Function of A.C. Superimposed on D.C. in the Anodic Oxidation of Lead in Sulfuric Acid

R. Vijayavalli, P. V. Vasudeva Rao, S. Sampath, and H. V. K. Udupa

Central Electrochemical Research Institute, Karaikudi, India

ABSTRACT

Superimposed a.c. is found to favor the dissolution of lead while d.c. helps the formation of lead dioxide. The role of a.c. is thus similar to that of a "forming agent," like nitrate, the use of which tends to boost the formation of lead dioxide. This view is supported by measurements of anode potentials and the time needed for passivation. The porous nature of the surface film, indicated by the resistance measurements, explains the continued formation of lead dioxide. A probable mode of attack of the lead surface is given based on the microscopic examination of the corroded surface.

In an earlier communication (1) it was shown that superimposition of a.c. on d.c. resulted in an increased formation of lead dioxide which was confirmed by the discharge capacity measurements and quantitative estimation of the lead dioxide formed. No explanation was offered, however, for the results obtained. It is the purpose of this paper to discuss the role of a.c. in increasing the formation of lead dioxide.

Alternating current superimposed on d.c. finds application in different fields by virtue of its effects on the electrode reactions. Effect of periodically reversed currents on the corrosion of underground cables has been reported (2, 3), and it has been shown that corrosion decreases with increasing frequency (2). Superimposed a.c. has been found to be useful in the electrodeposition of zinc, nickel, etc. (4), in the refining of gold (5) and in the preparation of inorganic compounds like lead chromate (6). Superimposed a.c. has been utilized to advantage in obtaining bright electrodeposits of metals (7). The a.c. superimposed has been found to have the following effects: (i) it enhances anodic corrosion of metals which depends on the frequency of the a.c. and the ratio of a.c. to d.c., etc.; (ii) it reduces both cathodic and anodic polarization and electrochemical passivity; (iii) it causes marked reduction of both hydrogen and oxygen overvoltages, and the extent of depolarization appears to be independent of the electrode (in the case of hydrogen overvoltage) and is primarily determined by the ratio of a.c. to d.c. (8). Corrosion by superimposed a.c. has been found at first to increase with increasing current density, reach a maximum, and then to decline at still higher current density in the case of lead in sulfuric acid (9). The effect of different wave forms on the anodic oxidation of aluminum (10) has also been studied and reported. An understanding of the function of a.c. in the anodic oxidation of lead may find application in the formation of Planté plates without the use of forming agent for the purpose.

Experimental

Lead foil guaranteed to contain less than 0.001% of silver was used in the investigation. The area of the electrode oxidized in every experiment was 1 cm^2, the rest of the surface being stopped off with nitrocellulose varnish. The electrolyte was prepared by diluting reagent grade sulfuric acid to 1.200 sp gr (5.66*N*). A large, formed negative plate of a lead-acid battery served as the cathode so that hydrogen evolution could not occur. Direct current was obtained from an electronic current regulator and a.c. (50 cps) from the mains through a voltage stabilizer. The circuit diagram is given in Fig. 1. The panels were cleaned by dipping in 70-80% ammonium acetate solution for a few minutes just before the experiment to remove the oxides of lead formed on the surface by atmospheric oxidation. Experiments were carried out at 30° ± 1°C with d.c. alone, with d.c. having superimposed a.c., and with d.c. and forming agent as employed in Planté plate formation. Reagent grade ammonium nitrate was used as the forming agent, as has been found to be effective for the purpose (13). Different current densities of d.c. tried were from 1 to 8 ma/cm^2. The current density of a.c. was varied from 0 to 3 ma/cm^2, forming a ratio of 0-300% of d.c. used. Four different concentrations of the forming agent, *viz.*, 1.5, 3, 6, and 12 g/l of ammonium nitrate, were employed.

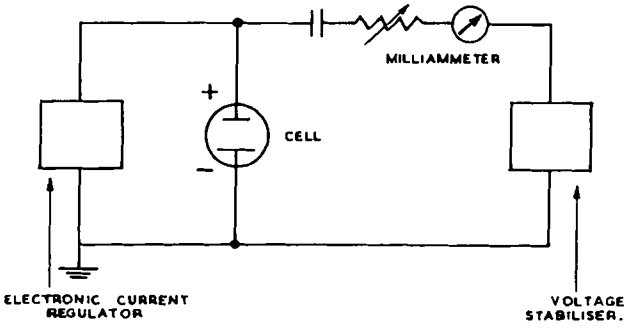

Fig. 1. Circuit diagram for superimposing a.c. on d.c. for anodic oxidation of lead in sulfuric acid.

During the experiment the anode potential was measured with reference to $Hg/Hg_2SO_4/1.200$ sp gr sulfuric acid using Philips V.T.V.M. GM 6010, and time was noted with a stopwatch which could read up to 0.02 sec. The peak or the maximum potential attained by the anode and the time required to reach the same (passivation time) were noted in every case.

Results and Discussion

The variations of peak potential and time of passivation with current density (d.c.) under different experimental conditions are graphically represented in Fig. 2 to 5. It is observed that with increase in current density the passivation time decreases (Fig. 2). The time required for attaining the peak potential is the lowest when d.c. alone is employed at any particular current density. The superimposition of a.c. raises the time of passivation which remains particularly high with 1 ma a.c. at all current densities studied. The anode potential is reduced by the superimposition of a.c. (Fig. 3), a marked lowering of the peak potential being effected by the use of 1 ma a.c.

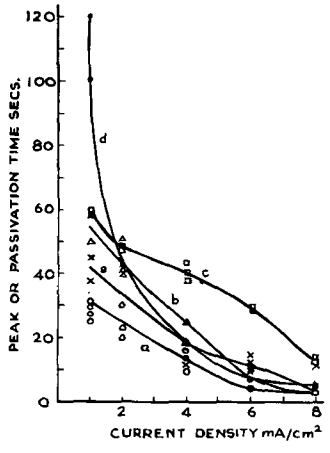

Fig. 2. Passivation time *vs.* direct current density with different amounts of superimposed a.c.: (a) d.c. only; (b) d.c. + 0.5 ma a.c.; (c) d.c. + 1.0 ma a.c.; (d) d.c. + 2.0 ma a.c.; (e) d.c. + 3.0 ma a.c.

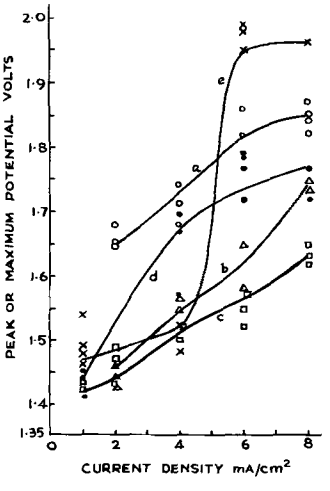

Fig. 3. Peak potential *vs.* direct current density with different amounts of superimposed a.c.; (a) d.c. only; (b) d.c. + 0.5 ma a.c.; (c) d.c. + 1.0 ma a.c.; (d) d.c. + 2.0 ma a.c.; (e) d.c. + 3.0 ma a.c.

The use of ammonium nitrate in different concentrations as a forming agent at varying current density leads to an increase in the time of passivation (Fig. 4) and to lower peak potentials compared to those obtained using d.c. without any forming agent (Fig. 5). Out of the concentration of the forming agent tried, it is found that the peak potential is the lowest and passivation time the highest in the case of 12 g/l ammonium nitrate in the bath.

It has been reported (11) that the potential-time curve for the anodic oxidation of lead in sulfuric acid under galvanostatic conditions consists of three distinct regions: the first a negative region, a second region comprising a rapid rise of potential to a maximum value followed by a sudden fall, and a third region of steady potential. The first region is said to correspond to the passivation of the surface due to the formation of an isolated layer of lead sulfate. During the rapid rise of potential, conversion of lead sulfate to lead dioxide commences. At the peak the pores get closed, and during the sudden fall lead dioxide is formed in between the crystals

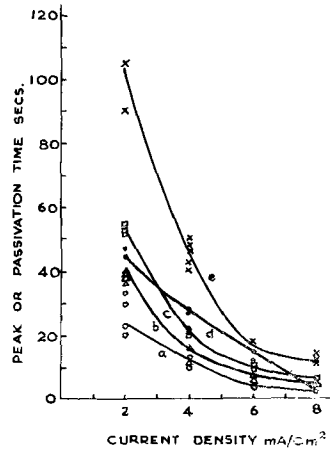

Fig. 4. Passivation time *vs.* direct current density with different concentrations of ammonium nitrate as the forming agent: (a) sulfuric acid only; (b) sulfuric acid containing 1.5 g/l ammonium nitrate; (c) sulfuric acid containing 3 g/l ammonium nitrate; (d) sulfuric acid containing 6 g/l ammonium nitrate; (e) sulfuric acid containing 12 g/l ammonium nitrate.

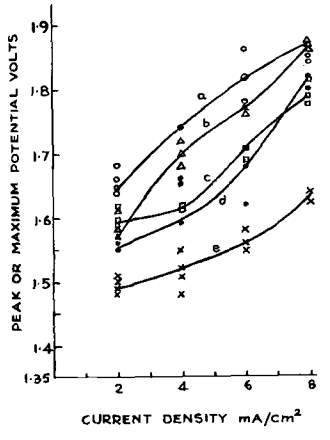

Fig. 5. Peak potential *vs.* direct current density with different concentrations of ammonium nitrate as the forming agent: (a) sulfuric acid only; (b) sulfuric acid containg 1.5 g/l of ammonium nitrate; (c) sulfuric acid containing 3 g/l of ammonium nitrate; (d) sulfuric acid containing 6 g/l of ammonium nitrate; (e) sulfuric acid containing 12 g/l of ammonium nitrate.

of lead sulfate. In the last region of the curve gas evolution and further formation of lead dioxide takes place. The film formed with d.c. alone in sulfuric acid is also reported to be compact and nonporous. It is well known that the addition of forming agents like nitrates and perchlorates increases the formation of lead dioxide in the case of Plante' plate formation. In the absence of forming agents the conversion of lead sulfate begins near the $Pb/PbSO_4$ interface and continues through the deposit without any further attack of the lead, but when a forming agent is present, the attack on the lead continues, thus maintaining a high concentration of Pb^{++} near the electrode surface (12). Chemical precipitation of lead sulfate takes place on the surface with subsequent oxidation to lead dioxide. Due to the simultaneous occurrence of the dissolution of the base metal, the anode potentials are lowered by the use of superimposed a.c. or of the forming agent. The continued attack of the anode results in a delay of the passivation of the surface and hence in an increase of the passivation time.

By increasing the concentration of the forming agent, the concentration of the nitrate ions available for the attack of the surface is increased. More of lead goes into solution, and a decrease of the anode potential should be expected as has been found experimentally (Fig. 5).

Alternating current is known to promote the dissolution of lead (9), and the potential with d.c. plus a.c. is also found to be less than that observed with d.c. alone for all ratios of a.c. to d.c. Increase of a.c., however, does not decrease the anode potential proportionately. This decrease of anode potential by the superimposed a.c. is an indication that the anodic attack of lead is favored by a.c. The negative value of the potential (−0.90v with reference to the $Hg/Hg_2SO_4/1.200$ sp gr H_2SO_4) obtained when only a.c. is used shows that oxidation to lead dioxide does not take place in this case.

The loss of weight suffered by the panels during oxidation was determined for d.c. alone, for d.c. with superimposed a.c., and for d.c. with the forming agent. The panels which were weighed before the experiment were oxidized anodically for the same duration under different conditions. The panels were weighed again after completely stripping off the oxide layer with ammonium acetate solution. The difference in weight of the panel obtained is given in Table I. It can be seen readily that the weight loss is the lowest in the case of the panel formed with d.c. alone.

The resistances of the films formed on lead using d.c. alone, d.c. with superimposed a.c., and d.c. with the forming agent were measured. Oscilloscopic transients were taken and the resistance computed from the initial potential jump under galvanostatic conditions. Approximate resistance values calculated are given in Table II. The results show that the films formed with the forming agent and with superimposed a.c. are more porous than that formed with d.c. alone and have lower resistances. The film formed with a.c. superimposition appears to be the most porous.

Table I. Weight loss of the panels under different conditions of anodic oxidation

Condition of formation	Duration of anodization, 2 hr Total weight loss, mg/cm²
D.C. 2 ma/cm²	5.2 5.0 5.6
D.C. 2 ma/cm² + A.C. 1 ma/cm²	9.6 8.2 7.8
D.C. 2 ma/cm² + "Forming agent" 12 g/l	10.2 9.0 9.8

Table II. Resistance of the films formed under different conditions

Condition of formation	Voltage jump, v	Resistance of the film, ohms
D.C. only, 2 ma	0.4	200
D.C. only, 2 ma	0.3-0.4	150-200
D.C. only, 2 ma	0.4	200
D.C. 2 ma +	0.1	33.3
A.C. 1 ma	0.1	33.3
D.C. 2 ma +	0.2	100
"Forming Agent" 12 g/l	0.2	100

The weight loss measurements as well as the estimated values of the resistance of the films formed during the oxidation process tend to indicate that superimposed a.c. attacks lead in a manner similar to a forming agent and promotes the formation of more lead dioxide as in the case of Planté plate formation.

A microscopic examination of the surfaces of panels just before the peak potential is reached and after the steady-state potential is reached under different conditions of oxidation revealed that there is uniform oxidation of the surface with formation of very little sulfate during the sharp rise of potential when d.c. alone was used. On the other hand only lead sulfate is formed if a.c. alone is employed. The potential in the latter case remains so low that oxidation to lead dioxide is not feasible. The use of superimposed a.c. produces a marked change in that both lead dioxide and lead sulfate are formed with lead dissolving out preferentially from a number of points. The surface of the panel oxidized using the

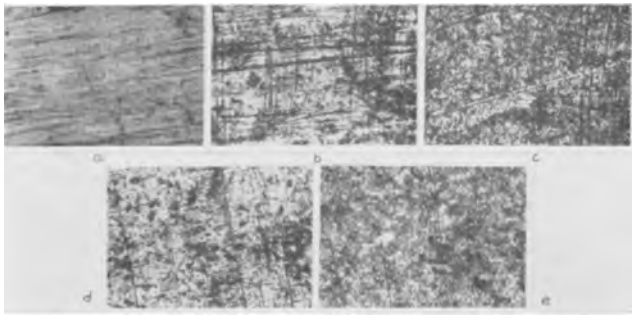

Fig. 6. Lead surface after removal of film formed: (a) initial surface; (b) d.c. 2 ma/cm², surface after removing the oxide film; (c) a.c. 1 ma/cm², surface after removing the sulfate film; (d) d.c. 2 ma/cm² + a.c. 1 ma/cm², surface after removing the oxide film; (e) d.c. 2 ma/cm², forming agent 12 g/l, surface after removing the oxide film. Magnification approximately 80X.

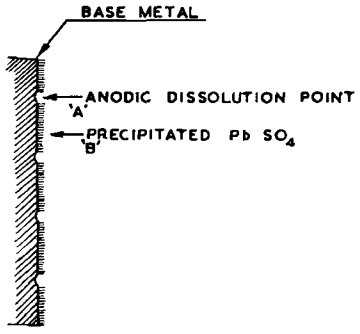

Fig. 7. Mode of attack of lead surface by a.c. or forming agent

forming agent appeared similar to that obtained with superimposed a.c. although the amount of sulfate on the surface was less in the former case. There was evidence of continued attack of the metal in both cases even after the steady potential was registered. The photomicrographs in Fig. 6 show the surface of the panels after removal of the film formed by oxidizing with d.c. alone, d.c. plus a.c., and d.c. plus forming agent. It may be seen that the surface shows a number of pits where the attack of the metal was concentrated in the cases where the forming agent and superimposed a.c. were employed. From the above consideration, it is possible to picture the mode of attack and the maintenance of the porosity of the film schematically as shown in Fig. 7. The lead is attacked at a point A and is precipitated chemically as lead sulfate at a spot B very near A. Subsequent dissolution of lead occurs preferentially at A rather than at other fresh spots which are covered by the film of sulfate. A number of such anodic dissolution points exist and hence the film remains porous.

As the mode of attack of the lead by superimposed a.c. is found to be similar to that of the forming agent, a.c. superimposed on d.c. can be used in the formation of Planté plates instead of the conventional forming agents like nitrate or perchlorate. A significant advantage of the use of a.c. would be the absence of the harmful effects of small quantities of the forming agents retained in the plate after formation.

Acknowledgment

The authors are thankful to Professor K. S. G. Doss, Director of the Institute, for suggesting the problem and helpful discussions during the investigation.

Manuscript received March 28, 1962; revised manuscript received Aug. 21, 1962. Paper presented at the Third Seminar on Electrochemistry at the Central Electrochemical Research Institute, Karaikudi, December 1961.

Any discussion of this paper will appear in a Discussion Section to be published in the December 1963 JOURNAL.

REFERENCES

1. (Miss) R. Vijayavalli, S. Ghosh, and H. V. K. Udupa, *Bull. acad. polon. sci.*, **10**, [1], 13 (1962).
2. Burton McCollum and G. H. Ahlborn, *Trans. Electrochem. Soc.*, **29**, 469 (1916).
3. E. R. Shepard, *ibid.*, **39**, 239 (1921).
4. R. Yu. Bek and N. T. Kudryavtsev, *Izvest Vysslikh Ucheb. Zavendenii, Khim. i Khim. Technol.*, **3**, 898 (1960); *C.A.*, **55**, 8115 (1961).
5. British Patent 6276 (1909).
6. N. F. Murphy and B. C. Doumas, *Bull. Va. Polytech. Inst.*, **49** [6], Eng. Expt. Ser. No. 108, 3-23 (1956); *C.A.*, **51**, 13617a (1957).
7. U. S. Patent No. 2,548,867, Apr. 17 (1951); *C.A.*, **45**, 5545 hi P (1951).
8. H. M. Goodwin and M. Knobel, *Trans. Am. Electrochem. Soc.*, **37**, 617 (1920).
9. J. Vene, *Bull. Soc. Sci., Bretagne*, **14**, 180 (1937) (Pub. 1938); *C.A.*, **33**, 9151a (1939).
10. Sakae Tajima, Fujio Satoh, Nobuyoshi Baba and Toshiro Fukushima, *J. Electrochem. Soc. (Japan)*, **27**, No. 10-12, E.262 (1959).
11. W. Feitknecht, *Z. Elektrochem.*, **62**, 795 (1958).
12. H. R. Thirsk and Wynne Jones, *J. Chim. Phys.*, **49**, C 131 (1952).
13. P. V. Vasudeva Rao, S. Ghosh, H. V. K. Udupa, and B. B. Dey, Proc. Symposium on "Electrolytic Cells," Central Electrochemical Research Institute, Karaikudi-3, S.Rly., p. 292 (1961).

The Effect of Alloying Elements on the Oxidation of Tin

W. E. Boggs, R. H. Kachik, and G. E. Pellissier

Applied Research Laboratory, United States Steel Corporation, Monroeville, Pennsylvania

ABSTRACT

Small amounts of certain alloying elements change the oxidation behavior of tin. If the formation of SnO is thermodynamically favored, elements that enter the oxide with valence greater than tin increase the rate of formation of SnO. When the formation of SnO is not favored, the alloying element is oxidized preferentially on the surface of the alloy in the form of a thin oxide film and discrete crystallites. The crystallites were found to be associated with dislocations in the metal.

In a search for means of improving the oxidation resistance of tin, the authors have investigated and previously reported the oxidation kinetics (1) and the morphology and mode of growth (2) of oxide films formed on pure-tin foils in pure dry oxygen. The oxidation process started with the nucleation and lateral growth of crystalline α-SnO. During this interval, the rate of oxidation increased with time. As the impingement of the laterally spreading oxide platelets became widespread, the rate of oxidation

began to decrease, conforming to a direct logarithmic rate law, and cavities began to develop at the oxide-metal interface. The authors have shown that the observed logarithmic behavior could be the result of an interplay between the throttling action of the expanding cavities at the base of the oxide film and the movement of tin ions through a thickening film of oxide (3). Evans (4) has suggested that such cavities might be the result of the coalescence of vacancies that had diffused through the oxide to the oxide-metal interface. The most likely source of vacancies would be the reaction between oxygen and tin ions at the oxide-oxygen interface, provided that stannous oxide, the compound formed under the experimental conditions, is a p-type, cation-deficient semiconductor.

In a subsequent phase of this investigation, the effects of small amounts of impurity and alloying elements on the oxidation of tin have been explored. Commercial tin sometimes contains impurities that may influence its oxidation resistance. Furthermore, alloying elements are often used to improve the oxidation and corrosion resistance of technologically important metals, and it was expected that elements could be found that had similar inhibiting effects on the oxidation of tin. Finally, the effects of certain alloying elements on the rate of tin oxide formation might help to establish the semiconductor classification of the oxide formed on tin below its melting point (α-SnO) and re-enforce the arguments already advanced (3) to explain the logarithmic oxidation behavior of tin. An extensive literature search had failed to reveal the semiconductor classification of stannous oxide, although this information is available for stannic oxide (5).

The first alloying elements investigated were selected using Hauffe's valency rule (6) as a guide. According to this rule, if an oxide contains cation vacancies (p-type), the introduction of a minor constituent of greater valency than the solvent metal should increase the oxidation rate, whereas the introduction of a minor constituent of lower valency should decrease the rate. The valency rule often has been useful in predicting the effects of minor alloying constituents on the oxidation rates of metals (4). It was realized that the application of the valency rule to the logarithmic oxidation of tin might not be valid, since theoretically the rule applies only to a diffusion-controlled process which would be expected to conform to the parabolic rate law. Nevertheless, since the logarithmic rate behavior observed in the earlier work on the oxidation of tin (1, 3) appeared to be a modification of parabolic behavior, as first suggested by Evans (4), it seemed worthwhile to attempt to apply the valency rule, as a first approximation, to predict the effects of various alloying and impurity elements on the oxidation rate of tin. After this preliminary survey the emphasis of the investigation was placed on a study of the mechanisms by which a few other alloying elements produce marked inhibition of tin oxidation, as had been reported in the literature (7).

Table I. Concentration of the alloying elements in the binary tin alloys

	Nominal concentration		Spectrographic concentration	
	Atom per cent	Weight per cent	Atom per cent	Weight per cent
Antimony	0.1	0.103	0.11	0.11
Bismuth	0.1	0.181	0.1	0.18
Cadmium	0.1	0.095	0.074	0.070
Indium	0.1	0.099	0.083	0.080
Iron	0.1	0.047	0.049	0.023
Lead	0.1	0.175	0.09	0.15
Manganese	0.1	0.046	0.086	0.040
Phosphorus	0.388	0.105	0.535	0.14
Thallium	0.1	0.172	0.029	0.050
Zinc	0.1	0.055	0.078	0.043

Table II. Free energy of formation of the oxides of the alloying elements and the reported solubilities in tin

Element	Free energy of formation per gram atom of oxygen, kcal at 25°C	Oxide	Solubility of element in tin, weight per cent	Temperature of solubility measurement, °C
Bismuth	—39	Bi_2O_3	21.5	—
Thallium	—43	Tl_2O	*	—
Lead	—45	PbO	2.6	183
Antimony	—50	Sb_2O_3	8.0	25
Iron	—59	Fe_2O_3	*	—
Cadmium	—60	CdO	1.0	—
Tin	—61	SnO	—	—
Phosphorus	—64	P_2O_5	*	—
Indium	—73	In_2O_3	12.00	117
Zinc	—77	ZnO	2.5	196
Manganese	—89	MnO	*	—
	—76	Mn_3O_4		

* The solid solubilities of these elements in tin are not reported in the technical literature.

Experimental Procedure

Table I shows the compositions of the binary alloys used in this investigation. These alloys were made by melting 10-g ingots of 99.999% pure tin (obtained from A. D. MacKay, Inc.) with the amount of the respective alloying element calculated to produce a concentration of 0.1 atomic per cent (a/o) in the tin. The solid solubilities (8) of these elements, together with the free energies of formation of the most likely oxides (9, 10), are given in Table II. Chemically pure (C. P.) grade metals were used as alloy additions, and no further purification was attempted. The melting was conducted in a quartz tube under an atmosphere of Matheson prepurified grade argon. When the tin became entirely molten and the alloying constituent had completely dissolved, as far as could be determined visually, the tube was agitated to achieve as much homogeneity of composition in the liquid alloy as possible. The melt then was allowed to cool and solidify under the argon atmosphere. The top surface of each of the ingots was filed clean to remove any dross or segregation of foreign element in the surface. Each ingot then was rolled, on a small rolling mill, into foil approximately 3 mils thick. In view of the relatively low melting point of tin, it is believed that the large amount of mechanical deformation provided by the rolling to foil thickness, coupled with the subsequent annealing treatment at 200°C for 1 hr in vacuum,

was sufficient to ensure uniform composition of the alloy foils.

Spectrographic analyses of electropolished specimens of the foils showed that the actual concentration of alloying constituent sometimes varied from the desired 0.1 a/o. These variations were not considered critical, since rigorous quantitative comparisons of the oxidation behavior of the various alloys were not of primary interest. The average grain diameter of the tin in these foils was 0.18 mm. To provide a sample of pure-tin foil for comparison with these alloys, an ingot of the pure tin used in the preparation of these alloys was remelted in the quartz tube and rolled into a 3-mil-thick foil. This material also had an average grain diameter of 0.18 mm. The curves for the oxidation kinetics of pure tin, which are used for comparison throughout this paper, were obtained from experiments in which this remelted tin was used.

The surface of each foil was prepared for controlled oxidation by abrasive grinding, electropolishing, and washing; the foil was then inserted in a vacuum microbalance system and annealed at 200°C in a vacuum of 10^{-7} torr,[1] or better, for 1 hr. Immediately after the vacuum-annealing step, the temperature of the system was adjusted to 190° or 220°C, and pure, dry oxygen was introduced at a pressure of 10 torr. The change in weight of the foil specimen, caused by the reaction with oxygen, was measured with the microbalance (1). The microbalance used in these experiments had a sensitivity of 0.1 μg per micron deflection. The weight gains in duplicate experiments usually agreed within 1%. After oxidation, the specimen was removed from the vacuum system and was prepared for electron microscopy and electron diffraction analysis by using the extraction-replication techniques discussed in an earlier paper (2).

Since the condition of the surface of the metal before the start of controlled oxidation is important in the subsequent growth of the oxide, an attempt was made to determine the composition of any initial surface films by using reflection electron diffraction. Pure tin and the tin alloys containing indium, zinc, and manganese were examined (i) after electropolishing and (ii) after vacuum annealing at 200°C.

Valuable information about the distribution of oxide in extraction replicas of the alloy surfaces was obtained by using dark-field electron microscopy. In this technique the objective-contrast aperture is displaced from the central electron beam to cover a preselected spot or ring segment in the diffraction pattern produced by the crystalline material in the film. The diffracted electrons producing this spot or ring are then focused on the viewing screen, forming an image in which the particular distribution of crystallographic planes responsible for the diffraction are illuminated in an otherwise dark field. Comparison of conventional and dark-field micrographs of the same area shows whether the illuminated crystallographic planes are associated with a continuous oxide film or only with a distribution of separated, discrete oxide particles on the surface of the metal.

[1] mm Hg; nomenclature recommended by the American Vacuum Society.

Results and Discussion

In all, the effects of the addition of about 0.1 a/o of some 10 alloying elements to 99.999% pure tin were investigated (Table I). As the kinetic and electron diffraction data for the oxidation of these binary alloys were accumulated, it became convenient to classify the alloying additions in two groups: (i) those that increased the rate of formation of stannous oxide, and (ii) those in which preferential oxidation of the alloying constituent inhibited the formation of stannous oxide.

Elements That Increased the Rate of Formation of Stannous Oxide

Initially, a number of alloying elements were investigated that might increase the oxidation rate if Hauffe's valency rule was assumed applicable to tin oxidation. The results of the investigation of the oxidation kinetics of the binary alloys of tin and antimony, bismuth, iron, lead, thallium, and cadmium, respectively, are plotted in Fig. 1 and 2. Each of these alloys gained weight in conformance with a direct logarithmic rate law (1, 3) after the usual "induction period" of oxide nucleation and lateral growth (2-4). The greatest increases in oxidation rate, as compared with that of pure tin, were produced by the addition of antimony and thallium. Bismuth and iron caused lesser increases, whereas lead and cadmium had only slight and probably insignificant effects. The increases in oxidation rate observed were in accord with the valency rule for a

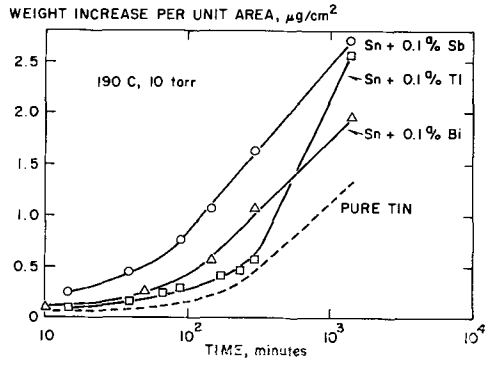

Fig. 1. Oxidation kinetics of tin-antimony, tin-thallium, and tin-bismuth alloys compared with that of pure tin.

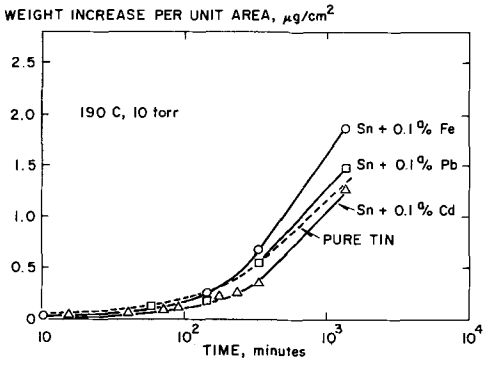

Fig. 2. Oxidation kinetics of tin-iron, tin-cadmium, and tin-lead alloys compared with that of pure tin.

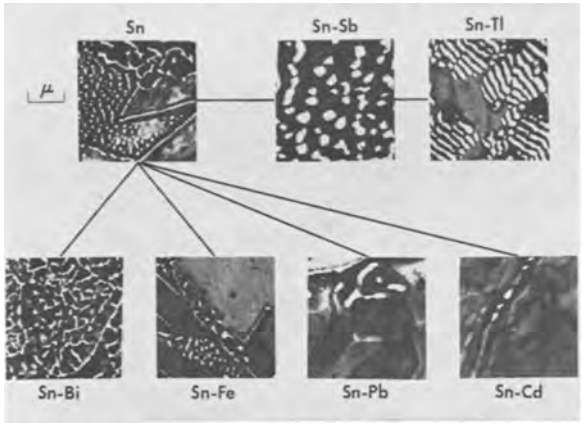

Fig. 3. Electron micrographs of the oxide stripped from pure tin and alloys containing antimony, thallium, bismuth, iron, lead, and cadmium after oxidation at 190°C and 10 torr for 1400 min.

cation-deficient oxide in a diffusion-controlled process.

Structure of oxide films.—Figure 3 shows electron micrographs of the oxide films isolated from the specimens of pure tin and of the alloys of tin with antimony, thallium, bismuth, iron, lead, and cadmium, respectively, which formed during oxidation for 1400 min at 190°C and an oxygen pressure of 10 torr. The microstructures of the oxide films formed on these tin alloys are not significantly different from the microstructure of oxide films formed on the pure tin. The structure consists of tin oxide grains of differing orientation and thickness. Many of the oxide grains contain cavities at the oxide-metal interface; these are arranged in parallel rows that presumably correspond to certain crystallographic directions or traces of crystallographic planes in the oxide. This type of structure has been discussed in more detail in an earlier paper (2). The small apparent differences among the micrographs of Fig. 3 are of degree and not of kind. Although an attempt was made in each case to choose a micrograph that would represent the "average" structure of the whole oxide film, the range of variation usually observed is so broad that this ideal can only be approximated in a single micrograph at the necessarily high magnifications used. Furthermore, even though the microstructures are compared on the basis of a single time of oxidation (1400 min), it should be noted that the progress of oxidation is different in general because of the varying effects of the alloying elements on the oxidation rate. For the alloying elements that increase the oxidation rate, it is to be expected that at a given time of oxidation the oxide films on the alloys will be thicker and the cavities will be larger and more coalesced than will those of the oxide film on pure tin. This indeed appears to be the trend in the micrographs of Fig. 3.

All the oxide films formed on these dilute tin alloys were identified as stannous oxide (α-SnO) by means of electron diffraction. Although slight changes in crystal-lattice parameters of the tin oxide might be expected because of the substitution of alloying-element ions for stannous ions, they were not detected within the limits of precision of the electron diffraction technique used.

Elements That Were Preferentially Oxidized

Since the ultimate objective of the present investigation was to find a practicable and generally useful means for improving the oxidation resistance of tin, further effort was concentrated on a determination of the mechanism(s) underlying the reported increase in oxidation resistance imparted to tin by the addition of a certain few alloying elements. According to Britton and Bright (7), the formation of colored temper films on tin heated in air is inhibited by alloying tin with small amounts of indium, phosphorus, or zinc. The simplest and intuitively most reasonable explanation of this effect is that the alloying element is preferentially oxidized (11) in the surface of the tin alloy.

If the formation of the oxide of a solute element is thermodynamically favored over the formation of the oxide of the solvent metal, a thin film of the oxide of the solute element may be formed preferentially over the surface of the alloy. If the diffusion rate of oxygen and/or solvent metal ions through this solute-element oxide film is less than the diffusion rate through the oxide of the solvent metal, then the oxidation rate of the alloy would be reduced to a value below the oxidation rate of the pure solvent metal. On the other hand, if the diffusion rate of solute ions through the solute-element oxide film is higher than the diffusion rate of solvent ions through the solvent or solute-element oxide, then the oxidation rate of the alloy would be expected to be higher than that of the pure metal, at least until the amount of solute at the oxide-metal interface would be greatly depleted. In either case, very little of the oxide of the solvent metal would be expected to form.

The free energies of formation, per gram atom of oxygen, of ZnO (—77 kcal), In_2O_3 (—73 kcal), and P_2O_5 (—64 kcal) are more negative than the free energy of formation of α-SnO (—61 kcal) (9, 10). Thus, the formation of the oxides of these alloying elements would be expected to be favored thermodynamically over the formation of tin oxide.

If preferential formation of alloying element oxide actually produced the effect observed by Britton and Bright (7), then some evidence of the alloying-element oxide should be found in films stripped from oxidized tin alloys. Accordingly, binary alloys of tin containing zinc, indium, and phosphorus were subjected to oxidation experiments similar to those previously performed with pure tin, and the oxidized surfaces were examined.

Condition of alloy surfaces at the start of controlled oxidation.—The presence of a coherent and stable film on the metal surface at the start of oxidation would be expected to have some influence on the course of subsequent oxide film growth. As reported in a previous paper (1), no electron diffraction patterns were obtained from extraction replicas of the electropolished and vacuum-annealed samples of pure tin. Since this technique places the sample film normal to the electron beam in the diffraction instrument, very thin (about 20Å or less) crystallites or crystalline films might not be detected. If a very smooth tin specimen covered with such a film

is placed nearly parallel to the beam so that the incident electron beam grazes its surface, the effective thickness of the surface film, and thus the sensitivity of the diffraction technique, is increased.

Specimens of freshly electropolished pure tin, tin-zinc, and tin-indium alloys were examined by this method. The major electron diffraction pattern obtained was that of β-tin. In addition, a weak pattern of hydrated tin oxide, $2SnO \cdot H_2O$, was detected in the pure-tin surface and on the tin-zinc alloy surface. After the electropolished specimens were vacuum annealed for 1 hr at 200°C, the hydrated tin oxide pattern no longer could be detected. However, one line, attributable to ZnO, was obtained from the surface of the tin-zinc alloy. The only other electron diffraction rings obtained from these surfaces correspond to β-tin. It is apparent that the surfaces of the alloys were cleaned somewhat by the vacuum-annealing treatment, but it is unlikely that any oxide resulting from electropolishing was completely eliminated. The results of these experiments are summarized in Table III.

Oxidation of the alloys.—The kinetic data obtained from the oxidation of binary alloys of tin with zinc, indium, and phosphorus at 190°C and an oxygen pressure of 10 torr (solid lines), compared with data for pure tin (broken lines) oxidized under similar conditions, are plotted in Fig. 4. The addition of about 0.1 a/o of these alloying elements resulted in a marked decrease in the oxidation rate. The rates of oxidation were so low that the rate laws involved could not be deduced from the kinetic data.

Extraction replicas were made of the oxide formed on each of the alloys during the kinetic studies. The oxides were then identified by electron diffraction. The diffraction pattern obtained from extraction replicas of the oxidized tin-zinc surface was entirely that of ZnO. The patterns obtained from the replica of the oxidized tin-indium alloy were attributable in the main to In_2O_3, although a few rings corresponding to α-SnO were also found. No diffraction pattern was obtained from an extraction replica of the tin-phosphorus surface. This latter result is not unexpected, since the oxides of

Table III. Summary of reflection electron diffraction results

	Diffraction pattern after treatment: Electropolished	Vacuum annealed
1. Pure tin	Total 17 rings 13 β-Sn 3 $2SnO \cdot H_2O$ 1 Unidentified	Total 10 rings 10 β-Sn
2. Tin + indium	Total 11 rings 11 β-Sn	Total 11 rings 10 β-Sn 1 Unidentified
3. Tin + zinc	Total 25 rings 11 β-Sn 11 $2SnO \cdot H_2O$ 3 Unidentified or ambiguous	Total 11 rings 10 β-Sn 1 ZnO?
4. Tin + manganese	Total 19 rings 11 $2SnO \cdot H_2O$ 6 β-Sn 2 Unidentified	Total 13 rings 12 β-Sn 1 Unidentified

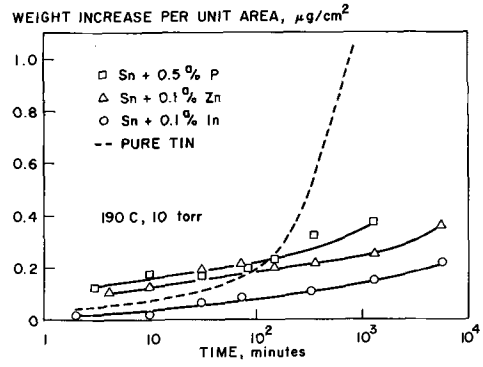

Fig. 4. Oxidation kinetics of tin-indium, tin-zinc, and tin-phosphorus alloys compared with that of pure tin.

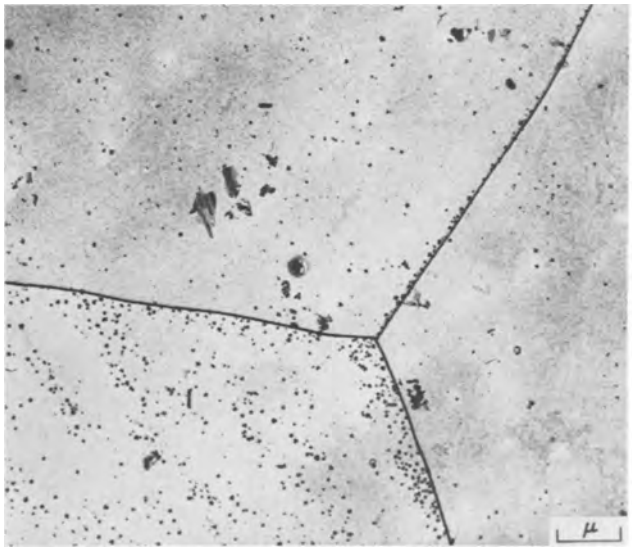

Fig. 5. Electron micrograph of the zinc oxide crystallites found on a tin-zinc alloy after oxidation at 190°C and 10 torr for 1400 min.

phosphorus most likely to be formed are very hygroscopic and probably are lost during preparation of the replica for electron optical examination. The replicas were also examined by electron microscopy.

Tin-zinc.—Discrete crystallites of zinc oxide (ZnO) were found in some areas of the oxidized tin-zinc alloy specimens, as shown in Fig. 5. However, an observation of seemingly greater significance is that the entire surface of the tin-zinc alloy was covered with a thin, continuous polycrystalline film of zinc oxide.

Evidence for the existence of the continuous ZnO film was obtained by conventional transmission electron diffraction and by dark-field electron microscopy. The diffraction patterns consisted of continuous rings, similar in appearance to the familiar powder patterns of x-ray diffraction. Such patterns are caused by a multitude of randomly oriented crystallites. The most convincing evidence of the continuous nature of the ZnO film was obtained by dark-field electron microscopy. Figure 6 shows a conventional electron micrograph and a dark-field micrograph of the same area of a ZnO film. The dark-field micrograph was obtained by using only the diffracted electrons that form the first strong line of the ZnO pattern, that is, the 2.816Å line from the (100) planes of the ZnO crystals.

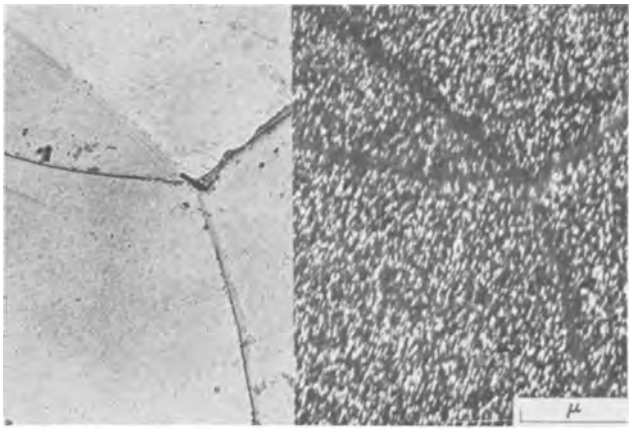

Fig. 6. Conventional and dark-field electron micrographs of the same area of the surface of a tin-zinc alloy after oxidation at 190°C and 10 torr for 1400 min, showing the recurrence of the (100) plane of ZnO in the oxide film.

The profusion of bright spots in the dark-field micrograph results from the frequent recurrence of the (100) planes in proper diffracting orientation in the zinc oxide film covering the surface of the metal. It is evident that the minute ZnO crystallites providing these (100) reflections are very uniformly distributed and closely spaced in the surface film. Although these crystallites are not resolved in the corresponding conventional bright-field micrograph, they probably are the reason for the mottled texture observed. These diffracting regions of zinc oxide detected by dark-field microscopy are so much smaller and more closely spaced than the idiomorphic zinc oxide crystallites observed by bright-field microscopy that it seems quite certain that they represent a continuous oxide film rather than separated, discrete particles. This thin film of zinc oxide effectively inhibits the formation of tin oxide on the surface of the tin-zinc alloy.

Tin-indium.—The oxide found on a specimen of the tin-indium alloy, which was oxidized for 5400 min at 190°C and 10 torr, consisted of small discrete rod- or plate-shaped crystallites of In_2O_3 such as are shown in Fig. 7. No direct evidence of any oxide could be found on the areas between the indium oxide particles. However, in some more recent work in this laboratory on additional tin alloys, notably tin-germanium, both continuous films and discrete particles of the solute-element oxide have been identified on the surface after oxidation; this information will be published at a later date. The oxide formed on pure tin oxidized under similar conditions is a film of α-SnO covering the entire surface of the metal, as is shown in the inset. The indium oxide particles that formed on this alloy under the above conditions were 1500-3000Å long and 700-1500Å wide. They protrude 700-1500Å above the plastic support, as is shown by the length of their shadows. Since similar shadows are not found on preshadowed specimens, it is evident that the indium oxide particles actually were imbedded in the metal and did not protrude appreciably above its surface.

The density of distribution of the particles varies from one alloy grain to another, as is shown in Fig. 7, where a grain boundary separates the grain in the upper right quadrant from a second grain in the lower left quadrant, but the over-all average density is about 5×10^7 particles/cm^2. This finding suggests that the indium oxide particles are associated with dislocations intersecting the surface of the tin-indium alloy. The tendency of impurities in crystals to diffuse to dislocations is well known (12). Young has demonstrated the correspondence between oxide "nuclei" and dislocations in copper single crystals doped with certain impurities (13).

Direct evidence of the association of the indium oxide particles with dislocations in the metal crystals is shown in Fig. 8, a transmission electron micrograph of an electrothinned specimen of the tin-indium alloy, which had been oxidized for 2800 min in oxygen at 10 torr and 190°C. The oxidized specimen was thinned by electropolishing from one side (14), using the standard 20% perchloric, 80% acetic acid tin electropolishing solution in a Zeiss (Jena)

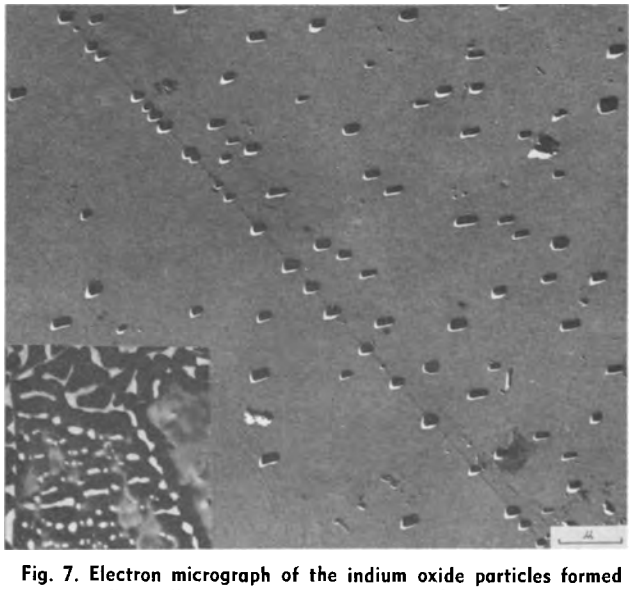

Fig. 7. Electron micrograph of the indium oxide particles formed on a tin-indium alloy during oxidation at 190°C and 10 torr for 5400 min with inset showing oxide formed on pure tin under similar conditions.

Fig. 8. Transmission electron micrograph of a tin-indium alloy foil after oxidation at 190°C and 10 torr for 2800 min.

"Elypovist" electropolishing microscope. The indium oxide particles at the ends of dislocations in the metal are clearly shown.

It might be hypothesized that indium atoms, since they are slightly larger than the tin atoms of the matrix (1.62Å *vs.* 1.40Å), produce symmetrical dilations of the tin lattice. Such oversized indium atoms are attracted to regions of hydrostatic tension and repelled from regions of compression in the crystal lattice, and so they diffuse to the tension side of edge dislocations where they are removed from the tin matrix by inclusion in indium oxide crystallites. Thus, dislocations may serve as "diffusion pipes" to facilitate transfer of indium atoms from the interior of the metal to the oxide crystallites in the surface.

Tin-phosphorus.—The results of the electron microscopic examination of the surface of the tin-phosphorus alloy were inconclusive. No electron diffraction patterns were obtained, and no clear evidence of oxide could be found with the electron microscope. As stated above, this might be expected because of the affinity of phosphorus oxides for water. It is believed that any oxide formed by preferential oxidation of phosphorus in the dry atmosphere of the balance system would absorb water from the laboratory air and either assume an amorphous character or be lost during the preparation of an extraction replica for electron microscopic examination.

Mechanism for inhibition of oxidation.—It is clear that preferential oxidation of zinc, indium, and phosphorus occurred when alloys of tin containing these elements were exposed to pure oxygen at elevated temperatures. A continuous film of ZnO was found on the oxidized tin-zinc alloy. Although it could not be demonstrated experimentally, it is believed that a similar, but even thinner, film of indium oxide formed on the tin-indium alloy. Such a film evidently impedes the movement of tin or oxygen ions through it to a greater degree than does a normal tin oxide film. It is reasonable to believe that this mechanism is operative in the early stages of the oxidation of these binary tin alloys, although it has been difficult to demonstrate the presence of these films on alloys that had been oxidized only for short times.

Preferential formation of alloying-element oxide was observed in the form of oxide crystallites imbedded in the surface of the tin-indium and tin-zinc alloys. It appears that these "plugs" grow at sites where dislocations emerge at the surface of the metal. Their role in the over-all mechanism of the inhibition of tin oxidation produced by small amounts of indium or zinc is not clearly established. However, it may be significant that none of the characteristic tin oxide growth centers (2) have been found on oxidized specimens of these alloys. Perhaps the sites normally involved in the nucleation of tin oxide growth centers are blocked by the preferential formation of these alloying-element oxide crystallites.

Tin-manganese.—Inasmuch as the oxides formed on only two tin alloys (Zn and In) were detected and positively identified, an effort was made to discover additional, verifiable examples of the preferential oxidation of alloying elements in tin. Additional elements were considered for study primarily on the basis of the free energies of formation of their oxides. A second consideration in the choice of the additional elements was the stability of the oxides in a moist atmosphere and/or in the film stripping procedure, in order to avoid the difficulties encountered with phosphorus. Managanese, selected according to these considerations, exhibited unusual and interesting behavior. The oxides which form on pure manganese are MnO and Mn_3O_4 (15); their free energies of formation, per gram atom of oxygen, are —89 kcal and —76 kcal, respectively, which are considerably more negative than that of tin oxide (—61 kcal). The tin-manganese alloy was prepared and investigated in the same manner as previously described. Electron diffraction examination of freshly electropolished surfaces of this alloy revealed the presence of a hydrated tin oxide ($2SnO \cdot H_2O$), as shown in Table III; after vacuum annealing, however, the pattern of this hydrated oxide disappeared, and only a pattern of β-tin was obtained.

In contrast to the tin-zinc, tin-indium, and tin-phosphorus alloys, the tin-manganese alloy exhibited a higher oxidation rate than pure tin, Fig. 9. The data for the oxidation of this alloy conformed initially to the parabolic rate law, Fig. 10. The rate became less than parabolic only after the weight increase corresponded to the consumption of about 13% of the total manganese present in the specimen. The value of the parabolic rate constant for this tin alloy at 190°C, 0.017 $\mu g^2\ cm^{-4}\ min^{-1}$, is fairly close to the value, 0.008 $\mu g^2\ cm^{-4}\ min^{-1}$, extrapolated to

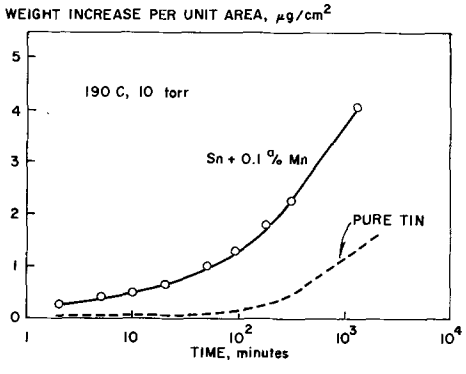

Fig. 9. Oxidation kinetics of a tin-manganese alloy compared with that of pure tin.

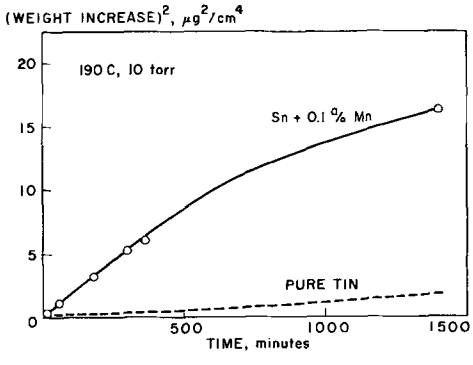

Fig. 10. Parabolic plots of the oxidation kinetics of a tin-manganese alloy and of pure tin.

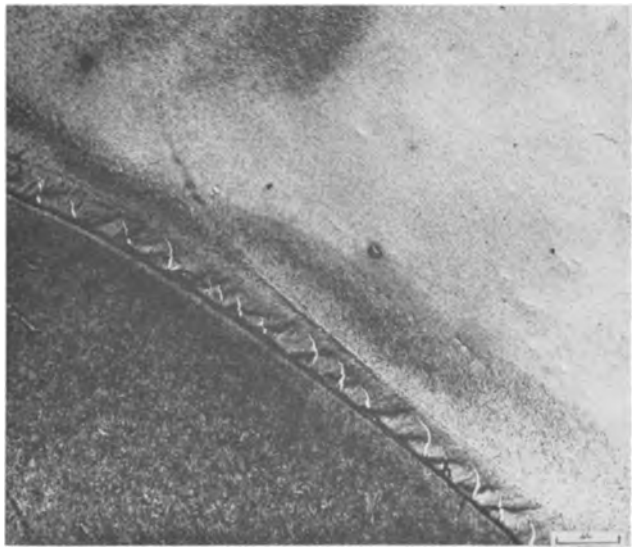

Fig. 11. Electron micrograph of the oxide films formed on a tin-manganese alloy during oxidation at 190°C and 10 torr for 240 min.

190°C from data given in the literature (15) for the oxidation of pure manganese. The surface of the oxidized tin-manganese alloy was found to be covered with a continuous film of the manganese oxides, MnO and Mn_3O_4, Fig. 11. The electron diffraction pattern of MnO was obtained from extraction replicas of the surface of this alloy after relatively short periods of oxidation at 190° and 220°C. The diffraction pattern of Mn_3O_4 appeared and became stronger after successively longer periods of oxidation. Apparently the oxide, MnO, formed first under the conditions of these experiments. It is interesting to note that the formation of Mn_3O_4 is reported to occur first on pure manganese (15). No trace of tin oxide was found in the oxide films stripped from this alloy. Thus, the oxide film formed on this alloy by preferential oxidation of the manganese is protective to the tin, although the over-all rate of oxidation is higher than that of pure tin because of the high rate of oxidation of manganese.

Summary

The rate of oxidation of tin can be markedly changed by alloying it with small amounts (about 0.1 a/o) of certain elements which exhibit appreciable solid solubility in tin. If the oxide of the alloying element was less stable thermodynamically than stannous oxide, the oxidation rate of the alloy was altered, perhaps fortuitously, in the direction predicted by Hauffe's valency rule. The ions of higher valence than stannous ion (antimony, bismuth, iron, and thallium) increased the oxidation rate of tin, while the ions of the same valence had no significant effect on the oxidation rate.

On the other hand, if an alloying element formed an oxide that was thermodynamically more stable than α-SnO, the alloying element was preferentially oxidized on the surface of the alloy, and the formation of tin oxide was inhibited. Thus, zinc was preferentially oxidized, forming a thin surface film covering the alloy surface. No tin oxide was found on this alloy, and the rate of reaction with oxygen was observed to be much less than that of pure tin. Similar reductions in oxidation rate and inhibition of tin oxide formation were observed with tin-indium, tin-phosphorus, and tin-germanium alloys. Thus, the solute element must have diffused to the surface of the alloy and was oxidized there to form a barrier to the movement of tin or oxygen ions, thereby inhibiting the formation of tin oxide.

Manganese also inhibited the formation of tin oxide. However, a relatively thick film of manganese oxides formed on the surface of a tin-manganese alloy. The rate of oxidation of this alloy was about as great as would be expected for the oxidation of pure manganese until the amount of manganese available in the alloy was considerably depleted.

In addition to the oxide films, discrete, idiomorphic oxide crystallites were observed in the surfaces of oxidized tin-zinc, tin-indium, and tin-germanium alloys. In the case of the tin-indium and tin-germanium alloys, these oxide crystallites formed in the same general pattern (that is, location and density of sites) as the tin oxide growth centers normally do during the oxidation of pure tin. Furthermore, dislocations in the tin alloy substrate have been observed directly associated with the indium oxide crystallites in the surface. These observations strongly suggest (i) that these crystallites nucleate and grow either from a thin continuous oxide film or in the metal surface itself at high-energy sites in the surface where dislocations emerge from the substrate, and (ii) that the formation of the alloying-element crystallites in these preferred high-energy sites may impede or preclude the nucleation of the α-SnO growth centers that normally form and grow rapidly, with large attendant weight increase, on the surface of pure tin.

Manuscript received May 11, 1962. This paper was prepared for delivery before the Boston Meeting, Sept. 16-20, 1962.

Any discussion of this paper will appear in a Discussion Section to be published in the December 1963 JOURNAL.

REFERENCES

1. W. E. Boggs, R. H. Kachik, and G. E. Pellissier, *This Journal*, **108**, 6 (1961).
2. W. E. Boggs, P. S. Trozzo, and G. E. Pellissier, *ibid.*, **108**, 13 (1961).
3. W. E. Boggs, *ibid.*, **108**, 124 (1961).
4. U. R. Evans, "The Corrosion and Oxidation of Metals," p. 836, St. Martin's Press, New York (1960).
5. T. Arai, *J. Phys. Soc., Japan*, **15**, 916 (1960).
6. K. Hauffe, *Progr. Metal Phys.*, **4**, 71 (1953).
7. S. C. Britton and K. Bright, *Metallurgia*, **56**, 163 (1957).
8. Equilibrium Data for Tin Alloys, Tin Research Inst., Sept. 1949.
9. A. U. Seybolt and J. E. Burke, "Procedures in Experimental Metallurgy," John Wiley & Sons, Inc., New York (1953).
10. J. F. Elliot and M. Gleiser, "Thermochemistry for Steel Making," Vol. I, Addison-Wesley (1960).
11. O. Kubaschewski and B. E. Hopkins, "Oxidation of Metals and Alloys," Butterworths Scientific Publications, London (1953).
12. A. H. Cottrell, "Dislocations and Plastic Flow in Crystals," Oxford, New York (1953).
13. F. W. Young, *Acta Met.*, **8**, 117 (1960).
14. J. T. Fourie, F. Weinberg, and F. W. C. Boswell, Jr., *Appl. Phys.*, **31**, 1136 (1960).
15. R. S. Gurnick and W. M. Baldwin, Jr., *Trans. ASM*, **42**, 308 (1950).

Porous Tantalum Anodes for Liquid and Solid Electrolytic Capacitors by Reaction in Situ

J. A. Pierret, A. Shtasel,[1] H. T. Knight, and A. B. Michael

Fansteel Metallurgical Corporation, North Chicago, Illinois

ABSTRACT

A new porous tantalum capacitor anode for liquid and solid electrolytic capacitors, prepared directly by the reaction *in situ* of Ta_2O_5 and C is described. Porous *in situ* anodes with total interstitial contents (C, O, and N) of less than 0.02%, metallic impurity contents less than the limit of chemical analytical detection, densities of approximately 4-12 g/cc, and specific capacitances of 1600-3200 μcoul/g were evaluated. Life tests of 1000 hr showed only slight changes in electrical characteristics for liquid electrolytic capacitors tested at 125v and 85°C and solid electrolytic capacitors tested at 34v and 125°C.

The electrical characteristics of porous anode tantalum capacitors are highly dependent on the purity and surface area of the tantalum anode, and considerable work has been directed toward preparing tantalum anodes having a maximum purity and optimum surface area. The general and current practice for preparing anodes is to compact powder particles of specified size, size distribution, and morphology into the desired shape and then to sinter under controlled conditions in vacuum at an elevated temperature. The selection of different combinations of powder particles, pressing pressures, and sintering conditions permits control of the surface area of the anode. Frequently, binders and lubricants are added to facilitate compaction, and these and other residual impurities must be removed during sintering.

The objective of the work reported here was to prepare high-purity porous tantalum anodes with controlled surface area by a simpler, more direct process than that currently used and, further, to prepare anodes with a high capacitance on a weight and volume basis. These objectives were met using a new approach based on the reduction *in situ* of a tantalum compound. The *in situ* process for preparing porous tantalum anodes is described. The characteristics of the anodes and of liquid and solid electrolytic capacitors prepared from these anodes are discussed. The investigation of columbium capacitor anodes prepared by reaction *in situ* is in progress and will be reported on in a later publication.

In Situ Process and Anode Preparation

Preliminary studies showed that the reduction of Ta_2O_5 with carbon was a more feasible reaction for preparing porous anodes by *in situ* reaction than the other systems examined, such as Ta_2O_5 with TaC and K_2TaF_7 with Na, and the major effort was concentrated on this system.

The *in situ* process consists of intimately blending high-purity Ta_2O_5 with graphite and compacting the blend into the shape of an anode, as shown in Fig. 1. Because of the compacting and lubricating properties of the blend, no additional lubricants or binders are required. The unreacted anode is heated in vacuum under a controlled temperature-time cycle to 2200°C to remove oxygen and carbon according to the reaction $Ta_2O_5 + 5C + 2Ta \rightarrow 5CO$. Reacted anodes are shown in Fig. 1. Considerable shrinkage occurs on reaction, but the cylindrical shape of the initial compact is retained.

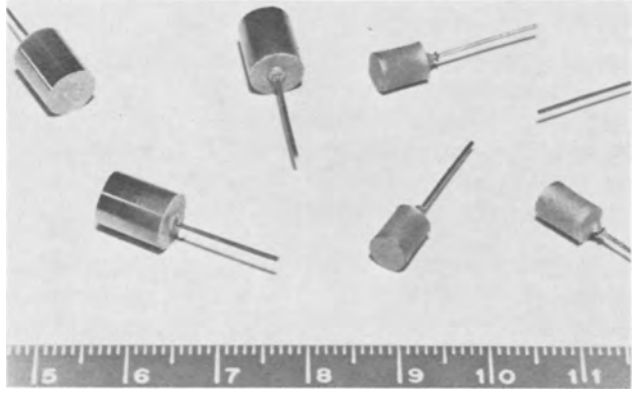

Fig. 1. Porous tantalum *in situ* anodes. Compacted Ta_2O_5 and C blend before reaction (left), as reacted anodes (right); scale in mm.

Characteristics of In Situ Anodes

The chemical purity, pore size, and pore size distribution of the reacted anode is a function of the particle size of the reactants, pressing pressure, and the temperature-time cycle for the reaction. Anodes with acceptable electrical characteristics were obtained when the carbon content was less than 0.004%, oxygen less than 0.02%, and nitrogen less than 0.001%. Metallic impurities were readily maintained less than the limit of chemical analytical techniques when high-purity reactants were used. A typical analysis of an *in situ* tantalum anode is given in Table I.

The *in situ* anodes are characterized by a thin sponge-like network of tantalum, as shown in Fig. 2A, whereas conventional anodes prepared from

[1] Present address: Cornell-Dubilier Electronics, Division of Federal Pacific Electric Company, Norwood, Massachusetts.

Table I. Typical analysis of *in situ* anodes[a]

O	0.014%	Zr	<0.002%
C	0.002	Si	<0.005
N	0.001	Ti	<0.002
Cb	<0.003	W	<0.005
Mo	<0.001	Mn	<0.005
Fe	<0.001	Cu	<0.0005
Co	<0.005	Al	<0.0005
Sn	<0.005	Ni	<0.005

[a]Methods of analysis: O-Leco oxygen analyzer, C-Leco carbon analyzer, N-Micro-Kjeldahl, Metallics-emission spectrographic using special carriers.

Table II. Density and wet electrical characteristics of *in situ* anodes

Density, g/cc	Electrical characteristics[a] Specific capacitance, μcoul/g at 120 cps	Specific capacitance, μcoul/cc at 120 cps	d-c Leakage, μa at 125v	Dissipation factor, %, at 120 cps
3.6	3200	11,800	20.0	1.7
5.6	2800	15,700	0.60	1.9
5.7	2800	16,000	0.50	1.6
5.9	3020	17,800	0.40	1.2
7.3	2560	18,700	1.0	N.D.
8.5	1970	16,700	0.6	2.0
9.6	1680	16,100	0.5	4.2
9.7	2250	21,800	1.15	3.3
11.0	2150	23,600	18.0	2.5
12.0	1280[b]	15,400[b]	2.5[b]	8.0[b]

[a] Anodized to 200v in ethylene glycol-oxalic acid, measured in sulfuric acid.
[b] Anodized to 100v, measured at 60v.

powder retain some of the characteristics of the initial powder particles, as shown in Fig. 2B and 2C.

Table II gives the densities and related electrical characteristics of *in situ* anodes. The useful range of anode densities is 5-10 g/cc. At densities less than 5 g/cc the capacitance per volume (μcoul/cc) is low, even though the capacitance per gram (μcoul/g) is acceptable. For high-density anodes the specific capacitance per gram is low. Both extremes of density showed high d-c leakages.

A comparison of the pore diameter distribution for *in situ* anodes and anodes prepared by conventional techniques is given in Table III. The higher specific capacitance of the sodium reduced powder and *in situ* anodes compared to the electrolytic powder anodes is attributed to the higher percentage of

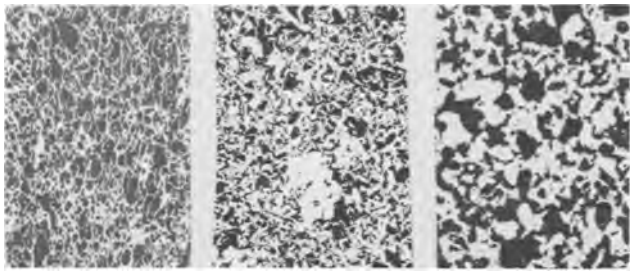

Fig. 2. Microstructure of *in situ* and conventional tantalum anodes. (A) (left), *in situ* anode; (B) (center), anode prepared from sodium reduced powder; (C) (right) anode prepared from electrolytically reduced powder. Magnification 100X before reduction for publication.

pore diameters in the range of 4-14μ. The *in situ* anodes have a pore diameter distribution similar to anodes prepared from sodium-reduced powder but a higher percent porosity, which results in a higher specific capacitance.

Performance of Anodes

Wet electrolytic capacitors were prepared from 1.05g *in situ* anodes having a density of 5.9 g/cc by forming to 200v in an ethylene glycol-oxalic acid electrolyte at 105°C. A specific capacitance of 3,020 μcoul/g was obtained. The anodes were encapsulated in a silver case containing a sulfuric acid electrolyte.

Solid electrolytic capacitors were prepared from 0.70g *in situ* anodes having a density 7.0 g/cc by forming to 200v, as above. A specific capacitance of 2660 μcoul/g was obtained. These anodes were fabricated into solid electrolytic capacitors with a MnO_2 solid electrolyte according to the procedure used by McLean (1), and encapsulated in a brass case.

The wet electrolytic capacitors were life tested for 1000 hr at 125v at 85°C. The results of this test, as shown in Table IV, indicate that these units have unusually good electrical characteristics. The initial capacitance values of the individual capacitors do not vary more than ±2.5% from the average, and after 1000 hr the variation remains equally as small. The change in capacitance after life testing is also unusually small. The remarkable uniformity of the dissipation factor both before and after testing, together with the capacitance regularity, is characteristic of the *in-situ* type of capacitor. The dissipation

Table III. Pore diameter distribution for conventional and *in situ* anodes[a]

Anode type	Total porosity, %	Apparent pore diameter per cent of total porosity >17μ	17-14μ	14-10μ	10-6μ	6-4μ	4-2μ	<2μ	Specific capacitance,[b] μcoul/g, at 120 cps
Electrolytically reduced powder	46.1	17.6	54.1	10.2	12.2	3.0	0.5	2.4	1185
	47.4	20.4	51.0	9.8	9.8	6.7	1.9	0.4	1270
Sodium reduced powder	40.0	7.8	3.4	1.2	35.7	38.8	11.4	1.7	1800
	40.1	4.2	2.3	0.5	33.1	43.5	14.6	1.8	1800
In situ	55.3	2.5	3.6	26.8	27.2	27.2	10.9	1.8	2600
	55.5	11.7	9.3	9.3	26.2	26.2	11.2	6.1	2600

[a] Measurements with an American Instrument Company Porosimeter.
[b] Anodized to 200v.

Table IV. Life tests of wet electrolytic capacitors[a]

	Initial values				After 1000 hr at 125v and 85°C			
	25°C					25°C		
	C, μf at 120 cps	Dissipation factor, %, at 120 cps	d-c Leakage, μa at 125v	85°C d-c leakage, μa at 125v	85°C d-c leakage, μa at 125v	C, μf at 120 cps	Dissipation factor, %, at 120 cps	d-c Leakage, μa at 125v
1	15.5	1.2	0.6	4.8	4.0	14.9	1.0	0.5
2	16.0	1.2	0.1	3.3	5.0	15.4	1.1	0.5
3	16.0	1.2	0.9	5.1	5.0	15.3	1.0	1.0
4	16.2	1.0	0.3	2.4	4.5	15.6	1.0	0.8
5	15.7	1.2	0.8	6.0	6.0	15.1	1.0	0.6
6	15.6	1.2	0.2	2.1	5.0	14.9	1.0	0.5
7	15.6	1.2	0.1	2.1	4.0	15.0	1.0	0.7
Avg	15.8	1.2	0.4[1]	3.7[2]	4.8[3]	15.2	1.0	0.7[4]

[a] *In situ* anodes of 1.05g anodized to 200v.
[1] 2×10^{-4} μa/μf-v.
[2] 1.9×10^{-3} μa/μf-v.
[3] 2.4×10^{-3} μa/μf-v.
[4] 3.6×10^{-4} μa/μf-v.

Table V. Life test of solid electrolytic capacitors [a]

	Initial values				After 1000 hours at 34 volts and 125°C			
	25°C					25°C		
	C, μf at 120 cps	Dissipation factor, %, at 120 cps	d-c Leakage, μa at 50v	125°C d-c leakage, μa at 34v	125°C d-c leakage, μa at 34v	C, μf at 120 cps	Dissipation factor, %, at 120 cps	d-c Leakage, μa at 50v
1	8.9	1.2	0.3	26.0*	29.0*	8.7	1.0	0.8
2	9.0	1.0	0.4	2.4	13.5	8.8	0.8	1.1
3	9.6	1.0	0.2	0.2	8.7	9.3	1.0	0.6
4	9.8	1.0	0.2	0.2	10.0	9.6	1.0	0.5
5	9.7	0.8	0.1	1.3	12.8	9.6	1.0	0.4
6	9.2	1.0	0.1	0.2	6.2	9.0	1.0	0.3
7	9.0	1.2	0.1	0.2	6.9	8.8	0.8	0.4
Avg	9.3	1.0	0.2[1]	0.8[2]	9.7[3]	9.1	0.9	0.6[4]

* Not included in averages.
[a] *In situ* anodes of 0.70g anodized to 200v.
[1] 4.3×10^{-4} μa/μf-v.
[2] 2.5×10^{-3} μa/μf-v.
[3] 3.1×10^{-2} μa/μf-v.
[4] 1.3×10^{-3} μa/μf-v.

factor values are less than those usually encountered in conventional tantalum wet slug capacitors, owing to the particular pore-size distribution of the *in situ* anode. The d-c leakage current of these units is also very low, about one tenth the value of conventional tantalum wet slug capacitors (1).

The results of the 1000-hr life tests on the solid electrolytic capacitors, as well as their initial electrical characteristics, are given in Table V. These 50v-9 μf solid capacitors are quite superior to solid capacitors prepared from conventional tantalum anodes. As with the wet capacitors prepared from *in situ* anodes, the solid electrolytic capacitors are characterized by unusually low leakage current values at 50v at room temperature and at the derated voltage of 34v at 125°C and a particularly low and stable dissipation factor. Even after 1000 hr at 125°C and 34v, the leakage current at room temperature has only increased by a factor of three. Also there is almost no change in capacitance values over this test period.

Discussion

The *in situ* process described in this paper shows great promise as a means for obtaining porous capacitor anodes with superior electrical characteristics as well as offering a cheaper and more efficient process for preparing porous anodes. It holds the further promise of being capable of extending the specific capacitance of porous slugs beyond the range now commercially feasible. On a weight basis, specific charge densities of 3000 μcoul/g are easily attained, and on a volume basis around 20,000 μcoul/cc can be reached. There are indications from experiments not as yet reported that a much higher specific capacitance is possible, approaching six times the normal specific capacitance-volt value on both a weight and volume basis.

The superior electrical characteristics can be explained by the unusual purity of these slugs and the special pore configuration of the reacted anode. The total interstitial impurity content is 170 ppm while the total metallic impurity content is less than 400 ppm. The tantalum purity, therefore, is better than 99.94% which is probably the highest purity reported in the literature for a porous anode and approaches the purity of electron beam-melted tantalum. There has been some speculation that the nature of the physical bonding between the tantalum metal particles has a direct bearing on both the leakage current values and the performance on life

test of wet and solid electrolytic capacitors. The improved leakage current and life test stability of the *in situ* anode is attributed to the sponge-like tantalum network and the increased porosity. The consistently low dissipation factor of both the wet and solid *in situ* capacitors is attributed to the uniform pore size.

Manuscript received July 3, 1962; revised manuscript received Sept. 10, 1962.

Any discussion of this paper will appear in a Discussion Section to be published in the December 1963 JOURNAL.

REFERENCE

1. D. A. McLean and F. S. Powers, *Proc. I.R.E.*, **44**, 872 (1956).

Electrical Properties of Thin Organic Films

Arthur Bradley and John P. Hammes

Radiation Research Corporation, Westbury, New York

ABSTRACT

Thin organic polymer film specimens were prepared for electrical conductivity measurements by the glow discharge polymerization process. The experimental procedure for film preparation is described in detail. Data on film properties and deposition efficiencies (g/kwhr) are presented for their possible bearing on the polymerization mechanisms. Dark conductivities (σ) were measured over the temperature range 75°-275°C. Plots of log σ *vs.* $1/T_{abs}$ generally gave straight lines above about 125° with slopes characteristic of the chemical composition of the polymer film. Conductivities at 150°C ranged from 10^{-17} mho/cm (films rich in halogen) to 10^{-13} mho/cm (ferrocene, tetracyanoethylene). A possible relationship between structure and conductivity is discussed.

It appears that semiconductive or photoconductive thin films will occupy a significant place in future technology. Both inorganic and organic materials are being evaluated for this application. The present communication describes convenient procedures for preparing thin organic films and their incorporation into specimens suitable for electrical measurements. Some representative data on conductivity as a function of temperature are included and discussed.

Uniformly thin organic films of good physical properties and generally high electrical resistance have been prepared by glow-discharge polymerization. Approximately forty different organic compounds were tested as potential "monomers." A variety of film specimens were prepared, differing in appearance and electrical parameters. Correlations were sought between these properties and the chemical nature of the polymer, as reflecting the choice of monomer. It was intended that this information would be applied to the synthesis of organic semiconductor films and might possibly lead to a better understanding of the source of free carriers and the mechanisms of charge transfer in amorphous solids.

Glow Discharge Polymerization

When an organic substance in the vapor phase is excited into luminescence by an electric discharge, a solid film tends to deposit on all surfaces exposed to the luminous plasma. This process has been the subject of considerable study at Radiation Research Corporation in recent years (1), and a film with composition and properties similar to Teflon is now being produced for use as a capacitor dielectric (trade name: "Glofilm") (2).

The solid deposit from the glow discharge need not be formed in the conventional manner of functional groups uniting with each other in a repeating chain reaction. In fact, no such functional groups are necessary (*e.g.*, methane and benzene gave solid films, the latter in relatively high yield). It is believed that ionic and ion-radical fragments are formed under the intense electron bombardment and recombine as they accumulate on the electrodes. The result is a complex intermolecular rearrangement of chemical bonds at more or less specific locations in the monomer molecule, leading to a macromolecule of fairly well defined structure: a three-dimensional network of atoms built up of the original compound (and/or its principal subsidiary units) in an irregular, but homogeneous pattern.

When the discharge conditions could be met (see below) most organic vapors deposited films. Unsaturated and aromatic compounds were "polymerized" at the fastest rate, that is, with the most efficient conversion of the energy dissipated in the discharge into new chemical bonds. The slowest or most inefficient materials were saturated aliphatics, particularly perhalogenated hydrocarbons.

The basic equipment for preparing glow-discharge films consisted of an evacuated chamber with a source of organic "monomer" vapor and electrodes wired to an external power supply. The electrodes were pairs of flat plates of any conductive material, placed approximately 1 cm apart. With a vapor pressure of about 1 mm Hg the glow discharge was usually initiated at 300-400v. Good films were ob-

tained when the discharge was sustained with a current density of the order of 1-3 ma/cm^2.

An alternating voltage in the ultra-audio frequency range (10-50 kc) was most satisfactory in the production of uniform, adhesive films. In most experiments, the two electrode plates became coated with identical "polymer" layers of thickness dependent only on the discharge current and time. The film thickness was self regulating through its own impedance, resulting in a high degree of uniformity and freedom from pinholes. The best films for electrical measurements were between 0.5 and 2.0μ thick.

The organic vapor was introduced through a needle valve from an external gas cylinder or liquid reservoir. Solid compounds were placed directly in the reaction chamber and their equilibrium vapor pressure adjusted to meet optimum discharge requirements by heating the entire system. All organics with vapor pressure approaching 1 mm Hg below 200°C without decomposition were satisfactory. Even then, the limiting factors were warping of the Teflon electrode holders and sublimation of monomer directly onto the electrodes. Discharges conducted at 200°C and above appeared to give as good films as at room temperature.

A detail view of the electrode holder assembly is shown in Fig. 1. An 8-in. bell jar constituted the discharge chamber. It was customary to evacuate the system to 10^{-5} mm Hg before admitting the monomer vapor to ensure that residual impurities from the previous deposition did not remain in the chamber. During each polymerization run the monomer pressure, voltage, and discharge current were monitored to control the film thickness and quality.

It was observed that films produced by glow discharge had higher melting points, greater thermal stability, and lower solubility than conventional polymers of similar composition. Most of them were hard and smooth and quite resistant to chemical attack. These good physical and chemical properties, coupled with the variety of fundamental structural elements and functional groups that could be incorporated into them, made them uniquely useful

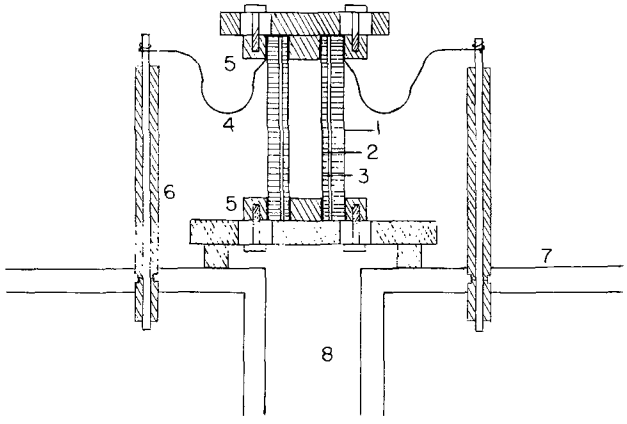

Fig. 1. Electrodes set up for glow discharge. 1, Quartz back up plate; 2, silica microscope slide specimen plate; 3, aluminized "bottom" electrode; 4, tinned copper strip electrical contact; 5, Teflon support pieces with adjustable jaws for clamping slides; 6, vacuum-tight electrical feedthru; 7, base plate for bell jar seal; 8, evacuation system and connection to monomer reservoir.

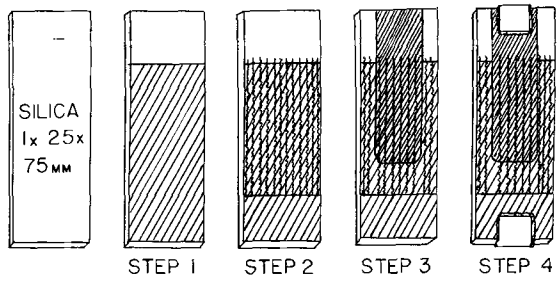

Fig. 2. Preparation of organic polymer film specimens. Step 1, application of vacuum metallized bottom electrode (Al); step 2, organic film from glow-discharge polymerization; step 3, top electrode (Al); step 4, electrical connections.

for a study of the electrical properties of organic solids.

Electrical Measurements

The electrodes used in the discharge were silica microscope slides (1 x 25 x 75 mm) coated with a thin conducting film of aluminum by standard evaporation techniques. The sequence of operations involved in preparing specimens from these slides is illustrated in Fig. 2.

As set up in the chamber, the Teflon holder masked the lower edge of the aluminized electrode during the deposition, permitting later electrical contact. At the higher edge of the electrodes the polymer fringe bridged over onto the silica substrate, allowing a top electrode to be evaporated directly over the organic film without shorting. The specimen was masked during the second aluminization to restrict the area of the top electrode to approximately one square inch and increase the surface path to the edges. When leads were attached at the ends of the specimen with the aid of silver paste they were ready for electrical measurements. The procedure for determining dark conductivities as a function of temperature was quite straightforward and need not be described in detail.

The measured electrical parameter was current, at 1.4v (dry cell less 0.1v drop across the electrometer). Most measurements were carried out on a General Radio 1520-A d-c amplifier, although a few specimens at higher temperature could be read directly on a microammeter. A typical specimen (naphthalene, 6.5 cm^2 area, 1.8 x 10^{-4} cm thick) gave 4 x 10^{-11} amp at 150°C and 1.4 x 10^{-8} amp at 250°, or dark conductivities of about 10^{-15} and 3 x 10^{-13} mho/cm at the respective temperatures. Intermediate values fell on the straight line joining these points on a plot of log conductivity *vs.* reciprocal of absolute temperature, with a slope corresponding to a thermal activation energy of conduction of 1.1 ev (Eq. [1]) (3).

$$\sigma = \sigma_0 e^{-E_a/kT} \qquad [1]$$

Conductivity *vs.* temperature points for naphthalene and acrylonitrile are plotted in Fig. 3. Similar plots for other monomers tested in this investigation (with experimental points omitted) are given in Fig. 4 through 8.

An accurate value of film thickness was required for the calculation of conductivity. This could be

determined either (a) from the measured capacitance of the specimen, assuming a reasonable dielectric constant, or (b) by counting interference fringes, and assuming a reasonable index of refraction. The two methods were used with fair agreement, as discussed below.

Film specimens were prepared from over 40 monomers, about 30 of which gave some useful conductivity data. A few invariably blistered or peeled during the temperature cycle (see below) or gave scattered or poorly reproducible currents. In most cases, the experimental points from duplicate films of the same monomer were essentially interchangeable on the linear portions of the log σ *vs.* $1/T$ plots. The curves presented in Fig. 4 through 8 were obtained with at least two specimens of each material.

Some comments on the discharge process and the properties of thin organic film specimens are presented in the following sections, followed by a concluding discussion of the conductivity results.

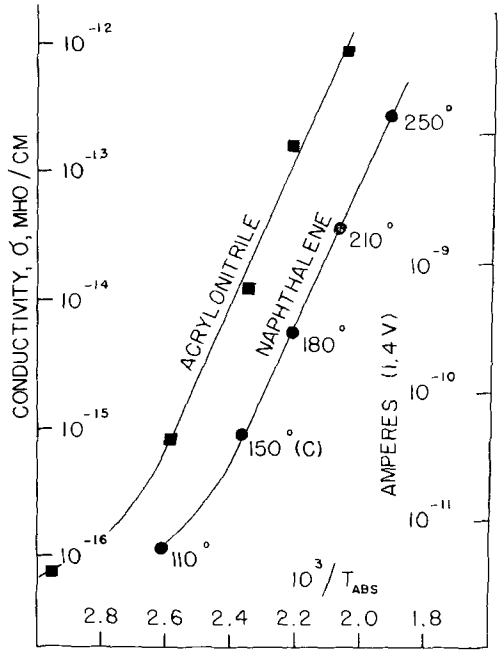

Fig. 3. Experimental current and conductivity *vs.* temperature points for naphthalene and acrylonitrile.

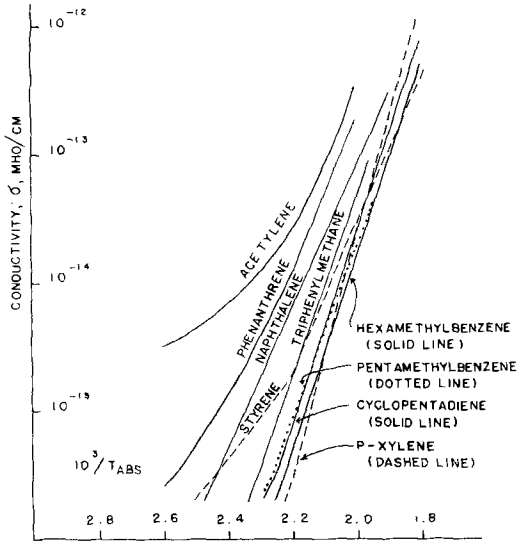

Fig. 4. Conductivity (σ) *vs.* temperature for organic polymer film specimens: hydrocarbons.

Discharge Parameters; Efficiency

As indicated above, the experimental procedures were essentially identical for the production of film from all monomers. When necessary, the entire system was heated to achieve the desired vapor pressure with the result that polymerization runs on certain high-molecular-weight solid monomers like triphenyltin chloride were carried out at relatively high temperatures (200°C and above). There were no definite indications that such heating had a significant influence on the properties of the films so deposited.

The voltage required to initiate the discharge with fixed electrode configuration was chiefly dependent on the pressure, as would be expected from

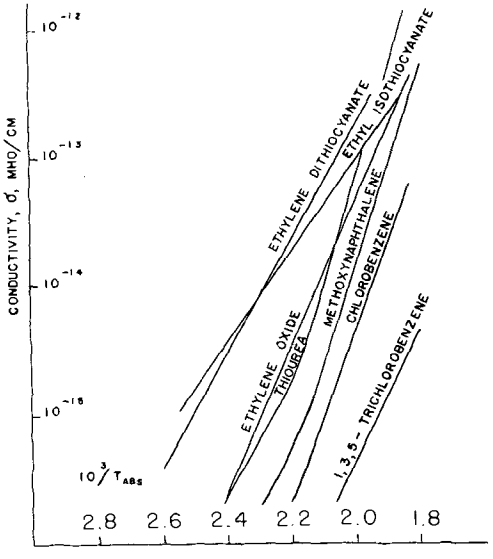

Fig. 5. Conductivity (σ) *vs.* temperature for organic polymer film specimens: oxygen, sulfur, and halogen compounds.

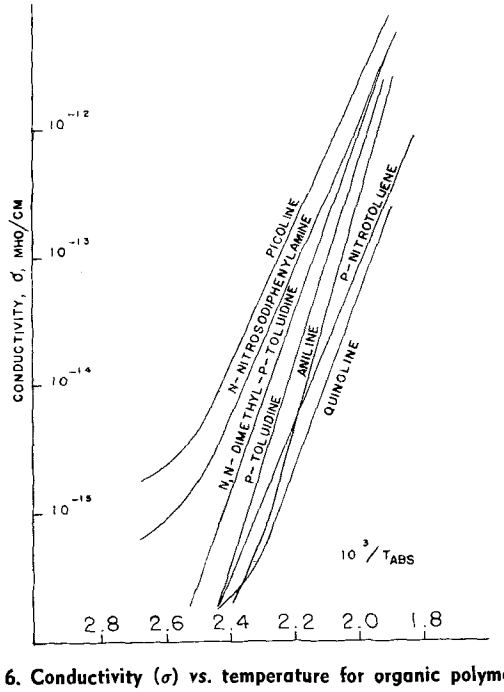

Fig. 6. Conductivity (σ) *vs.* temperature for organic polymer film specimens: amines.

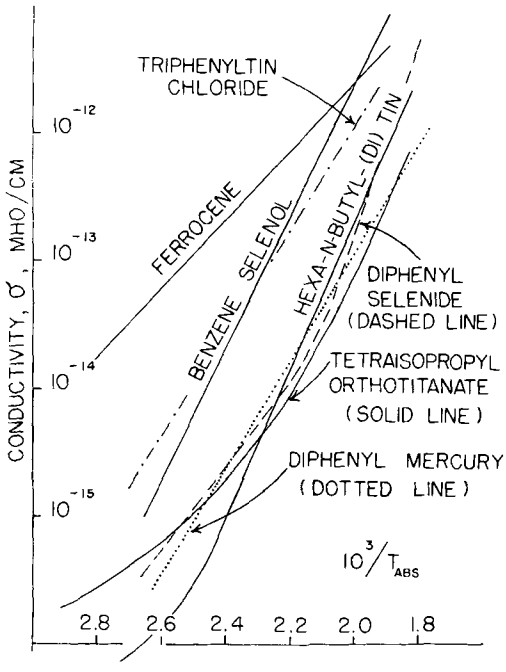

Fig. 7. Conductivity (σ) vs. temperature for organic polymer film specimens: complex compounds.

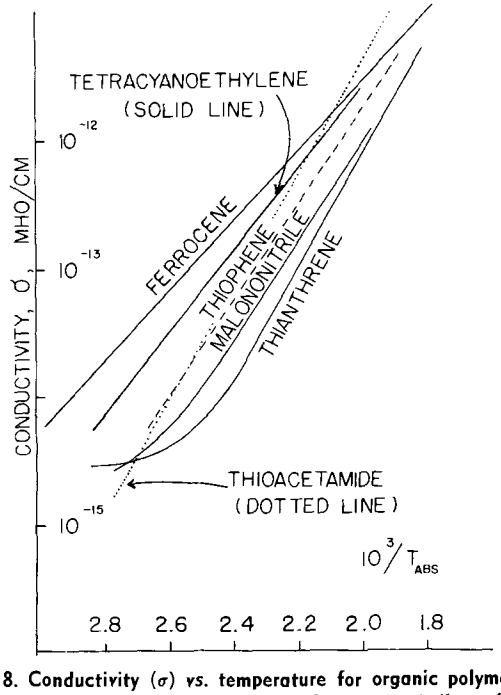

Fig. 8. Conductivity (σ) vs. temperature for organic polymer film specimens: high conductivity specimens (ferrocene, nitrile and sulfur compounds).

Paschen's law (4). The ionization characteristics of the monomer were probably also a factor in determining this voltage. The observed parameters of typical discharge runs are recorded in Table I. The discharge current and duration of each run were arbitrarily chosen according to the thickness of deposit desired and the anticipated efficiency of the polymerization. In duplicate experiments on a single monomer, it was found that the weight of polymer obtained was approximately proportional to the energy dissipated in the discharge, regardless of the rate of deposition.

The deposition "efficiency," or rate of accumulation of solid polymer per unit of electrical power, reflected both the molecular weight of the monomer and the ease with which it yielded ionized or radical fragments under electron bombardment. Most aromatic compounds yielded between 25 and 75 g/kwhr, as shown in Table II. Nitroso-substituted amines and ethylene compounds comprised a less efficient class, and it is noteworthy that there was no correlation between efficiency and film electrical properties. The difference between 1, 3, 5- and 1, 2, 4-trichlorobenzene was striking and will be discussed further below. The highest yield (300 g/kwhr) was obtained with vinyl ferrocene, a solid that required warming to above 60°C to give a sufficient vapor pressure to sustain a discharge. Completely saturated molecules such as propane were deposited with poor efficiency, as were most halogen-substituted compounds. For example, tetrafluoroethylene polymerized no faster than ethylene, despite its molecular weight advantage of 3.5:1. Saturated perhalogenated hydrocarbons such as carbon tetrachloride and even hexachlorobenzene gave no film at all. In general, polymer was obtained where the monomer contained any carbon-hydrogen bond, any carbon-carbon double bond, and any aromatic ring unless perhalogenated.

Special attention can be directed to the comparative efficiencies of 1, 3, 5- and 1, 2, 4-trichlorobenzene. The former was polymerized at the very high rate of 190 g/kwhr; the latter far below the related aromatics at only 5.5 g/kwhr. Both were solids that required mild heating to get sufficient vapor pressure. The essential difference appears to be the higher equilibrium concentration of the free radical intermediate from the symmetrical (1, 3, 5) compound, which could be stabilized by resonance more easily than the unsymmetrical (1, 2, 4) isomer. The former gave the most intense discharge color (bright red) of any monomer tested in this program. This observation suggests that the rate-determining step in the polymerization mechanism involved the consumption of a free radical intermediate.

In general the starting pressure was between 0.5 and 1.0 mm Hg or as close to this as could conveniently be obtained. During each polymerization run the system was closed off from the monomer reservoir ("static conditions"). Changes in pressure were frequently observed during the discharge to an extent that could be predicted fairly well from the structure. Monomers that had an easy route to ionization without breaking a carbon-hydrogen bond, such as acrylonitrile, showed a normal decrease in pressure as they were converted to solid film. On the other hand, saturated hydrocarbons showed pressure increases during a run. It may be assumed that more molecules of hydrogen and other gaseous fragments were formed in these experiments than monomer was consumed. In either case it will be evident that a static system will deposit polymer less efficiently with time, and therefore the most reliable efficiency data will be derived from runs of short duration.

Film Properties; Thickness; Thermal Effects

Besides the discharge variables, Table I also presents the raw measurements from which film thickness were computed: capacitance and number of

Table I. Discharge variables and film properties

Run No.	Monomer	Volts	ma-min	Avg rel P*	Cap. μF	Cap. after heating	Fringes 508 mμ
84	Tetraethyl orthotitanate	350	50	4.6	0.026	—	5
87	Ferrocene	340	10	2.2	0.078	—	4
89	Phenanthene	315	30	2.8	0.018	0.022	16
94	Naphthalene	370	10	2.3	0.011	0.020	12
96	Dicyclopentadienyl titanium dichloride	360	9	3.0	0.023	0.031	7
97	Pentamethylbenzene	340	9	1.7	0.0066	0.0059	13
102	Vinyl ferrocene	425	7.5	0.9	0.0037	—	20
110	Ethylene dithiocyanate	385	13.5	2.0	0.064	0.063	35
112	Triphenylmethane	420	16	2.2	0.0037	0.0058	13
136	Acetylene	275	23	1.9	0.105	0.115	25
141	Cyclopentadiene	340	16	1.8	0.016	0.015	7
147	Hexamethylbenzene	360	22	2.8	0.0058	0.0053	17
150	Methoxynaphthalene	385	12	2.0	0.0041	0.0077	22
156	Quinoline	305	60	1.9	0.066	Shorted	2
165	Styrene	350	15	2.7	0.021	0.022	12
167	*p*-Nitrotoluene	350	20	5.1	0.0079	0.011	16
168	*p*-Xylene	300	10	2.1	0.0094	Peeled	12
176	Acrylonitrile	350	5	1.5	0.005	0.013	5
201	Diphenyl selenide	400	14	1.4	0.0172	0.0171	9
203	Picoline	385	20	1.5	0.0087	0.0093	16
207	Malononitrile	415	5	3.5	0.0395	0.056	6
214	N, N-dimethyl-p-toluidine	355	42	3.7	0.0052	0.0058	19
222	Aniline	345	25	3.2	0.0115	0.0108	9
226	Dicyanoketene ethylacetal	450	11	1.2	0.0906	0.113	2
230	Cyamelurine	350	27	1.5	0.074	0.099	2
235	Diphenyl mercury	370	17	2.5	0.0187	0.0187	7
241	N-Nitrosodiphenylamine	445	57	1.6	0.0161	0.0139	8
247	Thiourea	325	150	1.3	0.0118	0.0125	10
251	1-Nitrosopiperidine	455	100	4	0.011	0.0120	11
254	Triphenylarsenic	355	250	1.1	0.0332	Shorted	4
260	Tetracyano ethylene	450	11	1.2	0.0906	0.113	2
267	N-Nitrosodiethylamine	365	96	1.8	0.038	0.038	6
277	Hexa-n-butyl (di) tin	305	150	1.3	0.014	0.0136	9
285	Thianthrene	330	300	1.0	0.098	0.098	7
304	Tetraisopropyl orthotitanate	350	90	—	0.015	0.017	6
306	Thioacetamide	385	210	1.1	0.020	Shorted	11
355	Thiophene	435	75	—	0.0071	0.0115	17
356	Benzene selenol	440	85	0.4	0.0049	0.0067	—

* Rough criterion of Relative Pressure, in units of 10^{-9} amp of ionization current (tritium vacuum gage, 45v applied). Calibration varies slightly for different monomers, and current is only approximately linear function of P. On the average, 4×10^{-9} amp corresponds to 1.0 mm Hg.

interference fringes. Each method requires an assumption of the magnitude of a basic property of the material: the dielectric constant (k) in the case of capacitance and the index of refraction in the case of fringes. Fairly consistent comparisons of the two methods were obtained when these numbers were chosen to be 3.0 and 1.5, respectively.

The capacitance method has the advantage of being based on approximately the same area-to-thickness ratio as the resistance measurements. It can also give an average thickness in the case of a nonuniform specimen. If parts of either the upper or lower electrode were not in good contact with the film, the capacitance method would lead to an erroneous conclusion of thickness but an accurate value for the conductivity. A typical capacitance for a specimen of 6.5 cm^2 (nominal) area might be 0.01 μF. Assuming $k = 3.0$, the average thickness would then be 1.7μ.

The fringe-counting method is most effective when the thickness is essentially uniform, with a steep taper at the edge, and the number of fringes lies between 3 and about 25. It is much closer to being a direct measurement than capacitance except that the index of refraction must be included to correct for the slower speed of light in the organic film medium. Each additional band appearing at the specimen edge represents an increment in thickness of one half wavelength. Using a 508 mμ green light source in a standard metallurgical microscope, and assuming IR = 1.5, the 1.7μ specimen referred to above would show between 10 and 11 fringes.

Certain runs, particularly at extremes of pressure where the discharge was difficult to sustain evenly over the electrode surface, gave nonuniform deposition of film. This was immediately evident on inspection, since interference bands could be observed across the entire face of the specimen. The usual pattern was a series of roughly concentric rings, or "bull's eye," clearly indicating the thickest (or thinnest) region. These patterns could be seen without the aid of a microscope or monochromatic light, especially after the heating cycle of a resistance *vs.* temperature measurement. As mentioned above, the capacitance method provided an average thickness and therefore accurate conductivities could be derived for bull's eye specimens.

The fringe count did not change after the heating

Table II. Polymerization efficiencies

Monomer	Yield, g/kwhr	Moles/kwhr
Vinyl ferrocene	300	1.4
1, 3, 5-Trichlorobenzene	190	1.05
Chlorobenzene	75	0.67
Styrene	69	0.66
Ferrocene	67	0.36
Picoline	65	0.70
Naphthalene	62	0.48
Pentamethylbenzene	61	0.44
Nitrotoluene	55	0.40
Acrylonitrile	55	1.04
Diphenyl selenide	52	0.20
p-Toluidine	47	0.44
p-Xylene	45	0.42
N, N-dimethyl-p-toluidine	39	0.29
Toluene	38	0.41
Aniline	38	0.41
Diphenyl mercury	30	0.08
Hexamethylbenzene	28	0.17
Malononitrile	25	0.38
Tetracyanoethylene	19	0.15
Thiophene	13.5	0.16
Benzene selenol	13.5	0.086
Tetrafluoroethylene	12	0.12
Ethylene	11	0.39
N-Nitrosodiphenylamine	10	0.05
Thianthrene	10	0.046
Acetylene	9	0.35
N-Nitrosopiperidine	9	0.08
Dicyanoketene ethylacetal	7	0.04
Cyamelurine	6	0.013
1, 2, 4-Trichlorobenzene	5.5	0.03
Propane	5.2	0.12
Thiourea	4.7	0.06
Thioacetamide	4.4	0.059
N-Nitrosodiethylamine	4.2	0.04
Hexa-n-butyl (di) tin	4.0	0.007
Triphenyl arsenic	3.4	0.19
Methyl mercaptan	1	—
Carbon tetrachloride	0	
Hexachlorobenzene	0	
Ammonia	0	

cycle, indicating that the thickness remained the same. There was a tendency for the capacitance and the power factor to increase during the conductivity runs, possibly due to chemical changes such as furthur oxidation at elevated temperatures. The conductivity was markedly independent of minor changes in composition, whereas increases in dielectric constant and power factor would be expected on introduction of polar impurities such as represented by new carbon-oxygen bonds.

There was evidence that some oxygen was taken up by the films even before heating. Both combustion and infrared absorption analyses showed the presence of oxygen (2-10%) in glow-discharge polymer prepared from hydrocarbons such as cyclopentadiene and p-xylene. Unfortunately, the infrared spectra were almost completely lacking in fine structure and so were of no value in clarifying the chemical nature of the film.

It was occasionally observed that temperature cycling affected the lower or nonlinear portions of the log σ *vs.* $1/T$ plots. Repeat runs on the same specimen sometimes showed higher currents in this region and thereby tended to raise the threshold of linearity from which activation energies were calculated. This again suggests the addition of impurities by heating, changing the conductivity in what for inorganic semiconductors might be referred to as the "extrinsic region."

A tendency to "peel" or separate from the substrate silica plate was observed in many of the hydrocarbon films. Among the most troublesome were toluene, p-xylene, and chlorobenzene. This difficulty rarely occurred with solid monomers, and even with liquids it could usually be controlled by restricting the thickness to $\frac{1}{2}\mu$. Another precaution that proved useful in preserving the life of the film specimens was storage in a dessicator. Most films were moderately sensitive to damage by moisture, especially in the first few days after preparation. Certain compounds (*e.g.*, *N*-nitrosoamines) formed surface bubbles after thermal cycling indicative of gaseous decomposition products.

In terms of the properties of these glow-discharge films, 1 to 2μ represented a substantial and useful thickness, with pinhole counts vanishingly small and capable of supporting 50v d.c. or more without breakdown. Thicker specimens could have been prepared, particularly from amine and solid hydrocarbon monomers, but only with the sacrifice of uniformity and efficiency. It may be estimated as a matter of general interest that the practical upper limit of thickness for such films (maintaining a certain degree of physical integrity as films) is of the order of 10μ.

Many of the thinner films (0.5μ and less) examined for conductivity *vs.* temperature were discovered to have become shorted during or after the heating cycle. On the other hand, the thickest specimens (above 2μ) tended to separate from the substrate due to differences in thermal expansion and contraction coefficients and were often found to have opened along the fringe area covered by the top aluminized electrode. These could generally be repaired, but the most reproducible results on repeated thermal cycling were obtained with those specimens in the optimum thickness range of $1\text{-}2\mu$.

Conductivity of Film Specimens

Although this program is barely out of the exploratory stage, it is felt that the conductivity *vs.* temperature relationships observed with these glow-discharge films are representative of the best information currently available on the electrical behavior of organic solids. The high thermal stability of the films made it possible to measure an accurate and significant activation energy of conduction for most specimens. The values of E_a determined from the slopes of the log σ *vs.* $1/T$ curves over large ranges of temperature were reproducible in different specimens of the same material prepared under variant conditions and were also found to be characteristically uniform in groups of structurally related compounds.

Absolute magnitudes of dark conductivity at 150°C ranged from below 10^{-17} mho/cm for polymer films prepared from 1, 3, 5-trichlorobenzene to above 10^{-13} for ferrocene. However, the great majority of monomer compositions led to films with conductivities between about 10^{-16} and 10^{-14} mho/cm at this temperature. This was particularly

Table III. Typical conductivity vs. temperature data

Monomer	σ, mho/cm 150°	σ, mho/cm 250°	E_a, ev	See fig.
Naphthalene	9×10^{-16}	2.7×10^{-13}	1.1	3, 4
Styrene	6×10^{-16}	9×10^{-14}	1.2	4
p-Xylene	5×10^{-17}	1.5×10^{-13}	1.8	4
Cyclopentadiene	1.0×10^{-16}	1.2×10^{-13}	1.5	4
Hexamethylbenzene	7×10^{-17}	7×10^{-14}	1.5	4
Ethylene oxide	4×10^{-16}	1.6×10^{-13}	1.1	5
Methoxynaphthalene	1.1×10^{-16}	7×10^{-14}	1.5	5
Thiourea	3.3×10^{-16}	4×10^{-13}	1.7	5
Chlorobenzene	8×10^{-17}	1.9×10^{-14}	1.4	5
Picoline	2.2×10^{-14}	6×10^{-12}	1.1	6
N-Nitrosodiphenylamine	8×10^{-15}	3.0×10^{-12}	1.2	6
p-Toluidine	7×10^{-16}	2.3×10^{-12}	1.5	6
Aniline	2.8×10^{-16}	1.4×10^{-12}	1.8	6
p-Nitrotoluene	5×10^{-16}	2.5×10^{-13}	1.2	6
Diphenyl selenide	3.1×10^{-18}	8×10^{-13}	0.75, 1.5	7
Diphenyl mercury	2.8×10^{-15}	2.7×10^{-13}	0.85	7
Ferrocene	2.7×10^{-13}	4.5×10^{-12}	0.55	7, 8
Benzene selenol	2.5×10^{-14}	7×10^{-12}	1.1	7
Hexa-n-butyl (di) tin	1.5×10^{-15}	7×10^{-13}	1.1	7
Tetracyanoethylene	1.8×10^{-13}	5×10^{-12}	0.60	8
Malononitrile	3×10^{-14}	1.8×10^{-12}	0.75	8
Thianthrene	1.5×10^{-14}	1.6×10^{-12}	0.85	8
Thiophene	6×10^{-14}	3×10^{-12}	0.75	8
Thioacetamide	8×10^{-14}	9×10^{-12}	0.85	8

true of the hydrocarbons and the amines, which constituted the two largest groups. Activation energies of conduction were more nearly uniform in these two sets. The average value of E_a for fifteen monomers (all except acetylene in Fig. 4 and 6) was 1.36 ± 0.06 ev. This magnitude of temperature response may be related to the energy required to create charge carriers in a structure consisting principally of carbon-carbon bonds.

It should be made clear that the conductivities and activation energies under discussion do not refer to the monomers themselves. The actual compositions and structures of the polymer films tested are unknown and may reflect much or little of the monomer, depending on the conditions and the mechanisms of glow-discharge polymerization. Moreover, these conductivity data were generally recorded in a temperature range where the monomer would not be available in the solid state. There is no contradiction, for example, between the value of 1.1 ev for the activation energy of a film derived from naphthalene (Table III) and the lower literature values on the crystalline monomer (3).

The results suggest that conduction in organics is determined only by gross compositional features common to a great variety of polymers. This investigation did not distinguish between films prepared from such contrasting monomers as cyclopentadiene and hexamethylbenzene on the basis of magnitude and temperature dependence of conductivity. This is not to be interpreted that the glow-discharge process converted all organic monomers to the identical polymer structure, for there were differences in appearance and stability that clearly set them apart, but that the conduction mechanism involved only certain chemical bond linkages which were approximately the same for all.

Moreover, impurities cannot be considered as participating in the conduction process. The proportions of whole molecules and fragments of different sizes would tend to vary according to the pressure and voltage in different runs but this was evidently not a consideration. Certain of these films were contaminated with as much as 10% oxygen, and there was no indication that it changed the conductivity as much as a factor of two.

In connection with the above, it was not surprising to find that films prepared from compounds already containing oxygen were electrically similar to those from hydrocarbon monomers (Fig. 5). It appears that in many cases the common "hetero" atoms of organic chemistry (O, N, S, halogens) can be incorporated into glow-discharge films in various mixtures and combinations without causing significant changes in the fundamental conductivity process. No doubt many exceptions to this generalization will be uncovered. The first one to be discussed involves compounds with two or more nitrile groups.

The conductivity of acrylonitrile film (Fig. 3) was comparable to the hydrocarbon-amine groups; in fact it was nearly identical to picoline (Fig. 6). However, the presence of an additional nitrile substituent in the monomers resulted in a lower slope and, at least in the case of tetracyanoethylene (Fig. 8), a significant increase in conductivity.

All materials tested in this program which gave relatively highly conductive films (Fig. 8) had activation energies of conduction below 0.9 ev. This was in marked contrast to the average of 1.36 ev for hydrocarbon and amine polymers. A different conductivity mechanism is indicated, and one of the first possibilities to be considered must be that the principal charge carriers are now becoming available from new sites in the molecular structure. This may be accompanied by a shift in the charge transfer path from the carbon-carbon bond skeleton to the functional groups (where the mobility may be higher).

The compounds with two or more nitrile groups may have formed polymer linkages that were rich in carbon-nitrogen bonds, perhaps with some degree of conjugated unsaturation. Other workers have observed high conductivity in substituted cyamelurines (high molecular weight compounds rich in aromatic nitrogen in condensed rings) (5). Our attempts to polymerize cyamelurine decomposition products at 200°C led to film specimens of varying appearance and stability and no consistent conductivity pattern.

A few sulfur-containing films were found in the highest conduction group (Fig. 8). Thiophene and thianthrene had conductivities higher than any hydrocarbon polymer, and thioacetamide was comparable to tetracyanoethylene and ferrocene at the higher temperatures. It appears that the sulfur atom, as a functional group with favorable charge transfer characteristics, is potentially capable of dominating the conduction mechanism. There is a distinct possibility that results showing no enhancement of conductivity with a sulfur compound (accompanied by a high E_a, as in thiourea, Fig. 5) were anomalous and represented a recombination of decomposition fragments which included little or no sulfur.

The presence of a metal or transition element in the polymer generally did not lead to special electrical properties. Various monomers containing tin, titanium, mercury, and selenium were tested (Fig. 7) and generally gave log σ *vs.* $1/T$ curves in the hydrocarbon region, although they were rarely as reproducible and not generally good exponentials. Diphenyl selenide showed a fairly sharp break in slope at about 200°C; tetraisopropyl orthotitanate and dicyclopentadienyl titanium dichloride were nonlinear, as was vinyl ferrocene; diphenyl mercury and the tin-containing compounds gave somewhat scattered points that were only approximately represented by single lines. By contrast, excellent agreement in conductivities over a wide temperature range was obtained from five different specimens of ferrocene.

The reproducibility and characteristic activation energy of ferrocene suggest that there was an essential difference between the polymerization mechanism for this monomer and other metal-organics. There may have been either less fragmentation or some favored linkage to join the surviving units in the film. On the other hand, ferrous ions may have functioned as preferred carrier sources by conversion to the ferric (+3) oxidation state with the loss of one electron. No more specific explanation of the high conductivity of ferrocene polymer can be offered at this time.

In summary, it is proposed that there is a characteristic magnitude and temperature dependence of conductivity for organic polymer films that is basically due to the preponderance of carbon-carbon bonds in the structure. This situation remains essentially the same even when a fair proportion (say 10%) of the atoms in the carbon network are replaced by other elements, whether metals or nonmetals. However, when special structural features begin to appear in significant competition with the cross-linked carbon skeleton and these features offer new sources of carriers or a preferred path for their transmission, new patterns in conductivity response may be expected. These phenomena were observed with films prepared from ferrocene, some sulfur compounds, and certain monomers containing nitrogen in a form likely to be incorporated into a condensed ring or conjugated chain structure.

None of these films would qualify for consideration as organic semiconductors. Extrapolated to room temperature, the highest conductivities achieved in this survey of glow-discharge films did not exceed 10^{-14} mho/cm. Nevertheless, certain trends are clearly indicated to guide a specific development to this end: the influence of the carbon-carbon backbone must be minimized and the possible categories of substituent atoms or functional groups classified for selection according to their relative charge transfer capabilities. The optimum composition for a semiconductive organic polymer film should consist of a high concentration of electronically active centers held together by a framework that includes no superfluous carbon.

Manuscript received April 24, 1962; revised manuscript received Sept. 6, 1962. This paper was prepared for delivery before the Boston Meeting, Sept. 16-20, 1962.

Any discussion of this paper will appear in a Discussion Section to be published in the December 1963 JOURNAL.

REFERENCES

1. J. Goodman, *J. Poly. Sci.*, **44**, 552 (1960).
2. *Electrical Design News*, October 1960, p. 6.
3. C. G. B. Garrett, "Organic Semiconductors," Chap. 15 in "Semiconductors," N. B. Hannay, Editor, Reinhold Publishing Co., New York (1959).
4. J. M. Meek and J. D. Craggs, "Electrical Breakdown of Gases," p. 82, Clarendon Press, Oxford (1953).
5. E. Beekman, Private communication.

A New Family of Self-Activated Phosphors

D. E. Harrison, N. T. Melamed, and E. C. Subbarao

Research Laboratories, Westinghouse Electric Corporation, Pittsburgh, Pennsylvania

ABSTRACT

A series of compounds were discovered which have the generalized formula $R_2^{2+}R^{4+}R_2^{5+}O_9$. Examination of single crystals of $Pb_2ZrP_2O_9$ showed it to have hexagonal symmetry with $a_H = 10.08$Å and $c_H = 23.29$Å. Five of the seven compounds studied ($Ba_2ZrP_2O_9$, $Sr_2ZrP_2O_9$, $Pb_2TiP_2O_9$, $Ba_2ZrAs_2O_9$, and $Pb_2ZrAs_2O_9$) were isostructural with $Pb_2ZrP_2O_9$, and the seventh, $Sr_2ZrAs_2O_9$, had optical properties closely related to the group. With the exception of $Pb_2TiP_2O_9$, all of the compounds exhibited a broad band blue fluorescence, with an intensity maximum near 4800Å, when excited by 2537Å radiation. By contrast, $Pb_2TiP_2O_9$ showed a weak orange fluorescence, more easily excited by 3650Å radiation. Emission, absorption, and excitation data are presented.

The following describes a new class of host-luminescent materials which have the generalized formula $R_2^{2+}R^{4+}R_2^{5+}O_9$. Their synthesis resulted from an attempt to prepare compounds isostructural with the self-activated phosphor $Ba_2TiP_2O_9$ (1, 2). Of the seven compounds reported here, $Ba_2ZrP_2O_9$, $Sr_2ZrP_2O_9$, $Pb_2ZrP_2O_9$, $Pb_2TiP_2O_9$, $Ba_2ZrAs_2O_9$, and $Pb_2ZrAs_2O_9$ are isostructural with one another, and the seventh, $Sr_2ZrAs_2O_9$, has optical properties closely related to the group. Because of certain features common to host luminescence, it is instructive to make some comparisons between the present system and other known host-luminescent systems.

The most comprehensive study of host luminescence is given by Kröger (3), and is concerned with the alkali and alkaline earth tungstates and molybdates. These materials are characterized by fairly broad emission bands and by very strong absorption bands which are characteristic of lattice absorption. The absorption bands commence in the u.v. exhibiting steep edges which rise rapidly to very high values and appear to maintain these high values toward shorter wavelengths. Excitation is stated to occur everywhere within the absorption bands to within the limits of measurements. Because of these features, no meaningful details are seen within either the absorption or the excitation bands. On the basis of fairly extensive comparisons between the tungstates and molybdates and their solid solutions, Kröger concludes that the $WO_4^=$ and $MoO_4^=$ ions are responsible for the observed luminescence. Indeed, it is difficult to see how anything else could be possible.

The present series of compounds differ from the tungstates and molybdates in several respects. The most notable differences are in the absorption and excitation bands. In the ternary zirconates, the absorption coefficients of the bands responsible for luminescence appear to be much weaker, but at the same time the bands are better defined than the corresponding bands in the tungstates or molybdates. The excitation bands, which are undefined in the tungstates or molybdates, are very well defined in the ternary zirconates and show a structure which is remarkably similar from compound to compound. In this respect, the present series adds to the previous work on host luminescence by providing additional information not seen, for example, in the tungstates and molybdates. The information is of a more detailed nature and may help toward characterizing the center in host-activated luminescence. Despite the preliminary and largely descriptive nature of the present work, one conclusion can readily be drawn, namely, that in the ternary zirconates the zirconium ion is the essential constituent of the luminescent center.

Crystal Chemistry

Preparation.—Compositions were made according to the general formula, $R_2^{2+}R^{4+}R_2^{5+}O_9$, where R^{2+} = Mg, Ca, Sr, Ba, Pb, Cd, Zn; R^{4+} = Ti, Zr, Sn; and R^{5+} = P, As, Sb, V. Those compositions which were examined are listed in Table I. Samples were prepared by calcination of the appropriate oxides or carbonates of reagent grade purity in fused silica crucibles at 1000°-1400° in a SiC resistance furnace.[1] X-ray diffraction data and petrographic techniques were used to identify phases.

Small single crystals of $Pb_2ZrP_2O_9$ (PZP) were grown from the melt by cooling at a rate of about 80°C/hr after fusion at 1400°C in a platinum crucible. The crystals formed as thin hexagonal platelets about 10 mm² in area by 0.2 mm in thickness.

Phase data.—Phase identification was made by means of standard x-ray diffraction techniques using CuKα radiation. These data showed that none of the compositions listed in Table I were isostructural with either of the forms of $Ba_2TiP_2O_9$ (2). The compositions listed in the first column of Table I are nonfluorescent and some of them are multiphase. Only those single phase materials which exhibited luminescence were selected for further study. Of this group, six form an isostructural series (see Table II) and the seventh, $Sr_2ZrAs_2O_9$, has optical properties closely related to the series. Both $Sr_2ZrAs_2O_9$

[1] The Zirconium Corporation of America supplied the hafnium-free ZrO_2 which contained 1000 ppm Ca, 300 ppm Mg, 150 ppm Si and other impurities each <100 ppm. The TiO_2 was fluorescent grade material obtained from Westinghouse Lamp Division, Bloomfield, N. J.

Table I. Compositions

Nonfluorescent materials of undetermined phase composition	Fluorescent compounds
$Mg_2TiP_2O_9$	$Ba_2ZrP_2O_9$ (BZP)
$Ca_2TiP_2O_9$	$Sr_2ZrP_2O_9$ (SZP)
$Sr_2TiP_2O_9$	$Pb_2ZrP_2O_9$ (PZP)
$Mg_2ZrP_2O_9$	$Pb_2TiP_2O_9$ (PTP)
$Ca_2ZrP_2O_9$	$Ba_2ZrAs_2O_9$ (BZA)
$Zn_2ZrP_2O_9$	$Pb_2ZrAs_2O_9$ (PZA)
$Cd_2ZrP_2O_9$	$Sr_2ZrAs_2O_9$ (SZA)
$Ca_2SnP_2O_9$	
$Sr_2SnP_2O_9$	Other compounds
$Ba_2SnP_2O_9$	ZrP_2O_7
$Pb_2SnP_2O_9$	$BaZrO_3$
$Ba_2TiV_2O_9$	$Ba_2P_2O_7$
$Ba_2ZrV_2O_9$	$Pb_2P_2O_7$
$Ba_2TiSb_2O_9$	ZrO_2
$Ba_2ZrSb_2O_9$	

Table II. Lattice parameters, angstrom units

Compound	a_H	c_H
$Ba_2ZrP_2O_9$	10.26	23.76
$Pb_2ZrP_2O_9$	10.08	23.29
$Sr_2ZrP_2O_9$	9.86	22.78
$Pb_2TiP_2O_9$	10.03	23.13
$Ba_2ZrAs_2O_9$	10.54	24.34
$Pb_2ZrAs_2O_9$	10.37	23.91

(SZA) and $Ba_2ZrAs_2O_9$ (BZA) are dimorphic. In BZA, the crystallographic inversion is at 1260° ± 15°C, and in SZA it is at 1225° ± 15°C. On the order of 20-30 hr is required for either inversion to reach completion even at 30°C above the transition temperature. The low-temperature form of BZA is isostructural with the other members of the series. The high-temperature form of BZA and both forms of SZA are of undetermined structure. Characteristic x-ray patterns of the high- and low-temperature modifications of BZA and SZA are listed in Table III. The low-temperature form of BZA is indexed on the basis of the single crystal measurements performed on PZP (see below). For purposes of discussion, the isostructural series is referred to as the β-structure, the high-temperature form of BZA as the α-structure, and the low- and high-temperature forms of SZA as β_1- and α_1-structures, respectively.

The ternary zirconium phosphates and $Pb_2ZrAs_2O_9$ (PZA) appear to be stable at temperatures approaching their melting points. In the case of the high-temperature forms of BZA and SZA partial decomposition occurred as revealed by the evolution of vapor during the sluggish crystallographic inversion and the presence of free ZrO_2 in the high temperature phases. In no case, however, could the excess ZrO_2 account for the optical properties which were observed.

Crystal structure data.—Rotation and Weisenberg photographs taken both parallel and perpendicular to the hexagonal faces of the single crystals established that $Pb_2ZrP_2O_9$ (PZP) has hexagonal symmetry. In PZP, the unit cell parameters are $a_H = 10.08$Å and $c_H = 23.29$Å. Assuming 33 formula weights per unit cell, the theoretical x-ray density

Table III. X-ray powder diffraction data, CuKα radiation

	(a) β-$Ba_2ZrAs_2O_9$			(b) α-$Ba_2ZrAs_2O_9$	
hkl	d_{obs}	d_{calc}*	I_{obs}	d_{obs}	I_{obs}
113	4.414	4.419	6	3.624	6
—	3.821	—	7	3.302	6
106	3.684	3.707	3	3.292	6
204	3.630	3.651	4	3.220	100
211	3.419	3.416	100	3.153	16
				2.875	60
116	3.229	3.214	15	2.829	10
213	3.157	3.175	15	2.348	16
108	2.891	2.886	56	2.253	6
				2.148	25
215	2.834	2.814	10	2.061	7
				1.948	22
220	2.618	2.635	3		
400	2.308	2.282	10	1.821	9
1, 1, 10	2.209	2.209	15	1.723	17
227	2.122	2.100	25		
319	1.847	1.848	3	1.710	7
				1.664	10
2, 1, 12	1.756	1.748	12	1.650	7
1, 0, 14	1.724	1.725	4	1.614	12
418	1.670	1.666	7		
3, 1, 11	1.666	1.666	5		

	(c) α_1-$Sr_2ZrAs_2O_9$		(d) β_1-$Sr_2ZrAs_2O_9$	
	d_{obs}	I_{obs}	d_{obs}	I_{obs}
	3.690	5	5.555	6
	3.633	5	3.684	8
	3.422	4	3.556	27
	3.197	8	3.422	10
	3.157	47	3.297	17
	3.078	80	3.179	62
	2.838	30		
	2.789	100+	3.070	52
	2.620	7	3.039	33
	2.603	6		
	2.538	4	2.940	100
	2.348	14	2.855	12
	2.221	7	2.838	6
	2.177	8	2.783	23
	2.069	35	2.582	25
	1.848	19	2.453	14
	1.818	7	2.417	10
	1.662	38	2.062	7
	1.612	13	2.005	6
			1.987	11
			1.914	9
			1.887	6
			1.843	10
			1.823	9
			1.788	15
			1.738	7
			1.657	6
			1.651	8
			1.646	8
			1.581	8

* Calculated using $a_H = 10.54$Å, $c_H = 24.34$Å.

of PZP is 6.35 g/cm^3. The measured density was 6.33 g/cm^3. The unit cell parameters of the members of the series are listed in Table II.

In Fig. 1 is plotted a_H *vs.* c_H lattice parameters for the series. The linear progression in unit cell dimensions from compound to compound is consistent with the ionic radii of the constituent elements. Beginning with the strontium-zirconium-phosphate member, the parameters increase in size from SZP

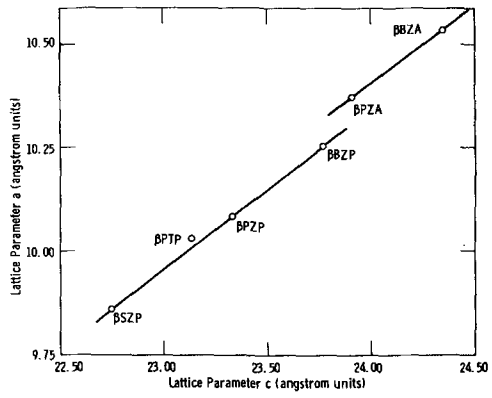

Fig. 1. a_H vs. c_H lattice parameters of the isostructural compounds

to PZP to BZP. The substitution of titanium for zirconium decreases the cell parameters placing PTP intermediate in size between SZP and PZP.

Similarly, the arsenates form a parallel series with larger unit cell sizes. Exclusion of α_1- and β_1-SZA and α-BZA from the isostructural series is probably a result of the inability of the β-lattice to accommodate the size differential between the divalent and pentavalent ions in these compounds.

Optical Properties

Emission spectra.—The emission spectra were obtained by placing the samples at the slit of a Beckman D.U. Monochromator equipped with a spectrally calibrated photomultiplier tube. A mineralite lamp rich in 2537Å radiation was used to excite the samples. The low-temperature spectra were obtained in a similar manner using a specially built fused silica Dewar with flat transparent end windows. A resolution of about 20Å was obtained both at 300° and 77°K. At low temperatures a blue fluorescence was produced by the fused silica in the region of 4000-4800Å which somewhat complicated the low-temperature spectra. This emission caused a comparatively small error in the samples which did not contain lead. Larger errors were involved in the spectra of the lead compounds because of their relatively lower brightnesses. The silica emission was determined separately, and for each sample it was subtracted from the total observed fluorescence.

The emission spectra of the six zirconates are shown in Fig. 2 at 300°K and at approximately 77°K. The low-temperature form of SZA does not fluoresce at room temperature and is not shown in Fig. 2. All of the data are shown on the same relative scale of intensity. The $Ba_2TiP_2O_9$ phosphor, which has a quantum yield near unity, has on this scale a peak intensity of 8.7 at room temperature. Included in the figure are the emission spectra of $Pb_2TiP_2O_9$ and ZrO_2.

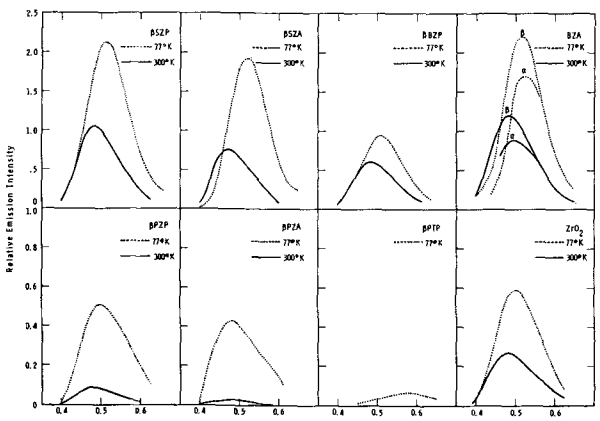

Fig. 2. Fluorescence emission spectra (2537Å radiation)

Examination of Fig. 2 shows the essential similarity in the positions, shapes, and temperature dependences of the emission spectra of all of the zirconium containing samples including ZrO_2 and a distinct difference in the position of the emission band of the isostructural titanium compound. With the exception of the lead compounds, there is an approximate twofold increase in peak intensity and a noticeable narrowing of band width on cooling to liquid nitrogen temperatures. The lead compounds show a very feeble luminescence at room temperature and undergo a far greater increase in intensity on cooling. This difference in the behavior of the lead compounds can be accounted for by the presence of a strong absorption band which is introduced by the lead ions and which overlaps the excitation band for the blue emission. A parallel behavior occurs in $PbWO_4$ and $PbMoO_4$ (4). This particular absorption is moderately temperature dependent and shifts to shorter wavelengths as the temperature is lowered. Even so, the emission intensity of the lead compounds is still low even at 77°K. For this reason, their emission bands were not very accurately obtained. Table IV summarizes the values for the peak wavelengths of emission for the various compounds. A more detailed description of the lead compounds is given below.

Absorption and excitation spectra.—Absorption coefficients, α, were obtained on powder samples from diffuse reflectance measurements, R, by means of a relationship between R and α (5) using a Beckman D. U. spectrophotometer with its diffuse reflectance attachment. The resolution was for the most part at least as good as for the emission spectra. Low-temperature measurements were again obtained by means of a fused silica Dewar, and appropriate corrections were made for the reflections from fused silica windows. Excitation spectra were obtained only at room temperature. The measurements consisted of irradiating the samples monochromatically at intervals within the region from 4000 to 2500Å and measuring their total luminescence output. A Perkin-Elmer quartz prism monochrometer served as the dispersing element, and an

Table IV. Emission peaks, excitation by 2537Å radiation

Compound	Approximate room temp emission peaks, Å	Approximate emission peaks at 77°K, Å
β BZP	4850	5100
β BZA	4850	5170
α BZA	4920	5200
β SZP	4900	5130
α_1 SZA	4870	5190
β PZP	(4840)	(5000)
β PZA	—	(4900)
β PTP	—	(5770)
ZrO_2	4850	5100

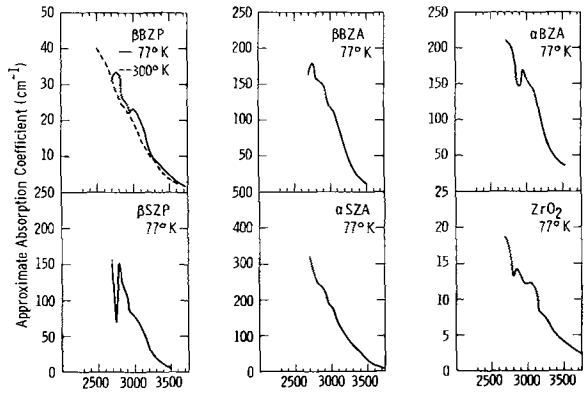

Fig. 3. Absorption spectra

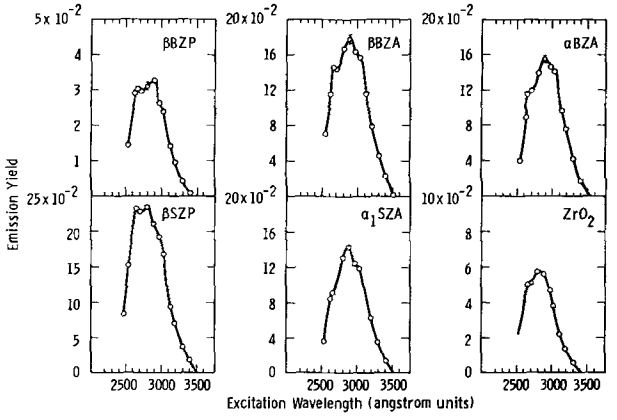

Fig. 4. Excitation spectra

internal thermocouple provided the reference for constant energy of irradiation. Corrections were later applied in order to present the data in the form of a constant number of photons at each irradiation wavelength. No corrections were made for changes in sample reflectance with wavelength.

The wavelength dependences of the absorption coefficients are shown in Fig. 3 for ZrO_2 and for those zirconates which do not contain lead. All of the spectra show evidence of three and possibly four absorption bands superimposed on a broad absorption which increases rapidly with decreasing wavelength. These bands are located at about the same wavelengths for all of the zirconium compounds (see Table V). They are poorly resolved at room temperature and are only a little better resolved at the low temperatures. The absorption spectrum of PTP is not shown, but it is appreciably different from the zirconates.

Evidence for the existence of at least three of the four possible absorption bands is much more clearly pronounced in the excitation spectra, where extraneous superimposed absorptions (which do not contribute to emission) produce less complication. The room temperature excitation spectra are shown in Fig. 4. Again, there is a close similarity in the positions of the bands and in the structural details of each of the compounds. The peaks of the excitation bands are tabulated in Table V and correspond sufficiently closely to the absorption bands to lead us to conclude that a one-to-one correlation exists between them.

The absorption bands of a typical lead compound, PZP, are shown in Fig. 5. The previously mentioned strong absorption is clearly seen masking, at room temperature, what appears to be two of the three or more absorption bands present in the other zirconates. At low temperatures, the lead absorption

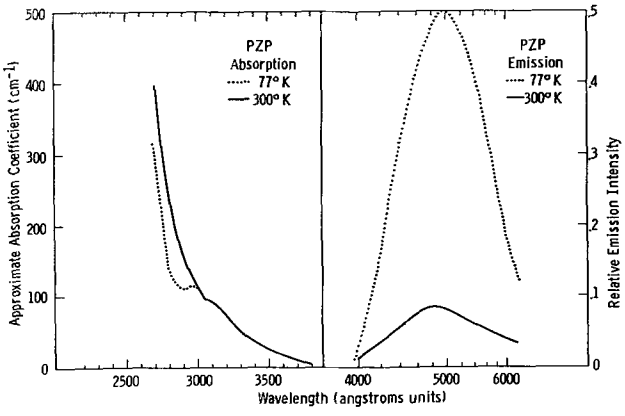

Fig. 5. Absorption and emission spectra of $Pb_2ZrP_2O_9$

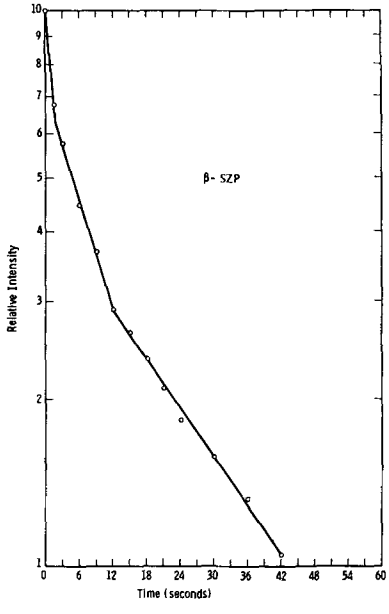

Fig. 6. Decay of fluorescence in $Sr_2ZrP_2O_9$

Table V. Absorption and excitation peaks

Compound	Approximate excitation peaks at room temperature, Å	Approximate absorption peaks at 77°K, Å
β BZP	2650, 2900, 3000	2750, 2900, 3000 (3400)
β BZA	2650, 2900, 3025	2750, 2900, 3050
α BZA	2650, 2900, 3025	2950, 3100
β SZP	2650, 2800, 3000	2900, 3000 (3400)
α1 SZA	2650, 2850, 3050	2900, 3025 (3400)
ZrO_2	2650, 2825, 3025	2850, 3050, 3250

shifts to shorter wavelengths exposing these absorption bands. The partial elimination, by cooling, of the obstructing effect of the lead absorption permits more efficient excitation of the blue emission, with a consequent increase in the intensity of the blue fluorescence. This results in a much more pronounced temperature dependence of the emission intensity which is illustrated in the accompanying portion of Fig. 5.

Table VI. Comparison of decay time and relative intensities

Compound	τ_1	I/I_0
β-$Ba_2ZrP_2O_9$	11.7	0.50
β-$Sr_2ZrP_2O_9$	5.96	0.71
α-$Ba_2ZrAs_2O_9$	4.06	0.84
α_1-$Sr_2ZrAs_2O_9$	3.75	0.83
β-$Ba_2ZrAs_2O_9$	3.67	1.00

Decay time.—Preliminary measurements of the decay times of luminescence again showed a group similarity. The decay process can be divided into two stages: the first stage is completed in the order of 1 sec. During this time, the intensity drops to about 5% of its initial value. The second stage lasts several minutes and consists of at least three components, each of which has an exponential decay. The results of the second stage of decay in SZP are shown in Fig. 6, as a typical case. Comparison of the initial exponential process, τ_1, in the second stage of decay with the relative fluorescence intensity is made in Table VI. The data show a distinct trend toward an inverse relationship between decay time and fluorescent brightness such that the shorter the decay time, the higher the brightness.

Discussion

The present series of isomorphous compounds allows for the substitution of various ions in each of the cation sites. This property makes possible some general remarks concerning the nature of the luminescent center.

The most striking feature seen in the ternary zirconate compounds is the remarkable similarity in the over-all characteristics of their absorption, excitation, and emission bands. These are very nearly independent of all substitutions except, of course, for the replacement of zirconium by titanium. The importance of the zirconium ion in determining the optical properties is further illustrated by the nearly identical emission, absorption, and excitation spectra of ZrO_2 when compared with the luminescent zirconium phosphates and by the similarities in the absorption spectra of the nonluminescent compounds, $BaZrO_3$ and ZrP_2O_7. The latter two compounds plus $Ba_2P_2O_7$ may be regarded as related binary compounds. Their absorption spectra at 77°K are shown in Fig. 7 and compared with BZP and ZrO_2. By contrast, the nonzirconium containing member, $Ba_2P_2O_7$, shows no absorption in the ultraviolet, to wavelengths at least as low as 2500Å. This leaves little doubt that the zirconium ion constitutes the most conspicuous component of the luminescent center. The absence of d electrons in the Zr^{4+} ion makes it very likely, however, that the luminescent center consists of a zirconium oxygen ion complex.

The absorption bands which produce excitation appear to be superimposed on a continuous background absorption which starts in the visible and rises rapidly toward shorter wavelengths. The magnitude of this background increases, and its tail extends further into the visible with increasing preparation temperature. We do not believe the background absorption is connected with the luminescence process; it was therefore subtracted from the

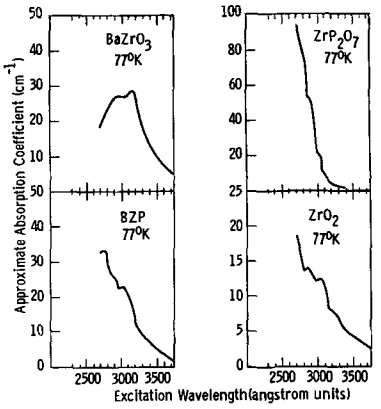

Fig. 7. Absorption spectra of $BaZrO_3$, ZrP_2O_7, $Ba_2ZrP_2O_9$, and ZrO_2.

total absorption. The absorption coefficients of the remaining bands, which are related to the excitation bands, are on the order of 10^{-1} cm or less. These values are surprisingly low for absorption into centers which are major lattice components. Such low absorption coefficients for major lattice components are suggestive of optical transitions which are normally forbidden. It is possible that the absorption bands are due to imperfections, but the strong similarities in the optical properties among the ternary compounds make this unlikely. Further, the long life times of these centers and their comparatively low quantum yields under steady-state excitation are consistent with weakly allowed transitions.

We might, therefore, picture the luminescence center as consisting of a zirconium ion and its surrounding oxygen ions, with the luminescence transitions arising from an essentially forbidden transition which becomes weakly allowed as the result of a perturbation determined by the details of the crystal structure. No clear evidence exists as to the nature of these perturbations, but two possibilities seem reasonable.

We note, in connection with the first possibility, that the crystal structures of the nonluminescent ZrP_2O_7 and $BaZrO_3$ compounds are both highly symmetric whereas the structure of ZrO_2 is of low symmetry. In ZrP_2O_7, Zr^{4+} is surrounded by 6 equally spaced oxygen ions at the corners of an octahedron, 2.018Å distant from the zirconium ion (6). In $BaZrO_3$, the ZrO_6^{8-} octahedra have 6 equally spaced oxygen ions located at 2.09Å from the Zr^{+4} ion (7). Monoclinic ZrO_2, on the other hand, has what amounts to a highly distorted fluorite structure in which Zr^{4+} is surrounded by 7 oxygen ions at distances ranging from 2.04 to 2.26Å (8). Thus, the occurrence of fluorescence in ZrO_2 may be a consequence of a distortion in the symmetry of the surrounding oxygen ions.

A second possibility, which is not incompatible with the first, is that the luminescence intensity is influenced by near neighbor interactions between luminescent centers. In $BaZrO_3$, the Zr^{4+}-Zr^{4+} ion separation is 4.18Å, and in ZrP_2O_7 it is 5.90Å. The Zr^{4+}-Zr^{4+} distance in monoclinic ZrO_2 varies from 3.43 to 4.03Å. The closer proximity of the Zr-O complexes in monoclinic ZrO_2 may, therefore, result in perturbations which favor fluorescence.

The relative importance of distortion and of near neighbor interactions in producing fluorescence in the ternary zirconates cannot be determined properly without more detailed crystal structure data. What is known about the ternary zirconates, however, is consistent with the behavior of the related tungstates. The expansion of the lattice produced by the substitution of Ba^{2+} for Sr^{2+} in SZP is attended by a decrease in fluorescent intensity which parallels the change from $CaWO_4$ to $SrWO_4$ to $BaWO_4$. Unfortunately, this is the only clear comparison that can be made; the complicating influence of the lead band in PZP and PZA prevents comparison between the series SZP-PZP-BZP and PZA-BZA. Substitution of As^{5+} for P^{5+} in BZP increases the lattice parameters and at the same time increases the fluorescent intensity, in apparent contradiction to the direction for SZP-BZP. This apparent contradiction may result from the fact that the substitution of $R = Sr^{2+}$, Pb^{2+} or Ba^{2+} in $R_2ZrP_2O_9$ or in $R_2ZrAs_2O_9$ produces isotropic expansions of the lattice whereas the substitution of either As^{5+} or Ti^{4+} produces changes in the lattice parameters which are anisotropic to the coordinates of the line SZP-PZP-BZP (see Fig. 1). The significance of an anisotropic expansion, from the viewpoint of near neighbor interactions, is only that it produces a change in the fluorescence intensity.

The degree of change in the optical properties attending ionic substitution in the ternary zirconates is much less than in the tungstates and molybdates, even though the optical properties appear to behave in a similar fashion. This suggests that if the zirconium-oxygen luminescent centers interact with one another, they do not interact as strongly as do the tungstate or molybdate centers. A much weaker interaction helps to explain the presence of better defined details in the absorption spectra of the zirconates, and their well-defined excitation spectra, in contrast to the smeared out and almost continuous absorption and excitation spectra of the tungstates and molybdates. It is clear, however, that a better understanding of the luminescence of the zirconates, molybdates, and tungstates will require a more accurate description of the luminescence process in these compounds. This, in turn, requires more detailed structure data.

Acknowledgments

Thanks are given to W. E. Snider for preparing the samples, to J. Hrizo for assisting in the x-ray work, and to H. H. Dorman for helping with the optical measurements.

Manuscript received July 16, 1962. This paper was prepared for delivery before the Los Angeles Meeting, May 6-10, 1962.

Any discussion of this paper will appear in a Discussion Section to be published in the December 1963 JOURNAL.

REFERENCES

1. D. E. Harrison, *This Journal*, **107**, 207 (1960).
2. D. E. Harrison and G. Shirane, *ibid.*, **108**, 788 (1961).
3. F. A. Kröger, "Some Aspects of the Luminescence of Solids," Elsevier Publishing Co., Inc., Chap. III (1948); Philips Research Repts., **2**, 177, 183, 340 (1947).
4. *Ibid.*, pp. 112, 117, 119.
5. N. T. Melamed, To be published in *J. Appl. Phys.*
6. G. R. Levi and G. Peyronel, *Z. Krist.*, **92**, 190-209 (1935).
7. H. D. Megaw, *Proc. Phys. Soc. (London)*, **58**, 133 (1946).
8. J. D. McCullough and K. N. Trueblood, *Acta Cryst.*, **12**, 507 (1959).

The Coactivator Emission of ZnS and (Zn,Cd)S Phosphors

S. Rothschild

Mullard Research Laboratories, Salfords, near Redhill, Surrey, England

ABSTRACT

ZnS(NaCl) phosphors show during excitation with u.v. 253.7 mμ at low temperatures a band between the edge emission and the self-activated emission. It was at first assumed that this band was connected with the presence of sodium, but it was then discovered that the band appeared with phosphors which contained no sodium, but halogen ions or ions of trivalent metals only. The band was called SAL band to distinguish it from the known self-activated emission which is usually designated SA band. Preparative conditions which tended to produce low coactivator concentrations favored the SAL band. The influence of the presence of oxygen on the relative intensities of the SA band and the SAL band is discussed. It is assumed that the SAL band is caused by transitions from nonassociated coactivator centers to the valence band.

Self-activated ZnS phosphors prepared by firing ZnS with NaCl in a stream of HCl at 900°C showed, according to Kröger (1), during excitation by u.v. 253.7 mμ at room temperature and at −180°C an emission consisting of a blue band at 460 mμ. If the phosphor was subsequently reheated in N_2 at 900°C, the luminescence spectrum changed. The blue band disappeared and a band peaked at shorter wavelengths with a maximum at 392 mμ appeared instead. If the phosphor was fired for prolonged periods in H_2, then the band at 392 mμ disappeared also. The peak at 392 mμ was found with ZnS phosphors

which had the sphalerite structure. If such phosphors were reheated at 1050°C in N_2, then the peak of the band moved to 380 mμ with the transformation of sphalerite into wurtzite. Kröger assumed that the band at 392 or 380 mμ was due to the incorporation of NaCl into the lattice with Na occupying Zn sites and Cl occupying S sites.

A band between the edge emission and the self-activated emission corresponding to Kröger's band was observed later on by several authors (2-4) with ZnS and ZnSCdS phosphors. In all cases NaCl with or without the addition of $MgCl_2$ had been added to the sulfides before firing.

Gill and Rothschild (5) found that a band in the same spectral position appeared at low temperatures with ZnS and ZnSCdS phosphors prepared with halide compounds other than NaCl and also with phosphors made without halides but with trivalent elements such as Al. This indicates that the assignment of the short wave band to a center involving sodium cannot be correct. In this paper the conditions under which the short wave band appears are studied in greater detail, and on the basis of these results together with a study of the physical properties of the band a model for the cause of the appearance of the band is proposed. In the following the short wave low-temperature emission band of the self-activated phosphors will be designated SAL band while the normal band due to self-activation will be called SA band.

Experimental

Preparation and measurements.—The phosphors were prepared from high-purity zinc sulfide and cadmium sulfide by firing in silica crucibles. The firing temperature was in most cases 975°C. For firing in a stream of N_2 or other gases, the crucibles were, if required, fitted with an inlet quartz tube at the bottom, the hole being covered with quartz wool. The crucibles were covered with a lid. The speed of the gas stream was usually 250 cc/min. The crucibles were inserted in vertical tube furnaces and removed from the furnace immediately after the firing was finished. This time was in most cases 1 hr, sometimes 30 min. Some phosphors were fired twice with grinding in between the firings to ensure complete reaction and uniformity. The crucibles were left to cool in air, with the gas still passing through the phosphors.

The ZnS:CdS ratio for most of the phosphors used during these investigations was 75 mole % ZnS/25 mole % CdS. These figures relate to the proportions in the mixture before firing. The composition changed slightly during firing. X-ray diffraction analysis and chemical analysis showed that the samples with 25 mole % CdS before firing contained after firing 24 mole % CdS (±1%). These variations were too small to have an appreciable effect on the spectral distributions. The accuracy of the analytical methods as well as of the optical measurements was in any case no better than 1%. Therefore the figures given in the present paper for the ZnS:CdS ratios refer always to the quantities used at the start.

The spectral distributions were measured with a Perkin Elmer spectrometer, type 4000A. The use of

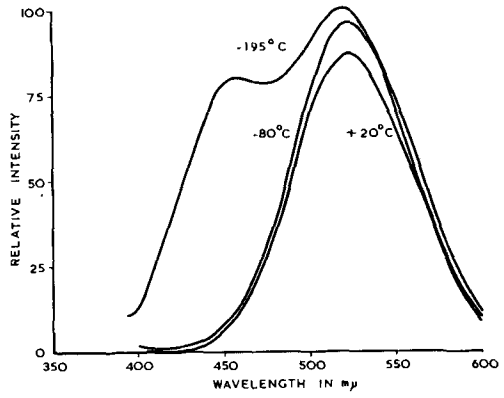

Fig. 1. Spectral distribution curves for the emission of ($Zn_{0.75}Cd_{0.25}$)S (NaCl) during excitation with u.v. 365 mμ at +20°, —80°, and —195°C (sample 44/2a).

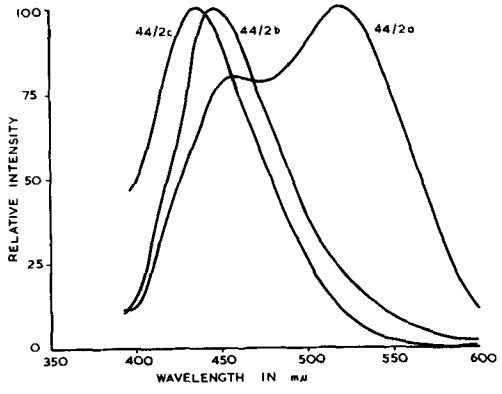

Fig. 2. Spectral distribution curves for the emission of ($Zn_{0.75}Cd_{0.25}$)S (NaCl) during excitation with u.v. 365 mμ at —195°C: 44/2a fired in a stationary atmosphere of N_2; 44/2b fired in a current of N_2; 44/2c fired in a current of N_2 (90%) + H_2 (10%).

($Zn_{0.75}Cd_{0.25}$)S phosphors simplified the optical measurements as the emission bands of such phosphors are situated mainly in the visible part of the spectrum and can be excited by 365 mμ u.v.

Phosphors prepared with halides as coactivators.—The spectral distribution at various temperatures of a ($Zn_{0.75}Cd_{0.25}$)S phosphor prepared by firing with the addition of 0.05 NaCl is shown in Fig. 1.

The effects of firing conditions on the spectral distribution of ($Zn_{0.75}Cd_{0.25}$)S phosphors prepared with the addition of NaCl are shown in Fig. 2. The figure clearly shows the appearance at —195°C of a short wave band with a maximum at approximately 450 mμ (the SAL band) next to the normal self-activation band at approximately 520 mμ (the SA band). If the phosphors were fired in a stationary atmosphere of N_2, the SA band and the SAL band both appeared in the low-temperature spectrum. The efficiency of the SA band was considerably reduced if the firing was carried out in a current of nitrogen. Phosphors prepared by firing in a current of 90% N_2 with 10% H_2 showed at room temperature no luminescence at all and at low temperature the SAL emission and a band at shorter wavelength (known as the "edge emission"). Firing in H_2S had a similar effect to firing in $N_2 + H_2$. After prolonged firing in H_2S the SAL emission disappeared as shown already by Kröger (1). Chemical analysis of the various

Table I. Effect of firing conditions on Cl content of $(Zn_{0.75}Cd_{0.25})S$ phosphors

Flux	Firing temp, °C	Atmosphere during firing	Cl content, g-at. Cl/mole $(Zn_{0.75}Cd_{0.25})S$
—	900	H_2, current	below 5×10^{-5}
NaCl not fired		—	3.7×10^{-2}
NaCl	975	N_2, stationary	3.2×10^{-2}
NaCl	975	N_2, current	1.75×10^{-2}
NaCl	975	N_2 (90%) + H_2 (10%), current	6×10^{-3}

phosphors after firing and without any further treatment such as washing showed the variations in the Cl content (Table I).

A comparison of the results of the optical measurements and the chemical analysis indicates that the SAL band tends to become more preponderant with decreasing Cl content while the intensity of the SA band decreases with lower concentrations of Cl until the band disappears. Kröger and Hellingman (6) also observed that the intensity of the SA band depended on the Cl concentration. If ZnS was fired in an atmosphere which contained HCl only, then the Cl content of the phosphor was, after washing with water, 27 x 10^{-5} gram atoms (g-at) Cl/mole ZnS, while after firing in a mixture of H_2 + 10% HCl the Cl content was 7.5 x 10^{-5} g-at Cl/mole ZnS. The efficiency of the SA emission in the second case was 28.5% of the efficiency of the SA emission in the first case.

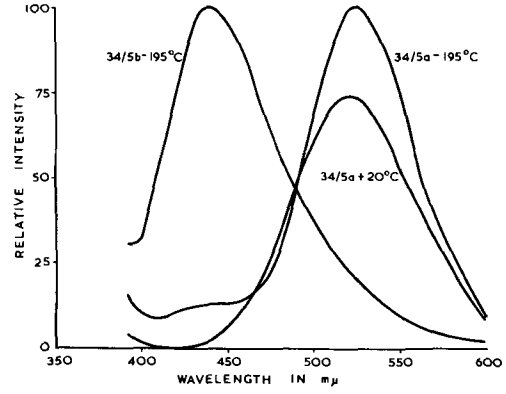

Fig. 3. Spectral distribution curves for the emission of $(Zn_{0.75}Cd_{0.25})S$ (KCl) during excitation with u.v. 365 mμ: 34/5a at +20° and —195°C, phosphor fired in a stationary atmosphere of N_2; 34/5b at —195°C, phosphor fired in a current of N_2.

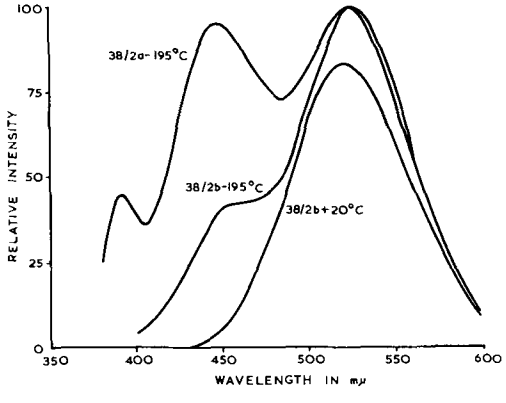

Fig. 4. Spectral distribution curves for the emission of $(Zn_{0.75}Cd_{0.25})S$ (NH_4Cl) during excitation with u.v. 365 mμ: 38/2a at —195°C, phosphor fired in a current of N_2; 38/2b at +20° and —195°C, phosphor fired in a stationary atmosphere of N_2.

Phosphors prepared with KCl instead of NaCl, if fired in a stationary atmosphere of N_2, showed like phosphors made with NaCl only the SA emission at room temperature. There is, however, as Fig. 3 shows, a difference between phosphors prepared with NaCl and phosphors prepared with KCl at low temperatures. With NaCl both the SA band and the SAL band appeared with high intensities while in the case of KCl the emission consisted mainly of the SA band with only a weak indication of the SAL band. The SAL band appeared, however, with strong intensity if the firing was carried out in a stream of N_2 or other gases, such as H_2S. The SAL emission was also observed with

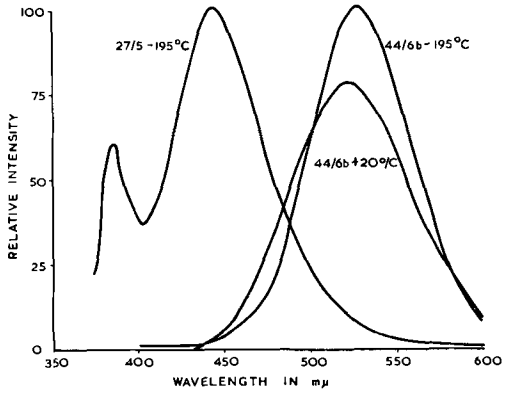

Fig. 5A. Spectral distribution curves for the emission of $(Zn_{0.75}Cd_{0.25})S$ during excitation with u.v. 365 mμ: 27/5 at —195°C, phosphor fired in N_2 + S_2Cl_2; 44/6b at +20° and —195°C, phosphor fired in N_2 + Br_2.

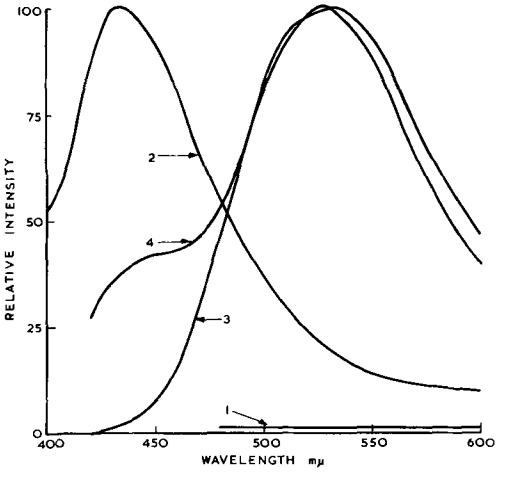

Fig. 5B. Spectral distribution curves for the emission of $(Zn_{0.75}Cd_{0.25})S$ (NaCl) during excitation with u.v. 365 mμ: curve 1, fired in O_2 free atmosphere, room temperature; curve 2, same phosphor, liquid nitrogen temperature; curve 3, same phosphor, refired in air, room temperature; curve 4, same phosphor, refired in air, liquid nitrogen temperature.

NH_4Cl (Fig. 4) as well as with CsCl, $CaCl_2$, $BaCl_2$, and S_2Cl_2.

$(Zn_{0.75}Cd_{0.25})S$ fired without any additions in a current of N_2 which contained HCl or Br_2 showed at room temperature and low temperatures the SA band only. If S_2Cl_2 was used instead of HCl, then the phosphor had no luminescence at room temperature, but showed the SAL band and the edge emission with a weak indication of the SA band at low temperatures (Fig. 5A). Phosphors which were fired in presence of bromine and which showed the SA band only gave a different spectral distribution after refiring in H_2S. The intensity of the SA band was much reduced, and the SAL band with the edge emission appeared in the low-temperature spectrum. Chemical analysis showed that the bromine concentration had dropped from 0.1% by weight of bromine to 0.01% bromine. It can generally be stated that any condition which tends to lower the halogen concentration in the phosphor favors the development of the SAL band.

The SA band which appeared in the spectrum of (Zn,Cd)S:Br phosphors and also of some other phosphors was found to vary in width and also slightly in the position of its peak with temperature during excitation. With decreasing temperature the band became narrower and the peak moved slightly to longer wavelengths. Similar observations have also been reported by other authors such as van Gool (7) who assumes that the SA emission consists at low temperatures of one band, while at higher temperatures a second band on the short wavelength side of the first band appears. This second band cannot be identical with the SAL band, as it disappears at low temperature.

Pure luminescent grade ZnS usually contains traces of Cl sufficient to give the SAL band after firing without any additions. If such ZnS was heated first in H_2S at 600°C for 2 hr and subsequently refired in N_2 at 975°C, then the SAL band did not appear unless chlorine was introduced before or during firing. Samples of pure ZnS supplied by RCA did not show the SAL band after firing without the addition of chlorides even if they were not heated first in H_2S. This material was apparently prepared from Cl-free starting materials. All ZnS or CdS used as starting material for the present investigations was tested first for the appearance of the SAL band without additions and, if necessary, the sulfides were prefired in H_2S or H_2.

Effect of oxygen on phosphors prepared with halides.—Other workers (8, 9) have shown that phosphors prepared by firing (Zn,Cd)S with NaCl do not show the SA emission unless oxygen was present during firing either in the atmosphere or in the form of compounds. Usually the ZnS or CdS used as starting materials contain sufficient oxides or sulfides to produce phosphors which show the SA band even if the firing was carried out in O_2-free N_2. During the present investigations it was found that, if the oxides were removed from the sulfides by prefiring in H_2S and the (Zn,Cd)S was subsequently fired with NaCl in oxygen-free argon, no luminescence was observed at room temperature, but the SAL band

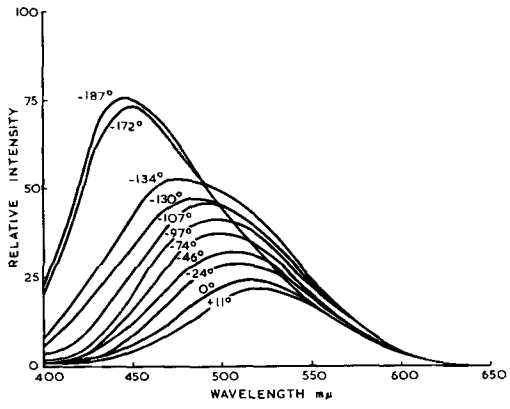

Fig. 6A. Spectral distribution curves for the emission of $(Zn_{0.75}Cd_{0.25})S$:Al during excitation with u.v. 365 mμ at various temperatures between +11° and —197°C (Sample 40/3, fired in H_2S only).

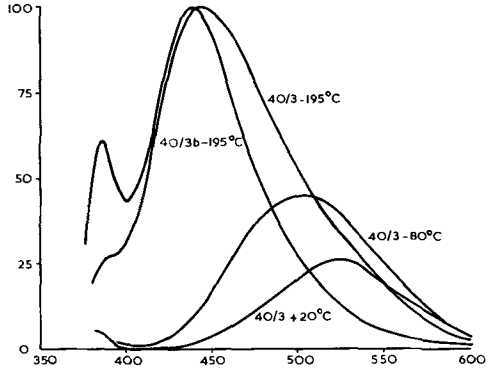

Fig. 6B. Spectral distribution curves for the emission of $(Zn_{0.75}Cd_{0.25})S$:Al during excitation with u.v. 365 mμ: 40/3 at +20°, —80°, and —195°C, phosphor fired in H_2S; 40/3b at —195°C, phosphor fired in H_2S (50%) + H_2(50%).

was present at low temperatures. If the phosphor was subsequently refired in air or after the addition of a small amount of ZnO in nitrogen, then the phosphor showed at room temperature the usual SA emission and at low temperatures the SA band with the SAL band (Fig. 5B).

Phosphors prepared with the addition of trivalent metals (Al,Ga,In).—$(Zn_{0.75}Cd_{0.25})S$ fired with 1.5 x 10^{-4} g-at Al for 1 hr in H_2S at 975°C showed at room temperature the SA band. If the phosphor was cooled down during excitation with u.v. 365 mμ, the center of gravity of the emission band gradually moved to shorter wavelength and nearly to the position of the SAL band found with $(Zn_{0.75}Cd_{0.25})S$:Cl (Fig. 6A). The band was, however, considerably wider on the long wavelength side than the SAL band due to the simultaneous presence of the SA band. If the $(Zn_{0.75}Cd_{0.25})S$:Al was reheated in 50% H_2S + 50% H_2 at 975°C for 1 hr then it showed barely any luminescence at room temperature, while the over-all structure of the spectrum at low temperatures was very similar to that of Cl coactivated phosphors fired in a reducing atmosphere (Fig. 2, curve 44/2c). The emission consisted of the SAL band with a peak in a similar position as the SAL band noticeable with Cl as coactivator and a band on the short wavelength side of the SAL band due to the edge emission (Fig. 6B, curve 40/3b).

Table II. Effect of Ga concentration on the position of the center of gravity of the low-temperature emission band with $(Zn_{0.75}Cd_{0.25})S$:Ga

Ga	g-at./mole	1.5×10^{-4}	1×10^{-3}	1×10^{-2}	5×10^{-2}	1×10^{-1}
	mμ	470	495	510	520	530

Phosphors coactivated with Ga or In showed the SAL band also. The effect of variations in the coactivator concentration with trivalent metals as coactivators was to a certain degree similar to the effects observed with halides. At low coactivator concentrations the SAL band was preponderant in the low-temperature spectrum, while at high concentrations the SA band and bands at the long wavelength side of the SA band were present. There was not such a clear replacement of one band by another with Ga or In as with Cl, although a shift in the center of the gravity was observed (5); this was rather gradual and at least partly due to self-absorption (Table II).

The concentrations given are those present in the materials at the start.

Further complications arise with Ga or In at high concentrations due to the appearance of bands on the long wavelength side of the SA band. These bands have previously been reported by Kröger and Dikhoff (10). Figure 7 shows the change in the spectral distribution of the low-temperature luminescence for $(Zn_{0.75}Cd_{0.25})S$:In containing various concentrations of In. These samples were fired at 1100°C.

A shift of the center of gravity of the low-temperature emission band with higher coactivator concentrations was also indicated with Al, but owing to the known difficulty of incorporating high concentrations of Al without the presence of a main activator, these results have been inconclusive. It has to be pointed out that it is also difficult to obtain reproducible results with Ga or In, since even using the same coactivator concentrations the spectral distribution was found to vary with firing time, firing temperature, rate of cooling after firing, and

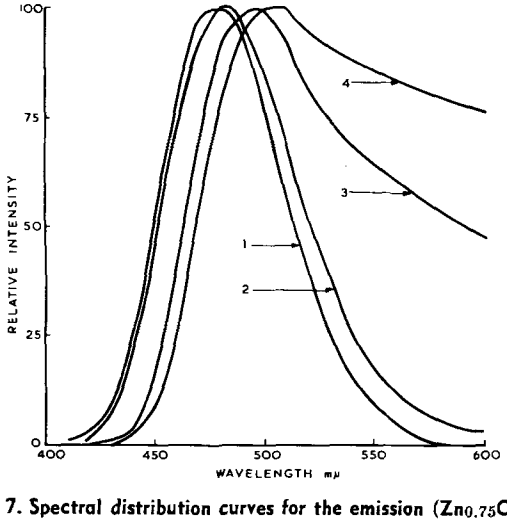

Fig. 7. Spectral distribution curves for the emission $(Zn_{0.75}Cd_{0.25})$: In during excitation with u.v. 365 mμ at —195°C. Amounts of In in g-at per mole (Zn,Cd)S: curve 1, 1.5×10^{-4}; curve 2, 1×10^{-3}; curve 3, 1.2×10^{-2}; curve 4, 2×10^{-2}.

Table III. Peak of the SAL bands with $(Zn_{0.75}Cd_{0.25})S$ phosphors

	Cl	Al	Ga	In
mμ	443	440	470	486

the type of atmosphere. Some of these variations are probably due to losses of Ga or In during firing. It was generally found, especially with higher coactivator concentrations, that the centers of gravity of the low-temperature emission bands moved to longer wavelengths with higher firing temperatures. This effect is probably due to an incomplete incorporation of the coactivators at lower firing temperatures. Unless temperature and time of firing are adequate the concentration of the coactivator incorporated in the phosphor remains low and an emission appears which corresponds to low coactivator concentrations even if high concentrations of the coactivator have actually been added at the start.

Table III lists the peak positions of the SAL band in various phosphors. A rather low concentration 1.5×10^{-4} g-at of coactivator per mole of sulfide was chosen for the trivalent elements in order to obtain the SAL band alone. The figure applies again for the concentrations used at the start. Due to all the various difficulties mentioned before, the figures for the peaks of the band should not be considered as entirely reliable, but there is clearly a trend toward longer wavelengths noticeable from Al to Ga and In.

Effect of the ratio of ZnS:CdS *on the appearance of the SAL band.*—For an investigation of the SAL band in samples with lower CdS content one has to take into account that with decreased CdS content and the corresponding increase of the forbidden gap the excitation spectra shift to shorter wavelengths. Therefore whereas u.v. 365 mμ is suitable to excite both the SA and SAL bands in $(Zn_{0.75}Cd_{0.25})S$:Al at lower CdS content or with ZnS alone this wavelength becomes too long to excite the SAL band. Thus during excitation of ZnS:Al phosphors at low temperatures with u.v. 365 mμ only the SA band appeared at 450 mμ and compared with room temperature it was shifted to slightly longer wavelengths (Fig. 8, curve B). If the ZnS:Al phosphor

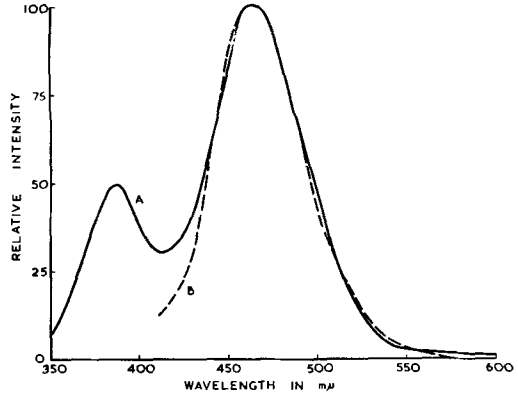

Fig. 8. Spectral distribution curves for the emission of ZnS:Al at —195°C (sample 31/3): A, during excitation with u.v. 253.7 mμ; B, during excitation with u.v. 365 mμ.

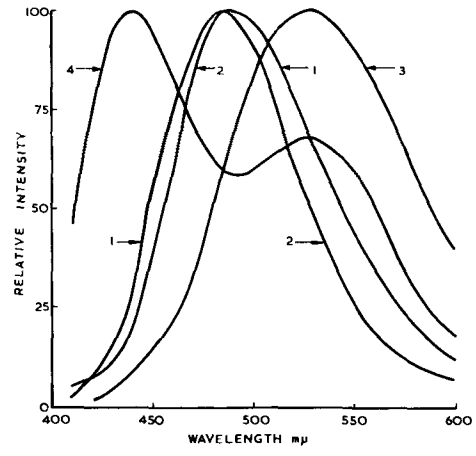

Fig. 9A. Spectral distribution curves for emission of ($Zn_{0.90}Cd_{0.10}$)S:Cl and ($Zn_{0.75}Cd_{0.25}$)S:Cl during excitation with u.v. 365 mμ: curve 1, ($Zn_{0.90}Cd_{0.10}$)S:Cl, (sample 82/1) room temperature; curve 2, same phosphor, liquid nitrogen temperature (SA band only); curve 3, ($Zn_{0.75}Cd_{0.25}$)S:Cl, (sample 34/6) room temperature; curve 4, same phosphor, liquid nitrogen temperature (SA band and SAL band).

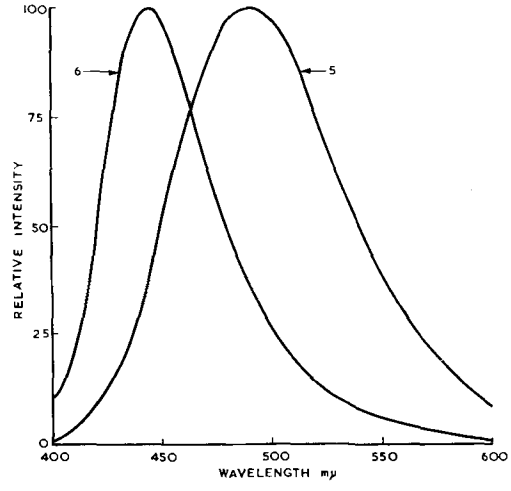

Fig. 9B. Spectral distribution curves for the emission of ($Zn_{0.90}Cd_{0.10}$)S:Ga during excitation with u.v. 365 mμ (sample 94/4): curve 5, room temperature (SA band); curve 6, liquid nitrogen temperature (SAL band).

was however excited with 253.7 mμ u.v., then the SAL band appeared beside the SA band (Fig. 8, curve A). Cl, Ga, or In coactivated ZnS phosphors also show the SAL band during excitation with short wave u.v., but not with 365 mμ u.v. Differences in the excitation properties between phosphors coactivated with different coactivators become apparent after the addition of 10% CdS. ($Zn_{90}Cd_{10}$)S:Cl behaves like ZnS:Cl and shows the SA band during excitation with 365 mμ u.v., but not the SAL band. With ($Zn_{90}S_{10}$)S:Ga the SAL band appears, however, even during excitation with 365 mμ u.v. (Fig. 9A and 9B). This effect is due to the fact that the addition of Ga causes an impurity absorption extending to longer wavelength than the impurity absorption produced by the addition of Cl as shown by the reflectivity spectrum (Fig. 9C). The SAL band moves in all cases like the SA band to longer wavelengths with increased CdS content.

The Cl coactivated phosphors used for these measurements were made by firing the sulfides after the

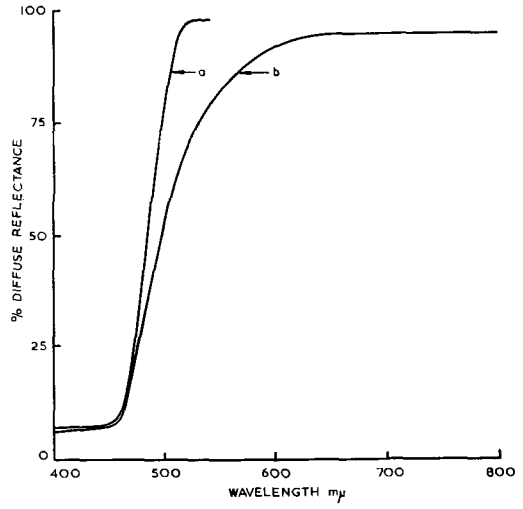

Fig. 9C. Diffuse reflectance spectra of ($Zn_{0.30}Cd_{0.70}$)S phosphors; measurements relative to MgO; a, activated with Cl; b, activated with Ga.

addition of 2 wt % NaCl in N_2 at 975°C for 1 hr. The ZnS:Al phosphor (31/3) was prepared from ZnS (RCA, Cl-free) to which 1.5 x 10^{-4} g-at Al/mole ZnS were added. The firing was carried out in H_2S first for 2 hr in H_2S at 800°C and then again for 1 hr in H_2S at 1100°C. The ($Zn_{0.75}Cd_{0.25}$)S phosphors were prepared by firing the sulfides after the addition of 1.5 x 10^{-4} g-at of Al or Ga/mole (Zn,Cd)S in H_2S at 975°C. The firing time for the Al coactivated phosphor was 1 hr, while the Ga coactivated phosphor was fired twice for 1½ hr.

Drozd and Levzhin (4) described the appearance of three bands in the low-temperature emission spectra of (Zn,Cd)S:Cl phosphors prepared with NaCl as flux during excitation with 365 mμ. Band I appeared with all phosphors including ZnS without CdS, while band II was found with phosphors containing more than 10% CdS, and band III with phosphors containing more than 50% CdS. Drozd and Levshin concluded that new centers are formed in the phosphors with higher CdS concentrations. The figures given by Drozd and Levshin indicate that band I is identical with the SA band, band II with the SAL band, and band III with the edge emission. The cause of the fact that bands II and III did not appear at the lower CdS concentrations was, according to the present investigations, not due to differences in the type of centers but to the irradiation with light of a wavelength too long to excite the particular emissions.

Discussion

After it had been established that the SAL band was not caused by sodium ions, the question arose as to which effects were responsible for the appearance of the SAL band. Zinc vacancies were considered at first, but the fact that the SAL band appeared after firing in a reducing atmosphere made this assumption unlikely. Sulfur vacancies also cannot be the cause of the appearance of the SAL band as the band was observed after firing under sulfurizing conditions. The SAL band also is not like the edge emission found in pure unactivated sulfides, but is observed in presence of coactivators only and must be con-

nected therefore with centers produced by the coactivators. Furthermore the investigations showed that the spectral distribution of the SAL band depended to some extent on the type of coactivator used. It was assumed accordingly (5) that the SAL band was due to the presence of single nonassociated coactivator centers and caused by transitions from the coactivator level to the valency band. The SA band is, according to Prener and Weil (11), due to the presence of centers consisting of associates of the coactivator and $(V_{Zn})^{-2}$ vacancies. Two types of variations of the intensity of the SAL/SA band emissions have to be considered: (i) Variations as a function of the preparative conditions during observation at a particular temperature. Such variations are due to changes in the relative concentrations of the centers leading to the emission of the SA or SAL bands. (ii) Variations as a function of the temperature of observation for given conditions of preparation. These variations are caused by changes in the kinetics of the luminescence processes.

Preparative conditions which tend to produce high concentrations of coactivator and $(V_{Zn})^{-2}$ vacancies are likely to produce phosphors with a high concentration of associated centers, and in such cases the SA band is either predominant or the only band present in the spectrum. On the other hand the number of next-nearest neighbor pairs [Prener-Weil model (11)] decreases with decreasing coactivator concentrations, and accordingly the SAL emission due to single coactivator centers is likely to become predominant. The changes in the spectral distributions with high concentrations of coactivators, in particular of Ga or In, are probably caused to some extent by self-absorption, which may produce some reduction in the intensity of the short wavelength part of the low-temperature emission, but self-absorption cannot be responsible for the appearance of emissions on the long wavelength side of the band where such emissions were not present with phosphors containing lower concentrations of coactivator.

The differences found between phosphors activated with halides and fired in static atmospheres and phosphors fired in a current of gas can be explained by these considerations. In a current of gas more halogen is lost during firing than in a static atmosphere, as the analytical results given in Table I show. Due to the drop in halogen concentration fewer associated centers are formed with the result that the SAL band becomes preponderant. Firing a halogen coactivated phosphor in $N_2 + H_2$ or in H_2S also removed halogen and produced accordingly a phosphor mainly emitting the SAL emission. Prolonged firing in H_2 or in H_2S reduced the halogen content still further until the SAL emission disappeared. If the phosphors were prepared under conditions which tended to produce high halogen concentrations, such as firing in HCl or Br, then the SA band only was observed in the spectra.

The effects of oxygen on the luminescence of (Zn,Cd)S phosphors which were described in the experimental part are understandable taking into account the previous work (8, 9) on the reaction of sulfides with halides and the ideas about the SAL and the SA centers. It has been stated by various authors (9, 12) that the products obtained by firing ZnS with NaCl in absence of oxygen are nonluminescent. The present investigations show that this is not the case. It is true that such materials showed little or no SA emission at room temperature, but the SAL band appeared at low temperatures (Fig. 5B, curves 1 and 2). Investigations by Riehl and Ortmann (9) and others have shown that little reaction takes place between ZnS and NaCl in the absence of oxygen at temperatures below 1000°C. Some Cl enters the lattice, however, but as the concentration of Cl centers is low no associated centers are formed. The SAL band alone appeared accordingly during excitation at low temperatures. The presence of oxygen prompted the reaction between ZnS and NaCl. According to Riehl and Ortmann (9) the following reactions occur

$$2ZnS + 3\,O_2 = 2ZnO + 2SO_2 \qquad [1]$$

$$2NaCl + SO_2 + O_2 = Na_2SO_4 + Cl_2 \qquad [2]$$

$$ZnS + Cl_2 = ZnCl_2 + S \qquad [3]$$

The concentration of Cl centers becomes high and the SA band appears accordingly at room temperature (Fig. 5B, curve 3). It follows from Eq. [3] that no oxygen is required to incorporate Cl into ZnS if the material is fired in Cl_2, and the same applies to Br_2 or HCl (6).

Similar effects of varying the coactivator concentration on the emission spectra as with halides were found with trivalent metals as coactivators. With very high concentrations of Ga or In however there appeared bands on the long wavelength side of the SA band. These bands were not found with Cl, Br, or Al, probably because insufficient quantities of these coactivators were incorporated into the phosphors. It has been suggested (13, 14) that the long wavelength bands are due to transitions from the coactivator level to the valence band, as for example the orange luminescence of ZnS:In, but according to the glow curve measurements by Hoogenstraaten (15) the distance of the indium level to the conduction band is smaller than for instance the distance of the Cu_{Zn}' level to the valence band. The indium emission should therefore have a shorter wavelength than the green Cu emission, *i.e.*, it should be blue and not orange. Van Gool (7) concluded accordingly that the Klasens-Schön model fails to explain the facts. The present investigations showed however that the coactivator emission with In coactivated phosphors is blue and therefore has a peak value at higher energies than the Cu emission in agreement with the Klasens-Schön model.

The bands which appear on the long wavelength side of the SA band are as proposed by Williams (16) probably due to transitions between the ground state of the donor and the acceptor in highly associated pairs and become predominant therefore in phosphors with very high coactivator concentrations. The shift of the center of gravity of the low-temperature emission toward longer wavelengths with increasing coactivator concentration (Fig. 7) is partly due to self-absorption but mainly due to

the increase in the number of associated centers. The intensity of the bands on the long wavelength side of the SAL emission becomes therefore higher and causes the peak of the composite band to move toward longer wavelengths.

The SAL bands of phosphor prepared with halides and the SAL bands of phosphor prepared with Al are very similar in their spectral positions. This similarity may be explained from the results of Hoogenstraaten's (15) investigations on the electron traps in ZnS phosphors. Hoogenstraaten calculated from glow curve measurements that the trap depth for Cl as well as for Al was 0.25 ev, while the trap depth for Ga was 0.42 ev and for In = 0.5 ev. If the SAL band is due to transitions from coactivator levels to the valency band, then transitions from bands with equal trap depth should give bands with peaks of equal wavelengths, as was indeed the case. Hoogenstraaten observed that the trap depth became shallower with increasing CdS content about 1.2×10^{-2} ev/mole % CdS. It could be expected therefore that the differences in trap depth between the various coactivators would be levelled out, provided that the distance of the trap levels from the valence band remains constant with phosphors of increased CdS content. The coactivator levels move, however, according to Hoogenstraaten (15) downward to a certain extent with increasing CdS content, and a difference between the trap depths of various coactivator levels therefore remains. As the trap depth of Ga or In is greater than the trap depth of Cl, the peaks of the coactivator emission are expected to be at longer wavelength. Measurements showed in accordance with this assumption that the SAL peak for $(Zn_{0.75}Cd_{0.25})S$:Cl was situated at 440 mμ (2.82 ev), while the peak of the SAL band with $(Zn_{0.75}Cd_{0.25})S$:Ga was found at 469 mμ (2.82 ev), and for $(Zn_{0.75}Cd_{0.25})S$:In at 483 mμ (2.57 ev). It should be borne in mind, however, that the figures given for the peaks of the SAL band may not represent the figures for the true peaks as other bands may be present.

The assumption that the SAL band is to be considered as a coactivator emission is also supported by the results of the calculation of the ratio of the optical trap depth (E_{abs}) to the thermal trap depth (E_{th}), (Franck-Condon ratio), using the figures for the SAL peaks as obtained during the present investigations. The Franck-Condon ratio lies between 1 for nonpolar crystals and 3 for very strongly polar crystals. Hoogenstraaten (15) calculated the Franck-Condon ratio with the figures for coactivator emissions as given by Kröger (10) and other authors (13, 14) and found that the ratio was higher than 3. Hoogenstraaten doubted therefore whether these emissions were really caused by transitions from the coactivator level to the valence band. As mentioned elsewhere these bands are indeed due to other transitions. If the Franck-Condon ratio is calculated from the values for the SAL peaks, then the ratio is found to be well below 3. For instance in the case of ZnS:Al the SAL band was peaked at 3.26 ev. If the value for the energy gap for ZnS (wurtzite) was taken as 3.70 ev, then the optical trap depth E_{abs} = 0.44 ev. The thermal trap depth E_{th} for Al was 0.25 ev. The ratio E_{abs}/E_{th} is therefore 1.76.

The measurements of paramagnetic resonance (EPR) in self-activated ZnS phosphors by Kasai and Otomo (17) are of interest in connection with the models for the centers in such phosphors. Kasai and Otomo found during the excitation of ZnS:Cl or ZnS:Br phosphors with 365 mμ u.v. at liquid nitrogen temperature two EPR signals A and B. They came to the conclusion that the A signals are caused by associated centers of the type proposed by Prener and Weil (11) which lose electrons during excitation to be trapped at the B center. The B resonances were assumed to be due to un-ionized donors (filled traps). Resonances of the B type were also observed by Lambe and Kikuchi (18) with CdS:Cl phosphors, and they also conclude that the resonances are caused by donor centers *i.e.*, Cl centers. Smith and Dieleman (19) extended the investigations to ZnS phosphors coactivated with trivalent metals and found A and B resonances with ZnS:Al phosphors. The EPR investigations did not reveal the presence of any other types of centers in self-activated ZnS phosphors, and it is suggested therefore that associated centers cause the A signal as well as the appearance of the SA band, while single donor centers cause the B signal and the SAL band.

Acknowledgments

The authors thanks are due to Dr. F. A. Kröger and Dr. B. A. Ridley for valuable discussions and to Mr. R. W. A. Gill who prepared all the phosphors described in this paper.

Manuscript received April 18, 1962; revised manuscript received Aug. 3, 1962.

Any discussion of this paper will appear in a Discussion Section to be published in the December 1963 JOURNAL.

REFERENCES

1. F. A. Kröger, *J. Opt. Soc. Am.*, **39**, 670 (1949).
2. E. B. Fehr, A. I. Friedman, F. J. Stucker, and C. R. Fonda, *ibid.*, **42**, 917 (1952).
3. S. T. Henderson, P. W. Ranby, and M. B. Halstead, *This Journal*, **106**, 27 (1959).
4. L. Drozd and V. L. Levshin, *Optics and Spectroscopy*, **10**, 408 (1961).
5. R. W. A. Gill and S. Rothschild, Enlarged Abstracts, Electrochemical Society, Chicago, 1960, Indianapolis, 1961.
6. F. A. Kröger and J. E. Hellingman, *This Journal*, **93**, 157 (1948).
7. W. van Gool, Fluorescence Centres in ZnS, Thesis Amsterdam, 1961.
8. A. Schleede, *Chem. Ber.*, **90**, 1162 (1957).
9. N. Riehl and H. Ortmann, Monographie "Uber den Aufbau der Zinksulfid-Luminophore," Verl. Chemie Weinheim, 1957.
10. F. A. Kröger and J. Dikhoff, *Physica*, **16**, 297 (1950).
11. J. S. Prener and D. J. Weil, *This Journal*, **106**, 409 (1959).
12. A. G. Lavrov, *Bull. Acad. Sci. USSR.*, Phys. Scr., **23**, 1351 (1959).
13. H. A. Klasens, *This Journal*, **110**, 72 (1953).
14. H. Koelmans, *J. Phys. Chem. Solids*, **17**, 69 (1960).
15. W. Hoogenstraaten, Electron Traps in Zincsulphide phosphors, Thesis, Amsterdam, 1958.
16. F. E. Williams, *J. Phys. Chem. Solids*, **12**, 265 (1959).
17. P. H. Kasai and Y. Otomo, *Phys. Rev. Letters*, **7**, 17 (1961).
18. J. Lambe and O. Kikuchi, *J. Phys. Chem. Solids*, **8**, 492 (1959).
19. W. V. Smith and J. Dieleman, To be published.

Effects of Ultraviolet Radiation on Fluorescent Lamp Phosphors

J. H. Singleton

Research Laboratories, Westinghouse Electric Corporation, Pittsburgh, Pennsylvania

and Lawrence Suchow[1]

Research Department, Westinghouse Electric Corporation, Bloomfield, New Jersey

ABSTRACT

Irradiation of halophosphate lamp phosphors by a low-pressure mercury arc causes a loss in luminescent efficiency, changes in the absorption spectra, and thermoluminescence. The 1849Å wavelength is primarily responsible for these changes, which are partially reversed by longer wavelength radiation or by heat. X-radiation produces larger changes in the absorption spectra, which are compared to observations on unactivated halophosphates. The relation between luminescent efficiency and color center formation is discussed.

The effect of ultraviolet radiation on phosphors is of considerable interest with respect to their stability in fluorescent lamps. The decrease in luminescent efficiency previously reported for several phosphors (1) was found to occur for the alkaline earth halophosphate phosphors. Production of color centers has been described resulting from u.v. and x-radiation of the luminescent (2, 3) and nonluminescent (4) forms of the halophosphates. The conditions which result in a decrease of luminescent efficiency and the formation of color centers have been examined further. These studies relate to the phosphors alone and are not directly applicable to operation in practical lamps where additional effects due to binders, gases, and the supporting glass may be of great importance.

Experiments and Results

Both commercially manufactured and laboratory-prepared halophosphate phosphors were studied. These have the general formula

$$M_5\,(PO_4)_3\,X\text{: Sb, Mn}$$

where M is Ca and/or Sr; X is Cl and/or F; Sb is a sensitizer as well as an activator which produces a blue luminescence in the region of 4800Å; and Mn is an activator which produces a peak in the 5800Å region. Table I shows the qualitative composition of the phosphors studied. In addition, a sample of self-activated barium titanium phosphate was examined.

Irradiation of the phosphors.—The phosphors were used as a thick layer on a quartz or Vycor support and maintained in an atmosphere of argon or a vacuum. The vacuum system was such as to allow the phosphors to be heated to 600°C, at pressures below 10^{-7} mm, without the introduction of impurities. Irradiation was carried out *in situ* through a window of Corning No. 7940 ultraviolet transmitting quartz. The window was not subject to solarization and had a constant transmission, for 1849Å radiation, of greater than 75%. The light sources were low-pressure mercury vapor lamps placed in close contact with the quartz window and maintained in a stream of dry nitrogen in order to eliminate oxygen absorption of the 1849Å radiation.

Measurement of relative efficiency of light production.—To determine a relative luminescent efficiency for excitation by 2537Å the phosphors were compared with a standard of the same phosphor which was initially well baked out and sealed in an atmosphere of helium. The standard so prepared was shown to be reproducible to better than 0.5% during the time of an experiment. Excitation of luminescence was produced by a weak source of 2537Å and a waveband in the emission was selected, using a monochromator, so as to exclude lines of the excitation source. The relative output so measured was repeatable to ±0.5%

The emitted radiation was observed from the same surface of the thick phosphor layer on which the excitation was directed. It was shown experimentally that the same quantitative data resulted when the emitted light was observed after transmission through a thinner phosphor layer as is normally the case when observing a fluorescent lamp.

Vacuum baking of phosphors.—The luminescent efficiency of the phosphors was only slightly affected by baking at 500°C *in vacuo* and usually decreased by less than 1%. Subsequent heating at the same temperature for many hours did not produce any further change in efficiency; in the case of halophosphates this baking was extended to beyond 100 hr. The phosphors are therefore stable up to at least 500°C *in vacuo*.

Table I. Qualitative composition of halophosphate phosphors

Phosphor	Ca	Sr	Cl	F	Mn	Sb
Westinghouse blue halo	x			x		x
Westinghouse white	x	x	x	x	x	x
Westinghouse cool white	x	x	x	x	x	x
Westinghouse warm white	x	x	x	x	x	x
Osram yellow halo	x			x	x	x
M-33 (experimental)	x			x	x	x

[1] Present address: Thomas J. Watson Research Center, International Business Machines Corporation, Yorktown Heights, New York.

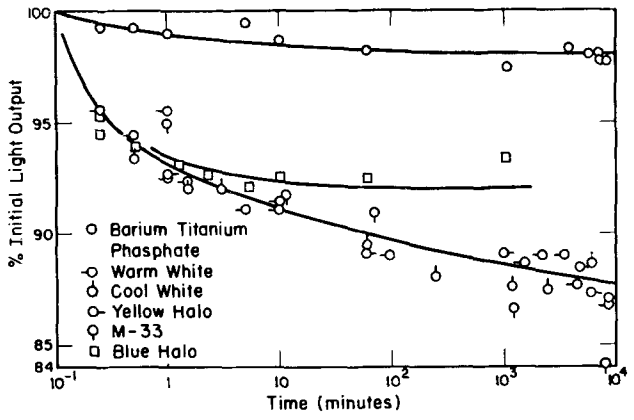

Fig. 1. Loss of light output during u.v. irradiation (2537Å~6000 μw/cm², 1849Å~1500 μw/cm²).

Change in luminescent efficiency by u.v. irradiation.—Irradiation at 2537Å[2] produced no detectable change in the efficiency of phosphors which had been exposed to 1849Å radiation.[2] Exposure to 1849Å radiation produced considerable depreciation in the halophosphate phosphors. The extent of this depreciation was not determined by the amount of previous heat treatment and was, therefore, not a function of the sorbed gaseous impurities. For example, a fresh sample of phosphor, evacuated to 10^{-5} mm pressure at room temperature, had the same characteristics as following exhaustive bake out at 500°C and less than 10^{-7} mm pressure. In all the subsequent experiments on u.v. irradiation each new phosphor sample was initially heated to 500°C, *in vacuo*, in order to eliminate subsequent changes in luminescent efficiency due to thermal effects.

Figure 1 shows the changes in luminescent efficiency of a group of phosphors during 1849Å irradiation. The appreciable scatter in the data was primarily due to the difficulty of maintaining a stable u.v. intensity for several hundred hours. The barium titanium phosphate showed very little depreciation. The blue halo, a calcium fluorophosphate activated with antimony, had a smaller decrease in luminescent efficiency than the remaining halophosphates in which calcium is partially substituted by strontium, and fluorine by chlorine, and manganese is present as an additional activator. A group of three halophosphate phosphors containing varying amounts of manganese and antimony, and a barium titanium phosphate phosphor were exposed under carefully controlled conditions for a limited time interval. The results, given in Table II, show no significant differences from each other in the rate of depreciation of these three halophosphates, irrespective of relative content of manganese and antimony.

The rate and extent of depreciation of halophosphate phosphors by 1849Å radiation increased with intensity, as shown in Fig. 2. A quantitative investigation was not possible because of the difficulty of obtaining an intense monochromatic source of 1849Å light. The effects of the additional wavelength

[2] For convenience throughout this discussion irradiation at 2537Å implies the use of a low-pressure mercury arc from which radiation below 2000Å has been removed, while irradiation at 1849Å signifies the unfiltered arc source, *i.e.*, including 2537Å. Although these are the principle lines present, there are appreciable intensities at other wavelengths, extending into the visible region.

Table II. Depreciation of lamp phosphors by u.v. irradiation

1849Å Intensity ~ 2400 μw/cm²; 2537Å Intensity ~ 2500 μw/cm²	% of initial output after stated irradiation time, min		
Phosphor	1	10	960
Westinghouse cool white halophosphate	91.3	88.7	85.7
Westinghouse white halophosphate	90.8	88.5	84.4
Westinghouse warm white halophosphate	90.2	88.2	84.8
Sylvania barium titanium phosphate	98.3	97.8	96.6

lines present in the irradiating source are discussed below.

Reversal of ultraviolet-induced depreciation by heating.—The depreciation of halophosphate phosphors was readily reversed by heating. This process was measurable at temperatures below 200°C and proceeded to completion, in most cases, in 1 hr at 450°C. The u.v. depreciation and its reversal by heating *in vacuo* was repeated several times on individual phosphor samples without any evidence of fatigue.

Influence of 2537Å radiation on a depreciated halophosphate phosphor.—Small losses in the luminescent efficiency of a halophosphate phosphor, caused by 1849Å, can be reversed quantitatively by exposure to 2537Å. For extensive depreciation only partial recovery was possible, as seen in the data of Table III where 2537Å irradiation was continued until no further recovery was observed. The results do not differentiate between phosphor depreciation occurring by a single mechanism, which can only be partially reversed by 2537Å, or by a series of processes, one of which is completely reversible, although the relatively constant recovery, irrespective of total depreciation, may favor the second alternative.

If during depreciation by 1849Å radiation the phosphor is also exposed to the same mercury spectrum as that which causes the recovery process, it is evident that some equilibrium must exist between at least part of the 1849Å induced depreciation and the 2537Å recovery. This hypothesis receives some support from the data of Table IV. A warm white halophosphate phosphor was subjected to three intensity levels of u.v. radiation in which the ratio of the

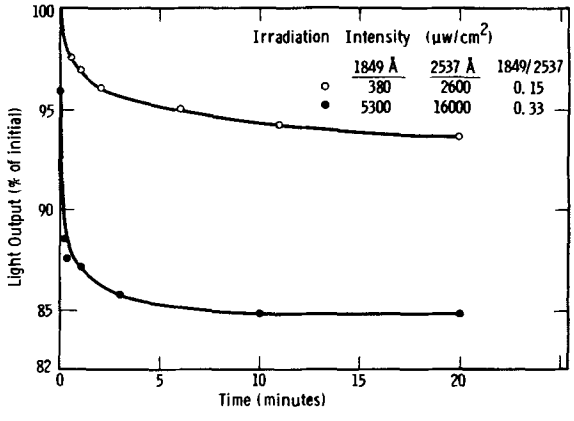

Fig. 2. Phosphor depreciation by u.v. light

Table III. Reversal of depreciation by irradiation at 2537Å and longer wavelengths

Phosphor	2537Å intensity, μw/cm²	Output intensity, % initial: Before irrad.	After irrad.	Increase
Westinghouse cool white	~6000	89.9	95.6	5.7
		84.9	91.7	6.8
Westinghouse warm white	~500	80.7	89.0	8.3
		88.1	95.6	7.5
		91.3	95.4	4.1
	~6000	80.3	87.5	7.2
		80.5	91.3	10.8
		83.1	90.7	7.6
		83.3	91.6	8.3
		84.4	92.0	7.6
		87.8	95.0	7.2
		88.7	94.9	6.2
		91.0	97.7	6.7
		92.4	97.0	4.6
M-33	~500	84.3	91.9	7.6
Osram yellow halo	~500	83.7	91.9	8.2
Westinghouse blue halo	~500	90.5	95.9	5.4
		92.3	97.7	5.4
		93.8	99.3	5.5

Table IV. Irradiation of a Westinghouse cool white halophosphate phosphor

Intensity, μw/cm²		Ratio		
2000-3000Å	1800-2000Å	1800-2000Å / 2000-3000Å	Irradiation time, hr	% Initial light output
190	30	0.16	184	90.6
740	120	0.16	60	90.8
3000	460	0.15	17	90.0

wavelength bands 1800-2000Å and 2000-3000Å was held constant at a value of 0.16 to 1. The 15-fold change in total intensity did not change the depreciation level significantly. Thus the rates of depreciation and recovery were dependent on the intensities of radiation in the 1800-2000Å and 2000-3000Å bands, respectively.

Color center formation in the phosphors.—In an earlier paper by Suchow (4) it was shown that 1849Å irradiation of unactivated alkaline earth halophosphates containing chloride caused formation of color centers which could be bleached out either optically or thermally. The reversal by 2537Å radiation or heat of the depreciation of phosphor light output by 1849Å radiation appeared to be an analogous case. Reversal of depreciation by longer wavelengths than 2537Å was therefore sought. Visible radiation was found to produce recovery, although not as completely as did 2537Å radiation. It was not possible to observe the relatively sharp color center bands found in unactivated base materials (4) either visually or in the diffuse reflectance spectrum measured with a Beckman DU spectrophotometer. However, a very slight general depression of the diffuse reflectance spectrum was noted, apparently with greater depression in the u.v.

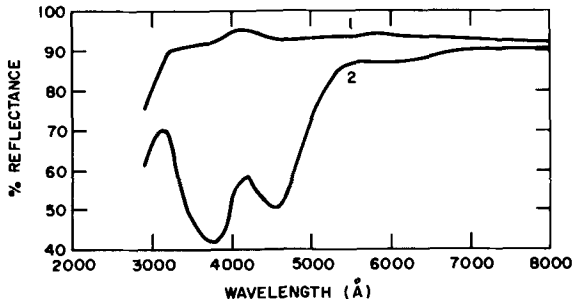

Fig. 3. Diffuse reflectance spectra of typical commercial halophosphate base material: 1, before exposure; 2, after exposure to tungsten x-rays for 15 hr (corrected to give absolute reflectance).

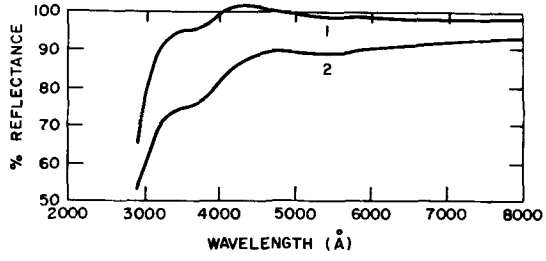

Fig. 4. Diffuse reflectance spectra of Westinghouse blue halo phosphor: 1, before exposure; 2, after exposure to tungsten x-rays for 15 hr (corrected to give absolute reflectance).

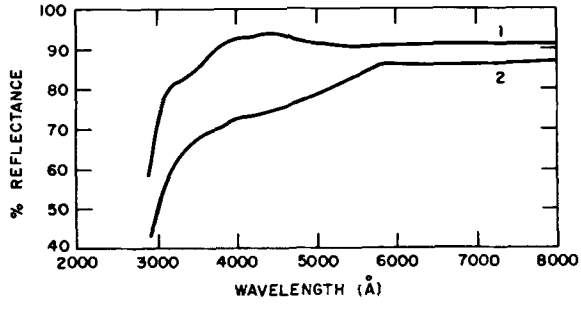

Fig. 5. Diffuse reflectance spectra of Westinghouse warm white halophosphate phosphor: 1, before exposure; 2, after exposure to tungsten x-rays for 15 hr. (corrected to give absolute reflectance).

region than at longer wavelengths. (This may correspond to the more pronounced effect observed with x-rays which is reported below.) Since phosphors in lamps and in the experiments described here are always bathed in visible light and 2537Å u.v. during exposure to 1849Å, it is probable that color center bleaching in halophosphate phosphors occurs simultaneously with formation, thus preventing a large build-up in concentration. The self-absorption involved in bleaching would of course be expressed as a decrease in luminescent efficiency.

In the halophosphate base materials it has now been shown that x-radiation produces the same color centers as 1849Å radiation (4) only in greater concentration [compare Fig. 3 with Fig. 1 of ref. (4)]. Because of these results and because x-radiation produces only weak visible fluorescence in halophosphate phosphors (and could therefore cause only little bleaching), it was thought that a high concentration of color centers might be obtained by exposure of the halophosphate phosphors to x-radiation. Exposure of the blue halo phosphor to tungsten x-rays for 15 hr caused the body color to turn

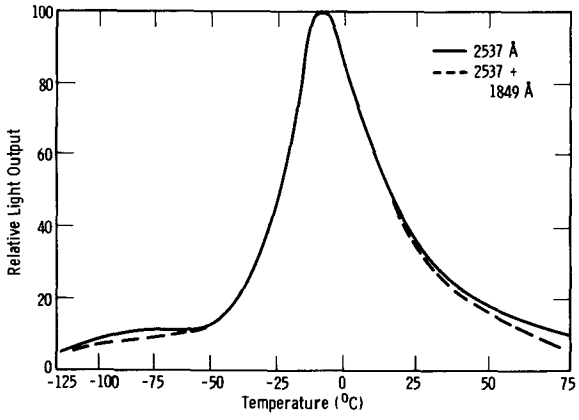

Fig. 6. Thermoluminescence of Osram yellow halophosphate

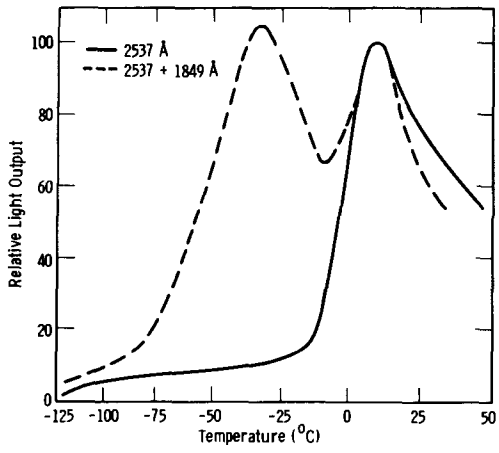

Fig. 7. Thermoluminescence of Westinghouse cool white halophosphate.

light gray-tan, and the fluorescence of the phosphor on exposure to 2537Å radiation was greatly reduced. However, no sharp absorption bands developed, but only a broad band from about 3000 to 4300Å, as shown in Fig. 4. Similar exposure of warm white halophosphate phosphor caused development of a rather deep yellowish-tan color which was due to broad absorption from about 2900 to 5500Å (see Fig. 5). Again the fluorescence on exposure of 2537Å was greatly reduced.

Comparison of the reflectance spectra in Fig. 5 with those given in ref. (4) and in Fig. 3 indicate the likelihood that the color centers produced in the base material are also produced in the phosphor, but that superimposition of additional overlapping absorption centers in the phosphor results in smeared-out absorption. In the case of the blue halo phosphor, in which no color centers would be expected to form in the chlorine-free base material [at least with 1849Å radiation (4)] the induced absorption band is much narrower than in warm white phosphor, and it must be assumed that the induced absorption is due only to a band or bands not found in the absence of antimony, or else that x-rays are capable of affecting an all-fluorophosphate phosphor as u.v. cannot. A qualitative experiment has shown that x-rays do produce slight coloration in unactivated $Ca_5(PO_4)_3F$; 1849Å u.v. radiation does not do this. [Johnson (2) has also reported formation of color centers in $Ca_5(PO_4)_3F$ by x-rays.]

Thermoluminescence of halophosphate phosphors.—Because of apparatus limitations it was found necessary to study the thermoluminescence of the phosphors over two temperature regions:

(*a*) *Low-temperature thermoluminescent: −125° to +100°C.*—The phosphors were deposited from a water suspension onto a copper disk. The lowest temperature of the phosphor was approximately −130°C and the rate of heating was 50°C/min. The phosphors were irradiated at the lowest temperatures, and the total visible light produced during subsequent heating was plotted as a function of temperature, the light intensities being normalized in each experiment to the value of the largest peak produced by 2537Å radiation.

The halophosphate phosphors studied fall into three types: (i) blue halo, containing Ca and F, with Sb as an activator, produced no detectable emission under any irradiation conditions; (ii) phosphors containing Ca and F, with Sb and Mn as activators, were found to have a single group of trapping sites after irradiation with either 1849 or 2537Å; the glow curve of irradiated yellow halophosphate, shown in Fig. 6, is typical; (iii) phosphors containing Ca, Sr, F, and Cl, with Sb and Mn as activators were found

Table V. High-temperature thermoluminescence measurements

Phosphor	Peak temperature, °C: After exposure to quartz low-pressure mercury-vapor lamp (1849Å and higher wavelengths)	After exposure to Vycor low-pressure mercury-vapor lamp (2537Å and higher wavelengths)
Westinghouse blue halo	260° and 370°C (second peak higher than first)	None
Westinghouse cool white	Broad emission from 70° to 260°C, perhaps with small peak at 230°C. Further emission starts at 320°C and disappears in incandescence of heater.	90°C
Westinghouse white	Broad emission from room temperature to 360°C, then disappearing in incandescence of heater.	Broad peak from 70° to 110°C, possibly with maximum at about 80°C.
Westinghouse warm white	Broad emission from 50° to 350°C with broad peak from 180° to 225°C; disappears into incandescence of heater above 350°C.	Broad peak from 100° to 200°C.
Osram yellow halo	Broad emission from 50° to 300°C; superimposed peak at 100°C.	Broad emission from 50° to 300°C.

to have a group of traps, similar to those in type (ii), after 2537Å irradiation, and an additional group following 1849Å irradiation. Figure 7 shows results for a cool white halophosphate. The traps resulting from 1849Å radiation were not observed if this treatment was followed by subsequent exposure to 2537Å, for 1 min, before making a thermoluminescent measurement. Thus the electrons trapped by 1849Å were rapidly released by 2537Å radiation.

The low-temperature thermoluminescence curves show some parallel behavior to the changes in luminescent efficiency by u.v. irradiation, but the extent of any correlation is not clear. For example, the appearance of additional traps after 1849Å radiation occurred only in the presence of chloride and not with fluoride alone, and the fluorophosphate base material did not exhibit color center formation during 1849Å radiation (4). Thus, if a simple correlation exists between depreciation and the formation of color centers by 1849Å radiation the above results would require low depreciation for phosphors containing only fluoride. This was not found to be the case for either the yellow halo or for M-33 (Fig. 1). Further comment on this will be made in the Discussion Section.

(b) *High-temperature thermoluminescence: +35° to +360°C.*—The exposure of phosphors to u.v. and subsequent measurement of high-temperature thermoluminescence curves were carried out as previously described for the base materials (4). The results obtained are summarized in Table V. Barium titanium phosphate did not exhibit any thermoluminescence under similar conditions.

The thermoluminescence in the calcium fluorophosphate phosphors is probably associated with effects on the antimony and manganese activator centers, for as shown earlier (4) similar irradiation of the unactivated base material did not result in either thermoluminescence or color centers. Such a superimposed effect on the activators would explain why the fluorophosphate phosphors discussed above did not exhibit better maintenance than those which also contained chloride.

Discussion

There appears to be reason to assert that the ultraviolet-induced depreciation of the halophosphate phosphors is an intrinsic property, typical of the phosphor crystal, and not produced by the presence of gaseous or other contaminants such as mercury. Further, the ease with which depreciation is reversed, by quite low temperatures or by irradiation, and the observed result that the cycle of depreciation and recovery may be repeated quantitatively many times with no evidence for fatigue, implies that whatever the mechanism it does not involve any migration or transfer of phosphor components over appreciable distances in the lattice. The minor change observed in the reflectance of the 2537Å line, following exposure to 1849Å, coupled with the very high absolute absorption at this wavelength, means that depreciation does not occur by a reduction of the efficiency of energy absorption. Also, the spectrum of a depreciated phosphor does not show any preferential decay of the antimony or manganese peaks although the excitation energy must be transmitted to the manganese centers, as distinct from the antimony centers, which are simultaneously responsible for energy absorption. It is evident that energy absorbed by the antimony centers is dissipated before radiation can occur at either antimony or manganese centers.

It is not clear what effect the electron traps observed in low-temperature thermoluminescence could have on the luminescent efficiency since the traps would presumably be empty at the normal temperature of observation. However, if the time electrons spend in these traps is comparable with the time of the electronic transitions in luminescence, the traps might still have an effect on the kinetics of the process. The high-temperature traps have been found in all of the halophosphate phosphors studied thus far. Once filled these traps would not be thermally emptied, but bleaching by visible or 2537Å wavelength light would be observed as depreciation in total light efficiency.

The parallels between depreciation and color center formation have been partly discussed above. The change in absorption spectrum of ultraviolet-irradiated halophosphate phosphors on irradiation with 1849Å u.v. is at most very slight. However, the experiments with x-rays imply that 1849Å radiation produces the same color centers as x-rays even though they are nearly invisible in the former case because most are bleached out by the visible light and 2537Å radiation which are always present. Although some light is expected to be lost in the bleaching process which occurs as a phosphor is exposed to both 1849 and 2537Å radiation simultaneously, this does not explain why a phosphor with almost unchanged absorption following exposure still shows depressed brightness when exposed to 2537Å radiation in the absence of 1849Å (prior to full recovery with 2537Å). There must therefore be a second type of efficiency loss due to some sort of interference with the electronic process of fluorescence by a very small concentration of trapped electrons (that is, color centers). It is only when all of these color centers are bleached that full recovery is observed.

The very low depreciation of barium titanium phosphate in these experiments is probably related to the absence of thermoluminescence and color centers following u.v. irradiation, but is at variance with the large depreciation during operation in a fluorescent lamp. It has not been possible to detect any unusual susceptibility of this phosphor to impurity gases, but it is distinguished from the halophosphates by a very high-temperature coefficient of the intensity of the emitted light. Thus, from room temperature to 100°C a typical halophosphate loses 5% of output while the barium titanium phosphate loses 35% (5). A phosphor subjected to u.v. radiation converts an appreciable amount to thermal energy. For example, a thin layer of phosphor irradiated *in vacuo* at intensities of u.v. only a half or less than those present in a 40w fluorescent lamp, rapidly reached a temperature of 50°C. This temperature would increase throughout the life of the

fluorescent lamp if its operation caused slow deposition of ultraviolet-absorbing materials such as mercury (6) or mercuric oxide on the phosphor surfaces. Thus it is conceivable that such a process would produce an apparent depreciation of the barium titanium phosphate due only to increased temperature of the phosphor surface, but which would have a negligible effect on the halophosphate phosphors.

Acknowledgment

The Bloomfield portion of this work was carried out with the capable assistance of Mr. John J. Minchak.

Manuscript received June 1, 1962; revised manuscript received Sept. 10, 1962. This paper was prepared for delivery before the Los Angeles Meeting, May 6-10, 1962.

Any discussion of this paper will appear in a Discussion Section to be published in the December 1963 JOURNAL.

REFERENCES

1. G. Meister and R. Nagy, *J. Opt. Soc. Am.*, **36**, 396 (1946); **37**, 403 (1947).
2. P. D. Johnson, *J. Appl. Phys.*, **32**, 127 (1961).
3. P. D. Johnson, *This Journal*, **108**, 159 (1961).
4. L. Suchow, *ibid.*, **108**, 847 (1961).
5. C. H. Haake, Private communication.
6. H. C. Froelich, *J. Appl. Phys.*, **17**, 573 (1946).

Pulse Excitation of Electroluminescent Films of ZnS:Cu(Cl,Br,I)

W. J. Harper

Research Laboratories, Westinghouse Electric Corporation, Pittsburgh, Pennsylvania

ABSTRACT

Thin electroluminescent films of ZnS:Cu, (Cl,Br,I) between tin-oxide-on-glass and aluminum electrodes were excited with unidirectional voltage pulses of either polarity. Results are given for the delay, rise, and decay time and the emission intensity of the light pulses under varying conditions of voltage, pulse duration, and repetition rate. The decay of the light pulse can be represented by a fast exponential superposed on a slower bimolecular form. Voltage pulses with the metal electrode positive suppress the longer wavelength emission band.

The objective in this work was to investigate the individual light pulses resulting from excitation of electroluminescent (EL) films with voltage pulses of microsecond duration, with the intent of utilizing such films in combination with photoconductive receptors in computer logic elements. Desirable attributes of EL films for this application are low voltage excitation with single unidirectional pulses, speed of microsecond order, and minor sensitivity to low temperatures. This paper presents the results of a study of such parameters.

Experimental Method

The evaporated EL films were similar in structure to those described previously (1, 2). The surface resistivity of the tin oxide electrode varied from 10 to 50 ohms, and the area of the film excited at one time was usually 0.1 cm^2. When exciting a cell the pulse generator could be adjusted to have either a voltage rise or fall time (to 1/e) as low as 0.02 μsec. This sharp rise or fall was accompanied by a rounding or by oscillations at the other end of the pulse. Generally, tests were made with voltage fall in the range of 0.05-0.1 μsec, particularly at high voltages. In this report results will be given for excitation by unidirectional, rectangular voltage pulses only. Where results are given without identification of the phosphor, it is implied that they are similar for any of the three halide coactivators, since this is generally true for most properties.

The light was detected with a multiplier phototube having an S-10 spectral response. The quantitative values given for light intensities should be considered approximations. In measuring delay and rise times of less than 1 μsec, the anode impedance of the multiplier was the 200 ohm input of a wide band amplifier. For detecting decay times of more than 1 μsec, the amplifier was not used, but the anode was connected directly to an oscilloscope with a short cable, with an anode resistance of 200 or 1000 ohms.

Many properties of EL films depend on the amount of insulation between the phosphor and the metal electrode. In this report only two conditions will be considered, either no insulation or 0.1μ of SiO insulation, both with an evaporated aluminum electrode. All the results given refer to room temperature conditions unless otherwise stated.

Results

Waveform.—Because of the asymmetric structure of the EL films, only a single dominant light pulse is obtained for each voltage pulse, and the waveform of the light pulse depends somewhat on the polarity of the voltage pulse. If a positive voltage pulse is applied to the tin oxide electrode (abbreviated SnO+),[1] there may be some light emitted while the voltage is on. As the voltage is returned to zero there is a delay, then a rise and fall of the dominant

[1] SnO is used as a symbol to represent the tin oxide electrode. The tin oxide material itself may be represented by $SnO_2(Sb)$.

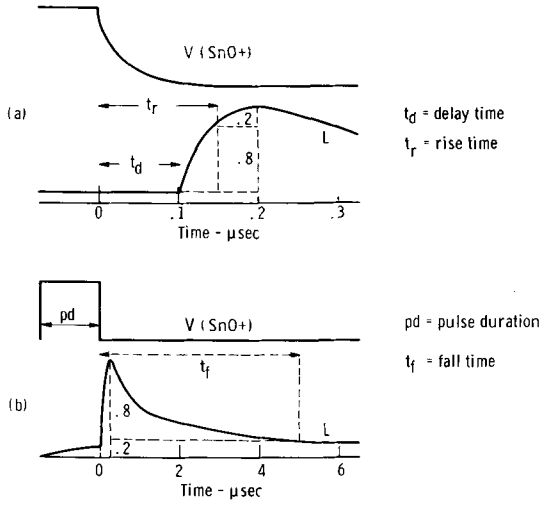

Fig. 1. Schematic diagram of the light pulse *L* due to the voltage pulse *V* showing how the delay, rise, and fall time are measured. The time scale shows representative values.

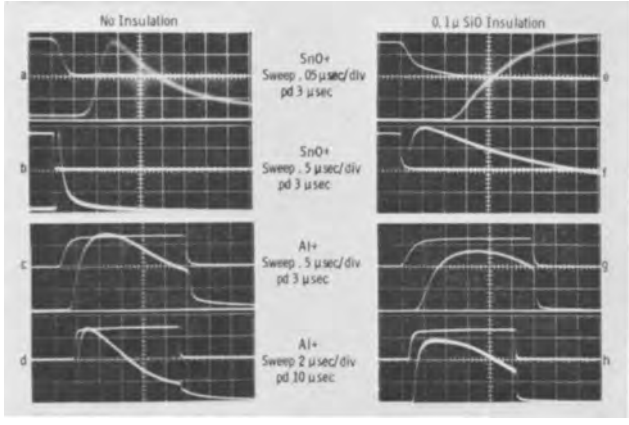

Fig. 2. Waveforms of voltage (upper trace) and light (lower trace) for an EL film of ZnS:Cu,Br 1.7μ thick. The symbol SnO+ (Al+) means that a positive voltage pulse is applied to the tin oxide (aluminum) electrode.

light pulse. Figure 1 shows how the delay time, rise time, and fall time[2] of the light pulse were interpreted in the measurements. If a short positive voltage pulse is applied to the aluminum electrode (abbreviated Al+), the dominant light pulse occurs while the voltage is on. As the voltage returns to zero, there may follow a minor light pulse or the dominant light pulse may be quenched. Examples of the form of the light pulse due to voltage pulses of either polarity are shown in Fig. 2.

With Al+ polarity the in-phase and the dominant light pulses are superposed, whereas with SnO+ polarity they are separated. For the latter the rise time of the in-phase light varies from about 20 μsec at low voltages to about 1 μsec at high voltages. In the remainder of this report, only the dominant light pulses will be discussed.

The decay or fall of the light pulse can be fitted to a bimolecular recombination formula, as is shown in Fig. 3(a). Narrow band filters were used to separate the blue and green components. If the values of the light L obtained from the extrapolated portion of Fig. 3(a) are subtracted from the measured light

[2] The decay time of the phosphor is being called the fall time to avoid the use of the two similar words decay and delay.

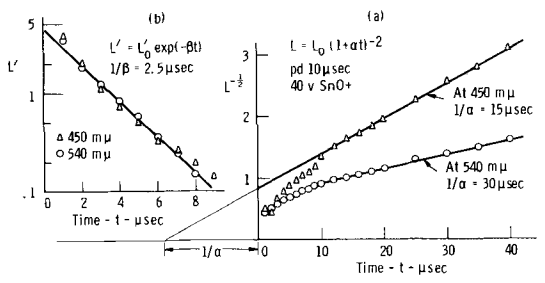

Fig. 3. Fitting the decay of the light pulse to (a) bimolecular and (b) exponential forms. The phosphor is ZnS:Cu,Cl 2.0μ thick with no insulation. In (a) the points represent the measured values of light amplitude. In (b) L' is the difference between the measured values and those found from the extrapolated portion of the curve in (a).

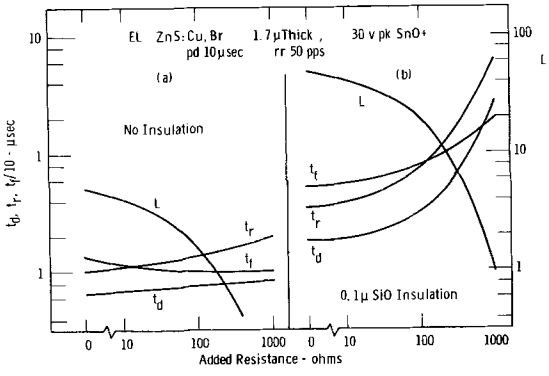

Fig. 4. Effect on a light pulse due to insulation and to an added series resistance. Cell area is 0.1 cm²; peak amplitude of the light pulse *L* is in microwatts.

values and the logarithm of the differences is plotted against time as in Fig. 3(b), a good fit for the exponential form of decay is usually obtained. The time constant is frequently the same for both blue and green components, being 2.5 μsec in the example shown. In Fig. 3(a) the quantity $1/\alpha$ gives the time in which L is reduced to 0.25 L_0. The values so obtained are usually greater than the fall time t_f measured on the same curve by the method of Fig. 1(b). The physical meaning of the constants α and β in Fig. 3 is discussed in ref. (3). The decay of light with Al+ polarity is similar to that with SnO+, but the initial exponential portion is relatively smaller in magnitude or sometimes negligible. The portion of the decay beyond 20 μsec could not be consistently fitted to any form. Results similar to the above were obtained for the blue and green bands of ZnS:Cu,Br and the blue band of ZnS:Cu,I.

The build-up of light during the first few pulses from a de-excited phosphor film is very pronounced for the Al+ polarity, the first voltage pulse giving no light pulse. With SnO+ the build-up is small by comparison, the first voltage pulse being followed by a light pulse.

Effect of insulating layer.—As the thickness of the insulating layer is increased, each of the time quantities, delay, rise, and fall is increased. They are also increased if a resistance is added in series with the tin oxide electrode. Figure 4 shows the magnitude of the effect. An insulating layer of 0.1μ SiO roughly doubles the values of delay and rise time.

It is believed that the nature of the contact between the aluminum and the phosphor has an effect

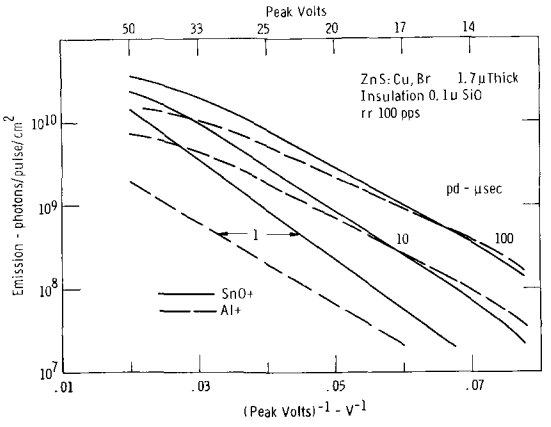

Fig. 5. Dependence of the integrated light emission on voltage. Results from unidirectional pulses of both polarities and three values of pulse duration are shown.

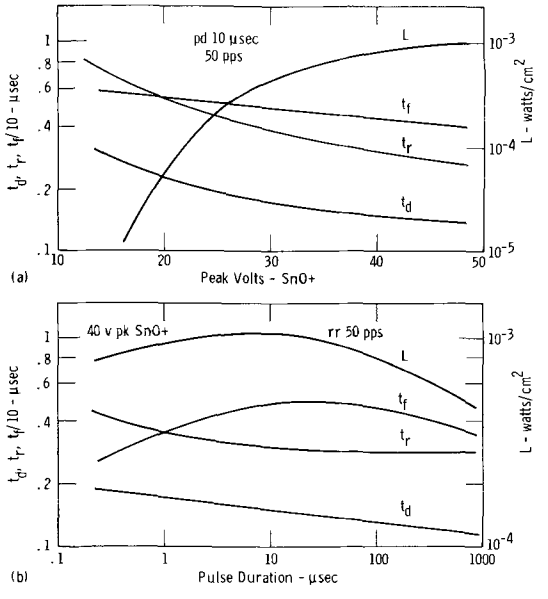

Fig. 6. Dependence (a) on voltage and (b) on pulse duration of the delay, rise, and fall time, and of the peak amplitude L of the light pulse. The phosphor film is ZnS:Cu,Br 1.7μ thick with 0.1μ of SiO insulation.

on the delay time since on the same phosphor layer different contacts with no insulation may have delay times ranging from 0.06 to 0.12 μsec. The delay time appears with the first application of low voltage to a new cell and is not a result of electrical forming. At the rising light pulse of a given cell, the minimum delay times obtained were the same for either voltage polarity and for the different spectral emission bands.

Effect of voltage, pulse duration, and repetition rate.—The dependence of the light pulse L (maximum amplitude or integrated light) on the voltage V, is represented reasonably well by

$$L = L_0 \exp(-a/V) \qquad [1]$$

where a and L_0 are constants. Deviations from [1], such as are shown in Fig. 5, are common at low and high voltages. For pulse durations less than about 5 μsec with Al+ polarity, voltage quenching reduces the light output.

Variations of voltage and pulse duration have only minor effects on the delay, rise, and fall times of the light pulse, as shown in Fig. 6 for a cell with 0.1μ SiO insulation. The variation with voltage is even less for cells with no insulation.

As the pulse duration is increased with SnO+ polarity the peak amplitude of the light pulse may reach a maximum at widths of 10-100 μsec and thereafter decline. The integrated light, however, remains at the maximum. This is due partly to an increase of the in-phase light but mostly to an increase in the very long decay component. The explanation is not evident from values of the fall time t_f in Fig. 6(b), but rather from plots as in Fig. 3(a). For example, on a specimen of ZnS:Cu,I at pulse durations of 1, 10, and 100 μsec, the values of t_f (to 0.2 of peak L) were 3.0, 3.5, and 5.5 μsec while the slower components (to 0.25 L_0) as shown by Fig. 3(a) were 12, 15, and 21 μsec. After deducting the slower components, the faster components (to 1/e) as shown by Fig. 3(b) were 1.2, 1.5, and 2.1 μsec. In addition to the slow component mentioned above, an even slower decay follows which contributes to the measure of the integrated light output.

The time constants of the light pulse are affected by the rate at which the voltage falls. For a cell with 0.1μ SiO insulation, as the voltage fall time (to 1/e) was increased in steps from 0.08 to 1 μsec, the rise and fall time of the light pulse increased in magnitude similarly to those shown in Fig. 4(b). This effect has previously been reported for powder cells (4). The delay time increase and the light amplitude reduction were considerably less than in Fig. 4(b). The voltage fall has an initial fast portion and then a slower one. The time constant of the latter and any ripple in it affect the delay time and the shape of the rise of the light pulse. For a voltage fall time of 0.02 μsec, the minimum delay and rise times observed were 0.06 and 0.09 μsec; that is, the rising portion was 0.03 μsec. These minimum values were also obtained for electrodes of several metals other than aluminum. On a similar phosphor film with RaD alpha particle excitation the rise time was also about 0.03 μsec.

If conditions are such that light is quenched at the end of a pulse with Al+ polarity, there is frequently also a delay, but shorter than for the rise of the light pulse. For example, when voltage fell to 1/e in 0.04 μsec, the light remained constant for 0.05 μsec and was then quenched to 1/e in 0.5 μsec.

As may be seen in Fig. 7, if the voltage is high, the light output per pulse with Al+ polarity is con-

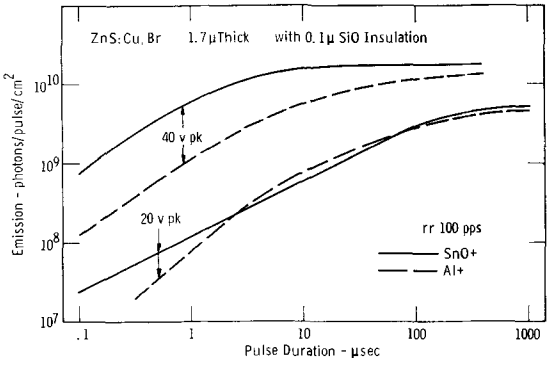

Fig. 7. Dependence of the integrated light emission on the pulse duration for both voltage polarities.

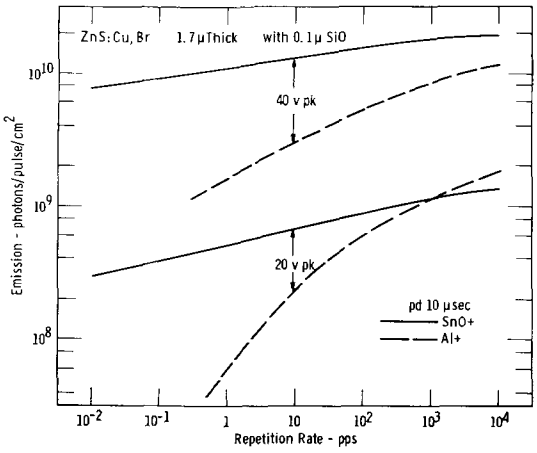

Fig. 8. Dependence of the integrated light emission on the repetition rate.

siderably less than with SnO+ for pulse durations from 0.1 to 1000 μsec. At low voltages, however, it is less only for pulse durations less than about 3 μsec, where quenching is important.

At moderate duty factors with SnO+ polarity, the repetition rate does not have a strong effect on either the form of the light pulse or its magnitude. An example of the total light emitted per pulse for both voltage polarities is shown in Fig. 8. With Al+ voltages the light output is comparable to that with SnO+ at high repetition rates, but falls off rapidly at low rates.

If the repetition rate is increased so that a new voltage pulse appears before the previous light pulse has decayed to zero, the decaying light is quenched both for blue and green. Just prior to the quenching and for both blue and green, as the voltage begins to change there is a delay of about 0.07 μsec, then a small rise in the light with a duration of about 0.1 μsec, and then the quenching which has a time constant of about 0.1 μsec. The small rise may be the minor delayed pulse appearing with voltage polarity opposite to that of the dominant delayed light pulse.

Spectral emission.—For SnO+ pulses the spectral emission from films is similar to that from the powder counterparts for ZnS:Cu,Cl and ZnS:Cu,Br (5).

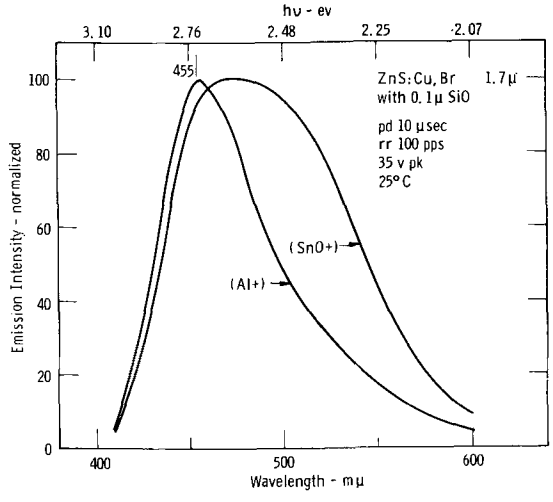

Fig. 9. Spectral emission of an EL film with pulse excitation of opposite polarities.

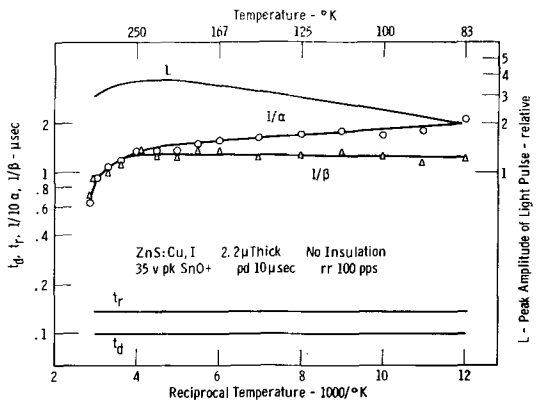

Fig. 10. Effect of temperature on the light pulse

In the ZnS:Cu,I films, the broad band of ZnS:Cu peaking in the red (6) was obtained in addition to the blue band. For Al+ pulses the longer wavelength emission band is suppressed. For sufficiently narrow pulses with Al+ polarity, films with any one of the three halide coactivators, Cl, Br, or I, give a similar emission band peaking at the wavelength 455 mμ at room temperature and having the same width at half maximum. An example is shown in Fig. 9.

Effect of temperature.—In the range 80°-330°K, temperature has a minor effect on the delay and rise of the light pulse. With increase of temperature from 80°K, the decay time is reduced and the light amplitude passes through a maximum. An example for the blue band of ZnS:Cu,I is shown in Fig. 10. In this specimen the hyperbolic and exponential decay constants differ approximately by a factor of 10. In the range 80°-300°K, log α varies as $T/14{,}000$. Because of the short pulse duration and the spectral sensitivity of the phototube, the influence of the red band in the emission of Fig. 10 is negligible. The temperature at which quenching of the emission takes place depends on the pulse duration, the voltage, and the amount of insulation.

Efficiency.—The efficiency of conversion of electrical energy absorbed to light energy emitted was measured for a ZnS:Cu,Br film, 1.7μ thick with 0.1μ of SiO insulation. At a pulse duration of 10 μsec, as the voltage was increased the efficiency (ratio of emitted to absorbed energy) passed through a maximum at about 30v for both polarities. At 30v as the pulse duration was increased from 0.1 to 5 μsec, the efficiency for SnO+ decreased from 3.10^{-3} to 10^{-3} while for Al+ it increased from 10^{-4} to 10^{-3}. As the pulse duration was further increased from 5 to 1000 μsec, for both polarities the efficiency decreased from 10^{-3} to 10^{-5}. This dependence of efficiency on voltage and pulse duration is somewhat different than that for pulse excitation of powder cells (4).

Discussion

Hoffman and Smith (7) have reported a delay between the voltage pulse and the light pulse in EL cells of powders and have discussed some of the factors which may contribute to it. From the work on thin films it is concluded that the delay is due to the effect of circuit constants at the cell and at the anode of the phototube on the transmission of the step voltage pulses and is not due to any property

of the phosphor. The shorter delay at the quenching of the light pulse may be due to the shape of the voltage pulse; quenching being the result of the initial fast change of the voltage while the rise of light reflects the slower portion of the voltage change. With the same equipment, delays of 0.05 μsec were also obtained on electroluminescent GaP and SiC.

The minimum observed time of the light rise was about 0.03 μsec. The slower rates usually obtained are apparently due to the shape of the voltage pulse, the effects caused by the cell circuit elements at the phosphor film, and perhaps the effects of trapping within the phosphor.

The kinetics of the decay of luminescence has been interpreted by many authors (3), particularly for photoluminescence. For EL powders Tanaka (8) has obtained a fairly good fit for the bimolecular form of decay, obtaining a time constant of about 10 μsec at room temperature. Other authors (9-12) have described the EL decay as hyperbolic or exponential, reporting decay constants of from 4 to 100 μsec. The results for thin films can be represented quite well by a fast exponential decay superposed on a slower bimolecular decay. This superposition indicates that the dominant light pulse with pulse excitation is due to two sources. The secondary pulse that is obtained with sine wave excitation is not one of them since with pulse excitation the superposition is present when the secondary pulse is negligible, as, for example, with insulation or at 80°K. The fast exponential decay may be determined by the escape rate of electrons from shallow traps with no retrapping and can, therefore, be the same for both the blue and green emission. At low temperatures the rate does not vary with temperature, indicating field release of electrons. The bimolecular decay may be evidence for deeper traps and for retrapping (13, 14) with the rate being determined by the number of luminescent centers as well as the number of electrons being released.

For pulse durations longer than about 100 μsec, the peak light amplitude declines while the fall time becomes longer. This may be due to transfer of holes from blue to green type luminescent centers according to the Schoen-Klasens model since the emission is more green at the longer pulse durations and the decay of green is slower. However, since the effect is observed in ZnS:Cu,I in which the green band is very weak, some other mechanism is also present. It would be expected that the long pulses would have a greater proportion of deep traps which would reduce the initial amplitude of the light pulse and increase its decay time.

In the pulse excitation of single crystals, there was reported (15) a quenching of blue light and a stimulation of green by the same voltage change. Such an effect was not observed here in the films. Any increase in light prior to a quenching can be attributed to the minor delayed light pulse. The blue and green components behaved qualitatively in the same manner.

When excitation is with Al+ polarity, the voltage change that returns the cell to zero applied potential excites the phosphor. The energy of excitation is stored during the period between the pulses. At low duty factors this allows time for any transfer of energy between centers within the phosphor. It also allows time for the thermal release of trapped electrons, and if no retrapping occurred, there would be a supply of free electrons for the next voltage change. This voltage change would, therefore, favor the transition from the conduction band. The blue emission from ZnS has been identified (16, 17) as due to the transition from the conduction band to a zinc vacancy center. This may be the explanation for the blue emission with Al+ polarity. Obtaining an efficiency comparable to that with SnO+ implies that the number of electrons available is small compared to the number of empty luminescent centers. The bimolecular decay obtained may not arise from the same conditions as for SnO+ polarity, but may be due to the relative number of empty traps and centers.

It appears that at low voltages the energy stored between pulses is retained longer in the absence of an externally applied voltage. The loss with an applied voltage may be due to the stronger field, greater conductivity, or the greater density of electrons initially in traps but released during the interval between pulses. That the space charge of trapped electrons forms only near the tin oxide electrode is confirmed by the effect of voltage polarity on the build-up of light.

Bowers and Melamed (18) attributed the green band from ZnS:Cu to substitutional Cu and the red band to interstitial Cu. Since the green band is strong with Cl and Br coactivators and the red band with I coactivation, it may be concluded that Cu enters ZnS crystals substitutionally when associated with Cl or Br and interstitially with I.

Acknowledgments

This work was supported by the United States Air Force Aeronautical Systems Division, under Contract No. AF 33(616)-8020, Project No. 1610-7062. The author is indebted to K. A. Rumon for a large part of the experimental work.

Manuscript received June 18, 1962. This paper was prepared for delivery before the Los Angeles Meeting, May 6-10, 1962.

Any discussion of this paper will appear in a Discussion Section to be published in the December 1963 JOURNAL.

REFERENCES

1. W. A. Thornton, *J. Appl. Phys.*, **30**, 123 (1959).
2. W. J. Harper, *This Journal*, **109**, 103 (1962).
3. G. F. J. Garlick, "Luminescent Materials," Oxford University Press, London (1949); Chapters 1, 2, and 4 contain a discussion of decay kinetics.
4. J. A. Rajchman, G. R. Briggs, and A. W. Lo, *Proc. I.R.E.*, **46**, 1808 (1958).
5. I. J. Hegyi, S. Larach, and R. E. Shrader, *This Journal*, **104**, 717 (1957).
6. H. C. Froelich, *J. Opt. Soc. Am.*, **42**, 982 (1952); *This Journal*, **100**, 280 (1953).
7. G. R. Hoffman and D. H. Smith, *J. Elec. Control*, **9**, 161 (1960).
8. Shoji Tanaka, *J. Phys. Soc. Japan*, **14**, 1123 (1959).
9. T. Kilburn, G. R. Hoffman, and R. E. Hayes, *Proc. I.E.E.*, **105B**, 136 (1958).
10. Shin-ichiro Narita, *J. Phys. Soc. Japan*, **15**, 128 (1960).

11. R. Zallen, W. T. Eriksen, and H. Ahlburg, *This Journal*, **107**, 288 (1960).
12. J. E. Johnson, *ibid.*, **108**, 852 (1961).
13. W. Hoogenstraaten, *Philips Research Repts.*, **13**, 515 (1958).
14. R. C. Herman, C. F. Meyer, and H. S. Hopfield, *J. Opt. Soc. Am.*, **38**, 999 (1948).
15. I. T. Steinberger, V. Bar, and E. Alexander, *Phys. Rev.*, **121**, 118 (1961).
16. H. Samelson and A. Lempicki, *ibid.*, **125**, 901 (1962).
17. I. Broser and H. J. Schulz, *This Journal*, **108**, 545 (1961).
18. R. Bowers and N. T. Melamed, *Phys. Rev.*, **99**, 1781 (1955).

A Comparison of the Intensities of Emission of Eu^{3+} and Tb^{3+} in Tungstates and Molybdates

L. G. Van Uitert

Bell Telephone Laboratories, Incorporated, Murray Hill, New Jersey

ABSTRACT

The intensity of emission of Eu^{3+} is shown to vary with its electrostatic binding energy in the tungstates which have the scheelite structure. Increasing the polarization of the oxygens toward Eu^{3+} or Tb^{3+} appears to decrease the total binding energies of these ions in the tungstates and molybdates. Brightness can either increase or decrease with binding energy depending on the effectiveness with which the host structure can capture excitation energy and communicate it to the rare earth ions involved.

Fluorescent emission from rare earth ions in oxides can be stimulated by ultraviolet excitation in a number of ways. The most familiar of these is by exciting the ion directly within a conveniently disposed absorption region. Recently Varsanyi and Dieke (1) have shown that rare earth ions can also be excited by excitation in pairs whose energy corresponds to the sum of the energies of two absorption transitions of the ions. Energy transfer from the host structure to the rare earth ion can also be important. Kroger (2), for example, has shown this to occur in $CaWO_4$:Sm. The intensity of emission of a rare earth ion is dependent on the character of the host environment whether it absorbs the excitation energy directly or not. The facility with which energy can be coupled to the f-electrons of the rare earth ion is, at least in part, dependent on the binding energy of the ion in the host structure and the symmetry of the site which it occupies. Intensity of emission measured under a given set of conditions may be dependent on crystal perfection and the impurities present. It is not always possible to avoid difficulties from these sources. However, in the hope of doing so, the present investigation has been carried out employing materials that had been prepared as well formed crystallites by flux growth methods under conditions[1] which insure reproducibility and as near to optimum a brightness as possible considering the purity of the starting materials (3, 4). This has made it possible to obtain reasonably quantitative comparisons of brightness for a large number of compositions.

In the present work, intensity of emission is shown to vary with the parameters of a simple electrostatic model in as far as this is possible. Where these qualitative relationships appear to hold for a large body of data, some significance can be attached to them. For the present study, it is assumed that the symmetry of the sites in which the rare earth ions are located are not significantly affected by changing the host structure cations as long as the scheelite structure is maintained. Where this assumption is applicable, the intensity of emission of an isolated rare earth ion can be expected to show a direct dependence on its interaction distances in the crystal. The related over-all binding energy of a given ion can be considered to be a combination of its electrostatic binding energy (such as can be calculated on the basis of a hard sphere model) (5) and the modifying effects due to the nonspherical distribution of charge about the given ion and its neighbors (6). Where rare earth ions can interact more complex effects may be expected.

Measurements

In general, the materials studied were in the form of crystallites not exceeding 1 mm in their major dimension. By filling a cavity 1 in. long by ½ in. wide by ¼ in. deep with these crystals, a sample of random orientation was obtained. Emission was excited by illuminating the samples with, alternately, a 3660Å rich H4 mercury spotlamp, a broadband longwave u.v. Mineralight or a 2537 Mineralight through a Corning 9863 filter. In general, the data presented were obtained under excitation from the H4 Spotlamp since fluorescence is much brighter with this source. In as far as possible, all of the relationships discussed have been confirmed by measurements employing the broadband longwave u.v. Mineralight.

Measurements were made with a Gaertner high dispersion spectrometer adapted with an AMINCO

[1] Melts containing about 30 mole % of the desired material and 70 mole % of the relevant alkali metal ditungstate or dimolybdate flux were cooled at about 5°C/hr from 1150°C.

photomultiplier microphotometer using a 931A tube. Ten micron slit widths were used at the entrance and exit to the spectrometer. The system was calibrated against a tungsten filament lamp whose output was assumed to behave as a black body. Data were obtained for both 300° and 77°K. Data for 300°K are employed where the dependences of brightness on temperature are small. Otherwise the 77°K data are employed.

The intensities reported are for the $^5D_0$ to $^7F_2$ transitions of Eu^{3+} (as measured for the emission of Eu^{3+} in the 6150Å region) and the $^5D_4$ to $^7F_2$ transitions of Tb^{3+} (as measured for the emission of Tb^{3+} in the 5450Å region). These values are relative to 100 for the 5450Å peak of $Na_{0.5}Tb_{0.5}WO_4$ in keeping with previous measurements (7). The above peaks are the most intense for the Eu^{3+} and Tb^{3+} ions in each structure discussed. Within the confines of a given structure, the intensities so obtained are proportional to the integrated emission from the same excited state. Photometric response spectra indicate approximately the same proportionality between the measured emission and the integrated emission for the different structures under consideration.

General

The dependence of the intensity of emission of Eu^{3+} on the size of the host structure cation has been reported previously (4, 8) for the series $M_{0.98}^{2+}Na_{0.01}Eu_{0.01}WO_4$ (where M = Ca, Sr, and Ba) and for the series $M_{0.5}^{+}Eu_{0.5}WO_4$ (where M = Li, Na, K, Rb, and Cs). Since the M^{2+} compositions all have the scheelite structure, the interaction distance between Eu^{3+} and its surroundings decreases with the lattice constants on going from Ba to Sr to Ca. Equivalently, one can infer that, since the Eu^{3+} ions occupy M^{2+} sites, the size of the hole in which Eu^{3+} finds itself decreases in the above order. Such a change is expected to produce an increase in binding energy whether considered from a coulombic (5), a covalent (9), or an empirical (10) point of view. Indeed, brightness increases approximately linearly with the reciprocal of the interaction distances between the M^{2+} ions and the neighboring oxygen ions for the M^{2+} series. In the $M_{0.5}^{+}Eu_{0.5}WO_4$ series, however, it is not possible to show a similar simple relationship. Here, structural changes, changes in polarization, and interactions between rare earth ions are involved. Nevertheless, it was found that under longwave u.v. excitation a linear relationship is obtained for both the M^+ and the M^{2+} series when the logarithm of the intensity of emission of Eu^{3+} is plotted against the volume (or cube of the radius-r^3) of the alkaline earth or alkali metal ions. This empirical relationship provides a useful starting basis for comparing the effects of environment on brightness. The above dependence for the $M_{0.98}^{2+}Na_{0.01}Eu_{0.01}WO_4$ series is shown in Fig. 1 along with data for a number of alkali metal rare earth tungstates which have comparable Eu^{3+} concentrations.

The M^{2+} ions in $M_{0.98}^{2+}Na_{0.01}Eu_{0.01}WO_4$ can be replaced by ½ M^+ plus ½ M^{3+} without changing the structure when the ions are comparable in size.

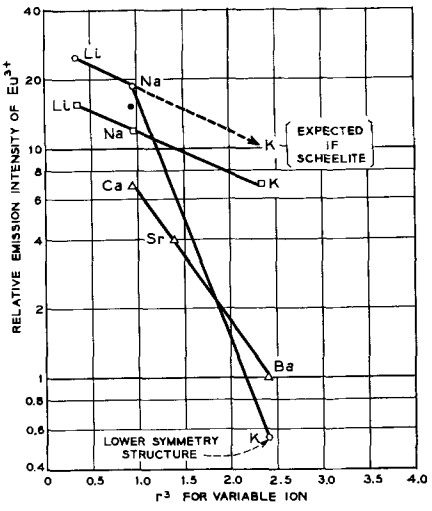

Fig. 1. Intensity of emission of Eu^{3+} as a function of r^3 for the variable ions under 3660Å excitation at 300°K. Open triangle, $M_{0.98}^{2+}Na_{0.01}Eu_{0.01}WO_4$; open square, $M_{0.5}^{+}La_{0.49}Eu_{0.01}WO_4$; open circle, $M_{0.5}^{+}Y_{0.49}Eu_{0.01}WO_4$; dark circle, $Na_{0.5}Gd_{0.49}Eu_{0.01}WO_4$.

For this to occur, the M^+ and M^{3+} ions must distribute themselves in a random fashion in the M^{2+} sites. However, on the average, each M^{3+} ion has more M^+ than M^{3+} ions in neighboring M^{2+} sites and *vice versa*. This is required to preserve short-range electrical neutrality. The distance between equivalently situated ions in $Na_{0.5}Gd_{0.49}Eu_{0.01}WO_4$ is about the same as that found in $Ca_{0.98}Na_{0.01}Eu_{0.01}WO_4$ as indicated by x-ray measurements. This may be expected as the radii of Na^+ (0.97Å, Gd^{3+} (0.97Å), and Ca^{2+} (0.99Å) are approximately equal (11).

On the basis of a hard sphere model, the contributions to electrostatic binding resulting from interactions between Eu^{3+} and the surrounding oxygen ions should be about the same in each of the above cases. But the ion-ion repulsion contributions between Eu^{3+} and the cations on the neighboring M^{2+} sites should be less in the sodium gadolinium composition. Consequently, Eu^{3+} should have a greater electrostatic binding energy in the sodium gadolinium than in the calcium composition. In keeping with the trend for brightness to increase with the electrostatic binding energy of Eu^{3+}, its intensity of emission in the sodium gadolinium composition is about twice that in the calcium composition.

The Na and K compositions of the $M_{0.5}^{+}La_{0.49}Eu_{0.01}WO_4$ series (Fig. 1) have the scheelite structure, whereas the Li compound does not. The indicated value for $Li_{0.5}La_{0.49}Eu_{0.01}WO_4$ is an estimate of the intensity of emission that Eu^{3+} would have if the indicated composition had the scheelite structure. This estimate was obtained by taking the ratio of the intensity for Eu^{3+} in $Li_{0.5}La_{0.4}Eu_{0.1}WO_4$ to that in $Na_{0.5}La_{0.4}Eu_{0.1}WO_4$ (both of which have the scheelite structure) and increasing the value obtained for $Na_{0.5}La_{0.49}Eu_{0.01}WO_4$ (which has the scheelite structure) by this factor.

The difference in slopes of the La^{3+} series and the M^{2+} series in Fig. 1 is at least in part due to the fact that only ½ of the ions in the M^{2+} sites are

varied in the La^{3+} series. The decrease in brightness with increasing r^3 may be associated with an increase in interionic distance as for the M^{2+} series. In the La^{3+} series, the size of all of the M^{2+} sites tend to increase with the average size of their occupants.

The intensities of emission of Eu^{3+} in the series $M_{0.5}{}^{+}Y_{0.49}Eu_{0.01}WO_4$ (where M = Li, Na, and K) are also shown in Fig. 1. The Li and Na compositions have the scheelite structure. The structure of the K composition, however, appears to be triclinic (4). The data for the Li and Na compositions of the yttrium series indicate a slope that is approximately parallel to that obtained for the lanthanum series. An extrapolation to the value expected for $K_{0.5}Y_{0.49}Eu_{0.01}WO_4$ (presuming a scheelite structure) is shown by the broken line. The intensity of emission of Eu^{3+} in the actual composition, however, is far weaker than the above extrapolation indicates. The marked decrease in brightness appears to be related directly to the change in structure. A study of the intensities of emission of Eu^{3+} in Ca and Cd tungstates and molybdates given elsewhere (8) has shown that there is a comparable large decrease in brightness on going from the scheelite structure to the monoclinic Ferberite structure. Eu^{3+} has eight neighboring oxygen ions in the former and only six in the latter. In keeping with the trend obtained so far, the reduction in the number of oxygen ions that are immediate neighbors of Eu^{3+} may effect a decrease in the binding energy of this ion. It is possible that a similar reduction in the number of neighboring oxygen ions occurs in $K_{0.5}Y_{0.49}Eu_{0.01}WO_4$.

Polarization

The hard sphere model considered so far does not take into account changes in binding energy that may result from changes in the polarization of the electron clouds about the oxygen ions which surround Eu^{3+}. It may be expected that, even though the lattice constants remain essentially the same, replacing Ca^{2+} ions by Na^+ and M^{3+} ions in the scheelite structure will cause the oxygen ions to be polarized to a greater extent toward Eu^{3+}. This is due to a reduction of the average charge on the cations in the neighboring M^{2+} sites. Such an increase in polarization can reduce the electrostatic binding energy between ions as a result of increased electron-electron repulsion. This is expected to be the case for interactions between the oxygen ions and the rare earth ions, since the nuclei of both are well shielded by their respective electron clouds. It can be inferred from Fig. 1 that the increased polarization of the oxygen ions toward Eu^{3+} (resulting from replacing M^{2+} ions with $M^+ + M^{3+}$ ions) does not override the effect of reducing the average charge of the ions in the neighboring M^{2+} sites in the tungstates.

It is possible to obtain more direct information concerning the effect of polarization by avoiding a change in the size or formal charge of the neighboring cations. This can be done by comparing the intensities of emission of Eu^{3+} or Tb^{3+} in tungstates and molybdates that have similar structures. Hexavalent tungsten and hexavalent molybdenum are considered to have equivalent ionic radii (0.62Å for six coordination and 0.59Å for four coordination) (11). The compositions in which the hexavalent metal ions have the lower electronegativity should show an increased polarizability of the anionic complexes. This occurs for the molybdates as indicated by the higher refractive indices (13) of $CaMoO_4$ (1.974 and 1.978) than that of $CaWO_4$ (1.918 and 1.934). Specific comparisons of the effects of polarization on brightness in the tungstates and molybdates, however, cannot be clearly drawn without first gaining some insight into the dependences of the intensity of emission of Eu^{3+} and Tb^{3+} on concentrations and the excitation processes involved.

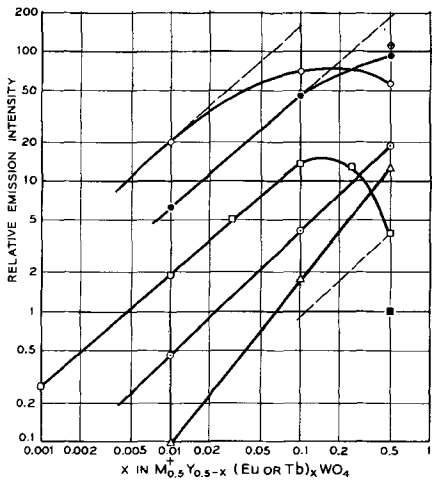

Fig. 2. Intensity of emission of Eu^{3+} or Tb^{3+} as a function of its concentration under 3660Å excitation. The data are for 300°K except for the point for $Cs_{0.5}Tb_{0.5}WO_4$ which is for 77°K.

	M^+	RE		M^+	RE
Circled plus	Li	Tb	Open triangle	Rb	Eu
Open circle	Na	Eu	Open square	Cs	Eu
Closed circle	Na	Tb	Closed square	Cs	Tb
Dotted circle	K	Eu			

Concentration Dependencies—Tungstates

Figure 2 shows the dependence of the intensity of emission of Eu^{3+} and Tb^{3+} on concentration for a number of alkali metal rare earth tungstates (7, 12, 14). The line for the $K_{0.5}Y_{0.5-x}Eu_xWO_4$ series has a slope of a little less than one. Such a slope can be expected where the fluorescing ions are excited only directly or from fixed volumes of their surroundings. There is a decrease in the availability of excitation to Eu^{3+} ions other than those in the surface layer as concentration increases. Dashed lines parallel to the curve for the $K_{0.5}Y_{0.5-x}Eu_xWO_4$ series are provided to facilitate comparison of the other curves to this one. The series $Na_{0.5}Y_{0.5-x}Eu_xWO_4$ and $Na_{0.5}Y_{0.5-x}Tb_xWO_4$ show negative deviations from the reference slope at high rare earth concentrations. Here the fluorescing levels of Eu^{3+} and Tb^{3+} are increasingly perturbed by increasing the concentration (7) of these ions. The resulting decrease in emission per rare earth ion is termed self-quenching. The greater self-quenching of Eu^{3+} as compared to that for Tb^{3+} is associated with a stronger coupling between the f-electrons of Eu^{3+} and the host structure. This in turn may be attributed to

the smaller gap in energy between the excited state and the ground manifold of Eu^{3+} than for Tb^{3+} (15, 16).

Self-quenching, as discussed herein, is not due to a rise in self-absorption of emission. This is shown by Tb^{3+}, for example (17), in the series $Ca_{1-2x}Na_xTb_xWO_4$. Here Tb^{3+} emits strongly from two excited states. As the concentration of Tb^{3+} increases above $x = 0.01$, the emission from the level lying higher in energy quenches (equally for all transitions). At the same time, emission from the lower level is enhanced. It receives part of the excitation lost from the upper level. Self-absorption, in general, only occurs for resonance transitions. The weakest emission transition from the upper level of Tb^{3+} is the only one in a position to excite transitions from the ground states of other Tb^{3+} ions to their lower excited levels. A comparable sequential quenching of the four emitting states of Eu^{3+} with increasing concentration is found in the series $Ca_{1-2x}Na_xEu_xWO_4$ (7). In general, the levels which lie higher in energy suffer self-quenching at lower concentrations.

In the series $Rb_{0.5}Y_{0.5-x}Eu_xWO_4$ (Fig. 2) the intensity of emission of Eu^{3+} increases faster than its concentration, the slope being approximately two. Slopes of greater than one arise as the absorption edge of the host structure is approached. They may be attributed to a reduction in the energy required to excite charge transfer processes as the absorption edge of the host structure moves to lower frequencies with increasing rare earth concentration. The edge lies in the neighborhood of 3000Å in the above Rb compositions, 2800Å in the comparable Li, Na, and K compositions, and 3400Å in the Cs compositions.

The series $Cs_{0.5}Y_{0.5-x}Eu_xWO_4$ shows a large negative deviation from linearity at high Eu^{3+} concentrations. This abrupt decrease in brightness is due to an increase in the interactions between the Eu^{3+} ions in a manner similar to that which occurs in self-quenching. However, in this case, quenching is not due to the excessive perturbation of the excited f-electrons of Eu^{3+} but to a decrease in the energy received by Eu^{3+} from the host structure (12). The processes by which a host structure captures energy in insulating crystals have been discussed in detail by Kroger (2) and by Wannier (18). Herein they will be referred to as "lattice" processes. Energy gained through these processes is subject to degradation by interaction with the phonon spectrum, which may result in its dissipation before it can be communicated to the fluorescing ions. As can be seen from Fig. 2, "lattice" processes enhance the intensity of emission per Eu^{3+} ion by a factor of 15 (up to x—0.10) in the series $Cs_{0.5}Y_{0.5-x}Eu_xWO_4$ under 3660Å excitation. In comparison, when the same materials are excited within the absorption edge of the host structure by the 2537 Mineralight, an enhancement by a factor of about 2000 is obtained (12). Under each excitation, the contribution to the emission of Eu^{3+} due to lattice processes fall off above $x = 0.10$. This shows that the extent to which the energy captured by

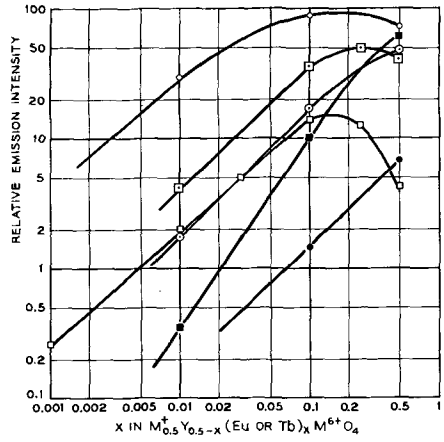

Fig. 3. Intensity of emission of Eu^{3+} or Tb^{3+} on concentration under 3660Å excitation at 77°K.

	M^+	RE	M^{6+}		M^+	RE	M^{6+}
Closed circle	Li	Eu	W	Open square	Cs	Eu	W
Dotted circle	Li	Eu	Mo	Dotted square	Cs	Eu	Mo
Solid Circle	Na	Tb	Mo	Solid square	Cs	Tb	Mo

the lattice is degraded by phonon processes increases with Eu^{3+} concentration. In a similar manner there is an enhancement of Eu^{3+} emission by a factor of 2 for the members of the series $Rb_{0.5}Y_{0.5-x}Eu_xWO_4$ under broadband longwave u.v. (up to x—0.25) which is not present under 3660Å excitation. This is excited by the short-wave components of the broadband u.v. source. A much greater enhancement is obtained under 2537Å excitation.

It is helpful to point out again that, in the absence of lattice processes, the intensity of emission of Eu^{3+} or Tb^{3+} increases with its binding energy. However, the contributions to the emission of Eu^{3+} (or Tb^{3+}) resulting from lattice processes decrease with increasing binding energy. Thus, brightness can vary in either direction with binding energy.

Comparisons

Concentration curves.—Figure 3 shows the dependences of the intensity of emission of Eu^{3+} or Tb^{3+} on its concentration for a number of alkali metal rare earth tungstates and molybdates. It can be seen that the self-quenching of Eu^{3+} is much less severe in the $Li_{0.5}Y_{0.5-x}Eu_xMoO_4$ series than for the comparable tungstates. Further, the intensities of emission of Eu^{3+} in the dilute region of the molybdates are about an order of magnitude weaker than in the comparable tungstates. Since lattice processes are not dominant in these series, the differences observed may be attributed to a smaller binding energy for the Eu^{3+} ions in the molybdates.

A comparison of the series $Cs_{0.5}Y_{0.5-x}Eu_xWO_4$ and $Cs_{0.5}Y_{0.5-x}Eu_xMoO_4$ (in Fig. 3) shows that the intensity of emission of Eu^{3+} in the molybdate series is greater by a factor of two than that in the tungstate series under 3660Å excitation. Furthermore, the contributions of the lattice processes are not as strongly quenched by increasing Eu^{3+} concentration in the molybdates. These relationships are also in keeping with a smaller binding energy in the latter.

Rather marked changes in the intensity of emission of Tb^{3+} occur on going from the tungstates to the comparable molybdates. A comparison of Fig. 2 and 5 shows that at 77°K $Li_{0.5}Tb_{0.5}WO_4$ is twenty times brighter than $Li_{0.5}Tb_{0.5}MoO_4$, and $Cs_{0.5}Tb_{0.5}MoO_4$ is sixty times brighter than $Cs_{0.5}Tb_{0.5}WO_4$. These changes are much larger than those observed for Eu^{3+} (1.5 and 10 respectively). The pronounced changes observed for Tb^{3+} are consistent with the weaker coupling of its f-electrons to the environment (15). This is also indicated by the slope of three obtained for the $Cs_{0.5}Y_{0.5-x}Tb_xMoO_4$ series. The ability of Tb^{3+} to derive energy from lattice processes increases with its concentration. The opposite is true for Eu^{3+} which is more strongly coupled to the environment. As previously indicated, increasing the concentration of Eu^{3+} in the $Cs_{0.5}Y_{0.5-x}Eu_x$ WO_4 series (above x = 0.1) results in a reduction in the contribution of lattice processes to the emission of Eu^{3+}.

The $M_{0.5}{}^{+}Y_{0.5-x}Eu_xWO_4$ *series.*—Figure 4 presents a comparison of the intensities of emission of the members of the series $M_{0.5}{}^{+}Eu_{0.5}WO_4$ and $M_{0.5}{}^{+}$ $Y_{0.4}Eu_{0.1}WO_4$ under 3660Å excitation and excitation from the 2537Å Mineralight. The intensity data are plotted against r^3 for the variable ion as in Fig. 1. There is an approximately logarithmic dependence of brightness on r^3 for the $M_{0.5}{}^{+}$ $Eu_{0.5}WO_4$ series under 3660Å excitation, but not for the $M_{0.5}{}^{+}Y_{0.4}Eu_{0.1}WO_4$ series. The relatively high intensity for the $Cs_{0.5}Y_{0.4}Eu_{0.1}WO_4$ composition is, at least in part, due to enhancement of Eu^{3+} emission by lattice processes as discussed in connection with Fig. 2. The large increases in relative brightness for Eu^{3+} in this and the comparable Rb composition under excitation from the 2537 Mineralight are due to an increase in lattice processes. This results from exciting the host structures within their continuous absorption regions. Lattice processes do not appear to enhance emission from Eu^{3+} in the Li, Na, and K compositions of the $Eu_{0.1}$ series.

In the $M_{0.5}{}^{+}Eu_{0.5}WO_4$ series enhancement of emission due to lattice processes does not appear to occur under 3660Å excitation. However, it does under excitation from the 2537 Mineralight.[2] In both the $Eu_{0.1}$ and $Eu_{0.5}$ series the contributions of lattice processes to the emission of Eu^{3+} are seen to decrease with decreasing r^3.

The fact that the intensities of emission of the several compositions of the $M_{0.5}{}^{+}Eu_{0.5}WO_4$ series under 3660Å excitation come close to falling on the same line might be considered coincidental. A number of structure changes occur in this series (4) and self-quenching effects are quite strong for the Li and Na compositions. However, the above relationship follows a definite trend for brightness to decrease with increasing electron-electron repulsion between Eu^{3+} and its neighboring oxygen ions. In each composition of this series, Eu^{3+} essentially determines its own site size. Hence, the interaction distance of Eu^{3+} with its surrounding oxygens is

[2] The relatively constant brightness of Eu^{3+} for this series under excitation from the 2537 Mineralight was formerly (4) attributed to excitation within the continuous absorption region of Eu^{3+}. However, such an explanation is not consistent with the variations in the $x = 0.1$ series.

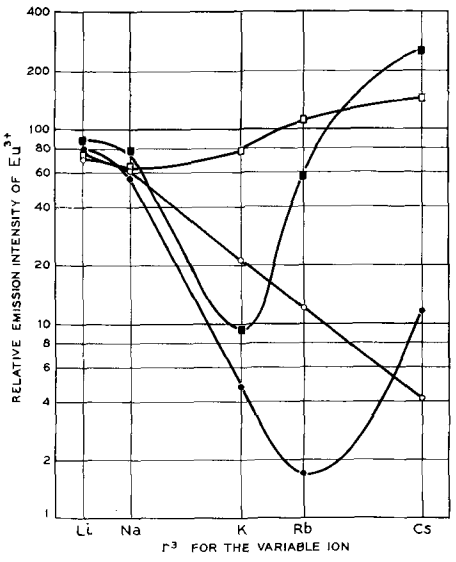

Fig. 4. Intensity of emission of Eu^{3+} as a function of r^3 for the variable ions in the indicated series under 3660Å excitation and excitation from the 2537 Mineralight at 300°K: open circle, $M_{0.5}{}^{+}Eu_{0.5}WO_4$ 3660Å; solid circle, $M_{0.5}{}^{+}Y_{0.4}Eu_{0.1}WO_4$ 3660Å; open square, $M_{0.5}{}^{+}Eu_{0.5}WO_4$ 2537; solid square, $M_{0.5}{}^{+}Y_{0.4}Eu_{0.1}$ WO_4 2537.

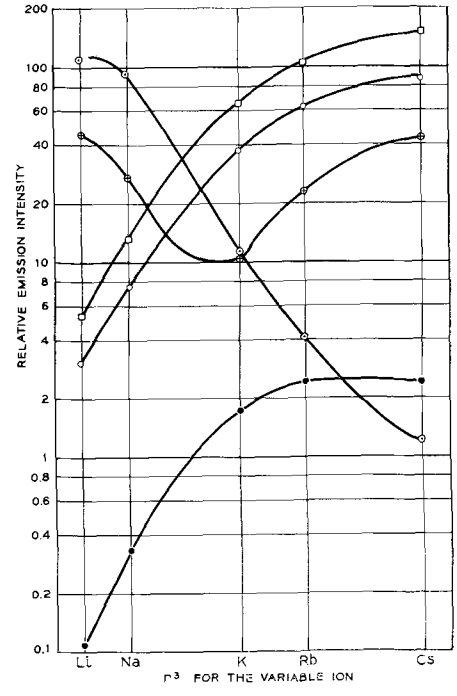

Fig. 5. Intensity of emission of Eu^{3+} or Tb^{3+} as a function of r^3 for the variable ions in the indicated series under 3660Å excitation. Circled plus, $M_{0.5}{}^{+}Eu_{0.5}MoO_4$, Eu —77°K; dotted circle, $M_{0.5}{}^{+}$ $Tb_{0.5}WO_4$, Tb —77°K; open circle, $M_{0.5}{}^{+}Tb_{0.5}MoO_4$, Tb —77°K; solid circle, $M_{0.5}{}^{+}Tb_{0.5}MoO_4$, Tb —300°K; open square, $M_{0.5}{}^{+}$ $Tb_{0.45}Eu_{0.05}MoO_4$, Eu —77°K.

in part determined by the ability of the alkali metal ions present to polarize the $WO_4{}^{2-}$ anions towards themselves. This ability decreases as the radius of the alkali metal ion increases. The polarization of the $WO_4{}^{2-}$ anions toward the Eu^{3+} ions and the effects of the interactions that occur between Eu^{3+} ions on their coupling to the environment seem to be more important than structural considerations in determining brightness in the $Eu_{0.5}$ series. Since

the interactions between Eu^{3+} ions are not effective in the dilute materials, structural factors are of increased importance in the x—0.10 and 0.01 series.

Comparisons-vs. r^3.—Figure 5 provides a comparison of the dependences of the intensity of emission of Tb^{3+} and/or Eu^{3+} on r^3 for the variable ions in the series $M_{0.5}{}^{+}Eu_{0.5}MoO_4$, $M_{0.5}{}^{+}Tb_{0.5}WO_4$, $M_{0.5}{}^{+}Tb_{0.5}MoO_4$, and $M_{0.5}{}^{+}Tb_{0.45}Eu_{0.05}MoO_4$ under 3660Å excitation. The data for the $Mo_{0.5}{}^{+}Eu_{0.5}MoO_4$ series show a dependence on r^3 that may be considered to be similar in character to that for the comparable tungstates under excitation from the 2537 Mineralight (Fig. 4). This is due to the absorption edges of the molybdates lying in the 3400-3600Å region. It is readily seen that the intensity of emission of Tb^{3+} in the tungstates follows the trend of the series $M_{0.5}{}^{+}Eu_{0.5}WO_4$ (and of the members of the $M_{0.5}{}^{+}Eu_{0.5}MoO_4$ series which have the smaller values of r^3) while that for Tb^{3+} in the molybdates follows the trend of the members of the $M_{0.5}{}^{+}Eu_{0.5}MoO_4$ series which have the larger values of r^3. These relationships show that the coupling of the rare earth ion to the host structure (as determined by the binding energy, polarization, and concentration effects) is the dominant factor controlling the intensity of emission of Tb^{3+} (as well as that for Eu^{3+}) in the tungstates. In the molybdates, (the coupling of Tb^{3+} being considerably weaker) the contributions of lattice processes are dominant for the entire series.

The data for the $M_{0.5}{}^{+}Tb_{0.45}Eu_{0.05}MoO_4$ series of Fig. 5 show that energy acquired by Tb^{3+} can be transferred to and emitted by Eu^{3+} in the molybdates as well as in the tungstates (19).

Temperature Dependencies

The data for the $M_{0.5}Tb_{0.5}MoO_4$ series of Fig. 5 are plotted for 300°K as well as for 77°K. It is apparent that the intensity of emission of Tb^{3+} under 3660Å excitation increases by a factor of approximately 25 on going from 300° to 77°K. The comparable factor ranges from 1.0 to 3.0 with increasing r^3 in the tungstate series. The difference in the temperature dependence of the two series is due to a difference in excitation processes. Lattice processes are not dominant in the tungstates, but they are in the molybdates. Hence, the degradation of excitation energy by interaction of excited states of the host structure with the phonon spectrum can greatly diminish the availability of energy to the Tb^{3+} ions in the molybdates. Lowering the temperature reduces competition from this source and, consequently, increases the availability of excitatior to Tb^{3+}. The effect of temperature on the intensity of emission of Eu^{3+} in the comparable molybdates is much smaller. This may be associated with the stronger coupling between Eu^{3+} and the host structure.

Summary

Employing a hard sphere ionic model, the intensity of emission of Eu^{3+} has been shown to vary with its electrostatic binding energy in the tungstates which have the scheelite structure when the Eu^{3+} is present in low concentrations. A relatively direct comparison of the effects of charge induced polarization of the anionic groups on the binding energy of Eu^{3+} and Tb^{3+} has been obtained for tungstates and molybdates which have similar structures. The ions, Mo^{6+} and W^{6+}, have equal radii and, hence, the substitution of one for the other can be made without changing structure, ion size, or charge type. However, the $MoO_4{}^{2-}$ groups are more polarizable than the $WO_4{}^{2-}$ groups. An increase in electron-electron repulsion between the oxygens and their neighboring rare earth ions in the molybdates (due to a greater charge induced polarization) reduces the coupling of Eu^{3+} or Tb^{3+} to their surroundings. Increasing the concentration of Eu^{3+} or Tb^{3+} acts to increase the ease with which these ions interact with each other and with the surroundings. This can result in self-quenching, an increase in emission per Eu^{3+} or Tb^{3+} ion with concentration, or the quenching of lattice processes.

Acknowledgments

The author wishes to thank R. R. Soden for preparing the materials considered herein and Miss A. D. Mills for providing x-ray data. He is particularly indebted to F. J. Schnettler, A. D. Liehr, and A. P. Ginsberg for helpful comments on the manuscript.

Manuscript received March 6, 1962; revised manuscript received July 10, 1962. This paper was prepared for delivery before the Los Angeles Meeting, May 6-10, 1962.

Any discussion of this paper will appear in a Discussion Section to be published in the December 1963 JOURNAL.

REFERENCES

1. F. Varsanyi and G. H. Dieke, *Phys. Rev. Letters*, **7**, 442 (1961).
2. F. A. Kroger, "Some Aspects of the Luminescence of Solids," Elsevier Publishing Co. Inc., New York (1948).
3. L. G. Van Uitert and R. R. Soden, *J. Chem. Phys.*, **31**, 328 (1960).
4. L. G. Van Uitert and R. R. Soden, *ibid.*, **36**, 517 (1962).
5. See, for example, "Introduction to Solid State Physics," C. Kittel, J. Wiley & Sons, Inc., London (1956).
6. G. E. Kimball and E. M. Loebl, *J. Chem. Ed.*, **36**, 233 (1959).
7. L. G. Van Uitert, *This Journal*, **107**, 803 (1960).
8. L. G. Van Uitert, *J. Chem. Phys.*, **37**, 981 (1962).
9. See, for example, "Valence," C. A. Coulson, Oxford, The Clarendon Press, London (1952).
10. See, for example, A. D. Walsh, *J. Chem. Soc. London*, **1949**, 398.
11. L. H. Ahrens, *Geochim. et Cosmochim. Acta*, **2**, [3] (1952).
12. L. G. Van Uitert, R. R. Soden, and R. C. Linares, *J. Chem. Phys.*, **36**, 1793 (1962).
13. "Handbook of Physics," E. V. Condon and H. Odishaw, Editors, McGraw Hill Book Co., Inc., New York (1958).
14. L. G. Van Uitert and R. R. Soden, *J. Chem. Phys.*, **36**, 1289 (1962).
15. G. H. Dieke and L. A. Hall, *ibid.*, **25**, 465 (1957).
16. L. G. Van Uitert and S. Iida, *ibid.*, **37**, 986 (1962).
17. L. G. Van Uitert and R. R. Soden, *ibid.*, **32**, 1161 (1960).
18. G. H. Wannier, *Phys. Rev.*, **52**, 191 (1937).
19. L. G. Van Uitert and R. R. Soden, *J. Chem. Phys.*, **36**, 1289 (1962).

Properties of Twin Boundaries in Silicon

H. J. Queisser

Shockley Transistor, Unit of Clevite Transistor, Palo Alto, California

ABSTRACT

Twin boundaries in a crucible-grown silicon crystal are investigated. A specimen was found to contain both low-energy boundaries in (111)-planes and high-energy boundaries in (221)-planes. This structure resulted from simultaneous twinning on the four lower octahedral planes during pulling along a [100]-growth axis. P-n junction diodes show "soft" reverse characteristics at the high-energy boundaries. This is attributed to precipitates. Neither preferential "softness" nor precipitation is detected on the (111)-boundaries. Neither boundary gives any enhancement of impurity diffusion.

Structural imperfections are of importance for performance and reliability of solid-state devices. One particular two-dimensional imperfection in a crystal is the twin boundary. Presented in this paper are some investigations concerning twin boundaries and their influence on structure and behavior of silicon devices.

Twinning is a phenomenon frequently observed in silicon. Several papers have dealt with the crystallographic structure of twin boundaries (1-6). The most common boundary between two twins lies in a (111)-plane. Figure 1 shows a model of this boundary, which is often called "first-order" or "coherent" boundary. It is seen that the two grains are mirror images of each other. No dislocations, broken or distorted bonds are required for this boundary. It is obvious from Fig. 1 that the atoms at the boundary violate only second-nearest neighbor relations. Therefore, it is plausible that the energy to create this twin boundary must be low, hence the frequent occurrence of this twin boundary.

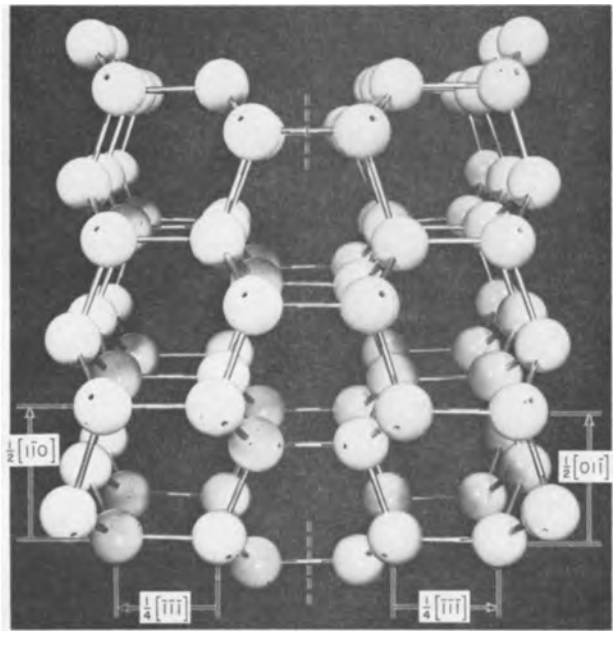

Fig. 1. Coherent, low-energy twin boundary in the diamond lattice. Boundary plane is mirror plane, it is (111)-plane for both grains. Common $[10\bar{1}]$-direction goes into paper.

Besides this low-energy fault, there are several other possible boundaries with higher energies, often generally categorized as "incoherent" or "high-order" twin boundaries. Kohn (1, 2) and Hornstra (3) have discussed these boundaries in detail. One particular type of boundary will be of interest for our investigations. This structure is called "second order twin join" by Kohn (2). Such a "join" is the interface between two grains ("individuals") which are in nonparallel first-order (111)-twin relations to a third individual. Kohn shows that three such second-order joins exist in the diamond lattice. He does not discuss the structure of these joins in terms of dislocations. Hornstra (3), on the other hand, maintains that all twin boundaries are only special cases of generalized grain boundaries, which are formed by regular arrays of dislocations.

This paper reports various measurements made on an unusual, twinned silicon crystal. The specimen showed very regular boundaries; both the coherent (111)-boundary and a second-order join were found within otherwise perfect crystalline material. Thus the crystal was particularly suitable for investigations of the two different kinds of boundaries. In the following, we shall first describe the structure of the sample and speculate about the causes of its peculiar growth. Measurements concerning electrical properties as well as precipitation and diffusion will be discussed next. Comparison with the structural models and some implications concerning p-n junction behavior at these boundaries conclude this paper.

Experimental

Description of the samples.—A silicon single crystal was grown with a [100] pull axis, utilizing the Czochralski technique (6, 7) with a quartz crucible. Some uncontrolled interference during the early stages of the growth process resulted in simultaneous twinning on the four lower octrahedral (111)-planes. This gave four coherent twin-boundaries propagating toward the axis as the pulling proceeded.

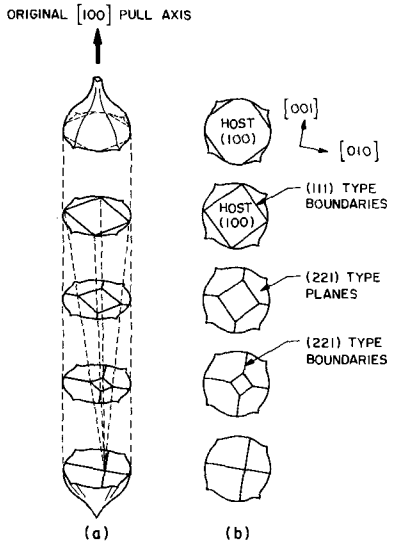

Fig. 2. (a), Sketch of silicon crystal with grown-in twin boundaries; (b), cross sections of crystal at different growth levels.

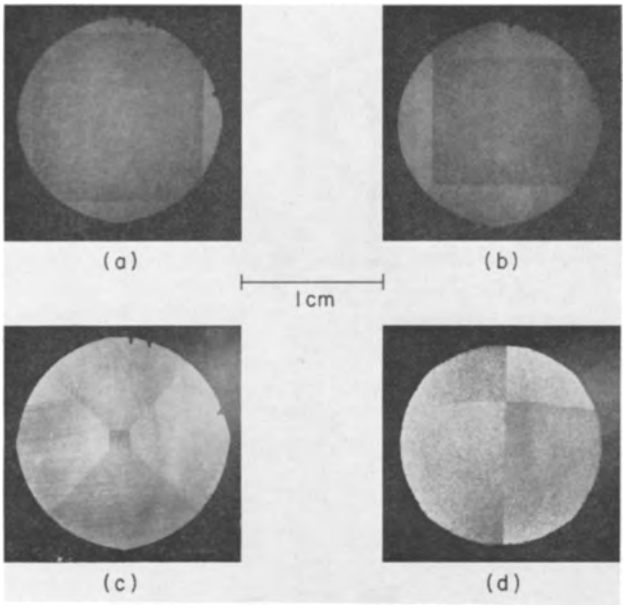

Fig. 3. Photographs of crystal slices with twin boundaries, corresponding to drawings of Fig. 3.

Figure 2 (a) illustrates this situation. As the four boundaries moved inward, four new boundaries were created. These are the interfaces between two adjacent twins, each of which is in a coherent twin-relation to the original crystal. We thus have created[1] four second-order joins, using Kohn's terminology (1, 2). The coherent boundaries vanish after meeting at a common point on the crystal axis. The four high-energy joins are left "locked" into the crystal. Figure 2(b) further illustrates this development by showing the cross sections of slices at different levels of the grown crystal. Figure 3 shows photographs of lapped slices, corresponding to the drawings of Fig. 2(b).

The growth of this unusual crystal was accidental. The unique character of the sample was not discovered until after slicing of the crystal boule. It may be speculated that a temperature shock or

[1] This is an experimental verification of Kohn's idealized drawing; see Fig. 4 of ref. (1).

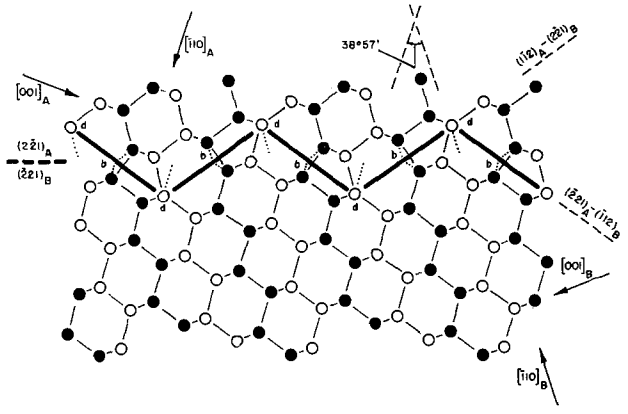

Fig. 4. Structure of the (221)-type second-order twin join after Kohn (1,2). A and B refer to the two individuals of the twin. Bonds are distorted at points d and b. [Reproduced from ref. (2), courtesy of Mineral. Soc. of America].

an inadvertent sudden contamination of the melt led to the simultaneous twinning (6). Such simultaneous twinning had frequently been found after deliberate introduction of "alloying mixtures" (8) into silicon melts. Although this seems a likely explanation, our data as well as those in the literature (8) are not sufficient to permit a conclusive statement.

The crystallographic evaluation of the slices was done first, roughly, by observing the slip patterns introduced by boron-diffusion (9). A complete evaluation was then done with x-ray techniques.[2] It was established that the initial twinning occurred along (111)-planes. The second-order joins were found to be of the $(2\bar{2}1)$-$(\bar{2}21)$ type. Both Kohn (1, 2) and Hornstra (3) give models for this type of twin boundary. Figure 4 is a reproduction of Kohn's proposal. It shows a zig-zag discontinuity with a resulting direction along $(2\bar{2}1)$ of twin individual A and $(\bar{2}21)$ of individual B. Arrays of nets with consecutively five and seven atoms are formed. No "dangling bonds" are necessary, but, as shown in the sketch, some bonds have to be distorted. Kohn does not speak of dislocations forming this boundary. Hornstra (3) derives a structure identical to Fig. 4, but discusses it in terms of a closely spaced zig-zag array of dislocations. He presents an alternative model for this second-order twin, which consists of overlapping double dislocations. This model is shown in Fig. 5.

Electrical Properties

Slices from the crystal were cut perpendicular to the pull axis. They were then lapped and finally polished with Linde A. The average electrical resistivity of the specimen was 1.5 ohm-cm, p-type. The doping element was boron.

Photoscanning measurements (10) were done with a light spot of 25μ diameter. Such measurements can give useful information about magnitude and type of conductivity of boundaries in semiconductors. For example, germanium grain boundaries show photovoltages of a polarity which are thought

[2] We are very much indebted to Mr. William R. Cook of the Electronic Research Division, Clevite Corporation, Cleveland, Ohio, who kindly performed these investigations.

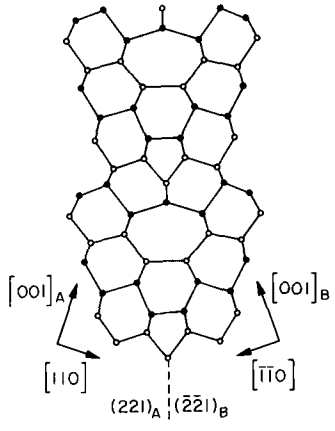

Fig. 5. Alternative structure of (221)-type second-order twin boundary after Hornstra (3), assuming double dislocations. (Reproduction by courtesy of "Physica.")

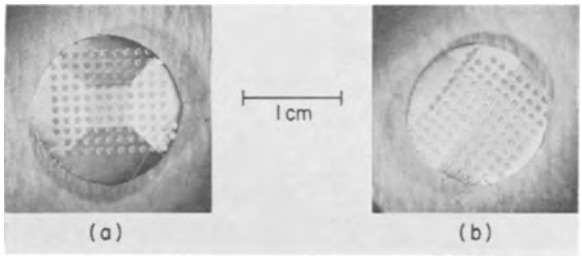

Fig. 6. Etched mesa-diodes on slice with different twin boundaries

to reveal the acceptor character of the dangling bonds in the boundaries. In our experiments, no photovoltage was measurable on either type of twin boundary (limit of detection about 10^{-6}v). Conclusions from this result should be drawn with caution, since boundaries in silicon seem to show photoeffects different from those in germanium (11). However, the absence of a photoresponse on the high-energy boundary indicates that this boundary is probably not made up of dislocations with dangling bonds. The lack of a photoresponse on the "coherent" twin boundary is to be expected from its small lattice disturbance.

P-n junction diodes were produced by diffusing phosphorus from a P_2O_5 source into the slices at 950°C for 1 hr. Mesa diodes were etched by means of wax masking techniques. Care was taken to obtain as many mesas as possible that included the boundaries. Figure 6 shows photographs of the mesa diode arrays on two slices. The (221)-boundaries are perpendicular to the plane of the p-n junction, whereas the (111)-boundaries intersect the junction at an angle of approximately 55°.

The properties of the p-n junctions were investigated by measuring the reverse characteristics of the diodes. The mesas are classified as either regular or containing the coherent boundary or the second-order join. A distinction in junction behavior is made by calling a junction "soft" or "hard." "Softness" (13) means that before avalanche breakdown is reached, a comparatively large (in our case > 1 ma) reverse current is flowing through the diodes. This "softness" is an undesirable feature and usually constitutes a device failure mechanism.

Table I. Evaluation of diodes with and without twin boundaries

Reverse current at 90% of breakdown voltage	<1 μa "hard," %	~1 μa, %	~10 μa, %	~100 μa, %	>1 ma "soft," %
Diodes on (221) boundary	30	—	21	10	39
Diodes on (111) boundary	100	—	—	—	—
Regular diodes	83	3	11	—	3

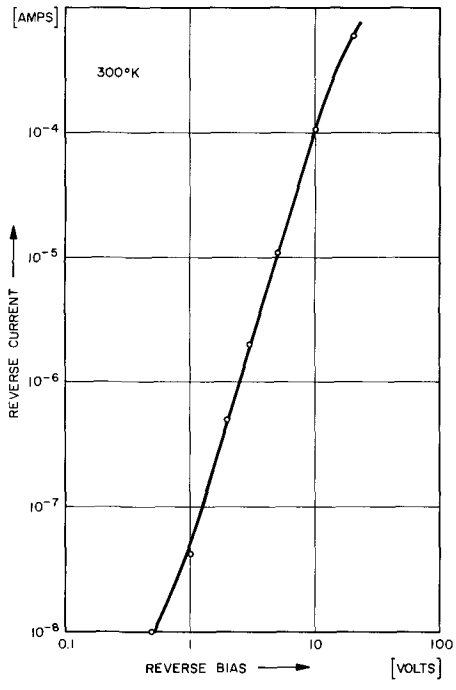

Fig. 7. Reverse characteristic of a soft diode on a (221)-boundary, exhibiting the V^n-dependence of current on voltage which is typical for metal precipitates (8).

Some typical results are shown schematically in Table I. It is seen that diodes on the coherent boundary were in all cases hard, as were most of the devices on the regular material. On the other hand, the diodes, which incorporated the high-energy boundary, show a higher percentage of softness. The reverse currents for these diodes were definitely higher than the average for the slice. From this set of measurements and similar ones on other slices we conclude the following. P-n junctions which incorporate a high-energy twin boundary are very susceptible to softness. Coherent boundaries do not have such a deleterious influence.[3] It is probable that the softness has been caused by metallic impurities in precipitated form (13). Detailed measurements of soft reverse characteristics support this hypothesis. Figure 7 shows, that the reverse current has a voltage dependence of approximately $V^{3.5}$. This is a dependence typical for metal precipitates (13). "Gettering" with glassy oxide layers is known (13) to harden such soft devices. Some diffusion runs under these gettering conditions yielded hard diodes on the (221)-boundaries as well. This proves that the softness is not caused by the structure of the boundary itself. By copper decoration and infrared microscopy

[3] E. Billig and M. S. Ridout, ref. 12 [*Nature*, 173, 496 (1954)] have also shown that coherent boundaries in germanium have no detrimental effects on electrical properties.

techniques (14) it was found that there is a tendency for preferential precipitation along the (221)-boundaries. No decoration was found on the (111)-twin boundary, in accordance with previous results (15). It is thus very likely that the difference in precipitation behavior explains the different susceptibility for softness of p-n junctions.

The forward current-voltage characteristics of diodes on high-energy boundaries show one peculiarity. These diodes obey a relation between current I and voltage V of the form

$$I = I_o' [\exp (qV/AkT) - 1] \qquad [1]$$

where q is the electronic change, kT the Boltzmann constant times absolute temperature, and I_o' a fitting parameter. Theory predicts (16) the parameter A to take values between 1 and 2, but these diodes show A-values of about 3. Similar deviations in the forward characteristics have been found with silicon solar cells; one hypothesis offered to explain these anomalies on solar cells involved the assumption of precipitates (17). The results on these twin boundary diodes thus seem to substantiate this hypothesis. Preliminary results, obtained in this laboratory with small angle grain boundaries, also indicate high A-values in connection with precipitates.

Diffusion along Twin Boundaries

Coherent twin boundaries are reported to show no anomalies for impurity diffusion (18). Several control experiments were performed with the silicon twin crystal described here. The techniques of previous grain-boundary investigations (19) were applied. No enhancement was found. Again, in view of the smallness of the disturbance which is introduced by the coherent boundary, this negative result is not surprising.

It is, however, not immediately obvious what kind of diffusion behavior should be anticipated at the high-energy second-order twin boundaries. If one considers these boundaries as being closely related to the artificially grown symmetrical grain boundaries, one should expect a diffusion enhancement similar to the one observed on the latter structures (19). It is, however, important to consider the strain field built up by the boundary, since the Cottrell-attraction of the dislocations has been shown to be a decisive factor for the diffusion enhancement at grain boundaries (19). Twin boundaries can be regarded as symmetrical grain boundaries with distinct angles of misfit. The grain boundary energy has minima at these angles (20). This means that the strain field must fall off more rapidly with distance from the boundary than for grain boundaries with a slightly differing angle of misfit. The "dislocation structure" of the twin boundary must be such that the strain fields of the very closely spaced dislocations almost cancel each other. In this case, one should expect a comparatively smaller diffusion enhancement, assuming that the Cottrell-attraction is the basic mechanism for the faster diffusion. In view of this unresolved situation it is of general interest to explore the structure of high-energy boundaries by making studies of impurity diffusion.

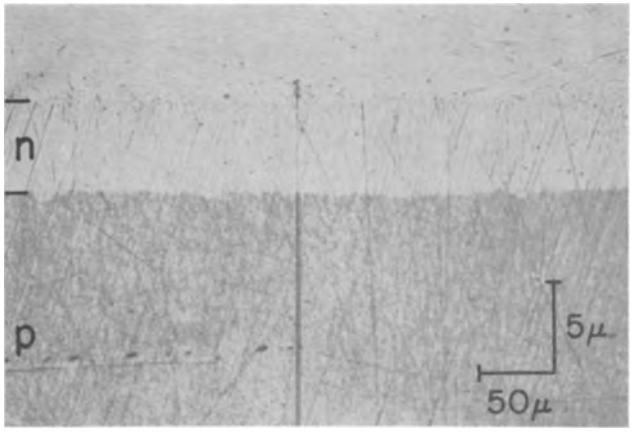

Fig. 8. Diffusion front at (221)-twin boundary. No evidence for diffusion enhancement.

Several diffusion runs were performed with slices containing (221)-boundaries. A typical result is demonstrated in Fig. 8 which shows a beveled and stained (19) section of a slice which was diffused for 1½ hr at 1050°C with a P_2O_5 source. The p-n junction is indicated by the staining, the n-type diffused top layer appears light. The (221) twin-boundary is made visible by preferential etching, and appears as a dark vertical line. No diffusion "spike" (19) is observed. Thus there is no detectable diffusion enhancement.

Control runs were made with several other slices. By beveling at various angles possible diffusion enhancements in other crystallographic directions would have been detected. However, no such anisotropy was found; a spike was never observed. We thus conclude that under these diffusion conditions there is no detectable enhancement for substitutional impurity diffusion at the (221)-second-order twin boundary.

Conclusions

It has been shown that coherent (111)-twin boundaries in silicon have no unusual diffusion properties nor influence on p-n junction behavior. They appear indistinguishable from regular crystalline material.

High-energy (221)-boundaries show a tendency for precipitation of impurities. This precipitation can induce softness in p-n junction diodes. The forward characteristics seem also to be influenced by precipitates. These twin boundaries do not enhance the diffusion of substitutional impurities. In this respect they differ strikingly from artificially grown grain boundaries which show strong diffusion enhancement.

The absence of photoresponse on either boundary type indicates that dangling bonds are unlikely. This is also substantiated by the fact that "hard" diodes are possible on uncontaminated boundaries which means that the grain boundary is not a good conductor. It can be summarized that the direct electrical effects on the "high-energy boundaries" are much weaker than expected (2, 4).

These results indicate that silicon devices should not be impaired by coherent boundaries. Similarly,

only small direct effects should result from the stacking faults on (111)-planes, which have recently been detected in epitaxial silicon (21, 22), since stacking faults are closely related to twins (4-6). The incoherent boundaries would be harmful for devices, but mostly indirectly through the action of impurity precipitates.

Acknowledgments

The reported work represents a combined effort of many people in this organization. R. F. Griffin and L. Weber grew the crystal specimen and called attention to this unusual sample. The experimental investigations were largely carried out by L. Amadei, R. H. Finch, W. W. Hooper, and P. van Loon. W. R. Cook (Cleveland) deserves the author's thanks for making the x-ray analysis.

Manuscript received July 3, 1962. Work supported by Rome Air Development Center (Physics of Failure Mechanisms in Silicon Semiconductors).

Any discussion of this paper will appear in a Discussion Section to be published in the December 1963 JOURNAL.

REFERENCES

1. J. A. Kohn, *Am. Mineralogist*, **41**, 778 (1956).
2. J. A. Kohn, *ibid.*, **43**, 263 (1958).
3. J. Hornstra, *Physica*, **25**, 409 (1959); **26**, 198 (1960).
4. For general review on elastic and defect properties of Si, see P. Haasen and A. Seeger in "Halbleiterprobleme," Vol. IV, p. 68, Vieweg. Braunschweig (1958) or (5).
5. H. G. van Bueren, "Imperfections in Crystals," North Holland Publishing Co., Amsterdam (1960).
6. A review on crystal growing and defects is given by E. Billig in "Semiconductors and Phosphors," M. Schön and H. Welker, Editors, p. 2, Interscience Publishing Co., New York and Fr. Vieweg, Braunschweig (1958).
7. J. Czochralski, *J. Phys. Chem.*, **92**, 219 (1918).
8. M. G. Mil'vidskii and L. V. Lainer, *Sov. Phys., Solid State*, **3**, 210 (1961).
9. H. J. Queisser, *J. Appl. Phys.*, **32**, 1776 (1961).
10. G. L. Pearson, *Phys. Rev.*, **76**, 459 (1949).
11. W. W. Hooper and H. J. Queisser, *Bull. Am. Phys. Soc.*, **7**, 211 (1962).
12. E. Billig and M. S. Ridout, *Nature*, **173**, 496 (1954).
13. A. Goetzberger and W. Shockley, *J. Appl. Phys.*, **31**, 1821 (1960).
14. W. C. Dash, *ibid.*, **27**, 1193 (1956).
15. W. C. Dash, *ibid.*, **30**, 459 (1959); also: R. Bullough *et al.*, *ibid.*, **31**, 707 (1960).
16. C. T. Sah, R. Noyce, and W. Shockley, *Proc. IRE*, **45**, 1228 (1957).
17. H. J. Queisser, *Solid State Electronics*, **5**, 1 (1962).
18. S. Amelinckx and W. Dekeyser in "Solid State Electronics," F. Seitz and D. Turnbull, Editors, Vol. 8, p. 468, Academic Press, New York and London (1959).
19. H. J. Queisser, K. Hubner, and W. Shockley, *Phys. Rev.*, **123**, 1245 (1961).
20. W. T. Read and W. Shockley, *ibid.*, **78**, 275 (1950).
21. H. J. Queisser, R. H. Finch, and J. Washburn, *J. Appl. Phys.*, **33**, 1536 (1962).
22. G. H. Schwuttke, *ibid.*, **33**, 1538 (1962).

Arsenic Purification by Crystal Growth from the Melt

L. R. Weisberg and P. R. Celmer[1]

RCA Laboratories, Radio Corporation of America, Princeton, New Jersey

ABSTRACT

Large arsenic crystals can be grown from the melt quite simply in sealed, heavy wall, transparent fused quartz ampoules by the Bridgman technique. Emission spectrographic analysis indicates that all detected impurities segregate to the ends of the crystals. Wet chemical and radiotracer analysis show sulfur to be deposited on the surface of the crystal and the inner quartz walls, with little entering the bulk of the crystal. Arsenic with a spectrographically determined purity exceeding 99.9999% has been prepared by this relatively simple procedure of crystal growth.

In recent years, considerable attention has been directed toward the purification of arsenic because of its use in the synthesis of semiconducting compounds such as GaAs and InAs. In general, the procedures have involved either the preparation and purification of arsenic compounds such as $AsCl_3$ (1), AsH_3 (2), and As_2O_3 (3) followed by reduction to the element, or else sublimation of arsenic by different methods (4-6). However, the very effective techniques of directional freezing or zone refining have not been previously applied to arsenic because of its high pressure of 36 atm at the melting point of 814°C (7). In this work, it is found that large arsenic single crystals (8) can be grown from the melt simply by the Bridgman technique by using heavy wall quartz tubes as growth ampoules. Evidence is adduced that impurities segregate effectively during this directional freezing, resulting in the preparation of very high purity arsenic (9). An abbreviated description is also presented of attempts at zone refining arsenic.

Experimental Procedure

To prepare the arsenic crystals, a two-sectioned transparent fused quartz vessel was used, consisting of a 7 mm bore quartz tube with a 3 mm wall and about 25 cm long, connected to a standard wall quartz tube of 16-18 mm bore, and 20 cm long. The free end of the heavy wall quartz was drawn out into a small sealed tip to facilitate seeding of single

[1] Present address: Material Electronic Products, Inc., Trenton, New Jersey.

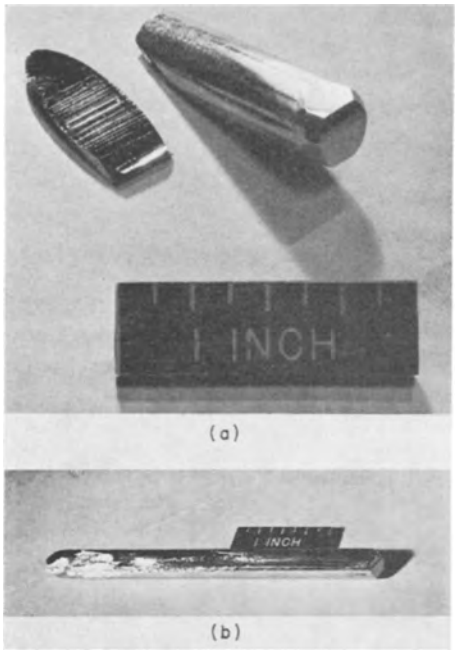

Fig. 1. Two single crystals of arsenic grown from the melt: (a) showing a cleaved section and facets at the tail end, and (b) an entire single crystal.

crystals at the bottom portion of the growth ampoule. The large bore tubing, in which were placed 20-30g of small pieces of metallic arsenic, was connected to a vacuum system, and the vessel was evacuated to a pressure below 10^{-5} torr. After removing the arsenic surface oxides by heating the entire quartz vessel during evacuation to 325°C for 1 hr, the large bore tube was sealed under vacuum. The arsenic was then sublimed from the large bore tube into the heavy wall section, which was, in turn, sealed and separated from the large bore tube, thus forming the growth ampoule.

The vertical growth furnace was constructed especially to provide a uniform temperature. The furnace was 18 in. long and had a center section 12 in. long wound with Nichrome ribbon in four sections, each separately controlled by a 1 amp autotransformer. These were adjusted to produce a temperature of 840°C, constant to within 5°C over a region 9 in. long. To grow the crystal, the growth ampoule was raised into this region so that the arsenic melted under a pressure of 60 atm, and then was lowered out of this region at a rate of 1 cm/hr. A total of 35 crystals was grown by this procedure without a single explosion. One of the ampoules was heated safely to 910°C representing a pressure of over 100 atm, corroborating other observations concerning the bursting strength of quartz (10).

Subsequent to growth, the arsenic crystals were removed by carefully cracking the ampoule. The crystals were silvery and lustrous, and their grain structure was visible in the as-grown condition. Facets were always evident at the tail end of a crystal, as shown in Fig. 1a, and may have been present because the final portion of the ingot grows from the vapor phase since over half a gram of arsenic occupies the vapor phase. The crystals could be cleaved fairly easily, usually at an acute angle to the longitudinal axis of the crystal. A typical cleaved section is shown in Fig. 1a. The horizontal markings on the cleaved section appear to be steps on the surface. A second single crystal of arsenic is shown in Fig. 1b.

The segregation of impurities in these crystals was observed mainly by emission spectrographic analysis. Samples for analysis were removed without metallic contamination by wrapping the crystal in filter paper, laying it on a metal plate, cleaving the crystal with a hammer blow, and collecting small chips of arsenic that were separated from the bulk. The emission spectrographic analysis, carried out each time for 37 elements, was semiquantitative and accurate to within a factor of three. One of the main impurities in arsenic is sulfur, which is not detectable in low concentrations by the emission spectrograph. The sulfur concentration was determined by either a chemical analysis sensitive to 0.5 ppm by weight (11), or else radiotracer techniques in which sulfur (S^{35}) was added to the ampoule in either an elemental or compound form.

Results

Metallic impurities.—To investigate the general segregation properties of impurities in the arsenic, a low-purity source of arsenic was used. The impurity segregation in a typical crystal grown from this arsenic is shown in Table I. The samples from the "Front" (or bottom) and "Tail" (or top) were removed from the very tips of the crystal. It can be seen that almost all the impurities segregate during growth, with the possible exception of silicon and magnesium, which might have been introduced from the quartz. High concentrations of impurities were always found at the front tip and are attributed to supercooling followed by sudden freezing of the melt at the front end, thereby trapping impurities. The center section of the crystal was always the purest. The only impurity that segregated completely to the front ends of several other crystals was aluminum, and is therefore believed to have a segregation coefficient >1.

Crystals were also grown from high-purity arsenic with care taken to avoid contamination. The arsenic, purchased from the American Smelting and Refining Company, had the following spectrographically detected impurities (in ppm by weight): Mg (0.1), Si (0.3), Cu (0.3), and occasionally Sb (1). In initial tests, it was found that, when the

Table I. Impurity segregation in a crystal of low-purity arsenic

Sample position	Impurity concentration, ppm											
	Ni	Pb	Mn	Sb	Ga	Zn	Bi	Ag	Fe	Cu	Si	Mg
Front	—	—	—	—	—	—	—	10	1	10	0.3	0.1
Center	—	—	—	—	—	—	—	1	—	1	10	1
Tail	3	10	3	10	30	3	30	100	100	300	3	1

Table II. Impurity segregation in a crystal of high-purity arsenic grown in a quartz ampoule etched with HF or with a carbon film

Sample position	Impurity concentration, ppm											
	With carbon film							With HF etch				
	Si	Mg	Cu	Sb	Pb	Ag	Fe	Si	Mg	Cu	Sb	Pb
Front	<0.1	<0.1	3	—	—	3	—	10	<0.1	—	—	—
Center	<0.1	0.1	—	—	—	—	—	—	<0.1	—	—	—
Tail	3	0.3	10	30	1	30	1	0.1	0.1	30	10	10

ampoule was treated with only aqua regia, the crystals were contaminated with 1-10 ppm of silicon. This contamination was successfully avoided by coating the inside of the growth ampoule with an adherent carbon film produced by cracking acetone. However, it was found that the contamination could also be eliminated by merely treating the growth ampoule with hydrofluoric acid for 20 min before the usual aqua regia treatment. This latter method is preferable since it avoids the possibility of carbon contamination. Impurity concentrations in a typical arsenic crystal grown by each method are given in Table II. It can be seen that the purity of the arsenic at the center exceeds that of the starting material. Furthermore, the concentration of impurities at the tail end of the crystals reveals the presence of impurities not detectable in the original arsenic. In almost all arsenic crystals, antimony, lead, and occasionally silver were detected at the tail ends.

As further evidence of the high purity of the crystals, InAs has been prepared with such arsenic with a mobility of 62,000 $cm^2\ v^{-1}\ sec^{-1}$ at 78°K which is among the highest values yet achieved (1, 2, 12). It is believed that with arsenic of this high purity, the mobility of the InAs is limited by impurities either in the indium or else introduced during growth.

Sulfur.—Six crystals of arsenic were grown to determine the segregation behavior of sulfur in arsenic. Four crystals were grown with high-purity arsenic, of which three were doped with elemental sulfur in quantities of 1, 20, and 50 ppm, and one was doped with 13 ppm of ZnS, all containing known quantities of radioactive sulfur (S^{35}). The high-purity arsenic used was found to initially contain <1 ppm of sulfur by chemical analysis. In addition, two crystals were grown from a low-purity source of arsenic that contained 6 ppm of sulfur. The concentration of the sulfur along these two crystals was determined by wet chemical analysis.

The distribution of the radioactive sulfur was determined by two procedures. First, a scan was made of activity *vs.* crystal length by translation of a Geiger tube and slotted aluminum plate along the crystal. In the second procedure, the sulfur was separated chemically from the arsenic as a precipitate of $BaSO_4$, and the activity of the precipitate was determined using a 2π windowless proportional counter, applying appropriate control tests.

The concentration of the sulfur was determined both according to its penetration into the surface and its longitudinal distribution. To determine the former, the arsenic crystals were progressively etched in a 1:1:1 solution of HCl, HNO_3, and H_2O. After each etch, the sulfur concentration in the etch solution was counted, and in addition, the crystal was scanned with the Geiger tube before and after the etching. Longitudinal distributions were determined both from scanning and from radiotracer and chemical analysis of pieces of arsenic removed from the bulk of the sample after removal of the surface.

The results of all the experiments were essentially identical and are typified by the scanning data shown in Fig. 2. It can be seen that the initial sulfur concentration along the ingot is very erratic. However, most of this sulfur is in the surface, since removal of the first 0.005 in. of the surface reduced the activity by an order of magnitude, and further etching had little effect. For these samples, less than 1 part in 10^4 of the total sulfur entered the bulk of the crystal. Examination of the quartz ampoule with a Geiger counter revealed that roughly half of the sulfur was imbedded in the quartz walls, and the other half was on the surface of the crystal. Finally, it can be seen in Fig. 2 that after the surface was removed the sulfur concentration was highest at both the front and tail ends of the crystal, which is similar to the segregation of metallic impurities.

Similar results were obtained from the crystals grown from the impure arsenic having 6 ppm of sulfur. After the surface was removed by etching, the crystal weighing 19.6g and therefore containing 118 μg of sulfur previous to growth was broken into five sections, and the sulfur concentrations were determined by wet chemical analysis. The data are shown in Table III. Again, the sulfur concentration is high at the two ends. However, Table III again

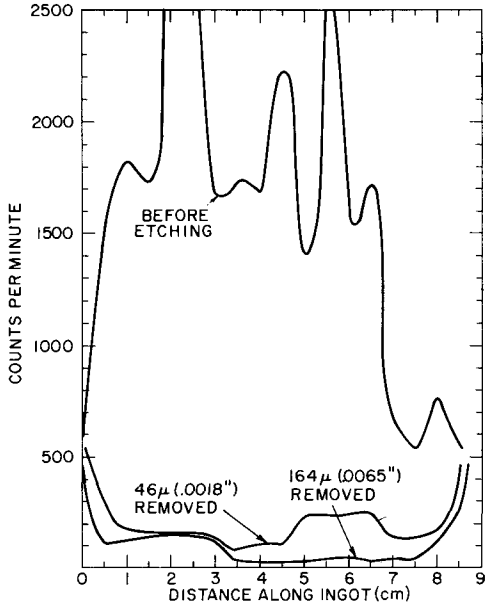

Fig. 2. Distribution of radioactive sulfur along an arsenic crystal before and after removal of the surface.

Table III. Sulfur distribution in an arsenic crystal

Fractional distance along crystal	Sample weight, g	Sulfur weight, μg
0.1	3.7	9
0.3	4.0	<2
0.5	4.3	2
0.7	4.6	<2
0.9	3.0	32

demonstrates that only a fraction of the sulfur entered the bulk of the crystal. In fact small red dots were observed inside the front tip of the growth ampoule, and these dots were found to contain 5 μg of sulfur, indicating that the red compound As_2S_2 may have been deposited from the vapor phase.

All of these results are consistent with the following viewpoint: When the arsenic is melted, the sulfur enters the vapor phase, possibly as an arsenic-sulfur compound, and is confined above the melt. However, only after the arsenic is completely solidified, can the sulfur then travel into the very constricted region between the arsenic crystal and quartz walls and eventually condense out in roughly equal portions between the walls and the surface of the crystal, but in an erratic fashion depending on surface factors. During the slow cooling of the crystal, the sulfur diffuses slightly into the crystal. Thus, as expected in a volatile constituent, the liquid-vapor distribution of the sulfur appears to dominate the sulfur behavior, rather than the usual solid-liquid distribution.

In most of the ampoules, a whitish band was observed around the inner wall near the top of the ampoule after growth. This band was suggestive of arsenic trioxide and, if so, indicates that melting of arsenic might help to remove arsenic oxides. To remove traces of oxides, in several tests the arsenic was heated at 700°C in the presence of titanium before sublimation into growth ampoule, since it was shown separately that titanium, similar to zirconium (13), will reduce arsenic oxides. For these tests, the whitish band was nearly entirely eliminated.

Zone refining of arsenic.—The rapid escape of arsenic from the melt would be expected to make horizontal zone refining difficult. Therefore, several attempts were carried out to zone refine arsenic vertically, since the solid arsenic filling the tube on both sides of the melt will slow down the rate of escape of arsenic from the melt. A nine-section vertical furnace was constructed to be at a uniform temperature of 800°C along its length, and 820°C at the center section. The growth ampoule was prepared in the same way as described previously, and usually lowered through the furnace at a rate of 1 cm/hr.

Five attempts at zone refining were carried out. In each case, the first pass went satisfactorily; however, the second pass was never completed successfully. In two cases, the ampoule exploded during the second pass, and in the other three cases the ampoule cracked and the arsenic rapidly burned. However, in two of these cases, the cracks in the ampoule were located as much as 3 and 5 cm away from the molten zone. The cause of the ampoule cracking was concluded to be as follows: After the first pass, the arsenic is formed into a solid crystal almost completely filling the cross section of the tube. When the second zone is melted, a small amount of arsenic escapes from the molten zone and fills the remaining space between the arsenic and the walls. Then as these regions are heated subsequently, the arsenic expands and cracks the tube. Slowing down the rate of travel by a factor of two did not solve this difficulty. Because of the efficacy of arsenic purification by crystal growth, attempts at zone refining were abandoned. This vertical procedure of zone refining has been reported to have been applied successfully to lower vapor pressure materials (6, 14).

Conclusions

Crystals of arsenic can be grown from the melt by the Bridgman technique by using sealed heavy wall (3 mm), transparent fused quartz tubing for the growth ampoule. Metallic impurities are observed to segregate effectively toward the ends of the crystals. The main volatile impurity, sulfur, remains in the vapor phase until the crystal is solidified and then deposits on the surface of the crystal and the inner walls of the ampoule. After removal of the surface containing sulfur, the center portions of the crystals are considerably purer than the starting material. Spectrographic purities exceeding 99.9999% have been achieved, indicating that crystal growth from the melt is a relatively simple, yet highly effective purification procedure for arsenic. Attempts at zone refining arsenic were not successful.

Acknowledgments

The authors are grateful to Mr. H. H. Whitaker for the spectrographic analyses, and to Dr. S. J. Adler for the wet chemical analyses of arsenic for sulfur. They are especially indebted to Mrs. M. Tiner for carrying out the radiotracer determination of S^{35} in the arsenic. The authors are also appreciative of the guidance and encouragement received from Dr. F. D. Rosi throughout the course of this work.

Manuscript received July 3, 1962; revised manuscript received Sept. 4, 1962. This research was sponsored by the Electronic Research Directorate of the Air Force Cambridge Research Laboratories under Contract AF 33(616)-5029.

Any discussion of this paper will appear in a Discussion Section to be published in the December 1963 JOURNAL.

REFERENCES

1. R. H. Harada and A. J. Strauss, *J. Appl. Phys.*, **30**, 121 (1959).
2. D. Effer, *This Journal*, **108**, 357 (1961).
3. D. P. Enright, NAVORD Report 6024, Jan. 15, 1958.
4. J. T. Edmond, R. F. Broom, and F. A. Cunnell, Report on Meeting on Semiconductors, Rugby, England, April, 1956, p. 109, London, The Physical Society.
5. L. R. Weisberg and F. D. Rosi, *Rev. Sci. Instr.*, **31**, 206 (1960).
6. T. C. Harman *et al.*, *J. Phys. Chem. Solids*, **2**, 181 (1957).
7. See, for example, "Handbook of Chemistry and Physics," 38 edition, p. 481, Chemical Rubber Publishing Co., Cleveland, Ohio (1956).
8. Small arsenic crystals were prepared from the melt by P. Kapitza, *Proc. Roy. Soc. (London)*, **A123**, 323 (1929).

9. Preliminary work was reported by L. R. Weisberg, F. D. Rosi, and P. G. Herkart, in "Properties of Elemental and Compound Semiconductors," p. 41, Interscience Publishing Co., New York (1959).
10. W. D. Lawsen, S. Nielsen, E. H. Putley, and A. S. Young, *J. Phys. Chem. Solids*, **9**, 325 (1959).
11. S. J. Adler, to be published.
12. T. C. Harman, H. L. Goering, and A. C. Beer, *Phys. Rev.*, **104**, 1562 (1956).
13. G. A. Geach, R. A. Jeffery, and R. J. Shelton, *J. Chem. Soc.*, **1950**, 1207.
14. F. K. Heumann, *This Journal*, **109**, 345 (1962).

Zone Refining of Gallium Trichloride

Radiochemical Method For Determining the Distribution of Components in a Column and Its Application in Analyzing the Zone Refining Effectiveness in Purifying Gallium Trichloride

Werner Kern

Semiconductor and Materials Division, Radio Corporation of America, Somerville, New Jersey

ABSTRACT

This paper describes a nondestructive radiotracer method for determining the distribution of components in a column of material. It is used to determine the effectiveness of zone refining purification of gallium trichloride in a sealed system. In this new analytical technique, gamma emitting radioisotopes are added to controlled amounts of specific impurities which are then equally distributed throughout the gallium trichloride ingot. A scintillation counter in a specially designed shield measures the tracer radioactivity as a function of ingot distance before and after zone refining treatments. Some of the radiotracer analyses are complemented by emission spectrographic experiments. Effective segregation coefficients are determined for zinc, iron, manganese, sodium, copper, nickel, aluminum, and magnesium at concentrations of 0.01-40 ppm and are shown to range between 0.02 and 0.5. Recommendations for purification on a production scale are made.

Zone refining of gallium trichloride is now an important intermediate purification process in the preparation of high-purity gallium (1). During the developmental and production phases of this process, quantitative impurity-segregation data were required to evaluate various types of zone refining. This paper describes a radiotracer method which was developed to supply this information.

Because gallium trichloride is a highly reactive, corrosive, and hygroscopic chemical which must be processed in all-quartz apparatus, a nondestructive, sealed-system analysis is particularly desirable. The method developed meets these requirements fully. Controlled quantities of radioactive impurity tracers were added to a gallium trichloride charge. The radiation emitted from the ingot was then measured as a function of ingot distance before and after zone refining. Massive lead shields minimized background radiation from the ingot which was sealed in a quartz tube. A gamma-scintillation counter was used as the radiation detector, in conjunction with a count-rate meter and a scaler. The resulting radioactivity data were then evaluated in terms of effective segregation coefficients and purification efficiency factors.

This nondestructive method of analysis can be applied readily to other similar problems. For example, we have used it to determine the distribution of radioactive adsorbates in chromatographic and ion-exchange columns in purification studies.

Experimental

Preparation of columns for zone refining.—As shown in Fig. 1, flat-bottomed tubes of fused silica having 1.2 cm inside diameter and 30 cm length were sealed to a quartz distillation apparatus. A small volume of aqueous solution which contained the trace element was introduced in the cleaned tube and vacuum-evaporated to dryness. The solutions contained 0.05-0.5 millicuries of radioactivity in the form of either $Fe^{59}Cl_3$, $Zn^{65}Cl_2$, $Mn^{54}Cl_2$, or $Na^{22}Cl$.

The iron deposit was specially prepared to prevent hydrolysis during evaporation. A $Fe^{59}Cl_3$ solution was adjusted to a concentration of 6*N* HCl and extracted with diethyl ether. These ether extracts were then chilled in liquid nitrogen, freed from the ice by filtration, and introduced in the zone refining tube before evaporation of the solvent.

Columns for combined spectrographic and radiochemical analyses were prepared with solutions containing 10 ppm of each element in the form of $AlCl_3$, $CuCl_2$, $NiCl_2$, $MgCl_2$, $PbCl_2$, and $MnCl_2$. Controlled quantities of $Mn^{54}Cl_2$ and $Fe^{59}Cl_3$ were added to these solutions as tracers. The apparatus which contained the zone refining tube and the impurity deposit was then evacuated and filled with purified chlorine gas to a pressure of 1 atm. The break seals were opened, and a predetermined quantity of gallium trichloride was distilled from the storage container into the zone refining tube which was then sealed. The contents were dissolved and mixed by repeated melting and rapid freezing so that the impurity solute was uniformly distributed throughout the gallium trichloride charge.

Zone refining.—The Fisher zone refiner used was designed for automatic upward, downward, and horizontal pass-cycling. Nichrome ribbon looped

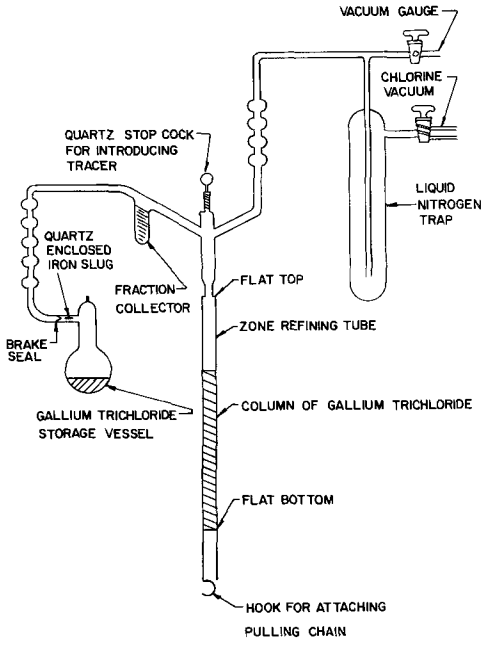

Fig. 1. Quartz apparatus for preparing the radiotracer zone refining columns.

around the tube and connected to a pair of terminals on a movable carriage served as the resistance-heating element. No means of stirring the melted zone was applied other than natural convection in the liquid. The melted zone section was quickly resolidified by a blast of room temperature air from a ring mounted behind the heater. The length of the melted zone was kept constant at one-tenth the total ingot length by close control of the heater power supply and the distance between the heater and the air blast. Zone travel velocities of 0.50, 1.0, and 2.0 in./hr were used. These travel rates were regulated by adjusting the movement of the heater with a timer-controlled variable-speed motor. Radiation measurements were usually conducted after each pass. Up to five consecutive passes were applied for a given set of experimental conditions.

Transport of the gallium trichloride by the molten zone was minimized to maintain the uniform charge thickness essential for the subsequent analytical evaluation. Material transport of this type is caused by density changes during melting and can be eliminated during horizontal zone refining by tilting the ingot container slightly (2).

Radiation measurement.—A thallium-activated sodium iodide crystal served as the gamma-radiation detector. The photomultiplier pulses were passed to the amplifier of a scaler assembly and to a count-rate meter with four-linear ranges. As shown in Fig. 2, the radiation detector was shielded from the zone refining tube by a 6 or 8-in. layer of lead bricks which were positioned to form a 6 or 10 mm slit above and across the center of the detector. The lead thickness required to minimize background radiation from the zone refining column and still maintain a sufficiently high tracer counting rate was determined experimentally from graphs which showed the radioactivity of standard sources as a function of distances from the slit under various shielding conditions.

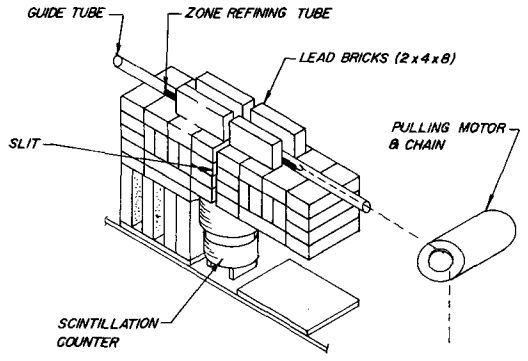

Fig. 2. Apparatus for radioactivity measurements of zone refining columns.

Two types of radiocounting techniques were employed; the first was a dynamic technique based on automatic scanning, and the second a static technique based on section counting.

In the radioscanning analysis, the columns were pulled slowly by a variable-speed motor across and perpendicular to the slit. A thin-walled glass tube was used as a guide canal for the column. Ingot profiles of radioactivity as a function of column distance were obtained by automatic plotting of the counting rates on a calibrated and synchronized strip-chart recorder. Suitable radioactivity standards and background scans were included on these charts before and after scanning of the column. Typical profiles for an ingot after 0, 1, and 3 passes are shown in Fig. 3.

The static counting technique was used for accurate analyses and low-level radioactivity measurements. In this technique, the column was positioned so that a single section could be counted until

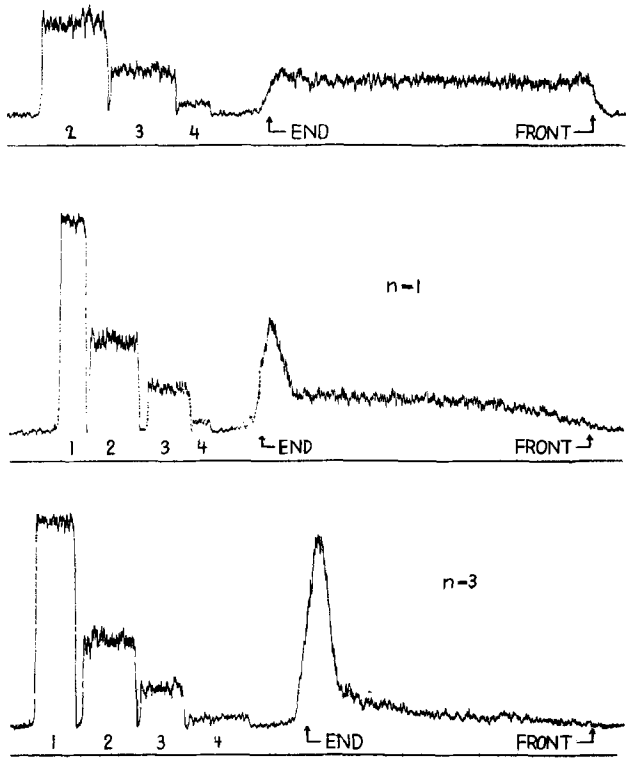

Fig. 3. Automatic radioactivity scanning profiles of activity vs. ingot distance for an ingot after 0, 1, and 3 zone-passes (n); radioactivity calibration standards [1,2,3,4] are also shown.

a desired number of counts were collected on the radioscaler; these counting periods depended on the activity level of the section and ranged from 3 to 60 min.

Emission-spectrographic analysis.—Some radiotracer experiments were complemented by emission spectrographic analyses. After radioscanning of the finished zone refining columns, single sections of the column measuring one tenth the ingot length were melted out with the zone refiner. The melted gallium trichloride was collected in weighed quartz beakers containing purified 6*N* HCl. The exact quantity of gallium trichloride was determined by weighing. The gallium trichloride and the ferric chloride complexes were separated from the other substances by two extractions with isopropyl ether so that emission spectrographic analysis of the added net impurities in the acid phases could be made (3). Radioactivity measurements of the solutions provided the concentration data, the acid phases yielding the $Mn^{54}Cl_2$ and the ether phases yielding the $Fe^{59}Cl_3$ concentrations.

Radiographic examination of ingots.—Columns from the vertical zone refining experiments sometimes contained gas-filled spaces which, if not detected, would lead to errors. X-ray radiography was initially used for examining the columns. Later, a rapid testing technique was designed for checking the column prior to analysis. A few millicuries of a nuclide which emitted low-energy gamma radiation was positioned 2 cm above the slit of the radiation-detector shield. The column was then pulled over the slit as described for the automatic scanning. Any increase in relative radiation transmission was indicated on the chart recorder which immediately verified the extent and location of voids. Columns with severe irregularities were excluded from analysis.

Determination of purification efficiency.—The effectiveness of zone refining for separation of specific trace impurities under various experimental conditions was evaluated by use of the effective segregation coefficients and the over-all purification factors.

First, the net concentration figures for each ingot section of the zone refined column were ascertained. The radioactivity measurements of each section were corrected for normal background activity and for the radiation from the adjacent sections. The corrected net tracer activity (C) was then proportional to the concentration of the element being traced. The original average tracer activity (C_o) of each ingot section before zone refining was calculated by dividing the sum of all section activities (C) by the number of sections. (As pointed out previously, the actual uniformity of the solute distribution was ascertained experimentally by radioscanning profiles.) The ratio values (C/C_o) represented the relative solute concentrations and were plotted for each ingot section as a function of ingot distance. This distance was expressed in terms of the number of zone lengths. Figures 4 and 5 show typical semilogarithmic graphs based on experimental and theoretical values.

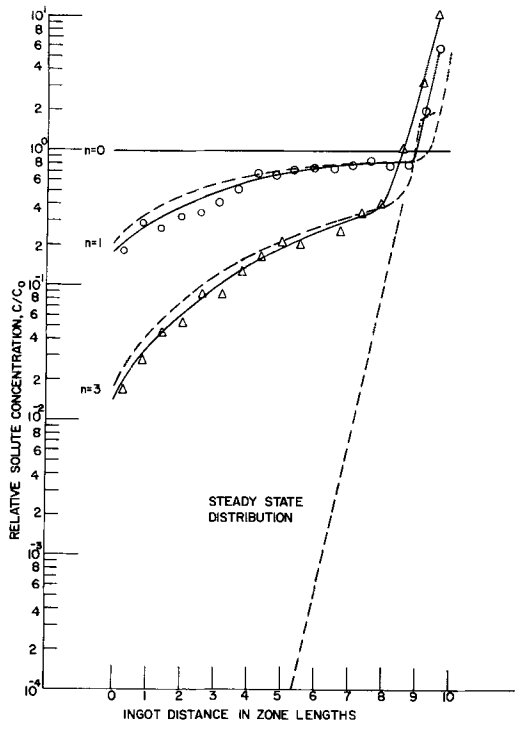

Fig. 4. Experimental zone refining curves for $Fe^{59}Cl_3$ in $GaCl_3$ after 0, 1, and 3 vertical zone passes at 2.0 in./hr velocity; also shown are theoretical curves calculated for 1 and 3 passes, and for the steady-state distribution with a k_e of 0.2; - - -, theoretical for k_e 0.2; ——— experimental.

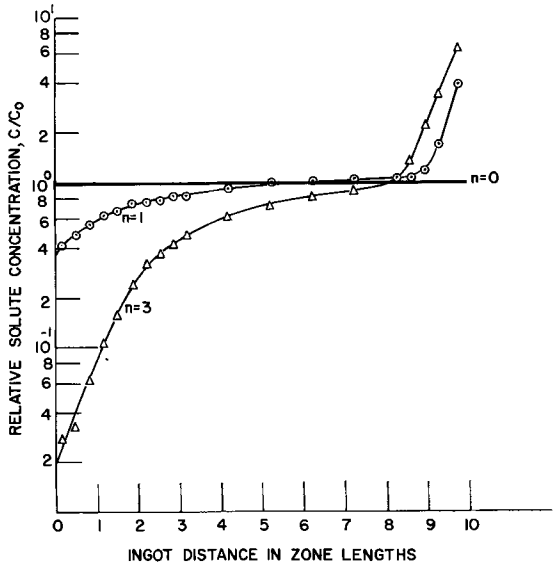

Fig. 5. Experimental zone refining curves for $Fe^{59}Cl_3$ in $GaCl_3$ after 0, 1, and 3 horizontal zone passes at 2.0 in./hr velocity.

The effective segregation coefficient (k_e) is an exact mathematical expression of the zone refining efficiency and is defined as C_s/C_l, the ratio of the impurity concentration of the solid at the interface to the concentration of the liquid beyond the diffusion layer. The value of k_e was normally determined from the interception of the extrapolated C/C_o curve with the ordinate at zero front-end distance of the ingot. Mathematical solution of the zone refining equation (2) yielded closely similar results for ingots that followed the theoretical impurity distribution.

In addition to k_e, the purification efficiency was expressed directly by calculation of the mean purifi-

cation C_o/C which was achieved in the first 80% and the first 90% of the ingot. These values were labelled as $P_{0.8}$ and $P_{0.9}$, respectively.

Accuracy and precision.—The accuracy of the static radioactivity measurements was good. Test results showed that the sum of the corrected radioactivity values from all ingot sections usually ranged within ±5% of the actual tracer quantity added to the gallium trichloride. The precision of the radiocounting data was statistically dependent on the background activity and the total counts collected. This figure was maintained within ±5% of the true value by choosing suitable lengths of counting periods.

The over-all reliability of the results of these experiments was primarily dependent on the reproducibility of various zone refining parameters, such as zone length, convection, temperature of melt, ingot uniformity, and single-crystal formation. Variations in these factors so reduced accuracy that the resultant effects were far more significant than those caused by any analytical errors. Because the data were obtained from various duplicate experiments, however, the reliability of the results is quite satisfactory.

Discussion of Results

Segregation of Iron

Because of practical implications, the zone refining segregation behavior of iron in gallium trichloride was investigated in greater detail than the other impurities. Table I presents the essential data and results.

At a zone travel velocity of 0.50 in./hr, zone refining in vertical downward direction proceeded at an effective segregation coefficient (k_e) of 0.10. At 1.0 in./hr, the k_e attained a value of 0.14, which indicated a slightly lower purification efficiency at double the zone rate. After four zone passes, the first 80% of this ingot showed a 20-fold decrease in the mean concentration of iron; the front end of the ingot showed a 500-fold decrease.

At a 2.0 in./hr vertical zone travel speed, a k_e of 0.17 was attained. Zone refining curves from this experiment are shown in Fig. 4 for 0, 1, and 3 zone passes. Except for some fluctuations in the C/C_o data because of ingot irregularities, the experimental curves follow nearly ideal zone refining behavior. For purposes of comparison, Fig. 4 also contains theoretical curves which were based on the zone refining equation (2) for a k_e of 0.2 for 1 and 3 passes. The corresponding steady-state distribution is indicated by the steep curve which represents the ultimate solute distribution achieved at a k_e of 0.2; this maximum segregation is limited by the back-reflection of the solute that accumulates in the last zone lengths.

Calculations for optimum zone refining conditions require a knowledge of the equilibrium distribution coefficient, k_o. By use of the above data and the Burton-Prim-Slichter equation (2, 4), k_o is calculated to be 0.08; this figure represents the segregation coefficient obtainable under the most favorable zone refining conditions. As shown in the experimental data (Table I), the segregation coefficient at a velocity of 0.5 in./hr is 0.10, a value quite close to the theoretical maximum. Calculations also indicate that eight passes under these conditions should result in a 10^6-fold purification in the first zone length.

Zone refining in horizontally positioned columns, which were slightly inclined to prevent transport of gallium trichloride, resulted in considerably lower segregation effectiveness than vertical zoning. The lower values are caused by the differences in stirring conditions of the molten zone; convectional stirring for a liquid in a horizontal tube is known to be poorer than in a vertical tube (2). As shown in Table I, the k_e values for horizontally positioned columns ranged between 0.3 and 0.4, depending on zoning conditions. Changes in zone-travel velocities did not have much effect on the k_e (probably because of the overriding influence of the poor stirring conditions). However, because a gas phase is maintained above the ingot in the horizontal zone refining approach, the horizontal technique prevents the formation of gas bubbles in the gallium trichloride charge. As a result, this approach produces considerably more uniform ingots than the vertical technique and reduces the danger of tube breakage. In addition, because multiple-pass horizontal zoning yields ingots of sufficiently high purity, this technique is well suited for production applications. Figure 5 shows a typical set of zone refining curves for these experiments.

Segregation of Zinc, Manganese, and Sodium

When zinc-65 chloride was added to gallium trichloride at a concentration of 0.020 ppm (as Zn) followed by vertical zone refining, a 16-fold mean

Table I. Zone refining results for $FeCl_3$ in $GaCl_3$

Experimental data are based on gallium trichloride column containing 0.14 ppm iron in form of $FeCl_3$, with $Fe^{59}Cl_3$ as tracer. The charge was remixed and the solute uniformly distributed before each zone refining experiment.

Zone refining conditions			Resulting purification			
			Purification factor			
Direction	Velocity, in./hr	Passes	$P_{0.8}$	$P_{0.9}$	C/C_o at front end	k_e
v	0.50	1	—	—	0.10	0.10
		2	—	—	0.014	
v	1.0	1	1.8	1.7	0.14	0.14
		2	4.7	3.8	0.050	
		3	7.2	5.3	0.015	
		4	20	10	0.002	
v	2.0	1	1.8	1.7	0.17	0.17
		2	2.5	2.0	0.045	
		3	6.3	3.5	0.014	
h	0.50	1	1.5	1.3	0.38	0.3-0.4
		2	2.3	1.9	0.11	
		3	2.6	2.0	0.05	
h	1.0	1	1.2	1.1	0.38	0.3-0.4
		2	1.4	1.3	0.11	
		3	1.8	1.6	0.02	
h	1.0	1	1.2	1.2	0.3	0.3-0.4
		3	3.0	2.0	0.04	
h	2.0	1	1.2	1.1	0.19	0.3-0.4
		2	1.6	1.4	0.045	
		3	2.6	1.7	0.012	

v, Vertical downward; h, horizontal (slightly inclined); $P_{0.8}$, mean purification in first 80% of ingot; $P_{0.9}$, mean purification in first 90% of ingot· C_o, solute concentration before zone refining; C, solute concentration after zone refining; k_e, effective segregation coefficient.

Table II. Zone refining results for $ZnCl_2$, $MnCl_2$, and NaCl in $GaCl_3$

Impurity added			Zone refining conditions			Resulting Purification		
Compound	Concentration, ppm	Tracer	Zone direction	Velocity, in./hr	Passes	Purification factor $P_{0.8}$	$P_{0.9}$	k_e
$ZnCl_2$	0.020	$Zn^{65}Cl_2$	v	1.0	1	16	16	<0.06
			h	1.0	1	4.8	3.7	0.04-0.10
$ZnCl_2$*	0.17	$Zn^{65}Cl_2$	v	1.0	1	1.2	1.2	~0.4**
			h	1.0	4	3.3	1.6	
$MnCl_2$	0.021	$Mn^{54}Cl_2$	v	1.0	1	11	8.7	0.02
			h	1.0	1	6.9	6.1	0.03
			h	0.50	1	5.6	4.9	0.04
$MnCl_2$	0.010	$Mn^{54}Cl_2$	h	1.0	1	6.4	6.4	0.07
NaCl	37	$Na^{22}Cl$	v	1.0	1	2.6	2.1	~0.1**
			h	1.0	1	1.3	1.3	~0.4**
NaCl*	40	$Na^{22}Cl$	h	1.0	1	1.1	1.1	~0.5**

* Contains water and some organic impurities.
** Abnormal zone refining behavior; k_e values were estimated from mean purification.

purification ($P_{0.9}$) with a k_e of less than 0.06 resulted. Horizontal zoning is considerably less efficient. The segregation inhibiting effect caused by water traces was demonstrated experimentally by contaminating a column of gallium trichloride with moisture. The results shown in Table II indicate a reduction in segregation effectiveness by a factor greater than 10; four vertical passes achieved a $P_{0.8}$ of only 3.3. Changes of this sort are to be expected because water hydrolizes gallium trichloride with ease.

Manganese-54 dichloride at concentrations of 0.010 and 0.021 ppm (as Mn) showed excellent segregation with a k_e of 0.02 and 0.03-0.04 for vertical and horizontal-zoning directions, respectively. Purification yielded clear, transparent single-crystal gallium trichloride after one zone pass. However, this analytical evaluation was complicated because of a small quantity of material that consistently segregated in the front portion of the ingots where manganese depletion was greatest. Gamma-ray spectrometric analysis showed that this radioactivity was definitely caused by manganese-54 and not by some other nuclide present as an impurity. Apparently, this phenomenon was caused by a small fraction of the manganese in an oxidation state different from that of the major portion of the manganese.

As shown in Table II, segregation for gallium trichloride which contained 37 ppm sodium in the form of sodium-22 chloride proceeded with a $P_{0.8}$ of 2.6 in the vertical direction, and 1.3 in the horizontal. This purification did not follow normal zone refining laws. The first half of the vertically processed ingot showed a 13-fold purification after one pass and an apparent k_e of well below 0.1; the concentration in the second half rose abruptly beyond the initial mean concentration. This abnormal behavior was attributed to the high concentration of sodium chloride that was added because of low specific radioactivity. The concentration level in the solvent was apparently beyond the solubility limit of sodium chloride in gallium trichloride. Evidence of incomplete solubility was indicated by the white-colored polycrystalline appearance of the ingots. Segregation curves of moist gallium trichloride ingots containing sodium chloride were similar to those of the impure zinc column in that the center portion of the ingot showed a concentration leveling effect. A mean k_e of approximately 0.5 was estimated for these ingots.

Segregation Effectiveness under Severe Impurity Concentrations

One ingot was prepared with a multiple mixture of elements which were added as chlorides to investigate effective segregation under extreme conditions of impurity concentrations. With the exception of iron, which was added at a concentration of 0.01 ppm, the other six impurities were present at concentrations of 10 ppm each. Manganese-54 was added as a tracer for the manganese. One vertical downward pass was applied at a zone-travel velocity of 1.0 in./hr. Under these conditions, an emission spectrographic analysis led to the following effective segregation coefficients: 0.11 for aluminum; less than 0.12 for copper; 0.30 for nickel. Lead and manganese results were not conclusive, and iron was not detected.

The radiochemical analysis, however, showed that the segregation of iron was not affected by the high concentrations of added impurities; the k_e of 0.12 checks closely with the values for iron listed in Table I. In the case of manganese, the purification effectiveness at the 10 ppm concentration was about one-half as compared to the values reported in Table II for 0.02 ppm manganese alone.

On the basis of the data presented in Tables I and II, the segregation effectiveness of horizontal zoning at the same impurity concentrations should be lower by a factor of about two.

Conclusions

Experimental results indicate that this radiotracer method is an effective nondestructive quantitative technique for determining the distribution of radioactive components in a column of material. In addition to evaluating zone refining processes, this technique can be readily used in other applications where the distribution of components needs to be measured, such as in chromatographic and ion-exchange columns, or in rods, ingots, and crystals of uniform thickness.

When used in the determination of zone refining parameters for gallium trichloride, the data obtained showed that chlorides of manganese, zinc, and iron, which were added at concentrations of 0.01-10 ppm, had effective segregation coefficients of 0.02-0.4. Similar results were obtained with aluminum, magnesium, copper, and nickel which were analyzed by emission spectrography. Because of its low solubility in gallium trichloride, sodium chloride did not adhere to normal zone refining laws; however, segregation did occur and sodium ions collected toward the rear of the ingot.

These results show that multiple-pass zone refining is a highly effective process for the preparation of high-purity gallium trichloride. For production-scale purifications, horizontal zone refining is considered more efficient than the vertical technique. Although the purification effectiveness in the horizontal direction is lower than that in the vertical, horizontal parameters are more easily controlled, and the danger of column breakage is reduced.

Acknowledgment

The author wishes to thank Mr. G. A. Lang for the spectrographic analyses. The work described in this paper was sponsored by the Manufacturing Technology Laboratory, Aeronautics System Division, Air Force Systems Command, United States Air Force.

Manuscript received July 19, 1962; revised manuscript received Sept. 7, 1962.

Any discussion of this paper will appear in a Discussion Section to be published in the December 1963 JOURNAL.

REFERENCES

1. N. Goldsmith, A. Mayer, and L. Vieland, *J. Less Common Metals*, **3** (1962) in press.
2. W. G. Pfann, "Zone Melting," John Wiley & Sons Inc., New York (1959).
3. E. B. Owens, *Appl. Spectroscopy*, **13**, 105 (1959).
4. J. A. Burton, A. C. Prim, and W. P. Slichter, *J. Chem. Phys.*, **21**, 1987 (1953).

Electrochemical Oxidation of Titanium Surfaces

Merle E. Sibert

Materials Sciences Laboratories, Lockheed Missiles and Space Company, Palo Alto, California

ABSTRACT

Films produced on titanium depend on the nature and concentration of electrolyte, forming voltage, current density, and temperature. In most cases, dense films of limited thickness are produced, but in some cases, thick, porous films result. Physical, chemical, and electrical nature of the coatings are discussed together with their relation to the substrate surface character. Evidence indicates that films prepared in aqueous electrolytes are not a pure rutile structure. These coatings are highly uniform, insulating, and adherent.

Anodic oxidation is a well-established procedure in the case of many metals, but in the case of titanium, relatively little conclusive information is available, and procedures are not well developed.

It was the purpose of this investigation to study anodic processes as applied to titanium surfaces and to learn something of the effects of various formation parameters on the character of anodic films produced.

The work to be described is largely a study concerning the effects of process parameters on the anodic oxidation of titanium metal. Such parameters include type and concentration of electrolyte, anodic current density, temperature, voltage, total current, and effects of superimposed a.c. In the study of anodic films on metals, factors of significance in evaluation of films include thickness, density, porosity, and electrical properties. A convenient means for evaluation of such factors is obtained by a measurement of capacitance and loss factors. In most cases, films prepared in this study were evaluated through capacity and loss measurements.

Much process data have been accumulated in the case of anodic processes as applied to certain metals. These include common metals such as aluminum and less common metals such as tantalum. Although a great deal of effort has been expended in anodizing investigations of titanium, little in the way of concrete results has been obtained. In most cases, films prepared have been semiconducting in nature and nonstoichiometric in composition. For the most part, anodized titanium films have been nonuniform, highly porous, very thin and conducting, or completely nonadherent.

It is beyond the scope of this paper to provide a complete literature background regarding anodic-conversion processes as applied to titanium metal. However, a few pertinent examples of work in this area are cited to illustrate the general trend of approaches previously made to this problem.

Ence (1) employed alcoholic-organic acid baths containing small amounts of phosphoric acid for imparting thin anodic films to titanium metal. Jacquet (2) employed acetic-perchloric acid baths for this purpose. These have been found to produce pure white oxidic films, but they are extremely poor in adherence. Ma (3) employed dilute sulfuric acid baths for titanium anodizing. Voltage attainable in this type of bath is limited to relatively low

values so that only thin noninsulating films are produced. McLean (4) utilized hydrochloric-nitric-sulfuric acid baths for polishing the surface followed by anodizing in a buffered borate solution. Films formed in excess of 150v were reported. However, these films were also said to be unstable in solution and during processing.

The Philco Corporation (5) reported favorable characteristics of anodic films formed in saturated oxalic acid-1-2-propanediol solutions. Such films were reported to have capacity values considerably in excess of comparable films formed on tantalum indicating a high-dielectric-constant film material. Wainer (6) recommended a two-step anodizing procedure employing first a phosphoric acid-glycol bath and, second, a boric acid bath for final film formation. High formation voltages and capacitance values in excess of those for comparable tantalum films were reported.

A variety of salt solutions have also been employed for imparting anodic films to titanium. Ence (1) employed a sodium cyanide bath. No details are given for results of this formation. Dummer (7) suggested aqueous solutions of common salt, potassium dichromate, and potassium orthophosphate. Again, formation voltages are extremely limited in solutions of this type. Examples are cited showing formation voltages in the vicinity of 10v. Beck (8) has patented anodizing procedures for titanium employing various phosphate salts in aqueous solutions. These include sodium and potassium orthophosphates, sodium, potassium and ammonium acid phosphates, and microcosmic salt. These materials are reported to produce stable films on titanium metal. Hass (9), in converting very thin films of titanium to oxides, utilized ammoniacal tartaric acid baths. Complete conversion of titanium films of the order of 500Å in thickness to titanium oxides was claimed.

A large number of other references to the anodizing of titanium metal exist in the literature. Films produced have been variously identified as rutile, anatase, and brookite. Existing evidence on the anodizing of titanium metal is, to a large degree, conflicting both from the standpoint of the effects involving process parameters and in film identification and properties.

Experimental

Materials

In order to provide titanium surfaces of varying purity for anodizing studies, a series of five different materials were utilized. These are listed in Table I along with available impurity data. The deposited film materials were of higher order of purity than the commercially available materials.

The commercially available sheet materials were employed as 3-, 5-, and 10-mil thickness sheets. These were generally utilized as 1- by 5-cm strips. The iodide material was used in the form of thin (approximately 50-mil) slices. The chemically deposited titanium films were applied to either glass or alumina substrates by a fused-salt deposition procedure. This procedure gives a uniform film following the contours of the original alumina substrate. Vapor-deposited films were on glass substrates and deposited by standard vapor-deposition techniques.

All electrolyte materials were formulated from standard CP chemicals in distilled water. Anodic films were formed utilizing a constant-current source capable of 300-ma current and 500-v. Bath temperature was controlled either by use of internal cooling coils or external, constant-temperature baths. Titanium cathodes were utilized throughout the work. The general preparation procedure involved presetting of the power supply to the desired voltage and current, inserting the electrode under voltage, allowing the film to build up to this specified voltage followed by current decay to a minimum value, usually of the order of less than 1 ma.

Since in most cases there were tendencies for excessive arcing to take place at the electrolyte-air interface, this interface was protected by use of a small jig clamping the anode between two pieces of silicone rubber.

When the anode had reached prespecified voltage-current conditions, it was removed under an applied voltage, washed in distilled water, boiling distilled water, and finally allowed to dry either in air or in a low-temperature oven.

In most cases, the capacity-loss measurements described later were obtained by application of a high-purity, low-firing silver electrode (DuPont No. 6730 silver paint) to the anodized film. As will be seen later, this electrode type does not strictly conform to anodized surfaces and results in capacity-measurement error. This is evident from the difference observed in measurements using these silver electrodes as compared with measurements in aqueous solutions.

Results

Electrolyte Types

Initially, a large variety of acid, basic, and salt-type electrolytes were surveyed to determine which general type of materials produced the most promising anodic films in the case of titanium. A number of electrolytes studied are tabulated in Tables II, III, and IV according to the three cited types. In

Table I. Purity of titanium metal substrates

Substrate	Source	Total Ti, %	O_2, %	C, %	N_2, %	Fe, %
75A	TMCA	99.0	0.5	0.05	0.03	0.35
55A	TMCA	99.2	0.3	0.03	0.02	0.25
Iodide	Foote Mineral	99.9	0.05	0.01	0.01	0.01
Chem. Dep. Film	LMSD	>99.9	0.5	Nil	—	Nil
Vapor Dep. Film	LMSD	>99.9	<0.05	<0.05	Nil	<0.05

Table II. Acid electrolytes

Electrolyte, room temp	Conc, %	Max, *E*	Initial c.d., ma/cm²	Final c.d., ma/cm²	Time, min	Gassing	Adherence	*R*[5], ohms	*C*[1], μf/cm²	*D*[1], %
HF	5	20	50	1	30	Mod.	None	—		
$HClO_4$	5	35	10	1.2	2	Heavy	None	—		
H_2SO_4	95	80	10	0.25	15	Mod.	Good	5-10	0.001	>25
	15	35	10	0.5	15	Heavy	Good	5-10	0.001	>50
HNO_3	70	20	120	2.5	15	Heavy	None[2]	20	—	—
H_3PO_4	85	150	20	0.04	40	Slight	Good	10^5	0.010	>5
CH_3COOH	95	—	10	0.4	30	Heavy	Poor[3]	—	—	—
H_3BO_3	Sat'd.	200	10	0.15	30	Heavy	Good[4]	10^3	0.0005	>10
Tartaric acid	5	200	30	0.5	30	Heavy	Good[4]	10^2	0.0002	>25
Oxalic-citric lactic acids	5.5-10	300	10	0.25	45	Heavy	Good[4]	20-40	0.0005	>20
Et acid phosphate	5-25	400	14	0.04	45	Slight	Good	10^5	0.004	<1

[1] Dry contact, at maximum obtained voltage.
[2] Etching.
[3] Electropolishing.
[4] Very thin.
[5] Measured through film between metal substrate and surface silver electrode.

Table III. Basic electrolytes

Electrolyte	Conc, %	Max, *E*	Initial c.d., ma/cm²	Final c.d., ma/cm²	Time, min	Gassing	Adherence	*R*, ohms	*C*[1], μf/cm²	*D*[1], %
K-Ti-oxalate, NH_4OH	Sat'd.	10	10	1.25	15	—	—[2]	—	—	—
NaOH	10	75	30	2.50	30	Heavy	Fair[3]	10^7	0.0003	5.7

[1] Dry contact at maximum obtained voltage.
[2] TiO_2 ppt.
[3] Spalling.

Table IV. Salt electrolytes

Electrolyte	Conc, %	Max, *E*	Initial c.d., ma/cm²	Final c.d., ma/cm²	Time, min	Gassing	Adherence	*R*, ohms	*C*[1], μf/cm²	*D*[1], %
Na_3BO_3	Sat'd.	100	10	0.025	30	Little	Good	5-20	0.0005	20
$TiCl_4$	5	50	10	0.5	30	Heavy	Good	40	0.0005	5-10
NaCN	10	10	10	0.25	20	Heavy	Good[2]	—	—	—
Na_3AlO_3	Sat'd.	100	10	0.5	20	Mod.	Poor[3]	—	—	—
Na_3PO_4	2	120	20	0.05	20	Slight	Good	10^6	0.005	5
NaH_2PO_4	5	145	20	0.07	30	Mod.	Poor	10^3	—	—
Na_2HPO_4	5	350	20	0.04	20	Mod.	Good	—	0.009	4

[1] Dry contact at maximum voltage obtained.
[2] Very thin.
[3] Reduced.

general, acid electrolytes gave by far the best results. However, a very strong acid such as HF or $HClO_4$ had strong tendencies toward dissolving the films produced. Thus, the anodic films in these cases were essentially nonadherent. The very weak acids, such as the usual organic acids, produced very adherent but limited thickness translucent films. Such films grow to some finite low voltage (usually <50v) and consequent thicknesses, at which point growth ceases. Acids, such as sulfuric, tended to yield heavy, opaque, amorphous, films which could be formed to high voltages, but here again, there was also a tendency toward dissolution of the films. Films so formed had a tendency to retain a very porous structure, and thus the electrical properties were somewhat undesirable. Of the acidic electrolytes tried, the phosphate-based materials gave by far the best results. These electrolytes allowed buildup of films to high voltages with a minimum of porosity. In particular, an aqueous methyl-ethyl acid phosphate electrolyte produced excellent anodizing characteristics.

Strongly basic electrolytes either resulted in precipitates of titanium oxide or reacted so rapidly with the titanium surface that the entire substrate was quickly converted to oxide. Thus, it was difficult to control the anodic process utilizing these electrolytes.

Most neutral or near neutral salt-type electrolytes yielded only very thin translucent films. These had poor electrical character and little protective value to the titanium substrate. Salts of an acidic nature produced improved-type films, particularly in the case of the phosphate salts. The effectiveness of a salt-type electrolyte seems to be largely controlled by its *p*H properties and ability to dissolve small amounts of the anodic product.

The titanium based anodic films produced have a finite solubility in the organic phosphate electrolyte. This is evidenced by the slow *p*H increase of

Table V. Effect of titanium purity on the anodizing process

Titanium type	Purity, %	100 Volts				200 Volts			
		Min c.d., ma/cm²	Time, min	C*, μf/cm²	D*, %	Min c.d., ma/cm²	Time, min	C*, μf/cm²	D*, %
Ti75A	99.0	0.16	30	0.0122	4.6	0.14	35	0.0075	2.6
Ti55A	99.2	0.11	20	0.0088	2.2	0.21	27	0.0058	1.2
Iodide	99.9	0.10	18	0.0075	—	0.04	30	0.0060	1.1
ChDepFilm	>99.9	0.30	15	0.0135	1.1	0.05	25	0.0056	1.3
VacEvapFilm	>99.9	0.28	2	0.0082	2.7	0.14	2.5	0.0065	1.5

* Ag counter electrodes.

Table VI. Surface-roughness effects

Forming voltage, v	Ti on as-rec'd Al_2O_3			Ti on grit-blasted Al_2O_3			Electropolished Ti on Al_2O_3		
	Min c.d., ma/cm²	C, μf/cm²	D, %	Min c.d., ma/cm²	C, μf/cm²	D, %	Min c.d., ma/cm²	C, μf/cm²	D, %
250	0.3	0.0087	3.1	0.25	0.0069	2.8	0.08	0.0061	1.8
300	0.2	0.0063	8.5	0.25	0.0044	3.4	0.12	0.0028	2.7
350	0.2	0.0029	6.9	0.17	0.0030	5.7	—	—	—

the bath accompanied by an increasing titanium concentration. When the electrolyte reaches a *p*H much above 1, it is no longer effective in generation of an effective dielectric film on titanium.

In general the effectiveness of an electrolyte for anodic oxidation of titanium metal appears to be largely a function of the electrolyte's ability to dissolve the anodic product. This is comparable to behavior observed in the case of aluminum and tantalum. Films formed anodically in electrolytes which do not dissolve the oxide to any extent build up to a finite thickness (< 1000Å) and block the flow of current except for a relatively small leakage current. In electrolytes which attack the oxides, relatively coarse coatings can be produced of up to 6000-8000Å estimated thickness (based on weight change data).

As a result of these investigations on electrolyte composition, the balance of the program was carried out in the methyl-ethyl acid phosphate-based electrolytes. It was found that films could be formed in these electrolytes up to at least 400v, and that final current densities of the order of 0.007-0.035 ma/cm² could be obtained.

The so-called ethyl acid phosphate is actually about a 50-50 mixture of the methyl, $CH_3H_2PO_4$, and ethyl, $C_2H_5H_2PO_4$, derivatives. The material performs best as an anodizing medium for titanium at low *p*H levels (<1) representing concentrations of > 5 v/o. For the study described, 20 v/o (*p*H ~ 0.4) solutions have been employed unless otherwise stated.

Substrate Surface Effects

Titanium substrate purity and surface character were found to have an effect on properties of the anodic films produced. Five types of titanium substrate were anodized to 100 and 200v and to minimum obtainable currents. It was found that the time required to reach these conditions varied by a factor of 10 or greater with purity of the substrate. Results of this study are shown in Table V. Capacity and loss values for films formed on these several materials also differ appreciably in comparing the minimum with maximum purity substrates. Data are generally reproducible within 10% for C & D values and within 15% for time values.

Although it is difficult to separate purity and surface effects, an effort was made to determine surface effects by anodizing the same type of chemically deposited film with varying surface preparations. Data are given in Table VI for anodized chemically deposited films on as-received alumina, on fresh grit-blasted alumina, and on electropolished titanium surfaces over alumina. Anodic film formation on different surfaces under identical conditions produced different results in terms of leakage current and loss factor.

Film Growth

Electrolyte effects.—As previously mentioned, the gross effects resulting from electrolyte constitution appear to reside primarily in ability of the electrolyte to dissolve the resultant anodic films. It is apparent that those electrolytes having some solvent action capabilities produce the most desirable results in terms of film thickness and electrical properties. Electrolytes possessing no solvent action produce relatively thin films with poor electrical characteristics. Electrolytes possessing extreme solvent action characteristics yield poorly adherent or nonadherent films.

There are also small effects resulting from concentration of the active electrolyte material. Electrolyte concentrations varying from 10 to 40 wt % produced small changes in capacity displayed by the resultant films. These changes are minimal compared to the gross changes resulting from voltage effects and are comparable to similar effects observed for other metals.

Anode current density.—Current density like solution concentration produces some small effects in resultant characteristics of the films as indicated by capacity measurements. There is probably also a relationship with oxide film density. Variation of the anode current density by a factor of 100 produces a capacity change of not more than a factor of 2.

Temperature.—Electrolyte temperature effects have only a small net effect on the anodic films. The

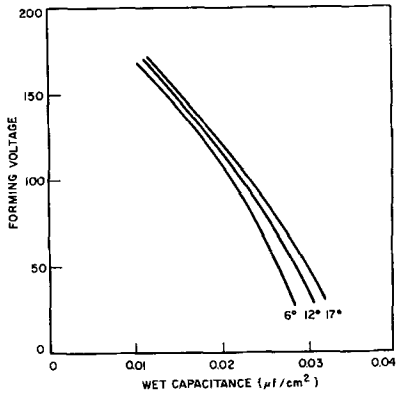

Fig. 1. Temperature effects on anodized films

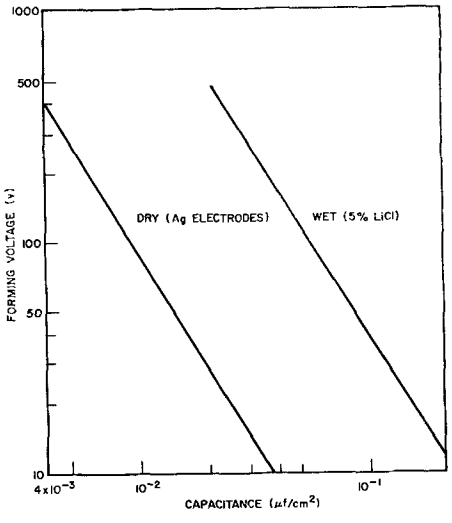

Fig. 2. Effect of forming voltage on film capacitance

three capacity curves in Fig. 1 show only minimal changes in film character employing formation temperatures from 6° to 17°C. The effect is somewhat greater at forming voltages below 100 than at higher formation voltages. The increase in capacitance probably indicates increased solvent action on the films. At much higher temperatures of the order of 80°-100°C, highly porous noninsulating films are formed, indicative of excessive solvent action.

Voltage.—As would be anticipated, voltage to which an anodic film on titanium is formed has by far the most profound effect on the net film character and, to a great extent, determines properties of the film produced. The effect of voltage on the film capacity is illustrated by the data in Fig. 2. Curves are shown for both dry measurements utilizing silver electrodes and wet measurements taken in 5% lithium chloride. It is evident that these values differ by about a factor of 5. This would indicate that surface areas between the two measurements differ by about a factor of 5. Microscopic examination of the films tends to confirm their highly roughened character and hence their grossly increased actual area as compared with geometric area. Surface character is revealed by the microscope which appears quite similar to that observed for anodized tantalum and aluminum. Typical electron micrographs are shown in Fig. 3 and 4. These areas illustrate typical blistering and

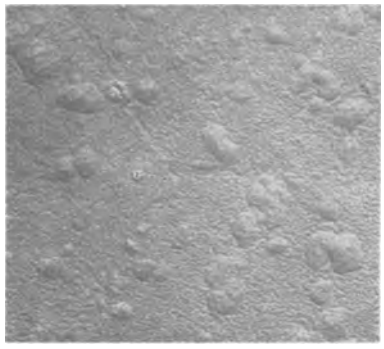

Fig. 3. Blisters and microcracks, anodized Ti surface, 150v. Magnification 3500X.

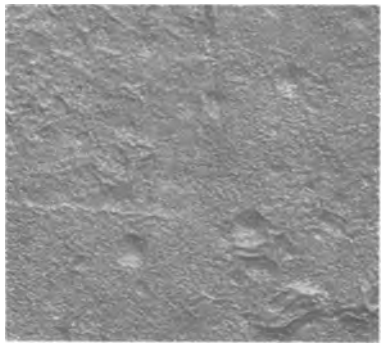

Fig. 4. Grain boundary area, anodized Ti surface. Magnification 3500X.

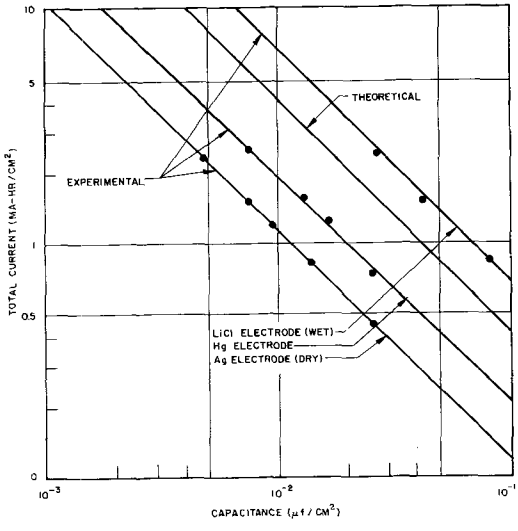

Fig. 5. Film capacitance as a function of total current

microcracks which are commonly detected on detailed examination of anodic films.

Total current.—Capacitance of films as a function of total current appears to follow Faraday's law as shown by the data in Fig. 5 comparing experimental results with the theoretical curve obtained by calculating the amount of TiO_2 deposited through a tetravalent change (average dielectric constant of 100 assumed). The curve obtained using an electrolyte is the only one providing for a true surface area contact; it indicates that the formation of TiO_2 takes place at a rate slightly less than the theoretically calculated rate. Oxygen evolution taking place during formation of the films indicates that efficiency of the reaction is less than 100%. This is

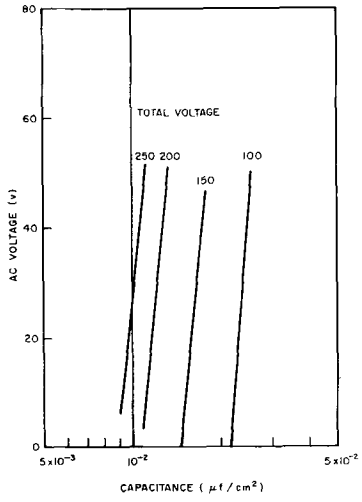

Fig. 6. Effect of superimposed a.c. on film capacitance

particularly true of films formed to greater than 100v. At less than 100v there is negligible gas evolution observed at the anode.

The total current passed in forming a given film is largely proportional to the formation voltage. The total current required to reach a minimum current value is also directly proportional to the magnitude of the formation voltage.

Superimposed a.c.—The beneficial effects of superimposed a.c. on d.c. in the case of both electrolytic deposition and electrolytic conversion processes are well known. These effects were briefly studied during this work. It was found that the presence of a.c. in the circuit tended to increase capacity value slightly. This value also increased for any given formation voltage as a percentage of a.c. was increased. An even more profound effect was observed in the case of changes in loss factors of the films. These observations are illustrated by the curves in Fig. 6 and 7.

Referring to Fig. 7, it is seen that for a 150-v film the loss factor decreased from 6 to 2% by raising the percentage of a.c. voltage from 0 to 60%. This behavior is probably explained by increased compaction and higher resultant densities for the films produced. The presence of a.c. would tend to produce cyclic solution-deposition actions which would, in turn, tend to result in increased film density.

Film Characteristics

Films produced by the procedures described are essentially insulating in character. Resistances of the order of megohms are generally measured. As would be expected, the electrical resistance is a direct function of the forming voltage. It is also a function of the final current obtained in the anodizing procedure. Minimum current values produce maximum film-resistance values. The two curves shown in Fig. 8 illustrate these tendencies for representative samples.

Electrical loss values appear to be largely a function of film porosity and, in turn, film density. They are largely dependent on final currents obtained in the forming process. Films at any given voltage may be formed to any loss value down to 0.5-1% de-

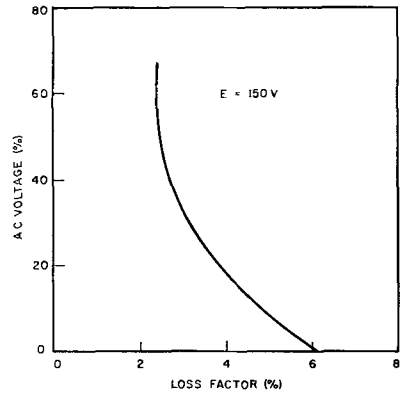

Fig. 7. Effect of superimposed a.c. on film-loss factor

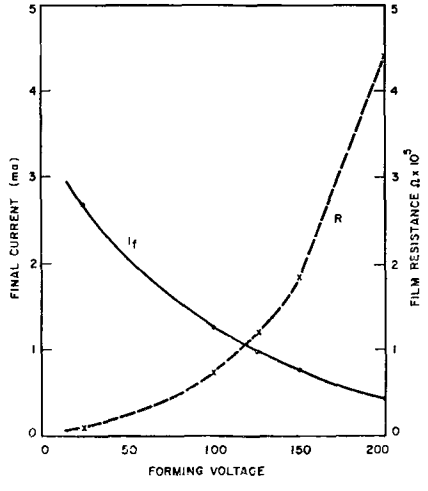

Fig. 8. Minimum current resistance for films formed to 200v; specimens 14 cm² area; 25% electrolyte.

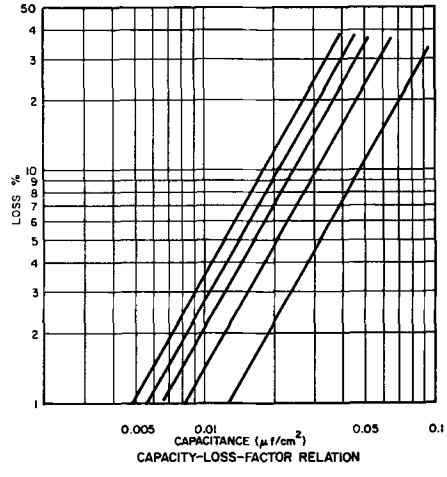

Fig. 9. Capacity-loss factor relation for Ti dielectric films, measured in 5% LiCl for 250, 200, 150, 100, and 50v formation, left to right.

pendent on formation voltage. As the loss value is lowered, capacity values are likewise lowered. The final part of the formation process during which the current drops from its maximum to its minimum value probably results in the filling in of pores and general compaction of the film. The data in Fig. 9 illustrate the capacitance-loss relationship for films formed at 5 different voltages.

Accurate values for film thickness have not yet been obtained in this work. However, approximate values have been obtained by calculations based on

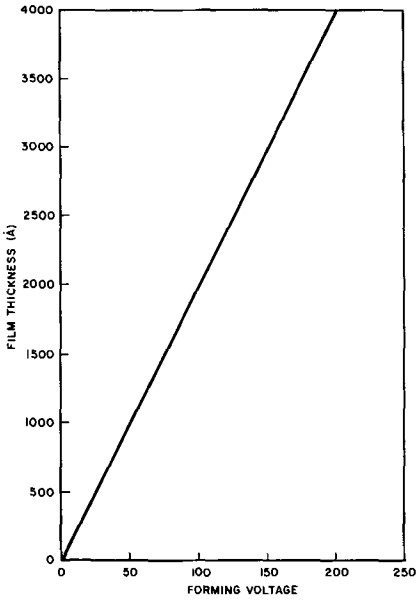

Fig. 10. Film thickness as a function of forming voltage

current-voltage relations, interference colors, and rough optical measurements. Currently available information indicates a voltage-thickness curve of the form shown in Fig. 10.

An indirect approach may be made toward calculation of effective dielectric constants for anodic films based on current density-voltage characteristics during the film formation. Current density for a typical process may be expressed as

$$\frac{i}{A} = \text{const} \exp \frac{\beta E}{x}$$

where i is the current, A is the surface area (cm^2), E is the voltage, x is the film thickness, and β is a constant. Then, since $x = k/C$, where C is capacitance

$$2.3 \log \frac{i}{A} = 2.3 \log \text{const} + \frac{\beta EC}{k}$$

and

$$EC = \frac{2.3\,k}{\beta} \left(\log \frac{i}{A} - \log \text{const} \right)$$

Thus, the voltage-capacitance product should be a linear function of the log of current density with a slope equal to $2.3k/\beta$ where k is $8.84\epsilon/10^8$ and ϵ is the dielectric constant.

On the basis of slope of the curve for the logarithm of current density as a function of the voltage-capacity product, it is possible to calculate values for the effective dielectric constant of anodic films. A value of 5×10^{-6} is assumed for β.

For 200-v films giving a capacitance value of 0.035 $\mu f/cm^2$ in 1% lithium chloride and showing leakage currents of 46.3 $\mu a/cm^2$, a value for the effective dielectric constant of 13.2 is calculated. Using this approach, one obtains values of 12-16 for the effective dielectric constant.

These calculations entail the use of certain approximations and are thus subject to errors. Such values would indicate that the oxide film produced is not entirely of the rutile form, although other evidence has shown rutile to be present (12).

Using approximate dielectric constant values as obtained in the above calculations, one may obtain some estimates of film thickness from the basic capacitance relationships: $C = K\epsilon/x$ where x is the thickness. Values obtained fall roughly on the curve shown in Fig. 10.

Conclusions

A study of anodic oxidation of titanium surfaces reveals that two types of films may be produced. Electrolytes with low solubility for the product film produce thin, translucent films with poor electrical and insulating characteristics. Electrolytes possessing solvent action with product film material produce thick, highly insulating films with a porous structure. These films have high resistivity values, but their indicated dielectric constants are not of sufficient magnitude to indicate the presence of a stoichiometric rutile structure. The film may consist of an amorphous structure over a rutile film layer.

The anodic oxidation procedure in the phosphate electrolyte is largely voltage controlled, the formation voltage governing the major film properties. There are smaller effects due to anodic current density, solution concentration, and temperature.

Films are indicated to form at the rate of about 20Å/v up to 200v. This value apparently decreases slightly as formation voltage increases. In the range up to 300v, the films appear to form at the rate of about 17Å/v. This is apparently due to decreased availability of titanium ions for film formation and to increased local solubility in the electrolyte due to thermal effects.

It has been demonstrated that formation of thick, adherent, high-voltage films is possible on titanium substrates. Further work is necessary to understand fully the mechanics of formation and to characterize and identify the resultant film structure fully.

Acknowledgment

This work was carried out as part of the Lockheed Microsystems Electronics program under the LMSC general research organization.

Acknowledgment is made to R. T. Lamoureux, W. J. Coy, R. A. Quinn, and D. A. Vance for contributions to this work. All are on the staff of the LMSC Research Laboratories.

Manuscript received Oct. 12, 1961; revised manuscript received July 10, 1962. This paper was prepared for delivery before the Detroit Meeting, Oct. 1-5, 1961.

Any discussion of this paper will appear in a Discussion Section to be published in the December 1963 JOURNAL.

REFERENCES

1. E. Ence and J. Margolin, *J. Metals*, **6**, 346 (1954).
2. P. A. Jacquet, *Metal Treatment*, **18**, 176 (1951).
3. C. Ma and E. M. Peres, *Ind. Eng. Chem.*, **43**, 675 (1951).
4. D. A. McLean, N. Schwartz, J. K. Werner, and M. Gresh, Bell Tel. Labs. Rpt. AD-232-690, Jan. 15, 1960, pp. 14-15.
5. Philco Corp., *Fifteen Month Summary Report on Electrolytic Capacitors*, H-2177F, AD-231-587, July 1, 1959.
6. E. Wainer, U. S. Pat. 2,874,102, Feb. 17, 1959.

7. G. W. A. Dummer and H. M. Nordenberg, "Fixed and Variable Capacitors," pp. 185-186, McGraw-Hill Book Co., New York (1960).
8. K. O. Beck, U. S. Pat. 2,949,411, Aug. 16, 1960.
9. G. Hass, *Vacuum* 11, [4] 331 (1952).
10. Boeing Airplane Co., *Protective Coatings for Titanium*, by E. C. Parr, Rpt. DR-2522, June 11, 1958.
11. S. Yamaguchi, *This Journal*, **108**, 302 (1961).
12. M. Tecotzky, Paper presented at the Detroit Meeting, Electrochemical Society, Oct. 1961.

A-C Methods in Interfacial Electrical Phenomena

Akira Watanabe

Institute for Chemical Research, Kyoto University, Takatsuki, Osaka-fu, Japan

ABSTRACT

The mechanical vibration of the electrical double layer gives rise to the generation of an alternating voltage. In the case of glass-liquid interfaces this effect can be used to measure the streaming potential by an a-c technique. For mercury-solution interfaces, an alternating current is generated, which provides new methods for double layer capacity measurements. These phenomena may also be used in various practical applications, such as mechano-electric transducers.

Very few a-c methods have been employed in interfacial electrical measurements; most of them, for instance, the streaming potential, electrophoretic mobility measurements, etc., have been carried out by using steady-state methods (1). During the course of experiments on the interfacial electrical phenomena from 1942 to 1943, it was found in our laboratory that the mechanical vibration of interfaces gave rise to the generation of an a-c voltage. This we called "U-effect" (2), since this phenomenon was discoverd by using a U-tube. In this paper stress is placed on the detailed description of the methods of these measurements rather than on the presentation and discussion of the results obtained from them.

A-C Streaming Potential

The generation of the d-c potential difference by the tangential displacement at solid-liquid interfaces is widely known as one of the electrokinetic phenomena, the streaming potential (1). The potential difference E between the two electrodes, a and b of Fig. 1, is given by

$$E = P\,\epsilon\,\zeta/4\,\pi\,\eta\,\lambda \qquad [1]$$

where P is the pressure applied to the liquid phase, ζ the so-called electrokinetic zeta potential, and ϵ, η, and λ are, respectively, the dielectric constant, the viscosity, and the specific conductivity of the liquid.

It was found in this connection that an a-c potential difference was obtained between these two electrodes when a periodically changing pressure was employed (3). This phenomenon is called "U-effect I" and is the generation of an a-c streaming potential. The potential had the same wave character as the original vibration in all experiments up to a frequency as high as 25,000 cps.

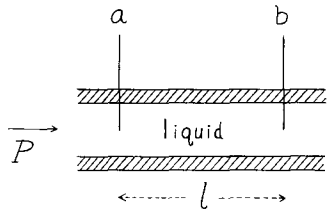

Fig. 1. Glass capillary for the streaming potential generation

Theoretical.—A simple derivation of the equation of the a-c potential, $e = \sqrt{2}\,\mathbf{E}\,\exp\,(j\omega t)$, is made by using Helmholtz's model of an electrostatic condenser for the electric double layer at the solid-liquid interface, *viz.*

$$\sigma = \epsilon\,\zeta/4\,\pi\,\delta \qquad [2]$$

where σ is the interfacial charge density and δ the gap distance of the equivalent condenser (1). Here, $j = \sqrt{-1}$, t is the time, $\mathbf{E}$ the complex effective value, and ω the circular frequency (*i.e.*, $\omega = 2\,\pi\,f$, f being the frequency in cps) of the a-c voltage e. If we take the x-axis in the direction tangent to the interface, the relative displacement at the interface, Δx, is given by

$$\Delta x = \sqrt{2}\,\mathbf{X}\,\exp\,(j\omega t) \qquad [3]$$

where $\mathbf{X}$ is the complex amplitude of vibration. The instantaneous transfer of the electric charge, *i.e.*, the current i, produced by this mechanical motion is given by

$$i = 2\pi r\sigma\,(d\Delta x/dt) = (j\omega\epsilon\zeta r\mathbf{X}/\sqrt{2}\delta)\,\exp\,(j\omega t) \qquad [4]$$

where r is the radius of the capillary. On the other hand the current i is also given by Ohm's law, *viz.*

$$i = e\lambda\pi r^2/l \qquad [5]$$

where l is the distance of the two electrodes. Equating Eq. [4] and [5], we obtain the following expression of the a-c streaming potential

$$\mathbf{E} = j\omega\epsilon\zeta l\mathbf{X}/2\pi\lambda\delta r \qquad [6]$$

This means that the a-c voltage is proportional to the zeta potential and the dielectric constant and

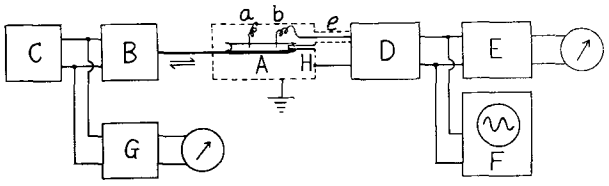

Fig. 2. Block diagram of zeta potential measurements by U-effect I.

inversely proportional to the specific conductivity of the liquid, if a constant mechanical vibration of a given vibrating element is employed.

Experimental.—As an example of streaming potential measurements by U-effect I, results of experiments on a glass capillary in contact with cationic surface active agent solutions will be given.

The experimental device is shown schematically in Fig. 2. The glass capillary element A, filled with the surface active agent solution, is forced to vibrate by an electrodynamic vibrator B, which is driven by an audiofrequency oscillator C. The frequency used was 200 cps in these experiments. The output voltage e is amplified by an amplifier D and read by means of a valve voltmeter E. The valve voltmeter G gives the relative magnitude of the vibrating amplitude **X**. The measurements of the absolute amplitude of vibration will be shown later. A fine glass rod H serves as the piston of the capillary to prevent the liquid from moving with the glass wall. The cathode ray oscilloscope F is for the purpose of observing the wave form of e.

The solutions used were $10^{-4}N$ KCl aqueous solutions, containing dodecyl- or cetylpyridinium chloride in various concentrations. The potassium chloride was added as an indifferent electrolyte in order to compress the thickness of the diffuse double layer, since otherwise the zeta potential data would be difficult to interpret (6).

It can be seen from Eq. [6] that the zeta potential is proportional to $\mathbf{E}\lambda$ when a constant vibration is employed, since ϵ can be assumed constant in the case of dilute aqueous solutions as in the present experiments. The relative ζ-value, *i.e.*, ζ/ζ^*, is therefore obtained by the ratio $\mathbf{E}\lambda/\mathbf{E}^*\lambda^*$, where the asterisk denotes the absence of surface active agents.

The ζ/ζ^*-values thus obtained are plotted against the logarithms of the surface active agent concentration in Fig. 3. On the same figure are plotted, for comparison, the ζ/ζ^*-values obtained by d-c measurements. These latter measurements were carried out by the ordinary constant pressure method using a plug of Pyrex glass powder (4). A marked parallelism can be found between the two sets of curves obtained by the a-c and d-c methods, except for the higher absolute values of ζ/ζ^* at higher concentrations in the case of the a-c data: this would probably be due to the difference in the qualities of glass used. The curves show the typical behavior of the effect of cationic surface active agents on zeta potentials, causing a change in sign at certain surface active agent concentrations (4, 5).

According to the author's theoretical treatment of the zeta potential, using the Stern and the Gouy-

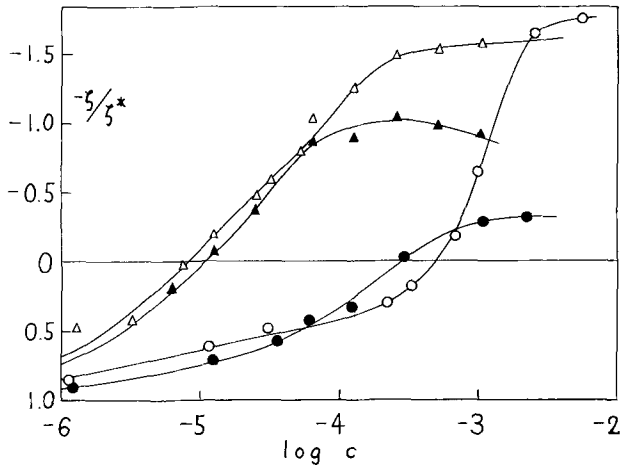

Fig. 3. Relative zeta potentials as functions of the logarithms of the surface active agent concentrations; indifferent electrolyte, $10^{-4}N$ KCl. •, Dodecylpyridinium chloride, d-c method; ○, the same, a-c method; ▲, cetylpyridinium chloride, d-c method; △, the same, a-c method.

Chapman theories of the electrical double layer, the following equation holds (4)

$$\zeta = [c_i/(c + c_i)]^{1/2}[\zeta^* + k_1 k_2 c/(1 + k_2 c)] \quad [7]$$

where

$$k_1 = (2\pi \cdot 1000\, kT/\epsilon c_i N)^{1/2} N_1 (z/|z_i|) \quad [8]$$

and

$$k_2 = \exp(\Delta G/kT)/55.6 \quad [9]$$

Here c and c_i are the concentrations, and z and z_i are the valencies (including signs), of the surface active agent and the indifferent electrolyte, respectively. ΔG and N_1 are the electrochemical free energy and the number of available sites of adsorption, and k, T, and N are the Boltzmann constant, the absolute temperature, and the Avogadro number. Here, the first order Debye-Hückel approximation was taken.

It is easy to derive simple equations to be used for estimations of ΔG and N_1 in the case of $c << c_i$, *viz.*

$$(d\zeta/d \log c)_o = -2.303\, \zeta^* [1 + (\zeta^*/k_1)] \quad [10]$$

and

$$1/c_o = -k_2 [1 + (k_1/\zeta^*)] \quad [11]$$

Here the subscript zero denotes the isoelectric point, *i.e.*, $\zeta = 0$. The values of ΔG and N_1 obtained from the experimental curves in Fig. 3 by using Eq. [10] and [11] are summarized in Table I. It will be seen that N_1-values are almost the same for the two cationic surface active agents of different chain lengths. The ΔG-values, on the other hand,

Table I. Adsorption characteristics of cationic surface active agents on a glass surface at the room temperature

Surface active agent		N_1, cm^{-2}	ΔG, cal/mole
DPC	d-c method	1.06×10^{12}	7810
	a-c method	1.60×10^{12}	6880
CPC	d-c method	0.69×10^{12}	9570
	a-c method	0.68×10^{12}	9720

DPC, dodecylpyridinium chloride; CPC, cetylpyridinium chloride; indifferent electrolyte, $10^{-4}N$ KCl.

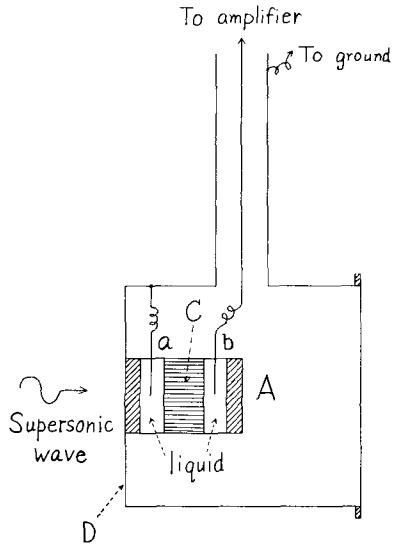

Fig. 4. Unit cell of the hydrophone of U-effect I

show a difference of approximately 2 ~3 kcal/mole for an increase in chain length from 12 to 16. These values of ΔG and the increase with chain length are sufficiently reasonable if we consider the relatively poor accuracy of interfacial electrical measurements in general (4, 5). The values of N_1 ($\cong 10^{12}$ cm^{-2}) are considerably smaller than those obtained on negatively charged silver iodide sols (5), indicating that only a very small portion of the glass surface provides adsorption sites for these cationic surface active agents.

It has been difficult to do electrokinetic measurements by d-c methods, especially in the case of solid-organic liquid interfaces, due to the high resistance of the plug, and hence of the circuit. However, this kind of difficulty can be reduced to a considerable amount by using the a-c method as given above. Figure 4 shows another type of such measurements. This is the unit cell of a hydrophone of a glass filter vibrating element A filled with various liquids, *i.e.*, distilled water, methanol, ethanol, acetone, pyridine, acetic acid anhydride, carbon tetrachloride, or benzene. The element has a pair of electrodes, a and b, immersed on both sides of the capillary system C, and attached vertically to the diaphragm D of the unit cell.

A supersonic wave of a constant power and frequency, here 13,500 cps, forces the diaphragm and hence the element to vibrate, giving rise to the generation of an a-c voltage by U-effect I at the two electrodes. This voltage is amplified and read by a valve voltmeter.

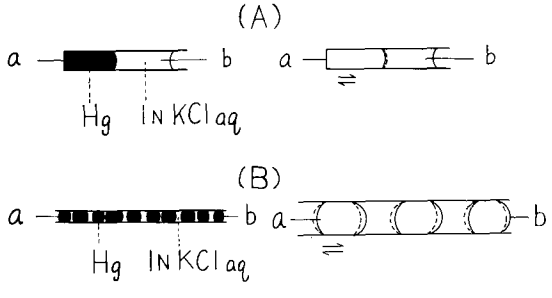

Fig. 5. Capillary elements of U-effect II

It was found that no a-c voltage generation was observed when benzene or carbon tetrachloride was used as the liquid phase. Moreover the relative value of zeta potential, $E\lambda/\epsilon$ (see Eq. [6]) was an increasing function of the dipole moment of the molecule of the liquid phase (6). This suggests that the zeta potential is intimately related to the dipole orientation of the organic molecules at the interface. This orientation takes place in order to minimize the free energy of the system, which gives rise to the "dipole double layer," including the diffuse part due to thermal agitation (6).

A-C Capacity Current

U-effects are not restricted to the case of solid-liquid interfaces, as shown above. If a glass capillary containing a mercury-salt solution interface, as shown in Fig. 5A, is forced to vibrate mechanically, an a-c voltage is generated between the two electrodes, a and b. The voltage has the same wave character as the mechanical vibration. This we called "U-effect II" (7). The principle is more or less the same as in the case of the condenser microphone, since the electrical double layer at the mercury-solution interface behaves as a perfect condenser (8). However, the total double layer capacity changes periodically by virtue of the interfacial area change in the present case, while it is due to the change in the condenser gap distance in the case of the condenser microphone.

The inner resistance of the element can be reduced by using a solution of high salt content, *e.g.*, 1*N* KCl or H_2SO_4. In addition it was found that the output voltage increased linearly with the number of interfaces, and hence a very efficient transducer could be made by using an element as is shown in Fig. 5B.

Theoretical.—The mercury-solution interface is equivalent to a perfect condenser, having a potential difference E, *vs.* the electrocapillary maximum. Its instantaneous integral capacity c is given by

$$c = C\,a = C\,A\,(1 + \rho) \qquad [12]$$

where C is the integral double layer capacity per unit area, a and A are the instantaneous and the average interfacial areas, and ρ is the time dependent term of vibration. The instantaneous current of the circuit i is given by

$$i = (d/dt)\,[c(E + e - i\,R_o)]$$
$$= (d/dt)\,[CAE\,(1 + \rho)\,\{1 + (e - i\,R_o)/E\}]$$
$$= CA\,[E(d\rho/dt) + d(e - i\,R_o)/dt] \qquad [13]$$

where R_o is the solution resistance and e the instantaneous potential drop at the load Z (see Fig. 6). Here the terms of higher orders in ρ have been neglected. In the case of the stationary state, com-

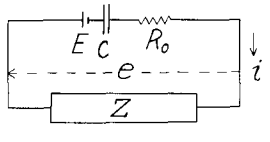

Fig. 6. Equivalent circuit of U-effect II

plex representations of the instantaneous quantities can be employed, as

$$i = \sqrt{2}\,\mathbf{I}\exp(j\omega t)$$

$$e = \sqrt{2}\,\mathbf{E}\exp(j\omega t)$$

and

$$\rho = \sqrt{2}\,\mathbf{P}\exp(j\omega t) \qquad [14]$$

where the phase differences are included in the corresponding complex amplitude terms, **I**, **E**, and **P**. Substituting Eq. [14] into Eq. [13], followed by rearrangements, we obtain

$$\mathbf{I} = j\omega CA\,(\mathbf{V} + \mathbf{E} - \mathbf{I}R_o) \qquad [15]$$

where

$$\mathbf{V} = E\,\mathbf{P} \qquad [16]$$

V is the "electromotive force of U-effect II." On the other hand, Ohm's law states that

$$\mathbf{E} = -\mathbf{I}Z \qquad [17]$$

Equating [15] with [17], we obtain the final equation, as

$$\mathbf{I} = \mathbf{V}/[(R + R_o) + j\{X - 1/(\omega CA)\}] \qquad [18]$$

where

$$Z = R + jX \qquad [19]$$

R and X being the resistive and reactive parts of the load. The a-c current **I** is, therefore, proportional to the electromotive force **V**, if a constant load is used. Since both **V** and C are functions of the polarization E, **I** is a complicated function of E.

Experimental.—Figure 7 is the block diagram of the circuit for the measurement of the **I**-E relation. The mercury-solution interface in a glass-capillary vibrating element A is polarized by a potentiometer B. The a-c current i generated by the mechanical vibration of this interface is measured by the a-c potential drop across a small load resistance R, amplified by the amplifier C, and read by the valve voltmeter D. The vibrating mechanism of the element is the same as in the case of Fig. 2, *i.e.*, E and F are, respectively, the vibrator and the oscillator. A constant amplitude of vibration was always used for each frequency.

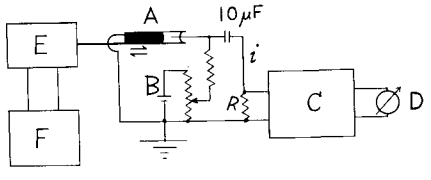

Fig. 7. Block diagram of the measurement of the current-polarization relationship of U-effect II.

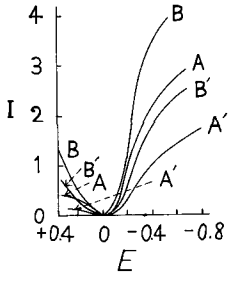

Fig. 8. A-c currents of U-effect II as functions of polarizations of the mercury surface. I is in an arbitrary scale. A, 1N KCl aq, 300 cps; A', 1N KCl aq, 500 cps; B, 1N KI aq, 300 cps; B', 1N KI aq, 500 cps.

Figure 8 shows the experimental relative **I**-values as functions of E. The curves A and A' are for 1N KCl aqueous and B and B' are for 1N KI aqueous. As expected from the theory, Eq. [16] and [18], the current **I** is zero at the electrocapillary maximum, where $E = 0$, and increases with increasing $|\mathbf{E}|$. The difference in the curves for KI and for KCl is explained by the higher integral capacity of the mercury-KI solution interface, as compared with that for the mercury-KCl solution interface (8, 10).

Double Layer Capacity Measurements by U-effect II

Impedance matching method.—If a purely resistive load is used, *i.e.*, $X = 0$ and hence $Z = R$ in Eq. [18], the power W supplied to the load is given by

$$W = I^2R = V^2R/[(R + R_o)^2 + 1/(\omega CA)^2] \qquad [20]$$

where the quantities shown by italic types are the moduli of the corresponding vectors. The condition of the maximum power supply, *i.e.*, $\partial W/\partial R = 0$, is then given by

$$R_o^2 + 1/(\omega CA)^2 = R^2 \qquad [21]$$

This is generally known as impedance matching since, when the modulus of the inner impedance and the load resistance are the same, the maximum power is supplied to the load.

This principle can be applied to double layer capacity measurements at mercury-solution interfaces (11). If we find the matched load resistance at two frequencies, it is an easy matter to solve for C and R_o by using Eq. [21].

Resonance method.—For an inductive load, *i.e.*, $Z = R + j\omega L$, the current is given by

$$\mathbf{I} = \mathbf{V}/[(R + R_o) + j\{\omega L - 1/(\omega CA)\}] \qquad [22]$$

The condition of the maximum current is widely known as the resonance phenomenon and is given by

$$\omega L = 1/(\omega CA) \qquad [23]$$

This principle is also applicable to double layer capacity measurements (12).

Experimental.— Figure 9 is the block diagram of the apparatus for double layer capacity measurements using U-effect II. The capillary element A containing a mercury-solution interface is inserted through a small hole into a glass vessel B. This

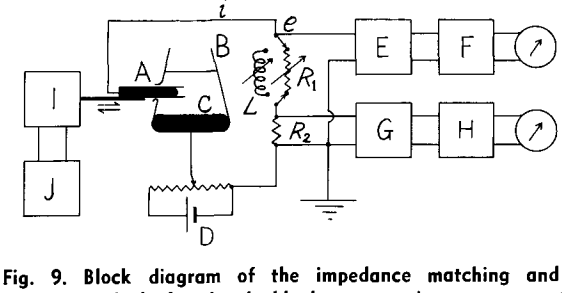

Fig. 9. Block diagram of the impedance matching and the resonance methods for the double layer capacity measurements at mercury-solution interfaces.

vessel contains the salt solution to be investigated, *e.g.*, 1*N* KCl aqueous. The interface in the capillary is polarized by a potentiometer D, the large pool of mercury C being the reference electrode.

The a-c current produced by the mechanical vibration of the element is supplied to the load, which consists of a variable resistance R_1 (40 k ohm var.) and a small resistance R_2 (100 ohm). The a-c potential drop e at the load $(R_1 + R_2)$ is amplified (by E) and read by means of a valve voltmeter F, while the current i is read by another amplifier (G)-valve voltmeter(H) system from the potential drop at the resistance R_2. By varying R_1 continuously, the condition of the maximum power supply is determined, *i.e.*, the value of $(R_1 + R_2)$ which gives the maximum power. The vibration of the element is produced by means of a vibrator I driven by an oscillator J.

If we use instead of R_1 a variable inductance L, and measure the current by the potential drop at R_2, we can easily determine the resonance condition by varying L, and hence the C-value by using Eq. [23]. It is also possible to work out the solution resistance R_o from the analysis of the shape of the resonance curve (9, 13).

Practical Applications of U-effects

Several characteristics of U-effect II.—In addition to the contributions to interfacial electrical measurements in supplying various new methods as given above, U-effects I and II can also be applied to various mechano-electric transducers (7). It is then important to know several characteristics of the capillary vibrating element for these purposes. From the view point of the practical application, however, U-effect II is far superior to the other due to the lower internal impedance of the element, the higher a-c voltage gain, etc. We shall, therefore, examine the characteristics of the elements of U-effect II in this section, although it has been proved by experiments that U-effect I is also applicable to various kinds of transducer devices (14).

Figure 10 shows the block diagram of the measurement circuit. The a-c voltage obtained by the mechanical vibration of the capillary element A is measured by an amplifier(B)-attenuator(C)-amplifier(D)-valve voltmeter(E) system. The current is measured by the potential drop across a small

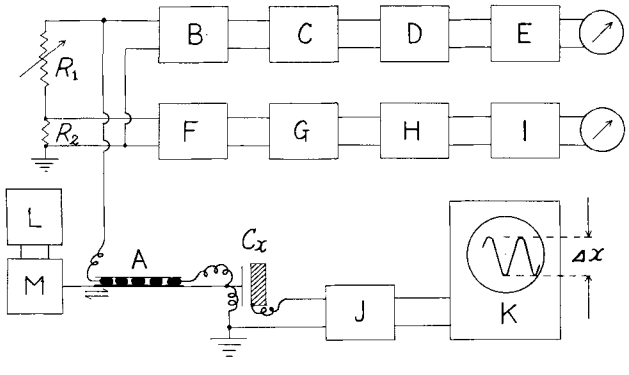

Fig. 10. Block diagram of characteristic measurements of U-effect II.

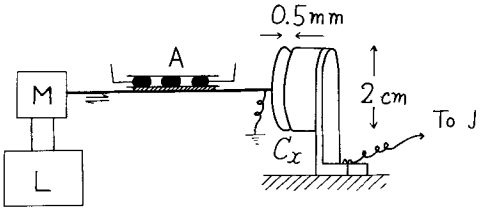

Fig. 11. Vibrating condenser for vibrational amplitude measurements.

constant resistance R_2, which is read by another amplifier (F)-attenuator(G)-amplifier(H)-valve voltmeter (I) system.

The amplitude of vibration was measured by a frequency modulation circuit J. The principle is as follows. The frequency of a self-oscillator is a function of the capacity of its tank circuit. Hence, the mechanical vibration of a condenser can be converted into a frequency change, which is further converted into a voltage change by a detector. This voltage change is supplied, after amplification, to the vertical axis of the cathode ray oscilloscope K, and read by the height of the trace on the screen. L and M are, respectively, the oscillator and vibrator for the mechanical vibration. Figure 11 shows the vibrating condenser C_x attached to the end of the vibrating rod. This condenser constitutes a part of the tank circuit of the self-oscillator set in the FM circuit. The symbols A, L, M, and J have the same meanings as in Fig. 10.

The inner impedance of the element was measured by the impedance matching method. The voltage at the load $(R_1 + R_2)$ in Fig. 10 is measured as before, and the current by the potential drop at R_2. Since the decibel readings, Db_1 and Db_2, of the attenuators C and G are the measures of logarithms of the voltage and current, the sum $(Db_1 + Db_2)$ is the measure of the power supplied to the load $(R_1 + R_2)$. By changing the load resistance by varying R_1, and maintaining the readings of the voltmeters E and I at constant values, a condition can be found which gives the maximum $(Db_1 + Db_2)$ value. The value of $(R_1 + R_2)$ under this condition is equal to the inner impedance of the element at the frequency used.

Table II shows the values of the inner impedance of capillary elements of large, medium, and small cross sections, *i.e.*, (I) 0.76, (II) 0.49, and (III) 0.37 mm in diameter, respectively. Each element contains forty mercury-1*N* HCl aqueous interfaces. It is seen from this table that the internal impedance is of the order of several thousand to several tens of thousand of ohms at 1000 cps and is inversely proportional to the cross-sectional area of the ele-

Table II. Inner impedance of the capillary elements of U-effect II at 1000 cps

Element No.	Diameter, mm	Impedance, k ohm
I	0.76	5
II	0.49	20
III	0.37	30

Number of interfaces, 40; solution phase, 1*N* HCl aqueous.

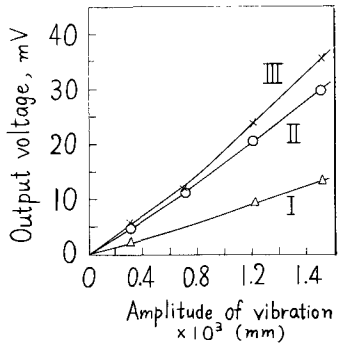

Fig. 12. Output voltages of U-effect II as functions of amplitudes of vibration at 1000 cps.

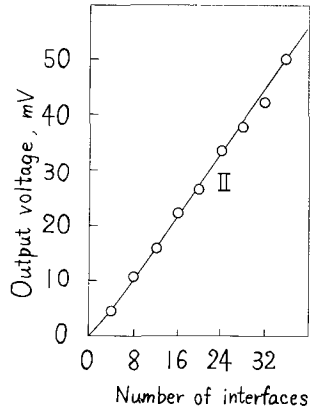

Fig. 13. Output voltage of U-effect II as a function of the number of interfaces at 500 cps. Element No. II.

ment. It was also found that the internal impedance was proportional to the number of interfaces.

Figure 12 shows the output voltages as functions of the amplitude of vibration for the three elements. This is not a linear relation, since the amplitude of the periodic interfacial area change is of an order higher than that of the one-dimensional amplitude measured by the FM circuit.

Figure 13 shows the linear relation between the output voltage and the number of interfaces contained in the capillary element, n. Here the element II was used, and the amplitude and frequency of vibration were kept constant at 2.6 x 10^{-3} mm and 500 cps, respectively. The load was always matched to the internal impedance of the element, since otherwise this impedance would become larger than the load for higher n-value, and a saturation effect would be observed.

The curves in Fig. 14 are logarithmic plots of the voltage-frequency relation at a constant amplitude of vibration, *i.e.*, 1.2 x 10^{-3} mm. In each case, the load resistance was matched to the internal impedance of the element at 1000 cps. It is clear from these curves that the response at lower frequencies is higher for larger elements, while that at higher frequencies is higher for smaller elements. This kind of frequency character is always shown by the free type of vibration employed here, which is mainly due to the natural frequencies of the elements. It will be shown later that flat frequency character curves are obtained by employing a piston type of vibration.

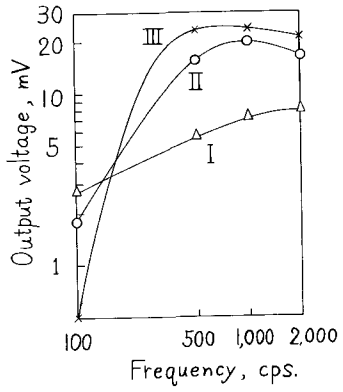

Fig. 14. Frequency character curves of U-effect II for the free type of vibration of the elements I, II, and III. Amplitude of vibration: 1.2 x 10^{-3} mm.

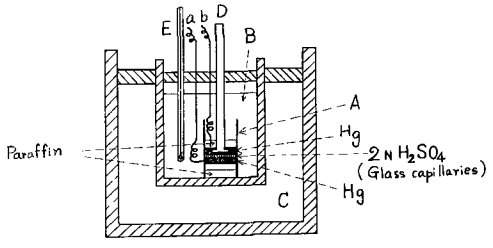

Fig. 15. Cooling experiments of U-effect II

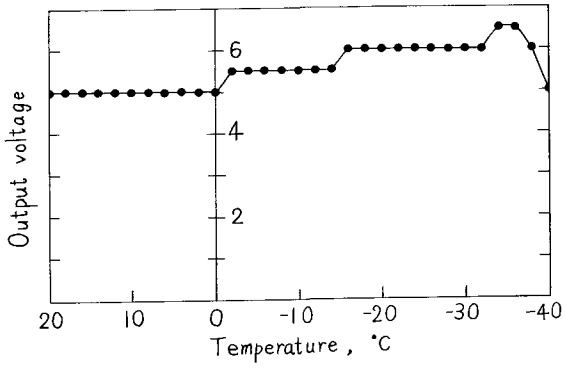

Fig. 16. Output voltage of U-effect II as a function of temperature.

Effect of cooling (15).—Figure 15 shows the experimental device. An element of U-effect II, A, made of a glass filter No. 2, was dipped in an alcoholic bath B, cooled by the dry ice C, and the receiving sensitivity measured as a function of the bath temperature. A constant mechanical pulse is delivered to the element by knocking the upper end of the glass pole D, and the pulse voltage generated at the two electrodes, a and b, was measured by the height of the trace at the screen of a cathode ray oscilloscope. E is the thermometer.

Figure 16 shows the results obtained. The output voltage is practically constant from 20 to *ca.* −40°C. The melting points of the mercury and the 2*N* H_2SO_4 aqueous, which was used as the solution phase of the element, were −38.89° and −19°C, respectively. The results indicate, therefore, that even if the solution is in the solid state, the output voltage of U-effect II does not diminsh.

Hydrophones.—An example of the practical application of U-effect I to a hydrophone device has

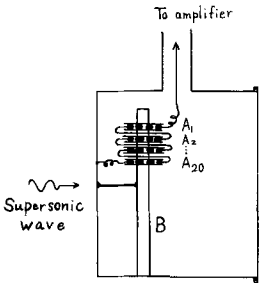

Fig. 17. Unit cell of the hydrophone of U-effect II

already been given in Fig. 4. A hydrophone using U-effect II is shown in Fig. 17. The unit cell has twenty capillary elements, A_1, A_2, . . . and A_{20}, which are fixed to a resonating plate B and connected in series. Each element contains twenty mercury-solution phases. The output voltage is amplified and read by a valve voltmeter.

The comparison of the receiving sensitivities of the unit cells of U-effects I and II and also of the Rochelle salt was made by 10-meter water tank tests. The unit cell and the supersonic source, using the magnetostriction of a nickel pole with the anode loss of about 1w and the frequency of 13,500 cps, confronted each other in the tank, and the readings of the output voltage were observed. Outdoor tests were also made at the *Yodo* river, in which the maximum receivable distance was tested by using the same supersonic source, with the anode loss of about 10w.

Table III shows the average results thus obtained. It is clear that the unit cell of U-effect II has a receiving sensitivity of twice to 1.5 times as high as that of the unit cell of the Rochelle salt.

Pickups of the electrophonograph.—In applying the U-effects to pickups of the electrophonograph, a uniform frequency response is demanded, avoiding the resonance of the vibrating system. A pickup of the free vibration type of the capillary element of U-effect II is shown in Fig. 18A. The curve I of Fig. 19 is its frequency character curve, indicating a marked peak at about 400 cps. It was also proved experimentally that this peak shifted toward the high-frequency region for a fine capillary (curve II) and toward the low frequency region for a large one (curve III). The internal diameters of these capillaries are 0.135, 0.148, and 0.182 mm, respectively.

The influence of the electrolyte of the solution phase of the element is also examined. A solution of high electrolytic conductivity and low viscosity is desirable. For instance the response at lower frequencies is lower in the case of sulfuric acid for low temperatures than in the case of hydrochloric acid.

Table III. Receiving sensitivities of the hydrophones of U-effects I and II and the Rochelle salt

Element	10-meter water tank test. (Readings of the valve-voltmeter)	Maximum receivable distance, km
U-effect I	42	1.9
U-effect II	143	3.8
Rochelle salt	68	2.5

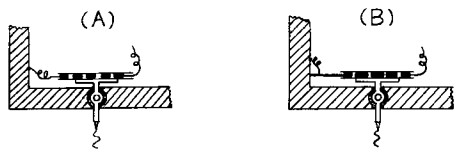

Fig. 18. Pickups of the electrophonograph using U-effect II: A, free type; B, piston type.

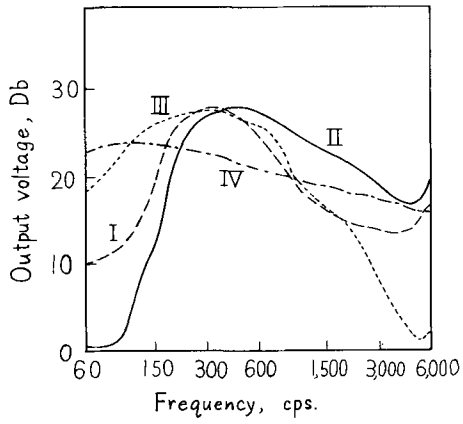

Fig. 19. Frequency character curves of the pickups of U-effect II. The output voltage is in an arbitrary scale.

This is due to the larger viscosity increase at low temperatures for the former solution.

A pickup of very high quality is made by employing the piston type of vibration to one of the electrodes as shown in Fig. 18B. The frequency character curve of this type of pickup is given by the curve IV in Fig. 19, showing a satisfactory linearity over the frequency range examined.

Summary

The mechanical vibration of the electrical double layer in a glass capillary gives rise to the generation of an a-c voltage between the two ends. This phenomenon is called in general "U-effect." In the case of glass-liquid interfaces, we call it "U-effect I," while in the case of mercury-salt solution interfaces "U-effect II." The former is an effect of an a-c streaming potential generation, and the latter is an a-c capacity current of the double layer at mercury-solution interfaces.

U-effect I can be used to measure streaming potentials by an a-c technique, providing an alternative method to compare with the ordinary d-c method. U-effect II has its application in providing new methods for the double layer capacity measurements at mercury-solution interfaces.

U-effects, both I and II, are applicable to all sorts of mechano-electric transducers, and it was shown that the hydrophone and pickup using U-effect II were equal to or even superior to those using Rochelle salt.

Acknowledgments

The author would like to thank the National Science Foundation and the Theoretical Division of this Society for giving him the opportunity of delivering this paper before the Indianapolis Meeting, by supporting the travel expenses from Japan to the States. He also wishes to express his gratitude

to Professor I. Tachi of Kyoto University for his continuous advice and encouragement. He is greatly indebted to Dr. S. Ueda and Mr. F. Tsuji, since the data used in this article were exclusively obtained by their cooperation.

Manuscript received April 17, 1962; revised manuscript received Sept. 17, 1962. This paper was prepared for delivery before the Indianapolis Meeting, April 30-May 3, 1961.

Any discussion of this paper will appear in a Discussion Section to be published in the December 1963 JOURNAL.

REFERENCES

1. H. A. Abramson, "Electrokinetic Phenomena," Chem. Catalog, New York (1934); J. A. V. Butler, "Electrocapillarity," Methuen, London (1940).
2. S. Ueda, F. Tsuji, and A. Watanabe, *Proc. 2nd Intern. Congr. Surface Activity*, London, **3**, 3 (1957).
3. S. Ueda, A. Watanabe, and F. Tsuji, *Bull. Inst. Chem. Res., Kyoto Univ.*, **20**, 28 (1950); *Mem. Coll. Agr., Kyoto Univ.*, **57**, 22 (1950); *J. Electrochem. Soc., Japan*, **19**, 142 (1951).
4. A. Watanabe, F. Tsuji, and S. Ueda, *J. Electrochem. Soc., Japan*, **29**, 777 (1961).
5. R. H. Ottewill and M. C. Rastogi, *Trans. Faraday Soc.*, **56**, 866 (1960).
6. S. Ueda, F. Tsuji, and A. Watanabe, *J. Electrochem. Soc., Japan*, **24**, 74 (1956).
7. S. Ueda, F. Tsuji and A. Watanabe, *Bull. Inst. Chem. Soc., Kyoto Univ.*, **20**, 28 (1950); *Mem. Coll. Agr., Kyoto Univ.*, **57**, 22 (1950); *Chem. & Chem. Ind.*, **4**, 316 (1951).
8. D. C. Grahame, *Chem. Revs.*, **41**, 441 (1947).
9. A. Watanabe, F. Tsuji, and S. Ueda, *J. Electrochem. Soc., Japan*, **22**, 179 (1954).
10. A. Watanabe, F. Tsuji, and S. Ueda, *J. Electrochem. Soc., Japan*, **22**, 521 (1954); *Proc. 2nd Intern. Congr. Surface Activity*, London, **3**, 94 (1957); *Bull. Inst. Chem. Res., Kyoto Univ.*, **34**, 1, 65 (1956).
11. S. Ueda, A. Watanabe, and F. Tsuji, *J. Electrochem. Soc., Japan*, **21**, 267 (1953); *Bull. Inst. Chem. Res., Kyoto Univ.*, **25**, 30 (1951); *Mem. Coll. Agr., Kyoto Univ.*, **60**, 13 (1951); **67**, 53 (1954).
12. A. Watanabe, F. Tsuji, K. Nishizawa, and S. Ueda, *Bull. Inst. Chem. Res., Kyoto Univ.*, **32**, 54 (1954); *Mem. Coll. Agr., Kyoto Univ.*, **67**, 79 (1954).
13. A. Watanabe, F. Tsuji, K. Nishizawa, and S. Ueda, *Bull. Inst. Chem. Res., Kyoto Univ.*, **32**, 62 (1954).
14. S. Ueda, A. Watanabe, F. Tsuji, and K. Nishizawa, *J. Electrochem. Soc., Japan*, **20**, 605 (1952); *Bull. Inst. Chem. Res., Kyoto Univ.*, **28**, 47 (1952); **31**, 103 (1953); *Mem. Coll. Agr., Kyoto Univ.*, **67**, 61 (1954).
15. S. Ueda, F. Tsuji, and A. Watanabe, *J. Electrochem. Soc., Japan*, **24**, 116 (1956).

Technical Notes

Some Effects of Zinc Atmospheres on Zinc Sulfide

Hideo Baba[1]

Thomas J. Watson Research Center, International Business Machines Corporation, Yorktown Heights, New York

Generally, nonstoichiometry of a compound semiconductor can be affected by the gas atmosphere in which the sample is heated. When ZnS is heated in a zinc atmosphere, surplus zinc may be introduced into the crystal, creating anion vacancies V_A and free electrons.

$$Zn^{2+}\,S^{2-} + Zn \rightleftarrows \begin{Bmatrix} Zn^{2+}\,S^{2-} \\ V_A\,Zn^{2+} \end{Bmatrix} + 2- \qquad [1]$$

As the V_A center formed is a missing S^{2-} ion, the V_A center has a change of $+2e$ relative to the normal lattice, and it can trap the two electrons.

This process also occurs in the case of lead sulfide. If surplus sulfur is added to the lattice by heating it in a sulfur atmosphere, free holes and cation vacancies will be created.

It has been reported that the conductivity type of PbS changes from n- to p-type very sharply when heated in a sulfur atmosphere of sufficient pressure (1). In the case of zinc oxide, it is known that its resistivity goes down remarkably by introducing interstitial zinc into the crystal by heating it in zinc vapor and quenching (2). Since the interstitial zinc atoms in zinc oxide crystals act as donors with a low ionization energy, they effect the increased conductivity (3). Similar phenomena have been reported with many other compound semiconductors (4, 5).

In the case of both lead sulfide and zinc oxide, their conductivity is high enough for the Hall coefficient to be measurable, and one can obtain quantitative information about the surplus carrier concentration. However, the conductivity of zinc sulfide is too low for such measurements except at elevated temperatures, making it difficult to clarify the influence of the environmental gas on the electrical character of this material. The pulsed Dember measurement is one possible tool for the study of the nonstoichiometry of this material. This effect was first observed by Dember in Cu_2O single crystals in 1931 (6, 7). The effect was used for the determination of the carrier sign of various materials by Burke (8) and Goodman (9). Morehead (10) showed that the Dember voltage of ZnS changed

[1] Present address: Sony Research Laboratories, Hodogaya-ku, Yokohama, Japan.

linearly with the square root of the sulfur pressure in which it was fired. The sample became more and more p-type as the sulfur pressure was increased.

If a p-type ZnS sample is fired in a zinc atmosphere of a certain pressure, the conductivity type should be changed to n-type by the introduction of excess zinc as described above. The purpose of this paper is to show how the nonstoichiometry of zinc sulfide is affected by heating it in a zinc atmosphere, as detected by pulsed Dember measurements.

Experimental

The experiment consisted of two parts: one was the in-diffusion process in which surplus zinc was incorporated in ZnS powder by heating in a zinc atmosphere, and the other was the out-diffusion process in which ZnS saturated with excess Zn was heated in vacuum to extract the zinc and to confirm the influence of zinc on conductivity type.

The In-Diffusion Process

Three kinds of zinc sulfide were used for the in-diffusion experiments. Each of them was made from the same lot of luminescent grade zinc sulfide (RCA 298): (i) as-received ZnS; this contained small amounts of free sulfur and sulfate. (S: 0.038%, $SO_4^=$: 0.29%); (ii) prefired samples; the original ZnS (i) was fired in flowing H_2S at 1250°C for 2 hr to eliminate the sulfate; this sample showed strong p-type conductivity; (iii) compensated sample; zinc sulfide powder is usually prepared by precipitation from solutions of zinc salts with hydrogen sulfide. As a result it usually contains much free sulfur, which can act as a source for an acceptor. The excess sulfur is removed from the material by heating it in vacuum at moderately high temperatures. The compensated sample was prepared by heating the original ZnS in running vacuum at 500°C for 96 hr. (It was confirmed by Dember measurements that the sample was just compensated.)

Control of zinc pressure.—ZnS powder was introduced in one side of a quartz tube and a sufficient amount of pure zinc was placed in the other side. The tube was then evacuated, sealed off, and placed in an electric furnace of desired temperature. In the case of low zinc pressures (390 mm Hg), a two-section furnace was used which provided two independently controllable heating regions. The portions of the tube with ZnS and Zn, respectively, were then brought into the constant temperature region of each furnace. For high pressures, the tube was at a uniform temperature. The zinc pressure was determined by the lowest temperature of the tube. The experimental conditions involved the equilibrium zinc vapor pressures of 2500, 1950, and 390 mm Hg, which correspond to zinc temperatures of 1075°, 1035°, and 850°C, respectively.[2] After the samples were fired under these conditions for the desired time, they were quenched to room temperature, and the Dember current was measured.

[2] These vapor pressures are calculated averages of values determined by C. Barnes, J. W. Richards, and R. E. Honig, respectively. Pressures calculated from Kubaschewski's formula are higher.

The Out-Diffusion Process

If the zinc sulfide is first fired in a Zn atmosphere and then heated in vacuum, the excess zinc will diffuse out from the material and will condense at the cool portion maintained at room temperature. Since the zinc pressure at room temperature is of the order of 10^{-12} mm Hg the process can be considered to be equivalent to one in a running vacuum. This out-diffusion process was carried out at 670°C using samples of zinc sulfide which had been fired in zinc atmospheres of either 390 mm Hg or 2500 mm Hg.

After the desired time at 670°C, the tube was taken out of the furnace and quenched to room temperature, and the Dember current measured using a part of the sample. Further heating at 670°C was continued using the remainder of the sample to get data for longer times. For a description of the Dember measurements see Appendix.

Results

In-Diffusion Process

Figure 1a shows the results of the in-diffusion process with the as-received zinc sulfide. The starting material is strongly p-type and as the time of firing in zinc vapor increases, the conductivity type becomes less p-type. After 40 hr, the concentrations of sulfur and zinc vacancies reach a compensated state. If the firing time and temperature are kept constant (44 hr and 1050°C, respectively) the p-typeness of the sample depends on the zinc pressure below about 1300 mm Hg, as shown in Fig. 1b.

When the ZnS which had been prefired in H_2S atmosphere was fired under various zinc pressures, the type changed to less p-type as the firing time increased and it approached different steady states depending on the zinc pressure in which the sample was fired. That is, the higher the zinc pressure, the more n-type or less p-type will the final state be, as shown in Fig. 2.

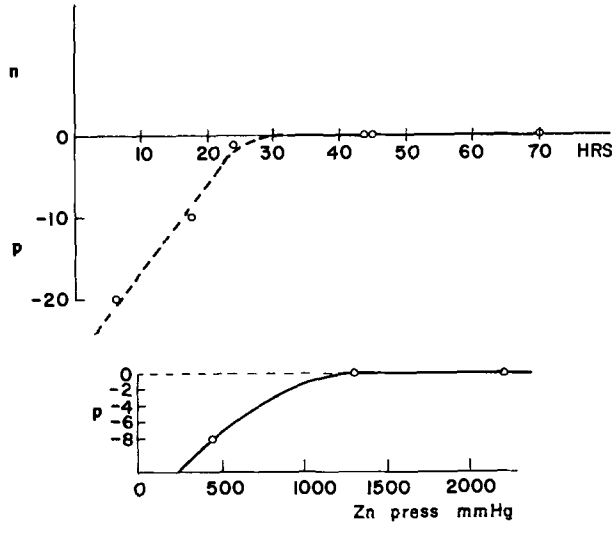

Fig. 1. Change of conductivity type with Zn pressure of "as received" ZnS. (a) (top) The ordinate represents the type of carrier and the abscissa is the length of firing time, firing temperature 1050°C, Zn pressure 220 mm Hg; (b) (bottom) The ordinate is the type of conductivity and the abscissa is the Zn pressure, firing temperature 1050°C, firing time 44 hr.

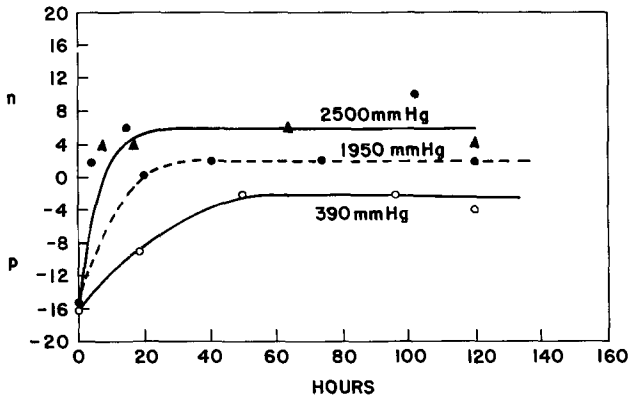

Fig. 2. Change of conductivity type as a function of firing time at various Zn pressures. The starting material was prefired ZnS. The firing temperatures associated with different Zn pressures were as follows: 2500 mm, 1075°C; 1950 mm, 1035°C; and 390 mm, 850°C.

If one starts with the compensated sample, the situation is rather complicated and, unfortunately, not very reproducible quantitatively. At high zinc pressures there is essentially no change in the conductivity type. There is apparently no way in which the possible introduction of excess donors can be detected from Dember effect measurements (see Appendix). At lower zinc pressures a tendency toward becoming more p-type was noted for short firing times; this trend was reversed for longer periods of firing, but the exact behavior was erratic. Uncontrolled impurities in the starting material and perhaps a natural tendency for excess zinc vacancies to form at high temperatures under conditions approximating a running vacuum (11) can explain these latter results.

The Out-Diffusion Process

In order to confirm the incorporation of Zn by the in-diffusion process, the ZnS which had been treated in a zinc atmosphere was heated in a high vacuum for a long time, to extract the excess zinc at 670°C. No significant changes in electrical activity (Dember effect) were noted as a result of the out-diffusion process. In every case, even for starting samples which showed p-type conductivity after treatment in a zinc atmosphere, an appreciable amount of zinc was observed at the cool portion of the tube which was kept at room temperature. This fact shows that only a small part of the zinc which diffused into the crystal is electrically active, and the rest of it is probably present as a precipitation at the boundary of the crystals, in dislocations, or at cracks in the crystal.

Discussion and Conclusions

If the excess zinc incorporated in the ZnS crystallites acts as a donor just as in the case of zinc oxide, the conductivity type should be changed to less p-type or more n-type by the in-diffusion process. That is true in the case of prefired samples as shown in Fig. 2.

It is difficult to make a quantitative argument about the results because the Dember measurements give only semiquantitative information, and the effect may depend strongly on the surface conditions of the particle.

In order to confirm the results, some other information such as photoconductivity is required.

Acknowledgments

The writer wishes to thank Dr. S. P. Keller and his group for much helpful discussion and many suggestions. The Dember measurements were made by F. F. Morehead and W. N. Hammer and the x-ray analysis by N. Stemple.

Manuscript received April 30, 1962; revised manuscript received Sept. 26, 1962.

Any discussion of this paper will appear in a Discussion Section to be published in the December 1963 JOURNAL.

REFERENCES

1. J. Bloem, *Philips Research Rept.*, **11** [4], 273 (1956).
2. R. Pohl, *Z. Phys.*, **155**, 120 (1959).
3. D. G. Thomas, *Phys. Chem. Solid*, **3**, 229 (1957).
4. F. A. Kroger, H. J. Vink, and J. van den Boomgaard, *Z. Phys. Chem.*, **203**, 1 (1954).
5. G. Heiland and E. Mollwo, *Solid State Physics*, **8**, 191.
6. H. Dember, *Physik. Z.*, **32**, 554 (1931).
7. H. Dember, *ibid.*, **33**, 207 (1932).
8. E. E. Burke, *Optica i Spektroskopia*, **3**, 334 (1957).
9. A. M. Goodman, *Phys. Rev.*, **120**, 1142 (1960).
10. F. F. Morehead and A. B. Fowler, *This Journal*, **109**, 688 (1962).
11. F. F. Morehead, to be published.

APPENDIX

Pulsed Dember Measurement Technique

These measurements were made by F. Morehead of this laboratory, using a technique described by Morehead and Fowler (10). Intense 320 mμ radiation is flashed onto the sample cell to obtain a Dember current pulse peak. The sign and size of the Dember pulse are noted both after a 1-min dark interval between pulses and after a 1-min exposure to broad band infrared radiation (~0.8μ). The I.R. ionizes and facilitates the return of deeply trapped holes (~1 e.v.) so that a much larger p-type signal (or smaller n-type pulse) is obtained after the I.R. exposure. If the two signals are of the same size and n-type, then there are no excess acceptors. If the peak obtained after I.R. is n-type and smaller or actually p-type, the algebraic difference between the two signals is taken as a measure of the excess acceptors. If both signals are p-type, the peak obtained after I.R. is always larger and its value is used to measure the p-type content. If both signals are n-type and the one obtained after I.R. is the larger, the sample may actually have a donor excess, but not necessarily. It is not possible to demonstrate an excess donor concentration in ZnS by means of Dember measurements alone. For more details on the method, the reader is referred to ref. (11).

Some Comments on Thermal Etching of Silicon Surfaces Treated in Sealed Quartz Tubes

A. N. Knopp

Semiconductor Division, Westinghouse Electric Corporation, Youngwood, Pennsylvania

Thermal etching or evaporation of metal and semiconductor single crystals results in the deterioration of certain crystal faces in favor of more stable ones (1). Dillon and Oman (1) were able to show that heat treatment in different ambient pressures resulted in different etch-pit patterns of silicon surfaces. To prevent interaction between silicon and quartz a molybdenum slice holder was used which separated the silicon from the quartz. The etch pit density of silicon treated in a poor vacuum ($10^{-5} - 10^{-6}$ mm Hg) was much greater than the pit density of silicon treated in high vacuum ($<< 10^{-6}$ mm Hg). Silicon temperatures were reported as 850°C in the first case and greater than 1000°C in the second case.

It is inferred that enhancement of thermal etching at higher ambient pressure is due to the formation and subsequent evaporation of volatile SiO, and that this effect becomes negligible when the vacuum is better than 1×10^{-6} mm Hg. In addition, any oxygen formed by outgassing of certain metals or oxygen which is present due to interaction between silicon itself and the ambient and between silicon and quartz must be excluded. On the other hand, thermal etching is reduced by increasing the oxygen content such that a protective SiO_2 layer is formed which protects the silicon from thermal etching. Consequently, in procedures which employ a very poor vacuum, the effect vanishes again. [Silicon which has been treated in pure O_2 (1) shows less triangular pits than silicon heated in atmospheres of N_2, He, or H_2.][1]

Since the revealing of special surface patterns is due to the removal of varying amounts of silicon, the same patterns should be obtained by applying either thermal or chemical etching.

In silicon, the [111] plane is the most densely populated of the low-index planes, therefore it is the most stable under high-temperature heating or a preferential chemical etching. The etching pattern shows the familiar triangular forms for the [111] face.

The present experiment is to demonstrate that thermal etching has been observed and compared to chemical etching. The significance of thermal etching in sealed tubes is discussed.

Experimental Procedure

It is assumed that thermal etching is determined by the silicon temperature and the amount of oxygen which is present. In order to get factual information, experiments have to be carried out in which temperature and oxygen content are varied in a controlled manner. The desired value of oxygen concentration is controlled by the vacuum quality and special surface treatments of the silicon.

The thermal treatment procedures were carried out in the following way: all quartz parts were soaked in boiling nitric acid, rinsed several times in hydrofluoric acid and deionized water, and finally dried in an inert atmosphere at elevated temperatures. The silicon was sliced, lapped, thoroughly cleaned, and slightly etched in a HNO_3-HF-CH_3-COOH mixture. The silicon was then inserted into the quartz tube; the tube was evacuated and backfilled with hyperpure dry argon the pressure of which was never varied. Two different arrangements of the sealed tubes are shown in the following sketch (a) and (b).

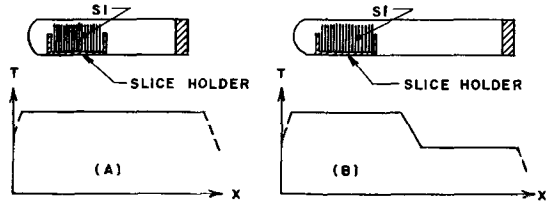

The slices were packed together vertically to contact each other across the whole area of the silicon face. The surface treatment prior to the heat treatment was different, resulting in various amounts of removal of the damaged layer resulting from lapping, and the heat treatment temperature of 1200°C was held for several hours. After heat treatment, the tubes were broken, and the silicon slices were evaluated without having applied any further surface treatment. The results obtained are best described by the photomicrographs, Fig. 1-5.

Discussion

It is obvious that thermal etching takes place when (a) silicon surfaces touch quartz (reaction with quartz); and/or (b) silicon is packed together resulting in special thermal etched areas either on the edges and/or center parts between silicon slices (poor contact areas). Due to the fact that the contact areas were not 100% uniform, we did not obtain uniform thermal etched surfaces. The oxygen affecting the localized equilibrium condition could result from the backfilled gas, the quartz parts, and the more or less oxidized silicon surfaces.

Generally, silicon with shiny (mirror finish) etched surfaces prior to a heat treatment shows

[1] A treatment in pure N_2 which has been carried out by the author yielded a white flaky coating on the entire surface consisting of Si_3N_4 which could be removed easily. However, neither thermal etching nor any stronger triangular pits could be detected.

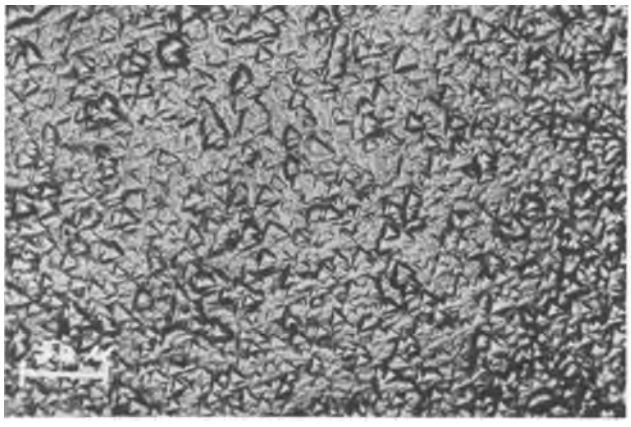

Fig. 1. Silicon having touched another silicon slice during heating. Special areas where triangles become larger indicate poor contact with the adjacent slice. Magnification 200X.

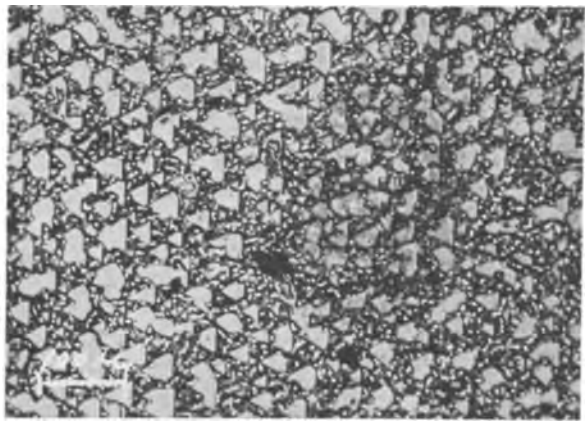

Fig. 4. Silicon having been exposed to a quartz plug: note the large triangles between the original "small" ones. Magnification 100X.

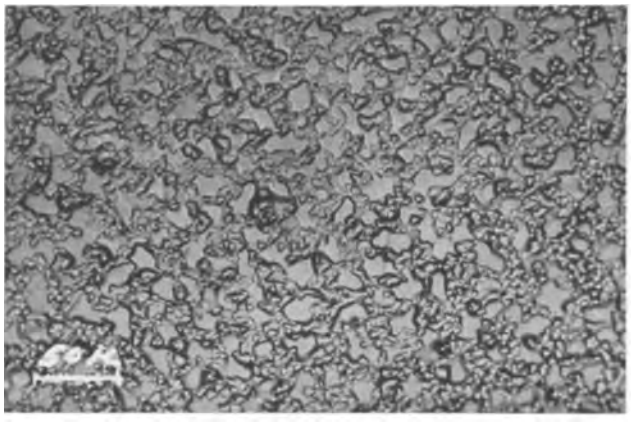

Fig. 2. Silicon slice in poor contact with another silicon slice during heat treatment: the strong etch pit pattern is due to stronger thermal etching. The triangles become larger, now touching each other. Magnification 200X.

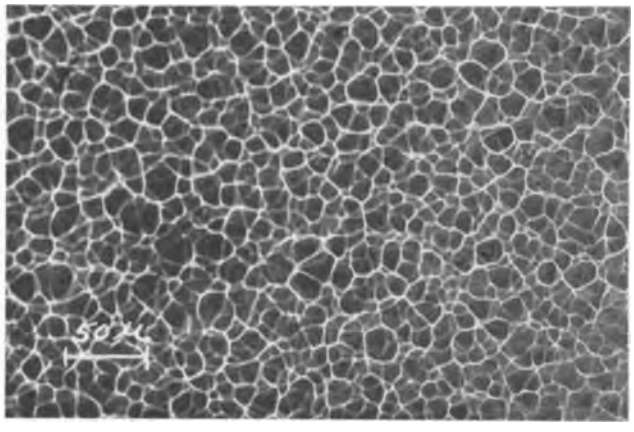

Fig. 5. Silicon slice having been chemically etched in a (1:1:1) $HF:HNO_3:CH_3COOH$ mixture for 6 sec; the etch pit pattern is similar to the thermal etched surface (compare with Fig. 3). Magnification 200X.

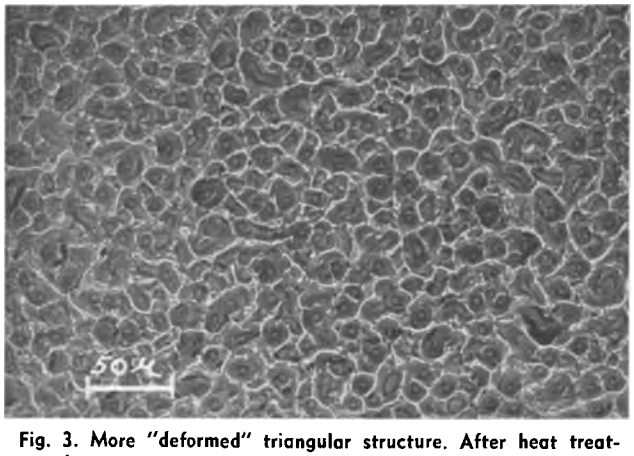

Fig. 3. More "deformed" triangular structure. After heat treatment, these areas are shiny, like a satin, chemically etched surface (compare with Fig. 5). Magnification 200X.

very little or no thermal etching, whereas, silicon with dull and/or rough surfaces exhibits severe thermal etching. Figures 2 and 3 were taken from slices which started with a very rough and dull surface. We may conclude that shiny etched surfaces are more stable than the rough ones, resulting in different thermal etching rates. However, this only holds true as long as the total amount of oxygen in the sealed tube is within a critical range as pointed out above. Thermal etching may be influenced by the volume of the quartz capsule, too. A sealed system at a certain equilibrium temperature determines the equilibrium vapor pressure of silicon that saturates the capsule to limit thermal etching. The effect is minimized when a small tube is used in a single temperature zone (see sketch above). In a two-zone system, thermal etching will continue as in Dillon's experiment, since silicon is "distilled" from the hot zone to the colder zone. This latter case is often used to advantage in diffusion when the low-temperature zone is used to control the vapor pressure.

As a comparison, Fig. 5 shows a chemical etched silicon surface which has been treated in a (2:1:1) $HF:HNO_3:CH_3COOH$ mixture for 6 sec after lapping. This pattern is very similar to that of Fig. 3. By modifying the etching solutions, patterns comparable to thermally etched patterns shown in Fig. 1 and 2 were also obtained. Thus, it clearly demonstrates the similar nature of the thermal treatment to that of a chemical etching.

Application

In application to diffusion, if the evaporation rate is very high, the impurity distribution in such diffusion process follows neither the well-known erfc-distribution nor the "Gaussian" distribution, but rather a solution of the diffusion equation

which considers simultaneously evaporating silicon (2). This results in a time-independent, constant impurity penetration due to equal rates of evaporating silicon and impurity penetration. This effect could be observed after our diffusion processes in some cases, since strong thermal etching has increased the rate of evaporating silicon such as to fulfill the above mentioned condition.

Although thermally etched surfaces yield excellent device properties because the etching process has yielded relatively clean silicon surfaces,[2] its effect should be acknowledged if control of uniformity is intended.

[2] A cleaning process occurs as soon as a certain amount of impurities distills off the surface and condenses on the quartz.

Manuscript received May 31, 1962; revised manuscript received Aug. 27, 1962.

Any discussion of this paper will appear in a Discussion Section to be published in the December 1963 JOURNAL.

REFERENCES

1. J. A. Dillon and R. M. Oman: "Thermal Etching of Silicon Crystals," Dept. of Physics, Brown University, Providence, Rhode Island. (Research directed toward the investigation of silicon and silicon carbide surfaces—AFCRC-TR-59-199.)
2. F. M. Smits, R. C. Miller, and R. L. Batdorf: "Surface Effects on the Diffusion of Impurities in Semiconductors," International Symposium on Semiconductors and Phosphors (1956), F. Vieweg, Braunschweig.

The Growth of Silicon Carbide from Molten Silicon

G. E. J. Beckmann

Central Research Laboratories, The General Electric Company Limited, Hirst Research Centre, Wembley, England

Carbon is slightly soluble in molten silicon; its solubility at a number of temperatures has been determined by Scace and Slack (1). These authors heated silicon isothermally in small graphite crucibles and so formed saturated solutions of carbon in silicon from which silicon carbide crystallized upon rapid cooling. From the weight of silicon carbide the solubility at the temperature of the experiment was evaluated. When their results were combined with that of Dash (2) at the melting point of silicon, a linear relation was found from 1408°C up to about 2430°C between the logarithm of the solubility and the reciprocal temperature; this is the kind of variation which might be expected on thermodynamic grounds. However at yet higher temperatures the solubility increased more rapidly until the peritectic point of silicon carbide was reached at 2830° ± 40°C with a solubility of 19(atomic)% (in argon at 35 atm). Above 2830° ± 40°C Scace and Slack observed that silicon carbide decomposed without congruent melting to form a silicon-rich liquid in equilibrium with graphite.

The problem of crystallization from a solution in contact with excess solute may be approached in two ways. Either a saturated isothermal solution may be cooled whereupon solute crystallizes out, or a temperature gradient may be established in the container while the temperature at any point is kept constant.

In the latter case the solution circulates, becomes supersaturated and deposits crystals in cooler regions, and is replenished with solute on returning to the hot zone.

In view of the very small solubility of carbon in silicon (only 1 part in 20,000 at the melting point of silicon and even at 2150°C it is only 1%) the first approach would clearly be futile for crystallizing substantial amounts of silicon carbide, unless an operating temperature approaching 2830°C were contemplated. The second approach however seemed more promising and was therefore adopted in the present investigation.

Experimental Details

Materials.—High-purity silicon was melted in graphite crucibles by an eddy current heating set supplying 18 kw at 0.5 Mc/s. The crucibles were mounted concentrically with a heating coil chosen so as to give the appropriate distribution of temperature, and were covered by a glass bell-jar resting on a copper base-plate. The ambient gas was dried argon at atmospheric pressure; this repressed the evaporation of silicon which would have been troublesome in vacuum. The temperatures were measured by an optical pyrometer focused successively at points on the crucible wall. The actual temperatures were somewhat higher than those mentioned here since no corrections were made for the emissivity of graphite or for absorption by the glass wall of the bell-jar. Films of silicon formed on the walls during the run, causing a gradual fall of between 20° and 60°C in the measured temperature, which was corrected accordingly.

At first there were difficulties in retaining the molten silicon as the crucibles cracked for two reasons. First, molten silicon seeps through the pores of most graphite in a matter of seconds; this problem was overcome by using less permeable graphite which held silicon at temperatures in excess of 2600°C. Second, silicon expands when it solidifies, and the resulting stresses tend to break the crucibles; this was avoided by making the walls thicker.

The graphite contained a few hundred parts of impurity per million, but the purity was much enhanced by preheating it to 2000°C; the smoke thus evolved indicated that volatile impurities were being expelled.

Results of initial experiments.—A series of experiments was carried out in which 30g lots of sil-

which considers simultaneously evaporating silicon (2). This results in a time-independent, constant impurity penetration due to equal rates of evaporating silicon and impurity penetration. This effect could be observed after our diffusion processes in some cases, since strong thermal etching has increased the rate of evaporating silicon such as to fulfill the above mentioned condition.

Although thermally etched surfaces yield excellent device properties because the etching process has yielded relatively clean silicon surfaces,[2] its effect should be acknowledged if control of uniformity is intended.

[2] A cleaning process occurs as soon as a certain amount of impurities distills off the surface and condenses on the quartz.

Manuscript received May 31, 1962; revised manuscript received Aug. 27, 1962.

Any discussion of this paper will appear in a Discussion Section to be published in the December 1963 JOURNAL.

REFERENCES

1. J. A. Dillon and R. M. Oman: "Thermal Etching of Silicon Crystals," Dept. of Physics, Brown University, Providence, Rhode Island. (Research directed toward the investigation of silicon and silicon carbide surfaces—AFCRC-TR-59-199.)
2. F. M. Smits, R. C. Miller, and R. L. Batdorf: "Surface Effects on the Diffusion of Impurities in Semiconductors," International Symposium on Semiconductors and Phosphors (1956), F. Vieweg, Braunschweig.

The Growth of Silicon Carbide from Molten Silicon

G. E. J. Beckmann

Central Research Laboratories, The General Electric Company Limited, Hirst Research Centre, Wembley, England

Carbon is slightly soluble in molten silicon; its solubility at a number of temperatures has been determined by Scace and Slack (1). These authors heated silicon isothermally in small graphite crucibles and so formed saturated solutions of carbon in silicon from which silicon carbide crystallized upon rapid cooling. From the weight of silicon carbide the solubility at the temperature of the experiment was evaluated. When their results were combined with that of Dash (2) at the melting point of silicon, a linear relation was found from 1408°C up to about 2430°C between the logarithm of the solubility and the reciprocal temperature; this is the kind of variation which might be expected on thermodynamic grounds. However at yet higher temperatures the solubility increased more rapidly until the peritectic point of silicon carbide was reached at 2830° ± 40°C with a solubility of 19(atomic)% (in argon at 35 atm). Above 2830° ± 40°C Scace and Slack observed that silicon carbide decomposed without congruent melting to form a silicon-rich liquid in equilibrium with graphite.

The problem of crystallization from a solution in contact with excess solute may be approached in two ways. Either a saturated isothermal solution may be cooled whereupon solute crystallizes out, or a temperature gradient may be established in the container while the temperature at any point is kept constant.

In the latter case the solution circulates, becomes supersaturated and deposits crystals in cooler regions, and is replenished with solute on returning to the hot zone.

In view of the very small solubility of carbon in silicon (only 1 part in 20,000 at the melting point of silicon and even at 2150°C it is only 1%) the first approach would clearly be futile for crystallizing substantial amounts of silicon carbide, unless an operating temperature approaching 2830°C were contemplated. The second approach however seemed more promising and was therefore adopted in the present investigation.

Experimental Details

Materials.—High-purity silicon was melted in graphite crucibles by an eddy current heating set supplying 18 kw at 0.5 Mc/s. The crucibles were mounted concentrically with a heating coil chosen so as to give the appropriate distribution of temperature, and were covered by a glass bell-jar resting on a copper base-plate. The ambient gas was dried argon at atmospheric pressure; this repressed the evaporation of silicon which would have been troublesome in vacuum. The temperatures were measured by an optical pyrometer focused successively at points on the crucible wall. The actual temperatures were somewhat higher than those mentioned here since no corrections were made for the emissivity of graphite or for absorption by the glass wall of the bell-jar. Films of silicon formed on the walls during the run, causing a gradual fall of between 20° and 60°C in the measured temperature, which was corrected accordingly.

At first there were difficulties in retaining the molten silicon as the crucibles cracked for two reasons. First, molten silicon seeps through the pores of most graphite in a matter of seconds; this problem was overcome by using less permeable graphite which held silicon at temperatures in excess of 2600°C. Second, silicon expands when it solidifies, and the resulting stresses tend to break the crucibles; this was avoided by making the walls thicker.

The graphite contained a few hundred parts of impurity per million, but the purity was much enhanced by preheating it to 2000°C; the smoke thus evolved indicated that volatile impurities were being expelled.

Results of initial experiments.—A series of experiments was carried out in which 30g lots of sil-

Fig. 1. Crystals of silicon carbide; Fig. 1a, top; Fig. 1b, center; Fig. 1c, bottom. Magnification 10X.

icon were heated in graphite crucibles to various maximum temperatures between 1450° and 2600°C for several minutes. When the silicon was etched away with a mixture of equal amounts of HF and HNO_3, silicon carbide appeared as a thin raft of tiny crystals at the surface and as dendritic clusters at the base and walls of the crucible. Sometimes there were platelets up to 1 mm across in the lower part of the ingot itself. Some examples may be seen

Fig. 2. Slices of a crucible. Magnification ¾X

in Fig. 1(a) and (b). Figure 1(c) shows larger crystals grown at the base of a nearly isothermal melt at 2300°C from yet purer materials. Their well-defined growth patterns are brought out in the photograph. The crystals of this batch are bright yellow apart from small bright red inclusions here and there.

Nucleation and growth of crystals of silicon carbide were observed at the tip of a graphite rod dipping just beneath the silicon surface (protected above by radiation shields). At 1860°C the growth was so rapid that within 1 hr it had extended to the base of the crucible, whereupon the rod seized. These crystals were easily separated into dark green torpedo-shaped grains and were later shown to be cubic.

Production of pure polycrystalline SiC.— Of particular interest is the combination of high maximum temperatures (2100°-2600°C) and great temperature gradients because these conditions give rise to profuse precipitation of silicon carbide.

For example in one such run a region about 1.2 cm long in the central part of the length of the crucible was maintained for 20 min at 2300°C, the temperature falling off above and below this region initially at a rate of about 300°C/cm, while the regions at the top and bottom of the melt were at a temperature of about 1800°C. In this experiment 15g of silicon carbide was made; *i.e.*, 1/3 of the silicon had been transformed into silicon carbide.

This experiment was then repeated to find out how the crystals were arranged. This time the crucible was cut vertically into slices 1 mm thick, and the silicon was etched from these. It was then apparent that the ingot had consisted of a mass of solid silicon in which were embedded two separate networks of silicon carbide crystals, one at the top and the other at the bottom of the melt, whereas the central region was almost free of silicon carbide and the graphite wall thereabouts was deeply eroded. Figure 2 shows two nearly axial slices after etching. The networks consisted mainly of bright yellow crystals, but a few green ones also had grown randomly among them; the proportion of green crystals increased both with the duration of the run and with the temperature.

The results of a preliminary spectroscopic analysis are shown in Table I. These results support the view (3) that there is substantial rejection of impurities from silicon carbide; thus the iron content was less than 10 ppm, whereas that of the graphite was about 200 ppm.

Table I. Preliminary spectroscopic analysis

Elements detected	Probable concentration in ppm
Aluminum	10-50
Iron	<10
Calcium	10-50
Magnesium	<10
Copper	<10
Elements sought but not detected	**Low limit of detection for the method employed**
Phosphorus	500
Arsenic	500
Antimony	100
Boron	100

The crystals were mostly cubic although there were a few hexagonal ones. One yellow crystal examined separately was found to be entirely cubic. These observations agree with those of Scace and Slack who grew crystals which were predominantly cubic even at 2830°C. They considered that this was the stable form of melt-grown crystals and that the transformation from cubic to hexagonal was via the vapor phase. Such opinions may be contrasted with the frequent assumption (4, 5) that cubic is stable below but unstable above 2000°C.

On the other hand, in the present investigation a few experiments carried out in impure conditions (in particular when the argon was delivered by rubber tubing instead of a copper pipe) had a different outcome. Only green crystals then resulted which were both smaller and nearly all hexagonal (6H, 15R and 4H, with 4H predominating) in spite of identical thermal conditions. This group of experiments offered support to the view expressed by Ellis (6) that the hexagonal form is impurity stabilized.

Conclusions

The high yields encountered can be understood by supposing the existence of very rapid transport processes within the melt; the most effective of these was probably convection which was deliberately encouraged. No doubt some transfer of material arose also on account of diffusion and the r.f. fields.

It is especially interesting to recall that Scace and Slack found that above about 2430°C the solubility increases more rapidly than at lower temperatures. They attributed this observation to nonideality of the solution. It is tentatively suggested here that this behavior may readily be explained in terms of the transport phenomena proposed in this paper. Now although Scace and Slack endeavored to maintain isothermal conditions, some temperature variation was of course unavoidable; they appear to imply that the temperature gradient on the walls of their (much smaller) crucibles might have been as much as 20°C/cm, and this is not negligible in the present context. It seems likely therefore that the true values of the solubility at the highest temperatures may lie somewhat lower than those reported by Scace and Slack.

Manuscript received July 23, 1962.

Any discussion of this paper will appear in a Discussion Section to be published in the December 1963 JOURNAL.

REFERENCES

1. R. I. Scace and G. A. Slack, *J. Chem. Phys.*, **30**, 1551 (1959); "Silicon Carbide," p. 24, J. R. O'Connor and J. Smiltens, Editors, Pergamon (1960).
2. W. C. Dash, *J. Appl. Phys.*, **30**, 459 (1959).
3. F. A. Halden, "Silicon Carbide," p. 115.
4. H. N. Baumann, *This Journal*, **99**, 109 (1952).
5. H. Jagodzinski and H. Arnold, "Silicon Carbide," p. 136.
6. R. C. Ellis, "Silicon Carbide," p. 124.

Room Temperature Evolution of Hydrogen from High-Purity Nickel

K. M. Olsen and C. F. Larkin

Bell Telephone Laboratories, Incorporated, Murray Hill, New Jersey

Low-temperature electrical resistance measurements made at 20°K have provided a sensitive means for detecting the presence of small quantities of hydrogen in pure nickel. The use of such measurements for evaluating "over-all" purity of metals has been previously described (1, 2). The low-temperature resistivity of a comparatively pure metal is very sensitive to minute amounts of impurities in solid solution and is generally insensitive to impurities present as a second phase, whether dispersed throughout the matrix or segregated in grain boundaries. It is also sensitive to lattice defects such as produced by cold deformation. However, this latter effect can be minimized and made substantially constant by properly annealing the test specimens prior to measurement.

The usual parameter employed in evaluating the purity of a metal is the resistance ratio. In this study this is the ratio of the electrical resistance of a given mass at liquid hydrogen temperature (20°K) to the resistance of the same mass of the same sample at ice water temperature (273°K). The lower this resistance ratio the higher the over-all purity of the metal.

Experimental Procedure

The 0.050 in. diameter wire and 0.020 in. thick x ½ in. wide strip used in this study were prepared from a high-purity nickel ingot obtained by melting and casting under controlled atmospheres (3).

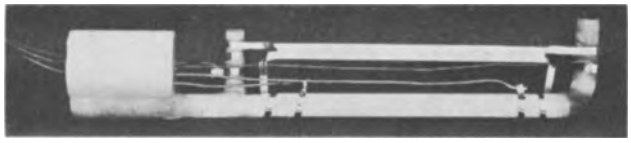

Fig. 1. Solder connections at extremities of separated slit strips

Chemical analysis of the wire and strip showed that no single impurity was present in amounts exceeding 0.005% by weight.

The wire to be tested was wound around a quartz fixture and cleaned by etching in a warm solution consisting of 3 parts glacial acetic acid, 1 part nitric acid, and 0.015 parts of hydrochloric acid. After cleaning, the entire assembly was heat treated 1 hr at 1000°C in dry hydrogen or dry helium (— 80°F dew point).

Resistance measurements at ice water temperature (273°K) and liquid hydrogen temperature (20°K) were made on the heat-treated wire without removing it from the quartz fixture. Current leads were soldered to the ends of the wire, and potential leads were similarly soldered at various points. The resistance at 273° and 20°K was measured using sensitive potentiometer-amplifier equipment capable of measuring voltages as low as 10^{-9}v.

Strip rather than wire was used for determining the resistance ratio changes associated with multiple heat treatments of the same specimen. In this procedure the 0.020 in. thick strip was slit part way down on both ends and mounted on a quartz fixture. After cleaning and heat treatment, solder connections are made at the extremities of the separated slit strips as shown in Fig. 1. After resistance measurements have been made the solder connections are cut off, the sample reheat-treated and a new set of solder contacts applied for another set of measurements.

Discussions of Results

Repeat measurements on the same wire which had been heat treated at 1000°C in dry hydrogen and rapidly cooled showed that the resistance ratio decreased steadily with length of time aged at room temperature. This aging effect was found to be due to gradual diffusion of hydrogen from the nickel. The hydrogen had been retained in the nickel by the rapid cooling after heat treatment. Evidence of this behavior is shown in the aging curves given in Fig. 2. A considerable difference in resistance ratio and aging characteristics was obtained by very slow furnace cooling in hydrogen after the 1000°C heat treatment. Of special significance is the lower resistance ratio obtained by either rapid or slow cooling after a similar heat treatment in helium. The helium treated samples showed no aging effect as contrasted with the continual drop in resistance ratio over a 70-day aging period for the hydrogen treated wire. The difference in level of resistance ratio between rapid and slow cooled helium treated samples is probably associated with lattice defects produced by the rapid cooling. It is of interest to note that these defects are not removed by room temperature aging.

An experiment using nickel strip was conducted to determine the reversibility of the hydrogen effect on resistance ratio. The first treatment in helium yielded the anticipated low resistance ratio. A reheating in hydrogen (after cutting off the solder leads) resulted in a marked increase in resistance ratio. Additional alternate heat treatments in helium and hydrogen yielded the same changes in resistance ratio and confirmed that hydrogen could be reversibly introduced or eliminated from the nickel. Three-days aging after a final hydrogen treatment resulted in a moderate decline of the resistance ratio. At this point the sample on the fixture was subjected to a 1-hr treatment in vacuum (10^{-6} mm Hg). This treatment produced no further decrease in the resistance ratio. This is a strong indication that the hydrogen atoms are tightly held in the nickel lattice and are evolved slowly by a diffusion process. Supporting evidence that the hydrogen is held in solid solution is the fact that the observed increase in resistance ratio associated with hydrogen absorption is too large to be caused by formation of a second phase or by retention in voids or grain boundaries. It appears

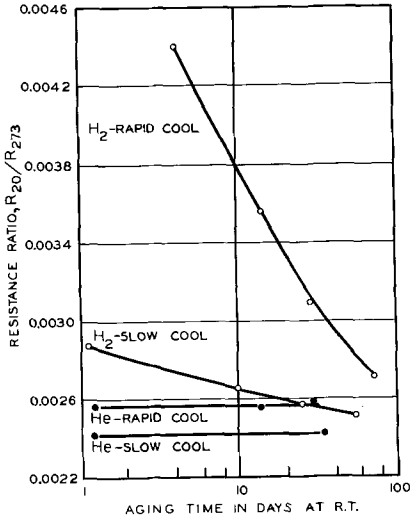

Fig. 2. Aging characteristics of acid-cleaned high-purity nickel wire from ingot CA550 after heat treatment at 1000°C in indicated atmosphere.

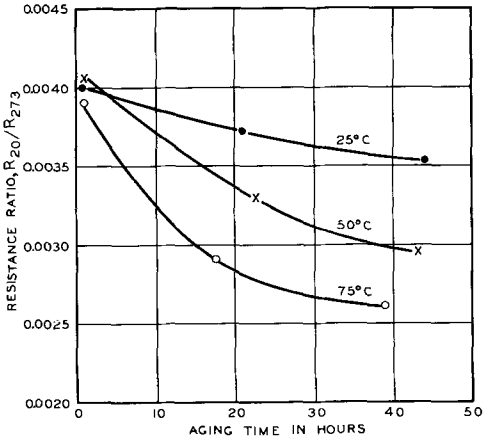

Fig. 3. Effect of aging temperature on resistance ratio of acid-cleaned high-purity nickel strip (CA550) rapidly cooled after 1 hr at 1000°C in hydrogen.

therefore that the absorbed hydrogen is retained in a supersaturated solid solution as a result of rapid cooling from elevated temperatures. Subsequent aging at lower temperatures induces gradual evolution of hydrogen by diffusion, the process continuing until equilibrium conditions are reached. Faster diffusion occurring during slow cooling results is less retention of hydrogen in the nickel.

Previous studies by Euringer (4) using gas analysis techniques, showed that hydrogen is slowly expelled from nickel at room temperature. Our mass spectrographic analysis on strip which had been rapidly cooled after the 1000°C treatment showed that hydrogen is continuously evolved from high-purity nickel during aging at room temperature. The analytical data indicate that approximately 0.0001% by weight of hydrogen in nickel is responsible for the observed change in resistance ratio. This indicates that the low-temperature resistance measurements are sensitive enough to detect the presence of 1 atom of hydrogen in 600,000 atoms of nickel.

The evolution of hydrogen from nickel during aging at 25°, 50°, and 75°C as indicated by resistance ratio measurements is shown in Fig. 3. Diffusion constants calculated from these data using the method employed by Allison and Samuelson (5) show the activation energy to be approximately 9500 calories per mole. The diffusion relationship for hydrogen in nickel can be expressed as

$$D = 3.8 \times 10^{-3} e^{\frac{-9500}{RT}}$$

At 25°C the diffusion coefficient D is 3.9×10^{-10} cm²/sec. These values are in good agreement with those obtained from gas analysis studies by Euringer (4), Grimes (6), and Hill and Johnson (7). The comparison is shown in the following table.

Source	H	Do	Temperature range, °C
Euringer	8,700	2.04×10^{-3}	85-165
Grimes	10,300	9.5×10^{-3}	430-850
Hill and Johnson	8,600	4.47×10^{-3}	380-1000
This work	9,500	3.8×10^{-3}	25-75

Conclusions

Low-temperature resistance measurements have shown that the hydrogen absorbed by high-purity nickel during a 1000°C heat treatment is liberated slowly at room temperature. The data indicate that the hydrogen is retained in solution interstitially and that evolution at room temperature occurs by a diffusion mechanism. Evolution of hydrogen as evidenced by change in resistance ratio occurred over a period as long as 70 days. Diffusion constants calculated from the observed changes in resistance ratio occurring during aging at 25°, 50°, and 75°C were in good agreement with those obtained by other investigators. Evolution of hydrogen at room temperature was confirmed by mass spectrographic analysis. The total amount of hydrogen liberated was found to be equivalent to approximately 0.0001% by weight in nickel.

This study has shown that low-temperature resistance measurements are sensitive enough to detect absorption and evolution of small quantities of gasses in metals.

Acknowledgment

The authors wish to express appreciation to Messrs. D. H. Wenny, W. C. Ellis, and D. F. Gibbons for their guidance and encouragement of this work; to Messrs. P. H. Schmitt and R. A. Hinrichsen for their help in preparing the high-purity nickel materials; and to Mr. E. E. Francois who conducted the mass spectrographic analysis.

Mansucript received May 23, 1962. This paper was prepared for delivery before the Los Angeles Meeting, May 6-10, 1962.

Any discussion of this paper will appear in a Discussion Section to be published in the December 1963 JOURNAL.

REFERENCES

1. J. E. Kunzler and C. A. Renton, *Bull. Am. Phys. Soc.*, Ser. II, **2**, 137 (1957).
2. J. E. Kunzler and J. H. Wernick, *Trans. AIME*, **212**, 866 (1958).
3. K. M. Olsen, *Met. Progress*, **72**, 105 (1957).
4. G. Euringer, *Z. Physic*, **96**, 37 (1935).
5. H. W. Allison and H. Samelson, *J. Appl. Phys.*, **30**, 1419 (1959).
6. H. H. Grimes, *Acta Met.*, **7**, 782 (1959).
7. M. L. Hill and E. W. Johnson, *ibid.*, **3**, 566 (1955).

The Dissociation Pressure of Zinc Antimonide

Chikara Hirayama

Research Laboratories, Westinghouse Electric Corporation, Pittsburgh, Pennsylvania

The thermoelectric properties of ZnSb have been reviewed recently by Miller (1). This compound is known to be a useful p-type material, whose crystal structure (2) is one of a distorted diamond structure with 16 atoms per unit cell. The compound ZnSb forms peritectically (2, 3), and it is known (4) that there is only a limited range of solid solution in the region of this compound.

Zinc antimonide dissociates according to the reaction ZnSb(s) = Zn(g) + Sb(s). Oelsen and Middel (5) have determined calorimetrically the standard heat of formation as −3.6 kcal/mole. DeWitt and Seltz (6) have determined the standard thermodynamic properties from emf measurements and report values of −3.07 kcal/mole, −3.36 kcal/mole, and 0.98 e.u./mole, respectively, for the heat, the free energy, and the entropy of formation. We have undertaken to measure the dissociation pressure of this compound and to calculate the heat of formation from the heat of dissociation of ZnSb(s) and the heat of sublimation of Zn(s).

Experimental

The ZnSb was kindly supplied by Dr. R. Mazelsky.[1] The material was prepared by melting stoi-

[1] Westinghouse Research Laboratories.

chiometric quantities of zinc and antimony at about 750°C in an evacuated Vycor tube which was subsequently air quenched. The material was ground, then cold-pressed and sintered at 500°C in an evacuated Vycor tube. The x-ray powder diffraction pattern showed only the ZnSb lines with crystal parameters $a = 6.161$Å, $b = 7.741$Å, $c = 7.986$Å.

The apparatus consisted of a 30 in. long vertical tube. This tube consisted of a 22 in. long, flanged Pyrex brand pipe of 1.5 in. ID (Corning Glass Works), to which was sealed a flat-bottomed mullite tube of 1⅛ in. ID, and 8 in. long. A stainless steel flange, containing the iron-constantan thermocouple and a hook for suspending the sample, was sealed to the flanged top of the Pyrex tube. A gasket of Viton-A (E. I. du Pont) was used to facilitate a vacuum seal. The tube was connected to a vacuum system just below the flanged top. Allowance was made also for introduction of argon to the system to break the vacuum.

The mullite section was heated by raising a tube furnace over it. The temperature of the furnace was controlled by ± 2° or better, and the bottom 4-in. section of the tube was at the same temperature.

The four Knudsen cells were machined from graphite rods supplied by the National Carbon Company. The dimensions were 1⅛ in. high, ¾ in. diameter with wall thickness of approximately 3/16 in. Two cells had 0.0625 in. orifice diameters and lengths of 0.250 and 0.219 in. The other two cells had orifice diameters of 0.125 in. and lengths of 0.250 and 0.185 in. The Clausing correction (7) was used to calculate the effective orifice area. The cells were heated above 850° in a vacuum of approximately 1×10^{-6} mm Hg for several hours until constant weight was obtained.

To obtain the effusion rate, the Knudsen cell was contained in a silica cup which was placed on a platinum pan. The pan was then lowered into the mullite tube. The thermocouple was placed adjacent to the cell. The system was flushed several times with oxygen-free argon and finally filled with the latter. The sample was then heated by raising the furnace over the tube and allowed to come to constant temperature. The time required was 20-30 min. The system was subsequently evacuated to about 3×10^{-5} mm Hg in about 3 min. The pressure during any run was maintained between 5×10^{-6} and 3×10^{-5} mm Hg. Check runs indicated no detectable loss of material during the heat-up time in the argon atmosphere. Each run was terminated by breaking the vacuum with argon and lowering the furnace to cool the tube with a forced draft. The effusion rate was determined from the weight loss over the heating period under vacuum. Results of the effusion measurements are summarized in Table I.

A sample of approximately 1g of ground material was used for each run. The effusion rates determined in the Knudsen cells of 0.0625 in. orifice diameter were independent of time over the temperature range measured. However, it was found that the effusion rates from the 0.125 in. orifice diameter at temperatures above 682°K decreased with time, while at 665°K it was apparently independent of time. This type of time-dependent evaporation rate has recently been observed by Dreger, Dadape, and Margrave (8) where they have found the rate of weight loss of BN to decrease with time. They attribute this time dependence to the formation of a surface crust of boron which inhibits the escape of nitrogen.

Table I. Effusion rate and dissociation pressure of ZnSb(s)

Run No.	Temp, °K	Time, sec	Weight loss, mg	Eff. orifice area, $cm^2 \times 10^3$	p, atm $\times 10^6$
1	688	2700	1.9	5.01	10.25
2	692	10,500	9.2	5.01	12.8
3	686	7200	4.5	5.01	9.11
4	687	7185	4.6	5.01	9.23
5	687	7200	5.2	5.01	10.5
6	687	7230	4.5	5.01	9.06
7	724	4500	10.9	5.01	36.3
8	724	4560	10.7	5.01	35.2
9	722	3330	8.7	4.44	44.0
10	739	3620	14.0	4.44	66.0
11	703	9860	11.6	4.44	19.6
12	692	6090	4.5	4.44	12.2
13	673	4360	1.4	4.44	5.24
14	745	1500	7.0	4.44	80.1
15	665	6420	8.3	27.84	3.34
16	682	3140	10.0	27.84	8.31
17	658	7950	6.5	27.84	2.10
18	695	1425	5.2	27.84	9.64
19	697	1480	7.4	33.7	10.9
20	665	5135	8.2	33.7	3.47
21	725	3660	9.6	5.01	39.3
22	697	7200	6.0	5.01	12.2
23	697	2910	13.0	33.7	9.75
24	676	3630	7.8	33.7	4.63

A single sample was used in runs 1-8 with an orifice of 0.0625 in. diameter and length of 0.219 in. New samples of approximately 1g were used in runs 9-14 with a cell of orifice diameter 0.0625 in. and length 0.250 in. Separate samples of approximately 1g were used in runs 15-18 in a cell of orifice diameter 0.125 in. and length 0.250 in., while a single sample was used for runs 19 and 20. Runs 21-24 were made on samples containing ZnSb and 30% excess of Sb powder.

The volatile species was ascertained by heating the zinc antimonide in a vacuum of approximately 10^{-5} mm Hg up to temperatures of 600°C. The x-ray powder diffraction patterns of the condensate showed only the zinc lines when approximately 10% of the solid was volatilized. The wet analysis of the residue confirmed the x-ray data. The x-ray diffraction pattern of the residue also shows the presence of only two phases, *i.e.*, ZnSb and Sb.

Results

The dissociation pressures, in atmospheres, were calculated with the equation $p_{atm} = 0.02255\ (m/At)\ (T/M)^{1/2}$ where m is the weight loss in grams after effusion time t, A is the effective orifice area, T the absolute temperature, and M the atomic weight of zinc. Table I summarizes the results. A least squares treatment of the data gives a good fit to the equation

$$\log p_{atm} = 7.71 - (8760 \pm 325)1/T$$

Table II. Free energy functions and heat of dissociation of ZnSb(s)

Run No.	Temp, °K	−RlnP	$-\left(\frac{F^\circ - H^\circ_{298}}{T}\right)_{Zn(g)}$	$-\left(\frac{F^\circ - H^\circ_{298}}{T}\right)_{Sb(s)}$	$-\left(\frac{F^\circ - H^\circ_{298}}{T}\right)_{ZnSb(s)}$	ΔH°_{298}
1	688	22.83	39.79	12.60	24.85	34.65
2	692	22.38	39.81	12.62	24.89	34.54
3	686	23.06	39.78	12.59	24.83	34.71
4	687	23.02	39.79	12.59	24.85	34.73
5	687	22.79	39.79	12.59	24.85	34.57
6	687	23.06	39.79	12.59	24.85	34.75
7	724	20.32	39.94	12.78	25.24	34.61
8	724	20.36	39.94	12.78	25.24	34.64
9	722	19.93	39.93	12.77	25.22	34.23
10	739	19.13	40.00	12.86	25.39	34.44
11	703	21.54	39.85	12.68	25.02	34.48
12	692	22.48	39.81	12.62	24.89	34.61
13	673	24.17	39.73	12.52	24.69	34.81
14	745	18.74	40.02	12.89	25.46	34.41
15	665	25.06	39.69	12.47	24.61	34.99
16	682	23.25	39.77	12.56	24.76	34.66
17	658	25.98	39.67	12.44	24.53	35.24
18	695	22.95	39.82	12.63	24.93	35.08
19	697	22.70	39.83	12.64	24.95	35.00
20	665	24.98	39.70	12.47	24.61	34.94
21	725	20.13	39.94	12.79	25.25	34.52
22	697	22.92	39.83	12.64	24.95	35.16
23	697	22.45	39.83	12.64	24.95	34.83
24	676	24.40	39.74	12.53	24.73	35.11

Avg = 34.74 ± 0.81 kcal/mole

between 658° and 745°K. The heat of reaction at 298°K was calculated by the third law method utilizing the free energy functions for Zn(g) and Sb(s) given by Stull and Sinke (9) and the free energy function for ZnSb(s) which was computed from the entropy (21.4 ± 1.4 e.u.) at 298°K (10) and its heat capacity (11). Results are summarized in Table II. The average heat of reaction at 298°K is ΔH°_{298} = 34.74 ± 0.81 kcal/mole.

The time dependence of the effusion rate through the 0.125 in. orifice is probably due to the formation of a surface crust or to a limited solubility of antimony which results in the decreasing effusion rate with time. As observed by Dreger *et al.* (8), the same behavior was found when a surface crust of boron formed on BN. The absence of the time dependence through the smaller orifice, which has a lower effusion rate, may be due to the fact that sufficient time is allowed for the nucleation and segregation of the Sb into discrete, separate crystals, whereas the rapid effusion rate through the larger orifice does not allow sufficient time to reach equilibrium.

Runs 21-24, where 30% excess of Sb was present, and the x-ray data show that the zinc pressure is measured over the two-phase system.

In the case of the effusion through the 0.125 in. orifice, which is time dependent, it is possible to approach the equilibrium dissociation pressure by using a sufficiently large sample run over a short time. The validity of this procedure is shown by the good agreement between the vapor pressures determined with cell orifice diameters of 0.125 and 0.0625 in., where the effusion through the latter cell is time independent. Other measurements (12) using the identical cells of 0.125 in. orifice shows that saturation pressure of zinc is measured.

Schulz and Searcy (13) have recently shown the validity of the Clausing correction, within experimental accuracy, up to 1/a ratios of 10.0. In the present work the good agreement of the data obtained with two orifice diameters and four different 1/a ratios suggests accommodation coefficients approaching unity.

The heat of formation of zinc antimonide, *e.g.*, for the reaction Zn(s) + Sb(s) = ZnSb(s) at 298°K, is obtained by subtracting the heat of sublimation (14), 31.189 kcal/mole, of Zn(s) from the heat of dissociation, 34.74 ± 0.8 kcal/mole. Thus ΔH°_f = −3.55 ± 1 kcal/mole for ZnSb(s), in excellent agreement with the previously reported values of −3.6 (5) and −3.07 (6) kcal/mole. This agreement lends further support to the present data.

Manuscript received March 28, 1962; revised manuscript received Aug. 30, 1962.

Any discussion of this paper will appear in a Discussion Section to be published in the December 1963 JOURNAL.

REFERENCES

1. R. C. Miller, in "Thermoelectricity: Science and Engineering," R. R. Heikes and R. W. Ure, Jr., Editors, pp. 405-407, Interscience Publishers, New York (1961).
2. M. Hansen, "Constitution of Binary Alloys," 2nd ed., pp. 1182-1185, McGraw-Hill Book Co., New York (1958).
3. R. L. Eisner, R. Mazelsky, and W. A. Tiller, *J. Appl. Phys.*, **32**, 1883 (1961).
4. I. M. Pilat, L. D. Chizh, and S. Yu. Voityschew, *Zhur. Tekh. Fiz.*, **28**, 786 (1958).
5. W. Oelsen and W. Middel, Mitt. Kaiser-Wilhelm-Inst. Eisenforsch. Dusseldorf, **19**, 1 (1937); [*C.A.*, **31**, 4941 (1938)].
6. B. DeWitt and H. Seltz, *J. Am. Chem. Soc.*, **61**, 3170 (1939).

7. S. Dushman, "Scientific Foundations of Vacuum Technique," p. 99, John Wiley & Sons, Inc., New York (1949).
8. L. H. Dreger, V. V. Dadape, and J. L. Margrave, *J. Phys. Chem.*, **66**, 1556 (1962).
9. D. R. Stull and G. C. Sinke, "Thermodynamic Properties of the Elements," Advances in Chemistry Series, 1959.
10. K. K. Kelley and E. G. King, "Contributions to the Data on Theoretical Metallurgy," U. S. Bureau Mines Bull. No. 592, 1961.
11. K. K. Kelley, *ibid.*, Bull. No. 584, 1960.
12. C. Hirayama, *J. Phys. Chem.*, **66**, 1563 (1962).
13. D. A. Schulz and A. W. Searcy, *J. Chem. Phys.*, **36**, 3099 (1962).
14. K. K. Kelley, "Contributions to the Data on Theoretical Metallurgy," U. S. Bureau Mines, Bull. No. 383, 1935.

Transport Numbers of Some Pure Fused Nitrates and Nitrites

F. R. Duke and George Victor

Institute for Atomic Research and Department of Chemistry, Iowa State University, Ames, Iowa

The transport numbers for the alkali nitrates, lithium through potassium, have been reported (1). In the corresponding chloride series, all of the salts, lithium through cesium, are known (2). It was considered to be of interest to complete the series of alkali nitrates, and in addition, to add $TlNO_3$ and NH_4NO_3 to the list of salts whose transport numbers are known. For comparative purposes, sodium and potassium nitrite are also included.

Experimental.—U-shaped cells made of fused silica or Pyrex and containing a centrally placed ultrafine disk were used in the experiments. The salt was placed on the anode side of the membrane; either the sodium or potassium salt of the same anion as the subject salt was placed in the cathode compartment. Platinum electrodes were used and currents of 80-160 ma were passed through the cells for 5,000 to 10,000 sec after the whole assembly was placed in a tube furnace. A copper coulometer was placed in series with the cell. After electrolysis, the cathode compartment was analyzed and the number of equivalents of the cation of the subject salt moving into the cathode compartment was determined.

The analyses were accomplished in some instances by flame photometry, the calibrations being done under conditions essentially identical to the unknowns. In other instances, wet chemical methods were used and in a number of cases, both methods were employed.

Results.—The results are listed in Table I.

An attempt was made to determine the transport numbers of NH_4NO_3. These values varied with the length of time of the run: 0.86 ± 0.08 for 8000 sec, 0.76 ± 0.05 for 6000 sec, 0.64 ± 0.04 for 4000 sec, all run at 100 ma. The variation was such as to indicate that NH_4NO_3 moved to the cathode compartment by other than electrical migration.

Table I. Transport numbers of the cations in pure fused salts

Salt	No. of runs	t_+	Values previously determined
$RbNO_3$	16	0.59 ± 0.04	—
$CsNO_3$	28	0.59 ± 0.07	—
$TlNO_3$ (3)	4	0.60 ± 0.05	—
KNO_2	20	0.62 ± 0.06	—
$NaNO_2$	16	0.75 ± 0.10	—
KNO_3	6	0.59 ± 0.02	0.60
$NaNO_3$	5	0.68 ± 0.05	0.70

Manuscript received July 23, 1962. Contribution No. 1171; work was performed in the Ames Laboratory of the United States Atomic Energy Commission.

Any discussion of this paper will appear in a Discussion Section to be published in the December 1963 JOURNAL.

REFERENCES

1. F. R. Duke and B. Owens, *This Journal*, **105**, 548 (1958).
2. F. R. Duke and A. L. Bowman, *ibid.*, **106**, 626 (1959).
3. Added in proof: J. G. Murgulescu and D. Topor [*Z. phys. Chem.*, **219**, 134 (1962)] report t_+ for $TlNO_3$ to be 0.30. We have rechecked our results and still find 0.60 ± 0.05.

Brief Communication

Thermodynamic Study of Phase Equilibria in the Titanium-Oxygen System within the $TiO_{1.95}$-TiO_2 Region

R. N. Blumenthal and D. H. Whitmore

Department of Materials Science, Northwestern University, Evanston, Illinois

Phase relationships in the titanium-oxygen system over the composition range $TiO_{1.90}$ to TiO_2 have been the subject of several x-ray diffraction investigations. In one of the first of these studies, Ehrlich (1) reported that the homogeneous TiO_{2-x} phase exists over the composition range $0.00 \leq x \leq 0.10$. More recently Straumanis and co-workers (2) have claimed that their diffraction study indicates that the homogeneous phase is stable over a much narrower composition range than previously supposed, x lying in the range $0.000 \leq x \leq 0.017$. Even though Magneli *et al.* (3) were unable to establish the existence of a two-phase region between $TiO_{1.90}$ and $TiO_{1.96}$ with x-ray techniques, they did report that the minimum oxygen content in nonstoichiometric rutile probably lies below $x = 0.04$. Assayag *et al.* (4), on the other hand, reported that the rutile phase is retained for compositions in the range $0.023 \leq x \leq 0.092$.

Isopiestic experiments.—The first indication of the existence of a two-phase region in the present study was obtained from the following isopiestic reduction experiment. A rutile specimen, nominally stoichiometric, was reduced by heating it in an evacuated-and-sealed quartz capsule together with a pellet consisting of a mixture of titanium oxides with a gross composition 37.2 wt % oxygen at 1100°C for 1½ hr. The reduced specimen experienced a weight loss of 0.79%, corresponding to O/Ti ratio of 1.960. Two samples, nominally stoichiometric, were sealed together with the aforementioned reduced sample, in an evacuated quartz capsule and heated at 1100°C for five days. As a result of this treatment, the two stoichiometric specimens experienced compositional changes to O/Ti ratios of 1.992 and 1.991, whereas the specimen with an initial O/Ti ratio of 1.960 oxidized to a ratio of 1.978. If, indeed, a single-phase region existed over O/Ti ratios ranging from 1.978 to 1.992, then each of the foregoing specimens should have reached identical compositions providing that the annealing time was sufficiently long for complete equilibration to have occurred. However, if this range of composition lies within a two-phase region, then the composition corresponding to a O/Ti ratio of 1.991 or 1.992 should represent one of the terminal compositions for the two-phase region at 1100°C.

The compositional state, or oxygen content of the specimens, prior to and following both the isopiestic and emf experiments (described below) was determined by means of weight measurements, assuming all of the detectable weight loss was due to a loss of oxygen from nominally stoichiometric TiO_2 (the state obtained by firing rutile in air at 1100°C). This assumption was verified by weighing specimens before reduction, after reduction, and again after reoxidation. The initial and final weights of the oxidized specimens for several cycles were identical within the precision of weighing (± 20 μg). The weight measurements were made on an Ainsworth type FDJ beam microbalance, the usual specimen weight being about 200 mg. With a specimen of this total weight and weight measurements of the aforementioned precision, determination of the O/Ti ratio of the specimen to a precision of ± 0.0005 may be achieved.

Emf measurements.—The galvanic cells employed here (5) involve a solid electrolyte and are of the type

Pt	Fe, wüstite	(0.85 ZrO_2 + 0.15 CaO)	TiO_{2-x} or 2-phase oxide mixture	Pt

Here the composition of the titanium oxide(s) electrode varied from an O/Ti ratio of 1.998 to 1.957. The preparation of the iron-wüstite reference electrode and the zirconia-calcia electrolyte has been discussed previously (6). The titanium oxide(s) electrode was prepared by pressing Fisher reagent grade anhydrous TiO_2 powder into pellets 0.25 in. diameter by 0.20 in. thick using a pressure of about 25,000 psi; these pellets were then placed in an alundum boat lined with TiO_2 powder and sintered in air at 1100°C for four days to insure formation of the rutile phase (7). The specimens were reduced to a predetermined O/Ti ratio with the aid of an isopiestic technique similar to that described above (8).

Using the above cell, emf measurements were conducted using titanium oxide specimens of varying O/Ti ratios between temperatures of 850° and 1050°C. The O/Ti ratio of the titanium oxide(s) electrode was preserved during the course of the measurements by conducting the experiment within

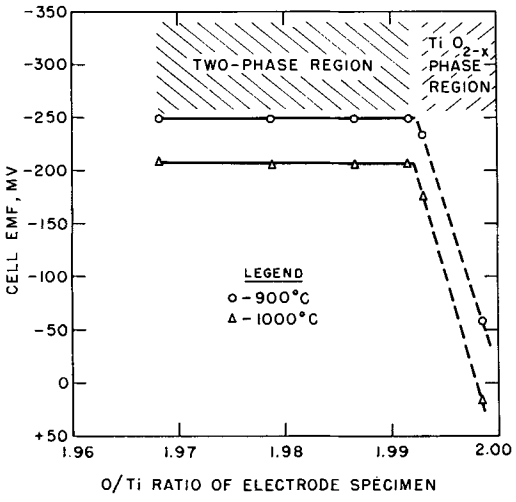

Fig. 1. Cell emf as a function of O/Ti ratio

a gas-tight assembly into which purified argon gas was continuously flowed. These results are summarized in Fig. 1 in which the cell voltage, E, is plotted as a function of the O/Ti ratio at two temperatures. The resulting curves reveal that: (i) in the case of electrode compositions with O/Ti ratios between about 1.998 and 1.992, the cell emf is a function of specimen composition, signifying the existence of a single-phase region (probably nonstoichiometric rutile); and (ii) specimens with O/Ti ratios lying between about 1.992 and 1.968 exhibited essentially constant emf's at the given temperatures (deviating by only ± 5 mv from one another), providing further evidence that a two-phase region exists over this compositional range. This latter observation completely substantiates the findings of the isopiestic experiments discussed above.

The relative partial molar free energy of oxygen ($\Delta\bar{G}_{O_2}$) and the partial pressure of oxygen (p_{O_2}) may be readily calculated as a function of temperature from the emf *vs.* temperature data (6). Values of $\Delta\bar{G}_{O_2}$ and p_{O_2} were calculated at 50°C intervals over the range 850°-1050°C from emf data for samples with compositions lying within the two-phase region; these are presented in Table I.

Finally, emf measurements, made on a reduced sample of a composition corresponding to a O/Ti ratio of 1.957, revealed emf values significantly more negative than those observed in the case of electrode samples with compositions lying within the two-phase region. It may be concluded from this that the lower limit of the two-phase region lies between O/Ti ratios of 1.968 and 1.957.

Table I. Variation of thermodynamic properties of titanium oxides exhibiting O/Ti ratios in the range 1.968 to 1.992

Temp, °C	Relative partial molar free energy of oxygen, $-\Delta G_{O_2}$, kcal/mole	Partial pressure of oxygen, p_{O_2}, atm
850	116.28	2.36×10^{-23}
900	112.73	9.95×10^{-22}
950	109.23	3.03×10^{-20}
1000	105.68	7.16×10^{-19}
1050	102.08	1.37×10^{-17}

The results of these and similar experiments now in progress on specimens in the homogeneous phase region will be reported on in greater detail in the near future.

Acknowledgment

This research was supported by Materials Central, Wright Air Development Center, under contract with Northwestern University.

Manuscript received Aug. 13, 1962; revised manuscript received Oct. 17, 1962.

Any discussion of this paper will appear in a Discussion Section to be published in the December 1963 JOURNAL.

REFERENCES

1. P. Ehrlich, *Z. Elektrochem.*, **45**, 363 (1939).
2. M. E. Straumanis, T. Ejima, and W. J. James, *Acta Cryst.*, **14**, 493 (1961).
3. S. Anderson, B. Collen, U. Kuilenstierna, and A. Magneli, *Acta Chem. Scand.*, **11**, 1641 (1957).
4. P. Assayag, M. Dode, and R. Faivre, *Compt. rend.*, **240**, 1212 (1955).
5. K. Kiukkola and C. Wagner, *This Journal*, **104**, 379 (1957).
6. R. N. Blumenthal and D. H. Whitmore, *J. Am. Ceram. Soc.*, **44**, 508 (1961).
7. N. F. H. Bright, Mineral Sciences Division Internal Report MS-60-66, Department of Mines and Technical Surveys, Mines Branch, Ottawa, Canada (July 1960) p. 24.
8. R. N. Blumenthal, Ph.D. Thesis, Northwestern University, Evanston, Illinois (1962).

The Anodic Behavior of Zinc in Potassium Hydroxide Solution

I. Horizontal Anodes

N. A. Hampson and M. J. Tarbox

Department of Applied Chemistry, College of Technology, Loughborough, England

ABSTRACT

A study of the anodic behavior of horizontal zinc electrodes in KOH solution has shown that the equation

$$(i - i_l)t^{1/2} = k$$

holds for concentrations in the range 1-13.8M and passivation times in the range 10-800 sec. The constant k depends on the KOH concentrations and attains a maximum value in the region of 8.5M KOH; i_l, the maximum current density attainable without passivation, from a least squares fit is very near zero in all cases. From the linear parts of the curves connecting anode potential and time, values of dE/dT indicate that the conductivity of the anodic product prior to passivation depends on the concentration of the KOH electrolyte. This conductivity passes through a maximum in the same region as that which produces the longest passivation times.

The anodic behavior of zinc in alkaline solution belongs to a general group of reactions usually classified by the formation of a soluble anodic product (1). Generally, if the current density is greater than the limiting value, initial anode dissolution is followed by passivation easily detected by a very rapid rise in anode potential.

The system, zinc in sodium hydroxide, has been fairly extensively studied (2-6). The system, zinc in potassium hydroxide has been less intensively studied, the investigations of Eisenberg, Bauman, and Brettner (7), Dirkse (8), and Sanghi and Wynne-Jones (9) appear to be the only ones recorded in the literature notwithstanding the importance of the system in connection with the silver oxide-zinc cell.

Huber (2, 3) and Fry and Whitaker (6) have considered the structure of the passive layer obtained under various conditions with sodium hydroxide solutions and concluded that the passive film consists of zinc oxide which may be dark if excess metal ions are present in the lattice. Landsberg (4, 5) has shown that for vertical electrodes the equation

$$(i - i_l)\ t^{1/2} = k \qquad [1]$$

holds from 0.05M-4M concentration of NaOH provided that i is not too high, k and i_l being dependent on concentration. At high current densities k was observed to increase markedly.

For the system, zinc in potassium hydroxide, Sanghi and Wynne-Jones (9) concluded that no general relationship exists between passivation time and current density whereas Eisenberg, Bauman and Brettner (7) show that Eq. [1] holds in 6.924M KOH for anodes with either vertical or horizontal orientation and passivation times of less than 20 sec.

Experimental

Materials.—All materials were of reagent (A.R.) quality. Zinc sheet was 99.95% containing less than 0.005% Cu, 0.005% Fe, 0.005% Cd, the major impurity being Pb. All solutions were prepared from ordinary distilled deionized water; no attempt was made to remove dissolved oxygen.

Passivation circuit.—Measurements were made with the anode in a horizontal position as shown schematically in Fig. 1. The anode potential was measured with reference to an Hg/HgO electrode or at a microporous zinc electrode (prepared by reducing an alkaline zinc oxide paste in a pure zinc frame using an electrolyte of aqueous KOH) in conjunction with a conventional luggin capillary

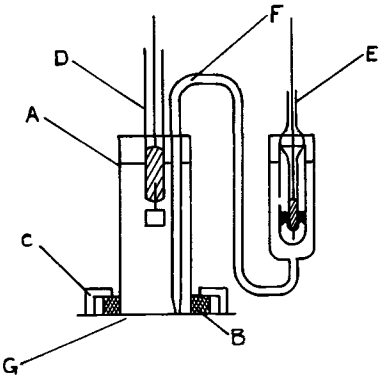

Fig. 1. Passivation cell (not to scale): A, glass (Pyrex) cylinder with accurately ground face pressing on zinc anode; B, tightly fitting rubber ring; C, clamps; D, cathode; E, reference electrode; F, luggin capillary; G, zinc anode.

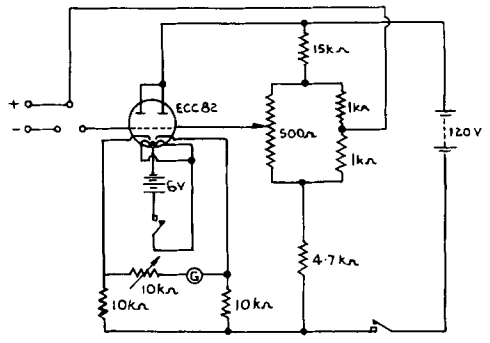

Fig. 2. Circuit for valve voltmeter

which was close to the anode surface. Voltage measurements were made with a valve voltmeter, the circuit for which is shown in Fig. 2. Current measurements were made with suitably shunted galvanometers manufactured by Cambridge Instrument Co. Ltd., with certified accuracy ± 0.2%. The cathode was platinum.[1]

Anode pretreatment.—Sanghi and Wynne-Jones (9) conclude that insufficient anode pretreatment is the major source of error in passivation experiments; they suggest a pretreatment routine employing six grades of emery paper lubricated with alcohol followed by a final rub with parchment and Selvyt cloth. The sample of zinc used in our experiments had a bright untarnished surface; however preliminary experiments were carried out in which a number of methods of surface preparation were investigated. Dissolution of the degreased surface in either HCl or H_2SO_4 for a series of times followed by careful washing and final degreasing produced surfaces identical in behavior with sheet which had been polished with filter paper and carefully degreased. Erratic results were obtained by abrading with emery paper; one brand used caused the zinc to react violently with aqueous KOH, hydrogen being evolved rapidly (10). The simple polish and degrease technique was, therefore, used in our experiments.

Experimental procedure.—Cleaned zinc sheet was fitted into the cell, aqueous KOH electrolyte (25 ml, changes in this volume did not affect the results), carefully thermostatted to 20°C, was added and the luggin capillary set up. The passivation time was determined from the time of closing the circuit to the instant the anode potential increased rapidly and coincided with the development of a film which was observed to flash across the anode surface. The anode potential was measured at convenient time intervals during the passivation experiments. After passivation the anode surface was examined, the cell being dismantled, thoroughly dried and cleaned before fresh zinc sheet was fitted prior to polarization at a preset rate.

Results

Figure 3 shows typical straight line plots relating $t^{-1/2}$ and current density; Table I records the complete results obtained from a least squares fit made with an IBM 1620 computer. The family of

[1] With these experimental conditions a number of variations in cathode shape made no difference in the value of t.

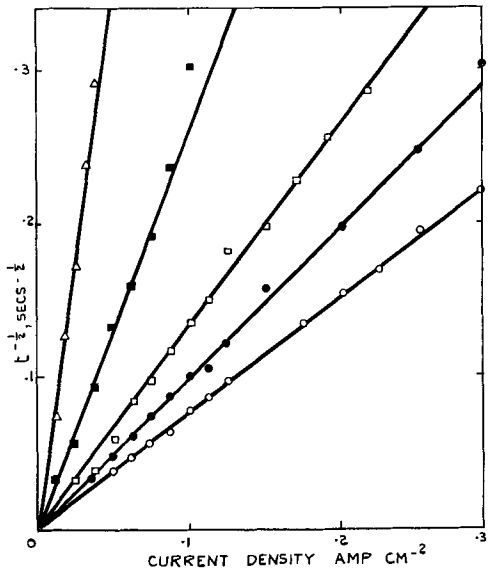

Fig. 3. (Passivation time)$^{-1/2}$ *vs.* current density. △, M; □, 3.5M; ■, 2M; •, 13.8M; ○, 10M.

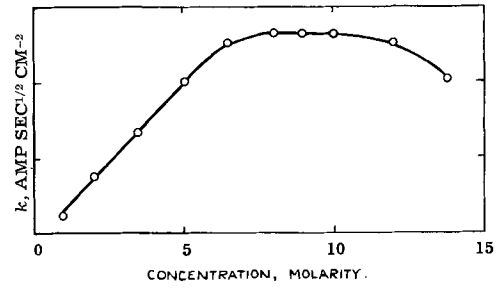

Fig. 4. k from $(i - i_e)t^{1/2} = k$ *vs.* concentration

curves form a pencil, indicating that the limiting current i_l is in the region of zero. Figure 4 shows a plot of k against concentration. It is evident that, for any current density, the passivation time reaches a maximum at 8.5M; k at this concentration has a value of 1.33 amp cm^{-2} sec$^{-1/2}$.

Film colors were observed to be generally dark in dilute electrolyte and at low current density, becoming white as the electrolyte concentration and current density were increased. If washed dark films were allowed to stand in contact with air for some time they became considerably lighter in color, indicating some oxidation of the zinc rich lattice.

Discussion of Results

The orientation of the anode in a horizontal plane with the mass of electrolyte above eliminates con-

Table I. Results of a least squares fit for constant current passivation trials

Concentration, M	Maximum current density investigated, amp cm^{-2}	k	i_l
1	0.038	0.1178	0.0005214
2	0.101	0.3773	0.00021
3.5	0.221	0.7660	0.00149
5	0.252	0.9930	0.00019
6.5	0.201	1.259	0.000118
8	0.302	1.323	0.000597
9	0.302	1.324	—0.000686
10	0.302	1.311	—0.000081
12	0.352	1.255	—0.000922
13.8	0.302	1.015	0.000207

vection currents. Before passivation the anodic products will diffuse away slowly relative to their rates of production until, at the instant of passivation, a critically thick layer of products surrounds the anode. At the electrode the products will diffuse away at a rate dictated by the concentration gradient and the diffusion coefficient. For a vertical electrode the removal of zincate rich electrolyte takes place continually and, unless critical conditions are reached when passivation occurs and hydroxyl ions are discharged, a steady state should be attainable then, provided that the current density does not exceed the limiting value when a net accumulation of anode products occurs. In the case of horizontal electrodes, conditions for passivation are always realizable, since in the absence of convection, however small the current, the critical concentration can theoretically always be realized.

For runs of short duration with a horizontal anode and a silver oxide cathode, Eisenberg, Bauman, and Brettner (7) find that in 6.924M KOH, i_l has a value of 0.06 whereas Landsberg and Bartelt (5) using a zinc plated copper wire as a vertical anode find i_l in the same concentration of NaOH to be 0.0080 (7). In the latter case convection as a means of zincate transfer from the anode can obviously occur in addition to diffusion; Eisenberg, Bauman, and Brettner's experiments are complicated by the possible uneven discharge of the silver oxide especially at high rates (this may explain the large amount of scatter in their results). The value of i_l for vertical zinc anodes in 7M KOH has been found to be in the region of 0.10 (11).

The observed maximum in the curves relating k and concentration indicates that t increases to a maximum at a concentration of about 8.5M and then falls off. (With vertical electrodes k increases to a maximum value in about 8.5M KOH; i_l in the vertical case goes through a fairly sharp maximum at about 8.5M. This investigation is still continuing.) This indicates that the supersolubility (7) of the anode products in the electrolyte passes through a maximum at this concentration. The degree of supersaturation required for passivation must be considerable as evinced by the addition of zinc oxide to 5M electrolyte which made remarkably little difference to t

Anion	Concentration	k
Nil	Nil	0.993
Zincate	0.25M	1.000
	0.60M	0.990

When the electrode undergoes polarization the initial step will be the production of soluble zincate. If there is a net accumulation of zincate at the anode the depletion of the OH^- concentration will cause the zincate to precipitate either as oxide or hydroxide (3); when this occurs the potential rises and the anode undergoes passivation. The rate of polarization and the concentration of the electrolyte will determine under what conditions the zincate is precipitated as a film; under conditions of low hydroxide concentration due to either electrolyte concentration or low polarization rates (more efficient removal of OH^- ions) the dark films observed will be due to precipitation under conditions resulting in the formation of zinc rich lattices.

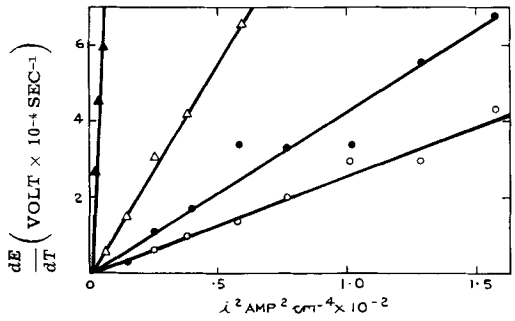

Fig. 5. dE/dT vs. i^2.○, 13.8M; •, 5M; △, 3.5M; ▲, 1M

Provided that a stationary state is rapidly established in the layers immediately surrounding the anode, the anode potential can be expressed as

$$E = E_r + E_c$$

Where E_r is that component of the anode potential due to the irreversible anode potential and E_c is the component due to the production of anode products. Treating E_c as purely ohmic in character, it can be shown that

$$E_c = \frac{1}{\kappa} K i^2 T$$

where κ is the conductance of the anode product layers, and K is a constant.

$$i^2 = \frac{\kappa}{K} \cdot \frac{dE}{dT} = A \cdot \frac{dE}{dT} \qquad [2]$$

An examination of the potential-time results for the passivation runs showed that for all except those in which t was relatively small a good value of dE/dT could be obtained; for short passivation times there was too much scatter for reliable gradients to be calculated.

Figure 5 shows typical dE/dT values plotted against i^2. It is evident from these curves that an equation of the form [2] is obeyed. Table II shows the slopes of curves relating dE/dT and i^2 calculated by the method of least squares using an IBM 1620 computer; the straight line correlations all passed through the origin. The maximum value of the constant, A, of Eq. [2] would imply that the conduc-

Table II. Results of a least squares fit for constant current passivation trials

$i^2 = A\ dE/dT$

Concentration, M	A, amps² sec volts⁻¹
1	0.9226
2	4.526
3.5	9.332
5	23.08
6.5	26.15
8	30.14
9	34.64
10	26.14
12	23.41
13.8	25.30

tivity of the anode product layers reaches a maximum in the region of 9M concentration and occurs in the same region as the maximum passivation time. These results show that the optimum concentration of KOH electrolyte for the discharge of horizontal zinc electrodes is 8.5M, when the duration of discharge and the conductivity of the anode product layers are at a maximum.

Acknowledgment

The authors wish to thank Dr. R. F. Phillips for his encouragement, and Messrs. Stewarts and Lloyds, Ltd., Corby, England, for a Sandwich Studentship to one of them (M.J.T.), during the final year of which this work was undertaken.

Manuscript received Jan. 22, 1962; revised manuscript received Aug. 13, 1962. This paper was prepared for delivery before the Boston Meeting, Sept. 16-20, 1962.

Any discussion of this paper will appear in a Discussion Section to be published in the December 1963 JOURNAL.

REFERENCES

1. J. O'M. Bockris, "Modern Aspects of Electrochemistry," No. 2, p. 262, Butterworth's Scientific Publications, London (1959).
2. K. Huber, *Z. Elektrochem.*, **48**, 26 (1942).
3. K. Huber, *This Journal*, **100**, 376 (1953).
4. R. Landsberg, *Z. Phys. Chem.*, **206**, 291 (1957).
5. R. Landsberg and H. Bartelt, *Z. Elektrochem.*, **61**, 1162 (1957).
6. H. Fry and Marjorie Whitaker, *This Journal*, **106**, 606 (1959).
7. H. Eisenberg, H. F. Bauman, and D. M. Brettner, *ibid.*, **108**, 909 (1961).
8. T. P. Dirkse, *ibid.*, **102**, 497 (1955).
9. Indra Sanghi and W. F. K. Wynne-Jones, *Proc. Indian Acad. Science, Sect. A*, **47**, (1958).
10. U. R. Evans, "The Corrosion and Oxidation of Metals: Scientific Principles and Practical Applications," p. 252, Edward Arnold, London (1960).
11. N. A. Hampson, Unpublished results.

NOMENCLATURE

E	anode potential, volts.
E_r	irreversible anode potential for the dissolution step, volts.
E_c	that component of the total anode potential due to the build-up of anode products, volts.
i	current density, amp cm^{-2}.
i_l	limiting current density, amp cm^{-2}.
k	constant in the equation: $(i - i_l)t^{1/2} = k$, amp cm^{-2} $sec^{1/2}$.
T	time, sec.
t	passivation time, sec.
κ	conductivity of the anode product layers, $ohms^{-1}$

Magnetic Properties of 97 Fe-3 Ni Thin Film Electroplate

A. Kolk and H. White

The National Cash Register Company, Hawthorne, California

ABSTRACT

Thin films of a 97 Fe-3 Ni alloy composition have been successfully electrodeposited on silvered glass Rod and on specially treated Be-Cu wire surfaces. With both substrates, the magnetic properties of the overplate met the requirements for a switching element in a computer memory. However, the process was simpler and much more uniform properties in the plate were obtained with the Be-Cu substrate than with the silvered glass. Optimum magnetic properties for the Rod device application were obtained by plating from an iron-nickel chloride bath, maintained at 80°C, pH = 1.0, and a current density of 90 ma/cm^2.

The use of magnetic memory elements in high speed digital computers has resulted in considerable interest in fast-switching magnetic materials. The switching of a magnetic element may often be related to the applied field, H, by the equation (1)

$$S_w = \tau(H - H_o)$$

The flux reversal time, τ, is defined as the time required to reverse a fixed percentage of the magnetic flux or the time between the points of 10% of peak voltage output on the voltage time curve. The switching coefficient, S_w, and the threshold field, H_o, are characteristics of the material. It is evident that the flux reversal time may be decreased by lowering S_w or by increasing $(H - H_o)$.

Much work has been conducted on uniaxially oriented permalloy films where, under certain conditions, the switching coefficient may be made quite small (2). However, the nature of the mechanism which gives the low switching coefficient requires good uniformity in the magnetic characteristics of the uniaxially oriented permalloy film; this uniformity requirement has slowed the development of permalloy film memory elements.

The device called the Rod has utilized the other technique for increasing the switching speed, namely, increasing the value of the excess field, $(H - H_o)$, which may be used while in a computer mode of operation. In normal computer modes of memory operation, the maximum permissible excess field is approximately equal to the coercive force, H_c, of the magnetic material. The Rod employs an approximately 97 Fe-3 Ni electroplate with a coercive force of about 15 oe as contrasted to the less than 2 oe generally found in the permalloy film devices.

The configuration of the Rod device is shown in Fig. 1. The 97 Fe-3 Ni alloy is deposited on a conductive substrate. Early work utilized a 10-15 mil

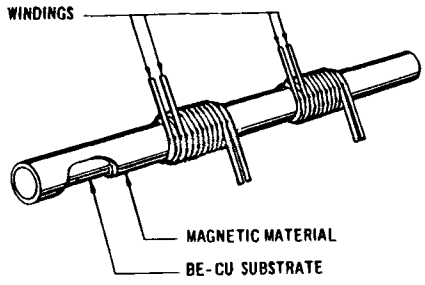

Fig. 1. Rod structure with solenoid windings

diameter silvered glass substrate, but the substrate used at present is Be-Cu wire.

The cylindrical configuration permits multiturn solenoid drive windings as contrasted with the one or two turn drive windings which are employed in a flat permalloy film memory. Therefore, the drive currents are similar in spite of the order of magnitude difference in the coercive forces of the two alloys.

This paper presents the results of a rather broad investigation of the effects of various deposition parameters on the magnetic properties of the plated alloys.

Experimental

Composition of plating bath.—An iron-nickel chloride bath with calcium chloride as the supporting electrolyte was used for much of the plating discussed below. The composition of this so-called "standard bath" was as follows: $FeCl_2 \cdot 4H_2O$, 285 g/l; $NiCl_2 \cdot 6H_2O$, 10 g/l; $CaCl_2 \cdot 2H_2O$, 238 g/l. The *p*H was adjusted to 1.0 ± 0.1 *p*H units by the addition of the proper amount of dilute HCl.

In every case in which a bath was used for more than one day, it was first regenerated. This process consisted of adding finely divided iron particles to reduce any ferric ions, heating with activated charcoal to remove organic impurities, filtering, cooling, and readjusting the *p*H. A coil of pure nickel wire was used as an anode. The rate of oxidation of the bath was not rapid in spite of the nickel anode because of the low rate of plating. Air oxidation was a much greater factor and was, in general, suppressed by using a nitrogen blanket over the bath.

The composition of the plating bath was checked at regular intervals by means of spectrophotometric analysis. The composition of the plate was checked by a number of methods: spectrographic, spectrophotometric, and x-ray fluorescence. The data indicated that, under the conditions discussed in this paper, the Fe/Ni ratio in the plate is the same as that in the bath. In the case of the "standard" 10 g/l $NiCl_2 \cdot 6H_2O$ bath, the nickel content of the plate was 2.5 to 3 weight per cent (w/o).

Batch process Rod production.—The Rods which were used in the first Rod memory application were prepared in a batch operation. Approximately 15 in. lengths of glass cane were coated with a thin layer of silver and then plated from the standard bath in the manner indicated in the schematic drawing, Fig. 2.

The method of applying the silver layer to the glass was as follows: Fifteen inch lengths of glass

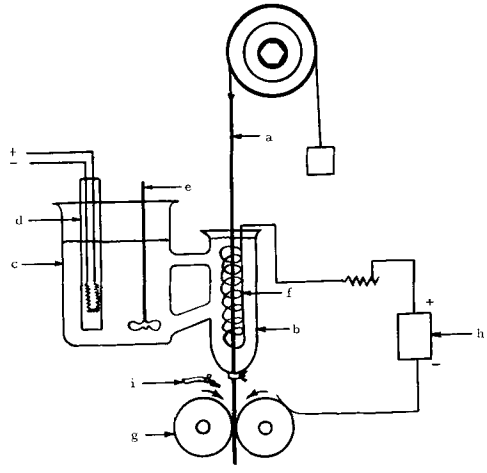

Fig. 2. Schematic of plating arrangement for silvered glass rod: a, cathode — 10 mil silvered glass Rod pulled at a uniform rate (5 in./min) through the plating cell; b, plating cell; c, reservoir containing bulk of plating solution; d, heater and thermo regulator which maintained bath temperature constant at 80° ± 1°C; e, stirrer which caused plating solution to circulate through cell; f, anode—coil of pure nickel wire; g, cathode drive and electrical contact; h, transistorized constant current source; i, jet of H_2O to remove any adhering solution from plated surface of Rod.

cane were cleaned by suspending them in hot chromic acid cleaning solution for approximately 1 hr. After first rinsing with distilled water, the surface of the glass was sensitized by immersing the cane for 1 min in a 2.5% solution of stannous chloride, followed by another rinse with distilled water. The silver was then applied to the glass surface by means of a spray process. Two separate streams of liquid, one containing a silver solution and the other a reducing agent, were directed so as to combine and impinge on or near the surface of the glass. As a result of the ensuing chemical action, metallic silver was deposited on the surface. In the early stages of this program, the spraying was a hand operation; later the process was mechanized.

Using the silvering procedure described above, problems were encountered in achieving uniform and reproducible magnetic properties. It was soon established that the principle cause of the nonuniform magnetic properties lay with the substrate rather than in the plating. Rods plated from the same bath with the same plating parameters but which had been silvered in different batches varied in coercive force readings by as much as 5 oe. This finding was not unexpected since the literature (3) on electrodeposition contains many references relating plating structure and stress to the nature of the substrate.

Since it was known that the magnetic properties of thin films are affected by the degree of surface roughness of the film substrate, it was decided to investigate the effects of electropolishing the silver surface before plating. When the original silver surface was rough, as revealed by inspection under a metallograph, the results of electropolishing were quite encouraging; reductions of as much as 10 oe in the coercive force of the magnetic plate were observed. However, when the original silvered surface was fairly uniform, no significant gain in mag-

Table I. Rod magnetic values

Series	No. of rods	Mercuricyanide dip	H_c, oe	1/0 Ratio
1	8	Yes	15.6	5.0
2	8	No	16.7	3.9

Plate thickness $\simeq 0.55\mu$.

netic properties resulted from the electropolishing treatment.

Electron micrographs of silver coated Rods before and after electropolishing revealed that the smoothing effect of the polishing was most pronounced in the areas thought to be crystallite clumps. Careful inspection of the micrographs indicated, however, that the larger raised areas were actually hollow blisters and not solid crystallites. The uniformity of the basal material, the shadowing, and the ragged filmy material around the edge of the polish plane all point to this conclusion.

Varying spray pressures, spray patterns, the concentrations of spray solutions, spatial positioning of nozzles as well as experimenting with different ways of cleaning and sensitizing the glass surface resulted in no great improvement in the uniformity of the silver substrate surface.

The one modification in the silvering process which did produce a significant improvement in the surface uniformity involved dipping the silvered Rods for approximately 20 sec in a 0.1% solution of potassium or sodium mercuricyanide. This treatment was suggested by Freund (4), who stated that the yellowish tinge frequently observed on silvered glass surfaces could be removed by immersing the surface in a mercuricyanide solution. It was also stated that the resulting oxide-free silver surface was particularly suitable for plating.

Table I presents values of the magnetic properties of two series of electroplates, one employing the mercuricyanide treatment before plating and the other series without the mercuricyanide.

The output/zero-disturb ratio[1] termed herein the 1/0 ratio, was appreciably larger for the Rods in which the mercuricyanide dip was used. A high 1/0 ratio is a necessary feature in any bistable switching element used in computer memories. In addition to an improved 1/0 ratio, Rods plated after the mercuricyanide dip displayed more uniform magnetic properties.

Electron micrographs of the silvered surface (Fig. 3 and 4) taken before and after the mercuricyanide dip treatment show that a bridging and smoothing of the larger silver crystallites had occurred as a result of this treatment. A spectrographic analysis of the silver after immersion in the mercuricyanide showed the presence of 5.6% mercury indicating that an exchange reaction or amalgamation with silver had taken place. That the reaction was no

[1] Output—Peak voltage across sense solenoid produced by the application of a switching magnetic field approximately 2 times the coercive force of the plate. Zero-disturb—The peak voltage measured across the sense solenoid and generated by the following pulse sequence: (*a*) starting with a magnetized state of the plate, a number of pulses ($<H_c$) are applied in the direction of switching; (*b*) the above half-select pulses are then followed by a full-select pulse ($\simeq 2H_c$) applied in a reverse direction (*i.e.*, direction of original magnetized state).

Fig. 3. Silver surface before mercuricyanide treatment

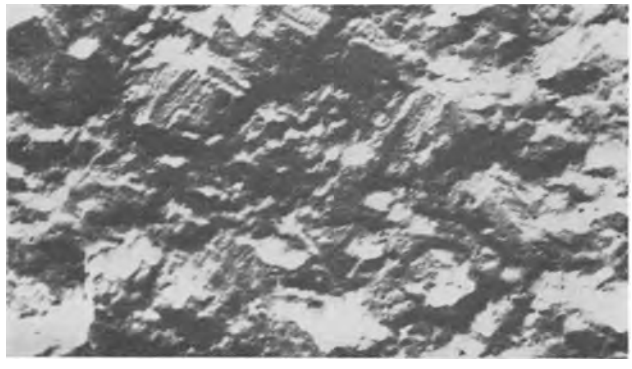

Fig. 4. Silver surface after mercuricyanide treatment

mere cleaning of the silver surface was indicated by the fact that other good silver cleaning solutions such as a thiourea-hydrochloric acid mixture, a sodium silver cyanide solution containing excess cyanide ion and others had no effect on the magnetic properties of the overplate.

Continuous process for Rod preparation.—In addition to the mercuricyanide dip treatment for the silvered-glass substrate surface, it was found that specially prepared beryllium-copper wire functioned equally well as a substrate material for the 97Fe-3Ni plate. Moreover, the process based on a Be-Cu substrate was more easily controlled and lent itself to continuous operation. The key steps in the continuous Rod plating process are illustrated in the line drawing shown in Fig. 5.

Heat-treated, prestraightened 10 mil Be-Cu wire is drawn from a 24 in. bicycle wire and pushed through carefully aligned holes in the plating tank array. One of the contact rollers is rubber and the other, which also serves as the electrical contact for the wire, is copper.

In the first tank, the wire is cathodically cleaned in a hot (90°C) alkaline cleaning solution (En-

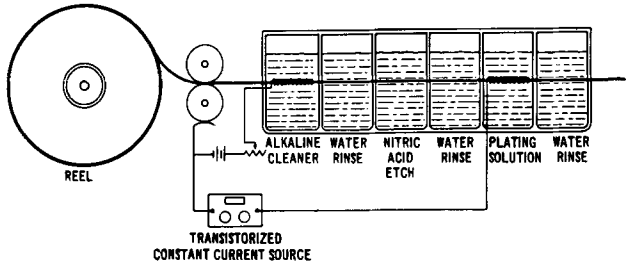

Fig. 5. Continuous Rod plating process

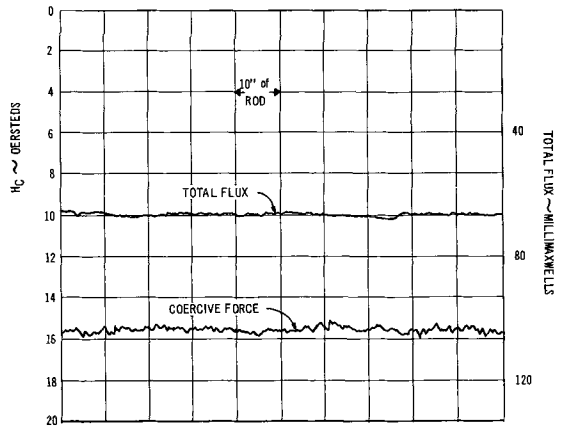

Fig. 6. Chart recording of Rod B-H characteristics

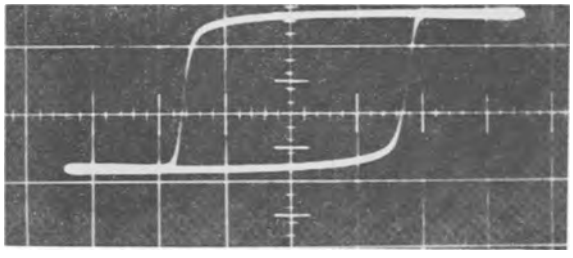

Fig. 7. Hysteresis loop; horizontal scale, 10 oe/large div.; vertical scale; ~ 30 millimaxwells/large div.

thone). After a water rinse, the wire then passes into a dilute (6.3*N*) nitric acid solution (room temperature). The action of nitric acid is twofold; it removes any oxide scale, and in addition, partially etches the wire surface. The degree of etching is a major factor in determining the coercive force and squareness of the plate. After another water rinse, the Be-Cu wire is plated with the 97Fe-3Ni alloy from the iron-nickel chloride bath.

After a final washing, the wire is passed through a magnetic test fixture which records on a strip chart the total magnetic flux and the coercive force of the plate. Figure 6 shows a chart recording for a typical section of the Rod passing through the test fixture. The magnetic flux and coercive force are also displayed in the form of a hysteresis loop on an oscilloscope. A typical hysteresis loop is shown in Fig. 7.

The final step in the process consists of applying a thin organic coating to protect the iron-rich magnetic film from corroding.

Effects of plating parameters on magnetic properties of film.—Plating in the presence of a magnetic field.—It is well known that the magnetic characteristics of permalloy films can be modified by plating in the presence of a magnetic field. However, axial magnetic fields as large as 600 oe produced no observable differences in the magnetic properties of the 97 Fe-3 Ni films.

Replacement of calcium chloride with potassium chloride as the supporting electrolyte.—Potassium chloride is often used in iron chloride baths when relatively stress-free plate is desired (5). Since it is known that stress in a magnetic film can affect the magnetic properties of the film, the effect of replacing calcium chloride with an equal number

Table II. Magnetic properties of plate as a function of Ni concentration in bath

Sample No.	$NiCl_2 \cdot 6H_2O$, g/l	Coercive force H_c, oe	Flux* ψR arbitrary units	1/0 Ratio
1	0	20	2.7	4.7
2	2.3	19.2	3.0	7.0
3	4.6	18.5	3.3	13.0
4	6.9	18.3	3.3	15.0
5	9.2	17.8	3.4	17.0
6	11.5	17.4	3.5	>18
7	13.8	17.0	3.5	>18.5
8	18.6	16.5	3.5	>20

it = 280 ma sec/in. of 10 mil BeCu wire; plate thickness ≃0.6μ.

* In this and subsequent tables, one arbitrary unit of flux corresponds to approximately 20 millimaxwells.

of equivalents of potassium chloride in our standard bath was investigated.

Except for an increase of approximately 3 oe in the coercive force of the plate deposited from the bath containing KCl, no other magnetic differences were noted. Output, squareness, and switching characteristics were essentially the same.

This bath was found to be quite sensitive to small changes in *p*H. At *p*H values of 1.0, excessive gassing and burning of the plate occurred. At higher *p*H values (3.0), objectionable hydroxide precipitates formed.

Varying Nickel Concentration.—A series of Rods were plated from the standard bath modified with respect to the concentration of $NiCl_2 \cdot 6H_2O$. The concentration of this salt was varied over the range 0-18.6 g/l. All of the other plating conditions remained unchanged. The effects of the nickel concentration in the bath on the magnetic properties of the film are shown in Table II.

Although the values for the 1/0 ratio improve with increasing Ni concentration in the bath, it was found that for $NiCl_2 \cdot 6H_2O$ concentrations in excess of 11 g/l the magnetic properties of the plate are very sensitive to externally applied stresses.

Increasing the Ni concentration had two effects on the physical properties of the plate: (i) a decrease in pitting was observed, and (ii) a change in the macroscopic stress in the plate was noted (Fig.

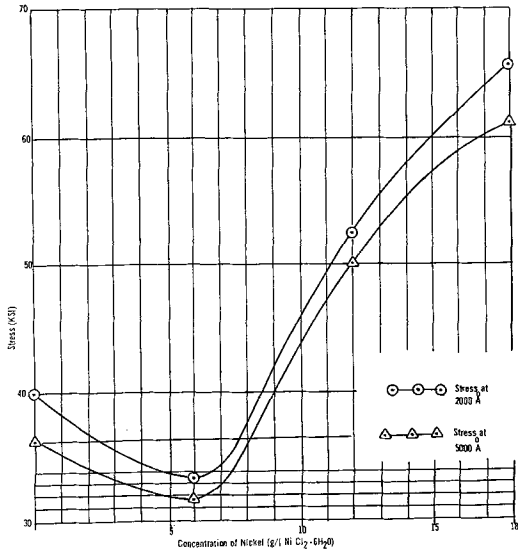

Fig. 8. Effect of nickel concentration on stress

8). Since the observed change in coercive force does not follow the stress-composition curve, particularly when the known behavior of the magnetostrictive coefficient is taken into account, the conclusion is drawn that stress does not play a significant role in the effects of composition on coercive force.

Effect of temperature of bath on magnetic properties of plate.—Several lengths of Rod were made at various bath temperatures, all other plating conditions being maintained constant. The results of these tests are shown in Table III. Rods with the best switching characteristics and squareness ratios were obtained when the bath temperature was maintained at approximately 80°C. With bath temperatures of 65°C and below, the physical properties of the plate also deteriorated as manifested by a blackening of the plate.

Effect of current density.—The magnetic properties of the plate are not affected by variations of ±25% in the normal current density (90 ma/cm^2). The speed of travel in the continuous plating process can therefore be adjusted for optimum conditions in the substrate etching tank.

The results of a study of the magnetic properties of the 97 Fe-3 Ni plate *vs.* the pH of the plating solution are shown in Table IV. Inspection of Table IV reveals that, whereas the coercive force shows a slight tendency to decrease with decreasing pH, the values for the magnetic output decrease appreciably for pH values less than 0.9.

Relation of coercive force and plate thickness.—The relationship between thickness and the coercive force of the coating is shown in Fig. 9 for three different substrate treatments. In the thinner regions, the relationship is roughly linear on a log-log plot. This is not unexpected since previous theoretical and experimental work on thin films has shown the following relation to hold (6)

$$H_c = Ct^{-n}$$

where H_c is the coercive force, C is a constant dependent on the nature of the roughness, t is the thickness, and n also depends on the nature of the roughness.

The slope of the linear portion and the break in the curve as the thickness is increased was found to be a function of the substrate preparation. The break is dependent on the roughness of the substrate and probably occurs at the initiation of multidomain behavior. Since the theoretical treatments only have validity where the roughness of the film or the substrate is small compared with domain wall thickness, which is not the case for the films studied, no quantitative conclusion can be drawn from the data. The slope after the break is similar for the three substrate treatments.

Switching kinetics.—The most important magnetic characteristics of the Rod as a computer component is the switching speed. The switching characteristics of the Rod have been measured in the laboratory in an apparatus described elsewhere (7). A typical switching pulse is shown in Fig. 10.

The switching time was determined as the interval between the points where the voltage was 10% of the peak value. A switching coefficient was then obtained assuming the usual linear relation

$$S_w = \tau(H - H_o)$$

The switching coefficient has also been measured on a 10-90% of the volt-sec area basis, and no sig-

Table III. Magnetic properties of plate as a function of bath temperature

Sample No.	Temp, °C	Flux ψ arbitrary units	Coercive force, oe
1	85	3.3	18.4
2	80	3.4	18.0
3	75	3.4	16.8
4	70	3.0	14.0
5	65	2.7	15.8
6	60	2.5	16.0
7	50	2.2	22.0

it = 280 ma sec/in. of 10 mil BeCu wire; plate thickness ≃0.6μ.

Table IV. Magnetic properties of plate as a function of pH of bath

Sample No.	pH	Flux ψ arbitrary units	Coercive force H_c-oe
1	1.1	3.5	18.2
2	1.05	3.5	18.2
3	0.95	3.5	18.6
4	0.5	3.0	17.8
5	0.3	2.8	16.3
6	0.15	2.8	17.8
7	0.10	2.9	18.2

it = 280 ma sec/in. of 10 mil BeCu wire; plate thickness ≃0.6μ.

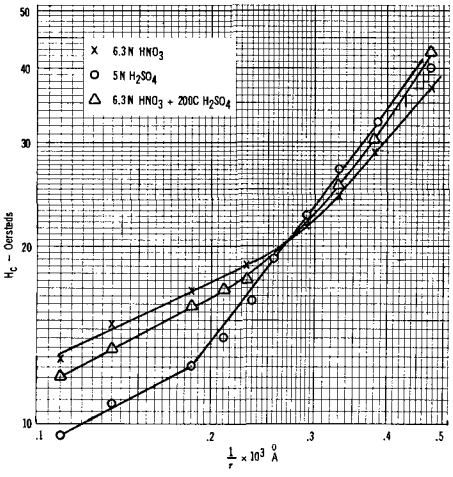

Fig. 9. Thickness and coercive force for three different substrate treatments.

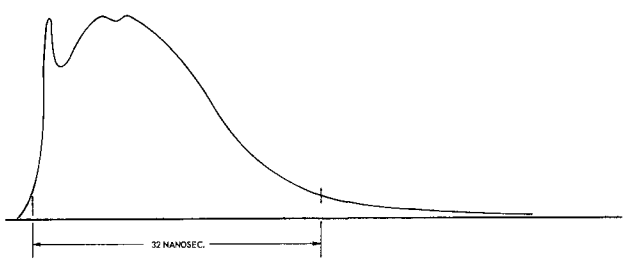

Fig. 10. Typical switching pulse

nificant difference in value is found as compared to the peak voltage method.

The observed switching behavior of the Rod may be summed up in general as quite closely approximating the behavior of a ferrite core. Two models have been suggested to describe the behavior of a core; one a nucleation and domain growth hypothesis developed by Goodenough and Menyuk (1), and many others; the other model, offered by Humphrey and Gyorgy (8), is based on the incoherent rotation mechanism.

The shape of the switching transient as well as data based on interrupted pulse measurements make a nucleation and growth hypothesis more tenable than incoherent rotation, at least down to switching times of 25 nanosec. Both the switching transients and the interrupted pulse measurements closely resemble the data obtained with ferrite cores (1).

Acknowledgments

The authors wish to thank Donal Meier, Richard Clinehens, George Schrader, Larry Douglas, Eric Chow, and Harry Watkins for their contributions and assistance. The work was partially supported by Air Force Cambridge Research Laboratories, Contract No. AF 19(604)-5896.

Manuscript received April 11, 1962; revised manuscript received Sept. 21, 1962. This paper was prepared for delivery before the Detroit Meeting, Oct. 1-5, 1961.

Any discussion of this paper will appear in a Discussion Section to be published in the December 1963 JOURNAL.

REFERENCES

1. N. Menyuk and J. B. Goodenough, *J. Appl. Phys.*, **26**, 1 (1955).
2. J. B. Goodenough and D. O. Smith, "Magnetic Properties of Metals and Alloys," Chap. 7, American Society for Metals (1958).
3. W. Blum and W. O. Meyer, "Modern Electroplating," pp. 26-43, John Wiley & Sons, New York (1953).
4. E. Freund, U.S. Pat. 2,063,034 (1934).
5. A. G. Gray, "Modern Electroplating," p. 278, John Wiley & Sons Inc. (1953).
6. J. C. Lloyd and R. S. Smith, *J. Appl. Phys.*, **30**, 274S (1959).
7. D. A. Meier and A. J. Kolk, "The Magnetic Rod—A Cylindrical Thin Film Element," ONR Symposium on Large Capacity Memory Techniques for Computing Systems, May 1961.
8. F. B. Humphrey and E. M. Gyorgy, *J. Appl. Phys.*, **30**, 6 (1959).

Effects of Additives on the Structure of Electrodeposited Silver

R. W. Hinton,[1] L. H. Schwartz,[2] and J. B. Cohen

Department of Materials Science, Technological Institute, Northwestern University, Evanston, Illinois

ABSTRACT

The structure of silver deposited from a cyanide bath was examined using x-ray diffraction techniques. Measurements were made of the effects of small concentrations of potassium ethyl xanthate (KEX), carbon disulfide, gelatin, and polyvinylpyridine on the mosaic size, density of faults in the (111) stacking sequence, macrostresses, and microstrains. Hardness of the deposit and plating efficiency were also determined. All deposits contained microtwin faults but no (one-layer) stacking faults. Dislocation densities were of the order of $10^9/cm^2$ in deposits without additive. With KEX there were 10^{10}-10^{11} dislocations/cm^2; these were more randomly distributed than in the deposit from a solution without additive. Small additions of additives increased the plating efficiency, but with increasing amounts the efficiency passed through one or more maxima. The twin-fault density, hardness, and line breadth changed in a similar manner and were highest when the effective current density (or plating efficiency) was greatest.

With additions of KEX, microstrains varied greatly over small distances, from 3×10^{-3} averaged over 20Å to 1×10^{-3} averaged over 150Å, but there was no variation of these microstrains with concentration of additive. Macrostresses followed the plating efficiency in an opposite manner to the microtwin density, hardness, and line breadth at low concentrations of KEX; macrostresses increased when the current efficiency decreased. At higher concentrations the macrostresses increased when current efficiency increased. The structures obtained with the four additives studied were similar.

The presence of residual stresses in electrodeposits has been known for a century (1). When the deposit is thin the magnitude and sign of these stresses depend on the substrate, but in thicker deposits the stresses depend only on the metal and deposition conditions (2). Four classes of theories have been proposed to account for these residual stresses. Observations indicate that all four are probably operative: (*a*) plastic deformation during the deposition process due to inclusions (such as additives), or to differences in local temperature (3); (*b*) evolution of hydrogen occluded during plating. [Some

[1] Present address: Universal Oil Products Company, Des Plaines, Illinois.

[2] Standard Oil Foundation Fellow.

stress relief after plating or during hydrogen charging has been observed (2)]; (c) Formation and occlusion of compounds (4, 5) and their subsequent reduction. Differences in the stresses in different metals could then arise due to the densities of different types of compounds and the amount of their reduction; (d) Dislocations due to growth accidents (6, 7). It is known that the dislocation density in a copper deposit is orders of magnitude greater than that in a well annealed metal (8, 9), (*i.e.*, 10^9-10^{10} dislocations/cm^2), and that the stored energy in electrodeposited silver is similar to that found in deformed silver (10). Thus we can expect microstresses to arise from the presence of dislocations, and macrostresses to arise from the dislocation arrangement and/or the excess of dislocations of one sign. [Dislocations can be produced by deformation associated with mechanisms (a) or (b) (11) as well as by mistakes during growth of the deposit.]

Additives to the solution have an important effect on most aspects of electrodeposition. It is well known that they are occluded in the plate (6, 8). Several authors have proposed that additives block growth steps during deposition (6, 12, 13), and Vermilyea *et al.* (14) have been able to show quantitatively that the rate of electrodeposition of metal whiskers is controlled by this process. When applied to the formation of a polycrystalline deposit (15), this concept explains the well-known decrease of grain size with increasing amounts of additives.

The dislocation density and twinning frequency have been observed to increase greatly in Cu deposits when additives are present in the bath (8); the dislocations seem to be associated with occluded additive, although whether this is true for the twins is not known. Growth around such an occlusion might lead to dislocations (6, 7). It is also interesting that with Cu deposits there seems to be a limiting dislocation density and occlusion density (8) of about 10^{11}/cm^2 and 10^{17}/cm^3, respectively; such defect concentrations can lead to large increases in strength and to residual stresses.

With copper deposits, there does not seem to be any correlation between hardness and residual macrostresses (16).

In this paper it will be shown that the use of additives in electrodeposition of silver can also increase the dislocation density. Also, twin faults, but not (one-layer) stacking faults, are present in the plate, and the concentration of twins increases to about the same limiting value for all additives. It will further be shown that the hardness of the deposit and its twin-fault density are directly related. Variations in both of these and in macrostresses in the plate will be discussed in relation to plating efficiency and its variation with concentration of additive. A supplementary purpose of the work was to demonstrate the use of modern techniques of analysis of the broadening of peaks in an x-ray diffraction pattern from a deposit in the study of its structure. These techniques, which have been invaluable in studies of deformation, are shown here to be very sensitive to small changes in the structure of the electrodeposit. Wood (17) was the first to observe x-ray line broadening in electro-deposits. To date, only approximate attempts have been made to analyze the diffraction patterns, often in cases involving alloy deposits where fluctuations in composition and associated variations in lattice parameter make a detailed interpretation in terms of defects difficult (18, 19).

Experimental Procedures

Sample preparation.—Plating solutions were made with distilled and deionized water having a resistivity of 2 x 10^6 ohm-cm. These were mixed, stored, and used in polyethylene containers. Separate containers were used for deposition with and without additive. Increasing amounts of additive were studied by successively increasing the concentration in one bath. All containers were rinsed in distilled water and kept covered when not in use. (No soap was ever used in the washing.) The initial composition of the plating solution was 1.4*N* KCN, 0.4*N* AgCN; it was freshly prepared (using Fisher reagents) for each sequence of studies with a given additive. Before any additions were made to such a fresh solution, the half-breadth of the 400 x-ray peak was checked under fixed plating conditions. This half-breadth varied by no more than ±5%. No change was noted if the solution was allowed to stand for periods up to two weeks. *p*H was measured with a meter; the additives had no effect.

The additives used in this study were potassium ethyl xanthate (KEX), CS_2, polyvinylpyridine (PVP),[3] and gelatin. These were added from aqueous solutions of 1-2 mg/ml. The KEX was prepared as suggested by Vogel (20). CS_2 and gelatin were of standard reagent quality. These additives have a wide range of affinity for silver ions and were expected to give rise to different structures if chemical adsorption of the additive on the deposit was important. The additives containing sulfur, KEX, and CS_2, are strongly attracted to silver ions, gelatin is next, and PVP has the weakest attraction (21). In the solutions used here, molecular weights of gelatin and PVP are not known, as the size of these macromolecules in any solution depends on *p*H and the presence of other ions in the solution (21). In the case of CS_2 and KEX, however, the molecular weights are those given by the simplest chemical formula. Thus for CS_2 (molecular weight = 76.1) 1 mg = 7.9 x 10^{18} molecules, while for KEX (molecular weight = 197.4) 1 mg = 3.05 x 10^{18} molecules.

The anodes and cathodes were strips of silver, 99.99 *w/o* pure, rolled to about 1 mm in thickness, roughened with emery paper, and annealed for 1 hr at 300°C. (The roughening provided a randomly oriented surface layer after recrystallization, as determined from x-ray pinhole patterns and comparisons of the intensities of the 222 and 400 peaks.) For x-ray studies of macrostress and hardness measurements, these strips were 1 cm wide and 3 cm long. For studies of x-ray line-broadening, cathodes 3 x 5 cm were used. Both sides of the cathode were

[3] PVP was obtained from Professor I. M. Klotz, Chemistry Department, Northwestern University, Evanston, Illinois.

plated (to about twice the infinite thickness for Cu Kα radiation, 0.001 cm) to avoid bending from residual stresses.

Unless otherwise mentioned, deposition was carried out at room temperature (24°-30°C) at current densities of 5-15 ma/cm^2. The current source was a d-c storage battery. Current was measured with an accuracy of ±3%; error in determination of sample area led to a total uncertainty of ±5% in current density. The solution was stirred with a glass paddle held far from the electrodes to minimize velocity effects. Cathodes were weighed before and after deposition, and the weight change was used as an indication of plating efficiency. The appearance of all deposits was recorded.

X-ray methods.—All x-ray data for studies of line broadening were obtained with a G. E. XRD-5 diffractometer using filtered Cu radiation. 111, 222, 200, and 400 peaks were chart recorded. Care was taken to use the same slits for each peak for both deposited silver and an annealed sample, and to record a sufficient angular range around each peak to be sure that the background was clearly established. Observations were made of peak positions, half-breadths, and intensities. Fourier analysis of the shape of x-ray peaks as a function of additive concentration was made for the KEX additive. The analysis has been recently reviewed by Warren (22), and only the pertinent procedures will be discussed here.

From a careful quantitative study of the diffraction pattern it is possible to determine concentrations of faults in the stacking sequence of (111) planes, mosaic sizes, and strains. The gross assumptions concerning defect distributions, necessary to correct the shape of the pattern for instrumental broadening when only line breadths are considered, are not necessary with this method. The analysis also provides details of the variation in strains over distances of atomic dimensions. Strains must in fact vary with the distance from an imperfection, and, if these are of atomic size, a variation of strain over atomic dimensions is an important indication of the presence of such imperfections.

The peak to be analyzed is a convolution of the true broadening due to structural defects and that due to instrumental factors (as represented by the shape of a peak from an annealed sample). The two peaks are represented by one dimensional Fourier series in terms of a new unit cell for each peak such that hkl = oo$L$. The true broadening function can be determined, as was shown by Stokes (23). The cosine and sine coefficients of the structural broadening function, A_n and B_n, can be obtained from the cosine and sine coefficients of the peaks from the sample [$H_r(n)$ and $H_i(n)$] and the annealed standard [$G_r(n)$ and $G_i(n)$]

$$A_n = \frac{H_r(n)\,G_r(n) + H_i(n)\,G_i(n)}{G_r^2(n) + G_i^2(n)} \qquad [1]$$

$$B_n = \frac{H_i(n)\,G_r(n) - H_r(n)\,G_i(n)}{G_r^2(n) + G_i^2(n)}$$

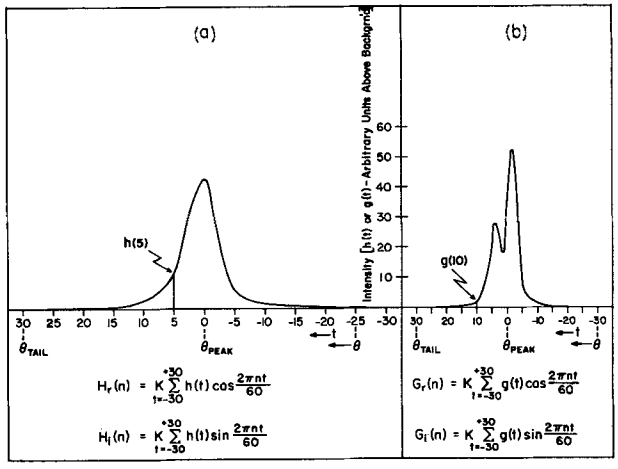

Fig. 1(a). 400 peak from silver deposited from a solution of 1.4*N* KCN + 0.4*N* AgCN; plating conditions: room temperature, C.D. = 10 ma/cm^2; Fig. 1(b). 400 peak from annealed silver specimen. Positions for determination of the fictitious lattice parameter a'$_3$ (for Fourier analysis), θ_{tail} and θ_{peak}, are shown. The sum used to evaluate the Fourier cosine and sine coefficients are indicated under each peak. The constant K, a scale factor, is unimportant as only the shape is of interest in the analysis (see text).

A unit cell parameter, a'$_3$, is determined for each peak from where the tails reach background. This point is taken as half the distance in reciprocal space from the center of oo$L$ peak to the next order

$$\left[\left(L + \frac{1}{2}\right) - L\right] = \frac{2\,a'_3}{\lambda}\,(\sin\theta_{tail} - \sin\theta_{peak}) \qquad [2]$$

In Fig. 1, a 400 peak from silver deposited from 1.4*N* KCN, 0.4*N* AgCN and the same peak from the annealed silver standard are presented. The angular positions for the determination of a'$_3$ are indicated. The intervals shown are used for the determination of the Fourier coefficients as indicated by the sums under each peak. Coefficients are compared for the same value of na'$_3$ = L (which is a true distance normal to the diffracting planes) rather than for the same n. Thus, using a different parameter a'$_3$ for each peak increases the accuracy of the analysis. After correction for instrumental effects the coefficients are normalized, setting A_o = 1, as only the shape of the peak is important. The sums for the determination of the Fourier coefficients for each peak were carried out with the aid of Beevers-Lipson strips (24) or with a computer (25). In Fig. 2

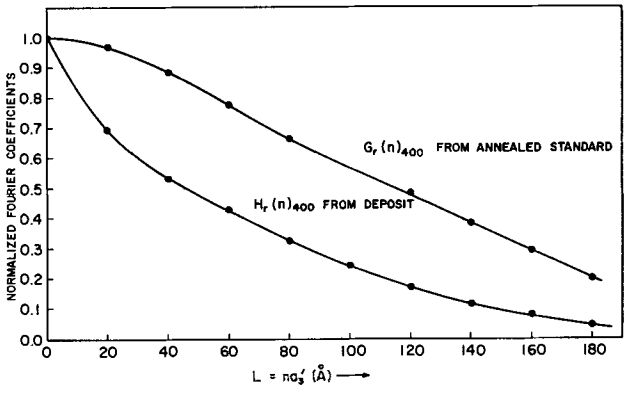

Fig. 2. Fourier cosine coefficients for the peaks shown in Fig. 1

the cosine coefficients for the data of Fig. 1 are presented.

The diffracted intensity per unit length of the cone of diffraction from a powder sample, $P'_{2\theta}$, can be written in terms of the corrected coefficients, A_n and B_n, by representing the diffraction in terms of coherently reflecting columns of cells normal to the (oo$L$) diffracting planes

$$P'_{2\theta} = K(\theta)\, N \sum_{n=-\infty}^{\infty} \{A_n \cos 2\pi n(h_3 - l - \delta) + B_n \sin 2\pi n(h_3 - l - \delta)\} \quad [3]$$

h_3 is a continuous variable along the oo$L$ direction in reciprocal space, δ represents a peak shift due to stacking faults (*i.e.*, one-layer faults in the normal —ABC—sequence in the fcc structure such as ABCABCBCABC), and N is the average number of unit cells in each diffracting domain.

$$K(\theta) = \frac{G f^2 (1 + \cos^2 2\theta)}{\sin^2\theta} \quad [4]$$

where θ is the diffraction angle, f is the atomic scattering factor, and G is a constant independent of θ.

Warren has shown that

$$A_n = \frac{N_n}{N_3} \langle \cos 2\pi l \epsilon_n \rangle \quad [5]$$

Here ϵ_n is the strain in a column of n cells, N_n is the average number of cells having an nth neighbor in a given column, and N_3 is the average number of cells in a column normal to the diffracting planes. The brackets signify averaging over all columns of length n under the x-ray beam. For small l and n the cosine can be expanded to give

$$A_n = \frac{N_n}{N_3}\left(1 - 2\pi^2(h^2+k^2+l^2)\frac{n^2 a'^2_3}{a_0^2}\langle \epsilon_n^2 \rangle\right) \quad [6]$$

where the substitution $l = a'_3 (h^2+k^2+l^2)^{1/2}/a_0$ has been made.

Thus it is possible to separate the term involving column size, N_n/N_3, from the strain, for each n. The slope of a plot of log A_n *vs.* $|h^2+k^2+l^2|$ using two orders of a peak, (111-222, or 200-400 for example), yields the rms strain, $\langle \epsilon_n^2 \rangle^{1/2}$. In Fig. 3 such a plot is presented using the data given in Fig. 2 for a 400, treated as in Eq. [1] and normalized to unity, and similar data for the 200 peak. If the origin of the peak being analyzed is chosen as the position from the deposit rather than the annealed position, any long range component is not included, *i.e.*, the strains are truly microstrains. The microstrains obtained from the slopes are indicated, and in the insert the intercepts at $|h^2+k^2+l^2| = 0$, N_n/N_3, are plotted for the determination of "particle size," $D_{\text{eff}\langle 200\rangle}$. The term N_n/N_3 is related to four quantities: (i) the mosaic size normal to the diffracting planes, D; (ii) the mosaic size parallel to the diffracting planes, T; (iii) the probability of finding a stacking fault between two (111) layers, α, (ABCABCBCABC); (iv) the probability of finding a twin or growth fault, β, *i.e.*, of finding *two* or more

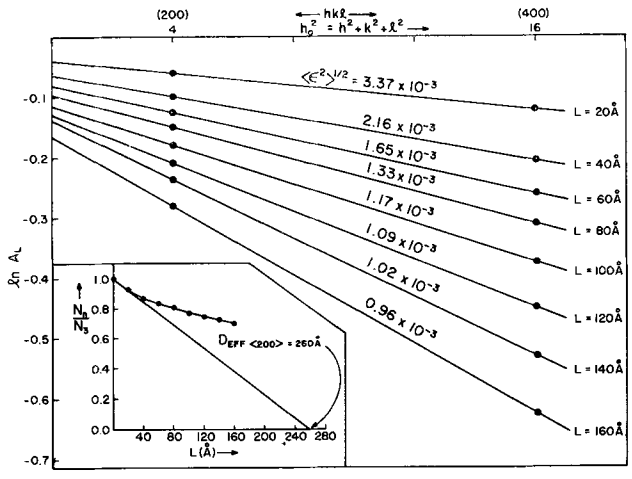

Fig. 3. In A_n *vs.* $h^2+k^2+l^2$ for silver deposited from a solution of 1.4*N* KCN + 0.4*N* AgCN; plating conditions: room temperature, C.D. = 10 ma/cm². Data from Fig. 2 for the 400 peak, treated as in Eq. [1] and normalized to unity, and similar data for the 200 peak are used. The strains obtained from the slopes using Eq. [6] in the text are shown. The values of the coefficients at $|h^2+k^2+l^2| = 0$, N_n/N_3 are presented in the insert. The initial slope of this function yields $D_{\text{eff}\langle 200\rangle}$ (See Eq. [6] and [8] in the text).

layers in an incorrect sequence (ABCABCBABC-ABC)

$$\left[\frac{d(N_n/N_3)}{dn}\langle 111\rangle\right]_{n\to 0} = \frac{1}{D_{\text{eff}\langle 111\rangle}} = \frac{1}{D} + \left(\frac{1.5\alpha+\beta}{a_0}\right)\frac{\sqrt{3}}{4} + \frac{1}{T\sqrt{2}} \quad [7]$$

$$\left[\frac{d(N_n/N_3)}{dn}\langle 200\rangle\right]_{n\to 0} = \frac{1}{D_{\text{eff}\langle 200\rangle}} = \frac{1}{D} + \frac{1.5\alpha+\beta}{a_0} + \frac{1}{T\sqrt{1.5}} \quad [8]$$

Note that when the terms in α and β are large in comparison to the terms in D and T, the ratio $D_{\text{eff}\langle 111\rangle}/D_{\text{eff}\langle 200\rangle}$ approaches the value 2.3.

It is difficult to estimate the error in particle size and strain. However, repeated measurements on samples prepared in the same manner indicate a reproducibility of ±10% in values of particle size and rms strain at distances of greater than about 60Å. Strains averaged over shorter distances are more strongly affected by the choice of background values in the x-ray pattern, and variations of as high as ±30% were found for distances below 60Å.

By combining the two equations [7] and [8] and measuring α and β separately as discussed below, D and T can be determined. Alternatively minimum values for D or T can be obtained by eliminating α and β in [7] and [8] and neglecting the term in T or D.

Stacking faults in fcc structures cause unusual shifts in peak positions as well as peak broadening. Whereas general strains shift all peaks to higher or lower angles, stacking faults cause different peaks to shift in different directions. For example, the 111 shifts to high angles and the 200 to low angles.

α can be determined by simply chart recording from the 111 to the 200 continuously, first with the standard and then with the sample to be analyzed, and then comparing the change in peak position:

$$\Delta(2\theta^\circ_{200} - 2\theta^\circ_{111}) = \frac{-45\sqrt{3}\,\alpha}{\pi^2}\left(\tan\theta_{200} + \frac{1}{2}\tan\theta_{111}\right) \quad [9]$$

$4/\alpha$ is a measure of the number of (111) planes between faults on any of the 4 possible {111}, assuming all four to be faulted. A change in peak separation of less than $\pm 0.01^\circ$ 2θ could not be detected; this corresponds to $\alpha = 4 \times 10^{-3}$ or one stacking fault per 1000 planes in any of the four <111> directions.

β causes an asymmetry in the peaks (*i.e.*, β is related to the coefficient B_n in Eq. [3]). Strains may do this also, but will cause all the peaks to be asymmetrical in one direction, whereas due to β, the 111 tails to high angles and 200 tails to low angles. It is possible to determine β from the difference in position of the center of gravity and peak maximum, (Δ C.G.) (27). Two peaks such as 111 and 200 generally overlap if there is any significant broadening. Also strains can cause an asymmetry as mentioned above. Therefore it is best to write an expression for the sum of these Δ C.G.'s for the two peaks, a procedure which minimizes the troubles in determining the center of gravity and partially cancels any effects due to general strains

$$\Delta\,\text{C.G.}(^\circ 2\theta)_{111} - \Delta\,\text{C.G.}(^\circ 2\theta)_{200} = \beta(11\tan\theta_{111} + 14.6\tan\theta_{200}) \quad [10]$$

Before determining the C.G. a peak must first be corrected by dividing through by the angular dependent portion of $K(\theta)$, f^2 $(1 + \cos^2 2\theta)/\sin^2\theta$. It is desirable to choose slits so that the corresponding annealed peaks are reasonably symmetrical. In this work it was found that the angular difference in (10) was 0.00° $2\theta \pm 0.01$ for the annealed standard. The error in β will then be a constant, about $3\text{-}4 \times 10^{-3}$ (27), and the percentage error will vary inversely to the magnitude of β. [It is worth mentioning that by using this change in separation of the C.G. and peak maximum, β can be measured more precisely than by previous methods (27)].

Measurements of macrostresses.—The stress in the surface of the plate, σ_s, was determined using a Picker x-ray diffractometer with NiKα radiation. The position of the 420 peak was measured in the normal Bragg-Brentano focusing position, and also with the sample rotated 45°. The receiving slit was placed at the correct focal position for each of the two sample positions to increase the observed intensity of the peak. The stress is given by the formula (28)

$$\sigma_s = K\Delta 2\theta \quad [11]$$

where $\Delta 2\theta$ is the difference in the two peak positions (corrected for the difference observed for an annealed sample) and $K = 640$ psi/$0.01^\circ 2\theta$ for the peak chosen. An error of $\pm 0.02^\circ 2\theta$ in the determination of peak maxima gave rise to a probable error of ± 2560 psi.

Hardness measurements.—Microhardness measurements were made on the deposits using a Leitz Miniload-Hardness Tester. The average Vickers hardness number (VHN) was the same for 15g and 25g loads; the 25g load gave more uniform indentations on the plated surface and therefore all hardness values reported here were determined using this load. Five to ten readings were made on each sample. The mean and the extremes are reported.

In summary, studies were made of the effects of small additions of KEX, CS_2, gelatin, and PVP on the diffraction patterns from electrodeposited silver. Diffraction peak shapes, breadths, and positions were examined. From the positions and shapes, information was obtained on stacking disorders (microtwins and stacking faults). With KEX added to the solution, the diffraction peaks from the deposit were also analyzed by Fourier techniques, and, from the coefficients, data on mosaic size and microstrains were obtained. In addition, microstresses in the deposits and their hardness were determined. From the weight of the deposits, information about the effects of additives or plating efficiency was obtained.

Results

No additives.—Before starting the study of the effects due to additives, it was considered important to determine the amount of broadening of diffraction peaks from silver deposited from solutions containing no additive, and to establish that the structure was stable during the period required for measurement.

Several qualitative observations were made on the effect of temperature and current density on deposits from solutions containing no additives. The 400 line breadth from a sample plated at 5 ma/cm^2 at room temperature was $0.60^\circ 2\theta$ compared to 0.90° at 15 ma/cm^2. Plating at 5 ma/cm^2 from a solution cooled to 4°C resulted in a 400 line breadth of 0.8°, and a twin fault probability twice that observed in a sample plated at room temperature at the same current density.

Subsequent experiments indicated that there was no appreciable recovery of such a plate, or of one made at room temperature, even after one day at room temperature. (However, after several months at room temperature the line breadths decreased to near those of annealed silver.) On plating at 60°C at 10 ma/cm^2 there was no appreciable x-ray line broadening, while a specimen plated at room temperature and held for 2 hr at 60°C recovered only a portion of its line sharpness. Thus the defects formed during plating are quite stable during the period of time necessary to make x-ray measurements, and the results are not complicated by simultaneous annealing.

In all further work to be discussed here the current density was 10 ma/cm^2 and plating was carried out at room temperature (24°C-30°C).

Figure 4 shows the rms strain, $\langle\epsilon_L^2\rangle^{1/2}_{\langle hkl\rangle}$, *vs.* distance in the <200> and <111> directions for a deposit from a solution containing no addi-

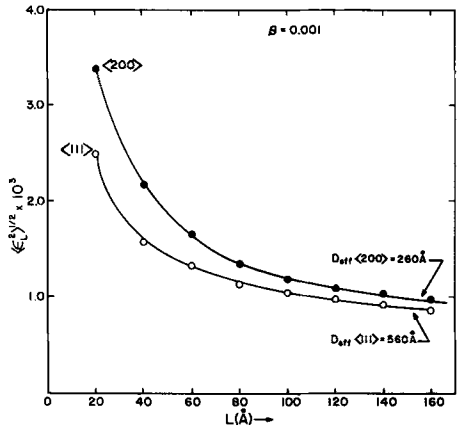

Fig. 4. rms strain $\langle \epsilon L^2 \rangle^{1/2}$ *vs.* the averaging distance normal to the diffracting planes (L), particle size (D_{eff}) and twin fault probability (β) for silver deposited from 1.4*N* KCN + 0.4*N* AgCN; plating conditions: room temperature, C.D. =10 ma/cm^2.

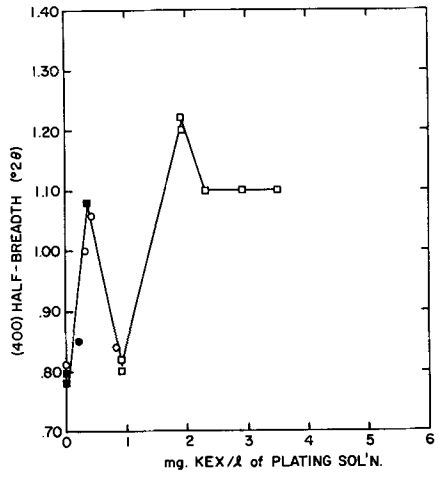

Fig. 5. Breadth of the 400 peak from electrodeposited silver *vs.* concentration of KEX in 1.4*N* KCN + 0.4*N* AgCN; plating conditions: room temperature, C.D. = 10 ma/cm^2. ■, solution G_1; □, solution J; ○, solution F; ●, solution H_1.

tive. The particle sizes in the two directions, $D_{eff<200>}$ and $D_{eff<111>}$, are given, as well as the twin fault probability, β. The significant observations to be made are these: (*a*) strains averaged over short distances are large, indicating the presence of defects with size of the order of atomic size, such as dislocations; (*b*) strains level off to about 1.0 x 10^{-3} at larger distances; (c) Deff <111>/Deff<200> = 2.2 indicating that faults are playing an important role in determining the particle sizes (see Eq. [7] and [8]).

These same characteristics were observed in all the results of the Fourier analysis reported here. Consequently, only the particle sizes, rms strain at two values of L (50Å and 150Å), and fault probabilities will be reported for the other deposits examined. As seen in Fig. 4 the strain in the <200> direction is greater than that in the <111> direction. The ratio is 1.2. As Young's modulus in these two directions is in the ratio 2.6 (29), this indicates the deposit is closer to a state of equal strains in all directions than equal stresses. For L>60Å this was true for all plots of strain *vs.* L. However for some samples the curves crossed at about L = 60Å and for L<60Å the strain in the <200> direction was less than that in the <111> direction. It is believed that this effect was due to inaccuracies in the choice of background for the 200 and 400 peaks. (Due to texture in the samples these peaks are of very low intensity.)

No stacking faults were detected in any of the deposits examined in this study (with or without additives in the plating solution). Long-range residual compressive strains normal to the deposit, or a decrease in lattice parameter, might cause peak shifts which would tend to mask out the change in 111-200 peak separation due to a small concentration of stacking faults. If this were the case, then the fault probability calculated from the 222-400 separation should be larger than that calculated from the 111-200 separation, as stacking faults increase the former separation and decrease the latter, whereas compressive strains or a decrease in lattice parameter would increase both separations. A careful examination of the data indicated that this was not the case within experimental error which means that the stacking fault probability α was of the order of 4 x 10^{-3} or less (no more than one faulted plane per 1000 planes in any of the four <111> directions).

For the sample considered in Fig. 4 the Vickers hardness was 92 as compared to 48 for fully annealed silver. The surface stress, σ_s, was found to be 3200 psi and tensile.

Addition of potassium ethyl xanthate (KEX).— In Fig. 5 the x-ray line breadth of the 400 peak is plotted for varying concentrations of KEX. The two maxima are reproducible from one plating solution to another. In Table I results are shown of Fourier analysis of several samples plated with varying additions of KEX. The mosaic size is a minimum and the twin fault probability is a maximum for the concentrations of KEX corresponding to a maximum

Table I. Results of Fourier analysis of diffraction patterns of electrodeposited silver with various KEX additions

Sample No.	Conc. KEX mg/l	$\langle \epsilon^2_{50A} \rangle^{1/2}_{<111>}$	$\langle \epsilon^2_{150A} \rangle^{1/2}_{<111>}$	$\langle \epsilon^2_{50A} \rangle^{1/2}_{<200>}$	$\langle \epsilon^2_{150A} \rangle^{1/2}_{<200>}$	D_{eff} <111> Å	D_{eff} <200> Å	β	T_{min}, Å	D_{min}, Å	D_F <111> Å	D_F <200> Å
135	0.00	1.4 x 10^{-3}	0.9 x 10^{-3}	1.9 x 10^{-3}	1.0 x 10^{-3}	560	260	0.001	3000	8000	9200	4000
137	0.34	1.7	0.9	1.6	1.1	250	140	0.011	392	1020	821	370
167	0.84	1.4	0.9	1.7	1.0	340	180	0.005	660	1720	1886	820
169	1.9	1.7	0.9	1.75	1.0	150	85	0.015	225	586	644	280
174	3.5	1.8	1.15	texture too great; not enough intensity to analyze 200-400		170	—	—	—	—	—	—

Plating conditions: 10 ma/cm^2, room temperature.

in line breadth. It is further seen that microstrains averaged over small and large distances are rather independent of other variations, being about the same for all concentrations of additive. In the last two columns the values of particle size calculated from twin fault probability, D_f, are presented. It is seen that the observed values of D_{eff} are due in part to the presence of twin faults, and in part to mosaic size, (D and T).

Measurements of plating efficiency, microhardness, and residual macrostress were made on freshly prepared samples.[4] In Fig. 6 microhardness is plotted as a function of concentration, once again repeating the two maxima. Figure 7 shows residual stress *vs.* concentration of KEX. For the first peak (0.2-1.5 mg/l) the residual macrostresses are low when hardness is high; however for concentrations of KEX greater than 1.5 mg/l the macrostresses follow the hardness. In Fig. 8 the data on deposition efficiency are presented. This parameter varies just as the twin fault probability, peak broadening, and hardness.

Some remarks on the effect of KEX additives on the appearance and texture of the plate are pertinent. While in general it can be said that increasing amounts of additive resulted in an improvement of the appearance of the plate (increasing brightness or luster), no correlation was observed between plate appearance and the maxima observed in other properties.

Texture was also considered by examining the ratio of x-ray peak intensities, $I_{222}/I_{400} = R$. For annealed substrate $R \simeq 3$. In general for the deposited silver R $\simeq$ 10, while in some extreme cases values of R as high as 40 were observed. However, it was found that while line breadth was quite reproducible, texture was not. A second sample prepared in the same manner as that giving $R = 40$ was found to have the same line breadths as the first, but $R = 10$. (X-ray measurements after storage at room temperature for 6 months showed $R < 1$ for samples whose line breadth had decreased to the values observed for annealed silver.) The lack of correlation of appearance and other parameters as well as the variability of texture was observed with all additives used in this study.

No accurate lattice parameters were measured in this program; however, an order of magnitude estimate of any change can be obtained from the lattice parameter calculated from the position of the 222 and 420 peaks as compared to those for an annealed silver sample. It must be emphasized that this procedure is justifiable only if no stacking faults are present so that the peak shift is due only to strain (as was the case here). For all samples examined, the 420 peak was shifted to higher angles while the 222 was shifted to lower angles, indicating a decrease in lattice parameter normal to the deposit. (Stacking faults would shift both the 420 and 222 peak to lower angles.) Other peaks shifted consistent with this observation. The magnitude of the observed change in parameter was 0.5 x 10^{-3} — 1.5 x 10^{-3}, in good agreement with the values of the strain obtained by Fourier analysis at large

[4] These observations were made six months following the preparation of the KEX. During this time the prepared KEX adsorbed considerable amounts of water making knowledge of the weight of additive uncertain. However when the 400 line breadth of these new samples was plotted *vs.* concentration of additive plus adsorbed water, Fig. 5 was reproduced. From this plot the true concentration of KEX was determined.

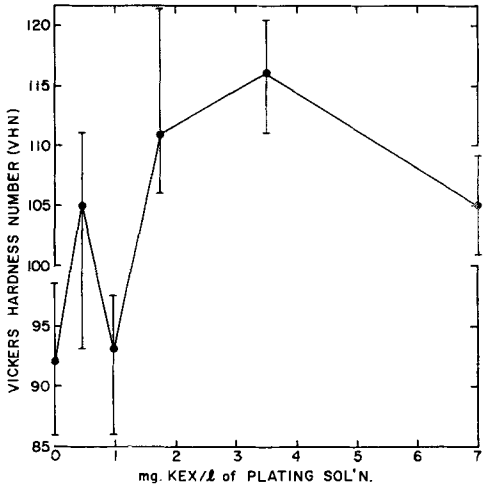

Fig. 6. Vickers hardness number (VHN) of electrodeposited silver *vs.* concentration of KEX in 1.4*N* KCN + 0.4*N* AgCN; plating conditions: room temperature, C.D. = 10 ma/cm^2; load, 25g. Vertical lines represent extreme values.

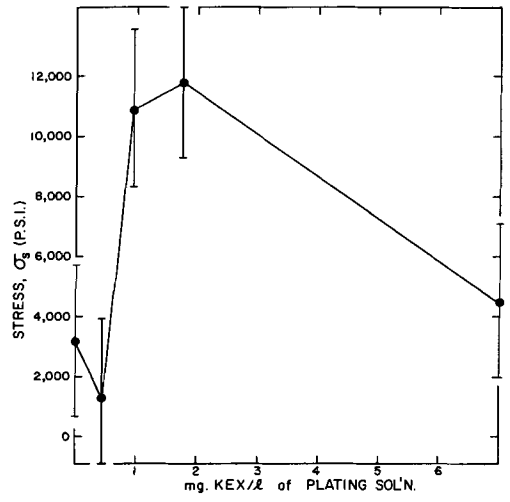

Fig. 7. Residual stress (σ_s) parallel to surface of silver deposit *vs.* concentration of KEX in 1.4*N* KCN + 0.4*N* AgCN; plating conditions: room temperature, C.D. = 10 ma/cm^2. Vertical lines represent estimated error.

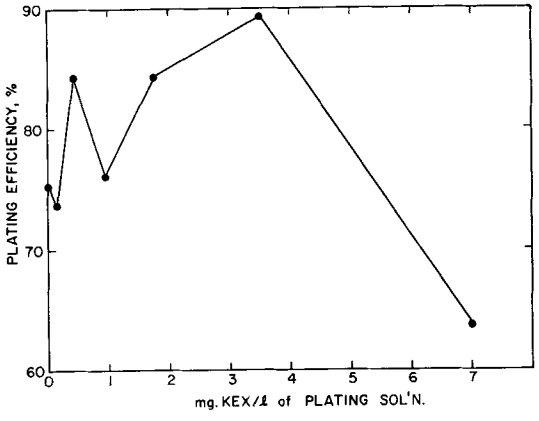

Fig. 8. Plating efficiency *vs.* concentration of KEX in 1.4*N* KCN + 0.4*N* AgCN; plating conditions: room temperature, C.D. = 10 ma/cm^2.

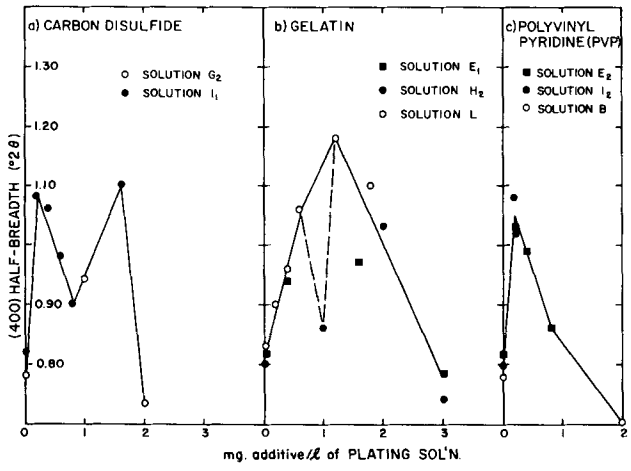

Fig. 9. Breadth of 400 peak from electrodeposited silver vs. concentration of additive in 1.4*N* KCN + 0.4*N* AgCN for: (a) CS_2, (b) gelatin, and (c) PVP; plating conditions: room temperature, 10 ma/cm^2.

values of L (1.0 x 10^{-3}). As the surface stresses were tensile this apparent decrease in parameter (normal to the surface) is probably due to the long-range (compressive) strains normal to the surface. (With a diffractometer, an hkl peak comes from those grains for which {hkl} planes are parallel to the surface of the sample.)

Other additives.—In Fig. 9 line breadth *vs.* concentration of additive is shown for deposits from solutions containing CS_2, gelatin, and PVP. From Fig. 9(a) the behavior of CS_2 is seen to be similar to that of KEX, with two maxima in the curve. Gelatin appears to have only one maximum at these low concentrations; however, the possibility of a minimum at 1.0 mg/l is suggested [dotted line Fig. 9(b)]. PVP [Fig. 9(c)] exhibits only one maximum at low concentrations. Indications of a second maximum at 75 mg/l were obtained.

Twin fault probability, hardness, and plating efficiency are given in Table II for deposits with concentrations of additive roughly corresponding to the maxima shown in Fig. 9. Once again, with the possible exception of the sample plated from a solution containing 0.2 mg/l CS_2, large values of line breadth, twin fault probability, and hardness are seen to correlate with high plating efficiency.

Discussion

If it is assumed that mosaic sizes, twin fault probabilities, and strains are due to dislocations, it is possible to calculate the densities (ρ) of these from the data reported. Assuming the dislocations are random (30)

$$\rho_s = \frac{16\langle \epsilon^2_{50A} \rangle^{5}}{b^2} \qquad [12]$$

where b is the Burger's vector of the dislocation ($a_0/2\langle 110\rangle$). Also if the mosaic size and faults are associated with dislocations, it has been shown by Warren (22) that the measured sizes are one-half the dislocation spacing. Therefore

$$\rho_1 = \frac{1}{4}\left(\frac{1}{D} + \frac{1}{T} + \frac{\beta}{a_0}\right)^2 \qquad [13]$$

or if the faults are not associated with dislocations

$$\rho_2 = \frac{1}{4}\left(\frac{1}{D} + \frac{1}{T}\right)^2 \qquad [14]$$

The values for various concentrations of KEX are gathered in Table III. (For D and T, values of D_{min} and T_{min} were taken from Table I.)

The assumption of a random distribution of dislocations seems valid in all cases except the deposit without additive, where the density calculated from the microstrain (Eq. [12]) is much larger than that calculated from Eq. [13] or [14]. This indicates a clustering of dislocations. Assuming n dislocations piled up $n = (\rho_s/\rho_{1 \text{ or } 2})^{1/2}$. There are then on the average about 8-12 dislocations in a cluster in the deposit without additive.

The nature of the effects observed appears to be nonspecific, *i.e.*, maxima of the same magnitude occur in the properties *vs.* concentration curves for the four additives used. The absolute position of these maxima in units of molecules per liter of plating solution is not known for gelatin and PVP, since the molecular weight of these organic molecules is not known in the specific ionic solution used here. For KEX and CS_2, however, the concentrations of additive are known in molecules per liter of solution, and the two maxima fall at about the same concentration of additive for both (the first maximum at 1.4 x 10^{-18} and the second at 12 x 10^{18}

[5] Strains around a dislocation fall off as $1/r$ whereas those due to elastic distortion from an occluded molecule decrease as $1/r^2$. Thus the strains averaged over 50Å should depend primarily on dislocations.

Table II. Effect of additives on twin fault probability, hardness, and plating efficiency

Additive	β	VHN	Plating efficiency, %
No additive	0.001	92 ± 6	75.2
0.2 mg/l CS_2 (1st peak Fig. 9a)	0.006	96 ± 8	76.0
1.6 mg/l CS_2 (2nd peak Fig. 9a)	0.007	107 ± 10	85.1
2 mg/l Gelatin (Fig. 9b)	0.008	103 ± 8	93.4
0.2 mg/l PVP (peak, Fig. 9c)	0.006	108 ± 5	92.6

Plating conditions: 10 ma/cm^2, room temperature.

Table III. Calculated dislocation densities for deposits with varying concentrations of KEX

Sample No.	Conc. KEX mg/l	ρ_1, cm^{-2}	ρ_2, cm^{-2}	ρ_s, cm^{-2}
135	0.00	0.12 × 10^{10}	0.05 × 10^{10}	6.9 × 10^{10}
137	0.34	5.6	3.0	4.9
167	0.84	1.7	1.0	5.5
169	1.9	15.0	9.2	5.8

$$\rho_s = \frac{16\langle \epsilon^2_{50A} \rangle}{b^2}$$

$$\rho_1 = \frac{1}{4}\left(\frac{1}{D} + \frac{1}{T} + \frac{\beta}{a}\right)^2$$

$$\rho_2 = \frac{1}{4}\left(\frac{1}{D} + \frac{1}{T}\right)^2$$

molecules per liter). The presence of similar maxima in properties for all additives suggests that chemical adsorption of the molecules is not an important factor in determining the structure of the deposit, in agreement with Vermilyea *et al.* (14). It appears that the additive molecules, or their dissociated products, are trapped in the deposit by metal atoms which surround them during the deposition.

If one visualizes the formation of twin faults and dislocations as accidents which occur as the metal ions arrange themselves on the lattice (6,7), then the number of defects which are found in the deposit would be expected to be proportional to the rate of deposition (or efficiency) as observed. Even assuming that the same number of defects are formed per unit thickness of plate, independent of deposition rate, a faster rate of metal ion arrival will "freeze in" defects which might be annealed out if allowed to remain near the surface of the plate for *longer* times. The observation of increasing line breadths with increasing current density (without additives) or decreasing temperature at a fixed current density agrees with this picture of the deposition process. The effect of additives (in the small concentrations used here) is thus seen as changing the number of silver ions deposited per unit time and thereby changing the effective deposition rate. The upper limit to the number of faults the deposit can retain is obtained only at 100% plating efficiency. The mechanism by which these additives affect the plating efficiency is, however, not known.

While it is possible that twin faults occur as random growth accidents, an alternative model may be important also. A (111) plane in a face-centered cubic structure is shown in Fig. 10. A silver atom deposited on such a plane will preferentially seek "B-sites" which would continue the structure in the correct stacking sequence. An additive molecule will have no such preference. In Fig. 10 a molecule somewhat larger than a silver atom is shown adsorbed at a "C-site" in the next layer. As an advancing growth step passes this molecule three possible configurations arise depending on the molecular size: (i) If the molecule's radius ≃silver atom's radius, silver atoms can fit onto sites 1, 2, and 3, and the region about the molecule may be strained, causing dislocations, but no faults will be produced. (ii) If the molecule's radius ≃ 1.5 x silver atom radius, sites 1, 2, and 3 are excluded, and as the growth step passes the molecule, silver atoms will be forced onto C-sites creating a fault which would continue for a few layers until the molecule was covered. (iii) For a molecular radius >2 silver atom radii either case (i) or (ii) applies, depending on the amount of disparity in size. There is a large variation in size of the molecules of additive used here, from the triatomic CS_2 molecule to the macromolecules of gelatin and PVP. The molecular radii of gelatin and PVP, although not known, must be considerably larger than that of the silver atom (which has a diameter = 2.9Å). The minimum dimension of KEX on the deposit surface is about 3.6-4.2Å (31), when the long dimension of the molecule is oriented normal to the deposit surface. CS_2 probably lies in the plane of the deposit surface with both sulfur atoms attracted to silver ions, and then has dimensions of 4.8Å by 1Å (32).

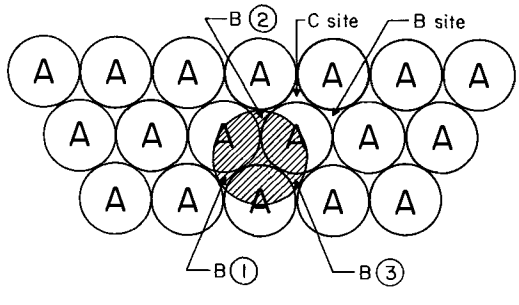

Fig. 10. Model for formation of twin or growth faults showing a large occluded molecule on a (111) plane. B is a correct site for the next layer. C is a wrong site. Note that the large molecule blocks sites B 1-3.

If the adsorbed molecule is at a B-site, the argument is similar; growth faults will occur if the adsorbed molecules have a radius greater than about twice that of the silver atom. The occurrence of adsorbed molecules is expected to be random on B and C sites. Some faulting should then occur regardless of the size of the molecule as long as it differs appreciably from the radius of the silver atom. The concentration of faults will then depend only on the number of molecules which are occluded in the plate. (Water attached to a silver ion may produce the same effects as deliberate additions.)

This model is in qualitative agreement with the observations that the maximum twin fault probability β is independent of the size of the additive for given plating conditions and that the maxima in properties occur at fixed numbers of molecules of additive per liter of solution for KEX and CS_2 additives. This model for the formation of twin faults predicts that a high concentration of twin faults is due to a high concentration of occluded molecules. Thus a detailed study of twin-fault concentration and the concentration of additive in the deposit as a function of additive concentration in solution would indicate whether this model or twinning due to growth accidents (which depends only on the rate of effective deposition) is the controlling factor.

Summary

Observations have been made of the effect of additions of organic molecules on the structure of the deposit from an argentocyanide plating bath. Maxima were found in the plots of x-ray line breadth, twin fault probability, hardness, macrostress, and plating efficiency *vs.* concentration of additive. The effect of various additives was shown to be nonspecific in the sense that the maximum values observed were roughly independent of which additive was used, even though the different additives had a wide range of sizes and affinity for silver. No evidence of the presence of stacking faults was

found, even though a frequency of twin faults as high as one every 260 (111) planes ($\beta = 0.015$) was detected. A model is suggested for the formation of twin faults by growth around additive molecules.

Dislocation densities were of the order of $10^9/cm^2$ in deposits without additive. The density was $10^{10} - 10^{11}/cm^2$ in the presence of additive and the distribution was more random.

Changes in line breadth, twin fault probability, mosaic size, and hardness followed changes in plating efficiency. Microstrains remained relatively constant during these changes. Macrostresses followed efficiency only for large additions. No correlation was observed between texture or appearance and the other properties studied.

Finally, Fourier analysis of x-ray line profiles has been shown to be a useful tool in studying the structure of electrodeposited metals. It is not necessary in x-ray studies to remove the deposit from the substrate, as is necessary for studies in transmission with the electron microscope. Furthermore, these diffraction studies are particularly adapted for high concentrations of imperfections where present resolution in transmission microscopy is not adequate.

Manuscript received July 30, 1962; revised manuscript Oct. 5, 1962. The research on which this paper is based was supported by the Advanced Research Projects Agency of the Department of Defence through the Northwestern University Materials Research Center.

Any discussion of this paper will appear in a Discussion Section to be published in the December 1963 JOURNAL.

REFERENCES

1. E. J. Mills, *Proc. Roy. Soc.*, **26**, 504 (1877).
2. J. B. Kushner, *Metal Finishing*, **56**, 46 (1959).
3. H. Wilman, *Proc. Phys. Soc.*, **B68**, 474 (1955).
4. M. R. J. Wylie, *J. Chem. Phys.*, **16**, 52 (1948).
5. J. B. Kushner, *Metal Progr.*, **81**, [2], 88 (1962).
6. H. Fischer, "Elektrolytische Abscheidung und Elektrokristallisation von Metallen," Springer, Berlin (1954).
7. N. Cabrera and D. A. Vermilyea, "Growth and Perfection of Crystals," John Wiley & Sons, Inc., New York (1958).
8. S. Steinemann and H. E. Hintermann, *Schweiz. Arch.*, **26**, 202 (1960).
9. L. Reimer, J. Ficker, and T. Pieper, *Z. Metallkunde*, **52**, 753 (1961).
10. W. F. Schottky and M. B. Bever, *Acta Met.*, **7**, 199 (1959).
11. A. S. Tetelman, C. N. J. Wagner, and W. D. Robertson, *ibid.*, **9**, 205 (1961).
12. W. Machu, *Osterr Chemiker-Ztg.*, **42**, 244 (1939).
13. K. M. Gorbunova and N. D. Dankov, *Progr. Chem. U.S.S.R.*, **17**, 710 (1948).
14. P. B. Price, D. A. Vermilyea, and M. B. Webb, *Acta Met.*, **6**, 524 (1958).
15. D. A. Vermilyea, *This Journal*, **106**, 66 (1959).
16. H. Fischer, P. Hubse, and F. Pawlek, *Z. Metallk.*, **47**, 43 (1956).
17. W. A. Wood, *Trans. Faraday Soc.*, **31**, 1248 (1935).
18. R. S. Smith, *I. B. M. J. Res. Dev.*, **4**, 205 (1960).
19. S. Steinemann, J. P. Renaud, H. E. Hintermann, and A. Braun, *Bull. Annuel de la S. S. C.*, **4**, 1 (1958).
20. A. J. Vogel, "A Textbook of Practical Organic Chemistry," p. 480, Spottiswoode, Ballantyne and Co., Ltd., London (1951).
21. I. M. Klotz, Private communication.
22. B. E. Warren in "Progress in Metal Physics," **8**, 147, Pergamon Press, New York (1959).
23. A. R. Stokes, *Proc. Phys. Soc.*, **61**, 382 (1948).
24. C. A. Beevers, *Acta Cryst.*, **5**, 670 (1952).
25. L. H. Schwartz and J. B. Cohen, Amer. Cryst. Assoc. Mark I Computer Listing.
26. B. E. Warren, *J. Appl. Phys.*, **32**, 2428 (1961).
27. J. B. Cohen and C. N. J. Wagner, *ibid.*, **33**, 2073 (1962).
28. B. D. Cullity, "Elements of X-Ray Diffraction," p. 446, Addison-Wesley, Reading, Mass (1956).
29. E. Schmid and W. Boas, "Kristallplastizität," Springer, Berlin (1935).
30. G. K. Williamson and R. E. Smallman, *Phil. Mag.*, **1**, 34 (1956).
31. S. Ruby, Ph.D. Thesis, Columbia University, 1954, p. 64.
32. L. Pauling, "The Nature of the Chemical Bond," pp. 167 and 197, Cornell University Press, Ithaca, N. Y. (1940).

SYMBOLS

A_n	nth cosine coefficient of the structural broadening function.
B_n	nth sine coefficient of the structural broadening function.
a'_3	Fictitious unit cell parameter, different for each x-ray peak.
a_o	True lattice parameter.
$na'_3 = L$	real distance in the crystal normal to the diffracting planes.
$\langle \epsilon^2_L \rangle^{1/2}_{\langle hkl \rangle}$	rms strain averaged over a distance L normal to the $\langle hkl \rangle$ planes.
$D_{\text{eff } \langle hkl \rangle}$	Particle size determined from Fourier coefficients.
D	Mosaic size.
$D_{F \langle hkl \rangle}$	Calculated particle size due only to the presence of faults.
T_{min}	T calculated from Eq. [7] and [8] assuming $D = \infty$.
D_{min}	D calculated from Eq. [7] and [8] assuming $T = \infty$.
α	Stacking fault probability.
β	Twin fault probability.
σ_s	Stress parallel to the sample surface.
$R = I_{222}/I_{400}$	Texture parameter.

A Study of Cadmium Chlorophosphate Phosphor

R. C. Ropp

Chemical and Metallurgical Division, Sylvania Electric Products Incorporated, Towanda, Pennsylvania

ABSTRACT

A study of the utilization of $CdCl_2$ in the formation of $Cd_5Cl(PO_4)_3$:Mn revealed that the quantum efficiency of luminescence can be related to the amount of incorporated chloride. The absorption site probably involves a charge transfer complex between a chloride on the c_o axis and one of the neighboring cadmium atoms.

Several authors have reported on the physical and optical properties of the apatite phosphors. Historically, cadmium chlorophosphate was the first synthetic apatite phosphor discovered (1), and many subsequent patents and publications have demonstrated its high efficiency in low-pressure mercury vapor lamps. Perhaps the most comprehensive study was that by Wollentin *et al.* (2) in which various modifications of the phosphor were studied.

The present work describes some new observations on the phosphor and correlates composition and structure with absorption properties. Cadmium chlorophosphate has the hexagonal structure with $a_o = 9.7$Å and $c_o = 6.4$Å (3, 4) and presumably has the theoretical formula $Cd_5Cl(PO_4)_3$:Mn.

Method of Preparation

The preparation of raw materials was described previously (5). The use of $(CdHPO_4)_3 \cdot 3NH_3 \cdot 3H_2O$ was preferred since the stoichiometry was more easily controlled. Particular care to exclude $Cd_5H_2(PO_4)_4(H_2O)_4$ was exercised since its firing product is a mixture of $Cd_2P_2O_7$ and $Cd_3(PO_4)_2$, and since inferior phosphors were obtained when this compound was employed as a raw material. The highly reactive CdO_2 (6) gave a more uniform product than any other source of cadmium oxide. $MnNH_4PO_4 \cdot H_2O$ was employed as a source of manganese activator.

There are several ways in which the apatite formula may be represented. These include: $Cd_5Cl(PO_4)_3$ and $Cd_3(PO_4)_2 \cdot 0.33CdCl_2$. The latter was preferred in the present case because of the greater facility in representing changes in formulation and because the solid-state reactions first form $Cd_3(PO_4)_2$ as a separate entity, as shown below, which is then subsequently converted to the apatite by $CdCl_2$. Thus, the phosphor formulation used was

$$(Cd+Mn)_{3.00}(PO_4)_{2.10} \cdot 0.75CdCl_2$$

with all quantities expressed in moles. Note that an excess of phosphate was employed. A larger than theoretical amount of $CdCl_2$ had to be used, partly to serve as a lattice constituent, partly to act as a flux, and partly in order to furnish a protective atmosphere of $CdCl_2$ vapor at the firing temperature. Firing was accomplished in air atmosphere in open 500 ml silica crucibles. Little difference was noted in plaque brightness between phosphors processed in open or closed crucibles. Measurements on the phosphors were obtained similar to the methods described in a previous paper (7).

Experimental Results

The compound $Cd_5Cl(PO_4)_3$ activated by Mn^{+2} fluoresces orange when excited by 254 mμ radiation. The excitation band is broad and contains two peaks in contrast to the rather narrow emission band at 588 mμ as shown in Fig. 1. These data correlate well with those given by Wollentin *et al.* (2).

The effect of manganese activator concentration, cadmium to phosphate ratios, and optimum cadmium chloride content were found to be similar to those reported by Wollentin *et al.* Preparation parameters are not critical. A minimum of 0.01 mole of Mn^{+2} per mole of apatite is required to obtain activation, and the maximum, where concentration quenching begins to take place, is about 0.30 mole of Mn^{+2}. The cadmium to phosphate ratio has little effect on brightness as long as the cadmium chlorophosphate structure is maintained. The amounts of cadmium chloride added before firing can vary between 0.40 mole and 1.40 mole per calculated mole of orthophosphate, depending on firing conditions, with little effect on brightness. At the higher ratios, $CdCl_2$ appeared as a separate phase, as determined by x-ray diffraction analysis.

A study of the solid-state reactions was made employing differential thermal analysis (DTA) and thermogravimetric analysis (TGA), with identifi-

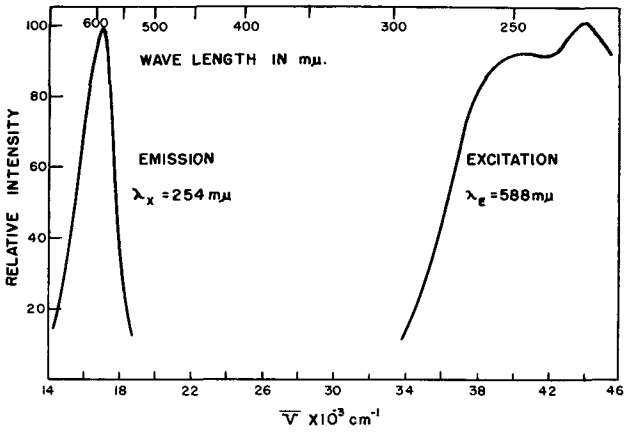

Fig. 1. Excitation-emission spectra of $Cd_5Cl(PO_4)_3$:Mn

cation of the products by x-ray diffraction techniques. The decomposition of the phosphate, $(CdHPO_4)_3 \cdot 3NH_3 \cdot 3H_2O$, is endothermic. The phosphate decomposes to the intermediate $(CdHPO_4)_3 \cdot NH_3$ between 205°-230°C and forms $Cd_2P_2O_7$ at 355°-360°C, as determined by DTA and TGA (5). The exothermic decomposition of CdO_2 to CdO is most rapid at 215°C, the temperature at which the endothermic heat absorption of the phosphate is maximum. The reaction product is the tribasic phosphate. The temperature at which the orthophosphate transforms to the apatite by reaction with cadmium chloride could not be definitely established. The following solid-state reactions were confirmed by x-ray diffraction methods

$$2[(CdHPO_4)_3 \cdot 3NH_3 \cdot 3H_2O] \xrightarrow{\Delta} 3Cd_2P_2O_7 + 6NH_3 + 9H_2O \quad [1]$$

$$4[(CdHPO_4)_3 \cdot 3NH_3 \cdot 3H_2O] + 6CdO_2 \xrightarrow{\Delta} 6Cd_3(PO_4)_2 + 12NH_3 + 18H_2O + 3\,O_2 \quad [2]$$

$$4[(CdHPO_4)_3 \cdot 3NH_3 \cdot 3H_2O] + 6CdO_2 + 2CdCl_2 \xrightarrow{\Delta} 2Cd_{10}Cl_2(PO_4)_6 + 12NH_3 + 18H_2O + 3\,O_2 \quad [3]$$

In general, the preparation parameters are not critical because cadmium chlorophosphate will form defect structures at ratios far from the theoretical composition for apatite, *i.e.*,

$$3Cd_2P_2O_7 + CdCl_2 \xrightarrow{\Delta} 2Cd_{3.5}Cl(PO_4)_3 \quad [4]$$

Therefore, when the cadmium content is sufficient to form the apatite structure, the chloride content is not very critical. At 2.95 gram-atoms of cadmium per 2.10 mole of phosphate, the optimum cadmium chloride content in the raw mix is 0.75 mole per mole of orthophosphate as shown in Fig. 2. The crucible size during firing had little effect on this value.

Effect of chloride.—$CdCl_2$ is volatile at the firing temperature, and the optimum amount in the raw mix is 2.27 times that theoretically required to produce the apatite. The vapor pressure of $CdCl_2$ as determined by Bloom and Welch (8), is shown in Fig. 3 along with the amounts of $CdCl_2$ removed by washing, and the plaque brightnesses [as indicated by the numbers at the points (in per cent)] of a series of phosphors fired at the various temperatures are indicated. Note that the vapor pressure is substantial (~60 mm at 760°C), and that a partial loss of $CdCl_2$ due to volatilization would be expected, depending on crucible size and the physical mass being fired. If the role of $CdCl_2$ during firing is traced, three forms of utilization can be found: (i) retention as an unreacted species in the fired product, removable by washing; (ii) incorporation in the phosphor phases; (iii) $CdCl_2$ lost by volatilization. A quantitative evaluation of the first two forms of utilization is feasible.

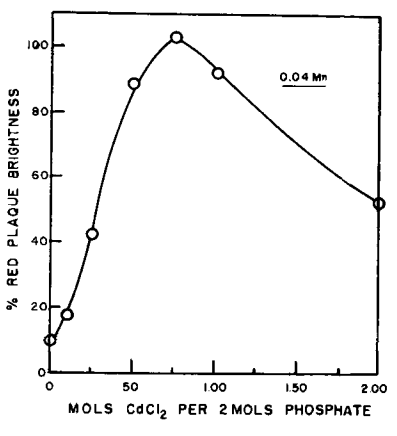

Fig. 2. Effect of $CdCl_2$ content on brightness of phosphors prepared with 0.04% Mn.

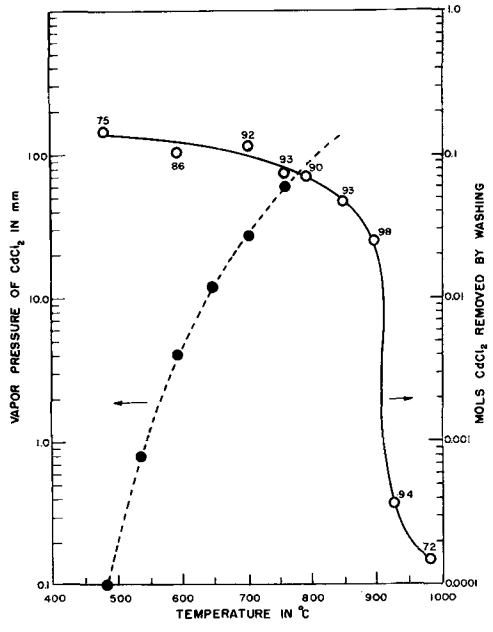

Fig. 3. Surface $CdCl_2$ as a function of firing temperature

The conductivity of an aqueous solution of $CdCl_2$ was measured and found to be linear with concentration over the range of 0.00001 to 0.2 moles per liter. Therefore, corrections to the specific conductivity, k, for effects of concentration, ionic mobilities or complexing in solution were not indicated. The data in Table I show the amounts of unreacted $CdCl_2$ removed from a typical phosphor by washing, as measured by solution conductivity.

It is presumed that washing in hot water removes all of the surface chloride present. This seems likely

Table I. Removal of $CdCl_2$ by washing

No. of washes	k (μmhos)	$CdCl_2$ removed per wash mole/l	ppm	Mole/4l
1 hot	2210	0.0170	3110	0.068
2 hot	168	0.0040	730	0.016
3 hot	18	0.00005	9	0.0002
4 hot	5	0.00001*	2	—
5 hot	6	0.000013*	2	—
				0.084 total
1 cold	1880	0.0140	2570	0.056
2 cold	130	0.0015	275	0.006
3 cold	9	0.00002*	4	—
4 cold	4	0.000007*	1	—
				0.062 total

* Extrapolated.

since the total amount removed was greater, for the same weight of phosphor, in hot water than in cold water. The wash water and the phosphor particle surface may be regarded as two phases between which the $CdCl_2$ distributes itself. The apparent difference between hot and cold washing could possibly be due to a difference in time required to establish equilibrium between the two phases. In the case of cold water washing, complete equilibrium was not attained.

The amount of $CdCl_2$ removed by washing is shown in Fig. 3 as a function of the firing temperature during preparation along with the corresponding vapor pressure of $CdCl_2$ at that temperature. At the lower temperatures, the sublimation process is important. In the firing temperature region (650°-875°C), the slope of the curve representing the amount of $CdCl_2$ removed by washing changes rapidly. This denotes a higher amount of volatilization at the higher temperatures with lower $CdCl_2$ retention on the phosphor surface.

Retention of chloride in the lattice was determined by chemical analyses of two specific phosphors selected from the series in Fig. 3. It is presumed that the chloride content found by analysis of the washed phosphors was in the lattice since x-ray powder diffraction analysis showed the phosphor to possess the apatite structure and no separate $CdCl_2$ phase was found.

Analysis of washed phosphor samples showed that the atom ratios of the most efficient phosphor closely duplicate those of the theoretical structural formula, $Cd_5Cl(PO_4)_3$. Thus the cadmium chloroapatite forms a defect structure, that is, it can exist with a deficiency of chloride, as has been shown for hydroxide in $Ca_5OH(PO_4)_3$ (10). Two significant points are evident: (*a*) although an excess of phosphate was employed during preparation, the final washed phosphor does not contain excess phosphate, and (*b*) the brightness is related to the lattice-incorporated chloride. In this case, the apparent loss of phosphate was not real since the cadmium from the incorporated cadmium chloride compensated for the initial calculated deficit of cadmium to give the theoretical ratios of the apatite, as found by chemical analysis. This may be more easily understood by reference to the alternate formula given in Table II under the "Added" column.

The utilization of $CdCl_2$ in the solid-state reaction may now be shown (Table III). It may be concluded that the optimum preparation conditions are those in which the incorporation of the stoichiometric amount of chloride is achieved. Note that the volatilized $CdCl_2$ varies between 67 and 85% of the original amount and depends on firing temperature at a given firing time (for a given mass being fired).

Table III. Utilization of $CdCl_2$ in $Cd_5Cl(PO_4)_3$:Mn

Moles added	Firing temp, °C	Plaque brightness, %	$CdCl_2$ Incorporated mole	ratio*	Soluble mole	Volatile mole**	% ***
0.75	480	75	0.106	0.935	0.145	0.50	67
	590	86	0.105	0.929	0.106	0.54	72
	700	92	0.109	0.962	0.115	0.53	71
	900	99	0.113	1.010	0.025	0.61	82
	1000	72	0.109	0.962	0.0002	0.64	85

* Calculated as $(Cd + Mn)_5Cl_x(PO_4)_3$.
** Calculated by difference.
*** % of original added $CdCl_2$.

The position of the emission peak was constant irrespective of stoichiometry and was not a function of lattice chloride, cadmium to phosphate ratios, or of manganese concentration. However, the plaque brightness did vary with incorporated chloride as may be seen by the comparisons given in Table III.

Absorption properties.—The absorption properties of the phosphors given in Table II are shown in Fig. 4. A shift in the absorption edge was observed as a function of chloride content. The measured absorption was shown experimentally to be the fundamental absorption edge of the matrix by measurement of the unactivated material. The spectral absorption band differs from the excitation band in that the former drops to the 50% point at 37,400 cm^{-1}, whereas the excitation band does not reach the 50% level until 36,300 cm^{-1}. In addition, very weak, but well-defined, absorption bands due to Mn^{+2} were observed at 358, 402, and 430 mμ. A change of 0.075 mole of lattice chloride causes a shift of approximately 1500 cm^{-1} in the absorption edge (see Fig. 4).

The unactivated matrix did not luminesce in the ultraviolet or visible portion of the spectrum, and no emission was noted under various excitation wave lengths for the material prefired in air and subsequently subjected to a reducing atmosphere during the second firing as was noted in a previous account for $Cd_2P_2O_7$ (11). The absorption edge for the unactivated chloroapatite drops to the 50% point at 37,000 cm^{-1}. Thus, a slight shift was noted due to the incorporation of the activator into the matrix.

Quantum efficiency.—The relative quantum efficiencies of the phosphors containing the varying chloride mole ratios of Table III show a linear dependence on lattice chloride. The data were obtained by making comparisons to a standard magnesium tungstate phosphor and assuming 100% quantum

Table II. Analysis of cadmium chlorophosphate phosphor calculated formulas for apatite

Added	Theoretical
$(Cd + Mn)_{3.00}(PO_4)_{2.10} \cdot CdCl_{2(0.75)}$	$(Cd + Mn)_{5.00}Cl_{1.00}(PO_4)_{3.00}$
or	
$(Cd + Mn)_{2.86}(PO_4)_{2.00} \cdot CdCl_{2(0.714)}$	

Firing temp, °C	Plaque brightness, %	Found
900	98	$(Cd + Mn)_{4.99}Cl_{1.01}(PO_4)_{3.00}$
480	75	$(Cd + Mn)_{4.98}Cl_{0.935}(PO_4)_{3.00}$

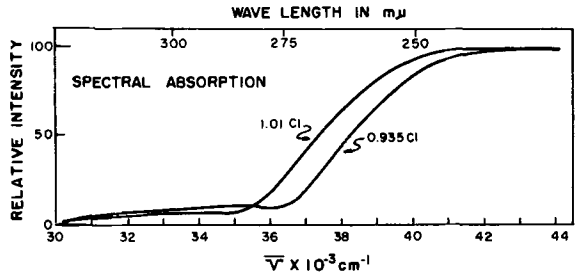

Fig. 4. Correlation of absorption with chloride content

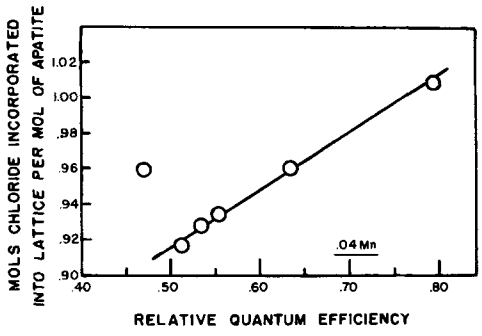

Fig. 5. Quantum efficiency as a function of lattice chloride, all phosphors prepared with 0.04 Mn.

efficiency for the latter. These data are given in Fig. 5.

The method of measurement was a variation of the methods used in the literature (12), as derived from the definition of quantum efficiency. In this method, quantum efficiency (QE) is defined as the ratio of quanta emitted to quanta absorbed. Relative quantum efficiency is obtained by comparison to a standard $MgWO_4$ phosphor, which is assumed to have 100% QE

$$QE_{rel} = \frac{\int E_1\lambda_1 d\lambda}{\int E_2\lambda_2 d\lambda} = \frac{\int E_1\lambda_1 d\lambda -}{100}$$

By measuring the quantum area (obtained from the emission spectrum), the relative emission peak heights at the excitation maximum (λ_x) of each phosphor, the relative absorption at λ_x (to correct for reflection), and the energy ratios of both excitation and emission, the relative quantum efficiency can be obtained.

Only one sample does not fall on the line connecting the points. This was the phosphor fired at 1000°C, as shown in Fig. 6 and given in Table III. The plaque brightness and the quantum efficiency of the 1000°C phosphor are not linear extensions of the other phosphor properties, nor was the stoichiometric phosphor obtained. It is probable that the 1000°C firing temperature was too high. Hence, due to the high vapor pressure of $CdCl_2$, a deficiency of lattice chloride resulted, leading to the poor efficiency.

Discussion

The phosphor $Cd_5Cl(PO_4)_3$:Mn is unusual in that it is one in which the activator, Mn^{+2}, is not associated with a sensitizer as is manganese in most other apatite phosphors (13). The x-ray powder diffraction patterns of the unactivated and the manganese-activated cadmium chlorophosphate compositions can be easily indexed as hexagonal. The structure is probably similar to apatite, $Ca_5F(PO_4)_3$. By analogy, the cadmium chlorophosphate structure includes two nonequivalent cadmium positions, although the exact site symmetry is not known. If it is the same as apatite, one site has a trigonal symmetry whereas the other involves a rhombic grouping. The equivalent CdII positions would then be arranged triangularly around the chloride, forming a screw axis along the c_o direction of the unit cell. Although Mn^{+2} can be incorporated up to 0.30 mole per 1.00 mole of apatite with little effect on the fluorescent properties, no definite assignment of position can be made for the manganous activator center, even though the (hkl) planes are known. The Mn^{+2} probably distributes itself between the CdI and CdII sites. No attempt was made to distinguish the actual distribution of activator sites in the phosphor.

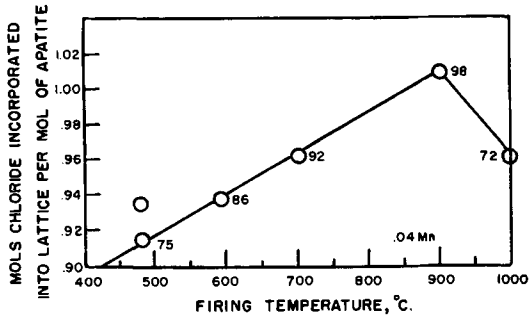

Fig. 6. Chloride incorporation as a function of firing temperature

It has been shown that there is a linear dependency of quantum efficiency on incorporated lattice chloride. Defect structures can exist in which the chloride content is less than stoichiometric. The quantum efficiency of $Cd_5Cl(PO_4)_3$:Mn depends on the chloride content of the structure. In the present work, this was found to depend on the phosphor-firing-temperature at a given firing time. The fact that the quantum efficiency as well as the position of the absorption edge depends on the chloride incorporated in the structure suggests that the absorption and emission processes may involve chloride in some manner. It appears unlikely that the chloride atom itself is the only species directly involved in the absorption process. A more logical process would involve the cadmium atoms of the structure. In a previous paper (11) it was shown that the luminescence process of $Cd_2P_2O_7$:Mn, prepared in a reducing atmosphere, probably involves host-sensitization, with formation of a localized absorption center, Cd^+. Resonance energy transfer processes were shown to be possible and account for the high efficiency observed. Such an explanation could be applied to $Cd_5Cl(PO_4)_3$:Mn. A possible mechanism would involve the formation of a localized absorption site in which a complex was formed by charge-transfer between a cadmium atom at a CdII site and a chloride atom on the c_o axis

$$Cd^{++} + Cl^- \rightarrow [(Cd^+) + Cl^\circ] \qquad [5]$$

The absorption bands of transition metal complexes are commonly of two kinds: those due to charge

transfer processes and those arising from transitions which, to a good approximation, can be considered as taking place within the d-shell of the ion. The formation of such an electronic species, Cd^+, would produce a center having an allowed transition, ($^2S_{1/2} \rightarrow {}^2P_{3/2}$) with an electronic configuration, $4d_{10}5s$. In the luminescence process, excitation of the Mn^{+2} emission center through a resonance process from the charge-localized (Cd^+) absorption center in an excited state would be expected to occur, similar to other well-known sensitization processes.

There is a certain correspondence of the present hypothesis to the theory proposed by Johnson (14) for $Ca_5F(PO_4)_3$:Sb:Mn. Using optical measurements on single crystals containing either or both activators, Johnson concluded that while Mn^{+2} may occupy either of the nonequivalent calcium positions when present alone, Sb^{+3} occupies primarily the CaII position in the presence of Mn^{+2} which prefers the CaI site. The inferences drawn for $Cd_5Cl(PO_4)_3$:Mn require the absorbing site to be at the CdII position since the whole luminescent process is dependent on chloride content.

While it is possible that the absorption center is composed of Mn^{+2} at a CdII site in association with the nearest neighbor chloride, this appears less likely since the actual absorption is strong, whereas the Mn^{+2} or Mn^+ transitions will be weak since both involve forbidden transitions.

Finally, although a Cd^+ species has not been observed in the oxygen-dominated phosphors, Lushchik and Lushchik (15) have investigated a series of homologous activators in alkali halides. Included in these activators was a species, Cd^+, which had an absorption band in the ultraviolet. The formation of a Z-center, involving a doubly charged cation such as Ca^{++} and a localized electron to give a Ca^+ species, was postulated.

Acknowledgments

The author is indebted to Dr. R. W. Mooney and M. A. Aia for discussions concerning the phosphor, to D. T. Palumbo for discussions on quantum efficiency, and to H. D. Layman and J. E. Webster for some of the preparations.

Manuscript received April 23, 1962; revised manuscript received Oct. 8, 1962.

Any discussion of this paper will appear in a Discussion Section to be published in the December 1963 JOURNAL.

REFERENCES

1. A. H. McKeag and J. T. Randall, British Pat. 495,706 (1937).
2. R. W. Wollentin, C. K. L. Wei, and R. Nagy, *This Journal*, **99**, 131 (1952).
3. A. H. McKeag, U. S. Pat. 2,201,698 (1940).
4. American Society for Testing Materials, Philadelphia, X-ray Powder Data File, 1957. Card No. 2-0793.
5. R. C. Ropp and R. W. Mooney, *J. Am. Chem. Soc.*, **82**, 4848 (1960).
6. C. W. W. Hoffman, R. C. Ropp, and R. W. Mooney, *ibid.*, **81**, 3830 (1959).
7. R. C. Ropp and R. W. Mooney, *This Journal*, **107**, 15 (1960).
8. H. Bloom and B. J. Welsh, *J. Phys. Chem.*, **62**, 1594 (1958).
9. L. Onsager, *Z. Physik*, **27**, 388 (1926); **28**, 277 (1927).
10. P. W. Arnold, *Trans. Faraday Soc.*, **46**, 1061 (1950).
11. R. C. Ropp, *This Journal*, **109**, 569 (1962).
12. See for example, A. Bril and W. Hoekstra, *Philips Research Repts.*, **16**, 356 (1961), or Y. Uehara, I. Masuda, and Y. Kobuke, *This Journal*, **107**, 1 (1960).
13. D. L. Dexter, *J. Chem. Phys.*, **23**, 1004 (1953).
14. P. D. Johnson, *This Journal*, **108**, 159 (1961); Also, talk given at "International Conference on Luminescence," New York Univ., October, 1961.
15. N. E. Lushchik and Ch. B. Lushchik, *Optika i Spektroskopiya*, **8**, 839 (1960).

The Phosphorous Dissociation Pressure over the System $GaP_{(s)}$-$Ga_{(l)}$

W. D. Johnston[1]

Research Laboratories, Westinghouse Electric Corporation, Pittsburgh, Pennsylvania

ABSTRACT

The phosphorous pressure derived from the dissociation of GaP according to the reaction

$$GaP_{(s)} \rightarrow Ga_{(l)} + \tfrac{1}{2}P_{2(g)}$$

has been measured by the Knudsen effusion method. In the temperature range 781°-1005°C the phosphorous pressure may be expressed as log pP_2mm = $-18{,}870/T°K + 13.60$.

The phosphorous pressure over GaP at its melting point (~1500°C) is quite high (estimated ~20 atm) (1). No dissociation pressures are available for lower temperatures. Such data would be particularly helpful for such lower temperature processes as junction preparation by diffusion, transport experiments, and epitaxial growth since in these cases phosphorous pressure may have to be applied to prevent decomposition.

Experimental

This study was made by the Knudsen effusion method (2). Effusion cells were made of quartz which were coated inside with aquadag to prevent the reaction of Ga or GaP with quartz forming Ga_2O^3. The two cells used in this work had the

[1] Present address: Pittsburgh Corning Research & Engineering Center, Pittsburgh, Pennsylvania.

transfer processes and those arising from transitions which, to a good approximation, can be considered as taking place within the d-shell of the ion. The formation of such an electronic species, Cd^+, would produce a center having an allowed transition, ($^2S_{1/2} \rightarrow {}^2P_{3/2}$) with an electronic configuration, $4d_{10}5s$. In the luminescence process, excitation of the Mn^{+2} emission center through a resonance process from the charge-localized (Cd^+) absorption center in an excited state would be expected to occur, similar to other well-known sensitization processes.

There is a certain correspondence of the present hypothesis to the theory proposed by Johnson (14) for $Ca_5F(PO_4)_3$:Sb:Mn. Using optical measurements on single crystals containing either or both activators, Johnson concluded that while Mn^{+2} may occupy either of the nonequivalent calcium positions when present alone, Sb^{+3} occupies primarily the CaII position in the presence of Mn^{+2} which prefers the CaI site. The inferences drawn for $Cd_5Cl(PO_4)_3$:Mn require the absorbing site to be at the CdII position since the whole luminescent process is dependent on chloride content.

While it is possible that the absorption center is composed of Mn^{+2} at a CdII site in association with the nearest neighbor chloride, this appears less likely since the actual absorption is strong, whereas the Mn^{+2} or Mn^+ transitions will be weak since both involve forbidden transitions.

Finally, although a Cd^+ species has not been observed in the oxygen-dominated phosphors, Lushchik and Lushchik (15) have investigated a series of homologous activators in alkali halides. Included in these activators was a species, Cd^+, which had an absorption band in the ultraviolet. The formation of a Z-center, involving a doubly charged cation such as Ca^{++} and a localized electron to give a Ca^+ species, was postulated.

Acknowledgments

The author is indebted to Dr. R. W. Mooney and M. A. Aia for discussions concerning the phosphor, to D. T. Palumbo for discussions on quantum efficiency, and to H. D. Layman and J. E. Webster for some of the preparations.

Manuscript received April 23, 1962; revised manuscript received Oct. 8, 1962.

Any discussion of this paper will appear in a Discussion Section to be published in the December 1963 JOURNAL.

REFERENCES

1. A. H. McKeag and J. T. Randall, British Pat. 495,706 (1937).
2. R. W. Wollentin, C. K. L. Wei, and R. Nagy, *This Journal*, **99**, 131 (1952).
3. A. H. McKeag, U. S. Pat. 2,201,698 (1940).
4. American Society for Testing Materials, Philadelphia, X-ray Powder Data File, 1957. Card No. 2-0793.
5. R. C. Ropp and R. W. Mooney, *J. Am. Chem. Soc.*, **82**, 4848 (1960).
6. C. W. W. Hoffman, R. C. Ropp, and R. W. Mooney, *ibid.*, **81**, 3830 (1959).
7. R. C. Ropp and R. W. Mooney, *This Journal*, **107**, 15 (1960).
8. H. Bloom and B. J. Welsh, *J. Phys. Chem.*, **62**, 1594 (1958).
9. L. Onsager, *Z. Physik*, **27**, 388 (1926); **28**, 277 (1927).
10. P. W. Arnold, *Trans. Faraday Soc.*, **46**, 1061 (1950).
11. R. C. Ropp, *This Journal*, **109**, 569 (1962).
12. See for example, A. Bril and W. Hoekstra, *Philips Research Repts.*, **16**, 356 (1961), or Y. Uehara, I. Masuda, and Y. Kobuke, *This Journal*, **107**, 1 (1960).
13. D. L. Dexter, *J. Chem. Phys.*, **23**, 1004 (1953).
14. P. D. Johnson, *This Journal*, **108**, 159 (1961); Also, talk given at "International Conference on Luminescence," New York Univ., October, 1961.
15. N. E. Lushchik and Ch. B. Lushchik, *Optika i Spektroskopiya*, **8**, 839 (1960).

The Phosphorous Dissociation Pressure over the System $GaP_{(s)}$-$Ga_{(l)}$

W. D. Johnston[1]

Research Laboratories, Westinghouse Electric Corporation, Pittsburgh, Pennsylvania

ABSTRACT

The phosphorous pressure derived from the dissociation of GaP according to the reaction

$$GaP_{(s)} \rightarrow Ga_{(l)} + \tfrac{1}{2}P_{2(g)}$$

has been measured by the Knudsen effusion method. In the temperature range 781°-1005°C the phosphorous pressure may be expressed as log pP_2mm = $-18{,}870/T°K + 13.60$.

The phosphorous pressure over GaP at its melting point (~1500°C) is quite high (estimated ~20 atm) (1). No dissociation pressures are available for lower temperatures. Such data would be particularly helpful for such lower temperature processes as junction preparation by diffusion, transport experiments, and epitaxial growth since in these cases phosphorous pressure may have to be applied to prevent decomposition.

Experimental

This study was made by the Knudsen effusion method (2). Effusion cells were made of quartz which were coated inside with aquadag to prevent the reaction of Ga or GaP with quartz forming Ga_2O^3. The two cells used in this work had the

[1] Present address: Pittsburgh Corning Research & Engineering Center, Pittsburgh, Pennsylvania.

dimensions: orifice area $A = 9.22 \times 10^{-3}$ cm^2, Clausing factor $K = 0.87$ and $A = 9.51 \times 10^{-3}$ cm^2, $K = 0.76$. The cells were partially filled with (0.3086 and 0.1587g) powdered, zone refined GaP and were individually suspended by a quartz fiber from a quartz spring having a constant of 19.72 cm/g in an all-glass vacuum system capable of 1×10^{-7} mm. Spring extensions were measured by a cathetometer which could be read to 0.001 cm. A 13-in. long tube furnace with a central 2-in. region having a temperature uniform to within ±2° was used to heat the sample. Temperatures were measured during an experiment by a chromel alumel thermocouple placed between the furnace heater and the quartz furnace tube. This temperature was found to be consistently 15° higher than the actual sample temperature by a separate series of experiments where a fine thermocouple replaced the sample.

The data reported here are computed from the average of large numbers of measurements (10-50) of Δ mass/Δ time at a given temperature. These measurements mainly reflect loss of phosphorus and were always well within ±10%. Further, there was no systematic change in Δ mass/Δ time as the sample slowly changed composition via phosphorus volatilization at a given temperature. This independence of vapor pressure with composition is evidence for the presence of two condensed phases. This was confirmed by visual inspection.

The loss of small quantities of gallium during effusion was noted. In the first experiment effusion was allowed to continue at the highest temperature until the rate of effusion decreased sharply due to the exhaustion of phosphorus from the sample. At this end point too much weight had been lost from the effusion cell. The extra weight loss of 0.0122g corresponds to 5.7% of the available gallium. Chemical analysis of a cream colored deposit in the furnace tube revealed 0.0123g of gallium. The red deposit of free phosphorus is much further removed from the hot region of the furnace tube than is this cream region which has been shown by x-ray diffraction to be GaP. A mass spectrometric study (3) of III-V compounds has not revealed any III-V vapor species. Thus it is believed that monatomic gallium vapor effuses from the cell and reacts with phosphorus at the furnace tube wall. This deposit is relatively nonvolatile and does not distill completely out of the heated region. The vapor pressure data have been corrected from gallium effusion by using the data of Cochran and Foster (4). This correction amounts in terms of pressure to 5.8% at the lowest temperature and 1.5% at the highest temperature, both of which are within experimental error.

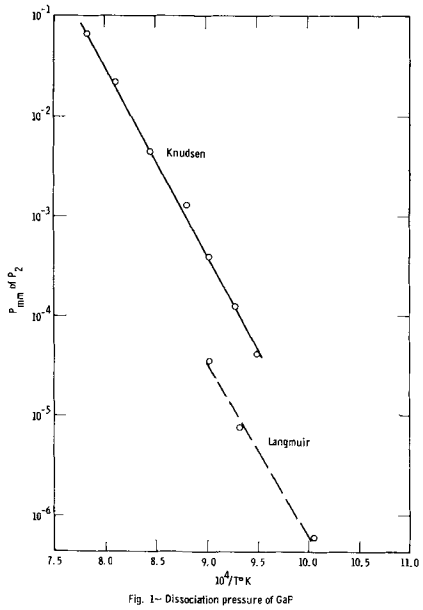

Fig. 1— Dissociation pressure of GaP

Fig. 1. Dissociation pressure of GaP

Table I. Knudsen cell data

T, °C	Pressure of P_2 in mm
781	4.27×10^{-5}
806	1.28×10^{-4}
836	3.93×10^{-4}
862	1.27×10^{-3}
910	4.40×10^{-3}
961	2.17×10^{-2}
1005	6.46×10^{-2}

In one series of experiments an attempt was made to increase the sensitivity necessary to determine the phosphorous dissociation pressure at lower temperatures by using the Langmuir method. This was done by suspending a slice of GaP on the quartz fiber. In this case, the correction for Ga vaporization amounts at the lowest temperature (722°C) to more than half of the total loss of mass. The phosphorous pressures so derived are about a factor of 10 lower than the Knudsen measurement suggesting an accommodation coefficient of 0.1. However, the magnitude of the gallium correction and the lack of knowledge of the accommodation coefficient for gallium make these results of qualitative significance only.

Results

A plot of the log vapor pressure as a function of $1/T$ is given in Fig. 1. Numerical data are given in Table I. The vapor pressure is given in terms of the P_2 species. Normally one would expect the P_4 species to be predominant at these temperatures, and this is the case at higher pressures. But at the low pressures involved in this work the reaction

$$P_4 \rightleftarrows 2P_2$$

is driven strongly to the right. Using thermodynamic data of Stull and Sinke (5) one can show that in this work P_4 is more than 99% dissociated.

The Knudsen data of Fig. 1 may be expressed mathematically as

$$\log p\,P_2\,\text{mm} = -18{,}870/T\ °\text{K} + 13.60$$

This leads to an average heat of decomposition in this temperature range of 43.2 kcal/mole for the reaction

$$GaP \rightarrow Ga(l) + 1/2\,P_2(g)$$

(The heat resulting from the very qualitative Langmuir work was 39.7 kcal/mole.) These may be compared with the values 43.1 and 41 for the decomposition of InAs and GaSb to the respective dimeric gas species (3).

In the equation as written GaP is indicated as decomposing into pure Ga (l). The phase diagram of the Ga-GaP system recently reported by Rubenstein (6) shows that the solubility of P in liquid Ga is quite small (1-2 mole %) at temperatures up to 1000°. Thus in the temperature range of this experiment pure Ga liquid is a reasonable approximation. As the temperature increases beyond 1000° and more phosphorus becomes dissolved in the liquid phase, it will be expected the plot of log pressure *vs.* $1/T$ will deviate from linearity in the direction of higher phosphorous pressures. Such an effect may be noted in the compilation of data on GaAs reported by Lyons and Silvestri (7). This behavior is magnified as one approaches the melting point as has been demonstrated by van den Boomgaard and Schol (8). Thus it is not correct to extrapolate this data to the GaP melting point to obtain the phosphorous pressure over GaP liquid.

Finally, it should be re-emphasized that the data reported here refer to the phosphorous pressure in equilibrium with the two condensed phases, GaP and a gallium rich liquid. Thus the pressure is invariant at a given temperature. Similarly, the stoichiometry of the condensed phases are invariant at a given temperature. If, however, one deals with only GaP as the condensed phase, stoichiometry will vary with phosphorous pressure. This will result in a corresponding variation in the electrical properties of the material (9). Thus, the pressures reported here may be considered as the lowest possible pressures in equilibrium with GaP at various temperatures.

Acknowledgments

The zone refined GaP was kindly supplied by Mr. D. Barrett. The chemical analysis was performed by Mr. E. Beiter. Many helpful discussions were held with Dr. M. Rubenstein. Mr. D. Sestrich assisted in much of the experimental work.

Manuscript received June 11, 1962; revised manuscript received Aug. 5, 1962.

Any discussion of this paper will appear in a Discussion Section to be published in the December 1963 JOURNAL.

REFERENCES

1. C. J. Frosch and L. Derick, *This Journal*, **108**, 251 (1961).
2. S. Dushman, "Vacuum Techniques," John Wiley & Sons, Inc., New York (1949).
3. P. Goldfinger and M. Jeunehomme in "Advances in Mass Spectrometry," J. D. Waldron, Editor, Pergamon Press, New York (1959).
4. C. N. Cochran and L. M. Foster, *This Journal*, **109**, 144 (1962).
5. D. R. Stull and G. C. Sinke, "Thermodynamic Properties of the Elements," Advances in Chemistry Series No. 8, American Chemical Society, Washington, D. C. (1956).
6. M. Rubenstein, *This Journal*, **109**, 69C (1962).
7. V. J. Lyons and V. J. Silvestri, *J. Phys. Chem.*, **65**, 1275 (1961).
8. J. van den Boomgaard and K. Schol, *Philips Research Repts.*, **12**, 127 (1957).
9. H. G. Grimmeiss and H. Koelmans, *ibid.*, **15**, 290 (1960).

Oxygen-Controlled Conduction in Thin Films of Cuprous Iodide: A Mixed Valency Anion Semiconductor

Carlyle S. Herrick and Arthur D. Tevebaugh

Research Laboratory, General Electric Company, Schenectady, New York

ABSTRACT

Oxygen present in cuprous iodide greatly increases the electrical conductivity. Copper films were formed with differing oxygen contents by copper vapor condensation at various oxygen pressures. After iodination to CuI the conductivity was found proportional to the 1/8.4 power of the oxygen pressure during condensation. Cuprous iodide with oxygen created conductors is a mixed valency anion semiconductor.

Cuprous iodide was recognized by Gudden and Schottky to be a stoichiometric imbalance semiconductor (1). Additional work has not yet brought satisfactory agreement between theory and experiment (2-4). In this report the electrical conductivity of CuI is shown to increase greatly due to the presence of small amounts of oxygen. In a gross sense this material may be regarded as CuI containing a small amount of Cu_2O. Since conduction is due to the presence of oxygen this appears to be an example of a mixed valency anion semiconductor, in a manner analogous to the well-known Li_2O-NiO system.

CuI-Cu_2O in thin films is optically transparent. Since only moderate temperatures are required to form this semiconductor from the elements, it can be applied readily to polymeric materials. Lyon earlier applied transparent conducting films of CuI to methacrylate polymer surfaces intended for aircraft window use (5). However CuI films as Lyon made them were neither reproducible nor stable electrically. CuI-Cu_2O films are reproducible and have improved stability.

Experiments and Results

In a series of experiments varying amounts of oxygen have been incorporated in CuI and measurements made of the resulting resistivities. It was experimentally convenient to use thin film techniques for this work.

Oxygen-free copper evaporated in a vacuum chamber was condensed on a transparent, inert-polymer substrate until the light transmission of the deposit fell to 5% of the no-deposit value. Oxygen gas flowed through the evaporation chamber at a constant rate controlled by its diffusion rate through a heated silver tube. Other gases were purged from the chamber by the continuous oxygen flow while the rate of flow in relation to the pumping speed established the chamber oxygen pressure. Evaporation time was less than 5 min for each experiment. During condensation each layer of copper atoms had opportunity to react with oxygen in proportion to the oxygen pressure.

The oxygen containing copper film was treated with iodine vapor, in equilibrium with solid iodine at 70°C (ca. 8 mm), for about 5 sec then allowed to stand in air. This treatment formed the CuI as tiny crystallites. The resulting film was clear, highly transmissive, and of brilliant coloring by reflected light. Prolonged iodine treatment produced a milky-hazy appearance due probably to formation of larger crystallites. Resistivity was not dependent on whether the film was clear or milky-hazy. Hydrogen iodide vapor was also used instead of iodine to form CuI films; however iodine was more convenient.

Measurements of d-c resistivity were made with an ohmmeter and a standard geometry contact. Film thickness was estimated in the usual way for thin transparent films using a refractive index of 2.35 together with the color complement wavelength of the reflected color. The film thicknesses chosen gave colors of the first order.

Resistivities as a function of oxygen pressure are given in Table I for two film thicknesses. Values at 1400Å are the average measurements from two experiments while the values at 1050Å are the average measurements from four experiments. Reproducibility was about ±250 ohms per square. The resistivity of CuI films prepared this way varies monotonically with oxygen pressure in the range between 6.0×10^{-5} and 1.0×10^{-2} mm Hg.

Computed electrical conductivities in Table I are independent of film thickness suggesting that surface conduction is a minor factor. These experimental data are well represented by the relation

$$\sigma \simeq [P_{O_2}]^{\frac{1}{8.4}} \qquad [1]$$

Table I

Oxygen pressure, mm	Resistivity, ohms/square	Conductivity per ohm-cm	Conductors/cm³, μ = 10 cm²/volt-sec
	1400Å		
1.0×10^{-2}	1900	38	2.4×10^{19}
1.0×10^{-3}	2600	28	1.7×10^{19}
1.5×10^{-4}	3100	23	1.4×10^{19}
6.0×10^{-5}	4000	18	1.1×10^{19}
	1050Å		
1.0×10^{-2}	2500	38	2.4×10^{19}
1.0×10^{-3}	3300	29	1.8×10^{19}
1.5×10^{-4}	4100	23	1.4×10^{19}
6.0×10^{-5}	4550	21	1.3×10^{19}

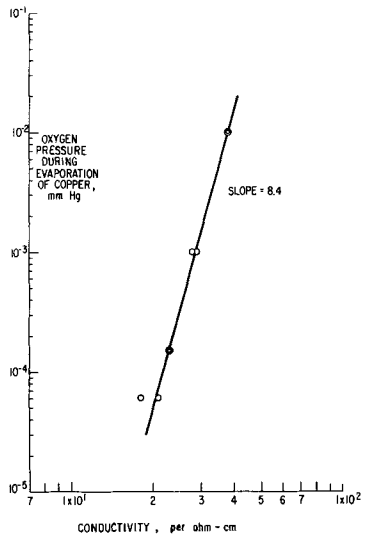

Fig. 1. Oxygen dependence of CuI conductivity

where σ is electrical conductivity and P_{O_2} is oxygen pressure during evaporation of copper (see Fig. 1).

Discussion

In view of the apparent similarity of our data to Dünwald and Wagner's data (6) for the Cu_2O-O_2 system, we attempted to apply their concepts to the problem of explaining Eq. [1]. Our data are not sufficient to verify a proposed mechanism; hence, we suggest the following alternative postulates as reasonable explanations for Eq. [1].

1. Oxygen may be present in the CuI as $O^=$ substituted for I^- on a regular lattice site analogous to the system NiO-Li_2O. With this model conductivity would be directly proportional to oxygen content; hence the amount of oxygen in the copper must vary as $[P_{O_2}]^{\frac{1}{8.4}}$. Oxygen analysis of the copper films to support this point appears difficult at the present time. The expected dependence is proportional to $[P_{O_2}]^{\frac{1}{2}}$.

2. Oxygen may be present in the CuI as electrically neutral interstitial atoms, a minor fraction of which ionize by electron capture from the lattice to create holes. Assuming the oxygen content of copper proportional to $[P_{O_2}]^{\frac{1}{2}}$, the expected dependence, the conductivity would be proportional to $[P_{O_2}]^{\frac{1}{6}}$.

3. Oxygen may be present in the CuI as electrically neutral interstitial atoms in equilibrium with cuprous ion vacancies which ionize by hole formation. The vacancies, two per oxygen atom, form rapidly during the iodine treatment. Assuming the oxygen content of copper proportional to $[P_{O_2}]^{\frac{1}{2}}$, the expected dependence, conductivity would be proportional to $[P_{O_2}]^{\frac{1}{8}}$ which agrees well with experiment. Not everyone will agree that the oxygen atoms can be in equilibrium with cuprous ion va-

cancies; however to the authors this postulate appears to be the most reasonable.

Conduction due to formation of cuprous ion vacancies and electron holes was suggested by Nagel and Wagner (7) for nonstoichiometric CuI containing excess iodine. Maurer's data (4) indicate that the chemical and thermal conditions used by us would, at equilibrium, create sufficient iodine induced vacancies to account for all of the observed conductivity. It is important then to identify what fraction of the conductivity might be due to iodine created vacancies.

All samples were exposed to identical iodine treatments. In each sample the conductivity due to excess iodine-created vacancies should be the same. If conductivity were all due to excess iodine, the slope of Fig. 1 would be infinite instead of 8.4.

In other experiments several samples were repeatedly exposed to the short iodine treatments, and conductivity did not change with the additional exposures. This suggests that formation of copper ion lattice vacancies due to the presence of Cu_2O is much more rapid than vacancy formation due to excess iodine.

When HI was the iodinating agent the resulting conductivity was the same as when iodine was used. Absorption of excess HI is not known to create conductors as does the absorption of excess I_2 in CuI.

For these reasons it seems quite probable that any conductivity induced by the presence of excess I_2 is of very minor magnitude. Then in Fig. 1 the conductivity can be said to be due almost entirely to oxygen.

The conducting species in Cu_2O are in equilibrium with oxygen gas according to the Dünwald and Wagner mechanism (6). The conducting species in nonstoichiometric CuI are in equilibrium with iodine gas according to the Nagel and Wagner mechanism (7). When these two are combined into a CuI lattice, the exact behavior to be expected is not clear. It does seem reasonable to expect some conducting species to be in equilibrium with iodine gas, hence some conductors may disappear with time when iodine is absent from the atmosphere. All samples in Fig. 1 were remeasured after six weeks in an iodine-free atmosphere. The new conductivity values were lower by exactly a factor of two while the slope remained unchanged. This is a very slow decrease in the number of conductive species compared with the decay of excess iodine induced conductors (8).

The number of conductors per cubic centimeter, Table I, column 4, was calculated from the conductivity using a mobility value of 10 cm^2 volt-sec given by Vine and Maurer (3) for the same physical condition in excess iodine induced conductivity. Caution is recommended in comparing numbers derived from a "bulk" value computed from thin film measurements with measurements made on larger specimens because of the well-known conductivity discrepancies of evaporated thin films.

Acknowledgment

Helpful discussions concerning selection of models were afforded by Professor Dr. Carl Wagner, Max Planck Institute, Göttingen. In this laboratory Dr. H. G. Pfeiffer offered helpful suggestions and discussions, Dr. K. B. Blodgett assisted with the thickness estimations, and H. Gooley performed the copper evaporations.

Manuscript received March 20, 1962; revised manuscript received Sept. 15, 1962. This paper was prepared for delivery before the Los Angeles Meeting, May 6-10, 1962.

Any discussion of this paper will appear in a Discussion Section to be published in the December 1963 JOURNAL.

REFERENCES

1. B. Gudden and W. Schottky, *Physik. Z.*, **36**, 717 (1935).
2. K. Weiss, *Z. Physik. Chem. (Frankfurt)*, **12**, 68 (1957).
3. B. H. Vine and R. J. Maurer, *Z. Physik Chem.*, **198**, 147 (1951).
4. R. J. Maurer, *J. Chem. Phys.*, **13**, 321 (1945).
5. D. A. Lyon, U.S. Pat. 2,756,165 (assigned to U.S.A.), July 24, 1956; U.S. Pat. 2,704,265, March 15, 1955.
6. H. Dünwald and C. Wagner, *Z. Physik Chem.*, **B22**, 212 (1933).
7. K. Nagel and C. Wagner, *ibid.*, **B25**, 71 (1934).
8. K. Bädeker, *Ann. Physik.*, **22**, 749 (1907); *Physik. Z.*, **9**, 431 (1908).

The Thermal Conductivities of Mg_2Si and Mg_2Ge

Richard J. LaBotz[1] and Donald R. Mason

The University of Michigan, Ann Arbor, Michigan

ABSTRACT

The thermal conductivities of relatively large homogeneous samples of Mg_2Si and Mg_2Ge have been measured in a dynamic calorimeter from 0°C to 300°C. In both samples, phonon scattering predominates, and the relationship, λT = constant was observed. For Mg_2Si, λT = 23.4 watts/cm, and for Mg_2Ge, λT = 19.8 watts/cm.

Although the electrical properties of Mg_2Si and Mg_2Ge have been measured by several investigators (1-5), the thermoelectric figure of merit for the materials could not be determined because their thermal conductivities had not been measured. In this paper, the results of thermal conductivity measurements made on Mg_2Si and Mg_2Ge in a dynamic calorimeter are presented.

The method which has been used to measure the thermal conductivity is an extensive modification

[1] Present address: Advanced Development Section, Liquid Rocket Plant, Aerojet-General Corporation, Sacramento, California.

of one first described by Ioffe (6). The sample is placed between two copper blocks, one of which has a resistance heater attached to it and is called the source. The second copper block is thermally isolated from the remainder of the system except for contact with the sample and is referred to as the sink.

A constant power input to the source heater establishes a steady-state thermal flux through the sample characterized by a constant rate of temperature rise in the blocks and a constant temperature differential across the sample. Once steady-state conditions exist it is possible to calculate the thermal conductivity, λ, from measurements of the temperature drop across the sample and the rate of temperature rise of the sink.

Preparation of Samples

Polycrystalline samples of the various compositions were prepared by fusion of the pure elements. Transistor grade silicon from the Allegheny Electronic Chemicals Company, transistor grade germanium obtained from the Eagle Picher Company, and sublimed magnesium with 99.99% or greater purity from the Dow Metal Products Company were used. The magnesium was cut into a few pieces totaling 20-25g etched until bright in dilute HNO_3, rinsed well in deionized water, dried, and weighed accurately. The amounts of germanium or silicon (used as received) required to give the correct final composition were then calculated and added.

Because of the high reactivity and high vapor pressure of the magnesium at elevated temperatures and the tendency of silicon to wet and react with various materials, considerable experimentation was required before a satisfactory combination of crucible and fusion cycle was obtained. After experimenting with alumina crucibles, thoria-lined crucibles, and boron nitride crucibles, graphite was finally selected because of ease of machining and sample removal, low cost, and availability in high-purity form. Although some silicon soaked into the graphite, it was possible to compensate for this by adding excess silicon to the charge, and minimizing the time at which the sample was at maximum temperature. Since the vapor pressure of magnesium is equal to 1 atm at 1105°C, it was necessary to enclose the graphite crucible in a pressurized container. After trying fused silica and zirconia containers, stainless steel was finally selected.

The system which was used is shown in Fig. 1. The open end of the spectrographically pure carbon crucible was closed by wedging a carbon plug with a 1° taper into it. This graphite crucible was held inside the stainless steel fusion container, to the closed end of which a ½ in. diameter stainless steel pipe was attached. The system could be evacuated and pressurized through this tube. After the graphite tube was inserted into the stainless steel tube the system was sealed by welding a steel disk over the open end of the tube. In order to remove the sample after the fusion was completed, the disk was ground off on a grinding wheel. Immediately before being used the crucible was baked for a few minutes in

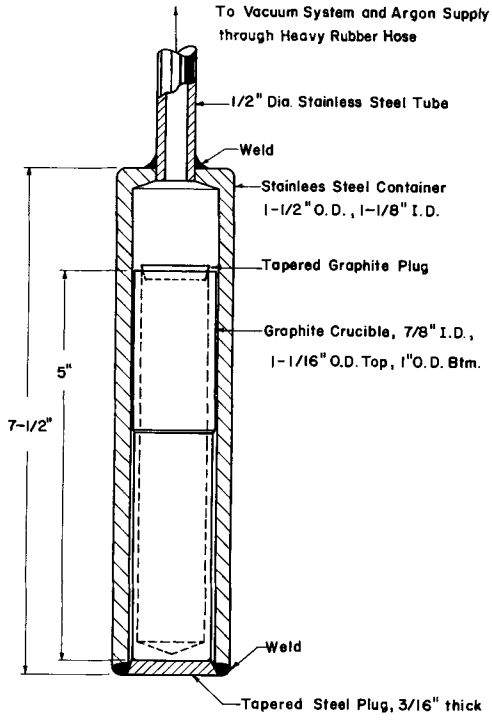

Fig. 1. Fusion crucible and container for preparing Mg_2Si and Mg_2Ge samples.

a fore-pump vacuum at 1400°C to remove any volatile materials and adsorbed gas. While the graphite crucible was cooling the system was backfilled with argon to minimize the readsorption of air during the time that the magnesium and germanium or silicon charge was being loaded into the crucible. After the crucible was loaded and welded into the stainless steel tube the system was evacuated. The stainless steel tube was then heated to 500°-600°C in an induction heater to drive off any additional gas. As soon as the tube had cooled back to room temperature the system was filled with argon to a pressure of 20 psia. Following this it was heated as rapidly as possible in the induction heater to a temperature 30°-40°C above the melting temperature of compound. Once this temperature was attained the tube was transferred to a resistance furnace which had been preheated to this same temperature. After soaking in this furnace for about 5 min the sample was inverted a few times to assure good mixing of the molten ingredients. The sample would then be placed near the end of the furnace so that the sample was subjected to a temperature gradient. The furnace was then cooled at 15°C/hr to a temperature 15°C below the freezing temperature. After the sample had been held at a temperature 30°C below the freezing temperature for approximately 12 hr in order to promote grain growth, it was cooled to room temperature at about 100°C/hr.

In order to compensate for the loss of silicon by penetration into the graphite it was necessary to add about 1% excess silicon to the melt for the Mg_2Si samples, when using a fusion cycle with a maximum temperature approximately 35°C above the liquidus temperature for about 5 min. The amount of silicon lost to the graphite depends very

strongly on the maximum temperature and time used during the fusion cycle.

Mg_2Ge tends to decompose in the presence of water vapor or when in contact with water, and these samples were stored in acetone to prevent the reaction with the water vapor in the atmosphere.

It was necessary to make over 90 samples in order to obtain a sufficient number which had high enough quality to permit meaningful measurements to be made. The most common difficulties were associated with porous samples, poor mechanical properties, and eutectic inclusions. Two series of samples were run. The first series was composed of about 40 samples and was used to screen various crucible materials and fusion methods. When the combination of a graphite crucible and stainless steel crucible holder was finally selected the second series of 52 samples was run. In the course of the investigation improvements were continually being made in the preparational procedures. As a result of this the latter samples had a much higher success ratio than the early samples.

Method

Under steady-state conditions the temperature profile across the sample can be calculated from a one-dimensional solution of the heat conduction equation for a sample with constant cross-sectional area.

$$\frac{d^2T}{dx^2} = \frac{\rho_s C_{p,s}}{\lambda} \frac{dT}{dt} \qquad [1]$$

Under conditions of steady-state operation appropriate boundary conditions are

$$\frac{dT}{dt} = R = \text{rate of heating, °C/sec} = \text{constant} \qquad [2]$$

which is valid over all values of x. Also the thermal flux across the face at $x = 0$ is equal to the sensible heat absorbed by the sample and the copper sink.

$$-\lambda A\, dT/dx = (m_s C_{p,s} + m_c C_{p,c})R \qquad [3]$$

where m_s is the mass of the sample, g; $C_{p,s}$, specific heat of the sample, cal/g °K; m_c, mass of the sink, g; $C_{p,c}$, specific heat of the sink, cal/g °K; A, cross-sectional area of the sample. Equation [1] can be integrated using the boundary conditions from Eq. [2] and [3].

The temperature difference across the sample can be obtained by evaluating T at $x = 0$ and $x = L$, and subtracting. Therefore, after integration, condensation of terms and rearrangement the solution is

$$\lambda = \frac{RL}{A\Delta T}\left(m_c C_{p,c} + \frac{m_s C_{p,s}}{2}\right) \qquad [4]$$

In practice the points $x = 0$ and $x = L$ need not correspond with the end faces of the sample, but need only be symmetrically placed about the midpoint, $x = L/2$. The sample from L to the sink then becomes part of the sink and the one-half factor is no longer applicable for that mass of the sample. However, by adding an equal amount of sample material ahead of the first thermocouple in the heat flux path, an equal mass which absorbs no heat is added to the sample, and the one-half factor is restored.

Seebeck voltage can be measured by attaching copper leads to the sample at the same locations as the thermocouples. The Seebeck coefficient is then obtained by dividing the potential read across the copper leads by the ΔT read from the differential thermocouple. That is

$$\alpha = \frac{V}{\Delta T} \qquad [5]$$

Description of Equipment

Figure 2 shows a sketch of the apparatus used to measure thermal conductivity and the Seebeck coefficient. The copper source block rests on a lavite disk, which in turn rests loosely on three steel rods supported by the brass base. The sink, sample, and source are held tightly together by two 30 gauge (0.010 in. diameter) chromel wires, which loop over the sink and under the lavite supporting disk. This insures good contact between the three elements and also removes the possibility that the sink may be jarred off the sample. The sample and sink are enclosed in Pyrex wool.

The source-sample-sink combination is enclosed in a radiation shield made from a 2 in. diameter copper tube. The tube fits into a silver-plated steel disk which in turn is kept from contacting the bottom brass plate by a lavite disk. The shield extends from slightly below the source to about 4 in. above the top of the sink and is covered inside and out with aluminum foil. The shield in turn is contained in a 4.5 in. diameter glass cylinder, which has "O" ring seals to both the bottom and top brass plates. The space between the glass cylinder and radiation shield is completely filled with Pyrex wool.

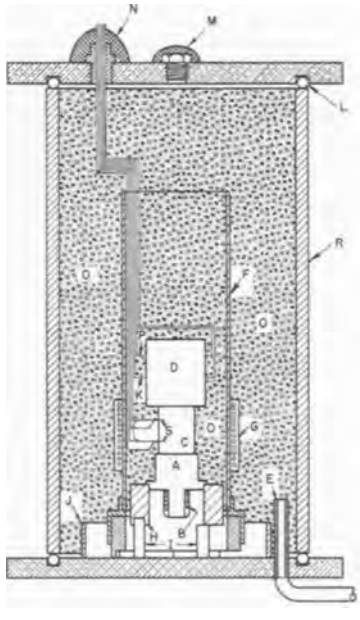

Fig. 2. Instrument for measurement of thermal conductivity and Seebeck coefficient. A, copper source block; B, source heater; C, sample; D, copper sink; F, shield; G, shield heater; K, shield control differential thermocouple; M, port for pouring in liquid N_2—sealed with Apiezon wax; N, thermocouple port sealed with Apiezon wax; P, sink thermocouple; R, glass cylinder; S, sample differential thermocouple and Seebeck probes.

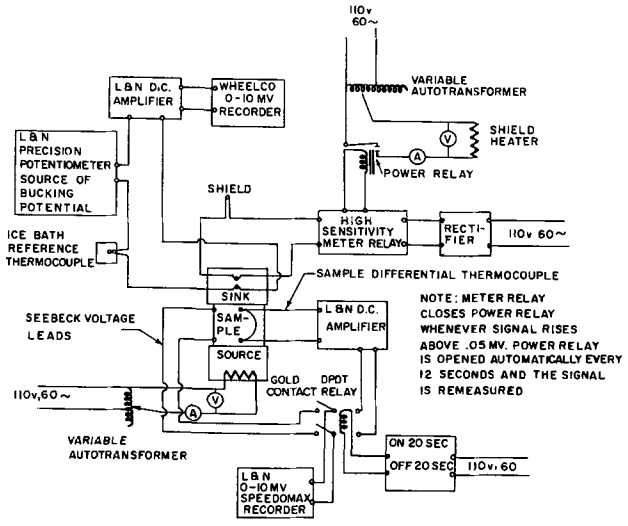

Fig. 3. Schematic diagram of measurement and control circuits for thermal conductivity apparatus.

The power leads to the source and shield heaters pass through the bottom plate by means of hermetically sealed connectors. The vacuum lead also passes through the bottom plate and is located between the glass cylinder and the copper shield. All thermocouple leads pass through the top plate where they are sealed by means of Apiezon sealing wax. Permanent hermetically sealed connectors were not used because the system must be dismantled each time the sample is changed. The large number of leads would make permanent hermetic seals impractical. In addition, the possibility of spurious thermal emfs arising as a result of the intermediate metal-to-metal contact is eliminated.

The measurement and control circuits are shown schematically in Fig. 3. The temperature of the sink is measured using a 30 gauge chromel-alumel thermocouple with an ice-water reference junction. A circuit comprising a L&N potentiometer, a L&N d-c amplifier, and a Wheelco recorder with a 0-10 mv range is used to measure the heating rate of the sink.

A 40 gauge (0.003 in. diameter) chromel-alumel differential thermocouple is used to measure the temperature drop across the sample. The junction of the couple is placed in 0.020 in. diameter holes drilled into the sample by means of an ultrasonic cutter. The output of the differential thermocouple is connected through a L&N d-c amplifier into a L&N Speedomax recorder. The Seebeck voltage is also measured with this recorder. The input to the recorder is switched automatically between the Seebeck voltage and the differential thermocouple output every 20 sec by means of a timer which controls a gold contact relay.

The differential thermocouples are made from bare chromel and alumel wire, calibrated by the manufacturer. As the junctions are inserted into holes in the sample the wires have to be insulated from the sample and from each other. By drawing the wire through a bead of molten borax glass ($Na_2B_4O_7$) and then quickly through a flame it is possible to deposit a thin, tough, high resistance film on the wires. When examined under a microscope this film appears to be approximately 0.0003 in. thick, has a brownish color, and does not break or crack when the wire is bent. The resistance of this coating is approximately 700,000 ohms at room temperature. If allowed to sit in the air for several weeks a white powder forms on the coating, probably due to the formation of one of the hydrates of sodium tetraborate. Because of this the thermocouples are used immediately after they are made. Several of the thermocouples were checked using boiling water and ice water junctions and were on calibration. In addition to this they gave accurate results to above 400°C when used in checking the thermal conductivity of Inconel.

The temperature control on the radiation shield is achieved by means of 30 gauge copper-constantan differential thermocouple. One junction of the thermocouple is embedded in the sink and the other junction rests against the radiation shield directly adjacent to the sink. The output of this thermocouple activates a very highly sensitive meter relay. Whenever the output of this differential thermocouple rises above 0.05 mv (a[$-\Delta T$] of approximately 1°C) the shield heater is switched on by the meter relay. The power relay is opened automatically every 12 sec and the signal remeasured. The magnitude of the shield heater power is controlled by use of an autotransformer.

Calibration and Operation

The instrument was checked by measuring the thermal conductivity of Armco iron, Inconel, and fused SiO_2, the thermal conductivities of which already have been rather firmly established by experimental measurements and reported in the literature. The results of these measurements agreed with values previously obtained within an accuracy of $\pm 6\%$. The measured values cover a range from 0.0138 to 0.71 w/cm °K, a range of a factor of 50. Armco iron has a thermal conductivity which decreases with rising temperature, that of Inconel increases slowly with temperature, while that of fused SiO_2 is nearly constant. Thus the instrument was able to measure all types of temperature dependence.

There is a twofold limitation on the upper temperature which can be attained by the instrument. The actual value of this limit for any given sample depends on the sample geometry and its thermal conductivity. As the rate of heat exchange between the sink and its surroundings increases with temperature due to increased radiation effects, the error introduced by this heat leak also usually increases with rising temperature. The temperature at which this spurious heat leak becomes sizeable relative to the total amount of heat passing from the sample to the sink is a function of the cross section, length, and thermal conductivity of the sample. In other words, when a large amount of heat is passing from the sample into the sink, the amount of heat exchanged between the sink and the surroundings does not reach significant proportions until a high measuring temperature is reached.

A second limitation on the maximum temperature is placed by the vacuum seals. The sealing method employed is satisfactory until the temperature of the seals reaches about 100°-150°C. When a sample with a low thermal conductivity or small cross section is measured, a heating rate of 1°-2°C/min is generally used. With this low heating rate the seal temperature reaches its limit when the sample temperature is slightly above 300°C. However, for material with a high thermal conductivity or samples with a large cross section, heating rates to 3°-4°C/min can be used. Under these conditions the sample temperature may be over 400°C before the vacuum seals reach their limiting temperature.

In order to make measurements from 0°C it was necessary to cool the instrument far enough below 0°C so that "steady-state" conditions could be attained by the time the sample had reached 0°C. This precooling was performed simply by pouring liquid nitrogen into an open port in the top cover plate. In a few instances it appeared as though there was frost formation within the instrument. This was indicated by a rise in the temperature gradient across the sample and a drop in the sink heating rate at temperatures from slightly below to slightly above 0°C. The apparent cause of this was the melting and vaporization of frost on the sink.

Good thermal contact between the sink, sample, and source was achieved by placing a thin layer of silicone grease impregnated with copper between the contacting surfaces.[2] This material had both a high thermal conductivity and a high electrical resistivity.

The samples of Mg_2Ge and Mg_2Si were run under the same conditions as the fused SiO_2. The heating rates varied from about 0.75° to 3°C/min, while the temperature drop across the sample varied from about 7° to 13°C.

In order to calculate λ by using Eq. [4] it is necessary to know $C_{p,s}$, the specific heat of the sample. In many cases this is not known, but it can be approximated as closely as necessary by the law of Dulong and Petit, which states that, for atomic lattices at temperatures above the Debye temperature, the specific heat should be 6 cal/g at. wt °K, and there is considerable experimental evidence to show that this is a reasonable approximation for a number of materials.

The uncertainty introduced in the thermal conductivity measurement by an uncertainty in $C_{p,s}$ is generally small. If, for example, the total heat capacity of the copper sink $(mC_p)_c$ is five times greater than that of the samples, then an uncertainty of 15% in C_{ps} would introduce an uncertainty of only about 1.5% in λ. By making the sink larger this uncertainty can be reduced to as low a level as desired.

Unfortunately, there are other considerations which would dictate the selection of a small sink. The first of these is that a finite heating rate must be obtained. The second consideration is that the ΔT across the sample should be kept rather small. A small ΔT minimizes thermal shielding difficulties and makes the value of λ which is obtained more nearly a differential value. A small sink is also favored by the fact that heat losses from the sink to the surroundings are proportional to the surface area of the sink. Therefore the sink should not only be small but also have a minimum surface-to-volume ratio. Hence the final selection of a sink size must be a compromise. The vacuum obtained generally was about 1 mm of mercury or better. Measurements were made up to 300°C which is felt to be a conservative estimate of the upper limit of reliability to within ±6% for the samples being measured.

[2] "Thermocopper Grease," obtained from I.T.T. Laboratories, 3700 East Pontiac Street, Fort Wayne, Indiana.

Results

The thermal conductivity of Mg_2Si was measured on a specimen which had a cross-sectional area of 1.57 cm^2 and a length of 1.61 cm between the differential thermocouples. It was large-grained and contained no visible cracks. When examined under 400X magnification only a trace of magnesium-rich eutectic could be observed in one corner of the sample and probably represented less than 0.01% of the total surface area examined.

Plots of both thermal conductivity *vs.* temperature and the product λT *vs.* temperature are given in Fig. 4. It can be seen that the expression λT = 23.4 w/cm describes the thermal conductivity as a function of temperature very well. It appears that heat conduction in this sample is due primarily to phonons and that the thermal resistance is the result of phonon-phonon scattering (8). A calculation of the electron component of the thermal conductivity gives a value λ_{el} = 0.000054 w/cm °K, which is negligible (electrical resistivity ρ = 0.07 ohm-cm) (9). Ambipolar thermal conductivity can also be neglected as the sample never exhibited intrinsic behavior, and there is no exciton contribu-

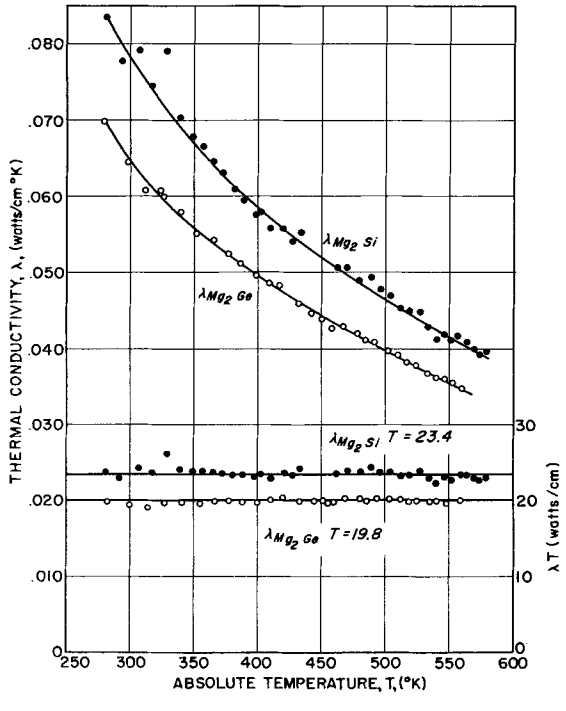

Fig. 4. Thermal conductivities for Mg_2Si and Mg_2Ge *vs.* absolute temperature.

tion to the thermal conductivity in this sample. Thus the lattice thermal conductivity is essentially equal to the measured values of thermal conductivity.

The thermal conductivity of Mg_2Ge was measured on a sample which had a cross-sectional area of 2.34 cm^2 and a length of 1.61 cm between the differential thermocouples. The grains in the sample were very large, and the specimen was almost a single crystal. There were no evidences of any eutectic inclusions either in the ingot from which the specimen was taken or in the specimen itself.

The experimental values of thermal conductivity for this sample are also given as a function of temperature in Fig. 4. Because of the high electrical resistivity of this sample (9), the charge carrier contribution to the thermal conductivity is negligible, and the lattice thermal conductivity is equal to the experimentally measured values. The thermal conductivity for this sample follows very well the relationship $\lambda T = 19.8$ w/cm, indicating that phonon-phonon interactions are the primary source of thermal resistance (8).

Samples containing as little as 1% of magnesium-rich inclusions as detected by microscopic examination had thermal conductivities which were as much as 50% greater than the values reported here. The thermal conductivity thus is quite sensitive to the purity of the materials.

These results are used in the following paper (9) which investigates the thermoelectric properties of the pseudobinary system $Mg_2Ge_xSi_{1-x}$.

Acknowledgments

The authors wish to express their gratitude to the General Motors Corporation for fellowship grants received during the doctoral work, to the Dow Metal Products Company for donating high-purity magnesium, to the Allegheny Electronic Chemicals Company for donating the high-purity silicon, and to the Institute of Science and Technology at the University of Michigan for their partial support of this study.

Manuscript received Jan. 23, 1962; revised manuscript received Sept. 24, 1962. This paper was prepared for delivery before the Detroit Meeting, Oct. 1-5, 1961. Contribution No. 9 from the Semiconductor Research Laboratory, College of Engineering, University of Michigan, Ann Arbor, Michigan. This work was done in partial fulfillment of the requirements for the Ph.D. degree at The University of Michigan by R. J. LaBotz.

Any discussion of this paper will appear in a Discussion Section to be published in the December 1963 JOURNAL.

REFERENCES

1. G. Busch and U. Winkler, *Physica*, **20**, 1067 (1954).
2. R. T. Ellickson and J. T. Nelson, "Semiconducting Properties of Intermetallic Compounds," Fifth Quarterly Progress Report, Department of Physics, University of Oregon, Eugene, Oregon, as quoted by Morris (3).
3. R. G. Morris, "Semiconducting Properties of Mg_2Si Single Crystals," Ph.D. Thesis, Iowa State University, University Microfilms, Inc., Ann Arbor, Mich. (1957).
4. R. D. Redin, "Semiconducting Properties of Mg_2Ge Single Crystals," Ph.D. Thesis, Iowa State University, University Microfilms, Inc., Ann Arbor, Mich. (1957).
5. C. R. Whitsett, "Electrical Properties of Magnesium Germanide and Magnesium Silicide," Ph.D. Thesis, Iowa State College, Ames, Iowa, as quoted by Morris (3) and Redin (4) (1955).
6. A. V. Ioffe and A. F. Ioffe, *Zh. Tekh. Fiz.*, **22** (1952). Original in Russian, English Abstract in *Sci. Abst.* (Physics), **56**, 772 (1953).
7. R. J. LaBotz, "The Thermoelectric Properties of the Pseudobinary System Mg_2Si-Mg_2Ge," Ph.D. Thesis, The University of Michigan, Ann Arbor, Mich. (1961).
8. P. G. Klemens, "Lattice Thermal Conductivity," in "Solid State Physics," Vol. 7, Academic Press, New York (1957).
9. R. J. LaBotz, D. R. Mason, and D. F. O'Kane, *This Journal*, **110**, 127 (1963).

The Thermoelectric Properties of Mixed Crystals of $Mg_2Ge_xSi_{1-x}$

Richard J. LaBotz,[1] Donald R. Mason, and Daniel F. O'Kane[2]

The College of Engineering, The University of Michigan, Ann Arbor, Michigan

ABSTRACT

The purpose of this work was to determine the thermoelectric properties of the pseudobinary system Mg_2Si-Mg_2Ge. The compositions investigated were Mg_2Si, $Mg_2Ge_{0.2}Si_{0.8}$, $Mg_2Ge_{0.4}Si_{0.6}$, $Mg_2Ge_{0.6}Si_{0.4}$, $Mg_2Ge_{0.8}Si_{0.2}$, and Mg_2Ge. X-ray diffraction lattice parameter measurements and differential thermal analysis measurements established the existence of complete solid solubility between Mg_2Si and Mg_2Ge. Both the lattice parameter and liquidus temperature show almost linear variation with composition in this system. The melting temperature of Mg_2Si was found to be 1070° ± 5°C, while that of Mg_2Ge was found to be 1102° ± 5°C.

Electrical resistivity and Hall effect measurements indicated that at 300°K the electron Hall mobility in the mixed crystals is essentially the same as that of the pure compounds. Maximum values obtained were slightly above 300 cm^2/volt sec. The forbidden energy gap appeared to vary monotonically from about 0.78 electronvolt (ev) for Mg_2Si to about 0.70 ev for Mg_2Ge. Thermal conductivity measurements on the pseudobinary system showed that the lattice thermal conductivity of the solid solutions is substantially lower than that of either of the pure compounds at 300°K. At this temperature the lattice thermal conductivity of $Mg_2Ge_{0.6}Si_{0.4}$ was found to be 0.0268 watt/cm °K. The maximum thermoelectric figure of merit which could be obtained with these materials is not as good as that of other materials now in use.

Lattice parameter determinations, differential thermal analysis measurements, and microscopic examinations at six different compositions in the system Mg_2Ge-Mg_2Si showed that there was complete solid solubility between Mg_2Si and Mg_2Ge; thermal conductivity, Seebeck coefficient, electrical conductivity, and Hall effect were measured on these samples, and all data were analyzed to correlate the results with theory.

No prior work has been reported in the literature on the Mg_2Ge-Mg_2Si mixed crystals, although previous investigators have made many measurements on Mg_2Ge and Mg_2Si. The electrical properties of single crystals of Mg_2Ge have been measured by Whitsett (1) and by Redin (2), while the electrical properties of polycrystalline samples of Mg_2Ge have been measured by Busch and Winkler (3). The electrical properties of single crystals of Mg_2Si have been investigated by Whitsett (1), by Morris (4), and by Ellickson and Nelson (5). The electrical properties of polycrystalline samples of Mg_2Si have been measured by Busch and Winkler (3).

Lattice parameter measurements have been performed on Mg_2Ge by Busch and Winkler (3), Klemm and Westlining (6), Brauer and Tiesler (7), Zintl and Kaiser (8), and Farrel (9). Similar measurements were performed on Mg_2Si by Owen and Preston (10), Klemm and Westlining (6), Busch and Winkler (3), and Farrel (9).

[1] Present address: Advanced Development Section, Liquid Rocket Plant, Aerojet-General Corporation, Sacramento, California.

[2] Present address: Thomas J. Watson Research Center, International Business Machines, Inc., Yorktown Heights, New York.

Melting temperature determinations were made on Mg_2Ge by Klemm and Westlining (6). The melting temperature of Mg_2Si has been measured by Vogel (11), by Klemm and Westling (6), and by Wohler and Schliephake (12). The thermal conductivities of Mg_2Ge and Mg_2Si have been measured in conjunction with this work and are reported in the previous paper (13).

The only mixed crystal system containing either Mg_2Ge or Mg_2Si that has been reported is the system Mg_2Ge-Mg_2Sn. The electrical properties and lattice parameter of mixed crystals of this system were measured by Busch and Winkler (14).

Experimental Results

The technique used to prepare the samples has been described in the previous paper (13). It was necessary to prepare 115 ingots before 13 satisfactory specimens of compositions Mg_2Si, $Mg_2Si_{0.8}Ge_{0.2}$, $Mg_2Si_{0.6}Ge_{0.4}$, $Mg_2Si_{0.4}Ge_{0.6}$, $Mg_2Si_{0.2}Ge_{0.8}$, and Mg_2Ge were obtained for measurements. The latter three compositions all tended to decompose in water or humid air, and these samples were stored in acetone to protect them.

The results of the x-ray lattice parameter measurements and the differential thermal analyses established the isomorphous nature of the pseudobinary system $Mg_2Ge_xSi_{1-x}$.

X-ray lattice parameter measurements.—The lattice parameter of each of the six different compositions tested was determined by use of x-ray powder diffraction techniques (15). The results of these measurements, shown in Fig. 1, indicate complete

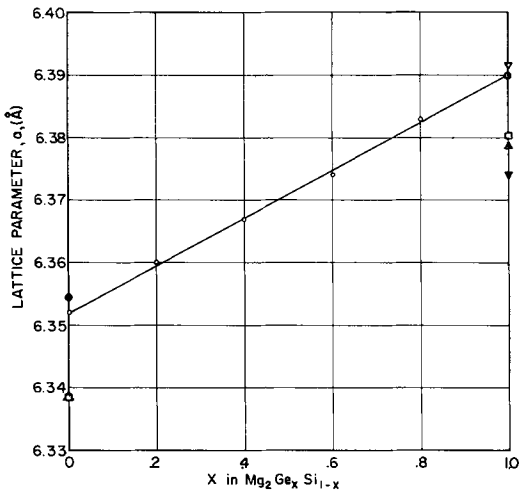

Fig. 1. Lattice parameter *vs.* composition for the system $Mg_2Ge_xSi_{(1-x)}$. Open circle, this work; solid circle, Farrel (9); open square, Klemm and Westlining (6); open triangle, Busch and Winkler (3); inverted open triangle, Owen and Preston (10); solid triangle, Zintl and Kaiser (8); inverted solid triangle, Brauer and Tiesler (7).

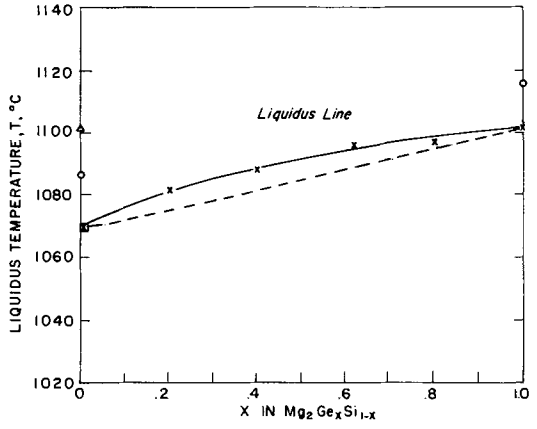

Fig. 2. Liquidus temperature *vs.* composition for the system $Mg_2Ge_xSi_{(1-x)}$. X. This work; open circle, Klemm and Westlining (6); open triangle, Vogel (11); open square, Wohler and Schiephake (12).

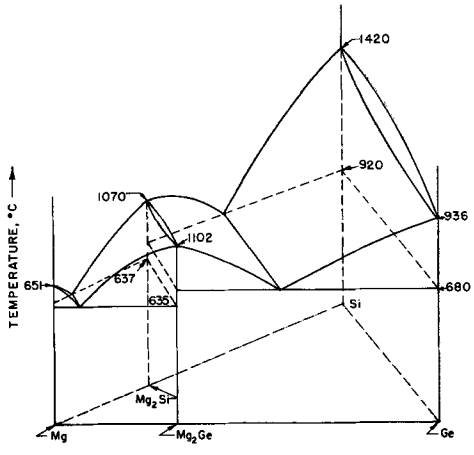

Fig. 3. Mg-Ge-Si ternary phase diagram

solid solubility between the compounds Mg_2Si and Mg_2Ge, the slight variation in results being due to experimental error.

The measured lattice parameter of the mixed crystals varies linearly with the composition, showing unusually good agreement with Vegard's law. This type of behavior can be expected in substitutional solid solutions with atoms of similar size and electronic structure (15). Similar results were obtained by Busch and Winkler (14) in their work on the pseudobinary system Mg_2Ge-Mg_2Sn.

Differential thermal analysis measurements.— Differential thermal analysis measurements were made on each of the six compositions in order to construct the pseudobinary phase diagram. The samples were held in a boron nitride crucible using an empty boron nitride crucible as a reference. The sample crucible and the reference crucible were heated inside a low carbon steel block which in turn was contained in a zirconia tube that was closed at one end. The other end of the zirconia tube was fitted with an "O" ring seal so that the tube could be evacuated and backfilled with argon in order to suppress the vaporization of magnesium as much as possible. Measurements were made under about 1½ atm. of argon. Samples were heated in a Kanthal resistance furnace which had an automatic control to provide a substantially linear heating rate of about 3°K/min. The results of these measurements and those of previous investigators are plotted in Fig. 2.

Since there was a fair amount of supercooling and a loss of magnesium vapor from the molten material, only heating curves were used for the phase diagram determination, and it was not possible to determine the solidus temperature accurately.

No transitions other than the melting phenomenon were observed in the heating curves, but the cooling curves showed a very slight transition at the magnesium-deficient eutectic temperature whenever magnesium had been lost at elevated temperatures.

These results also indicate that Mg_2Ge and Mg_2Si form an isomorphous system. A complete Mg-Ge-Si ternary phase diagram is given in Fig. 3.

Electrical measurements.—Electrical resistivity and Hall effect measurements are carried out using conventional direct current techniques (16). The direct current supplied by a Lambda Model 65M power supply was filtered to reduce ripple by use of an 8.5 h choke and a 40 μf capacitor. Resistors in series with the sample were used to obtain the desired current level. Switches were available for reversing the polarity of the current, the Hall probes, and the electrical resistivity probes. The potential readings were taken with a L&N K-2 potentiometer.

The magnetic field used in the Hall effect measurements was obtained by use of a 2100 gauss permanent magnet. This magnet had a pole face diameter of 2½ in. and a 2¾ in. gap. To facilitate reversing the magnetic field the magnet was mounted on a large roller bearing, and the magnet could be rotated exactly 180° without moving the sample.

Electrical contacts were made to the test specimens by leaf springs made from rhodium-plated beryllium copper. These leaf springs were fastened to small copper blocks which in turn are mounted

on a lavite platform. The rectangular specimen was held in place by pressure contacts which also served as current leads. The sample holder was patterned after the design published by Brooker, Clay, and Young (17). The sample holder is mounted with stainless steel screws. Directly over the sample holder are two molybdenum tubes containing 30 gauge chromel-alumel thermocouples, which were used to check the temperature gradient along the sample.

A 2½ in. long copper shield is placed over the sample holder while a solid copper rod with a heater mounted on it is connected to the lower end of this shield. The heater is made on a threaded piece of lavite which is wrapped with 28 gauge chromel heating wire. The large mass of solid copper rod is used to damp out temperature fluctuations.

Connected to the top end of the copper shield is a ½ in. copper tube with a copper spacer and a lavite heater similar to the lower heater. A lavite spacer prevents thermal conduction up the copper tube. A Vycor tube encloses the sample and supporting apparatus and is wrapped with Pyrex wool to reduce heat losses. The open end of the Vycor tube is sealed by means of "O" ring seals to a mounting coupling. The ½ in. copper tube passes through this coupling by means of seals which allow the vertical positioning of the sample directly between the poles of the magnet. An outlet from the coupling leads to a pressure gauge, a vacuum system, and the hydrogen supply. The samples were measured under a hydrogen atmosphere. Oxygen and water vapor are removed from the hydrogen by passing it through a "Deoxo" catalyst and then through molecular sieves.

The thermal conductivities and Seebeck coefficients were measured with the apparatus described in the preceding paper (13).

The results of electrical resistivity measurements on the six different compositions are plotted in Fig. 4. The onset of intrinsic behavior follows no consistent pattern since the impurity concentration was an uncontrolled variable in the investigation.

The measurements of the Seebeck coefficient are presented in Fig. 5. The Hall coefficient data were sufficiently extensive in the intrinsic region of only $Mg_2Ge_{0.4}Si_{0.6}$ and Mg_2Ge to permit an evaluation of the energy gap. Plots of log $|R_HT^{3/2}|$ against reciprocal absolute temperature are shown in Fig. 6, and the derived energy gaps are also tabulated in Table

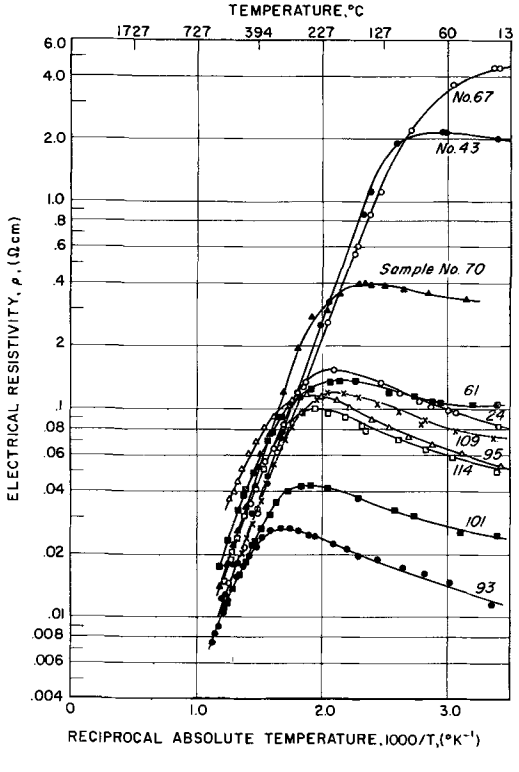

Fig. 4. Logarithm of electrical resistivity vs. reciprocal absolute temperature.

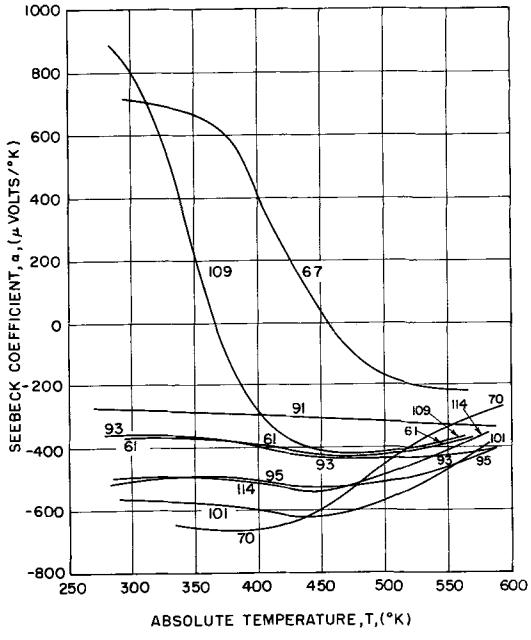

Fig. 5. Seebeck coefficient vs. absolute temperature

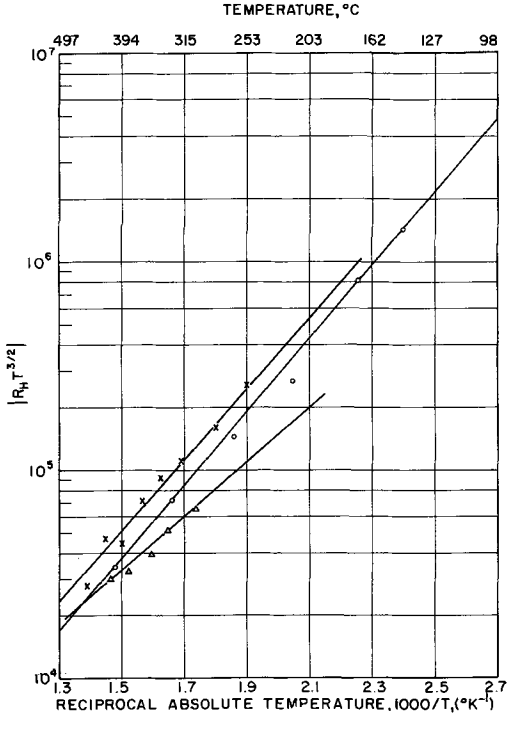

Fig. 6. Logarithm of $|R_HT^{3/2}|$ vs. reciprocal absolute temperature

Table I. Summary of results obtained from measurements on the system $Mg_2Ge_xSi_{1-x}$

	E_{g_o}, ev ρ vs. $1/T$	E_{g_o}, ev $\lvert R_H T^{3/2}\rvert$	Extrinsic mobility $\mu_H = \mu_o T^\gamma$ cm²/v sec	Intrinsic mobility $\lvert R_H/\rho\rvert = \lvert R_H/\rho\rvert_o T^\gamma$ cm²/v sec	$\lambda_{300°K}$, w/cm °K	Sat'n impurity conc'n $\lvert N_D - N_A\rvert$, carriers/cm³	Z_{max}, °K⁻¹	m_n*	Resistivity, $\rho_{300°K}$, ohm-cm	Seebeck Coef. $\alpha_{300°K}$, μv/°K
Mg_2Si										
No. 95	[~0.72]		[160](T/300)$^{-1.7}$	[420](T/300)$^{-3.1}$		9×10^{17}	3.3×10^{-4}	$1.0m_o$	0.06(n)	−505
No. 24	[~0.65*]		350*			2.6×10^{17}			0.09(n)*	
No. 91					0.0792					−275
$Mg_2Ge_{0.2}Si_{0.8}$										
No. 93	0.79		310(T/300)$^{-1.5}$			2×10^{18}	6.7×10^{-4}	$0.51m_o$	0.0114(n)	−370
No. 115					0.0355					
$Mg_2Ge_{0.4}Si_{0.6}$										
No. 70	0.75	0.74	[187](T/300)$^{[-1.0]}$	[350](T/300)$^{-2.4}$		1.4×10^{17}	[2.6×10^{-3}]	[$0.15m_o$]	0.035(n)	−650
No. 101	[0.72]	[0.58]	273(T/300)$^{-1.4}$	640(T/300)$^{-2.6}$	0.0289	1.3×10^{18}		$0.58m_o$	0.026(n)	−570
$Mg_2Ge_{0.6}Si_{0.4}$										
No. 61	[0.70]		[70]	[160](T/300)$^{[-2.1]}$		1×10^{18}	9.4×10^{-4}		0.11(n)	−375
No. 114	0.75		280(T/300)$^{-1.6}$	530(T/300)$^{-2.5}$	0.0289	5.8×10^{17}		$0.85m_o$	0.051(n)	−500
$Mg_2Ge_{0.8}Si_{0.2}$										
No. 109	0.71*	0.72*	310*(300/T)$^{-1.4*}$	620*(T/300)$^{-2.7*}$	0.0405*	3.5×10^{17}			0.07(n)	+800(p)*
No. 108			342*			2.9×10^{17}				
Mg_2Ge	Sample going from p to n over range of Hall measurements.									
No. 43	0.70					1.3×10^{17}			2.0(p)	
No. 67	[0.71]	0.70	[175](T/300)$^{[-1.2]}$	[360](T/300)$^{-2.4}$	0.0628	9.5×10^{15}			4.0(n)	+710(p)
Average			300(T/300)$^{-1.5}$	600(T/300)$^{-2.5}$						

* Single crystal data.
Values in brackets are doubtful.

I. The saturation impurity carrier concentration in the extrinsic region as determined from the Hall effect measurements (16) is also tabulated in Table I for each sample that was measured. The impurity concentration varied erratically from 10^{16} to 10^{18} carriers/cm³.

The Hall mobility factor, R_H/ρ, is plotted against absolute temperature on logarithmic coordinates in Fig 7. The extrinsic Hall mobility at 300°K is given as a function of composition in Table I. The amount of variation from one composition to the next is no greater than the variation observed from one sample to another of the same composition. The maximum mobilities observed for the mixed crystals of $Mg_2Ge_{0.2}Si_{0.8}$, $Mg_2Ge_{0.4}Si_{0.6}$, and $Mg_2Ge_{0.6}Si_{0.4}$ are lower than those observed in Mg_2Si and $Mg_2Ge_{0.8}Si_{0.2}$. It appears as though this reduction in the maximum observed mobility is not due to the formation of mixed crystals because relatively high mobilities were observed for the mixed crystal samples of $Mg_2Ge_{0.8}Si_{0.2}$. A more satisfactory explanation is that the mobility difference is associated with the form of the material being measured. The higher mobilities for Mg_2Si and $Mg_2Ge_{0.8}Si_{0.2}$ were measured in single crystals, whereas the slightly lower maximum mobilities measured in the other mixed crystals were measured in polycrystalline specimens. If all mobility measurements had been made on single crystals it is quite likely that no decrease in the maximum mobility would have been observed, and that the average mobility would be slightly greater than 300 cm²/volt sec at 300°K. The average temperature dependence of the mobility (−3/2 power) indicates that lattice scattering is the predominant scattering mechanism.

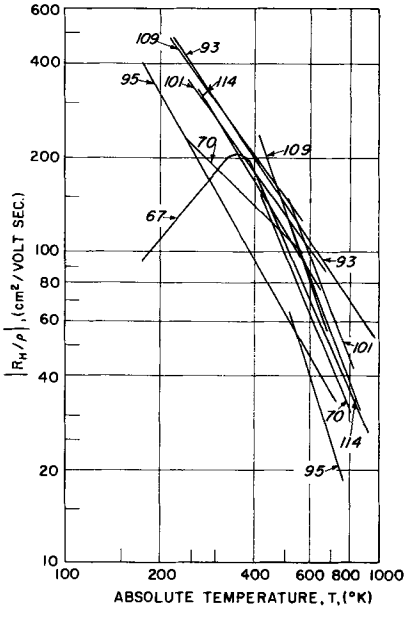

Fig. 7. Logarithm of $|R_H/\rho|$ vs. logarithm of absolute temperature

The high mobilities reported by Winkler (3) for polycrystalline Mg_2Si (370 cm²/volt sec) and Mg_2Ge (530 cm²/volt sec) were obtained by extrapolating high-temperature data to obtain a room temperature value, and are actually intrinsic mobility values extrapolated to room temperature rather than measured extrinsic mobilities.

When a similar extrapolation is applied to the data obtained in this investigation, room temperature mobilities which are two to three times higher than those actually measured are obtained, and the results of this extrapolation are also tabulated in Table I. The average temperature dependence of the intrinsic Hall mobility (−5/2 power) indicates that hole-electron scattering is apparently the predominant scattering mechanism.

Once the temperature dependence of the mobility is known (−γ), a plot of log ($\rho T^{3/2-\gamma}$) against reciprocal absolute temperature can be made. The straight line in the intrinsic conductivity region then has a slope of $E_{g_o}/4.6k$, and the energy gaps for these materials were determined in this way. The value of energy gap from this investigation for Mg_2Si is not very precise, and Morris' value of

0.78 ev[4] is undoubtedly more correct. From Table I then it can be noticed that the energy gap decreases from a value of about 0.78 ev for Mg_2Si to about 0.70 ev for Mg_2Ge. On the basis of this data it is difficult to state whether the energy gap varies linearly with composition or not. Busch and Winkler (14) in their work on the Mg_2Ge-Mg_2Sn solid solution found a nonlinear variation of energy gap with composition. However, it should be pointed out that the energy gap in the Mg_2Ge-Mg_2Sn system changes from 0.70 ev for Mg_2Ge to 0.36 ev for Mg_2Sn, which is considerably greater than that experienced in going from Mg_2Si to Mg_2Ge.

The Seebeck coefficient data show the temperature at which intrinsic behavior commences in each sample (18). Also in conjunction with the saturation impurity concentration, the Seebeck coefficient can be used to determine the effective mass of the electrons. The results are also tabulated in Table I.

Thermal Conductivity

The thermal conductivity of a semiconductor at moderate temperatures is generally considered to be the sum of the lattice and charge carrier components. For nondegenerate materials these components are essentially independent of each other.

The charge carrier component is made up of contributions from various mechanisms such as the normal thermal diffusion of charge carriers as described by the Wiedeman-Franz relationship, ambipolar diffusion, and diffusion of excitons. The methods of calculating these contributions from measured electrical and thermal conductivity data are given in the literature (19).

The lattice thermal conductivity is the result of energy transport by phonons. The magnitude of the lattice thermal conductivity is a function of the amount of phonon scattering which takes place within the lattice. The nature of the scattering which exists in the lattice can be determined to a large extent by an examination of the temperature dependence of the lattice thermal conductivity, as various scattering mechanisms have different temperature dependencies (20).

The substitutional solid solutions examined in this investigation would be expected to have a strong point defect scattering due to the large mass difference between the silicon and germanium. As pointed out by Klemens (21)

$$\lambda \propto T^{-1/2}\epsilon^{-1/2}$$

for temperatures above the Debye temperature. The term ϵ accounts for the concentration of point defects and is given by

$$\epsilon = \sum_j C_j(M_j - M)^2/M^2 \qquad [1]$$

$$M = \sum_j C_j M_j \qquad [2]$$

where C_j and M_j are the concentration and mass of atoms of type j. This is in contrast to the

$$\lambda \propto T^{-1} \qquad [3]$$

which would be expected for the pure compounds.

Thermal conductivity of $Mg_2Ge_{0.2}Si_{0.8}$.—The thermal conductivity of $Mg_2Ge_{0.2}Si_{0.8}$ was measured on sample No. 115. However, due to a lack of reproducibility in the electrical measurements made on this sample there is some question as to the quality of the ingot. For this reason the results are presented in Fig. 8 without comment simply for the sake of completeness.

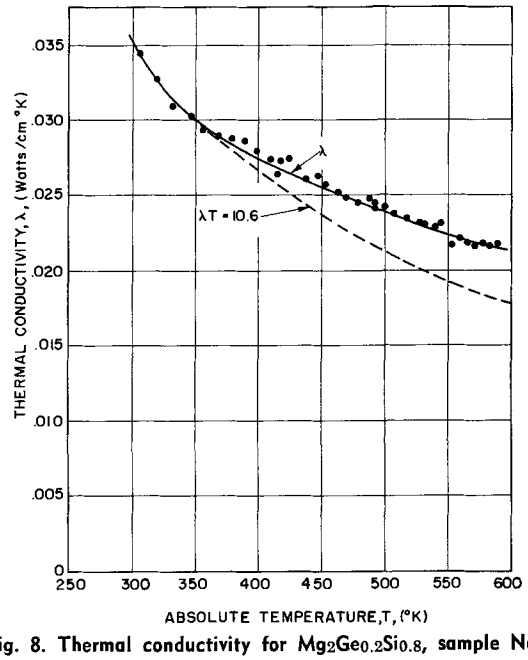

Fig. 8. Thermal conductivity for $Mg_2Ge_{0.2}Si_{0.8}$, sample No. 115, vs. absolute temperature.

Thermal conductivity of $Mg_2Ge_{0.4}Si_{0.6}$—The thermal conductivity of $Mg_2Ge_{0.4}Si_{0.6}$ was measured on sample No. 101. This sample was large grained and contained no visible eutectic. It was 1.67 cm long and had a cross-sectional area of 2.30 cm^2.

In Fig. 9 the experimentally determined values of thermal conductivity and the calculated values of the electron component are given as functions of temperature. The quantity $(\lambda_{th} - \lambda_{el})$ is not plotted as this value is very close to λ_{th}.

By matching curves at 300°K the relationship $\lambda_{lattice} = 0.512T^{-1/2}$ watts/cm °K was determined. The experimental values follow this relationship

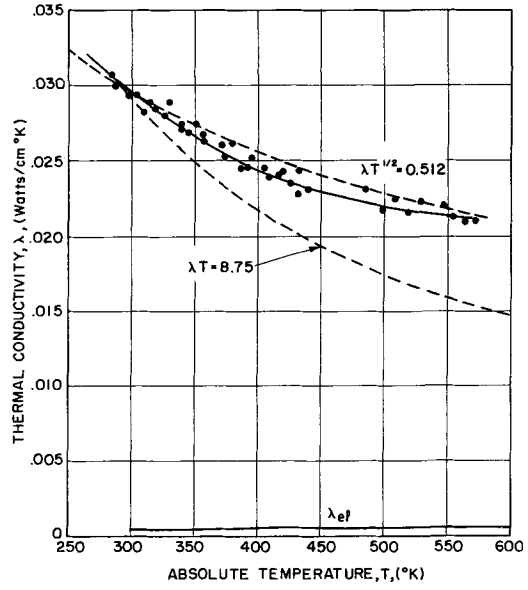

Fig. 9. Thermal conductivity for $Mg_2Ge_{0.4}Si_{0.6}$, sample No. 101, vs. absolute temperature.

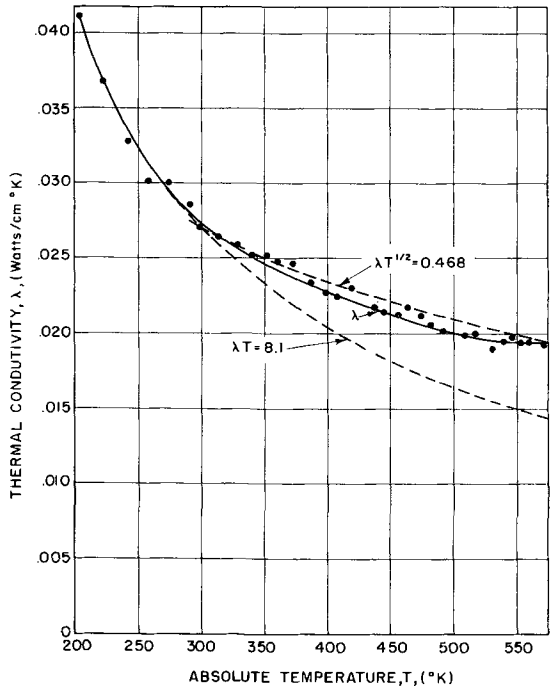

Fig. 10. Thermal conductivity for $Mg_2Ge_{0.6}Si_{0.4}$, sample No. 114, vs. absolute temperature.

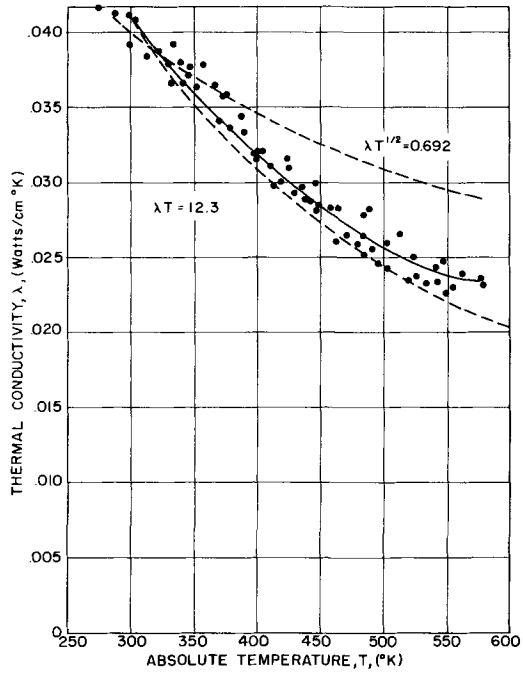

Fig. 11. Thermal conductivity for $Mg_2Ge_{0.8}Si_{0.2}$, sample No. 109, vs. absolute temperature.

rather well, indicating that point defect scattering predominates.

Thermal conductivity of $Mg_2Ge_{0.6}Si_{0.4}$.—The thermal conductivity of $Mg_2Ge_{0.6}Si_{0.4}$ was measured on sample No. 114. This sample was large grained and free of eutectic, had a cross-sectional area of 1.65 cm^2, and was 1.37 cm long.

A plot of the experimental values of thermal conductivity as a function of temperature for this sample is given in Fig. 10. The electron component of thermal conductivity for this sample is negligible. Thus lattice thermal conductivity is essentially equal to the measured values.

Due to a rather unusual set of experimental circumstances it was possible to make thermal conductivity measurements from 200°K. The results are rather interesting.

From 200°K to 300°K the lattice thermal conductivity is proportional to T^{-1}, while above 300°K the lattice thermal conductivity is proportional to $T^{-1/2}$. Thus above about 300°K $\lambda = 0.468T^{-1/2}$ watts/cm °K, while from 200°K to 300°K $\lambda = 8.10T$ watts/cm °K. Although the behavior above 300°K is explainable in terms of the mass difference point defect scattering, the reason for the sharp transition at 300°K is not apparent.

Thermal conductivity of $Mg_2Ge_{0.8}Si_{0.2}$.—The thermal conductivity of $Mg_2Ge_{0.8}Si_{0.2}$ was measured on sample No. 109. This sample appeared to be a single crystal. As all the better ingots of this composition were composed of a number of relatively large single crystals which were very weakly bound together, it was decided to use the largest crystal available for making the thermal conductivity specimen. For this reason, this specimen was the smallest one which was tested in the whole sequence. It had a cross-sectional area of 0.87 cm^2. The small cross section resulted in very low heating rates being used in the thermal conductivity measurements. These low heating rates made heating rate determinations difficult, producing a large amount of scatter in the final results.

The experimentally determined thermal conductivity is given as a function of temperature in Fig. 11. Due to the fact this was a single crystal its thermal conductivity would not necessarily correlate very well with that of the other samples, as its properties were nonisotropic.

The exact temperature dependence of the thermal conductivity is difficult to determine due to the scatter of the experimental data. However, it does lie between the $T^{-1/2}$ and T^{-1} temperature dependence lines. This suggests that possibly the thermal resistance could be a combination of point defect and normal Umklapp scattering.

Variation of lattice thermal conductivity with composition.—The variation of lattice thermal conductivity with composition and temperature is shown in Fig. 12. As just pointed out the values for $Mg_2Ge_{0.8}Si_{0.2}$ do not correlate very well with the other samples due to its nonisotropic nature.

The temperature-composition variation is not in good agreement with the expression given by Klemens. According to this expression the ratio of the conductivity from one composition to the next should be the same at any given temperature. However, this is not the case with the experimental data. As can be seen from Fig. 12 the differences in thermal conductivity from one composition to the next become significantly smaller as the temperature is raised. This would seem to indicate some sort of saturation effect in the phonon scattering at elevated temperatures as has been suggested by Ioffe (22).

Thermoelectric Figure of Merit

The final property which will be considered is the maximum thermoelectric figure of merit, Z_{max}, by the correlations presented by Simon (23). This

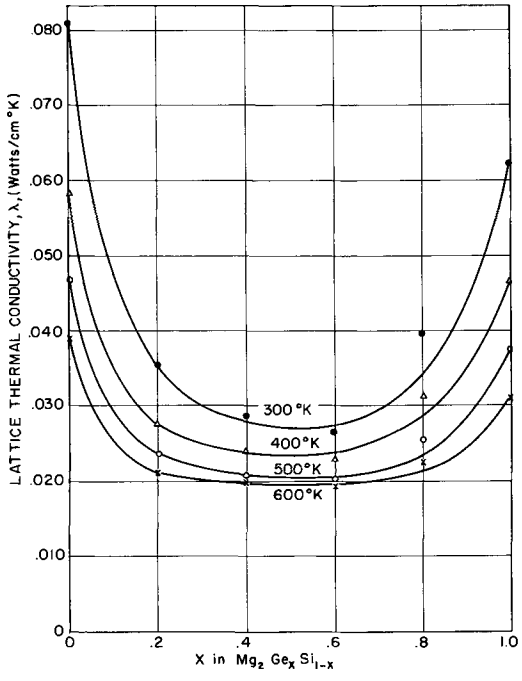

Fig. 12. Lattice thermal conductivity as a function of composition and temperature in the system $Mg_2Ge_xSi_{(1-x)}$.

quantity is also given in Table I for the four materials for which sufficient correlatable data are available. The variation in the maximum thermoelectric figure of merit should be proportional to the variation in the ratio μ_n/λ_{ph}. In going from Mg_2Si to $Mg_2Ge_{0.4}Si_{0.6}$ and $Mg_2Ge_{0.6}Si_{0.4}$ the ratio μ_n/λ_{ph} increases by a factor of about 2.4. Due to the nearly identical lattice thermal conductivity and electron mobility for $Mg_2Ge_{0.4}Si_{0.6}$, sample No. 101, and for $Mg_2Ge_{0.6}Si_{0.4}$, sample No. 114, it would be expected that these two samples would have almost identical values of Z_{max}. However, the optimized thermoelectric figure of merit increases by a factor of about 8.0 in going from Mg_2Si to $Mg_2Ge_{0.4}Si_{0.6}$ while it increases by a factor of 2.8 in going from Mg_2Si to $Mg_2Ge_{0.6}Si_{0.4}$. This indicates the value of Z_{max} for $Mg_2Ge_{0.6}Si_{0.4}$ is probably correct while that for $Mg_2Ge_{0.4}Si_{0.6}$ is probably too large by a factor of about 3.

As the value of Z_{max} is calculated on the basis of the extrinsic properties of the material, a difference in impurity carrier concentration between the specimens used to measure electrical resistivity and thermal conductivity could give rise to this discrepancy. In this case the electrical specimen should have a higher impurity level than the thermal conductivity specimen. It should be noted that such a difference in impurity levels would not have any effect on the intrinsic properties of the material.

Since the value of Z_{max} for the mixed crystals is considerably higher than that for Mg_2Si, the mixed crystals would be much better as thermoelectric materials than the pure compound if all the materials had the optimum impurity levels. Even under these optimized conditions, however, the mixed crystals would have a thermoelectric figure of merit somewhat lower than that of materials now in use.

Effects of nonstoichiometric specimens.—Since six of the samples on which measurements were made were either slightly nonstoichiometric or were taken from ingots which were nonstoichiometric as determined by microscopic examination, the effects of nonstoichiometry should be examined. Three of these samples were slightly silicon-rich, while the other three may have contained a trace of excess magnesium.

Morris (4) and Redin (2) in their work at Iowa State University found that an excess of silicon or an excess of germanium in an ingot does not affect the electrical properties of the Mg_2Si or the Mg_2Ge taken from the ingot. Morris in his work on single crystals of Mg_2Si took his single crystals from ingots containing large amounts of excess silicon. Redin obtained his single crystals of Mg_2Ge from ingots containing up to 66% of the germanium-rich eutectic. The low impurity carrier concentrations found in these investigations seem to indicate that neither the excess silicon nor the excess germanium enter the lattice as donors or acceptors. The data of Morris and Redin say nothing about the solubility of magnesium in either Mg_2Si or Mg_2Ge.

The electrical properties of polycrystalline samples of both stoichiometric and nonstoichiometric Mg_2Si and Mg_2Ge have been measured by Winkler (3). His measurements were made on Mg_2Si, Mg_2Ge, Mg_2Si + 2% Si, Mg_2Si + 2% Mg, Mg_2Ge + 1%Ge, and Mg_2Ge + 0.5% Mg. Due to the extremely low limits of solubility found by Morris and Redin it must be concluded that the excess silicon and germanium in Winkler's samples showed up as eutectic inclusions in the grain boundaries.

Winkler's silicon-rich sample of Mg_2Si has an impurity carrier concentration only 15% higher than that of the pure Mg_2Si in the extrinsic region, while the Hall mobilities of the pure and the silicon-rich Mg_2Si are essentially identical. Although the silicon-rich specimen has a lower extrinsic resistivity due to its higher carrier concentration, it has identical properties with the pure material in the intrinsic region.

The magnesium-rich sample of Mg_2Si has an impurity carrier concentration approximately 40% higher than that of the pure sample. This indicates the solubility of magnesium in Mg_2Si is very slight, and that the excess magnesium probably shows up as eutectic inclusions in the grain boundaries. In the extrinsic region the mobility of magnesium-rich material is about 30% higher than that of the pure materials. Again in the intrinsic region the pure and impure material approach the same behavior.

The magnesium-rich sample of Mg_2Ge does not follow completely the trend set by the corresponding Mg_2Si sample. Although the impurity carrier concentration in the extrinsic region is about 25% higher than that of the pure Mg_2Ge, the electron Hall mobility is 10% lower than that of the pure material. The two samples again behave similarly in the intrinsic region.

Winkler found that the germanium-rich Mg_2Ge had an impurity carrier concentration which was

twice as high as that of the pure Mg_2Ge while the charge carrier mobility was 10% higher than that of the pure Mg_2Ge. None of the samples tested in this investigation had an excess of germanium.

Winkler made Seebeck coefficient measurements on only two samples of Mg_2Si the pure material and the silicon-rich sample. The impure sample had a value 5-10% lower than the pure material. This is better agreement than Winkler found between his pure samples of Mg_2Ge.

A few conclusions can be drawn from Winkler's data for samples containing eutectic inclusions. The presence of small eutectic inclusions of either silicon or magnesium does not affect the electrical properties in the intrinsic region. In the extrinsic region the excess magnesium and the excess silicon seem to cause a slight increase in the impurity carrier concentration. However, as the impurity carrier concentrations normally vary by an order of magnitude from one stoichiometric melt to another this change does not seem particularly significant. The excess silicon did not seem to have any effect on the charge carrier mobility, while the excess magnesium increased the mobility a slight amount in one case and decreased it a slight amount in another. In view of this it is possible that very small magnesium-rich eutectic inclusions do not materially affect the mobility and that the changes in mobility which were observed represent normal variations from one sample to the next.

The results of this investigation are in fairly good agreement with those of Winkler for the effects of nonstoichiometry. An excess of silicon did not seem to have any effect on the saturation impurity carrier concentration, although it did appear to produce a reduction in charge carrier mobility. The excess magnesium appeared to raise the saturation impurity carrier concentration to about 10^{18} electrons/cm^3, indicating a solubility of magnesium in the lattice of about 1 part per 100,000. The excess magnesium had no noticeable effect on the charge carrier mobility. The intrinsic properties of the material were not affected by the presence of either the excess silicon or the excess magnesium.

The thermal conductivity specimens measured in this investigation were either of stoichiometric composition or contained only a trace (0.01%) of excess magnesium. An analysis of the thermal conductivity data did not indicate any contribution to the thermal conductivity which could be attributed to the trace of magnesium.

Acknowledgments

The authors wish to express their appreciation to General Motors Corporation for fellowship grants received during the doctoral work, to the Dow Metals Company for donating high-purity magnesium, to the Allegheny Electronic Chemicals Company for donating a large quantity of high-purity silicon, to the Michigan Institute of Science and Technology for their partial support of this study, and to both the Department of Mechanical Engineering and the Department of Chemical and Metallurgical Engineering at the University of Michigan for their financial support.

A special word of appreciation is also due Mr. Gerald Schmitt for his assistance with the x-ray studies.

Manuscript received Jan. 23, 1962; revised manuscript received Sept. 24, 1962. This paper was prepared for delivery before the Detroit Meeting, Oct. 1-5, 1961. Contribution No. 8 from the Semiconductor Materials Research Laboratory, College of Engineering, University of Michigan, Ann Arbor, Michigan. This work was done in partial fulfillment of the requirements for the Ph.D. degree at The University of Michigan by R. J. LaBotz.

Any discussion of this paper will appear in a Discussion Section to be published in the December 1963 JOURNAL.

REFERENCES

1. C. R. Whitsett, "Electrical Properties of Magnesium Germanide and Magnesium Silicide," Ph.D. Thesis, Iowa State College, Ames, Iowa, as quoted by Morris (4) and Redin (2) (1955).
2. a. R. D. Redin, "Semiconducting Properties of Mg_2Ge Single Crystals," Ph.D. Thesis, Iowa State University, University Microfilms, Inc., Ann Arbor, Mich. (1957).
   b. R. D. Redin, R. G. Morris, and G. C. Danielson, *Phys. Rev.*, **109**, 1916 (1958).
3. a. G. Busch and U. Winkler, *Physica*, **20**, 1067 (1954).
   b. U. Winkler, *Helv. Phys. Acta*, **28**, 633 (1955).
4. a. R. G. Morris, "Semiconducting Properties of Mg_2Si Single Crystals," Ph.D. Thesis, Iowa State University, University Microfilms, Inc., Ann Arbor, Mich. (1957).
   b. R. G. Morris, R. D. Redin, and G. C. Danielson, *Phys. Rev.*, **109**, 1909 (1958).
5. R. T. Ellickson and J. T. Nelson, "Semiconducting Properties of Intermetallic Compounds," Fifth Quarterly Progress Report, Department of Physics, University of Oregon, Eugene, Ore. as quoted by Morris (4).
6. W. Klemm and H. Westlining, *Z. anorg. Chem.*, **245**, 364 (1941).
7. V. G. Brauer and J. Tiesler, *Z. anorg. Chem.*, **262**, 319 (1950).
8. E. Zintl and H. Kaiser, *ibid.*, **211**, 125 (1933).
9. P. Farrel, "Lattice Parameter of Mg_2Si and Mg_2Ge," as quoted by Redin (2) and Morris (4).
10. E. A. Owen and G. D. Preston, *Proc. Phys. Soc.*, **36**, 341 (1924).
11. R. Vogel, *Z. anorg. Chem.*, **61**, 46 (1909).
12. L. Wohler and O. Schliephake, *ibid.*, **151**, 11 (1926).
13. R. J. LaBotz and D. R. Mason, *This Journal*, **110**, 121 (1963).
14. G. Busch and U. Winkler, *Helv. Phys. Acta*, **26**, 578 (1953).
15. C. Barrett, "The Structure of Metals," McGraw-Hill Book Co., New York (1952).
16. O. Lindberg, *Proc. I.R.E.*, **40**, 1414 (1952).
17. A. Brooker, R. Clay, and A. Young, *J. Sci. Inst.*, **34**, 512 (1957).
18. A. F. Ioffe, "Semiconductor Thermoelements and Thermoelectric Cooling," Infosearch, Ltd., London (1957).
19. A. F. Ioffe, "Physics of Semiconductors," Academic Press, New York (1960).
20. P. G. Klemens, "Lattice Thermal Conductivity," *Solid State Physics*, Vol. 7, Academic Press, New York (1957).
21. P. G. Klemens, *Phys. Rev.*, **119**, 507 (1960).
22. A. V. Ioffe and A. F. Ioffe, *Izv. Akad. Nauk. SSSR Ser Fig.*, **20**, 55 (1956).
23. R. Simon, "Maximum Figure of Merit of Thermoelectric Materials," Symposium on Thermoelectric Power Conversion, Dallas, Texas (January 1961). Paper obtained from Battelle Memorial Institute, Columbus, Ohio.

Filament Temperatures from Geometry-Independent Electron Emission Functions

A. F. Reid

Division of Mineral Chemistry, Chemical Research Laboratories,

Commonwealth Scientific and Industrial Research Organization, Melbourne, Australia

ABSTRACT

By expressing the surface area of an electrically heated body in terms of its current-voltage characteristics and substituting in the Richardson equation, electron emission functions $f(i)$ having the linear form $\log f(i) = \alpha - \beta/T$ are derived which fix the temperature of the body independent of its cross-sectional area or dimensions. The functions $f(i)$ can be directly determined experimentally; α and β are logarithmic functions of resistivity, emissivity, and the electron emission constants. In the simplest case a simultaneous measurement of electron emission and heating current is sufficient to fix the temperature. The method has particular application to vapor deposited filaments, and experimental determination of the emission functions has been made for "as-deposited" zirconium and thorium. For the former a spread in temperature prediction at 1600°K of ±5° was obtained from filaments 2-18 cm in length and 0.03-0.17 cm in diameter; for similar thorium filaments the spread was ±30°. Resistivities, emissivities, and electron emission constants were measured for both metals from 1300° to 1800°K and found to be consistent with literature data and the derived functions.

The temperatures of unviewable filaments of known geometry have been estimated variously (1) by measurement of heating current I, resistance R, voltage drop E or heat dissipation W, making use of either an initial calibration or of known values of resistivity or emissivity. In cases where a filament of length L is of unknown diameter, it is in principle possible to regard the function $EI^{1/3}/L$ as being constant at a fixed temperature (1-3) for a cylindrical filament; the function can be determined experimentally for filaments of irregular surface (2). Although this function can be used to regulate the growth temperature in a vapor deposition process (2, 4) it is found to give variable temperature definition (5, 6) and to be impurity sensitive (5). In the converse case of filament vaporization (3) the function was found to decrease in value as vaporization proceeded.

In the present work four electron emission functions are derived which enable the temperature of an unseen filament of unknown diameter or dimensions to be determined from the measurement of its electron emission and, variously, heating current, voltage drop, or both. It is shown experimentally that the functions derived can be applied to "iodide" zirconium and thorium filaments, giving somewhat better temperature estimation for filaments of comparable purity than the $EI^{1/3}/L$ function, and considerably less temperature spread for filaments of differing purity. Physical and emission data determined for "as-deposited" filaments of both metals are presented, together with the experimentally determined values of the emission functions for each.

Application of the method and the choice of emission function are discussed.

Derivation of Functions

Three diameter independent functions are derived, two of these requiring only one variable, besides electron emission, to be measured. A fourth, geometry independent function is also obtained. To derive a function of electron emission and electrical characteristics which is independent of dimension, the surface area of a heated body must first be expressed in terms of its electrical characteristics. Then, for a surface of area S the saturated emission per unit area, J, is a constant at a given temperature, and where i is the total emission from the surface, is given by the Richardson-Dushman equation (7)

$$J = i/S = AT^2 \exp - (\phi/kT) \qquad [1]$$

Here A is a constant, theoretically 120 amp/cm^{2}deg^2 for a pure metal surface, ϕ the apparent work function, k the Boltzmann constant, 8.63 x 10^{-5} ev/deg, and T the absolute temperature. Substitution in Eq. [1] of the expression for area in terms of heating current or voltage drop will give the required functions. For a right circular cylinder of diameter D, resistance and resistivity are related by the expression $R = 4\rho L/\pi D^2$ and thus for the surface area we have

$$S = (4\pi\rho L^3/R)^{1/2} \qquad [2]$$

Combination of Eq. [1] and [2] gives the result that

$$(i^2R/L^3)^{1/2} = (4\pi\rho)^{1/2} AT^2 \exp - (\phi/kT) \qquad [3]$$

This function is independent of cylinder diameter and is a constant at a given temperature. Thus knowledge of filament length and measurement of the total electron emission and the resistance allow the estimation of filament temperature.

Minimum variable functions.—Consideration of the relationship between diameter and heat radiated (2) shows that the diameter of a cylindrical filament can be expressed as

$$D = 4\rho\epsilon\sigma T^4 L^2/E^2 = I^{2/3}(4\rho/\pi^2\epsilon\sigma T^4)^{1/3} \quad [4]$$

where ϵ is the total emissivity, and σ the Stefan-Boltzmann constant, 5.672 x 10^{-12} w/cm^{2}deg^4. Hence, multiplying by πL and cancelling areas we obtain

$$i/LI^{2/3} = (4\pi\rho/\epsilon\sigma T^4)^{1/3} AT^2 \exp - (\phi/kT) \quad [5]$$

and

$$iE^2/L^3 = 4\pi\rho\epsilon\sigma T^6 A \exp - (\phi/kT) \quad [6]$$

Equations [5] and [6] are diameter independent and require the measurement of only one electrical characteristic other than electron emission. Since the function of Eq. [6] contains E^2, it is the most sensitive to error in potential drop measurement and is not considered subsequently.

Geometry-independent function.—A function which is independent of the shape of the heated body, provided it has no re-entrant surfaces, is obtained from a simple consideration of the heat radiated. To a good approximation the latter, in w/cm^2 is given by

$$W/S = \epsilon\sigma T^4 \quad [7]$$

The ratio i/W, where W is the total heat radiated, will be a constant at a given temperature, with surface areas cancelling. Combining Eq. [1] and [7] we have

$$i/W = A \exp - (\phi/kT)/\epsilon\sigma T^2 \quad [8]$$

Practical Form of the Emission Functions

The Richardson plot of log J/T^2 is linear, with slope $(\phi/1.984)$ x 10^4deg^{-1}, and it will now be shown that the plots of log $f(i)$ *vs.* $1/T$, where $f(i)$ represents the functions $(i^2R/L^3)^{1/2}$, $i/LI^{2/3}$, and i/W, are linear, with negligible error, as is the plot of log i *vs.* $1/T$. Extracting log J/T^2 from the logarithmic forms of Eq. [3], [5], and [8] and separating the remaining temperature dependent terms, it can be seen that these latter have at most the values 2 log T, 1/2 log ρ and log ϵ. It can readily be deduced that, if between T_1 and T_2 the plot of log T *vs.* $1/T$ is assumed linear, the error in the value of log T obtained at the mid-range is log $[(T_1+T_2)/2(T_1T_2)^{1/2}]$. For the range 1500°-2000°K this error is 0.0045 log units, and to combine a 2 log T *vs.* $1/T$ plot with a Richardson plot, with ϕ = 4 ev, leads to a departure from linearity equivalent to a temperature error of less than 2°; the slope of the 2 log T *vs.* $1/T$ plot is $-2T/2.303$, and thus the change in slope is 0.0435 x 10^4deg^{-1}. At the temperatures at which thermionic electron emission is significant, the high melting point metals have resistivity *vs.* temperature plots (8) approximated by the form

$$\rho_{T_2} = \rho_{T_1}[1 + \theta\,(T_2 - T_1)], \text{ with } \theta \leq 10^{-3}\ \text{deg}^{-1}$$

Neglecting cubic and higher terms in the series expansion of log ρ_{T_2} we obtain that in the range T_1 to T_2 the slope of the plot of log ρ *vs.* $1/T$ is given by

$$d\log\rho_{T_2}/d(1/T) = -0.434\,T_2^2\,[\theta - \theta^2(T_2 - T_1)]$$

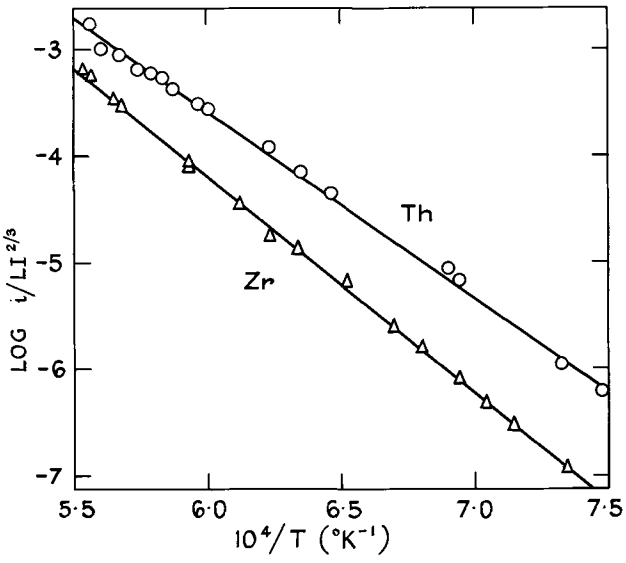

Fig. 1. Electron emission function values for zirconium and thorium filaments as a function of the reciprocal of the temperature.

Inserting $\theta = 10^{-3}$, deg^{-1}, T_1 = 1500°K, and T_2 = 2000°K, it is found that the change in slope of this plot between T_1 and T_2 is $\approx$ 0.01 x 10^4 deg^{-1}, and therefore completely negligible. A similar argument obtains for emissivity, which for most substances has a temperature coefficient of $\leq$5 x 10^{-4} deg^{-1}. Semiconductors at elevated temperatures will show intrinsic conduction, and therefore the plots of log ρ *vs.* $1/T$ will be linear (9), as required. For boron (10) for example, the plot is linear from 600° to 2000°K.

For both metals and semiconductors therefore, the plots of log $f(i)$ *vs.* $1/T$ can be expressed, as is confirmed experimentally, by the useful linear form,

$$\log f(i) = \alpha - \beta/T \quad [9]$$

The forms of α and β can be derived from the considerations given above, but values are more simply obtained by insertion in the logarithmic forms of Eq. [3], [5], and [8] of values of ρ, ϵ, ϕ, and A at two temperatures. Experimentally, plots of log $f(i)$ *vs.* $1/T$ (see Fig. 1) for a filament of a given substance are obtained by direct measurement of electron emission current and heating current (and voltage drop if required) without reference to filament diameter, resistivity, or emissivity. Values of the latter properties were, in fact, measured in the present work and were used to check the forms of the emission functions.

For iodide metal filaments the assumption of smooth cylindrical geometry is not valid (nor, of course, is it valid in the derivation of the function $EI^{1/3}/L$), but filaments of the same metal grown under comparable conditions do exhibit similar crystalline surfaces, and can be expected to have similar true to apparent surface area ratios. Calculation of area ratios is possible for a plane surface covered with random sized crystals of a given form (11), but variation in the forms observed makes the calculation approximate in practice. Values between 2 and 3 are typical for a number of the cube-octa-

Table I. Geometry factor to replace 4π in the expressions for $(i^2R/L^3)^{1/2}$, $i/LI^{2/3}$, and $EI^{1/3}/L$ for filaments with cross sections other than circular

Section	Factor	T[a]
Circle	4π	
Rectangle of sides ratio (m)	$4(m+1)^2/m$	8° ($m=2$)
Square ($m=1$)	16	5°
Hexagon	13.9	2°
Octagon	13.25	1°

[a] Temperature decrease which would result from the application of a function for circular section to filaments with other given cross-sections, assuming the filament resistance to be unaltered.

hedra forms observed (5) on thorium filaments. However it is shown in Table VII that a moderate variation in surface area ratios will not markedly affect the temperature derived from a given value of log $f(i)$.

It has been shown (2, 3) that the function $EI^{1/3}/L$ is given by

$$EI^{1/3}/L = [4\pi\rho(\epsilon\sigma T^4)^2]^{1/3} \qquad [10]$$

The factor 4π in this and the expressions for $f(i)$ can be shown to be the special solution for circular section of the general factor (perimeter)^2/(cross-sectional area) which is applicable for any cross section. In Table I are given the values of this factor for filaments of various cross sections. It can be seen that moderate departures from circular section, as sometimes occurs for iodide metal filaments (12), have relatively small effects.

Experimental

Zirconium filaments were grown by the iodide process both from unidentified hafnium-containing zirconium chips and from hafnium-free reactor grade zirconium turnings obtained from the Wah-Chang Corporation. This material had an analysis of 1250 ppm Fe, <800 ppm all other metals, 900 ppm O, 100 ppm C, 25 ppm N, and <100 ppm Hf. On the basis of the transfer coefficients given by Shapiro (2) and his typical analysis values, it can be concluded that iodide zirconium grown under careful conditions from this feed will contain <200 ppm Fe, <200 ppm all other metals, <200 ppm O,<10-100 ppm C, 3 ppm N, and <100 ppm Hf.

Thorium filaments were grown by the carbide-iodide process which gives thorium metal of exceptional purity (5, 13, 14). Total metal impurity has been shown to be <<100 ppm; filaments exposed to moisture and air contained <20 ppm O, <20 ppm C, 3-7 ppm N, and 1 ppm H. For filaments *in situ* the nonmetal contents will be still lower.

Filaments were grown in 5 cm diameter Pyrex bulbs, on 0.01 cm tungsten starting wire, in either straight or hairpin form. The wire was taken in a single outward turn over the thinned down tips of the 3 mm tungsten current leads and on to 1 mm tungsten leads for voltage drop measurement. A cylindrical sheet molybdenum anode containing a wide viewing slot was held in position by 2 mm tungsten rods. Before growth of a filament the bulbs and feed material were outgassed at less than 10^{-6} mm for 15-20 hr, and the starting wire heated at 1600°-1800°C until the pressure fell below 10^{-6} mm. Bulbs and zirconium *in situ* were held at 500°C and thorium carbide separately at 850°C. Metal iodides were formed *in situ* at 250°-300°C by admission of vacuum-dried iodine, and the bulbs were repumped to below 10^{-6} mm via a glass break-seal before final sealing. Filaments were grown at a fixed temperature in the range 1200°-1400°C. Immediately after growth the bulbs were cooled in 5-15 min to 250° below the growth temperature to condense out metal iodides, and measurements commenced. Stabilized filament heating current, voltage drop, and emission current were each read on instruments accurate to ±1% full scale. Temperatures were read with a calibrated optical pyrometer. For thorium the emissivity at 0.65μ was taken as 0.36[15], and for zirconium the brightness temperature plot given by Shapiro (2) for crystal bar zirconium was used. In the range 1400°-1800°K this gives corrected temperatures agreeing within ±2° of those obtained by use of the value $\epsilon_{0.65} = 0.426$ determined (8, 16) for smooth zirconium surfaces. End corrections were made by observing the filament temperature 0, 7, and 15 mm from the support leads using the optical pyrometer at a fixed distance with a calibrated viewing field, and applying a simple graphical integration to determine the corrections to the emission, heat radiated, and resistance. The emission was also corrected for the Schottky effect.

Observations were usually made over at least two temperature cycles and for a period of up to 2 hr. In a number of bulbs growth was re-started to give filaments of various diameters grown under strictly comparable conditions. Once the bulbs had cooled and the filaments were heated in the resulting vacuum, the initial resistance of thorium filaments fell by 20-30%, and that of zirconium filaments by somewhat less, but the emission functions remained constant within the limits shown in the various tables. Thorium filaments when removed showed well-formed crystal facets (5) with mirror-bright surfaces; the faceting on zirconium filaments was less pronounced, although the metal appeared equally bright.

From the emission-current-voltage-temperature observations and subsequent determination of filament lengths and weights (5), values of ρ, ϵ, ϕ, and A were obtained for a number of filaments, calculations being based on smooth cylinder geometry. Room temperature resistivities were also determined using an accurate potential drop apparatus. Resistance per unit length for the filaments *in situ* or for a selected length when removed agreed within 1%.

Results

Three hafnium-containing and three hafnium-free zirconium filaments of lengths from 2 to 18 cm and diameters 0.03 to 0.15 cm were examined in three separate bulbs. Filament behavior was practically independent of hafnium content, and the data are treated together. Table II gives the value of α and β in the electron emission function equations for the combined data for all filaments, and for a representative single filament, bulb 4, No. 1. The plot

Table II. Electron emission function equations for zirconium filaments; log $f(i) = \alpha - \beta/T$

	All data combined	
log $(i/LI^{2/3})$	=	$8.196 \pm 0.013 - (2.073 \pm 0.024)\ 10^4/T$
log $(i^2R/L^3)^{1/2}$	=	$8.648 \pm 0.013 - (2.165 \pm 0.024)\ 10^4/T$
log (i/W)	=	$6.958 \pm 0.013 - (1.834 \pm 0.022)\ 10^4/T$
	Single filament[a]	
log i	=	$10.573 \pm 0.019 - (2.124 \pm 0.030)\ 10^4/T$
log $(i/LI^{2/3})$	=	$7.946 \pm 0.018 - (2.026 \pm 0.028)\ 10^4/T$
log $(i^2R/L^3)^{1/2}$	=	$8.480 \pm 0.019 - (2.135 \pm 0.030)\ 10^4/T$
log (i/W)	=	$7.824 \pm 0.015 - (1.804 \pm 0.023)\ 10^4/T$

[a] Bulb 4, No. 1; hafnium-free zirconium.

Table III. Zirconium filaments. Temperatures required to give values of log $i/LI^{2/3}$ corresponding to those for the least mean squares line for all data combined

Filament No.	Diam, cm	Length, cm	Temp, °K		
Values of T for LMS line for all data			1800 ± 17[a]	1600 ± 8[a]	1400 ± 17[a]
Bulb 2, No. 1[b]	0.030	16	1798	1604	1410
No. 2[b]	0.085	16	1795	1600	1400
No. 3[b]	1.10	16	1791	1599	1400
Bulb 3, No. 1[c]	0.060	2	—	1599	—
Bulb 4, No. 1[c]	0.091	18	1794	1595	1392
No. 2[c]	0.169	9	1804	1602	1397

[a] 99% confidence level for the combined data.
[b] Hafnium containing.
[c] Hafnium free.

of log $i/LI^{2/3}$ *vs.* $1/T$ for this filament is shown in Fig. 1. In Table III are shown the temperatures derived from plots of log $i/LI^{2/3}$ *vs.* $1/T$ for each of the zirconium filaments at values of this function corresponding to 1400°, 1600°, and 1800°K for the best line through all data. At 1600°K the observed spread of temperature values is ±5°, corresponding to 99% confidence limit for the position of the best line through all data of ±8°. For the single zirconium filament, the rms deviations given in Table II correspond, for emission and emission functions, respectively, to temperature deviations of ±8.6°, ±8.6°, ±8.7°, and ±8.0° for a single observation at 1600°K, showing that little or no additional scatter is introduced from current and voltage measurements, and that experimentally the plots of log $f(i)$ *vs.* $1/T$ show negligible departure from linearity. These values are typical of those obtained for both zirconium and thorium.

Thorium filaments of lengths from 17 to 19 cm were grown in four separate bulbs to the diameters shown in Table IV, which gives the temperatures required for each filament to produce a given value of the function log $i/LI^{2/3}$; at 1600°K a spread of plot positions of ±30° about the mean plot through all data was observed. This spread was in part attributable to observed impurity effects in bulb 2 introduced by a departure from normal preparative procedure, and resulting in changes in physical and emission properties, but also caused in part by apparently random variations in the surface morphology of thorium filaments (5). The function values obtained for bulb 3, filament No. 2, presented in Table V, represent the mean of all values within a few degrees over the temperature range.

Table IV. Thorium filaments. Temperatures required to give nominal values of log $i/LI^{2/3}$ and $EI^{1/3}/L$

Filament No.	Diam, cm	Temp, °K		
Nominal temperature		1800 ± 40[a]	1600 ± 30[a] log $i/LI^{2/3}$	1400 ± 20[a]
Bulb 2, No. 1	0.05	1799	1596	1403
Bulb 1, No. 1	0.07	1764	1577	1389
Bulb 3, No. 1	0.07_5	1775	1580	1385
Bulb 3, No. 2	0.09_6	1800	1600	1400
Bulb 2, No. 2	0.10	1843	1629	1423
Bulb 4, No. 1	0.11	1812	1609	1409
Bulb 1, No. 2	0.15_2	1781	1600	1410
Bulb 2, No. 3	0.15_3	1832	1613	1414
			$EI^{1/3}/L$[b]	
Bulb 3, No. 2	0.09_6	1800	1600	1400
Bulb 1, No. 2	0.15_2	1850	1635	1440
Bulb 2, No. 3[c]	0.15_3	1715	1525	1300

[a] Range of observed values of T required to give the nominal value of log $i/LI^{2/3}$.
[b] Values for filaments annealed to constant resistivity.
[c] $\rho_{20°C} = 27\ \mu\Omega$ cm, *cf.* 16-18 $\mu\Omega$ cm for bulbs 1, 3, and 4.

Table V. Electron emission function equations for a representative thorium filament, bulb 3, filament No. 2; $f(i) = \alpha - \beta/T$

log i	$= 9.628 \pm 0.015 - (1.852 \pm 0.023)\ 10^4/T$
log $i/LI^{2/3}$	$= 7.051 \pm 0.015 - (1.772 \pm 0.022)\ 10^4/T$
log $(i^2R/L^3)^{1/2}$	$= 7.611 \pm 0.014 - (1.880 \pm 0.021)\ 10^4/T$
log i/W	$= 5.887 \pm 0.019 - (1.546 \pm 0.026)\ 10^4/T$

Table VI. Iodide zirconium:[a] physical properties, electron emission constants and $EI^{1/3}/L$ values for "as-deposited" filaments

T°K	1400	1600	1800
ϵ_{total}	0.26_5	0.27_0	0.28_0
ρ, $\mu\Omega$ cm[b]	120	126	131
$EI^{1/3}/L$	0.37_2	0.54_6	0.78_0
	(0.47)[c]	(0.67)[c]	(0.90)[c]

$\phi = 3.91$ ev, $A = 270$ amp cm²/°K²

[a] Averaged values for hafnium-free zirconium, vacuum annealed to constant resistance.
[b] At 20°C, $\rho = 44.8\ \mu\Omega$ cm.
[c] Value of $EI^{1/3}/L$ during growth.

The physical constants obtained for zirconium filaments are given in Table VI and are in general agreement (2, 8, 17) with literature values. A reasonable value of 2.25 for the true:apparent area ratio of zirconium filaments allows the theoretical value of 120 amp/cm²deg² for A. The physical data for thorium filaments are discussed in detail elsewhere (5), for bulb 3, filament No. 2 (Table V) the values obtained at 1600°K were: $\rho = 95\ \mu\Omega$cm, $\epsilon = 0.31$, $\phi = 3.37$ ev, $A = 37$ amp/cm²deg². The same value of ϕ was obtained from an analysis of all thorium data, and is in agreement with that generally accepted, 3.39 ev (15).

Discussion

The comparisons between zirconium filaments given in Table III show that the electron emission functions provide a fairly accurate means of de-

termining the temperature of an unseen filament. A similar spread of values was found for each of the functions, and for hafnium-free zirconium the values are consistent with the physical constants given in Table VI with less than 2° differences in temperature prediction at 1600°K. From the 99% confidence limit of ±8° at 1600°K and the rms deviation for a single observation of ±8°, it appears that a group of m observations made on an unknown filament in the vicinity of 1600°K will give a temperature within ±8° $\pm(8°/\sqrt{m})$ of the true temperature. The differences between the last two filaments, which were grown in the same sealed bulb, correspond to a difference in the true:apparent surface area ratio of approximately 16%. A reverse trend with diameter is observed for bulb 2, and it does appear that the results over-all are random with respect to filament diameter.

In Table IV, the spread of log $i/LI^{2/3}$ vs. $1/T$ plots for thorium filaments shows that considerably less precise values are obtained than for zirconium; this appeared in part due to the greater variation in surface morphology (5) of thorium filaments. The data show a small trend in values from the smaller diameters to those of approximately 1 mm and above. These last show random variation with diameter, indicating that further diameter increase should not alter the range of values observed.

It is evident that the function $EI^{1/3}/L$ is much more sensitive to variation in ρ or ϵ than are the electron emission functions log $f(i)$; the effect of variation in, or measurement error on, the various quantities comprising the functions are compared in Table VII. Experimentally, also, $EI^{1/3}/L$ has a considerably different value for a growing thorium filament than for the same filament annealed in vacuum (5), and the same effect was observed for zirconium, Table VI. In Table IV it can be seen that the temperature prediction differences between the filaments grown in bulb 2, in which impurity effects were evident, and those grown in bulb 3 for example, were much greater when based on $EI^{1/3}/L$ than on log $f(i)$. Even for filaments of comparable purity, bulbs 1 and 3, the values derived from $EI^{1/3}/L$ show 2-4 times the scatter of those derived from log $f(i)$.

Residual Atmosphere in Iodide Bulbs

It was found (14) that outgassing rates for empty bulbs at room temperature were approximately 10^{-9} mm/hr. Both thorium and zirconium at filament growth temperatures will act as getters for residual gases containing oxygen, for residual hydrocarbons, and for nitrogen; thus on cooling a bulb to condense the metal halides, the residual atmosphere should be in the region of ultrahigh vacuum. However there was a residual pressure of hydrogen approaching 10^{-3} mm in a bulb after growth of a thorium filament (14). The residual hydrogen content of the thorium, calculated by extrapolation of the data of Mallet and Campbell (18) was 0.3 ppm; hydrogen, being almost completely expelled at high temperatures, will act as inert gas toward the thorium. Similar behavior is expected for zirconium, whose hydrides are similarly decomposed at elevated temperatures. For both metals Schottky plots made from 0 to 300v showed normal vacuum diode behavior once metal halide vapors were condensed out. As the bulbs cooled there was a steady rise in emission to a final value which remained constant for up to 2 hr and was unaffected by further cooling. For thorium iodide this condition was reached at temperatures below 240°C, and for zirconium iodide, below 60°C. The estimated vapor pressures at those temperatures were $\approx 10^{-9}$ mm.

Whether or not the observed electron emission is dependent on the residual atmosphere of vapors other than the iodides does not invalidate the conclusions derived above, provided that emission functions are observed and applied under similar conditions. It does appear, however, that iodide metal filaments grown and observed in vacuum can provide the clean surfaces required for work function determination and, of course, consist of high-purity metal which has never been exposed to atmosphere and on which observations can be made within 5-10 min of deposition.

Table VII. Effect on temperature definition of measurement error or variation in the quantities comprising the functions log $i/LI^{2/3}$ and $EI^{1/3}/L$

Property or quantity	Measurement error or inherent variation,[b] %	Temp. error at 1600°K log $i/LI^{2/3}$	Temp. error at 1600°K $EI^{1/3}/L$
i[a]	10	5.2	
I	2	0.8	2.6
L	1	0.5	3.7
ρ	20	3.3	32
ϵ	6	1.0	15

[a] Or true:apparent surface area ratio.
[b] Arbitrarily assigned for calculation purposes.

Applications of the Emission Function Method

It is evident that for filaments produced under similar conditions with surfaces of reasonable uniformity or reproducible structure, such as zirconium crystal bar, the electron emission functions can give a quite accurate measure of the surface temperature independent of the filament diameter. For metal reactors with both filament heating leads insulated from the vessel body, the electron emission collecting voltage can be applied simply between the filament transformer and the vessel shell. However for growth control in a vapor deposition process it would be necessary to freeze out the carrier vapor temporarily; cooling of the whole vessel could be avoided by the use of a re-entrant tube cooled by air or liquid flow to an appropriate temperature.

The temperature determined from the electron emission functions, while not able to be determined during growth proper, provides a more reliable means of temperature determination than the $EI^{1/3}/L$ function and could be used to apply periodic corrections to an operating schedule based on the latter. Although the value of $EI^{1/3}/L$ at a given temperature decreases on heating an iodide metal filament in vacuum, this effect is not marked during short periods below 1650°K, and is less evident for

zirconium than for thorium. For both metals the value of $EI^{1/3}/L$ was found to rise to approximately its former value once growth was resumed.

The method is not restricted to vapor deposition systems, but is applicable to the determination of the temperature of any electron emitting body of suitable shape held in a vessel from which the atmosphere can be removed by condensation or pumping. The material need not be a metal, but could for example be an elemental semiconductor, or a boride, carbide, or oxide. The body need not be increasing in size, but could be evaporating or undergoing reduction in section by chemical reaction. The emission-wattage function is applicable in principle to shapes other than cylindrical or prismatic and is independent of the body dimensions provided it does not have re-entrant surfaces which are not of constant form.

Choice of Emission Function

The function log $i/LI^{2/3}$ offers the greatest practical advantage in that only the emission current and the filament heating current need be measured. It is independent of any potential drop in the current leads, and does not require the use of voltage measuring leads. The function log i^2R/L^3 is independent of the actual or effective emissivity of the heated body and thus of its surroundings or the use of radiation shields, but since the other functions depend on log ϵ they are themselves insensitive to moderate changes in the value of ϵ, as shown in Table VII.

Summary

It is shown that emission functions determined by experimental measurement of the electron emission and heating current for an electrically heated body can be used to define its temperature independent of its diameter, and if potential drop is also measured, independent of its dimensions. For vapor deposited zirconium filaments the observed deviation in temperature prediction at 1600°K was ±5°, and for thorium, ±30°. Electron emission constants, resistivities, and emissivities were determined in the temperature range 1400°-1800°K for the "as-deposited" metals, and found to be closely consistent with the derived forms of the temperature prediction equations and in general agreement with literature values.

Acknowledgment

The author is greatly indebted to G. H. Bush, Royal Armament Research and Development Establishment, England, for vacuum fusion analyses.

Manuscript received July 16, 1962.

Any discussion of this paper will appear in a Discussion Section to be published in the December 1963 JOURNAL.

REFERENCES

1. H. A. Jones and I. Langmuir, *Gen Elec. Rev.*, **30**, 310 (1927).
2. Z. M. Shapiro, Chap. 4 in "The Metallurgy of Zirconium," Lustman and Kerze, Editors, McGraw-Hill Book Company Inc., New York (1955).
3. F. T. Worrell, *Phys. Rev.*, **61**, 520 (1942).
4. N. D. Veigel, E. M. Sherwood, and I. E. Campbell, *This Journal*, **102**, 687 (1955).
5. A. F. Reid, R. E. Wilmshurst, and A. W. Wylie, "High Temperature Physical Properties of Carbide-Iodide Thorium," to be published.
6. E. M. Sherwood and I. E. Campbell, Chap. 4 in "The Metallurgy of Hafnium," D. E. Thomas and E. T. Hayes, Editors, U.S.A.E.C. (1959).
7. E. B. Hensley, *J. Appl. Phys.*, **32**, 301 (1961).
8. A. Goldsmith, T. E. Waterman, and H. J. Hirschhorn, Editors, "Handbook of Thermophysical Properties of Solid Materials," Vol. 1, p. 751, MacMillan, New York (1961).
9. D. A. Wright, "Semi-Conductors," p. 37, John Wiley & Sons, Inc., New York (1958).
10. A. G. Hagenlocher, p. 129 in "Boron; Synthesis, Structure and Properties," J. A. Kohn, W. F. Nye, G. K. Gaule, Editors, Plenum Press, Inc., New York (1960).
11. L. Tonks, *Phys. Rev.*, **38**, 1030 (1931).
12. R. F. Rolsten, "Iodide Metals and Metal Iodides," p. 72, p. 383, John Wiley & Sons, Inc., New York (1961).
13. D. E. Scaife and A. W. Wylie, "Proc. 2nd Internat. Conf. on the Peaceful Uses of Atomic Energy, Geneva 1958," Vol. 4, pp. 215-36.
14. A. F. Reid, "Self-Gettering and Impurity Transfer in the Vapour Deposition of Thorium by the Carbide-Iodide Process," to be published.
15. O. N. Carlson, P. Chiotti, G. Murphy, D. Peterson, B. A. Rogers, J. F. Smith, M. Smutz, M. Voss, and H. A. Wilhelm, "Proc. Internat. Conf. on the Peaceful Uses of Atomic Energy, Geneva 1955," Vol. 9, pp. 74-106.
16. C. R. Tipton, Jr., Editor, "Reactor Handbook," Vol. I, p. 711, Interscience Publishers Inc., New York (1960).
17. A. Wahl, *Phys. Rev.*, **82**, 575 (1951).
18. M. W. Mallett and I. E. Campbell, *J. Am. Chem. Soc.*, **73**, 4851 (1951).

The Reaction of Lithium with Water Vapor

W. R. Irvine and J. A. Lund

Department of Metallurgy, The University of British Columbia, Vancouver, British Columbia, Canada

ABSTRACT

This paper describes a thermal balance and x-ray diffraction study of the reaction of lithium with water vapor. Water was carried at partial pressures of up to 12.6 mm Hg in oxygen and argon gases, and runs were conducted between 20° and 45°C. The reaction was found to proceed in three distinct successive stages: (*a*) the formation at constant rate of a lithium hydroxide (LiOH) film believed to be coherent with the underlying lithium metal lattice; (*b*) the localized nucleation and growth by spreading of lithium hydroxide monohydrate ($LiOH \cdot H_2O$) at the outer surfaces of the hydroxide; and (c) the simultaneous formation and hydration of the hydroxide at constant rate, culminating in complete conversion of the metal to the hydroxide monohydrate.

The reaction of lithium metal with water vapor has been studied previously by Deal and Svec (1) who employed a manometric technique. The reaction was observed to conform to a logarithmic rate law. However, at times exceeding approximately 2 hr, the reaction rate became erratic. This behavior coincided with the formation of a white reaction product over an initially black glossy reaction layer, and it was suggested that the white product was a recrystallized lithium hydroxide. The rate constant for the initial stage of the reaction was found to be independent of the partial pressure of water vapor in the system over a range from 22 to 55 mm Hg. At higher pressures the rate increased with increasing pressure. The energy of activation for the initial reaction was calculated at 6.2-5.5 kcal/mole depending on the vapor pressure.

The reaction of lithium with dry and moist gases has been studied by various investigators. It is reported that lithium does not react with dry oxygen below approximately 100°C, although it reacts rapidly at higher temperatures (2). In contradiction to this, Yamaguti (3) reports finding mixed crystals of hydroxide (LiOH) and oxide (Li_2O) on a lithium surface which had been exposed to laboratory air for 5 min.

Belyaev *et al.* (4) studied the reaction of lithium with moist air using a gravimetric method. For humidities greater than 80% the reaction products were reported to be lithium hydroxide and carbonate. At lower moisture levels lithium nitride was formed.

The present investigation is concerned with studies of the reaction of lithium with moist argon and oxygen, using water vapor partial pressures of up to 12.6 mm Hg, *i.e.*, lower pressures than those employed by Deal and Svec.

Materials and Procedure

Lithium in the form of 1-lb ingots was supplied by the Foote Mineral Company. Principal impurities in the as-received material were potassium (340 ppm) and sodium (70 ppm). The ingot was sectioned, and pieces were cold formed by die-pressing to obtain rectangular blocks of uniform grain size. In a glove-box, under a positive pressure of purified argon, rectangular wafers approximately 0.040 in. thick were cut from the cold-pressed blocks using fine piano wire. A cork-borer was then used to cut circular disks from the wafers. The disks which served as specimens for reaction studies had only freshly cut faces and edges exposed to reaction. To remove any dust particles which may have collected on the samples during preparation, the disks were washed in lithium-dried benzene before admitting them to the reaction vessel, which also opened into the argon-filled dry box in which the specimens were prepared.

The reaction vessel, constructed of glass, was immersed for most of its length in an immersion-heated oil bath. The temperature of the bath was controlled to within ±0.2°C using a mercury thermoregulator. A mechanical stirrer was employed to ensure uniformity of temperature. Reaction gases were preheated by passing them through a spiral copper tube immersed in the oil bath.

Specimens were placed in an aluminum basket lined with platinum gauze, which was suspended inside the reaction vessel by means of a chain attached to one arm of a chainomatic balance. Automatic weighing of the specimen assembly was provided by using two opposed photoelectric cells situated behind a vented vane mounted at the end of the balance pointer. The imbalanced voltage from the photocells was used to drive a recording potentiometer. Mechanical linkage between the recorder and the balance was provided by a pair of synchromotors, one of which was geared to the drive shaft of the recorder and the other to the chain drive of the balance. The accuracy of the balance, assessed by using calibrated weights to drive the balance up and down scale, was within ±0.3 mg.

Moisture content of the reaction gases was controlled by bubbling the carrier gas (oxygen or argon from a cylinder) through a water tower and then through bubble towers containing ice water at 0°C or saturated salt solutions at 20°C. The solutions used and the corresponding equilibrium water

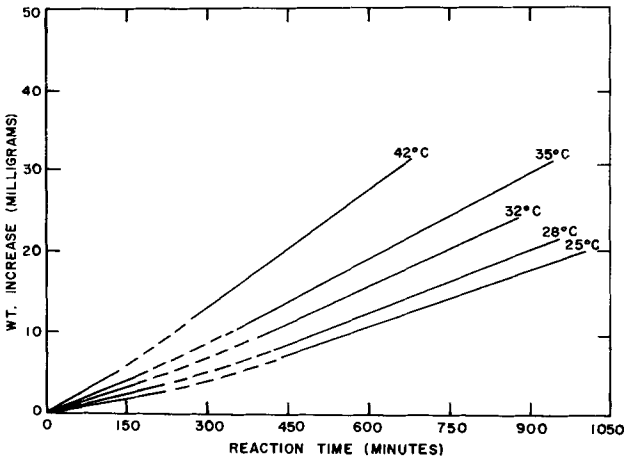

Fig. 1. Reaction curves for specimens reacted in moist oxygen at various temperatures; P_{H_2O} = 4.6 mm Hg; specimen area = 2.792 cm^2.

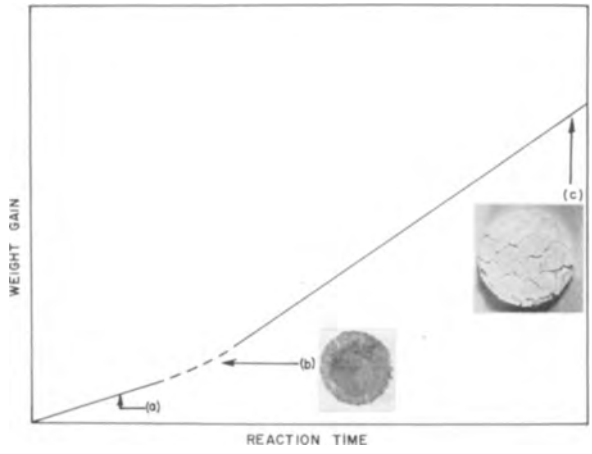

Fig. 2. Changes in surface appearance of specimens in relation to a typical reaction curve.

partial pressures were: lithium chloride solution (2.6 mm Hg), ice water (4.6 mm Hg), potassium thiocyanate solution (8.2 mm Hg), and ammonium chloride solution (12.6 mm Hg). Flow rates were controlled at 0.2 lpm with calibrated capillary flow meters.

After first admitting the reaction gas to the chamber, approximately 2 min elapsed before the first weight reading could be obtained. Except for runs which were interrupted in order to obtain photographs of specimens, the reactions were followed for approximately 24 hr.

Results

A specimen heated in dry oxygen at 40°C exhibited no increase in weight over a period of 16 hr. Moreover for the same conditions of temperature and pressure, reaction rates in moist argon and oxygen were comparable. Accordingly in the experiments with moist gases which are described below, both oxygen and argon were considered as inert carrier gases.

General characteristics of the reaction.—Some typical reaction curves obtained using moist (P_{H_2O} =4.6 mm Hg) oxygen at temperatures from 25° to 40°C are shown in Fig. 1.

It is apparent from these curves that the reaction proceeded in three distinct steps: (*a*) an initial stage, of 3-4 hr duration, in which the reaction rate was approximately constant; (*b*) an intermediate stage during which, over a period of 1-4 hr depending on the temperature, the reaction rate increased continuously; and (*c*) a third stage during which the reaction proceeded at a constant rate approximately 1½ times that of the initial stage.

Visual examination revealed a characteristic sequence of changes in the appearance of the specimens which corresponded with the observed changes in the reaction rates. Some runs were interrupted in order to obtain photographs of the samples, and these are shown in Fig. 2. During the initial stage of approximately constant rate, the specimens acquired a black glossy tarnish. At a time corresponding approximately to the commencement of the intermediate (rate increasing) stage, a white reaction product appeared. This product formed first at the edges and grew laterally across the surface. The final stage of constant rate commenced when the entire surface was covered with the white product, which then thickened uniformly over the surface as the reaction proceeded. The specimen swelled appreciably during this period as evidenced in Fig. 2.

X-ray diffraction patterns of the surface film were obtained at various stages of the reaction. For the black film characteristic of early stages of the reaction, the calculated d-spacings for the important diffraction lines compared closely with those reported for lithium hydroxide (LiOH). The white layer which was present at advanced stages gave two sets of diffraction lines corresponding to lithium hydroxide (LiOH) and lithium hydroxide monohydrate ($LiOH \cdot H_2O$). A sample reacted to completion at 35°C (P_{H_2O} = 8.2 mm Hg) was found to consist entirely of the hydroxide monohydrate.

Effect of temperature.—Lithium specimens were reacted with moist oxygen at temperatures from 22° to 42°C with the results summarized in Table I.

Graphs (Fig. 3) of the logarithm of the rate constant against the reciprocal of the absolute reaction temperature gave straight lines in accordance with an Arrhenius relationship. The apparent activation energies were 11,700 ± 2,500 and 7,700 ±

Table I. Summary of data for reaction in moist (4.6 mm H_2O) oxygen

Temp, °C	Linear reaction-rate constants (k_1 (mg/cm^2-min))	(k_2 (mg/cm^2-min))	k_2/k_1
22	0.00417	0.00716	1.7
22	0.00391	0.00738	1.9
25	0.00461	0.00837	1.8
28	0.00573	0.00955	1.7
30	0.00674	0.0118	1.8
30	*	0.0107	—
32	0.00836	0.0114	1.4
35	0.0107	0.0126	1.2
35	0.0104	0.0131	1.3
40	0.0122	0.0158	1.3
42	*	*	—

* Nonlinear reactions.

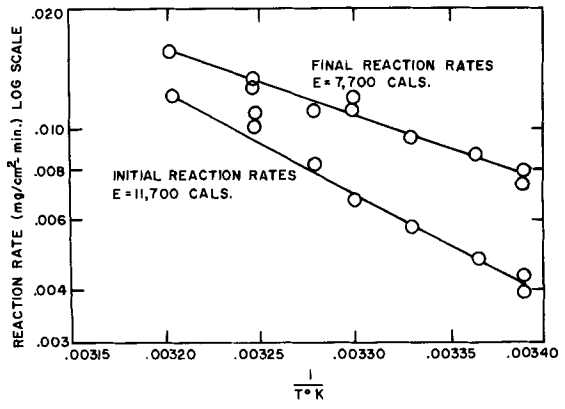

Fig. 3. Arrhenius plots for reaction rate constants; runs carried out in moist oxygen; P_{H_2O} = 4.6 mm Hg.

1,800 cal for the initial and final stages of reaction, respectively.

Effect of the partial pressure of water vapor.—Samples were reacted at 35°C in argon gas saturated to give moisture levels of 2.6, 4.6, 8.2, and 12.6 mm Hg. All reactions displayed the three characteristic stages described previously. Rate constants were determined, and a graph illustrating the dependence of these rates on the partial pressure of water is presented as Fig. 4.

In a previous investigation (1) it was reported that the rate constant for the reaction (the initial rate constant only was determined) was pressure-independent from 22 to 55 mm Hg. The rates increased with pressure above 55 mm Hg, but a lower limit to the pressure-independent range was not established.

In the present work, the rate constants for both the initial and the final stages of oxidation were found to increase rapidly with pressure in the range 2.6-4.6 mm Hg. With further increases in pressure the rate constants continued to increase, but rather slowly.

In another run, a specimen was reacted in moist (4.6 mm Hg) oxygen at 35°C until the white product characteristic of an advanced reaction had formed. A shift was then made to dry oxygen. The rate dropped to zero indicating that lithium oxide would not form even under these conditions.

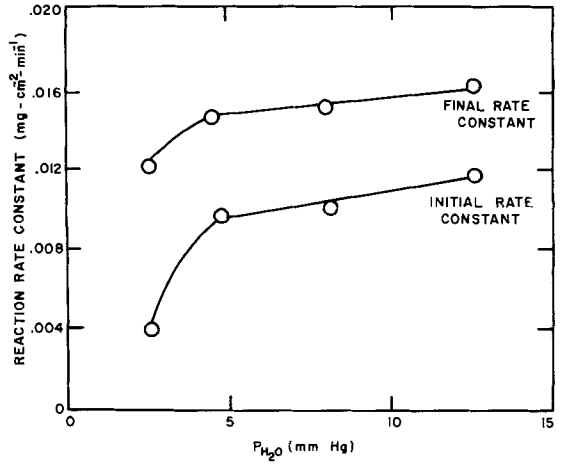

Fig. 4. Dependence of reaction rate constants at 35°C on water vapor pressure; runs carried out in moist oxygen.

Discussion

General considerations.—It was shown in the present work that the lithium hydroxide (LiOH) film which forms initially undergoes hydration to lithium hydroxide monohydrate ($LiOH \cdot H_2O$). Deal and Svec (1) do not report having observed this phase, but they did note the formation of a white product at relatively advanced stages of reaction.

Deal and Svec followed the reaction by measuring the increase in pressure in a static system due to hydrogen evolved according to

$$Li + H_2O \longrightarrow LiOH + \tfrac{1}{2} H_2$$

Their investigation was concerned only with the early stages of the reaction during which, according to the present results, no hydrated product formed. It is clear, however, that a manometric method could not have sensed that the hydration reaction $LiOH + H_2O \longrightarrow LiOH \cdot H_2O$ was proceeding simultaneously. The authors stated that with the appearance of the white product the rate of the reaction became unpredictable. The present results, obtained using a gravimetric method, do not exhibit erratic behavior; rather an initial constant reaction rate (during which only the reaction $Li + H_2O \longrightarrow LiOH + \tfrac{1}{2} H_2$ is involved), gradually increases to a higher steady-state value (during which the outer layers of the LiOH film undergo hydration).

The relative magnitude of the reaction rates at advanced stages can be explained from the above considerations. The increase in weight associated with hydration of the film may be considered to proceed at a constant rate which is superimposed upon the initial rate. Then the new rate would not exceed twice the initial rate. In Table I it is shown that the ratios of the observed reaction rate constants vary from 1.3 to 1.9, the higher value being associated with low reaction temperatures. The only exception is the ratio of 3.1 which was obtained for a reaction at 35°C with a water partial pressure of 2.6 mm Hg. This result was obtained in the region of extreme pressure dependence, and its significance is not understood.

Suggested mechanism.—From a comparison of the lattice constants of lithium hydroxide (tetragonal, c — 4.34Å, a = 3.55Å) and lithium metal (cubic, a = 3.50Å) it appears possible that the initial film of hydroxide is coherent with the underlying metallic lattice. Such a film would be in a state of lateral compression. It was mentioned earlier that the white product ($LiOH \cdot H_2O$) formed first at the edges of a specimen and grew laterally across the faces, after which it thickened uniformly over the surface. This behavior suggests that a nucleation and growth process is involved, nucleation of $LiOH \cdot H_2O$ being favored at sites of high surface energy. The pronounced swelling which accompanied formation of the hydroxide monohydrate leads to the formation of cracks, at least in the outer layers of the film. Although the disposition of lithium hydroxide and its monohydrate in the reaction layer could not be inferred from x-ray diffraction data, it is reasonable to suppose that a concentration gradient existed such that only the

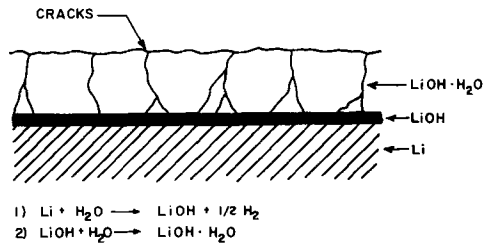

Fig. 5. Assumed distribution of reaction products

outer portion of the film was hydrated. The assumed distribution of reaction products is shown in Fig. 5.

During early stages of the reaction (*i.e.*, during formation of the initial lithium hydroxide film) the reaction rate, according to Deal and Svec (1), decreases logarithmically with time implying that the initial film is a protective one. In the present investigation constant reaction rates were observed. This suggests that some hydration of the film occurred very early during the reaction starting, as discussed previously at the edges of the sample. Apparently the additional weight gains associated with hydration of the film distorted the rate law from its normal logarithmic form (as observed using a manometric method) into an approximately linear form.

Later during the reaction (that is, for a distribution of reaction products as depicted in Fig. 5) a linear rate law was also observed. For continued thickening of the reaction product layer, transport of water molecules (or OH^- ions) to the lithium metal interface is necessary. The outer hydrated portion of the reaction layer is porous or permeated by cracks, and it is reasonable to suppose that water molecules would have ready access to the coherent lithium hydroxide film which overlies the metal surface. Then the consecutive steps involved in the reaction should include:

1. Transport of water molecules from the gas phase through the porous outer portion of the film to the coherent lithium hydroxide interface.
2. Adsorption at this interface (the present results do not permit identification of the adsorbed species as H_2O molecules or OH^- ions).
3. Diffusion of the reacting species across the lithium hydroxide film.
4. Reaction with lithium.

Generally a linear reaction law, such as was observed for the present results, implies that the reaction film overlying the metal surface is completely permeated by cracks so that gas molecules always have ready access to the metal. However, as has been pointed out by Evans (5), a linear rate law is consistent with a reaction controlled by lattice diffusion provided that the diffusing distance remains constant. This is true for example when a network of cracks penetrates the reaction film to reach almost but not quite to the metal surface. For the present results a modified version of this concept could apply. That is, the coherent lithium hydroxide layer could remain constant in thickness as the reaction proceeds, its outer portions undergoing hydration to form porous lithium hydroxide monohydrate.

The measured reaction rates were approximately pressure independent in the range of partial pressures of water vapor from 4.6 to 12.6 mm Hg, and this result is consistent with the notion of a diffusion-controlled reaction of this type. For lower pressures the reaction rate constant was pressure dependent, and this result indicates a rate-controlling step other than diffusion (*i.e.*, one of steps 1 or 2 above). Again, at higher pressures (>22 mm Hg) as reported by Deal and Svec (1) the reaction rate is apparently pressure independent and is probably diffusion controlled.

Conclusions

The attack of lithium by water vapor involves two reactions. Initially a lithium hydroxide film forms which is believed to be coherent with the underlying metallic lattice. During this stage the reaction rate is constant. Subsequently the outer portions of this film undergo hydration to lithium hydroxide monohydrate. The increased weight gains associated with water of hydration are superimposed on those due to the simultaneous formation of lithium hydroxide, and the over-all rate of the reaction, as measured by weight changes, increases to approximately 1½ times the initial rate. Results are consistent with the notion of a reaction controlled by lattice diffusion across a lithium hydroxide film of constant thickness.

Acknowledgment

The authors gratefully acknowledge the financial support of this research which was provided by the Foote Mineral Company. Thanks are also extended to Mr. R. G. Butters, Research Associate at the University of British Columbia, who designed the automatic-recording thermal balance used in this work.

Manuscript received May 2, 1962; revised manuscript received July 16, 1962. This paper was prepared for delivery before the Boston Meeting, Sept. 16-20, 1962.

Any discussion of this paper will appear in a Discussion Section to be published in the December 1963 JOURNAL.

REFERENCES

1. B. E. Deal and H. J. Svec, *J. Am. Chem. Soc.*, **75**, 6173 (1953).
2. "Rare Metals Handbook," C. A. Hampel, Editor, Reinhold Publishing Co., London (1961).
3. S. Yamaguti, *Nature*, **145**, 742 (1940).
4. A. I. Belyaev, L. A. Firsanova, and I. N. Pomerantsev, *Sbornik Nauch. Trudov Moskov. Inst. Tsvetnykh Metal. i Zolota*, **25**, 172 (1955).
5. A. R. Evans, *This Journal*, **91**, 547 (1947).

Electrochemical Oxidation of Hydrogen on Partially Immersed Platinum Electrodes

I. Experiments and Interpretation

Fritz G. Will

Research Laboratory, General Electric Company, Schenectady, New York

ABSTRACT

The mechanism of the ionization of molecular hydrogen has been studied on partially immersed platinum electrodes in acidic solutions, serving as an idealized model for a gas diffusion electrode. The formation of the electrolyte meniscus is observed microscopically and compared to the large current increase which occurs when the electrode is partly raised above the liquid level. Potentiostatic current-voltage curves obtained with partially immersed electrodes differ drastically from those obtained with completely submerged electrodes. The temperature dependence of the current is the same for partially and completely immersed electrodes. The findings suggest that the diffusion of molecular hydrogen through the upper edge of the meniscus and a thin liquid film above the intrinsic meniscus is the rate-determining step. The contribution of surface diffusion of hydrogen atoms and of the diffusion of hydrogen through the bulk electrolyte to the current is negligible.

Current-voltage characteristics of platinum group metals completely immersed in electrolytes which are saturated with molecular hydrogen are well known (1-3) (compare, also, curve 2 in Fig. 5). A large number of studies has been devoted to the mechanism of this electrochemical system in the past. Only a few studies have been concerned with the subject of partly immersed electrodes, although the understanding of this system would lead to a better understanding of the working mechanism of gas diffusion electrodes.

Grove discovered that a marked increase in current takes place when part of a platinum sponge electrode is exposed to hydrogen gas above the level of the electrolyte (4).

Nobis (5) and later Schmid (6) observed the same effect and measured the current as a function of the "unwetted" part of the platinum sponge electrode. Almost no current increase was found on smooth platinum electrodes. The attempt of a qualitative interpretation of these findings by Schmid calls for an adsorption of hydrogen molecules on the unwetted part of the electrode, followed by a "rapid capillary diffusion of the molecules into the microporous structure of the platinum sponge." The molecules were then assumed to "penetrate the intramolecular spaces and thereby be electrochemically activated." The latter molecular diffusion was supposed to be the slow step. On the basis of his experiments Schmid constructed the first successful gas diffusion electrode.

More recently Justi, Pilkuhn, Scheibe, and Winsel (7) carried out a theoretical treatment of the reaction mechanism of gas diffusion electrodes. According to this study, the dissociation of hydrogen molecules and subsequent chemisorption of hydrogen atoms takes place on the electrode surface above the electrolyte meniscus. This part of the electrode may or may not be covered with a thin film of electrolyte, but in either case it is assumed that no electrochemical reaction takes place above the intrinsic meniscus. The hydrogen atoms are supposed to diffuse along the electrode surface to the area below the liquid meniscus where the electrochemical reaction occurs. As rate-determining steps the chemisorption and the surface diffusion of the hydrogen atoms are discussed. Both cases lead to the existence of an anodic limiting current. The contribution to the current by diffusion of hydrogen molecules through the meniscus is considered negligible. The authors did not find an agreement between the theoretical results and experiments performed on their high-drain hydrogen diffusion electrodes.

The marked current increase on partially raising an electrode above the electrolyte was also observed in the case of oxygen reduction on copper, silver, and nickel electrode sheets by Weber, Meissner, and Sama (8). These authors believe that the gas molecules diffuse through the liquid meniscus prior to the electrochemical reaction on the electrode surface and that diffusion of atoms along the unwetted electrode surface or of molecules through the bulk of the electrolyte is not predominant. It is assumed that a three-phase boundary forms at the upper meniscus edge and that the existence of this three-phase zone has essentially no effect on the current. It is suggested that mass transport of oxygen through the meniscus may be the rate-limiting step.

In view of this controversial picture of the mechanism of gas reactions involving partially immersed electrodes and gas diffusion electrodes the present work was undertaken. The study is specifically concerned with the ionization of molecular hydro-

gen on cylindrical platinum electrodes in sulfuric acid solutions. This system has the advantage that the rate of dissociation of molecular hydrogen and the rate of ionization of the hydrogen atoms are relatively high. It was hoped, therefore, that one or the other of the disputed transport mechanisms would be rate controlling and that a distinction between them could be made by designing suitable experiments. Several possible reaction paths for the ionization of hydrogen are shown in Fig. 7.

The electrochemical system chosen here has some important features in common with the complex gas diffusion electrodes. The meniscus formation and the effect of a possible thin liquid film above the meniscus are essentially the same as for an ideal capillary. The difficulties encountered in trying to make measurements on a single pore, on the other hand, are avoided.

Experimental

Measurements were made in a glass electrolytic cell consisting of four compartments, separated from each other by fritted glass disks. The compartment containing the hydrogen reference electrode was connected by a Luggin capillary with the main compartment in which only the test electrode was located. The two remaining compartments contained two symmetrically arranged counter electrodes.

The test electrodes consisted of platinum tubing (99.99% pure), 1.2 cm long, 0.635 cm (¼ in.) in diameter and 0.0127 cm (0.005 in.) in wall thickness. Electrical connection was made by spot-welding a platinum wire on the inner surface of the tubing. Closely fitted Teflon stoppers and Teflon tubing were then used to prevent the inner surface and the wire from making contact with the electrolyte. Measurements were made on five differently pretreated electrodes: (i) surface covered with platinum sponge, obtained by platinization in chloroplatinic acid (plus traces of lead acetate) with a current density of 20 ma/cm^2 for 120 sec; (ii) platinum sponge surface obtained with 20 ma/cm^2 for 12 sec; (iii) electrode No. 2 heated in a hydrogen flame so that a smooth platinum surface was restored; (iv) surface sandblasted with No. 150 Carborundum; and (v) surface smooth, highly polished. A cathetometer enabled the test electrode to be raised and lowered accurately to within ±0.01 cm.

Sulfuric acid of two normalities (1N and 8N) was made up from C. P. reagent grade stock solution using double distilled water of 7.9×10^{-8} ohm^{-1} cm^{-1} conductivity at 25°C.

The hydrogen used in these experiments was prepurified, containing <8 ppm O_2, <1 ppm CO_2 + CO, and <1 ppm hydrocarbons.

A specially designed forced-air thermostat controlled the temperature to within ±0.1°C.

To carry out the polarization measurements, an ultra stable potentiostat was designed having an output of ±0.4 amp and ±6v with a noise of 2×10^{-5}v (rms), an internal resistance of 0.03 ohm, and an amplifier bandwidth of 30 kcps. This instrument is an improved version of earlier designs (3, 9). Surface area measurements on the different platinum electrodes were made with the triangular voltage sweep method (10) using the potentiostat in conjunction with a Hewlett Packard Function Generator 202A.

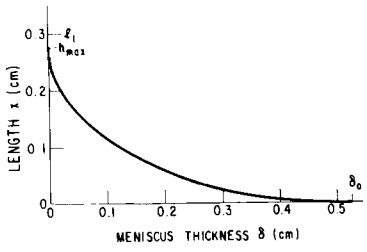

Fig. 1. Actual meniscus formation of 1N H_2SO_4 on a platinized platinum cylinder according to microscopic observation.

Results

Meniscus and film formation.—The formation of the electrolyte meniscus and of a possible film of electrolyte above the intrinsic meniscus was observed microscopically. A freshly platinized and thoroughly cleaned platinum test electrode and 1N H_2SO_4 were used in the following experiment.

Starting with the electrode completely submerged, but just touching the undisturbed liquid level ($l_1 = 0$), the electrode is progressively raised to positions $l_1 > 0$.[1] The meniscus height increases to a maximum h of 0.275 ± 0.01 cm; further raising of the electrode does not visibly affect the meniscus geometry. Figure 1 shows the actual meniscus for $l_1 = 0.3$ cm with its maximum height according to microscopic observation.

Shortly after raising the electrode to a new position $l_1 > h$, a liquid film can be detected. This film decreases in thickness with time until it can no longer be detected with the microscope. From this experiment, it can therefore only be concluded that an upper limit for the thickness of a possible liquid film above the meniscus is about 1μ which was the resolution of the microscope, but there may be no liquid film.

Because of edge effects and especially for small values of l_1, the observed meniscus deviates from the theoretical meniscus. Starting at about l_1 =0.13 cm, small regions of the electrode surface near the upper edge occur where the thickness of the liquid layer is at least much smaller than would correspond to the regular meniscus. Whether these regions of the surface are actually covered with a thin liquid film or are unwetted could again not be decided. Between 0.13 and 0.27 cm more such regions occur until the meniscus is fully developed at 0.27 cm.

The following experiments were performed in order to find out to which extent the meniscus formation would affect the electrode current.

Current as a function of electrode position.—The electrolyte was saturated with hydrogen and then hydrogen continuously blown through the gas volume above the liquid. The temperature was held at 25° ± 0.1°C.

A constant potential of 0.4v was applied between the test electrode and a hydrogen reference elec-

[1] The length l_1 is counted from the undisturbed liquid level to the upper edge of the platinum tubing.

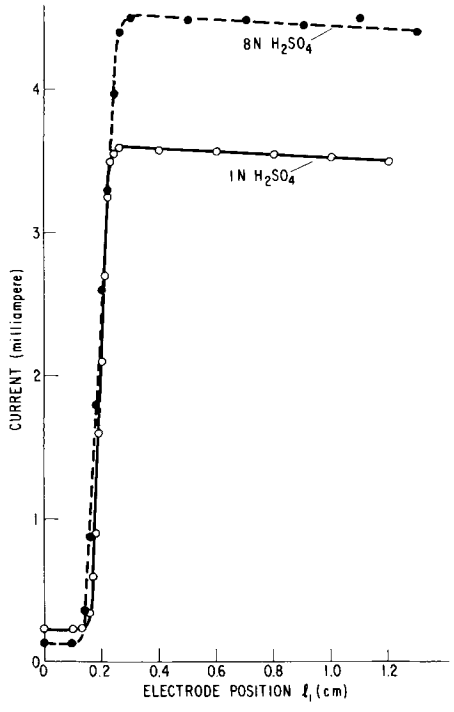

Fig. 2. Current as a function of electrode position for an applied potential of 0.4v; platinized platinum cylinder (r.f. 88) in 1*N* and 8*N* H_2SO_4 at 25°C.

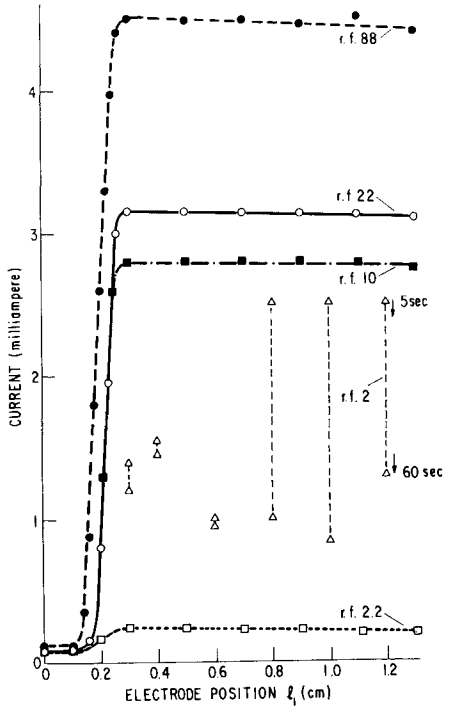

Fig. 3. Effect of surface roughness on the electrode current for 0.4v in 8*N* H_2SO_4 at 25°C.

trode, and the current was measured as a function of the electrode position.

Figure 2 shows two curves which were obtained with the heavily platinized electrode No. 1 in 1*N* and in 8*N* H_2SO_4. For the completely immersed electrode, $l_1 \leqq 0$, a small residual current is measured which is about 50% smaller in 8*N* H_2SO_4 than in 1*N* H_2SO_4. When raising the electrode, the current initially remains constant. For electrode positions beyond about $l_1 = 0.13$ cm, the current increases steeply and reaches a maximum value at about 0.26 cm. On raising the electrode further the current stays almost constant. There is a 16-fold (1*N* H_2SO_4) respectively 36-fold (8*N* H_2SO_4) increase in current compared to the completely immersed electrode. The currents for positions $l_1 >$ 0.26 cm are some 25% larger in 8*N* H_2SO_4 than in 1*N* H_2SO_4.

Figure 3 shows the effect of surface roughness[2] on the magnitude of the currents for 8*N* H_2SO_4 under otherwise unchanged conditions. While the residual currents are essentially unaffected, there is a pronounced influence of the surface roughness on the other parts of the curves, which correspond to partial immersion of the electrodes.

Compared with the heavily platinized electrode No. 1 which has a roughness factor (r.f.) of 88, the less platinized electrode No. 2 with r.f. 22 draws 30% less current (for $l_1 \geqq 0.26$ cm); and the same electrode, after heating in a hydrogen flame has a r.f. of 2.2 and shows only 1/18 of the current of the heavily platinized electrode. The currents for the sandblasted electrode No. 4 with r.f. 10 are 38% smaller than those through the electrode with r.f. 88.

The currents in Fig. 2 and 3 are stationary values and in most cases are obtained after a few seconds. Within the first few seconds after raising the electrode to a new position, transient currents are observed which are smaller than the stationary values. On lowering the electrode, transient currents occur which are much larger (up to 100 ma) than the stationary values. No transient currents are noticed for electrode positions $l_1 \leqq 0.13$ cm. Except for smooth platinum, the curves are the same for raising and lowering the electrode and are well reproducible. The currents do not show the fluctuations which are known to occur on completely immersed electrodes in hydrogen-stirred solutions. However, the residual currents have a tendency to drift slowly.

The results obtained on smooth platinum electrodes are irregular and, in general, irreproducible. The mechanically polished electrode No. 5 with r.f. 2, immediately after raising to a new position, showed currents up to 2.5 ma. Sometimes after several seconds, sometimes after 15 min these currents suddenly decreased to much smaller values. At the same time electrolyte was seen to glide down along the surface above the meniscus. On lowering of the electrode, the currents are small from the beginning and decrease little with time. The smooth electrode with r.f. 2.2 behaved less irregularly. Although currents up to 1.2 ma were observed initially, quasi-stationary values were obtained eventually and plotted in Fig. 3.

Essentially no influence of surface roughness is found if the electrodes are completely submerged and the hydrogen bubbled through the electrolyte.

[2] The surface roughness factor (ratio of true and geometric surface area) for the five platinum electrodes was measured with the triangular voltage sweep method (10) with about ±5% accuracy. Electron micrographs of surface replica were made for electrodes No. 1 and 2. The average diameter of the platinum black particles was found to be 0.5μ for electrode No. 1 with r.f. 88 and 0.3μ for electrode No. 2 with r.f. 22.

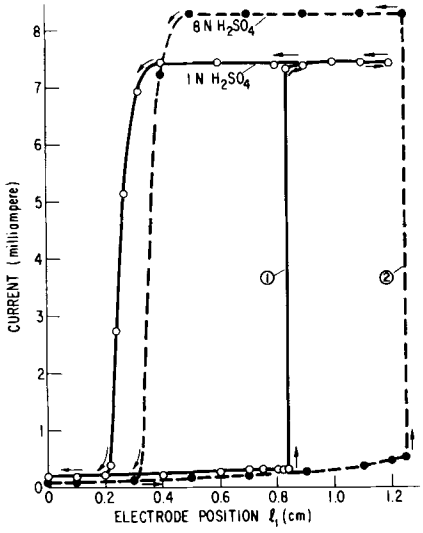

Fig. 4. Current as a function of electrode position for an applied potential of 1.3v; platinized platinum cylinder (r.f. 88) in 1*N* and 8*N* H_2SO_4 at 25°C.

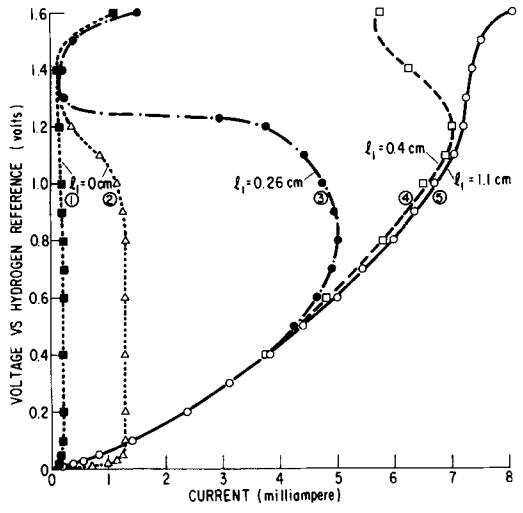

Fig. 5. Current as a function of applied voltage for different constant electrode positions; platinized platinum cylinder (r.f. 88) in 1*N* H_2SO_4 at 25°C. Curves 1 and 2 for submerged electrode; curve 2, solution stirred with H_2; all other curves, H_2 blown through gas phase.

In this case, the current for all of the electrodes is 1.25 ma in 1*N* H_2SO_4 and 0.85 ma in 8*N* H_2SO_4 for a moderate gas flow rate and strongly dependent on the stirring rate.

The experiments described hitherto were performed at a constant potential of 0.4v. Each electrode position shows only one reproducible value of the current. However, a characteristic hysteresis loop is observed when a constant potential of 1.3v is applied. Figure 4 shows the currents for electrode No. 1 with r.f. 88 in 1*N* and 8*N* H_2SO_4, again as a function of electrode position.

In 1*N* H_2SO_4, the residual current (lower branch of the curve) for the submerged electrode has about the same value as for 0.4v applied potential. The current increases only a little on raising the electrode as high as 0.8 cm. For $l_1 = 0.84$ cm the current is initially 0.35 ma and rises to 0.5 ma within 30 sec. Then, within a fraction of a second, the current suddenly increases to 7.35 ma where it stays constant. Raising the electrode to 1.2 cm or lowering to 0.4 cm has almost no influence on the current now, and the upper branch of the curve is obtained. Below 0.4 cm the current drops steeply, and below 0.2 cm the original small current is measured again. This pronounced hysteresis loop is reproducible, although the electrode positions corresponding to the steep rise and drop of the current are observed to shift somewhat.

An important observation concerns the transient currents: No transient currents occur for the lower branch of the hysteresis loop ($0 \leqq l_1 < 0.84$ cm), when the electrode is either raised or lowered intermittently. Large transient currents are observed for the upper curve branch ($0.2 \leqq l_1 \leqq 1.2$ cm), especially on lowering the electrode.

In 8*N* H_2SO_4 the residual current is smaller than in 1*N* H_2SO_4. The steep rise of the current occurs only for definitely higher electrode positions. In some cases, no current rise is observed at all, and only the lower branch of the curve is obtained. However, the upper branch of the curve could always be realized by raising the electrode completely into the gas volume above the liquid and then making contact with the electrolyte again.

In general, stationary values of the current are obtained sluggishly, and slow drifting is common. Over-all reproducibility of the currents is better than 5%.

Current as a function of applied voltage.—Potentiostatic current voltage curves were obtained for fixed electrode position in order to substantiate the characteristic differences between partially and completely immersed electrodes found above.

Figure 5 shows the curves which were obtained in 1*N* H_2SO_4 with the platinized electrode No. 1 having a roughness factor of 88.

For the completely immersed electrode ($l_1 = 0$), the dotted curve 1 is obtained. It exhibits the limiting current of hydrogen diffusion between 0.1 and 0.8v, the subsequent decline of current as a consequence of adsorption of atomic oxygen, and the increase in current at 1.4v because of the evolution of molecular oxygen. The dotted curve 2, included in Fig. 5 for reasons of comparison, is obtained with hydrogen gas bubbling through the electrolyte at a moderate rate (1-3, 10, 11, 13). The character of the curve is the same as in the case of hydrogen flowing through the gas volume above the liquid. Because of the decreased diffusion layer thickness, however, the currents are larger.

The character of the curve changes completely when the electrode is partly drawn out of the electrolyte. No limiting current of diffusion appears in curves 3, 4, and 5. The adsorption of atomic oxygen at potentials above 0.8v has an effect on the current which depends on the electrode position. For $l_1 = 0.26$ cm, the current decreases above 0.8v, and the curve joins the curves for $l_1 = 0$ at about 1.3v. For $l_1 = 0.4$ cm, the current decrease sets in only at 1.2v and is not as drastic as for $l_1 = 0.26$ cm. For $l_1 = 1.1$ cm, no negative resistance region occurs at all: the current increases steadily with increasing

voltage and reaches values which are almost three orders of magnitude larger than the corresponding currents for a completely immersed electrode (curve 1). All curves show the increase of current at higher anodic potentials which is connected with visible evolution of molecular oxygen.

Below 0.8v, stationary currents are obtained in all cases rather fast. Above 0.8v, for a completely immersed electrode (curves 1 and 2), stationary values were very often not obtained, and the reported currents are somewhat higher than the expected stationary values. In contrast, for a partially immersed electrode (curves 3, 4, and 5), stationary currents were attained within a few minutes. Reproducibility of the curves proved to be good.

A study of the effect of surface roughness on the current-voltage curves gave the following results: For a completely immersed electrode, there is no influence of surface roughness; curves 1 and 2 in Fig. 5 remain unchanged. If partly immersed, the electrodes with r.f. 10 and 22 (compare Fig. 3) yield curves similar to curves 3, 4, and 5 in Fig. 5. The only major difference is that the magnitude of the currents decreases with decreasing surface roughness. With partly immersed smooth platinum electrodes, in some cases curves of type 3, 4, and 5 were observed; in other cases, however, curves very similar to curve 1 were found.

The effect of different acid concentration is such, that for $8N$ H_2SO_4 curves 1 and 2 in Fig. 5 (obtained in $1N$ H_2SO_4) are shifted toward smaller currents and curves 3, 4, and 5 are shifted toward larger currents. In other words, the effect of varying the concentration is reverse for completely immersed electrodes on the one hand and partially immersed electrodes on the other.

Current as a function of temperature.—The temperature dependence of the current was studied for different electrode positions at a constant potential of 0.4v. The measurements were performed in $1N$ H_2SO_4 with the platinized electrode, having a roughness factor of 88.

In Fig. 6 the logarithm of the current in milliampere is plotted against the reciprocal of the absolute temperature.

Curve 1 for electrode position $l_1 = 0.4$ cm is representative for all electrode positions $l_1 \geqq 0.26$ cm. Between 20° and 40°C the curve is almost linear and declines between 40° and 60°C. Excessive thermal expansion of the Teflon parts and changes in the liquid level limited the measurements to temperatures below 60°C.

Curve 2 is obtained for a completely immersed electrode. Note that in this case log 10 I is plotted against $1000/T$. The error in the current measurement is relatively much larger than for curve 1: as mentioned before, the small rest currents of curve 2 are subject to slow drift.

Breiter and Hoffmann (11) studied the diffusion of hydrogen in sulfuric acid with a completely immersed rotating platinum disk electrode. Using data from these authors in $5N$ H_2SO_4 at 0.4v, the dotted curves 3 and 4 in Fig. 6 are obtained. Curve 3 corresponds to a disk rotation of 480/min, curve 4 to a rotation of 2400/min.

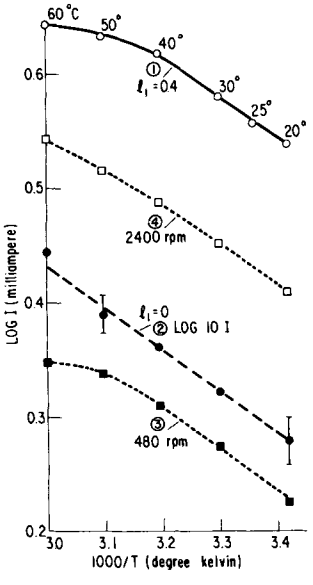

Fig. 6. Current as a function of temperature for an applied potential of 0.4v. Curves 1 and 2, platinized platinum cylinder (r.f. 88) in $1N$ H_2SO_4; curves 3 and 4, rotating platinum disk in $5N$ H_2SO_4.

Discussion

An idealized model of the electrode surface s covered with a liquid film f and a liquid meniscus m in contact with the bulk electrolyte b is shown in Fig. 7.

Several imaginable reaction paths for the over-all reaction

$$ {}_0H_2 \rightarrow 2\,{}_0H^+ + 2e^- $$

are included in the picture. ${}_0H_2$ is hydrogen in its equilibrium concentration in the gas phase, ${}_0H^+$ are the hydrogen ions in their equilibrium concentration in the bulk electrolyte. Reaction paths a, b, c, and d occur in parallel and contribute to the foregoing over-all reaction according to their reaction rates. Each reaction path consists of several reaction steps in series; the slowest of these steps determines the

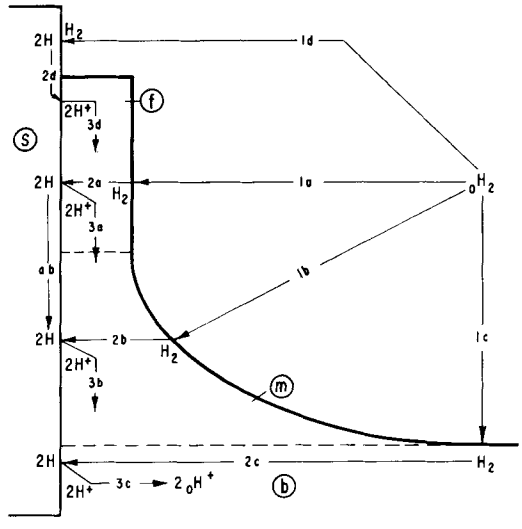

Fig. 7. Idealized model of the electrode surface s with liquid film f, meniscus m, and bulk electrolyte b. Several possible reaction paths for the ionization of hydrogen are indicated.

rate of the reaction path. As an example, path d consists of the following steps: Transport of hydrogen molecules to the gas-solid interface—dissociation and adsorption—surface diffusion of hydrogen atoms on the solid phase—ionization on the solid-liquid interface—transport (diffusion and migration) of hydrogen ions through liquid film and meniscus into the bulk electrolyte. This case was discussed by Justi *et al.* (7).

An attempt will be made in the following to decide on the basis of the experimental results which reaction paths are the prevailing ones.

The small residual current in Fig. 2 for electrode positions $l_1 \leqq 0$ at 0.4v is a direct measure of the maximum possible contribution of the diffusion of molecular hydrogen through the bulk electrolyte to the over-all current in a still solution. As can be seen from Fig. 2, this path contributes only 6% (1*N* H_2SO_4) or 3% (8*N* H_2SO_4) to the current of a partially immersed electrode.

The increase of the current at about $l_1 = 0.13$ cm coincides with the electrode position where, according to microscopic evidence, small regions of the upper electrode edge are only covered with a thin liquid film or are even unwetted. When raising the electrode further, more thin film or unwetted area is created, and the current increases further. In the steep part of the curve the current increases by 0.57 ma each time the electrode is raised 0.1 mm. This corresponds to a current density of at least 28.5 ma/cm^2, but confined to these upper parts of the electrode, while the current density on the lower electrode parts is by more than two orders of magnitude smaller. Between $l_1 = 0.26$ and 0.3 cm, the current reaches a maximum which coincides with the maximum meniscus length of 0.275 cm, observed microscopically. Beyond this electrode position, the current stays almost constant. Even for $l_1 = 1.45$ cm, when only less than 0.1 cm of the electrode is in contact with the upper meniscus (electrode length is 1.2 cm), the current is still the same. The minor decrease of the current above 0.3 cm is due to the decrease of surface area which is available for step 2c, the bulk diffusion of hydrogen.

These findings show that only a small part of the electrode close to the meniscus edge which is less than 1 mm in length is responsible for 94 to 97% of the total current of a partially immersed electrode. On the basis of experiments with an air-depolarized copper plate, Weber *et al.* (8) come to similar conclusions.

These and all the other experimental results can be interpreted as follows. Any thin liquid film above the meniscus and the upper parts of the meniscus have a comparatively large electrolytic resistance. The electrolytic current which consists of the migration of hydrogen ions from the reaction zone into the bulk electrolyte (compare Fig. 7) causes a large ohmic drop of the potential parallel to the electrode surface. Consequently, the current density and, in the case of slow transport mechanisms, the concentrations of molecular and atomic hydrogen at the electrode surface will vary along the surface.

The results shown in Fig. 2 indicate that the potential decays from the value of the applied potential, 0.4v, to essentially zero potential over a length of about 0.1 cm. All parts of the electrode above $l_1 = 0.27$ cm are at zero potential and therefore do not contribute to the current. The concentrations of molecular and atomic hydrogen at these parts are constant and equal to their equilibrium concentrations. The decrease of the residual currents in Fig. 2 and Fig. 4 with increasing electrolyte concentration is due to the decrease of the diffusion coefficient of molecular hydrogen by about 45%. The fact that for a partially immersed electrode the currents increase with increasing electrolyte concentration can be explained with the large increase of the conductivity (roughly four times) when going from 1*N* to 8*N* H_2SO_4. As a consequence the potential drop in meniscus and film is much smaller for 8*N* H_2SO_4 and the currents are therefore larger.

The hysteresis curves for an applied potential of 1.3v shown in Fig. 4 are strong evidence for the existence of a liquid film which covers the whole electrode surface above the intrinsic meniscus and therefore evidence against the existence of a "three-phase-boundary." At 1.3v the surface of a submerged electrode is covered with a monolayer of atomic oxygen (10, 12, 13). The current is small because the dissociation of hydrogen molecules on such a layer is hindered. When raising the electrode, the potential at the upper film edge decreases because of the potential drop in meniscus and film. At a certain electrode position (0.84 cm in 1*N* H_2SO_4 and 1.25 cm in 8*N* H_2SO_4) the potential at the upper film edge has decreased to such a value [about 0.7v (10)] that a rapid electrochemical reduction of the oxygen layer takes place. The current increases steeply, the reaction zone is again confined to a small region close to the meniscus edge, and the electrode position, over a wide range of positions, does not affect the large observed currents. For 8*N* H_2SO_4 the steep increase of the current occurs at a higher electrode position because the potential drop in the film is smaller.

If the diffusion of hydrogen atoms along an unwetted surface above the meniscus according to Justi *et al.* (7) would be important the pronounced effect of the acid concentration could not be explained. Also, if surface diffusion would be rate controlling one would expect the currents to increase approximately proportionally to the surface roughness. However, as one can see from Fig. 3, the currents increase only by a factor of 1.6 for an increase of the surface roughness from 10 to 88, and for smooth platinum currents are sometimes found which are almost as large as those for an electrode with r.f. 10.

If molecular diffusion through a thin liquid film controls the rate, on the other hand, a small effect of the surface roughness on the currents is expected. A thin film will probably adapt somewhat to the surface roughness. Direct evidence for the importance of a liquid film, finally, is the observation that the current on smooth platinum decreases at the same

moment when electrolyte is seen to glide down along the surface above the meniscus.

The shape of the current-voltage curves shown in Fig. 5 can also be fully understood on the basis of slow molecular diffusion through a thin liquid film. The assumption of surface diffusion of atoms as rate controlling step by Justi *et al.* (7) calls for the existence of an anodic limiting current. The nonoccurrence of such a current limit is additional evidence against surface diffusion.

Experimental evidence that neither the dissociation of H_2 nor the ionization of H are rate-controlling steps is obtained from the temperature dependence of the currents at 0.4v as shown in Fig. 6.

Curve 2 for a completely immersed electrode shows a very similar temperature dependence as curve 1 which is representative for partly immersed electrodes. In fact, between 20° and 40°C both curves are linear and have the same slope, corresponding to an activation energy of 0.7 kcal/mole H_2. This suggests that the same s low reaction step occurs on the completely and on the partially immersed electrode. The slow step, however, determining the current of the completely immersed electrode (curve 2) is known (2, 3, 10) to be the diffusion of molecular hydrogen through the electrolyte. This is in favor of reaction paths a and b in Fig. 7a and suggests that the diffusion of molecular hydrogen through the meniscus and the liquid film is the rate-controlling step.

Correcting for the temperature dependence of the solubility of hydrogen in the electrolyte, a value of 1.25 kcal/mole H_2 for the activation energy of H_2-diffusion is obtained. A value for H_2-diffusion in water was calculated from published data (14, 15) as 1.95 kcal/mole H_2.

Curves 3 and 4 in Fig. 6 which were obtained using H_2-diffusion measurements from Breiter and Hoffmann (11) on rotating platinum electrodes also compare favorably with curves 1 and 2. These authors, however, do not give values for the activation energy.

The small activation energies mentioned above make it unlikely that the dissociation of H_2 or the ionization of H are rate-controlling steps.

Conclusions

The described experiments suggest the following model for the ionization of molecular hydrogen on partly immersed platinum electrodes:

1. The electrode surface above the intrinsic electrolyte meniscus is covered with a thin electrolyte film of a thickness comparable to or smaller than the surface roughness. Essentially the whole electrode surface is therefore wetted with electrolyte; there is no "three-phase boundary."

2. The electrochemical oxidation of hydrogen takes place almost exclusively in a narrow region of the electrode at the upper edge of the meniscus and the adjacent film close to it; the current density there is comparatively high.

3. The reaction mechanism consists of the diffusion of molecular hydrogen through the upper edge of the meniscus and the adjacent film, followed by dissociation and ionization at this narrow region of the electrode surface. The diffusion of molecular hydrogen is the rate-controlling step, although ionization hindrance could be an additional factor at potentials close to zero.

4. The migration of the hydrogen ions causes a large ohmic voltage drop in film and meniscus along the electrode surface. This voltage drop is responsible for the fact that the reaction zone is limited to a narrow region at the meniscus edge.

5. Diffusion of hydrogen atoms along the electrode surface as assumed and treated theoretically by Justi *et al.* (7) is not a determining factor.

6. Diffusion of hydrogen molecules through the bulk of the electrolyte presents a very small and measurable contribution to the over-all current.

The above conclusions can be applied to hydrogen ionization on other platinum group metals. On metals other than those, however, slow dissociation and slow ionization can play an essential role. In the process of electrochemical reduction of oxygen, activation polarization will, as usual, occur at low current densities, but at higher current densities, the model as developed above, should apply. Taking these restrictions into account, the proposed mechanism should generally be encountered in gas diffusion electrodes.

Manuscript received May 16, 1962; revised manuscript received Oct. 1, 1962. This paper was prepared for delivery before the Los Angeles Meeting, May 6-10, 1962.

Any discussion of this paper will appear in a Discussion Section to be published in the December 1963 JOURNAL.

REFERENCES

1. O. Sackur, *Z. physik. Chem.*, **54**, 641 (1906).
2. E. Wicke and B. Weblus, *Z. Elektrochem.*, **56**, 169 (1952).
3. M. Breiter and F. G. Will, *ibid.*, **61**, 1177 (1957).
4. W. R. Grove, *Phil. Mag.*, **14**, 127 (1839); **21**, 417 (1842).
5. Nobis, Dissertation, Dresden (1909).
6. A. Schmid, "Die Diffusionsgaselektrode," F. Enke, Stuttgart (1923).
7. E. Justi, M. Pilkuhn, W. Scheibe, and A. Winsel, "High-Drain Hydrogen-Diffusion-Electrodes Operating at Ambient Temperature and Low Pressure," Verl. d. Akad. d. Wissensch. u.d. Lit., Wiesbaden (1959).
8. H. C. Weber, H. P. Meissner, and D. A. Sama, Abstract No. 21, Battery Division, Electrochemical Society, Fall Meeting, Detroit, October, 1961.
9. F. G. Will, *Z. Elektrochem.*, **63**, 484 (1959); **63**, 689 (1959).
10. F. G. Will and C. A. Knorr, *ibid.*, **64**, 258 (1960); **64**, 270 (1960).
11. M. Breiter and K. Hoffmann, *ibid.*, **64**, 462 (1960).
12. A. Obrutschewa, *J. Phys. Chem. (U.S.S.R.)*, **26**, 1448 (1952).
13. M. Becker and M. Breiter, *Z. Elektrochem.*, **60**, 1080 (1956).
14. R. C. Reid and T. K. Sherwood, "The Properties of Gases and Liquids," McGraw-Hill Book Co., New York (1958).
15. C. R. Wilke and Ping Chang, *J. Am. Inst. Chem. Eng.*, **1**, 264 (1955).

Electrochemical Oxidation of Hydrogen on Partially Immersed Platinum Electrodes

II. Theoretical Treatment

Fritz G. Will

Research Laboratory, General Electric Company, Schenectady, New York

ABSTRACT

The mechanism of the anodic oxidation of molecular hydrogen on partially immersed platinum electrodes in acidic solutions, serving as an idealized model for a gas diffusion electrode, has been treated theoretically. The mechanism, which earlier experiments had suggested, consists of the slow diffusion of molecular hydrogen through the upper edge of the electrolyte meniscus and a thin liquid film covering the electrode surface above the intrinsic meniscus. On the basis of this model, the relationship $I = K_1[E_a - K_2(1 - e^{-K_3E_a})]^{1/2}$ between current and applied potential is derived which agrees with experimental data over a potential range from zero to 1.8v. The relative contributions of meniscus and film to the total current are calculated. The reaction takes place mainly at a few tenths of a millimeter length of the electrode close to the upper meniscus edge. The true current density at this narrow band and the thickness of the liquid film are calculated. The surface diffusion of hydrogen atoms as rate-determining transport mechanism has also been treated, and it is shown that the results of this treatment are not in agreement with the experimental data.

The purpose of the following theoretical account is to contribute to the understanding of the working mechanism of gas diffusion electrodes. So far, there is only one known example for a theoretical treatment of this problem: Justi, Pilkuhn, Scheibe, and Winsel (1) treated slow dissociation of hydrogen molecules and slow surface diffusion of hydrogen atoms in special cases for an idealized model of a single straight pore. They could not find an agreement between the results of this treatment and experiments performed with their high-drain hydrogen diffusion electrodes.

The case of slow ionization or discharge has been studied by Ksenzhek and Stender (2) for a system not involving gas-liquid interfaces and gas transport phenomena [compare also (3)]. These authors calculated the current and potential distribution inside of pores which are completely filled with electrolytes. A comprehensive theoretical treatment of discharge hindrance was also given most recently by Winsel (4).

A preceding experimental study (5) was concerned with the electrochemical oxidation of hydrogen on partially immersed platinum-tube electrodes in sulfuric acid solutions. The formation of the electrolyte meniscus and of any liquid film above the intrinsic meniscus at such electrodes is in general the same as that inside of a single straight pore of a gas diffusion electrode. The electrochemical system chosen here can be considered as an "inverse pore" and can thus, for the purpose of treating reaction mechanisms, serve as an idealized model for a hydrogen gas diffusion electrode.

The qualitative interpretation of the experimental results (5) suggested that the rate-determining step of the over-all reaction $_oH_{2\,gas} \rightarrow 2_oH^+{}_{bulk} + 2e^-$ consists of the diffusion of molecular hydrogen through the upper edge of the electrolyte meniscus and a thin liquid film covering the electrode surface above the intrinsic meniscus. The migration of the hydrogen ions subsequent to dissociation and ionization of the hydrogen causes an ohmic voltage drop in film and meniscus parallel to the electrode surface.

For electrochemical systems other than the platinum-hydrogen system, hindrance of the dissociation or ionization step may occur and cause the currents to be smaller for a given polarization than in the case of slow diffusion alone which will be treated below.

A quantitative agreement between the results of a theoretical treatment of this concept and the experimental results would be a strong support for the correctness of the concept, while a successful treatment of the surface diffusion concept would possibly eliminate surface diffusion as a determining transport mechanism. Such a treatment would furthermore answer the following questions which could not be resolved on the basis of the experiments alone: What are the relative contributions of the meniscus and the film to the total current; what is the length of the reaction zone and the thickness of the liquid film; what is the true current density; and finally, what can surface diffusion of hydrogen atoms contribute to the total current?

General Differential Equation for Potential in Film and Meniscus

Figure 1 shows schematically the platinum tube electrode (length $L = l_1 + l_2$, diameter $2r$), the meniscus [height h, thickness $\delta(x)$, maximum thick-

ness for $x = 0$: δ_o, minimum thickness for $x = h$: δ_h] and the film (length H-h, thickness δ_h). The emerging length of the electrode is l_1, the immersion depth $-l_2$. The coordinate origin has, for convenience, been shifted from the cylinder axis into the electrode surface.

Each infinitesimal length element dx of the electrode contributes the current

$$dI = -2\pi r\, i\, dx \qquad [1a]$$

to the total electrode current I_t, where $i = f(E, x)$ is the local current density which is a function of the local electrode potential $E(x)$. One can rewrite Eq. [1a] as

$$dj/dx = -i \qquad [1b]$$

if one introduces the current per unit circumference of the electrode

$$j = I/2\pi r = f(E, x) \qquad [2]$$

Each length element dx of meniscus and film adds the increment dR to the total resistance R_t, and the current I causes an ohmic drop in the potential parallel to the electrode surface of

$$dE = -IdR = -I\rho dx/2\pi r\delta(x) \qquad [3]$$

It is assumed that the resistivity ρ of the electrolyte is constant in the meniscus and in the film which means that the limiting diffusion current of the hydrogen ions must be large compared to the actual electrode current. It is further assumed that for $x > 0$ any potential gradient perpendicular to the electrode surface can be neglected compared to the potential gradient parallel to the surface.

When substituting Eq. 3 in Eq. 2, one obtains

$$j = -\rho^{-1}\delta(x)dE/dx \qquad [4]$$

When Eq. [4] is differentiated and substituted in Eq. [1b], one gets the second order differential equation

$$\delta(x)d^2E/dx^2 + [d\delta(x)/dx]dE/dx = \rho i = \rho f(E, x) \qquad [5]$$

In order to integrate this differential equation, the thickness δ as a function of x and the local current density i as a function of E and x must be known. Depending on the complexity of these functions, an analytical integration may or may not be possible.

A mathematical expression describing the shape of a meniscus is known (6), but in a cartesian coordinates this expression becomes far too complicated in order to be practical. A good approximation of the actual meniscus [compare Fig. 1 (5)] can be obtained with the parabola

$$\delta(x) = \delta_o(1 - x/h)^2 + \delta_h \qquad \text{for } 0 \leq x \leq h \qquad [6a]$$

with $\delta_o = 0.253$ cm and $h = 0.275$ cm, and the liquid film of thickness δ_h above the meniscus is described by

$$\delta(x) = \delta_h \qquad \text{for } h \leq x \leq H \leq l_1 \qquad [6b]$$

Diffusion of Hydrogen Molecules Rate-Limiting

It is assumed that the rate of diffusion of hydrogen molecules through the electrolyte in meniscus and film determines the current. With Nernst's

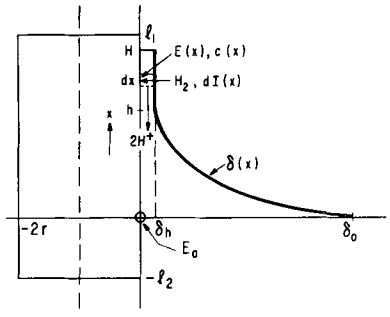

Fig. 1. Schematical drawing of the platinum tube electrode (length $l_1 + l_2$, diameter $2r$), the meniscus (height h, thickness $\delta(x)$) and the film (length $H - h$, thickness δ_h); x = length counted from bulk level.

equation and Fick's diffusion law the local current density i then becomes

$$i = k_{od}\delta^{-1}(x)\ (1 - e^{-2\phi E}) \qquad [7]$$

where

$$k_{od} = 2_ocFD \qquad [7a]$$

and

$$\phi = F/RT \qquad [7b]$$

The diffusion coefficient D of the hydrogen in the electrolyte is assumed to be independent of x; $_oc$ is the equilibrium concentration of hydrogen in the bulk electrolyte.

If one substitutes [6a] and [7] in [5], a complicated nonlinear differential equation results which cannot be solved analytically. Two limiting cases will be discussed as follows in which an integration is possible:

1. The existence of the meniscus is disregarded, the film forms a right angle boundary with the bulk electrolyte at $x = h$ (Fig. 1).

2. Meniscus and film are taken into account; however, the applied potentials or total polarizations are comparatively large ($E_a > 0.1$v).

Case 1. Film forms a right-angle boundary with the bulk electrolyte.—Hence, the integration has only to be performed over the film with its constant thickness δ_h from $x = h$ to $x = H$. With [6b] and [7] differential Eq. [5] simplifies to

$$d^2E/dx^2 = \rho k_{od}\delta_h{}^{-2}\ (1 - e^{-2\phi E}) \qquad [8]$$

With E_a as the applied potential (or the total polarization) the boundary conditions are

$$E = E_a \text{ for } x = h \qquad [9]$$

$$dE/dx \propto j = 0 \quad \text{for} \quad x = H \qquad [10]$$

Since the variable x does not occur explicitly in [8], the first integration can readily be performed and gives

$$dE/dx = -\left[2\rho k_{od}\delta_h{}^{-2}\left(E + \frac{1}{2}\phi^{-1}\, e^{-2\phi E}\right) - K_1\right]^{1/2} \qquad [11]$$

where K_1 is an integration constant.

Current and potential distribution in film and current-potential relation for small potentials.—An exact second integration of [11] is not possible. However, for small values of E an approximate solution of [11] can be given by approximating the ex-

ponential term in [11] with the parabola $1 - 2\phi E + 2a\phi^2E^2$. For $a = 0.785$ the parabola deviates by less than 1.5% from the exponential term for potentials $0 \leq E \leq 0.01$v and is somewhat better than the usual MacLaurin approximation with $a = 1$. One obtains for the potential E and from [4] for the current per unit circumference j as a function of the variable x for applied potentials $0 \leq E_a \leq 0.01$v

$$E = E_a \frac{\cosh [2\sigma_c^{1/2}\rho^{1/2}(H - x)/\delta_h]}{\cosh [2\sigma_c^{1/2}\rho^{1/2}(H - h)/\delta_h]} \quad [12]$$

$$j = 2\sigma_c^{1/2}\rho^{-1/2}E_a \frac{\sinh [2\sigma_c^{1/2}\rho^{1/2}(H - x)/\delta_h]}{\cosh [2\sigma_c^{1/2}\rho^{1/2}(H - h)/\delta_h]} \quad [13]$$

The abbreviation $\sigma_c = a_0cF^2D/RT$ has the dimension ohm^{-1} cm^{-1}. For $x = h$ (lower film edge) one obtains $E = E_a$ from [12] and for $x = H$ (upper film edge) $j = 0$ from [13]. The boundary conditions [9] and [10] are therefore fulfilled. The residual potential E_H at the upper film edge is obtained from [12] with $x = H$

$$E_H = E_a/\cosh [2\sigma_c^{1/2}\rho^{1/2}(H - h)/\delta_h] \quad [14]$$

and the total electrode current j_t as a function of the applied potential $E_a \leqq 0.01$v from [13] with $x = h$

$$j_t = 2\sigma_c^{1/2}\rho^{-1/2}E_a \tanh [2\sigma_c^{1/2}\rho^{1/2}(H - h)/\delta_h] \quad [15]$$

For $H - h >> \delta_h$, the tanh in [15] tends toward one and j_t assumes its maximum value

$$j_{t\,opt} = 2\sigma_c^{1/2}\rho^{-1/2}E_a \quad [16]$$

When substituting [16] in [15] one can write the total current as

$$j_t/j_{t\,opt} = \tanh [2\sigma_c^{1/2}\rho^{1/2}(H - h)/\delta_h] \quad [15a]$$

With $(H - h)/\delta_h > 180$ and $E/E_a > 0.01$, one can approximate the hyperbolic functions in [12] and [13] with one and the same exponential function

$$E/E_a \approx j/j_{t\,opt} \approx \exp[2\sigma_c^{1/2}\rho^{1/2}(h - x)/\delta_h] \quad [17]$$

which results in an error of less than 1%.

The exponential decay of the potential and of the current in the film parallel to the surface according to [12] and [13] or [17] is shown in Fig. 2 for three different film thicknesses δ_h and 8N H_2SO_4 at 25°C. For the constants D, $_oc$, and ρ published data

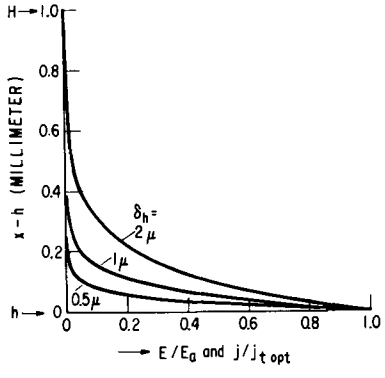

Fig. 2. Decay of the potential E and the current j in the film in relative units of the applied potential E_a and the optimum total current $j_{t\,opt}$ for different film thicknesses δ_h for 8N H_2SO_4 at 25°C.

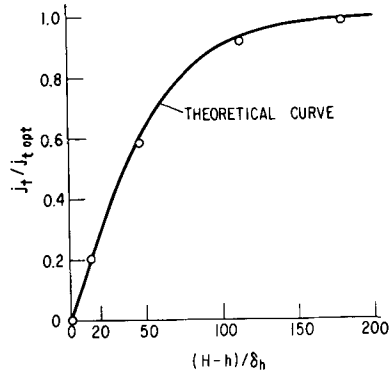

Fig. 3. Total current j_t (in units of $j_{t\,opt}$) as a function of the ratio of film length and film thickness for 8N H_2SO_4 at 25°C. Curve calculated from [15a]; points are experimental values.

(7-9) were used and extrapolated, where necessary. For 1N H_2SO_4, $D = 3.1 \cdot 10^{-5}$ cm^2/sec, $_oc = 7.67 \cdot 10^{-7}$ mole H_2/cm^3 (at $p_{H_2} + p_{H_2O} = 1$ atm), $\rho = 4.65$ ohm-cm; for 8N H_2SO_4, $D = 2.2 \cdot 10^{-5}$, $_oc = 7.17 \cdot 10^{-7}$, and $\rho = 1.21$ were employed. The film thicknesses 0.5, 1, and 2μ are close to the actually expected (5) thickness of about 1μ. The potential decays to 1% of the applied potential E_a over a film length of a few tenths of a millimeter. The parts of the film above this length are essentially at zero potential and contribute less than 1% to the total current $j_{t\,opt}$. The potential E_H at the upper film edge according to [14] is only 3×10^{-7} E_a. For acid concentrations smaller than 8N, curves analogous to those in Fig. 2 are obtained from [17]. However, the increase of the resistivity and of the diffusion coefficient (entering into σ_c) causes a steeper exponential decay than for 8N H_2SO_4.

Equation [15a] describes how the total current depends on the film length and the film thickness. In Fig. 3, $j_t/j_{t\,opt}$ is plotted against the ratio $(H - h)/\delta_h$ of film length and film thickness for 8N H_2SO_4 at 25°C. For $H - h = 180\delta_h$, the total current j_t deviates by less than 1% from the maximum value $j_{t\,opt}$ and approaches $j_{t\,opt}$ exponentially for $H - h > 180\delta_h$. For a fixed film thickness, Fig. 3 shows how the current varies with the film length according to [15a]. As experimental check for the theoretical curve, the upper part of the plot of the experimental current against the electrode position for 8N H_2SO_4 and $E_a = 0.4$v [(5), Fig. 2] was used. The parts of the film close to the upper film edge meet the condition $E < 0.01$v for which [15a] can be applied. Figure 3 shows that the experimental points agree well with the theoretical curve. The curves were fitted assuming a film thickness of 1.5μ; other values of δ_h did not fit the curves, and 1.5μ can therefore be considered as a semi-empirical value for the film thickness.

For film lengths $H - h > 180\delta_h = 0.27$ mm, the total current j_t is approximately equal to $j_{t\,opt}$ and from [16] should depend linearly on the applied potential in the range $0 \leqq E_a \leqq 0.01$v. An experimental check of [16] can readily be performed.

Figure 4 shows two curves which were calculated from [16] for 1N and for 8N H_2SO_4. The experimental curves were obtained with a sandblasted

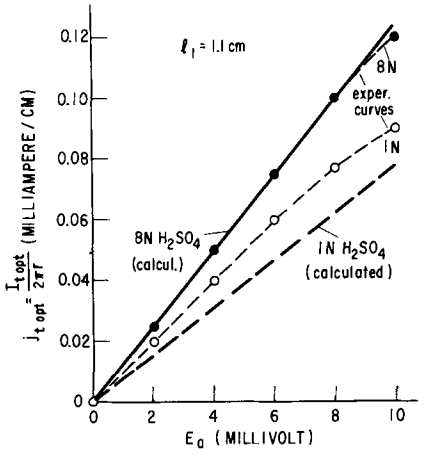

Fig. 4. Optimum total current $j_{t\,opt}$ as a function of the applied potential E_a for 8N and 1N H_2SO_4 at electrode position l_1 = 1.1 cm. Heavy lines, theoretical curves; points are experimental values.

platinum electrode with a roughness factor of 10 for an electrode position $l_1 = 1.1$ cm (compare Fig. 1). For this position, the undesired contribution to the current of H_2-diffusion through the bulk electrolyte is negligible and the condition $(H - h) > 180\delta_h$ is met. Both experimental curves show the required linearity for small potentials, but begin to deviate above 8 mv. The quantitative agreement between experiment and theory is very good for 8N H_2SO_4. For 1N H_2SO_4, the experimental currents are some 30% larger than the calculated ones. This can be understood if one assumes that the smaller diffusion rate of hydrogen ions in the less concentrated electrolyte starts to be comparable with the over-all reaction rate. As a consequence of this, the concentration of the electrolyte in the film increases over the concentration in the bulk. Since the simultaneous decrease of the resistivity outweighs the decrease of the diffusion coefficient, the current increases according to [16]. Such an increase of the current was observed experimentally for larger applied potentials and will be discussed later.

Current-potential relation over whole potential range.—At potentials E_a above 0.01v, the experimental curves deviate more and more from the calculated curves. This is to be expected because [15] and [16] are only approximate solutions of differential Eq. [11] for $E_a \leq 0.01$v. The current as a function of the potential over a wider range would be given by [11] because of $j = -\rho^{-1}\delta_h\, dE/dx$, if the integration constant K_1 in [11] would be known. With $dE/dx = 0$ for $x = H$ (boundary condition [10]) and $E = E_H$ for $x = H$, the constant K_1 becomes

$$K_1 = 2\rho k_{od}\delta_h^{-2}\left(E_H + \frac{1}{2}\phi^{-1}\, e^{-2\phi E_H}\right)$$

According to Fig. 2 the potential E decays steeply along the liquid film and from [14] E_H is vanishingly small for $E_a \leq 0.01$v. For larger applied potentials E_a, the potential E might not decay as steeply, and E_H might therefore be somewhat larger than, for instance, the 3×10^{-7}v calculated from [14] for $(H - h) = 0.1$ cm and $E_a = 1$v. Nevertheless, one can expect that for sufficiently large film lengths the potential E_H at the upper film edge is close to zero potential and that one can write K_1 approximately as $K_1 = \rho k_{od}\delta_h^{-2}\phi^{-1}$. The total current j_t is obtained when one substitutes [11] with $E = E_a$ in [4]

$$j_t = 2({}_oc\, FD/\rho)^{1/2}\,[E_a - (1 - e^{-2\phi E_a})/2\phi]^{1/2} \qquad [18]$$

For small values of the applied potential E_a one can again approximate the exponential term with the parabola $1 - 2\phi E + 2a\phi^2E^2$, and one can readily see that in this case j_t from [18] becomes identical with $j_{t\,opt}$ from [16]. For $E_a > 0.05$v, the exponential term can be neglected with an error of less than 2%, and for $E_a > 0.3$v, one can further simplify [18] and obtains

$$j_t \approx 2({}_oc\, FD/\rho)^{1/2}\sqrt{E_a} \qquad [18a]$$

The error of about 4% for $E_a = 0.3$v decreases with increasing potentials.

The linear relationship between the experimental values of j_t and E_a at small potentials has already been shown in Fig. 4. According to Eq. [18] the experimental values of j_t should fall on a straight line when plotted against $[E_a - (1 - e^{-2\phi E_a})/2\phi]^{1/2}$. Figure 5 shows two curves for 1N and 8N H_2SO_4 which were calculated from [18] and in the square root plot are straight lines with a slope of $2({}_oc\, FD/\rho)^{1/2}$. The constants D, ${}_oc$, and ρ are the same as those used before. The experimental curve for 8N H_2SO_4 and an electrode position $l_1 = 1.1$ cm is in good quantitative agreement with the calculated curve over the entire range of potentials from zero to 1.8v. The experimental values of the current for 1N H_2SO_4 fall on a straight line as required, but the currents are roughly 30% larger than the calculated currents. The same observation was mentioned above for potentials smaller than 0.01v and was interpreted as the consequence of an increase of the acid concentration due to slow hydrogen ion diffusion. In favor of this explanation is the finding that the currents

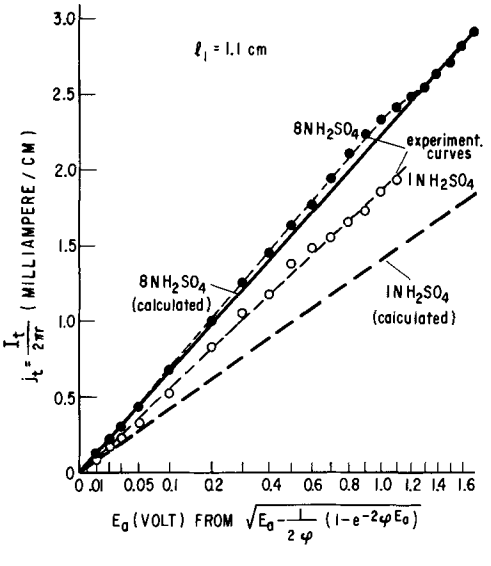

Fig. 5. Optimum total current $j_{t\,opt}$ as a function of $[E_a - \frac{1}{2}\phi^{-1}(1 - e^{-2\phi E_a})]^{1/2}$ for 8N and 1N H_2SO_4 at electrode position l_1 = 1.1 cm. Heavy lines, theoretical curves; points are experimental values.

have a tendency to increase slightly with time. This was especially noticeable after the electrode had been completely submerged in the electrolyte shortly before the current was measured at $l_1 = 1.1$ cm. In this case, the electrolyte concentration in the film was supposedly the same as that in the bulk immediately after raising the electrode to 1.1 cm, and then the concentration increased slowly. No such effect was found in $8N$ H_2SO_4, and this might indicate that in this case the diffusion of the hydrogen ions is still fast enough to prevent appreciable changes of the electrolyte concentration.

The currents at a platinized platinum electrode with a roughness factor of 88 were found larger than the calculated currents by a factor of more than 2 in $1N$ H_2SO_4 and by a factor of 1.65 in $8N$ H_2SO_4. This influence of the surface roughness on the currents can be explained by assuming that the true circumference of the electrode is larger than the geometric circumference and that the liquid film covering the surface is so thin that it adapts the shape of the true circumference. The area available for the diffusion of hydrogen then increases with the surface roughness. Furthermore, the large "internal" surface of the platinum sponge is also likely to contribute somewhat to the current. According to a calculation based on electron micrographs, the surface of the electrode with r.f. 88 consists of 10 layers of platinum black particles with an average diameter of 0.5μ [compare (5)].

It is noteworthy that the current does not depend on the film thickness [18]. However, this is only true as long as the potential at the upper film edge tends toward zero.

Case 2. Diffusion of hydrogen molecules through film and meniscus for large potentials.—The contribution to the current by diffusion of hydrogen through the meniscus and the potential gradient in the meniscus will now be considered together with diffusion through the film for the special case of applied potentials $E_a > 0.1$v. In this case, an approximate solution of the problem is possible.

In the following treatment, the local current density i which is given by [7] will be assumed to be independent of the local potential $E(x)$; i will be considered $\neq 0$ for all potentials $E(x) \geqq +0$ and equal to zero for $E(x) = -0$ (step function). This approximation is very good for potentials $E(x) > 0.05$v because the exponential term in [7] is then much smaller than unity (limiting current density). The error which arises for $E(x) < 0.05$v is the smaller the larger the applied potential E_a; in this case, most of the electrode surface lies at potentials $E(x) > 0.05$v since the potential decays especially steeply along the electrode surface for small $E(x)$ (compare Fig. 2 and Eq. [17]).

Current and potential distribution in meniscus and film and current-potential relation.—Under the foregoing assumption, Eq. [7] simply becomes $i = k_{od}/\delta(x)$ and with the expression [6a] for $\delta(x)$ and with [1b] one obtains

$$dj/dx = -k_{od}/[\delta_o(1 - x/h)^2 + \delta_h] \qquad [19]$$

For $x \leqq h$ this equation describes dj/dx in the meniscus. When substituting [6b] instead of [6a] one obtains the equation $dj/dx = -k_{od}/\delta_h$ which describes the film for $x \geqq h$. If one postulates that the term $\delta_o(1 - x/h)^2$ is zero for $x > h$, then [19] can be applied to meniscus and film. The first integration of [19] yields the current j per unit circumference as a function of x, and the potential E as a function of x is according to [4] given by $E = -\rho \int j dx/\delta(x)$. The boundary conditions are

$$E = E_a \text{ for } x = 0 \qquad [20a]$$

$$E = 0 \text{ for } j = 0 \text{ with } E_a \leqq \hat{E}_a \qquad [20b]$$

The position of zero potential depends on the applied potential E_a. For a certain applied potential $E_a = \hat{E}_a$, zero potential $E = 0$ is obtained for $x = \mathrm{H}$ (upper film edge) and for $E_a = E_{mo}$, zero potential is obtained for $x = h$ (upper meniscus edge).

The integration of [19] yields the current as a function of x

$$j = (2k_{od}/\rho)^{1/2} [T_m(x) - T_f(x) + \sqrt{E_a} - \sqrt{E_{mo}}] \qquad [21]$$

with

$$T_m(x) = h(k_{od}\rho/2\delta_o\delta_h)^{1/2} \operatorname{arc\,tan} [(\delta_o/\delta_h)^{1/2} (1 - x/h)] \qquad [21a]$$

$$T_f(x) = h(k_{od}\rho/2\delta_h^2)^{1/2} (x/h - 1) \qquad [21b]$$

and

$$\sqrt{E_{mo}} = h(k_{od}\rho/2\delta_o\delta_h)^{1/2} \operatorname{arc\,tan} (\delta_o/\delta_h)^{1/2} \qquad [21c]$$

For the decay of the potential E parallel to the electrode surface one obtains

$$E = [T_m(x) - T_f(x) + \sqrt{E_a} - \sqrt{E_{mo}}]^2 \qquad [22]$$

Equations [21] and [22] are, similar to [19], composed of two analytical functions, one of them describing j and E in the meniscus ($x \leqq h$) and the other function describing j and E in the film ($x \geqq h$). In order to apply [21] and [22] one has to set $T_f(x) = 0$ for $x < h$ and $T_m(x) = 0$ for $x > h$. For $x = h$, where $\delta(x)$ is identically δ_h for meniscus and film, $T_m(x)$ and $T_f(x)$ are identically zero as one can readily see from [21a] and [21b].

The current as a function of the potential at any point x

$$j = (2k_{od}/\rho)^{1/2} \sqrt{E} \qquad [23]$$

is obtained by eliminating x from [21] and [22]. This means that the same square root relationship applies at any point in meniscus and film; Eq. [23] is an analytical function for all x for which $0 \leqq x \gtreqless h \leqq \mathrm{H}$.

In particular, for $x = 0$, the potential E from [22] equals the applied potential E_a (boundary condition [20a]) and the current j from [23] becomes

$$j_t = 2(FD_oc/\rho)^{1/2} \sqrt{E_a}, \text{ with } E_a \leqq \hat{E}_a \qquad [23a]$$

This is the same relationship between the total current j_t and the applied potential E_a which was obtained for exclusive diffusion through the film [18a]. For $x = h$, the potential at the lower film edge

$$\sqrt{E_f} = \sqrt{E_a} - \sqrt{E_{mo}} \qquad [22a]$$

and the total film current

$$j_f = (2k_{od}/\rho)^{1/2}\sqrt{E_f} \qquad [23b]$$

are obtained from [22] and [23]. The maximum meniscus current $\hat{j}_m$ follows directly from [23a] with $E_a = E_{mo}$.

The applied potential $E_a = \hat{E}_a$ for which the potential E at $x =$ H vanishes is from [22]

$$\sqrt{\hat{E}_a} = \sqrt{E_{mo}} + \sqrt{E_{fo}} \qquad [24]$$

where

$$E_{fo} = \frac{1}{2} k_{od}\rho(\mathrm{H} - h)^2/\delta_h^2 \qquad [25]$$

For $E_a = \hat{E}_a$, the largest possible total current $\hat{j}_t$ is obtained from [23a]. For $E_a > \hat{E}_a$, the potential E at $x =$ H will exceed zero; however, the current cannot increase above $\hat{j}_t$ because the current density i is independent of $E(x)$ for all potentials $E(x) > +0$ according to the original assumption. Once the whole electrode surface is at potentials $E(x) > +0$ the current has therefore reached its optimum value $\hat{j}_t$. In practice, this situation should arise when the potential for $x =$ H has reached values larger than about 0.05v. It has been observed experimentally [compare Fig. 5 (5)] that the current for low electrode positions indeed reaches such a maximum while a maximum does not occur at higher electrode positions, where another electrode process (oxygen evolution) sets in before the maximum can occur.

The current j and the potential E as a function of x according to [21] and [22] are shown in Fig. 6 for $\delta_h = 1\mu$ and applied potentials E_a of 0.1 and 0.4v in 1N and in 8N H_2SO_4. One can see that H_2-diffusion through the lower part of the meniscus from $x = 0$ to $x = 2.5$ mm contributes less than 3% to the total current j_t and that the main contribution comes from the upper 0.2 mm of the meniscus and several tenths of a millimeter of the liquid film. What the relative contributions of the meniscus and the film are depends on the applied potential, acid concentration, and film thickness. For a given concentration and film thickness, the contribution of the meniscus to the current depends on the applied potential for $E_a < E_{mo}$ only; for $E_a = E_{mo}$, the meniscus contributes a maximum current $\hat{j}_m$ which is not exceeded for $E_a > E_{mo}$. Table I gives values for E_{mo} and $\hat{j}_m$ which were calculated from [21c] and [23].

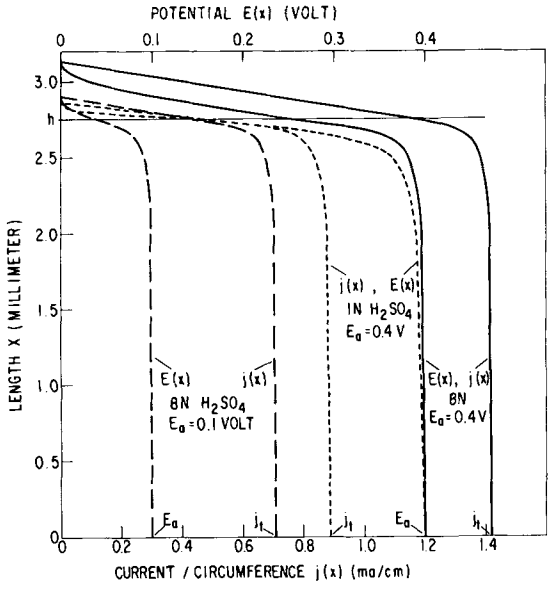

Fig. 6. Decay of the potential E and the current j in film and meniscus for 8N H_2SO_4 at $E_a = 0.1$ and 0.4 v and for 1N H_2SO_4 at $E_a = 0.4$v.

As one would expect, E_{mo} and $\hat{j}_m$ increase with decreasing film thickness. With decreasing concentration, the resistivity increases which causes an increase of E_{mo}. The change in resistivity does not affect $\hat{j}_m$ as one can show readily by substituting [21c] in [23]. However, the diffusion coefficient of hydrogen increases with decreasing concentration, and this causes an increase of $\hat{j}_m$.

Diffusion of H_2 through the film does not contribute to the current for $E_a \leq E_{mo}$. However, the film current increases steeply with increasing applied potentials $E_a > E_{mo}$ and is given quantitatively by $j_f = j_t - \hat{j}_m$ or, which is the same, by substituting [22a] in [23b].

The potential parallel to the electrode surface decreases very little over the larger length of the meniscus as one can see from Fig. 6. The potential change, like the current change, occurs mainly over a few tenths of a millimeter of the meniscus edge and the adjacent film. The potential decay in the film is parabolic as follows from [22] with [21b] and is the steeper, the smaller the acid concentration and the film thickness are.

Below $E(x) = 0.05$v, the true decay of the potential and of the current will differ more and more from that shown in Fig. 6, because the exponential term in [7] can no longer be neglected. As a consequence, potential and current decay exponentially

Table I. Values for E_{mo} and $\hat{j}_m$

δ_h, μ		10	5	2	1	0.5	0.2	0.1
E_{mo}, mv	8N H_2SO_4	1.26	2.56	6.6	13.34	26.85	67.5	135.7
$\hat{j}_m$, ma/cm	8N H_2SO_4	0.080	0.114	0.182	0.259	0.368	0.584	0.826
E_{mo}, mv	1N H_2SO_4	7.31	14.83	38.25	77.4	155.8	392	786
$\hat{j}_m$, ma/cm	1N H_2SO_4	0.120	0.171	0.275	0.390	0.553	0.878	1.245

for these small values of E as it is shown in Fig. 2 (compare also [17]).

Calculation of film thickness and true current density.—From Fig. 6 and [21] the current should increase linearly with the electrode length x for $x \geqq h$ in the film (and like the arc tan for $x \leqq h$ in the meniscus). This is found experimentally and speaks for the existence of a liquid film. From the slope of the measured straight line the film thickness can be deduced as follows: The maximum possible current $\hat{j}_f$ that a film of a given length H — h can contribute to the total current is obtained by substituting [25] in [23b]

$$\hat{j}_f = k_{od}(\mathrm{H} - h)/\delta_h \qquad [26]$$

This maximum film current occurs when the applied potential E_a is equal to or larger than the optimum applied potential $\hat{E}_a$ according to [24], and the film length, necessary to produce the maximum current, can be calculated from [24] and [25] for any given applied potential. For $E_a = 0.4$v, for example, this film length is 108μ in 1N H_2SO_4 and 378μ in 8N H_2SO_4. For larger film lengths the current must stay constant, and for smaller film lengths the current is expected to decrease linearly with decreasing film length. The slope of this straight line is, from [26], given by k_{od}/δ_h. The experimental slopes [compare Fig. 2 (5)] are 0.285 ma/cm/0.1 mm film length in 1N H_2SO_4 and 0.205 ma/cm/0.1 mm length in 8N H_2SO_4. The ratio of these two figures is 1.4 which agrees well with the ratio $k_{od}(1N)/k_{od}(8N) = 1.5$ from [26]. A film thickness of 1.5μ can be calculated from [26] when one uses the experimental slopes mentioned above. The same film thickness was calculated above based on different considerations. The limiting local current density which is constant over the whole film is obtained from [7] as k_{od}/δ_h. One obtains 20 ma/cm^2 in 8N H_2SO_4 and 30 ma/cm^2 in 1N H_2SO_4.

The treatment of diffusion of molecular hydrogen through the meniscus and a liquid film above the meniscus as the rate-limiting step leads to a quantitative agreement between the calculated and observed current potential curves. It will now be investigated whether the treatment of slow surface diffusion of hydrogen atoms leads to a disagreement with the experimental results.

Surface Diffusion of Hydrogen Atoms as Rate-Limiting Step

Justi *et al.* (1) showed that the treatment of surface diffusion of hydrogen atoms as slow transport mechanism followed by hindered ionization leads to a complicated nonlinear differential equation which cannot be integrated analytically. The differential equation was obtained for a single straight pore in which the electrolyte forms a right angle boundary with the pore wall (the actually existing meniscus is therefore disregarded) and under the assumption that the contribution to the current by diffusion of molecular hydrogen can be neglected. In order to solve the differential equation, approximations to the physical model have to be made. Justi *et al.* (1) made the simplifying assumptions that the ionization of the hydrogen atoms occurs essentially in a narrow band close to the "three-phase boundary" and that in this band the surface activity of the hydrogen atoms, the polarization, and the current density are constant.

These assumptions are not expected to describe the physical model properly. The activity of the hydrogen atoms must be assumed to vary along the electrode surface, even if the reaction zone is assumed to be very small. Without activity gradient, no surface diffusion of hydrogen is possible. Then, as a consequence of the activity gradient, the current density has to vary along the electrode surface, too. Under the assumptions made by Justi *et al.*, the relation between total polarization and total pore current is simply the known expression for simultaneous discharge (ionization) and concentration polarization (10) plus a term which takes into account the ohmic drop in the pore electrolyte. A decision whether surface diffusion is determining as transport mechanism does not seem possible on the basis of the equations derived by Justi *et al.* (1).

Different approximations are made in the following treatment so that an upper limit can be set for the expected currents as a function of the polarization, and it will be shown that for the smaller polarizations the theoretical currents are much smaller than the measured currents.

The approximations are as follows: (i) The existence of meniscus and film is disregarded; this means, the bulk electrolyte in Fig. 1 forms a right angle boundary with the electrode surface at $x = 0$. Consequently, the potential gradient parallel to the electrode surface can be neglected which is not possible for a narrow pore. (ii) The diffusion of molecular hydrogen is neglected; surface diffusion of atomic hydrogen is the determining transport mechanism.

In contrast to the treatment of Justi *et al.*, the surface activity of the hydrogen atoms and the current density are considered to vary parallel to the electrode surface. Close to the three-phase boundary, $x = 0$, the activity is expected to be high (close to the equilibrium activity) and the concentration polarization is therefore small. For $x < 0$ the activity decreases; this means that the concentration polarization increases. According to assumption (i), the total polarization E_a is constant along the electrode surface. Hence, the discharge (ionization) polarization is the difference between E_a and the concentration polarization for each x.

The current density in the presence of concentration and ionization polarization may, under certain assumptions (10), be written as

$$i(x) = i_{oi}[(a(x)/{}_oa)e^{\alpha\phi E_a} - e^{-(1-\alpha)\phi E_a}] \qquad [27]$$

where i_{oi} is the exchange current density of the discharge (ionization), α the transfer coefficient and ${}_oa$ the equilibrium activity. The current as a function of x is

$$I(x) = I_t - 2\pi rFD'\, da(x)/dx \qquad [28]$$

where I_t is the total electrode current and D' the diffusion coefficient of the hydrogen atoms on the platinum surface. When using [1b] and [2] and when substituting the differential Eq. [28] in [27], one obtains

$$d^2a/dx^2 = i_{oi}[(a/{}_oa)e^{\alpha\phi E_a} - e^{-(1-\alpha)\phi E_a}]/FD' \quad [29]$$

With the boundary conditions

$$a(x) = a(0), \text{ for } x = 0 \quad [30a]$$

$$da(x)/dx = 0, \text{ for } x = -l_2 \quad [30b]$$

the solution of the differential equation is

$$a(x) = [a(0) - {}_oae^{-\phi E_a}] \cosh \lambda\,(l_2 - |x|)/\cosh \lambda\, l_2 + {}_oae^{-\phi E_a} \quad [31]$$

with

$$\lambda = (i_{oi}\, e^{\alpha\phi E_a}/{}_oaFD')^{1/2} \quad [32]$$

The boundary condition [30b] means that the current for $x = -l_2$ is equal to the total current I_t which follows from [28]. The current as a function of x can be obtained simply by differentiating [31] and substituting da/dx in [28]. The total current I_t as a function of the total polarization

$$j_t = (a(0)/{}_oa - e^{-\phi E_a})({}_oaFD'\, i_{oi}\, e^{\alpha\phi E_a})^{1/2} \tanh \lambda l_2 \quad [33]$$

is then simply obtained from [28] by observing the fact that $I(x) = 0$ for $x = 0$ and that $I_t = 2\pi r j_t$ from [2].

The activity $a(0)$ at the three-phase boundary in [31] and [33] depends in a complicated manner on the rate of dissociation and surface diffusion and upon the total current I_t, as Justi *et al.* (1) have shown. If the rate of dissociation is assumed to be fast compared to the rates of surface diffusion and ionization, then $a(0)$ is equal to the equilibrium activity ${}_oa$.

For $\lambda l_2 >> 1$, $\tanh \lambda l_2$ in [33] becomes very nearly one. Using $i_{oi} = 0.6$ amp/cm^2 (8) and assuming that ${}_oa$ is equal to the equilibrium surface concentration of hydrogen, ${}_oc_H = 6 \times 10^{-4}$ coul/cm^2 (11, 12), a lower limit for λ is obtained for $E_a \to 0$ as $\lambda = 33/\sqrt{D'}$ (1/cm). Unfortunately, not much information is available for the surface diffusion of hydrogen on metals. Gomer *et al.* (13, 14) studied the surface diffusion of hydrogen on single crystals of tungsten and nickel with the field emission microscope. They found diffusion coefficients of the order of 10^{-8} cm^2/sec at room temperature. Since the diffusion coefficient depends strongly on the degree of coverage, the value given above is merely an average value. For a depth of immersion l_2 of the order of a few millimeter, the condition $\lambda l_2 >> 1$ is indeed fulfilled and [33] together with $a(0) = {}_oa$ assumes the simple form

$$j_{t\,\mathrm{opt}} = (1 - e^{-\phi E_a})\,({}_oaFD'\, i_{oi}\, e^{\alpha\phi E_a})^{1/2} \quad [34]$$

This is an upper limit for the total current per unit circumference as a function of the total polarization which can be expected for surface diffusion as transport mechanism. The existence of meniscus and film, which was disregarded in this treatment, leads to a potential gradient parallel to the electrode surface so that the potential across the interface is smaller than E_a for all $-l_2 < x \leqq 0$. Consequently, j_t is smaller in this case than under the assumption of a constant E_a. The assumption of $a(0) = {}_oa$ also sets an upper limit for j_t.

Using the same numerical values as above and accounting for the roughness factor 10 of the studied sandblasted electrode, $j_{t\,\mathrm{opt}}$ becomes 0.23 ma/cm for $E_a = 0.4$v, 0.025 ma/cm for 0.1v, and 0.012 ma/cm for 0.01v as compared to the measured values 1.45 ma/cm, 0.67 ma/cm, and 0.12 ma/cm. In the case of a smooth platinum electrode with a roughness of 2, the calculated currents are smaller by a factor of 5 than for the sandblasted electrode, while the experimental currents are almost the same in both cases. In either case the calculated currents are much smaller than the measured currents.

From the treatment given above one may conclude therefore that the surface diffusion of hydrogen atoms is much too slow a transport process to account for the actually measured currents. However, because of the stringent approximation (meniscus and film disregarded) which had to be made in order to solve the differential equation, the treatment has only the value of setting an upper limit for the current; the theoretical current-potential relations [33] and [34] would not be expected to conform with experimental current-potential curves if the surface diffusion were fast enough to account for the large measured currents.

Conclusions

The theoretical treatment of the concept of rate-limiting diffusion of molecular hydrogen through the electrolyte meniscus and a liquid film above the meniscus (5) leads to the following results:

1. For applied potentials smaller than 0.01v the decay of potential and current in the film is exponential with the height. The parts of the film above a length of 0.35 mm are essentially at zero potential and contribute less than 1% to the total current.

2. The relationship $I_t = K_1[E_a - K_2(1 - e^{-K_3E_a})]^{1/2}$ between total current and applied potential is derived for the existence of a liquid film which agrees quantitatively with experimental results obtained on a sandblasted platinum electrode in 8N H_2SO_4 over a potential range from zero to 1.8v.

3. For applied potentials smaller than 0.01v, a linear dependence of the total current on the applied potential is calculated which also checks quantitatively with the experimental results on platinum in 8N H_2SO_4.

4. For applied potentials or total polarizations larger than 0.1v the relation $I = K\sqrt{E}$ is derived which is applicable to any part of film and meniscus.

5. The potential decays parallel to the surface like the square of the arc tan in the meniscus and parabolically in the film, as long as the polarization is larger than 0.05v. The current decays like the arc tan in the meniscus and linearly in the film.

6. The relative contributions of meniscus and film to the total current depend on film thickness, acid

concentration, and applied potential. For a film thickness of 1μ, $8N$ H_2SO_4 and $E_a = 0.4$v, the meniscus contributes 0.26 ma and the film 1.16 ma.

7. The reaction zone is confined to a narrow band close to the upper meniscus edge. In the numerical example given in 6, 0.35 mm of the meniscus and 0.38 mm of the film are responsible for 98% of the total current.

8. From the theoretical treatment, the current should increase linearly with the electrode length x above the bulk electrolyte. This is found experimentally, and from the slope of the measured straight line, a film thickness of 1.5μ is deduced.

9. With this film thickness, a current density of 20 ma/cm^2 for platinum in $8N$ H_2SO_4 and of 30 ma/cm^2 in $1N$ H_2SO_4 is calculated.

10. A theoretical treatment of the surface diffusion of hydrogen atoms as a rate-determining transport mechanism shows that the surface diffusion is much too slow a process to account for the actually measured currents. A similar treatment of slow surface diffusion by Justi *et al.* (1) employs approximations which are too stringent and therefore cannot be used to arrive at such a decision.

Manuscript received July 20, 1962; revised manuscript received Oct. 1, 1962. This paper was prepared for delivery before the Boston Meeting, Sept. 16-20, 1962.

Any discussion of this paper will appear in a Discussion Section to be published in the December 1963 JOURNAL.

REFERENCES

1. E. Justi, M. Pilkuhn, W. Scheibe, and A. Winsel, "High-drain hydrogen diffusion electrodes operating at ambient temperature and low pressure," p. 33, Verlag d. Akademie d. Wissenschaften u.d. Literatur, Wiesbaden (1959).
2. O. S. Ksenzhek and V. V. Stender, *Doklady Akad. Nauk SSSR*, **107**, 280 (1956); *Zhur. Fiz. Khim.*, **31**, 117 (1957).
3. W. Stein, *Naturwissenschaften*, **45**, 459 (1958).
4. A. Winsel, *Z. Elektrochem.*, **66**, 287 (1962).
5. F. G. Will, *This Journal*, **110**, 145 (1963).
6. K. L. Wolf, "Physik und Chemie der Grenzflächen," Vol. II, Springer, Berlin (1959).
7. M. Breiter and K. Hoffmann, *Z. Elektrochem.*, **64**, 462 (1960).
8. R. C. Reid and T. K. Sherwood, "The Properties of Gases and Liquids," McGraw-Hill Book Co., New York (1958).
9. Gmelins Handbuch der anorganischen Chemie, "Schwefel," 8 Aufl. B2, Verlag Chemie, Weinheim (1960).
10. M. Breiter and R. Clamroth, *Z. Elektrochem.*, **58**, 493 (1954).
11. M. Breiter, C. A. Knorr, and W. Völkl, *ibid.*, **59**, 681 (1955).
12. F. G. Will and C. A. Knorr, *ibid.*, **64**, 258 (1960); **64**, 270 (1960).
13. R. Wortman, R. Gomer, and R. Lundy, *J. Chem. Phys.*, **27**, 1099 (1957).
14. R. Gomer, *Discussion Faraday Soc.*, **28**, 23 (1959).

Electrochemistry in Pyridine

I. Polarography and Macroscale Electrolysis of Inorganic Salts

Andrzej Cisak[1] and Philip J. Elving

Department of Chemistry, The University of Michigan, Ann Arbor, Michigan

ABSTRACT

The use of pyridine as a typical aprotic solvent for polarographic and macroscale electrolysis has been investigated. The silver electrode in $1M$ silver nitrate in pyridine (NAgE) is a reliable reference electrode; its potential *vs.* the aqueous saturated calomel electrode is +0.09v (liquid junction potentials included). Lithium chloride and nitrate, and tetra-*n*-butylammonium iodide are satisfactory as background electrolytes; decomposition potentials at the dropping mercury electrode (DME) *vs.* NAgE are Li(I) —2.0v and Bu_4NI —2.3v. Tl(I) and Pb(II) are apparently reversibly reduced in diffusion-controlled processes to the metal, *i.e.*, amalgam, whereas Zn(II) is reduced in two one-electron steps; half-wave potentials at the DME *vs.* NAgE are Tl(I) —0.48v, Pb(II) —0.61v (nitrate media) and —0.96v (chloride media), and Zn(II) —1.61v (wave I) and —1.70v (wave II). Solutions of Al(III) give a well-defined polarographic wave, which is due not to reduction of the Al(III) but to that of the solvent.

In recent years interest in the investigation of electrochemical and, in particular, polarographic behavior in nonaqueous media has greatly increased as a result of both practical and theoretical demands. Practically, water is not a satisfactory solvent for many organic compounds, and the possibility of hydrolysis complicates evaluation of data. The theoretical reasons are, however, probably more important.

The solvent plays an important role in polarography. It controls the mass transfer process through its effect on the diffusion coefficient *via* viscosity and solvation and affects the potential in a variety of ways, the most important of which are its effect on the structure of the electrical double layer and its participation directly or *via* derived species in the primary electrochemical reaction, in accompanying chemical reactions, and in polarization of the reactant molecule. For example, in solvents of low proton availability the addition of electrons can be studied with little or no complication due to protonation.

Solvents which have been studied can be divided into three types: (*a*) proton-releasing solvents such

[1] Permanent address: Laboratory of Inorganic Chemistry, University of Warsaw, Warsaw, Poland.

Table I. Physical properties of pyridine

Molecular weight	79.10
Density, 15°C	0.988 g/ml
30°C	0.973 g/ml
Melting point	−41.8°C
Boiling point	115.6°C
Electrical conductivity, 25°C	4.8×10^{-8} ohm^{-1}
Dielectric constant, 25°C	12.3
Dipole moment	2.30
Viscosity, 25°C	0.878 cp
Heat of vaporization at bp	8.43 kcal/mole
Trouton's constant	21.7
Vapor pressure, 13.2°C	10 mm
57.8°C	100 mm
Dissociation constant, K_a, in water, 25°C	4.2×10^{-6}

as water, ammonia, and acetic acid; (*b*) nonproton-releasing solvents, the most popular of which have been acetonitrile and dimethylformamide; and (*c*) nonproton-containing solvents, the only one of which to have been studied being sulfur dioxide.

During the past year, study was started of pyridine as a nonproton-releasing solvent of a type sufficiently different from acetonitrile and dimethylformamide to warrant its investigation, *e.g.*, it is apparently the first aromatic-type solvent to be systematically considered for polarography.

In spite of its low dielectric constant (Table I) (1-3), pyridine is a good solvent for a relatively large number of inorganic and organic substances. In the case of many salts the solubility is due in at least part to the solvating, *i.e.*, complexing, ability of the pyridine for cations. The conductivity of such solutions is relatively poor as would be expected from the low dielectric constant. Pyridine has a convenient liquid range and relatively low vapor pressure at room temperature, although its odor is unpleasant for most observers. The normal value of Trouton's constant indicates a relative lack of association of the molecules of pyridine in the liquid. Pyridine has a density and a viscosity similar to that of water. Pyridine-water mixtures have greater viscosities with a maximum at 66.6 w/o (weight per cent) pyridine: 2.23 cp at 25°C (4). The solvation and viscosity behavior of pyridine would be expected to reveal itself in the polarographic properties of the half-wave potential and diffusion current constant as compared to the values of such properties in aqueous solution.

The following metals have been successfully electrodeposited from pyridine solutions using platinum, mercury, and iron electrodes (5): lithium, sodium, potassium, copper, silver, magnesium, calcium, barium, zinc, lead, and iron. However, Müller (6) was not able to confirm the reported successful deposition of Ba (7).

As a polarographic solvent, pyridine is little used, most work involving it having been done in pyridine-water mixtures. At the beginning of the present study, the only known published paper on polarography in pyridine was a study of some organosilanes by Abrahamson and Reynolds (8). The recent thesis by Willeboordse (9) deals briefly with the polarography of Cd(II), Zn(II), and Co(II) in pyridine-water mixtures and in pure pyridine.

The present investigation was primarily concerned with establishing conditions for future studies involving polarography, coulometry, macroscale electrolyses, and other voltammetric-related technics, as well as in locating and defining a suitable reference electrode, satisfactory background electrolytes, and the behavior of a few metallic ions which could serve as reference ones in future studies.

Experimental

Reagents.—Good, reproducible polarographic waves could be obtained in the pyridine used (J. T. Baker analytical reagent grade) without further purification; however, the results given in the present paper were obtained with pyridine, which was dried by being shaken with Linde molecular sieves type 4A (a synthetic metal-alumino-silicate) and left standing over them for two or three days. The dryness of pyridine and pyridine solutions was checked by floating clean, freshly cut metallic potassium on them; pyridine which gave no reaction after several hours contact with potassium was considered to be satisfactory. Potassium hydroxide is insoluble in pure pyridine (1).

LiCl (Baker & Adamson reagent) and $LiNO_3$ (J. T. Baker analyzed reagent) were used without further purification; the salts were dried at 150°-200°C and the warm crystals were dissolved; the dried salts were kept in a desiccator and were reheated prior to use. TlOAc (Fisher Scientific), $Pb(NO_3)_2$ (Mallinckrodt), and $Pb(OAc)_2$ (Baker & Adamson) were also used without further purification. $ZnCl_2$ (Baker & Adamson reagent) was dried at about 150°C and dissolved while warm. Tetra-*n*—butylammonium iodide was purified by recrystallization from ethyl acetate by Dr. P. G. Grodzka, who also supplied tetramethylammonium iodide and tetraethylammonium bromide.

Oiled pumped nitrogen and argon (claimed 99.998% purity) were used to purge solutions and cells of oxygen.

Since the densities of water and pyridine are almost the same, there is little difference between volume and weight per cent of mixtures of the two solvents except for volume change on mixing. In the present study, volume per cent is used, *i.e.*, the 67% pyridine solution was prepared by mixing 50 ml water and 100 ml pyridine.

Apparatus.—Two types of polarographic cells were used: (*a*) an all-glass jacketed one-compartment cell (Fig. 1; capacity 8 ml) with conventional inlet and outlet for nitrogen and a standard taper cap through which was sealed a capillary (only measurements *vs.* the mercury pool could be made in this cell); and (*b*) a jacketed H-cell with the two legs separated by a fritted glass disk (one leg contained the polarographic test solution and the other the reference electrode).

The capillaries used (made from marine barometer tubing) had *m* values at the heights of mercury used (30-60 cm) of 0.9-2.5 mg/sec (3.5 mg/sec was used in a few Zn(II) runs). Values of *t* were measured at the same potential as that of current measurement and varied between 3 and 5 sec.; in

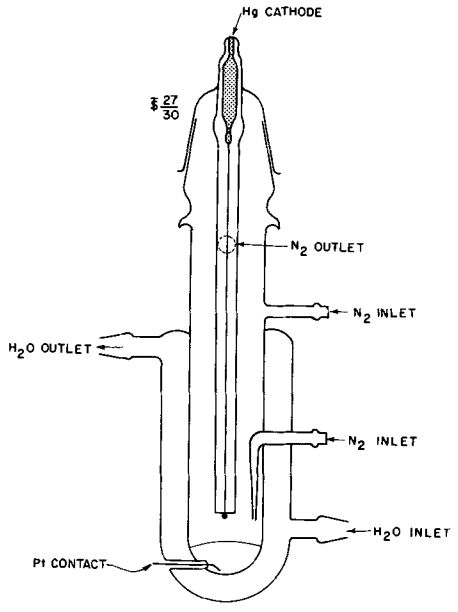

Fig. 1. All-glass one-compartment polarographic cell

a few cases t was as small as 2 or as large as 6 sec. The product $m^{2/3}t^{1/6}$ was generally between 1.3 and 2.2.

Polarograms were recorded with a L&N Electro-Chemograph Type E; those for $AlCl_3$ solutions were recorded on a Metrohm Polarecord. The minimum resistance, *i.e.*, that between cathode and anode at the end of the drop growth, was measured with a General Radio No. 650 inpedance bridge. The mean resistance, which is 4/3 of the minimum resistance, was used to calculate the iR drop.

Electrolysis cell.—For macroscale electrolyses an all-glass, three-compartment cell was used, which essentially consisted of three telescoping glass tubes (Fig. 2). The two inner tubes were closed on the bottom with fritted glass disks and on top with glass joints and standard taper caps; the joints were held together by plastic rings. The cell was mounted vertically with cathodic compartment (provided with magnetic stirrer) at the bottom, the bridge compartment between the two fritted glass disks, and the anodic compartment on top. All three compartments were air-tight and provided with deaeration inlets and outlets, which were standard taper joints, so that the gases evolved in each compartment could be collected individually for analysis. The cathodic compartment, which was surrounded by a glass cooling jacket, had a platinum contact to the mercury pool, an outlet for the reference electrode, and an arm in which a 10-ml buret could be inserted. When not in use, all outlets were closed with standard taper glass caps.

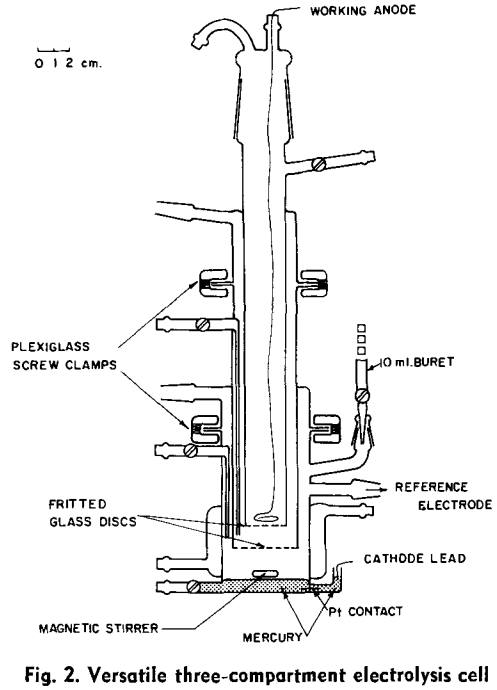

Fig. 2. Versatile three-compartment electrolysis cell

In some electrolysis experiments, the top section or the top two sections were omitted and their place taken by stoppers.

Potentiostat.—For low-voltage controlled-potential electrolysis, the Fisher controlled potential electroanalyser was used; this instrument has a maximum working d-c potential of 15v. Since the electrolysis was performed in a nonaqueous solvent, the resistance was large and the currents flowing through the cell were small (less than 20 ma).

To obtain larger amounts of products (about 0.01 mole), 110v from storage batteries was fed to a 150-ohm, 150-watt rheostat arranged as a potential divider. The resulting manually controlled potential, read on a Weston Model 931 voltmeter, was applied to the electrolysis cell through a silver coulometer and a Weston Model 45 milliammeter. The potential of the working cathode *vs.* NAgE was monitored with a RCA Senior Voltohmyst and checked with a Rubicon Model B potentiometer.

Reference electrode.—A silver wire (18 gauge thick for the electrolysis cell and 2-mm diameter for the H-cell) immersed in a 1*M* solution of $AgNO_3$ in pyridine was used as a reference electrode and will be referred to as the NAgE. The reported reversibility (10) and the reproducible potential of this electrode were confirmed. The influence of small amounts of water on the pool potentials and the potential of the NAgE was not investigated. However, Willeboordse's work (9) indicates that pool potential in pyridine becomes less negative with increasing water content. The potentials reported in the present investigation were made under normal laboratory conditions with the precautions indicated and are therefore not as definitive as if they had been measured in a totally closed system from which water could be rigorously excluded. It is hoped that a study of the effect of water using such a system can be initiated in the near future; such a system would also permit a thorough investigation of the electrochemistry of oxygen in pyridine.

To avoid mixing of solutions and precipitation of silver halides, the electrolytic bridges between the electrolyzed solution and the reference electrode in the H- and electrolysis cells were filled with ignited asbestos soaked with 1*M* $LiNO_3$ in pyridine.

Results and Discussion

Lithium.—The behavior of Li(I) at the DME was studied in solutions containing 0, 1, 20, 66, 90, and

100% pyridine with water as the second constituent. The reference electrode was a mercury pool, the NAgE, or an aqueous S.C.E.; the latter was separated from the pyridine solution by a double bridge of $LiNO_3$ in water and $LiNO_3$ in pyridine, both slurried with asbestos.

In 0.1*M* LiCl pyridine-water solutions (1-90% pyridine), the decomposition potential decreases from −1.6v to about −1.5v *vs.* the mercury pool; under similar conditions, the potential of the pool anode *vs.* S.C.E. becomes increasingly negative (9). The decomposition current observed in aqueous pyridine solutions is generally ascribed to the catalytic evolution of hydrogen (11). In pyridine solution containing 1% H_2O a sharp maximum is observed at −1.6v *vs.* pool, followed by a minimum in the i-E curve, during which the current decreases during the increase of the mercury drop. Such behavior, which is characteristic of an adsorption process, is probably indicative of formation of a strongly adsorbed film on the surface of the mercury drop. The nature of this phenomenon was not further investigated, but should be considered at some future time. In dry pyridine, the maximum and minimum disappear; a fairly small residual current (less than 1 μa) is observed up to about −1.5v *vs.* pool with a rapid rise in current occurring at more negative potential due to the start of the electrolytic deposition of lithium. Traces of water (air moisture) result in an ill-defined wave starting at −1.5v *vs.* pool.

The macroscale reduction of LiCl in dry pyridine was investigated, using the macroscale electrolysis cell with silver wire or platinum sheet as anode and mercury pool or copper wire as cathode. The current intensity was varied up to 200 ma; the applied d-c potential *vs.* NAgE at zero current after initial electrolysis was −2.2v.

Lithium was deposited as a metal amalgam in mercury or as a metal on copper. The presence of elemental lithium was confirmed by reaction of the amalgam or deposit formed with water, e.g., evolution of hydrogen, alkaline reaction of the resulting aqueous solution, and persistent crimson-red coloration of the Bunsen flame, when the amalgam free of solution was introduced into the flame. In agreement with earlier data (12), the electrolytic reduction of Li(I) in pyridine proceeds to the metal.

No change in the appearance and weight of the copper cathode was observed after the deposits were decomposed and the cathode was washed with water.

Lithium chloride has been reported to have a molar conductivity of 0.35 in pyridine (13).

When nitrogen was used for deaeration in the macroscale electrolysis, a red-to-black precipitate appeared, which was decomposed by water and which was probably a mixture of Li_3N and metallic lithium (14). When argon was used for deaeration, this deposit was not formed.

Potential scale.—The potential of the NAgE ($Ag/AgNO_3$, 1*M* in pyridine) is +0.09v *vs.* S.C.E. (saturated calomel electrode in aqueous solution).

The following summary of potentials found for the mercury pool in contact with the indicated salt solutions in pyridine, when measured against the reference electrode shown, will be useful as a frame of reference for the discussion of potentials in this and future papers (these values include liquid junction potentials):

Solution in contact with mercury pool	Potential of mercury pool *vs.* S.C.E., v	Potential of mercury pool *vs.* NAgE, v
0.1*M* LiCl	−0.36	−0.45
0.3*M* LiCl	−0.40	−0.45
0.1*M* $LiNO_3$		−0.09
0.15*M* Bu_4NI		−0.65

Consequently, to convert potentials measured *vs.* the mercury pool in iodide solution to read *vs.* NAgE, −0.65v should be added; in the case of chloride solutions, −0.45v should be added; for nitrate solution, −0.09v should be added.

Willeboordse (9) reported −0.28v *vs.* S.C.E. for the mercury pool in contact with 0.1*M* LiCl solution. The appreciable difference of 0.08v between the latter value and that of the present study may be due to differing trace amounts of water present in the pyridine used. The test for dryness of the pyridine used in the present study is described under "Experimental."

Electrocapillary curve.—Figure 3 is a typical electrocapillary curve obtained for a 0.1*M* LiCl solution in pyridine in the absence of air. The rather flat nature of the top of the curve precludes an exact determination of the electrocapillary zero, which for the solution indicated is *ca.* −0.2v *vs.* mercury pool, *ca.* −0.65v *vs.* NAgE or *ca.* −0.56v *vs.* S.C.E.

In the presence of normal laboratory air, the electrocapillary curve is distorted, due probably to the presence of some adsorbable species in the solution, *e.g.*, water absorbed from the air.

Tetraalkylammonium salts.—Tetraethylammonium bromide, tetra-*n*-propylammonium bromide, and tetra-*n*-butylammonium iodide were also tested as background electrolytes with the DME in pyridine; NAgE was used as reference electrode. Best

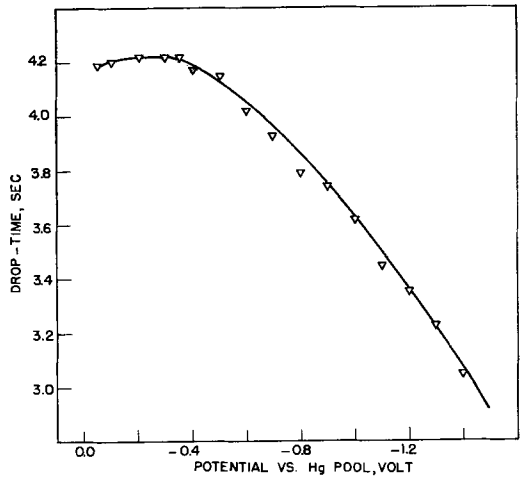

Fig. 3. Electrocapillary curve for 0.1M LiCl in pyridine, DME vs. mercury pool, in the absence of air.

results in respect to small residual currents were obtained with the butyl compound.

A 0.15*M* Bu_4NI solution has a very good conductivity, *i.e.*, its resistance in the H-cell is about one-tenth of that of comparable solutions containing LiCl (17 kohms) or $LiNO_3$ (12 kohms). The decomposition potential of Bu_4NI is −1.65v *vs.* mercury pool, *i.e.*, −2.30v *vs.* NAgE. However, at −1.45v *vs.* pool a small wave began (i = 1.5 μa at −1.6v *vs.* pool), which is probably due to traces of moisture.

Thallium (I).—Solutions of thallous acetate up to 2 m*M* are obtained in pyridine without difficulty; at higher concentration, turbidity results. The sulfate is almost insoluble.

Tl(I) in $LiNO_3$ solution gives a well-developed polarographic wave (*cf.* Table II, which contains typical data for three metallic ions). The limiting current is directly proportional to the depolarizer concentration (0.2-2 m*M*) and to the square root of the mercury height and has a temperature coefficient of 1.4%, indicating diffusion control.

Table II. Polarographic data for metallic cations in pyridine

Cation conc., m*M*	$LiNO_3$ conc., *M*	Temp, °C	h,[a] cm	$-E_{1/2}$,[b] v	i_d, μa	I[c]	Slope,[d] mv
				Thallium			
0.23	0.5	25	30	0.48	0.56	1.87	57
0.23	0.5	25	60	0.48	0.76	1.77	52
0.4	0.1	25		0.48[i,g]	1.42	2.60	61
0.50	0.5	25	60	0.48	1.96	2.10	[e]
1.0	0.07	5		[e]	3.04	1.66	[e]
1.0	0.07	5		[e]	2.36	1.74	[e]
1.0	0.07	20		[e]	2.88	2.12	[e]
1.0	0.07	20		[e]	3.76	2.04	[e]
1.0	0.5	25	30	[e]	2.64	2.03	[e]
1.0	0.5	25	60	0.49	3.60	1.93	[e]
1.0	0.5	25		0.51[g]	3.20	1.95	[e]
2.0	0.1	25		0.54	4.60	1.83	93
2.0	0.1	25	60	0.52	6.65	1.78	141
2.1	0.5	25	60	0.54[g]	7.56	1.93	[e]
				Lead			
0.15	0.1	25	60	0.59	0.98	2.97	34
1.5	0.1	25	60	0.63	10.4	3.15	74
1.5	0.1	25	30	0.63	7.8	2.88	70
1.5	0.1	25	60	0.58[g]	10.3	3.12	82
1.5	0.1	3	60	0.54[g]	8.3	2.53	47
5.0	0.5[f]	25	60	0.97[g]	28.8	2.62	40
5.0	0.5[f]	25	30	0.95[g]	19.8	2.19	38
				Zinc			
0.15	0.3[f]	25		max.	0.88[h]	2.03	NM
0.5	0.3[f]	25		I 1.60	1.56	1.91	41
				II 1.68	1.20		40
0.95	0.3[f]	7		max.	2.96[h]	2.06	NM
0.95	0.3[f]	7		I 1.63	2.40	2.28	49
				II 1.72	2.04		62
1.0	0.3[f]	25		I 1.60	3.00	1.83	58
				II 1.69	2.28		45
1.38	0.3[f]	6		max.	5.52[h]	1.95	NM

[a] Uncorrected for back-pressure.
[b] Measured *vs.* mercury pool and adjusted to be *vs.* NAgE.
[c] Diffusion current constant, I, = $i_d/cm^{2/3}t^{1/6}$. In the case of Zn, it was calculated from the sum of waves I and II.
[d] Calculated from variation of log $[i_d/(i_d - i)]$ *vs.* E, using the relationship of $(E_{1/4} - E_{3/4})$ = − slope/0.056 at 25°C. NM = not measurable.
[e] Not measured because a maximum of the first kind was present.
[f] Run in LiCl solution.
[g] Uncertain value due to a very large iR drop correction when run directly *vs.* the NAgE, *e.g.*, 0.3v.
[h] Sum of currents for waves I and II.
[i] Maximum of the second kind present.

Satisfactory waves are obtained in solutions up to 0.5*M* in $LiNO_3$; above 0.5*M* $LiNO_3$ or 1 m*M* Tl(I), a sharp maximum of the first kind appears.

The half-wave potential of −0.48v *vs.* NAgE, *i.e.*, −0.39v *vs.* S.C.E., is comparatively less negative than that of Tl(I) in aqueous media, *i.e.*, −0.46v *vs.* S.C.E. in 0.1*M* background electrolyte and −0.48v in 1*M* electrolyte. However, such comparisons must be made with caution, *e.g.*, the magnitudes of the junction potentials may be controlling. It will, though, be interesting to compare the differences between pairs of ions in water and in pyridine.

The diffusion current constant of *ca.* 2.0 in pyridine is less than the 2.7 found in aqueous solution.

The data indicate a 1*e* reduction of Tl(I), likely to the amalgam. The wave slope at low Tl(I) concentration may indicate reversibility.

Lead(II).—Solutions of lead acetate and nitrate in pyridine are readily obtained. Lead(II) in 0.1*M* $LiNO_3$ and in 0.5*M* LiCl solutions gives a well-developed polarographic wave (Table II), whose limiting current is directly proportional to depolarizer concentration (with some deviation between the two background electrolytes) and to the square root of the mercury height, and has a temperature coefficient of 1.0%, indicating diffusion control.

The data obtained with lead acetate are not included in Table II since the compound used was the trihydrate and the presence of the water would have introduced a possible complicating factor. Typical data at 25°C for 2 m*M* $Pb(OAc)_2$ in 0.1*M* LiCl solution, which is also 6 m*M* in H_2O, are $E_{1/2}$ = −0.77v *vs.* NAgE, I = 3.25, and slope = 37 mv.

A sharp maximum of the first kind often appears at the beginning of the limiting current of the Pb(II) reduction; this maximum disappears at lower temperature, *e.g.*, 0°C, and at lower Pb(II) concentrations.

In aqueous solution Pb(II) has nearly identical half-wave potentials and diffusion current constants in nitrate and chloride media (I in parentheses), *e.g.*, −0.38 and −0.40 (3.7) in 0.1*M* and 1*M* nitrate, and −0.40 (3.9) and −0.44 in 0.1 and 1*M* chloride. In pyridine, however, $E_{1/2}$ is much more negative in chloride, −0.87v, than in nitrate solution, *ca.* −0.52v; I is also less, *ca.* 2.4 *vs.* 3.1. (All potentials are *vs.* S.C.E.)

The data indicate a 2*e* reduction of Pb(II), likely to the amalgam. The wave slope of 34 mv at low Pb(II) concentration may indicate reversibility. However, at higher concentrations of the depolarizer the wave slope is less steep, possibly because of the increasing influence of the error in the measurement of the resistance of the solution, which necessitated iR drop corrections of several hundred millivolts.

Zinc(II).—The polarographic behavior of zinc in pyridine is more complicated than those of thallous and lead ions (Table II; Fig. 4). Two reduction waves are observed in 0.3*M* LiCl; these are separated by an inflection rather than by a limiting current, due to the small difference of *ca.* 0.1v in $E_{1/2}$. When the waves can be separately measured, wave I is somewhat larger than wave II, comprising *ca.* 55% of the total current.

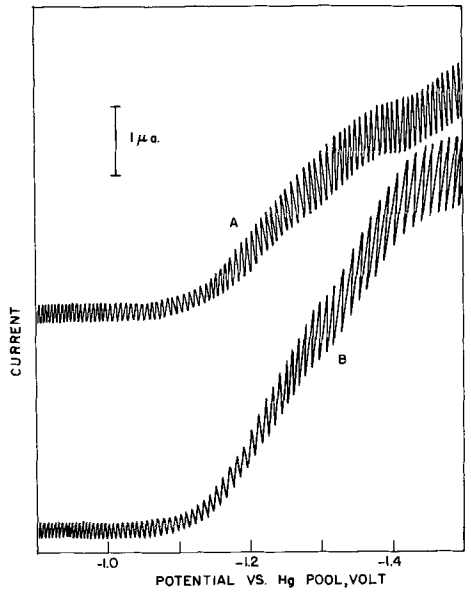

Fig. 4. Polarograms of $ZnCl_2$ in 0.3M $LiNO_3$ at 25°: A, 0.5 mM Zn(II), $E_{1/2}$ = —1.60 and —1.68v, i_d = 1.56 and 1.20 μa; B, 1.0 mM Zn(II), $E_{1/2}$ = —1.60 and —1.69v, i_d = 3.00 and 2.28 μa.

At higher concentrations of Zn(II) and of background electrolyte, *e.g.*, greater than 1 m*M* Zn and 0.3*M* LiCl, the first wave appears as a sharp maximum on the rising portion of the polarographic wave. It is an open question, whether the apparent first wave originates from a damped, *i.e.*, partially suppressed, maximum which sometimes appears as a wave, or whether it is a real reduction wave, which is very apt to develop maxima. Attempts to improve resolution of the waves by varying temperatures, concentration of depolarizer, concentrations of $LiNO_3$ and Bu_4NI as background electrolytes, mercury height (30-60 cm), and polarization rate (20-200 v/min) were not decisive. The waves in Bu_4NI solution were poorly separated; those in $LiNO_3$ were similar to those in LiCl solution.

The diffusion current constant for the total current (sum of the two waves) is somewhat less than that for lead in chloride media. This may be due to the decreased mobility of Zn(II) as a result of strong complexation by pyridine. This is supported by the more negative $E_{1/2}$ (*ca.* —1.6v) and lower I (*ca.* 2.0) in pyridine as compared to aqueous solution (—1.00v and 3.4 in 1*M* KCl solution).

Willeboordse (9), who studied the polarographic reduction of $ZnCl_2$ in 0-100% pyridine (0.1*M* in LiCl), observed only one Zn(II) wave even in 100% pyridine and does not mention any maxima associated with the wave. He reported an $E_{1/2}$ of —1.46v *vs.* S.C.E.; I could not be measured accurately, but was probably 2.5 or less based on the data for pyridine-water mixtures. This value of —1.46v checks the values of *ca.* —1.52 and —1.61v found in the present study when cognizance is taken of the difference of 0.08v found in the two studies for the potential of the mercury pool *vs.* S.C.E.

The macroscale electrolytic reduction of solutions of $ZnCl_2$ in pyridine was run, using a silver anode and a mercury cathode. These solutions show poor conductivity, *i.e.*, the resistance is about fifty times that of comparable solutions of $AlCl_3$ in pyridine. (The resistance of 0.1*N* $ZnCl_3$ in the three-compartment cell used for macroscale electrolysis was *ca.* 50 kohms; that of a comparable $AlCl_3$ solution was *ca.* 3 kohms.) Zinc probably exists in pyridine largely as an undissociated complex with the solvent, *e.g.*, $ZnCl_2pyr_4$.

After prolonged electrolysis, the presence of metallic zinc in the mercury cathode was established as follows: The mercury, free from electrolyzed solution and stirred with a magnetic stirrer, was short-circuited to a large platinum electrode in an aqueous 6*M* HCl solution. Thus, "internal electrolysis" should occur and zinc should dissolve into the acidic solution. However, it was found that actual external short-circuiting of the platinum and mercury was unnecessary. After 3 hr the acidic solution was quantitatively transferred to a volumetric flask, neutralized with an excess of concentrated aqueous ammonia, and diluted with water to obtain a solution approximately 1*M* in NH_3 and 1*M* in NH_4Cl; this solution was polarographed to give a zinc wave.

The presence of what are probably two polarographic waves for zinc suggests a two-stage reduction

$$ZnCl_2pyr_4 + e = [ZnCl_2pyr_4]^- \quad [1]$$

$$[ZnCl_2pyr_4]^- + e + (Hg) = Zn(Hg) + 2Cl^- + 4\,pyr \quad [2]$$

Comparison of behavior in aqueous and pyridine solution.—Values of the half-wave potentials and diffusion current constants found for the three cations, (Tl(I), Pb(II), and Zn(II), in aqueous and pyridine solutions are summarized in Table III. Although potential data must be compared with caution because of the presence of unknown liquid junction potentials in the data for pyridine solution, the half-wave potentials show little difference where complexation involving the anion is apparently not involved, *e.g.*, Tl(I) and Pb(II) in nitrate media. For Zn(II) and Pb(II) in chloride media the difference is appreciable.

Similarly, although all of the diffusion current constants are less in pyridine than in water, the relative decrease is greater where complexation is more pronounced.

Aluminum.—The polarography of aluminum has attracted considerable interest from investigators for the past three decades. Aluminum cannot be electrodeposited from aqueous solution. The polaro-

Table III. Comparison of polarographic constants in aqueous and pyridine solution

	$-E_{1/2}$ *vs.* S.C.E., v			$I = i_d/cm^{2/3}t^{1/6}$		
	Pyridine	Water	Difference	Pyridine	Water	Ratio
Tl (I)	0.39[a,b]	0.46	0.07	2.0	2.7	0.74
Pb (II)	0.52[a]	0.39	—0.12	3.1	3.7	0.84
	0.87[b]	0.42	—0.45	2.4	3.9	0.61
Zn (II)	I 1.52[b]	1.00[c]	—0.52	2.0[d]	3.4[c]	0.59
	II 1.61[b]		—0.61			

[a] Nitrate solution. [b] Chloride solution. [c] Only one wave observed. [d] Combined waves I and II.

Table IV. Polarographic data for solutions of aluminum chloride in pyridine[a]

$AlCl_3$, mM	Wave I $-E_{1/2}$,[b] v	Wave I i_l, μa	Wave I I^d	Wave I Slope, mv	Wave II $-E_{1/2}$,[b] v	Wave II i_l, μa	Wave II I^d	Wave II Slope, mv
0.25	1.35	1.4	2.61	160	Obscured by Wave I			
0.96	1.25	1.4		102	1.45	6.9	3.35	46
2.80	1.25	1.4		100	1.45	21.5	3.57	57
3.00		1.6		90	1.44	24.1	3.73	67
3.00[c]		1.4		170	1.43	16.8	3.64	74
6.68	Not measurable				1.49	51.0	3.48	80

[a] Temperature: 25°C; background electrolyte: 0.6M LiCl.
[b] Measured *vs.* the mercury pool and adjusted to be *vs.* NAgE.
[c] Run at h = 30 cm. Ratio of the Wave II currents in the two experiments on 3.00 mM is 1.43; ratio of the square roots of the corresponding mercury height is 1.41.
[d] The apparent diffusion current constant is slightly low, since the $AlCl_3$ used contained small amounts of insoluble material.

graphic reduction wave obtained for aqueous Al(III) solutions has been ascribed to a variety of electrode processes; one of the more recent and thorough studies, that of Heyrovsky (15), has shown that the wave is due to the reduction of hydrogen ions from the aquo-complex, which is catalyzed by the adsorbed reaction product, aluminum hydroxide. Consequently, the electrochemistry of aluminum(III) was investigated with considerable interest since a successful electrodeposition of aluminum metal from pyridine has also not been reported, although unsuccessful experiments have been described (6).

Surprisingly enough, solutions of $AlCl_3$ in pyridine containing LiCl as background electrolyte give two polarographic waves (Table IV), the first of which seems to be a small, extraneous prewave. The limiting current of this first wave, which is constant and independent of the $AlCl_3$ concentration, may be a catalytic hydrogen discharge due to the presence of traces of moisture absorbed in preparing the original stock solution of aluminum salt. Solutions of $AlCl_3$ in pyridine containing small amounts (1%) of water do give two waves with the half-wave potentials observed.

The second, well-defined wave is proportional in height to the Al(III) concentration and has a diffusion current constant, which would correspond to an n value of about two; its height is proportional to the square root of the mercury head; its slope is 57±10 mv. These properties correspond to those expected for a reversible one-electron, diffusion-controlled reduction. However, metallic aluminum could not be obtained on macroscale electrolysis at potentials on the crest of the second polarographic wave. Further investigation of the nature of the faradaic process which was occurring indicated that it may involve solvent. Work is now in process on determining the exact nature of the electrochemical reduction which occurs in solutions of Al(III) in pyridine.

Acknowledgment

The authors wish to thank the U.S. Atomic Energy Commission, which helped support the work described.

Manuscript received May 12, 1962; revised manuscript received Aug. 15, 1962.

Any discussion of this paper will appear in a Discussion Section to be published in the December 1963 JOURNAL.

REFERENCES

1. L. F. Audrieth and J. Kleinberg, "Non-Aqueous Solvents," pp. 123-9, John Wiley & Sons, New York (1953).
2. G. Jander, "Die Chemie in wasserähnlichen Lösungsmitteln," pp. 209-307, Springer-Verlag, Berlin (1949).
3. A. Weissberger, E. S. Proskauer, J. A. Riddick, and E. E. Toops, "Organic Solvents: Physical Properties and Methods of Purification," Interscience Publishers, New York (1955).
4. H. Hartley, N. G. Thomas, and M. P. Applebey, *J. Chem. Soc.*, **93**, 538 (1908).
5. L. F. Audrieth and H. W. Nelson, *Chem. Revs.*, **8**, 335 (1931).
6. R. Müller, F. Hölzl, W. Knaus, F. Planiszig, and K. Prett, *Monatsh.*, **44**, 219 (1923).
7. H. Hevesy, *Z. Elektrochem.*, **16**, 672 (1910).
8. E. A. Abrahamson and C. A. Reynolds, *Anal. Chem.*, **24**, 1827 (1952).
9. F. Willeboordse, "Polarography in Some Non-aqueous Solvents," Ph.D Thesis, University of Amsterdam, 1959.
10. U. Bertocci, *Z. Elektrochem.*, **61**, 431 (1957).
11. I. M. Kolthoff and J. J. Lingane, "Polarography," 2nd ed., Vol. 1, p. 812, Interscience Publishers, New York (1952).
12. S. Laszcynski and S. Gorski, *Z. Elektrochem.*, **4**, 290 (1897); L. Kahlenberg, *J. Phys. Chem.*, **3**, 602 (1899).
13. H. C. Mandell, W. M. McNabb, and J. F. Hazel, *This Journal*, **102**, 263 (1955).
14. F. W. Dafert and R. Miklauz, *Monatsh.*, **31**, 981 (1910).
15. M. Heyrovsky, *Collection Czech. Chem. Communs.*, **25**, 3120 (1960).

The Reduction of Oxygen on Passive Zirconium

Robert E. Meyer

Chemistry Division, Oak Ridge National Laboratory,

Operated by Union Carbide Corporation for the U. S. Atomic Energy Commission, Oak Ridge, Tennessee

ABSTRACT

The reduction of oxygen on film-covered zirconium was investigated by the measurement of the rate as a function of potential and concentration. The amount of hydrogen peroxide produced was measured and compared to the theoretical amount. The results showed two distinct polarization regions, a very low-current region with a Tafel slope of about 1.4 (2.3 RT/F) and an oxygen order of unity, and a higher current region with a much larger Tafel slope and a fractional oxygen order. Equations accounting for the general features of the data are derived based on a model which considers the separate potential drops across the film and the solution double layer.

Zirconium is known to form a film, presumably of ZrO_2, when in contact with O_2 in aqueous solution. The standard potential (1) for the half-reaction $Zr + 2H_2O = ZrO_2 + 4H^+ + 4e^-$ is -1.43v. It is evident from this potential that ZrO_2 is thermodynamically stable under potentials at which such oxidizing agents as O_2, H_2O_2, and H^+ are easily reduced. Furthermore, measurements made in O_2-saturated 0.1M Na_2SO_4 (pH $\sim$ 4) showed that the rate of formation of ZrO_2 at potentials in the vicinity of S.C.E. falls off to values on the order of 10^{-8} to 10^{-9} amp/cm^2 after a few days (2). Therefore it should be possible to study reduction processes on film-covered zirconium without significant interference from the film-forming reactions. It is found, in practice, that determinations of reduction rates are reasonably reproducible on a given sample, and therefore it is safe to conclude that the effect of reduction experiments on the surface of the electrode is slight.

In a previous paper (3), experiments were described concerning the reduction on zirconium of several oxidizing agents including oxygen. Because the primary purpose of that paper was to present and illustrate kinetic equations resulting from consideration of a two-barrier model for film-covered electrodes, specific mechanisms were not discussed. In the present paper, additional experiments concerning the reduction of oxygen on zirconium are described, and the mechanism of this reaction is discussed. This reaction was chosen because of its importance for the film-formation process in oxygenated aqueous solutions.

The reduction of oxygen on metals has not received a great deal of attention. On mercury in acid solutions, Iofa *et al.* (4) and Agar (5) found Tafel regions of slopes equal to about $2(2.3RT/F)$, a first-order reaction with respect to oxygen, and a slight pH dependence. This led to the following postulated mechanism

$O_2 + e^- = O_2^-$	(slow)	[1]
$O_2^- + H^+ = HO_2$	(fast)	[2]
$HO_2 + e^- = HO_2^-$	(fast)	[3]
$HO_2^- + H^+ = H_2O_2$	(fast)	[4]

The reduction of oxygen on platinum has been studied by Winkelmann (6) and on platinum, silver, gold, and nickel by Krasilshchikow and co-workers (7). In general, the above system of equations is postulated and Eq. [1] is considered the slow step if the reaction is pH independent and if the Tafel slope is about $2(2.3\ RT/F)$. In alkaline solution it is sometimes found that the Tafel slope is $2/3(2.3\ RT/F)$ and that the reaction is pH dependent. In this case, the application of elementary kinetics shows that Eq. [3] is the probable slow step. An excellent summary of the oxygen electrode has been presented by Vetter (8).

In order to determine whether this mechanism was applicable to zirconium, it was necessary to measure the potential dependence and the orders with respect to oxygen and hydrogen ion. It was also desirable to determine whether hydrogen peroxide could be detected. Delahay and Stagg (9) reported that little hydrogen peroxide was produced by the reduction of oxygen on zirconium in phosphate buffered 0.2M KCl, pH 6.9.

Experimental

The experimental techniques used in determining the potential-current curves and in measuring the kinetic orders have been described in detail (3). The only new type of experiment was the determination of the hydrogen peroxide concentration in solution. A modification of the method described by Winkelmann (6) was used. Two cells similar to those described in ref. (3) were used, one of 10 cc and the other of 100 cc capacity. The anodic polarization curve representing the oxidation of hydrogen peroxide on a small platinum electrode (area $\sim$0.2 cm^2) was recorded at various known concentrations. External polarizing electrodes were necessarily used. The same cells were used for the reduction of oxygen on zirconium, and whenever it was desired to determine the hydrogen peroxide concentration, the same platinum electrode used in determining the standard curves was polarized anodically. The resulting potential-current curve was compared to the set of standard curves, and the exact amount of hydrogen peroxide produced was determined by inter-

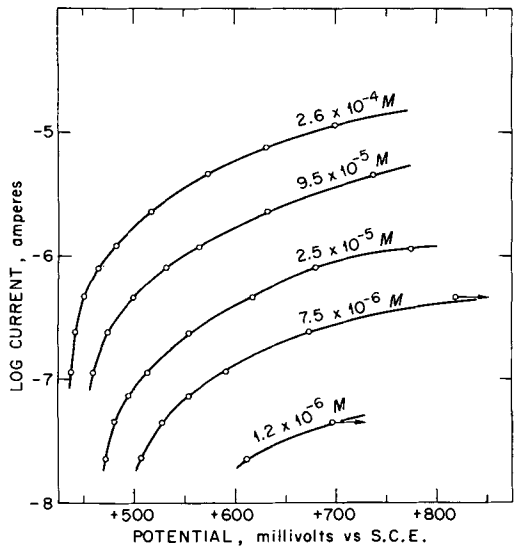

Fig. 1. Anodic oxidation of H_2O_2 on Pt. Concentration of the H_2O_2 is given in moles per liter above each curve. Arrows on the two lower curves represent slight drifting of the potential at constant current. 0.1M Na_2SO_4; pH, 3.12; T, 25°C.

polating at several potentials. Interpolation was possible because the reaction was first order, as can be seen by comparing currents on constant-potential lines on the set of standard polarization curves shown in Fig. 1. At the lowest concentrations encountered, the accuracy of this method was not very great for almost the entire anodic curve was under the influence of diffusion, and it was found quite difficult to reproduce stirring conditions in the 10 cc cell. The accuracy was sufficient for the present purposes however.

In these experiments, the preparation of the zirconium electrodes was of crucial importance. If the electrodes were merely cleaned after machining or abrading, the results were completely irreproducible, and potentials at constant current drifted and showed frequent sharp jumps. If, in addition to the cleaning, the electrodes were chemically polished (10 volume parts HF, 50 parts conc. HNO_3, and 50 parts H_2O), the results were better, but considerable drifting remained. Only if the electrodes were also annealed in a vacuum of 10^{-6} mm Hg or better at 800° for an hour, were the results acceptable. The electrodes were always placed in the cell immediately after removal from the vacuum system. Measurements were begun as soon as the rate of the film formation process decayed to a small enough value to allow polarization with small currents.

A few experiments were conducted with Zircaloy-II instead of crystal bar zirconium. In all cases, there was no significant difference between crystal bar zirconium and Zircaloy-II.

In all experiments, the solutions were 0.1*M* in Na_2SO_4 and, unless otherwise stated, enough H_2SO_4 was added to give a *p*H value of 3. Although some experiments were conducted at *p*H values other than 3, *p*H values close to 3 were selected as a compromise between various complications. In more acid solutions, hydrogen discharge becomes more possible with consequent possible transient effects due to hydrogen penetration into the metal. In fact, it was observed that with lower *p*H values the meaurements tended to be less reproducible. In solutions more alkaline than *p*H 3, there was the possibility in long term reduction experiments at the higher current densities that the *p*H would change because hydrogen ion is consumed in the reduction of oxygen.

Whenever possible, experiments were conducted both at 25° and at 75°C. Unless otherwise noted, general conclusions in this paper refer to both temperatures.

In the case of the 75° experiments, a saturated calomel electrode at room temperature (25°C) was used as a reference electrode. Thermal junction was maintained through capillary glass tubing leading into the water bath and then into the cell which was immersed almost completely in the bath. The constancy of the ambient temperature maintained more than sufficient reproducibility for the establishment of a constant although unknown junction potential.

Results

Potential dependence.—Determinations of the cathodic reduction current of oxygen on film-covered zirconium as a function of the potential showed a Tafel region when the electrodes were polarized sufficiently far from the open-circuit potential. It was not possible to make measurements earlier than several hours after initial immersion because the initial rates of film formation were quite large (2). These first measurements, taken usually from 2 to 4 hr after initial immersion, always showed a Tafel slope of from 2.5 to 2.7(2.3 RT/F). There was then a slow increase of the Tafel slope extending over several days with the final determinations giving slopes of 3 to 4(2.3 RT/F) and an occasional sample giving 5(2.3 RT/F). Although the Tafel slopes for different samples were reasonably reproducible, the magnitude of the current for the same potential and temperature varied somewhat depending on the condition of the electrode. This was probably due to the fact that the nature and thickness of the film present on the surface had a profound influence on the rate of charge transfer. Further, it is obviously impossible to duplicate precisely a solid electrode and in particular to reproduce exactly the film that grows on the electrode. For this reason, a large number of measurements were made in order to determine the general trends in the Tafel slope mentioned above. An example of one of these measurements is shown in Fig. 2. These data were taken 26 hr after initial immersion. The electrode had an area of 2.2 cm^2, and apparent current densities may be obtained by dividing the experimental currents by 2.2.

If the electrodes were allowed to remain in solution until the rate of film formation decayed to about 10^{-8} amp/cm^2 or less, another phenomenon was noted. This is illustrated in Fig. 3 where the very low-current region of polarization is plotted. (The run shown in Fig. 3 is not the same as that shown in Fig. 2.) Both anodic and cathodic branches are shown. The anodic points drift slightly, of course, due to anodizing, but at these low currents the amount of charge passed through the electrode is so small that the drift is negligible and a fairly accurate plot can be obtained. As can be seen, the

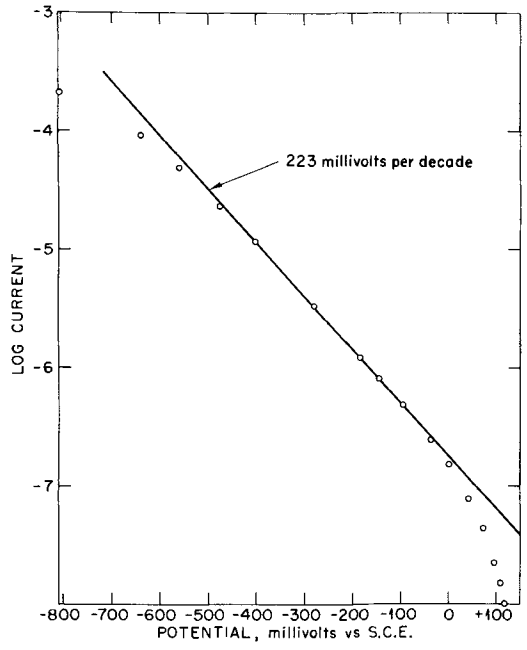

Fig. 2. Cathodic reduction of oxygen on passive zirconium. *T*, 75°C; 0.1*M* Na_2SO_4; *p*H, 2.75; O_2 saturated; electrode area, 2.2 cm^2.

experimental points can be analyzed by assuming an anodic region of slope 3.5(2.3 *RT/F*) and a cathodic region of 1.3(2.3 *RT/F*). At higher currents, the cathodic points bend off to a region of greater Tafel slope. This low-current change of slope would not be noticed if the film-formation rate stayed above 10^{-7} amp/cm^2. Other determinations of the Tafel slope in this low current density region gave values of 1.3, 1.4, 1.4, 1.3, and 2(2.3 *RT/F*).

In the high-current density region, the time to reach a steady state was usually longer than the time in the low-current region. This effect was particularly noticeable for electrodes of very low corrosion rate, *i.e.*, more than about three days old.

Order determinations.—These experiments were described in ref. (3). The general conclusion arrived at was that the reaction is first order in the low-current density region and fractional in the high-current region. Values of these fractional orders ranged

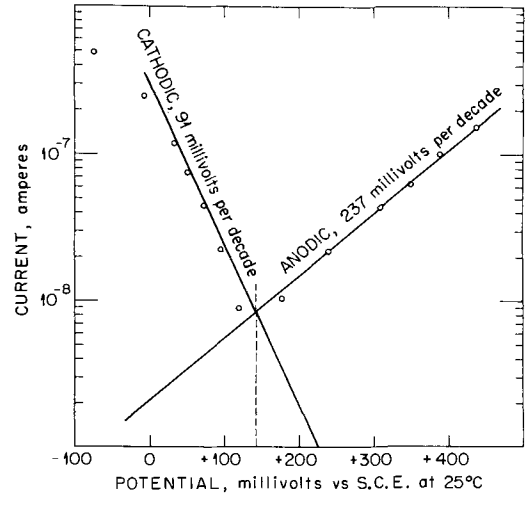

Fig. 3. Low-current polarization of zirconium. *T*, 75°C; 0.1*M* Na_2SO_4; *p*H, 5.12; O_2 saturated; electrode area, 2.2 cm^2.

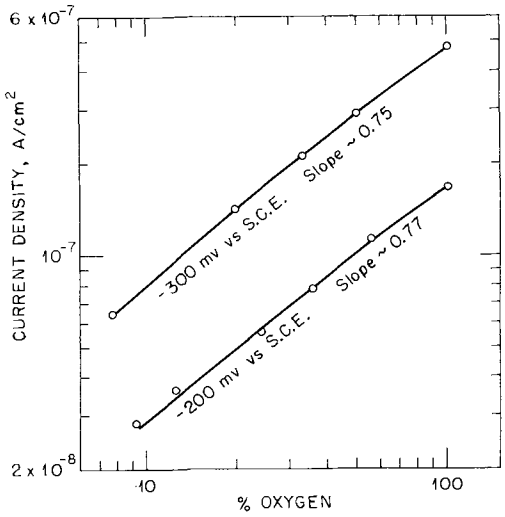

Fig. 4. Determination of order of oxygen reduction on passive zirconium. 0.1*M* Na_2SO_4; *p*H, ~4; *T*, 25°C.

from 0.66 to 0.9 in different experiments. In a given experiment, the fractional orders were constant and showed no tendency to increase or decrease with changes of the current. In Fig. 4 an example of an order determination in the high-current density region is shown. Points were taken using a gas flow method in which varying proportions of oxygen and helium were passed through the cell. The current was determined as a function of per cent oxygen at constant potential. At lower currents, varying quantities of oxygen were introduced into a closed cell by anodic evolution on platinum. Constant current density was used so that the total amount of oxygen present was proportional to the total charge passed. The order was then equal to the slope of the line obtained by plotting the logarithm of the increase in current *vs.* the logarithm of the total charge passed at various times. A determination using this method and showing unit order is shown in Fig. 5. In order to check both methods, oxygen was reduced on platinum and unit order was found using both techniques.

It was observed that the transition current region between unit and fractional orders increased to higher currents at the higher temperatures. As

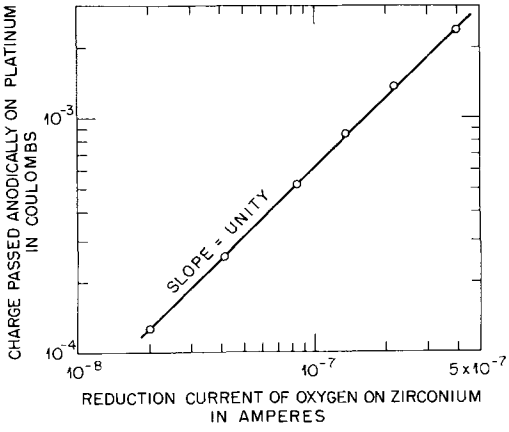

Fig. 5. Determination of order of oxygen reduction on passive zirconium. Potential, —400 mv *vs.* S.C.E. at 25°C; *p*H, 3.98; *T*, 75°C; electrode area, 2.2 cm^2.

shown in Fig. 4 and 5, fractional orders persist at 25° at currents which show unit orders at 75°.

Hydrogen peroxide determinations.—About fifteen determinations of hydrogen peroxide concentration were made at current densities as low as 2×10^{-8} amp/cm^2. In each of the experiments below 3×10^{-7} amp/cm^2, less than 10% of the maximum possible hydrogen peroxide was found. At current densities above 10^{-6} amp/cm^2, significant quantities were found, but the usual quantity was 35-40%, and in no experiment was the full possible amount found.

These experiments were performed under conditions at which the bulk decomposition rate was small compared to the formation rate. Under all conditions studied, the reduction of hydrogen peroxide was also small as determined by adding hydrogen peroxide to solution. These experiments were performed only at 25°C because of the rapid increase in the rate of the bulk decomposition of hydrogen peroxide as the temperature was raised.

pH Effect.—Attempts were made to determine if the reduction of oxygen on zirconium had an order with respect to hydrogen ion. The method used consisted of measuring the current as a function of pH at constant potential. Although a complicated small increase in rate was noted with increasing acidity, the effect was not sufficiently reproducible or well defined to say even that a fractional order was involved. For the purposes of discussing the mechanism of the reduction of oxygen, the order will be considered essentially as zero.

There is a pH effect, however, on the electrode, and it is shown in Fig. 6. In these experiments a freshly prepared electrode was used at 75°, and a series of experiments was conducted in which the potential was measured as a function of pH while constant current was applied to the zirconium electrode. The pH of the solution was estimated by drawing out a small portion of the solution into a separate compartment also maintained at 75°. The potential of a platinum-hydrogen electrode in this compartment was then measured against the same saturated calomel electrode used to measure the zirconium electrode. The results are plotted as the potential of this platinum-hydrogen electrode *vs.* the potential of the zirconium electrode. The pH of one of the solutions was measured at 25° with a glass electrode, and this value is indicated on the figure by the point indicated by the arrow. These experiments were done in the cathodic region where oxygen was being reduced and in the anodic region under helium atmosphere where the reaction is mainly film formation (2). In all cases, the change of potential of the zirconium electrode was approximately equal to the change of potential of the platinum-hydrogen electrode, *i.e.*, the plots of Fig. 6 had a slope of about unity. This indicates that the potential of the zirconium electrode changed by approximately 2.3 RT/F for every unit change in pH. This effect was difficult to measure at 25° because of the slow response of the electrode. Therefore, it is not certain whether this effect exists for all experimental conditions encountered in this study.

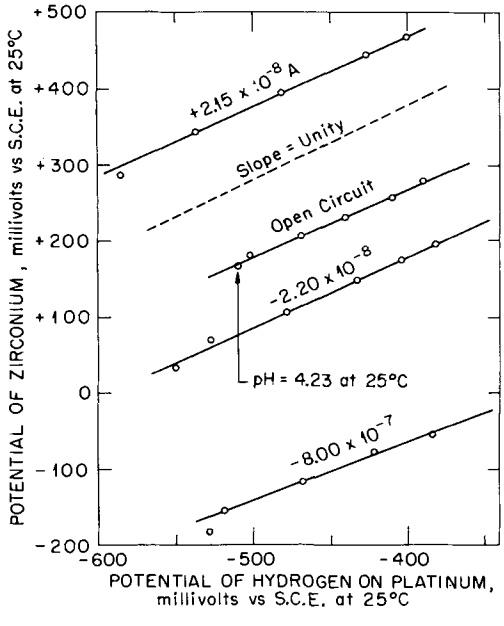

Fig. 6. Effect of pH on potential of zirconium. The numbers above each curve refer to the constant current that was applied to the zirconium electrode while the pH was changed. The electrode area was 2.2 cm^2; *T*, 75°C; 0.1*M* Na_2SO_4. See text for further explanation.

Discussion

These measurements show two regions, a low-current region with a Tafel slope of about 1.4(2.3 RT/F) and a high-current region with a much greater and somewhat variable Tafel slope. The transition between these regions is in the neighborhood of $1\text{-}5 \times 10^{-7}$ amp/cm^2 at 75°. Also, in the low-current region, little hydrogen peroxide is found in solution and unit order with respect to oxygen is observed. At higher currents, fractional orders are observed, and more hydrogen peroxide is produced.

It is evident that in the low-current region at least, the reaction of an electron with oxygen to form O_2^- (Eq. [1]) is the most probable slow step. The potential dependence, the unit order with respect to oxygen, and the absence of a significant pH effect all support this conclusion. It is not evident, however, what the succeeding steps are, since so little hydrogen peroxide is found.

The fact that some hydrogen peroxide is found suggests that all of the O_2^- is reduced at least to HO_2^-. It is reasonable to suppose that the HO_2^- is adsorbed on the surface of the film for it is known that zirconium can form stable peroxy compounds in which the zirconium is bonded directly to one of the oxygen atoms of the peroxy structure (10). Three possible paths are available for the removal of HO_2^-, further reduction, desorption, and decomposition. Reduction does not seem reasonable at the more anodic potentials because the addition of hydrogen peroxide does not increase the cathodic current materially. It might be argued that the HO_2^- absorbed on the surface is more easily reduced than added hydrogen peroxide, but then one must explain why the amount of H_2O_2 found in solution is small at the more anodic potentials but then increases at more cathodic potentials. It appears more

reasonable to assume that most of the adsorbed HO_2^- either decomposes on desorption or that it decomposes immediately after desorption. It is possible that conditions in the immediate vicinity of the electrode are such as to favor considerable decomposition. Since the electrode will have its most positive charge at anodic potentials, hydroxyl ion, desorbed HO_2^-, and possibly some desorbed O_2^- will tend to accumulate in the solution side of the double layer. The presence of OH is also a possibility. These factors would, therefore, favor the decomposition of HO_2^- in the environment near the electrode for it is well known that free radical decomposition reactions can contribute significantly to the decomposition of H_2O_2. At more cathodic potentials, the concentration of these negatively charged species will tend to decrease, and the decomposition will be less favored. A great variety of possible mechanisms and chain reactions could be postulated at this point, but the decomposition of H_2O_2 is so complicated that any suggestion would be little more than pure speculation. Therefore, the remainder of the discussion will be confined to a presentation of how the change in slopes and the fractional order can be derived using the above considerations.

It is assumed that the over-all reaction consists of two potential dependent steps. The first of these involves a slow transfer of an electron to an oxygen molecule at the surface (Eq. [1]). This reaction depends on the potential difference between the metal and the position of the oxygen molecules at the surface, V_f.[1] The appropriate rate equation is

$$r_f = K_f(O_2)\,(1-\theta)\,\exp(-\alpha_f F V_f/RT) \qquad [5]$$

Here r_f is the rate, K_f is a constant, θ is a coverage term assumed to be representative of the fraction of the surface covered by HO_2^-, and the rest of the terms have the usual significance. The desorption reaction is assumed to depend on the potential difference between the solution and the position of the adsorbed HO_2^- ions, V_s. The appropriate rate equation is

$$r_s = K_{des}\theta\,\exp(-\alpha_s V_s F/RT) \qquad [6]$$

In the steady state, the measured rate, r, equals r_s and r_f and under all conditions $V_s + V_f = V_t$ where V_t is the over-all potential drop between the metal and the solution. Implicit in the discussion is the reasonable and usual assumption that changes in V_t are equal to changes in the potential as measured by the electronic potentiometer.

In the high-current region, a simple solution can be obtained if it is assumed that the value of θ stays relatively constant during an experiment. The adsorption of a charged particle should become more difficult at high coverage because of the mutual repulsion of the charges. If it is assumed, therefore, that θ tends to a constant maximum value at high-current densities, then Eq. [5] and [6] may be combined as shown in ref. (3) to give the following equation

$$r = K_t(O_2)^{\frac{\alpha_s}{\alpha_f+\alpha_s}}(1-\theta)^{\frac{\alpha_s}{\alpha_f+\alpha_s}}(\theta)^{\frac{\alpha_f}{\alpha_f+\alpha_s}}\exp\frac{-\alpha_f\alpha_s F V_t}{(\alpha_f+\alpha_s)RT} \qquad [7]$$

This equation predicts both a fractional order and a large Tafel slope as shown by the following derivatives:

$$\frac{2.3}{(\text{Tafel slope})} = \frac{\partial \ln r}{\partial V_t} = -\frac{\alpha_f\alpha_s F V_t}{(\alpha_f+\alpha_s)RT} \qquad [8]$$

$$\frac{\partial \ln r}{\partial \ln O_2} = \frac{\alpha_s}{\alpha_f+\alpha_s} \qquad [9]$$

If $\alpha_s = 1$ and $\alpha_f = \frac{1}{2}$, then the order[2] would be two-thirds and the Tafel slope $3(2.3\,RT/F)$.

The function, $f(\theta) = (1-\theta)^{\frac{\alpha_s}{\alpha_f+\alpha_s}}(\theta)^{\frac{\alpha_f}{\alpha_f+\alpha_s}}$, is not a very sensitive function of θ, and even if small changes in θ did occur, the pre-exponential factor would not change significantly. However, it would change values of the Tafel slope from that predicted by Eq. [8]. This may be the reason for some of the variations of the Tafel slope observed.

It would be desirable to combine the relationships given above to give the over-all rate as a function of V_t without including θ in this over-all rate function. In order to do this, an additional relationship can be found by considering the following idealized model.[3] The charge distribution is assumed to be represented by three layers of charge density, a layer of charge at the metal film interface, σ_1, a layer of charge on the outer surface of the film at the plane of the HO_2^- ions and the O_2 molecules, σ_2, and the charge on the solution side of the double layer, σ_3. It is assumed that σ_2 is made up solely of HO_2^- ions and that any space charge in the film is negligible. Then

$$\sigma_1 + \sigma_2 + \sigma_3 = 0 \text{ (algebraic sum)} \qquad [10]$$

$$V_f = \frac{\sigma_1 l_f}{D_f \epsilon_o} \qquad [11]$$

and

$$V_s = -\frac{\sigma_3 l_s}{D_s \epsilon_o} \qquad [12]$$

Here l_f, l_s, D_f, and D_s are the thicknesses and dielectric constants of the film and solution double layers, respectively. The constant ϵ_o is the usual constant relating potential and charge density. Combining Eq. [10], [11], and [12]

$$\sigma_2 = \epsilon_o\left(\frac{V_s D_s}{l_s} - \frac{V_f D_f}{l_f}\right) \qquad [13]$$

Although Eq. [13] is the additional needed relation, an explicit relationship between r and V_t, not including (θ), cannot be found. Certain special cases can be considered, however. It is possible to com-

[1] The arguments for taking this potential difference, V_f, are somewhat lengthy. They are given in ref. (3) and are therefore not repeated here.

[2] In some respects, this treatment is similar to the classical Frumkin correction [cf. Parsons (11)] for the potential drop existing across the diffuse double layer. This effect, which considers the separate potential drops across the diffuse double layer and the inner or Helmholtz double layer, can lead to unusual orders and Tafel slopes. Although it is possible that this effect could be the cause of the fractional orders found in the present work, the evidence seems to favor the model given here.

[3] A model very similar to the model given here, and leading to Eq. [13], was used by Kimball, *et al.* (12) in their discussion of hydrogen evolution on metals.

bine these equations to obtain V_t as a function of θ. We then obtain

$$V_T = \frac{RT}{F}\frac{D_s l_f + l_s D_f}{\alpha_f l_f D_s - \alpha_s l_s D_f}\ln\frac{K_F(O_2)(1-\theta)}{K_{des}(\theta)} + \frac{\theta\sigma_{max}}{\epsilon_o}\frac{\alpha_f l_s l_f + \alpha_s l_s l_f}{\alpha_f l_f D_s - \alpha_s l_s D_f} \quad [14]$$

here σ_{max} is the maximum possible charge on the surface. This equation has the form

$$V_t = \gamma\frac{RT}{F}\ln\frac{K_F(O_2)(1-\theta)}{K_{des}(\theta)} + \beta\theta \quad [15]$$

where $(\gamma RT/F)$ is easily seen to be of the order of magnitude of 2 RT/F volt and is probably positive because the film will normally be much thicker than the double layer. The value of β is quite uncertain since it depends on values of dielectric constants and thicknesses, all of which are difficult to estimate. However, arbitrarily assuming that $\sigma_{max} = -10^{-4}$ coulomb/cm^2, $\alpha_f = \alpha_s = \frac{1}{2}$, $D_s = D_f = 10$, $l_f = 100$Å, and $l_s = 5$Å, the value of β is roughly -100v.

If the first term on the right side of Eq. [15] is small compared to the second, then θ will be proportional to V_t and Eq. [7] would contain two preexponential terms in V_t. This would change the Tafel slope to give

$$\frac{2.3}{\text{Tafel slope}} = \frac{\partial \ln r}{\partial V_t} = \frac{\alpha_f}{(\alpha_s+\alpha_f)V_t} - \frac{\alpha_s\alpha_F F}{(\alpha_s+\alpha_f)RT} - \frac{\alpha_s}{(\alpha_f+\alpha_s)(\beta - V_t)} \quad [16]$$

Thus, the Tafel slope would depend to some extent on the value of V_t. The departure from linearity could, however, scarcely be detected over the one to two decade current ranges used in these experiments unless V_t was quite small. The order is not affected by this substitution.

In the event that the second term of the right side of Eq. [15] is small, *e.g.*, if θ is very small, then

$$V_t = \gamma\frac{RT}{F}\ln\frac{K_f(O_2)}{K_{des}(\theta)} \quad [17]$$

where

$$\gamma = \frac{D_s l_f + l_s D_f}{\alpha_f l_f D_s - \alpha_s l_s D_f}$$

and combining Eq. [7] and [17], one obtains

$$r = K'_t\,(O_2)\exp -\left\{\frac{1}{\gamma} + \frac{\alpha_s\alpha_f}{(\alpha_f+\alpha_s)}\right\}\frac{FV_t}{RT} \quad [18]$$

Equation [18] predicts that the oxygen order will be unity and that the Tafel slope will be

$$2.3 \times \frac{(\alpha_f+\alpha_s)\gamma}{\alpha_f+\alpha_s+\alpha_f\alpha_s\gamma}\frac{RT}{F}$$

If $\alpha_f = \frac{1}{2}$, $\alpha_s = 1$, and γ is about 2, the Tafel slope will be 1.2(2.3 RT/F). Thus Eq. [18] predicts a Tafel slope and oxygen order in good agreement with the low-current density region of the data.

There is one other possible explanation for the unit oxygen order and 1.4(2.3 RT/F) Tafel slope observed in the low-current region. In the pH experiments shown in Fig. 6 a change of about 2.3 RT/F occurred in the potential of the zirconium electrode for every unit change in pH. Such an effect can be explained by the existence of the equilibrium, $O^= + 2H^+ = H_2O$, at the surface of the electrode. This reaction was proposed by Vetter (13) for the explanation of a similar pH effect on passive iron. If the "exchange current" of this equilibrium is sufficiently large, the potential V_s will be determined by this reaction rather than the desorption of HO_2^-, and V_s will, therefore, remain constant at a given pH value. Only the film potential will change during polarization under these conditions and, therefore, the rate will be given by Eq. [5]. Since V_s is a constant, then if $\theta << 1$

$$\frac{2.3}{\text{Tafel slope}} = \frac{\partial \ln r}{\partial V_t} = \frac{\partial \ln r}{\partial V_f} = -\frac{\alpha_f F}{RT}$$

and

$$\frac{\partial \ln r}{\partial \ln (O_2)} = 1$$

These conditions, therefore, provide an alternative explanation for the low-current region since agreement with the experimentally determined Tafel slope can be obtained with $\alpha_F = 2/3$, a not unreasonable value.

Manuscript received Feb. 2, 1962; revised manuscript received Aug. 6, 1962.

Any discussion of this paper will appear in a Discussion Section to be published in the December 1963 JOURNAL.

REFERENCES

1. W. M. Latimer, "Oxidation Potentials," p. 271, Prentice-Hall, New York (1952).
2. R. E. Meyer, *This Journal*, **106**, 930 (1959).
3. R. E. Meyer, *ibid.*, **107**, 847 (1960).
4. Z. A. Iofa, Ya. B. Shimshelevich, and E. P. Andreeva, *Zhur. Fiz. Khim.*, **23**, 828 (1949).
5. J. N. Agar, "Soviet Electrochemistry," Consultants Bureau, **Vol. I**, p. 235 (1961).
6. D. Winkelmann, *Z. Elektrochem.*, **60**, 731 (1956).
7. A. I. Krasilshchikow *et al.*, *J. Phys. Chem. USSR*, **21**, 849 (1947); **23**, 332 (1949); **26**, 216 (1952); **27**, 389 (1953).
8. K. J. Vetter, "Elektrochemische Kinetik," pp. 513-525, Springer-Verlag, Berlin, (1961).
9. P. Delahay and L. J. Stagg, *This Journal*, **99**, 546 (1952).
10. W. B. Blumenthal, "The Chemical Behavior of Zirconium," D. Van Nostrand, New York (1958).
11. R. Parsons in "Advances in Electrochemistry and Electrochemical Engineering," P. Delahay, Editor, Vol. I, Chap. 1, Interscience, New York (1961).
12. G. E. Kimball, S. Glasstone, and A. Glassner, *J. Chem. Phys.*, **9**, 91 (1941).
13. K. J. Vetter, *Z. Elektrochem.*, **58**, 230 (1954).

Technical Notes

The Anodic Oxidation of Boron

Leung Cheng Chen and R. E. Salomon

Department of Chemistry, Temple University, Philadelphia, Pennsylvania

The apparent inertness of crystalline boron in the presence of many powerful oxidizing agents is not easily explained. Boron is not attacked by concentrated HF, HNO_3, and boiling NaOH solutions. Several fused alkali salt mixtures, however, have been found to etch boron crystals (1).

The electrode potential for the couple $B \rightarrow B^{+3} + 3e$ has been estimated using free energy data to be about −1.7v in alkaline solution and −0.8v in acidic solution (2). The oxidation of boron by the above reagent is thermodynamically feasible, and therefore the apparent inertness of boron is due to an immeasurably slow rate of reaction. Many metals with large positive oxidation potentials fail to dissolve in oxidizing solutions because of the formation of a protective oxide coating that separates the two phases. In order for good protection of this type to occur it is necessary that the oxide be insoluble and nonporous. Boric oxide, the likely oxidation product of boron in aqueous solutions, is however slightly soluble in water (1.1g per 100 ml of water at 0°C) (3) and hydrolyzes readily to boric acid. However, the rate of dissolution of a thin oxide film supported by an active substrate may differ from the behavior of bulk material.

In order to ascertain whether or not the oxidation product of boron affords any protection against further oxidation, polycrystalline samples were anodized at constant voltage and the current efficiency for the process was determined.

Experimental

Polycrystalline boron of 99.1% purity, made by the United States Borax and Chemical Corporation, was used. The bulk crystal was mechanically cleaved, and samples were selected for uniformity of thickness. The samples were of the order of 1 cm^2 in area and 0.1 cm thick. Electrical contact was made with an evaporated layer of silver. Subsequent tests established that the contacts were ohmic. The samples were mounted on the edge of a thin glass tube and held in place by silicone rubber. The latter also served to insulate the contact and to define the electrode area.

The electrodes were cleaned first with concentrated nitric acid and then with 95% ethanol. The anodization was carried out in a 0.1*N* LiOH solution at 30.0°C. A platinum foil served as the cathode. Prior to and during the electrolysis nitrogen was bubbled through the solution. The cell container and bubbling tube were made of polyethylene because of the possible contamination of the electrolyte by borate leached from glass. The anodization was carried out for periods of several hours. A Sorenson Nobatron provided the d-c power. The current was followed with a Speedomax recorder. Polarization voltages ranged from 100 to 250v. Most of the voltage drop was found to occur across the electrode itself and approximately 1-2% across the interface. The latter was based on a measurement of the bulk resistance of the sample with evaporated silver contacts on both sides.

Table I. Current efficiency data

Voltage applied, v	Average current, ma	Time, sec	Charge passed, coul	Amount borate (calc.), μg	Amount borate (found), μg	Current efficiency, %
100	0.38	4000	1.52	56.7	54.5	95.9
100	0.44	6000	2.64	98.7	94.0	95.2
100	0.30	8400	2.52	94.2	97.0	103.0
100	0.39	3500	1.36	50.6	52.0	102.7
100	0.34	5500	1.88	70.2	72.0	102.6
150	0.72	5400	3.89	145	122	84.1
150	0.44	3630	1.60	59.7	58.5	98.0
150	0.41	5460	2.24	84.2	84.5	100.4
150	0.72	7200	5.18	193	195	101.0
150	0.75	5000	3.75	139.6	143	102.5
200	0.48	5400	2.59	94.1	113.4	121.0
200	1.02	6000	6.12	228.6	221	96.7
200	1.19	4000	4.76	117	152	85.9
200	0.99	2000	1.98	73.8	62.0	84.0
250	2.36	2100	4.96	184.8	172	93.1

After anodization the solution was analyzed for borate by coulometric titration with fructose solution. The method is described by Swann (4). A L&N Electrochemograph Type E was used.

Results and Discussion

From the amount of charge passed and the amount of borate found in the electrolyte the current efficiency was calculated. It was assumed that boron was oxidized to the plus three state. The method of analysis was unaffected by the occasional flaking of boron into the electrolyte. The results are given in Table I. The current efficiencies in each run were fairly close to 100%. With a given electrode the current increased slightly with time of anodization. It is suggested that this is due to an increase in the effective surface area with flaking. Photomicrographs of the surface before and after anodization seem to confirm this.

The anodic behavior of a boron in alkaline solution differs markedly from that of aluminum, tantalum, and other valve metals when anodized under similar conditions. In the latter the ionic current efficiency at constant voltage decreases rapidly with time of anodization (5). This is attributed to the growth of a nonporous insoluble oxide film.

If boron forms a duplex type of oxide similar to that formed on aluminum when anodized in acidic solution then the theory proposed by Mott and Hoar (6) may be applicable. The duplex film consists of a thin compact oxide followed by a porous open structure which is in contact with the electrolyte. During anodization the thickness of the compact film remains constant while the pores get deeper. The porous film may dissolve readily in the case of boric oxide, and this could lead to a 100% current efficiency as determined by the borate found in solution. The compact film may protect the unpolarized electrode from oxidation and still permit a field enhanced migration of boron or oxide ions.

Manuscript received June 28, 1962; revised manuscript received Nov. 8, 1962.

Any discussion of this paper will appear in a Discussion Section to be published in the December 1963 JOURNAL.

REFERENCES

1. R. C. Ellis, Jr., "Boron," p. 135, Plenum Press Inc., New York (1960).
2. W. M. Latimer, "Oxidation Potentials," 2nd ed., Prentice Hall, Inc., Englewood Cliffs, N. J. (1952).
3. "Handbook of Chemistry and Physics," 42nd ed., Chemical Rubber Publishing Co. (1960).
4. W. B. Swann, W. M. McNabb, and J. F. Hazel, *Anal. Chim. Acta*, **22**, 76 (1960).
5. L. Young, "Anodic Oxide Films," p. 7, Academic Press, New York (1961).
6. T. P. Hoar and N. F. Mott, *J. Phys. Chem. Solids*, **9**, 97 (1959).

Lead Selenide Evaporated Layer Photoconductive Detectors for Room Temperature Operation

D. G. Coates

Royal Radar Establishment, Malvern, Worcestershire, England

The spectral response of photoconductive layers of PbSe has been well known for some time (1). Sensitive PbSe detectors have been in use for a number of years, and brief general outlines of the methods of preparing such cells by chemical and evaporation techniques have been described (2). The present note describes in detail a method of preparing evaporated layers of lead selenide with a high sensitivity at room temperature out to 4.8μ, the limit of response at that temperature.

Initial Preparation of the Layer

The layers are formed in small borosilicate Dewar-type cell blanks fitted with thin glass bubble windows or sapphire windows. Dewar cells are used since it is necessary to deposit the layer on a cooled substrate. The vacuum system to which the cell blanks are sealed provides an ultimate vacuum of better than 10^{-6} mm Hg and is fitted with a side arm containing potassium chlorate which acts as a source of oxygen. The system is also fitted with a movable oven capable of reaching 600°C in about 15 min for heat treatment of the layer. Before sealing to the vacuum system the cell blank is charged with approximately 5 mg of finely ground melt-grown PbSe crystal (3) tapped into a "pip" in the cell wall. Manipulation of the powder within the cell is made easier if the cell is first given a rough vacuum pump to remove adsorbed water vapor. After sealing to the system the cell is vacuum baked to outgas the powder, at about 350°-400°C, until a pressure better than 10^{-6} mm Hg is maintained. Slight loss of PbSe occurs during this process, and also some selenium is liberated from the remaining powder.

Oxygen is introduced at a pressure of 10^{-2} mm Hg and a cold air jet directed on to the cell window from an 1/8 in. glass nozzle positioned about 3/8 in. away. Air pressure for the jet is about 3-4 lb/in.^{2}.

A layer of PbSe is then formed on the front window by baking the cell in the oven to a temperature of 580°C. Evaporation is assisted by briefly flaming the pip containing the PbSe charge when the oven has reached a temperature of about 450°C. The PbSe is now transferred from the front window to the final substrate, which is now cooled with liquid nitrogen, by heating the front window with a moderate flame for 5 to 10 sec. The window and cell end must be heated quickly and evenly to ensure that the bulk of the PbSe is transferred to the graphite electrode area and not to other regions of the cell walls. The layers so formed are normally

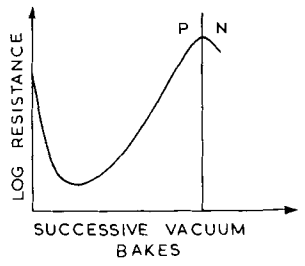

Fig. 1. Typical effect of a succession of vacuum bakes on the resistance of a layer.

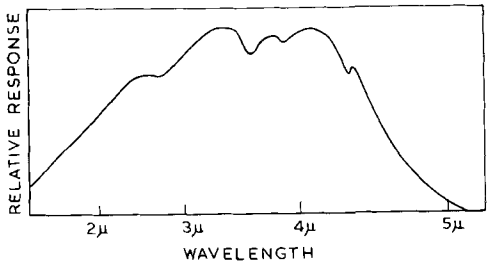

Fig. 2. Typical spectral response of a photoconductive PbSe cell at room temperature.

quite opaque, gray in appearance, with an average thickness of about a micron. At this stage a typical room temperature resistance for a layer with an area of 6 x 6 mm between electrodes is 90 kohm, although the resistance may vary between 50 and 120 kohm. Photoconductive sensitivity is usually negligible at this stage.

Sensitization

High photoconductive sensitivity is achieved by subjecting the layer to a succession of short rapid bakes *in vacuo* (about 10^{-6} mm Hg). This is normally done by raising the cell temperature to between 300°-400°C in about 10 min and then cooling rapidly with the aid of a low-pressure air stream. The room temperature resistance of the layer is noted after each bake together with its thermoelectric sign, determined by applying a cooled probe to one electrode and noting the direction of the thermoelectric current. The succession of vacuum bakes causes the resistance of the layer to fall initially and then rise to a maximum value as shown in Fig. 1. Vacuum baking beyond this point changes the layer from initially p- to n-type. The process should be stopped when the layer is still p-type (Fig. 1) and just on maximum resistance, as it has been found, by monitoring sensitivity during processing, that sensitivity is highest at this point. Table I gives typical values of layer resistance after successive vacuum bakes for a cell area of 6 x 6 mm.

Table I. Values of layer resistance for successive vacuum bakes

Vacuum bake at, °C	Resistance at room temperature, kohms
300	4 p
325	10 p
350	15 p
375	50 p
375	70 p
375	100 p
380	200 p
380	250 p
400	100 n

It is likely that the initial preparation introduces excess oxygen into the layer (4, 5) and that subsequent vacuum baking reduces the amount of oxygen and selenium until it is near a "compensated" stoichiometric composition, *i.e.*, lead Pb balanced by selenium and oxygen. Vacuum baking also extends the long wave spectral response due probably to an increase in crystallite size of the layer (6). If the baking is carried too far so that the layer becomes n-type, it can be made p-type again by baking in oxygen at any temperature up to 300°C followed by high vacuum sensitization bakes until the optimum state is again achieved. The necessity for re-introducing oxygen should, however, be avoided as layers of high sensitivity rarely result.

Figure 2 shows a typical spectral response for a room temperature cell made by the method described. A monochromator system with a constant energy output in 0.7-7μ region was used to measure the spectral response. Cells with D^* values (7) up to 4.1 x 10^8 cm $cps^{1/2}$ $watt^{-1}$ at 4.4μ have been prepared by this method and average values of 2.2 x 10^8 cm $cps^{1/2}$ $watt^{-1}$ have been regularly achieved.

Manuscript received Aug. 6, 1962.

Any discussion of this paper will appear in a Discussion Section to be published in the December 1963 JOURNAL.

REFERENCES

1. A. F. Gibson, W. D. Lawson, and T. S. Moss, *Proc. Phys. Soc.*, **A64**, 1054 (1951).
2. T. S. Moss, *Research*, **6**, 258 (1953).
3. W. D. Lawson, *J. Appl. Phys.*, **22**, 1444 (1951).
4. R. H. Jones, *Proc. Phys. Soc.*, **B70**, 704 (1957).
5. R. H. Jones, *ibid.*, **B70**, 1025 (1957).
6. W. D. Lawson, F. A. Smith, and A. S. Young, *This Journal*, **107**, 206 (1960).
7. P. L. Kruse, L. D. McGlauchlin, and R. B. McQuiston, "Elements of Infrared Technology," p. 270, John Wiley & Sons, New York (1962).

Isolation and Examination of Alloy Layers from Electrolytic Tinplate

Charles Luner[1] and M. V. Murray

Applied Research Laboratory, United States Steel Corporation, Monroeville, Pennsylvania

The alloy layer formed during the melting of electrodeposited tin on a steel substrate (tinplate) has been shown to be essentially $FeSn_2$ (1, 2), but owing to its thinness (about 1500Å), investigation of its properties has largely depended on specially prepared material. For example, electrochemical and physical measurements reported by Covert and Uhlig (3) were made on alloy that had been grown in molten tin. Recently, Bright and Britton (4) reported some electrochemical measurements on alloy isolated from hot-dipped plate. Small areas of alloy layer suitable for transmission electron microscopy have also been isolated from electrolytic tinplate (2).

This paper describes the development of a suitable method for stripping relatively large areas of tin alloy layer from electrolytic tinplate and reports preliminary optical and electrochemical measurements on isolated alloys. Although this technique has been developed primarily for the isolation of the alloy from commercial tinplate, it is believed that the method has wider applications in other systems where it is desirable to separate the intermetallic compound or alloy from the substrate.

Experimental

Specimen preparation and procedure.—The procedure for isolating the alloy from tinplate consists of cleaning the tinplate, removing the tin anodically, mounting the sample, and removing the steel substrate (low carbon steel).

The specimens (¾ x ¾ in.) are first degreased in acetone, then treated cathodically for about 1 min at about 1 amp/ft² in 0.5% sodium carbonate solution to remove any chemical treatment that may be present. This procedure is repeated until the sample may be completely wetted by water. The specimen is then washed with distilled water and dried. If the plate has not been properly cleaned, areas of tin will remain on the surface of the alloy after the detinning operation.

Following the cleaning, the tin from both surfaces of the specimen is removed electrolytically. Detinning will take place conveniently at room temperature in a 5% solution of sodium hydroxide at constant voltage, 0.4v, between the tinplate specimen as anode and the stainless steel cathode. A higher voltage may result in passivation of the tin layer and possible attack on the alloy. Complete detinning occurs in about 3 min. Detinning is determined by visual observation. It has been reported that this method of removing the tin should not attack the alloy (5, 6). However, work at the Laboratory has shown that an attack on the alloy layer occurs when the specimens being detinned are left in the detinning solutions for any length of time after the detinning has been completed. This attack can be avoided by connecting a piece of pure tin in parallel with the specimen being detinned. After the specimen is completely detinned, the detinning action will continue at the pure-tin anode, thus preventing the cell voltage from rising too high and causing damage to the alloy.

After detinning, the specimen is mounted in a Lucite block, using a conventional metallographic press. The specimen is mounted so that the alloy surface to be isolated is bonded to the mount while the outer surface remains free from the mounting material. A schematic representation of the mounted specimen is shown in Fig. 1.

A number of investigators (7, 8) have reported the relative inertness of $FeSn_2$ to attack by normal etching agents, dilute aqua regia, and dilute nitric acid, compared with the corrosion behavior of pure tin and iron. After considerable experimentation, it was found that a nitric acid-copper sulfate mixture would dissolve the steel preferentially without attacking the alloy. First, the alloy on the surface that is not protected by the mount is removed by abrasion to facilitate the corrosion of the steel. The specimen is then placed in a solution of 75% by volume of saturated copper sulfate and 25% by volume of concentrated nitric acid. Upon immersion of the specimen, copper plates on the steel. Additional concentrated nitric acid is then added, 1 ml at a time, until dissolving action starts on the specimen. To prevent the alloy from flaking off the mount because of a severe dissolving action, care should be taken not to add too much acid at one time. More acid may be added as the etching action on the specimen decreases. After the steel is completely removed, as indicated by the absence of any copper deposit on the surface of the specimen, the specimen is immediately removed from the solution, washed thoroughly with distilled water, and dried. The alloy remains intact and bonded to the transparent mount, the steel-alloy interface being exposed.

Preparation of electrodes.—To obtain electrode potentials, the mounted specimens were prepared in the following manner: electrical connection with the mounted isolated alloy was made with a Mueller No. 88 clip, a piece of tin foil placed over the edge of the alloy serving as a contact material between the clip and the specimen. The clip was connected to an alligator clip that in turn was connected to a

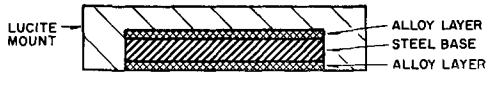

Fig. 1. Cross section of mounted specimen

[1] Present address: Argonne National Lab., Argonne, Illinois.

brass bolt. Around this bolt was a stopper, so that the whole assembly could be placed in a glass cell.

The cell was a glass container 6 in. in diameter and 6 in. high. An inlet and an outlet tube were placed ½ in. from the top of the container. A piece of micarta with six holes to accommodate the electrodes served as a lid for the cell.

The solution, 0.1M citric acid, in which the potentials were measured was deaerated for about 3 to 5 hr with commercially prepurified nitrogen or prepurified nitrogen that was further purified by passing it over heated (350°-400°C) copper. The specimens and holder, which were waxed completely except for an area of 42 mm^2, were placed in the solution while a positive pressure of nitrogen was maintained above the solution. Deaeration was then continued for at least another hour. The potentials were measured and recorded every 3 min with a L&N Micromax Recorder with a high input impedance. A positive pressure of N_2 was maintained in the space above the solution during the measurements. A saturated calomel electrode was used as a reference electrode and was situated in the center of the cell. The measurements were made at ambient temperature, 25° ± 2°C.

Results and Discussion

A transmission photomicrograph of the alloy isolated from electrolytic tinplate is shown in Fig. 2. The substrate had been annealed and chemically polished prior to tinplating. Although the average thickness of the alloy as determined by chemical analysis is about 1500Å, certain areas show a high degree of porosity. The areas which are quite porous appear to have grainlike shapes. That such areas do indeed correspond to the grain structure of the substrate is shown by the photomicrographs in Fig. 3. Figure 3a shows a photomicrograph of the steel substrate before plating, and Fig. 3b shows a photograph of the alloy from the same area which had been isolated after plating and melting. It is obvious that there is a one-to-one correspondence between the grains of the steel substrate and the alloy structure.

To show that little, if any, structural damage occurred during the stripping operation, a photomicrograph was taken of a preselected area of the alloy on the steel substrate (alloy-tin interface), Fig. 4a. (For convenience, the alloy was formed by melting an evaporated tin deposit.) The specimen was then mounted in a Lucite mount with the preselected area facing the mount. The steel was removed in the manner outlined above, and the same area rephotographed in transmission, Fig. 4b. It should be noted that in this instance the alloy-steel interface is exposed, thus showing a mirror image of the alloy-tin interface. It can be concluded that within the resolution of the optical microscope it appears that little, if any, structural damage resulted from the stripping operation.

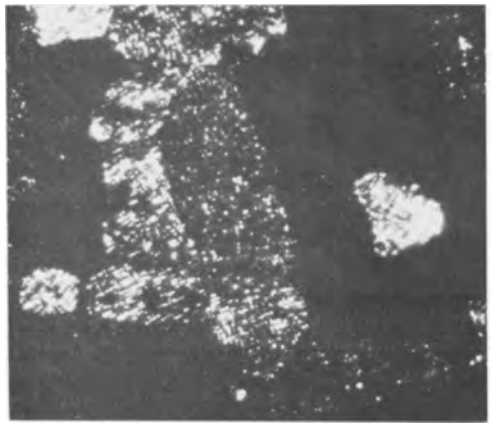

Fig. 2. Transmission micrograph of alloy isolated from tinplate; substrate annealed in vacuum and chemically polished prior to plating. Magnification 200X.

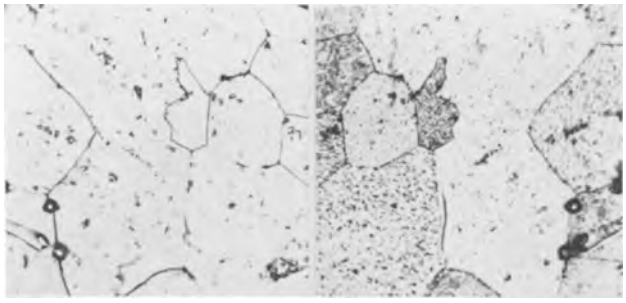

Fig. 3. Micrographs showing a one-to-one correspondence between ferrite grains and alloy: (a) (left) steel substrate; (b) (right) isolated alloy. Magnification approximately 330X.

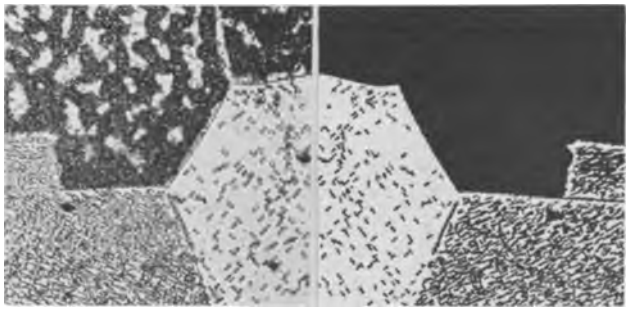

Fig. 4. Micrograph showing that no structural damage occurs during stripping operation. Tin deposited by vacuum evaporation on a vacuum annealed substrate: (a) (left) alloy-tin interface (reflection); (b) (right) alloy-steel interface (transmission). Magnification approximately 330X.

A number of observations on the above micrographs are worth noting. The alloy particles on neighboring ferrite grains were oriented in various directions, but on each grain one direction was preferred. The density of alloy varied from grain to grain, thus showing that the rate of growth depends on crystallographic direction. Certain grain boundaries appear to be preferred sites for alloy growth. Certain defects visible in the steel base are also apparent in the alloy layer. A full account of factors affecting the growth and morphology of the alloy is now under investigation and will be reported later.

It is more difficult to determine the extent to which the alloy might be contaminated during the stripping procedure. Because of the large number and intensity of diffraction lines in the $FeSn_2$ pattern, diffraction methods were not feasible for identifying small amounts of impurities that may have been present on the surface. The corrosion potentials, which are shown in Fig. 5, give some indication of the condition of the surface after stripping.

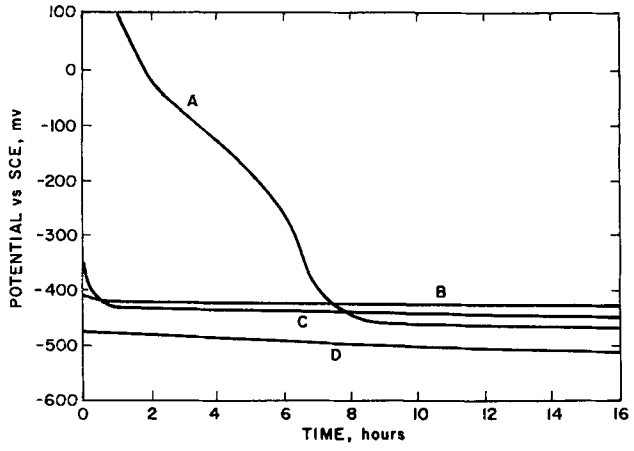

Fig. 5. Corrosion potentials of alloy ($FeSn_2$) isolated from tinplate. Surface preparation: A, no pretreatment; B, 6*N* HCl; C, 10% HNO_3 + HCl; D, HCl-N_2 laboratory purified.

For instance, if the corrosion potential of the isolated alloy is measured without further treatment of the alloy after it is isolated from the substrate, curve A in Fig. 5, the initial potential is about 430 mv positive (cathodic) to the saturated calomel electrode (S.C.E.). The potential becomes negative to the S.C.E. after about 1 hr and gradually becomes more negative for 5 hr, after which time it becomes relatively constant. If, however, the alloy was dipped in 6*N* HCl for 30 sec and then washed prior to the measurement, curve B in Fig. 5, the initial positive portion of the potential-time curve is eliminated and the final negative corrosion potential is attained sooner. In another experiment the specimen, after being isolated from the substrate, was dipped for 30 sec in 10% HNO_3, washed, immersed in 6*N* HCl, and rinsed. The corrosion potential of this specimen is shown in curve C, Fig. 5. It would appear from the results of the last two experiments that the presence of copper on the alloy as an impurity is unlikely. However, there is no doubt that a passive film exists on the surface of the alloy after the alloy is removed from the substrate.

The potentials reported above were obtained in a citric acid solution which had been deaerated with commercially prepurified nitrogen. If the nitrogen, further purified by passing it over heated copper was used to deaerate the citric acid, the final potentials were about 70 mv more negative, curve D in Fig. 5. The initial positive portion of the potential-time curve was similar to that obtained when commercially prepurified nitrogen was used to deaerate the solution. The corrosion potential obtained in this instance was in fair agreement with that obtained by Covert and Uhlig (3).

Manuscript received Aug. 2, 1962.

Any discussion of this paper will appear in a Discussion Section to be published in the December 1963 JOURNAL.

REFERENCES

1. W. E. Hoare and E. S. Hedges, "Tin and Its Uses," Edward Arnold and Co. (1959).
2. P. A. Stoll, American Society for Testing Materials, Special Publication No. 262.
3. R. A. Covert and H. H. Uhlig, *This Journal*, **104**, 537, (1957).
4. K. Bright and S. C. Britton, *Chem. & Ind.*, London, **1958**, 1362.
5. A. W. Hothersall and W. N. Bradshaw, *J. Iron Steel Inst., London*, **133**, 225 (1936).
6. C. T. Kunze and A. R. Willey, *This Journal*, **99**, 354 (1952).
7. A. W. Hothersall and V. C. Prytherch, *J. Iron Steel Inst., London*, **133**, 205 (1936).
8. W. E. Hoare, *ibid.*, **129** (1934).

Some Factors Affecting the Degradation of GaAs Tunnel Diodes

A. Pikor, G. Elie, and R. Glicksman

Semiconductor and Materials Division, Radio Corporation of America, Somerville, New Jersey

Irreversible degradation of GaAs tunnel diodes has been observed during prolonged operation in the forward injection region. This degradation is characterized by a large decrease in peak current and small decreases in junction capacitance and voltages. The conditions under which degradation occurs have been established, and the changes have been quantitatively correlated with a widening of the junction space-charge region during degradation (1).

The purpose of this note is to point out that the degradation rate of GaAs tunnel diodes depends on the ratio of peak current to capacitance (Ip/C), the forward voltage (V_F), and the forward current past the valley point (I_F). In addition, a figure of merit for safe operation of GaAs tunnel diodes has been established.

The GaAs tunnel diodes used in these tests were made by two techniques. In the first, zinc was diffused into GaAs wafers to produce a highly p-doped wafer surface. The wafers were then diced into pellets, and tin was alloyed into the GaAs to form the highly doped p-n junctions (2). The units were then electrochemically etched to the desired peak current values, washed, dried, and sealed in a low inductance case. Typical electrical characteristics of 50 ma GaAs tunnel diodes made by this diffusion process are given in Table I.

Table I. Typical electrical characteristics of 50 ma GaAs tunnel diodes used in the life studies

	Diffused crystal	Epitaxial crystal
Ip, ma	50 ± 5%	50 ± 5%
Ip/Iv	13/1	25/1
Vp, mv	165	145
V_v, mv	530	560
V_F', mv	1080	1270
R_s, ohms	1.5	1.3
C, pf	25	25

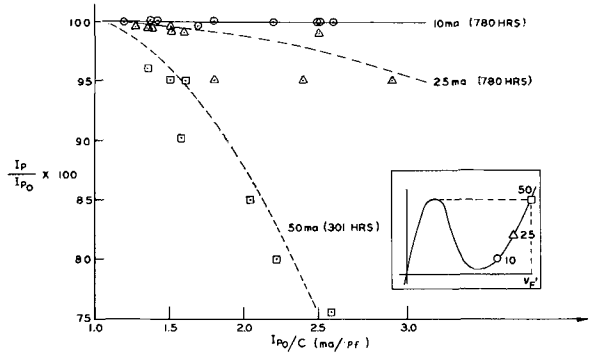

Fig. 1. Life data of 50 ma GaAs tunnel diodes (diffused crystal) tested at various operating (d.c.) currents beyond the valley (V_F' = 1020 — 1150 mv).

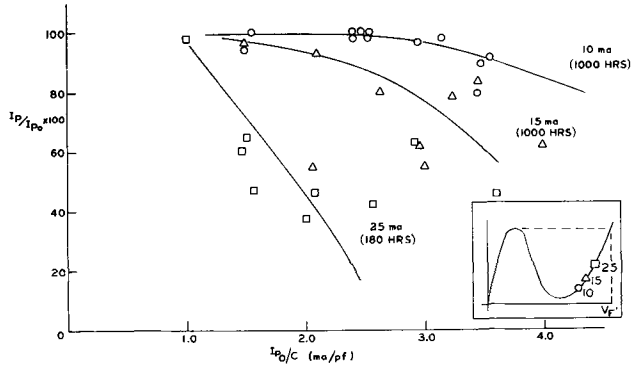

Fig. 2. Life data of 50 ma GaAs tunnel diodes (epitaxial process) operated at various forward currents (V_F' range 1220-1360 mv).

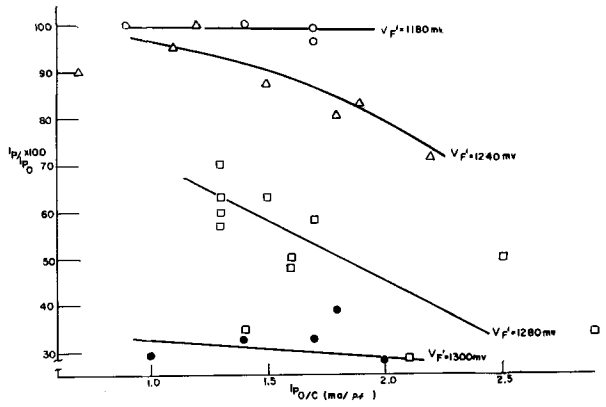

Fig. 3. Life data of 50 ma GaAs tunnel diodes (epitaxial crystal) operated at 25 ma forward current for 252 hr.

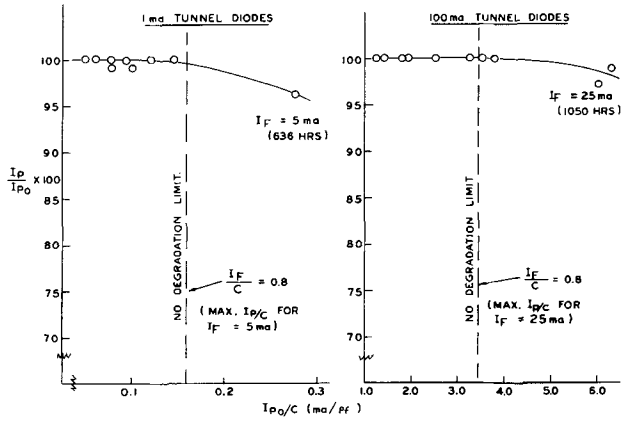

Fig. 4. Application of figure of merit ($I_F/C \leq 0.8$) for operating GaAs tunnel diodes (diffused crystal) under d.c. forward bias with no degradation.

In the second technique, diodes were fabricated by growing a thin epitaxial layer of GaAs heavily doped with zinc onto a substrate of p-type GaAs crystal (3). A tin dot was then alloyed into the epitaxial layer to form the junction, which was then electrochemically etched to the appropriate peak current value. Typical electrical characteristics of these diodes are also shown in Table I. In general, GaAs tunnel diodes made by the epitaxial process have typical Ip/Iv ratios of 25/1 and voltage swings of ($V_{F'} - V_P$) of 1100-1150 mv, compared to ratios of 13/1 and voltage swings of 900-950 mv obtained with diodes made by the diffusion process.

Figure 1 shows life data for 50 ma GaAs tunnel diodes made with zinc-diffused GaAs. The diodes, which covered a range of speed indices, were tested at various d-c operating currents beyond the valley voltage. The degradation rate, expressed as the percentage change of initial peak current (Ip/Ip_o x 100), is greater for diodes having higher speed ratios, Ip/C, and for diodes operated at higher forward currents. For these diodes the degradation rate also increases with increasing ambient temperatures. However, high ambient temperatures with no current (*i.e.*, shelf life tests at 175°C) does not cause any degradation.

Figure 2 shows similar curves for 50 ma tunnel diodes made with epitaxial crystal. Although the general trends are the same, these diodes show more severe degradation than diodes made with the diffused crystal. These greater degradation rates are attributed to the higher forward voltages of diodes made from epitaxial crystal. This fact is further borne out by the life data shown in Fig. 3 for 50 ma epitaxial tunnel diodes; for comparable diode speeds, degradation is greatest in diodes having the highest forward voltages. Other tests indicate that it is improbable that the greater power dissipation (and higher resultant junction temperatures) alone could account for the higher degradation rates of these diodes (4). However, such rates can be explained in terms of the degradation model proposed by Gold and Weisberg (5).

On the basis of extensive life data, a figure of merit for safe operation of GaAs tunnel diodes made with diffused crystal has been established empirically. This figure of merit was found to be applicable to tunnel diodes having peak currents which range from 0.1 to 250 ma. The requirement to be satisfied is $I_F/C \leq 0.8$ ma/pf, where I_F is the forward current past the valley, and C is the junction capacitance measured at the valley. When this condition is met, degradation is negligible. This figure of merit applies to diodes having high peak currents which are operated at less than Ip in the forward direction. It also applies to low current units operated at currents greater than Ip. Figure 4 shows typical degradation curves for 100 ma units operated at 25 ma past the valley and 1 ma units operated at a forward current of 5 ma. In both cases, diodes for which this figure of merit was exceeded, showed degradation.

Based on the life test data gathered to date, the following generalizations can be made: (*a*) degradation rate is a function of I_F, I_p/C, and V_F; (*b*) for similar values of forward voltage degradation of diffused and epitaxial GaAs tunnel diodes are comparable; (c) operation of a GaAs tunnel diode from the origin to the valley voltage (V_V) is completely safe; and (*d*) for given operating conditions, GaAs tunnel diodes can be designed for safe operation beyond the valley voltage.

Acknowledgments

The authors wish to acknowledge the help of F. Carlson who performed the life tests and the guidance of Dr. A. Blicher under whose direction this work was done. Thanks are also due to R. D. Gold for his helpful comments in the preparation of this note.

Manuscript received October 22, 1962.

Any discussion of this paper will appear in a Discussion Section to be published in the December 1963 JOURNAL.

REFERENCES

1. R. D. Gold, B. Goldstein, L. R. Weisberg, and R. M. Williams, *Bull. Am. Phys. Soc.*, II, **6**, [3], 312 (1961).
2. A. Wheeler, *RCA Engineer*, **6**, [2], 18 (August 1960).
3. H. Nelson, "Epitaxial Growth From the Liquid Phase," Presented at the IRE Solid State Device Research Conference, Stanford University, June 1961.
4. R. D. Gold and A. E. Roswell, Private communication.
5. R. D. Gold and L. R. Weisberg, *IRE Trans. On Electron Devices*, **ED-8** [5], 428 (Sept. 1961). A more complete discussion of this model will be published shortly.

On the Defect Structure of ZrO_2 and HfO_2

P. Kofstad and D. J. Ruzicka

Central Institute for Industrial Research, Oslo, Blindern, Norway

ABSTRACT

The defect structure of ZrO_2 and HfO_2 has been studied through measurements of electrical conductivity as a function of oxygen pressure. The electrical conductivity exhibits an unusual and complex oxygen pressure dependence, and to explain the results it has been proposed that these oxides are ionic conductors and that a coupled transport of oxygen vacancies and interstitials is faster than an independent transport of these defects. Thermogravimetric measurements on ZrO_2 suggest that the nonstoichiometry of this oxide is more than a factor of ten smaller than that observed by Aronson.

The oxidation mechanism of zirconium is not well understood. This is partly due to a lack of knowledge of the relative importance of and interplay between oxygen dissolution in the metal and oxide (ZrO_2) formation (1). From various studies (1-9) it is reasonable to conclude that the ZrO_2 layer has a protective effect and that a transport of ions through the scale at least partially determines the rate of oxidation of zirconium.

The elucidation of the oxidation mechanism of a metal forming a protective oxide scale of course requires knowledge of the defect structure of the oxide. From the literature it does not appear that the defect structure of ZrO_2 is known. In interpretations of the oxidation mechanism of zirconium this is commonly assumed to involve oxygen vacancies and a corresponding n-type conductivity (4-9). However, recent studies by Rudolph (10) have shown that the electrical conductivity of ZrO_2 is proportional to about $p_{O_2}^{1/5.2}$ at 900°-1000°C in the oxygen pressure range 760-0.1 torr. This may suggest that ZrO_2 is a p-type conductor under these conditions.

Although a large number of studies of oxidation of zirconium and zirconium alloys and corresponding attempts to elucidate the oxidation mechanism have been carried out, relatively little effort has been made to obtain a good working knowledge of the defect structure of ZrO_2. The present work is an attempt in this respect by measuring the electrical conductivity as a function of oxygen pressure. Studies on HfO_2 have also been included as this oxide closely resembles ZrO_2. In addition, attempts to make thermogravimetric measurements of the defect structures of these oxides have been made.

Materials and Methods

ZrO_2 powder was obtained from Johnson, Matthey & Company Limited. According to the suppliers estimates of impurities are as follows: Hf, 1.7%; Si, 5 ppm; Na, 1 ppm; and Cu and Mg, <1 ppm.

HfO_2 powder was supplied by the Wah Chang Corporation, and estimates of impurities contents are: Zr, <1000 ppm; Fe, <100 ppm; W, <50 ppm; Si, 50 ppm; Cu, <40 ppm; Al, <25 ppm; Ti, <20 ppm; Cr, Mg, Mn, Mo, Ni, and Sn, <10 ppm; Pb, Co, and V, <5 ppm, and Cd, <1 ppm.

Specimens were prepared by sintering cold-pressed powders in air at 1400°C.

In the studies of electrical conductivity 2 Pt-10% Rh plates served as electrodes, and these were pressed against the ends of the specimens by a spring-loading method. The resistance was measured with a Wheatstone bridge using direct current. The ZrO_2 specimen had a cylindrical shape with a diameter of 1.70 cm and a height of 1.65 cm. The density was 4.70 g/cm^3. The HfO_2 specimen had a diameter of 1.9 cm and a height of 2.1 cm. The density was 5.81 g/cm^3.

Measurements of the electrical conductivity as a function of oxygen pressure were made in pure oxygen gas at different pressures, in mixtures of argon and oxygen, and in mixtures of CO + CO_2 to obtain low partial pressures of oxygen (11). The equilibration periods varied from ½ hr to 1 day depending on the temperature.

The thermogravimetric measurements were carried out in a quartz helix type apparatus (12). The weight of the oxide was measured in O_2, in mixtures of CO + CO_2, and in pure CO. All measurements were made at a total gas pressure of 1 atm. Particular care was taken to avoid buoyancy due to thermomolecular or radiometer effects, which may cause serious errors in thermogravimetric measurements (12).

Results and Discussion

Electrical conductivity studies.—In the measurements of electrical conductivity of ZrO_2 hysteresis in the monoclinic-tetragonal transformation was observed. This is shown in Fig. 1, where the resistance of the specimen is plotted as a function of decreasing and increasing temperatures at a constant partial pressure of 0.009 atm + O_2. The measurements in Fig. 1 were taken at rapid heating and cooling (~3°C/min), but essentially the same curve was obtained by equilibrating the specimen for about 24 hr at each temperature. At increasing temperature the transition was very rapid and occurred at 1200°-1205°C, while at decreasing temperature the transition was more sluggish and took place at 1000°-1050°C. The observed transition temper-

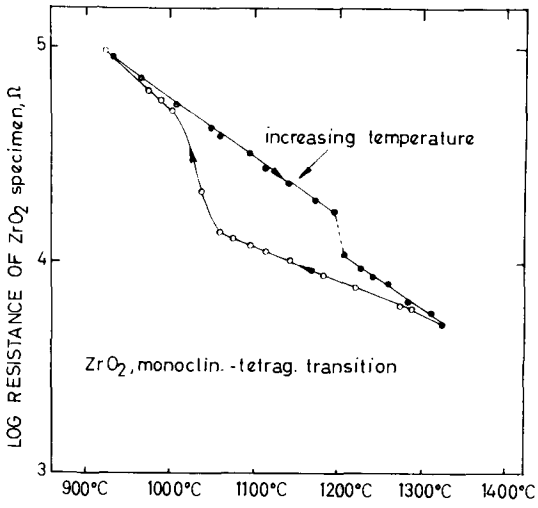

Fig. 1. Resistance of the ZrO_2 specimen as a function of increasing and decreasing temperature at a partial pressure of oxygen of 0.009 atm.

ature of 1200°C is in good agreement with recent studies of this phase transformation (13, 14).

The results of the studies of conductance of the ZrO_2 and HfO_2 specimens as a function of oxygen pressure are shown in Fig. 2 and 3, respectively. During measurements the system was kept at constant temperature. In order to avoid hysteresis effects associated with the ZrO_2 phase transformation, the results in Fig. 2 only include measurements taken under a sequence of increasing temperature.

If one expresses the conductance of the specimen as

$$\sigma = \text{const. } p_{O_2}^{1/n}$$

it is seen that for HfO_2 n has negative values at oxygen pressures above 10^{-3}-10^{-4} atm. At 800°-900°C and close to 1 atm O_2 n has a value of about −4, while at higher temperatures the value of n becomes larger. At 10^{-3}-10^{-4} atm O_2 the conductance goes through a maximum and again decreases with decreasing oxygen pressure. Below 10^{-6}-10^{-8} the conductance becomes approximately independent of oxygen pressure.

ZrO_2 shows the same general type of behavior. For tetragonal ZrO_2 n has negative values close to

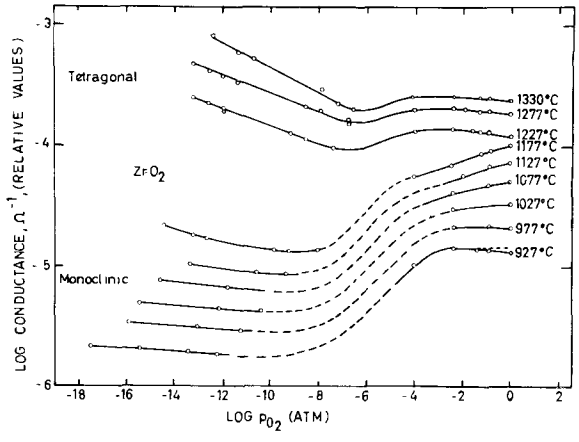

Fig. 2. Conductance of the ZrO_2 specimen as a function of the partial pressure of oxygen.

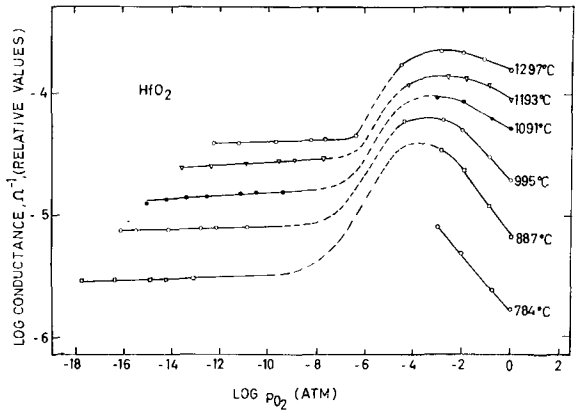

Fig. 3. Conductance of the HfO_2 specimen as a function of the partial pressure of oxygen.

1 atm O_2. The conductance goes through a slight maximum at about 10^{-3} atm O_2 and goes through a minimum at about 10^{-6}-10^{-7} atm O_2. Below this pressure n takes on negative values.

For monoclinic ZrO_2 n has in general positive values above 10^{-8}-10^{-9}, but the conductance becomes less oxygen pressure dependent with increasing oxygen pressure. The results also suggest a slight maximum at 10^{-2} atm at 927° and 977°C, similar to the maximum observed for HfO_2. Below 10^{-8}-10^{-9} atm O_2 n again takes on negative values.

Compared with other oxide semiconductors the conductivity of HfO_2 and ZrO_2 shows a very complex oxygen pressure dependence. This is indicative of a complex defect structure and interrelated effects of charge carrier mobilities.

Ionic defects whose concentrations are dependent on the oxygen pressure include oxygen and cation vacancies and interstitials. Oxygen defects may be described by the equations

$$O_I^{=} = Ov^{p+} + pe^{-} + \tfrac{1}{2}\, O_2^{(g)} \quad \text{Equil. const.} = K_2 \; [2]$$

$$\tfrac{1}{2}\, O_2^{(g)} = O_i^{-q} + qe^{+} \quad \text{Equil. const.} = K_3 \; [3]$$

where $O_I^{=}$ designates an oxygen ion in a normal lattice position, Ov an oxygen vacancy, O_i an oxygen interstitial, e^- an electron in the conduction band, and e^+ an electron hole. p and q may have values from 0 to 2. In addition one should also consider intrinsic ionization in the oxides. This may be written as

$$\text{Nil} = e^{+} + e^{-} \quad \text{Equil. const.} = K_4 \; [4]$$

A qualitative consideration of these defect equilibria gives the following limiting conditions:

1. If intrinsic ionization (Eq. [4]) predominates, the electrical conductivity is independent of oxygen pressure and the concentration of electrons (or electron holes) is given by

$$[e^{-}] = K_4^{1/2} \qquad [5]$$

2. If intrinsic ionization is negligible, the electrical conductivity is determined by Eq. [2] and [3]: (*a*) At very high pressures Eq. [3] will predominate and the defect equilibrium will essentially be given by

$$[O_i^{-q}][e^{+}]^q = K_3 p_{O_2}^{1/2} \qquad [6]$$

Under these conditions both the concentration of electron holes and interstitial oxygen ions will be proportional to $p_{O_2}^{+\frac{1}{2(q+1)}}$; (b) At very low pressures Eq. [2] will predominate, and the defect equilibrium will essentially be given by

$$[O_v^{+p}][e^-]^p = K_2 p_{O_2}^{-1/2} \qquad [7]$$

Under these conditions both the concentrations of electrons and of oxygen vacancies will be proportional to $p_{O_2}^{-\frac{1}{2(p+1)}}$

On the basis of the above defect structure model one would thus expect that the electrical conductivity is proportional to $p_{O_2}^{\frac{1}{2(q+1)}}$ at very high oxygen pressures. Similarly at very low oxygen pressures the electrical conductivity would be proportional to $p_{O_2}^{-\frac{1}{2(p+1)}}$. At the transition from p- to n-type conductivity one would also expect a minimum in conductivity. A defect structure of this type has been proposed for Ta_2O_5 (15).

A corresponding analysis of a defect structure involving cation vacancies and interstitials would lead to the same general conclusions, *i.e.*, one would expect p-type conductivity at high oxygen pressures and n-type at low oxygen pressures. Similarly a minimum in the conductivity *vs.* p_{O_2} curves would be expected at the p-n transition. The same oxygen pressure dependence would be expected regardless of whether one has predominant electronic conduction or a predominant ionic conduction with independent migration of the defects.

As seen in Fig. 3 the conductivity of HfO_2 shows a maximum at 10^{-3}-10^{-4} atm O_2 and with an apparent n-type conductivity at higher oxygen pressures and p-type at lower oxygen pressures. This experimentally observed pressure dependence is thus the opposite of the expected behavior discussed above. Therefore it does not appear possible to the authors to explain the observed behavior in terms of predominant electronic conduction or predominant ionic conduction with independent migration of the defects or in terms of a combination of such transport processes. A possible interpretation of the results may, however, be made by assuming that ionic conduction takes place through a "coupled" transport of vacancies and interstitial ions.

If one assumes that HfO_2 and ZrO_2 has an anti-Frenkel defect structure, i.e., oxygen vacancies and interstitials, the defect structure is described by Eq. [2]-[4]. The concentration of oxygen vacancies will increase with decreasing oxygen pressure, while the concentration of oxygen interstitial ions will increase with increasing oxygen pressure. However, Eq. [3] will not be applicable up to extremely large oxygen pressures as this would assume an unlimited solubility of interstitial oxygen ions. One must assume that the solubility of interstitial oxygen ions approaches a limiting value with increasing oxygen pressure. The valence of the interstitial oxygen ion, *i.e.*, the value of q, may vary from 0 to 2. Considering the size of an oxygen ion, small values of q would be favored.

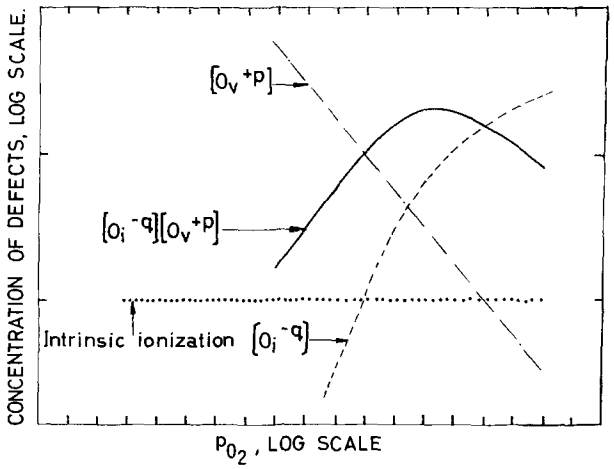

Fig. 4. Proposed model for variations in defect concentrations with partial pressure of oxygen.

The concentration of oxygen vacancies and interstitial ions will be a very complex function of oxygen pressure and will depend on the values of q, p, K_2, K_3, and K_4. The exact relationship may be evaluated by applying the condition of electroneutrality and the law of mass action to Eq. [2], [3], and [4] (12, 15).

A qualitative representation of the concentrations of oxygen vacancies and interstitial ions is shown in Fig. 4. In drawing the curves it is assumed that $q < p$ and that the concentration of interstitial oxygen ions approaches a solubility limit.

As discussed above an independent transport of defects will under no circumstances result in a maximum in the electrical conductivity as a function of oxygen pressure. However, if one assumes that "coupled" or simultaneous transport of the defects is much faster than the independent migration, the electrical conductivity will be given by the product of the defect concentrations, thus $\sigma \alpha [O_i^{-q}][O_v^{+p}]$. This product is shown as the fully drawn line in Fig. 4 and, as seen, one obtains a maximum in the conductivity curve.

At higher and lower pressures than that of the maximum, the conductivity will decrease with pressure until the total conductivity will be determined by another transport process. For HfO_2 it is proposed that when the conductivity due to the coupled transport becomes too small, the conductivity due to intrinsic ionization will predominate and the conductivity will become essentially independent of oxygen pressure (Eq. [5]). This behavior is observed for HfO_2 at $p_{O_2} < 10^{-6}$-10^{-8} atm. According to this model one would also expect that the conductivity becomes independent of oxygen pressure and that it is determined by the intrinsic ionization at very high oxygen pressures. The total conductivity on the basis of this model will be as shown in Fig. 4.

The same general interpretation is also proposed for ZrO_2. For the monoclinic phase a maximum in the conductivity is suggested only at the lower temperature. Compared to HfO_2 it thus appears that the

maxima are displaced toward higher oxygen pressures for monoclinic ZrO_2. This may be explained by a somewhat higher solubility of interstitial oxygen ions in monoclinic ZrO_2 than in HfO_2.

At $p_{O_2} < 10^{-8}$-10^{-14} ZrO_2 exhibits increasing conductivity with decreasing oxygen pressure. This may be explained qualitatively by effects of independent migration of oxygen vacancies. From Eq. [2], [3], and [4] it is obvious that at sufficiently low oxygen pressures the oxygen vacancy defect equilibrium (Eq. [2]) will eventually predominate, and if the mobility of oxygen vacancies is larger than that of the electrons, the conductivity will be given by that of the oxygen vacancies.

Due to the complexity of the defect equilibria and the transport processes, the above discussion is at the present stage necessarily qualitative in nature. The observed temperature dependence and activation energies also are composites and reflect the relative importance of the defect equilibria and the mobilities of the charge carriers. Furthermore the different equilibria will most likely have different "activation energies," and the oxygen pressure dependence of the conductivity will therefore show variations with temperature, as shown for HfO_2 and ZrO_2.

Thermogravimetric studies.—The nonstoichiometry of ZrO_2 as a function of oxygen pressure at 900°-1100°C has been studied by Aronson (7). These results suggest that the nonstoichiometry (*i.e.*, the concentration of defects) increases with decreasing temperature. Thermodynamically this is extremely unlikely. It was therefore considered worthwhile to attempt to reproduce the results of Aronson by means of thermogravimetric measurements in the same manner as for Nb_2O_5 (12) and TiO_2 (16).

Thermogravimetric measurements were made at 1100°-1300°C by measuring the weight change of ZrO_2 and HfO_2 specimens when successively equilibrating the specimens in 1 atm O_2, in mixtures of $CO + CO_2$ (p_{O_2} ranging from 10^{-7} to 10^{-18} depending on temperature), and in pure CO. Equilibration periods up to 1 day were used.

In all cases very small weight changes were observed, and in most cases the weight changes were within the limits of error of the measurements. Because of these small weight changes it was impossible to evaluate the oxygen pressure dependence of the nonstoichiometry.

If the formula of the oxide is written as ZrO_{2-z}, the results suggest that the maximum weight loss in going from a partial pressure of oxygen of $1\text{-}10^{-15}$ atm at 1175°C corresponds to a value of $z < 0.001$. This value suggests a nonstoichiometry which is more than a factor of 10 smaller than that observed by Aronson at 900°-1100°C (7).

Summary and General Considerations

In the above interpretation it has been proposed that the defect structures of ZrO_2 and HfO_2 involve oxygen vacancies and interstitials. The formula of the oxides should correspondingly be written MeO_{2-x+y}, where x represents oxygen vacancies and y interstitial oxygen.

In order to explain the oxygen pressure dependence of the conductivity it has been found necessary to assume a predominant ionic conductivity and that a coupled transport of oxygen vacancies and interstitial ions is much faster than an independent transport of these defects.

In order to confirm the proposed mechanism it would be highly desirable to study the relative importance of ionic and electronic conduction as a function of the partial pressure of oxygen. In this connection it is important to note that ZrO_2 highly doped with Ca is essentially an ionic conductor involving the transport of oxygen via oxygen vacancies (17).

The proposed mechanism and defect structure would also be of importance as regards the elucidation of the mechanisms of oxidation of these metals. In this respect it is particularly important to ascertain the relative importance of ionic and electronic conduction.

A remark should also be made with regard to the use of the Wagner-Hauffe semiconductor approach to alloy oxidation in attempts to improve oxidation resistance of metals. This approach has frequently been applied in recent years, but it has been seemingly unsuccessful in disappointingly many cases. The above discussion emphasizes that a firm knowledge of the defect structure and transport mechanism in oxides is necessary before attempts to apply the semiconductor approach is made. All in all, in order to obtain a more fundamental understanding of protective oxidation of metals and alloys, more emphasis should be placed on the study of diffusion, defect structures, and electrical conductivity in oxides and the effect of impurities and oxide additions on such phenomena.

Manuscript received March 12, 1962; revised manuscript received July 30, 1962.

Any discussion of this paper will appear in a Discussion Section to be published in the December 1963 JOURNAL.

REFERENCES

1. K. Östhagen and P. Kofstad, *This Journal*, **109**, 204 (1962).
2. E. A. Gulbransen and K. F. Andrew, *Trans. AIME*, **185**, 515 (1949); **209**, 394 (1957).
3. D. Cubiciotti, *J. Am. Chem. Soc.*, **72**, 4138 (1950).
4. J. Belle and M. W. Mallett, *This Journal*, **101**, 339 (1954).
5. M. W. Mallett and M. M. Albrecht, *ibid.*, **102**, 407 (1955).
6. H. A. Porte, J. G. Schnizlein, R. C. Vogel, and D. F. Fisher, *ibid.*, **107**, 506 (1960).
7. S. Aronson, *ibid.*, **108**, 312 (1961).
8. D. Flint and J. H. O. Varley, *J. Phys. Chem. Solids*, **6**, 213 (1958).
9. O. Flint and J. H. O. Varley, *Nature*, **179**, 145 (1957).
10. J. Rudolph, *Z. Naturforsch.*, **14a**, 727 (1959).
11. P. Kofstad, *J. Phys. Chem. Solids*, **23**, 1571 (1962).
12. P. Kofstad and P. B. Anderson, *ibid.*, **21**, 280 (1962).
13. F. A. Humpton and R. Roy, *J. Am. Ceram. Soc.*, **43**, 234 (1960).
14. C. T. Lynch, F. W. Vahldick, and L. B. Robinson, *ibid.*, 44 (1961).
15. P. Kofstad, *This Journal*, **109**, 776 (1962).
16. P. Kofstad, *J. Phys. Chem. Solids*, **23**, 1579 (1962).
17. W. D. Kingery, T. Pappis, M. E. Doty, and D. C. Hill, *J. Am. Ceram. Soc.*, **42**, 393 (1959).

High-Pressure Oxidation of Metals, Nickel in Oxygen

J. P. Baur,[1] R. W. Bartlett, J. N. Ong, Jr., and W. M. Fassell, Jr.

Aeronutronic, A Division of Ford Motor Company, Newport Beach, California

ABSTRACT

The oxidation of Mond nickel was studied between 1000° and 1200°C at oxygen pressures from 6.5 x 10^{-3} to 20.4 atm. The oxidation rate was controlled by diffusion through the oxide and had a gross activation energy of 50 ± 4 kcal/mole. Least squares straight line fitting over the entire pressure range indicated the rate was proportional to $P_{O_2}^{1/5}$. However, the rates above 1 atm appeared insensitive to pressure. On this basis, the measured rates below 1 atm more closely follow the $P_{O_2}^{1/4}$ dependence expected from electrical conductivity studies in NiO. The oxide oriented in a preferred manner with 100 planes parallel to the polycrystalline nickel base.

In the early work of Wagner and Grünewald (1) on the oxidation of nickel, the observed parabolic rate was derived on the basis of diffusion of nickel ions by a vacancy exchange mechanism through a uniform layer of NiO. Below 1000°C, the parabolic relation has been observed by other investigators (2-4). The role of cation vacancies has been confirmed by electrical and thermoelectric studies on NiO (5-7), which is a p-type semiconductor, and by the close correspondence of the activation energies for oxidation and for diffusion of radioactive nickel in NiO (8, 9). Nevertheless, there are some anomalies. Gulbransen and Andrew (10) have observed that at 900°C and higher, parabolic rate law plots of the data show increasing values of the rate constant with time. The dissociation of two electron holes from each cation vacancy and a resulting oxidation rate and electrical conductivity dependence on $P_{O_2}^{1/6}$ which was assumed by Wagner and Grünewald are not clearly supported by electrical conductivity measurements or oxidation rate measurements.

Since most of the previous studies of nickel oxidation have been confined to temperatures below 1000°C and no known studies have been made at oxygen pressures above 1 atm, the present study was conducted at temperatures to 1200°C and oxygen pressures from 6.5 x 10^{-3} to 20.4 atm to clarify further the pressure dependence of the oxidation of nickel.

Experimental Procedure

Mond nickel sheet containing the impurities listed in Table I was vacuum annealed at 10^{-6} mm Hg for 24 hr and cold rolled to approximately 0.010 in. Samples were cut, abraded with 8/0 garnet paper, washed in acetone, and dried. The weight and apparent geometric area were determined, and the sample was suspended by a quartz hook from a quartz helical spring into a platinum wound tube furnace. The rate was determined from the weight increase measured by monitoring the extension of the spring with a Gaertner cathetometer. For pressures above 1 atm, the entire furnace and suspension train were enclosed in a steel vessel capable of operation at 40.8 atm which was flooded with dry oxygen to the desired pressure after vacuum purging (11). The furnace for subatmospheric pressure work and its suspension train were of zirconium silicate and glass construction (12).

[1] U.S. Bureau of Mines, Salt Lake City, Utah.

Table I. Analysis of Mond nickel

Cobalt	0.20
Manganese	0.03
Iron	0.04
Sulfur	0.005
Silicon	0.02
Copper	0.01
Magnesium	0.005
Aluminum	0.005

Results

Oxidation rate measurements were made at 1000°, 1100°, 1150°, and 1200°C. Only one oxide phase, NiO, was produced. For each sample, the weight increments were area normalized, squared, and plotted against time. The results for an oxygen pressure of 0.125 atm are shown in Fig. 1. The shape of the resulting curves is similar at other oxygen pressures. With the exception of a brief initial period, a parabolic relation is followed, indicating that diffusion

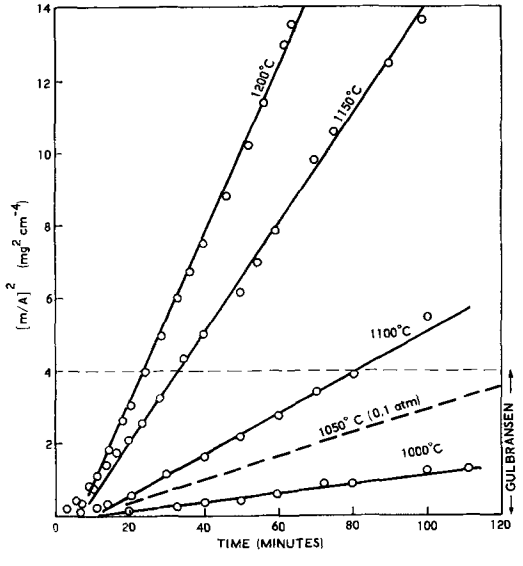

Fig. 1. Parabolic oxidation of nickel; P_{O_2} = 0.125 atm; dashed line represents data of Gulbransen and Andrew (10) at 1 atm.

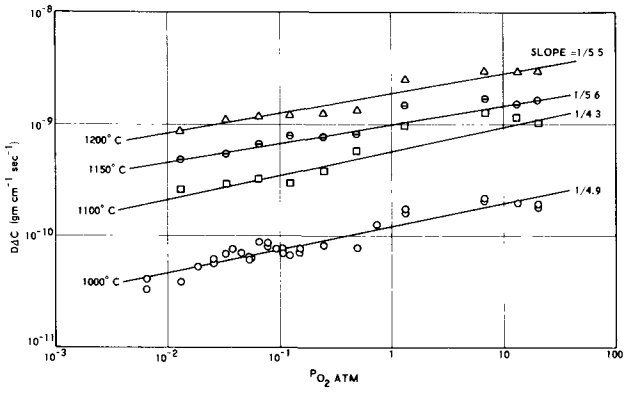

Fig. 2. Nickel oxidation rate log ($D\Delta C$) *vs.* log oxygen pressure (P_{O_2}); average slope 1/5.0.

through the oxide layer controls the rate of oxidation for films thicker than 3-5μ. Plots of area normalized weight gain *vs.* time (linear plot) and log-log plots of the same parameters did not indicate a linear to parabolic or other transition in the rate. The initial deviation from a parabolic plot is not ascribed to impurities since Johnson-Mathey nickel with no impurities present in amounts greater than 0.0002% behaved in the same manner.

By assuming a uniform concentration gradient and integrating the steady-state one-dimensional diffusion equation, after substituting $\Delta X = m/A\rho_0$, the following parabolic relation is obtained:

$$(m/A) = (2D\Delta C\rho_0)^{1/2}\, t^{1/2} \qquad [1]$$

where m is the weight gain, ρ_0 is the density of oxygen in NiO, D is the diffusion coefficient, A is the sample area, and ΔC is the difference in concentrations of the diffusing species across the oxide. From this equation and the terminal slopes of the curves in Fig. 1 and similar data at other pressures from 6.5 x 10^{-3} to 20.4 atm, log $D\Delta C$ was plotted against log P_{O_2}, Fig. 2. The drawn lines represent least squares fitting of the data.

Because the cation vacancy concentration is small, the diffusion coefficient is not expected to depend on concentration. However, it is expected to vary with temperature exponentially. An Eyring plot of the logarithm of $D\Delta C/T$ *vs.* $1/T$ at several oxygen isobars is shown in Fig. 3. From the slopes, an experimental activation enthalpy of 50.5 ± 4 kcal/mole was determined.

Oxide Orientation

A preferred orientation of the NiO crystals growing on nickel was observed above 1000°C. A series of photomicrographs were taken of the surfaces of samples oxidized at various temperatures and pressures without polishing, etching, or otherwise altering the existing surface. The oxide film formed at 850°C and 1 atm oxygen during 37.5 hr in the furnace was green, extremely thin, and fine grained. X-ray diffraction studies indicate a random orientation of the oxide. Samples oxidized at 1000°C and 20.4 atm show well-defined oxide grains, some preferred orientation, and a large number of flat crystal faces. The preferred orientation and grain growth both increase with temperature. One of these

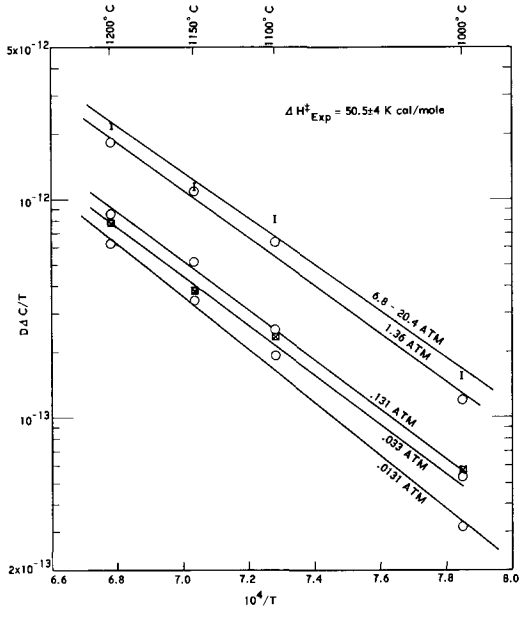

Fig. 3. Experimental activation enthalpy for oxidation of nickel

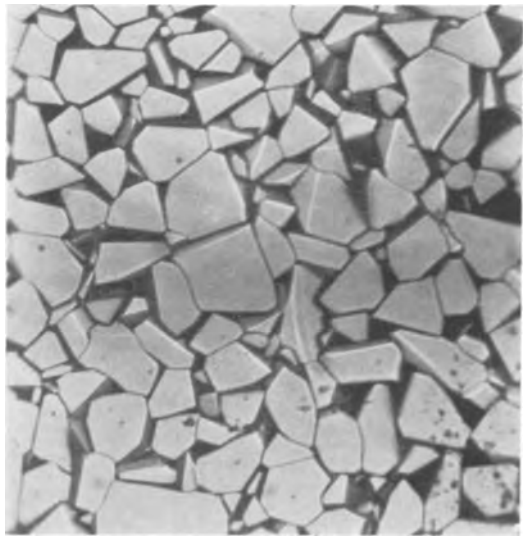

Fig. 4. Oxide film on nickel oxidized 14 hr at 1200°C and oxygen pressure of 13.6 atm. No polishing or etchant was used. X300

photomicrographs, representing a sample oxidized 14 hr at 1200°C and 13.6 atm oxygen is reproduced in Fig. 4, and several striking features can be seen. The grains of NiO are very large, and sharp edges and recesses are preserved except where the crystals join. At these junctions the boundaries are often curved. Large flat faces predominate and are about the same height above the base metal, lying within the focal plane of the microscope objective. These films adhere tenaciously to the metal and will withstand considerable handling without chipping.

The x-ray diffraction intensities for the oxide film found at three different temperatures are reproduced in Fig. 5 with the peaks resulting from diffraction of the nickel metal base deleted. The following changes occur with increasing temperature and pressure. The {111}, {220}, {331}, and {422} peaks disappear. The {200} and {400} peaks increase markedly until the {200} peak predominates. The {311} and {420} peaks initially increase and sub-

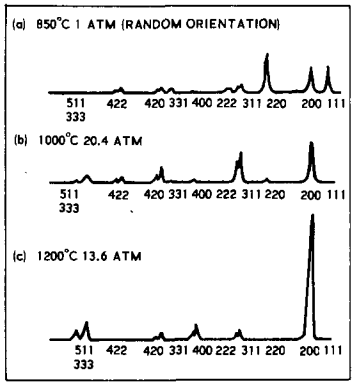

Fig. 5. X-ray diffraction diagrams of NiO films at various temperatures and P_{O_2}; nickel peaks deleted.

sequently decrease. The {511} and {333} peaks increase somewhat.

A comparison of these diagrams and the photomicrographs indicates the {100} planes form the large flat faces of the grains and grow at the expense of the other planes. This orientation provides the densest possible nickel atom packing parallel to the nickel sheet. Evidently the {311} and {420} planes increase and then decrease because the angles made by these planes with the {100}, *i.e.*, 25°14′ and 26°34′, respectively, are less than those of the others, *i.e.*, {111} 54°44′; {220} 45°; {331} 46°30′; and {422} 35°16′. The increase of the {511} peak with that of {100} is due to the fact that this family of planes, {511}, makes an angle of only 5°49′ with the appropriate {100} planes.

Figure 6 represents a sample oxidized 33¼ hr at 1200°C and 13.6 atm oxygen. It is a good example of the structure of the boundaries between oxide grains. The projected angles between the faces of the tetrahedral pit are 120° and the faces of the pit are {111} planes. An x-ray diffraction of this sample showed complete orientation of the {100} parallel to the surface of the nickel base. A fold appearing in the lower left-hand corner suggests some ductility in NiO at these temperatures.

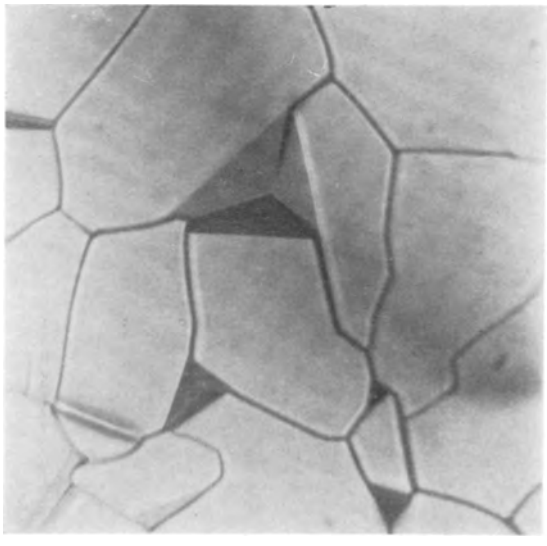

Fig. 6. Growth pits in oxide film on nickel oxidized 33¼ hr at 1200°C and oxygen pressure of 13.6 atm. No polishing or etchant was used. X300

Discussion

The 1050°C data of Gulbransen and Andrew (10) are superimposed on Fig. 1. The approximate magnitude of the rate and change in the rate constants are consistent with the results of this study. Gulbransen and Andrew did not report data at higher temperature or longer oxidation periods. As a result, the change in rate constant came approximately midway during their experiments, and they postulated oxide film breaking as the cause of the deviation. Under this premise the curve should continue to curve upward indefinitely as successive layers of oxide form and break away. However, the higher temperature parabolic plots of Fig. 1 remain straight over a considerable oxide film thickness and suggest that the deviation from parabolic behavior occurs with the initial film growth. A similar relationship was observed in the oxidation of iron at 1000°C by Benard (13). At high temperatures, when the NiO layer is thinner than about 3-5μ, transport of nickel ions is evidently more rapid than some other reaction step in the oxidation process, *e.g.*, adsorption of oxygen on NiO, dissolution of oxygen or nickel in the NiO lattice at their respective interfaces. Moreover, the morphology of film growth, particularly if oxide domains or clusters form, has been shown to affect the oxidation kinetics in several systems (14) and may retard the initial oxidation of nickel by lowering the area available for reaction.

The oxidation rate is expected to depend on the concentration gradient of cation vacancies. For the temperatures of this investigation, the oxygen pressure at the NiO/Ni interface is below 10^{-20} atm and, hence, well below the pressure range investigated. As a result, the cation vacancy concentration at the NiO/Ni interface is negligible compared to the O/NiO interface. The oxidation rate will effectively depend only on the latter concentration. Thus, using the Kröger-Vink atomic notation (15)

$$\Delta C = \{V_{Ni} + V'_{Ni} + V''_{Ni}\}_{O/NiO} \qquad [2]$$

where we have included the possibility of nonionized, singly and doubly ionized nickel vacancies. Over a limited temperature range, only one state of the vacancy is likely to predominate. The concentration of vacancies at the O/NiO interface will be affected by the oxygen pressure, impurities, and the extent of ionization of electron holes from the cation vacancy. Wagner and Grünewald (1) reported a $P_{O_2}^{1/6}$ dependence which was explained on the basis of the equilibrium at the O/NiO interface between oxygen, vacancies, and two free electron holes for each vacancy

$$\tfrac{1}{2}\,O_2 \rightleftharpoons NiO + V''_{Ni} + 2\,\oplus \qquad [3]$$

However, Moore and Lee (3) have shown that the data of Wagner and Grünewald actually follow a $P_{O_2}^{1/5.3}$ dependence and have suggested the possibility of ionization of only one, instead of two, electron holes from each vacancy. This requires the vacancy concentration to depend on $P_{O_2}^{1/4}$.

Electrical conductivity measurements offer additional evidence on the oxygen pressure dependence of the oxidation rate. Mitoff (6) measured electrical conductivity at 1300°C from 10^{-4} to 1 atm. Metered

amounts of oxygen and inert gas were mixed to obtain the desired oxygen pressure at a total flow rate of 1 liter/min and total pressure slightly above 1 atm. Mitoff's data fit a $P_{O_2}^{1/6}$ dependency, but if the 10^{-4} atm readings were deleted, the remaining data fits $P_{O_2}^{1/4}$ much better. Some difficulty in maintaining a pressure of 10^{-4} atm might attend this method since an O_2 flow rate of only 0.1 cc/min must be maintained. Baumbach and Wagner (16) measured the conductivity of NiO in oxygen pressures from 2 x 10^{-4} to 1 atm at 900° and 1000°C. The conductivity was proportional to $P_{O_2}^{1/4}$.

It is difficult to determine the pressure dependence of the oxidation rate or conductivity when the exponential argument of the pressure is small. Studies of the temperature dependence on electrical conductivity and, in particular, carrier concentration, measure the extent of ionization of electron holes from the vacancy more precisely. The electrical conductivity varies with the charge carrier concentration, and since electron concentration is negligible

$$\sigma = p|e|\mu \qquad [4]$$

The temperature dependence of the mobility, μ, is usually small, and conductivity measurement becomes a crude measure of hole concentration. Morin (7) studied the electrical conductivity of several NiO samples treated in different atmospheres. Of the high-purity samples sintered in H_2, the sample with the lowest conductivity was assumed to represent NiO whose electrical conductivity was not influenced by impurities. This sample was compared with lithium doped material and pure NiO sintered above 1200°C in oxygen and air. A log σ *vs.* $1/T$ plot was made, and typical intrinsic and extrinsic curves resulted. The intrinsic conductivity varied from 10^{-7} to 1 ohm^{-1} cm^{-1} between 200° and 1100°C. Below 600°C the vacancy concentration is frozen. It was concluded that most of the 22 kcal/mole intrinsic activation energy is for ionization of the first hole from the field of the nickel ion vacancy. About 5 kcal/mole were attributed to mobility activation energy. The latter value was deduced from the high-temperature slope of lithium doped NiO. On the basis of this and similar data reported by Mitoff, a temperature in excess of 600°C is required before an appreciable fraction of the first holes are ionized. Assuming the Bohr model for the vacancy-hole dissociation and neglecting any changes in the dielectric constant of the material, the second hole ionization energy is expected to be about four times larger than the first hole ionization energy. Consequently, appreciable second hole ionization should not occur below about 2100°C, well beyond the temperature range of investigation. Thus, electrical conductivity measurements indicate that the O/NiO interface reaction in the oxidation of nickel is likely to produce a singly ionized nickel vacancy and one electron hole and require a rate dependence on $P_{O_2}^{1/4}$.

The pressure dependence may also be altered by chemisorption of oxygen on the NiO surface. Chemisorption and splitting of the oxygen molecule is required before reaction with a nickel ion can occur. Employing the Langmuir equilibrium, the surface concentration of oxygen atoms $[\frac{1}{2}\ O_2]_s$ may be expressed as

$$[\tfrac{1}{2}\ O_2]_s = \frac{k_o K_a P_{O_2}^{1/2}}{1 + K_a P_{O_2}^{1/2}} \qquad [5]$$

where k_o includes surface roughness and the total available active surface site concentration, and K_a is the adsorption equilibrium constant. The chemisorbed oxygen reacts to form singly ionized nickel vacancies

$$\tfrac{1}{2}\ O_2|_S \overset{K_1}{\rightleftharpoons} V'_{Ni} + \oplus + NiO \qquad [6]$$

$$p[V'_{Ni}] = \frac{K_1 k_o K_a P_{O_2}^{1/2}}{1 + K_a P_{O_2}^{1/2}} \qquad [7]$$

$$[V'_{Ni}] = \left\{\frac{K_1 k_o K_a P_{O_2}^{1/2}}{1 + K_a P_{O_2}^{1/2}}\right\}^{1/2} \qquad [8]$$

or doubly ionized vacancies

$$\tfrac{1}{2}\ O_2|_S \overset{K_2}{\rightleftharpoons} V''_{Ni} + 2\oplus + NiO \qquad [9]$$

$$p^2[V''_{Ni}] = \frac{K_2 k_o K_a P_{O_2}^{1/2}}{1 + K_a P_{O_2}^{1/2}} \qquad [10]$$

$$[V''_{Ni}] = \left\{\frac{\tfrac{1}{4} K_2 k_o K_a P_{O_2}^{1/2}}{1 + K_a P_{O_2}^{1/2}}\right\}^{1/3} \qquad [11]$$

For either of Eq. [8] and [11] at low pressures or high temperatures, $K_a P_{O_2}^{1/2} << 1$, and the surface vacancy concentration and oxidation rate are pressure sensitive. At sufficiently high pressures or low temperatures, $K_a P_{O_2}^{1/2} >> 1$, and the surface vacancy concentration and oxidation rate are independent of further pressure increase.

The literature does not provide information on the adsorption of oxygen on NiO at the investigation temperatures.

Least squares straight line fitting of the data in Fig. 2 gave an average pressure dependence of $P_{O_2}^{1/5.0}$ in good agreement with the least squares analysis of Wagner and Grünewald data by Moore and Lee. This fit does not agree with the low-pressure limits of either Eq. [8] or [11]. Careful in-

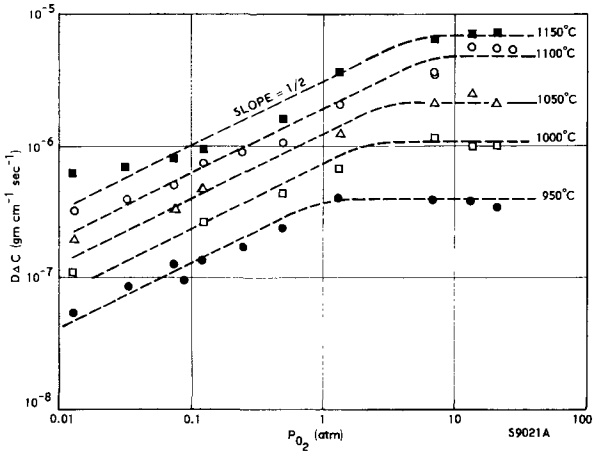

Fig. 7. Cobalt oxidation rate log ($D\Delta C$) *vs.* log oxygen pressure (P_{O_2}); from data of Bridges, Baur, and Fassell (12); lines drawn at slope of ½.

Table II. Comparison of experimental activation energies

Activation enthalpy, kcal/mole	Investigators	Method
41.2 (400°-750°C)	Gulbransen and Andrew (4)	Oxidation
45	Kubaschewski and Goldbeck (2)	Oxidation
41.2; 68 (750°-1050°C)	Gulbransen and Andrew (10)	Oxidation
44.2	Shim and Moore (8)	Ni diffusion
55.4 (800°-1000°C)	Ipatev and Ivanova (17)	Oxidation
41 (700°-1050°C)	Kofstad (18)	Oxidation
51 (800°-1400°C)	Frederick and Cornet (19)	Oxidation
56 (700°-1400°C)	Lindner and Akerstrom (9)	Ni diffusion
35	Moore and Lee (3)	Oxidation
50 (1000°-1200°C)	This work	Oxidation

spection of the region of Fig. 2 above 1 atm indicates that the rate is independent of pressure. If this correlation is assumed, the rate data below 1 atm fit a $P_{O_2}^{1/4}$ dependence, in good agreement with the $P_{O_2}^{1/4}$ dependence expected from electrical property measurements. Additional data at very high pressures are required before a definite conclusion may be made. This change in rate sensitivity to oxygen pressure is more pronounced with a similar transition metal, cobalt. The data of Bridges, Baur, and Fassell (12) have been replotted in the form of log $D\Delta C$ *vs.* log P_{O_2} in Fig. 7. The rate is proportional to $P_{O_2}^{1/2}$ at pressures below about 1 atm which indicates that both electron holes are strongly bound by the cobalt ion vacancy at oxidizing temperatures

$$\tfrac{1}{2}\, O_2|_S \rightleftharpoons V_{Co} + CoO \qquad [12]$$

Above 10 atm, the oxidation rate is independent of the oxygen pressure, indicating complete coverage of surface active sites by oxygen.

The measured nickel oxidation activation enthalpy of 50.5 kcal/mole includes the activation enthalpy for diffusion, $\Delta H_D^{\ddagger}$, and the enthalpies for the equilibrium reactions for adsorption, ΔH_a, and vacancy creation, ΔH_1, at the O/NiO interface. Since the measured value is close to the activation energy for diffusion of nickel in NiO, the sum of the adsorption and vacancy reaction enthalpies must be small. A comparison of experimental activation energies is given in Table II.

Summary

For an equivalent uniform oxide film thickness greater than 5μ, the oxidation rate of nickel between 1000° and 1200°C is controlled by diffusion through the oxide with the observed rate approximately proportional to $P_{O_2}^{1/5}$. The rate-controlling mechanism is presumed to be nickel ion-vacancy exchange. A rate dependence on $P_{O_2}^{1/4}$ is explained by the ionization of one electron hole from the vacancy while a $P_{O_2}^{1/6}$ dependence results if 2 electron holes are ionized. The large variation of electrical conductivity with temperature in NiO indicates the former mechanism. The data suggest that the rate is independent of pressure above 1 atm, but the evidence is not conclusive. The activation enthalpy was 50.5 ± 4 kcal/mole. The nickel oxide grew with {100} planes parallel with the polycrystalline nickel base.

During growth of the initial 3-5μ of oxide, the rate is slower than required by the thick film diffusion process.

Manuscript received April 3, 1962; revised manuscript received Aug. 31, 1962. This paper was prepared for delivery before the Boston Meeting, Sept. 16-20, 1962.

Any discussion of this paper will appear in a Discussion Section to be published in the December 1963 JOURNAL.

REFERENCES

1. C. Wagner and K. Grünewald, *Z. Physik Chem. B*, **40**, 455 (1938).
2. O. Kubaschewski and O. Goldbeck, *Z. Metallkunde*, **39**, 158 (1948).
3. W. J. Moore and J. K. Lee, *Trans. Faraday Soc.*, **48**, 916 (1952).
4. E. A. Gulbransen and K. F. Andrew, *This Journal*, **101**, 128 (1954).
5. M. Verwey, M. Haaijman, H. Romeijnan, and M. von Oosterhout, *Phillips Research Repts.*, **5**, 173 (1950).
6. S. P. Mitoff, *J. Chem. Phys.*, **35** [3], 882 (1961).
7. F. J. Morin, *Phys. Rev.*, **93** [6], 1199 (1954).
8. M. T. Shim and W. J. Moore, *J. Chem. Phys.*, **26**, 802 (1957).
9. R. Lindner and A. Akerström, *Discussions Faraday Soc.*, **23**, 133 (1957).
10. E. A. Gulbransen and K. F. Andrew, *This Journal*, **104** [7], 451 (1957).
11. R. C. Peterson, W. M. Fassell, Jr., and M. E. Wadsworth, *J. Metals*, **6**, 1038 (1954).
12. J. P. Baur, D. W. Bridges, and W. M. Fassell, Jr., *This Journal*, **103**, 273 (1956).
13. J. Benard, *Bull. soc. chim. France*, p. D89 (1949).
14. H. F. Fischmeister, "Reactivity of Solids," J. H. deBoer *et al.*, Editors, p. 195-206, Elsevier Publishing Co., New York (1961).
15. F. A. Kröger and H. J. Vink, "Solid State Physics," Vol. 3, p. 310, F. Seitz, and D. Turnbull, Editors, Academic Press, New York (1956).
16. H. H. Von Baumbach and C. Wagner, *Z. Phys. Chem.*, **B24**, 59 (1934).
17. V. B. Ipatev and M. A. Ivanova, *Uchenye Zapiski Leningrad. Gosudarst. Univ. No. 175, Ser. Khim. Nauk.*, **14**, 80 (1954).
18. P. Kofstad, *Nature*, **179**, 1362 (1957).
19. S. F. Frederick and I. Cornet, *This Journal*, **102**, 285 (1955).

The Electrochemistry of Tin

I. Effects of Nonionic Addition Agents on Electrodeposition from Stannous Sulfate Solutions

Stuart Meibuhr,[1] Ernest Yeager, Akiya Kozawa, and Frank Hovorka

Department of Chemistry, Western Reserve University, Cleveland, Ohio

ABSTRACT

The kinetics of the electrodeposition of tin were studied from simple acid solutions containing various nonionic organic additives. Many of these substances produced a large increase in the cathodic polarization. The similar behavior at solid polycrystalline tin and liquid tin-amalgam cathodes implies that the rate-determining step responsible for the polarization is substantially the same at each electrode in the presence of the adsorbed organic additive. Qualitative evidence is presented for the adsorption of nonionic organic molecules on the electrode surface. A probable rate-determining step is the transfer of cations through a barrier of adsorbed organic molecules to the electrode surface. The formation of this barrier is kinetically limited rather than diffusion-limited.

Tin is electrodeposited with little activation polarization from acid stannous solution in the absence of addition agents. The deposits obtained under such conditions are nonadherent, coarse, and usually treed. The presence of certain organic addition agents results in a substantial increase in the polarization even at moderately low current densities. Furthermore, the quality of the tin deposits may be greatly improved in terms of adherence, decreased grain size, and freedom from treeing. Although considerable effort has been directed toward finding addition agents for tin plating and examining the effects of these addition agents on the structural properties of the deposits, relatively little attention has been focused on establishing how such organic addition agents influence the kinetics of the electrodeposition process.

The purpose of the present investigation has been the fundamental study of the kinetics of tin deposition from solutions containing nonionic organic additives. Tin is deposited from acid solutions at moderate cathodic potentials, and therefore, many organic agents can be used as addition agents without the complications associated with the formation of reduction products at the cathode. Furthermore, the electrocapillary maximum for tin is relatively close to the reversible potential in such solutions as the acid stannous sulfate, and frequently, nonionic additives are readily adsorbed on the electrode.

This paper presents the results of measurements of the steady-state cathodic polarization in sulfate solutions containing various addition agents as a function of current density, temperature, type and concentration of addition agents, stannous ion concentration, supporting electrolyte concentration, and chloride ion concentration with both pure polycrystalline tin and liquid tin amalgam. Some differential capacity measurements also have been made.

The over-all cathodic polarization associated with the deposition of tin from various acid stannous solutions including chloride, sulfate, and perchlorate baths has been measured by various workers including Esin and Loshkarev (1), Loshkarev and co-workers (2-5), Izmaylov (6), Kovalenko and Bogdasarov (7), Piontelli and co-workers (8-11), and Bertocci and Serrevalle (12). In the absence of addition agents, the activation polarization on polycrystalline and single-crystal tin as well as on liquid tin amalgam is of such small magnitude that concentration polarization is usually predominant in steady-state polarization measurements, and Tafel linearity is not observed. Under such circumstances, the interpretation of the small activation polarization in terms of a unique rate-determining step is very difficult.

Loshkarev and his co-workers (2, 3) have measured the cathodic polarization for the deposition of tin from a solution containing cresolsulfonic acid and glue. They found Tafel linearity for both polycrystalline tin and liquid tin-amalgam cathodes at apparent current densities above 20 ma/cm^2, although the range of Tafel linearity was limited. Loshkarev and his co-workers concluded that at current densities greater than 20 ma/cm^2, charge transfer is rate determining even in the presence of the cresolsulfonic acid and glue.

Loshkarev and Kryukova (4, 5) have studied the deposition of tin on solid tin and liquid tin-amalgam cathodes in the presence of organic additives. Their study showed a sharp decrease in the differential capacity associated with the double layer at potentials close to the electrocapillary maximum. Loshkarev and Kryukova concluded that the differential capacity data and the high polarization in solutions containing some nonionic organic additives confirm the existence of a compact, adsorbed layer of organic additives. In their opinion, this layer or film caused the discharge step to be retarded because of the slow diffusion of tin through the layer. As the potential becomes significantly more cathodic than the electrocapillary maximum, the differential capacity as-

[1] Present address: Fuel Cell Corporation, St. Louis, Missouri.

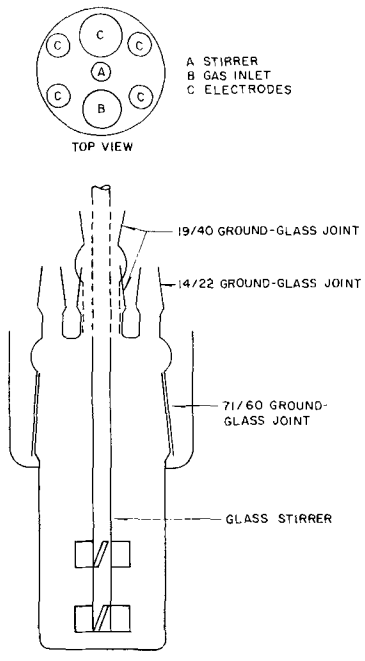

Fig. 1. Polarization cell

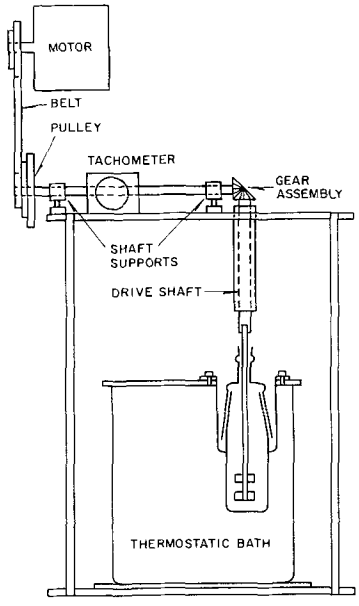

Fig. 2. Cell assembly and stirrer drive system. (Note details of cell cap are not shown, see Fig. 1).

sociated with the electrode again increases. This was explained in terms of the breakdown of the adsorbed film with increasing cathodic potential. Loshkarev and Kryukova attributed this behavior not to the reduction but rather to the desorption of the additive from the electrode surface, the potential range for the desorption being dependent on the structure of the organic addition agent. When the concentration of the organic addition agent was decreased, they observed a displacement of the potential of desorption to values less cathodic relative to the point of zero charge.

In an article concerned primarily with the applied aspects of tin plating, Gurevich (13) reported that the mechanism of addition agent action is the same in stannous chloride and stannous sulfate solutions. His results led him to agree with the theory advanced by Loshkarev and Kryukova that the large increase in polarization produced by nonionic organic addition agents may be attributed to the retarded diffusion of tin through the adsorbed layer of organic molecules.

Experimental

Apparatus.—All the present measurements were conducted in a Pyrex glass cell, Fig. 1. Provisions were made in the cell design for pre-electrolysis electrodes, two cathodes for duplicate measurements, a hydrogen bubbler, an anode, and a reference electrode. All the electrodes and the hydrogen bubbler were introduced into the cell through ground glass joints in the cap of the cell.

Purified hydrogen gas was passed through the solution by means of a glass bubbler tube submerged below the surface of the solution. The hydrogen was purified by passing it through a gas train consisting of a Deoxo[2] catalytic unit for the conversion of O_2 to H_2O at room temperature and three packed columns; the first column contained $Mg(ClO_4)_2$ to remove water, the second Hopcalite[3] to oxidize CO to CO_2, and the last soda ash to remove CO_2. The gas next flowed through three traps maintained at liquid-nitrogen temperature. The second trap contained activated charcoal that had previously been outgassed, whereas the first and third traps were empty. The purified gas then passed directly to the cell through glass tubing connected to the cell with a few centimeters of polyethylene tubing. The use of polyethylene tubing expedited assembly and disassembly of the system. The authors believe that a few cm of tubing would not introduce into the hydrogen gas stream any impurities that would have an appreciable effect on the polarization measurements.

The cell was mounted in a thermostatic bath, Fig. 2, that could be adjusted to any temperature from 5° to 45°C with an accuracy of ± 0.2°C. All polarization measurements were made at a fixed stirring rate that corresponded to an estimated flow rate of 400 cm/sec in the bulk of the solution in the immediate vicinity of the cathode. Gas bubbles were whipped through the solution and probably increased the effectiveness of the forced convection in reducing the boundary-layer thickness at the electrode surface.

Polarization measurements were made by the steady-state, indirect method with an electronic interrupter represented by the block diagram in Fig. 3. This unit is similar to that described by Staicopoulus and co-workers (14), except that the bridge null detector was replaced by a Tektronix oscilloscope (Type 532), with a differential vertical plug-in amplifier (Type 53/54D). A Dumont oscilloscope camera with a Polaroid back was used to photograph the oscilloscope traces from which the differential capacities were calculated.

The polarization of the cathode could be measured with this equipment with an accuracy of ± 1

[2] Manufactured by the Baker Platinum Division of Englehard Industries, Inc.

[3] Manufactured by Mine Safety Appliance Corporation.

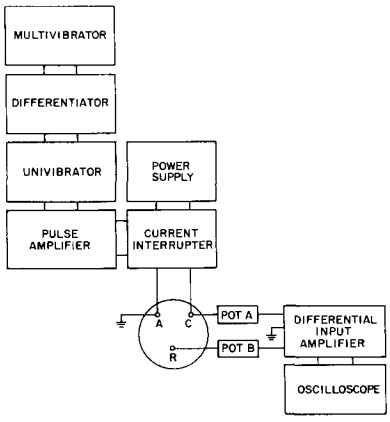

Fig. 3. Block diagram of electronic commutator and associated equipment. A, anode; C, cathode; R, reference.

mv within 2-3 μsec after the interruption of the polarizing current. The current-on period was 2 msec and the current-off period was 100 μsec for all the measurements by the interrupter technique presented in this paper.

Procedure.—The electrodes were prepared by sealing chemically pure platinum wire (24 gauge Brown and Sharp) in Pyrex glass tubing, Fig. 4, which in turn was attached to a ground glass joint that fitted into the cell cap. A glass bead was secured to the ends of each of the platinum wires used as cathodes to minimize extraneous edge effects that otherwise would cause extremely high local current densities. The anode and reference electrodes were prepared by attaching chemically pure tin foil to a platinum wire, which in turn was sealed in the Pyrex glass tubing. These electrodes were immersed in chromic acid cleaning solution and then washed profusely with distilled water before introducing them into the cell.

The glass assembly used in the work with the amalgam cathode is shown in Fig. 4. The tin amalgam was prepared by electrodepositing tin from a stirred solution containing 0.4M $SnSO_4$ and 1.0M H_2SO_4 into a pool of triple-distilled mercury for sufficient time to yield a 0.1% by weight amalgam. The potential of the amalgam electrode relative to a reversible polycrystalline-tin electrode in the same solution was about −3 mv at 25°C. If the potential deviated by more than ±1 mv from this value, the amalgam was discarded.

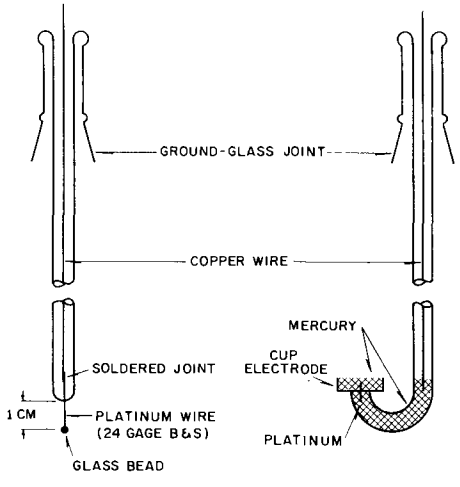

Fig. 4. Electrode design

For the measurements made with addition agents, the solid tin cathodes were prepared by electrodepositing tin from the same solution as that used for the subsequent measurements onto a platinum surface at a current density of 25 ma/cm² for 60 sec. The potential at which this preplate procedure was performed was always greater than −200 mv relative to a tin reference electrode. If the potential was lower than this, a grainy, rough deposit was often obtained, and this was not satisfactory as a base for the subsequent polarization measurements. At potentials more negative than −200 mv with an effective addition agent present, a relatively smooth, adherent deposit was always produced.

For polarization measurements made in solutions void of organic addition agents, the tin cathodes were prepared by electrodepositing tin from a separate solution that contained 0.1% Pluronic L64 in 0.4M $SnSO_4$ and 1.0M H_2SO_4 under conditions that resulted in a smooth deposit.

The organic additives for which polarization-current density plots were obtained and their manufacturers are listed in Table I. These materials were 98-100% pure as specified by their manufacturer; the main impurities were compounds that had a structure similar to the structure of the primary substance.

The electrolyte was prepared by dissolving purified $SnSO_4$[4] in 1.0M H_2SO_4, which was prepared by diluting reagent grade concentrated H_2SO_4 with distilled water. The cloudy solution that resulted was stirred for ½ hr. Then 1 g/l of active carbon Nuchar C190A[5] was added and the solution was stirred for ½ hr. The material was suction-filtered to yield a clear solution. This treatment (*a*) removed the insoluble stannic compounds, and (*b*) should have been reasonably effective in reducing the concentration of the trace metals and chlorides to a very low level. The resulting solution was analyzed by titrating it with 0.05M $KMnO_4$. The electrolyte was stored in fully-stoppered Pyrex bottles. Solutions stored in this manner were not used for polarization measurements unless they remained clear.

The solutions used in this investigation were not subjected to all of the extensive purification procedures (for example, multiple recrystallizations) usually considered desirable in fundamental studies of the kinetics of electrode reactions in the absence of organic additives. Such purification procedures did not appear to be justified in the present work with organic additives, since the organic additives were not available in the ultrapure form. Pre-electrolysis was used in the measurements with addition agents in only one test involving 0.1% (by weight) Pluronic L64. In this test, 500 ml of solution were pre-electrolyzed in the polarization cell with agitation for 90 hr at a current of 5 ma with a tin-foil

[4] The principal impurities designated by the supplier, City Chemical Corporation, Brooklyn, New York, in the $SnSO_4$ crystals from which the solutions were prepared were stannic content, 4.35%; iron, 0.0006%; antimony, 0.0003%; lead, 0.002%; and chloride, 0.008%.

[5] West Virginia Pulp and Paper Company.

Table I. Organic compounds used as additives and their manufacturers

Compound	Source	Chemical type
Triton X114	Rohm & Haas Co.	$R—\bigcirc—(OC_2H_5)_xOH$ 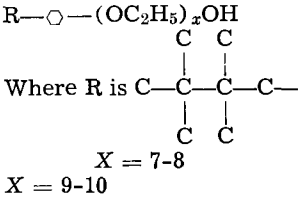 Where R is $C—C(C)—C(C)—C—$ $X = 7\text{-}8$
Triton X100	Rohm & Haas Co.	$X = 9\text{-}10$
Triton X102	Rohm & Haas Co.	$X = 12\text{-}13$
Triton X165	Rohm & Haas Co.	$X = 16$
Triton X205	Rohm & Haas Co.	$X = 20$
Triton X305	Rohm & Haas Co.	$X = 30$
Polyglycol P400	Dow Chemical Co.	$HO(C_3H_6O)_xC_3H_6OH$ $X = 6$
Polyglycol P750	Dow Chemical Co.	$X = 12$
Pluronic L61	Wyandotte Chemical Corp.	A block polymer $HO(C_2H_4O)_a(C_3H_6O)_b(C_2H_4O)_cH$ $b = 30$ $a + c = 4\text{-}5$
Pluronic L62	Wyandotte Chemical Corp.	$b = 30$ $a + c = 10$
Pluronic L64	Wyandotte Chemical Corp.	$b = 30$ $a + c = 26$
Pluronic F68	Wyandotte Chemical Corp.	$b = 30$ $a + c = 160$
Pluronic P75	Wyandotte Chemical Corp.	$b = 33$ $a + c = 44$
Pluronic L44	Wyandotte Chemical Corp.	$b = 19$ $a + c = 20$
Trimethyl nonyl ether of polyethylene glycol (TMN)	Union Carbide Corp.	$C_{12}H_{25}—O—(C_2H_4O)_xC_2H_4OH$ $X = 6\text{-}7$
Polyglycol E300	Dow Chemical Co.	$HO(C_2H_4O)_xC_2H_4OH$ $X = 6\text{-}7$
Polyglycol E600	Dow Chemical Co.	$X = 12\text{-}14$
Polyglycol E4000	Dow Chemical Co.	$X = 90\text{-}95$
Polyglycol E9000	Dow Chemical Co.	$X = 200\text{-}210$
Dowanol EB	Dow Chemical Co.	$n\ C_4H_9—O—C_2H_4OH$
Dowanol TPM	Dow Chemical Co.	$CH_3(OC_3H_6)_3OH$
Dowanol DPM	Dow Chemical Co.	$CH_3(OC_3H_6)_2OH$

cathode of 1.00 cm^2 area with the same tin anode as that used for the polarization measurements. The pre-electrolysis-cathode was withdrawn from the solution at the conclusion of the pre-electrolysis before the polarization measurements were made.

Prior to a polarization run, the cell, cap, and stirrer were washed with chromic acid cleaning solution to remove any organic material, rinsed several times with distilled water, and then finally rinsed with the solution to be investigated. The complete cell assembly together with the solution was then transferred to the constant-temperature bath. Purified hydrogen gas was introduced through the bubbler, and the solution was stirred for ½ hr to permit the temperature of the electrolyte within the cell to reach equilibrium. The addition agents and the electrodes were then introduced into the cell. The polarization measurements were almost always taken by adjusting the current through the electronic interrupter to the desired value with the electrodes disconnected from the circuit to minimize cathode-area changes due to continued deposition. After the current had stabilized at the desired value, the cell was switched into the circuit, and the potential between the various electrodes was measured. The time required for current stabilization in the electronic equipment was 30 sec or less; that is, the current did not flow through the cell for periods of this time between each of the polarization measurements. The time required for the actual potential measurement in each polarization test was about 20 sec, which was more than ample in the present work for the cathode to approach a steady value. Unless otherwise indicated, all polarization data were recorded with increasing current. Duplicate polarization measurements were made for all the work involving organic additives. The potential difference between the solid tin cathode and the reference electrode was measured at zero current before and after each run. If this potential was greater than ±5 mv, new electrodes were prepared. The potential of the solid tin cathode was usually within ±1 mv of that of the reference tin electrode.

If the differential capacities were to be determined, a photograph of the cathode-polarization decay curve was made.

Experimental Results

Polarization Measurements

Figures 5, 6, and 7 show typical S-shaped polarization-current density curves obtained for various organic additives at 25°C. Duplicate measurements

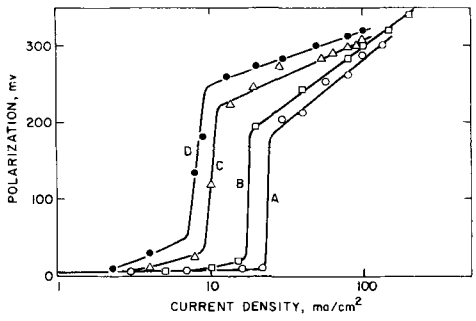

Fig. 5. Polarization measurements with various Tritons. Temperature, 25.0° ± 0.2°C; electrolyte, 0.4M $SnSO_4$ plus 1.0M H_2SO_4 plus 0.5% (by weight) addition agent. Curve A, Triton X305; B, Triton X165, C, Triton X100; D, Triton X114.

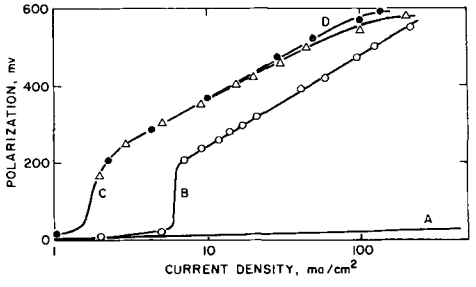

Fig. 6. Polarization measurements with Polyglycol P400. Temperature, 25.0° ± 0.2°C; electrolyte, 0.4M $SnSO_4$ plus 1.0M H_2SO_4 plus Polyglycol P400. Curve A, 0.01% by weight; B, 0.1%; C, 0.5%; D, 2.0%.

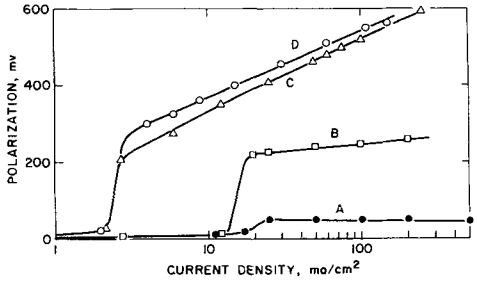

Fig. 7. Polarization measurements with Pluronic L64. Temperature, 25.0° ± 0.2°C; electrolyte, 0.4M $SnSO_4$ plus 1.0M H_2SO_4 plus Pluronic L64. Curve A, 0.01% by weight; B, 0.04%; C, 0.1%; D, 0.5%.

were always within 2% of the polarization values reported in these graphs. The curves show an inflection point that shifts to lower current densities as the concentration of the organic additive is increased. This dependence of the inflection point on additive concentration indicates that the rapid rise of the polarization with increasing current density does not correspond to a simple diffusion limited process involving either the stannous ion or the organic additive.

Tafel linearity was obtained with every additive that caused an increase in polarization. The Tafel slope, however, was a function of the particular additive and differed even for additives of the same generic formula. If charge transfer was the rate-determining step associated with the deposition process, then this dependence of the Tafel slope on the type of organic additive is not surprising, since the height and symmetry of the potential-energy barrier probably should be a function of the particular additive adsorbed on the electrode surface. The apparent exchange current densities and the Tafel slopes for all the organic additives used in this investigation are listed in Table II. The Tafel linearity almost always extends over at least one decade of current density and often over two decades. With the exception of the Tritons, the Tafel slopes for the addition agents fall in the range 170-230 mv per decade.

The Tin Research Institute gives the formulation of a tin-plating solution for obtaining mirror-bright deposits with wood tar as an additive (15). The cathodic polarization for this solution is shown in Fig. 8. There was no evidence of simultaneous hydrogen evolution even at the extreme cathodic polarization of −600 mv that was obtained for the measurements with wood tar.

Current efficiency measurements were made by weighing the cathode in the work with Pluronic L64 at 0.1% by weight concentration. At a current density of 100 ma/cm² duplicate measurements indicated an efficiency of 100 ± 0.5%.

The polyethylene glycols (E Series, Dow Chemical Company) did not affect the cathodic polarization. The compound trimethyl nonyl ether of polyethylene glycol (TMN) is related to Polyglycol E300; both have the same polyglycol chain length of 6. The TMN exhibits hydrophobic-hydrophylic character, whereas the Polyglycol E300 does not. The TMN differs sufficiently in structure from the Polyglycol E300 to cause a marked increase in the polarization. The polarization data for the TMN are shown in Fig. 9.

These results may suggest that micelle formation is involved in the action of such addition agents. For example, Heydegger and Dunning (16) reported

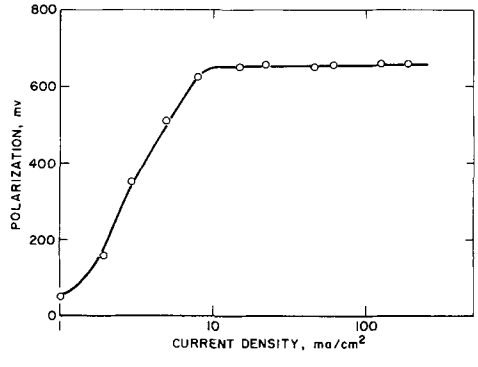

Fig. 8. Polarization measurements with hardwood tar DEV 193 with solution prepared according to specification of the Tin Research Institute (15). Temperature, 25.0° ± 0.2°C; electrolyte, 0.4M $SnSO_4$ plus 8 g/l wood tar, plus 35 ml per liter Tergitol 08.

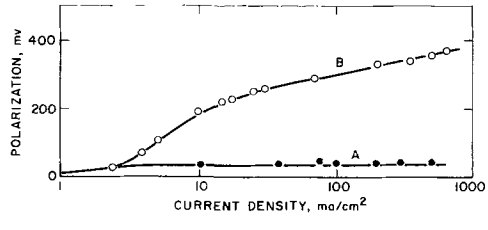

Fig. 9. Polarization measurements with ethoxylated trimethyl nonyl alcohol (TMN). Temperature, 25.0° ± 0.2°C; electrolyte, 0.4M $SnSO_4$ plus 1.0M H_2SO_4 plus TMN. Curve A, 0.01% by weight; B, 0.03%; higher concentrations yield same results as Curve B.

Table II. Apparent exchange current densities and slopes of the Tafel curves

Compound	Percent concentration	i_o, ma/cm²	Slope	Remarks
Triton X165	0.5	1.0	0.15	Pure, solid, tin cathode
Triton X100	0.5	0.043	0.095	Pure, solid, tin cathode
Triton X114	0.5	0.003	0.070	Pure, solid, tin cathode
Triton X305	0.5	2.0	0.164	Pure, solid, tin cathode
Polyglycol P400	0.1	1.0	0.24	Pure, solid, tin cathode
	0.5	0.18	0.21	Pure, solid, tin cathode
Polyglycol P750	0.5	0.50	0.24	Pure, solid, tin cathode
Polyglycol P400 + Cl^-	0.1 0.001M	1.5	0.236	Pure, solid, tin cathode
P400 + Cl^-	0.1 0.01M	3.3	0.236	Pure, solid, tin cathode Pure, solid, tin cathode
Pluronic L44	0.1	0.22	0.157	Pure, solid, tin cathode
	0.5	0.15	0.170	Pure, solid, tin cathode
Pluronic L61	0.1	0.20	0.211	Pure, solid, tin cathode
Pluronic L62	0.1	0.07	0.170	Pure, solid, tin cathode
	0.5	0.03	0.170	Pure, solid, tin cathode
Pluronic L64	0.1	0.19	0.190	Pure, solid, tin cathode
	0.5	0.03	0.170	Pure, solid, tin cathode
Pluronic P75	0.1	0.17	0.250	Pure, solid, tin cathode
Pluronic F68	0.1	No appreciable linear section		Pure, solid, tin cathode
	0.5	0.05	0.28	
Pluronic L64	0.1	0.11	0.20	7.5°C Pure, solid, tin cathode
		0.26	0.190	25°C Pure, solid, tin cathode
		0.30	0.196	35°C Pure, solid, tin cathode
		0.61	0.202	45°C Pure, solid, tin cathode
Polyglycol P400	0.1	0.34	0.23	7.5°C Pure, solid, tin cathode
		1.0	0.24	25°C Pure, solid, tin cathode
		4.0	0.23	35°C Pure, solid, tin cathode
		12.5	0.23	45°C Pure, solid, tin cathode
TMN	0.1	—	0.083	Pure, solid, tin cathode
Triton X165	0.1	1.0	0.105	Liquid tin amalgam
Pluronic L64	0.1	0.20	0.154	Liquid tin amalgam
Polyglycol P400	0.1	0.75	0.16	Liquid tin amalgam
TMN	0.1	0.4	0.095	Liquid tin amalgam
Pluronic L64				
0.025M $SnSO_4$	0.1	0.036	0.240	Pure, solid, tin cathode
0.05M $SnSO_4$	0.1	0.15	0.265	Pure, solid, tin cathode
0.20M $SnSO_4$	0.1	0.29	0.235	Pure, solid, tin cathode
0.40M $SnSO_4$	0.1	0.41	0.225	Pure, solid, tin cathode
0.60M $SnSO_4$	0.1	0.52	0.220	Pure, solid, tin cathode

that micelle formation occurred at concentrations above 0.03% for Pluronic L64, for which the polarization curve is shown in Fig. 7. Their studies indicated that the adsorption isotherm for Pluronic L64 on quartz in water showed no further increase in the amount of adsorbant with increasing solution concentration above 0.03%. This behavior can be explained on the basis that no further increase in the concentration of the free molecules occurred above the critical micelle concentration. The concentration of the organic additive at which micelle formation becomes significant is affected by the presence of the $SnSO_4$ and H_2SO_4, but the dependence should be relatively small with nonionic agents such as Pluronic L64. Although micelle formation may strongly influence the adsorption isotherms for some organic additives on the electrode surface, nonionic agents that do not form micelles can also be readily adsorbed on the electrode surface and can also exhibit effective addition agent action. For example, Polyglycol P400 should not form micelles, yet it is effective as an additive, Fig. 6.

The effect of pre-electrolysis on a solution containing Pluronic L64 is shown in Fig. 10. The polarization values with and without pre-electrolysis for this solution are virtually identical. However, this is no assurance that the results with and without pre-electrolysis would be the same with the other addition agents if pre-electrolysis had been tried, but it is doubtful whether any major changes would

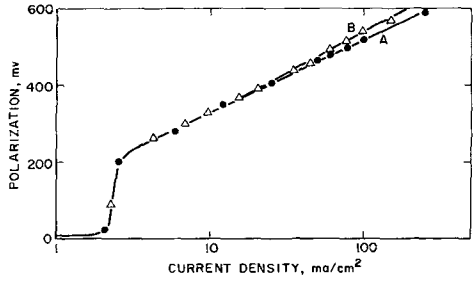

Fig. 10. Effects of pre-electrolysis on polarization measurements with Pluronic L64. Temperature, 25.0° ± 0.2°C; electrolyte, 0.4M $SnSO_4$ plus 1.0M H_2SO_4 plus 0.1% Pluronic L64. Curve A, without pre-electrolysis; B, with pre-electrolysis.

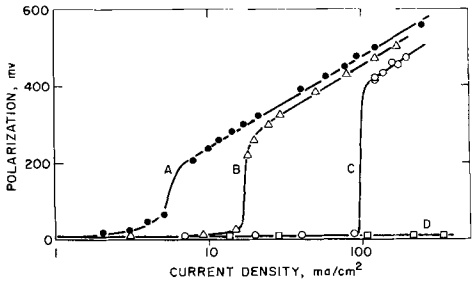

Fig. 11. Effect of chloride ion on polarization measurements with Polyglycol P400. Temperature, 25.0° ± 0.2°C; electrolyte, 0.4M $SnSO_4$ plus 1.0M H_2SO_4 plus 0.1% Polyglycol P400. Curve A, no Cl^-; B, 10^{-3}M Cl^-; C, 10^{-2}M Cl^-; D, 2 x 10^{-2}M Cl^-.

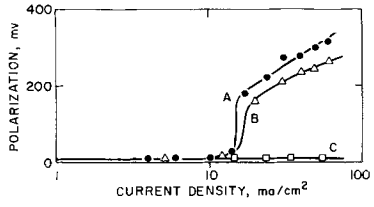

Fig. 12. Effect of chloride ion on polarization measurements with Triton X102. Temperature, 25.0° ± 0.2°C; electrolyte, 0.4M $SnSO_4$ plus 1.0M H_2SO_4 plus 1.0% Triton X102. Curve A, 10^{-4}M Cl^-; B, 10^{-3}M Cl^-; C, 10^{-2}M Cl^-.

have been found with pre-electrolysis for the other agents.

Effect of Chloride Ions on Cathodic Polarization in Sulfate Solutions Containing Organic Additives

The addition of small amounts of chloride ions to solutions containing effective organic additives caused the polarization to decrease and the inflection point to shift to higher current densities. Figures 11 and 12 show typical data for the effects of increasing amounts of chloride ion on the cathodic polarization in solutions containing Polyglycol P400 and Triton X165, respectively. The modification of the polarization curves is probably caused by the preferential adsorption of chloride ion on the electrode surface.

Other addition agents (Triton X165 at 0.5%, Polyglycol P400 at 0.1%, and Pluronic L64 at 0.1%), which greatly affected the polarization in the acid sulfate bath, were also tested in an acid chloride bath containing 0.4M $SnCl_2$ and 2.0M HCl. The steady-state polarization at current densities up to 400 ma/cm² (the highest examined) was identical with that obtained without the organic additive. This was anticipated from an examination of the results of the experiments involving the addition of small amounts of the chloride ion to the sulfate solution. The presence of the organic additives in the chloride solution had no apparent effect on the structure; it continued to be highly treed.

Effect of Concentration of Stannous Ion

The dependence of the polarization on the concentration of the stannous ion is shown in Fig. 13 for a solution containing Pluronic L64 at a concentration of 0.1%. The Tafel slopes varied from 0.24 for 0.025M $SnSO_4$ to 0.22 for 0.6M $SnSO_4$ with the exception of the slope for the 0.05M $SnSO_4$ solution (Curve B), which had a slope of 0.26. The somewhat higher slope for curve B probably represents experimental error.

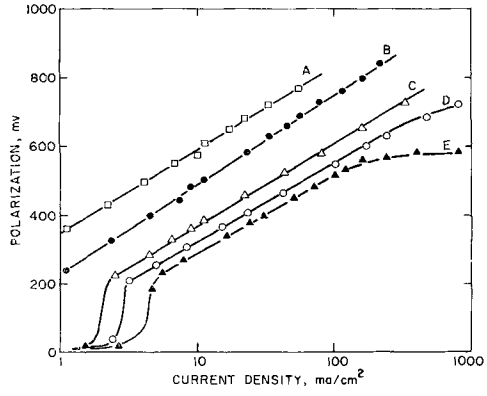

Fig. 13. Effect of stannous ion on polarization measurements with Pluronic L64. Temperature, 25.0° ± 0.2°C; electrolyte, 1.0M H_2SO_4 plus 0.1% Pluronic L64 plus $SnSO_4$. Curve A, 0.025M $SnSO_4$; B, 0.05M; C, 0.20M; D, 0.40M; E, 0.6M.

In the more dilute $SnSO_4$ solutions, the structure of the double layer was established predominantly by the H_2SO_4, which was held constant in concentration. From curves A and C in Fig. 13, the value for $[\partial \log i/\partial \log (C_{Sn^{+2}})]$ at constant electrode potential is 1.1, where i is the current density and $C_{Sn^{+2}}$ is the bulk concentration of the stannous ion. A comparable calculation based on curves A and B in the midrange of polarization in Fig. 13 yields a value for this derivative of 1.0. Thus, the reaction order with respect to Sn^{+2} appears essentially to be one, as would be expected. Likewise, $[\partial \eta/\partial \log (C_{Sn^{+2}})]$ is about equal to 0.24 mv per decade on the basis of curves A and C in Fig. 13, where η is the polarization.

Effect of Sodium Sulfate

The effect of adding Na_2SO_4 to the acid stannous sulfate solution with 0.5% Triton X165 present is shown in Fig. 14. When the Na_2SO_4 was added to this solution, the activity coefficient of Sn^{+2} was depressed, and at the same time some modification was produced in the structure of the double layer in terms of both the Sn^{+2} ion concentration in the Helmholtz plane and the potential drop across the diffuse layer. This modification of the double layer structure may have been caused directly by the added Na_2SO_4 or indirectly by affecting the ionization of HSO_4^- to H^+ and $SO_4^=$.

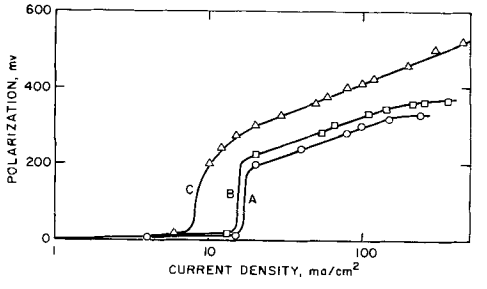

Fig. 14. Effect of supporting electrolyte on polarization measurements with Triton X165. Temperature, 25.0° ± 0.2°C; electrolyte, Curve A, 0.4M $SnSO_4$ plus 1.0M H_2SO_4 plus 0.5% Triton X165; B, same as A plus 0.5M Na_2SO_4; C, same as A plus 1.0M Na_2SO_4.

Structure of Deposits

All the addition agents in Table II that caused a significant increase in the polarization produced a pronounced improvement in the quality of the electrodeposits at current densities above the inflection points in the polarization-current density curves. Many of the deposits at these current densities were semibright with no evidence whatsoever of treeing or coarse-grain structure on visual examination. Even at current densities somewhat below those corresponding to the inflection points, these organic agents produced some improvement in the quality of the deposits, which in their absence would have been characterized by extreme treeing. Deposits obtained below the inflection points, however, were generally very coarse, regardless of which particular organic additive in Table II was present in the solution. This correlation of the structure of the deposits with the polarization persisted even when chloride ions were added to the sulfate solution during the course of the measurements reported in Fig. 11 and 12; that is, deposits obtained at current densities above the inflection point were very superior to those obtained below the inflection point.

Polarization Measurements on Liquid Tin Amalgams

The polarization associated with the deposition of tin into a 0.1% (by weight) tin amalgam is shown in Fig. 15 for Triton X165, Polyglycol P400, the trimethyl nonyl ether of polyethylene glycol (TMN), and Pluronic L64 in a sulfate solution. These measurements were made after the electrode had been in contact with the electrolyte for a relatively short but unknown amount of time. In the absence of any organic additive, the polarization was only a few

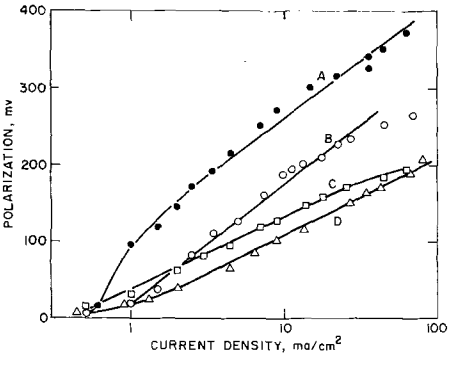

Fig. 15. Polarization measurements on a liquid tin-amalgam cathode. Temperature, 25.0° ± 0.2°C; amalgam, 0.1% by weight tin; electrolyte, 0.4M $SnSO_4$ plus 1.0M H_2SO_4 plus addition agent (curve A, 0.1% Pluronic L64; B, 0.1% Polyglycol P400; C, 0.1% TMN; D, 0.1% Triton X165).

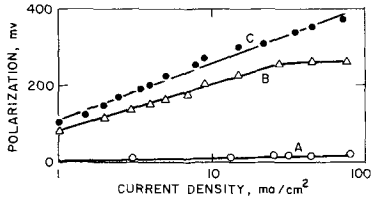

Fig. 16. Polarization measurements with Pluronic L64 on liquid tin amalgam. Temperature, 25.0° ± 0.2°C; amalgam, 0.1% tin; electrolyte, 0.4M $SnSO_4$ plus 1.0M H_2SO_4 plus Pluronic L64 (curve A, 0.0001%; B, 0.01%; C, 0.1%).

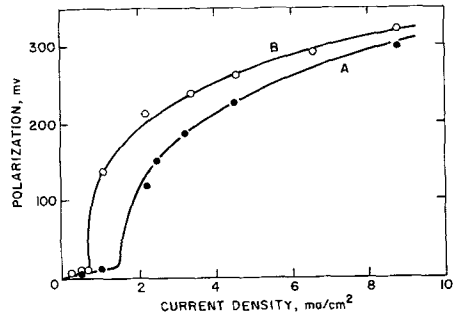

Fig. 17. Effect of cathode immersion time on polarization measurements with a pure tin cathode. Temperature, 25.0° ± 0.2°C; electrolyte, 0.4M $SnSO_4$ plus 1.0M H_2SO_4 plus 0.1% Pluronic L64. Curve A, polarization measurements immediately after immersion of cathode; B, 20 hr immersion with no polarizing current prior to measurements.

millivolts even at current densities of 100 ma/cm². A comparison of the results in Fig. 16 with those in Fig. 7 indicates that Pluronic L64 is effective in increasing the polarization at much lower concentrations with the liquid tin-amalgam cathode than with the pure solid tin cathode. This is also true with all the other organic additives represented in Fig. 15 and is probably due to a difference in the adsorption isotherms of the organic additives on the two different surfaces. The Tafel slopes for the amalgam cathodes were generally much lower than the corresponding values for the solid tin cathodes.

Time Dependence of Polarization

All the polarization measurements heretofore presented in this paper have been obtained with increasing polarizing current and with not more than a few minutes of time elapsing between the immersion of the cathode in the solution and the beginning of the polarization measurements. The effects of delaying the measurements after the introduction of the cathode into the solution are shown in Fig. 17 for a pure tin cathode in a sulfate solution containing Pluronic L64. Similar shifts in the polarization curves could be produced by prepolarizing the pure tin cathode at a current density well above that of the inflection point for a few minutes, and then immediately obtaining the polarization-current density data in the usual way.

The effects of immersion time prior to polarization measurements are shown in Fig. 18 for a liquid tin-amalgam cathode in a solution containing Poly-

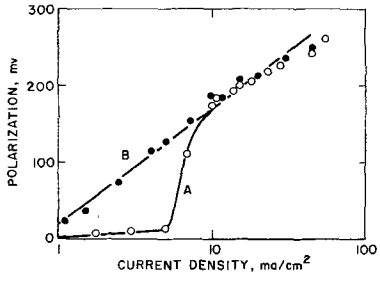

Fig. 18. Effect of cathode immersion time on polarization measurements with a liquid tin-amalgam cathode. Temperature, 25.0° ± 0.2°C; amalgam, 0.1% tin; electrolyte, 0.4M $SnSO_4$ plus 1.0M H_2SO_4 plus 0.1% Polyglycol P400. Curve A, polarization measurements immediately after exposing amalgam surfaces; B, 3 hr immersion with no polarizing current prior to measurements.

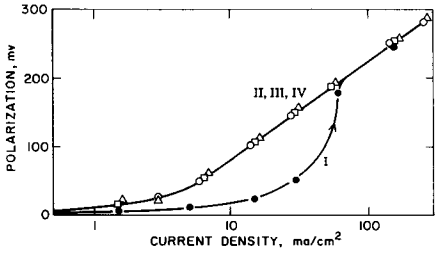

Fig. 19. Repeated polarization measurements on a liquid tin-amalgam cathode. Temperature, 25.0° ± 0.2°C; amalgam: 0.33% tin; electrolyte, 0.4M $SnSO_4$ plus 1.0M H_2SO_4 plus 0.002% Pluronic L64. Curve I, measurements with increasing current density; II, decreasing; III, repeat increasing; IV, repeat decreasing.

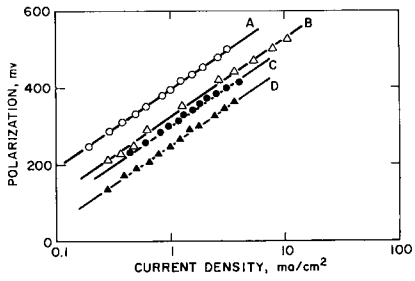

Fig. 20. Effect of temperature on polarization measurements on pure tin cathode with Pluronic L64. Electrolyte, 0.4M $SnSO_4$ plus 1.0M H_2SO_4 plus 1.0% Pluronic L64. Curve A, 7.5°C; B, 25.0°C; C, 35.0°C; D, 45.0°C.

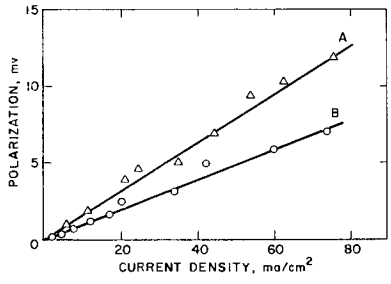

Fig. 21. Polarization measurements on a pure tin cathode and liquid tin-amalgam cathode without addition agents. Temperature, 25.0° ± 0.2°C; electrolyte, 0.4M $SnSO_4$ plus 1.0M H_2SO_4. Curve A, 0.1% tin amalgam; B, pure solid tin.

glycol P400. Similar results have been obtained in solutions containing TMN and Pluronic L64. The curves in Fig. 15 do not show as clearly the characteristic inflection points as the curve A in Fig. 18 because some unknown time had elapsed before the measurements reported in Fig. 15 were made. The polarization-current density data obtained in repeated runs with increasing and decreasing current densities for a liquid tin-amalgam cathode (0.33% tin) in a pre-electrolyzed solution containing 0.002% Pluronic L64 are shown in Fig. 19. (The data presented in this figure were obtained by Dr. F. Hine at Western Reserve University by using substantially identical equipment and techniques to those described in this paper with pre-electrolysis for 24 hr prior to immersing the cathode in the solution.) After the initial series of polarization measurements was made with increasing current, the inflection point was completely missing in subsequent measurements made with either increasing or decreasing current. Similar results have been obtained with a liquid amalgam containing 0.33% tin in a sulfate solution continuing 0.001% Pluronic L64.

Effect of Temperature on Polarization

The effect of temperature on the polarization for pure solid tin and liquid tin-amalgam cathodes was studied with Pluronic L64 and Polyglycol P400 as the additives. Typical polarization data for various temperatures are presented in Fig. 20.

The enthalpy of activation at zero polarization (ΔH^*_0) has been calculated from these results by means of the equation

$$\frac{\partial \ln i_o}{\partial (1/T)} = \frac{\Delta H^*_0}{R} \qquad [1]$$

where i_o is apparent exchange current density obtained from the extrapolation of the linear portion of the Tafel plots to zero polarization, T the absolute temperature, and R the gas constant. Values obtained for ΔH^*_0 for a solution containing 0.1% Pluronic L64 are 8.5 ± 1 kcal/mole for a solid tin cathode and 9.0 ± 1 kcal/mole for a liquid tin-amalgam cathode.

The data obtained with Polyglycol P400 at temperatures above 25°C were sparse, and the Tafel slopes were somewhat uncertain. Therefore, values for i_o at temperatures above 25°C were calculated by extrapolating the polarization *vs.* log i plots to zero polarization with the same Tafel slope as that obtained experimentally at 25°C. The enthalpy of activation for the solid tin cathode in a solution containing 0.1% Polyglycol P400 was calculated to be 11 ± 2 kcal/mole.

The relative agreement between the values for the enthalpy of activation for the deposition of tin into a liquid tin amalgam and on the pure tin indicates that the height of the energy barrier for the rate-determining step is probably the same for the two types of electrodes within experimental error. The difference in the energies of activation for the solid tin cathode with Pluronic L64 and Polyglycol P400 also probably is within the limits of experimental error and does not represent a true difference.

Measurements without Addition Agents

Polarization curves obtained for pure tin and tin-amalgam cathodes in a solution containing 0.4M $SnSO_4$ and 1.0M H_2SO_4 without any organic addition agent present are shown in Fig. 21. Despite the extreme agitation in the cell, concentration polarization probably was significant although it was not the major factor because the diffusion limiting current density was greater than 600 ma/cm². The lower limits for the exchange current densities can be obtained by assuming that the curves in Fig. 21 represent only activation polarization. This yields values of 110 ma/cm² for pure tin and 80 ma/cm² for the liquid tin-amalgam cathode (0.1% by weight tin) at 25°C. A stoichiometric number of one for an over-all 2-electron process was used to calculate these values.

In the same electrolyte, Piontelli and co-workers (8-10) have reported an exchange current density

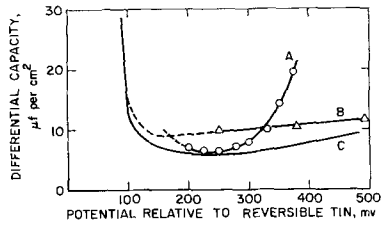

Fig. 22. Differential capacity curves. Temperature, 25°C. Curve A, 0.1% tin-amalgam in 0.40M $SnSO_4$ plus 1.0M H_2SO_4 plus 0.1% Pluronic L64; B, pure tin in same solution; C, data of Deriaz and Randles (18) for pure tin in 0.001M $KClO_4$ plus 0.1M amyl alcohol.

of 5.0 ma/cm² for electrodeposition on pure tin, the polarization being determined by an essentially steady-state technique. The explanation for this discrepancy of more than two orders of magnitude is not immediately evident. Differences in surface structure would not be expected to be sufficient to account for such a large difference in the exchange current densities. Although concentration polarization may have been somewhat greater in the work of Piontelli and his associates, this does not represent an adequate explanation for such a large difference. Impurities adsorbed on the electrode surface, however, can easily produce such a difference. Such adsorbed impurities usually tend to increase the polarization and decrease the exchange current density in systems with low polarization.

Differential-Capacity Measurements

The differential capacity of the cathode was determined from the rate of decay of the potential immediately after the interruption of the polarizing current according to the equation

$$C = i/(\partial E/\partial t)_0 \qquad [2]$$

where C is the differential capacity per unit apparent area, i the current density before interruption, and $(\partial E/\partial t)_0$ the slope of the potential-time curve the instant after interruption. The variation of the capacity with potential for liquid tin amalgam and pure solid tin in a solution containing Pluronic L64 is shown in Fig. 22. These values were obtained during polarization measurements made with increasing current immediately after the cathode was immersed in the solution. Unfortunately, accurate capacity measurements could not be made at potentials below about —200 mv for the system represented in Fig. 22 because of the small decay rates. Although part of the decrease in the decay rate with decreasing polarization was associated with the decrease of the current density in Eq. [2] the most important factor was a large increase in the differential capacity because of a Faradaic component. This increase has been approximated by the dashed lines in Fig. 22, but the values represented by the dashed lines may be in considerable error.

All the nonionic addition agents examined (Triton X165, Polyglycol P400, and Pluronics L61, L62, L64, and F68) exhibited a minimum in the differential capacity curves for the liquid tin-amalgam cathodes in the vicinity of —0.25v relative to the potential of the reversible solid pure tin electrode in the same solution or —0.75v relative to the normal calomel electrode (liquid junction potentials were neglected). It is difficult to establish the potential of the minimum in the capacitance curve for solid tin in the present work because of insufficient accuracy at the lower potentials in Fig. 22.

Frumkin (17) has predicted for the electrocapillary maximum a value of —0.34v relative to the standard hydrogen electrode or —0.62v relative to the normal calomel electrode in the absence of specific adsorption on the basis of the work function of tin. Deriaz and Randles (18) have found that the minimum in the differential capacity curve for pure tin in dilute $KClO_4$ and K_2SO_4 solutions (0.01-0.001M) was in the range —0.7 to —0.8v relative to the normal calomel electrode. These workers found that the addition of 0.1M amyl alcohol to the solutions broadened the minimum, but did not produce any appreciable shift in the potential at which it occurred.

The differential-capacity measurements reported in Fig. 22, as well as others conducted during the course of the present investigation, provide qualitative evidence for the adsorption of nonionic organic molecules on the electrode surfaces. The quantitative interpretation of the data in Fig. 22 is not readily possible, or for that matter, warranted because of the limited accuracy.

Discussion

The experimental results with both pure tin and liquid tin-amalgam cathodes indicate that the adsorption of the nonionic addition agents on the electrode surface produces a large increment in the polarization. The somewhat similar behavior of pure tin and liquid tin-amalgam cathodes implies that the rate-determining step responsible for the polarization is substantially the same at each electrode in the presence of the adsorbed organic addition agents. This would indicate that a process of crystal growth is not the rate-determining step responsible for the polarization for the solid as well as liquid-amalgam cathodes in the presence of the nonionic organic addition agent.

The Tafel linearity observed with the pure tin and amalgam cathodes in the presence of the addition agents can be explained in terms of a charge-transfer step as rate determining. Tafel linearity, however, does not constitute unique evidence for such a rate-determining step. The adsorbed addition agent may produce the large increment in the cathodic polarization (a) by greatly reducing the number of sites on the electrode surface where charge transfer can occur and thus produce a very high current density on the unblocked sites, and (b) by presenting a barrier to the transfer of cations to the electrode surface. The first is unlikely as an explanation for the polarization. If surface coverage is not substantially complete, then the fraction of the surface not blocked by the organic molecules should depend on the potential, and this would prevent Tafel linearity from being observed over any significant range of potentials.

The second mechanism appears more likely, provided the electrode surface is covered with a rela-

tively thin, complete layer of organic molecules for the range of conditions for which Tafel linearity is observed. If the transfer of stannous ions occurs through a relatively thick layer of adsorbed organic molecules under the influence of an electric field or by diffusion, the polarization would not be expected to depend logarithmically on the current density. In a thick layer, as the cation approaches the electrode surface, a number of positions exist within the organic layer where the potential energy is a minimum. With progressively thinner layers, however, the number of such minima decreases until finally the potential energy function for the cation does not exhibit a minimum in the organic layer. Under these latter circumstances, the transfer of charge through the organic layer involves transmission over a single barrier and can give rise to a linear Tafel plot over a significant range of current densities.

The Tafel slope, and hence the transfer coefficient, depend on the nature of the organic additive. The lack of correlation between the Tafel slopes for pure tin and the liquid tin amalgam in the experimental data may indicate differences in the state of packing or in the orientation of the organic molecules on the surface. The large deviation of the Tafel slope from the usual value of 120 mv per decade at 25°C is not surprising if transfer of stannous ions through a layer of adsorbed organic molecules is rate determining. The constancy of the Tafel slope over a relatively wide range of potentials with both the pure tin and liquid tin-amalgam cathodes, however, is surprising and indicates that the configuration of the adsorbed molecules as well as the extent of coverage must not change under these conditions.

The nonionic addition agents used in this work are expected to be adsorbed on the electrode surface in an uncoiled, rather elongated configuration. Under some conditions, most segments of the chain may lie on the surface so as to provide maximum overlap of the unshared p-orbitals of oxygen and π-orbitals of the aromatic portions with localized orbitals of the metal. This arrangement should be favored by using potentials close to the electrocapillary maximum and a relatively large number of ether linkages within the molecules. An alternative arrangement is to have only a limited portion of each polymer molecule in proximity to the metal surface with the remainder of the molecule extending some distance into the solution phase.

With either of these arrangements, complete coverage of the surface should be difficult. A relatively high entropy of adsorption is anticipated for such polymeric species, and the value should increase very substantially as complete coverage is approached because of the ordering required for monolayer coverage. Adsorption is expected to be relatively slow, particularly at high surface coverage.

The time and hysteresis effects associated with the solid tin cathodes can be explained in terms of area and crystallographic changes. Such changes are not possible with the liquid-amalgam cathode. Furthermore, the composition of the amalgam remained substantially constant throughout a given series of polarization measurements. The results for the amalgam cathode in Fig. 18 and 19 lead to the conclusion that the adsorption of such organic molecules as Pluronic L64 and Polyglycol P400 is a slow process and that the rate of adsorption increases with increasing cathodic potential. The polarization does not show any appreciable change with increased stirring rate in the range of current densities in which the time dependence has been observed. Thus, the adsorption of the addition agent does not appear to be diffusion-limited, but rather is kinetically limited. The apparent increment in the rate of adsorption with increasing cathodic potential may indicate that at electrode potentials above the electrocapillary maximum, various segments of the polymer molecules are oriented at the interface in such a way as to lead to rather complete coverage of the surface. As long as this layer of adsorbed organic molecules remains intact, the polarization appears to follow the Tafel equation down to current densities at which the back reaction becomes appreciable, compared with the net current.

Heydegger and Dunning (16) have reported that periods of up to 10 days are required for equilibrium to be reached in the adsorption of Pluronic L64 on quartz powder from aqueous solutions. Adsorption isotherms obtained by these workers after they allowed only a few hours for equilibration exhibit false minima of a kinetic origin.

During the deposition on solid tin, the surface is in a constant state of renewal except possibly at very low current densities. The time of immersion of the solid tin cathode in the solution prior to the start of the polarization measurements, therefore, would not be expected to have any appreciable effect on the amount of addition agent adsorbed per unit true area for a given surface topography. The S-shaped portion of the cathodic polarization curve for pure tin probably would disappear in much the same manner as with liquid tin amalgam if the layer of organic additive would remain intact over the complete range of conditions involved in a given series of polarization measurements. The slow adsorption of organic molecules during electrodeposition has been considered by other workers (19, 20).

If the transfer of Sn^{+2} across a thin barrier consisting of the adsorbed organic molecules is rate determining, the net current density (i) may be expected to depend on the polarization (η) according to the equation

$$i = i_o \exp(-2\alpha f\eta/RT) \qquad [3]$$

for conditions in which the back reaction is negligible and the transfer coefficient (α) is constant. The apparent exchange current density (i_o) should depend on the bulk concentration of Sn^{+2} according to the equation

$$i_o = k_1 (C_{Sn^{+2}})^{1-\alpha} \qquad [4]$$

provided the concentration of Sn^{+2} in the Helmholtz plane is proportional to the bulk concentration ($C_{Sn^{+2}}$). Such a condition may be approached in the

present work when the concentration of the Sn^{+2} is small compared with that of the sulfuric acid.

The Tafel slopes observed with the nonionic addition agents listed in Table II range from 0.07 for Triton X114 to 0.24 for Polyglycol P750. For the transfer of Sn^{+2} across a potential energy barrier as the rate-determining step, these Tafel slopes correspond to values of α ranging from 1/2 to 1/6. Such a range of transfer coefficient is possible if the potential energy barrier is associated with a thin layer of adsorbed organic molecules.

The value of the derivative

$$\frac{\partial \log i_o}{\partial \log (C_{Sn^{+2}})}$$

may be obtained from Fig. 13 for a solution containing 0.1% Pluronic L64. If curves A and B are extrapolated to zero polarization, the value for this derivative is 0.96. Since curves A and B both have Tafel slopes of about 0.24, the interpretation of these curves in terms of the mechanism just described yields a transfer coefficient of 1/8 and a value for the derivative $[\partial \log i_o/\partial \log (C_{Sn^{+2}})]$ of 0.88 provided that the double layer structure is assumed to be relatively independent of $C_{Sn^{+2}}$. Although the difference between the experimental and quasi-theoretical values for the concentration dependence of i_o may be associated with the failure to meet completely this assumption, the difference is probably within the experimental error of the measurements.

The effects of chloride ions on the characteristic polarization curves obtained with the addition agents, Fig. 11 and 12, can be interpreted on the basis that the chloride ions modified the adsorption of the organic molecules on the electrode surface. In the solutions involved in the work with Cl^-, however, much of the Cl^- is in the form of chlorocomplexes of Sn^{+2}. From the published equilibrium constants (21), assuming activity coefficients of 1, the concentrations of the various chlorocomplexes are estimated to be as follows for the 0.02M chloride solution, the most concentrated used in Fig. 11:

$$SnCl^+ = 1.7 \times 10^{-2}M$$
$$SnCl_2 = 10^{-4}M$$
$$SnCl_3^- = 10^{-8}M$$

It is possible that the chlorocomplexes may play a direct role in the electrode kinetics and may be the predominant species in the Helmholtz plane at relatively cathodic potentials. This question, however, cannot be resolved on the basis of the present data.

Summary

A fundamental study was made of the kinetics of tin deposition from solutions containing nonionic organic additives. Measurements were made of the steady-state cathodic polarization in sulfate solutions containing various addition agents as a function of current density, temperature, type and concentration of addition agents, stannous ion concentration, supporting electrolyte concentration, and chloride ion concentration with both pure polycrystalline tin and liquid tin amalgam. The principal observations made were as follows:

1. The rate-determining step for the electrodeposition of tin from acid stannous solutions that contain an addition agent is probably charge transfer through a layer of adsorbed organic molecules. This layer of adsorbed organic molecules is reasonably complete in the range of current densities in which Tafel linearity is maintained.

2. The forms of the S-shaped curves as shown in Fig. 5 and subsequent figures are not due to limiting current densities, but rather the forms of the S-shaped curves are related to the buildup of the film of adsorbed organic molecules, and this film is both potential and time dependent.

3. On tin-amalgam cathodes the layer of adsorbed organic molecules is complete after a length of time. The layer can also be completed by applying a prepolarization potential. This layer or film is stable (in a steady state of adsorption and desorption); the metal is deposited beneath the film.

4. On solid tin cathodes, some of the adsorbed organic molecules undoubtedly are occluded into the deposit during the deposition process. This indicates that the film is in a steady state of adsorption, desorption, and occlusion. In addition to the potential and time dependence of the adsorption process, crystallographic changes of the surface may also be important.

Acknowledgments

This research has been sponsored by the United States Steel Corporation. The authors express their appreciation to Dr. F. Hine and Dr. E. Schwartz for their suggestions relative to the experimental work.

Manuscript received June 18, 1962; revised manuscript received Oct. 10, 1962. This paper was prepared for delivery before the Detroit Meeting, Oct. 1-5, 1961.

Any discussion of this paper will appear in a Discussion Section to be published in the December 1963 JOURNAL.

REFERENCES

1. O. Esin and M. Loshkarev, *Acta Physicochim. U.S.S.R.*, **10**, 513 (1939).
2. M. Loshkarev, O. Esin, and V. Sotnikova, *J. Gen. Chem. U.S.S.R.*, **9**, 1412 (1939).
3. M. Loshkarev, V. Sotnikova, and A. Kryukova, *Zhur. Fiz. Khim.*, **21**, 219 (1947).
4. M. Loshkarev and A. Kryukova, *ibid.*, **22**, 805 (1948).
5. M. Loshkarev and A. Kryukova, *ibid.*, **23**, 209 (1949).
6. A. Izmaylov, Reports of University of Ministry of Higher Education of USSR, *Chem. and Chem. Tech.*, No. 4, p. 568 (1959).
7. P. Kovalenko and K. Bogdasarov, *Ukrain. Chem. J.*, **26**, 573 (1960).
8. R. Piontelli, *Gazz. Chim. ital.*, **29**, 210 (1949).
9. R. Piontelli, G. Serravalle, and R. Ambrossetti, *Metal ital.*, **47**, 200 (1955).
10. R. Piontelli and G. Poli, "Comite intern. thermodynam. et cinet. electrochim.," Compt. rend. reunion, 2e Reunion, Milan, 1950, pp. 136-148, C. Tambruini, Milan, 1951.
11. R. Piontelli, G. Poli, and G. Serravalle, "A Contribution to the Study of the Electrode Behavior of Metallic Single Crystals," pp. 67-103, Chap. 4 in "Transactions of the Symposium on Electrode Processes," E. Yeager, Editor, John Wiley & Sons, Inc., New York (1961).
12. U. Bertocci and G. Serravale, *Metal ital.*, **49**, 95 (1957).

13. I. Gurevich, *Zhur. Priklad, Khim.*, **28**, 285 (1955).
14. D. Staicopoulus, E. Yeager, and F. Hovorka, *This Journal*, **98**, 68 (1951).
15. A. M. Harper, A. Mohan, and S. C. Britton, *Trans. Inst. Metal Finishing*, **34**, 273 (1957).
16. H. Heydegger and H. Dunning, *J. Phys. Chem.*, **63**, 1613 (1959).
17. A. Frumkin, *J. Phys. Chem.* U.S.S.R., **5**, 240 (1934).
18. M. Deriaz and J. Randles, Private communication.
19. A. Frumkin, "Proceedings of the Second International Congress on Surface Activity," Vol. III, pp. 58-65, Academic Press, New York (1957).
20. A. Vagramian and A. Solovieva, *Zhur. Fiz. Khim.*, **26**, 560 (1952).
21. R. S. Tobias and L. L. Hugus, Jr., *J. Phys. Chem.*, **65**, 2165 (1961).

Electrolytically Regenerated Manganic Sulfate for the Oxidation of Aromatic Hydrocarbons

II. Oxidation of Xylenes to Tolualdehydes

R. Ramaswamy, M. S. Venkatachalapathy, and H. V. K. Udupa
Central Electrochemical Research Institute, Karaikudi, India

ABSTRACT

A two-stage process for the oxidation of xylenes to tolualdehydes is described which consists of the oxidation of manganous sulfate to manganic sulfate in the cell and reacting the manganic sulfate obtained with xylene outside the cell. The reason for low current efficiency for the in-cell oxidation is explained on the basis of anode potential measurement. Measurement of the oxidation potential of manganic sulfate in presence of xylene indicates that the steady potential attainable during the reaction makes it possible to control the oxidation of xylene to tolualdehyde. A large laboratory cell is described.

The oxidation of p-xylene to the half aldehyde has been the subject of considerable study (1). With chromates and permanganates the product is p-toluic acid. Vapor phase oxidation of xylene in the presence of vanadium or molybdenum catalysts even with careful control always gives some p-toluic acid (2).

Etards' method (3) using chromyl chloride for the oxidation to the aldehyde is too hazardous and expensive. Law and Perkin (4, 5) were the first to study the oxidation of p-xylene electrolytically and reported a 25% yield at a current density of 1-2 amp/dm^2 with a platinum anode. Other references (5-8) give little further information.

Various electrochemical factors governing the direct oxidation of p-xylene to p-tolualdehyde in the cell itself using manganous sulfate as "oxygen carrier" were studied in this laboratory earlier (9), but the current efficiency for the in-cell oxidation could not be maintained high in sustained electrolysis. However, it has been noticed by the authors (10) that a two-stage process is a more feasible approach for electroorganic oxidations involving inorganic reagents and aromatic hydrocarbons to give, in particular, aromatic aldehydes. The oxidation of manganous sulfate both in the form of a clear solution and in the form of a suspension of manganous sulfate in sulfuric acid to manganic sulfate was studied in this laboratory earlier (11, 12), and kinetic studies of the reaction of manganic sulfate with toluene (13) and with p-xylene (14) led to a possible mechanism for the reaction. The preparation of benzaldehyde by reacting toluene with a paste of manganic sulfate prepared electrolytically was reported in ref. (15). Now a two-stage process for the preparation of p-tolualdehyde and other tolualdehydes using electrolytically regenerated manganic sulfate is described.

Experimental

Materials.—Xylenes were redistilled. The *p*-compound had bp 137°-38°C, *m*- 138°-140°, o- 142°-144°, and mixed xylenes 138°-140°C.

Procedure.—The cell and the experimental techniques adopted for the oxidation of manganous sulfate were similar to those described in the earlier papers (12, 15). In the small cell, only 750 cc of the electrolyte could be taken, and the maximum quantity of *p*-tolualdehyde isolated was 18g. *p*-Tolualdehyde, obtained by the decomposition of the bisulfite addition compound and steam distillation, was dried with anhydrous calcium chloride. The fraction, bp 201°-205°C, was stored in a closed bottle with the addition of a few crystals of hydroquinone.

Mixed tolualdehydes similarly prepared had bp 200°-203°C.

Large-scale trials.—A lead lined cylindrical iron vessel suitably lead-lined and having the inner dimensions 19 cm diameter x 18 cm depth (Fig. 1) was used as combined cell and reactor. A cathode frame having 4 lead-covered copper rods 7 mm diameter x 21 cm long (length immersed 14 cm) fitted to it was held on the asbestos cement lid with openings for the rods, stirrer, and thermometer. The vessel itself was made the anode (effective area, 9 dm^2).

Three liters of 55% sulfuric acid containing 900g manganous sulfate (anhydrous basis) was the electrolyte. Direct current was passed from a selenium rectifier capable of giving 50 amp at 0-12v. Temperature was maintained at 50°C by means of a water jacket. Vigorous agitation was effected with a blade-

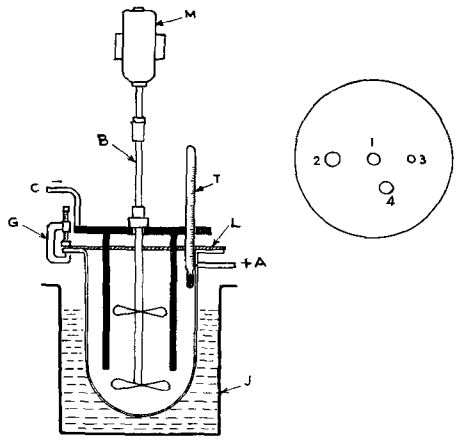

Fig. 1. Large-scale cell: A, lead lined vessel as anode; B, blade-type stirrer; C, cathode frame; L, asbestos cement lid; G, G-clamp; T, thermometer; M, motor. 1, Opening for stirrer in the lead lined lid, 2, opening for condenser, 3, opening for thermometer, 4, opening for dropping funnel.

type stirrer. After the oxidation was over an aliquot portion was removed for estimation of the manganic sulfate formed.

The asbestos cement lid was then replaced by a lead-lined lid (inset in Fig. 1) having openings for a thermometer, stirrer, condenser, and a dropping funnel for xylene addition. Xylene was added slowly keeping the temperature at 30°-35°C. After the reaction was over, the aldehyde was isolated, and the spent electrolyte was purified as described earlier (15).

Results and Discussion

The first step consisted of electrolytically oxidizing manganous sulfate to manganic sulfate and may be represented by Eq. [1].

$$4Mn^{2+} \rightarrow 4Mn^{3+} + 4e \qquad [1]$$

The chemical reaction of trivalent manganese with xylene can be represented by Eq. [2].

$$4Mn^{3+} + p\text{-}C_6H_4(CH_3)_2 + H_2O \rightarrow 4Mn^{2+} + p\text{-}C_6H_4(CHO)(CH_3) + 4H^+ \qquad [2]$$

Table I. Influence of temperature on the oxidation of xylene by manganic sulfate

Conditions: Manganic sulfate, 30g in 700 cc of electrolyte; xylenes, 20 cc in each case.

Temp, °C	Current efficiency, %		
	Para	Ortho	Meta
20	42	35	25
25	45	35	30
30	45	40	30
35	40	45	35
40	30	40	35

On the basis of these two equations it is possible to arrive at an over-all current efficiency for aldehyde formation, and up to 45% current efficiency could be obtained for the oxidation of p-xylene to p-tolualdehyde. Detailed investigation on the oxidation of xylenes by manganic sulfate was then carried out.

The results of the influence of temperature on the oxidation of xylenes are given in Table I. p-Xylenes gave the highest current efficiency at a temperature of 25°-30°C, and a temperature of 35°-36°C was found suitable for the oxidation of o-xylene to o-tolualdehyde. In the case of m-xylene, a temperature range of 35°-40°C was found necessary for oxidation to proceed. Higher temperature was found to give resinous products in addition to toluic acids.

The first two experiments in Table II represent the oxidation of p-xylene by repeated use of a clear reagent. An average of nearly 42% over-all current efficiency was obtained. In the subsequent experiments, different quantities of manganous sulfate are used in the same volume of acid.

p-Xylene oxidation efficiency based on the manganic sulfate has been calculated on the basis of Eq. [2] by which four equivalents of manganic ion are required to give 1 mole of p-tolualdehyde.

Results obtained in the large-scale runs with mixed xylenes, containing predominantly m-xylene, are given in Table III.

Potential measurements.—The low current efficiency in the one-step oxidation process can be explained by the potential measurements given in curve 1, Fig. 2, where the anode potentials are plotted against time. The potential is uniformly high (2.3v) and is near that for oxygen evolution.

Table II. Preparation of p-tolualdehyde by the two-stage process

Same electrolyte, after purification, was used for regeneration of manganic sulfate. Interelectrode distance, 1.5 cm; volume of electrolyte, 700 cc of 55% H_2SO_4; anode, lead dioxide on lead (area, 1.2 dm^2); cathode, two lead strip (area, 0.15 dm^2); current density, 5 amp/dm^2.

Total current passed, amp-hr	Cell voltage, v	$MnSO_4$, g	Current efficiency for manganic sulfate formation, %	p-tolualdehyde isolated, g	Oxidation efficiency for aldehyde formation based on manganic sulfate, %	Over-all current efficiency for aldehyde formation, %*
5	3.1	29	78	2.2	60	44
5	3.1	29	75	2.0	59	40
10	3.3	58	75	4.2	60	42
15	3.4	70	73	6.0	58	40
20	3.8	100	75	8.1	60	40
40	3.9	200	70	18	60	45
40	3.9	200	68	17	59	43

* This refers to the ratio of the theoretical current required for the aldehyde isolated to the actual current used for the oxidation of manganous to manganic sulfate.

Note: The first two and the last two experiments represent the oxidation of p-xylene by repeated use of a clear reagent and a reagent in the form of a slurry, respectively.

Table III. Large-scale oxidation of xylenes to tolualdehydes

Electrolyte, 3 liters of 55% H_2SO_4 containing 900g of manganous sulfate; cell voltage, 3.5v; amperage, 45 amp.

Run No.	Nature of electrolyte	Quantity of current passed, amp-hr	Manganic sulfate formed, g	Current efficiency for oxidation of manganous sulfate, %	Yield of manganic sulfate, %	Oxidation efficiency for aldehyde formation based on manganic sulfate, %	Tolualdehyde isolated, g	Energy consumption, d.c., kwh/kg
1.	Fresh	300	1256	56.3	99	44	83	16.0
2.	Fresh	270	1118	56.1	93	51	85	11.1
3.	Purified regenerated electrolyte	270	1103	55.4	92.4	53	90	10.5
4.	Purified regenerated electrolyte	250	766	41.4	64.2	57	65	13.5

In the two-stage process, the oxidation potential of manganic sulfate is measured during the course of reaction with p-xylene using platinum as an inert electrode. The oxidation potential of Mn^{3+} ion has been reported (16) to be 1.51v in 15*N* H_2SO_4 at 12°C. We have obtained a value of 1.48v in acid of more or less same strength at 30°-35°C. This value of the potential remains constant during the course of reaction (Fig. 2, curve 2), since a solid phase of manganic salt is present. Once the manganic sulfate in suspension is exhausted, further reaction of manganic ion with p-xylene leads to a lowering of the concentration of manganic ion and a sudden drop in the potential of the inert electrode ultimately to that due to the manganous salt in suspension in 55% H_2SO_4. The upper steady potential (lower than the anode potential in direct electrolytic oxidation) during the major part of the oxidation of xylene explains the better over-all current efficiency for the formation of p-tolualdehyde. The redox potential of the Mn^{2+}-Mn^{3+} system appears to be 1.30-1.32v as read out from curve 2 of Fig. 2.

Acknowledgment

The authors thank Professor K. S. G. Doss, Director of the Institute, for his keen interest in the investigation and Professor Christopher L. Wilson for very kindly presenting the paper at the Detroit Meeting, October 1-5, 1961.

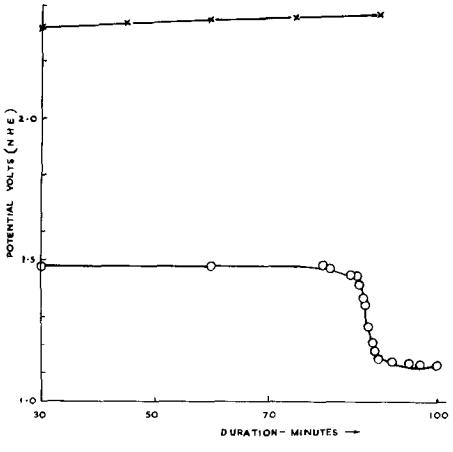

Fig. 2. Potential *vs.* duration of reaction: anode potential, curve 1; oxidation potential, curve 2.

Manuscript received Sept. 28, 1961; revised manuscript received Oct. 31, 1962. This paper was prepared for delivery before the Detroit Meeting, Oct. 1-5, 1961.

Any discussion of this paper will appear in a Discussion Section to be published in the December 1963 JOURNAL.

REFERENCES

1. A. H. Blatt, Editor, "Organic Syntheses," Vol. II, p. 586, John Wiley & Sons, Inc., New York (1950).
2. W. G. Parkes and C. E. Allard, *Ind. Eng. Chem.*, **31**, 1162 (1939).
3. C. Weygand, "Organic Preparations," p. 134, Interscience Publishers, New York (1945).
4. H. D. Law and F. M. Perkin, *Trans. Faraday Soc.*, **1**, 31 (1905).
5. F. Fichter and R. Stocker, *Ber.*, **47**, 400 (1914).
6. F. Fichter, "Organiche Elektrochemie," Steinkopff, Dresden 1942, Lithoprinted by Edwards Bros., Ann Arbor 1946.
7. C. J. Brockman, "Electro-Organic Chemistry," John Wiley & Sons, Inc., New York (1926).
8. F. Fichter and H. Erlenmeyer, "Handbuch Der technischen Elektrochemie," Band, 2. Teil 2, Leipzig (1933).
9. M. S. Venkatachalapathy and H. V. K. Udupa, Proc. Symposium on "Electrolytic Cells," Central Electrochemical Research Institute, Karaikudi-3, S.Rly., India, p. 204 (1961).
10. H. V. K. Udupa, M. S. Venkatachalapathy, and R. Ramaswamy, Indian Pat. 62,379 (1959) and 62,426 (1959).
11. M. S. Venkatachalapathy, R. Ramaswamy, and H. V. K. Udupa, *Curr. Sci. (India)*, **28**, 63 (1959).
12. M. S. Venkatachalapathy, R. Ramaswamy, and H. V. K. Udupa, Proc. Symposium on "Electrolytic Cells," Central Electrochemical Research Institute, Karaikudi-3, S.Rly. India, p. 147 (1961).
13. M. S. Venkatachalapathy, R. Ramaswamy, and H. V. K. Udupa, *Bull. acad. Polon. Sci.*, **6**, 487 (1958).
14. M. S. Venkatachalapathy, R. Ramaswamy, and H. V. K. Udupa, *ibid.*, **7**, 629 (1959).
15. M. S. Venkatachalapathy, R. Ramaswamy, and H. V. K. Udupa, *ibid.*, **8**, 361 (1960).
16. J. W. Mellor, "A Comprehensive Treatise of Inorganic and Theoretical Chemistry," Vol. 12, p. 428, Longmans Green & Co., London.

The Formation of a Zinc Oxide-Niobium Pentoxide Spinel

Robert W. Harrison and Eugene J. Delgrosso

Materials Laboratory, CANEL, Pratt & Whitney Aircraft, Division of United Aircraft Corporation, Middletown, Connecticut

ABSTRACT

The spinel $7ZnO \cdot Nb_2O_5$ ($Zn_7Nb_2O_{12}$ or $Zn_{2.33}Nb_{0.67}O_4$) was synthesized. The reactions occurring between ZnO and Nb_2O_5 were investigated as a function of temperature and composition. Evidence is presented to demonstrate the important role ZnO vapor played in formation of the spinel. It would appear that in the Nb_2O_5-ZnO system spinel formation was the last stage in a sequence of reactions in which the lowest symmetry oxide structure was formed first and the highest symmetry oxide, the cubic spinel, formed last. This reaction sequence agreed with Goldschmidt's "oxide structure sequence" proposed for the NiO-Nb_2O_5 and MgO-Nb_2O_5 systems.

The importance of double oxides with a spinel structure in the improvement of oxidation resistance of metallic materials is a well-established fact. It would appear that improvements in oxidation resistance may be attributed to the fact that the diffusion rates of the reactants are lower in double oxide compounds than in the constituent oxides (1). Of the double oxide types, spinels have been observed to offer the greatest improvement in oxidation resistance.

As part of a general investigation of various aspects of niobium oxidation, an oxide program was initiated to investigate the possibility of forming a spinel double oxide, one oxide being Nb_2O_5. A recent paper by Bayer (2) described the formation of double oxides of the II/V type having a spinel structure. One of the spinel oxides reported was $Zn_7Sb_2O_{12}$, formed by reacting seven moles of ZnO and one mole of Sb_2O_5 at high temperature. The possibility of producing a similar spinel with niobium pentoxide was investigated, and a spinel $Zn_7Nb_2O_{12}$ was produced.[1] This paper describes this investigation.

Oxide mixes were prepared by weighing analytical grade[2] niobium pentoxide and zinc oxide powders on an analytical balance in the desired mole proportions. Intimate mixing was achieved by hand grinding the powders in an isopropyl alcohol slurry in a dia-mon-ite mortar. The powders were dried and sieved through a 200 mesh screen. Any necessary regrinding was performed in the manner described until all powders passed through the screen. One half inch diameter pellets were pressed in a hydraulic compacting press in hardened steel dies at 20,000 psi. Oxide mixes were reacted in powder or pellet form in a globar box furnace in air or encapsulated in quartz tubes or Inconel bombs in a vacuum of 5×10^{-5} to 5×10^{-7} mm Hg. Specimens were removed, cooled in air, and could be handled in 5 or 6 min.

[1] The initial phase of this work involved partial substitution of Nb^{5+} for Sb^{5+} in the $Zn_7Sb_2O_{12}$ spinel. This work is described in the Appendix, Section 1.

[2] Chemical compositions of the oxides are presented in Appendix, Section 2.

Analysis of reacted mixes was performed by x-ray diffraction using a Norelco diffractometer, high density CuK α-radiation ($\lambda = 1.5405$Å) operated at 50 kv and 40 ma. A Geiger-Muller counter was used as a detector. Spectrographic analyses of these specimens were performed to check the composition and determine the presence of impurities.

Experimental Results and Discussion

Mixed Oxide Reactions

Pellets composed of ZnO and Nb_2O_5 in a 7:1 mole ratio when heated slowly from 1400° to 2200°F in relatively still air form a spinel $Zn_7Nb_2O_{12}$; whereas, rapid heating to 2200°F does not form the spinel. As a result, a step by step analysis of the reactions taking place was performed. The results of this analysis are depicted in Fig. 1. At 1400°F, the first reaction to take place, as determined by x-ray diffraction, was the formation of a compound later identified as $ZnNb_2O_6$. At 1600°F the relative amount of this compound increases with very little free Nb_2O_5 remaining. After ½ hr at 1800°F, the formation of a new compound $Zn_3Nb_2O_8$ occurs by reaction between $ZnNb_2O_6$ and ZnO. At this point all available Nb_2O_5 has reacted with ZnO. Continuing to heat at 1800°F results in a mixture of ZnO, $Zn_3Nb_2O_8$, and a trace of

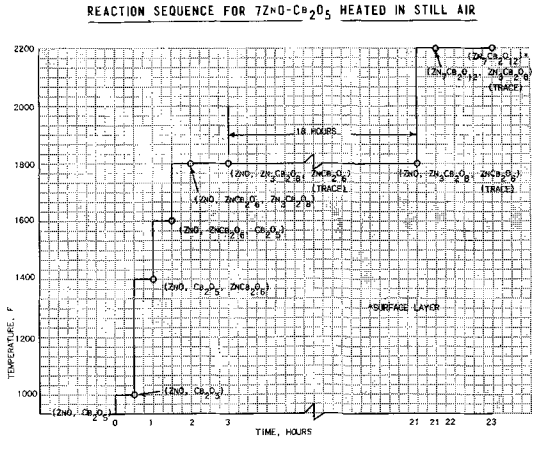

Fig. 1. Reaction sequence for $7ZnO$-Cb_2O_5 heated in still air

Table I. Solid-state oxide reactions

All reactions conducted in still air

Composition, moles	Heat treatment	Constitution, x-ray diffraction	Remarks
$1ZnO\text{-}Nb_2O_5$	18 hr at 1900°F 36 hr at 2200°F	$ZnNb_2O_6$	Resembles the iron columbite structure.
$3ZnO\text{-}Nb_2O_5$	18 hr at 1900°F 36 hr at 2200°F	$Zn_3Nb_2O_8$	Tetragonal
$4ZnO\text{-}Nb_2O_5$	18 hr at 1900°F 36 hr at 2200°F	$Zn_3Nb_2O_8$ and ZnO	
$5ZnO\text{-}Nb_2O_5$	18 hr at 1900°F 36 hr at 2200°F	$Zn_3Nb_2O_8$ and ZnO	
$6ZnO\text{-}Nb_2O_5$	18 hr at 1900°F 36 hr at 2200°F	$Zn_3Nb_2O_8$, ZnO, and trace $Zn_7Nb_2O_{12}$	
	2 hr at 2200°F (slowly heated from 1400° to 2200°F	$Zn_3Nb_2O_8$, $Zn_7Nb_2O_{12}$, trace ZnO	
$7ZnO\text{-}Nb_2O_5$	18 hr at 1900°F 36 hr at 2200°F	$Zn_3Nb_2O_8$, ZnO, and trace $Zn_7Nb_2O_{12}$	
	2 hr at 2200°F (slowly heated from 1400° to 2200°F	$Zn_7Nb_2O_{12}$	Spinel structure (surface) inner portions of pellet same as first heat treatment.
$8ZnO\text{-}Nb_2O_5$	2 hr at 2200°F (slowly heated from 1400° to 2200°F	$Zn_7Nb_2O_{12}$	Same as above except more spinel in the inner portions of the pellet.

$ZnNb_2O_6$. After 2 hr at 2200°F the formation of the spinel $Zn_7Nb_2O_{12}$ on the surface has occurred.

As a further clarification of the compound formation in the $ZnO\text{-}Nb_2O_5$ system, pellets of $1ZnO\text{-}Nb_2O_5$, $3ZnO\text{-}Nb_2O_5$, $4ZnO\text{-}Nb_2O_5$ to ——— $8ZnO\text{-}Nb_2O_5$ were reacted and analyzed. Results of this investigation are shown in Table I. Three compounds were found in this system: $ZnO \cdot Nb_2O_5$ ($ZnNb_2O_6$), $3ZnO \cdot Nb_2O_5$ ($Zn_3Nb_2O_8$), and $7ZnO \cdot Nb_2O_5$ ($Zn_7Nb_2O_{12}$). The diffraction analysis for each compound oxide is shown in Tables II, III, and IV, respectively. The spectrographic analyses could not be performed readily on a quantitative basis due to the difficulty in separating completely reacted individual oxide compounds in the reacted pellet; however, qualitative results indicated the atomic ratios were correct to approximate the compositions shown. No major impurities were found in any of the analyzed pellets.

Table II. X-ray diffraction results

$ZnO \cdot Nb_2O_5$ ($ZnNb_2O_6$) niobite

Observed d	I/I_o	hkl	Calculated d
3.6686	38	002	3.669
3.5672	6	400	3.566
2.9683	100	222	2.968
2.8750	23	500	2.854
2.5252	32	440	2.523
2.4953	35	521	2.493
2.3719	13	112	2.378
2.2275	10	540	2.229
2.2077	16	223	2.201
2.0768	18	442	2.079
1.8937	22	721	1.894
1.8287	17	650	1.827
1.7729	37	651	1.773
1.7262	44	224	1.724
1.7178	49	810-740	1.721
1.6726	8	830	1.670
1.5262	37	662	1.529
1.4784	15	444	1.484
1.4576	32	105	1.460
1.4495	50	940	1.449
1.4459	27	614	1.445
1.3789	19	833	1.379

Indexed as tetragonal $A_o = 14.27$, $C_o = 7.34$

Table III. X-ray diffraction results

$3ZnO \cdot Nb_2O_5$ ($Zn_3Nb_2O_8$)

Observed d	I/I_o	hkl	Calculated d
5.639	3	101	5.639
4.324	10	220	4.319
3.824	9	310	3.862
3.326	24	311	3.302
3.202	40	002	3.180
2.728	80	420	3.732
2.5989	50	331	2.623
2.568	60	222	2.561
2.281	6	501	2.281
2.259	15	520	2.268
2.017	25	610	2.009
1.949	12	601	1.939
1.901	5	223	1.902
1.879	3	313	1.880
1.749	100	532	1.749
1.656	2	622	1.651
1.607	5	503	1.601
1.593	4	004	1.590
1.524	30	214	1.526
1.494	28	642	1.495
1.476	14	820	1.481
1.450	35	613	1.458
1.420	20	750	1.420
1.370	18	424	1.374
1.359	77	900	1.357
1.351	8	910	1.349

Indexed as tetragonal $A_o = 12.23$, $C_o = 6.37$

Table IV. X-ray diffraction results

$7ZnO \cdot Nb_2O_5$ ($Zn_7Nb_2O_{12}$) spinel

Observed d	I/I_o	hkl	Calculated d
4.9566	3	111	4.9489
3.0354	9	220	3.0367
2.5902	100	311	2.5897
2.4793	6	222	2.4794
2.1454	89	400	2.1473
1.9705	2	331	1.9705
1.9395	1	420	1.9206
1.7533	6	422	1.7532
1.6537	86	511-333	1.6530
1.5181	26	440	1.5183
1.4515	5	531	1.4518
1.4312	1	600-442	1.4315
1.3582	12	620	1.3581
1.3101	6	533	1.3098
1.2949	18	622	1.2949
1.2387	2	444	1.2397
1.2031	4	711-551	1.2027
1.1824	1	640	1.1911
1.1480	2	642	1.1478
1.1188	21	731-553	1.1182

Cubic (spinel) structure $A_o = 8.589$

The compound $ZnO \cdot Nb_2O_5$ was indexed as tetragonal in structure. Although Goldschmidt (3) has identified a $ZnO \cdot Nb_2O_5$ compound as a niobite, the diffraction results (d spacings) found in this study fit a tetragonal lattice more accurately than that of a classical niobite such as $FeO \cdot Nb_2O_5$. Goldschmidt's method of synthesization, namely, arc meltings, is conducive to a greater degree of reactivity and hence a more complete reaction than could be produced using the solid-state reaction method described in this study. The compound $3ZnO \cdot Nb_2O_5$ was also indexed as tetragonal for much of the same reasons described above.

Although some spinel is found at isolated locations in the inner portions of reacted $7ZnO$-Nb_2O_5 pellets, complete reaction takes place only at the surface. The situation is illustrated in Fig. 2. The surface layer (reaction zone) of complete spinel can be seen under the microscope and was approximately 2 mils thick for pellets heated slowly to 2200°F and held for 2 hr at temperature. Holding pellets at 2200°F for times up to 100 hr did not increase the thickness of this layer appreciably. As a result no pellets could be reacted to complete spinel. Pellets of $7ZnO$-Nb_2O_5 reacted in vacuum in quartz capsules under similar temperature-time conditions did not form a spinel. However each quartz capsule contained an appreciable deposit of oxide, which was identified by x-ray diffraction analysis as ZnO.

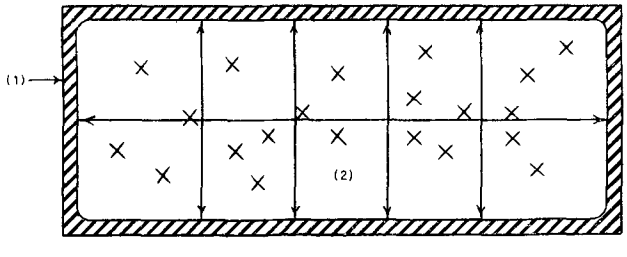

Fig. 2. Illustration of the reactions in $7ZnO$-Cb_2O_5 pellet. 1, Spinel shell, completely reacted in $Zn_7Cb_2O_{12}$; 2, this zone has been depleted in ZnO by gaseous diffusion through interconnected pore passages prior to densification by sintering. As a result, only small clusters of spinel are found at areas where the necessary stoichiometry exists; the remaining oxides are ZnO and $Zn_3Cb_2O_8$. x, Cluster of spinel, $Zn_7Cb_2O_{12}$. Arrows denote directionality of decreasing ZnO concentration.

ZnO *Volatility*

Due to its great volatility, ZnO is believed to play the determinant part in the spinel formation. As a $7ZnO$-Nb_2O_5 pellet is heated, a ZnO partial pressure will be produced by the vaporization of ZnO throughout the interstices of the unsintered low density compacted pellet. As the spinel reaction temperature (2200°F) is reached, the pellet sinters and little interconnected porosity remains. Further vaporization from the inside of the pellet is thus prevented. As a result, the spinel reaction takes place inside the pellet only at those locations where the necessary stoichiometry exists. At the surface, however, the existence of the ZnO vapor will supply the necessary ZnO to form the spinel. Thus a thin spinel layer is produced comparatively rapidly on the surface, since the accessibility and the reactivity of the ZnO in the vapor is much greater than that of the ZnO in the pellet interior, where solid-state diffusion must occur to supply the ZnO necessary for the spinel reaction. Any thickening of the surface spinel layer, once it is completely adherent and continuous, can only occur by solid-state diffusion. This is a very slow process in comparison to the initial spinel formation.

Several different experiments were performed to corroborate the above reasoning. A pellet of $7ZnO$-Nb_2O_5 was suspended in a thermobalance at 1400°F in moving air (1200-1400 cc/min). The temperature was slowly increased to 2200°F and the weight loss measured continuously. The rate of weight loss at 1400°F is much greater than the loss rate at 2200°F, when the pellet is sintering rapidly. The rate remains relatively constant as the pellet is held at 2200°F. To show further that the role of ZnO was connected to sintering considerations and concomitant blocking of interconnected pores, a pellet of the same composition was sintered initially at 2200°F prior to being placed in the thermobalance and subjected to the same conditions as the previous pellet. Its initial weight losses were much less, as can be seen in Fig. 3. It can be noticed that the weight loss

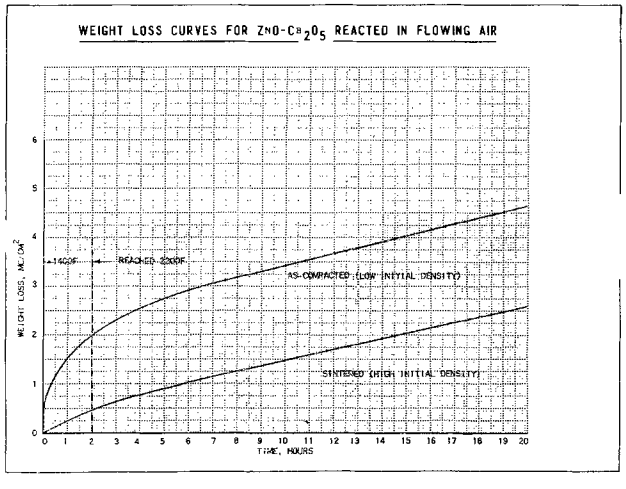

Fig. 3. Weight loss curves for ZnO-Cb_2O_5 reacted in flowing air

rate, after the 2200°F temperature is reached, is comparatively the same for both pellets. This experiment also indicated the necessity of a ZnO vapor supply to achieve spinel layer formation. In both cases, no spinel layer was formed, since the moving air environment constantly removed the vapor away from the pellet. As stated previously, by reacting pellets of the same composition under similar temperature-time conditions in a box furnace in a still air environment a spinel layer is produced.

When $8ZnO\text{-}Nb_2O_5$ pellets are reacted in the box furnace in the designated manner a spinel layer is produced; however, a greater amount of spinel is found throughout the $8ZnO\text{-}Nb_2O_5$ pellet than in a $7ZnO\text{-}Nb_2O_5$ pellet. Similar results were found when a $7ZnO\text{-}Nb_2O_5$ pellet and a ZnO pellet were placed in an evacuated quartz tube at 5×10^{-5} mm Hg. Spinel formed because the ZnO pellet provided the necessary ZnO to maintain the equilibrium partial pressures at the reaction temperature and to react with the mixed oxide pellet, so that the stoichiometry of the $7ZnO\text{-}Nb_2O_5$ pellet was not depleted. In contrast, when only a $7ZnO\text{-}Nb_2O_5$ pellet was reacted in an evacuated capsule under similar conditions the high loss of ZnO from the pellet prevented any appreciable amount of spinel from forming.

Additional experiments were made to investigate the effect of ZnO vapor on the growth of the spinel layer. A series of $7ZnO\text{-}Nb_2O_5$ plus ZnO pellets were reacted in evacuated quartz capsules for various lengths of time at 2200°F.

Results were obscured by the formation of zinc silicate from the reaction between ZnO vapor and SiO_2 (quartz). This reaction only became a problem when reaction times at 2200°F exceeded 10 hr. This experiment was repeated in an Inconel tube furnace. After 18 hr of heating all the ZnO initially present in the hot zone of the furnace tube (including that contained in the mixed oxide pellet) was depleted by a gaseous mass transfer and condensed at the water cooled O-ring flange on the end of the furnace tube. Thus all future experiments of this type in Inconel tubes were performed under isothermal conditions.

Diffusion Couples

A study of $ZnO\text{-}Nb_2O_5$ diffusion couples was fruitful as it showed the spinel formed by the reaction of Nb_2O_5 and ZnO vapor. Pellets of ZnO and Nb_2O_5, in constant intimate contact, were sealed in an evacuated (5×10^{-5} mm Hg) Inconel tube about 4 in. in length. These tubes could be heated isothermally at 2200°F for long periods of time. The first diffusion couple, heated 40 hr, was examined by metallographic and x-ray diffraction techniques; three zones could be distinguished in the Nb_2O_5 pellet. Starting at the interface between this pellet and the ZnO pellet the zones in the Nb_2O_5 were analyzed to be: $Zn_3Nb_2O_8 + ZnNb_2O_6$, $ZnNb_2O_6$, and Nb_2O_5 plus trace amounts of $ZnNb_2O_6$. A spinel layer was produced on the top and sides of the Nb_2O_5 pellet. A second diffusion couple, heated for 60 hr at 2200°F, showed somewhat different results. This time only two zones were detected: $ZnNb_2O_6$, and NbO_2 plus trace amounts of $ZnNb_2O_6$. No spinel layer was produced, and the Nb_2O_5 was reduced to NbO_2. An examination of the inside of the Inconel tube showed oxidation of the metal surface had occurred. It is believed that the oxygen produced from the dissociation of ZnO vapor reacts with the Inconel, upsetting the equilibrium concentrations of gaseous vapors and resulting in an excess partial pressure of zinc which, in turn, reduces the Nb_2O_5 and possibly any previously formed spinel. The volatilization and dissociation of ZnO at high temperature has been shown to be extensive by such investigators as Stahl, Kowalke, Doeltz, and Graumann (4). Although side reactions were a problem in these diffusion experiments, the experiments showed that the reaction of ZnO vapor with Nb_2O_5 is responsible for the formation of the spinel layer on mixed oxide pellets as previously postulated.

The volatility of ZnO may contribute to the self-healing properties of the Zn-coated columbium specimens when exposed to oxidizing atmosphere as described by Sandoz (5).

Conclusions

Two major factors are involved in the formation of the spinel $Zn_7Nb_2O_{12}$: (i) the formation of the intermediate compounds prior to the spinel reaction induced by slow heating $7ZnO\text{-}Nb_2O_5$ pellets, and (ii) the volatilization of ZnO and its influence on the spinel reaction. Goldschmidt (3) has shown in the $NiO\text{-}Nb_2O_5$ and $MgO\text{-}Nb_2O_5$ type of systems that the over-all sequence in terms of structures:

$$\underset{1}{Nb_2O_5} \rightarrow \underset{2}{\frac{\text{Rutile}}{\text{Niobite}}} \rightarrow \underset{3}{\text{Hematite}} \rightarrow \underset{4}{\frac{\text{Rocksalt}}{\text{Spinel}}}$$

exists with the proviso that the allotropy may or may not exist, and the series may terminate at stage 3. As found in this investigation, the above sequence describes in general terms the compound formation in the $ZnO\text{-}Nb_2O_5$ system terminating in the spinel structure. The slow heating and ZnO volatilization factors are interrelated in that by slow reaction a considerable amount of free ZnO is absorbed in compound formation at lower temperatures, before a high volatilization rate is attained and, therefore, does not contribute to the ZnO partial pressure when higher temperatures are reached. It can be concluded that the formation of a spinel layer occurs by the reaction of Nb_2O_5 and ZnO, the majority of which is supplied at the mixed oxide pellet surface by ZnO vapor. Subsequent growth of this layer can only occur by solid-state diffusion of the ZnO being supplied at the surface of the pellet.

Acknowledgment

This investigation was sponsored by the A.E.C. under Contract AT(30-1)-2789. The authors wish to thank Mr. L. M. Raring for permission to conduct this work and Messrs. D. Fornwalt and R. Granger for x-ray examinations of the oxide structures. Special appreciation is due to Dr. J. B. Wagner and Mr. R. Gambino for helpful discussions.

Manuscript received July 23, 1962; revised manuscript received Oct. 10, 1962.

Any discussion of this paper will appear in a Discussion Section to be published in the December 1963 JOURNAL.

REFERENCES

1. O. Kubachewski and B. E. Hopkins, "Oxidation of Metals and Alloys," Butterworths Scientific Publications, London (1953).
2. G. Bayer, *Naturwiss.*, **48** (2), 46 (1961) (in English).
3. H. J. Goldschmidt, *Metallurgia*, p. 218-250, November and December 1960.
4. J. W. Mellor, "Comprehensive Treatise on Inorganic and Theoretical Chemistry," Vol. 4, p. 515, Longman, Green and Company, London (1957).
5. G. Sandoz, *J. Metals*, **12**, 340 (1960).

APPENDIX

Section 1.—A recent paper by Bayer (2) described the formation of double oxides of the II/V type having a spinel structure. One of the spinel oxides reported was $Zn_7Sb_2O_{12}(Zn_{2.33}Sb_{0.67}O_4)$, formed by reacting 7 moles of ZnO and 1 mole of Sb_2O_5 at high temperatures. This work was reproduced prior to this study by reacting a mixed oxide pellet of $7ZnO-Sb_2O_5$ at 2200°F for 2 hr in air. X-ray diffraction analysis showed the spinel structure had formed with an $A_o = 8.603$. An oxide pellet composed of ZnO, Sb_2O_5, and Nb_2O_5 in a 7:0.5:0.5 mole ratio was reacted under similar conditions to a spinel structure $Zn_7(Sb,Nb)_2O_{12}$. From this preliminary investigation it was believed that a spinel oxide could be produced between ZnO and Nb_2O_5 without the Sb_2O_5 addition.

The reactivity of the $ZnO-Sb_2O_5$ mixed oxide pellets is much greater than that of $ZnO-Nb_2O_5$ pellets due to the instability of Sb_2O_5 at the temperature of reaction. As a result, a complete reaction to spinel could be produced in a mixed oxide pellet using Sb_2O_5 whereas incomplete reactions were found with Nb_2O_5 in this work.

Section 2.—The following is a list of the major impurities in the raw materials used in this investigation:

Nb_2O_5-Ta, 0.08% (by weight); Si, 0.053%; Ti, 0.0008%; Fe, 0.004%.

ZnO-chloride (Cl), 0.0008%; sulfur (SO_4), 0.003%; Pb, 0.002%; Mn, 0.0000%; substances not pptd by ammonium sulfate, 0.04%.

Electrolytes for Low-Temperature Fuel Cells

K. R. Williams and D. P. Gregory[1]

"Shell" Research Limited, Thornton Research Centre, Chester, England

ABSTRACT

It is suggested that because of concentration polarization only strong acids or strong bases are suitable as electrolytes for commercially acceptable low-temperature fuel cells. If carbonaceous fuels are employed, acid electrolytes must be used, since alkaline electrolytes would react with the carbon dioxide produced. Experimental results are quoted to show that high performance oxygen and hydrogen electrodes can be made which operate satisfactorily in acid electrolytes.

The general problem of concentration polarization in electrolytic cells has been discussed by Agar and Bowden (1), and the particular case of the oxygen electrode in alkaline electrolytes considered by Witherspoon *et al.* (2). The problem is also briefly mentioned by Austin (3). However, to the best of the authors' knowledge, the implications of concentration polarization in fuel cells have not been discussed in the literature. As this effect can severely limit the performance of electrodes, it is important that it should be considered in the design of practical fuel cells.

Although the arguments which we shall give are to some extent applicable to high-temperature as well as low-temperature cells, it is the low-temperature cells which we shall consider in detail. We believe that it is only the low-temperature cell that can compete economically with existing mobile power units. This is because easy starting is a feature of existing mobile power units and, hence, must be a characteristic of any competitive unit.

Theoretical Considerations

In the first instance, it is useful to consider the hydrogen-oxygen cell. The primary sources of concentration polarization are the supply of gas to the electrode and the removal of ions from the electrode. Because of the high mobility of gases, it should be possible to supply gas as fast as it is consumed by the electrode at practical power densities. On the other hand, ions in solutions are very much less mobile than the molecules of a gas and would be expected to be more liable than gases to cause concentration polarization. In practical electrodes limitation from gas supply may well occur however. The argument is much simplified if we assume an ideal gas supply, perfect catalysis, and plane electrodes. In this way the results obtained will be representative of the best performance that could be expected. Practical electrodes will always fall short of the theoretically possible.

Consider first the alkaline electrolyte system. Concentration polarization results from the changes in OH^- concentration which occur in the vicinity of the electrodes. The OH^- concentration is increased near the oxygen electrode and decreased near the hydrogen electrode. Since the concentration cannot fall below zero at the hydrogen electrode, a limiting current will be reached.

If it is assumed that a linear concentration gradient exists over a boundary layer of thickness δ cm, application of Fick's law makes it possible to calculate the concentration at the electrode and hence the concentration polarization η_c. The expressions obtained are of the form

oxygen electrode:

$$\eta_c = -\frac{2.303RT}{\mathbf{F}} \log_{10}\left[1 + \frac{(1 - t_{OH^-})I\delta}{(C^o_{OH^-})(\mathbf{F}D_{KOH})}\right] \quad [1]$$

[1] Present address: Pratt and Whitney Aircraft, East Hartford, Connecticut.

hydrogen electrode:

$$\eta_c = -\frac{2.303RT}{\mathbf{F}} \log_{10}\left[1 - \frac{(1 - t_{OH-})I\delta}{(C^o_{OH-})(\mathbf{F}D_{KOH})}\right] \quad [2]$$

Where t_{OH-}, C^o_{OH-} are the transport number and bulk concentration of the hydroxyl ion, I is the current density, D_{KOH} is the diffusion coefficient of KOH, and R, T and $\mathbf{F}$ have their usual significance.

Similar expressions may be derived for the acid electrolyte system, in which case it is the oxygen electrode which exhibits the limiting current.

We may now consider the effect of the choice of electrolyte on the concentration polarization. Some advantage may be gained from the choice of electrolyte with a large transport number (such as an ion exchange resin), but in an aqueous electrolyte the dominant influence is that of the concentration of the active ion. Not only must its initial concentration be high, but the electrolyte must be able to maintain this concentration at a steady value when a current is flowing. At high current densities ions are produced by one electrode and removed by the other at a high rate. This implies a large concentration difference across the cell, but it must not be allowed to cause an appreciable change in pH, which would result in concentration polarization. This is analogous to the problem of making solutions which maintain their pH when substantial additions of acid or alkali are made. Electrolytes which are suitable in this respect include strong bases, strong acids, and certain buffer solutions. Conventional neutral buffer solutions are unsuitable because they have a very low ionic conductivity.

Taking , as examples, KOH, H_2SO_4, and K_2CO_3, we may insert numerical values into Eq. [1] and [2]. The following values have been assumed: $\delta = 0.03$ cm (4). This is the lowest value for boundary layer thickness that can be assumed for an unstirred system; temperature 25°C.

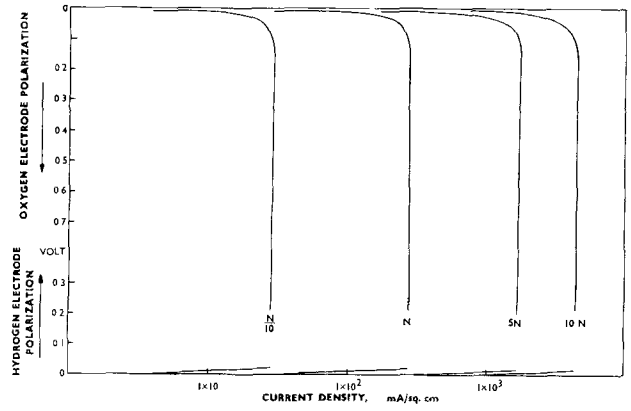

Fig. 1. Theoretical concentration polarization curves in H_2SO_4 electrolyte (assuming $\delta = 0.03$ cm).

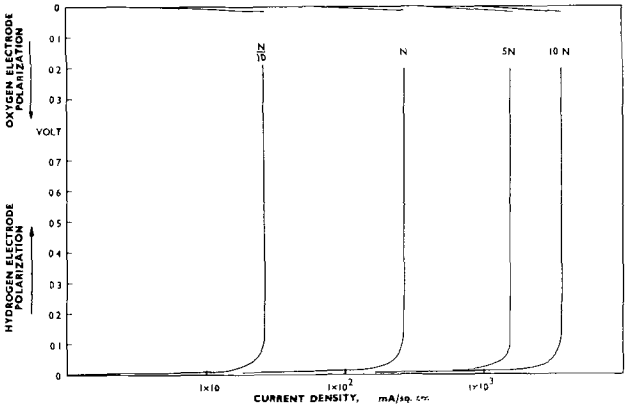

Fig. 2. Theoretical concentration polarization curves in KOH electrolyte (assuming $\delta = 0.03$ cm).

Inserting these values in Eq. [1] and [2] we obtain theoretical curves for polarization *vs.* current density (Fig. 1 and 2). It should again be stressed at this stage that all the assumptions we have made tend to give a low value of η_c, so that in an actual electrode greater polarization is to be expected. For

H_2SO_4

Molarity	0.05	0.5	2.5	5.0	Ref.
D (cm²/sec) *	1.6×10^{-5}	1.6×10^{-5}	2.2×10^{-5}	2.7×10^{-5}	(7)
t_{H+}	0.82	0.81	0.80	0.80	(6)
C^o_{H+} g ions/cc	0.1×10^{-3}	1.0×10^{-3}	5.0×10^{-3}	10.0×10^{-3}	

KOH

Molarity	0.1	1.0	5.0	10.0	Ref.
D (cm²/sec) *	2.2×10^{-5}	2.2×10^{-5}	2.7×10^{-5}	3.0×10^{-5}	(7)
t_{OH-}	0.737	0.737	0.737	0.737	(5)
C^o_{OH-} g ions/cc	0.1×10^{-3}	1.0×10^{-3}	5.0×10^{-3}	10.0×10^{-3}	

K_2CO_3

Molarity	2.5
$D_{K_2CO_3}$	0.8×10^{-5} cm²/sec
t_{OH-}	0 (assume current carried entirely by K^+ and CO_3^{--})
C^o_{OH-}	10^{-5} g ions/cc (since pH = 12)
C^o_{CO3--}	2.5×10^{-3} g ions/cc

* Some of these diffusion coefficients may not be entirely accurate, but are the only values available in the literature.

example, we have assumed that dissociation is complete, whereas it is undoubtedly not. We must also consider the effect in practice of concentration polarization due to the gas supply, the removal and supply of water to the electrodes, activation polarization, and resistive polarization.

It will be seen that the polarization value is markedly dependent on the concentration of the active ion in the electrolyte. In both alkaline and acid cells one electrode exhibits a limiting current density, which severely restricts the usefulness of the cell as a useful power source. The parameters defining this limiting current cannot be changed by mechanical design of the cell or by development of electrode structure or catalysts. We have not been able to predict the performance of electrodes when the electrolyte is a carbonate, but this special case will be dealt with in detail later on.

Practical requirements.—We should consider here the minimum current density which is required before a fuel cell becomes of practical interest. In order to compete with existing mobile power units, a power/volume ratio of 5 kw/ft^3 is required (0.2 w/cc.). The power/volume ratio, p/v, of a fuel-cell is given by the expression:

$$p/v = \frac{IeS}{d}$$

where I is the current density obtained at a cell potential, e, d is the thickness of each cell, and S is a space factor (the ratio of the working surface of the electrode to the over-all cross section of the whole cell assembly). We have found experimentally that the following values can be realized $S = 0.8$, $d = 0.4$ cm. Maximum power is obtained when $e = 0.5$v. The required current density is therefore 200 ma/cm^2 at normal operating temperatures. At 25°C, therefore, a figure of at least 100 ma/cm^2 is likely to be necessary. Our predicted polarization curves show that current densities of this order are achieved only in acid or alkali stronger than about 0.7N. For economic reasons, the most promising fuels for a competitive fuel cell are the liquid fuels containing carbon. It is well known that strongly alkaline electrolytes cannot be used with such fuels owing to the formation of carbonate and bicarbonate. The evidence so far suggests the use of concentrated acidic electrolyte or a carbonate solution. (Although in principle a redox system is also possible, the authors know of no redox couple which could satisfy the requirements of a high power density fuel cell.)

Performance of Practical Electrodes

We shall now compare these theoretical predictions with some experimentally determined figures. Electrodes were examined in a half-cell arrangement in which the experimental electrode and its gas supply were mounted at one end of the electrolyte bath and a platinum electrode at the other end. This cell was so arranged that a reference electrode could be placed at the same point in the electrolyte in each experiment. An "interruption" technique, employing a high-speed relay and a cathode-ray oscillograph, was used to determine the ohmic polarization due to the electrolyte. This was subtracted from the results.

The electrodes which we have used are not simple plane surfaces, and they differ from the ideal model we have been considering. The principal difference is that they are porous and trap a stagnant layer of electrolyte which increases the boundary layer thickness.

We know that in these electrodes the effective reaction zone is about 0.07 cm from the interface between the free electrolyte and the pore-structure, and adding this dimension to the boundary layer in the free electrolyte we obtain an effective diffusion gradient extending over some 0.10 cm. The value of $\delta = 0.10$ cm has therefore been used to recalculate theoretical concentration polarization curves for our electrodes in order to compare their performance with the theory. The predicted curves (solid lines) and the experimental curves (broken lines) are shown in Fig. 3 and 4.

In the case of $N/10$ and N solutions of potassium hydroxide, the calculations of limiting current on the hydrogen electrode are moderately well confirmed. However, the limiting current reached with the 5N electrolyte was less than might be expected from the concentration polarization due to ionic transport. Polarization may, therefore, be due also to failure of gas transport to the catalyst. The oxygen electrode in 5N KOH shows a similar but unexpected limiting current which again points toward gas transport polarization. (This view is borne out by the experimental observation that a fuel cell incorporating a similar hydrogen electrode to those tested, when run with gas supplies at 60 psi, operated quite satisfactorily at 180 ma/cm^2 at 25°C

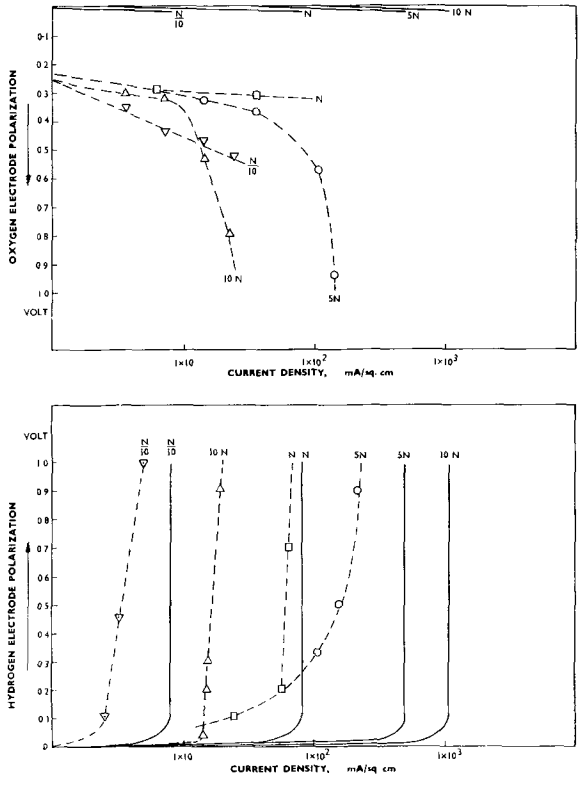

Fig. 3. Theoretical concentration polarization curves in KOH electrolyte (assuming $\delta = 0.10$ cm) and experimental curves.

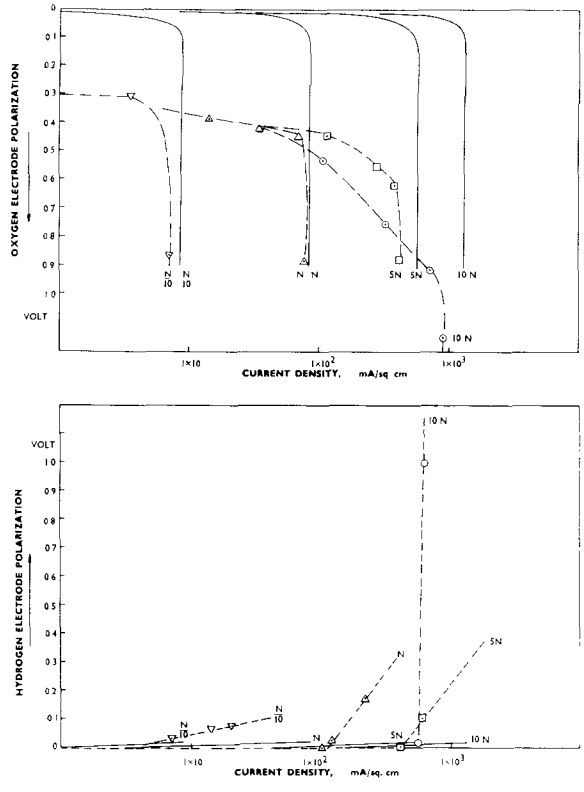

Fig. 4. Theoretical concentration polarization curves in H_2SO_4 electrolyte (assuming $\delta = 0.10$ cm) and experimental curves.

in 6*N* KOH.) The performance of the hydrogen electrode in 10*N* electrolyte was much worse than in 5*N*. If concentration polarization due to gas transport is the cause, then this may be attributed to the reduced solubility of hydrogen in the more concentrated solution of potassium hydroxide. The best performance is obtained at about 5*N*, which is also the optimum concentration for conductivity. It may be seen that, under optimum conditions, electrodes can be made which just approach the power density requirements for a high performance cell.

The experimental results for hydrogen and oxygen in sulfuric acid are shown in Fig. 4. Here there is better agreement in the limiting current values on the oxygen electrode, but the initial polarization is largely due to imperfect catalysis of the electrode reaction. The agreement in limiting currents at the higher concentrations of acid suggests that limitation due to gas transport is not severe, but may be affecting performance of 10*N* acid. This may well be due to the fact that oxygen and hydrogen are about 5 times more soluble in acid than in alkali. Limitation due to gas transport certainly occurs on the hydrogen electrode in 10*N* acid.

Figure 4 shows that there is no theoretical reason why high performance acid cells should not be practicable, and the experimental curves indicate that it is experimentally possible to make electrodes which give satisfactory power density figures. Kordesch (6) has pointed out that the rate of peroxide decomposition is slow below *p*H 13, so that one might expect a greater polarization of oxygen electrodes in acid than in alkali. Our results indicate that this effect is a function of the catalyst used.

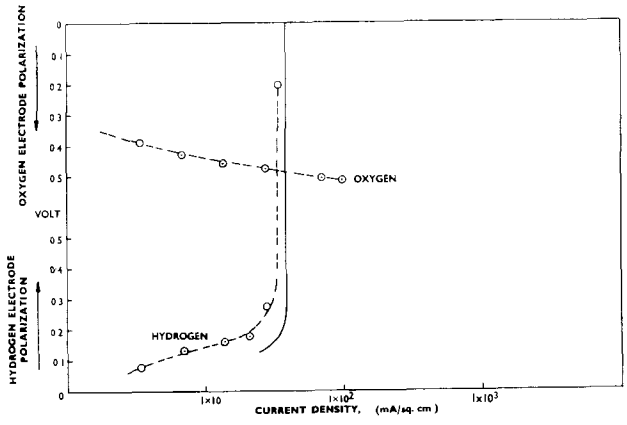

Fig. 5. Polarization curves for 5*N* potassium carbonate electrolyte

Carbonate Electrolytes

We may now consider the use of carbonate and bicarbonate electrolytes. It appears at first sight that the very low value of the hydroxyl ion concentration will give rise to a very large degree of polarization and a very small limiting current. The position is not straightforward, however, since the hydroxyl ions are in equilibrium with carbonate and bicarbonate ions

$$CO_3^{--} + H_2O \rightleftharpoons OH^- + HCO_3^-$$

$$HCO_3^- + H_2O \rightleftharpoons OH^- + H_2CO_3$$

and as the hydroxyl ions are removed from solution at the electrode, more are formed rapidly by hydrolysis. The limiting current density is controlled by diffusion of potassium carbonate across the boundary layer, and a value of 39 ma/cm^2 is predicted for 5*N* K_2CO_3 at 25°C when $\delta = 0.10$ cm. The electrode potential will also be controlled by the concentration of carbonate ion if the hydrolysis is very rapid.

The experimentally observed polarization curve is shown in Fig. 5 and confirms the predicted limiting current (solid line). At low current densities, the relatively low polarization obtained indicates a very rapid hydrolysis of carbonate ions to form hydroxyl ions. In spite of this, the limiting current obtained is too low for carbonate electrolytes to be satisfactory in low-temperature cells.

Conclusions

We conclude, therefore, that in order to have a satisfactory power/volume ratio, the low-temperature fuel cell must use either a strong acid or strong alkali electrolyte. On economic grounds, a carbonaceous fuel is essential, but this precludes the use of alkali. Our experimental results have shown that it is possible to construct oxygen and hydrogen electrodes which have the necessary performance in acidic electrolytes at low temperatures, so that there is no fundamental objection to the acid fuel cell.

Acknowledgment

In conclusion the authors would like to acknowledge the helpful discussions they have had with Dr. J. N. Agar.

Manuscript received Aug. 11, 1961; revised manuscript received Sept. 28, 1962. This paper was prepared

for delivery before the Indianapolis Meeting, April 30-May 3, 1961.

Any discussion of this paper will appear in a Discussion Section to be published in the December 1963 JOURNAL.

REFERENCES

1. J. N. Agar and F. P. Bowden, *Proc. Roy. Soc.*, **A169**, 206 (1938).
2. R. R. Witherspoon, H. Urbach, E. Yeager, and F. Hovorka, ONR Contract No. NONR 581 (00) Project No. NR.359-277, Technical Report No. 4, October, 1954.
3. L. G. Austin, "Fuel-Cells," Chap. 4, Reinhold Publishing Co., New York (1960).
4. L. L. Bircumshaw and A. C. Riddiford, *Quart. Rev. London*, **6**, 157 (1952); A. Hickling, *ibid.*, **3**, 95 (1949).
5. M. Knobel, *J. Am. Chem. Soc.*, **45**, 70 (1923); M. Knobel, D. K. Worcester, and F. B. Briggs, *ibid.*, **45**, 77 (1923).
6. Landolt-Bornstein Physikalische und Chemische Tabellen, Ergb 3 II 2149 (1936).
7. International Critical Tables V, 64.
8. K. Kordesch, "Fuel-Cells," Chap. 2, Reinhold Publishing Co., New York (1960).

Calorimetric Determination of Half-Cell Entropy Changes

J. M. Sherfey[1]

Metallurgy Division, National Bureau of Standards, Washington, D. C.

ABSTRACT

The reversible heat effects ($T\Delta S$) of half-cell processes have been measured in a twin calorimeter consisting of a Dewar flask divided into two halves by means of a vertical partition. Both compartments contain the same electrolyte and each has an electrode. A hole in the partition, covered by filter paper, permits the passage of electrolytic current between the compartments. The total heat effect and the heat due to irreversible phenomena are measured separately for each compartment. The difference between these two gives the desired reversible heat.

The half-cells studied include copper in acid copper sulfate, silver in acid silver perchlorate, and silver-silver chloride in various chloride solutions. The effect of "transport entropies" on these measurements is outlined. Presently accepted theories of the "irreversible" or "steady-state" thermodynamics of electrolytic cells predict the equivalence of half-cell entropy data obtained by the present calorimetric method and data obtained from thermocell studies. This predicted agreement was not obtained in the case of the half-cell silver-silver perchlorate.

The work reported in this paper is part of a continuing investigation of the heat effects of dynamic electrochemical processes. A previous paper (1) dealt with the calorimetric measurement of electrode polarization and with the determination of the heat (enthalpy change) of electrochemical reactions. The present paper is concerned with the measurement of the entropy change of half-cell processes.

The purpose of these researches is to demonstrate the usefulness of calorimetry in studies of electrochemical phenomena and to develop the necessary apparatus and techniques. Therefore there has been no attempt to accumulate a large mass of data or to refine the measurements unduly.

Ionic entropies are ordinarily calculated from free energy and enthalpy data, using the second law of thermodynamics. The values obtained, however, refer to molecular species as they exist in solution and are not applicable to individual ions. In order to avoid this difficulty, a convention has been adopted which arbitrarily assigns a value of zero to the standard state entropy of the hydrogen ion at all temperatures. All other ions are then given values relative to the hydrogen ion on this scale.

Calculated ionic entropies can be no more accurate than the free energy and enthalpy data from which they are obtained, and because such calculations often involve the difference between two relatively large numbers the percentage error is increased proportionately.

A direct method for the determination of individual ionic entropies would, therefore, be very valuable. This is particularly true if the values obtained were on the "absolute" scale rather than the arbitrary scale described above. Such absolute ionic entropies would be of considerable theoretical interest. Also, the determination of only one ionic entropy on both scales would fix the absolute entropy of the hydrogen ion and thus relate one scale to the other.

Method

One method for measuring so-called "absolute" ionic entropies was proposed by Lange (2). His approach to the problem was as follows: A calorimeter was divided into two symmetrical halves by a vertical partition. Both sides contained the same electrolyte and the same type of electrode. A hole in the partition permitted the passage of current from one electrode to the other, and a sensitive thermopile with junctions on both sides of the partition made it possible to maintain temperature equality on the two sides by means of a heater on that side which tended to be cooler. Changes in the concentrations of the electrolyte caused by electrolysis were negligible.

[1] Present address: National Aeronautics Space Administration, Goddard Space Flight Center, Greenbelt, Maryland.

The electrolytic process was essentially reversible because of the very low current densities employed. It was therefore possible to relate the heat developed (or absorbed) on either side to the $T\Delta S$ of the half-cell reaction taking place on that side. Since the reactions on the two sides were identical except for direction, the heat absorbed on one side equaled the heat evolved on the other, and the energy supplied to the heater used to maintain temperature equality could be related to twice the $T\Delta S$ of either half-cell reaction. The entropy of nonionic reactants and products is known in most cases. Thus, the entropy of the ion evolved in the half-reaction was readily calculated.

Basically, the method used in the investigation reported here is like Lange's. Our use of much higher current densities is the most important difference. This makes possible the study of a relatively large number of reactions which approach 100% current efficiency only at moderate current densities. It also simplifies the problem of determining the current efficiency. These advantages are partially balanced, however, by the fact that irreversible effects become too large to be ignored. Heat effects due to electrode polarization and to the passage of current through the solution must both be determined and subtracted from the total heat in order to obtain the desired reversible heat.

The method used to measure these irreversible effects is similar to that used to measure polarization with a Luggin capillary. The tip of the half-cell probe, however, is not pressed against the working electrode as in polarization studies, but is placed midway between the electrodes at a point which effectively divides one half of the calorimeter from the other. The potential between this probe and each working electrode is determined before the experiment is started (static or reversible potential) and periodically during the experiment (dynamic or irreversible potential). Then for either side the difference between the former and the time-weighted average of the latter gives the effective irreversible voltage during the run. This voltage, for any given side, includes not only the electrode polarization, but also the resistive drop in the solution between electrode and probe. When multiplied by the current and time, this equals the total irreversible heat due to electrolysis on that side.

Our method also differs from that of Lange in that we use two sheets of hardened filter paper to cover the hole in the partition. This prevents gross mixing of the solutions on the two sides without introducing a significant impediment to the passage of current between the electrodes.

Both methods are sensitive to nonstoichiometry of the electrode reactions, and both require that the electrodes be reversible in the sense that they have a reproducible and thermodynamically significant potential under static conditions.

Lange's work was confined to cells having identical electrodes on the two sides. The half-cell process on one side was thus the reverse of that on the other, and there was no net reaction in the cell as a whole. Therefore, the reversible cell voltage, the free energy change, and the enthalpy change were all zero. We have studied the cell

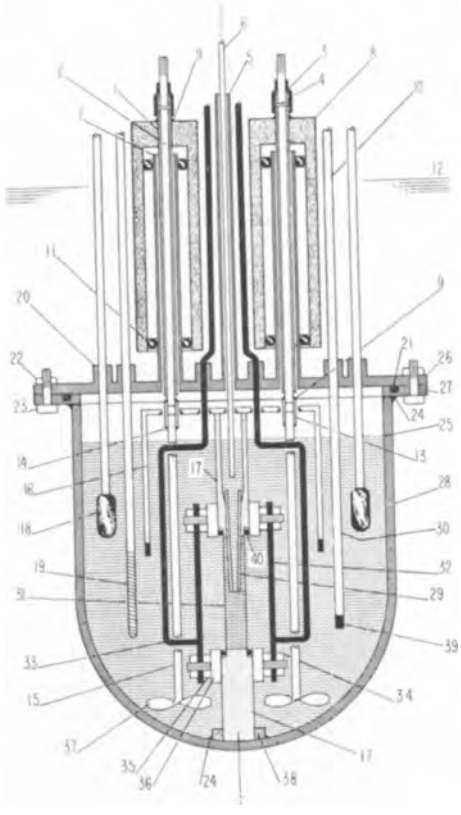

Fig. 1. The calorimeter: 1, Stirrer shaft guide tube, stainless steel; 2, stirrer shaft, stainless steel; 3, seal, rubber tubing; 4, drive pin, steel; 5, probe chimney, brass; 6, probe; 7, stirrer chimney, brass; 8, inverted cup seal, copper; 9, solder joint; 10, adiabatic thermopile; 11, ball bearing assembly; 12, oil bath level; 13, coupling sleeve, stainless steel; 14, wax joint; 15, Stirrer shaft, glass; 16, left-right thermopile; 17, partition, poly (methyl methacrylate); 18, heater; 19, platinum resistance thermometer; 20, compression seal; 21, "O" ring; 22, nut; 23, bolt; 24, polysulfide rubber sealant; 25, electrolyte level; 26, calorimeter lid, brass; 27, flange, brass; 28, Dewar flask, glass; 29, capillary, glass; 30, adiabatic thermopile; 31, filter paper disk; 32, electrode; 33, electrode lead; 34, nut, poly (methyl methacrylate); 35, washer, poly (methyl methacrylate); 36, support ring with studs, poly (methyl methacrylate); 37, propeller, glass; 38, gasket, sponge rubber; 39, adiabatic thermopile junctions; 40, "O" ring, neoprene rubber.

$$Cd, CdCl_2(1M), AgCl, Ag$$

The use of different electrodes on the two sides makes it possible to determine in one experiment the cell voltage, and thus the free energy change (ΔF), the heat of reaction (ΔH), the half-cell entropy change (ΔS) at each electrode, and, from the sum of the half-cell entropy effects, the total entropy change for the cell.

Apparatus

The apparatus used in making these measurements is described in detail in the appendix. Figure 1 is a diagrammatic representation of the calorimeter. One of the thermopiles can be seen to have a set of junctions on each side of the partition. The calorimeter also has a heater on each side, and one of these is used to maintain temperature equality on the two sides. The other thermopile (Fig. 1) has one set of junctions in the right compartment and the

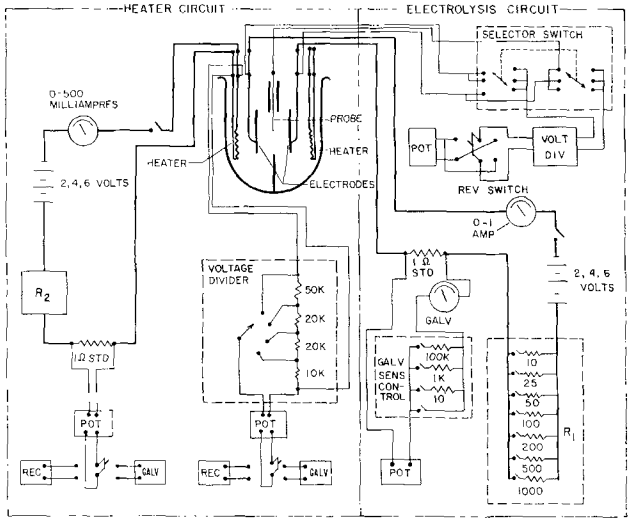

Fig. 2. Electrical circuit

other in the oil bath in which the calorimeter is immersed. The temperature difference between these two is kept at a minimum by means of a heater in the oil bath. Both sides of the calorimeter are thus maintained in an adiabatic condition, and no correction for heat leak is necessary.

The essential parts of the electrical circuit are shown in Fig. 2. This can be divided into two parts, the "heater circuit" and the "electrolysis circuit." The latter makes it possible to pass a known constant current between the electrodes and to measure the voltages between the electrodes and the probe. The heater circuit provides current to one of the calorimeter heaters and measures the energy supplied.

Procedure

Each determination requires at least three experiments. The first two (stirrer and calibration) experiments are used to determine four quantities, the rate of heat generation of each stirrer and the heat capacity of each compartment of the calorimeter. The third (electrolysis) experiment supplies the desired thermodynamic data. Procedures for these experiments are as follows.

Stirrer experiment.—A stirrer experiment is started by bringing the system to an adiabatic steady state with both stirrers running. Because the heat capacities of the two sides and the stirrer heats are not perfectly matched, there will be a tendency for one side to heat more rapidly than the other. This is counteracted by the heater on that side which tends to be cooler, using the "heater circuit" as a source of power. The voltage across this heater is adjusted as necessary to maintain a minimum temperature difference between the two sides. Maximum excursions of this difference are ordinarily about 10^{-3}°C (see Appendix).

When it appears that a steady state has been established, the initial readings of both time and the temperature (platinum resistance thermometer, Fig. 1, No. 19) are recorded. Temperature equality of the two sides is maintained by suitable adjustments of the heater voltage. It is desirable to take periodic time-temperature readings during the experiment, but this is not necessary. After about 30 min, the experiment is terminated by taking a final time-temperature reading.

Calibration experiment.—The calibration experiment is similar to the stirrer experiment except that the heaters in both compartments of the calorimeter are operated. The current for one of these is supplied by the "electrolysis circuit" and is held constant. The heat output of the other is adjusted as necessary to maintain temperature equality. As in the stirrer experiment, it is desirable to take periodic time-temperature readings, and the experiment is terminated with a final time-temperature reading.

Electrolysis experiment.—During the electrolysis experiment the constant current from the electrolysis circuit is directed through the cell. The heater on that side which tends to be cooler is operated by means of the heater circuit. The voltages between anode and probe, cathode and probe, and anode and cathode are noted periodically and in sequence throughout the experiment. These three voltages are also measured before (and preferably after) the experiment when no current is passing through the cell. In other respects the electrolysis experiment is similar to the stirrer and calibration experiments.

Reverse Electrolysis Experiment.—A fourth experiment, during which the electrolysis current is reversed, is very desirable but not essential. Such a "reverse electrolysis experiment" serves to disclose sources of error and doubles the amount of data obtained.

Calculations

The first step in the calculations is the determination of the total electrical energy supplied by the heaters in each of the various experiments. The method used is described in the appendix. The heat capacity of each compartment of the calorimeter and the rate of heat generation of each stirrer can then be calculated by means of Eq. [1] through [4] below. The subscripts "L" and "R" refer to the left and right sides of the calorimeter and the subscripts "1", "2", "3," and "4" refer to the corresponding experiments described under "Procedure." Also, it is assumed that experiment number one required the use of the left heater.

Then for experiment No. 1,

$$C_L \Delta\theta_1 = Z_L t_1 + [eit]_{L1} \qquad [1]$$

and

$$C_R \Delta\theta_1 = Z_R t_1 \qquad [2]$$

The symbol $\Delta\theta$ represents the difference between the initial and final temperatures of the calorimeter, expressed in terms of the resistance of the platinum resistance thermometer (ohm). The heat capacity of one compartment of the calorimeter is given by C and has the dimensions volt amp min ohm^{-1}. Thus $C\Delta\theta$ represents the total energy supplied to one side of the calorimeter in volt amp min. The symbol Z represents the rate of heat generation of a stirrer (volt amp) and t is the time (min). The energy supplied to a heater during the experiment is given by $[eit]$ (volt amp min). The brackets indicate that this quantity is obtained by integrating the recorder curves as described in the appendix.

For experiment No. 2, using the same notation

$$C_L \Delta\theta_2 = Z_L t_2 + [eit]_{L2} \quad [3]$$

$$C_R \Delta\theta_2 = Z_R t_2 + e_{Ave} i_2 t_2 \quad [4]$$

The product $e_{Ave} i_2 t_2$ represents the energy supplied to the right heater at constant current by means of the electrolysis circuit; e_{Ave} being the time-weighted average voltage (assuming a significant voltage variation), i_2 the current (ampere), and t_2 the time (min).

The only unknowns in Eq. [1] through [4] are the two C terms and the two Z terms. The heat capacities and stirrer heating powers are therefore uniquely determined by those four equations.

The half-cell entropy changes are calculated from the following equations. The subscripts a and c refer to anode and cathode, respectively. It is assumed that the anode is on the left in experiment No. 3 and, with the current reversed, on the right in experiment No. 4. It is also assumed that the anodic process is exothermic, requiring the use of the heater on the side with the cathode.

Then for experiment No. 3

$$C_L \Delta\theta_3 = -\frac{T_3 \Delta S_a I_3 t_3}{\mathbf{F}} + E_{a3} I_3 t_3 + Z_L t_3 \quad [5]$$

$$C_R \Delta\theta_3 = -\frac{T_3 \Delta S_c I_3 t_3}{\mathbf{F}} + E_{c3} I_3 t_3 + Z_R t_3 + [eit]_{R3} \quad [6]$$

Two similar equations can be written for experiment [4].

The average temperature during an electrolysis run is obtained from the initial and final readings of the platinum resistance thermometer. This is given by T and is in °K. The ΔS term has the usual significance and has the dimension joule deg^{-1} equiv^{-1}. The electrolysis current is represented by I (amp), $\mathbf{F}$ is the faraday (amp sec equiv^{-1}), and E is the irreversible voltage between the probe and either electrode obtained by subtracting the reversible probe-electrode potential from the time-weighted, average, dynamic probe-electrode potential. The quantity EIt thus represents the irreversible heat due to electrode polarization and the resistance of the solution. It is always positive. The quantity $[eit]$ again represents the energy dissipated by the heater.

If both sides of the calorimeter contain the same kind of electrode, Eq. [5] and [6], together with two equations for experiment (4), yield four independent values of ΔS since all other quantities represented are known.

If the two electrodes are different, however, two different values for ΔS are involved, and experiments 3 and 4 will yield two independent values for each. In this case, there is a net cell reaction, the entropy change of which equals the sum of the two half-cell entropy changes. The free energy change of the cell is given by the familiar equation

$$\Delta F = -n\mathbf{F}E_r \quad [7]$$

in which E_r is the reversible cell voltage. The enthalpy change ΔH of the cell is obtained from the difference between the total energy added to the calorimeter and the energy equivalent of the temperature rise. Thus,

$$\frac{\Delta H\, I_3 t_3}{\mathbf{F}} = -(C_L + C_R)\Delta\theta_3 + E_3 I_3 t_3 + [eit]_{R3} + (Z_L + Z_R) t_3 \quad [8]$$

A similar equation can be written for experiment 4.

The dimension of ΔH is joules·equiv^{-1}. The quantity E_3 in Eq. [8] represents the time-weighted average voltage across the cell and does not involve subtraction of a reversible potential as do E_c and E_a in Eq. [5] and [6]. The significance of the other quantities is unchanged. It should be noted parenthetically that the above method for determining reaction enthalpy is superior to either of the two methods described in a previous communication [1].

The order of magnitude of the various quantities in the equations above can be obtained from Table I which gives the numerical values for the terms in Eq. [6]. These data were obtained from the system Ag, AgCl, HCl(a=1) which requires that the heater be on the anode side, so that the anodic analogue of Eq. [6] must be used.

Table I. Numerical values in Eq. [6] from half cell Ag, AgCl, HCl (a=1)

C_R	= 492.6 volt amp min ohm^{-1}
$\Delta\theta_3$	= 0.0100 ohm (0.100°C)
T_3	= 299.47°K
ΔS_c	= −4.83 joule equiv^{-1} deg^{-1} (= $-\Delta S_a$)
I_3	= 0.300 amp
t_3	= 23.33 min
$E_{a3} I_3 t_3$	= 0.495 volt amp min
Z_R	= 0.0143 volt amp
$[eit]_{R3}$	= 3.993 volt amp min

Results

The various systems that have been studied, together with the cell currents employed and the half-cell entropy changes calculated are given in Table II. The ΔS values have the sign of the cathodic half-reaction. All measurements were made at approximately 25°C. The values given represent a selection "best results" from a much larger accumulation of data. Results that showed internal inconsistencies were discarded.

Table II does not include the results of our work with the cell Cd, 1M $CdCl_2$, AgCl, Ag. This cell, with different electrodes on the two sides, is the only one of its type studied. The following half-cell entropy changes were obtained.

	ΔS(joules·equiv^{-1}·deg^{-1})
½ Cd = ½ Cd^{++} + e^-	−49.1
Ag + Cl^- = AgCl + e^-	−31.2

The enthalpy change was calculated using Eq. [8]. For the reaction ½ Cd + AgCl = ½ $CdCl_2$ (1M) + Ag, we find ΔH = −17.68 kcal equiv^{-1}. For the same reaction at 25°C, using the above half-cell entropy changes, $T\Delta S$ = −1.28 kcal equiv^{-1}, and ΔF = ΔH − $T\Delta S$ = −17.68 + 1.28 = −16.40 kcal equiv^{-1}. The observed reversible potential was 0.7094v, corresponding to a ΔF of −16.36 kcal equiv^{-1}.

Table II. Half-cell entropy changes from electrochemical calorimetry

System No.	Electrode	Solution	Electrolysis current,* amp	Cathodic ΔS (joules equiv^{-1} deg^{-1}) Left side	Right side
1	Cu	0.75*M* $CuSO_4$, 1.0*M* H_2SO_4	0.4	+67.7	+65.0
		0.75*M* $CuSO_4$, 1.0*M* H_2SO_4	1.0	+75.3	+71.5
		0.75*M* $CuSO_4$, 1.0*M* H_2SO_4	1.0	+68.3	+67.0
2	Ag	1*M* $KAg(CN)_2$, 0.33*M* KCN	0.3	+12.3	+19.0
		1*M* $KAg(CN)_2$, 0.33*M* KCN	0.3	+19.3	+26.0
3	Ag	1*M* $KAg(CN)_2$, 1.0*M* KCN	0.5	+44.6	+41.6
4	Ag	1*M* $AgClO_4$, 0.05*M* $HClO_4$	0.5	−24.8	−25.2
		1*M* $AgClO_4$, 0.05*M* $HClO_4$	0.5	−30.1	−27.7
5	Ag	1*M* $AgClO_4$, 1.0*M* $HClO_4$	0.2	−42.3	−38.1
		1*M* $AgClO_4$, 1.0*M* $HClO_4$	1.0	−39.2	−40.7
		1*M* $AgClO_4$, 1.0*M* $HClO_4$	1.0	−34.5	−33.0
		1*M* $AgClO_4$, 1.0*M* $HClO_4$	3.0	−44.2	−41.7
6	Ag	1*M* $AgClO_4$, 4.0*M* $HClO_4$	0.2	−30.7	−30.5
		1*M* $AgClO_4$, 4.0*M* $HClO_4$	0.2	−34.5	−34.6
		1*M* $AgClO_4$, 4.0*M* $HClO_4$	0.5	−30.8	−31.5
		1*M* $AgClO_4$, 4.0*M* $HClO_4$	0.5	−32.7	−33.0
		1*M* $AgClO_4$, 4.0*M* $HClO_4$	0.5	−30.2	−32.2
		1*M* $AgClO_4$, 4.0*M* $HClO_4$	0.5	−33.1	−33.6
7	Ag, AgCl	1.15*N* (a = 1.0) HCl	0.3	−2.4	−4.8
		1.15*N* (a = 1.0) HCl	0.3	−4.4	−3.2
8	Ag, AgCl	1.21*N* (a = 1.0) LiCl	0.3	+32.8	+34.2
		1.21*N* (a = 1.0) LiCl	0.3	+24.4	+23.0

* The electrode disks have an area of 0.87 dm^2 (diameter = 10.5 cm) and thus, the currents indicated roughly equal the current density in amp dm^{-2}.

There are no data in the literature that can be compared directly with the above results. Data on the heat of formation of $CdCl_2$ in more dilute solutions (3) can be extrapolated to 1*M*, however, without introducing a significant error. Using −48.10 kcal equiv^{-1} for half of this constant and −30.36 kcal/eq as the heat of formation of AgCl(c) (3) gives −17.74 kcal equiv^{-1} for heat of the above reaction. This agrees with our value (−17.68 kcal equiv^{-1}) within the expected experimental error.

In order to compare our value of ΔF with the literature, it was necessary to calculate half the free energy of formation of $CdCl_2$ (1*M*) from that of the hypothetical ideal solution at unit activity. Using a value of −40.64 kcal equiv^{-1} (3) and a mean ionic activity coefficient of 0.0664 (4) gives half the free energy of formation of $CdCl_2$ (1*M*) as −42.6 kcal equiv^{-1}. With this value, and −26.2 kcal equiv^{-1} as the free energy of formation of AgCl(c) (3), the free energy change of the reaction was calculated to be −16.4 kcal equiv^{-1}. A ΔF of −16.4 kcal equiv^{-1} corresponds to a cell voltage of 0.711v which is in satisfactory agreement with the observed cell voltage, 0.7094v.

The literature value for the entropy of $CdCl_2$ (1 mole/liter) was calculated from the standard state value, 11.6 e.u. (3), by means of the relation $S = S° - R \ln a - RT\, d \ln a/dT$. The term $-R \ln a$ was found to equal 13.4 e.u., again using 0.0664 as the activity coefficient. The term $-RT\, d \ln a/dT$ was evaluated from the relation $H = H° - RT^2\, d \ln a/dT$. Both H and $H°$ were obtained from ref. (3), the former by extrapolation. Thus $-RT^2\, d \ln a/dT$ = 1.2 kcal mole^{-1} and $-RT\, d \ln a/dT$ = 4.02 e.u. Then S = 11.6 + 13.4 + 4.0 = 29.0 e.u. or 14.5 e.u. on an equivalent basis. The entropy change of the reaction was then found to be −4.45 cal equiv^{-1} deg^{-1} by using the following additional entropy values [3]: ½Cd = 6.15 cal equiv^{-1} deg^{-1}, AgCl = 23.0 cal equiv^{-1} deg^{-1}, and Ag = 10.2 cal equiv^{-1} deg^{-1}. The difference between this calculated literature value for entropy change of the reaction, −4.45 cal equiv^{-1} deg^{-1}, and the value given by our measurements, −4.3 cal equiv^{-1} deg^{-1}, is well within the estimated uncertainty of 1 cal equiv^{-1} deg^{-1}.

Discussion of Errors

In general the total spread of the ΔS values obtained for a given half-cell reaction does not exceed 8 joules equiv^{-1} deg^{-1} or 2 cal equiv^{-1} deg^{-1}. Those obtained toward the end of the program reflect the various improvements made in the apparatus and are somewhat better. It is probable that additional improvements in the apparatus, along the lines suggested in the Appendix, would increase precision by as much as an order of magnitude.

Such improvements, however, would not reduce errors caused by nonstoichiometry of the electrode processes. This type of measurement is particularly sensitive to side reactions involving chemical attack of the electrodes in the absence of an electric current. The heats (ΔH) of such side reactions are usually large compared to the reversible ($T\Delta S$) heats, and the consequent errors in the latter are therefore correspondingly great.

Three of the half-cells involved in these studies were nonstoichiometric because of this type of side reaction. These were copper in copper sulfate, silver in silver cyanide and cadmium in cadmium chloride. Current efficiency studies showed that

this source of error is eliminated, in all three cases, by excluding oxygen. The calorimeter was modified to permit the use of a helium atmosphere only after the studies of the first two systems had been completed.

It was noted while making current efficiency studies on the cell Cd, $CdCl_2$ (1*M*), AgCl, Ag that the solubility of AgCl in 1*M* $CdCl_2$ is great enough to cause the deposition of silver metal on the cadmium electrode by displacement. It was therefore necessary to assemble the calorimeter with an uncoated silver electrode and to obtain the data before the AgCl formed by electrolysis had time to diffuse to the cadmium electrode.

Since the results obtained are internally consistent and in good agreement with the literature, it is apparent that the heat effect due to the dissolution of the AgCl is not sufficient to affect the results materially.

The precision of these measurements is influenced by the electrode current density. For example, side reactions such as those mentioned above will tend to be masked at high current densities. Even in the case of a stoichiometric cell reaction, however, there will be an optimum current density at which data should be taken to obtain minimum error in the calculated entropy values. An excessively high current density increases the ratio of irreversible to reversible heat: an excessively low current density increases the percentage error in the measurement of the temperature rise and exaggerates other errors such as those due to imperfect adiabatic control. Numerous factors such as the nature of the reaction, the roughness of the electrode surfaces, and the geometry of the cell, will bear on the true optimum, but in the work reported here the best precision was obtained at 0.3 to 0.5 amp/dm^2. Errors due to weaknesses in the design of the apparatus are discussed in the Appendix.

Discussion

Theoretical aspects of Lange's work.—The most significant findings by Lange (2) grew out of his study of the half-cells Ag, AgCl, HCl, and Ag, AgCl, LiCl. At a given temperature and concentration, he found that the entropy changes of these two half-cells differ by about 8 cal $equiv^{-1}$ deg^{-1}. The ΔS values given for systems 7 and 8 of Table II confirm this 8 e.u. difference. If it is assumed that the activities of the chloride ion in these solutions equal the activities of the respective solutes, it follows that conventional chemical thermodynamics offers no explanation of his results. Lange therefore concluded that the difference between the entropy changes of the two half-cells was due to "transport entropies" as defined by Eastman (5).

In view of the fact that single ion activities are not thermodynamically defined, Lange's position cannot be defended rigorously. The practical fact remains, however, that single ion activities are widely used, for example in *p*H measurements. Further, common sense rebels against the supposition that there is a one-hundred fold difference between the chloride ion activities in HCl and LiCl solutions, both dilute and at the same concentration. Such a difference would be necessary to explain Lange's results in terms of classical thermodynamics. It is, therefore, logical to conclude that Lange's measurements entail an effect such as that described by Eastman and that such effects can only be treated by the methods of "irreversible" or "steady-state" thermodynamics.

The literature on this subject, as it is related to this paper, has been reviewed in two recent articles by deBethune (6, 7). Adopting his nomenclature and notation, the quantity measured by Lange, and by the experiments described in this paper, is S^*_I, the molal entropy change of a thermocell with the Soret effect hindered. In our experiments the temperature gradient is essentially zero and the driving force is the applied voltage.

The quantity S^*_I is the sum of two effects, S^*_E, the entropy of electrochemical transport, and S^*_M, the entropy of migration transport which, it is generally agreed, are not separately determinable. The subscripts E and M denote, respectively, the portion of the entropy change which is predicted by reversible thermodynamics, *i.e.*, the effect caused by the electrode reaction, and the portion which is a consequence of the irreversible transport of matter in the electrolyte.

An alternative explanation of the anomalous heat effect has been proposed by Brenner (8). He also divides the observed half-cell Peltier heat P_t into two components both of which are reversible. One, P_e, is caused by the electrolytic reaction or change in state. The other, P_c, is associated with the electrode-solution interface and is phenomenologically identical to the heat effect at a metal-metal junction. There is no way to divide the observed P_t into its two components or to measure them individually. However, the ordinary laws of thermocouples applies to the P_c component. One such law is that in a complete circuit at uniform temperatures the summation of the P_c components equals zero. Therefore, these components cancel out in a completed cell and cannot contribute to the voltage of a cell at uniform temperature.

This view of the reversible heat effects of a half-cell measured at constant temperature is expressed in the following relations:

$$P_t = P_e + P_c$$

For a complete cell:

$$P_c = 0$$

$$P_t = T\Delta S$$

For a thermocell, both P_e and P_c are operative, hence,

$$P_t = T\mathbf{F}dE/dT$$

where E is voltage, $\mathbf{F}$ is the faraday, and T the temperature.

This view of the composite nature of the Peltier heat of an electrolytic half-cell differs from the one embodying the concept of an entropy of transport in two ways: (i) it ascribes the location of the P_c contribution to the electrode-solution interface, not to a transport of heat through the body of the solution; (ii) for a cell consisting of two half-cells each with a different electrode in contact with a different elec-

trolyte, and thus including a liquid junction, the summation of P_c must still equal zero. However, the entropy of transport would not necessarily be the same for the two different electrolytes.

The measurements on systems 1 and 5 of Table II were made first and were completed without a knowledge of the anomalous effect discovered by Lange. Those two sets of measurements were therefore designed in the belief that they would afford a direct measure of the quantity S^*_E. Had this been true we would have attained our original goal, a determination of the "absolute" entropy of an ion. Systems 2, 3, 4, 6, and 7 were studied to determine the effect of complexing and of variations of the transport numbers involved. The results from systems 7 and 8 are in good agreement with values obtained by extrapolation of Lange's data and therefore serve to confirm his finding.

As an additional confirmation of Lange's results, we measured the voltage of the isothermal cell Ag, AgCl, HCl ($a = 1$)/LiCl ($a = 1$) AgCl, Ag. The difference between the entropy effects of the two half-cells is about 8 cal equiv^{-1} deg^{-1} (Table II, systems 7 and 8). If it is assumed that the heat of formation of the chloride ion is the same in both solutions and the entropy of migration (S^*_M) is ignored, this 8 ev would correspond to a potential of 0.1v across this cell. A variety of techniques were used to form the liquid junction between these two half-cells, including the use of selectively permeable membranes, but a cell potential in excess of approximately 35 mv was never detected. This experiment definitely indicates that the reversible operation of a half-cell entails a heat effect which is not predicted by conventional chemical thermodynamics and which does not contribute to the cell emf under static isothermal conditions. This can be explained either in terms of a transport entropy (S^*_M) or in terms of contact Peltier heat P_c.

Thermocell results.—Another finding of this research bears on the validity of presently accepted theories of irreversible phenomena in electrolytic cells. This finding was a consequence of a comparison of the calorimetric ΔS values in Table II with ΔS values calculated from the potentials of the corresponding thermocells (Soret effect hindered). Accepted theory holds that the same value of ΔS should be obtained from both types of measurement.

The thermocells were set up as in the configuration indicated below, using system 8 of Table II as an example.

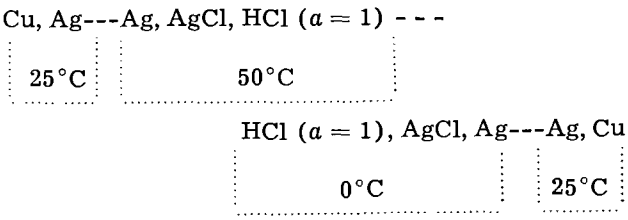

Temperatures were determined with calibrated mercury-in-glass thermometers and potentials with a precision potentiometer.

The dE/dT values obtained were checked by varying the indicated temperatures and by reversing the electrodes. The reproducibility of the temperature coefficients was found to be about ±0.01 mv/deg corresponding to a ΔS of 1 joule deg^{-1} equiv^{-1} (mv deg^{-1} x 96.5 amp sec milliequivalents^{-1} = joules equiv^{-1} deg^{-1}). The results are given as averages in Table III. These are compared with the average calorimetric values taken from the data in Table II. A positive sign for a thermocell ΔS value indicates that the hot electrode has the positive polarity.

It can be seen from Table III that the agreement predicted by theory was obtained for all systems studied except those which involve a silver electrode in an acid silver perchlorate solution. The latter three systems produced a consistent difference of about 9 joules equiv^{-1} deg^{-1}. No explanation is offered for these anomalous results.

The results obtained from the study of these three perchlorate systems are also interesting in that the solution of intermediate acidity gave a maximum ΔS. This was unexpected but can be attributed to variation in the activity of the silver ion due to complex formation. Transference measurements that were made on these solutions pointed strongly to the existence of complexing since the total equivalents of silver plus hydrogen transported, exceeded the faradays of current passed. This could be caused by an ion such as $[HAgClO_4]^+$.

Another experiment, which was planned but not carried out, entailed the use of permselective membranes in place of the filter paper. Such an experiment would be complicated by heat effects, both reversible and irreversible, caused by the membrane, but the results might throw light on transport processes.

Acknowledgment

The financial support for this project came from the U. S. Atomic Energy Commission. The author offers grateful acknowledgment. The author is greatly indebted to Dr. Abner Brenner of the Na-

Table III. Comparison of thermocell and calorimetric half-cell entropies

	Half-cell	Cathodic ΔS (joules equiv^{-1} deg^{-1}) Thermocell	Calorimetric	Difference
1)	Ag, $AgClO_4(1.0N)$, $HClO_4(0.05N)$	—18.8	—26.9	—8.1
2)	Ag, $AgClO_4(1.0N)$, $HClO_4(1.0N)$	—29.4	—39.2	—9.8
3)	Ag, $AgClO_4(1.0N)$, $HClO_4(4.0N)$	—23.4	—32.3	—8.9
4)	Ag, AgCl, HCl(1.15N, $a = 1.0$)	—2.7	—3.7	—1.0
5)	Ag, AgCl, LiCl(1.21N, $a = 1.0$)	26.6	28.6	2.0
6)	Cd, $CdCl_2(1M)$	49.8	49.1	—0.7
7)	Ag, AgCl, $CdCl_2(0.91M)$	33.6	31.2	—2.4

tional Bureau of Standards who conceived this project and gave constant help and encouragement. Sincere thanks are also due to Drs. Ray M. Hurd and Andre J. deBethune for valuable discussions.

Manuscript received Jan. 10, 1962; revised manuscript received Sept. 15, 1962. This paper was prepared for delivery before the Indianapolis Meeting, April 30-May 3, 1961.

Any discussion of this paper will appear in a Discussion Section to be published in the December 1963 JOURNAL.

REFERENCES

1. J. M. Sherfey and A. Brenner, *This Journal*, **105**, 665 (1958).
2. E. Lange and Th. Hesse, *Z. Elektrochem.*, **39**, 374 (1933).
3. Selected Values of Chemical Thermodynamic Properties. Circular of the National Bureau of Standards No. 500, U.S. Government Printing Office, Washington, D. C.
4. H. S. Harned and B. B. Owen, "The Physical Chemistry of Electrolytic Solutions," 3rd ed., Reinhold Publishing Corp., New York, N. Y. (1958).
5. E. D. Eastman, *J. Am. Chem. Soc.*, **50**, 283 (1928).
6. A. J. deBethune, T. S. Licht, and N. Swendeman, *This Journal*, **106**, 616 (1959).
7. A. J. deBethune, *ibid.*, **107**, 829 (1960).
8. A. Brenner, Private communication (1962).
9. R. E. Nelson, T. J. Kildoff, and A. A. Benderly, *Ind. Eng. Chem.*, **50**, 329 (1958).

APPENDIX

The calorimeter.—Figure 1 is a diagrammatic representation of the calorimeter. The entire drawing, and particularly the central partition and electrode support assembly, is shown proportionately too wide for the sake of clarity. The actual interior dimensions of the container are 12 cm wide by 20 cm high (nominal capacity = 2 liters).

The electrolyte shown in the top of the partition is contained by a vertical hole (about 1 cm x 1 cm). The stirrer shafts, 2, are enclosed in sleeves, 1, to stiffen them and to permit disassembly of the stirrer assembly after removal of the drive pins, 4. The support rings, 36, surround the circular hole in the partition and are attached to the partition by stainless steel machine screws. Cemented into each support ring, 36, are four studs which pass through corresponding holes in each electrode. The hole through the partition is 7.5 cm in diameter.

A Dewar flask is not ordinarily used in precision calorimetry because of its excessive thermal lag and the consequent errors in the heat-leak calculations. In the work reported here, this objection to the Dewar flask is invalid. This is due primarily to the adiabatic nature of the measurements. It is also important that the steady-state conditions at the beginning and end of a run are essentially the same. This leads to a cancellation of lag effects.

The Dewar flask is preferable to an all-metal calorimeter in that its rate of heat leak is about one-fifth as great and, because it is made of glass, it does not have to be protected from chemical and electrochemical attack.

Coolers.—The calorimeter is equipped with two "coolers," one on each side, which are not shown. These consist of glass thimbles through which cold water can be passed in order to cool the calorimeter between experiments. With this arrangement, the measurements can all be made at approximately 25°C.

Oil bath.—The electrode leads must be fairly heavy, about ⅛ in., in order to prevent errors due to joule heating. Such heavy leads do not come to bath temperature if passed through a chimney. It was found, instead, that the temperature of the calorimeter is influenced by the temperature of the room. These considerations led to the adoption of an oil bath as an adiabatic environment. The bare leads pass through the oil and come to thermal equilibrium with it before passing into the calorimeter.

Reference half-cell and probe.—It is important that the tip of the capillary be at a point which effectively divides one-half of the calorimeter from the other in order that the irreversible electrolytic heat be properly proportioned between the two sides. The arrangement shown, with a glass capillary cemented into the proper position, insures such centering.

The probe which passes down through the central chimney and into the electrolyte in the upper part of the partition can be either a wire electrode or a glass capillary filled with a solution containing agar. The latter must connect with a suitable half-cell outside the calorimeter. The former is the more convenient arrangement but requires that the wire passing through the chimney be small to avoid heat effects caused by variations in the temperature of the room.

Heaters.—The first heaters used were based on a widely used design consisting of a manganin coil in a glass thimble. These were found to be inadequate in that their excessive lag rendered impossible the maintenance of adequate temperature equality on the two sides.

The final design utilized a small 12v, 50w light bulb, weighing about 2.5g. Plastic insulated lead wires were first soldered to the base, after which the exposed metal parts were encapsulated in epoxy resin. The glass bulb was then etched and given two coats of flat black paint, followed by two coats of varnish. These heaters were very satisfactory.

It is probable that even better performance would be obtained from an open coil of manganin wire, supported by a suitable plastic "spider," and encased in "Teflon" spaghetti tubing.

Thermopiles.—The fabrication of satisfactory thermopiles was a particularly troublesome problem. The final design, however, was very satisfactory and because it might be useful to others, it will be described in some detail. The discussion that follows applies to the thermopile used to maintain temperature equality on the two sides (left-right thermopile). The thermopile that was used to detect temperature differences between the oil bath and the right side of the calorimeter (adiabatic thermopile) has the same basic construction.

The finished thermopile takes the form of an inverted "U," with the "cold" junctions at the bottom on one side and the "hot" junctions at the bottom on the other. These junctions are indicated by the solid black portion of item 16 in Fig. 1. The thickness shown in Fig. 1 is that of a single covered junction. There are 24 such junctions in each compartment side by side, extending into and out of the plane of the paper.

The method of construction can be illustrated by means of Fig. 3 which shows a partially constructed four-couple (eight junction) thermopile. Four of the junctions are hidden behind the form. The wires initially are wound as a continuous rectangular spiral on a form such as that indicated, alternating copper (No. 32, S.C.C.) and constantan (No. 32, bare). The former is shown as heavy lines, the latter as light ones. After they have been anchored with pressure-sensitive tape all the wires are cut near the bottom of the form and the insulation is stripped from the copper up to the point where the junctions are to be prepared. Alternate wires are then twisted together and soldered, using soft solder and a flux consisting of pure rosin mixed with ethanol to form a paste. The wires are then cut immediately below the soldered junctions thus formed.

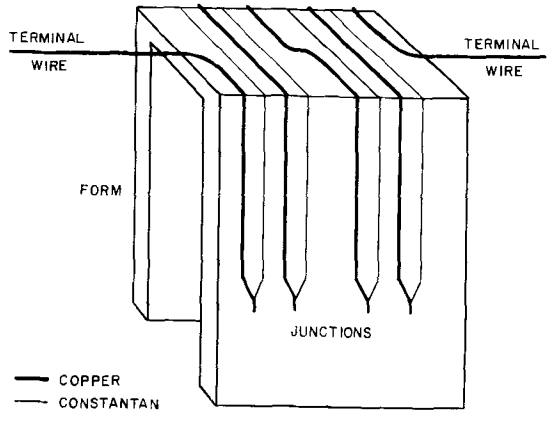

Fig. 3. Thermopile construction

A suitable length of Teflon spaghetti tubing (about 1.8 mm OD x 0.2 mm wall) is treated on its exterior surface only with a solution (9) which conditions it for subsequent bonding to epoxy resin. The distance, along the wires, from the junctions to the point where the thermopile crosses the calorimeter partition is then measured, and the treated spaghetti tubing is cut into lengths equal to twice this distance. These lengths are then bent double to form a sharp "V," and one of two adjacent junctions is slid into each side of the "V" until they nearly touch at the bend. There are thus 12 Teflon loops and 24 junctions on each side of the calorimeter. After attaching suitable leads to the two copper end-wires, the entire assembly, with the exception of the junctions, is encased in epoxy resin.

The thermal emf of the wires used is 41.3 μv deg^{-1}, with a galvanometer sensitivity of 0.125 μv/mm and 24 couples, this gives a thermopile sensitivity of 1.3 x 10^{-4}°C mm^{-1}. The performance of the heaters and thermopile described above is such that numerous runs were made during which the thermopile galvanometer was held within 1 mm of its zero point. With both sets of junctions at the same temperature, there was no detectable deflection of the galvanometer.

The sensitivity of the adiabatic thermopile-galvanometer system is about 1.5 x 10^{-3} °C/mm, which is adequate. The galvanometers used in conjunction with these thermopiles must both be connected to suitable shunts. These serve to protect the galvanometers when the system is out of balance.

Stirrers.—The stirrer shafts enter the calorimeter through a device based on the principle of a "mercury seal stirrer." The upper part of each shaft is thus provided with an "inverted cup seal, copper" (Fig. 1). The open end of each cup extends a few centimeters below the surface of the oil and thus effects a seal against the egress or ingress of gas. These cups have a heavy cross section (about 1 cm) to avoid effects due to the temperature of the room. Both stirrers are driven by the same synchronous motor through a gear train.

The inefficiency of the stirrers is one of the most serious weaknesses in the design of the calorimeter. Because of space limitations, the propellers do not operate inside of tubes, and, as a consequence, adequate temperature uniformity is attainable only with a relatively large heat of stirring.

A closely related and more serious source of error is a consequence of poor placement of the various calorimeter components relative to one another. Because the measurements are made under steady-state conditions, it is not essential that the various temperature sensing elements be surrounded by solution, the temperature of which is representative of the entire compartment. If it is not representative, however, this situation must be the same at the beginning and end of the experiment.

In the calorimeter described here, for example, the placement of the left heater relative to the resistance thermometer is such that the temperature of the latter is influenced by the rate of heat evolution of the former. Thus, if this rate is greater at the end of the experiment than it was at the beginning, the apparent temperature rise of the compartment is too large. An error of only 0.001°C in this measurement would cause a significant error, 0.7 cal, in the reversible heat.

This source of error was not detected until late in the program and, because a major modification of the calorimeter would have been necessary, it was never completely eliminated.

Filter paper membranes.—Filter paper serves adequately as a membrane material except for one fault; it tends to bulge or warp when wet. This leads to two types of error. First, the irreversible electrolytic heat, as indicated by the probe-electrode potentials, is improperly proportioned between the two sides. The second source of error is caused by an increase in the heat capacity of one side and a corresponding decrease in the heat capacity of the other. This source of error is of course eliminated if the degree of bulging is the same for all experiments in a given determination; stirrer, calibration, and electrolysis. It was minimized in the latter part of this research by "sandwiching" each filter paper disk between two disks of glass cloth, each of which was held flat by cementing it to a plastic ring.

Thermometry and timing.—All temperature measurements are made by means of a platinum resistance thermometer connected to a Mueller bridge and a sensitive galvanometer. Each temperature measurement is timed by means of a stop watch which has been described (1). The watch was calibrated periodically using the standard radio time signal. Time-temperature measurements are made by setting the Mueller bridge to a reading which corresponds to a temperature higher than that of the calorimeter. The bridge key is then locked down, and the moment when the galvanometer light passes through its zero is noted with the stop watch.

Electrical circuit.—The various parts of the electrical circuit are shown in Fig. 2. Heavy lines indicate wires that carry a significant current; light lines are those used only in connection with voltage measurements. The connections shown are those which would be made for an electrolysis experiment requiring the heater on the left side of the calorimeter. Reversing the electrolysis current would require use of the right-hand heater instead of the left. During a heater experiment, the current from the electrolysis circuit would be directed through one of the heaters and that from the heater circuit through the other. During a stirrer experiment, only the heater circuit is used, and it is connected to the heater on that side which tends to be cooler.

Electrolysis circuit.—Current in the electrolysis circuit passes through the following elements, all in series; the electrolytic cell in the calorimeter, an "off-on" switch, one or more lead cells, an ammeter, a bank of resistors (R_1), and a 1-ohm standard resistor. The current in this circuit is measured indirectly by balancing the voltage across the 1-ohm standard with a constant, known voltage from a potentiometer. Balance is indicated by a nul position of the galvanometer and is maintained by means of the rheostats in (R_1). The parallel resistors in series with the galvanometer protect the latter when the system is badly unbalanced.

The voltages between anode and cathode, anode and probe, and cathode and probe, are measured by means of the circuit in the upper right corner of Fig. 2. Any one of these three can be measured, depending on the position of the selector switch. The voltage divider is identical to that shown as a part of the heater circuit. This divider is ordinarily used only during a heater experiment when this circuit is used to measure the voltage across one of the heaters.

Heater circuit.—Like the electrolysis circuit, the heater circuit is divided into two parts; one to control and measure the current, and the other to measure the voltage. The box "R_2" represents a bank of resistors, like that shown as a part of the electrolysis circuit.

The purpose of the two potentiometer-recorder combinations (see Fig. 2) is to measure both heater current and heater voltage as a function of time. The former is obtained indirectly as the voltage across the 1-ohm standard. This permits the calculation of the total energy dissipated by the heater during the time of the experiment. In use, each potentiometer dial is set at a reading that is 0-10 mv less than the voltage being measured, and this unbalance is imposed on the associated recorder through the galvanometer terminals of the potentiometer. The desired voltage at a given time is thus the sum of the readings of the potentiometer-recorder combination. When the heater current is changed in order to maintain temperature equality on the two sides of the calorimeter, these changes are followed by the recorder. If the recorder goes off scale, the potentiometer setting is changed in such a way as to bring it back. The calculations are simplified if the heater voltage is changed by whole numbers of millivolts and held constant between changes. The various potentiometer settings are noted on the recorder chart and the time axis of the chart must be keyed to the time-temperature readings.

The total energy supplied to a heater during an experiment can be calculated from the data on the recorder charts by adding the current-time-voltage products corresponding to each setting of the heater wattage.

Analog Solutions for the Growth of Activation Overpotential

John M. Matsen

Central Basic Research Laboratory, Esso Research and Engineering Company, Linden, New Jersey

ABSTRACT

The equation for build-up of activation overpotential

$$C\frac{d\eta}{dt} = i - i_o \exp(\alpha Z\mathbf{F}\eta/RT) + i_o \exp(-[1-\alpha]Z\mathbf{F}\eta/RT)$$

has been solved on an analog computer to obtain η as a function of t, for cases where C, i_o, and α remain constant during the charging process. The analog solution involves no approximations, in contrast to the several analytic solutions which have been developed, and hence gives a true picture of the charging curves resulting from the theoretical model. The solutions indicate that any attempt to calculate deposition parameters from a single charging curve would be subject to large errors. Curves of $d\eta/dt$ *vs.* η seem to promise greater accuracy in analyzing experimental data and are certainly simpler from a mathematical standpoint.

The relationship between steady-state current density and activation overpotential for electrodeposition processes is usually written as:

$$i = i_o \exp(\alpha Z\mathbf{F}\eta\infty/RT) - i_o \exp(-[1-\alpha]Z\mathbf{F}\eta\infty/RT) \quad [1]$$

where i is the net current density, amp/cm^2, i_o the exchange current density, amp/cm^2, α the transfer coefficient ($0 \leq \alpha \leq 1$), Z the electrons transferred in rate-determining step, $\eta\infty$ the steady-state activation overpotential, volts. The sign convention used here is that η is positive for deposition of cations. R is the gas constant, 8.314 ergs/°K mole, T the temperature, °K, and $\mathbf{F}$ the Faraday, 96,500 coulombs/equivalent. This merely says that the net reaction rate, i, is the sum of the forward and reverse reaction rates, which are derived according to the theory of absolute reaction rates. In the unsteady-state case, the overpotential is changing, and some of the net current is consumed in charging the double layer. An equation for this case may be written (1) as

$$i = i_o \exp(\alpha Z\mathbf{F}\eta/RT) - i_o \exp(-[1-\alpha]Z\mathbf{F}\eta/RT) + C\frac{d\eta}{dt} \quad [2]$$

where C is the differential capacity of double layer, Farads/cm^2, t the time, seconds, and η the unsteady state overpotential, volts. Thus for a specified net current i, usually held constant, a relationship between η and $d\eta/dt$ is given in terms of the electrodeposition parameters i_o, α, and C. Even in the simple case where these parameters are constant, the differential Eq. [2] is nonlinear and has no exact analytic solution. Thus, the desired relationship of η as an explicit function of t has heretofore been only approximated.

In the present case, as in most of science, solutions of theoretical relationships are of value for two reasons. First, they permit comparison between experiment and theory. Second, if theory is borne out, they usually permit necessary information to be derived with much less experimental observation. The general validity of Eq. [2] is accepted for many cases, and it would be desirable to use the equation or its solution in determining i_o and α from a single charging curve. This not only would save a good deal of labor; it would also permit more meaningful results in cases where reproducibility between successive runs is low, *e.g.*, in the case of plating on soiled electrodes.

Approximate solutions to Eq. [2] have been proposed most recently by Linford and Karasyk (2), with others having been developed by Bockris and Potter (1), Agar (3), and Roiter, Juza, and Polujan (4). These are of some mathematical interest and give, in certain regions, fair agreement with experimental charging curves. These solutions do involve approximations, however, which limit their accuracy and applicability in the determination of plating parameters from a single charging curve. Equation [2] can be solved exactly on an analog computer, however, and this approach was taken in the present work. It was hoped that this would permit a better picture of the effects of the parameters on the shapes of charging curves, and it might indicate limitations or new approaches to estimating these parameters from experimental curves.

Procedure

Equation [2] was programmed on an Electronic Associates Model 231 R computer. Results were automatically recorded on 10 x 15 in. plotting tables as η *vs.* t and also $d\eta/dt$ *vs.* t and $d\eta/dt$ *vs.* η.

The two most significant features of an experimental charging curve are its final value, $\eta\infty$, and its initial slope, $(d\eta/dt)_{t=0} = i/C$. Since i is known and constant, C may be obtained from the initial slope. Knowing $\eta\infty$, Eq. [1] gives a relationship be-

Table I. Values of deposition parameters used in solutions

i_o for selected combinations of η and α
i = 0.1 amp all solutions; C = 50 × 10^{-6} Farads all solutions; Z = 1; F/RT = 38.93 volt^{-1} all solutions

$\eta\infty$, volts	0.2	0.1	0.05	0.02
α 0.0	0.10004 amp	0.1020 amp	0.1167 amp	0.1849 amp
0.1	0.04593	0.06916	0.09604	0.1710
0.2	0.02108	0.04686	0.07905	0.1582
0.3	0.009679	0.03175	0.0651	0.1464
0.4	0.004443	0.02251	0.05356	0.1354
0.5	0.002039	0.01458	0.04409	0.1252
0.6	0.0009364	0.009876	0.03629	0.1159
0.7	0.0004299	0.006692	0.02987	0.1072
0.8	0.0001973	0.004534	0.02459	0.09918
0.9	0.00009059	0.003072	0.02024	0.09174
1.0	0.00004159	0.002081	0.01666	0.08486

tween α and i_o. The approach therefore was to use constant values of i, C, and $\eta\infty$ in a series of solutions and find the effect of changing α on the shape of the charging curve. The values of the various parameters used in the solutions are shown in Table I.

Results

Examples of charging curves, η *vs.* t, are shown in Fig. 1 and 2. In each figure the parameter is α, with i_o being adjusted to give the desired value of $\eta\infty$.

Perhaps the most significant characteristic of these solutions is the small effect on shape of charging curves due to variation of α, especially for $0.4 \leq \alpha \leq 1$. This means that it will be difficult to determine α accurately from a single charging curve. For instance assume a value of α of about 0.5 and examine the curves at the point $\eta = 0.9\ \eta\infty$ where the greatest differentiation between curves occurs. Variation of α by ±20% would have the effects listed in Table II.

Table II. Effect of variation of α at $\eta = 0.9\ \eta\infty$

$\eta\infty$	α	η	i_o
0.2	±20%	±2.5%	±86%
0.1	±20%	±2.5%	±43%
0.05	±20%	±2%	±20%
0.02	±20%	±1%	±8%

In other words, in order to determine α with an error of ±20%, η must be obtained from a charging curve with the accuracy listed, and the error in i_o will be as noted. This assumes that C, $\eta\infty$, and t are known exactly and that the only error would be in obtaining η. Even then, an error of ±1% in η (probably about the limit of experimental accuracy) would still result in intolerably large errors in α and i_o. It should be noted that, although α has a greater effect on charging curve shape for high $\eta\infty$, it also has a greater effect on i_o, so that as α becomes easier to determine accurately, i_o becomes more difficult.

The conclusion to be reached from this is that it will be exceedingly difficult to determine deposition parameters with satisfactory accuracy from a single charging curve, even if these parameters stay constant throughout the charging process. Furthermore there is reason to believe that these parameters do not remain constant in many cases, *e.g.*, plating on soiled electrodes, and then the task would become hopeless. The results also indicate that even quite accurate analytical solutions of Eq. [2] will have little use in experimental work, although they may be of mathematical interest.

Analysis of Charging Curve Derivatives

The situation may be slightly more promising if one examines curves of $d\eta/dt$ *vs.* t, Fig. 3 and 4.

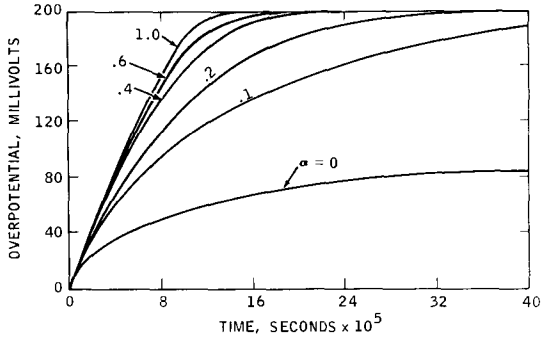

Fig. 1. Charging curve; $\eta\infty$ = 200 mv

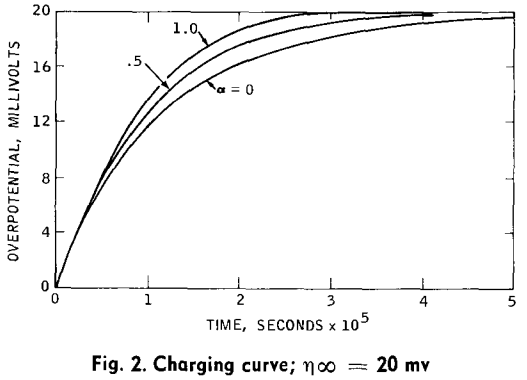

Fig. 2. Charging curve; $\eta\infty$ = 20 mv

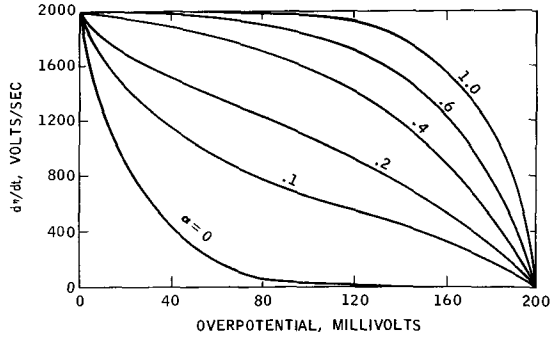

Fig. 3. $d\eta/dt$ *vs.* η; $\eta\infty$ = 200 mv

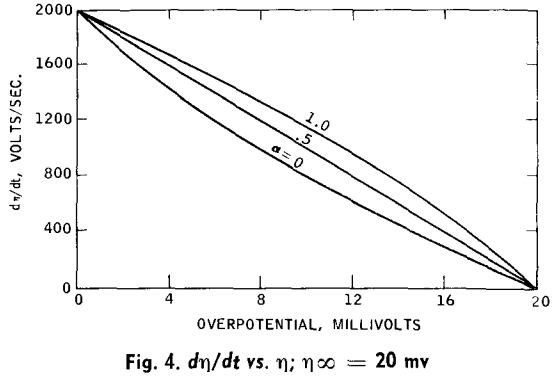

Fig. 4. $d\eta/dt$ *vs.* η; $\eta\infty$ = 20 mv

These may be obtained by numerical substitution into Eq. [2], but in the present case they were calculated on the analog computer.

These curves are much more sensitive to changes in α. For instance, in the case $\alpha = 0.5$ and $\eta\infty = 0.2$, a variation of α by $\pm$ 20% will cause a maximum variation in $d\eta/dt$ of $\pm$10% as opposed to a variation of only $\pm$2.5% in η.

In this case C may be determined from the initial value of the curve. From the initial slope of this curve one may determine i_o independently of α

$$\left[\frac{d(d\eta/dt)}{d\eta}\right]_{t=0} = -\frac{i_o ZF}{CRT} \qquad [3]$$

If one studies possible variation of parameters during charging, the data will be much easier to handle in the form $d\eta/dt$ *vs.* η than in the form η *vs.* t, because the value of $d\eta/dt$ depends only on the existing values of η, i, i_o, and C, and not on their past behavior.

The trick in this approach lies in obtaining the derivative $d\eta/dt$ experimentally, differentiation being a rather imprecise operation. The most direct approach would be graphical differentiation of an enlarged photograph of the charging curve as recorded on an oscilloscope. With care the graphical method can be fairly accurate. Figure 3 could be reproduced to within 1% by graphical differentiation of Fig. 1.

A second possibility would be to generate $d\eta/dt$ electronically, feeding this to the y input of the scope and feeding η to the x input. A simple differentiator may be assembled from a resistor and capacitor, and more elaborate ones may be built with operational amplifiers. It should be noted that differentiators are inherently troublesome, because they differentiate high-frequency noise as well as the signal. Properly designed filters would reduce this source of error somewhat, although perhaps not enough. It would be a relatively simple experiment, however, and seems worth a try.

Curves of $d\eta/dt$ *vs.* t were also determined, and one is shown in Fig. 5. They seem to have no advantages from the standpoint of either mathematical manipulation or experimental work.

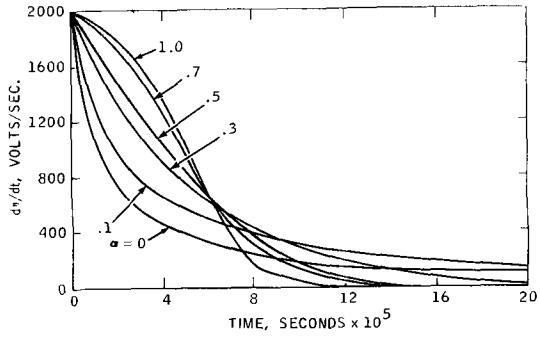

Fig. 5. $d\eta/dt$ *vs.* t; $\eta\infty$ = 100 mv

Conclusion

Accurate charging curves have been obtained by analog solution of the theoretical differential equation. The significant (and previously unemphasized) result of these solutions is that changes in α and i_o have such a small effect on the shape of the charging curve. This indicates that solutions of the differential charging equation, whether analog or analytical, will be of little use in obtaining accurate deposition parameters from a single charging curve. A more promising approach to the determination of these parameters may well be to analyze curves of the derivative $d\eta/dt$ *vs.* η, a method which has yet received little attention.

Manuscript received Feb. 26, 1962; revised manuscript received Sept. 28, 1962. This paper was prepared for delivery before the Pittsburgh Meeting, April 14-18, 1963.

Any discussion of this paper will appear in a Discussion Section to be published in the December 1963 JOURNAL.

REFERENCES

1. J. O'M. Bockris and E. C. Potter, *This Journal*, **99**, 169 (1952).
2. H. B. Linford and L. Karasyk, American Electroplaters' Society Project 12, Research Report No. XV (1961).
3. J. N. Agar, *Ann. Repts. Prog. Chem.*, **44**, 5 (1947).
4. W. A. Roiter, W. A. Juza, and E. S. Polujan, *Acta Physicochim. U.R.S.S.*, **10**, 389, 845 (1939).

Polarographic Reduction of the Phenyl-Substituted Ethenes

I. Relation of Postulated Mechanisms to Theoretical Behavior Patterns

Philomena G. Grodzka[1] and Philip J. Elving

Department of Chemistry, The University of Michigan, Ann Arbor, Michigan

ABSTRACT

The theoretically expected variations of the criteria of reversibility for electrochemical reduction, which have been proposed for inorganic systems on the basis of direct current polarography, have been developed for the various possible mechanisms, which might be expected for the reduction of the phenyl-substituted ethenes at the dropping mercury electrode. These criteria of reversibility include the beta function (ratio of mean current to instantaneous current), the dependence of the current on the drop-time (mercury column height), the slope of the plot of the familiar log current function, *i.e.*, log $[(i_d - i)/i]$ *vs.* potential, and the variation of half-wave potential in relation to proton availability. The situation for irreversible waves is considered on the basis of the equations derived for both the planar electrode and the expanding spherical electrode. Since the mechanisms considered are generalized approaches which can be applied to the reduction of various types of functionalities, both inorganic and organic, the equations developed and conclusions reached are of general utility.

In continuation of an investigation of the electrochemical reduction mechanisms of conjugated double bond systems, which has included studies of alifatic unsaturated acids and esters (1-4), phenyl ketones (5, 6), β-diketones (7), and aromatic N-nitrosohydroxylamines (8), the reduction of the phenyl-substituted ethene series, members of which have been frequently studied polarographically, was systematically investigated in respect to mechanism.

In order to facilitate decision on the basis of experimental data as to the reaction mechanisms operative for the reduction of the ethenes at the dropping mercury electrode (DME) in nonaqueous and aqueous-organic media, the theoretically expected variations of the criteria of reversibility for electrochemical reduction, previously proposed on the basis of direct current polarography for simple inorganic systems, have been developed for various possible reduction mechanisms. The forms thus assumed by the various postulated criteria are summarized in Table I, which will afford a convenient reference for the subsequent discussion.

Since the mechanisms considered are generalized approaches which can be applied to the reduction of various types of functionalities, both inorganic and organic, the equations developed and conclusions reached are of general utility. Consequently, the present paper and the succeeding experimental study (9), in which the criteria discussed are applied to the behavior of the five phenyl-substituted ethenes, represent an attempt to determine the value of contemporary direct current polarographic theory when applied to the problem of the elucidation of mechanism for the polarographic reduction of organic compounds.

Electrode kinetics and thermodynamics.—The observed behavior of the majority of polarographic processes depend primarily on the rate of mass transfer of the electroactive substance and the kinetics of the electrochemical reaction. Polarographic waves are generally classified as reversible or irreversible according to whether the rate of mass transfer or that of electrochemical reaction is current-controlling (currents controlled by the rate of conversion at the electrode interface of the species being supplied by mass transfer to a reducible species constitute a special class).

In recent years, elaboration of the theory of electrode processes has resulted in the development of criteria for the reversibility or irreversibility of a polarographic wave. Experimental verification of these criteria, which are discussed subsequently, has been rather sparse, especially in respect to the behavior of organic compounds.

The defined transition from a reversible to an irreversible process occurs over a relatively narrow range of magnitude of the heterogeneous rate constant, $k_{s,h}$, for the electrochemical reaction: 2×10^{-2} to 3×10^{-5} cm sec^{-1} (10). Therefore, most polarographic waves are readily classifiable by this criterion as either reversible or irreversible. The behavior of reversible waves is characterized mathematically by the Nernst equation. The situation for irreversible waves is complicated by the existence of two sets of equations, one based on the planar electrode (10) and the other on the expanding spherical electrode (11); the latter set is generally admitted as being the more rigorous in the case of the DME. Consequently, in the subsequent discussion recourse will be had to the expanding spherical electrode theory insofar as possible; in cases where application of the latter theory has not yet been developed, reference will be made to the planar electrode theory. Reference will frequently be made to both theories since both have been used in the literature, and it is of value to contrast their different predictions. Application of the equations

[1] Present address: Avco Corporation, Wilmington, Massachusetts.

Table I. Variation of criteria of reversibility, log plot slopes, and $E_{1/2}$ expected on the basis of various possible mechanisms

No.	Mechanism[a]	Conditions[b]
1.	$R \xrightarrow[k]{n_a e} R^-$	k v fast, $D_R = D_{R^-}$ k slow
2.	$R \xrightarrow[k_1]{\alpha_1 n_1 e} R^- \xrightarrow[k_2]{\alpha_2 n_2 e} R^=$	k_1 v fast, k_2 slow k_1 slow, k_2 v fast k_1 slow, k_2 slow
3.	$R \underset{}{\overset{n_1 e}{\rightleftharpoons}} R^- \xrightarrow[k]{\alpha n_2 e} R^=$	
4.	$R \overset{n_1 e}{\rightleftharpoons} R^- \overset{n_2 e}{\rightleftharpoons} R^= \xrightarrow[k_1]{H^+} RH^- \xrightarrow[k_2]{H^+} RH_2$	A—S A—O—B A—O—UB
5.	$R \overset{n_1 e}{\rightleftharpoons} R^- \xrightarrow[k_1]{H^+} RH \xrightarrow[\text{very fast}]{\alpha n_2 e} RH^- \xrightarrow[k_2]{H^+} RH_2$	A—S A—O—B A—O—UB
6.	$(R) + H^+ \underset{k_1}{\rightarrow} (R \ldots H)^+ \xrightarrow[k_2]{\alpha_1 n_1 e} RH \xrightarrow[\text{very fast}]{\alpha_2 n_2 e} RH^- \xrightarrow[k_3]{H^+} RH_2$	k_1 slow, $[H^+]$ large k_1 v fast, $[H^+]$ large
7.	$(R) + HA \underset{k_1}{\rightarrow} RHA \xrightarrow[k_2]{\alpha_1 n_1 e} RHA^- \xrightarrow[k_3]{} RH + A^-$ $RH \xrightarrow[\text{very fast}]{\alpha_2 n_2 e} RH^- \xrightarrow[k_4]{H^+} RH_2$	k_2 slow, other rates fast k_3 slow, other rates fast [HA] large in both cases
8.	$R \overset{n_1 e}{\rightleftharpoons} R^- \xrightarrow[\text{or HA, } k_1]{H_2O} RH + OH^- \text{ or } A^-$ $RH \xrightarrow[\text{very fast}]{\alpha n_2 e} RH^- \xrightarrow[\text{or HA, fast}]{H_2O} RH_2 + OH^- \text{ or } A^-$	A—S $[H_2O]$ large

[a] Parentheses indicate polarization at the electrode surface.
[b] A—S = anhydrous solvent; A—O—B = aqueous organic buffered solution; A—O—UB = aqueous organic unbuffered solution; v = very.

based on the expanding spherical electrode theory (11) to irreversible current-potential curves permits calculation of the heterogeneous rate constant and the transfer coefficient for the electrochemical reaction.

Electrochemical Processes Involving One Electrochemical Reaction: Criteria of Reversibility

The β function.—The β function is defined as the ratio of $(\bar{i}/i)_E$. For reversible processes involving a soluble reduced product, the expanding spherical electrode theory (12) predicts that β should be nearly constant and slightly less than 0.857, *i.e.*, 6/7, throughout the whole wave. On the basis of this theory β can be represented by the equation

$$\beta = (6/7)[\overline{f(X_m)}/f(X_m)] \qquad [1]$$

where $\overline{f(X_m)} = \bar{i}/\bar{i}_d$ and $f(X_m) = i/i_d$. At the toe of an irreversible wave, where the ratio, $\overline{f(X_m)}/f(X_m)$, is approximately 0.75, β values of approximately 0.64 are to be expected; at the head of the wave, $\overline{f(X_m)} = f(X_m)$, and β approaches 0.857.

According to planar electrode theory, β should be 3/5 at the base of an irreversible wave and 6/7 at the head (13); these predictions agree with those of the spherical electrode theory. Although the observed experimental variation of β along the wave in both reversible and irreversible reductions is not in too good quantitative agreement with theory, the qualitative agreement has been considered adequate to have verified the predictions of this theory (13).

Experimental determination of β, measured at the limiting current, for a number of substances showed, however, that no one β value seems to apply to all electroactive substances (14).

Dependence of current on the mercury column height.—A sensitive criterion of reversibility for electrode processes is the dependence of the average or instantaneous current on the flow of mercury. For reversible processes involving a soluble reduced product, the relation of i to h, in terms of i/i_o and h/h_o, at the beginning of the wave is (12)

$$i/i_o = \frac{(h^{1/2}/h_o^{1/2}) + Q\, D_R^{1/2} m_o^{-1/3} (t_m)_o^{1/6}}{1 + Q\, D_R^{1/2} m_o^{-1/3} (t_m)_o^{1/6}} \qquad [2]$$

where

$$Q = (3\pi/7)^{1/2} (4\pi d/3)^{1/3} \qquad [3]$$

At the head of the wave, the relationship becomes

$$i/i_o = \frac{(h^{1/2}/h_o^{1/2}) + Q\, D_O^{1/2} m_o^{-1/3} (t_m)_o^{1/6}}{1 + Q\, D_O^{1/2} m_o^{-1/3} (t_m)_o^{1/6}} \qquad [4]$$

When $D_O = D_R$, Eq. [2] and [4] become identical, and the slopes of plots of (i/i_o) *vs.* $(h^{1/2}/h_o^{1/2})$ would be expected to be nearly constant at 0.87 at all points along the wave. Such plots for trisethylenediaminecobalt (12) (the reduced product is soluble in the solution phase and it was assumed that $D_O = D_R$) do give straight lines, whose slopes of 0.93 do not agree too well with the theoretical slope of 0.87.

(Table I. Con't)

Variation of β from toe to head of wave[c]	Variation of slopes of current ratios from toe to head of wave[c]	Log plot slopes	Variation of $E_{1/2}$ as function of proton availability[d]
con; < 6/7	con; < 1	$n/0.059$	—
3/5 → 6/7	0 ⟶ 1	$\alpha n_a/0.059$	—
3/5 → 6/7	0 ⟶ 1	$(n_1 + \alpha_2 n_2)/0.059$	—
3/5 → 6/7	0 ⟶ 1	$\alpha_1 n_1/0.059$	—
3/5 → 6/7	0 ⟶ 1	$(n_1 + \alpha_2 n_2)/0.059 \longrightarrow \alpha_1 n_1/0.059$	—
con; < 6/7	con; < 1	$(n_1 + \alpha_2 n_2)/0.059$	—
con; < 6/7	con; < 1	$(n_1 + n_2)/0.059$	—
incr < 6/7	incr < 1	$(n_1 + n_2)/0.059$	* pH or [R∞] decr
incr < 6/7	incr < 1	$0.5(n_1 + n_2)/0.059 \longrightarrow (n_1 + n_2)/0.059$	* [H_2O] incr or [R∞] decr
con; < 6/7	con; < 1	$n_1/0.059$	—
incr < 6/7	incr < 1	$n_1/0.059$	* pH or [R∞] decr
incr < 6/7	incr < 1	$0.5n_1/0.059 \longrightarrow n_1/0.059$	* [H_2O] incr or [R∞] decr
3/5 → 6/7	0 ⟶ 1	$\alpha_1 n_1/0.059$	* H^+ availability incr
incr < 6/7	incr < 1	$n_1/0.059$	* H^+ availability incr
3/5 → 6/7	0 ⟶ 1	$\alpha_1 n_1/0.059$	* HA availability incr
incr < 6/7	incr < 1	$n_1/0.059$	* HA availability incr
con; < 6/7	con; < 1	$n_1/0.059$	—
incr < 6/7	incr < 1	$n_1/0.059$	* [H_2O] or [HA] incr

[c] con = constant; incr = increases to; → = varies between the values given at the toe and head of the wave, respectively.
[d] * = $E_{1/2}$ becomes less negative as; decr = decreases; incr = increases.

For irreversible waves, planar electrode theory predicts current-independence of h at the beginning of the wave and direct proportionality to $h^{1/2}$ at the limiting current (13). Thus, plots of (i/i_o) *vs.* $(h^{1/2}/h_o^{1/2})$ would be expected to give a series of lines of ever increasing slope as the limiting current is approached. Although good experimental verification has been obtained in the few cases tested, anomalies have been observed for nitromethane and 2-methyl-2-nitropropane in methanol (15).[2]

Since the planar electrode theory prediction of the β function is in accord with that of the expanding spherical electrode, both theories will be in accord regarding current dependence on the mercury head.

Log plots.—A plot of log $[(i_d - i)/i]$ or log $[(\bar{i}_d - \bar{i})/\bar{i}]$ *vs.* E for a reversible wave has a slope of $n_a/0.059$ at 25°C.[3] However, a log plot slope of $n_a/0.059$ is a necessary but not sufficient condition for a reversible polarographic process.

For irreversible waves, expanding spherical electrode theory predicts a log plot slope of $\alpha n_a/0.059$ (16).

Other criteria.—Other criteria of reversibility such as the dependence of $E_{1/2}$ on drop-time and the variation of the instantaneous current with time have not been sufficiently investigated or are apparently insufficiently sensitive to warrant application in the present study.

Electrochemical Processes Involving Two or More Reactions

Two consecutive slow electrochemical reactions: Equivalent reaction pair.—If the rate of one step in a series of consecutive reactions is controlling, an "equivalent reaction pair" may be written which embodies all of the kinetic properties of the mechanism (17). For example, an equivalent reaction pair for the series of reactions,

$$R^{\infty} \xrightarrow{\text{diffusion to electrode surface}} R \qquad [5]$$

$$R + \alpha_1 n_1 e \xrightarrow{k_1} R^{-} - (1 - \alpha_1 n_1)e \qquad [6]$$

$$R^{-} + \alpha_2 n_2 e \xrightarrow{k_2} R^{=} - (1 - \alpha_2 n_2)e \qquad [7]$$

where the rate of diffusion of R^{∞} to the electrode surface is much larger than k_1 and where k_1 is much less than k_2, is

$$R^{\infty} + \alpha_1 n_1 e \underset{k'}{\overset{k'}{\rightleftharpoons}} R^{=} - (2 - \alpha_1 n_1)e \qquad [8]$$

R^{∞} represents the electroactive species in the bulk of the solution. The rate constants in Eq. [6] and

[2] Greater current dependence on the mercury head was observed along the beginning of the nitroalkane reduction waves than at the plateaus. Such behavior may not necessarily be an anomaly, but might represent a different reduction mechanism than the expected one.

[3] Such plots of logarithmic functions of the current *vs.* potential are generally called "log plots"; the slope of the plot has important implications as subsequently discussed. The term, RT/F, is generally evaluated for 25°C.

[7] refer to the equilibrium state in which $E = 0$, and the activities of products and reactants are unity. The net rate of the reaction represented by Eq. [8] is

$$k_{net} = k'[R^{\circ}]\exp[-\alpha_1 n_1 \mathbf{F}(E - E^{\circ})/RT] - k'[R^{=}]\exp[(2 - \alpha_1 n_1)\mathbf{F}(E - E^{\circ})/RT] \quad [9]$$

At very negative potential, the second term on the right hand side of Eq. [9] becomes very small and can be neglected. A plot of log k_{net} (or of the experimental log $k_{f,h}$) *vs.* E should then be a straight line of slope equal to $-\alpha_1 n_1/0.059$ at 25°C, while a log $[i_d - i)/i]$ *vs.* E plot should have a slope of $\alpha_1 n_1/0.059$.

If k_1 and the rate of diffusion of R° to the electrode surface are very large compared to k_2, the equivalent reaction pair is

$$R^{\circ} + (n_1 + \alpha_2 n_2)e \underset{k''}{\overset{k''}{\rightleftharpoons}} R^{=} - (1 - \alpha_2 n_2)e \quad [10]$$

and

$$k_{net} = k''\,[R^{\circ}]\exp[-(n_1 + \alpha_2 n_2)\mathbf{F}(E - E^{\circ})/RT] \quad [11]$$

The log current or log $k_{f,h}$ plots, therefore, would have slopes equal to $(n_1 + \alpha_2 n_2)/0.059$. The latter is the same as the log plot slope predicted by expanding spherical electrode theory for a mechanism in which a reversible electrochemical reaction precedes an irreversible one (16).

In cases where k_1 and k_2 are of the same order of magnitude, and the rate of diffusion of R° to the electrode surface is very large, the net rate of the reaction represented by Eq. [7] at the toe of the wave would be much smaller than that of the reaction represented by Eq. [6]. Hence, the third reaction would be rate-controlling, and log plot slopes should equal $(n_1 + \alpha_2 n_2)/0.059$.

At the head of the wave, the following equation applies (17),

$$1/k_{net} = 1/(k_{net})_1 + 1/(k_{net})_2 \quad [12]$$

where $(k_{net})_1$ refers to the net rate if only the second reaction were rate-determining and $(k_{net})_2$ if only the third reaction were. The log plot slope at the head of the wave, obtained by substituting Eq. [9] and [11] into Eq. [12] and differentiating the resulting expression, is $\alpha_1 n_1/0.059$.

Because of the disagreement noted between the log plot slope predictions of the planar and expanding spherical electrode theories in the case of a very fast, *i.e.*, reversible, electrochemical reaction preceding an irreversible one (16), the conclusions regarding log plot slopes for two consecutive slow electrochemical reactions arrived at by the equivalent reaction pair theory are to be preferred to those deduced from planar electrode theory (18), even though the equivalent reaction pair equations for currents would not be of the correct form according to expanding spherical electrode theory.

Current-ratio and β plots in cases where two consecutive slow electrochemical reactions are operative would be identical generally with those expected on the basis of only a single slow electrochemical reaction.

Reversible electrochemical reaction followed by irreversible electrochemical reaction.—A log plot slope for a polarographic wave, in which the mechanism

$$R \underset{}{\overset{n_1 e}{\rightleftharpoons}} R^{-} \xrightarrow[k]{\alpha n_2 e} R^{=} \quad [13]$$

is operative, would be equal to $(n_1 + \alpha_2 n_2)/0.059$ (16). Current-ratio and plots may be deduced from the approximate expanding spherical electrode formula (11)

$$\bar{i}/\bar{i}_d = X_m/(1.5 + X_m) \quad [14]$$

and the approximation (16)

$$X_m = (7/12)^{1/2}\, k_{f,h}/\exp\,[n_1(E - E^{\circ})\mathbf{F}/RT] \quad [15]$$

Since X_m is independent of time, the average current $\bar{i}$ depends on time in the same manner as does $\bar{i}_d$. Therefore, current-ratio plots and β values would be expected to remain constant.

Chemical reactions involving hydrogen ions preceded by reversible electrochemical reactions.—The following mechanism has been thoroughly discussed (19) with regard to the types of log plots obtained:

$$R \overset{n_1 e}{\rightleftharpoons} R^{-} \overset{n_2 e}{\rightleftharpoons} R^{=} \xrightarrow[k_1]{H^+} RH^{-} \xrightarrow[k_2]{H^+} RH_2 \quad [16]$$

In unbuffered solution containing water, log plot slopes are predicted to change from approximately $0.5(n_1 + n_2)/0.059$ at the toe of the wave to $(n_1 + n_2/0.059$ at the head. $E_{1/2}$ is expected to become more negative as the bulk concentration of R increases.

If the rate of the chemical reaction is greater than the rate of diffusion of $R^{=}$, current-ratio slopes and β values would be expected to increase because the chemical reaction would have the effect of making the diffusion coefficient of $R^{=}$ appear larger than if the rate of the chemical reaction were small (*cf.* Eq. [2]).

Two chemical reactions alternating between two electrochemical reactions.—For a mechanism of the type

$$R \overset{n_1 e}{\rightleftharpoons} R^{-} \xrightarrow[k_1]{H^+} RH \xrightarrow[\text{very fast}]{\alpha n_2 e} RH^{-} \xrightarrow[k_2]{H^+} RH_2 \quad [17]$$

the same type equations as were developed for the mechanism represented by Eq. [16] are applicable, since the reversible addition of n_1 electrons to R is the potential-determining step. In aqueous-organic unbuffered solvents, the mechanism represented by Eq. [17] would, therefore, be expected to exhibit a log plot slope equal to $0.5n_1/0.059$ at the toe of the wave and $n_1/0.059$ at the head. The height of the polarographic wave would increase as the *p*H decreased. Current-ratio slopes and β values should approximate those in the case of a chemical reaction following a reversible electrochemical reaction (*cf.* preceding section).

Another mechanism in the category of two chemical reactions alternating between two electrochemical reactions, which deserves considerations, is

$$R \underset{}{\overset{n_1e}{\rightleftharpoons}} R^- \xrightarrow[k_1]{H_2O \text{ or } HA} RH + OH^- \text{ or } A^- \quad [18]$$

$$RH + OH^- \text{ or } A^- \xrightarrow{n_2e, \text{ very fast}} RH^- \xrightarrow[k_2]{H_2O \text{ or } HA} RH_2 + OH^- \text{ or } A^-$$

In anhydrous solvents the chemical reaction of Eq. [18] involving water would not occur. In organic solvents containing 10% or more water, the concentration of water at the electrode surface may be considered as essentially constant. Thus, log plot slopes in such aqueous organic solvents would equal $n_1/0.059$ if reaction [18] occurs; current-ratio plots and β would vary as predicted in the case of a mechanism represented by Eq. [16] in buffered solution. For a mechanism represented by Eq. [18] $E_{1/2}$ would be independent of pH, but would become more positive as the H_2O or HA concentration increased; the dependence of $E_{1/2}$, however, would have to be tested under conditions where the water content was quite small and precisely known. In polarography with organic solvents minute indeterminate traces of water are probably practically inevitable.

Electrochemical processes controlled by diffusion and activation.—A mechanism originally proposed for the reduction of phenyl ketones in acidic solution (5), adapted for the case of phenyl-substituted ethenes, is

$$(R) + H^+ \xrightarrow[k_1]{} (R \ldots H)^+ \xrightarrow[k_2]{n_1e} RH \xrightarrow[\text{very fast}]{n_2e} RH^- \xrightarrow[k_3]{H^+} RH_2 \quad [19]$$

where (R) is a polarized molecule. In this mechanism, the reducible species diffuses into the field of the electrode, the latter initiating polarization of the reducible group. Simultaneously, the polarized group attracts protons, a process which increases the polarization. The reducible species then completes diffusion to the electrode surface and acquires an electron. The preceding processes are continuous and involve a transition state. The involvement of hydrogen ion in the transition state is inferred from the pH-dependence of $E_{1/2}$. Polarographic waves resulting from such a mechanism would be diffusion controlled throughout the whole wave.

It is difficult at present to say exactly what factors are important in determining the rate of formation of $(R \ldots H)^+$ and what influence the manner of formation of $(R \ldots H)^+$ would have on the log plot slope, since electrical double layer effects, which are not easily evaluated, undoubtedly play an important role. However, if formation of $(R \ldots H)^+$ may be assumed to occur as a simple chemical reaction at the electrode surface, log plot slopes in cases where the rate of formation of $(R \ldots H)^+$ is very fast would reflect the rate of addition of an electron to $(R \ldots H)^+$, *e.g.*, if k_2 is slow compared to all other rates, a log plot slope would equal $\alpha_1 n_1/0.059$. If k_2 is very fast, the addition of n_1e is reversible, and a log plot slope would vary as in the previously discussed case of a chemical reaction preceded by a reversible electrochemical reaction.

An alternating current polarographic study (20) of the benzophenone reduction suggests that the following mechanism, which has been adapted for the case of the phenyl-substituted ethenes, is more representative of ketone reduction in nonaqueous media in the presence of undissociated proton donors:

$$(R) + HA \underset{k_1}{\rightarrow} RHA \xrightarrow[k_2]{\alpha_1 n_1 e} RHA^- \underset{k_3}{\rightarrow} RH + A^- \xrightarrow{n_2e, \text{ very fast}} RH^- \xrightarrow[k_4]{H^+} RH_2 \quad [20]$$

where HA represents an undissociated acid. Again, determining factors in the rate of formation of RHA and its influence on slopes are uncertain. If the rates of formation of RHA and RH_2 are assumed to be very rapid, k_2 or k_3 will determine the log plot slopes, *i.e.*, log plot slopes would equal $n_1/0.059$ if k_3 is rate-determining, and $\alpha_1 n_1/0.059$ if k_2 is.[4]

In both of the mechanisms of Eq. [19] and [20], it is difficult to predict current-ratio slopes and β values, although behavior approximating that expected for a single slow electrochemical reaction is most likely.

Electrochemical processes in which a change of electron transfer mechanism occurs.—In the case of the phenyl-substituted ethenes, this type of mechanism would be equivalent to two possibly concurrent mechanisms represented by Eq. [19], [20], and [16]; reaction [19] or [20] predominates during the earlier part of the wave and reaction [16] during the latter part. The reaction products, RH^- and $R^=$, are capable of diffusion away from the electrode surface or of further reaction in the interface with H^+. Log plots would be expected to show two intersecting linear lines, the slopes of which would be equal to the corresponding $\alpha n_a/0.059$ values, with perhaps a curvilinear portion near the intersection region.

Current-ratio and β plots would be generally the same as those expected for a mechanism controlled by a single slow electrochemical reaction.

Nonspecific Salt Effects

Recently, a number of studies of the influence of the structure of the electrical double layer on electrochemical reactions have appeared. The situation is complicated by the fact that most of the theories evolved have not yet been rigorously tested experimentally. It is of value, however, to consider the conclusions set forth for the general case of an irreversible electrochemical reaction (21) as an indication of the probable effect of the double layer structure on an electrochemical reaction.

For the irreversible electrochemical reaction (backward reaction neglected)

$$Ox^* \xrightarrow[\text{transfer}]{\text{mass}} Ox \xrightarrow{n_ae} Red \quad [21]$$

where Ox^* indicates bulk species and Ox the species being reduced, the expression for $E_{1/2}$ is

$$E_{1/2} = E^0 + \phi_{sb}[1 - (2z/n_a)] - (2RT/n_a\mathbf{F}) \ln [K D_0^{1/2}/(5 \times 10^4 pt^{1/2})] - \lambda/n_a\mathbf{F} \quad [22]$$

[4] The predicted log plot slopes are easily derived by equivalent reaction pair treatment.

where ϕ_{sb} is the electrostatic potential difference between the reaction site and the bulk of the solution (computed in the absence of the reacting species), z the charge on Ox, p the probability of electron-transfer during the life-time of Ox, λ the fraction of the charge separation attained in the transition state, and K a constant dependent on the choice of reference electrode.

The expression for αn_a is

$$\alpha n_a = n_a/2 + \tfrac{1}{2}(2z - n_a)(\delta\phi_{sb}/\delta E) - \tfrac{1}{2}\mathbf{F}(\delta\lambda/\delta E) \quad [23]$$

Thus, $E_{1/2}$ depends on ϕ_{sb} and αn_a on $\delta\phi_{sb}/\delta E$. On the negative side of the electrocapillary maximum, increasing the ionic strength or changing the electrolyte composition to favor greater adsorption makes ϕ_{sb} more positive, and thus makes $E_{1/2}$ more negative if $2z/n_z$ is greater than 1.

It is apparent that the criteria of reversibility presented in the preceding sections are to be regarded with caution, since the influence of the double layer structure on such parameters as $E_{1/2}$, α, and n_a has not yet been fully evaluated.

Acknowledgment

The authors wish to thank the U.S. Atomic Energy Commission which helped support the work described.

Manuscript received April 25, 1962; revised manuscript received Sept. 24, 1962.

Any discussion of this paper will appear in a Discussion Section to be published in the December 1963 JOURNAL.

REFERENCES

1. P. J. Elving and I. Rosenthal, *Anal. Chem.*, **26**, 1454 (1954).
2. P. J. Elving, I. Rosenthal, and A. J. Martin, *J. Am. Chem. Soc.*, **77**, 5218 (1955).
3. I. Rosenthal, J. R. Hayes, A. J. Martin, and P. J. Elving, *ibid.*, **80**, 3050 (1958).
4. P. J. Elving, I. Rosenthal, J. R. Hayes, and A. J. Martin, *Anal. Chem.*, **33**, 330 (1961).
5. P. J. Elving and J. T. Leone, *J. Am. Chem. Soc.*, **80**, 1021 (1958).
6. M. Suzuki and P. J. Elving, *J. Phys. Chem.*, **65**, 391 (1961).
7. P. J. Elving and P. G. Grodzka, *Anal. Chem.*, **33**, 2 (1961).
8. P. J. Elving and E. C. Olson, *J. Am. Chem. Soc.*, **79**, 2797 (1957).
9. P. G. Grodzka and P. J. Elving, *This Journal*, **110**, 231 (1963).
10. P. Delahay, "New Instrumental Methods in Electrochemistry," Interscience Publishers, New York, 1954.
11. J. Koutecky, *Collection Czechoslov. Chem. Communs.*, **18**, 597 (1953).
12. K. B. Oldham, P. Kivalo, and H. A. Laitinen, *J. Am. Chem. Soc.*, **75**, 5712 (1953).
13. P. Kivalo, K. B. Oldham, and H. A. Laitinen, *ibid.*, **75**, 4148 (1953).
14. H. A. McKenzie, *Australian J. Chem.*, **2**, 271 (1958).
15. A. F. Findeis, Jr. and T. DeVries, *J. Am. Chem. Soc.*, **80**, 797 (1958).
16. D. M. H. Kern, *ibid.*, **76**, 4234 (1954).
17. K. B. Oldham, *ibid.*, **77**, 4697 (1955).
18. T. Berzins and P. Delahay, *ibid.*, **75**, 5716 (1953).
19. G. J. Hoijtink, J. van Schooten, E. de Boer, and W. Y. Aalbersberg, *Rec. trav. chim.*, **73**, 355 (1954).
20. A. C. Aten, Ph.D. Thesis, Free University of Amsterdam, 1959.
21. W. H. Reinmuth, L. B. Rogers, and L. E. I. Hummelstedt, *J. Am. Chem. Soc.*, **81**, 2947 (1959).

GLOSSARY OF TERMS

1. *Equation for the electrochemical half-cell reaction:*

$$\mathrm{Ox} + ne \underset{k_{b,h}}{\overset{k_{f,h}}{\rightleftharpoons}} \mathrm{Red} \quad [24]$$

Ox	oxidized form
Red	reduced form
n	total number of electrons transferred
n_a	number of electrons involved in the activation step of Eq. [24]
D_O	diffusion coefficient of Ox in $cm^2\ sec^{-1}$
D_R	diffusion coefficient of Red in $cm^2\ sec^{-1}$
$k_{f,h}$	formal heterogeneous rate constant (cm sec^{-1}) of the forward process at potential E
$k_{b,h}$	formal heterogeneous rate constant (cm sec^{-1}) of the backward process at potential E

2. *Rate constant relationships:*

$$k_{f,h} = k^o_{f,h} \exp(-\alpha n_a \mathbf{F}E/RT) \quad [25]$$

$$k_{b,h} = k^o_{b,h} \exp[(1-\alpha) n_a \mathbf{F}E/RT] \quad [26]$$

$k^o_{f,h}$ and $k^o_{b,h}$	formal heterogeneous rate constants at $E = 0$
$k_{s,h}$	rate constant at $E = E^o_c$
E	measured electrode potential *vs.* the normal hydrogen electrode (NHE)
E^o_c	potentials *vs.* NHE at which the concentrations of Ox and Red are equal
E^o	potential *vs.* NHE at which the activities of Ox and Red are equal
$E_{1/2}$	half-wave potential *vs.* NHE
α	transfer coefficient, *i.e.*, fraction of the potential which favors the cathodic reaction of Eq. [24]

3. *Current definitions and factors:*

i	instantaneous current at time t_m
i_t	instantaneous current at time t
i_d	instantaneous diffusion-limited current at time t_m
$\bar{i}$	mean current over drop life
$\bar{i}_d$	mean diffusion-limited current over drop life
i_o	instantaneous current at effective mercury height h_o and time $(t_m)_o$
I	diffusion current constant $= i_d/Cm^{2/3}t^{1/6}$
t	time in sec
t_m	drop time in sec
$(t_m)_o$	drop time in sec at mercury height h_o
m	rate of flow of mercury in mg sec^{-1}
m_o	rate of flow of mercury in mg sec^{-1} at mercury height h_o
h	effective mercury height (mercury column height corrected for back-pressure)
h_o	reference effective mercury height
β	$(i/i)_E$ at a given value of E

4. *Miscellaneous:*

R	aromatic-olefinic hydrocarbon (the gas constant is also R but no trouble should be encountered)
R	gas constant (8.314v coulomb $mole^{-1}\ °C^{-1}$)
T	absolute temperature, °K
$\mathbf{F}$	Faraday (96,500 coulombs $equivalent^{-1}$)
d	density of mercury (13,534 mg cm^{-3} at 25°C)

Polarographic Reduction of the Phenyl-Substituted Ethenes

II. Electrochemical Kinetic Parameters and Mechanism in Dimethylformamide

Philomena G. Grodzka and Philip J. Elving

Department of Chemistry, The University of Michigan, Ann Arbor, Michigan

ABSTRACT

The polarographic behavior of the five phenyl-substituted ethenes (styrene, stilbene, 1,1-diphenylethylene, triphenylethylene, and tetraphenylethylene) at the dropping mercury electrode has been examined in dimethylformamide (DMF) and DMF-water solution containing 0.2*M* tetra-*n*-butylammonium iodide as background electrolyte on the basis of the various criteria for reversibility based on direct current polarography. Heterogeneous rate constants and αn_a values have been calculated on the basis of the spherical expanding electrode theory.

None of the reversibility criteria predictions for the various possible mechanisms are entirely in accord with the experimental results. Although polarographic reduction of the phenyl-substituted ethenes is indicated to occur by processes which involved a change of electron transfer mechanisms, a definite decision regarding the actual mechanisms cannot be reached because of the lack of adequate theoretical bases for such a mechanism change and for the effects of variation in double layer structure on any given mechanism.

Considerable effort has been expended on the search for correlations between polarographic half-wave potentials and various structural and kinetic parameters of compounds containing conjugated double bonds. Most correlations, however, have been based on electrochemical reduction mechanisms which are questionable because either the effects of experimental variables were not fully considered or the mechanisms were deduced from insufficient experimental data. For example, in the correlation of $E_{1/2}$ of aromatic and aromatic-olefinic hydrocarbons with the coefficient of the molecular orbital resonance integral in the expression for the energy of the lowest unoccupied electron level of the molecules (1, 2), the calculations are based for most of the compounds investigated on a reduction mechanism model, in which addition of the first electron is assumed to be reversible. There is some question, however, as will be evident subsequently, that this addition is actually reversible.

The polarographic reduction mechanism originally proposed by Laitinen and Wawzonek (3) for phenyl-substituted olefins and acetylenes in aqueous dioxane solution is[1]

$$R + e \rightleftarrows R^- \text{ (reversible, potential determining} \quad [1]$$

$$R^- + e \rightarrow R^= \text{ (irreversible} \quad [2]$$

$$R^= + H_2O \rightarrow RH_2 + 2\,OH^- \text{ (irreversible, rapid)} \quad [3]$$

This mechanism was inferred from the facts that (*a*) slopes of plots of log $[\bar{i}/(\bar{i}_d - \bar{i})]$ *vs.* E for the observed single waves of stilbene and diphenylacetylene were approximately equal to 1/0.059, (*b*) the waves were apparently independent of *p*H, and (*c*) the Ilkovic n was 2. This mechanism, which was one of the first proposed to elucidate an organic polarographic process, has been used by many investigators as a prototype for other organic electrochemical reductions. It has been well suited for this purpose, since it emphasizes that the first step is formation of a free radical which may then be reduced to a carbanion; such a sequence is characteristic of many organic electrode reactions (4).

However, subsequent studies showed the experimental behavior of the phenyl-substituted ethenes to be more complicated, *e.g.*, stilbene gives not one but two polarographic waves, whose heights depend on the solvent used and the amount of water present (5, 6).

The following mechanism has been advanced by Wawzonek (6) to explain the two 1*e* waves of stilbene in anhydrous acetonitrile and N,N-dimethylformamide (referred to hereafter as DMF):

$$R + e \rightarrow R^- \text{ (slow)} \quad [4]$$

$$R^- + e \rightarrow R^= \text{ (slow)} \quad [5]$$

$$R^= + \text{solvent} \rightarrow RH_2 \text{ (slow)} \quad [6]$$

The mechanism advanced (6) for the one 2*e* wave of styrene under similar conditions is

$$R + e \rightarrow R^- \text{ (slow)} \quad [7]$$

$$R^- + e \rightarrow R^= \text{ (fast)} \quad [8]$$

$$R^= + \text{solvent} \rightarrow RH_2 \text{ (slow)} \quad [9]$$

In acetonitrile containing water, the two 1*e* stilbene waves merge into a single 2*e* wave; the mechanism inferred (6) is

$$R + e \rightarrow R^- \text{ (slow)} \quad [10]$$

$$R^- + H_2O \rightarrow RH + OH^- \text{ (fast)} \quad [11]$$

$$RH + e \rightarrow RH^- \text{ (fast)} \quad [12]$$

$$RH^- + H_2O \rightarrow RH_2 + OH^- \quad [13]$$

A mechanism proposed by Hoijtink (7) for the reduction of aromatic hydrocarbons in water-dioxane

[1] The symbols used in this paper have been defined in the previous paper, ref. (8).

solution can be considered to apply to reduction of phenyl-substituted ethenes. The first step involves reversible addition of an electron; this may be followed by one or more of three other processes:

1. Diffusion of the resulting carbanion into the bulk solution, where

$$R^- + H^+ \rightarrow RH \rightarrow \text{dimerization or disproportionation} \quad [14]$$

2. Interfacial neutralization and reduction:

$$R^- + H^+ \rightarrow RH \quad [15]$$

$$RH + e \rightarrow RH^- \quad [16]$$

$$RH^- + H^+ \rightarrow RH_2 \quad [17]$$

3. Immediate reversible reduction,

$$R^- + e \rightleftarrows R^= \quad [18]$$

followed by diffusion of the doubly charged carbanion into the bulk solution, where

$$R^= + 2H^+ \rightarrow RH_2 \quad [19]$$

or

$$R^= + H^+ \rightarrow RH^- \xrightarrow{H^+} RH_2 \quad [20]$$

For those conjugated hydrocarbons which give two 1*e* waves, $E_{1/2}$ for the reversible addition of an electron to R is assumed to be less negative than $E_{1/2}$ for the reversible addition of an electron to R^-. Hence, when the rate of addition of a proton to R^- is slower than the rate of diffusion of R^- away from the electrode surface layer, two waves are observed: the first involves reduction to R^-; the second reduction to $R^=$. When the rate of proton addition to R^- is faster than the rate of diffusion of R^-, the radical RH is formed in the electrode layer and immediately adds an electron; the one wave now observed involves the over-all addition of two electrons.

The mechanisms represented by Eq. [15]-[17] and [18]-[20] would result in polarographic waves, whose $E_{1/2}$ would become more positive as *p*H decreased (8). However, only slight tendencies for $E_{1/2}$ to become more positive with decreasing *p*H were noted for anthracene, fluoranthene, dibiphenyleneethylene and pyrene in dioxane-water and alcohol-water (9); it was concluded that Hoijtink's mechanism is acceptable if the first electron uptake is assumed to proceed irreversibly.

The postulated reversible reduction of various conjugated hydrocarbons in DMF-$(Bu)_4NI$ solution was tested by alternating current polarography (10-12). For stilbene and some other compounds, addition of the first electron was very rapid ($k = 1$ cm sec^{-1}); that of the second electron was much slower (10^{-2} to 10^{-3} cm sec^{-1}). These results tend, on the whole, to confirm the mechanism postulated by Hoijtink (7), if addition of the second electron is assumed to proceed more or less irreversibly.

It was, consequently, of considerable interest to determine which of the previously discussed mechanisms is best substantiated for the phenyl-substituted olefins by their d-c polarographic behavior in DMF-$(Bu)_4NI$ solution, and to evaluate the usefulness of proposed d-c polarographic reversibility criteria for moderately complex organic molecules. Consequently, the better defined d-c polarographic criteria of reversibility were applied to the analysis of the behavior at the DME of the five phenyl-substituted ethenes, *i.e.*, styrene, stilbene, 1,1-diphenylethene, triphenylethene, and tetraphenylethene, in DMF and in DMF-water solutions.

The behavior patterns expected for various possible mechanisms have been examined elsewhere (8), and detailed account has been taken of how the various parameters, which can be measured or calculated from the polarographic behavior, will vary. This information, summarized in Table I of ref. (8), provides a convenient framework in which to examine the polarography of the phenyl-substituted ethenes.

In the present study, log plot slope predictions based on the "equivalent reaction pair" treatment (8) are used only as qualitative guides, for the latter treatment does not apply rigorously to substances which produce primary reduction products which, although capable of further electrochemical reaction, are stable enough for a fraction of the amount present to diffuse away from the electrode surface; styrene and stilbene are undoubtedly, to some degree, such substances.

Discussion of Experimental and Calculated Data

The basic experimental and calculated data for the five phenyl-substituted ethenes in DMF and DMF-water solutions containing 0.2*M* tetra-*n*-butylammonium iodide as background electrolyte are summarized in Table I.

Styrene.—In both DMF and 90% DMF styrene gives one 2*e* wave. In DMF, plots of i/i_0 *vs.* $(h)^{1/2}/(h_0)^{1/2}$ for various points along the wave show a series of lines whose slopes, with one exception, increase as the limiting current is approached; at i_1, the slope is 0.87. At *ca.* —1.92v *vs.* Hg pool, *i.e.*, near $E_{1/2}$, the current ratios fall below those at lower potentials. In 90% DMF similar plots show essentially the same behavior, except that the current ratios at —1.92v only fall below the current ratios found at potentials more positive than —1.92v by some 20 mv or so. The slope at i_1 is approximately 0.81.

The β function is approximately 0.64 at the toe of the wave in DMF, increasing to 0.79 at i_1. Essentially the same variation is observed in 90% DMF.

Log plot slopes observed in DMF and 90% DMF consist of two straight lines, which intersect just prior to $E_{1/2}$; αn_a calculated from these slopes is 0.59 at the toe of the wave and 1.02 at the head in DMF, and 0.62 and 1.02 in 90% DMF.

Since the styrene wave is a 2*e* wave, mechanisms 2, 3, or 4 [Table I of ref. (8)] seem most likely to be operative. However, αn_a values expected on the basis of these mechanisms are not in accord with the observed values.

If the presence of traces of water in the supposedly anhydrous DMF is assumed, mechanism [5] is a possibility, although it is unlikely that enough water is present to account for the entire wave. Mechanism [5] at the toe of the wave and mechanism [4] or [3] at the head would seem more likely in DMF con-

Table I. Polarographic, rate constant, and related data for the phenyl-substituted ethenes in dimethylformamide and dimethylformamide-water solution, 0.2M in tetrabutylammonium iodide

Compound	Solvent	$-E_{1/2}$, v[a]	Wave I: $\Delta E_{1/2}$, v	I[c]	$D_0^{1/2} \times 10^8$, cm $sec^{-1/2}$	αn_a[d]	αn_a[e]	$-\log k_{f,h}$ at $E_{1/2}$	$-\log k^\circ_{f,h}$ vs. N.H.E.
Styrene	DMF	2.451 ± 0.016[b]		5.63 ± 0.12	3.98	0.59	0.59	2.82	24.7
			0.106 ± 0.029			1.02	0.95		38.1
	90% DMF	2.345 ± 0.013		4.37 ± 0.13	3.09	0.62	0.67	2.83	26.7
						1.02	1.00		36.1
Stilbene	DMF	I 2.141 ± 0.013		2.64 ± 0.11	3.42	I 0.62	0.67	2.96	23.5
						0.96	1.03		36.1
		II 2.498 ± 0.022		1.69 ± 0.14		II 1.20	1.18	2.85	47.8
			0.007 ± 0.022						
	80% DMF	2.134 ± 0.009		2.97 ± 0.11	2.60	1.20	1.12	3.18	38.9
1,1-Diphenyl-ethylene	DMF	2.302 ± 0.016		4.01 ± 0.20	2.90	I 0.68	0.64	2.97	25.4
						0.92	0.84		32.0
						0.09	0.13		7.02
						II 0.60	0.60		25.1
			0.060 ± 0.029						
	90% DMF	2.242 ± 0.013		3.54 ± 0.22	2.50	0.92	0.88	3.05	32.7
Triphenyl-ethylene	DMF	2.084 ± 0.018		3.22 ± 0.04	2.28	I 0.79	0.74	3.10	26.2
						0.23	0.23		9.85
						II 1	[f]	[f]	[f]
			0.025 ± 0.029						
	80% DMF	2.059 ± 0.011		2.65 ± 0.05	1.87	1.17	1.09	3.20	36.6
Tetraphenyl-ethylene	DMF	2.020 ± 0.012		3.75 ± 0.09	2.65	0.94	0.89	3.03	29.8
			0.032 ±0.023						
	80% DMF	1.988 ± 0.011		2.55 ± 0.07	1.80	2.20	2.01	3.23	62.5

[a] Versus S.C.E.
[b] Errors represent standard deviations.
[c] Calculated from maximum instantaneous limiting currents.
[d] Calculated from slopes of log $[(i_d - i)/i]$ *vs.* E curves. Multiple αn_a values for a given wave indicate a change of slope; values are calculated for each slope.
[e] Calculated from slopes of log $k_{f,h}$ *vs.* E curves.
[f] The second wave was so small that $k_{f,h}$ values could not be calculated.

taining traces of water; however, the observed αn_a values are not in accord with the predicted values.

In an anhydrous medium such as DMF, the possibility that protons are furnished by the solvent rapidly enough to necessitate consideration in mechanisms [4] or [5], does not seem likely for the following reasons. First, phenyl-substituted carbanions have been demonstrated to be quite stable in anhydrous dimethylformamide (6). Secondly, proton availability would be greater in a DMF-water solvent than in DMF, so that a radical difference in the log plot slope would be expected with styrene in going from DMF to DMF-water. Since the log plot slopes do not change appreciably, the donation of protons to phenyl-substituted carbanions by solvent would appear to be very slow.

Mechanism [7] can be ruled out on the grounds that a 1*e* wave would result in DMF. Mechanism [6] does not seem likely in view of the very similar behavior of the log plot slope in both DMF and 90% DMF. Apparently none of the mechanisms presented in Table I (8) is entirely capable of explaining the observed polarographic behavior of styrene. The slight variation of log plot slopes and the moderately large shift of $E_{1/2}$ toward more positive potential in going from DMF to 90% DMF may indicate that double layer phenomena involving H^+ or H_2O are affecting the styrene reduction processes.

Stilbene.—Stilbene gives two diffusion-controlled waves in DMF and one in 80% DMF. Comparison of stilbene's I values (Table I) with styrene's indicates that the two waves in DMF are 1*e* waves and the one in 80% DMF is a 2*e* wave.

Plots of current-height ratios show two lines of different slope. At the toe of wave I in DMF the slopes are constant at about 0.93; near $E_{1/2}$ the slopes decrease to about 0.85 and then increase to 0.93 at the upper portions of the wave. Slopes for wave II in DMF increase as i_l is approached, becoming 0.93 at i_l. In 80% DMF, current-ratio plot slopes increase as i_l is approached, becoming 0.83.

In DMF, β increases from 0.60 at the toe of wave I to 0.70 in the region corresponding to $E_{1/2}$, levels off for approximately 0.04v, and then increases to 0.74; β for wave II decreases from 0.74 to 0.70 and then increases to 0.79. In 80% DMF, β increases from 0.54 to 0.75.

The log plot exhibits a change of slope for wave I in DMF; αn_a is 0.62 at the toe and 0.96 at the head of the wave; αn_a for wave II is 1.20. The log plot for the wave in 80% DMF is a single straight line; αn_a is 1.20.

If the presence of traces of water is assumed in the DMF, the behavior of stilbene wave I in DMF may be explained on the basis of a change of electron transfer mechanism, *i.e.*, at the toe of the wave, mechanism [5], [6], [7], or [8] predominates, while at the head of the wave, mechanism [1], in which the electron addition occurs reversibly, predominates.

In 80% DMF, mechanism [5], [6], [7], or [8] would predominate throughout the wave. Mechanism [5] seems unlikely because a change of log plot slope would be expected in 80% DMF. The fact that the $E_{1/2}$ is unchanged in going from DMF to 80% DMF would, however, tend to rule out mechanisms [6], [7], or [8].

If allowance is made for the fact that $D^{1/2}{}_{R^-}$ probably is not equal to $D^{1/2}{}_{R^=}$, the αn_a value of 1.20 for the stilbene wave II in DMF indicates that the wave is nearly reversible, *i.e.*,

$$R^- + e \rightleftarrows R^= \qquad [21]$$

1,1-Diphenylethylene.—In DMF 1,1-diphenylethylene gives one large rather distorted wave, whose shape suggests the probable presence of a small unresolved second wave near the head of the large first wave followed by a very small third wave. A mathematical treatment involving subtraction of the first wave height from the total wave height was not considered justifiable in view of the large errors that would probably result. The first two waves, therefore, were considered together as one.

In 90% DMF, the one wave observed decreases slightly in height about 0.25v before the background takeoff and an almost indistinguishable small second wave becomes evident. For calculation purposes, the latter was generally considered as part of the major wave.

Comparison of the I values for 1,1-diphenylethylene with those of the other phenyl-substituted ethenes indicates that the waves in both DMF and 90% DMF are essentially 2*e* waves.

In DMF, slopes of the current-ratio plots, on the whole, increase as i_l is approached, with a few of the slopes in the toe region of the wave being less than those at more positive potentials; the slope at i_l is 0.96. In 90% DMF, the plot slopes increase as i_l is approached, becoming 0.86 at i_l.

In both DMF and 90% DMF, β increases from 0.60 to 0.78.

The log plot for the wave in DMF shows four changes of slope; αn_a, calculated from these, is 0.68, 0.92, 0.09, and 0.60 from the toe to the head of the wave; 0.60 refers to the small third wave. The change from 0.68 to 0.92 occurs just before $E_{1/2}$ at *ca.* −2.28v *vs.* S.C.E., while that from 0.92 to 0.09 occurs just after $E_{1/2}$ at *ca.* −2.35v. For the first wave in 90% DMF, a single straight line, giving αn_a of 0.92, is obtained for the log plot; the second wave was too small for a log plot computation to have any meaning.

The αn_a values obtained for the first wave in DMF and 90% DMF are not in accord with any of the mechanisms presented in Table I (8) or any combination thereof. The small third wave αn_a of 0.60 in DMF implies that addition of an electron to the carbanion R^- occurs irreversibly.

Triphenylethylene.—In DMF, triphenylethylene gives one large wave of distorted shape, which, as in the case of 1,1-diphenylethylene, is suggestive of the presence of a small unresolved wave near its head; this is followed by a very small second wave. In 80% DMF, one wave is observed.

Although a current-ratio plot at a constant potential anywhere along the triphenylethylene wave in DMF shows a change of slope, even at the limiting current, the slopes increase as the potential is increased; the slope at i_l changes from approximately 1.2 to 1.4. In 80% DMF, the current-ratio plot slopes increase to a value of 0.89 at i_l.

In DMF β increases from 0.64 to 0.73, levels off at 0.73 near the head of the wave, and increases thereafter to 0.78; the latter increase is undoubtedly due to the small second wave. In 80% DMF, β increases from 0.60 to 0.79.

The log plot shows a change of slope near the head of the first wave in DMF, which can be attributed to the small unresolved wave; αn_a calculated from the slopes are 0.79 and 0.23. In 80% DMF, the log plot exhibits a single straight line; αn_a is 1.17.

The αn_a of 0.23 obtained for the small unresolved wave in DMF probably indicates an irreversible addition of the second electron.

Tetraphenylethylene.—Tetraphenylethylene gives one wave in both DMF and 80% DMF.

Slopes of current-ratio plots in both DMF and 80% DMF increase as i_l is approached; the slopes at i_l are approximately 0.95 and 0.88, respectively.

β increases from 0.63 to 0.77 in DMF and from 0.61 to 0.79 in 80% DMF.

The log plots in both DMF and 80% DMF consist of single straight lines, whose slopes give αn_a values of 0.94 and 2.20, respectively. The latter value is rather unexpected in view of the αn_a values of about 1 obtained with the lower members of the series and is not readily explainable in terms of any of the mechanisms advanced. The possibility that both electrons are added very rapidly in DMF to give $R^=$ (mechanism [4] with K_1 and K_2 being slow) was excluded because it would lead to an αn_a value of 2, whereas one of 0.94 is observed.

Conclusions

None of the reversibility criteria or log plot slope predictions for the various possible mechanisms presented in Table I of ref. (8) or combinations thereof is entirely in accord with the experimental results. Thus, a simple decision as to the actual mechanisms involved is not possible. However, the observed change of slopes of the log plots in DMF strongly suggests that reduction of the phenyl-substituted ethenes at the DME in DMF involves a change of electron-transfer mechanism during the course of reduction, *i.e.*, mechanism [6] or [7] accounts for the process at the toe of the polarographic waves and mechanism [2], [3], or [4] for that at the head. If reduction in DMF occurs as indicated, reduction in DMF-water solutions would have to be accounted for entirely by means of mechanisms [6] and [7]. Unfortunately, an explanation of the polarographic waves in DMF-water solutions in terms of mechanism [6] or [7] is not possible at present because of lack of an adequate theoretical basis for correlation of electrochemical parameters with such mechanisms. It may be pointed out that mechanisms [6] and [7] have much in common with various postulated mechanisms for the reduction of solvated H^+ to H_2; elucidation of the latter process has been the subject of numerous investigations.

The possibility exists that the observed $E_{1/2}$ shifts and αn_a variations, when the DMF solvent medium is altered, are the result of alteration of the structure of the electrical double layer, rather than only the result of a pH change. As was indicated in ref (8),

variation in the double layer structure would be reflected in variation of the potential difference, ϕ_{sb}, which represents the potential difference between the reaction site and the bulk of the solution. Variations in ϕ_{sb} and $\delta\phi_{sb}/\delta E$ may cause variations in $E_{1/2}$ and αn_a. Direct determination of ϕ_{sb} and $\delta\phi_{sb}/\delta E$ is a complicated matter. Even if such data were available, it would still be problematical if a definite decision could be reached regarding the actual mechanisms involved because of the lack of an adequate theory for mechanisms [6] and [7].

The contention that surface effects are responsible for the bent log plot slopes of the phenyl-substituted ethenes is supported by the work of Meites and Israel (13), who found that the log plot slopes of an irreversible system (1 m*M* Ni(II) in 0.1 *F* KCl) depend on the concentration of maximum suppressor.

Although the present investigation has not permitted a decision to be reached as to the actual mechanisms involved in the polarographic reduction of the phenyl-substituted ethenes, it has demonstrated the difficulty of directly applying criteria of reversibility postulated for inorganic systems to organic systems. Such difficulties have been previously encountered in the examination of the behavior of nitromethane (14) and of benzophenone (15).

Experimental

Chemicals.—Styrene (Eastman white label) was distilled under reduced pressure; the fraction boiling at 51.5°C was collected. Stilbene (Eastman white label), triphenylethylene (Aldrich), and tetraphenylethylene (Aldrich) were used as received, since their polarographic waves were identical to those observed with recrystallized samples. 1,1-Diphenylethylene (Aldrich) was used without further purification for runs in DMF since a fraction, distilled under reduced pressure at 156°C, gave a polarographic wave identical to the one obtained with the unpurified compound; the distilled material was used for the runs in 90% DMF.

N,N-dimethylformamide (DuPont, technical grade) was fractionally distilled after being dried over anhydrous potassium carbonate for several days; the fraction boiling at 151°-153°C was collected.

Tetra-*n*-butylammonium iodide was prepared as described by Laitinen and Wawzonek (3). Recrystallization from anhydrous ethyl acetate revealed a puzzling phenomenon. Sometimes the iodide dissolved readily in the hot ester, but at other times resisted dissolution. In the latter, ethanol was added dropwise until the iodide just dissolved.

Nitrogen was purified, dried, and equilibrated by successive passage through alkaline pyrogallol, concentrated sulfuric acid, indicating Drierite, and a portion of the test solution.

Apparatus.—A water-jacketed mercury pool cell, maintained at 25° ± 0.1°C, was used in conjunction with a L&N Type E electrochemograph. The validity of using this instrument for measurement of instantaneous and average currents has been verified (16-18). Applied constant potentials were checked potentiometrically.

The cell resistance, measured at the peak of the mercury drop formation in 0.2*M* Bu_4NI in DMF, 90% DMF, and 80% DMF, were 450, 520, and 600 ohms, respectively. The increased resistance with increased water content may be due to preferential solvation of the ions.

At potentials varying from open circuit to −2.2v, m for the various capillaries used varied from 0.80 to 0.95 mg/sec; m for a given capillary varied by not more than 1%. Drop-times at the applied constant potentials, at which currents were measured, were determined from the fall of ten drops and ranged from 5 sec at the wave toe to 2.5 sec at the limiting current.

The capillaries (Corning marine barometer tubing) became clogged easily; drawing concentrated nitric acid up past the clogged area and then rinsing repeatedly by drawing up and expelling distilled water resulted in excellent functioning over a considerable length of time. (Drawing concentrated nitric acid up a capillary is rather an art, for the capillary is easily ruined for further use if the intake and expulsion of nitric acid are not rapid and continuous.) After such cleaning, mercury should be allowed to drop from the capillary overnight before further use to insure that residual traces of water do not remain.

Procedures.—The compound concentrations varied between 0.52 and 1.13 m*M*. For styrene and stilbene in DMF, the potential interval between current measurements was 0.02v; each point on the log plot was the average of the i/i_d ratios for 6 runs. For the other compounds and for styrene and stilbene in aqueous DMF, the potential interval between points was 0.01v, and each point on the log plot was the average of 3 runs; the latter actually represent 6 runs at 0.02-v intervals, which were spaced 0.01v apart between 2 sets of 3 runs each.

Test solutions were deoxygenated by passing nitrogen through a sintered glass bubbler into the solution for 10 min. The mercury pool was then introduced and nitrogen purging continued for 5 min more. A nitrogen atmosphere was maintained over the solution throughout the run.

Currents used in obtaining the log plots were corrected for iR drop; those used in obtaining current-ratio and β plots were not, since in these cases only the variation of the functions was of interest.

The potentials at 25° ± 0.1°C of the reference pool electrode, when covered with solutions of 0.2*M* Bu_4NI in DMF, 90% DMF, and 80% DMF, were 0.535 ± 0.008, 0.497 ± 0.007, and 0.463 ± 0.008v, respectively, *vs.* the aqueous saturated calomel electrode, using a Laitinen bridge (19) filled with saturated KCl, in general agreement with the value of −0.50v found for a reference pool covered with 0.1*N* Et_4NI in DMF (20); the variation in potential (standard deviation) may be due to junction potentials. The potentials reported in Table I as *vs.* S.C.E. were obtained by adding to the potential *vs.* the mercury pool, the measured potential between the pool and the S.C.E. for the solution concerned.

Calculation of kinetic parameters.—In Koutecky's mathematical treatment (21) of totally irreversible waves, *i.e.*, waves due to a single rate-determining

electrode process, for which $k_{s,h}$ is less than 3×10^{-5} cm sec^{-1} (22), $(i/i_d)_{tm} = f(X_m)$. It is customary to assume that the rate of the backward electrochemical reaction is negligible; X_m is then given by

$$X_m = (12/7)^{1/2} k_{f,h} (t_m/D_O)^{1/2} \quad [22]$$

From the conveniently constructed table given by Koutecky (21) and reproduced by Delahay (22), the value of X can be determined for a given experimental value of $(i/i_d)_{tm}$; hence, $k_{f,h}$ can be calculated for a given potential if the value of D_O is known.

For stilbene, D_O was calculated by the equation

$$D_O = \{(I_1/708) + [I_{total}/(2 \times 708)]\}/2 \quad [23]$$

where I_1 refers to the diffusion current constant of the first wave, and I_{total} refers to the sum of I_1 and I_2. This procedure is advisable because the second wave is smaller in height than it should be as the result of some diffusion of the reduction products of the first wave away from the electrode into the bulk solution, where some dimerization undoubtedly occurs. For the other compounds, $D_O^{1/2}$ was calculated by means of the Ilkovic equation on the assumption that the total wave involves two electrons.

The forward heterogeneous rate constant is related to α by the equation

$$k_{f,h} = k^\circ_{f,h} \exp(-\alpha n_a \mathbf{F} E/RT) \quad [24]$$

Thus, a plot of log $k_{f,h}$ *vs.* potential for an electrode process involving one rate-determining step would yield a straight line, whose slope is $-0.434\ \alpha n_a \mathbf{F}/RT$, from which the product αn_a can be calculated.

Rather than attempting to determine log $k^\circ_{f,h}$ by a straight graphical extrapolation over a 2-v interval to $E = 0$ *vs.* N.H.E., the relation was used

$$\log k_{f,h} = [\Delta(\log k_{f,h})/\Delta E]E + \log k^\circ_{f,h} \quad [25]$$

where E equals the potential compared to the N.H.E., at which $k_{f,h}$ was measured, *i.e.*, E = (E *vs.* mercury pool) -0.290v. The latter value is derived from the facts that for a solution of 0.2*M* Bu_4NI in DMF the pool potential is -0.535v, and the potential of S.C.E. is 0.245v compared to N.H.E.; the former value, as already mentioned, contains unknown junction potentials.

In addition to the values of $k^\circ_{f,h}$, which may involve considerable error due to the required range of extrapolation, values of $k_{f,h}$ are given in Table I, which were measured at the half-wave potential. These values of the rate constant provide a realistic measure of the rate of the electrode reaction in the potential region of most interest.

Calculation of the $(i/i_d)_{tm}$ ratios requires correction of the observed i_d values for electrocapillarity, *e.g.*, by the equation

$$(i_d)_{tm} = (i_d)_{td} (t_m/t_d)^{1/6} \quad [26]$$

where t_d refers to the drop-time measured on the diffusion current plateau.

Reproducibility of data.—Although the reproducibility of the individual i/i_d ratios is only fair, the log plots for each individual run show the same variation, differing only in displacement along the potential axis; this behavior may be due to the variation in reference electrode potential already mentioned. The average values of the i/i_d ratios for a given compound give excellent log plots.

Potential displacement at currents less than the limiting current is also evident in the determination of current-ratios as a function of $h^{1/2}$ and β values. However, the diagnostic value of the plot obtained in a single run is not impaired.

Acknowledgment

The authors wish to thank the U. S. Atomic Energy Commission which helped support the work described.

Manuscript received April 25, 1962; revised manuscript received Sept. 24, 1962.

Any discussion of this paper will appear in a Discussion Section to be published in the December 1963 JOURNAL.

REFERENCES

1. G. J. Hoijtink, *Rec. trav. chim.*, **73**, 895 (1954).
2. G. J. Hoijtink and J. van Schooten, *ibid.*, **72**, 903 (1953).
3. H. A. Laitinen and S. Wawzonek, *J. Am. Chem. Soc.*, **64**, 1765 (1942).
4. P. J. Elving and B. Pullman, "Advances in Chemical Physics," Vol. III, pp. 1-31, Interscience Publishers, New York (1961).
5. P. H. Given and M. E. Peover, "Proceedings of Second International Polarography Congress," Vol. 3, pp. 948-54, Pergamon Press, London (1961).
6. S. Wawzonek, E. W. Blaha, R. Berkey, and M. E. Runner, *This Journal*, **102**, 235 (1955).
7. G. J. Hoijtink, J. van Schooten, E. de Boer, and W. Y. Aalbersberg, *Rec. trav. chim.*, **73**, 355 (1954).
8. P. G. Grodzka and P. J. Elving, *This Journal*, **110**, 225 (1963).
9. K. Schwabe and E. Schmidt, *Z. physik. Chem.*, Sonderheft, 278 (1958).
10. A. C. Aten, Ph.D. Thesis, Free University of Amsterdam, 1959.
11. A. C. Aten, C. Buthker, and G. J. Hoijtink, *Trans. Faraday Soc.*, **55**, 323 (1959).
12. A. C. Aten and G. J. Hoijtink, *Z. physik. Chem.*, **21**, 192 (1959).
13. L. Meites and Y. Israel, *J. Am. Chem. Soc.*, **83**, 4903 (1961).
14. M. Suzuki and P. J. Elving, *Collection Czechoslov. Chem. Communs.*, **25**, 3202 (1960).
15. M. Suzuki and P. J. Elving, *J. Phys. Chem.*, **65**, 391 (1961).
16. A. F. Findeis, Jr., and T. DeVries, *J. Am. Chem. Soc.*, **80**, 797 (1958).
17. P. Kivalo, K. B. Oldham, and H. A. Laitinen, *ibid.*, **75**, 4148 (1953).
18. H. A. McKenzie and M. C. Taylor, *Australian J. Chem.*, **2**, 260 (1958).
19. H. A. Laitinen, *Ind. Eng. Chem., Anal. Ed.*, **13**, 393 (1941).
20. P. H. Given, M. E. Peover, and J. Schoen, *J. Chem. Soc.*, **80**, 797 (1958).
21. J. Koutecky, *Collection Czechoslov. Chem. Communs.*, **18**, 597 (1953).
22. P. Delahay, "New Instrumental Methods in Electrochemistry," Interscience Publishers, New York (1954).

Influence of Indifferent Electrolytes on Transfer Coefficient of $Fe(CN)_6^{---}$ / $Fe(CN)_6^{----}$ System

H. P. Agarwal

Department of Chemistry, Motilal Vigyan Mahavidyalaya, Bhopal, India

ABSTRACT

The nature of a supporting electrolyte has an effect on transfer coefficient and rate constant of the redox system. The transfer coefficients of $Fe(CN)_6^{---}$ and $Fe(CN)_6^{----}$ (0.001M equimolecular concentration) in 1*N* KCl, 1*N* KNO_3, and 1*N* K_2SO_4 are equal and the value is 0.49 at 35°C. The rate constant at equilibrium in 1*N* KNO_3, having 0.001M concentration of the redox couple, is 6.6 x 10^{-2} cm sec^{-1} at 35°C. The value of α, transfer coefficient in 1*N* KBr and 1*N* KI, is 0.50 and 0.47, respectively, at 35°C. The different transfer coefficient in potassium iodide is due to the combined action of the $Fe(CN)_6^{---}$, $Fe(CN)_6^{----}$, and KI, KI_3. The latter was produced as a result of reaction between potassium ferricyanide and potassium iodide. In KCNS and KCN medium, however, the ferro-ferri cyanide redox system was not stable, hence the determination of α was not possible.

When a sinusoidal alternating current is made incident on two electrodes dipped in a solution containing reversible redox reactants, a small shift in the mean potential is observed (1) at each of the electrodes. As the phenomenon is caused by the nonlinearity of redox processes it was called a "redoxokinetic effect" (1), but it is now more commonly known as faradaic rectification (2, 3). Doss and Agarwal (4) worked out its theory for the particular case of small a-c fields corresponding to equal concentrations (of the order of a few millimoles per liter) and equal diffusion coefficients of the reactants. Barker (3) generalized the treatment and combined it with his ingenious experimental technique for developing his new and powerful analytical process called RF polarography. The faradaic rectification method has an advantage over the conventional methods (5) since it is free from errors associated with the resistance of the solution. If the change in mean potential is measured for a platinum/electrolyte interface instead of a mercury/electrolyte interface as described earlier (2, 3), the correction suggested by Matsuda and Delahay (6) for high frequencies (of the order of 1 megacycle) will not be necessary since the observations are limited to the audio frequency range. Furthermore, for a moderately fast redox reaction (K_s of the order of 0.01-0.1 cm sec^{-1}), the correction for the double layer structure in the solution of the boundary value problem need not be applied for finding out the correct value of transfer coefficient. In the present work, the transfer coefficients of ferrocyanide and ferricyanide redox mixtures prepared in 1*N* solutions of several indifferent electrolytes have been determined for the platinum/electrolyte interfaces to study the influence of supporting electrolytes on transfer coefficients. The rate constant K_s of the redox couple in 1*N* KNO_3 solution has been determined to show that the reactions under study are only moderately fast.

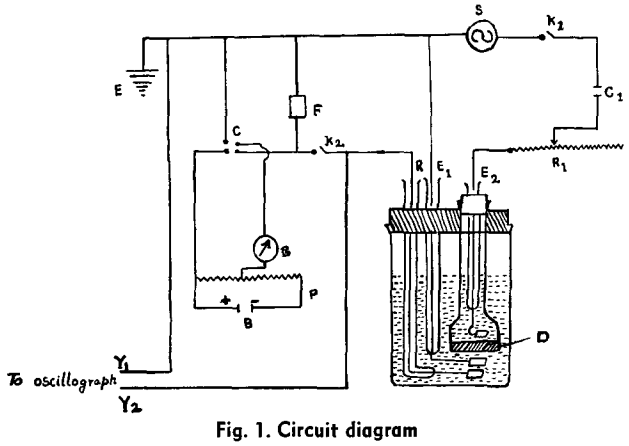

Fig. 1. Circuit diagram

Experimental

The circuit diagram is given in Fig. 1. A Philips audio oscillator, S (type GM 2315) serves as an a-c source, and the current is controlled by the variable resistance R_1. A condenser C_1 is provided to cut off any d-c component that may be associated with the alternating current. The electrolytic cell contains three electrodes E_1, E_2, and R. All of them are of polished bright platinum foil, each of size 1.6 cm^2. E_1 and E_2 are separated from each other by a sintered glass disk D (porosity 1G4), so that there may be a uniform distribution (7) of current density. R is the reference electrode. The iR drop in between the reference electrode and polarized electrode E_1 was avoided (7) by keeping the two close together within a distance of 0.5 cm. On pressing keys K_1 and K_2, the d-c potential developed between E_1 and R is measured by the potentiometer P, after filtering off a-c through low-frequency pass filter F. The sign of the potential is that of the reference electrode. The potentiometer used could measure correctly potentials of the order of 1 μv using a Pye & Co. moving coil mirror galvanometer G (sensitivity: 4.5 mm/μv at a distance of 1.1 meter and resistance

= 1840 ohms) as a null instrument. C is the commutator used in the potentiometer circuit for reversing the current. On pressing key K_1, keeping K_2 open, the a-c potential incident between E_1 and R is measured by connecting them to the Y-axis of a highly sensitive Philips oscillograph-type GM 3156 whose sensitivity was 1 mv (rms)/cm. The same solution was filled in the partitioned compartment of electrode E_2 and the cell. The cell was immersed in a thermostat maintained at a desired temperature. For protection from atmospheric oxidation, the solution in each compartment was covered with liquid paraffin.

Before each experiment, the electrodes are cleaned by dipping in hot chromic acid. Then the electrodes are washed thoroughly with distilled water, rinsed with absolute alcohol, and heated red hot in flames. The solution of potassium ferrocyanide (A.R.) and potassium ferricyanide (A.R.), the concentration of each being 0.001M, were prepared in 1*N* solution of the supporting electrolyte (A.R.). The indifferent electrolytes chosen for the study were KCl, KNO_3, K_2SO_4, KBr, KI, KCNS, and KCN. The values of the d-c potential ψ, obtained at varying frequencies and at 4 mv of a-c, are given in Table I for the first five indifferent electrolytes. The readings for ψ at 8 mv of a-c were also obtained to see the proportionality of ψ to square of the a-c voltage incident. As the values of ψ at 8 mv of a-c were exactly four times to those obtained at 4 mv of a-c at the corresponding frequencies, they are not shown in Table I. In potassium thiocyanate and potassium cyanide solutions, values of ψ are not stable and reproducible hence they have not been incorporated in Table I.

The diffusion of 0.001M potassium ferricyanide in 1*N* KNO_3 was studied by the porous diaphragm cell method (8), and the values of mean concentration gradient (0.04×10^{-6}) and mean concentration (18×10^{-6}) were obtained.

Results and Discussion

In all the supporting electrolytes used, ψ, the shift in mean potential becomes constant at a frequency of 1000 cps or above (Table 1). In KCl, KNO_3, and K_2SO_4 solutions, ψ acquires constancy even at 500 cps, and below it ψ decreases proportionately to the square root of frequency. The values of ψ at a frequency of 100 cps are only approximate since it was difficult to read correctly the fractions of a microvolt. Hence observations at the still lower frequencies have not been taken. The values of α transfer coefficient can be calculated from the theoretical equation applicable at high frequencies (4)

$$\alpha = 0.5 - \frac{2\psi RT}{V^2 n\mathbf{F}} \qquad [1]$$

where ψ is the shift in mean potential, R is the gas constant, T is the absolute temperature, V is the a-c voltage incident, n is the valency, and $\mathbf{F}$ is the Faraday. The transfer coefficient of ferrocyanide and ferricyanide reaction in KCl, KNO_3, and K_2SO_4 medium will be of the same order as ψ; the shift in mean potential at high frequencies (above 500 cps) in these media remains almost unaffected. On substituting the values of ψ at 1000 cps (from Table I) in Eq. [1], the values of transfer coefficient obtained are 0.49 in KCl, KNO_3, or K_2SO_4 medium, 0.50 in KBr, and 0.47 in KI solution. The results obtained with KI are not conclusive as potassium ferricyanide reacts with potassium iodide leading to the evolution of iodine, and this also brings about the changes in concentration of the two reactants. As a result of the reaction there will be in the solution ferricyanide-ferrocyanide and potassium iodide-tri-iodide redox mixtures; consequently the variation in ψ at any frequency will be the result of the combined effect of the two. It is interesting to note, however, that the system is stable as compared to that obtained with either of the two (KI, I_3 or $Fe(CN)_6^{---}$, $Fe(CN)_6^{----}$ separately.

On using KCNS and KCN as the supporting electrolytes, no reproducible values for ψ, shift in mean potential, could be obtained, thereby showing that in such a medium the system (ferrocyanide-ferricyanide) is unstable.

The value of K_s, the rate constant at equilibrium, is obtained for the redox reaction in 1*N* KNO_3 solution, by applying the theoretical equation (4) for low-frequency range, *i.e.*,

$$\psi = (0.5 - \alpha)\frac{V^2 n\mathbf{F}}{2RT}\frac{1}{2K}\sqrt{\frac{\omega D}{2}} \qquad [2]$$

provided D, the diffusion coefficient of the reactants, and ω ($\omega = 2\pi f$ where f is the frequency of a.c.), the angular frequency are known. The diffusion coefficient of 0.001M ferricyanide in 1*N* KNO_3 was determined from values of the mean concentration gradient and mean concentration using the method adopted by Hartley and Runnicles (9). The value of the mean diffusion coefficient thus obtained is 12.2×10^{-6} cm^2 sec^{-1}. The value of K_s, the rate constant at equilibrium (concentration of each reactant being 0.001M), was determined by substituting the values of α (transfer coefficient), D, V, and ψ at 200 cps in Eq. [2]. The value thus obtained is 6.6×10^{-2} cm sec^{-1} which shows that it is a moderately fast reaction. Hence the values of transfer coefficient obtained for the reactions under study are independent of correction for the double layer structure in the solution of the boundary value problem (6).

In potassium iodide and potassium bromide solutions, the value of ψ, shift in mean potential, increases in magnitude with the lowering in frequency

Table I. Temperature of the thermostat 35° ± 0.05°C

Frequency of a.c. used, cps	Values of shift in mean potential ψ in microvolts at 4 mv of a.c. when equimolecular quantities of $K_4Fe(CN)_6$ and $K_3Fe(CN)_6$ (each 0.001M) are dissolved in 1*N* solution of KCl	KNO_3	K_2SO_4	KBr	KI*
100	+1	+1	+2	−7	+26
200	+2	+2	+3	−6	+19
500	+3	+3	+4	−3	+12
1000	+3	+3	+4	0	+8
2000	+3	+3	+4	0	+8
5000	+3	+3	+3	0	+7

* Some I_2 seems to have liberated as solution became slightly brownish.

of a-c, rather than being proportional to the square root of frequency; hence in such cases it is not possible to calculate the values of K_s, the rate constant at equilibrium.

Manuscript received Sept. 11, 1961; revised manuscript received June 29, 1962.

Any discussion of this paper will appear in a Discussion Section to be published in the December 1963 JOURNAL.

REFERENCES

1. K. S. G. Doss and H. P. Agarwal, *J. Sci. Ind. Research, India*, **9B**, 280 (1950).
2. K. B. Oldham, *Trans. Faraday Soc.*, **53**, 80 (1957).
3. G. C. Barker, R. L. Faircloth, and A. W. Gardner, *Nature*, **181**, 247 (1958); G. C. Barker, *Anal. Chim. Acta*, **18**, 118 (1958).
4. K. S. G. Doss and H. P. Agarwal, *Proc. Indian Acad. Sci.*, **34**, 263 (1951); *ibid.*, **35**, 45 (1952).
5. P. Delahay, "New Instrumental Methods in Electrochemistry," pp. 146-168, Interscience Publishers, New York (1954).
6. H. Matsuda and P. Delahay, *J. Am. Chem. Soc.*, **82**, 1547 (1960).
7. P. Delahay, "New Instrumental Methods in Electrochemistry," p. 358, Interscience Publishers, New York (1954).
8. H. P. Agarwal, *Proc. Indian Acad. Sci.*, **56**, 108 (1962).
9. G. S. Hartley and D. F. Runnicles, *Proc. Roy. Soc.*, **168**, 401 (1938).

Technical Notes

A Method for the Preparation of Low-Temperature Alloyed Gold Contacts to Silicon and Germanium

W. Mehl, H. F. Gossenberger, and E. Helpert

RCA Laboratories, Radio Corporation of America, Princeton, New Jersey

For many practical purposes the preparation of low resistance "ohmic" metal-semiconductor contacts has been of great interest. As a criterion for the ohmic nature of the contact a linear I-V-characteristic is used. The presence of a linear I-V-characteristic, however, does not exclude the existence of a contact resistance due, for instance, to a thin insulating film between the metal and the semiconductor (1). A thin oxide film is unfortunately present on germanium and silicon during most methods of contact preparation so that a metal-oxide-semiconductor structure is almost always obtained. For many applications such a contact resistance can be neglected. There are, however, device applications where even low series resistances are quite undesirable because of the large currents involved. One such device is the tunnel diode where currents of the order of 10^4 amp/cm^2 are not unusual (2) and where contact resistances must be kept as small as possible.

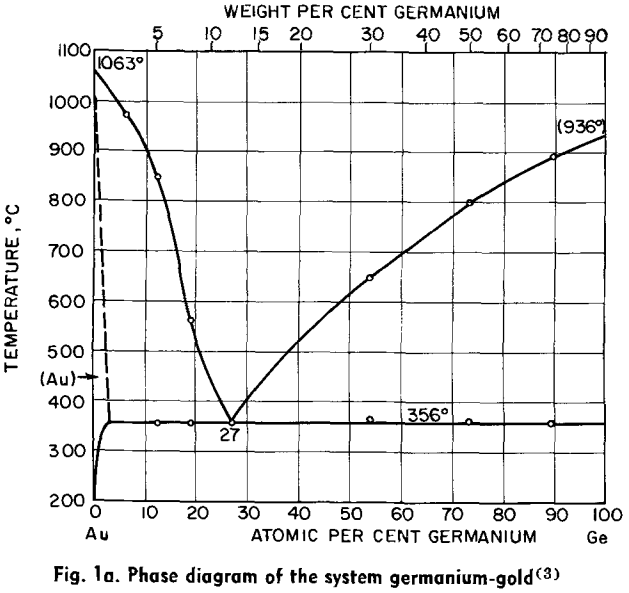

Fig. 1a. Phase diagram of the system germanium-gold[3]

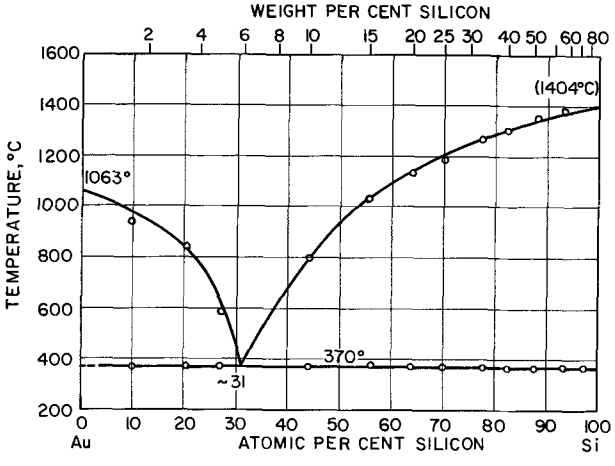

Fig. 1b. Phase diagram of the system silicon-gold[3]

The contact resistance associated with oxide films can usually be avoided if alloying techniques are used. One such technique is discussed in this paper.

Alloying through Oxide Films

In forming contacts to tunnel diodes, the alloying temperature must be kept low in order not to damage the concentration gradient at the junction. As can be seen from the phase diagrams in Fig. 1a and 1b (3) the gold-germanium and gold-silicon system allows this condition to be fulfilled. In both systems a eutectic containing about 30 at. % of the

semiconductor will form at temperatures between 350° and 400°C.

No alloying is observed, however, if gold is electroplated onto germanium or silicon and the structure heated to 400°C. Similarly, no alloying is observed below 400°C if gold is deposited on germanium or silicon by the replacement procedure discussed by various authors (4). The following experiment shows that the failure of the germanium-gold and the silicon-gold structure to form an alloy at 400°C can be related directly to the presence of an oxide film on the germanium and silicon surface:

A piece of germanium or silicon is cleaved (5) in a gold plating bath during cathodic polarization, *i.e.*, while the metal is being plated onto it. At the cleavage plane the gold is then deposited directly onto a fresh oxide-free surface. On surfaces prepared in this way alloying of the gold to the semiconductor can be obtained at temperatures of about 400°C.

Etching While Plating

The problem thus seems to be to prepare an oxide free germanium or silicon surface by a more conventional method prior to gold deposition. In the course of this work it was found that the replacement method can be modified in such a manner that a gold deposit is obtained which will permit low-temperature alloy formation with both germanium and silicon.

The principle of the method can be developed from the following discussion of the replacement reaction:

If germanium is in contact with a solution containing gold ions, the following processes occur

$$4Au^{3+} + 12e^- \rightarrow Au_{metallic} \text{ (cathodic partial reaction)}$$
$$3Ge \rightarrow 3Ge^{4+} + 12e^- \text{ (anodic partial reaction)} \quad [1]$$

It can thus be seen that during replacement plating the gold ions play the same role as the oxidizing agent during chemical etching (6). We can thus apply to this reaction the models developed for the discussion of corrosion processes (7).

During a corrosion process an anodic (oxidation) and a cathodic (reduction) partial reaction proceed with equal rate at the corroding electrode. Unless local cell action occurs, the loci of cathodic and anodic processes are distributed randomly over the surface. Partial current density-potential curves can be determined for both the anodic and the cathodic process. They permit prediction of the response of the system to a change of potential. Figure 2 shows a schematic plot of cathodic and anodic partial current-potential curves for systems [1].

Curve a represents the potential dependence of the rate of gold deposition and curve b represents the potential dependence of germanium (or silicon) dissolution. E_0 is the corrosion potential which is established when germanium is brought in contact with a solution containing Au^{3+} ions. When a negative potential is applied to this system (E_1), the rate of gold deposition is enhanced while the rate of germanium dissolution is reduced (cathodic protection). When a positive potential is applied, the rate of germanium dissolution is enhanced and the rate of gold deposition is reduced.

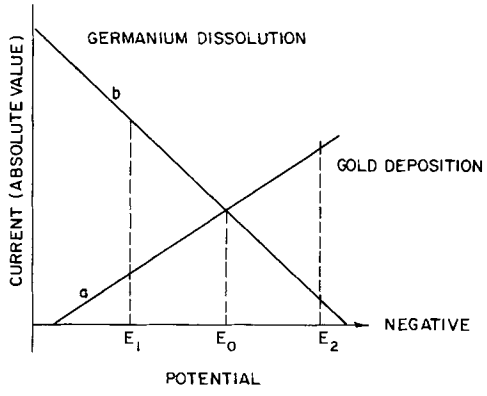

Fig. 2. Schematic current potential diagram for germanium corrosion in a solution containing gold ions.

Previously (10) it has been shown that during electrolytic germanium dissolution in the presence of HF parts of the germanium surface are at least temporarily free of oxide film [see also Turner (8)] so that intimate contact between germanium (or silicon) and gold may occur. The spots at which gold deposition occurs are distributed randomly over the semiconductor surface, separated by anodic sites at which dissolution proceeds. The gold plated parts of the crystal are blocked for further germanium dissolution but not for further metal deposition. During this procedure gold is deposited on both the cathode and the anode of the plating cell which appears to be rather a paradox. The final product of this kind of plating process is a rather porous metal structure the pores of which can, however, be closed by normal electroplating procedures. At longer plating times the dissolution process undercuts the deposited metal, and finally the metal defoliates.

Procedure

The final composition of the plating bath developed in this work was 2.7 g/l $HAuCl_4 \cdot 3H_2O$ in an aqueous solution containing 50% hydrofluoric acid (49% HF) by volume. The following procedure was found to give quite reliable results: (*A*) Clean the semiconductor surface by standard procedure, *e.g.*, etching. If etching is not possible, cleaning with boiling chloroform gives excellent results. (*B*) Immerse for 15 sec in the gold plating solution (see above) while passing an anodic current of 2 ma/cm^2 through the wafer. (*C*) Rinse thoroughly with distilled water. (*D*) Electroplate for 30 sec at 4 amp/cm^2 in a standard gold cyanide plating bath (11). (*E*) Heat for 30 sec to 400°C in a flowing hydrogen stream.

There seemed to be only a negligible amount of oxide trapped between the gold and the semiconductor because on heating the structure the gold alloyed completely with the germanium (or silicon).

Rate of Plating

The effect of the $HAuCl_4$-concentration, the HF concentration, and the anodic current on the rate of gold deposition was investigated experimentally. For this purpose round silicon wafers of 20 mm diameter and 0.5 mm thick were immersed in plat-

ing solutions of various compositions. After removal from the bath the wafers were rinsed immediately with conductivity water. The gold deposit was dissolved with aqua regia and then determined by a method developed by Cheng (9). From this analysis the thickness of the gold film was estimated. Figure 3 shows that at longer plating times the diffusion of gold ions to the semiconductor surface becomes rate-determining. At high gold concentrations complications seem to occur which are not yet well understood. Figure 4 shows that the rate of plating increases with increasing HF-concentration presumably because the partial current-potential curve for dissolution is shifted to more negative potentials (10). Figure 5 shows the effect of an anodic current on the rate of deposition. The rate of gold deposition decreases with increase in anodic polarization which is easily understandable on the basis of Fig. 2.

Results

For a tunnel diode structure alloyed gold contacts prepared in the manner here discussed showed a contact resistance of 10^{-5} to 10^{-6} ohms/cm^2. If ohmic contacts to material of higher resistivity are desired, the gold deposit has to be doped according to the procedure described by Pudvin and Biondi (4).

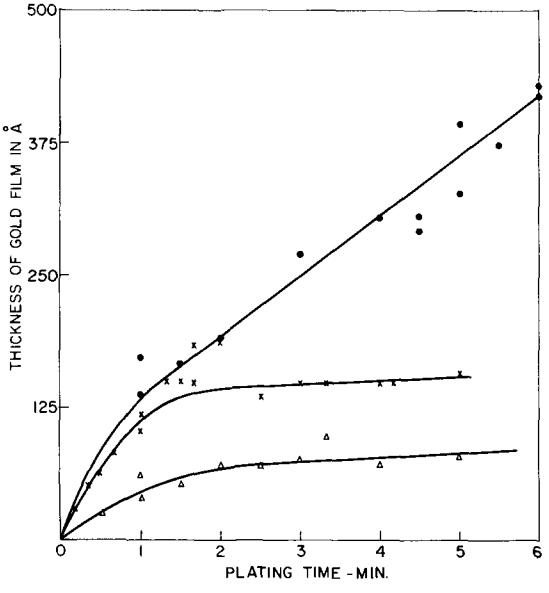

Fig. 3. Effect of concentration of gold ions on rate of gold deposition. △, 0.0035M $HAuCl_4$ in 25% HF; X, 0.007M $HAuCl_4$ in 25% HF. •, 0.014M $HAuCl_4$ in 25% HF.

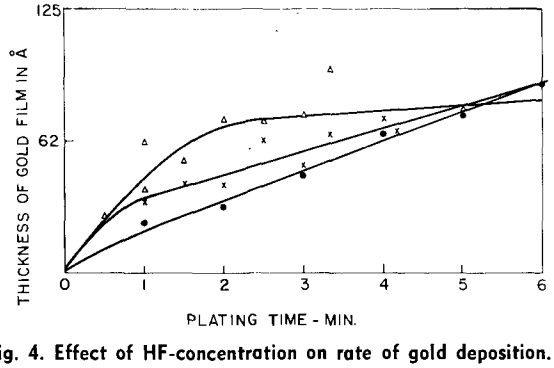

Fig. 4. Effect of HF-concentration on rate of gold deposition. △, 25% HF; X, 12.5% HF; •, 6.25% HF.

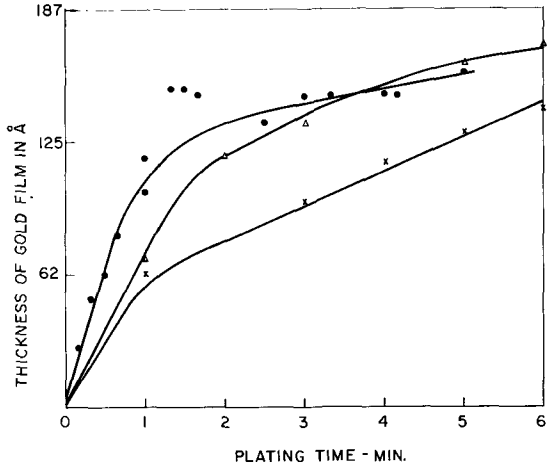

Fig. 5. Effect of anodic polarization on rate of gold deposition. •, No current; △, 1.7 ma/cm^2; X, 3.0 ma/cm^2.

Acknowledgment

The authors are indebted to M. E. Szekely and H. S. Sommers, Jr., for several valuable discussions of this work. The research reported in this paper has been sponsored in part by the U.S. Army Ordnance District, Philadelphia, Pa., under contract DA 36-034-ORD-3283RD.

Manuscript received Sept. 7, 1962; revised manuscript received Nov. 12, 1962.

Any discussion of this paper will appear in a Discussion Section to be published in the December 1963 JOURNAL.

REFERENCES

1. N. J. Harrick, *Phys. Rev.*, **115**, 876 (1959).
2. H. S. Sommers, Jr., *RCA Engineer*, **6**, 4 (1960).
3. M. Hansen and K. Anderko, "Constitution of Binary Alloys," pp. 206, 232, McGraw-Hill Publishing Co. (1958).
4. J. F. Pudvin and F. J. Biondi in "Transistor Technology," Vol. III, pp. 172-173, D. Van Norstrand Co., Inc. (1958).
5. S. J. Silverman and D. R. Benn, *This Journal*, **105**, 170 (1958); S. L. Mathew and E. L. Ralph, *Solid State Electronics*, **2**, 202 (1961); G. Gobeli and F. G. Allen, *J. Phys. Chem. Solids*, **14**, 23 (1960).
6. J. F. Dewald in "Semiconductors," N. B. Hannay, Editor, Chap. 17 (1958).

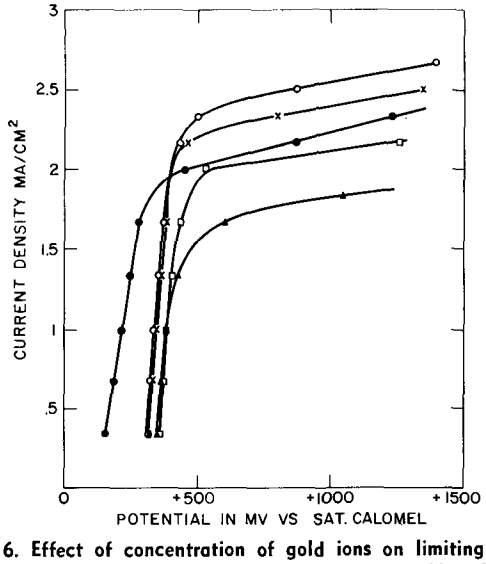

Fig. 6. Effect of concentration of gold ions on limiting current during anodic dissolution of n-type germanium. •, 1*N* H_2SO_4; ▲, 0.059M $HAuCl_4$; □, 0.105M $HAuCl_4$; X, 0.143M $HAuCl_4$; ○, 0.182M $HAuCl_4$.

7. C. Wagner and W. Traud, *Z. Elektrochem.*, **44**, 391 (1938).
8. D. R. Turner, *This Journal*, **103**, 252 (1956).
9. K. L. Cheng and P. F. Lott, Proc. Int. Symposium Microchemical Techniques, Pennsylvania State University, 1961, To be published.
10. W. Mehl, To be published.
11. Mohler and Sedusky, "Electroplating," p. 196, Chemical Publishing Co., New York (1951).
12. Yu V. Pleskoz, *Doklady Akad. Nauk S.S.S.R.*, **126**, 112 (1959); H. Gerischer and F. Beck, *Z. physik. Chem. (Frankfurt)*, **13**, 389 (1957); D. R. Turner, *This Journal*, **107**, 810 (1960).

APPENDIX

Electronic Interaction between Germanium and Gold Ions

An important step in the replacement plating reaction is the transfer of electrons from the germanium to the gold ions resulting in the formation of metallic gold.

Electrons can exist in germanium in two energy bands, the valence and the conduction band (neglecting surface states, and the question therefore arises whether these gold ions accept electrons from the valence band or from the conduction band (6). The following experiment decides this question in favor of a valence band reaction. N-type germanium shows on anodic polarization in an electrolyte a light-sensitive limiting current. From this observation it has been concluded that holes are needed for breaking the covalent Ge-Ge bands (8). Figure 6 shows how this limiting current changes with increasing concentration of gold ions in the plating. solution. After a relatively small addition of gold ions the limiting current drops, presumably because parts of the germanium surface are now covered by gold. On further increase of the gold ion concentration the limiting current increases above the value measured for the free germanium surface in absence of gold ions. During the reduction of gold ions, therefore, more holes must be available for germanium dissolution than in the absence of gold ions. We thus have to conclude that gold ions accept electrons from the valence band, *i.e.*, inject holes into the valence band. These holes are then available for germanium dissolution resulting in an increase of the anodic limiting current. Similar results have previously been found for other oxidizing agents (12).

Vapor Pressure of Molybdenum Trioxide

E. A. Gulbransen, K. F. Andrew, and F. A. Brassart

Research Laboratories, Westinghouse Electric Corporation, Pittsburgh, Pennsylvania

The vapor pressure of solid and liquid molybdenum trioxide is one of the important quantities in evaluating the kinetics of oxidation of molybdenum at temperatures above 600°C. During the course of these studies we have measured the vapor pressure of pure $MoO_3(s)$. A number of papers in recent years have dealt with this problem (1-6). Two recent studies on the vapor pressure of solid molybdenum trioxide are the papers of Blackburn, Hoch, and Johnston (1) and Hörbe, Knacke, and Prescher (2). Both groups used the Knudsen effusion method. The former obtained an enthalpy of sublimation of 79.74 kcal/mole of vapor while the latter found a value of 88.6 kcal/mole of vapor. This difference is outside the range of the experimental errors. The vapor pressure of liquid molybdenum trioxide has been studied recently by Selikman, Gorowitsch, and Prosenkova (3). An enthalpy of vaporization of 35.2 kcal/mole was calculated by Hörbe, Knacke, and Prescher (2) using this data and the corrected data of Feiser (4). The boiling point has been given as 1155°C and the melting point as 795°C (2).

Berkowitz, Inghram, and Chupka (5) have determined the vapor species using the mass spectrometer method. The trimer, $(MoO_3)_3$, is the main gaseous species for the temperature range of 600°-700°C. Smaller quantities of $(MoO_3)_4$ and $(MoO_3)_5$ and the dimer and monomer also are present.

Method

The vapor pressure above $MoO_3(s)$ was measured by the Knudsen effusion method using a vacuum microbalance (7). Pressures of about 10^{-6} Torr were obtained at temperature. The Knudsen cells were made from 0.005 in. thick Pt sheet with the effusion orifice in the top. The orifice was 0.06 cm in diameter and was not beveled. The cell was 0.686 cm long and had a diameter of 0.681 cm. The molybdenum trioxide was obtained by collecting the condensed volatile oxides after oxidation of pure molybdenum rod at temperatures of 1000°-1600°C. The oxide was collected in the form of thin plates of whitish-yellow crystals. Before each use and between each measurement the Knudsen cell + sample was treated with pure oxygen at temperature. Changes in weight of the Knudsen cell alone were checked by weighing the cell before and after the series of experiments. No changes were observed. These observations also indicate the high purity of the molybdenum trioxide used since no residue could be observed visually or by weighing. The weight change measured externally agreed precisely with the weight change resulting from the effusion measurements. Temperature was measured to ±2°C by means of platinum-10% rhodium platinum thermocouple. The thermocouple was calibrated against a NBS standard thermocouple. Weight change measurements were accurate to about 2%.

Results—Vapor Pressure of Molybdenum Trioxide Solid

Vapor pressures were calculated from the measured rates of evaporation at 5 temperatures between 600° and 700°C using the equation

$$P = m\sqrt{\frac{2\pi RT}{M}}$$

Here P is the pressure in atmospheres, R is the gas constant, T is the temperature in °K, and m is the rate of evaporation in g cm^{-2} sec^{-1}. M is the molecular weight of the vapor as calculated by Hörbe, Knacke, and Prescher (2). The accuracy of these M values has been questioned by one of the readers of this paper.

Table I. Vapor pressure data for solid molybdenum trioxide

Temp, °K	Time, sec	Wt loss, g × 10^{-3}	Effective area, $cm^2 \times 10^2$	$\bar{n}$ of $(MoO_3)_{\bar{n}}$ (2)	$(MoO_3)_{\bar{n}}$ pressure, atm
873.1	1200	0.578	0.2860	3.238	6.08×10^{-6}
898.1	3000	3.423	0.2861	3.277	1.47×10^{-5}
923.1	900	4.838	0.2862	3.323	6.82×10^{-5}
948.1	480	7.258	0.2864	3.375	2.02×10^{-4}
973.1	180	6.588	0.2866	3.438	4.69×10^{-4}

The effective area of the effusion orifice was determined by multiplying the area at room temperature by the thermal expansion factor and by the Clausing factor.

Table I and Fig. 1 show the vapor pressure data for solid molybdenum trioxide. To calculate the heat of sublimation of $(MoO_3)_s$ the method of least squares was applied to the data. Figure 1 also shows values for $MoO_3(s)$ and $MoO_3(l)$ from the literature. Using the data of Berkowitz, Inghram, and Chupka (5), Hörbe, Knacke, and Prescher (2) calculated the average molecular weight of the species from 600° to 700°C and have used this value to calculate their vapor pressure data. The data of Berkowitz, Inghram, and Chupka are not plotted in the figure. Their data fall close to line B of Fig. 1. Hörbe, Knacke, and Prescher (2) have also recalculated the older data of Feiser (4) for both $MoO_3(s)$ and $MoO_3(l)$. When recalculated the older data of Feiser for $MoO_3(l)$ agree very well with the newer data of Selikman, Gorowitsch, and Prosenkowa (3). The data for $MoO_3(l)$ are shown as curve D in Fig. 1. At the melting point the vapor pressure of $MoO_3(l)$ is given as 11.4 Torr or 0.015 atm. At the melting point the vapor pressures of the solid and liquid molybdenum trioxide should be equal. We have used this fact to help construct the extrapolated part of curve A of Fig. 1. Our least square treatment of the data extrapolates to a pressure of 11.7 Torr at the melting point and is in excellent agreement with the older data of Feiser (4) as corrected by Hörbe, Knacke, and Prescher (2). The Clausius-Clapeyron equation for the vaporization of the solid as determined from the method of least squares is

$$4.576 \log P\ (MoO_3)_{\bar{n}} = -\frac{75{,}400}{T} + 62.3 \pm 0.2$$

where P is in atmospheres and $\bar{n}$ is the average molecular association number. $\Delta H_{s\to g}$ is 75.4 kcal/mole ± 1 kcal/mole. The corresponding equation for the vaporization of the liquid oxide is

$$4.576 \log P\ (MoO_3)_3 = -\frac{35{,}200}{T} + 24.60$$

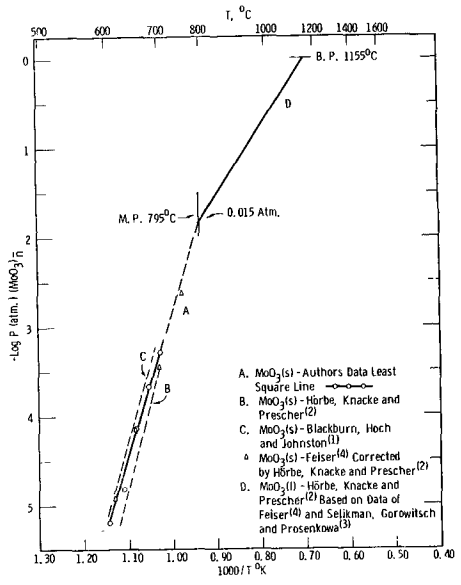

Fig. 1. Vapor pressure curves, solid and liquid MoO_3. ΔH_{s-g} = 75.4 kcal/mole, ΔH_{l-g} = 35.2 kcal/mole.

The difference in heat of vaporization of the solid and liquid molybdenum trioxide is 40.2 kcal/mole of $(MoO_3)_{\bar{n}}$ or 12.4 kcal/mole of MoO_3. The value of the latent heat of fusion according to Cosgrove and Snyder (8) is 12.6 kcal/mole of MoO_3. The agreement gives further evidence for the existence of the trimer $(MoO_3)_3$ and tetramer $(MoO_3)_4$ species in the vapor state of the oxide.

Figure 1 indicates a considerable discrepancy in $\Delta H_{s\to g}$ and in the absolute values of the vapor pressure of molybdenum trioxide as determined by the several authors. The reasons for these discrepancies are not clear.

Manuscript received July 23, 1962.

Any discussion of this paper will appear in a Discussion Section to be published in the December 1963 JOURNAL.

REFERENCES

1. P. E. Blackburn, M. Hoch, and H. L. Johnston, *J. Phys. Chem.*, **62** [7], 769 (1958).
2. Von R. Hörbe, O. Knacke, and K. E. Prescher, *Metall u. Erz.*, **14**, 232 (1961).
3. A. N. Selikman, N. N. Gorowitsch, and T. J. Prosenkowa, *Z. anorg. Chem., USSR*, **1**, 632 (1956).
4. J. Feiser, *Metall u. Erz.*, **28**, 297 (1931)
5. J. Berkowitz, M. G. Inghram, and W. A. Chupka, *J. Chem. Phys.*, **26** [4], 842 (1957).
6. K. Ueno, *J. Chem. Soc. Japan*, **62**, 990 (1941).
7. E. A. Gulbransen, "Advances in Catalysis," Vol. V, p. 119, Academic Press, New York (1953).
8. L. A. Cosgrove and P. E. Snyder, *J. Am. Chem. Soc.*, **75**, 1227 (1953).

A Study of the Rest Potentials in the Gold-Oxygen-Acid System

James P. Hoare

Research Laboratories, General Motors Corporation, Warren, Michigan

ABSTRACT

Two different electrode systems are found. One is the Au/Au-O system in which the gold surface is covered with a hydrated monolayer of adsorbed oxygen atoms. Here, the rest potential is a mixed potential, 980 ±20 mv. The other is the Au/Au_2O_3 system in which the gold surface is covered with a multilayer of hydrated Au_2O_3. In this case, the rest potential is an equilibrium metal-metal oxide potential, 1350 ±10 mv. The electrical properties of the Au-O layer are such that the O_2/H_2O reaction proceeds with great difficulty on it, and the reversible value of 1230 mv is not expected to be observed on gold electrodes.

Since most electrode reactions which involve an adsorption step are extremely complicated, a complete unified picture is still not obtained from the literature for the processes occurring at oxygen electrodes. It is interesting to note that relatively little work has been done on the potential-determining processes responsible for the rest potentials observed at noble-metal-oxygen electrodes. This situation may exist because, in this region of investigation, minute changes in the properties of the system cause large changes in the observed potentials.

As Vetter (1) points out, one must be able to reproduce the experimental conditions, that is, be able to obtain a reproducible electrode surface. A technique for obtaining a reproducible electrode surface in the platinum-oxygen-acid system has been demonstrated (2).

In much of the older work, care was not taken to control impurities in the system. This is a very important step in such investigations, as was pointed out by Bockris (3), because the oxygen potentials are so noble that the possibility of less noble electrode processes occurring is great.

It was suggested (2) that the rest potentials observed in the $Pt-O_2$-acid system could be explained in terms of a mixed potential (4) and the assumption that the monolayer of adsorbed oxygen on Pt is a good electronic conductor (5). The question now arises, how is the rest potential influenced by an adsorbed oxygen layer that is a poor electronic conductor? The gold-oxygen-acid system has been chosen as a representative of this situation.

Investigations of the rest potentials of an electrochemically prepared gold-oxide electrode are scarce in the literature. Much of the early work was done with gold wires dipping in a slurry of chemically prepared Au_2O_3 in H_2SO_4 solution (6-9). Since the noble metal oxides are quite unstable when chemically prepared (10), it is reasonable to suppose that the electrochemically prepared species may be different from the chemically prepared ones. Therefore, estimates of the standard potentials from standard chemical thermodynamic data (11) may be in error. Certainly the adsorbed oxygen and oxide layers on the electrode are hydrated, and the standard free energies of such adsorbed species are not known.

Most of the work in the literature on Au/O_2 electrodes has been concerned with obtaining polarization data and estimating rate-determining steps. Only Barnartt (12) has given serious thought to the potential-determining reactions of an electrochemically produced Au/Au_2O_3 electrode at rest. However, this analysis was not complete.

In this work, the rest potential of a gold bead in oxygen-saturated 2N H_2SO_4 solution was studied as a function of time, *p*H, partial pressure of oxygen, and the history of preparation of the electrode under conditions of rigorous control of impurities.

Experimental

Small gold beads (0.08-0.15 cm in diameter) were melted at the end of a gold wire (99.9+% pure) in a hydrogen flame because natural gas contains intolerable mercaptans. After the bead was cleaned by dipping it into concentrated nitric acid followed by heating to red heat in the hydrogen flame several times, it was mounted along with two other similarly cleaned beads, as checks, in one side of the dual Teflon cell, as described before (2). Trace impurities were leached from the cell by soaking it in water, which had been triply distilled from an all-quartz still, for at least 48 hr with frequent changes of this water.

An alpha-palladium-hydrogen reference electrode (13, 14) was used because the use of this system avoids the problems encountered with other reference systems used previously. Because the α-Pd-H electrode is reversible to hydrogen ions, junction potentials are not involved as in the case with saturated calomel electrodes nor is contamination with mercury a problem as in the case with Hg/Hg_2SO_4 electrodes. Besides, since the α-Pd-H electrode is independent of the partial pressure of hydrogen (15), the depolarizing effect on the oxygen elec-

trode by dissolved hydrogen from a Pt/H_2 reference electrode is avoided because hydrogen need not be bubbled over α-Pd-H. A Pd bead was mounted in the other side of the dual cell as described before (2). After the cell had been filled with the electrolyte and sealed, all electrodes on both sides were pre-electrolyzed against a removable auxiliary platinum cathode for at least 24 hr. Then, hydrogen was bubbled in the reference side of the cell until the potential of the Pd bead had remained constant at 50 mv against a Pt/H_2 electrode in the same solution (15) for 2 hr. The H_2 flow was stopped, the reference side of the cell sealed off, and measurements on the test electrode begun. It is to be noted that the Pt lead wire and the weld area were imbedded in virgin polyethylene to prevent solution contact with the Pt and the resulting polarization of the α-Pd-H electrode (16).

Cell, electrode, and solution preparations and the gas purification were all carried out as before (2). The potential was measured with a model 1230-A General Radio electrometer with an input impedance variable between 10^4 and 10^{14} ohms. The *p*H of the solutions was changed by diluting the $2N$ H_2SO_4 with $2N$ Na_2SO_4 to keep the ionic strength constant. At the end of a run, the *p*H was determined from the potential difference between the Pt/H_2 electrode and a saturated calomel (SCE) electrode. With this measurement the potential with respect to the α-Pd-H electrode may be converted to that with respect to the normal hydrogen electrode (NHE). Unless otherwise stated all potentials are reported *vs.* the NHE. All experiments were carried out at 25° ± 1°C. The partial pressure was changed by diluting the oxygen with nitrogen since the molecular weight of N_2 is closer to that of O_2 than is that of He, and the problems of the segregation of the gases were reduced. The cleanliness of the test electrode was monitored by observing the pseudocapacitance (17) when the test electrode was polarized with hydrogen bubbling over it by an electronic current interrupter.

Results and Discussion

Rest potential as a function of time.—If the circuit was broken in which a gold bead was anodized at about 2v in oxygen-saturated $2N$ H_2SO_4 acid, the potential fell to a steady value of about 1280 mv within about 2 hr. A sample of the electrolyte gave a positive test with titanium sulfate reagent (18) for the presence of peroxide. As in the case of Pt/O_2 (2), it was found that a reproducible system could be obtained only after the peroxides in solution and higher oxides on the metal surface were removed by bubbling purified hydrogen over the test electrode for about 20 min. In this case, purified hydrogen was bubbled through the test side of the cell for 15 min at about 200 cc/min. At this point the potential between two Pt electrodes was zero, but the potential of the Au was still 1200 mv. The test for peroxide was negative. Apparently, treatment with hydrogen removed the peroxide from solution, but did not remove all of the oxide from the metal surface.

If, now, H_2-stirring was replaced with O_2-stirring, the potential rose to a steady value of 1350 ± 10 mv which was time invariant for over 48 hr. This is in good agreement with the potential value of 1360 mv assigned by Hickling (9) to the Au/Au_2O_3 couple and with the potential values observed by those workers (6-9) who used slurries of chemically prepared Au_2O_3 in H_2SO_4 solutions. Evidently the hydrogen reduced some of the Au_2O_3 to Au, and the intimate mixture of Au and Au_2O_3 on the surface of the Au bead produced a good Au/Au_2O_3 electrode equivalent to the slurry experiments. In physical appearance, such a bead was covered with a reddish brown deposit. This reddish brown deposit has been shown (12, 19) to be Au_2O_3.

Next, the system was stirred with hydrogen until the potential of the Au bead had reached the hydrogen potential (—50 mv *vs.* α-Pd-H) and all oxides had been removed from the system (over 2 hr at H_2 flow = 200 cc/min). Then the H_2-stirring was replaced with O_2-stirring, and the potential was followed as a function of time. The potential rose quickly to about 600 mv (5 min) and more slowly (several hours) to about 800 mv. After being in contact with O_2-saturated acid solution for over two days the potential came to a steady value of 980 ± 20 mv. When such an electrode system was stirred with H_2 at about 200 cc/min, the potential of the Au bead reached the hydrogen potential within 500 sec. This reduction time, required to remove the oxide from such a Au bead, is of the same magnitude as that required to remove the monolayer of adsorbed oxygen from a Pt bead (2).

Vetter (20) has pointed out that various workers (1, 9, 21) have found from coulombmetric measurements that a monolayer of oxide is formed on Au before oxygen gas is evolved. Inspection of the charging curves at low current densities, in Fig. 9 of ref. (1), shows a small kink near 1v before the large kink appears at about 1.35v. The first kink may be interpreted as the beginning of the formation of a monolayer of adsorbed oxygen atoms on gold, Au-O. With increased polarization the monolayer of Au-O is converted to a monolayer of Au_2O_3 which begins at the second kink. The Au-O, most likely, is not a true oxide since gold atoms are not pulled out of the gold surface. It is reasonable to assume, then, that a gold electrode which exhibits 980 ± 20 mv has its surface covered by a monolayer of adsorbed oxygen atoms. Such a system will be referred to as a Au/Au-O electrode. In appearance, such an electrode was either bright or covered with a black deposit which may be assumed to be finely divided Au resulting from the complete reduction of Au_2O_3 with hydrogen.

A clean gold electrode was allowed to oxidize in air at room temperature and was then plunged into oxygen-saturated $2N$ H_2SO_4 solution. The potential came immediately to about 600 mv and in about 24 hr came to a steady potential of 980 ± 20 mv. When this system was stirred with H_2, the hydrogen potential was reached within 500 sec. These data indicate that in the absence of anodic polarization a gold surface is covered by a film of adsorbed ox-

Table I. Dependence of the potential on the partial pressure of O_2

Rotameter reading* O_2	N_2	Potential *vs.* α-Pd, mv Au_1	Au_2	P_{O_2}
4.4	0	1300	772	1
10.8	0	1300	772	1
3.8	4.7	1300	772	0.45
3.7	10.7	1300	772	0.26
10.2	9.6	1300	772	0.51
0	7.0	1280	760	0
4.3	0	1300	772	1

* The rotameter calibration curves are fairly linear from a reading of 3.0 corresponding to 95 cc/min to one of 13.0 corresponding to 600 cc/min.

ygen atoms rather than by a film of Au_2O_3 or some other oxide.

Using coulombmetric measurements, El Wakkad and El Din (22) reported three arrests in their charging curves which they attributed to the successive formation of Au_2O, AuO, and finally Au_2O_3. These data were not confirmed by other workers (1, 6, 9, 23) who found only one arrest near 1.35v. Therefore, in the Au-O_2-acid system one may be concerned only with one true oxide, Au_2O_3, and this is obtained only by anodic polarization.

Dependence of rest potential on partial pressure of oxygen.—The partial pressure was determined from the rotameter readings as described before (2). In Table I is presented the partial pressure, P_{O_2}, data in the order in which the experiments were performed. Each potential had been constant for about 10 min before being recorded. Au_1 is a Au/Au_2O_3 electrode exhibiting a potential of 1347 mv (1300 *vs.* α-Pd-H), and Au_2 is a Au/Au-O electrode exhibiting 819 mv (772 mv *vs.* α-Pd-H). Au_1 and Au_2 were obtained in the same cell by mounting two gold beads side by side in the test side of the Teflon cell. After the two gold beads had been preelectrolyzed anodically, hydrogen gas was bubbled through the cell for 15 min which converted both beads to Au/Au_2O_3 electrodes as described above. With the H_2 still flowing, Au_2 was cathodized by an external current until it registered −50 mv *vs.* α-Pd-H. When O_2-stirring replaced the H_2-stirring, Au_2 became a Au/Au-O electrode. The data in Table I were obtained under identical conditions for both electrodes after the potentials had become fairly steady. These data show that the rest potential is independent of the rate of stirring and of P_{O_2}. These results seem to indicate that the over-all potential-determining reaction does not involve a process which uses molecular oxygen.

In the case of the Au/Au_2O_3 electrode, at least two situations may occur which could give these observed results. In one, if the rest potential is a mixed potential similar to that suggested for the platinum case (2), it may be made up of the O_2/H_2O reaction

$$O_2 + 4H^+ + 4e \rightleftarrows 2H_2O \qquad [1]$$

and the Au/Au_2O_3 reaction

$$Au_2O_3 + 6H^+ + 6e \rightleftarrows 2Au + 3H_2O \qquad [2]$$

In addition, if the i_o for Eq. [1] proceeding on a Au-Au_2O_3 surface is very low (highly irreversible), then the local cell current will polarize the O_2/H_2O potential up to the Au/Au_2O_3 potential. The mixed potential will then be determined by Eq. [2] and will be independent of the partial pressure of oxygen. In the other situation, the properties of the Au-Au_2O_3 surface are such that Eq. [1] is not established on this surface and the electrode behaves as a true metal-metal oxide electrode. In this case a local cell is not set up, and the potential is an equilibrium potential and not a mixed potential. The second situation is favored for reasons given later on in this report.

In the case of the Au/Au-O electrode the same sort of analysis can be made. Here the mixed potential would be made up of Eq. [1] and the Au/Au-O reaction

$$Au\text{-}O + 2H^+ + 2e \rightleftarrows Au + H_2O \qquad [3]$$

Data are presented later which indicate that the rest potentials observed in this case are mixed potentials determined by the potential of Eq. [3] since a dependency on P_{O_2} was not found.

The slow change of potential with time from 800 to 980 mv exhibited by the Au/Au-O system in O_2-saturated 2N H_2SO_4 acid may be explained in terms of the activity of the Au-O layer. The extreme slowness of this transition is indicative of a molecular rearrangement in the surface layer. As time passes, the activity of this layer increases, probably under the influence of Eq. [1]. This may be true since the local cell is set up such that Eq. [1] is cathodized and Eq. [3] is anodized. Evidence for this is found in the case where O_2-stirring is replaced with pure N_2-stirring. Here the potential of the Au/Au-O system falls to a value near 800 mv (780 ± 20 mv) in about 24 hr since the O_2/H_2O reaction is suppressed. As soon as the system is stirred with oxygen again the potential rises once more. This behavior is shown in the last two lines in Table I for Au_2.

If an Au/Au_2O_3 electrode is allowed to stand in unstirred O_2-saturated 2N H_2SO_4 solution for about a week, the deposit on the Au bead changes from a reddish brown to a black color, and the potential falls from 1350 mv to about 980 mv. When this system is stirred with H_2, the hydrogen potential is obtained in about 500 sec. These data indicate that the Au_2O_3 oxide layer is unstable in contact with the acid electrolyte and that it interacts with the acid to form finely divided gold. Therefore, a Au/Au_2O_3 electrode is converted spontaneously to a Au/Au-O electrode. This process is hastened in a N_2 atmosphere as indicated in Table I for Au_1.

Dependence of the rest potential on pH.—Measurements of the rest potential were repeated in solutions composed of 0.1*N* H_2SO_4 + 2*N* Na_2SO_4 and 0.01*N* H_2SO_4 + 2*N* Na_2SO_4. The pH and the rest potential with respect to both α-Pd-H and NHE are presented in Table II for a Au/Au_2O_3 electrode, Au_1, and for a Au/Au-O electrode, Au_2. It is seen that the potential with respect to α-Pd-H is independent of pH in both cases. This means that the potential-determining reactions of gold-oxygen-acid electrodes have the same dependence on hydrogen ion activity as that of α-Pd-H (9), *i.e.*, a hydrogen ion is involved for every electron transferred.

Table II. Dependence of potential on pH

Solution composition	Pt/H_2 vs. SCE, mv	pH	Potential Au$_1$ vs. α-Pd	Au$_1$ vs. NHE	Au$_2$ vs. α-Pd	Au$_2$ vs. NHE	ΔE/ΔpH
2N H_2SO_4	245	0	1306	1353	805	852	—
0.1N H_2SO_4 + 2N Na_2SO_4	342	1.6	1300	1250	800	750	64
0.01N H_2SO_4 + 2N Na_2SO_4	395	2.5	1300	1197	798	695	62

Therefore, there should be a change of RT/F for each unit change in pH. In the last column of Table II, it is seen that the behavior is obeyed for the experimental data. It is to be noted that Eq. [1]-[3] fulfill this requirement as potential-determining reactions.

Polarization at low current densities.—If a system is in a steady-state condition on open circuit, it may be polarized at very low current densities with some assurance that the process being polarized is the same as that which determines the steady-state or rest potential. By varying the input impedance of the electrometer, minute currents were passed between the α-Pd-H reference electrode and the gold test electrode such that the test electrode was cathodically polarized. As shown before (2) under these conditions, it is safe to assume that the observed polarization is due entirely to that on the test electrode. A plot of the difference between the open-circuit potential and the polarized potential, $E_{oc} - E$, as a function of the logarithm of the apparent current density (estimated from the value of the input impedance, the exposed geometric area of the test electrode, and the potential reading) is presented in Fig. 1.

Curve A in Fig. 1 shows the polarization of a Au/Au_2O_3 electrode (1350 mv at rest) in O_2-stirred 2N H_2SO_4 solution in the absence of a detectable amount of peroxide. These points could be reproduced within 3 mv in both directions as indicated by the arrowheads on the curve. When O_2-stirring was replaced with N_2-stirring, a curve identical with curve A was obtained. These data indicate that the O_2/H_2O reaction is not established on a $Au\text{-}Au_2O_3$ surface, probably because such a surface is not a good enough electronic conductor (23), and that all the current goes into the Au/Au_2O_3 reaction, Eq. [2]. It is suggested that the observed rest potential for the Au/Au_2O_3 system is not a mixed potential but an equilibrium metal-metal oxide potential. In this case, the potential-determining reaction is given by the reaction in Eq. [2] with a standard potential of 1.36v.

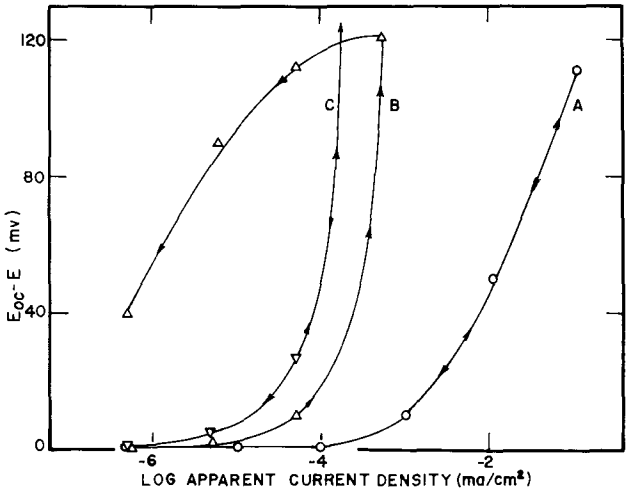

Fig. 1. Cathode polarization data at low current densities for Au-O_2 system: curve A, Au/Au_2O_3 stirred with O_2 or N_2; curve B, Au/Au-O stirred with O_2; and curve C, Au/Au-O stirred with N_2.

A plot of the polarization data taken on a Au/Au-O electrode (850 mv at rest) in O_2-stirred acid solution is presented in Fig. 1 as curve B. The unidirectional arrows indicate that in coming back down the curve the same points are not obtained unless one waits 15 or 20 min per point. One observes a temporary hysteresis. When a Au/Au-O electrode was polarized in N_2-stirred solution, the same curve as found in O_2-stirring was not obtained. Instead, a curve with higher polarization, curve C in Fig. 1, was obtained. Here the hysteresis is much larger than in curve B and permanent since even after standing in N_2-stirred solution for several hours the points coming down the curve were not the same as going up. To reproduce curve C, one had to stir with O_2 until the original rest potential was obtained. These data indicate that part of the current goes into the O_2/H_2O reaction and also, since the O_2 curve is different from the N_2 curve, that the adsorbed monolayer of oxygen, Au-O, has enough electronic conductivity to permit Eq. [1] to be established on this surface. It is suggested that the rest potentials observed in the Au/Au-O system are mixed potentials whose component potential-determining reactions are those represented by Eq. [1] and Eq. [3]. The i_o for Eq. [1], the O_2/H_2O reaction, is so low at the Au-Au-O surface that on open circuit the local cell current polarizes the potential of Eq. [1] down to that of Eq. [3]. Effectively, then, the rest potential is determined by the potential of the Au/Au-O reaction. It is further suggested that the standard potential for Eq. [3] lies near 980 mv since this is the point where it has been assumed that the activity of the Au-O layer is at a maximum value (activity→unity).

The hysteresis observed in curves B and C may be interpreted in terms of the activity of the Au-O layer. When the Au/Au-O electrode is cathodized some of the current goes into the reduction of Au-O with a resulting lowering of the activity of the Au-O layer. Then the same potential as before was not obtained on open circuit. In O_2-stirred solutions, the changes in activity produced during polarization were rectified in minutes due to the influence of the O_2/H_2O reaction. In N_2-stirred solutions, however, all the current went into Eq. [3] with a greater change in the activity of the Au-O layer. Here, since O_2 was not present, the activity did not increase again, as discussed above, and a permanent hysteresis was observed.

The oxygen reactions are more irreversible on Au than on Pt surfaces because the hydrated monolayer of adsorbed oxygen atoms on Pt is a good elec-

tronic conductor (5) while that on Au is a poor electronic conductor (23). In the absence of anodic polarization, the oxygen layers on Pt and Au surfaces do not grow much beyond a monolayer because enough energy is not realized in the reaction between Au or Pt and oxygen to remove a metal atom from the lattice. If additional energy is added to the system by anodic polarization, the film on a Pt surface does not build up because the field across the Pt-O monolayer is too small, since, being a good electronic conductor, the dielectric constant of the Pt-O layer approaches infinity. Most of the current goes into an oxygen reaction. However, when a gold surface is anodized, because the dielectric constant of the Au-O layer is comparatively small, the field across the Au-O layer is large enough to pull Au atoms out of the lattice. As shown in the work of Vetter and Berndt (1), the Au-O layer is converted to a Au_2O_3 layer which then continues to grow with further anodic polarization (12). Because the Au_2O_3 is not an adherent film (12), much of the current goes into the formation of Au_2O_3 which flakes off and falls to the bottom of the cell exposing new sites to attack. A barrier layer such as that found on aluminum is not found. This supports the conclusion that the oxygen layers on Au are better ionic than electronic conductors (23). Supporting evidence for these conclusions may be found in the observation that Pt and Au surfaces heated in air and anodized Pt surfaces remain bright and smooth while anodized Au surfaces become dull and rough.

The rest potential of Au-O_2 electrodes in acid solution to which peroxide was added behaved in the same way as the Pt-O_2 electrodes (2). That is, the rest potential fell close to the standard potential of 628 mv (11) of the O_2/H_2O_2 reaction,

$$O_2 + 2H^+ + 2e \rightleftarrows H_2O_2 \qquad [4]$$

and, for a given current density, the polarization was lowered.

It was found that the potential of the Au/Au-O system was more sensitive to the presence of impurities than the Au_2O_3. In general, however, the presence of impurities had a similar influence on the rest potential in either case, as was found for Pt/Pt-O electrodes.

From this work it is concluded that the theoretical value of the O_2/H_2O reaction, 1230 mv, cannot be realized on a gold electrode because of the electrical properties of the gold-oxygen layers.

Acknowledgment

The author is indebted to the late Mr. Cleveland F. Nixon and to Dr. Seward E. Beacom of the Electrochemistry Department of the General Motors Research Laboratories for their many helpful comments and for their continued support of this work. He is also grateful to Dr. Paul Delahay, Dr. Raymond Thacker, and Dr. John L. Griffin for many interesting and fruitful discussions.

Manuscript received June 6, 1962; revised manuscript received Oct. 6, 1962. This paper was prepared for delivery before the Boston Meeting, Sept. 16-20, 1962.

Any discussion of this paper will appear in a Discussion Section to be published in the December 1963 JOURNAL.

REFERENCES

1. K. J. Vetter and D. Berndt, *Z. Elektrochem.*, **62**, 378 (1958).
2. J. P. Hoare, *This Journal*, **109**, 858 (1962).
3. J. O'M. Bockris and A. K. M. S. Huq, *Proc. Roy. Soc. London*, **A237**, 277 (1956).
4. C. Wagner and W. Traud, *Z. Elektrochem.*, **44**, 391 (1938).
5. H. A. Laitinen and C. G. Enke, *This Journal*, **107**, 773 (1960).
6. T. F. Buehrer, F. S. Wartman, and R. L. Nugent, *J. Am. Chem. Soc.*, **49**, 1271 (1927).
7. R. H. Gerke and M. D. Rourke, *ibid.*, **49**, 1855 (1927).
8. T. F. Buehrer and W. E. Roseveare, *ibid.*, **49**, 1221, 1989 (1927).
9. A. Hickling, *Trans. Faraday Soc.*, **42**, 518 (1946).
10. N. V. Sidgwick, "Chemical Elements and Their Compounds," Oxford Press (1950).
11. W. H. Latimer, "Oxidation Potentials," Prentice-Hall, New York (1952).
12. S. Barnartt, *This Journal*, **106**, 722 (1959).
13. D. J. G. Ives and G. J. Janz, "Reference Electrodes," p. 112, Academic Press, New York (1961).
14. J. P. Hoare, *G. M. Eng. J.*, **9** [1], 14 (1962).
15. S. Schuldiner, G. W. Castellan, and J. P. Hoare, *J. Chem. Phys.*, **28**, 16 (1958).
16. J. P. Hoare, *J. Phys. Chem.*, **64**, 1780 (1960).
17. D. C. Grahame, *Chem. Rev.*, **41**, 441 (1947).
18. F. D. Snell and C. T. Snell, "Colorimetric Methods of Analysis," Vol. II, 3rd ed. (1949).
19. A. Hickling and S. Hill, *Discussion Faraday Soc.*, **1**, 236 (1947).
20. K. J. Vetter, "Elektrochemische Kinetik," p. 502, Springer Verlag, Berlin (1961).
21. G. Armstrong, F. R. Hinsworth, and J. A. V. Butler, *Proc. Roy. Soc.*, **A143**, 89 (1939).
22. S. E. S. El Wakkad and A. M. S. El Din, *J. Chem. Soc.*, **1954**, 3098.
23. H. A. Laitinen and M. S. Chao, *This Journal*, **108**, 726 (1961).

Flaws in Anodic Ta_2O_5 Films

D. A. Vermilyea

Research Laboratory, General Electric Company, Schenectady, New York

ABSTRACT

Electron microscopy has shown that the flaws in Ta_2O_5 formed anodically on contaminated or roughened tantalum surfaces are thin spots in the film. At the thin spots, which have a diameter about equal to the film thickness, the two surfaces of the film have roughly conical indentations of considerable depth so that the minimum thickness may be less than half the film thickness elsewhere on the specimen. There is probably a gap between the metal and the film under the thin spots. Flaws, which form around a point where film growth is prevented, can be produced by carbide and oxide particles only a few hundred angstroms in diameter, or by surface roughness resulting from abrasion, chemical etching, or a crack in a pre-existing oxide film. The formation behavior and dielectric properties of films containing many flaws differ considerably from those of flaw-free films.

Many of the chemical and physical properties of thin insulating films depend on processes which occur at flaws in the films. Flaw, as used in this paper, refers to a region larger than an atom in size which is chemically or physically different from the remainder of the film. Examples of flaws are voids and regions of different composition or crystal structure.

Among the properties determined by flaws are electrical conduction and resistance to chemical attack. The electrical conductivity of flaw-free regions of many thin films is extremely low, and yet the films on the whole are poor insulators because of the voids and cracks which they contain. Electrolytic rectification does not occur at flaw-free regions of anodic films but only at the flaws. Scintillation, or electrical breakdown, of anodic films also starts at flaws. The chemical protection afforded the substrate by a film is often lost or greatly diminished by flaws for two reasons. First, the corrosion of the substrate usually involves removal of both ions and electrons, and the high electrical conductance of the flaws makes electron removal easy. Second, the original film may transform to one which is physically or chemically different, and such transformation often starts at flaws in the film. Examples of such losses of protection which start at flaws are the "breakaway oxidation" in gases (1) and the formation of porous oxide films on aluminum (2).

This paper describes the flaws present in anodic tantalum oxide films and tells how flaw generation is related to the chemical and physical state of the substrate surface. A subsequent paper will describe electrical conduction in these flaws and provide information about the nature of electrolytic rectification.

Experimental

Tantalum from three sources was used in these studies. The first material was 0.005 in. annealed sheet from Fansteel; a typical analysis shows (in parts per million) carbon 300, oxygen 70, nitrogen 20. The second material, arc melted in this Laboratory, analyzed carbon 20, oxygen 481, and nitrogen 33. The third material was zone refined in this Laboratory seven passes by a floating zone technique; the starting material was NRC tantalum analyzing carbon 8, oxygen 53, nitrogen 15. For chemical polishing a solution of $5H_2SO_4$, $2HNO_3$, 1½ HF, parts by volume of concentrated commercial acids was used. Unless otherwise noted chemical polishing was always followed by a 10-sec HF etch to remove the polishing film. It was necessary to add about 50% more HF to the polishing solution in order to polish arc melted or zone refined material.

Anodizing was performed using a variety of dilute aqueous solutions, including sodium borate, sodium sulfate, phosphoric acid, and perchloric acid; in most experiments 0.2% Na_2SO_4 was used. No effect of different solutions or forming rates was observed. All films were formed at room temperature, usually at 10-50Å/sec.

The thicknesses of anodic films were estimated by color comparison with a previously described optical step gage (3). Values obtained were increased by the factor 8.74/7.93 to take account of the better estimate of film density published by Young. Capacitance measurements were made using a solution of 1% H_2SO_4, saturated with hydrogen gas, and a platinum counter electrode.

Results

Nature of Flaws

Optical microscopy.—It has been found that many different surface treatments, for instance, oxidation, carburization, abrasion, and addition of contaminants such as grease or particles of various materials, result in the generation of flaws in the subsequently formed anodic films. Flaw concentrations vary from 10^4 cm^{-2} for the purest materials to 10^{10} cm^{-2} for heavily contaminated specimens. The flaws formed by all surface treatments are very similar in appearance and behavior. In the optical microscope the flaws can be observed at a magnification

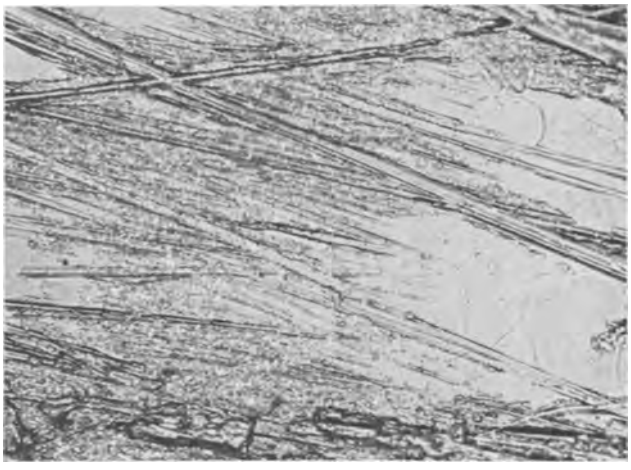

Fig. 1. Thin spots (light colored) in a 3100Å film on 0.005 in. chemically polished Fansteel sheet, scratches produced by abrasion against a similar specimen. 500X (all magnifications before reduction for publication).

of about 500 provided the film thickness selected is one which provides good contrast between the flaws and the rest of the film. Films of about 3100Å, formed at 195v, are especially suitable for they are purple while the flaws are pink or yellow. Figure 1 shows flaws in a film formed at 195v on 0.005 in. Fansteel sheet which had been chemically polished and abraded against another specimen of the same material. The flaws, which appear light in the photograph, may be seen in profusion in the abraded areas and in smaller concentration elsewhere on the surface. The colors of the flaws, yellow to pink, correspond to a film thickness of about 2400Å; they are thus thin spots in the film. Flaws of greater diameter appear to be thinner.

The difference between the thickness of the film at a particular thin spot and the rest of the film increases as the thickness of the rest of the film increases. This effect can be observed on individual flaws as the voltage of film formation is raised; it is even easier to observe on specimens containing about 10^{10} flaws/cm^2. When such large concentrations of flaws are present the entire film appears to the unaided eye to have a color which does not match precisely any of the colors for normal films, but which clearly corresponds to a smaller film thickness than would be present on a normal specimen. Figure 2 shows the difference between the thicknesses of heavily flawed and flaw free films as a function of formation voltage. (The methods of carburizing and oxidizing the specimens are explained below.) Examination at high magnification shows that the colors of such specimens are not uniform, but are mottled and vary from grain to grain of the substrate. For example, a 195v film may show purple grains with yellow spots and yellow grains with purple spots. In addition to the variation in color from grain to grain each flaw exhibits a variation of thickness from its periphery (thicker) to its center (thinner). The macroscopically observed colors are thus an average, and the data in Fig. 2 do not give maximum values of the deviation of film thickness from normal. The exact form of the curves in Fig. 2 probably depends on the concentration, size, and nature of the particles in the metal surface which give rise to the flaws.

Electron microscopy.—Observations with the electron microscope using preshadowed direct carbon positive replicas made it possible to determine the detailed geometry of the flaws. Figures 3 and 4 show the top surface of a film 2400Å thick formed on chemically polished 0.005 in. Fansteel tantalum sheet. The flaws are seen to be depressions in the film surface; in Fig. 4 they lie along a grain boundary of the substrate, while in Fig. 3 they are distributed throughout the grain. Figure 5 shows the surface of the specimen before film formation. The very large, round, shallow pits are characteristic of chemical polishing. Several particles, perhaps carbides, can be seen on the surface, especially at the grain boundaries. These particles are evidently the sources of the flaws; note that they are only of the order of a few hundred angstrom units in size. When

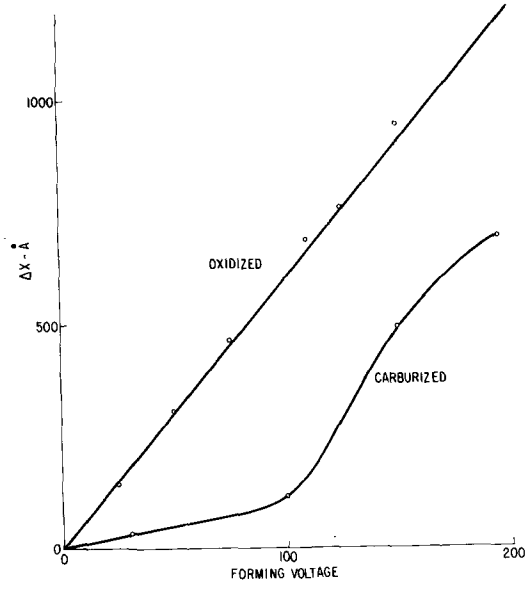

Fig. 2. Difference, ΔX, between the thicknesses of heavily flawed and flaw free films as a function of forming voltage.

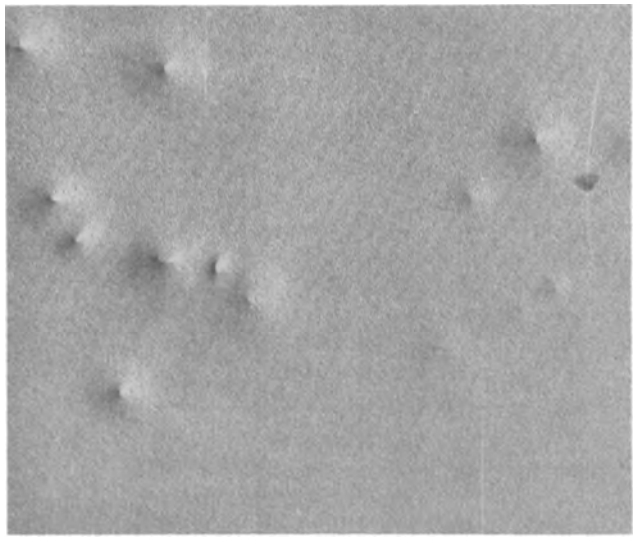

Fig. 3. Flaws on a 2400Å film. 75,000X (All electron micrographs are preshadowed direct carbon replicas, except as noted. The shadowing was always from the top or right side.)

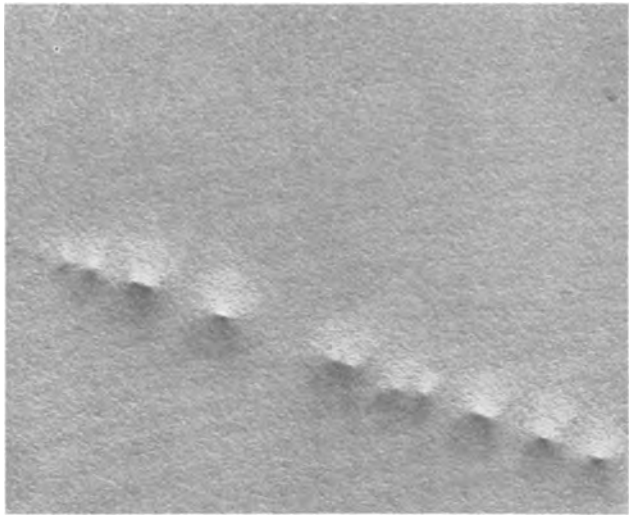

Fig. 4. Flaws at a substrate grain boundary on a 2400Å film. 75,000X.

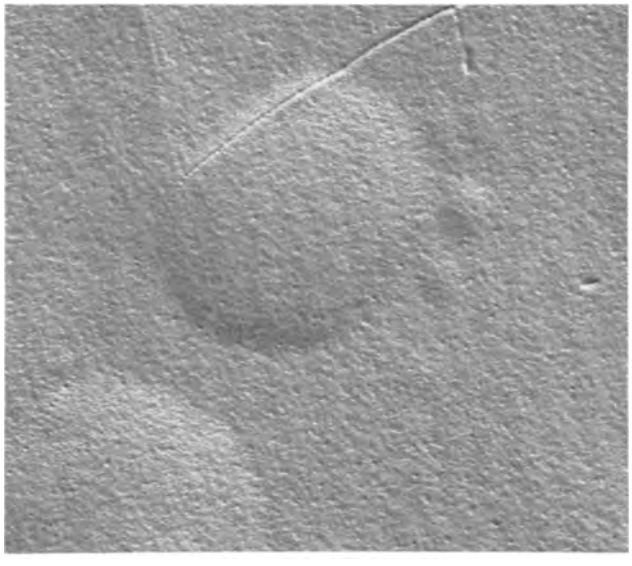

Fig. 5. Chemically polished 0.005 in. Fansteel sheet. 75,000X

the particles are very small the flaws are circular and symmetrical, the center being a point, while larger particles produce flaws which are not quite symmetrical and with elongated or irregularly shaped centers (see also Fig. 9, 10, and 11).

The surface of the metal after film formation is shown in Fig. 6. This picture was obtained by forming the film on a chemically polished specimen which was not given the 10-sec HF etch; the film left by chemical polishing reduces the adherence of the subsequently formed anodic film. After formation the film was stripped with cellulose tape and the metal surface was examined. The general appearance of the metal surface is very similar to that of the film surface, but there are two major differences. On the metal surface the flaws appear as elevations, and surrounding the elevation is an annular depressed area. The particles responsible for the flaws have been seen on many micrographs; they range in size up to several hundred angstroms and in shape from spheres to rods.

The flaws appear from these observations to have a shape like that shown schematically in Fig. 7. The shadows cast by the flaws reveal their shape and

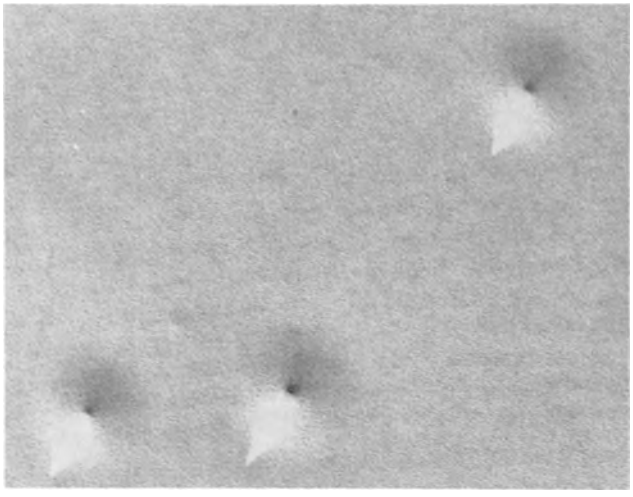

Fig. 6. Metal surface underneath a 3100Å film. 75,000X

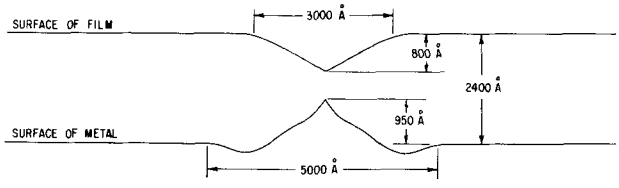

Fig. 7. Cross section of flaw in a 2400Å film

show that the maximum height of the projections on the metal surface under a 3100Å film is about 1200Å. In order to form 3100Å of tantalum oxide about 1200Å of metal must be used, and it therefore appears likely that the peaks of the highest elevations on the metal surface represent the position of the original surface before film formation. The maximum depression on the upper surface of a 2400Å film appears to be about 800Å. The flaw diameter on the upper surface is slightly larger than the film thickness, while the diameter of the flaw on the metal surface, including the annular depression, is about twice the film thickness. The shape of the annular depression on the metal surface could not be determined; the absence of shad-

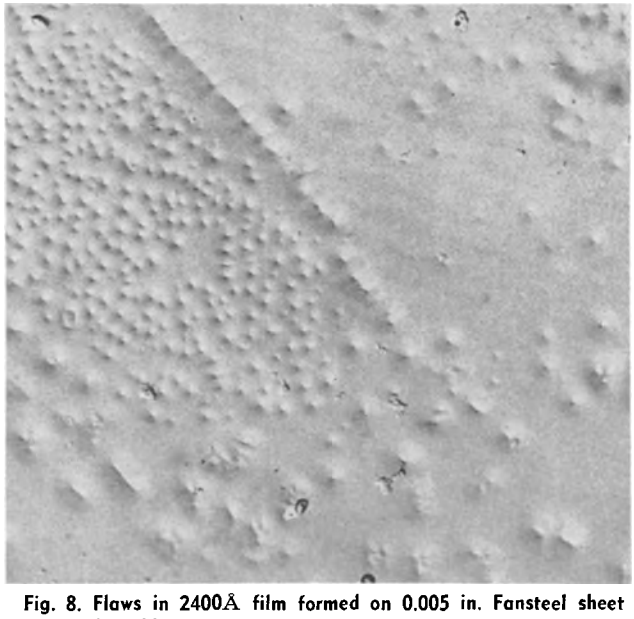

Fig. 8. Flaws in 2400Å film formed on 0.005 in. Fansteel sheet as received. 35,000X.

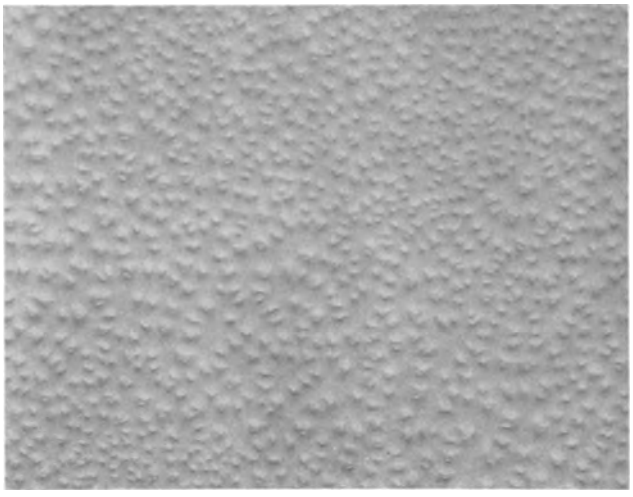

Fig. 9. Flaws in 3100Å film formed on carburized arc melted tantalum. 35,000X.

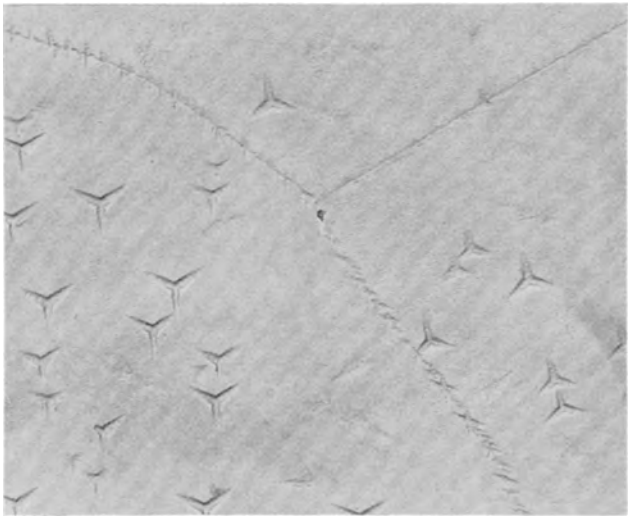

Fig. 10. Surface of tantalum heated 1 hr in argon at 800°C. 35,000X.

ows places an upper limit of about 450Å on the depth.

When more and larger particles are present on the surface, so that the macroscopic color of the specimen is abnormal, the electron microscope shows that the flaws are so close together that they impinge upon each other. Figure 8 shows the surface of a 150v film formed on 0.005 in. Fansteel sheet as received. Some metal grains have a very high flaw density (these grains appear blue instead of yellow), but the general flaw shape appears the same as on the chemically polished material. Probably the annealing operation resulted in surface contamination. Figure 9 shows the surface of 0.010 in. arc melted sheet which was heated under carburizing conditions (graphite wool present near specimen). The apparent thickness of individual grains on this specimen varied from 2400 to 3100Å. The flaws here are no longer symmetrical, probably because the particles were not symmetrical. That nonsymmetrical particles cause nonsymmetrical flaws is shown by Fig. 10 and 11. Figure 10 shows the surface of a chemically polished 0.005 in. Fansteel sheet specimen which was heated for 1 hr in unpurified welding grade argon; the platelets are presumed to be

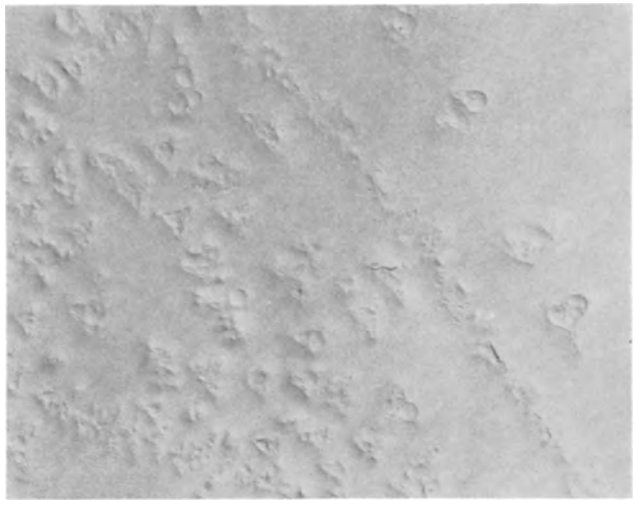

Fig. 11. Flaws in 2400Å film formed on specimen of Fig. 10. 35,000X.

a suboxide of tantalum. Figure 11 shows the surface of a 150v oxide film formed on a similar specimen; the apparent thickness varied from 1900 to 2400Å. The triangular shape of the flaws, corresponding to the triangularly shaped particles, is clearly visible. Note that cracks are present in some flaws; it is likely that cracked flaws are sites of electrolytic rectification and leakage.

When the contamination is even more extensive the colors present on some grains of a specimen show a still greater variation from pink through yellow, green, blue, and purple. Figure 12 shows the surface of such a specimen, which has been heated to 800°C for 1 hr in a vacuum of 10^{-5} mm Hg and then formed at 195v. On one grain the flaws appear separate and distinct, while on the other the entire area simply appears rough. It is believed that such films are at least partly porous; the evidence is presented below.

On specimens formed to higher voltages, for instance 300v, a few surface markings have shapes

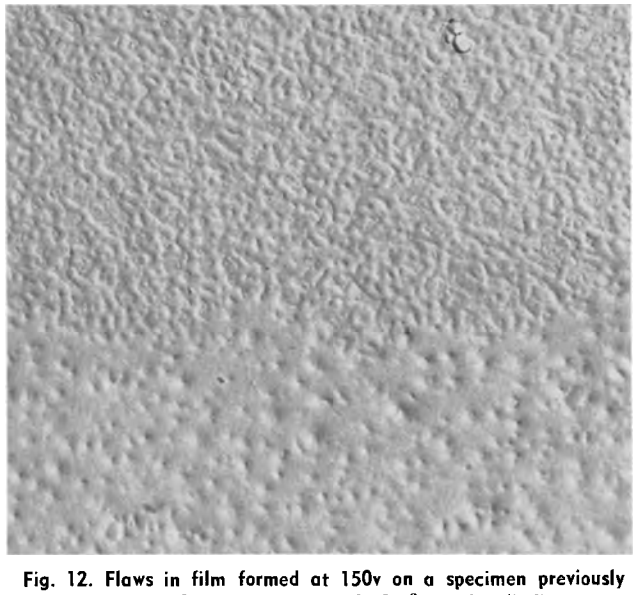

Fig. 12. Flaws in film formed at 150v on a specimen previously heated 1 hr at 800°C at a pressure of 10^{-6} mm Hg (indirect carbon replica). 35,000X.

suggestive of the collapse or healing of some flaws. For example, such films contain some slightly depressed areas with flat bottoms which may have resulted from the removal of the particle responsible for the flaw and subsequent healing of the flaw. A second type of spot in such films shows concentric circular depressions, which may have resulted from a sequence of flaw formation, healing, and new flaw formation at the same spot. Such a sequence might occur if very small particles were precipitated along a dislocation line in the substrate.

Attempted chemical analysis of flaws.—Electron beam microprobe analysis did not detect any elements other than tantalum at flaws on 0.005 in. Fansteel sheet. Such a result is not surprising both because of the very small size of the particles which can apparently cause flaws and because the device used was not sensitive to elements having atomic weights less than 40.

Behavior of Flaws

Etching in HF.—The chemical resistance of the flaws to all strong mineral acids except hydrofluoric is very great. No change is effected in either the electrical capacitance or leakage current of a specimen upon dipping into concentrated HCl, HNO_3, or H_2SO_4 for several minutes. Etching in hydrofluoric acid, however, increases the capacitance at a rate greater than would be expected from the decrease in thickness, so that the product of capacitance and thickness is increased. This effect was studied using 150v films 2400Å thick and an etching time of 120 sec in 50% HF; such an etch reduces the optical thickness from 2400 to about 400Å. If a relatively pure substrate such as arc melted or zone refined tantalum is used, the CX product stays constant at about 240 mfd Å/cm^2. On impure or abraded surfaces, however, the CX product after such a treatment may rise to 10^4 or more. Table I gives some typical results of such experiments. Observation with the optical microscope after etching reveals that holes have been etched through the film at the flaws; it is possible to see the holes developing in the thin spots during etching. The increased CX product results from the opening of holes at the flaws; the capacitance at the hole is about 22 mfd/cm^2 under the test conditions. Figure 13 shows the appearance of these holes after etching a film formed on chemically polished 0.005 in. Fansteel sheet which had been scratched with a diamond; holes can be seen both at the scratches and elsewhere, often at grain boundaries. The rough estimates in Table I of the numbers of flaws on the various specimens were obtained by counting either the holes produced by HF etching or the depressions in an electron micrograph.

Table I. Results of etching 2400Å films in HF

Material	Surface condition before film formation	Etching time, sec	Capacitance times thickness, mfd Å/cm^2	No. of flaws/cm^2
1. Zone refined	Chemically polished	120	236	10^4
2. Arc melted	Chemically polished	120	241	10^4
3. Arc melted	Chem. pol. & abraded against similar specimen	120	3600	Very high in scratches
4. Arc melted	Carburized, 2200°C	50	10,000	10^{10} on some grains; 10^4 on others
5. Arc melted	Carburized as above, formed 150v, then etched clean & reformed	120	242	10^6 on some grains; 10^4 on others
6. Arc melted	Carburized as above, chem. polished	120	243	10^6 to 10^4
7. Arc melted	800°C, vacuum of 10^{-6} mm Hg	120	2040	—
8. 0.005 in. Fansteel	Chemically polished	120	336	10^7
9. 0.005 in. Fansteel	Chem. pol. + 10 min HF	120	555	10^7
10. 0.005 in. Fansteel	Chem. pol. + 20 min boiling H_2O	120	323	10^7
11. 0.005 in. Fansteel	Chem. pol. + 5 min boiling 50% NaOH	120	500	10^7
12. 0.005 in. Fansteel	Chem. pol. + seven cycles of forming, etching, reforming	120	1020	10^8
13. 0.005 in. Fansteel	Chem. pol. + 5 min 550°C in air	120	3800	10^8
14. 0.005 in. Fansteel	Same spec. reformed & etched	120	4550	10^8
15. 0.005 in. Fansteel	Chem. pol. + Ta_2O_5 crystals	120	6100	10^9
16. 0.005 in. Fansteel	Chem. pol. + 1μ Al_2O_3 powder sprinkled on	120	3000	—
17. 0.005 in. Fansteel	Chem. pol., ground Pyrex, —200 mesh sprinkled on	120	400	10^7
18. 0.005 in. Fansteel	Chem. pol. + diamond abraded one side	120	1590	High in scratches
19. 0.005 in. Fansteel	Chem. pol. + abraded against similar spec.	120	6200	High in scratches
20.	Specimen 19 reformed	120	575	10^7
21. 0.005 in. Fansteel	Chem. pol. + grease	120	3900	—
22. 0.005 in. Fansteel	2200°C, 15 min in vacuum of 10^{-6}	120	242	10^5
23. 0.005 in. Fansteel	As received	120	6800	10^8
24. 0.005 in. Fansteel	Chem. pol. + 800°C vacuum for 1 hr	20	(~19,000) capacitance = 10 mfd/cm^2	
25.	Specimen 24 etched clean & reformed	120	390	—
26. Ta_2C		5	C = 62.5 mfd/cm^2	
27. TaC		5	C = 66 mfd/cm^2	

The data in Table I reveal that flaws are made either by the presence of some foreign matter on the surface, by abrasion, or by any treatment such as etching which roughens the surface. The contaminant can evidently be almost anything, particles such as Al_2O_3 or Ta_2O_5, thick layers of grease, and overgrowth or precipitates of carbides, oxides, and possibly nitrides. Not shown in the table is the fact that even very fine electrodeposited gold particles will cause flaws. The nature of the contamination and the relationship between the substrate structure and contaminant will be discussed in more detail in a later section.

At one time in the course of these studies it was thought possible that fluoride contamination on the surface might be the source of some flaws. The experiments using an NaOH etch and a 20-min leach in boiling water seem to rule out such an effect, for such treatments remove the film left by chemical polishing without introducing HF.

The rate of increase of the extra capacitance due to holes is very instructive. Figure 14 shows curves of excess capacitance as a function of time for several surface treatments. The excess capacitance is determined by estimating the thickness optically, calculating the capacitance which corresponds to the optical thickness, and subtracting this capacitance from the measured value. Consider first the data for the 0.005 in. chemically polished Fansteel sheet. The excess capacitance, ΔC, is very small after 5 sec and increases at an increasing rate to about 0.1 mfd/cm^2. After about 40 sec the slope of the log-log plot is about 2, as would be expected if all of the flaws had been penetrated by the HF and if the diameter of the growing hole at each flaw increased at a constant rate. The lower initial slope probably arises because not all of the flaws are completely penetrated in 5 sec, some requiring as much as 40 sec.

All of the heavily contaminated or abraded specimens show a very much larger ΔC after 5 sec, presumably because many more flaws are very quickly penetrated. The slopes of the log-log plots for heavily contaminated or abraded specimens are less than 2, probably because of impingement of the

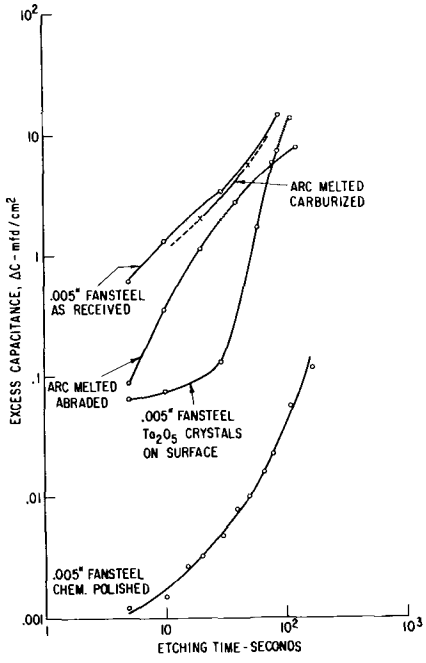

Fig. 14. Excess capacitance, ΔC, caused by etching in HF. ΔC = measured capacitance less capacitance calculated from optical thickness.

growing holes, and after 120 sec ΔC reaches a value of about 10 mfd/cm^2.

The specimen on which crystals of Ta_2O_5 were sprinkled evidently has some flaws which are quickly penetrated by HF and some which require more than 30 sec. During the last 90 sec the slope of the log-log plot is greater than 2; such slopes could mean either that an increasing number of flaws are becoming active or that the hole starts with some finite diameter at time zero. This latter condition might obtain if the interface between the amorphous and crystalline film at the periphery

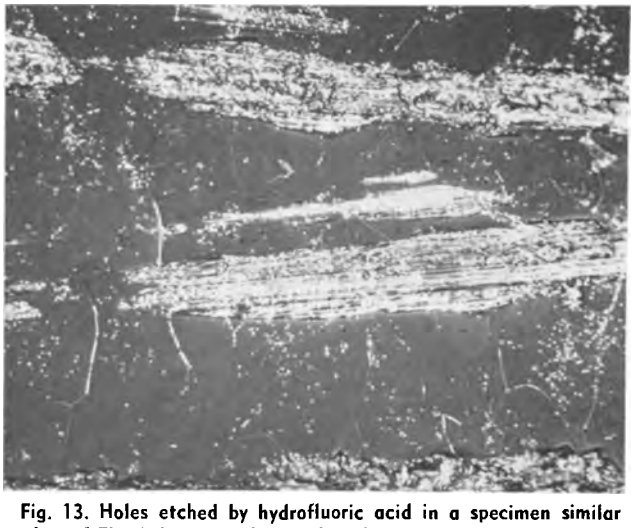

Fig. 13. Holes etched by hydrofluoric acid in a specimen similar to that of Fig. 1 but scratched with a diamond. 500X.

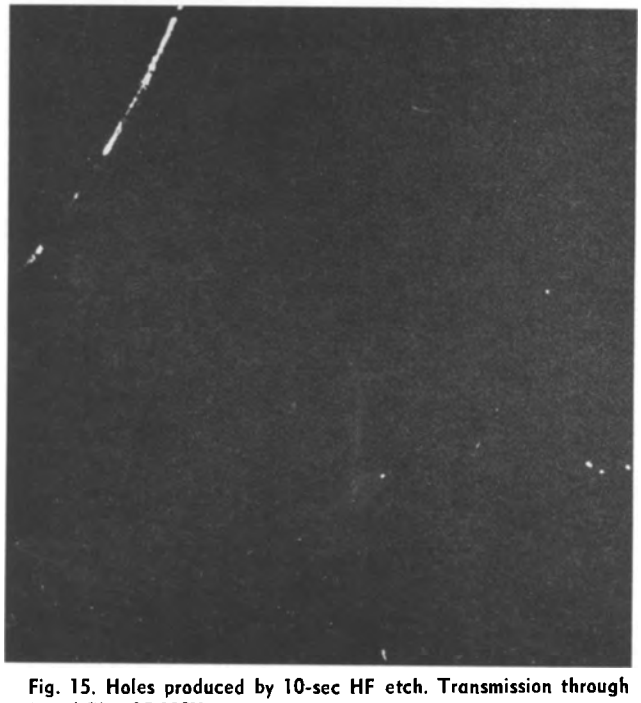

Fig. 15. Holes produced by 10-sec HF etch. Transmission through stripped film. 35,000X.

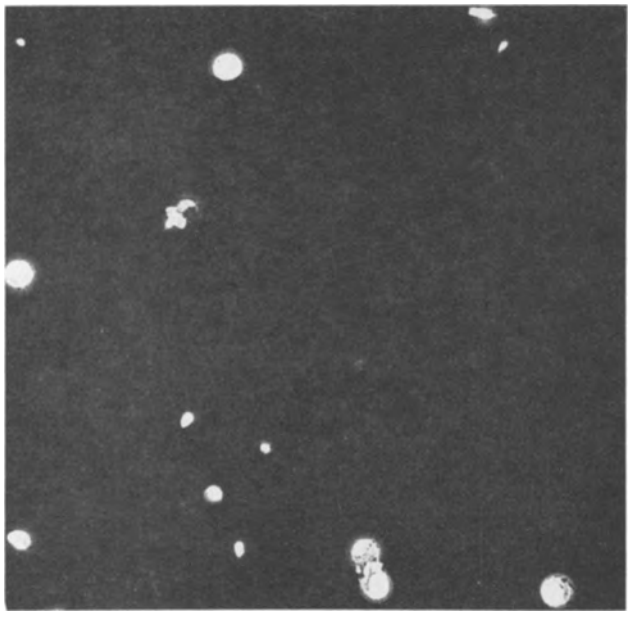

Fig. 16. Same as Fig. 15 except 30-sec etch.

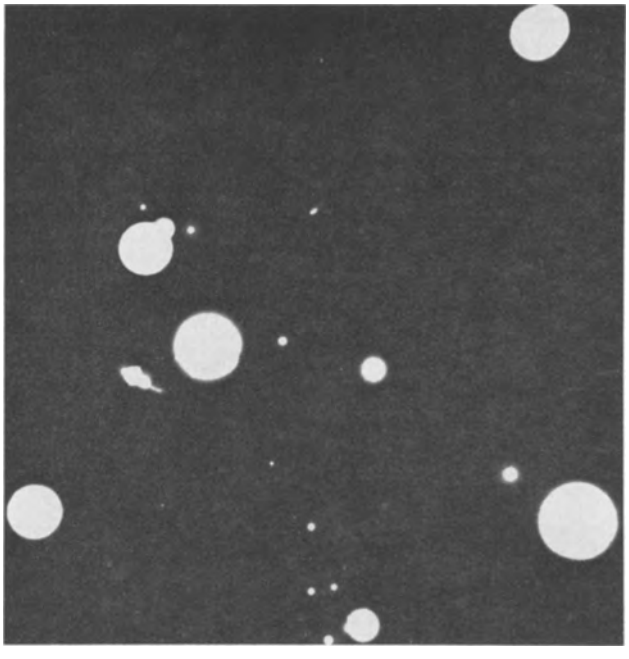

Fig. 17. Same as Fig. 15 except 50-sec etch.

of the crystal was attacked very quickly and the hole started with the diameter of the crystal.

It is concluded from these experiments that some flaws are penetrated in a very few seconds, while others require many seconds, and that heavily contaminated or abraded specimens contain many of the former. Electron microscope observations of films stripped with cellulose tape from 0.005 in. chemically polished Fansteel sheet which was not given the 10-sec HF etch after the chemical polish show how the flaws are opened. Transmission micrographs of such films stripped from the substrate after etching for 10, 30, and 50 sec are shown in Fig. 15, 16, and 17. After 10 sec the flaws are well opened and the edges are irregular. After 30 sec the holes are mostly circular, but note that there is a region of thinner oxide around the periphery. After 50 sec most of the holes appear circular with sharp edges, and they are about the same size as the depressions observed on the surface of the oxide before etching, about 3000Å. Electron microscope examination of surface replicas of etched specimens supplement the results obtained by transmission; after 10 sec the holes are open but jagged, with diameters to 600Å; after 30 sec the diameters are as great as 3000Å, while after 120 sec the maximum diameter is 6000Å. After 30 sec the holes are circular with steep sides at their periphery. These surface replicas also reveal that the flaw-free oxide remains remarkably flat during etching.

These and other electron micrographs have shown that the radii of the holes formed at flaws by HF etching initially increase at a rate of about 30 Å/sec to a radius of about 1500Å and then at a rate of about 15 Å/sec. The dissolution rate of the amorphous Ta_2O_5 in the film is about 15 Å/sec, and hence the final rate of growth of the hole represents dissolution of the Ta_2O_5 along the radius. The more rapid initial growth rate of the hole is a result of the decrease in thickness of the tapered oxide in the flaw (see Fig. 7).

It is believed that the HF penetrates under the oxide some distance from the center of the flaw, since observation of the colors of flaws during dissolution indicates that they get thinner initially about twice as fast as the rest of the oxide. This effect could conceivably arise from a composition difference, but the fact that the rate appears to be the same regardless of the source of the flaws makes such a cause unlikely. In addition, the fact that these large flaws are made by very tiny particles makes it unlikely that impurities would be present so far from the center of the flaw. It has been observed occasionally that a flaw dissolves at the same rate as the rest of the film for a minute or so and then more rapidly; presumably such a flaw was not immediately penetrated by the HF. The fact that some flaws, otherwise indistinguishable from the rest, dissolve at the same rate as the bulk of the film also supports the idea that the material in the flaws is normal Ta_2O_5. Rarely a flaw is seen to dissolve at about five times the rate of the film; this behavior was observed with some flaws produced by grease on the surface. Perhaps chunks of the film in the flaw were dislodged in such cases, leaving a smaller average thickness to be seen by the eye. All of these optical microscope observations of thickness changes during etching of flaws are not very accurate since the size of the flaw is about at the limit of resolution of the microscope. However, many instances of apparent dissolution rates twice that of the bulk film have convinced me that such behavior really does occur. Rapid penetration of HF through the center of the flaw could occur because of stress in the film at that point, because of a composition difference, or because of a crack or pore.

Two final observations should be made with respect to the HF etching experiments. The first is that the effects of abrasion and most of the surface contaminations studied were removed by a few cycles of forming, etching, and reforming. The only exception seemed to be that, once crystalline Ta_2O_5 had been produced at the surface whether by oxida-

tion at high temperature, sprinkling on Ta_2O_5 powder, or by field crystallization (5), the number of flaws only increased on repeated cycling. In fact, repeated cycling of a specimen not intentionally contaminated resulted in the development of some crystalline Ta_2O_5, probably by field crystallization during each formation of the specimen. The permanence of the effect of crystalline Ta_2O_5 probably results from the fact that it is unaffected by the HF; a stripped porous crystalline film produced by scintillation was intact after 8 hr in 50% HF.

The second point to notice is that the very rapid change in capacitance which may occur when a heavily contaminated specimen is etched in HF does not necessarily mean that the film substance dissolves at a very high rate. When films formed on Ta_2C and TaC are etched, for example, the capacitance increases to about 60 mfd/cm^2 in 5 sec, but on continued etching a white film is dislodged. Hence severe contamination may produce a porous oxide. Figure 18 shows a nontypical transmission electron micrograph of a stripped film which has not been etched in HF at all. Probably the large cracks were produced during stripping, but note the porous film within the largest crack. Presumably this porous film formed on some large impurity particle in the substrate (0.005 in. chemically polished Fansteel tantalum).

Formation behavior of films with flaws.—Gas evolution during film formation occurs with most substrates which have been contaminated or abraded in such a way that flaws form in the film. Gas evolution is copious on specimens containing crystalline Ta_2O_5, on abraded specimens, on specimens containing large precipitates visible in the optical microscope, and on TaC and Ta_2C. When large amounts of gas are evolved the efficiency of formation is low and the rate of voltage increase at constant current is abnormally low.

When only small amounts of gas are evolved the rate of voltage increase at constant current is often as much as 50% higher than normal for smooth uncontaminated specimens. This effect was reported for abraded surfaces some time ago (6) and was thought due to growth around oxygen bubbles which blocked part of the surface. Examination at a magnification of 600X during formation showed that no bubbles were present at the thin spots, and hence such an explanation is not tenable. Growth of the film around an entrapped bubble, as proposed by Young (7), would account for the high rate of voltage increase, but the geometry of the flaws is not like that suggested by Young. Gas evolution during the first few seconds of HF etching on specimens which are so heavily contaminated that the macroscopic color is abnormally low do indicate that gas is sometimes trapped in the film, however. Such trapped gas could be present between the film and the metal in the region around the flaw.

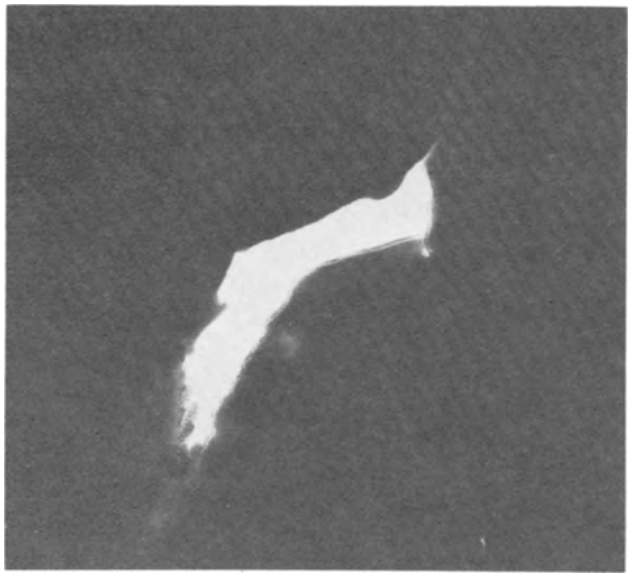

Fig. 18. Porous region in a cracked film stripped from the substrate. 35,000X.

Capacitance of flawed films.—It has already been pointed out by Young (8) that the capacitance per unit area of films formed on rough surfaces is abnormally low. The present experiments confirm this result and have shown much larger anomalies when heavily contaminated specimens are used. For example, a specimen heated to 1200°C for 1 hr at a pressure of 10^{-6} mm was formed at 240v. The optical thickness for an uncontaminated specimen should have been about 3800Å, the capacitance 0.064 mfd/cm^2. For the contaminated specimen the optical thickness was 2280Å, the capacitance 0.042 mfd/cm^2; both values are abnormally low! The specimen was etched clean in HF, then formed to 26v. The optical thickness was 286Å, the capacitance 0.44 mfd/cm^2 while the values expected for an uncontaminated specimen are 420Å, 0.57 mfd/cm^2. Such behavior, abnormally low values of both optical thickness and capacitance, is expected for films containing flaws which are thinner than the rest of the film, but which are separated from the metal by a gas filled gap. The gap would have to be of the order of 100Å wide to give the decrease in capacitance observed with a 3000Å film.

While most contaminated or abraded surfaces produce films with low capacitances the opposite behavior is sometimes observed. For instance, films formed at 150v on TaC and Ta_2C had capacitances of 2.4 and 2.9 mfd/cm^2 *vs.* a normal value of 0.1 mfd/cm^2, while a specimen heated at 800°C in unpurified argon yielded a film with a capacitance of 0.18 mfd/cm^2. This latter specimen is the one of Fig. 10 and 11. A particular treatment may give different results at different formation voltages. For example, heating in vacuum at 800°C for 1 hr followed by formation to 10v gave a capacitance of 1.62 mfd/cm^2 *vs.* the expected 1.53; formation at 30v gave an initial value of 0.4 mfd/cm^2 *vs.* the expected 0.52, but in a few seconds the capacitance drifted to 0.96; and formation at 80v gave a stable capacitance of 0.15 *vs.* the expected 0.198. Probably the particles producing the flaws were not well covered at 10v, only partially at 30, but well covered at 80 v.

Those specimens which have abnormally large initial capacitances are those which also show a very large capacitance change on etching a few seconds in HF, as with the tantalum carbides; presumably such films are cracked or porous. Those specimens which

have an abnormally low capacitance show a fairly small capacitance increase after 5-10 sec in HF, but the rate of capacitance change increases greatly, and by 50 sec such specimens may be "bare," *i.e.*, give capacitances of about 20 mfd/cm^2. Such behavior suggests a relatively coherent outer layer over an inner porous one.

Healing the flaws.—The large holes produced by HF attack at the flaws can be healed by reforming the specimen. Changes in the capacitance can be detected at very low voltages. For example, a specimen formed to 200v and etched to a film thickness of 450Å showed an excess capacitance of 0.176 mfd/cm^2. Application of 0.5v *vs.* the hydrogen electrode reduced ΔC to 0.15 mfd/cm^2, while 5v reduced ΔC to 0.015 mfd/cm^2.

The optical thickness of flaws can be changed markedly by a short etch plus reformation. This effect is observable on individual flaws, but is most striking on heavily contaminated specimens. For instance, the 0.005 in. as-received Fansteel sheet formed to 195v has a pink color because of the great number of flaws, while the color of an uncontaminated specimen is purple. If the pink specimen is etched 5 sec and reformed to 195v, it is purple and only slightly different in color from a chemically polished specimen formed to 195v. Examination with the microscope shows that a large fraction of the flaws have been healed by the etch and reformation. Presumably the etch allows access of the electrolyte to the gap between the oxide and the metal, and on reformation the gap is filled with oxide and the film over the gap can grow to the normal thickness. The specimen still contains many flaws, as shown by the behavior on etching subsequently, and it is not possible to produce a flaw-free film by repeated cycles of forming and etching. The reason for this lack of complete healing is discussed in the section on Surface Geometry.

Effect of strain on flaws.—The amorphous Ta_2O_5 films are brittle and crack if the specimen is bent substantially. The report by Young (9) that such films can flow plastically is probably in error. The film does change color and appears thinner when a specimen of tantalum is plastically deformed, but examination at high magnification reveals that the thin areas are mottled in such a way as to suggest that the film is extensively cracked on a very fine scale in such regions. Many macroscopic cracks are also caused by such deformation. Presumably the film cracks where a slip band arrives at the surface, and cracks of various sizes result from slip bands of different activity. Edeleanu and Law (10) have studied cracks produced by deformation of anodic aluminum oxide films.

Because of the cracks produced, plastic deformation of a relatively pure specimen causes changes in capacitance and leakage current. For example, a film 2400Å thick formed on 0.005 in. chemically polished Fansteel sheet had a capacitance of 0.1 mfd/cm^2. When the specimen was placed in a solution containing a 10^{-2}M ferrous-ferric redox system the current at —0.7v with respect to the redox potential was —0.2 μa/cm^2. After bending the specimen the capacitance was 0.17 mfd/cm^2, and the current was —2.0 μa/cm^2. Reformation to 150v resulted in a return to the original values.

Similar plastic deformation of a specimen on which a heavily flawed film had been formed produced much more startling changes. For example, a specimen heated to 800°C for 1 hr at a pressure of 10^{-6} mm Hg was formed to 150v. The capacitance was 0.081 mfd/cm^2 and the current in the redox test was —0.016 μa/cm^2. After bending the capacitance was 0.2 mfd/cm^2 and the redox current was —12 μa/cm^2. Reformation resulted in a return of the capacitance and current to their initial values, but also caused a change in the color of the specimen near the bend. The original color was blue instead of the normal yellow; bending and reformation resulted in the formation of a nearly normal yellow color in the deformed area. In areas at the periphery of the deformed area it was possible to see the slip bands which had been active in the area because the flaws had been healed and hence changed color along the slip bands. Figure 19 shows such an area on the carburized specimen of Fig. 20 after bending and reforming. The gray bands, purple in the microscope, are normal flaw free film and were not affected by the strain. The mottled areas are flawed as shown in

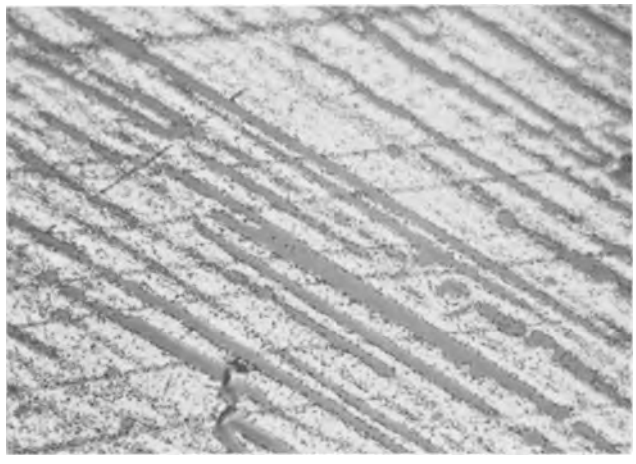

Fig. 19. Flaws in carburized specimen after deformation and reformation. Slip bands are horizontal. 500X.

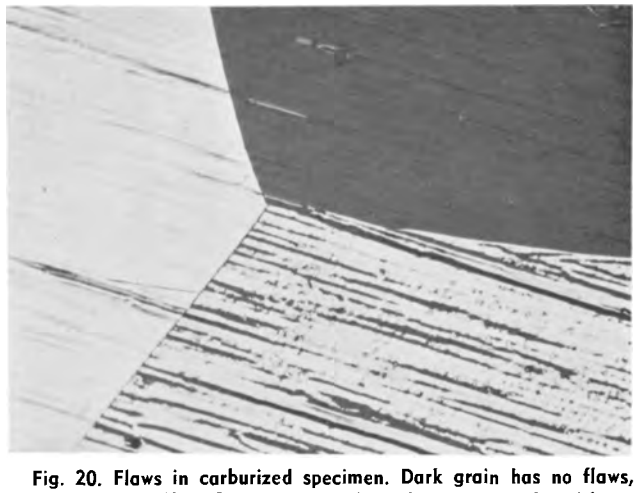

Fig. 20. Flaws in carburized specimen. Dark grain has no flaws, light grain ~10^{10}/cm^2, other grain has alternate streaks with no flaws and high flaw density along rolling grooves. 250X.

Fig. 9; they are yellow. Slip bands crossing yellow areas are purple and green.

The effect of deformation on the flaws is very similar to the effect of HF etching, the capacitance and current increase, and on reforming the color becomes more nearly normal. Evidently the deformation opens up many of the flaws to penetration by the electrolytic solution, and reformation heals these open flaws.

Origin of Flaws

In this section the nature of the surface conditions yielding flaws are discussed in more detail. These considerations and conclusions are uncertain and incomplete because of the fact that an extremely small volume of the metal is involved and chemical and structural analyses have not been possible. Tantalum is an excellent "getter" and forms innumerable binary and ternary compounds with carbon, oxygen, nitrogen, and hydrogen. In addition, precipitation from solid solution is very likely involved in the formation of many particles, and we know little about the solubilities and rates of precipitation in such complicated systems. The discussion to follow only points out some possibilities.

Oxygen and nitrogen.—Tantalum specimens of any purity available in this work, heated for 1 hr in the temperature range 800°-1200°C in an atmosphere of unpurified welding grade argon or nitrogen, a vacuum of 10^{-6} mm Hg, or sealed in an evacuated quartz capsule all yield heavily flawed films. The most likely contaminant is oxygen in most experiments, but specimens of 0.005 in. chemically polished Fansteel sheet heated 4½ hr at 800°C in nitrogen were found to contain 350 ppm of nitrogen along with 2650 ppm of oxygen. Hence nitrogen will be taken up by the tantalum at these temperatures. The experiments using sealed quartz capsules make it likely that oxygen contamination alone will cause flaws, since the most likely reactant is water liberated from the quartz. Most such heated specimens did not contain any surface phase visible in the optical microscope, and while electron diffraction sometimes gave lines the identification was not certain. Platelets were sometimes observed. Formation on such platelets appeared entirely normal, but flaws were often observed at the edges of the platelets.

When the surface of a specimen is oxidized sufficiently to produce crystalline Ta_2O_5 then flaws are produced at the oxide particles. Previous studies (5) have shown that cracks and stripping of the amorphous film are caused by the different growth kinetics of the crystalline and amorphous oxides (the crystalline oxide grows twice as thick as the amorphous for a given voltage). Flaws are evidently produced in such regions, probably because of loss of contact between the oxide and the metal in a region near the amorphous-crystalline boundary.

Carbon.—The following series of experiments makes it very likely that carbon produces flaws. Specimens were heated in a vacuum of 10^{-5} mm Hg at 2200°C for 15 min inside a tantalum cylinder which in turn was inside a sleeve of graphite wool. The first batch of specimens, heated in a new tantalum cylinder, had only about 10^5 flaws/cm^2, a reduction from 10^7 for the unheated material (0.005 in. Fansteel). The second batch of specimens heated in the same cylinder had tremendous numbers of flaws on some grains while there were practically none on other grains. Figure 20 shows a dark grain, which had the normal purple color for a 195v formation, a light grain, which was yellow, and a light and dark grain which had purple and yellow streaks along the rolling grooves. Evidently there is a marked sensitivity to orientation; such a finding is not surprising since surface nucleation of a precipitate could be very orientation dependent. X-ray analysis showed both the purple and yellow grains to have a (112) plane nearly in the plane of the sheet, but the purple grain was about 10° closer to a (111) orientation than the yellow grain. Note that the yellow areas are not uniform but mottled on a very fine scale.

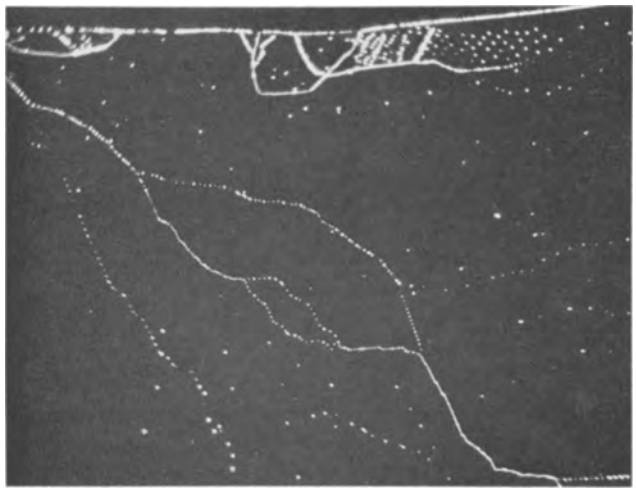

Fig. 21. Holes produced by HF attack at flaws in a film formed on decorated dislocations in a carburized arc melted specimen. 500X.

Two cycles of etching this specimen in HF and reforming resulted in a film which was almost entirely uniform but which did contain flaws at grain boundaries and low angle boundaries, as shown in Fig. 21. This figure shows holes etched through a film originally 2400Å thick by 120 sec of HF etching. Chemical polishing, reforming, and re-etching gave a very similar pattern with many identical spots, showing that the contamination extended some distance into the specimen along a line. (Chemical polishing removed about 1μ.) The persistence of the location of flaws on this specimen and their peculiar distribution along lines makes it very likely that the flaws are formed at carbide precipitates at dislocations in low-angle boundaries.

The third set of specimens heated in this cylinder contained 450 ppm of carbon, and the surface was covered with the platelets shown in Fig. 22. Formation resulted in thin spots at these platelets, which are probably carbides. It is interesting that the rate of decrease in thickness of the thin spots in the film on these platelets was about twice that of the rest of the film, while on Ta_2C and TaC the dissolution is apparently very much more rapid. Such a difference is not unexpected; on a small carbide platelet, covered with a normal dense film produced by growth

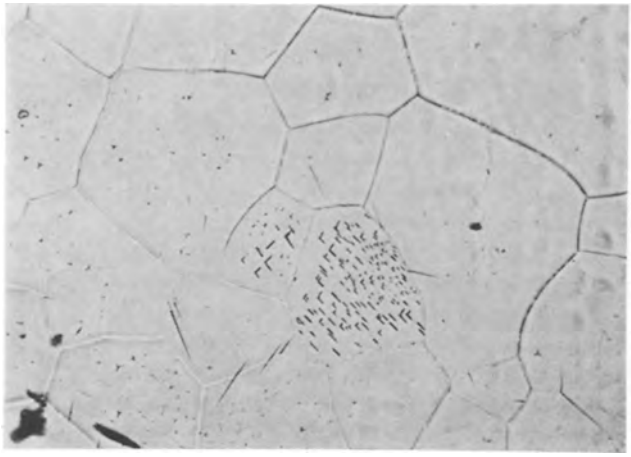

Fig. 22. Carbide platelets in a carburized arc melted specimen. 500X.

from the sides around the platelet the dissolution rate would be different from that on a bulk carbide phase where the poor, probably porous, film cannot be covered over.

After these cycles the tantalum cylinder was very brittle, contained 4.1% carbon (Ta_2C and TaC contain 3.2%C and 6.2%C, respectively), and x-ray diffraction revealed the presence of both Ta_2C and TaC. The outside, golden in color, was probably TaC, while the inside, silvery, was Ta_2C; a sharp interface separated these phases. The first specimens heated in the new cylinder were not carburized, but the second and third sets were increasingly carburized as the carbon content of the cylinder increased.

Hydrogen.—Hydrogen was charged electrolytically into tantalum to such an extent that platelets of a hydride were visible. Formation on these specimens was normal, and no preferred association of flaws with platelets was observed.

Grease.—Heavy layers of grease are initially impervious to the electrolytic solution. As the voltage is raised to perhaps 50v the grease is suddenly penetrated and then pushed aside. In this process some grease is evidently trapped and subsequent formation gives rise to the thin spots shown in Fig. 23. From their HF etching (most etch at twice the rate of the rest of the film) and other characteristics they

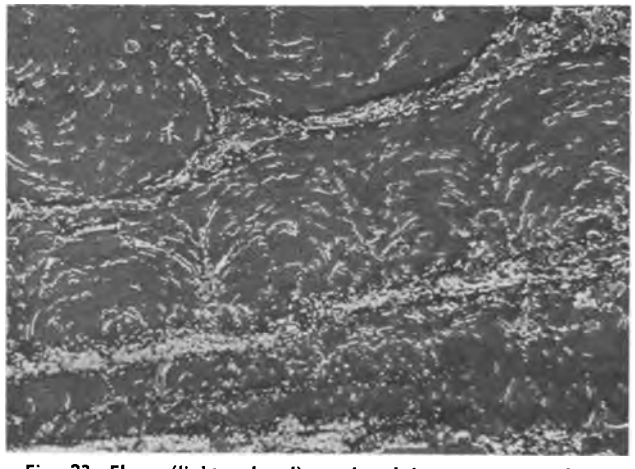

Fig. 23. Flaws (light colored) produced by grease on substrate surface. 500X.

appear to be very similar to other flaws produced by other types of contamination.

Surface geometry.—A certain degree of surface roughness produces flaws. Etching arc melted tantalum in 50/50 HF/HNO_3 produces a surface which on formation yields 10^6 flaws/cm^2 while chemical polishing gives only 10^4.

Any kind of abrasion which produces a sufficiently rugged surface produces many flaws. It is possible that contamination is sometimes introduced by the abrasion, but the roughness alone seems to be sufficient to cause flaws. Contamination might result because of high local surface temperatures; Bowden and Tabor (11) found that temperatures as high as the lowest melting point of the couple and lasting 10^{-3} sec were produced during rubbing one material on another. In order to prevent high temperatures tantalum was abraded with low melting metals like Zn, Cd, and Bi which were chilled to 77°K, and also by a glass with a softening point of 311°C (Minnesota Mining and Manufacturing SK 201). An aqua regia etch to remove surface contamination followed all abrasions using materials different from tantalum. Various atmospheres were tried, and arc melted tantalum was scratched on arc melted tantalum to reduce contamination. The atmospheres used included argon purified over hot Ti-Zr turnings at 800°C, oil, benzene, carbon tetrachloride, water, liquid nitrogen, and air. All abrasions resulted in copious flaw generation. The generation of flaws in the pure argon atmosphere makes it likely that contamination is not required, but that surface roughness alone is sufficient, for the only source of contamination in those experiments was the naturally formed air oxide film about 8Å thick. The abrasion was performed in a closed vessel through a metal bellows, and a positive argon pressure of 2 cm Hg was maintained. The 500 cc vessel was flushed for 5 hr with 120 liters of argon prior to the abrasion.

Not all surface roughness will produce flaws; evidently some minimum ruggedness is necessary. For instance, 0.0005 in. cold rolled foil with a very smooth surface made on highly polished rolls yields a film with only 10^5 flaws/cm^2.

It is interesting that recent studies by Eubanks, Moore, and Pennington (12) of the oxidation of iron have shown that surface roughness generates a porous oxide. Even more important is their observation that loss of contact between the oxide and the metal does occur at the corners of intentionally cut rectangular grooves and at the peaks of triangular grooves. Their photographs show directly that the oxide film cannot follow perfectly a rough receding surface.

Flaws are also introduced upon reforming a specimen containing a crack in a previously formed film. Figure 24 shows such flaws on a specimen which had been formed to 195v to produce a 3100Å film, bent to crack the film, and reformed to 195v; the crack is the horizontal line in the photograph. Most of the flaws appear dark in this photograph because of the small sizes of the flaws. Under the microscope the pink color of the flaws can be seen. The crack in the film is necessary for the creation of such flaws, since

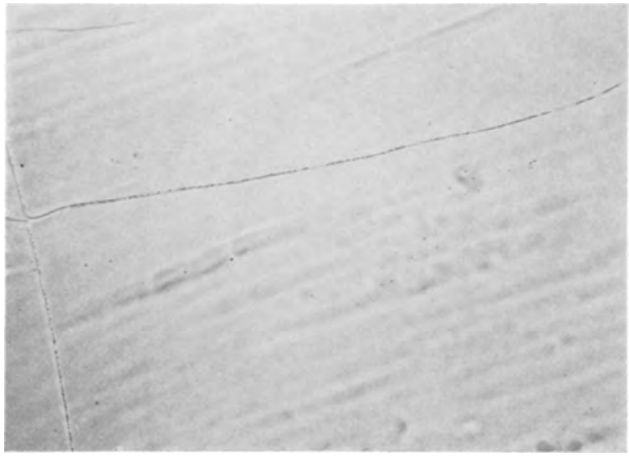

Fig. 24. Flaws (dark colored) in a reformed crack in a 3100Å film. 500X.

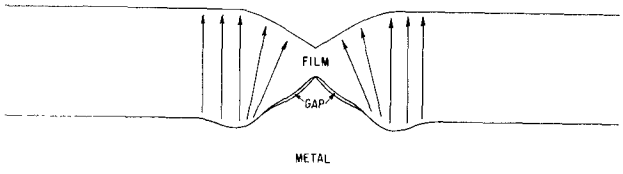

Fig. 25. Arrows show direction of ionic motion during growth of a flaw.

plastic deformation of a specimen prior to any film formation does not introduce flaws along slip lines. Flaws are produced at the crack on reformation because the new film being formed is constrained by the sides of the crack and hence cannot follow the receding metal surface at the base of the crack. It is probably for this reason that flaws cannot be entirely removed from a film by repeated cycles of forming and etching.

Summary

The picture of flaws and their formation which emerges from these studies is the following. If the surface of the tantalum contains some region on which film formation is strongly hindered for some reason, then this region can be surrounded by growth of the film parallel to the surface. The film thickness in the region of the flaw is diminished because the field must pull tantalum ions from outside the region of the flaw into its center, as shown schematically in Fig. 25. The annular depression on the metal surface surrounding the flaw results from the added metal consumption in that region, which must supply the film both immediately above itself and also above the flaw. Note that it is essential to this model of the flaw that no contact exist between the film and the metal in the immediate vicinity of the flaw, for if such contact did exist the thin region could thicken to the normal value.

Many surface conditions can hinder film formation and create flaws. Formation on compounds is presumably hindered by the residue (for instance, carbon or nitrogen) left after some of the tantalum is extracted. The oxygen of an oxide may not be able to find its proper positions in the growing film and hence disrupt film formation. Foreign substances such as grease and particles can block film formation mechanically. The different growth rates of crystalline oxides, suboxides, and amorphous oxides can cause stresses which could crack the film or cause it to separate from the substrate. Very small particles are evidently effective. Surface roughness may result in cracks or losses of contact because of stresses generated as the film attempts to follow the metal surface which is not only receding but also changing shape as formation proceeds. Cracks in pre-existing films present geometries which cause flaws on reformation. Possibly oxygen gas bubbles formed at some of these surface regions are embedded in the growing film.

During the growth of a heavily flawed film at constant current the voltage often rises abnormally rapidly because a thinner film is produced on some regions of the surface so that fewer coulombs are required to reach a given voltage. Despite the fact that the average thickness of a film containing flaws is less than that of a perfect film formed under the same conditions, the capacitance of the flawed film is less than that of the perfect film. The decreased capacitance presumably results from the loss of contact between the film and the metal in the vicinity of the flaw.

Most of the flaws apparently are closed so that contact between electrolytic solutions and the metal is prevented. Hydrofluoric acid opens many of the flaws in a 2400Å film in a few seconds and most flaws in 30 sec. Possibly the center of the flaw is only thinly covered with a bridge of oxide. Some of the flaws are cracked and apparently open to the electrolyte. It is likely that the oxide film immediately over the center of the flaw is under a tensile stress, since the oxide must bend with the center of the flaw as a pivot point in order to follow the receding metal surface. Such stress may lead to cracking as the film thickens, and may also accelerate corrosion of the film in hydrofluoric acid.

While most of the observations described in this paper were made on films thicker than 2000Å flaws are also present in thinner films. Flaws can be seen in the optical microscope in 750Å films. The presence of flaws can be inferred in 100Å films by the effect of a 1-sec etch in hydrofluoric acid on the current in a redox electrolyte. Finally even a 20Å film has some areas, presumably flaws, of easy metal electrodeposition.

Flaws have been observed in anodic films on niobium and zirconium, and presumably they occur in other anodic films where their observation is made difficult by the absence of suitable interference colors.

Acknowledgment

The writer is indebted to J. J. Becker and R. E. Hoffman for many stimulating discussions during these studies and to them and F. G. Will for their critical comments on the manuscript.

Manuscript received Aug. 15, 1962. This paper was prepared for delivery before the Pittsburgh Meeting, April 15-18, 1963.

Any discussion of this paper will appear in a Discussion Section to be published in the December 1963 JOURNAL.

REFERENCES

1. P. Kofstad, ARL Report #240, 1961; D. W. Aylmore, S. J. Gregg, and W. B. Jepson, *This Journal*, **107**, 495 (1960); R. E. Pawel, J. V. Cathcart, and J. J. Campbell, *ibid.*, **107**, 956 (1960).
2. T. A. Renshaw, *ibid.*, **108**, 185 (1961).
3. D. A. Vermilyea, *Acta Met.*, **1**, 282 (1953).
4. D. A. Vermilyea, *This Journal*, **101**, 389 (1954).
5. D. A. Vermilyea, *ibid.*, **102**, 207 (1955).
6. D. A. Vermilyea, *Acta Met.*, **2**, 476 (1954).
7. L. Young, "Anodic Oxide Films," p. 124, Academic Press, New York (1961).
8. L. Young, *ibid.*, p. 123.
9. L. Young, *ibid.*, p. 69.
10. C. Edeleanu and T. J. Law, *Phil. Mag.*, **7**, 573 (1962).
11. F. P. Bowden and D. Tabor, "The Friction and Lubrication of Solids," Clarendon Press, Oxford (1950).
12. A. G. Eubanks, D. G. Moore, and W. A. Pennington, *This Journal*, **109**, 382 (1962).

Studies on the Structure of Anodic Oxide Films on Aluminum, II

R. W. Franklin and D. J. Stirland

Caswell Research Laboratories, The Plessey Company Limited, Towcester, Northants, England

ABSTRACT

The apparent optical anisotropy of porous oxide films on anodized aluminum is shown to be due to variations in the inclination of the pores above different crystal orientations in the metal substrate. This variation is an additional factor which must now be included in the basic picture of the cellular structure of these films. The conditions necessary for the observation of this phenomenon by means of electron microscopy are discussed.

It has been known for several years that certain anodizing treatments produce aluminum surfaces which appear to be optically anisotropic since, when viewed under polarized light, grains of differing orientation are revealed in differing contrast. Various authors (1-6) have advanced explanations of this effect, although little conclusive experimental evidence has been provided.

The present investigation has used electron microscopic methods to demonstrate directly the reason for this apparent anisotropy.

Hone and Pearson (1) used a phosphoric acid based electrolyte to anodize aluminum and reveal its grain structure. The electrolyte was kept at 20°C; formation was begun at 20v and increased to 50v after a few seconds. A film of sufficient thickness to disclose the grain structure developed after about 5 min, but for optimum results the treatment was prolonged to 20 min. Lacombe (2) and Lacombe and Beaujard (3) found that short anodization times in sulfuric acid, giving a film thickness of the order of a wavelength of visible light, produced grain visibility in natural light. At a moderate current density (*e.g.*, 1.5 amp/dm^2) the effect disappeared, but it reappeared at high current densities (*e.g.*, 27 amp/dm^2 for 5 min).

Herenguel and Lelong (4) claim to have shown by means of an interference method that the color differences are due solely to variations in the oxide thickness from grain to grain, the refractive index of the oxide being constant at 1.58. Huber (5) rejected the possibility that the material of the anodic film was birefringent, and hence responsibility for the anisotropy, on the grounds that the substance of the film is an isotropic oxide. He also showed that the birefringence disappeared when the film was impregnated with a liquid having the same refractive index as that of the oxide and suggested that the birefringence was directly connected with the presence of pores in the film. Hone and Pearson (1) consider that the pores control the film thickness at each grain and suggest that there is "some relationship between the angle of a pore-like structure and the film thickness. It might be that the length of pore-like units is constant from grain to grain: when the pores are vertical to the polished face, the film would then reach its maximum thickness; when the pores are at an angle, the film accordingly would be thinner."

Perryman (6) however, takes the view that the anisotropy effect may be due entirely to the topography of the anodized surface, and not due to anisotropy of the oxide film.

Edwards and Keller (7) and Keller *et al.* (8) used optical and electron microscope examination of cross sections, stripped oxide films, and replicas of the metal surface beneath films to show that the anodic film consisted of a close packed array of oxide cells, each containing a central pore. Confirmation of this structure has been obtained by Booker *et al.* (9) from examination of replicas taken from cross section of thick ($\sim 30\mu$) porous coatings produced in sulfuric acid electrolytes. However, neither of these groups of workers give any indication that they detected change in pore direction or distribution with grain orientation, and this might have been expected if previous explanations of the anisotropy effect are correct.

Experimental Details

Aluminum.—The aluminum used throughout the investigation was 99.99% pure rolled annealed foil 0.002 in. thick. With one exception the specimens were prepared from strips of this foil cleaned by immersion in 3% sodium hydroxide at 30°C for 2 min. A single specimen was electropolished in a standard ethyl alcohol-perchloric acid bath (10).

Electrolytes and forming conditions.—Two different electrolytes were used: (*a*) 2% chromic acid and 3% phosphoric acid, and (*b*) 4% phosphoric acid. Electrolyte (*a*) had previously been used in other experiments and had been found to produce an oxide containing large diameter pores. After the effects to be described had been observed with this electrolyte the investigations were repeated and extended using the phosphoric acid electrolyte to ensure that the observations were not due to artifacts caused by the high solubility of the anodic coating in the mixed acid solution.

Electrolyte (*a*) was employed with a variety of temperature, time and current density conditions. For electrolyte (b) the temperature and formation voltage were standardized at 20°C, 40v, and only the time of anodization was varied.

Film Thickness Measurement

It was found necessary, for reasons which will appear later, to have an accurate measurement of the thickness of each anodic film specimen.

Anodic films were stripped from the aluminum by the well-known amalgamation method (11) with mercuric chloride, washed thoroughly in distilled water, and finally floated on a clean water surface. A glass cover slide was dipped into the water at about 45°C to the surface and the oxide fragments coaxed near to the glass surface with a needle. When the slide was gently withdrawn the wet fragments flattened against the glass. They were then dried with a warm air blast directed normally on to the slide. Care had to be taken not to overheat the oxide fragments, as they then peeled off the glass.

The film thickness was measured directly by means of a Taylor Hobson Talysurf (12, 13). The instrument proved to be eminently suitable for quick and accurate film thickness measurements. Curled edges and folds in the films (a possible source of error) could easily be identified from the traces. A convenient vertical magnification was X20,000, which gave a thickness measurement accurate to about ± 10%, on films ranging from 1500 to 8300Å. The average of five readings across several different fragments was obtained for each specimen.

Electron Microscopy

The electron microscope used for the present investigation was an RCA EMC-2 operating at 30 kv. This microscope has no double condenser lens, and heating of the specimens presented some problems since the comparatively thick oxide films were observed to buckle and slide around on their support grids if they were mounted dry. To overcome this each film was mounted on one grid while wet, dried in air, and then transferred to a second grid, made sticky with acetone-moistened "sellotape" adhesive, by pressing the second grid on top of the mounted film. The original grid was then discarded. It was also found necessary to use a film which completely covered the grid, so that the grid holder gripped the edges of the film and held it flat.

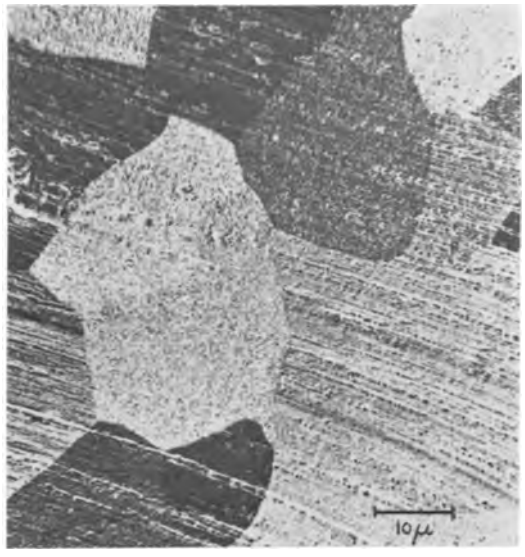

Fig. 1. Typical transmission micrograph of a porous film 1μ thick. Magnification approximately 1000X.

The films were examined in the following way. A suitable area was selected at a magnification of X500, and micrographs obtained of this area in the five possible "stereo-tilt" positions, *i.e.*, −10°, −5°, 0°, +5°, +10° (angles between the incident electron beam and a normal to the specimen surface). If required, the same area was then photographed in these five positions at a higher magnification.

The topography of the aluminum beneath the anodic coatings was examined by dissolving the coatings in a hot phosphoric-chromic acid mixture (8) and taking direct carbon replicas (14) from the metal surfaces. These replicas were subsequently shadowed at a glancing angle with chromium.

Experimental Results

The stripped oxide films viewed in transmission in the electron microscope appeared as opaque solids pierced with tiny holes and corresponded in most cases with the transmission micrographs shown by Keller *et al.* (8). However, it was found that under certain conditions low magnification micrographs revealed a grain structure similar to that given by an anisotropic coating viewed under polarized light. Figure 1 shows such a micrograph, obtained from a film formed in the mixed phosphoric-chromic acid bath at 90°C and current density of 0.25 amp/cm^2 for 1 min. These conditions give a film 1μ thick. The parallel scores across the micrograph are the traces of scratches on the original aluminum surface, produced during the production of the foil, and replicated by the oxide film.

Figures 2a, 2b, and 2c show a different area of this film, and its appearances in three of the five stereo-positions. Examination of these micrographs indicates that both actual and relative contrast of each "grain" changed with the angle of the specimens to the incident electron beam. Optical examination of the original anodized aluminum under polarized light gave a similar effect when the specimen was rotated.

Fig. 2. Effect of tilting specimen relative to incident electron beam: 2a (top) + 10° tilt; 2b (center) 0° tilt; 2c (bottom) — 10° tilt. Magnification approximately 1000X.

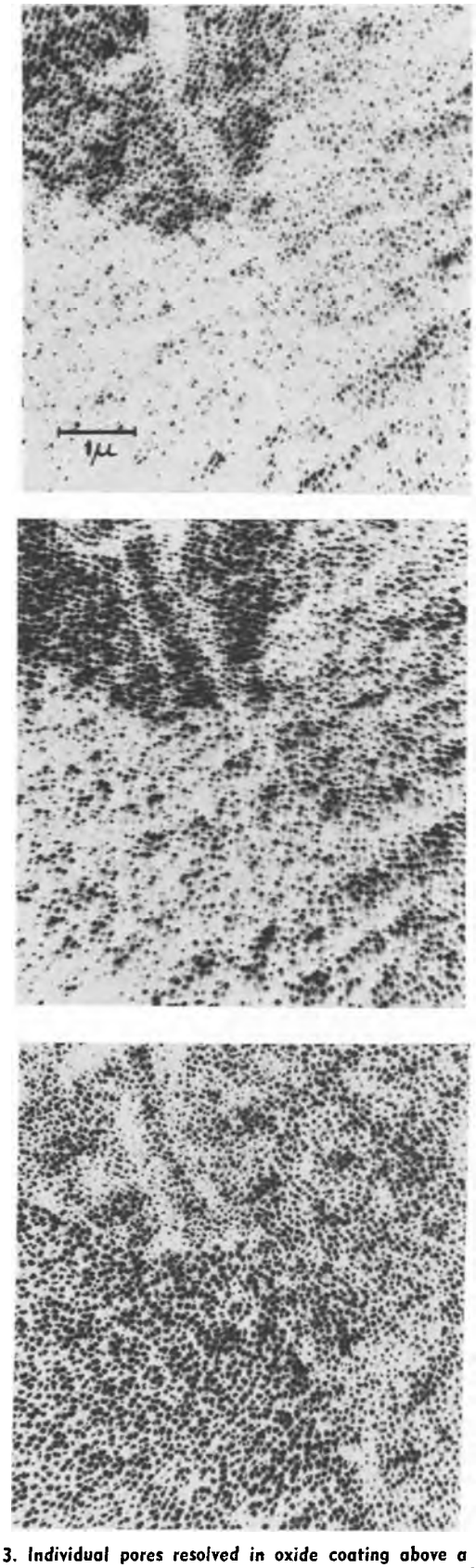

Fig. 3. Individual pores resolved in oxide coating above a triple grain boundary area: 3a (top) + 10° tilt; 3b (center) 0° tilt; 3c (bottom) — 10° tilt. Magnification approximately 11,000X.

Figures 3a, 3b, and 3c show individual pores resolved, at higher magnification, in three grains meeting at a triple boundary. The appearance of specific pores can be followed in the three tilt positions, as shown in Fig. 4a, 4b, and 4c.

The grain contrast effect was examined in detail for the 4% phosphoric acid electrolyte. Five different anodization times were employed, to give five films of different thickness, at a constant formation voltage of 40v (20°C). Each film was stripped from the aluminum, and its thickness determined with the Talysurf. They were then examined in the five dif-

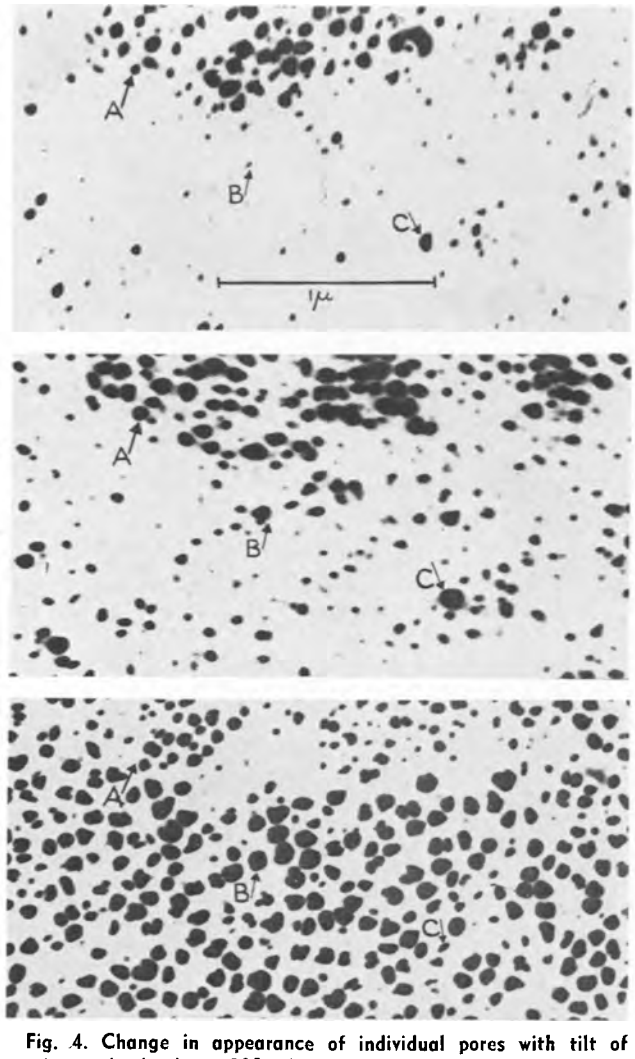

Fig. 4. Change in appearance of individual pores with tilt of specimen: 4a (top) + 10° tilt; 4b (center) 0° tilt; 4c (bottom) — 10° tilt. Magnification approximately 28,500X.

ferent tilt positions in the electron microscope. The results of these examinations are shown in Fig. 5.

Explanation of Grain Contrast Effect

If the anodic specimens were completely nonporous, then their thickness would render them opaque to the electron beam. In fact, an image is only produced because part of the incident beam can pass through both pores and the barrier layer (8) at the

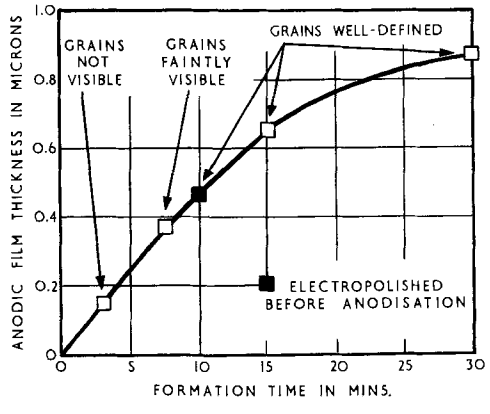

Fig. 5. Variation of oxide film thickness with formation time. Anodization at 40v 20°C in 4% phosphoric acid.

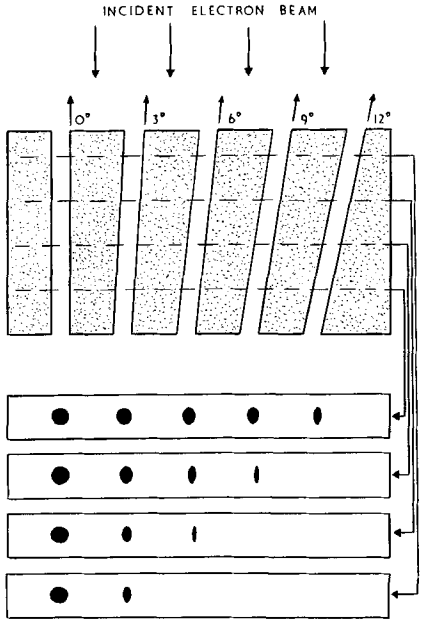

Fig. 6. Appearance of pores at four different film thicknesses.

pore bases. The barrier layer for a 40v formation in phosphoric acid is not greater than 500Å thick, and probably much less, and will transmit most of the beam. Thus the pores themselves must be sensibly parallel to the incident electron beam. However, slight tilting of the pores will not completely eliminate transmission of the beam, and the proportion allowed through will then depend both on the angle of tilt of the pores and the thickness of the film. Figure 6 illustrates this diagrammatically (the barrier layer has been omitted for simplicity and the pores have not been drawn to scale).

The explanation of the contrast differences between grains therefore appears to be that (*a*) pores in the oxide film on different grains are tilted with respect to one another, although the pores corresponding to any one grain are all parallel to each other, and (*b*) the oxide thickness is sufficient to produce a detectable difference between the projected pore images of different grains.

The crux of this explanation is that both factors (*a*) and (*b*) must be fulfilled in order to get the contrast effect. It is believed that failure to satisfy condition (*b*) is the reason why no grain effect is to be seen in the transmission oxide micrographs of Keller *et al.* (8). Although no times of formation or coating thicknesses were given in this paper, Hunter (15) has stated that times of the order of 5 min were used for the phosphoric acid formations. Figure 5 shows that this time is insufficient to reveal the grain structure clearly, although by examination of such specimens in the extreme tilt positions (±10°) the structure might just be apparent. Another possibility is that the grain size of the aluminum was too large for the effect to be apparent in electron microscope examinations.

An additional parameter which influences the proportion of the electron beam transmitted through an oxide film in the various tilt positions is the diameter of the pores. The 4% phosphoric acid oxide film con-

tains pores of diameter ~ 330Å (see later). If such a set of parallel pores are tilted 5° from a position parallel with the incident beam complete blacking out of the pores will occur if the film thickness is greater than (330 cot 5°)Å *i.e.* ~0.38μ. For this reason most of the micrographs shown are of the phosphoric-chromic acid films in which the much larger (~ 900Å) pore diameter enabled the full tilting range to be employed for a wide range of film thicknesses.

Cell Base Structure

Keller *et al.* (8) have shown that each cell in the porous oxides consists of a hexagonal column of oxide containing an axial pore, mounted above a nonporous cell base. Thus, if groups of pores are tilted with respect to each other, their corresponding cell bases might also be tilted. Examination of replicas of aluminum surfaces beneath such oxide layers has shown that this does occur, although again the layers must be greater than a certain minimum thickness for the effect to be observed.

Figure 7 shows a typical example of the cell base structure beneath a phosphoric-chromic acid coating at a triple grain boundary pq, rq, sq, separating grains A, B, and C. Although it is difficult to assess quantitatively the tilt between grains A and B, the effect is visually evident. Boundaries pq and rq are also clearly delineated. Boundary sq is less distinct, partly because the shadowing direction is nearly parallel with the boundary and partly because the angular crater-tilt difference between B and C is smaller than that between A and B or A and C.

Optical examination of the aluminum surfaces after dissolution of the anodic films showed the grain boundaries clearly, although of course the cell bases were not resolved.

Porous Oxide Cell Structure

It has been previously considered that three parameters are sufficient to specify the porous structure produced by a particular set of formation conditions: (i) pore diameter, (ii) cell size, (iii) number of pores (or cells) per unit area.

It is now apparent that the angle of tilt of the pores should also be included in this list. Table I shows values obtained in this investigation compared with the corresponding values of Keller *et al.* (8) for the 4% phosphoric electrolyte formations at 20°C and 40v. Agreement is generally very good.

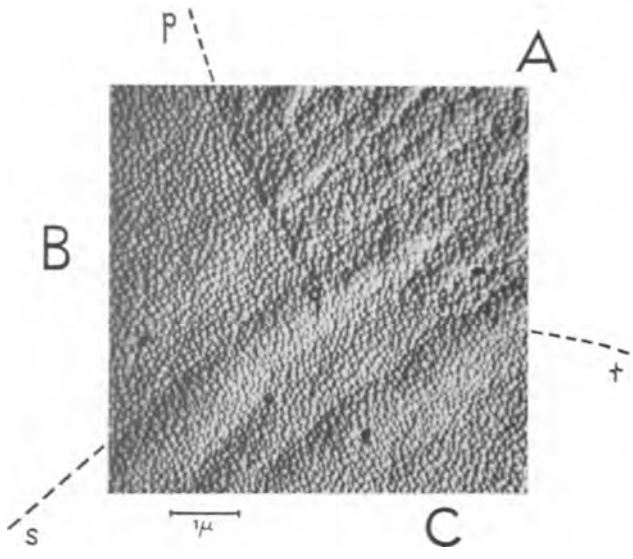

Fig. 7. Replica of cell base structures on three grains A, B, and C. Grain boundaries are pq, rq, and sq. Magnification approximately 9000X.

There is experimental evidence, *e.g.*, Booker *et al.* (9), that the pores widen on the electrolyte side of the film. This has not been investigated in the present work, and the pores have been considered as parallel tubes. If the pores do widen at the outer surface, then the films can be tilted through greater angles with respect to the incident beam of electrons before grains "black-out" completely. However, this only affects the actual magnitude of the angular tilt of the pores, not the qualitative basis of the argument.

Conclusions

This investigation has demonstrated directly that the direction of pores through porous anodic films is related to the grain orientation of the aluminum beneath the films. It is suggested that this is the reason for the apparent optical anisotropy of such films.

Table I. Values obtained here compared with Keller *et al.*

Parameter	Method of measurement	Keller *et al.* (8) results	Present results
Pore diameter	(i) Direct measurement from stripped anodic film.		
	(ii) Measurement from intercept on forming-voltage/cell-size plot.	(ii) 330Å	(ii) 330 ± 20Å
Cell size	Distance between cell base centers measured from micrographs of		
	(i) oxide replicas	(i) 1130Å	
	(ii) carbon replicas		(ii) 1260 ± 200Å
No. of pores per unit area	(i) Direct counting of pores in stripped oxide micrographs.		74 ± 15 × 10^8/cm^2
	(ii) Direct counting of cell bases on micrographs of carbon replicas.		79 ± 12 × 10^8/cm^2
	(iii) No details given	(iii) 78 × 10^8/cm^2	

Acknowledgments

The authors wish to acknowledge the assistance of R. E. Martin in preparing some of the oxide films and are grateful to the Plessey Company Limited for permission to publish this work.

Manuscript received July 11, 1962; revised manuscript received Oct. 10, 1962.

Any discussion of this paper will appear in a Discussion Section to be published in the December 1963 JOURNAL.

REFERENCES

1. A. Hone and E. C. Pearson, *Metal Prog.*, **53**, 363 (1948).
2. P. Lacombe, *Trans. Inst. Metal Finishing*, **31**, 208 (1954).
3. P. Lacombe and L. Beaujard, *Journée des États de Surface (Paris)*, 44 (1945).
4. J. Herenguel and P. Lelong, Congrès de Métallurgie (Paris 1953); *Compt. rend.*, **232**, 248 (1951); *Rev. Mét.*, **49**, 374 (1952); *Rev. Mét.*, **51**, 411 (1954).
5. K. Huber, *Helv. Chim. Acta*, **28**, 1416 (1945); *Bull. Soc. Chim. France*, **D183** (1949).
6. E. C. W. Perryman, "Polarised light in Metallography," Butterworths, London (1952); *J. Inst. Metals*, **85**, 567 (1956-7).
7. J. D. Edwards and F. Keller, *Trans. AIME*, **156**, 288 (1944).
8. F. Keller, M. S. Hunter, and D. L. Robinson, *This Journal*, **100**, 411 (1953).
9. C. J. L. Booker, J. L. Wood, and A. Walsh, *Brit. J. Appl. Phys.*, **8**, 347 (1957).
10. A. de Sy and H. Haemers, *Stahl u. Eisen*, **61**, 185 (1941).
11. H. Mahl, *Naturwiss.*, **30**, 207 (1942).
12. R. E. Reason, M. R. Hopkins, and R. I. Garrod, "Measurement of Surface Finish by Stylus Methods," p. 44, Taylor and Hobson Ltd., Leicester, England.
13. R. E. Reason, "Properties of Metallic Surfaces," Institute of Metals Monograph (London) p. 327 (1953).
14. D. E. Bradley, *Brit. J. Appl. Phys.*, **5**, 65 (1954).
15. M. S. Hunter, Private communication.

Control of Al Corrosion in Caustic Solutions

L. Bockstie,[1] D. Trevethan,[2] and S. Zaromb[3]

Philco Scientific Laboratory, Blue Bell, Pennsylvania

ABSTRACT

In aqueous solutions of 1-10M NaOH or KOH the corrosion of Al can be accelerated by chemical promoters such as $S^=$ (or SH^-) ions and/or by a thermal runaway mechanism, and inhibited by surface amalgamation, especially with ZnO-saturated solutions, and/or by alkyldimethylbenzylammonium salts. Corrosion is also markedly reduced at high anodic current densities.

The use of Al anodes in alkaline primary batteries, as discussed in an earlier paper (1), depends in large part on adequate corrosion control. The present studies deal first with the acceleration and then mainly with the inhibition of Al corrosion in aqueous solutions containing 1-10M NaOH or KOH.

Experimental Procedure

The experiments were performed at room temperature with standard strips of 10 cm^2 total surface area Al grade 1145 containing at least 99.45% Al, $\leq$0.55% (Si + Fe), $\leq$0.20% Mn, and $\leq$0.09% other impurities. For quick comparative tests, several Craig cells (2), modified as shown in Fig. 1, were used to read directly the volume of H_2 formed by the corrosion reaction

$$Al + 3H_2O + OH^- \rightarrow Al(OH)_{4-} + \frac{3}{2}H_2 \quad [1]$$

as a function of time of immersion in the tested solution. These readings were converted both into average rate of consumption of Al and average local action corrosion current by means of the conversion factors: 1 cc H_2 at 300°K and 1 atm/10 cm^2-sec is equivalent to 2.71 x 10^{-5} cm (or 0.271μ) Al reacted/sec or 785 ma/cm^2, *i.e.*, 1μ Al/hr is equivalent to 0.805 ma/cm^2.

[1] Present address: Corning Glass Works, Bradford, Pennsylvania.

[2] Present address: Radio Corporation of America, Moorestown, New Jersey.

[3] Present address: Research and Consulting Corporation, 1125 East 102 Street, Brooklyn 36, New York.

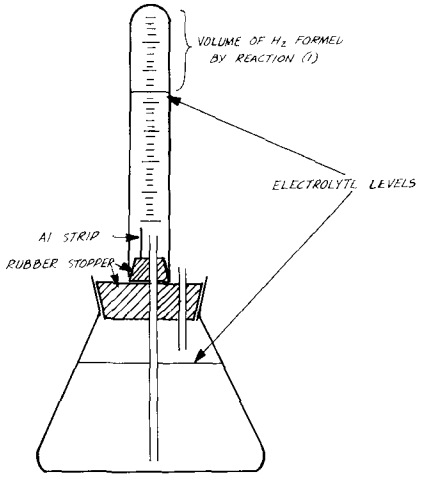

Fig. 1. Modified Craig cell for comparative corrosion tests

The corrosion rate as a function of anode current density was measured with the apparatus shown schematically in Fig. 2. Two porous Ni air cathodes mounted on thin, flat, solid Ni frames were clamped between rubber gaskets and glass flats on each side of a vertical surface-amalgamated Al anode strip held firmly at the lower (shorter) edge between an Fe nail and a glass tube passing through a rubber stopper. A shallow pool of Hg just above the stopper assured continued anode surface amalgamation and satisfactory electrical contact between the Al and the Fe nail. With the cathodes connected in parallel,

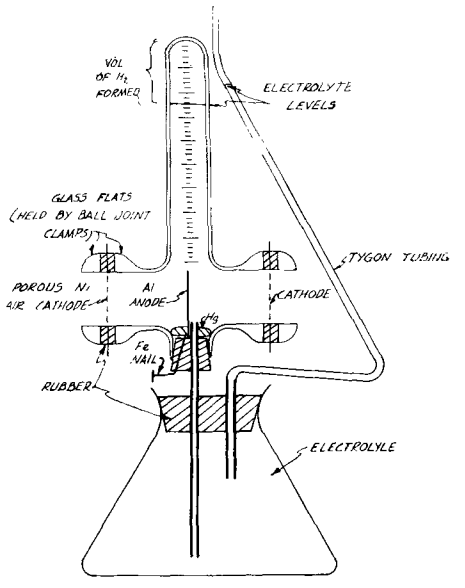

Fig. 2. Apparatus for simultaneous current density and corrosion rate determinations.

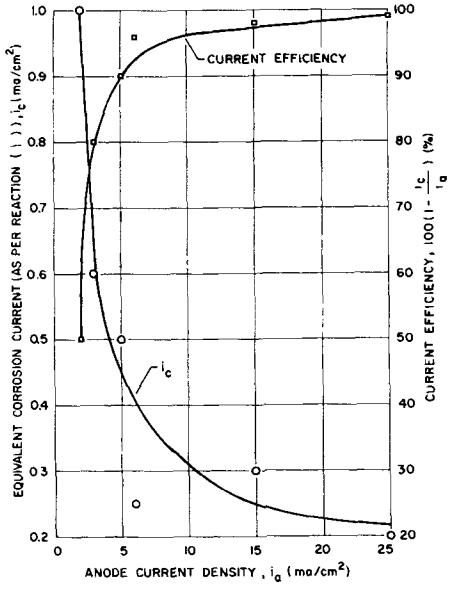

Fig. 3. Corrosion rate and current efficiency at room temperature as functions of current density at surface-amalgamated Al grade 1145 anodes in 3M KOH plus 0.5M $Al(OH)_3$ plus an excess of ZnO.

the cell was discharged through a resistance decade box. Simultaneous recordings of the voltage across a given standard resistance and of the volume of H_2 as a function of time yielded the data shown in Fig. 3.

Thermal and chemical corrosion acceleration.—It is worth noting first of all that the corrosion reaction [1] dissipates about 1.5 ev or 36 kcal/g-equivalent of free energy (1, 3) corresponding to 4 kcal/(g Al reacted). This tremendous energy dissipation is localized at the Al-electrolyte interface and may thus give rise to hot spots if the rate of corrosion is sufficiently high and/or the rate of heat removal sufficiently low. Since reaction rates increase rapidly with temperature, the hot spots may give rise to a kind of chain reaction mechanism which may come to end only after formation of large bubbles of H_2 and/or boiling H_2O. In view of the high free energy of reaction [1], this type of chain mechanism would be expected at any Al-aqueous solution interface were it not for the protective layer of oxide strongly adhering to the Al. Even in highly alkaline solutions in which the oxide readily dissolves, a thin, slowly dissolving oxide layer may still account for observed steady corrosion rates at low temperatures. The action of chemical acceleration of Al corrosion probably consists then of weakening the coherence and/or adherence of the protective layer. It was thus observed in the present studies that addition of 0.1-1.0M Na_2S to solutions of 1.0-3.0M NaOH renders them several times more corrosive to Al,[4] probably due to the weakening of the protective film on substitution of an $O^=$ (or OH^-) by a $S^=$ (or SH^-) ion.

Corrosion Inhibition.—Inorganic inhibitors.—Limited inhibition of Al corrosion in caustic solutions by ZnO is known to occur in the Zn immersion process (4) based on the reaction

$$2Al + 3Zn(OH)_4^= \rightarrow 2Al(OH)_4^- + 4OH^- + 3Zn \quad [2]$$

In preliminary experiments, the use of ZnO in 10M alkali solutions was partly effective in inhibiting the corrosion of Al. However, the layer of Zn formed on the Al tends to flake off on continued immersion, with a resulting corrosion of the Al at a rate of the order of 10 ma/cm². This is about 6 times lower than without the ZnO, but still too high for battery applications. However, when Hg_2SO_4 was added to the solution, there was no sign of flaking and the bubbling of H_2 appeared quite low.

To clarify the role of Hg_2SO_4 in the corrosion inhibiting mechanism, identical Al strips were placed in three beakers containing 10M NaOH saturated with ZnO and either one of the following: (a) HgO, (b) Hg_2SO_4, and (c) Hg. The rate of corrosion appeared slowest in beaker (c) and fastest in beaker (a). Hence it was the metallic Hg formed on decomposition of Hg_2SO_4 that was effective in beaker (b). Furthermore, direct contact of the Hg with Al was found to be more protective than mere presence of Hg in the container.

When properly amalgamated and in contact with Hg, completely submerged Al (grade 1145) anodes corroded at room temperature in ZnO-saturated 10M KOH or NaOH solutions at a rate of less than 0.15μ/hr. If the corrosion rate could be maintained indefinitely at such a low value, then an Al sheet 0.3 cm thick would lose less than 10% of its weight by corrosion from both sides over a period of 1000 hr. However, very rapid corrosion frequently occurred at unpredictable times (cf. the preceding section and discussion of Table I below).

The inhibiting effect of Hg in alkaline solutions may seem surprising at first sight in view of its known corrosion accelerating effects (3, 5) in neutral and acidic solutions. The probable explanation is that, with most of the protective oxide layer already removed by the strong alkali, any further

[4] *E.g.*, addition of 0.1M Na_2S to 1M $Ba(OH)_2$ and 1M NaOH + 0.1M $Ba(OH)_2$ solutions increased the corrosion rates from 5μ/hr to 30μ/hr and from 10μ/hr to 25μ/hr, respectively. Addition of 1M Na_2S to a 10M NaOH solution in a Lucite container caused partial melting of the Lucite from the uncontrollably fast Al corrosion rate.

Table I. Typical average rates of corrosion of Al (Grade 1145) in alkaline solutions at room temperature

Nomenclature: Hyamine 3500 is a 50% aqueous solution of mixed ($C_{12\ to\ 14}$ alkyl)NMe_2BzCl; Hyamine 1622 is (di-isobutylphenoxyethoxyethyl)NMe_2BzCl; Hyamine 10X is (di-isobutylcresoxyethoxyethyl)NMe_2BzCl; Hyamine 2389 is a mixture of 4 parts

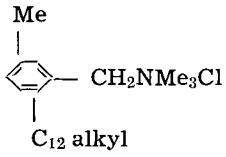

+ 1 part

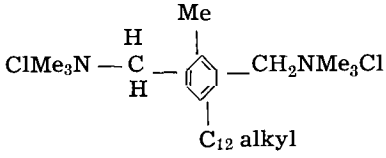

Hyamine 1450 is a mixture of C_{14} alkyl NMe_2BzCl and carbamide; Triton X-400 is (stearyl, *i.e.*, n-C_{18} alkyl)NMe_2BzCl; Aliquat 4 is (C_{12} alkyl)NMe_3Cl; Aliquat 6 is (palmityl, *i.e.*, n-C_{16} alkyl)NMe_3Cl.

A. Plain vs. surface-amalgamated Al

Set No.	Additive	Avg corrosion rate (μ/hr) in 3M solutions of KOH: Plain Al	KOH: Amalgamated Al	NaOH: Plain Al	NaOH: Amalgamated Al
1	None	25	13-15	75	13-15
2	0.5M $Zn(OH)_4^=$	25	—	25	—
3	0.5M $Al(OH)_4^-$	60	13-25	75	25-60
4	0.5M $Zn(OH)_4^=$ + 0.5M $Al(OH)_4^-$	20	0.6-1.0	20	0.6-1.5
5	10% Hyamine 3500	35-38	0.05-0.25	25-38	0.03-0.13
6	10% Hyamine 3500 + 0.5M $Zn(OH)_4^=$	5	0.13-0.5	2.5	0.25-0.5
7	10% Hyamine 3500 + 0.5M $Al(OH)_4^-$	25	7.5-25	25	2.5-10
8	10% Hyamine 3500 + 0.5M $Zn(OH)_4^=$ + 0.5M $Al(OH)_4^-$	5	0.13	5	0.13
9	1% Hyamine 1622	—	—	25	0.08-0.13
10	1% Hyamine 1622 + 0.5M $Zn(OH)_4^=$	—	0.06-0.18	5	0.06-0.2
11	1% Hyamine 1622 + 0.1M $Zn(OH)_4^=$	—	—	75	0.1
12	0.1% Hyamine 1622	—	—	50	0.1-0.5
13	1% Hyamine 10X	—	—	33-38	0.13-0.25
14	1% Hyamine 10X + 0.5M $Zn(OH)_4^=$	—	0.05-0.18	5	0.08-0.18
15	1% Hyamine 10X + 0.1M $Zn(OH)_4^=$	—	—	10	0.08
16	0.1% Hyamine 10X	—	—	50	0.08
17	0.1% or 1% Triton X-400	—	—	30-50	3
18	10% Hyamine 2389	—	—	50	0.025
19	10% Hyamine 2389 + 0.5M $Al(OH)_4^-$	—	—	38	0.13
20	10% Hyamine 2389 + 0.5M $Zn(OH)_4^=$	—	—	7.5	0.08
21	10% Hyamine 2389 + 0.5M $Zn(OH)_4^=$ + 0.5M $Al(OH)_4^-$	—	—	2.5	0.25
22	1M KI + 0.1M HgO	0.5	—	—	—
23	100% MeOH (nonaqueous solution)	1.3	0.25	—	—
24	100% EtOH (nonaqueous)	5	1.3	—	—
25	50% MeOH + 10% Hyamine 3500	40	0.1	43	0.08
26	50% EtOH + 10% Hyamine 3500	38	0.05	100	0.13

B. Surface-amalgamated Al

Set No.	Organic corrosion inhibitor	Avg corrosion rate (μ/hr) in solutions of 3M NaOH	4M NaOH + 0.5M ZnO	3.5M NaOH + 0.5M $Al(OH)_3$	4.5M NaOH + 0.5M ZnO + 0.5M $Al(OH)_3$
27	None	5	0.3-1.8	5-7.5	0.6-1.8
28	1% $Me_3(C_{16}H_{33})NBr$	0.1-0.25	0.18-0.6	0.4-1.3	0.5
29	1% $Et(C_{16}H_{33})Me_2NBr$	0.25	0.25	0.25	0.25
30	1% $Me_2(Bz)N$	4	0.25	6.3	0.5
31	1.2% Me_3NBzCl	1.5	0.25	2.5	0.8
32	5% $PhNMe_3OH$	2.5	2.5	5	1.8
33	1% $PhNMe_3Cl$ (or I)	2.5	0.8	2.5	0.8
34	1% Me_4NI	5	0.13	8	0.25
35	1% Hyamine 1450	0.13	0.25	0.25	0.13
36	1% Aliquat 4	0.8	0.08	1.3	0.2
37	1% Aliquat 6	0.13	1	0.8	1.3
38	1% Triton X-400	0.8-3	0.5	0.5	0.25

weakening of this layer by amalgamation is outweighed by the Hg-induced increase in overvoltage for the H_2 evolution reaction

$$H_2O + e^- \rightarrow OH^- + \frac{1}{2}H_2 \qquad [3]$$

which then becomes the rate-limiting step in the corrosion mechanism.

Unfortunately, amalgamation of Al presents several practical disadvantages. Lack of reproducibility would result from improper amalgamation (the best procedure consisting of pre-etching the Al in 10M

KOH, dipping immediately into Hg, leaving the Al in contact with at least a drop of Hg, and immersing immediately in the electrolyte). Exposure to air results in rapid attack of the amalgamated Al by atmospheric O_2. Hence, an inert gas atmosphere was used both during and after the amalgamation procedure prior to immersion in electrolyte. Amalgamation in the electrolyte by a displacement reaction with dissolved $HgI_4^=$ appeared satisfactory at first (cf. set 22 of Table I), but rapid corrosion suddenly occurred after several hours (probably due to a contaminating corrosion accelerator introduced into the solution from the contacting rubber stopper or from impurities in the dissolving Al and resulting in the type of thermal chain reaction described in the preceding section). However, even if amalgamation with $HgI_4^=$ or Hg_2SO_4 were entirely successful, the above-mentioned reactivity with atmospheric oxygen made it desirable to search for a more suitable inhibitor.

Organic corrosion inhibitors.—The average corrosion rates given in Table I can only serve for comparative rather than predictive purposes. The most commonly observed irreproducibility would arise from suddenly accelerating corrosion, probably initiated by an accelerator. Improper surface amalgamation (cf. the preceding section) also accounts for some of the irreproducibility with amalgamated Al (sets 2, 4-7, 10, 12-14, 27, and 28).

Nevertheless, significant conclusions may be drawn from Table I. Sets 2, 4, etc., show reduced H_2 evolution but serious Zn sponge formation with ZnO as additive in absence of Hg. Comparison of sets 5-8 with 1-4 shows a marked reduction of corrosion rate upon addition of 10% Hyamine 3500. Sets 9-16 show similar corrosion inhibition with 1% Hyamine 1622 or 1% Hyamine 10 X, but poorer inhibition with only 0.1% of these Hyamines. Sets 17-21 show similar though somewhat poorer results with 1% Triton X-400 or 10% Hyamine 2389. Comparison of adjacent columns in sets 1-26 shows the remarkable effect of amalgamation, especially in conjunction with the same Hyamines. Sets 36-38 show distinct corrosion inhibition by 1% Aliquat 4 or 6 or 1% Triton X-400 when compared with the control sets 1-4. Similarly, sets 28, 29, and 31 compared with sets 1-4 show inhibition by 1% $Me_3C_{16}H_{33}NBr$, 1% $Et(C_{16}H_{33})Me_2NBr$, and 1.2% Me_3NBzCl, sets 32-34 show some inhibition by $PhNMe_3OH$, $PhNMe_3Cl$ or $PhNMe_3I$, and Me_4NI, set 30 shows a questionable advantage of Me_2BzN, and set 35 shows distinct inhibition by Hyamine 1450.

Corrosion abated markedly in nonaqueous MeOH or EtOH solvents (sets 23 and 24), but not in 1:1 water-alcohol solutions (sets 25-26). Similarly replacement of water by 100% MeOH reduced the attack on plain (Hg-free) Al in 2M Li_2S from 18 μ/hr to <0.03 μ/hr.

No significant effect was caused by 0.5M $Al(OH)_3$ in sets 3, 8, 21, 27, 29, 32, and 33, but distinct interference with the inhibiting effect of Hyamine 3500 is shown in set 7 and also with other inhibitors in sets 19, 28, 30, 31, and 34-37. On the other hand, 10-20% polyvinylbenzene trimethylammonium chloride showed no significant effects when added in conjunction with the Hyamines or with Triton X-400.

A number of similarly tested additives such as $CrCl_3$, $CrO_4^=$, $VO_4^=$, $Na_2B_4O_7$, Na_4SiO_4, Na_2SiF_6, dibutylsulfide, and several quinolinium, pyridinium, and indolium compounds showed no corrosion inhibiting effects.

In summary, the organic amine compounds which inhibit the corrosion of Al in caustic solutions either by themselves or in combination with ZnO and Hg belong mainly to the group of derivatives of Me_4NOH and Me_3NBzOH where Me = methyl and Bz = benzyl. Further marked improvements may result from substituting one of the methyls in Me_4NOH or Me_3NBzOH by a long chain group including 12 to 18 C atoms such as dodecyl, tetradecyl, hexadecyl, steryl, di-isobutylphenoxy-ethoxy-ethyl, di-isobutylcresoxy-ethoxy-ethyl, etc. Substitution of a H atom in a Bz radical of Me_3NBzOH by a long chain group such as listed above also appears satisfactory.

Corrosion inhibition by means of current drain.—A marked decrease of corrosion rate with increasing anode current density was reported by Hisamatsu (5) for amalgamated Al in sea water (pH values between 4 and 10), who related this effect to anode polarization. The same decrease was observed in the present studies. In 10M KOH containing no inhibitors, the corrosion of an unamalgamated Al abated to a minimum local action corrosion current of approximately 10 ma/cm^2 for anode current densities of the order of 50 ma/cm^2.

A more accurate determination of the corrosion rate dependence on anode current density was achieved by measuring the rate of H_2 evolution during current drain. The results for surface-amalgamated Al grade 1145 anodes in a ZnO-saturated solution containing 3M KOH plus 0.5M $Al(OH)_3$ are given in Fig. 3, which shows current efficiencies of at least 80% for anode current densities of 3-25 ma/cm^2.

Other examples of corrosion inhibition with increasing current density are shown in Fig. 7 and 9 of an earlier paper (1).

Conclusions

Although corrosion inhibition is quite effective with both the fairly large number of additives listed in Table I and with a number of alcohol solutions, it is most frequently accompanied by increased anode polarization. Nevertheless, several of the inhibitors included in Table I, as well as the observations on chemical and thermal acceleration and on inhibition by current drain may lead to the development of practical Al batteries (1).

Manuscript received Feb. 12, 1962; revised manuscript received Nov. 1, 1962.

Any discussion of this paper will appear in a Discussion Section to be published in the December 1963 JOURNAL.

REFERENCES

1. S. Zaromb, *This Journal*, **109**, 1125 (1962).
2. G. Vinal, "Primary Batteries," p. 96, John Wiley & Sons, Inc., New York (1951).

3. W. M. Latimer and J. H. Hildebrand, "Reference Book of Inorganic Chemistry," Macmillan Co., New York (1950).
4. F. Keller in "Modern Electroplating," pp. 514-517, A. G. Gray, Editor, John Wiley & Sons, Inc., New York (1953).
5. Yoshihiro Hisamatsu, *J. Electrochem. Soc. (Japan)*, 27, E73-75 (1959).

Correction

In the papers "Theory and Design Principles of the Reversible Electroplating Light Modulator" and "Geometric Requirements for Uniform Current Densities at Surface-Conductive Insulators or Resistive Electrodes" by Solomon Zaromb, published in Vol. 109, pp. 903-918, October 1962 *Journal*, the following changes should be made:

p. 908, Eq. (V') should read

$$\frac{1}{2}I_3^- + Ag\left(+\frac{3}{2}I^-\right) \rightarrow (3I^- + Ag^+) \rightarrow AgI_3^= \quad (V')$$

Page 909: Boundary condition [40'] is:

an amount $q_d/\mathbf{F}$ injected at $x = a$ and $t_p = \tau_p$ [40']

Eq. [42] is:

$$c_{ox}(x, t_p') = \frac{2q_d}{\mathbf{F}a}\sum_{n=0}^{\infty}(-1)^n e^{-(2n+1)^2\pi^2 Dtp'/4a^2}\sin\frac{(2n+1)\pi x}{2a} + \frac{4c_i}{\pi}\sum_{n=0}^{\infty} e^{-(2n+1)^2\pi^2 Dtp'/4a^2}\sin\frac{(2n+1)\pi x}{2a} = \sum_{n=0}^{\infty}\left(\frac{2q_d(-1)^n}{\mathbf{F}a} + \frac{4c_i}{\pi}\right) e^{-(2n+1)^2\pi^2 Dtp'/4a^2}\sin\frac{(2n+1)\pi x}{2a} \quad [42]$$

The last line of footnote 4 should read:

in C and J'^s Eq. §36 (2), and adding + c_i.

The line preceding Eq. [50] should read:

[42], results in a solution of the form[5]

and Eq. [50'] is

$$c_{ox}(x, t_p') \simeq \left[\frac{2q_d}{\mathbf{F}a} + 2c_i\right]\frac{x}{a} + \left[\frac{2q_d}{\mathbf{F}a}\left(1 - \frac{8}{\pi^2}\right) + \frac{4c_i}{\pi}\left(1 - \frac{4}{\pi}\right)\right] e^{-\pi^2 Dtp'/4a^2}\sin\frac{\pi x}{2a} \quad [50']$$

Page 910, column 2, Eq. [50''''] is

$$c_{ox}(x, 0) \simeq \frac{2q_d}{\mathbf{F}a}\left[1 + \frac{1}{2}e^{-\pi^2 Dtp'/4a^2}\right]\frac{x}{a} \text{ for } t_u = 0 \quad [50'''']$$

On p. 914, fourth line from bottom of column 1, Eq. [19] should read Eq. [9].

On p. 916, column 2, in the line following Eq. [77'] insert) following [7]; in the next line delete the , following [39].

Properties of Evaporated Thin Films of SiO

D. B. York

Components Division, International Business Machines Corporation, Kingston, New York

ABSTRACT

The absorption coefficient and transmission of vacuum deposited films of SiO were used as a measure of the reproducibility of the relative composition of the resulting films. The optical properties of the films can be reproduced by controlling the evaporation rate and partial pressure of oxygen. Reproducibility of optical properties does not insure reproducible electrical properties since the surface condition of the electrode material greatly affects the electrical properties.

Recently, SiO has received considerable attention in the fabrication of thin films by vacuum evaporation technique due to its low vapor pressure, relative chemical inertness, sublimation of bulk material, and flexibility of boat design. Vacuum deposited thin films of SiO have been widely used in the areas of optical coatings, encapsulation of electrical and optical devices, and as an insulator or dielectric in thin film electrical devices.

Although this material has found wide application in the thin film area, there is a question concerning the existence of a true chemical compound SiO in the solid state (1-13). It has been established that SiO does exist in the gas phase (7-8) whereas on condensation the compound probably disproportionates according to the following reaction

$$2SiO \rightarrow Si + SiO_2$$

The condensed material obtained for the experiments to be discussed varied in composition depending on conditions of preparation. As would be expected, this variation in composition greatly affected the optical and electrical properties of the thin films.

The purpose of this investigation was to study the influence of the partial pressure of oxygen and the evaporation rate of the SiO and to relate these findings to their optical and electrical properties.

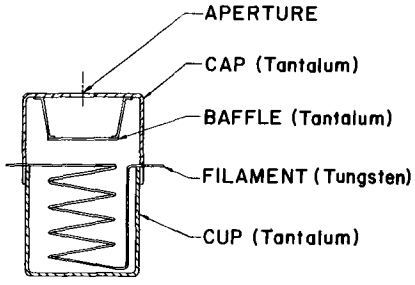

Fig. 1. SiO boat used to fabricate films

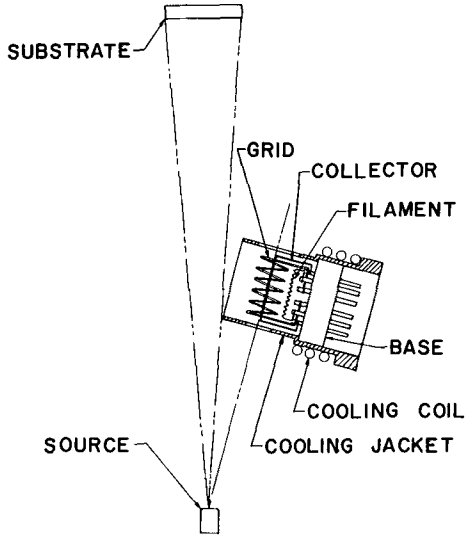

Fig. 2. Position of sensing element relative to evaporant stream

Experimental Procedures and Equipment

The films were fabricated in a conventional vacuum system, consisting of a glass bell jar 18 in. in diameter and 36 in. high, and mounted on a stainless steel base plate. The system was evacuated by a 6-in. oil diffusion pump backed by a mechanical pump. With the aid of a Meissner trap (14) and a Ti pump, the bell jar could be evacuated to a pressure of about 10^{-8} mm Hg. A pressure of 5 x 10^{-7} mm Hg was maintained throughout the evaporation process.

Figure 1 illustrates the SiO boat used in the fabrication of the films. This design met the necessary requirements of evaporation rate, input power, and prevention of particles of the bulk material from leaving the boat before they are in the gas phase. The evaporation rate of SiO from this boat was controlled automatically by an evaporation rate monitor and controller (15). The sensing element of the rate monitor was located in the path, and parallel to, the evaporant stream as shown in Fig. 2.

Production of the films was aided by a mask changer shown in Fig. 3, which permitted the fabrication of the entire device during a single pump down of the vacuum system. The mask changer had ten mask positions which worked in conjunction with three source positions, had a source-to-substrate distance of 36 cm, and held a single substrate which could be heated to 200°C or cooled to liquid N_2 temperature.

The base plate contained a port through which oxygen could be bled into the vacuum chamber by

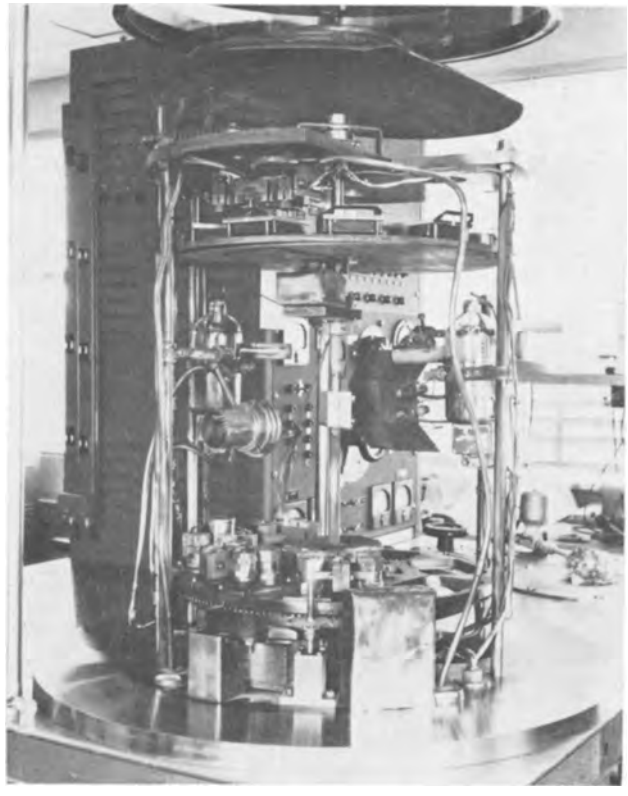

Fig. 3. Mask changer

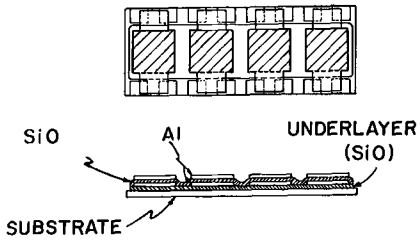

Fig. 4. Parallel plate capacitor

a manually operated needle valve. Due to the gettering action of the evaporated SiO and the limitations of the manually operated needle valve it was impractical to attempt to maintain a partial pressure of oxygen lower than 1 x 10^{-6} mm Hg during evaporations. Higher pressures, however, could be controlled manually without difficulties. This enabled us to study the effects of oxidation of the deposited films over a limited range ($10^{-3} \rightarrow 10^{-6}$ mm Hg).

Two types of geometry were employed for the fabrication of the films: one for the optical measurements and one for the electrical measurements.

The SiO films were deposited on Vycor[1] substrates in order to study the optical transmission of the films in the uv and visible regions. The transmission curves were produced by a double beam spectrometer using Vycor glass as the reference material, and standard testing procedures were followed.

The geometry chosen to obtain the electrical measurements was the parallel plate capacitor as illustrated in Fig. 4. The soda-lime glass substrate on which the capacitors were fabricated contained baked silver lands which aided in making electrical connection to the device. These silver lands were

[1] Corning 7910.

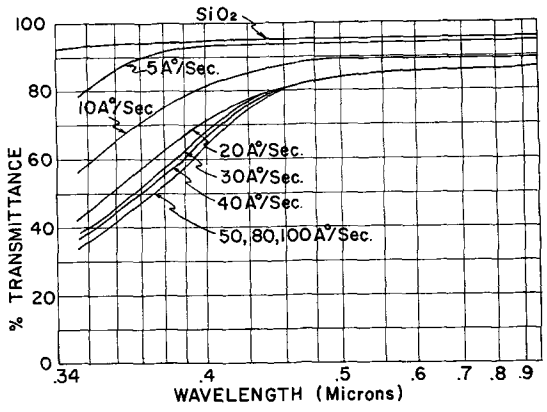

Fig. 5. % Transmittance vs. wavelength (microns): thickness, 920Å; residual pressure 5 x 10^{-6} mm Hg.

necessary if the device was to be tested repeatedly, since thin films by themselves cannot maintain the mechanical adhesion necessary for multiple soldering and point probing. The thick underlayer of SiO is used to produce a clean smooth surface for the electrode material. Each substrate was 0.75 x 2 x 0.04 in. and contained four capacitors. Each capacitor had an insulation area of one square centimeter.

Capacitance measurements were taken with a reliable impedance bridge operating at 1 kc. The maximum test voltage applied to the film by the bridge was 10v. The d-c voltage and current measurements were taken with a sensitive electrometer and ammeter, respectively.

Results

A literature search revealed no method of determining the percentages of Si, SiO, Si_2O_3, and SiO_2 in an evaporated thin film sample. However, since Si and SiO are strong absorbers in the uv and visible regions, it was felt that the optical properties could be used as a measure of the relative composition of the films. Films having the optical characteristics of SiO_2 in the uv, visible, and near infrared were prepared by evaporating SiO at a slow evaporation rate (2 Å/sec) in a high partial pressure of oxygen (10^{-4} mm Hg). The composition of the resulting film may consist of SiO_2, Si_2O_3, or both (3, 4). Figure 5 shows a typical curve of the transmittance *vs.* wavelength for films prepared in the residual gas pressures in the system at various evaporation rates. For a constant wavelength in the uv region, the percentage of transmittance increases with a decrease in the evaporation rate. As the evaporation rate decreases more SiO is allowed to be oxidized, and the transmittance of the film approaches that of SiO_2 in the uv and visible regions. The degree of oxidation of the SiO will be determined by the ratio of the number of SiO to oxygen atoms arriving at the substrate and is a function of the partial pressure of oxygen in the system.

Figures 6 and 7 compare the transmittance of films evaporated in a high oxygen atmosphere to the transmittance of those evaporated in the atmosphere of the normal residual gases in the system. These curves are characteristic of a particular vacuum system depending on the residual gases, source to

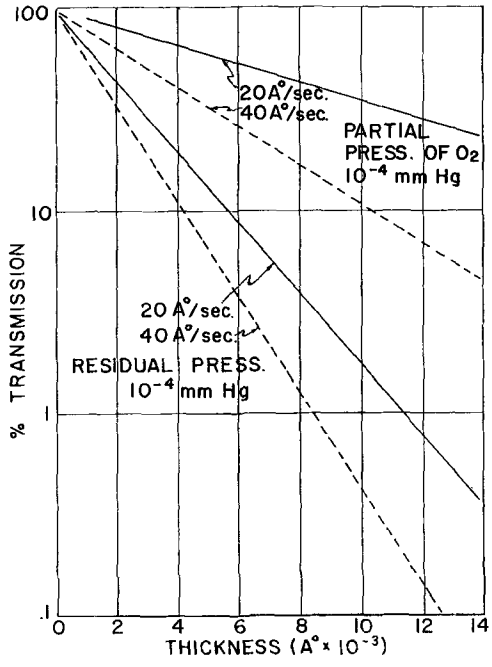

Fig. 6. % Transmission vs. thickness (Å x 10^{-3}); wavelength, 0.4μ.

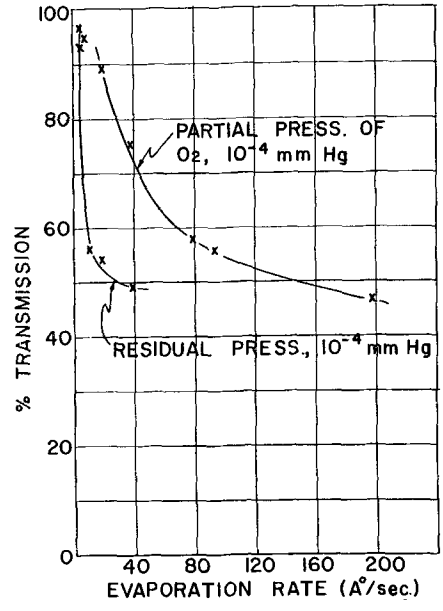

Fig. 7. % Transmission vs. evaporation rate (Å/sec); thickness, 1250Å; wavelength, 0.4μ.

substrate distance, and spacing of the shutter from the substrate.

From these curves we conclude that the composition of the deposited films is affected by the evaporation rate and the partial pressure of oxygen in the system, and this composition lies somewhere between Si and SiO_2.

If the electrical properties of these films (when used in capacitors) are to be reproducible, it is necessary that the composition of the films be reproducible. It was found that the optical transmittance of these films was reproducible when the evaporation rate and partial pressure of oxygen were controlled. This indicated that the composition of the deposited films could be controlled in a similar manner. Reproducible electrical properties did not fol-

low directly, however, until the surface roughness of the electrodes was reduced.

It was found that special consideration must be given electrodes used in the thin film capacitors. The surface of vacuum deposited metals is affected by such parameters as evaporation rate, substrate temperature, substrate material, and pressure. Since the vacuum deposited materials that we were most concerned (In,Pb, Sn, Al) with result in surface irregularities of the same order of magnitude as the dielectric thickness (2000Å) used to obtain the experimental results, it was necessary to reduce surface roughness to a minimum before the electrical properties of the capacitors were reproduced. Aluminum was chosen for the electrode material because of its small grain size which results in a smooth surface compared to the dielectric thickness. Figure 8 illustrates vividly the difference in surface roughness of several metals vacuum deposited in the form of thin films. All electrical measurements were taken from devices that were fabricated with Al electrodes. These pictures were prepared by the indirect carbon replica technique, with the initial replica containing 5% collodion shadowed with Pt/Pd at 15°.

Figure 9 is a graph of dielectric constant and dissipation factor measured at room temperature (300°K) and liquid N_2 temperature (77°K), *vs.* the evaporation rate. The dielectric constant and dissipation factor both increase with increasing evaporation rate.

This again is as expected and is in agreement with the results obtained from the optical measurements. The dielectric constant lies between that of Si(11.6) and SiO_2(3.8). Since it is not expected that the composition of the deposited film would ever reach that of Si, but some intermediate oxidation state Si_xO_y, the dielectric constant should not exceed 11.6.

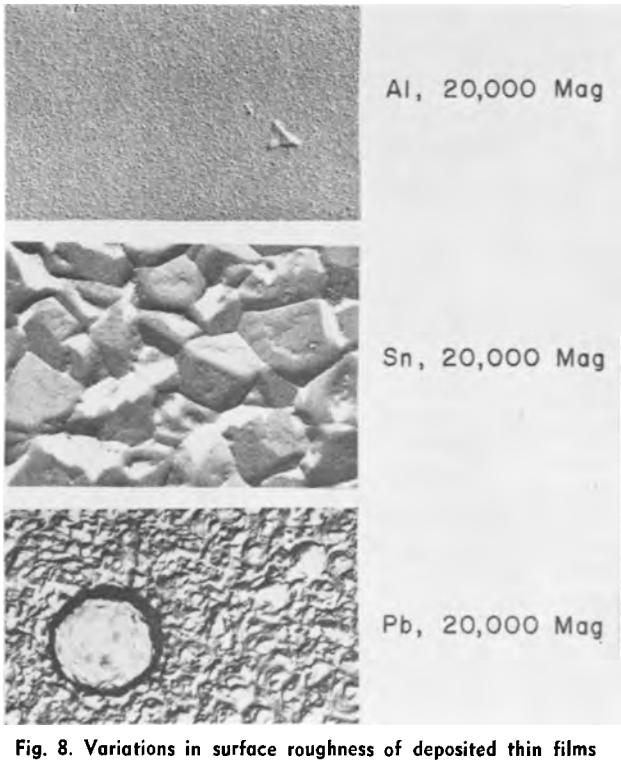

Fig. 8. Variations in surface roughness of deposited thin films

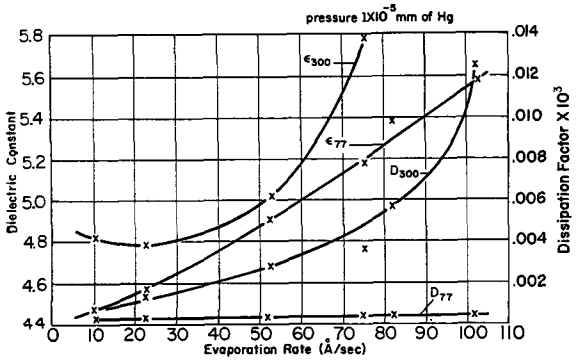

Fig. 9. Dielectric constant *vs.* evaporation rate (Å/sec); pressure, 1 x 10^{-5} mm Hg; D_{77} dissipation factor measured at 77°K; D_{300} dissipation factor measured at 300°K; C_{77} dielectric constant measured at 77°K; C_{300} dielectric constant measured at 300°K.

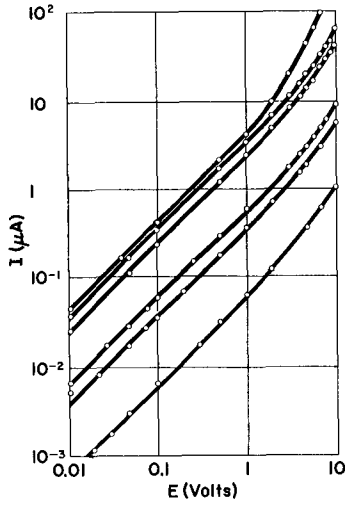

Fig. 10. I (μa) *vs.* *E* (v); thickness between 1500 and 3000Å

The upper limit of the dielectric constant measured in the laboratory has been 8.0 while the lower limit was 4.1. Due to experimental difficulties of controlling the very slow evaporation rates, physical geometry inside the bell jar, and stresses in the highly oxidized films, films could not be prepared that had a dielectric constant of 3.8 which would agree with that of SiO_2.

The voltage-current relationship of the capacitors is shown in Fig. 10 and 11. These films followed

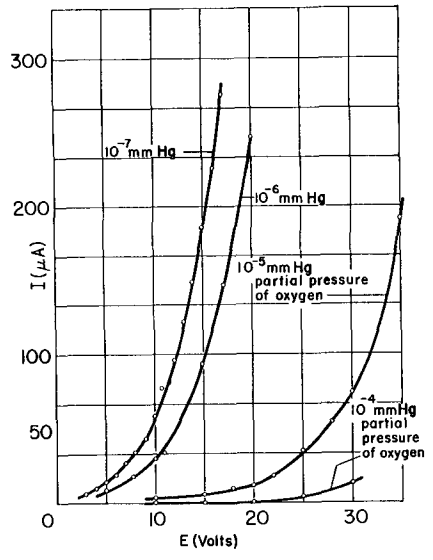

Fig. 11. I (μa) *vs.* *E* (v); thickness between 1500 and 3000Å

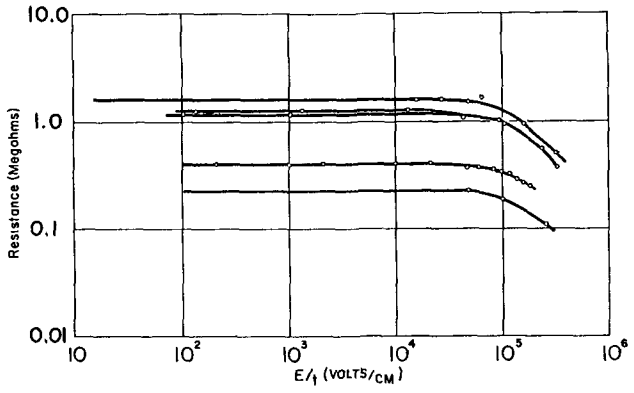

Fig. 12. Resistance (megohms) vs. E/t (v/cm); thickness between 1500 and 3000Å.

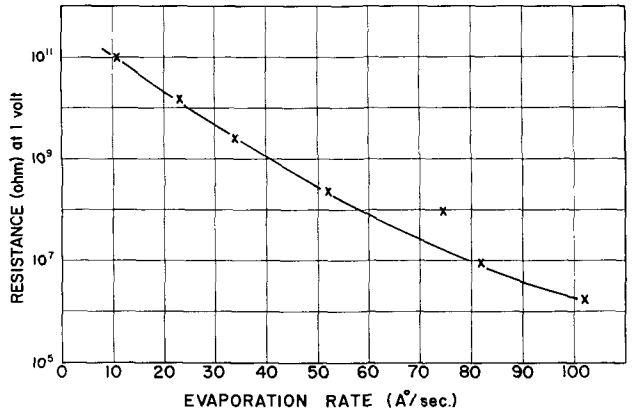

Fig. 13. Resistance (ohm) vs. evaporation rate (Å/sec); thickness, 2500Å; pressure, 1 x 10^{-5} mm Hg.

Ohm's law at low voltages (electric field), but became nonlinear at higher voltages. Figure 12 is a plot of resistance *vs.* electric field. We are not able to explain the shape of these curves, but it can be observed that the break in the curves is from one to two orders of magnitude below the voltage breakdown point (1-5 x 10^{-6} v/cm). It is possible that this break is largely determined by the roughness of the electrode surface compared to the dielectric thickness. A poor surface condition could cause high localized fields resulting in both field emission and heating effects.

Figure 13 indicates that the resistance of the films increased as the evaporation rate decreased. This graph shows a general trend and is another example of the fact that the films approach the properties of SiO_2 as the evaporation rate decreases.

Conclusions

If the electrical properties of vacuum deposited thin films of silicon oxides are to be reproducible, the composition of the film must be controlled. The composition is reproducible if the evaporation rates of silicon monoxide and the partial pressure of oxygen in the vacuum system is controlled. By controlling these parameters and insuring that the surface of the electrodes is smooth (1:10) compared to the dielectric thickness, reproducible capacitors have been fabricated.

Acknowledgments

The author wishes to thank Mr. W. Clark to whom he is greatly indebted for assistance in fabrication of these devices.

Manuscript received Dec. 15, 1961. This paper was prepared for delivery before the Indianapolis Meeting, April 30-May 3, 1961.

Any discussion of this paper will appear in a Discussion Section to be published in the December 1963 JOURNAL.

REFERENCES

1. G. Hass, *J. Am. Ceram. Soc.*, **33**, 353 (1950).
2. G. Hass and C. D. Salzberg, *J. Opt. Soc. Am.*, **44**, 181 (1954).
3. E. Cremer, J. Kraus, and E. Ritter, *Z. Elektrochem.*, **62**, 939 (1958).
4. E. Cremer, A. Faessler, and H. Kramer, *Naturwissenschaften*, (1959).
5. G. Siddal, *Vacuum*, **9**, 274 (1960).
6. L. Bulbs and W. Isler, "The Application of Vacuum Evaporation Techniques to Microminiaturization," Diamond Ordnance Fuze Lab., Washington 25, D. C.
7. L. Brewer and R. K. Edwards, *J. Phys. Chem.*, **48**, 351 (1954).
8. L. Brewer and F. J. Greene, *J. Phys. Chem. Solids*, **2**, 286 (1957).
9. G. W. Brady, Private communication.
10. K. F. Bonhoeffer, *Z. Phys. Chem.*, **131**, 368 (1928).
11. H. N. Potter, *Trans. Am. Electrochem. Soc.*, **12**, 191 (1907).
12. C. A. Zapffe and C. E. Sims, *Iron Age*, **5**, 34 (1942).
13. H. DeWet Erasmus and J. A. Persson, *J. (and Trans.) Electrochem. Soc.*, **95**, 316 (1949).
14. C. R. Meissner, *Rev. Sci. Instr.*, **26**, 305 (1955).
15. M. H. Perkins and G. R. Giedd, *ibid.*, **31**, 8773 (1960).

Electrical Resistivity of Stabilized Zirconia at Elevated Temperatures

J. M. Dixon, L. D. LaGrange, U. Merten, C. F. Miller, and J. T. Porter, II

John Jay Hopkins Laboratory for Pure and Applied Science,
General Atomic Division of General Dynamics Corporation, San Diego, California

ABSTRACT

The electrical resistivity of stabilized zirconia of various compositions has been measured by a four-probe technique in the temperature range 550°-1200°C. Resistivities of fully stabilized compositions are found to increase with increasing additions of the stabilizing oxide, and the lowest resistivities appear to occur in materials stabilized with small cations.

It is generally accepted that the conductivity of zirconia stabilized in the fluorite structure by additions of divalent and trivalent oxides is essentially ionic over a wide temperature range and that the mobile ions are the anions. Kiukkola and Wagner (1) argued that the observed insensitivity of the resistivity of zirconia-calcia solutions to the oxidizing power of the ambient atmosphere was proof of the absence of a significant electronic contribution to the conductivity; and the good agreement observed by these workers between thermodynamic data obtained with galvanic cells using these electrolytes and data obtained by other methods over a considerable temperature range is, in itself, confirmation of the essentially ionic nature of their conductivity. Pal'guev and Neuimin (2) recently used the galvanic-cell approach to study several solid electrolytes and found no significant electronic contribution in a zirconia-15 mole % calcia solution in the 600°-1000°C range. Similar measurements made in this Laboratory (3) on a zirconia-10 mole % yttria solution yielded the same result. Hund found that the oxygen deficiency of the fluorite phase in the zirconia-yttria (4) and zirconia-calcia (5) systems gives rise to anion vacancies (rather than cation interstitials). Kingery *et al.* (6) were able to demonstrate that the mobile carrier in zirconia-15 mole % calcia is the oxide ion moving through these vacancies by showing that the tracer diffusion coefficient for oxygen is sufficiently large to account for the entire observed conductivity.

Only meager quantitative information is available on the resistivity of these materials. Noddack *et al.* (7) obtained relative data for a series of zirconia-yttria solutions, while Kingery *et al.* (6) and Hund (5) obtained extensive data on a zirconia-15 mole % calcia solution, and Volchenkova and Pal'guev (8) determined resistivities in this system as a function of temperature and composition. Trombe and Foex (9) determined resistivities at 1000°C in zirconia-calcia solutions. Most of this work has been carried out by a two-probe technique, in some cases with direct current, and is open to question on the basis of the possible importance of contact resistance.

In the present investigation, the two systems most commonly suggested as electrolytes, zirconia-calcia and zirconia-yttria, were investigated in the compositional range where the lowest resistivities are encountered and at temperatures up to about 1200°C. A cursory study of solutions with some alternative stabilizing oxides was also carried out.

Experimental Procedures

The samples studied were prepared from a variety of oxide, nitrate, and carbonate starting materials, all of which had contents of the desired metal greater than 98% of total metal content. The zirconia-calcia, zirconia-neodymia, and most of the zirconia-yttria samples were prepared by a cold-press-and-sinter technique. The desired mixed oxide was prepared by a final firing of several hours' duration in air at 1500°-1700°C. The resulting mass was ground to −100 mesh, mixed with a few per cent stearic acid binder, cold-pressed at 15,000 psi, and fired in air for several hours at ~1700°C. The other samples were hot-pressed from previously prepared mixed oxide powders in graphite dies at 3000-5000 psi and ~1400°C. Porosities of the samples were determined by a modification of the ASTM-C20-46 water-absorption procedure (10), which indicated that the open porosity of the cold-pressed and sintered samples was 10-20% of their volume, while that of the hot-pressed samples was <5% in most cases.

The resistivity measurements were made on bars ~1 in. long by ~⅛ in. square. The samples were mounted in a holder of high-purity alumina and were heated in air by a platinum-wound resistance furnace. Pressure contacts were made with four platinum leads spaced along the length of the sample, the two end leads being used to supply current and the two center ones serving as voltage taps (*i.e.*, these leads served as reference electrodes at the oxygen activity of the ambient air). Alternating current of 1-1000 cps was employed, and the resistivity determined by the four-probe technique was found to be independent of frequency in this range on several samples and at several temperatures where this effect was checked. The sample re-

sistance was determined by measuring the voltage drop across the sample and across a known series resistor with a calibrated oscilloscope, and resistivities were calculated from these results, the sample cross sections, and the distance between the voltage probes. The resistivities so calculated on individual samples are accurate to ±10%, well within the observed variations between nominally identical samples.

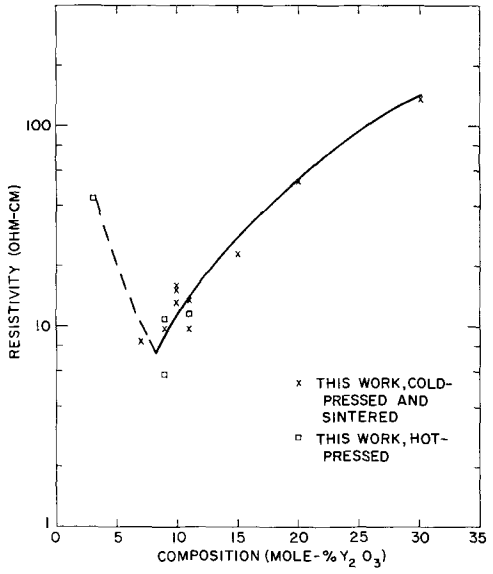

Fig. 1. Resistivities of zirconia-yttria solutions at 1000°C

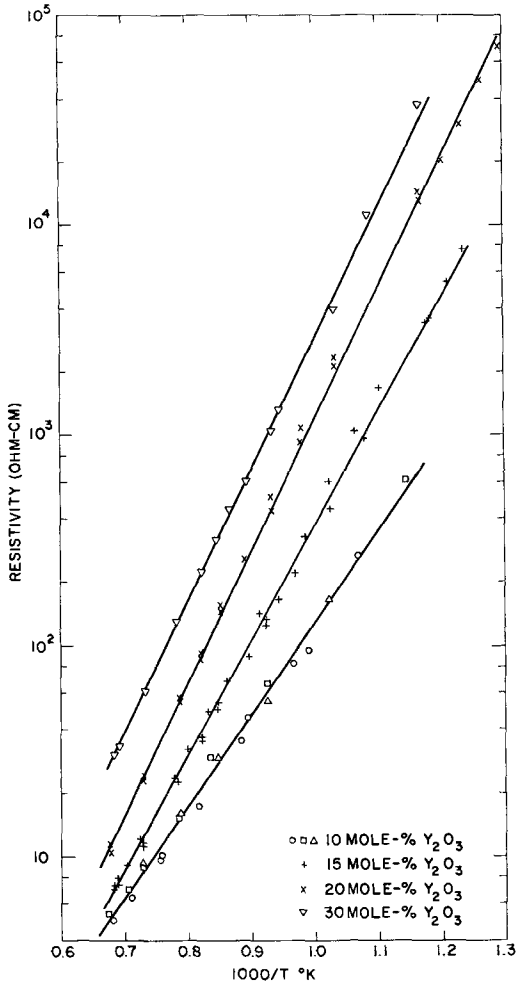

Fig. 2. Temperature-dependent resistivities of cold-pressed and sintered zirconia-yttria solutions.

Table I. Apparent activation energies for zirconia-yttria solutions

Composition, mole % Y_2O_3	Activation energy, kcal/mole
7	~18*
9	~19*
10	19.8
11	20.7
15	24.7
20	28.5
30	28.4

* Based on data for which $0.65 < 1000/T < 0.95$ only.

Experimental Data

Zirconia-yttria solutions.—The resistivities of zirconia-yttria solid solutions at 1000°C are shown in Fig. 1. A minimum occurs in the resistivity curve at ~8 mole % Y_2O_3, which coincides with the low-yttria boundary of the cubic zirconia field in the phase diagram of Duwez *et al.* (11). Thus, in this system the lowest resistivities appear to be obtained when the minimum amount of Y_2O_3 needed to stabilize the cubic solid solution is added.

In Fig. 2 the temperature-dependent data for three samples of the 10 mole % Y_2O_3 solution and for one sample each of the 15, 20, and 30 mole % solutions are presented. The data for each composition can be represented by an Arrhenius equation within experimental uncertainty, the apparent activation energies increasing with increasing yttria content as indicated in Table I.

At lower yttria contents, deviations from this simple behavior are observed. This is suggested by the data of Fig. 3 and is quite apparent in Fig. 4, where data for the three hot-pressed samples, one containing 11 mole % Y_2O_3 and two nominally identical 9 mole % Y_2O_3 samples, are given. Apparently

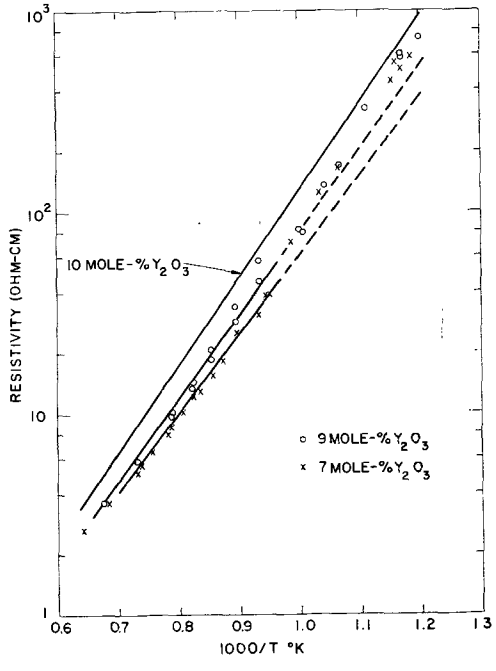

Fig. 3. Resistivities of low-yttria solutions

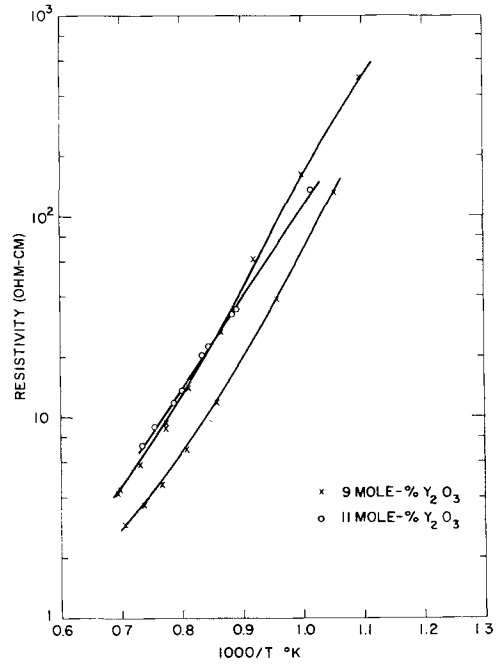

Fig. 4. Resistivities of hot-pressed zirconia-yttria solutions

some decomposition of the cubic solution occurs for these lower yttria contents at temperatures below 800°C.

Zirconia-calcia solutions.—The resistivities of zirconia-calcia solid solutions at 1000°C are shown in Fig. 5. As with yttria, the minimum resistivity appears to be at the lower limit of the single-phase cubic region, which these data place at ~12 mole % CaO. This is in reasonable agreement with Duwez *et al.* (12), who report that the boundary is at 15 mole % CaO in this temperature range. Volchenkova and Pal'guev (8) and Trombe and Foex (9) also find a resistivity minimum near this composition, but their reported resistivities are much higher than ours.

The temperature-dependent data for the 12-15 mole % CaO samples can be represented by Arrhenius equations, as is shown in Fig. 6, the resulting apparent activation energies being generally higher than those for the yttria solutions, as is indicated in Table II. Our activation energy of 30.0

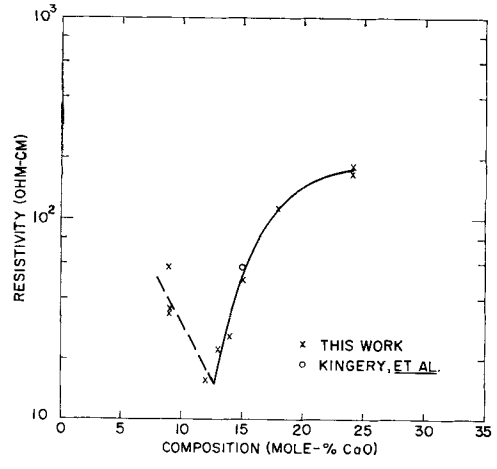

Fig. 5. Resistivities of zirconia-calcia solutions at 1000°C

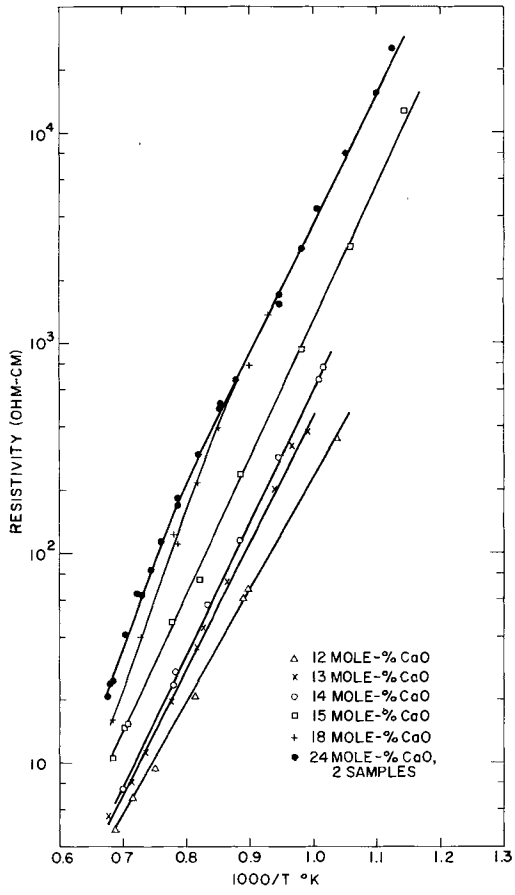

Fig. 6. Temperature-dependent resistivities of zirconia-calcia solutions.

kcal/mole for the 15 mole % CaO solutions is in very satisfactory agreement with the 29.1 kcal/mole reported by Kingery *et al.* (6). The 18 and 24 mole % CaO solutions show deviations from this exponential relationship, despite the fact that both compositions are well within the single-phase region of Duwez *et al.* (12). Again this may be an indication that these compositions undergo some decomposition of the cubic solid solution at the lower temperatures, and indeed the older work of Hund (5) places this phase boundary at about 20 mole % at 1200°C.

Zirconia solutions with other stabilizing elements.—The effect of the identity of the added cation on the conductivity of zirconia solutions was examined in a preliminary way by determining the resistivity of samples containing 10 mole % Nd_2O_3, 9 and 15 mole % Yb_2O_3, and 10 and 15 mole % Sc_2O_3. The

Table II. Apparent activation energies for zirconia-calcia solutions

Composition, mole % CaO	Activation energy, kcal/mole
12	24.5
13	27.4
14	29.0
15	30.0
18	~38*
24	~39†

* Based on data for 1000/T <0.85 only.
† Based on data for 1000/T <0.80 only.

phase diagrams for all these systems are in some question. Monoclinic zirconia transforms to tetragonal at 1000°C. Above this temperature small additions of rare-earth oxides apparently go into solution in the tetragonal phase or cause modification of this structure to the closely related cubic form. Collongues *et al.* (13), have reported that in a number of systems, including ZrO_2-Yb_2O_3 and ZrO_2-Nd_2O_3, the miscibility gap between the tetragonal and cubic forms disappears at higher temperatures (1500°C in the Yb_2O_3 case; >2000°C for Nd_2O_3 solutions). This close crystallographic similarity suggests that the ion-transport processes in the two structures may be similar.

According to Roth (14) the equilibrium structure for the 10 mole % neodymia solution studied here is essentially single-phase tetragonal solid solution at temperatures above ~300°C. The results of Collongues *et al.* (13), on the other hand, suggest the presence of a large amount of the cubic phase. The latter data would place our 9 and 15 mole % ytterbia samples entirely in the cubic-solid-solution field at 1200°C. Duwez *et al.* (11) contend that 7 mole % scandia is sufficient to stabilize the cubic phase in the ZrO_2-Sc_2O_3 system.

Room-temperature x-ray examination of the samples employed in this investigation showed only the cubic fluorite phase in ZrO_2·10 mole % Nd_2O_3 with a lattice parameter of 5.197Å. The 9 and 15 mole % Yb_2O_3 samples also showed only the fluorite structure with lattice parameters of 5.127 and 5.134Å, respectively. The patterns of the 10 and 15 mole % Sc_2O_3 samples were essentially those of a fluorite phase, with lattice parameters of about 5.09 and 5.06Å, but there was considerable splitting of the lines, which suggests lattice distortion or the presence of a second closely related phase.

The resistivity data for these samples are presented in Fig. 7 and 8. In all cases there are marked deviations from simple Arrhenius behavior, suggesting that the samples are not single-phase solid solutions over the entire range of measurement. Results for the 10 mole % Sc_2O_3 sample were not reproducible on thermal cycling and annealing, particularly at the lower temperatures. At the highest temperatures, where only the tetragonal and cubic solutions are likely to exist, the resistivities at a single composition fall in the order Nd >Y ≧ Yb > Sc. The ionic radii of the added cations fall in the same order, as do the lattice parameters of the respective cubic phases at a given composition. A similar correlation between lattice parameter and resistivity exists within the calcia-zirconia and yttria-zirconia systems where the resistivity and lattice parameter both increase with added lower valent oxide in the single-phase region.

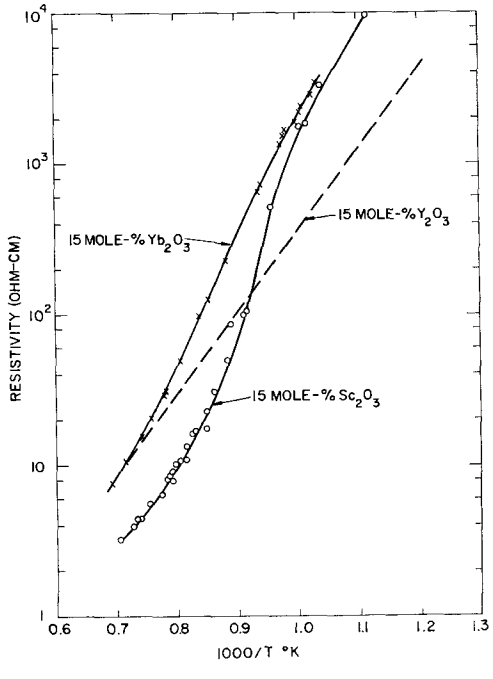

Fig. 7. Resistivities of some 15 mole % zirconia solutions

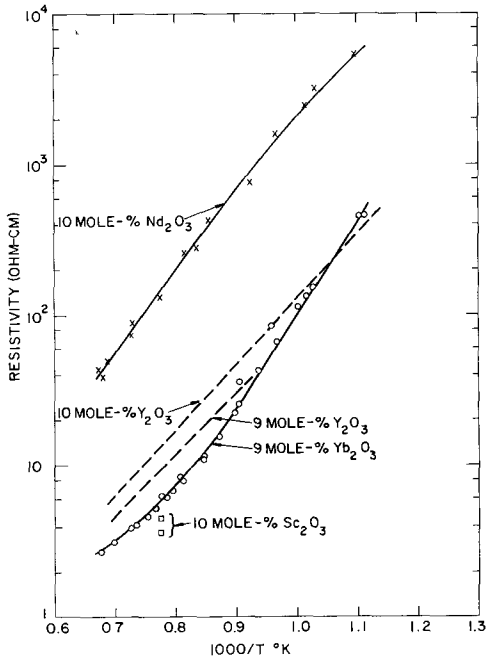

Fig. 8. Resistivities of some 9 and 10 mole % zirconia solutions

Conclusions

The present results indicate that the cubic solid solutions of yttria and calcia in zirconia have their lowest resistivities when the minimum amount of lower-valent oxide needed to stabilize the solution is added, and that the resistivities of fully stabilized solutions follow Arrhenius equations over a wide range of temperature.

The effect of varying the identity of the added cation is difficult to assess because of the scarcity of phase equilibrium information and the meagerness of the present results. The present work suggests, however, that in the neighborhood of 1000°C, solutions made with the smallest added cations have the lowest resistivities.

Acknowledgments

The authors are indebted to W. A. Steele and J. F. Quirk for preparing some of the conductivity samples.

Manuscript received August 20, 1962.

Any discussion of this paper will appear in a Discussion Section to be published in the December 1963 JOURNAL.

REFERENCES
1. K. Kiukkola and C. Wagner, *This Journal*, **104**, 379 (1957).
2. S. F. Pal'guev and A. D. Neuimin, *Trans. (Trudy) Institute of Electrochemistry*, No. 1, p. 90 (translation from the Russian by Consultants Bureau, New York, 1961).
3. D. T. Bray, Private communication.
4. F. Hund, *Z. Elektrochem.*, **55**, 363 (1951).
5. F. Hund, *Z. physik. Chem.*, **199**, 142 (1952).
6. W. D. Kingery, J. Pappis, M. E. Doty, and D. C. Hill, *J. Am. Ceram. Soc.*, **42**, 393 (1959).
7. W. Noddack, H. Walch, and W. Dobner, *Z. physik. Chem. (Leipzig)*, **211**, 180 (1959).
8. J. S. Volchenkova and S. F. Pal'guev, *Trans. (Trudy) Institute of Electrochemistry*, No. 1, p. 97 (translation from the Russian by Consultants Bureau, New York, 1961).
9. F. Trombe and M. Foex, *Compt. rend.*, **236**, 1783 (1953).
10. *ASTM Standards*, Pt. 3, p. 648 (1952 ed.), American Society for Testing Materials.
11. P. Duwez, F. H. Brown, Jr., and F. Odell, *This Journal*, **98**, 356 (1951).
12. P. Duwez, F. Odell, and F. H. Brown, Jr., *J. Am. Ceram. Soc.*, **35**, 107 (1952.)
13. R. Collongues, M. Perez y Jorba, and J. Lefevre, *Bull. Soc. Chim. France*, No. 1, 70 (1961).
14. R. S. Roth, *J. Research Natl. Bur. Standards*, **56**, 24 (1956).

Thorium Phosphate Phosphors

P. W. Ranby and Doreen Y. Hobbs

Thorn Electrical Industries Ltd., Enfield, Middlesex, England

ABSTRACT

Some thorium phosphate phosphors activated by a number of different elements are described. Most important of these are the copper activated materials which show unusual fluorescent properties by emitting strongly in the orange when excited by short ultraviolet. Lower concentrations of copper in the presence of lithium give the more usual blue emission associated with lower valent copper activation of phosphates, while with copper and silver an emission occurs in the yellow. The fluorescent intensity of some of these materials is high, and their use in lamps is discussed.

Only a few thermally prepared phosphors have been described in which thorium is the main metallic component of the matrix. Outstanding among these are thorium oxides activated by certain of the lanthanon elements (1) and some thorium silicates capable of activation by a number of different metals (2). There are some cases in which thorium appears to function as an activator or coactivator, especially in conjunction with cerium; one example of the latter is in a magnesium pyrophosphate matrix (3).

The following paper describes some thorium phosphate phosphors (4) which are strongly excited by u.v. radiation. The matrix of these materials corresponds to the orthophosphate and can be activated by a number of different metals of which copper in the lower valent form is most effective. When activated by copper the intensity of the luminescence is remarkably stable to increases in temperature; the system also provides an example of three elements, which individually are often able to function as activators, producing a specific luminescent effect when present together in the matrix.

Preparation

A typical method of preparing these phosphors is to heat an intimate mixture of thorium oxide and ammonium phosphate with compounds of the activators at about 800°C in air followed by reheating at 1100°C. After comminuting, the material is reheated at 1100°C. As is usual in the preparation of phosphate phosphors, relatively short periods of heating, *e.g.*, an hour, are sufficient. In order to avoid the formation of hard products it is sometimes preferable to use only part of the ammonium phosphate in the initial mixture and then incorporate the remainder after the first heat treatment. Alternatively, thorium phosphate can be coprecipitated with the activators by using a solution of the metal nitrates and a soluble phosphate. The precipitate is washed and dried and then mixed with additional ammonium phosphate before heating.

The composition of the mixture used for the preparation of these phosphors can be varied over wide limits. For example, fluorescent products can be obtained when the molecular ratio of ThO_2 to $(NH_4)_2HPO_4$ used in the initial mixture is varied widely as from 1:0.2 to 1:1.9, but the optimum ratio corresponds to 1 ThO_2:0.66 P_2O_5 with some additional phosphate to allow for the activators present. Chemical analysis of the products after heating shows that practically no phosphorus is lost during the preparation, and the results reported in the present paper are for phosphors having a molar composition of 1 ThO_2:0.66 P_2O_5, *i.e.*, $Th_3(PO_4)_4$.

The activators can be incorporated in the initial mixture before heating as the oxides, *e.g.*, Sb_2O_3 or, in the case of copper, the acetate is a convenient form.

The optimum concentration of copper depends on the presence of other activators and is dealt with later, but no appreciable loss of copper occurs during the thermal preparation of the phosphor. In the case of antimony activation, a concentration in the initial mixture of 0.12 atoms Sb to 1 Th is reduced to approximately 0.04 Sb:1 Th by volatilization during the preparation. Similarly, in the case of thallium activated materials from an initial concentration of 0.1 atoms Tl:1 Th only approximately 0.01 Tl:1 Th remains in the finished phosphor. The other activators are used in concentrations of the

order of 0.04 atoms to 1 atom Th except silver where a ratio of about 0.15 Ag:1 Th is required.

When copper is used as the activator or as one of the activators the final heating is carried out in a mildly reducing atmosphere, such as steam and hydrogen. A similar atmosphere is required during the preparation of the cerium activated phosphors.

Structure of Matrix

Because the composition of these phosphors can be varied over a fairly wide range of metal to phosphorus ratios without producing marked changes in the fluorescent emission it is difficult by chemical means alone to establish the true nature of the matrix. However, x-ray analysis indicates that except in the case of the lithium containing materials it corresponds to the normal orthophosphate $Th_3(PO_4)_4$. The x-ray pattern of thorium phosphates prepared with decreasing concentrations of copper activator are virtually indistinguishable from that of the unactivated material. The pattern for a copper activated orange fluorescent thorium phosphate is given in col. 1 of Table I while in col. 2 are listed the characteristic x-ray diffraction lines of thorium orthophosphate as given by Burdese and Borlera (5).

In all columns, d represents the interplanar spacing in Angstrom units. The terms in col. 1 correspond approximately to the intensity values as follows: very strong, 100-80; strong, 80-60; medium, 60-40; weak, 40-20; very weak, below 20.

Table I

1 Thorium phosphate (Cu) (orange fluorescence)		2 Thorium orthophosphate (5) $Th_3(PO_4)_2$		3 Thorium phosphate (Cu, Li) (blue fluorescence)	
d	Intensity	d	Intensity	d	Intensity
		8.50	1	8.57	Medium
6.44	Weak			6.29	Strong
5.49	Medium	5.35	40	5.45	Weak
5.23	Medium	5.08	44	5.11	Medium
		4.56	2	4.77	Weak
				4.34	Medium
4.34	Strong	4.25	100	4.26	Medium
3.98	Weak	3.90	8	3.99	Medium
		3.66	2	3.58	Weak
3.54	Medium	3.49	35	3.48	Weak
3.36	Weak	3.33	11	3.37	Medium
				3.24	Medium
3.24	Weak	3.19	7	3.18	Medium
3.05	Weak	3.03	13	3.00	Medium
2.97	Weak	2.93	12	2.92	Weak
2.93	Strong	2.90	80		
				2.84	Medium
2.81	Medium	2.79	33	2.80	Weak
				2.75	Medium
				2.70	Weak
2.61	Weak	2.59	10	2.55	Very weak
2.56	Medium	2.53	25		
				2.43	Weak
		2.36	2		
2.31	Weak	2.29	8		
2.17	Medium	2.15	18	2.18	Weak
2.10	Medium	2.08	18		
		2.05	3		
		1.99	5		
1.95	Weak	1.93	10	1.94	Medium
1.91	Weak	1.90	11		
		1.89	12		
1.87	Weak	1.85	10		
1.83	Very weak	1.82	7	1.82	Medium
1.81	Weak	1.80	7		
1.79	Weak	1.77	10	1.79	Weak
1.77	Very weak	1.76	7		
1.73	Weak	1.72	6		
1.67	Weak	1.66	8	1.69	Medium
1.62	Weak	1.61	8	1.62	Very weak
		1.60	7		
1.57	Weak	1.56	8		
1.54	Weak	1.55	7	1.55	Very weak
1.52	Weak	1.52	9		
		1.51	8		
		1.49	9	1.47	Very weak
				1.33	Very weak

Table II

Matrix	Peak of main emission band due to activation by Sb	Mn	Gap between peaks in cm^{-1}	Reference
Calcium pyrophosphate	4150	5750	6700	(6)
Calcium fluophosphate	4870	5700	3000	(7)
Thorium phosphate	4760	5420	2600	Fig. 1

Cerium, Antimony, and Lead Activated Systems

Thorium phosphates activated by cerous cerium or lead, fluoresce blue, manganese is effective as a secondary activator and shifts the emission to longer wavelengths, but none of these are efficient phosphors at room temperature. Activated by antimony alone, thorium phosphate emits a fairly wide blue band with a maximum at 4760Å when excited by 2537Å; when manganese is present as an additional activator a band in the yellow appears with a maximum at 5420Å and at the same time suppression of the blue band occurs (Fig. 1). It is of interest to compare the position of the peaks of these main emission bands with those reported for the same activator combination in other phosphate matrices similarly excited (see Table II).

When manganese is present in these materials they show a weak yellow fluorescence under cathode ray excitation.

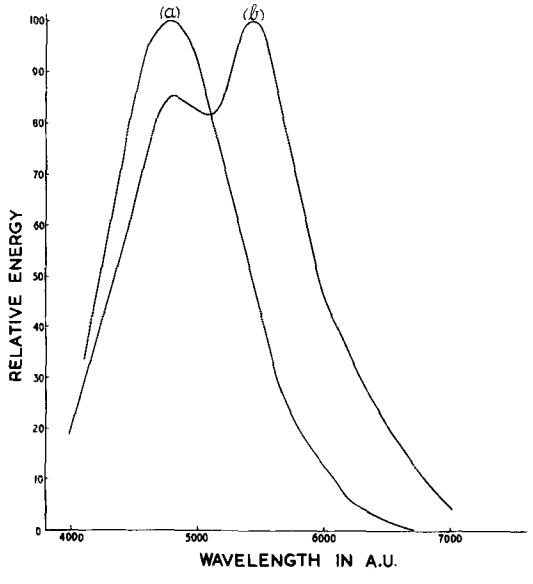

Fig. 1. Spectral energy distribution curves of thorium phosphate activated by (a) antimony (0.04Sb:1 Th) and (b) antimony and manganese (0.04Sb:0.02Mn:1Th) (2537Å excitation at room temperature).

Table III

Phosphor	Relative brightness measured through filters* Chance OGr2	Chance orange OY1	Ilford green No. 404 + 801	Ilford blue No. 304
Thorium phosphate (Sb) (0.04Sb:1Th)	75	20	40	30
Thorium phosphate (Cu, Li) (0.01Cu:0.36Li:1Th)	110	20	40	160
Calcium tungstate	100	20	40	120

* The transmission characteristics of these filters are:
Chance OGr2, 0% at 4100Å; 63% at 5400Å; 13% at 7000Å
Chance OY1, 0% at 5400Å; 65% at 5800Å; 85% beyond 6100Å
Ilford 404 + 801, 0% at 4700Å; 52% at 5300Å; 0% at 6200Å
Ilford 304, 0% at 3600Å; 50% at 4300Å; 0% at 5300Å

In Table III the relative brightness of the blue phosphor at room temperature measured through a number of standard filters is compared with that of calcium tungstate. The intensity of luminescence steadily decreases as the temperature of the phosphor increases (Fig. 2).

Activation by Copper

Thorium phosphate activated by univalent copper emits a bright orange which peaks at about 5920Å when excited by 2537Å at room temperature. The spectral energy distribution of this emission is shown in curve (a) of Fig. 3. As the temperature of the phosphor is raised this emission moves to shorter wavelengths, but the intensity of luminescence remains high; these changes are shown by the curves of Fig. 4. When the phosphor is cooled to liquid air temperatures, the fluorescence becomes brick-red in color, and the intensity is maintained. At room temperatures the intensity of fluorescence of this phosphor compares very favorably with established lamp phosphors such as the halophosphates (see Table IV).

The proportion of copper required for activation of thorium phosphate is relatively high, and ratios of 0.125 atoms Cu per atom Th are suitable although the exact concentration is not critical.

The presence of traces of manganese in this material exerts a quenching effect on the fluorescence.

At room temperature the phosphor is only feebly excited by long wavelength u.v. (*e.g.*, 3650Å) and

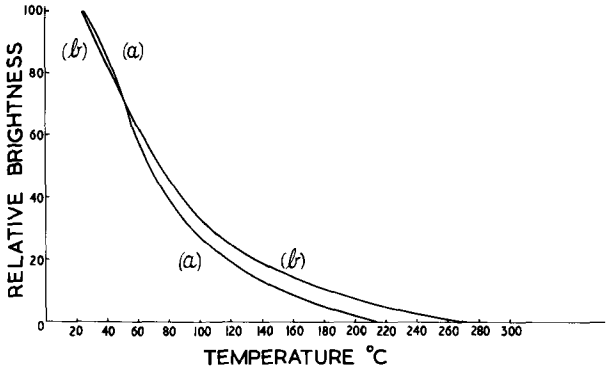

Fig. 2. Effect of temperature on intensity of fluorescence of (a) thorium phosphate (antimony) (0.04Sb:1Th) and (b) thorium phosphate, (antimony, manganese, 0.04Sb:0.02Mn:1Th), (2537 Å excitation measurements through Chance OGr2 filters.

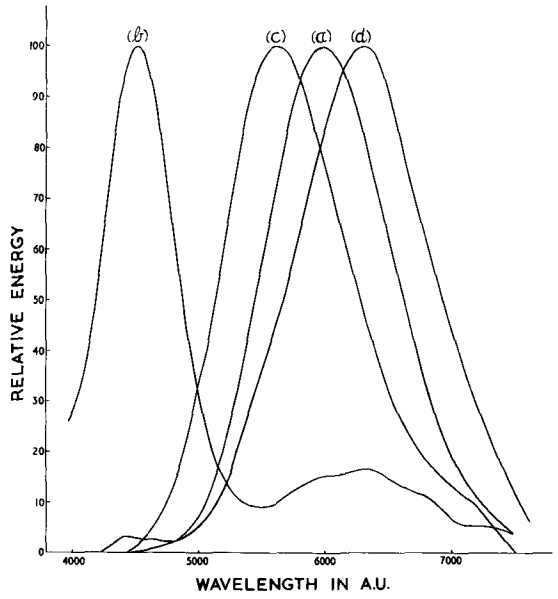

Fig. 3. Spectral energy distribution curves of thorium phosphate activated by (a) copper, (0.12Cu:1Th), (b) copper in the presence of lithium (0.01Cu:0.36Li:1Th), (c) copper and silver, (0.01Cu:0.16Ag:1Th), (d) copper, thallium and manganese (0.04Cu:0.02Mn:0.01Tl:1Th), (2537Å excitation at room temperature).

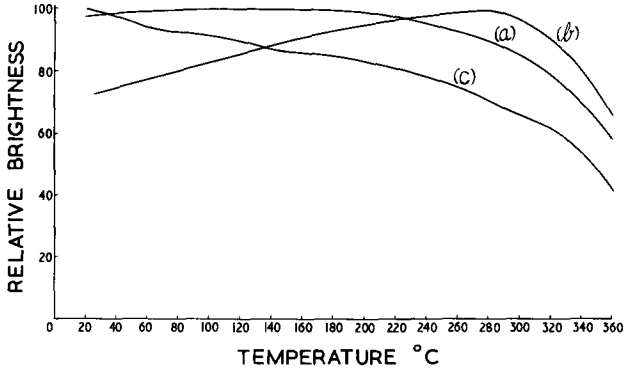

Fig. 4. Effect of temperature on intensity of fluorescence of thorium phosphate (copper) (0.12Cu:1Th) excited by 2537Å radiation; measurements through (a) Chance OGr2 filter, (b) Ilford green filter Nos. 404+801 and (c) Chance orange filter No. OY1.

becomes even weaker as the temperature is reduced, but when the temperature is raised the intensity increases and the color changes from an orange-yellow to a greenish-yellow. Under cathode-ray excitation the phosphor emits in the yellow.

The fluorescence normally associated with activation by univalent copper is blue-green in color and thorium phosphate (Cu), is one of the few efficient phosphors whose emission is predominantly in the long wavelength region of the visible spectrum. Other copper activated phosphate phosphors which emit in the long wavelength region of the visible spectrum are barium halophosphates of the apatite-type of structure (8), but these materials are excited primarily by long wavelength u.v. although like thorium phosphate (Cu) the fluorescence tends to shorter wavelengths as the temperature of the phosphor is raised.

Table IV

Phosphor	Relative brightness measured through filters*			
	Chance OGr2	Chance OY1	Ilford green No. 404 + 801	Ilford blue No. 304
Thorium phosphate (Cu) (0.12Cu: 1Th)	100	110	23	0
Thorium phosphate (Cu, Ag) (0.01Cu: 0.16Ag: 1Th)	74	55	25	2
Thorium phosphate (Cu, Tl, Mn) (0.04Cu: 0.01Tl: 0.02Mn: 1Th)	45	65	7	0
Calcium halophosphate (Sb, Mn) (3500°K)	100	100	24	6

* See footnote to Table III.

Activation by Copper in the Presence of Lithium

If lithium is incorporated in thorium phosphate-copper phosphors, the orange emission band due to cuprous copper which peaks at 5920Å is suppressed, and a new emission in the deep blue appears. This blue emission is due to a fairly narrow band with a peak at about 4550Å [curve (b), Fig. 3]. There is also a lesser band in the red peaking at about 6360Å. The brightness of this blue phosphor compares favorably with calcium tungstate (Table III). The blue emission band is not as stable to increases in temperature as the orange band; it is also excited only by short wavelength u.v. Under cathode-ray excitation the phosphor emits in the blue.

The concentration of copper required for optimum intensity of luminescence is much less for the blue than for the orange phosphor and is of the order of 0.01 atoms Cu per atom Th (cf. 0.125 atoms Cu per atom Th in orange phosphors).

Additions to the initial mixture before the thermal preparation of the blue phosphor may be made as lithium phosphate Li_3PO_4 or as the carbonate if sufficient ammonium phosphate is also added to yield the orthophosphate. Although it is convenient to use a concentration of the order of 0.3 atoms Li per atom Th, in the preparation it is not critical. In fact this change in the emission can also be brought about in the absence of lithium by preparing the phosphor at a higher temperature than normal, *e.g.*, 1250°C, but the products are not as bright as the lithium containing materials.

The x-ray diffraction pattern of this blue phosphor differs from that of the normal thorium orthophosphate and the lines are listed in col. 3 of Table I. This pattern is obtained when the phosphor is prepared with as little as 0.05 atoms Li per atom Th at the normal firing temperature of 1100°C; it is also obtained in the absence of lithium if the preparation is carried out at 1250°C. Consequently it cannot be due to the formation of a thorium lithium phosphate, but at the same time the x-ray diffraction does not agree with that of the other reported (5) thorium phosphates such as the pyrophosphates, $Th_2P_2O_9$, $(ThO)_2P_2O_9$, etc. It is thought most likely that this blue phosphor is a thorium orthophosphate of modified crystal structure.

A blue or blue-green emission is much more usual than orange for univalent copper activated phosphate phosphors; for example, calcium hydroxyphosphate (Cu) (9) and strontium magnesium fluophosphate (Cu) both emit strongly in the blue when excited by short wave u.v., and the peaks of their main emission bands are at 4800 and 4850Å, respectively [compared with 4550Å for thorium phosphate (Cu, Li)]. Also, with the other phosphors there is little evidence of a lesser band in the red analogous to that shown by the thorium phosphate (Cu, Li) (see Fig. 3).

Activation by Silver in the Presence of Copper

In the absence of copper, thorium phosphate is not activated by silver, for excitation by u.v. or cathode rays, but materials containing copper concentrations of the order of 0.01 atoms Cu per atom Th and silver concentrations of the order of 0.15 atoms Ag per atom Th are strongly excited by a wide range of u.v. radiation, *e.g.*, both 2537 and 3650Å are effective sources of excitation; the emission is in the yellow. The phosphor also emits a weak yellow under cathode rays. The spectral emission curve of a sample excited by 2537Å radiation at room temperature is shown in Fig. 3. The peak of the main band of this emission is at about 5710Å and there is a lesser band in the red. The brightness of this phosphor relative to some others is shown in Table IV.

The optimum proportion of copper required for sensitizing this silver emission is only about a tenth of that required for efficient activation by copper alone.

Activation by Copper and Manganese in the Presence of Thallium

When thallium is present in the thorium phosphate matrix, copper and manganese can be incorporated together, and a red emitting phosphor is obtained which is excited by short but not long wavelength u.v. The red emission consists of a new band peaking at about 6300Å (see Fig. 3), and the intensity of this band is reduced by raising the temperature of the phosphor.

In the absence of thallium, manganese, as indicated earlier, acts as an inhibitor of the normal copper fluorescence, while in the presence of thallium alone manganese is not effective as an activator of thorium phosphate.

Use of Thorium Phosphate Phosphors in Lamps

The orange copper activated phosphor can be used as the coating in conventional tubular fluorescent lamps and the color of a 48T12 40w lamp lies just above the black body locus at $x = 0.463$ $y = 0.423$. Initial efficiencies of 58 lpw with a maintenance of 93% at 100 hr are typical of this phosphor. The relatively low initial efficiency and maintenance are due to the difficulties inherent in conventional lamp coating techniques when applied to phosphors with a low resistance to oxidation. However, by suitable surface treatments of the glass wall of the lamp bulbs before coating these losses can be reduced to some extent (4).

An alternative application for this phosphor is in partially color corrected high-pressure mercury vapor lamps. When used in lamps of this type some color correction is achieved although not to the same extent as with manganese activated magnesium arsenate or fluogermanate, but the high brightness of the phosphor at elevated temperatures adds materially, *e.g.*, up to 10% to the lumen output of the uncorrected lamp. The color of 125w high-pressure mercury vapor lamps coated with this phosphor is around $x = 0.348$, $y = 0.400$ compared with $x = 0.302$, $y = 0.347$ for uncoated lamps.

Discussion

For calcium and strontium orthophosphates activated by univalent copper it has been suggested (10) that the half-height band width of 700-800Å of these phosphors is less than that of most phosphors and is associated with a good temperature dependence of fluorescence. However, the band width of the blue fluorescent thorium phosphate is of the same order (700Å), but the fluorescence of this phosphor is not remarkable for its temperature stability, whereas the orange emitting copper activated thorium phosphate has a band width of 1180Å and this phosphor has a temperature stability at least as high as that of any of the alkaline earth orthophosphate phosphors. It would seem unlikely then that the narrow band width of the blue copper emission in phosphate phosphors can be associated with a good temperature dependence of fluorescence.

It is interesting to note that by Gaussian analysis of the emission, the peaks of the blue and orange bands due to univalent copper activation of thorium phosphate excited by short u.v. at room temperatures are at 22,000 and 16,510 cm^{-1}, respectively; these are very close to the values for the peaks of the blue and orange bands (22,400 and 17,000 cm^{-1}, respectively) which are supplementary (11) to the main green emission from copper activated hexagonal zinc sulfide excited by long u.v. at room temperature. This may indicate that the supplementary emission bands of copper activated zinc sulfide are associated with univalent copper while the main green emission of zinc sulfide is due to divalent copper. The relatively mild reducing conditions necessary in the thermal preparation of phosphors activated by univalent copper would not conflict with this possibility.

From a study of the halophosphates activated by univalent copper the occurrence of both a blue and an orange-red emission have been attributed (8) to two different types of univalent copper centers; that is copper ions occupy alternative lattice sites. This would seem to be a possible explanation with the present phosphors especially as there is a difference in x-ray diffraction patterns between the orange and blue emitting structures and a much higher concentration of copper is required for orange than for blue emission.

Acknowledgments

The authors wish to thank Miss M. B. Halstead for spectral energy measurements, Mr. P. J. Clewer for x-ray analyses, and the Directors of Thorn Electrical Industries Limited, for permission to publish these results.

Manuscript received June 6, 1962; revised manuscript received Nov. 9, 1962.

Any discussion of this paper will appear in a Discussion Section to be published in the December 1963 JOURNAL.

REFERENCES

1. F. G. Wick and C. G. Throop, *J. Opt. Soc. Am.*, **25**, 57 (1935).
2. H. Meyer, British Pat. 601042 (14.9.45).
3. H. C. Froelich, *This Journal*, **95**, 254 (1949).
4. P. W. Ranby and D. Y. Hobbs, British Pat. 827,967, (22.2.56); 834,024 (27.7.56).
5. A. Burdese and M. L. Bolera, *Atti. Accad. Sci.* (Torino), **94**, 107 (1960).
6. D. E. Kinney, *This Journal*, **102**, 676 (1955).
7. K. H. Butler and C. W. Jerome, *ibid.*, **97**, 265 (1950).
8. B. E. Hunt and A. H. McKeag, *ibid.*, **106**, 1032 (1959).
9. H. G. Jenkins, A. H. McKeag, and P. W. Ranby, *ibid.*, **96**, 1 (1949).
10. W. L. Wanmaker and C. Bakker, *ibid.*, **106**, 1027 (1959).
11. S. T. Henderson, P. W. Ranby, and M. B. Halstead, *ibid.*, **106**, 27 (1959).

Brief Communications

The JOURNAL accepts short technical reports having unusual importance or timely interest, where speed of publication is a consideration. The communication may summarize results of important research justifying announcement before such time as a more detailed manuscript can be published. Consideration also will be given to reports of significant unfinished research which the author cannot pursue further, but the results of which are of potential use to others. Comments on papers already published in the JOURNAL should be reserved for the Discussion Section published biannually.

Submit communications in triplicate, typewritten double-spaced, to the Editor, Journal of The Electrochemical Society, 30 East 42 St., New York 17, N. Y.

A Dember Effect Study of Shifts in the Stoichiometry of ZnS

F. F. Morehead

International Business Machines Corporation,
Thomas J. Watson Research Center, Yorktown Heights, New York

ABSTRACT

An attempt was made to follow, by pulse Dember effect measurements, the changes in vacancy concentration in ZnS resulting from variations of temperature and sulfur pressure. The p-type Dember pulse increases at constant temperatures roughly as the square root of the sulfur pressure; it decreases with temperature for a constant sulfur pressure so as to indicate a reaction energy of 0.6 ev per zinc vacancy formed. The "n-type" pulse measured in material with no added sulfur increases with temperature, yielding an activation energy of 1.1 ev for each pair of vacancies formed. Firing the "pure" ZnS in a running vacuum at 900°C, on the other hand, yields p-type material, indicating that the formation of an isolated Zn vacancy is energetically considerably more favorable than the formation of an isolated S vacancy. This conclusion agrees with the reaction energies mentioned above.

A previous work (1) has described both the technique and some applications of the pulsed Dember effect in the study of compounds of the ZnS type. The present work represents a detailed example of such applications. In general, one would prefer to make quantitative and unambiguous electrical measurements of the Hall effect on well-characterized, homogeneous single crystals. In the case of materials like ZnS, however, it is experimentally difficult if not impossible to produce homogeneously a change in the number and type of carriers in single crystals of sufficient size for conventional galvanomagnetic measurements. The time required for the crystal interior to come to equilibrium with the surface and the surrounding atmosphere is prohibitively long, especially at lower temperatures, which may be the temperature region of most interest. Therefore, a measurement such as the Dember effect which can be used on powders, even though it gives considerably less information than Hall effect measurements on large single crystals, can be of considerable value in at least identifying and following trends in stoichiometry in a semiquantitative fashion.

For ZnS which contains a sufficient number of uncompensated acceptors, the sign of the Dember pulse indicates a diffusion current of holes away from the illuminated surface. Since the electron mobility is greater than that of the holes, most ZnS materials show only electronic Dember pulses. For small, but compensated doping levels, the amplitude of the n-type signal increases with the concentration of added impurities. This increase arises from the fact that for most impurity systems, *e.g.*, copper and chlorine, the thermal depth of the hole traps that are introduced is much greater than that of the electron traps, typically 1 ev *vs.* 0.3 ev). Under the circumstances, the net number of electrons in excess of the holes flowing in the concentration gradient produced by the strongly absorbed light may be increased. For still larger concentrations the effect of increasing concentration is simply to decrease the effective mobility of the electrons, hole motion being negligible at this point. For concentrations greater than about 1000 ppm, a decrease in signal with increasing concentration is observed.

The purpose of this present work is to follow changes produced in purified, undoped ZnS by a variety of simple treatments, within the limitations of the Dember effect method. It is hoped that despite the limitations, some light will have been shed on the factors determining the defect structure of ZnS.

Experimental

The exact details involved in the measurement of the Dember pulse current of powdered samples have been given elsewhere (1). In outline the procedure is as follows. The ZnS powder is mixed with an inert, viscous liquid binder to give a volume concentration of 30% ZnS. The mixture is compressed between two planar electrodes, one of which is transparent, so that the electrode separation is about 100μ. By means of a shutter a constant intensity of band gap (0.32μ) light is flashed onto the sample, and the peak diffusion current is observed on a scope. The direction and magnitude of the current pulse peak are recorded for two dark intervals between flashes, one of 1 sec and the other 60 sec. A third datum is also recorded for the condition in which the sample has been allowed to relax for 60 sec under intense infrared radiation. If the third reading is smaller algebraically than the second, the difference is taken as a measure of the p-type content of the sample, that is, the excess of acceptors over donors. The 60-sec dark period allows the electrons which have diffused away from the surface to return; the holes, which are more deeply trapped, require a much longer period or the application of infrared radiation, (which ionizes both holes and electrons from traps) to effect their return. If only

electrons flow, as in an n-type or compensated sample in the range of defect concentration investigated, on application of the band gap light, then 60 sec of infrared radiation between applications of band gap light should result in the same or a large n-type signal as that resulting from a 60-sec dark interval. If as in a p-type sample both holes and electrons flow away from the illuminated surface on the application of the band gap light to a completely relaxed sample, then infrared relaxation will give a smaller n-type (or a larger p-type) signal than the same period of relaxation in the dark.

The magnitude of the n-type signal obtained after the 60-sec dark interval is assumed to be a measure of the concentration of compensated donors or acceptors. This latter correlation, as mentioned in the introduction, applies only to low "doping" levels. It is assumed that the vacancy concentrations produced by the treatments to be described fall within this doping limit.

The 0.32μ radiation used to produce the Dember pulse was obtained with a high-pressure Xe arc lamp with a 250 mm Bausch and Lomb monochromator. The infrared light peaked at 0.85μ to relax the samples came from a Sylvania DXL movie light and a Perkin Elmer Model 98 monochromator with a quartz prism.

Sample Preparation and Experimental Results

It had been noticed that some unactivated samples of ZnS fired in sealed quartz capsules at 900°C showed n-type Dember currents while the same material fired in an H_2S atmosphere at 1200°C gave p-type signals in a Dember effect measurement. To determine what effects were due to atmosphere and to temperature the experiments given in Fig. 1 were performed. For this particular batch of RCA luminescent grade ZnS, the sealed, evacuated capsule firings led to a nearly exponential increase in n-type response with firing temperature. Practically the same result was obtained in an atmosphere of N_2 flowing over the samples at a rate of 0.04 ft^3/min. Firing in flowing H_2S atmosphere (0.025 ft^3/min) produced strikingly different results. The data plotted as H_2S-A, as well as the other two curves, are the peak Dember pulses obtained for 1-min dark intervals between pulses. The data plotted as H_2S-B are assumed to measure the p-type content of the samples and are obtained by subtracting the Dember pulse obtained for a 1-min dark interval from that

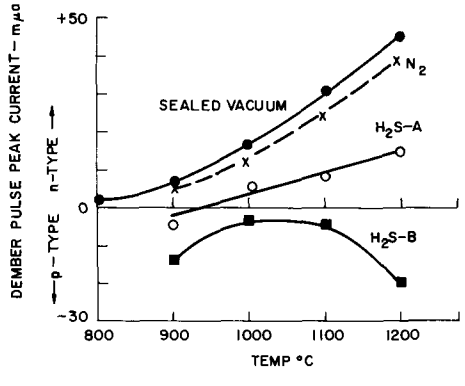

Fig. 1. Dember pulse as a function of temperature and atmosphere

measured after a 1-min period of exposure to infrared. The basis for this procedure has been described in the measurements section, above. Thus the effect of increasing temperature in a sealed vacuum or inert atmosphere is to increase the n-type response of the sample, which can be due, as stated in the introduction, to an increase in the concentration of either compensated or uncompensated donors, *e.g.*, sulfur vacancies. In view of the large amount of energy (virtually the band gap) released when an electron is transferred from a filled donor to a compensating acceptor, the former possibility, compensated donors, is considered most likely.

The H_2S firings plainly favor the formation of some uncompensated acceptors, probably zinc vacancies, the formation of which is favored by an atmosphere containing S_2. The effect of temperature is ambiguous here since, although one expects the solubility of S_2 in ZnS to decrease with increasing temperature for a given pressure of S_2 [from the endothermic dissociation of $(ZnS)_s$ to $(Zn)_g$ and $(S_2)_g$], p_{S_2} is increasing with temperature since the dissociation of H_2S into H_2 and S_2 is also endothermic. The occurrence of the maximum near the temperature of the cubic-hexagonal phase change is probably not significant.

In order to continue this investigation, it was found necessary to use another batch of the RCA material. This second batch, as well as a third, was found to give small p-type pulses as received, in contrast to the original material which gave small n-type signals. Wet chemical analysis of this second batch showed the presence of about 2% excess sulfur, probably present as polysulfides coprecipitated with the ZnS. Other impurities found to be present were 1% $ZnSO_4$ and 0.4% S by weight from wet chemical analysis. From spectrographic analyses 3 ppm Si, less than 1 ppm of Mg or B, and less than 3 ppm of Pb were detected. No Cu or Al were detected and were, therefore, present to the extent of less than 2 ppm. An earlier analysis of the ZnS batch used in the first series of experiments showed 10 ppm Cu, but a recent recheck showed this result to be in error; none was detected. No analysis for halides was made.

Baking at temperatures in excess of 800°C, either in a running vacuum, sealed vacuum, or open system, produced material which gave rather large p-type pulses, indicating that excess sulfur (as zinc vacancies) was still present. Firing at temperatures below 700°C, either in running vacuum or open systems, did produce ZnS which gave small n-type pulses which were consistent with expectations for stoichiometric material. The excess sulfur present as polysulfides is removed by vacuum baking, but as will be shown, baking in a running vacuum at temperatures higher than 700°C also removes more zinc from ZnS than sulfur. Material used in subsequent experiments was first fired at 500°C for 96 hr in a running vacuum.

In the next series of experiments prebaked material was sealed into evacuated quartz capsules of about 5 ml volume with sufficient elemental sulfur to give the desired S_2 pressure at the firing temperature. The ratio of volume occupied by the S_2 to

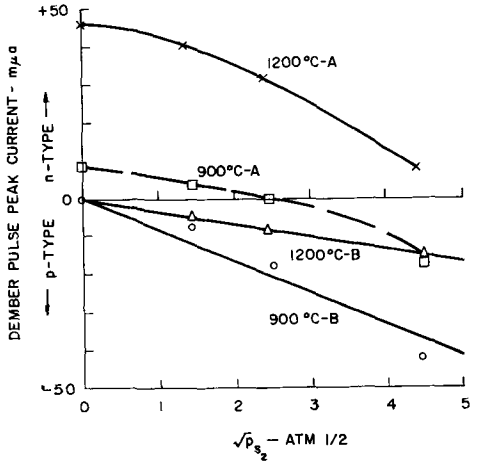

Fig. 2. Dember pulse data as a function of sulfur pressure and temperature.

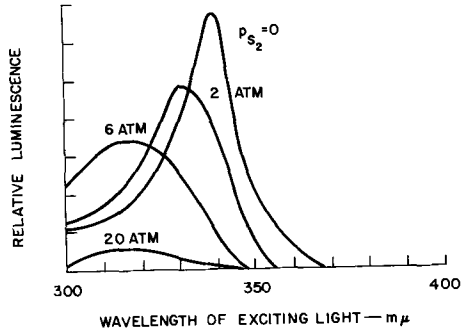

Fig. 3. Excitation spectra of ZnS samples fired at 1200°C under different sulfur pressures. The relative heights of the different curves are meant to be significant.

that of the ZnS was maintained at 4:1. At least two different firing times were used for each point to assure that a steady-state condition had been attained. Results are shown in Fig. 2.

In Fig. 2 the curves marked A give the size and sign of the Dember pulse obtained after 1 min of relaxation in the dark between pulses. Those marked B give the difference between the 1-min dark interval pulse and that obtained after the same period of exposure to infrared radiation. Later we will use B to indicate values of these differences. Hence the value of B is assumed to measure the uncompensated acceptor concentration in the samples. If this latter assumption is true, then it can be seen that the zinc vacancy concentration at a given sulfur pressure decreases with increasing temperature and that it increases at constant temperature roughly as the square root of the sulfur pressure, which is as expected (2). Since we can write

$$(ZnS)_s = (Zn)_g + 1/2(S_2)_g, \text{ and}$$
$$Zn_{Zn} = (Zn)_g + V_{Zn}, \text{ from which}$$
$$p_{Zn}p_{S_2}^{1/2} = K_{ZnS} \text{ and}$$
$$[V_{Zn}] = k_{Zn}/p_{Zn} = k_{Zn}p_{S_2}^{1/2}/K_{ZnS}$$

The same starting material which, when fired in a sealed vacuum at 900°C, gives n-type pulses with no indication of any uncompensated acceptors ($B = 0$), also gives definite p-type Dember pulses ($B = 10$ nanoamp) when fired at the same temperature in a running vacuum. The value of B at 700°C under the same circumstances is less than 0.1 nanoamp. These experiments indicate the difference of steady-state composition resulting from firing ZnS in sealed or running vacuum. Further, the fact that firing at 900° produces a higher p-type signal and thus a larger Zn vacancy content than the firing at 700°C indicates that the energy required to remove a zinc atom from the ZnS lattice is less than that required to remove a sulfur atom.

Some Luminescence Measurements

The samples fired in sealed capsules at 1200°C without sulfur exhibit appreciable blue-green luminescence at room temperature in two bands peaking at 4500 and 4900Å. With decreasing firing temperature the luminescence diminishes and shifts toward the blue; it is hardly detectable at 1000°C. At 1200°C with increasing sulfur pressure the luminescence excited by extrinsic radiation decreases and again shifts toward the blue. The excitation spectra for samples fired at 1200°C under various sulfur pressures are shown in Fig. 3. While the luminescence produced by extrinsic radiation steadily decreases with sulfur pressure, that excited by intrinsic light appears to go through a maximum at around 6 atm. The luminescence is probably due to vacancy levels and may also be connected with the presence of copper (less than 1 ppm as an impurity originally, but perhaps higher after the quartz firings), although in what way is not clear at this point.

The luminescence quenching spectrum of the sample fired at 1200°C with no sulfur is typical of ZnS (3), showing a broad band with a low energy edge at around 1.3 ev and a small peak at 1.05 ev. The wavelength dependence of the effect of the infrared radiation in allowing the measurement of larger p-type Dember signals for the sulfur-fired samples is also typical (1) and corresponds closely to the quenching spectrum for the luminescence described above.

Discussion

A thoroughly rigorous consideration of all of the possible effects, both in luminescence and in Dember measurements, of both vacancies and trace impurities will not be attempted. The following discussion assumes only negligible effects of the trace impurities, including those originally present, those which can diffuse in from the quartz capsules, and those which are sufficiently volatile to be removed during the firings in running vacuum, such as halogens.

An examination of the available data will show that they are consistent with the indication that the energy cost of an isolated sulfur vacancy is significantly greater than that of an isolated zinc vacancy. This experimental indication is the observation that firing ZnS presumed to be compensated with respect to vacancy content in a running vacuum at above 800°C produces p-type material, that is, zinc vacancies.

Figure 4 shows an activation energy analysis of the increase with temperature of n-type Dember signals for samples fired in sealed evacuated capsules with no sulfur. There is no indication of any

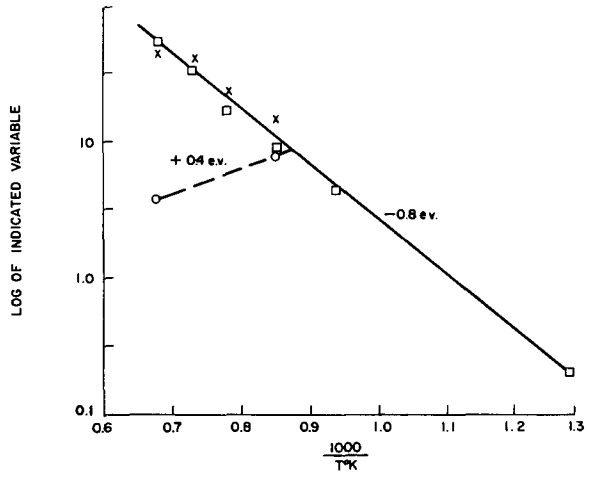

Fig. 4. Activation energy analyses of available data. Samples fired in capsules, no sulfur: □, n-type Dember signal; x, epr measurements; sulfur fired samples: ○, slope of B vs. $\sqrt{P_{S_2}}$.

uncompensated acceptors in any of these samples, *i.e.*, $B = 0$. In accordance with the assumption made in the introduction that at low concentration levels the n-type signal will increase with concentration of compensated donor and acceptor levels, we assume that this curve shows the increase with temperature of V_{Zn}^- and V_S^+. EPR measurements on the same samples are also plotted to show the increase in concentration of a paramagnetic species, which is consistent with the assumption immediately above. A single line 10 gauss wide at $g = 2$ was observed. A large number of paramagnetic species give such a signal. The slope indicates an activation energy of 0.8 ev, so that we may write for the energy of the reaction

$$\text{Vacuum} = V_{Zn}^- + V_S^+ - 1.6\text{ ev}$$

Assuming that the energy lost by the system in transferring one electron from the double donor V_S to the double acceptor V_{Zn} is nearly the band gap (4), say 3.0 ev, we can also write

$$\text{Vacuum} = V_{Zn} + V_S - 4.6\text{ ev}$$

From the change with temperature in the slope of the B *vs.* $\sqrt{p_{S_2}}$ curves in Fig. 2, we obtain a negative activation energy of 0.4 ev, (It should be noted that only two points were available to derive this energy. As a result, the actual numbers subsequently derived should merely indicate trends.) This value then is the energy for the reaction

$$1/2(S_2)_g + 1/\delta(ZnS)_s = V_{Zn} + 1/\delta(ZnS_{1+\delta})_s + 0.4\text{ ev}$$

where δ represents the mole fraction of excess sulfur and is very small. With these equations and from available thermodynamic data we can write

$$(ZnS)_s = (Zn)_g + 1/2(S_2)_g \qquad -1.0\text{ ev} \quad a$$
$$\text{Vacuum} = V_{Zn} + V_S \qquad -4.6\text{ ev} \quad b$$
$$1/2(S_2)_g + 1/\delta\,(ZnS)_s = V_{Zn} + 1/\delta\,(ZnS_{1+\delta})_s \qquad +0.4\text{ ev} \quad c$$
$$(Zn)_g + 1/\delta\,(ZnS_{1+\delta})_s = V_S + (1 + 1/\delta)\,(ZnS)_s \qquad -4.0\text{ ev} \quad b—a—c=d$$
$$Zn_{lat} = V_{Zn} + (Zn)_g \qquad -0.6\text{ ev} \quad c+a$$
$$S_{lat} = V_S + 1/2(S_2)_g \qquad -5.0\text{ ev} \quad d+a$$

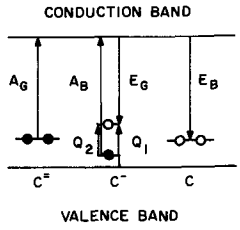

Fig. 5. Transitions in the doubly ionizable center model

The reaction energy of the first equation above was obtained from thermodynamic data (2), the energies for the following two are from the present data and those for the last three equations follow from the first three in the indicated fashion. These data, therefore, support the assertion that it costs much more energy to form an isolated V_S than V_{Zn}.

The luminescence data support a currently proposed doubly ionizable center (3,5) as the origin of the blue and green emission in ZnS. This model is shown in Fig. 5. The extrinsic absorption A_G by the completely filled $C^=$ center leads to green emission E on recombination. Absorption A_B by the singly occupied center C^- leads to the promotion of the single electron into the conduction band and to blue emission E_B on recombination. The promotion of valence electrons into C^- via absorption Q_1 leads to a quenching of E_G as does the absorption Q_2 within C^-, since at room temperature there is sufficient thermal energy to promote a valence electron into the lower level (now unoccupied after Q_2) which fills C^- to give $C^=$. A lowering of the Fermi level by adding uncompensated acceptors such as V_{Zn} with increasing sulfur pressure will lower the concentration of $C^=$ centers and increase that of C^-. With further lowering of the Fermi level, the concentration of C^- will decrease and that of C will correspondingly increase. The emission excited by A_G radiation will, therefore, steadily decrease. The emission excited by intrinsic radiation will increase and shift from green to blue as observed. Why the emission excited by intrinsic radiation for samples prepared at 20 atm of S_2 should become so low cannot be understood without making further assumptions.

Acknowledgment

The author wishes to thank Dr. S. P. Keller for his valuable discussion and encouragement and to acknowledge the help of Dr. R. S. Title, who made the EPR measurements, Mr. J. A. Kucza, who prepared the samples, and Mr. W. N. Hammer, who assisted in making the measurements.

Manuscript received Sept. 7, 1962.

Any discussion of this paper will appear in a Discussion Section to be published in the December 1963 JOURNAL.

REFERENCES

1. F. Morehead and A. Fowler, *This Journal*, **109**, 688 (1962).
2. W. Van Gool, Thesis, Univ. of Amsterdam, January 1961.
3. I. Broser and H. J. Schulz, *This Journal*, **108**, 545 (1961).
4. J. S. Prener and F. E. Williams, *Phys. Rev.*, **101**, 1427 (1956).
5. F. Morehead, *J. Phys. Chem. Solids*, in press.

X-ray Study and Thermoelectric Properties of the $W_xTa_{1-x}Se_2$ System

L. H. Brixner

Pigments Department, Experimental Station, E. I. du Pont de Nemours & Company, Wilmington, Delaware

ABSTRACT

A wide range of compositions of the title system have been prepared with x ranging from 0.10 to 0.99, and x-ray parameters and pertinent thermoelectric properties such as Seebeck coefficient, electrical resistivity, and thermal conductivity were determined. Particular emphasis was given to the range of x from 0.95 to 0.99, where useful thermoelectric properties yielding figures of merit between 0.5-0.9 x 10^{-3} deg^{-1} are experienced at elevated temperatures.

In a previous publication (1), we described the preparation, structure, and thermoelectric properties of the individual compounds WSe_2 and $TaSe_2$. The lattice parameters of WSe_2 have also been previously reported by Glemser (2), and $TaSe_2$ was described by Ariya (3). On the basis of the single-crystal work in ref. (1), WSe_2 and $TaSe_2$ are isostructural and crystallize in the D^4_{6h} — P $6_3/mmc$ space group of the MoS_2 type. However, when prepared in a polycrystalline state by a powder-metallurgical route, $TaSe_2$ more commonly crystallizes in the D^5_{3d} space group of the $CdCl_2$ type. $CdCl_2$ and MoS_2 are known to crystallize in layer structures and in the case of $TaSe_2$ and WSe_2, the layers formed of tantalum, tungsten, and selenium atoms are identical in both modifications, only the sequence of layers is different. The hexagonal lattice dimensions are also in perfect agreement: $a_{CdCl_2} = a_{MoS_2}$ and $c_{CdCl_2} = 3/2\, c_{MoS_2}$. Since the unit cell of $CdCl_2$ contains three molecules and MoS_2 has two molecules, the molecular volume is identical in both structures. Thus, with this close relationship of the structures of $TaSe_2$ and WSe_2, the extended formation of solid solutions could be expected. Such compositions were to be of particular interest, since the components thereof exhibit greatly different electrical characteristics. WSe_2 is a rather well behaved semiconductor with a relatively low electrical conductivity, increasing with temperature, and a high Seebeck coefficient, whereas $TaSe_2$ shows almost metallic conductivity, decreasing with temperature, and a corresponding very low Seebeck coefficient.

It was therefore our intention to see if the two components, $TaSe_2$ and WSe_2, could be combined advantageously in the form of single-phase, solid solutions with optimized or at least improved overall thermoelectric properties.

Experimental

Preparation.—The standard experimental technique for the preparation of all solid solutions was to vacuum-seal the constituent elements, W, Ta, and Se, weighed to the nearest tenth of a milligram, into a quartz ampoule, 15 mm in diameter, 20 cm long. All tubes were carefully heat-treated under vacuum in order to eliminate moisture as much as possible. The components were of the best commercially available purity, usually 99.9%+ and were not given any special purification treatment prior to the reaction. Charges of approximately 20g were fired at 600°-700°C for 10-15 hr, after which time generally a black-looking, free-flowing reaction product was obtained that could be effectively remixed inside the quartz tube by shaking. A second firing step at 1000°-1200°C for another 10-15 hr assured completeness of the reaction and a homogeneous polycrystalline product of gray metallic luster was obtained.

Crystallographic characterization.—All x-ray data are based on powder diffraction patterns obtained with a Phillips 114.6 mm diameter camera at 25°C. The samples, which were taken from the center portions of the final reaction product, were ground to −325 mesh and were sealed into 0.2 mm diameter Lindemann glass capillaries. Exposure times to the K_α radiation of copper (λ = 1.5418Å) varied between 5 and 8 hr. All film patterns were of excellent quality with rather sharp splitting of the α_1 and α_2 lines in the high angle region. Accurate parameters were obtained by extrapolating both a_0 and c_0 according to the function $1/2(\cos^2\theta/\sin\theta + \cos^2\theta/\theta)$ given by Nelson and Riley (4). The lattice parameters of the investigated compounds are given in Table I, and the over-all structural picture of the $WSe_2/TaSe_2$ system is best summarized by Fig. 1. The parameters for $W_{0.97}Ta_{0.03}Se_2$ were also determined as a function of temperature up to 600°C. No structural transition was experienced up to this point and the results are best represented by Fig. 2.

The expansion coefficient in the a-direction is 6.82 x 10^{-6} and 10.56 x 10^{-6} in the c-direction.

Inspection of the data represented by Fig. 1 shows that the $CdCl_2$ structure is retained up to $x = 0.55$; we then have a rather narrow two-phase region ($W_{0.60}Ta_{0.40}Se_2$ clearly contained both phases at about equal intensities); and from $x = 0.65$, we change over to the single phase MoS_2 type.

Densities were determined by vacuum-distilling CCl_4 onto the powdered specimen contained in a 5 ml pycnometer. This procedure yielded experimental values which were generally 1-3% lower

Table I. Lattice parameters of the $W_xTa_{1-x}Se_2$ System

Composition	a_o	c_o	c/a	Type	$\rho_{x\text{-ray}}$	Unit cell volume
$TaSe_2$	3.446	19.101	5.543	$CdCl_2$	8.59_3	196.43
$Ta_{0.90}W_{0.10}Se_2$	3.423	19.107	5.567	$CdCl_2$	8.64_1	194.89
$Ta_{0.75}W_{0.25}Se_2$	3.408	19.132	5.614	$CdCl_2$	8.79_0	192.43
$Ta_{0.50}W_{0.50}Se_2$	3.367	19.186	5.698	$CdCl_2$	8.99_9	188.36
$Ta_{0.49}W_{0.51}Se_2$	3.366	19.186	5.700	$CdCl_2$	9.00_5	188.25
$Ta_{0.48}W_{0.52}Se_2$	3.365	19.188	5.702	$CdCl_2$	9.01_0	188.15
$Ta_{0.47}W_{0.53}Se_2$	3.363	19.189	5.706	$CdCl_2$	9.02_2	187.94
$Ta_{0.46}W_{0.54}Se_2$	3.362	19.189	5.707	$CdCl_2$	9.02_7	187.83
$Ta_{0.45}W_{0.55}Se_2$	3.360	19.192	5.712	$CdCl_2$	9.03_8	187.64
$Ta_{0.40}W_{0.60}Se_2$	3.353	19.194	5.724	$CdCl_2$	9.08_4	186.87
		(12.796)	(3.816)	(MoS_2)	(9.07_8)	(124.583)
$Ta_{0.35}W_{0.65}Se_2$	3.345	12.806	3.828	MoS_2	9.11_9	124.086
$Ta_{0.30}W_{0.70}Se_2$	3.336	12.836	3.848	MoS_2	9.15_0	123.71
$Ta_{0.25}W_{0.75}Se_2$	3.329	12.852	3.861	MoS_2	9.19_1	123.22
$Ta_{0.10}W_{0.90}Se_2$	3.303	12.899	3.905	MoS_2	9.30_7	121.87
$Ta_{0.09}W_{0.91}Se_2$	3.302	12.902	3.907	MoS_2	9.30_9	121.82
$Ta_{0.08}W_{0.92}Se_2$	3.300	12.908	3.911	MoS_2	9.31_7	121.73
$Ta_{0.07}W_{0.93}Se_2$	3.298	12.912	3.915	MoS_2	9.32_5	121.62
$Ta_{0.06}W_{0.94}Se_2$	3.297	12.920	3.919	MoS_2	9.32_6	121.62
$Ta_{0.05}W_{0.95}Se_2$	3.295	12.923	3.922	MoS_2	9.33_6	121.50
$Ta_{0.04}W_{0.96}Se_2$	3.293	12.928	3.926	MoS_2	9.34_5	121.40
$Ta_{0.03}W_{0.97}Se_2$	3.292	12.938	3.930	MoS_2	9.34_4	121.42
$Ta_{0.025}W_{0.975}Se_2$	3.291	12.941	3.932	MoS_2	9.34_8	121.38
$Ta_{0.02}W_{0.98}Se_2$	3.290	12.945	3.935	MoS_2	9.35_1	121.34
$Ta_{0.015}W_{0.985}Se_2$	3.288	12.950	3.938	MoS_2	9.35_9	121.24
$Ta_{0.01}W_{0.99}Se_2$	3.288	12.966	3.943	MoS_2	9.34_8	121.39
WSe_2	3.286	12.976	3.949	MoS_2	9.35_3	121.34

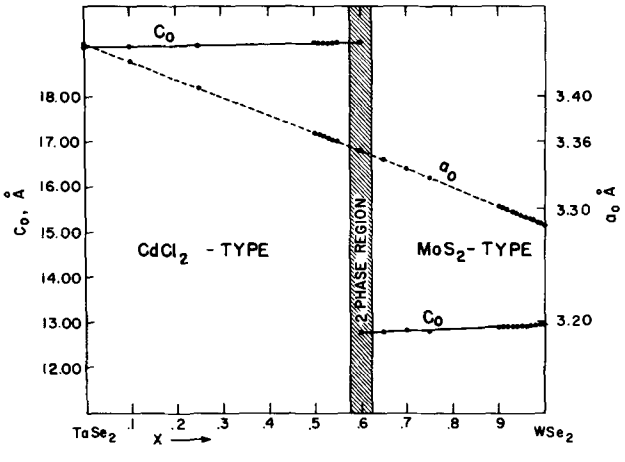

Fig. 1. Lattice parameters as a function of composition for $W_xTa_{1-x}Se_2$ system.

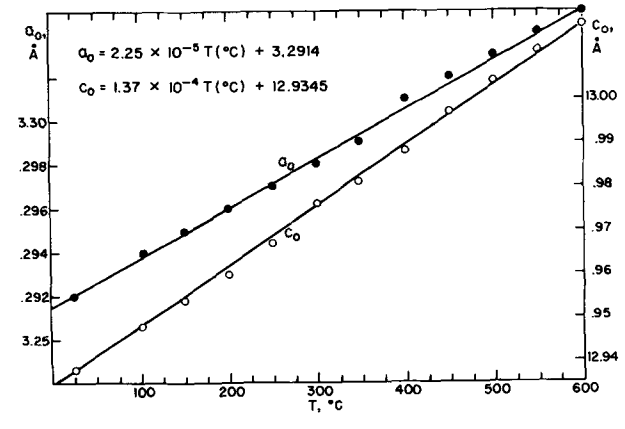

Fig. 2. Lattice parameters as a function of temperature for $W_{0.97}Ta_{0.03}Se_2$.

than the densities calculated from the x-ray data. This can be considered rather good agreement. Some of these results are as follows:

$W_{0.50}Ta_{0.50}Se_2$, ρ pycn. = 8.8_5; ρ x-ray = 8.99_9
$W_{0.75}Ta_{0.25}Se_2$, ρ pycn. = 8.9_7; ρ x-ray = 9.19_1
$W_{0.99}Ta_{0.01}Se_2$, ρ pycn. = 9.2_9; ρ x-ray = 9.34_8

Electrical properties and thermal conductivity.— In order to evaluate the title compositions as possible thermoelectric candidates, we determined the pertinent parameters; namely, electrical resistivity ρ(ohm-cm), Seebeck coefficient S(μv/°C) and thermal conductivity κ(watts/cm-deg). The combination of these parameters in form of the equation $S^2 \cdot \rho^{-1} \cdot \kappa^{-1} = Z$ permitted then to calculate a "Figure of Merit." The samples used for the electrical measurements were bars, ¼ x ¼ x 2 in., which were cold-pressed at 40-60 tsi and subsequently sintered at 600°-800°C for 10-15 hr. The green densities of the as-pressed bars were usually 85-90% of theoretical and generally did not change upon sintering.

The d-c resistivities were measured by a two-point method, using a standard 0.01 ohm resistance, a 1½v battery as power source and determining the potential drop with a L&N type K-2 potentiometer.

The thermal emf output (from which the Seebeck coefficient was calculated) was measured with a Type K-2 potentiometer in combination with a galvanometer. Voltage was generated by butting the bars between two copper blocks, turned from the same piece of stock, one of which was heated by means of a heating tape, the other water-cooled by a coil soldered onto the block. The temperature gradient was measured by means of two thermocouples (copper/constantan) located in holes

drilled to the center of the bar immediately behind the contact faces. Thus, all Seebeck coefficients are measured with respect to copper. The correction of +2 μv/°C to obtain absolute values was generally not applied.

For the measurement of thermal conductivity, two techniques were available. For elevated temperature measurements, we used a technique which was first described by Francl (5) and can be considered a series comparative method. The test cylinder (usually ¾ in. diameter, 1 in. long) was sandwiched between two standard alumina rods of the same dimensions, which were obtained from the Norton Company and had a reported thermal conductivity over the investigated temperature range of 0.02 w/cm-deg. As soon as the thermal current was established as equal through both standards, the thermal current through the sandwiched unknown, together with the temperature difference gave the thermal conductivity. In the equilibrium state when the temperature in the specimen is independent of the time, we have the following conditions

$$k_u a_u \, (\Delta T/\Delta X)_u = k_s a_s \, (\Delta T/\Delta X)_s$$

where k_u and k_s are the thermal conductivities of unknown and standard, a_u and a_s are the contact areas and ΔX_u and ΔX_s are distances between which the temperatures have been measured. Room temperature values derived from this technique were obtained by extrapolation only, since the lowest point of the measurement was generally not below 100°C. Mainly due to problems in the contact areas, accuracies of not better than ± 20% can be claimed.

For more accurate numbers at room temperature, we also employed an absolute technique similar to the one described by Weiss (6); it used smaller samples (generally ½ in diameter, 3-5 mm thick cylinders) operated under vacuum, and the heater input (I·V) could be determined rather accurately. Errors here were mainly due to radiation losses, and the accuracy is probably ±5%. The room temperature properties of some 26 different compositions of $W_xTa_{1-x}Se_2$ with x varying from 0.1 to 0.99 were measured in order to get a good general idea on the electrical behavior of the over-all system.

These data are given in Table II and Fig. 3 gives a graphical representation of the situation. Assuming a relatively constant thermal conductivity, the product $S^2\sigma$ can be considered a truncated figure of merit, and it clearly indicates that the thermoelectrically interesting region is between $x = 0.90$ to 0.99. It is for this reason that only compositions with $x \geqq 0.90$ were investigated in some more detail, particularly as to their behavior at elevated temperatures. The scattering of the data around the solid line, particularly in the regions of minor stoichiometry variations, is mainly due to fluctuations in densities, and it should be borne in mind that all numbers are characteristic of this "pressed condition" only since no extrapolation to 100% density was attempted. As can best be seen from a comparison of Fig. 1 and Fig. 3, the structural transition from the $CdCl_2$-type to the MoS_2-type does not quite

Table II. Electrical properties of the $W_xTa_{1-x}Se_2$ compounds

x	ρ, m ohm-cm, 25°C	ρ, m ohm-cm, −196°C	S, μv/°C, 25°C	S^2/ρ	Type
0	0.40	0.31	−10	$2.50\cdot10^{-7}$	n
0.10	0.60	0.45	−9	$1.35\cdot10^{-7}$	n
0.25	0.55	0.42	−6	$6.5\cdot10^{-8}$	n
0.50	0.72	0.59	−2	$5.5\cdot10^{-9}$	n
0.51	0.82	0.53	−1.5	$2.7\cdot10^{-9}$	n
0.52	0.83	0.51	−1.0	$1.2\cdot10^{-9}$	n
0.53	0.75	0.54	−0.6	$4.8\cdot10^{-10}$	n
0.54	0.79	0.57	−0.2	$5.1\cdot10^{-10}$	n
0.55	0.80	0.58	+0.5	$3.1\cdot10^{-10}$	p
0.60	0.95	0.80	+2	$4.2\cdot10^{-9}$	p
0.65	0.92	0.83	+6	$3.9\cdot10^{-8}$	p
0.70	0.88	0.80	+10	$1.13\cdot10^{-7}$	p
0.75	1.01	0.93	+14	$1.94\cdot10^{-7}$	p
0.90	1.10	0.95	+33	$9.9\cdot10^{-7}$	p
0.91	1.10	0.96	+36	$1.18\cdot10^{-6}$	p
0.92	1.15	0.97	+39	$1.32\cdot10^{-6}$	p
0.93	1.23	0.96	+44	$1.57\cdot10^{-6}$	p
0.94	1.40	1.09	+48	$1.64\cdot10^{-6}$	p
0.95	1.49	1.18	+56	$2.10\cdot10^{-6}$	p
0.96	1.70	1.58	+65	$2.48\cdot10^{-6}$	p
0.97	1.90	1.83	+75	$2.96\cdot10^{-6}$	p
0.975	3.50	2.90	+90	$2.31\cdot10^{-6}$	p
0.98	4.51	4.00	+100	$2.22\cdot10^{-6}$	p
0.985	5.71	6.02	+110	$2.12\cdot10^{-6}$	p
0.99	6.92	7.21	+120	$2.09\cdot10^{-6}$	p
1	719	$1.2\cdot10^{-5}$	+700	$6.82\cdot10^{-7}$	p

coincide with the electronic transition from n-type to p-type at room temperature. Determination of the Seebeck coefficients as a function of temperature for the compositions with $x = 0.50$, 0.51, 0.52, 0.53, and 0.54 indicated that it changed sign from minus to plus at 70°, 81°, 102°, 153°, and 175°C, respectively. All p-type samples examined over a temperature range from 25° to 600°C stayed p-type.

Figure 4 gives the variation of the Seebeck coefficients of some of the preferred compositions over an average temperature range between about 40° and 170°C. It can be seen that the gradient $\Delta S/\Delta T$ increases significantly even within this narrow range from 0.08 to 0.48 μv/°C. For compositions with $x < 0.91$, this gradient becomes consistently smaller yet until it is finally negative for the n-type samples with $x = 0.54$, 0.53, 0.52, 0.51, and 0.50. $TaSe_2$ itself and $Ta_{0.90}W_{0.10}Se_2$ stayed n-type over the same investigated temperature range.

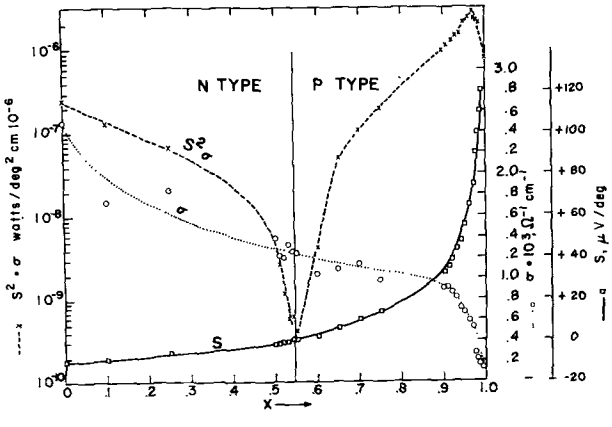

Fig. 3. Electrical properties of $W_xTa_{1-x}Se_2$ system

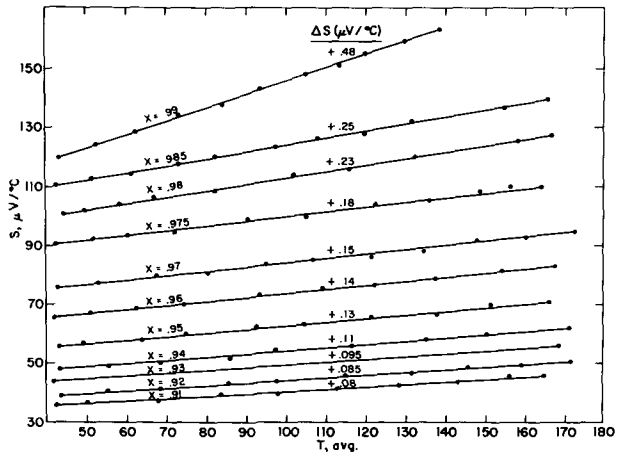

Fig. 4. Seebeck coefficient as a function of temperature and x for some preferred compositions of $W_xTa_{1-x}Se_2$ system.

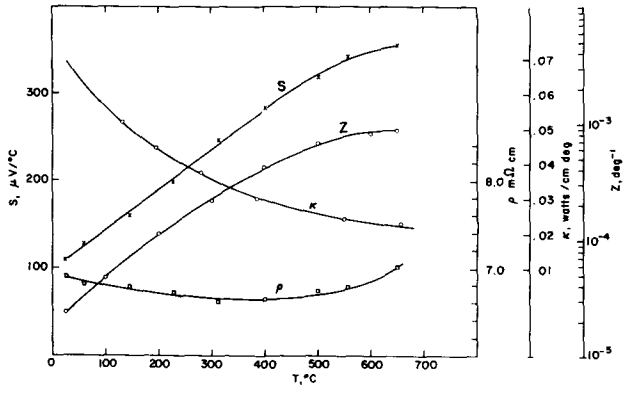

Fig. 5. Thermoelectric properties of $W_{0.99}Ta_{0.01}Se_2$ as function of temperature.

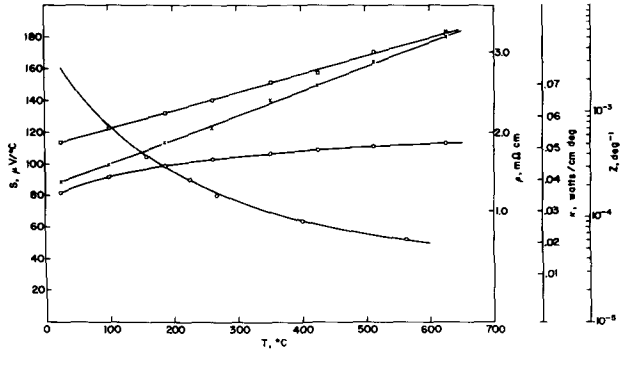

Fig. 6. Thermoelectric properties of $W_{0.97}Ta_{0.03}Se_2$ as function of temperature.

Since Fig. 4 indicated that at least S improves with increasing temperature, we studied all three properties, S, ρ, and k, as a function of temperature for four of these compositions with $x = 0.99$, 0.98, 0.97, and 0.96. Characteristic plots are given for $W_{0.99}Ta_{0.01}Se_2$ and $W_{0.97}Ta_{0.03}Se_2$ in Fig. 5 and 6.

We can see that $W_{0.99}Ta_{0.01}Se_2$ exhibits a rather flat resistivity profile, which actually goes through a minimum at about 400°C. All other compositions with tungsten concentrations <0.99 showed a positive temperature gradient of the electrical resistivity. The highest Figure of Merit of $0.90 \cdot 10^{-3}$ at 650°C was observed for $W_{0.99}Ta_{0.01}Se_2$. A summary of the high-temperature properties for this composition, together with three others, is given in Table III.

Table III. Thermoelectric properties at 650°C for some compositions of the $W_xTa_{1-x}Se_2$ system

x	S, μV/°C	ρ, m ohm-cm	k, mw/cm-deg	Z, deg^{-1} × 10^3
0.99	370	7.02	0.02	0.98
0.98	260	5.30	0.02	0.64
0.97	184	3.27	0.02	0.52
0.96	174	3.10	0.02	0.49

Anisotropy.—It should be pointed out that all properties quoted to this point are essentially only characteristic of the crystallographic a-direction. The fact that the inherent crystallographic anisotropy is rather strongly reflected, even in the powder compacts for both the electrical and thermal properties was first pointed out by Carlson (7). Our own measurements on a 1 in. cube of $W_{0.97}Ta_{0.03}Se_2$ (89% dense) gave the results summarized in Table IV, which are in good agreement with those obtained earlier by Carlson. Since the individual crystallites are small, flat hexagonal plates with the crystallographic c-axis normal to the plane, this indicated that the crystals orient themselves with the plates stacking up in the direction of pressing. This was proven by means of Laue back-reflection photographs taken in the direction of pressing and perpendicular to it with both Cr and Cu radiation, using V and Ni filters, respectively. The picture taken with chromium radiation yielded the 0 0 10 line, and the one taken with copper radiation gave the 1 0 14 line, each of which was significantly stronger in the direction of pressing, indicating that the crystallites do orient themselves with the c-axis in the direction of pressing. Even implosive compaction with PETN (pentaerythritoltetranitrate) failed to give compacts with random distribution of properties. However, densities as high as 95% of theoretical were achieved.

The data in Table IV indicate that there is an over-all advantage in using these compositions in the a-direction. Since the thermal conductivity in this direction of some 70 mw/cm-deg is quite high, further experiments should be directed toward lowering this number by introducing new phonon scattering sites, both in the anion and cation lattice. This investigation led to the more complicated system $W_{x/2}Mo_{x/2}Ta_{1-x}Se_2$ and $W_{x/2}Mo_{x/2}Ta_{1-x}Se_yTe_{2-y}$ which will be subjects of separate publications.

Other metal substitutions in WSe_2.—Finally, the influence of metals such as Gd, Hf, Zr, Ti, Re, V, Nb, and Sb on WSe_2 was studied. Due to lack of solubility in the WSe_2 lattice, as evidenced by unchanged lattice parameters, most elements had no or only

Table IV. Anisotropy data for $W_{0.97}Ta_{0.03}Se_2$

Resistivity, m ohm-cm		Seebeck coefficient, μV/°C		Thermal conductivity, watts/cm-deg		Figure of Merit, deg^{-1} × 10^3	
Crystallographic direction		Crystallographic direction		Crystallographic direction		Crystallographic direction	
a	c	a	c	a	c	a	c
2.11	7.63	+79	+60	0.07	0.02	0.042	0.024

Table V. Structural and thermoelectric properties of $W_{0.97}Nb_{0.03}Se_2$ and $W_{0.97}V_{0.03}Se_2$

Composition	a_0, Å	c_0, Å	25°C ρ, m ohm-cm	25°C S, μv/°C	600°C ρ, m ohm-cm	600°C S, μv/°C
$W_{0.97}Nb_{0.03}Se_2$	3.292	12.941	2.3	+68	4.7	+178
$W_{0.97}V_{0.03}Se_2$	3.288	12.948	3.7	+74	5.6	+188

a very minor effect. The only element which made WSe_2 n-type at room temperature (it changed to p-type at 230°C) was Re, and only Nb and V, the two other Group VB metals, had similar resistivity lowering effects as tantalum. The lattice parameters and electrical properties of the two compositions $W_{0.97}Nb_{0.03}Se_2$ and $W_{0.97}V_{0.03}Se_2$ are summarized in Table V.

Discussion

In an attempt to explain the electrical behavior of WSe_2 and $TaSe_2$, we have previously assumed (1) that both metals are in their tetravalent state. Magnetic susceptibility measurements, showing WSe_2 to be diamagnetic and $TaSe_2$ paramagnetic, at least qualitatively indicate that this assumption has some value, although we cannot state to which degree these compositions are ionic or covalent. Since Seebeck coefficient measurements indicated that WSe_2 is of p-type, the conduction mechanism is by holes, which can rather easily be understood in view of the WSe_2 structure. The Group VB metal tantalum, with one electron less, if introduced in the WSe_2 lattice, acts as a p-type doping agent (as do V and Nb) and thereby contributes to the increase of the carrier concentration and consequently the electrical conductivity. At the same time, we notice that the Seebeck coefficient decreases, since it varies as the logarithm of the reciprocal of the charge-carrier concentration. The energy gap of undoped pure WSe_2 as derived from Hall measurements *vs.* temperature was calculated to be 1.4 ev. The room temperature mobility was 100 cm^2/volt-sec and dropped significantly by the introduction of Ta as doping agent. So it was a matter of establishing the region of maximum for the product $S^2 \cdot \sigma$. This was found in a rather empirical fashion as being between $x = 0.95$-0.99. In this region, we experience Seebeck coefficient (at elevated temperatures) in the neighborhood of 180 μv/°C. According to Ioffe (8), this is considered near the optimum, which occurs at a carrier concentration of $n = 10^{19}/cm^3$, and we can, therefore, assume that the concentration of holes for the best materials from this investigation is in the neighborhood of $10^{19}/cm^2$. The actual carrier concentration as derived from Hall measurements for $W_{0.99}Ta_{0.01}Se_2$ was found to be 6×10^{19} cm^{-3}.

Further attempts at optimization of Z have to be made by altering the lattice to increase the ratio of phonon scattering to carrier scattering. Airapetiants (9) showed that with semiconductor compounds, which can be regarded as consisting of a cation sublattice and an anion sublattice, electrons tend to follow the former while holes follow the latter; *i.e.*, electron scattering will be strongly affected by changes in the anion sublattice. The phonons, being uncharged, show no preference. Since we were concerned essentially with only p-type materials, new attempts at lowering the thermal conductivity will have to be concerned with substitutions in the cation lattice of the type $W_{x/2}Mo_{x/2}Ta_{1-x}Se_2$. These studies will be the subject of a separate forthcoming paper.

Since the compositions of this investigation are selenides and, therefore, tend to decompose like most other power-generating candidates of the telluride or selenide category, they would definitely have to be encapsulated for use at elevated temperature. Compared to p-type PbTe, there would be some other shortcomings or disadvantages. For instance, the average atomic weight of PbTe is 161.41 as compared to 113.51 of $W_{0.99}Ta_{0.01}Se_2$. PbTe has an isotropic cubic structure as compared to the anisotropic hexagonal structure of the discussed selenides. The lead telluride density is 8.17 g ml^{-1} against 9.35 g ml^{-1} of $W_{0.99}Ta_{0.01}Se_2$. For both materials, resistivity and Seebeck coefficient increase with temperature and both need to be encapsulated. The biggest disadvantage of $W_{0.99}Ta_{0.01}Se_2$ as compared to PbTe is the fact that it does not melt congruently; and therefore, it is almost impossible to obtain truly dense and consistently reproducible samples. Attempts to prepare single crystalline ternaries by the previously described (1) transport technique failed, since WSe_2 was transported preferentially.

In summary, we can say that the solid solutions described in this paper constitute a group of compounds with interesting thermoelectric properties in the intermediate temperature range of 300°-600°C, which seem to be worthy of some further investigations.

Acknowledgments

The assistance of Dr. G. Teufer and Mr. A. T. Weinmann in obtaining the x-ray data was greatly appreciated. For carrying out the Hall measurements, thanks are also due to Dr. W. T. Hicks, who is planning to publish a detailed account of his studies in a forthcoming issue of this JOURNAL.

Manuscript received June 6, 1962; revised manuscript received Nov. 9, 1962. This paper was prepared for delivery before the Los Angeles Meeting, May 6-10, 1962.

Any discussion of this paper will appear in a Discussion Section to be published in the December 1963 JOURNAL.

REFERENCES

1. L. H. Brixner, *J. Nuclear and Inorganic Chem.*, **24**, 257 (1962).
2. O. Glemser, H. Sauer, P. König, *Z. Anorg. Chem.*, **257**, 241 (1948).
3. S. M. Ariya, A. I. Zaslavsky, I. I. Matveeva, *J. Gen. Chem.*, **26**, 2651 (1956).
4. J. B. Nelson and D. P. Riley, *Proc. Phys. Soc.*, **57**, 160 (1945).
5. J. Francl and W. D. Kingery, *J. Am. Ceram. Soc.*, **37**, No. 2, 80 (1954).
6. H. Weiss, *Ann. Phys. Lpz.*, **4**, 121 (1959).
7. R. O. Carlson, General Electric Company, Private communication.
8. A. F. Ioffe, "Semiconductor Thermoelements and Thermoelectric Cooling," Infosearch Limited, London (1957).
9. S. V. Airapetiants *et al.*, *Soviet Physics*, **2** [9], 2009, (1957).

Improvement in the Electrolytic Preparation of Iodoform

R. Ramaswamy, M. S. Venkatachalapathy, and H. V. K. Udupa

Central Electrochemical Research Institute, Karaikudi, S.Rly., India

ABSTRACT

Use of lead dioxide anode with a graphite substrate in the electrolytic preparation of iodoform is described. Influence of bath composition, current density, temperature, and pH on the current efficiency has been investigated. Results are compared with those obtained with the conventional anodes like platinum and graphite. The effect of rotation of the anode is discussed.

Schering (1) obtained a German patent in 1884 for the electrolytic production of iodoform, and in 1885 Theodore Kempf patented the same process in the United States. Later, an attempt was made to substitute (2) acetone for alcohol, and Abbot obtained a current efficiency of 59.7% of iodoform from acetone by electrolysis in an alkaline solution. In 1904 Teeple (3) obtained a current efficiency of 94.5% by using acetone. He employed low anodic current density and kept the electrolyte slightly acidic, cold, and well stirred. In 1905 Roush (4) obtained a current efficiency of 95% by using two cathodes, one enclosed in a diaphragm cell and thus regulating the amount of alkali which mixed with the main electrolyte. All these methods employed low current density with the use of expensive material, platinum, as anode and are run only for short durations.

Electrolytic manufacture of iodoform (5-12) is usually carried out, either at a platinum or at a graphite anode. In the electrolytic preparation of iodoform from ethyl alcohol, an attempt (13) was made to replace the costly platinum anode by graphite (14), but the product obtained was slightly gray in color, and further purification was necessary. It is also reported (13) that nickel, copper, and silver were unsatisfactory, and nichrome was too poor a conductor.

On account of the above difficulties involved in the production of iodoform without platinum, it appeared worthwhile to investigate a cheaper lead dioxide anode prepared by depositing the same on graphite and carbon substrates. This process has been developed in this Institute (15) and used in perchlorate preparation (16). This has now been done, and the influence of rotation of the anode (17) also has been studied.

Factors in the Electrochemical Formation of Iodoform

The anodic reactions (18) in the iodide electrolyte, during electrolysis may be represented as Eq. [1]

$$2I^- - 2e \longrightarrow I_2 \qquad [1]$$

After the iodide discharge, the iodine formed comes into equilibrium with the hydroxyl ions in the alkaline medium to give hypoiodite ion, Eq. [2] and [3]

$$I_2 + OH^- \rightleftharpoons HIO + I^- \qquad [2]$$

$$HIO + OH^- \rightleftharpoons IO^- + H_2O \qquad [3]$$

The hypoiodite ion is both an oxidizing and an iodinating agent. It can decompose at a measurable rate (19, 20) to give iodate and iodide, Eq. [4] and [5], or it can (Eq. [6] and [7])

$$6IO^- + 3H_2O \rightleftharpoons 2IO_3^- + 6H^+ + 1\tfrac{1}{2}\,O_2 + 4I^- + 6e \qquad [4]$$

i.e.,

$$3\,OI^- \rightleftharpoons IO_3^- + 2I^- \qquad [5]$$

iodinate (21) acetone and alcohol.

$$CH_3 - CO - CH_3 + 3\,OI^- \longrightarrow CH_3 - CO - O^- + CHI_3 + 2\,OH^- \qquad [6]$$

$$CH_3 - CH_2 - OH + 5\,OI^- \longrightarrow CHI_3 + H_2O + 2I^- + CO_2 + 3\,OH^- \qquad [7]$$

As the electrolysis proceeds, the electrolyte becomes increasingly alkaline and favors reaction [5]. When, therefore, formation of iodoform is desired, it is necessary to maintain the electrolyte at moderate alkalinity (*p*H 10-11) so as to favor reactions [2], [3], and [7], giving a high current efficiency. Reactions [4] and [5] can be minimized by increasing the concentration of alcohol and preventing the build up of hypoiodite concentration. At the same time occurrence of reactions [4] and [5] cannot be altogether prevented as seen by the detection of iodate in the electrolyte at the conclusion of electrolysis, especially at high current densities.

Experimental

Anodes.—The lead dioxide anodes were made essentially as described earlier (15) by electrolytic deposition on a rotating graphite anode of 1 cm diameter and 15.5 cm long, which had been precleaned with alkali solution and dilute nitric acid. A solution containing 350-400 g/l lead nitrate and 25-30 g/l copper nitrate was used as electrolyte. The temperature of electrodeposition was 50°-60°C, and the rpm of the anode was 700-750. A copper

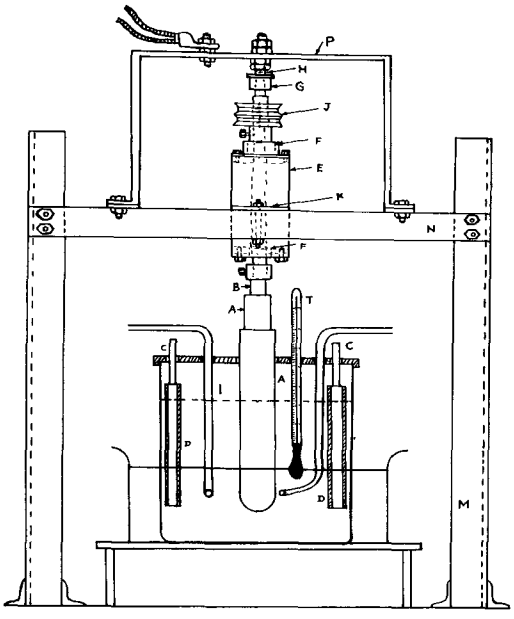

Fig. 1. Electrolytic cell with rotating anode assembly: A, lead dioxide anode; B, rotating shaft; C, cathodes; D, closely fitted diaphragm; I, inlet for CO_2 gas; T, thermometer; F, ball bearings; E, flat angle iron frame work; K, support for the frame work; J, pulley; G, mercury cup for contact; H, lead to the anode; P, anode bus-bar; N, horizontal wooden beam; M, stand.

plate surrounding the anode was used as cathode, and the rate of circulation of electrolyte was 2 to 3 l/hr. The anodic current density was 4-5 amp/dm^2, and the thickness of the deposit obtained was about 0.2 mm for 2 hr of duration. The deposit was quite adherent and free from holes, and during deposition the pH was kept between 4 to 5 by neutralizing the electrolyte with carbonates of copper and lead outside the cell. The assembly for rotation is the same as in Fig. 1.

Cell.—A 600 cc beaker, 8 cm in diameter and 14 cm in height, with a perspex lid having five holes for the electrodes, thermometer, and gas inlet served as the electrolytic cell. Two cylindrical lead rods, 5 mm in diameter and 14 cm in height, were used as cathodes. By using a closely fitting nylon cloth diaphragm (22) on the cathodes, a build-up of hydroxyl ion concentration occurs only in the pores of the diaphragm. Adverse potential gradient in the pores is thus sufficient to prevent the reduction of hypoiodite ion. A diaphragm used in this way is very effective and does not cause an excessive IR drop or polarization potential. Lead dioxide electrodeposited on graphite substrate with an effective area of immersion of 0.25 dm^2 was used as anode. The pH of the electrolyte was maintained at the desired level by passing in CO_2. The cell was kept in an electric waterbath and the temperature maintained in the required range. The rotating anode assembly and the cell is shown in Fig. 1.

While investigating the use of the stationary anode, the same cylindrical lead dioxide anode was used, but a glass stirrer was included for agitating the electrolyte. Current was obtained from a selenium rectifier capable of giving 25 amp at 0-12v.

Isolation of the product.—After electrolysis the iodoform obtained was separated, using a sintered

Table I. Current efficiency for the formation of iodoform at various anodes

Electrolyte, 10% NaI (250 cc); pH, 11-11.5; temperature, 60°-63°C; rectified spirit, 30 cc; current density, 20 amp/dm^2; current, 5 amp; duration, 2 hr; rpm of anode, 1000; cell voltage, 5-5.5v.

Run No.	Anode material	Iodoform obtained, g	Current efficiency, %	Color of product
1.	Platinum	13.45	91.6	Bright yellow
2.	Graphite	11.5	80.2	Greenish yellow
3.	Lead dioxide on graphite	12.0	81.4	Bright yellow
4.	Lead dioxide formed on lead*	1.0	—	Orange yellow

* Cell voltage increased abnormally, so that theoretical current could not be passed.

funnel, and dried to a constant weight in a vacuum desiccator over anhydrous calcium chloride. The iodate content in the filtrate was also estimated in some of the experiments by iodimetry. Current efficiency was calculated on the basis that 10F and 6F are required for the formation of iodoform and iodate, respectively.

Anode potential was measured using a Crompton potentiometer and a saturated calomel electrode and results expressed on the hydrogen scale. The different experimental conditions employed are given in the tables.

Results and Discussion

Influence of anode material.—The current efficiency for the electrosynthesis of iodoform at various anode materials is shown in Table I. The product obtained in the case of graphite anode was rather greenish yellow. But in the case of electrodeposited lead dioxide anode, the product was bright yellow, and the anode loss was almost negligible. When lead dioxide formed on lead was used as anode, the lead substrate was attacked giving lead iodide which prevented electrolysis. The difference in current efficiency between platinum and lead dioxide anodes could be explained on the basis of anode potential measurements as given in Fig. 2.

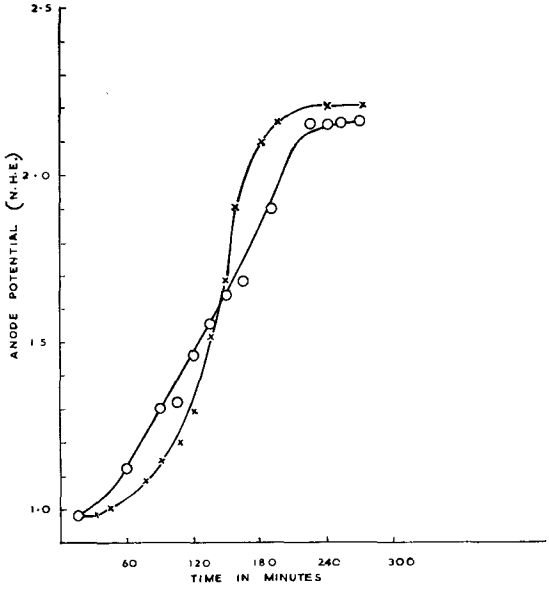

Fig. 2. Plot of anode potential vs. duration. —○——○—, Lead dioxide anode; —x——x—, platinum anode.

Table II. Effect of rotation on the current efficiency of formation of iodoform

Anode, lead dioxide on graphite; other conditions, same as in Table I.

Run No.	Motion of anode	Current density, amp/dm²	Current efficiency for iodoform, %	Current efficiency for sodium iodate, %	Current, amp	Duration, hr
5.	Rotating	10	98	1	2.3	5
6.	Stationary	10	90	8	2.3	5
7.	Rotating	20	78-80	14-16	4.6	2.5
8.	Stationary	20	53	46	4.6	2.5
9.	Rotating	30	69	30.2	6.9	1.45
10.	Stationary	30	44	55.8	6.9	1.45
11.	Rotating*	20	74	24.3	4.6	2.5

* In this case, the concentration of NaI was maintained constant.

In the case of platinum anode, anode potential first increases exponentially, but after 2 hr it increases rapidly, indicating the depletion of the iodide ion. Finally it becomes constant. With lead dioxide, there is an almost linear increase of potential throughout. The higher initial potential with lead dioxide anode is due to simultaneous oxidation of hypoiodite ion to iodate in addition to iodide discharge.

Influence of rotation on anode potential and current efficiency.—The current efficiency for the electrochemical preparation of iodoform with a rotating and a stationary anode are given in Table II. The influence of rotation is quite significant, and the difference in the current efficiency between rotating and stationary anode is high at 20 amp/dm² and above. This could also be explained on the basis of data on anode potential measurements given in Fig. 3, where the logarithm of current density (amp/dm²) is plotted against corresponding anode potential for the rotating and stationary anodes. At a stationary anode without alcohol (curve I), anode potential *vs.* log current density is linear up to a certain current density at which a sudden break occurs due to superimposition of hypoiodite discharge on iodide discharge. On the addition of alcohol, the primary reaction at the anode remains the same, namely, discharge of iodide ion, but removal of the

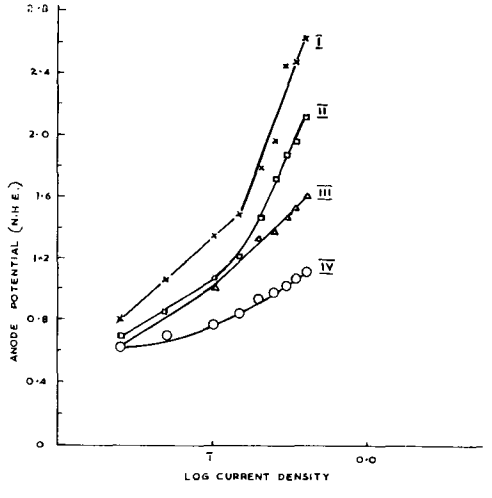

Fig. 3. Plot of anode potential *vs.* log current density: I, stationary anode without alcohol; II, stationary anode with alcohol; III, rotating anode without alcohol; IV, rotating anode with alcohol.

Table III. Effect of current density on current efficiency

Rotating anode, lead dioxide on graphite; rpm, 900-1000; other conditions, same as in Table I.

Run No.	Current, amp	Cell voltage, v	Current density, amp/dm²	Duration, min	Iodoform obtained, g	Current efficiency, %
12.	2.5	4.5	10	216	13	98.5
13.	3.75	5.0	15	162	13	98.5
14.	5	7.0	25	120	11.5	78
15.	7.5	7.5	30	80	11.1	76
16.	5	8.0	35	144	10.9	66

hypoiodite ion by reaction with alcohol gives somewhat lower anode potentials at the same current density (curve II).

With a rotating anode an almost linear relationship is obtained with only slight indications of a break. With the addition of alcohol, removal of hypoiodite ion keeps the potential low up to quite high current densities (curve IV). At very high current densities when hypoiodite concentration is high for the same alcohol content, simultaneous iodate formation also occurs as seen by the upward trend of anode potential curves.

It is believed that rotating the anode (23) reduces the thickness of the diffusion layer and facilitates transfer of the iodide ions and escape of hypoiodite. This reacts with the alcohol to give iodoform as in [7]. Reaction [4] therefore occurs to a minimum extent.

Influence of current density on current efficiency.—Current efficiency for the formation of iodoform at a rotating anode at several current densities are shown in Table III. The current efficiency is high up to 15 amp/dm² and then decreases as the current density is increased up to 35 amp/dm². At higher anode current densities iodate formation increases, accounting for the lowering of current efficiency for iodoform formation. Since the increase of current density for the same anode area shortens the duration of electrolysis, it should be possible in practice to employ high current density up to 20 amp/dm² which will be quite economical.

Influence of temperature.—The influence of temperature on the current efficiency for the formation of iodoform is shown in Table IV. A temperature range of 60°-62°C gave optimum current efficiency.

Influence of sodium iodide concentration.—The current efficiency for the formation of iodoform at different concentrations of sodium iodide solution is shown in Table V, and it can be seen that a 10% solution not only gives the highest current efficiency

Table IV. Effect of temperature on current efficiency

Anode, lead dioxide on graphite; current density, 20 amp/dm²; other conditions, same as in Table I.

Run No.	Temperature, °C	Cell voltage, v	Iodoform obtained, g	Current efficiency, %	Remarks
17.	50-52	6.5	4.2	29	Reaction slow. Yellowish orange product.
18.	60-62	5.2	11.25	78	Bright yellow. Reaction is fast.
19.	70-72	5.0	11.30	79	Reaction is very fast.

Table V. Effect of sodium iodide concentration on current efficiency

Anode, lead dioxide on graphite; current density, 20 amp/dm²; other conditions, same as in Table I.

Run No.	Sodium iodide concentration, %	Cell voltage, v	Total current passed, amp-hr	Iodoform obtained, g	Current efficiency, %
20.	2.5	10	2.5	1.32	36
21.	5	8	5	4.15	65
22.	7.5	7.5	7.5	8.5	77
23.	10	7.0	10	11.5	78

Table VI. Effect of alcohol concentration on the current efficiency

Anode, lead dioxide on graphite; current, 4.6 amp; duration, 2.5 hr; other conditions, same as in Table I.

Run No.	Volume of alcohol, cc	Iodoform obtained, g	Current efficiency for iodoform, %	Amount of $NaIO_3$, g	Current efficiency for $NaIO_3$, %
24.	5 (theoretical)	5.6	33	8.5	63
25.	25	11.8	70	3.6	27
26.	35	12.6	74	2.0	16
27.	50	12.6	74	1.8	14

but also the lowest cell voltage. Addition of excess of sodium iodide to maintain its concentration constant during the electrolysis did not increase the current efficiency for the formation of iodoform, but did increase that for the formation of iodate, due to excess concentration of IO^- being maintained toward the end of reaction when the alcohol concentration was low (Run No. 11, Table II).

Influence of alcohol concentration.—The effect of alcohol concentration in the electrolyte on the current efficiency for the formation of iodoform can be seen from the results in Table VI. When the theoretical quantity of alcohol is used, very low current efficiency is obtained. This is increased by using an excess of alcohol (reaction [7]).

Influence of pH.—The pH of the electrolyte during electrolysis plays a very important part in the formation of iodoform as seen from Table VII. A pH range of 10-11 should be maintained for good current efficiency.

Effect of current concentration.—Table VIII gives the results obtained at different current concentrations using the same current density. The current efficiency of iodoform formation is not affected by lowering the current concentration.

Acknowledgment

The authors thank Professor K. S. G. Doss, Director of the Institute, for his keen interest in the investigation and Professor Christopher L. Wilson for very kindly presenting the paper at the Detroit Meeting, October 1-5, 1961.

Manuscript received Sept. 28, 1961; final revised manuscript received Oct. 26, 1962. This paper was prepared for delivery before the Detroit Meeting, Oct. 1-5, 1961.

Any discussion of this paper will appear in a Discussion Section to be published in the December 1963 JOURNAL.

Table VII. Effect of pH on the current efficiency of formation of iodoform

Anode, lead dioxide on graphite; other conditions, same as in Table I.

Run No.	pH during electrolysis	Cell voltage, v	Iodoform obtained, g	Current efficiency, %
28.	8-8.5	8.5	6	41
29.	9-9.5	8.5	10	68
30.	10-10.5	8.0	11.3	77
31.	11-11.5	7.0	11.5	78
32.	11.5-12	7.0	11.6	79

Table VIII. Influence of current concentration on the current efficiency for the formation of iodoform

Anode, lead dioxide on graphite; current density, 20 amp/dm²; temperature, 60°-62°C; sodium iodide, 10% solution; all other conditions, same as in Table I.

Run No.	Current concentration, amp/l	Theoretical amount of iodoform, g	Iodoform obtained, g	Current efficiency, %
33.	15.65	14.68	11.5	78.3
34.	7.82	30.82	22.9	74.3
35.	5.21	46.32	35.7	77.1

REFERENCES

1. E. Schering, D.R.P. 29771 (1884); T. Kempf, U.S. Pat. 372,940 (1885).
2. K. Elbs and W. Herz, *Z. Elektrochem.*, **4**, 113 (1897).
3. J. E. Teeple, *J. Am. Chem. Soc.*, **26**, 170 (1904).
4. G. A. Roush, *Trans. Am. Electrochem. Soc.*, **8**, 283 (1905).
5. F. Fichter, "Organische Elektrochemie," p. 139, Steinkopff, Dresden (1942).
6. N. I. Putokhin and A. S. Maslennikov, *Zhur. Obshchei Khim.*, **11**, 1047 (1941); *C.A.*, **36**, 6446 (1942).
7. J. B. Lucas and Irving Gray, *Virginia J. Sci.*, **2**, 194 (1941); *C.A.*, **36**, 2209 (1942).
8. G. Lazzarini, *Ind. chim.*, **4**, 771 (1929); *C.A.*, **24**, 334 (1930).
9. A. R. Johnson, *Trans. Wisconsin Acad. Sci.*, **16** [1], 253 (1908).
10. K. Elbs and F. Foerster, *Z. Elektrochem.*, **7**, 341 (1900).
11. Octave Dony-Henault, *ibid.*, **7**, 57 (1900).
12. F. Foerster and W. Meves, *ibid.*, **4**, 263 (1897); *J. prakt. Chem.*, **56**, 353 (1897).
13. A. Vyskocil, *Chem. listy*, **23**, 212-5, 249-51 (1929); *C.A.*, **23**, 4896 (1929).
14. M. Wiekiera and W. Mazewska, *Przemysl Chem.*, **31** [8], No. 6, 305 (1953); *C.A.*, **47**, 9823 (1953).
15. K. C. Narasimham and H. V. K. Udupa: Proc. Symposium on "Electrolytic Cells," p. 22, Central Electrochemical Research Institute, Karaikudi-3, S. Rly., India (1961); H. V. K. Udupa and K. C. Narasimham, *Indian*, **66**, 195, Dec. 22 (1958).
16. K. C. Narasimham, S. Sundararajan, and H. V. K. Udupa, *This Journal*, **108**, 798 (1961).
17. H. Debauge, Brit. Pat. 148,760 (1919); *C.A.*, **15**, 212 (1921); Ital. Pat. 172,916 (1919).
18. M. J. Allen, "Organic Electrode Processes," p. 156, Chapman & Hall Ltd., London (1958).
19. C. H. Li and C. F. White, *J. Am. Chem. Soc.*, **65**, 335 (1943).
20. W. G. Chomiakov, W. P. Maszowiec, and L. L. Kuzmin, "Technologia Przemyslu Electrochemicznego," Warszawa, p. 308 (1953).
21. R. P. Bell and H. C. L. Higgins, *J. Chem. Soc.*, **1946**, 636.
22. M. S. Venkatachalapathy, Doctoral Dissertation, Silesian Technical University, Gliwice, Poland (1960).
23. H. V. K. Udupa and B. B. Dey, *Proc. 6th Meeting Interna. Comm. Electrochem. Thermodynam. and Kinetics*, p. 87, Butterworths Scientific Publications, London (1955).

The Formation of Silicon Carbide in the Electric Arc

W. E. Kuhn

Applied Research Branch, Research and Development Division,

The Carborundum Company, Niagara Falls, New York

ABSTRACT

The formation of silicon carbide in an electric arc from consumable anodes composed of silica and graphite was investigated in a special consumable electrode arc furnace, the design and operation of which are described. The electrical and erosion characteristics of the arc are described in detail. Phenomenological observations of events occurring at the anode termination were made with the assistance of high-speed motion pictures. Possible reactions occurring at the anode termination, the arc column, and vapor jet regions of the arc are discussed in terms of the thermodynamic and kinetic factors dominant in three critical temperature regions, namely, temperatures greater than 3000°K, between 2000° and 3000°K, and less than 2000°K. The composition and morphology of the arc vaporized product are discussed in relation to the various reactions and phenomena believed to occur at the anode termination and in the vapors produced in the arc.

Interest in the vapor phase formation of silicon carbide from silica and carbon was first aroused by Ruff's reference to arcing within the silicon carbide resistance furnace in which he stated "in the neighborhood of these arcs, SiC vaporizes and dissociates bringing about a cooling effect. At the same time graphite is produced." Ruff further suggested that the silicon carbide crystals are too large to attribute their growth to a solid state diffusional process and concluded that a gas phase accounts for their growth (1).

Although the investigations of Lely (2) and others have both confirmed and refuted much of Ruff's early findings and provided new knowledge on the formation of silicon carbide, the mechanism and kinetics of formation of silicon carbide crystals are still little understood.

Much of the disagreement revolves around whether silicon monoxide exists as an intermediate compound in the reaction sequence, and if so, the precise role it plays. The question of its existence and its role in the reaction sequence remain with us largely because of the inability of researchers to produce direct experimental evidence of silicon monoxide and its role. The present work was primarily undertaken to produce an ultrafine powder of silicon carbide crystallites. However, the techniques and procedures employed in this work offer another approach to the study of this reaction. Confining the chemical reactions to the anode termination of a consumable electrode and the products of the reaction to a fast moving vapor stream emanating from the reaction surface provide a convenient accessible arrangement of reactants, reaction, and reaction products for observation, measurement, and analysis. Morphological studies as a means of identifying various species found in the reaction products with specific reactions have also been a useful approach.

The information available from thermodynamic studies utilizing a mass spectrometer indicates that the reactions occurring at high temperatures between silicon and carbon are highly complex involving various combinations of silicon and carbon atoms and molecules (3). The mechanism of growth of the silicon carbide crystals from embryos to nuclei and thence to seed crystals and larger is still much of a mystery. Such considerations suggested that much would be learned about the initial stages of formation of silicon carbide from the vapor state by vaporizing silica and carbon in stoichiometric proportions and studying the resultant condensed products. An arc furnace was thereupon designed and constructed to facilitate such an investigation.

This paper is concerned with a description of an experimental apparatus for vaporizing consumable anodes of silica and carbon, its operation, and the product. Arc characteristics and phenomena observed at the anode termination and in the plasma flame are discussed. The possible reactions occurring in the arc column, anode termination, and plasma jet of a direct current arc between a graphite cathode and an anode consisting of a nearly stoichiometric mixture of silica and graphite are discussed in the light of existing pertinent knowledge of the over-all thermodynamics of silicon carbide and silica reactions.

Apparatus and Experimental Procedure

Arc Reactor.—A diagrammatic sketch of the arc reactor is shown in Fig. 1. The salient features of the furnace are described below.

The arc chamber was designed to be used *in vacuo* or at pressures up to 200 psi. Ports for the electrode contact device, gas inlets, fume collecting system, and viewing windows were sealed with O-ring seals. Construction was brass except where noted in Fig. 1.

The contact device shown in Fig. 2 utilized spring loaded multiple graphite contact brushes housed in a cross-shaped water-cooled vacuum-tight copper sleeve. The ⅜ in. diameter consumable anodes were

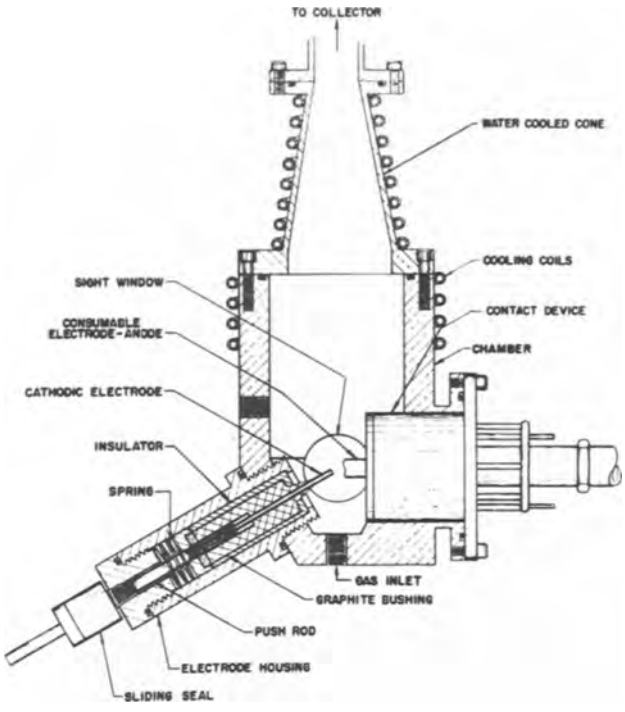

Fig. 1. Construction and detail of arc test cell

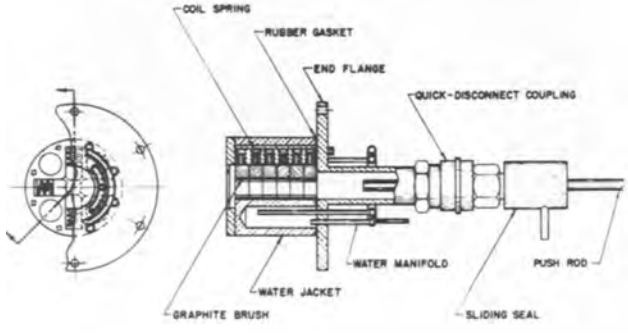

Fig. 2. Design of multiple contact device for feeding consumable anodes.

advanced into the arc manually by means of a steel push rod operating through a vacuum-tight sliding seal. A boron nitride face plate protected the metal components from the arc plasma and prevented secondary arcing between the cathode and the copper housing. The multiple contacts permitted electrodes with undulating surfaces and wide tolerances to be used thereby reducing electrode preparation problems significantly.

The ⅛ in. diameter graphite cathode was held in a graphite bushing which in turn was supported in, and insulated from, the arc chamber by boron nitride bushings as shown in Fig. 1. The cathode was positioned in a vertical plane common to the anode and inclined 45° below the horizontal. Adjustment of the cathode was made outside the arc chamber.

A transition duct shown in Fig. 1 leads from the top of the furnace to a 1 in. diameter duct to an electrostatic dust collector 3 in. ID by 18 in. long. A 30 kw dc Spellman Model PN-30R power supply was used to charge a 0.010 in. diameter axial steel electrode. Normally 7-10 kv were used, the output being variable between 0 and 30 kv.

The control panel consisted of pressure and gas flow gauges, meters for measuring the arc current and voltage, and valves for atmosphere control.

Power was supplied at 70v d-c open circuit by a Westinghouse Type RA Welding Rectifier rated at 300 amp. Higher voltages were obtained by series connecting two or more rectifier units.

Materials and their preparation.—The mix proportions and chemical analysis of the materials used in the preparation of the consumable anodes are given in Table I. The analyses of the silica, graphite, and binder are given in Table II.

The silica and graphite powders were thoroughly dry mixed in a Lancaster mixer for about 10 min. Corn syrup binder was slowly added while mixing for about 20 min. The mix was considered suitable for extrusion into ⅜ in. diameter rods after balling commenced and firm spheres could be packed from the mix by hand. The anodes were extruded into 2 ft lengths at 3000 psi onto corrugated drying trays. The rods were air dried for 1 hr, oven dried at 220°F for 29 hr, and finally fired at 800°C for 16 hr in a reducing atmosphere provided by a graphite powder packing. The electrical properties of the rods after firing are given in Table I.

Table I. Consumable electrode composition and properties

Silica content, %		Graphite content, %		Binder* content, % of SiO_2 plus graphite	Physical properties			
					After oven drying for 24 hr at 220°F	After firing at 800°C for 16 hr		
Mix	After firing**	Mix	After firing**	before firing	Density, g/cc	Density, cc	Resistivity, ohm-cm	Shrinkage, %
71	65	29	35	43	3.05	2.5	0.018 to 0.027	3 to 4

* Corn syrup, specific gravity 1.31 g/cc.
** Increase in the carbon to silica ratio is caused by the loss of volatiles and the conversion of organic material to carbon.

Table II. Chemical Analyses of silica, graphite and binder

Material	C	SiO_2	Fe	Al	Si	B	Mn	V	Ca	Residue	H_2O	Al_2O_3	CaO
Silica	Nil	99.77	—	—	—	—	—	—	—	—	—	0.07	0.06
Graphite	99.8	—	0.01 to 0.05	0.001	0.01 to 0.05	0.01 to 0.05	0.005 to 0.01	0.005 to 0.01	0.005 to 0.01	0.2	—	—	—
Corn syrup* binder	5.32	—	0.0002 to 0.001	0.0002 to 0.001	0.002	0.00002 to 0.0001	0.0001 to 0.0002	—	0.002	0.21	11.4%	—	—

* Volatiles and combustibles at 950°C, 94.5%.

Experimental procedure.—The arc chamber was purged and filled with argon which was maintained at 1 psig while allowing a flow of about 4 s.c.f.h. into the arc chamber whence it flowed through to the duct work and electrostatic precipitator into the atmosphere. Before each experiment the cathode and anode tips were positioned to facilitate ignition of the arc by simply touching the anode to the cathode tip. The open circuit potential of the power supply (75 v) was then applied to the electrodes with the current set at a predetermined value. Upon ignition of the arc the anode was withdrawn and the arc gap maintained between ⅜ and ½ in. while maintaining the anode overhang at ½ in.

Ignition caused the voltage across the arc to drop to between 30 and 40 v. No difficulties were experienced in either starting the arc or maintaining it in operation. The time to consume the maximum permissible length of the electrode (*ca.* 75% of the original length) was noted and the rate of consumption calculated. The electrical and vaporization characteristics of the anode were observed during each experiment. After each experiment the electrodes and the product of vaporization were examined and the behavior of the arc during the experiment recorded.

High-speed motion pictures recorded the arc behavior at the anode termination of the plasma region of the arc. A Wollensak Fastax® WF-3 16 mm. high-speed camera was employed using a speed setting of 1440 frames/sec.

Results of Experiments

Operation of arc reactor.—The experimental data are summarized in Table III for open-circuit d-c voltages of 75 and 145v. Arc behavior is similar at both 75 and 145v, except that the arc can be operated in the region of unstable arcs[1] at higher currents using the higher voltage. The dependence of consumption rate and voltage on arc current is given in Fig. 3. Figure 4 shows the change in the shape of the electrode tip with arc current at 75v, open circuit. The anodes burned cleanly without spatter or the slag loss typical of some oxidic materials vaporized in the arc (4).

[1] "Region of unstable arcs" is that region in which the current is high enough to cause the anode spot to overlap the tips and begin to rotate around the sides of the anode termination.

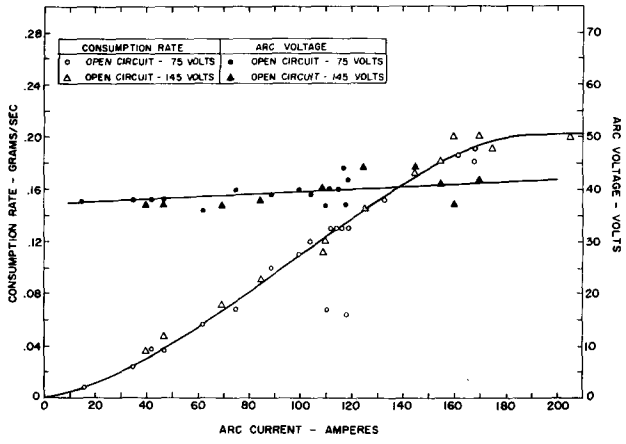

Fig. 3. Dependence of consumption rate of consumable electrodes as arc current.

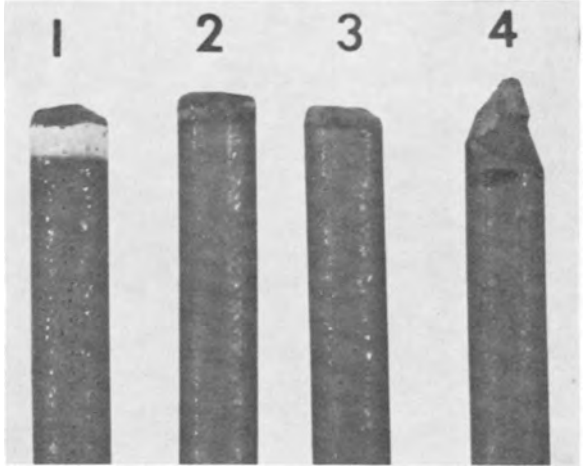

Fig. 4. Appearance of anode tip after arc vaporization. 1. Current range 16-42 amp, voltage 38; 2. current 47-89 amp, voltage 36-40; 3. current 104-162 amp, voltage 37-45; 4. current 170-205 amp, voltage 32-48.

Morphology of arc vaporized products.—The product of vaporization was tan in color having the

Table III. Summary of experiments conducted at 75 and 145v open circuit

Current (average values), amp	Voltage range of (average values), v	Time of run, sec	Anode weight loss, g	Consumption, g/sec	Remarks
16-42	38	320-1005	8-12.4	0.008-0.038	Unsteady movement of tail flame, powdery deposit of SiC formed on cathode tip; general appearance of anode tip shown in Fig. 4-1. At low currents deposit is formed on anode also.
47-89	36-40	115-330	12.1-12.9	0.037-0.110	Straight, projecting tail flame, crystalline deposit of SiC formed on cathode tip; appearance of anode termination shown in Fig. 4-2.
104-162	37-45	45-150	7.6-12.5	0.11-0.19	Straight, projecting tail flame, crystalline deposit of SiC formed on cathode tip; hard crusty deposit formed on interior walls. Appearance of anode shown in Fig. 4-3.
170-205	32-48	10-30	2.0-6.0	0.19-0.20	Violent, unsteady movement of arc. Anode spot rolled over edge of anode and onto sides to give the tapered tip shown in Fig. 4-4.

Table IV. Chemical composition of typical product from the arc vaporization of silica and carbon anodes*

Total carbon	18.65
Uncombined carbon	Not detected
Total silicon	64.41
Free silicon	14.43
Silica	25.6
Silicon carbide (based on C)	62.2
Iron	0.12
Aluminum (all other oxides as Al)	0.24
Nitrogen**	0.65

* In duplicate.

** Nitrogen is believed to originate from the electrodes, slight air leakage and adsorption on the surface of the powder after exposure to air.

analysis given in Table IV. X-ray diffraction studies of the powder identified the beta or cubic modification of silicon carbide. Electron micrographs of the product are shown in Fig. 5-9. The product is very similar to that described in detail elsewhere (5) and consisting of a mixture of beta silicon carbide crystallites and fibers of disproportionated silicon monoxide (Si + SiO_2). The silicon carbide particles are predominantly platelike having triangular and hexagonal configurations. The tan color

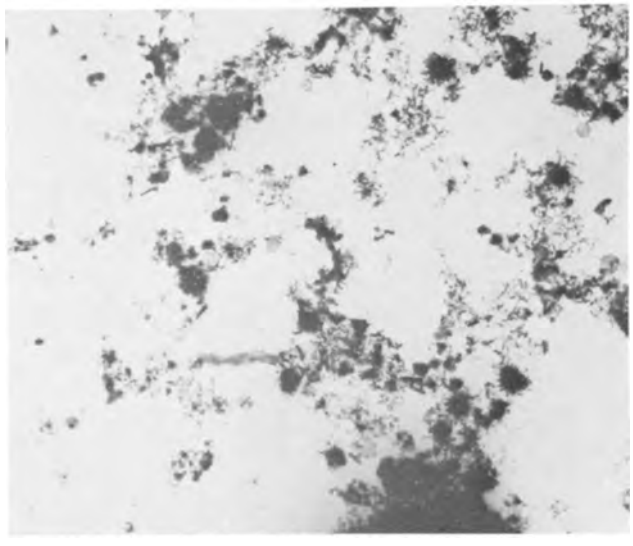

Fig. 5. Electron micrograph of product produced by arc vaporization of (SiO_2 + 3C) anodes. Magnification 8500X.

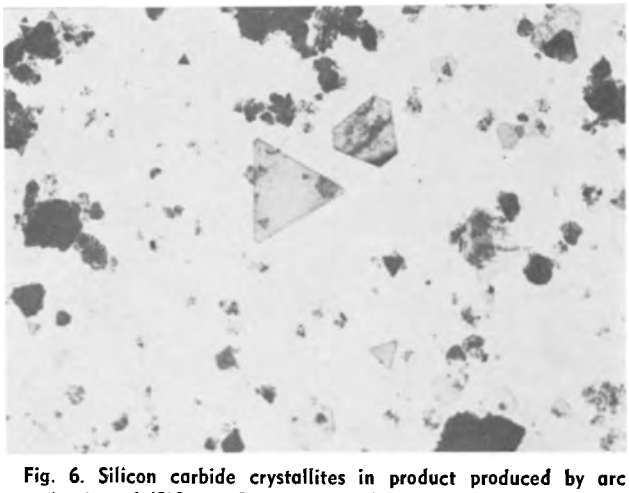

Fig. 6. Silicon carbide crystallites in product produced by arc vaporization of (SiO_2 + 3C) anodes, after leaching in hydrofluoric acid. Magnification 12,760X.

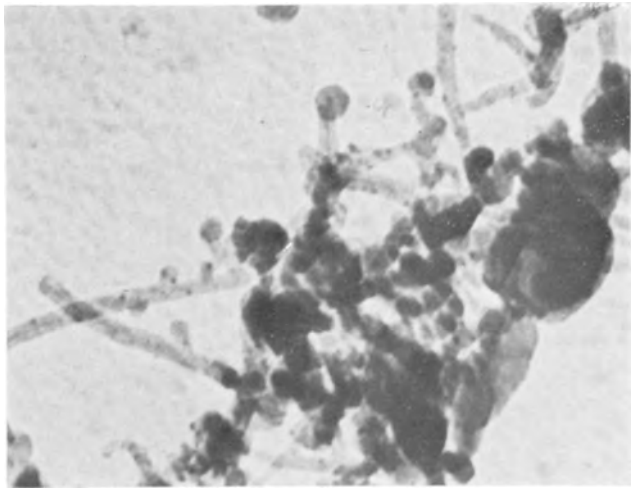

Fig. 7. Fibrous component of arc vaporized product believed to consist of disproportioned silicon monoxide. Magnification 160,000X.

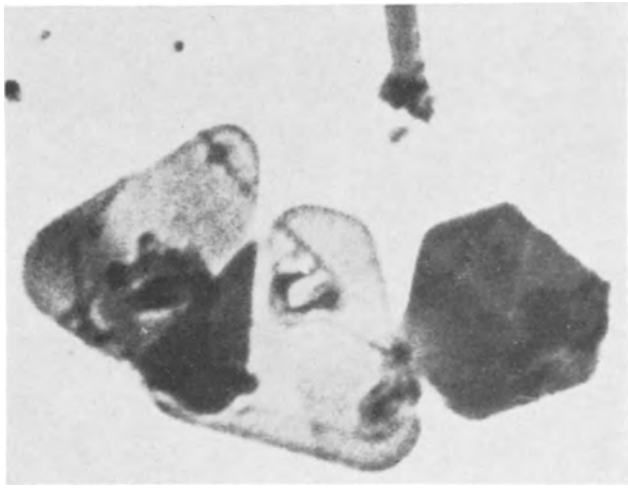

Fig. 8. Typical single crystals of silicon carbide found in arc vaporized product. Magnification 52,000X.

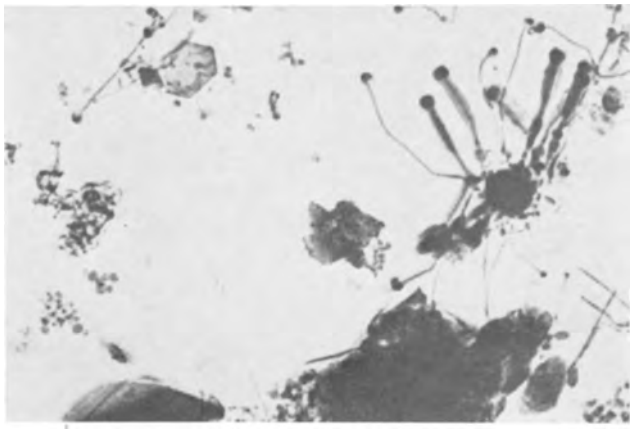

Fig. 9. Typical appearance of silicon carbide crystallites and fibrous component observed in arc vaporized product. Magnification 40,000X.

is imparted by the disproportionated silicon monoxide fibers shown in Fig. 5, 7, and 9. Leaching with aqueous hydrofluoric acid containing a small amount of nitric acid removes the silica and silicon leaving a very fine beta silicon carbide powder. Typical single crystals are shown in Fig. 8.

Discussion of Results

Arc characteristics.—The erosion characteristics given in Fig. 3 differ from those of the high intensity arc exhibited by carbon and some other materials in that the voltage rises only slightly with arc current and the erosion rate levels off or decreases after reaching a peak at high current levels, whereas the voltage and erosion rate of the high intensity arc rise steeply at a fairly critical current (6, 11). The anode spot area apparently grows in diameter with increasing current while maintaining a flat frontal area at the anode termination. At higher currents the arc begins to spill over and rotate on the sides of the anode termination thereby forming a pointed tip as shown in Fig. 4-4. As the current increases, the area of the anode spot continues to expand over the tip with little increase in anode consumption rate or arc voltage. This produces a broad, unsteady anode flame rather than the stiff vapor jet associated with the high erosion arc.

Phenomena at the anode termination and in the vapor jet.—A possible explanation for the behavior of the arc involves the events occurring at the surface of the anode. The temperature at the anode face was assumed to be equal to or slightly greater than the boiling point of silica (3070° ± 25°K), the lowest boiling point material in the anode. X-ray and petrographic examination of successive scrapings from the anode face indicates that the reaction zone is less than 0.1 mm below the porous surface of the anode face. The nature of successive layers as determined by x-ray diffraction and petrographic examination is given in Table V.

It is conceivable that sudden expansion of the gases generated by the SiO_2 + 3C reaction overcomes the compressive forces exerted by the arc's own magnetic field giving a flaring rather than a sharply defined vapor jet. This was evident from a high speed motion picture frame of an arc produced in an argon atmosphere between a carbon cathode and a (SiO_2 + 3C) composition anode.

High speed motion picture studies of the arc reveal a stream of particles and vapor from the surface of the anode, but none from the cathode. The speed of these particles was estimated from both

Fig. 10. Appearance of 55 amp arc photographed at high speed. Time interval represented is 0.0007 sec. Anode is at the right of the photograph. Magnification approximately 7X.

measurements of streaks of maximum length and the displacement of particles from one frame to the next to be about 940 cm/sec at an anode current density of about 77 amp/cm^2. The streaks are believed to represent incandescent particles of carbon propelled by the vapor stream. Comparison of a series of frames revealed occasional streaks to disappear in the vapor stream as if consumed by reaction with the vapors. This may explain the absence of free carbon in the product. The anode spot is indistinguishable *per se,* either occupying the entire frontal area of the anode or consisting of multiple spots moving rapidly and randomly over the surface at such high speed as to give it a uniform appearance. The latter is suggested by the multitude of incandescent "microspots" moving rapidly over the surface. The microspots though clearly visible in the projected film are barely visible in Fig. 10.

Relatively larger particles, also seen in Fig. 10, broke away from the edge of the anode, many of which collided with the cathode, producing a silicon carbide formation just below the tip of the cathode.

The absence of fusion or bubbling of liquid phases at the anode termination is taken as evidence that the silica is either directly vaporized and/or reacts instantaneously with carbon to produce silicon monoxide vapor, carbon monoxide, and nutrient

Table V. Composition of the anode termination after partial consumption of electrode*

Cumulative weight of material removed from anode tip, g	Estimated axial distance from anode tip surface, mm	X-ray diffraction intensity				Petrographic examination
		βSiC	Si	Graphite	Quartz	
0.006	< 0.1	Major	Weak/mod.	Major	N.D.	Beta SiC, glassy substance, and graphite present.
0.019	ca. 0.1	Weak	N.D.	Major	N.D.	Minor amount of quartz present. Glassy material and graphite present.
0.044	ca. 0.3	N.D.	N.D.	Major	N.D.	Similar to above.
0.100	ca. 0.6	N.D.	N.D.	Major	Strong	Quartz increased to a significant proportion.
Unreacted material away from tip.		N.D.	N.D.	N.D.	Major	Alpha quartz and graphite are major phases. No glass or beta SiC observed.

* Arc current approximately 55 amp.
N.D. = not detected or determined.

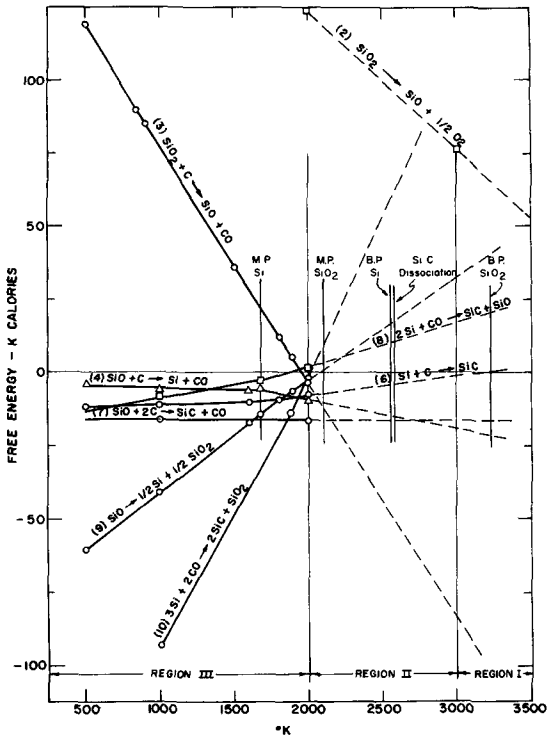

Fig. 11. Free energies of formation of possible reactions occurring in three temperature regions of an electric arc between a consumable anode composed of silica and carbon and a graphite cathode.

species for the formation of silicon carbide crystals. Additional evidence of this is given in Table V showing that silicon carbide has either formed or deposited on the tip of the anode from vapors at the instant the arc was quenched. These data also indicate that the gradient is very sharp rising from the fusion temperature of silica (*ca.* 2000°K) to the temperature at the surface of the anode termination (*ca.* 3000°K) within a distance of 1 or 2 mm. The depth of penetration of the reaction zone is dependent on the thermal conductivity of the anode and the rate of consumption of the anode reactants.

It was concluded from the preceding observations that at the anode face, vaporization and reaction proceed simultaneously and these processes are almost instantaneous.

Possible reactions occurring at the anode termination, arc column, and vapor jet.—The reactions at the anode termination, the arc column, and vapor jet can be conveniently discussed in terms of three temperature regions derived from the thermodynamic data in Fig. 11 and reference (10). These are at temperatures greater than 3000°K where all reactants are in the gaseous state with possibly the exception of carbon; the temperature range between 2000° and 3000°K where solid SiC crystallizes and silicon monoxide is a stable compound; and below 2000°K where silicon monoxide disproportionates into silicon and silica and silicon reacts with carbon monoxide.

Reactions occurring at temperatures greater than 3000°K.—The important reactions believed to occur in region I are given as follows

$$SiO_{2(s)} \rightarrow SiO_{2(g)} \quad [1]$$

$$SiO_{2(g)} \rightarrow SiO_{(g)} + 1/2\ O_{2(g)} \quad [2]$$

$$SiO_{2(g)} + C_{(s\ or\ g)} \rightarrow SiO_{(g)} + CO_{(g)} \quad [3]$$

$$C_{(g\ or\ s)} + SiO_{(g)} \rightarrow Si_{(g)} + CO_{(g)} \quad [4]$$

$$C_{(s)} \rightarrow C_{(g)} \quad [5]$$

Above 3000°K reactions [1], [2], [3], and [4] should proceed strongly to the right according to the free energy values given in Fig. 11. Also graphite begins to vaporize appreciably above 3000°K. The main reaction sequence is believed to be in the order [1] → [3] → [4] above 3000°K. Hence the partial pressure of silicon and silicon monoxide in the vapor phase is probably very high. Complex Si-C molecular ions are reported to exist at small partial pressures in the gas phase at these temperatures (3). Reaction [2] is the most important reaction when silica is vaporized. Under neutral and oxidizing conditions it is reported for silica that the partial pressure of SiO is about 1 atm at 3150°K (7). Dissociation of the $SiO_{(g)}$ to monomeric, dimeric, or larger aggregates of silicon has been shown to be negligible. At 3000°K under neutral conditions and a pressure of 0.4 atm of $SiO_{(g)}$ the pressure of silicon is 1.30×10^{-6} atm (7). Also, the formation of dimers and trimers is reported not to be important above 3000°K (7). In the presence of excess carbon SiO will not react with carbon to produce SiC since the latter is unstable at these temperatures.

Reactions occurring at temperatures between 2000° and 3000°K.—As the temperature drops into region II between 3000° and 2000°K the following reactions became important

$$C_{(g\ or\ s)} + SiO_{(g)} \rightarrow Si_{(g\ or\ l)} + CO_{(g)} \quad [4]$$

$$Si_{(g)} + C_{(g\ or\ s)} \rightarrow SiC_{(g\ or\ s)} \quad [6]$$

$$SiO_{(g)} + 2C_{(g\ or\ s)} \rightarrow SiC_{(g\ or\ s)} + CO_{(g)} \quad [7]$$

$$2Si_{(g\ or\ l)} + CO_{(g)} \rightarrow SiC_{(g\ or\ s)} + SiO_{(g)} \quad [8]$$

The vapors entering region II are composed largely of SiO, silicon, carbon vapors, and CO gas. According to the free energy of the various reactions given in Fig. 11 the tendency for silicon carbide formation is very weak at 3000°K becoming stronger as the temperature decreases. Smith has observed that silicon carbide crystallites begin to form in visible clouds at 2973°K in substantial agreement with the thermodynamic data, whereas dissociation of large crystals begins about 2573°K (8). The morphology of crystallites produced by Smith is, except for their larger size, very similar to the triangular and hexagonal crystallites shown in Fig. 6. Thus the region between about 2573° and 3000°K is the region of small crystallite formation. These may form by reactions [6], [7], and [8]. Reactions [7] and [8] are believed to have a minor role kinetically since the probability of a trimolecular reaction is much less than that of dimolecular reactions. Also the thermochemical potential of reaction [8] does not favor the formation of SiC and SiO above 2000°K. Thus reactions [6] and [7] will

compete for the available carbon in the environment.

At 3000°C the thermodynamic potential for the formation of silicon carbide is small while that for silicon is high in the presence of silicon monoxide and carbon, whereas the high temperature and concentration of reactants are favorable for both reactions. Therefore, the composition of the vapor phase at this temperature probably does not depart greatly from equilibrium conditions. However, as the temperature drops the thermodynamic potential for silicon carbide formation increases and that for silicon formation decreases. The formation of solid silicon carbide crystallites, however, lowers the kinetic potential of reaction [6] as the crystals grow in size and as the available carbon becomes less. Thus as the temperature lowers more time is needed to give the silicon and carbon an opportunity to locate at nucleation and growth sites on the growing crystallites. Under equilibrium conditions the two final phases would be silicon carbide and carbon monoxide. However, the steep temperature gradients, high velocity gas flows, and varying energy states of the molecular, atomic, and ionic species provide conditions for complex, nonequilibrium conditions and hence an incompleted over-all reaction. This explains the presence of disproportionated silicon monoxide, silicon, carbon monoxide, and silicon carbide in the product as the temperature rapidly falls below 2000°K into the third region.

Reactions occurring at temperatures less than 2000°K.—The important reactions in region III also include reactions important in regions I and II and are listed as follows

$$SiO_{(g\text{ or }s)} + C_{(s)} \rightarrow Si_{(l\text{ or }g)} + CO_{(g)} \quad [4]$$

$$Si_{(g\text{ or }l)} + C_{(s)} \rightarrow SiC_{(s)} \quad [6]$$

$$SiO_{(g\text{ or }s)} + 2C_{(s)} \rightarrow SiC_{(s)} + CO_{(g)} \quad [7]$$

$$2Si_{(g\text{ or }l)} + CO_{(g)} \rightarrow SiC_{(s)} + SiO_{(s\text{ or }g)} \quad [8]$$

$$SiO_{(s)} \rightarrow 1/2\ Si_{(s)} + 1/2\ SiO_{2(s)} \quad [9]$$

$$3Si_{(g\text{ or }l)} + 2CO \rightarrow 2SiC_{(s)} + SiO_{2(s\text{ or }l)} \quad [10]$$

The bulk of the silicon carbide is believed to form in the region II where the mobility of the nutrient species is high. It may be seen from Fig. 11 that the thermodynamic potential of silicon carbide forming reactions [6], [7], and [8] and silicon forming reaction [4] is quite low at temperatures less than 2000°K. Residual carbon would be solid at these temperatures and silicon would be liquid or solid. Thus both thermodynamic and kinetic factors are relatively unfavorable to further significant production of silicon carbide below 2000°K in rapidly cooling gases. However, if the reactants could be held at these lower temperatures for relatively long periods of time it is well known that the reactions would go to completion with silicon carbide and carbon monoxide the final products (9).

As the gases cool below 2000°K the potential for the disproportionation of silicon monoxide increases. The equilibrium pressure for reaction [9] in Fig. 11 has been calculated to be 1 atm at 2090°K. According to Schick (7) excess silicon monoxide will disproportionate at low temperatures after reaction [9]. Solid silicon monoxide is considered to be unstable relative to solid silicon and silica below 1450° and 1573°K, respectively. Above these temperatures solid silicon monoxide is considered the stable phase. Although the thermodynamic data are somewhat uncertain the equilibrium pressure for the reaction $SiO_{(s)} \rightarrow SiO_{(g)}$ has been calculated to be 1 atm at 2300°K (7). Thus above 2300°K silicon monoxide probably exists as a vapor, between 2090° and 2300°K as both a solid and vapor, and below 2090°K exists in equilibrium with silicon and silica. However, reaction [9] is believed to be sluggish at the higher temperatures and silicon monoxide may exist down to about 400°C before disproportionation occurs rapidly (7). The fibrous material in Fig. 7 and 9 is believed to be condensed silicon monoxide which has disproportionated.

The foregoing analysis suggests that the silicon carbide content of the anode flame is largely dependent on the reactions occurring between 2000° and 3000°K, particularly reactions [6] and [4]

$$Si_{(g)} + C_{(g\text{ or }s)} \rightarrow SiC_{(s)} \quad [6]$$

$$SiO_{(g)} + C_{(s\text{ or }g)} \rightarrow Si_{(g)} + CO_{(g)} \quad [4]$$

of which reaction [6] is probably rate determining since the probability of finding a reaction site on the silicon carbide crystallites is believed to be less than collisions between silicon monoxide molecules and carbon atoms or particles.

Reaction [10] is unlikely below 2000°K because of the extremely low probability of occurrence of a reaction between three silicon atoms and two carbon monoxide molecules. Actually, reaction [10] represents the sum of reactions [8] and [9], hence silicon carbide formation is controlled essentially by reaction [8].

Experiments have been performed by the author whereby silicon and carbon monoxide have been reacted in an electric arc above a liquid bath of silicon in a "cold" crucible arc furnace, the resultant product consisting of very fine silicon carbide (*ca.* 300Å by x-ray line broadening measurements) and disproportionated silicon monoxide fibers. The appearance of the former is shown in Fig. 12 and the

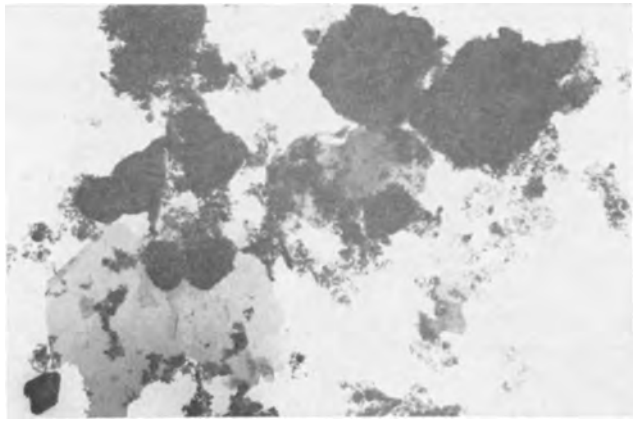

Fig. 12. Silicon carbide particles produced by reaction between carbon monoxide and silicon. Magnification approximately 10,000X.

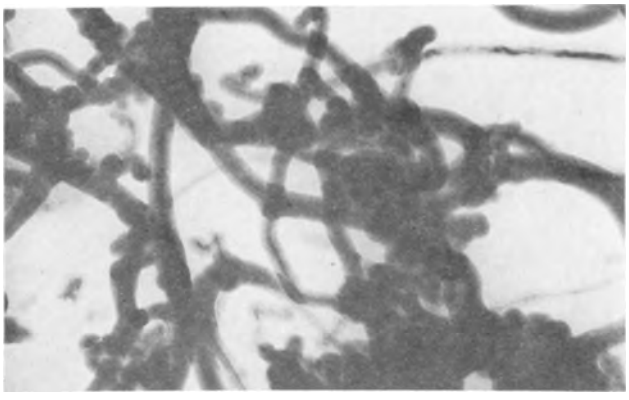

Fig. 13. Disproportionated silicon monoxide fibers formed by reaction between carbon monoxide and silicon metal. Magnification approximately 80,000X.

latter in Fig. 13. Similar experiments have shown that when silica is reacted over a pool of silicon metal in the presence of carbon monoxide, disproportioned silicon monoxide and a small amount of silicon carbide are produced. These experiments establish that the fibrous product is associated with the formation of silicon monoxide gas and its subsequent condensation and that silicon carbide may be produced by reaction between silicon and carbon monoxide. In both the preceding reactions silicon was identified in the product and the silicon and silica contents were in nearly stoichiometric proportions as required by the reaction

$$2SiO \rightarrow Si + SiO_2 \qquad [2]$$

It has not been established directly that silicon monoxide exists in the solid state, but observations of the structure of the fibrous product strongly suggest that solid state reactions are responsible for the cored structure revealed in Fig. 13.

The above analysis reasonably accounts for the composition of the final arc vaporized product. Silicon carbide may originate from reaction of silicon and carbon and silicon and carbon monoxide; silicon monoxide from reaction between silica and carbon or silicon and carbon monoxide; silica from vaporization of silica, reaction between silicon and carbon monoxide, or disproportionation of silicon monoxide. Strong evidence for these reactions would be provided if the morphology of the silicon carbide and silica could be shown to be characteristic of each reaction. The predominant species identified in the arc product are triangular, hexagonal, and irregular thin crystallites of silicon carbide and fibrous particles resulting from condensation of silicon monoxide. There are relatively small amounts of extremely fine spherical particles and infrequent spikes, ribbons, and other odd shapes.

There is no evidence of significant amounts of free silicon metal which would be expected to be present as spherical particles. Earlier work has shown that the major part of the free silicon in the product is associated with the fibers of disproportionated silicon monoxide (5).

The chemical analysis of the reaction products reveals no free carbon from which it may be concluded that silicon carbide formed in the arc is not subsequently dissociated. Morphological data reveals the silica to be present in an amorphous fibrous form suggesting that it originates with reactions [8] and [9].

Table VI. Comparison of carbon/silica ratios of mixes

Source of data, Table No.	Description	%SiO_2	%C	C/SiO_2 ratio
1	Electrode mix	71	29	2.05
1	Electrode mix after firing	65	35	2.69
4	Electrode mix back calculated from product analysis	68	32	2.36
	Stoichiometric mix composition	62.5	37.5	3.00

Added support for the proposed reaction steps might have been obtained from careful material balance studies and the exercise of various precautions. Unfortunately, this additional effort was not within the scope of this investigation. However, it is instructive to briefly review some of the problems and considerations that would be involved in obtaining accurate data for stoichiometric and materials balance calculations.

Table VI obtained from values found in other tables compares several carbon to silica ratios. It is a problem to produce an electrode containing carbon and silica in stoichiometric proportions by the procedure outlined in this investigation because of the difficulty of predicting and controlling the carbon contribution resulting from the conversion of organic binder materials to carbon. Assuming stoichiometric proportions of carbon and silica in the electrode, the carbon contribution from the cathode, though small, will react with or be added to the anode vapor products and thereby influence the composition of the product. The large specific surface area of the ultrafine silicon carbide and silicon in the product reacts with and adsorbs oxygen and nitrogen on exposure to air resulting in an unknown increase in the silica content and a proportionate decrease in the carbon to silica ratio. For accurate analysis of the condensed vapors either precautions must be taken to exclude oxygen during handling of the powder and/or accurate determination of the oxygen pick-up just prior to chemical analysis must be made.

The silicon carbide yield is highly dependent on the rate of cooling of the gases in regions II and III close to the anode face, and will not be affected appreciably by the surrounding environment. Since the velocity of the vapor streaming from the anode probably varies little, the silicon carbide content should not vary greatly. However, gas sucked into the vapor jet will dilute, react with, and cool the vapors in the gas streaming away from the anode spot, the effect depending on the gas introduced into the system. The degree of quenching will also depend on the physical properties of the gas introduced into the system. It has been shown that some gases will react with the vapors and affect the composition and morphology of the product (11).

Conclusions

1. Silicon carbide can be produced in a direct current open arc between a graphite cathode and con-

sumable anodes composed of nearly stoichiometric proportions of silica and carbon for the formation of silicon carbide.

2. Silicon carbide cannot be produced by arc vaporization in an open arc of the type under consideration without silica and silicon being present in the product as a consequence of nonequilibrium conditions characteristic of an arc plasma environment.

3. The product of vaporizing a stoichiometric mixture of silica and carbon in an electric arc consists predominantly of beta silicon carbide crystallites intermixed with disproportionated silicon monoxide ($Si + SiO_2$).

4. The direct current open arc between a graphite cathode and a consumable ($SiO_2 + 3C$) anode is characterized by the almost constant value of the voltage with rising current and erosion rate and the leveling off or drop in the erosion rate at higher current levels.

5. Vaporization and reaction occur simultaneously and instantaneously in a layer, less than 1 mm thick at the anode termination producing a jet stream having a velocity estimated at 940 cm/sec at a current density of approximately 77 amp/cm^2.

6. The fibrous form of amorphous silica in the product resulting from arc vaporization of silica and carbon is associated with reactions involving silicon monoxide gas. Circumstantial evidence suggests that the silicon associated with disproportionated silicon monoxide is precipitated by a solid state reaction within the fibers.

Acknowledgment

The author wishes to acknowledge the assistance of Edward Stofka, Bettis Atomic Power Laboratory, Westinghouse Electric Corporation, Pittsburgh, Pennsylvania, in the design and construction of the consumable electrode arc reactor and for much of the data contained in this paper.

Manuscript received May 24, 1962. This paper was prepared for delivery before the Los Angeles Meeting, May 6-10, 1962.

Any discussion of this paper will appear in a Discussion Section to be published in the December 1963 JOURNAL.

REFERENCES

1. Otto Ruff, *This Journal*, **68**, 87 (1935).
2. J. A. Lely, *Ber. Deut. Keram. Ger.*, **32**, No. 8, 229 (August 1955).
3. J. Drowart, J. De Maria, and M. G. Inghram, J. *Chem. Phys.*, **29**, No. 5, 1015 (November 1958).
4. V. Harris, J. D. Holmgren, S. Korman, C. Sheer, *This Journal*, **106**, 874 (1959).
5. W. E. Kuhn, "The Morphology of Ultrafine Silicon Carbide Produced by Vaporization of Silica and Carbon in the Electric Arc" to be published in book "Ultrafine Particles", W. E. Kuhn, H. Lamprey, C. Sheer, Editors, John Wiley & Sons, Inc., New York (1963).
6. C. Sheer and S. Korman, "Arcs in Inert Atmospheres and Vacuum," pp. 169-183, John Wiley & Sons, Inc., New York (1956).
7. H. L. Schick, *Chem. Rev.*, **60**, 331 (August 1960).
8. A. H. Smith, *This Journal*, **106**, 526 (June 1959).
9. H. N. Baumann, *ibid.*, **99**, 109 (March 1952).
10. G. L. Humphrey, S. S. Todd, J. P. Coughlin, and E. G. King, "Some Thermodynamic Properties of Silicon Carbide," B.M.R.I. 4888 (July 1952).
11. Unreported research by the author.

Electrode Kinetics for Chlorides of Tungsten, Antimony, and Phosphorus

S. W. Mayer and W. E. Brown, Jr.
Laboratories Division, Aerospace Corporation, El Segundo, California

ABSTRACT

Chronopotentiometry has been utilized to measure the rate constants for the first electroreduction step at platinum in dimethylformamide solution of several chlorine compounds of interest for regenerable fuel cell systems. The chronopotentiometric curves were also used to determine the diffusion coefficients and the products of the transfer coefficients with the number of electrons involved in the rate-determining steps. Tungsten hexachloride obeyed the chronopotentiometric equation of reversible reactions, with an $E_{1/4}$ of —0.159v (*vs.* a gold reference electrode) for its one-electron first reduction step. The reduction of $SbCl_5$ to $SbCl_3$ was irreversible and occurred in two steps, suggesting the intermediate formation of $SbCl_4$. The reductions of phosphorus chlorides and several group IV A chlorides were also found to be irreversible. Some correlation was noted between bond energies and the reciprocals of the rate constants. The electrode surface-area requirements for minimizing activation polarization for PCl_5 and $SbCl_5$ were calculated from the rate constants and chronopotentiometric data. Using Latimer's method, it was estimated that the WCl_6 fuel cell could produce 40% higher open-circuit voltage than the PCl_5 fuel cell.

Regenerable fuel cells potentially can provide the high specific energy important for vehicles in longer satellite and solar system flights. Several halides have been considered for nonaqueous regenerable fuel cell systems (1). For example, the reaction between PCl_3 and Cl_2 to form PCl_5 can produce 0.27v at open circuit in a fuel cell at 25°C; the PCl_3 and Cl_2 can then be regenerated by decomposing the

PCl_5 thermally (at 300°C), photolytically or electrolytically, and recycled in a closed system to the fuel cell (1).

As part of a research effort on regenerable fuel cells using polyvalent halides, a fundamental study of the electrode kinetics for the reduction of WCl_6, $SbCl_5$, $SbCl_3$, PCl_5, PCl_3, $POCl_3$, and group IV A chlorides was considered desirable inasmuch as fuel cell efficiency would be poor, because of activation polarization, for those halides which have relatively low rates of electrode reactions (1). Delahay (2) reported in 1953 that chronopotentiometry can be used to determine the kinetics of electrode reactions for typical inorganic ions in aqueous solutions. The dropping mercury electrode has been used occasionally to provide some of the rather scarce measurements of electrode reaction kinetics (2), but chronopotentiometry has a key advantage for fuel cell research in that it is applicable to reactions at solid electrodes. Accordingly, the reductions of several polyvalent chlorides in nonaqueous systems were examined to determine whether they followed chronopotentiometric theory for noncomplex electrode reactions. When suitable methods were used to prevent hydrolysis of the halides, chronopotentiometry was found to give reproducible results from which rate constants could be readily calculated for the first reduction step in accordance with chronopotentiometric theory. Diffusion coefficients and the products of the transfer coefficients with the number of electrons involved in the rate-controlling steps were also calculated from the potential-time curves at platinum electrodes.

Experimental

The chronopotentiometric apparatus was a modernized version of that previously employed (2). A calibrated X-Y recorder (Model 2D-2, F. L. Moseley Co., Pasadena, Calif.) with a 15 x 10-in. recording area, was used to obtain the potential-time curves. The pen voltage-response speed (Y axis) was 2 v/sec at a scale setting of 10 in./v; maximum pen travel speed (X axis, time axis) was 2 in./v. The power supply for providing constant current maintained its voltage output constant within 0.1% at the 375v setting used. Current was measured by using a precision potentiometer to determine the potential drop across standard resistors accurate to 0.1%. An amplifier having an impedance of more than 100 megohms was utilized in the circuit between the reference electrode and the polarized electrode in order to minimize the current between these electrodes.

A calomel electrode was not used as the reference electrode because of the rapid decomposition of the polyvalent halides by water. Instead, the reference electrode (Fig. 1) consisted of a gold sheet helix having an area of 75 cm^2. The platinum electrode used for the kinetic studies was a polished circular disk with an area of 0.216 cm^2. It was sealed into the end of a 5-in. length of soft glass tubing and was maintained in a horizontal position for upward diffusion (3). Preliminary tests with aqueous ferricyanide solutions and nonaqueous PCl_5 solutions demonstrated that this electrode behaved in accordance with chronopotentiometric theory; for the transition time range of 3-30 sec covered in this study, the product of current density with the square root of transition time was constant (3) within a standard deviation of 1%. Furthermore, the reciprocal slope (2) for the reversible one-electron reduction of ferricyanide was found to be 0.0590 with this electrode; the transition time for the anodic step following the cathodic step was found to be 0.333 of the cathodic transition time, in accordance with theory (2). The transition time was determined graphically from the chronopotentiogram by Delahay's procedure (2).

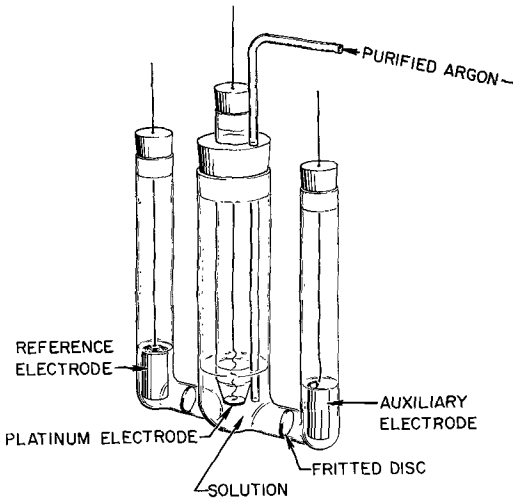

Fig. 1. Cell for chronopotentiometry

Oxygen was removed from the dimethylformamide solution in the electrolysis cell (Fig. 1) by bubbling argon through the solution for at least 30 min. The argon was pretreated to remove any oxygen and water by passage through a 50-cm bed of calcium chips in a quartz tube maintained at 650°C by a horizontal tube furnace. The argon was then allowed to cool, saturated with dimethylformamide vapor, and passed into the dimethylformamide solution, which was maintained at 25°C. This argon was also used to stir the solution between the recording of each chronopotentiogram.

All the chlorides were reagent grade, anhydrous compounds. A dry box was used for the preparation and transfer of solutions. Reagent grade lithium nitrate was dried by heating in vacuum at 160°C for 48 hr. The dimethlylformamide was the spectroscopically pure grade, dried and distilled in accordance with the procedure of Wawzonek *et. al.* (4).

Results

Preliminary investigations with nonaqueous solvents.—In order to select a suitable solvent for these studies, preliminary experiments were made to determine the solubility and reactivity of phosphorus pentachloride and other chlorides in dimethylformamide, dimethylsulfoxide, pyridine, and acetonitrile. Dimethylsulfoxide was found to react strongly with these chlorides. Solubilities in the other solvents were adequate, and acetonitrile was found to be an especially strong solvent for PCl_5 and $SbCl_5$. Since conductivity measurements (5) suggest, however,

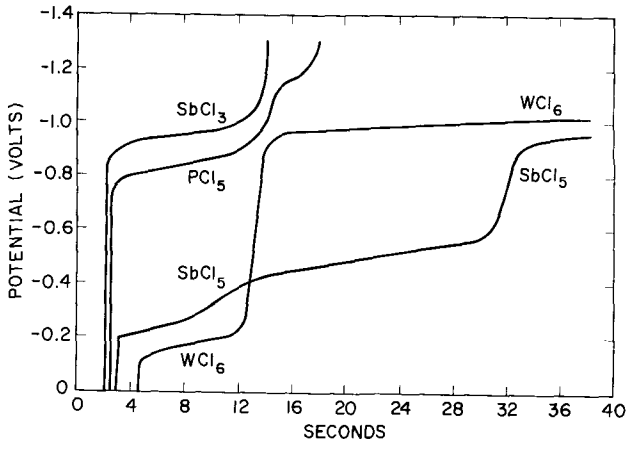

Fig. 2. Representative chronopotentiograms. Each curve begins at the origin, but has been shifted along the x-axis for clearer presentation.

that PCl_5 slowly reacts with acetonitrile, this solvent was not employed for the chronopotentiometric measurements. Dimethylformamide was used because it has a higher dielectric constant (6) than pyridine (36.7 *vs.* 12.3 at 25°C), and preliminary chronopotentiograms indicated that the reduction of PCl_5 in pyridine was considerable more irreversible than in dimethylformamide.

The supporting electrolyte used was 1.000M $LiNO_3$ in dimethylformamide since chronopotentiometric "blank" runs for this electrolyte (with no polyvalent chloride solute present) showed no reduction or oxidation transitions from −3.1v to +0.9v. Tests of silver-silver chloride or mercury as reference electrodes showed troublesome drifts in potential for successive chronopotentiograms, whereas the gold helix electrode gave potentials reproducible within a standard deviation of 3 mv. The potential of the gold helix electrode in the 1.000M $LiNO_3$ solution in dimethylformamide was found to be +0.38v when compared with a saturated KCl aqueous calomel electrode.

Measurement of rate constants.—Representative chronopotentiometric curves are shown in Fig. 2. (Each curve actually begins at the origin. They have been sketched displaced horizontally to avoid overlapping.) Date and results are summarized in Table I. Tungsten hexachloride was the only one of these halides which exhibited chronopotentiometric behavior corresponding to the potential-time relationship for reversible electrode reactions (2)

$$E = E_{1/4} + \frac{2.303RT}{n\mathbf{F}} \log \frac{\tau^{1/2} - t^{1/2}}{t^{1/2}} \qquad [1]$$

where τ is the transition time, t is the time elapsed since the beginning of the electrolysis, n is the overall number of electrons involved in the electrode-reaction equation, E is the observed potential, and $E_{1/4}$ is the observed potential at t equal to $\frac{1}{4}\tau$. The slope of the straight line obtained by plotting E against the logarithmic term was 0.0590 for WCl_6, compared to the theoretical value of 0.0591 for a one-electron process. When that logarithmic plot was attempted for the chronopotentiograms of all the other chlorides in Table I, the experimental points deviated significantly from a straight line. An "approximate slope" was calculated by applying the least squares method to the logarithmic plot from $t = \frac{1}{4}\tau$ to $t = \frac{3}{4}\tau$. The results are listed in Table I and show considerable deviation from $0.0591/n$.

The chronopotentiometric curve for totally irreversible processes follows the relationship (2)

$$E = \frac{2.303RT}{\alpha n_a \mathbf{F}} \log \frac{n\mathbf{F}Ck^\circ_f}{i_o} + \frac{2.303RT}{\alpha n_a \mathbf{F}} \log \frac{\tau^{1/2} - t^{1/2}}{\tau^{1/2}} \qquad [2]$$

where α is the transfer coefficient, n_a is the number of electrons involved in the rate-determining charge transfer step, C is the bulk concentration in moles per cubic centimeter, i_o is the current density in amperes per square centimeter, and k°_f is the formal heterogeneous rate constant of the reduction process at E equal to zero, *vs.* the gold reference electrode. The potential-time curve for the first reduction step of each chloride of Table I, except WCl_6, was found to agree with Eq. [2] when the potential was plotted against the logarithmic term involving $t^{1/2}$. From the slope of the resulting straight line, αn_a was calculated.

Table I lists the observed potential, E_o, at t equal to zero. From Eq. [2], at t equal to zero

$$E_o = \frac{2.303RT}{\alpha n_a \mathbf{F}} \log \frac{n\mathbf{F}Ck^\circ_f}{i_o} \qquad [3]$$

The rate constant, k°_f, was then calculated from Eq. [3] since all of the required factors were available. Inasmuch as electrode processes are heterogeneous,

Table I. Chronopotentiometric data

	Concentration, moles/cc × 10^6	Current density, amp/cm² × 10^3	Transition time, sec	E_o, v	Approximate slope	αn_a	Diffusion coefficient, cm²/sec × 10^5	Log of rate constant, cm/sec	Bond energy, kcal
$SbCl_5$	7.72	0.329	5.66	−0.205	0.066	0.618	0.14	−5.49	38
$SbCl_3$	3.99	0.994	3.17	−0.875	0.168	0.184	2.68	−5.30	74
PCl_5	3.85	0.893	11.36	−0.730	0.076	0.536	2.10	−9.53	40
PCl_3	3.95	0.327	10.80	−0.960	0.053	0.776	1.01	−15.68	86
$POCl_3$	3.87	0.466	6.11	−0.925	0.084	0.434	0.30	−10.02	
$SiCl_4$	4.06	0.259	28.5	−1.135	0.282	0.121	1.58	−5.50	86
$GeCl_4$	9.89	2.41	15.12	−0.810	0.106	0.402	12.3	−8.11	77
$SnCl_4$	8.74	0.371	10.20	−1.190	0.014	1.94	0.06	−42.8	77
WCl_6	5.32	0.263	8.52	$E_{1/4} = -0.159$	0.059		0.28		

the units of the rate constants are cm sec^{-1}. In Table I the logarithms of the rate constants are given. The diffusion coefficient, D, for each halide was calculated from the Sand equation (7)

$$\tau^{1/2} = \frac{\pi^{1/2} n \mathbf{F} C D^{1/2}}{2 i_o} \qquad [4]$$

Discussion

Magnitudes of Rate Constants and Diffusion Coefficients

The magnitudes of the rate constants in Table I extend over a wide range and, in view of the complexity of factors affecting the activation energy for electrode reactions of polyvalent halides, only a qualitative consideration of the relative magnitudes can be expected. Since the reduction of a covalently bonded polyvalent chloride involves breaking a bond to the chlorine atom, the bond energy probably affects the activation energy. Accordingly, the energy of each chlorine bond is listed in Table I. These are single-bond energies and are calculated in accordance with the procedure of Pauling (8) from the appropriate thermodynamic data (9). In the cases of PCl_5 and $SbCl_5$, the bond energies of the last two bonds are given since, as demonstrated by thermodynamic data, those bonds have a lower energy than the first three bonds (8). Consequently, the higher rate constant for PCl_5 relative to PCl_3 is not unexpected. This correlation is not found for the rate constants of $SbCl_5$ and $SbCl_3$. The ionic contribution to the bonding of $SbCl_3$ (as indicated by the fact that the melting point of $SbCl_3$ is considerably higher than that of PCl_3) may be a factor in lowering the activation energy for reduction since the reduction of an Sb^{+3} ion would involve only charge transfer rather than bond breaking.

The very small rate constant for $SnCl_4$ may arise from the possibility that two or more bonds are broken for each reduction, as indicated by the value of 1.94 for αn_a. The energy of two disrupted bonds for $SnCl_4$ is 154 kcal, with a consequent slower rate of reaction. The bond energies for $SiCl_4$ and $GeCl_4$ do not correlate well with the rate constants, relative to PCl_5 and $SbCl_5$. Reverse polarity chronopotentiometry (10) showed that the anodic transition times were one-third the cathodic transition times for WCl_6, $SbCl_5$, and PCl_5, but were more than one-third for the other chlorides of Table I. This suggests that products with low diffusion coefficients were formed from the other chlorides; conceivably, these products could be colloids (*i.e.*, insoluble) or polymers. Alternatively, the electrode reactions for these chlorides may not be diffusion controlled.

The comparatively rapid electrode reaction for WCl_6 could be attributed to its ionic nature, as indicated by its relatively high melting point. For example, if WCl_6 were ionized to the extent of forming significant proportions of WCl_5^+ and WCl_7^- the reduction could proceed by a charge transfer (with no activation energy required for bond breaking) as in the following equation

$$WCl_5^+ + 1e^- = WCl_5 \qquad [5]$$

There is some evidence (5) that polyvalent chloride solutes in nonaqueous solvents can ionize rapidly, but to a limited extent, in the manner indicated above.

The magnitudes of the diffusion coefficients (Table I) in dimethylformamide solution are similar to those found in aqueous solutions. In ideal nonelectrolyte solutions, diffusion coefficients would vary inversely as the square root of molecular weight of the solute. Although its high molecular weight is a factor in the low diffusion coefficient of WCl_6, the general lack of correlation with molecular weight for these polyvalent chlorides can be attributed to such interactions as ionic forces, induction and dispersion effects, and dipole forces which produce nonideal solutions (11).

The chronopotentiometric curves in Fig. 2 demonstrate that only for $SbCl_5$ did the second step in the reduction agree with the transition time relationship for a first-order, noncomplex second step (2, 12)

$$\frac{\tau_2}{\tau_1} = \frac{2n_2}{n_1} + \left[\frac{n_2}{n_1}\right]^2 \qquad [6]$$

where the subscripts, 1 and 2, denote the first and second step. For $SbCl_5$ the transition time of the second step was three times that of the first step, in agreement with Eq. [6] for two successive one-electron reductions. E_o's were −0.205, −0.40, and −0.87 for the first, second, and third steps, respectively, in the chronopotentiometric reduction of $SbCl_5$. E_o for $SbCl_3$ was −0.875v, which agrees with the third step for $SbCl_5$. These observations suggest that pentavalent antimony was reduced to tetravalent antimony in the first one-electron step. [Tetravalent antimony has been reported (13) as Sb_2O_4.] In the third step of the reduction, the trivalent antimony would be reduced to lower valent or metallic antimony. The existence of lower valent antimony chlorides has not been established, although there is evidence that group 5 elements can form divalent and univalent halides such as P_2Cl_4 (14) and BiCl (15). In these chronopotentiometric reductions, no indication could be obtained of deposition of group IV, V, or VI elements on the electrodes.

For the chronopotentiometric reduction of PCl_5 at the C/i_o ratio of 4.01 x 10^{-3} moles cm^{-1} amp^{-1}, E_o was −0.73v for the first step followed at −1.15v by a second step. The reduction of PCl_3 was found to occur at −1.15v for the same C/i_o ratio. This supports the view that the first step in the reduction of PCl_5 produces PCl_3. Since PCl_3 has a lower diffusion constant than PCl_5 (Table I), the C/i_o ratio used for PCl_3 to obtain a chronopotentiogram with a 10 sec transition time was 12.1 x 10^{-3} moles cm^{-1} amp^{-1} which, because of the irreversibility of the reduction, produced a lower E_o of −0.96v. Stannic chloride also appeared to reduce to stannous chloride in the first step since the second step for $SnCl_4$ had an E_o of −1.30, which corresponded to the E_o of $SnCl_2$.

Activation Polarization Estimates

Since no free energy data exist for WCl_6 and WCl_5, the theoretical voltage is not known for the reaction of WCl_5 with chlorine to form WCl_6. Enthalpy meas-

urements for these compounds have been made, however, and it is possible to estimate the entropy difference between WCl_6 and WCl_5 well enough by Latimer's method (16) to make a useful estimate of the free energy change. At 300°K the change in enthalpy for the reaction of WCl_5 with $\frac{1}{2}Cl_{2(g)}$ to form WCl_6 is −14.7 kcal/mole (9). The entropy of WCl_6 is estimated to be 8 cal/mole deg more than that of WCl_5 by Latimer's method. Since the entropy of $\frac{1}{2}Cl_{2(g)}$ is 26.6 cal/mole deg (9), the entropy change of the reaction is calculated to be −18.6 cal/mole deg. The free energy change can then be estimated to be 9.1 kcal/mole at 300°K. At unit activities the open-circuit potential of the cell would be 0.39v, which is 40% higher than the 0.27v open-circuit potential of the PCl_5-PCl_3 system (1).

Since the reversible potential for the reduction of WCl_6 to WCl_5 is −0.16v (Table I) using the gold reference electrode, the reversible potential of the chlorine electrode is estimated to be +0.23v relative to the gold electrode, to agree with the thermodynamic estimate. On that basis the reversible potential for the reduction of PCl_5 should be about −0.05v relative to the gold electrode, if the solvation effects for PCl_5 are comparable to those for WCl_6. The experimentally observed potential for PCl_5 was −0.73v which would correspond to the high overvoltage of 0.68v. Consequently, the PCl_5 system would form a markedly inefficient fuel cell at a current density or 0.89×10^{-3} amp/cm² (Table I) since the overvoltage produces a high drop in fuel cell voltage at that current density.

The rate constant and transfer coefficient results, however, can now be utilized for estimating the minimum surface area required to make activation polarization negligible for a porous platinum fuel cell electrode. It is, of course, essential to distinguish between the actual current density of a porous electrode and the apparent current density. The actual current density, i_o, is equal to i_a/A where i_a is the apparent current density and A is the measured surface area per square centimeter of apparent electrode area. The apparent current density is merely the current divided by the apparent electrode area calculated from the over-all dimensions of the electrode, neglected its roughness factor or porosity. In Eq. [3] the factor, i_o, is the actual current density. Equation [3] can be rearranged to calculate the actual surface area corresponding to any fuel cell voltage or current.

$$\log A = \frac{\alpha n_a E_o}{2.303RT} - \log \frac{n\mathbf{F}Ck^\circ_f}{i_a} \qquad [7]$$

For fuel cell estimates, i_a can be set equal to unity, which corresponds to the useful apparent current density of 100 amp/cm². For PCl_5, the rate constant and transfer coefficient results of Table I can be utilized along with the E_o value of −0.05v, estimated above as its reversible reduction potential. A concentration of 4M and a porous platinum electrode 0.93 mm thick with a 50% void volume were selected for convenience in calculation. Insertion of these numbers in Eq. [7] leads to the estimate that a platinum electrode having an actual surface area of 155 m²/g would have negligible activation polarization. Although obtaining this value for the specific surface area would require that the platinum be extremely finely divided, it appears feasible to attain this specific area since values of 270 m²/g have been reported (17). The fine pores in such electrodes would tend to impede diffusion, however; consequently, concentration polarization problems could be severe.

The thermodynamic data in the literature is inadequate for calculating the free energy and voltage for the formation of $SbCl_5$. A rough estimate (18) suggests that the voltage is slightly less than for the formation of PCl_5. Accordingly, for the purpose of utilizing Eq. [7] to make a practical estimate of A, E_o can be chosen as equal to +0.02v. Then, in a manner similar to that used for PCl_5, the minimum specific surface area required to avoid activation polarization is estimated to be 0.13 m²/g for a 4M solution of $SbCl_5$. Since the electrode surface area estimate for $SbCl_5$ is less than one-hundredth of the specific area estimate for PCl_5, the mean diameter of the platinum particles can be approximately ten times larger for $SbCl_5$ than for PCl_5. Thus, the platinum electrode for $SbCl_5$ would probably be less difficult to fabricate. It would also have less tendency to impede diffusion and could be made thicker to have greater structural strength. The $SbCl_5$ electrode reduction reaction was less polarized during chronopotentiometry than that for PCl_5; the E_o was −0.205v for the former compared with −0.730v for the latter, and the estimated overvoltage for $SbCl_5$ was 0.23v whereas that for PCl_5 was 0.68v. Consequently it is not surprising that a smaller specific surface area would be needed to obtain thermodynamically ideal voltages from $SbCl_5$ than from PCl_5.

The Tafel equation, which has long been used empirically to predict the effect of current density on overvoltage (19), has the following form

$$E_o = a + b \log i_o \qquad [8]$$

where a and b are constants. It can be shown that the empirical Tafel equation can be derived from Eq. [3] which is based on established electrochemical principles. Equation [3] can be written in the form

$$E_o = \frac{2.303RT}{\alpha n_a \mathbf{F}} \log n\mathbf{F}Ck^\circ_f - \frac{2.303RT}{\alpha n_a \mathbf{F}} \log i_o \qquad [9]$$

Comparison of Eq. [8] and [9] shows that the chronopotentiometric data of Table I can be used to obtain the constants which are needed for the calculation of overvoltages from the Tafel equation since

$$a = \frac{2.303RT}{\alpha n_a \mathbf{F}} \log n\mathbf{F}Ck^\circ_f \qquad [10]$$

and

$$b = -\frac{2.303RT}{\alpha n_a \mathbf{F}} \qquad [11]$$

The chronopotentiometric apparatus has been used to test these equations by decreasing i_o from the values of Table I by the factors 10, 100, and 1000. These studies were made for $SbCl_5$, $SbCl_3$, PCl_5, and PCl_3. It was found that substituting into Eq. [9] the chronopotentiometric data from Table I

for each of these compounds gave calculated values of E_o which agreed with the measured values within an average deviation of 0.01v, when i_o was decreased by these factors. Thus, the chronopotentiometric apparatus can be used for evaluating relatively rapidly the polarization problem in fuel cells in addition to measuring fundamental kinetic constants for the electrode reactions.

Manuscript received June 20, 1962; revised manuscript received Sept. 26, 1962.

Any discussion of this paper will appear in a Discussion Section to be published in the December 1963 JOURNAL.

REFERENCES

1. J. N. Pitts, J. D. Margerum, and W. E. McKee, *J. Am. Rocket Soc.*, **31**, 890 (1961); L. Schieler "Direct Conversion of Chemical Energy to Electrical Energy," Report No. A61-1840.8-41, Aerospace Corp., El Segundo, Calif., June 1961.
2. P. Delahay and T. Berzins, *J. Am. Chem. Soc.*, **75**, 2486 (1953); P. Delahay, "New Instrumental Methods in Electrochemistry," Interscience Publishers, Inc., New York (1954).
3. A. J. Bard, *Anal. Chem.*, **33**, 11 (1961).
4. S. Wawzonek, E. W. Blaha, R. Berkey, and M. E. Runner, *This Journal*, **102**, 235 (1955).
5. D. S. Payne, *J. Chem. Soc.*, **1953** 1052.
6. A. A. Maryott and E. R. Smith, *Nat. Bur. Standards Circ. 514*, 1951.
7. H. J. S. Sand, *Phil. Mag.*, **1**, 45 (1901).
8. L. Pauling, "The Nature of the Chemical Bond," 3rd ed., Cornell University Press, 1960.
9. F. D. Rossini *et al.*, *Nat. Bur. Standards Circ. 500*, 1952.
10. W. H. Reinmuth, *Anal. Chem.*, **32**, 1514 (1960).
11. J. H. Hildebrand and R. L. Scott, "The Solubility of Nonelectrolytes," 3rd ed., Reinhold Publishing Corp., New York (1950).
12. T. Berzins and P. Delahay, *J. Am. Chem. Soc.*, **75**, 4205 (1953).
13. R. Anderson, *ibid.*, **52**, 2712 (1930).
14. A. Besson and L. Fournier, *Compt. rend.*, **150**, 102 (1910).
15. S. W. Mayer, S. J. Yosim, and L. E. Topol, *J. Phys. Chem.*, **64**, 238 (1960).
16. W. M. Latimer, "Oxidation Potentials," 2nd ed., p. 363, Prentice-Hall, Inc. Englewood Cliffs, N. J. (1952).
17. H. L. Gruber, *J. Phys. Chem.*, **66**, 48 (1962).
18. A. Glassner, "The Thermochemical Properties of the Oxides, Fluorides and Chlorides to 2500°K," ANL-5750, Argonne National Lab., Argonne, Ill. 1958.
19. E. C. Potter, "Electrochemistry," 128ff, Cleaver-Hume Press Ltd. (1956).

Transference Numbers and Ion Association in Pure Fused Alkaline Earth Chlorides

Edward D. Wolf[1] and Frederick R. Duke

Institute for Atomic Research and Department of Chemistry, Iowa State University, Ames, Iowa

ABSTRACT

The transference number of the chloride ion was determined in pure fused $MgCl_2$, $CaCl_2$, $SrCl_2$, and $BaCl_2$ utilizing radioactive chloride ions in a porous quartz membrane cell. On the basis of a two-step dissociation for these salts, $MCl_2 \rightleftarrows MCl^+ + Cl^- \rightleftarrows M^{++} + 2Cl^-$, the extent of the second dissociation was predicted qualitatively from a consideration of the relative mobilities of the ions.

There is some controversy about the physical significance of Hittorf-type transference experiments in pure single component fused salts. It is obvious that ambiguity about the reference frame for the velocities of the ions could result, since in the pure fused salt the solvent, to which ion motion is generally referred, is absent. Indeed one might consider the phenomenon as electroosmosis, since experimentally there is no distinction. On this basis Sundheim (1) has extended conventional hydrodynamic equations of motion to describe the movement of the ions and has found that the transference numbers defined in the reference frame of the cell (*i.e.*, porous plug experiments) can be expressed in terms of partial viscosities of the ions.

Laity (2) has discussed the conceptual difficulties of defining transference numbers in pure single component fused salts. The idea conveyed is that the conventional porous plug transference experiments do indeed measure a property of the salt, but the significance of this property has not yet been clarified. However, Esin *et al.* (3) in a short review expressed the view that there is no basis for considering it impossible in principle to measure transference numbers in pure single component fused salts using the porous plug method.

In the present paper the transference number measured with respect to the porous plug will be interpreted as a measure of the mobility of the ion relative to the salt immobilized at the membrane surfaces. Further comments on transference numbers in pure fused salts will be reserved for a future publication.

The purpose of this paper is to report the experimental values of the transference number of the chloride ion in pure fused alkaline earth chlorides and then to infer certain structural properties (*i.e.*, association) of the melts.

Experimental

Materials.—"Baker Analyzed" reagent grade alkaline earth chloride hydrates were recrystallized

[1] Present address: Department of Chemistry, Princeton University, Princeton, New Jersey.

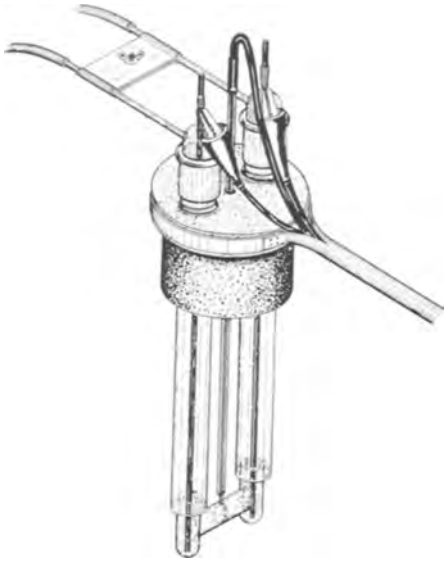

Fig. 1. Cell holder and cell

and dried under vacuum to remove surface water and some hydration water. Complete dehydration was realized for barium, strontium, and calcium chloride during the course of the transference experiments during which a dry argon atmosphere covered the salt at all times. Vacuum fusion analyses (4) after sample runs indicated a total oxygen content (calculated as MO) of less than 1 mole % for each of these salts.

Pure anhydrous magnesium chloride was prepared by vacuum sublimation of the chloride (near 800°C) away from the dehydration impurities. Similar vacuum gas analyses gave an oxygen contamination of less than 0.5 mole % MgO.

Radioactive salts were prepared in the same manner except that prior to recrystallization a predetermined amount of HCl^{36} was added to the aqueous solution.

Apparatus.—A Vycor cell holder which extended about 10 in. into an upright tube furnace was used to support the quartz transference cell, Fig. 1. This arrangement allowed for a dry inert atmosphere over the salt at all times. The construction of cells and the porosity reduction treatment of the quartz disks have been described previously (5). Spectroscopic graphite rods 12 in. in length and ⅛ in. in diameter were used for the electrodes.

The 230v furnace was controlled by a Bristol Electronic Controller sensitized by a Chromel-Alumel thermocouple.

Initially a Heathkit Model PS-5 variable voltage regulated power supply served as the d-c source. In some of the later work a full-wave selenium rectifier in conjunction with a pi-section filter circuit was employed. A silver coulometer was used to determine the charge passed through the cell.

A Model 181A Nuclear-Chicago Decade Scaler and a Tl Dual Timer were used with a Tracerlab TGC-1 Geiger-Mueller tube for determining the beta activity.

Procedure.—The anode and cathode compartments were filled with inactive and radioactive salts, respectively. In the case of the magnesium chloride experiments the filling of the cells was done in a dry box followed by a rapid transfer to the cell holder through which dry argon was flowing. The cell was attached to the cell holder with small Nichrome springs and the entire assembly lowered into the furnace. After the desired temperature was reached and sufficient time allowed for the salt to come to equilibrium temperature, the graphite electrodes were lowered into the melt, and a measured d-c current was passed through the cell. The electrolysis time varied from 500 to 2000 sec depending on the current used. Generally a total charge of approximately 100 coulombs was employed. After electrolysis the electrodes were lifted out of the melt and the cell was removed from the furnace to cool and freeze quickly. The dry argon flush was continued during the cooling process. The cell was then split carefully at the disk so as not to contaminate the anolyte with the more radioactive catholyte salt. The electrolyte in both parts was dissolved in water. The anolyte weight was found by weighing the half cell before and after the salt was dissolved with corrections made for adsorption of the salt by the electrode. The solutions were buffered below *p*H 10 with ammonium acetate and ammonium hydroxide, and the chloride ion was precipitated with excess silver nitrate. Three samples from each anolyte and catholyte were prepared for counting. Standard coincidence, self-absorption, and background corrections were made and the specific activities of the samples recorded.

To be consistent with the operational definition of transference numbers all conditions of the experiment must be referred to the disk. It was discovered during the experiments that the standardized Pt, Pt-Rh thermocouple did not sense the rather large temperature rises within the disk even though it was in contact with the cell directly above the disk. In order to follow the temperature of the disk a fading element Pyro Micro-Optical Pyrometer was mounted directly above the furnace. Readings were taken by focusing on the disk through the small thermocouple well in the top of the cell holder. In a few cases in which the membrane porosity had been substantially reduced, arcing was observed in a few "hot" spots in the disk. However, for most experiments the heating was moderate (0-50°C, with no arcing) and uniform throughout the disk. Cell resistances varied from 100 to 1000 ohms and the current was generally 100 ma; however, even a sixfold variation of 50-300 ma caused no appreciable change in the equivalents of Cl^- ion transported. The temperature of the disk varied linearly with the power dissipation within the disk which was usually less than 5w.

Previous transference experiments have been done with little or no consideration for this dissipation of energy within the disk. Lunden (6) did attempt to measure it by wrapping the leads of a small thermocouple around the disk with the thermocouple in contact with the outer surface of the cell. It is reasonable to assume similar heating in Pyrex disks. Experiments with Pyrex cells in which a high current density was maintained near the softening point of Pyrex should be viewed with

this in mind. Under extreme heating the fused Pyrex glass would act as an ion exchange medium exhibiting only cationic conduction.

Diffusional and viscous flow due to gravity can play a major role in the experimental error of the data. However, for sufficiently fine disks, blank runs for diffusion and experiments in which hydrostatic heads of several millimeters were used, indicated negligible corrections for these effects during the short duration of each transference experiment.

Results and Discussion

For most uni-univalent molten salts complete dissociation is generally assumed. However, for molten salts containing multivalent ions incomplete dissociation (or association) may occur. Consider possible reactions for the alkaline earth chlorides in the molten state

$$\begin{array}{l} MCl_2 \rightleftarrows MCl^+ + Cl^- \quad \alpha_1 \\ \quad\quad\uparrow\downarrow \\ \quad\quad M^{++} + Cl^- \cdot \alpha_2 \end{array} \qquad [1]$$

There are three species, M^{++}, MCl^+, and Cl^-, to which transference numbers, t_{++}, t_+, and t_-, may be assigned.

The equivalents of chloride ion transferred from cathode to anode compartment during a radioactive chloride traced electrolysis of a pure fused alkaline earth chloride can be shown to be

$$m = (C_a/C_c)(W_a/M) \qquad [2]$$

where C_a and C_c are the specific activities of the anolyte and catholyte salts, respectively, at the end of the experiment, W_a is the weight of the salt in the anode compartment at the end of the experiment, and M is the equivalent weight of the salt.

Cathodic migration of radioactive chloride was not observed in experiments in which the radioactive salt was initially in the anode compartment. This does not exclude the existence of the MCl^+ ion. On the contrary this is consistent with rapid equilibration of the MCl^+ ions with its chloride ion environment. The only conditions required are that the rate of exchange of Cl^- ions is rapid with respect to the time required (a few seconds) for the ion to pass through the disk and that $t_- > t_+$. The first condition is satisfied by the very nature of these fused salts. Had the last condition been reversed (*i.e.*, $t_- < t_+$) then anodic migration of radioactive chloride would not be observed. And finally if $t_- = t_+$ the radioactive tracer would not migrate, other than by diffusion, from either compartment. Thus the net motion of the chloride ion may be described by defining the net equivalents of chloride ion transferred as

$$m = t_-Z - t_+Z \qquad [3]$$

where Z is the number of Faradays of electricity passed through the cell.

The experimentally determined quantity, m/Z, is listed in Table I for each of the four alkaline earth chlorides over the indicated temperature range. Included also are values obtained from the data of Lunden (6) for $ZnCl_2$ and Duke and Laity (7) for $PbCl_2$. Although the m/Z values are reported as temperature independent, it should be mentioned that a slight linear increase of m/Z with temperature was observed for $CaCl_2$.

The probability of existence of doubly negative vacancies in the liquid seems small with univalent anions present. On this basis, if the mobility of the M^{++} ion is assumed to be negligible in comparison with the mobilities of the MCl^+ and Cl^- ions, then the relative concentrations of the ions may be estimated. For the mobility of the MCl^+ ion satisfying the condition $u_-/2 < u_+ < 2u_-$, values of the degree of dissociation for the reaction, $MCl^+ \rightleftarrows M^{++} + Cl^-$, were found to range between zero and unity as shown in Table I. Dissociation increased for each salt progressively down the Group II_A chlorides. One may conclude from the small value found for $ZnCl_2$ that an appreciable concentration of associated $ZnCl_2$ molecules exists in the melt. Equivalent conductivity and viscosity data argue in favor of this conclusion also. The dissociation for $MgCl_2$ was somewhat greater than for $ZnCl_2$, and the dissociation for $PbCl_2$ was approximately that found for $BaCl_2$.

Degrees of dissociation for the alkaline earth chlorides have been predicted by Markov and Delimarskii (8). From a consideration of a semi-empirical expression for the electrical conductivity and the rather drastic assumption that the chloride ion will have the same mobility in the corresponding states (*i.e.*, in the neighborhood of the melting points) for the different salts, they conclude that $BeCl_2$ is mostly molecular while $BaCl_2$ exists mainly as Ba^{++} and Cl^- ions with about 30% of the Ba^{++} ions associated as $BaCl^+$. While their results are compatible with those proposed in this paper, the

Table I. Chloride transference numbers and per cent dissociation in fused alkaline earth chlorides

Salt	No. of experiments	m/Z	t_-††	$\alpha_2 \times 100$ Case I $u_+ = u_-/2$	Case II $u_+ = u_-$	Case III $u_+ = 2u_-$	Temp. range, °C
$ZnCl_2$* (6)		0.27 ± 0.08**	0.64	0	27	55	435-673
$MgCl_2$	6	0.52 ± 0.04	0.76	23	52	73	730-920
$CaCl_2$	29	0.58 ± 0.09	0.79	31	58	76	780-1100
$SrCl_2$	19	0.74 ± 0.07	0.87	54	74	86	880-1165
$BaCl_2$	15	0.77 ± 0.09	0.89	59	77	88	960-1100
$PbCl_2$† (7)		0.76 ± 0.01	0.88	57	76	87	565-635

* Tracer method.
** Standard deviation errors.
† Bubble-cell method.
†† Calculated as MCl^+ and Cl^- from the experimental data.

means by which they were obtained are questionable.

In conclusion, analogous dissociation could be predicted by assuming Stokes' law and effective ion radii for the singly charged species after setting $u_{++} \doteq 0$. However, the use of Stokes' equation for describing the motion of ions in fused salts is fundamentally unsound even though order of magnitude agreement is generally found between observed and calculated values.

Manuscript received May 1, 1962; revised manuscript received Oct. 23, 1962. Work was performed in the Ames Laboratory of the U. S. Atomic Energy Commission, Contribution No. 1142.

Any discussion of this paper will appear in a Discussion Section to be published in the December 1963 JOURNAL.

REFERENCES

1. B. R. Sundheim, Private communication.
2. R. W. Laity, *J. Chem. Ed.*, **39**, 67 (1962).
3. O. A. Esin, G. A. Teterin, and I. N. Zakharov, *Zhurn. Fiz. Khim.*, **33**, 1887 (1959).
4. V. M. Horrigan, V. A. Fassel, and J. M. Goetzinger, *Anal. Chem.*, **32**, 787 (1960).
5. F. R. Duke and A. L. Bowman, *This Journal*, **106**, 626 (1959).
6. A. Lundén, U.S.A.E.C. Rept. IS-114, April 1960.
7. F. R. Duke and R. W. Laity, *J. Phys. Chem.*, **59**, 549 (1955).
8. B. F. Markov and Yu K. Delimarskii, *Ukrain. Zhurn. Khim.*, **19**, 255 (1953).

Electrochemistry and Reactions in Molten Li_2SO_4-Na_2SO_4-K_2SO_4

K. E. Johnson[1] and H. A. Laitinen

Department of Chemistry and Chemical Engineering, University of Illinois, Urbana, Illinois

ABSTRACT

Sulfur and oxide are produced by electroreduction of the solvent at 550° whereas active metals, *e.g.*, Mg, yield sulfide and oxide ions. Current-voltage curves of dilute solutions of heavy metal sulfates show reduction waves corresponding to the formation of either (*a*) metal or (*b*) metal sulfide and oxide, the course of the reaction apparently being determined by the solubility of the sulfide. For the case (*a*), an electromotive force series on a molality scale was established for temperatures between 550° and 580° as follows: Pd(II), Rh(III), Cu(II), Ag(I), Cu(I), Co(II) [Pd(II) being the strongest oxidizing agent]. The properties of solutions of higher transition metal oxides in the sulfate melt and the electrolysis of oxyanion melts in general are discussed.

Considerable attention has been given to the properties of molten halide systems in recent years, but the basic chemistry of common oxyanion salts in the molten state is not well known. The range of thermal stability of nitrates and carbonates is relatively small, but alkali sulfates are stable in air to 800° (1) and were expected to contain less complex species than phosphates, borates, and silicates. Thus, sulfate melts appeared to be convenient systems for electrochemical studies and might provide information on the contact process and the possible production of sulfuric acid from metal sulfates and steam (2).

The relative thermal decomposition temperatures of a number of divalent metal sulfates have been determined by thermogravimetric and differential thermal analysis (3); the range of 537° for $FeSO_4$ to 1374° for $SrSO_4$ suggested that many metal ions could be studied in mixed alkali sulfate solvents. All of the data on thermal stability can be explained in terms of the electronegativities and crystal radii of the cations (4).

Sulfate melts have been employed to set up an electrode reversible to oxide ions (4, 5). Flood, Førland, and Motzfeldt (6) obtained satisfactory results with the system Na_2SO_4-Na_2CO_3 in equilibrium with a constant CO_2 pressure, oxide-ion activity being given by $a_{O2-} = Ka_{CO3^{2-}}/p_{CO_2}$. This is one example of an acid-base equilibrium in melts; other relevant examples are the formation of PO_4^{3-} and SO_3 from PO_3^- and SO_4^{2-} (5) and of SO_3 and Al_2O_3 from Al(III) and Na_2SO_4 at 900° (7). In this connection it was surprising to be able to form stable solutions of Cr(III) and Fe(III) in the ternary alkali sulfate at 550°, but this stability could merely be a consequence of a lower temperature. Hill *et al.* (8) used the system $Pt/O_2/O^{2-}$ in Li_2SO_4-K_2SO_4 at temperatures of 600°-700° to measure standard formation potentials of various metal oxides.

Pushkareva (9), in the course of studying the effect of sulfate on the current efficiency of magnesium production from carnallite melts, observed that various compounds of sulfur yield the element when added to the system, either by thermal decomposition (*e.g.*, sulfite, thiosulfate) or by reaction with dissolved magnesium (sulfate). The sulfur formed dissolved to give a blue color detectable at 0.03 wt % S, but it slowly distilled from the melt. Measurements of the double layer capacity at Mo in this system (NaCl-KCl-$MgCl_2$-$MgSO_4$) as a function of potential (10) showed two desorption peaks and the nature of the curve was ascribed to the presence of surface active polymers S_n.

[1] Present address: Department of Chemistry, Sir John Cass College, Aldgate, London E.C.3., England.

Very recently, Liu (11) has made electrode potential measurements in Li_2SO_4-K_2SO_4 and has shown that certain metals, *e.g.*, Ni, reduce SO_4^{2-}. Andrieux (12) implied that certain metal sulfates yield metals on electrolysis of melts containing them, whereas others yield sulfites or sulfides. Similar phenomena have been observed with borate (12), phosphate, and silicate melts (13).

The present study concerns the fundamental electrochemical properties of one sulfate melt as shown by current-voltage curves and emf measurements on the Li_2SO_4-$NaSO_4$-K_2SO_4 system. Some simple reactions are discussed qualitatively.

Experimental

Reagent grade chemicals were used. The solvent was a mixture of 78% Li_2SO_4, 8.5% Na_2SO_4, and 13.5% K_2SO_4 with mp 512.[2] Its preparation has already been described (15) except for the addition of a few milligrams of potassium pyrosulfate to the melt to scavenge traces of oxide, excess pyrosulfate decomposing to sulfate and sulfur trioxide gas. $NiSO_4$ and $CoSO_4$ were prepared as previously described (15), and $PbSO_4$ and Ag_2SO_4 were obtained by double decomposition reactions.

The sulfate content of a compartment was determined by exchanging hydrogen ions for cations through Amberlite C9-120 and titrating with barium chloride solution using alizarin red S as indicator (16). Molarities and mole fractions were calculated using a density value of 2.13 g/ml estimated from the data of Jaeger and Kahn (17).

Two furnaces were used: a Hoskins pot furnace (Hoskins Manufacturing Company, Detroit, Michigan, Type FD 104) and a Hevi-Duty split-tube furnace (Hevi-Duty Electric Company, Milwaukee, Wisconsin, Type M-3012-S). The latter was mounted on pulleys in a steel frame and counterbalanced with two large weights so that it could be raised or lowered easily as well as opened. An electrolysis beaker was supported on glass wool in a glass envelope, itself suspended by its ground glass flange in a copper cooling jacket. A head for electrodes and connections to vacuum and argon lines fitted the flange (18). The method of compartmenting an electrolyte and details of the remaining equipment are described elsewhere (19).

Results and Discussion

Reduction of sulfate.—Electrolysis of the solvent at 550° between two large platinum electrodes at a current density of ~5 $\mu a/cm^2$ yielded a small quantity of sulfite but mainly sulfur and oxide in the cathode compartment. It was verified that sulfur dissolves to some extent in a molten sulfate even when added in air. Further, sodium sulfite yielded sulfur and sulfur dioxide (*a*) when heated in a closed tube or, (*b*) added to a molten sulfate or, (*c*) mixed with sulfate and heated to melting. Any significant quantity of sulfur appeared as a blue color rapidly turning brown.

The addition of magnesium powder to the solvent produced considerable darkening and sulfide and a little sulfur were found in the cooled product. The solvent was also reduced by Fe, Cd, Ni, Zn, Tl, and Pb metals, but not so rapidly.

[2] According to Akopov and Berman (14) this composition is a eutectic, but this was not confirmed in a recent x-ray measurement (15).

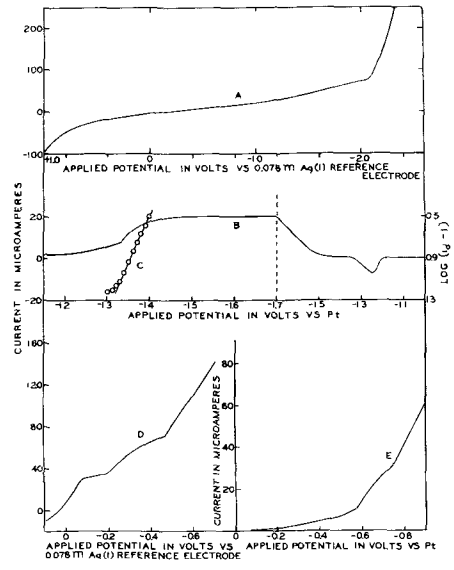

Fig. 1. Current-voltage curves of Li_2SO_4-Na_2SO_4-K_2SO_4 at 550°. A, B pure solvent; C potential *vs.* log (id-i) for solvent wave; D solution of K_2CrO_4; E solution of V_2O_5.

Liu (19), however, obtained sulfite and sulfide but not sulfur by electrolysis of Li_2SO_4-K_2SO_4 at 625°.

It then appears probable that sulfate is first reduced to sulfite which then disproportionates to yield sulfate and sulfide or is further reduced directly to yield sulfur. The disproportionation reaction no doubt would be temperature dependent. When a large quantity of metal is the reducing agent, sulfide is the most likely product because of a reaction such as

$$Mg + S \rightarrow MgS$$

Current-voltage curves.—Figure 1A shows a typical current-voltage curve of the pure solvent obtained with a Pt microelectrode. It was unchanged by bubbling with argon, indicating the absence of electroactive dissolved water or oxygen. The limiting anodic process was observed from macro-electrolysis to be the oxidation of sulfate

$$SO_4^{2-} - 2e^- \rightarrow SO_3 + \tfrac{1}{2}O_2$$

The limiting cathodic process was the reduction of sulfate. The first stage of this with a limiting current and "half-wave potential" of ~ −0.6v *vs.* Ag/Ag(I) is magnified in Fig. 1B. The slope of the *E vs.* log (*id-i*) plot for the wave (Fig. 1C) was about 0.110v whereas 2.303 *Rt*/**F** at this temperature is 0.163v. The shape of the curve on reversal of polarization resembles that obtained in the irreversible reduction of nitrate (20). It appears that the first stage of the reduction is irreversible, but the insoluble product on the electrode is capable of electro-oxidation.

Current-voltage curves of a number of dilute solutions of metal ions and oxides were also recorded. Platinum microelectrodes were used except in the case of V_2O_5 when W was substituted for Pt. Potassium chromate dissolved to give a red melt

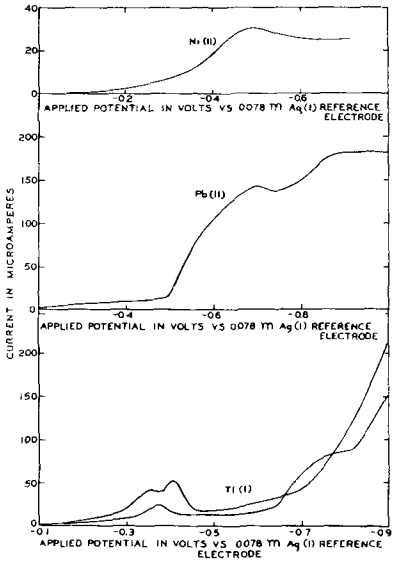

Fig. 2. Current-voltage curves of solutions in Li_2SO_4-Na_2SO_4 at 550°: $NiSO_4$ (top), $PbSO_4$ (center), Tl_2SO_4 (bottom).

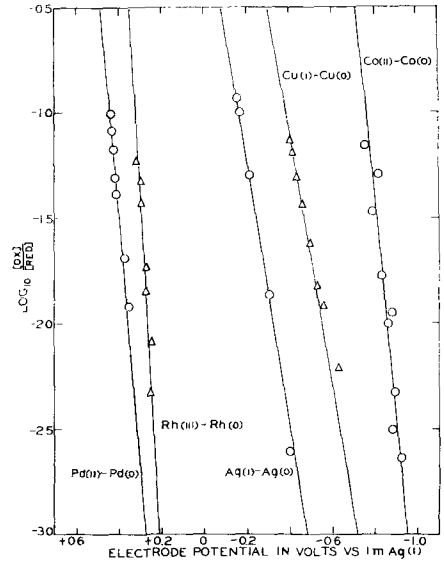

Fig. 3. Nernst equation plots for couples in Li_2SO_4-Na_2SO_4-K_2SO_4.

cooling to a yellow solid. This suggests that the equilibrium

$$2CrO_4^{2-} \rightleftharpoons Cr_2O_7^{2-} + O^{2-}$$

may be significant in this system (4). A multiple wave was obtained (Fig. 1D). Vanadium pentoxide dissolved to a brown solution and showed reduction waves at quite negative potentials (Fig. 1E). Solutions of Cr(VI), V(V), and Mo(VI) were reduced to Cr(III), V(IV) and Mo(IV) as insoluble oxides by Mg and Tl metals. Nickel sulfate and cobalt sulfate dissolved to red and violet solutions, respectively, and gave single waves (Fig. 2). Lead sulfate gave a colorless solution and double wave while thallous sulfate gave a colorless solution and a wave initially changing with time, the split peak at ~ −0.4v fell and a permanent wave appeared at ~ −0.7v (Fig. 2).

Emf measurements.—It was found that a silver coil could be anodized to silver (1) with 100% current efficiency and concentration cell measurements on the Ag/Ag(I) system were made in the mixed solvent at temperatures of 545°-585°. The Nernst relation

$$E = E^\circ + \frac{RT}{\mathbf{F}} \ln \frac{[Ag(I)]}{[Ag(O)]}$$

was obeyed at the various temperatures for concentrations of 10^{-3} to 10^{-1}M. Thus any activity coefficient term is constant. The theoretical line and experimental points for 550° are shown in Fig. 3. The solutions of silver (1) were colorless, but in time the glass in contact with them developed a brown color with violet fluorescence. This can be ascribed to exchange of silver and sodium ions with subsequent discharge and neutralization to form silver atoms in dispersion (21, 22). The rate of this migration was not sufficient to affect the validity of measured concentrations so that silver (I)-silver (0) could be used as a reference couple in other emf studies with confidence.

A platinum foil was stained brown after long contact with the solvent and usually took up a potential of ~ −0.2v *vs.* Ag/Ag(I). It was used as a reference electrode only in exploratory work, the potential-determining process being unknown.

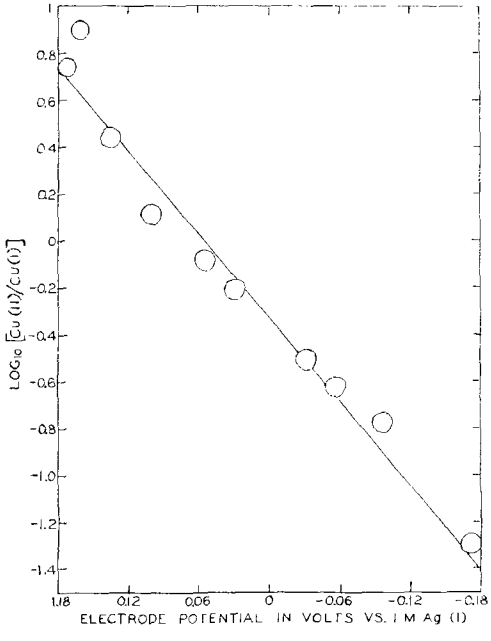

Fig. 4. Nernst equation plot for Cu(II)/Cu(I) in Li_2SO_4-Na_2SO_4-K_2SO_4 at 575°.

Palladium, rhodium, copper, and cobalt were also anodized to palladium (II), rhodium (III), copper (I), and cobalt (II) and copper (I) was oxidized to copper (II) at a palladium foil anode, all with close to 100% current efficiency. Electromotive forces as a function of concentration were measured *vs.* a silver (I)-silver (0) reference electrode and the Nernst relation was found to hold in all cases. Theoretical lines and experimental points are shown for this in Fig. 3 and 4. Standard electrode potentials (E°) for these systems with respect to silver (I)-silver (0) were calculated on three concentration scales and are summarized in Table I. This may be done either by correcting all measurements to unit

Table I. Electromotive force series in molten Li_2SO_4-Na_2SO_4-K_2SO_4

Couple	Temperature, °C	$E°_{m,V}$	$E°_{M,V}$	$E°_{X,V}$
Co(II) - Co(0)	550	−0.689	−0.662	−0.764
Cu(I) - Cu(0)	580	−0.220	−0.220	−0.220
Ag(I) - Ag(0)	545-585	0	0	0
Cu(II) - Cu(I)	575	+0.055	+0.110	−0.099
Rh(III) - Rh(0)	575	+0.370	+0.407	+0.267
Pd(II) - Pd(0)	580	+0.518	+0.546	+0.441

concentration of silver (I) (since activity coefficients are incorporated in $E°$) or from relations such as

$E°_{Rh(III)/Rh(0)} = E_{cell}$ when $[Rh(III)] = [Ag(I)_{Reference}]$[3]

The mean values of the standard potentials had deviations of 0.004v except in the case of cobalt (II)-cobalt (0) when the deviation was 0.017v. The electromotive force series obtained is very similar to Liu's (11) and a close relationship between displacement reactions in various melts is suggested by the values of the equilibrium constants calculated from emf data and presented in Table II.

The part played (in this relationship) by coordination of the transition metal ions is not yet clear: palladium (II) gives brown solutions indicating square planar coordination in chloride and sulfate melts, cobalt (II) is tetrahedrally coordinated in chloride and sulfate melts (15) and shows the greatest diversity of K values. The coordination in the pink rhodium (III) and green copper (II) sulfate solutions is under investigation.

Attempts to generate a number of other metal ions from the metals coulometrically in this solvent were unsuccessful because the metals, *e.g.*, Ni, Cd, reduced sulfate to insoluble sulfides. The criterion for the reduction of sulfate by a metal is not merely that the reduction of the metal sulfate ($NiSO_4$) occurs at a potential close to the sulfate potential but rather than the metal sulfide has a low solubility product. The oxides of the metals studied are more soluble than the sulfides and so do not determine the course of reaction.

Thus, current-voltage curves of metal ions in sulfates represent either the process

$$M^{z+} + ze^- \rightarrow M$$

or a process such as

$$SO_4^{2-} + 5Ni^{2+} + 8e^- \rightarrow NiS + 4NiO$$

Some idea of the likely course of reaction of a few metals is given by calculations of the cell potentials of the over-all processes. Free energy data for solids at 25° (25) have been used to compile the relative values given in Table III. These values do suggest that silver will be stable in contact with sulfate, that sodium and zinc will reduce it, and that the reaction of lead and cobalt will probably be very sensitive to conditions. In this connection, cobalt appears to be fairly stable in contact with the ternary melt at 550°.

The results given here and the findings of other workers discussed previously suggest that the electrolysis of oxy-anion melts in general can be represented by the following scheme written for a typical ion XO_n^{m-}:

$$XO_n^{m-} \rightleftharpoons XO_{n-1}^{2-m} + O^{2-}$$

$$XO_{n-1}^{2-m} + (2n - m)e^- \rightarrow X + (n - 1)O^{2-} \quad \text{at cathode}$$

$$O^{2-} - 2e^- \rightarrow \tfrac{1}{2}O_2 \text{ at anode}$$

$$(2n + q)M^{p+} + pXO_n^{m-} + p(q + 2n - m)e^- \rightarrow M_qX_p + nM_2O_p \text{ for certain M.}$$

Acknowledgment

The authors are grateful to the Office of Ordnance Research and the Army Research Office (Durham) for financial support of this work.

Manuscript received Aug. 9, 1962; revised manuscript received Oct. 29, 1962. This paper was prepared for delivery before the Los Angeles Meeting, May 6-10, 1962.

Any discussion of this paper will appear in a Discussion Section to be published in the December 1963 JOURNAL.

REFERENCES

1. V. I. Spitsyn and V. I. Shostak, *Zhur. Obschei Khim.*, **19**, 1801 (1949).
2. A. B. Suchkov, B. A. Borok, and Z. I. Morozova, *Zhur. Priklad. Khim.*, **32**, 1616 (1959).
3. A. G. Ostroff and R. T. Sanderson, *J. Inorg. Nucl. Chem.*, **9**, 45 (1959).
4. H. Flood and T. Førland, *Acta Chem. Scand.*, **1**, 592, 781 (1947).
5. H. Lux, *Z. Elektrochem.*, **45**, 303 (1939); **52**, 220 (1948); **53**, 41 (1949).
6. H. Flood, T. Førland, and T. Motzfeldt, *Acta Chem. Scand.*, **6**, 257 (1952).

Table II. Equilibrium constants of reactions in molten salts

Reactants	(This study) $\log_{10} K_x$	(This study) $\log_{10} K_m$	Li_2SO_4-K_2SO_4 at 625°C (11) $\log_{10} K_m$	LiCl-KCl at 450°C (23) $\log_{10} K_x$	NaCl-KCl at 700°C (24) $\log_{10} K_x$
Ag + Co(II)	−9.37	−8.45	—	−4.94	−5.35
Ag + Cu(I)	−1.30	−1.30	−1.13	−1.49	−1.35
Ag + Rh(III)	+4.77	+6.61	+6.52	—	—
Ag + Pd(II)	+5.21	+6.13	+6.07	+5.90	—

Table III. Decomposition potentials of sulfates

Net reaction	M = Na	Zn	Pb	Co	Ag
$MSO_4 \rightarrow M + SO_3 + 1/2\,O_2$	−4.65	−2.60	−2.28	−2.03	−1.27
$4MSO_4 \rightarrow 4MO + S + 3SO_3 + 3/2\,O_2$	−4.27	−1.90	−2.38	−1.87	−2.26
$5MSO_4 \rightarrow 4MO + MS + 4SO_3 + 2\,O_2$		−1.82	−2.34	−1.80	−1.96

7. K. Grjøtheim, T. Halvorsen, and S. Urnes, *Can. J. Chem.*, **37**, 1170 (1959).
8. D. G. Hill, B. Porter, and R. S. Gillespie, Jr., *This Journal*, **105**, 408 (1958).
9. S. A. Pushkareva, *J. Applied Chem. U.S.S.R.*, **32**, 1079 (1959).
10. S. A. Pushkareva and E. A. Ukshe, *Doklady Akad. Nauk. S.S.S.R.*, **124**, 370 (1959).
11. C. H. Liu, *J. Phys. Chem.*, **66**, 164 (1962).
12. J. L. Andrieux, Colloq. intern. centre natl. recherche sci. (Paris) 39, Electrolyse C7-C10 (1952).
13. S. S. Hsu, P. N. Yocom, T. C. C. Cheng, K. B. Oldham, C. E. Myers, K. Gingerich, C. H. Travaglini, J. C. Bailar, Jr., H. A. Laitinen, and S. Swann, Jr., Final Report, Contract N6 ori-071(50), Project NR 052-341, Office of Naval Research, Department of the Navy (1958).
14. E. K. Akopov and A. G. Bergman, *Zhur. Neorg. Khim.*, **2**, 193 (1957).
15. K. E. Johnson and T. S. Piper, *Disc. Faraday Soc.*, **32**, 32 (1962).
16. J. S. Fritz and M. Q. Freeland, *Anal. Chem.*, **26**, 1593 (1954).
17. F. M. Jaeger and J. Kahn, *Proc. Acad. Sci.* Amsterdam, **19**, 381 (1916).
18. G. J. Hills and K. E. Johnson, *This Journal*, **108**, 1013 (1961).
19. H. A. Laitinen and B. B. Bhatia, *Anal. Chem.*, **30**, 1995 (1958).
20. H. A. Laitinen and H. S. Swofford, Jr., To be published.
21. W. Eitel, The Physical Chemistry of the Silicates, p. 173, University of Chicago Press, Chicago (1952).
22. W. A. Weyl, J. H. Schulman, R. J. Ginther and L. N. Evans, *This Journal*, **95**, 70 (1949).
23. H. A. Laitinen and C. H. Liu, *J. Amer. Chem. Soc.*, **80**, 1015 (1958).
24. S. N. Flengas and T. R. Ingraham, *This Journal*, **106**, 714 (1959).
25. National Bureau of Standards Circular No. 500 (1952).

Surface Studies on Passive Iron

Norvell E. Wisdom, Jr.[1] **and Norman Hackerman**

Department of Chemistry, University of Texas, Austin, Texas

ABSTRACT

Surfaces of zone-refined iron in sulfate solutions of pH between 1 and 15 have been studied by measurement of electrode capacity and by chronopotentiometry. Capacities were measured as a function of potentiostatically controlled average electrode potential by a recently developed pulse technique. The capacity curves thus obtained were approximately plateaus over potential regions in which oxygen or hydrogen evolution occurred at >10 μa cm^{-2}. In intermediate potential regions the curves had shallow minima as low as 4 μfarad cm^{-2} near the potential region of oxygen evolution and peaks with maxima as great as 165 μfarad cm^{-2} near the potential region of hydrogen evolution. The capacity values depended on the history of the potential variations applied to the electrodes. Chronopotentiometry indicated the presence of at least two sorts of reducible surface material under most of the experimental conditions. Results are interpreted to indicate the presence of a surface material with properties which depend on the electrode potential and solution environment during its formation and which are significantly different from those of any known crystalline, stoichiometric iron oxide. Such properties of the material of a passive iron surface may be reasonably explained by a previously presented hypothesis of a surface material formation sequence initiated by the adsorption of solution species.

Despite the lengthy history of the investigation of passive iron, no postulate to explain the nature of the passive surface has yet received sufficient experimental support to make it universally acceptable. A previous paper from this laboratory presented a hypothesis reconciling the two principal classical theories of the passivity, *i.e.*, the oxide film and adsorbate film theories (1). A series of further papers (2, 3) experimentally examining aspects of this hypothesis is continued in the present work, in which the surface of passive iron has been studied by measurements of electrode capacity and by chronopotentiometry. Although several previous capacity measurements on iron have been reported (3-12), they have been characterized by severe experimental difficulties, poor reproducibility, and consideration of only a very limited number of environments, usually aggressive ones. In this work solutions of a wide pH range have been used at a low temperature to include environments less aggressive toward iron than those usually considered. Good reproducibility has been obtained under most of the experimental conditions, and both the chronopotentiometric behavior of the electrodes and the capacity values obtained proved significantly different from most of the results previously observed in other environments. The results are believed to indicate a greater complexity in the passivation process than has generally been thought to be the case heretofore.

Materials, Apparatus, and Procedure

Water used in the experiments was distilled water distilled from alkaline permanganate in a block tin system. It had no contact with ion exchange resins

[1] Present address: Central Basic Research Laboratory, Esso Research and Engineering Company, Linden, New Jersey.

and had a specific resistance of $> 3 \times 10^6$ ohm-cm. Other chemicals used were of Analytical Reagent grade and were recrystallized from water if feasible. The electrodes were machined from a stock of zone-refined iron supplied by Battelle Memorial Institute. The analysis furnished with the material showed the following impurities: 10 ppm carbon, 23-28 ppm oxygen, 2 ppm nitrogen, and 0.1 ppm hydrogen. The cells used for pre-electrolysis and measurement were constructed entirely of Pyrex glass, platinum, and Teflon.

Potentials were measured with respect to the half cell: Hg(l); Hg_2SO_4(s); Hg_2SO_4 (sat'd sol'n), K_2SO_4 (sat'd sol'n) with the use of a Luggin capillary and a potentiometer. The reference cell was maintained at 25° during use. The measured potentials were converted to the standard hydrogen scale at 25° by adding 0.65v. This value for the potential of the reference half cell was determined by comparison with a saturated calomel half cell. The error due to neglecting the thermal potential and junction potentials should be less than 0.01v.

The electrodes were mounted during use to expose only a cylindrical surface 2-4 mm in both length and diameter. When inserted into the test cell, the electrode surface was centered inside a cylindrical platinum gauze polarizing electrode 4 cm in diameter and 7 cm long.

The electrical apparatus and circuit used are shown schematically in Fig. 1. A detailed description of the individual items of electrical equipment and of the construction of the cells, electrode mounts, and reference electrodes is available (13).

The electrodes were prepared for use by abrading with emery paper to a final mechanical finish of 4/0 grit and then electropolishing according to the method of Sewell *et al.* (14). Electrodes received a final electropolish for 8 to 15 sec immediately before they were inserted in the test solution. Fresh bath solution for this final electropolish was necessary for best reproducibility of capacities. However, the acid etch recommended in the original procedure was not generally used, since it had no effect on the steady values obtained. Its effect on kinetics is considered later.

Special care was taken to prevent contamination of the experimental systems by foreign substances. The use of grease was avoided entirely. All test solutions were pre-electrolyzed before use between platinum foil electrodes at a current density of ~25 ma cm^{-2} for 12-150 hr. No difference due to pre-electrolysis for more than 12 hr could be detected. The test solutions were saturated with flowing helium during use. The helium used was stated by the supplier (U.S. Bureau of Mines) to be of 99.99% purity and was used as supplied. All measurements were made at 4.5° ± 0.2°C unless otherwise noted.

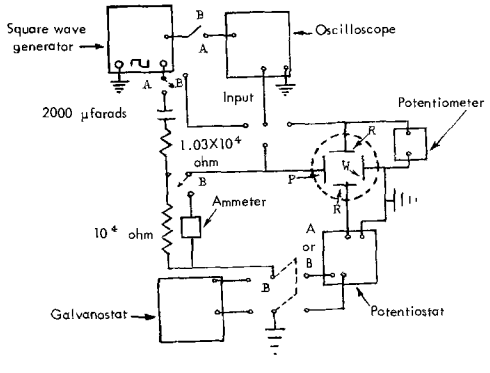

Fig. 1. Apparatus and circuit diagram; R, reference electrode; P, polarizing electrode; W, test electrode. A and B, switch positions.

Electrode capacities were measured by the method of Riney *et al.* (15). The current pulses required by this method necessarily effect some change in the potential of the electrode to which they are applied. Therefore no useful results could be obtained if a potentiostat were also connected directly to the electrodes, because the large current output induced from the potentiostat would violate the condition of constant total current between pulses required for the validity of the method. This difficulty was overcome by the use of a current-time function which averaged nearly to zero over times > 1 sec and by inserting a resistor between the potentiostat and the cell. The resistor partially decoupled the potentiostat from the current pulse system and slowed the instrument's response to rapid potential changes without severely affecting its ability to control average potential. A 480 sec^{-1} current pulse of 680 μa was usually used, and under these conditions the minimum satisfactory resistance was 10^4 ohm. This resistance limited the cyclic variations in potentiostat output to < 4 μa.

A comparison of this method of measuring capacity with the use of an impedance bridge or other charging methods has been given (15). In theory the method used here should be equivalent to a bridge method at infinite frequency, since the capacity is calculated from the instantaneous values of the slopes of a voltage-time curve on each side of a discontinuity in the applied current. In practice, of course, the initial slope cannot be measured exactly, and an average slope over approximately the first microsecond was used. A few attempts were made to use higher frequency current pulses. These appeared to give the same results, but the voltage variation becomes too small to measure conveniently with current pulses more frequent than ~5000 sec^{-1}.

Capacities were measured at frequent time intervals at constant potential until values steady for at least 5 min were obtained. This time interval was used as a criterion for "apparent equilibrium" in most cases because preliminary work indicated that values steady for this time would usually persist for an hour or more. At certain specific potentials, capacities drifted rather slowly for long times, and the times then used as criteria for apparent equilibrium will be stated individually later. The term equilibrium will be used for convenience to refer to all these steady states; its use is not intended to imply any thermodynamic significance.

The measured capacity values were converted to the specific capacity of the test electrode by dividing by its measured area (0.2-0.5 cm^2). No correction for roughness factor was attempted.

Electrode potential was measured as a function of time during galvanostatic charging. For determination of these charging curves, the switches in the

Table I. Composition of test solutions

	pH at 5°C
1.0*M* NaOH	14.5*
0.1*M* NaOH + 0.03*M* Na_2SO_4	13.6*
0.07*M* Na_2SO_4 + 0.05M H_3BO_3 + 0.002*M* NaH_2BO_3	7.9**
0.10*M* Na_2SO_4 adjusted to *p*H with H_2SO_4	2.2**
0.10*M* Na_2SO_4 + 0.025*M* $Na_2Cr_2O_7$ adjusted to *p*H with H_2SO_4	2.2**
0.50*M* H_2SO_4	1.0**

* Calculated from the data of Conway (18).
** Measured with a glass electrode.

circuit diagram (Fig. 1) were set to position B. The test electrode was polarized with the potentiostat to a desired potential and allowed to remain there for a sufficient length of time to give reproducible results as determined by preliminary experiments. Usually 5-10 min were sufficient. The electrode was then switched rapidly from the potentiostat to the galvanostat, which had been pre-set to deliver a known current. The potential-time display on the oscilloscope was recorded photographically. Calculations made from the photographs are considered in the presentation of results.

The composition and *p*H of the test solutions are shown in Table I. The *p*H of the four more acid solutions used was measured before and after use and found not to have changed. It is reasonable to assume that the two more alkaline solutions also did not change significantly in *p*H during use.

Results

As noted above, the theory of the capacity measurements requires pulses of current which are constant between discontinuities, but the use of potentiostatic control of average potential did not permit the current to be rigorously constant. Therefore an experimental check to demonstrate the minor effect of the unavoidable small fluctuations in current seemed desirable. For this purpose, the capacity measurements of Laitinen and Enke (16) on platinum in 1*M* $HClO_4$ at 25°C were repeated, except that platinum wires prepared by the method of Popat and Hackerman (17) were used rather than foils. The results of Laitinen and Enke for both ascending and descending potential traverses were reproduced within the precision limits they reported.

Preliminary experiments with iron showed that the environmental history of the specimens often had an important effect on the results. A particularly important influence was the exposure of the specimens in solution to certain potentials or potential regions. Consequently standard programs of potential variation were adopted. These are described below. The programs used, which involve initial polarization near one extreme of the potential range studied, were adopted both because they appeared to yield the most reproducible results and because of theoretical interest. In a few circumstances, the effects of variation from the standard programs were both reproducible and interesting, and such results will be given with individual specifications of conditions.

In each of the three alkaline solutions studied, two potential variation programs were used. In the first, designated as "after cathodic polarization," the electrode was polarized immediately after insertion into the cell to a potential 0.5-0.3v negative to the reversible hydrogen evolution potential for the solution. Any initial potential in this range produced the same final results, but more time was required for equilibration at less negative potentials. After the initial equilibration, the electrode potential was altered in 0.1v steps always in the anodizing direction until the desired final potential was reached. In the reverse, designated as "after anodic polarization," initial polarization of the electrode was to a potential at which oxygen evolution at >2 μa cm^{-2} occurred. Any such initial potential produced the same subsequent results. After this initial equilibration, the potential was altered in steps always in the cathodizing direction.

In the three acid solutions, initial polarization of the electrodes was always to an oxygen evolution potential. Again any potential of readily detectable oxygen evolution produced the same subsequent results. After the initial equilibration, the electrode potential was varied in a loop, first in steps always cathodizing, then in steps always anodizing back to the original potential. The negative boundary of the potential loop was a potential empirically determined so that 1 hr after reaching it the current required to maintain it was 10-100 μa cm^{-2} anodic. This was done so as nearly but not entirely to activate the iron. Polarization as little as 0.02v negative to this empirically selected potential resulted in loss of passivity of the electrodes within 5 min or less, and during such loss of passivity the electrode mount developed leaks and led to erratic results.

Measurement of the potential of an electrode during galvanostatic charging, as performed here, is of course a well-known procedure of both electroanalytical chemistry and previous studies of passivity. The general principles of interpretation of such measurements as presented by Delahay (19) are used in considering the present results.

The forms of the charging curves obtained under various conditions with a charging current of 1 ma cm^{-2} are shown in Fig. 2, parts (a) to (e). In the alkaline solutions the form of the charging curve varied as shown with the potential of the electrode before the beginning of the charging. No such variation occurred within the narrower range of initial potentials studied in the acid solutions. For convenience of reference, the various arrests, characterized by the potentials of their midpoints, are coded as shown in the figure. The arrest potentials for 1 ma cm^{-2} were polarized 0.1v more than those obtained with 0.01 ma cm^{-2} charging current. The total polarization is difficult to estimate, because current densities substantially less than 0.01 ma cm^{-2} produced such slow changes that the arrests were almost impossible to distinguish. A very rough estimate of 0.2v total polarization at 1 ma cm^{-2} may be made from the difference between the potential of the least negative arrest in charging in acid solutions and the potential at which activation of the

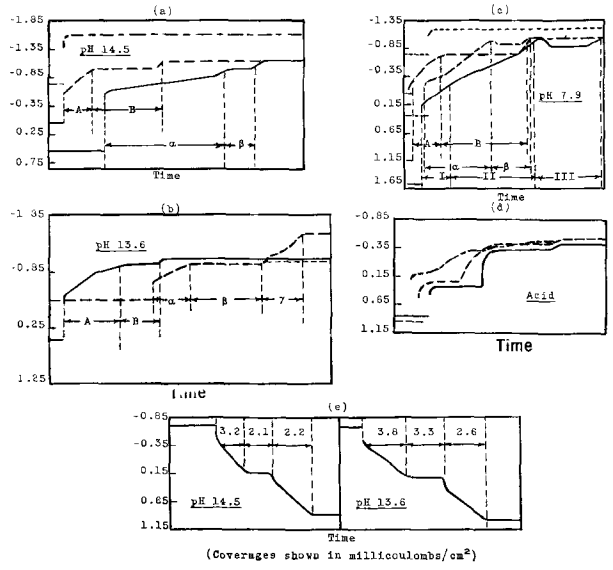

Fig. 2. Form of charging curves and arrest codes: (a) cathodic charging, pH 14.5; — - potentials < —0.60v from cathodic equilibrium; — — potentials between —0.55 and 0.05 from cathodic equilibrium; —— potentials > 0.15 from cathodic equilibrium or > —0.55 from anodic equilibrium; (b) cathodic charging, pH 13.6; — — potentials —0.65 to —0.15 from cathodic equilibrium, and with - - - all potentials > —0.65 from anodic equilibrium; —— potentials between —0.05 and 0.55 from cathodic equilibrium; (c) cathodic charging, pH 7.9; - - - - potentials < —0.45; — — potentials —0.45 to —0.05; — - potentials 0.25 to 1.25. —— potentials >1.35; potentials of 0.05 and 0.15 were intermediate, with an arrest at —0.80 and —0.85, respectively. All potentials are from cathodic equilibrium; (d) cathodic charging, acid solutions; — — pH 2.2; — - pH 2.2 + $Cr_2O_7^=$; —— pH 1.0; same from all initial potentials in range 0.65 to 1.85; (e) anodic charging pH 14.5 and pH 13.6. The charging current was ~ 1 ma cm^{-2} for all curves. The time scales are from 0.2 to 5 sec cm^{-1}. Voltages are referred to the NHE at 25°C. In parts (a) to (c) the potentials of the subcaptions refer to the potential of the electrode before charging curve was taken. The initial potentials before charging were reached after equilibration either at extreme cathodic or extreme anodic polarizations as indicated. The codes A, α, I, etc., are used in Fig. 3-6 to refer to various arrests. All ordinates are expressed in volts vs. NHE.

specimens apparently would have occurred, given sufficient time.

In the three alkaline solutions, the product of charging current density and the time length of the various arrests (charge) was independent of charging current density from 10 to 0.01 ma cm^{-2}. Also, both the charge and the potentials of the arrests were independent of stirring up to the maximum rate obtainable with a magnetic stirrer. For these reasons the arrests are ascribed to reactions limited in extent by creation or consumption of a surface material on the electrodes. The charge per unit area of electrode surface is denoted as surface coverage. In these solutions the charge in arrests did not change because of interruptions of the charging current for as much as a minute at any point during the charging.

In the three acid solutions, in contrast to the alkaline ones, the charge in arrests increased sharply with increasing charging current density and were poorly reproducible even at constant current density. Furthermore, in acid solutions at least part of the charge of the more negative arrest disappeared if the charging was interrupted after passing the less negative arrest. These phenomena are consistent with previous reports (2, 8) that once a small fraction of the coverage on iron in acid solutions has been destroyed, the remainder disappears without further charge consumption.

The surface coverages of the various arrests in cathodic charging in the alkaline solutions are shown in Fig. 3-5 as functions of the electrode potential before charging. The logarithmic ordinates were adopted for convenience, and no special implication in their use is intended. The values shown are averages of two determinations with average deviations of <10%. Electropolishing and repeating the potential variation program after each charging curve determination was necessary to obtain reproducible results. It is apparent from the form of the charging curves that in some cases the division between two arrests is fairly arbitrary, and this contributes to the relative imprecision of the coverage results as compared to the capacity values considered later.

Anodic charging curves were obtained in the two more alkaline solutions. With anodic charging the

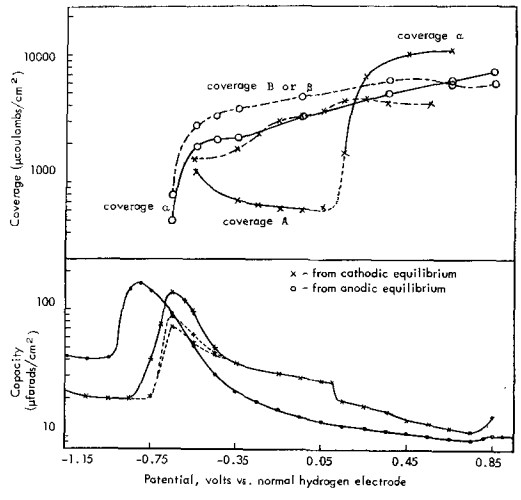

Fig. 3. Capacities and surface coverages in pH 14.5; × — values at potentials reached after cathodic polarization; O — potentials reached after anodic polarization. For the coverages, the values connected by the solid line are for arrest A or α; dashed line is for arrest B or β (see Fig. 2).

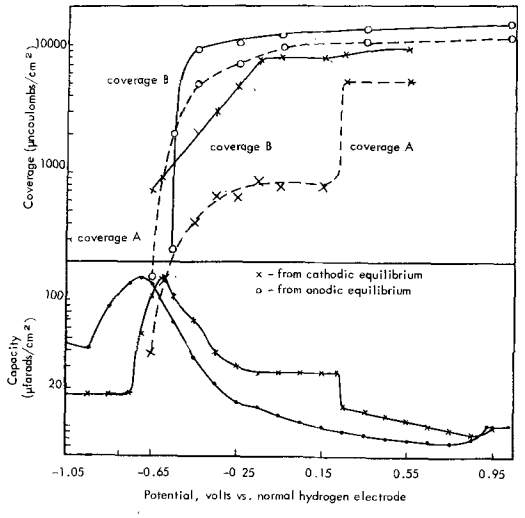

Fig. 4. Capacities and surface coverages in pH 13.6; × — potentials reached after cathodic polarization; O — potentials reached after anodic polarization. For the coverages, solid line is for arrest B or β; dashed line is for arrest A or α (see Fig. 2).

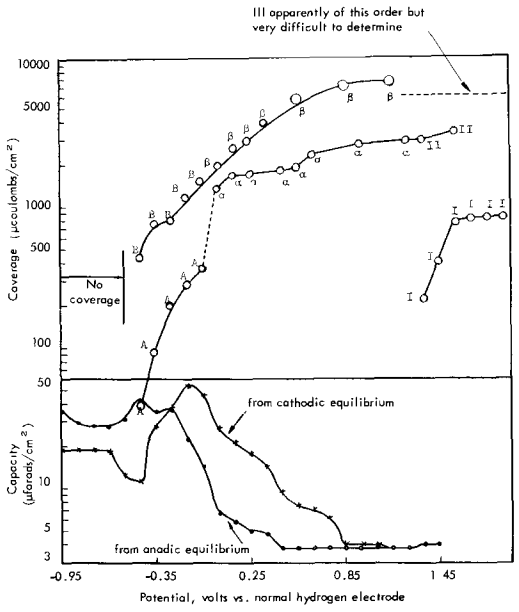

Fig. 5. Capacities and surface coverages in pH 7.9. For capacities: O — potentials reached after anodic polarization, and × — potentials reached after cathodic polarization. For the coverages, upper line is for arrest B, β, or III, middle curve is for arrest A, α, or II, bottom curve is for arrest I. All potentials were reached after cathodic polarization.

same curve was obtained from any initial potential more negative than those shown on the curve, and the remaining applicable portion of the curve was obtained in charging from any point shown on it, with allowance for polarization. Consequently the surface coverages corresponding to various arrests are shown with the form of the charging curves in Fig. 2.

The values of specific capacity in various solutions are shown as a function of electrode potential in Fig. 3-6. Again the use of logarithmic ordinates is for convenience only. The curves were drawn directly through the experimental points with no attempt at smoothing, and the details of the variation may not be significant. Except for the small potential region in pH 14.5 solution where individual runs are shown, each point on the capacity curves is the average of values obtained in at least three runs with different electrodes and batches of test solution each time. The average deviation of these values was generally less than 2% or 0.2 μf cm^{-2}, whichever is greater. Only for the potential region 0.1v or more negative to the capacity peak in runs after anodic polarization in the two more alkaline solutions was the deviation 5-6%. Capacity values, like surface coverages, were independent of stirring rate up to the maximum available with a magnetic stirrer.

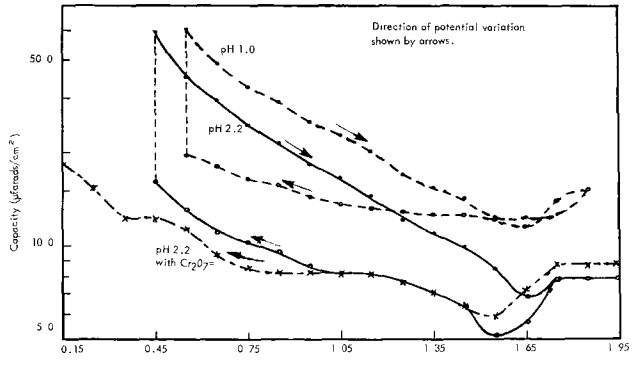

Fig. 6. Capacities in acid solutions. The lower dashed line is for pH 2.2 with added dichromate ion; the upper dashed line is for pH 1.0 solution; solid line is for pH 2.2 solution. Arrows show direction from which the potential of each capacity value was reached.

Certain qualitatively reproducible features of the kinetic behavior of the capacities and of the potential maintaining currents were noted during the capacity measurements. These are described below, as are the potentials at which deviations were made from the usual time used as a criterion for equilibrium of the capacity values.

Immediately after the initial polarization in runs after cathodic polarization, capacities of ~50 μf cm^{-2} were observed. The capacities declined steadily for about an hour to ~20 μf cm^{-2}. This value persisted for at least an additional hour and usually for several hours. One hour of steady capacity value was used as a criterion for equilibrium at these potentials. About half an hour was usually required to attain steady values in these runs at the most negative potential at which the capacity exceeded the value of the initial plateau region. Fifteen minutes was used as a criterion here, at the initial potential of runs begun from an oxygen evolution potential, and at the first potential >0.1v negative to the capacity peak in runs after anodic polarization. Steady values were not attained only at the negative boundary of the potential variation loop used in acid solutions. In this case the capacity value found after 1 hr at the boundary potential was used arbitrarily. At all potentials not noted above, equilibration of capacity values occurred within 10 min and often within 1 min after reaching the potential.

Outside the potential regions of gas evolution or rapid dissolution of iron, currents required to maintain potential were <5 μa cm^{-2}. The currents declined in magnitude for several hours at potentials where they were small, and no attempt to obtain equilibrium values was made. In all the solutions except that of pH 1, the currents were <0.1 μa cm^{-2} throughout a potential region of several hundred millivolts negative to the region of oxygen evolution. Currents for oxygen evolution were fairly reproducible, came to equilibrium quickly, and did not depend on the direction from which an oxygen evolution potential was approached. Currents for hydrogen evolution declined from initial values of ~300 to ~10 μa cm^{-2} during the initial equilibration in runs begun by cathodic polarization and depended greatly on the previous treatment of the electrode.

Several qualitative phenomena were noted in connection with cathodic polarization. If an electrode was treated anodically to produce a thick surface film, the change in current density with time at any potential negative to the capacity peak was much slower than on freshly electropolished electrodes. On the other hand, if an electropolished electrode was etched in dilute nitric acid in which the film formed during polishing is soluble (14) and inserted into the cell, unrinsed and with electrical contacts in place, the time required for decline of the current and equilibration of the capacity was considerably re-

duced. After the equilibration at cathodic polarization, the initial high currents could be restored by polarizing the electrode to any potential more positive than a critical potential. This critical potential corresponded to the potential of the first appearance of an arrest during cathodic charging. Finally, the capacity value during any short time interval during the equilibration time required at cathodic polarization was almost independent of potential within the region of the capacity plateau observed after equilibration.

Discussion

The general features of the variation of capacity with potential have been fairly well established for two groups of metals. One of these is the "clean-surfaced" group typified by mercury (20) and possibly also including platinum (17) and stainless steel (3). The other group includes aluminum and tantalum, which have been successfully treated by consideration of the growth of surface layers with properties like those of bulk oxide (21). From the results here it appears that iron cannot reasonably be assigned to either of these groups. The variation of capacity (and also of chronopotentiometric behavior) observed as a function of potential is much more complex than is expected from members of either of the two well-understood groups. No complete explanation of all the results observed here can be offered, but some of the inferences which can be drawn from them are discussed below.

The first potential region in runs after cathodic polarization is characterized in all three alkaline solutions by a capacity plateau at a value of 20 ± 3 μf cm^{-2}. This value is typical of double layer capacity values found on clean-surfaced metals on the cathodic side of the zero point of charge (20, 22). Also there is no arrest in cathodic charging to hydrogen evolution from this potential region, and most of the region is negative to the reversible potential for oxidizing iron to any possible compound (23). Thus it may be reasonably concluded that under these conditions the iron surface is free from extensive films and covered only with some hydrogen evolution intermediates.

The fall in potentiostat current associated with the attainment of equilibrium capacity values at extreme cathodic polarization must correspond to an increase with time of the overvoltage of the hydrogen evolution reaction. This is because no other process can reasonably account for the charge consumption observed ($\sim$1 coulomb cm^{-2}). Such an increase with time of the overvoltage of hydrogen evolution has been noticed several times before. It has been variously ascribed to the formation of surface hydrides, penetration of hydrogen into the metal, and adsorption of impurities leached from glass cells (9).

Although these causes of overvoltage increase may well contribute to the over-all effect, none of them seems particularly satisfactory for explaining all the effects noted here during cathodic polarizations. With a view toward a single simple explanation for all these effects, the following hypothesis is presented: From this work and others (14, 24), it seems apparent that reducible surface "coverages" form on iron during surface preparation by most techniques or by exposure of even clean surfaces to air or aqueous solutions. From Fig. 2-6, it appears that the coverages must be reduced prior to, or at least during, hydrogen evolution. It is proposed that (i) reduction of the film material in solutions in which it is insoluble produces initially a layer of disordered surface iron atoms, (ii) that this layer has considerable surface roughness and greater activity for hydrogen evolution than normal iron, and (iii) that with sufficient time, the disordered layer transforms into conformance with the substrate, with more time required for thicker layers. Such a hypothesis furnishes a ready explanation for all the effects noted.

It is notable in the runs after cathodic polarization that the end of the capacity plateau is marked by the simultaneous appearance of arrests in the cathodic charging curves. The form of the curves in this and all other cases studied indicates that the coverage is reduced in two stages. There is no consistent ratio between the charge product of the two arrests for the charging curves from different initial potentials. Thus, the coverage itself consists of at least two types of material. The first arrest involves a linear change of potential with time, indicating a continuing change in the activity of reduced material or its product during the reduction. Such a change is very suggestive of the reduction of an adsorbate for which the specific adsorption energy decreases with increasing coverage. The second part of the reduction, however, proceeds at a constant potential.

One of the most striking features of the runs after cathodic polarization is the sharp transition in coverage and capacity values at 0.12 ± 0.02v in pH 14.5 solution and at 0.24 ± 0.02v in pH 13.6 solution. The changes shown in the figures occur within 1 min after polarization to the stated potentials and cannot be reversed by small cathodic polarizations after they have occurred. These effects are among those which might be expected from migration of metal ions into a sorbed surface layer according to the surface film formation sequence theory (1). The migration should be irreversible and favored by anodic potential, as was observed. The stabilization of film material so produced ought to result in considerable increase in the total amount of surface film and to heighten the constancy of activity during reduction, as is indicated by the difference in charging curves before and after the transition.

A point of interest may be made by estimating the dielectric properties of the surface material. From elementary electric theory: if k is the dielectric constant of the dielectric of a parallel plate capacitor, d is the thickness of the dielectric in angstroms, and C is the specific capacity of the capacitor in μfarad cm^{-2}, $k/d = 0.113C$. At a given potential, the electrical double layer may be treated approximately as a parallel plate capacitor with surface material (if any) as a dielectric (20-22). From the charge products of arrests measured here, the thickness of the films may be calculated with appropriate assumptions as to the nature of the reduction process.

Table II. Minimum formal dielectric constants* of surface material

Potential, v vs. NHE	pH 14.5		pH 13.6		pH 7.9
	k_c**	k_a***	k_c**	k_a***	k_c**
−0.15	69	65	129	110	
−0.05	64	58	129	110	
0.05	65	60	129	110	
0.15	64	67	129	110	54
0.25	107	68	101	101	47
0.35	115	68	101	96	42
0.45	106	70	96	98	33
0.55			95	101	28
0.65					32
0.75					29
0.85					21
0.95					21

* See text for assumptions made in calculation.
** Values for the potential as reached after cathodic polarization.
*** Values for the potential as reached after anodic polarization.

To estimate a minimum thickness it is assumed that the film material should have a density no greater than that of FeO, the densest stoichiometric iron oxide, and an equivalent weight for reduction no less than that of Fe_2O_3 to Fe. The values of Table II were obtained by such calculation using the measured capacity.

The dielectric constants of stoichiometric iron oxides have been variously reported (25-27) to be in the range 7-20. The values of Table II are higher than this and much higher in the two more alkaline solutions. They show some evidence of a transition potential like that of the other data in runs after cathodic polarization. Either an adsorbed layer of oxygen-containing species, at least part of which are ions or dipoles, or an amorphous mixture of such species with iron ions could rationalize such dielectric behavior. Specifically, such mobile charges could shift about in response to applied potential variations which were too small or too rapid to permit film growth or destruction. In this way the material would behave as a dielectric of high dielectric constant in differential capacity measurements even though it might have to be considered as an additional capacitance in series with the double layer for integral capacity measurements. It is not unreasonable even to suppose that the film would be restricted to growing in such a fashion as to preserve total charge neutrality, and in this case it could act as a dielectric even for integral capacity.

The capacity peaks found in all runs in the three alkaline solutions are similar in magnitude and potential range covered to peaks previously observed with stainless steel (3). These were interpreted as due either to ion adsorption-desorption processes or to dielectric constant changes. From the present results the latter interpretation is more likely in view of the hysteresis observed in the position of the peaks and the close relationship between the presence of the peaks and the presence of relatively thin surface coverage. A thin surface film of sufficiently high dielectric constant could increase the capacity of an electrode since the greater separation of charges would be more than compensated by the dielectric effect. Because of the hysteresis of the potential of the peaks especially, it is unlikely that the high capacity can be ascribed to reversible charge transfer processes, although these cannot be excluded on the basis of the present data.

A region of constant capacity at extreme anodic polarization would be expected from double layer effects (22). The constant capacity observed here in the potential region of oxygen evolution probably indicates both that this region has been reached and that the surface coverage has grown to its maximum extent and ceased to change in properties when potentials sufficiently positive for oxygen evolution have been reached.

In contrast to the report of Engell and Illschner (5), whose measurements were made at 25°C in 0.5*M* H_2SO_4, no potential region in which reciprocal capacity varied linearly with potential could be found in the present work. However, in 0.5*M* H_2SO_4 in the potential range considered by Engell and Illschner, a line could have been drawn through a plot of reciprocal capacity *vs.* potential (not shown) without great inaccuracy. In any case, the conclusion of these workers that their observed linearity supported an oxide model for the passive film does not seem entirely justifiable. Such linearity implies only that a regular relationship is obeyed for film growth dependence (or some qualitative change in film properties) on potential. This circumstance is quite compatible with many possible models for the nature of the film.

The effects observed on addition of $Cr_2O_7^=$ to acid solution suggest that the protective action of this ion is due to its reduction, in preference to film material. In the presence of dichromate, much rather than little charge is required to force the electrode potential into the active region.

If one considers "corresponding potentials" for the various solutions studied as potentials positive to the capacity peak by the same amount, it is apparent from Fig. 3-6 that there is a minimum in capacity near neutral *p*H and a fairly symmetrical increase with either acid of alkaline *p*H. There is at best a poor correlation of capacity with quantitative surface coverage, and it seems likely that the constitution plus the dielectric and similar properties of the surface material depend on the solution environment of its formation. Such dependence could well be expected from a model of film formation in which adsorption of solution species played an initiating role. In this connection it must be emphasized that the effects of buffer ions required in working near neutral *p*H have not been considered because they are not known. The borate system was chosen to avoid the known iron ion complexing effects of other common buffers such as phosphate and ammonia. It is unlikely, however, that the electrode surface should be entirely unaffected by the borate.

The variation with *p*H of the two most negative arrests observed in cathodic charging is shown in Fig. 7. Only the more negative of these is linearly dependent on *p*H within experimental error. Its standard potential (corrected by 0.2v for polarization) and *p*H coefficient are consistent with reduction of magnetite by several possible mechanisms (28). This supports previous postulates of magnetite as the inner layer of a duplex protective surface ma-

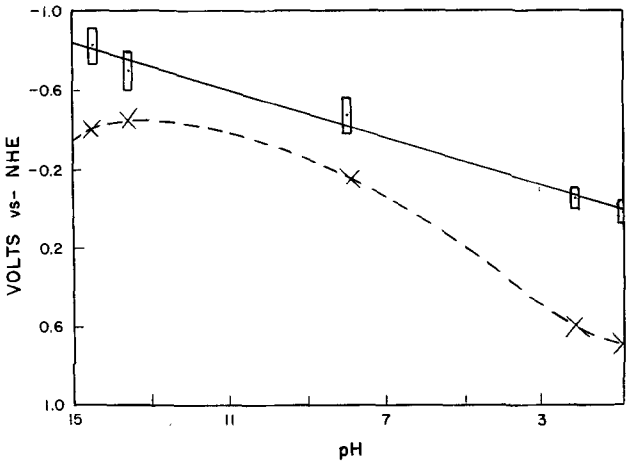

Fig. 7. Variation of arrest potentials with pH. □ — potential of more negative arrest; × — potential of less negative arrest. Potentials at the center of the arrests obtained with ~ 1 ma cm^{-2}.

terial (29). Nevertheless, the observed disappearance of this arrest in acid solution after passing the first arrest only, indicates at least that this material alone is not protective. The nonlinearity of the variation of the potential of the less negative arrest with pH further emphasizes the likelihood that the composition of this part of the surface material depends on solution environment during its formation.

Conclusion

A general view of the results obtained here makes it clear that the capacity behavior of iron cannot be treated entirely in analogy to that of either the clean-surfaced or bulk oxide-covered metals. The results indicate that at all but the most negative potentials the iron surface is indeed covered with a film, but that the film is of complex structure and has properties which depend on the environment in which it is formed and which differ from those of known bulk oxides in many significant respects. All the results are consistent with and support a model for the formation of the film involving initiation by adsorption of solution species and transformation by the migration of metal ions into a protective layer capable of resisting further external attack for considerable periods of time.

Acknowledgment

The authors are pleased to acknowledge the financial support of this work by fellowship from the National Science Foundation (for NEW) and by research grants from The Robert A. Welch Foundation and the Office of Naval Research. The gift of the iron used in the work by Battelle Memorial Institute is also gladly acknowledged.

Manuscript received April 26, 1962; revised manuscript received July 26, 1962.

Any discussion of this paper will appear in a Discussion Section to be published in the December 1963 JOURNAL.

REFERENCES

1. Norman Hackerman, *Z. Elektrochem.*, **62**, 632 (1958).
2. E. S. Snavely and Norman Hackerman, *Can. J. Chem.*, **37**, 268 (1959).
3. P. V. Popat and Norman Hackerman, *J. Phys. Chem.*, **65**, 1201 (1961).
4. L. Gougerot and R. Alfieri, *J. Chim. Phys.*, **52**, 382 (1955).
5. W. J. Engell and B. Illschner, *Z. Elektrochem.*, **59**, 716 (1955).
6. M. Prazak, V. Prazak, and V. Cihal, *ibid.*, **62**, 739 (1958).
7. H. A. Christiansen *et al.*, *Acta Chem. Scand.*, **15**, 300 (1961).
8. K. F. Bonhoeffer, "Soviet Electrochemistry," II, p. 210, Consultant's Bureau, New York (1961).
9. V. V. Sobol' and Z. A. Iofa, *Proc. Acad. Sci. USSR*, **138**, 480 (1961).
10. E. O. Ayazyan, *Doklady Akad. Nauk SSR*, **100**, 473 (1955).
11. V. E. Past and Z. A. Iofa, *Zhur. Fiz. Khim.*, **33**, 1230 (1959).
12. A. M. Sukhotin and K. M. Kartashova, *ibid.* **33**, 2649 (1959).
13. N. E. Wisdom, Jr., Dissertation, University of Texas, 1962.
14. P. D. Sewell, C. D. Stockbridge, and M. Cohen, *Can. J. Chem.*, **37**, 1813 (1959).
15. J. S. Riney, G. M. Schmid, and Norman Hackerman, *Rev. Sci. Instr.*, **32**, 588 (1961).
16. H. A. Laitinen and C. G. Encke, *This Journal*, **107**, 773 (1960).
17. P. V. Popat and Norman Hackerman, *J. Phys. Chem.*, **62**, 1198 (1958).
18. "Electrochemical Data," B. E. Conway, Editor, p. 88, Elsevier Publishing Co., Houston (1952).
19. Paul Delahay, "New Instrumental Methods in Electrochemistry," p. 179-217, Interscience Publishers, Inc., New York (1950).
20. D. C. Grahame, *Chem. Rev.*, **41**, 441 (1947).
21. L. Young, "Anodic Oxide Films," Academic Press, Inc., New York (1961).
22. Roger Parsons, "Properties of Electrified Interfaces" in "Modern Aspects of Electrochemistry," p. 103, Butterworths Scientific Publications, Inc., London (1952).
23. W. M. Latimer, "Oxidation Potentials," 2nd ed., Prentice-Hall, Inc., New York (1952).
24. T. P. Hoar, "Anodic Behavior of Metals" in "Modern Aspects of Electrochemistry," II, p. 280, Academic Press, Inc., New York (1959).
25. T. Takei, *J. Inst. Elec. Engrs. Japan*, **66**, 121 (1946).
26. F. Wagenknecht, *Kolloid-Z.*, **112**, 35 (1948).
27. A. W. Kohlschutter, *Z. inor. allgem. Chem.*, **278**, 270 (1951).
28. A. M. Sukhotin, "Soviet Electrochemistry, II," p. 243, Consultants Bureau, New York (1961).
29. K. J. Vetter, *Z. Elektrochem.*, **62**, 642 (1958).

The Role of Displacement Reactions in the Determination of Activities in Alloys with the Aid of Galvanic Cells

Carl Wagner and Alfred Werner

Max-Planck-Institut für physikalische Chemie, Göttingen, Germany

ABSTRACT

The determination of the activity a_A of the less noble component A in a binary alloy A-B with the aid of the cell

A | A-salt | A-B

involves a certain error because of a displacement reaction which tends to increase the concentration of A in the alloy and to decrease the concentration of A-salt in the electrolyte. The magnitude of the error is estimated and is found to be appreciable if the difference in the nobility of metals A and B is not sufficiently large. The basic assumptions for the estimate of the error are tested by measuring the emf of cells with initially pure metal B on the right-side for the pairs Cd-Sn, Zn-Cd, Zn-Pb, and Zn-Sn.

Statement of the Problem

The activity a_A of the less noble component A in a binary alloy A-B is usually deduced from the emf E_I of the galvanic cell

A(pure)	electrolyte + A-salt	electrolyte + A-salt	A-B alloy	[I]

with the help of the formula

$$E_I = -(RT/z_A F) \ln a_A \qquad [1]$$

where z_A is the valence of ions of metal A in the electrolyte.

At the right-hand electrode of cell I, there is the possibility of the displacement reaction

$$(1/z_B)\,B(\text{alloy}) + (1/z_A)\,A(X) = (1/z_A)\,A(\text{alloy}) + (1/z_B)\,B(X) \qquad [2]$$

where z_B is the valence of ions of metal B and the salts of A and B with the appropriate amount of anion X present in the electrolyte are denoted by A(X) and B(X), respectively. Thus in the case of a one-phase alloy the concentration of A in the alloy is increased and the concentration of A-salt at the right-hand electrode is decreased. Both changes tend to decrease the emf of cell I below the value pertaining to the nominal composition of the alloy. By and large, changes resulting from displacement reaction [2] are considered to be negligible if component B is much more noble than component A (1). This is a qualitative formulation which should be replaced by a quantitative formulation. Therefore, in what follows, the error due to displacement reaction [2] is estimated for known differences of the nobility of metals A and B, *i.e.*, for known ΔF° values of reaction [2].

As a limiting case, one may consider cell I with pure metal B at the initial stage, *i.e.*, $a_A = 0$ corresponding to $E_I = \infty$ according to Eq. [1]. The displacement reaction [2], however, produces a finite concentration of A in the alloy next to the alloy-electrolyte interface and, therefore, the actual value of E_I is finite. Calculated and observed values of E_I for cell I set up with pure metal B on the right-hand side are compared below in order to test the assumptions which are introduced for estimating the error due to the displacement reaction [2] if Eq. [1] is used for the calculation of a_A from E_I.

Since the experimental conditions determining concentration changes resulting from displacement reaction [2] are in general not adequately defined, one obtains only the order of magnitude of the error but not a correction term. Thus one may eliminate objectionable measurements.

Calculation of the Error of Activity Determinations

It is shown below that the relative error in the activity of A is expected to be especially large if the concentration of A in the alloy is low. Therefore, calculations are confined to mole fractions of A in the alloy lower than 0.1. The following simplifying approximations are introduced.

(i) The activity a_A in the alloy is approximated by

$$a_A = x_A f_A \qquad [3]$$

where x_A is the mole fraction of A in the alloy and f_A is the limiting value of the activity coefficient of A in B-rich alloy for a vanishing concentration of A.

(ii) The activity a_B in the alloy for $x_B \cong 1$, $f_B \cong 1$ is approximated by

$$a_B \cong x_B f_B \cong (1 - x_A) \cong 1 \qquad [4]$$

(iii) A large excess of supporting electrolyte is assumed so that the activities of A(X) and B(X) are virtually proportional to the mole fractions, $y_{A(X)}$ and $y_{B(X)}$, respectively.

(iv) It is assumed that equilibrium between the alloy and the electrolyte at the alloy-electrolyte interface is virtually established, *i.e.*, the single electrode potential can be calculated from Nernst's formula with the respective mole fractions at the inter-

face, which will be indicated by a star superscript, whereas the initial mole fractions used for setting up cell I are marked by a degree superscript.

If there were no displacement reaction, one would have the nominal emf $E_{I(nom)}$ to be calculated as

$$E_{I(nom)} = -(RT/z_A F) \ln (x^\circ_A f_A) \quad [5]$$

whereas according to the general Nernst equation the actual emf E_I is

$$E_I = -\frac{RT}{z_A F}\left[\ln \frac{y^\circ_{A(X)}}{y^*_{A(X)}} + \ln x^*_A f_A\right] \quad [6]$$

If the mole fractions at the alloy-electrolyte interface deviate from the initial mole fractions only to a minor extent, the difference between actual and nominal emf is found to be

$$\begin{aligned} E_I - E_{I(nom)} &= \frac{RT}{z_A F}\left[\ln \frac{y^*_{A(X)}}{y^\circ_{A(X)}} - \ln \frac{x^*_A}{x^\circ_A}\right] \\ &= \frac{RT}{z_A F}\left[\ln\left(1 + \frac{y^*_{A(X)} - y^\circ_{A(X)}}{y^\circ_{A(X)}}\right)\right. \\ &\quad \left. - \ln\left(1 + \frac{x^*_A - x^\circ_A}{x^\circ_A}\right)\right] \\ &\cong \frac{RT}{z_A F}\left[\frac{y^*_{A(X)} - y^\circ_{A(X)}}{y^\circ_{A(X)}} - \frac{x^*_A - x^\circ_A}{x^\circ_A}\right] \\ &\quad \text{if } x^*_A \cong x^\circ_A,\ y^*_{A(X)} \cong y^\circ_{A(X)} \quad [7] \end{aligned}$$

Using Eq. [1] without additional terms one obtains only an apparent value a'_A of the activity of metal A in the alloy at the right-hand side of cell *I*

$$a'_A = \exp(-z_A E_I F/RT) \quad [8]$$

From Eq. [7] and [8] it follows that the relative error in the activity is

$$\begin{aligned} \epsilon \equiv \frac{a'_A - a_A}{a_A} &= \exp\left[-\frac{z_A(E_I - E_{I(nom)})F}{RT}\right] - 1 \\ &\cong -\frac{z_A(E_I - E_{I(nom)})F}{RT} = \frac{y^\circ_{A(X)} - y^*_{A(X)}}{y^\circ_{A(X)}} \\ &\quad + \frac{x^*_A - x^\circ_A}{x^\circ_A} \quad [9] \end{aligned}$$

The equilibrium condition for the displacement reaction in Eq. [2] is

$$\left(\frac{x^*_A}{y^*_{A(X)}}\right)^{1/z_A}\left(\frac{y^*_{B(X)}}{x^*_B}\right)^{1/z_B} = \frac{K}{f_A^{1/z_A}}\frac{(f_{A(X)})^{1/z_A}}{(f_{B(X)})^{1/z_B}} \quad [10]$$

where f_A, $f_B \cong 1$, etc., are the activity coefficients of A, B, etc., and K is given by the standard free energy change ΔF° of displacement reaction [2] with pure A, B, A(X), and B(X)

$$K = \exp(-\Delta F^\circ/RT) \quad [11]$$

The value of ΔF° may be calculated as the difference of the standard free energies of formation of B(X) and A(X) per equivalent. Alternatively, one may deduce ΔF° from emf measurements, *e.g.*, by using the cell

B	electrolyte with B(X)	electrolyte with A(X)	A

[II]

with a large excess of supporting electrolyte of the same type as used in cell I. Since in the presence of a large excess of supporting electrolyte there is virtually no diffusion potential, the emf E_{II} of cell II is given by the formula

$$E_{II} = -\frac{\Delta F^\circ}{F} + \frac{RT}{z_A F}\ln y_{A(X)} f_{A(X)} - \frac{RT}{z_B F}\ln y_{B(X)} f_{B(X)} \quad [12]$$

Defining the standard states of the salts A(X) and B(X) so that the activities equal the mole fractions at infinite dilution, the standard value E°_{II} of the emf of cell II is given by

$$E^\circ_{II} = \left[E_{II} - \frac{RT}{z_A F}\ln y_{A(X)} + \frac{RT}{z_B F}\ln y_{B(X)}\right] \quad \text{for } y_{A(X)} \to 0,\ y_{B(X)} \to 0 \quad [13]$$

Upon substituting Eq. [12] and [13] in Eq. [11], it follows that

$$K\frac{(f_{A(X)})^{1/z_A}}{(f_{B(X)})^{1/z_B}} = \exp\left[\frac{E^\circ_{II} F}{RT}\right] \quad [14]$$

If the concentrations at the alloy-electrolyte interface differ only slightly from the respective nominal concentrations, one may use the approximations $x^*_A \cong x^\circ_A$, $y^*_{A(X)} \cong y^\circ_{A(X)}$ and $x^*_B \cong 1$ in order to calculate the concentration of B-salt at the alloy-electrolyte interface from Eq. [10]. Thus

$$y^*_{B(X)} \cong \left(\frac{y^\circ_{A(X)} f_{A(X)}}{x^\circ_A f_A}\right)^{z_B/z_A}\frac{K^{z_B}}{f_{B(X)}} \quad [15]$$

In order to calculate the differences $(x^*_A - x^\circ_A)$ and $(y^\circ_{A(X)} - y^*_{A(X)})$ required for the evaluation of Eq. [9], it is necessary to introduce special assumptions. In what follows calculations are made for two different sets of conditions which are amenable to a mathematical analysis. Actually, conditions may be more involved. A careful study would be needed in order to specify the conditions in a given cell in a more realistic manner.

In the first place, we consider conditions under which the concentrations at the alloy-electrolyte interface are determined by the interplay of diffusion in a virtually semi-infinite alloy and a virtually semi-infinite electrolyte. Thus, the time elapsed after assembling the cell is supposed to be not excessively long so that concentration changes due to displacement reaction [2] do not extend to the boundaries of the alloy or the electrolyte. Constant cross sections of both the alloy and the electrolyte are assumed so that equations for one-dimensional diffusion apply.

Fick's second law for the alloy with the interdiffusion coefficient D reads

$$\partial x_A/\partial t = D(\partial^2 x_A/\partial \xi^2) \quad \text{at } \xi < 0 \quad [16]$$

where t is the time and ξ is the distance from the alloy-electrolyte interface in the direction of the interior of the electrolyte.

The equations for diffusion in the electrolyte with the diffusion coefficients $D_{A(X)}$ and $D_{B(X)}$ are

$$\partial y_{A(X)}/\partial t = D_{A(X)}\ (\partial^2 y_{A(X)}/\partial \xi^2) \qquad \text{at } \xi > 0 \quad [17]$$

$$\partial y_{B(X)}/\partial t = D_{B(X)}\ (\partial^2 y_{B(X)}/\partial \xi^2) \qquad \text{at } \xi > 0 \quad [18]$$

These equations are to be solved for the initial conditions

$$x_A = x^o_A \qquad \text{at } \xi < 0, t = 0 \quad [19]$$

$$x_{A(X)} = x^o_{A(X)} \qquad \text{at } \xi > 0, t = 0 \quad [20]$$

$$x_{B(X)} = x^o_{B(X)} \qquad \text{at } \xi > 0, t = 0 \quad [21]$$

In view of the displacement reaction [2], two boundary conditions at the metal-electrolyte interface are obtained from the material balance of the fluxes

$$(-z_A j_{A(X)} = -z_A j_A = z_B j_B)_{\xi=0} \quad [22]$$

where j_A, $j_{A(X)}$, and $j_{B(X)}$, respectively, are the transport rates in the ξ-direction in moles per unit area per unit time for metal A in the alloy, A-salt in the electrolyte, and B-salt in the electrolyte. In view of Fick's first law, Eq. [22] becomes

$$\frac{z_A D_{A(X)}}{V''_m}\left(\frac{\partial y_{A(X)}}{\partial \xi}\right)_{\xi=0} = \frac{z_A D}{V'_m}\left(\frac{\partial x_A}{\partial \xi}\right)_{\xi=0} = -\frac{z_B D_{B(X)}}{V''_m}\left(\frac{\partial y_{B(X)}}{\partial \xi}\right)_{\xi=0} \quad [23]$$

where V'_m and V''_m are the molar volumes of the alloy and the electrolyte, respectively. In addition, Eq. [15] at $\xi = 0$ is to be obeyed.

Eq. [15] to [21] and [23] determine the mole fractions of A and B in the alloy and of A(X) and B(X) in the electrolyte as functions of ξ and t. Eq. [15] to [21] are satisfied by

$$x_A = x^o_A + (x^*_A - x^o_A)\ \mathrm{erfc}[|\xi|/2(Dt)^{1/2}] \quad [24]$$

$$y_{A(X)} = y^o_{A(X)} - (y^o_{A(X)} - y^*_{A(X)}) \times \mathrm{erfc}[\xi/2(D_{A(X)}t)^{1/2}] \quad [25]$$

$$y_{B(X)} = y^*_{B(X)}\mathrm{erf}[\xi/2\,(D_{B(X)}t)^{1/2}] \quad [26]$$

Substitution of Eq. [24] to [26] in Eq. [23] yields

$$z_A(y^o_{A(X)} - y^*_{A(X)})\,(D_{A(X)})^{1/2}/V''_m = z_B y^*_{B(X)}(D_{B(X)})^{1/2}/V''_m = z_A(x^*_A - x^o_A)D^{1/2}/V'_m \quad [27]$$

Upon substitution of Eq. [15] in Eq. [27], one obtains the differences $(x^*_A - x^o_A)$ and $(y^o_{A(X)} - y^*_{A(X)})$ which in turn are substituted in Eq. [9]. Thus the relative error ϵ of the activity a_A is found to be

$$\epsilon = \frac{z_B K^{z_B}}{z_A f_{B(X)}}\left(\frac{y^o_{A(X)} f_{A(X)}}{x^o_A f_A}\right)^{z_B/z_A} \times \left[\frac{1}{y^o_{A(X)}}\left(\frac{D_{B(X)}}{D_{A(X)}}\right)^{1/2} + \frac{1}{x^o_A}\left(\frac{D_{B(X)}}{D}\right)^{1/2}\frac{V'_m}{V''_m}\right] \quad [28]$$

where the first term in brackets is due to the difference between the actual mole fraction $y^*_{A(X)}$ of A-salt at the alloy-electrolyte interface and the nominal mole fraction $y^o_{A(X)}$, and the second term in brackets is due to the difference between the actual mole fraction x^*_A of metal A at the alloy-electrolyte interface and the nominal mole fraction x^o_A.

In order to estimate the order of magnitude of ϵ for liquid alloys, one may introduce the approximations $V'_m \cong V''_m$, $D \cong D_{A(X)} \cong D_{B(X)}$ whereupon Eq. [28] becomes

$$\epsilon \cong \frac{z_B K^{z_B}}{z_A f_{B(X)}}\left(\frac{y^o_{A(X)} f_{A(X)}}{x^o_A f_A}\right)^{z_B/z_A}\left(\frac{1}{y^o_{A(X)}} + \frac{1}{x^o_A}\right) \quad [29]$$

In contradistinction to the foregoing calculation, one may assume that diffusion equilibrium within each phase in the right-hand compartment of cell I has been attained at the time of the measurement of E_I, if the volumes of the respective phases are small. Since the mole fractions in each phase are locally constant and equal to those at the alloy-electrolyte interphase, the equation of material balance resulting from Eq. [2] is

$$z_A(x^*_A - x^o_A)n' = z_B y^*_{B(X)} n'' = z_A(y^o_{A(X)} - y^*_{A(X)})n'' \quad [30]$$

where n' and n'' are the number of moles of the alloy and the electrolyte in the right-hand compartment of cell I. Substitution of Eq. [15] in Eq. [30] yields the differences $(x^*_A - x^o_A)$ and $y^o_{A(X)} - y^*_{A(X)}$, which in turn are substituted in Eq. [9]. Thus

$$\epsilon = \frac{z_B K^{z_B}}{z_A f_{B(X)}}\left(\frac{y^o_{A(X)} f_{A(X)}}{x^o_A f_A}\right)^{z_B/z_A}\left[\frac{1}{y^o_{A(X)}} + \frac{1}{x^o_A}\frac{n''}{n'}\right] \quad [31]$$

Eq. [31] becomes identical with Eq. [29] if $n' = n''$.

Hence, Eq. [29] is recommended in order to estimate the order of magnitude of the relative error ϵ except under special conditions which are in striking conflict with one of the foregoing assumptions.

According to Eq. [28], [29], and [31], the error ϵ is especially large in the case of low concentrations of A.

Expressing K in terms of ΔF^o according to Eq. [11], one obtains from Eq. [29] for $f_{A(X)} \cong f_{B(X)} \cong 1$

$$\epsilon \cong \frac{z_B}{z_A}\left(\frac{y^o_{A(X)}}{x^o_A f_A}\right)^{z_B/z_A}\left(\frac{1}{y^o_{A(X)}} + \frac{1}{x^o_A}\right) \times \exp\left(-\frac{z_B \Delta F^o}{RT}\right) \quad [32]$$

Expressing K in terms of E^o_{II} with the help of Eq. [14], one obtains from Eq. [29]

$$\epsilon \cong \frac{z_B}{z_A}\left(\frac{y^o_{A(X)}}{x^o_A f_A}\right)^{z_B/z_A}\left(\frac{1}{y^o_{A(X)}} + \frac{1}{x^o_A}\right) \times \exp\left(\frac{z_B E^o_{II} F}{RT}\right) \quad [33]$$

Laitinen and Liu (2) have published standard single electrode potentials of the most important metals with respect to a Pt-Pt^{2+} reference electrode for a eutectic KCl-LiCl melt as solvent at 450°C. From these data, the value of E^o_{II} for many metal pairs can readily be calculated. Hence Eq. [33] is of special practical importance. A small value of ϵ is obtained if the value of the exponential function is small, *i.e.*, $-z_B E^o_{II} F/RT$ is large. Hence the lower the valence z_B of the more noble metal, the greater

must be the value of E°_{II}, *i.e.*, the difference of the standard single electrode potentials of metals A and B in order to have a permissible error for given values of x°_A, $y^{\circ}_{A(X)}$, and T.

According to Eq. [28], [29], and [31] to [33], the error depends on x°_A and $y^{\circ}_{A(X)}$ as well. Under all conditions, ϵ is especially large if x°_A is low. In order to investigate the dependence of ϵ on $y^{\circ}_{A(X)}$, the following cases for the special conditions $f_{A(X)} = f_{B(X)} = 1$ and $f_A = 1$ are discussed.

(*a*) If $z_A = z_B$, Eq. [29] becomes

$$\epsilon \cong \frac{K^{z_A}}{x^{\circ}_A}\left(1 + \frac{y^{\circ}_{A(X)}}{x^{\circ}_A}\right) \qquad [34]$$

To minimize ϵ, let $y^{\circ}_{A(X)} << x^{\circ}_A$. Thus

$$\epsilon \cong K^{z_A}/x^{\circ}_A \qquad \text{if } y^{\circ}_{A(X)} << x^{\circ}_A \qquad [35]$$

(*b*) If $z_A = 2$, $z_B = 1$, Eq. [29] becomes

$$\epsilon \cong \frac{K}{2x^{\circ}_A}\left[\left(\frac{x^{\circ}_A}{y^{\circ}_{A(X)}}\right)^{1/2} + \left(\frac{y^{\circ}_{A(X)}}{x^{\circ}_A}\right)^{1/2}\right] \qquad [36]$$

The expression in brackets has a minimum value equal to 2 if $x^{\circ}_A = y^{\circ}_{A(X)}$. Hence

$$\epsilon \cong K/x^{\circ}_A \qquad \text{if } y^{\circ}_{A(X)} = x^{\circ}_A \qquad [37]$$

Equation [37] holds with sufficient approximation also if $y^{\circ}_{A(X)}$ is four times greater or smaller than x°_A.

(*c*) If $z_A = 1$, $z_B = 2$, Eq. [29] becomes

$$\epsilon \cong \frac{2K^2}{x^{\circ}_A}\left[\frac{y^{\circ}_{A(X)}}{x^{\circ}_A} + \left(\frac{y^{\circ}_{A(X)}}{x^{\circ}_A}\right)^2\right] \qquad [38]$$

The error is minimized if $y^{\circ}_{A(X)} << x^{\circ}_A$. Thus

$$\epsilon \cong 2K^2\, y^{\circ}_{A(X)}/(x^{\circ}_A)^2 \qquad [39]$$

Hence the error can, in principle, be made as small as one desires by using a low mole fraction of A-salt in the electrolyte in accord with the fact that for $z_B > z_A$ the displacement reaction [2] becomes less favorable at low concentrations of A(X) and B(X) in the electrolyte. There are obvious limits, however. If $y^{\circ}_{A(X)}$ is very low, a small amount of oxide at one of the electrodes of cell I may effect a much greater nonuniformity of the concentration of A(X) than displacement reaction [2]. In practice, values of $y^{\circ}_{A(X)}$ lower than 0.03 or possibly 0.01 do not seem recommendable.

Calculation of the Emf of Cell I Set up with Pure Metals A and B

As a limiting case, one may investigate cell I set up with pure metals A and B. A finite concentration of A next to the metal-salt interface at the right-hand side is attained by virtue of displacement reaction [2].

In the first place, one may assume conditions corresponding to diffusion in semi-infinite phases of the metal and the salt. For $x^{\circ}_A = 0$, one has in view of Eq. [27]

$$z_B y^{*}_{B(X)} D_{B(X)}{}^{1/2}/V''_m = z_A x^{*}_A D^{1/2}/V'_m \qquad [40]$$

From Eq. [10] with $y^{*}_{A(X)} \cong y^{\circ}_{A(X)}$ and $x^{*}_B \cong 1$ and Eq. [40] one may calculate the values of x^{*}_A and $y^{*}_{B(X)}$. For the special case $z_A = z_B = 2$ for which measurements are reported below, one has

$$x^{*}_A = \left(\frac{y^{\circ}_{A(X)}}{f_A}\right)^{1/2} K \left(\frac{f_{A(X)}}{f_{B(X)}}\right)^{1/2} \times \left[\left(\frac{D_{B(X)}}{D}\right)^{1/2} \frac{V'_m}{V''_m}\right]^{1/2} \qquad [41]$$

Second, one may assume that diffusion equilibrium in each phase in the left-hand compartment of cell I has been attained. For $x^{\circ}_A = 0$, one has in view of Eq. [30]

$$z_B y^{*}_{B(X)} n'' = z_A x^{*}_A n' \qquad [42]$$

From Eq. [10] with $y^{*}_{A(X)} \cong y^{\circ}_{A(X)}$ and $x^{*}_B \cong 1$ and Eq. [42] one may calculate the value of x^{*}_A and obtains for $z_A = z_B = 2$

$$x^{*}_A = \left(\frac{y^{\circ}_{A(X)}}{f_A}\right)^{1/2} K \left(\frac{f_{A(X)}}{f_{B(X)}}\right)^{1/2} \left(\frac{n''}{n'}\right)^{1/2} \qquad [43]$$

In order to obtain the order of magnitude of x^{*}_A, one may let $D_{B(X)} = D$ and $V'_m = V''_m$ in Eq. [41] and $n' = n''$ in Eq. [43] whereupon in view of Eq. [14]

$$x^{*}_A \cong \left(\frac{y^{\circ}_{A(X)}}{f_A}\right)^{1/2} \exp\frac{E^{\circ}_{II}F}{RT} \qquad [44]$$

Substitution of Eq. [44] in Eq. [6] with $y^{*}_{A(X)} = y^{\circ}_{A(X)}$ yields

$$E_I(x^{\circ}_A = 0) \cong -\frac{1}{2}E^{\circ}_{II} - \frac{RT}{4F}\ln y^{\circ}_{A(X)} f_A \qquad [45]$$

Experimental

In order to test the applicability of Eq. [45], the emf of cells of type I with $x^{\circ}_A = 0$ and cells of type II with the metal pairs Cd-Sn, Zn-Cd, Zn-Pb, and Zn-Sn has been measured at 510°C. The supporting electrolyte was an eutectic mixture of 42 mole % KCl and 58 mole % LiCl. The mole fraction $y^{\circ}_{A(X)}$ in cells of type I was 0.03. Likewise, the mole fractions $y_{A(X)}$ and $y_{B(X)}$ in cells of type II were 0.03 each.

In order to avoid side reactions, special care was taken in order to prepare the salt mixtures free of water or oxide. To dehydrate LiCl, KCl, and $CdCl_2$, the salts were mixed with NH_4Cl and heated to about 350°C until all NH_4Cl had vaporized in the form of $NH_3 + HCl$. $PbCl_2$ was used without pretreatment because it is not hygroscopic. $ZnCl_2$ free of water was prepared by dissolving Zn in ether containing HCl according to Hamilton and Butler (3). Since no convenient method for preparing $SnCl_2$ free of water was found, $SnCl_2 \cdot 2H_2O$ was melted with LiCl and KCl in the vessels used for the cells, purified HCl was bubbled through the melt, and finally HCl was removed with the help of a stream of purified N_2. The same procedure was used for the other salt mixtures in order to remove traces of H_2O possibly left over during the pretreatment or picked up during the preparation of the mixtures.

The set-up for cells of type I consisting of Pyrex vessels 1, 2, and 3 is shown in Fig. 1. To assemble the cell, the electrolyte was melted in vessel 3 in a stream of purified HCl and subsequently in a stream of purified nitrogen. The small vessels 1 and 2 containing metals A and B with sealed-off side arms

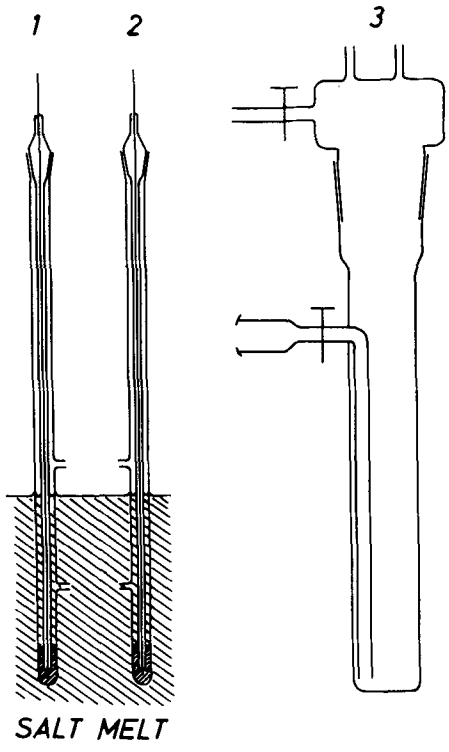

Fig. 1. Vessels for cell of type I

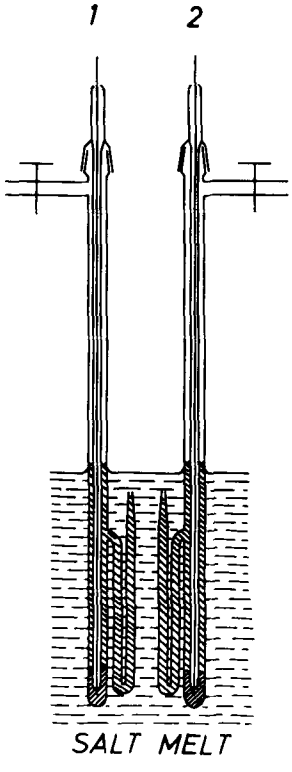

Fig. 2. Vessels for cell of type II

were heated in a separate furnace in order to melt the metals under purified nitrogen. Then the side arms were opened and vessels 1 and 2 were transferred into vessel 3. The salt melt moved into vessels 1 and 2. Thereupon the cell was ready for measuring the emf with the help of a potentiometer.

The set-up for cells of type II, designed after a cell used by Lorenz and Michael (4), consisted of vessels 1 and 2 shown in Fig. 2 and a larger Pyrex

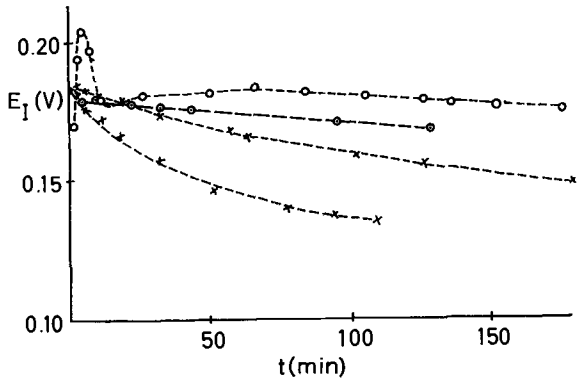

Fig. 3. Emf E_I of cells of type I for $x^\circ_A = 0$ as a function of time t (○, ⊙ Cd-Sn; X Zn-Cd).

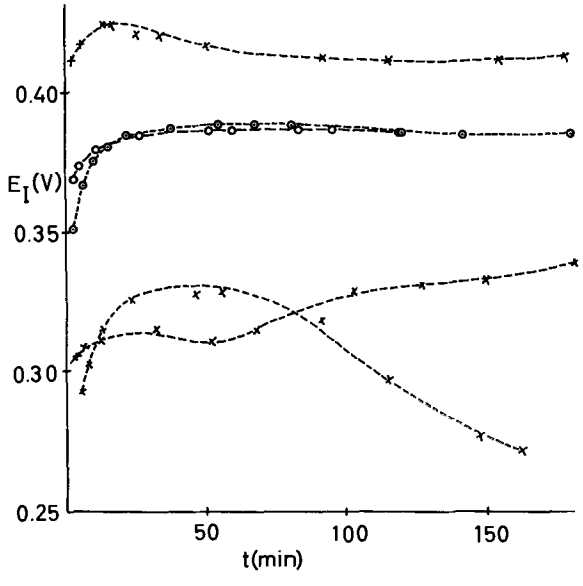

Fig. 4. Emf E_I of cells of type I for $x^\circ_A = 0$ as a function of time t (○, ⊙ Zn-Sn; X Zn-Pb).

tube closed at one end. The latter tube contained an eutectic melt of KCl and LiCl. The vessels 1 and 2 with sealed-off side arms were charged with the respective metals, the KCl-LiCl base electrolyte, and additions of $CdCl_2$, $PbCl_2$, $SnCl_2$, or $ZnCl_2$ and were heated in a separate furnace to the experimental temperature. During these operations, first HCl and subsequently purified N_2 was bubbled through the melts. After opening the side arms and transferring vessels 1 and 2 into the larger Pyrex tube containing the KCl-LiCl melts, the cell was ready for measuring the emf.

Electromotive force readings of cells of type I varied with time as is shown in Fig. 3 and 4. Seemingly, concentrations of A, A(X), and B(X) at the alloy-electrolyte interface were not determined by one-dimensional diffusion in virtually semi-infinite spaces of alloy and electrolyte alone as assumed in the foregoing theoretical analysis, Eq. [16] to [28]. Possibly, three-dimensional rather than one-dimensional diffusion is to be considered in view of the curvature of the meniscus of the alloy. It is also possible that convection is not negligible. The highest quasi-stationary emf readings for cells of type I are listed in Table I as representative values for a comparison with values calculated from Eq. [45].

Table I. Emf of cells of type I and II at 510°C

Metal pair A-B	$E_{II} = E^{\circ}_{II}$, v obs.	f_A	x^*_A from Eq. [44]	$E_I(x^{\circ}_A = 0)$, v Obs.	Estimated from Eq. [45]
Cd-Sn	—0.234	1.9	$4 \cdot 10^{-3}$	0.18;0.18	0.165
Zn-Cd	—0.250	3.4	$2 \cdot 10^{-3}$	0.18;0.18	0.165
Zn-Pb	—0.467	12	$5 \cdot 10^{-5}$	0.33;0.42;0.33	0.288
Zn-Sn	—0.480	1.9	$1 \cdot 10^{-4}$	0.39;0.39	0.251

In contrast, emf values of cells of type II were virtually steady with irregular variations of less than 2 mv, see Table I. These values are essentially equal to values determined by Laitinen and Liu (2) at 450°C.

Values f_A of the activity coefficients of metal A needed for the evaluation of Eq. [44] and [45] were extrapolated to zero mole fraction of A by using data reported by various authors (5-9), see Table I.

Discussion

For the metal pairs Cd-Sn and Zn-Cd, observed values of $E_I(x^{\circ}_A = 0)$ listed in Table I agree, within reasonable limits, with values calculated from Eq. [45]. In contrast, values of $E_I(x^{\circ}_A = 0)$ observed for the metal pairs Zn-Pb and Zn-Sn are considerably greater than values calculated from Eq. [45]. For the latter metal pairs, values of E°_{II} and likewise the standard free energy changes ΔF° for displacement reaction [2] are about twice as much as those for the metal pairs Cd-Sn and Zn-Cd. Accordingly, values of x^*_A estimated with the help of Eq. [44] are considerably lower for Zn-Pb and Zn-Sn than for Cd-Sn and Zn-Cd. It is obvious that low values of x_A are very susceptible to changes by virtue of side reactions. In particular, presence of oxidizing agents, *e.g.*, molecular oxygen or traces of water or oxides of metal B may lower the mole fraction of A in the alloy next to the alloy-electrolyte interface considerably whereupon an emf greater than the value calculated from Eq. [45] results. This readily explains the divergence between observed and calculated values of $E_I(x_A = 0)$ for Zn-Pb and Zn-Sn.

Since Eq. [45] has been shown to be applicable if $x^*_A \gtrsim 0.002$ and since the basic assumptions for the derivation of Eq. [32], [33], and [45] are the same, one may conclude that Eq. [32] or [33] can be used with reasonable confidence in order to estimate the order of magnitude of the error of activity measurements due to displacement reactions in cells of type I if x°_A is greater than 0.01. At lower concentrations of metal A, however, additional errors may occur owing to oxidation of metal A by impurities unless extraordinary precautions are taken in order to prevent the presence of oxidizing agents.

The estimate of the error ϵ of activity determinations in liquid alloys with the help of Eq. [33] for liquid alloys is illustrated by the following examples, assuming a mole fraction $y^{\circ}_{A(X)} = 0.03$ in an eutectic melt of KCl and LiCl as electrolyte in cell I.

(a) For the system Cd-Sn ($E^{\circ}_{II} = -0.234$v; $f_A = 1.9$) at 510°C, one obtains $\epsilon \cong 0.015$ for $x^{\circ}_A = 0.1$ and $\epsilon \cong 0.12$ for $x^{\circ}_A = 0.01$. Thus it seems reasonable to confine activity determinations with the help of cell I to mole fractions of cadmium greater than 0.1. Activities for lower concentrations are to be obtained by means of extrapolation.

(b) For the system Zn-Sn ($E^{\circ}_{II} = -0.480$v; $f_A = 1.9$) at 510°C, one obtains $\epsilon \cong 2 \cdot 10^{-5}$ for $x^{\circ}_A = 0.1$ and $\epsilon \cong 2 \cdot 10^{-4}$ for $x^{\circ}_A = 0.01$. Thus measurements may be extended to values of x°_A as low as 0.01.

(c) For the system Pb-Ag, one has $E^{\circ}_{II} = -0.467$v at 450°C according to Laitinen and Liu (2). As an approximation, the same value may be adopted for 1000°C. According to Chipman (10) f_A equals about 2. Thus, for $x^{\circ}_A = 0.1$, ϵ is found to be as high as 0.12. In spite of a relatively high value of E°_{II}, the error is large because z_B is equal to 1 instead of 2 as in the foregoing examples, and the temperature is higher. Thus reliable activity measurements cannot be made in the conventional manner. However, one may combine the results of measurements of the displacement reaction

$$2Ag(\text{alloy}) + PbCl_2(\text{salt melt}) = Pb(\text{alloy}) + 2AgCl(\text{salt melt})$$

with the results of emf measurements in order to calculate activities in both the alloy and the salt melt as has been shown in a previous paper (11).

In the case of solid alloys, the diffusion coefficient D for the alloy is much lower than the values $D_{A(X)}$ and $D_{B(X)}$ pertaining to the salt melt. Therefore, the second term in brackets in Eq. [28] prevails. Substituting Eq. [14] in Eq. [28], one has

$$\epsilon = \frac{z_B}{z_A} \left(\frac{y^{\circ}_{A(X)}}{f_A} \right)^{z_B/z_A} \left(\frac{1}{x^{\circ}_A} \right)^{1+z_B/z_A} \times \left(\frac{D_{B(X)}}{D} \right)^{1/2} \frac{V'_m}{V''_m} \exp \left(\frac{z_B E^{\circ}_{II} F}{RT} \right) \quad [46]$$

For the sake of illustration, Eq. [46] may be applied to solid Ag-Au alloys with $z_A = z_B - 1$. The value $E^{\circ}_{II} = -0.948$v found by Laitinen and Liu (2) at 450°C is adopted also for higher temperatures. According to White, Orr, and Hultgren (12) $f_A = f_{Ag}$ for $x_{Ag} = 0$ may be represented by

$$RT \ln f_A \text{ (cal)} = -7250 - 1.375\, T \text{ (°K)} \quad [47]$$

According to Johnson (13) the diffusion coefficient D of the alloy is given by

$$D \text{ (cm}^2\text{/sec)} = 0.14 \exp (-41700/RT) \quad [48]$$

where RT is to be taken in cal/mole. In view of data for self-diffusion of sodium ions in liquid NaCl (14), one may assume that

$$D_{B(X)}\text{(cm}^2\text{/sec)} = 7 \cdot 10^{-4} \exp (-3500/RT) \quad [49]$$

Substituting Eq. [47] to [49] in Eq. [46] and letting $V'_m/V''_m = 0.3$, one has for $x^{\circ}_A = 0.1$

$$\epsilon \cong 2.7 \cdot 10^{-2} \exp \left[\frac{3625 - 1750 + 20850 - 21850}{RT} \right] \quad [50]$$

where the four terms of the numerator of the quotient in the exponential function are due to the temperature dependence of f_A, $D_{B(X)}$, D, and K according to Eq. [14], respectively. The sum of the four terms is 875 cal. Thus ϵ is estimated to be 0.04 at 800°C and nearly independent of temperature.

The situation for solid Ag-Au alloys is especially favorable since $-z_B E^\circ_{II}$ is large. For most other solid alloys a considerably less favorable situation is expected, especially at lower temperatures where diffusion coefficients for solid alloys are small.

To overcome limitations of cells with conventional electrolytes, new types of cells involving other electrolytes than chloride melts may be used. For instance, a cell of type I with an eutectic KCl-LiCl melt as base electrolyte cannot be used for the determination of the activity of Cu in solid Cu-Ni alloys because $E^\circ_{II} = -0.056$ at 450° according to Laitinen and Liu (2). With the help of a cell involving solid ZrO_2 doped with CaO as auxiliary electrolyte, however

$$\begin{array}{l|l|l} \text{Ni(s)}, & & \text{Cu-Ni(s)}, \\ \text{NiO(s)} & \text{ZrO}_2\ (+\text{CaO}) & \text{NiO(s)} \end{array} \qquad \text{[III]}$$

Rapp and Maak (15) have determined the activity of Ni in solid Ni-Cu alloys between 700° and 1000°C. It seems possible to use the same type of cell for the determination of the activity of Pb in liquid Ag-Pb alloys.

Manuscript received June 12, 1962; revised manuscript received Aug. 15, 1962.

Any discussion of this paper will appear in a Discussion Section to be published in the December 1963 JOURNAL.

REFERENCES

1. C. Wagner, "Thermodynamics of Alloys," p. 91 f. Addison-Wesley Press, Cambridge, Mass. (1952).
2. H. A. Laitinen and C. H. Liu, *J. Am. Chem. Soc.*, **80**, 1015 (1958).
3. R. T. Hamilton and J. A. V. Butler, *J. Chem. Soc.*, **1932**, 2283.
4. R. Lorenz and F. Michael, *Z. physik. Chem.*, **137**, 1 (1928).
5. N. W. Taylor, *J. Am. Chem. Soc.*, **45**, 2865 (1923).
6. J. F. Elliott and J. Chipman, *Trans. Faraday Soc.*, **47**, 138 (1954).
7. S. Mellgren, *J. Am. Chem. Soc.*, **74**, 5037 (1952).
8. M. Fiorani and V. Valenti, *Gazz. chim. ital.*, **85**, 607 (1955).
9. O. J. Kleppa, *J. Am. Chem. Soc.*, **74**, 6052 (1952).
10. J. Chipman, *Discussions Faraday Soc.*, **4**, 154 (1948).
11. C. Wagner, *Z. physik. Chem. N. F.*, **8**, 342 (1956).
12. J. L. White, R. L. Orr, and R. Hultgren, *Acta Met.*, **5**, 747 (1957).
13. W. A. Johnson, *Trans. A.I.M.E.*, **147**, 531 (1942).
14. A. Borucka, J. O'M. Bockris, and J. A. Kitchner, *Proc. Roy. Soc.* (London), **A241**, 554 (1957).
15. R. A. Rapp and F. Maak, *Acta Met.*, **10**, 63 (1962).

Transition from Hydrogen Ionization to Oxygen Evolution on a Platinum Electrode

Sigmund Schuldiner and Robert M. Roe

U. S. Naval Research Laboratory, Washington, D. C.

ABSTRACT

With pulse techniques, determinations were made of double layer capacitance and numbers of hydrogen and oxygen atoms associated with a platinum surface undergoing anodic transitions to the oxygen evolution reaction. The complexity of hydrogen sorption on platinum was shown together with quantitative determinations of various hydrogen sorption regions. An improved definition of true surface area was possible because of the linearity of the atomic oxygen adsorption region and the precision with which the number of oxygen atoms on a fully covered surface could be determined quantitatively.

Recently developed experimental techniques were applied to a study of the transition from the hydrogen ionization to the oxygen evolution reactions on a platinum electrode in acid solution. Anodic charging curves and other transient techniques [see ref. 1-3) for literature surveys] have been used widely for such work, but it was felt that an increase in instrumental resolution and precision, as well as rigorous control of the conditions of electrolysis, were necessary for a better understanding of the details of these reactions.

In this investigation relations, between the open-circuit potentials and (*a*) the number of hydrogen and oxygen atoms sorbed, and (*b*) the double layer capacitance on a platinum electrode were determined. This work verified that the method used by Butler and co-workers (1, 4) for the determination of the true surface area of a platinum electrode, by measurement of the number of oxygen atoms deposited, does operationally provide an improved definition of true surface area for this electrode.

Experimental

One of the aims of this investigation was to build an electrochemical system in which a rigorous control was possible of the factors which went into the electrode process. Since diffusion of air into the cell may have deleterious effects, pains were taken to build a vacuum-tight system. The gas distribution (Fig. 1) and purification system was constructed

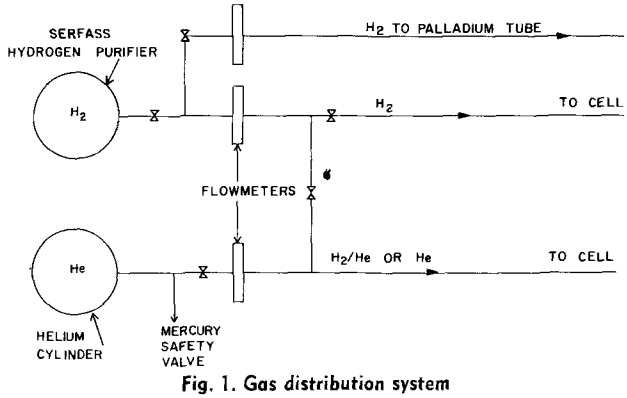

Fig. 1. Gas distribution system

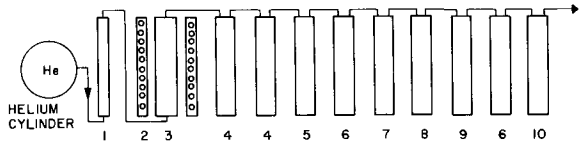

Fig. 2. Helium purification train : 1, flowmeter; 2, furnace (200°C); 3, Meyer-Ronge Cu catalyst column; 4, molecular sieves; 5, liquid nitrogen trap; 6, trap; 7, saturater (water); 8, oxygen generator (electrolytic); 9, electrolytic cell; 10, bubbler.

entirely of copper and Pyrex glass, free of ground glass stopcocks and connectors. Copper tubing connections were made from the gas sources to the flowmeters where the lines were connected to an all-glass system through Kovar seals. The all-glass system was constructed of ¼ in. flanged glass pipe joined to the various components of the purification system and the electrolytic cell. All joints were sealed with Viton A O-rings with the necessary glass pipe couplings. The entire system was vacuum-tight under a moderate vacuum. No diffusion of air through the joints was observed during a 30-day period prior to the first experimental run. The entire system was frequently checked for leaks with a leak detector developed at the Naval Research Laboratory.

Tank hydrogen was passed through a Serfass Hydrogen Purifier (heated palladium-silver tubes), saturated with conductivity water, and then passed through the electrolysis cell. The normal flow rate for pure hydrogen in the cell was 420 ml/min. By suitable manipulation of the manifold valves hydrogen could be made to flow in any one or all of the three gas lines shown in Fig. 1.

Figure 2 gives the details of the helium purification train. Water-pumped, Grade A helium entered the system from storage tanks through a pressure reducing gauge to a flowmeter. From the flowmeter the helium passed through a Meyer-Ronge copper catalyst bed (5) which was maintained at 200°C, then through two traps containing Linde 5A molecular sieve, and then through an additional molecular sieve column immersed in liquid nitrogen. After passing the liquid nitrogen-cooled trap, the gas was saturated with water vapor then sent through an arm of an electrolytic cell, which could be used as an oxygen generator, and then into the electrolysis cell. A water trap on the gas exit side of the cell prevented diffusion of air into the system.

In the "pre-electrolysis" treatment the platinum (99.99% pure) bead and counterelectrode were connected together and made the anode with respect to a platinum wire cathode substituted for the palladium reference electrode. Current of 15 to 180 ma was passed through the hydrogen-saturated electrolyte in the cell for at least 24 hr. After the palladium reference electrode is substituted for the pre-electrolysis cathode, the electrodes were permitted to remain in the hydrogen-saturated electrolyte until the potential between the platinum electrodes was equal to zero and the potential of each palladium electrode was 50 mv positive (the potential of the maximum α Pd-H electrode) to each Pt/H_2 electrode. These α Pd-H electrodes were used as reference electrodes because their potential in the electrolyte used is 50 mv positive to the normal hydrogen electrode (NHE) and is independent of the partial pressure of hydrogen (6).

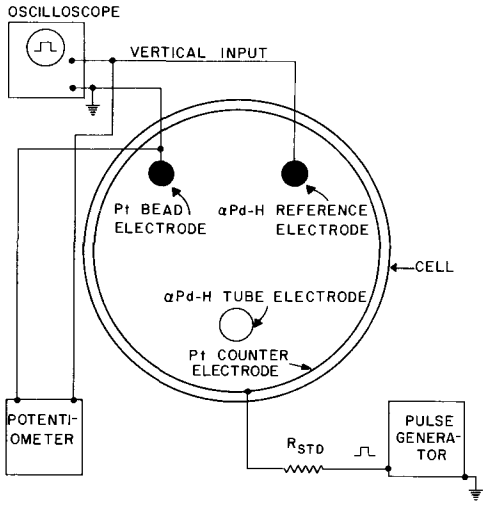

Fig. 3. Circuit diagram

The wiring diagram and cross section of the electrolytic cell is shown in Fig. 3. The electrolytic cell was made from two 2 in. ID flanged glass pipe caps secured by a suitable coupling and Viton A O-ring. The platinum counterelectrode was made from platinum gauze in the form of a cylinder approximately 2¼ in. high and 1⅞ in. in diameter. Electrical connection was through the wall of the glass cap. The Pt and Pd bead electrodes had apparent areas of about 0.1 cm^2. The Pd tube electrode was 2 in. in length, ¼ in. OD and 0.005 in. wall thickness.

The upper half of the cell was a similar flanged glass pipe cap with three flanged glass pipe nipples of varying length projecting from the top of the cap. Two gas inlet ports which led to the bottom of the cell were diametrically opposite one another with an outlet port at right angles.

The platinum bead electrode which was tightly mounted in a drilled Teflon rod was then sealed off with molten polyethylene, the palladium bead electrode and the palladium tube electrode were all inserted through the glass nipples into the cell.

The electrolyte was 2.3N H_2SO_4 made with distilled water that was further purified by redistillation with alkaline permanganate followed by a double distillation in a quartz still. The ambient cell temperature was 25° ± 1°C.

Pulses from an Electro-Pulse Model 3450C pulse generator were passed first through a series of four 1N252 diodes to eliminate a residual d-c current from the generator and then through a current-controlling resistor (R_{std} in Fig. 3). Since the potential drop across this resistor was about two orders of magnitude higher than the voltage drop across the cell, constant current pulses were applied. Changes of potential with time were photographed from the screen of a carefully calibrated Tektronix 535 oscilloscope. A L&N electronic pH indicator was used to observe open-circuit potentials.

Double Layer Capacitance

In order to determine accurately the coulombic equivalent of hydrogen atoms ionized and of oxygen

atoms formed during a charging curve, the number of coulombs used to charge the double layer in these potential regions must be determined. A determination of double layer capacitance *vs.* potential is then necessary because the number of coulombs used to charge the double layer can be considered to be equal to the product of the average double layer capacitance over the applied potential region multiplied by the change in potential.

The double layer capacitance was determined by a single pulse method similar to that used by Schmid and Hackerman (7). Single five microsecond constant current pulses of low current density were applied to the platinum electrode. These pulses were applied at various open-circuit potentials. Since Presbrey and Schuldiner (8) showed that at small overvoltages essentially all of the applied current goes to charging of the double layer in the first 10 μsec, faradaic effects due to the ionization of hydrogen would be negligible.

The open-circuit potential on the platinum electrode was varied from the equilibrium hydrogen potential at 1 atm partial pressure of hydrogen to other equilibrium hydrogen potentials by decreasing the hydrogen partial pressure with hydrogen-helium mixtures. By this means the open-circuit potential was made more noble to a limit of about 0.1v positive to NHE. More positive rest potentials were achieved by bubbling pure helium through the solution mixed with from 0.01 to 1.5% oxygen. For low oxygen concentrations such mixtures caused the rest potential to change to more noble values very slowly (about 16 hr were required to change the potential to about 0.8v positive to NHE).

Higher rest potentials were achieved by anodically polarizing the platinum electrode with a series of 5 μsec pulses, turning them off and letting the potential decay to a point where it changed very slowly with time. Double layer capacitance values were obtained in this way up to about 1v. Higher open-circuit values were determined in the same way, but in these cases the change in potential with time was preceptible in a matter of seconds so that double layer capacitance values had to be taken rapidly during this period. It was difficult to coordinate potential with double layer capacitance in this region and only relatively few values were obtained in this way.

Double layer capacitances also were obtained in helium-saturated solutions in the absence of oxygen by the above polarization and decay technique at potentials below 0.8v. These results checked with values obtained with rest potentials. Double layer capacitances were effectively the same for cathodic or anodic polarization, although most of the values were determined with anodic pulses. The capacitances were independent of current densities, which ranged from about 10 to 40 ma/cm^2. It did not matter if rest potentials were preceded by a more or less positive rest potential.

Figure 4 depicts these 5 μsec charging curves at two open-circuit potentials. The double layer capacitance, C, in microfarads was determined by the relation

$$C = I\Delta t/\Delta E \qquad [1]$$

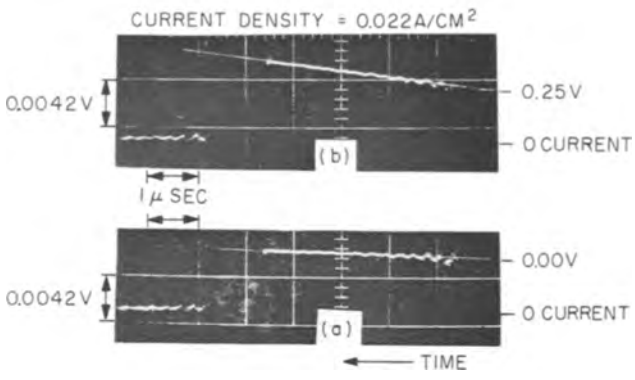

Fig. 4. Typical charging curves used to determine double layer capacitance. Note: The direction of the time scale on this and succeeding oscilloscope traces is reversed from its normal direction. Zero time is on the right side of the pulses. The time scale reads from right to left.

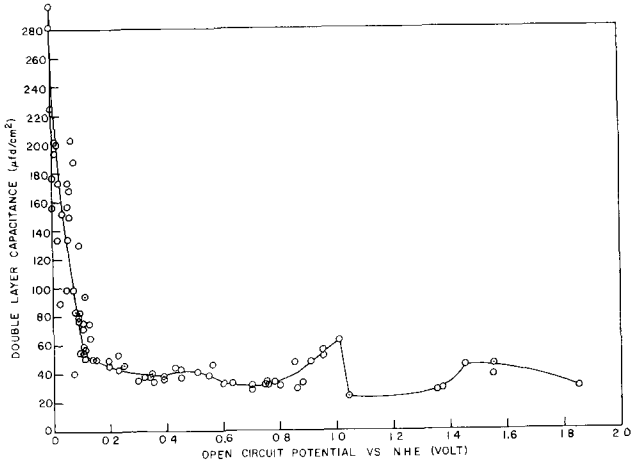

Fig. 5. Double layer capacitance *vs.* open circuit potential

where I is the applied current in amperes, Δt is the change in time in microseconds, and ΔE is the change in potential in volts during Δt. The less steep curve Fig. 4a indicates a higher capacitance than the curve shown in Fig. 4b. The area of the electrode was determined by a method which will be described later.

Figure 5 shows the double layer capacitance *vs.* open-circuit potential relation obtained. As can be seen, reproducibility was reasonably good except near zero potential. Here poor reproducibility can be attributed to the extreme sensitivity of the platinum electrode surface. It is believed that in this region the double layer capacitance on platinum does change drastically from moment to moment and that these large variations are not due to experimental error or to impurities. The impurity effect was discounted because an increase in double layer capacitance was just as likely from one measurement to a succeeding one as was a decrease.

Anodic Charging Curves

A typical anodic charging curve in hydrogen-saturated solution is shown in Fig. 6. Similar curves have been obtained by Pearson and Butler (4), Breiter, Knorr, and Völkl (2), and others. However, it is felt that some additional details, which could be measured with a reasonable degree of accuracy, are apparent. This charging curve depicts a series of events occurring at the platinum anode. The per-

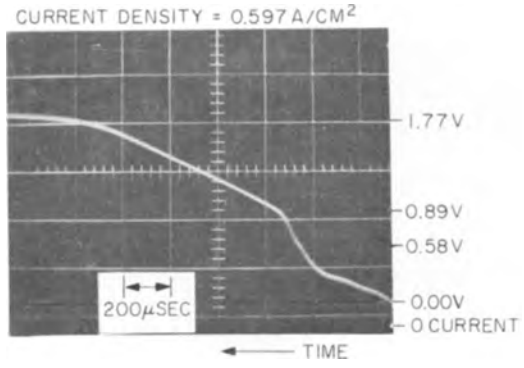

Fig. 6. Typical anodic charging curve for $P_{H_2} = 1$ atm

pendicular rise from the foot of the pulse at open circuit (zero current) to the point at zero potential is due to the solution *IR* drop between the working and reference electrode. All polarization potentials have been corrected for this solution resistance polarization. The potentials shown on the charging curves represent these corrected polarization potentials.

The portion of the curve shown in Fig. 6 from 0 to 0.58v represents the ionization of hydrogen atoms sorbed on the platinum electrode. At 0.58v a slightly detectable arrest is apparent followed by a sharp rise to 0.89v. This rise is usually considered to represent the charging of the double layer to a potential at which oxygen atoms can be formed. However it will be shown that when hydrogen is sorbed on the platinum at open circuit, the bulk of the coulombs represented by this potential rise is owing to hydrogen atoms being ionized. Only about one-third of the number of coulombs go to charging the double layer. However, in respect to tradition, the potential range from about 0.55 to 0.88v will be referred to as the double layer charging region. The linear rise from 0.89 to 1.77v is caused by the formation of a monolayer of oxygen atoms (1, 9). Molecular oxygen is evolved above 1.78v.

At an open-circuit potential of about 0.35v (these were varied as in the determination of double layer capacitance) no hydrogen remains sorbed on the platinum. This can be seen from Fig. 7 where the hydrogen ionization region is absent. The sharp linear rise between 0.34 and 0.85v here truly represents the charging of the double layer capacitance. The calculation, using Eq. [1], of the double layer capacitance from a number of similar curves gave

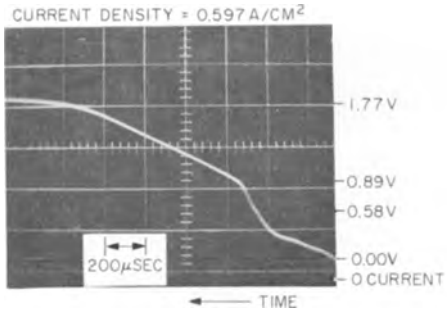

Fig. 7. Typical anodic charging curve for $P_{H_2} = 0$ atm

Table I. Values of potential regions (*vs.* NHE)

Hydrogen ionization region	0 to 0.55 ± 0.07v
Double layer charging region	0.55 to 0.88 ± 0.04v
Oxygen atom adsorption region	0.88 to 1.76 ± 0.07v
Molecular oxygen evolution	Starts at 1.76 ± 0.07v

an average C close to 40 μF/cm². This value is in good agreement with the independently determined average double layer capacitance shown in Fig. 5 for the same potential region.

Average potential values of the boundaries of the various regions taken from over one hundred separate charging curves, using pulse widths from 400 to 2000 μsec and current densities from 0.6 to 2 amp/cm², are given in Table I. The percentage error is most marked for the limit of the hydrogen ionization region. This is not only because a separation between two sharply rising curves is necessary, but also because the arrest between the two curves was just perceptible.

Determination of True Surface Area

Butler and co-workers proposed that the surface area of a platinum electrode could be determined by the number of oxygen atoms deposited on the surface in the linear oxygen atom formation region. This proposal assumes that a monolayer of oxygen atoms is formed in this region and that there is a one-to-one correspondence between platinum and oxygen atoms. The experimental validity of these assumptions is given in references (1-3, 10) and in the literature quoted therein. There is some question, however, as to whether the monolayer of oxygen was chemisorbed or a unimolecular layer of PtO was formed (9). The double layer capacitance *vs.* potential relationships shown in Fig. 5 as well as the results in perchloric acid given by Laitinen and Enke (10) support the chemisorbed oxygen atom proposal, since both investigations do not indicate a falling off of double layer capacitance in the oxygen formation region. If a true oxide were formed, one would expect a falling off in double layer capacitance as the surface became covered with the oxide.

In this investigation, the areas of the platinum electrodes were determined in the following way. The transition times, in microseconds, of linear oxygen atom adsorption regions (as shown in Fig. 6 and 7) were determined. Multiplying these transition times by the applied currents, in amperes, gave the total numbers of microcoulombs consumed in these regions. These microcoulombs were consumed in two processes, (*a*) by the charging of the double layer in the potential region from about 0.88 to 1.76v, and (*b*) in the formation of oxygen atoms. The number of microcoulombs consumed in charging the double layer was determined from the average double layer capacitance in the potential region from 0.88 to 1.76v. This average was determined by plotting a double layer capacitance *vs.* potential relation, integrating under this curve in the required potential region and dividing by ΔE (0.88v). The number of microcoulombs required to charge the average double layer capacitance from 0.88 to 1.76v

was then subtracted from the total number of microcoulombs consumed in the oxygen atom adsorption region of the charging curves. The resulting number of microcoulombs represented the number of oxygen atoms adsorbed as a monolayer on the platinum electrode. Using the value of 1.31 x 10^{15} platinum atoms/cm^2 (11) and assuming a one-to-one correspondence between oxygen and platinum atoms on the surface, the true area of the electrode was readily determined. Areas of the electrodes used were all determined in this way as were all current density values given in this paper. Calculations of the true electrode area were made also by taking a geometric area of the electrodes and multiplying by a roughness factor of two; these calculations gave values which were close to those found above.

Oxygen Atom Adsorption Region

The oxygen atom adsorption regions on the charging curves were very linear when no oxygen was present in the gas bubbling through the electrolyte. However, when oxygen was added and the open-circuit potential was above 0.175v this region was slightly convex, as a close examination of Fig. 7 will show. This effect is probably due to the coverage of some sites with molecular oxygen or other oxygen containing species. This is borne out by the results shown in Fig. 8. This figure shows a plot of the relation between the number of oxygen atoms adsorbed as a result of coulombic charging and the open-circuit potential for two platinum electrodes of different sizes. The resulting curves show that the number of atoms adsorbed is virtually independent of hydrogen partial pressure and of even a small amount of oxygen up to an open-circuit potential of about 0.175v. At higher open-circuit potentials there is a significant decrease in the number of oxygen atoms formed during anodic charging. This decrease undoubtedly is due to the partial covering of the platinum with molecular oxygen and/or oxygen bearing species. The curves in Fig. 8 clearly show that during the time of charging the reaction of molecular hydrogen with the chemisorbed atomic oxygen is negligibly slow.

In the open-circuit region from 0 to 0.175v, the slope of the oxygen atom adsorption region gives an average oxygen atom adsorption capacitance of 478 μFd/cm^2. The fact that this region is so linear (except, of course, for the slight rounding off at each

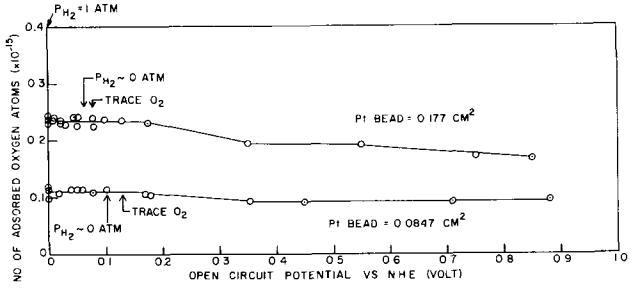

Fig. 8. Dependence of the number of oxygen atoms adsorbed during anodic charging on the open-circuit potential. Note: Arrows indicate hydrogen partial pressure limits (1 atm at zero potential decreasing to zero atm at points indicated on each curve) and potentials at which oxygen was first introduced into the cell.

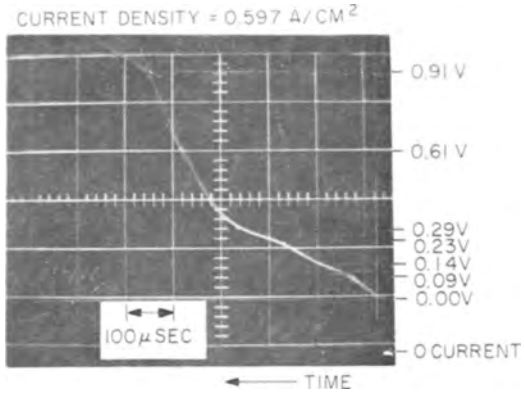

Fig. 9. Anodic charging curve in hydrogen ionization region

end) indicates that this adsorption capacitance is independent of potential. In fact, it strongly indicates that the potential is determined by the degree of surface coverage with adsorbed oxygen atoms.

Hydrogen Ionization Region

A close examination of the hydrogen ionization region (Fig. 9) shows that there is indeed a very complex relation between hydrogen atom sorption and potential. The total number of hydrogen atoms ionized up to the start of the double layer region (0.55v) was determined by taking the total number of coulombs/cm^2 in the transition region as determined from the charging curves, subtracting the number of coulombs/cm^2 used to charge the double layer from the open-circuit potential to 0.55v (average double layer capacitance/cm^2 from integration of appropriate potential regions under curve in Fig. 5) and multiplying by 6.25 x 10^{18} (factor for converting coulombs to number of atoms).

The relation between the number of hydrogen atoms ionized up to the double layer region and the open-circuit potential is given in Fig. 10 (middle curve). The number of hydrogen atoms which were ionized in the double layer region (0.55 to 0.88v) was determined after subtraction of the number of charges used to raise the potential of the double layer by this additional 0.33v. The average value of capacitance/cm^2 again was determined from Fig. 5.

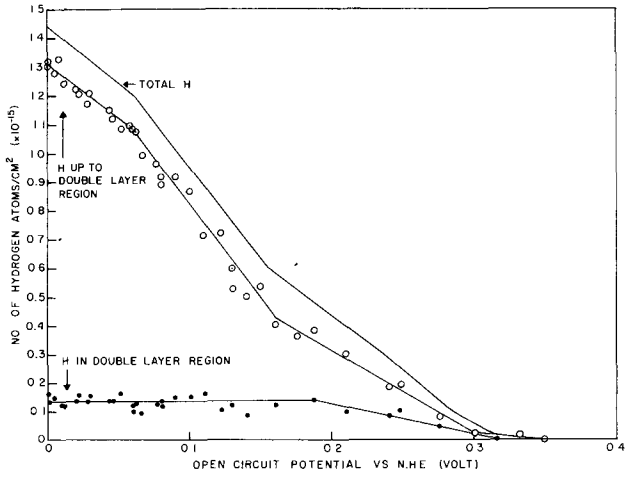

Fig. 10. Dependence of the number of hydrogen atoms per cm^2 of electrode surface on the open circuit potential.

Table II. Number of hydrogen atoms in each section of the charging curve up to the oxygen formation reaction

Open-circuit potential *vs.* NHE, v	Limiting potential of each section						No. of H atoms/cm² (× 10^{-15})					
	E_{H_1}	E_{H_2}	E_{H_3}	E_{H_4}	E_{H_5}	E_{H_6}	H_1	H_2	H_3	H_4	H_5	H_6
0.000	0.09	0.14	0.23	0.29	0.61	0.91	0.09	0.23	0.26	0.34	0.36	0.16
0.020	0.08	0.13	0.21	0.27	0.60	0.88	0.09	0.21	0.23	0.32	0.39	0.14
0.022	0.08	0.14	0.21	0.27	0.59	0.88	0.09	0.24	0.17	0.32	0.37	0.16
0.130	—	—	0.22	0.31	0.55	0.89	0.00	0.00	0.14	0.23	0.18	0.12

The bottom curve in Fig. 10 shows the relation between the number of hydrogen atoms ionized in the double layer region and the open-circuit potential. The fact that the number of hydrogen atoms in the double layer region is essentially independent of the hydrogen partial pressure up to an open-circuit potential of about 0.2v, proves conclusively that the number of hydrogen molecules which dissociate to give hydrogen atoms during the charging period is insignificant. Even a small amount of oxygen in this potential range does not affect the number of hydrogen atoms ionized. This shows that the reaction rate between oxygen and adsorbed hydrogen atoms at these low oxygen partial pressures and short transition times is so slow that this reaction has a negligible effect. Previous work (8, 12) indicated that in the 400 μsec or shorter interval used in removing the hydrogen by anodic charging, about 2×10^{12} hydrogen molecules will dissociate to hydrogen atoms. This means that to see the effects of dissociation of hydrogen molecules one would have to increase the precision of the data shown in Fig. 10 by about 100 times.

The uppermost curve in Fig. 10 represents the relationship between the total amount of hydrogen ionized and the open-circuit potential. Breiter's data (13) gives points which correspond closely to the upper and lower parts of the middle curve in Fig. 10. Intermediate points on Breiter's curve appear to lie between the middle and upper curves.

An examination of each section of the complex hydrogen ionization curves, as shown in Fig. 9, was made at several open circuit potentials. These data, corrected for double layer charging, are summarized in Table II. These results show that the six relatively linear parts of the over-all hydrogen ionization region occurred in well-defined potential ranges which were independent of the open-circuit potential (hydrogen partial pressure) on the platinum. It is instructive to note that even though the partial pressure of molecular hydrogen has been reduced to about two-tenths of an atmosphere for the 0.020 and 0.022v equilibrium open-circuit values, the effects of molecular hydrogen atomization are not apparent in the zero potential curve. This further supports our contention that dissociation of molecular hydrogen is of insignificant effect on our charging curves. Also, it is interesting to note in the 0.13v open-circuit charging curve that while sections 1 and 2 are completely gone, a lowering of hydrogen content in sections 3, 4, and especially 5 all occur. Hence it appears that as the open-circuit potential becomes increasingly positive, some hydrogen (but not in relatively equal amounts) is lost from each of these regions.

Even though this investigation has shown that the hydrogen ionization region can be broken down into six well-defined potential sections and the hydrogen content of each can be determined with reasonable accuracy, this still does not indicate the different ways in which the hydrogen atoms are associated with the platinum surface. Presbrey and Schuldiner (8) discuss this in some detail. In the present paper we can only say that hydrogen is sorbed on platinum, most of this sorption is probably a combination of strongly and weakly bonded chemisorbed H atoms, and part is probably hydrogen atoms alloyed with the surface layers of platinum. The fact that the first section has only 0.09 $\times 10^{15}$ H atoms/cm² (the degree of surface coverage, θ, would be about 0.07) indicates that only relatively few of the H atoms are active near the NHE equilibrium potential. The total hydrogen curve in Fig. 10 indicates four major hydrogen sorption regions. Each of these regions can be represented by essentially a linear atom number *vs.* potential relation.

Acknowledgments

The authors are indebted to Dr. J. C. White for his suggestions and advice during the course of the work. They are also grateful for the assistance given by C. H. Presbrey, Jr. on instrumentation.

Manuscript received June 11, 1962; revised manuscript received Aug. 2, 1962. This paper was prepared for delivery before the Pittsburgh Meeting, April 15-18, 1963.

Any discussion of this paper will appear in a Discussion Section to be published in the December 1963 JOURNAL.

REFERENCES

1. J. A. V. Butler, "The Behavior of Oxygen and Hydrogen at Electrodes," in "Electrical Phenomena at Interfaces." J. A. V. Butler, editor, p. 204, Macmillan, New York (1951).
2. M. Breiter, C. A. Knorr, and W. Völkl, *Z. Electrochem.*, **59**, 681 (1955).
3. K. J. Vetter, "Elektrochemische Kinetik," p. 500, Springer-Verlag, Berlin (1961).
4. J. D. Pearson and J. A. V. Butler, *Trans. Faraday Soc.*, **34**, 1163 (1938).
5. F. R. Meyer and G. Ronge, *Angew. Chemie*, **52**, 637 (1939).
6. S. Schuldiner, G. W. Castellan, and J. P. Hoare, *J. Chem. Phys.*, **28**, 16 (1958).
7. G. M. Schmid and N. Hackerman, *This Journal*, **109**, 243 (1962).
8. C. H. Presbrey, Jr. and S. Schuldiner, *ibid.*, **108**, 985 (1961).

9. A. Hickling, *Trans. Faraday Soc.*, **41**, 333 (1945).
10. H. A. Laitinen and C. G. Enke, *This Journal*, **107**, 773 (1960).
11. W. F. Meggers, "Key to the Welch Periodic Chart of the Atoms," 1959 ed., Welch Scientific Co., Chicago (1959).
12. S. Schuldiner, *This Journal*, **106**, 891 (1959).
13. M. Breiter, "Kinetics of Hydrogen Evolution and Dissolution at Activated Platinum Metals," in "Transactions of the Symposium on Electrode Process." E. Yeager, editor, p. 316, John Wiley & Sons, New York (1961).

Technical Notes

Phenomena at a Solid-Melt Interface

J. R. O'Connor

Lincoln Laboratory,[1] Massachusetts Institute of Technology, Lexington, Massachusetts

The general theory of crystal growth distinguishes between two mechanisms (1): (*a*) the growth interface is singular and advances by the lateral motion of steps or (*b*) the growth interface is diffuse and can advance normal to itself without the need of steps. Two experiments, which were designed to investigate such phenomena, have been performed.

One experiment studies the distribution coefficient, k, of Sb in Ge as a function of crystal orientation. Anisotropy in this coefficient was first reported by Hall (2). In this experiment tricrystals are grown from an Sb doped Ge melt. The simultaneous growth of tricrystals minimizes variations in several crystal growth parameters. The distribution coefficient is then calculated from the variation of conductivity along the growth axis. The seeds of these crystals were oriented in the [111], [100], [110], and [112] directions. When a [112] seed was used, the crystal invariably twinned to a [$\bar{1}\bar{1}$2] direction. Several crystals were grown at various growth rates. The data on these crystals are shown in Fig. 1. In particular one notes that (*a*) a minimum k is obtained for a [$\bar{1}\bar{1}$2] crystal direction, (b) a small but finite difference exists between [$\bar{1}\bar{1}$2] and [112] crystal orientations, (*c*) for growth rates, f, between 2 and 7 in./hr, the distribution coefficient rises at a rapid rate, (*d*) the coefficients for [100], [110], and [$\bar{1}\bar{1}$2] orientations are intermediate between those for [111] and [112] directions, and (*e*) at large growth rates the slopes of all the curves appear equal. The anisotropy in k as well as the value of k extrapolated to zero growth rate, k_0, are in agreement with previous work (2, 3). For different tricrystals grown at the same rate, variations in the anisotropy of k varied as much as 5%. To investigate this discrepancy [111] crystals were grown from low and high thermal gradient melts. For a high gradient the anisotropy in k was reduced by a factor of two. Other parameters (*e.g.*, differences in melt concentration, variations in crystal diameter, etc.) were not investigated.

[1] Operated with support from the U.S. Army, Navy, and Air Force.

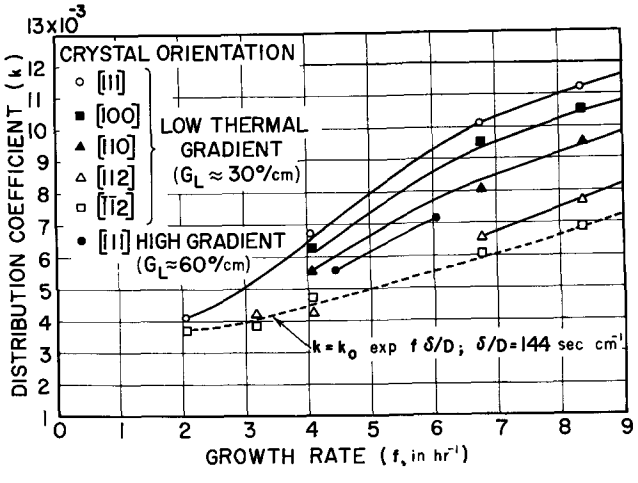

Fig. 1. Distribution coefficient of Sb in Ge is plotted as a function of growth rate for several crystal orientations.

The data of Fig. 1 are interpreted as follows. The [$\bar{1}\bar{1}$2] interface of Ge is nonsingular and can advance normal to itself. For low growth rates the theory of Burton *et al.* (3) indicates that k should increase exponentially with growth rate. This dependence is shown as a dashed curve in Fig. 1 for a value of $\delta/D = 144$ sec cm^{-1}. The [111] interface is singular and requires the nucleation of growth steps in order to advance. The lateral motion of these growth steps, which is much larger than the actual growth rate of the crystal (4), causes a nonequilibrium amount of Sb to be frozen into the crystal. This mechanism can account for the increased value of $k_{[111]}$. Interfaces normal to [100] and [110] poles are probably stepped surfaces (5) comprised of segments oriented in [111] and [$\bar{1}\bar{1}$2] directions. For these surfaces k should be intermediate $k_{[111]}$ and $k_{[\bar{1}\bar{1}2]}$ and it is reasonable that $k_{[100]} > k_{[110]}$. In addition to growth phenomena one should consider anisotropy in the adsorption of Sb on different Ge crystal faces. This type of experiment cannot distinguish between these two mechanisms.

To treat this problem theoretically is a rather formidable task. For example, one should simultaneously consider (*a*) fluid flow in the melt, (*b*) solute concentration gradients and the resultant un-

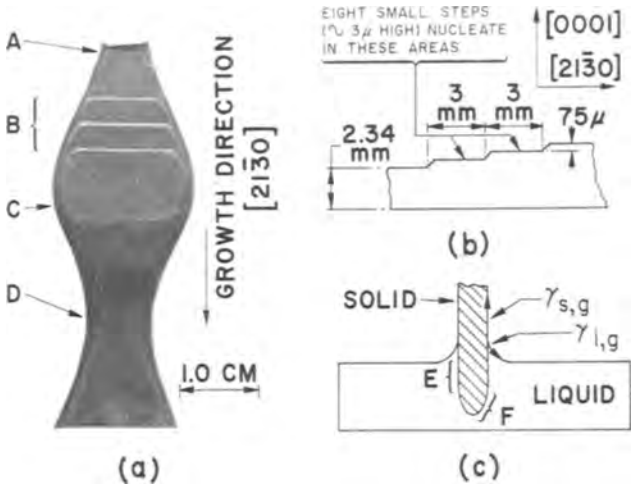

Fig. 2a. Single crystal of Bi_2Te_3 grown from the melt under varied conditions. The upper half of the crystal has been etched so as to reveal dislocations; b, schematic diagram of growth steps through section B; c, schematic diagram of the growth interface.

dercooling at the interface, (c) phenomena at the interface involving adsorption, diffuseness, nucleation, re-entrant corners, etc., (*d*) the effect of impurities on these properties as well as changes in interfacial energy, and finally (*e*) solid-state diffusion. Additional experiments of the type described are necessary before one could attempt a complete analysis.

The following experiment deals with the morphology of Bi_2Te_3 crystals grown from the melt. This is an interesting system in that the structure of Bi_2Te_3 is analogous to α-II SiC, whose properties have been studied so extensively (6). That is, both materials have faulted, hexagonal crystal structures and tend to grow as platelets oriented in the [21$\bar{3}$0] direction. For SiC screw dislocations are required for growth normal to the basal plane whereas for Bi_2Te_3 a two-dimensional nucleation process is observed.

Several single crystals have been grown in a hydrogen atmosphere from stoichiometric melts. At growth rates greater than 1 in./hr the crystals assumed a ribbonlike "dendritic" form. From these growth rates the melt is undercooled and the crystals have flat, mirrorlike (0001) faces. Figure 2a shows some of the more interesting features of these crystals. Prior to point A the crystal was grown from the melt with uniform width and thickness. However, throughout the entire growth process the crystal thickness slowly increases at a rate of 8 μ/mm. This is due to the nucleation of ~3μ steps at the rotating solid-liquid interface. That is, the period of this step formation coincides with the pulling and rotation rates. At point A the melt temperature was lowered and for some time the crystal becomes wider, but not thicker. In the range B, however, the undercooling has increased sufficiently so that large steps are nucleated. A cross section along the growth axis through this region is shown in Fig. 2b. Each large step is composed of at least three smaller steps of ~25μ height. The morphology of these steps is undoubtedly modified as they pass through the solid-liquid interface because the liquid-gas interfacial energy, $\gamma_{l,g}$, is reasonably large. It should also be noted that the large steps are nucleated on either one face or the other, but not simultaneously on both. At point C the melt temperature has been raised and the crystal width slowly decreases, but the thickness remains constant. At point D the melt temperature is again lowered. The crystal now grows out to a width greater than that at C before new large steps are nucleated. Figure 2c shows a side view of the interface geometry. Region *E* is flat and in contact with undercooled melt. The geometry at F depends on thermal and crystallographic factors. During growth a new plane may be nucleated on E when the undercooling is sufficiently large. The rate of growth is limited only by the rapidity with which the latent heat is dissipated in the undercooled melt. It appears that the 25μ layers interact thermally and that these layers require appreciable undercooling for nucleation to take place. The upper half of the crystal in Fig. 2a has been etched to reveal dislocations. There is no evidence for screw dislocations; however, a large density of edge dislocations is present. Bi_2Te_3 seems to be an ideal material to study in regard to dendritic and nucleation processes.

Acknowledgment

These experiments were performed several years ago with the assistance of W. A. McLaughlin, F. D. Shepherd, and A. C. Yang of the Air Force Cambridge Research Laboratories. The writer also acknowledges several recent discussions with A. J. Strauss at Lincoln Laboratory.

Manuscript received Nov. 19, 1962. This paper was prepared for delivery before the Boston Meeting, Sept. 16-20, 1962.

Any discussion of this paper will appear in a Discussion Section to be published in the December 1963 JOURNAL.

REFERENCES

1. W. K. Burton, N. Cabrera, and F. C. Frank, *Phil. Trans. Roy. Soc., London*, **A243**, 299 (1950).
2. R. N. Hall, *Phys. Rev.*, **88**, 139 (1952).
3. J. A. Burton, R. C. Prim, and W. P. Slichter, *J. Chem. Phys.*, **21**, 1987 (1953).
4. R. L. Longini, A. I. Bennett, and W. J. Smith, *J. Appl. Phys.*, **31**, 1204 (1960).
5. W. A. Tiller, *ibid.*, **29**, 611 (1958).
6. See for example the papers by Amelinckx *et al.*, Verma, and Jagodzinski *et al.* in "Silicon Carbide —A High Temperature Semiconductor," J. R. O'Connor and J. Smiltens, Editors, Pergamon Press, New York (1960).

The Thermoluminescence of CaF_2:Mn

William F. Schmid and Richard W. Mooney

Chemical and Metallurgical Division, Sylvania Electric Products Inc., Towanda, Pennsylvania

In 1957 Ginther and Kirk (1) reported the preparation of CaF_2:Mn phosphor and the dependence of its thermoluminescence on manganese content and added substituents. Schulman and co-workers (2) used CaF_2:Mn in the development of a radiation dosimeter tube. Recent work in these laboratories has led to an alternate method of preparation and to the discovery that the addition of chloride ion improves the thermoluminescent efficiency of the phosphor.

In Ginther's method of preparation (3), the raw materials were contained in a covered Pt crucible. This Pt crucible was placed in a recrystallized alumina crucible which in turn was placed in a larger alumina crucible containing carbon to provide a reducing atmosphere. The exterior crucible was tightly fitted with a Pt cover. By firing overnight at 1200°C, Ginther obtained a phosphor with a white body color. Repeated attempts in this laboratory to duplicate Ginther's technique and results were invariably unsuccessful. The method was also extremely destructive to platinum.

An alternate procedure was developed as follows. Calcium fluoride was precipitated by the simultaneous dropwise addition of purified $CaCl_2$ solution and NH_4F solution to boiling deionized water. The CaF_2 thus prepared contained less oxygen in the form of hydroxide or carbonate (see analyses below) than CaF_2 prepared in this laboratory using Ginther's method (4) or a commercial electronic grade CaF_2.

	% $Ca(OH)_2$	% $CaCO_3$
CaF_2 prepared from $CaCO_3$ + HF(sol.)	7.78	3.21
CaF_2, commercial electronic grade	2.68	1.34
CaF_2 prepared from $CaCl_2$(sol.) + NH_4F(sol.)	2.55	0.48

When CaF_2 having a high oxygen content was used, the manganese reacted preferentially with the oxygen forming the colored oxides of manganese instead of entering the CaF_2 lattice. Ammonium manganous fluoride, NH_4MnF_3, was prepared by Ginther's method (4).

The nonmodified phosphor was prepared by mortaring 1.0 mole of CaF_2 with 0.03-0.10 mole of NH_4MnF_3 and blending. The dry mix was fired in recrystallized alumina crucibles or boats for 4 hr at 1200°C in a 2% H_2-98% N_2 atmosphere. A richer H_2 content reduced manganese to the metal. The product had a very faint greenish color and was washed to whiteness with 10% HCl solution.

The apparatus for the measurement of thermoluminescence is illustrated in Fig. 1. The phosphor

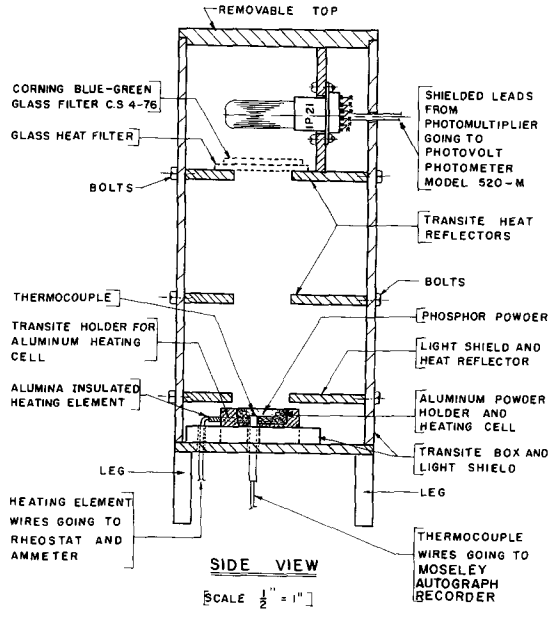

Fig. 1. Apparatus for the detection of thermoluminescence

to be tested was packed into the Al holder and exposed for 1 min to radiation from a W x-ray tube at 60 kv and 40 ma. X-ray irradiation produced two color centers in most of the phosphors. The brown color centers disappeared when the low-temperature traps were emptied, and the green centers vanished when the higher temperature traps were emptied. The Al sample holder containing the undisturbed phosphor was transferred directly to the detection apparatus. The advantage of using the same holder for irradiation by x-rays and measurement of thermoluminescence is the elimination of any movement of powder which results in triboluminescence. A heating rate of 0.5°C/sec was used.

The brightest unmodified phosphor, obtained within the range 3.5-6.7 mole % Mn, was only 42% of the peak height of Ginther's phosphor (3). At

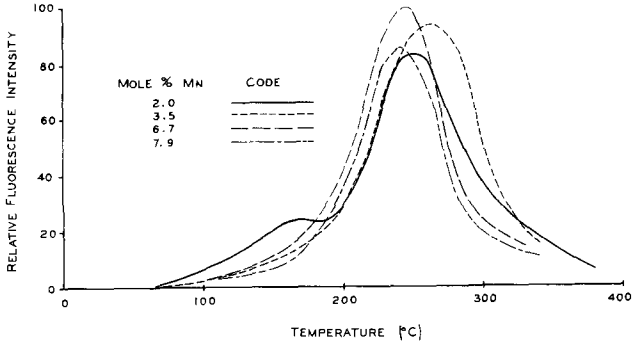

Fig. 2. Thermoluminescence curves of CaF_2:Mn at various activator concentrations.

Table I. Effect of added chloride ion on Mn concentration and peak height of thermoluminescent emission

	Moles of added chloride compound*					
	0	0.01	0.02	0.04	0.06	0.08
NH_4Cl						
mole % Mn	4.97	4.34	4.33	3.97	3.44	3.10
Rel. pk. int.	62	56	56	115	490	250
$CaCl_2$						
mole % Mn	4.97	4.07	2.50	1.78	1.05	0.86
Rel. pk. int.	62	300	740	540	570	520
NaCl						
mole % Mn	4.97	4.21	4.20	2.90	2.28	2.06
Rel. pk. int.	62	33	22	25	42	66

* The chloride compound was added to 1.0 mole of CaF_2 and 0.06 mole of NH_4MnF_3.

low manganese concentrations of 2 mole %, a low-temperature emission occurs at about 160°C. Ginther (1) also reports this effect at manganese concentrations of 1 mole % or less. Representative curves of thermoluminescent intensity *vs.* temperature are shown in Fig. 2. The temperature at which maximum emission is observed plotted as a function of the phosphor's manganese content revealed that the manganese concentration for maximum emission also roughly corresponded to that of the maximum temperature peak.

The addition of NH_4Cl in the authors' synthesis procedure greatly improved the brightness of the phosphor, but the presence of chloride (0.18 mole % or greater) produced low-temperature emission peaks. However, the use of NH_4Cl as a flux, with most of the chloride volatilized out, gave no low-temperature peaks and higher temperature emission than without the use of the flux. A CaF_2:Mn phosphor with 0.09 mole NH_4Cl added, prepared in this laboratory, was measured at 76% of the peak height of Ginther's phosphor (3).

In order to determine if the effect was specifically attributable to NH_4Cl or was associated with the chloride ion only, a series of phosphors was prepared incorporating various amounts of NH_4Cl, $CaCl_2$, and NaCl. The results, summarized in Table I, lead to the following conclusions:

1. The Mn content decreases with increasing chloride concentration indicating volatilization of $MnCl_2$.
2. The use of $CaCl_2$ gave a thermoluminescent phosphor with the greatest peak height.
3. It required considerably more NH_4Cl than $CaCl_2$ to produce a comparable decrease in Mn content and increase in peak height of thermoluminescence.
4. The use of NaCl did not produce an improvement.

The thermoluminescence glow-curves showed a characterisic temperature spectrum for CaF_2:Mn, consisting of very low intensity peaks between 80°-160°C, a high intensity peak between 245°-290°C, and a very low intensity peak at temperatures greater than 360°C. The relative intensities given in the table are those of the highest emission peak. When $CaCl_2$ is added, the low-temperature emission peak is enhanced along with the main peak. In addition, a high intensity peak at about 320°C is observed overlapping the main band. Two high intensity bands at about 250° and 290°C were clearly evident when NaCl was added. The relative intensities of these two bands varied with the concentration of Na and Mn. As in the original series, the addition of NH_4Cl to the phosphor mix increased the thermoluminescence without producing low-temperature emission bands.

The chief conclusion to be drawn from the results is that, although the Mn concentration is the main determining factor for brightness, the addition of chloride ion in the form of $CaCl_2$ or NH_4Cl improves the thermoluminescent efficiency possibly by acting to minimize the amount of oxides of manganese that are formed. An alternate explanation is that the chloride ion present in the final phosphor to the extent of 0.02-0.11 mole % by analysis may be producing a defect CaF_2 lattice similar to the proposed defect effect of halide in ZnS (5).

Acknowledgment

The authors are indebted to Dr. R. J. Ginther of the Naval Research Laboratories for discussions of his techniques and measurements on some of the early samples.

Manuscript received Nov. 7, 1962.

Any discussion of this paper will appear in a Discussion Section to be published in the December 1963 JOURNAL.

REFERENCES

1. R. J. Ginther and R. D. Kirk, *This Journal*, **104**, 365 (1957).
2. J. H. Schulman, F. H. Attix, E. J. West, and R. J. Ginther, *Rev. Sci. Instr.*, **31**, 1263 (1960).
3. R. J. Ginther, Private communication.
4. R. J. Ginther, *This Journal*, **101**, 248 (1954).
5. R. H. Bube, *J. Phys. Chem.*, **57**, 788 (1953).

Surface Masking in Gallium Arsenide During Diffusion

T. H. Yeh

Components Division, International Business Machines Corporation, Poughkeepsie, New York

The publication of several recent papers (1, 2) indicates a growing interest in the subject of impurity diffusion in gallium arsenide. Progress in making planar-type diode and transistor structures for gallium arsenide would be significantly accelerated by the development of a diffusion-masking technique analogous to that which has proved so useful for the silicon-diffusion technology. Studies at IBM's laboratory show that silicon monoxide can be used as a masking material against the diffusion of cadmium and zinc in gallium arsenide.

Undoped, as well as tellurium-doped, n-type single crystals of gallium arsenide with (111) orientation were used for these studies. The undoped

gallium arsenide crystal (used in the study of cadmium) had a net impurity concentration of 2.2×10^{17} cm^{-3} and an electron mobility of 4430 cm^2/volt-sec. The tellurium-doped crystal (used in the study of zinc) had a net impurity concentration of 1.8×10^{18} cm^{-3} and an electron mobility of 2600 cm^2/volt-sec. Etched wafers ($H_2SO_4/H_2O_2/H_2O$ solution), as well as optically polished wafers, were used in this study. Silicon monoxide film thicknesses of approximately 10,000, 8250, 2250, 1500, and 1000Å have been tested for the effect of masking against the diffusion of cadmium and zinc in gallium arsenide. The silicon monoxide films were evaporated onto half of the wafer surfaces. Two wafers were used in each diffusion run: one wafer had silicon monoxide covering half of the wafer surface; the other had none. Two diffusion experiments were carried out for each particular film thickness in the study.

Wafers were placed on a flat quartz plate which was then inserted into a quartz capsule. A small quartz capillary containing either 1.5 mg of zinc or 3-4 mg of cadmium, and a small quartz cup containing the necessary amount of arsenic (3) to suppress the wafers' decomposition, were placed underneath the quartz plate. The quartz capsule (about 20 ml) was attached to a high-vacuum system, pumped down to about 2.0×10^{-6} mm Hg, and then sealed off.

Zinc diffusion experiments were carried out at 718°C for 6 hr. Cadmium diffusion experiments were carried out at 718°C for 72 hr. The capsules were cooled with a cold zone at one end to avoid condensation of arsenic, cadmium, or zinc on the gallium arsenide wafers. After the diffusion was completed, the silicon monoxide on the wafer surface was removed with hot concentrated HF solution. The optically polished or etched surface was retained after the diffusion process. Hall measurements and p-n junction delineation by an aqueous copper sulfate solution plus HF or diluted nitric acid without HF were performed on each wafer. Junction depths (where wafer surface was not protected by the silicon monoxide) were then determined by the copper-plating or nitric acid staining and by the interference fringe method. Some typical examples are shown in Fig. 1-3.

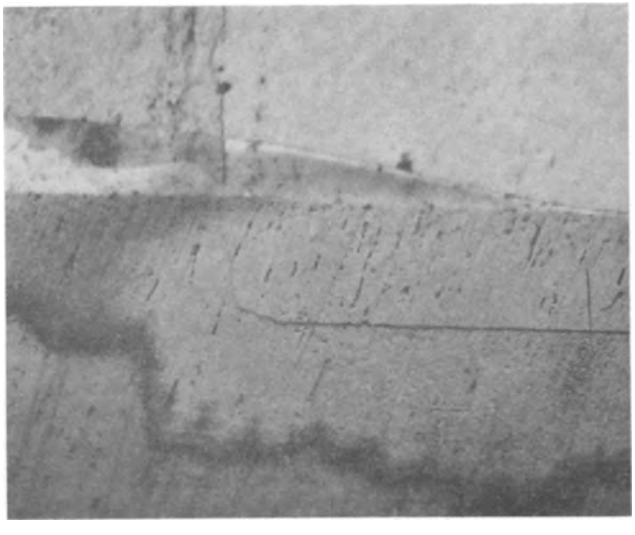

Fig. 1. GaAs wafer treated with copper sulfate solution. P-N junction delineated at right; no junction at left because of masking effect of SiO. Magnification 150X.

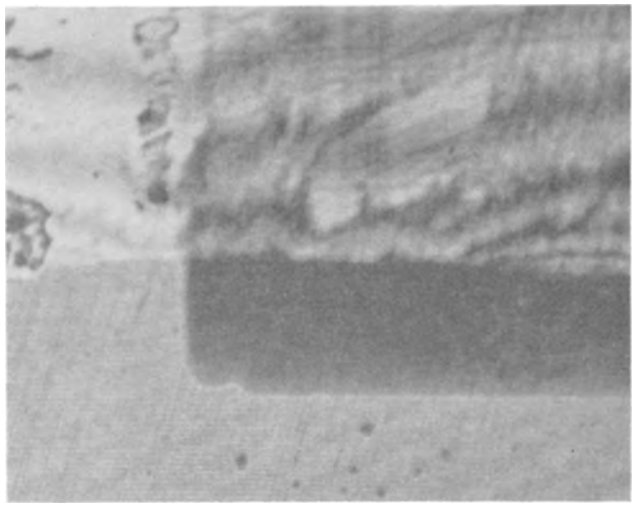

Fig. 2. GaAs wafer treated with diluted nitric acid. P-N junction delineated at right; no junction at left because of masking effect of SiO. Magnification 150X.

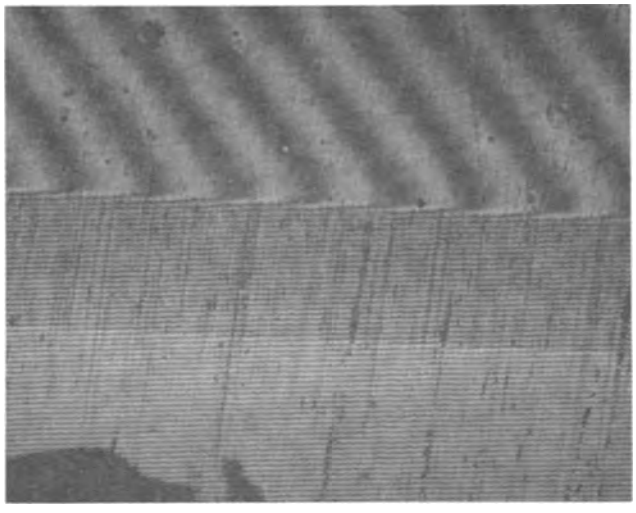

Fig. 3. P-N junction delineated on GaAs wafer by diluted nitric acid and superimposed interference fringes. Magnification 150X.

The results indicated that n-type gallium arsenide wafers remained n-type[1] after the diffusion (4, 5), with nearly the same electron mobility and impurity concentration as before the diffusion if the wafer surface had approximately 2250Å, or more, of silicon monoxide. A thickness of 1500Å, or less, of silicon monoxide did not completely mask against the diffusion of cadmium or zinc. Spotted areas of diffused p-layer were formed on the surface. Otherwise, with no silicon monoxide for protection, a p-layer of 0.3 ~ 0.4 mil would materialize on n-type gallium arsenide wafers from the zinc or cadmium diffusion.

Acknowledgment

The author wishes to thank Dr. G. A. Silvey and Dr. A. E. Blakeslee for their valuable discussions and R. M. DeFries and E. F. Gorey for their assistance in performing the experiments and the Hall measurements, respectively.

[1] No thermal conversion was observed in this study.

Manuscript received Oct. 11, 1962.

Any discussion of this paper will appear in a Discussion Section to be published in the December 1963 JOURNAL.

REFERENCES

1. F. A. Cunnell and C. H. Gooch, *J. Phys. Chem. Solids*, **15**, 127 (1960); F. A. Cunnell and C. H. Gooch, *Nature*, **188**, 1096 (1960).
2. B. Goldstein, *Phys. Rev.*, **121**, 1305 (1961).
3. J. Van den Boomgaard and K. Schol, *Philips Research Repts.*, **12**, 127 (1957).
4. J. T. Edmond, *J. Appl. Phys.*, **31**, 1428 (1960).
5. J. J. Wysocki, *ibid.*, **31**, 1686 (1960).

High-Purity CdTe by Sealed-Ingot Zone Refining

M. R. Lorenz and R. E. Halsted

Research Laboratory, General Electric Company, Schenectady, New York

Single crystal CdTe can be grown both from the vapor and from the melt. Attempts to prepare high-purity CdTe have generally been confined to the purification of the elemental components. Recently, however, limited purification was achieved by zone melting of the compound (1). The problem of dissociation at melt temperatures and the consequent necessity of minimizing transport of material from the melt was met with a three-zone furnace permitting control of Cd pressure, ingot temperature, and molten zone temperature. There are several problems associated with this method, now current in compound semiconductor technology. The maintenance and control of three temperature zones over relatively long periods of time is attended with difficulties. Also, the whole ingot is hot, a condition favoring impurity back diffusion through the solid. Furthermore, the ingot is located in an open boat, a condition permitting vapor transport of impurities. Recently a simple technique of zone melting decomposable compounds has been described (2) which appears to overcome these limitations. The preparation of high-purity CdTe by this technique is described below and evidence for its effectiveness is presented.

Procedure

Starting from elemental Cd and Te, multiple zone refined CdTe was obtained containing single crystals of suitable size for optical and electrical measurements. High-purity tellurium (99.999 + % American Smelting and Refining Company) and cadmium (99.9999% Cominco Products, Inc.) were used. The suppliers' spectrographic analyses of materials indicated the presence of 0.1 to 0.2 ppm lead, copper, and silver in the cadmium and less than 1 ppm of magnesium and copper in tellurium. In addition it was found that CdTe prepared from these materials, utilizing well-cleaned quartzware, always contained aluminum of the order of 1 ppm.

Elemental cadmium and tellurium corresponding to about 110g of CdTe were placed in 9/16 in. ID quartz tubes previously coated with pyrolytic graphite. In addition, 100 mg or less of spectrographically pure graphite powder was added to the charge. The graphite was employed for a dual purpose. It prevented the ingot from sticking to the quartz walls. It may also help reduce any oxygen content of the ingot. A 1 in. long cylindrical quartz plug was inserted in the tube and rested just above the charge. The filled tube was evacuated to less than 10^{-6} mm Hg pressure and, after repeated flaming, was sealed off at the quartz plug. The sealed tube was suspended from a wire in a resistance furnace, heated slowly to about 1150°C, and held at that temperature for at least 2 hr. Slow heating is necessary to allow the reaction between the elemental components without violence. Holding at 1150°C assures complete melting of the CdTe (mp 1092°C). The tube was then slowly lowered to produce directional freezing from the bottom up. After complete solidification of the charge, the tube was removed and cooled to room temperature. The solid ingot, approximately 7 in. in length, occupied the lower half of the tube. The upper part was void. To enclose the ingot completely without any major voids the tube was cut open at the top. A quartz plug was positioned to rest on the ingot and a ground joint fused onto the tube. The tube was then evacuated to a pressure less than 10^{-6} mm Hg and sealed at the quartz plug after repeated flaming.

For the formation of a narrow molten zone, while keeping the rest of the ingot cold, an induction heater was most convenient. The complete assembly is shown in Fig. 1. Briefly, the enclosed ingot was suspended from a shaft driven by a variable speed motor and centered over a graphite susceptor. The susceptor inner diameter was cut to provide not more than 1 mm clearance for the quartz tube. The susceptor ring height of 0.5 in. provided a melted zone estimated at 1-1.5 cm length. A quartz tube served as a susceptor holder. Another quartz tube enclosed these components. Flowing N_2 isolated the system from oxygen. Other details of the assembly are self-explanatory from Fig. 1.

A typical zone pass consisted of positioning the sealed ingot with the tip just in the susceptor ring, and activation of the induction coil by means of a 450 kc oscillator. The power drawn was less than 5 kw. When operating temperature was reached, the ingot was lowered at a uniform rate. It was found that 1150°-1200°C was sufficient to maintain the molten zone at a temperature about 30°-40°C above the melting point of 1092°C. The ingot speed was varied from pass to pass for best utilization of time, but ranged between 1.5 and 2.5 cm/hr. After the ingot had completed a pass through the hot zone, the operation was repeated until the desired number of passes was achieved. For the final pass the 0.5 in. high susceptor ring was replaced by one 1 in. in height and the rate of zone travel was reduced to 5

Manuscript received Oct. 11, 1962.

Any discussion of this paper will appear in a Discussion Section to be published in the December 1963 JOURNAL.

REFERENCES

1. F. A. Cunnell and C. H. Gooch, *J. Phys. Chem. Solids*, **15**, 127 (1960); F. A. Cunnell and C. H. Gooch, *Nature*, **188**, 1096 (1960).
2. B. Goldstein, *Phys. Rev.*, **121**, 1305 (1961).
3. J. Van den Boomgaard and K. Schol, *Philips Research Repts.*, **12**, 127 (1957).
4. J. T. Edmond, *J. Appl. Phys.*, **31**, 1428 (1960).
5. J. J. Wysocki, *ibid.*, **31**, 1686 (1960).

High-Purity CdTe by Sealed-Ingot Zone Refining

M. R. Lorenz and R. E. Halsted

Research Laboratory, General Electric Company, Schenectady, New York

Single crystal CdTe can be grown both from the vapor and from the melt. Attempts to prepare high-purity CdTe have generally been confined to the purification of the elemental components. Recently, however, limited purification was achieved by zone melting of the compound (1). The problem of dissociation at melt temperatures and the consequent necessity of minimizing transport of material from the melt was met with a three-zone furnace permitting control of Cd pressure, ingot temperature, and molten zone temperature. There are several problems associated with this method, now current in compound semiconductor technology. The maintenance and control of three temperature zones over relatively long periods of time is attended with difficulties. Also, the whole ingot is hot, a condition favoring impurity back diffusion through the solid. Furthermore, the ingot is located in an open boat, a condition permitting vapor transport of impurities. Recently a simple technique of zone melting decomposable compounds has been described (2) which appears to overcome these limitations. The preparation of high-purity CdTe by this technique is described below and evidence for its effectiveness is presented.

Procedure

Starting from elemental Cd and Te, multiple zone refined CdTe was obtained containing single crystals of suitable size for optical and electrical measurements. High-purity tellurium (99.999 + % American Smelting and Refining Company) and cadmium (99.9999% Cominco Products, Inc.) were used. The suppliers' spectrographic analyses of materials indicated the presence of 0.1 to 0.2 ppm lead, copper, and silver in the cadmium and less than 1 ppm of magnesium and copper in tellurium. In addition it was found that CdTe prepared from these materials, utilizing well-cleaned quartzware, always contained aluminum of the order of 1 ppm.

Elemental cadmium and tellurium corresponding to about 110g of CdTe were placed in 9/16 in. ID quartz tubes previously coated with pyrolytic graphite. In addition, 100 mg or less of spectrographically pure graphite powder was added to the charge. The graphite was employed for a dual purpose. It prevented the ingot from sticking to the quartz walls. It may also help reduce any oxygen content of the ingot. A 1 in. long cylindrical quartz plug was inserted in the tube and rested just above the charge. The filled tube was evacuated to less than 10^{-6} mm Hg pressure and, after repeated flaming, was sealed off at the quartz plug. The sealed tube was suspended from a wire in a resistance furnace, heated slowly to about 1150°C, and held at that temperature for at least 2 hr. Slow heating is necessary to allow the reaction between the elemental components without violence. Holding at 1150°C assures complete melting of the CdTe (mp 1092°C). The tube was then slowly lowered to produce directional freezing from the bottom up. After complete solidification of the charge, the tube was removed and cooled to room temperature. The solid ingot, approximately 7 in. in length, occupied the lower half of the tube. The upper part was void. To enclose the ingot completely without any major voids the tube was cut open at the top. A quartz plug was positioned to rest on the ingot and a ground joint fused onto the tube. The tube was then evacuated to a pressure less than 10^{-6} mm Hg and sealed at the quartz plug after repeated flaming.

For the formation of a narrow molten zone, while keeping the rest of the ingot cold, an induction heater was most convenient. The complete assembly is shown in Fig. 1. Briefly, the enclosed ingot was suspended from a shaft driven by a variable speed motor and centered over a graphite susceptor. The susceptor inner diameter was cut to provide not more than 1 mm clearance for the quartz tube. The susceptor ring height of 0.5 in. provided a melted zone estimated at 1-1.5 cm length. A quartz tube served as a susceptor holder. Another quartz tube enclosed these components. Flowing N_2 isolated the system from oxygen. Other details of the assembly are self-explanatory from Fig. 1.

A typical zone pass consisted of positioning the sealed ingot with the tip just in the susceptor ring, and activation of the induction coil by means of a 450 kc oscillator. The power drawn was less than 5 kw. When operating temperature was reached, the ingot was lowered at a uniform rate. It was found that 1150°-1200°C was sufficient to maintain the molten zone at a temperature about 30°-40°C above the melting point of 1092°C. The ingot speed was varied from pass to pass for best utilization of time, but ranged between 1.5 and 2.5 cm/hr. After the ingot had completed a pass through the hot zone, the operation was repeated until the desired number of passes was achieved. For the final pass the 0.5 in. high susceptor ring was replaced by one 1 in. in height and the rate of zone travel was reduced to 5

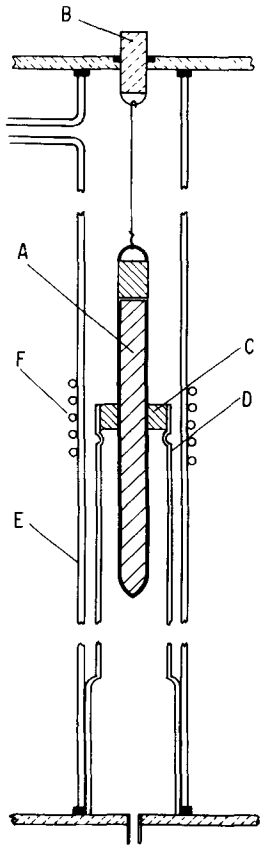

Fig. 1. Zone refining assembly; A, quartz enveloped ingot; B, shaft to variable speed drive mechanism; C, graphite susceptor; D, quartz susceptor holder; E, quartz for protection from atmosphere; F, induction coil.

mm/hr or less. Special care was necessary for the last pass to assure the production of single crystals of sufficient size for property measurement purposes.

Results

Single crystal grains of several centimeter length were found in every ingot. Evidence for effective zone refining has been obtained by spectrographic analysis, by observation of fluorescent emission spectra, and by electron mobility measurements.

Results of spectrographic analysis for the common impurities found in II-VI compounds indicate the presence of traces of Cu, Ag, Al, Sb, and Bi in the initial ingot. Upon zoning ingots with a minimum of 7 and no more than 22 passes, the tip and center sections show no detectable concentration of these impurities except for one ingot where Cu and Al were found in concentration at the detection limit, *i.e.*, 0.1 ppm. Analysis of the tail sections, however, reveals these impurities in concentrations of the order of several ppms. The results show that the detected impurities have segregation coefficients less than unity.

Further confirmation of effective zoning was gained by measuring the 80°K fluorescent emission spectra of various ingot sections from 0.75 to 2.50μ. In the short wavelength region three bands were observed with peaks at 0.81, 0.87, and 1.12μ. The emission bands have been correlated with native defects and can be varied by changes in stoichiometry. At 1.45μ, however, a well-defined band is observed in all tail sections. This is a characteristic Cu band which we have observed in our Cu doped CdTe crystals. It was detected with Cu concentrations as low as 0.1 ppm. Sections from the tip and center regions of the ingots show either the absence or at least a tenfold decrease in the intensity of this band.

Perhaps the best comparison of the relative merits of this and prior methods of CdTe preparation can be derived from resistivity and Hall coefficient measurements. Earlier work has yielded maximum room temperature Hall mobilities of 1000 (1) and 800 (3) cm^2/volt sec, and a maximum value of 1500 (3) at lower temperatures in agreement with results obtained on nonzone refined CdTe here. In a sample from a recent 20-pass run the electron Hall mobility was observed to increase from a 300°K value of 1050 cm^2/volt sec to a maximum value of 57,000 at 20°K. The large increase of mobilities, especially at low temperatures, indicates that impurity or defect scattering of electrons has been substantially reduced by the present method of preparation.

As noted in the introduction, the present method of CdTe purification appears to have several important advantages over a three-zone furnace technique. First, it should minimize back-diffusion of impurities *via* the solid phase since the main body of our CdTe ingots was below 200°C. Second, CdTe is more dense in the liquid state than as a solid. Therefore, vapors generated in the molten zone should be confined to a small, self-sealed, free volume travelling with the zone. This should minimize back-diffusion of volatile impurities, *via* vapor phase transport. Third, but not least, the method is simple and requires a minimum of supervision. The results on CdTe provide clear evidence for the value of this method.

Acknowledgments

The authors wish to thank F. K. Heumann and F. H. Horn for helpful discussions. L. H. Esmann and B. B. Binkowski provided valuable assistance in the experimental work. This work was supported by the Aeronautical Systems Division, Air Force Systems Command, U. S. Air Force.

Manuscript received Sept. 13, 1962.

Any discussion of this paper will appear in a Discussion Section to be published in the December 1963 JOURNAL.

REFERENCES

1. D. de Nobel, *Phillips Research Repts.*, **14**, 361, 430 (1959).
2. F. K. Heumann, *This Journal*, **109**, 345 (1962).
3. S. Yamada, *J. Phys. Soc. Japan*, **15**, 1940 (1960); **17**, 645 (1962).

Stresses in Anodic Films

D. A. Vermilyea

Research Laboratory, General Electric Company, Schenectady, New York

Stresses in anodic films produced on several metals were measured by clamping the upper end of a thin foil of the metal and observing the motion of the lower end through a telescope.[1] Foils were about 10 cm long, and one side was coated with stopcock grease to prevent anodization. (Grease is preferable to lacquer which shrinks on drying and can support some stress.) Deflections were of the order of a millimeter in most experiments; the minimum measurable deflection was about 0.005 cm. No twisting of the foil was observed. The stress measured on the second side of a specimen, using the first anodic film on the other side to prevent anodization, was the same as that on the first side. In such experiments, however, the effect of applied field on the stress is more complicated to analyze, since it acts on both films. Hence, only experiments conducted on greased specimens are reported. Stresses were computed from the formula (2)

$$\sigma = \frac{h^2 E}{6r\epsilon} \qquad [1]$$

where σ is the stress in the anodic film, h is the foil thickness, E is Young's modulus of the foil, r is the radius of curvature, and ϵ is the oxide film thickness. Some data on the metals, values of Young's moduli, and film thickness per volt used in these studies are given in Table I. Unless noted otherwise, films were formed at 2 ma/cm^2 in an aqueous solution of 2% H_3BO_3 plus 0.5% $(NH_4)_2B_4O_7 \cdot 4H_2O$. No effect of changes in the forming solution were observed as long as dilute aqueous solutions were used. "Glycol borate" in Fig. 1 refers to a solution of 2% each of water and ammonium borate in ethylene glycol. The initial surface condition had an important effect, as shown by the results for tantalum. Unless otherwise noted the specimens were chemically polished and etched to remove the polishing film. Results were the same whether or not the polishing film was removed. No chemical polish for tungsten is known to me.

Table I. Data on the metals

Metal	Thickness, in.	Source, purity, condition	Young's modulus, psi	Film thickness, A/v
Tantalum	0.002	Fansteel, 99.9, annealed	27	16.5
Niobium	0.0016	Wah-Chang, 99.9, cold rolled	15	21
Aluminum	0.003	United Mineral and Chemical, 99.9999, annealed	10	13
Zirconium	0.0016	Foote Mineral, Iodide, annealed	13	21
Titanium	0.002	Titanium Metals, Iodide, annealed	16	20
Tungsten	0.002	Rembar, 99.9+	55	18

[1] Similar experiments on aluminum have been performed by J. S. L. Leach of Imperial College (1).

Typical results, shown in Fig. 1, exhibit the following salient features. First, the stress in all films was tensile at small film thickness. For most metals the sign of the stress was independent of formation voltage, but the stress in anodic films on zirconium decreased steadily from strong tension at low voltages to strong compression at higher voltages. Except for films formed on tantalum, the reproducibility was generally poor, variations of ±25% from specimen to specimen being typical. Stresses reported for tantalum are reproducible to ±10%.

Second, the stress with forming voltage applied was always more compressive than at zero voltage except for tungsten where no effect of the applied field was observed. It is tempting to interpret this compressive component due to the field as being caused by the electrostatic pressure resulting from the field. (Such pressures are calculated to be about 3500 to 7000 psi normal to the film, depending on the metal and field.) If Poisson's ratio for the film is 0.2, however, then the compressive stress parallel to the film is much too small to account for the effects observed, which are sometimes larger than the entire electrostatic pressure. Moreover, the electrostatic pressure should be proportional to the square of the electric field, whereas actually the change in deflection on increasing the field is very small until about half or three-quarters of the forming field is reached, after which it increases at a rate corre-

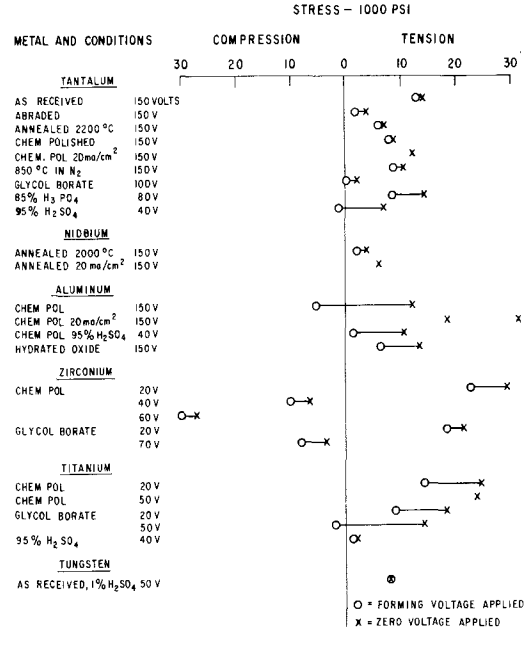

Fig. 1

sponding to a much higher power of the field. These changes are also accompanied by hysteresis. Hence, while electrostatic pressure may play some role it probably is not responsible for all these effects.

A third general characteristic is that a high formation rate increases the final tensile stress observed at zero field. Such increases were observed to range from about 20% for tantalum to more than a factor of two for aluminum. Holding at a constant voltage to allow the field to decrease results in a decrease in the stress. The behavior under changing field is thus very complicated. As noted above the stress is more compressive at high fields; nevertheless the stress finally observed after growth at the high field is more tensile. Films often are under compression with a field applied and tension at zero field.

Fourth, when much gas is evolved the stress is more compressive. The effect can be seen on the abraded tantalum specimen and was observed especially often with aluminum, zirconium, and titanium. In fact, when rolled or abraded foils of these metals were used the stress was often compressive even at small film thicknesses. Furthermore, the reversal of the sign of the stress on zirconium coincides approximately with the start of substantial oxygen evolution. Perhaps this effect results from gas trapped under pressure; however, evolution of hydrogen on a 60v zirconium specimen did not change the deflection.

The final general characteristic is that the stress is a strong function of the forming electrolyte if very concentrated solutions are used. This fact can best be seen from the data presented for tantalum. Not all of the data are for the same film thickness or formation voltage, but the magnitude of the stress for tantalum oxide films was nearly independent of film thickness. For instance, the stresses measured in Ta_2O_5 films formed on a single specimen at 50, 150, and 250v were 6250, 7110, and 7800 psi, respectively.

For tantalum oxide films the tensile stress after formation in aqueous solution is higher on films known to contain many flaws (3) (the as-received specimen and the one heated at 850°C in nitrogen) than on relatively perfect ones (the specimen annealed at 2200°C).

Discussion

These complicated phenomena add to the mounting evidence (4, 5) that the picture of a uniform, rigid, unchanging oxide film through which only cations move is untenable. If only cations moved in a uniform oxide, it would be expected that the stress in the film with forming voltage applied would be zero (6), and that a final slight net compressive stress might result from the release of the electrostatic pressure.

A hypothesis which might explain some of the observations described above is the following. Assume that each newly deposited layer is hydrated. As the layer becomes buried it is dehydrated by proton migration, producing tension in the film. Experiments with aluminum on which a hydrated film was produced by boiling for 1 hr in distilled water support this idea.[2] Subsequent anodic formation of such films (which should have been about 3000Å thick) did produce tension in the film, and such a treatment is thought to dehydrate the films (7). The higher stress produced by high formation rates would, on this picture, result from increased trapping of water. Solutions containing much less water should produce less stress, as observed. Zirconium oxide, for which the hydration free energy is highest, shows the largest tensile stress as might be expected on such a picture.

[2] This experiment was suggested by W. E. Tragert, and J. R. Rairden kindly supplied the specimens.

Manuscript received Oct. 22, 1962; revised manuscript received Dec. 11, 1962.

Any discussion of this paper will appear in a Discussion Section to be published in the December 1963 JOURNAL.

REFERENCES

1. J. S. L. Leach, Private communication.
2. Stoner, *Proc. Roy. Soc.*, (A) **82**, 172 (1909).
3. D. A. Vermilyea, *This Journal*, **110**, 250 (1963).
4. J. A. Davies, J. P. S. Pringle, R. L. Graham, and F. Brown, *This Journal*, **109**, 999 (1962).
5. N. J. M. Wilkins, *This Journal*, **109**, 998 (1962).
6. D. A. Vermilyea, *Acta Met.*, **5**, 492 (1957).
7. W. E. Tragert, Private communication.

The Mechanism of the Nickel-Fluorine Reaction

R. L. Jarry, J. Fischer, and W. H. Gunther

Chemical Engineering Division, Argonne National Laboratory, Argonne, Illinois

Nickel is commonly employed as a material of construction for laboratory and plant equipment in which fluorine is used because it has a low rate of reaction with fluorine up to the region of 500°C. The resistance of nickel to attack by fluorine is attributed to the formation of an adherent scale of nickel fluoride on the nickel surface. The rate of the nickel-fluorine reaction has been studied at Argonne National Laboratory (1) and at Union Carbide at Oak Ridge (2). The rate of reaction of nickel with fluorine was found to follow the parabolic rate law; therefore, it was deduced that the rate is controlled by the diffusion of either metal or nonmetal species through the adherent fluoride scale as described in the Wagner (3) theory of metal oxidation.

The work described in this report was undertaken to elucidate the mechanism of the nickel-fluorine reaction, with respect to which species, metal or nonmetal, is the principal migrant through the nickel fluoride scale. In order to establish the validity of the experimental approach experiments were also performed with the nickel-oxygen system. Other workers (4, 5) have established that the

nickel-oxygen reaction proceeds *via* the diffusion of metal ions through the nickel oxide scale to the gas-solid interface where it reacts with oxygen. Simultaneously, there is a counter flow of cation vacancies to the metal-oxide interface.

Two different experimental techniques were used in this work. In the first experimental approach metallographic examination was used to determine whether two scales of the same material, nickel fluoride or nickel oxide, growing toward each other from nearly parallel nickel surfaces would fuse into one continuous scale or form an interface between the two scales. If metal atoms were the principal species migrating through the film to react at the film gas interface, the two scale surfaces growing toward one another would fuse into one scale as the metal from one scale surface migrated into the other scale. If the mechanism were dependent on the movement of the nonmetal across the forming scales, then the two scales would come together but not fuse, and an interface would be present. This technique was similar to that used by Schnizlein (6) to identify the diffusing species in the oxidation of uranium. The second technique employed a radioactive tracer. nickel-63, which was plated on the surface of the nickel specimens. These specimens were then fluorinated or oxidized, and the scales were examined autoradiographically to determine the location and distribution of the radioactivity. If the reaction were controlled by metal diffusion, the activity would be distributed through the scale as found by Bardeen (7) for the copper-oxygen system. Bardeen calculated, using the Wagner theory, and confirmed experimentally that the activity would be distributed in the scale in a diminishing concentration as measured from the scale-gas to the metal-scale interface. If the reaction were not controlled by metal ion diffusion but rather by the nonmetal, then the activity would remain in a narrow band at the scale-gas interface.

The nickel used in these experiments was commercial grade A-nickel of a purity of 99.4%. The principal impurities, in weight per cents, were manganese, 0.28; carbon, 0.07; iron, 0.10; silicon, 0.08; and copper, 0.05. The fluorine used was 98.2% pure. The principal impurities were nitrogen and oxygen. The oxygen used was passed through Molecular Sieves to remove water. Nickel-63 was obtained from the Oak Ridge National Laboratory as an acidic chloride solution. The oxidation and fluorinations were carried out in electrically heated nickel tubular reactors.

Impinging scale experiments.—Reaction specimens were prepared by welding two coupons, 1x3x 16 cm, together along the 1-cm edge. The opposing 1x3 cm faces of the coupons, which had been polished through 1μ diamond paste, were nearly parallel and separated by a gap of about 0.1 mm. The samples were then either fluorinated at 700°C for 36 hr, or oxidized at 1000°C for 48 to 72 hr. After the reaction period the samples were mounted in Bakelite, sectioned normal to the scale between the opposing surfaces, and photomicrographs were taken of the sectioned specimens. Figure 1 is a representative photomicrograph of the fluorinated sample and Fig. 2 of the oxidized sample. It is apparent from Fig. 1 that the impinging fluoride scale is separated by an interface, which indicates that fluorine migrated from the gas-solid interface through the fluoride film to the nickel-nickel fluoride interface and that any metal migration was negligible.

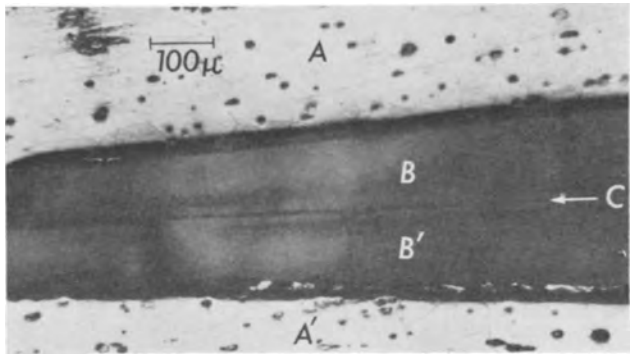

Fig. 1. Photomicrograph of impinging nickel fluoride scales. A and A', nickel substrates; B and B', nickel fluoride scales; C, interface between nickel fluoride scales.

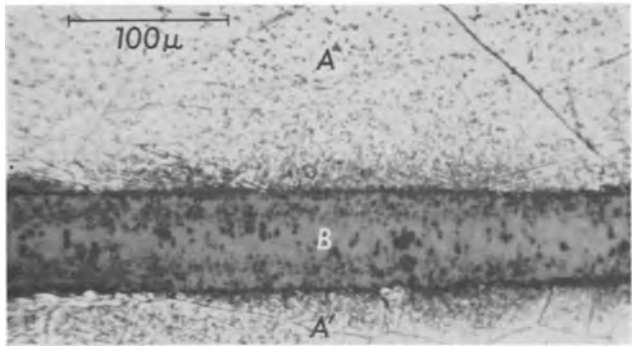

Fig. 2. Photomicrograph of impinging nickel oxide scales. A and A', nickel substrates; B, continuous nickel oxide scale.

In Fig. 2 it is seen that there is a continuous oxide film from one metal surface to the other which confirms that the metal migrates through the metal oxide scale and reacts at the metal oxide-gas interface to produce a continuous oxide film.

Further examination of the photomicrograph reproduced in Fig. 2 reveals a considerable porosity in the nickel oxide scale. The adjacent metal surfaces, which were etched to provide more contrast with the scale, also exhibit porosity. The porosity of the oxide scale can be attributed to the removal of cation vacancies by condensation and precipitation within the oxide phase. Birchenall (8) has proposed this as a mechanism by which cation vacancies are removed from the metal oxidation system. The vacancies are present in the system as a result of the cation diffusion mechanism of the reaction.

Radioactive tracer experiments.—Specimens for the radioactive marker experiments were prepared by plating nickel-63, a low energy beta emitter, onto nickel coupons, 1x5x0.16 cm. The plating solution was prepared by adding concentrated ammonia to the acidic chloride solution of nickel-63 to form the tetra-amine chloride complex. These coupons,

plated with a layer of nickel-63, about 2μ thick, were then either fluorinated at 600°-700°C for about 50 hr or oxidized at 1000°C for 80 to 100 hr. Following the reaction period, which resulted in fluoride or oxide scales of about 100μ in thickness, the specimens were mounted in a supporting medium and sectioned normal to the surface of the scale. Autoradiographs were made by a technique similar to that described by Gomberg and associates (9). In brief, the autoradiographic technique comprised the following steps: (*a*) stripping film emulsion[1] was placed in direct contact with the sectioned surface of the specimen; (*b*) the film was exposed to the sample for a period of five days; and (c) the exposed emulsion was developed in place. Figure 3 is a photomicrograph of the autoradiograph of the nickel fluoride scale. This photomicrograph clearly shows a narrow band of activity at the position of the scale-fluorine interface. The line, indicated by arrow E in Fig. 3, locates the position of the scale-gas interface. The width of the darkened portion of the emulsion is greater than the thickness of the portion of the nickel fluoride scale occupied by the radioactive nickel because of the dispersion of the beta rays in the 5μ thick emulsion. From the location and distribution of the radioactivity it can be deduced that fluorine is the migrating species in this reaction and that it migrates through the nickel fluoride scale to the metal surface where it reacts with the nickel.

Figure 4 is a photomicrograph of an autoradiograph of the nickel oxide scale. The nickel activity is seen to penetrate into the nickel oxide scale. The linear penetration normal to the surface of the scale is as much as 70% of the thickness of the oxide scale.

Bardeen (7) predicted that the activity would extend to the nickel-nickel oxide interface. However, the diminution of the activity close to the interface may not be resolved in the autoradiograph. Birchenall (8) has also pointed out that the expected distribution of radioactive tracer has been found by other workers to drop off rapidly in the region near the metal-oxide interface. He has postulated that this effect is due to an abrupt change in the diffusion coefficient due to porosity in the scale near the metal-oxide interface. Porosity has been observed in the nickel oxide scales produced in these experiments and could therefore account for the activity distribution found in Fig. 4.

[1] Two types of stripping film were used in this work, Kodak Experimental Permeable Base Stripping Film and Kodak Autoradiographic Film AR-10.

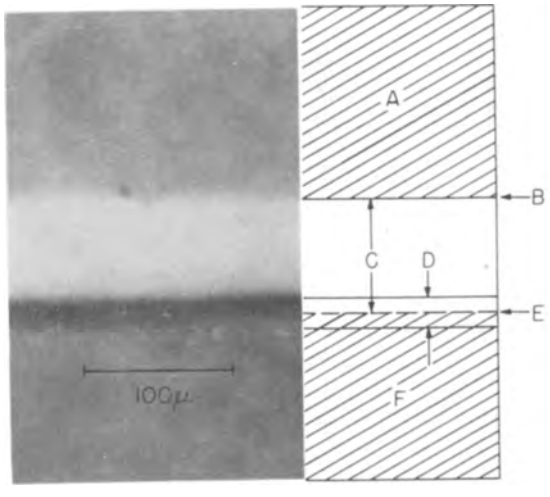

Fig. 3. Micrograph of autoradiographic emulsion showing nickel-63 activity in nickel fluoride scale. A, original location of nickel substrate; B, nickel-nickel fluoride interface; C, nickel fluoride scale; D, darkened zone in emulsion due to radioactivity; E, location of nickel fluoride-fluorine gas interface; F, original location of dental rubber mounting.

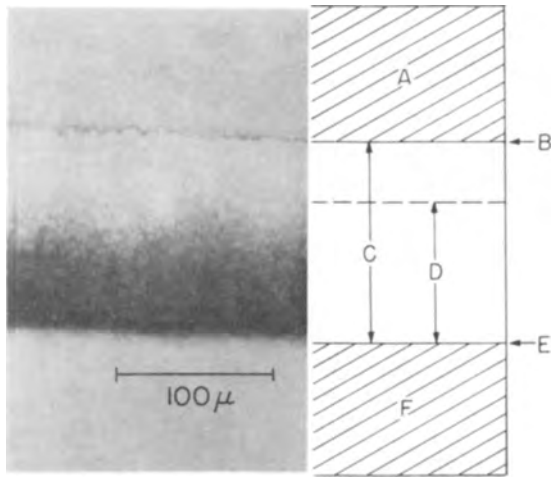

Fig. 4. Micrograph of autoradiographic emulsion showing nickel-63 activity in nickel oxide scale. A, original location of nickel substrate; B, nickel-nickel oxide interface; C, nickel oxide scale; D, darkened area of emulsion due to radioactivity; E, location of nickel oxide-oxygen gas interface; F, original location of Bakelite mounting.

The results obtained for both types of marker experiments indicate that fluorine, rather than nickel, migrates through the fluoride scale during the course of the reaction. Fluorine could reach the metal surface by gross movement through pores and cracks in the fluoride scale or by some transport process through the bulk of the scale. Since the kinetics of the reaction have been shown to follow a parabolic rate it is most probable that the mechanism involves the transport of fluorine through the bulk of the nickel fluoride scale. Stipulation of the mode of transfer of fluorine from the gas phase through the fluoride scale requires further experimental work. The evidence obtained from the marker experiments for the nickel-oxygen reaction is in accord with the accepted metal ion diffusion mechanism for that reaction.

Acknowledgment

The authors wish to express their appreciation to Dr. M. D. Adams for his assistance with the autoradiographic technique preparations.

Manuscript received Sept. 6, 1962. Work performed under the auspices of the U. S. Atomic Energy Commission.

Any discussion of this paper will appear in a Discussion Section to be published in the December 1963 JOURNAL.

REFERENCES

1. R. K. Steunenberg, L. Seiden, and H. E. Griffin, ANL-5924 (1958); R. L. Jarry, J. Fischer, and W. H. Gunther, ANL-6477 (1961).
2. C. F. Hale *et al.*, AECD-4292 (1959).

3. C. Wagner, *Z. physik. Chem.*, **B21**, 25 (1933).
4. E. A. Gulbransen and K. F. Andrews, *This Journal*, **104**, 451 (1957).
5. M. O'Keefe and W. J. Moore, *J. Phys. Chem.*, **65**, 1438 (1961).
6. J. G. Schnizlein, J. D. Woods, J. D. Bingle, and R. C. Vogel, *This Journal*, **107**, 783 (1960).
7. J. Bardeen, W. H. Brattain, and W. Shockley, *J. Chem. Phys.*, **14**, 714 (1946).
8. C. E. Birchenall, *This Journal*, **103**, 619 (1956).
9. H. J. Gomberg *et al.*, "High Resolution Autoradiography for Study of Grain Boundaries in Metals, Project 2029," University of Michigan (February 1954).

Brief Communications

Measurement of "Pressure-EMF" in Pure Fused Salts

Paul Duby and Herbert H. Kellogg

Department of Mineral Engineering, Columbia University, New York, New York.

Determination of transport numbers in a pure fused salt, by the method of Duke and Laity (1), is based on the measurement of the volumetric flow produced by an electric potential difference in the absence of a pressure gradient. One of us recently suggested (2) that the application of the theory of irreversible processes and Onsager's theorem to a system composed of a pure fused salt, at constant temperature, predicts an effect reciprocal to that measured by Duke and Laity, *i.e.*, a pressure gradient imposed on the system should produce not only a volumetric flow but also an electrical potential difference (herein called a pressure-emf).

For a cell comprising the electrolyte MX, and electrodes of the metal M, the following equation has been shown to apply

$$\left(\frac{\Delta E}{\Delta P}\right)_{I=0} = -\frac{\Delta V}{\mathbf{F}} = \frac{V_M - T_X\, V_{MX}}{\mathbf{F}} \qquad [1]$$

where ΔE is the pressure-emf developed for a pressure difference ΔP. $\mathbf{F}$ is the Faraday equivalent, ΔV is the volume change accompanying the passage of one faraday, V_M and V_{MX} are the equivalent volumes of metal and salt, and T_X is the transport number of X. This equation can be derived (2) either from the theory of irreversible processes or by application of classical thermodynamics to a cell in which the electrode compartments are maintained at different pressures.

The pressure-emf in a fused salt is a phenomenon related to the emf of a galvanic cell in a gravitational or centrifugal field. MacInnes and others have studied the latter phenomenon in aqueous electrolytes and used it to evaluate transport numbers (3).

Our experiments with pressure-emf have been confined, so far, to studies of molten silver nitrate and lead bromide. The results have proven so promising that we report them here briefly, in anticipation of a fuller account at a later date.

The melt is contained in an H-shaped Pyrex cell with a medium or fine-porosity fritted Pyrex disk inserted in the horizontal tube. The cell is maintained at constant temperature in a bath of molten wax or molten tin. The two vertical legs extend upward out of the bath. The pressure difference across the porous plug is obtained by connecting one side of the cell either with a large vessel under argon pressure or with another vessel under partial vacuum. The two electrodes are made of silver wire in the case of $AgNO_3$, and they consist of pieces of tungsten wire dipping in molten lead in the case of $PbBr_2$. The potential difference between the two electrodes is measured by a Keithley type 150 A microvoltmeter, and it is recorded continuously. A slowly drifting background emf exists between the electrodes as a result of small temperature differences within the cell. When pressure is applied, however, the potential changes abruptly by the amount of the pressure-emf.

For $PbBr_2$ at 494°C, the pressure-emf is -11.6 ± 0.2 μv/atm. In a less precise experiment, we found 0 ± 1 μv/atm for $AgNO_3$ at 230°C. In the case of $PbBr_2$, the emf is proportional to the applied pressure difference within the range we studied, *i.e.*, 0-1 atm.

These emf values have been used, along with reported values for the equivalent volumes of metal and salt, in Eq. [1] to calculate the transport numbers for lead and silver. The results are given in Table I and compared with independent measurements of the transport number in the same salts by Laity and Duke (4) and by the weighing method (5) of the authors. The results of all three methods are in good agreement, and suggest that the pressure-emf method is a promising and reliable technique for measurement of transport numbers in molten salts. The agreement of values is also a new illustration of Onsager's reciprocal relations.

The pressure-emf for the cell, which we measure, is made up of two parts, one of which describes the effect of pressure on the electrode potentials and the other the effect of pressure on the transport mechanism. The latter may be thought of as a liquid junction potential resulting from the pressure

Table I. Comparison of transport numbers obtained by different methods

	T_{Pb} in $PbBr_2$	T_{Ag} in $AgNO_3$
Pressure-emf	0.372 ± 0.006 (494°C)	0.757 ± 0.025 (230°C)
Weighing technique (5, 6)	0.355 ± 0.015 (504°C)	0.781 ± 0.006 (219°C)
Bubble technique (4)	0.347 ± 0.013 (500°C)	0.76 ± 0.05 (225°C)

gradient, and we call it the pressure-diffusion potential.

The pressure-diffusion potential arises from the difference between the self-diffusion coefficients of anions and cations which, under the effect of the pressure gradient, migrate with different velocities relative to the bulk of the liquid. If the mechanism proves to be correct, the agreement among the different methods of measuring transport numbers should offer important implications for the validity of the Nernst-Einstein equation in pure fused salts.

Although the measurement of pressure-emf is analogous to the measurement of streaming potential in aqueous solution we believe the two phenomena are fundamentally different. Streaming potential and related electrokinetic phenomena are surface phenomena. We believe our pressure-emf to be a bulk phenomenon, independent of surface effects. We mean to prove this by experiments with porous plugs of different substances but the same molten salt. It is the apparent absence of surface double-layers in fused salt media which makes possible the measurement of pressure-emf, which would otherwise be obscured by the larger streaming potential.

Acknowledgment

This work is supported by the National Science Foundation under grant NSF G 20879. Mr. L. J. Howell provided valuable assistance with the measurements on lead bromide.

Manuscript received Dec. 7, 1962.

Any discussion of this paper will appear in a Discussion Section to be published in the December 1963 JOURNAL.

REFERENCES

1. F. R. Duke and R. W. Laity, *J. Am. Chem. Soc.*, **76**, 4046 (1954); *J. Phys. Chem.*, **59**, 549 (1955).
2. P. Duby, Eng. Sc. D. Thesis, Columbia University (1962).
3. D. A. MacInnes, "The Principles of Electrochemistry," pp. 174-180, Dover Publications, New York (1961).
4. R. W. Laity and F. R. Duke, *This Journal*, **105**, 97 (1958).
5. H. H. Kellogg and P. Duby, *J. Phys. Chem.*, **66**, 191 (1962).
6. Results on $PbBr_2$, to be published.

Preparation of Spherical Single Crystal Electrodes For Use in Electrocrystallization Studies

D. K. Roe[1] and H. Gerischer

Max-Planck-Institut für Metallforschung, Stuttgart, Germany

Single crystal electrodes have obvious importance in studies of electrochemical processes which are influenced by crystal orientation (1-6). Both flat and spherical crystal surfaces have been used; the latter exhibits all crystal orientation and may be advantageous in certain cases. Elaborate procedures used in preparing single crystal electrodes usually involve mechanical or chemical pretreatment which causes indefinite surface changes and can put the results into question quite seriously. It seemed, therefore, an interesting problem to develop an experimental method which allows convenient preparation of single crystal electrodes so that systematic investigations with a great number of freshly prepared crystals can be done in reasonable time.

The method described here has been used to prepare single crystal spheres, with a diameter of 2-3 mm, of silver, copper, or gold. The method makes use of the technique first applied by Kaischev and Mutaftshiev (7), who prepared single crystal spheres by melting the end of a wire containing single crystal segments. Upon cooling, the sphere was a single crystal if nucleated by a single crystal segment. The concept of this technique has been combined with the procedure described by Conway, Bockris, and Mehl (8) for preparing polycrystalline spherical electrodes. These authors melted the end of a polycrystalline wire in a hydrogen stream by heating the surrounding quartz tube with a gas burner and thereby obtained clean, smooth electrodes free of contamination from mechanical or chemical pretreatment.

The procedure was as follows: Single crystal wires were prepared by the Bridgman method of slow cooling. The wire, 1-2 mm in diameter, was held in a graphite mold in an evacuated quartz tube. The mold was made from spectroscopic graphite electrodes previously baked out at 1000°C in vacuum. Split molds are preferred to bored rods since the latter can produce strains in the wire; the crystals are often held fast in the mold by surface irregularities. There are no major problems associated with the preparation of single crystal wires of silver, copper, or gold. X-ray diffraction patterns

[1] Present address: Department of Chemistry, Massachusetts Institute of Technology, Cambridge 39, Mass.

taken by back reflection show sharp, symmetrically oriented spots.

For convenience in subsequent manipulation, the single crystal wire was attached to the end of a silver or platinum wire; the two ends can simply be melted together in a small flame so that the junction is about the diameter of the wire. A Teflon plug, enlarged in Fig. 1b, was made to fit tightly around the wire and served to hold it to the end of a glass tube. Control of the vertical position of the end of the crystal was possible through the use of a parallel ground K.P.G. tube (Schott and Gen., Mainz), sealed to the inner part of the ground glass joint at the top of the apparatus shown in Fig. 1a. Quartz, Pyrex, or Jena glass is suitable for construction of the apparatus, depending on the diameter.

The end of the wire was located in the center of a tungsten spiral heater made from about 30 cm of 0.4 mm diameter wire and silver-soldered to thick tungsten leads which are sealed through the inner part of a Pyrex joint, as shown. Approximately 80w was necessary to melt the end of the crystal, but the required power will be greatly dependent on the geometry. Hydrogen or an inert gas was used to purge the apparatus. When pure hydrogen was not used, it was found necessary to mix a per cent or two of hydrogen with argon or nitrogen flowing through the tube. Otherwise, as the tungsten heater operated at an extremely high temperature, there was some oxidation of tungsten by traces of oxygen, which caused evaporation of tungsten oxide.

Temperatures, relative to the melting of the silver crystals, were determined by trial and thereafter reproduced by measuring the heater current. The end of the crystal was allowed to melt until a sphere of metal formed, two or three times the diameter of the wire. Freezing times of 10-30 sec were sufficient for the formation of single crystal spheres. The rate of freezing for a given heater current can be estimated by gently tapping the support stand and observing the vibrations in the liquid portion of the sphere. Approximately the same freezing rate will occur in subsequent operations with crystals of the same size. After some experience it was found possible to remelt a sphere without further melting of the crystal wire.

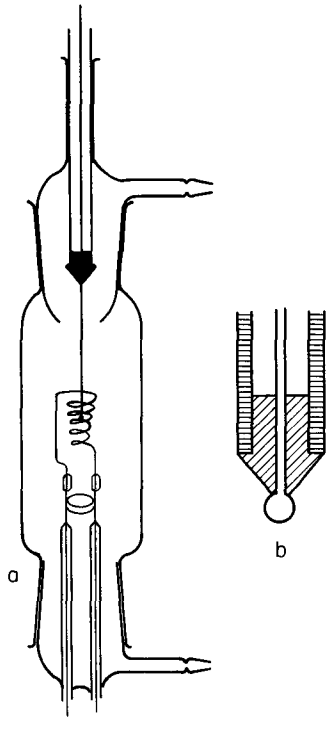

Fig. 1a. Cross section of furnace tube; Fig. 1b. detail of crystal sphere in Teflon holder.

Although the crystal wires were cleaned in nitric acid prior to forming the spheres, dull deposits were sometimes found on the surface after the first melting. These impurities can be removed by further cleaning in acid, followed by remelting of the sphere. The deposits are apparently due to condensation on the crystal of any volatile oxides which might be formed. Deposits were minimized by a thorough gas purge with the heater on, before the crystal wire is placed in the apparatus. Also a long pretreatment of heating of the spiral helps a great deal.

Cleaning of silver spheres in nitric acid revealed the crystallization state in addition to removing surface deposits. From the symmetry of the etched surface it was possible to see if the sphere was a single crystal. A more selective etch (9) is hot (70°C), concentrated sulfuric acid, which clearly reveals the (100) and (111) planes. Acid cleaning or etching followed by remelting of the sphere can be repeated until a satisfactory crystal is formed. After some experience one usually obtains a crystal sphere ready for immediate use.

After cooling, the wire was pulled up until the crystal sphere contacted the Teflon plug. The glass tube was also drawn upwards until the crystal was close to the end of the K.P.G. tube. Removal of the top portion of the apparatus and transfer to an electrochemical cell was thus possible without exposing the crystal to the atmosphere, provided an adequate flow of inert gas was maintained.

The surface of the crystal sphere was specular like a drop of mercury and, in the case of silver at least, the crystal planes (111) and (100) were often observable as small facets. With microscopic techniques it may be possible to use these individual crystal planes as electrodes. The appearance of these planes gives immediate information about the orientation of the spherical crystal.

The degree of perfection of the surfaces of crystals grown in this manner is, of course, not known. It seems reasonable to assume that gross surface irregularities are less likely on these spheres than on cut and polished metal crystals. Comparative measurements, which are dependent on surface structure, will help to estimate how closely the ideal crystal surface is approached. Preliminary potential and current-potential measurements have indicated that the (111) and (100) planes on silver crystal spheres are relatively free of growth sites. Microscopic examination of the spheres reveals a number of steps surrounding the (111) and (100) facets. The height of each step is estimated to be less than 0.5μ. The facets themselves appear microscopically flat.

Such spherical electrodes are in use in our laboratory for the study of electrocrystallization pro-

cesses. Some preliminary experiments have also been conducted with small capillaries attached to different parts of the surface for studying the polarization behavior of selected areas on the sphere. The method allows a rapid and quite reproducible preparation of an uncontaminated single crystal surface, which may be useful also in other studies.

Acknowledgment

One of the authors (D.K.R.) expresses thanks to the National Science Foundation for a postdoctoral fellowship during the period of this work.

Manuscript received Nov. 26, 1962.

Any discussion of this paper will appear in a Discussion Section to be published in the December 1963 JOURNAL.

REFERENCES

1. T. Erdey-Gruz *et al., Z. physik. Chem.*, **A172**, 157 (1935); **A178**, 255, 266 (1937).
2. R. Kaischev, E. Budevski, and S. Malinovski, *Compt. rend. acad. bulgare sci.*, **2**, 29 (1949).
3. W. Kossel, in "Zur Struktur und Materie der Festkörper," p. 56, Springer Verlag, Berlin-Göttingen-Heidelberg (1952).
4. A. T. Gwathmey and H. Leidheiser, *Trans. Electrochem. Soc.*, **91**, 95 (1947); *This Journal*, **98**, 225 (1951).
5. R. Piontelli, G. Poli, and G. Serravalle in "Transactions of the Symposium on Electrode Processes," E. Yeager, Editor, p. 67, John Wiley & Sons, New York (1961).
6. N. A. Economou and D. Trivich, *Electrochim. Acta*, **3**, 292 (1961).
7. R. Kaischev and B. Mutaftshiev, *Z. physik Chem.*, **204**, 334 (1955).
8. B. E. Conway, J. O'M. Bockris, and W. Mehl, *J. Sci. Instr.*, **33**, 400 (1956).
9. M. Yamamoto and J. Watanabe, *J. Japan Inst. Metals*, **17**, 425 (1953).

Investigation of the Electrochemical Characteristics of Organic Compounds

X. Sulfur Compounds

R. Glicksman

Semiconductor and Materials Division, Radio Corporation of America, Somerville, New Jersey

ABSTRACT

Anodic half-cell potential discharge data are presented for various classes of organic sulfur compounds, such as the thiophenols, mercaptans, and thioureas in alkaline electrolyte. The effect of group substitution and aromaticity on the anode potential of the thiophenol compounds is interpreted in terms of the electron density distribution in the molecule. Half-cell potential discharge data for the reversible thiourea-formamidine disulfide and dithiobiuret-thiuret systems in different electrolytes of varying *p*H are also presented.

The importance of sulfhydryl compounds in biological systems has led to considerable interest in the following equilibrium (1).

$$2RSH = RSSR + 2H^+ + 2e^- \qquad [1]$$

Many attempts have been made to measure the oxidation-reduction potentials of theoretically reversible systems of this type, but, for the most part, the data of such investigations do not conform to the criteria for freely reversible systems (2).

The compounds of these oxidation-reduction systems are also of interest as anode and cathode materials in galvanic cells. In this paper, anodic half-cell potential data for various organic sulfur compounds discharged in alkaline solution, as well as data for reversible thiol-dithio systems discharged in electrolytes of varying *p*H, are presented.

Apparatus and Technique

A previously described technique (3) has been used to measure the operating potential during current flow of the various organic sulfur compounds. This technique consists in discharging a 0.5g sample of the sulfur compound mixed with 0.05g of Shawinigan acetylene black in a large volume of electrolyte at a constant current drain of 0.005 amp/g. The change in anode or cathode potential with time was measured with a L&N type-K potentiometer using a saturated calomel reference electrode. The measured potentials were corrected for the IR drop associated with the apparatus and electrolyte by means of an oscillographic technique.

All half-cell potential data reported are referred to the normal hydrogen electrode and include a liquid junction potential. For most of the anode potential measurements, an aqueous 1.44*M* NaOH electrolyte ($a_{OH^-} = 1$)[1] was used as the electrolyte and a manganese dioxide bobbin wrapped in cheesecloth served as the cathode. For the cathod half-cell potential studies, aqueous $MgBr_2$, NH_4Cl-$ZnCl_2$, and NaOH electrolytes were used with compatible magnesium and zinc anodes.

[1] Calculated from the data given by Latimer (4).

Experimental Data and Discussion of Results

Thiourea-formamidine disulfide system.—Although most sulfhydryl compounds do not form truly reversible redox systems, there are some systems of this type which establish reproducible potentials as postulated theoretically. The first system of this kind, discovered by Preisler and Berger (2), is the thiourea-formamidine disulfide system.

In the acid range (0.05-1*N* HCl) studied by Preisler and Berger, thiourea does not ionize to any appreciable extent, whereas formamidine disulfide exists as the acid salt of a divalent base. The reaction is as follows

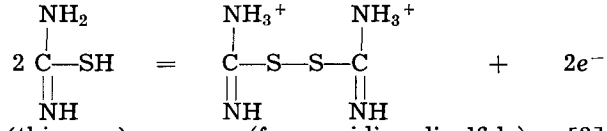

(thiourea) (formamidine disulfide —acid form) [2]

Because H^+ is not involved in the process (within the *p*H range studied) the potential is unaffected by change of *p*H.

The equation for the electrode potential, *E*, may then be written as follows

$$E = E_o' + \frac{RT}{2F} \ln \frac{(RSSR)}{(RSH)^2} \qquad [3]$$

where (RSSR) and (RSH) are the concentrations of formamidine disulfide and thiourea, respectively, and the constant E_o' is the potential when the logarithmic term becomes zero. For this system the E_o' value was found by Preisler and Berger to be +0.420v for solutions of 0.05-1*N* HCl.

Figure 1 shows half-cell potential discharge curves of the compounds in this reversible oxidation-reduction system obtained by discharging thiourea as an anode and formamidine disulfide dihydrochloride as a cathode in three electrolytes of different *p*H. As a cathode material, formamidine disulfide dihydrochloride operates at a potential close to its theoretical value in the 14% $MgBr_2$ (*p*H = 8.2) and 25% NH_4Cl-20% $ZnCl_2$ (*p*H = 4.5)

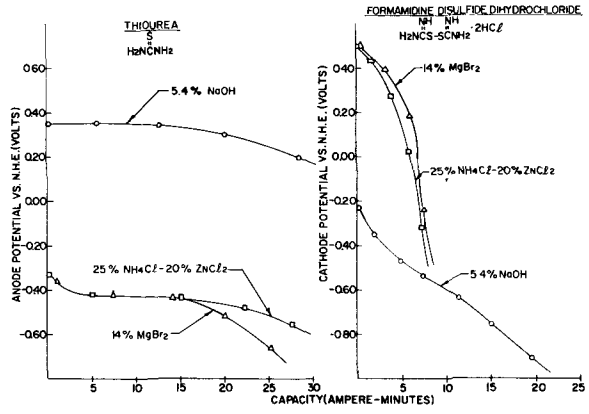

Fig. 1. Anode and cathode half-cell potential curves for the system thiourea-formamidine disulfide discharged at a rate of 0.005 amp/g in various aqueous electrolytes.

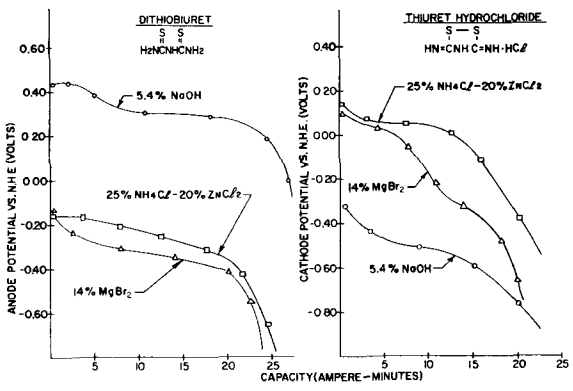

Fig. 2. Anode and cathode half-cell potential curves for the system dithiobiuret-thiuret discharged at a rate of 0.005 amp/g in various aqueous electrolytes.

electrolytes and at electrode efficiencies of 56 and 53%, respectively, as shown by the theoretical capacity and electrode efficiency data in Table I. As an anode material in the 5.4% NaOH electrolyte, thiourea has a potential of +0.35v and an electrode efficiency of 89% under these conditions of discharge. In the $MgBr_2$ and NH_4Cl-$ZnCl_2$ electrolytes, thiourea operates at considerably lower anode potentials; however, it provides approximately the same coulombic capacity to lower end potentials as in the strongly alkaline electrolyte.

Dithiobiuret-thiuret system.—The oxidation of dithiobiuret to thiuret (3,5-diimino-1,2,4-dithiazoline) investigated by Preisler and Bateman (5) indicates that the system apparently involves the opening and closing of a ring system as a part of the oxidation-reduction equilibrium, according to the following reaction

$$\underset{\text{(dithiobiuret)}}{\overset{\text{SH SH}}{\overset{|\quad|}{\text{HN=CNHC=NH}}}} = \underset{\text{(thiuret)}}{\overset{\text{S—S}}{\overset{|\quad|}{\text{HN=CNHC=NH}}}} + 2H^+ + 2e^- \qquad [4]$$

Table I. Theoretical capacities and electrode efficiencies of various organic sulfur compounds

Compound	Theoretical capacity, amp-min/g	Electrode efficiency,‡ %		
Anode materials		$ZnCl_2$†	$MgBr_2$†	NaOH§
Thiourea	21.1		88.6	
1-Methyl-2-thiourea	17.9		91.1	
1-Acetyl-2-thiourea	13.6		55.1	
1-Allyl-2-thiourea	13.8		81.2	
1-Phenyl-2-thiourea	10.6		97.2	
Thioacetamide	21.4		74.8	
Mercaptoacetic acid-Na salt	14.1		76.6	
Cysteine	13.3		100**	
Dithioloxalic acid dipotassium salt	16.2		93.8	
Dithiooxamide	26.8		53.7	
Dithiobiuret	23.8		93.7**	
Benzenethiol	14.6		—	
1-Hexanethiol	13.6		—	
Cathode materials		NH_4Cl-$ZnCl_2$†	$MgBr_2$†	NaOH§
Formamidine disulfide dihydrochloride	14.4	52.8	56.3	100
Thiuret hydrochloride	18.9	100	86.8	97.9
Cystine	13.4	—	—	100

‡ Experimental capacity calculated on the basis of the following end potentials: * +0.30v; ** +0.25v; † −0.40v; § −0.70v.

The reaction proceeds by a reversible two-step process. The potentials, within the pH range studied, are stable and follow the equations applicable to systems of this type. Preisler and Bateman measured the oxidation-reduction potential of this system over the pH range of 0.05-5.2 and obtained E_o' values of +0.251v at pH 0 and +0.102v at pH 5. The values indicate that dithiobiuret would act as a strong reducing agent in chemical reactions.

Figure 2 shows half-cell potential discharge curves of dithiobiuret and thiuret hydrochloride obtained by discharging these compounds at a current drain of 0.005 amp/g in various electrolytes. Thiuret hydrochloride operates at cathode potentials close to its theoretical value in both the NH_4Cl-$ZnCl_2$ and $MgBr_2$ electrolytes and at electrode efficiencies of 100 and 87%, respectively. Dithiobiuret, which initially has a higher anode potential than thiourea in the NaOH electrolyte, operates at an electrode efficiency of 94%. As in the case of thiourea, the anode potentials of dithiobiuret in the more acidic electrolytes are 0.5-0.6v lower than in the NaOH electrolyte, while the coulombic capacities obtained from dithiobiuret in all three electrolytes (to low end-potentials) are comparable.

Cysteine-cystine system.—The oxidation-reduction potential of the cysteine-cystine system, shown below, has been the subject of many investigations (6).

$$\underset{\text{(cysteine)}}{2HSCH_2CHCOOH} = \underset{\text{(cystine)}}{\overset{NH_2}{\overset{|}{S—CH_2CHCOOH}}\quad\overset{NH_2}{\overset{|}{S—CH_2CHCOOH}}} + 2H^+ + 2e^- \qquad [5]$$

From potential measurements carried out in the classical way, it is apparent that the reaction is not strictly reversible thermodynamically. However,

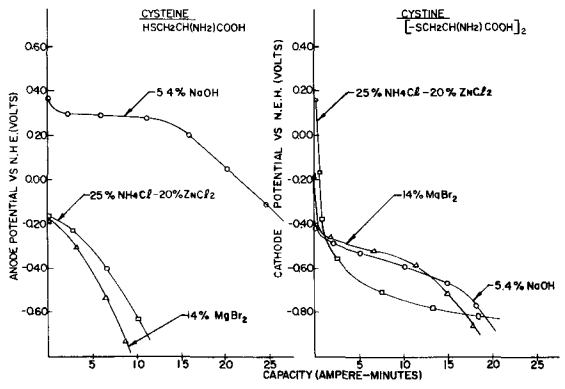

Fig. 3. Anode and cathode half-cell potential curves for the system cysteine-cystine discharged at a rate of 0.005 amp/g in various aqueous electrolytes.

the reaction can be reversed chemically with the expenditure of large amounts of energy.

As shown in Fig. 3, the half-cell potential discharge data for cysteine and cystine indicate that cystine is a weak oxidizing agent, even in the more acidic electrolytes. On the other hand, the anode potential of cysteine in NaOH electrolyte is only 0.07v lower than that of thiourea, whereas it operates at an electrode efficiency of 100%. Like thiourea and dithiobiuret, cysteine operates at considerably lower potentials in NH_4Cl-$ZnCl_2$ and $MgBr_2$ electrolytes.

Organic sulfur compounds as reducing agents.—Organic derivatives of sulfur are of two types, those related to the corresponding oxygen compounds by the substitution of S for O and those corresponding to the oxidized forms of sulfur. In this section, compounds of the first group, such as the mercaptans, thioacids and thioamides, are evaluated as anode materials. Figures 4 through 8 show half-cell potential discharge curves of these compounds, obtained by discharging them as anodes in 5.4% NaOH electrolyte at a rate of 0.005 amp/g. Theoretical capacity and electrode efficiency data for the compounds, based on a theoretical two-electron oxidation step to the disulfide state, are shown in Table I.

Thiophenols.—Figure 4 shows half-cell potential discharge data for various aromatic thiophenol compounds compared with phenol and 1-hexanethiol. Of the various compounds tested, the alkyl derivative, 1-hexanethiol, had the highest anode potential (+0.45-0.50v) in the NaOH electrolyte, whereas the thiophenol derivatives had anode potentials of +0.25-0.40v.

The higher anode potential of thiophenol in comparison to phenol is to be expected on the basis of their different behavior toward oxidizing agents; the sulfur atom can be oxidized whereas the oxygen atom cannot. This ability makes possible compounds such as the sulfoxides, sulfones, and sulfonic acids. In addition, the —S—S—linkage is stable whereas the —O—O—linkage is very unstable.

Thus the mercaptans can be readily oxidized to disulfides in alkali electrolyte by mild oxidizing agents such as air, halogens, and hydrogen peroxide. Stronger oxidizing agents convert the disulfides into sulfonic acids.

The discharge curves of the various para substituted thiophenol compounds indicate that the effect of substituted groups on the anode potential of thiophenol closely parallels their effect on the anode potential of aromatic hydroxy and amine compounds (3). For example, the higher potential of p-toluenethiol and the lower potential of p-nitrothiophenol as compared to benzenethiol can be readily explained in terms of the effect of the electron repelling —CH_3 group and the electron attracting —NO_2 group on the electron density in the vicinity of the oxidizable —SH group. Similarly, the higher potential of 2-naphthalenethiol as compared to benzenethiol can be explained on the basis of the higher ring electron density in the vicinity of the naphthalene —SH group than around the —SH group on the benzene ring. As a consequence of this higher electron density, 2-naphthalenethiol has a lower electron affinity than benzenethiol and is a stronger reducing agent.

Thiourea derivatives.—Figure 5 shows half-cell potential discharge curves for various 1-substituted thiourea derivatives. These compounds operate at anode potentials of +0.32-+0.37v, and (assuming end potentials of +0.30v), at electrode efficiencies of 80-90%. Unlike the effect of substituted groups on the anode potential of the thiophenols, the effect of substituted groups on the potential of thiourea does not follow any established pattern. However, as in the case of methyl and phenyl hydrazine (7), the anode potentials of these compounds increase in the

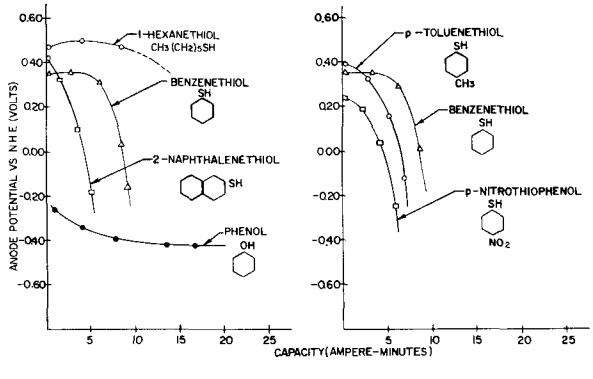

Fig. 4. Half-cell potential discharge curves of various thiophenol derivatives discharged at a rate of 0.005 amp/g in 1.44M NaOH.

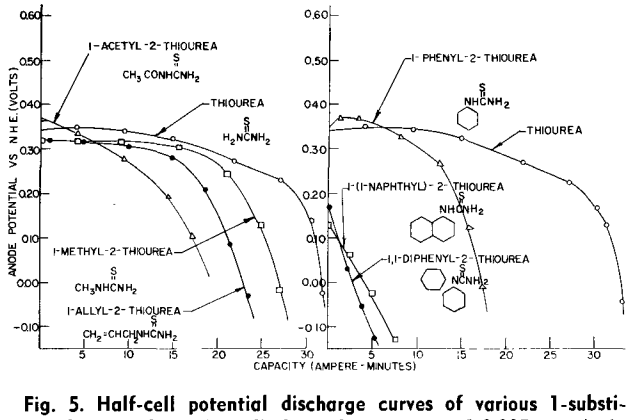

Fig. 5. Half-cell potential discharge curves of various 1-substituted thiourea derivatives discharged at a rate of 0.005 amp/g in 1.44M NaOH.

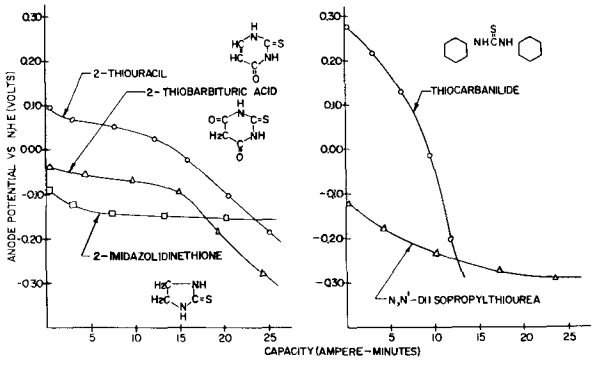

Fig. 6. Half-cell potential curves of various N,N'-disubstituted thiourea derivatives discharged at a rate of 0.005 amp/g in 1.44M NaOH.

order of 1-methyl-2-thiourea, thiourea, and 1-phenyl-2-thiourea.

The addition of another phenyl group to the 1-position of 1-phenyl-2-thiourea results in a compound which polarizes readily under these conditions of discharge. Unlike 1,1-diphenyl-2-thiourea, the symmetrical diphenylthiourea compound (thiocarbanilide) shown in Fig. 6, operates at a considerably higher electrode potential and has a greater coulombic capacity in the NaOH electrolyte.

Also shown in Fig. 6 are half-cell potential discharge curves for 2-thiouracil, 2-thiobarbituric acid, and 2-imidazolidinethione. These compounds may be considered as cyclic N,N' disubstituted thiourea derivatives. As in the case of phenol and thiophenol, 2-thiouracil and 2-thiobarbituric acid operate at higher anode potentials than their comparable hydroxy compounds uracil and barbituric acid (8), giving further indication that the —SH group is a stronger reducing agent than the —OH group.

The half-cell potential discharge curves for two other substituted thiourea compounds of interest are shown in Fig. 7. These compounds, thiocarbohydrazide and thiosemicarbazide, contain, in addition to the —SH group, the hydrazino group (—$NHNH_2$), which is also oxidizable. For thiocarbohydrazide this results in a compound which has a higher initial anode potential than the thiourea derivatives shown in Fig. 5 and 6 and a higher anode potential than the other hydrazine compounds previously studied (7). Similarly, thiosemicarbazide operates at a higher anode potential than the simple semicarbazide hydrochloride compound.

Thioacid and thioamide derivatives.—The introduction of one sulfur into a carboxyl group might be expected to yield two different products; however, thiocarboxylic acids are tautomeric, and only one substance has been isolated because the two forms readily interconvert (9) as follows

$$R-\overset{\overset{O}{\|}}{C}-SH \rightleftarrows R-\overset{\overset{OH}{|}}{C}=S \qquad [6]$$

This interconversion is also true of the thioamides, as shown below

$$R-\overset{\overset{S}{\|}}{C}-NH_2 \rightleftarrows R-\overset{\overset{SH}{|}}{C}=NH \qquad [7]$$

Figure 8 shows half-cell potential discharge data for various thioamide and thioacid derivatives obtained by discharging these compounds at a rate of 0.005 amp/g in 5.4% NaOH electrolyte. The data indicate that simple thioamides such as thioacetamide and dithiooxamide operate at potentials 0.10-0.15v more anodic than thiourea; however, they provide less coulombic capacity, as evidenced by the half-cell potential discharge curve of thioacetanilide.

Compared to thioacetamide and thiourea, thioacetic acid operates at a considerably lower anode potential. Similarly, dithioloxalic acid dipotassium salt operates at a potential +0.15v less anodic than dithiooxamide.

A curve for mercaptoacetic acid-Na salt is included in Fig. 8 for comparison, although this compound is a mercaptan and not a thioacid. The high anode potential of this compound is comparable to that obtained for 1-hexanethiol (Fig. 4) and is a further indication of the strong reducing power of the mercaptans.

Conclusion

Compared to inorganic anode materials, organic sulfur compounds are not as good both on the basis of theoretical and experimentally obtained coulombic capacities. In addition, the anode potentials of the more strongly reducing organic sulfur derivatives range from +0.3 to +0.5v, values considerably

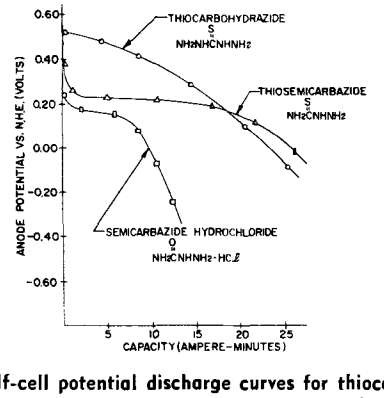

Fig. 7. Half-cell potential discharge curves for thiocarbohydrazide and thiosemicarbazide discharged at a rate of 0.005 amp/g in 1.44M NaOH electrolyte.

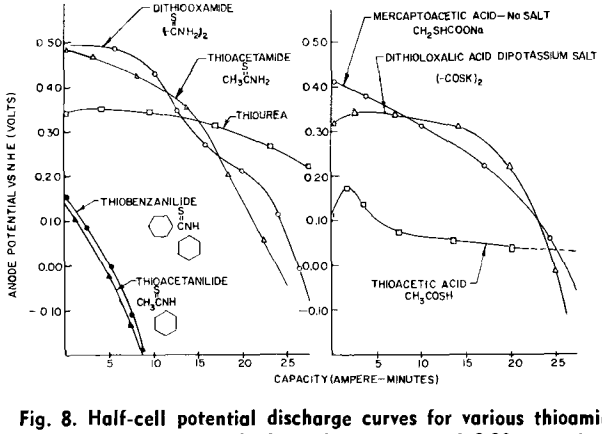

Fig. 8. Half-cell potential discharge curves for various thioamide and thioacid derivatives discharged at a rate of 0.005 amp/g in 1.44M NaOH electrolyte.

lower than those of conventional inorganic metal anodes.

Of the solid compounds tested, thiourea and dithiobiuret offer the most promise as anode materials because of their comparatively high anode potentials and coulombic capacities. High potential liquid mercaptan compounds such as 1-hexanethiol are also of interest because of their possible use as anodes in continuous feed electrochemical cells. Although the theoretical coulombic capacities of these compounds are low, the use of mercaptans with two or three functional —SH groups in the molecule would allow for higher capacity compounds having higher anode potentials.

Acknowledgment

The author wishes to acknowledge support of this research by the U.S. Army Signal Engineering Laboratories under Contract No. DA-36-039-sc-78048.

Manuscript received Oct. 2, 1962.

Any discussion of this paper will appear in a Discussion Section to be published in the December 1963 JOURNAL.

REFERENCES

1. L. D. Freedman and A. H. Corwin, *J. Biol. Chem.*, **181**, 601 (1949).
2. P. W. Preisler and L. Berger, *J. Am. Chem. Soc.*, **69**, 322 (1947).
3. R. Glicksman, *This Journal*, **108**, 1 (1961).
4. W. M. Latimer, "Oxidation Potentials," p. 354, Prentice-Hall, Inc., New York (1952).
5. P. W. Preisler and M. B. Bateman, *J. Am. Chem. Soc.*, **69**, 2632 (1947).
6. A. E. Remick, "Electronic Interpretations of Organic Chemistry," 2nd Ed., pp. 566-569, John Wiley & Sons, Inc., New York (1949).
7. R. Glicksman, *This Journal*, **108**, 922 (1961).
8. R. Glicksman, *ibid.*, **109**, 352 (1962).
9. C. R. Noller, "Chemistry of Organic Compounds," p. 271, W. B. Saunders Co., Philadelphia, Pa. (1951).

Disintegration of Magnesium While Dissolving Anodically in Neutral and Acidic Solutions

M. E. Straumanis and B. K. Bhatia

Department of Metallurgical Engineering,
University of Missouri School of Mines and Metallurgy, Rolla, Missouri

ABSTRACT

A closer investigation of the dark deposits which separate from a magnesium anode in the form of leaflets in neutral and in acidic solutions showed that the views set forth by Baborovsky (1905) concerning metallic Mg in the deposits are correct. A multitude of Mg particles of about 6×10^{-5} mm in diameter were visible in the flakes, causing their dark color. In perchloric acid the magnesium anodes first turned slightly dark at the rim. Beautiful patterns of deformation twins appeared. At high current densities flakes containing innumerable metallic particles separated from the anode. The particles broke off from anodic regions leaving a series of dark holes where the metal was locally strained or deformed or where the interatomic bonding was weakened. The partial disintegration of Mg into fine particles contributes to the explanation of the negative difference effect; it explains the apparent deviation from Faraday's law and shows that the assumption of expulsion of lower valency ions from the anode during anodic dissolution is unnecessary at present. The active metal particles themselves have great reducing ability.

Several explanations have appeared in the literature for the anodic behavior of metals dissolving in aqueous solutions, especially with regard to decrease or increase of the self-dissolution rate during the passage of anodic currents. The latter are referred to as the positive and negative difference effects, respectively (1). This seemingly theoretical problem is of practical importance, *e.g.*, in cathodic protection. The efficiency of sacrificial Mg anodes is low, sometimes less than 50% (2). It can be shown that such Mg anodes exhibit the negative difference effect.

To explain the negative difference effect, assuming Faraday's law to hold, some investigators have proposed that the electrodes under anodic current expel ions of lower valency (3-7), which then are oxidized by the electrolyte under hydrogen evolution to their normal valency. However, this hypothesis cannot be sufficiently backed by experimental facts, and it becomes less probable when the positive difference effect is also considered (8, 9).

The difficulties connected with an explanation of the negative difference effect or with the apparent deviation from Faraday's law, or with the appearance of ions of seemingly lower valency disappear if another phenomenon is considered: the partial disintegration of metals into fine particles under conditions of free dissolution and dissolution under an anodic current. Disintegration was observed previously, *e.g.*, by Hoey and Cohen (10, 8), and is mentioned by Evans (11). However, only relatively large chunks were found. What is new now is the partial disintegration into finest metallic particles observable only under high magnifications using oil immersion objectives. The disintegration of electrodes was proposed by Marsh and Schaschl (12) for the ex-

planation of the negative difference effect and corrosion of steel in aqueous solutions was mentioned as an example. Disintegration of metals was first recognized as such with Be, dissolving in HCl (13, 14). Soon afterward the same phenomenon was observed with Mg.

Disintegration of Mg in NaCl Solutions

All the dissolution experiments were performed with 99.995% pure Mg, and all acids and salts used were of reagent grade.

It has been reported that during anodic dissolution of Mg metal in aqueous solutions a black corrosion product is given off by the anode (15). Qualitative studies were carried out here to produce the black deposit and to examine it for the possible presence of Mg particles. The electrolysis was carried out with a Mg anode and a Pt cathode in about 3% NaCl aqueous solution. The current varied from 250 to 300 ma/cm^2. In order to reduce the reaction rate of the Mg particles with water, the electrolysis was performed at lower temperatures by immersing the reaction beaker in ice water. A black corrosion product separated from the anode at the start, but soon the solution exhibited a white turbidity. To avoid further hydrolysis, the electrolysis was stopped and the black deposit decanted with ice water several times in order to remove the salt and then quickly dried, using 95% ethanol. Nevertheless the deposit turned partially white during this operation. In a dry state the flake-like deposit was stable for months. In water, hydrolysis was complete within a few hours. X-ray powder patterns showed the white product to be $Mg(OH)_2$.

The dark, sometimes completely black flakes were examined under the microscope. However, only at highest magnifications (oil immersion) and in reflected light could the structure of the flakes be resolved; it consisted of innumerable particles of metallic luster, held together by the substance of the flakes, in all probability $Mg(OH)_2$ (see Fig. 1). In the transmitted light these particles, excepting the holes, appeared dark. The whiter the flakes, the less dense was the accumulation of the reflecting particles (see Fig. 2). No movement of the agglomerations in the oil was observed, but rather a movement of the whole "cloud," which clearly shows that the particles were held fixed by the hydroxide of the

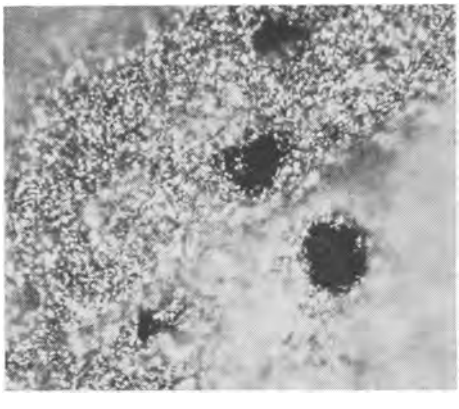

Fig. 1. Highly reflecting metallic particles in the black anodic corrosion product, 250-300 ma/cm^2, electrolyte 3% NaCl aqueous solution. Holes in the film. Magnification 1430X.

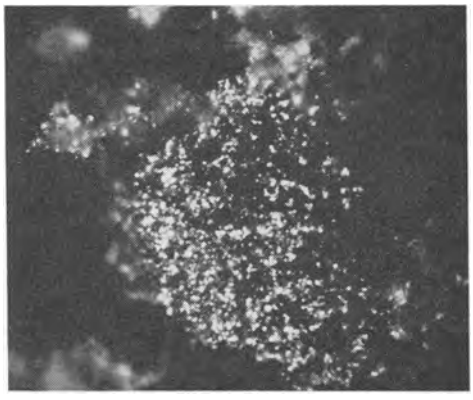

Fig. 2. Less dense accumulation of particles in nearly white flakes. Magnification 1430X.

film. Separate particles and even large chunks floating in the oil could also be observed. The particle size was quite uniform, as shown in Fig. 1 and 2. In the denser accumulations there were more than 200,000 particles/cm^2. The diameter of the smallest particles was around 6 x 10^{-5} mm. From the behavior of the free particles floating in the oil it could be deduced that they were platelets.

Disintegration in Dilute Aqueous Solutions of HCl and $HClO_4$

The concentration of HCl was approximately 0.05N. The conditions of electrolysis were the same as described above. The Mg electrode developed a black coating, as observed through the solution, and dark flakes separated from the anode while the current was flowing. The flakes turned white quickly on settling and could not be collected in the black state for microscopic observation. The white flakes did not contain any shiny particles.

However, it was possible to observe the particles directly in the film of the Mg electrode when the latter was subjected to anodic dissolution in $HClO_4$ (0.2-0.4N) at current densities above 300 ma cm^{-2}. Around the edges of the electrode, at the highest current densities, a black adherent saltlike film was formed. The electrode was then removed from the beaker, washed, dried, and examined microscopically under low magnifications to reveal the presence of a cracked film of a structure resembling that of the etched Mg surface (see Fig. 3). In the same films, observed under oil at high magnification, innumerable shiny particles of the size and shape shown in Fig. 1 and 2 could be detected (Fig. 4). These particles gave the dark film (Fig. 3) a slight metallic luster (16). Evidently the shiny particles are covered by some thin film which protects them from dissolution in the $HClO_4$. By crushing the thick saltlike coatings, the particles were released and observed under the microscope. There was no difference in their appearance as compared with those formed in NaCl solutions. The same picture was obtained with flakes peeled off the anode during electrolysis in $HClO_4$.

Nature of the Particles

In the case of Be it could be shown by x-ray diffraction that the shiny particles separating from the anode were metallic Be (13, 14). In the present case

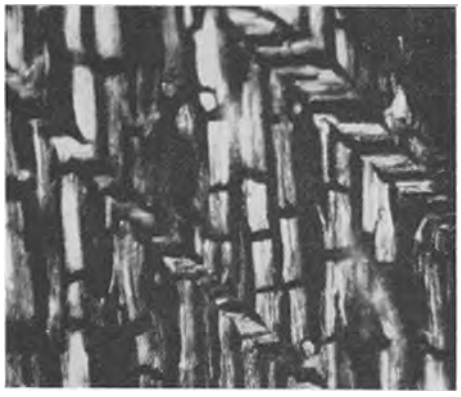

Fig. 3. Dark edge of a Mg electrode etched anodically in 0.3-0.4*N*. $HClO_4$ for 0.5 min, 350 ma cm^{-2}. Magnification 320X.

Fig. 4. Dark edge of a Mg electrode etched anodically in $HClO_4$ (Fig. 3). Shiny particles are present. Magnification 1430X.

it was more difficult to prove the metallic nature of the Mg particles, because they were much smaller than the Be particles and were entangled in the $Mg(OH)_2$ network. The x-ray analysis yielded diffraction lines belonging to $Mg(OH)_2$ and in addition two lines, the positions of which coincided with the two strongest lines of pure Mg, having relative intensities of 100 and 40. On the patterns obtained with the black substance, the first of these lines was weak, although sharp, and the second was very weak. The third strong line of pure Mg with a relative intensity of 20 and all other lines of still lower intensity could not be observed on the films. This was not surprising because only a very small amount of Mg was present in the flakes. Furthermore, broad and relatively strong lines of $Mg(OH)_2$ overlapped the weak Mg lines, and there was also a background created by fluorescent radiation on the films.

Further evidence of the metallic nature of the particles was found in their strong metallic luster; they behaved as if they were tiny mirrors.

In addition, the particles, after separating from the anode, reacted with the electrolyte to evolve gas (in all probability, hydrogen). Simultaneously the flakes turned white [$Mg(OH)_2$]. Of course, this property (evolving hydrogen) could also be exhibited by lower valency ions, but would only occur at the proximity of the anodic surface (3-7) as these ions are only of a very short life (10^{-3} to 10^{-1} sec) (7). The dark flakes observed here reacted only slowly with H_2O, even with acids ($HClO_4$), and were very stable in a dry state. This is exactly the behavior of fine particles of active metals and not of lower valency ions.

Origin and Break-Out Spots of Metallic Particles

In previous work it was shown that Be particles break out of a massive Be plate while it is dissolving in HCl (13, Fig. 3) and are not formed subsequently in a secondary reaction (14). In the present case, Mg particles also could not be formed in a secondary reaction in aqueous solutions. Furthermore the sharpness of the two diffraction lines of the particles indicates that the lattice of particles was not distorted and, hence, originated from the metal electrode itself.

There is a further question as to where on a metallic surface the particles will break out. It has to be expected that this should occur on such places of the metallic lattice where the metal is strained or distorted, *e.g.*, along glide planes, or lines, caused by mechanical deformation, possibly along dislocation lines and their accumulations, or where the interatomic bonding is somewhat weakened as along concentrations of vacancies and impurities. These places may be attacked preferentially by the process of dissolution, and particles may break out because of partial undermining (10). An uneven place should be left on the sample which should appear black in the light of the opaque illuminator. This is exactly what is observed. The anodic dissolution of Mg under certain conditions can be so directed that the break-out of particles occurs not throughout, but preferentially at the above-mentioned locations on the surface of the sample (Fig. 5). Evidently the tiny particles break out side by side leaving the relatively large spots looking dark on the photomicrograph. It can be seen clearly that this break-out occurred in preferred directions, frequently along straight lines. On the right side of Fig. 5 there is another grain with a different crystallographic direction. It is assumed that the break-out of the Mg particles occurred on the black places. A similar Mg plate treated anodically at lower current densities looked, especially in the center, as if it had been electropolished, although the grain boundaries were clearly defined (Fig. 6).

Another pattern of Mg, showing deformation twins, is pictured in Fig. 7. Thus the consequences of the deformation of Mg and of other metals (Zn, Cd, Be) can be studied by making electrodes of

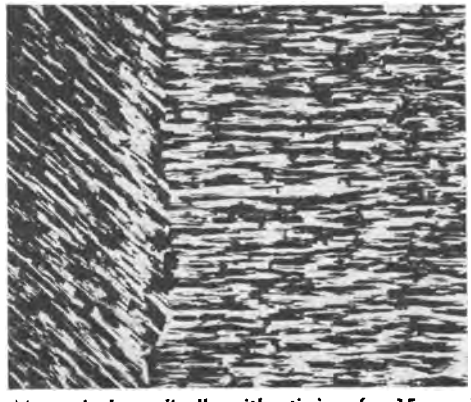

Fig. 5. Mg etched anodically with stirring for 15 sec in 0.4*N* $HClO_4$, 520 ma cm^{-2}. Magnification 90X.

Fig. 6. The middle of a Mg electrode etched anodically with stirring for 15 sec in 0.3*N* $HClO_4$, 330 ma cm^{-2}. Magnification 60X.

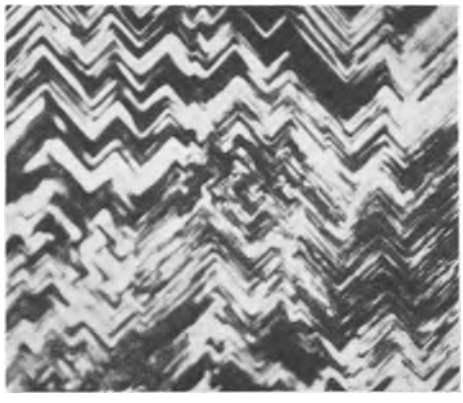

Fig. 7. Mg etched anodically with stirring for 30 sec in 0.3*N* $HClO_4$, 350 ma cm^{-2}. Magnification 320X.

them and by applying anodic currents of such a density in a certain electrolyte that partial disintegration of the anode occurs.

Conclusions concerning the deformation process can then be drawn from the microscopic picture of the etched surface of the anode.

Conclusions

This investigation shows that Mg disintegrates partially into very small metallic particles under certain conditions of dissolution or corrosion. The dark color of the flakes separating from the anode is caused by the presence of minute Mg particles held in a matrix of $Mg(OH)_2$. Baborovsky, who assumed that the dark color of the anodic films was caused by the presence of metallic Mg, was therefore correct (17).

The break-out of particles explains in part the negative difference effect, that is the increased rate of dissolution of Mg when an anodic current of sufficiently high density is passed through the electrode. The current, as also observed with Al (8), partially but continuously breaks down the regenerating oxide coating which contains a multitude of metallic particles. Due to the breakdown of the film the reacting surface of Mg increases and with it the self-dissolution rate of Mg; the rate is increased still more by the separate dissolution of the metallic particles of the film. The disintegration also explains the low efficiency of Mg anodes used for cathodic protection and some other phenomena observed during dissolution of metals (18).

Taking into account the increased dissolution rate while the current is flowing, no deviation from Faraday's law would be found and, therefore, there is at present no need for the assumption of expulsion of ions of a charge lower than normal (19). Vice versa, to prove the presence of such ions, at least the increased rate of fragmentation of the anode while the current is flowing has to be taken into account as by Hamer and associates in the case of silver when they redetermined Faraday's constant (20, 21).

The reducing ability of the anolyte does not prove the existence of lower valency ions because the fine particles of active metals observed in the anolyte have even a greater reducing ability than the lower valency ions.

Acknowledgments

The authors wish to thank the Office of Naval Research for partial support of this research work, and Director Dr. R. Gadeau, Paris, for supplying the magnesium. They are also grateful to Dr. W. J. James, Professor of Physical Chemistry at the School, for presenting the essence of this investigation at the Gordon Research Conference in July, 1962, and for assistance with the manuscript.

Manuscript received Oct. 1, 1962. This paper was prepared for delivery before the Boston Meeting, Sept. 16-20, 1962.

Any discussion of this paper will appear in a Discussion Section to be published in the December 1963 JOURNAL.

REFERENCES

1. M. E. Straumanis and N. Y. Wang, *This Journal*, **102**, 304 (1955).
2. C. S. Roberts, "Magnesium and its Alloys," pp. 199 and 200, John Wiley & Son, Inc., New York (1960).
3. P. Brouillet, G. Epelboin, and M. Froment, *Compt. rend.*, **239**, 1795 (1954).
4. J. N. Greenblatt, *This Journal*, **103**, 539 (1956).
5. D. V. Kokoulina and B. N. Kabanov, *Dokl. Akad. Nauk. SSSR*, **112**, 692 (1957)
6. D. T. Sorensen, A. W. Davidson, and J. Kleinberg, *J. Inorg. Nucl. Chem.*, **13**, 64 (1959).
7. K. E. Heusler, *Z. Elektrochem.*, **65**, 192 (1961).
8. M. E. Straumanis, *This Journal*, **105**, 284 (1958).
9. M. E. Straumanis, *ibid.*, **108**, 1087 (1961).
10. G. R. Hoey and M. Cohen, *ibid.*, **105**, 245 (1958).
11. U. R. Evans, "Corrosion and Oxidation of Metals," p. 883, Edward Arnold, London (1960).
12. G. A. Marsh and E. Schaschl, *This Journal*, **107**, 960 (1960).
13. M. E. Straumanis and D. L. Mathis, *J. Less-Common Met.*, **4**, 213 (1962).
14. M. E. Straumanis and D. L. Mathis, *This Journal*, **109**, 434 (1962).
15. L. R. Petty, A. W. Davidson, and J. Kleinberg, *J. Am. Chem. Soc.*, **76**, 363 (1954).
16. M. E. Straumanis and B. K. Bhatia, *Metall*, **16**, 535 (1962).
17. G. Baborovsky, *Z. Elektrochem.*, **11**, 465 (1905).
18. B. Roald and M. A. Streicher, *This Journal*, **97**, 283 (1950).
19. J. L. Robinson and P. F. King, *This Journal*, **108**, 36, 41 (1961).
20. D. N. Craig, J. I. Hoffman, C. A. Law, and W. J. Hamer, *J. Research Natl. Bur. Standards*, **64A**, 381 (1960).
21. D. A. Vermilyea, *This Journal*, **105**, 547 (1958).

Pyrolytic Deposition of Silicon Dioxide for 600°C Thin Film Capacitors

Charles R. Barnes and Charles R. Geesner

Electronic Technology Laboratory, Aeronautical Systems Division, Wright-Patterson Air Force Base, Ohio

ABSTRACT

Silicon dioxide thin films have been deposited by pyrolytic hydrolysis of silicon tetrabromide vapor on hot substrates at 950°C by using a mixture of hydrogen and argon gases in the presence of water vapor. Nitrogen may be substituted for the argon to form an equally efficient dielectric. In either case chemical and physical analytical procedures show that the dielectric is amorphous and mainly silicon dioxide.

Further research on dielectrics suitable for 600°C capacitors has revealed that the dielectric previously described by the authors (1) as silicon nitride is actually silicon dioxide formed as a result of small traces of residual water vapor in the carrier gas. This conclusion has been verified by chemical and physical analyses of the films as well as by the fact that argon or other inert gases may be substituted for the nitrogen carrier to produce a film with equivalent dielectric properties.

To deposit a nonporous silicon dioxide thin film with optimum dielectric properties, it is essential to supply a controlled amount of moisture to the pyrolytic reaction between hydrogen, water, and silicon tetrabromide vapors at the hot substrate surface. Due to considerable variation of the water and oxygen contents of commercially available compressed gases, it was found necessary to develop a method to control these contaminants.

Deposition of Silicon Dioxide Dielectric

The method of moisture and oxygen control developed by the authors, as illustrated by Fig. 1, consists of entering four drying towers (E) following the deoxidizers (B) and (C) in order to overdry the mixed carrier gases. Then by by-passing a portion of the mixed carrier gases over a 55% (by weight) solution of sulfuric acid (S) the amount of water vapor entering the plating chamber may be controlled accurately.

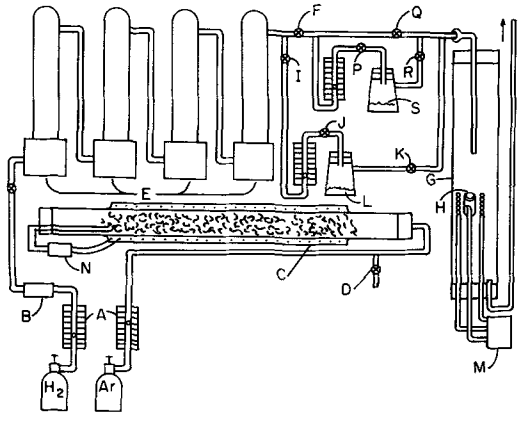

Fig. 1. Apparatus for depositing silicon dioxide: A, flowmeters for hydrogen and argon, B and C, deoxidizers; D, back-flush valve; E, calcium hydride drying towers; F, I, J, and K, vapor control valves; G, deposition chamber; H, substrate; L, silicon bromide evaporator; M, induction heater and temperature controller; N, deoxidizer temperature control; P, Q, and R, humidity control valves; S, sulfuric acid solution.

Table I. Dielectric properties of silicon dioxide thin film capacitors vs. heat exposure

Temp of heat exposure, °C	Capacitor No. 1 Capacitance-pf	Capacitor No. 1 Dissipation factor	Capacitor No. 2 Capacitance-pf	Capacitor No. 2 Dissipation factor
25	2691	0.0001	3090	0.0001
100	—	—	—	—
200	2699	0.0001	3102	0.0001
300	2711	0.0001	3110	0.0001
400	2723	0.0002	3120	0.0001
500	2732	0.0005	3132	0.0006
600	2741	0.0057	3150	0.0063

To deposit silicon dioxide thin film dielectric at the rate of 0.7 mil thickness per hour with the present apparatus the flow rates of hydrogen and argon should be approximately 400 and 1300 ml/min, respectively. At the same time the amounts of mixed gases by-passed over the silicon tetrabromide (L) and the 55% sulfuric acid solution should be 100 and 1000 ml/min, respectively.

Dielectric Properties of Thin Silicon Dioxide Films

To measure and compare the dielectric properties of a silicon dioxide thin film made with hydrogen and argon with that formed with hydrogen and nitrogen by the above procedure, encapsulated capacitors were constructed of each using the method previously described. The results in Table I showing the effect of temperature increase over the range of 25°-600°C on capacitance and dissipation factor indicate that the dielectric in capacitor No. 1 made using hydrogen and nitrogen carrier is equivalent to capacitor No. 2 in which hydrogen and argon were employed.

In order to determine the chemical composition of the dielectric, two films were deposited on molybdenum by the exact procedures followed for capacitors No. 1 and 2. The films were removed mechanically and analyzed for chemical composition following common analytical and investigative techniques such as spectrographic analysis, microchemical analysis, infrared absorption, and x-ray diffraction.

The results of the analytical examinations show that both films are amorphous and consist mainly of silicon dioxide. Microchemical analysis showed nitrogen contents of less than 0.3% for film No. 1 and less than 0.1% for film No. 2. Due to the smallness of the sample available, it is estimated that the nitrogen analyses were accurate to ±0.1%. Therefore if any silicon nitride does exist in film No. 1, it is only present in an amount less than 0.25% of the film. Infrared inspection showed only the presence of silicon dioxide. X-ray diffraction examination showed that the films were noncrystalline.

Conclusion

Thin films of silicon dioxide are deposited at 950°C by pyrolytic hydrolysis of silicon tetrabromide in the presence of small amounts of water vapor regardless of whether argon or nitrogen carrier gas is used. Such films form dielectrics suitable for 600°C capacitors.

Acknowledgment

Analyses of the films were performed by Battelle Memorial Institute, Columbus, Ohio.

Manuscript received May 25, 1961; revised manuscript received Dec. 3, 1962. This paper was delivered before the Los Angeles Meeting, May 6-10, 1962.

Any discussion of this paper will appear in a Discussion Section to be published in the December 1963 JOURNAL.

REFERENCE

1. C. R. Barnes and C. R. Geesner, *This Journal*, **107**, 98 (1960).

The Electrodeposition of Nickel-Molybdenum Alloys

Nelson W. Hovey, Albertine Krohn, and George M. Hanneken, Jr.[1]

Chemistry Department, University of Toledo, Toledo, Ohio

ABSTRACT

Pyrophosphate solutions have been used for the successful deposition of iron-molybdenum and cobalt-molybdenum alloys. This investigation shows that a similar bath can be used to deposit nickel-molybdenum alloys. Hydrazine sulfate was added to prevent anodic oxidation of Ni(II). This greatly improved the cathode current efficiency, but lowered the molybdenum content of the deposits. Efficiency is further increased by wiping the cathode during plating. The average content of the deposits was about 60% molybdenum, 35.5% nickel, 4.5% nonmetallic material. The cathode current efficiency was about 37.5%. The deposits were bright and adherent.

The codeposition of molybdenum with iron and with cobalt from pyrophosphate solutions has been studied extensively (1, 2). A specially designed plating cell incorporating cathode rotation, stirring, and wiping increases the efficiency of the plating process. The present study is part of a continuing research program concerned with the deposition of molybdenum with various metals from pyrophosphate baths using this specially designed plating apparatus.

Experimental

Apparatus.—The plating cell and auxiliary equipment used in this study have been described in a previous publication (1).

Plating bath.—The bath used at the beginning of this investigation was similar to that established by Krohn and Brown (2) as the optimum bath for the electrodeposition of cobalt-molybdenum alloys. Preliminary experiments showed that Ni(II) in the bath was anodically oxidized unless hydrazine sulfate was added as a potential buffer.

Analysis of the deposits.—The alloy deposits were dissolved from the platinum cathodes with 5*N* nitric acid. Both molybdenum and nickel were analyzed colorimetrically. Mercaptoacetic acid was used for the determination of molybdenum (3) and beta-mercaptopropionic acid for nickel (4).

[1] Present address: Rocky Mountain Arsenal, Denver, Colorado.

Experimental Results

Unless otherwise stated, the plating runs were made using a current density of 16.1 amp/dm^2 (150 amp/ft^2) and a bath temperature of 60°C. Most of the plating runs were of 10-min duration. The speed of rotation of the cathode was 1750 rpm, which continued to be optimum (1). As with other electrodeposited molybdenum alloys, all the deposits contained a small amount of nonmetallic material (NMM) which may have been oxygen, hydrogen, or both. The percentage of NMM was obtained by subtracting the total percentage of molybdenum and nickel from 100. The calculation of cathode current efficiency (CCE) was based on the oxidation states of Mo(VI) and Ni(II). The effects of changes in plating conditions and solution composition on the deposits and on cathode current efficiency are summarized by the following graphs and discussion. When conditions encountered were better than those previously used, these were retained for the remainder of the investigation.

Effect of current density.—The plating solution in this series of tests had the following composition: 32.2 g/l (0.80*N*) $Na_2MoO_4 \cdot 2H_2O$, 11.9 g/l (0.10*N*) $NiCl_2 \cdot 6H_2O$, 70.0 g/l (0.63*N*) $Na_4P_2O_7 \cdot 10H_2O$, 80.0 g/l (0.95*N*) $NaHCO_3$, and 2.5 g/l $N_2H_4 \cdot H_2SO_4$.

Seven runs were made at current densities varied from 5.4 to 21.5 amp/dm^2 (50-200 amp/ft^2). The

length of plating time was varied so that 2000 coulombs passed during each run. Except at the lower current densities where the deposits were thin and dark, this is not a critical variable. As shown in Fig. 1, there is a slight increase in the molybdenum content and in the CCE in the range 13.5 to 18.8 amp/dm^2 (125-175 amp/ft^2). At higher current densities, evolution of hydrogen decreases the efficiency and the quality of the alloy plates.

Effect of the length of plating time.—Using the same bath composition as for the above study, six runs were made from 2.5- to 20-min duration. It was necessary to double the concentration of hydrazine sulfate in the 40- and 60-min runs to prevent the formation of an anode deposit.

The deposits obtained at the shorter plating times were shiny and adherent. The 60-min deposit was light gray with a rough surface. Figure 2 shows that, as the length of plating time was increased, the molybdenum content of the deposits decreased. Changes are not significant in runs of 10 or more minutes.

Effect of temperature.—The plating bath for this study contained 20.2 g/l (0.50*N*) $Na_2MoO_4 \cdot 2H_2O$, 5.95 g/l (0.050*N*) $NiCl_2 \cdot 6H_2O$, 16.7 g/l (0.15*N*) $Na_4P_2O_7 \cdot 10H_2O$, 80.0 g/l (0.95*N*) $NaHCO_3$, and 2.5 g/l $N_2H_4 \cdot H_2SO_4$. Runs were made at varying temperatures from 28° to 70°C. Deposits obtained at temperatures below 60° were dull gray. The efficiency increased as the bath temperature increased, but the molybdenum content of the deposits decreased slightly (Fig. 3).

Effect of molybdenum (VI) concentration.—Seven runs were made with the concentration of Mo(VI) varied from 0.0*N* to 1.5*N* (0-60.6 g/l $Na_2MoO_4 \cdot 2H_2O$). The other bath components were the same as for the current density study. With no molybdate present, the deposit was a blistered, dull brown, and difficult to dissolve in 5*N* HNO_3. It contained 88.3% Ni and 11.7% NMM. As the Mo(VI) content of the deposits increased (Fig. 4), the nickel content decreased, and the CCE dropped considerably. Deposits became brighter and more metallic looking up to bath concentrations of 0.10*N* Mo(VI); above this concentration they were dark and spotted. The molybdenum content of the deposits remains nearly constant above bath concentrations of 0.50*N*.

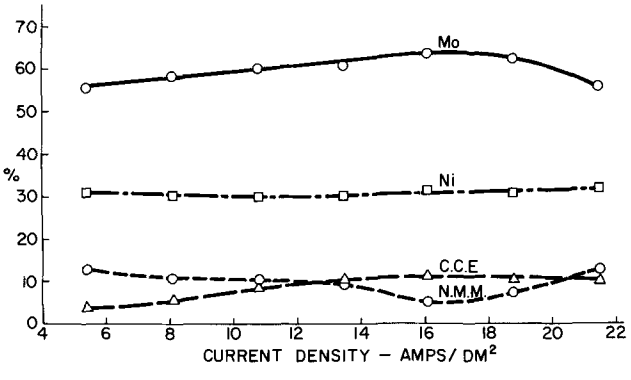

Fig. 1. Effect of current density

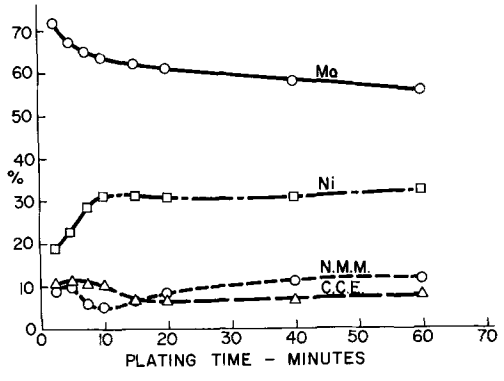

Fig. 2. Effect of length of plating time

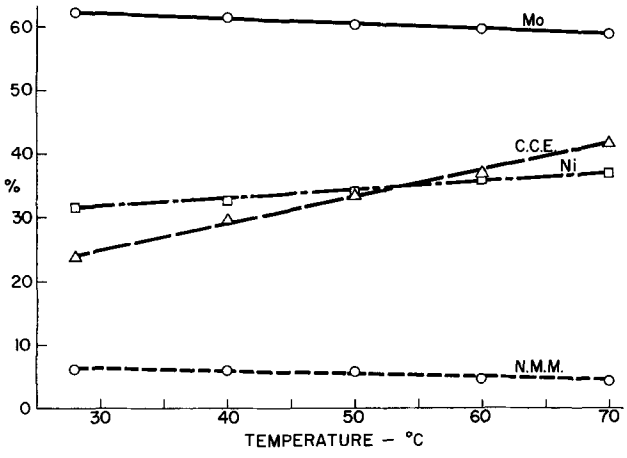

Fig. 3. Effect of temperature

Effect of nickel (II) concentration.—The concentration of Ni(II) was varied between 0.0*N* and 0.2*N* (0-23.8 g/l $NiCl_2 \cdot 6H_2O$). The amount of pyrophosphate also was varied to keep the nickel complexed to the same degree. Except in the solution containing no Ni(II) where 70 g/l $Na_4P_2O_7 \cdot 10H_2O$ was added, the normality of the pyrophosphate was six times the normality of the Ni(II) used. The plating solutions also contained 20.2 g/l (0.50*N*) $Na_2MoO_4 \cdot 2H_2O$, 80.0 g/l $NaHCO_3$, and 2.5 g/l $N_2H_4 \cdot H_2SO_4$.

Only a flash deposit was obtained without Ni(II) in the bath. The best looking deposits were obtained with Ni(II) concentrations of 0.050*N* and 0.075*N*. At higher and lower concentrations, they were darker and more dull. As Fig. 5 shows, varying the Ni(II) content of the bath has comparatively little effect on the composition of the alloy plates. Current efficiency tends to decrease with increasing bath concentration of Ni(II).

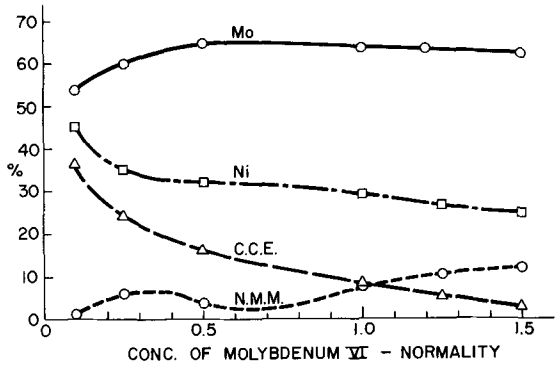

Fig. 4. Effect of Mo(VI) concentration

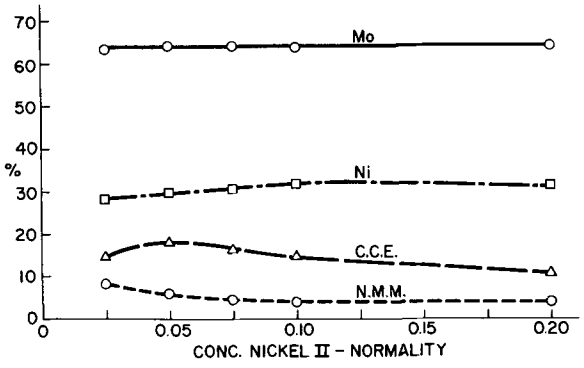

Fig. 5. Effect of Ni(II) concentration

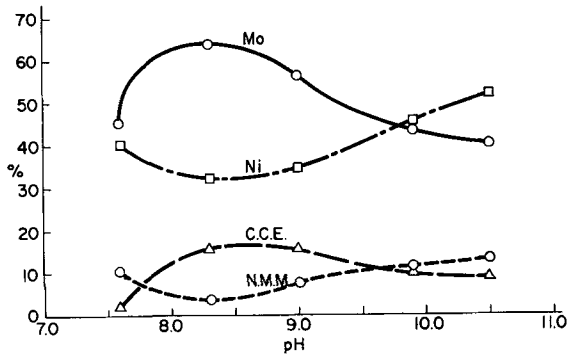

Fig. 7. Effect of pH

Effect of sodium pyrophosphate concentration.—Pyrophosphate concentration was varied on the basis of its molar ratio to Ni(II). The range studied was from 0 to 8 moles of sodium pyrophosphate per mole of Ni(II). The other bath components were: 20.2 g/l (0.50*N*) $Na_2MoO_4 \cdot 2H_2O$, 5.95 g/l (0.50*N*) $NiCl_2 \cdot 6H_2O$, 80.0 g/l $NaHCO_3$, and 2.5 g/l $N_2H_4 \cdot H_2SO_4$.

With no pyrophosphate present, $Ni(OH)_2$ formed, and the expected black anode deposit formed during plating. The deposit was dark and nonadherent. At a mole ratio of 0.05 pyrophosphate: 1 Ni(II), the hydroxide still formed, but there was no anode deposit. A ratio of 1:1 kept all the Ni(II) in solution. The deposit was still gray and not adherent. Increasing the mole ratio to 1.5:1 decreased the current efficiency, but produced a shiny adherent deposit. Additional pyrophosphate further decreased the current efficiency and produced darker deposits.

Figure 6 clearly shows the formation of the complex $NiP_2O_7^{=}$. The CCE is the highest when just enough pyrophosphate is present to form this complex. At higher ratios, the nickel is more tightly bound, and both current efficiency and nickel content of the deposits diminish.

Effect of pH.—Using a bath having the composition 20.2 g/l (0.50*N*) $Na_2MoO_4 \cdot 2H_2O$, 11.9 g/l (0.10*N*) $NiCl_2 \cdot 6H_2O$, 70.0 g/l (0.63*N*) $Na_4P_2O_7 \cdot 10H_2O$, and 2.5 g/l $N_2H_4 \cdot H_2SO_4$, five runs were made over a pH range of 7.6-10.5. The pH of 7.6 was achieved by replacing the $NaHCO_3$ with an equivalent amount of NaCl (36.5 g/l). This bath produced a black, streaked deposit of poor quality. The plating solution containing the usual amount of $NaHCO_3$ had a pH of 8.3. Higher pH values were obtained by replacing part of the $NaHCO_3$ with Na_2CO_3. When the bath pH exceeded 9, some $Ni(OH)_2$ precipitated. Alloy deposits were dark but very shiny, and a black deposit also formed on the anode. As Fig. 7 shows, the maximum molybdenum content is obtained at pH 8.3, easily reproducible by adding an excess of $NaHCO_3$.

Effect of hydrazine concentration.—The plating solution had the following composition: 20.2 g/l (0.50*N*) g/l $Na_2MoO_4 \cdot 2H_2O$, 5.95 g/l (0.050*N*) $NiCl_2 \cdot 6H_2O$, 16.7 g/l $Na_4P_2O_7 \cdot 10H_2O$, 80.0 g/l $NaHCO_3$, and amounts of hydrazine sulfate varied from 0 to 8.0 g/l. The bath containing no hydrazine sulfate was a light yellow green. During the run, it became black as colloidal oxides of nickel were formed. The oxide also deposited on the anode. The cathode deposit was dark, rough, and flaky. The addition of 1-4 g/l $N_2H_4 \cdot H_2SO_4$ gave good alloy deposits with no anodic oxidation of Ni(II). As Fig. 8 shows, increasing the hydrazine sulfate concentration has only a slight effect on the composition of the deposits. The efficiency is lower without the hydrazine, and it again decreases at higher concentrations.

Reproducibility.—Four identical runs were made keeping all factors as nearly constant as possible. The composition of the deposits was found to be reproducible within ±0.5% which was within the experimental error of the analytical methods used. The four deposits were nearly identical in appearance.

Summary and Conclusions

Eight variables as given in Table I were examined. Since the primary purpose of this investiga-

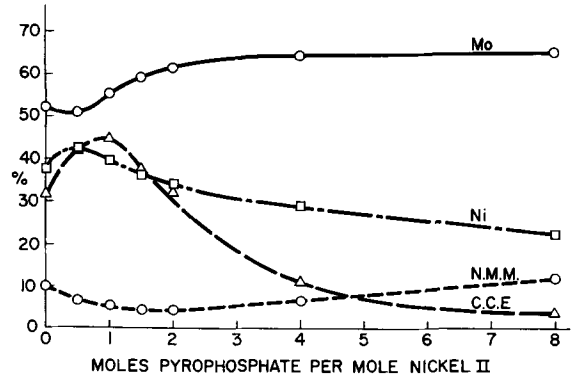

Fig. 6. Effect of sodium pyrophosphate concentration

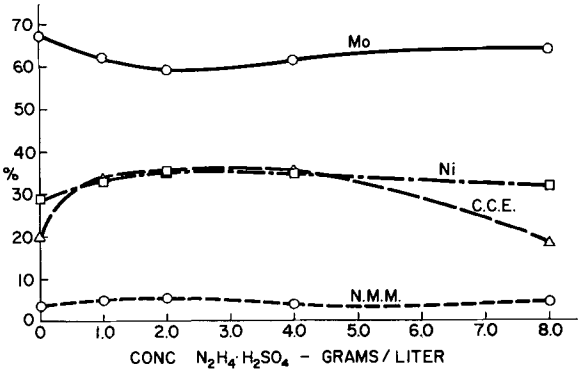

Fig. 8. Effect of hydrazine concentration

Table I. Optimum solution composition and plating conditions using cathode stirring and wiping

Variable	Value for highest % Mo	Value for greatest % CCE	Value for practical operation
Current density	16.1 amp/dm^2	16.1 amp/dm^2	16.1 amp/dm^2
Length of plating time	2.5 min	5 min	10 min
Temperature	28°C	70°C	60°C
Mo(VI) conc.	0.50*N*	0.10*N*	0.50*N*
Ni(II) conc.	0.050*N*	0.050*N*	0.050*N*
Sodium pyrophosphate conc.	0.80*N*	0.10*N*	0.15*N*
*p*H	8.3	8.3	8.3
$N_2H_4 \cdot H_2SO_4$ conc.	0.0 g/l	3.0 g/l	3.0 g/l

tion was to obtain a deposit containing a high percentage of molybdenum with the greatest current efficiency possible, values of each variable are given for the conditions under which the highest molybdenum content and the greatest CCE were obtained. Finally, there appears the value chosen as the one best suited for practical operation. It was not possible in all cases to choose a value for practical operation which gave both the maximum molybdenum content and the maximum current efficiency.

Using the solution composition and conditions indicated in the last column of Table I, deposits weighing about 0.16g were obtained using a platinum electrode having an effective plating area of 21.7 cm^2. Such deposits were about 7μ thick. A typical deposit is shown in Fig. 9. The average composition of such deposits was 60.2% Mo, 35.5% Ni, and 4.3% nonmetallic material, which may have been oxygen or hydrogen. If this material is oxygen and if it is tied up with the molybdenum, calculations show that each per cent of oxygen would tie up 4% of molybdenum. Assuming that all of the oxygen is combined with molybdenum, the composition would be about 44% Mo, 36% Ni, and 20% Mo_2O_3.

The current efficiency under the conditions of Table I averaged 37.6%. Deposits were bright and adherent.

These results compare favorably with those of other investigators. Seim and Holt (5) reported alloys containing about 20% Mo plated at current efficiencies of 20-25% from citric acid baths. The efficiency was claimed to increase to 75-80% if ammoniacal sodium citrate baths were used (6). A Russian paper (7) reports Ni-Mo alloys containing up to 25% Mo from ammoniacal citrate baths using alloy anodes. The efficiencies ranged from 30 to 40%.

Fig. 9. Typical nickel-molybdenum deposit

Ammoniacal citrate baths also were studied by Imanaga (8) who states that the maximum Mo:Ni ratio in the alloys he obtained was 1. Previous work with pyrophosphate solutions (9) had produced alloys containing up to 50% Mo and efficiencies generally below 20%.

Photomicrographs (1) and x-ray analysis (10) indicate that these alloys are single-phase solid solutions having the lattice of the corresponding iron-group metal (cubic or hexagonal). Russian researchers (10) believe that when molybdenum-containing ions are discharged on freshly deposited nickel, the Mo atoms simultaneously enter the two-dimensional lattice of the latter as a consequence of vacancies present in it.

There is, as yet, no theoretical explanation which satisfactorily describes the mechanism of the electrodeposition of molybdenum alloys. The various theories which have been proposed for this type of deposition were described and compared previously (1). Additional ideas were presented at the Fourth Soviet Conference on Electrochemistry where Krasovskii (11) concluded that the deposition of pure molybdenum from aqueous solutions is impossible owing to the high overvoltage of Mo on Mo together with the low overvoltage of hydrogen on Mo. The main gain in energy in codeposition comes through reduction of overvoltage as a result of alloy formation rather than by reduction in equilibrium potential. Relative to thermodynamically calculated normal potentials of Mo, this depolarization amounts to 300-400 mv (10). The main reason for alloy deposition is suggested to be the formation of supplementary *d*-electron bonds, as shown by a considerable gain in energy and a positive shift in the deposition potential of the iron-group metals relative to their standard potentials. The greater depolarization of Ni-Mo alloys as compared to Fe-Mo alloys is ascribed to fewer vacancies in the *d*-orbital and to energy effects caused by Mo filling them (12-15).

With the completion of extensive studies on the codeposition of molybdenum with Fe, Co, Ni, Cu, and Zn, it is hoped that the mechanism of the process may become more apparent.

Manuscript received Aug. 24, 1962; revised manuscript received Nov. 5, 1962. This paper was prepared for delivery at the Boston Meeting, Sept. 16-20, 1962. It is abstracted from a thesis presented by George M. Hanneken, Jr., to the University of Toledo in partial fulfillment of the requirements for the degree of Master of Science.

Any discussion of this paper will appear in a Discussion Section to be published in the December 1963 JOURNAL.

REFERENCES

1. L. O. Case and A. Krohn, *This Journal*, **105**, 512 (1958).
2. A. Krohn and T. M. Brown, *ibid.*, **108**, 60 (1961).
3. F. Will, III, and J. H. Yoe, *Anal. Chem.*, **25**, 1363 (1953).
4. J. B. Lear and M. G. Mellon, *ibid.*, **25**, 1411 (1953).
5. H. J. Seim and M. L. Holt, *J. (and Trans.) Electrochem. Soc.*, **96**, 205 (1949).
6. D. W. Ernst, R. F. Amlie, and M. L. Holt, *This Journal*, **102**, 461 (1955).
7. I. N. Frantsevich, T. F. Frantsevich-Zabludovskaya, and E. F. Zhelvis, *J. Appl. Chem. U.S.S.R.*, **25**, 387 (1952).
8. H. Imanaga, *Kogo Kagaku Zasshi*, **63**, 1336 (1960).
9. H. S. Myers, "The Electrodeposition of Molybdenum," unpublished Ph.D. thesis, Columbia University (1941).
10. T. F. Frantsevich-Zabludovskaya and A. I. Zayats, *Trudy Chetvertogo Soveshchaniya po Elektrochemii*, Moscow 1956, 524 (Pub. 1959).
11. A. I. Krasovskii, *ibid.*, 530 (Pub. 1959).
12. T. F. Frantsevich-Zabludovskaya, *Zhur, Priklad. Khim.*, **28**, 700 (1955).
13. T. F. Frantsevich-Zabludovskaya, A. I. Zayats, and K. D. Modylevskaya, *ibid.*, **29**, 1684 (1956).
14. T. F. Frantsevich-Zabludovskaya, A. I. Zayats, and V. T. Barchuk, *Ukrain. Khim. Zhur.*, **25**, 713 (1959).
15. A. T. Vagramyan, A. I. Krasovskii, Yu. S. Petrova, and Z. A. Solov'eva, *Fiz. Khim.*, **34**, 1255 (1960).

Infrared Effects on Luminescence and Conductivity of UV Excited ZnS Phosphors

Bernard Kramer and Alva Turner

Department of Physics and Astronomy,
Hunter College of the City University of New York, New York, New York

ABSTRACT

Simultaneous measurements of the photoconductivity and light emission of ZnS phosphors under various conditions of u.v. excitation and simultaneous infrared radiation show some discrepancies with the usually accepted Schön-Klasens model. The results of these measurements are given and discussed in light of a transition model for these phosphors.

The quenching effect of infrared radiation on the light emission and conductivity of excited ZnS phosphors is well known (1). However, unless the light emission and conductivity are measured simultaneously, it is difficult to compare the experimental results with a particular transition model. Apparatus was therefore developed to measure conductivity and light emission at the same time as functions of the u.v. exciting intensity, the infrared intensity, and the wavelength of the infrared radiation. All measurements were made at room temperature.

The main points of interest obtained in this investigation follow:

1. The photoconductivity is reduced more than the light emission when infrared is added to the u.v. excitation.

2. The ZnS:Mn phosphor shows a slight enhancement of light emission with a simultaneous decrease in photoconductivity.

3. Increasing the infrared intensity never completely quenches the light emission induced by u.v. excitation.

Apparatus and Phosphors

Light emission measurements.—The output current of a 1P21 photomultiplier (which was proportional to the emitted light) passes through resistances (10^{10}-10^5 ohms) which are the input grid resistances of a Raytheon CK 5886 electrometer tube. One beam of a Dumont 411 oscilloscope is used to detect this signal. Corning glass filters 4-96 and 3-73 are placed between the photomultiplier and phosphor to pass only the visible light emission and cut out the exciting light and the near infrared.

Conductivity measurements.—The conductivity was determined by use of a-c impedance measurements since the impedance changes observed on excitation were shown to have been primarily due to changes in the conductivity (2). The phosphor is placed between two conducting glass sheets, or a conducting glass sheet and metal electrode, and the capacitance and dissipation factor measured with the General Radio Capacitance Bridge 716-C. The second beam of the Dumont 411 scope was used to detect the unbalance.

Light sources.—A mercury arc with a Corning 7-60 filter was used to obtain the 3660Å line used for excitation: Wratten neutral filters ND1 and ND2 cut down this excitation by factors of 1/28 and 1/740, respectively.

The infrared beam was obtained by using a 750w projector using Corning filter 7-56 for wavelengths greater than 8000Å and Corning filter 7-69 for wavelengths between 7000 and 10,000Å. Intensity was controlled by varying the voltage of the light bulb. For infrared wavelength measurements, the projector was used with a Bausch and Lomb monochromator.

Phosphors.—The seven phosphors used, their known composition, and their source of supply are listed in Table I.

Results and Discussion

Comparison of luminescence and conductivity quenching with full infrared intensity.—The quenching of the light emission can be readily obtained, but the values for the quenching of the con-

Table I. ZnS phosphor composition and source

Phosphor	Source	Activator
MS-17	Prof. Riehl, Technische Hochschule (Munich)	0.1% Cu
MS-19	Prof. Riehl, Technische Hochschule (Munich)	0.1% Ag, 0.003% Cu
GE-1127	Dr. Froelich, G. E.	0.005% Cu
GE-3-202	Dr. Froelich, G. E.	0.01% Ag, 0.2 ppm Cu
RCA-2040*	RCA-Commercial	0.01% Cu
Fink No. 29	Solid State Lab., N. Y. U.	0.005% Cu
D1-14-1	U.S. Radium Co.	0.5% Mn

* All except this phosphor are definitely known to be prepared with NaCl as a flux.

ductivity are more difficult to obtain since the conductivity is a complicated function of the measured capacitance and dissipation factor for nonhomogeneously excited phosphors (2). The method used for obtaining conductivity quenching is the following: the capacitance change divided by the dark capacitance ($\Delta C/Co$) is plotted against the logarithm of the u.v. intensity (see Fig. 1) with no simultaneous infrared. A smooth curve is obtained relating $\Delta C/Co$ and intensity. The value of $\Delta C/Co$ when infrared is added is then marked on the curve, and the corresponding u.v. intensity picked off. Thus, the u.v. intensity which would account for the reduced conductivity is obtained. If the relationship between exciting intensity and conductivity were known, the conductivity quenching could be determined. Since this relationship is not exactly known, the conductivity is assumed to vary as

$$\sigma \propto I^{V}_{uv}$$

where V is a value between ½ and 1 (3).

Table II gives the data for the light emission quenching for all the phosphors at both bands of infrared wavelengths. At the higher u.v. intensity the reduction in light L_{uv+1R}/L_{uv} is considerably less than the reduction in conductivity $\sigma_{uv+1R}/\sigma_{uv}$. Even

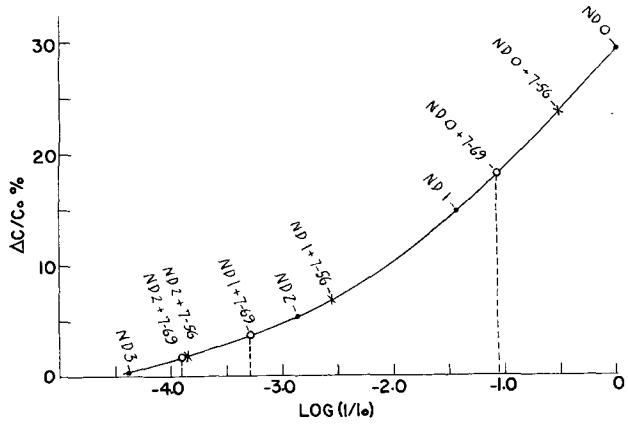

Fig. 1. Capacitance change as a function of u.v. intensity (full intensity = 45 μw/cm^2) for sample Fink-29. Curve is drawn for solid circles (u.v. only); crosses indicate u.v.+7-56 infrared and open circles indicate u.v.+7-69 infrared $\Delta C/C_0$ values; dotted lines indicate corresponding effective intensity for 7-69 case.

at the lower u.v. intensity, the light quenching is less than the current quenching for all but one phosphor, GE-3-202.

In terms of the Schön-Klasens model, the light emission is determined by $L = \beta n P_t$, where n is the density of free electrons, and P_t is the density of ionized activators. The conductivity is determined

Table II. Light and conductivity quenching

Phosphor	Comp.	ND-0 L_{uv+IR}/L_{uv}	ND-0 $\sigma_{uv+IR}/\sigma_{uv}$	ND-1 L_{uv+IR}/L_{uv}	ND-1 $\sigma_{uv+IR}/\sigma_{uv}$	IR filter
MS-17	ZnS:Cu	0.88	0.60-0.36	0.64	0.45-0.20	7-56
		0.85	0.41-0.17	0.50	0.27-0.072	7-69
RCA-2040	ZnS:Cu	0.92	0.49-0.24	0.53	0.23-0.053	7-56
		0.89	0.42-0.18	0.37	0.12-0.015	7-69
Fink No. 29	ZnS:Cu	0.89	0.55-0.30	0.51	0.28-0.078	7-56
		0.72	0.29-0.085	0.21	0.12-0.015	7-69
GE-1127	ZnS:Cu	0.73	0.46-0.21	0.46	0.25-0.063	7-56
		—	—	0.34	0.36-0.13	7-69
MS-19	ZnS:Ag	0.95	0.60-0.36	0.78	0.58-0.27	7-56
		0.90	0.67-0.50	0.64	0.50-0.25	7-69
GE-3-202	ZnS:Ag	0.79	0.68-0.46	0.31	0.69-0.47	7-56
		0.88	0.77-0.60	0.60	0.75-0.56	7-69
D1-14-1	ZnS:Mn	1.0	0.81-0.65	1.02	0.49-0.24	7-56
		1.0	0.61-0.37	1.02	0.43-0.19	7-69

Intensity of infrared (7-56), 6.0 mw/cm^2; intensity of infrared (7-69), 13 mw/cm^2; intensity of u.v. (ND 0), 45 μw/cm^2; intensity of u.v. (ND 1), 1.6 μw/cm^2.

by n (hole density is assumed negligible), and since this model assumes P_t is decreased by infrared (release of trapped holes to valence band), the product nP_t should be more strongly reduced than n. Table II shows that the contrary is true; the conductivity is quenched more than the light emission. If holes as well as electrons contribute to σ_{uv+IR}, then n is even more strongly reduced than the ratios in Table II indicate.

That P_t is decreased by infrared can be deduced from other experiments (4, 5), where the number of trapped electrons (n_t) was determined by deficiency areas and glow curves and found to decrease with the addition of infrared.

The suggestion that β is increased by infrared irradiation has been made (6); this would decrease the amount of light quenching and would explain some of the experimental results obtained.

Another possibility is that levels always exist in these phosphors which can accept electrons from the valence band. These levels differ from the so-called activator levels in that the latter are filled unless ionized by excitation.[1] If such acceptor levels exist, and recent experiments (7) on photoconductivity may be explained on this basis, the addition of infrared could produce holes which may be trapped at nonionized activator levels leading to an increase in light emission. This effect, in addition to the nonradiative recombination of these holes with trapped electrons, could provide for the smaller decrease of light emission than conductivity with simultaneous infrared. Still another possibility is discussed in the next section.

The enhancement of the light emission in the Mn activated phosphor combined with the simultaneous decrease in conductivity (see Table II) can also be explained on this latter assumption. (Since the Cu concentration is less than 1 ppm, it is unlikely to be due to a shift from Cu to Mn centers, and no spectral shift was observed.) However, if levels are always available to valence band electrons, and if we assume that the probability of capture of a hole by a nonionized Mn center is large, the creation of new ionized Mn centers may be greater than the radiationless transitions so that light is enhanced while the current would be decreased.

Effect of infrared intensity.—The changes obtained in light emission and $\Delta C/Co$ when the infrared intensity is varied are given in Fig. 1 for phosphor MS-17 (using the short wavelength infrared band) and in Table III for all the phosphors with both short and long wavelength infrared. Quenching of light emission is defined as $(1 - L_{uv+IR}/L_{uv})$ 100.

Table III and Fig. 1 show the relatively rapid rise followed by an approach to saturation of the quenching (both of light emission and conductivity) with increasing infrared intensity.

It may be noted that for weaker u.v. intensity, the quenching rises more rapidly with increasing infrared excitation than for stronger u.v. intensity and reaches a higher value.

[1] It could also be assumed that these are, in fact, ionized centers whose recombination coefficient is very small.

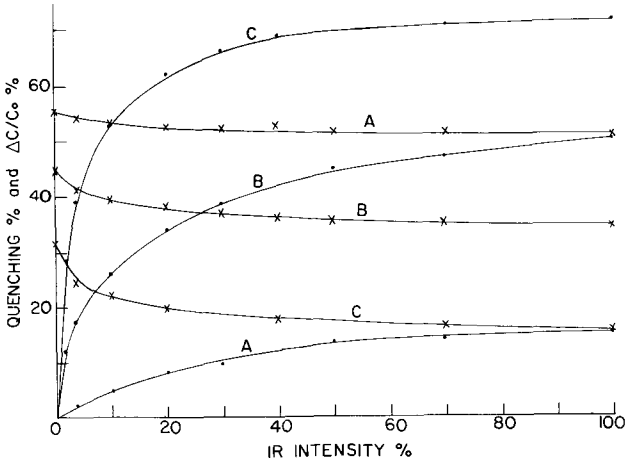

Fig. 2. Light quenching and capacitance change for MS-17 as a function of 7-69 (infrared) intensity; maximum infrared intensity = 13 mw/cm². Curve A, u.v. intensity = 45 μw/cm²; curve B, u.v. intensity = 1.6 μw/cm²; curve C, u.v. intensity = 0.061 μw/cm².

In addition, Fig. 1 and Table III show that the infrared quenching reaches a limiting value well below 100% for all phosphors except Fink No. 29.

Any theory must account for these two characteristics, and the following equations (based on some simple mechanisms) fit the data rather well.

Let us assume that the infrared absorption is due to the ionized activators; thus, the number of free holes produced would be $\gamma I_R P_t$ where γI_R is proportional to the infrared intensity. If we assume that the light emitting process is 100% efficient when no infrared is added, it would be equal to the u.v. energy absorbed (αI_{uv}). With simultaneous u.v. and *IR*, the light emission may be written as

$$L = \beta n P_t = \alpha I_{uv} - \gamma I_R P_t \qquad [1]$$

where we assume that every freed hole results in one radiationless transition. This yields

$$L = \frac{\alpha I_{uv}}{1 + \dfrac{\gamma I_R}{\beta n}} \qquad [2]$$

The value for the quenching then becomes

$$Q = \left(1 - \frac{L_{uv\,+\,IR}}{L_{uv}}\right) 100\% = \frac{100\%}{\dfrac{\beta n}{\gamma I_R} + 1} \qquad [3]$$

This expression yields the steeper rise in the Q *vs.* γI_R curve with weaker u.v. intensities (because n is smaller) but has the disadvantage that it always leads to 100% quenching at strong infrared intensities. Therefore, Eq. [1] must be modified. We assume that infrared not only produces free holes but also gives rise to a radiative transition proportional to the infrared absorption ($K I_R P_t$).

We then re-write Eq. [1] as follows

$$L = \beta n P_t + K I_R P_t \qquad [4]$$

which leads to the following expression for the quenching

$$Q = \frac{100\%}{\dfrac{\beta n}{\gamma I_R} + \dfrac{K}{\gamma} + 1} \qquad [5]$$

Table III. Light and capacitance quenching as a function of infrared intensity

Phosphor	ND filter	IR intensity, %	Light quenching, % 7-56	Light quenching, % 7-69	ΔC/Co, % 7-56	ΔC/Co, % 7-69
MS-17	ND-0	0	0	0	57	56
		20	5.0	8.2	56	52
		50	8.2	14	55	51
		100	12	16	54	51
	ND-1	0	0	0	45	45
		20	18	34	42	38
		50	28	45	40	36
		100	36	50	39	34
	ND-2	0	0	0	31	32
		20	40	62	24	20
		50	57	70	21	17
		100	67	72	19	15
RCA-2040	ND-0	0	0	0	106	106
		20	2.6	4.4	98	93
		50	4.7	7.6	94	89
		100	7.8	11	91	86
	ND-1	0	0	0	69	68
		20	18	39	57	45
		50	32	54	51	37
		100	47	63	45	31
Fink No. 29	ND-0	0	0	0	29	29
		20	3.9	13	27	23
		50	7.8	21	25	20
		100	12	29	24	18
	ND-1	0	0	0	15	15
		20	24	54	9.6	5.5
		50	36	69	8.0	4.4
		100	49	80	6.8	3.7
	ND-2	0	0	0	5.4	5.4
		20	74	93	1.9	1.6
		50	86	95	1.7	1.6
		100	91	97	1.7	1.6
GE-1127	ND-0	0	0	—	39	—
		20	12	—	36	—
		50	18	—	34	—
		100	26	—	34	—
	ND-1	0	0	0	28	31
		20	30	44	24	26
		50	44	58	21	25
		100	54	67	20	23
	ND-2	0	0	0	18	18
		20	60	74	9.1	12
		50	76	84	6.9	10
		100	85	88	5.0	9.0
MS-19	ND-0	0	0	0	28	30
		20	1.9	2.9	26	27
		50	3.7	5.7	25	26
		100	5.7	9.5	24	26
	ND-1	0	0	0	16	18
		20	7.8	17	14	14
		50	15	26	13	13
		100	22	36	13	13
	ND-2	0	0	0	9.3	7.9
		20	39	55	7.6	6.1
		50	52	63	7.4	6.1
		100	60	67	7.8	7.1
GE-3-202	ND-0	0	0	0	51	60
		20	5.8	4.5	43	54
		50	12	8.4	41	52
		100	21	12	39	51
	ND-1	0	0	0	17	21
		20	29	20	14	19
		50	49	30	14	18
		100	69	39	14	17
	ND-2	0	0	0	5.4	6.0
		20	76	43	4.1	5.8
		50	88	52	3.9	5.6
		100	93	60	3.9	5.0

Table III (Con't)

Phosphor	ND filter	IR intensity, %	Light quenching, % 7-56	Light quenching, % 7-69	ΔC/Co, % 7-56	ΔC/Co, % 7-69
D1-14-1	ND-0	0	0	0	18	17
		20	0	0	17	15
		50	0	0	17	14
		100	0	0	17	14
	ND-1	0	0	0	9.1	8.6
		20	−0.80	−1.9	7.5	5.8
		50	−1.4	−1.1	6.5	5.8
		100	−2.0	0	6.3	5.8
	ND-2	0	0	0	3.1	3.2
		20	−4.1	−4.4	3.1	3.2
		50	−4.3	−2.4	3.1	3.2
		100	−3.6	−1.8	3.1	3.2

3660Å. The intensity of the u.v. light is approximate'y 45 μw/cm^2 for ND-0, 45/28 μw/cm^2 for ND-1, and 45/740 μw/cm^2 for ND-2. For 7-56, 100% is equivalent to 6.0 mw/cm^2. For 7-69, 100% is equivalent to 13.0 mw/cm^2.

which not only gives the steeper rise for low u.v. intensities, but does not reach a value of 100% as long as K is not zero.

Since infrared stimulation and quenching are found together, the assumption that a portion of the infrared irradiation induces a slight emission process is not unlikely. The ratio K gives the relative probability of stimulation to quenching.

This infrared light induced process may also account for the stronger quenching of conductivity than light discussed above. Both processes (KI_RP_t and γI_RP_t) must lead to a reduction in the concentration of free electrons since the number freed depends only on αI_{uv}, but only γI_RP_t leads to a reduction in light. Thus, the quenching of conductivity may be considerably stronger than that of light, as experimentally found.

Summary

Experimental results obtained with simultaneous u.v. and infrared irradiation of ZnS phosphors lead to some contradictions with the Schön-Klasens model, and some modifications are proposed.

Acknowledgments

The authors want to acknowledge gratefully the encouragement of the late Professor Gertrude B. Wertenbaker in this research undertaking. In addition, they thank Mr. Paul Balkin and the physics students for their help in constructing equipment and taking data. They also want to thank Professor Hartmut Kallmann for many stimulating discussions.

Manuscript received Aug. 31, 1962; revised manuscript received Oct. 15, 1962.

Any discussion of this paper will appear in a Discussion Section to be published in the December 1963 JOURNAL.

REFERENCES

1. F. F. J. Garlick, "Luminescent Materials," Oxford (1949); P. Pringsheim, "Fluorescence and Phosphorescence," Interscience Publishing Co. (1949); I. Broser, Symposium on Solid State Phenomena in Electric Circuits, Polytechnic Institute of Brooklyn, April 1957; R. Bube, *Proc. Inst. Radio Engrs.*, **43**, 1836 (1955).

2. H. Kallmann, B. Kramer, and A. Perlmutter, *Phys. Rev.*, **99**, 391 (1955); H. Kallmann, B. Kramer, and P. Mark, *J. Phys. Chem. Solids*, **10**, 59 (1957); B. Kramer and H. Kallmann, Photoconductivity of ZnCdS, in "Luminescence of Organic and Inorganic Materials," pp. 430-442, John Wiley & Sons, New York (1962).
3. M. Schön, "Halbleiter Probleme," Schottky, Editor, (1959); H. Kallmann and B. Kramer, *Phys. Rev.*, **87**, 91 (1952).
4. S. Shionoya, H. Kallmann, and B. Kramer, *ibid.*, **121**, 1607 (1961).
5. M. Schön and B. Kramer, *Z. Physik*, **160**, 145 (1960).
6. H. Kallmann and K. Luchner, *Phys. Rev.*, **123**, 2013 (1961).
7. F. G. Ullman and J. J. Dropkin, *This Journal*, **108**, 154 (1961).

Some Aspects of Electroluminescence in ZnS

W. A. Thornton

Research Department, Westinghouse Electric Corporation, Bloomfield, New Jersey

ABSTRACT

Four rather disparate aspects of electroluminescence are described. Multiple primary peaks are found in the electroluminescence of a typical ZnS:Cu,Cl phosphor and are explained on the basis of field-controlled thermal release of trapped electrons. Carrier transit times between traps and centers are shown to be negligible in ordinary electroluminescence. By means of a model of a p-i-n junction, carrier injection is shown to be consistent with normal delayed emission and buildup in electroluminescence. A typical electroluminescent phosphor is made photoconductive by the blue component of its own emission.

Electroluminescence in copper activated zinc sulfide (1-3) involves, as do all luminescence processes in photoconducting phosphors, an ionizing event in which energy is absorbed and a majority carrier is removed from some sort of luminescence center. At a later time the inverse, or recombination, process takes place with the emission of light. The ionization process in electroluminescence is still unidentified. Much more is known about the events following ionization, namely, trapping of the carriers, release from traps, transit back to the ionized centers, and recombination, and it is with these processes that this paper is primarily concerned.

The four aspects of electroluminescence in ZnS to be described briefly, all emphasize the importance of trapping processes in electroluminescence; aside from this, the four topics are not closely related, but contribute to the general picture of ordinary electroluminescence in zinc sulfide.

Multiple Primary Peaks in the Electroluminescence Waveform

Generally most of the electroluminescence excited by a sinusoidal voltage occurs in a burst of emission, called the primary peak, immediately preceding the two voltage maxima per cycle. This emission has been shown to be delayed (4, 5) and is often considered to be due to carriers which were previously freed, swept to a different region of the crystal, trapped, released from the traps, and finally returned to recombine in or near the region from which they originated; this cyclic process takes about one-third cycle for completion, and occurs only once each cycle (4, 6) in any particular phosphor crystal region. The shape, phase, and amplitude of the primary peak seem best explained as controlled primarily by the release process of trapped carriers from a single trapping level; the release is thermal, but the effective depth of the trap varies with the electric field and so the release rate is field-controlled (7). This release of carriers governs the timing and extent of their return and recombination at the empty luminescence centers.

If there are several trap depths in an electroluminescent phosphor, then there should be as many distinguishable primary peaks observable under appropriate conditions. For more than one primary peak to be visible simultaneously in the waveform, one must depend on phase differences for their resolution and would expect also that often one primary is increasing while another is diminishing as voltage, frequency, or temperature is varied.

These additional primaries have been observed in several standard (production lot) electroluminescent ZnS:Cu,Cl phosphors emitting in the blue, blue-green, or green. These additional primaries are favored by increasing voltage, increasing frequency, and decreasing temperature, as shown in the waveforms of Fig. 1 for the standard green ZnS:Cu,Cl phosphor; with any one or any combination of such variation of voltage, frequency, and temperature the new primary appears earlier in the cycle than the normal primary, grows in amplitude relative to the normal primary, moves later in phase relative to the main primary, and often overwhelms the normal primary. A single additional primary develops with increasing voltage or frequency in Fig. 1A and 1B; the temperature range of Fig. 1C is sufficient that two additional primaries develop sequentially as the temperature is reduced. Assuming the field-controlled thermal release (7) of trapped carriers as governing the primary peaks, a peak associated with a shallower trap should appear earlier in the cycle because of release from the traps at lower field strength. The new primary should grow with increasing voltage as stronger excitation provides sufficient carriers to fill shallow traps in addition to the deeper ones associated with the

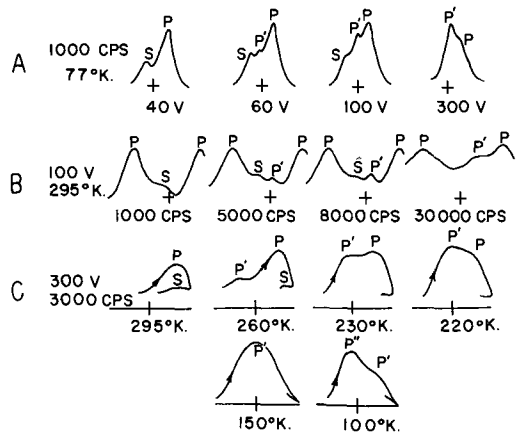

Fig. 1. Oscilloscope traces of the electroluminescence waveform of the standard green ZnS:Cu,Cl phosphor. (A) and (B) are light emission *vs.* time traces, corresponding to about one half-cycle of the sinusoidal voltage. The traces in (C) are light emission (Y-plates) *vs.* applied voltage (X-plates, zero center, baseline proportional to voltage) with the zero-light baseline shown below each trace, and also correspond to about one half-cycle. Peaks are designated by P (normal primary), S (normal secondary), and P′ or P″ (additional primaries). Points are V=0, L=0.

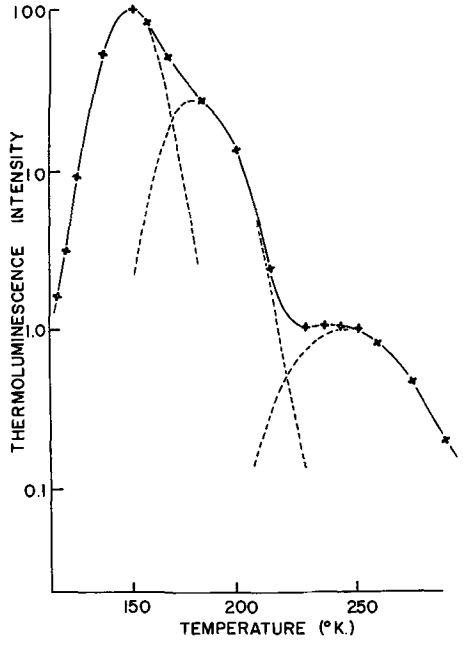

Fig. 2. Thermoluminescence (glow curve) of the phosphor of Fig. 1 excited by electroluminescence at 300v rms, 3000 cps and liquid nitrogen temperature, heating rate 14°C/min.

normal primary. The new primary should grow with increasing frequency both because a shorter period favors the more rapid release from shallower traps, and because higher frequency seems to involve higher excitation per unit volume of the phosphor (8, 9). The new primary should grow with decreasing temperature since then release from the deeper traps is retarded compared to that from the shallower traps. All of these characteristics are demonstrated in Fig. 1.

The electroluminescence buildup (10) of the additional primary is slower than that of the normal primary; that is, the normal primary reaches a steady state, after application of voltage, while the additional primary is still increasing in magnitude. This observation also suggests that the additional primary involves shallow traps which fill and become active only after there are sufficient carriers in circulation.

The two additional primaries of Fig. 1C dominate the waveform in the regions 180°-210°K and below 150°K, respectively. The field-excited glow curve for this phosphor (Fig. 2) shows peaks at approximately 250°, 180°, and 150°K; the indicated trapping levels may be associated with the normal primary and the two additional primary peaks, respectively. However, the release of carriers from a given trapping level at zero field (glow curve) may occur at a different temperature than that of release from the same level in the presence of a field (electroluminescence), so correlation might be difficult.

An additional primary is often first seen as it begin to develop near the normal position of the preceding secondary peak (see Fig. 1). To be identified as an "additional primary" the new peak must therefore be distinguished from this secondary peak, and some evidence should exist that the new peak is related to the primary which follows it rather than to the secondary (and primary) which precede it. The additional primary can be distinguished from a secondary peak in three ways:

1. Both the additional primary and the secondary adjacent to it are, under certain conditions, seen side by side and their individual behavior can be followed. This is demonstrated in Fig. 1B, where the first trace is a typical primary-secondary sequence. The following traces, representing progressively higher frequencies, show the appearance and growth of an additional primary and, except at highest frequencies, the normal secondary still present. The normal secondary is masked out, at highest frequencies, by the additional primary following.

2. The additional primary is predominantly blue emission, while the normal secondary is predominantly green emission. This is shown in Fig. 3B where the trace is the waveform through a violet filter (Corning 5970) and shows the additional primary but no secondary, and Fig. 3A is the same waveform under the same conditions but through an orange filter (Corning 3482) and shows the secondary but no additional primary.

3. The new primaries are favored by high voltage, high frequency, and low temperature (Fig. 1), while the normal secondary is favored by low voltage, high frequency, and high temperature.

The fact that the additional primaries are predominantly blue emission (Fig. 3B) serves to establish their position among the peaks representing a given ionization event. It is known that excitation of ZnS:Cu phosphors, which emit in both the blue and green bands, leads to early blue emission and delayed green emission in photoluminescence (11), glow curves (11), and the normal electroluminescence waveform (7). The effect in photoluminescence is illustrated by Fig. 3C in which the photoluminescence excited by chopped 3650Å radiation on the standard green phosphor is resolved by filters into blue and green components, detected by separate photomultipliers, and the green signal im-

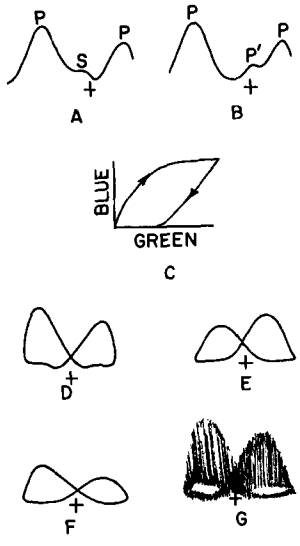

Fig. 3. Oscilloscope traces of the standard green phosphor. (A) and (B) are light emission *vs.* time traces as measured through a Corning 3482 orange filter or a Corning 5970 violet filter, respectively, at 1000 cps, 200v. (C) is a trace showing the more rapid rise of blue photoluminescence relative to green photoluminescence. (D) and (E) are light emission *vs.* applied voltage (see Fig. 1C) at 1000 cps, 800v and 0.008 cps, 200v, respectively. The conditions for (F) are 1 cps, 100v, and for (G) are the same as (F) but with the addition of 400 cps, 5v.

pressed on the X-plates and the blue signal on the Y-plates of an oscilloscope; the blue luminescence always precedes the green luminescence. In the electroluminescence waveform, the leading edge of the normal primary is bluer than the trailing edge, and the following secondary peak contains, in general, only green light. These observations, together with the fact that the new peaks are predominantly blue emission, show that the new peaks are related to those following them in the waveform (normal primary and secondary) rather than to the secondary (and primary) preceding the new peaks. Finally, by the reasoning in this and the preceding paragraph, the new peaks can be identified unambiguously as additional primaries.

Negligible Carrier Transit Time

The release and return of trapped carriers to the centers from which they were previously freed seem to govern many of the characteristics of normal electroluminescence. In the previous section, the idea of field-controlled thermal release (7) of trapped carriers has been extended to deal with the additional primary peaks which are observed. However, Zalm (5), and later Morehead (12), proposed that the transit time of the released carriers[1] from traps to recombination centers varies with the electric field in such a way as to be the determining factor in the electroluminescence waveform. It is the purpose of this section to show (i) that the trapped carriers are not released until the electric field is applied, no matter how prompt or delayed this application may be after the carriers are trapped, and (ii) that the carrier transit time back to the centers cannot be significantly involved.

The first argument involves the electroluminescent waveform with sinusoidal voltage of very low frequency. Figure 3D and E shows that the waveforms for the same phosphor layer at 1000 cps, 800v rms and at 0.008 cps, 200v rms are basically the same. At 1000 cps, Fig. 3D, the trapped electrons must be released in a fraction of a millisecond and traverse the distance back to the recombination centers in a time no longer than that. Conversely, at 0.008 cps, Fig. 3E, the trapped electrons must again be released in a fraction of a millisecond if the electric field is not necessary to assist in the release, since the temperature (300°K) is the same. Recombination is still occurring, at low frequency, almost a minute after it commences, and this intervening time must be accounted for. It seems unlikely that the carrier transit time could vary from the order of 1 min in one case to 10^{-5} min in the other, even though the applied voltages are different. It is much more plausible that release of the trapped carriers is controlled by the electric field; put in another way, the time rate of release from the traps increases with the applied electric field. For this reason 800v rms is required at 1000 cps to generate the same waveform as 200v rms at 0.008 cps. Light output per cycle at 0.008 cps is at least half as great as at 1000 cps so trapped carriers are stored without much loss at least for minutes in this phosphor at room temperature.

Further evidence that recombination is critically controlled by the effect of electric field on the release rate from traps, rather than transit time to the centers, is shown in Fig. 3F, which is the electroluminescence waveform of the standard phosphor at 1 cps, 100v rms. Figure 3G shows the effect of adding 400 cps, 5v rms to the low-frequency voltage; almost 100% modulation is observed. The effect of field variation of release rate of trapped carriers is exponential (7), so near 100% modulation of light emission (recombination) with only 5% field modulation is not unexpected, if carrier transit time is negligible. However, if the only effect of the field is on transit time of the carriers, it should require near 100% modulation of the field to cause near 100% modulation of the emission. In fact, Zalm (5) shows 70% modulation by a 15% pulse, in the section immediately preceding his proposal of the transit time effect. Further, Ivey (3) has calculated that if Zalm is correct then carrier mobility would be only 3.5×10^{-5} cm²/v-sec instead of about 100 cm²/v-sec as measured by many workers; one cannot assume a priori that retrapping reduces mobility by this factor of 10^6.

Transit time from traps to centers at zero applied field is normally quite rapid, since a phosphor irradiated with 3650Å at 80°K and then very rapidly warmed gives a burst of thermoluminescence which can be made at least as short as 100 msec, and probably far shorter. Hence transit time effects cannot account for the very low-frequency EL waveform and thus are presumably not involved in the similar high-frequency EL waveform either.

Delayed Emission and Buildup in Injection Electroluminescence

It has been proposed (13) that normal electroluminescence in ZnS is injection electrolumines-

[1] All carriers considered to be free (detrapped) at V = 0.

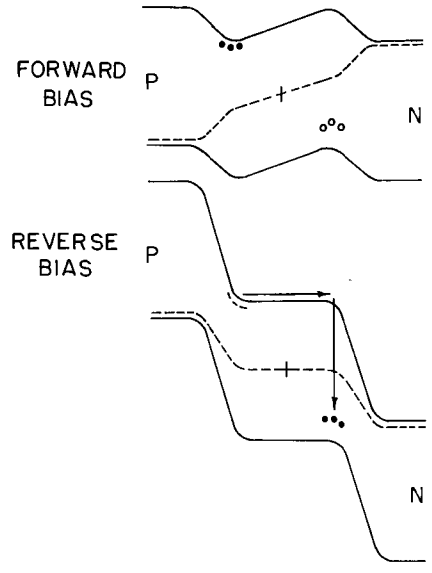

Fig. 4. Proposed p-i-n junction and the mechanism of normal a-c electroluminescence in ZnS or other materials, whether insulated from the electrodes or not.

cence, whether phosphor particles or layers are insulated from or in contact with the electrodes, and that the major currents flowing are due to forward bias of some sort of junctions in the phosphor crystal. This picture can be consistent with the mass of evidence for delayed (4, 5) emission and buildup (10) in normal electroluminescence. It is probably generally agreed that efficient injection electroluminescence is most likely in a p-i-n junction (14), where the p and n regions are relatively good semiconductors and the i region is a relatively good phosphor. Forward bias of such a junction is shown in Fig. 4. Most of the applied potential difference appears in the transition regions which therefore cause the observed approximately exponential current-voltage relationship (13); because of the large current flowing under forward bias conditions and because of the high resistivity, there is, however, a substantial electric field in the i region. Carriers of both signs enter and cross the i region; some are trapped at the appropriate potential minimum, not many recombine while crossing because of the high field, and those which pass the potential minimum and enter the semiconductor as minority carriers are not likely to cause visible emission. On reversal of polarity of the field, the field in the i region reverses sign but remains smaller than before because of the very much smaller reverse currents passed by the transition regions. On disappearance of the potential minima, the more mobile and easily detrapped carriers will be released, flow toward the trapped carriers of opposite sign, and recombine radiatively with them, causing the usual burst of electroluminescence.

With excitation by an alternating voltage, the forward bias half-cycle accounts for the "ionization" (largely by thermal energy) and charge separation, while recombination and light emission are delayed by about one half-cycle and occur during reverse bias conditions; this is the so-called primary peak. Field-controlled thermal release, during the reverse half-cycle, of electrons trapped in the i region still accounts for the shape of the primary (major) peak of electroluminescence emission.

In the case of a-c excitation of insulated phosphor particles or layers, at least one of two conditions may have to be fulfilled if this model is to apply: (*a*) the resistivity of the i region(which is expected to be high in any case) must be great enough that an appreciable fraction of the applied potential difference appear across this region through most of the forward bias half-cycle, or (*b*) the resistivity and/or permittivity of the i region must be great enough that the transient forward currents persist through most of that half-cycle; that is, the time constant of the junction must be as long as one period of the lowest frequency utilized.

If one type of carrier is more deeply trapped in the i region, then it is possible that buildup of a reservoir of such carriers at the potential minimum should occur before efficient radiative recombination at that location is possible; this would explain buildup (10) of electroluminescence. Such a buildup would imply that not all the reservoir of carriers is recombined each cycle; therefore some residual recombination immediately following field reversal from reverse to forward bias conditions can account for the secondary peak. This peak was ascribed by Zalm (5) to overshoot of returning carriers, a very similar picture.

The diagram of Fig. 4 represents only a very small volume within a phosphor particle or layer and does not depend on whether the a-c excited phosphor is insulated or in contact with the electrode.

Self-Excited Photoconductance of Electroluminescent Phosphors

Photoconductance of a good electroluminescent phosphor is excited by its own emission, providing that emission contains a "blue band" component. The a-c conductance of an electroluminescent lamp (same phosphor as Fig. 1-3) increased by as much as 10% when illuminated by the electroluminescence of an adjacent identical lamp, unless the blue emission was filtered out, whereupon the effect disappeared. This may be related to the observation that voltage excited (9, 15) thermoluminescence in good electroluminescent phosphors is very strong, at least 85% of the light sum of thermoluminescence following saturation at 80°K by 3650Å; in this case, blue emission may empty centers and fill traps in phosphor regions experiencing only small electric fields.

Summary

There is evidence that each trapping level in an electroluminescent phosphor leads to a peak in the emission waveform, as is to be expected if that waveform is due to field-controlled thermal release of trapped carriers (7); the emission is to be thought of as a voltage driven glow curve recurring each half-cycle (or each cycle in a given volume element). Carrier transit time from traps to centers is shown to be negligible, and thus to confirm that it is their release rate from traps which controls the shape and phase of the emission waveform. Carrier injection in a p-i-n junction is shown to be

at least consistent with the normal observations of electroluminescence, including delayed emission and buildup. Finally, considerable filling of traps and freeing of carriers occurs by cascade processes in these phosphors; that it, light generated during electroluminescence is reabsorbed and contributes to trap population and photoconductance.

Acknowledgment

Thanks are due H. F. Ivey for helpful comment.

Manuscript received Aug. 23, 1962; revised manuscript received Dec. 5, 1962.

Any discussion of this paper will appear in a Discussion Section to be published in the December 1963 JOURNAL.

REFERENCES

1. G. Destriau, *Phil. Mag.*, **38**, 100, 774, 800, 885 (1947).
2. H. F. Ivey, *IRE Trans. Electron Devices*, **ED6**, 203 (1959); *This Journal*, **108**, 590 (1961); *Electrochemical Technology*, **1**, No. 1 (1963) (Bibliography, Parts I, II and III).
3. H. F. Ivey, "Advances in Electronics and Electron Physics," L. Marton, Editor, Supplement No. 1 (Review article) Academic Press, in press.
4. J. F. Waymouth and F. Bitter, *Phys. Rev.*, **95**, 941 (1954).
5. P. Zalm, *Philips Research Repts.*, **11**, 353, 417 (1956).
6. W. A. Thornton, *Phys. Rev.*, **103**, 1585 (1956).
7. W. A. Thornton, *ibid.*, **102**, 38 (1956)
8. G. F. Alfrey, I. Cooke, and K. N. R. Taylor, *J. Electronics and Control*, **4**, 417 (1958).
9. W. A. Thornton, "Solid-State Physics in Electronics and Telecommunications," M. Desirant and J. L. Michiels, Editors, vol. 4, p. 658, Academic Press, New York (1960).
10. C. H. Haake, *J. Appl. Phys.*, **28**, 245 (1957).
11. H. Arbell and A. Halperin, *Phys. Rev.*, **117**, 45 (1960).
12. F. F. Morehead, *This Journal*, **105**, 461 (1958).
13. W. A. Thornton, *ibid.*, **108**, 636 (1961).
14. L. Patrick, *J. Appl. Phys.*, **28**, 765 (1957).
15. P. M. Jaffe, *This Journal*, **108**, 711 (1961).

Observations on the Formation of Color Centers in Calcium Halophosphates

E. F. Apple

Large Lamp Department, General Electric Company, Cleveland, Ohio

ABSTRACT

This paper concerns the effects of Cl/F ratio, stoichiometry, incorporation of Mn, Sb, and Cd, and of thermal treatment on the formation of color centers in calcium halophosphates. Short wavelength u.v. radiation, or the discharge from a Tesla coil, induces three color centers in the 2500-7000Å region. The spectral distributions of these centers depend on the Cl/F ratio. Incorporation of Sb and Cd and/or rapid quenching of the samples from elevated temperatures leads to a decrease in induced color center formation.

The formation of color centers in calcium halophosphate when exposed to either 1850Å or x-ray radiation has been observed by Johnson (1) and Suchow (2). Johnson reported on the optical properties of the color centers formed either under 1850Å or x-ray radiation in single crystals of calcium fluoro- and chlorophosphates. Suchow was concerned with the effects of halogen and cation identities on color center formation induced in Ca, Sr halophosphate powders by 1850Å radiation.

Although much basic information such as the orientation and concentration of color centers can be obtained precisely only with macroscopic single crystals, some useful information can be obtained on powder samples using reflectivity measurements. Single crystals of the halophosphates are hard to obtain in well-defined stoichiometry and with activator concentrations of the order of 1 wt %, so that the use of powders still affords an advantage in both time of preparation and in sample definition. One concern in the growth of single crystals would be the identity and variation of vapor over the sample during crystal growth. Neither the components nor the halophosphate are as volatile in the lower temperature range where powder samples are prepared.

This paper concerns the effects of halogen identity, stoichiometry, thermal treatment, and impurity substitution on the intensity and spectral distribution of the color or absorbing centers induced in Ca halophosphate powder samples by short wavelength u.v. radiation.

Experimental Procedures

The calcium halophosphate powder samples reported in this paper were prepared from the following raw materials: $CaHPO_4$, $CaCO_3$, CaF_2, NH_4Cl, Sb_2O_3, $MnCO_3$, and CdO. In a particular sample, the appropriate raw materials were blended thoroughly and put in a quartz beaker which was covered by an inverted telescoping beaker of slightly larger diameter. In general, the samples were fired in air at 1100°-1200°C for periods of 1-4 hr, after which they were usually air cooled to room temperature, then ground and screened through a 200-mesh nylon screen.

Diffuse reflectivities in the 2500-7200Å region were measured on a Beckman DK-1 spectrometer with reflectance attachment. Below 2500Å, the reflectivities were measured on a vacuum monochromator previously described by Johnson (3).

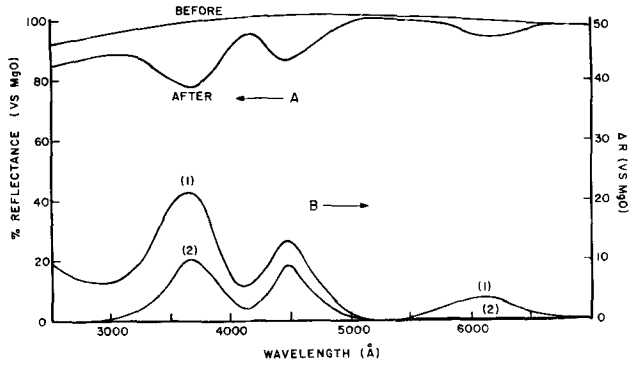

Fig. 1A. Diffuse reflectance (vs. MgO) of unactivated $Ca_5(PO_4)_3F$ before and after 1-min exposure to the discharge from a Tesla coil. Fig. 1B. Reflectance before minus reflectance after (ΔR) exposure to (1) discharge from a Tesla coil for 1-min and (2) 1850Å radiation from a quartz low pressure mercury lamp for 1 hr.

1850Å radiation was obtained from a 15w, unfiltered, low-pressure mercury discharge lamp with a quartz envelope. For irradiation studies, the plaques of sample were placed 1 in. from the 1850Å source in an atmosphere of flowing nitrogen at room temperature. In addition to the 1850Å radiation, this source gave all other Hg line emissions in the u.v. and visible parts of the spectrum, a fact which in some cases seriously affects the data obtained since the color centers can be bleached by radiation of the appropriate wavelength.

As an alternate source of radiation for the damage studies, the discharge from a Tesla coil in rough vacuum was used. Although complex in nature, this discharge probably produces electrons as well as short wavelength u.v. radiation. It does not produce appreciable radiation in the 2500-7000Å region which virtually eliminates the bleaching effects observed with the mercury lamp discharge. Further, the results were reproducible to ±2% and consistent and were very similar to those obtained under cathode-ray bombardment. Usually 1-min exposure to the discharge from the Tesla coil resulted in as much or more damage than 2-3 hr exposure to the 1850Å source. The depth of penetration of the absorption induced by either Tesla coil discharge or 1850Å during the above-mentioned exposure times was of the order of 0.5 mm as determined by visual observation.

The plaque brightnesses of the phosphors used in the brightness depreciation studies were measured under 2537Å excitation obtained from a 20w low-pressure Hg lamp with Corning filter No. 9-54. The emission passed through a filter with average-eye-response transmission and was detected by a photovoltaic cell (G.E. 8PV1AAF) connected to a sensitive galvanometer. A plaque of the unirradiated phosphor under test was used as the comparison standard (100% brightness).

Experimental Results

Effects of Cl/F Ratio

In Fig. 1-A the diffuse reflectances (*vs.* MgO) of an unactivated calcium fluorophosphate before and after 1-min exposure to a Tesla coil discharge at

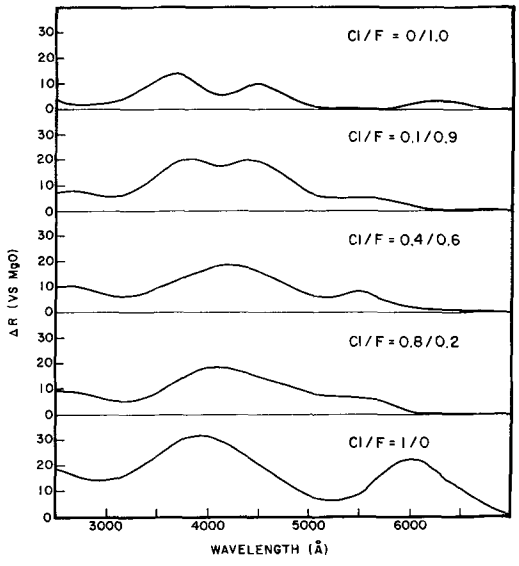

Fig. 2. Difference in reflectance, ΔR (R before minus R after 1-min exposure to Tesla coil), of unactivated Ca halophosphates vs. wavelength as a function of Cl/F.

room temperature are shown. Three absorption bands are introduced. The difference in diffuse reflectance, ΔR (R before minus R after irradiation), is a measure of the absorption introduced. Figure 1-B plots ΔR against wavelength using Tesla coil and 1850Å irradiation. In the latter case, the sample was exposed to the u.v. discharge for 1 hr. With Tesla coil radiation, the three absorptions in the 2500-7000Å region are observed to peak at 3700, 4500, and 6100Å, while with 1850Å irradiation only the bands at 3700Å and 4500Å are present in this sample. Except for the number and speed of formation of color centers there is very little difference in the effects produced by the two sources for the centers which are considered in most detail.

The effect of changing Cl/F ratio on the spectral distribution of the absorption centers introduced by the discharge from a Tesla coil is shown in Fig. 2. The Cl/F ratio is in general fixed by the original F content of the phosphor mix. As this ratio increases, the two induced absorption bands peaking at 3700Å and 4500Å move together and change in relative intensity.

In Ca chlorophosphate only one very broad absorption peaking at 3900Å is observed. In the latter case, ΔR is greater than 30%. It is also interesting to note that the induced absorption peaking at 6100Å in Ca fluorophosphate is also observed in Ca chlorophosphate, but is not observed in the chlorofluorophosphate. Instead, another minor absorption peaking at about 5500Å is observed. It appears then that at least three absorption bands are introduced by suitable radiation in the 2500-7000Å region in unactivated Ca halophosphate. In addition to being severely damaged by Tesla coil discharge, it was observed that the chlorophosphate was damaged by 1850Å and to a lesser extent by 2537Å radiation. Damage was severe on exposure to x-ray radiation. It was also observed that bleaching of the 3900Å band in this sample was very rapid in room light.

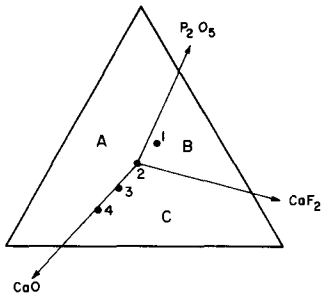

Fig. 3. Segment of composition diagram. Points indicate samples with increasing CaO content. Sample 2 is stoichiometric $Ca_5(PO_4)_3F$.

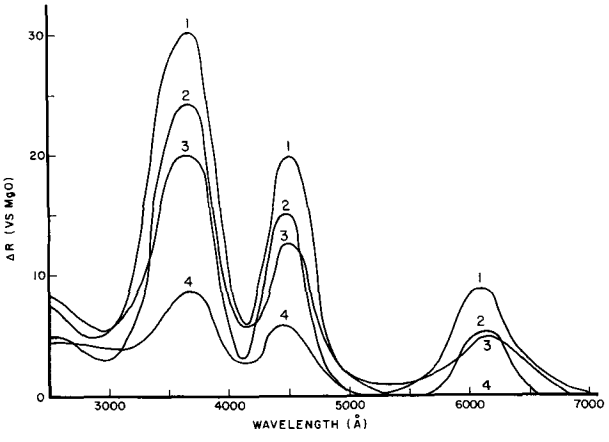

Fig. 4. Difference in reflectance, ΔR (R before minus R after 1-min exposure to Tesla coil), vs. wavelength as a function of CaO content. Numbers refer to samples shown in Fig. 3 and Table I.

Effects of Stoichiometry

Stoichiometric calcium fluorophosphate has the formula $Ca_5(PO_4)_3F$ in which the ratio of Ca/PO_4 = 5/3 and PO_4/F = 3/1. The measure of stoichiometry in this paper is based on the analysis of the raw materials used in making the fluorophosphate, coupled with x-ray diffraction analysis of the finished product. Of course, the limit of detection of extraneous phases by x-ray techniques is rather high and probably above the concentration range of defects and of induced absorption centers.

In Fig. 1 it was shown that stoichiometric (with respect to starting materials) Ca fluorophosphate was susceptible to radiation damage. It was the purpose of this portion of the investigation to examine the effects of deviations from this stoichiometric point. Using the common triangular plot, the initial composition of the fluorophosphate can be represented by a three-component system of end members P_2O_5, CaF_2, and CaO. A small segment of this triangular plot is shown in Fig. 3. Samples with initial compositions completely surrounding the stoichiometric point were prepared and irradiated with a Tesla coil discharge. As an example of the change in the intensity of the absorption peaks with changing composition, points 1, 2, 3, and 4 represent increasing CaO content (from 68.99 to 69.69 mole %) in the starting composition. Figure 4 shows the induced absorption curves for these four samples. It is evident that ΔR decreases with increasing CaO content. Table I summarizes the results obtained from 35 samples with initial compositions completely surrounding the stoichiometric point. The minimum intensity of induced absorption of color center formation is found in the C region of Fig. 3 where the CaO plus CaF_2 content is greater than in stoichiometric fluorophosphate. The data suggest that the important parameter is the total Ca content, and it is concluded that color center formation is minimized in samples with a much higher Ca content than $Ca_5(PO_4)_3F$.

Table I. Relative intensities of the color centers (induced by 1-min exposure to discharge from a Tesla coil) in Ca fluorophosphate as a function of the initial composition

	Region in Fig. 3	Mole % CaO	Mole % CaF_2	Mole % CaO + CaF_2	ΔR_{3800}-ΔR_{4500}-ΔR_{6100}
1*	B	68.99	7.75	76.74	30-20-9
2*		69.23	7.69	76.92	24-15-5
3*	C-A	69.47	7.63	77.10	20-13-5
4*	C-A	69.69	7.58	77.27	10- 6-0
	A	69.30	7.00	76.30	19-14-2
	A	69.50	7.40	76.90	17-12-2
	B	69.00	7.40	76.40	26-18-5
	B	68.85	8.08	76.93	23-14-4
	C	69.10	8.10	77.20	6- 3-0
	C	69.40	7.90	77.30	6- 3-0
	C	69.50	7.72	77.22	10- 6-0

* Numbers refer to samples shown in Fig. 3, 4.

It is interesting to note that $\Delta R_{3700}/\Delta R_{4500}$ is about constant with CaO increase in the fluorophosphate samples. This is not true with increase of CaO in unactivated chlorofluorophosphate (Cl/F = 1/9) where the over-all absorption decreases in intensity, but the ratio of the absorption bands changes also ($\Delta R_{3800}/\Delta R_{4500}$ decreases).

Effects of Impurities

The results reported thus far were obtained on unactivated Ca halophosphate with no impurities or activators added intentionally. This does not preclude the presence of Sb or Mn which may be present in the original raw materials in the ppm range. In this part of the paper the effects of larger amounts of Mn, Sb, and Cd incorporation in Ca fluorophosphate or chlorofluorophosphate on the formation of color centers are presented. Figure 5 shows the absorptions induced by 1-min exposure

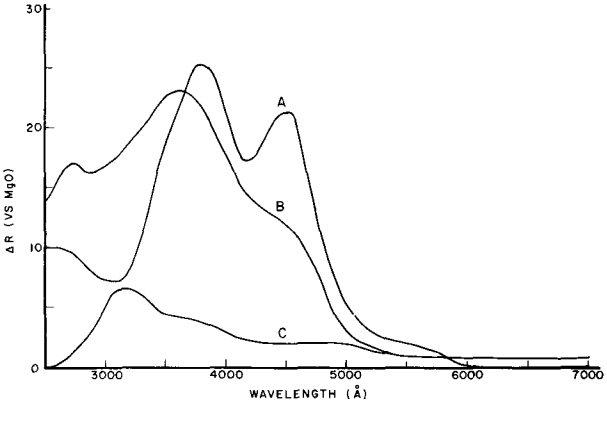

Fig. 5. Change in reflectance, ΔR, vs. wavelength caused by 1-min exposure of Ca chlorofluorophosphate to the discharge from a Tesla coil. A, Unactivated; B, Mn-activated; C, Sb-activated.

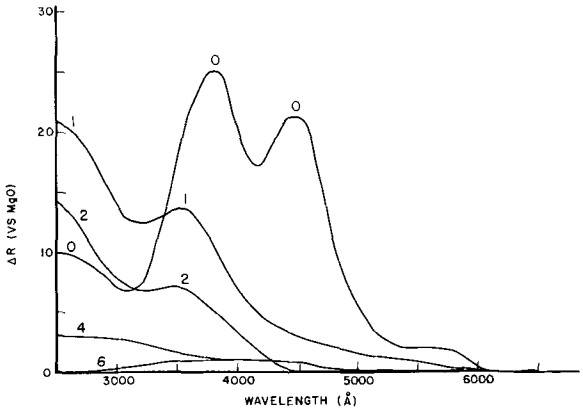

Fig. 6. Change in reflectance, ΔR, vs. wavelength for Ca,Cd chlorofluorophosphates exposed for 1-min to discharge from a Tesla coil. Numbers indicate atom per cent Cd added in place of Ca.

to Tesla coil discharge for unactivated, Mn-activated, and Sb-activated Ca chlorofluorophosphate (1Cl; 9F). The effect of 1 at. % Mn (replacing Ca) is to decrease the induced absorption peaking at 4500Å, while the intensity of the absorption peaking at about 3800Å is about the same as in unactivated Ca halophosphate. Incorporation of about 1 at. % Sb (for Ca) with or, as shown here, without Mn reduces the intensity of all three induced absorption bands. Notice in Fig. 5 that the biggest change in reflectance, ΔR, is now at 3000-3200Å on the edge of the impurity absorption introduced by Sb and that the absorption bands at 3800Å, 4400Å, and 6100Å are broad and practically structureless.

Because of the rapid change in reflectance with wavelength in the region below 3200Å, it would perhaps be more meaningful to plot $\Delta R/R_{original}$ in which case the curve would increase continually below 3100Å.

Figure 6 shows the effect of Cd substitution for Ca on the induced absorption in unactivated Ca fluorophosphate. The numbers represent atom per cent Cd added in place of Ca. Because of partial volatilization of cadmium during firing, the actual Cd content is slightly less. The intensity of the color centers in the 2500-7000Å region decreases gradually with increasing Cd content. Virtually no absorption is induced by Tesla coil or 1850Å irradiation in the sample with 6 at. % Cd substituted for Ca.

The diffuse reflectance curves of several of the samples shown in Fig. 6 are plotted in Fig. 7. Note

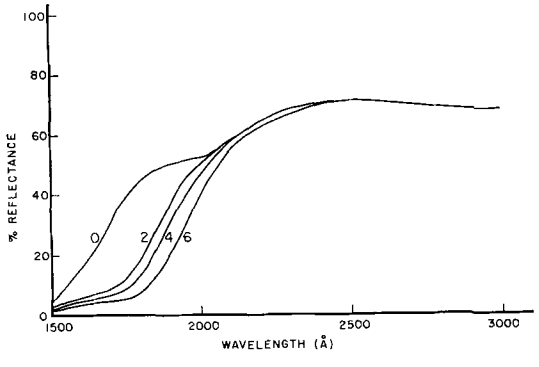

Fig. 7. Diffuse reflectance of Ca,Cd chlorofluorophosphates. Numbers indicate atom per cent Cd added in place of Ca.

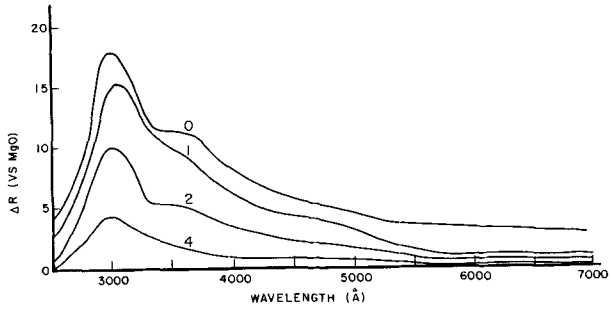

Fig. 8. Change in reflectance, ΔR, vs. wavelength of (Ca,Cd) halophosphate:Sb,Mn as a result of 1-min exposure to discharge from a Tesla coil. Numbers indicate atom per cent Cd added in place of Ca.

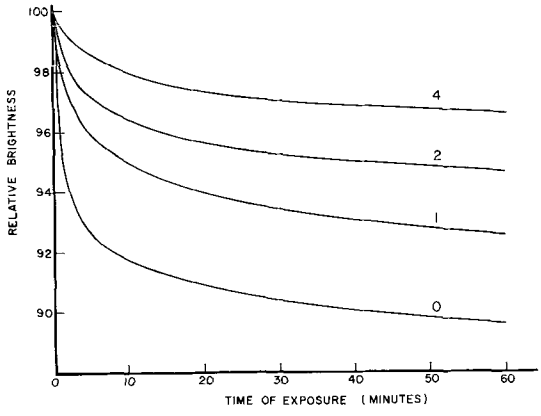

Fig. 9. Relative plaque brightness (under 2537Å excitation) of samples listed in Fig. 8 as a function of exposure time to 1850Å radiation.

that the effect of Cd substitution is to decrease the reflectance, *i.e.*, increase the absorption, in the 1700-1900Å region. It should also be mentioned that an emission band which peaks at about 3600Å is observed in the samples listed in Fig. 6 and 7. This emission, which is excited by 1850Å or cathode rays, is greatly enhanced in the samples containing Cd.

Figure 8 shows the effect of Cd on the induced absorption in calcium chlorofluorophosphate phosphor with Sb and Mn activators. Again the effect of increased Cd is to reduce the induced absorption. As was pointed out before, the largest change in reflectance induced by the irradiation is in the 3100Å region but the induced absorption extends throughout the entire visible spectrum.

As in Fig. 5-C, a plot of $\Delta R/R_{original}$ would lead to increasing values in the region below 3200Å because of the rapid decrease in reflectances of the original samples in this region.

Figure 9 shows the relative plaque brightness (under 2537Å excitation) of the samples listed in Fig. 8 as a function of exposure time to 1850Å radiation. Brightness measurements were made after 1, 3, 5, 7, 10, 15, 30, 60 min exposure, and it was found that the brightness measured depended only on the total exposure time and not on the sequence of measurements during that time. It is evident from Fig. 9 that the major depreciation takes place in the first few minutes of exposure to 1850Å radiation and that with increasing Cd content the rate of depreciation decreases. It should also be mentioned

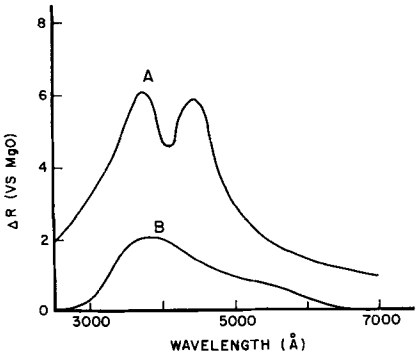

Fig. 10. Change in reflectance, ΔR, in $Ca_5(PO_4)_3F$ as a result of 1-hr exposure to 1850Å radiation. A, Slowly cooled from 1100°C; B, rapidly quenched from 1100°C to room temperature.

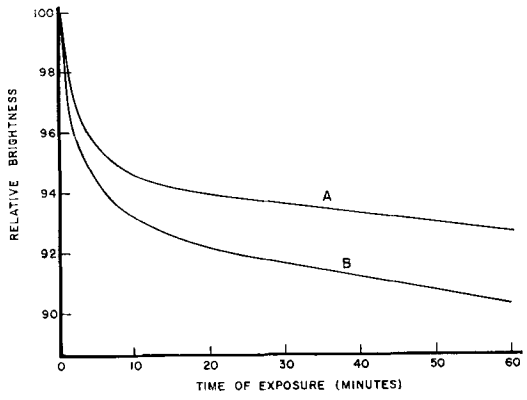

Fig. 11. Relative plaque brightness (under 2537Å excitation) of Ca chlorofluorophosphate:Sb,Mn as a function of exposure time to 1850Å radiation. A, Slowly cooled from 1150°C; B, rapidly quenched from 1150°C.

that the rate of formation of color centers in unactivated halophosphate or the rate of formation of the broad absorption in Sb, Mn-activated Ca halophosphate is approximately the same as the rate of plaque brightness depreciation of phosphors.

Effects of Heat Treatment

It has been reported previously that variations in heat treatment also affect the formation of color centers in calcium halophosphate (4). Figure 10 shows absorptions introduced by 1-hr exposure to 1850Å radiation in unactivated Ca fluorophosphate, one sample slowly cooled from 1100°C and the other quenched rapidly from the same temperature to room temperature. To assure rapid quenching, the samples were either dumped directly from the firing beaker into a water bath or, to avoid possible effects of reaction with the water, samples in sealed-off quartz tubes were also quenched in a water bath. These tubes are double-walled cylindrical firing vessels with phosphor in the annular space and sealed both at top and bottom. On plunging the tubes into water, high-temperature gradients are produced in opposite directions within the charge of about 3 mm total thickness, thus allowing faster quenching than in a normal quartz test tube. The two methods of quenching gave essentially the same results. Note in Fig. 10 that the induced absorption is lower in intensity, and it is more diffuse in the quenched sample. The effect of heat treatment on the induced absorption is reversible in a slowly cooled, quenched, slowly cooled sequence. It should also be mentioned that preliminary observations show that the absorption induced by 1850Å radiation in unactivated Ca fluorophosphate decreases with increasing quenching temperature in the range 500°-1150°C.

In addition to the effects of quenching on the induced absorption in unactivated samples, similar results were obtained on Ca fluorophosphate and chlorofluorophosphate with Sb and Mn activators. In phosphors of a regular cool white formulation, it was observed that the induced absorption, ΔR, is less at all wavelengths between 2500-7000Å in the quenched than in the slowly cooled samples. Figure 11 shows the effect of duration of exposure to 1850Å radiation on the relative plaque brightnesses of a quenched and a slowly cooled Ca chlorofluorophosphate:Sb, Mn of cool white color. The brightness measurements, as mentioned previously, were made under 2537Å excitation. Note the difference in depreciation between the quenched and slowly cooled samples. The quenched sample shows less depreciation under 1850Å irradiation which is consistent with the change-in-reflectivity measurements.

Discussion

In the present work it was observed that 1850Å radiation or the discharge from a Tesla coil induces absorption bands in Ca fluorophosphate which peak at 3700, 4500, and 6100Å (not in all samples). Johnson (1) reports absorption bands peaking at about 4500, 6100, and 7500Å in x-rayed CaF_2-deficient fluorophosphate. Although his reported data do not extend below 3900Å there is evidence for another absorption band in this range (5). The fact that the spectral data obtained from powder samples are qualitatively consistent with those obtained from single crystal samples justifies in part the use of the more easily prepared powder samples. Quantitative differences in band widths and relative intensities between Johnson's absorption data and the present reflectance minima are observed however. These differences may be due to precision of measurement as well as sample variations. The results suggest that the induced absorptions in the powders in the 2500-7000Å range are due mainly to volume rather than surface defects. In addition to being consistent with Johnson's single crystal data, the present spectral data are also for the most part consistent with those reported by Suchow on powder samples (2).

The data on the rate of formation of color centers in unactivated Ca halophosphate suggest strongly that the primary effect of both 1850Å radiation and the discharge from the Tesla coil is to produce charge carriers which are subsequently trapped at defects (vacancies, etc.) already present in the lattice. Since almost all of the radiation damage observed occurs during the first few minutes of exposure to either of the two sources, it is concluded that few if any defects are created by either source of radiation. In contrast, irradiation with x-rays (Cu K α radiation) at room temperature produces more extensive coloration which increases continually over the entire exposure time of three hours. These preliminary data suggest that x-rays produce

defects in Ca halophosphate at room temperature.

The data on the effect of the Cl/F ratio show that there are three absorption bands induced in Ca chloro-, chlorofluoro-, and fluorophosphate in the 2500-7000Å region. Both the ratios of relative intensities and the spectral distribution of these bands depend on the Cl/F ratio. In Ca fluorophosphate, the absorption bands peak at 3700, 4500, and 6100Å. As the Cl/F ratio is increased, the bands peaking at 3700 and 4500Å (in fluorophosphate) move together; their overlap becomes larger. In samples whose Cl/F ratio is 0.4/0.6 or greater, only one broad composite absorption is observed. Also of interest, but as yet unexplained, is the apparent shift of the induced absorption band which peaks at 6100Å in both chloro- and fluorophosphates but is found at 5500Å in chlorofluorophosphate.

The results for unactivated Ca chlorophosphate reported here differ from those reported by Suchow (2) who observed an absorption (induced by 1850Å) extending across the visible part of the spectrum and peaking at about 6100Å. He did not observe the major absorption band peaking at 3900Å. The apparent difference arises from the difference in radiation sources, coupled with the ease of bleaching of the absorption band peaking at 3900Å by self-absorption. In our experiment using a Tesla coil, no or little bleaching is observed since no radiation in the 3500-4500Å region is produced. In Suchow's experiment, the band peaking at 3900Å was undoubtedly bleached during exposure to the unfiltered radiation from the low-pressure Hg arc lamp. When the 1850Å source was used, results similar to those of Suchow were obtained. Further, when the plaque of Ca chlorophosphate was irradiated simultaneously with the discharge from a Tesla coil and a source of 3650Å radiation, the absorption band peaking at 3900Å was markedly decreased in intensity. Thus the advantage of the Tesla coil over 1850Å irradiation in avoiding self-bleaching is emphasized.

The experimental results indicate that color center formation is minimized in a region of excess Ca either introduced as CaO or CaF_2. Under the conditions of sample preparation, where H_2O vapor is not scrupulously avoided or eliminated, the effect of excess CaO may be to shift the equilibrium vacancy concentration by supplying both Ca(II) and OH^-. The latter would occupy fluorine sites and thus charge compensation would be maintained. Excess Ca as CaF_2 may involve a shift to lower Ca and F vacancy concentrations by providing a driving force for the completion of reaction, *i.e.*, the formation of the halophosphate phase.

It is difficult to deduce ideas of the nature of the color centers in Ca halophosphate from the available data. Although the present work was concerned with the three centers in the 2500-7000Å region, other centers are induced by the radiation sources used. An absorbing center peaking at 7500Å has been reported (1). In addition, an induced absorption peaking at about 2200Å has been observed in some samples in the present work. Little is known at present about the relationships of relative intensities, rates of formation, ease of thermal and optical bleaching, etc., of the five absorption bands mentioned above. The fact that color center formation in the region 2500-7000Å is minimized in samples which originally contained excess Ca either as CaO or CaF_2 suggests strongly that both Ca and halogen vacancies may be involved in the absorbing centers. In addition, the spectral distributions of the centers are dependent on the Cl/F ratio. Since it is thought that F and Cl atoms occupy different lattice positions [(0, 0, ¼; 0, 0, ¾) and (0, 0, ½; 0, 0, 0), respectively] (5) it would be expected that F and Cl vacancies may be located at different lattice sites. Consequently the interaction of the neighboring atoms on the vacancy would be different in the two cases. This difference would probably lead to a dependence of the spectral distribution of the color center on the halogen identity as is observed. It has been suggested that the exact position of the halogens in chlorofluorophosphates depends on the halogen ratio (4, 7). Chlorine at its normal site would require at least an adjacent fluorine to occupy a next nearest chlorine site also. Thus a relatively small amount of incorporated chlorine may have a relatively large influence in determining the lattice positions of the halogens. The same effect may influence the location of the halogen vacancies on the two possible sites. The experimental data shown in Fig. 2 indicate not only a dependence of the spectral distribution of the color centers on Cl/F but also a similarity in the color centers in samples with a Cl/F ratio of 0.4/0.6 and above. Perhaps the vacancies are preferentially oriented on one of the halogen sites (probably the Cl site) in these samples.

The quenching experiments suggest that the color centers peaking at 3700, 4500, and 6100Å in Ca fluorophosphate may involve associated defects or perhaps clusters of defects. Quenching from high temperatures to room temperature gives samples more resistant to discoloration under 1850Å radiation than samples slowly cooled from the same high temperature. This result would be expected if the color centers were due to defects which tended to associate during slow-cooling. The preliminary experiment mentioned heretofore in which it was pointed out that the degree of color center formation was inversely proportional to the quenching temperature supports the idea of associated defects being involved in the observed color centers.

The data on the substitution of Mn, Sb, and Cd indicate that both the relative intensities and spectral distributions of the color centers present in unactivated Ca halophosphate can be altered by impurity incorporation. It is believed that the incorporation of these elements probably leads to defects which may provide, in place of color center formation, alternate and competing mechanisms for energy absorption and dissipation. All three elements, for instance, introduce absorption bands or change the absorption in the region below 2000Å and also give rise to emission bands in the u.v. and visible parts of the spectrum. Similar effects have been reported by Delbecq (8) for KCl where F cen-

ters are essentially prohibited from forming in samples containing one part in 10^3-10^4 of Ag(I), Pb(II), or Tl(I). These impurities undoubtedly produce centers which compete with color center formation for energy absorption and dissipation. Incorporation of Cd in unactivated, Mn-activated, Sb-activated, and Sb, Mn-activated halophosphates leads to a decrease in the induced absorptions in all cases.

Of practical importance is the relationship of absorbing centers induced by 1850Å radiation to the phosphor performance. The data suggest a close relationship in that the rate of brightness depreciation is similar to the rate of formation of induced absorption. The rate of change of both processes is large during the first few minutes of exposure to 1850Å radiation. Also, the magnitude of brightness depreciation in all cases is proportional to the magnitude of the induced absorption. Compare Fig. 8 and 9, 10 and 11, for example. It is suggested that the depreciation in brightness arises both from self-absorption of emission by the induced absorption in the visible as well as a decrease in excitation efficiency to 2537 and 1850Å radiation. Although the over-all absorption of 2537Å radiation increases, the useful absorption decreases during irradiation.

The data show that the effect of Cd incorporation is to reduce brightness depreciation caused by exposure to 1850Å radiation. Aia and Poss (9) reported that incorporation of up to 5 at. % Cd for Ca in Ca halophosphate phosphors produced little or no change in plaque brightness. However, when the phosphors were incorporated in low-pressure mercury lamps, the Cd-containing phosphor (about 1% Cd) yielded lamps of higher brightness and efficiency. Their observations are consistent with the results of the present work regarding reduction of discoloration by Cd incorporation in that plaque brightness was measured under 2537Å excitation whereas both 1850 and 2537Å excitation are present in the lamps. As was shown in the present work, the Cd-containing phosphors are more resistant to depreciation under 1850Å radiation, which explains the observed improvement in lamp performance.

In addition to the inhibiting effect of Cd on the brightness depreciation in Ca halophosphate phosphors, it was observed that quenching Ca halophosphate phosphors from elevated temperatures also leads to improved maintenance under 1850Å radiation. It has already been pointed out that quenching unactivated Ca halophosphates leads to a decrease in color center formation. In addition to the effect of randomizing lattice defects, *i.e.*, vacancies, interstitials, quenching phosphors from elevated temperatures may affect both the solubility and distribution of Mn and Sb activators. Preliminary experiments show that the concentration of incorporated Sb(III) is slightly higher in quenched samples. It has been suggested that the distribution of both Mn and Sb between the two Ca sites may be a function of thermal treatment (10). In addition, there is indication of a slight structural change in Ca chloro- and chlorofluorophosphate toward the fluorophosphate structure as a result of quenching (7).

Summary

Irradiation of unactivated Ca halophosphates with 1850Å radiation or the discharge from a Tesla coil leads to the formation of three absorbing centers (in the 2500-7000Å wavelength region) whose spectral distributions and relative intensities depend on the Cl/F ratio. The magnitudes of the color centers are reduced when the samples are prepared with excess Ca, either as CaF_2 or CaO, which suggests that both Ca and halide vacancies are involved in color center formation. Quenching the samples from elevated temperatures also decreases the magnitude of the color centers (compared to slowly cooled samples) which suggests that the centers may involve associated defects or clusters of defects. Incorporation of impurities such as Mn, Sb, and Cd (singly or in combination) leads to a change both in magnitude and spectral distribution of the induced absorption due probably to the introduction of processes which compete with the color center formation for energy absorption and dissipation. Both Cd and Sb incorporation, either individually or together, reduce color center formation.

Brightness depreciation of phosphors when exposed to 1850Å radiation closely parallels observations on color center formation in unactivated halophosphates. Improved brightness maintenance toward 1850Å radiation is observed in phosphors quenched rapidly from elevated to room temperature and in phosphors containing Cd partially substituted for Ca.

Acknowledgments

The author is grateful to Mr. T. W. Luscher for preparation of the samples, to Miss Betty Walsh and Dr. P. D. Johnson for reflectance measurements, and to Dr. H. C. Froelich for suggestions about the work and the manuscript.

Manuscript received Sept. 21, 1962. This paper was prepared for delivery before the Los Angeles Meeting, May 6-10, 1962.

Any discussion of this paper will appear in a Discussion Section to be published in the December 1963 JOURNAL.

REFERENCES

1. P. D. Johnson, *J. Appl. Phys.*, **32**, 127 (1961).
2. L. Suchow, *This Journal*, **108**, 847 (1961).
3. P. D. Johnson, *J. Opt. Soc. Amer.*, **42**, 228 (1952).
4. E. F. Apple and W. E. Ishler, "Luminescence of Organic and Inorganic Materials," p. 587, H. P. Kallmann and G. M. Spruch, Editors, John Wiley & Sons, Inc., New York (1962).
5. P. D. Johnson, Private communication.
6. S. Naray-Szabo, *Z. Krist.*, **75**, 387 (1930); S. B. Hendricks, M. E. Jefferson, and V. M. Mosley, *ibid.*, **81**, 352 (1931).
7. W. E. Ishler, E. F. Apple, and H. C. Froelich, Conference on Luminescence, Balatonvilagos, Hungary (1961); *Acta Phys. Hung.*, **14**, 295 (1962).
8. C. Delbecq, "Proceedings of the International Conference on Color Centers and Crystal Luminescence," p. 9, Torino, Sept. 8-12, 1960.
9. M. A. Aia and S. M. Poss, U. S. Pat. 2,965,786, 1960.
10. P. D. Johnson, "Luminescence of Organic and Inorganic Materials," p. 563, H. P. Kallmann and G. M. Spruch, Editors, John Wiley & Sons, Inc., New York (1962).

Properties of ZnO Phosphors Doped with Li, Ni, and Cu

Arnold Pfahnl

Bell Telephone Laboratories, Incorporated, Murray Hill, New Jersey

ABSTRACT

The relative luminescent intensity, I, and the absolute value of the decay time, τ, were determined for the green emission of ZnO phosphors doped with Li, Ni, and Cu. It was found that doping with Li has practically no influence on these parameters, but that Cu and Ni doping reduced I, and Ni also reduced τ. The spectrum, the temperature dependence of I, and the surface conductivity were also measured. Results are discussed on the basis of a model for ZnO phosphors.

ZnO is used as a fast decay phosphor and as a photoconductor in addition to other applications, such as a catalyst, a nonlinear conductor, and a pigment. Some of the properties of the green luminescence of ZnO (Zn) prepared by providing excess Zn in ZnO according to the formula $2ZnO + ZnS = SO_2 + 3Zn$ (excess) were described in a previous paper (1).

The purpose of the present work was to investigate the influence of doping with Li, Ni, and Cu on the luminescent properties of similar phosphors, as it was thought that, in analogy to the quenching action of Ni and Co observed with ZnS phosphors (2), such doping could possibly reduce the decay time without a proportional reduction of the intensity of the green emission band. No study of the relation between the green and the u.v. emission was attempted, as it was found that in general the intensity of the latter was small compared to the former.

The various samples were also studied for the dependence of the conductivity on the preparation conditions, doping levels, and doping materials. This is of interest for the controlled variation of the conductivity, such as when these materials are used as photoconductors.

Experimental Procedures

The samples were prepared by firing reagent pure (r.p.) ZnO and luminescent pure ZnS at various temperatures ranging from 700° to 1400°C for 1 hr in an atmosphere of nitrogen. All samples used in the present experiments were prepared from the same batches of ZnO and ZnS. Use of different batches of ZnO showed only relatively small variations of the intensity, I, but use of r.p. ZnS instead of l.p. ZnS resulted in a strong decrease of I (1).

Ni and Cu were introduced by impregnating the base material ($ZnO + X\%ZnS$, $X = 1,5,10$) with solutions of $Cu(NO_3)_2$ and $Ni(NO_3)_2$ of various strengths and drying them at 120°C. Doping with Li was done by mixing appropriate amounts of Li_2CO_3 to the base material. After the firing, the samples were cooled rapidly.

For several selected samples, the content of the doping material remaining after the firing process was determined by spectrographic analysis. Results showed that the quantity of Ni, Li, and Cu introduced before the firing was not altered by the heat treatment.

For measurements of cathodoluminescent properties, the samples were suspended in potassium silicate solutions and settled on glass slides with $Ba(NO_3)_2$ as the coagulant. For measurements of the conductivity, samples were pressed into pellets with pressures of the order of 250 kg/cm^2.

The conductivity was measured in a Dewar which could be evacuated or filled with gas under known pressure. The material used for electrical contact to the pellets was graphite, pressed on as a dry powder.

Parameters measured were the relative emission intensity, I, and the decay time, τ, under cathode-ray excitation (10 kv, 5 ma/cm^2, 5 μsec pulse length, repetition frequency 1000 times/sec). The green emission was detected by a photomultiplier with S11 response. The u.v. emission band was filtered out (Corning filter CS3-72, 2.9 mm thick). The photocurrent was displayed on an oscilloscope. The time constant of the circuit was small enough to permit measurements of decay times down to 50 nanosec. Determined were also the temperature dependence of I under u.v. excitation (3650Å), the green emission spectrum, and the conductivity, σ, of samples pressed into pellets.

Results

Luminescent properties.—Figure 1 shows the variation of the intensity, I, for the green emission

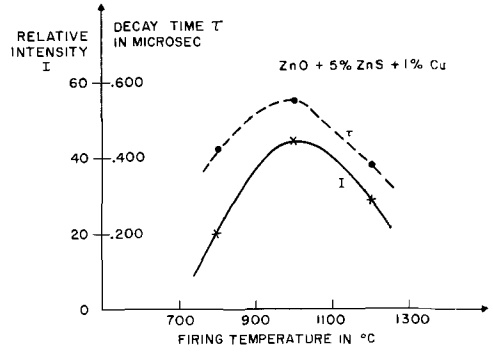

Fig. 1. Relative emission intensity I and decay time τ of ZnO(Zn,Cu) phosphors doped with 1% Cu as a function of the firing temperature.

band and the decay time, τ, of a series of ZnO(Zn) phosphors doped with 10^{-2}g Cu/g ZnO and fired at various temperatures. For increasing firing temperatures, the intensity and the decay time go through a maximum at about 1000°C similar to the behavior of the undoped green luminescent ZnO(Zn) prepared according to the same formula (1). Doping with Li and Ni results in similar curves.

Figure 2 shows the influence of doping with various quantities of Cu on the green luminescence of these ZnO(Zn) phosphors. The intensity rises first and reaches a maximum at a doping level of 10^{-5}g Cu/g ZnO. For higher Cu doping levels the intensity falls off. It is interesting to note that a similar maximum was found for the dipolar Debye absorption in Cu doped ZnO (3). Cu doping practically does not affect the decay time. Ni doping first increases slightly the intensity and decay time, similar to doping with Cu. This is followed by a reduction of the intensity and, at higher concentrations above 10^{-4} Ni/g ZnO, by a decrease of the decay time. Doping with Li in quantities up to about 10^{-2}g Li/g ZnO has practically no influence on I or τ.

If the decay time is plotted as a function of the intensity, it becomes clear (Fig. 3) that the quality of the doped phosphor samples when compared to the characteristics of the undoped samples was not improved. (Higher quality is defined here as higher emission intensity at equal decay time.)

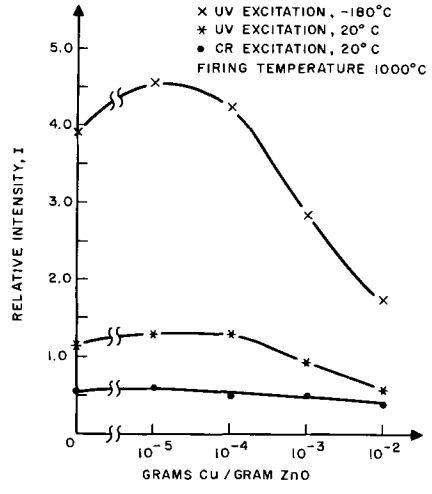

Fig. 2. Relative emission intensity I of ZnO(Zn) phosphors as a function of the Cu doping level.

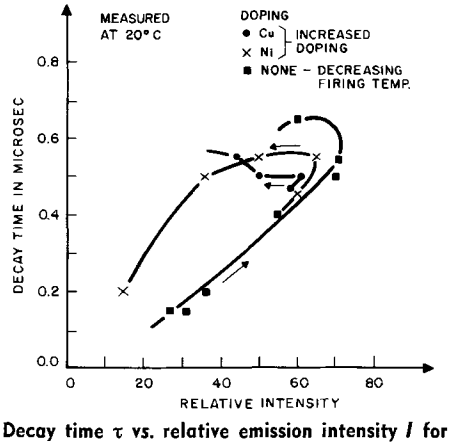

Fig. 3. Decay time τ vs. relative emission intensity I for ZnO(Zn) without doping and ZnO(Zn) doped with Ni and Cu. The various points for a given dopant were obtained by varying the doping level.

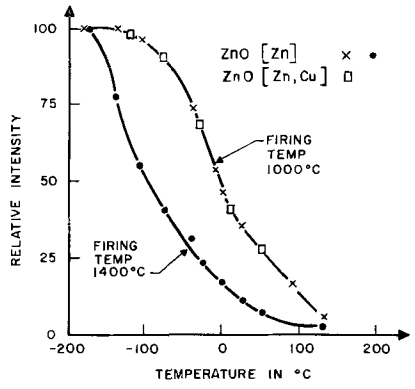

Fig. 4. Relative emission intensity I of ZnO(Zn) and ZnO(Zn, 10^{-3}Cu) fired at 1000°C, and of ZnO(Zn) fired at 1400°C.

Comparison of the relative intensities obtained under CR and u.v. excitation shows that the general shape of the intensity *vs.* doping curves remains the same, regardless of the type of excitation (Fig. 2). It may be noted that the peak in I is greatly enhanced as the sample temperature is decreased.

If the sample temperature is lowered, the intensity increases and reaches a maximum in the vicinity of —180°C. For the undoped samples (Fig. 4), this maximum value of I is always the same regardless of the firing temperature. The firing temperature strongly influences the intensity at higher sample temperatures. For example, at 20°C the intensity of the sample fired at 1000°C is 37 relative units, and that of the sample fired at 1400°C is 12.5 relative units. These results indicate that firing at higher temperatures introduces a quenching mechanism which acts on the luminescence center; this quenching can be eliminated by lowering the temperature of the sample.

For the doped samples, the rate of increase of the intensity with decreasing sample temperature is practically the same as that of the undoped sample (curve for 1000°C firing temperature in Fig. 4). This could indicate that some luminescent centers have been replaced by doping atoms, without influencing the behavior of the remaining luminescent centers.

An additional experimental observation was that the shape of the green emission spectrum, with a peak at 500 mμ, remains unchanged for doped or undoped samples.

Preliminary conductivity measurements.—To determine the influence of the pressure used to form pellets on the properties of the ZnO powders, a series of pellets were prepared using pressures up to 400 kg/cm^2. After this treatment, the pellets were broken up gently and the powder settled on slides. The cathodoluminescent emission intensity was then determined and compared to that of the unpressed material. Results are shown in Fig. 5: the intensity decreases with pressure, and those samples fired at higher temperatures are slightly more sensitive than those fired at lower temperature. For pressures up to 250 kg/cm^2 and a 1000°C firing temperature, the effect does not exceed a reduction of 5% of the intensity and was therefore considered as negligible. In turn, it is assumed that

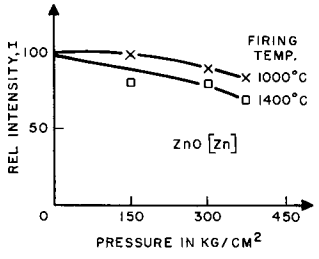

Fig. 5. Influence of pressure used to form pellets on the emission intensity of ZnO(Zn) phosphors. CR excitation.

the pellet-forming process does not affect other properties of the ZnO powders.

Another important factor to be determined is the influence of the ambient atmosphere on the conductivity. To insure reproducible conditions, the pellets were placed in a vacuum. Under these conditions an increase of the conductivity is observed which follows, after an initial steeper increase, the relation $\log \sigma = c_1 . \log t$, with c_1 being a constant and t being the time. The increase of the conductivity can be explained by a desorption of oxygen from the surface of the ZnO powder (4), and the results indicate that the effects from desorption of H_2O were negligible. The time at which the conductivity measurements were made was then selected for practical reasons at ½ hr after the sample was placed in the vacuum chamber.

The reproducibility of the results was typically ±15% for the conductivity measurements, if pellets formed from ZnO powder prepared from the same base materials and fired under similar conditions were used. To eliminate the influence of different base materials, all samples shown in the curves were prepared from the same batch of ZnO and ZnS.

In one experiment samples were prepared with a different ZnO batch and fired at various temperatures. The absolute value of the conductivity increased, but the form of the curve σ *vs.* firing temperature remained the same.

It was also investigated how the properties of the pellets formed from the various ZnO powders would be influenced by a further heat treatment. It was found that such sintering in a nitrogen atmosphere changes the sample properties strongly. The luminescent intensity decreases, and the conductivity increases up to a value which corresponds to the calculated σ for donors at 0.05 ev in concentrations of 10^{15}-10^{18}/cm³ (Fig. 6). The result depends, of course, on the sintering time and the atmosphere. This shows clearly how heat treatments after the preparation change the properties of the material and must therefore be investigated systematically if such samples are to be used in measurements. One of the reasons for this behavior is that during the sintering process the grains become connected by thin necks the size of which depends on the various conditions during the sintering treatment.

Conductivity of doped and undoped samples.— Figure 7 shows that the conductivity of pressed r.p. ZnO pellets is not influenced by firing the powder, before pressing, at temperatures up to 1300°C. For

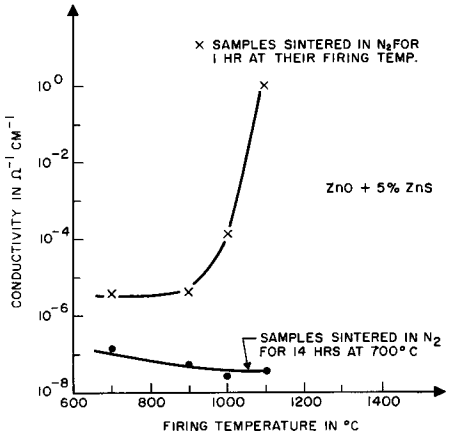

Fig. 6. Influence of sintering on the conductivity of ZnO(Zn)

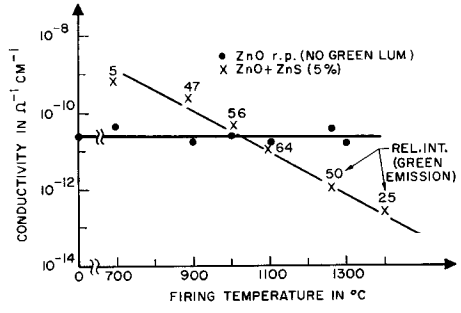

Fig. 7. Conductivity of reagent-pure ZnO and ZnO(Zn) as a function of the firing temperature. Samples are fired before forming them into pellets for the conductivity measurements.

the ZnO(Zn), an increase of the firing temperature decreases σ by nearly four decades. It may be emphasized that the conductivity shows no simple relation to the luminescent intensity of the green emission which goes through a maximum when the conductivity is about 10^{-11} ohm^{-1} cm^{-1}.

Doping with Cu in concentrations up to 10^{-5}g Cu/g ZnO increases the conductivity (Fig. 8). Doping with larger Cu concentrations then produces a decrease of σ of nearly six decades. Lithium has a similar but somewhat smaller effect, which appears only at higher Li concentrations of 10^{-3}g Li/g ZnO. Ni doping in concentrations of up to 10^{-3} g/g ZnO has no effect on σ (Fig. 8). If σ is plotted against $1/T$, activation energies, ϵ, in the order of 1 to 2 ev are obtained. As it is to be expected, larger ϵ values are associated with lower σ.

Discussion

ZnO is an n-type semiconductor with interstitial Zn acting as a donor (5). If it is fired under reducing conditions, as was the case in the present experiments, a further excess of Zn is produced through the creation of oxygen vacancies. The green emission which is observed after such a reducing treatment has been attributed to a transition within the excess Zn ions (6) or oxygen vacancies (7).

As an alternative explanation, it has been advanced that the green band could be the result of a small amount of ZnS (0.1% or less) present in solid solution in the ZnO (8). On the basis of previously reported experiments, where green luminescent ZnO was prepared by the oxidation of high-purity

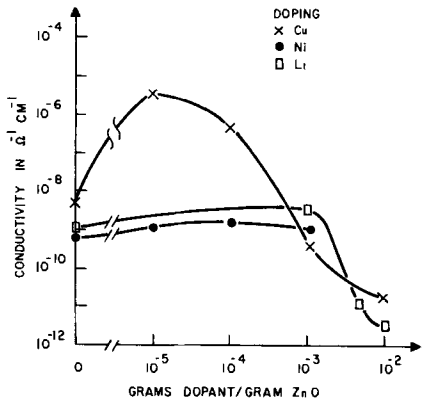

Fig. 8. Conductivity of ZnO(Zn) phosphors doped with Cu, Ni, and Li, as a function of the doping concentration.

Zn (1, 7), it is not possible to eliminate this possibility completely as it is not possible to ascertain the absence of small quantities of sulfur which may already be luminescent active. The following discussion is based on the assumption that the luminescent process takes place in the ZnO crystal.

Since there always is a great number of electrons present in the conduction band, it is assumed that the green emission takes place whenever a hole has been captured by the luminescent center (13).

In the presence of reducing agents, Li is incorporated interstitially into the ZnO lattice and acts as a donor with an activation energy of 0.05 ev (9) or less (3). Doping with Li should, therefore, simply increase the electron concentration in the conduction band, but should have no influence on I or τ. This is in agreement with the present and other (10) experiments.

Cu enters the ZnO lattice substitutionally (11), but may possibly also enter interstitially (12). The observed reduction of the conductivity with increasing Cu doping indicates that it may introduce levels which act as traps for electrons. The decrease of I at approximately constant τ and the form of the temperature dependence of I indicate that it replaces activator centers (13) or that it acts also as an independent nonradiative recombination center. It is interesting to note that the increase of the luminescent intensity with an increase of Cu doping from 0 to 10^{-5} is similar to the increase of the intensity of the dipolar Debye absorption, which suggests that the Cu doping introduces a level of about 0.20 ev (14). The intensity of the dipolar Debye absorption band also decreases with higher Cu doping levels. Further measurements, especially of absorption, stimulation, and quenching spectra, would be necessary to elucidate this question. A similar mechanism and similar conclusions can be assumed for the action of Ni.

The conductivity of pressed ZnO pellets is determined essentially by chemisorbed oxygen which acts as an acceptor and forms a surface and depletion layer (4). The depth and the height of this layer depend on the concentration of electrons in the conduction band and are therefore functions of the preparation and doping conditions, as well as of the surface-to-volume ratio. The present simple measurements of σ show that such effects exist, but are insufficient to permit an exact interpretation of the phenomena. It has been established that the electrical conductivity of ZnO is primarily a surface effect and that the σ of pressed pellets can be controlled by doping with Li or Cu. This result may be useful when ZnO powders are used in photoconductive applications.

The pressure and sintering experiments show that, as expected, the powders are sensitive to all treatments after preparation. It should be emphasized especially that heat treatments after sample preparation can affect the luminescent properties critically. Hence, sample processing should be considered carefully in experiments of this nature.

Manuscript received Sept. 12, 1962; revised manuscript received Nov. 14, 1962. This paper was presented in part before the Los Angeles Meeting, May 6-10, 1962.

Any discussion of this paper will appear in a Discussion Section to be published in the December 1963 JOURNAL.

REFERENCES

1. A. Pfahnl, *This Journal*, **109**, 502 (1962).
2. L. A. Levy and D. W. West, *Brit. J. Radiol.*, **6**, 85 (1933).
3. M. Blanchard and M. Martin, *J. phys. radium*, **19**, 677 (1958).
4. S. R. Morrison, *Advances in Catalysis*, **7**, 259 (1955). D. J. M. Bevan and J. S. Anderson, *Discussions Faraday Soc.*, **8**, 238 (1950).
5. E. Scharowsky, *Z. Physik*, **135**, 318 (1953); E. E. Hahn, *J. Appl. Phys.*, **22**, 855 (1951).
6. F. I. Vergunas and G. A. Konivalov, *J. Exptl. Theoret. Phys., U.S.S.R.*, **23**, 712 (1952).
7. E. Mollwo and F. Stöckmann, *Ann. Phys.*, **3**, 240 (1948); F. A. Kröger and H. J. Vink, *J. Chem. Phys.*, **22**, 250 (1954).
8. S. M. Thomsen, *J. Chem. Phys.*, **18**, 770 (1950).
9. J. J. Lander, Private communication.
10. A. R. Hutson, *Phys. Rev.*, **108**, 222 (1957).
11. G. Bogner and E. Mollwo, *J. Phys. Chem. Solids*, **6**, 136 (1956); G. Heiland, *Z. Physik*, **148**, 15 (1957).
12. C. G. B. Garrett, Private communication.
13. E. Mollwo, *Z.Physik.*, **162**, 557 (1961).
14. B. Hagene, H. Corneteau, and M. Blanchard, *J. phys. radium*, **17**, 450 (1956).

Solubility of III-V Compound Semiconductors in Column III Liquids

R. N. Hall

Research Laboratory, General Electric Company, Schenectady, New York

ABSTRACT

The solubilities of InSb, InAs, and InP in In, and of GaSb, GaAs, and GaP in Ga have been measured at low temperatures, covering the atom fraction solubility range 10^{-4} to 10^{-1}. Near the melting temperature these systems exhibit negative departures from ideality which are most pronounced for InSb and InAs and are relatively small for the others. The measured solubilities can be represented by a two parameter formula describing the behavior of regular solutions.

In the preparation and processing of III-V compound semiconductors, it is often important to know the solubility of the semiconductor in the liquid phase of its column III constituent as a function of temperature. Phase diagrams of these systems have been published (1-5), but in general they do not extend to low temperatures which is the region of principal interest here. In this paper we report measurements of the solubility of InSb, InAs, and InP in In, and of GaSb, GaAs, and GaP in Ga, with particular attention being paid to the low-temperature region where the solubility becomes quite small.

Experimental Procedure

At each temperature liquid Ga or In was saturated with a sample of the III-V semiconductor using the equipment shown in Fig. 1, and the solubility was calculated from the weight loss of the sample. A charge of 15-20g of In or Ga was placed in a quartz tube of inside diameter 1.5 cm. Hydrogen was introduced through a side tubulation and burned at the open end at the top. A quartz thermocouple tube, T, was immersed in the Ga or In. It contained a chromel-alumel thermocouple which was used to measure the temperature of the liquid. A carefully weighed sample, S, of the III-V semiconductor being studied was floated on the surface of the melt until the liquid was saturated, and the solubility was calculated from the measured weight loss of the crystal. Quartz tube, T, also had a "foot" consisting of a loop of quartz which was used to stir the melt and to remove the sample for weight loss measurements. Heat was applied using a nichrome heater, wound on an alumina tube 20 cm long and 2.5 cm ID. The furnace power was supplied from a regulated voltage source in order to maintain a steady temperature during each measurement.

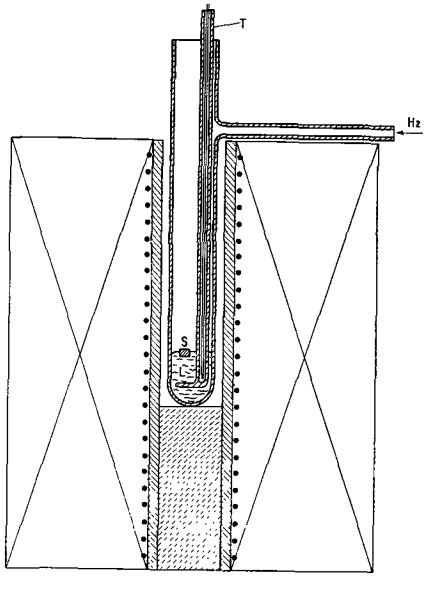

Fig. 1. Equipment for measuring solubility: S, sample of III-V semiconductor; L, liquid Ga or In; T, thermocouple well.

A slight modification of this procedure was often employed at higher temperatures, where solubilities were a few per cent or more. An appropriate size crystal was introduced, and the temperature was increased slowly and with frequent mixing until it was seen to be completely dissolved by visual observation through the open end of the tube. The temperature was then decreased gradually until crystals formed again and then increased to redissolve them. By repeating this cycle several times it was possible to determine the solution temperature with an uncertainty of less than $\pm$ 5°C.

Gallium of 99.99% purity from the Aluminum Company of America and In of 99.97% purity from the Indium Corporation of America were used in these experiments. Since the principal impurities present in these metals are expected to be those closely related to In and Ga, they should have little effect in this concentration range on the solubilities of the III-V compounds under study. The III-V compound semiconductor crystals which were used were often polycrystalline. They were given a chemical polish before the initial weighing and were free of visible chips or crevices which might trap inclusions of Ga or In as judged by careful examination using a 20X binocular microscope.

The procedure used in determining a solubility curve was to saturate the solution at the lowest temperature and then remove the sample and determine the weight loss. The furnace temperature

was then raised to the next temperature and the procedure was repeated, and so on throughout the desired temperature range. Small samples were used in the lower temperature ranges in order to minimize weighing errors.

Discussion of Experimental Errors

Weight loss determination.—In the low-temperature range, crystals, S, weighing 50-200 mg were used and were weighed to the nearest tenth milligram. Since weight losses in the data which we report were seldom less than a few milligrams, the measurement itself is not regarded as a serious source of error. Important errors could arise if traces of In or Ga remained on the sample after removal from the melt, and care was taken to insure that this was properly done. Gallium was relatively easy to remove using an air blast followed by etching in HCl. GaSb, GaAs, and GaP are not attacked appreciably by HCl. In is more difficult to remove because of its higher melting point and because the chemical etchants that we tried for dissolving the In also attacked InAs and InP. We therefore immersed the samples in Hg to dissolve the In, and any Hg which remained on the sample after this treatment was removed with an air blast. Errors due to solution of In or Ga in the crystals are quite negligible because of the high degree of stoichiometry of the III-V semiconductors.

Temperature measurement.—The thermocouple voltage was measured with a Rubicon potentiometer with reference junction in an ice bath. Since the end of the thermocouple was 1 cm below the surface of the melt, and since the melt and a considerable length of the thermocouple leads were located in a low thermal gradient portion of the furnace, it is felt that the potentiometer reading gave an accurate value for the melt temperature. The principal temperature uncertainty resulted from temperature fluctuations, usually $\pm$ 3°C or less, during the holding period while melt saturation was established. Using this equipment we measured the melting points of GaSb and Ge as being 712° and 936°C, respectively. These values agree within 1°C with the results of other investigators (6, 7).

Completeness of saturation.—During each measurement the semiconductor sample was held in contact with the melt, either floating on the surface or submerged within it, for at least 20 min, and occasionally for an hour or more with frequent stirring of the melt by means of the foot on the thermocouple well. Weight losses measured after saturation for 20 min were indistinguishable from those made after saturation for an hour or more, and consequently it is believed that saturation was reasonably complete in nearly all cases. Lack of complete saturation may, however, have occurred in some of the lowest temperature determinations, due to limited wetting of the sample surface by the melt.

Loss of Sb, As, or P.—Due to the high vapor pressures of Sb, As, and P, there may be appreciable loss of the column V constituent during the course of the experiment, particularly as the temperature approaches that of the pure compound and the melt becomes correspondingly rich in the column V element. This loss was quite noticeable in the case of experiments involving InP and GaP, with a fairly heavy deposit being left at the upper end of the quartz tube by the conclusion of the highest temperature measurements. However, the actual weight of material found in such deposits was rather small, being 10 to 50 mg, compared with several grams of InP or GaP in solution at these temperatures. Furthermore, we were unable to observe any change in solution temperature with time over periods of several hours at the highest temperatures reached in our experiments and conclude that the loss of these elements during our experiments amounted to a negligible fraction of the total amount in the system and therefore did not contribute appreciably to the experimental error.

In summary, we feel that errors in temperature measurement are less than 5°C over most of the temperature range, although they may be as high as 10° above 1000°C. Near the low-temperature limit, where the atom fraction of P, As, or Sb in the melt is of the order of 10^{-4}, weight loss errors and lack of complete equilibration may become appreciable. Other sources of error are believed to be relatively negligible.

Results

We first conducted preliminary measurements in each of the systems under study in order to work out the experimental procedures required for each material. These results are not reported here, since they include errors which are now recognized and which have been eliminated in the later measurements. A second and in most cases a third series of measurements was then carried out in each system giving the results shown in Fig. 2. We have also included the high-temperature measurements of other workers on InSb (1), InAs (2), InP (3), GaSb (4, 6), GaAs (4), and GaP (5). Except in the cases of InP and GaSb, these measurements are in good agreement with ours in the temperature range where they overlap. The disagreement in the InP data is in the direction anticipated by van den Boomgaard and Schol (3) as the result of phosphorous condensation during cooling in their experiments. In the case of GaSb, the discrepancy

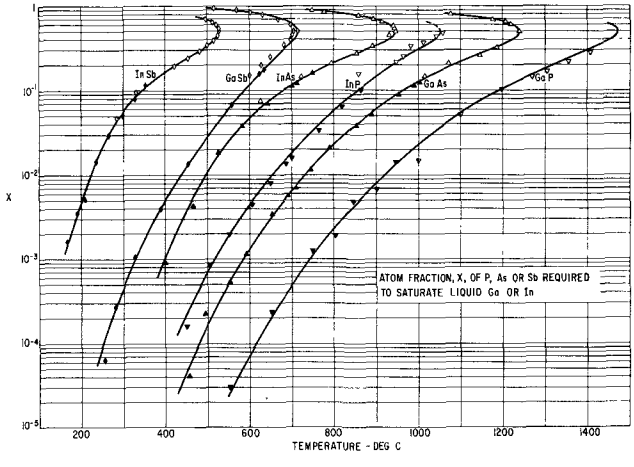

Fig. 2. Solubility of III-V compounds in Ga or In. Solid points are our measurements; open points are from ref. (1)-(6).

disappears if the temperatures given by Köster and Thoma (4) are increased by 9°C to make the melting point of GaSb agree with the measurement of Bedner and Smirous (6).

Discussion

Wagner has given a theoretical treatment of the solubility of an AB binary compound in each of its constituents (8). His results suggest the following form for the liquidus curve of a regular solution in which the excess free energy of solution is proportional to the product of the atom fractions of the two constituents in the liquid phase, $F^E = -wx(1-x)$.

$$-\ln [4x(1-x)] = \frac{\Delta S^{f*}}{R}\left(\frac{T_m}{T} - 1\right) - \frac{w}{4RT}(1-2x)^2 \qquad [1]$$

T_m is the melting temperature of the pure compound, and x is the atom fraction of one component in the liquid phase. In the derivation of this equation the temperature dependence of the interaction parameter, w, and the difference in specific heats of the solid and liquid phases of the compound are neglected. Because of these approximations, the effective entropy of fusion, ΔS^{f*}, may differ significantly from the true entropy of fusion, ΔS^f.

In the case of an ideal solution, where $w = 0$, a plot of $\ln[4x(1-x)]$ against T_m/T gives a straight line having a slope equal to $-\Delta S^f/R$. The regular solution assumed above gives a curve which is convex upward for positive values of w (negative departures from ideality) and which approaches a limiting slope, $-(\Delta S^{f*}/R) + (w/4RT_m)$ at low temperatures. The data of Fig. 2 in the region $x <$ 0.5 are plotted in this way in Fig. 3 and 4. In Fig. 3, the high-temperature GaSb data given by ref. (4) have been increased by 9°C as discussed above. These experimental curves can be fitted quite accurately by Eq. [1], using values for the parameters ΔS^{f*} and w which are given in Table I. The discrepancies between the experimental values of $4x(1-x)$ and those calculated from Eq. [1] and Table I are less than 10% everywhere, except in the case of InSb at low temperature where it amounts to 15%. If values of ΔS^{f*} are used which differ by 10% from those listed in Table I while readjusting w to give the best fit under these circumstances, the agreement with the experimental curves becomes significantly worse.

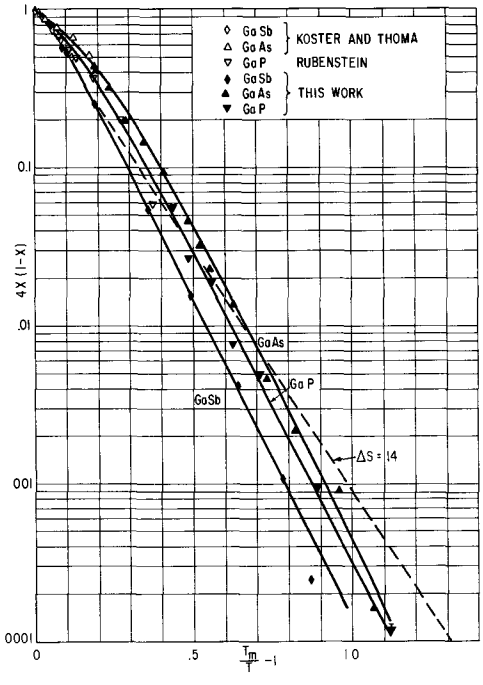

Fig. 3. Solubility curves of GaSb, GaAs, and GaP in dimensionless form.

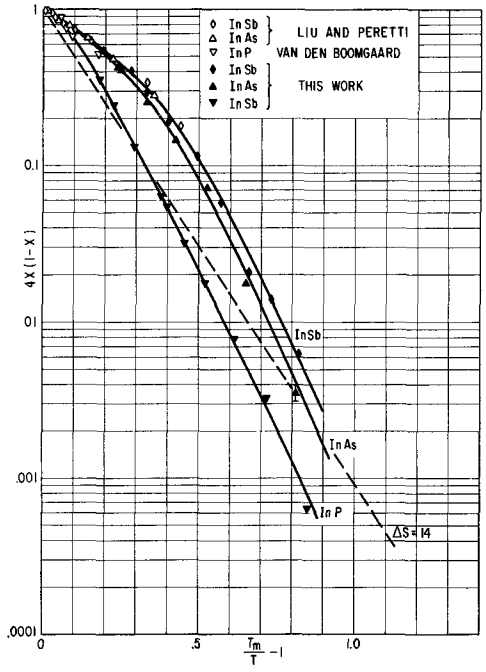

Fig. 4. Solubility curves of InSb, InAs, and InP in dimensionless form.

The entropies of fusion of InSb and GaSb are reported to be 15.3 and 12.3 cal/deg-mole, respectively (9). The other members of the III-V semiconductors are expected to have entropies of fusion of approximately this same magnitude. In order to illustrate the departures of the experimental curves from ideality, a dashed line is shown in Fig. 3 and 4 with a slope corresponding to an ideal solution with $\Delta S^f = 14$ cal/deg-mole.

Schottky and Bever (9) have also evaluated the interaction parameter, w, from the liquidus curves of InSb and GaSb. Only the high-temperature data

Table I

Compound	T_m, °K	ΔS^{f*}, cal/deg-mole	$w/4T_m$, cal/deg-mole
GaSb	985	19.8	4.4
GaAs	1510	22.2	13.4
GaP	1743	20.1	7.8
InSb	798	29.9	31.0
InAs	1215	30.0	29.2
InP	1323	21.1	8.1

of ref. (1) and (4) were available at that time and the procedure used was to set $\Delta S^{f*} = \Delta S^f$ and then select w so as to give a satisfactory fit. The resulting values of w/T_m (9 and 1.4 cal/deg-mole, respectively) are quite different from those listed in Table I. They agree with the experimental data only in the nearly linear high temperature region of the curves in Fig. 3 and 4.

In conclusion, we find that the liquidus curves of the III-V compound semiconductors can be represented over an extended temperature range by a formula representing the behavior of regular solutions, and which contains two adjustable parameters. One of these corresponds to an effective entropy of solution, but differs substantially from the measured entropy of solution. The other is a measure of the excess free energy of solution.

Acknowledgments

This research was sponsored by the Electronics Research Directorate of the Air Force Cambridge Research Laboratories. Much of the experimental work was performed by Miss S. Schwarz.

Manuscript received July 27, 1962; revised manuscript received Oct. 22, 1962. This paper was prepared for delivery before the Boston Meeting, September 16-20, 1962.

Any discussion of this paper will appear in a Discussion Section to be published in the December 1963 JOURNAL.

REFERENCES

1. T. S. Liu and E. A. Peretti, *Trans. Am. Soc. Metals*, **44**, 534 (1952).
2. T. S. Liu and E. A. Peretti, *ibid.*, **45**, 677 (1953).
3. J. van den Boomgaard and K. Schol, *Philips Research Repts*, **12**, 127 (1957).
4. W. Köster and B. Thoma, *Z. Metallk.*, **46**, 291 (1955).
5. M. Rubenstein, Electrochem. Soc. Abstracts, **11**, 129 (1962).
6. J. Bednar and K. Smirous, *Czech. J. Phys.*, **5**, 546 (1955).
7. F. X. Hassion, C D. Thurmond, and F. A. Trumbore, *J. Phys. Chem.*, **59**, 1076 (1955).
8. C. Wagner, *Acta Met.*, **6**, 309 (1958).
9. W. F. Schottky and M. B. Bever, *ibid.*, **6**, 320 (1958).

Stacking Faults in Vapor Grown Silicon

T. L. Chu and J. R. Gavaler

Research Laboratories, Westinghouse Electric Corporation, Pittsburgh, Pennsylvania

ABSTRACT

The stacking faults in vapor grown silicon on silicon substrates have been investigated using chemical etching and optical microscope tehniques. The etch figures are generally in the form of equilateral triangles, isosceles triangles, squares, and isosceles triangles for grown material on {111}, {110}, {100}, and {211} substrates, respectively. The stacking faults take place along {111} planes in all cases. The majority of the stacking faults initiate from the substrate-deposit interface. Dislocations associated with the stacking faults are not all revealed by dislocation etches. Experimental results indicated that the surface defects of the substrate, the impurities on the substrate surface, and the local stress developed during the growth process are probably the principal causes of faulting.

The vapor growth or epitaxial growth of semiconducting materials, such as silicon, germanium, and III-V compounds, has received considerable attention during the past few years. However, the structural perfection of the vapor grown crystals is not yet equal to that of the best melt-grown crystals. In general, the crystals grown from the vapor phase, particularly the thin films deposited by the vacuum evaporation technique (1), often contain stacking faults as shown by transmission electron microscopy. The stacking faults in vapor grown silicon have been investigated recently by optical (2, 3), electron transmission (2, 4), and x-ray diffraction techniques (5). It is now well established that the defects in vapor grown silicon of {111} orientation, observable as triangular etch figures, are stacking faults. The thickness determination of {111} oriented epitaxial silicon films by measuring the etch figures has been reported (6). Some fundamental properties of stacking faults in the diamond lattice have been reviewed by van Bueren (7).

We have investigated the stacking faults in vapor grown silicon on substrates of {111}, {110}, {100}, and {211} orientations, using chemical etching, cross-sectioning, and optical microscope techniques. Since the stacking fault planes exhibit faster etch rates than the bulk crystal, they are readily revealed by appropriate chemical etching. Thus, conventional metallographic techniques are valuable for the investigation of stacking faults in the vapor grown crystals. This paper describes briefly the geometry of, the interactions among, and the dislocations associated with the stacking faults. The probable causes of faulting are discussed. Many specimens were examined in detail; however, only the commonly observed results are summarized.

Experimental

The vapor growth of silicon was carried out by the conventional method, *i.e.*, the thermal reduction of a silicon chloride with hydrogen on a heated substrate surface in a flow system (8). Chemically etched silicon wafers of {111}, {110}, {100}, and {211} orientations were used as substrates. The grown layer was usually 100-250μ in thickness.

The stacking faults are usually not visible on the as grown surface with an optical microscope. They can be detected, however, by etching the grown

surface with suitable etchants. The intersections of the stacking fault planes with the grown surface are revealed as grooves. Many chemical etchants, such as CP_4 etch,[1] Dash etch,[2] iodine etch,[3] etc., serve this purpose. The Dash etch was used in most of this work. With this etchant, the stacking faults are brought out clearly by etching the specimen for 15 to 20 min at room temperature. Upon prolonged etching, 2-4 hr, the Dash etch also reveals dislocation pits on surfaces of all orientations under study. In addition to the Dash etch, the Sailer etch[4] was also used on {111} surfaces, as this etch brings out more clearly the structures of the intersections of stacking fault planes and the grown surface, and also the structure of dislocation pits.

In the cross-section studies, the specimens were potted in a plastic material, sectioned, and polished with diamond abrasives. The polished surface was then etched with the Dash etch for 15 to 20 minutes, or CP_4 etch for 3 to 5 sec, and examined with an optical microscope.

Geometry of the Stacking Faults

{111} Oriented substrates.—On etching the grown surface, most of the stacking faults are brought out in the form of equilateral triangles of one orientation. In some cases, the etch figures are incomplete triangles, single lines parallel to a side of the triangles, or complicated geometrical configurations.

A typical triangular etch figure is shown in Fig. 1, where the growth thickness is approximately 200μ. The dimension of the triangle decreased proportionally as the grown material was gradually removed, and the thickness of the grown layer was always approximately 80% of the length of a side of the etch figure. On approaching the deposit-substrate interface, the etch figure was no longer detectable. These results indicated that the fault originated from the interface and propagated along the three adjacent {111} planes, each making an angle of 70°32′ with the substrate surface. These three planes and the grown surface form a regular tetrahedron with one apex at the interface. The traces of the intersections of the stacking fault planes with the grown surface are in $<\bar{1}10>$ directions. The stacking faults can also be revealed on the cross-sectioned surfaces of the specimen. For instance, the vertical cross section through the origin of a stacking fault and an apex of the triangular etch figure yields a $\{\bar{1}10\}$ plane. Such a cross section is shown in Fig. 2 where two lines intersecting at the interface are seen. The interface line is revealed due to the resistivity difference between the substrate and the grown layer. The line at the left making an angle of approximately 70° with the interface line results from the intersection of a $\{11\bar{1}\}$ faulting plane with the $\{\bar{1}10\}$ plane. The other line results from the intersection of two $\{11\bar{1}\}$ faulting planes. This line should make an angle of 54°44′ with the interface line. The angle shown is slightly off due to the errors involved in making this type of cross section (the triangular etch figure is usually less than 0.03 mm² in area).

[1] 5 parts HNO_3, 3 parts CH_3COOH, and 3 parts HF.

[2] 3 parts HNO_3, 12 parts CH_3COOH, and 1 part HF. W. C. Dash, *J. Appl. Phys.*, **27**, 1193 (1956).

[3] 110 ml glacial CH_3COOH, 100 ml HNO_3, 50 ml HF, and 0.3g I_2. P. Wang, *Sylvania Tech.*, **11**, 50 (1958).

[4] 300 ml HNO_3 + 600 ml HF + 2 ml Br_2 + 23g $Cu(NO_3)_2$, dilute 10:1 with deionized water before use and etch for 4 hours. Allegheny Electric Chemicals Company, Technical Bulletin No. 6.

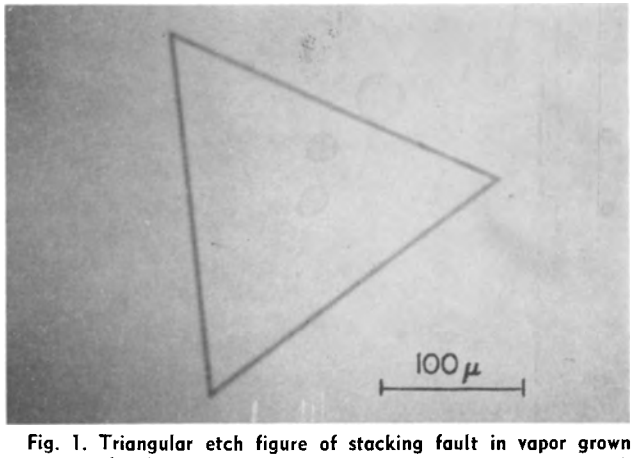

Fig. 1. Triangular etch figure of stacking fault in vapor grown silicon on {111} substrate (as grown surface etched 15 min with Dash etch; approximate growth thickness, 200μ).

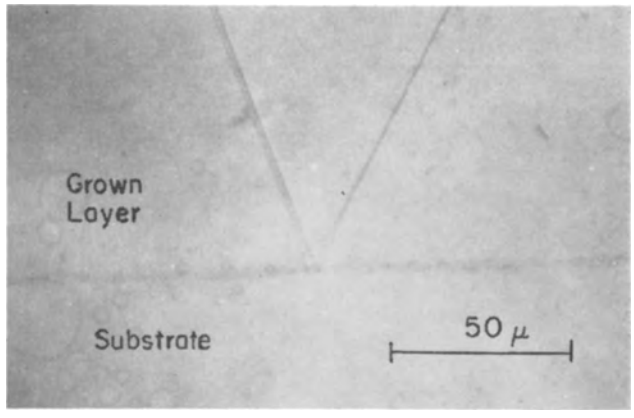

Fig. 2. Vertical cross section of vapor grown silicon on {111} substrate showing interface and stacking fault (see text).

The linear etch figures exhibited by some faults are parallel to a side of the triangular etch figures, *i.e.*, they are oriented along $<\bar{1}10>$ directions. During the gradual removal of the grown material, they decrease in length in the same manner as the triangular etch figures. These faults also take place along one of the {111} planes adjacent to the substrate surface. Other etch figures due to the interactions of faults will be discussed later.

The stacking faults in the vapor grown silicon do not all originate from the growth interface as is shown by the different sizes of the triangular etch figures and by cross-section studies. When the faults originate from the interface, the growth thickness can be calculated from the dimensions of the triangular etch figure on the grown surface. If one side of the equilateral triangle is of length a, the thickness of the grown layer is then $\sqrt{\frac{2}{3}}\,a$.

{110} Oriented substrates.—The etch figures of the stacking faults in vapor grown silicon on {110} substrates are usually in the form of isosceles tri-

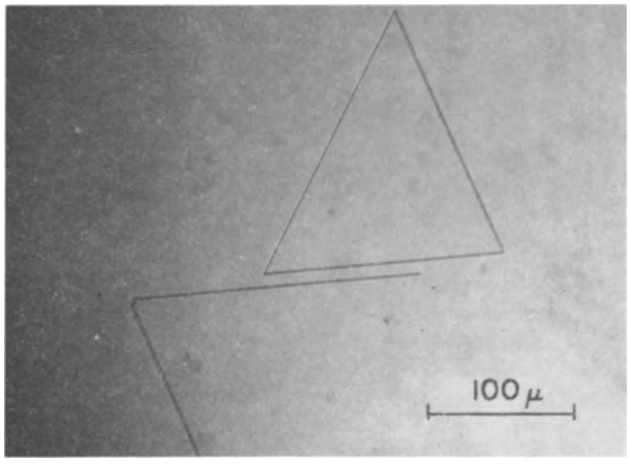

Fig. 3. Etch figure of stacking faults in vapor grown silicon on {110} substrate (as grown surface etched 15 min with Dash etch).

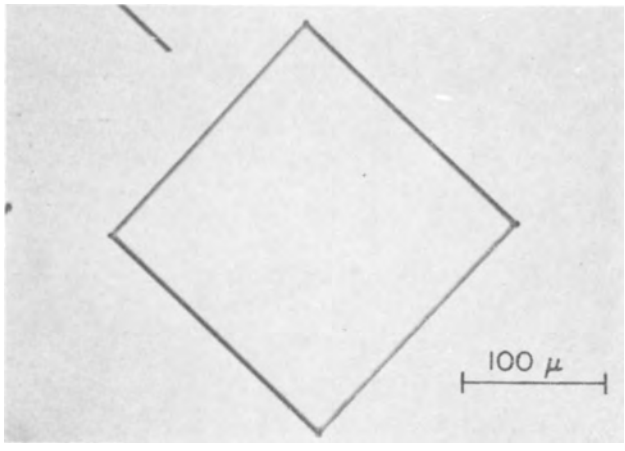

Fig. 4. Etch figure of stacking fault in vapor grown silicon on {100} substrate (as grown surface etched 15 min with Dash etch; approximate growth thickness, 130μ).

angles of two opposite orientations. The equal sides of the triangle form an angle of approximately 70°. Figure 3 shows two nearly isosceles triangles of opposite orientations; these etch figures are not exactly isosceles due to the slight deviation of the grown surface from the {110} orientation. Besides isosceles triangles, lines, partial triangles, and complicated etch figures, due to interactions of closely spaced faults, have also been observed.

The gradual removal of the grown material indicated that the two faulting planes intersecting on the grown surface at 70° are perpendicular to the substrate surface. A vertical cross section bisecting this apex of the triangular etch figure indicated that the other faulting plane makes an angle of approximately 35° with the substrate surface. Therefore the stacking faults in the vapor grown silicon on {110} substrates also propagate along three {111} planes. In this case, two combinations of {111} stacking fault planes yield triangular etch figures. On a (110) surface, the faulting takes place along $(11\bar{1})$, $(\bar{1}1\bar{1})$, and $(1\bar{1}\bar{1})$ planes or (111), $(1\bar{1}1)$, and $(\bar{1}11)$ planes. The $(\bar{1}1\bar{1})$, $(1\bar{1}\bar{1})$, $(1\bar{1}1)$, and $(\bar{1}11)$ planes are perpendicular to the substrate surface, and $(11\bar{1})$ and (111) planes make an angle of 35°16′ with the substrate surface. Each set of the three planes forms a pyramid, and the pyramids intersect with the grown surface to form two isosceles triangles, one being the mirror image of the other. The sides of the triangular etch figure are along <110> and <211> directions.

The stacking faults in the vapor grown silicon on {110} substrates also do not all initiate from the interface. When the faults do initiate from the interface, the growth thickness is equal to $a/\sqrt{3}$, where a is the length of the equal sides of the triangular etch figure.

{100} Oriented substrates.—The etch figures of the stacking faults in vapor grown silicon on {100} substrates are usually in the form of squares. Lines and partial squares have also been observed. A typical example is shown in Fig. 4, where the growth thickness is approximately 130μ. The dimension of the square decreased as the grown material was gradually removed, and the thickness of the grown material was approximately 70% of the length of a side of the square. The faults seen in many specimens all originated at the deposit-substrate interface. The stacking fault planes are thus the four {111} planes adjacent to the substrate surface. On a (100) substrate surface, the stacking fault planes are (111), $(11\bar{1})$, $(1\bar{1}1)$, and $(1\bar{1}\bar{1})$ planes. They form a pentahedron and intersect with the grown surface along <110> directions forming a square. Since the faults initiate from the interface, the growth thickness is $a/\sqrt{2}$, where a is the length of one side of the square.

{211} Oriented substrates.—The predominant etch figures of stacking faults in vapor grown silicon on {211} substrates are isosceles triangles of one orientation, the angle between the equal sides of the triangle being 44°. Considerations of the geometry of the faulting planes indicated that, on a (211) substrate surface, the fault propagates along $(\bar{1}11)$, $(1\bar{1}1)$, and $(11\bar{1})$ planes. The $(\bar{1}11)$ plane is perpendicular to the substrate surface, and each of the other two planes makes an angle of 61°50′ with the substrate surface. Another combination of {111} stacking fault planes, namely, the (111), $(1\bar{1}1)$, and $(11\bar{1})$ planes, would yield the same orientation and interior angles of the etch figure. However, none of the vertically cross-sectioned faults observed showed this combination. These results indicated that the stacking faults are less likely to form on the (111) plane making a shallow angle with the substrate surface. In contrast to stacking faults in vapor grown silicon of other orientations described previously, none of the triangular etch figures observed in the grown layer of {211} orientation originated at the growth interface.

Dislocations Associated with Stacking Faults and the Interactions of Stacking Faults

The stacking faults in the crystal always terminate at partial dislocations, and the partial dislocations can have several structures (9). Attempts were made to reveal the dislocations associated with stacking faults by etching the vapor grown silicon on {111} substrates with Sailer's etch. It is generally recognized that all dislocations present in

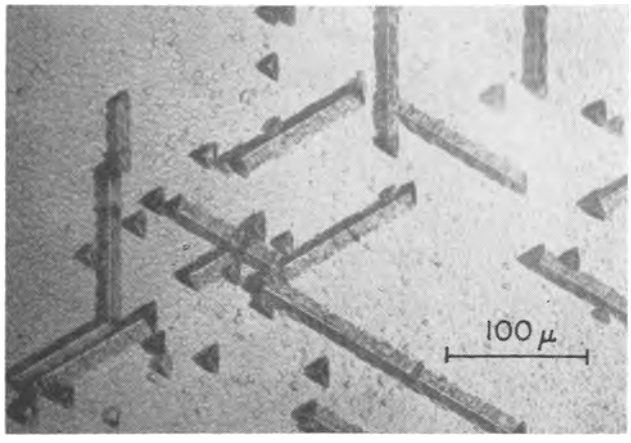

Fig. 5. Linear etch figures of stacking faults in vapor grown silicon on {111} substrate (as grown surface etched 4 hr with Sailer's etch).

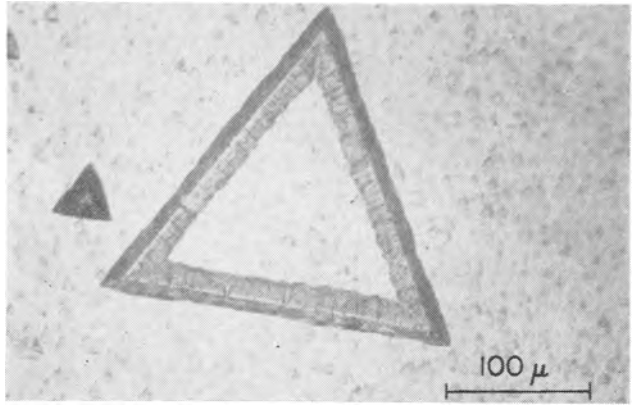

Fig. 7. Triangular etch figure of stacking fault in vapor grown silicon on {111} substrate (as grown surface etched 4 hr with Sailer's etch; approximate growth thickness, 180μ).

the silicon crystal, except those meeting the surface at shallow angles, are revealed by this etch.

The stacking faults yielding the linear etch figures are considered first. A number of lines and dislocation pits are shown in Fig. 5 where the grown surface was etched with Sailer's etch for 4 hr. If the grown surface were etched with the Dash etch for 15 to 20 min, these lines would have the same appearance as one side of the triangular etch figure shown in Fig. 1. It is noted from Fig. 5, and more clearly in Fig. 7 and 10, that the two sides of the etched "valley" are different in appearance. This difference enables one to determine the direction of propagation of the stacking faults with linear etch figures. The majority of the linear etch figures show a deep pit at each end, and the opposite sides of the ends are at 60° to each other. Schwuttke (5) and Booker and Stickler (4) have reported that the partial dislocations terminating the faults with linear etch figures possess $\frac{1}{6}$<112> Burgers vectors. On the basis of this result, it appears that this type of partial dislocation is revealed by Sailer's etch. During the gradual removal of the grown material, the etch pits at the position of the partial dislocations associated with the linear etch figure became close together. Figure 6 shows two linear etch figures where approximately 7μ of the grown material remained. On complete removal of the grown material, no imperfections could be detected in the substrate immediately below these faults.

Contrary to the linear etch figures of the stacking faults, deep pits are not associated with the vast majority of triangular etch figures. A typical etch figure is shown in Fig. 7 where three valleys form an equilateral triangle. No dislocation pits are seen along the valleys and inside the triangle. When the grown material was removed and subjected to Sailer's etch at various intervals, the etch figure retained the same structure. No imperfections were found immediately below the fault after complete removal of the grown material. Apparently, the partial dislocations associated with this type of fault are different from those associated with the faults with linear etch figures. In this case, the partial dislocations at the intersections of the adjacent {111} faulting planes have been shown to be of stair-rod type with $\frac{1}{6}$<110> Burgers vectors (4, 5). Presumably, this type of partial dislocation is not etched deeper by the Sailer etch than the stacking fault planes, thus making them undistinguishable.

Among the large number of specimens examined, a small percentage of the triangular etch figures

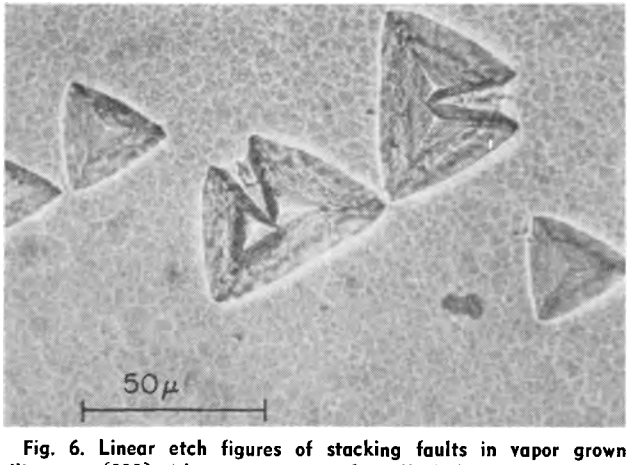

Fig. 6. Linear etch figures of stacking faults in vapor grown silicon on {111} substrate near interface (Sailer's etch 4 hr).

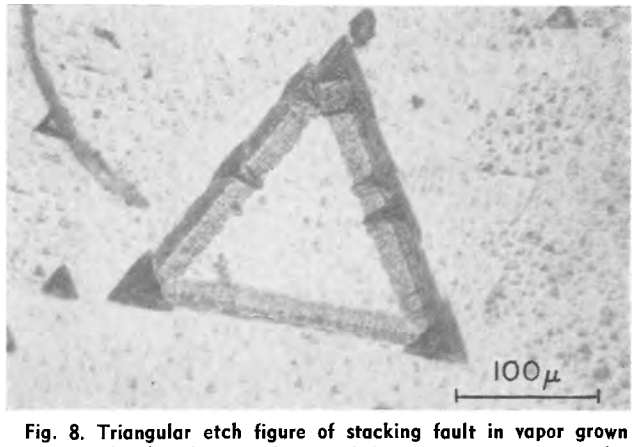

Fig. 8. Triangular etch figure of stacking fault in vapor grown silicon on {111} substrate showing dislocation pits at apexes (as grown surface etched 4 hr with Sailer's etch; approximate growth thickness, 180μ).

exhibited dislocation pits at one or more apexes. The interactions of faults may be responsible for the observed pits. Figure 8 shows the dislocation pits associated with the triangular etch figure where the grown surface was subjected to Sailer's etch. On partial removal of the grown material and subsequent etching with CP_4, nonintersecting lines resulted. Although the dislocation pits persisted through the grown material, no dislocation pits were found in the substrate immediately below the faults after complete removal of the grown material. Triangular etch figures with dislocation pits associated with two apexes have also been observed. It is possible in this case that a fault with a linear etch figure and a fault with a triangular etch figure are formed simultaneously at very small separations. The linear etch figure would not be distinguishable from a side of the triangular etch figure, and the pits seen could be associated with the linear etch figure.

The interactions of closely spaced faults usually yield complicated etch figures; an example is shown in Fig. 9 (Sailer's etch). In this figure, the regions ABCDEF and GHI resulted from the interactions of at least six and three faults, respectively. It is noted that the dislocation pits are not associated with the apexes of the component triangles, and that these faults were partially annihilated when interacting with each other. As the grown material was gradually removed, the complex faults resolved into their components, and the regions J and K increased in areas. If further growth had been allowed to take place, the triangular regions J and K would have eventually disappeared. On the other hand, when the faults had dislocation pits at the apexes of the triangular etch figure, the sides of the triangle interacting with other faults were not annihilated (Fig. 10).

Causes of Faulting

It has been mentioned previously that after complete removal of the grown material from the substrate, no structural imperfections, such as dislocations, could be detected in the substrate in the region below the stacking faults. Thus the faulting is not directly related to the structural defects in the substrate. It has been found that the growth parameters, such as substrate temperature, substrate doping level, reactant composition, growth rate, etc., do not have an observable influence on the concentration of stacking faults in the grown material.

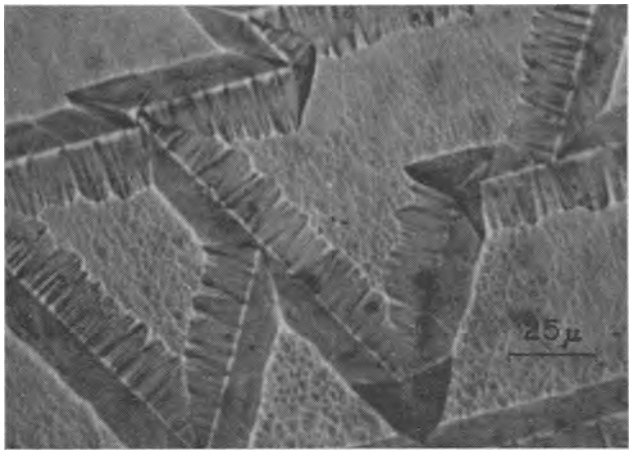

Fig. 10. Etch figure showing interactions of stacking faults in vapor grown silicon on {111} substrate (Sailer's etch 4 hr).

Most of the substrates used in this work were chemically etched. When mechanically polished substrates were used, the grown material generally had a high concentration of stacking faults. Furthermore, the faults with linear etch figures predominated. Since the mechanically damaged layer is believed to contain high concentrations of dislocations, it is possible that the stacking faults are caused by the splitting of these dislocations into partials. The two partials then continue at 60° to each other during the growth process, and a fault is formed between them. This mechanism has been suggested for the stacking fault formation in thin films deposited by vacuum evaporation technique (1).

When the substrate is free from mechanically damaged material, the impurities on the substrate surface and in the growth system were found to be mainly responsible for the stacking faults originating at the interface. Many sources of impurities, such as insufficiently cleaned substrate, solvent residue on the substrate surface, impure hydrogen, etc., could increase the fault concentration in the grown material.

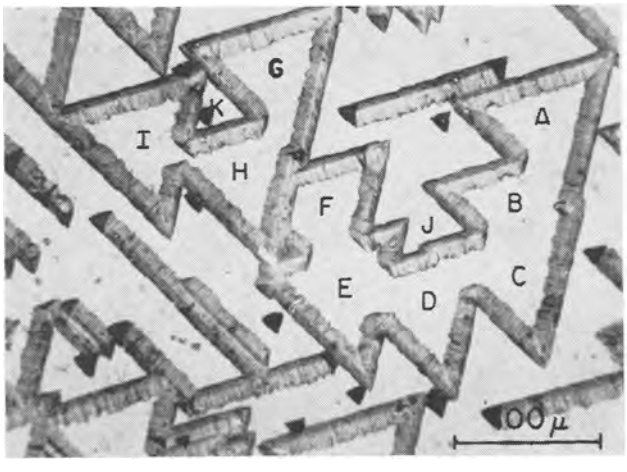

Fig. 9. Etch figure showing interactions of stacking faults in vapor grown silicon on {111} substrate (as grown surface etched 4 hr with Sailer's etch).

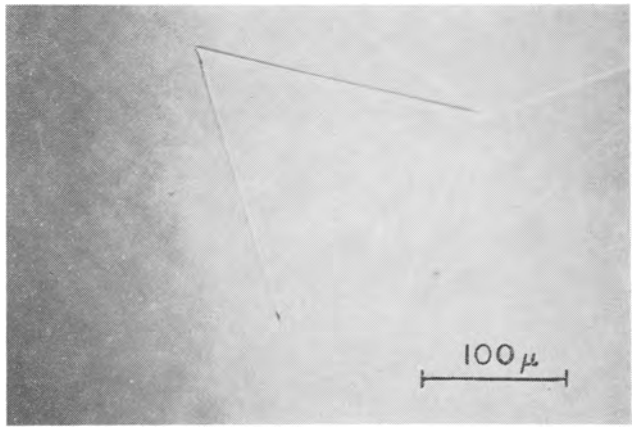

Fig. 11. Growth pyramid on the as grown {111} surface with a stacking fault at the apex; growth thickness, approximately 160μ).

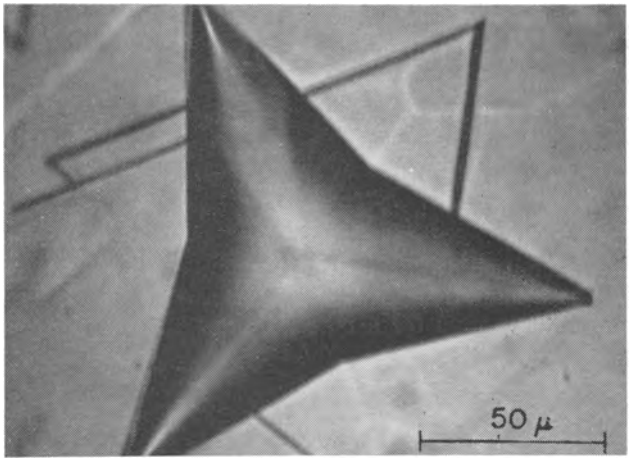

Fig. 12. Etch figure showing stacking faults associated with star-like hillock on the {111} surface (as grown surface etched 20 min with the Dash etch).

It has been pointed out previously that the stacking faults in the grown material do not all originate from the interface. The faults not originating at the interface were sometimes arranged in a straight line, along a <110> direction and this region of the grown material often had a very low dislocation density. It is unlikely that these faults were caused by impurities. Thus, the generation of local stress during the growth process apparently caused the formation of stacking faults. It is conceivable that some of the faults originating at the interface may also be caused by local stress.

Stacking faults are frequently found to be associated with other imperfections in vapor grown silicon. Figures 11 and 12 show the stacking faults associated, respectively, with a growth pyramid and a star-like hillock commonly observed on {111} oriented grown surfaces. These studies will be described in detail elsewhere (10).

The mechanism of the fault formation has been discussed by several investigators. Booker and Stickler (4) proposed that stacking faults form on the {111} plane parallel to the substrate surface and explained many of the experimental observations on the basis of this model. Queisser *et al.* (2) also suggested this type of growth mistake as one of the possible mechanisms.

Summary

The stacking faults in the vapor grown silicon on substrates of {111}, {110}, {100}, and {211} orientations take place along {111} planes in all cases, presumably because they are the lowest energy planes in silicon. The majority of the faults initiate from the growth interface. Impurities on the substrate surface, surface defects of the substrate, and deformation of the substrate are probably the principal causes of faulting.

Acknowledgments

The authors wish to thank G. R. Booker, J. W. Faust, H. F. John, S. O'Hara, and R. Stickler for discussions.

Manuscript received Sept. 13, 1962; revised manuscript received Nov. 2, 1962.

Any discussion of this paper will appear in a Discussion Section to be published in the December 1963 JOURNAL.

REFERENCES

1. See, for instance, G. A. Bassett, J. W. Menter, and D. W. Pashley, in "Structure and Properties of Thin Films," C. A. Neugebauer, J. W. Newkirk, and D. A. Vermilyea, Editors, p. 11, John Wiley & Son, New York (1959).
2. H. J. Queisser, R. H. Finch, and J. Washburn, *J. Appl. Phys.*, **33**, 1536 (1962).
3. T. B. Light, in "Metallurgy of Semiconductor Materials," T. B. Schroeder, Editor, Metallurgical Society Conferences, Vol. 15, p. 137, Interscience Publishing Co., New York (1962).
4. G. R. Booker and R. Stickler, to be published.
5. G. H. Schwuttke, *J. Appl. Phys.*, **33**, 1538 (1962). G. H. Schwuttke and V. Sils, Electrochem Soc. Electronics Division Abstracts, **11**, No. 1, 186 (1962).
6. W. C. Dash, *ibid.*, **33**, 2395 (1962).
7. H. G. van Bueren, "Imperfections in Crystals," p. 599, Interscience Publishing Co., New York (1961).
8. See, for instance, H. C. Theuerer, *This Journal*, **108**, 649 (1961).
9. W. T. Read, Jr., "Dislocations in Crystals," p. 92, McGraw-Hill Book Co., New York (1953).
10. T. L. Chu and J. R. Gavaler, to be published.

Correction

In the article by C. O. Thomas, D. Kahng, and R. C. Manz "Impurity Distribution in Epitaxial Silicon Films" which was published in the November 1962 issue of the *Journal*, Eq. [10] on page 1059 should read

$$N_y = N_o\alpha^y + \alpha bn\,(1 + \alpha + \ldots + \alpha^{y-1}) \quad [10]$$

Epitaxial Silicon Junctions

D. Kahng, C. O. Thomas, and R. C. Manz

Bell Telephone Laboratories, Incorporated, Murray Hill, New Jersey

ABSTRACT

In a preceding paper, the effect of the epitaxial silicon growth process on impurity distribution in the epitaxial film was treated in terms of a countercurrent model, and experimental results were presented for n-type films on n-type substrates. In the present paper, additional experimental data are presented for p-on-p, n-on-p, and p-on-n growth conditions.

For n-on-p, or p-on-n growth, the electrical junctions are shifted by the process a distance of x_j microns (the junction lag) from the substrate-film interface. The process-dominated junction lag may be much larger than that predicted from diffusion considerations. It is dependent on the film growth temerature and the doping levels in the substrate and in the gas phase. As predicted by the countercurrent distribution expression, it is greater for lower growth temperatures.

Junction lags from immeasurably small values up to greater than 30μ have been generated. There is quantitative agreement between the observed magnitude of the junction lag and the value predicted by use of the countercurrent distribution expression. Also, for those samples measured electrically (with junction lags of 1.8-4.8μ) the agreement between the measured mean impurity concentration level (by four-point probe measurements) in the epitaxial layer and the mean impurity level predicted on the basis of the distribution expression is quantitative.

At present there is considerable experimental evidence that in the growth of epitaxial silicon films by the hydrogen silicon-tetrachloride process in a flow system, dopant is able to exchange between the solid and the gas phase as indicated by the following expression.

$$(\text{dopant})_{\text{gas}} \underset{\text{b}}{\overset{\text{c}}{\rightleftarrows}} (\text{dopant})_{\text{reservoir}} \underset{\text{a}}{\overset{\text{d}}{\rightleftarrows}} (\text{dopant})_{\text{solid}} \qquad [1]$$

The exchange probably involves an intermediate reservoir which may be either an adsorbed layer or some working volume of gas near the surface. The results of such an exchange are illustrated by the effect of the silicon pedestal, of adjacent wafers in certain multislice systems, and of the back side of the substrate wafer itself on the epitaxial film doping (1, 2). In other words, the doping level in the epitaxial film is affected not only by the silicon-tetrachloride saturator doping level [or the injection level with phosphine or diborane doped hydrogen (3, 4)], but also by contributions from other sources in the system. Also, the doping level and distribution in the epitaxial film will be determined not only by the doping level of the ambient gas, but also by redistribution of dopant from the substrate surface on which the film is grown, since the exchange process indicated in Eq. [1] also will occur at the growing surface.

The chemical kinetics of epitaxial silicon growth have been discussed by Bylander (5) in terms of available experimental data. The chemical kinetics of epitaxial germanium growth have been discussed by Matovich and Andres (6), and by Grossman (7), who refer to the process dominated redistribution of substrate dopant as "autodoping." The kinetics of the germanium iodide disproportionation in a closed system have been discussed by Lever (8). However, the experimental chemical kinetics data at present appear to be inadequate for quantitative treatment of the dopant distribution in terms of specific chemical reactions. Nevertheless, it is possible to deal with the problem by means of a countercurrent approach, making no particular assumptions about the specific chemical reactions involved in the growth process.

We have previously described the countercurrent approach in detail (9). In this approach, we treat the film growth process as if the film grew by a series of discontinuous steps, with a, b, c, and d of Eq. [1] constituting a complete cycle, and a number of these cycles constituting film growth. It was also shown that this method leads to the generalized impurity distribution expression, Eq. [2].

$$N_x = N^*_o \, e^{-\phi x} + A(1 - e^{-\phi x}) \qquad [2]$$

where N_x is the doping concentration at x-microns from the substrate film interface. The first term on the right is the substrate contribution to the film doping, and the second term on the right is the total gas phase contribution to the film doping. Equation [2] defines the film doping distribution, exclusive of a thin diffusion dominated region near the film substrate interface (10), in terms of three measurable system parameters, N^*_o, ϕ, and A.

Previously, we have discussed the measurement of these three parameters and experimental determination of the doping profiles for n-type films on n-type substrates. In this paper we will discuss: (*a*) additional data relative to the experimental

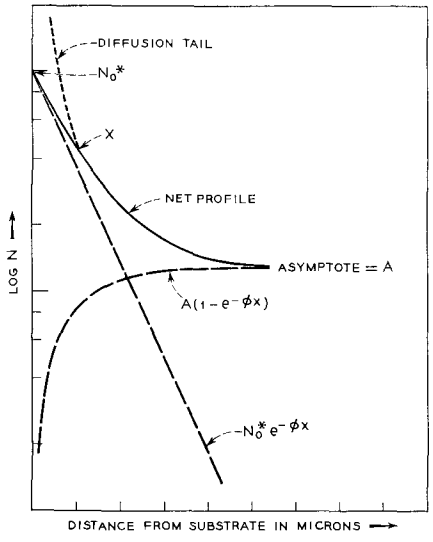

Fig. 1. Impurity profile components for epitaxial silicon film

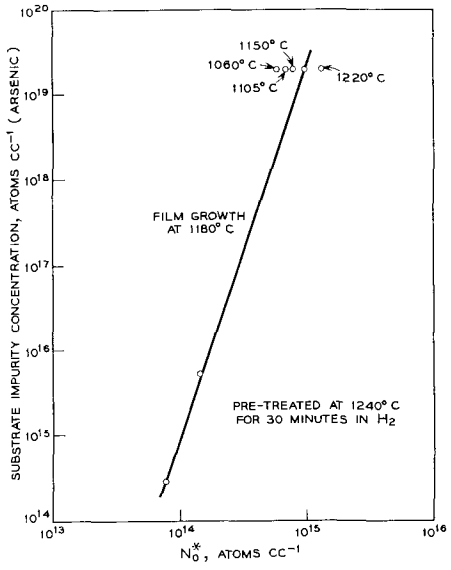

Fig. 2. Relationship between the intercept, N^*_o, and the substrate impurity level for films grown at 1180°C. Additional points for other film growth temperatures are shown at a substrate level of 2 x 10^{19}.

system parameters, including data for p-type doping; (b) the doping distribution for electrical junctions prepared by growing an epitaxial film of one conductivity type on a substrate of the other conductivity type; and (c) general aspects of the countercurrent redistribution of substrate dopant in an epitaxial film.

Experimental System Parameters

Figure 1 illustrates the profile components as given by Eq. [2] for an n-type film on an n-type substrate (or a p-type film on a p-type substrate). From the substrate-film interface out to about X the diffusion tail over rides the process effect. However, throughout the remainder of the film the profile is dominated by the process. For a film grown from a "pure" gas phase ($A < \sim 0.01$-$0.05\ N^*_o$) the profile is defined very closely by

$$N_x = N^*_o\ e^{-\phi x} \qquad [3]$$

Under this condition the intercept parameter (N^*_o) may be determined by extrapolation of the profile to the substrate film interface, and the slope parameter (ϕ) may be determined from the slope of the profile. The asymptote parameter (A) is determined by growing films thick enough to reach a steady-state doping level. For purified silicon tetrachloride (11) the asymptote, or steady-state level, appears to be less than about 5 x 10^{13} in the station used for these experiments.

The profiles are conveniently and accurately measured by means of a differential capacitance-voltage method described earlier (9). For n-type films on n-type substrates, shallow ($\frac{1}{4}\mu$) boron diffused diodes are used. For p-type films on p-type substrates aluminum surface barrier diodes are used.

Figure 2 shows the relationship between N^*_o and the substrate doping level for films grown at 1180°C on arsenic doped substrates. The relationship is somewhat sensitive to the film growth temperature as shown by the additional points at the 2 x 10^{19} level. The variation is probably real, since each point is an average based on 6-8 separately prepared films, with at least 6 diodes measured on each film. The sensitivity to the growth temperature is less for more lightly doped substrates. The line slope is about 10^4 for the range of growth temperatures indicated.

The relationship shown in Fig. 2 is quite sensitive to the heat treatment which the substrate receives prior to film growth. If the indicated heat treatment time is cut in half, the N^*_o value (for a 2 x 10^{19} substrate) may rise to more than 10^{16}. Consequently, we have used great care in maintaining run-to-run reproducibility of the pretreatment time and temperature. These observations suggest that the effective surface concentration at time-zero is determined by thermal leaching, and that, as the film grows, diffusion from the usually more heavily doped substrate over-rides the process profile near the interface.

Figure 3 illustrates the relationship between the film growth temperature and the profile slope parameter, ϕ, in μ^{-1} for both arsenic and boron doped substrates. This relationship is found experimentally to be independent of substrate doping level over about four orders of magnitude ($\sim 10^{15}$ to $\sim 10^{19}$). The points for arsenic doped substrates have been reported earlier (9). The points for boron doped substrates may lie on a line slightly divergent

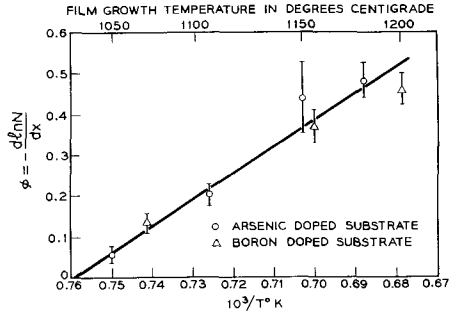

Fig. 3. Effect of film growth temperature upon the profile slope parameter, ϕ in μ^{-1}, for both arsenic and boron doping.

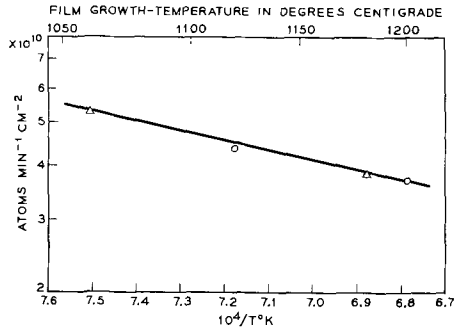

Fig. 4. Effect of film growth temperature on impurity deposition rate. ○, boron doped saturator. △, arsenic doped saturator. Rates are calculated for the asymptote or steady-state doping level in thick films.

from that for arsenic doped substrates. However, in view of the data spread we have not felt justified in making this distinction and have fitted one least squares line to the points. Thus, throughout the remainder of this paper the slope parameter, ϕ, at a given growth temperature is taken to be the same for both n-type and p-type dopants.

Figure 4 illustrates the observed variation of the steady-state doping level with film growth temperature in thick films. The rate parameter as plotted contains a correction for the variation in film growth rate with temperature. The n-type and the p-type saturators were chosen to give approximately the same doping levels for experimental reasons related to the junction studies discussed in the next section. Therefore, the agreement between the arsenic and boron points has no fundamental chemical significance. Figure 4 should not be interpreted as an activation energy plot for the impurity deposition for reasons to be considered in the Discussion section.

The numerical values of the three system parameters, (N^*_o, ϕ, and A) are characteristic of a given station and experimental conditions. All of the data shown in Fig. 2, 3, and 4 were obtained in one vertical, RF-heated, single slice station using a silicon pedestal without a doped insert. The gas flow rate was 2.5 l/min through a 32 mm ID deposition chamber. The total gas flow passed through the silicon tetrachloride saturator which was maintained at −40°C for all of the work.

Electrical Junctions

In a preceding paper we considered the impurity distribution for n-type films on n-type substrates. In this case, the net distribution expression is the sum of the two terms in Eq. [2]. In this section, making use of the additional data presented above, we will consider the case for electrical junctions prepared by growing a film of one conductivity type on a substrate of the opposite conductivity type. For this case, the first right-hand term of Eq. [2] gives the substrate contribution, for example, donors, and the second right-hand term of Eq. [2] gives the gas phase contribution, for example, acceptors. The net doping level at points on either side of the electrical junction will be given by the difference of these two terms as shown in Eq. [4].

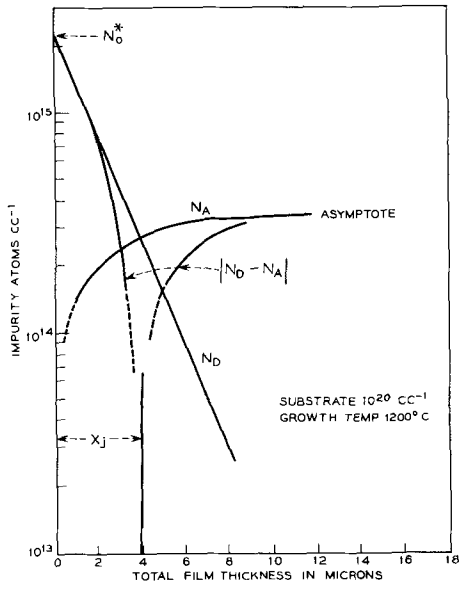

Fig. 5. Hypothetical profile components for p-type film on n-type substrate. Diffusion tail near interface not shown. Components are calculated from known values of N^*_o and ϕ, and an arbitrary value of the asymptote.

$$|N|_x = |N_D - N_A|_x = |N^*_o\ e^{-\phi x} - A(1 - e^{-\phi x})|_x \quad [4]$$

At the electrical junction the net doping concentration is zero, and we have

$$0 = |N_D - N_A|_j = |N^*_o\ e^{-\phi x_j} - A(1 - e^{-\phi x_j})|_j \quad [5]$$

Figure 5 illustrates the hypothetical profile components for a p-type film on an n-type substrate. The junction is located at x_j-microns from the substrate where $N_D = N_A$. The net profile on either side of the junction is also shown. There will also be a diffusion tail near the substrate.

The distance x_j is referred to in this paper as the junction lag. For a wide range of conditions, it may be much larger than that predicted from diffusion considerations alone, even allowing for anomalously high diffusion rates near the interface (10). For those situations where the process junction lag is greater than that predicted by diffusion, the value of x_j is determined almost entirely by the growth process itself.

Equation [5] may be solved explicitly for x_j in terms of the three experimental system parameters.

$$x_j = \phi^{-1} \ln(\eta + 1) \quad [6]$$

where

$$\eta = N^*_o/A \quad [7]$$

Figure 6 shows the predicted junction lag distance as a function of the system parameter η for selected film growth temperatures. A control line for a given system will cut across this family of curves on a bias rather than on the horizontal, since the value of η is a function of the film growth temperature (Fig. 2 and 4).

Figure 7 is a bevelled and stained cross section of a p-type film on an n^+-type substrate. The distance from the film surface to the electrical junction will be called the junction depth or p-layer

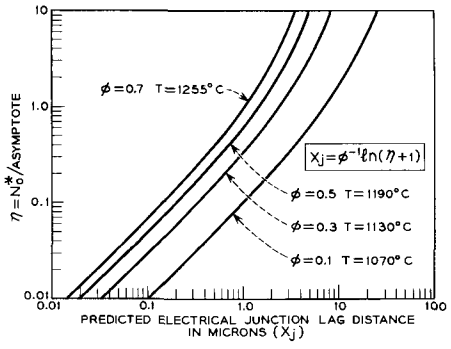

Fig. 6. Predicted junction lag distance computed for four growth temperatures.

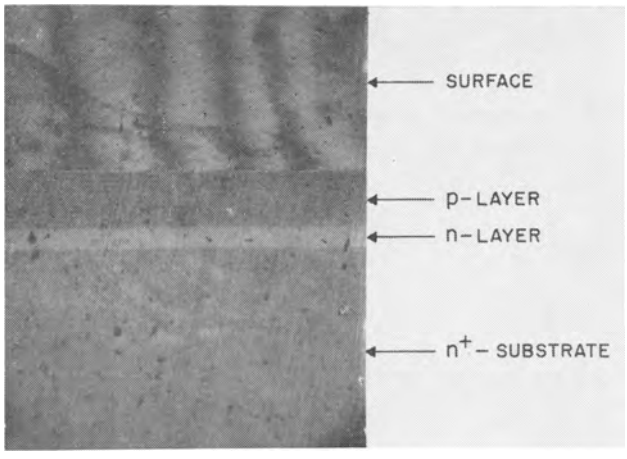

Fig. 7. Bevelled and stained cross section of a p-type film on an n^+-type substrate.

thickness. An n-layer in the film also is shown in Fig. 7. The thickness of this n-layer, or the distance from the substrate to the junction, is the junction lag distance. It is not always possible to bring out a triple stain as shown in Fig. 7, particularly with n-type films on p-type substrates. Furthermore, there may be some question as to whether the n-layer thickness as shown in Fig. 7 is in fact equal to the junction lag distance as defined by the distribution expression. Therefore, the junction lag distance also is determined experimentally as follows.

A number of individual films are grown for different growth times and growth temperatures under otherwise identical conditions. The growth times and temperatures are randomized to minimize the effect of system drift. The samples are then bevelled and stained as shown in Fig. 7. The p-layer thickness for a given growth temperature is then plotted *vs.* growth time as shown by the upper curve in Fig. 8. The straight line for the upper curve is fitted by least squares, which also yields a calculated slope and intercept for the line. The slope is the film growth rate at the given temperature, and the intercept is the distance to the substrate from the electrical junction, the junction lag. Similar rate plots for n-type films on n^+-type substrates yield calculated intercepts of $0 \pm 0.2\mu$, which indicates that extrapolation of a rate plot to zero time is a valid method for locating the substrate film interface within the precision stated here. Also, in Fig.

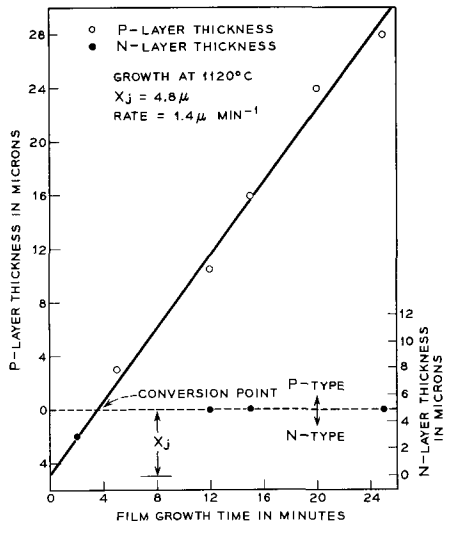

Fig. 8. Plot illustrating experimental determination of junction lag for a p-type film grown at 1120°C on an n^+-type (2×10^{19} arsenic) substrate.

8 we have plotted the directly measured n-layer thicknesses from the photographs for the same samples. For films thick enough to have developed a junction, the n-layer thickness is constant and equal to the junction lag within the accuracy of the measurement. The junction lag for these particular conditions is found to be 4.8μ. For films too thin to have developed a junction, the n-layer thicknesses follow a curve with a slope equal to the film growth rate.

Figure 9 illustrates the junction lag at a higher growth temperature. Here again, for films thick enough to have developed a junction, the n-layer thickness is constant and equal to the junction lag within the accuracy of the measurement. The junction lag here is 4.3μ. For films too thin to have developed a junction, the n-layer thickness again follows a curve with a slope equal to the film growth rate.

The data in Fig. 8 and 9 show that the junction lag, as predicted, is greater at the lower growth

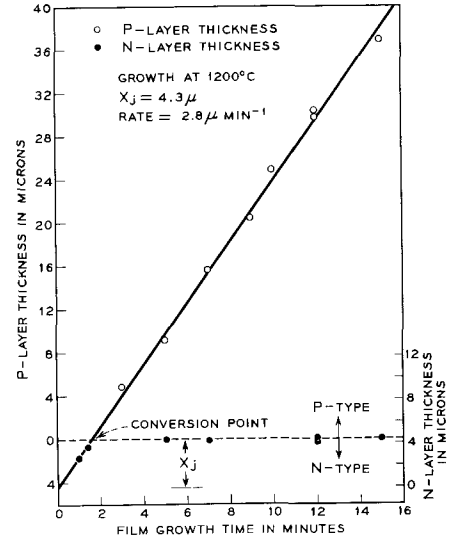

Fig. 9. Plot illustrating experimental determination of junction lag for a p-type film grown at 1200°C on an n^+-type (2×10^{19} arsenic) substrate.

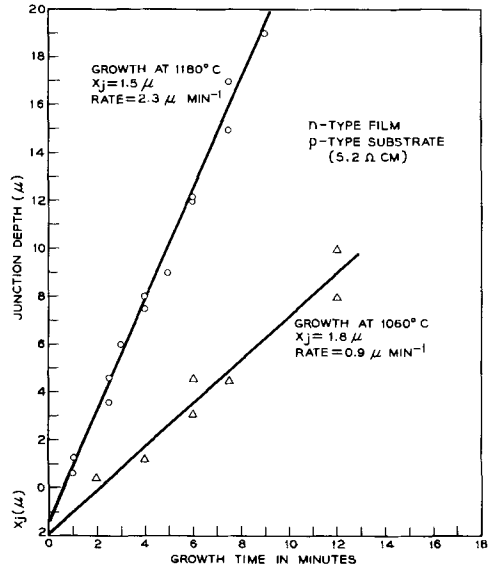

Fig. 10. Plot illustrating experimental determination of junction lag for n-type films grown at 1060°C and at 1180°C on p-type (3 x 10^{15} boron) substrates.

temperature. This fact plus the magnitude (4-5μ) of the lag indicate that it is not a diffusion-dominated phenomenon.

Figure 10 illustrates the junction lag effect for n-type films on p-type substrates. Here again, the lag is greater at the lower growth temperature. For these samples, we were not able to stain the intermediate p-layer, and so only the upper rate curves are shown. The slope and intercept for these two curves are again calculated by least squares.

The data in Fig. 8, 9, and 10 were selected for presentation here because the junction lag is large enough to illustrate the effect but small enough for convenient plotting. However, by proper choice of the substrate and gas-phase doping levels, we have been able to generate junction lags from values too small to measure up to greater than 30μ.

The experimental measurement of the junction lag has been described above. For a quantitative comparison of experiment and theory, we proceed as follows, using the data in Fig. 8 for illustration. The value of x_j is 4.8μ at 1120°C (from least squares calculation). The required value of η can then be found from Fig. 6, or by solving Eq. [6], and is 2.49. The value of N^*_o for the stated experimental conditions (Fig. 2) is 8 x 10^{14}. The required value of A is then calculated to be 3.2 x 10^{14}. The experimental value of ϕ (Fig. 3) for this growth temperature is 0.26 μ^{-1}. Now from the two experimentally known system parameters, N^*_o and ϕ, and the calculated value of A required to satisfy the observed junction lag condition, we construct the profile components shown by the solid lines in Fig. 11. These are the substrate contribution

$$N_{D,x} = (8 \times 10^{14})\, e^{-0.26x} \qquad [8]$$

and the gas-phase contribution

$$N_{A,x} = (3.2 \times 10^{14})\,(1 - e^{-0.26x}) \qquad [9]$$

The net profile on either side of the junction is given by

$$|N|_x = |N_{D,x} - N_{A,x}| \qquad [10]$$

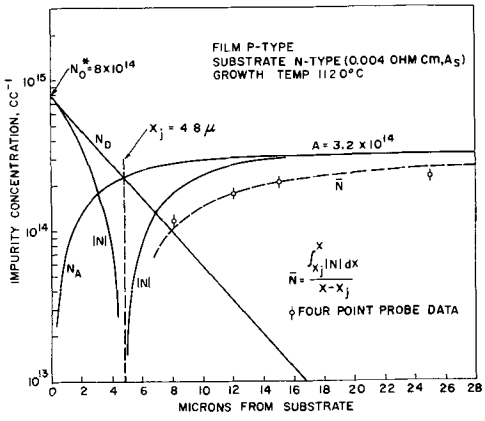

Fig. 11. Plot illustrating use of mean film resistivity (four-point probe) measurements for verification of impurity profiles.

These are the profile components calculable from the distribution expression for the particular experimental conditions.

If these in fact are the true distributions of donors, acceptors, and net impurity levels, then the mean impurity level in a p-layer $(x - x_j)$-microns thick, is given by

$$\overline{N}_x = \frac{\int_{x_j}^{x} \left| N^*_o\, e^{-\phi x} - A(1 - e^{-\phi x}) \right| dx}{x - x_j} \qquad [11]$$

The dashed line in Fig. 11 is the calculated required $\overline{N}_x$ curve. The circles indicate four-point probe[1] measurements on samples from this set of experiments at 1120°C, and the vertical lines indicate the spread in the measurements. The agreement between the measured mean impurity level in the p-layer and the mean impurity level predicted on the basis of the distribution expression is quite good. Similar agreement for the data in Fig. 9 and 10 also is found.

Discussion

Countercurrent concept.—Here and in the preceding paper we have used the concept of a discontinuous countercurrent process as a model from which a mathematical analysis of a continuous process is developed. There are a number of chemical separation processes, such as extraction, which may be experimentally conducted in either a discontinuous or a continuous manner. In the mathematical treatment of the discontinuous process, one may assume that the process is allowed to reach an equilibrium condition at each step before proceeding to the next step. In a continuous process, equilibrium generally is not attained. However, the effectiveness of the continuous process is rated in terms of the number of theoretical equilibrations needed to produce the distribution or degree of impurity separation observed experimentally in the process. Furthermore, if the individual steps of a discontinuous process are decreased in size and increased in number, then the mathematical distribution expression and the experimentally observed distribution approach the form of those in a con-

[1] Data of J. C. Irvin, published in *Bell System Tech. J.*, **41**, 387 (1962), were used to convert resistivity to impurity concentration.

tinuous process (12-14). There are other chemical separations, such as distillation (15, 16) or chromatography (17-19) which are normally conducted in a continuous manner, but for which the distribution mathematics can be successfully treated in terms of a hypothetical discontinuous process.

In addition to the above, the various processes have received extensive treatment (20-23) in terms of their kinetics and mechanisms. It has been shown that there is similarity in form between the conclusions reached from a discontinuous countercurrent argument, and those one reaches starting with kinetics assumptions. We have not considered the specific kinetics of the epitaxial process in terms of its effect upon impurity distribution since we feel that the experimental data is inadequate at this point.

Etch-back.—There is implicit in the discontinuous countercurrent model, as we have stated it, the concept of an "etch-back." We have shown (9) that for a substrate with a uniform impurity level of 2 x 10^{19} the required hypothetical etch-back distance is only 1-2Å. However, the substrate donor impurity level probably is reduced near its surface due to thermal leaching during the preheat treatment. Consequently, the required etch-back distance will be greater than the minimum 1-2Å. The effective substrate surface concentration at time-zero, obtained by profile extrapolation, is about 10^{15} for a 2 x 10^{19} substrate. This sets a maximum upper limit of about a micron for the etch-back, with a probable value somewhere between the two limits.

The estimation of etch-back distance involves data from experiments where the gas-phase contribution is insignificant. Hence, the total number of impurity atoms available for redistribution must come initially from the substrate. Furthermore, at time-zero the reservoir is empty. However, after the film growth is started, some of these impurity atoms are present in the reservoir. Therefore, one may not calculate an etch-back distance for the y^{th} cycle in the process by integration of the profile from x_y to x_∞. To do so would imply that the reservoir is empty at this point, which is no longer the case.

The occurrence of a literal physical etch-back for some small distance early in the growth process could, from chemical arguments, be a reasonable possibility (24). However, it is not a required feature of a countercurrent model. For example, assume the reservoir to be an adsorbed layer of impurity atoms at the surface. These may have originated, for example, from thermal leaching of the substrate, although specification of a particular mechanism of their origin again is not a necessary requisite for the countercurrent model. Earlier experimental results indicate that the postulated adsorbed layer must contain about 2 x 10^{11} impurity atoms per square centimeter, (for our experimental conditions) or a very small fraction of a monolayer. In this case, the steps of the hypothetical discontinuous process involve equilibration of the layer with its immediate environment, rather than an etch-back.

General system effects.—The magnitude of the process-controlled redistribution of impurity is dependent on the specific experimental conditions, such as substrate doping level, growth temperature, and gas-phase doping level. It also should be dependent on the specific chemistry of the process. For example, it is reasonable to expect that quantitatively significant differences may exist between germanium and silicon growth processes, and that such differences may also exist, for example, between a chloride and an iodide process. Therefore, the numerical results reported here and in the preceding paper should clearly be understood to apply to the process and the experimental conditions as stated in these papers. However, for a film growth process which operates as indicated by Eq. [1], the process effect on the impurity distribution will be qualitatively described by the countercurrent distribution expression. The quantitative magnitude of the process effect will, however, depend on the specific experimental conditions.

Impurity deposition rate.—In Fig. 4, we have shown the manner in which the steady-state doping level is observed to vary as a function of the growth temperature. If one interprets this plot literally as showing the temperature dependence of the reduction of the gas-phase doping compound to solid-state doping atoms, then a negative activation energy is implied. However, two other possible explanations are immediately obvious. It is known that there is a significant amount of side reaction in the H_2-$SiCl_4$ process. If the side reactions compete more effectively for dopant at the higher temperatures, then results as shown in Fig. 4 might be expected. Also it is possible that the vapor pressure of the dopant over the solid increases with temperature sufficiently to cause the effects shown in Fig. 4 by a reduction in the "sticking probability" for the dopant atoms relative to that for silicon.

Apparent activation energy.—In the measurement of the junction lag as shown in Fig. 8, 9, and 10 one obtains as by-product information the film growth rates at four temperatures. These silicon growth rates are plotted *vs.* the reciprocal temperature in Fig. 12. The apparent activation energy calculated from Fig. 12 is 30.5 kcal/mole which is in agreement with the value found from growth rates of n-type films on n^+-type substrates. The comparison is for an air-cooled wall in both film growth stations. The vertical displacement of the lines relative to each other is accounted for by the fact that absolute film growth rates vary from one apparatus to another. However, the slope, which should be characteristic of the reaction, remains constant.

Theuerer (25) has reported a value of 37 kcal/mole for the apparent activation energy of this reaction. Theuerer's data includes two points at growth temperatures below 1050°C. Two of our data points for film growth temperatures below about 1050°C lie below the lines shown in Fig. 12 and have been omitted in calculating the activation energy. If these points were included, the line slope and the apparent activation energy would be higher. We have omitted these points since there appears to be a bend in the curve at about 1000°-1050°C. Also,

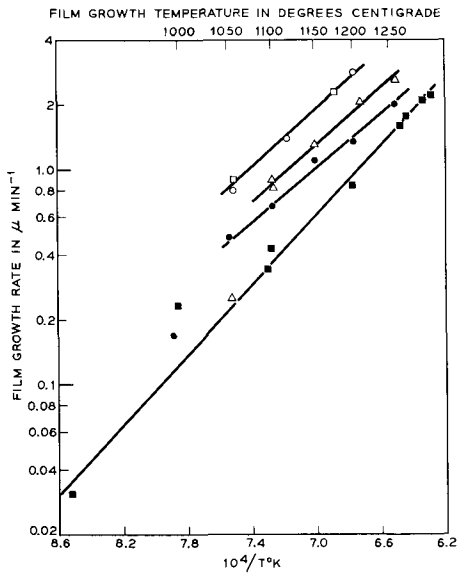

Fig. 12. Rate plots for calculation of effective activation energy. From present junction lag work with air-cooled station, E_a = 30.5 kcal/mol for ○ = p-type film on n-type substrate, and □ = n-type film on p-type substrate. For n-type films on n^+-type substrates in a separate air-cooled station (△) E_a = 30.5 kcal/mole. For n-type films grown on n^+-type substrates in a separate water-cooled station (•) E_a = 29.5 kcal/mole. ■ = Theuerer (25).

for the experimental conditions described here, 1000°-1050°C is an approximate minimum growth temperature for the preparation of smooth epitaxial silicon films of acceptable device quality.

Summary

We have reported the extension of earlier experimental work to n-type films on p-type substrates and to p-type films on both n and p-type substrates. The impurity distribution expression reported earlier was found to be applicable to these three situations also. In addition, the three empirical system parameters were found (within the precision of the measurements) to be numerically interchangeable for p-type and n-type impurities if all other film growth conditions are held constant.

A specific consequence on the process-dominated distribution of impurities in the film is illustrated by the "junction lag." The junction lag is the distance from the electrical junction to the substrate-film interface for films of one conductivity type grown on substrates of the other conductivity type. Diffusion from the normally more heavily doped substrate into the film will, of course, produce such a shift. However, under a wide range of conditions the film growth process itself may produce a much larger shift than does diffusion. In these cases, the magnitude of the process effect varies inversely with the film growth temperature.

There are experimental conditions for which the process effect on the impurity profiles, discussed here and in the preceding paper, may be minor. There are other conditions under which the effects may be quite significant. The countercurrent distribution approach has been shown to provide a practical and quantitatively usable tool for dealing with the problem, making use of only three experimentally measurable system parameters.

Acknowledgments

The authors appreciate the assistance of C. D. Thurmond in discussion of the theory and implications of this work, and of A. Loya in making electrical measurements.

Manuscript received Sept. 13, 1962; revised manuscript received Nov. 2, 1962. This paper was prepared for delivery before the Los Angeles Meeting, May 6-10, 1962.

Any discussion of this paper will appear in a Discussion Section to be published in the December 1963 JOURNAL.

REFERENCES

1. H. Basseches, R. C. Manz, C. O. Thomas, and S. K. Tung, "Proceedings of the AIME Technical Conference on the Metallurgy of Semiconductor Materials," Interscience Publishers, New York (1962).
2. V. Y. Doo, Paper presented at Semiconductor Symposium (Recent News Note), Electrochemical Society Meeting, Los Angeles, May 1962.
3. V. Sils, R. Berkstresser, and P. Wang, *ibid.*
4. W. J. Corrigan, *ibid.*
5. E. G. Bylander, *ibid.*
6. E. Matovich and R. J. Andres, Paper presented at Semiconductor Symposium, Electrochemical Society Meeting, Detroit, October 1961.
7. J. J. Grossman, Paper presented at Semiconductor Symposium, Electrochemical Society Meeting, Los Angeles, May 1962.
8. R. F. Lever, *ibid.*
9. C. O. Thomas, D. Kahng, and R. C. Manz, *This Journal*, **109**, 1055 (1962).
10. D. Kahng, C. O. Thomas, and R. C. Manz, *ibid.*, **109**, 1106 (1962).
11. H. C. Theuerer, *J. Metals*, **8**, 688 (1956).
12. L. C. Craig and D. Craig in "Techniques of Organic Chemistry," Vol. III, Part I, pp. 171-173, 185-197, A. Weissberger, Editor, Interscience Publishers, New York (1956).
13. E. G. Scheibel, *ibid.*, p. 334ff.
14. L. C. Craig, *J. Biol. Chem.*, **155**, 519 (1944).
15. A. Rose and E. Rose in "Techniques of Organic Chemistry," Vol. IV, Chap. I and pp. 109-111, A. Weissberger, Editor, Interscience Publisher, New York (1951).
16. A. Rose and L. M. Welshans, *Ind. Eng. Chem.*, **32**, 671 (1940).
17. A. J. P. Martin and R. L. M. Synge, *Biochem. J.*, **35**, 1358 (1941).
18. A. I. M. Keulemans, "Gas Chromatography," p. 106-115, Reinhold Publishing Co., New York (1957).
19. C. Phillips, "Gas Chromatography," pp. 11-16, Academic Press, New York (1956).
20. A. Klinkenberg and F. Sjenitzer, *Chem. Eng. Sci.*, **5**, 258 (1956).
21. E. Glueckauf, *Trans. Faraday Soc.*, **51**, 34 (1955).
22. J. C. Giddings and H. Eyring, *J. Phys. Chem.*, **59**, 416 (1955).
23. J. J. van Deemter, F. J. Zuiderweg, and A. Klinkenberg, *Chem. Eng. Sci.*, **5**, 271 (1956).
24. H. Schafer and J. Nickl, *Z. anorg. u allgem. Chem.*, **274**, 255 (1953).
25. H. C. Theuerer, *This Journal*, **108**, 649 (1961).

SYMBOLS

N	atoms cc^{-1} of dopant in the solid phase.
N^*_o	effective dopant concentration at the interface, atoms cc^{-1}.
x	distance in microns from the substrate.
A	asymptotic limit of doping profile, atoms cc^{-1}.
ϕ	profile slope parameter, μ^{-1}.
x_j	junction lag distance in microns produced by the film growth process.
η	N^*_o/A.
$\overline{N_x}$	mean impurity level, atoms cc^{-1}, for a film thickness of x microns with the junction at x_j microns from the substrate.

Epitaxial Growth and Properties of ZnTe-CdS Heterojunctions[1]

M. Aven and W. Garwacki

Research Laboratory, General Electric Company, Schenectady, New York

ABSTRACT

Epitaxial junctions between ZnTe and CdS have been prepared by vapor deposition of CdS on ZnTe single crystals. Study of the growth habits of CdS on ZnTe have shown that an epitaxial deposit of CdS can be obtained only on the $(111)_{Zn}$ faces of ZnTe under the employed experimental conditions. Double injection behavior has been observed in heterojunctions with wide compensated regions between the p and the n parts of the junction. A tentative band model has been proposed for the ZnTe-CdS junctions on the basis of the experimental findings.

Recent interest in semiconductor devices prepared from wide band gap semiconductors has led to active work on several binary compounds of the IV-IV and III-V class. In the II-VI family of compounds similar work has been lagging because of the difficulty of preparing them in both strongly n-type and p-type form at room temperature. While several of the wide band gap II-VI compounds have been prepared with good n-type conductivity, the only compound which has shown low enough resistivity in p-type form to be useful in p-n junction devices is ZnTe. Unfortunately, ZnTe is also the only II-VI compound which cannot be made easily in n-type form. Therefore the attempts in preparing well-defined p-n homojunctions from II-VI compounds have not been successful in the past.

A different approach to this problem is to prepare the junctions from two different compounds one of which can be made n-type and the other p-type with suitable carrier concentrations and transport properties. In the past such heterojunctions have been prepared from Ge-GaAs by Anderson (1), from GaAs-GaP by Holonyak *et al.* (2), and from Ge-GaP by Van Ruyven and Dekker (3). Preliminary work on the ZnTe-CdS system has been reported by Aven and Cook (4).

In the preparation of junctions from two different materials it is important to choose these materials so as to minimize the difference in lattice constants and bandgaps between the p-type and the n-type side of the junction. Of the wide bandgap II-VI compounds the most suitable combination from this standpoint is the junction between n-type CdS and p-type ZnTe. These two compounds differ by less than 0.2 ev in bandgap, and by 0.08Å in average bond length. ZnTe is cubic and CdS is hexagonal which, however, is no impediment for epitaxial junction formation, as will be shown below. ZnTe can be made p-type with as low as 0.1 ohm-cm resistivity and a hole mobility of about 100 cm²/volt sec. CdS is a well-known n-type semiconductor and can be prepared with doping levels from near-intrinsic to degenerate. It has a room temperature intrinsic mobility of 350 cm²/volt sec.

[1] Sponsored by the Air Force Cambridge Research Laboratories Contract No. AF-19(604)-8512.

Experimental

The experimental arrangement for growing the ZnTe-CdS junctions is shown in Fig. 1. It consists of a 2.2 cm ID quartz tube which can be connected, through appropriate valving, to high vacuum, or a source of purified hydrogen. Placed concentrically around the tube are two resistance furnaces, approximately 20 cm apart. One end of the tube is provided with a magnetically operated device which serves to transfer the crystals inside the tube from the etch into the charge furnace. In a typical junction growing run, a quartz boat containing 10g of prefired CdS powder is placed in one end of the tube, and a similar boat with a diamond-polished single crystal of ZnTe in the other. The tube is evacuated, and the temperature of the charge and the etch furnace is slowly raised to 500° and 700°C, respectively. During this period the tube is flushed three or four times, and left with approximately 600 mm Hg of purified hydrogen. The etch furnace then is raised to 740°C, at which temperature the ZnTe crystal starts evaporating at a slow rate. While the ZnTe crystal is kept at this temperature, the CdS powder

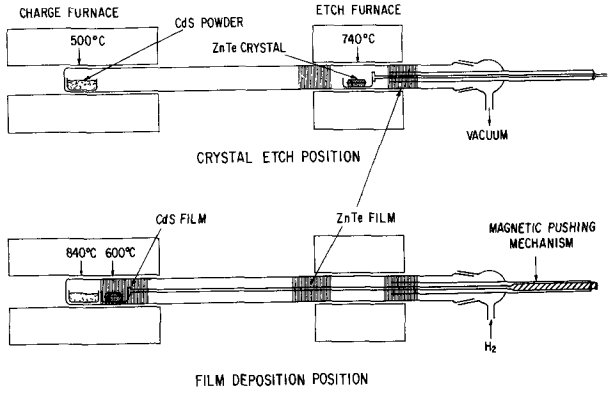

Fig. 1. Experimental arrangement for growing epitaxial ZnTe-CdS junctions.

is raised to 840°C. When a CdS film starts depositing on the walls of the tube, the ZnTe crystal is pushed into the position in the charge furnace corresponding to approximately 600°C, whereupon CdS starts growing on the ZnTe crystal. At this temperature the rate of growth of CdS on ZnTe is approximately 1.5 μ/min.

The choice of the above temperatures was based on the following considerations. The reaction CdS + ZnTe → CdTe + ZnS proceeds in the indicated direction with a free energy change of approximately −10 kcal/mole. Therefore, since CdS and ZnTe will react to form CdTe and ZnS if provided with sufficient activation energy, the film deposition should be carried out at as low a temperature as possible (ΔF does not vary significantly with temperature). On the other hand, the ZnTe crystal has to be kept at as high temperature as possible to prevent surface contamination by adsorbed impurities. It was found by experimentation that a suitable compromise was to keep the evaporating CdS and ZnTe spacially separated during the period of thermal etch, and to execute the transfer of the ZnTe crystal from the etch to the charge furnace so as to have the crystal temperature below 700°C but above 600°C when it arrives in the etch furnace. Adherence to this schedule has always produced junctions which show no extraneous phases under x-ray or electron diffraction analysis. Accidental deviations from the indicated temperature schedule, however, have often produced readily observable deposits of ZnS.

The p-type conductivity of the ZnTe substrate crystals was controlled by suitable doping with Cu and firing in Zn or Te atmospheres prior to film deposition. The n-type conductivity of the CdS film could be varied by varying either the partial pressure of hydrogen in the film growing apparatus or by varying the concentration of the Ga dopant in the CdS powder charge. An increase in either produced an increase in the n-type conductivity of the film. As changing the partial pressure of hydrogen during film deposition changed the film growth rate, it was preferred to perform the deposition runs at a constant hydrogen pressure (600 mm Hg) and modify the conductivity of the film by Ga doping alone.

Figure 2 shows a schematic sketch of a ZnTe-CdS junction with electrodes attached. The In contact to the CdS film is attached immediately after the film deposition run by pressing an In dot on the surface of the film and fusing it in under argon atmosphere at 250°C. The In contact and a small area of the film around the contact is then masked off with glyptal cement. After the cement has dried, the crystal is etched with cold 1:1 HCl to remove the CdS film from the ZnTe crystal, except under and around the In contact, and with 50% warm NaOH to clean the ZnTe face opposite the CdS film. The contact to ZnTe is made by chemically forming a large area deposit of Au on it, and fusing a dot of Ag-In alloy to the Au. If prepared by the above described technique, the resistance of the In contact to CdS is completely negligible (4-probe and 2-probe resistivity measurements give identical results). The Au contact to ZnTe is also ohmic but since its resistance is not negligible, it is preferred to make it a large area (2-4 mm^2) contact.

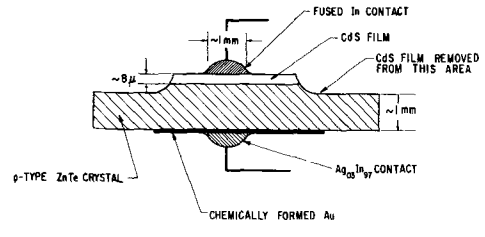

Fig. 2. External structure of ZnTe-CdS diodes

Results

By growing the CdS film on different crystallographic faces of the ZnTe substrate it was found that the quality of the film depended critically on the orientation of the substrate crystal. Film depositions on the (110) cleavage planes, on the (112) planes, or the (111) planes containing the Te atoms invariably resulted in multicrystalline deposits. Only the (111) planes containing the Zn atoms led to single-crystalline CdS films, as evidenced by spot Laue patterns under x-ray diffraction analysis. Figure 3A shows a photomicrograph of one such single-crystalline CdS deposit. As a contrast, Fig. 3B displays a photomicrograph of a CdS deposit on a ZnTe crystal containing a mis-oriented twin. The film growth on the twin is polycrystalline and extends in many places even beyond the twin boundary onto the correctly oriented face.

In order to determine the reason for this growth habit, the reactivities of the $(111)_{Zn}$ and the $(111)_{Te}$ crystallographic faces were studied under chemical and thermal etch conditions. Figure 4 shows the photomicrographs of a ZnTe crystal treated with hot NaOH. Figure 4A displays the $(111)_{Te}$ face and Fig. 4B the $(111)_{Zn}$ face. The Te side contains large shallow triangular structures and is almost specularly reflecting, while the Zn face has a silvery sheen produced by the many reflections off the sides of the small deep etch pits.

The appearance of a pair of ZnTe crystals, oriented with the $(111)_{Zn}$ and the $(111)_{Te}$ faces up, respectively, and thermally etched under conditions

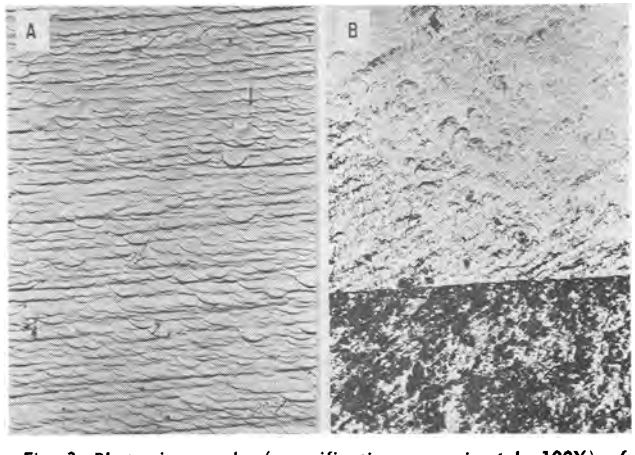

Fig. 3. Photomicrographs (magnification approximately 100X) of CdS deposits on ZnTe: A, Epitaxial deposit on $(111)_{Zn}$ face; B, polycrystalline growth on a misoriented twin (dark area).

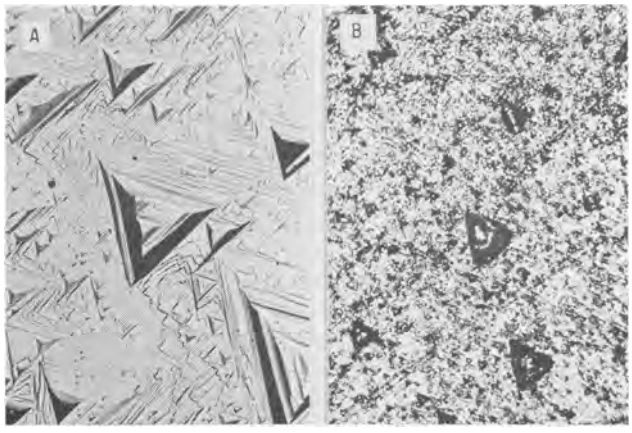

Fig. 4. Photomicrographs (magnification approximately 110X) of a ZnTe crystal treated with NaOH; A, $(111)_{Te}$ face; B, $(111)_{Zn}$ face.

identical to a regular junction fabrication run is shown in Fig. 5. Now the crystal oriented with the $(111)_{Zn}$ face up has a relatively smooth finish, with occasional shallow triangular etch pits. The $(111)_{Te}$ face, on the other hand, exhibits deep canyon-like structures with a few triangular etch pits at the bottoms of the canyons. The distance between the bottoms and ridges of the canyons is between 0.1 and 0.2 mm.

Figure 6 shows a schematic representation of the internal structure of a ZnTe-CdS junction. This junction was lapped at an angle of 1° to the junction plane to produce a magnified cross-section through the film. Under u.v. excitation the outer surface of the CdS film is green-luminescent,[1] while the ZnTe substrate crystal shows no luminescent response in the visible spectral range. Between the outer CdS layer and the ZnTe substrate one can see a red-luminescent streak which has a width (in the actual crystal) of approximately 4μ. The total thickness of the film in this crystal was 8μ. From separate experiments with CdS films it was established that under the employed conditions of film deposition, red luminescence was observed in CdS films which were compensated to a high degree. Green-luminescent films, on the other hand, were obtained under conditions which minimized compensation.

[1] Heavily Ga-doped films are green-luminescent at both room and liquid N_2 temperatures, while lightly doped films show green luminescence only at liquid N_2 temperature.

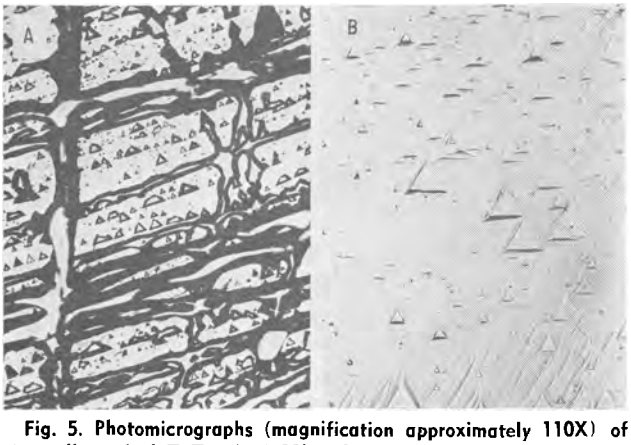

Fig. 5. Photomicrographs (magnification approximately 110X) of thermally etched ZnTe: A, $(111)_{Te}$ face; B, $(111)_{Zn}$ face.

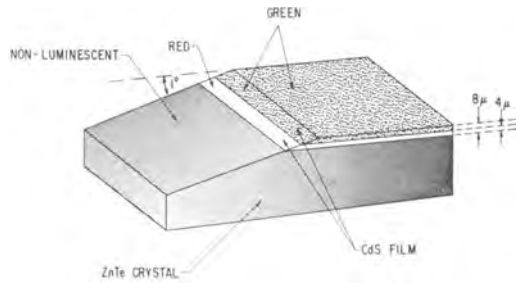

Fig. 6. Pattern of fluorescent response of angle-lapped ZnTe-CdS junctions.

The red-luminescent films were weakly n-type or insulating, while the green-luminescent films were strongly n-type.

Figure 7 shows the current-voltage characteristic of a ZnTe-CdS junction at room temperature. The characteristic exhibits an exponential region between approximately 10^{-7} and 10^{-4} amp, with a slope of $q/2kT$, where q is the electronic charge, k is the Boltzmann constant, and T is the temperature. At both low and high voltages the characteristic deviates from exponential behavior, showing excess current at low voltages and a gradual transition to linear behavior at high voltages. The extrapolated intercept of the exponential portion of the curve on the current axis, often referred to as the saturation current I_o, is approximately 10^{-9} amp. The forward to reverse current ratio at 1v is about 10^4. Many of the ZnTe-CdS diodes have also shown exponential portions of the forward characteristic with slopes lower than $q/2kT$, the lowest slopes usually being exhibited by diodes in which the resistivity of the CdS film is very low. The saturation currents have, generally, ranged between 10^{-8} and 10^{-10} amp (for 1 mm^2 junctions), and have shown very little change with temperature at or below room temperature.

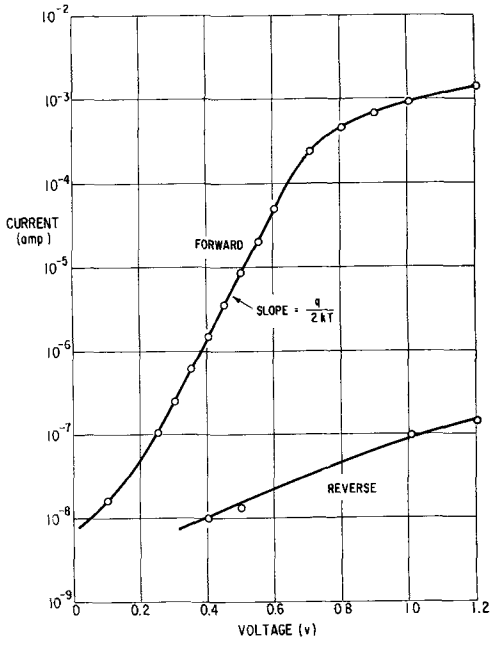

Fig. 7. Current-voltage characteristic of a ZnTe-CdS diode. Junction area ~1 mm^2; p-type side: ZnTe crystal, Cu-doped; n-type side: CdS film, undoped.

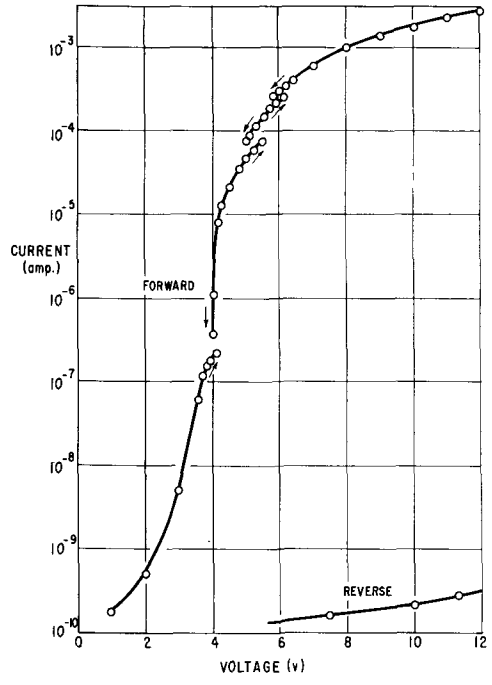

Fig. 8. Current-voltage characteristic of a ZnTe-CdS double-injection diode. Junction area ~1 mm²; p-type side: ZnTe crystal, Cu-doped; n-type side: CdS film, Ga-doped.

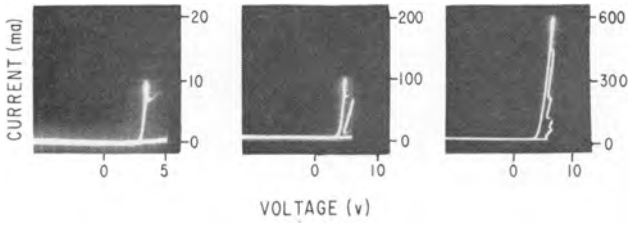

Fig. 9. Oscilloscope traces of a ZnTe-CdS double-injection diode

In Fig. 8 is shown the current-voltage characteristic of a ZnTe-CdS diode in which the nearly compensated region of the CdS film between the ZnTe crystal and the more strongly n-type outer portion of the CdS film was intentionally made wider than the usual 4μ (it is estimated to be approximately 10μ). The characteristic shows several features which distinguish it from the thinner junctions. First, it exhibits an unusually large rectification ratio, approximately 10^7 at 10v. Second, the forward characteristic, if measured point-by-point with a d-c circuit, consists of four segments isolated by gaps which are difficult to breach by smooth tie-lines. If displayed on an oscilloscope, as shown in Fig. 9, these segments appear one after another as the voltage across the junction is increased, with some of the traces interconnecting the segments showing a course corresponding to negative resistance. By setting the voltage across such a diode to a critical value (*e.g.*, 4.1v, 5.5v, or 6.1v in Fig. 8) it is possible to make the diode oscillate between the high and low current regimes. The diode can be made to switch from one branch of the characteristic to another by illumination of the junction area with an incandescent source.

Discussion

Epitaxial growth.—The general features of the above described growth habit of CdS on ZnTe can be understood in terms of the tetrahedral bonding structure of II-VI compounds. When CdS is deposited on a substrate on which epitaxial growth is unlikely or impossible (*e.g.*, glass), the deposit is, in most cases multicrystalline, with the crystallites oriented so that their c-axis forms an angle close to 90° with the substrate plane. It is, therefore, reasonable to assume that the best conditions for epitaxy would be realized if one took advantage of the habit of CdS to grow with the c-axis near normal to the substrate plane and presented to the growing CdS film a crystallographic plane of the cubic ZnTe substrate crystal which corresponds, in its atomic arrangement, to the planes perpendicular to the c-axis in the hexagonal crystalline modification. Such a plane in the cubic crystalline modification is the plane perpendicular to the [111] cubic axis. In the II-VI compounds both the planes perpendicular to the c-axis in the hexagonal structure and the planes perpendicular to the [111] axis in the cubic structure are composed of alternating layers of the group II and group VI atoms. A junction between a hexagonal and a cubic crystal along such planes is, therefore, essentially equivalent to a stacking fault, which is not expected to catastrophically disrupt the lattice periodicity.

The presented experimental evidence supports these views. Single-crystalline growth of CdS on ZnTe was obtained only on the (111) crystallographic planes of ZnTe. Of the two (111) faces of different polarity, however, only the (111) faces containing Zn atoms led to epitaxial CdS films. The reason for this is evident from Fig. 5. Thermal etch of the $(111)_{Zn}$ faces produces a smooth surface with long-range order conducive to relatively fault-free joining of the growing CdS nuclei. The deep furrows and ridges produced by thermal etch on the $(111)_{Te}$ faces, on the other hand, are likely to lead to spurious nucleation of CdS on the ridges, and the bottoms and the sides of the furrows, with little likelihood for the nucleated CdS to grow together to form a single-crystalline film.

Because of the greater volatility of Zn as compared to Te, it is possible that the dark ridges in Fig. 5B represent bunched chains of Te molecules, which would represent a completely mismatching base for the overgrowth by CdS. As can be seen in Fig. 4A, the dark ridges are absent from the $(111)_{Te}$ face subjected to an alkaline etch because of the good solubility of Te in hot alkalies.

Electrical properties.—The appearance of angle-lapped ZnTe-CdS junctions under u.v. irradiation, as illustrated in Fig. 6, indicates that they are not sharp p-n junctions, but junctions of the p-s-n or p-i-n type.[2] The red-luminescent highly compensated layer between the p-type ZnTe substrate crystal and the outer strongly n-type layer of the CdS film is believed to originate from the diffusion of the Cu dopant from the ZnTe crystal into the portion of the CdS film closest to the interface of the two materials. It is also conceivable, however, that the red luminescence is due to the formation of Cd vacancies in CdS by the diffusion of Cd into ZnTe.

[2] In the used notation, s stands for semi-insulating and i for intrinsic.

ZnTe is known to always have an excess of Zn over Te vacancies, and could thus readily accommodate extra Cd atoms. Detailed analysis of the luminescence spectra would be helpful in deciding this point.

Because of the p-s-n character of the ZnTe-CdS junctions, their current-voltage behavior should be analyzed on the basis of the charge recombination theory rather than the more common diffusion theory which is applicable to sharp p-n junctions. In its simplest form the current-voltage relation of a p-s-n diode, in which the carrier recombination takes place in the s region, can be expressed as (5)

$$I = I_0 \left(e^{\frac{qV}{2kT}} - 1\right) \qquad [1]$$

where the saturation current, I_0, is given by

$$I_0 = Aq\frac{w}{\tau}n_i \qquad [2]$$

In this expression A is the junction area, w is the width of the junction, τ is the lifetime of carriers in the s region and n_i is the intrinsic carrier concentration in the s region. The shape of the current-voltage characteristic of the ZnTe-CdS diode, illustrated in Fig. 7, is qualitatively very similar to the current voltage characteristics of p-n or p-s-n junction diodes prepared from more conventional semiconductor materials (6). In such diodes the deviation from exponential behavior at low voltages is accounted for by bulk or surface leakage currents. At high voltages the departure from exponential behavior and the gradual transition to a linear current-voltage relationship is due to the current limiting effect of series resistance. In the ZnTe-CdS junctions the series resistance effect, which sets in at about 1v, is believed to be due to bulk resistance of the CdS film in diodes with high CdS film resistivity and due to the resistance of the external contact to ZnTe in other diodes. The exponential portion of the forward characteristic which, in the present case, extends over approximately three decades of current, has a slope of $q/2kT$ as required by Eq. [1]. The saturation current I_0 however, does not have the magnitude or the temperature dependence required by Eq. [2]. With reasonable estimates of the involved parameters, the calculated saturation current turns out many orders of magnitude smaller than the observed value and has a much steeper variation with temperature than observed experimentally.

The reasons for these discrepancies may be, at least partly, understood in reference to the behavior of the diode whose characteristic appears in Fig. 8. In a recent article, Lampert (7) has theoretically analyzed double injection phenomena in insulators and semiconductors and proposed a mechanism by which the increasing lifetime of carriers with increasing injection levels may lead to negative resistance. According to the proposed mechanism at low voltages such double injection devices pass a one-carrier space charge limited current. As the voltage across the device is increased, the recombination centers in the insulating region, which usually have much higher capture cross sections for holes than for electrons, gradually become saturated with holes. Once all the recombination centers are filled with holes, the device switches over to the so-called semiconductor regime and starts operating on the basis of a two-carrier recombination-limited current. While the saturation region sweeps through the semi-insulating region of the crystal, negative resistance is observed.

Experimental observation of related phenomena have been reported by a number of workers (8, 9). In most of these cases the observed current-voltage characteristics have showed pronounced hysteresis between rising and descending I-V traces, or exhibited spontaneous oscillations with applied d.c. In some instances well-defined regions of negative resistance were also observed.

As can be seen in Fig. 8 and 9, the ZnTe-CdS diode with the wide compensated region clearly exhibits double injection behavior. The appearance of as many as five branches in the I-V characteristic is indicative of the presence of several sets of recombination centers with different hole capture cross sections and level depths. Referring to Fig. 9, as the voltage across the junction is increased, one can first see a trace near the zero current axis which presumably represents space charge limited traverse of electrons from n-type CdS to p-type ZnTe *via* the semi-insulating region of the CdS film. At about 3v the diode switches over to the first semiconductor regime with electron-hole recombinations occurring *via* the first set of recombination centers. At higher voltages new recombination centers come in to play with the recombination switching from one set to another during each sweep of the applied 60 cps a.c. The described multiple branch switching in the ZnTe-CdS diodes is thus quite analogous to that found by Holonyak (10) in GaAs and Si, and interpreted as being due to the presence of several sets of recombination centers.

The presence of several sets of recombination centers in compensated CdS is not unexpected. There are two known Cu centers which have been observed in compensated CdS (11), and one, possibly two self-activated centers promoted by the presence of donors (coactivators) like Ga (12). The semi-insulating layer of the CdS film in the ZnTe-CdS diodes contains Ga from the CdS powder charge, and Cu (or possibly, Cd vacancies) which diffuse in from ZnTe. Therefore it is almost certain that this portion of the film will contain at least two recombination centers of the above-mentioned kind. In addition to this the film may contain centers due to isolated Cu or Ga, centers responsible for the well-known CdS "edge emission" and possibly also centers due to partial diffusion of Zn or Te into the CdS film near the ZnTe phase boundary. Except for the width of the semi-insulating layer, the regular narrow ZnTe-CdS junctions are identical with the double injecting junctions and should therefore also contain a multiplicity of recombination centers. Thus it is not surprising to find that the saturation current in such junctions does not fit the simple charge recombination expression of Eq. [2], which is based on a model with only one set of recombination centers at the middle of the forbidden zone with equal capture cross sections for electrons and holes.

In the foregoing discussion it was tacitly assumed that, although the ZnTe-CdS diodes represented junctions between two dissimilar materials with rather limited solid solubility in each other, they behaved as homojunctions as far as their current-voltage relationship was concerned. In the following discussion it will be shown that this is, indeed, a satisfactory first approximation.

In recent years reports about the properties of several heterojunction systems have appeared in literature (1-4). Yet there exists no thorough theoretical treatment of the subject of lining up of the band edges in dissimilar materials. The only paper which deals with this subject explicitly is due to Anderson (1). Anderson prepared Ge-GaAs heterojunctions and determined the relative positions of the conduction and the valence bands in the two materials by estimating the built-in voltages at the conduction and valence band edges. Implicit in his treatment was the idea that the band profile at the junction was not only determined by the positions of the Fermi levels and the charge densities, but also by the relative electron affinities of the two materials. This is not the place to speculate as to the theoretical justification of such a treatment. From the practical standpoint it is clear that in heterojunctions like Ge-GaAs or Ge-GaP, where the bandgap of one material is more than twice that of the other, and the electron affinities differ considerably (this is another way of saying that the materials are chemically rather different from each other), an exact solution to this problem is quite difficult.

In the ZnTe-CdS system the situation is fortunately much simpler because here the mismatch in bandgaps is less than 10% of the average of the two materials. In addition the electron affinities of ZnTe (13) and CdS (14) differ by only 0.3 ev. This is, of course, not surprising in view of the similar chemical nature of these two compounds. The solid solubility of ZnTe in CdS and *vice versa* is not very extensive. However, the type of bonds which may occur adjacent to each other at the interface of the ZnTe crystal and the CdS film, *i.e.*, Zn-S, Te-Cd, Zn-Te, and Cd-S are again quite similar and would not be expected to disrupt the tetrahedral bonding order of the structure as a whole or form patches of abnormally high recombination rate. Therefore, it is believed that a satisfactory first approximation is to smoothly join the valence and conduction band edges of the two compounds taking into account only the relative positions of their Fermi levels and the fixed charge densities. The more sophisticated treatment by Anderson, which takes into account the difference in electron affinities, is depicted in Fig. 10. Here the 0.3 ev difference in electron affinities between CdS and ZnTe is carried over into the actual junction space charge region where it produces a small spike in the conduction band edge and a 0.1 ev discontinuity in the valence band edge. The existence of these would not be easily observed by the measurements described in the preceding text, so that the question of their existence is academic at this point.

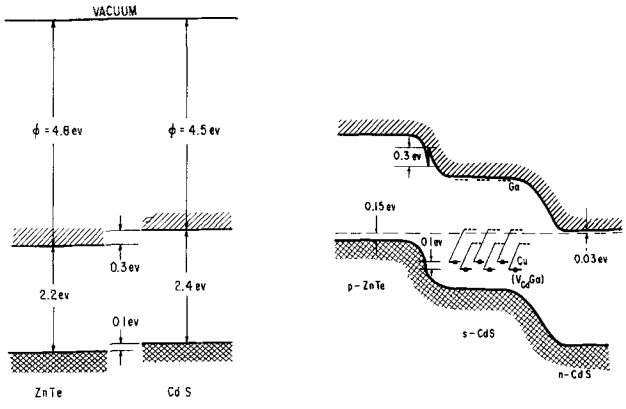

Fig. 10. Band model for ZnTe-CdS heterojunctions

The other features of the band model shown in Fig. 10 afford an illustrative summary of the pertinent conclusions regarding the ZnTe-CdS heterojunctions. From the experimental evidence of Fig. 6 and 7, it was concluded that the junctions have a p-s-n structure, with the s part representing a heavily compensated region with the Fermi levels near or slightly above the middle of the band gap of CdS. The indicated positions of the Fermi levels in ZnTe and the outer layer of the CdS film were determined from Hall measurements with similarly doped single crystals. The experiments with the junctions showing double injection and negative resistance indicated that the s regions of the junctions contain several sets of recombination centers. The approximate positions of two such sets of recombination centers are shown in the figure. The short horizontal lines with dots indicate the positions of the levels when occupied by electrons, while the dashed lines indicate their positions after hole capture (after the Stokes shift has occurred). Because the recombination centers have larger capture cross sections for holes than electrons, there is always a supply of holes waiting in these centers (in the regular narrow ZnTe-CdS junctions) for the electrons to be injected over the potential hill between the n and the s parts of the junction, as the voltage across the junction is increased. The s-layer in these junctions may, therefore, behave like a material with approximately one half of the band gap of intrinsic CdS, thus affording a possible explanation for the large observed saturation currents.

Acknowledgment

We wish to thank Dr. R. E. Halsted for stimulating our interest in the double injection phenomenon and for performing the electrical measurements on the double injection diodes.

Manuscript received August 6, 1962; revised manuscript received Nov. 23, 1962. This paper was prepared for delivery at the Los Angeles Meeting, May 6-10, 1962.

Any discussion of this paper will appear in a Discussion Section to be published in the December 1963 JOURNAL.

REFERENCES

1. R. L. Anderson, *IBM J. Research Develop.*, **4**, 283 (1960).

2. N. Holonyak, Jr., D. C. Jillson, and S. F. Bevaqua, "Halogen Vapor Transport and Growth of Epitaxial Layers of Intermetallic Compounds and Compound Mixtures," in "Metallurgy of Semiconductor Materials," Vol. 15, p. 49, Interscience Division of J. Wiley & Sons, Inc., New York (1962).
3. L. J. Van Ruyven and W. Dekker, *Physica*, **28**, 307 (1962).
4. M. Aven and D. M. Cook, *J. Appl. Phys.*, **32**, 960 (1961).
5. C. Sah, R. N. Noyce, and W. Shockley, *Proc. IRE*, **45**, 1228 (1957).
6. J. S. Saby, Report Meeting on Semicond., p. 39, Rugby, 1956.
7. M. A. Lampert, *Phys. Rev.*, **125**, 126 (1962).
8. *Ibid.*, ref. 9-16.
9. N. Holonyak, Jr., S. W. Ing, Jr., R. C. Thomas, and S. F. Bevaqua, *Phys. Rev. Letters*, **8**, 426 (1962).
10. N. Holonyak, Jr., In press, *Proc. IRE*, Dec. (1962).
11. M. Avinor, Thesis, p. 59, Univ. of Amsterdam, 1959.
12. W. van Gool *Philips Research Repts. Suppl.*, 1961, No. 3.
13. J. A. Dillon, Jr., *J. Appl. Phys.*, **33**, 669 (1962).
14. J. J. Scheer and J. van Laar, *Philips Research Repts.*, **16**, 323 (1961).

Vacuum Evaporation of Cadmium Telluride

Reinhard Glang, John G. Kren, and William J. Patrick

Components Division, International Business Machines Corporation, Kingston, New York

ABSTRACT

Structural and electrical properties of CdTe films prepared by vacuum evaporation of the compound were studied. Films 0.1-1μ thick were deposited on glass substrates between 25° and 250°C at ambient pressures below 10^{-6} Torr. The deposition rate was controlled by an ionization rate monitor. Film thickness, uniformity, adhesion, and infrared absorption were determined. X-ray diffraction techniques were used to analyze the structure, grain size, and orientation of the films. These properties were found to be related to the deposition temperature. Film resistivities were greater than 10^7 ohm-cm at all deposition temperatures, even if impurities were added during evaporation. Possible causes for this behavior are discussed.

Recent advances in thin film circuit technology have created a strong interest in evaporated semiconductor films (1-4). Of the materials amenable to vacuum evaporation, cadmium telluride seemed promising because the electrical properties of single crystals have been varied over a wide range. This study was made to evaluate CdTe as a material for evaporated thin film devices. The objective was to establish a controllable evaporation process and to correlate film properties with deposition parameters.

Cadmium telluride is a II-VI compound semiconductor with zinc blende structure (5) and a band gap of about 1.5 ev (6-8). Single crystals of both conductivity types have been grown by various methods, and p-n junctions showing rectification and photovoltaic effects have been demonstrated (6-11). Extrinsic conductivity has been produced by deviation from stoichiometry or by incorporation of foreign atoms.

Electrical properties associated with various defects in the CdTe lattice are shown below. Impurity concentrations up to 5 x 10^{17} cm^{-3} and mobilities up to 700 cm^2/v sec for electrons and 65 $cm^2/v \cdot sec$ for holes have been reported (6).

Element	Mechanism of incorporation	Conductivity type produced	Activation energy, ev	Reference
Excess Te	Cd-vacancy	p	0.15	(6)
Li	Substit. for Cd	p	0.27	(8),(9)
Cu	Substit. for Cd	p	0.34	(6)
Ag	Substit. for Cd	p	0.30-0.35	(6),(8),(9)
Au	Substit. for Cd	p	0.27-0.35	(6),(9)
Pb	Substit. for Te	p	0.51	(8)
P	Substit. for Te	p	0.38	(8)
Sb	Substit. for Te	p	0.36	(6),(8),(9)
Excess Cd	Interstitial	n	0.02	(6)
In	Substit. for Cd	n	0.02	(6),(9),(11)
I	Substit. for Te	n	0.003	(8),(9),(11)

Small CdTe crystals and polycrystalline films have been condensed by mixing Cd and Te_2 vapors (12), or by vacuum evaporation of the compound at pressures from 10^{-5} to 10^{-4} Torr (13, 14). When evaporating, CdTe dissociates into the elements (6, 17)

$$CdTe\ (s) \rightleftharpoons Cd\ (g) + \tfrac{1}{2}\ Te_2\ (g) \qquad [1]$$

Approximate equilibrium pressures for 700° to 1000°C have been calculated from the standard free energy of formation (6). Previous attempts to evaporate CdTe have produced semiconducting films with dark resistivities typically between 10^7 and 10^8 ohm-cm at room temperature. Under certain deposition conditions, these films have shown unusually large photovoltages (13-16).

Evaporation Process

The CdTe films were prepared in a commercial vacuum system with an 18 in. diameter bell jar shown in Fig. 1. Vacua of 1x10^{-7} Torr could be produced by cooling the baffle of the oil diffusion pump and a Meissner trap located near the top of the bell jar with liquid nitrogen.

The films were deposited on 1 x 3 x 0.04 in. borosilicate glass slides. Parallel experiments with soda lime glass substrates yielded identical results. Substrate cleaning started with soaking the slides in a cold saturated solution of sodium dichromate in sulfuric acid followed by a rinse in demineralized water. After ultrasonic cleaning in detergent solution, the slides were rinsed in distilled water and

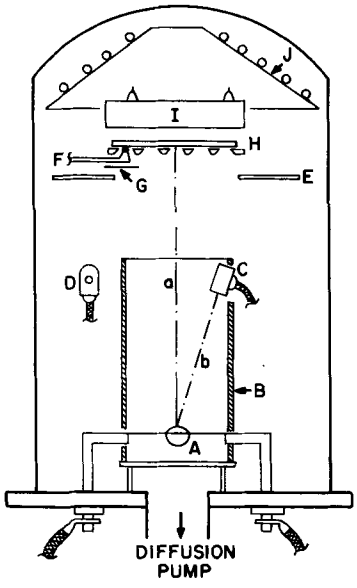

Fig. 1. Evaporation system used for CdTe film deposition. A, source; B, glass cylinder; C, rate sensor; D, ionization gauge; E, shutter; F, thermocouple; G, thermocouple shield; H, substrate and mask; I, substrate heater; J, Meissner trap. The distances a and b are 15 and 7 in., respectively.

stored in absolute isopropanol. Immediately prior to loading into the evaporator, the substrates were rinsed in pure toluene and dried under a heat lamp. For each experiment, two substrate slides were placed in the evaporator in close contact with metal evaporation masks. The deposit was obtained in the form of several strips or squares and such patterns as commonly used for Hall and resistivity measurements. The substrates were radiation heated by tantalum filaments mounted about 1 in. above the glass slides. A thermocouple springloaded against the deposit side of one substrate and attached to a recorder-controller provided temperature constancy within ±5°C. This arrangement permitted convenient loading and unloading of substrates. At temperatures above 150°C, reproducibility and accuracy of measurements gradually deteriorated due to the thermocouple contact area being small compared to the lead diameter, and to nonuniform heat absorption.

Two types of evaporation sources were tried. An open cylindrical alumina or quartz crucible, resistance heated by a tantalum strip, proved unsatisfactory because particles were ejected and deposited on the film surface even at moderate evaporation rates. This problem was greatly reduced by using a spherical tantalum boat with an internal baffle as shown in Fig. 2. The source temperature

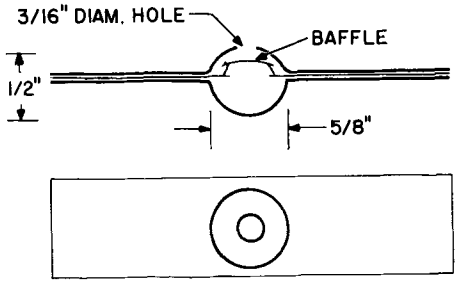

Fig. 2. Tantalum boat used as evaporation source

was measured during evaporation by a thermocouple spot welded to the boat. Depending on the evaporation rate, initial temperatures varied between 750° and 850°C. Due to a nonuniform temperature distribution in the boat, a gradual increase of 30°-50°C was observed toward the end of each run, when material in contact with the cooler portions of the source evaporated.

The source material was high-purity grade CdTe powder from various suppliers. X-ray fluorescence and spectroscopic analysis of a typical product revealed an excess of about 5 at. % tellurium and the following impurities (in ppm): 5 Cu, 4 Sn, 3 Ag, 3 Pb, and less than 0.5 Mg, Al, Fe, Ni, Bi.

The CdTe charge, usually 2.5g, was evaporated to completion. The first and the last 25% of the evaporating charge were excluded from condensation on the substrate by keeping the shutter closed. Prior to an evaporation, the system pressure was reduced to about 2 x 10^{-7} Torr; immediately after evaporation, pressures between 4 x 10^{-7} and 1 x 10^{-6} Torr have been measured.

The evaporation process was controlled by an ionization rate monitor (18). As shown in Fig. 1, the ionization gauge C measured the particle density in the evaporant stream. Another ionization gauge D mounted outside the glass cylinder B indicated the background pressure. The difference of ionization currents in both gauges was fed into a recorder-controller which kept the net ionization current constant to within ±1% by varying the power input to the source. To prevent condensation of CdTe on the inner sensor C, all electrodes of this ionization tube were heated during evaporation (19).

With this arrangement the evaporation rate, calculated from the amount of CdTe in the source and the total evaporation time, could be controlled through the ionization current; the relationship is shown in Fig. 3. The scatter is due to small differences in the respective positions of source and rate sensor and to condensation of CdTe on the source baffle, thus restricting the orifice and affecting the directionality of the evaporant stream. Most experiments were made with evaporation rates of about 10 micromole CdTe per second; at higher rates, spattering occurred frequently.

The condensation rate depends on the number of molecules in the evaporant stream and is there-

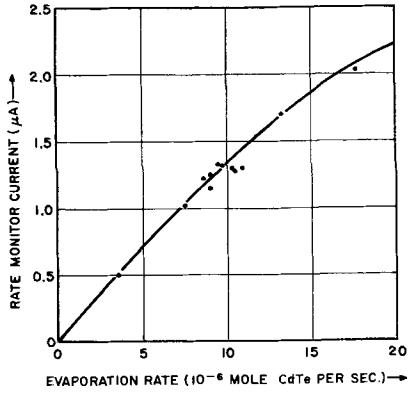

Fig. 3. Rate monitor current as a function of the evaporation rate

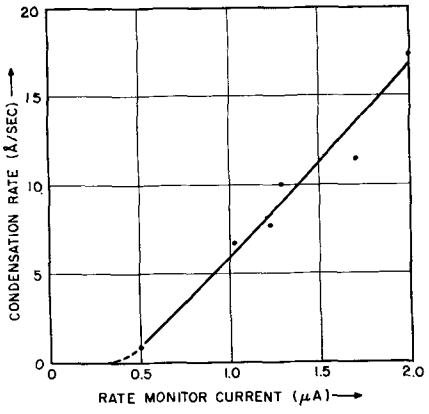

Fig. 4. Condensation rate at 200°C on glass as a function of rate monitor current. These rates were determined from 10-min deposition runs.

fore related to the ionization current. This is shown in Fig. 4 for CdTe films deposited on glass surfaces at 200°C. Reproducibility was limited by the method of measuring the substrate temperature. As shown in Fig. 5, condensation rates above 150°C are quite sensitive to temperature fluctuations and drop sharply above 200°C. The slight maximum at 100°C is genuine and has been confirmed repeatedly.

For constant substrate temperatures and evaporation rates, the film thickness increased linearly with deposition time as shown in Fig. 6. At the higher temperatures, there is indication of delayed condensation of the first few hundred angstroms.

Properties of CdTe Films

The CdTe films had very smooth shiny surfaces; they were continuous and dense. An electron microscope picture of a surface replica taken from a typical film is shown in Fig. 7. Films thinner than about 4000Å were transparent with a brownish color. Thicker films had a metallic gray appearance. Thicknesses have been determined by the Tolanski interference method (20) and with a profilometer. Both methods gave results in excellent agreement. Thickness variations over the entire 3 x 3 in. substrate area were ±1% for deposition temperatures up to 200°C.

Film adhesion was tested qualitatively with cellophane tape pressed over the deposit and then stripped off (21). CdTe films deposited at temperatures of 100°C or higher adhered firmly to the substrate. However, if no chromic acid had been employed in the substrate cleaning procedure, films

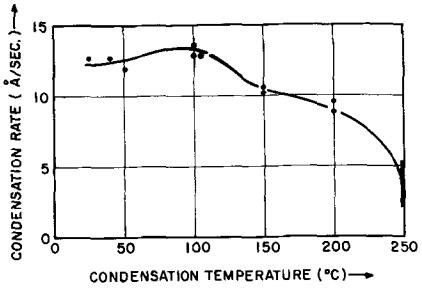

Fig. 5. Condensation rate vs. condensation temperature on glass surfaces, determined from 10-min deposition runs. Data normalized for 10 micromole/sec evaporation rate.

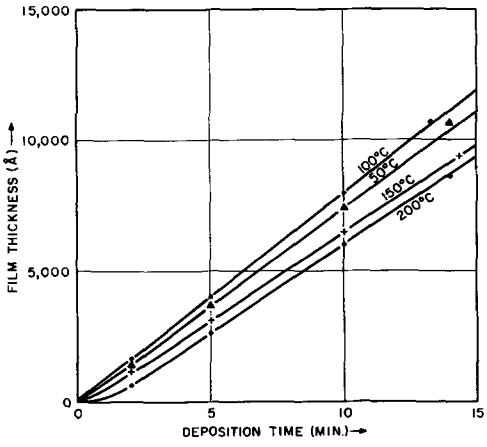

Fig. 6. Film thickness vs. deposition time at various substrate temperatures for constant evaporation rates of 10.3 ± 0.1 micromole/sec.

Fig. 7. Surface of CdTe film 5000Å thick, deposited at 200°C. Magnification 10,000X before reduction for publication.

prepared at these temperatures were partially stripped off the glass. Films deposited below 100°C did not adhere regardless of the cleaning procedure. Baking the substrates in vacuum prior to deposition did not improve this behavior. In addition, all low-temperature films were heavily strained; mechanical or thermal action caused them to wrinkle and peel.

Structure and crystallinity of the films were investigated with an x-ray diffraction unit and pulse height analyzer using Cu $K\alpha$ radiation. All films showed diffraction maxima characteristic for CdTe. The deposition temperature had a pronounced influence on the crystallinity of the films. Table I shows the relative intensities of the first three diffraction maxima for films of comparable thicknesses. The other maxima were always very weak or missing. All films deposited at 150°C or above exhibit preferential (111) orientation. At lower condensation temperatures, particularly at 100°C, (110) and (311) orientations compete with (111).

Also listed in Table I are the average grain sizes of these films. These have been calculated from the width of the (111) diffraction maxima by comparison with a commercial silicon powder x-ray stand-

Table I. X-ray diffraction data of CdTe films

Film No.	Deposition temperature, °C	Relative intensities (111)	(220)	(311)	Film thickness, A	Grain size, A	Reflections from crystalline Te, hkl
Standard*	—	100	80	70	—	—	—
13	25	100	54	21	8000	200	(100)
41	25	100	50	40	7300	300	(101)
14	100	3	100	2	7700	700	(100), (101)
43	100	65	100	70	7750	600	—
51	100	100	43	61	8000	500	—
17	150	100	10	13	7250	800	(100), (101), (102), (111)
44	150	100	0.4	0.5	5950	2500	—
52	150	100	—	—	6450	2200	—
15	200	100	—	0.2	6150	1200	—
49	200	100	0.3	0.7	6250	2600	—
18	250	100	—	1	5000	1000	—
54	250	100	10	7	4000	1700	—

* Relative intensities for randomly oriented CdTe powder, from ASTM X-Ray Powder Data File, Card No. 10-20, Fe $K\alpha$ radiation.

ard. There is a general increase of grain size with temperature, but no quantitative relationship between temperature and grain size is apparent.

X-ray diffraction diagrams revealed the presence of a second crystalline phase in low-temperature films. The additional maxima have been identified as characteristic for hexagonal tellurium, and the corresponding crystal planes are listed in the last column of Table I. If deposited at room temperature, part of the excess tellurium is probably amorphous, and its crystallinity improves with deposition temperature. At 100° and 150°C, condensation of excess tellurium is not reproducible and was found only if one particular CdTe powder was used for evaporation. Substrate temperatures of 200°C or higher consistently prevented the condensation of a tellurium phase.

Similar results have been published by Semiletov (22), who evaporated CdTe on NaCl, mica, celluloid, and glass. He found the intensity of the (222) x-ray reflection to be unusually high, which indicates preferred (111) orientation. Furthermore, he reports the presence of one unidentified interference associated with an interplanar spacing of 3.95Å. In this investigation, the same interference was found in combination with additional maxima and therefore could be attributed to the (100) plane of tellurium.

The influence of the condensation temperature on the composition of CdTe films has been confirmed

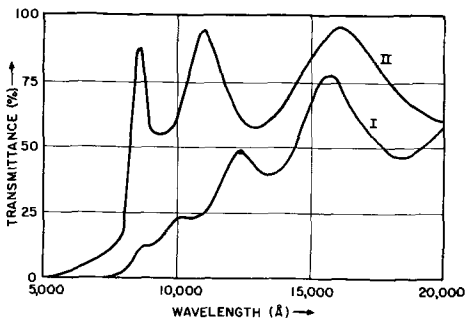

Fig. 8. Transmittance of CdTe films. I is typical of films deposited at room temperature or 100°C. II is typical of films deposited at 150°, 200°, or 250°C. Maxima and minima are due to interference effects superimposed on the transmittance characteristics.

by infrared transmittance measurements. Figure 8 shows the two types of transmittance curves obtained with films 4000-8000Å thick. Those films deposited at 150°C or above had a sharp absorption edge at wavelengths around 0.83μ. This corresponds to a transition energy of 1.5 ev, which is the width of the energy gap of CdTe and in agreement with photo-absorption and photosensitivity data of CdTe single crystals (6, 23, 24). CdTe films produced at lower substrate temperatures showed a transmittance which decreased gradually in the wavelength range from 1.5 to 0.8μ. In accordance with the results of the x-ray analysis, absorption in this region is attributed to the presence of free tellurium.

Contrary to expectations, the electrical properties of CdTe films did not reflect differences in composition Regardless of deposition temperature, all films had resistivities greater than 10^7 ohm-cm. If sandwiched between two metal electrodes, the films had equally high resistivities until the applied electric field approached 10^5 v/cm. Beyond this limit electrical breakdown occurred, and the films were destroyed. Attempts were made to produce films with lower resistivities by adding impurities to the CdTe charge in the boat. However, additions of 0.05% Cd, 0.3% In, 1% $CdCl_2$, and 1-20% CdI_2 were found to be completely ineffective.

The high film resistivities indicate either very low effective carrier mobilities, or low carrier concentrations, or both. The low effective mobilities may be caused by electrical barrier layers at the grain boundaries similar to those postulated by Goldstein and Pensak (15) and Hutsin (16) to explain large photo voltages in CdTe films prepared under an oblique angle of deposition. deNobel, too, found large potential drops across grain boundaries in CdTe crystals (6).

Small carrier concentrations would mean that, at the condensation temperatures used, CdTe does not have the ability to dissolve an appreciable excess of its constituents. Although differences in the accommodation coefficients of Cd atoms and Te_2 molecules are large enough to allow the condensation of unreacted tellurium up to 150°C, a significant de-

viation from stoichiometry in the compound is not produced. This conclusion is supported by data published by deNobel (6), who observed the melting temperatures of CdTe crystals in equilibrium with Cd and Te_2 vapors. From Hall measurements, he determined the excess of Cd or Te dissolved in these crystals and he found that the solubilities of both constituents decrease toward lower temperatures. For example, near the melting point of the stoichiometric compound at 1090°C, the solid solubility for Te in CdTe is approximately 7×10^{17} cm^{-3}; it decreases to about 10^{16} cm^{-3} at 700°C. For excess Cd, the solubility is also in the order of 10^{17} cm^{-3}, but the decrease is less drastic. Assuming that the trend of decreasing solubilities extends to temperatures below the investigated interval, deviations from stoichiometry in CdTe films condensed between 25° and 250°C must be considerably smaller than 10^{16} cm^{-3}.

In those cases where impurities had been added to the evaporated CdTe charge, it is questionable whether they have also been deposited on the substrates. Assuming that some condensation of impurities took place, an electrical effect is not necessarily to be expected. Kroeger (25) has shown that, in contrast to silicon and germanium, the incorporation of impurities into semiconductor compounds may occur by different mechanisms. It depends on the ambient conditions during preparation, whether the incorporation of an impurity will contribute charge carriers or not. In CdTe, deNobel found indium to be an effective donor only if the crystal had been annealed in Cd vapor to establish a metal excess. Similarly, crystals containing Cu or Au showed p-type conductivity only if a tellurium excess had been formed by heating the compound at very low Cd or high Te pressures. If CdTe films condensed at or below 250°C do not show significant deviations from stoichiometry, neither acceptor not donor impurities are electrically effective.

Various postdeposition treatments have been tried to lower film resistivities. Up to 400°C, CdTe films could be heated in a stream of dried helium without sublimation, but no permanent resistivity changes have been observed. Several films were sealed into evacuated quartz tubes together with small quantities of Cd, Ga-In, or Te, and heated to 500°-575°C for 1 hr. This procedure lowered dark resistivities to about 10^3 ohm-cm and increased the average grain size of films up to about 1μ. Films annealed in the presence of Cd alone or Cd plus Ga-In showed n-type conductivity, whereas those baked in Te-vapors were p-type. Hall measurements could not be made because the high film resistance produced voltages between the Hall contacts which were several orders of magnitude greater than the Hall voltages to be expected.

This method of increasing the conductivity of CdTe films has several shortcomings. Some of the films heated under identical conditions did not show lower dark resistivities nor larger grains than they had had initially. Some films peeled as a result of annealing in Cd-vapor, others were severely riddled with pinholes. It is also questionable what impurities were responsible for the conductivity increase, because the resistivity of n-type films produced by treatment in Cd-vapor either did not change or even decreased slightly after heating in a high vacuum up to 300°C. If interstitial Cd had been present as donor impurity, it should have been re-evaporated and resulted in a resistivity increase. Finally, evaporated gold contacts to be used in connection with CdTe films cannot be subjected to the Cd-vapor treatment because they alloy with the free metal and peel off.

Summary and Conclusions

CdTe can be vacuum evaporated under controlled conditions using an ionization rate monitor. The vapors, although dissociated into the constituents, form stoichiometric, crystalline CdTe films with zinc blende structure. The films are continuous, uniform, and adhere well to glass surfaces if deposited at or above 100°C. To avoid condensation of free tellurium, substrate temperatures above 150°C are required. At these condensation temperatures, films about 0.5μ thick have grain sizes of 1000-2500Å, and their (111) crystal faces are oriented parallel to the substrate surface. Above 200°C, the accommodation coefficient of condensation decreases sharply. Regardless of deposition temperature, all films have resistivities of 10^7 ohm-cm or higher, even if impurities are added to the source material. This behavior may be due to barrier layers at the grain boundaries, or to narrow solubility limits of excess Cd and Te in the compound at the condensation temperatures. The high resistivities seriously limit the usefulness of CdTe as a semiconductor for thin film device applications.

Acknowledgment

The authors wish to thank Dr. A. Reisman of the IBM Research Center in Yorktown Heights for supplying samples of CdTe powder. Valuable cooperation in various phases of film analysis has been received from their colleagues in Kingston and Poughkeepsie and is gratefully acknowledged.

Manuscript received Oct. 24, 1962. This paper was prepared for delivery before the Pittsburgh Meeting, April 15-18, 1963.

Any discussion of this paper will appear in a Discussion Section to be published in the December 1963 JOURNAL.

REFERENCES

1. "Thin Film Circuit Functions," Final Report, Signal Corps Contract DA36-039-sc-84547, IBM Corp., August 1959-July 1960. ASTIA AD 248733.
2. B. Miller, *Aviation Week*, July 4, 1960.
3. M. M. Perugini and N. Lindgren, *Electronics*, November 25, 1960.
4. P. K. Weimer, *Proc. IRE*, **50**, 1462 (1962).
5. M. Hansen, "Constitution of Binary Alloys," p. 444, McGraw-Hill Book Co., New York (1958).
6. D. deNobel, *Philips Research Repts.*, **14**, 361 and 430 (1959).
7. R. H. Bube, *Proc. IRE*, **43**, 1836 (1955).
8. D. A. Jenny and R. H. Bube, *Phys. Rev.*, **96**, 1190 (1954).
9. Yu. A. Vodakov, G. A. Lomakina, G. P. Naumov, and Yu. P. Maslakovets, *Soviet Physics—Solid State*, **2**, 1 (1960).
10. G. B. Dubrowski, *Soviet Physics—Solid State*, **2**, 536 (1960).
11. D. A. Jenny, U. S. Pat. No. 2,840,496, June 24, 1958.

12. R. T. Lynch, *J. Appl. Phys.*, **33**, 1009 (1962).
13. V. M. Lyubin and G. A. Fedorova, *Soviet Physics—Doklady*, **135**, 1343 (1960).
14. P. P. Konorov and I. B. Shevchenko, *Soviet Physics—Solid State*, **2**, 1027 (1960).
15. B. Goldstein and L. Pensak, *J. Appl. Phys.*, **30**, 155 (1959).
16. A. R. Hutsin, *Bull Am. Phys. Soc.*, Series II, **6**, 110 (1961).
17. P. Goldfinger and C. Drowart, Final Report ARDC, AF 61(514)-868, October 1956. [See ref. (6), p. 492]
18. G. R. Giedd and M. H. Perkins, *Rev. Sci. Instr.*, **31**, 773 (1960).
19. M. H. Perkins, "An Evaporation Rate Control System Employing a Heated Electrode Sensing Gauge." 2nd Intern. Congress on Vacuum Technology, Washington, D. C., Oct. 16-19, 1961.
20. S. Tolansky, "Multiple Beam Interferometry of Surfaces and Films," Clarendon Press, Oxford (1948).
21. L. Holland, "Vacuum Deposition of Thin Films," p. 99, John Wiley & Sons, Inc., New York (1958).
22. S. A. Semiletov, *Trudy Inst. Krist., Akad. Nauk S.S.S.R.*, **1955**, [11], 121.
23. P. W. Davis and T. S. Shilliday, *Bull, Am. Phys. Soc.*, Series II, **4**, 133 (1959).
24. R. H. Bube, *Phys. Rev.*, **98**, 431 (1955).
25. F. A. Kroeger, H. J. Vink, and J. van den Boomgaard, *Z. Phys. Chem.*, **203**, 1 (1954).

An Electropolishing Technique for Germanium and Silicon

M. V. Sullivan, D. L. Klein, R. M. Finne, L. A. Pompliano, and G. A. Kolb

Bell Telephone Laboratories, Incorporated, Murray Hill, New Jersey

ABSTRACT

An electrochemical technique has been developed for polishing germanium and silicon to yield smooth and flat semiconductor surfaces. This technique is based on the anodic dissolution of a semiconductor whose surface is close to a moving cathode. The average surface roughness of electropolished semiconductors was found to be ±25Å and the deviation from flatness was typically 1 μ/cm.

For n-type samples, the holes necessary to support uniform electrolysis of the surface were injected by illuminating the anode surface. For both n- and p-type anodes the average current efficiencies were found to be between 103 and 105%. Practical current densities are about 0.1 amp/cm^2. At this value, the etch rates were about 2.2 μ/min for germanium and 1.9 μ/min for silicon.

The techniques of diffusion, evaporation, and epitaxial growth have made improved transistors possible. However, the active regions of devices made by these processes are so close to the surface of the semiconductor that previously ignored minor imperfections in the surface structure may now be significant with regard to the physical and electrical properties of the semiconductor devices.

At the present time mechanical lapping and polishing are commonly used for the preparation of smooth and flat semiconductor surfaces (*i.e.*, surfaces containing a minimum of short- and long-range irregularities). The surfaces are then chemically etched to a depth just sufficient to remove all of the mechanical damage introduced by the polishing procedure. Deeper chemical etching is undesirable because of the difficulty in maintaining the surface smoothness and flatness acquired mechanically. When the lapping and polishing damage is deeper than expected, the chemical etching treatment can fail to remove all of the mechanical damage and this can lead to poor quality transistors.

The present paper describes an electropolishing procedure developed for both germanium and silicon that can be used for the preparation of smooth and flat surfaces that contain a minimum of residual surface damage. The technique makes use of an intensive stirring action near the semiconductor anode surface. This form of electropolishing is based on, and is a combination of, some of the principles outlined in a number of published papers (1-7). These papers have described the use of shaped cathodes and/or intensive stirring to obtain special effects during anodic dissolution processes. A comprehensive review of electrolyte-semiconductor behavior, including a bibliography of over 100 references, has been made by Turner (8).

The electropolishing procedure which has been developed for germanium and silicon employs a moving flat cathode which is spaced very close to the surface of the semiconductor anode. Semiconductor surfaces prepared with this intensively stirred system are comparable to the finest mechanically polished surfaces with regard to smoothness and flatness, but they are free of the mechanical damage which always accompanies mechanical polishing.

Experimental Procedure

An intensive stirring action between the electrodes was desired. This was accomplished by rotating a large motor-driven cathode next to a smaller nonconducting disk on which the semiconductor anode was mounted. These electrodes and their relative positions can be seen in Fig. 1 and 2.

Anode.—The surface of the semiconductor that was to be electropolished was made the anode of the electrochemical cell. The samples to be polished were waxed (usually with paraffin) to the forward

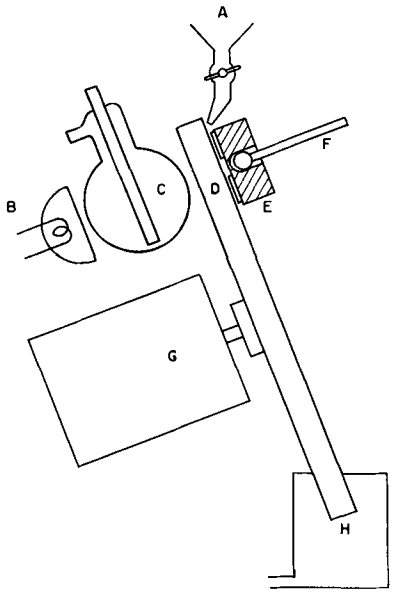

Fig. 1. Schematic arrangement of electropolishing equipment: A, dropping funnel containing etchant; B, light; C, heat absorber; D, rotating disk; E, polishing block holding 3 or more specimens; F, support rod for polishing block; G, motor drive; H, drip pan.

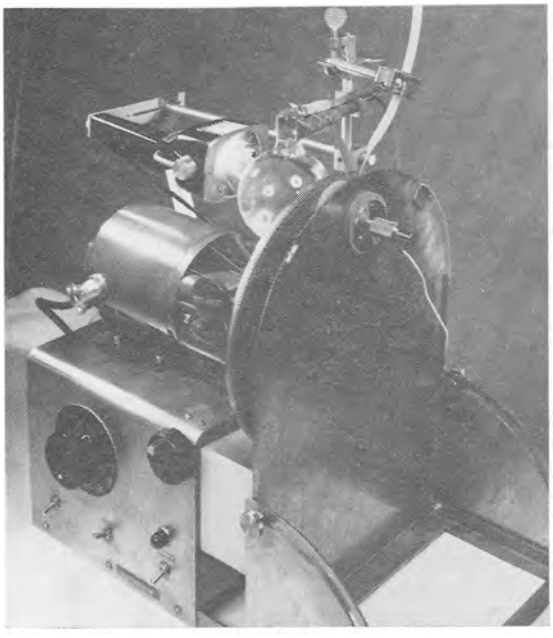

Fig. 2. Photograph of electropolishing equipment

surface of a phenolic-fiber disk 7 cm in diameter. Wires passing through the disk made electrical contact to the semiconductor samples. These wires were terminated on the rear surface of the disk at a centrally located socket of a ball-and-socket joint. Figure 3 is a photograph showing the disk with and without semiconductor samples and a view of the rear surface of the disk.

In operation, the anode disk was supported near the periphery of the cathode on a ball joint. By tilting the cathode slightly (10°-20°) gravity helped to maintain the anode disk in close proximity to the cathode. Rotation of the anode was caused by the differential velocity developed across the anode disk due to the rotation of the motor-driven cathode. Although the apparatus shown in Fig. 2 has only

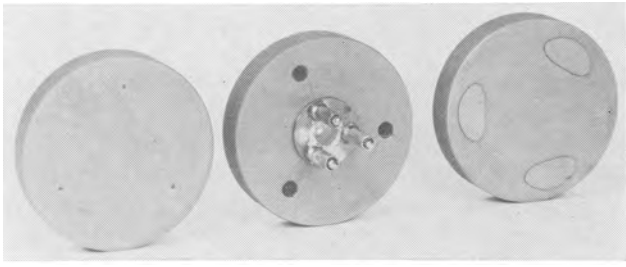

Fig. 3. Several views of anode disk assembly

one anode disk, additional disks could be mounted along the periphery of the cathode. Electrical contact to the anode was made through the ball-and-socket joint which contained a small amount of an electrically conductive lubricant.[1]

A point contact made directly to the rear surface of the samples was found to be sufficient for samples of less than about 0.01 ohm-cm resistivity. For higher resistivity samples the effect of the spreading resistance caused a slight depression to appear on the polished surface in a position opposite to the point contact on the rear of the sample. To avoid this effect on higher resistivity samples the rear surfaces were metallized with electroless nickel (9) prior to mounting the slices on the anode disk. After electropolishing, the nickel can be stripped from the rear of the polished slices by immersion in a $FeCl_3$ solution (National Formulary, 10-11%). This solution did not degrade the quality of the polished silicon surfaces. However, for germanium it was necessary to protect the polished surfaces with wax prior to removal of the nickel plate from the back surface.

Cathode.—As will be explained later, the anodic dissolution of germanium and silicon consumes holes. When these carriers cannot be supplied by the semiconductor anode (*e.g.*, for most n-type samples) it is necessary to generate the carriers by external means in order to sustain a uniform electropolishing of the entire surface. Light injection was chosen for the present work as the most convenient and practical method of carrier generation. For this type of injection a semitransparent cathode was evolved that was operated in a near-vertical position. With this form of electrode, the radiation from a light source placed behind the cathode could illuminate the anode surface.

Several types of transparent conductive cathodes were constructed and tested. One form employed a thin conducting film (gold, tin oxide, chrome alloy, or Inconel) on flat glass disks. This type of cathode could be made very flat and had over 70% transmission in the visible region. It was not considered practical, however, because with repeated electropolishing the conductive film of this cathode either separated from the glass or became opaque. Another type of cathode which was investigated employed a metal grid structure on disks of either glass or plastic. This type of cathode could not be prepared readily with the degree of surface flatness required for the process and likewise was abandoned. The third method employed a metal disk with an array

[1] "Conducto-Lube" obtained from the Conducto-Lube Company, Portland 19, Oregon.

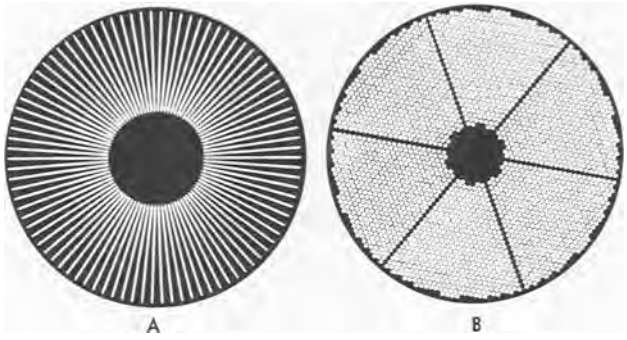

Fig. 4. Two forms of perforated metal cathode disks

of holes or slots throughout the surface. Stainless steel, gold-plated cast iron, and gold-plated brass have been used successfully. Figure 4 illustrates two types of perforated 20 cm metal cathodes. Of the two types shown, the slotted disk (Fig. 4A) was easier to fabricate and gave slightly flatter semiconductor surfaces than were obtained from the cathode with the close packed array of holes (Fig. 4B).

The perforations in the cathode served an additional function. The gas liberated at the cathode surface could readily escape through the holes or slots in the electrode. Thus, even for semiconductor samples not requiring carrier injection, the perforated disks were superior to solid disks and this type of cathode was employed for all varieties of samples polished.

Cathode velocity.—With equipment of good mechanical tolerances, no large change in the quality of the electropolish was found for cathode speed variations between 25 and 500 rpm. All the data reported were obtained at speeds of less than 100 rpm where the mechanical tolerances were not critical.

Anode-cathode separator.—It was established that the close anode-cathode separation necessary for polishing could be maintained by the viscous film of electrolyte developed between the spinning electrodes. In order to avoid any direct electrical contact of the two electrodes it was necessary, however, to maintain a rigid control over the mechanical tolerances associated with both electrode surfaces, and all moving and supporting parts. A more practical method to assure anode-cathode separation was to employ a thin sheet of cloth or paper to cover the cathode surface. The use of such a separator eased the mechanical and operating tolerances.

A number of materials have been used as separators. These have included paper, silk, Nylon, Orlon, Dacron, cotton, felt, and gelatin. The chief requirements of the separator are that it be as thin as practicable, exhibit a smooth surface texture, have the ability to withstand the chemical action of the electrolytes, and have the necessary wet-strength to withstand the rubbing action of the spinning anode.

Light source.—Tungsten light sources offered the most effective means of carrier injection for both germanium and silicon. A variety of ordinary illuminating and projecting lamps were tested. The lamp which proved most satisfactory had a power rating of 625w.[2] When mounted as shown in Fig. 2 the size of the illuminated area was adjusted to include the entire anode area. A round-bottom flask through which cooling water could be circulated was mounted between the lamp and the anode. This flask removed a large portion of the heat from the projected beam of light. Without the cooling filter it was found that the semiconductor samples often became warm enough to melt the wax which held them to the anode disk. In addition, the heat from the unfiltered beam caused an uncontrolled decrease in the resistivity of the electrolyte film.

To increase the life of the light source it was expedient to operate the lamp from a variable autotransformer at a voltage not much beyond that necessary to support the desired rate of electrolysis. Also, a blast of air was directed on the lamp housing to facilitate the cooling of the lamp and extend its useful life.

Electrolytes.—A wide variety of electrolytes can be used for the electropolishing of germanium (6). Solutions of KOH, HCl, HNO_3, H_2SO_4, and the sodium salt of ethylenediaminetetraacetic acid have all been investigated during the course of the present study. Dilute potassium hydroxide was chosen for the anodic dissolution of germanium because it is easily handled, presents little if any safety hazard, produces a minimum of corrosion on the various parts of the electropolishing apparatus, and is not a preferential etch (10). A solution containing 25% glycerine and 0.1% KOH has been found to be satisfactory for germanium. Incorporation of glycerine into the electrolyte composition increased the viscosity and, therefore, enhanced the mechanical coupling between the anode disk and the cathode. The glycerine also increased the film thickness of the electrolyte and in this way helped to prevent anode-cathode shorts.

For silicon it was found that acidic solutions containing fluoride ion were satisfactory for electropolishing. Dilute solutions (between 0.5 and 3 wt %) of HF or NH_4HF_2 have both been employed during the current investigation. As was the case with germanium, the addition of glycerine helped secure smoother rotation of the anode disk. Also, the presence of the glycerine increased the cell impedance. A further discussion of this point will be made later. A 1% solution of NH_4HF_2 in 30% glycerine-70% water was found to produce a good polish on p-type and on less than 0.1 ohm-cm n-type silicon. For higher resistivity n-type silicon, it was found desirable to increase the resistivity of the electrolyte by decreasing the NH_4HF_2 concentration.

The electrolytes were gravity-fed at a rate of about 10 to 30 ml/min to a point close to where the anode was positioned on the cathode disk. The electrolyte was caught below the cathode disk in a polyethylene container and disposed of through a waste line. These features can be seen in Fig. 1. Recirculation of the electrolyte was not considered practical because of the adverse effects which have been caused by metal ion contamination. For example, as

[2] Sylvania Sun Gun.

little as 0.001% of Cu^{++} in the electrolyte degraded the polish on a germanium surface. It is interesting to note that the resistivities of the preferred electrolytes for both germanium and silicon were higher than the resistivities of the bulk semiconductor.

Semiconductor materials.—The majority of semiconductor samples used during this investigation were zone leveled or pulled single crystals oriented and cut in the {111} plane. The {100} and {110} planes have also been electropolished. Both n- and p-type material in the resistivity range of 0.004-47 ohm-cm Ge and 0.001-300 ohm-cm Si have been polished.

Results and Discussion

Surface Characteristics

On a microscale, the surface of a semiconductor appears as a series of peaks and valleys. The short range peak/valley ratio is an index of the smoothness of a surface. The long range irregularities of a surface determine the over-all flatness. Electropolishing with intensive stirring operates in such a way as to minimize both forms of irregularities.

In electropolishing there is formed in the region close to the surface being polished a concentration of the products of electrolysis which is greater than in the bulk of the electrolyte. By introducing intensive stirring, brought about with a flat moving cathode, the concentration of electrolysis products is reduced and the concentration of the active electrolyte species is increased in the vicinity of the anode. In this manner a high polishing rate can be achieved. Good polishing has been obtained with current densities as high as 1.6 amp/cm^2. If the surface being polished contains discontinuities, the hills or high points will receive the most intensive stirring. In addition, the local electric fields and temperatures are higher near the peaks. Thus, on a microscale the action is that of a differential etch rate whereby the peaks are electrolyzed at a faster rate than the valleys. Over-all flatness is developed by the application of this same mechanism operating over larger areas. That is, any group of peaks which extend beyond the average peak height will be acted on more rapidly, since the stirring action will be more intensive in those regions.

Electropolishing has been accomplished starting with slices that had previously been mechanically polished, lapped, sawed, or chemically etched. The amount of material that must be removed in order to achieve a well-polished surface was found to be related to the peak/valley ratio of the starting surfaces. For mechanically polished surfaces (0.1μ particle size abrasive) up to 50μ had to be removed in order to obtain a good electropolish. For semiconductors lapped with 12μ particle size Al_2O_3 between 50 and 75μ had to be removed. Saw-cut surfaces required the removal of up to 250μ of material. Presumably, the damage had been removed from all of these surfaces with less than the polishing actually used. The removal of the additional material was required in order to obtain the desired smoothness and flatness.

Figures 5A and 5B compare a typical mechanically polished surface (0.05μ particle size Al_2O_3)

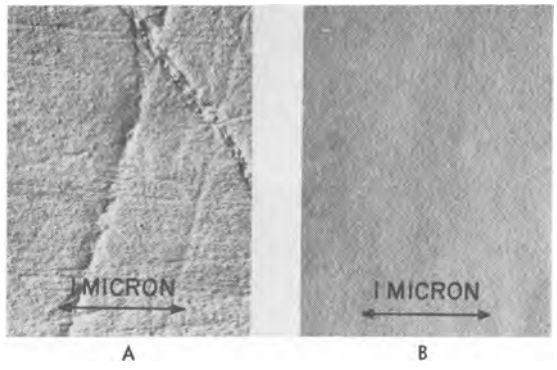

Fig. 5. Electronmicrographs of polished surfaces: A, mechanically polished with 0.05μ Al_2O_3; B, electrochemically polished.

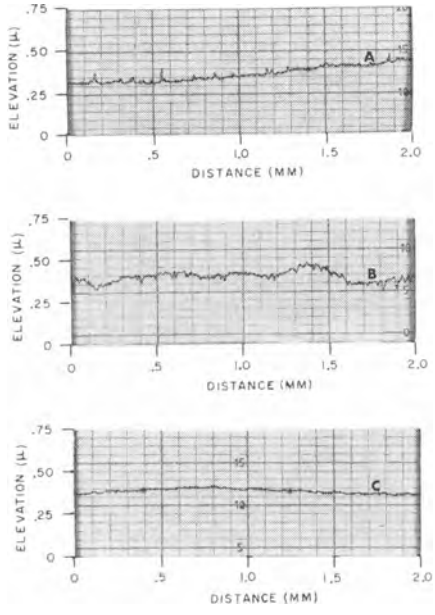

Fig. 6. Profilimiter patterns of several germanium surfaces: A, mechanically polished; B, mechanically polished followed by a chemical etch; C, lapped with 1800 alumina and electropolished.

and an electropolished surface as seen in the electron microscope using a surface replica technique. The residual grain in the photograph of the electropolished surface is typical of all nearly perfect surfaces examined by this technique. Figure 6 compares the surface profiles of mechanically polished, chemically polished, and electropolished germanium as determined by a Talysurf instrument, Model 3.

These surfaces were also examined with a Brush Surface Analyzer and the characteristics obtained are shown in Table I. Thus, it was found that it was possible to achieve surfaces by electropolishing that were as smooth as those obtained by the usual mechanical polishing techniques. For n-type silicon in the rather limited range of 0.1 to 1 ohm-cm, this degree of surface polish was not obtained. The best

Table I. Surface characteristics

Surface treatment	Average roughness, Å
Lapped with Al_2O_3, 12μ	2100
Polished with Al_2O_3, 0.05μ	25
Electropolished after lapping with Al_2O_3, 12μ	25

material in this range has a roughness of 75Å. The reason for this difficulty is not known but may be related to the fact that as the resistivity decreases the need for externally supplied holes decreases (see section on Electrolytic Dissolution) while the presence of crystal imperfections increases.

Except for the rounding of the edges of samples (see Fig. 7), good control of flatness was achieved. Electropolished samples with diameters in excess of 2 cm have a flatness of ± 1 μ/cm across 80% of their surface. A typical interference photograph, Fig. 8, indicates the degree of flatness control on 1 cm^2 of germanium. The control of material removal was such that it was found possible to prepare slices of less than 25μ thickness. It was also possible to remove from thicker specimens as much as 250μ by electropolishing and still maintain the degree of flatness indicated above.

Material Imperfections

An important difference between mechanical polishing and electropolishing was noted when semiconductor slices containing imperfections such as grain boundaries, twins, and inclusions were polished. Whereas mechanical polishing will not reveal such crystal defects, they are readily observed after electropolishing. However, the definition and sensitivity to these types of imperfections is lower than that which is obtained with standard crystallographic etches. The ability to discern these

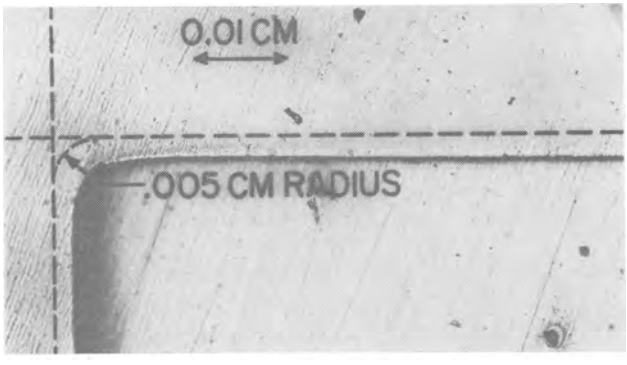

Fig. 7. Sectioned electropolished slice indicating degree of edge rounding.

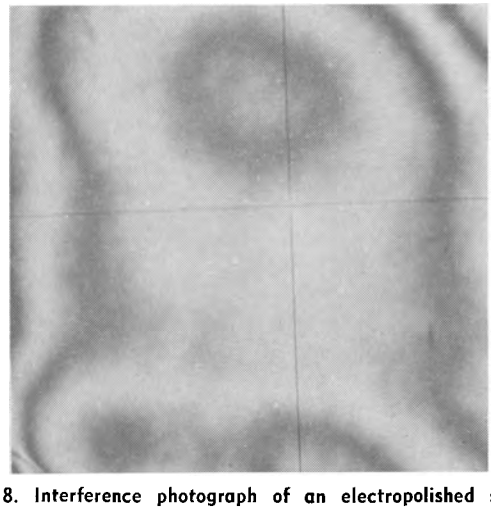

Fig. 8. Interference photograph of an electropolished surface. Field of view is 1 cm x 1 cm. Each fringe indicates an elevation difference of 0.27μ.

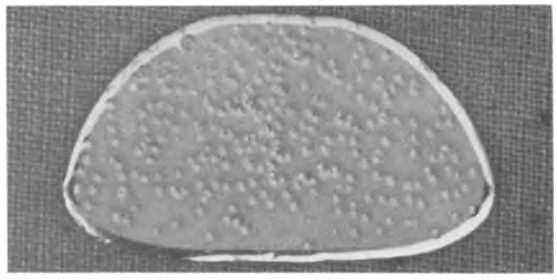

Fig. 9. N-type sample electropolished without carrier injection. The long dimension of the sample is 2.5 cm.

imperfections after electropolishing can be used to advantage in grading the quality of semiconductor slices for device application.

Electrolytic Dissolution

The electrolytic dissolution process for Ge and Si involves both electron and hole carriers (11). The electrons are supplied by broken semiconductor bonds. The holes are available in sufficient quantity for p-type materials of lower than intrinsic resistivity and electrolysis of this material proceeds uniformly. Initially, this is also true for damaged surfaces, such as freshly lapped material. For such surfaces there are numerous carrier generator sites present to support a good rate of electrolysis independent of the bulk resistivity and conductivity type. However, once the damaged layer has been removed from n-type material greater than about 0.01 ohm-cm,[3] the anodic etching becomes very nonuniform. Continued anodization will result in the formation of deep etch pits. Such a condition is shown in Fig. 9 for an n-type Ge sample of 1 ohm-cm. A possible explanation of the pitting follows.

To achieve electropolishing the semiconductor is made positive in the electrolysis cell. Under this biasing condition there is built up in the electrolyte, near the semiconductor surface, an excess of negatively charged ions from the electrolyte. These negatively charged ions in turn repel electrons in the outermost layer of the semiconductor and cause the energy bands to bend upward near the surface. In the case of p-type samples, this merely results in a p+ surface layer. However, in the case of n-type materials an inversion layer is produced. The p-n junction so formed is reverse biased by the etching current. In order to etch at a reasonable rate (greater than 0.03 μ/min) it is necessary to use voltages in excess of the junction breakdown voltage. At these voltages the surface p-n junction breaks down at its weakest point or points. This concentrates a major portion of the etching current through the local breakdown regions and produces deep etch pits.

It is possible to supply carriers to the entire surface layer by using either heat, or an injecting contact, or a "chemical etching" solution, or light. In this way, uniform etching can be achieved rather than the local junction breakdown which results in pitted surfaces. From practical considerations the first method of hole generation was rejected because

[3] For n-type material with resistivities below 0.01 ohm-cm sufficient carriers appear to be available to support uniform anodization.

it would have severely limited the maximum etching rate. The use of an injecting contact was not employed because not enough carriers would survive passage through thick specimens of the semiconductor to the semiconductor-electrolyte interface. The chemical etching solution approach for n-type germanium was attempted using the HCl-KI electrolyte, described by Efimov and Erusalimchik (12), but it was unsuccessful. Therefore, light injection of carriers, the only technique that gave practical etching rates and smooth nonpitted surfaces, was employed. To illuminate the surface of the semiconductor, it was necessary to devise a cathode that was transparent and conductive. As was explained in the experimental section the most effective cathode was a metal disk containing a series of slots. When the semiconductor moved over this perforated metal, all parts of the anode surface received the same average illumination and were equally etched.

A good illustration of the effect of carrier injection can be observed in Fig. 10. Initially, the lapped surface of an n-type germanium anode provided sufficient hole generation sites to support uniform electrolysis. As the damaged region was consumed the cell resistance rose to, and remained at, a high value. At the end of 15 min the light source was turned on and the cell resistance dropped to the low value initially observed on the lapped surface. After 1 min the illumination was discontinued and the cell resistance returned to a high value. A slightly higher impedance value was observed immediately after the light was turned off compared with the value before the light was turned on. The slow return to the steady-state condition was probably caused by the rapid buildup of reaction products while the light was on followed by their slow removal after the light was turned off.

Cell Resistance

An examination of the voltage-current characteristic of the electropolishing cell was made. Figure 11 is a plot of the cell resistance *vs.* voltage for germanium and Fig. 12 for silicon. The best electropolishing was found in the region where a general leveling in the resistance value was observed. This region exists above 2v for germanium and above 7v for silicon. This general pattern and the location

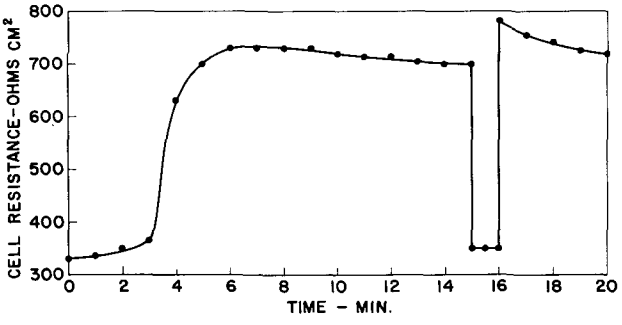

Fig. 10. Effect of damage and illumination when electropolishing an n-type semiconductor anode. Electropolishing was begun from a lapped surface without illumination. Illumination was begun at 15 min and discontinued at 16 min.

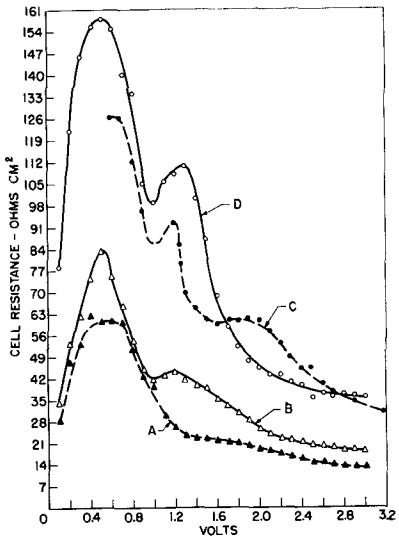

Fig. 11. Cell resistance as a function of voltage for the electropolishing of germanium: A, 0.1% KOH; B, 0.1% KOH, 5% glycerine; C, 0.1% KOH, 25% glycerine; D, 0.1% KOH, 50% glycerine.

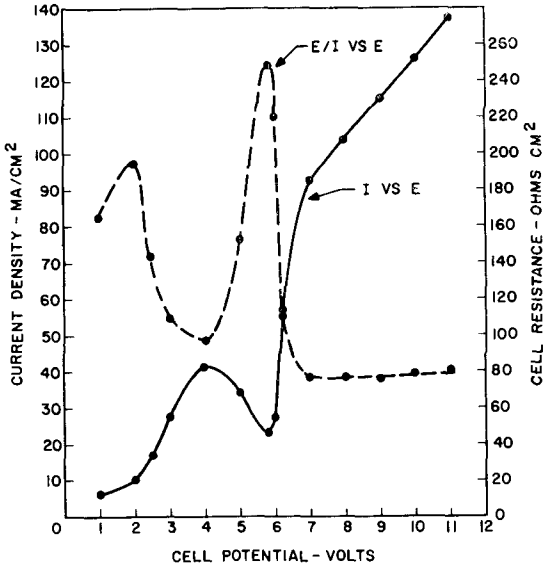

Fig. 12. Current density and cell resistance as a function of voltage for the electropolishing of silicon.

of the best polishing region have been observed in other systems (13).

Current Efficiency

The current efficiency for the dissolution process was measured at several constant current density levels in the range from 1.5 ma/cm² to 1.5 amp/cm². For both germanium and silicon the efficiencies were found to be between 103 and 105%. These efficiencies were computed on the basis of an oxidation state change of 4. Efficiencies greater than 100% can result from dissolution with less than 4 electronic charges per atom. For germanium and silicon the formation of a small amount of the divalent species would account for the high efficiencies observed. A discussion of the number and kind of carriers involved in semiconductor dissolution has been made by Dewald (11).

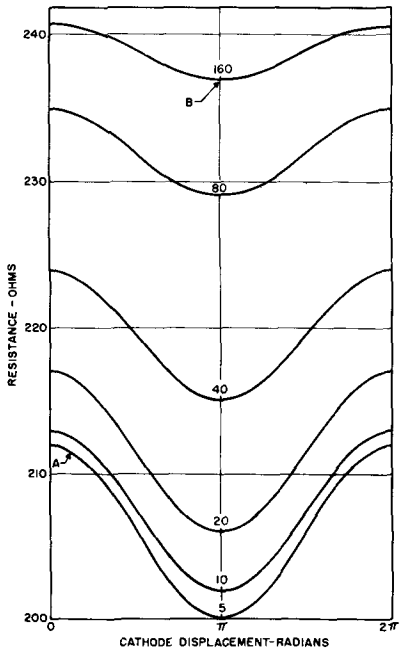

Fig. 13. Cell resistance as a function of cathode displacement. Point of closest approach is indicated in microns at center of each curve.

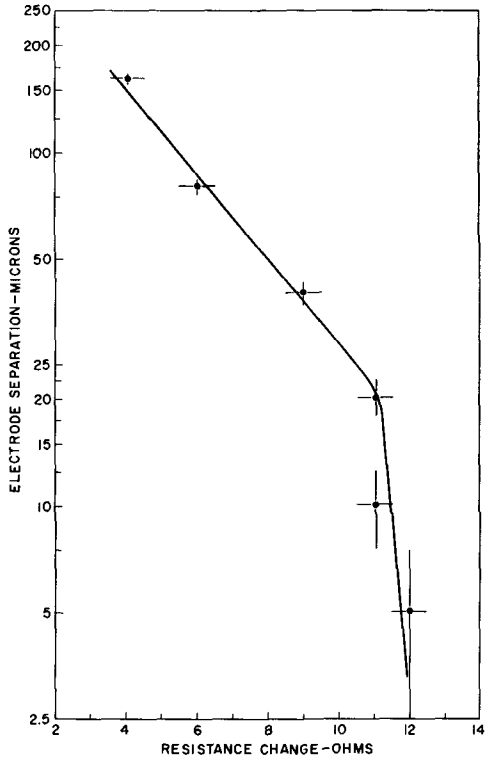

Fig. 14. Change in cell resistance as a function of minimum electrode separation.

Anode-Cathode Spacing

It is believed that the degree of polishing improves as the anode-cathode spacing is decreased. In the polishing system described here, this spacing is a function of the fluid mechanics of the system and cannot be varied easily without changing other properties of the electrolyte. However, the improvement in polishing, which results from a small spacing, was demonstrated by holding the semiconductor specimen at several fixed distances from the cathode.

Another interesting observation was made by holding the semiconductor anode fixed and using a rotating cathode which was centrally supported by a shaft arbitrarily set at 89° 53′ to the plane of the cathode. When rotated, this cathode produced a cyclically varying anode-cathode spacing. The voltage-current characteristics of this cell were continuously monitored on an oscilloscope. A typical set of tracings from an oscillograph record is shown in Fig. 13. In each curve the anode-cathode spacing varied by 160μ throughout one rotation of the cathode (0-2π). The separate curves are for positions of the anode such that the points of closest approach to the cathode were 5, 10, 20, 40, 80, and 160μ.

After inspection of a single curve, it might be concluded that the cell resistance is a simple function of the anode-cathode spacing. An examination of the remainder of the curves, however, leads to the suggestion that the cell resistance is also a function of the stirring history. For example, at point A in Fig. 13 the cell resistance is 211 ohms for an anode-cathode spacing of 160μ, whereas at point B the cell resistance is 237 ohms for the same spacing. The anode-cathode spacing at the time of the measurement was the same for both points. The difference in cell resistance is probably due to the fact that at point A the anode was very intensively stirred π radians ago (spacing ~5μ) whereas at point B the anode was very poorly stirred π radians ago (spacing 320μ). This same mechanism should lead to an asymmetric appearance of each curve. If this is the case, the degree of asymmetry was so small that it was lost in the recording error.

Another presentation of these same data is shown in Fig. 14 where the anode-cathode separation at the point of closest approach was plotted against the change in resistance throughout one cycle of the wheel rotation. The data suggest that the mechanism is different at small anode-cathode spacings (below 20μ). This may, for example, be the distance below which turbulent stirring becomes predominant. Another interpretation of the change in slope may be that it occurs at a distance from the anode equivalent to the thickness of the diffusion layer. An excellent discussion of the effect of stirring on metal dissolution is given by King (14).

Device Applications

A variety of semiconductor devices have now been made using materials which had been electropolished with intensive stirring. In every case the quality of the finished device was equal to or better than that obtained when mechanical polishing was used. For example, Fig. 15 shows the distribution of saturation currents on one type of high-frequency germanium transistor. This transistor was particularly sensitive to surface damage because its junction was only 0.25μ below the surface. The standard surface preparation for this transistor was a mechanical polish followed by a short chemical etch. When electropolishing was used in the preparation of this device, the distribution shown in Fig. 16 was obtained. Note that the median value of the satura-

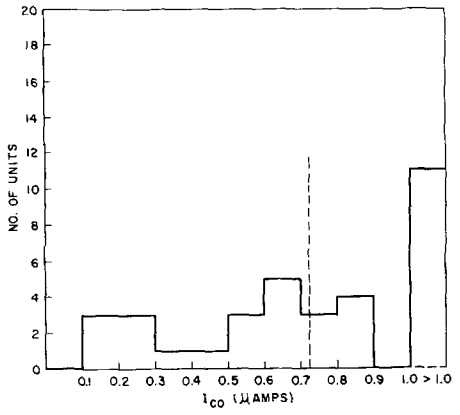

Fig. 15. Distribution of saturation currents for high-frequency diffused-base germanium transistors. Surfaces had been mechanically and then chemically polished. Median value is indicated by the dotted line.

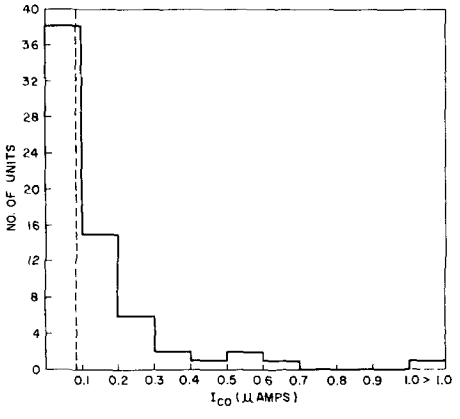

Fig. 16. Distribution of saturation currents for the same type of transistors as in Fig. 15 made with electropolished germanium.

tion current had improved by a factor of 10 as the result of replacing the mechanical operation with electropolishing. Presumably the chemical etch did not remove all of the mechanical damage from the standard transistors. A longer chemical polish would seem to be a simple solution. Unfortunately, however, there is no chemical polish available for germanium which leaves a smooth surface after a prolonged etch. Therefore, for germanium, electropolishing is the most desirable from the standpoint of surface quality. It is significant also that the cost of electropolishing is less than half the cost of mechanical polishing.

In the case of silicon, a chemical polishing technique has been recently developed which is able to produce very fine damage-free surfaces directly from lapped material (15). These surfaces are quite comparable with electropolished surfaces and the selection of a polishing method must, therefore, depend on the particular application. Both chemical and electropolishing of silicon are significantly less expensive than mechanical polishing.

Summary

One of the major problems in the manufacture of semiconductor devices is the maintenance of an undamaged surface on a semiconductor slice. In conventional practice the slices are lapped with coarse abrasives and then polished with fine abrasives until a smooth and flat surface is obtained. The mechanical damage is then removed by a short chemical etch. This is usually accomplished at some sacrifice to the smoothness and flatness obtained in the mechanical polishing operation. If the mechanical damage were deeper than expected, the short chemical etch would fail to remove all of the damage and poor quality devices might result. By using electropolishing instead of mechanical polishing all of the damaged material is removed during the polishing operation.

In order to obtain a high degree of polish and flatness, the cathode-anode spacing was kept very small and intensive stirring was developed between the rotating electrodes. The small spacing was obtained by allowing the anode to ride on a thin film of the electrolyte whose thickness was determined principally by the viscosity of the solution. Additional mechanical spacers such as thin sheets of paper or cloth were also used.

Germanium or silicon, n- or p-type, can be electropolished in this manner to give a very high degree of polish in about 30 min.

Manuscript received Nov. 7, 1962. This paper is based on a paper presented before the Indianapolis Meeting, April 30-May 3, 1961.

Any discussion of this paper will appear in a Discussion Section to be published in the December 1963 JOURNAL.

REFERENCES

1. J. W. Tiley and R. A. Williams, *Proc. I.R.E.*, **41**, 1706 (1953).
2. E. Billig and J. J. Dowd, *Nature*, **172**, 115 (1953).
3. A. Uhlir, Jr., *Rev. Sci. Inst.*, **26**, 965 (1955).
4. M. V. Sullivan and J. H. Eigler, *This Journal*, **103**, 132 (1956).
5. A. Uhlir, Jr., *Bell System Tech. J.*, **35**, 33 (1956).
6. E. C. Wurst, Jr. and E. H. Borneman, *J. Appl. Phys.*, **28**, 235 (1957).
7. I. A. Lesk and R. E. Gonzales, *This Journal*, **105**, 469 (1958).
8. D. R. Turner, in "Electrochemistry of Semiconductors," P. J. Holmes, Editor, Academic Press, Inc., New York (1962).
9. M. V. Sullivan and J. H. Eigler, *This Journal*, **104**, 226 (1957).
10. W. W. Harvey, Private communication.
11. J. F. Dewald, "Semiconductors," N. B. Hannay, Editor, p. 733, Reinhold Publishing Corp., New York (1959).
12. E. A. Efimov and I. G. Erusalimchik, *Doklady Akad. Nauk SSSR*, **128**, 124 (1959).
13. I. Epelboin, *J. Chem. Phys.*, **49**, C214 (1952).
14. C. V. King, in "Surface Chemistry of Metals and Semiconductors," H. C. Gatos, Editor, John Wiley & Sons, Inc., New York (1960).
15. D. L. Klein and D. J. D'Stefan, *This Journal*, **109**, 37 (1962), and another paper to be published.

Polarographic Studies in Acetonitrile and Dimethylformamide

VII. The Formation of Benzyne

S. Wawzonek and J. H. Wagenknecht

Department of Chemistry, State University of Iowa, Iowa City, Iowa

ABSTRACT

Polarographic studies of the three isomeric dibromobenzenes and bromochlorobenzenes have been carried out in acetonitrile and dimethylformamide. The results with o-dibromobenzene in these solvents point to an intermediate which eliminates a bromide ion and forms benzyne. The intermediate from o-bromochlorobenzene under the same conditions undergoes partial elimination to benzyne. The elimination reaction also occurs to a slight extent for o-dibromobenzene in aqueous dioxane. The formation of benzyne was verified by a large-scale electrolytic reduction of o-dibromobenzene in dimethylformamide in the presence of furan. The tarry product obtained on acid hydrolysis gave a 1% yield of α-naphthol.

Saturated hydrocarbons containing halogens on adjacent carbon atoms undergo polarographically a two-electron reduction and form an olefin (1,2). Similarly 1,2-dihaloethylenes give acetylenes as indicated by coulometric data for *trans*-2,5-dimethyl-3,4-dibromo-3-hexen-2,5-diol (3) and the polarographic behavior of α,β-dichloroacrylonitrile (4), dibromomaleic and dibromofumaric acids and their ethyl esters (5).

In the present study, the polarographic behavior and large-scale electrolytic reduction of o-dihalobenzenes have been investigated in both aprotic and protic solvents to determine whether benzyne is formed as an intermediate. Polarographic data for the other isomeric dihalobenzenes and monohalobenzenes were also obtained as an aid in formulating the mechanism of reduction.

Experimental

The solutions were studied in a cylindrically shaped cell with a mercury pool anode as previously described (6). All measurements were made in a water thermostat at 25° ± 0.1°C.

The current-voltage curves were obtained with a Sargent Model XXI polarograph. The gas chromatograph was a Perkin-Elmer Model 154 with helium as a carrier gas.

The dropping mercury electrode was operated at 72 cm pressure and had a drop time of 5.5 sec and an m value of 1.17 mg sec^{-1} with a calculated value of $m^{2/3}\ t^{1/6}$ of 1.468 $mg^{2/3}\ sec^{-1/2}$.

The solvents and supporting electrolytes were purified and prepared in a manner to that described previously (6). The various dihalobenzenes were obtained from stock, Eastman Kodak Company and Aldrich Chemical Company. The purity was verified by gas chromatography using a Perkin-Elmer Column C (silicone oil DC 200) at 176°.

Electrolytic reduction of o-dibromobenzene.—The electrolytic reduction was carried out with a platinum anode and mercury cathode as described previously (6). The cell was cooled in a mixture of ethylene glycol and dry ice at −35°C. A solution of 300 ml dimethylformamide, 22g of tetra-*n*-butylammonium iodide, 10g of o-dibromobenzene, and 50 ml of furan was degassed for 2 hr with pure nitrogen. The direct current of 0.4 amp used at the start of the electrolysis dropped to 0.25 amp after 6 hr, and the electrolysis was terminated.

The catholyte and anolyte were combined and the solvent was removed by distillation at atmospheric pressure through a 1-ft Vigreux column. The remaining black oily residue was refluxed with 100 ml of ethanol saturated with hydrogen chloride for 5 hr. Removal of the solvent was followed by a steam distillation of the black tarry residue. The steam distillate was extracted with ether, and the ether extract was analyzed for α-naphthol by gas chromatography on a 4-ft silicone grease column at 160° with a flow rate of 1.4 ml/sec of helium. A peak with a retention time of 2 min 32 sec was obtained which agreed with that obtained with an authentic sample. The yield based on the area of the peak was 1%. The ether extract in ethanol gave an adsorption peak in the ultraviolet region at 215 mμ in agreement with that found for α-naphthol.

Electrolysis of o-dibromobenzene was also carried out in the absence of furan, but no triphenylene could be found in the black oily product by gas chromatography, polarography, fluorescent analysis, and ultraviolet spectroscopy.

Results

The polarographic results obtained in various solvents for the isomeric dihalobenzenes and monohalobenzenes are given in Table I.

The waves observed were well defined for most of the examples. o-Dibromobenzene gave a maximum in dimethylformamide and acetonitrile which still persisted at a concentration of 0.00026*M*. o-Bromochlorobenzene gave a maximum for the first wave in dimethylformamide but not in acetonitrile.

p-Dibromobenzene gave a well-defined first wave which, at the start of its limiting value, developed into a drawn out second wave at a slightly more positive potential than that for bromobenzene.

Table I. Polarographic behavior of halogenated benzenes in various solvents containing 0.2M tetra-n-butylammonium bromide

Benzene[a]	Solvent	1st Wave $-E_{1/2}$	1st Wave I_d[b]	2nd Wave $-E_{1/2}$	2nd Wave I_d[b]
o-Dibromo	DMF[c]	1.28	6.53	—	—
	CH_3CN	1.41	9.77	—	—
	82% Dioxane	1.40	4.15	—	—
	75% Dioxane	1.40	3.84	—	—
	60% Dioxane	1.40	3.42	—	—
o-Bromochloro	DMF	1.38	4.50	2.02	1.44
	CH_3CN	1.54	5.5	—	—
m-Dibromo	DMF	1.40	3.79	1.88	2.68
	CH_3CN	1.55	5.0	2.05	3.9
	82% Dioxane	1.56	2.66	—	—
	75% Dioxane	1.56	2.57	—	—
	60% Dioxane	1.56	2.28	—	—
m-Bromochloro	DMF	1.49	3.32	2.04	2.83
	CH_3CN	1.65	4.85	—	—
p-Dibromo	DMF	1.53	3.02	1.82	3.49
	CH_3CN	1.70	4.12	2.02	4.12
p-Bromochloro	DMF	1.60	3.09	2.02	2.61
	CH_3CN	1.81	4.5	—	—
Bromo	DMF	1.85	3.28	—	—
Chloro	DMF	2.00	2.95	—	—

[a] Concentrations varied from 0.0005M to 0.0011M.

[b] $I_d = \frac{i_d}{Cm^{2/3}t^{1/6}}$.

[c] Dimethylformamide.

The break between the two waves was difficult to estimate. p-Bromochlorobenzene, however, gave well-defined waves in both solvents.

To help formulate the electrode reaction for the reduction of o-dibromobenzene and to obtain proof for the intermediate specie a large-scale electrolytic reduction of o-dibromobenzene was carried out in the presence of furan in dimethylformamide.

Discussion and Results

Examination of the results in Table I indicates that the polarographic reduction of m-dibromobenzene, m-bromochlorobenzene, and p-bromochlorobenzene is normal in dimethylformamide and acetonitrile. The reduction of the halogens proceeds stepwise through bromo- and chlorobenzene to benzene since the half-wave potentials of the second waves in dimethylformamide occur at the same point as those

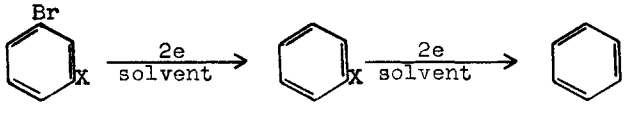

for bromo-and chlorobenzene. The behavior of these compounds in acetonitrile was quite similar except that the reduction wave for chlorobenzene was not observed since this compound is not reducible in this medium.

The height of the second wave in dimethylformamide for these compounds is smaller than that of the first wave. This behavior parallels that observed for the two-step reduction of hydrocarbons (7), quinones (8), and ketones (9) in this solvent and is probably caused by a similar partial repulsion of the intermediate carbanion from the electrode.

o-Dibromobenzene in contrast to the meta isomer gives only one wave with a diffusion current constant equivalent to the sum of the diffusion current constants of the two waves for m-dibromobenzene. This behavior points to the formation of benzyne by the elimination of a bromide ion from the first reduction intermediate. Benzyne is then reduced more easily than o-dibromobenzene and the net reaction is a four-electron wave. The elimination reaction is a rapid one since phenol had no effect on the height of the wave in dimethylformamide and the wave is diffusion controlled.

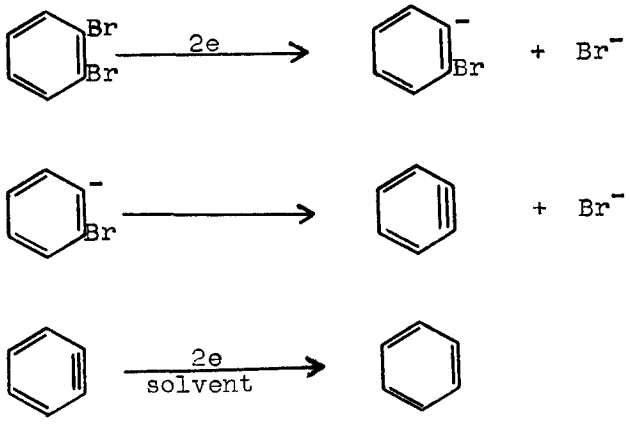

o-Bromochlorobenzene undergoes only partial elimination of chloride ion and gives a small second wave for the reduction of chlorobenzene. The extent of this elimination is not influenced by the presence of phenol, but seems to be a function of the solvent; the amount, for example, is less in acetonitrile. A similar behavior occurs for o-dibromobenzene even in aqueous dioxane; the wave height is larger than that observed for m-dibromobenzene.

Further proof for the formation of benzyne was the large-scale electrolytic reduction of o-dibromobenzene in dimethylformamide in the presence of furan. Benzyne has been found by others (10) to add to furan and yield 1,4-epoxy-1,4-dihydronaphthalene which on acid hydrolysis yields α-naphthol.

The products from electrolysis upon acid hydrolysis gave a 1% yield of α-naphthol. Vigorous stirring of the catholyte was necessary to produce this product since the benzyne formed is easily reduced electrolytically to benzene.

Electrolysis in the absence of furan gave a series of fluorescent products which could not be identified. Triphenylene which has been isolated in some preparation of benzyne (11), could not be detected by v.p.c. analysis, polarography, fluorescent analysis, or ultraviolet spectroscopy.

The polarographic behavior of p-dibromobenzene in dimethylformamide and acetonitrile indicates that the bromine substituents are removed stepwise. The drawn out second wave, which occurs at slightly more positive potentials than that for bromobenzene, suggests that the bromine substituent in the intermediate carbanion may become more labile to re-

duction by the tendency of the intermediate to form p-benzyne.

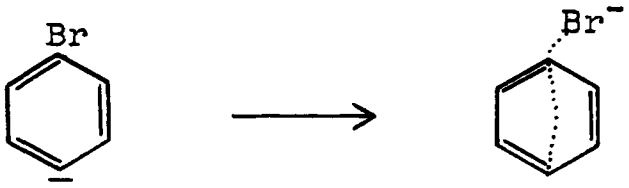

Manuscript received Sept. 4, 1962; revised manuscript received Nov. 12, 1962.

Any discussion of this paper will appear in a Discussion Section to be published in the December 1963 JOURNAL.

REFERENCES

1. M. von Stachelberg and W. Stracke, *Z. Elektrochem.*, **53**, 118 (1949).
2. I. Rosenthal and R. J. Lacoste, *J. Am. Chem. Soc.*, **81**, 3268 (1959).
3. S. G. Mairanovski and L. D. Bergel'son, *Zhur. Fiz Khim.*, **34**, 236 (1960).
4. W. A. Jura and R. J. Gaul, *J. Am. Chem. Soc.*, **80**, 5402 (1958).
5 I. Rosenthal, J. R. Hayes, A. J. Martin, and P. J. Elving, *ibid.*, **80**, 3050 (1958).
6. S. Wawzonek and R. C. Duty, *This Journal*, **108**, 1135 (1961).
7. S. Wawzonek, E. W. Blaha, R. Berkey, and M. E. Runner, *ibid.*, **102**, 23 (1955).
8. S. Wawzonek, R. Berkey, E. W. Blaha, and M. E. Runner, *ibid.*, **103**, 456 (1956).
9. S. Wawzonek and A. Gundersen, *ibid.*, **107**, 537 (1960).
10. G. Wittig, *Angew. Chem.*, **69**, 245 (1957).
11. A. Luttringhaus and K. Schubert, *Naturwissenschaften*, **42**, 17 (1955).

Electrochemical Degradation of Aryl Sulfonium Salts

Manuel Finkelstein, Raymond C. Petersen, and Sidney D. Ross

Research Laboratories, Sprague Electric Company, North Adams, Massachusetts

ABSTRACT

The products of the electrochemical degradation of several aryl sulfonium salts at an aluminum cathode were studied. In each case a phenyl radical was cleaved with the subsequent formation of benzene. Dimethylformamide was found to be an excellent solvent for these reactions. The rate of formation of benzene in the electrochemical decomposition of triphenylsulfonium trifluoroacetate in dimethylformamide has been shown to be independent of the concentration of sulfonium salt. A brief discussion of the mechanism is presented with reference to the observed current efficiency.

In connection with a study of the mechanism of the electrochemical degradation of quaternary ammonium salts (1, 2), the electrolysis of several aryl sulfonium salts was investigated. Previous work by Bonner (3) had shown that in aqueous solution triphenylsulfonium nitrate is decomposed at a platinum cathode to diphenyl sulfide and some alkali-soluble tars. His experimental technique did not permit the detection of benzene.

We wish to report some results obtained from the electrolysis of triphenylsulfonium and ethyldiphenylsulfonium salts at an aluminum cathode in various solvents and under conditions which allow the formation and quantitative detection of benzene. Since our major interest in this work was the fate of the phenyl radical, we have not studied the sulfur-containing products quantitatively. In most cases only the identification of the sulfur product is reported.

Experimental

Electrode materials.—The aluminum sheet used for cathodes was obtained from either Aluminum Foils Inc., Jackson, Tennessee, or AIAG Metals, Inc., Zurich, and was 99.999% Raffinal, 0.05 cm thick. Platinum wire 0.1 cm in diameter was used for anodes.

Solvents.—Dimethylformamide (DMF) was purified by Method I of Thomas and Rochow (4). Methanol was A.C.S., reagent grade.

Compounds.—Triphenylsulfonium bromide and nitrate were prepared according to Wildi, Taylor, and Potratz (5).

Ethyldiphenylsulfonium fluoborate was made by the method of Franzen (6).

Triphenylsulfonium trifluoroacetate was prepared by treatment of a methanolic solution of the bromide with an equivalent quantity of silver trifluoroacetate in methanol, filtering off the silver bromide and removing the methanol *in vacuo*. Two crystallizations from acetone-ether afforded white crystals, mp 119°-120°.

Analysis.—Calculated: for $C_{20}H_{15}F_3O_2S$; C, 63.82; H, 4.02; S, 8.52. Found: C, 63.52, 63.47; H, 3.51, 3.42; S, 8.57, 8.64.

The solution of triphenylsulfonium methoxide in methanol was prepared by magnetically stirring an excess of silver oxide with a methanolic solution of the sulfonium bromide. The silver bromide and excess silver oxide were filtered with the aid of Celite through sintered glass, and the clear solution was analyzed for basicity.

Ethyl phenyl sulfide was prepared by treating a solution of thiophenol in excess aqueous sodium hydroxide with a solution of ethyl iodide in ethanol, n_D^{26} 1.5627 [reported (7), n_D^{20} 1.5666].

Electrolysis Procedure

The electrolysis cell consisted of a jacketed tall-form beaker 10 cm high and 5 cm in diameter with

an enlarged top 1 cm high. The electrodes were attached to a circular piece of Bakelite which fitted in the enlarged top. Two strips of aluminum 2.5 cm apart served as cathodes with a platinum wire anode centered between them. The immersed area of each cathode was 12.5 cm^2 (5 cm high and 2.5 cm wide) and the anode also was immersed to a depth of 5 cm. Cold tap water was constantly circulated through the jacket and stirring was provided by a Teflon-covered magnetic bar. Current was provided by a variable voltage-regulated power supply and an ammeter (Sensitive Research Instrument Corporation D.C. Polyranger Model "Univ.") was connected in series with the electrolysis cell. The current was maintained constant at 0.50 amp throughout each electrolysis.

Electrolysis of triphenylsulfonium nitrate in DMF.—A solution of 16.3g (0.050 mole) of triphenylsulfonium nitrate in 128 ml of DMF was electrolyzed for 14.5 hr. The initial applied voltage was 100v. This was increased as the reaction proceeded to maintain constant current, and it reached 155v by the end of the electrolysis. The reaction mixture was analyzed directly for benzene by VPC (vapor phase chromatography), and the yield was found to be 96.2% of theoretical (assuming one phenyl radical to be cleaved from each triphenylsulfonium ion).

In a separate experiment, an identical electrolysis was performed and the reaction mixture poured into a liter of water and extracted four times with ether. The ether was dried over magnesium sulfate and distilled through a Vigreux column. The residue was distilled at 0.18 mm to give 3.78g of a yellow liquid, bp 80°-90°, n_D^{21} 1.6230. The liquid was redistilled and a middle cut, bp 85°, n_D^{23} 1.6276 taken, the infrared spectrum of which was identical with that of diphenyl sulfide. The crude yield was 40.6%.

The yield of benzene obtained and the electrolysis time for each of the experiments is presented in Table I.

The experimental procedure in each case was similar to that described in detail for triphenylsulfonium nitrate in DMF. Ethyldiphenyl sulfide was identified by isolation and comparison with an authentic sample.

Electrolysis of diphenyl sulfide.—A solution of 9.1g of diphenyl sulfide, 4.5g of sodium nitrate and 130 ml of DMF was electrolyzed for 6 hr. The dark solution was poured into water and extracted. Distillation of the extract gave a maximum recovery of 42% of the diphenyl sulfide.

Decomposition of Benzoyl Peroxide in DMF.—A solution of benzoyl peroxide (12.11g, 0.05 mole) in 130 ml of DMF was kept for 30 hr at 78°-83°. Analysis by VPC indicated the presence of 0.0196 mole of benzene. Also isolated were 6.7g (0.055 mole) of benzoic acid and 4.3g (0.022 mole) of N-benzoyloxymethyl-N-methylformamide, n_D^{27} 1.5324 [reported (8) n_D^{20} 1.5401].

Table I. Sulfonium Salt Electrolyses

Salt	Solvent	Time, hr	% Yield of benzene
Triphenylsulfonium nitrate	DMF	14.5	96.2
Triphenylsulfonium nitrate	Water	14.2	40.5
Triphenylsulfonium trifluoroacetate	DMF	13.3	99.8
Triphenylsulfonium trifluoroacetate	Methanol	2.7	11
Triphenylsulfonium methoxide	Methanol	15.5	28
Ethyldiphenylsulfonium fluoborate	DMF	16.2	75.1
Ethyldiphenylsulfonium fluoborate	Water	11.8	10.3

Results and Discussion

The electrolysis of triphenylsulfonium nitrate in DMF at an aluminum cathode produced benzene in 96% of the theoretical yield and diphenyl sulfide in 41% yield. In contrast, the electrolysis of the same salt in water gave 40% of benzene and almost 60% of diphenyl sulfide. These products can be rationalized by an electrolysis mechanism involving the discharge of the cation, cleavage of a phenyl radical and subsequent abstraction of a hydrogen atom to form benzene. An alternative source of hydrogen in the aqueous system could be the concurrent discharge of hydrogen ions provided by the water.

The hydrogen atoms in DMF are all bonded to carbon and the average C-H bond energy is 98.8 kcal/mole (9). In the case of water, however, the hydrogens are bonded to oxygen. To remove a hydrogen atom from water requires 119.9 kcal/mole (10). It would thus be easier for the phenyl radical to remove a hydrogen atom from DMF than from water, and a higher yield of benzene would be expected in the former case.

The possibility of such a reaction is demonstrated by decomposition of a known source of phenyl radicals, benzoyl peroxide, in DMF. We found conversion of 20% of the phenyl radicals in the peroxide to benzene. Clearly phenyl radicals can abstract hydrogen from DMF.

Further examples of the ability of radicals to effect this reaction are given by Friedman and Schechter (11) and by Schwetlick (12) in their work on the decomposition of *t*-butyl peroxide in DMF.

The fact that a higher yield of diphenyl sulfide is obtained from the aqueous system is best explained by the insolubility of diphenyl sulfide in water. It was shown that diphenyl sulfide could be recovered in a maximum of only 42% yield after its electrolysis in a solution of sodium nitrate in DMF. In the aqueous system the sulfide forms a separate phase and does not react further.

A similar distinction between DMF and water was observed in the case of ethyldiphenylsulfonium fluoborate, and the same explanation is applicable. It is of some interest to note that in DMF the phenyl is cleaved rather than the ethyl, as shown by the identification of benzene and ethyl phenyl sulfide as the products. In this sense sulfonium compounds behave much like ammonium compounds, which also split off phenyl in preference to alkyl radicals (13, 14).

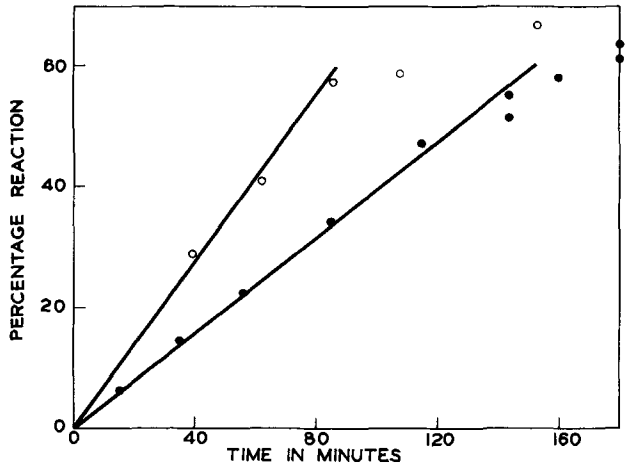

Fig. 1. Rate of benzene production from electrolysis of triphenylsulfonium trifluoroacetate in DMF, Al cathode, 0.50 amp, 130 ml DMF in each case; ○, 0.0212 mole salt; ●, 0.0419 mole salt.

The electrolysis of triphenylsulfonium trifluoroacetate in DMF at an aluminum cathode gave benzene in 99.8% yield. This was followed kinetically by periodic vapor phase chromatographic analysis of the reaction solution for benzene.

This experiment represents a departure from the ordinary polarographic type of reduction. A solid metal electrode is used to obviate undesirable complications which might arise from the involvement of mercury in the reaction, perhaps through the aryl-mercury radicals postulated by Colichman and Maffei (15) in their reduction of diphenyliodonium ion.

Figure 1 shows for two different salt concentrations that a plot of percentage reaction (based on benzene production) *vs.* time gives a straight line for a substantial part of the reaction. This is the expected behavior for the situation in which the rate of discharge of sulfonium ions is independent of the sulfonium ion concentration.

The solid lines drawn on the plot correspond to current efficiencies for benzene production of 47% for the solution containing 0.0212 mole and 53% for the solution containing 0.0419 mole. If we call these identical within experimental error, this result is again consistent with a reaction zero-order in sulfonium ion concentration.

It is apparent from the plot that at about 50% reaction there is a sudden decrease in the current efficiency for benzene production. Additional points at later times, omitted from Fig. 1 for convenience, continue the trend of the later points shown. At this point the two solutions have only one obvious common denominator. In each case the total charge passed by the solution has been just about the amount required to discharge all of the sulfonium ions, assuming 100% current efficiency for the discharge reaction. We do not yet choose to draw any conclusion from this fact.

Mechanistically the observed current efficiency of 50% for the formation of benzene can be explained by either a one-electron transfer for the discharge (path A) with diversion of the remainder of the current through side reactions or a two-electron transfer for the discharge of the sulfonium ion (path B).

$$\begin{array}{ccc} (C_6H_5)_3S^+ & \xrightarrow[\text{Path A}]{+1e} & (C_6H_5)_2S + C_6H_5\cdot \\ {\scriptstyle +2e}\ \downarrow\ \text{Path B} & & \downarrow \\ (C_6H_5)_2S + C_6H_5^- & \longrightarrow & C_6H_6 \end{array}$$

While the 50% current efficiency is strongly suggestive of path B, and while we hesitate to dismiss it as a mere coincidence, we are equally hesitant about insisting that path B is required.

Among the possible side reactions which could occur is the electrochemical reduction of DMF. That this is a feasible reaction has been shown, albeit under different conditions, by Gavrilov and Koperina (16). Traces of water present in the DMF could also account for side reactions.

The polarographic reduction of trimethylsulfonium ion has been carried out by Colichman and Love (17). Relating their results to the Colichman and Maffei data (15) on diphenyliodonium ion and assuming equal diffusion coefficients for the two ions, they decided that the reduction of trimethylsulfonium involved a two-electron step.

In previous work with quaternary ammonium salts (2) optical results and dimerization reactions permitted the assignment of path A as the probable mechanism. With the more reactive phenyl radical, hydrogen abstraction reactions are favored over coupling reactions, and the failure to find diphenyl as a product of the electrochemical reaction is no indication that a phenyl radical is not involved as an intermediate.

It appears that, while there is experimental basis for tentative conclusions concerning the mechanisms of some specific electrochemical 'onium' ion reductions, there is still a great deal of confusion and no significant generalization can yet be made.

Acknowledgment

The authors are indebted to Dr. E. Robert Coburn of Bennington College for the preparation of some of the salts.

Manuscript received May 1, 1962; revised manuscript received Nov. 20, 1962.

Any discussion of this paper will appear in a Discussion Section to be published in the December 1963 JOURNAL.

REFERENCES

1. M. Finkelstein, R. C. Petersen, and S. D. Ross, *J. Am. Chem. Soc.*, **81**, 2361 (1959).
2. S. D. Ross, M. Finkelstein, and R. C. Petersen, *ibid.*, **82**, 1582 (1960).
3. W. A. Bonner, *ibid.*, **74**, 5078 (1952).
4. A. B. Thomas and E. G. Rochow, *ibid.*, **79**, 1843 (1957).
5. B. S. Wildi, S. W. Taylor, and H. A. Potratz, *ibid.*, **73**, 1965 (1951).
6. V. Franzen, H-J Schmidt, and C. Mertz, *Chem. Ber.*, **94**, 2942 (1961).
7. A. I. Vogel, *J. Chem. Soc.*, **1948**, 1822.
8. C. H. Bamford and E. F. T. White, *ibid.*, **1959**, 1860.
9. L. Pauling, "The Nature of the Chemical Bond," 3rd Ed., p. 85, Cornell University Press, Ithaca, N. Y.

10. L. Pauling, *ibid.*, p. 622.
11. L. Friedman and H. Schechter, *Tetrahedron Letters*, 238 (1961).
12. K. Schwetlick, *Angew. Chem.*, **72**, 208 (1960).
13. B. Emmert, *Ber.*, **42**, 1507 (1909).
14. B. Emmert, *ibid.*, **45**, 430 (1912).
15. E. L. Colichman and H. P. Maffei, *J. Am. Chem. Soc.*, **74**, 2744 (1952).
16. N. I. Gavrilov and A. W. Koperina, *C.A.*, **34**, 1615 (1940).
17. E. L. Colichman and D. L. Love, *J. Org. Chem.*, **18**, 40 (1953).

Electrochemical Reduction of the Benzene Ring

Heinz W. Sternberg, Raymond Markby, and Irving Wender

Pittsburgh Coal Research Center, Bureau of Mines, Pittsburgh, Pennsylvania

ABSTRACT

Reduction of benzene and tetrahydronaphthalene (tetralin) was achieved by electrolysis in ethylenediamine saturated with lithium chloride. This reduction could also be carried out with tetrabutylammonium iodide as the supporting electrolyte. In the absence of a substrate, electrolysis of a solution of lithium chloride in ethylenediamine produced the blue color of the solvated metal.

In recent years electrolytic methods have been applied in the reduction and structural elucidation of coal and coal extracts (1, 2). However, the usefulness of these methods is limited by the fact that the benzene ring (that is, the isolated benzene ring as in benzene or tetralin), which may represent a large portion of the coal structure, has not been reduced electrolytically. We therefore became interested in developing a method for the electrolytic reduction of the benzene ring.

The fact that benzene is not reduced in solvents such as dimethylformamide or dioxane-water is due to the high reduction potential of the benzene ring. This has been estimated (3) to be about 1v more negative than the reduction potential of naphthalene which can be readily reduced electrolytically. Solvents such as dimethylformamide or dioxane-water are not stable at the high potential required for the reduction of the benzene ring. On the other hand, reduction is readily achieved chemically by treating benzene with an alkali metal in ammonia (4) or amine solution (5, 6). The mechanism proposed for the chemical reduction of aromatic hydrocarbons in liquid ammonia (7) is similar to that proposed for the electrolytic reduction (8, 9); in the former, the solvated alkali metal furnishes the electron while, in the latter, the cathode is the electron source.

Since solutions of alkali metals in ammonia can also be obtained electrolytically (10), it occurred to us that electrolytic reduction of alkali metal ions might provide a means for the reduction of the benzene ring. Our own observations, described below, show that blue solutions of lithium can be obtained by electrolysis of a solution of lithium chloride in ethylenediamine. This led us to investigate the possibility of reducing the benzene ring electrolytically in ethylenediamine in the presence of lithium chloride.

Experimental

Apparatus.—The apparatus used for electrolysis is shown in Fig. 1. The arrangement of stopcock and adapters permitted the electrolysis to be carried out in an inert atmosphere and the measurement of the evolved gas. A carbon anode was used in all experiments. Smooth platinum wire (20 gauge), graphite and carbon rods (maximum impurity 6 ppm) were used as cathodes. The surface area of each cathode was 7.0 cm^2. In one experiment (Experiment No. 3, Table I) an anode compartment was used. It consisted of a basket made by cutting off the stem of a micro Buchner funnel (capacity 3 ml, medium porosity).

All electrolyses were carried out at manually controlled constant current.

Polarograms were recorded on a L&N Electrochemograph Type E.

Reagents.—Lithium chloride and tetrabutylammonium iodide were reagent grade materials. Anhydrous ethylenediamine was purified by refluxing

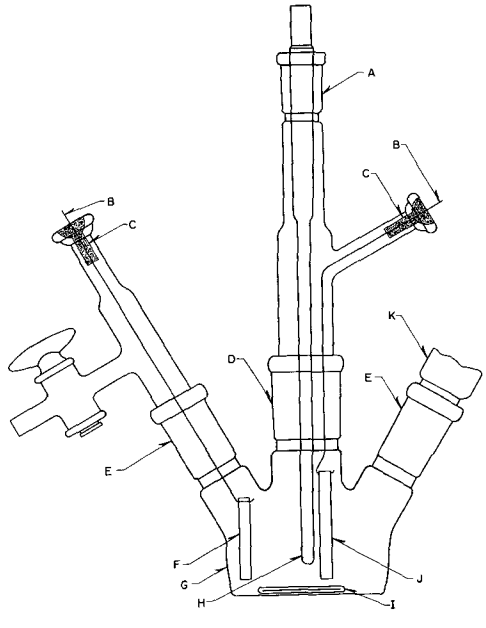

Fig. 1. Electrolysis vessel. A, 12/30 joint; B, platinum wire; C, epoxy resin seal; D, 24/40 joint; E, 19/38 joint; F, carbon anode; G, three-necked 100 ml flask; H, thermocouple well; I, glass enclosed stirring bar; J, carbon cathode; K, condenser.

Table I. Electrochemical reduction of tetralin and benzene in ethylenediamine saturated with lithium chloride

Experiment No.	Substrate	Cathode material	Temp, °C	Applied potential, v	Current, amp	Time, min	Current used, % Reduction	Current used, % Hydrogen formation	Total current accounted for, %
1	Tetralin	Platinum	33	105	0.500	60	52.9	16.5	69.4
2	Tetralin	Graphite	33	125	0.500	60	70.5	7.5	78.0
3*	Tetralin	Graphite	33	210	0.250	120	64.3	22.0	86.0
4	Tetralin	Carbon	33	125	0.500	60	80.3	7.6	87.9
5	Tetralin	Carbon	23	190	0.500	60	81.3	6.2	87.5
6	Tetralin	Carbon	35	185	0.850	35	79.0	7.6	86.6
7	Benzene	Carbon	33	105	0.500	60	52.4**	8.6	61.0

* Anode compartment used. See Experimental.
** This figure represents a minimum conversion due to incomplete recovery.

over sodium followed by distillation under nitrogen.

Electrolysis of Lithium Chloride and Tetrabutylammonium Iodide in Ethylenediamine

When a saturated solution of lithium chloride (1.4g) in ethylenediamine (100 ml) was electrolyzed at room temperature, deep blue globules formed at the cathode and then dissolved, imparting a blue color to the solution in the immediate vicinity of the electrode. On stirring, the blue color of the solution quickly disappeared. The formation of blue globules seemed to be independent of cathode material (platinum, graphite, or carbon) and of the applied voltage and only dependent on the current. At currents of less than 0.050 amp, the blue color could no longer be observed. In this connection, the observations of Putnam and Kobe (11) are of interest. They electrolyzed lithium bromide in ethylenediamine at 100° between a lithium amalgam anode and a copper cathode and obtained at the cathode a brown deposit without metallic luster, which reacted explosively with water and with alcohol to give hydrogen. It appears that cathode material and/or temperature determine whether lithium is solvated or plated out.

When tetrabutylammonium iodide was used instead of lithium chloride no color was observed at the cathode.

Reduction of Tetralin

Solutions of 100 ml of ethylenediamine containing 1.4g (0.033 mole) of lithium chloride and 3 ml (0.022 mole) of peroxide-free tetralin were electrolyzed under various conditions. When tetrabutylammonium iodide was used, 11.5g (0.031 mole) was dissolved. During electrolysis the cell was cooled by an ice bath. To maintain constant current, little regulation of applied voltage (about ±5v of the average voltage given in Tables I and III) was necessary. To isolate the reduction products, the solution was poured onto ice and the resulting aqueous solution extracted with pentane; the extract was treated in turn with dilute acid, bicarbonate, and water, dried over "Drierite," filtered, and the bulk of the pentane removed by fractional distillation. The residue was analyzed mass spectrometrically. The reaction mixtures contained octa- as well as hexahydronaphthalenes. The starting material, tetralin, contained some dihydronaphthalene as an impurity, the bulk of which was reduced to tetralin.

In a typical example (run 1, Table I), mass spectrometric analysis of the starting tetralin ($C_{10}H_{12}$) and of the recovered material (on a pentane-free basis) gave the following results:

	Mass	Volume % Starting material (tetralin)	Volume % Recovered material
$C_{10}H_{10}$	130	1.8	0.3
$C_{10}H_{12}$	132	98.0	80.9
$C_{10}H_{14}$	134	0.05	15.3
$C_{10}H_{16}$	136	0.0	3.4

In calculating current efficiencies, all of these conversions were taken into account. The results are summarized in Tables I-IV. To determine whether any chlorination of substrate had occurred at the anode, samples of residues from various electrolyses were analyzed for chlorine. In all cases, chlorine was

Table II. Supplement to Table I. Breakdown of current used for reduction

Experiment No.	Substrate	Current used, % Reduction of tetralin to hexahydronaphthalene	Reduction of hexahydronaphthalene to octahydronaphthalene	Reduction of dihydronaphthalene* to tetralin	Reduction of all available organic substrates
1	Tetralin	41.6	7.5	3.8	52.9
2	Tetralin	55.4	11.6	3.5	70.5
3	Tetralin	51.8	8.7	3.8	64.3
4	Tetralin	67.3	9.5	3.5	80.3
5	Tetralin	70.0	7.9	3.4	81.3
6	Tetralin	67.0	8.8	3.2	79.0
		Reduction of benzene to cyclohexadiene	Reduction of cyclohexadiene to cyclohexene		
7	Benzene	38.0	14.4		52.4

* Impurity in starting material. See Experimental.

Table III. Effect of electrolyte on reduction of tetralin*

Experiment No.	Electrolyte	Concentration, mole/liter	Temp, °C	Applied potential, v	Current used, %		Total current accounted for, %
					Reduction	Hydrogen formation	
4	LiCl	0.3	33	125	80.3	7.6	87.9
8	$(C_4H_9)_4NI$	0.31	28	90	17.5	46.1	63.6
9	NH_4Cl	0.33	20	60	0.0	122.0**	—
10	NH_4Cl	0.17	33	120	0.0	118.0**	—
11	NH_4Cl + LiCl	0.17 Saturated	21	75	70.5	26.4	—

* Standard conditions: carbon cathode; current, 0.500 amp; time of electrolysis, 60 min.
** Excess hydrogen possibly due to side reaction involving ammonium radical.

Table IV. Supplement to Table III. Breakdown of current used for reduction

Experiment No.	Electrolyte	Current used, %			
		Reduction of tetralin to hexahydronaphthalene	Reduction of hexahydronaphthalene to octahydronaphthalene	Reduction of dihydronaphthalene to tetralin	Reduction of all available organic substrates
4	LiCl	67.3	9.5	3.5	80.3
8	$(C_4H_9)_4NI$	13.0	1.8	2.7	17.5
9, 10	NH_4Cl	0.0	0.0	0.0	0.0
11	NH_4Cl + LiCl	62.9	6.4	1.2	70.5

found to be absent, a fact which allowed us to carry out the electrolysis without a diaphragm cell. Mass spectrometric analyses of the gas samples showed that only hydrogen was evolved during electrolysis.

As cathode material, graphite proved to be less resistant than carbon. Visual inspection of carbon and graphite electrodes after several electrolyses showed little, if any, corrosion in the carbon electrode and considerable erosion in the graphite electrode. No erosion was noticed when either carbon or graphite was used as an anode.

Reduction of Benzene

Reduction of benzene and isolation of the reduction products was carried out as described under tetralin. In contrast to tetralin, we were unable to obtain quantitative recovery; only 50% of the material could be accounted for. The current efficiency listed in Table I is based on the amount of material recovered and therefore represents a minimum figure.

Polarographic Data

Polarograms were run in ethylenediamine solution 0.15M in tetrabutylammonium iodide. There was a wave with an $E_{1/2}$ of about −1.4v *vs.* the mercury pool, probably due to some impurity in the $(C_4H_9)_4NI$, since the latter gave the same wave in dimethylformamide. Since neither the position nor the height of this wave interfered wtih the following runs, no attempt was made to eliminate this wave by further purification of the electrolyte. All voltages were measured *vs.* the mercury pool at 27° ± 0.5°C. No corrections were made for cell resistance. Results are summarized in Table V, and the essential features of the curves sketched in Fig. 2 for ready reference in the following discussion.

Table V. Half-wave potentials, diffusion currents (i_d), and diffusion current constants (I_d) in ethylenediamine (0.15M $(C_4H_9)NI$ as supporting electrolyte)

Compound	Concn. (mmole/liter)	i_d	$i_d/Cm^{2/3}t^{1/6}$	$E_{1/2}$ *vs.* Hg pool
Tetralin	50.0	—	—	—
Naphthalene	2.00	4.4	1.4	−1.89
Li^+	1.97	9.0	2.9	−1.90
Li^+ and tetralin	1.97 50.0	9.0	2.9	−1.90

i_d, limiting diffusion current, μa; *C*, concentration in millimoles per liter; *m*, flow rate of mercury, mg sec^{-1}; *t*, drop time in seconds; $m^{2/3}t^{1/6}$, 1.57.

Discussion

Table I reveals some interesting facts regarding influence of cathode material on current efficiency. There is a noticeable difference in current efficiency between a platinum cathode on the one hand and

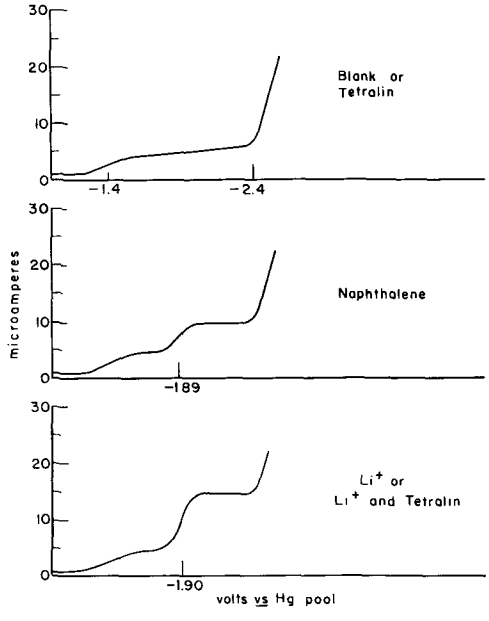

Fig. 2. Polarographic reduction waves in anhydrous ethylenediamine (0.15M tetrabutylammonium iodide).

graphite and carbon cathodes on the other. It is surprising that this difference is not greater in view of the fact that the hydrogen overvoltage (12) of platinum (0.29) is considerably lower than that of carbon (0.89), and that platinum catalyzes the reaction of amines with alkali metals to form amides. The lower current efficiency obtained with the graphite electrode as compared to that of the carbon electrode in conjunction with the fact that hydrogen production remained constant suggests that partial hydrogenation of graphite may have taken place. This view is supported by the fact that the graphite in contrast to the carbon cathode showed considerable erosion.[1]

Table I also shows that a 10° change in temperature has little, if any, influence on current efficiency. In Table III, current efficiencies obtained with various electrolytes are compared with that of lithium chloride.

The electrochemical reduction of the benzene ring in ethylenediamine described above, involves, we believe, prior reduction of solvated lithium cation to solvated lithium

$$Li_s^+ + e^- \rightarrow Li_s^+ \ldots e_s^- \quad [1]$$

Electron transfer to and protonation of the benzene ring may then proceed according to a mechanism similar to that proposed by Krapcho and Bothner-By (7) for the reduction of the benzene ring (R) by alkali metals in liquid ammonia:

$$Li_s^+ \ldots e_s^- + R \rightleftharpoons Li_s^+ \ldots R_s^- \quad [2]$$

$$Li_s^+ \ldots R_s^- + NH_2(CH_2)_2NH_2 \rightarrow RH + NH_2(CH_2)_2NHLi \quad [3]$$

$$RH + Li_s^+ \ldots e_s^- \rightarrow Li_s^+ \ldots RH_s^- \quad [4]$$

$$Li_s^+ \ldots RH_s^- + NH_2(CH_2)_2NH_2 \rightarrow RH_2 + NH_2(CH_2)_2NHLi \quad [5]$$

The main difference between the present system and that studied by Krapcho and Bothner-By is that in the former ethylenediamine and in the latter alcohol is the proton source.

The mechanism of electroreduction in the presence of lithium chloride may be similar to that in the presence of salts of metals such as titanium or vanadium. These cations are reduced at the cathode from a higher to a lower valence state and in this latter state reduce the organic material (15, 16). In the case of lithium in ethylenediamine, the two valence states are solvated lithium cation, Li_s^+ and solvated lithium, $Li_s^+ \ldots e_s^-$.

The assumption that reduction of the benzene ring does not take place by direct electron transfer from cathode to substrate is based on the following observations and facts. (i) Electrolysis of a solution of lithium chloride in ethylenediamine produces the blue color characteristic of solvated lithium metal. In the presence of tetralin or benzene, this color is not observed. (ii) No reduction takes place when ammonium chloride is used. However, reduction does take place when lithium chloride is added (Table III). (iii) No wave attributable to reduction of tetralin occurs at any potential less negative than the decomposition potential (−2.4v) of ethylenediamine, while naphthalene and lithium cation give rise to well-defined waves (Fig. 2). Electron addition to tetralin, if it occurs by direct electron transfer, must take place at about −2.9v [1v more negative than the reduction potential of naphthalene (3)], *i.e.*, at a potential considerably more negative than the decomposition potential of ethylenediamine. It seems therefore that in ethylenediamine, little, if any, reduction of the benzene ring takes place by direct electron transfer from cathode to substrate, and that electron transfer occurs predominantly between solvated lithium and the benzene ring.

In this connection it is of interest that tetrabutylammonium cation can also serve as an electron transfer agent (Table III). This is surprising in view of the difference in size and structure between these two ions and may shed light on the mechanism of electron transfer from alkali metal to the benzene ring. That tetraalkylammonium cations can be reduced to form stable solvated radicals, $R_4N^+ \ldots e^-$, in liquid ammonia was demonstrated by Schlubach (17) in 1920. The fact that tetrabutylammonium cation did not prove as effective as lithium cation may be due to decomposition (18) of the radical

$$R_4N^+ \ldots . e^- \rightarrow R_3N + R\cdot \quad [6]$$

prior to electron transfer to the benzene ring.[2] Another reason may be a lower stability toward the solvent. The radical $R_4N^+ \ldots e^-$ may react faster than $Li^+ \ldots e^-$ to form amide and hydrogen

$$2R_4N^+ \ldots e^- + 2NH_2(CH_2)_2NH_2 \rightarrow 2R_4N^+ + 2^-NH(CH_2)_2NH_2 + H_2 \quad [7]$$

Indeed, a considerable increase in hydrogen production was observed when tetrabutylammonium iodide was used in place of lithium chloride.

The electrochemical reduction of tetralin in the presence of tetrabutylammonium iodide amounts to the first "metal-amine" reduction of an organic compound using a tetraalkylammonium radical as the metal. It will be of interest to study reductions using variously substituted tetraalkylammonium and trisubstituted sulphonium radicals.

Acknowledgments

Helpful discussions with Professors A. E. Remick and G. J. Hoijtink are gratefully acknowledged.

Manuscript received July 13, 1962; revised manuscript received Nov. 13, 1962. This paper was prepared for presentation at the Detroit Meeting, Oct. 1-5, 1961.

Any discussion of this paper will appear in a Discussion Section to be published in the December 1963 JOURNAL.

REFERENCES

1. P.H. Given and M. E. Peover, *Fuel*, **39**, 463 (1960).
2. W. Fuchs, I. Schmidt, and O. Veiser, *Erdol u. Kohle*, **12**, 542 (1959).
3. L. E. Lyons, *Nature*, **166**, 193 (1950).

[1] These observations are consistent with the fact that graphite can be partially hydrogenated by lithium in ethylenediamine (13) and that graphite swelled and disintegrated when used as a cathode material in the electrolysis of sodium amide in liquid ammonia (14).

[2] The reaction according to Eq. [6] should give rise to the formation of butene and butane (18). The fact that mass spectrometric analysis of the reaction products did not reveal any peaks attributable to butane or butene does not exclude their presence, since these gases would have escaped during recovery of the reaction products which involved ether extraction followed by removal of the ether by distillation.

4. A. J. Birch, *J. Chem. Soc.*, **1944**, 430.
5. R. A. Benkeser, R. E. Robinson, D. M. Sauve, and O. H. Thomas, *J. Am. Chem. Soc.*, **76**, 631 (1954).
6. L. Reggel, R. A. Friedel, and I. Wender, *J. Org. Chem.*, **22**, 891 (1957).
7. A. P. Krapcho and A. A. Bothner-By, *J. Am. Chem. Soc.*, **81**, 3658 (1959).
8. G. J. Hoijtink, J. Van Schooten, E. DeBoer, and W. I. J. Aalbersberg, *Rec. trav. chim.*, **73**, 355 (1954).
9. S. Wawzonek, E. W. Blaha, R. Berkey, and M. E. Runner, *This Journal*, **102**, 235 (1955).
10. C. A. Kraus, *J. Am. Chem. Soc.*, **30**, 1323 (1908).
11. G. L. Putnam and K. A. Kobe, *Trans. Electrochem. Soc.*, **74**, 609 (1938).
12. W. M. Latimer, "Oxidation Potentials," 2nd ed., Prentice-Hall, Englewood Cliffs, N. J. (1952).
13. R. Raymond, L. Reggel, W. A. Steiner, S. Ergun, and I. Wender, *Nature*, **185**, 379 (1960).
14. W. Rudorff in H. J. Emeleus and A. G. Sharpe, "Advances in Inorganic Chemistry and Radiochemistry," Vol. 1, 242, Academic Press, Inc., New York (1959).
15. F. D. Popp and H. P. Schultz, *Chem. Rev.*, **62**, 19 (1962).
16. S. Glasstone and A. Hickling, "Electrolytic Oxidation and Reduction," p. 190, D. Van Nostrand Co., Inc., New York (1936).
17. H. H. Schlubach, *Ber.*, **53B**, 1689 (1920).
18. E. Grovenstein, Jr. and R. W. Stevenson, *J. Am. Chem. Soc.*, **81**, 4850 (1959).

High-Temperature Physical Properties of Carbide-Iodide Thorium

A. F. Reid, R. E. Wilmhurst,[1] and A. W. Wylie

Division of Mineral Chemistry, Commonwealth Scientific and Industrial Research Organization, Melbourne, Australia

ABSTRACT

Methods have been developed for measuring several of the physical properties of pure, freshly deposited carbide-iodide thorium over a range of temperatures without exposing the metal to atmospheric or other contamination. The allotropic transition of such material has been located at 1325° ± 10°C, the transition from fcc thorium to bcc thorium being complete at 1335°C in less than 1 min. New values are given for the electrical resistivity and total emissivity of thorium, these properties being markedly influenced by impurities in materials used by previous investigators. The morphology of the deposits has been studied and related to the composition and physical properties of the metal.

An essential requirement for accurate determination of the physical properties of reactive metals is a degree of purity notably superior to that of current production grade materials. Superficial contamination of thorium for instance occurs if it is exposed to the atmosphere, and Evans and Raynor (1) have shown that filings of iodide thorium subsequently annealed at a pressure as low as 5×10^{-6} mm may give lattice spacings as high as 5.089 kX in place of the currently accepted value 5.0741 kX. Nitrogen is the most serious offender in this instance. Similar effects however are likely to arise whenever thorium is heated to high temperatures in an inadequate vacuum, even if it has never been exposed to the atmosphere.

To overcome the difficulties of making reliable physical measurements on such reactive material the measurements described in this paper have been made *in situ* on freshly deposited carbide-iodide thorium prepared as described by Scaife and Wylie (2). The quality of this material meets the standards of purity required, and the modified iodide "vapor deposition" bulbs used in the work provide an ideal means of carrying out measurements on thorium metal which has never been exposed to the atmosphere or contacted with refractories which could alter its composition.

The first part of the paper describes the application of resistance measurements to the study of the transformation of fcc carbide-iodide thorium to the bcc modification. Investigators point out the difficulty of avoiding contamination of separately mounted specimens, for example with vapors from oil diffusion pumps. Also stressed is the effect of carbon and other nonmetallic impurities in progressively raising the transformation temperature after each temperature cycle through this point. With the techniques and material used in this work it has been found that the transformation temperature remains unaltered after three complete cycles totalling 2 hr.

In conjunction with the phase transformation study, resistivity measurements have been made on freshly deposited thorium over a wide range of temperatures. The resistivity in all cases is sensitive to the care taken in out-gassing the bulb and reactants. The effect of annealing the filament after growth was studied, and a decrease in resistivity due to recrystallization of initially poorly coherent grains was found. This effect does not appear to have been noted in earlier literature.

The rate of phase transformation has also been investigated. For the small filaments used in this work the transition from fcc to bcc thorium is found to be completed in approximately 0.5-0.7 min at 1335°C. Transition in the reverse direction is at least as rapid.

Other measurements have been made on the total emissivity over a range of temperature, since few

[1] Seconded from Australian Mineral Development Laboratories, Adelaide.

values can be found in the literature, and on the electron emission, both above and below the phase transformation temperature. No discernable change was observed in apparent work function or emissivity at the transformation point.

The final section of the paper describes the crystal habit of carbide-iodide thorium. The characteristic development of cube and octahedron faces, the random orientation of the purest deposits, and the preferred orientation of less pure material are described and correlated with the physical properties of the metal.

Experimental

Thorium carbide and thorium tetraiodide were prepared as described by Scaife and Wylie (2, 3) all material transfers being made via glass break-seals. Thorium oxide was made from analytical grade thorium nitrate by ignition of precipitated thorium oxalate. Graphite was of reactor grade. Analytical grade iodine was dried and further purified by a technique of Reid (4) in which outgassed material is sublimed *in vacuo* through a column of well-outgassed Linde molecular sieves. Thorium filaments were grown by the carbide-iodide process previously described (3). Higher outgassing temperatures and longer outgassing times at lower pressures were used than in earlier work.

Temperatures were read on a calibrated L&N optical pyrometer, the spectral emissivity of thorium being taken, after Smithells (5) as 0.36 at 0.65μ. Yosim and Milne (6) give 0.35 at 0.63μ; if this emissivity is taken to be applicable to 0.65μ appropriate changes, amounting to 3° at 1300°K, and 6° at 1800°K, must be made to the corrected temperatures given in this paper. Corrections were made for absorption in the glass wall of the bulb. Periodical checks on the transmission of the wall were made throughout an experiment, and the effect of condensed films was overcome by occasional use of a microflame on the window area. Figure 1 shows a typical filament-growing bulb.

Observation of even the roughest filament shows that the tips of projecting crystals do not differ in temperature from the bulk of the filament by more than 8°C. The intervention of black body cavities is therefore precluded, and the use of the spectral emissivity factor adopted above (5, 6) is justified. In this connection it is worthy of note that the brightness temperature of crystal bar zirconium given by Shapiro (18) coincides to within a few degrees over the range 1000°-1500°C with that estimated from the spectral emissivity of a smooth polished zirconium surface.

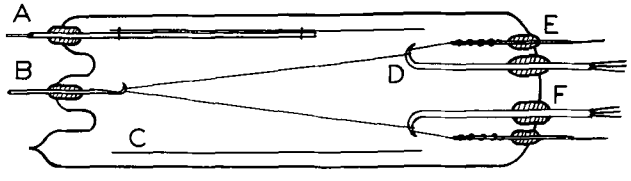

Fig. 1. Filament-growing bulb for carbide-iodide thorium: A, seal for tungsten anode support; B, seal for tungsten filament support hook; C, cylindrical molybdenum anode; D, tungsten starting wire wound over thin terminal hook on tungsten electrode; E, seal for tungsten potential measuring electrode spot-welded to filament; F, seal for current-carrying electrode (A,C included only for electron emission work).

Measurement of various physical quantities was carried out as follows.

Resistivity.—Above 1000°C resistances were determined from the readings of an ammeter and vacuum-tube voltmeter, accurate to ±1% full scale. In several experiments two 0.005 in. tungsten potential leads were attached to the starting wire at its midpoint but about 1 cm apart. Thorium grew over the junctions with virtually no change in cross section, and heat loss along the potential leads was negligible. In general the arrangement shown in Fig. 1 was more satisfactory. Contact potentials were negligible, as thorium grew over the tips of the current leads. A correction which never exceeded 0.7% and was often much smaller was made for the end-cooling effect of these current leads on the filament.

The measuring technique was checked at a number of temperatures by determining the resistivity of pure platinum filaments mounted in a vacuum system resembling in essentials that used for thorium. Values within ±1% of published values were obtained.

Resistances at room temperature were measured by use of an accurate potentiometer to determine the voltage drop (500-1500 μv) when a small current was passed through selected lengths of filament removed from the bulb. Current was measured with a precision milliammeter, resistances being independent of current in the range 50-500 ma. Contact potentials at the 0.005 in. copper potential probes were less than 1 μv. Resistance determined in this way agreed to within 1% of those determined on a filament *in situ*.

All filaments were annealed until the resistivity at any temperature was constant.

The resistance of the filaments was corrected for that of the substrate wire. Consideration of conductivity sums shows that, at any temperature,

$$\frac{1}{R'_{\text{corr.}}} = \frac{1}{R_{\text{obs.}}} - \frac{[\rho_{\text{Th}}/\rho_s] - 1}{[\rho_{\text{Th}}/\rho_s]R_S}$$

where $R'_{\text{corr.}}$ is the resistance of a filament of the observed dimensions but consisting entirely of thorium, ρ_{Th}, ρ_s are the resistivities at a given temperature of the filament metal and the substrate wire, and R_S is the resistance of the substrate wire alone. This form of correction, which was usually less than 0.5%, makes unnecessary the measurement of physical dimensions of the filament and substrate. A correction was also made for the change in dimension of the filament with temperature. In bulbs with hairpin filaments the same resistivity was obtained for the filament as a whole as for the two halves separately. As the weights per unit length were the same within 0.5% the filaments could be regarded as having uniform physical properties over their length.

Resistivities were calculated using dimensions obtained from weighing measured lengths of filaments. A correction for cross-section irregularity was made on the assumption that the projecting

crystals occupied half the volume between base and peak diameters, D_0 and D, and that the observed resistance could thus be approximated to that of two cylinders, of equal length and diameters D_0 and D, taken in series. For the usual value $D/D_0 = 1.1$ this correction was usually about 2½%.

The total resistivity correction does not exceed 6%, of which 2% can be determined precisely. The remaining 4% correction is less precisely determinable, but its application will not lead to an error in the final resistivity exceeding 2%.

Transition rate.—An estimate of the transition rate at a temperature 10° above the transition point was obtained by measuring the time taken for a filament to achieve voltage-current equilibrium after an incremental change in the applied voltage. This was done by balancing a signal representing the voltage drop across the filament against the voltage developed by the shunted secondary winding of a current transformer in the filament circuit. With the system balanced and at equilibrium, a small change was made in the voltage applied to the filament, and the time to establish a new equilibrium was measured. Temperature equilibrium as observed with the pyrometer was attained in 6-10 sec whether or not the change included the transition; when it did not, current-voltage equilibrium was attained in the same time. When the transition temperature was included, the longer time taken to reach current-voltage equilibrium was taken as a measure of the transition rate.

Electron emission.—Emission currents were measured with an accurate multirange meter, 200v d.c. being applied between filament and anode of the bulb shown in Fig. 1. The vapor pressure of thorium tetraiodide, approximately 10^{-9} mm at 240°C, had a negligible effect below this temperature. These measurements are discussed in greater detail elsewhere (4).

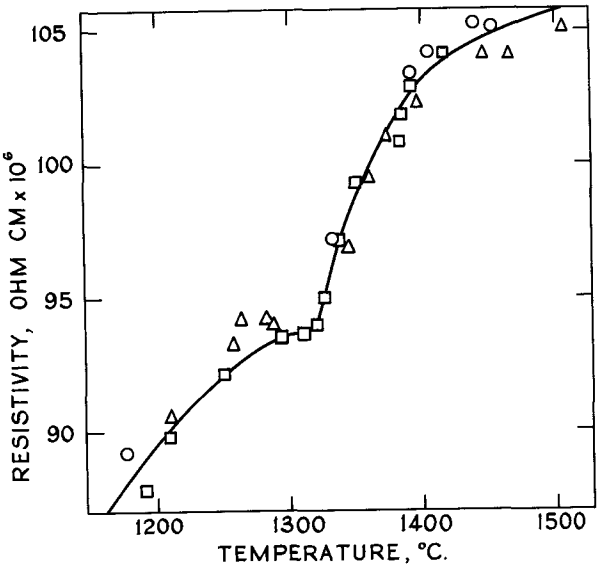

Fig. 2. Variation of resistivity of carbide-iodide thorium with temperature. Three successive heating cycles, points for rising temperatures only shown.

Results and Discussion

Allotropic Transition

A typical curve of resistance *vs.* temperature is shown in Fig. 2. Each point was plotted only when no further change in resistivity could be observed at a given temperature. For clarity only points for increasing temperatures are shown, but the curve for decreasing temperatures closely follows that for rising temperatures, even after three complete temperature cycles between 20° and 1550°C. For remounted filaments the transition temperature was found to be 1360° ± 10°C. For filaments prepared *in situ* in six different bulbs, including those prepared under the most stringent conditions, the transition temperature was found to lie in the range 1325° ± 10°C for filaments having diameters be-

Table I. High-temperature phase transition in thorium

Authors	Ref.	Technique*	Transition temp, °C	Sample source and purity (ppm) C	O	N	Metals
				Ames thorium, cast			
Chiotti (1954)	(7)	Resistivity and x-ray (T.C.)	1400 ± 25	345	1000	195	1000
				Iodide thorium, drawn, polished			
Deem and Winn (1955)	(8)	Resistivity (O.P.)	1400 approx.	200	90-200	6-8	?
				Thorium carbon alloys			
Chiotti, via Rough and Bauer (1958)	(9)	Resistivity (X-ray)	1360 ± 10	**			
				Ames iodide thorium, arc melted			
McMasters and Larsen (1961)	(10)	Resistivity (T.C.)	1363 ± 10	75-100	50-150	75-150	100
				"Commercial thorium"			
Bentle (1958)	(11)	Resistivity (T.C.)	1365 ± 10	400	1300	80	?
				Iodide thorium, arc melted			
			1330 ± 10	50	290	10	?
				Carbide-iodide thorium†			
This paper		Resistivity (O.P.)	1325 ± 10	10-25	11-22	3-7	<<100

* Temperature by optical pyrometer (O.P.) or thermocouple (T.C.).
** Transition temperature by extrapolating data to zero carbon content.
† Hydrogen 1.1 ppm.

tween 0.05 and 0.15 cm. This value derives from a brightness temperature range of 1208° ± 5°C, as observed through a Pyrex glass window. The transition temperature was independent of recrystallization or vacuum annealing phenomena, although these processes reduced the actual resistance. Variations of approximately 10% in the room temperature resistivity caused no change in the transition point. As the observed transition temperature is in accord with the value 1330° ± 10°C given by Bentle (Table I), it seems unlikely that further lowering of the impurity level will alter it significantly.

Transition rate.—For specimens of the size and composition used in this work, and for a final temperature 10°C above the transition point, the transition time, or time for establishment of current voltage equilibrium with the arrangement described, was found to be 30-40 sec. The observed voltage increment reached 0.63 of its final value in approximately half this time. A typical energy increment was 0.65w, and this was sufficient to supply the heat of transition, stated by Kelley (12) to be 670 cal/mole, in about 4 sec. Under similar conditions the electron emission (q.v.) became steady in 6-10 sec, the time required for attainment of steady temperature, indicating that the emission characteristics do not alter measurably with the allotropic transition.

Transition of bcc to fcc thorium at temperatures 50°-100°C below the transition point was found to take less than 30 sec. X-ray examination of samples quenched by shutting off the heating power after annealing the specimens at 1550°C confirmed that only the fcc form was present at 20°C.

Effect of tungsten or tantalum starting wire.—Rough and Bauer (9) in their summary of work on the tungsten-thorium system observe that there is little solid solubility in the terminal phases. Scaife and Wylie (2) observed that after thorium growth the tungsten starting wire could be almost completely recovered by dissolving off the thorium in hydrochloric acid solution, and that metallographic examination of a cross section of filament revealed a diffusion region of less than one diameter around the starting wire.

McMasters and Larsen (10), who quote a value of 1363° ± 10°C for the transformation temperature of arc-melted Ames iodide thorium (Table I), state that tantalum lowers the transition temperature to 1338° ± 5°C. The equilibrium solubility of tantalum in thorium and of thorium in tantalum was found to be less than 0.2 wt. % at 1340°C, but to obtain equilibrium repeated remelting followed by milling and refabrication was required. Thus interaction between tantalum and thorium is slow and homogenization is difficult to achieve. In the present work it has been found that thorium could be reacted off a tantalum starting wire by iodine vapor at 480°C to leave the tantalum apparently completely unaltered.

Thus the bulk of the thorium on a filament should contain negligible quantities of either a tungsten or tantalum substrate and the transformation temperature should be unaffected. This is confirmed by the fact that no systematic differences in resistivity could be observed between annealed thorium filaments grown on 0.012 cm tungsten starting wire to diameters varying from 0.07 cm to 0.15 cm, even after repeatedly heating to 1400°C. Nor was any effect due to substitution of tantalum for tungsten observed.

Effect of annealing on resistance.—In all cases after cessation of growth the resistance of thorium filaments decreased on heating them in the vacuum produced by cooling the bulb. Typically an initial value at 1400°C of 135 μ-ohm-cm fell after 2-3 min to a constant value of 94 μ-ohm-cm. Below this temperature however annealing was much slower. The annealing effect is presumably due to recrystallization of the incompletely coherent crystals of a growing filament, the structure of which is described in the final section of this paper. In a separate experiment a filament in hairpin form was grown at

Table II. Effect of preparative procedure on resistivity of thorium[a]

Bulb No.	Outgassing procedure: Carbide, pretreated in quartz	Outgassing procedure: Bulb and contents: Before admission of outgassed carbide	Outgassing procedure: Bulb and contents: After ThI_4 formation	Resistivity, μ-ohm-cm at 20°C (fcc thorium)
1	20 hr at 3×10^{-7} mm 1000°C, 2 hr at 1100°C	20 hr at 10^{-6} mm 500°C	1 hr at 10^{-7} mm 300°C	15.7(i)
2	20 hr at 10^{-6} mm 850°C	20 hr at 10^{-6} mm	0.5 hr at 10^{-6} mm	16.7(ii)
3	As in 2	As in 2	Not repumped	27(iii)
4	As in 2	As in 2	3 hr at 5×10^{-6} mm 500°C[b]	17.8
5[c]	As in 2	As in 2	As in 2	18.3
6	3 hr at 10^{-5} mm 850°C	3 hr at 10^{-5} mm 500°C	0.5 hr at 10^{-5} mm 300°C	25
7	1 kg of pelleted carbide; p fell to 10^{-5} mm after 3 hr at 800°C	Inconel reactor[d] 10 hr at 10^{-5} mm 550°C	16 hr at 10^{-5} mm while reactor cooled to 100°C	32(iv)

[a] Unless otherwise stated bulb temperature during growth 480°C, filament deposition temperature 1315°C. All filaments except 5 then heated above transition point and quenched by shutting off heating power. Starting wires tungsten. Over-all deposition rate 50-60 mg/cm/hr.

[b] Inadvertent admission of air after ThI_4 formation, followed by immediate repumping with ThI_4 held at 350°C and the body of the bulb at 500°C.

[c] Deposition temperature 1435°C.

[d] Carbide transferred to reactor in dry nitrogen stream, filament temperature 1400°C as indicated by the function $EI^{1/3}$, rising during deposition until a portion of the filament melted; temperature 600°C; starting wire tantalum; deposition rate 50-120 mg/cm/hr.

(i) Fig. 4a; (ii) Fig. 4b; (iii) Fig. 5a; (iv) Fig. 5b.

1400°C and quenched by turning off the heating current. After the bulb had cooled one leg only of the filament was annealed at 1400°C for 30 min and quenched. At 20°C this then had a resistance 16% lower than that of the quenched leg. X-ray examination confirmed that both legs of this filament were in the fcc form. No marked difference in the appearance of the two legs could be seen under the microscope, although crystals on the annealed leg appeared to be less sharply faceted. In spite of the considerable decrease in resistivity after annealing, the final resistivity of this and other filaments at any temperature was constant even after three complete temperature cycles between 1550° and 20°C.

Low- and High-Temperature Resistivities

As shown in Tables II and III the resistivity at room temperature was found to be notably sensitive to the care taken in preparation of the metal.

The purest specimens have a resistivity even lower than the recent carefully determined value of Wallace (13). Although it seems likely that improved degassing and vacuum techniques could lower the resistivity still further, it is doubtful whether the resistivity estimated by Carlson *et al.* (14) would be reached. Danielsen *et al.* (15), who give resistivity values of 19.7-20.5 μ-ohm-cm at 25°C for several lots of the much less pure Ames billet thorium cast in beryllia crucibles, report that further additions of either carbon, nitrogen, oxygen, or metals almost invariably raise the resistivity. However the changes in resistivity at the high prevailing level of impurities (several hundred to several thousand ppm of each) were relatively small, and it is now suggested that the resistivity of thorium is most sensitive to the presence of impurities when these are present at low concentrations. This is logical since resistivity is very sensitive to the presence of impurities in solid solution (16) and much less sensitive to segregated impurities likely to be present at the high concentrations discussed by Danielsen.

The resistivity of thorium at high temperatures is given in Table IV. At 1000°C the resistivity falls within 3% of the value derived from the curve drawn by Goldsmith *et al.* (17) and within 9% of the value given by Wallace (13). Above 1000°C resistivities are significantly higher than those given by other investigators (17). The reasons for this are not clear, but it seems highly unlikely that the effect can be attributed to impurities in view of the precautions taken in preparation, in view of the actual low impurity levels found by analysis, and in view of the low resistivity at 20°C.

Table III. Composition and hardness of carbide-iodide thorium

Bulb No.[a]	Oxygen ppm	Nitrogen ppm	Hydrogen ppm	Microhardness VPN[b]
2	11-22	3-7	1.1	41
3	55-97	11-31	4.9-13	40
7	430-446	26	3.3-4.9	44

[a] Numbers as in Table II.
[b] Load 10 g.

Table IV. Resistivity of thorium at high temperatures

T°K	1273	1300	1400	1500	1590	1650	1700	1800
μ-ohm-cm	72	73	78	82	85.5	91	93	96

Use of the Function $EI^{1/3}$ for Control of Filament Temperature

This function, in the form $EI^{1/3} = KL$, where E is the applied voltage, I the current flowing, and L the length of the filament, has been used by Shapiro (18), following Jones and Langmuir (19), to control the temperature of an unseen filament in a metal reactor. The constant K is independent of filament diameter at a given temperature and for an ideal filament *in vacuo* radiating heat to cold surroundings can be calculated to have the value

$$K = (4\pi\rho\epsilon^2\sigma^2T^8)^{1/3}$$

where ρ is the resistivity, ϵ the total emissivity, σ the Stefan-Boltzmann constant, and T the absolute temperature. Heat losses by conduction in thorium iodide vapor at a pressure of 1 mm are negligible in comparison with radiation losses.

The spread of $EI^{1/3}$ values per unit length for five carefully prepared and annealed filaments is shown in Fig. 3, curve 1. The $EI^{1/3}$ values during growth of these filaments (Fig. 3, curve 2), were consistently higher than in the annealed state. The opposite would apply if the filaments were smooth cylinders during growth since the bulb temperature is then high enough to reduce filament radiation significantly. However the change in resistance produced by vacuum annealing after growth is of the order required to produce the observed reduction in $EI^{1/3}$; in addition there is probably a 2-3% reduction in emissivity.

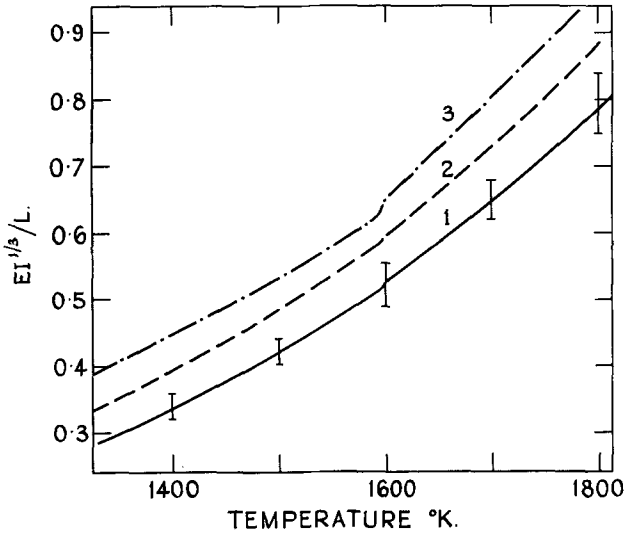

Fig. 3. Variation of function $EI^{1/3}$ with temperature: curve 1, averaged values for fully annealed filaments of highest purity (resistivity less than 18 μ-ohm-cm at 20°C); curve 2, values for same filaments during growth; curve 3, values for filaments from Bulb No. 3 (Fig. 5) during growth.

For "contaminated" filaments having resistivities of 25-27 μ-ohm-cm (Bulb 3, Table II) the $EI^{1/3}$ values were considerably higher both during and after growth than those for clean filaments (Fig. 3, curve 3). This sensitivity to resistance is thus shown to be the basis of the criticism of Sherwood and Campbell (20) since the function $EI^{1/3}$ cannot be other than unreliable for temperature control of filaments whose resistance is not known accurately.

A small but definite inflection in the function $EI^{1/3}$ was observed at the transition temperature, as would be expected from its proportionality to $\rho^{1/3}$.

Electron Emission and the Transition Point

It was found that Richardson plots of log (emission/T^2) *vs.* $1/T$ were strictly linear through the range 1000°-1550°C with no change in slope, as determined by regression analysis, at the transition point. The apparent work function for the polycrystalline thorium, determined within 2-10 min of deposition, was 3.37 ± 0.025 ev over this range and did not alter for periods of up to 2 hr. Riviere (23), using stringent ultrahigh vacuum evaporation techniques reports the work function, as determined by contact potential measurements, to be 3.46 ev. In work described elsewhere (4) it was found that the procedures described here lead to bulb outgassing rates of approximately 10^{-9} mm/hr, and that heated thorium carbide and heated thorium iodide remove gases adsorbable on hot thorium. This action, and especially the gettering action of the growing filament, ensure that after metal deposition residual gas pressures will be in the ultrahigh vacuum region. Moreover it was found that electron emission from the filament of a bulb which was rapidly cooled after deposition of thorium was observable as the last traces of thorium tetraiodide condensed at 350°-240°C, and increased to a final value which remained constant for at least 2 hr irrespective of further cooling. Since fresh thorium surfaces are continuously deposited as the bulb cools to 350°C it appears that carefully prepared "iodide" metal filaments may be used directly for work function determinations. More elaborate outgassing techniques might alter the value given, but the bulk purity of thorium used in this work is certainly higher than that of any other thorium yet examined.

Total Emissivity

Emissivity of polycrystalline filaments were calculated from the relationship

$$W = EI = A\epsilon\sigma T^4$$

where W equals watts radiated between voltage probes, E volts, I current, A projected surface area of filament, ϵ total emissivity, σ Stefan-Boltzmann constant, (5.672 x 10^{-12} w/cm^2 deg absolute^{-4}), T absolute temperature.

For two of the best filaments (Table II, No. 2 and 3) of projected area 6 cm^2 and 8.5 cm^2, respectively, the values of ϵ agreed to within ±3%. Average values are given in Table V.

No data could be found in the literature on thorium to compare these results with, but the values appear reasonable in comparison with those for other metals.

Table V. Total emissivity of carbide-carbide thorium filaments

Temp, °K	1400	1500	1600	1700	1800
ϵ, ±3%	0.30	0.30_5	0.31	0.32	0.34

A small reduction in emissivity (2-3%) occurs on annealing a filament of freshly deposited thorium. Any change in emissivity at the phase transition point is probably less than 0.5%.

Morphology of Iodide Thorium

Both the low-temperature and the high-temperature allotropic modifications of thorium exhibit similar characteristic development of crystal forms which persist essentially unchanged after three thermal cycles of the specimens through the transition point, or after quenching from above this point. Calculations based on the unit cell dimensions given by Chiotti (7) for fcc thorium at 1200°C and for bcc thorium at 1400°C show that the volume of the unit cell per atom differs in the two modifications by only 1.8%.

The most stringent degassing procedures,[2] which gave thorium of resistivity 15.7 μ-ohm-cm, produced deposits showing prominent development of both cube and octahedron faces, all of which were smooth and lustrous (Fig. 4a). Triangular octahedral faces frequently truncated the vertices of cubic crystals and occasionally showed striations parallel to the cube faces as described in greater detail for specimen No. 7. Orientation of these crystals appeared to be random. This was confirmed by x-ray examination of specimens grown at 1250° or 1315°C and cooled without further treatment. A few similar filaments showed small regions of deposition where "en echelon" arrays of distorted octahedral crystals showed faces subparallel to the filament axis, the remainder of the crystals being randomly oriented.

Thorium specified by the data for Bulb No. 2 in Tables II and III showed prominent development of symmetrical and distorted octahedral faces, the cube faces occurring only as facets truncating the junction of {111} faces, either at corners or along edges. There was a well-marked arrangement of crystals in an "en echelon" array (Fig. 4b), distorted, often six-sided octahedron faces approximately parallel to the axis of the filament being bordered on either side by vertices of octahedra, again in parallel array. In all cases the orientation of the octahedral axes of symmetry of the crystals was approximately perpendicular to the axis of the filament.

Examination of a filament of intermediate purity (Bulb No. 3, Tables II and III) showed radial arrays of columnar crystals approximately perpendicular to the filament axis. However, the prominent faces subparallel to the filament axis consisted of both cube and octahedron faces in approximately equal numbers (Fig. 5a). Both types of faces were about equally developed, and re-entrant forms on octahedral faces were rare. In this specimen, there-

[2] See earlier discussion on effect of preparative procedure on resistivity.

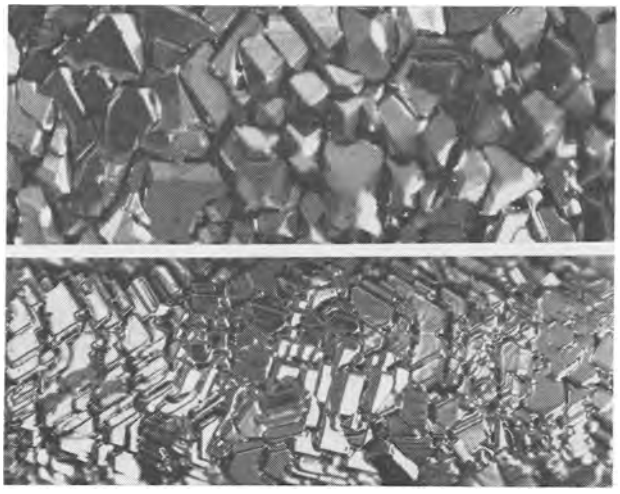

Fig. 4a. (top) Pure thorium (resistivity 15.7 μ-ohm-cm) showing randomly oriented cube and octahedron faces. Magnification 75X. Fig. 4b. (bottom) Pure thorium (resistivity 16.7 μ-ohm-cm) showing distorted octahedral faces in sub-parallel orientation to filament axis. Magnification 50X.

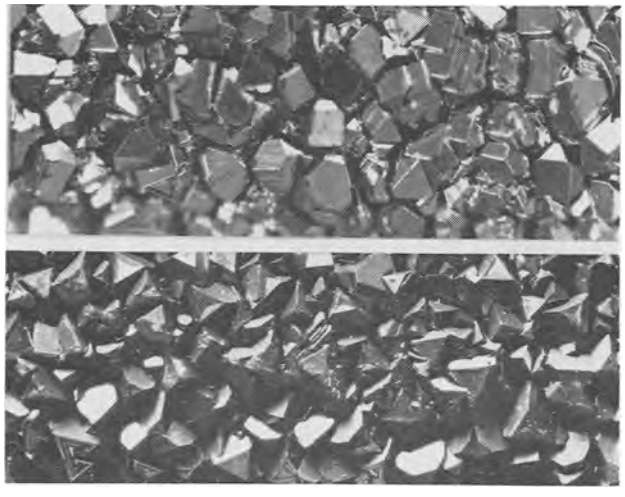

Fig. 5a. (top) Thorium of intermediate purity (resistivity 27 μ-ohm-cm) showing cube and octahedron faces in subparallel orientation to filament axis. Magnification 50X. Fig. 5b. (bottom) Relatively impure thorium (resistivity 32 μ-ohm-cm) showing cubic crystals oriented with an octahedral axis of symmetry perpendicular to filament axis. Magnification 10X.

fore, two preferred orientations appear to be present, either a cubic or an octahedral axis of symmetry of the crystal tending to be perpendicular to the filament axis.

The least pure material examined is specified by the data for Bulb No. 7 in Tables II and III. This product consists of dull crystals which have grown in radial array perpendicularly outward from the axis of the filament. Terminal faces of the crystals are the three faces {100} of a simple cube, the corner of the cube forming the tip of the crystal. Most of these tips are truncated by triangular octahedron faces (Fig. 5b), the marked preferred orientation of the lattice in these crystals with the octahedral axes perpendicular to the axis of the filament thus being the same as for material from Bulb No. 2. Only rarely in this type of material can cube faces bounded by four octahedron faces be seen.

A notable feature of the triangular octahedron faces is the number of striations parallel to the cube faces. These are caused by stepped growth which results in a hollow center. Rhombohedral {110} forms in combination with cube and octahedron are believed to be responsible. Another feature of these crystals is the presence of smooth, curved anhedral boundaries roughly parallel to the direction of elongation, the boundaries occurring close to the junction of a columnar crystal with its neighbors and extending well downward toward the root of the crystal. Cohesion between crystals is mechanically weak along these boundaries in unannealed specimens.

It is evident from the description of the various deposits that traces of gaseous and other impurities present in an iodide bulb before deposition of thorium notably influence both the relative development of cube and octahedron faces and the orientation of the deposited crystals with respect to the axis of a supporting tungsten or tantalum filament. X-ray examination of such filaments confirms the existence of a simple fiber texture with [110] parallel to the filament axis (21), despite grain growth occurring after "flashing" the filament for 30 minutes at 1800°C. Nevertheless random orientation, rather than epitaxial growth on the substrate, prevails in the purest specimens of thorium[3] while preferred orientation, usually with an octahedral axis of symmetry of the crystal approximately perpendicular to the filament axis, is observed with less pure material. It must be concluded, therefore, that increasing concentrations of impurity atoms on clean tungsten or tantalum surfaces can cause the development in thorium of a preferred orientation which would not otherwise result.

Summary

Pure thorium metal has been grown by the carbide-iodide process, and methods have been developed for determining a number of its physical properties without exposing the freshly deposited metal to atmospheric or other contamination.

The allotropic transition of fcc thorium to the bcc modification has been located by resistivity measurements at 1325° ± 10°C. Study of the rate of transition near the transition point shows that the phase change to bcc thorium is complete in less than 1 min.

The resistivity of the best specimens of carbide-iodide thorium at 20°C has been found to be 15.7 μ-ohm-cm. The resistivity values above 1000°C are significantly higher than those given in the literature.

Both transition temperature and resistivity are sensitive to the mode of preparation, especially at low contamination levels. Resistivity, but not transition temperature, is sensitive at high temperatures to annealing conditions used to convert the loosely coherent grains of iodide metal to more coherent metal.

The unreliability of the function $EI^{1/3}$ for control of filament temperature is shown to be caused by resistivity, annealing, and other changes in a newly formed filament.

[3] Although the degree of mismatch between (111) of fcc thorium, or (110) of bcc thorium, on (110) of bcc tungsten is 31% at 20°C, it does not exceed that reported for numerous other epitaxially related systems (21, 22). Corresponding mismatch for thorium on tantalum is 27%.

The electron emission of polycrystalline thorium has been measured, and the apparent work function has been found to be 3.37 ev. No change in work function was detectable at the phase transition temperature.

The total emissivity of thorium has been found to rise from 0.30 to 0.34 over the range 1400°-1800°C. Both the electron emission and the emissivity of thorium vary with the purity of the specimen and its surface condition.

The morphology of carbide-iodide thorium has been described. The purest material consisted of lustrous, randomly oriented cubic crystals. Slightly less pure material consisted of arrays of distorted octahedral crystals whose faces were approximately parallel to the axis of the filament. The least pure deposits consisted of radial arrays of cubic crystals whose orientation resembled that of purer specimens showing faces subparallel to the filament axis in having an octahedral axis of symmetry approximately perpendicular to the filament axis. Development of orientation is attributed to the intervention of layers of impurity atoms on the tungsten or tantalum surfaces rather than to epitaxial growth on the substrate.

Acknowledgment

The authors wish to acknowledge financial support (for R.E.W.) from Consolidated Zinc Pty. Ltd. They gratefully acknowledge assistance from Dr. J. McAndrew and Dr. I. R. Garrod and are deeply indebted to Mr. G. H. Bush, Royal Armament Research and Development Establishment, England, for vacuum fusion analyses.

Manuscript received Oct. 9, 1962.

Any discussion of this paper will appear in a Discussion Section to be published in the December 1963 JOURNAL.

REFERENCES

1. D. S. Evans and G. V. Raynor, *J. Nucl. Mater.*, **3**, 281 (1959).
2. D. E. Scaife and A. W. Wylie, *Proc. Second Intern. Conf. Peaceful Uses At. Energy*, **4**, 215, United Nations, Geneva (1959).
3. D. E. Scaife and A. W. Wylie, "Australian Atomic Energy Symposium," p. 172, Australian Atomic Energy Commission, Melbourne (1958).
4. A. F. Reid, to be published.
5. C. J. Smithells, "Metals Reference Handbook," Butterworth, London (1949).
6. S. J. Yosim and T. A. Milne, NAA-SR-2124 (1957).
7. P. Chiotti, *This Journal*, **101**, 567 (1954).
8. H. W. Deem and R. A. Winn, BMI-1052, p. 104, (1955).
9. F. A. Rough and A. A. Bauer, BMI-1300 (1958).
10. O. D. McMasters and W. L. Larsen, *J. Less-Common Metals*, **3**, 312 (1961).
11. G. G. Bentle, NAA-SR-2069 (1958).
12. K. K. Kelley, *U. S. Bur. Mines, Bull 584*, Washington, D. C. (1960).
13. D. C. Wallace, *Phys. Rev.*, **120**, 84 (1960).
14. O. N. Carlson, P. Chiotti, G. Murphy, D. Peterson, B. A. Rogers, J. F. Smith, M. Smutz, M. Voss and H. A. Wilhelm, *Intern. Conf. Peaceful Uses At. Energy*, **9**, 74, United Nations, Geneva (1955).
15. G. C. Danielsen, G. Murphy, D. Petersen, and B. A. Rogers, ISC-297 (1952).
16. J. E. Kunzler and J. H. Wernick, *Trans. Met. Soc. AIME*, **212**, 856 (1958).
17. "Handbook of Thermophysical Properties of Materials," A. Goldsmith, T. E. Waterman, and H. J. Hirschhorn, Editors, Vol. I, pp. 635, 647, The MacMillan Co., New York (1961).
18. Z. M. Shapiro, in "The Metallurgy of Zirconium," B. Lustman and F. Kerze, Editors, Chap. 5, McGraw-Hill Book Co., Inc., New York (1955).
19. H. A. Jones and I. Langmuir, *Gen. Elec. Rev.*, **30**, 310 (1927).
20. E. M. Sherwood and I. E. Campbell, in "The Metallurgy of Hafnium," D. E. Thomas and E. T. Hayes, Editors, Chap. 4, U. S. Atomic Energy Commission, Washington (1959).
21. C. S. Barrett, "Structure of Metals," pp. 442, 510, McGraw-Hill Book Co., Inc., New York (1952).
22. D. W. Pashley, "Advances in Physics," **5**, 173, 199, 219 (1956).
23. J. C. Riviere, *U. K. At. Energy Authority Rept.* AERE-R 3910 (1961).

Electro-Oxidation of Ethylenediaminetetraacetocobalt(II) at Platinum Electrodes. Effects of Anion Adsorption

Fred C. Anson

Division of Chemistry and Chemical Engineering,
California Institute of Technology, Pasadena, California

ABSTRACT

Adsorbed bromide ion is shown to act catalytically on the electro-oxidation of ethylenediaminetetraacetocobalt(II) ion at platinum electrodes although no bromide is incorporated in the cobalt(III) product of the electrode reaction. Adsorbed bromide is also shown to inhibit the oxidation of platinum electrodes especially in acid solutions.

As part of a study in these laboratories of the effects of anion adsorption on electrode reactions an investigation of the electro-oxidation of several chelates of cobalt(II) with amino acids such as ethylenediaminetetraacetic acid was undertaken. The electro-oxidations were carried out in the absence and presence of anions known to be adsorbed on platinum electrodes, *e.g.*, I^-, Br^-, Cl^-. It was anticipated that participation of such anions as electron bridges in the electrode reaction might be detected by analysis of the substitution-inert cobalt (III) chelates obtained as products of the electrode

reaction. Thus, if bromide ion were adsorbed on the electrode during the cobalt(II) oxidation and participated in the electron transfer in the form of an electron bridge (1), it might be expected that the product of the electrode reaction would be $CoHYBr^-$ [H_4Y represents ethylenediaminetetraacetic acid; the properties and synthesis of $CoHYBr^-$ have been described in the literature (2)]. Conversely, if bromide ion did not act as an electron bridge in the electrode reaction the expected product would by CoY^-.

The experimental results demonstrate that adsorbable anions produce very pronounced effects on the kinetics of the electrode reaction, although none of the adsorbed anions studied was incorporated in the cobalt(III) products of the electrode reaction.

Experimental

The chronopotentiometric technique was used to investigate the electrode reactions. The procedure, two-compartment cell and circuitry were of the conventional type (3). The working electrode was a piece of 0.030 in. diameter platinum wire sealed in soft glass to give an exposed area of 0.1 cm^2. The auxiliary electrode was a large platinum gauze cylinder surrounding the working electrode.

Controlled-potential electrolyses were performed in a three-compartment cell with the aid of a Duffers Associates Inc. Potentiostat. A platinum gauze electrode, with an area of *ca.* 200 cm^2, served as the working electrode in these electrolyses.

Solutions were prepared with triply distilled water and were deaerated with pre-purified nitrogen. $KCoHYBr \cdot 2H_2O$ was synthesized according to the procedure of Schwarzenbach (2) and twice recrystallized from aqueous ethanol. A purer product was obtained by substituting $CoBr_2$ (prepared from $CoCO_3$ and HBr) for the $CoCl_2 \cdot 6H_2O$ called for by Schwarzenbach. $Ba[CoY]_2 \cdot 2H_2O$ was prepared by the procedure in Inorganic Syntheses (4). Reagent grade chemicals were used without further purification.

Results

Anion effects.—Collected in Fig. 1 are chronopotentiograms showing the effect of bromide ion on the oxidation of 0.01M $CoY^=$ in phosphate buffer solutions of *p*H 3, 6, and 12 and a borate buffer solution of *p*H 9. The concentration of bromide required to cause a noticeable cathodic shift in the quarter-wave potential of the anodic chronopotentiograms is clearly a function of the *p*H of the solution: more bromide being required at higher *p*H values. At *p*H 12 no effect of bromide was observable up to 1M NaBr. It should be pointed out in a 0.01M solution of the cobalt(II) chelate of EDTA the chelate is less than 1% dissociated at *p*H 3 or greater (5).

Similar cathodic shifts in the potential at which $CoY^=$ is oxidized were also obtained upon addition of chloride, iodide, azide, and iodine. Iodide is oxidized before the cobalt chelate so that iodine is the active species at the electrode surface in solutions containing iodide. The concentrations of the various species needed to produce a given potential shift increase in the order $I^- < Br^- < Cl^- < N_3^-$.

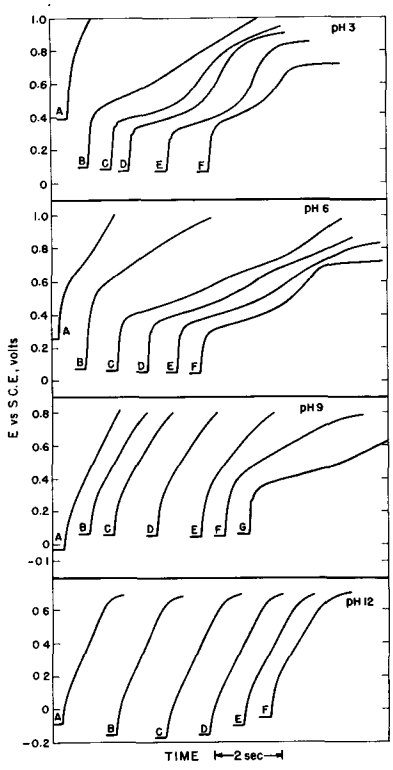

Fig. 1. Anodic chronopotentiograms for the oxidation of $CoY^=$ in the presence of bromide. Current density was 1.2 ma/cm^2 throughout. A, Buffer solution blank; $[CoY^=] = [Br^-] = 0$; B, $[CoY^=] = 7 \times 10^{-3}$M; $[Br^-] = 0$. *p*H 3 and 6 -C-F: $[Br^-] = 10^{-4}$, 10^{-3}, 10^{-1}, 1 M. *p*H 9 -C-G: $[Br^-] = 10^{-4}$, 10^{-3}, 10^{-2}, 10^{-1}, 1 M. *p*H 12 -C-F: $[Br^-] = 10^{-3}$, 10^{-2}, 10^{-1}, 1 M.

Behavior quite similar to that depicted in Fig. 1 was obtained with the anionic cobalt(II) chelate of N-(2-hydroxyethyl)ethylenediamine-NN'N'-triacetic acid as well as the cationic chelate of cobalt(II) with tetraethylenepentamine. The latter chelate was studied at *p*H values of 6 and above because of its lesser stability.

Electrode reaction products.—The products of the anodic electrode reaction were identified in the case of $CoY^=$ oxidation by reversing the direction of the current and comparing the resulting cathodic chronopotentiograms with those obtained from solutions containing samples of CoY^- or $CoHYBr^-$. The ion $CoHYBr^-$ is an acid with a pK_a near 3 (2). Thus at *p*H values greater than 3 the ion is present predominantly as $CoYBr^=$. The reduction of CoY^- to $CoY^=$ occurs at about −0.05v *vs.* S.C.E. while $CoHYBr^-$ and $CoYBr^=$ are both reduced at about +0.2v *vs.* S.C.E. The reduction waves for the two species are thus adequately separated for reverse-current chronopotentiometry to be used to examine the product of the electrode reaction immediately after its formation. The reverse-current waves obtained following the oxidation of $CoY^=$ occurred at −0.05v *vs.* S.C.E. whether or not bromide was present in the solution. The anodic electrode reaction product was thus CoY^- in all cases.

The product of the electrode reaction which results from the oxidation of $CoY^=$ in the presence of bromide was also identified by means of controlled-potential electrolyses of solutions of $CoY^=$ and bromide followed by visual examination of the resulting

solutions. The deep purple CoY^- ion could be readily distinguished from the blue-green $CoYBr^=$ and $CoHYBr^-$ ions. In every case CoY^- was the observed electrode reaction product.

The generally sluggish rate at which the complexes of cobalt(III) attain equilibrium with respect to substitution reactions is known to be catalyzed by activated carbon (6). It is conceivable that the large platinum gauze electrode employed in the controlled potential electrolyses, although not intentionally platinized, could nevertheless act as a catalyst for the decomposition of any $CoYBr^=$ formed at its surface into the more stable CoY^- ion. However, this possibility was ruled out by immersing the electrode in a solution of $CoYBr^=$ for a period three to four times longer than was required for the controlled potential electrolysis and observing no significant increase in the rate of the slow conversion of $CoYBr^=$ to CoY^-.

Effect of oxidation of the electrode.—To study the effect of added bromide on the behavior of the platinum electrode in the absence of cobalt chelates the amount of adsorbed oxygen[1] produced on the electrode surface during constant-current oxidation of the electrode to a fixed potential was determined by reversing the current and measuring the cathodic transition times corresponding to reduction of the adsorbed oxygen layer. The results of a series of such experiments run at various *p*H values and bromide concentrations are summarized in Fig. 2. At each *p*H value the electrode was oxidized with a constant current to a potential corresponding to an oxygen coverage of 10-20%. Under these conditions, the ratio of coulombs of adsorbed oxygen produced in the presence of various concentrations of bromide to the coulombs produced in the absence of bromide is plotted as a function of the bromide concentration in Fig. 2. Bromide clearly inhibits the formation of the oxygen layer up to *p*H 9, the inhibition being stronger at the lower *p*H values. Breiter has reported a similar inhibition of the formation of the adsorbed oxygen layer on platinum electrodes by adsorbed organic molecules including methanol, amyl alcohol, diphenylamine, and capryllic acid (7).

[1] The question as to whether oxidation of platinum electrodes leads to platinum oxides as distinguished from adsorbed oxygen has yet to receive a totally unambiguous answer. Recent experiments in the author's laboratory indicate the likely presence of both platinum oxide and adsorbed oxygen on oxidized electrodes. (The details of these experiments will be reported elsewhere). In this paper the term "oxidation of the electrode" means: to make the electrode sufficiently anodic to produce the oxide or oxygen film on its surface. No specification or commitment is intended regarding the composition of the film. For the sake of consistency the film is referred to throughout as "the adsorbed oxygen layer" although all of the data would be equally compatible with a film consisting of platinum oxides.

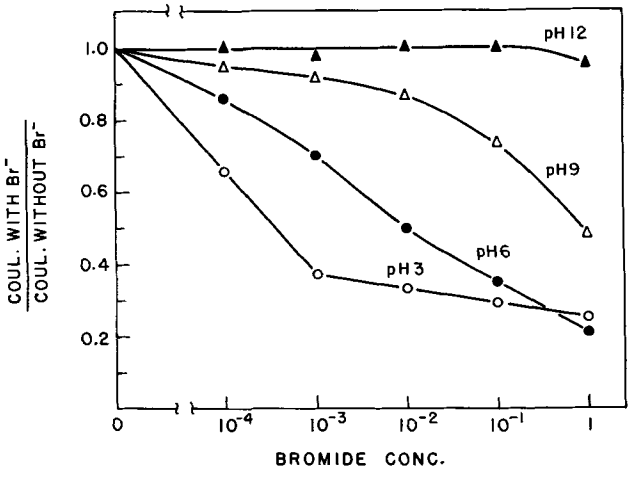

Fig. 2. Effect of bromide concentration on oxidation of platinum electrode.

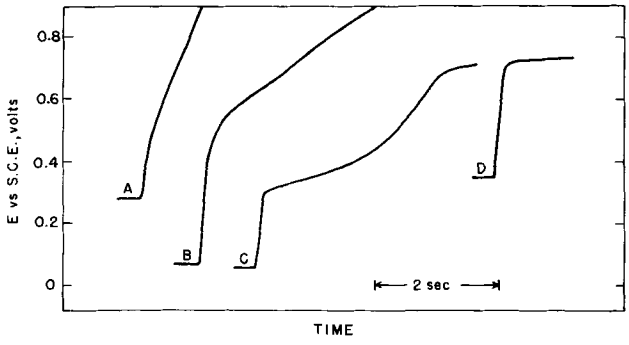

Fig. 3. Effect of oxidation of the electrode on anodic chronopotentiograms for the oxidation of $CoY^=$ at *p*H 6. A, *p*H 6 buffer solution blank; $[CoY^=] = [Br^-] = 0$; B, $[CoY^=] = 7\times10^{-3}$M; $[Br^-] = 0$; C, $[CoY^=] = 7\times10^{-3}$M; $[Br^-] = 1$ M; D, repeat C after oxidation of the electrode. Current density was 1.2 ma/cm^2 throughout.

This apparent inhibition of electrode oxidation by added bromide could be a part of the explanation of the effect of bromide on $CoY^=$ oxidation if it were established that oxidation of the electrode inhibits the oxidation of $CoY^=$. Results of experiments conducted to test this possibility are shown in Fig. 3. Curves B and C show the pronounced effect bromide has on $CoY^=$ oxidation at *p*H 6 when the electrode is initially unoxidized. However if the electrode is preoxidized in a separate, bromide-free, *p*H 6 buffer solution to a potential of 1.0v *vs.* S.C.E. and then placed in the $CoY^=$-Br^- solution and immediately used to record an anodic chronopotentiogram, curve D results. (On standing the oxygen film is chemically removed by 1M Br^- at *p*H 6 so the oxidized electrode must be used immediately.) Curve D shows that the bromide is no longer effective in facilitating the oxidation of $CoY^=$ at a partially oxidized electrode.

Discussion

All of the experimental evidence indicates that the effect of bromide arises as a result of its adsorption on the electrode surface. The fact that the transition time of the anodic oxidation wave for $CoY^=$ in the presence of bromide is essentially independent of the bromide concentration (see Fig. 1) argues against any mass-action conversion of the $CoY^=$ to a more easily oxidized bromo-complex. It was also established that the product $i\,\tau^{1/2}$ for the anodic chronopotentiograms in the presence of 0.1F NaBr at *p*H 3 is independent of the current density for transition times from 1 to 10 sec, thus ruling out chemical kinetic complications.

That anions are adsorbed on platinum electrodes through a considerable potential range has been well established (8). Adsorption of bromide is presumably responsible for the smaller quantities of adsorbed oxygen produced when the electrode is oxidized in the presence of bromide as shown in Fig. 2. The adsorbed bromide prevents the formation of

the oxygen layer until more anodic potentials are reached, probably by a simple blocking of the electrode surface.

At pH 9 a larger concentration of bromide is required to inhibit the formation of the adsorbed oxygen layer (see Fig. 2) as well as to produce a potential shift in the oxidation of $CoY^=$ (see Fig. 1). At pH 12 even 1M NaBr has little effect on the oxygen layer formation or the oxidation of $CoY^=$. This behavior is to be expected because as the pH increases the oxidation of the electrode can commence at less anodic potentials, while the potential at which $CoY^=$ is oxidized is independent of pH above pH 3. Thus at pH 9 a larger concentration of bromide is required to inhibit electrode oxidation prior to the oxidation of $CoY^=$. At pH 12 even 1M NaBr is insufficient to prevent oxidation of the electrode before the $CoY^=$ can be oxidized.

One can account in part for the effect of bromide on the oxidation of $CoY^=$ by observing that in the absence of bromide the oxidation of $CoY^=$ is accompanied by formation of the adsorbed oxygen layer on the electrode which inhibits the oxidation of $CoY^=$ and thus causes the chronopotentiometric wave to occur at more anodic values. In the presence of bromide the formation of the inhibiting oxygen film is itself inhibited and oxidation of $CoY^=$ proceeds at the more cathodic values observed. The curves in Fig. 3 clearly demonstrate the strongly inhibiting effect of the oxygen layer on the oxidation of $CoY^=$. Curve D in Fig. 3 shows that even in the presence of bromide, $CoY^=$ oxidation is inhibited at an electrode which has been pre-oxidized. This inhibition is partly due to the displacement of adsorbed bromide by adsorbed oxygen, but experiments in bromide-free solutions at pH 3 showed that the oxygen layer also eliminates the $CoY^=$ oxidation wave under conditions where displacement of adsorbed bromide plays no part.

Inhibition of oxidations at platinum electrodes by films of adsorbed oxygen is well known in numerous other instances which include the oxidations of oxalic acid (10), iodine (11), ferrous iron (12), hydrogen (13), and thiocyanate (14). (The only case known to the author in which the presence of an oxygen layer on platinum electrodes does not inhibit oxidation reactions at the electrode is in the oxidation of the ferrous o-phenanthroline complex; this oxidation appears to proceed equally as well on oxygen-covered as on oxygen-free electrodes.)

Anion catalysis of electron transfer.—There is evidence that in the case of $CoY^=$ oxidation the adsorbed bromide (and other anions) does more than just prevent the formation of the inhibiting oxygen layer; positive catalysis of the electron transfer reaction by adsorbed bromide is indicated. Comparison of curves A and C in Fig. 1 shows that at pH 3 and in the presence of bromide, oxidation of $CoY^=$ occurs at about +0.4v *vs.* S.C.E. while no oxygen layer is formed in the absence of bromide and $CoY^=$ before *ca.* +0.6v *vs.* S.C.E. at pH 3. In this case the bromide must function as more than just an inhibitor of oxygen layer formation.

It should be pointed out that in all cases studied here the catalysis of $CoY^=$ oxidation by bromide ion occurs at potentials several hundred millivolts less anodic than corresponds to the oxidation of bromide itself. Furthermore the rate of reaction between $CoY^=$ and Br_2 is only moderate at the concentration levels prevailing in the electrochemical experiments. It is thus not possible to explain the catalysis by bromide in terms of electrogenerated bromine.

Negative, but nevertheless persuasive evidence favoring positive catalysis by adsorbed bromide was obtained by studying the effect of amyl alcohol on the oxidation of $CoY^=$ at pH 3. Amyl alcohol is known to be adsorbed on platinum electrodes (7), and anodic charging curves showed that a 0.1M solution of amyl alcohol was, like bromide, an effective inhibitor of the electrode oxidation. However the oxidation of $CoY^=$ proceeds at more anodic potentials in a 0.1M amyl alcohol solution than in solutions containing neither amyl alcohol nor bromide. These experiments show that an adsorbed substance must do more than just inhibit the formation of the oxygen layer in order to provide for the earlier oxidation of $CoY^=$.

Mechanism.—The mechanism of the catalysis of the oxidation of $CoY^=$ by adsorbed halide is puzzling. One would expect that if the adsorbed halide served as a bridge for transfer of the electron from $CoY^=$ to the electrode, the resulting cobalt(III) species would contain bromide. Just such behavior has been observed in experiments involving the oxidation of Cr(II) to Cr(III) at mercury electrodes in the presence of halide; the inert Cr(III) ions produced contained bound halide (15, 16). Yet when $CoY^=$ is oxidized in the presence of large excesses of bromide, no bromide is contained in the Co(III) product. To test the possibility that any bromide which may be bound to the cobalt during the electron-transfer step is displaced by the sixth coordinating group of the hexadentate EDTA, controlled potential oxidations of the chelates of cobalt(II) with N-(2-hydroxyethyl) ethylenediamine-NN'N'-triacetic acid and tetraethylenepentamine were carried out in the presence of excess bromide. Both of these chelates can be at most pentadentate. The bromide strongly catalyzed the oxidations but no bromide was attached to the cobalt(III) species that were formed.

Large effects on rates of electrode reactions can result from the addition of specifically adsorbed anions such as bromide (17) because of changes in the effective potential of the electrode. The present experimental results can not be accounted for in this way, however, because adsorbed bromide would be expected to decrease the rate of electro-oxidation of anionic reactants and increase the rate of cationic reactants relative to their rates in bromide free solutions. In fact, bromide increases the rate for the anionic $CoY^=$ ion and the cationic tetraethylenepentamine cobalt(II) ion.

Vlcek (18) has demonstrated that changes in ligand fields in transition metal complexes can be correlated with changes in the ease of their polarographic reduction. It is possible that in the present case the adsorbed, polarizable bromide ion, although apparently not forming a cobalt-bromide bond, could nevertheless perturb the ligand field of $CoY^=$

ions near the electrode so that it resembles more closely that of the CoY^- ion, thereby facilitating the electrode reaction. The same would then be true for adsorbed chloride which mimics the behavior of bromide.

The bromide catalysis of $CoY^=$ oxidation could be used advantageously in electro-analysis of cobalt(II) solutions by means of controlled potential electrolysis. One-hundred per cent current efficiency for the oxidation of $CoY^=$ is not obtainable in bromide-free solutions of any pH (19) but it should be easily achieved at pH 3-6 in the presence of bromide ion.

Acknowledgment

This investigation was supported in part by the U. S. Army Research Office under Grant No. DA-ARO(D)-31-124-G315.

Manuscript received July 25, 1962; revised manuscript received Nov. 9, 1962.

Any discussion of this paper will appear in a Discussion Section to be published in the December 1963 JOURNAL.

REFERENCES

1. H. Taube, "Advances in Inorganic and Nuclear Chemistry," Vol. 1, Chap. 1, Academic Press, Inc., New York (1959).
2. G. Schwarzenbach, *Helv. Chim. Acta*, **32**, 839 (1949).
3. J. J. Lingane, "Electroanalytical Chemistry," Chap. 22, Interscience Publishers, Inc., New York (1958).
4. "Inorganic Syntheses," T. Moeller, Editor, Vol. 5, p. 186, McGraw-Hill Book Co., New York (1957).
5. H. Laitinen, "Chemical Analysis," p. 229, McGraw-Hill Book Co., New York (1960).
6. J. Bjerrum, "Metal Ammine Formation in Aqueous Solution," p. 240, P. Haase and Son, Copenhagen (1941).
7. M. Breiter, *This Journal*, **109**, 42 (1962).
8. A. Frumkin, "Trans. Symposium on Electrode Processes," Chap. 1, p. 1, John Wiley & Sons, New York (1959).
9. F. C. Anson, Ph.D. Thesis, Harvard Univ., 1957.
10. J. J. Lingane, *J. Electroanalyt. Chem.*, **1**, 379 (1960).
11. F. C. Anson and J. J. Lingane, *J. Am. Chem. Soc.*, **79**, 1015 (1957).
12. F. C. Anson, *Anal. Chem.*, **33**, 934 (1961).
13. M. Breiter, *This Journal*, **109**, 425 (1962).
14. F. C. Anson, Unpublished experiments.
15. D. Aikens and J. Ross, *J. Phys. Chem.*, **65**, 1213 (1961).
16. J. Jones, H. Keller and F. C. Anson, Experiments to be published.
17. L. Gierst, "Trans. Symposium on Electrode Processes," Chap. 5, p. 109, John Wiley & Sons, New York (1959).
18. A. A. Vlcek, *Discussions Faraday Soc.*, **26**, 164 (1958).
19. F. C. Anson and T. Tebben, Unpublished experiments.

Electrical Double Layer Capacities and Adsorption of Alcohols on Gold

G. M. Schmid[1] and Norman Hackerman

Department of Chemistry, The University of Texas, Austin, Texas

ABSTRACT

The differential capacity of polycrystalline gold in 1*N* $HClO_4$ was studied and compared to the behavior of (100) and (110) gold surfaces. Retardation of "oxygen" adsorption on the polycrystalline material is attributed to localized adsorption, preferential on the (100), (110), and possibly other crystal faces. Changing the temperature from 25° to 5°C leads to an exclusion of ClO_4^- from the double layer. The addition of alcohols, methanol through n-pentanol, causes the appearance of new capacity peaks at −0.1 and +0.5v *vs.* SCE at 25°C. This is taken as evidence for the zero point of charge of gold in $HClO_4$ being at or very close to 0.0v. An adsorption peak with added aniline at +0.2v gives additional support.

In principle, the adsorption of substances at a metal-electrolyte interface can be followed as a function of potential by both surface tension and capacity measurements (1). However, adsorption and desorption from solution almost always constitute a replacement step. Consequently the number of adsorbed molecules does not undergo large changes, and at the potential regions at which an adsorption or desorption step occurs no significant variations in surface tension are found (2). On the other hand, adsorption of charged particles, thus replacement of charged particles by neutral molecules, leads to a significant change of the charge in the inner double layer and manifests itself by a more or less pronounced peak in the differential capacity-potential curve. Moreover surface tension measurements of the required accuracy are restricted to liquid metals. No such limitation exists for differential capacity measurements.

In the past, differential capacity measurements on solid electrodes have been hampered largely by poor reproducibility. This problem is being overcome slowly by use of single crystal electrodes, by improved surface preparation, by especially purified electrolytes, and by special measuring techniques. Increasingly valuable data on the potential dependent adsorption of substances at the solid metal/electrolyte interface are being obtained (3, 4).

Solid electrodes are often far from being ideally polarizable. It is usually assumed that passage of current through the electrode/solution interface does not disturb the equilibrium in the electrical double

[1] Present address: University of Alberta, Department of Chemistry, Edmonton, Alberta, Canada.

layer. A thermodynamic treatment for reversible systems has been published (5). Lack of ideal polarizability leads to a frequency dependent capacity with the "true" differential capacity being obtained at infinite frequencies. Frequencies of the required magnitude are difficult to handle experimentally. It has been shown in this laboratory that a square wave method (6) or a fast risetime single pulse technique (7) gives capacities corresponding to infinite frequency values in some cases. Difficulties have been encountered during oxygen evolution and aniline oxidation, reactions that seem to be very fast thus causing the potential-time curve to show curvature even in the first microsecond. However, these methods are limited at present only by the sensitivity and bandwidth of the available measuring equipment and can be easily made to correspond to capacity values taken at 500 kcps.

It is frequently forgotten in the interpretation of differential capacity measurements that the values obtained are not an indication of the change of charge with potential on the solution side of the double layer, but rather give the change of charge with potential on the metal side of the interface (1, 2). Electroneutrality requires the charge on the solution side to be equal and of opposite sign, but does not permit conclusions as to the amount of anions and cations present. A quantitative interpretation of the amount adsorbed requires a detailed knowledge of the components of charge on the solution side of the double layer. An analysis of this type requires knowledge of the zero point of charge and detailed data of the variation of the capacity with activity of the adsorbed substance (8). Both are difficult to obtain on solid electrodes, largely because of poor surface reproducibility. Interpretation of differential capacity data have therefore remained rather qualitative.

In a recent paper from this laboratory (9) the zero point of charge of (110) and (100) gold in $HClO_4$ was tentatively identified as being at 0.00 and −0.05v *vs.* SCE, respectively. The present paper is a study of the adsorption of a series of aliphatic alcohols on gold from 1*N* $HClO_4$ furnishing experimental proof for this identification.

Experimental

The electrodes were polycrystalline mint gold purchased from Engelhard Industries, Inc., Newark, New Jersey. Rods were pressure sealed into Kel-F and joined to a Pyrex glass holder using a Teflon washer, brass rod, and nut. The x-ray analysis of the exposed cross section showed a perfect powder pattern indicating a random orientation of the gold crystallites. The electrodes were abraded with 4/0 emery paper, etched in aqua regia, washed in conductivity water, and degreased with acetone in a soxhlet.

The base electrolyte, 1*N* $HClO_4$ in all cases, was prepared from 70% A. R. Mallinckrodt perchloric acid and water from a Barnstead conductivity still ($\sim 2 \times 10^{-7}$ ohm^{-1} cm^{-1}). The resulting solution was pre-electrolyzed between Pt electrodes with at least 35 coulombs/ml, degassed with a steady stream of grade A helium for 12 additional hours. The alcohols, n-C_1 through n-C_4, were Baker Analyzed Reagent. They were redistilled and the fractions finally used had a boiling range of C_1, C_2: 0.1°C; C_3: 0.2°C; C_4: 0.3°C. The n-C_5 alcohol was obtained from Eastman, a fraction with a boiling range of 0.3°C being used. Some experiments were performed with redistilled aniline, Baker Analyzed Reagent. The adsorbents were added to the base electrolyte using a hypodermic syringe with a Pt needle. Unless otherwise stated the experiments were performed at 25° ± 0.5°C.

The all-Pyrex glass cell contained a large platinized Pt wire gauze as polarizing electrode. Polarizing current was supplied by the pulse generator, or by a potentiometer and by a large SCE whenever the total required current was less than 1 μa (from about −0.2 to 1.4v, or −0.2 to 0.3v with aniline added). The potentials were measured with a second SCE and a Haber-Luggin capillary, using a Keithley 610A electrometer. They are reported with respect to SCE at 25°C. A stream of grade A helium presaturated with adsorbent served as stirrer.

The single pulse method and equipment used here have been described elsewhere (7). The differential capacity, C, was calculated with

$$C\,(t{-}0) = \Delta Q'(0)/\Delta e'(0)$$

where $\Delta Q'(0) = I_2 - I_1$ with I_1 the current density at time $t<0$ (before the pulse) and I_2 at $t>0$ (during the pulse). $\Delta e'(0)$ is the change in slope of the potential-time curve at $t{-}0$. A resistor and a capacitor in parallel were taken as the circuit analog for the electrical double layer in this analysis. The potential-time function of the test electrode was displayed on a Tektronix Type 531 A oscilloscope using a Type-D preamplifier. The trace was photographed with a Dumont Polaroid oscilloscope camera.

Charging curves were obtained by applying to the cell a 50v cathodic bias and a 100v anodic pulse, 10 sec long, both dropped through an appropriate series resistor. The current density was 17.5 ma/cm^2, both cathodic and anodic.

Each run was started at about −0.6v, and the capacity measurement was taken 10 min after the potential became steady. The electrode potential was then gradually made more anodic in steps of 50 mv every 10 min. Generally the capacity had reached a stable value after less than 5 min. Runs with 1N $HClO_4$ alone or with alcohol added were interrupted at +1.4v. Capacity-potential curves with added aniline were taken between −0.2 and +0.3v only, to prevent oxidation of the additive.

The precision of the capacity measurement is limited by the nonlinearity of the scope amplifiers to ±3%. The reproducibility is not as good for polycrystalline gold as it was for single crystals (9). It is generally ±5% except for the height of the maxima which is reproducible to only ±10%. A roughness factor of 1.5 was estimated under the microscope and used for converting measured capacity to capacity per true unit area.

Results and Discussion

Figure 1 shows a comparison of capacity data in 1*N* $HClO_4$ at 25°C obtained with single crystal gold

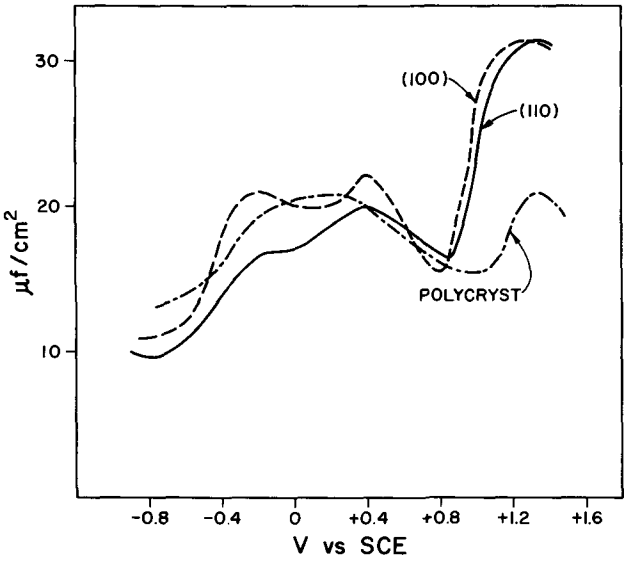

Fig. 1. Differential capacity-potential curves of (100), (110), and polycrystalline gold in 1*N* $HClO_4$, 25°C.

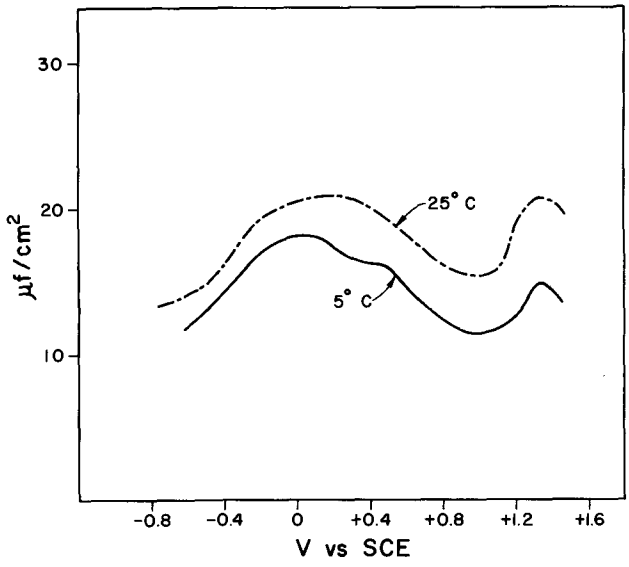

Fig. 2. Differential capacity-potential curves of polycrystalline gold in 1*N* $HClO_4$ at 25°C and 5°C.

electrodes reported previously (9) and the polycrystalline gold used in this work. The most striking feature is the much lower maximum at +1.35v for the polycrystalline electrode, a result which is more in keeping with data published by Laitinen and Chao (4) for a polycrystalline electrode with predominant (111) surface orientation. As stated already, no such orientation could be found on the electrodes used in this work.

In the potential region −0.6 to +0.4v the polycrystalline electrode is very similar to a (100) face. According to our previous explanation this indicates hydrogen adsorption in the left portion and ClO_4^- adsorption in the right portion of the broad maximum at +0.25v. No direct proof can be offered for this interpretation. The broad peak is followed by a minimum at +1.0v as compared to minima at +0.8v on the single crystal electrodes. This indicates a certain reluctance of the polycrystalline electrode to adsorb "oxygen," which is also emphasized by the diminished height of the following oxygen adsorption maximum. It seems that oxygen adsorption on gold is rather localized with preferred sites being on the (100), (110), and possibly other crystal faces. This point of view is supported by the immobility of oxygen on Pt reported by others (10).

The temperature dependence of the capacity of polycrystalline gold in 1*N* $HClO_4$ is shown in Fig. 2. The capacity values at 5°C are generally lower than those at 25°C. The right hand part of the broad maximum, attributed to specific adsorption of ClO_4^-, is lowered more than other parts of the curve. This can be attributed to an "anion exclusion" due to Grahame's "ice-like" layers (11). The relative height of the oxygen adsorption peak is slightly less also and this matter will be taken up in a forthcoming paper.

The alcohols used in this work are not oxidized on gold up to +1.4v. This was ascertained by obtaining anodic and cathodic charging curves. No difference was detected between pure base electrolyte and the same with added alcohol up to 0.1M. The charge involved in the cathodic reduction of the anodized electrode was 3.8 mcoul/cm² from an anodization potential of +1.9v, in excellent agreement with the literature (4). Charging curves for base electrolyte with 0.1M aniline showed oxidation of aniline at +0.4v. These experiments were therefore terminated at +0.3v.

The dependence of the capacity on the concentration of added methanol is shown in Fig. 3. Two new peaks point to adsorption-desorption at about −0.1v and at about +0.5v. The capacity is strongly dependent on methanol concentration, the peaks being higher with increasing concentration. The maxima are rather broad and closely spaced, preventing the capacity at intermediate potentials from reaching the low values expected for the adsorption region of neutral organic molecules (1).

The maximum nonspecific adsorption of neutral substances on a metal-electrolyte interface takes

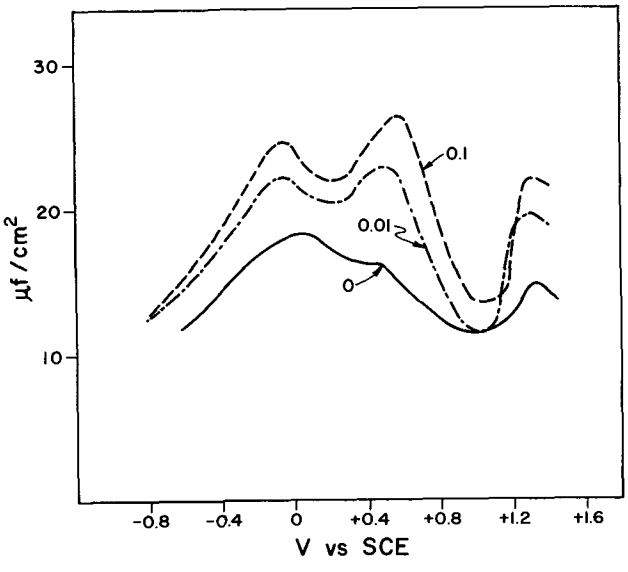

Fig. 3. Differential capacity-potential curves of polycrystalline gold in 1*N* $HClO_4$ at 5°C with 0M, 0.01M, and 0.1M methanol added.

place at or around the zero point of charge (z.p.c.) of the metal. At potentials anodic and cathodic to this z.p.c. the adsorbed substance is expelled from the (inner) double layer, presumably through replacement by anions, cations, or water dipoles. This expulsion expresses itself in maxima in the capacity-potential behavior of the system. The z.p.c. is to be found in the potential region enclosed by the capacity peaks caused by adsorption or desorption of neutral molecules. The z.p.c. of (110) and (100) gold in $HClO_4$ has been tentatively identified as being at 0.00 and —0.05v, respectively (9). This point is between the two peaks observed (on polycrystalline Au) with methanol, as expected, but it lies very close to the peak at —0.1v, a matter which is discussed below.

It is seen from Fig. 3 that the peaks at +1.3v due to oxygen adsorption are markedly enhanced in methanol-containing solutions. No definite explanation can be offered for this phenomenon. Methanol is oxidized on Pt between +0.8 and +1.0v (12) whereas no oxidation could be observed on gold up to +1.4v as judged from the charging curves. This high overpotential of the oxidation of methanol on gold suggests coverage of the electrode with methanol oxidation intermediates similar to the coverage just before oxygen evolution, with oxygen, observed on many metals with high oxygen evolution overvoltage. Coverage with methanol oxidation intermediates could very well lead to a higher peak in the capacity-potential curve. However, cathodic and anodic charging curves show no difference between methanol-free and methanol-containing solutions.

Figure 4 shows the very similar behavior of the capacity-potential curves observed with methanol and the other alcohols used in this work. The maximum on the left is seen to decrease when going from C_1 to C_5, a phenomenon which can be explained by a spread of the adsorption region over an increasingly wider potential range. For example, the corresponding adsorption of n-butanol on mercury occurs over a region of 0.6v (13). The desorption

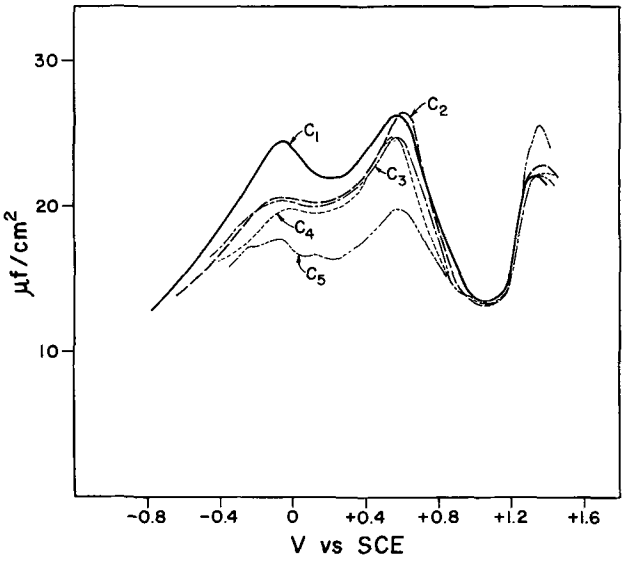

Fig. 4. Differential capacity-potential curves of polycrystalline gold in 1N $HClO_4$ at 5°C with 0.1M n-C_1 through n-C_5 added.

range of the alcohols on the anodic side is quite narrow as indicated by the steep fall of the capacity to the minimum at +1.1v. This again is similar to the behavior shown by n-butanol on mercury (13).

Alcohols in acid are protonated to a certain extent, more so with increasing chain length. This also causes an increase in the hydration of the molecule which should lead to a decrease in adsorbability, making the adsorption of the neutral molecule energetically more favorable. Moreover, since hydrogen adsorption does not seem to be very pronounced on gold (14), the protonated species should be adsorbed far into the cathodic region, that is more than just 0.6v cathodic from the anodic desorption peak. The reason for the smaller peaks of amyl alcohol can be sought in the lower dipole moment (15) if one is willing to assume that the adsorption bond is established by electronic interaction of the metal with the dipole, this leading to a (small) increase in the charge on the metal. The oxygen adsorption peak is slightly higher for amyl alcohol than for the other alcohols, the difference being just outside the experimental error. This may be for the same reasons discussed above for the difference between methanol and pure base electrolyte.

The desorption of n-butanol from mercury on the cathodic side starts at potentials slightly anodic to the z.p.c. (13). Moreover, a shift of the z.p.c. to more positive potentials in $HClO_4$ containing alcohols appears to be feasible. Also, a small shift as compared to single crystal electrodes may be allowed for because of the polycrystallinity of the electrodes used in this work. For these reasons we do not believe that a serious argument can be made against identification of the z.p.c. of gold in $HClO_4$ from the fact that this z.p.c. is close to one of the peaks observed with added alcohols.

To obtain further experimental evidence, 0.1M aniline was added to the base electrolyte. Aniline should be protonated almost completely in 1N $HClO_4$ and should also show at least some specific adsorption due to π electron interaction. A desorption peak on the anodic side of the z.p.c. potential should therefore be expected whereas the peak on the cathodic side should be displaced to higher cathodic potentials. Since aniline is oxidized at +0.4v and the polarizing electrode was in the same compartment with the gold electrode, data were taken only between —0.2 and +0.3v (region of nearly ideal polarizability). The results are shown in Fig. 5 and are entirely in keeping with the point of view presented here.

Summary

The differential capacity of a polycrystalline gold electrode in 1N $HClO_4$ was studied and compared to data on single crystal electrodes obtained previously. The capacity-potential behavior is similar, except in the oxygen adsorption region where the polycrystalline electrode shows a marked retardation of oxygen uptake. This is taken as evidence for oxygen adsorption on fixed sites with the (100), the (110), and possibly other crystal faces preferred. The difference in the capacity-potential curve at 25° and at 5°C is attributed to ClO_4^- exclusion at the lower temperature caused by Grahame's "ice-like" layers.

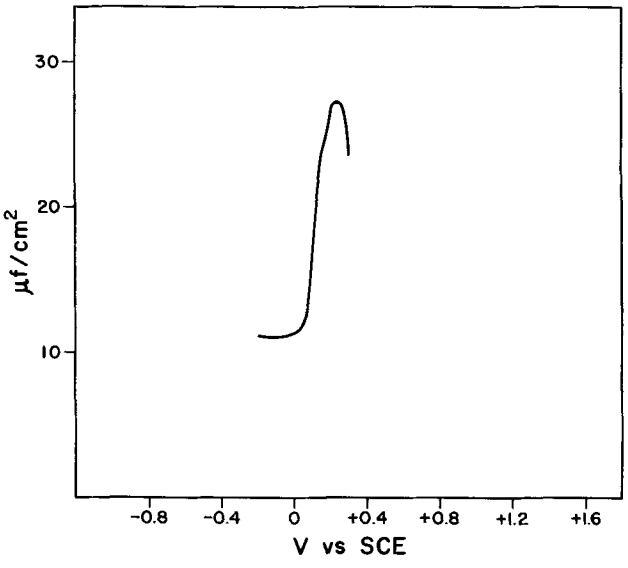

Fig. 5. Differential capacity-potential curves of polycrystalline gold in 1N $HClO_4$ at 5°C with 0.1M aniline added.

The adsorption of alcohols, n-C_1 through n-C_5, from 1N $HClO_4$ was investigated. New capacity peaks at −0.4 and +0.5v were found with the height being strongly dependent on alcohol concentration up to 0.1M, at least for methanol. Gradual disappearance of the new cathodic peak with increasing chain length is attributed to a broadening of the potential region of adsorption. The effect of the alcohols on the oxygen adsorption peaks is presumably caused by adsorption of alcohol oxidation intermediates.

The appearance of the alcohol adsorption peaks, one cathodic and one anodic to the suggested z.p.c. of (100) and (110) gold in $HClO_4$ is taken as experimental proof for the z.p.c. of gold being at or very close to 0.0v. This is supported by a capacity peak on the anodic side of this z.p.c. observed in 1*N* $HClO_4$ with aniline added.

Acknowledgment

The authors take this opportunity to express their appreciation for financial help to the Robert A. Welch Foundation of Houston, Texas, and to the Office of Naval Research (Contract Nonr 375(15)). They are indebted to Mr. E. F. Meyer for the x-ray analysis and to Mr. J. S. Riney for many helpful discussions regarding the electronic equipment used in this work.

Manuscript received Aug. 13, 1962; revised manuscript received Nov. 9, 1962.

Any discussion of this paper will appear in a Discussion Section to be published in the December 1963 JOURNAL.

REFERENCES

1. For reviews see: D. C. Grahame, *Chem. Revs.*, **41**, 441 (1947); A. N. Frumkin, *This Journal*, **107**, 461 (1960); B. B. Damaskin, *Uspekhi Khimii*, **30**, 220 (1961).
2. A. N. Frumkin and B. B. Damaskin, *J. Electroanal. Chem.*, **3**, 36 (1962).
3. H. A. Laitinen and C. G. Enke, *This Journal*, **107**, 773 (1960); H. A. Laitinen and M. S. Chao, *ibid.*, **108**, 726 (1961); *Anal. Chem.*, **33**, 1836 (1961).
4. M. W. Breiter, *This Journal*, **109**, 42 (1962).
5. D. M. Mohilner, *J. Phys. Chem.*, **66**, 724 (1962).
6. R. J. Brodd and Norman Hackerman, *This Journal*, **104**, 704 (1957).
7. J. S. Riney, G. M. Schmid, and Norman Hackerman, *Rev. Sci. Instr.*, **32**, 588 (1961).
8. D. C. Grahame and B. A. Soderberg, *J. Chem. Phys.*, **22**, 449 (1954).
9. G. M. Schmid and Norman Hackerman, *This Journal*, **109**, 243 (1962).
10. A. I. Shlygin and M. A. Kerdivarenko, *Uchenye Zapiski Kishinev Gosudorst. Univ.*, **7**, 7 (1953). *C.A.*, **49**, 10098c.
11. D. C. Grahame, *J. Am. Chem. Soc.*, **79**, 2093 (1957).
12. M. W. Breiter and S. Gilman, *This Journal*, **109**, 622 (1962).
13. E. Blomgren, J. O'M. Bockris, and C. Jesch, *J. Phys. Chem.*, **65**, 2000 (1961).
14. F. G. Will and C. A. Knorr, *Z. Elektrochem.*, **64**, 270 (1960).
15. Landolt-Börnstein, "Zahlenwerte und Funktionen," 3. Teil, Molekeln II, p. 386 ff, Springer Verlag, Berlin (1951).

Electrochemical Study of the Nickel-Hydrogen System

Z. Szklarska-Smialowska and M. Smialowski

Polish Academy of Sciences, Institute of Physical Chemistry, Warsaw, Poland

ABSTRACT

A study has been made to determine the potential of a mixed nickel-hydrogen electrode containing up to about 0.7 H atoms per Ni atom. Nickel layers electrodeposited on copper foils were charged cathodically in sulfuric acid solutions containing thiourea or selenium dioxide as catalytic poisons of the hydrogen recombination reaction. The electrode potential of nickel charged with hydrogen and kinetics of decomposition of the hydride phase were studied as functions of time of hydrogen desorption and pH of the electrolyte. The results show that the nickel-hydrogen system behaves electrochemically like the palladium-hydrogen system. The open-circuit potential of $NiH_{0.4}$, i.e., of a nickel-hydrogen electrode presumably containing a mixture of alpha and beta phases, is a linear function of *p*H, with a value approximately 0.13v less noble than that of the hydrogen electrode. The desorption rate of hydrogen from Ni-H depends on the *p*H.

It has been reported in preceding publications (1, 2) that massive nickel samples (wires, sheets, and rods of polycrystalline nickel, electroplated layers, and single crystals obtained by a slow solidification from the melt) may be charged with hydrogen to contents as high as 0.7-0.8 H atoms per Ni

atom. The conditions bringing out such a high saturation degree of the metal with hydrogen are as follows: (i) cathodic polarization at a sufficiently high current density; (ii) presence of catalytic poisons having the ability to restrain the recombination reaction of hydrogen into molecules; (iii) temperature not higher than about 80°C.

Under these conditions hydrogen penetrates interstitially into the nickel crystals, and if the chemical potential of atomic hydrogen at the electrolyte/metal interface is high enough, a hydride phase of the approximate composition $NiH_{0.7}$ is produced.

As shown by x-ray (3) and electron diffraction studies (4), the nickel hydride $NiH_{0.7}$ has a fcc crystal lattice with a spacing about 6% greater than that of pure nickel. The formation of this phase inside of the massive metal is therefore accompanied with the creation of very high compression stresses (5). These decrease the amount of hydrogen which may be absorbed interstitially within the nickel crystals (6), and, therefore, a further production of the hydride during cathodic polarization stops after a certain depth within the given nickel specimen is attained. The limiting thickness of the nickel layer, which may be transferred into the hydride phase, depends on the poison added to the electrolyte in which the cathodic charging is performed. For example, this thickness is of the order of 2μ in the case of arsenic trioxide used as poison, about 25μ in that of selenium dioxide, and about 30μ in that of thiourea (7).

Catalytic poisons, P, S, As, Se, Te, Bi, are thought to inhibit the hydrogen recombination reaction $2H \rightarrow H_2$, and thus to increase the chemical potential of atomic hydrogen at the working cathode. Anions SO_4^{2-} and PO_4^{3-} having a high degree of oxidation and stability are not reduced at the cathode and do not influence the process of hydrogen penetration, but lower oxides, such as sulfur dioxide, and oxidized anions of other elements mentioned, give by cathodic reduction free elements and hydrides, for instance

$$As_2O_3 \rightarrow As \rightarrow AsH_3$$

Evidently, the formation of a volatile hydride is decisive for the poisoning effect and for the increased ability of hydrogen to penetrate the cathodic metal. Thus, arsenic trioxide is active as poison only at potentials less noble than −0.4v, at which the AsO_2^- ion is reduced into arsine (8). Thiourea is active due to its reduction at the cathode into hydrogen sulfide.

It has been found by Baranowski (9) that electroplated nickel layers, when charged cathodically with hydrogen at room temperature in $1N$ H_2SO_4 solution containing thiourea as a catalytic poison, absorb hydrogen in amounts dependent on the cathodic current density. The isotherms, concentration of hydrogen absorbed *vs.* current density, show two distinct changes in slope: one at the atomic ratio H:Ni $\approx$ 0.03, and another one at H:Ni $\approx$ 0.7. These isotherms and the curves of the dependence on the temperature of the amount of hydrogen absorbed at a constant current density suggest the existence of a fargoing similarity of the nickel-hydrogen system to the well-known palladium-hydrogen one.

At room temperature and standard pressure palladium and hydrogen form two separate phases: the alpha phase containing 0.025 atoms of hydrogen per one palladium atom, and the beta phase in which the atomic ratio H:Pd is approximately 0.69 (10). The beta phase in Pd-H has a fcc crystal lattice with a spacing about 3.5% greater than that of pure palladium. This phase is simply formed at room temperature when gaseous molecular hydrogen at standard pressure is brought into contact with massive palladium. In similar conditions nickel absorbs only 6.10^{-5} hydrogen atoms per metal atom. Recent experimental data (11) seem to suggest that the high atomic ratio H:Ni $\approx$ 0.7 corresponding to the presence of the hydride phase may be obtained at a pressure of gaseous hydrogen of the order of 2.10^4 atm in contact with nickel.

Palladium is believed to have 0.55 holes per atom in the d shell, and since the magnetic susceptibility of the Pd-H system drops to zero when there are about 0.6 hydrogen atoms absorbed per each palladium atom (12), Mott and Jones (13) made the assumption that hydrogen atoms give up their electrons to the d shell of palladium, *i.e.*, that the hydrogen dissolved in palladium is completely ionized.

Similarly one might assume that, since nickel has an average of 0.6 holes per each Ni atom, the filling up of these holes by electrons taken from hydrogen atoms is attained at an atomic ratio H:Ni $\approx$ 0.6, *i.e.*, not far from the limiting concentration found experimentally for the Ni-H system. This assumption is supported by the fact that the electrical conductivity becomes considerably increased (14), and the saturation magnetization is reduced eventually to zero, by the cathodic introduction of hydrogen into nickel (15).

Hence, there are many experimental indications as to the qualitative similarity of both the systems Pd-H and Ni-H. We, therefore, thought it useful to compare the electrochemical behavior of these systems.

Electrochemical studies of the palladium-hydrogen alloys have been made by Frumkin and Aladjalova (16), Breiter *et al.* (17), Hoare and Schuldiner (18), and others. If palladium is immersed in an acid solution and brought into contact with gaseous hydrogen at standard pressure, a gradual shift of the potential can be observed to values characterizing the hydrogen electrode. The curves of the potential values plotted as functions of charging time or of hydrogen concentration show three parts corresponding to three successive stages of palladium hydrogenation, namely, to the alpha phase, the presence of two immiscible phases (alpha plus beta), and the beta phase. The beta phase, $PdH_{0.69}$, has been reported to reveal the potential of a hydrogen electrode, whereas within the range of immiscibility of the alpha and beta phases, the potential has been found about 0.05 to 0.058v more noble than that of the hydrogen electrode.

In the case of nickel, one might expect more involved effects due to the fact that nickel is less noble than both palladium and hydrogen, and that the beta phase (hydride phase) in the Ni-H system is unstable at ordinary conditions. This phase starts

to decompose immediately after interruption of the cathodic charging. The kinetics of its decomposition corresponds to a first-order reaction (9). It is more stable in single crystals than in a polycrystalline nickel, and the rate of its decomposition seems to depend on the crystal orientation (19).

Experimental

Main experiments were performed using nickel layers electrodeposited on copper. A copper foil, 0.05 mm thick, was degreased for 10 min in a 10% boiling solution of KOH. Further, the foil was washed in distilled water and in absolute alcohol and electropolished for 2 min in orthophosphoric acid (density of the acid 1.4, current density 0.13 amp/cm^2). The foil was then quickly immersed in distilled water and in absolute alcohol, dried, and heated for 1 hr at 400°C and normal pressure in a hydrogen atmosphere. After cooling to room temperature, the copper foil was coated electrolytically by a bright nickel plate. A solution of 75g ammonium-nickel sulfate per liter at 40°-45°C and at a current density of 0.004 amp/cm^2 was applied. The electroplated foils were further heated for 1 hr in vacuum at 300°C. The thickness of the electrodeposited nickel layer was usually of the order of 0.017mm.

The above procedure was chosen for the following reasons. As known, the surface of electropolished copper shows different structures. On the other hand, the structure of the basic surface is continued to a certain degree by the electrodeposited metal. Thus, the heating of the copper foil was done to produce a more homogeneous structure on the metal. The heating was undertaken at a not too high temperature, since the absorption of too great amounts of hydrogen by the basic metal had to be avoided. Heating of the nickel plate was performed in order to remove stresses usually present in electrodeposited metals. Stresses were shown to effect the absorption of hydrogen by nickel (6). The upper limit of the applied heating temperature was determined by the reciprocal diffusion rates in the Cu-Ni system. During 1 hr at 300°C the diffusion depth was certainly not greater than 1% of the nickel plate thickness.

The specimens were charged cathodically at room temperature in an aqueous solution of 1N H_2SO_4 containing 0.001g selenium dioxide or 0.2g thiourea per liter. A large amount of electrolyte was used for charging, namely 2 liter per each 30 cm^2 of the treated sample, since during electrolysis there occurs a slight evolution of H_2Se or H_2S, and the concentration of the poison in the electrolyte gradually decreases. The charging with hydrogen was carried out at a cathodic current density of 0.05 amp/cm^2 for a sufficiently long time to obtain the limiting concentration of about 0.7 H atoms per each Ni atom, *i.e.*, about 140 cm^3 gas at S.T.P. per 1g nickel. The hydrogen content of samples was determined after the interruption of the cathodic charging by measurement of the volume of gas desorbing under ordinary conditions from the charged specimens. Usually, a "training," *i.e.*, a preparatory treatment of the specimens by several successive chargings and dischargings, was performed in order to obtain reproducible results. Such a preparatory charging was made in 1N H_2SO_4 with poison at a current density of 0.02 amp/cm^2 for 12 hr or more. For discharging, the specimen was immersed in distilled water, and the volume of escaping hydrogen was observed. Once the limiting hydrogen concentration was attained in the given sample, it next behaved quite reproducibly and could be used for kinetic and electrochemical measurements. For these, specimens prepared in the above way were charged several hours in 1N H_2SO_4 with or without poison at 0.05 amp/cm^2. After charging, the specimens were quickly rinsed with distilled water, and the hydrogen content was determined by measurement of the volume of desorbing gas at 25° ± 0.05°C and at atmospheric pressure. The amount of evolved gas was determined with an accuracy of 0.01 cm^3. An interval of 0.5 min usually elapsed between the interruption of electrolytic charging and beginning of the measurement of desorption rate and open-circuit potential.

The rate of hydrogen desorption was measured on specimens immersed in aqueous electrolytes differing in *p*H, namely, sulfuric acid, water, and sodium hydroxide solutions.

Measurements of the open-circuit potential were made at 25°C in a vessel represented in Fig. 1. Immediately after interruption of the charging current, the specimen was transferred into this vessel containing 150 cm^3 of a pure deaerated electrolyte (sulfuric acid, sodium hydroxide, or a mixture of both), and the potential was measured simultaneously with volume measurements of the evolving hydrogen gas. A mercury sulfate reference electrode was used. Both for kinetic and electrochemical measurements, samples 5 mm in width and 15 cm in length were applied. Some comparative experiments have been carried out on massive nickel wires 0.2 mm in diameter and up to 50 cm in length. In this case the limiting H:Ni ratio corresponding to a complete transformation of nickel in the whole wire section into $NiH_{0.7}$ could not be obtained.

Results and Discussion

A typical curve of changes in the open-circuit potential of a hydrogen charged nickel layer *vs.* time

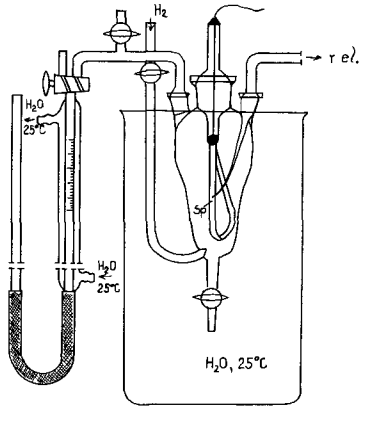

Fig. 1. Vessel used for the measurement of the open-circuit potential of nickel charged with hydrogen. Sp, specimen; r.el., reference electrode.

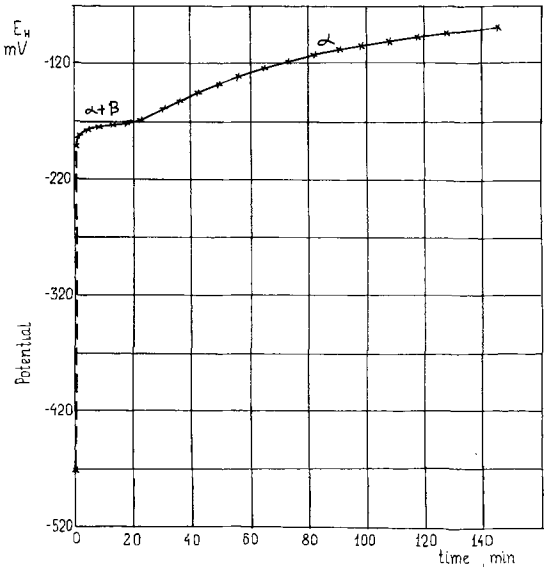

Fig. 2. Effect of time after interruption of cathodic charging on the open-circuit potential (hydrogen scale) of nickel. Specimen immersed in 0.1*N* H_2SO_4 solution.

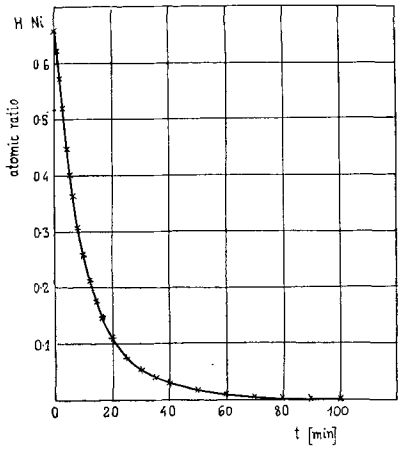

Fig. 3. Effect of time of desorption in 0.1*N* H_2SO_4 solution on the hydrogen content of nickel charged cathodically.

of desorption is shown in Fig. 2. Similarly as it has been observed by Frumkin (16) and others for palladium, the potential rises initially very quickly, and this corresponds to the discharge of the electric double layer. Next, there appears a part of the curve with less slope, followed by an almost horizontal part which is related to the presence in the electrode of both the alpha and beta phases. Later still, the potential changes very slowly with escaping hydrogen, tending to a not very well reproducible value of the electrode potential of pure nickel.

Specimens charged with hydrogen in the presence of thiourea gave results identical to those charged in the presence of selenium in sulfuric acid solution. There occurred a slight incorporation of sulfur or selenium on the nickel surface, but these elements evidently had a minor effect on the electrode potential of the nickel-hydrogen electrode. The reproducibility of potential values of the mixed Ni-H electrode was quite good, about ±2 mv in alkaline solutions and ±3 mv in acids. Experiments performed on massive nickel wires gave similar results, but, as mentioned above, in this case a transformation of the whole wire section into the hydride $NiH_{0.7}$ could not be attained.

As may be seen in Fig. 3 which illustrates the relationship between the atomic ratio H:Ni and the time of desorption in 0.1*N* H_2SO_4 solution, after 25 min there remains in the sample an average hydrogen content lower than $NiH_{0.1}$. When immersed in alkaline solutions, the samples evolved hydrogen at a greater rate than in acids, see Fig. 6.

In Fig. 4, the potential is plotted as function of the hydrogen content. Here again, similarly as found for palladium, one may observe three parts corresponding to the alpha phase, the range of immiscibility of the alpha and beta phases, and the beta phase.

Figure 5 shows the effect of *p*H of the solution on the open-circuit potential of the nickel-hydrogen electrode containing both the alpha and beta phases. This plot was drawn using potential values for electrodes containing 0.4 H atoms per one Ni atom. As may be seen, the relationship between the potential of the $NiH_{0.4}$ electrode and *p*H is represented by a straight line shifted some 0.13v toward less noble values than those characterizing the hydrogen electrode. If the assumption were made that Ni-H behaves like a reversible electrode, one would obtain 10^4 atm as the pressure of hydrogen gas in equilibrium with $NiH_{0.4}$. This order of magnitude was also found in a recent observation by Baranowski (11) who showed that under a pressure of 2.10^4 atm the nickel hydride does not decompose at room temperature any more.

The above results show that, despite the fact that nickel is less noble than hydrogen, not nickel, but

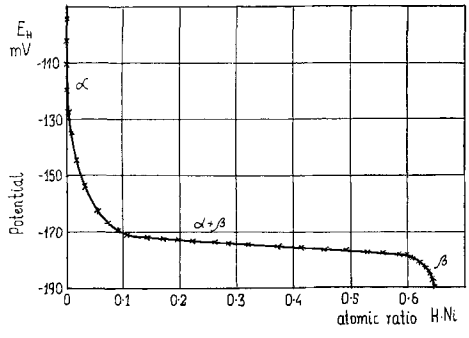

Fig. 4. Relationship between the electrode potential of nickel in 0.1*N* H_2SO_4 solution, and hydrogen content.

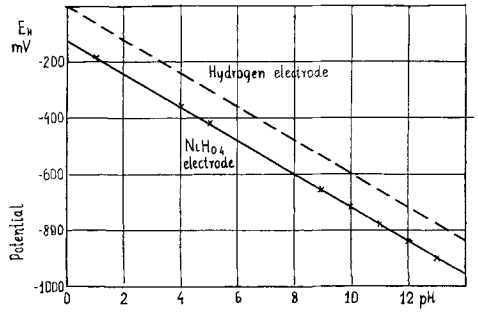

Fig. 5. Relationship between the electrode potential of $NiH_{0.4}$, and *p*H of the solution. For comparison, the straight line for the hydrogen electrode is also plotted.

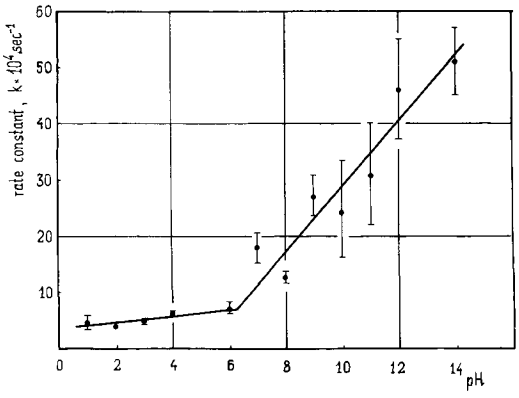

Fig. 6. Relationship between the rate constant k of hydrogen desorption from $NiH_{0.7}$, and pH of the solution in which the specimen is immersed after interruption of the cathodic charging. Ranges indicated on the diagram illustrate the scattering of experimental results when three different specimens of electrodeposited nickel have been used. The reproducibility was much better in the case of one specimen used for all the experiments.

primarily hydrogen is ionized, when a mixed Ni-H electrode is immersed in an aqueous electrolyte.

The desorption rate of hydrogen from Ni-H depends on the pH of the surrounding aqueous medium. This effect is illustrated in Fig. 6, in which the rate constant k from the equation

$$\frac{dv}{dt} = -k \cdot v$$

(v is volume of hydrogen comprised by the given sample, and t, time) is plotted as function of pH. As may be seen, the desorption rate is much greater in alkaline media than in acids, and at pH $\approx$ 6 there occurs a change in slope of the curve $k \sim$ pH. As shown in Fig. 6, the reproducibility of experimental results was better in acid than in alkaline solutions.

It is worth mentioning that recently Bagotskaia (20) observed a greater rate of hydrogen permeation through an iron membrane when its outgoing surface was brought into contact with an alkaline solution (2N NaOH), as compared with the case when an acid medium (2N H_2SO_4) was applied. Bagotskaia suggests that this effect is due to a greater energy of the Me-H_{ads} boundary in alkaline than in acid solutions (21).

Manuscript received June 22, 1962; revised manuscript received Sept. 7, 1962.

Any discussion of this paper will appear in a Discussion Section to be published in the December 1963 JOURNAL.

REFERENCES

1. B. Baranowski and M. Smialowski, *J. Phys. Chem. Solids*, **12**, 206 (1959); *Bull. Acad. Pol. Sci., Ser. Sci. Chim.*, **7**, 663 (1959).
2. B. Baranowski, Z. Szklarska-Smialowska, and M. Smialowski, Paper 115, Second Intern. Congress of Catalysis, Paris 1960.
3. A. Janko, *Naturwissenschaften*, **47**, 225 (1960); *Bull. Acad. Pol. Sci., Ser. Sci. Chim.*, **8**, 131 (1960).
4. A. Janko and P. Michel, *Compt. rend.*, **251**, 1001 (1960).
5. Z. Szklarska-Smialowska and M. Smialowski, *Bull. Acad. Pol. Sci., Ser. Sci. Chim.*, **6**, 427 (1958).
6. Z. Szklarska-Smialowska and M. Smialowski, *ibid.*, **6**, 187 (1958).
7. H. Jarmolowicz and M. Smialowski, *J. Catalysis*, **1**, 165 (1962).
8. H. Angerstein-Kozlowska, *Bull. Acad. Pol. Sci., Ser. Sci. Chim.*, **7**, 881 (1959).
9. B. Baranowski, *ibid.*, **7**, 887, 891, 897, 907 (1959); *Naturwissenschaften*, **46**, 666 (1959).
10. T. B. Flanagan and F. A. Lewis, *Trans. Faraday Soc.*, **55**, 1400 (1959).
11. B. Baranowski, *Bull. Acad. Pol. Sci., Ser. Sci. Chim.*, **10**, 451 (1962).
12. B. Svensson, *Ann. Physik*, [5], **18**, 299 (1933).
13. N. F. Mott and H. Jones, "The Theory of the Properties of Metals and Alloys," p. 200, Dover Publications Inc., New York (1958).
14. Z. Szklarska-Smialowska, *Bull. Acad. Pol. Sci., Ser. Sci. Chim.*, **8**, 305 (1960).
15. H. J. Bauer and E. Schmidbauer, *Z. Physik*, **164**, 367 (1961).
16. A. N. Frumkin and N. Aladjalova, *Acta Physichochim. U.S.S.R.*, **19**, 1 (1944).
17. M. Breiter, H. Kammermaier, and C. A. Knorr, *Z. Elektrochem.*, **58**, 702 (1954).
18. J. P. Hoare and S. Schuldiner, *J. Phys. Chem.*, **61**, 399 (1957).
19. A. Janko, *Bull. Acad. Pol. Sci., Ser. Sci. Chim.*, **10**, 613 (1962).
20. I. A. Bagotskaia, Private communication, March 1962.
21. V. E. Past and Z. A. Iofa, *Zhur. Fiz. Khim.*, **33**, 1230 (1959).

Anodic Oxidation of Methanol on Platinum

III. Adsorption Kinetics in Acidic Solution

M. W. Breiter

Research Laboratory, General Electric Company, Schenectady, New York

ABSTRACT

The rate of methanol adsorption during low-speed, periodic potential sweeps was computed on the basis of the measured current density and the methanol coverage in the potential region of the prewave during the anodic sweep and of the shoulder of the wave during the cathodic sweep. The rate of adsorption was analyzed as a function of free surface area, potential, and methanol bulk concentration. The found dependence suggests that each methanol molecule covers two platinum atoms on the average. The rate of adsorption is potential-dependent. It decreases with potential on both sides of 0.65v. The rate constant of the discharge step of adsorbed methanol molecules is smaller during the anodic sweep than during the cathodic sweep while the rate constant of the adsorption step shows the opposite behavior. This effect is interpreted by the concept that the heat of adsorption of methanol molecules on a surface whose oxygen coverage has just been reduced has a lower value initially than some time later.

Results on the adsorption of methanol molecules, oxygen atoms, and hydrogen atoms on smooth platinum wire electrodes in unstirred perchloric acid solutions with different additions of methanol were reported for the potential region of the anodic methanol oxidation in the first paper of this series (1). The methanol coverage θ_M was obtained as a function of potential U and methanol bulk concentrations ${}_oc_M$ from experiments in which a periodic voltage of triangular waveform with a sweep rate of 30 mv/sec was applied potentiostatically to the test electrode. The shape of potentiostatic current-potential curves which were measured under the same conditions was interpreted on the basis of the adsorption results in the second paper (2). It was shown there that the current density obeys the following equation in the potential region of the rising part of the first oxidation wave during the anodic sweep for $0.3 \leq \theta_M < 0.9$ and $0.01M \leq {}_oc_M \leq 1M$:

$$I \approx I_1 = k_1\theta_M \exp \frac{\alpha nFU}{RT} \qquad [1]$$

Here, I designates the net current density, which is essentially equal to the current density I_1 due to the oxidation of adsorbed molecules; k_1 is the rate constant of the discharge step, n is the number of electrons involved in the discharge step, and α is the transfer coefficient. It was concluded from the decrease of θ_M with increasing potential in the oxidation region and from the validity of Eq. [1] that a discharge step and an adsorption step are rate-determining simultaneously. In the mentioned region the difference between the rates of adsorption and of discharge can be related to the change in coverage through

$$F\Gamma \frac{d\theta_M}{dt} = I_a - I_1 \qquad [2]$$

where I_a is the rate of adsorption which depends on ${}_oc_M$, θ_M, and U, and $F\Gamma$ corresponds to a surface coverage of a monolayer of methanol molecules. As ${}_oc_M$, θ_M, U, and I_1 are known the rate of adsorption is computable on the basis of Eq. [2] in a simple way.

It is the purpose of this paper to determine and discuss the dependence of I_a on free surface area, potential, and methanol bulk concentration in order to get information on the adsorption mechanism. Values of θ_M, I_1, and U which were determined previously (1) under the same conditions of a periodic, low-speed potential sweep are used for the analysis. While the rate of adsorption of organic species on mercury has been the subject of extensive studies (3) in recent years, few results on the rate of adsorption have been reported for solid electrodes. Many studies dealt with the question of whether or not the rate of the anodic oxidation of molecular hydrogen on platinum could be interpreted by the hindrance of adsorption steps (4, 5). Munson's recent treatment (6) considered the influence of an adsorption step on transition times, as determined by a galvanostatic technique, but, for reasons of simplicity, did not take into account the influence of the surface coverage on the adsorption rate. Gilman (7) developed a new technique and carried out an intensive study of the rate of CO-adsorption on smooth platinum wire electrodes in 1N $HClO_4$. As for many organic substances on mercury, the adsorption step was found to be less hindered than other processes on platinum for most of the systems (4, 6, 7) studied so far. However, methanol and other alcohols or species of similar nature appear to undergo adsorption steps on platinum with sufficiently large activation energies to influence the rate of oxidation.

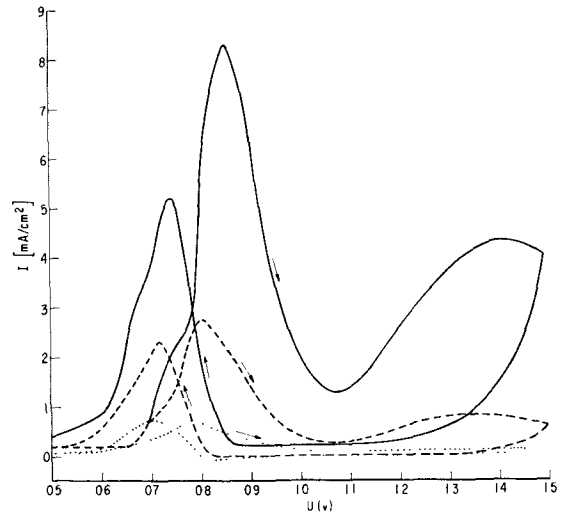

Fig. 1. Potentiostatic current-potential curves at 30 mv/sec on smooth platinum in 1N $HClO_4$ with different amounts of methanol: ——— 1M CH_3OH; — — — 0.1M CH_3OH; ..... 0.01M CH_3OH.

Results

Potentiostatic I-U curves which were measured at 30 mv/sec in unstirred solutions (1N $HClO_4$ with different concentrations of CH_3OH) at 30°C are plotted in Fig. 1. The electrode potential is referred to a hydrogen electrode in the same solution as the test electrode throughout this paper. The curves have the characteristic shape with two oxidation waves during the anodic sweep and one oxidation wave during the cathodic sweep. It was shown (2) that the first anodic peak cannot be interpreted on the basis of diffusion control. The same arguments hold for the interpretation of the peak during the cathodic sweep which has nearly the same height as the first peak of the anodic sweep in the same solution.

To see if Eq. [1] is applicable for part of the wave of the cathodic sweep, plots of log I/θ_M *vs.* U were made in the respective potential regions for the three I-U curves of Fig. 1. These curves are given in Fig. 2. For purposes of comparison the corresponding plots for the first wave of the anodic sweep which were published already (2) are given also. The experimental points of the anodic sweep scatter around a straight line. The systematic deviations at more anodic potentials were attributed (2) to the influence of an additional oxidation reaction of methanol with the rate I_2 on the free surface. Figure 2 demonstrates the applicability of Eq. [1] for the waves of the cathodic sweep at potentials which are more cathodic than the peak potential (see Fig. 1). However, the parallel log I/θ_M-U lines do not coincide as for the anodic sweep. The slopes of the linear parts of the log I/θ_M-U curves differ somewhat for the anodic and cathodic sweep. The differences in k_1 and α for the anodic and cathodic sweep can be understood as follows. Methanol oxidation during the cathodic sweep occurs on a surface freshly "activated" by the preceding reduction of the oxygen layer. The higher activity leads to larger k_1 values (compare the location of the linear parts of the log I/θ_M-U curves in Fig. 2).

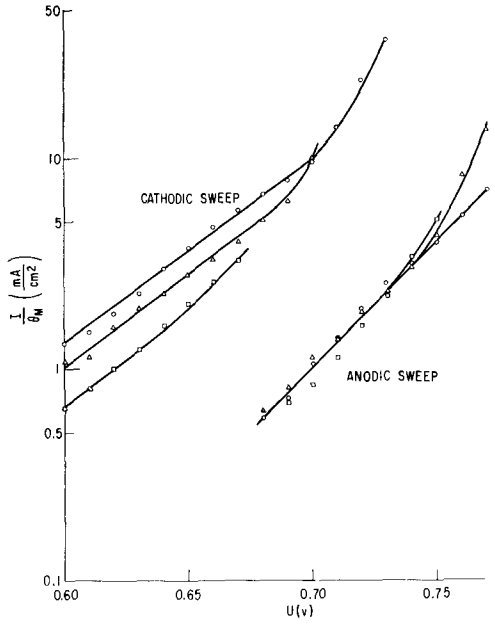

Fig. 2. Logarithmic plot of I/θ_M *vs.* U in the potential region of the first oxidation wave during the anodic sweep and of the wave during the cathodic sweep. ○, 1M CH_3OH; △, 0.1M CH_3OH; □, 0.01M CH_3OH.

Nearly a monolayer of methanol molecules has been present for some time in all solutions when the oxidation starts during the anodic sweep. Correspondingly the deviations of the experimental points at a given potential for 0.01M, 0.1M, and 1M CH_3OH from an average value are larger during the cathodic sweep than during the anodic one. The height of the peak during the cathodic sweep was found more sensitive to a change of the potential of reversal in the oxygen region than the height of the peak of the anodic sweep in the same solution.

A closer comparison between the results in Fig. 2 and Fig. 1 for 1M CH_3OH shows that Eq. [1] is applicable in the potential region of a prewave during the anodic sweep and of a shoulder on the left side of the wave of the cathodic sweep. The systematic deviations of the experimental points from the straight lines in the vicinity of the peaks can be attributed for the cathodic sweep as well as for the anodic sweep to the occurrence of an additional oxidation reaction of methanol molecules on the free surface which obeys other kinetic laws than Eq. [1]. Since the kinetics of this reaction are not known, the discussion of I_a will be restricted to the respective potential regions where Eq. [1] holds.

The results of the computation of I_a are plotted in Fig. 3 for the anodic sweep. There is an uncertainty in the $F\Gamma$ value and therefore in I_a. The charge for the anodic removal of a monolayer of adsorbed molecules was determined by fast potentiostatic potential sweeps (1). The obtained $F\Gamma$-value of 0.3 mcoul/cm² is rather small. This suggests that the oxidation during the fast sweep does not lead primarily to carbon dioxide (six electrons) as it is true for the measurements at low sweep rates which correspond nearly to steady-state conditions. As formaldehyde is the first stable intermediate in the anodic methanol oxidation, the two

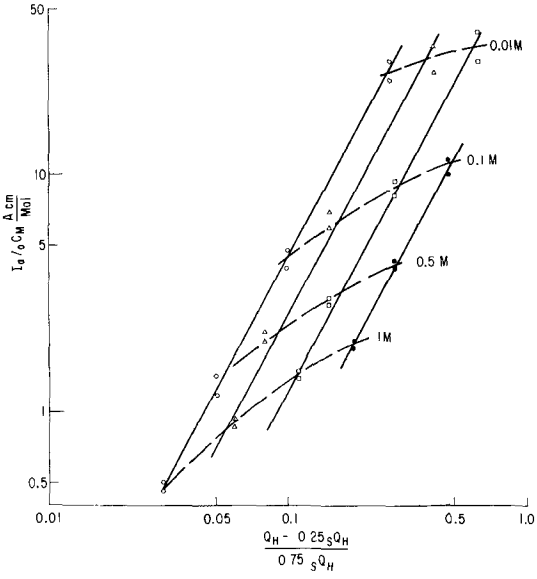

Fig. 3. Plot of $I_a/{}_oc_M$ for $m = 1$ and $m = 3$ vs. θ_f on a double logarithmic scale for different potentials and methanol concentrations. ○, 0.68v; △, 0.70v; □, 0.72v; •, 0.74v.

limits for the rate of adsorption are obtained for $m = 1$ and $m = 3$ from the more general formula

$$I_a = I_1 + m\ F\Gamma \frac{\Delta\theta_M}{\Delta t} \qquad [3]$$

with $F\Gamma = 0.3$ mcoul/cm². The logarithm of the two limiting values for $I_a/{}_oc_M$ is plotted in Fig. 3 *vs.* the logarithm of the relative free surface area at four different potentials for the curves in Fig. 1 and for ${}_oc_M = 0.5$M. The relative free surface θ_f which is proportional to the number of Pt-atoms on the 75% of the surface which become covered by adsorbed methanol molecules (1) was computed from

$$\theta_f = \frac{Q_H - 0.25 \cdot {}_sQ_H}{0.75\ {}_sQ_H} \qquad [4]$$

Here, Q_H is the amount of adsorbed hydrogen atoms in mcoul/cm², ${}_sQ_H$ is the value for a monolayer. A correction for the change of the methanol concentration in the diffusion layer was not applied because it is smaller than 5% for ${}_oc_M = 0.01$M and negligible for 0.1M $\leq {}_oc_M \leq$ 1M as follows from an estimate of the limiting diffusion current density of methanol molecules from the formula

$$I_l = \frac{6D_MF}{\delta}\ {}_oc_M \qquad [5]$$

with $D_M \approx 10^{-5}$ cm²/sec and $\delta \approx 0.06$ cm for unstirred solutions. I_l is equal to 10 ma/cm² for ${}_oc_M =$ 0.01M. The experimental points in Fig. 3 scatter around straight lines with equal slope at the same potential.

Conclusions

Figure 3 demonstrates that the rate of adsorption can be described in a good approximation by the equation

$$I_a = f(U) \cdot \theta_f^p \cdot {}_oc_M \qquad [6]$$

Here, the potential-dependent rate constant is represented by $f(U)$; p is a constant. The value of p was found equal to 1.85. This value is close to 2 and suggests that each adsorbed methanol molecule

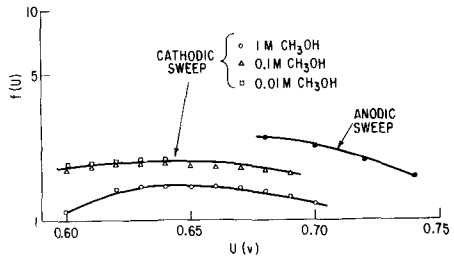

Fig. 4. Logarithmic plot of the rate-constant of the adsorption step vs. potential for the anodic and cathodic sweep.

covers two adsorption sites (platinum atoms). Then, the respective m-value in Eq. [3] should be close to 3. This conclusion is in fair agreement with the experimental values of ${}_sQ_H = 0.34$ mcoul/cm² and ${}_sQ_M = 0.30$ mcoul/cm² as the ratio $\frac{2 \cdot {}_sQ_M}{2 \cdot 0.75 \cdot {}_sQ_H} =$ 1.17 is nearly equal to 1.

The logarithm of $f(U)$ is plotted *vs.* U in Fig. 4. For the anodic sweep $f(U)$ was determined from the straight lines in Fig. 3, for the cathodic sweep $f(U)$ was computed with the aid of Eq. [6] for the different methanol concentrations. As log $f(U)$ does not differ much for $m = 1$ and $m = 3$ during the cathodic sweep, only the values for $m = 1$ are plotted. As expected from the results in Fig. 2, $f(U)$ has the same value for 0.01 $\leq {}_oc_M \leq$ 1M during the anodic sweep while the curves during the cathodic sweep lie close but do not coincide. The rate of adsorption, as a function of potential, decreases with increasing potential above 0.68v during the anodic sweep and above 0.65v during the cathodic sweep. The curve at 1M during the cathodic sweep shows a maximum at about 0.645v. On mercury a maximum rate of adsorption (as a function of potential alone) occurs at a potential (8) close to the electrocapillary maximum. The curve at 1M, taken with the fact that a similar situation exists on mercury, is evidence for the existence of a maximum on platinum. Figure 4 shows that $f(U)$ is greater at 0.68v and 0.69v during the anodic sweep than during the cathodic one. The opposite is true for the rate-constant of the discharged step of adsorbed molecules (see Fig. 2). These results suggest that an "activated" (just reduced) surface has a lower heat of methanol adsorption initially than some time later. Then, the activation energy of the discharge step of the oxidation of adsorbed molecules is smaller and that of the adsorption step is larger during the cathodic sweep than during the anodic one, as it is observed. A theoretical treatment of the above argument can be found in papers (9) about the influence of the heat of hydrogen adsorption on the kinetics of hydrogen evolution.

Manuscript received Aug. 27, 1962; revised manuscript received Nov. 5, 1962.

Any discussion of this paper will appear in a Discussion Section to be published in the December 1963 JOURNAL.

REFERENCES

1. M. W. Breiter and S. Gilman, *This Journal*, **109**, 622 (1962)

2. S. Gilman and M. W. Breiter, *ibid.*, **109**, 1099 (1962).
3. See the recent review of R. Parsons "Advances in Electrochemistry and Electrochemical Engineering," P. Delahay, Editor, Vol. 1, pp. 17-25, Interscience Publishers, New York (1961).
4. A. Frumkin and E. Aikasyan, *Doklady Akad. Nauk SSSR*, **100**, 315 (1955).
5. K. J. Vetter and D. Otto, *Z. Elektrochem.*, **60**, 1072 (1956).
6. R. A. Munson, *J. Phys. Chem.*, **66**, 727 (1962).
7. S. Gilman, Interim Report No. 3, Contract No. DA-44-009-ENG-4853, ARPA ORDER No. 247-61, U. S. Army, Engineer Research and Development Laboratories, Ft. Belvoir, Virginia.
8. W. Lorenz and F. Möckel, *Z. Elektrochem.*, **60**, 507 (1956).
9. See M. I. Temkin and A. N. Frumkin, *Zhur. fiz. Khim.*, **29**, 1513 (1955); H. Gerischer, *Z. physik. Chem. N.F.*, **8**, 137 (1956); R. Parsons, *Trans. Faraday Soc.*, **54**, 1053 (1958).

Molten Carbonates as Electrolytes: Viscosity and Transport Properties

George J. Janz and Fumihiko Saegusa[1]

Department of Chemistry, Rensselaer Polytechnic Institute, Troy, New York

ABSTRACT

The melt viscosities for Li_2CO_3, Na_2CO_3, and K_2CO_3 as a function of temperature to 950°C have been precisely determined. The temperature dependence of the viscosities can be expressed by the Arrhenius-type equation: $\eta = Ae^{E/RT}$, the values for $A(\times 10^7)$ and E(kcal mole^{-1}) being respectively: Li_2CO_3, 141, 16.9; Na_2CO_3, 4.9, 25.7; K_2CO_3, 1.35, 29.1. The experimental values for E correspond closely to those predicted theoretically for the transport process, assuming that viscous flow is primarily controlled by migration of the carbonate ion in these melts. Electrical transport and viscous flow in carbonate and chloride melts are briefly examined.

Some melt viscosities for the ternary eutectic mixture are reported, but interpretation awaits precise density data. The present results indicate that simple average fluidity relations based on pure carbonates are not likely applicable to mixtures of carbonates in the molten state.

Carbonate melts have approximately the same kinetic energy content as the corresponding molten chlorides but differ in the interesting aspect that the anions are disk-shaped polyatomic species rather than the rare-gas type spherical ions of the molten halides. The properties of surface tension, density, and electrical conductance for Li_2CO_3, Na_2CO_3, K_2CO_3 and selected mixtures have been reported in a recent paper (1) from this laboratory. Current surveys (2-4) show that data for the viscosities of these melts, essential to characterize the transport properties of this class of molten electrolytes, are entirely nonexistent, most likely due to the experimental difficulties associated with melts of such reactivity and relatively high liquid state ranges. The present communication reports the determination of the melt viscosities for Li_2CO_3, Na_2CO_3, K_2CO_3 and for the ternary mixture (5) as a function of temperature to 950°C. Results are examined relative to melt structure and the transport processes in viscous flow and electrical conductance.

Experimental

Materials.—As described in the preceding papers in this series (1, 5), the alkali carbonates, Reagent Grade chemicals, were dried to constant weight under CO_2 atmosphere at 600°C and stored over P_2O_5 until required for use. The melting points were: Li_2CO_3, 726°C; Na_2CO_3, 858°C; K_2CO_3, 899°C; and Li, Na, K/CO_3 ternary mixture (mole ratio, 4:3:3), 397°C.

Apparatus.—Preliminary corrosion studies (6) had shown that pure gold and alloys such as 80% Au-20% Pd withstood attack after contact with molten carbonates at 900°C for periods up to 60 hr. In the present work the metal components of the viscometer containing the melts were made from 80% Au-20% Pd alloy, since its properties (melting point, tensile strength) are somewhat more favorable than pure gold for measurements at 1000°C.

Of the methods available for the determination of viscosities, the principle of the oscillating crucible seems best suited for high temperatures with reactive melts. This method, in which the viscosity is gained from observations of the logarithmic decrement of the oscillations of the crucible (containing the liquid under investigation) was first used for liquid metals (7-9), and more recently has been applied satisfactorily to molten salts (10-12). Some aspects of the assembly designed and constructed in this laboratory are illustrated in Fig. 1. The details of the apparatus are as follows. The melt under investigation is contained in the cylindrical crucible, A, of 80% Au-20% Pd alloy with a flat bottom and cover 2.5 cm ID, 6.5 cm high and 0.015 in. thick. The crucible fits snugly in an Inconel cradle, B, the top of which screws to the bottom of the nickel rod, C, of ¼ in. diameter and 22 in. length. The upper end of this rod is fixed to a brass piece which carries adjustable brass inertia pieces, D,D', of 1 in. diameter and

[1] Post-doctorate research associate, 1958-1961. Present address: Electrochemical Research Department, Watervliet Arsenal, Watervliet, New York.

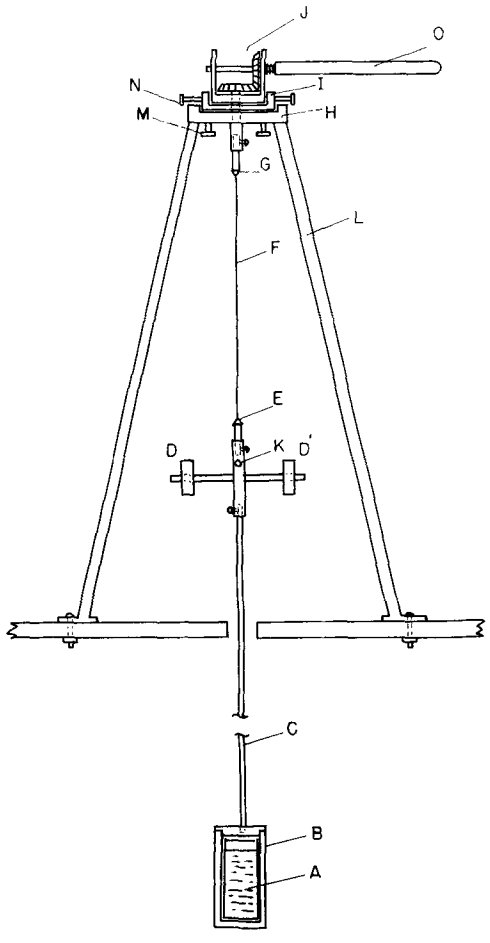

Fig. 1. Cross-sectional view of the torsion head, suspension system and crucible of the "oscillating" viscometer. A, Cylindrical crucible, 80%-20% Au-Pd; B, Inconel cradel; C, nickel rod, ¼ in. diameter and 22 in. long; DD', inertia piece, 1 in. and ½ in. thick; E, pinchuck; F, tungsten suspension wire, 40 s.w.g.; G, pinchuck; H, torsion head; I, aluminum base-plate; J, gear assembly; K, mirror; L, tripod; M,N, screws; O, aluminum rod.

½ in. thickness (113.157 and 113.224g) both on threaded arms. The pinchuck, E, on the top of the brass piece holds a 12 in. long suspension wire, F, of tungsten wire hanging from the torsion head, H, by a pinchuck G. A small concave mirror, K, is attached to the brass axis to indicate the damping of oscillations by means of a beam of light reflected to a millimeter scale.

The torsion head consists of a base-plate, I, and a gear assembly, J, connected to the oscillating system. The base-plate is an aluminum cup, 3½ in. in diameter, positioned on the head-plate of the tripod, L. Three vertical screws, M, through the tripod head permitted the horizontal adjustment of the base-plate. The tripod consists of 1 in. angle steel legs of 25 in. length mounted rigidly on a 1 in. thick soapstone platform directly above the furnace. The aluminum disk of 2¾ in. diameter which holds a precision radial ball bearing (Nice type 1602 DC) of ¼ in. ID in the center, is placed in the base-plate and is centered by means of four screws, N, through the plate wall. The gear assembly, consisting of two brass miter gears (Boston type G465y). set at right angles, is mounted in the center of the disk so that the vertical shaft is attached to the upper pinchuck, G. The horizontal shaft is fixed to an aluminum rod, O, ¾ in. diameter and 12 in. long, which was knurled at its outermost end. The pure oscillation could be started by a slight twist of the knurled rod, which protruded through a hole in the side of the plexiglass draft shield.

The furnace consisted of 1¾ in. bore and 24 in. long alundum core surrounded by a nickel tube of 2½ in. diameter and 10 in. length to allow a uniform temperature zone along the length of the cradle. The heating elements were five separate sections of resistance wire winding in parallel. A series of alundum baffles was mounted in the empty space of the core to minimize heat losses. Free suspension of the system through the baffle holes could be cross-checked by means of an electrical circuit between the suspension rod and baffle walls. Temperature control and measurement were made with two separate Pt-Pt, 10% Rh thermocouples in an alundum sheath inserted from the furnace bottom. A mixture of dry argon and carbon dioxide was introduced through a bottom inlet to protect the system from oxidation and decomposition. A copper water-cooling coil (¼ in.) was fused to the upper end of the furnace core. To guard against air-turbulence, the whole of the assembly above the furnace was enclosed in a plexiglass draft shield.

Procedure.—Amplitude and time period.—As indicated, a slight rotation of the gear shaft of the torsion head set the crucible in oscillation. The amplitudes of the swings were observed visually on a scale fixed 1m from the vertical axis of oscillation. For time periods greater than 8 sec it was possible to read the scale at the momentary halt of the image on both sides of the swing with an accuracy of 0.1 mm. Amplitudes were recorded over the range of 20-10 cm corresponding to the angular deflection of 0.032 and 0.016 radian respectively. The time period was measured by a manual stopwatch with an accuracy of 1/10 sec.

Moment of Inertia.—The moment of inertia of the whole suspension system must be known for absolute viscosity calculation. The total moment of inertia, I, is a sum of the inertia of a variable part, I_n, due to the adjustable disks, and a fixed part, I_o, due to the rest of the system. In the present work, these were determined in the conventional manner, for three different positions of the inertia pieces, using 100 complete swings in each determination. The values of I_n and I_o were 6148.6 and 1163.9 ± 1.7 g cm^2, respectively.

Logarithmic decrement.—The logarithmic decrement is defined by the logarithm of the ratio of successive amplitudes. This was determined by the relation: $\delta = 1/r \ln A_n/A_{n+r}$ where r, the number of oscillations, was taken as at least 30 to reduce the experimental error. The amplitudes for these swings were in the range 19 to 10 cm in the observation scale. For the empty crucible, the logarithmic decrement was 3.221×10^{-3}.

Calibration.—The oscillating crucible method is capable of absolute viscosity values, but the underlying theory is complicated and the computations are tedious. Alternately, the viscosities may be determined by the relative method in which the apparatus constant is found from measurements using a series of

Table I. Logarithmic decrement of liquids of known viscosity and density

Liquid	Temp, t, °C	Viscosity, poise	Density at temp, t, g cm^{-3}	Density at mp	Decrement δ	Period, T, sec
Toluene	25.0	0.005516	0.86106	0.97491	0.001622	11.12
Chloroform	21.7	0.00553	1.4858	1.64443	0.002341	11.14
Water	21.7	0.009648	0.99784	0.99984	0.002302	11.11
KNO_3	359	0.02585	1.8457	1.8710	0.006206	11.15
KNO_3	401	0.02080	1.8173	1.8710	0.005654	11.15
KNO_3	457	0.01615	1.7711	1.8710	0.004755	11.15
KNO_3	491	0.01420	1.7533	1.8710	0.004468	11.15

"standardizing" liquids, as given by the equation (13)

$$(\delta + \Delta)\ \rho_t/\rho_{tm} = K\sqrt{\eta T \rho_t} \qquad [1]$$

in which ρ_t, ρ_{tm} are the densities at the measuring temperature and the melting point, respectively, T is the time-period, and Δ, K, the apparatus constants.

The standardizing liquids used were toluene, chloroform, and water at ambient temperatures (14) and KNO_3 at elevated temperatures (3) (to 500°C). The temperatures used and the values for the densites and viscosities, together with the logarithmic decrements δ, (corrected for that of the empty vessel) are summarized in Table I. These data, fitted to Eq. [1], using the method of least squares, gave 8.74×10^{-4} and 9.59×10^{-3} for the values of the apparatus constants, Δ and K, respectively.

Molten carbonates.—For the carbonates, as for KNO_3, the procedure was as follows. A weighed amount of the melt (about 100g) was prepared in the gold-palladium cylindrical crucible under a CO_2 atmosphere in an auxiliary (Hoskins-type) muffle furnace. At all times the CO_2 atmospheres were above the carbonate-CO_2 dissociation pressures, as reported elsewhere (1). The depth of the melts was adjusted to be the same for all samples at the respective melting point temperatures. The crucible and sample, thus prepared, were placed in the Inconel cradle of the suspension system, and kept in the argon-CO_2 atmosphere. The argon-CO_2 gas flow in the furnace was only interrupted during the period of time over which the amplitude decrement was recorded. A period of about 1 hr at each temperature was allowed for thermal equilibration prior to measurements.

Table II. Viscosities of molten carbonates

Temp, t, °C	a_n/a_{n+30}	δ obs.	ρ_t/ρ_{ts}	η, poise
	(a) Lithium carbonate (m. 726°C)			
773	1.4288	0.011894	0.99038	0.04810
781	1.4145	0.011560	0.98880	0.04472
782	1.4120	0.011500	0.98858	0.04413
807	1.3827	0.010801	0.98350	0.03745
815	1.3695	0.010481	0.98191	0.03462
828	1.3460	0.009905	0.97924	0.02981
849	1.3402	0.009761	0.97497	0.02854
	(b) Sodium carbonate (m. 858°C)			
879	1.3920	0.011024	0.99523	0.03705
885	1.3805	0.010748	0.99386	0.03468
905	1.3478	0.009949	0.98934	0.02827
925	1.3216	0.009294	0.98478	0.02350
940	1.3034	0.008832	0.98139	0.02041
972	1.2743	0.008079	0.97408	0.01582
	(c) Potassium carbonate (m. 899°C)			
913	1.3583	0.010208	0.99678	0.03168
919	1.3435	0.009843	0.99536	0.02877
957	1.2962	0.008648	0.98640	0.02014
974	1.2760	0.008124	0.98238	0.01686
984	1.2685	0.007928	0.98001	0.01570
(d) Ternary mixture, Li, Na, K|CO_3 (4:3:3 mole ration) (m. 397°C)				
483	1.5082	0.010479	0.97852	0.0584
484	1.4918	0.010114	0.97829	0.0547
539	1.3839	0.007611	0.96499	0.0323
598	1.3359	0.006434	0.95118	0.0237
600	1.3166	0.005949	0.95071	0.0207

Results

The temperatures, observed amplitude ratios, logarithmic decrements (uncorrected for air-damping) are summarized in Table II, with the density data (1), and the values thus found for the carbonate viscosities. In the calculations, the values for T and δ_{air} used were $T = 11.15$ sec (as for KNO_3) and $\delta = 3.221 \times 10^{-3}$. The temperature dependence of the viscosity for the three pure carbonates is illustrated in Fig. 2. It is apparent that the viscosities of the carbonate melts can be expressed by the Arrhenius-type rate expression

$$\eta = A\, e^{E_\eta/RT} \qquad [2]$$

The values found for E_η, the energy of activation for viscous flow, and the pre-exponential constant A, both by graphical analysis and the least squares calculation, are

	A (x10^7)	E_η (kcal mole^{-1})
Li_2CO_3 (770°-850°C):	141 ± 7	16.9 ± 0.1
Na_2CO_3 (875°-975°C):	4.9 ± 0.6	25.7 ± 0.6
K_2CO_3 (910°-985°C):	1.35 ± 0.2	29.1 ± 0.3

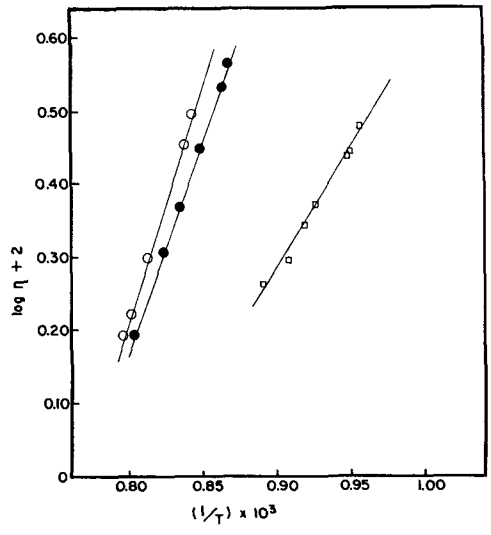

Fig. 2. Plot of logarithmic viscosities vs. reciprocal absolute temperature. ○, Na_2CO_3, ●, K_2CO_3, □, Li_2CO_3.

The results for the ternary mixture (Table II) must be regarded as more qualitative than quantitative in view of the assumptions involved in the calculations relative to the required density data. No experimental densities for the ternary mixture have been reported so that estimation of these data was necessary. The values were calculated from the data of three pure salts, assuming the temperature dependence for each could be extrapolated to the temperatures of the ternary melt, and that molar additivity could be invoked. The energy of activation for viscous flow thus approximated is 11 ± 1 kcal $mole^{-1}$.

Discussions

It is of interest to examine the viscosities of these carbonate melts both relative to melt structure and the transport processes.

The ionic nature of the molten carbonates is well established (5) and need not be developed in detail. It is sufficient to note that such physical properties as surface tension, density, and electrical conductance of these melts are understood if the carbonate melts are completely ionized molten electrolytes, with the species M^+ and $CO_3^=$ as the predominant ionic species, with some evidence that "contact ion pairs," *e.g.* $[M^+CO_3^=]^-$ contribute to the mechanism of electrical transport. The latter are not unlike the "pair-interactions" detected spectroscopically in molten nitrates (15) and are predicted statistically most probable in Li_2CO_3 (16), for which the electrostatic ion core potential (17) interactions are most pronounced. A consequence of the statistical theoretical theory of fused salts (17) is the prediction that the ion core potentials effectively force the ions into local close-packed lattice-like arrangements of relatively high order, persisting as a quasicrystalline lattice much as a memory of the highly organized crystalline structure but with the long range order of the solid state entirely absent. Evaluation of the present results for viscosity in the light of such concepts follows.

In the theory of rate processes, viscous flow is seen as a transport process in which a basic act is the passing of a molecule (or other "unit of flow") from one equilibrium position to another over a potential energy barrier. This requires an availability of holes or empty sites in the quasi-crystalline lattice and may be pictured as jump of a single flow species, or some cooperative rotational act such as by a molecular pair. The act of hole formation in the melt and the jump or movement of the molecular flow unit into the hole theoretically account for, in large part, the activation energy. The free energy for hole formation and the enthalpy for hole formation in a liquid can be calculated from a knowledge of the surface tension according to Fürth (18) by the relations

$$\Delta F_h = 4\pi r^2\gamma \quad \text{and} \quad \Delta H_h = 4\pi r^2\left(\gamma - T\frac{d\gamma}{dT}\right) \qquad [3]$$

where r and T are the ionic radius and temperature (°K), respectively, and γ is the surface tension. The results of this calculation for Na_2CO_3, using the surface tension data recently reported elsewhere (1) are given in Table III, together with the experimental values for the energies of activation for electrical conductance and viscous flow. It is clear that the observed value of the activation energy for viscous flow compares closely with the theoretical heat of hole formation for $CO_3^=$; that viscous flow is primarily controlled by the migration of the $CO_3^=$ ion is strongly supported by this evidence, although a cooperative anion-cation act is not ruled out.

The entropies of activation for viscous flow, $\Delta S^{\ddagger}$, may be gained from the equation developed (19) from the theory of rate processes

$$\eta = \left[\frac{Nh}{V}\exp\left(\Delta S^{\ddagger}/RT\right)\right]\exp\left(\Delta H^{\ddagger}/RT\right) \qquad [4]$$

since the molar volumes can be calculated from the density data for carbonate melts (1) and the values of $\Delta H^{\ddagger}$ are known from the present study. The values for $\Delta S^{\ddagger}$ thus found are: 3.8, 9.9, 11.9 cal deg^{-1} mole $^{-1}$ for Li_2CO_3, Na_2CO_3, and K_2CO_3, respectively. The values for $\Delta S^{\ddagger}$ support a transport process common to the three carbonate melts; the positive values, characteristic of association, are independent support for the formation of species such as the paired ions $[M^+CO_3^=]^-$ in these molten electrolytes as proposed elsewhere from electrical conductance (15) and x-ray (16) studies.

In general, for molten electrolytes, electrical transport is determined largely by the mobility of the smallest ionic species, whereas viscous flow involves migration of paired anionic-cationic species (as required by electrical neutrality), and is more closely related to the lower mobility of the larger ionic species. Comparison of the activation energies for electrical conductance and viscous flow for corresponding chloride and carbonate melts, as shown in Table IV, is of interest since these molten salts have approximately the same thermal (kT) energy.

Table III. Free energy and enthalpy of hole formation for N_2CO_3

Ion	r, A	ΔF_h (kcal $mole^{-1}$)	ΔH_h (kcal $mole^{-1}$)	$\Delta E^{\ddagger}_{(obs)}$ (kcal $mole^{-1}$)
Na^+	0.95	3.42	4.36	(a) conductance, 4.17
$CO_3^=$ (a)	2.05	15.9	20.3	(b) viscosity, 25.7
$CO_3^=$ (b)	2.44	22.6	28.9	

(a) Smallest hole (to accommodate a disk-ion).
(b) Largest hole (sphere evolved by three dimensional rotation of disk-ion.

Table IV. Activation energies for electrical conductance and viscous flow for chloride and carbonate melts

Salt	mp, °C	E_λ, kcal $mole^{-1}$	E_η, kcal $mole^{-1}$	E_η/E_λ
LiCl	610	2.06*	5.6**	2.7
NaCl	808	2.92*	12.2**	4.2
KCl	772	3.36*	7.6**	2.3
Li_2CO_3	726	4.40†	16.9	3.8
Na_2CO_3	858	4.18†	25.7	6.1
K_2CO_3	899	4.65†	29.1	6.3

* From E. R. van Artsdalen and I. S. Yaffe, *J. Phys. Chem.*, 59 118 (1955).
** From C. E. Fawsitt, *J. Chem. Soc.*, 93, 1299 (1908); and R. S. Dantuma, *Z. Anorg. Chem.*, 175 1 (1928).
† From ref. (1).

It is apparent that the larger values of the ratio in the carbonate melts may be attributed in large part to the increased spatial requirements of the carbonate ion (*viz.*, r Cl^-, 1.8Å r $CO_3^=$, 2.05-2.44Å). Compared with the alkali chlorides the energies of activation for electrical conductance for the carbonate melts are almost invariant. This suggests that the mobility of the cationic species in carbonate melts is very nearly constant in Li_2CO_3, Na_2CO_3, and K_2CO_3, but it is not at present possible to distinguish whether this is because the rate-determining process for electrical transport is a cooperative jump-rotation mechanism as advanced earlier (1) or whether it is simply because the mobility of the smaller Li^+ species has been markedly decreased by the pronounced ion-core interactions in such melts containing planar polyatomic anionic species.

For the ternary mixture, the value for the activation energy for viscous flow, 10.7 kcal $mole^{-1}$ is considerably smaller than the values for the pure component carbonates. The value for the ternary mixture is an approximation in view of the estimates made to gain the required density data. If significance can be attached to this value it is apparent that simple average fluidity relations, based on the pure carbonates, are not likely applicable for mixtures of carbonates in the molten state. This point awaits further information on mixtures.

Acknowledgments

This work was made possible, in large part, by support received from the Office of Naval Research, Division of Chemistry, Washington, D.C. The authors wish to thank Roger Reeves of this laboratory for assistance in the calculations.

Manuscript received October 18, 1962.

Any discussion of this paper will appear in a Discussion Section to be published in the December 1963 JOURNAL.

REFERENCES

1. G. J. Janz and M. R. Lorenz, *This Journal*, **108**, 1052 (1961).
2. G. J. Janz, C. Solomons, and H. J. Gardner, *Chem. Revs.*, **58**, 461 (1958).
3. H. Bloom and J. O'M. Bockris, "Modern Aspects of Electrochemistry," Vol. 2, Academic Press, Inc. (1959).
4. H. Bloom, *Revs. Pure and Appl. Chem.*, **9**, 139 (1959).
5. G. J. Janz and M. R. Lorenz, *J. Chem. Eng. Data*, **6**, 321 (1961).
6. G. J. Janz and M. R. Lorenz, *Rev. Sci. Inst.*, **31**, 18 (1960).
7. H. Thielman and A. Wimmer, *Stahl u. Eisen*, **47**, 389 (1927).
8. E. N. da C. Andrade and Y. S. Chiong, *Proc. Phys. Soc.*, **48**, 247 (1936).
9. G. Cavalier, "Physical Chemistry of Metallic Solutions and Intermetallic Compounds," Vol. II, p. 54, Chem. Publishing Co., N. Y. (1960).
10. G. J. Janz and J. D. E. McIntyre, *This Journal*, **109**, 842 (1962).
11. M. M. Vetyukov, S. N. Shkal'nikev, R. G. Chuvilyaer, and A. N. Nivikov, *Russ. J. Phys. Chem.*, **34**, 221 (1960).
12. J. O'M. Bockris, W. L. White, and J. D. MacKenzie, "Physico-Chemical Measurements at High Temperatures," Ch. 15. p. 323, Academic Press, N. Y. (1959).
13. T. P. Yao, *Tech. Wiss. Beih. Giessereiw. u. Metallk.*, **16**, 837 (1956).
14. International Critical Tables, Vol. III (1933).
15. G. J. Janz and D. W. James, *J. Chem. Phys.*, **35**, 739 (1961); see also G. P. Smith and C. R. Boston, *ibid.*, **30**, 1396 (1961).
16. G. Zarzycki, Faraday Society Discussions, "Ionic Melts," Liverpool, Sept. 1961.
17. F. H. Stillinger, J. Kirkwood, and P. J. Wojtowicz, *J. Chem. Phys.*, **32**, 1837 (1960).
18. R. Fürth, *Proc. Roy. Soc. Camb. Phil. Soc.*, **27**, 252 (1941).
19. S. Glasstone, K. Laidler, and H. Eyring, "Theory of Rate Processes," McGraw-Hill Book Co., Inc., New York (1943).

Technical Notes

Photoconductivity Performance in Large Single Crystals of Cadmium Sulfide

Arthur B. Dreeben and Richard H. Bube[1]

RCA Laboratories, Radio Corporation of America, Princeton, New Jersey

There has been widespread interest in increasing the speed of response of photoconductors when excited by low light intensities. Previous research has indicated that low-light photoconductivity performance (gain-bandwidth product) can be improved up to two orders of magnitude in CdS crystals by taking special precautions in purity, especially as concerns oxygen and water vapor (1). The crystals grown in this previous investigation by reaction between cadmium and sulfur vapor were very small and fragile crystals, suitable only for laboratory examination. Having demonstrated the feasibility of improved performance, it became a natural second step to attempt to obtain these im-

[1] Present address: Stanford University, Department of Materials Science, Stanford, California.

proved characteristics in larger crystals. The work described in this paper grew out of this attempt and indicates a measure of success in this direction.

A variety of methods have been described for growing CdS single crystals. Of these, sublimation procedures (2-4) are attractive because they can be accomplished at lower temperatures and with less complicated apparatus than melt growth, are generally easier to control, and yield larger stronger crystals than vapor phase reaction (Frerichs) techniques. Chemical transport (5) can be accomplished at relatively low temperatures, but the transport agent (*e.g.*, I_2) is necessarily a contaminant of the crystals. The present paper describes some of the properties of CdS and CdS:Cu single crystals produced by sublimation in Ar or H_2S atmospheres at several different pressures.

Experimental

The crystals were grown by a technique similar to one previously described (3) which was, however, modified to provide improved temperature regulation to within ± 0.5°C with West or L&N proportional controllers. Growth took place in quartz liners which were precleaned in HNO_3 and HF and used only once.

Pressure measurements of the atmosphere gas were made with a Monel Bourdon tube gauge. The CdS starting material was prepared either (*a*) by precipitation from aqueous solution followed by prefiring in an H_2S atmosphere at 900°C before use, or (*b*) by vapor phase reaction of the purified elements (6). Tank Ar and H_2S were dried by passing through a trap immersed in a dry-ice, alcohol mixture. It is clear that more elaborate precautions could be taken to insure the purity of these gases and hence to improve even further the reported performance of the grown crystals.

Crystals were grown in two general temperature ranges: above 1100°C and between 800° and 950°C. Growth times ranged from 4 to 7 days depending on the temperature, but were terminated before the CdS charge sublimed completely, to avoid releasing impurities which may have concentrated in the charge. X-ray diffraction showed that all crystals reported on were hexagonal.

Crystals Grown in Argon

At about 1200°C and 760 Torr in Ar, crystals generally grow out of or near the powder charge in the form of large transparent pieces with centimeter dimensions and weighing several grams. They often have well-developed faces and hexagonal cross section. A quartz wool substrate inserted in the growth tube provides nucleation sites from which some of the largest crystals grow. Rectangular pieces cut from these specimens can be polished for measurements.

Single crystal plates and needles can be grown by lowering the temperature of the crystallization zone to about 1100°C. The procedure of Fochs (4) has also been useful in producing crystals with these habits.

Purity of the crystals varied with the type. In general, as a result of fractional sublimation processes occurring during growth, impurities are lowest in samples which do not grow in contact with the powder charge. Table IA lists the growth conditions for some typical crystals for which spectrographic analyses are given in Table IIA. It is not unreasonable to expect that nonspectrographically detectable impurities may have at least an equal effect with that caused by the impurities listed in Table II. Spectrographic analysis can, therefore, be considered as only a partial indication of total purity. The actual photoconductivity performance is a much more sensitive test.

Type-1A crystals were grown with sublimation and crystallization temperatures exceeding 1100°C. Type-58-3C grew at a lower temperature (943°-

Table I. Preparation and some properties of CdS crystals

Sample	Temp, °C Subl.	Temp, °C Growth	CdS*	Atm, gas	Press., torr	Time, hr	Crystal type	*S*, cm²/ohm-watt	Low light Figure of Merit, $S/(T_0L)$**
A. Ar grown crystals									
1A	1200	1160	P	Ar	760	95	Sublimed plate	—	—
58-3C	950	943-50	P	Ar	350	174	Plate growing out of charge	—	—
53-2C	1200	1200	P	Ar	760	95	Chunk growing out of charge	10^{-1}	0.077
65-4xA	1200	1160-80	P	Ar	760	120	Sublimed chunk	2×10^{-1}	0.083
B. H_2S grown crystals									
50	950	808-70	V	H_2S	700	168	Plate	5×10^{-2}	—
55DE-1	950	826-84	V	H_2S	304-80	170	Plate	2×10^{-2}	65
55DE-2	950	826-84	V	H_2S	304-80	170	Plate	1.3×10^{-1}	—
64CD-1	950	800-70	V	H_2S	500-30	144	Plate	1.4×10^{-1}	45
64CD-2	950	800-70	V	H_2S	500-30	144	Plate	1	133
29	950	870	P	H_2S	200	168	Ribbon	7×10^{-6}	—
37CD-1	950	810-20	P	H_2S	200	168	Ribbon	7×10^{-5}	—
37CD-2	950	810-20	P	H_2S	200	168	Ribbon	10^{-3}	—

* V, vapor phase reaction starting material; P, precipitated and prefired starting material.

** A hybrid number obtained by dividing the specific sensitivity in cm²/ohm-watt by the decay time in seconds and by the light intensity in ft-c in the low light range 10^{-2}-10^{-4} ft-c. A standard CdS:Cu,Cl crystal has a Figure of Merit on this basis between 10-30; the highest Figure of Merit ever measured was 2400 for a small fast CdS crystal prepared by a special technique (1).

Table II. Spectrographic analyses of CdS crystals

Sample	Impurity, ppm Ag	Cu	Zn	Al	Fe	Mg	Si
A. Ar grown crystals							
1A	0.1-1	<1	0.3-3	—	0.3-3	0.6-6	1-10
58-3C	<1	1-10	2-20	<1	<1	0.03-0.3	0.3-3
53-2C	1-10	3-30	3-30	—	0.3-3	2-20	30-300
65-4XA	1-10	1-10	3-30	<1	<1	0.3-3	6-60
R_1*	3-30	100-1000	100-1000	—	2-20	0.3-3	20-200
B. H_2S grown crystals							
50	3-30	3-30	—	—	<1	0.3-3	10-100
55-DE	0.3-3	1-10	—	1-10	0.3-3	1-10	1-10
64-CD	—	<1	—	—	<1	<0.1	0.1-1
29	<1	<1	—	—	—	0.03-0.3	2-20
37CD	0.3-3	<1	—	<1	<1	1-10	0.03-0.3
R_2*	3-30	30-300	—	<1	1-10	1-10	1-10
C. Starting materials							
Precipitated and prefired CdS	<1	3-30	10-100	3-30	1-10	2-20	10-100
Vapor phase CdS	<1	1-10	—	<1	1-10	3-30	10-100

* R_1 and R_2, typical after-run residues of original CdS charges.

50°C) but directly out of the powder charge. Crystals of type-1A had a very high dark resistivity of the order of 10^{12} ohm-cm or higher. The spectral response of a typical 1A specimen is given in Fig. 1. The sharp drop in photosensitivity for wavelengths longer than the absorption edge is consistent with a relatively high purity for these crystals, whereas the low level, long wavelength response is commonly found in crystals which are reasonably photosensitive. This response may be associated with small proportions of an impurity such as copper or may arise from excitation from crystal defects such as compensated vacancies.

The trap distribution of the 1A crystal is shown by the curve of thermally stimulated current in Fig. 2. The trap depths and densities indicated by this curve are summarized in Table III. Comparison of the trap depths found in this crystal with those

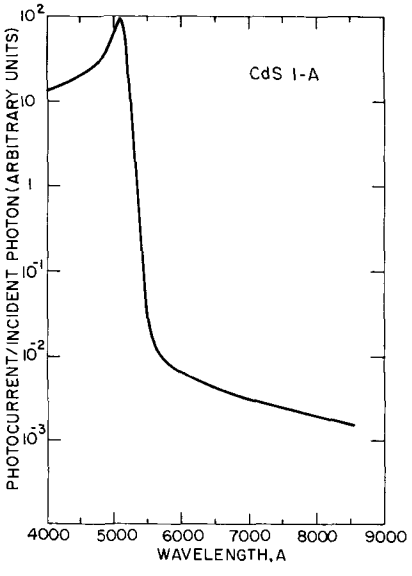

Fig. 1. Spectral response of CdS 1-A

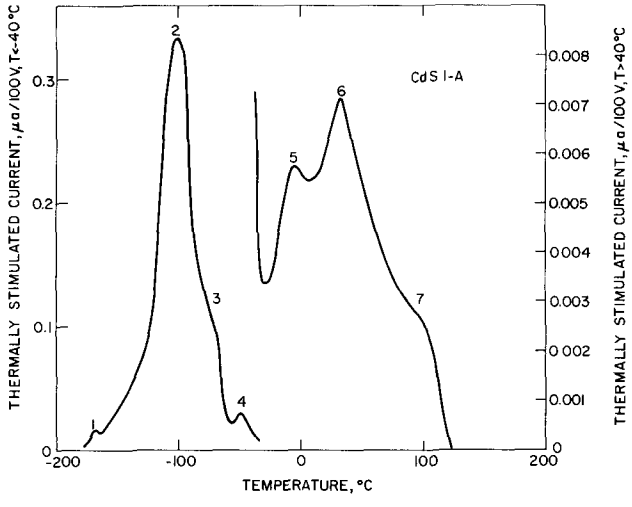

Fig. 2. Thermally stimulated current curve for CdS crystal 1-A

of previous investigators (1) shows a close correlation with all 7 major trap depths to within a few hundredths of a volt, which is within experimental error. There is increasingly good evidence, therefore, that this is the order of complexity of the trap structure in CdS. The trap densities in the crystal are not very high, and it will be shown later that still lower densities and improved performance result from growth at lower temperature in an H_2S atmosphere.

The spectral response curve for 58-3C crystals is given in Fig. 3. These crystals were highly photosensitive, low light specific sensitivity of 0.7 and 2.5 cm^2/ohm-watt being typical values of two crystals at room temperature. Type 58-3C crystals were grown at a lower temperature than 1A crystals, but grew in contact with the CdS powder charge. As a result they were less pure than 1A crystals particularly for Cu and Zn impurities as indicated in Table II, and this lack of purity overshadows any effect

Table III. Summary of traps in CdS 1-A crystals

Trap No.*	T_m, °C	E_t, ev**	N_t, cm^{-3}†
1	−170	0.21	10^{12}
2	−100	0.30	10^{14}
3	−75	0.37	2×10^{13}
4	−50	0.43	5×10^{12}
5	−5	0.56	3×10^{15}
6	+30	0.63	4×10^{15}
7	+95	0.79	2×10^{15}

* In Fig. 2.

** Trap depth calculated as the location of the quasi-Fermi level at the thermally stimulated current maximum, assuming a mobility of 100 cm²/v-sec.

† Trap densities calculated from the total thermally stimulated charge, using a suitable gain factor derived from steady-state excitation.

of the lower growth temperature on their properties. It also accounts for the higher trap densities (10^{16} — 10^{17} cm^{-3}) measured for 58-3C crystals. These results emphasize the great importance of crystal purity and mode of growth in minimizing trapping and consequently the response time of the photoconductor.

Crystals Grown in H_2S

Pure CdS.—At growth temperatures in the vicinity of 800°C, CdS crystals were grown in H_2S atmospheres at several pressures, in the form of needles, rods, and plates. The largest ribbon and platelike crystals were formed from the dry process CdS. Only crystals which grew at some distance from the powder charge will be considered. Preparation conditions and spectrographic analyses for some typical crystals are given in Table IB and IIB, respectively.

With respect to the improvement in crystal size obtained with the use of the dry-process CdS, it may be noted that with the exception of zinc, the two materials are not sufficiently dissimilar in cationic impurities for these to account for the difference in size of the resulting crystals. In addition not all impurities are harmful. It was found for example, that crystals doped with copper grow with the same habits as pure crystals. Further, Woods

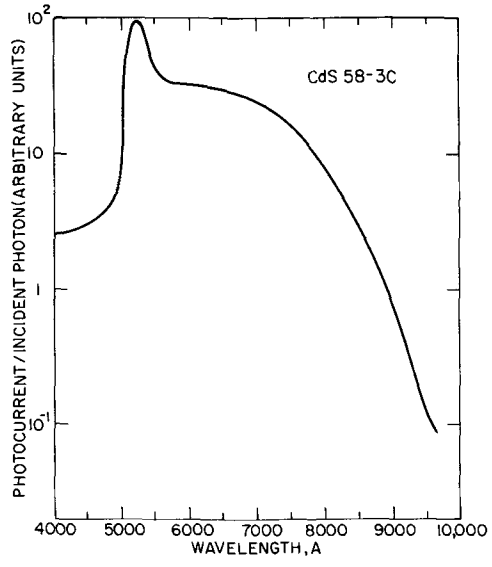

Fig. 3. Spectral response of CdS 58-3C

(7) reports that his largest Frerichs-type crystals were obtained when gallium or indium was used as an impurity additive. It is well known that halogens promote CdS crystal growth. The results from this and other work in these laboratories (8), indicate that anionic impurities such as sulfate, oxide, and hydroxyl ions, which are not revealed by spectrographic analysis, may affect crystal growth. The precipitated product, for example, originates from aqueous solution, after which it is dried. It is probable, therefore, that the oxy-anions previously mentioned are all present and may not be completely removed by the pregrowth treatment. On the other hand, the formation of oxy-anions would be minimized in the material produced by the vapor phase reaction.

In contrast with a previous report (3) it was found that H_2S pressures in the range between 200-700 Torr did not appreciably affect the size of the crystals. (The initial H_2S pressure decreases by about 20-100 Torr during an experiment as a result of diffusion through the quartz of H_2 formed by dissociation of H_2S.) The most sensitive crystals, however, were grown with H_2S pressures over 300 Torr. Some of the H_2S grown crystals are characterized by good speed of response as well as by good sensitivity as indicated by the Figures of Merit listed in Table IIB. The Ar grown crystals have considerably lower speed of response for equivalent sensitivity.

Thermally stimulated current measurements were made on a number of these crystals. Crystal 50 grown at 700 Torr, showed a broad distribution of traps from 0.2 to 0.7 ev. In this and another specimen total trap densities of 7×10^{15} cm^{-3} and 4×10^{16} cm^{-3} were found with deep trap densities of 2×10^{14} cm^{-3} and 5×10^{15} cm^{-3}, respectively. These densities are not very low, and particularly, the deep trap densities are such as to prevent fast response (1).

Crystals made with H_2S pressures between 300 and 500 Torr, on the other hand, appear to have both sensitivity and good speed. Crystal 55DE-1, for example, has a total trap density of 5×10^{15} cm^{-3}, but a deep trap density of only 3×10^{13} cm^{-3}. This low deep trap density results in an improvement by a factor of 2 to 6 over standard CdS:Cu,Cl crystals. It is encouraging that this superior performance has been achieved in crystals with an area of 30 mm² and up to 0.2 mm thick which are appreciably larger than previous standards.

CdS:Cu *crystals.*—The growth procedure has also been used to obtain single crystals of CdS:Cu by intimately mixing Cu_2S with the CdS powder charge. Crystal growth occurred over a temperature range from 800°-890°C, and conditions are summarized in Table IV. The crystal habits varied with temperature in the same manner as the pure crystals. The presence of copper, however, may alter the temperature range in which a particular habit will grow. A similar result has been noted by Woods (7) for Frerichs type CdS crystals grown in HCl.

An interesting feature is that the amount of copper in a crystal depends strongly on the growth

Table IV. Preparation and some properties of CdS:Cu crystals

Sample	Growth, T, °C	Crystal type	[Cu]-ppm	s, cm²/ohm watt	Low light Figure of Merit, $S/(T_0L)$*
60-AB	800-20	Thin, clear light yellow plates	2-200	8×10^{-2}	196
60-EF	820-40	Thick, striated dark yellow plates	1500-3000	4×10^{-2}	10
60-3	840-70	Dark brown rods	12,000	3×10^{-3}	0.09
60-DE	860-90	Black cones, some with hollow centers	33,000	3×10^{-4}	0.002

Notes: Starting material, vapor phase, CdS; initial [Cu], 1% by weight as Cu_2S; atm Gas, H_2S, 380 Torr; growth time, 144 hr; sublimation T, 950°C; * see definition Table I.

temperature. Estimates from spectrographic analyses are included in Table IV. Chemical analyses on a crystal with the highest concentration indicated, however, that the copper may not be homogeneously distributed throughout a crystal. Since it is likely that some elements in addition to Cu will also segregate in higher temperature crystal fractions, these data demonstrate the advantage in purity gained from low temperature growth.

Results of some photoelectronic measurements are summarized in Table IV. As the proportion of Cu in the crystals increases: (*a*) the sensitivity decreases; (*b*) the low light Figure of Merit drops sharply because of a decrease in both speed and sensitivity; (*c*) optical quenching of photoconductivity by long wavelength light becomes much more pronounced, and the spectral response changes principally because of impurity interaction at high Cu concentrations (9). The spectral response of typical crystals from each of the four groups is given in Fig. 3. Because of the variation of the importance of optical quenching with Cu concentration, a fairly sharp maximum in response at 7000-8000Å is found as a function of Cu concentration in the crystals. Crystal 60AB has a low Cu concentration and as a result shows a high, low-light Figure of Merit consistent with the fact that these crystals were prepared in an H_2S pressure of 330-380 Torr.

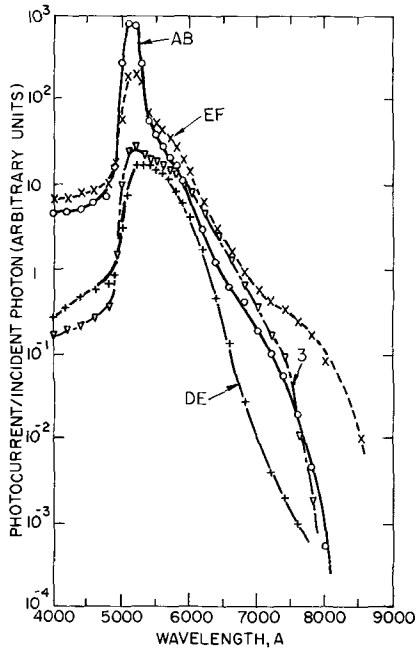

Fig. 4. Spectral response of CdS:Cu crystals

Summary

Sublimation techniques have been utilized to grow CdS and CdS:Cu single crystals with the following results. (*A*) Improved photoconductivity performance for low-light excitation has been achieved in 30 mm² x 0.2 mm CdS crystals grown at 800°-850°C under 300-500 Torr H_2S. These crystals have a relatively low density of deep traps. (*B*) Very sensitive crystals with centimeter dimensions can be grown in argon. (*C*) Copper impurity has been shown to segregate strongly as a function of growth temperature, the concentration of incorporated Cu increasing with temperature. (*D*) The absence of oxyanionic impurities in the CdS starting material appears to be important in the production of larger crystals.

Acknowledgment

The authors wish to thank H. Whitaker for spectrographic analyses, R. J. Paff for x-ray diffraction data, S. Adler and K. L. Cheng for spectrochemical analyses, and W. M. Anderson for help in preparing samples.

Manuscript received Oct. 4, 1962; revised manuscript received Dec. 17, 1962. The research reported in this paper was sponsored by the Electronic Research Directorate, Air Force Cambridge Research Laboratories, Office of Aerospace Research, U. S. Air Force under Contract AF 19(604)8353.

Any discussion of this paper will appear in a Discussion Section to be published in the December 1963 JOURNAL.

REFERENCES

1. R. H. Bube and L. A. Barton, *RCA Rev.*, **20**, 564 (1959).
2. L. C. Greene, D. C. Reynolds, S. J. Czyzak, and W. M. Baker, *J. Chem. Phys.*, **29**, 1375 (1958).
3. D. R. Boyd and Y. T. Sihvonen, *J. Appl. Phys.*, **30**, 176 (1959).
4. P. D. Fochs, *ibid*, **31**, 1733 (1960).
5. R. Nitsche, *J. Phys. Chem. Solids*, **17**, 163 (1960).
6. W. E. Medcalf and R. H. Fahrig, *This Journal*, **105**, 719 (1958).
7. J. Woods, *Brit. J. Appl. Phys.*, **10**, 529 (1959).
8. Scientific Report No. 2 to AFCRL, Contract No. AF19(604)8353 (1962).
9. R. H. Bube, E. L. Lind, and A. B. Dreeben, *Phys. Rev.*, **128**, 532 (1962).

Effect of an Electric Field on the Oxidation of Zinc

Paul J. Jorgensen

Research Laboratory, General Electric Company, Schenectady, New York

Recently Cismaru and Cismaru (1) concluded that an electric field does not influence the oxidation rate of zinc. Uhlig and Brenner (2) have also concluded that an electric field does not influence the rate of oxidation of copper. On the other hand, Jorgensen (3) and Schein, LeBoucher, and Lacombe (4) have demonstrated that electric fields can influence oxidation rates of silicon and iron, respectively.

In all the above cases, it seems most reasonable to this author that the rates of oxidation are controlled by the diffusion of ions through the oxide layers. Therefore, if an electric field is to affect the rates of reaction, it must influence the diffusion of the ions or change the rate-controlling mechanisms.

Both Uhlig and Brenner, and Cismaru and Cismaru attempted to establish an electric field across the oxide layer by capacitive coupling of the metal to be oxidized to a potential source. The experimental arrangement resulted in a parallel plate capacitor with the oxide layer and an air gap as the dielectric. In this arrangement virtually all of the potential drop occurs across the air gap, and hence no sizeable electric field develops across the oxide layer. This lack of electric field explains Uhlig and Brenner's and Cismaru and Cismaru's results. It is the purpose of this note to show that an electric field applied across a zinc oxide layer, where diffusion of ions is the rate-controlling mechanism, does influence the rate of oxidation.

Experimental Procedure and Results

Oxide layers were formed simultaneously on a number of freshly cleaved 99.999% zinc crystals by oxidizing in 1 atm oxygen at 375°C for a few seconds. The thickness of the oxide layers on these crystals was less than 1% of the total thickness finally formed, and due to the uniform experimental conditions it was assumed that all oxide layers were equivalent in thickness. Counter electrodes were formed by sputtering platinum on the oxide surfaces. Rate constants determined from data for further oxidation should therefore be slightly lower than if the rate had been measured exactly beginning at time zero. The slope of a parabolic plot of the data ideally should show some curvature, but the deviation from linearity caused by 1% of the oxide being initially present is negligible. A diagram of the experimental arrangement is shown in Fig. 1. A constant current density of 1.05 amp/cm^2 was applied which gave a field of 3.3 x 10^3 v/cm at 375°C. A platinum wire buried inside the zinc allowed the same polarity to be applied to both sides of the zinc crystal.

In order to determine whether the sputtered platinum electrode interfered with the process of oxidation, a further zinc crystal was sputtered with platinum and oxidized without an electric field at 400°C in oxygen at which temperature the parabolic rate constant is well known. Results are shown in Fig. 2. The rate constant of 8.5 x 10^{-11} g^2/cm^4/hr measured by a weight gain method compares favorably with the data of Pilling and Bedworth (5) and Wagner and Gruenwald (6), who obtained 8.8 x 10^{-11} and 7.2 x 10^{-11} g^2/cm^4/hr, respectively. It was therefore concluded that the sputtered platinum allowed the passage of oxygen through the electrode, and the electrode did not interfere with oxidation.

The rate of oxidation for the remainder of the work was followed, under constant current conditions, by measuring the change in voltage across the zinc oxide layer with time. A relationship between voltage and time can be derived, assuming the oxide layers exhibit uniform resistivity and the rate of oxidation is parabolic (7), *i.e.*

$$X^2 = kt \qquad [1]$$

where X is the thickness of the oxide layer, t is time, and k is the rate constant. Hence

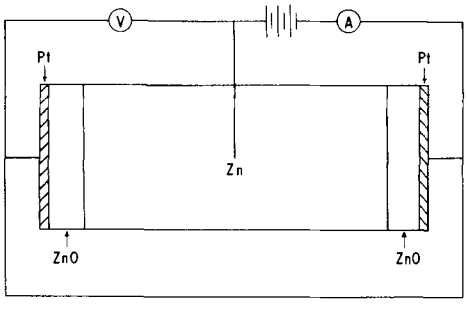

Fig. 1. Illustration showing experimental arrangement for studying the effect of an electric field on the oxidation of zinc.

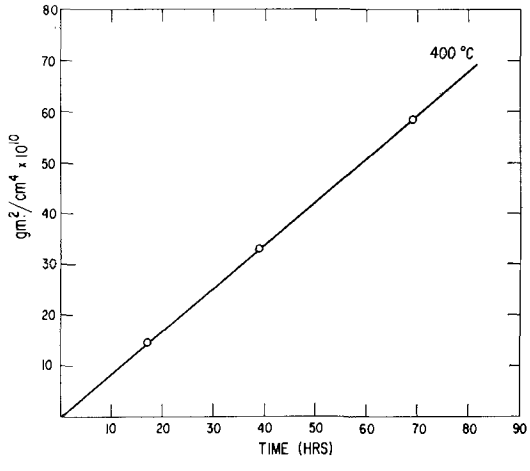

Fig. 2. Parabolic plot of the weight gain per unit area vs. time for zinc oxidation at 400°C.

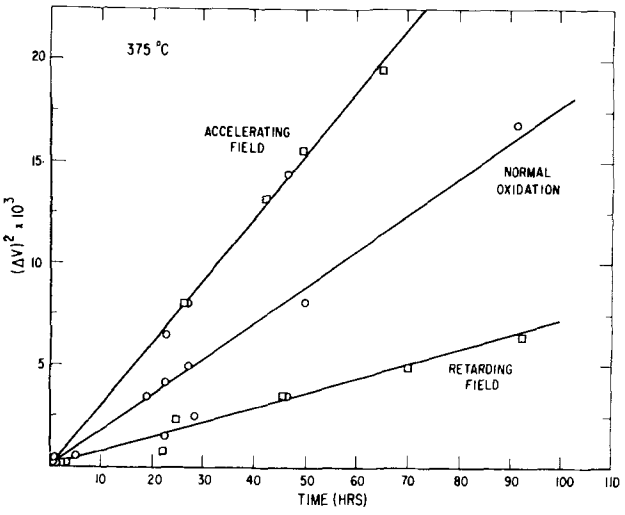

Fig. 3. Parabolic plot of the voltage measured across a growing zinc oxide layer *vs.* time, illustrating oxidation under an accelerating electric field, a retarding electric field, and normal oxidation.

$$E = IR = I\ \rho X/A \qquad [2]$$

where E is the voltage, I is current (0.5 amp), ρ is the resistivity (3.16 x 10^3 ohm-cm at 375°C) (8), and A is the electrode area (0.477 cm^2), and

$$E^2 = \frac{4\ I^2\ \rho^2}{A^2}\ kt \qquad [3]$$

The factor of four enters Eq. [3] due to the parallel arrangement of zinc oxide layers in the experimental setup. This method of following the rate of reaction necessitates the assumption that the contact resistance at a constant temperature is constant with time. This assumption appears to be valid because good parabolic plots of the data were obtained in accordance with Eq. [3].

A series of experiments were conducted at 375°C in an oxygen atmosphere in which the rate of oxidation was followed without an electric field and with both an accelerating and a retarding field. The field is termed accelerating when the metal-metal oxide interface is positive with respect to the metal oxide-gas interface and retarding when the metal-metal oxide interface is negative with respect to the oxide-gas interface. Results are shown in Fig. 3. The rate of oxidation for normal oxidation was measured by intermittently applying the current when the voltage was to be measured. The square and circles indicate different runs under the same conditions showing the reproducibility of the results. The total thickness of oxide produced for example under an accelerating field, calculated from the data shown in Fig. 3, was 4170Å.

Table I. Rate constants obtained from slopes of data plotted in Fig. 3

Condition	Rate constant
Accelerating field	2.25×10^{-10} $g^2/cm^4/hr$
Normal oxidation	1.30×10^{-10} $g^2/cm^4/hr$
Retarding field	5.40×10^{-11} $g^2/cm^4/hr$

Table I lists the rate constants obtained from the slopes of data plotted in Fig. 3, multiplied by the square of density of ZnO. These rate constants are uniformly high due to neglecting contact potentials in the calculation. Comparison of the data of Fig. 2 and 3 would suggest a total contact resistance of approximately 0.15 ohm.

It is clearly evident from Fig. 3 that the rate of oxidation can be either accelerated or retarded depending on the orientation of the electric field. Therefore, it is concluded than an electric field does influence the rate of oxidation of zinc. In the case of Cismaru and Cismaru's and Uhlig and Brenner's work, the lack of influence of an electric field on zinc and copper oxidation may be attributed to the manner in which the electric field was applied and not to an inherent property of the oxidizing systems.

Acknowledgment

The author is indebted to R. E. Carter and R. J. Charles for their encouragement and assistance.

Manuscript received Nov. 5, 1962; revised manuscript received Dec. 28, 1962.

Any discussion of this paper will appear in a Discussion Section to be published in the December 1963 JOURNAL.

REFERENCES

1. D. Cismaru and G. D. Cismaru, 1st International Congress on Metallic Corrosion, Butterworths', London, p. 237 (1961).
2. H. H. Uhlig and A. E. Brenner, *Acta Met.*, **3**, 108 (1955).
3. P. J. Jorgensen, *J. Chem. Phys.*, **37**, 874 (1962).
4. F. Shein, B. LeBoucher, and P. Lacombe, *Compt. rend.*, **252**, 4157 (1961).
5. N. B. Pillig and R. E. Bedworth, *J. Inst. Metals*, **29**, 529 (1923).
6. C. Wagner and K. Gruenwald, *Z. phys. Chem.*, **B40**, 455 (1938).
7. W. J. Moore and J. K. Lee, *Trans. Faraday Soc.*, **47**, 501 (1951).
8. H. H. von Baumbach and C. Wagner, *Z. phys. Chem.*, **B22**, 199 (1933).

Brief Communications

Growth Twins in the F.C.C. Metals

J. W. Faust, Jr., and H. F. John

Research and Development Center, Westinghouse Electric Corporation, Pittsburgh, Pennsylvania

Although there are numerous references to annealing and deformation twins in metals, there are only a few examples of the presence of growth twins. Price (1) reports them in cadmium needles grown from vapor phase, Herenquel and Lacombe (2) in chill cast aluminum, and the authors (3) in silver dendrites grown by electrodeposition. The authors have presented the general conditions under which growth twins may play a dominant role during the growth of dendrites of other materials in addition to semiconductors (4). In metals several crystal systems meet these conditions. It is the purpose of this communication to present further evidence of growth twins in metals crystallizing in the fcc system.

Wranglen (5) has grown dendrites of the fcc metals Pb, Cu, and Ag. These were faceted by {111} planes and grew in the <110> or <100> direction depending on the current density and concentration of the electrolyte. Based on x-ray examination these dendrites were reported to be single crystals. It has been shown (4) that dendrites of the fcc materials growing in the <110> direction, or in any direction of general index <h, h-l, l>, could contain twin planes while those growing in the <100> direction could not. In a preliminary investigation of dendrites grown by electrodeposition, dendrites of Cu and Pb were grown, and dendrites of Al were obtained from Dötzer (6). The electrolytes, current density and other data on the electrodeposits are given in Table I. For lead, the conditions given by Wranglen (5) were used.

Figure 1 shows an example of a lead dendrite that grew in the <110> direction. This is somewhat similar to the one shown by Wranglen. Figure 2 shows a typical cross section of a lead dendrite that has been polished and etched to reveal the microstructure. Several twin planes can be seen by following the changes in etch pattern across the cross section.

Fig. 1. Lead dendrite grown in <110> direction

Table I. Summary of data on electrodeposited metals

Metal	Electrolyte	C.D., ma/cm²	Growth form	Growth directions	Twin planes
Pb	0.5 m $Pb(NO_3)_2$ 2 m NH_4NO_3	100	dendrites	<110>	yes
Cu	$CuSO_4$	100	sponge	—	yes
Al	organic	—	dendrites	<100> <h, h-l, l>	no yes
Au	0.05 m $KAu(CN)_2$ 0.2 m KCN 0.1 m K_2CO_3	30-60	dendrites		yes

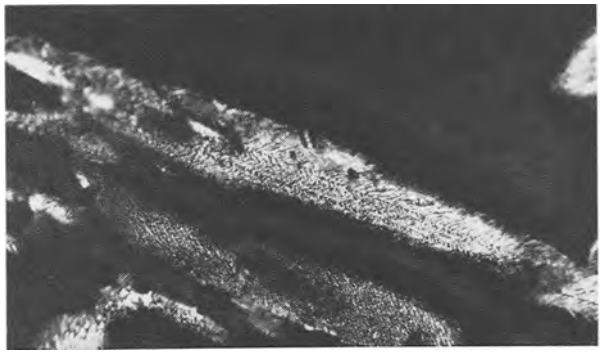

Fig. 2. Cross section of lead dendrite showing twin planes

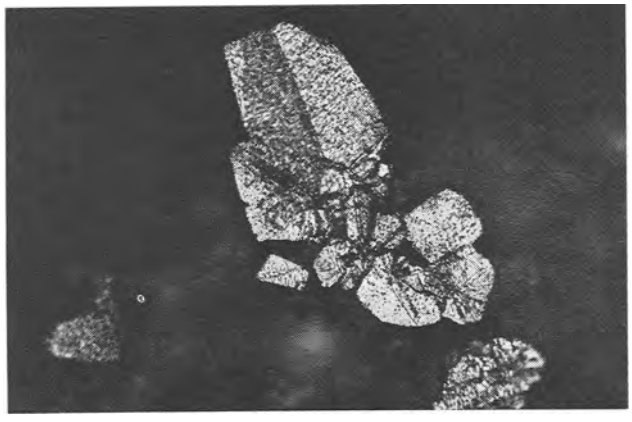

Fig. 3. Cross section of copper sponge showing twin planes

In the case of copper, we obtained the familiar spongy deposit instead of the elongated dendrites found by Wranglen. Perhaps the reason for this lies in the fact that Wranglen used a copper nitrate solution rather than the copper sulfate used by us. Pieces of the spongy deposit were cross-sectioned, polished, and etched to reveal the microstructure. Examination of these cross sections showed that the crystallites of Cu contained twin planes, as shown in Fig. 3, and for some reason were inhibited from extended growth. No attempt was made in this preliminary investigation to determine the limits over which dendrites could be produced.

Dötzer studied the electrodeposition of Al from organic solutions. He obtained good solid growth, long needles, or polyhedral growth depending on the current density. He kindly supplied us with material grown at a current density between long needle growth and polyhedral growth. We examined this material and found the polyhedral growth to be single crystal dendrites grown in a <100> direction faceted by {111} planes. Some of the non-<100> dendrites were cross-sectioned, polished, and etched to reveal their microstructure and found to contain twin planes as shown in Fig. 4. It was not possible to determine whether the growth direction was <211>, <110>, or another direction of the general indices <h, h-l, l>.

We also examined some metals with other crystal structures. Dendrites of Ta, Ti, Mn, and In were found to be single crystal as would be predicted from the general conditions for twin plane growth.

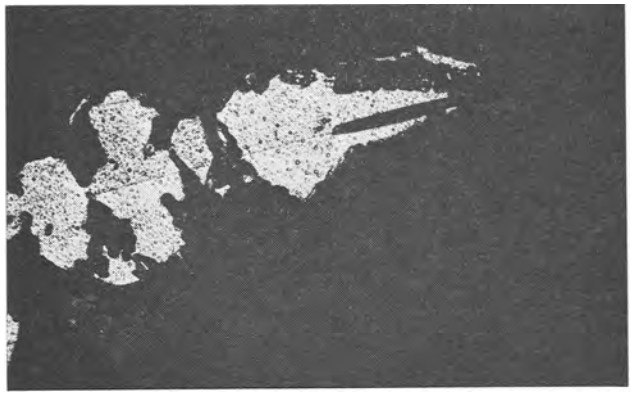

Fig. 4. Cross section of non <100> aluminum dendrite showing twin planes.

As yet we have not examined any other materials whose crystal structure allows twin planes.

This work shows that growth twins can be produced and play a predominant role in the electrodeposition of fcc metals. For such to be the case suggests that re-entrant edges are formed at twin planes similar to that found in semiconductor dendrites (4). It is relatively easy to understand how such re-entrant edges can act as sites for easy nucleation during growth from the melt. It is more difficult to imagine, however, how the re-entrant edges act similarly in electrodeposition where the highest deposition rate would be expected at the corners and edges. One might speculate that ions sit down in half crystal positions at the corners and edges and then migrate. Certainly the re-entrant edge at the twin plane would be a good site for any mobile ions to go into lattice positions where they would form a nucleus for layer growth. Such a process would be easier than two-dimensional nucleation. In such a case, a certain minimum surface mobility would be needed before the re-entrant edge would present any advantage.

Acknowledgment

The authors are indebted to Dr. S. Barnartt for helpful discussions, to Dr. R. Dötzer of Siemens Schuckertwerke for supplying the aluminum dendrites, and to Mrs. H. Larson and Mrs. S. Hillbeck for valuable assistance.

Manuscript received Jan. 14, 1963. This paper was prepared for delivery before the Boston Meeting, Sept. 16-20, 1962.

Any discussion of this paper will appear in a Discussion Section to be published in the December 1963 JOURNAL.

REFERENCES

1. P. B. Price, *Phil. Mag.*, **4**, 1229 (1959).
2. J. Herenquel and P. Lacombe, *Compt. rend.*, **228**, 846 (1949).
3. J. W. Faust, Jr., and H. F. John, *This Journal*, **108**, 109 (1961).
4. H. F. John and J. W. Faust, Jr., in "Metallurgy of Elemental and Compound Semiconductors," E. Grubel, Editor, p. 127, Interscience Publishing Co., New York (1961).
5. G. Wranglen, *Acta Polytech.*, **182**, 1 (1955).
6. R. Dötzer, Private communication.

Low-Temperature Deposition of Silicon Oxide Films

Leslie L. Alt, Samuel W. Ing., Jr., and Karl W. Laendle[1]

Semiconductor Products Department, General Electric Company, Syracuse, New York

Silicon oxide films play an important role in semiconductor device technology. Surface passivation and diffusion masking are the most prominent applications for these amorphous films. There are several methods by which such oxide films may be obtained, but only the elevated temperature processes give satisfactory oxide films for the above-mentioned applications.

Decomposition of organic compounds on the absorption of energy is a well-known phenomenon. The necessary energy may be supplied as chemical energy, thermal energy or in the form of radiation (ultraviolet, gamma radiation, etc.). The composition of the decomposition products depends on the nature of the starting material, as well as on the experimental conditions. Consequently, it is difficult if not impossible to predict the nature and composition of all the products of such decomposition. Nevertheless, one can expect the formation of certain compounds from thermodynamic considerations. Thus, the thermal decomposition of aluminum isopropoxide is expected to give aluminum oxide under favorable conditions.

The difficulties encountered in electron optical systems lead to the discovery (1, 2) that organic compounds decompose when subjected to an electron beam. The discovery was followed by the development of the method of forming thin polymeric and metallic films by electron bombardment of suitable chemical compounds (3-5).

The well-known phenomenon of direct current glow discharge was used for preparation of thin films at the Electronics Laboratory of General Electric Company (6). The work reported here followed the same basic principle, except that R.F. induced gaseous plasma was used in order to eliminate the undesirable sputtering observed with d-c glow discharge.

We have developed a method by which a uniform and amorphous silicon oxide film may be deposited at nearly room temperature. In our process a suitable organo-silicon compound is decomposed in a low energy gaseous plasma to give a silicon oxide film and various other decomposition products which are prevented from depositing on the substrate by the continuous bombardment of the surface. Among the many organo-silicon compounds alkoxy-silanes were found to be most suitable. Due to the favorable silicon to oxygen ratio, these compounds may be used successfully with argon plasmas. It follows that oxygen must be added to the system if the silicon to oxygen ratio is too low.

We propose the following tentative mechanism for the reaction. The excited or ionized gas atoms of the carrier gas collide with the organo-silicon molecules. Some of these collisions result in the formation of free radicals which in turn are adsorbed by the surface of the substrate. Further decomposition takes place on the substrate under the influence of the continuous bombardment. Thus, a stable Si-O-Si network is built up on the surface.

In order to avoid the introduction of undesirable impurities the plasma is generated in a fused quartz reaction chamber by an applied R.F. field. In our experiments, frequencies of 1-5 mc were employed although both lower as well as higher frequencies may be used. Reasonable deposition rates were obtained in the 1-20 x 10^{-2} Torr pressure range. The rate of deposition is a function of flow rates, power input, substrate temperature, and equipment geometry. Under controlled conditions the film growth is a linear function of time. Deposition rates of 1000-3000 Å/hr on unheated substrates gave satisfactory films. The films obtained are quite uniform; the variation in film thickness over 1 in.^{2} area is estimated to be less than 300Å. In some experiments, ion currents as high as 80 ma have been measured.

These films were evaluated by several methods. Electron diffraction studies have confirmed that the films are indeed amorphous. Infrared transmission measurements failed to show the presence of C-H bonds. Nevertheless, the absence of organic groups in these films cannot be accepted solely on the basis of the IR data.

The deposited films protected silicon substrates in chlorine atmosphere at 900°-950°C, a test often used for the evaluation of silicon oxide films. The films were also used successfully as masking films in phosphorous diffusion of silicon at 1250°C. Similar experiments in boron diffusion masking gave inconclusive results.

This investigation is being extended to other oxide systems including mixed oxide films since it seems to offer some exciting possibilities for the preparation of novel glassy films not obtainable by conventional methods of preparation.

Manuscript received Jan. 2, 1963.

Any discussion of this paper will appear in a Discussion Section to be published in the December 1963 JOURNAL.

REFERENCES

1. K. M. Poole, *Proc. Phys. Soc. London*, **B66**, 541 (1953).
2. A. E. Ennos, *Brit. J. Appl. Phys.*, **5**, 27 (1954).
3. R. W. Christy, *J. Appl. Phys.*, **31**, 1680 (1960).
4. A. G. Baker and W. C. Morris, *Rev. Sci. Instr.*, **32**, 458 (1961).
5. R. W. Christy, *J. Appl. Phys.*, **33**, 1884 (1962).
6. V. A. Russell and D. L. Stockman, Unpublished Internal Report, Jan 2, 1962.

[1] Present address: Electronics Laboratory, General Electric Company, Syracuse, New York.

A New Method for the Determination of the Zero Charge Point of Metal Electrodes

Mino Green and Harald Dahms

Electrochemistry Laboratory, University of Pennsylvania, Philadelphia, Pennsylvania

Several methods are available for the determination of the zero charge point (zcp) of metal-electrolyte electrodes (1). Each method has limitations which restrict the range of its applicability. We have developed a method for the determination of the zcp which extends the number of systems amenable to investigation.

Our method depends on the fact that, under suitable conditions, an organic molecule adsorbed at the metal-electrolyte interface can be used as a probe of the electrostatic field in the compact Helmholtz double layer (cHdl), *i.e.*, between the outer Helmholtz plane and the metal surface. It has been demonstrated (2, 3) that the potential dependent adsorption of neutral, organic molecules at the metal-electrolyte interface can be interpreted in terms of field/dipole interaction across the cHdl. At the zcp the field across the double layer arising from excess charge is zero, whence for a fixed solution concentration of organic material the amount of organic material adsorbed will be independent of the supporting electrolyte concentration. Thus potential dependent organic material adsorption curves obtained using various concentrations of supporting electrolyte will have a common point of intersection at the zcp.

The requirements for this method are: (i) The zcp should not be markedly (< 10 mv) affected by adsorption of the organic material (low surface coverages). (ii) Change of the concentration of the supporting electrolyte should cause little shift of the zcp. If specific adsorption of ions of the supporting electrolyte is extensive, the adsorption should be insensitive to electrolyte concentration changes.

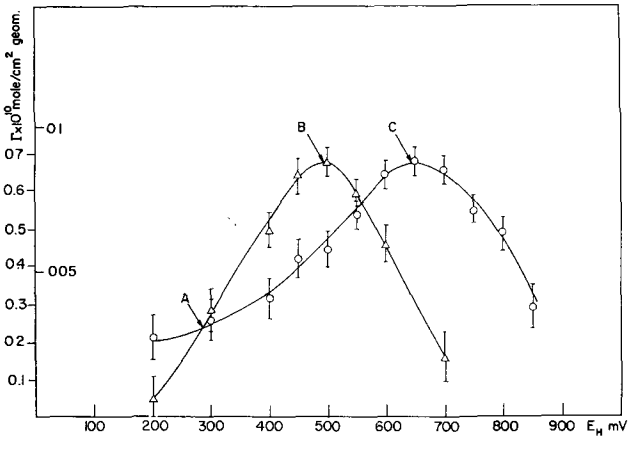

Fig. 1. Adsorption of naphthalene (mole/cm² and in terms of surface coverage) on gold at different ionic strengths. Concentration of naphthalene, 10^{-5} moles/l. ○, 10^{-3}M $HClO_4$; △, 10^{-3}M $HClO_4$ + 1M $NaClO_4$.

The technique of measurement uses C^{14}-labeled organic material. The electrode, a thin gold foil, is exposed to the solution on one side while a radiation detector is placed on the back side of the foil. The total radiation passing through the foil arises partly from adsorbed species and partly from material in solution; these two contributions are separated readily. The gold foil was cleaned by alternate anodic/cathodic pulsing terminating on a cathodic pulse. Accuracies of ~ 0.02 monolayer can be obtained (see Fig. 1).

The electrode investigated was Au|10^{-3} M $HClO_4$ c M $NaClO_4$, 10^{-5}M naphthalene, where c in one case was 0 and in another case was 1. The amount of naphthalene adsorbed on the gold was measured as a function of potential (4). This system obeys the criteria required for the applicability of this method. For naphthalene adsorption the potential corresponding to the adsorption peak does not change more than 10 mv on going from zero to 1/10 coverage. Perchlorate solutions were used because ClO_4^- does not usually specifically adsorb. High, but variable, ClO_4^- adsorption would result in the peaks for the two curves having different values, but this is not so (cf. Fig. 1).

Experimental results are shown in Fig. 1. Point A, at 300 ± 50 mv, is the zcp of the gold-electrolyte electrode. The electrode potential, E_H, may be described as follows:

$$E_H = E_{zcp} + \Psi_{M-2} + \Psi_{2-S} \qquad [1]$$

where Ψ_{M-2} and Ψ_{2-S} are the potential differences arising from excess charge across the cHdl and the Gouy layer, respectively; potential changes associated with changes in dipole orientation (*e.g.*, water) are neglected since these are accounted for in the selection of values for ϵ and d in Eq. [2]. For a 1:1 electrolyte (5)

$$\Psi_{M-2} = \left(\frac{32\, kT\, n_S\, \epsilon_{2-S}\, d\pi}{\epsilon_{M-2}} \right)^{1/2} \sinh\{e_o\, \Psi_{2-S}/2kT\} \qquad [2]$$

where ϵ is the dielectric constant ($\epsilon_{M-2} = 6$ and $\epsilon_{2-S} = 78$), d the thickness of the cHdl (3.4Å), n_S the concentration of anions, e_o, k and T the charge on the electron, Boltzmann constant, and absolute temperature, respectively. The peaks B and C of the curves correspond to identical conditions in the cHdl, *i.e.*, the values of Ψ_{M-2} are the same. Since, for c = 1, $\Psi_{M-2} \geqslant 20\, \Psi_{2-S}$ and therefore Ψ_{2-S} can be neglected

$$(E_H)_C - (E_H)_B = [\Psi_{2-S}]_{c=0} \; (= 160 \text{ mv}) \qquad [3]$$

Knowing $[\Psi_{2-S}]_{c=0}$ at the adsorption peak, we obtain Ψ_{M-2} at the peak using Eq. [2]: (Ψ_{M-2} = 240 mv) whence E_{zcp} = 250 mv which, within experimental error, is in agreement with the point A. Similar calculations can be made for E_{zcp}, over an entire pair of adsorption curves.

Manuscript received Nov. 29, 1962.

Any discussion of this paper will appear in a Discussion Section to be published in the December 1963 JOURNAL.

REFERENCES

1. A. N. Frumkin, *This Journal*, **107**, 461 (1960).
2. A. N. Frumkin, *Z. Physik*, **35**, 792 (1926); J. A. V. Butler, *Proc. Roy. Soc.*, **A122**, 399 (1929).
3. M. A. V. Devanathan, K. Müller, and J. O'M. Bockris, Paper presented at the Los Angeles Meeting, Electrochem. Soc., May 1962.
4. For a full account of the method and the results obtained see H. Dahms, M. Green in course of publication.
5. A. N. Frumkin, "Kinetika elektrodnych prozessov" § 3, p. 12 ff, Moscow 1952.

Extension of Iridium Crucible Lifetime

R. S. Horwath and C. Whiteley

Sperry Electronic Tube Division, Sperry Rand Corporation, Great Neck, New York

Iridium crucibles are used extensively in single crystal growth of many high melting point materials such as calcium tungstate and calcium fluoride. The lifetime of such crucibles is very short under such conditions. We wish to report that by rhodium plating a new or slightly used crucible the useful lifetime is increased 4 to 5 times. The repair of a cracked crucible may also be achieved by brazing with platinum or rhodium metal.

While operating at high temperatures in air, small black needle crystals of IrO_2 are observed at the base of the crucible. The wall thickness of the crucibles is found to decrease due to volatilization of iridium. Cracks of unknown origin appear in the crucibles at various times and under various conditions. Due to the initial high cost of large crucibles, a method of retarding the volatilization and repairing the cracks is desirable.

Possible materials for such retardation and repair are platinum and rhodium since they are also used frequently for high-temperature crucibles. Since rhodium has a higher melting point than platinum and a lower vapor pressure (1) than iridium, rhodium was chosen as the best plating material. An iridium crucible is cleaned, first chemically, then with a liquid honing process. The crucible is electroplated with a thin layer (0.0002 in.) of rhodium metal, heated to 1650°C for 16 hr, and the cycle, except for a slightly thicker plating, is repeated. This completes the processing for a relatively new crucible. This treatment will increase the life of an iridium crucible from 50 hr to about 300 hr.

If the crucible fails by cracking, further lifetime extension may be obtained by repairs. The repair is accomplished by first cleaning the crucible, then spot welding a piece of platinum or rhodium wire into the crack, which has been filed until it is a V-shaped groove. The crucible is then heated in an R.F. field to the melt temperature of the filler metal used (platinum or rhodium). The metal flows as in a normal braze and seals the cracks. The crucible lifetime is often extended beyond 300 hr with the use of this repair method. Eventually the crucible becomes irreparable due to a "porosity," causing general leakage.

Acknowledgment

The authors wish to thank G. R. Wirtenson for helpful discussions.

Manuscript received Jan. 10, 1963.

Any discussion of this paper will appear in a Discussion Section to be published in the December 1963 JOURNAL.

REFERENCE

1. K. Nassau and A. M. Broyer, *J. Appl. Phys.*, **33**, 3064 (1962).

Electrode Reactions and Iron Oxide Selection for the Thermal Cell Mg/LiCl-KCl/FeO_x, Ni

Sidney M. Selis[1] and Laurence P. McGinnis

United States Army Materiel Command, Harry Diamond Laboratories, Washington, D. C.

and Elmer S. McKee and James T. Smith

Catalyst Research Corporation, Baltimore, Maryland

ABSTRACT

In this system magnesium is oxidized to a soluble form ($MgCl_2$). The iron oxide is reduced to an insoluble species containing lithium ion. Electrode efficiencies are high. A specially designed cell was used to examine the characteristics of iron oxide samples. The broadly important considerations are ferric ion content and specific resistance of the iron oxide powder. For example, energy output with γ-Fe_2O_3 is generally larger than with Fe_3O_4. Highly conductive samples, such as synthetically prepared spinel forms, those containing titanium(IV) ion in the lattice, and those which include conducting carbon provide higher voltages than poorly conducting samples such as α-Fe_2O_3 and those which contain silica as an impurity. Certain samples are highly absorbent and extra electrolyte is needed. The results provide a basis for selecting samples for particularly desired cell characteristics.

Thermal cells have normally solid electrolytes and become activated when these solid electrolytes are melted. Such cells have been described by several authors, including Vinal (1), Goodrich and Evans (2), and McKee (3). The negative electrode is generally calcium or magnesium since these metals are relatively stable in the electrolytes and afford large cell voltages.[2] The material reduced at the positive electrode may either be dissolved in the electrolyte, or if insoluble, may be located on the positive electrode metal.

Selis and McGinnis (5) have discussed the behavior of a soluble oxidant (potassium chromate) in the thermal cell system Mg/LiCl-KCl-K_2CrO_4/Ni. The present paper is concerned with a slightly soluble or "solid" cathode reactant, iron oxide, located on a nickel metal substrate. When they afford satisfactory voltage and discharge characteristics, the solid reactants are of special advantage for thermal cells because they do not attack the negative electrode when the cells are activated and because they do not raise the liquidus temperature of the electrolyte (as does potassium chromate); some serious design problems are thus avoided.

However, characterizing the iron oxide component is a complex task. First there are three different higher oxides which are available from commercial sources; these include Fe_3O_4 (magnetite), α-Fe_2O_3 (hematite), and γ-Fe_2O_3. With each one, the ratio of iron to oxygen can vary. Impurities will also vary. Furthermore, there will be different particle size distributions. Such variations result from different modes of preparation for different commercial uses and provide a wide selection of samples for the construction of thermal cells.

There were two objectives for this work. The first was to shed some light on the nature of the electrode reactions for the system Mg/LiCl-KCl/Fe_2O_3, Ni, and the experiments were done with more or less conventional arrangements. The second objective was to consider iron oxide samples as cathode reactants in thermal cells of more practical geometry. For that particular purpose some iron oxide lots are of little value; the use of others allows the building of cells of capabilities as desired. In the present paper, performance will be correlated with physical and chemical parameters of the oxidant. These can provide a basis for specifying iron oxide lots satisfactory for the fabrication of thermal cells for different applications. The cell construction used here has been referred to by Goodrich and Evans (2) and is discussed below.

Experimental

Studies of electrode reactions.—Materials.—The negative electrodes were constructed from sheet magnesium which was 0.37 mm in thickness and of a commercially pure grade (99.8% Mg; minor amounts of Ca and Zn). The magnesium surfaces were abraded with fine emery, thoroughly rinsed in cold water, and wiped dry before immersion in the electrolyte. The positive electrodes were prepared with reagent grade iron oxide (α-Fe_2O_3) and commercially pure nickel gauze (98-99% Ni; minor amounts of Co, Fe, and Zn).

The lithium and potassium chlorides were of reagent grade and were handled in a "dry room" (relative humidity of 4-5% at ambient temperature).

Cell construction and discharge.—Porcelain crucibles were used for cell containers. The electrolyte

[1] Present address: Research Laboratories, General Motors Corporation, Warren, Michigan.

[2] Some formation of a liquid calcium-lithium alloy does occur in molten LiCl-KCl. However, the calcium can still be a very useful electrode material and, in fact, the alloy is desirable since its fluid properties serve to keep the anode from being excessively polarized (4).

consisted of 60g of the lithium chloride-potassium chloride eutectic mixture (58 mole % LiCl, 42 mole % KCl) accurately weighed out. A cell contained two pairs of electrodes; one pair was discharged under load and the other pair remained on open circuit and served as references. Each pair included a magnesium negative and an iron oxide, nickel positive electrode. The magnesium electrodes each presented an area of 12.9 cm^2 (including front and back surfaces); the positive electrodes had a projected area of 6.4 cm^2 and were made by spreading 3.40g of iron oxide into a nickel cup, covering with a piece of nickel gauze, and crimping the edges of the cup over the gauze.[3] These were then dried at 105°C. Nickel wire leads were spot-welded to all electrodes. The electrodes were positioned on the edges of a square with dissimilar electrodes facing each other and separated by four centimeters. A chromel-p-alumel thermocouple in a Pyrex protection tube was located in the center.

Discharges were made with constant currents of 0.50 or 1.00 amp, and values of coulombic passage were calculated. Potentials between electrodes that were discharged and not discharged were recorded as a function of time, and typical curves are shown in Fig. 1.

Chemical analysis.—After a discharge the electrolyte was dissolved in 250 ml of distilled water. The solution was filtered and the residue was analyzed quantitatively for magnesium. The pH of the filtrate was measured, and the filtrate also was analyzed for magnesium. The magnesium electrodes were rinsed in cold distilled water, dried, and weighed. The iron oxide electrodes were washed and then analyzed quantitatively for ferrous and ferric iron and also submitted to spectrochemical analysis and to x-ray powder diffraction studies. The results of the various qualitative and quantitative analyses will be presented, and the inferred electrode reactions are discussed below.

Thermal cell studies.—Cell design and procedure. As with the work on electrode reactions, the lithium and potassium chlorides were of reagent grade and handled in a low-humidity room. The eutectic mixture was melted in a large porcelain crucible, and into the fused salts some lengths of glass tape were dipped. The glass tape saturated with electrolyte was allowed to cool in a desiccator charged with calcium sulfate. The glass tape can be described as tightly woven from fine yarn, heated to nearly 600°C to remove sizing, and having a thickness of 0.08 mm before saturation. After saturation the thickness was 0.25 mm and an annular piece, as described below, contained 200 mg (3.6 millimoles) of electrolyte.

The various iron oxides will be discussed later. The preparation of the cathode material was as follows. A mixture of 3.14g of the iron oxide sample, 0.04g of Pyrex glass fiber, and 0.5 ml of a 5% aqueous solution of Ninol 1281 wetting agent in 500 ml of distilled water was agitated for 30 sec in a food blender. The slurry was then poured into a suction funnel fitted with a 12.5-cm circle of Whatman No. 40 filter paper. Filtration was fast and there was even distribution on the paper. The filter paper was removed and heated in an oven for 15 min at 120°C and then put in a calcium sulfate desiccator for at least 18 hr. The sheet was cut with a die prior to stripping away the deposit which could then be handled as a wafer. The thickness of these disks was 0.2-0.3 mm. This spread is caused by the variation in the density of the samples.

The several components of the thermal cells are shown in Fig. 2. The nickel cup was constructed of commercially pure metal partially annealed and 0.13 mm in thickness. The diameter of the base of the cup was 3.43 cm and the hole diameter was 1.27 cm. The notched wall had a height of about 0.25 cm with special notches to accommodate the nickel ribbon leads spot-welded to the nickel and magnesium disks.

In the nickel cup was laid an iron oxide disk. Next were placed one or two pieces of electrolyte-saturated glass cloth; the matter of using single or double electrolyte will be discussed. The iron oxide and electrolyte pieces had an outside diameter of 3.38 cm and a hole diameter of 1.27 cm and presented an apparent area of 7.68 cm^2 on each face. The weight of iron oxide in each disk was 0.195-0.198g.

[3] In principle the nickel substrate does not participate in the overall cell reactions, and in practice the behavior of the iron oxide electrode is essentially unchanged when such metals as stainless steel or gold replace the nickel in short-period discharges. With discharges of longer time duration, local couples between the metal and the iron oxide do have a small effect on the positive electrode potential.

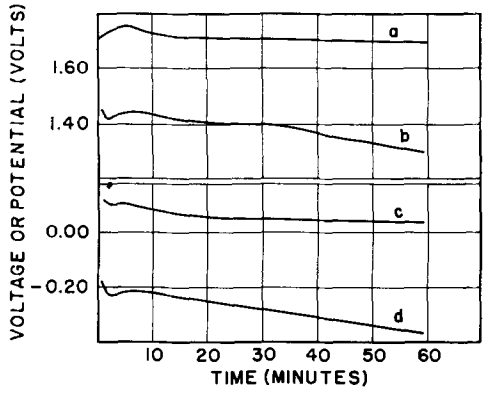

Fig. 1. Magnesium and iron oxide potentials and voltages under no load and under constant current discharge of 0.50 amp. (a) Zero-current voltage between reference electrodes; (b) closed-circuit cell voltage; (c) Mg potential vs. Mg reference; (d) Fe_2O_3 potential vs. Fe_2O_3 reference.

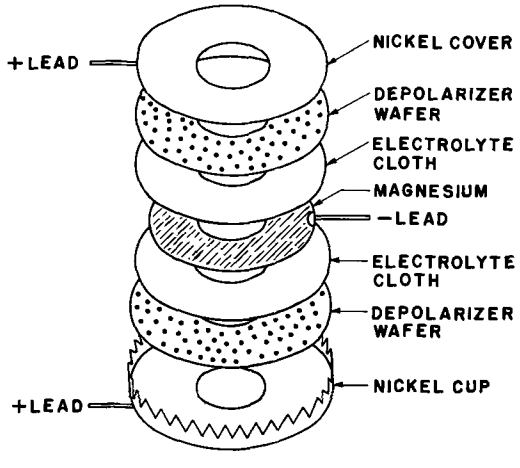

Fig. 2. Exploded view of thermal cell

Next is the magnesium negative electrode, somewhat smaller than the other components so that short-circuiting is avoided. This was of commercially pure metal and 0.13 mm thick. On it was placed one or two pieces of electrolyte cloth and an iron oxide disk laid so that the surfaces that were against the filter paper were now against the electrolyte cloth. Finally the nickel cover was positioned and the cell was closed under a hydraulic ram with a total force of 4500 kg. The cells had a thickness of 2-3 mm. The leads were wrapped with asbestos paper to avoid short circuiting during discharge, and the assembled cells were stored in a desiccator prior to activation.

The cells were activated under load between two massive steel blocks, each presenting to the cell a flat circular heating surface of 60-mm diameter. The steel blocks were kept hot in individual electric crucible furnaces, separately controlled at a temperature of 420°C. During discharge the cells were pressed under a force of 12 kg. The external load was a fixed resistance of 3.5 ohms. Voltages were measured with a good quality voltmeter having an internal resistance of 3000 ohms and were read every 5 sec after activation for a 2-min period. In addition, the time required for the cell voltage to reach 1.35v was registered, and the peak voltage was also recorded.

It should be noted that these annular cells were discharged at 420°C while the studies of electrode reactions were done with a temperature of 500°C. Nothing has been found in the course of the work to indicate that the results of electrode reaction studies are not wholly valid for 420°C. Attention is also called to one other basic difference in experimental method. When chemical analyses and stoichiometric comparisons were to be done for the purpose of establishing half-cell reactions then the electrodes were discharged at constant current. This gives the advantage of simple calculation of total passed charge and delivered energy. In use, however, batteries are discharged through loads which are more like fixed resistances. For such a situation it is understood that current changes continuously due to change in cell voltage as well as total circuit resistance (since there are variations in resistance within the cell). The authors have been careful to interpret the behavior of the annular cells in terms of discharge through constant external load resistance.

Modification of iron oxide samples.—Brief reference has already been given to the various forms of iron oxide, natural and synthetic, which are commercially available for widely different applications. Modifications were also made in the laboratory in terms of changing crystal structure, incorporating foreign elements, removing impurities, and blending of different iron oxide samples.

A synthetic Fe_3O_4 was converted to γ-Fe_2O_3 or to α-Fe_2O_3 by heating in air. The transformations were indicated by color changes and verified by x-ray powder diffraction studies and differential thermal analyses and will be discussed below in somewhat more detail.

The addition of carbon to an iron oxide sample was a simple dry blending procedure. Highly conductive carbon powders, such as Statex Black and Shawinigan Black, were used in the amount of 16.5 wt % (72 mole % with Fe_2O_3; 79 mole % with Fe_3O_4). The mixing of two depolarizer samples was also done by dry blending; these mixtures contained 50.0 wt % of each component.

Naturally occurring iron oxides generally contain a few weight per cent of silica. With one such sample silica was removed by warming with an excess of aqueous hydrofluoric acid solution followed by a thorough washing and drying of the residue at 125°C.

An α-Fe_2O_3 lot was prepared by precipitation of ferric ion from HCl solution with ammonium hydroxide. Another such sample included a small amount of coprecipitated TiO_2. The precipitates were heated in oxygen overnight at 550°C or higher and then pulverized and passed through a 200-mesh sieve.

X-ray powder diffraction and differential thermal analysis studies.—X-ray powder diffraction measurements were made by conventional methods. Values of d/n were compared with those given in published tables.

The differential thermal analysis technique used here has been described by Newman and Wells (6). Reference will be made below in regard to applying the results of DTA to verify the modifications of iron oxide samples.

Oil absorption.—This technique is used by the Federal Supply Service (7) for evaluating the ability of a paint pigment to absorb oil. A good grade of linseed oil is added dropwise to a known weight of solid material which is constantly stirred with a spatula. The end point is the point at which a homogeneous paste is formed, and the oil absorption number is defined as the number of weight units of oil needed for 100 weight units of powder. Since the composition of linseed oil varies somewhat, the same lot of oil must be used to obtain comparative measurements. This test is pertinent in describing the ability of a depolarizer sample to absorb electrolyte (8). Its application will be discussed later.

Results and Discussion

Electrode Reactions

The magnesium electrode.—The dissolution of magnesium on open circuit has been measured in the LiCl-KCl electrolyte at 500°C. The loss of metal is slow, and for periods up to 1 hr it is linear with time. On the basis of twelve experiments the dissolution rate is $1.0 \pm 0.2 \times 10^{-6}$g ($8 \times 10^{-8}$ equivalent)/cm^2 of exposed surface per minute. At reasonable discharge rates this side reaction is not very important as can be shown with the data in Table I. The first four sets of results in this table are typical for the twelve experiments. Electrode efficiency was never found below 91%, and in most cases it was above 96%.

Within experimental accuracy essentially all of the oxidized magnesium is found in the electrolyte

Table I. Analysis of magnesium electrode efficiency at 500°C

Experiment No.	Duration of experiment, min	Coulombic passage for electrode under load, faraday	Loss of weight of electrode not under load, equivalent	Loss of weight of electrode under load, equivalent	Magnesium recovered from electrolyte	
					Water-soluble, equivalent	Water-insoluble, equivalent
M 8	20.0	6.22×10^{-3}	0.33×10^{-3}	6.76×10^{-3}	—	—
M 10	20.0	12.4	0.21	12.4	—	—
M 2	62.0	19.3	0.92	20.1	—	—
M 1	71.0	22.1	1.18	24.2	—	—
M 13	30.0	18.6	—	—	18.3×10^{-3}	0.15×10^{-3}
M 14	30.0	18.6	—	—	18.8	0.26

and in a water-soluble form. Reaction [1] is written for the negative electrode process. Formation of

$$Mg(c) + 2Cl^-(l) \rightarrow Mg^{++}(l) + 2Cl^-(l) + 2e^- \quad [1]$$

magnesium oxide at the electrode or in the electrolyte does not seem possible. In the first place, very little of the oxidized magnesium was water-insoluble, and in the second place the pH of the water solution of electrolyte was 4.9 instead of a value of 11-12 presented by a saturated aqueous solution of MgO. Therefore, neither MgO nor oxide ion exist in the discharged cell electrolyte.

The iron oxide, nickel electrode.—Table II presents results which are typical for eight separate experiments. The positive electrodes were matched in regard to content of active material (Fe_2O_3). From the table it is seen that not enough ferric ion was expended nor was quite enough ferrous ion formed to account for the current passage, and therefore some uncharacterized electrode process must occur to a relatively minor extent. No elemental iron was detected with the x-ray powder diffraction technique.

While α-Fe_2O_3 is readily detected by x-ray analysis of electrode material which has not been discharged, this phase is not found in a discharged electrode. Fe_3O_4 is found and there is a very strong possibility of $(Li_2O)(Fe_2O_3)_5$. There are also some unidentified lines in the diffraction pattern.

There is the material in the discharged electrodes which does not contain metallic iron and which is probably a compound of lithium. Spectrochemical analysis shows the collection of lithium in a water-insoluble form; in fact, discharged electrodes were heavier than those not discharged. A water-insoluble compound of lithium oxide and an iron oxide would explain the absence of oxide ion in the electrolyte; oxide ion would otherwise be expected consequent to positive electrode discharge.

In terms of the x-ray observations summarized above, reaction [2]

$$2Li^+(l) + 8Fe_2O_3(c) + 2e^- \rightarrow 2Fe_3O_4(c) + (Li_2O)(Fe_2O_3)_5(c) \quad [2]$$

would be reasonable, but it is not strongly supported and cannot be the complete description of the cathode process. Not enough Fe_2O_3 was included in the electrode to account for the coulombic passage on the basis of reaction [2]. Indeed, if all the Fe_2O_3 were reduced to Fe_3O_4, the coulombic passage would still not be accounted for. Furthermore, Fe_3O_4 potentials are generally more cathodic under load than those of α-Fe_2O_3, as will be seen later.

As a matter of fact, the phase in which ferrous ion exists in the discharged electrode is not known. Reduction to FeO is not possible below 560°-580°C because FeO would disproportionate to α-Fe and Fe_3O_4 (9). Much could be explained in terms of a species $(Li_2O)(FeO)_x$, but this has not been reported in the literature nor has an attempt been made by the present authors to prove its existence.

Iron Oxide as a Cathode Reactant

The iron oxide samples.—Table III lists the synthetic and naturally occurring iron oxides that were obtained for this study. The first part of the table is for the synthetic materials which are in three groups: pure or mainly γ-Fe_2O_3, pure or mainly Fe_3O_4, and α-Fe_2O_3. For each sample there is given the supplier, his designation of the lot, and the suggested use for that lot. Next are some of the parameters measured by the authors. These are the oil absorption number, the time required for the voltage to reach 1.35v when the cell was activated

Table II. Analysis of iron oxide electrode efficiency

Experiment No.	Weight of electrode after run, g	Coulombic passage: 0.01865 faraday				Residual weight after run, g
		Weight of Fe^{+++} as Fe_2O_3 after run, g		Weight of Fe^{++} as FeO after run, g		
		Calc.	Obs.	Calc.	Obs.	
F7 (not under load)	3.418	—	3.295	0.000	0.049	0.074
F7 (under load)	3.626	1.807	2.130	1.339	1.215	0.281
F8 (not under load)	3.482	—	3.358	0.000	0.050	0.074
F8 (under load)	3.660	1.870	2.169	1.339	1.200	0.291

Table III. Commercial iron oxides as cathode reactants

Form	Impurities	Supplier and designation	Suggested use	Oil adsorption No.	Activation time to 1.35v, sec	Peak voltage, v	Voltage (v) at indicated time (sec)								
							10	20	30	45	60	75	90	105	120
γ-Fe_2O_3		Williams IRN 210	Recording	65	5	1.80	1.80	1.74	1.70	1.63	1.55	1.48	1.42	1.34	1.25
γ-Fe_2O_3		General Aniline P1719		45	4	1.72	1.72	1.70	1.68	1.64	1.52	1.39	1.25	1.16	1.15
γ-Fe_2O_3		Williams IRN 110	Recording	42	12	1.66	1.00	1.63	1.64	1.66	1.64	1.62	1.58	1.51	1.45
γ-Fe_2O_3, Fe_3O_4		Columbian Carbon 421	Paint	28	11	1.52	1.30	1.52	1.50	1.44	1.40	1.30	1.32	1.30	1.28
γ-Fe_2O_3, α-Fe_2O_3		Columbian Carbon 422	Paint	26	10	1.54	1.38	1.54	1.54	1.50	1.46	1.43	1.41	1.40	1.39
Fe_3O_4		Williams IRN 100	Recording		9	1.82	1.80	1.72	1.52	1.24	1.18	1.16	1.16	1.15	1.14
Fe_3O_4		Williams IRN 200	Recording		9	1.78	1.70	1.76	1.71	1.54	1.38	1.19	1.14	1.12	1.10
Fe_3O_4		Columbian Carbon Mapico Black 592	Paint	33	9	1.69	1.66	1.69	1.65	1.45	1.24	1.19	1.18	1.16	1.15
Fe_3O_4		Columbian Carbon Mapico Black 401	Paint	33	8	1.62	1.60	1.62	1.61	1.54	1.45	1.26	1.20	1.19	1.18
Fe_3O_4		Williams Black 250	Paint	20	4	1.59	1.52	1.57	1.58	1.52	1.35	1.20	1.15	1.13	1.11
Fe_3O_4, γ-Fe_2O_3		Columbian Carbon 419	Paint	28	9	1.57	1.52	1.56	1.57	1.55	1.52	1.44	1.27	1.22	1.20
Fe_3O_4, γ-Fe_2O_3		General Aniline 55		30	9	1.56	1.56	1.51	1.43	1.34	1.29	1.24	1.20	1.16	1.14
Fe_3O_4, α-Fe_2O_3		Reichard 82046		36	10	1.42	1.40	1.38	1.32	1.28	1.24	1.22	1.20	1.18	1.17
α-Fe_2O_3		J. T. Baker Co.	Reagent	23		1.33	1.20	1.31	1.27	1.26	1.26	1.26	1.26	1.26	1.24
α-Fe_2O_3		Columbian Carbon 347	Paint	22		1.33	1.30	1.33	1.32	1.32	1.31	1.31	1.30	1.29	1.29
α-Fe_2O_3		Columbian Carbon 567	Paint	20		1.31	1.20	1.29	1.31	1.30	1.29	1.28	1.28	1.28	1.28
α-Fe_2O_3	TiO_2	National Lead	Ti ore	12	10	1.45	1.39	1.32	1.28	1.23	1.19	1.15	1.10	1.00	0.90
α-Fe_2O_3	TiO_2, SiO_2	Whittaker, Clark, and Daniels S100 JM2594	Paint	15		1.28	1.26	1.26	1.22	1.21	1.20	1.20	1.19	1.18	1.18
α-Fe_2O_3	TiO_2, SiO_2	Whittaker, Clark, and Daniels S175 JM2561	Paint			1.24	1.21	1.24	1.22	1.19	1.18	1.18	1.17	1.16	1.14
α-Fe_2O_3	SiO_2, $PO_4^{\equiv}$	National Bureau of Standards 27-B	Standard sample			1.16	0.60	1.10	1.15	1.13	1.11	1.10	1.09	1.08	1.07
α-Fe_2O_3	TiO_2, SiO_2	Williams N-3185	Paint	12		1.05	1.05	1.03	0.99	0.93	0.90	0.88	0.87	0.86	0.87
Fe_3O_4	TiO_2, SiO_2	National Lead-MacIntyre Magnetite Concentrate	Ti ore	12		0.84	0.84	0.78	0.66	0.55	0.48	0.45	0.41	0.40	0.38

under load, the peak voltage observed, and the voltage after different lapses of time (10-120 sec).

The second part of the table is for the naturally occurring samples. The additional information given here is on the major impurities. Some of these samples were analyzed for silica which was found to the extent of 3-5 wt %. It should be noted that these descriptions pertain to the material as received from the suppliers. Modifications of samples as made by the present investigators will be specifically referred to below, and data for the modified ones will be given there.

Characteristics of unmodified synthetic samples.—It is at once obvious that the γ-Fe_2O_3 and the Fe_3O_4 samples provide higher cell voltages than does α-Fe_2O_3, and the differences cannot possibly be accounted for on the basis of thermodynamics. The γ-Fe_2O_3 and Fe_3O_4 are very similar in their spinel-type structures and have relatively high electronic conductivities. On the other hand, α-Fe_2O_3 has a hexagonal structure, contains only trivalent ions, and has a conductivity which is several orders of magnitude less than that of magnetite or γ-Fe_2O_3. It is this large difference in conductivity to which the authors ascribe the basic difference in electrode performance at the beginning of discharge. In this regard it will be seen that the four samples suggested for recording tape application give higher voltages than do the materials simply used as pigments.

Both γ-Fe_2O_3 and Fe_3O_4 exhibit peak load voltages as high as 1.80v. However, with Fe_3O_4 the voltage drops much faster. At the end of 60 sec, the average voltage for the γ-Fe_2O_3 samples was above 1.5v; for the Fe_3O_4 samples this average was well below 1.4v. At 120 sec the corresponding averages were 1.3 and 1.15v, respectively. The explanation may be in terms of the amount of reducible iron. With γ-Fe_2O_3 there are 4.96 mg-ions of Fe(III) per cell, but with Fe_3O_4 there is only 69.0% of that amount.

With α-Fe_2O_3 the initial voltages are much lower than with the samples of higher conductivity. However, the discharge curves are very flat and at 120 sec α-Fe_2O_3 voltages are as high as those of γ-Fe_2O_3 and are higher than the Fe_3O_4 voltages. Open-circuit voltage with α-Fe_2O_3 is 1.70 ± 0.03v (measured with a meter of high impedance), and the initially lower closed-circuit voltage can be reasonably accounted for by the larger IR drop through the α-Fe_2O_3 cells. The larger circuit resistance with α-Fe_2O_3 cells will also explain the flatter discharge curves.

The unmodified synthetic samples have oil absorption numbers from 20 to 65. These numbers reflect the ability of a material to absorb electrolyte, and depletion of electrolyte from the magnesium electrode occurs when single electrolyte disks are used with samples having oil absorption numbers greater than 35-40. Excessive polarization of the magnesium electrode under these circumstances has been demonstrated by the use of the micro reference electrode developed by Walker (8). Any such difficulty is circumvented by using double electrolyte disks with the more absorbent samples, and if this is done, no particular irregularities are observed. Such samples as Williams IRN 210 and IRN 110 and General Aniline P1719 were discharged with double electrolyte.

Characteristics of unmodified natural samples.—The naturally occurring samples of α-Fe_2O_3 provide less power than do the pure ones. This is particularly evident after 30 sec of discharge, and even with lower peak voltages, the drop of voltage with time is more severe than with pure α-Fe_2O_3. (The sample giving the lowest voltages is actually an Fe_3O_4 containing some TiO_2 and SiO_2.)

Apparently the decreased performance of the impure iron oxides is again based on differences in resistance. Wagner and Koch (10) measured the specific conductance of similar magnetite samples. The

pure ones gave values of 125-215 $ohm^{-1}cm^{-1}$ at room temperature. A sample with 4 at. % of SiO_2 had a value of 52 $ohm^{-1}cm^{-1}$. It has been suggested that the silica may coat the outsides of the iron oxide particles. This is reasonable inasmuch as the impure oxides are improved by the relatively superficial treatment with aqueous HF.

Characteristics of modified samples.—Three general types of modifications were used. The first was the simple blending of an iron oxide with conductive carbon powder or another iron oxide. A second type of modification resulted from the application of heat to change allotropic form. Still other modifications consisted of chemical treatment to add or remove foreign ions.

Seven iron oxide samples were discharged with and without being mixed with 16 wt % of conducting carbon powder. Enough of the blend was used so that the normal amount of iron oxide was included in the cells. Figure 3 shows two typical pairs of discharge curves (for a γ-Fe_2O_3 and an α-Fe_2O_3); one curve of a pair is for the unmixed sample and the other is for the iron oxide blended with Statex Black or Shawinigan Black.

It will be noted that an effect of adding carbon is to increase initial voltages. This may be due in part to an increase in actual electrode area with a concomitant decrease in current density and mass transfer polarization; it may also be due to a decreased resistance and smaller IR loss across the iron oxide layer. However, voltages fall away more rapidly than with the unmixed samples; this second effect may be the result of depletion of iron oxide because of nongalvanic reaction with the carbon.

When two samples give somewhat parallel discharge curves, it is possible to blend them and record intermediate behavior. Such a situation can be seen in Fig. 4 which includes discharge curves for an Fe_3O_4 (Columbian Carbon Mapico Black 401), an α-Fe_2O_3 (J. T. Baker Company), and a 1:1 weight mixture. The important implication here is that a cathode material of selected galvanic properties can be prepared by suitable blending.

It is well known that synthetic magnetite can be converted to γ-Fe_2O_3 and γ-Fe_2O_3 can be converted

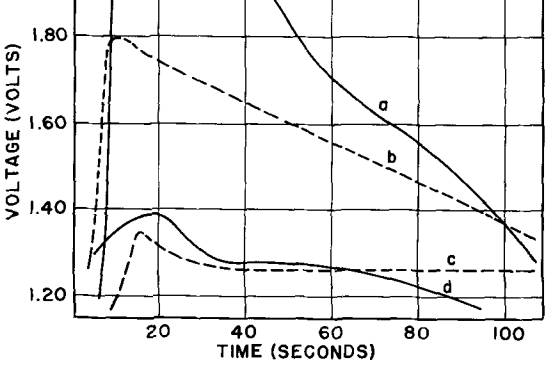

Fig. 3. Effect of conductive carbon powder on depolarizer behavior. (a) γ-Fe_2O_3 with carbon; (b) γ-Fe_2O_3 (Williams IRN-210); (c) α-Fe_2O_3 (J. T. Baker); (d) α-Fe_2O_3 with carbon.

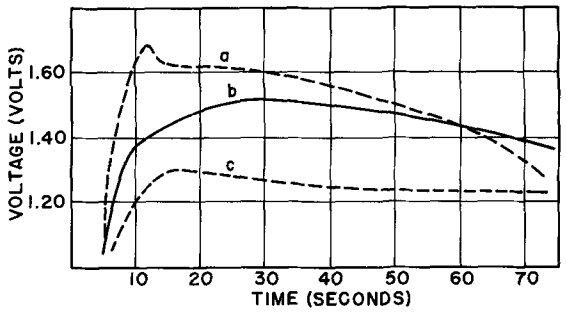

Fig. 4. Behavior of depolarizer mixtures. (a) Fe_3O_4 (Columbian Carbon Mapico Black 401); (b) 1:1 mixture; (c) α-Fe_2O_3 (J. T. Baker).

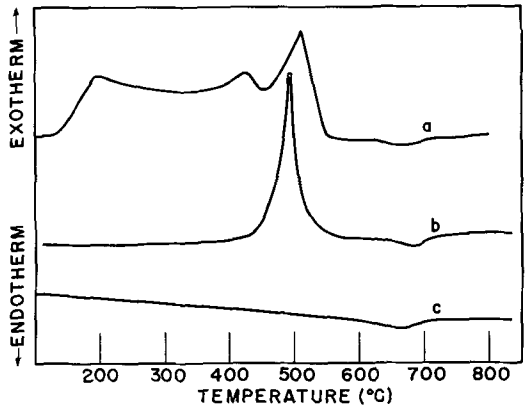

Fig. 5. DTA curves for a synthetic magnetite and for γ-Fe_2O_3 and α-Fe_2O_3 thermally prepared from that magnetite. (a) Fe_3O_4 (Columbian Carbon Mapico Black 401); (b) γ-Fe_2O_3; (c) α-Fe_2O_3.

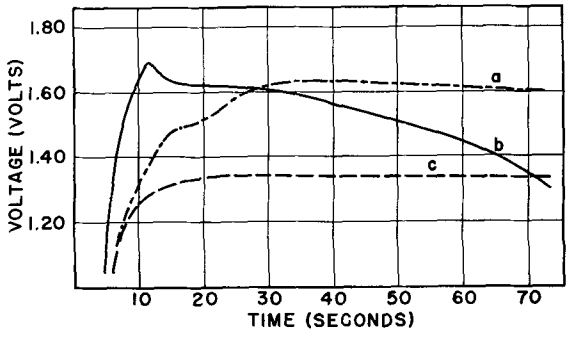

Fig. 6. Cell discharge with a synthetic magnetite and with γ-Fe_2O_3 and α-Fe_2O_3 thermally prepared from that magnetite. (a) γ-Fe_2O_3; (b) Fe_3O_4 (Columbian Carbon Mapico Black 401); (c) α-Fe_2O_3.

to α-Fe_2O_3 by heating in air or oxygen (11). In this work an Fe_3O_4 sample (Columbian Carbon Mapico Black 401) was heated for 3 hr in air at 380°C to prepare γ-Fe_2O_3 and was heated for 1 hr at 800°C to prepare α-Fe_2O_3. The conversions were verified by x-ray powder diffraction as well as differential thermal analysis. Figure 5 shows the DTA curves which have the general characteristics described by Lepp (12) for the three forms; with the Fe_3O_4 a broad exothermic peak begins at 140°C and culminates at 500°C; the γ-Fe_2O_3 displays a sharp exotherm at 500°C; α-Fe_2O_3 is relatively stable in the range of temperatures shown. Figure 6 presents discharge curves for the three depolarizer samples thus obtained. Differences in behavior are generally typical of those shown in Table III. The original Fe_3O_4 gives a noticeable voltage maximum and a

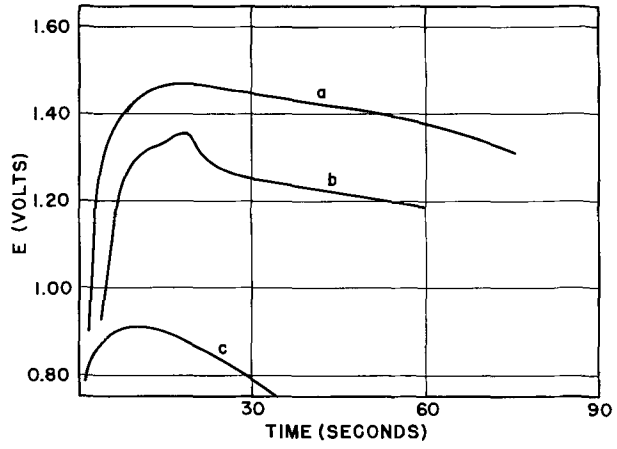

Fig. 7. Effect of the silica impurity on depolarizer behavior. (a) Synthetic Fe_3O_4; (b) natural Fe_3O_4 treated with HF; (c) untreated natural Fe_3O_4.

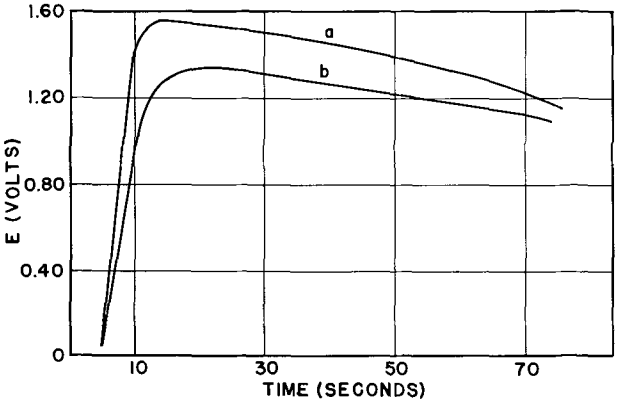

Fig. 8. Effect of titanium(IV) ion on depolarizer behavior. (a) α-Fe_2O_3 + TiO_2 (coprecipitated); (b) α-Fe_2O_3.

relatively fast voltage drop. A large voltage is also obtained with the γ-Fe_2O_3, and this voltage falls more slowly. With α-Fe_2O_3 the voltage is decidedly lower and the discharge curve is flat.

Reference has been made to the very low voltages obtained with naturally occurring iron oxide samples. It was of interest to determine the effect of removing the silica impurity which, as noted above, can increase the resistivity of the sample. A quantity of the National Lead-MacIntyre Magnetite Concentrate was treated with aqueous hydrofluoric acid as described above. Behavior approached that for a synthetic Fe_3O_4. This is shown in Fig. 7 which also gives the discharge curve for the unpurified material.

Verwey *et al.* (13) and Morin (14) discuss the lowered resistivity of α-Fe_2O_3 due to the inclusion of small amounts of tetravalent titanium ion in the hematite lattice; an n-type conductor results with a specific resistance which is four or more orders of magnitude less than that for pure α-Fe_2O_3. In the present work several mole per cent of TiO_2 was coprecipitated with α-Fe_2O_3. Another quantity of α-Fe_2O_3 was precipitated but without TiO_2. The samples were washed, dried and baked and discharged in cells. Figure 8 compares the behavior of the two. The pure material performs in a manner generally typical of synthetic α-Fe_2O_3. The sample containing TiO_2 gives a peak voltage which is 0.25v higher, and after 1 min the voltage falls faster than it does in the case of the pure iron oxide cell.

Conclusions

This work has provided an insight as to the electrode reactions in the thermal cell system Mg/LiCl-KCl/Fe_2O_3,Ni. More than that, it outlines the capabilities which one can expect from these cells, pointing out that a cathode material can be selected or prepared according to desired discharge behavior.

The physical and chemical reasons for differences in this behavior can be discussed on the basis of two broad considerations. One of these is the amount of available reducible iron. Thus a magnetite cell containing only 3.42 mg-ions of Fe(III) polarizes more rapidly than a γ-Fe_2O_3 cell with 4.96 mg-ions. The addition of conductive carbon enhances behavior at the beginning of a discharge, but voltage drop is very fast presumably because of nongalvanic reduction of the iron oxide.

The other general consideration is the specific resistance of the oxide. In each instance discussed above, those effects which enhance conductance lead to higher cell voltage and those which increase resistance result in lower terminal voltages, albeit flatter curves because of decreased discharge current. In this regard the performance of the magnetite and γ-Fe_2O_3 spinels is to be compared with that of α-Fe_2O_3 obtained as such or thermally prepared; samples containing small amounts of silica have a higher resistivity than pure samples, and this is reflected in cell performance; small amounts of titanium ion decrease resistivity, and this is also reflected in cell performance. Unfortunately, this resistance parameter, which is of primary interest, is difficult to measure directly. It is affected by such things as compacting pressure, particle size, and porosity. Bevan *et al.* (15) state that absolute values have little significance since the geometry of the powder sample is indeterminate. In fact, much experimental difficulty was encountered in making broadly relative measurements, and even such results as those cannot be reported here.

These results will have an important connotation in the building of a thermal cell as a source of power. It can be inferred that one may select a cathode reactant to yield electrical characteristics which are particularly desired in a given instance. For example, if a large voltage is wanted with greater energy output during a short-time discharge, then a γ-Fe_2O_3 or magnetite might be chosen. If a flat discharge curve is more important than large voltage, then an α-Fe_2O_3 should be used. The voltage can be shifted up or down to some extent by incorporating small amounts of TiO_2 or SiO_2 and a high peak voltage of short duration may be had by blending the iron oxide with conductive carbon. Behavior which is between that of two separate samples can be obtained by mixing the samples. It is emphasized that no particular iron oxide is suggested as the "best" one; this depends strictly on the special application.

Acknowledgments

The authors are indebted to Dr. I. A. Denison for many stimulating discussions regarding this work. They acknowledge the contributions of Mr. H. E. Swanson and Mr. E. S. Newman of the National

Bureau of Standards who performed the x-ray powder diffraction analyses and differential thermal analyses, respectively. Appreciation is also expressed to C. K. Williams & Company and the Columbian Carbon Company who graciously supplied some of the iron oxide samples.

The study of single electrode reactions was done at the Catalyst Research Corporation under sponsorship by the U.S. Army Electronics Research and Development Laboratory under Contract DA 36-039 sc-42602. The study of iron oxide as a thermal cell cathode material was done at the Harry Diamond Laboratories.

Manuscript received Sept. 4, 1962; revised manuscript received Nov. 24, 1962. This paper was presented in part at the 12th Annual Battery Research and Development Conference, U. S. Army Electronics Research and Development Laboratory, Fort Monmouth, N. J., May 21-22, 1958, and at the 114th Meeting of the Society, Ottawa, Sept. 28-Oct. 2, 1958.

Any discussion of this paper will appear in a Discussion Section to be published in the December 1963 JOURNAL.

REFERENCES

1. G. W. Vinal, "Primary Batteries," pp. 324-329, John Wiley & Sons, Inc., New York (1950).
2. R. B. Goodrich and R. C. Evans, *This Journal*, **99**, 207C (1952).
3. E. S. McKee, Proc. 10th Ann. Battery Res. and Dev. Conf., Power Sources Div., Signal Corps Engineering Laboratories, Fort Monmouth, N. J. (1956), p. 26.
4. S. M. Selis and L. P. McGinnis, *This Journal*, **108**, 191 (1961).
5. S. M. Selis and L. P. McGinnis, *ibid.*, **106**, 900 (1959).
6. E. S. Newman and L. S. Wells, *J. Research Natl. Bur. Standards*, **36** [2], 137 (1946) (RP 1696).
7. Method 419.1 of Federal Spec. TT-P-141b, Federal Supply Service, Washington (January 15, 1949).
8. R. D. Walker, Private communications (1956).
9. M. Hansen, "Constitution of Binary Alloys," 2nd ed., p. 687, McGraw-Hill Book Co., New York (1958).
10. C. Wagner and E. Koch, *Z. physik. Chem.*, **B32**, 439 (1936).
11. L. A. Welo and O. Baudisch, *Phil. Mag.*, **24**, 80 (1937).
12. H. Lepp, *Am. Mineralogist*, **42**, 679 (1957).
13. E. J. Verwey, P. W. Haaijman, F. C. Romeijn, and G. W. van Oosterhout, *Philips Research Repts.*, **5**, 173 (1950).
14. F. J. Morin, *Phys. Rev.*, **83**, 1005 (1951).
15. D. J. M. Bevan, J. P. Shelton, and J. S. Anderson, *J. Chem. Soc.*, **1948**, 1729.

The Oxidation of Graphite at Temperatures of 600° to 1500°C and at Pressures of 2 to 76 Torr of Oxygen

E. A. Gulbransen, K. F. Andrew, and F. A. Brassart

Physical Chemistry Department, Research Laboratory, Westinghouse Electric Corporation, Pittsburgh, Pennsylvania

ABSTRACT

The oxidation of graphite is an interesting reaction due to its technological importance. Volatile reaction products of carbon monoxide and carbon dioxide are formed at all temperatures above 25°C. Below 800°C a small amount of surface oxide is also formed. The rate of oxidation below 800°C is limited by a chemical process having an energy of activation of 39 kcal/mole. Above 800°C the reaction is limited, by either a chemical process or by gaseous diffusion of oxygen through the products of reaction. The transition between the two processes depends on the pressure, sample size, and the nature of the reaction system.

Gravimetric, pressure change, and mass spectrographic methods were used to study the kinetics of the oxidation reaction. The discovery of the surface area effect greatly aided the study of the primary chemical reaction up to 1000°C and the diffusion-controlled region of oxidation. Using small samples having surface areas of 0.13 cm^2 rates of oxidation of 5.9 x 10^{18} atoms/cm^2/sec were measured in a static system. Experimentally the rate of oxidation of carbon is governed by three factors (i) the primary chemical reaction, (ii) the diffusion-controlled reaction, and (iii) the theoretical rate based on collision theory.

Due to current interest in the use of graphite at high temperatures many papers (1-9) have appeared in recent years on the reactions of graphite with oxygen, carbon dioxide, and other gases. Few studies have been made on graphite above 1200°C. This paper presents a study of the high-temperature oxidation of graphite. Of special interest is the region of high reaction rates between 10^{16} to 10^{20} atoms of carbon reacting per square centimeter per second. The transition between chemical- and diffusion-controlled oxidation is investigated to extend the range for the study of the chemical controlled reaction. Comparison is made between the chemical-controlled and diffusion-controlled rates of oxidation and values calculated from kinetic theory.

Walker, Rusinko, and Austin (1) made an extensive survey in 1959. They also pointed out some of the proposed mechanisms of oxidation.

Gulbransen and Andrew (9) studied the oxidation of artificial graphite in 1952 using micrograv-

metric methods over the temperature range 425°-575°C. The object of the work was to determine the mechanism of the primary chemical reaction under conditions where transport processes were not rate controlling. The rate of oxidation followed a nearly linear rate law, while the temperature dependence followed an exponential rate law. An energy of activation of 36.7 kcal/mole was calculated. A rate analysis showed the rate-limiting process was the adsorption of oxygen on the graphite surface.

Recently Blyholder and Eyring (2, 3) presented a different mechanism for the primary chemical reaction. They studied the oxidation of spectroscopic purity graphite between 800° and 1300° at low oxygen pressures using a flow method and thin specimens of low porosity. An energy of activation of 80 kcal/mole was calculated for the rate of oxidation. For thick specimens where pore diffusion can occur, a ½ order reaction was observed and an energy of activation of 42 kcal/mole was calculated. Carbon monoxide was the reaction product. For thin specimens desorption of carbon monoxide was proposed as the rate-controlling mechanism.

Thermochemical Calculations

Five reactions involving graphite, carbon dioxide, carbon monoxide, and oxygen are of interest in the interpretation of the experimental results. These are shown in Table I together with values of the equilibrium constant, K_R, for the temperature range 600°-1600°C. The thermodynamic data are taken from JANAF (10) tables. β-Graphite was used as the standard state for graphite. Volume changes associated with each reaction are also listed.

Carbon dioxide and carbon monoxide are stable to decomposition according to reactions [A], [B], and [C]. Reaction [C] shows carbon monoxide can be oxidized at all temperatures given in Table I. The reaction of carbon dioxide with graphite, reaction [D], is possible above 700°C. In a static system where the products of reaction can accumulate, the percentage of carbon monoxide should increase with temperature. The dissociation of oxygen molecules, reaction [E], becomes appreciable above 1200°C.

Experimental

Figure 1 shows the balance and associated reaction system used for determining the rates of oxidation of graphite. The apparatus and balance are changed greatly from our earlier work in order to measure the faster rates of reaction and to extend the temperature range of the system. Since a pressure change occurs if carbon monoxide is formed, pressure gauges are also used to follow the course of the reaction. To determine the composition of the reaction products, samples are taken for mass spectrometer analysis after reaction. The reaction system is essentially static with the products of reaction accumulating in the system. Some gas circulation is maintained by thermomolecular flow processes.

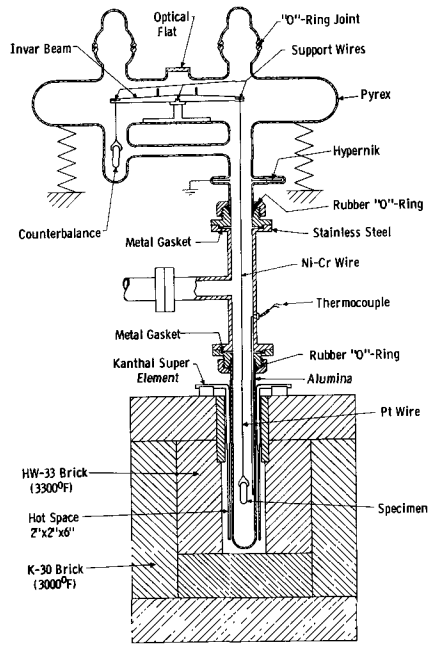

Fig. 1. Reaction system

Table I. Thermodynamic calculations

$C(s) + \frac{1}{2}O_2(g) \leftrightarrows CO(g)$	$\Delta V = +\frac{1}{2}$	[A]
$C(s) + O_2(g) \leftrightarrows CO_2(g)$	$\Delta V = 0$	[B]
$CO(g) + \frac{1}{2}O_2(g) \leftrightarrows CO_2(g)$	$\Delta V = -\frac{1}{2}$	[C]
$CO_2(g) + C(s) \leftrightarrows 2CO(g)$	$\Delta V = +1$	[D]
$\frac{1}{2}O_2(g) \leftrightarrows O(g)$	$\Delta V = +\frac{1}{2}$	[E]

$Log_{10}K_R$ for reactions

Temp, °C	[A]	[B]	[C]	[D]	[E]
600	11.27	23.64	12.37	−1.10	−11.725
800	10.05	19.25	9.20	0.85	−8.92
1000	9.20	16.27	7.07	2.13	−6.97
1200	8.55	14.04	5.49	3.06	−5.56
1400	8.06	12.38	4.32	3.74	−4.48
1600	7.66	11.00	3.34	4.32	−3.63

Balance.—A special gold plated Invar beam balance is used (11). This balance is 14.5 cm long, weighs 46g, and has a sensitivity of 75μg/0.001 cm deflection at 7.25 cm for a 1.4g weight. Sections of 8 and 20 mil platinum wire in the hot zone and a section of 2 mil nickel-chromium wire were used to suspend the specimen. Above 1500°C platinum wire either reacted with graphite or was too weak to support the load.

Furnace tubes.—The furnace tubes shown in Fig. 1 were 1 in. diameter, high density mullite or alumina. Alumina tubes were used above 1200°C.

Furnace and controls.—A special furnace using molybdenum disilicide furnace elements was built (12). This furnace could be used without a temperature controller at temperatures up to 1600°C. The furnace elements are mounted directly in the hot zone which is 5 cm square and 15 cm long.

Temperature measurement.—Calibrated Pt-Pt + 10% Rh thermocouples were used. They were mounted adjacent to the specimen as shown in Fig. 1. The temperature was controlled by setting the current to the heater elements. The temperature varied ± 3°C.

Specimens and analyses.—Spectroscopic grade of graphite (AGKSP) obtained from National Carbon Company was used. The specimens were carefully

machined from rods. The standard specimens were about 0.62 cm in diameter, 2.65 cm long, and had hemispherical ends. They weighed 1.4g and had surface areas of about 6.3 cm^2. Several experiments were made on one sample. New surface areas were calculated for each experiment. Smaller samples having surface areas of about 3.37, 1.74, 0.947, 0.232, and 0.136 cm^2 were used for studying the transition between chemical and diffusion controlled reactions.

Spectroscopic analyses showed the following impurities in (ppm): Fe, 0.2; Mg, 0.6; and Si, 0.2 with a confidence level of 95%. No traces were found for Al, Ba, Ca, Cu, Pb, Mn, K, Ag, Na, Ti, Sn, or V.

Gas source.—Tank oxygen was used. Water vapor was removed and the dried gas passed over a dry ice trap before using.

Method.—The specimen was placed on the balance beam and the system closed and evacuated to a pressure of 1 x 10^{-6} Torr or better. At frequent intervals the furnace tube and system were heated without sample to test the furnace tube for cracks not observable in the room temperature evacuation test.

The furnace was kept at temperature. For the oxidation experiment the furnace was raised about the furnace tube and the pressure read on the ion gauge or McLeod gauge. At 1500°C the pressure was 1 x 10^{-5} mm of Hg or lower. After thermal equilibrium was achieved, oxygen was added. Weight and pressure changes were recorded as a function of time.

The weight change curves were found to be reproducible to ± 3%. One sample was used for a series of runs. For the 6.3 cm^2 samples, the total burn off for the series of runs was less than 6%. For the smaller samples, complete oxidation occurred. Only the initial rate of reaction has meaning due to extensive changes in the surface area and temperature.

Results

Test of Reaction System and Method

The study of fast gas-solid reactions where volatile reaction products are formed presents several problems. Due to the rapid reaction, heat effects occur which make an evaluation of the surface temperature difficult. As a result, conflicting data are found in the literature. Ideally, the physical dimensions of the reaction system itself should be considered as variables. An alternative procedure is to study the reaction system by varying the sample size and shape and consequently the surface area to mass ratio. We have used this procedure to test our system for several oxidizing conditions.

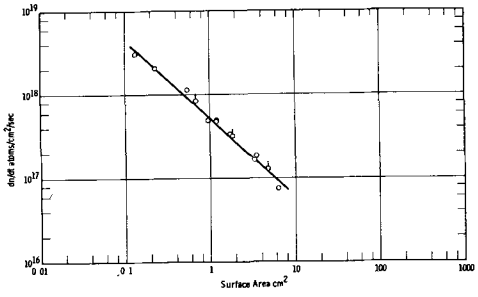

Fig. 2. Effect of surface area on rate of oxidation at 1200°C and 38 Torr; $dn/dt = 5.1 \times 10^{17}/A$; open circle, cylinders; open circle with line on top, spheres.

Table II summarizes our study of the effect of sample size and shape on the rate of oxidation of graphite at 1200°C and oxygen at 38 Torr pressure. Long and short cylinders and spheres of three diameters are used in addition to two flat plates of different thickness. The initial rates of oxidation are given in units of atoms/cm^2/sec. The dimensions, surface area, mass and surface area to mass ratio are given in the table. The weight loss *vs.* time curves show a decreasing slope as oxygen is used and the specimen area decreases. A wide variation is found for the rates of oxidation given in Table II. Considering surface area, mass and surface area to mass ratio as system variables, a good correlation is found between the rate of oxidation and the surface area.

Figure 2 shows a log-log plot of the initial rates of reaction *vs.* surface area. The following equation fits the data

$$\frac{dn}{dt} \cdot A = 5.1 \times 10^{17} = K(p, T) \qquad [1]$$

Table II. Effect of sample shape and sample area on rate of oxidation, 1200°C. 38 Torr

Dimension, cm Length	Diameter	Area, cm^2	Mass, g	A/M, cm^2/g	dn/dt, atoms/cm^2/sec	Log dn/dt
3.2	0.617	6.215	1.4001	4.439	7.31×10^{16}	16.86
Sphere	1.228	4.737	1.8102	2.617	1.278×10^{17}	17.107
1.54	0.617	3.570	0.7193	4.963	1.772×10^{17}	17.248
3.216	0.318	3.366	0.3833	8.773	1.629×10^{17}	17.212
0.72	0.615	1.985	0.3686	5.385	3.15×10^{17}	17.500
1.59	0.316	1.735	0.1912	9.074	3.33×10^{17}	17.523
a	*a*	1.188	0.0839	14.159	4.93×10^{17}	17.693
Sphere	0.614	1.185	0.2245	5.278	4.655×10^{17}	17.668
b	*b*	1.198	0.402	29.8	4.718×10^{17}	17.674
0.79	0.317	0.949	0.0955	9.937	4.923×10^{17}	17.692
Sphere	0.4695	0.6925	0.1017	6.809	8.326×10^{17}	17.920
0.397	0.3165	0.552	0.0492	11.22	1.118×10^{18}	18.048
0.396	0.156	0.232	0.0123	18.86	2.05×10^{18}	18.312
0.198	0.156	0.135	0.0063	21.42	3.016×10^{18}	18.479

a Flat plate 1.01 × 0.383 × 0.149.
b Flat plate 1.015 × 0.514 × 0.051.

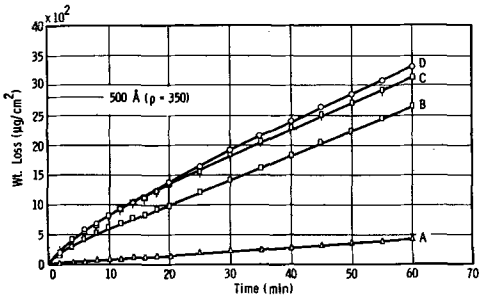

Fig. 3. Effect of temperature on oxidation of graphite, 600°-1000°C, 76 Torr; A, 600°; B, 700°; C, 800°; D, 1000°C.

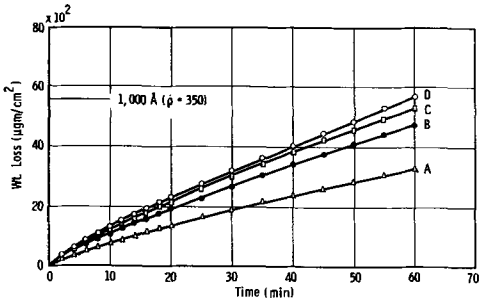

Fig. 4. Effect of temperature on oxidation of graphite, 1000°-1500°C, 76 Torr; A, 1000°; B, 1200°; C, 1400°; D, 1500°C.

Here dn/dt is the rate of oxidation in atoms/cm²/sec and A is the surface area. We have defined $K(p, T)$ as the capability constant of the reaction system (13). For reactions under diffusion control the specimen area uniquely determines the maximum rate of reaction for a given pressure, temperature, and reaction system. This equation suggests that small samples can be used to increase dn/dt provided dn/dt is less than the limiting value for chemical control.

We conclude that it is essential for studies on the oxidation of carbon at temperatures above 800°C to define the reaction system, gas flow, specimen area, temperature, pressure, and source of carbon.

Kinetic Studies 600° to 1500°C, Large Samples

Effect of time and temperature.—Specimens of 6.3 cm² were used to extend the temperature range of our earlier oxidation studies and to study the transition between chemical and diffusion controlled oxidation.

Figures 3 and 4 show the results at a pressure of 76 Torr. Weight loss is given in units of micrograms per square centimeter, and time is given in minutes. The rates of oxidation decrease as time increases since oxygen is consumed and carbon dioxide and carbon monoxide are produced. The change in oxygen concentration was largest for the low pressure experiments at high temperatures.

Figure 3 shows a large increase in the rate of oxidation, dW/dt, between 600° and 700°C and much smaller increases above 700°C. Similar results were found in experiments at 38, 19, 9.5, and 2 Torr pressures. A major change occurs in the mechanism near 700°C. Figure 4 shows the rate of oxidation increases slowly between 1000° and 1500°C.

The thickness of carbon removed can be estimated from the density, 1.6 g/cm³, and the surface roughness value, ρ, of 350 (9). Thickness markers based on these estimates are placed on Fig. 3 and 4.

The existence of a change in mechanism of reaction at 825°C was reported by Tu, Davis, and Hottel (14). These authors reported a change from a chemical reaction below 825°C to a diffusion-controlled reaction above 825°C. Kuchta, Kant, and Damon (15), Levy (16), and Blyholder and Eyring (2, 3) also report a change in mechanism near 825°C. Our results suggest a transition from chemical to diffusion control at about 700°C for a pressure of 76 Torr and a sample area of 6.3 cm². Using 0.136 cm² samples we have been able to raise this transition temperature to 1000°C. The fact that earlier workers found a transition temperature near

Table III. Summary of data, oxidation of graphite, 600°-1500°C 6.3 cm² area

Temp, °C	Pressure, Torr	dw/dt (initial), μg/cm²/sec	dn/dt (initial), at./cm²/sec	ΔP, Torr	Temp, °C	Pressure, Torr	dw/dt (initial), μg/cm²/sec	dn/dt (initial), at./cm²/sec	ΔP, Torr
600	38	0.033	1.65×10^{15}	0	1200	2	0.63	3.16×10^{16}	1.4
600	76	0.118	5.9×10^{15}	0	1200	5	0.85	4.26×10^{16}	2.0
700	2	0.16	8.0×10^{15}	0	1200	9.5	1.07	5.37×10^{16}	3.5
700	5	0.15	7.5×10^{15}	0	1200	19	1.34	6.72×10^{16}	3.75
700	9.5	0.20	1.0×10^{16}	0	1200	38	1.57	7.88×10^{16}	5.4
700	19	0.37	1.86×10^{16}	0	1200	76	2.07	1.04×10^{17}	4.0
700	38	0.59	2.96×10^{16}	0	1400	2	0.75	3.76×10^{16}	1.5
700	76	1.17	5.87×10^{16}	0	1400	5	1.24	6.22×10^{16}	2.8
800	2	0.45	2.26×10^{16}	0	1400	9.5	1.47	7.37×10^{16}	4.05
800	5	0.57	2.86×10^{16}	0	1400	19	1.72	8.63×10^{16}	5.1
800	9.5	0.72	3.61×10^{16}	0	1400	38	1.90	9.53×10^{16}	6.6
800	19	0.88	4.41×10^{16}	0	1400	76	2.65	1.33×10^{17}	6.0
800	38	1.03	5.17×10^{16}	0	1500	2	0.63	3.16×10^{16}	1.1
800	76	1.59	7.98×10^{16}	0	1500	5	0.90	4.52×10^{16}	5.0
900	38	1.09	5.47×10^{16}	0	1500	9.5	1.40	7.02×10^{16}	4.1
900	76	1.31	6.57×10^{16}	0	1500	19	1.57	7.88×10^{16}	5.0
1000	2	0.44	2.21×10^{16}	0	1500	38	1.90	9.53×10^{16}	6.6
1000	5	0.70	3.51×10^{16}	0	1500	76	2.33	1.17×10^{17}	6.5
1000	9.5	0.80	4.01×10^{16}	0					
1000	19	0.86	4.31×10^{16}	0					
1000	38	1.08	5.42×10^{16}	0					
1000	76	1.50	7.53×10^{16}	0					

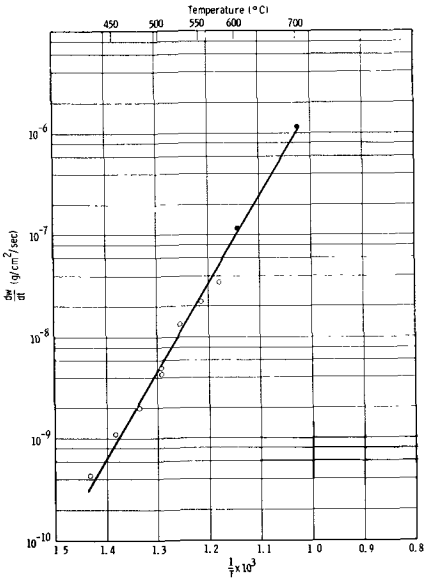

Fig. 5. Log *dw/dt* vs. 1/*T*, 425°-700°C, 76 Torr, *E* = 39 kcal/mole; •, new date; ○, Gulbransen and Andrew (9).

825°C indicates their reaction systems, specimen areas, and oxidation conditions were similar.

Table III gives a summary of the results. The initial rates of reaction are given in units of micrograms per square centimeter per second and in atoms of carbon reacting per square centimeter per second. Pressure changes occurring in the system are also given. According to the equations of Table I, pressure increase indicates carbon monoxide formation in addition to carbon dioxide. No change indicates carbon dioxide formation. Mass spectrometer studies were also made. These will be presented later. Pressure increases were found at 1200°C and higher.

Temperature dependence and energy of activation.—A log *dW/dt vs.* 1/*T* graph of the data at 76 Torr is shown in Fig. 5. Here *dW/dt* in grams per square centimeter per second, is used to compare

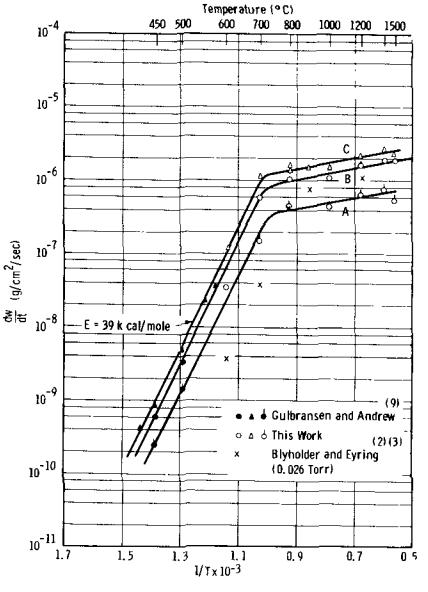

Fig. 6. Log *dw/dt* vs. 1/*T* oxidation of graphite; A, 2 Torr; B, 38 Torr; C, 76 Torr.

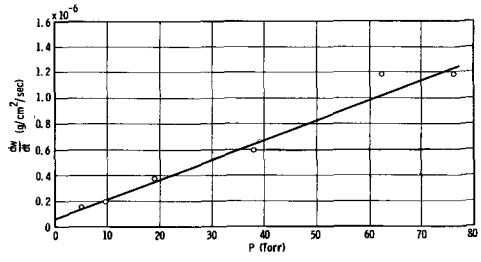

Fig. 7. Effect of pressure, *dw/dt vs. P* (Torr), *dw/dt* = (0.06 + 0.01565 *P*) 10^{-6} 700°C, 0-76 Torr.

with our older data, and *dn/dt*, in atoms per square centimeter per second, can be calculated by using Avogadro's number. Good agreement was found with the earlier data of Gulbransen and Andrew (9). An energy of activation of 39.0 kcal/mole is calculated. This may be compared to our earlier value of 36.7 kcal/mole.

Figure 6 shows the data for three pressures on a log *dW/dt vs.* 1/*T* plot for the complete temperature range of 425°-1500°C. Below 725°C the data fall on parallel straight lines. The data of Blyholder and Eyring (2, 3) are consistent with our results, although a pressure of 0.026 Torr was used. Above 725°C a change is noted in the kinetics of oxidation at all pressures. For this region an energy of activation of 3.6 kcal/mole is calculated. A decrease was noted in the rate of oxidation between 1400° and 1500°C.

Pressure dependence.—Linear plots of the effect of pressure on the initial rates of reaction are shown in Fig. 7 and 8. The initial rates of oxidation were determined from large-scale plots of the data using the first few minutes of oxidation.

This confirms our earlier results (9) at 500°C. Above 700°C a new pressure relationship is observed. This is shown in Fig. 8 for four temperatures between 1000° and 1500°C. To establish the pressure relationship, a log *dW/dt vs.* log *P* plot is given in Fig. 9 for the data at 800°, 1200°, and 1500°C. Combining the pressure and temperature coefficients we have the following equation for the data at 800°C and higher temperatures

$$\frac{dw}{dt} = 1.86 \times 10^{-6} P^{0.32} e^{-\frac{3600}{RT}} \qquad [2]$$

Here *P* is the pressure in Torr and *R* is the gas constant. The fractional exponential power suggests a complex mechanism for the reaction.

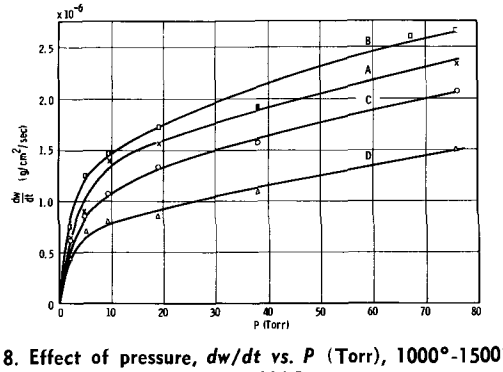

Fig. 8. Effect of pressure, *dw/dt vs. P* (Torr), 1000°-1500°C; A, 1500°; B, 1400°; C, 1200°; D, 1000°C.

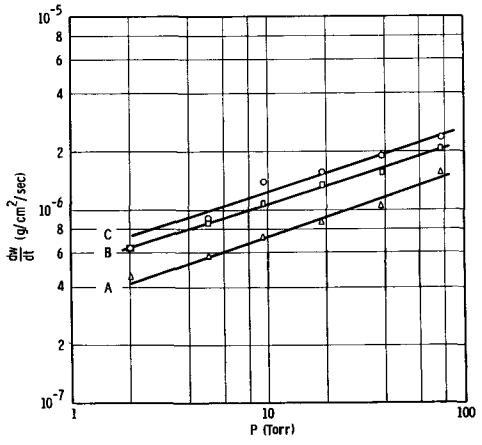

Fig. 9. Log dw/dt vs. log pressure, ($dw/dt = 1.86 \times 10^{-6} P^{0.32} e^{-3600/RT}$) 800°-1500°C; A, 800°; B, 1200°; C, 1500°C.

Effect of pretreatment.—Gulbransen and Andrew (9) showed that certain pretreatments of the graphite have an important influence on the rate of oxidation below 575°C. This is to be expected since heat treatments and oxidation can effect the surface area and the extent of surface oxide formation. Above 800°C the surface oxide is unstable, and the rate of oxidation is probably controlled by transport of reacting gas through the boundary layer of reaction product to the reacting interface.

Table IV shows a series of experiments to test the effects of pretreatment on the oxidation reaction. No important effect was found above 800°C. This evidence supports the proposal that transport processes are rate controlling.

Transition Between Chemical and Diffusion Controlled Oxidation Above 800°C

Studies on the gaseous diffusion-controlled oxidation of graphite have limited use, unless the rates of reaction are related to the chemical-controlled reaction and to the theoretical values calculated from kinetic theory. Kinetic theory gives the following equation for the number of impacts n of oxygen molecules with a square centimeter of surface per second

$$n = 3.52 \times 10^{22} \frac{P}{(MT)^{1/2}} \qquad [3]$$

Here M is the molecular weight, T is the temperature in °K, and P is the pressure in Torr. At 1500°C and 76 Torr $n = 1.21 \times 10^{22}$ collisions/cm²/sec. If CO is formed, each collision results in reaction with two atoms of C; therefore the theoretical value of dn/dt at 1500°C and 76 Torr is 2.4×10^{22} atoms of C/cm²/sec. This is equivalent to 3 mm ablated per second for graphite of density 1.6.

Table IV. Effect of pretreatment on rates of oxidation 800°C, 76 Torr

Treatment	Wt. loss, 20 min, g/cm²	Initial dw/dt, g/cm²/sec
New sample	1.28×10^{-3}	1.50×10^{-6}
After 1 oxidation	1.33×10^{-3}	1.575×10^{-6}
After 4 oxidations	1.32×10^{-3}	1.53×10^{-6}
Preheat 1300°C 16 hr	1.29×10^{-3}	1.46×10^{-6}

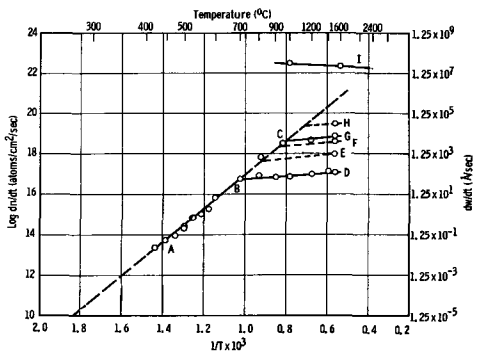

Fig. 10. Log dn/dt vs. $1/T$, oxidation of graphite, 76 Torr; line ABC, chemical control. Sample areas: D, 6.2 cm²; E, 0.947 cm²; F, 0.232 cm²; G, 0.136 cm²; H, estimated 0.0316 cm²; I, theory $C + O_2$.

We have investigated the diffusion region by determining the rate of oxidation, dn/dt, for a series of samples of different areas at several reaction temperatures. In these experiments, we have used sample areas of 6.3-0.136 cm². Smaller samples lead to large sample temperature increases due to the heat of reaction.

Table V and Fig. 10 show the surface area studies for an oxygen pressure of 76 Torr. At 1500°C the sample area was varied by a factor of 44 to determine the transition between diffusion- and chemical-controlled reaction. Since the value of dn/dt increased on reducing the specimen size we conclude the oxidation is still under diffusion control for the smallest sample. Reaction rates up to 5.9×10^{18} were measured. These rates of oxidation produced appreciable changes in surface temperatures. Observations on the thermocouple near the sample showed temperature changes of up to 7°C for the 0.136 cm² sample during oxidation.

Estimates of the surface temperature can be made on the following basis. First, carbon monoxide

Table V. Effect of surface area on initial rates of oxidation

Pressure, Torr	Furnace temp, °C	Calc. temp, °C	Sample area, cm²	dn/dt, atoms/cm²/sec	Log dn/dt
76	800	800	6.25	7.98×10^{16}	16.90
76	800	809	0.135	7.48×10^{17}	17.87
76	900	900	6.25	6.57×10^{16}	16.82
76	900	960	0.136	3.28×10^{18}	18.52
76	1100	1197	0.135	4.83×10^{18}	18.68
76	1500	1500	6.044	1.17×10^{17}	17.07
76	1500	1501	0.947	7.93×10^{17}	17.90
76	1500	1513	0.232	4.15×10^{18}	18.62
76	1500	1518	0.136	5.85×18^{18}	18.77
38	1200	1200	6.22	7.31×10^{16}	16.86
38	1200	1200	3.37	1.63×10^{17}	17.21
38	1200	1200	1.74	3.33×10^{17}	17.52
38	1200	1202	0.95	4.92×10^{17}	17.69
38	1200	1207	0.55	1.12×10^{18}	18.05
38	1200	1211	0.232	2.05×10^{18}	18.31
38	1200	1216	0.135	3.02×10^{18}	18.48
38	1500	1500	6.08	1.06×10^{17}	17.02
38	1500	1501	0.95	7.33×10^{17}	17.87
38	1500	1507	0.236	2.36×10^{18}	18.37
38	1500	1509	0.136	3.25×10^{18}	18.51
2	1500	1500	6.3	3.16×10^{16}	16.50
2	1500	1501	0.942	2.25×10^{17}	17.35
2	1500	1502	0.234	6.96×10^{17}	17.84
2	1500	1506	0.136	1.79×10^{18}	18.25

is assumed as the primary reaction product. Heats of formation of gaseous carbon monoxide were taken from the JANF (10) tables. Second, the emissivity was assumed to be 0.5. Third, radiation was assumed as the major source of heat loss. The calculated surface temperatures based on the measured rates of oxidation are given in Table V. Except for the small sample sizes, temperature increases due to oxidation were calculated to be less than 13°C.

Figure 10 shows a log *dn/dt vs.* $1/T$ graph of the data obtained at 76 Torr oxygen pressure together with our earlier data at lower temperatures (9). Line AB and its extension represents the data for the chemical controlled region of oxidation. Line ABD was obtained using 6.0-6.3 cm^2 samples. Line BCG was obtained using 0.136 cm^2 samples. Points E, F, and G were obtained by using samples of different surface areas. Point H is an estimated value for a 0.032 cm^2 particle.

Line ABC represents chemical-controlled oxidation with an energy of activation of 39 kcal/mole. Reaction rates to the right of line ABC, area BCHD, represent diffusion-controlled oxidation. In this region, temperature has only a minor effect on the rate of reaction. The important variable is the surface area.

The measured rate of reaction for a 0.136 cm^2 sample at a furnace temperature of 1500°C and 76 Torr pressure was 5.9 x 10^{18} at./cm^2/sec. The ablation rate in Ångstroms per second is given at the right in the figure.

Curve I of Fig. 10 shows the calculated *dn/dt* values from kinetic theory for 76 Torr pressure. A value of 2.4 x 10^{22} at./cm^2/sec is found at 1600°C.

Figures 11 and 12 and Table V give the rate data for pressures of 38 and 2 Torr oxygen pressure. These data support the picture of the oxidation reaction already developed.

Mass Spectrometer Studies

Several experiments were made to test the composition of the gas atmosphere after reaction. The samples were collected by opening a valve to an evacuated flask, after reaction. Table VI shows a summary of the results. Experiments 1 and 2 show CO_2 was the gas formed in the reaction at 800° and 900°C. These results confirm the observations on the reaction pressure. Calculations show that the amount of CO_2 in the gas sample was in the range

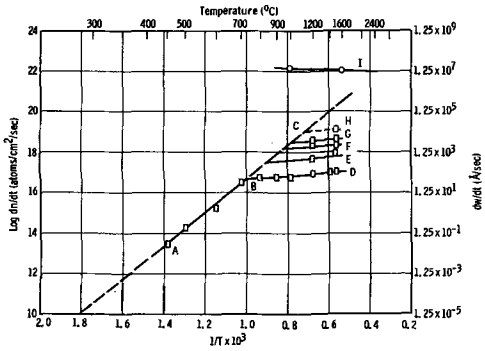

Fig. 11. Log *dn/dt vs.* $1/T$, oxidation of graphite, 38 Torr; line ABC, chemical control. Sample areas: D, 6.2 cm^2; E, 1.19 cm^2; F, 0.232 cm^2; G, 0.136 cm^2; H, estimated 0.0316 cm^2 particle; I, theory, C + O_2.

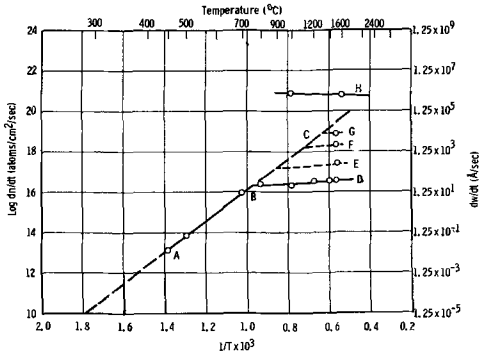

Fig. 12. Log *dn/dt vs.* $1/T$, oxidation of graphite, 2 Torr; line ABC, chemical control. Sample areas: D, 6.2 cm^2; E, 1.19 cm^2; F, 0.136 cm^2; G, estimated 0.0316 cm^2 particle; H, theory, C + O_2.

of the expected values. Due to lack of complete mixing, quantitative calculations cannot be made.

Two interpretations are possible. First, CO_2 is the primary reaction product. Second, CO is the primary reaction product and CO_2 is formed by the slow wall reaction of CO and O_2. Since CO was present only in traces, we favor the interpretation that CO_2 is the gas formed for these conditions.

At higher temperatures both CO and CO_2 are formed as shown in Table VI for oxidations at 1200° and 1400°C. The mass spectrometer results confirm the pressure change experiments. At 1200° and 1400°C, CO_2 can react with graphite to form CO.

Experiments 5 and 6 were made as control experiments on the possible formation of carbon gases by reaction of oxygen with impurities in the alu-

Table VI. Mass spectrometer results

Experiment	Gases present	Ratio CO_2/CO	Remarks
1. Oxidation 800°C, 76 Torr, 1 hr	O_2, CO_2, (traces CO and H_2)	115	CO_2 formed
2. Oxidation 900°C, 76 Torr, 1 hr	O_2, CO_2, (traces CO and H_2)	43	CO_2 formed
3. Oxidation 1200°C, 76 Torr, 1 hr	O_2, CO_2, CO, (traces N_2 and H_2)	1	CO and CO_2 formed
4. Oxidation 1400°C, 76 Torr, 1 hr	O_2, CO, CO_2, (traces H_2)	0.73	CO and CO_2 formed
5. Oxygen + tube 1200°C, 76 Torr, 1 hr (no graphite present)	O_2, (traces CO, CO_2, N_2, H_2)	—	No reaction
6. Oxygen + tube 1400°C, 76 Torr, 1 hr (no graphite present)	O_2, (traces CO, CO_2, N_2, H_2)	—	No reaction

mina tube. Mass spectrometer results showed no measurable reaction.

Discussion and Summary

Summary of Kinetic Data

Figures 10-12 summarize in graphical form our data on the kinetics of oxidation of graphite. The results can be explained in terms of chemical-controlled oxidation and gaseous diffusion-controlled oxidation. Discovery of the surface area effect made possible the investigation of the transition between the two types of oxidation phenomena. The transition temperature between chemical- and diffusion-controlled reaction depends on the specimen area and the nature of the reaction.

Rate expressions.—At 700°C the following expression is derived from the pressure dependence of the rate of oxidation as shown in Fig. 7

$$\frac{dn}{dt} = 5.02 \times 10^{16} (0.06 + 0.01565\,P) \qquad [4]$$

Here dn/dt is in atoms per square centimeter per second and P is the pressure in Torr.

At 500°C, the following expression is derived using the earlier data of Gulbransen and Andrew (9)

$$\frac{dn}{dt} = 5.02 \times 10^{13} (1.35 + 0.0505\,P) \qquad [5]$$

At 800°C and higher temperatures, the oxidation reaction is under diffusion control. A more general form of the rate expression can be used. Combining the pressure and temperature coefficient we have the following equation for samples with an area of 6.3 cm^2

$$\frac{dn}{dt} = 9.33 \times 10^{16} P^{0.32} e^{-3600/RT} \qquad [6]$$

Here T is the absolute temperature, R is the gas constant, and P is the pressure in Torr. To put the equations on an absolute basis of real area, we divide Eq. [4], [5], and [6] by the surface roughness factor of 350 (9).

Fast reactions.—For diffusion-controlled oxidation the rate of oxidation is inversely proportional to surface area. Fast reactions of 5.9×10^{18} at./cm^2/sec were measured on small samples of 0.136 cm^2 area, at a furnace temperature of 1500°C and an oxygen pressure of 76 Torr. Kinetic theory calculations indicate a maximum reaction rate of 2.4×10^{22} at./cm^2/sec at 1600°C and 76 Torr. This value is 3000 times the observed value for a 0.136 cm^2 specimen area.

Mechanism of Reaction

Two mechanisms have been proposed for the chemical-controlled oxidation process. Gulbransen and Andrew (9) showed that the rate-controlling process was probably one of two adsorption processes for thick specimens, mobile adsorption or immobile adsorption with dissociation. Blyholder and Eyring (2, 3) suggested desorption as the rate-controlling process for thin specimens. The present study supports the earlier conclusions of Gulbransen and Andrew (9). However, the new energy of activation is 39 kcal/mole instead of the earlier value of 36.7 kcal/mole. The present work does not conflict with the mechanism suggested by Blyholder and Eyring since the experimental samples were very different.

Interpretation of Surface Area Effect

Equation [1] relates the observed rate of oxidation to specimen area when the reaction is under diffusion control. Under diffusion control the specimen is surrounded by both carbon monoxide and carbon dioxide. If carbon monoxide is the primary reaction product, carbon dioxide is formed by gas phase oxidation or at the furnace wall by a surface reaction. For reaction to occur, oxygen molecules must diffuse to the sample through this region of reaction products. The immediate region surrounding the sample is very turbulent due to the heat of reaction and to the formation of two molecules of carbon monoxide for each oxygen molecule arriving at the surface. In this turbulent region the specimen reacts with all of the oxygen gas arriving in the reaction zone provided the specimen area is small compared to the dimensions of the reaction system. Fast reactions can be measured using small samples.

Manuscript received Oct. 5, 1962. This paper was prepared for delivery at the Boston Meeting, Sept. 16-20, 1962.

Any discussion of this paper will appear in a Discussion Section to be published in the December 1963 JOURNAL.

REFERENCES

1. P. L. Walker, F. Rusinko, Jr., and L. G. Austin, "Advances in Catalysis," Vol. XI, p. 133, Academic Press, New York (1959).
2. G. Blyholder and H. Eyring, *J. Phys. Chem.*, **61**, 682 (1957).
3. G. Blyholder and H. Eyring, *ibid.*, **63**, 1004 (1959).
4. G. Blyholder, J. S. Binford, Jr., and H. Eyring, *ibid.*, **62**, 263 (1958).
5. J. Nagle and R. F. Strickland-Constable, "Proc. Fifth Carbon Conference," Pergamon Press, (In Press).
6. N. R. Laine, F. J. Vostola, and P. L. Walker, *ibid.*
7. G. Hennig, G. J. Dienes, and W. Kosiba, *Proc. Second Intern. Conf. Peaceful Uses Atomic Energy*, Geneva, Switzerland, 1958, Paper No. 1778.
8. G. Hennig, "Proc. 1st and 2nd Carbon Conference," p. 103, University of Buffalo, (1956); "Proc. Third Carbon Conference," p. 265, Pergamon Press (1959); and "Proc. Fourth Carbon Conference," p. 145, Pergamon Press (1960).
9. E. A. Gulbransen and K. F. Andrew, *Ind. Eng. Chem.* **44**, 1034 (1952).
10. JANAF Interim Thermochemical Tables—Prepared under auspices of Joint Army-Navy-Air Force Thermochemical Panel, December 31, 1960, Dow Chemical Co., Midland, Michigan.
11. E. A. Gulbransen and K. F. Andrew, "Vacuum Microbalance Techniques," Vol. II, Plenum Press, Inc., New York (1962).
12. E. A. Gulbransen, K. F. Andrew, and F. A. Brassart, Westinghouse Research Labs. Report 62-123-121-R1.
13. E. A. Gulbransen, K. F. Andrew, and F. A. Brassart, Westinghouse Research Labs., Report 62-123-121-P5.
14. C. M. Tu, H. Davis, and M. C. Hottel, *Ind. Eng. Chem.*, **26**, 749 (1934).
15. J. M. Kuchta, A. Kant, and G. H. Damon, *ibid.*, **44**, 1559 (1952).
16. M. Levy, *ibid.*, Product Research and Development **1**, 19 (1962).

Effect of Crystal Structure on the Anodic Oxidation of Nickel

J. L. Weininger and M. W. Breiter

Research Laboratory, General Electric Company, Schenectady, New York

ABSTRACT

The formation of $Ni(OH)_2$ and NiOOH on different crystal planes of nickel, and of polycrystalline nickel, was studied in alkaline solution. Oxide films of less than two monolayers were reduced potentiostatically, then current-potential curves were measured in the range —200 to 1600 mv at different rates of the linearly increasing potential. Electron diffraction and microscopy were used to develop a suitable experimental procedure for dealing with bare and smooth nickel surfaces. The extent of oxide film formation in air on different planes was in the order (110) > (100) > (111). The reactivity on anodization, characterized by the potential at which the equivalent of one monolayer of hydroxide is formed, was in the same order. On continued oxidation the structure of the crystal surface is lost; subsequent reduction forms a strongly disordered surface. The results are discussed with regard to the mechanism of anodization, the extent of differences between crystal planes, and the conditions under which they are maintained or lost.

In the course of a study of the mechanism of electrode reactions of nickel, and of its oxides and hydroxide in an alkaline solution, experiments on single crystals of nickel were performed because these offer the best possible characterization of the surface. In recent years an increasing emphasis on crystal orientation and structure has developed in electrochemical studies. To date the most thorough work of this nature is that of Piontelli and coworkers (1) on the electrode behavior of metallic single crystals. They investigated anodic and cathodic overvoltages during dissolution and deposition and hydrogen evolution on different crystal planes of metals and found systematic differences in the overvoltages with high exchange currents for deposition and dissolution, *e.g.*, lead, tin, and cadmium. With nickel the overvoltage for the cathodic deposition at the (100) plane was about 30 mv lower than for the (110) plane in a chloride solution at pH 3.1.

Oxidation of single crystals has been studied extensively by Gwathmey and associates (2) in the gas phase, but there are only few reports of anodic formation of oxides on single crystals. Examples of the latter are the reported epitaxial growth of very thin layers of ZnO on Zn crystals, studied by Huber and Bieri (3), and the growth of AgCl on Ag crystals reported by Fleischmann and Thirsk (4). Such a study is appropriate for nickel crystals in alkaline solutions. Recently Kuchinskii and Ershler (5) made microscopic observations of single grains of $Ni(OH)_2$ during anodization. Extensive studies of cathodic polarization of nickel oxide were made by Wynne-Jones and co-workers (6), and by Lukovtsev (7), who separately suggested proton diffusion in the hydroxide as a step in the mechanism of oxidation of $Ni(OH)_2$ to NiOOH. This was verified experimentally by Lukovtsev and Slaiden (8). X-ray diffraction studies of the anodization of nickel in alkaline solution were performed by Briggs and Wynne-Jones (9), by Salkind and Bruins (10), and by Falk (11), who elucidated the electrode process in the nickel-cadmium cell. Recent measurements by Conway and Bourgault (12) of the discharge of nickel oxide electrodes at open circuit also gave information on the structure of the oxide. Their results illustrate the role of surface layers in the electrode reactions.

This paper presents experimental results showing the differences between crystal planes in the initial oxidation of nickel to the hydroxide and to higher oxides. The mechanism of anodic oxidation in this system, which is limited to only a few layers of oxyhydroxide (NiOOH) is also discussed.

Experimental

The following procedure gave reproducible results. After chemical polishing nickel electrodes were polarized at —200 mv in 0.2*N* KOH solution saturated with argon. (The electrode potential is referred to a hydrogen electrode in 0.2*N* KOH throughout this paper.) The electrodes were then anodized cyclically in a controlled "potentiodynamic" program. The potential was increased linearly at a given rate as a ramp (or saw-tooth voltage) from —200 to 1600 mv and the current was recorded on an oscilloscope. At the end of the potential increase, the potential dropped instantaneously to —200 mv. The electrode was kept for 2 min at —200 mv so that the oxide film was reduced. Then the next potential sweep was applied. This cycle was repeated several times. The potential was controlled with a Wenking potentiostat; the oscilloscope was a Type 502 Tektronix. This procedure was developed in conjunction with electron diffraction analyses mentioned below.

Single crystals of nickel of 99.9% purity (principal impurity Co ~ 0.05%) were supplied by the Virginia Institute for Scientific Research. The polycrystalline sample was a 0.005 in. cold-rolled 99.97% nickel foil from Sigmund Cohn Corporation. The principal impurity in the foil was 0.02% Fe. The

crystals were cylindrical with [100] axes. Other planes, (110) and (111), were either spark-cut or sawed and mechanically polished before surface treatment. The cylindrical walls of the crystals were masked with Teflon sleeves. Appropriate crystal planes were then etched and polished to a depth of about 1 mm below the original surface in a solution of 50 ml acetic acid, 30 ml HNO_3, 10 ml H_2SO_4, and 10 ml H_3PO_4 (13). The chemical polishing removed damage and strain in the surface layers. Polishing was performed at 80°-100°C for different periods, depending on the relative reactivity of the surfaces which was observed visually during the polishing. Electron micrographs showed that polishing yielded exceptionally smooth surfaces. The polishing solution was washed off, and the crystals were transferred to the electrochemical cell in distilled water saturated with hydrogen to minimize oxide formation. This was necessary because layers of oxide form rapidly on virgin surfaces of nickel in air or oxygen-containing solutions. In the present procedure the electrode was immersed in the KOH solution at a negative potential, and the exposure of the wet nickel surface to atmospheric oxygen was limited to the fraction of a second necessary to accomplish the transfer to the cell.

The existence of oxide and hydroxide films after chemical polishing was shown by 50 kev electron diffraction measurements. It was found that nickel crystals had patterns of single crystal surfaces after polishing, and also after the crystals were dipped with a negative potential into 0.2*N* KOH solution. Without an externally applied potential the hydroxide formed spontaneously. After only 1-min immersion there was still a nickel pattern, but also a trace of $Ni(OH)_2$ with a strongly preferred orientation, approximating pseudomorphic growth of the hydroxide on the metal substrate. After 30-min immersion the patterns indicated some texture of $Ni(OH)_2$, and after 16-hr immersion surfaces showed random polycrystalline patterns of $Ni(OH)_2$. Electrons with 50 kev energy penetrate to a depth of about 50Å. Consequently, the diffraction patterns do not describe the surface alone. They result from an array of about 15 atom layers. In the 1-min example above probably most of the pattern is due to the nickel substrate, but $Ni(OH)_2$ is formed immediately on immersion to the extent of at least 1 or 2 layers, by a local cell mechanism.

To arrive at quantitative values for the number of oxide layers formed on anodization, as well as for the amount of oxygen adsorbed or oxide formed in transfer, it is necessary to have a reasonable estimate of surface roughness. In the present work we assume a roughness factor of one. This is the ideal case, but such a surface is closely approached in the experimental procedure. After extensive chemical polishing no asperities exist at the surface and, except for a very occasional etch pit, the surface presents an extremely smooth appearance. This is shown in electron micrographs. Within their limits of sensitivity there is no indication that polishing introduced a different or preferential surface orientation.

Results

Electron microscopy.—Figures 1 through 5 are electron micrographs of carbon replicas of nickel electrodes, which after chemical polishing were shadow-cast with platinum. The three crystal planes appear to be exceptionally smooth. This is seen in Fig. 1, 2, and 3, which are the electron micrographs of the (110), (100), and (111) planes, respectively. At a magnification of 75,000, near the limit of the instrument and technique, what surface texture there is may be due to the method itself. The (111) plane has a few etch pits, some of them triangular. Figure 4 presents the polycrystalline surface at lower magnification (X 10,000), showing grain boundaries, including triple points. At larger magnification (Fig. 5, X 75,000) surface roughness is observed. It is restricted mostly to the neighborhood of the grain boundaries.

Current-time curves measured at constant potential after immersion.—Current-time curves of crystals immersed in the electrolyte were measured at controlled potentials of —280, —200, —100, and

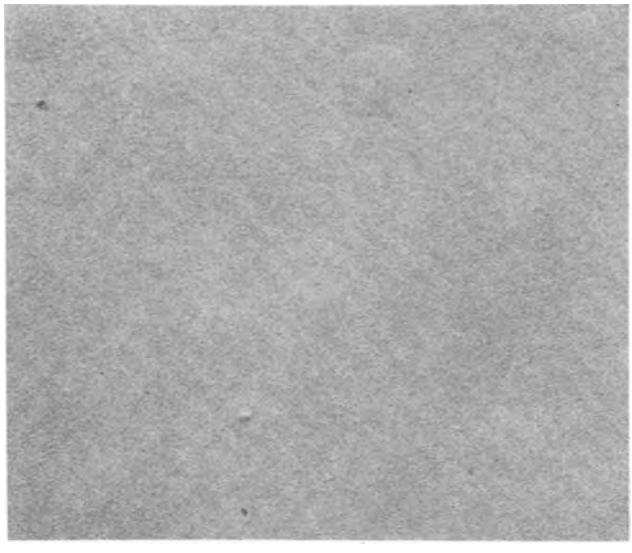

Fig. 1. Electron micrograph of a carbon replica of the (110) crystal plane of nickel after chemical polishing. Magnification 4800X. Arrow indicates direction of shadow casting.

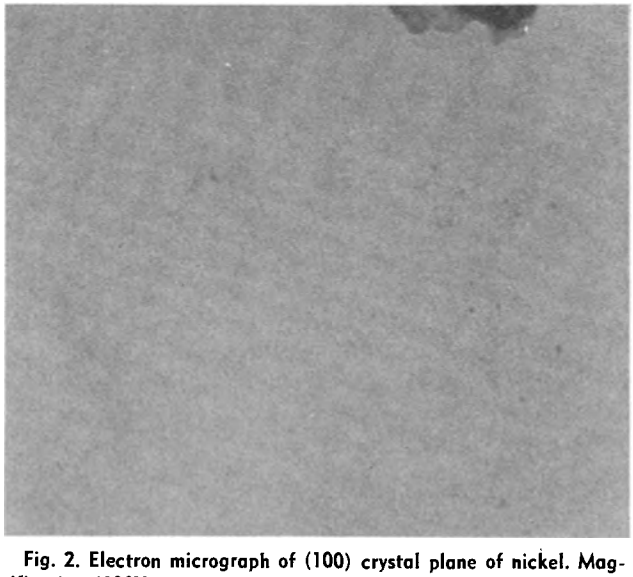

Fig. 2. Electron micrograph of (100) crystal plane of nickel. Magnification 4800X.

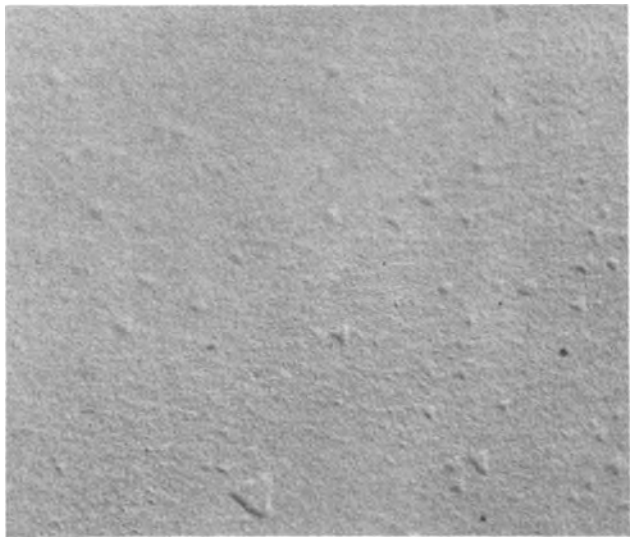

Fig. 3. Electron micrograph of (111) crystal plane of nickel. Magnification 4800X.

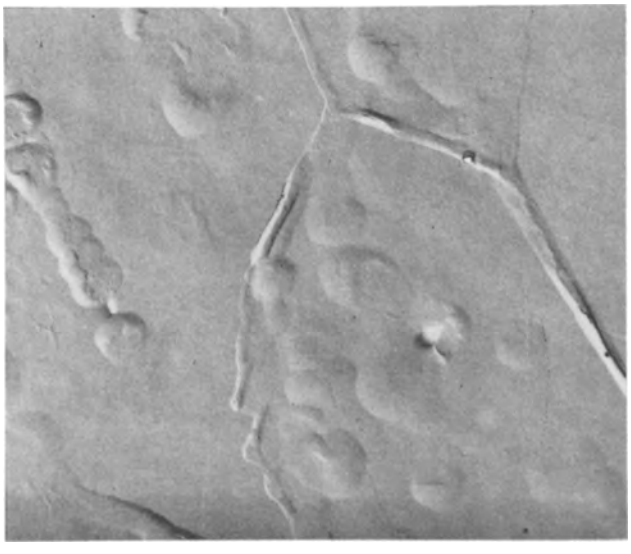

Fig. 4. Electron micrograph of polycrystalline nickel electrode. Magnification 4800X.

Fig. 5. Electron micrograph of grain boundary in polycrystalline nickel electrode of Fig. 4. Magnification 36,000X.

0 mv. A value of −200 mv was then chosen for the final series of experiments as the potential at which hydrogen evolves freely and at which oxide films are completely reduced within 2 min.

Figure 6 is a typical curve for the (111) crystal. Three traces are shown. The lowest (a) defines zero current. Trace (b) is due to hydrogen evolution in the steady state. The more or less exponential decay curve (c) shows the reduction of oxygen picked up in the transfer of the electrode from the hydrogen-saturated distilled water to the argon-saturated 0.2*N* KOH electrolyte. Integration of the curve yields 0.24 mC/cm^2 which corresponds to a coverage of 0.4 monolayers of oxide.

Although there is considerable experimental error, both due to the method of immersion of the crystal and the integration of the curves with a planimeter, the number of layers of oxide formed was reproducibly different for the four surfaces studied. This is shown in Table I, which gives the charges required to reduce the oxide layers. Each value is an average of about 7 determinations with a limit of reproducibility of ±10%. Oxide-reduction measurements were also made by exposing the crystals to air for times up to 90 sec and measuring current-time curves after immersion. The results were not, however, sufficiently reproducible to arrive at reliable conclusions.

Table I. Charges required to reduce oxide layers formed during the transfer of electrode

Surface	(110)	(100)	(111)	Polycrystalline
mC/cm^2	0.73	0.58	0.36	1.09

Anodic current-potential curves during single potential sweeps.—In the anodic sweeps which were carried out at a rate of about 110 mv/sec from −200 mv to about 1600 mv a marked difference was found between the first sweep on a virgin crystal surface and later sweeps. The oscillograms of Fig. 7 are the initial traces for the four different nickel surfaces. On repeating these after 2 min of polarization at −200 mv, the traces of Fig. 8 were obtained. The most important changes in the shape of the curves occur immediately after the first sweep. On subsequent repetition, without repolishing the crystal surface, only the high-voltage peak (at 1440 mv) increased in magnitude.

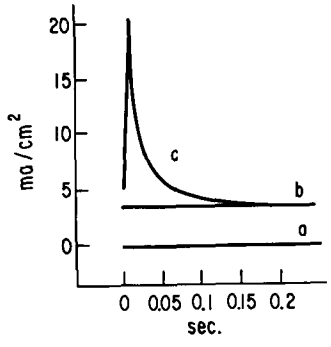

Fig. 6. Current-time curve of cathodic polarization of the (111) nickel crystal plane after immersion in 0.2*N* KOH at −200 mv: (a) zero current; (b) current due to hydrogen evolution; (c) current due to reduction of oxide film.

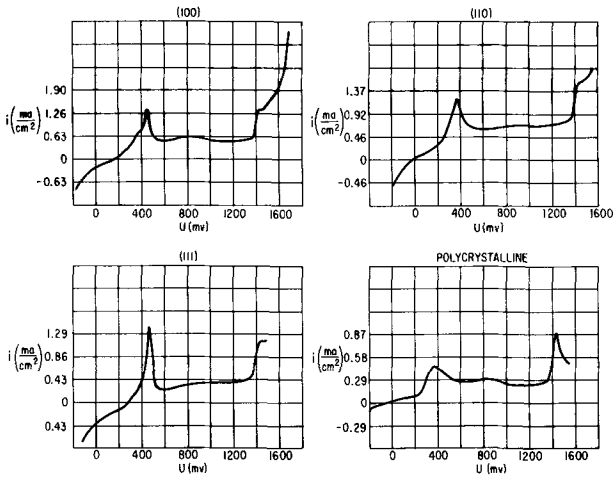

Fig. 7. Anodic current-potential curves during single potential sweeps at 110 mv/sec. Nickel crystal planes and polycrystalline foil in 0.2*N* KOH. Initial sweeps on virgin surfaces.

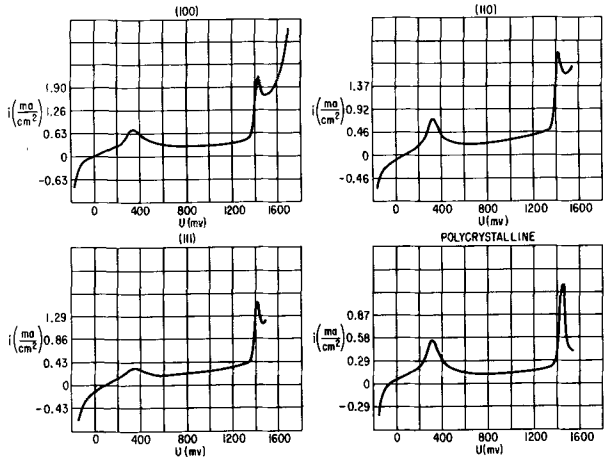

Fig. 8. Anodic current-potential curves during single potential sweeps at 110 mv/sec. Nickel crystal planes and polycrystalline foil in 0.2*N* KOH. Sweeps subsequent to those of Fig. 7.

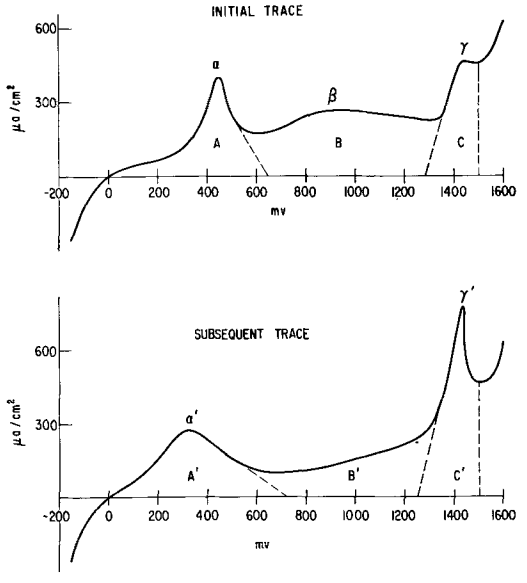

Fig. 9. Schematic current-potential curves of single crystal (initial trace) and disordered surfaces (subsequent trace) of nickel.

The significant features of the curves are shown schematically in Fig. 9. The curves may be divided into three parts, an area at low potential (A), one at a higher one (C), and an intermediate region (B). In the initial sweep there are characteristic peaks (at potentials α, β, γ) for each of these regions, but the intermediate peak disappears on subsequent traces. The numerical values for these potentials and the number of coulombs required to form the oxide on the electrode surfaces are tabulated in Table II. Since potential was increased linearly with time, therefore, the areas of the three regions, and hence the charges, could be obtained by integrating over the contours and along extrapolated lines from the maxima indicated by the dashed lines of Fig. 9. This necessarily arbitrary procedure introduces considerable error in the relative values of the individual areas, but comparison of the total integration (*i.e.*, A + B + C *vs.* A′ + B′ + C′) indicates good reproducibility.

It would be desirable to convert the charge-data of Tables I and II into the actual number of hydroxide or oxide layers formed, but this cannot be done accurately since the actual structure of the very few atomic or molecular layers covering the electrode surface is not known. In fact, this lack of knowledge is a principal reason for undertaking the present work. However, good estimates can still be made. For example, a reasonable assumption for surface coverage of a bare nickel electrode would be a 1:1 correspondence of nickel and oxygen atoms or ions. Thus weighting crystal planes according to their different geometry, and normalizing with respect to the (100) plane, the number of atoms per unit area are in the ratio of $1/\sqrt{2}:1:2/\sqrt{3}$ for the planes (110):(100):(111). Based on the lattice

Table II. Characteristic features of current-voltage curves for anodization of nickel

		(110)	(100)	(111)	Polycrystalline
Voltage measurements, mv	α	370 ± 20	450 ± 20	480 ± 20	370 ± 20
	β	880 ± 20	815 ± 20	870 ± 20	850 ± 20
	γ	1440 ± 20	1430 ± 20	1435 ± 20	1435 ± 20
	α'	325 ± 20	320 ± 20	340 ± 20	320 ± 20
	γ'	1435 ± 20	1445 ± 20	1425 ± 20	1450 ± 20
Charge measurements, mC/cm²	A	1.4 ± 30%	1.6 ± 30%	1.3 ± 30%	1.3 ± 30%
	B	3.9 ± 30%	3.6 ± 30%	2.7 ± 30%	1.5 ± 30%
	C	0.8 ± 30%	0.7 ± 30%	1.1 ± 30%	1.0 ± 30%
	A′	1.2 ± 30%	1.9 ± 30%	1.1 ± 30%	1.1 ± 30%
	B′	2.9 ± 30%	2.2 ± 30%	2.7 ± 30%	1.4 ± 30%
	C′	2.0 ± 30%	1.6 ± 30%	1.2 ± 30%	1.0 ± 30%
	A + B + C	6.1 ± 10%	5.9 ± 10%	5.1 ± 10%	3.8 ± 10%
	A′ + B′ + C′	6.1 ± 10%	5.7 ± 10%	5.0 ± 10%	3.5 ± 10%

constant of fcc nickel the surface coverage from the data of Table I would then be 2.0:1.1:0.6 for the above planes. The same assumption carried out for the initial anodization to the hydroxide (A and A' in Fig. 7, 8, and 9, and Table II) leads to the conclusion that about two layers of hydroxide are involved in the potential region defined by area A or A' (1 layer is approximately equivalent to 0.6 mC/cm^2). Furthermore potentials α and α' are reached on coverage equivalent to about 1 monolayer. On continued oxidation other structures and other conversion factors come into play. Within reasonable limits of error the curves can be interpreted, however, to the extent that about 3 or 4 layers of hydroxide are formed up to 600-800 mv during the potential sweep, and about 10 layers of oxyhydroxide at the end of the sweep, at 1600 mv.

The tabulated data were obtained with voltage sweeps at rates of 101 to 125 mv/sec. At slower rates, when the electrode is closer to steady-state conditions, the peaks are also reproducible. They are sharper and smaller with respect to the magnitude of both potential and current density. This is inherent in the potentiodynamic technique and consistent with the mechanism of oxidation discussed below.

Whereas the (110) and (111) crystals are believed to have single crystal structure there was some indication that the (100) crystal contained subgrain boundaries representative of some surface disorder. This may explain the shape of the low-voltage peak, which contained a shoulder in the case of a fast sweep (Fig. 10a, voltage rate 150 mv/sec). This peak could be resolved into two separate peaks at a slow sweep (Fig. 10b, voltage rate 12.4 mv/sec).

The following measurements were made to see whether a gradual transition of the electrochemical behavior between the two curves shown in Fig. 10 is possible. After polishing the (100) surface an initial sweep was traced from −170 to 380 mv at 12.5 mv/sec. The oscillogram showed a slight peak at 340 mv (see Fig. 11a). This maximum grew slowly on the next two sweeps, not shown in Fig. 11. Then, without re-polishing, the voltage range was increased from −170 to 510 at 10.4 mv/sec, *i.e.*, now the range included the second or "single crystal" peak at 450 mv (Fig. 11b). The next sweep shown in Fig. 11c showed that this peak persisted on recycling al-

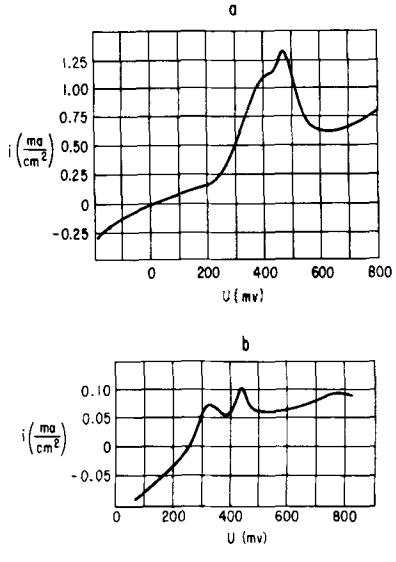

Fig. 10. Current potential curve of formation of $Ni(OH)_2$ on a (100) nickel face in 0.2*N* KOH: (a) sweep rate 150 mv/sec; (b) sweep rate 12.4 mv/sec.

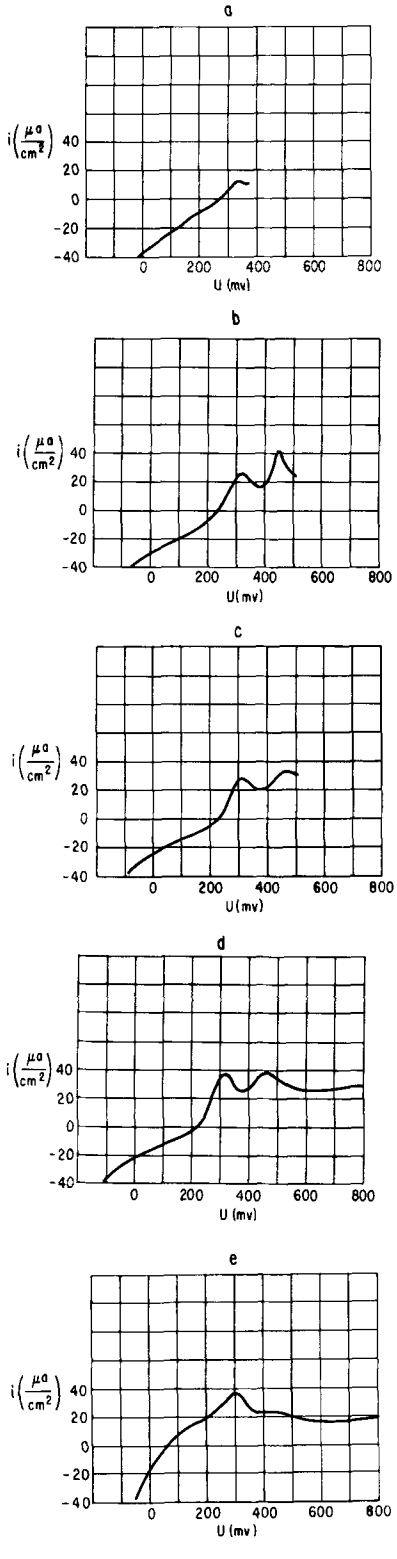

Fig. 11. Current potential curves of a series of anodizing sweeps: (a) initial anodization of (100) surface in 0.2*N* KOH at about 12 mv/sec; (b) fourth sweep in oxidation-reduction cycle without repolishing to higher potential; (c) fifth sweep to the same potential as Fig. 11b; (d) sixth sweep to still higher potential; (e) seventh sweep to the same potential as Fig. 11d.

though it decreased in magnitude. On a further voltage increase from −170 to 880 mv on the next sweep at 12.2 mv/sec (Fig. 11d), both peaks, as well as that of the intermediate range in Fig. 9, showed up. On the following sweep the higher peaks identified as α and β in Fig. 9 disappeared (Fig. 11e). With the sensitive current density scale of Fig. 11 negative currents at low potentials are noticed. This is due to oxygen diffusion, which could not be prevented even in argon-stirred and saturated solution. The experimental difficulties of immersing crystals rapidly into the electrolyte prevented a more elaborate setup needed to suppress oxygen diffusion entirely.[1]

Discussion

The questions regarding the present experiments which may be answered are: (*a*) what is the mechanism of anodization at surfaces of nickel crystals when only a few layers of reaction product are formed under the influence of a linearly increasing potential; (*b*) how do oxygen adsorption and anodization differ on different planes of a single crystal, and (*c*) how long, and under what conditions, are the crystal surfaces maintained?

Mechanism of anodization.—The current-voltage curves consist of at least three separate regions. The low-voltage region (A and A′ in Fig. 9) represents the formation of $Ni(OH)_2$ on the bare Ni surface

$$Ni + 2\,OH^- = Ni(OH)_2 + 2e^-$$

About one monolayer of the hydroxide is formed when the potential α or α' (Fig. 10) is reached. The rate of formation, reflected by the current density, then decreases as the reaction is sustained by the mobility of Ni(II) ions through the hydroxide surface cover.

The intermediate-voltage region (B and B′, Fig. 9) begins when about two layers of $Ni(OH)_2$ are formed. With increasing potential the oxyhydroxide NiOOH is produced

$$Ni(OH)_2 + OH^- = NiOOH + H_2O + e^-$$

This process is sustained by proton diffusion to the hydroxide/solution interface which has been demonstrated by Lukovtsev and Slaidin (8). In the present work it is postulated that in the broad intermediate region this process occurs simultaneously or consecutively with the oxidation of Ni to $Ni(OH)_2$. Thus, under the present experimental conditions, up to a potential of about 1v both Ni(II) ions and protons are mobile, $Ni(OH)_2$ is formed and partially converted to NiOOH in a quasi-solid solution.

Finally, at sufficiently higher potentials Ni is converted directly to NiOOH according to

$$Ni + 3\,OH^- = NiOOH + H_2O + 3e^-$$

At about 1.5v oxygen is evolved. The current resulting from this process masks the small contribution by still higher oxidation of Ni(III) to Ni(IV), for which Lukovtsev and Slaidin (8) give a current efficiency of 1 or 2%.

Oxide formation during transfer of electrode.—In spite of the large experimental error in determining the number of oxide layers the values of Table I still indicate clearly that oxide is formed on nickel crystal planes in the order (110) > (100) > (111). The reactivity is in that order, from least to closest-packed planes. If roughness were taken into account the value for the polycrystalline surface, which is rougher, would be reduced correspondingly.

Crystal structure in anodization.—$Ni(OH)_2$ forms spontaneously (*i.e.*, on open circuit) on nickel single crystals in KOH solution. For this reason crystals must be immersed in the electrolyte at a negative potential. On potentiodynamic oxidation the voltage and extent of surface coverage at which the unique properties of single crystals are lost can be located fairly accurately. This is discussed below. Initially, $Ni(OH)_2$ is formed at different rates on the crystal planes. The location of the $Ni(OH)_2$ peaks α in Fig. 2 and 4 is a rough measure of this varying degree of hindrance of the reaction. The α peaks occur at 480 > 450 > 370 mv for the planes (111) > (100) > (110) in the order of closest to least-packed planes. Experimentally, this is consistent with the above data and also with growth and dissolution rates of some fcc crystals measured by Piontelli (1). This is generally explained by assuming that atoms in the closest-packed planes have maximum bond energies in the plane, minimum for a constituent out of the plane. Hence their residual affinity for oxidation, *e.g.*, for the closest-packed (111) plane, is also a minimum.

Loss of crystal surface structure on anodization.—The most pronounced effect that can be attributed to the structure of the crystal planes is the change of shape in current-voltage curves, from the first anodic sweep (Fig. 7) to the second sweep (Fig. 8). In the second sweep all three crystal planes show the same general shape which is similar to the first sweep of the polycrystalline nickel electrode. The sweeps extend to 1600 mv and encompass 8 to 10 layers of oxide. It is clear that on subsequent reduction the nickel planes are not regenerated but that a disordered surface is formed. It should be mentioned that nickel ions did not go into solution. This was tested by cycling a nickel electrode for several hours, evaporating the electrolytic solution, and analyzing the precipitate by x-ray fluorescence. Nickel could not be detected. For the given experimental conditions the limit of detection was 0.1 ppm.

Knowing that surface structure of the crystals is lost at the end of an anodic sweep, one can locate the change in structure in the potential range at 600-800 mv (corresponding to 3-4 monolayers) where the higher oxidation of Ni to NiOOH comes to the fore. This is illustrated by the series of measurements shown in Fig. 11a to 11e. Cycling at lower voltages up to 380 and 510 mv, respectively, does not influence drastically the location of the α-peak. It is characteristic of the single crystal surface. On going past this potential range the α-peak disappears on the very next sweep. From this we conclude that a single crystal surface of fcc nickel can support, for reasonably short times, a few $Ni(OH)_2$ layers, ordered pseudomorphically on nickel, but not ordered with respect to the hexagonal structure of $Ni(OH)_2$,

[1] Note added in proof: This is not due to oxygen diffusion in the solution. Evidence to that effect is in the process of publication.

although the actual dimensions involved are not far apart. On further oxidation of $Ni(OH)_2$ a drastic irreversible step takes place. This is also indicated by the appearance of the current maximum β in the intermediate voltage region (see Fig. 7 and 9), which occurs only on first sweeps. It may signify a singular transformation of cations in the hydroxide film, of unknown origin, which for that particular potential and history of the oxide film accelerates the rate of oxidation. It is plausible to associate it with a loss of the original surface structure, resulting in a disordered polycrystalline surface, since the β-maximum also appears during the first sweep on the polycrystalline electrode, and disappears on it as well. A related effect may be a general change in electrochemical behavior as a result of aging $Ni(OH)_2$ electrodes observed by Briggs, Stott, and Wynne-Jones (14).

In summary, the potentiodynamic technique is a sensitive tool for the study of surface changes which involve only a few monolayers of reaction products. Using it in anodization of nickel in alkaline solution it was found that there are significant differences in the rate of oxidation of different crystal planes initially, but that after building up only a few layers of hydroxide and oxyhydroxide the crystal surface becomes disordered.

Acknowledgments

The authors wish to thank Mrs. R. K. DiCerbo for electron diffraction analyses and A. Holik for electron microscopic analyses and D. A. Vermilyea for a critical reading of the manuscript.

Manuscript received Sept. 27, 1962; revised manuscript received Dec. 21, 1962. This paper was prepared for delivery before the Boston Meeting, Sept. 16-20, 1962.

Any discussion of this paper will appear in a Discussion Section to be published in the December 1963 JOURNAL.

REFERENCES

1. R. Piontelli, G. Poli, and G. Serravalle, Trans. Symp. Electrode Processes (1959), E. Yeager, Editor, John Wiley & Sons, New York, (1961).
2. A. T. Gwathmey and K. R. Lawless, Symp. Surface Chem. of Metals and Semiconductors (1959), H. C. Gatos, Editor, John Wiley & Sons, New York (1960).
3. K. Huber and B. Bieri, *Helv. Phys. Acta,* **21,** 375 (1948).
4. M. Fleischmann and H. R. Thirsk, *Electrochim. Acta,* **2,** 22 (1960).
5. E. M. Kuchinskii and B. V. Ershler, *Zhur. Fiz. Khim.,* **20,** 539 (1946).
6. E. Jones and W. F. K. Wynne-Jones, *Trans. Faraday Soc.,* **52,** 1260 (1956).
7. P. D. Lukovtsev, Proc. 4th Conf. Electrochem., 1956, Acad. Sci. Moscow (Published 1959).
8. P. D. Lukovtsev and G. J. Slaiden, *Electrochim. Acta,* **6,** 17 (1962).
9. G. W. D. Briggs and W. F. K. Wynne-Jones, *Trans. Faraday Soc.,* **52,** 1276 (1956); *Electrochim. Acta,* **7,** 241 (1962).
10. A. J. Salkind and P. F. Bruins, *This Journal* **109,** 356 (1962).
11. S. U. Falk, *ibid.,* **107,** 661 (1960).
12. B. E. Conway and P. L. Bourgault, *Trans. Faraday Soc.,* **58,** 593 (1962).
13. W. J. M. Tegart, "Electrolytic and Chemical Polishing of Metals," Pergamon Press, New York (1959).
14. G. W. D. Briggs, G. W. Stott, and W. F. K. Wynne-Jones, *Electrochim, Acta,* **7,** 249 (1962).

The Oxidation Behavior of Tantalum at 700°-1000°C

Per Kofstad

Central Institute for Industrial Research, Blindern, Oslo, Norway

ABSTRACT

The oxidation behavior of tantalum has been studied at 700°-1000°C at oxygen pressures ranging from 1 atm to 0.01 Torr O_2. The oxidation involves oxide formation and oxygen dissolution in the metal. The rate of oxygen dissolution is governed by diffusion of oxygen in the tantalum metal. Except for the very initial stage of the oxidation, the weight gain due to oxygen dissolution is of minor importance compared to the total weight gain during oxidation. However, the relative importance of oxygen dissolution increases with decreasing oxygen pressure. The oxide scale consists of Ta_2O_5. At and below 800°C the metallic oxide phase TaO_z is formed at the metal/oxide interface, while above this temperature TaO gradually becomes the intermediate reaction product at the metal/oxide interface. Below 800°C and at the higher oxygen pressures the Ta_2O_5 formation follows a linear rate from the start of the reaction. At about 800°C one begins to observe a change in the oxidation behavior, and at higher temperatures the initial Ta_2O_5 formation is parabolic. The parabolic oxidation is concluded to be governed by a rate-determining diffusion of oxygen through the oxide scale. The parabolic stage is followed by a linear oxidation. The paralinear transition is due to cracking of the protective scale down to the metal/oxide phase boundary, and the subsequent linear oxidation above 800°C is concluded to be determined by the rate of nucleation and growth of Ta_2O_5 on TaO at the metal/oxide interface. The linear oxidation is dependent on oxygen pressure and the pressure dependence is interpreted in terms of an oxygen chemisorption equilibrium prior to the rate-determining part-process. The linear rate of oxidation at 1 atm O_2 exhibits a reversal in the temperature dependence at 700°-750°C. At 100 Torr O_2 the oxidation rate is independent of temperature and at lower pressures the reversal is absent. Above 800°C the linear rate constant increases rapidly with temperature at all oxygen pressures. The reversal in temperature dependence is a result of the change in oxygen pressure dependence associated with the change in the reaction scheme at about 800°C. An additional factor may be a decreased thermal stability of the intermediate reaction product TaO_z with increasing temperature.

Studies of the oxidation behavior of tantalum is of primary importance in evaluating the potentials of this metal as a high-temperature material.

The present work is part of a series of investigations on oxidation of tantalum in the temperature range 300°-1300°C (1-5). The experimental work comprises gravimetric reaction rate measurements coupled with x-ray diffraction, electron microscope, metallographic, and microhardness studies on reacted specimens.

Summaries of previous studies of the tantalum-oxygen system and of oxidation of tantalum and descriptions of the materials and experimental methods employed have been given in previous papers (1, 2).

Experimental Results

Reaction rate measurements.—The studies were made on electron beam melted tantalum. The specimens measured approximately 1.2 x 1.2 x 0.14 cm. Prior to oxidation the specimens were polished and etched (1).

The results of the gravimetric oxidation rate measurements on unannealed tantalum are shown in Fig. 1-6. In all cases the results represent averages of 3 or more (in a few cases as many as 10) different runs. All values were evaluated using the original geometrical dimensions of the specimens.

The effect of oxygen pressure (1 atm to 0.01 Torr) on the rate of oxidation at 800°C is shown in Fig. 1 and 2, at 900°C in Fig. 3 and 4, and at 1000°C in Fig. 5 and 6. At higher oxygen pressures oxidation was followed for relatively short periods of

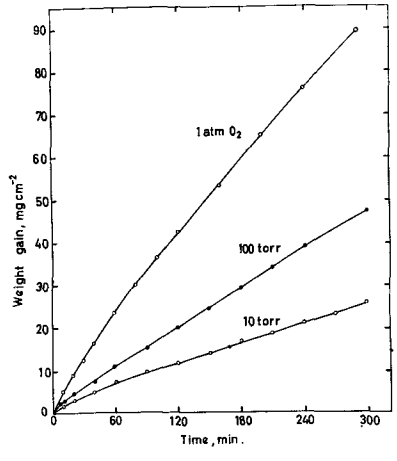

Fig. 1. Effect of oxygen pressure on the oxidation of tantalum at 800°C.

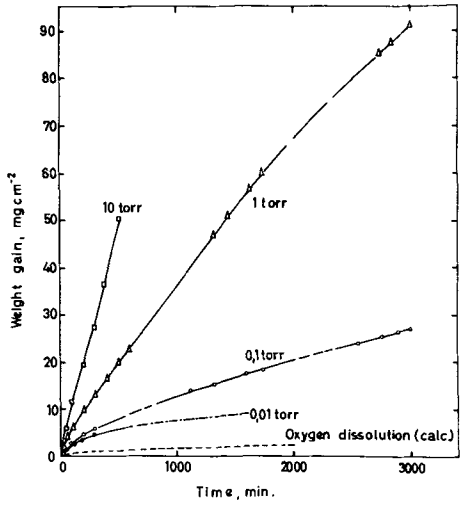

Fig. 2. Effect of oxygen pressure on the oxidation of tantalum at 800°C.

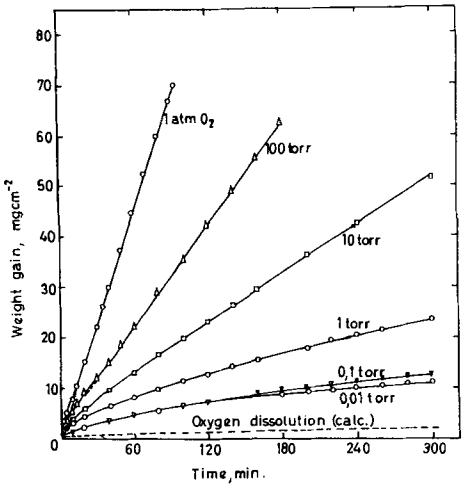

Fig. 3. Effect of oxygen pressure on the oxidation of tantalum at 900°C.

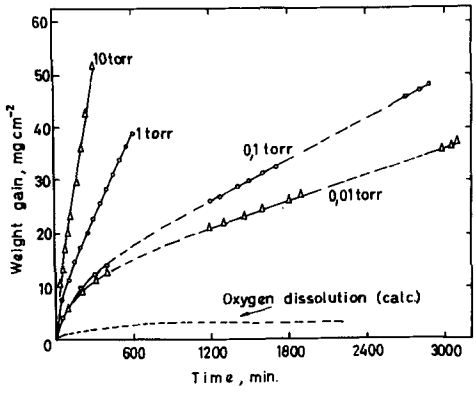

Fig. 4. Effect of oxygen pressure on the oxidation of tantalum at 900°C.

time due to the rapid oxidation. At lower oxygen pressures it was necessary to follow the oxidation for periods up to 3 days in order to get a good description of the kinetics.

Measurements were also made at a few oxygen pressures at 750°, 850°, and 950°C. The results of corresponding studies on the oxidation behavior as a function of oxygen pressure in the temperature

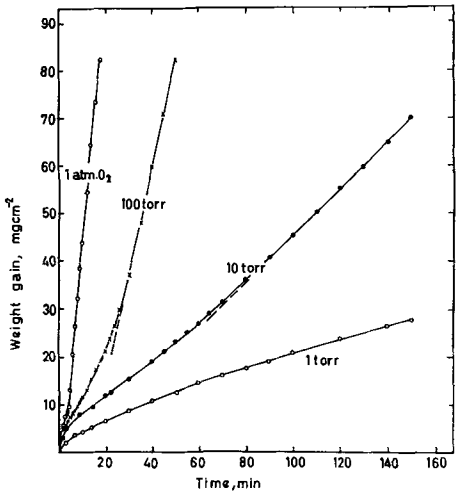

Fig. 5. Effect of oxygen pressure on the oxidation of tantalum at 1000°C.

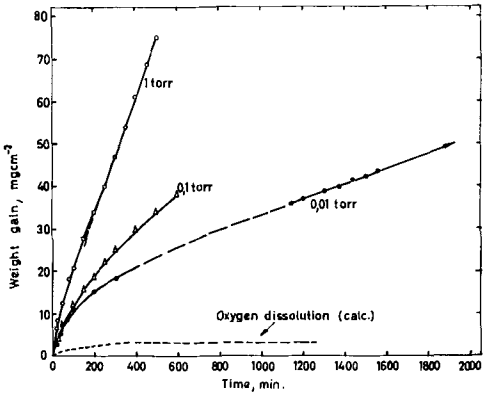

Fig. 6. Effect of oxygen pressure on the oxidation of tantalum at 1000°C.

range 500°-700°C have been published previously (1).

At 700°C the oxidation (Ta_2O_5 formation) follows, within the limits of error, a linear rate from the start of the reaction at the higher oxygen pressures (1). In the present study the same behavior was also observed at 750°C. However, at about 800°C a change in the kinetics begins to take place, and at higher temperature the initial oxidation conforms with a parabolic-type behavior. This is seen in Fig. 7 and 8, in which the initial oxidation at 900° and 1000°C has been plotted parabolically

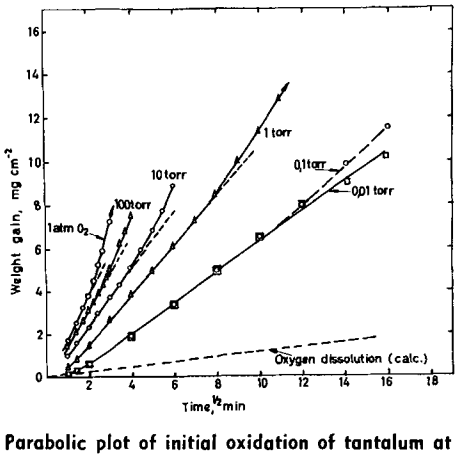

Fig. 7. Parabolic plot of initial oxidation of tantalum at 900°C

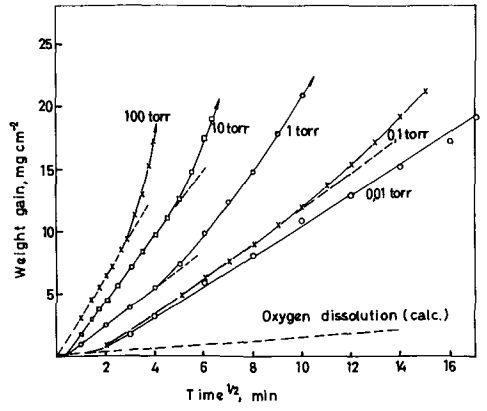

Fig. 8. Parabolic plot of initial oxidation of tantalum at 1000°C

(weight gain *vs.* square root of time). In general the duration of the parabolic oxidation becomes longer with decreasing oxygen pressure and with increasing temperature.

The initial parabolic oxidation is followed by an approximately linear oxidation. At higher oxygen pressures at 900° and 1000°C this transition from parabolic to linear oxidation exhibits a breakaway-type behavior (Fig. 3 and 5), while at the lower oxygen pressures one observes more gradual transitions.

Reproducibility during parabolic oxidation was relatively good and may be estimated to be within 15%. However, the reproducibility of the linear oxidation was relatively poor. Despite careful preparations of specimens and control of experimental conditions, the reproducibility was under some conditions only within 50%. This poor reproducibility was particularly marked at the higher oxygen pressures at 800°-850°C and 1000°C.

X-ray studies.—The oxide scales were in all cases found to consist of the low-temperature modification of tantalum pentoxide, β-Ta_2O_5. This oxide is isomorphous with the low-temperature modification of niobium pentoxide, γ-Nb_2O_5.

Diffractograms of powdered oxide scales gave reflection lines which were in excellent agreement with the published data for β-Ta_2O_5. At 600°-800°C the reflection lines became somewhat sharper with increasing temperature.

Diffractograms directly on the scales indicated oriented growth of the scale. The β-Ta_2O_5 at the metal/oxide interface proved to be strongly oriented. If β-Ta_2O_5 is indexed on the basis of a pseudohexagonal unit cell, the results suggest a preferred orientation where the hexagonal axis lies parallel to the metal surface.

At 700°C and below the metallic oxide phase, TaO_z, is formed at the metal/oxide interface (1, 2, 4, 5). TaO_z was also detected at the metal/oxide interface on specimens oxidized at 800°C. It appeared that the amount of TaO_z was larger in specimens oxidized at the lower oxygen pressures.

On specimens oxidized at 900°C traces of TaO_z could in some cases be detected after oxidation at the lower oxygen pressures. In some cases additional reflections which indicate the presence of TaO were observed. However, the presence of TaO could not be established in all specimens and particularly those which were oxidized at the higher oxygen pressures.

Table I. Tantalum lattice parameter at metal/oxide interface, in Å

Temp, °C	p_{O_2}, torr	Time, min	(321)	(222)
800	0.01	300	3.317	
800	0.1	300		3.317
800	1	300		3.313
900	0.01	300	3.317	
900	0.1	300		3.317
1000	0.01	300		3.316

At 1000°C TaO_z was not detected. Presence of TaO was established by measurements on the oxidized surface in specimens oxidized for short periods of time ($< \sim 20$ min) at low oxygen pressures. But on specimens with relatively large amounts of Ta_2O_5 it was in general difficult to ascertain the presence of TaO. The identification of TaO under such conditions was also made difficult by the numerous reflections from Ta_2O_5.

The above examinations were all made on specimens cooled in the oxidation apparatus by lowering the furnace from the reaction zone. By quenching oxidized specimens in Octoil (diffusion pump oil) it was in many cases easier to detect TaO. This may suggest that TaO has a decreased thermal stability at lower temperature.

From these studies it is concluded that TaO is present at the metal/oxide interface in trace or small amounts above 800°C, and that TaO is an intermediate oxidation product in the reaction scheme at such temperatures.

Oxidation of tantalum also involves dissolution of oxygen in the metal. In order to estimate the concentration of oxygen at the metal/oxide interface, determinations of the lattice parameter were made after removing and polishing off the scale. Results of the lattice parameter determinations are shown in Table I. The lattice parameters were determined from the (321)- and (222)-reflections using nickel-filtered copper radiation.

The parameter determined on the surface of unoxidized tantalum was 3.306Å. Thus an appreciable increase in the lattice parameter takes place during oxidation. By comparison with the results of Gebhardt and Seghezzi (6) and Vaughan, Stewart, and Schwartz (7), who determined the changes in lattice parameter with oxygen content, it follows that values of 3.313-3.317Å correspond to oxygen concentrations of 2.2-3.0 (7) or 2.8-3.6 at. % oxygen (6).

Surface appearance of oxidized specimens.—Specimens oxidized at 800°C had a white and porous oxide scale. After prolonged oxidation the β-Ta_2O_5 scale had a flakelike appearance. After cooling to room temperature the scale was easily detached from metal, and the exposed metal was covered in spots by white oxide.

With increasing temperature the oxide appeared to become more sintered. Concurrently the oxide exhibited pronounced cleavages at the edges, thereby causing raised oxide edges. This is also charac-

teristic of niobium specimens oxidized under similar conditions (8). The raised oxide edges were white, while the oxide closer to the center had more grayish color. The oxide also adhered better to the metal at the center of the surface. With decreasing oxygen pressure the oxide tended to have darker color; however, after prolonged oxidation the oxide edges tended to become white.

Electron microscope studies.—The oxide surface of a few specimens was examined by electron microscope techniques (1). In general the surface had a very uneven appearance and exhibited a large number of cracks. The surface appeared more sintered at 1000° than at 800°C. Examples of oxide surfaces after oxidation at 800° and 1000°C are shown in Fig. 9 and 10, respectively. In a few cases oxide whiskers also appeared on the surface.

Metallographic studies.—Studies of metallographic cross sections of oxidized tantalum specimens indicated that the oxide scales were porous after extended oxidation at all oxygen pressures from 1 atm to 0.01 Torr O_2. This is shown in Fig. 11-15, which represent various examples of the metallographic observations. The apparent porosity is larger the higher the oxygen pressure. Under such conditions the oxide scales were also often exfoliated and broken up and adhered poorly to the metal (Fig. 15). Specimens oxidized for short periods corresponding to the initial parabolic period had well adhering scales, and the scale thickness agreed to within 10-15% of the thickness calculated from observed weight gains when assuming theoretical density for Ta_2O_5.

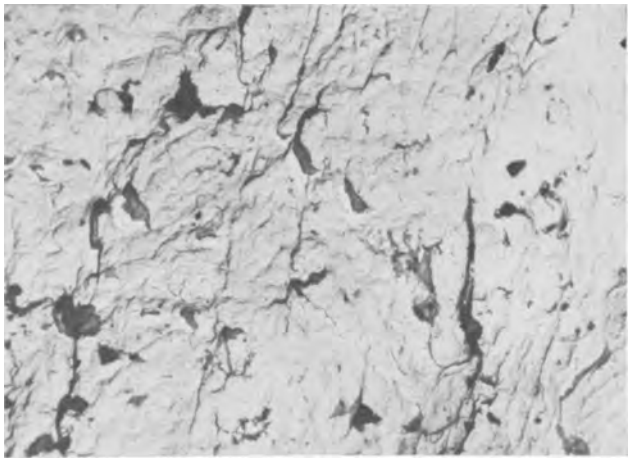

Fig. 9. Electron micrograph (replica) of oxide surface after oxidation of tantalum for 75 min at 800°C and 1 atm O_2. Magnification approximately 2730X.

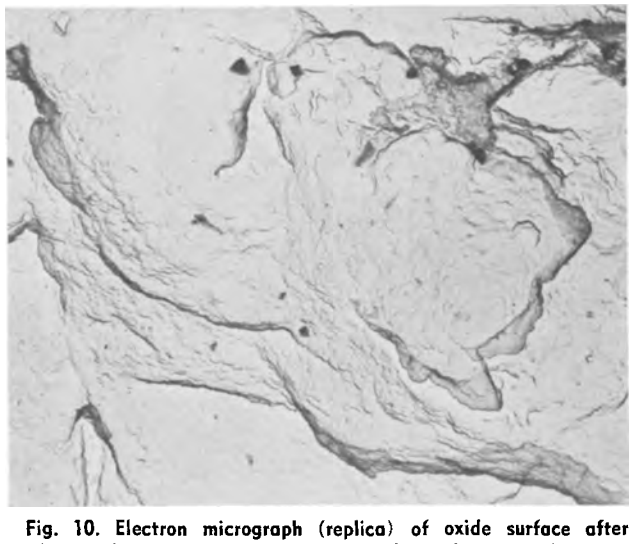

Fig. 10. Electron micrograph (replica) of oxide surface after oxidation of tantalum for 50 min at 1000°C and 10 Torr O_2. Magnification approximately 10,500X.

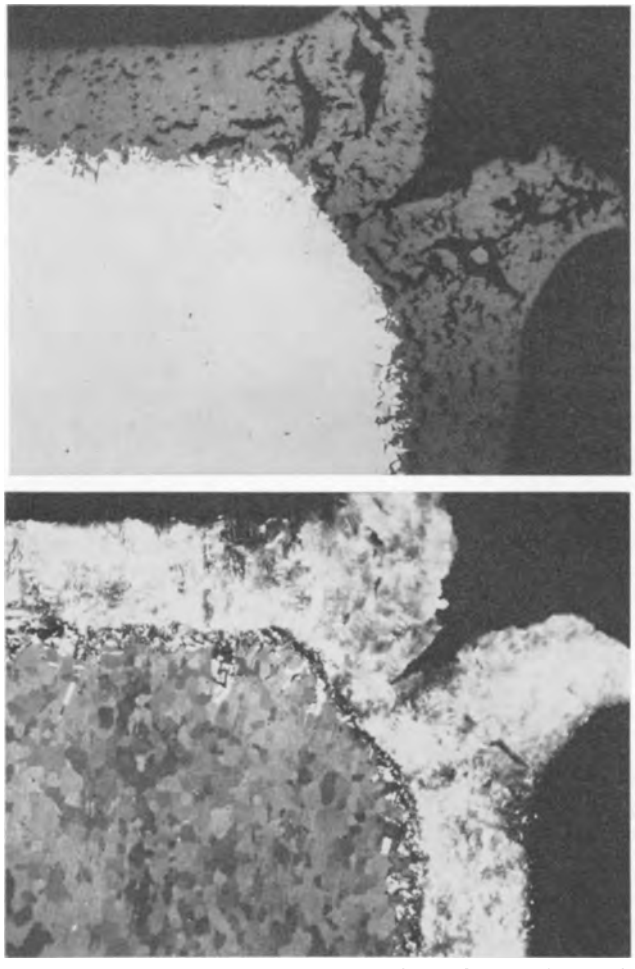

Fig. 11. Metallographic cross section of tantalum specimen oxidized for 1620 min at 900°C and 0.01 Torr O_2. Magnification approximately 120X. (a) (top) Vertical illumination; (b) (bottom) polarized light.

There was no pronounced occurrence of an inner compact oxide barrier with a thickness corresponding to that of the weight gain at the end of the parabolic oxidation. When examining the cross sections in polarized light, the oxide at the metal/oxide interface in some cases appeared to have a structure or orientation different from that of the bulk oxide (Fig. 11b). This may indicate either that the pentoxide is heavily oriented at the metal/oxide interface (see section on x-ray diffraction) or it may reflect the presence of TaO.

The cross sections showed an uneven oxidation of the metal surface. This became increasingly pronounced the longer the time of oxidation and was also characterized by an oxide growth into the metal and an internal oxidation (Fig. 11-15). In unannealed specimens the oxide penetration into the metal preferentially occurred along the rolling direction (Fig. 14 and 15). The internal oxidation, oc-

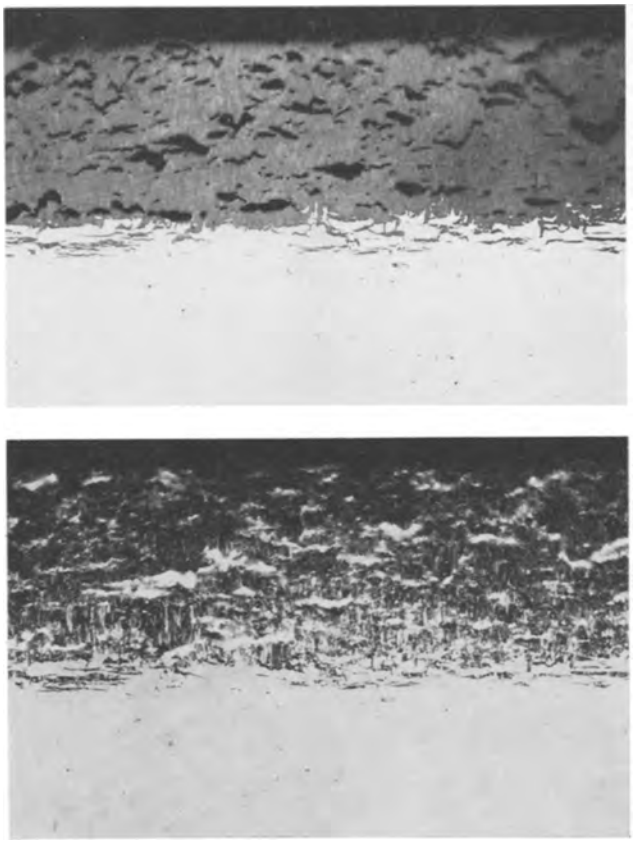

Fig. 12. Metallographic cross section of tantalum specimen oxidized for 2300 min at 900°C and 0.01 Torr O_2. Magnification approximately 120X. (a) (top) Vertical illumination; (b) (bottom) polarized light.

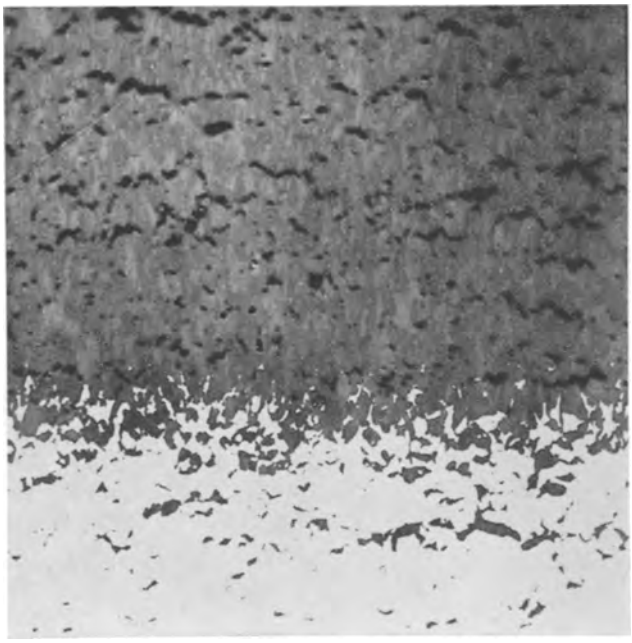

Fig. 13. Metallographic cross section of tantalum specimen oxidized for 3000 min at 1000°C and 0.01 Torr O_2. Magnification 150X.

curring after longer periods of oxidation, was characterized by apparently isolated oxide particles in a zone beneath the surface oxide (Fig. 11-13).

The oxidized specimens showed a preferred oxidation of the edges of the specimens, and this resulted in a rounding off of the originally square edges of

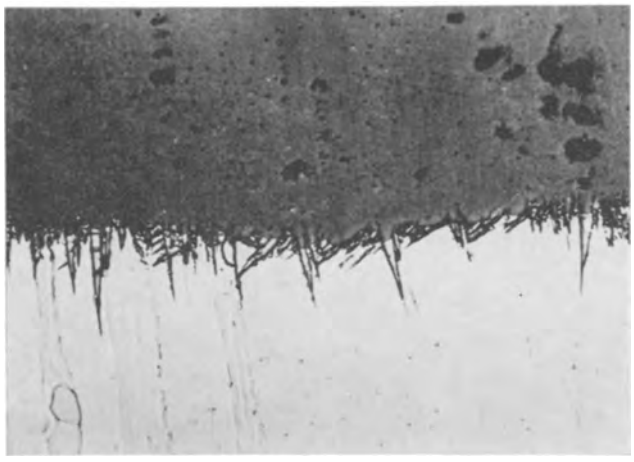

Fig. 14. Metallographic cross section of tantalum specimen oxidized for 30 min at 1000°C and 0.01 Torr O_2. Magnification approximately 550X.

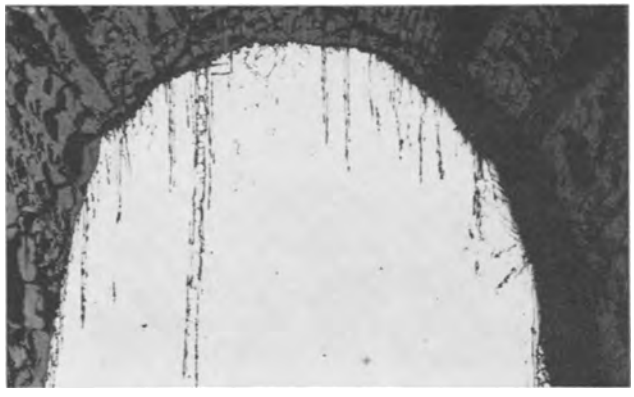

Fig. 15. Metallographic cross section of tantalum specimen oxidized for 300 min at 1000°C and 10 Torr O_2. Magnification approximately 80X.

the specimens (Fig. 11 and 15). This preferred oxidation is believed to reflect that oxide formation takes place at the metal/oxide interface following a saturation of an outer layer of the metal with oxygen. The very edges become saturated faster with oxygen due to the simultaneous diffusion from the intersecting surfaces, and this causes a faster oxidation at such places.

Microhardness studies.—Gebhardt and Seghezzi (6) have shown that the microhardness of tantalum increases almost linearly with increasing oxygen content. Microhardness traverses on metallographic cross sections may therefore by used to study the diffusion and dissolution of oxygen during oxidation of tantalum.

The results of microhardness measurements of tantalum specimens oxidized for various lengths of time at 800°C at oxygen pressures of 0.1 Torr and 1 atm are shown in Fig. 16 and 17. An appreciable oxygen penetration takes place, and the penetration relative to the metal/oxide interface increases with time.

Discussion

Tantalum exhibits a complex oxidation behavior. In the temperature range 700°-1000°C the total oxidation reaction is composed of several part-processes which include oxygen dissolution in the metal and oxide (TaO_z, TaO, and Ta_2O_5) formation. For an elu-

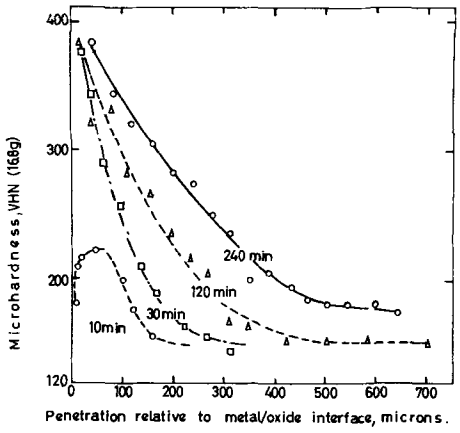

Fig. 16. Microhardness traverses on tantalum specimens oxidized for different lengths of time at 800°C and 0.1 Torr O_2.

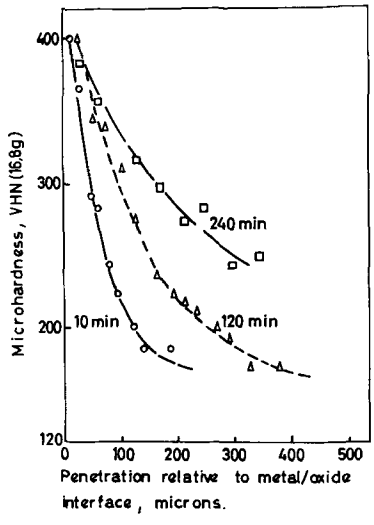

Fig. 17. Microhardness traverses on tantalum specimens oxidized for different lengths of time at 800°C and 1 atm O_2.

cidation of the oxidation mechanism it is necessary to estimate the relative importance of these part-processes.

Dissolution of oxygen in tantalum during oxidation.—From the lattice parameter determinations it is found that the oxygen content in the metal at the metal/oxide interface amounts to 2.2-3.0 at. % at 800°-1000°C. The maximum solubility of oxygen in tantalum as determined by Vaughan *et al.* (7) increases from about 2.8 at. % at 800°C and close to 3 at. % at 1000°C. Thus at these temperatures it is concluded that the oxygen concentration at the metal oxide interface is equal to the solubility limit. This is also to be expected thermodynamically.

During oxidation at temperatures below 700°C the oxygen concentration at the metal surface has in cases been found to be 5-7 at. % (1, 2), and thus it appears that the solubility limit has been exceeded in such cases. However, the measured solubilities at high temperatures refer to equilibria with Ta_2O_5 (7), while the large oxygen concentration at the metal surface has been found only during oxidation when the main reaction product has been TaO_z and when little or no Ta_2O_5 has been present on the metal surface. Thus the large oxygen concentration probably pertains to an "equilibrium" of Ta-O solid solution with TaO_z. This again infers that TaO_z is metastable. In this connection it should also be noted that small supersaturations of oxygen in tantalum are necessary to initiate oxide nucleation.

From internal friction measurements the diffusion coefficient of oxygen in tantalum has been determined to be $D = 0.01 \exp(-27{,}700/RT)$ (9). This value also adequately describes diffusion of oxygen in tantalum during oxidation at and below 700°C (1, 2).

The mean square displacement during diffusion as a function of time, t, is given by $\bar{x} = \sqrt{Dt}$. Using the above value for D, the value of $\bar{x}$ after 30 min at 800°C is calculated to be 64μ. This value may be compared with the penetration distances observed in the microhardness measurements (Fig. 16). One obtains satisfactory agreement between calculated and experimental values, and the above value for D will thus also be used to describe diffusion of oxygen in tantalum at 700°-1000°C.

By combining the solubility and diffusion data the weight gain due to oxygen diffusion alone may be estimated. The amount of material diffusing into a semi-infinite specimen is given by the equation (10)

$$n = 1.1284 \sqrt{Dt}\,(c_s - c_o) \qquad [1]$$

c_s represents the oxygen concentration at the metal surface, *i.e.*, the maximum solubility of oxygen in tantalum at the particular temperature, and c_o is the oxygen impurity content in the unoxidized material [0.006 at. % oxygen (1)].

Using the solubility limits determined by Vaughan *et al.*, calculated weight gains (Eq. [1]) due to oxygen dissolution alone at 800°, 900°, and 1000°C are shown as broken curves in Fig. 2 to 4 and 6 to 8. In estimating the contribution of oxygen dissolution it has been neglected that some of the metal is consumed by oxide formation. Furthermore, the curves have not been corrected for the fact that the oxygen penetration reaches the middle of the specimen during the later stages of the reaction. Such saturation effects decrease the concentration gradient and slow down the rate of oxygen dissolution.

From the calculated values it is seen that oxygen dissolution is of minor relative importance compared to the total weight gain. However, the oxide formation has a large oxygen pressure dependence (see later section), while oxygen dissolution may be considered independent of oxygen pressure as long as oxide is present on the surface. Consequently the relative importance of oxygen dissolution increases with decreasing oxygen pressure. This is also clearly evident from Fig. 2 to 4 and 6 to 8.

It should of course be borne in mind that, although the weight gain due to oxygen dissolution is relatively small, the oxygen penetration is quite rapid. Figures 16 and 17 show that oxygen penetration relative to the metal/oxide interface is approximately the same at 1 atm and 0.1 Torr O_2 at 800°C and this shows that oxygen penetration into the metal is much faster than the rate of metal consumption through oxide formation. At 900° and 1000°C the specimens also become saturated with

oxygen within the time period of the experiments (Fig. 4 and 6). Dissolved oxygen greatly affects the mechanical properties of the metal, and thus with regard to using tantalum for constructional purposes, oxygen dissolution is an important part-process.

Although the weight gain due to oxygen dissolution in general is of minor importance, the dissolution process is the predominant part-process during the very initial stage of the oxidation (Fig. 7 and 8). This feature becomes more marked with decreasing oxygen pressure as has also previously been shown by Gebhardt and Seghezzi (11). Thermodynamically it is also to be expected that oxygen dissolution and saturation of an outer layer of the metal precedes oxide formation, as the free energy of formation of tantalum-oxygen solid solutions is larger than that of the oxides. The higher free energy of the solid solutions is evidenced by the well-known fact that thin oxide films on tantalum metal are dissolved in the metal during heat treatment in high vacuum.

Oxide formation.—As shown in the proceeding section oxide formation is responsible for the main weight gain during oxidation at 700°-1000°C. The oxide scale consists of β-Ta_2O_5. Traces or small amounts of TaO_z and TaO may be detected at the metal/oxide interface depending on the temperature.

At 700°C and below the oxidation has been found to involve the following reaction scheme (1)

$$Ta + O_{chem.} \rightarrow Ta—O \text{ sol. sol'n} \rightarrow TaO_y \rightarrow TaO_z \rightarrow Ta_2O_5 \quad [2]$$

TaO_y is formed predominantly below about 500°C (1, 2, 4, 5). TaO_z grows as platelets parallel to {320} sets of planes of the metal (5, 12), and the platelets extend into the metal from the surface (1, 2, 4, 5). Ta_2O_5 grows on the TaO_z platelets, and the rate-determining reaction is interpreted to involve nucleation and growth of Ta_2O_5 nuclei (1). The Ta_2O_5 layer is very porous and has no protective properties, and within the limits of error of the measurements the Ta_2O_5 formation follows a linear rate from the start of the reaction at the higher oxygen pressures.

At about 800°C one begins to observe a change in the reaction mechanism. At higher temperature the initial oxidation conforms with a parabolic rate which is subsequently followed by a linear rate. At the same temperature the amount of TaO_z at the metal surface becomes smaller. In addition, at 900°-1000°C traces or small amounts of TaO are observed at the metal/oxide interface. These results are concluded to reflect gradual change in the reaction scheme with increasing temperature from Eq. [2] to

$$Ta—O \text{ sol. sol'n} \rightarrow TaO \rightarrow Ta_2O_5 \quad [3]$$

This proposed reaction scheme thus suggests that TaO_z becomes less thermally stable and/or that the formation of Ta_2O_5 through TaO becomes a faster reaction with increasing temperature.

Parabolic oxidation.—Figures 7 and 8 show that the initial oxidation conforms with a parabolic behavior. The parabolic rate curves do not extrapolate back to zero time, but are preceded by an incubation period, which becomes longer with decreasing oxygen pressure. This incubation period involves oxygen dissolution in the metal, TaO formation, and the initial nucleation of Ta_2O_5.

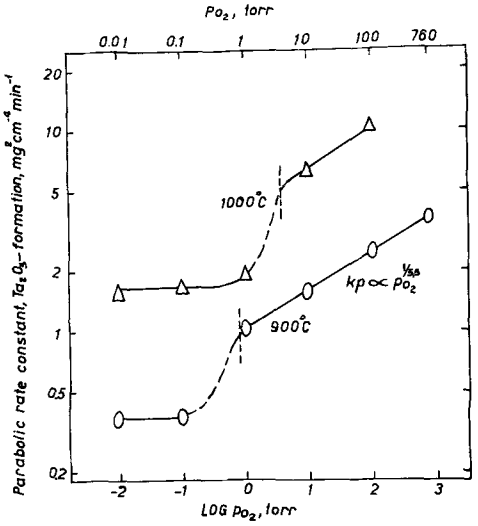

Fig. 18. Parabolic rate constant for initial Ta_2O_5 formation at 900° and 1000°C as a function of oxygen pressure.

The parabolic oxidation probably reflects a Wagner-type oxidation mechanism. Judging from the growth of the Ta_2O_5 scale and as small scratches on the unoxidized metal can be clearly observed on the oxide surface, it is concluded that oxygen ions are the faster moving ionic species. The same conclusions have been drawn by Albrecht *et al.* (13).

The formation of an initially compact Ta_2O_5 scale above 800°C may be due to two factors: (i) TaO facilities the formation of a more continuous, compact layer of Ta_2O_5. This is in contrast to formation of Ta_2O_5 on TaO_z platelets at lower temperatures which results in more isolated Ta_2O_5 nuclei and a porous scale (1, 2). (ii) Higher temperatures results in increased sintering of the oxide scale.

By subtracting the estimated weight gain due to oxygen dissolution from the total weight gain, the contribution due to oxide formation is obtained (Fig. 7 and 8). In Fig. 18 the values for the parabolic rate constant for Ta_2O_5 formation at 900° and 1000°C have been plotted as a function of oxygen pressure. At 900°C the parabolic rate constant is proportional to $p_{O_2}^{1/5.5}$ at and above 1 Torr O_2. In going from 1 to 0.1 Torr O_2 one observes a relatively large drop in the value of the parabolic rate constant, and at 0.1 Torr O_2 the parabolic rate constant is essentially independent of oxygen pressure. At 1000°C a similar change in oxygen pressure dependence takes place between 10 and 1 Torr O_2. This change in oxygen pressure dependence is probably related to the defect structure of Ta_2O_5.

The defect structure of Ta_2O_5 has been studied by measurements of the electrical conductivity as a function of the partial pressure of oxygen (14). Ta_2O_5 exhibits p-type conductivity at pressures close to 1 atm O_2 and n-type conductivity at lower oxygen pressures. From these studies it has been concluded that Ta_2O_5 has an anti-Frenkel defect structure involving interstitial oxygen ions (p-

type) and oxygen vacancies (n-type). At 900° and 1000°C the transition from p- to n-type conductivity takes place at about 0.8 and 3.5 Torr O_2, respectively. Transition pressures are indicated by broken vertical lines in Fig. 18.

The semiconducting properties of the Ta_2O_5 scale should, on this basis, be dependent on the oxygen pressure. At oxygen pressures lower than that of the p-n transition the oxide scale should consist of n-type Ta_2O_5, while at higher oxygen pressures an outer part of the scale should be predominantly p-type oxide, while an inner part should be n-type Ta_2O_5.

According to the Wagner theory, parabolic oxidation involving the formation of n-type oxide is essentially independent of oxygen pressure, while when p-type oxide is formed, the parabolic rate constant is proportional to $p_{O_2}^{1/n}$, where the value of n is given by the defect structure of the oxide. As seen in Fig. 18 a change in the oxygen pressure dependence of the parabolic rate constant takes place at oxygen pressures close to those of the p-n transition, and the observed oxygen pressure dependence is in agreement with the Wagner theory. It is to be noted that a gradual transition in the oxygen pressure dependence is expected corresponding to a gradual change in the defect structure.

In terms of the above interpretation transport of oxygen through the compact Ta_2O_5 scale predominantly occurs *via* vacancies at 0.1 and 0.01 Torr O_2 at 900°C, while at 1 Torr O_2 and above the transport of oxygen in addition takes place through interstitial positions in an outer layer of the oxide. The drop in the value of the parabolic rate constant at the transition suggests that the rate of diffusion of oxygen vacancies is slower than that of interstitial oxygen.

An Arrhenius plot of the parabolic rate constant at 0.1 and 10 Torr O_2 is shown in Fig. 19. At both oxygen pressures the activation energy is about 45 kcal/mole. If vacancy diffusion is the slower process, as suggested above, it is reasonable that the activation energies are the same at the two pressures. In the same terms, the activation energy corresponds to that for vacancy diffusion.

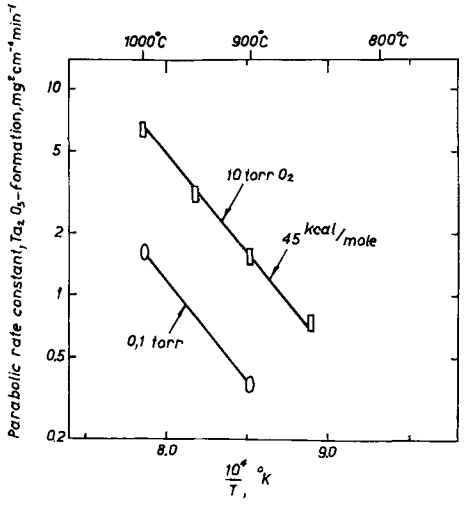

Fig. 19. Arrhenius plot of the parabolic rate constant for initial Ta_2O_5 formation during oxidation of tantalum.

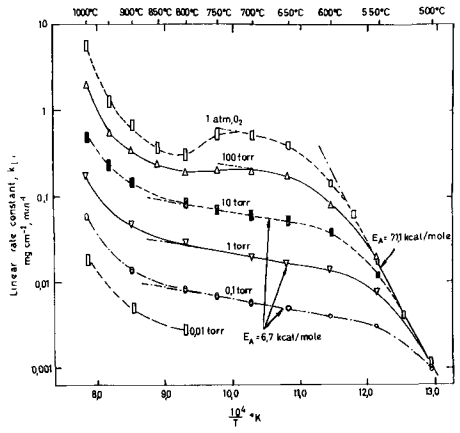

Fig. 20. Arrhenius plot of the linear rate constant at 1 atm, 100, 10, 1, 0.1, and 0.01 Torr O_2 during oxidation of tantalum.

Linear oxidation.—At the higher oxygen pressures below 800°C the oxidation, which reflects Ta_2O_5 formation on TaO_z, is linear from the start of the reaction. Above 800°C the oxidation is initially parabolic, but this is subsequently followed by a linear oxidation. Under the latter conditions TaO also becomes the intermediate reaction product (Eq. [3]).

An Arrhenius plot of the linear rate constant at 1 atm, 100, 10, 1, 0.1, and 0.01 Torr O_2 at 700°-1000°C is shown in Fig. 20. Results at 500°-700°C (1) are also included in the plot to give a more over-all description of the oxidation behavior of tantalum.

Figure 20 shows that at 1 atm O_2 a reversal in the temperature dependence takes place at about 700°-750°C. At 100 Torr O_2 the rate constant is essentially independent of temperature, and at 10 Torr O_2 and below no reversal takes place. At all pressures the linear rate constant increases rapidly with temperature above 800°C.

Figure 21 shows a plot of the linear rate constant as a function of oxygen pressure. At 700° and 1000°C the linear rate constant is proportional to $p_{O_2}^{1/2}$ over the pressure range 1 atm — 0.01 Torr

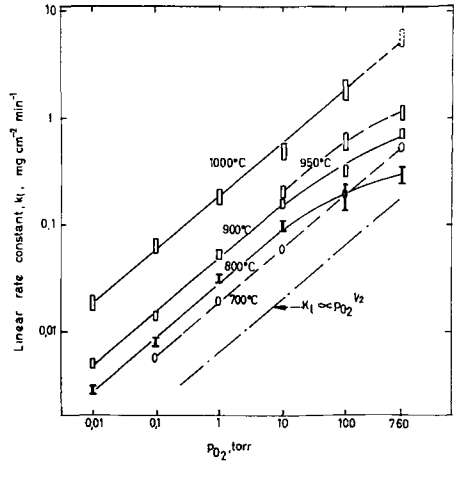

Fig. 21. The linear rate constant of oxidation of tantalum at 700°-1000°C as a function of oxygen pressure.

O_2. The same relationship applies to intermediate temperature at 10 Torr O_2 and lower pressures, but at 10-750 Torr O_2 the linear rate constant is less dependent on oxygen pressure. By comparing Fig. 20 and 21 it is seen that the reversal in temperature dependence at 1 atm O_2 also may be considered to arise from differences in the oxygen pressure dependence above 10 Torr O_2.

At and below 750°C the linear oxidation is interpreted as a rate-determining nucleation and growth of Ta_2O_5 on TaO_z platelets (1). The linear rate constant below 750°C is given by

$$k_l = \frac{ak_2 K \cdot p_{O_2}^{1/2}}{(RT)^{1/2} + Kp_{O_2}^{1/2}} \quad [4]$$

The oxygen pressure dependence is explained by assuming an oxygen chemisorption equilibrium prior to the rate-determining reaction (1). K denotes the chemisorption equilibrium constant for chemisorption of oxygen on TaO_z, a is the number of chemisorption sites, and k_2 the rate constant for the rate-determining reaction. According to this relationship k_l is approximately proportional to $p_{O_2}^{1/2}$ at low oxygen pressure and/or high temperature, while at low temperatures and/or high oxygen pressures the Ta_2O_5 formation is approximately independent of oxygen pressure. As indicated in Fig. 20 and as discussed in detail elsewhere (1), the activation energy for the linear oxidation below 750°C is equal to 6.7 kcal/mole when $k_l \propto p_{O_2}^{1/2}$ and equal to 71.1 kcal/mole when k_l is independent of the oxygen pressure.

Above 800°C the linear oxidation follows an initial parabolic stage. The paralinear transition may be due to (i) a breakdown of the protective scale through cracking due to stresses in the oxide scale or (ii) a linear depletion of a compact barrier layer into an outer porous layer (15).

The paralinear transition for tantalum at 800°-1000°C is best described by alternative (i). The transition to linear oxidation exhibits a breakaway-type behavior which is consistent with alternative (i) but inconsistent with alternative (ii). A breakdown of the protective scale through cracking due to mechanical stresses is not unreasonable when considering that the molar volume ratio of $1/2Ta_2O_5/Ta$ is 2.31. Presence of mechanical stresses in the scale is furthermore evidenced by the cleavages at the oxide edges. A mechanical cracking mechanism also explains the relatively poor reproducibility for the linear oxidation. A further evidence for the cracking mechanism is that the metallographic examination of specimens oxidized well into linear stage suggest porous scales with no evidence of an inner compact barrier as required by alternative (ii). As to the latter argument it is of course realized that the appearance of the oxide scale may change during cooling to room temperature and that the metallographic cross section may not represent the true status during oxidation.

The duration of the parabolic stage becomes longer and in general the weight gain at the paralinear transition also becomes larger with decreasing oxygen pressure. In terms of a mechanism involving cracking of the scale, this behavior is interpreted as a result of plastic flow in the oxide. One would expect the oxide to have more time to alleviate stresses through plastic flow at the lower oxygen pressures when the reaction rates are smaller, and consequently the onset of cracking would occur during later stages at lower oxygen pressures. Plastic flow may also be affected by differences in the amount of ionic disorder with oxygen pressures.

The linear oxidation after the onset of cracking and loss protective properties reflects a rate-determining part-process which either involves (*a*) formation, e.q. nucleation, and growth of Ta_2O_5 on TaO, or (*b*) diffusion through a thin, inner compact scale with an approximately constant thickness.

On the basis of the observed oxygen pressure dependence (at 1000°C $k_{lin} \propto p_{O_2}^{1/2}$ over an oxygen pressure range of almost 5 powers of ten) it is difficult to explain the reaction in terms of alternative (*b*). Thus if the oxygen pressure dependence reflects a chemisorption equilibrium prior to the rate-determining part-process, alternative (*b*) would infer that the thickness of the inner compact film is approximately constant at all oxygen pressures. This appears unlikely. In terms of alternative (*b*) one would also expect to observe effects of the change of defect structure of Ta_2O_5 associated with p-n transition on the linear rate of oxidation. Such effects are not observed. It is therefore concluded that the rate-determining part-process during the linear oxidation involves the formation, e.q. nucleation and growth of Ta_2O_5 on TaO.

The linear oxidation above 800°C is thus interpreted to involve a repetitive, continuous, and probably statistically distributed cracking of the scale down to the metal whereby the metal/oxide interface beneath the cracks is exposed to oxygen. Oxygen chemisorbs on active sites (TaO) and subsequently takes part in the rate-determining part-process. This mechanism also explains the uneven oxidation of the metal surface which is observed in the metallographic cross sections of oxidized tantalum specimens.

The proposed mechanism may be described by the equations

$$\text{site} + 1/2\ O_2^{(g)} \overset{K_1}{\longleftrightarrow} O_{chem} \cdot \text{site} \quad [5]$$

$$O_{chem} + TaO \xrightarrow[k_3]{\text{rate-determining}} Ta_2O_5 \quad [6]$$

Equations [5] and [6] neglect the oxygen consumed through oxygen dissolution in the metal.

This reaction scheme leads to an expression for the linear rate constant which is identical to Eq. [4], but which contains different values for a, k_2, and K. The difference in the linear oxidation below and above 800°C thus lies in the change of reaction scheme (Eq. [2] and [3], *i.e.*, that Ta_2O_5 is formed *via* TaO_z and TaO below and above 800°C, respectively.

The oxygen pressure dependence above 800°C is thus qualitatively the same as at lower temperature: at high temperatures and/or low oxygen pressures [when $(RT)^{1/2} >> Kp_{O_2}^{1/2}$], the linear

rate constant is proportional to $p_{O_2}^{1/2}$, while at low temperatures and/or high oxygen pressures $[(RT)^{1/2} < Kp_{O_2}^{1/2}]$, the oxidation becomes less dependent on oxygen pressure. This behavior is in accordance with the observed oxygen pressure dependence at and above 800°C (Fig. 21). However, the result does not permit an accurate evaluation for the corresponding values of k_2 and K.

Figure 20 shows that the activation energy of the linear oxidation above 800°C increases with temperature. This is interpreted as a gradual transition in the oxidation mechanism from Eq. [2] to Eq. [3]. In terms of Eq. [4] this means that the number of TaO chemisorption sites gradually increases with temperature at 800°-900°C.

During late stages of the linear oxidation apparently isolated oxide particles appear in a zone beneath the surface oxide. Whether these particles are direct continuations of the surface oxide is difficult to verify experimentally, but theoretically they must at least be connected to the surface oxide through microcracks in the metal. Such cracks in the outer, oxygen-saturated, and brittle layer of the metal may possibly arise from the growth stresses of the oxide.

Reversal in temperature dependence.—On the basis of the proceeding discussion it is concluded that the reversal in temperature dependence at 700°-750°C and 1 atm is primarily a result of the change in oxygen pressure dependence associated with the change in reaction scheme at about 800°C. An additional factor causing such a reversal may be a decreased thermal stability of TaO_z with increasing temperature.

When Ta_2O_5 is formed *via* TaO_z (Eq. [2]), the rate of formation of Ta_2O_5 will not be affected by changes in the stability of TaO_z as long as the metal surface is "saturated" with TaO_z, *i.e.*, when the rate formation of TaO_z is faster than that of Ta_2O_5. This situation is concluded to exist below 750°C. However, if the thermal stability and the rate of formation of TaO_z becomes smaller with increasing temperature, the situation may arise when the concentration of TaO_z begins to affect and limit the oxidation.

The concentration of TaO_z may be described by

$$\frac{d(TaO_z)}{dt} = k_n - k_3 \cdot p_{O_2}^{1/2} \qquad [7]$$

k_n denotes the rate of formation, *i.e.*, the rate of nucleation and growth of TaO_z nuclei from Ta-O solid solutions; k_3 designates the rate of depletion of TaO_z through the formation of Ta_2O_5 which at 700°C is proportional to $p_{O_2}^{1/2}$.

As long as $k_n > k_3 \cdot p_{O_2}^{1/2}$ the metal surface will be "saturated" with TaO_z platelets. If the thermal stability of TaO_z decreases with increasing temperature, k_n will, according to the general theory of nucleation and growth of nuclei, have an associated activation energy which decreases with temperature. Thus as temperature is increased, k_n will eventually become of the same order of magnitude as that of k_3. Under such conditions the metal surface may, depending on the oxygen pressures, no longer be saturated with TaO_z platelets. The total rate of reaction may be determined by the rate of formation of TaO_z, and because of the decreased thermal stability of TaO_z this may result in a reversal in the temperature dependence of the total oxidation reaction.

The occurrence of a reversal will be dependent on the oxygen pressure because of the term $k_3 \cdot p_{O_2}^{1/2}$. At high oxygen pressures the value of $k_3 p_{O_2}^{1/2}$ is large and may therefore cause a reversal; at low oxygen pressures the term $k_3 \cdot p_{O_2}^{1/2}$ will become of minor importance, and under such conditions the metal surface will still be saturated with TaO_z and no reversal will take place. This interpretation is also qualitatively in agreement with the x-ray studies which show larger concentration of TaO_z at the lower oxygen pressures at 800°C.

A qualitatively similar interpretation based on decreased thermal stability of metallic oxide phases of niobium and assuming a rate-determining nucleation and growth of oxide has previously been given to explain a corresponding reversal in the temperature dependence of oxidation of niobium (16). For niobium the reversal takes place at 1 atm O_2 at 600°C, while corresponding reversals are absent below 10 Torr O_2 (8).

Comparison with previous investigations.—Oxidation of tantalum under conditions similar to those of the present study has previously been studied by Peterson, Fassell, and Wadsworth (17) and by Albrecht, Klopp, Koehl, and Jaffee (13).

Petersen *et al.* found tantalum to oxidize linearly at 500°-1000°C at oxygen pressures from ½ to 40.8 atm. The oxidation was interpreted as involving an equilibrium adsorption process preceding the rate-determining step of the linear oxidation. The pressure-dependence was fitted to a Langmuir type-I adsorption isotherm.

Albrecht *et al.* studied the reaction of pure tantalum with oxygen and air at 500°-1300°C. The reaction in pure oxygen at 1 atm was found to follow a linear rate in the range 500°-1250°C. The reaction of tantalum with air at 400°-800°C was initially parabolic and showed a transition to linear oxidation after a time depending on the temperature. At 800°-1400°C linear oxidation only was noted for the reaction in air. The reaction in oxygen at 1000°C followed a square root of pressure dependence.

Cowgill and Stringer (18) studied the pressure dependence of the oxidation of tantalum at 600°-860°C at 760-1 Torr O_2. At sufficiently low pressures the rate was found to depend on the square root of the oxygen pressure.

A comparison between the present results and those of Peterson *et al.* and Albrecht *et al.* is shown in Fig. 22 where the linear rate constant has been plotted as a function of the reciprocal absolute temperature. There is fair agreement between the results of the three different studies. The result of Peterson *et al.* and of Albrecht *et al.* also suggest reversals in the temperature dependence.

Ong has presented two discussions of the oxidation mechanism of tantalum (19, 20). In the first treatment (19), as in the equivalent interpretation

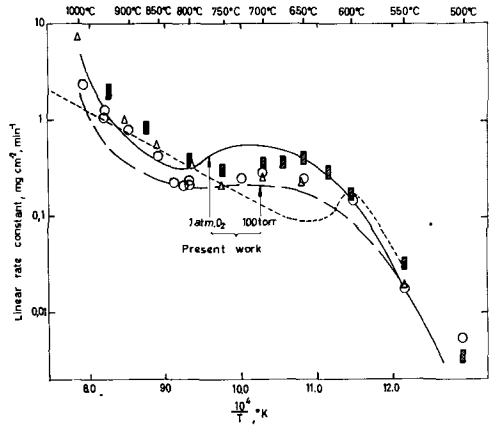

Fig. 22. Arrhenius plot of the linear rate constant during oxidation of tantalum. Comparison between present results (1 atm and 100 Torr O_2) and those of Peterson *et al.* (1 and 0.5 atm O_2) and Albrecht *et al.* (1 atm O_2). ○, Albrecht *et al.*; ■, △, Peterson *et al.*, - - - - - - -, 0.5 atm O_2, theoretical curve, Ong.

of the oxidation mechanism of niobium (21), the oxide scale is considered nonprotective, and interstitial oxygen atoms in the metal in the immediate region of the metal/oxide interface are assumed to be the intermediate species involved in the rate-determining step. It is furthermore proposed that the concentration of interstitial oxygen is related to the oxygen pressure through an oxygen adsorption equilibrium on the surface. Dilute solutions of oxygen in tantalum are considered nonideal.

By estimating and assuming values for the enthalpy of adsorption of oxygen, the entropy and enthalpy of solution of oxygen in tantalum, and the interaction energy between interstitial oxygen atoms, Ong calculated values for the linear rate constant as a function of temperature and oxygen pressure. The treatment predicts a cusp or reversal in the temperature dependence at all oxygen pressures and that the reversal takes place at decreasing temperature the lower the oxygen pressure. The values at 0.5 atm are shown as a stippled curve in Fig. 22.

This interpretation of the oxidation mechanism is not consistent with and does not give a satisfactory description of the present experimental results. The fundamental assumption that the concentration of interstitial oxygen in the metal is related to the oxygen pressure through an oxygen adsorption equilibrium at oxygen pressures of the order of magnitude of 1 atm also appears erroneous. By extrapolating the results of Pemsler (23) on the thermodynamics of the interaction of tantalum with oxygen, it may be estimated that the equilibrium pressure of oxygen at 700°C over tantalum containing 2 at. % oxygen is of the order of 10^{-22}-10^{24} atm. Thermodynamically, tantalum should thus be saturated with oxygen at any oxygen pressure above 10^{-22} atm at 700°C. Although kinetic factors are very important in considerations of oxidation mechanisms, it appears highly unlikely that the tantalum metal at the metal/oxide interface is anything but saturated with oxygen at pressures of the order of magnitude of 1 atm O_2. The concentration of interstitial oxygen should thus not be related to the oxygen pressure through an adsorption equilibrium. These same remarks also apply to Ong's corresponding interpretation of the oxidation mechanism of niobium (22).

On the basis of more recent experimental evidence Ong (20) in a later treatment assumed the oxidation of tantalum to occur by four simultaneous first-order chain reactions: solution of oxygen in the metal, nucleation and growth of a suboxide phase at the metal surface, and two phase boundary processes which give rise to two different modifications of Ta_2O_5. As in Kofstad's qualitatively similar interpretation of the oxidation mechanism of niobium (16), the cusp or reversal in the temperature dependence at about 700°C is explained in terms of a thermal instability of the intermediate suboxide phase at higher temperatures. This treatment also predicts a cusp in the temperature dependence regardless of oxygen pressure. As shown above this prediction is not confirmed by the present work.

Acknowledgment

The work has been sponsored by the Aeronautical Division AFSC, through the European Office, Office of Aerospace Research, United States Air Force.

Manuscript received Oct. 30, 1962; revised manuscript received Jan. 7, 1963.

Any discussion of this paper will appear in a Discussion Section to be published in the December 1963 JOURNAL.

REFERENCES

1. P. Kofstad, *J. Inst. Metals*, **90**, 253 (1962).
2. P. Kofstad, *ibid.*, **91**, 209 (1963).
3. P. Kofstad, *J. Less-Common Metals*, **5**, 158 (1963).
4. N. Norman, *ibid.*, **4**, 52 (1962).
5. N. Norman, P. Kofstad, and O. J. Krudtaa, *ibid.*, **4**, 124 (1962).
6. E. Gebhardt and H-D. Seghezzi, Plansee Proceedings, Reutte, Tyrol, p. 280 (1958).
7. D. A. Vaughan, O. M. Stewart, and C. M. Schwartz, *Trans. AIME*, **221**, 937 (1961).
8. P. Kofstad and H. Kjollesdal, *ibid.*, **221**, 285 (1961).
9. R. W. Powers and M. V. Doyle, *ibid.*, **215**, 655 (1959).
10. L. S. Darken and R. W. Gurry, "Physical Chemistry and Metals," p. 445, McGraw-Hill Publishing Co., New York and London (1953).
11. E. Gebhardt and H-D. Seghezzi, *Z. Metallk.*, **50**, 248 (1959).
12. R. E. Powel, J. V. Cathcart, and J. J. Campbell, *Acta Met.*, **10**, 149 (1962).
13. W. M. Albrecht, W. D. Klopp, B. G. Koehl, and R. I. Jaffee, *Trans. AIME*, **221**, 110 (1961).
14. P. Kofstad, *This Journal*, **109**, 776 (1962).
15. E. W. Haycock, *ibid.*, **106**, 771 (1959).
16. P. Kofstad, Paper presented at the First International Congress on Metallic Corrosion, London, April 1961, p. 181, Butterworths, London (1962).
17. R. D. Peterson, W. H. Fassell, Jr., and M. E. Wadsworth, *Trans. AIME*, **200**, 1038 (1954).
18. M. G. Gowgill and J. Stringer, *J. Less-Common Metals*, **2**, 233 (1960).
19. J. N. Ong, Jr., Paper presented at February 1961 Meeting of the AIME, St. Louis.
20. J. N. Ong, Jr., *Trans. AIME*, **224**, 991 (1962).
21. J. F. Brady and J. N. Ong, Jr., "Columbium Metallurgy," Metallurgical Society Conferences (AIME), vol. 10, p. 719, Interscience Publishers, New York-London.
22. J. P. Pemsler, *This Journal*, **108**, 744 (1961).

The Structure of Oxide Layers on Tungsten

E. A. Kellett and S. E. Rogers

Central Research Laboratories, Hirst Research Centre,

The General Electric Company Limited, Wembley, England

ABSTRACT

The oxidation of tungsten metal becomes appreciable at about 600°C. A thin, black adherent layer is first formed and at higher temperatures is eventually overlain by a bright yellow scale. The structure of these oxides has been studied by x-ray diffraction. It is concluded that the essential difference between the black and yellow oxides is one of structural perfection and orientation rather than composition. The observations are shown to be consistent with the protective nature of the black film.

The oxidation of tungsten metal in air or oxygen becomes appreciable at about 600°C. A thin, black (or blue-black) tightly adherent surface oxide is first formed, and this is normally "protective," *i.e.*, further attack on the tungsten base proceeds by diffusion of oxygen through the oxide layer.

The rate of formation of the black oxide increases rapidly with temperature. Eventually it ceases to grow and gradually becomes overlain by a bright yellow deposit, generally accepted to be tungstic oxide, WO_3.

The composition and structure of the black oxide film have been the subject of several investigations in recent years. The distinction between it and its yellow overlay has usually been considered on stoichiometric grounds, but various opinions are held. Of the thermodynamically stable oxides of tungsten (Table I), the black film has been claimed to be the γ-form (1), and the δ form (2). It has also been surmised to be a metastable modification of one of the intermediate oxide phases (3).

In the present work, the structure of the black oxide, in relation both to the yellow layer and the metal substrate, has been studied by x-ray analysis. It is concluded that the essential difference between the black and yellow oxides is one of structural perfection and orientation rather than of composition. The observations are shown to be consistent with the protective nature of the black film as compared with the nonprotective yellow oxide.

Preparation of Specimens

The metal used was commercial tungsten of better than 99.9% purity. It was received as centerless-ground rod of 1 mm diameter and was electropolished to a surface finish of center-line-average value about 10 μin. Short test lengths were cut by means of a diamond-impregnated slitting disk. Sharp edges were removed by filing, but the flat ends were not polished.

The specimens were oxidized at 650°, 700°, and 800°C in a stream of cylinder oxygen dried by activated alumina.

The black oxide only was formed after short times at 650° and 700°C, and the yellow overlay at higher temperatures. The overlay was "spongy" and cracked and could be removed readily. One specimen, completely converted to oxide, gave a product which was yellow throughout, with no evidence of either black oxide or a cavity at the center.

X-Ray Examination

For the rods oxidized at 650° and 700°C x-ray powder patterns were obtained from the black film *in situ* on the rods and also from a few flakes detached from the 700°C sample. For the rods oxidized at 800°C patterns were obtained from (i) the coatings removed as a whole from the rods, (ii) the yellow coatings *in situ*, and (iii) the underlying black coatings *in situ*. The x-ray examinations were all carried out at room temperature.

The films and scales, whether black or yellow in appearance, gave x-ray patterns showing that they consisted essentially of tungstic oxide of composition approaching WO_3. There were however wide differences in the details of crystal structure, both as regards orientation features and structural perfection. These textural and structural differences are

Table I. Stable oxides of tungsten

Designation	Formula	Color	Structure	Approximate lattice parameters a, Å	b, Å	c, Å	β	No. of mol. per unit cell	Space group	Reference
α	WO_3	Yellow	Monoclinic	7.28	7.51	3.83	90°	4	$P2_1/a$-C^5_{2h}	(6-8)
β	$WO_{2.90}$ ($W_{20}O_{58}$)	Light blue		12.1	3.8	23.4	95°	20	Laue^2/m	(9, 10)
γ	$WO_{2.72}$* ($W_{18}O_{49}$)	Violet	Monoclinic	18.32	3.79	14.04	115°2′	18	C^1_{2h}-P^2/m	(11)
δ	WO_2		Monoclinic	5.56	4.884	5.546	118°56′	4	$P2_1$	(9)

* Several compositions between $WO_{2.88}$ and $WO_{2.50}$ have been claimed, and thus the oxide has been variously described as W_2O_5, W_4O_{11}, etc. Magnéli (11) has shown that the formula $WO_{2.72}$($W_{18}O_{49}$) is consistent with the crystal structure and claims (9) that there is no evidence for extended homogeneity ranges for any of the tungsten oxides.

very significant from the point of view of the physical properties of the scales. For simplicity all the scales are denoted by the formula "WO_3," but it is emphasized that in some instances this is a very approximate description, particularly where the three-dimensional arrangement of well-crystallized WO_3 is obviously primitive or feebly developed. In these circumstances a distinction between WO_3 and the other structurally related tungsten oxides, such as $WO_{2.90}$ (Table I) is academic.

Strong diffraction patterns from the underlying tungsten were observed in the patterns obtained from black films *in situ*, showing that the maximum thickness of the black films was a few microns under the conditions of the present experiments.

Oxidation at 650°C.—Rod specimens were oxidized at 650°C for 1, 2½, and 4 min. X-ray diffraction patterns obtained from the black films *in situ* showed that the oxide crystal structure was relatively very feebly developed. The majority of the diffraction maxima were very weak and diffuse, so that growth of a true three-dimensional structure had apparently been much retarded.

The structural condition of this oxide layer was essentially similar to that described below for the specimen oxidized at 700°C.

A slight increase in development of the crystal structure was observed with increasing time of oxidation from 1 to 4 min.

Oxidation at 700°C.—A specimen was oxidized for 2 min at 700°C. While in broad appearance the x-ray pattern representing the film resembled that of WO_3, the really striking feature was that the OkO reflections [identifiable with the (OkO) planes of the orthorhombic structure of WO_3] were very strong and sharp and showed arcing, in marked contrast with the diffuse character of most of the other reflections. This indicated a marked directionally oriented arrangement of the "WO_3" crystallites; (010) planes tended to be aligned parallel to the surface of the oxidized rod. The diffuse character of reflections other than those of OkO type indicated a very imperfect development of the WO_3 structure in directions normal to the direction [OkO]. Gross lattice strains were implied by the imperfections of structure across the direction [OkO].

This black oxide film retained directional orientation features when rolled intact on to a glass fiber for x-ray examination. The flakes were thus parallel to (010) planes of the WO_3 structure.

Oxidation at 800°C.—At this temperature, the yellow coating formed readily over the thin black film on the rod surface. Specimens were oxidized for 5, 7, and 10 min.

The coating as a whole comprised "WO_3." From the details of the x-ray diffraction pattern, there was a suggestion of some slight deficiency in oxygen with respect to stoichiometric WO_3: signs of the presence of the lower oxide $WO_{2.95}$ were noticeable in some of the x-ray patterns.

On stripping away the main layer of oxide, the underlying film was exposed and examined *in situ*. It exhibited textural and structural features essentially similar to the black film on the 700°C specimens.

There was an indication in the pattern of the 10-min specimen of some lessening of the broadening of cross-lattice reflections, so that some slight advance in the perfecting of the structure perpendicular to the [010] direction may have started.

Examination *in situ* of the yellow oxide showed that directional orientation characteristics similar to those of the black film were only feebly noticeable. The diffraction pattern was now that of "WO_3" with crystallites in nearly random orientation. Crystal growth appeared to have occurred to a level at which the true three-dimensional structure of WO_3 was comparatively well-developed. Cross-lattice strains had been largely removed and the average crystal domain size was probably approaching 1μ.

Discussion

The formation of layered oxides of different colors is a feature of a number of metals. The layers can sometimes be distinguished as different oxide phases, but for tungsten it seems clear from the present results that the distinction between the black and yellow phases is essentially one of degree of structural perfection and orientation. Variations from the stoichiometric composition WO_3 do not appear to be significant.

Orientation effects as such are well known in thin oxide films, the degree of randomness increasing with distance from the metal surface. The only other reported instance of such effects being used to distinguish between oxide layers of different color appears to be that of niobium (4). When a specimen of rod or sheet was oxidized for 5 min at 800°C a black adherent film of α-Nb_2O_5 was formed. This showed marked preferred orientation. After 10 min oxidation, the oxide formed was a loose yellow deposit, again α-Nb_2O_5, but free from orientation.

The present x-ray investigations on tungsten oxides have shown that in the black film the oxide has grown with a pronounced directionally oriented texture. For simplicity the oxide has been described as "WO_3," but perfection of the WO_3 atomic arrangement is obviously poor, except perpendicular to the (010) layers in the orthorhombic structure. The directionally oriented growth is such that (010) planes of the structure tend to be parallel to the surface of the tungsten rod. In some respects the structure condition may be regarded as basically a two-dimensional one. Layers of atoms are stacked parallel to one another to give the normal interplanar spacing along the [010] direction of the WO_3 structure, but are not in proper register laterally; thus cross-lattice atomic spacings remain relatively ill-defined. This primitive lateral development probably accommodates a large degree of strain (or a high density of dislocations) such as is likely to be generated in a growing and expanding film of oxide.

By contrast considerable crystal growth has taken place when the yellow scale stage is reached. True three-dimensional development of the WO_3 structure is advanced, and the average size of the crystallites approaches the micron level. The strain condition present in the black film can be considered to have been largely eliminated, and the directional orientation features have been lost.

The evidence thus suggests that the change-over from the adherent black oxide to the nonadherent yellow oxide is associated with an advance in crystal growth in which the normal three-dimensional crystal structure of "WO_3" becomes substantially perfected. The adherence and protective character of the black layer probably depend on the ability of the film to retain and accommodate a high degree of lattice strain and directional orientation.

The observations on rod oxidized at 650°C show that the first trace of oxide scale which forms is this black, protective film possessing similar textural and structural features to the black scale formed on the rod surface at higher temperatures.

Magnéli (5) has discussed the analogy between the ReO_3-type structure and the structures of the oxides of molybdenum and tungsten. He shows how recurrent dislocations in an atomic pattern of the ReO_3-type can lead to atomic arrangements of the kind found in oxygen-deficient oxides of molybdenum and tungsten. The atomic patterns of these oxides are formed of metal-oxygen octahedra joined by corners to give blocks of the ReO_3-type. The blocks extend infinitely through the crystals in two dimensions and have a finite characteristic width in a third direction (at an angle to the a and c axes and in the a-c plane of the pseudo-orthorhombic structure). Magnéli states that a common feature of the x-ray diffraction patterns of the structures of such oxides will be the appearance of a substructure effect caused by the dominating influence of the ReO_3-type arrangement of the atoms.

It is of interest to note that the OkO reflections of WO_3, which exhibited such pronounced arcing in patterns obtained from the black oxide film, persist through the series of diffraction patterns of oxides deficient in oxygen with respect to the composition WO_3. Further, the interplanar spacing of such reflections are allmost identical with the hOO spacings of the primitive cubic substructure (a = 3.75Å) proposed by Magnéli for the blocks of the ReO_3-type structure. The value of a is a measure of the space diagonal of WO_6 octahedra in the tungsten oxide structures.

Webb *et al.* (3) recorded five diffraction lines from a dark-blue oxide layer, using x-ray powder diffractometry, which were sharp and which could be indexed on the assumption of a cubic lattice with a parameter 3.77Å. They state that the composition and structure were not definitely determined, but they surmise that the oxide is a metastable modification of one of the intermediate oxide phases. In view of the present observations on the arcing of certain reflections in the WO_3 pattern which can be indexed on the basis of a cubic substructure of parameter 3.77Å, (the interplanar spacings of the arced reflections recorded in the present study are $3.77, 1.88_5, 1.25_8$, and 0.94_3Å) it now seems likely that Webb *et al.* were observing a similar phenomenon, but that it was not recognized then as an orientation effect. The diffraction effects produced by such orientation might remain undetected by the diffractometer technique adopted by Webb *et al.*

Acknowledgment

The work described forms part of a program sponsored by the Director of Materials Research and Development, Ministry of Aviation.

Manuscript received Oct. 25, 1962; revised manuscript received Jan. 28, 1963.

Any discussion of this paper will appear in a Discussion Section to be published in the December 1963 JOURNAL.

REFERENCES

1. V. I. Arkharov and Yu. D. Kozmanov, *Fiz. Metal. i Metalloved., Akad. Nauk S.S.S.R., Ural Filial,* **2,** 361 (1956).
2. J. W. Hickman and E. A. Gulbransen, *Trans. AIME,* **171,** 371, (1947).
3. W. W. Webb, J. T. Norton, and C. Wagner. *This Journal,* **103,** 107 (1956).
4. H. J. Goldschmidt, *J. Inst. Metals,* **87,** 235 (1958-9).
5. A. Magnéli, *Acta. Cryst.,* **6,** 495 (1953).
6. G. Andersson, *Acta. Chem. Scand.,* **7,** 154 (1963).
7. R. Ueda and J. Kobayashi, *Phys. Rev.,* **91,** 1565 (1953).
8. H. Bräkken, *Z. Krist.,* **78,** 484 (1931).
9. G. Hägg and A. Magnéli, *Arkiv Kemi, Minerali. Geoli.,* **19A** (1944).
10. A. Magnéli, *Arkiv Kemi,* **1,** 513 (1950).
11. A. Magnéli, *ibid.,* **1,** 223 (1949).

A Method for Calculating Paralinear Constants for the Formation of Volatile Scale

Dominik Wajszel

Institute of Fertilizers, Tarnów, Poland

ABSTRACT

When a lead specimen is exposed to a chlorine stream at 300°C, a coherent layer of volatile $PbCl_2$ is formed. The consumption of metal follows paralinear kinetics. The parabolic constant A and linear constant B of Haycock's equation were calculated from the maximum on the experimental curve of weight change *vs.* time obtained by means of a thermal balance. A was $4.2 \times 10^{-11} g^2 \cdot cm^{-4} \cdot sec^{-1}$, and B was $2.8 \times 10^{-9} g \cdot cm^{-2} \cdot sec^{-1}$.

In the scaling system in which a coherent barrier layer of scale is formed, the rate of the process is commonly controlled by diffusion and obeys the so-called parabolic law. The rate of metal consumption is inversely proportional to the thickness of the compact layer (1) in accordance with the standard equation

$$\frac{dW_m}{dt} = \frac{K_p}{\xi} \qquad [1]$$

where W_m is the weight of consumed metal per unit

The evidence thus suggests that the change-over from the adherent black oxide to the nonadherent yellow oxide is associated with an advance in crystal growth in which the normal three-dimensional crystal structure of "WO_3" becomes substantially perfected. The adherence and protective character of the black layer probably depend on the ability of the film to retain and accommodate a high degree of lattice strain and directional orientation.

The observations on rod oxidized at 650°C show that the first trace of oxide scale which forms is this black, protective film possessing similar textural and structural features to the black scale formed on the rod surface at higher temperatures.

Magnéli (5) has discussed the analogy between the ReO_3-type structure and the structures of the oxides of molybdenum and tungsten. He shows how recurrent dislocations in an atomic pattern of the ReO_3-type can lead to atomic arrangements of the kind found in oxygen-deficient oxides of molybdenum and tungsten. The atomic patterns of these oxides are formed of metal-oxygen octahedra joined by corners to give blocks of the ReO_3-type. The blocks extend infinitely through the crystals in two dimensions and have a finite characteristic width in a third direction (at an angle to the a and c axes and in the a-c plane of the pseudo-orthorhombic structure). Magnéli states that a common feature of the x-ray diffraction patterns of the structures of such oxides will be the appearance of a substructure effect caused by the dominating influence of the ReO_3-type arrangement of the atoms.

It is of interest to note that the OkO reflections of WO_3, which exhibited such pronounced arcing in patterns obtained from the black oxide film, persist through the series of diffraction patterns of oxides deficient in oxygen with respect to the composition WO_3. Further, the interplanar spacing of such reflections are allmost identical with the hOO spacings of the primitive cubic substructure (a = 3.75Å) proposed by Magnéli for the blocks of the ReO_3-type structure. The value of a is a measure of the space diagonal of WO_6 octahedra in the tungsten oxide structures.

Webb *et al.* (3) recorded five diffraction lines from a dark-blue oxide layer, using x-ray powder diffractometry, which were sharp and which could be indexed on the assumption of a cubic lattice with a parameter 3.77Å. They state that the composition and structure were not definitely determined, but they surmise that the oxide is a metastable modification of one of the intermediate oxide phases. In view of the present observations on the arcing of certain reflections in the WO_3 pattern which can be indexed on the basis of a cubic substructure of parameter 3.77Å, (the interplanar spacings of the arced reflections recorded in the present study are $3.77, 1.88_5, 1.25_8$, and 0.94_3Å) it now seems likely that Webb *et al.* were observing a similar phenomenon, but that it was not recognized then as an orientation effect. The diffraction effects produced by such orientation might remain undetected by the diffractometer technique adopted by Webb *et al.*

Acknowledgment

The work described forms part of a program sponsored by the Director of Materials Research and Development, Ministry of Aviation.

Manuscript received Oct. 25, 1962; revised manuscript received Jan. 28, 1963.

Any discussion of this paper will appear in a Discussion Section to be published in the December 1963 JOURNAL.

REFERENCES

1. V. I. Arkharov and Yu. D. Kozmanov, *Fiz. Metal. i Metalloved., Akad. Nauk S.S.S.R., Ural Filial,* **2,** 361 (1956).
2. J. W. Hickman and E. A. Gulbransen, *Trans. AIME,* **171,** 371, (1947).
3. W. W. Webb, J. T. Norton, and C. Wagner. *This Journal,* **103,** 107 (1956).
4. H. J. Goldschmidt, *J. Inst. Metals,* **87,** 235 (1958-9).
5. A. Magnéli, *Acta. Cryst.,* **6,** 495 (1953).
6. G. Andersson, *Acta. Chem. Scand.,* **7,** 154 (1963).
7. R. Ueda and J. Kobayashi, *Phys. Rev.,* **91,** 1565 (1953).
8. H. Bräkken, *Z. Krist.,* **78,** 484 (1931).
9. G. Hägg and A. Magnéli, *Arkiv Kemi, Minerali. Geoli.,* **19A** (1944).
10. A. Magnéli, *Arkiv Kemi,* **1,** 513 (1950).
11. A. Magnéli, *ibid.,* **1,** 223 (1949).

A Method for Calculating Paralinear Constants for the Formation of Volatile Scale

Dominik Wajszel

Institute of Fertilizers, Tarnów, Poland

ABSTRACT

When a lead specimen is exposed to a chlorine stream at 300°C, a coherent layer of volatile $PbCl_2$ is formed. The consumption of metal follows paralinear kinetics. The parabolic constant A and linear constant B of Haycock's equation were calculated from the maximum on the experimental curve of weight change *vs.* time obtained by means of a thermal balance. A was $4.2 \times 10^{-11} g^2 \cdot cm^{-4} \cdot sec^{-1}$, and B was $2.8 \times 10^{-9} g \cdot cm^{-2} \cdot sec^{-1}$.

In the scaling system in which a coherent barrier layer of scale is formed, the rate of the process is commonly controlled by diffusion and obeys the so-called parabolic law. The rate of metal consumption is inversely proportional to the thickness of the compact layer (1) in accordance with the standard equation

$$\frac{dW_m}{dt} = \frac{K_p}{\xi} \qquad [1]$$

where W_m is the weight of consumed metal per unit

area after time t, ξ the thickness of the compact product, and K_p the parabolic rate constant. There are systems in which linear depleting of a compact scale layer occurs by sublimation or recrystallization, with formation of a layer that has negligible resistance to the transport of reactants. This gives rise to paralinear kinetics. Qualitative arguments for such kinetics were given by Evans (2) and Loriers (3). Quantitative analysis of paralinear scaling was carried out by Webb, Norton, and Wagner in the case of oxidation of tungsten (4), and by Haycock in the case of iron-H_2S scaling system (5) and oxidation of aluminum and hafnium (6). In such systems there is a simple relation between W_m and the weight change of the specimen W, and the parabolic and linear constants of paralinear equations can be estimated from experimental data.

In a system where the barrier scale layer MeX_n is partially volatile, it is possible to adapt a new method for calculating the paralinear constants. The rate of weight change of the specimen in such systems is equal to

$$\frac{dW}{dt} = \frac{1}{a}\frac{dW_m}{dt} - \frac{dW_s}{dt} \qquad [2]$$

where a is a stoichiometric conversion factor from gas to metal and W_s is the weight lost per unit area by sublimation. On the curve of W *vs.* time there is a maximum, as observed by Spretnak *et al.* (7) in the case of the oxidation of molybdenum. In the case of chlorination of lead at 300°C a similar maximum is found from which the paralinear constants can be calculated.[1]

Mathematical Treatment

The following analysis will be applied to systems where scale sublimation appears to be the only mechanism of barrier layer depletion. The rate of metal consumption in this case can be given by the general paralinear equation (6)

$$\frac{dW_m}{dt} = \frac{A}{W_m - Bt} \qquad [3a]$$

where $A = K_p \cdot d_p \cdot a/b$ is Haycock's parabolic constant, $b = a + 1$ is a stoichiometric conversion factor from gas X_2 to product MeX_n, d_p is the density of the product and $B \cdot b/a$ is a linear rate constant of sublimation of MeX_n.

Equation [3a] can be transformed after integration (see Eq. [7]) and re-differentiation into

$$\frac{dW_m}{dt} = \frac{B}{1 - e^{-W_m \cdot B/A}} \qquad [3b]$$

or expressed in terms of the thickness of the product

$$\frac{dW_m}{dt} = \frac{b}{a} \cdot \frac{A}{W_p} \qquad [4]$$

where W_p is the thickness of product in units of weight gain per unit area. The rate of thickening of the remaining product can be written (3, 4)

[1] Another case of oxidation with volatilization was discussed by Bernstein and Cubbicciotti (8) (scaling system Ge/O_2) and by Wagner (9) (scaling system Si/O_2). In both these systems the metal becomes oxidized to a volatile product MeO, or further to a nonvolatile product MeO_2 which covers the surface forming a protective layer.

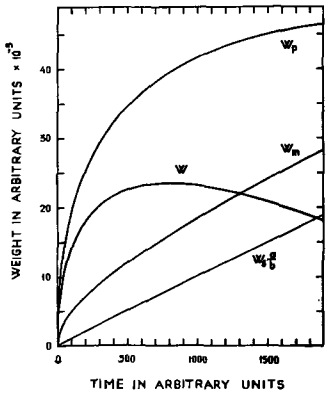

Fig. 1. Illustrating the curves for the rate of weight change. The curves of W_m, W_p, and W against time are calculated from Eq. [7], [8], and [9], respectively. The curve of $W_s \cdot a/b$, which demonstrates the sublimation of the product, expressed in units of weight loss of metal against time, is calculated from $W_s = b/a \cdot Bt$.

$$\frac{dW_p}{dt} = \frac{b}{a}\left(\frac{b}{a}\frac{A}{W_p} - B\right) \qquad [5]$$

from which the limiting thickness of the product can be calculated (3, 4)

$$W_{p(max)} = \frac{b}{a} \cdot \frac{A}{B} \qquad [6]$$

The integration of Eq. [3] and Eq. [5] yields, respectively,

$$\frac{A}{B^2}(-1 + e^{-W_m \cdot B/A}) + \frac{W_m}{B} = t \qquad [7]$$

$$\frac{A}{B^2}\ln\left[\frac{A}{A - \frac{a}{b} \cdot B \cdot W_p}\right] - \frac{W_p}{B} \cdot \frac{a}{b} = t \qquad [8]$$

The weight gain of the specimen at time t is given by

$$W = W_p - W_m \qquad [9]$$

and typical curves of W, W_m, W_p, and W_s are shown in Fig. 1.

From Eq. [2] and [3b] we have

$$\frac{dW}{dt} = \frac{B}{a}\left(\frac{1}{1 - e^{-W_m \cdot B/A}} - b\right) \qquad [10]$$

At the time $\bar{t}$, $dW/dt = 0$; the corresponding value of W_m, W_p, and W are equal to $\bar{W}_m$, $\bar{W}_p$, and $\bar{W}$, respectively, and can be expressed in terms of Haycock's paralinear constants, and in terms of a stoichiometric factor as calculated from Eq. [2], [4], [10]

$$\bar{W}_m = \frac{A}{B}\ln\frac{b}{a} \qquad [11]$$

$$\bar{W}_p = \frac{A}{B} \cdot \frac{1}{a} \qquad [12]$$

$$\bar{W} = \frac{A}{B} \cdot \alpha \text{ where } \alpha = \frac{1}{a} - \ln\frac{b}{a} \qquad [13]$$

From Eq. [7] and [11] we obtain expression for $\bar{t}$

$$\bar{t} = \frac{A}{B^2} \cdot \beta \text{ where } \beta = \ln\frac{b}{a} - \frac{1}{b} \qquad [14]$$

The above expressions lead to the equations for A and B

$$A = \frac{(\overline{W})^2}{\overline{t}} \cdot \frac{\beta}{\alpha^2} \quad [15]$$

$$B = \frac{\overline{W}}{\overline{t}} \cdot \frac{\beta}{\alpha} \quad [16]$$

Experimental

To check the proposed method for computing the paralinear constants, lead samples were corroded in chlorine at 300°C at a flow of 100 ml/min.

Materials.—Metallic lead (silver-free lead supplied by POCH Gliwice, Poland) with an analysis of better than 99.98% Pb was vacuum melted on a molybdenum boat at $5 \cdot 10^{-5}$ Torr of total pressure and cold rolled to the thickness of about $5 \cdot 10^{-3}$ cm. This foil was cut into a rectangular coupon 2.5 cm long and 1.6 cm wide.

Reagent grade lead chloride for the determination of the sublimation rate was melted in the stream of dried chlorine, powdered, and pressed at a pressure of about 6 tons/cm^2 to tablets $5 \cdot 10^{-2}$ cm in thickness and 1 cm in diameter. Chlorine was taken from commercial cylinder and dried over phosphorus pentoxide.

Apparatus.—Measurements of the curve of total gain in the weight of lead sample were by means of a quartz-spiral microbalance in a flowing system (see Fig. 2). The outer tube in which the specimens were corroded was of glass, 4 cm in outer diameter. In the middle of the tube there was attached a moveable micrometer microscope. The lower part of the tube was wound with Nichrome wire in a manner to eliminate temperature gradients in the hot zone. In addition a thick aluminum cylinder was placed around the glass tube at the middle of the furnace. The temperature was controlled by a Pt resistance thermometer connected to a commercial electronic controller. The temperature of the gas below the sample was measured by means of a Pt-Pt-10% Rh thermocouple introduced through the lower part of the tube and connected to a precision potentiometer. The inner tube of glass, 3 cm in diameter, in which the quartz helix was hung, had in the lower part a capillary with a row of glass shields. Another row of shields was placed on the thermocouple jacket leaving in the middle of the furnace a free space above 6 cm height. A quartz fiber chain which was connected to the helix was supplied in the upper part with a cylindrical glass scale 0.15 cm in diameter and 2 cm in length. (Such a scale can be made by means of a sapphire phonograph needle mounted on a micrometer screw.) The movement of the scale was observed through the windows in the tubes.

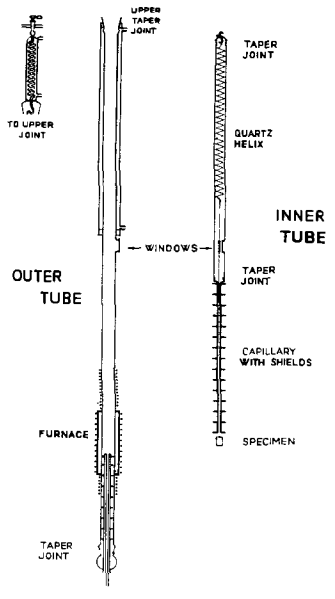

Fig. 2. Diagram of quartz-spiral microbalance

The upper part of the tube, the furnace walls, and the stream of gas were thermostatted with water.

The main characteristic of the described thermal balance was as follows: by measuring the elongation with an accuracy of $\pm 1 \cdot 10^{-4}$ cm an accuracy of $\pm 3 \cdot 10^{-6}$g could be obtained. There was no shift of zero point in a period of 100 hr at 300°C when the helix was loaded with a 200 mg quartz rod and a stream of thermostatted nitrogen was passed downward. However, the vibration of the helix reduced the accuracy to $\pm 6 \cdot 10^{-6}$g. The balance was sensitive to temperature changes in the upper part giving an error of $3 \cdot 10^{-4}$g/5°C of temperature decrease. (Usually in spiral microbalances the importance of temperature constancy is not generally realized leading to reading errors; these can be minimized by a stream of thermostatted gas and shields.)

The helix was calibrated by loading with known weights of aluminum and measuring the corresponding elongation, which was found to be satisfactorily proportional to the load.

Procedure.—The sequence of operations in an experiment was as follows: (i) heating the furnace to desired temperature and establishing the chlorine flow; (ii) rolling, cutting, and degreasing the lead sample in benzene; (iii) weighing the lead sample and the quartz fiber chain; (iv) introducing the sample under the stream of chlorine into the furnace and then measuring the time; (v) reading the elongation; (vi) raising the inner tube after chlorination to the cool zone, removing it from the system and reweighing the sample and the chain. The first reading was done after 1 hr to achieve thermal equilibrium. Further readings were taken at 5 hr intervals to 20 hr, and later at 10 hr intervals.

The sample was then observed under a microscope and metallographically in an epoxy-resin mount.

Results and Discussion

The kinetic data for the chlorination of lead at 300.0° ± 0.2°C and at a chlorine rate flow of 100 ml/min are shown in Fig. 3. The reproducibility of the curve of W measured in the period of two days was ±5% from the mean, as determined on the thermal balance, and ±8% from the mean value when using a fresh sample for each experimental point. This is greater than the relative error of readings which varied from 3% for the first point to about 1% for the maximum point. The maximum on the curve of W was reached at time $\overline{t} = 59$ hr and at $\overline{W} = 7.2 \cdot 10^{-4}$ g/cm^2 yielding $A = 4.2 \cdot 10^{-11}$ g$^2 \cdot$cm$^{-4} \cdot$sec^{-1} and $B = 2.8 \cdot 10^{-9}$ g$\cdot$cm$^{-2} \cdot$sec^{-1} ac-

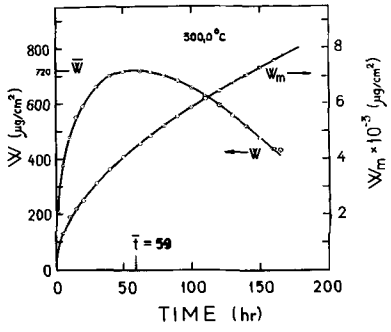

Fig. 3. Chlorination rate curves of lead at 300°C and at a flow rate of chlorine of 100 ml/min. The experimental W points demonstrate the change of weight of lead sample. The corrosion curve W_m which illustrates the metal consumption is calculated according to Eq. [7] using A and B obtained from Eq. [15] and [16]. The points on this curve are obtained from the experimental W points by use of $W_m = a(W+W_s)$.

cording to Eq. [15] and [16]. These values were used to calculate the W_m for Haycock's curve (Fig. 3). The points on this curve were obtained from the experimental W points by means of the equation $W_m = a(W + W_s)$, showing reasonable agreement with the calculated curve.

The value of B obtained from the sublimation measurements of pressed tablets was $3.4 \cdot 10^{-9}$ $g \cdot cm^{-2} \cdot sec^{-1}$.

Microscopic examination showed that the scale was relatively smooth and consisted of one layer without macrodiscontinuities at the metal/scale interface and without whiskers at the scale/gas interface. The thickness of the remaining product was not constant, ranging from 7.5 to $15 \cdot 10^{-4}$ cm, in reasonable agreement with the calculated value of $1.4 \cdot 10^{-3}$ cm. It must be pointed out that at the maximum on the W curve the thickness of the product reaches $100/b\%$ of its limiting value as evaluated from Eq. [6] and [12]; for the $PbCl_2$ layer this value is 26%.

The experimental results with the Pb/Cl_2 system at 300°C appear to show conclusively that the described method of evaluating the paralinear constants can be used in systems in which a nonporous layer of volatile MeX_n is continuously formed. If after time t_0 an additional cracking of the scale occurs, the rate of metal consumption will be greater and could be described by the equation

$$\frac{dW_m}{dt} = \frac{A}{W_m - Bt - R(t - t_0)}$$

where R is a linear rate constant of recrystallization. In this case the above derived formulas for A and B cannot be used if $t_0 < \bar{t}$.

Acknowledgments

The author's thanks are due to Dr. Ulick R. Evans, F.R.S., and to Professor A. D. McQuillan for their critical suggestions; to Dr. J. Nedoma for helpful discussion; and to Dr. L. Czuchajowski for friendly advice.

Manuscript received Sept. 4, 1962; revised manuscript received Nov. 30, 1962.

Any discussion of this paper will appear in a Discussion Section to be published in the December 1963 JOURNAL.

REFERENCES

1. C. E. Birchenall, "Metal-Gas Reactions," p. 278 in "Kinetics of High-Temperature Processes," W. D. Kingery, Editor, John Wiley & Sons Inc., New York (1959).
2. U. R. Evans, *This Journal*, **91**, 547 (1947).
3. J. Loriers, *Compt. rend.*, **231**, 522 (1950).
4. W. W. Webb, J. T. Norton, and C. Wagner, *This Journal*, **103**, 107 (1956).
5. E. W. Haycock, *ibid.*, **106**, 764 (1959).
6. E. W. Haycock, *ibid.*, **106**, 771 (1959).
7. E. S. Jones, J. F. Mosher, R. Speiser, and J. W. Spretnak, *Corrosion*, **14**, 20 (1958).
8. R. B. Bernstein and D. Cubbicciotti, *J. Am. Chem. Soc.*, **73**, 4112 (1951).
9. C. Wagner, *J. Appl. Phys.*, **29**, 1295 (1958).

Corrosion Inhibition in HCl Using Methyl Pyridines

Robert C. Ayers, Jr.,[1] and Norman Hackerman

Department of Chemistry, The University of Texas, Austin, Texas

ABSTRACT

The inhibiting effect of pyridine and seven of its methyl derivatives on the corrosion of iron in O_2-free, 6.08*N* HCl at 35°C was determined. Corrosion rates were measured by colorimetric analysis for iron with mercaptoacetic acid. The relative inhibitor efficiency and cathodic potential shift increased with increasing inhibitor concentration and, for a given concentration, with increasing electron density at the nitrogen atom. Both increased slightly with decreasing HCl concentration, but a temperature increase of 10°C had no effect on either. The proposition that chemisorption is involved in corrosion inhibition is supported by these experiments. As a supplementary item the great importance of careful purification of the organic compounds used in such researches as this is documented.

Organic amines act as inhibitors of the dissolution of iron in acid by adsorbing at the metal-solution interface. There is some difference of opinion as to the details of the mechanism of inhibition and the nature of the adsorbed species. Some workers hold that the organic cation is electrostatically adsorbed (1-3). This species is believed to inhibit the cathodic reaction. This laboratory does not deny the participation of the organic cation, but maintains that inhibition is attributed in part to chemisorption, probably of the neutral species (4, 5). The sorption predominantly polarizes the anodic process

[1] Present address: Humble Oil & Refining Company, Production Research, Houston, Texas.

in view of the generally observed cathodic shift seen with organic inhibitors.

Correlation of inhibitor efficiency with molecular structure has not yet been an outstanding success. Perhaps this comes from trying to stretch the limited knowledge of such a complex system too far. The basic problem of relating structure to properties is aggravated by these problems depending on proper knowledge of zero point of charge (zpc) for the system (6) and on the effect of nonbulk concentration in the electrical double layer (edl) on equilibria and kinetics. It was advantageous, therefore, to investigate closely related compounds on the premise that small changes in molecular properties lead to correspondingly small changes in inhibition and little or no change in systemic zpc. Thus, this work is concerned with inhibition by pyridine and seven of its methyl derivatives on the reaction of iron with 6*N* HCl. An advantage of aromatic molecules is that charge density at the nitrogen atom may be varied by changing the location of a substituent rather than by changing the molecular weight or structure type.

Materials

The electrode assembly was similar to that described by Stern and Makrides (7). Cylindrical electrodes of approximately 4.5 cm^2 area were cut from 99.9% Armco iron rod. The open end was protected from the solution by a Teflon plug which screwed into the electrode. Electrical contact was made through a steel rod which screwed into the other end. The steel rod was protected from the solution by a Teflon gasket and a glass electrode holder.

The constant boiling HCl (6.08*N*) was prepared with reagent grade HCl and distilled water, and purified by distillation.

The organic materials were obtained from Eastman Organic Chemicals and from Matheson, Coleman, and Bell. All the pyridine derivatives contained small amounts of sulfur compounds that greatly influenced inhibition. This requires a very important precaution, the lack of which may obviate a considerable amount of the information now in the literature. In order to remove these, as well as all nonbasic organic impurities, all the inhibitors were treated in the following manner. Steam was passed through a boiling mixture of the organic base dissolved in 1.2 equivalents of 22% sulfuric acid until about 10% of the base had been removed (6). After cooling, the acid solution of the amine was treated with an excess of hot, concentrated NaOH (9). The liberated organic base was separated and dried over solid sodium hydroxide. At this point in the purification process the several inhibitors were treated differently, as detailed below.

(*a*) Pyridine: The dry base was refluxed for 30 min in the presence of 1.5% $KMnO_4$ (8) distilled, and allowed to stand in a bottle containing iron powder (about 4g/100g of pyridine) for about 30 hr. Then the compound was redistilled out of a flask containing fresh iron powder.

(*b*) 2- and 4-Picoline: Each dry base was distilled, treated with iron powder, and redistilled out of a flask containing fresh iron powder.

(*c*) 3-Picoline: To remove traces of 4-picoline and 2,6-lutidine 400g of the dry base was refluxed with 27g phthalic anhydride and 30g acetic anhydride for 12 hr. 3-Picoline was separated by adding sodium hydroxide and steam distilling it out of the mixture. Then the compound was distilled, treated with iron powder, and redistilled.

(*d*) 3,5-, 2,4-, and 2,6-Lutidine; 2,4,6-collidine: Each dry base was distilled and then crystallized as the hydrochloride out of reagent grade benzene using dry HCl gas. The amine hydrochlorides were twice recrystallized out of an ethanol-ether mixture.

All distillations were carried out in a Pyrex fractionating column having 30 theoretical plates. The temperature could be read to 0.2°C and the fraction of distillate used in the experiments had a constant boiling point within this range.

To determine the effect of further purification, pyridine and 4-picoline, after being treated in the manner described, were crystallized as the hydrochloride out of reagent grade benzene using dry HCl gas. The crystals were washed several times with dry ether and dried in a vacuum desiccator. This last measure did not change the inhibitor properties of either compound.

Experimental

Corrosion rates were determined by withdrawing samples of solution from the cell and analyzing them colorimetrically for iron. The potential of the iron electrode with respect to a saturated calomel electrode (SCE) was measured with an L&N Student Type potentiometer.

The iron electrodes were polished successively with 1/0, 2/0, and 4/0 emery paper, washed with Alconox, and thoroughly rinsed in distilled water and acetone. They were then placed in a Vycor tube, and annealed in a hydrogen stream at 630°C for 12 to 15 hr. The electrodes were allowed to cool under hydrogen, removed from the furnace, and stored in a desiccator until needed. Electrodes treated in this way were re-used several times since they showed no change in their corrosion properties. Before each experiment the electrode apparatus was assembled, placed in a Soxlet extractor containing acetone, and degreased overnight. Thus some oxide existed but relatively little, and this dissolved within the first few minutes of the experiment.

The cell is shown in Fig. 1. Before each experiment it was cleaned with sodium dichromate-sulfuric acid solution, rinsed, and allowed to leach in distilled water for 12 to 14 hr. After this 700 cc of the HCl solution was poured into the cell, which was then placed in a water bath maintained at 35° ± 0.1°C. Grade A helium (99.997% pure) flowed through the solution continuously to maintain an inert atmosphere. It also provided mild agitation as well as pressure for withdrawing samples. After about 30 min the electrode assembly was removed from the degreaser and inserted into the cell. After

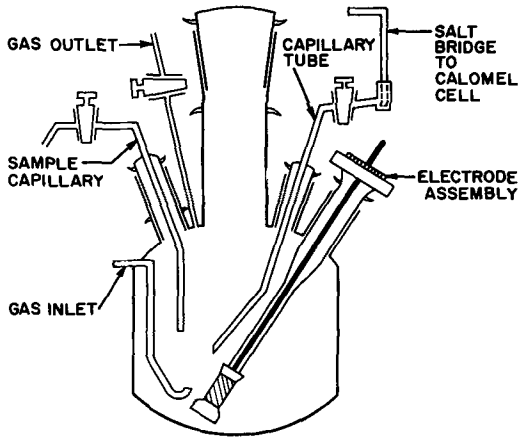

Fig. 1. Corrosion cell

150 min the corrosion rate and corrosion potential had become constant, and samples were withdrawn by forcing solution out through a capillary tube. The sample volume was 8 cc. The cell volume was lowered about 10% by removing samples during a run. Samples were taken every 10 min for 1 hr to establish the uninhibited rate. Approximately 15 sec were required to take a sample.

After the uninhibited rate was established, an HCl solution of the amine hydrochloride was added to the cell through the gas outlet with a hypodermic syringe. Immediately thereafter the potential was measured at 1 min intervals until it had become constant. After 1 hr, samples were taken at regular intervals to establish the inhibited rate. Stock amine hydrochloride solutions were made up to approximately 1*N* in HCl. The hydrogen ion concentration in the cell was never lowered more than 3% by addition of inhibitor solution.

The samples were analyzed using the mercaptoacetic acid method for iron. The percent transmittance of each sample, as determined on a Bausch & Lomb Spectronic 20 colorimeter at a wavelength of 525 mμ, was compared to a standard Lambert-Beer law curve to determine the iron concentration. The presence of inhibitors in concentrations used here had no effect on the analysis.

The method described here yields more reproducible values for the relative rate than would be obtained by simply immersing the electrode in the solution containing the inhibitor, measuring the inhibited rate, and comparing it to an average uninhibited rate. In the present method the uninhibited rate was always determined first; therefore, uncertainties due to differences in rates between individual electrodes were eliminated. Electrodes differing in initial rates by as much as 12% would yield the same relative inhibited rate. For the same reason the potential shift was reproducible to ± 1 mv, while the corrosion potential was reproducible to only ± 5 mv.

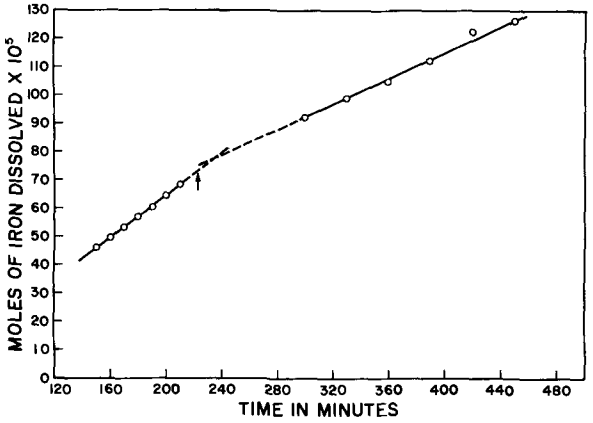

Fig. 2. Typical rate curve in 6.08*N* HCl at 35°C

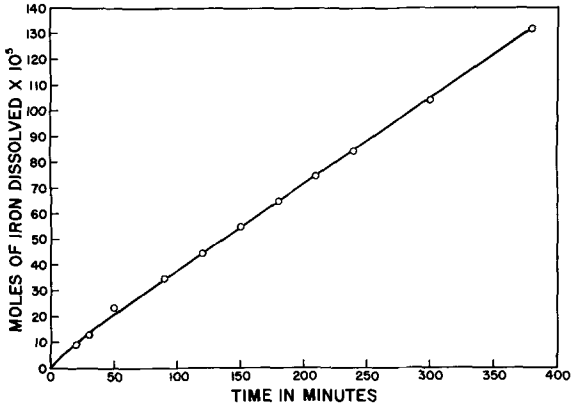

Fig. 3. Uninhibited rate curve in 6.08*N* HCl at 35°C

Results

Results of a typical run are given in Fig. 2. The portion of greater slope represents uninhibited corrosion. The arrow marks the time at which the inhibitor was added. Figure 3 gives the rate curve in uninhibited 6.08*N* HCl at 35°C. The rate became constant after about 90 min and remained so for at least 600 min, the longest time the uninhibited rate was followed. The rate was 4.3 x 10^{-5} moles/cm² hr with an average deviation of 4%. Deviations as high as 12% were observed in a few cases.

The steady-state, uninhibited, corrosion potential vs. SCE was −0.461 ± 0.005v. The uninhibited corrosion rate and the potential reached their steady values at approximately the same time. Upon addition of inhibitor, the potential shifted rapidly in the cathodic direction, reaching a steady value within 2 or 3 min. However, the shift was 80% or more complete in 2 sec.

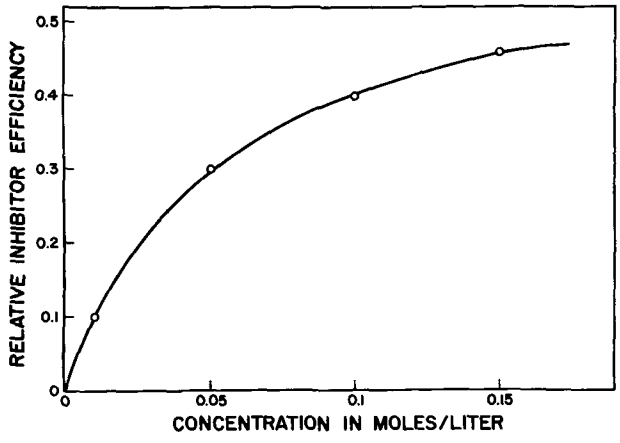

Fig. 4. Effect of inhibitor concentration on relative inhibitor efficiency, θ, with 2,6-lutidine.

The relative inhibitor efficiency, θ, is defined here as

$$\theta = \frac{r - r_i}{r}$$

where r is the uninhibited rate and r_i is the inhibited rate. Figure 4 shows the variation of θ with concentration of 2,6-lutidine. Data for all the compounds are shown in Table I. The cathodic potential shift, ΔE, is the difference in the steady state corrosion potential before and after addition of the inhibitor. All potential shift data are listed in Table II.

Effect of HCl concentration.—To determine the effect of lower acid strength, runs were made in 2.0*N* HCl at 35°C. The compounds investigated were pyridine and collidine. The inhibitor concentration was 0.1M, and just as with the more concentrated acid, the inhibited steady state potential shifts to within a millivolt or two of its final value within 2 sec after the addition of inhibitor. A comparison of the corrosion parameters in 2.0*N* and 6.08*N* HCl is shown in Table III.

Effect of temperature.—To determine the effect of increasing temperature, runs were made in 6.08*N* HCl at 45°C. The compounds investigated were pyridine and 2,4-lutidine. The inhibitor concentration was 0.1M. A comparison of these results with those at 35°C is shown in Table IV.

To determine the effect of a large temperature increase, inhibition tests were carried out on 2,4-lutidine in boiling 6.08*N* HCl. These 107°C runs were made in a 500 ml flask equipped with a reflux condenser. Rectangular shaped specimens of 1.8 cm² apparent area were cut from Armco iron sheet. They were polished with 1/0 emery paper, rinsed with water, dried, weighed, and stored in acetone. Before each run, 250 ml of 6.08*N* HCl was poured into the flask and refluxed for 10 min. To start a run the condenser was removed, an iron specimen dropped into the flask, and the condenser replaced. The duration of the test was 4 min. A run was terminated by removing the condenser and pouring the solution and specimen into a large beaker of cold water. The relative inhibitor efficiency at an inhibitor concentration of 0.1M calculated from weight loss measurements was 0.42.

Effect of purification.—Other experiments were performed in 6.08*N* HCl at 35°C with the same group of organic compounds purified only by distillation. Values of θ determined from these experiments at 0.15M are compared with the values of the purified compounds in Table V. The relative inhibitor efficiencies in these experiments were reproducible to a little better than ± 0.02. Also, in general all potential shifts were small and with the exception of pyridine, collidine, and 2,6-lutidine were anodic. After an initial cathodic surge, the potential slowly drifted in the anodic direction for 5 to 10 min after addition of the inhibitor.

Table I. Relative inhibitor efficiency

Inhibitor	0.01M	0.05M	0.1M	0.15M
Pyridine	0.05	0.18	0.31	0.36
3-Picoline	0.07	0.23	0.33	0.40
2-Picoline	0.08	0.26	0.36	0.44
4-Picoline	0.09	0.26	0.37	0.44
3,5-Lutidine	0.09	0.27	0.37	0.44
2,6-Lutidine	0.10	0.30	0.40	0.46
2,4-Lutidine	0.10	0.30	0.41	0.46
2,4,6-Collidine	0.12	0.32	0.43	0.48

Reproducibility = ±0.01

Table II. Cathodic potential shift in mv

Inhibitor	0.01M	0.05M	0.1M	0.15M
Pyridine	1	2	5	6
3-Picoline	1	2	6	6
2-Picoline	1	4	6	7
4-Picoline	1	4	6	8
3,5-Lutidine	1	6	9	11
2,6-Lutidine	2	7	10	12
2,4-Lutidine	2	6	10	13
2,4,6-Collidine	2	8	12	16

Reproducibility = ±1 mv

Table III. Comparison of corrosion parameters

HCl concentration	6.08*N*	2.0*N*
Rate, mole/cm² hr	4.3×10^{-5}	5.5×10^{-6}
Potential *vs.* SEC, v	−0.461	−0.496
θ for pyridine	0.31	0.33
ΔE for pyridine, mv	5	11
θ for collidine	0.43	0.45
ΔE for collidine, mv	12	17

Table IV. Comparison of temperature effect

Temperature	35°C	45°C
Rate, mole/cm² hr	4.3×10^{-5}	7.7×10^{-5}
Potential *vs.* SCE, v	−0.461	−0.469
θ for pyridine	0.31	0.30
ΔE for pyridine, mv	5	4
θ for 2,4-lutidine	0.41	0.42
ΔE for 2,4-lutidine, mv	10	10

Discussion and Results

The relative inhibitor efficiency and cathodic potential shift increased with concentration for all eight materials. The rate of increase dropped off with increasing concentration. The rapid attainment of steady potential suggests that the initial adsorption involves the protonated species. Free amine adsorption may also be taking place, but if this were the only species being adsorbed, a longer time lag for diffusion would be expected. The total number of molecules of free pyridine that would have time to diffuse to the surface amounts only to about 0.04% of a monolayer based on a diffusion

Table V. Effect of purification on relative inhibitor efficiency

Inhibitor	Distilled	Purified
Pyridine	0.48	0.36
3-Picoline	0.58	0.40
2-Picoline	0.74	0.44
4-Picoline	0.74	0.44
3,5-Lutidine	0.78	0.44
2,4-Lutidine	0.80	0.46
2,6-Lutidine	0.56	0.46
2,4,6-Collidine	0.62	0.48
Reproducibility	±0.02	±0.01

Table VI. Molecular areas, Å², and relative inhibitor efficiencies at 0.15M (see text)

Inhibitor	θ	A_1	A_2	A_2'	A_3
Pyridine	0.36	30	37	37	37
3-Picoline	0.40	60	49	49	68
2-Picoline	0.44	60	49	49	68
4-Picoline	0.44	30	41	49	68
3,5-Lutidine	0.44	60	58	58	68
2,6-Lutidine	0.46	60	58	58	68
2,4-Lutidine	0.46	60	58	58	68
2,4,6-Collidine	0.48	60	68	68	68

coefficient of 2×10^{-5} cm²/sec and an effective boundary layer thickness of 0.005 cm.

Effect of molecular area.—In Table VI approximate molecular areas are compared with values of θ at amine concentrations of 0.15M. The areas were calculated from Stuart and Briegleb atom models. A_1 is the projected area with the ring structure oriented perpendicular to the plane of the metal surface with free rotation allowed (1). A_2 and A_3 are areas based on ring orientation parallel to the surface. The area of the smallest possible circle containing the molecule is A_2, the cation oriented the same way gives A_2'. A_3 is the circular area with the ring oriented parallel to the surface and allowing free rotation about the center of the ring.

Which, if any, of these orientations is correct cannot be deduced from these data. Although poor, the parallel orientation offers the best correlation between area and inhibitor efficiency. For this type of orientation whether the cation or the free amine is involved, π interaction would have to be stronger than electrostatic or charge transfer interactions. However, it is difficult to understand why the stronger type of interaction in pyridine would involve π bonding when most saturated amines of comparable size and solubility are better inhibitors. None of the area sets is a single valued function of the relative inhibitor efficiency. Perhaps all orientations are incorrect. However, it is difficult to imagine any orientation where the area of 3,5-lutidine would be equal to that of 4-picoline while the area of 4-picoline would be greater than that of 3-picoline. It is concluded that as far as differences in inhibition properties in this series of compounds are concerned, differences in area are not of first order importance.

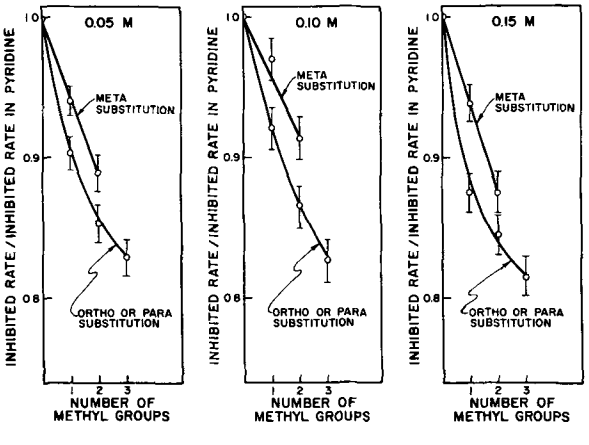

Fig. 5. Effect of methyl substitution on inhibitor power of pyridine

Effect of methyl substitution.—To show how methyl substitution increases inhibition, the ratio of the inhibited rate to the inhibited rate with pyridine, $\frac{1-\theta}{1-\theta \text{ pyridine}}$, is plotted as a function of the number of substituted methyl groups in Fig. 5. It is seen that inhibition increases with the number of methyl groups. Also methyl substitution ortho or para to the nitrogen increases inhibition more than does meta substitution. The data at 0.01M are not included due to the fact that at low inhibitor concentrations the θ values are near zero. The same trend is present, but in most cases differences in inhibition are inside the error limits.

The effect of resonance is pyridine is to concentrate charge at the nitrogen atom, largely at the expense of the 2 and 4 positions on the ring. A substituted methyl group at the 2 or 4 position would donate charge through hyperconjugation and by the inductive effect. A methyl group substituted at the 3 position would donate charge inductively, but should not increase the electron density at the nitrogen atom as much as does a 2 or 4 substitution. Several of the compounds are arranged in order of increasing nitrogen atom electron density:

pyridine < 3-picoline < 2-picoline = 4-picoline

This is also the order of relative inhibitor efficiencies and suggests a relationship between electron density at the nitrogen and inhibition.

It is generally believed that in these compounds the electron released during the first ionization is one of the "lone pair" electrons (10). Therefore, differences in ionization potential, I, should be a measure of differences in charge density at the nitrogen. Nakajima and Pullman (11) calculated values of I for seven of the eight compounds investigated in these experiments. A plot of θ *vs.* I at amine concentrations of 0.05, 0.10, and 0.15M is shown in Fig. 6. θ increases as I decreases. This

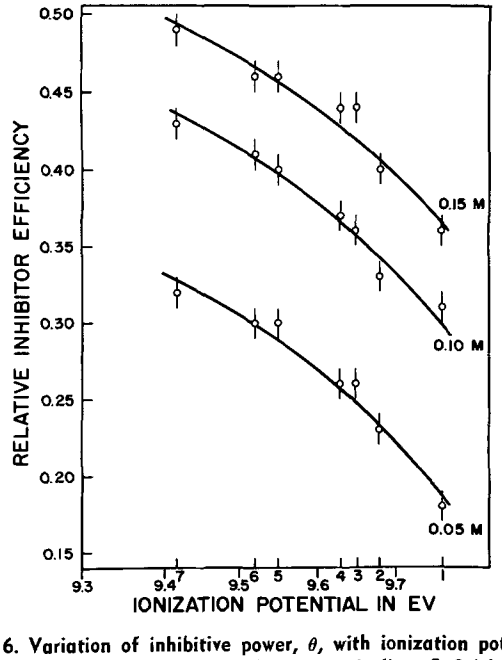

Fig. 6. Variation of inhibitive power, θ, with ionization potential. 1, Pyridine; 2, 3-picoline; 3, 2-picoline; 4, 4-picoline; 5, 2,6-lutidine; 6, 2,4-lutidine; 7, 2,4,6-collidine.

fact, combined with the apparent lack of an area effect, points clearly to the participation of the free amine in the inhibition process. If the free amine were not involved, one would not expect any correlation between inhibition and the resonance effects described above. Since the free amine would probably not have time to diffuse to the electrode surface without being protonated, it must be assumed that the chemisorbed free amine is generated from the cation at the metal surface. This generation process could occur most easily if the adsorbed pyridinium ions are oriented with the ring perpendicular to the surface with the N next to the metal. The zpc for iron is generally believed to lie about 0.25v positive to the observed corrosion potential (6). If this is the case cations would be preferentially adsorbed and the above type of orientation would be most likely.

Going on the assumption that the free amine is chemisorbed and important in inhibition, the increase in inhibition with nitrogen atom electron density may be due to one or both of the following effects: (*a*) an increase in the number of chemisorbed molecules, (*b*) an increase in the ability of chemisorbed molecules to inhibit corrosion. The first describes inhibition in terms of a molecule's chemisorption "constant" and the second in terms of the molecule's ability to inhibit corrosion once it has been adsorbed. That is, the second separates adsorption and inhibition. Due to a lack of knowledge of actual surface coverage it can be stated only that at a constant bulk concentration of inhibitor, inhibition and perhaps adsorption, is increased by an increase in the electron density at the nitrogen atom.

Other effects.—The fact that ΔE is cathodic indicates that the anodic reaction is inhibited more than the cathodic reaction. However, both reactions are surely affected, because ΔE is small among other reasons. From Tables I and II it is seen that in general ΔE increases with θ. However no quantitative relation between θ and ΔE was found.

Values of both θ and ΔE were slightly greater in 2.0*N* than in 6.08*N*. This result could be due to an increase in availability of free amine, keeping in mind always the role of the surface in the general equilibria and thus to an increase in the number of chemisorbed molecules.

Temperature had little effect over the 10° range, suggestive more of chemisorption than of physical adsorption. The value of θ for 2,4-lutidine at 107°C was still appreciable, although it must be remembered that a different type of experiment was used. However, it is important to note that inhibition is still pronounced at 107°C. This is further evidence for the existence of chemisorption.

Effect of impurities.—In every case the compounds purified only by distillation were considerably better inhibitors than the corresponding compounds subjected to extensive purification. Some of the compounds purified only by distillation developed a slight color if allowed to stand for several days or developed color when dissolved in HCl. Neither effect occurred with the extensively purified compounds, even after several months.

The impurities contained in pyridine are discussed in detail by Coulson and Ditcham (8). They found that the major impurity was tetrahydrothiophen in concentrations varying from 0.06% in technical grade to less than 0.005% in the purest reagent grade. All of the compounds studied come from coal tar, and it is quite likely that the sulfur contaminants in all the compounds studied are also thiophene derivatives. Other workers have found that these contaminants cannot be completely removed by distillation (14). Tetrahydrothiophen was found in this laboratory to be an effective corrosive inhibitor at low concentration (15).

In order to see how the addition of thiophene affects the system, the following experiment was performed. A run was made in 6.08*N* HCl at 35°C in the usual way. After the establishment of the uninhibited rate, the inhibited rate in the presence of 4-picoline, and the cathodic potential shift, enough thiophene was added to the cell to make up a concentration of 0.019M. This caused the potential to shift about 7 mv anodic to the uninhibited corrosion potential and increased the value of θ from 0.45 to 0.69. The true thiophene concentration was considerably less than 0.019M since drops of thiophene were detected floating on the surface. Thiophene is not necessarily the particular contaminant in 4-picoline that causes greater inhibition but the contaminant is probably a thiophene derivative.

Conclusion

It appears that the Hackerman and Makrides' inhibition mechanism is the most applicable to these results (4, 13). The following two step mechanism of the inhibition process is postulated.

1. Diffusion of the cation to the surface where it is weakly adsorbed.
2. A transformation of the weakly adsorbed cation to the strongly adsorbed free amine. An equilibrium is rapidly set up at the surface between these species.

Inhibition through chemisorption occurs either because of stabilization of the iron atom in the surface lattice, complex ion formation *in situ*, or by the arrest of emergent ferrous ions.

Whether the cation or free amine is most important in inhibition cannot be surely stated, but adsorption of the neutral species accounts for the differences observed in inhibition and for the cathodic potential shift.

Acknowledgment

The authors are grateful for the financial support of this work by the Office of Naval Research under Contract Nonr 375(15), and the Robert A. Welch Foundation of Houston.

Manuscript received Nov. 13, 1962. This paper was prepared for delivery before the Boston Meeting, Sept. 16-20, 1962.

Any discussion of this paper will appear in a Discussion Section to be published in the December 1963 JOURNAL.

REFERENCES

1. C. A. Mann, *Trans. Electrochem. Soc.*, **69**, 115 (1936).
2. J. O'M. Bockris and B. E. Conway, *J. Phys. & Colloid Chem.*, **53**, 527 (1949).
3. L. I. Antropov and A. T. Petrenko, *J. Appl. Chem.*

(*U.S.S.R.*), **31**, 1839 (1958).
4. N. Hackerman and A. C. Makrides, *Ind Eng. Chem.*, **46**, 523 (1954).
5. N. Hackerman, Comptes Rendus du Symposium Eupoeen sur les inhibiteurs de Corrosion, Ferrara (Italia) 1960.
6. L. I. Antropov, Kinetics of Electrode Processes and Null Points of Metals, Council of Science and Industrial Research, New Delhi, India (1960).
7. M. Stern and A. C. Makrides, *This Journal*, **107**, 782 (1960).
8. E. A. Coulson and S. B. Ditcham, *J. Applied Chem.*, **2**, 236 (1952).
9. O. Kruber, D.R.P., **551**, 606 (1929).
10. A. Streitwieser, "Molecular Orbital Theory for Organic Chemists," p. 196, John Wiley & Sons, New York (1961).
11. K. Nakajima and A. Pullman, *J. Chim. Phys.*, **55**, 793 (1958).
12. H. F. Finley and N. Hackerman, *This Journal*, **107**, 259 (1960).
13. A. C. Makrides and N. Hackerman, *Ind. Eng. Chem.*, **47**, 1773 (1955).
14. D. P. Biddiscombe, E. A. Coulson, R. Handley and E. F. G. Herrington, *J. Chem. Soc.*, 1957 (1959).
15. H. F. Finley, "Adsorption of Polar Organic Compounds on Steel," Ph.D. Dissertation, University of Texas (June 1958).

The Influence of Point Defects on the Kinetics of Dissolution of Semiconductors

George Simkovich[1] and J. Bruce Wagner, Jr.[2]

Hammond Metallurgical Laboratory, Yale University, New Haven, Connecticut

ABSTRACT

The kinetics of dissolution of semiconductors as a function of point defects introduced by varying the stoichiometry and/or by doping additions have been studied. Experiments on two ionic semiconductors, lead sulfide and zinc oxide, are described. Under conditions involving a relatively large change in the oxidation states of the constituents in the solid-liquid reaction, the kinetics have been shown to vary markedly with point defect concentration.

In the case of heterogeneous reactions between a gas and a solid, the role of point defects has been demonstrated especially in the oxidation of metals and also in catalytic reactions (1, 2). The role of line defects has also been studied (3). In the case of reactions between liquids and solids, specifically dissolution processes, much research has been devoted to an understanding of the role of dislocations in the formation of etch pits. However, aside from the work of Engell and co-workers (4) on the dissolution of wüstite as a function of oxidation or reduction potential and the studies of Cretella and Gatos (5) and Dewald and Turner (6) on the dissolution of germanium, little work has been carried out on the kinetics of dissolution of semiconductors containing well-defined concentrations of point defects (7). These types of data are needed for both practical and theoretical purposes. It is the purpose of this paper to report initial results of such a study which demonstrates that, in certain cases, the presence of point defects has a striking influence on the rate of liquid-solid reactions.

Two very different systems were chosen for this study in order to test the generality of the effect. These were the dissolution of lead sulfide in concentrated nitric acid and in aqueous hydrochloric acid and the dissolution of zinc oxide in aqueous hydrochloric acid. Lead sulfide, an amphoteric semiconductor, was investigated as a function of stoichiometry and as a function of doping additions, silver sulfide (Ag_2S) and bismuth sulfide (Bi_2S_3). Zinc oxide, pure and doped with either aluminum oxide (Al_2O_3) or with lithium oxide (Li_2O), was also investigated. In addition, an attempt was made to study the dissolution of pure and doped nickel oxide, but the experiments were unsuccessful because the rate of reaction was quite slow and the reaction was difficult to follow in the apparatus employed.

Experimental

Lead sulfide was prepared by slowly heating an evacuated tube containing lead and sulfur (both of 99.999 + purity) to 400°C where it was held for approximately one week. Bismuth sulfide and silver sulfide were synthesized in a similar manner. From this material, single crystals of pure lead sulfide, or lead sulfide to which appropriate amounts of either bismuth sulfide or silver sulfide had been added, were grown by the Bridgman technique utilizing evacuated quartz tubes as crucibles and a lowering rate of approximately 1 iph.

The single crystals so obtained were cleaved into smaller sections and were then equilibrated under known partial pressures of sulfur by methods described elsewhere (8). The data of Bloem and coworkers (9) were employed directly for the sulfur pressures. Conditions under which the crystals were annealed are tabulated in Table I.

The annealed single crystals were cleaved along their natural cleavage planes, the [100] planes. Any grinding necessary to obtain rectangular specimens was performed at this time on number 4/0 metallographic paper. It should be remarked that dissolution may be a function of crystal orientation. The cold-worked layers were removed by dissolution in concentrated nitric acid at room temperature. The

[1] Present address: Edgar C. Bain Laboratory for Fundamental Research, United States Steel Corporation Research Center, Monroeville, Pennsylvania.

[2] Present address: Department of Materials Science, Northwestern University, Evanston, Illinois.

Table I. Dissolution of lead sulfide single crystals in acid solutions

Sample	No.	Equil. PbS	Temp, °C S res.	Predominant carrier	Cross-sectional area, cm^2	Dissolving media	Dissolution temp, °C	RPM
PbS, stoich.	11	700	192.5	n = p	0.1571_8	500 cc conc. HNO_3	60 ± 0.5	
PbS, stoich.	10	700	192.5	n = p	0.2272_9	500 cc conc. HNO_3	60 ± 0.5	
PbS + excess Pb	9	700	82.5	n	0.1912_6	500 cc conc. HNO_3	60 ± 0.5	
PbS + excess S	8	700	400	p	0.2194_2	500 cc conc. HNO_3	60 ± 0.5	
PbS + 1/2 mole % Bi_2S_3	7	700	192.5	n	0.2091_5	500 cc conc. HNO_3	60 ± 0.5	
PbS + 1/2 mole % Ag_2S	6	700	192.5	p	0.2280_2	500 cc conc. HNO_3	60 ± 0.5	
PbS + 1/20 mole % Ag_2S	5	700	192.5	p	0.2272_9	500 cc conc. HNO_3	60 ± 0.5	
PbS, stoich.	20	700	192.5	n = p	0.1622_1	250 cc conc. HCl, 250 cc H_2O	45 ± 0.5	900 ± 25
PbS + 1/2 mole % Bi_2S_3	19	700	192.5	n	0.2748_3	250 cc conc. HCl, 250 cc H_2O	45 ± 0.5	900 ± 25
PbS + 1/2 mole % Ag_2S	21	700	192.5	p	0.2787	250 cc conc. HCl, 250 cc H_2O	45 ± 0.5	900 ± 25

length and width of the cleaved and polished specimens were measured at a minimum of four points using a micrometer accurate to a ten thousandth of an inch, and the area of the cleaved plane to be used for dissolution was calculated from an average of these measurements. Polyethylene was used as a mounting material.

For the experiments on lead sulfide, two dissolving media were used. These were concentrated nitric acid and aqueous hydrochloric acid. Because qualitative experiments had shown the dissolution reaction to be controlled by a phase boundary reaction under conditions reported herein, an apparatus was designed to ensure a well mixed dissolution medium of sufficiently large volume that samples could be withdrawn conveniently. For the dissolution of lead sulfide in aqueous nitric acid, a holder was made of Teflon. Beneath this holder was placed a Teflon-covered magnet which was used to stir the solution.

For the experiments on the dissolution of lead sulfide crystals and on the zinc oxide pellets in hydrochloric acid the samples were mounted in a room temperature setting plastic (Kold-Mount) along with a magnet, and the entire assembly was rotated by means of the magnetic stirrer beneath the solution. The zinc oxide pellets were pressed from U.S.P. grade powder in a steel die at 60,000 psi. Doping additions were made to the zinc oxide powder before pressing. The resulting pellets were sintered in air at 500°C for 12 hr. The pellets were cooled and placed inside quartz tubes which were evacuated and sealed off. These tubes containing the pellets were then heated for 24 hr at 1200°C. This procedure was followed to ensure a dense final product and to prevent the loss of material due to evaporation during the high-temperature anneal.

The cylindrical pellets of zinc oxide were measured with a micrometer and mounted as indicated above with one end exposed as the plane for dissolution.

A water bath provided with a temperature controller was used as a thermostat (±0.5°C) and the 800 ml beaker containing dissolution medium was immersed in this thermostat. To begin a run, a sample was placed in the beaker and the stirrer activated. For the experiments in which the sample was rotated, the rotational velocity was determined using a stroboscope arrangement. To follow the rate of dissolution, 10 ml samples of the dissolving medium were withdrawn from the solution at definite times. Chemical analyses were made on the initial dissolution medium and on the withdrawn samples by the Bridgeport Testing Laboratory, Bridgeport, Connecticut.

Results and Discussion

The p-T-x data of Bloem and Kroger (9) have shown that PbS annealed at 700°C under a S_2 partial pressure of $10^{-2.69}$ atm (corresponding to a sulfur reservoir at 192.5°C) is intrinsic and stoichiometric. These data also show that excess sulfur increases the hole concentration while excess lead increases the electron concentration. Likewise silver and bismuth enter the host lattice as acceptor and donor, respectively. Simkovich and J. B. Wagner (8) have shown that PbS exhibits a Frenkel disorder on the cation sublattice. Consequently the following equations must hold for both pure and doped crystals (8, 14)

$$[Pb^{+}_{(i)}] \propto 1/\{[\text{excess } \theta] \cdot p^{1/2}_{S_2}\} \quad [1]$$

and

$$[V_{Pb+}] \propto \{[\text{excess } \theta] \cdot p^{1/2}_{S_2}\} \quad [2]$$

where the symbol $Pb^{+}_{(i)}$ denotes a singly ionized lead interstitial, θ denotes an electron, and V_{Pb+} denotes a lead vacancy with an excess negative charge.

The defect structure of zinc oxide has been reported by von Baumbach and C. Wagner (10), by K. Hauffe (11), and others. A recent summary of the data has been presented by Thomas (12). Under an excessive zinc pressure the reaction may be formulated as

$$Zn\ (g) = Zn^{+}_{(i)} + \theta \quad [3]$$

where the $Zn^{+}_{(i)}$ denotes a singly ionized interstitial zinc atom (interstitial zinc acts as a donor). The introduction of a trivalent solute to a stoichiometric crystal of zinc oxide creates cation vacancies and thereby lowers the concentration of interstitial zinc ions as has been discussed by C. Wagner (13) for solid solutions of gallium oxide, Ga_2O_3, in ZnO. Conversely, the introduction of a monovalent solute such as lithium oxide, Li_2O, will increase the concentration of interstitial zinc ions. Under a fixed

Table II. Dissolution of pure and doped zinc oxide in aqueous hydrochloric acid solution (150 cc concentrated HCl plus 350 cc H_2O) at 37°±0.5°C. Samples rotated at 950±25 rpm

Sample	No.	Cross-sectional area, cm²
Pure ZnO	23	0.2824
Pure ZnO	27	0.3269
ZnO + 1/10 mole % Al_2O_3	26	0.6491
ZnO + 1/2 mole % Al_2O_3	24	0.8928
ZnO + 1/2 mole % Li_2O	25	0.5799

oxygen partial pressure the trivalent solute increases the concentration of electrons whereas the introduction of a monovalent solute will decrease the concentration of electrons.

Therefore, in the two different systems, PbS and ZnO, there is the possibility to vary the concentration of both electronic and atomic defects by varying the stoichiometry and/or doping as discussed briefly above. Furthermore, if these changes in point defects affect the solid-liquid reaction, there is a sufficiently wide range of concentrations and types that the effect should be readily observable.

Tables I and II list sample sizes and experimental conditions. The kinetics of dissolution are shown graphically in Fig. 1, 2, and 3. Figure 1 shows the dissolution kinetics of lead sulfide crystals in concentrated nitric acid. Note that these curves tend to show an exponential increase in rate with time. This behavior may be attributed to the formation of HNO_2 during the reaction and the subsequent catalysis of the reaction. During the reaction, large amounts of gas were evolved and free sulfur was liberated. Consequently we write the following tentative equation

$$3PbS + 8HNO_3 = 3S^\circ + 3Pb(NO_3)_2 + 4H_2O + 2NO \quad [4]$$

for the dissolution process. As can be seen from Fig. 1, the samples which were doped with silver dissolve much more rapidly than the undoped or the bismuth doped samples. Especially because of the catalytic effect of the HNO_2, a comparison of the

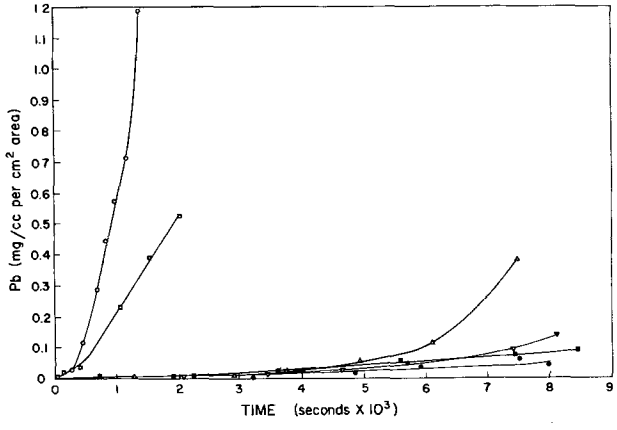

Fig. 1. Kinetics of dissolution of single crystals of lead sulfide in concentrated nitric acid at 60° ± 0.5°C. ○, PbS plus ½ mole % Ag_2S; □, PbS plus 1/20 mole % Ag_2S; △, PbS stoichiometric; ▽, PbS sulfur excess; •, PbS lead excess; ■ PbS plus ½ mole % Bi_2S_3.

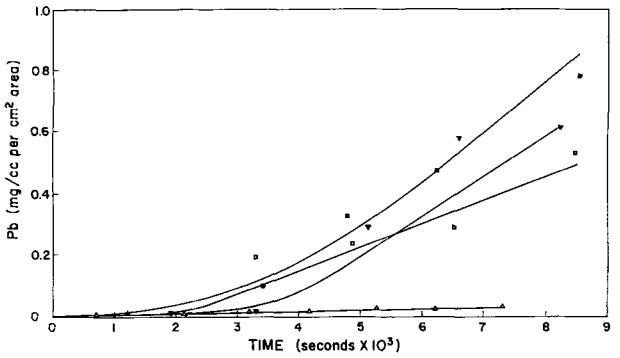

Fig. 2. Kinetics of dissolution of single crystals of lead sulfide in aqueous hydrochloric acid at 45° ± 0.5°C. Open triangle, PbS; solid inverted triangle, PbS; open square, PbS plus ½ mole % Ag_2S; solid square, PbS plus ½ mole % Bi_2S_3.

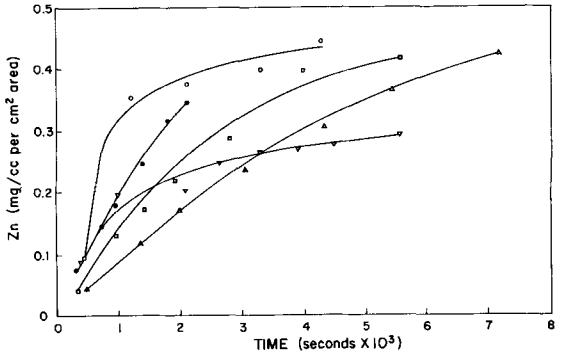

Fig. 3. Kinetics of dissolution of zinc oxide pellets in concentrated hydrochloric acid at 37° ± 0.5°C. ○, ZnO; •, ZnO; □, ZnO plus ½ mole % Li_2O; △, ZnO plus ½ mole % Al_2O_3; ▽, ZnO plus ½ mole % Al_2O_3.

initial slopes of the curves is more meaningful as a measure of the effect of the influence of defect structure. Also, as the reaction progresses, the surface area of all samples may change. Rate data obtained from the initial slopes are presented in Table III. The data are reported as milligrams of lead per cubic centimeter of solution per second for 1 cm² of initial surface area of sample.

For the analogous compound, lead selenide (14), Seltzer and Wagner (15) found that the bismuth doped crystals dissolved much more rapidly than the silver doped or the undoped crystals. The reaction in the latter case also evolved large quantities of gas, but there was no free selenium apparent, and we write the tentative dissolution equation as

$$3PbSe + 8HNO_3 = 3PbSeO_4 + 8NO + 4H_2O \quad [5]$$

In both systems the reaction is markedly affected by the introduction of doping agents which change

Table III. Initial rates of dissolution of doped and undoped lead sulfide single crystals in concentrated nitric acid

Test No.	Composition	Dissolution rate, mg/cc/cm²/sec
6	PbS + 1/2 mole % Ag_2S	$7.9_7 \times 10^{-5}$
5	PbS + 1/20 mole % Ag_2S	$1.7_6 \times 10^{-5}$
9	PbS (Pb excess)	$1.2_5 \times 10^{-6}$
10	PbS (Stoich)	$3.8_3 \times 10^{-6}$
11	PbS (Stoich)	$4.5_4 \times 10^{-6}$
8	PbS (S excess)	$1.6_3 \times 10^{-6}$
7	PbS + 1/2 mole % Bi_2S_3	$3.8_1 \times 10^{-6}$

the defect structure. The reason for this apparent inversion in behavior or the fact that one dope is more effective than another is not known.

Figure 2 shows the kinetics of dissolution of single crystals of lead sulfide in concentrated hydrochloric acid. In this case there was a much less pronounced difference between the dissolution rates of the doped and undoped crystals, and a tentative reaction equation may be formulated as

$$PbS + 2HCl = PbCl_2 + H_2S \qquad [6]$$

Likewise the kinetics of dissolution of the zinc oxide pellets in aqueous hydrochloric acid were not markedly affected by the doping agents as can be seen in Fig. 3. A tentative equation for this process is

$$ZnO + 2HCl = ZnCl_2 + H_2O \qquad [7]$$

Note that in both the PbS and PbSe systems where there was a large change in the oxidation states of the reactants and products, the kinetics were altered markedly by the introduction of doping agents (and to a less extensive way by changes in stoichiometry in the case of the PbS crystals) while those reactions in which there was only a small change in the oxidation states of the reactants and products, there was no effect of doping additions nor of deviations from stoichiometry.

A comparable study (16) using etchants which react slowly has been made on the rate of etch pit formation in doped and undoped crystals of lead sulfide. In that study, the dissolution medium was a mixture of aqueous hydrochloric acid and thiourea. The rate of etch pit growth was linear in time, and there was no effect of doping or deviation from stoichiometry on the rate of etch pit growth. This behavior may be expected on the basis of the foregoing discussions if the thiourea-hydrochloric acid etch removes the lead by means of a complex formation (17) involving an "addition compound" of lead and thiourea which does not involve a large change in the oxidation state of lead. Unfortunately, the exact electronic state of lead in this complex is not as yet known. (17).

Summary

The kinetics of dissolutions of semiconductors as a function of point defects introduced by varying the stoichiometry and/or by doping additions of foreign impurities have been studied. In particular, experiments on two ionic semiconductors, zinc oxide and lead sulfide, having different defect structures have been carried out in two different dissolution media, nitric acid and hydrochloric acid. These data show that when there is a large change in the oxidation state of the reactants and products during the solid-liquid reaction there may be a pronounced influence of point defects on the kinetics of the reaction. Further study on other systems are needed to test the generality of this working hypothesis.

Manuscript received Sept. 4, 1962; revised manuscript received Nov. 30, 1962. This work was supported by the Office of Naval Research.

Any discussion of this paper will appear in a Discussion Section to be published in the December 1963 JOURNAL.

REFERENCES

1. C. Wagner, *J. Chem. Phys.*, **18,** 69 (1950).
2. H. Kobayashi and C. Wagner, *ibid.*, **26,** 1609 (1957).
3. F. Young, *Acta. Met.*, **8,** 117 (1960).
4. H. J. Engell, *Z. Elektrochem.*, **63,** 835 (1959); *Arch. Eisenhüttenw.*, **28,** 109 (1957).
5. M. Cretella and H. Gatos, *This Journal*, **105,** 487 (1958).
6. J. F. Dewald and D. R. Turner in "Semiconductors," N. B. Hannay, Editor, p. 750, Rheinhold Publishing Corp., New York (1959).
7. B. A. Irving in "The Electrochemistry of Semiconductors," P. J. Holmes, Editor, p. 269, Academic Press, New York (1962).
8. G. Simkovich and J. B. Wagner, Jr., "The Diffusion of Lead-210 into Single Crystals of Lead Sulfide as a Function of Stoichiometry and Doping Additions" submitted to *J. Chem. Phys.*, July 1962.
9. J. Bloem, Thesis, University of Utrecht (1956); J. Bloem and F. Kröger, *Z. physik. Chem. (N.F.)*, **7,** 1 (1956); J. Bloem and F. Kröger, *ibid.*, **7,** 15 (1956); J. Bloem, F. Kröger, and H. J. Vink, Report on the Conference on Defects in Crystalline Solids (Bristol, 1954), p. 273 (1955).
10. H. H. von Baumbach and C. Wagner, *Z. physik. Chem. (B)*, **22,** 199 (1933).
11. K. Hauffe, "Reaction in und an Festen Stoffen," Springer-Verlag, Berlin (1955).
12. D. G. Thomas, in "Semiconductors," N. B. Hannay, Editor, p. 300, Rheinhold Publishing Corp., New York (1959).
13. C. Wagner, *J. Chem. Phys.*, **18,** 62 (1950).
14. M. Seltzer and J. B. Wagner, Jr., *ibid.*, **36,** 130 (1962).
15. M. Seltzer and J. B. Wagner, Jr., Unpublished data.
16. W. Franklin and J. B. Wagner, Jr., "Dislocations and Glide in Single Crystals of Lead Sulfide as a Function of Stoichiometry and Doping Additions," To be published.
17. R. C. Haworth and F. G. Mann, *J. Chem. Soc.*, **1943,** 661.

December 1963 Discussion Section

A Discussion Section, covering papers published in the January-June 1963 JOURNALS, is scheduled for publication in the December 1963 issue. Any discussion which did not reach the Editor in time for the June 1963 Discussion Section will be included in the December 1963 issue.

Those who plan to contribute remarks for this Discussion Section should submit their comments or questions in triplicate to the Managing Editor of the JOURNAL, 30 East 42 St., Rm. 1806, New York 17, N. Y., *not later than September 2, 1963.* All discussion will be forwarded to the author(s) for reply before being printed in the JOURNAL.

Photoluminescence of α-SiC

Arrigo Addamiano, Ralph M. Potter, and Vernon Ozarow

Lamp Research Laboratory, General Electric Company, Nela Park, Cleveland, Ohio

ABSTRACT

The room temperature photoluminescence of single crystals of SiC was investigated. Broad emission bands peaking from 5450 to 6700Å were observed for crystals containing grown p-n junctions prepared by alternate doping with BCl_3 and N_2. Only the n-part of the junctions showed appreciable luminescence. Changes in photoluminescence spectra were found to be associated with changes in crystal structure and optical absorption edge. Analysis of the emission and absorption spectra and the temperature dependence of brightness suggests that photoluminescence involves transitions from a deep donor level to a boron acceptor level about 0.3 ev above the valence band. At temperatures from 77°K to room temperature, the quantum efficiency of the photoluminescence is of the order of 1%.

Lely and Kröger (1) investigated the photoluminescence of α-SiC at liquid nitrogen temperature. For crystals grown in an atmosphere of Ar + N_2 they reported emission in bands peaking at 4800Å, 5200Å, 6000Å, and 6600Å. At room temperature none of the crystals showed appreciable luminescence. More recently Choyke, Hamilton, and Patrick (2) reported for crystals grown in Ar or H_2 a band at 5000Å [1] plus a series of lines at shorter wavelengths at 77°K, but only an extremely weak orange emission at room temperature. The present paper reports some observations on α-SiC crystals which show moderately bright photoluminescence peaking at 5450Å, 6100Å, and 6700Å, and having about the same brightness at room temperature as at 77°K.

Experimental and Results

The crystals studied were originally prepared as part of a program for making rectifiers and related devices and thus were not intentionally doped to obtain photoluminescence. The method used for growing these crystals was similar to that of Lely (3) and of Chang and Kroko (4-5) but modified in the growth chamber as illustrated in Fig. 1.

The purpose of the central tube was to facilitate the exchange of gases between the ambient and the growth chamber and to offer some control over the temperature gradient. The data reported here were taken with crystals grown in an argon ambient to which boron trichloride and nitrogen were added to effect p- and n-type doping respectively. The argon was purified by passing over a titanium getter at 900°C. The boron trichloride was added to the argon during the initial part of the crystal growing run and replaced with nitrogen toward the end so that a p-n junction was formed during the time of dopant change. The n-type region was therefore on the exterior of the crystal platelets.

The concentration of the nitrogen in the argon admitted to the growth chamber was about 10% and the boron trichloride about 15% by volume. The boron-doped p-type region was purple-black and the nitrogen-doped n-type region was various shades of green depending on the nitrogen concentration. Only the n-type region was photoluminescent under 3650Å excitation.

The majority of these platelets were of the types schematically represented in Fig. 2. The type shown in Fig. 2a has been reported previously (4-5). The

[1] For comparison with the other emission spectra, the curves of Choyke *et al.* were replotted as energy per unit wavelength interval; this plot shows the peak at 5000Å.

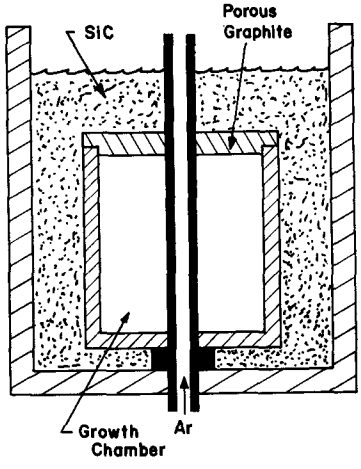

Fig. 1. Schematic drawing of the modified growth chamber used with a conventional Lely type furnace.

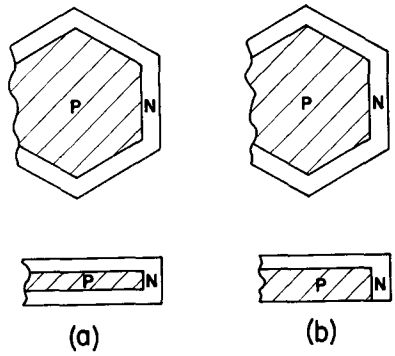

Fig. 2. Schematic drawing of the two most typical types of platelets obtained with consecutive BCl_3 and N_2 doping during growth. In case a the fluorescent n-type layer grows on both faces of the crystal while in case b it grows on only one face.

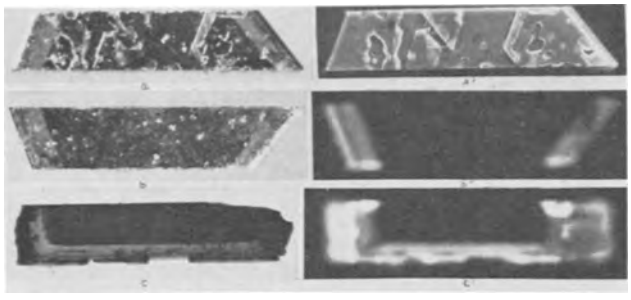

Fig. 3. Various views of a section cut from a hexagonal SiC platelet. In a, a', b, and b' the c axis is perpendicular to the plane of the paper. In c and c' an edge on view of the crystal section is displayed. Photographs a and a' are of the same surface of the crystal with a taken in reflected light and a' under 3650Å excitation. Photographs b and b' represent corresponding conditions on the other surface of the crystal. Photograph c was taken in transmitted light and c' under 3650Å excitation. (The edge of the platelet chipped off during polishing between c' and c and thus the transparent portion which should appear on the right edge of c is missing.)

more unusual type shown in Fig. 2b is further illustrated in Fig. 3 where the presence of the n-layer is shown in various ways by transmission and photoluminescence under 3650Å excitation. In some crystals the n-type layer appeared as two distinct regions, one light green in color and the other a darker green with a distinct boundary between them. This was also manifested in the photoluminescence where the lighter colored region was brighter than the other.

To eliminate any doubt that the observed photoluminescence might be due to some hitherto unknown compound or to an oxide layer, some crystals were boiled in conc HCl, conc HNO_3, conc HF, aqua regia, 10% Na_3PO_4, and 10% $(NH_4)_2HPO_4$. No change of photoluminescence occurred after these treatments. One week firing of the crystals at 900°C in air or in a stream of O_2 produced an extremely thin oxide layer which was easily removed by HF treatment without loss of photoluminescence. The luminescent layer could be removed by abrasion with diamond paste; the resulting powder was luminescent. An x-ray powder photograph of this material showed all the lines of the 6H-SiC polytype.

Single crystal oscillation, rotation and moving film x-ray photographs of photoluminescent crystals were in most cases consistent with the existence of an hexagonal 6H structure. A few 4H crystals were also identified. In every case disorder was present, as evidenced by the presence of diffuse scattering and streaks across the reflections.

The emission spectra of selected crystals under 3650Å excitation at room temperature are shown in Fig. 4 and consist of broad bands peaking at 5450Å, 6100Å, and 6700Å. The band peaking at 5450Å is typical of crystals which gave the diffraction pattern of the 4H polytype, while for the crystals giving the 6100Å and 6700Å peak the diffraction patterns were those of the 6H polytype. The optical transmission of the n part of the crystals investigated was different for crystals having different photoluminescence. Figure 5 shows that the absorption edge follows the same trend as the emission peaks. The other features of the transmission spectra for our 6H crystals are similar to those reported by Lely and Kröger (1) and Groth and Kauer (6).

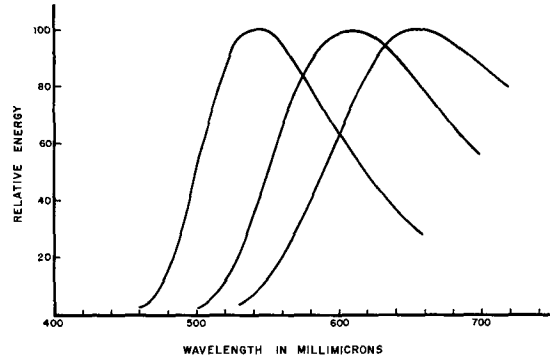

Fig. 4. Emission spectra of SiC crystals at room temperature under 3650Å excitation. (The ordinate is relative energy per unit wavelength interval.)

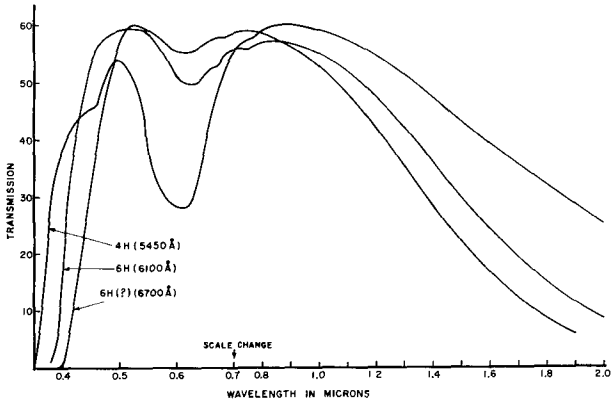

Fig. 5. Transmission spectra of the n-type region of crystals showing the indicated emission peaks. (Thickness: 4H, 100μ; 6H, 114μ; 6H(?), 122μ.)

Between 77°K and room temperature the brightness (and, therefore, the efficiency) of the photoluminescence of our crystals did not change very much. Typically a room temperature quantum efficiency of about 1% was measured for the crystals emitting at 6100Å. Figure 6 gives the temperature dependence of the brightness for the crystals exhibiting the 6700Å, 6100Å, and 5450Å emission bands. The curves are very similar for the 6100Å and 5450Å emissions, while for the 6700Å emission the curve has its inflection at an appreciably lower temperature. If the relation $B=[1+s(\exp-\epsilon/kT)]^{-1}$ is assumed for the high temperature part of the curves, where B is the relative brightness at the

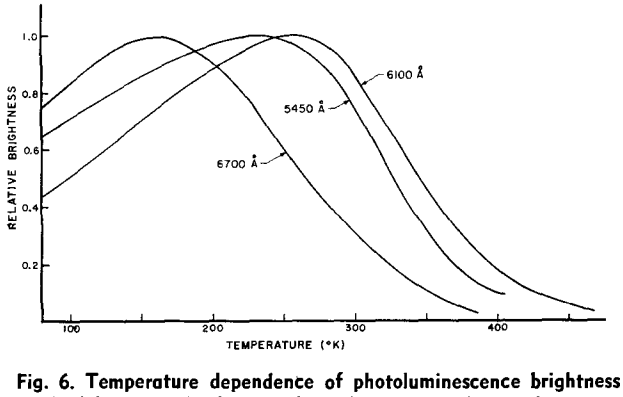

Fig. 6. Temperature dependence of photoluminescence brightness typical of SiC crystals showing the indicated emission peaks.

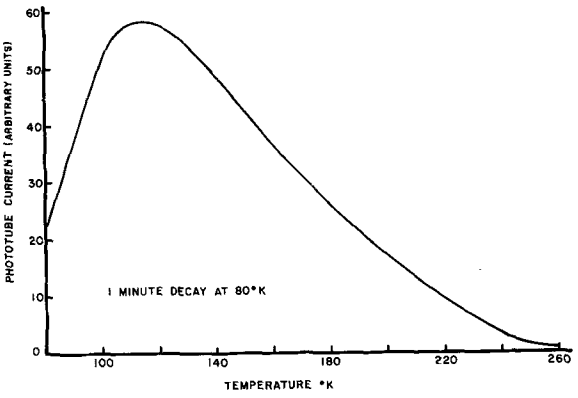

Fig. 7. Glow curve typical of both the 5450Å and 6100Å emitting crystals. Heating rate 1°/sec.

temperature T, a plot of log $(1/B-1)$ *vs.* $1/T$ should give a straight line, whose slope is a measure of the activation energy ϵ for thermal quenching of luminescence. When the data were so plotted, straight lines were obtained with $\epsilon \sim 0.3$ electron volt(ev) for the 6100Å and 5450Å emissions, and $\epsilon \sim 0.2$ ev for the 6700Å emission.

Glow curves were measured in crystals exhibiting 5450Å and 6100Å emissions; there was no significant difference in the glow curves for these two crystals. The data for a typical case are shown in Fig. 7. The trap depth was estimated by the method of initial rise slope (7). The values of trap depth found after allowing decay at various temperatures up to about 170°K were all about the same, *i.e.*, 0.1 ev. Further experiments will be necessary to decide whether we are dealing with electron traps or with hole traps.

Discussion

The preparative condition which appears to correlate with the growth of an n-layer of α-SiC showing relatively bright room temperature photoluminescence is alternate doping with BCl_3 and N_2. Crystals grown at the same temperature in the same furnace with only Ar or Ar + N_2 during the entire run showed little or no room temperature photoluminescence, although they did show blue, green, and orange emission at lower temperatures. Crystals grown in Ar + BCl_3 only showed no photoluminescence at room temperature or lower temperatures.

Presumably, after the change of doping gases the composition of the crystals varied in relative as well as in absolute concentrations of boron and nitrogen. These variations are reflected in the transmission color and photoluminescent brightness changes in the n-region of the crystal.

The variation in the emission peaks of the three crystals shown in Fig. 3 may be related to their structure through the variation of band gap with

Table I. Approximate band-gaps of different SiC polytypes at 300°K

Cubic	3C	2.3ev
Hexagonal	6H	3.0ev
Hexagonal	4H	3.2ev
Rhombohedral	15R	2.8ev
Rhombohedral	21R	2.7ev

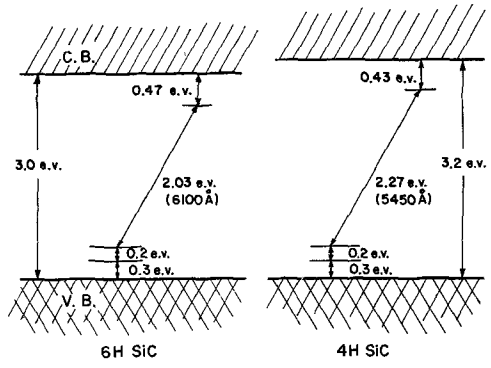

Fig. 8. Proposed energy level diagram for 4H and 6H SiC showing the observed emissions.

structure. Table I gives the values reported for different polytypes of SiC (9-11) corrected from 77° to 300°K when necessary. The two crystals emitting at 5450Å and 6100Å are 4H and 6H polytypes, respectively, according to x-ray diffraction analysis and the relative values of their band edges shown in Fig. 5. Although the crystal emitting at 6700Å also appeared to be 6H according to x-ray diffraction, its band edge is seen to be at a longer wavelength than the other 6H crystal, and it may be postulated that its structure is intermediate between 6H and a phase with a smaller band gap such as 3C.

On the assumption that the same acceptor forms part of the activator system in both 6H and 4H crystals, an energy level diagram was constructed for them (Fig. 8). The model of the luminescence center is an associated donor-acceptor pair analogous to that proposed by Apple and Williams (12) for a group of ZnS phosphors. The acceptor in the present case is probably boron. The transition responsible for the emission takes place between the ground state of the donor and an excited vibrational state of the acceptor. The ground state of the acceptor is taken to be 0.3 ev above the valence band edge, in accord with the activation energy for thermal quenching of luminescence in 6H and 4H crystals.[2] The terminal vibrational state is assumed to be 0.2 ev above the acceptor ground state; this represents a guess as to the polarization energy loss. If the sum of the emission peak energy (2.03 or 2.27 ev) and the terminal state energy (~0.5 ev) is subtracted from the band gap, about the same energy difference, 0.4 to 0.5 ev, is found for both 6H and 4H stuctures. This value is taken as the depth of the donor level.

As yet we have no other evidence for a donor of this depth in our crystals. According to Lely and Kröger (1), the nitrogen donor level is only 0.085 ev deep. However, Patrick and Choyke (14) reported a Fermi level 0.5 ev below the conduction band for the low conductivity n-region in their electroluminescent junctions. This suggests that some impurity level probably lies at this position. Chlorine and oxygen are two impurities which might be present and which could be expected to lead to deep donor levels in SiC. Chlorine from the BCl_3 might well be present in an appreciable concentration, while oxygen is not likely to be present in

[2] Values close to 0.3 ev have been reported by Lely and Kröger (1) and by van Daal *et al.* (13) from Hall effect measurements on α-SiC containing boron.

greater than trace amounts. Either impurity would have an energetic advantage over nitrogen for formation of donor-acceptor pairs because of the greater charge on the fully ionized donors (+3 or +2 compared to +1).

Summary

Certain samples of n-type SiC show a photoluminescence quantum efficiency of the order of 1%, which holds nearly to room temperature before thermal quenching sets in. The emission color depends markedly on crystal structure, varying from red to green for different structures. Emission and absorption spectra, and temperature dependence of brightness are interpreted in terms of a center consisting of an acceptor introducing a level about 0.3 ev above the valence band edge associated with a deep donor. It is suggested that the acceptor is boron.

Note Added in Proof. Measurements in progress in this laboratory on the brightness-temperature relation *vs.* excitation intensity on luminescent crystals and on the temperature dependence of electrical conductivity of crystals doped with boron only suggest an alternate energy level diagram in which the ~0.3 ev activation energy for quenching is assigned to the donor level and the boron acceptor level is deeper than 0.3 ev.

Manuscript received Sept. 26, 1962. Revised manuscript received Nov. 28, 1962.

Any discussion of this paper will appear in a Discussion Section to be published in the December 1963 JOURNAL.

REFERENCES

1. J. A. Lely and F. A. Kröger, "Semiconductors and Phosphors," M. Schon and H. Welker, Editors, p. 514; p. 525, Interscience, New York (1958).
2. W. J. Choyke, D. R. Hamilton, and L. Patrick, *Phys. Rev.*, **117**, 1430 (1960); *Bull. Am. Phys. Soc. II*, **7**, 77 and 185 (1962).
3. J. A. Lely, *Ber. Deutch. Keram. Ges.*, **32**, 229 (1955).
4. H. C. Chang and L. J. Kroko, Paper presented at the Semiconductor Device Research Conference, Boulder, Colorado, July 15-17, 1957.
5. H. C. Chang and L. J. Kroko, Am. Inst. Elec. Engrs. Conference Papers 57-1131, Chicago (1957).
6. R. Groth and E. Kauer, *Physica Status Solidi*, **1**, 445 (1961).
7. W. Hoogenstraaten, *Philips Research Repts.*, **13**, 515 (1958).
8. W. J. Choyke and L. Patrick, Proc. Int. Conf. on Semiconductor Physics, Prague 1960, p. 432, Academic Press, New York (1961).
9. W. J. Choyke, *Bull. Am. Phys. Soc.*, **7**, 185 (1962).
10. H. R. Philipp and E. A. Taft, "Conference on Silicon Carbide," J. R. O'Connor and J. Smiltens, Editors, p. 366, Pergamon Press, New York (1960).
11. H. Lipson, AFCRL 10, Jan. 3, 1961, pp. 43-46.
12. E. F. Apple and F. E. Williams, *This Journal*, **106**, 224 (1959)
13. H. J. van Daal, C. A. A. J. Greebe, W. F. Knippenberg, and H. J Vink, *J. Appl. Phys. Suppl. to Vol.*, **32**, 2225 (1961).
14. L. Patrick and W. J. Choyke, "Conference on Silicon Carbide," J. R. O'Connor and J. Smiltens, Editors, p. 281, Pergamon Press, New York (1960).

Carrier Compensation in Germanium Telluride

M. S. Lubell and R. Mazelsky

Research Laboratories, Westinghouse Electric Corporation, Pittsburgh, Pennsylvania

ABSTRACT

Changes in the Seebeck coefficient and Hall constant have been studied for the system $(1-x)M_{0.024} + (1-x)Ge_{0.976}Te + x\,Bi_2Te_3$ where M stands for the metals, germanium, tin, indium, gallium, titanium, and silver. The solubility of these metals is shown to increase with the addition of "neutral vacancies" introduced via bismuth telluride. A linear relationship is obtained between the log of the carrier concentration and the amount of neutral vacancies. The initial solubility is determined only by the ion charge and radius of the solute metal, and the initial carrier concentration is inversely proportional to the charge/radius ratio. An expression satisfying the data is obtained for the solubility as a function of charge, radius, neutral vacancy, and known constants.

Although there are extensive data available on tin and lead tellurides, there has been little reported on germanium telluride. The available data on germanium telluride have been summarized recently (1). For the purposes of the present work, the important information is that the congruently melting compound corresponds to the composition $Ge_{0.976}Te$ (2). Alloys of $Ge_{0.976}Te$ and GeTe with bismuth telluride were investigated recently (3). On the basis of this work, it was shown that the favorable thermoelectric properties and low carrier concentration of pressed and sintered GeTe-Bi_2Te_3 alloys were due to germanium metal initially present as a second phase dissolving into the lattice and filling the cation vacancies. This solubility was attributed to the "neutral vacancies" introduced via Bi_2Te_3.

The present work was undertaken (i) to determine if other metals are also soluble in $Ge_{0.976}Te$-Bi_2Te_3 alloys; (ii) to obtain the dependence of carrier concentration and solubility on the valence state and radii of the solvent atom introduced; and (iii) to obtain the dependence of carrier concentration and solubility on the amount of "neutral vacancies" added.

Experimental

The procedure used for the sample preparations and the experimental techniques employed for the Seebeck, Hall, and resistivity measurements have been described previously (3).

Results

The solid solutions prepared with germanium telluride were of the following general type

$$(1-x)M_{0.024} + (1-x)Ge_{0.976}Te + x\,Bi_2Te_3 \quad [1]$$

Here M stands for the metal solutes, germanium, tin, indium, gallium, titanium, and silver. An ex-

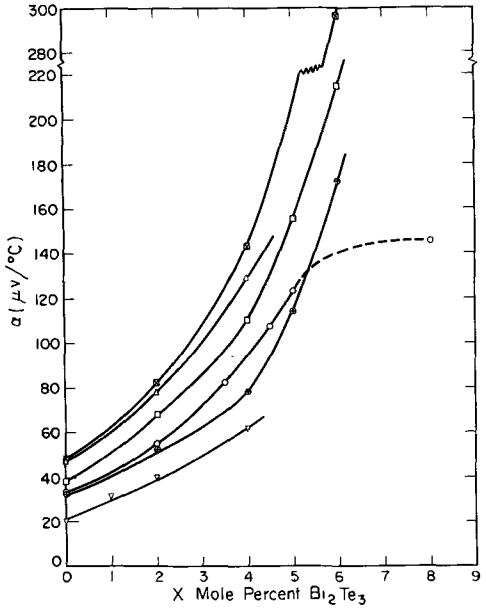

Fig. 1. Room temperature absolute Seebeck coefficient in μv/°C vs. x, the mole per cent of Bi_2Te_3. Open circle, Ge; open circle with plus sign, Sn; open square, Ga; open square with times sign, In; open triangle, Ti; open inverted triangle, Ag, in all 5 figures.

ception was made for gallium in that only 2.0 at. % Ga was used rather than 2.4 at. %.

Figure 1 shows the variation of the room temperature Seebeck coefficient [α] with x, the mole per cent of bismuth telluride for the various metal solutes. All the samples are p-type. In marked contrast to previous doping of germanium telluride (1-3) room temperature Seebeck values in excess of +150 μv/°C could be obtained for most of the above metals. Indeed, the $x = 6\%$ compound with indium has a value of 296 μv/°C. Another point worth noting is that the silver doped compound, $Ag_{0.024}Ge_{0.976}Te$ has a lower Seebeck coefficient than $Ge_{0.976}Te$ itself (21 compared to 32 μv/°C).

On Fig. 2, the electrical resistivities (ρ) measured at liquid nitrogen temperature are drawn *vs.*

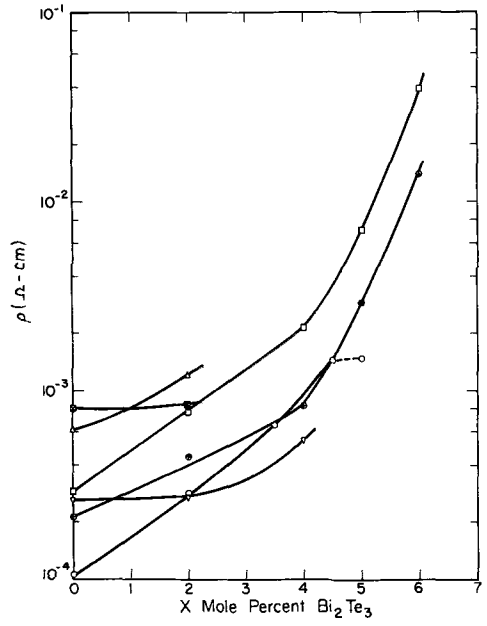

Fig. 2. Electrical resistivity in ohm-cm vs. x, the mole per cent of Bi_2Te_3 at $T = 77°K$.

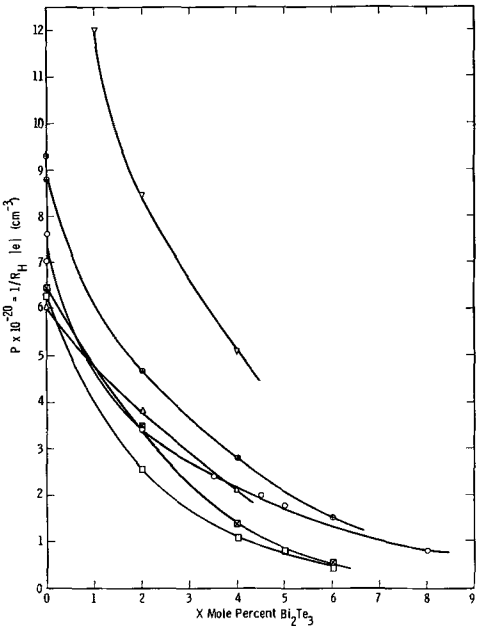

Fig. 3. Carrier concentration in cm^{-3} vs. x, the mole per cent of Bi_2Te_3 at $T = 77°K$.

x. These data are presented in order to estimate the mobility of the carriers and also for completeness. It has generally been our experience that Seebeck and Hall data taken on pressed and sintered material reproduce well and compare favorably with measurements on crystals; however, this is not always the case for resistivity measurements.

On Fig. 3, calculated hole carrier concentrations are shown *vs.* x. These were calculated from the Hall measurements on the basis of a degenerate, single band model using the expression $P = \frac{1}{R_H|e|}$, where $|e|$ is the absolute value of the electronic charge, 1.6×10^{-19} coulombs. The few low values of carrier concentration which corresponded to Seebeck values of $2(k/e)$μv/°C or larger were corrected for nondegeneracy by the usual factor $3\pi/8$. Owing to the fact that most of the Hall measurements showed an anomalous rise with temperature (possibly due to two-phase material), all calculations of carrier concentrations were made using Hall values taken at liquid nitrogen temperature. In the nondegenerate region the change in Seebeck coefficient with change in carrier concentration approximately follows the theoretical formula for an extrinsic, single band semiconductor, *i.e.*, $\Delta\alpha = -(k/e)\Delta \ln P$. In the degenerate region fair agreement is obtained by using the expression $\Delta\alpha = -0.7(k/e)\Delta \ln P$.

Discussion

It has been shown for $Ge_{0.976}Te$ that the carriers calculated from the nonstoichiometry on the assumption of two holes per germanium vacancy agree well with the Hall measurements of both Bridgemann grown ingots and pressed and sintered samples (1-3). For purposes of calculation the carrier concentration of $Ge_{0.976}Te$ (equivalent to $GeTe_{1.025}$) was assumed to be the theoretical value, $P = 9.25 \times 10^{20}$ cm^{-3}. It was previously found that

there is a dependence between the vacancies in the $Ge_{(1-y)}Te$ lattice hereafter referred to as "empty Ge sites" ($V^{2+}{}_c$) and the carrier concentration calculated from Hall measurements (3). Thus, changes in the carrier concentration are assumed to result from a metal dissolving into the lattice on cation sites and ionizing. For the series of alloys $M_{0.024}Ge_{0.976}Te$, the solubility of the metal M is not very large. In order to increase the solubility, it is necessary to increase the number of available vacancy sites. It also is important that the additional vacancies do not create a charge imbalance upon their introduction. Such a procedure is possible through alloying with Bi_2Te_3.

For clarification, Eq. [1] is recalculated on the basis of one tellurium atom/molecule; *i.e.*,

$$\frac{M_{0.024(1-x)}}{1+2x}\frac{Ge_{0.976(1-x)}}{1+2x}\frac{Bi_{2x}}{1+2x}Te \qquad [2]$$

Hence, the solid solutions of germanium telluride with Bi_2Te_3 result in cation vacancies because for every three tellurium ions introduced into the lattice, only two bismuth ions are added to cation sites. Since Bi_2Te_3 by comparison with $Ge_{0.976}Te$ is essentially an electrically neutral material, this alloying does not diminish the carrier concentration (3). Although the cation vacancies added may be physically indistinguishable from the initial "empty Ge sites," for convenience, they will be called "neutral vacancies" $\left(V^{\circ}{}_c = \frac{x}{1+2x}\right)$.

The solubility of the donors in atom per cent (Ag, the only acceptor will be discussed separately) is calculated from the difference between the initial "empty Ge sites" [$V^{2+}{}_c$ (initial) = 2.4 at. %] and the final charged vacancies present. At any composition the charged vacancies are simply proportional to the carrier concentration. In symbols the carriers and solubility take the form

$$P = 2AV^{2+}{}_c \qquad [3]$$

$$S = \frac{1}{|e|}[2B - 2V^{2+}{}_c] \qquad [4]$$

where B = 2.4 at. % (the initial empty Ge sites), $|e|$ is the ion charge or number of donor electrons/atom, and $A = 1.93 \times 10^{22}$ cm^{-3}, the carriers/defect/charge based on one formula weight of the congruently melting composition, $Ge_{0.976}Te$. In Fig. 4 the solubility S in atom per cent is plotted against

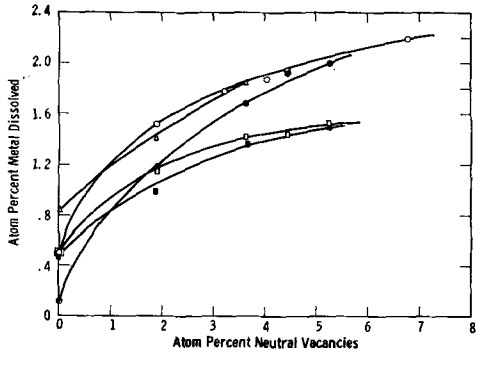

Fig. 4. Solubility of donors in atom per cent vs. the neutral vacancies ($V^{\circ}{}_c$) in atom per cent.

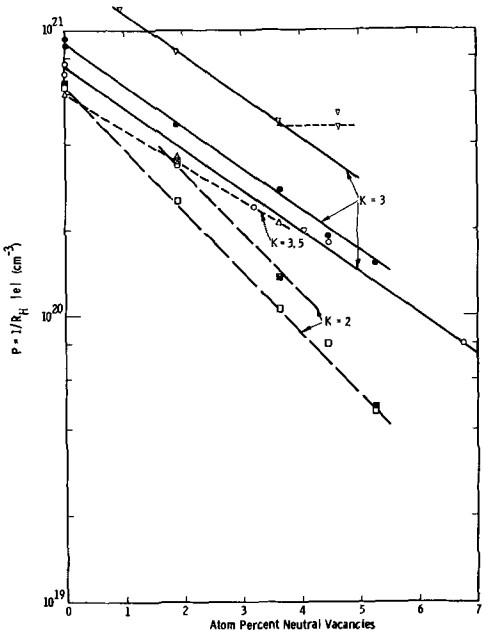

Fig. 5. The log of the hole carrier concentration in cm^{-3} vs. the neutral vacancies in atom per cent at T = 77°K.

$V^{\circ}{}_c$, the neutral vacancies, assuming that $|e| = 2$ for Ge, Sn, and Ti; $|e| = 3$ for Ga and In. We offer as justification for these assumptions the fact that not enough Ga or In was added to account for the low carrier concentration on the basis of just 2 carriers/atom when the concentration of the alloy reached $x = 6\%$. The solubility limits were tested by preparing $x = 4\%$ alloys with varying amounts of the solute. Below the limit the Seebeck coefficient and carrier concentration changed continuously with increasing amounts of the solute. When the solubility limit was exceeded, no changes in the Seebeck coefficient and carriers were found.

In Fig. 5, the log of the hole carrier concentration is plotted against the neutral vacancies, and it can be seen that a set of straight lines fit all the data. The lines in Fig. 5 are drawn according to the equation

$$P = P_0 \exp(-V^{\circ}{}_c/K) \qquad [5]$$

where P_0 is the initial carrier concentration for each of the various metal solutes when no neutral vacancies are added ($V^{\circ}{}_c = 0$), and K is a constant for a particular metal solute. The various K values conform to a simple relationship

$$(K|e|)_M = (K|e|)_{Ge} = 6 \qquad [6]$$

We may ask ourselves how the lattice is being changed as the metal solutes are added. The only difference the lattice detects in the end point compounds ($x = V^{\circ}{}_c = 0$) are the charge and radius of the solute metal. It is natural to expect then that both the initial carrier concentration and solubility will depend on these parameters. In Table I, the assumed ion charge, octahedral covalent radii, and carrier concentration data are tabulated for each of the solute elements in order to determine the relationship between P_0 and S_0, the initial solubility for $V^{\circ}{}_c = 0$ on these parameters. The radii were taken as 1.03 times the tetrahedral covalent radii. The data are presented as a ratio of the $|e|/R$ for Ge

Table I. Dependence of carrier concentration on charge and radius for the system (1 — x) $M_{0.024}$ + (1 — x) $Ge_{0.976}$ Te + x Bi_2Te_3

Element	Charge	Octahedral covalent radius, Å*	e/R	$\frac{(e/R)_{Ge}}{(e/R)_M}$	P_M/P_{Ge} for x=0	x=1	x=2 %	x=3	x=4
Ge	2	1.26	1.59	1.0	1.0	1.0	1.0	1.0	1.0
Sn	2	1.44	1.39	1.1	1.2	1.3	1.4	1.3	1.3
Ga	3	1.30	2.31	0.7	0.9	0.9	0.7	0.6	0.5
In	3	1.48	2.02	0.8	0.9	1.0	1.0	0.8	0.6
Ti	2	1.32	1.52	1.0	0.8	1.0	1.1	1.1	1.0
Ag	1	1.57	0.637	2.5	2.6	2.3	2.5	2.4	2.3

* Calculated from Tetrahedral Covalent Radii obtained from ref. (4), p. 246.

to the $|e|/R$ for the metal. This value is compared with the ratio of the P for the metal to the P for Ge at various alloy compositions. Although the e/R varies by as much as a factor of four, and the carrier concentration by a factor of three for $x = V°_c = 0$, the following simple relationship holds remarkably well

$$(P_o\,|e|/R)_M = (P_o\,|e|/R)_{Ge} = 11.6 \times 10^{20}\ \text{cm}^{-3}\ \text{Å}^{-1} \quad [7]$$

In fact, this type of relationship is seen to hold fairly well for values of P to neutral vacancy concentrations of 2.8 at. %. Although initially the value for the charge was assumed, Eq. [7] will now predict the ion charge of a metal dissolved in germanium telluride if one has a measurement of the carrier concentration. The deviations of P_M from this simple relation at higher neutral vacancies is of course due to the exponential term of Eq. [5] being omitted. At constant $V°_c$ the exponential term has a dependence on charge expressed by the relationship of Eq. [6].

It is important to note that Eq. [7] is not compatible with simple solubility for a univalent donor unless the effective radius is smaller than 0.8Å. A donor with an ion charge of one dissolving into "empty Ge sites" would reduce the hole carrier concentration below the initial value of 9.25×10^{20} cm^{-3}. However, Eq. [7] predicts values greater than this for reasonable values of R ($R > 1.0$Å). The univalent case will be discussed below.

Equations [3] through [7] can now be combined to yield an expression for S as a function of the parameters, charge, radii, neutral vacancy concentration, and known constants.

$$S = \frac{1}{|e|}\left[4.8 - \frac{6.02}{|e|/R}\exp -\left(\frac{|e|\,V°_c}{6}\right)\right] \quad [8]$$

All the data in Fig. 4 have the form of the above equation.

Although the data for silver, the only acceptor investigated, conforms with most of the above equations, there are some essential differences in interpretation. The initial hole carrier concentration for silver (not shown in Fig. 5) is 18.7×10^{20} cm^{-3}, *i.e.*, twice that of $Ge_{0.976}Te$. By means of Eq. [7], the proper ion charge is one but since the carrier concentration for some of the alloys also drops below that of $Ge_{0.976}Te$, silver cannot be regarded as having a negative valence. A possible explanation is that Ag^{+1} replaces the germanium which either remains un-ionized in interstitial sites ($R_{Ge} = 1.26 < 1.33 \equiv$ the tetrahedral site), or else comes out of the lattice forming a second phase. In this manner one hole is created for each Ag atom that dissolves. If it is assumed that initially all the Ag is soluble, then the calculated concentration is $P_o = 14 \times 10^{20}$ cm^{-3}. In Fig. 5, it can be seen that for large neutral vacancies the carrier concentration of the silver doped alloys drops rapidly and above $V°_c = 1.5$ at. % falls below that for $Ge_{0.976}Te$. We interpret this to mean that as the neutral vacancies are increased the displaced Ge dissolves back into the lattice providing 2 electrons/Ge. The constant, $K = 3$ for this range, is consistent with a charge of two for carrier compensation. It seems reasonable to expect that all the Ge is soluble since there will still be a considerable hole concentration due to the 2.4% Ag^{+1} ions. On this model, when all the Ge metal dissolves back into the lattice, the minimum hole carrier concentration, $P = 4.62 \times 10^{20}$ cm^{-3} should be obtained. This value corresponds to the dotted line drawn across the Ag doped alloy in Fig. 5. If, instead, the model is wrong and compensation continues beyond this value, then the value $P = 3.4 \times 10^{20}$ cm^{-3} would be expected for the $x = 5\%$ alloy. As seen in Fig. 5, the carrier concentration for the $x = 5\%$ alloy is in good agreement with the proposed model. It is evident then that the univalent metal unlike the divalent and trivalent metals is not simply soluble. This is in verification of Eq. [7].

Summary

1. We have shown that a variety of elements (both donors and acceptors) are soluble in $Ge_{0.976}Te$.

2. Furthermore, the solubility is shown to increase with the addition of neutral vacancies introduced via bismuth telluride.

3. A linear relationship is obtained between the log of the carrier concentration and the amount of neutral vacancies.

4. The initial solubility is determined only by the ion charge and radius of the metal and the initial carrier concentration is inversely proportional to the charge/radii ratio.

5. An expression satisfying all the data is obtained for the solubility as a function of charge, radius, neutral vacancy, and known constants.

6. The doping by silver, although compatible with most of the expressions used for the donors, is interpreted differently. The initial increase in carrier concentration is due to Ag^{+1} replacing Ge, and then the decrease at large neutral vacancy concentration is attributed to Ge dissolving back into the lattice.

Acknowledgment

The authors wish to thank W. E. Kramer for technical assistance; they also appreciate helpful discussions with F. L. Carter.

Manuscript received Oct. 23, 1962; revised manuscript received Jan. 21, 1963. This paper was prepared for delivery before the Boston Meeting, Sept. 16-20, 1962.

Any discussion of this paper will appear in a Discussion Section to be published in the December 1963 JOURNAL.

REFERENCES

1. "Thermoelectricity: Science and Engineering," R. R. Heikes and R. W. Ure, Jr., Editors, pp 434-439, Interscience Publishers, New York (1961).
2. J. P. McHugh and W. A. Tiller, *Trans. Met. Soc. AIME*, **218**, 187 (1960).
3. R. Mazelsky and M. S. Lubell, Am. Chem. Soc. Symposium on Nonstoichiometric Compounds, Washington, D. C., March 1962. To be published in Advances in Chemistry Series.
4. L. Pauling, "The Nature of the Chemical Bond," 3rd ed., p. 246, Cornell University Press, Ithaca, N. Y. (1960).

Surface Energy of Germanium and Silicon

R. J. Jaccodine

Bell Telephone Laboratories, Incorporated, Allentown, Pennsylvania

ABSTRACT

Surface energy is one of the most fundamental parameters of a solid since it depends directly on the binding forces of the material. Indeed, it is a measure of the work necessary to separate a material into two parts along a plane. Very few measurements have been made of this quantity and these by indirect means, because of difficulties of measurement and interpretation. This report deals with a direct measurement of specific surface energy of Ge and Si made by the cleavage technique. By measuring the force just necessary to move a crack "in reversible fashion" the surface energy can be obtained. The measured value for the {111} planes of Ge and Si are 1060 ergs/cm^2 and 1230 ergs/cm^2. From these measured values the energy of the planes {100} and {110} can be estimated. They are:

	{100}	{110}
Ge	1835 ergs/cm^2	1300 ergs/cm^2
Si	2130 ergs/cm^2	1510 ergs/cm^2

Using the measured value of specific surface energy, assuming this is due to the appropriate number of broken bonds/cm^2, the bond strength of Ge and Si was obtained as Ge-Ge = 42.6 kcal/mole; Si-Si = 45.5 kcal/mole.

The surface energy of a solid is a fundamental property which depends on the nature of the bonding of the material. It is for this reason that many theoretical treatments have been made to calculate this parameter. These treatments range from simple atomistic theories (1) to more sophisticated calculations reviewed by Van der Hoff and Benson (2) and by Ewald and Juretschke (3). Another reason for the large amount of theoretical work in this area is that attempts to calculate energy of cohesion involve the same approach. The surface energy is the work required to separate a crystal into two parts along a plane and is equal to half the energy of cohesion.

The attempts at theoretical calculations antedate the experimental attempts to measure this energy in part due to difficulties in measurement and interpretation. One of the earliest attempts was by Lipsitt, Johnson, and Maass (4) who used the difference of heat of solution between finely ground and coarse sodium chloride as a measure of the surface energy. Most successful attempts have been made by this and similar indirect techniques.

In view of the definition of surface energy, a direct technique would be a measurement of the work necessary to cleave in "reversible" fashion a unit area of surface. In practice this means making the force measurement just at the point where an already present cleavage crack begins to move again with such dissipative factors as step formation, plastic strain, heat, etc., held to a minimum or absent.

An early measurement made this way on mica was by Obreimov (5), and recently Bailey (6) checked and found good agreement with Obreimov's values. More recently Gilman (7) has applied this technique to a series of simple crystals (mainly ionic crystals) and compares theoretical with experimental values made by various workers. Gilman also applies the cleavage mechanics of Benbow and Roesler (8) to the case of the various crystals he measured. It must be mentioned that Gilman includes two measurements on Si specimens and gives a value of 1240 ergs/cm^2 (the average of the two) for {111} plane. He cites experimental difficulty in obtaining suitable cracks for limiting the number of measurements.

In passing, mention should be made of the work of Udin, Shaler, and Wulff (9) which measures the force necessary to balance the surface tension of a wire near its melting point. This method has been applied by Udin and co-workers to measure a variety of metals including refractory metals. Some recent reviews of this and similar work can be found in the literature (10).

The purpose of this paper is to give results of surface energy measurements made on {111} planes of Si and Ge. Further, this information is used to obtain energy of {110} and {100} planes and to determine the Si-Si and Ge-Ge bond energy.

Experimental Technique

The technique of measuring surface energy depends on determining the force necessary (in "reversible fashion") to just move a crack that is al-

ready present in the specimen under test. Determining this force and the lever arm to the crack tip, along with other specimen geometry measurements, allows one to calculate the surface energy.

A major obstacle in brittle material is the formation of a suitable cleavage crack arrested in the specimen. Attempts at cracking specimen bars only resulted in complete cleavage or fracturing. A more successful system consisted of using carefully prepared {111} slices, clamping these rigidly, and initiating a crack in the exposed top surface. When successful, the constraints slowed and stopped the crack from propagating through the slice. Polishing slices in acid and using thinner cross sections increased the yield of usable specimens. When a slice contained a proper cleavage crack, then a specimen of suitable geometry was cut. Small holes were machined in either side of the crack to be used with tungsten wire hooks as places for application of force. At this stage, the specimen is ready for a measurement. It must be remarked that no one system could be considered really satisfactory for producing cracked specimens. With care and patience, a fair number of specimens could be brought to the point of measurement.

The specimen to be tested was just immersed with tungsten grips in liquid N_2. During the measurement, liquid N_2 vapor is played over the specimen continuously to maintain it below room temperature and in the vicinity of liquid N_2 (−196°C). Since the cracking was not done in vacuum, the possibility of adsorption on the freshly cleaved surface must be considered. More particularly, the region at the very tip of the fracture would have to be affected to change the force necessary to move the crack. For specimens cracked and left standing in air for periods greater than several hours, no consistent trend was noted in measured surface energy values. However, specimens oxidized to a thickness of several thousand angstroms showed a marked decrease in measured surface energy value which can be attributed to the oxide acting as a wedge to help spread the crack sides.

Force is applied to the specimen by slowly adding links of chain (1.7 g/link) onto the specimen. This system is simple, easy to use, and allows weight as small as half a link to be added and held for as long as one wishes before additional weight is added. A very good determination of force could be made in this way. After the specimen is cracked, the two sections are examined for evidences of steps, tear marks, etc. Then a second measurement of crack length is made using evidence on the cracked face of the place where the initial crack stopped and restarted. This could be conveniently done with a toolmaker's microscope. Finally, specimen dimensions are rechecked using micrometer or toolmaker's microscope. From the measured force and geometry, surface energy is determined and the value recorded provided the specimen did not show large numbers of steps, tear marks, and dissipative signs. Since dissipative factors tend to raise the measured value of surface energy, more credence is placed on the lower values. For this reason, determinations which resulted in higher values are not included in the data.

Interpretation of Experiments

In order to derive the surface energy from the measured values, an analysis of the mechanics of a cleaved specimen must be made. This has been done rather thoroughly by Benbow and Roesler (8) using isotropic elasticity and modified by Gilman (7) for crystalline material. Briefly, following Gilman, the cracked crystal is treated as two cantilever beams of length L, height t, width w, and moment of inertia $I = wt^3/12$. Under the force F applied at $x = 0$ the bending moment in each beam is $M(x) = Fx$ and the strain energy U due to this moment is

$$U = \frac{1}{2EI}\int_0^L M^2(x)\,dx = \frac{F^2L^3}{6EI}$$

Here E is Young's modulus for the cleavage plane in the direction of crack propagation. The deflection δ due to bending at the point of application of the force is

$$\delta_0 = \left.\frac{\partial U}{\partial F}\right|_{x=0} = \frac{FL^3}{3EI}$$

and incremental work dW is given by:

$$dW = Fd\delta_0 = \frac{F^2L^2dL}{EI}$$

Now to satisfy the conditions that crack motion be "reversible," we make an energy balance for the system at the point where the crack just begins to move. The work done (neglecting dissipative factors) when a crack moves dL must be equal to the change in strain energy plus the energy of the newly created surface.

This balance equation gives

$$\gamma = \frac{6F^2L^2}{Ew^2t^3}$$

This is the required relation used to interpret the measured values.

Now in order to take into account the crystalline nature of a cleavage crack, the value of Young's modulus E must be that for the cleavage plane {111} in the direction of crack propagation. We can calculate Young's modulus using the following relations between elastic constants and compliance coefficients (11)

$$S_{11} = \frac{C_{11} + C_{12}}{C_{11}(C_{11} + C_{12}) - 2C_{12}^2};$$

$$S_{12} = \frac{-C_{12}}{C_{11}(C_{11} + C_{12}) - 2C_{12}^2};\quad S_{44} = \frac{1}{C_{44}}$$

where the elastic coefficients are taken from McSkimin (12) for liquid N_2 temperature as:

Si	C_{11} = 16.74	× 10^{11} dynes/cm^2
	C_{12} = 6.495	× 10^{11} dynes/cm^2
	C_{44} = 8.00	× 10^{11} dynes/cm^2
Ge	C_{11} = 13.16	× 10^{11} dynes/cm^2
	C_{12} = 4.95	× 10^{11} dynes/cm^2
	C_{44} = 6.84	× 10^{11} dynes/cm^2

Then the compliance coefficients can be calculated from the above expressions and values as:

$$\begin{aligned} \text{Si}\ S_{11} &= 7.64 \times 10^{-13}\ \text{cm}^2/\text{dyne} \\ S_{12} &= -2.14 \times 10^{-13}\ \text{cm}^2/\text{dyne} \\ S_{44} &= 12.50 \times 10^{-13}\ \text{cm}^2/\text{dyne} \\ \text{Ge}\ S_{11} &= 9.59 \times 10^{-13}\ \text{cm}^2/\text{dyne} \\ S_{12} &= -2.62 \times 10^{-13}\ \text{cm}^2/\text{dyne} \\ S_{44} &= 14.60 \times 10^{-13}\ \text{cm}^2/\text{dyne} \end{aligned}$$

The value for Young's modulus in the {111} is invariant and given by

$$E_{\{111\}} = \frac{4}{2S_{11} + 2S_{12} + S_{44}}$$

Which then gives

$$\begin{aligned} \text{Si}\ E_{\{111\}} &= 16.8 \times 10^{11}\ \text{dynes/cm}^2 \\ \text{Ge}\ E_{\{111\}} &= 14.0 \times 10^{11}\ \text{dynes/cm}^2 \end{aligned}$$

Results

The measured quantities and resulting determination for Si and Ge are given in Tables I and II. Measurements were made in the manner described previously. It should be noted that specimens with different surface finishes did not show any trend, and also room temperature measurements yielded approximately the same results as those at liquid N_2. These facts are probably due to the brittle nature of these materials and their lack of plastic behavior at room temperature. Only "successful" measurements are included in Tables I and II. As previously pointed out, dissipative factors would tend to raise the measured value of surface energy. Therefore, stronger reliance is put on the group of lower values with the authors' choice being 1230 ergs/cm², and for Ge a value of 1060 ergs/cm².

Table I. Cleavage surface energy for Si (in order of increasing value)

Specimen No.	w, cm	t, cm	L, cm	F, g	γ, ergs/cm²
Si 2	0.025	0.40	0.25	477	1220
14	0.057	0.50	1.20	100.5	1230
15	0.037	0.40	0.585	95	1230
6	0.025	0.35	0.65	151	1230
10	0.0215	0.35	0.215	384	1235
12	0.0405	0.30	0.52	244	1240
5	0.025	0.60	0.037	190	1250
9	0.023	0.40	0.35	333	1245
7	0.016	0.40	2.50	310	1250
3	0.0215	0.60	0.64	305	1270
8	0.016	0.40	0.014	580	1270
13	0.0605	0.40	0.445	212	1270
4	0.025	0.65	0.75	338	1280
16	0.020	0.22	0.206	193.6	1290
1	0.025	0.305	0.515	160	1300

Preferred value 1230 ergs/cm²

Table II. Cleavage surface energy for Ge (in order of increasing value)

Specimen No.	w	t	L	F, g	γ, ergs/cm²
Ge 2	0.0175	0.20	0.40	60.5	1000
3	0.0113	0.40	0.50	90.5	1020
7	0.0114	0.40	0.85	54	1045
4	0.011	0.40	0.60	73	1050
1	0.010	0.15	0.475	20	1060
5	0.0115	0.40	1.10	42	1060
6	0.0112	0.35	0.40	93	1080
9	0.010	0.55	0.154	135	1085
8	0.0127	0.20	0.30	62	1090
10	0.010	0.30	0.35	77	1120
11	0.010	0.55	0.30	70.8	1130

Preferred value 1060 ergs/cm²

Discussion

Using the measured value of surface energy for {111} we can derive additional information about the bond energy and surface energy of {110} and {100}. Since in cleaving a crystal we form twice the area of surface, we can say that the surface energy is equal to one half the cohesive energy. Now we make the simplifying assumption following Harkins (13) that this energy is due to a given number of bonds per unit area of the cleavage plane. Knowing this density and attributing our surface energy to breaking this number of bonds allows us to calculate the respective Ge-Ge and Si-Si bond energy. Having this energy and knowing the bond density of the other principal planes we can then determine their specific surface energies.

By this process we calculate the strength of the Ge-Ge and Si-Si bond as

$$\text{Ge-Ge} = 42.6\ \text{kcal/mole}$$
$$\text{Si-Si} = 45.5\ \text{kcal/mole}$$

With this value and the bond density of {110} and {100} plane we get the surface energy for these planes as

	{110}	{100}
Ge	1300 ergs/cm²	1835 ergs/cm²
Si	1510 ergs/cm²	2130 ergs/cm²

These values can be compared favorably with the theoretically arrived at values given by Viatkin and Vertopakhov (14) of

	{110}	{100}
Ge	1330 ergs/cm²	1900 ergs/cm²
Si	1465 ergs/cm²	2085 ergs/cm²

Conclusions

The surface energy of Ge and Si was measured by cleavage techniques and value of $\text{Ge}_{\{111\}} = 1060$ ergs/cm² and Si = 1230 ergs/cm² were obtained. From the measured values, the values of surface energy for {110} and {100} and the respective bonding energy were also estimated. The estimated values for Ge and Si bond energies are 42.6 and 45.5 kcal/mole, respectively. These values can be compared with like values of 46 and 52 kcal/mole obtained from heat of sublimation data listed by R. Honig (15). It should again be remarked that these measurements were biased in the direction of low surface energy. This would account for the lower values obtained for the bond energies. Although Ge and Si are both very brittle, which tends to minimize dissipative factors, it complicates the problem of obtaining properly cleaved, usable specimens in

sufficient numbers to obtain suitable distribution of measurements.

Manuscript received Nov. 1, 1962; revised manuscript received Jan. 12, 1963.

Any discussion of this paper will appear in a Discussion Section to be published in the December 1963 JOURNAL.

REFERENCES

1. M. Born and O. Stern, *Sitzber. preuss. Akad. Wiss. Physik.-math. Kl.*, 901 (1919).
2. B. M. Van der Hoff and G. C. Benson, *J. Chem. Phys.*, **22**, 475 (1954).
3. P. P. Ewald and H. Juretschke, "Structure and Properties of Solid Surfaces," p. 82, University of Chicago Press (1953).
4. S. G. Lipsitt, F. M. G. Johnson, and O. Maass, *J. Am. Chem. Soc.*, **49**, 925 (1927); **50**, 270 (1928).
5 J. W. Obreimov, *Proc. Roy. Soc. London*, **A127**, 290 (1930).
6. A. I. Bailey, Second Intern. Congr. Surf. Act., 3, 406, (1957).
7. J. J. Gilman, *J. Appl. Phys.*, **31**, 3208 (1960).
8. J. Benbow and F. C. Roesler, *Proc. Soc.*, **B70** [2], **70**, 201 (1957).
9. H. Udin, A. J. Shaler, and J. Wulff, *Trans. AIME*, **185**, 186 (1949).
10. "Metal Interfaces," A.S.M. (1952). "Structure and Properties of Solid Surfaces," University of Chicago Press (1953); Second Intern. Congr. Surf. Activity, **2, 3,** Butterworth Scientific Publications (1957).
11. W. G. Cady, "Piezoelectricity," McGraw-Hill Publishing Co., New York (1946).
12. H. J. McSkimin, *J. Appl. Phys.*, **24**, 988 (1953).
13. W. Harkins, *J. Chem. Phys.*, **10**, 268 (1942).
14. A. Viatkin and V. N. Vertopakhov, *Izv. Vysshikh Uchebn. Zavedenii Fiz.*, **2**, 169 (1959).
15. R. Honig, *RCA Rev.*, **18**, [2], 203 (1957).

The Oxidation of Silicon in Dry Oxygen, Wet Oxygen, and Steam

Bruce E. Deal[1]

Semiconductor Division, Raytheon Company, Mountain View, California

ABSTRACT

The oxidation of single crystal, n-type silicon has been investigated in the temperature range 900°-1200°C. These studies involved the use of three different oxidizing atmospheres, dry oxygen, wet oxygen, and steam, all at atmospheric pressure. Kinetic data, including thickness and weight rate constants, activation energies, and oxidation efficiencies, were compared among the three systems. The silicon oxides produced by the different methods were characterized by certain properties, such as density, dielectric strength, masking ability, and number of imperfections. It was demonstrated that the wet oxygen process produces oxides exhibiting the best protective properties relative to semiconductor device applications. No effects on oxidation characteristics were found due to impurity type or concentration, but a surface orientation effect was observed.

A number of investigations have been reported concerning the oxidation of silicon, including reaction kinetics, surface passivation, and masking of diffusing species, as related to semiconductor technology (1-18). However, in none of these has a direct comparison been made of the common high-temperature processes for silicon oxidation. Presented here, therefore, are the results of a study concerned with the reaction kinetics and properties of oxides produced in dry oxygen, wet oxygen, and steam atmospheres, at atmospheric pressure and at temperatures ranging from 900° to 1200°C. These studies are part of a general program designed to clarify some of the surface problems associated with semiconductor device fabrication.

Materials and Apparatus

Silicon used for the majority of these studies was single crystal Czochralski pulled, n-type phosphorus doped, (111) surface oriented, with a resistivity range of 1.5-2.5 ohm-cm. Ingots were cut into circular slices about 20 mm in diameter. The thickness of the slices after lapping and polishing was about 0.20 mm.

The oxidation procedure was as follows. The appropriate atmosphere was directed into a 45 mm ID quartz reaction tube contained in a silicon-carbide type, three-zone furnace. The temperature of the reaction zone was controlled to within ± 1°C. The silicon slices were placed flat on a quartz boat. Special experiments demonstrated that both sides of the slices, placed flat in this manner, oxidized at equal rates, and uniform heat distribution was obtained across the slices.

The inlet system of the apparatus was so arranged that the oxidizing atmosphere could be changed instantaneously at any time. Tank oxygen, whose dew point was maintained at less than − 60°C by a drying unit, was used at a linear flow rate of 62.9 cm/min for the dry oxygen process. Steam was obtained by boiling deionized, distilled water. The steam flow rate was approximately 570 cm/min at atmospheric pressure and room temperature. For all the oxidations reported here involving a wet oxygen atmosphere, oxygen was bubbled through water maintained at 95° ± 0.2°C, at 1 l/min. This resulted in a total linear flow rate of 315 cm/min (oxygen plus water) at atmospheric pressure and room temperature.

[1] *Present address:* Fairchild Semiconductor, Palo Alto, Calif.

Procedure

All silicon slices were mechanically polished to assure a uniform surface and reproducible area. After polishing, the slices were cleaned, using organic solvents and inorganic acids, the last step being an HF rinse followed by a deionized water rinse. Diameters and thicknesses were then determined and areas calculated. At least three slices were oxidized per run. One was for weight measurements. A second slice was used for oxide thickness measurements, dielectric strength determinations, and visual observation. Additional samples were prepared during each oxidation for subsequent masking and miscellaneous experiments. At least two runs were made for each oxidation condition.

Immediately prior to oxidation, the samples used for weight determinations were weighed on a microbalance having an accuracy of ± 0.002 mg. The slices then were placed in the reaction tube, and oxidation was carried out under the required temperature and time conditions. After oxidation, the weight samples were again weighed, the oxide removed in an HF solution, and the samples weighed again. Thus it was possible to calculate weight gain due to oxygen, $(W_2 - W_1)$, silicon oxide weight $(W_2 - W_3)$, and weight of silicon consumed during the reaction $(W_1 - W_3)$. The precision of weight per unit area measurements (which depended largely on the accuracy of the area determination) was better than ± 0.5% for a 1μ thick oxide.

Oxide thicknesses were obtained using the groove-chord method, similar to that described by McDonald and Goetzberger for measuring diffused junctions (19). Accuracy of this type of oxide thickness determination was considered to be within ± 2% for a 1μ oxide. Dielectric strength values were obtained using the Anodicator.[2] This instrument is based on the A.S.T.M. method for measuring dielectric strengths of insulating coatings on metals. An a-c voltage is impressed across the coating, starting with zero volts and increasing at a uniform rate until breakthrough occurs. The instrument then indicates the voltage at which breakthrough occurs. Reproducibility and accuracy depend on the nature of the coating, type of probe used, and other factors.

Results—Reaction Kinetics

Rate data.—All three oxidation processes were found to obey parabolic rate laws in the temperature range 1000°-1200°C. The parabolic law, indicating a diffusion controlled reaction (20), may be expressed as follows

$$w^2 = kt$$

where w is oxide weight or thickness, t, oxidation time; and k, rate constant. A parabolic plot of oxide thickness-oxidation time data for the wet oxygen process is shown in Fig. 1. Straight lines are obtained, which means the oxidation rates are controlled by the diffusion of one of the reactants through the oxide. Weight data for the same oxidations are plotted in Fig. 2. It can be noted that

[2] Manufactured by the R. O. Hull Company, Rocky River, Ohio.

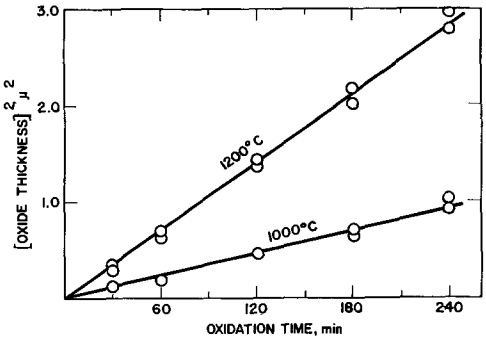

Fig. 1. Parabolic plot of thickness-time data for wet oxygen (95°C H_2O) oxidation of silicon.

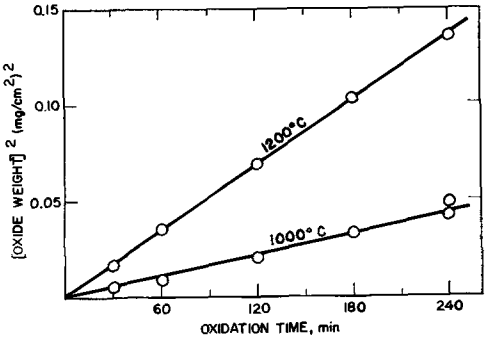

Fig. 2. Parabolic plot of weight-time data for wet oxygen (95°C H_2O) oxidation of silicon.

weight values are more reproducible than thickness values, due to the greater precision of weight measurements.

The data for dry oxygen and steam oxidations also provided parabolic curves. The steam rates were greater than those of wet oxygen, while the oxidation rates for the dry oxygen process were considerably less. Table I presents a summary of parabolic rate constants for the three processes at two temperatures. Both weight and thickness data are included. In general the precision of these determinations was ± 4%. The reproducibility of the dry and wet oxygen values from one set of experiments to another was also ± 4%. The steam rate constants varied more from one time to another, depending largely on the experimental conditions. These variations will be considered in the Discussion Section. A more practical comparison of oxidation rates is presented in Table II. Here, oxidation times required to produce certain oxide thicknesses are listed for the three processes.

Oxidation efficiencies.—The term "oxidation efficiency" was introduced in this program. It is de-

Table I. Parabolic rate constants for three types of silicon oxidation

Oxidation type	Temperature, °C	Rate constant from Thickness data, μ^2/min	Rate constant from Weight data, (mg/cm^2)^2/min
Dry oxygen	1000	1.48×10^{-4}	0.077×10^{-4}
	1200	7.64×10^{-4}	0.351×10^{-4}
Wet oxygen (95°C H_2O)	1000	38.5×10^{-4}	1.82×10^{-4}
	1200	117.5×10^{-4}	5.72×10^{-4}
Steam	1000	54.5×10^{-4}	2.35×10^{-4}
	1200	159.0×10^{-4}	6.67×10^{-4}

Table II. Time required to obtain specific silicon oxide thicknesses using three types of oxidation

Oxidation type	Temperature, °C	Time required to obtain 0.5μ, min	Time required to obtain 1.0μ min
Dry oxygen	1000	1800	—
	1200	320	1320
Wet oxygen (95°C H_2O)	1000	70	252
	1200	22	85
Steam	1000	55	195
	1200	16	60

fined as the ratio of measured weight of silicon oxide to that amount of SiO_2 which should have been produced from the measured weight of silicon consumed during the oxidation. In terms of weights obtained

$$\text{Oxidation efficiency} = \frac{(W_2 - W_3)}{2.139\ (W_1 - W_3)}$$

where W_1 is the weight of sample before oxidation; W_2, weight of sample after oxidation; and W_3, weight of sample after oxide is removed with HF. An oxidation efficiency of less than unity (or 100%) indicates either that the silicon is not oxidized completely to SiO_2, or that part of the SiO_2 produced is subsequently eroded by the oxidizing atmosphere. Results indicated that dry oxygen oxidation efficiencies are extremely close to 100%, wet oxygen values are 95-100%, while oxidation efficiencies of steam oxidations range from 75 to 100%. An interpretation of these results is presented in the Discussion Section.

Activation energies.—Activation energies have been determined for the three types of oxidations by plotting the logarithms of the parabolic rate constants *vs.* reciprocals of absolute temperatures. Values are listed in Table III. Good agreement is obtained between weight and thickness data. The values of activation energies are in general lower than those reported by Atalla (6) for a similar process, but are more in line with values found by Thurston (18). During the course of our experiments, a possible cause of disagreement among various investigators concerning activation energies was found. Above 1000°C all oxidations proceed according to a parabolic rate law. Below 1000°C, however, the oxidation mechanism apparently changes to a combination parabolic-linear type reaction. This relationship is expressed as (20)

$$w^2 + k_1 w = k_2 t$$

where w is amount of oxide formed, t, oxidation time, and k_1 and k_2 are constants. Such a growth law indicates that the rate of reaction is controlled by both a diffusion process and a surface or interface reaction. If this is the case, then activation energies determined over a temperature range extending both above and below 1000°C may be in error. It would be difficult to separate out the two activation energy values corresponding to two rate-controlling processes occurring simultaneously, as indicated by a mixed parabolic-linear rate law. Therefore, activation energies have been determined and reported here for the temperature range 1000°-1200°C only.

Table III. Activation energies for different types of silicon oxidation in the temperature range 1000°-1200°C

Oxidation type	Activation energy from Thickness data, kcal/mole	Activation energy from Weight data, kcal/mole
Dry oxygen	30.2	28.2
Wet oxygen (95°C H_2O)	20.8	21.4
Steam	19.9	20.0
Atalla's data (6)		
Dry oxygen	40	—
Steam (16 mm Hg)	40	—
Steam (50-120 atm)	23	—
Thurston's data (18)		
Dry air	28	—
Steam	25	—

Combination and interrupted oxidations.—The question arose as to whether the characteristics of one type of oxide are altered if the oxidized slice were subsequently subjected to a second type of oxidation process. This procedure is required in the fabrication of certain oxide-protected devices. An example of the results for one particular combination oxidation is shown in Fig. 3. Here, silicon slices were oxidized in steam at 1200°C for 15 min. Then, without removing them from the reaction chamber, the oxidation was continued in dry oxygen. The oxide thickness (and weight) values obtained during the dry oxygen portion were compared with a curve representing an all-oxygen oxidation. (This curve is labeled theoretical and is superimposed through the point of change-over). From the figure it is shown that the initial steam oxidation does not affect the subsequent dry oxygen oxidation. Other evaluations indicated also that the oxide properties were similar to dry oxygen oxides.

The results of the reverse procedure are shown in Fig. 4. An initial dry oxygen oxidation was followed by a steam oxidation. When compared with an all-steam curve, the denser dry oxygen oxide (see next section comparing oxide densities) apparently slowed down the diffusing reactants, and thus the steam oxidation rate was decreased. Again the oxide properties resembled those characteristics of the second type of oxidation (steam).

Other experiments were conducted where an oxidation was interrupted by removing the sample from the furnace, allowing it to cool, and then con-

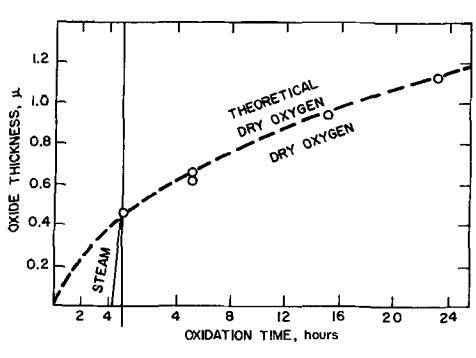

Fig. 3. Thickness-time data for steam-dry oxygen combination oxidation of silicon (1200°C).

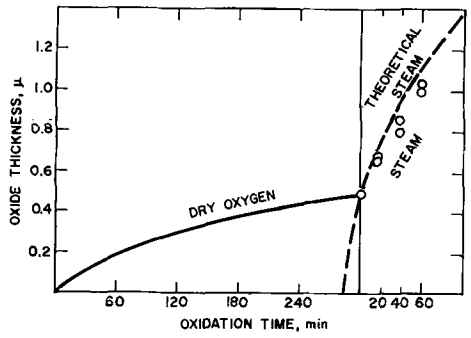

Fig. 4. Thickness-time data for dry oxygen-steam combination oxidation of silicon (1200°C).

tinuing the oxidation. No differences in oxidation characteristics were found due to this procedure, even when the oxidation was interrupted several times for the same sample.

It was also desired to know if oxidation characteristics would change if one sample were oxidized a number of times. This was accomplished by oxidizing a slice in wet oxygen for a long enough time to produce a 1μ thick oxide, then removing the oxide with HF, and re-oxidizing. The oxidation was repeated at least six times for each of several slices, resulting in a removal of at least 3μ per side per sample. The results indicated absolutely no difference in oxidation characteristics, from the standpoint of oxide thicknesses, weights, oxidation efficiencies and densities, within experimental error. In fact, this procedure helped to establish precision or reproducibility limits of the experimental measurements. It also demonstrated that any damage of the silicon caused by the mechanical polishing either did not affect oxidation or else provided a constant effect through the 3μ of silicon oxidized.

Results—Oxide Properties

General appearance of oxides.—Generally, oxides formed on silicon at high temperatures tend to follow the contour of the surface quite closely. The oxides in the dry and wet oxygen atmospheres were very uniform and reproducible as indicated by the interference colors and thickness-weight measurements. The steam oxides, however, (and occasionally, but to a lesser extent, the wet oxygen oxides) exhibited many spots and defects. Moreover, these spots appeared on both the top and bottom sides of the slices (placed horizontally in the reaction chamber). The number and size of these defects could be minimized, however, by certain process changes, and these are discussed later.

Oxide densities.—Bulk silicon oxide densities, as calculated from the weight and thickness data, are listed in Table IV. The average deviation from the mean for these values is ± 0.05 g/cc. The density values for dry oxygen and wet oxygen are similar and do not change appreciably with temperature. For these particular experiments the densities of steam oxides were found to be considerably less. However, as other oxidations were carried out at later times and with modified procedures, the steam oxide densities changed, as did other characteristics of the process. The over-all density range for steam

Table IV. Apparent densities of silicon oxides produced by three types of oxidation

Oxidation type	Temp, °C	Density, g/cc
Dry oxygen	1000	2.27
	1200	2.15
Wet oxygen (95°C H_2O)	1000	2.18
	1200	2.21
Steam	1000	2.08 (2.00-2.20)
	1200	2.05 (2.00-2.20)

oxides is therefore listed in parentheses in Table IV. The steam process is treated more completely in the Discussion Section.

Dielectric strengths.—As mentioned above, dielectric strengths were compared among the three types of oxides using the Anodicator. For oxides of similar densities, a linear relationship was found to exist between breakthrough voltage and oxide thickness or weight. If the densities varied, then the dielectric strength was proportional to oxide weight. Figure 5 shows the relationship between dielectric strength per unit thickness and oxide density, which is equivalent to plotting total breakthrough voltage against oxide weight. The points shown represent the average of a number of samples.

Masking properties.—Another comparison of properties among different types of oxides is the masking ability against certain diffusing impurities used in transistor fabrication. Representative samples of oxides produced by the three oxidation methods were examined for their ability to mask phosphorus and boron. The depth of penetration, if any, of the diffusing species into the silicon beneath each oxide was determined by junction depth and sheet resistance measurements. (Silicon used for the phosphorous experiments was p-type.) Unoxidized samples were used as standards. Results of the phosphorous masking experiments are presented in Fig. 6. Here, phosphorous junction depth is plotted against oxide thickness for steam and wet oxygen oxides. The phosphorous diffusion was a one-step process and the conditions were as follows: diffusion temperature, 1150°C; source temperature, 260°C; diffusion time, 145 min; carrier gas, dry oxygen at 1 l/min. If the difference in curves shown in Fig. 6 is related to oxide density,

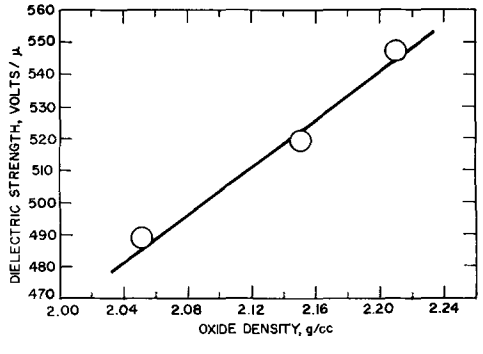

Fig. 5. Dielectric strength as a function of silicon oxide density

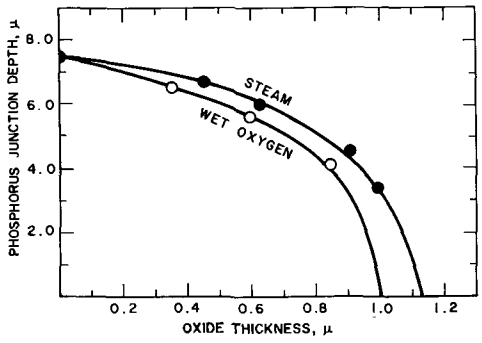

Fig. 6. Effect of silicon oxide thickness on phosphorous junction depth.

then a junction depth-oxide weight plot should result in one curve. This was found to be the case as shown in Fig. 7. Similar results are obtained using sheet resistance, oxide thickness, and weight data.

Additional analysis of the phosphorous masking data demonstrated that the movement of the phosphorous species through the oxides is linear with time for these conditions of diffusion.

For the particular conditions of boron diffusion used in these studies, all oxides having thicknesses of 0.4μ or greater completely masked the boron. The boron diffusion was a two-step process and resulted in a 12μ junction in an unoxidized silicon sample. Since most of the oxides selected for these particular experiments were thicker than 0.4μ, no additional results can be reported at this time regarding boron masking.

Chlorine etch test.—Samples of the three types of oxidation were subjected to chlorine gas for 3 min at 800°C. This procedure, as suggested by Atalla (6), is a sensitive test for imperfections in the oxide. Results indicated that the wet oxygen oxides were practically free from any defects. A fair number of pits were produced in the steam oxide. Both the wet oxygen and steam results were fairly reproducible. However, it was shown that the dry oxygen oxides are extremely sensitive to the cleaning process and samples subjected to the chlorine test ranged from some completely free of etch pits in the oxide to others severely attacked. This same finding was reported by Ing and co-workers (10).

Oxidation Dependence on Silicon Composition and Structure

Impurity type and concentration.—The oxidation characteristics of a series of silicon samples containing both n-type (phosphorus) and p-type (boron) impurities with resistivities ranging from 0.001 to 50 ohm-cm were compared for the three processes. No differences in either reaction kinetics or oxide properties were found due to impurity type or concentration over the above resistivity range.

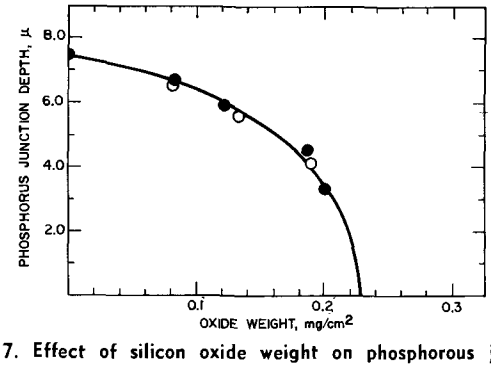

Fig. 7. Effect of silicon oxide weight on phosphorous junction depth; •, steam; ○, wet oxygen.

Epitaxial surface.—Limited experiments were carried out in which oxidation characteristics of epitaxial deposited silicon were compared with those of conventional silicon of the same impurity type and concentration. Results indicated that there is probably no difference between the epitaxial and nonepitaxial surfaces as related to thermal oxidation. The epitaxial deposits used for these experiments were 3 ohm-cm n-type and about 12μ thick. The substrates were 0.01 ohm-cm n-type (Sb doped). The epitaxial layer was deposited on both sides of the slices (by two separate depositions).

Surface orientation.—The effect of crystal orientation on oxidation characteristics was studied briefly. Slices with surfaces oriented in the (111), (110), and (100) planes were oxidized using the three processes, and the results compared. Figure 8 shows the dependence of the wet oxygen process on surface orientation. Very little difference in rates is noted at 1200°C. However, at 1000°C, the (100) values are definitely lower than those of (111) and (110). In addition, the (100) rate at 1000° no longer obeys a parabolic law, but rather indicates the mixed parabolic-linear relationship described previously.

Lizenza has predicted (14) that for the high-pressure steam oxidation, the oxidation rate on a (100) surface would be less than (110) or (111) surfaces. He proposed that there are fewer surface bonds or reaction sites available for the water species to react. Evidently, this dependence also carries over to atmospheric pressure oxidations of (100) surfaces, where the rate law suggests the reaction is partially controlled at the interface.

The same orientation effects are also noted in Fig. 8 for the 900°C oxidation data. In addition, all curves at this temperature are found to be mixed parabolic-linear. This substantiates the probability of a change in oxidation mechanism around 1000°C for all three types of oxidation.

Discussion

The results obtained in this program have shown that oxides produced in steam atmospheres are usu-

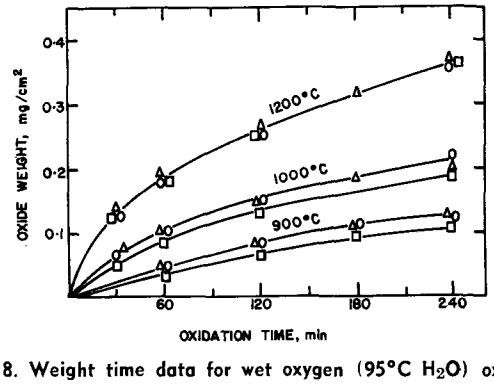

Fig. 8. Weight time data for wet oxygen (95°C H_2O) oxidation as a function of surface orientation and temperature: △, (111); ○, (110); □, (100).

ally less perfect and have lower densities than those formed in dry or wet oxygen atmospheres. As a result of the apparent lower densities of steam oxides, other properties dependent on the density are also affected. A reasonable correlation was found to exist between densities and oxidation efficiencies. This indicates that an erosion of the oxide by the wet oxidizing atmosphere occurs. Water and hydrogen are the two principal gaseous components of the steam-silicon oxidation system. To determine the extent of SiO_2 erosion by this atmosphere, special experiments were conducted where oxides previously formed were exposed to a water-hydrogen mixture at high temperatures. It was difficult to obtain quantitative data from the experiment, since the H_2O-H_2 mixture also oxidizes silicon. It was determined, however, that the gas mixture definitely attacked the oxide. This helped to support the theory of erosion in the steam atmosphere.

During the course of the entire program, holes and other defects could be observed in the steam oxides. These imperfections could be traced many times to some form of contamination, but more often to water droplets. The prevalence of these holes was emphasized during the dielectric strength determinations. Initially a large ball probe, with a ⅛ in. radius, was used, as recommended by the A.S.T.M. for such measurements. However, the majority of the steam oxides broke through at much lower voltages than would be expected even with lower densities. On changing to a needle probe, the results were much more consistent, however. A possible reason for this difference is as follows. If it is assumed that holes and defects are spaced at random throughout the oxide, it would be difficult to place the large ball probe in an area not containing such a defect. Thus a portion of the oxide thickness would be shorted out. The needle probe, on the other hand, covers a much smaller area and the probability of contacting a defective area is much less. Thus, it would provide a more consistent and reliable measurement of dielectric strength.

It was reasoned that better steam oxides, more dense and freer from defects, could be formed by providing closer control of the process. This was accomplished first by improving cleanliness conditions. Second, the system was modified in such a way as to prevent water droplets from depositing out on the slices. The latter was found to be important both during the oxidation as well as the time when the slices were placed in or removed from the reaction zone. A marked improvement in steam oxides was noted by these changes. Densities and oxidation efficiencies increased. At the same time, however, reaction rates decreased, since parabolic rate constants are inversely proportional to oxide density.

The chlorine test helped to identify the imperfections in the steam oxides mentioned above. In addition, a second type of defect was established to be present in dry oxygen oxides using this test. Insufficient cleaning of the silicon surface before oxidation resulted in the formation of small crystallites in the oxide during the long oxidation time. While these crystallites are not readily visible and do not lower the density, it is reasonable to expect that they might be attacked by certain diffusing species which are normally masked by amorphous SiO_2. Thus, severe difficulties might result during fabrication of oxide protected devices, if such imperfections were present in the oxide. The wet oxygen and steam oxidations, which require considerably shorter treatment times at high temperatures, are apparently much less sensitive to surface contamination which results in crystallite formation.

It should be emphasized that the silicon dioxides formed by the three methods undoubtedly have the same structure and density on a molecular scale. The differences in densities and other properties found in this investigation are probably due to macromolecular voids and defects of various orders of magnitude. Many are microscopic, others visible to the eye. Whatever their cause and size, however, the effect is most important during device fabrication and later when the surface of the finished device must be protected.

In conclusion, it has been demonstrated that the wet oxygen process produces silicon oxides with the best protective characteristics, from the standpoint of density, dielectric strength, masking ability, and freedom from defects. Oxides produced in dry oxygen are much more sensitive to the cleaning treatment, in that any surface contamination prior to oxidation results in oxide imperfections. The steam oxidation process is more difficult to control, is less reproducible, and oxides produced tend to be less perfect. These can be improved, however, with very close process control.

Acknowledgments

The author wishes to thank Mrs. D. S. Sklar and Philip J. Fleming for their assistance in the experimental portion of this program.

Manuscript received Oct. 8, 1962. This paper was prepared for delivery at the Los Angeles Meeting, May 6-10, 1962.

Any discussion of this paper will appear in a Discussion Section to be published in the December 1963 JOURNAL.

REFERENCES

1. R. B. Allen, N. Bernstein, and A. D. Kurtz, *J. Appl. Phys.*, **31,** 334 (1960).
2. R. J. Archer, *This Journal,* **104,** 619 (1957).
3. M. M. Atalla, E. Tannenbaum, and E. J. Scheibner, *Bell System Tech. J.*, **38,** 749 (1959).
4. M. M. Atalla and E. Tannenbaum, *ibid.*, **39,** 933 (1960).
5. M. M. Atalla, A. R. Bray, and R. Lindner, *Proc. Inst. E. E.*, **106,** (Part B, Supplement No. 17), 1130 (1960).
6. M. M. Atalla, "Properties of Elemental and Compound Semiconductors," Vol. 5, H. Gatos, Editor, pp. 163-181, Interscience Publishing Co., New York (1960).
7. L. A. D'Asaro, *Solid-State Electronics,* **1,** 3 (1960).
8. J. W. Evans and S. K. Chatterji, *J. Phys. Chem.*, **62,** 1064 (1958).
9. C. J. Frosch and L. Derick, *This Journal,* **104,** 547 (1957).
10. S. W. Ing, R. E. Morrison, and J. E. Sandor, *ibid.*, **109,** 221 (1962).
11. J. T. Law, *J. Phys. Chem.*, **61,** 1200 (1957).
12. J. R. Ligenza and W. G. Spitzer, *J. Phys. Chem. Solids,* **14,** 131 (1960).

13. W. G. Spitzer and J. R. Ligenza, *ibid.*, **17**, 196 (1961).
14. J. R. Ligenza, *J. Phys. Chem.*, **65**, 2011 (1961).
15. J. R. Ligenza, *This Journal*, **109**, 73 (1962).
16. C. T. Sah, H. Sello, and D. A. Tremere, *J. Phys. Chem. Solids*, **11**, 288 (1959).
17. J. L. Sprague, J. A. Minahan, and O. J. Wied, *This Journal*, **109**, 94 (1962).
18. M. O. Thurston, J. C. C. Tsai, and K. D. Kang, "Diffusion of Impurities into Silicon Through an Oxide Layer," Report 896-Final, Ohio State University Research Foundation, U. S. Army Signal Supply Agency Contract DA-36-039-SC-83874, March 1961.
19. B. McDonald and A. Goetzberger, *This Journal*, **109**, 141 (1962).
20. V. R. Evans, "The Corrosion and Oxidation of Metals," pp. 819-859, Edward Arnold Ltd., London (1960).

Gettering of Metallic Impurities from Planar Silicon Diodes

S. W. Ing, Jr.,[1] R. E. Morrison, L. L. Alt, and R. W. Aldrich[1]

Semiconductor Department, General Electric Company, Electronics Park, Syracuse, New York

ABSTRACT

Experimental studies are presented in which reverse leakage currents in diffused silicon planar diodes are reduced by orders of magnitude via an intermediate temperature (800°-1000°C) gettering of metallic impurities which presumably cause excess leakage. Inorganic oxides having melting points below the gettering process temperature have been employed as the getters. Life test data on gettered diodes are also presented. The effectiveness of such gettering processes is further demonstrated by experiments in which radioactive copper is utilized as the diffused contaminant.

In the modern day manufacturing of diffused silicon devices, one or more gettering steps are usually incorporated in the process to prevent introduction of undesirable metal impurities into the junction region or to remove any metal impurities that may be already there. Goetzberger and Shockley (1) have shown that a number of fast diffusing metals, such as Cu, Fe, Mn, and Au, when introduced into silicon diodes can cause excess reverse leakage current below avalanche breakdown. This current varies directly with reverse voltage raised to the *n*th power where "*n*" was between 4 and 7. They attribute the cause of this rise to localized high field points which cause Zener tunneling current to flow. They have further demonstrated that the excess reverse current can be reduced considerably by gettering with phosphorus or boron silicate at temperatures of 1000°C and higher. In their case, the lower limit on the gettering temperature was governed mainly by the liquidus temperature of their gettering glasses as it was found that the formation of a low viscosity oxide mixture was essential for the process to be effective.

The purpose of our work was to investigate the possibility of effecting gettering at temperatures lower than those which have been reported, which would be of great practical interest, by using suitable inorganic oxide compositions that have lower liquidus points. Furthermore, this process would be applied to the planar type of diodes in which the junctions terminate at the interface between the silicon and the thermally grown silicon dioxide.

The metal oxides and oxide mixtures used in this investigation as the gettering agents are listed along with their melting points, if known, in Table I. When one of these oxides is applied to the silicon wafer surface at elevated temperatures, one would expect some chemical reaction to occur which would incorporate silicon into the oxide, thus altering its liquidus point. Since the gettering treatments are carried out in an air ambient, the reaction products could therefore be considered as binary oxide mixtures of the silicon and the metal oxides. Only a few of these systems have been investigated in regard to their phase relationships. For example, in the lead oxide and silicon dioxide system, Geller and his co-workers (2) have found liquid-solid eutectics at 8, 15, and 30% silicon dioxide concentrations, all occurring within the temperature range of approximately 720°-740°C. For the boron trioxide and crystalline silicon dioxide system, Giellise and his coworkers (3) have presented a tentative phase diagram showing a continuous liquidus curve starting from pure silicon dioxide to pure boron oxide. It is therefore possible within a certain period of time from the start of the gettering process, to have the applied glass remain in its liquidus state, at or slightly above its initial melting point, while the concentration of the silicon in the glass is still low. A gettering temperature range of 800°-1000°C was then chosen. The metal impurities that diffuse via an interstitial mechanism should have sufficiently high

[1] Present address: Electronics Laboratory, General Electric Company, Electronics Park, Syracuse, New York.

Table I. Oxides and oxide mixtures used for gettering

Compound	B_2O_3	B_2O_3-P_2O_5	P_2O_5	V_2O_5	V_2O_5-BaO	$Pb_2P_2O_7$	PbO
Melting point, °C	577	—	563	690	—	824	888

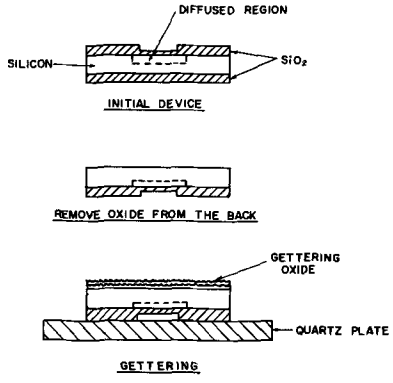

Fig. 1. Schematics of the procedure

diffusion rates at these temperatures to allow capture by the liquid oxides.

Experimental Procedure

In our experiments, 0.9 ohm-cm n-type silicon wafers approximately 9 mils thick, were used as the starting material. These wafers went through a standard process of steam oxidation, window cutting, boron predeposition, and final diffusion under oxidizing ambient. The oxide thicknesses were about 10,000Å and the junction depths were 7-8μ. After diffusion, the wafer was cut into quarters, each quarter containing a number of diodes of 2-4 mm^2 area. One piece was retained as a control sample, and the other pieces were used for gettering.

All the oxides except V_2O_5 were applied by a paint-on technique using the oxides in a saturated solution, or slurry, in ethylene glycol monoethyl ether. The boron and phosphorus oxide mixture was prepared by mixing equal volumes of the saturated solutions of the individual oxides in ethylene glycol monoethyl ether at room temperature. The experimental procedure is depicted in Fig. 1. The thermal oxide which covered the junction area was not touched. The oxide on the back side of the wafer was removed, the gettering agent was applied, and the wafer was inserted into the furnace under an air ambient. Following the gettering period, which usually lasted around 30-60 min, the wafer was withdrawn from the furnace and air quenched. In the case of V_2O_5 gettering, the wafer was simply floated on top of the melt in a quartz crucible, with only the back side of the wafer contacting the melt. In a few runs BaO was added (in a ratio of 3-8, BaO-V_2O_5) to the V_2O_5 for the purpose of reducing creeping of the V_2O_5 onto the top surface of the wafer. In all cases, excepting those with P_2O_5 and $Pb_2P_2O_7$, the glasses formed could be easily removed by using suitable chemical etches. P_2O_5 and $Pb_2P_2O_7$ glasses were relatively difficult to etch chemically, so these were lapped off. Reverse bias and current measurements and life tests were then performed on the diodes.

Results and Discussion

The results, in general, showed considerable improvement in the reverse characteristics of the diodes gettered with the above mentioned oxides. The reverse leakage currents decreased by orders of magnitude and became much less voltage dependent.

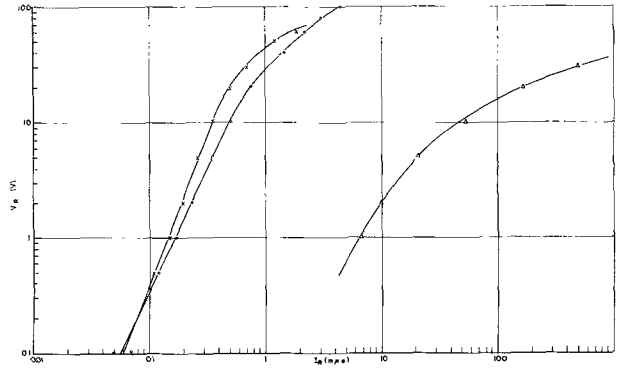

Fig. 2. Reverse bias characteristics of diodes gettered with boron oxide and boron-phosphorus oxide mixture. x, B_2O_3 30 min, 900°C; ○, B_2O_3-P_2O_5 30 min, 900°C; △, ungettered.

I_R, the reverse current, became proportional to V_R, the reverse bias, raised to a power of 0.5 or less prior to the onset of avalanche multiplication condition. This reverse current and bias relationship is typical of space charge layer carrier generation phenomena (4). As a check on the possibility that the observed gettering might be independent of the presence of the oxides, some wafers were subjected to the entire process except no oxide was applied to the back side. No improvement in diode characteristics was observed.

Following are a number of curves which show the extent of gettering under various process conditions as reflected in the electrical characteristics of the diodes. Each curve represents measurements taken on one of the ten or so diodes on a wafer that has undergone the same treatments. Generally about 80% of the diodes on one single wafer show similar breakdown voltages, and the variations in reverse currents are within a factor of two. The major difference of a few of the diodes from the majority is their lower breakdown voltages. In Fig. 2, the current is plotted *vs.* the reverse voltage for diodes gettered with boron-oxide and with a boron and phosphorus oxide mixture at 900°C for 30 min. The characteristic of an ungettered diode also is shown here for comparison. The gettered devices show vast improvement over the ungettered device. The reduction in the current is especially pronounced at high biases. However, there is no significant difference here, prior to life test, between the two diodes gettered with different oxides.

In Fig. 3 we compare phosphorus pentoxide with the boron and phosphorus oxide mixture as getter. Again, we initially observe no real difference between the two; both show considerable improvement over the ungettered material.

In Fig. 4 the characteristics of diodes gettered with the boron and phosphorus oxide mixture for 30 min at 800°, 900°, and 1000°C are presented. If we focus our attention at the higher bias region, which is the region of greater interest, we see considerable improvement in the leakage current by going from 800° to 900°C. However, no appreciable gain is observed by increasing the gettering temperature to 1000°C.

A series of runs also were made to see the effect of the gettering time duration of the diode reverse

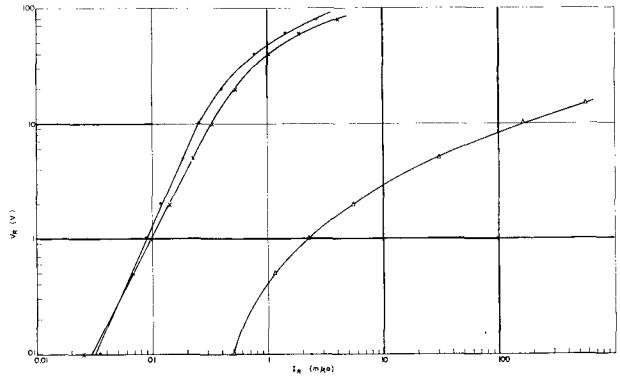

Fig. 3. Reverse bias characteristics of diodes gettered with phosphorus oxide and boron-phosphorus oxide mixture. x, P_2O_5 30 min, 900°C; ○, P_2O_5-B_2O_3 30 min, 900°C; △, ungettered.

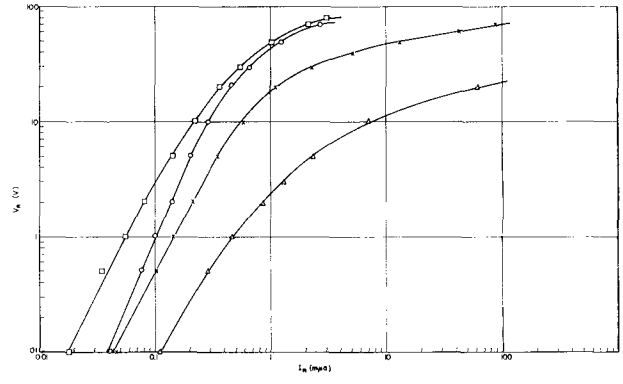

Fig. 4. Reverse bias characteristics of diodes gettered with boron-phosphorus oxide mixture at various temperatures. x, B_2O_3-P_2O_5 30 min, 800°C; ○, B_2O_3-P_2O_5 30 min, 900°C; □, B_2O_3-P_2O_5 30 min, 1000°C; △, ungettered.

current. Gettering was done at 800°C for 60, 150, and 300 min using the boron, phosphorus oxide mixture. Figure 5 shows the reduction of the leakage current by increasing the period of gettering time from 60 to 150 min. However, a 300 min gettering period proves to be too long; all diodes showed soft characteristics and are not shown on this plot. Too long a heating time could cause extensive evaporation of the oxides which may seriously limit their gettering action and, in this case, apparently a reverse process took place after the gettering action had stopped during the latter half of the 300 min heating time.

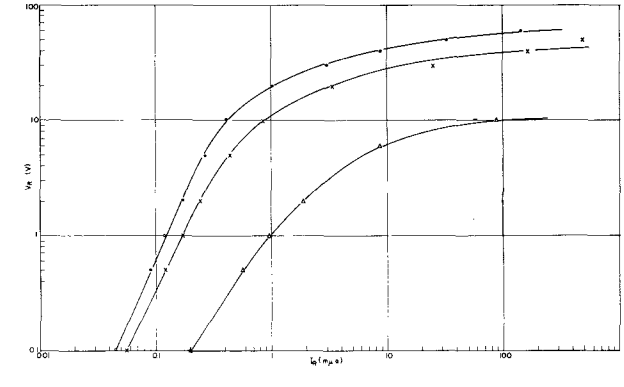

Fig. 5. Reverse bias characteristics of diodes gettered with boron-phosphorus oxide mixture for different periods. ×, B_2O_3-P_2O_5 60 min, 800°C; ○, B_2O_3-P_2O_5 150 min, 800°C; △, ungettered.

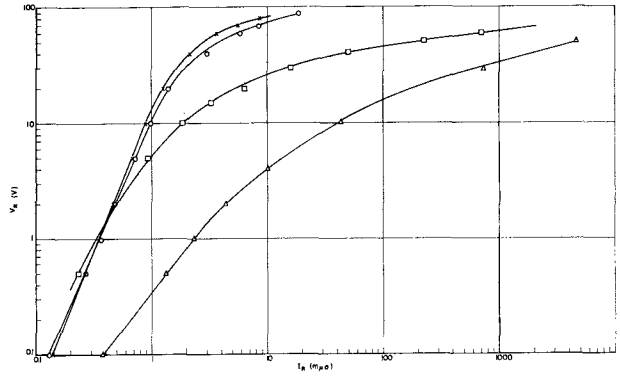

Fig. 6. Reverse bias characteristics of diodes gettered with various oxides. x, $Pb_2P_2O_7$ 30 min, 900°C; ○, V_2O_5-BaO 30 min, 900°C; □, PbO 30 min, 900°C; △, ungettered.

Figure 6 shows the effect of gettering using $Pb_2P_2O_7$, V_2O_5-BaO mixture and PbO at 900°C. Again a vast decrease in leakage current is observed by gettering; however, PbO seems to be the least effective among all the oxides used.

We have seen so far the results prior to life testing. We can summarize the results by saying that all the oxides used in the experiment are effective and a gettering temperature of 900°C and a time period of 30-60 min seems to be quite adequate. If conditions necessitate a lower temperature, 800°C gettering can be used, although it is less effective. The limiting factors in using gettering temperatures lower than 800°C can, perhaps, be itemized as follows: (*a*) higher oxide viscosity, (*b*) slower diffusion rate of the metal impurities, and (c) increased gettering time required, resulting in the depletion of oxide due to volatilization.

The gettered diodes were subjected to heat testing in room ambient at temperatures of 190°-300°C with or without reverse bias. All diodes showed good stability after many hundreds of hours of heating at 300°C, if no bias was applied. When a 50v reverse bias was applied during heat soaking at 190°C, with the exception of diodes gettered by P_2O_5, and the P_2O_5-B_2O_3 mixture, all gettered diodes tend to fail after 50 or more hours. Some typical test results are shown in Table II. Each of the results shown represents a group of four to six diodes. At 300°C the failure rate accelerated and became quite rapid. The reverse leakage current increase could be catastrophic. Heating to 200°-300°C for a few hours with the bias removed usually would restore these failed diodes, but they are subsequently even more susceptible to degradation. The failures are most probably due to some chemical interaction occurring in the thermal oxide and silicon interface region of the junction. The reversible nature of the failure strongly suggests ionic movements under the influence of a high electric field. These ionic species could have formed or introduced into the thermal oxide and silicon transition region during the gettering process. At the heat test temperature and high electric field ionic polarization could occur and gives rise to the formation of a silicon surface inversion layer. This proposed failure mechanism is just a conjecture. We have no direct evidence to substantiate it. However, diodes gettered with P_2O_5 seem to

Table II. Typical life test results of gettered diodes

Gettered with	Life test temperature, °C	Life test bias, v		Time, hr 0	20	60	150	330
B_2O_3	300	0	I_R*	0.54			0.11	
			V_B**	80			75	
B_2O_3	190	50	I_R	0.3			300	
			V_B	80			80	
$Pb_2P_2O_7$	300	50	I_R	0.85	1200			
			V_B	95	100			
P_2O_5	190	0	I_R	0.38				0.1
			V_B	85				90
P_2O_5	300	50	I_R	0.59		0.79		
			V_B	85		85		
$B_2O_3 + P_2O_5$	190	0	I_R	0.44				0.15
			V_B	85				88
$B_2O_3 + P_2O_5$	300	0	I_R	0.35				0.24
			V_B	82				82
$B_2O_3 + P_2O_5$	190	50	I_R	0.27				0.28
			V_B	95				92
$B_2O_3 + P_2O_5$	300	50	I_R	0.90			0.36	6.4
			V_B	83				81

* I_R ($m\mu$ amp) measured at V_R = 10v.
** V_B (v) diode breakdown voltage.

be more stable. As shown in Table II, for a P_2O_5 gettered diode, slight degradation is observed after, for example, life tested at 300°C and 50v bias for 60 hr. Even more stable devices resulted from using the boron-phosphorus oxide mixture as the gettering agent. Here we see no change in leakage current after soaking at 190°C for over 300 hr with 50v reverse bias applied. The diodes also stood up well after 150 hr at 300°C and 50v bias but started to degrade after over 300 hr. This test condition of 300°C air ambient and 50v bias could be overly severe. The heat dissipation at the junction itself would amount to a tenth of a watt or more under these conditions. Hence, the temperature at the junction could well substantially exceed that of the environment.

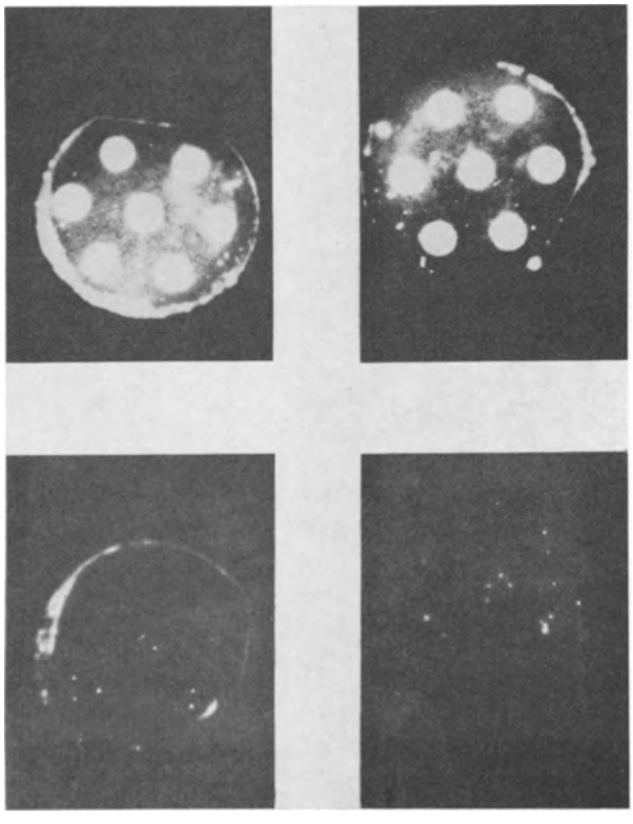

Fig. 7. (Upper and lower left) Before and after boron-phosphorus oxide mixture gettering of Cu^{64} in silicon diodes. (Upper and lower right) Before and after boron oxide gettering of Cu^{64} in silicon diodes.

The oxide gettering action we have shown so far yields no quantitative measurements on the actual metal impurities depleted. Therefore, a radio tracer technique was used to obtain such data. Radio Cu^{64} was used as the metal impurity and was plated onto the back side of the diode wafer followed by indiffusion at 600°-700°C. After the diffusion, the excess copper was removed and the wafer subjected to gettering in the same manner as described previously. Following the gettering and removing of the gettering oxide, a radioautogram was taken of the wafer. Radioactivity counting was usually taken before and after gettering to give indications of change in copper concentration. In Fig. 7 we have two pairs of radioautograms showing the initial and final copper distribution after gettering at 900°C for 1 hr using boron oxide alone and the boron and phosphorus oxide mixture. As is evident, the copper tends to concentrate in the boron diffused region. This is probably due to, first, enhanced copper solubility in the heavier doped p-region (5) and second, more dislocations and hence, more copper precipitation in the diffusion induced stress region first demonstrated by Queisser (6) and then by Prussin (7). The effectiveness of gettering is obvious. The remaining copper appears as dots, probably clusters of precipitates scattered within the diffused region.

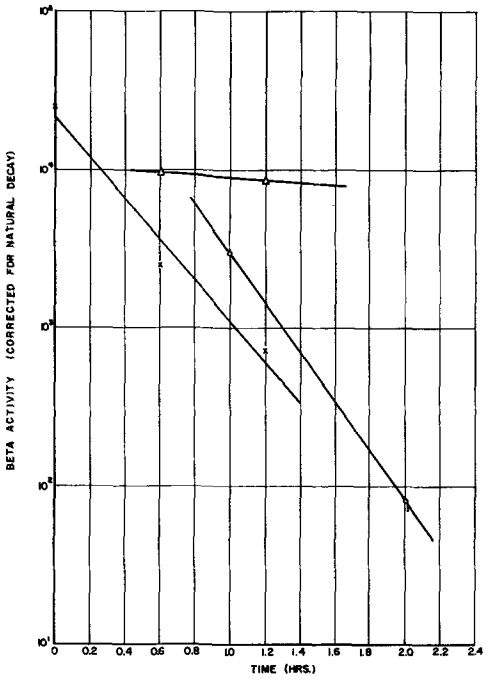

Fig. 8. Boron-phosphorus oxide mixture gettering rates of Cu^{64} in silicon diodes. x, Gettered with B_2O_3-P_2O_5 at 870°C; ○, gettered with B_2O_3-P_2O_5 at 1000°C; △, ungettered, but heated in air at 870°C.

We have observed no significant difference in the results using the two different oxides. Some preliminary results on the gettering rate are shown in Fig. 8. Here we have plotted the log of the activity, which is proportional to the copper concentration, *vs.* gettering time duration at two different temperatures, 870° and 1000°C. The radioactivity plotted here refers to the β particle counting taken on the top surface where the planar diodes were located. For a first approximation we fit the points with straight lines, which is equivalent to assuming a first order depletion rate. A small positive temperature coefficient is apparent by comparing the slopes of these lines. We also have shown here the activities of the wafer before and after going through the heat cycle at 870°C without the gettering oxide applied. We see no significant change in the copper concentration level.

Conclusion

In conclusion, we have shown the feasibility of reducing the reverse leakage current of planar diodes by using suitable oxide gettering of metal impurities in the temperature range of 800°-1000°C. The boron and phosphorus oxide mixture seems to be the outstanding gettering agent in that the gettered devices show good stability during life test. A radio tracer technique is shown to be a useful tool for studying the metal impurity distribution and the gettering kinetics.

Acknowledgment

The authors wish to express their deep appreciation to Dr. Robert Hall of the General Electric Research Laboratory for his contribution in obtaining the radio tracer data. They are also appreciative of Air Force Cambridge Research Center for their partial support of this work.

Manuscript received Oct. 22, 1962; revised manuscript received Dec. 27, 1962. This paper was prepared for delivery before the Boston Meeting, Sept. 16-20, 1962.

Any discussion of this paper will appear in a Discussion Section to be published in the December 1963 JOURNAL.

REFERENCES

1. A. Goetzberger and W. Shockley, *J. Appl. Phys.*, **31**, 1821 (1960).
2. R. F. Geller, A. S. Breamer, and E. N. Bunting, *J. Research Natl. Bur. Standards*, **13**, 243 (1934).
3. P. J. Gielisse, T. J. Rockett, T. S. Shevlin, and W. R. Foster, Ohio State University, Report No. 931-2, Contract No. AF33(616)-6509, Oct. 1959-Dec. 1959.
4. A complete treatment of this phenomena is given by C. T. Sah, R. N. Noyce, and W. Shockley, *Proc. IRE*, **45**, 1228, (1957), where further references to earlier work may also be found.
5. W. Shockley and J. L. Moll, *Phys. Rev.*, **119**, 1480, (1960).
6. H. J. Queisser, *Bull. Am. Phys. Soc.*, **6**, 106, (Mar. 1961); and H. J. Queisser, *J. Appl. Phys.*, **32**, 1776, (1961).
7. S. Prussin, *J. Appl. Phys.*, **32**, 1876 (1961).

Brief Communications

The JOURNAL accepts short technical reports having unusual importance or timely interest, where speed of publication is a consideration. The communication may summarize results of important research justifying announcement before such time as a more detailed manuscript can be published. Consideration also will be given to reports of significant unfinished research which the author cannot pursue further, but the results of which are of potential use to others. Comments on papers already published in the JOURNAL should be reserved for the Discussion Section published biannually.

Submit communications in triplicate, typewritten double-spaced, to the Editor, Journal of The Electrochemical Society, 30 East 42 St., New York 17, N. Y.

A Novel Four-Point Probe for Epitaxial and Bulk Semiconductor Resistivity Measurements

P. A. Schumann, Jr., and J. F. Hallenback, Jr.

Components Division, International Business Machines Corporation, Poughkeepsie, New York

ABSTRACT

A novel configuration for a four-point probe with points on opposite sides of the wafer is proposed. The potential distribution from a small area contact on a two resistivity epitaxial structure is given. The effects of the layer and substrate parameters on this potential distribution are discussed. A consideration of these potential distributions indicates that a probe of this design would be usable for epitaxial layer resistivity measurement under the design considerations discussed. These same potential distributions indicate that a two-point probe is also usable. Brief experimental results of the over-under four-point probe on bulk silicon are given. The two point probe is contrasted experimentally with the P-type control wafer, and three point breakdown for measurement of N on N^+ epitaxial silicon.

The use of semiconductor materials in the fabrication of solid-state devices has created a need for resistivity measurements of that material. Since the material on which measurements are made is to be used for fabrication purposes, it is essential that this measurement be nondestructive and, if possible, simple. Valdes (1) introduced an inline four-point probe technique for measurement of resistivity on finite samples with insulating or conducting bottom surfaces. This theory was expanded to a square array probe and further developed to incorporate sheet resistance measurements (2-5). A convenient technique for finding the solution to many sample and probe geometries was introduced by Uhlir (6). Uhlir found a general class of solutions for point contact potential distributions and finite sample geometry with conducting or insulating bottom surfaces. The four-point probe as developed is adequate for most resistivity measurements on bulk material. However, the measurement of epitaxial layers on substrates of the same type has created a new problem which cannot be solved by the normal four-point probe unless the probe spacing is of the order of the layer thickness.

The measurement of N on P or P on N epitaxial material can be made with a normal four-point probe and appropriate correction factors. However, this measurement itself is open to question due to the resistivity profile in the epitaxial layer and the effects of the substrate. The resistivity of N on N^+ or P on P^+ epitaxial material has not been measured on the sample with a nondestructive technique which is predictable from theory. The most common technique is to place an opposite-type substrate in the reaction chamber with the normal wafers. The sheet resistance of this sample is then measured with a four-point probe, and the resistivity is calculated. This technique is not advantageous because it does not measure the sample of interest and because of the different resistivity profiles obtained from growing on different types of substrates. A technique has recently been proposed by Brownson (7) whereby N on N^+ or P on P^+ epitaxial material may be measured. This technique involves a three-point probe and makes use of the point contact peak inverse voltage as a function of resistivity. But, as no adequate theory of point contact breakdown is available, this technique must be calibrated on known resistivity samples.

A normal four-point probe with extremely small spacing would be ideal for epitaxial layer measurement. However, the problems of holding a small probe spacing for four probes in a conventional array are many. The smallest published probe spacing (8) is 254μ (10 mils) which is not small enough to measure an epitaxial N on N^+ or P on P^+ structure. Also, there is no published solution to the four-point probe problem with a finite conducting substrate of finite thickness. Some of the mechanical problems of a small spacing probe may be eliminated if two probes are placed on the top surface of the wafer and two on the bottom surface. Then one need only maintain two probe spacings that are small. Also, because the substrate is low resistivity, the probe spacing on the epitaxial surface will be the most important, and tolerances on the substrate surface probe may be relaxed.

The theory of operation and design considerations of this probe when used to measure epitaxial N on N^+ or P on P^+ layers is developed here. The potential distribution for a finite area contact on an epitaxial structure with a finite conducting substrate of finite thickness and the dependence of this distribution on layer and substrate parameters is solved and related to probe design.

The aforementioned distributions suggest an alternate technique involving only two probes. A discussion of the same parameters shows that this technique can be used for the measurement of epitaxial layer resistivity.

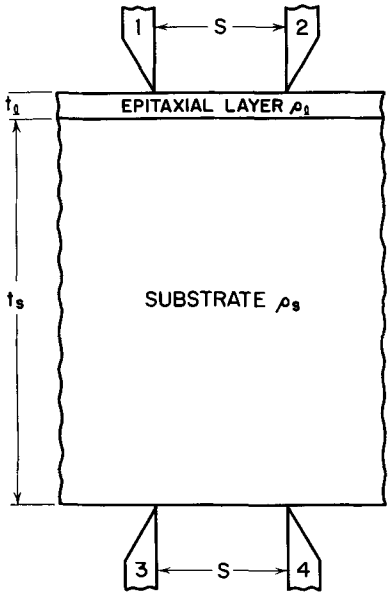

Fig. 1. Over-under four-point probe

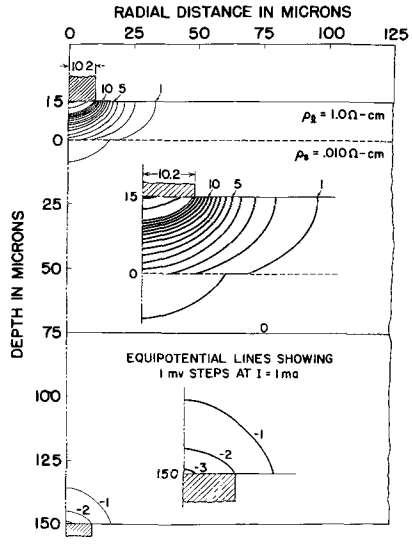

Fig. 2. Equipotential plot for over-under probe

Four-Point Probe

Theoretical

In the over-under configuration, probes are placed in pairs on opposite sides of the wafer, as shown in Fig. 1. Current is passed through probes 1 and 3, and voltage is measured between probes 2 and 4. The subscript l denotes layer parameters, and the subscript s denotes substrate parameters.

The boundary conditions used in the solution of Laplace's equation for this configuration are shown below.

The normal field at all surfaces except under the contacts is made to vanish by

$$\left.\frac{\partial\phi}{\partial r}\right|_{r=r_o} = 0 \quad \text{(Field at edge of wafer)}$$

and

$$\left.\frac{\partial\phi}{\partial Z}\right| = 0 \quad \text{(Field at surface of wafer excluding contact)}$$

$$r > a$$
$$Z = 0 \text{ and } Z = t_l + t_s$$

The average normal field under the contact is given by

$$\left.\frac{\partial\phi}{\partial Z}\right| = -\frac{I\rho_l}{\pi a^2} \qquad \left.\frac{\partial\phi}{\partial Z}\right| = -\frac{I\rho_s}{\pi a^2}$$

$$r \leq a \qquad r \leq a$$
$$Z = 0 \qquad Z = t_l + t_s$$

The conditions at the interface are

$$\sigma_l \frac{\partial\phi_l}{\partial Z} = \sigma_s \frac{\partial\phi_s}{\partial Z}$$

$$\phi_l = \phi_s$$

The problem was solved using cylindrical symmetry. It was assumed that the junction between the substrate and layer was abrupt with uniform resistivity on either side. The contact was assumed to be planar with an effective radius a; the radius of the wafer is r_o. The numerical solutions presented here were obtained.

Figure 2 shows a typical potential distribution for stated boundary conditions, nominal resistivity, and dimensions. The equipotential lines shown are at millivolt increments when the current is 1 ma. The enlargement details the structure of the equipotential surfaces near the contacts. It should be remembered that the field lines, which give an indication of the current flow, would be drawn perpendicular to the potential lines. This figure indicates that the current flows almost directly through the layer with very little spreading, while there is a wide current spread in the substrate. The equipotential lines are very closely spaced in the layer within a radial distance of 50μ and very widely spaced in the substrate. This indicates that the probe spacing on the substrate is not as critical as that on the layer. Thus, the probe spacing on the epitaxial layer will have to be less than 50μ (about 2 mils) in order to gain sensitivity to the layer.

Figure 3 shows the dependence of the equivalent resistance on probe spacing for various layer resistivities with all other parameters held constant. The equivalent resistance is the probe voltage divided by the sample current. For this plot the effective contact radius is 10.2μ, substrate thickness is 203μ, layer thickness is 10.2μ, and substrate resistivity is 0.010 ohm-cm. Calculations are shown for layer resistivities of 0.1, 1.0, and 10.0 ohm-cm. It can be seen from this graph that in order to have sensitivity to 0.10 ohm-cm layers, probe spacing must be less than 50μ. However, if higher resistivities are to be measured, larger probe spacing may be tolerated.

Figure 4 shows the layer resistivity as a function of the equivalent resistance for various probe spacings. Calculations were made for the same parameters used in Fig. 3. The slope of the line indicates the sensitivity to the layer resistivity. The best sensitivity is obtained with the zero probe spacing. Sensitivity decreases with an increase in probe spacing and at 102μ is practically zero. Calculations

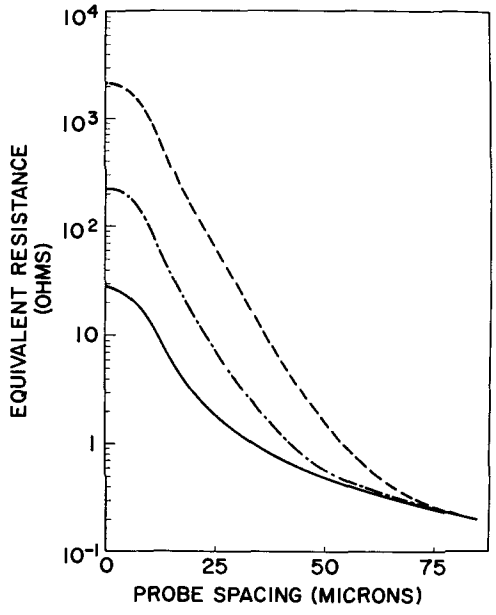

Fig. 3. Equivalent resistance as a function of probe spacing and layer resistivity. ———ρ_l, 0.10 ohm-cm; — - —ρ_l, 1.0 ohm-cm; — — —ρ_l, 10 ohm-cm; a, 1.02μ; t_l, 10.2μ; t_s, 203.2μ; ρ_s, 0.010 ohm-cm.

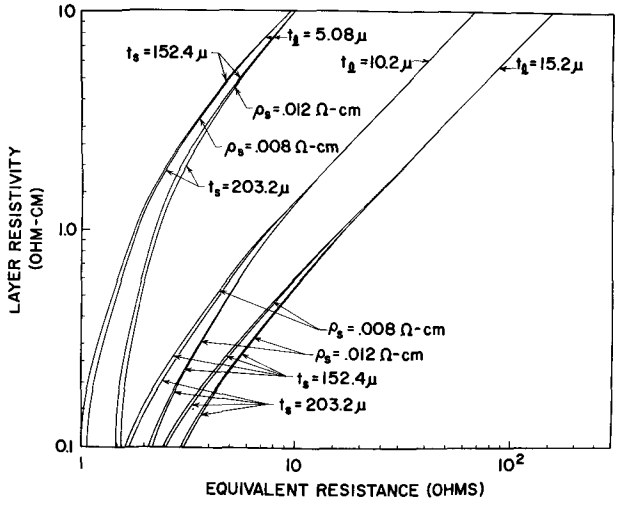

Fig. 5. Layer resistivity as a function of equivalent resistance, layer thickness, substrate resistivity, and substrate thickness; s, 25.4μ; a, 10.2μ.

have been made for various effective contact radii. As anticipated, the strongest dependence on the contact radius is at zero probe spacing. With a probe spacing of 25-50μ, dependence is not as great.

Figure 5 shows in more detail the layer resistivity as a function of the equivalent resistance for a probe spacing of 25.4μ (1 mil) and an effective radius of contact of 10.2μ. The three groups of lines are for layer thicknesses of 5.08, 10.2, and 15.2μ. It can be seen from this that the thicker layer makes the equivalent resistance more sensitive to the layer resistivity. The finer structure shows the dependence on substrate parameters. The largest horizontal separation is due to the substrate resistivity, and a lesser effect is due to the substrate thickness. The curves here are shown for substrate resistivities of 0.008 and 0.012 ohm-cm, and substrate thicknesses of 152 and 203μ. There is less splitting of the curves for all three thicknesses as the layer resistivity is increased and less splitting at all layer resistivities as layer thickness is increased.

Figure 6 shows much the same data except for a probe spacing of 50.8μ (2 mils) and a constant substrate thickness of 178μ. With this probe spacing, a change in resistivity produces a smaller change in the equivalent resistance than with a 25.4μ spacing. It can be seen that the effects of the substrate become more important.

As seen from Fig. 1 through 6, a probe spacing of 25-50μ is needed to emphasize the effects of layer resistivity on the equivalent resistance. Within this range of probe spacing the effect of layer resistivity is large while the effects of the substrate and contact radius are small.

The effects of the radius of the wafer are shown in Table I for various probe spacing. The correction factor necessary for a probe spacing of 50μ is 0.99 when a wafer with a radius of 208μ (8 mils) is

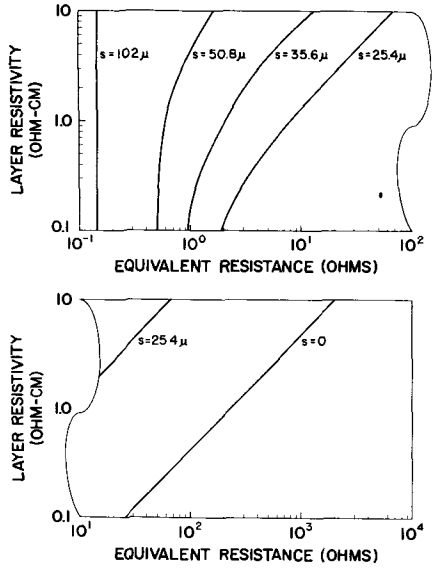

Fig. 4. Layer resistivity as a function of equivalent resistance and probe spacing.

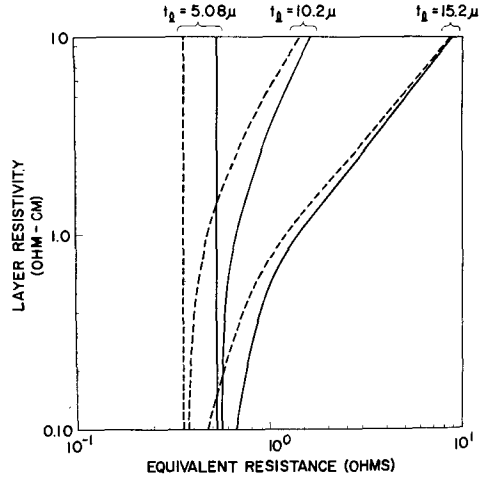

Fig. 6. Layer resistivity as a function of equivalent resistance, layer thickness, and substrate resistivity for a probe spacing of 50.8μ. — —ρ_s, 0.008 ohm-cm; ———ρ_s, 0.012 ohm-cm; t_s, 178μ; a, 10.2μ; s, 50.8μ.

Table I. Size correction factors for over-under four-point probe on epitaxial material

Wafer radius, μ	Probe spacing, μ 254	203	152	102	50.8	25.4
508	0.98	1.00	1.00	1.00	1.00	1.00
406	0.97	1.00	1.00	1.00	1.00	1.00
305	0.79	0.95	0.99	1.00	1.00	1.00
203	—	0.42	0.78	0.94	0.99	1.00

C.F. = $R\infty/R_s$; ρ_l = 0.5 ohm-cm; ρ_s = 0.006 ohm-cm; t_l = 10.2μ; t_s = 203μ; a = 15.2μ.

used. With these small correction factors, the radius of the wafer is not important for most applications.

Experimental

A probe is being designed to meet the conditions for measurement of epitaxial layer resistivity. A model of this probe has been constructed to test the feasibility of the probe design. The probe is constructed with tungsten carbide points which are independently loaded by lever arms and weights. Point loading and spacing is individually adjustable. The probe spacing and reproducibility is controlled by the action of a bearing on which each point mechanism rotates. Probe spacing on this first attempt is adjustable down to 62μ.

The reproducibility of the probe spacing was studied by observing the damaged areas the points make on polished silicon. Measurement was made with a 100 X microscope and an X-Y stage calibrated to 2.54μ (0.1 mil). Reproducibility was better than 2.54μ (0.1 mil) which includes the errors due to the finite size and irregular shape of the damaged area of contact. The reproducibility of the probe spacing was studied also by applying the probe to bulk wafers. Since there is no theory available for this case, the equivalent resistance is shown in Fig. 7 plotted against resistivity as measured with a normal four-point probe. The reproducibility in this case was ± 5% as averaged over 23 wafers with resistivities between 0.005 and 100 ohm-cm. This spread of course includes the variation of resistivity within the wafers.

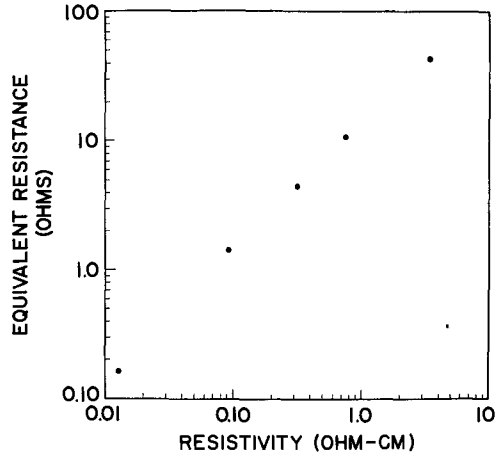

Fig. 7. Experimental equivalent resistance as a function of resistivity for bulk wafers; s, 110μ; $t \approx 305\mu$.

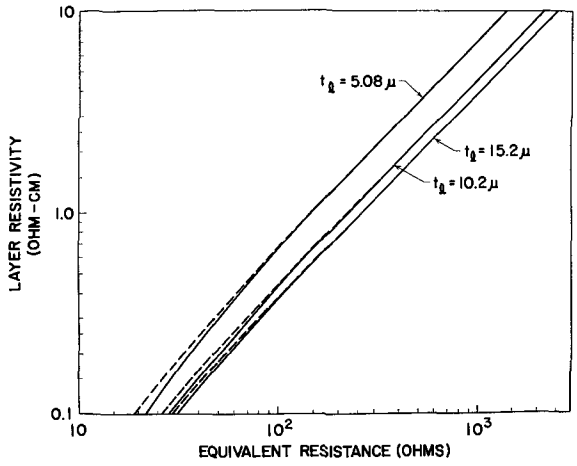

Fig. 8. Layer resistivity as a function of equivalent resistance, layer thickness, and substrate resistivity for over-under two-point probe. — —ρ_s, 0.008 ohm-cm; ———ρ_s, 0.012 ohm-cm. s equals 0; a, 10.2μ; 152.4$\mu \leq t_s \leq$ 203.2μ.

The application of this probe to bulk wafers offers some advantages which cannot be had by a normal four-point probe. The effects of the radius of the wafer will not be as pronounced, and the radial gradients may be mapped accurately. With the small probe spacing obtainable in this configuration, small samples may be measured with no size correction factors.

Two-Point Probe

Theoretical

As was seen in Fig. 4, the greatest sensitivity to the layer and the least sensitivity to the substrate was obtained with a zero probe spacing, reducing the four-point over-under probe to a two-point over-under probe. Calculations shown in Fig. 8 are given for zero probe spacing and layer thicknesses of 5.08, 10.2, and 15.2μ. The fine splitting at low layer resistivities is for substrate resistivities of 0.0080 and 0.012 ohm-cm. For substrate thicknesses between 152 and 203μ, no variance is observed for a change in substrate thickness. Similar conditions can be met by placing two probes on the epitaxial surface a great distance apart. In this way, the current still flows almost directly through the layer to the substrate. With this configuration the current flows through the layer twice, gaining more sensitivity to the layer.

Experimental

Measurements were made on epitaxial silicon wafers (N on N^+) using two points of a Fell 0.159 cm (62.6 mils) in-line probe. Results are shown in Table II with the three-point breakdown measurement (8) and resistivity measurements made on a N on P control wafer grown with the N on N^+ wafers. Resistivity was calculated from the theoretical data and effective contact radius. The effective contact radius was obtained by measurement of the constriction resistance on N-type polished bulk silicon. With this probe, the effective contact radius was nominally 5μ. Good agreement between the three-point breakdown and two-point probe measurements was obtained in the 0.10-0.60 ohm-

Table II. Experimental results obtained on N-N$^+$ epitaxial wafers with two-point probe compared with three-point breakdown and P-type control

Layer thickness, μ	Layer resistivity, ohm-cm: P-type control	Three-point breakdown	Two-point probe
6.09	0.75	0.47	0.48
7.36	0.85	0.64	0.44
7.87	0.95	0.68	0.86
8.38	0.47	0.41	0.41
12.5	0.23	0.18	0.18
9.40	0.34	0.29	0.23
7.36	0.020	0.022	0.0093
9.90	6.0-8.2	—	3.3
8.88	0.39	0.35	0.36
10.2	0.10	0.09	0.11
9.90	0.10	0.09	0.15
10.7	0.12	—	0.12
10.7	4	—	8.8
10.9	0.75	0.53	0.52

cm range. Very poor agreement was obtained between either of these methods and the P-type control. The thickness of the epitaxial layer was measured with the infrared reflectance technique (9, 10). If the effective area of contact is calculated before each measurement, repeatability is about ±15%.

Some measurements have been made on P-type epitaxial germanium. The results indicate that the two-point probe measurement should be easier on germanium than on silicon. However, no theoretical calculations have been made for the low resistivity substrates normally used for germanium. The repeatability of measurement on germanium ranges within ± 10%.

Summary

The over-under probe has the advantage in the measurement of epitaxial layer resistivity as its range is large and is bounded on the high end only by injection effects. In fact, the sensitivity at high layer resistivity is greatest. It is bounded on the lower end by the resistivity of the substrate. Measurement of layer resistivities less than 0.1 ohm-cm is not feasible. As was seen in Table I, the effects of wafer size are negligible. Because of its size, it is possible to bring the probe down in the very small window of a diffusion mask.

Besides these advantages, it is similar to the normal four-point probe in that it is a four-terminal resistance measurement predictable from potential theory.

Its application to bulk wafers is limited by the same conditions that limit the normal four-point probe. However, it may be more usable at high resistivities where surface leakage may be a problem for normal four-point probe measurements. Its usefulness for mapping wafers is increased by the fact that it averages the resistivities over a smaller area than the normal four-point probe. The effect of wafer size is reduced when the over-under configuration is used.

The small probe spacing needed for epitaxial layer resistivity measurement is certainly more easily obtained when only one probe spacing need be held accurately. It is easier to place two points close together than to hold four points in line with a small probe spacing.

The two-point probe technique is usable for reasons that make a normal four-point probe useless. The fact that a high resistivity layer is placed on a low resistivity substrate is why the two-point probe can even be considered. Because the current is largely confined to the region below the contact in the layer and because the current spreads widely in the substrate, the voltage between the two probes is a primary function of the layer. Since this is true, the voltage measured between the two points is almost independent of probe spacing as long as the spacing is much greater than the layer thickness. Therefore, refinements can be made on probe points to achieve optimum measurement conditions which will be a function of material and type.

The calculations presented here will be refined to obtain better accuracy and a wider range of parameter variation and will include calculations of the bulk resistivity case.

Both techniques will be applied to various epitaxial material and evaluated for their usefulness. The mechanical design of the over-under probe will be improved, and the present model will be altered to achieve smaller probe spacing.

Acknowledgments

The authors wish to thank W. H. Stocklin for programming the calculations presented here for the IBM 7090 computer. They also wish to thank E. E. Gardner for the three-point probe breakdown measurements, and J. C. Shelton for his assistance in the collection of the data presented here. Acknowledgment is also given to L. S. Sheiner, of the tool design group, for the mechanical design of the over-under probe. Grateful appreciation is expressed to Mr. M. Ranaldi for many valuable and encouraging discussions of this problem.

Manuscript received Oct. 29, 1962; revised manuscript received Feb. 2, 1963. This paper was prepared for delivery before the Boston Meeting, Sept. 16-20, 1962.

Any discussion of this paper will appear in a Discussion Section to be published in the December 1963 JOURNAL.

REFERENCES

1. L. B. Valdes, *Proc. IRE*, **42**, 420 (1954).
2. D. E. Vaughn, *Brit. J. Appl. Phys.*, **12**, 414 (1961).
3. F. Keywell, and G. Dorosheski, *Rev. Sci. Inst.*, **31**, 883 (1960).
4. F. M. Smits, *Bell System Tech. J.* **37**, 711 (1958).
5. M. A. Logan, *ibid.*, **40**, 885 (1961).
6. A. Uhlir, *ibid.*, **34**, 105 (1955).
7. J. Brownson, Paper presented at the Los Angeles Meeting of the Society, May 1962.
8. J. K. Kennedy, *Rev. Sci. Inst.*, **33**, 773 (1962).
9. E. Grochowski and W. A. Pliskin, Paper presented at the Detroit Meeting of the Society, October 1961.
10. M. P. Albert and J. F. Combs, *This Journal*, **109**, 709 (1962).

Photoconductivity in Thin Organic Films

Arthur Bradley and John P. Hammes

Radiation Research Corporation, Westbury, New York

ABSTRACT

Organic films of approximately 1μ thickness were prepared by glow-discharge polymerization of monomers containing nitrogen, sulfur, selenium, and certain metals and tested for photosensitivity. Conductivities (in the dark ranging from 10^{-17} to 10^{-13} mho/cm at room temperature) were enhanced by as much as three orders of magnitude by 10 w/in.^{2} of white light excitation. Nitrile groups and sulfur appeared most promising as chemical substituents in the polymer films for promoting conductivity to useful levels. Addition of traces of iodine to the discharge during the deposition of a polynaphthalene film increased its dark and photoconductivity over a thousandfold. Activation energies of photoconduction of the order of 0.25 ev were found (25°-175°C). Short-circuit photocurrents of consistent polarity in all films were observed and attributed to a photovoltaic effect at the interface between the film and the transparent electrode.

Glow discharge polymerization has been shown to be a useful technique for the preparation of thin organic films (1, 2). These films have been characterized by good chemical and thermal stability and generally high electrical resistance. Their first commercial application has been as a capacitor dielectric foil when deposited on an aluminized Mylar substrate (3), but they are also being investigated for possible use in micromodule electronic components (printed and evaporated circuits), as protective coatings on metal surfaces, as vapor-blocking deposits on otherwise porous substrates, as the dielectric element in electroluminescent panels, as the charge-storing layer in photosensitive information storage tape, and for many other purposes. A recent publication from this laboratory described procedures for carrying out electrical measurements on glow-discharge films and reported typical deposition efficiency and dark conductivity data for specimens of various chemical composition (4). The present communication deals with the photoconductive properties of these films.

Glow discharge films, as a class of insulating materials, have the characteristic patterns of dark and photoconductivity represented with slight variations in Fig. 1 through 4. A moderate photosensitivity, or additional current under light excitation, was a general property of all specimens, and its magnitude was not obviously related to the dark current (or resistivity). Dark and photocurrents varied to some extent with the composition of the films, tending to be higher with more polar substituted mon-

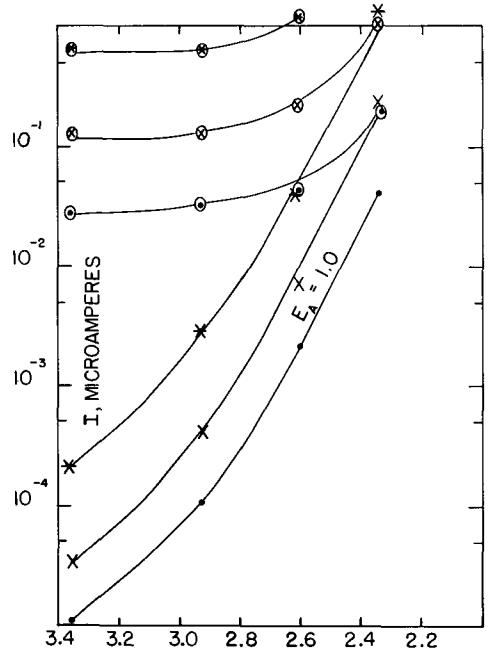

Fig. 1. Dark current and photocurrent (encircled points) vs. temperature for polymer film derived from thioacetamide; $10^3/T_{ABS}$; *, 24v; x, 6v; •, 1.5v.

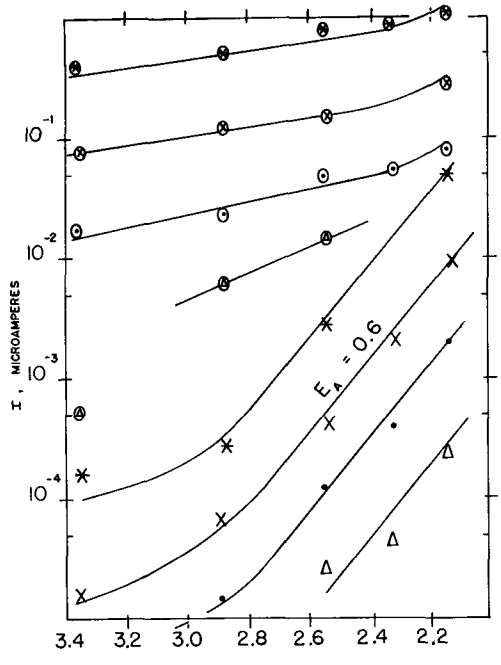

Fig. 2. Dark current and photocurrent (encircled points) vs. temperature for polymer film derived from thiophene; $10^3/T_{ABS}$; *, 24v; x, 6v; •, 1.5v; △, 0v.

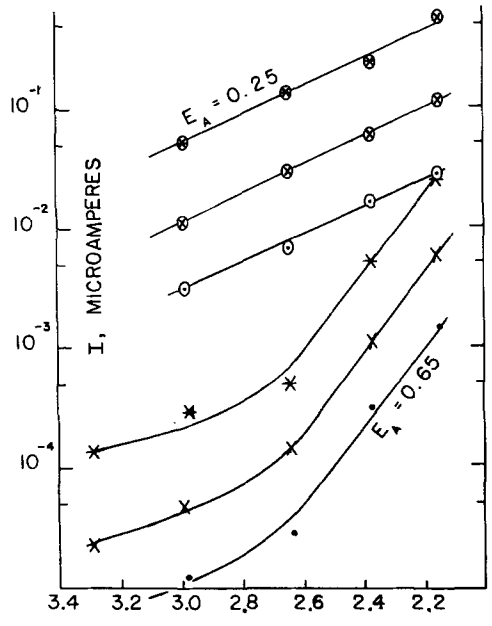

Fig. 3. Dark current and photocurrent (encircled points) vs. temperature for polymer film derived from pyrrole; $10^3/T_{ABS}$; *, 24v; x, 6v; •, 1.5v.

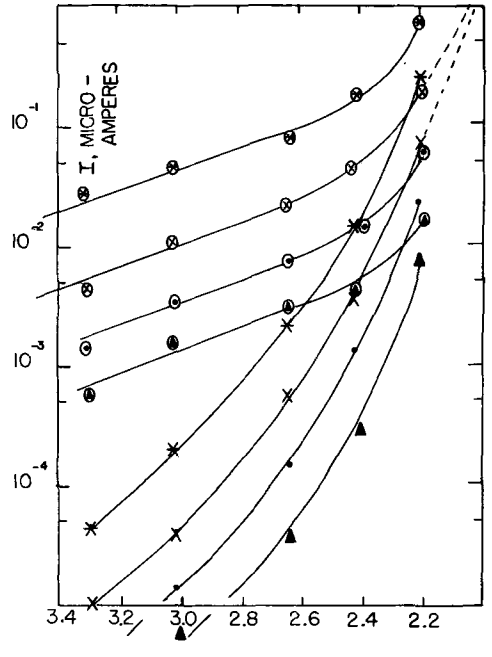

Fig. 4. Dark current and photocurrent (encircled points) vs. temperature for polymer film derived from pyrazole; $10^3/T_{ABS}$; *, 24v; x, 6v; •, 1.5v; ▲, 0v.

omers (Table I). Some apparent relationships between structure and conductivity are discussed below.

Since dark conductivity in all cases increased more rapidly with thermal activation than photoconductivity, the apparent sensitivity, or "gain," was most pronounced at room temperature. The increments tended to decrease with temperature and in some cases had fallen to insignificant levels above 200°C. As an example, a thioacetamide specimen had photo:dark current at room temperature of 2500:1, falling to about 200:1 at 90°C and 5:1 at 150°C (Fig. 1). On the other hand certain films still retained significant photosensitivity at the top of the temperature cycle range.

Table I. Ambient dark and photocurrents of typical specimens (6v applied, currents in units of 10^{-9} amp)

Compound	I_d	I^*_{W}[a]	I^*_{UV}[a]
1. N-Methyl-alanine nitrile	0.003	0.25	0.12
2. Hexa-n-butyl (di) tin	0.01	1.5	1.7
3. Naphthalene	0.01	2	0.7
4. Pyrazole	0.005	2	0.4
5. Pyrrole	0.02	5	3
6. Tetraisopropyl orthotitanate	0.03	5	5
7. p-Acetoxy-mercuri-aniline	0.01	6	8
8. Tributylamine	0.04	8	7
9. N-Nitrosopiperidine	0.01	2.5	0.2
10. N-Formylpiperidine	0.03	10	0.8
11. N-Nitrosodiethylamine	0.03	12	15
12. Dicyanoketene ethylacetal	0.025	15	3
13. Diphenyl selenide	0.003	16	5
14. Ferrocene	0.2	15	5
15. Thianthrene	0.05	70	16
16. Malononitrile	2	250	75
17. Thioacetamide	0.1	250	35
18. Tetracyanoethylene	10	1500	400
19. 2,4-Thiazolidone dione	20	2000	1500
20. Naphthalene-iodine	40	7000	1200

[a] Currents corrected for w (white light) = UV = 10 w.

Dark conductivity was related to temperature by the familiar expression

$$\sigma = \sigma_0 e^{-E_a/kT} \qquad [1]$$

in which E_a is best described as the "activation energy for conduction" (5). The activation energy (E_a) for dark conduction for the thioacetamide specimen was calculated to be just under 1.0 electron volt (ev) from the straight line section of the plot in Fig. 1.

In the temperature range where an activation energy of photoconduction (E_a^*) could be calculated or reasonably estimated, it fell in the range of 0.2-0.3 ev (Fig. 1-4). An example of a material with manifest activation energies for both dark and photoconduction is given in Fig. 3 (pyrrole). The values of E_a and E_a^*, respectively, for the pyrrole film were 0.65 and 0.25 ev.

The zero-voltage currents exhibited the same temperature dependence as those observed with an externally applied field. This is particularly well demonstrated in the case of a pyrazole specimen (Fig. 4) where the log I *vs.* $1/T$ curves were nonlinear, but the dark zero-voltage current followed the exact contour of the ohmic currents. The source of the internal voltage (of the order of 0.5v) may have been at the interface between the glow-discharge film and one of the electrodes.

Experimental

Photocurrents were measured under equilibrium conditions with illumination from a tungsten-filament white light source (additional work with pulsed excitation using a xenon flash lamp has been initiated and will be reported at a later date). Photosensitivity of one to more than three orders of magnitude above dark conductivity was observed at room temperature, depending on the composition of the film. Since the dark conductivities also

varied over a range of perhaps 10^4, there was great variety in the absolute magnitudes of the static photocurrents measured.

Specimens for electrical measurements were prepared on silica or other high-surface-resistivity glass. These substrates were conveniently in the shape of microscope slides 1 x 25 x 75 mm, with a transparent conducting film electrode covering approximately two-thirds of one face. Some preliminary work was carried out with transparent electrodes of gold and Nesa, but by far the greatest success was obtained with Corning EC coating, which was provided on Corning 1723 glass substrate, the electrode have a surface resistance of less than 100 ohms/square. This arrangement for measuring photoconductivity was originally described in 1951 by Weimer and Cope (6).

Pairs of aluminized or EC-coated slides were mounted about 1 cm apart in a glass bell jar for deposition of organic polymer film by glow-discharge in the manner previously described (4). A top electrode was applied by evaporation of aluminum. The complete specimen was essentially a capacitor of approximately 1 in.^{2} area, and 0.5-2μ thick. Typical capacitances were in the range of 0.003-0.03 μF.

Photoconductivities at varying temperatures were measured with the aid of a special Vycor apparatus in which the specimen could be mounted and maintained under voltage in an inert gas atmosphere. An outline drawing of the experimental setup is given in Fig. 5. Measurements were carried out with the Vycor "finger" immersed in a glycol bath warmed over a hot plate.

The illumination-source for most of these measurements was an Argus 200 slide projector, focusing light from a 200w Sylvania projector lamp bulb. The front of the lens system of the projector was positioned about 2 in. from the transparent face of the specimen in the glycol bath. Neither the walls of the Vycor finger nor the half-inch or so of glycol in the path of the beam absorbed any appreciable fraction of the illumination. It may be estimated that the photoconductivity excitation consisted of approximately 25w (over an area of 1 in.^{2}) of luminous power more or less uniformly distributed across the visible spectrum.

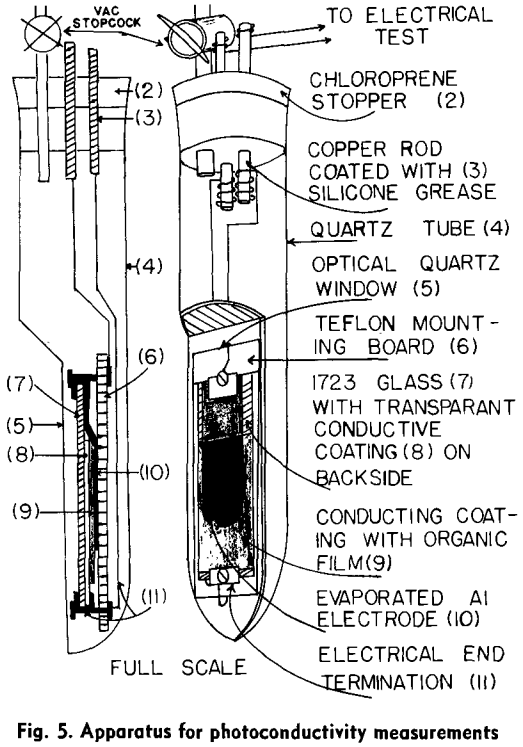

Fig. 5. Apparatus for photoconductivity measurements

Photocurrents and dark currents were taken on a General Radio 1230-A d-c amplifier. In all cases the shielded input lead to the electrometer was connected to the aluminized "back" electrode of the specimen, and the dry-cell voltage (between 1.5 and 24v) connected to the transparent electrode, which was therefore the frame of reference. As recorded in the figures, "positive" current was obtained when the transparent electrode was biased positively with respect to ground and to the aluminized face. The short-circuit currents (photo and dark) were invariably "negative" and therefore reflected a consistent internal polarization tendency in the specimens.

Currents were monitored visually to help determine the time necessary to wait for equilibration between voltages and after turning the illumination on or off. The recorder tracings revealed typical depolarization effects, requiring about an hour to stabilize when approaching new equilibrium current at reduced voltage. Most specimens showed delays of the order of 15 min in returning to their dark current levels after photocurrents of three orders of magnitude. These times tended to be shorter at elevated temperatures and at higher applied fields.

Most good specimens were essentially ohmic in their response to voltages between 1.5 and 24v (approximately 10^4-10^5 v/cm). An exception was pentachlorothiophenol, for which both dark and photocurrents were sensitive functions of voltage (Table II).

With the zero-voltage currents all tending to be "negative" it was not surprising that the currents observed at ±1.5v also reflected a certain bias in the negative direction. It was not uncommon for −1.5v currents to exceed +1.5v by about 50%. This was the only noticeable trend toward rectification. At higher voltages the currents were symmetrical both in the dark and under illumination.

A Pen-ray uv lamp dissipating 14w was mounted directly on the silica window of the Vycor finger to survey uv sensitivity in the film specimens. Temperature control was poor, even with the lamp apparatus immersed in the glycol bath. The uv excitation available to the specimen was estimated at 2.5w (sensitive area 1 in.^{2}). For comparison purposes, the currents assembled in Table I have been corrected to a uniform input excitation level of 10w.

Table II. Field effect in pentachlorothiophenol (25°, current in μa)

Voltage	I_d	I^*_w
1.5	0.00041	0.0063
6	0.021	0.32
24	1.7	21

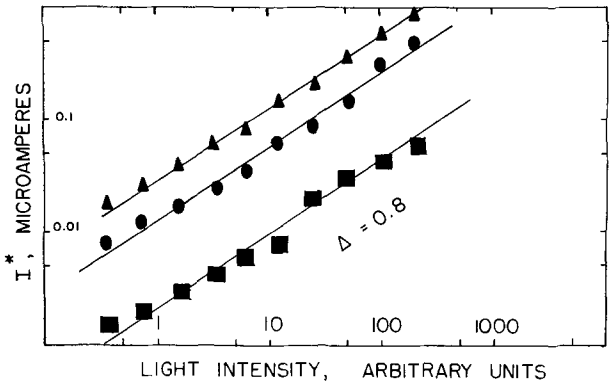

Fig. 6. Ambient photocurrent *vs.* light intensity. Thianthrene. ▲, 22½v; ●, 10½v; ■, 3v.

A series of variable illumination levels for a plot of photoconductivity *vs.* light intensity (Fig. 6) was achieved by adjusting the proximity of a small microscope lamp. Assuming the latter to be a point source, relative light levels at distances from filament to specimen face between 0.7 and 7.0 in. were calculated from the inverse square relationship and plotted (log log) *vs.* photocurrent. The specimen in this case was thianthrene (323A). The slope of Fig. 6, $\Delta = 0.8$, corresponds to the power of the illumination level proportional to the current. The experiment was repeated with a malononitrile specimen (370A), giving the same result.

Discussion and Summary

It is an interesting aspect of this work that all specimens gave zero-voltage or short-circuit currents, the ratios photo:dark and the temperature dependence being essentially identical to those obtained with an applied field. These currents were always in the direction of spontaneous flow of electrons from the transparent electrode into the specimen. In magnitude they usually comprised one-fifth to one-third of the normal ohmic current observed with 1.5v applied.

The self-generated currents under illumination may be regarded as resulting from a photovoltage: the effect of photon excitation on the junction emf originating at the interface between the film and the transparent electrode. The incident photon radiation creates free carrier in the bulk to a much larger extent than in the narrow barrier region, and this appears as a lowering of the electrical resistance of the specimen. With applied fields of 1.5v and larger this "photoconductivity" dominates the effect of the internal emf. Even at zero applied field both effects are important in determining the magnitude of the self-generated photocurrent. When the source of illumination is removed, the free carriers in the bulk quickly recombine and the residual current (at V=0) drops in a few minutes to below the level of equilibrium dark current at 1.5v. However, it does not fall to zero for several days, and sometimes appears to last indefinitely.

The existence of a permanent zero-voltage dark current would be of considerable theoretical interest. A system at equilibrium with its surroundings could not, according to the second law of thermodynamics, maintain a steady electrical output consuming heat alone. It must be assumed that either a chemical reaction was occurring at the electrode interface or there was a long-term residual current decreasing too slowly to measure in time intervals less than days, or, in some cases, weeks. Most of the data on zero-voltage dark conductivity, such as with pyrazole, Fig. 4, were recorded between 30 and 60 min after discontinuing the illumination. These currents appeared to be steady at the time of measurement but further investigation might have revealed a long time constant decay that eventually would have fallen to zero.

The persistent short-circuit currents after illumination was discontinued may have been due to charges released from long-lived traps in the barrier region maintaining a pseudo-photovoltage. Alternatively, the zero-voltage dark currents may have been no more than the minimum required to discharge the energy stored in the photovoltage across the barrier through the high resistance of the bulk of the specimen. An estimate of the orders of magnitude involved will help rationalize this point of view. The capacitance of a 1μ thick specimen was about 0.01μF. The barrier layer, however, may have been only 10-100Å thick (10^{-3}-$10^{-2}\mu$) with a corresponding increase in capacitance to 1-10 μF. A typical resistance for the specimen would be between 10^{11} and 10^{12} ohms. The RC time constant therefore could reasonably be expected to lie in the range of 10^{5}-10^{7} sec. Thus it would be possible for some specimens to continue to show short-circuit dark currents after a week that were as much as half those observed soon after discontinuing the illumination.

It was predicted by early workers (7, 8) that the majority carriers in anthracene were positively charged, on the basis of higher photocurrents being observed when the illuminated electrode was positive. This was later confirmed by direct measurements (9). On the other hand, evaporated film sandwich specimens of hydrocarbons such as ovalene and violanthrene were found to give higher photocurrents when the illuminated electrode was negative and therefore a negative carrier sign was suggested (10).

It is equally convenient on the basis of the direction of the zero-voltage photocurrent in these glow-discharge films to consider that the majority carriers are negatively charged. This would require that electrons generated in the barrier layer at the transparent electrode migrate into the bulk rather than holes originating at the aluminum electrode traversing the film in the opposite direction.

Activation energies for dark conduction were found in the range of 0.6-1.0 ev for the best photoconductors, prepared from sulfur and polynitrile-containing monomers. Hydrocarbons and amines were usually somewhat higher (1.0-1.4 ev). These figures are in agreement with previous data reported for similar types of films (4), and for organic "semiconductors" in general (5). The best interpretation of this approximately 1v activation energy that can be offered at present is that it is probably related to the average depth of carrier ground states below the bottom of a "conduction band" conceived by

analogy with the theory of conduction in single crystals.

Inorganic semiconductors like germanium, with good crystal order and high dielectric constant, have loosely bound donor and acceptor orbitals and corresponding impurity activation energies as low as 0.01 ev. Organic molecular crystals, however, with short range order and low dielectric constant tend toward localized orbitals (tightly bonded electrons), resulting in activation energies of the order of 1 ev even for impurity mechanisms. Hence the high activation energies shown by these polymer films do not necessarily imply intrinsic conductivity.

Photocurrents increased with temperature in roughly the same manner as dark currents, except that the apparent activation energies up to about 150°C were quite low, of the order of 0.2 ev. Kommandeur *et al.* (11) found E_a^* varied between 0.08 ev for naphthalene and 0.35 for pyrene in a series of photoconductivity measurements on aromatic hydrocarbons. It was suggested that such activation energies of photoconduction were associated with hindrances to charge transport arising from polarization of the molecules of the lattice by charge carriers.

The existence of an activation energy of photoconduction suggests that the carrier-generating mechanism does not require a band transition but rather a molecular excitation to an intermediate nonconducting state from which there is further thermal activation to produce free carriers. An equivalent sequence involving such "excitons" is well established in anthracene and other molecular crystals (12).

Evidence of a threshold of photoconductivity has often been observed (5). In this investigation, however, there was, on the average, less photocurrent from near ultraviolet excitation than from a comparable intensity of white light. This indicates somewhat less efficient charge carrier production by the higher energy radiation.

It was found that the photocurrent (I^*) was related to the intensity of illumination (L) by an exponential factor $\Delta = 0.8$, as in Eq. [2]

$$I_w^* \propto L^{\Delta} \qquad [2]$$

According to Rose (13), a photoconductor at low free carrier densities will give $0.5 < \Delta < 1.0$ if there is predominantly one class of ground states. Previous work in this Laboratory led to a value of $\Delta = 0.7$ for beta ray bombardment-induced conductivity in polystyrene (14), and many other organic polymer films have given approximately this value (15).

It does not appear that high photocurrents can be obtained from films prepared from hydrocarbon monomers, or from common oxygen or nitrogen compounds. Many other elements, metals and nonmetals can also be incorporated in substantial amounts without materially enhancing this property. The photoconductivity of ferrocene, for example, was disappointingly low. However, with multiplication of polar functional groups, such as the unsaturated —C≡N (nitrile) group, a definite trend toward higher currents was observed. This was also true of compounds containing sulfur. Some slight enhancement of conductivity occurred when mixed substituents (S and N; S, N, and O) were available from the monomer.

The factor most directly related to conductivity, dark or photo-excited, appeared to be the concentration of unsaturated (or charge-sharing) groups in the polymer. Second to the chemistry was the physical state. as reflected in the appearance. Hard, glossy, and moderately opaque films gave the best photoconductivity; cloudy or smoky films often had high dark conductivity but poor dielectric strength and little photosensitivity.

The thickness and area of the film specimens were such that conductances (I/V) obtained from the figures and tables can be converted to conductivities by dividing by the factor 10^5. Thus the room-temperature dark conductivities corresponding to the experimental results given in Table I ranged from as low as 10^{-17} mho/cm for naphthalene, pyrazole, diphenylselenide, and others to nearly 10^{-13} for the polynitrile, sulfur, and iodine-treated films. The spread in magnitudes and relationship to composition were similar to those previously reported (4). The photoconductivities (corrected to approximately 10w of white light) ranged from 10^{-15} to 10^{-11} mho/cm.

The 2,4-thiazolidone dione specimen 318B was representative of the best semi(photo)conductors prepared. At room temperature it had $\sigma = 4 \times 10^{-14}$ and $\sigma^* = 4 \times 10^{-12}$ mho/cm (10w input). Thus it was still, technically, an insulator according to the convenient classification of Hannay (16), in which a "semiconductor" lies in the range $10^3 > \sigma > 10^{-9}$. It is evident that the best glow-discharge films are still of only borderline interest for consideration as conductive components in solid state devices.

There may already be applications for these films in high temperature photosensitive detectors. Thiophene and pyrrole films had photo:dark ratios in excess of 20:1 at 190°C (Fig. 2 and 3), and at the highest temperatures studied many films did indeed enter the arbitrary "semiconductor" category.

The future of this research involves a search for higher conductive films, for better photosensitivity, and for more detailed investigation of related semiconductor parameters, such as carrier lifetime, mobility, and trap density. A preliminary investigation of possible electronic applications will also constitute a portion of the next phase of this program.

Acknowledgment

The authors have been privileged to discuss this work in depth with Professor David Fox of the State University of New York at Stony Brook. The able technical assistance of Miss Marlene Hiller is also gratefully acknowledged.

Manuscript received Oct. 9, 1962; revised manuscript received Dec. 17, 1962.

Any discussion of this paper will appear in a Discussion Section to be published in the December 1963 JOURNAL.

REFERENCES

1. J. Goodman, *J. Polymer Sci.*, **44**, 551 (1960).
2. J. J. Spokas, Paper presented at the Conference

on Semiconduction in Molecular Solids, Princeton University, February 1960.
3. "Glow Discharge Deposits Thin Film," p. 6, *Electrical Design News*, October 1960.
4. A. Bradley and J. P. Hammes, *This Journal*, **110**, 15 (1963).
5. C. G. B. Garrett, "Organic Semiconductors," Chap. 15, in "Semiconductors," N. B. Hannay, Editor, Reinhold Publishing Co., New York (1959).
6. P. K. Weimer and A. D. Cope, *RCA Rev.*, p. 316, (September 1951).
7. A. G. Chynowith and W. G. Schneider, *J. Chem. Phys.*, **22**, 1021 (1954).
8. D. C. Northrup and O. Simpson, *Proc. Roy. Soc.*, **A244**, 377 (1958).
9. O. H. LeBlanc, Jr., *J. Chem. Phys.*, **33**, 626 (1960).
10. H. Inokuchi and H. Akamatu, "Electrical Conductivity of Organic Semiconductors," in "Solid State Physics," F. Seitz and D. Turnbull, Editors, vol. 12, p. 129, Academic Press, New York (1961).
11. J. Kommandeur, G. J. Korinek, and W. G. Schneider, *Can. J. Chem.*, **35**, 998 (1957).
12. D. M. J. Compton, W. D. Schneider, and T. C. Waddington, *J. Chem. Phys.*, **27**, 160 (1957).
13. A. Rose, "Performance of Photoconductors," Chap. 1-A p. 26, "Photoconductivity Conference," R. G. Breckenridge *et al.*, Editors, John Wiley & Sons. New York (1956).
14. A. Bradley, *Plastics Design and Processing*, p. 18, November 1961.
15. J. F. Fowler, *Proc. Roy. Soc.*, **A236**, 464 (1956).
16. N. B. Hannay, ref. (5), p. 1.

Optical and Electrical Properties of Semiconducting Cadmium Oxide Films

T. K. Lakshmanan

Weston Instruments, Division of Daystrom Inc., Newark, New Jersey

ABSTRACT

Indium-doped, copper-doped, and undoped cadmium oxide films were prepared by reactive sputtering. The oxygen vacancy concentration in these films was changed by varying the oxygen pressure in the sputtering chamber. Electrical properties, spectral transmittance, and Hall effect were measured on doped and undoped specimens. Both the conductivity and the Hall coefficient were found to vary monotonically with the oxygen pressure at the time of film formation. Copper doping increased the Hall constant and indium doping decreased it. Stoichiometric and impurity effects on carrier concentrations are discussed. Spectral transmittance curves are given for the doped and undoped oxide films.

Not much is known about the basic properties of cadmium oxide as a semiconductor. The reason for this lack of knowledge is that good single crystals have not been grown yet. Gas phase oxidation of "cadmium metallicum in bacillis" as well as sublimation of the oxide in a stream of oxygen have been reported recently by Haul and Just (1) but these methods yielded only small and highly impure crystals.

Several papers have appeared during the past few years on studies on powder material, sintered blocks, compressed tablets, or sputtered films. Preston (2), Helwig (3), Holland and Siddall (4), Miloslavskii and Ranyuk (5), and Lappe (6) used thin films produced by reactive sputtering. Sintered blocks or compressed and sintered tablets were used by Wright (7) and Wright and Bastin (8), while Cimino and Marezio (9) used powder material. The results published so far seem to indicate that cadmium oxide is a nonstoichiometric semiconductor with excess, interstitial cadmium or vacancies in the anion sublattice ranging in concentration between 0.01 and 0.05%. Depending on purity and method of preparation, carrier concentrations range between 10^{18} and 10^{21}. Some known constants, taken from the International Tables of Constants and Numerical Data (10), are shown in Table I.

The effects of doping on the electronic properties have not been reported yet. The paper by Cimino and Marezio (9) describes the effect of incorporating indium, silver, and sodium on the lattice parameter. These authors prepared the oxide from the precipitated hydroxide and purified it subsequently by heating and quenching in air. They ascribed the observed changes in the lattice parameter on increasing additions of indium to the initial elimination of excess cadmium followed by a controlled valence process corresponding to a decrease of valence of cadmium ions. Kroger, Vink, and van

Table I. Some properties of cadmium oxide (10)

Energy gap	2.5 ± 0.1 (T, 300°)	(Dunstadter)
Electron effective mass	0.1	(Wright and Bastin)
Electron mobility	120	(Winkler)
Lattice parameter, a	4.6953 (T, 300°)	(Swanson and Fuyat)
Refractive index	2.49 (λ 671)	(Wyckoff)
Density	8.238 (T, 300°) (calc)	(Swanson and Fuyat)

den Bloomgaard (11) have shown that the controlled valence description of Verwey and coworkers (12) is basically the same as the quasi-free carrier description.

Very recently, Hall and Just (1) reported on lattice diffusion studies in cadmium oxide furnishing strong evidence for a transport mechanism involving vacancies in the anion sublattice. They doped the oxide with indium and lithium and found that Li^+ created additional oxygen vacancies while In^{3+} decreased their concentration. These workers favor the oxygen vacancy scheme against the postulate of cadmium excess in order to explain the nonstoichiometry.

The purpose of the present investigation was to develop a novel technique for introducing oxygen and metallic impurities simultaneously into cadmium oxide and to study empirically the effects of these additions on the electrical properties of the oxide. Reactive sputtering of alloys of cadmium in the presence of oxygen was used because it was found to yield uniform large-area specimens. The cadmium oxide was doped with cadmium or indium in this manner. The main advantage of the technique was that doping and deviations from stoichiometry were both accomplished during film formation and not subsequent to it.

Experimental Results

The sputtering chamber was provided with a cadmium-indium or cadmium-copper alloy cathode which was water-cooled. Water-cooling was found to improve reproducibility of the films. A mixture of pure argon and oxygen was fed into the chamber at a steady rate maintaining the chamber pressure at 10μ. In the earlier experiments nitrogen was used as the sputtering gas since higher film conductivities were thereby produced.

Since many variables exist in the reactive sputtering technique, it was necessary to keep most conditions constant and vary only one at a time. One variable investigated was the partial pressure of oxygen in the chamber using a given cathode. Volumetric ratios of oxygen in the argon-oxygen mixtures were maintained at 1%, 2%, 5%, 10%, and 100%. For a given proportion of oxygen three electrodes were used: 100% cadmium, 95 Cd-5 Cu by weight, and 95 Cd-5 In by weight. The remaining sputtering parameters were optimized for maximum deposition rate and kept constant throughout the entire series of experiments (Table II). The substrates were optical cover glass slides (Corning No. 0211) with fired-on platinum (Du Pont No. 7553) electrodes.

The following measurements were made on the resulting films: conductivity, spectral transmittance, thickness, Hall coefficient, and impurity concentration. The specimens used for most measurements were 2.5 cm long and 0.5 cm wide. Conductivity measurements were made by means of the two-terminal technique under ambient room conditions. The amount of copper or indium introduced into the mixed oxide films was measured by means of x-ray emission spectrography. Large area films of about 50 cm^2 were prepared for this purpose. The film material, weighing several milligrams, was dissolved in dilute HCl and distilled water, evaporated down, dried under heat lamps, and gently ignited. Then it was ground to a fine powder in an agate mortar and exposed to x-rays. The fluorescence peaks obtained were compared with those from known standards. The second order spectrum was necessary for separating indium from cadmium since these are adjacent elements in the periodic table.

The specimens analyzed were those prepared in the 10% oxygen mixture. The films prepared using the 95 Cd-5 Cu cathode yielded a proportion of 95.5 Cd-4.5 Cu. While the proportion of copper to cadmium in the film remained approximately the same as in the cathode, the films prepared using the 95 Cd-5 In cathode contained 78 Cd-22 In as the proportion of the two metals by weight. Whether these films contained a second indium-rich phase is not known.

The Hall effect was measured under d-c conditions. Several preliminary measurements showed that the Hall coefficient was independent of the specimen currents in the range used. For purposes of tabulation all Hall coefficients were calculated for a specimen current of 1 ma and a field of 12,000 oe. Film thickness was measured using the Tolansky multiple beam interference technique.

Table II shows the conductivities of the various specimens. For doped as well as undoped films the conductivities decrease monotonically with an increasing proportion of oxygen in the sputtering chamber. This dependence seems reasonable if it is

Table II. Electrical properties of doped and undoped oxide films

Cathode	Argon:Oxygen	Film thickness, Å	Ohms/square	Conductivity, σ, ohm^{-1} cm^{-1}	Hall constant, R_H, cm^3/cb	Hall mobility, $R_H\sigma$, cm^2/v sec
Cd	98:2	2430	88	467	0.017	7.9
Cd	95:5	1850	490	110	0.045	5.0
Cd	90:10	2030	590	83	0.051	4.2
Cd	0:100	1390	22,400	0.64	0.251	0.16
95 Cd-5 Cu	98:2	2430	390	106	0.030	3.2
95 Cd-5 Cu	95:5	2620	800	48	0.067	3.2
95 Cd-5 Cu	90:10	2810	1500	24	0.101	2.4
95 Cd-5 In	99:1	2810	188	189	0.012	2.3
95 Cd-5 In	98:2	2250	240	131	0.013	1.7
95 Cd-5 In	95:5	1690	466	127	0.017	2.2
95 Cd-5 In	90:10	1390	630	117	0.018	2.1

the cadmium excess or the oxygen deficiency that gives cadmium oxide its high conductivity. As the departure from stoichiometry is reduced the conductivity decreases. The nature of the variation for undoped oxide is in agreement with the findings of Holland and Siddal (4) and Helwig (3). No results have previously been reported for the mixed oxide. For a given proportion of oxygen, copper doping decreases the conductivity and indium doping increases it excepting for very low amounts of oxygen where departure from stoichiometry plays a part.

The room temperature Hall coefficients are also tabulated in Table II. All specimens were found to be N-type. For any given electrode the Hall coefficient increases with increasing proportion of oxygen. In other words, the carrier concentration decreases with decreasing oxygen deficiency in the lattice. The high value of the Hall coefficient for 100% oxygen is noteworthy. For a given oxygen proportion, the Hall constant increases on doping with copper and decreases with indium doping. The dependence of the Hall mobility on stoichiometry is striking for the undoped samples. In the doped samples the effect of stoichiometry is clouded by impurity effects which seem to play a significant role.

For undoped oxide with the least amount of oxygen deficiency the carrier concentration is approximately 10^{19}. It is noteworthy that Wright and Bastin (8) obtained the same value for sintered specimens. This value agrees with the value of 4×10^{-4} for oxygen defect or metal excess concentration determined by Haul and Just (1) and by Cimino and Marezio (9) on crystals and powder specimens respectively. With increasing oxygen deficiency the carrier concentration in the present samples increases to 10^{20}. Miloslavskii and Ranyuk (5) obtained values ranging from 10^{20} to 10^{21} on sputtered films depending on the method of preparation.

The spectral transmittance curves for doped and undoped specimens are seen superimposed in Fig. 1. All three specimens were sputtered at a constant oxygen proportion of 10% and the plots were normalized to approximately equal film thickness namely 2800Å. The absorption edge is not sharp but, for the undoped oxide, it generally agrees with the reported energy gap of 2.5. It is significant here that Mollwo (13) had shown that, with zinc oxide films, increasing amounts of zinc excess make the absorption edge less steep and extend it toward lower energies. The copper-doped sample shows a weak absorption in the region of 600 mμ possibly due to copper itself.

Doped and undoped specimens were found to form photovoltaic junctions when applied to a specially prepared selenium layer. Open circuit voltages as high as 0.7v have been observed with the undoped specimens in sunlight. Measurements made at 10, 100, and 1000 ftc show that copper doping reduces the open circuit potential, whereas indium doping increases it.

A certain amount of empirical work has previously been reported on this photovoltaic effect at

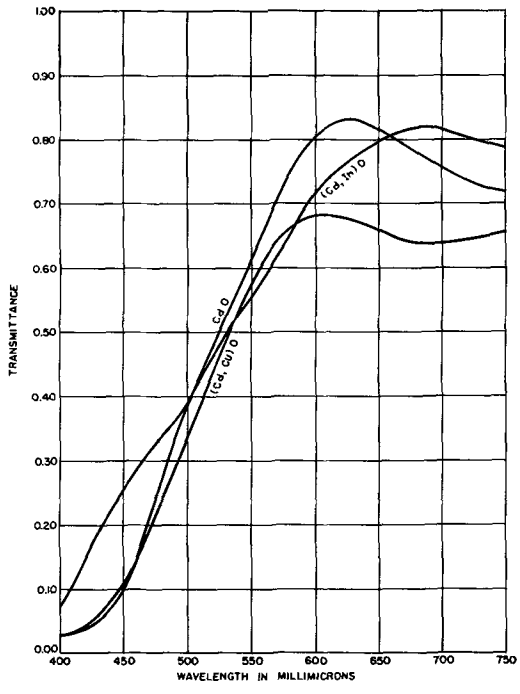

Fig. 1. Spectral transmittance of undoped and doped films

the selenium-cadmium oxide junction. The tendency has been to regard this as similar to a metal P-type semiconductor contact. The energy gap of selenium is 1.7 ev and of cadmium oxide 2.5 ev. If certain specimens of CdO should be nondegenerate, the question would arise as to what type of a complex or heterojunction existed between the two types. Since the crystal class is different for the two semiconductors, the picture becomes even more complicated. A very elementary model has been proposed by the author (14). A good deal of further investigation is necessary to establish the nature of the contact.

The manner in which the impurities are introduced is not known. The effect of heat treatment is now under study. One has to be careful in looking for temperature effects on the electrical properties of oxides, sulphides and selenides because of variations in stoichiometry at high temperatures. A very recent paper by Becker and Frederikse (15) points out the complications with nonstoichiometric semiconductors.

Summary

The reactive sputtering technique has been extended to form mixed or doped oxide films through the use of alloy cathodes in the sputtering chamber. Indium and copper have been introduced into cadmium oxide films in this manner and their respective amounts determined by x-ray emission spectrography. By varying the oxygen pressure in the chamber the stoichiometry of the resulting oxide is believed to be altered. Both doping and variations in stoichiometry are effected during the formation of the film and not subsequently.

When the partial pressure of oxygen is increased, the resulting films show a decrease in the N-type conductivity and an increase in the Hall coefficient. These results are explained qualitatively by noting that the carriers result from an oxygen deficiency

in the film and that the deficiency concentration decreases with increasing amounts of oxygen in the chamber. For a given pressure of oxygen, indium doping increases the carrier concentration and copper doping decreases it.

The absorption edge of the undoped film corresponds roughly with the reported energy gap for cadmium oxide. The doped and undoped films were found to form highly photovoltaic junctions with selenium.

Acknowledgment

The author wishes to acknowledge earlier contributions of Robert T. Luedeman to an initial sputtering technique for undoped cadmium oxide. Film deposition and several of the measurements were made by Joseph M. Mitchell.

Manuscript received Nov. 16, 1962; revised manuscript received Dec. 8, 1962. This paper was prepared for delivery before the Boston Meeting, Sept. 16-20, 1962.

Any discussion of this paper will appear in a Discussion Section to be published in the December 1963 JOURNAL.

REFERENCES

1. R. Haul and D. Just, *J. Appl. Phys. Suppl.*, **33,** 1, 487 (1962).
2. J. S. Preston, *Proc. Roy. Soc.*, **202A.,** 449 (1950).
3. G. Helwig, *Z. Physik*, **132,** 621 (1952).
4. L. Holland and G. Siddal, *Vacuum*, **11,** 4, 375 (1953).
5. V. K. Miloslavskii and A. I. Ranyuk, *Soviet Optics and Spectroscopy*, p. 536 (Nov. 1960).
6. F. Lappe, *Z. Physik*, **137,** 380 (1954).
7. R. W. Wright, *Proc. Phys. Soc.* **64A.,** 350 (1951).
8. R. W. Wright and J. A. Bastin, *ibid.*, **71A.,** 109 (1958).
9. A. Cimino and M. Marezio, *J. Phys. Chem. Solids*, **17,** 57 (1960).
10. "International Tables of Constants and Numerical Data," Vol. 12, Pergamon Press (1961).
11. F. A. Kroger, H. J. Vink, and J. van den Boomgaard, *Z. Phys. Chem.*, **203,** 1, (1954).
12. E. J. W. Verwey, P. W. Haayman, F. C. Romeigin, and G. V. van Osterhout, *Philips Research Repts.*, 5, 174 (1950).
13. E. Mollwo, "Photoconductivity Conference," John Wiley & Sons, Inc., New York (1956).
14. T. K. Lakshmanan, *Proc. I.R.E.*, **48,** 1646 (1960).
15. J. H. Becker and H. P. R. Frederikse, *J. Appl. Phys. Supp.*, **33,** 1, 447 (1962).

Stress Generation in Tantalum During Oxidation

R. E. Pawel, J. V. Cathcart, and J. J. Campbell

Metals and Ceramics Division, Oak Ridge National Laboratory,[1] Oak Ridge, Tennessee

ABSTRACT

Thin rectangular specimens of tantalum were oxidized on one side at 500°C and 1 atm oxygen pressure. From curvature measurements, the bending stresses arising as a consequence of the oxidation process were determined and correlated with known oxidation rate behavior and oxide morphology. The simplest stress model, that of a uniform film on a substrate, was shown to be an inadequate description of the stress source, thus reflecting the complexity of the tantalum-oxygen reaction. A model relating the stress gradient to the oxygen concentration gradient was tested and shown to be reasonably consistent with the experimental data.

The fact that high stresses may exist in surface layers of a material as a result of gaseous oxidation has been pointed out by several previous investigators (1-4). Also, indirect evidence of large stresses, existing as a result of an oxidation process or exerting an influence on the process, is available (5-8). If the kinetics of a reaction depend on the state of the reaction product, it seems certain that variables which control the characteristics of mechanical film rupture and repair become important. Stress buildup either on a local or general scale during the reaction is thus recognized as a likely influence on both the oxidation kinetics and the oxide morphology.

Quantitative data on the magnitude of the stresses arising during oxidation are limited. Dankov and Churaev (9) attempted to describe quantitatively the oxidation of Fe, Mg, and Ni in terms of stresses in the oxide film. Despite some questionable assumptions regarding the thickness of the oxide layer and the stress distribution, their data were consistent with arguments based on volume ratios of metal and oxide. Jaenicke and Leistikow (10) investigated the state of stress in copper oxide films formed on copper as a function of time at elevated temperatures (300°-500°C). These data confirm the presence of extremely high stresses in these films. More recently, x-ray diffraction and optical studies of thin films of Cu_2O formed on copper (11, 12) revealed the presence of large epitaxially induced strains.[2] The existence of strain gradients and strain anisotropy in the films was also noted. Evans (2) likewise observed a stress gradient in thin nickel oxide films; however, he concluded that the origin of this stress gradient was not epitaxial forces, but an "inheritance" of a stress gradient that existed in the metal prior to oxidation.

In an effort to characterize the nature of stresses arising as a result of oxidation processes in several metal-oxygen systems, an apparatus, similar to that used by Dankov and Churaev (9), was constructed in which the deformation resulting when a speci-

[1] Operated by the Union Carbide Corporation for the United States Atomic Energy Commission.

[2] The data in these investigations relate directly to atom positions and thus strictly reflect "strain." Although a description of the interface and the mechanical properties of the thin-film state is somewhat obscure, undoubtedly the word "stress" could be substituted here.

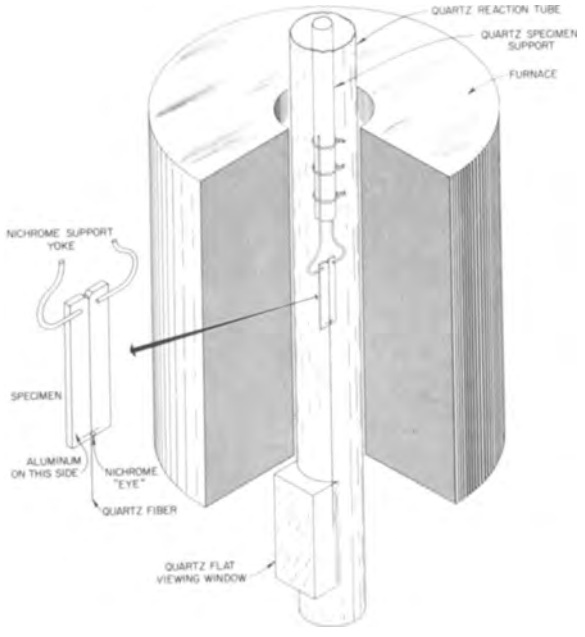

Fig. 1. Schematic drawing of apparatus

men is oxidized on one side only is measured as a function of time. This paper includes a description of the equipment and some preliminary results for oxidation of polycrystalline tantalum. The data also demonstrate that stress measurements provide a useful method for characterizing further the oxidation behavior of metals.

Experimental Procedure

Tantalum specimens[3] were cut from 0.020-in. sheet as rectangular coupons 1 x 4 cm, and annealed in vacuum for 2 hr at 1600°C. These coupons were mechanically polished through 0.3μ levigated alumina and prepared for the apparatus in the following way: A support yoke of heavy (0.060 in.) Nichrome wire was discharge-welded to one end of the specimen and a small V-notch filed at that end (see Fig. 1). At the other end, on the same side, a small "eye" was fashioned from 30 gauge Nichrome. The specimen was electropolished in a 90% H_2SO_4-10% HF solution, placed in the vacuum evaporator, and plated on one side with a thin film of aluminum. The aluminum layer served as adequate protection from oxidation for the tantalum beneath it, as has been reported previously for oxidation studies on niobium (6). The results of experiments in which specimens were protected on one side with aluminum or gold layers and held at 500°C in vacuum showed also that the thin metal layer exerted no measurable mechanical effect on the specimen; furthermore, no change in curvature was observed when the aluminum layer was dissolved in HCl after a specimen had cooled to room temperature.

The specimen was suspended in the apparatus by firmly attaching the Nichrome support yolk to the quartz positioning rod with several sections of wire. A quartz fiber, 20-30 cm long, was hung onto the specimen with the free end through the "eye" located at the bottom end of the aluminum-coated side. The purpose of the eye was to restrict lateral motion of the fiber along the edge of the specimen as bending proceeded. The fiber extended so that deflection measurements could be made through the quartz window in the part of the apparatus beneath the furnace. Deflections could be measured with a standard cathetometer to an accuracy of about ± 0.05 mm up to a total deflection of about 2 cm. Radii of curvature of the specimen, and thus the bending stresses, were determined directly from the deflection measurements.

With the specimen in position, the system was evacuated to a pressure of approx. 10^{-6} mm Hg, and the temperature was raised to 500°C. Small and erratic fiber deflections were sometimes observed during the heating period; however, after temperature was reached, any drift was uniform and quite small. A "zero" reading was taken immediately before dry oxygen was admitted at slightly less than atmospheric pressure. Cathetometer readings were then taken intermittently for the duration of the experiment.

Data and Interpretation

Preliminary experiments in which tantalum specimens were oxidized on one side only showed that bending could be observed very shortly after the specimens were exposed to oxygen at 500°C. Figure 2 is a photograph of a series of specimens oxidized for various times at this temperature. The curvature can be easily detected with the eye even in the first specimen. Thus in a qualitative sense it was obvious that large stresses are generated in the specimen as a result of the oxidation process.

The quantitative evaluation of the stress in the specimens was made in view of the following considerations. If a rectangular specimen is subjected to uniform bending about one axis by an external force and if the material obeys Hooke's law, the maximum stresses in the outermost fibers of the specimen are given by a simple flexure formula

$$\sigma_s = \pm \frac{hE}{2\rho} \qquad [1]$$

where σ_s is maximum bending stress, h the thickness of specimen, E Young's modulus, 24.8 x 10^6 psi for Ta at 500°C (13), and ρ the radius of curvature. However, stresses which exist as a result of a surface reaction are two-dimensional in nature, and the simple beam theory must be modified in order to take into account the deviation from cylindrical bending. The action of the lateral (Poisson) strain

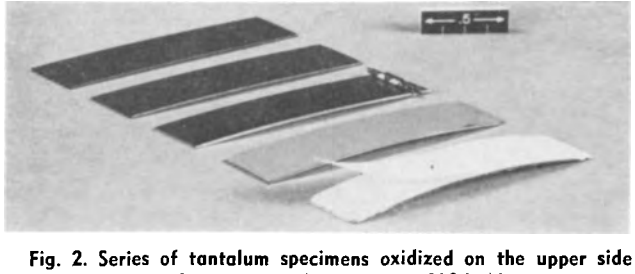

Fig. 2. Series of tantalum specimens oxidized on the upper side for ½ hr, 1 hr, 7 hr, 24 hr, and 168 hr at 500°C. Note separation of a layer of oxide in the last specimen.

[3] Nominal analysis: approx 99.7-99.8 wt % Ta, with Nb, Fe, and W being major metallic impurities. Oxygen content after vacuum anneal: approximately 200 ppm.

components during even one dimensional bending of thin strips is sufficient to alter the above equation by a factor of $1/(1-\gamma^2)$ (14), where γ is Poisson's ratio (0.35 for tantalum) (15). The correction factor would be increased even more, to $1/(1-\gamma)$, if the bending in two dimensions occurred without distortion. As distortion does occur for coupon-shaped specimens, the true relationship between stress and measured curvature becomes dependent on the geometry of the specimen. For the specimen geometry reported in this paper, a four-to-one length-to-width ratio, the correction is undoubtedly closer to $1/(1-\gamma^2)$. We have chosen, however, because of the uncertainty in the correction which exists at present, to analyze the stresses and report the results based on Eq. [1] with the realization that the actual stresses may be higher by 11% or more.

If the stress system which leads to bending originates in the vicinity of the specimen surface and a suitable stress distribution model is chosen, then the existence of a state of static equilibrium permits the magnitude and distribution of stresses in both the layer and the underlying material to be computed. The significance of the numbers arising from such a calculation, however, depends primarily on the accuracy of the model used to describe the stress distribution in the base material and the reaction products.

The data were initially analyzed in the customary fashion (16) under the assumptions that all oxygen absorbed by the specimen was present as a uniform surface layer of oxide and that a uniform stress existed in the oxide. However, for a specimen containing sufficient oxygen to produce a 1200Å layer of oxide at its surface, this model for stress distribution required the existence of the very large compressive stress of about 2,000,000 psi in the oxide layer in order to account for the observed bending of the specimen during oxidation. Further evidence for the inadequacy of this simple stress model was provided by the observation that, while chemical removal of the surface layers of the specimen resulted in a decrease in the amount of bending, more than 20 times the "ideal oxide thickness" had to be removed in order to eliminate the curvature of the specimen. It was concluded, therefore, that the processes responsible for the observed increase in stress level as oxidation proceeds on polycrystalline tantalum at 500°C occur in a relatively thick "surface region" and are not confined to any surface oxide films which may form.

Thus, since the source of the general stress build-up obviously must in some way be associated with the tantalum-oxygen reaction, factors other than those related to classical film formation must be taken into consideration. For example, it is well known that the solution of oxygen in the metal with the resulting expansion of the metal lattice is an important step in the oxidation of tantalum at 500°C. Furthermore, the early stages of oxidation of tantalum involve the formation and growth of platelets of oxide into the metal, producing a non-uniform interface which persists as oxidation proceeds. The geometry of the platelets is such that a "wedge" effect could result at the surface of the specimens.

For the purposes of the present paper, the region of stress generation during the early stages of oxidation of tantalum at 500°C is considered to be that layer of material in which an oxygen concentration gradient exists and in which platelets of oxide are forming. The stress model is based on the assumption that the lattice expansion accompanying oxygen solution is the major source of stress generation. It is, therefore, postulated that the thickness of the affected layer is controlled by the diffusion of oxygen into the tantalum and that the stress gradient in this region is proportional to the oxygen concentration gradient. It is further assumed that the macroscopic oxygen concentration gradient is not affected appreciably by the presence of the oxide platelets.

The oxygen concentration in the outermost surface layers of tantalum undoubtedly reaches a high level in a very short time. Thus, the results of previous investigations (8, 17, 18) indicate that the first oxides to form on tantalum at these temperatures and pressures do so from a metal already supersaturated with respect to oxygen and that on a macroscopic scale this supersaturation persists during the period of platelet formation. In the stress model it was assumed, therefore, that the time required for the attainment of the maximum oxygen concentration at the tantalum surface was negligibly small, and that the oxygen concentration at the surface and, consequently, the maximum surface stress, remains essentially constant throughout the course of the experiment.

These same experimental results along with the observation (see Fig. 4) that the bending of the specimen was initiated at the very beginning of the oxidation process, prior to the appearance of the first oxide platelets, likewise suggest that the "wedge effect" due to the presence of the platelets in the surface layers of the tantalum may be a less important source of stress generation than the lattice expansion associated with oxygen solution. Should this not be the case, however, the model described above probably still provides at least a first approximation of the stress distribution since the stress gradient would then be proportional to the platelet-density gradient which in turn must be related in some way to the oxygen concentration gradient.

As shown in Fig. 3, the stress in the specimens consists of two component parts, the stress σ_1, occasioned by the solution of oxygen in the specimen, and the bending stress, σ_2, which arises as a consequence of σ_1. The actual stress at any point in the bending specimen will be the algebraic sum of the two stresses

$$\sigma_1 = \sigma_I \frac{c - c_o}{c_s - c_o} = \sigma_I - \sigma_I \operatorname{erf} \frac{x}{2\sqrt{Dt}} \qquad [2]$$

$$\sigma_2 = \sigma_B + \left(\frac{\sigma_D - \sigma_B}{h}\right) x \qquad [3]$$

where h is the thickness of specimen, x the position in specimen with respect to surface in contact with oxygen, t time, D the diffusion coefficient of oxygen

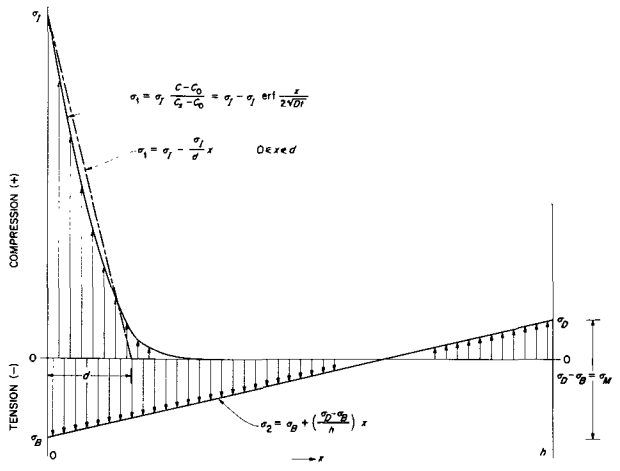

Fig. 3. Schematic diagram of stress distribution across tantalum specimen oxidized on one side. Experiment No. 225: specimen length, 4.0 cm; specimen thickness, 0.0445 cm; fiber length, 19.5 cm; temperature, 500°C; pressure, 1 atm.

in tantalum at 500°C, $D = 3.2 \times 10^{-10}$ cm^2/sec (19), c_s the surface concentration of oxygen when specimen is in contact with O_2 gas, σ_I the surface stress (at $x = 0$ and $c = c_s$), σ_B the component of bending stress at convex surface, σ_D the component of bending stress at concave surface, c oxygen concentration, and c_o residual oxygen concentration prior to oxidation. It should be pointed out that the stress distribution is expressed independently of the actual concentration values, which permits calculations to be made in terms of diffusivity data alone. The conditions for mechanical equilibrium, *i.e.*, the sum of forces and moments for the system must be equal to zero, require that

$$\int_0^h \left[\sigma_I - \sigma_I \operatorname{erf} \frac{x}{2\sqrt{Dt}} \right] dx + \int_0^h \left[\sigma_B + \left(\frac{\sigma_D - \sigma_B}{h} \right) x \right] dx = 0 \qquad [4]$$

and

$$\int_0^h \left[\sigma_I - \sigma_I \operatorname{erf} \frac{x}{2\sqrt{Dt}} \right] x\, dx + \int_0^h \left[\sigma_B + \left(\frac{\sigma_D - \sigma_B}{h} \right) x \right] x\, dx = 0 \qquad [5]$$

It is possible to simplify the solution of the equations by noting (see Fig. 3) that σ_1 may be approximated by a linear function of x, viz.,

$$\sigma_1 = \sigma_I - \frac{\sigma_I}{d} x \qquad 0 \leq x \leq d \qquad [6]$$

where d is determined as a function of time from available oxygen diffusivity data. At 500°C, $d \cong 3.23 \times 10^{-4} \sqrt{t}$ cm (t in minutes). Using Eq. [6], the simultaneous solution of the static equilibrium Eq. [4] and [5] in terms of the d parameter yields the following working equations

$$\sigma_I = \sigma_M \frac{h^2}{d(3h - 2d)} \qquad [7]$$

$$\sigma_I + \sigma_B = \sigma_M \frac{(h - d)^2}{d(3h - 2d)} \qquad [8]$$

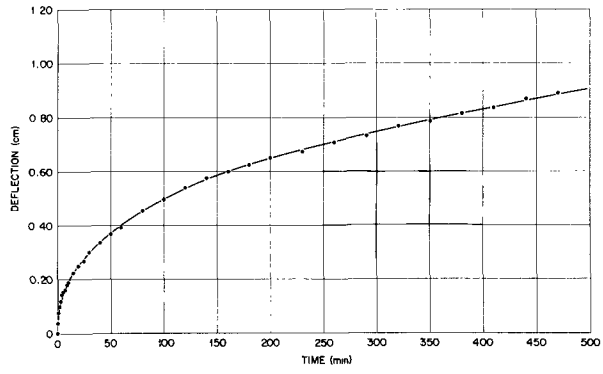

Fig. 4. Deflection-time curve for oxidation of polycrystalline tantalum at 500°C and atmospheric pressure.

where $\sigma_M = \sigma_D - \sigma_B = hE/\rho$. (Note, from Eq. [1], that $\sigma_M = 2\sigma_s$. Thus, for the case under consideration, the surface stress σ_I is related by a very simple equation to the maximum bending stress σ_s.) $\sigma_I + \sigma_B$ is the maximum stress which exists at the surface of the bent specimen. σ_I better represents the maximum surface stress if the specimen were not allowed to bend as would be the case for a thick specimen oxidized on both sides, and the data will be reported in terms of this parameter.

The inherent accuracy of the foregoing simplified procedure for computing stresses based on this model was tested by solving Eq. [4] and [5] simultaneously for several periods of time and comparing the resulting figures with those obtained from Eq. [7]. For oxidation times up to 8 hr, an error of less than 2% from this source was indicated.

Results and Discussion

A typical deflection-time curve is illustrated in Fig. 4 for a tantalum specimen oxidized at 500°C in 1 atm of dry oxygen. The degree of bending is a smooth function of time with the maximum bending rate established very early in the process. The curve of maximum bending stress computed with Eq. [1] for this experiment is shown in Fig. 5 and compared with the oxidation rate curve. It is significant to note that the "breakaway" inflection in the oxidation rate curve, associated phenomenologically

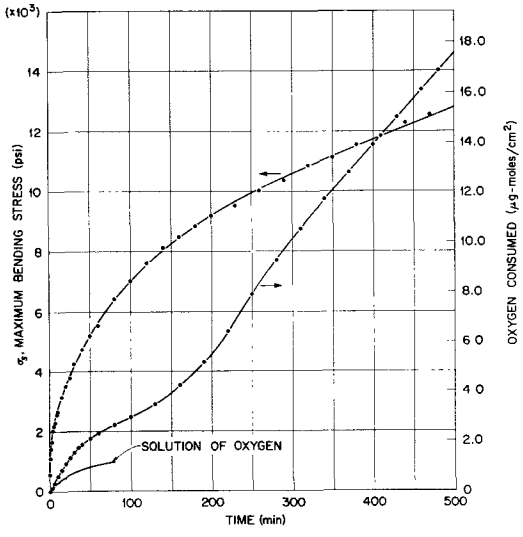

Fig. 5. Oxidation rate and bending stress curves for polycrystalline tantalum.

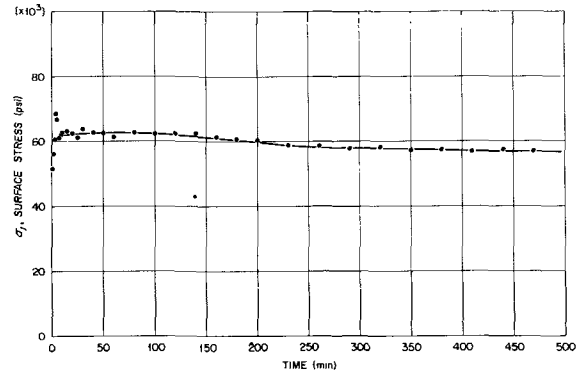

Fig. 6. Surface stress-time curve for the oxidation of polycrystalline tantalum.

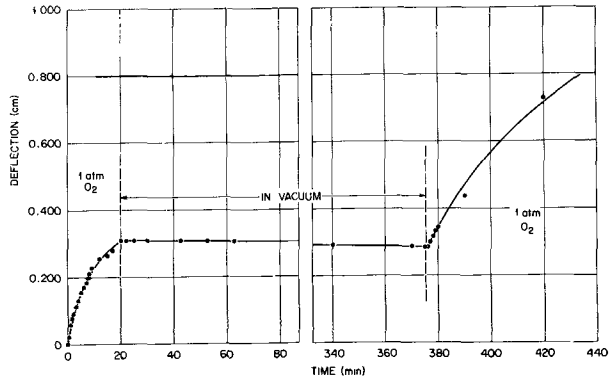

Fig. 7. Deflection-time curve for interrupted oxidation experiment. Experiment No. 229: specimen length, 4.0 cm; fiber length. 28.5 cm.

with localized cracking of the surface oxide (5), has no obvious counterpart in the bending stress curve. Neither can it be associated with an inflection in the surface stress curve, see Fig. 6.

The third curve in Fig. 5 shows as a function of time the amount of oxygen which dissolves in tantalum as calculated from existing values for the diffusion coefficient (19) with the surface concentration of oxygen in tantalum taken as 1800 ppm. As may be seen from Fig. 5, the solution of oxygen is an important part of the reaction in the early stages, accounting for at least half of the total oxygen consumed. The calculations of Kofstad (20) indicate that this ratio may be even higher.

Figure 6 is a plot of the surface stress, σ_I, computed from Eq. [7], as a function of time for the same set of data. The surface stress reached its maximum value of 60,000-65,000 psi compression after the first minute or so of oxidation and remained virtually constant for the remainder of the experiment, in agreement with the proposed model. During the first few minutes of oxidation the deflection measurements from which the surface stresses are calculated are particularly sensitive to small experimental errors arising from such sources as transient heating effects or slight mechanical displacements of the quartz pointer caused by the introduction of oxygen to the system. The scatter of data points in the first part of the stress curve in Fig. 6 can probably be explained most simply in these terms.

In order to test further the validity of the proposed stress distribution model, an interrupted oxidation experiment was performed. In this experiment, the specimen was oxidized in the usual fashion for 20 min; the system was then evacuated to a pressure of approx. 10^{-6} mm Hg and the specimen allowed to remain at temperature. After a total of 375 min oxygen was again admitted to the system. Deflection measurements were made throughout the three stages of this experiment and are plotted in Fig. 7. During the vacuum anneal, the amount of bending was observed to decrease slightly. Upon the re-admission of oxygen, the specimen continued to bend; however, the change in the initial slope of the curve showed that the anneal represented more than simply a lapse in the oxidation reaction. Presumably, the principal events occur-

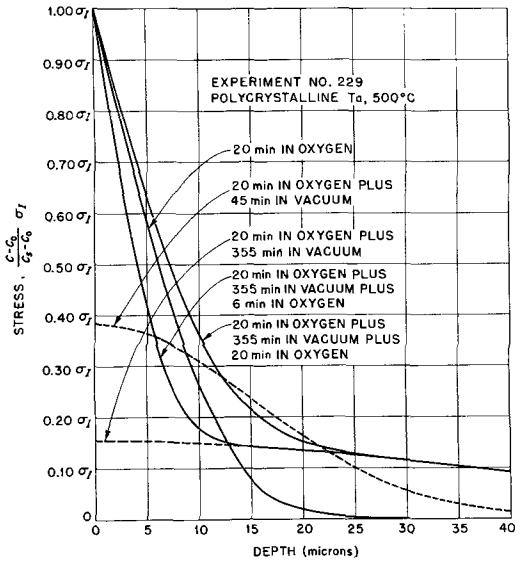

Fig. 8. Stress distributions pertinent to interrupted oxidation experiment computed on oxygen concentration basis.

ring during the anneal were the change in the oxygen concentration gradient caused by diffusion and, to a lesser extent, the solution of some of the oxide present.

The oxygen concentration gradient in the specimen at various times during the experiment was computed using existing diffusivity data (19) and expressed in terms of the corresponding stress gradient (*via* Eq. [2]); the results shown in Fig. 8 are thus simply representations of oxygen penetration curves where the ordinate is given in terms of fractional values of σ_I, the surface stress when the oxygen concentration in the surface layers of the specimen is at its maximum value, c_s. The values of the stress defined by these curves for each particular time were substituted for σ_I in Eq. [2] (see also Fig. 3), and corresponding values of σ_I were determined from the bending data by applying the conditions of mechanical equilibrium. The results of these computations are summarized in Fig. 9. During the first period of oxidation, σ_I increased rapidly to a constant value in excess of 50,000 psi and remained essentially invariant both during the subsequent vacuum anneal and the second period of oxidation. It should also be pointed out that, al-

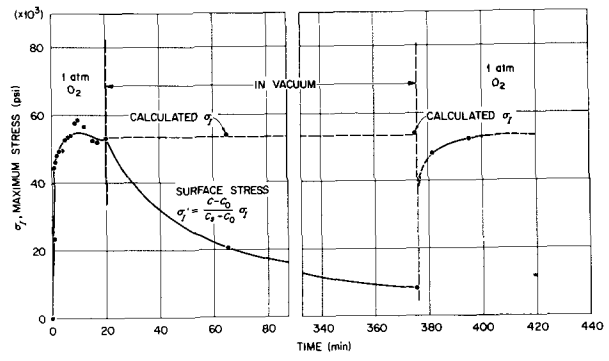

Fig. 9. Maximum stress-time curve for interrupted oxidation experiment.

though the actual surface stress during annealing, σ_I', decreased greatly, the bending stresses were not proportionately affected. Bending stresses are less sensitive to this sort of stress redistribution.

The most significant feature of these results was the constancy of the computed σ_I values. As outlined above, the stress model is based on the assumption that the stress gradient is proportional to the oxygen concentration gradient and, consequently, that

$$\sigma = K\,(c - c_o)$$

where the proportionality constant $K = \sigma_I/(c_s - c_o)$. For fixed values of c_s and c_o, the model obviously requires that σ_I likewise remain constant even when the oxygen concentration gradient in the specimen is considerably altered. The results of this experiment are, thus, entirely consistent with the requirements of the stress model and are regarded as further evidence for the validity of the assumption that the stress gradient in the specimens is proportional to the oxygen concentration gradient as defined in terms of the diffusion constant.

While this study indicates that the oxidation of tantalum under the aforementioned conditions results in the development of very high compressive stresses at and near the surface, the question remains as to how these stresses specifically affect the oxidation process. The answer to this question obviously lies with the results of a more complete investigation; for the present, however, it may be mentioned that the concept of the initiation of oxide platelet formation by a shear mechanism (8) is consistent with and considerably strengthened by these observations. Thus the existence of large stresses in tantalum during oxidation may dictate the morphology of the oxide formed.

It should also be mentioned that in the evaluation of the effects of stresses on the oxidation of tantalum, the purity of the tantalum may be an important factor, particularly with regard to the effects of purity on the elastic stress which the material can sustain. In very high-purity tantalum, for example, the yield stress might vary from 6000 to 30,000 psi (13) or higher along the oxygen concentration gradient arising as a consequence of oxidation. Thus, the actual elastic stress gradient may be influenced by the "mechanical property gradient" which could exist during oxidation. In the case of this particular investigation, however, the initial concentration of interstitial impurities was sufficiently high so as to minimize this effect.

Finally, the influence in the latter stages of oxidation of stresses in the oxide films themselves has not been considered in this paper, although such effects may also be quite important. That such stresses exist may be deduced from the appearance of the oxide film on the heavily oxidized specimen shown at the extreme right in Fig. 2. Note that the oxide film was partially separated from the substrate and exhibited a pronounced curvature opposite that shown by the remainder of the specimen. Similar behavior has been observed on specimens oxidized on both sides. Although several explanations fit the observation, the result suggests that a stress gradient existed in the film prior to separation. Further experiments should yield information on the nature and magnitude of the stresses involved as well as the mechanical properties of the films.

Summary

Bending stresses caused by the oxidation of one side of polycrystalline tantalum specimens at 500°C and 1 atm oxygen pressure were measured as a function of time. The surface stress, based on a model in which the stress is assumed proportional to the oxygen concentration, was found to increase to a high value, approximately 50,000 psi compression, during the first few minutes of oxidation. This value did not change appreciably as oxidation continued. The existence of appreciable stresses in the specimen during oxidation is in agreement with the proposed mechanism for oxide formation in the initial stages of tantalum oxidation.

Acknowledgment

The authors would like to thank R. O. Williams and J. R. Weir of the Metals and Ceramics Division, Oak Ridge National Laboratory, for their helpful discussions and assistance with the manuscript.

Manuscript received Oct. 29, 1962; revised manuscript received Jan. 14, 1963. This paper was presented before the Pittsburgh Meeting, April 15-18, 1963.

Any discussion of this paper will appear in a Discussion Section to be published in the December 1963 JOURNAL.

REFERENCES

1. U. R. Evans, *Trans. Electrochem. Soc.*, **91**, 547 (1947).
2. U. R. Evans, Institute of Metals Symposium on Internal Stresses in Metals and Alloys, p. 291 (1947).
3. U. R. Evans, "The Corrosion and Oxidation of Metals," particularly Chap. II and X, St. Martens' Press, Inc., New York (1960).
4. O. Kubaschewski and B. E. Hopkins, "Oxidation of Metals and Alloys," especially p. 61 *et. seq.*, Academic Press, Inc., New York (1953).
5. J. V. Cathcart, J. J. Campbell, and G. P. Smith, *This Journal*, **105**, 442 (1958).
6. R. E. Pawel, J. V. Cathcart, and J. J. Campbell, AIME Symposium Columbium Metallurgy, p. 442, Interscience, New York (1961).
7. J. A. Sartell *et al.*, *Trans. AIME*, **215**, 420 (1959).
8. R. E. Pawel, J. V. Cathcart, and J. J. Campbell, *Acta Met.*, **10**, 149 (1962).
9. P. D. Dankov and P. V. Churaev, *Doklady Akad.*

Nauk. SSSR, **73**, 1221 (1950); and P. V. Churaev, *Uchenye Zapiski Rostov-na-Donu Pedogog 1957*, No. 1, p. 143 [See *C. A.* 13934f (1959)].
10. W. Jaenicki and S. Leistikow, *Z. physik. Chem. N. F.*, **15**, 175 (1958).
11. B. Borie, C. J. Sparks, and J. V. Cathcart, *Acta Met.*, **10**, 691 (1962).
12. J. V. Cathcart, J. E. Epperson, and G. F. Petersen, *ibid.*, **10**, 699 (1962).
13. C. A. Hampel, Editor, "Rare Metals Handbook," 2d ed., Chap. 25, Reinhold Publishing Co., New York (1961).
14. S. Timoshenko and J. M. Lessells, "Applied Elasticity," Westinghouse Technical Night School Press, East Pittsburgh, Pa. (1925); and S. Timoshenko, *Mech. Engr.*, **45**, 259 (1923).
15. W. Koster, *Appl. Sci. Res.*, **A-4**, 329 (1954).
16. A review of the techniques and procedures useful for calculations of stress in growing surface films is given by A. Brenner and S. Senderoff, *J. Research Natl. Bur. Standards*, **42**, pp. 105, 189 (1949).
17. P. Kofstad, *J. Inst. Metals*, **90**, 253 (1961-62).
18. G. R. Wallwork and A. E. Jenkins, *J. Aust. Inst. Metals*, **7**, 71 (1962).
19. C. Y. Ang, *Acta Met.*, **1**, 123 (1953); and J. W. Marx, J. S. Baker, and J. M. Sivertsen, *ibid.*, **1**, 193 (1953).
20. P. Kofstad, Oxidation of Tantalum at 300-500°C, Tech. Note, Central Institute for Industrial Research, Blindern, Oslo, Norway, ARL-240 (Nov., 1961).

Electrodeposition of Dispersion-Hardened Nickel-Al_2O_3 Alloys

F. K. Sautter

Research Branch, Research & Engineering Division, Watervliet Arsenal, Watervliet, New York

ABSTRACT

Nickel-Al_2O_3 alloys were electrodeposited from a Watt's-type nickel-electrolyte, which contained the second phase particles suspended in the solution. The effects of particle concentration, particle size, and plating conditions on microstructure and physical properties of the deposits were studied. Using submicroscopic Al_2O_3 particles, the room temperature yield strength increased from 8 kg/mm^2 for pure nickel to 35 kg/mm^2 for alloys containing 3.5-6.0 v/o (volume per cent) Al_2O_3. It is believed that this increase was due to dispersion strengthening effects similar to those observed in sintered or internally oxidized metal-metal oxide systems.

Since Irmann (1) and von Zeerleder (2) in 1949 first published data relating to the superior high-temperature properties of SAP (Sintered Aluminum Powder), the subject of dispersion strengthening and hardening has won increasing interest in recent years (3).[1] The main advantage of this method of strengthening lies in the high temperature strength, the resistance to recrystallization, and in the creep resistance at elevated temperatures.

Dispersion hardening is obtained by uniform dispersion of a submicroscopic, hard and inert second phase in the metallic matrix. In contrast to precipitation hardened alloys, the second phase reacts very slowly or not at all with the matrix and is nearly or completely insoluble at high temperatures. Thus the mechanical properties are superior even at temperatures close to the melting point.

The two best-known methods for dispersing a second phase in a metallic matrix are "mechanical mixing" and "internal oxidation." Strengthening by internal oxidation is more effective than by mechanical mixing, probably due to more uniform structure and smaller interparticle spacings. An exception has to be made for SAP alloys, which are obtained by mechanical mixing, but show the greatest strengthening effects hitherto obtained for dispersion hardened alloys. The reasons are thought to be the very small size and the shape of the Al_2O_3 particles and the fact that there exists coherency between the matrix and the oxide. There are also indications of SAP being a honeycomb of alumina filled with aluminum, rather than a dispersion of Al_2O_3 in aluminum (4).

This report deals with another way of obtaining dispersion hardened alloys, namely, electrodeposition. The second phase particles are kept in suspension in a conventional electrolyte, and during the electrolytic crystallization the particles come in contact with the cathode and are so imbedded in the metallic deposit. Depending on the concentration and the size of the particles in suspension, dispersion hardened alloys of various concentrations and interparticle spacings can be obtained.

Equipment and Materials

Electrolyte: 300 g/l $NiSO_4$ x $6H_2O$ A.R.; 45 g/l $NiCl_2$ x $6H_2O$ A.R.; 30 g/l H_3BO_3 A.R.; 0.2 v/o N13 (Wetting Agent by Harshaw Chemical Co.)

Al_2O_3: 1. Linde Alumina Type A-5175, α, particle size 0.3μ; 2. Linde Alumina Type B-5125, γ, particle size 0.1μ; 3. Cabot Alumina Alon C, $\alpha + \gamma$, particle size 0.01-0.04 μ.

Anodes: rolled nickel 99.9%

Cathode: stainless steel, polished

Stirrers: magnetic, with Teflon coated stirring bars

*p*H meter: Beckman Zeromatic

Power supplies: 3-phase rectifiers

Heaters: quartz immersion heater

Electrolyte tanks: Pyrex, 4-liter capacity

Experimental Procedure

Specimen preparation.—In order to obtain specimens which could be used for determination of the yield strength of the electrodeposited material,

[1] A very extensive survey of the subject was published in March 1960 as a WADC Technical Report 59-414 by R. F. Bunshah and C. C. Goetzel of New York University.

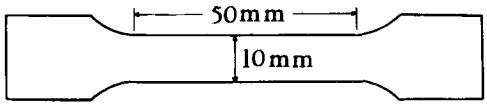

Fig. 1. Size and shape of tensile specimen

stainless steel cathodes were used. The adhesion of nickel coatings on stainless steel is very poor without special surface treatment, and therefore it was very easy to strip the deposit from the cathode by filing off the edges. The size of the cathode was 200 x 100 mm and the cathode was immersed 150 mm in the electrolyte. This gave a cathode area of 3 dm^2 considering both sides of the cathode. By filing off the edges after plating, two sheets 100 x 150 mm in size were obtained from which tensile specimens of the size and form shown in Fig. 1 were stamped out with a punch and die set. The thickness of the specimens varied between 80-120μ.

Preparation of the suspensions.—Linde Al_2O_3.— The aluminum oxides manufactured by Linde Corporation were very easily suspended in the electrolyte by stirring with a conventional laboratory stirrer. The particles did not agglomerate in the solution and no special precautions were needed. *Alon C.*— According to the literature, Alon C has a particle size between 0.01-0.04μ and a surface area of 50-100 m^2/g. These properties make is necessary to use a blender for dispersion of the oxide particles in the electrolyte. A Waring blender was used for this purpose. The following three different methods of dispersion were tried and were found to give no particular difference in the final suspension: (i) dispersing Al_2O_3 directly in the electrolyte, (ii) dispersing Al_2O_3 in water and adding to the electrolyte, and (iii) dispersing Al_2O_3 in water and adding electrolyte to the dispersion.

With the latter technique, a coagulation was observed after adding a small amount of electrolyte to the aqueous suspension, but by continuous blending the same grade of dispersion was achieved as by methods (i) and (ii). (In these cases settling time was used as the criterion for determining the grade of dispersion.)

Plating conditions.—The temperature of the nickel-electrolyte was kept at 50°C, the pH at 3.5, and the current density at 2 amp/dm^2 unless otherwise noted.

After preparing the suspension with Alon C, the electrolyte had to be stirred for 48 hr because of entrapment of air by the blending process. Addition of a wetting agent to prevent pitting was necessary at the beginning, but no additional wetting agent had to be added later. The anodes were hung in diaphragms made of dacron-cotton cloth to prevent contamination of the electrolyte with anode sludge. A steady decrease in the oxide concentration of the electrolyte was observed due to accumulation of the oxide particles inside the diaphragms.

Plating procedures.—The mechanically and electrolytically polished stainless steel cathodes were electrolytically degreased in an alkaline solution containing 50 g/l NaOH and 25 g/l Na_2CO_3 for 1-2 min. After rinsing in running water, followed by an acid dip in 10% H_2SO_4, and a second water rinse, the cathode was transferred to the plating tank. Plating time was approximately 4 hr for a deposit of 100μ thickness.

Analysis.—In order to determine the amount of Al_2O_3 in the test samples, these samples were dissolved in 50% HNO_3 after testing. The aluminum oxide was separated from the nickel nitrate solution by centrifuging and after sufficient washing and drying was weighed in the centrifuge tube on a microbalance.

According to the manufacturer's literature the different kinds of Al_2O_3 were anhydrous, with an ignition loss of less than 3% at 1000°C. A specific density of 3.5 was therefore assumed for the conversion of weight per cent in volume per cent. Tests were also made to insure the insolubility of the aluminum oxides in the 50% HNO_3 used for dissolving the samples.

Results

Influence of Al_2O_3 *content of the electrolyte on* Al_2O_3 *content of the deposit.*—Since it was supposed that the codeposition of Al_2O_3 depends solely on the number of collisions between particles and cathode, it was expected that increasing the concentration of Al_2O_3 in the electrolyte would also increase the amount of Al_2O_3 imbedded in the nickel matrix. As Fig. 2 shows, this is the case within certain limits of error, which are probably due to the above mentioned fact that the fine Al_2O_3 suspension penetrated the anode diaphragms and the particles accumulated inside the diaphragms. An upper limit was set by the viscosity of the suspensions, which made it, for example, impossible to maintain good stirring action above 50 g/l Alon C. The use of mechanical instead of magnetic stirrers will probably permit obtaining alloys of a higher Al_2O_3 content than those reported here.

Influence of temperature, pH, and current density on Al_2O_3 *content of deposit.*—The electrolyte used to study the influence of temperature, pH, and current density contained 50 g/l Alon C. As can be seen from Fig. 2, the oxide concentrations are greatly scattered from 2.0-2.75 v/o Al_2O_3 in the deposit. Figures 3 and 4 show generally that there was little or no ef-

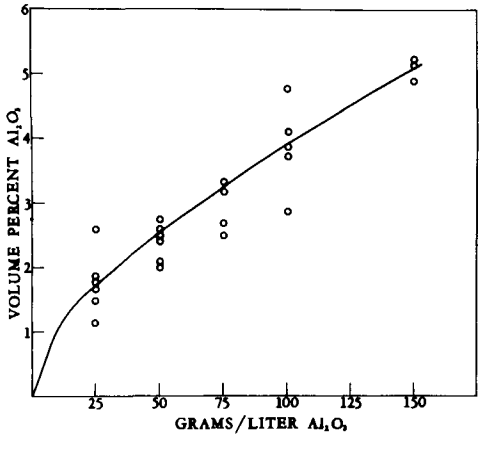

Fig. 2. Oxide content of deposit as a function of oxide content of electrolyte; 2 amp/dm^2; pH, 3.5; temperature, 50°C.

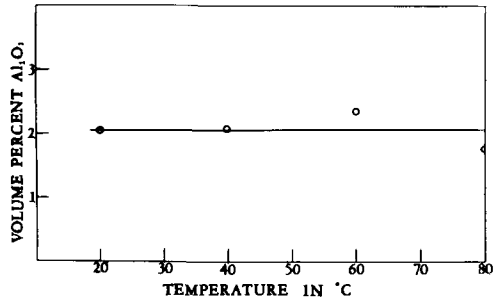

Fig. 3. Influence of temperature of the electrolyte on oxide content of deposit; 50 g/l Al_2O_3; 2 amp/dm^2; pH, 3.5.

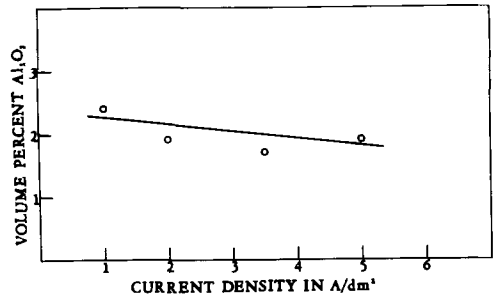

Fig. 4. Dependence of oxide content on current density; 50 g/l Al_2O_3; pH, 3.5; temperature, 50°C.

fect of temperature and current density on the codeposition of the Al_2O_3 with nickel. In addition, the pH value appeared to have no influence on the Al_2O_3 concentration in the deposit between pH 2.0 and 5.0 (see Fig. 5). Below pH 2.0, however, a sharp decrease in Al_2O_3 concentration was observed. This is in agreement with observations made with $CuSO_4$-type electrolytes which contained SiC and Al_2O_3 suspensions. No codeposition of copper and carbide or oxide was obtained from these electrolytes, which are also operated at pH values below pH 2.0.

Influence of Al_2O_3 on yield strength.—The strengthening effect of dispersed Al_2O_3 in nickel was investigated by measuring the yield strength of the alloys at 0.1% offset. The equipment used was an Instron Tensile Testing machine and the applied strain rate was 0.010 in./in./min. All tests were carried out at room temperature (22°C). To eliminate the effect of the plating conditions on the yield strength by different grain structure and orientation, all specimens were given a heat treatment prior to testing by annealing at 750°C for 1 hr in dry, pure nitrogen.

Figure 6 shows the dependence of the yield strength on the interparticle spacing. It is evident

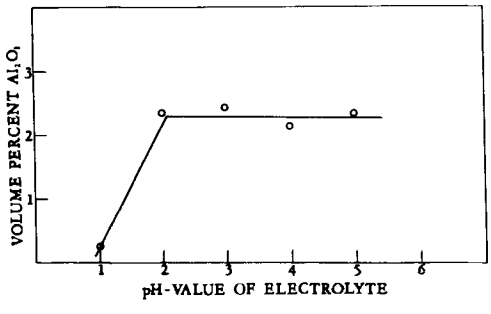

Fig. 5. Effect of pH value on oxide content of deposit; 50 g/l Al_2O_3; 2 amp/dm^2; temperature, 50°C.

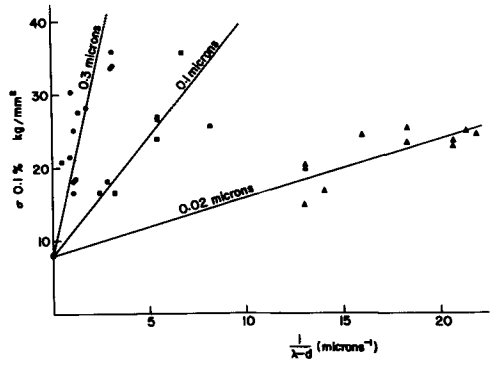

Fig. 6. Dependence of the yield strength on the interparticle spacing.

that a dependence based on the distance between two particles is only valid for a given particle diameter. Based on results obtained from dispersion of electrodeposited iron particles in mercury, Meiklejohn and Skoda (5) proposed a relationship, where the yield strength is also a function of the particle diameter, and arrived at the equation

$$\sigma_y = \frac{f(d)}{\lambda - d} + \sigma_o$$

where σ_y is the yield strength of the alloy, λ is the average distance between centers of two neighboring particles, assuming a cubic array of the particles, d is the particle diameter, and σ_o the yield strength of the matrix, and $f(d)$ is the slope of the lines and a function of the particle diameter.

Figure 7, in which the slope of the lines are plotted *vs.* the particle diameter, shows that also in this investigation $f(d) = ad$ where a is constant.

Since it has been shown (5) that $\lambda/d = 0.82/f^{1/3}$, where f is the volume fraction of the dispersed phase, Fig. 8 represents the plot of the yield strength as a function of the volume fraction according to the equation by Meiklejohn and Skoda

$$\sigma_y = \frac{a \cdot f^{1/3}}{(0.82 - f^{1/3})} + \sigma_o$$

Discussion

The results of this investigation are obtained from dispersions of spheres of discrete size and relatively uniform distribution as shown in Fig. 9, which shows an electronmicrograph of a dispersion of Alon C in

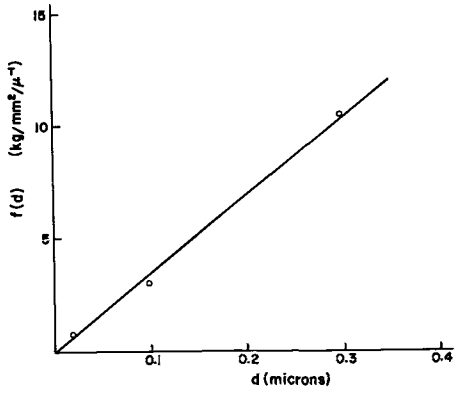

Fig. 7. Slope of the lines of Fig. 6 plotted *vs.* particle size

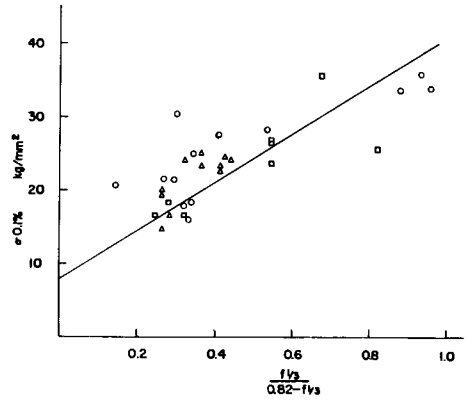

Fig. 8. Yield strength as a function of the volume fraction; △, 0.02μ; □, 0.1μ; ○, 0.3μ.

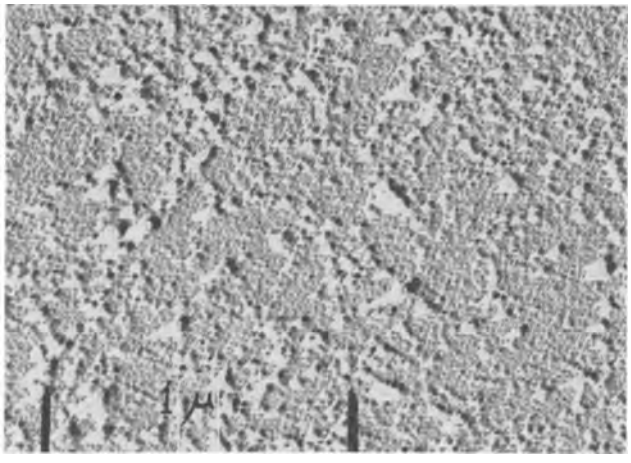

Fig. 9. Electromicrograph of Ni-Al_2O_3 alloy containing 2.5 v/o Alon C. Magnification approximately 50,000X.

nickel at 50,000 magnification. The particle size measurements from this picture show a sharp peak at a particle size of 210Å compared to the literature value of 200Å for the undispersed powder. It is probably this fact that gives the good agreement with the results reported for dispersion of iron particles in mercury. Coherency problems are eliminated, since there is definitely no coherence between matrix and dispersed phase throughout the entire particle size range.

It is therefore believed that electrodeposition is a suitable process to compete with sintering and internal oxidation in order to obtain dispersion hardened alloys both for models in studying mechanisms of dispersion strengthening and for technical applications.

Two factors are considered especially favorable for this processing method.

a. The suspension of the second phase in aqueous solutions reduces clustering and agglomeration of the submicroscopic particles, thus producing a very uniform dispersion of the second phase in the matrix.

b. The economical way of electrolysis. By using dispersion strengthened sheets of 0.1 mm thickness as cathodes, plates up to 10 mm thickness have been obtained.

The improved room temperature properties and the microstructure of these alloys indicate that similar improvements for the high temperature behavior can be expected, as were reported for both sintered and internally oxidized metal-metal oxide alloys.

Manuscript received Oct. 26, 1962; revised manuscript received Jan. 15, 1963. This paper was prepared for delivery before the Boston Meeting, Sept. 16-20, 1962.

Any discussion of this paper will appear in a Discussion Section to be published in the December 1963 JOURNAL.

REFERENCES

1. R. Irmann, *Tech. Rundschau Bern*, **36**, 19 (1949).
2. A. v. Zeerleder, *Z. Metallk.*, **8**, 228 (1950).
3. R. F. Bunshah and C. C. Goetzel, WADC Tech. Rept. 59-414.
4. C. L. Meyers and O. D. Sherby, *J. Inst. Metals*, **90**, 380 (1962).
5. W. H. Meiklejohn and R. E. Skoda, *Acta Met.*, **7**, 675 (1959).

The Mutual Solid Solubility of Hafnium Carbide and Uranium Monocarbide

N. H. Krikorian, W. G. Witteman, and M. G. Bowman

University of California, Los Alamos Scientific Laboratory, Los Alamos, New Mexico

ABSTRACT

In contrast to the miscibility gap which earlier workers have reported for the system HfC-UC, the present work demonstrates complete solid solubility of these carbides at 2000°C. Included are the preparation, heating conditions, x-ray data, and chemical analysis of the starting materials and the solid solutions.

The pseudobinary systems of uranium carbide with the carbides of zirconium, tantalum, and niobium have been investigated by Nowotny, Kieffer, Benesovsky, and Laube (1), as well as Brownlee (2). The mutual solubility of uranium carbide and zirconium carbide has also been confirmed by Witteman, Leitnaker, and Bowman (3). Work on uranium carbide with hafnium carbide has been reported by Nowotny, Laube, Kieffer, and Benesovsky (4); Nowotny, Kieffer, Benesovsky, Brukl, and Rudy (5) followed by a study of the ternary uranium-hafnium-carbon by Benesovsky and Rudy (6). The last three references based presumably on the same data indicate a miscibility gap in the HfC-UC system.

Table I. Atomic diameters of Group 4a and 5a transition metals

Metal	Diameter in Å for metal	Lattice parameters in Å for MC
V	2.63	4.166
Ti	2.79	4.332
Ta	2.92	4.456
Nb	2.93	4.471
Hf	3.10	4.641
Zr	3.16	4.702
U	3.42	4.958

Assuming $d_c = 1.54$ from Pauling

Table II. Size difference for the metals in carbide pairs

Carbide pair	% Difference smaller as solvent	% Difference larger as solvent
UC-ZrC	8.2	7.6
UC-HfC	10.3	9.4
UC-NbC	16.7	14.3
UC-TaC	17.1	14.6
UC-TiC	22.2	18.4
UC-VC	30.0	23.1

This finding seemed to contradict earlier work by the present investigators and the predictions of the empirical "size factor" rule of Hume-Rothery (7).

There are several methods of quantitatively expressing "size factor," all of which are based on how the atom size is defined. The authors have chosen to use the diameter of the metal from the monocarbides assuming Pauling's value for the carbon diameter to be 1.54Å (8). Table I shows the atomic diameters of the Group 4a and 5a transition metals and the cell dimensions for their cubic monocarbides.

Using the differences in the metallic diameters on the basis of the monocarbides, the percentage size differences can then be calculated for the listed carbide pairs shown in Table II.

The systems VC-UC and TiC-UC are outside the limit of the size factor rule and would therefore be expected to have a miscibility gap. These gaps have been experimentally observed by Nowotny *et al.* (1). Although TaC-UC and NbC-UC are at the limit of the size factor rule, mutual solid solubility has been observed (1, 2) for these systems as well as ZrC-UC which falls well within this rule (1-3). Thus, the behavior of HfC-UC would appear to be anomalous as reported by the previous (4-6) investigators.

Experimental

This investigation can thus be divided into two areas. The first involved the use of hafnium carbide prepared from HfO_2 (containing 1.8% Zr) which was reacted with carbon. Since the hafnium contained 1.8% zirconium, it might be possible to infer that it contributed to increased solubility of the hafnium carbide-uranium carbide system. Thus a definitive experiment would be one on which the zirconium content of the hafnium carbide would be negligible. In the second phase, extremely high-purity hafnium metal (<200 ppm Zr) was reacted with outgassed graphite to form $HfC_{0.97}$. The UC used with both batches of HfC was prepared by arc-melting uranium with carbon to give a nominal UC. A long time interval between the earlier work and later work necessitated using UC of different initial compositions. Table III gives analytical data for the starting materials.

The carbide powders used were −325 mesh. The experiments consisted essentially in heating a mixture of finely divided carbide powder in an outgassed tungsten crucible at 2100° ± 100°C at 10^{-3} Torr for most of the work. For the work using high-purity hafnium carbide, the heating was done at 2000° ±50°C at 10^{-5} to 10^{-6} Torr. One-half per cent of analytical reagent grade reduced iron powder was added to the mixtures to accelerate achievement of solid solutions (9). Analyses of the reacted specimens showed that practically all the iron was evaporated during the heating process.

The analytical data disclosed a slight tungsten pickup on heating using a tungsten crucible. Consequently, the heating using high-purity HfC was done in a tantalum crucible whose interior and lid were carbided to a few mils depth. The carbiding minimized the pickup of metallic tantalum.

The heating was done inductively using an eddy current concentrator as engineered by Donald Hull, Jr. of this Laboratory.[1]

In all cases the entire compact was removed from the crucible after cooling and crushed in a "diamond" or hardened steel mortar in a dry box. A representative sample was ground into powder for lattice parameter measurements. The x-ray samples were sealed in Lindemann glass capillaries, and the x-ray diffraction studies were carried out on a Norelco unit using nickel filtered copper radiation and a 114.59 mm Debye-Scherrer camera.

The x-ray wavelengths used in calculating the lattice parameters were: $K\alpha_1 = 1.54051$Å; $K\alpha_2 = 1.54433$Å and a weighted value (for unresolved doublets) of $K\alpha = 1.54178$Å.

Results

The reported a_o values are the arithmetic average of the calculated a_o values based on the last 3 or 4 doublets (reflections greater than 60°). The error is reported as the average deviation from this value for those reflections. The results are expressed in ang-

[1] Drawings of an early design may be obtained from Cooper-Trent Blueprint and Microfilm Corporation, 2701 Wilson Blvd., Arlington, Virginia, Drawings 26Y-70250-1 through 32.

Table III. Analytical data on starting materials

Lattice parameter and carbide	% Metal	% Total carbon	% Free carbon	Major impurity
UC $a_o = 4.958 \pm 0.002$	93.2	6.2	0.4	600 ppm Fe
HfC $a_o = 4.641 \pm 0.001$	92.3	5.4	—	1.8% Zr
UC $a_o = 4.961 \pm 0.001$	94.23	5.42	<500 ppm	200 ppm Fe, Si and Mo 100 ppm
HfC $a_o = 4.640 \pm 0.001$	93.84	6.31	0.19	<200 ppm Zr

Table IV. Solid solubility of UC-HfC at 2100° ± 100°C

Mole fraction HfC	Mole fraction UC	Heating time, hr	X-ray pattern	Lattice constant found Å	Calculated lattice constant Vegard	Calculated lattice constant Zen
1.00	—	—	Doublets resolved	4.640 ± 0.001	—	—
0.90	0.10	2.5	Doublets resolved	4.674 ± 0.002	4.672	4.674
0.70	0.30	5.0	Doublets resolved	4.714 ± 0.002	4.735	4.739
0.50	0.50	2.0	Doublets resolved	4.796 ± 0.002	4.799	4.804
0.50*	0.50	2.0	Doublets unresolved	4.798 ± 0.002	4.799	4.804
0.35	0.65	10.0	Doublets unresolved	4.843 ± 0.003	4.847	4.851
0.20	0.80	8.0	Doublets unresolved	4.903 ± 0.001	4.894	4.898
0.10	0.90	10.0	Doublets resolved	4.918 ± 0.001	4.926	4.928
—	1.00	—	Doublets resolved	4.958 ± 0.002	—	—

* Using high-purity HfC (<200 ppm Zr).

strom units. Table IV summarizes the conditions and findings of these experiments compared to the calculated lattice parameters assuming the normal straight line relationship of Vegard (10). Also shown in Table IV are values for the lattice parameters of the solid solutions based on a mathematical treatment for Vegard's relationship formulated by Zen (11). Using Vegard's relationship the expressed lattice parameter is proportional to the mole fraction itself, whereas Zen's equation makes the lattice parameter proportional to the cube root of the mole fraction. The net result, at least in this system, is about the same. The data from Table IV are also shown in Fig. 1.

Several samples were chemically analyzed after heating for hafnium, uranium, carbon, and possible contaminants. The mixtures had originally been weighed assuming conformation to theoretical composition. On the basis of the analytical data listed in Table V, the composition after heating remained essentially constant except for the slight tungsten pickup.

Discussion

Both pure HfC and HfC containing zirconium form continuous solid solutions with UC at 2000°-2100°C. It would be desirable to reconcile these findings with the miscibility gap extending from 35 to 65 m/o reported by the Austrian investigators (5). Since they did not give complete analytical data, it is difficult to compare the various starting carbides. For instance, the authors have found a lattice parameter of 4.6406 ± 0.0009 for $HfC_{0.90}$. Yet the lattice parameter reported by the Austrian investigators (4, 5) for $HfC_{0.97}$ (on the basis of their analysis for only carbon) gives a value of $a_o = 4.632$ which is low when compared with the data of Cotter and Kohn (12) (4.640Å) and Curtis, Doney, and Johnson (13)

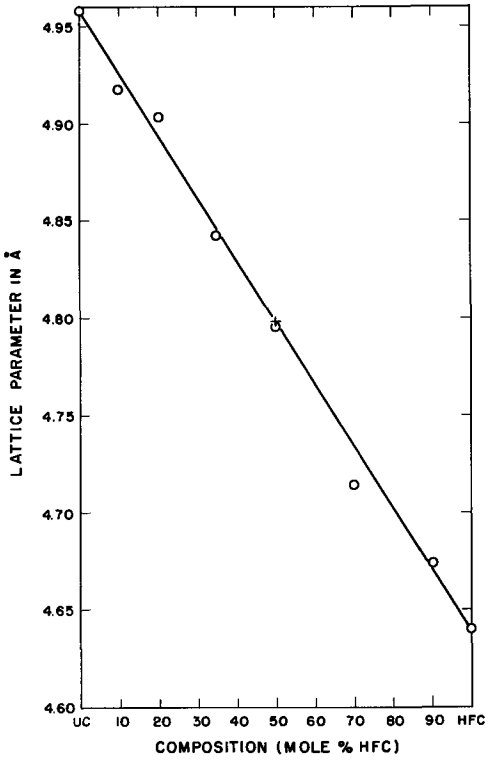

Fig. 1. Lattice parameter vs. nominal molar composition; ○, HfC (1.8% Zr); +, HfC (< 200 ppm Zr).

(4.6365 ± 0.0002). Indeed using the data of Cotter and Kohn, a value of $HfC_{0.73}$ can be ascribed to the HfC reported by the Austrian group. The explanation of the difference in findings on the basis of nonintegral stoichiometry is obviously not definitive.

Yet another difference in experimental technique is the addition of the ½% reduced iron powder in the present work to accelerate solid solution forma-

Table V. Analytical data on solid solutions

Nominal solid solution, mole %		Calculated in w/o			Found in w/o				Summation
HfC	UC	U	Hf	C	U	Hf	C	W	
10	90	87.77	7.31	4.92	86.1	8.2	4.84	0.64	99.78
35	65	67.49	27.26	5.24	65.6	28.8	5.18	0.96	100.5
50	50	54.02	40.52	5.45	54.1	40.6	5.16	<0.1*	99.86
70	30	34.26	59.98	5.76	32.1	58.5	5.73	3.7	100.0

* Tantalum.

tion. Therefore, it is possible that the miscibility gap others have reported represents a nonequilibrium condition due to insufficient heating time.

Possible differences in temperature readings were also considered as was a miscibility gap at lower temperatures. In order to investigate this possibility, a solid solution nominally 40 m/o HfC-60 m/o UC was first formed at 2000°C. This was then heated for 333 hr at 1700°C in high vacuum. Some uranium was lost, tungsten was picked up, but the solid solution continued to persist in the range where the gap had been reported.

Conclusions

From this study, it is apparent that the pseudobinary carbide system UC-HfC forms a continuous solid solution. The composition *vs.* lattice parameter plot closely approximates Vegard's relationship.

Acknowledgment

The authors wish to acknowledge the aid given by Mr. W. H. Ashley for the analytical data and Mrs. M. J. Jorgensen for reading the x-ray films. Thanks should be expressed to Dr. C. P. Kempter and Mrs. Bertha G. Fagan for the Zen method calculations. The authors also wish to thank Professor Hans Nowotny of the University of Vienna for a lengthy discussion of this system and for encouraging its presentation.

Manuscript received Dec. 3, 1962; revised manuscript received Feb. 4, 1963. This paper was prepared for delivery before the Los Angeles Meeting, May 6-10, 1962. This work was done under the auspices of the United States Atomic Energy Commission.

Any discussion of this paper will appear in a Discussion Section to be published in the December 1963 JOURNAL.

REFERENCES

1. H. Nowotny, R. Kieffer, F. Benesovsky, and E. Laube, *Monatsh. Chem.*, **88,** 336 (1957).
2. L. D. Brownlee, *J. British Nuclear Energy,* **4,** 35 (1959); *J. Inst. Metals,* **87,** 58 (1958-59).
3. W. G. Witteman, J. M. Leitnaker and M. G. Bowman, Los Alamos Scientific Lab. Report LA-2159 (1957).
4. H. Nowotny, E. Laube, R. Kieffer, and F. Benesovsky, *Monatsh. Chem.*, **89,** 701 (1958).
5. H. Nowotny, R. Kieffer, F. Benesovsky, C. Brukl, and E. Rudy, *ibid.*, **90,** 669 (1959).
6. F. Benesovsky and E. Rudy, *Planseeber. Pulvermet.*, **9,** 65 (1961).
7. W. Hume-Rothery, "Structure of Metals and Alloys," 2nd ed., Revised, Institute of Metals Monograph No. 1, p. 59, London (1950).
8. L. Pauling, "Nature of the Chemical Bond," p. 165, 2nd ed. Cornell University Press (1940).
9. J. T. Norton and A. L. Mowry, *Trans. AIME,* **185,** 133 (1949).
10. L. Vegard and H. Dale, *Z. Krist.*, **67,** 148 (1928).
11. E. Zen, *Am. Mineralogist,* **41,** 523 (1956).
12. P. G. Cotter and J. A. Kohn, *J. Am. Ceram. Soc.*, **37,** 415 (1954).
13. C. E. Curtis, L. M. Doney, and J. R. Johnson, *ibid.*, **37,** 464 (1954).

Interpretation of Knudsen Vapor-Pressure Measurements on Porous Solids

Gerd M. Rosenblatt

Department of Chemistry, and Inorganic Materials Division of the Lawrence Radiation Laboratory, University of California, Berkeley, California

ABSTRACT

A simple steady-state model is used to describe the vaporization, in a Knudsen cell, of a porous solid having a low vaporization coefficient. The description is in terms of the effective vaporizing area of the solid. The nature of the effective area and the assumptions in the model are investigated. Procedures to obtain the equilibrium pressure and vaporization coefficient from pressures measured by varying the cell and sample geometry are discussed. A one-parameter, empirical equation is presented which accurately represents measurements of the vapor pressure of porous arsenic taken over a large range of Knudsen-cell orifice areas.

The Knudsen effusion method is widely used to measure low vapor pressures. It is sometimes difficult to relate the pressures obtained from such measurements to the equilibrium vapor pressure. This is particularly true when the substance under investigation has a low vaporization coefficient. Motzfeldt (1) has used a steady-state approach to relate the measured and equilibrium pressures for a liquid having a low vaporization coefficient. The vaporizing area of the liquid was taken to be equal to the cross-sectional area of the Knudsen cell. Thus the results do not apply to porous solid samples.

In this paper Motzfeldt's equation is generalized to include solid samples with an effective vaporizing area different from the cross-sectional area of the cell, and the nature of the effective vaporizing area is investigated. Although the equations derived from the rough model employed should not be used to calculate the equilibrium pressure and the vaporization coefficient from the measured pressure and other experimentally amenable quantities, they may serve as some guide to proper experimental procedure and will serve to point out the quantities which are sensitive to the particular model chosen.

Recognition and inspection of the assumptions in the simple model also help to interpret experimental results and to determine the type of information which is obtained from nonequilibrium Knudsen measurements.

In addition a simple empirical equation is presented which has been found to represent accurately the measured vapor pressure of porous, solid arsenic as a function of the orifice area of the Knudsen cell.

Background and Definitions

The pressure measured in a Knudsen effusion experiment is

$$P_m = qG/W_a a \qquad [1]$$

where q is the number of moles of vapor which escape through the orifice of area a in unit time, W_a is the fraction of the molecules entering the orifice which exit from it, and $G = (2\pi RMT)^{1/2}$ where M is the molecular weight of the gaseous species. The fraction W_a was first calculated by Clausing (2) under the assumption that the molecules enter the orifice with a cosine angular distribution. The equilibrium vapor pressure shall be denoted by P_e.

The vaporization coefficient, α_v, may be defined as the ratio of the number of molecules actually evaporating from unit area of plane surface in unit time to the number of molecules which are calculated to strike that surface in unit time when the surface is in equilibrium with vapor at P_e. The coefficient α_v is closely related to α_c, the condensation coefficient, which is the fraction of molecules striking a plane surface which sticks to the surface. At equilibrium, $\alpha_v = \alpha_c$. As vaporization and condensation coefficients reflect the activation energy needed for these processes, the coefficients are expected to vary with temperature. The discussion in this paper is restricted to vaporization and condensation coefficients at a single temperature.

Although most metals have been found to have vaporization and condensation coefficients close to unity, materials which vaporize to molecular gaseous species sometimes have very small vaporization coefficients. This appears to be particularly likely when the structure of the gaseous molecule differs appreciably from the structure existing in the solid lattice (3, 4).

Other factors may cause substances to vaporize more slowly than would be calculated from the equilibrium vapor pressure: The temperature of a vaporizing surface may not be the same as the temperature of the bulk sample if there is a large net flux of vaporizing material, resulting in an apparent low vaporization coefficient (5). Or, with samples containing more than one component, solid-state diffusion may be the rate-determining process, particularly if the sample does not vaporize congruently.

Motzfeldt's equation.—Motzfeldt (1) considered the effect on P_m of a low vaporization coefficient and of the resistance to flow of the Knudsen cell proper. It was assumed that the vaporization coefficient is independent of pressure, *i.e.*, of the extent of saturation of the vapor over the evaporating surface, and thus, that $\alpha_v = \alpha_c$ at all pressures. Motzfeldt's result, for a cylindrical cell of cross-sectional area B containing a sample of the same vaporizing area, with cell Clausing factor W_B and orifice area a, is

$$\frac{P_e}{P_m} = 1 + \frac{W_a a}{B}\left(\frac{1}{\alpha} - 2 + \frac{1}{W_B}\right) \qquad [2]$$

The symbol α without a subscript represents the vaporization and/or condensation coefficient when these are equivalent and constant, and distinction is unwarranted. Whitman (6) had obtained an equivalent result previously by a more complex derivation. A somewhat simpler equation has been presented by Speiser and Johnston (7), and Rossman and Yarwood (8), and others. These authors considered the case where the cell resistance can be neglected ($W_B = 1$) and where the orifice is sufficiently small so that the pressure throughout the cell is essentially uniform ($W_a a << B$). In that case, only a low vaporization coefficient causes P_m to deviate from P_e. At these limits, Eq. [2] reduces to their result

$$\frac{P_e}{P_m} = 1 + \frac{W_a a}{\alpha B} \qquad [3]$$

All these authors mention that the effective vaporizing area of a porous solid with a low vaporization coefficient will be greater than the cross-sectional area of the cell.

Assumptions.—The derivation of Eq. [2] involves assumptions additional to those of a plane vaporizing surface and $\alpha_v = \alpha_c$ independent of pressure. Some of these are the assumptions usually made in calculating the properties of dilute gas systems, such as: collisions between molecules can be neglected, and molecules are reflected from a surface with a cosine angular distribution independent of the incident directions. These conditions can be closely realized at low pressures where the mean free path of the vapor is greater than the dimensions of the cell. The molecules are also assumed to rebound from the same point at which they strike a surface, without skidding or diffusing over the surface. Sears (9) and Winterbottom and Hirth (10) have questioned this assumption and have calculated the contribution of surface diffusion along the walls of the orifice to the total flow from a Knudsen cell.

The derivations cited above invoke further assumptions. The molecular flow across a horizontal plane of the cell is considered uniform over the plane. Carlson (11) has demonstrated that rigorous application of the cosine reflection law in a calculation of the type carried out by Clausing (2) leads to a radial dependence of the mass flow across a plane perpendicular to the axis of a cylindrical Knudsen cell. The derivation of Eq. [2] which makes use of the Clausing factor for the cell, W_B, also requires that the Clausing factor for the molecules rebounding off the top of the cell after a certain fraction have been lost through the orifice be the same as if the rebounding molecules had vaporized uniformly from the whole cell cross-sectional area. The magnitude of the error due to these last two assumptions has been discussed by Whitman

(6), Carlson (11), and Balson (12). Balson presents numerical calculations of the fraction escaping through the orifice which should be more accurate than the use of the cell Clausing factor, W_B.

Model Applicable to Solid Samples

In this section the steady-state approach used by Motzfeldt is extended to cover the general case in which the sample has an effective vaporizing area different from the cross-sectional area of the cell. The assumptions made in deriving Eq. [2] are also made here. The effect of these assumptions will be discussed further below. It is assumed that $\alpha_v = \alpha_c =$ constant α at all pressures, not because a steady-state approach requires this assumption, but because the functional form of the possible variation of α_c and α_v with pressure is unknown. The model presented here can be solved readily with $\alpha_v \neq \alpha_c$. In that case α_v and α_c might be interpreted as functions of the extent of saturation in the cell, which have different values for every steady-state attained. As the functional form of this variation is unknown, however, such an interpretation lacks concrete meaning and introduces conceptual difficulties. These difficulties might lead to inconsistencies in physical interpretation of the solution or in the definition of auxiliary quantities such as the effective area.

Consider a Knudsen cell, shown in Fig. 1, of cross-sectional area B, which contains a sample which has an effective vaporizing area A'. The definition and nature of the effective vaporizing area are discussed in the next section. Note that A' can be vastly different from B. The Clausing factor of the orifice of area a is W_a and the Clausing factor of the cell is W_B. Consider the two planes represented by dotted lines in Fig. 1. Plane 1 is just below the orifice and plane 2 is just above the sample surface. Let u_1 be the number of moles of vapor which pass upward through unit area of plane 1 in unit time. The total mass flux upwards through plane 1 is then u_1B. It is assumed that the vapor density across planes 1 and 2 is uniform. Let d_1 be the number of moles of vapor which pass downward through unit area of plane 1 in unit time. Similarly define u_2 and d_2 for plane 2.

The number of moles of vapor which escape through the orifice in unit time, q, will be equal to the number that enter the orifice, u_1a, times the fraction which get through the orifice, W_a. Thus $q = u_1W_aa$ and the measured pressure, $P_m = u_1G$ (cf. Eq. [1]). The equilibrium pressure is related to the number of moles of gas, r, which evaporate from area A' in unit time by the Langmuir equation

$$P_e = rG/\alpha_vA' \qquad [4]$$

The number of moles which vaporize from unit area in unit time is thus given by α_vP_e/G.

Now apply a mass balance to the flow of vapor through the cell after a steady-state has been attained. The number of moles of vapor which escape from the cell in unit time equals the net number crossing planes 1 and 2 and equals the number vaporizing minus the number condensing.

$$u_1W_aa = (u_1 - d_1)\ B \qquad [5]$$

$$= (u_2 - d_2)\ B \qquad [6]$$

$$= \alpha_vP_eA'/G - \alpha_cd_2A' \qquad [7]$$

The total number of moles which pass downward through plane 2 is equal to the number from plane 1 which reach plane 2 plus the number passing upward through plane 2 which do not reach plane 1.

$$d_2B = d_1\ W_BB + u_2\ (1 - W_B)\ B \qquad [8]$$

This equation assumes the applicability of Clausing factors to the situation inside a Knudsen cell.

Equating u_1 with P_m/G and α_c with α_v these four equations can be solved to yield[1]

$$\frac{P_e}{P_m} = 1 + W_aa\left(\frac{1}{\alpha A'} - \frac{2}{B} + \frac{1}{W_BB}\right) \qquad [9]$$

This equation reduces to Motzfeldt's result, Eq. [2], as expected, when the effective vaporizing area is equal to the cell area, that is when $A' = B$. Equation [9] reduces to the simple form used by Speiser and Johnston, Eq. [3], when $\alpha A' << W_BB$, showing that the area appropriate to that equation is the same effective area used here. This last limit is the most important result of equations of this type because of the ambiguities involved in the estimation of the resistance to flow of the cell proper. The cell resistance may be particularly difficult to calculate when the sample has a low vaporization coefficient, as in that case the vaporizing molecules might not cross plane 2 with a cosine angular distribution.

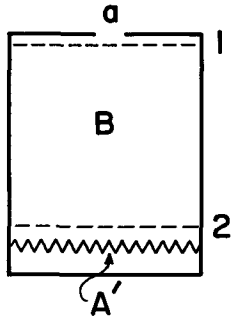

Fig. 1. Diagram of effusion cell

The Effective Vaporizing Area

The effective vaporizing area of a porous solid is defined to be the area of plane sample surface which would give rise to the same gross rate of vaporization. The pressure above, and temperature of, the porous solid and the plane surface being compared should be equal. The gross rate of vaporization of the plane surface is taken to include all the molecules vaporizing from the surface, but does not include molecules in the ambient vapor which strike the surface and are reflected without condensation.

[1] The vaporization coefficient α_v defined in this paper is determined only by the primary vaporization process. A somewhat different vaporization coefficient α_v^* can be defined by specifying that the net number of moles of sample vaporizing from unit area in unit time is $\alpha_v^*(P_e - P)/G$. That is, $\alpha_v^*(P_e - P)/G$ is the observed weight loss, in moles per unit area per unit time, of a sample with a plane surface surrounded by its vapor at pressure P. When the ambient pressure is not negligible ($P \neq 0$) α_v^* involves both vaporization and condensation processes. The coefficient α_v^* is related to the vaporization and condensation coefficients defined in the text by

$$\alpha_v^* = (P_e\alpha_v - P\alpha_c)/(P_e - P)$$

In terms of α_v^* Eq. [7] becomes $u_1W_aa = \alpha_v^*A'(P_e/G - d_2)$ and α in Eq. [9] can be designated as α_v^*.

If the gross rate of evaporation is r moles/sec, the evaporation coefficient has been determined by vaporization from a plane surface, and the equilibrium vapor pressure is known, the effective area can be evaluated from the Langmuir equation [4], $A' = rG/\alpha_v P_e$. Usually, the evaporation coefficient is not known from other experiments and the product $\alpha_v A'$ is determined. This definition of the effective vaporizing area implies that the gross rate of vaporization is always given by $P_e \alpha_v A'/G$.

The magnitude of the effective vaporizing area is a function of the condensation coefficient, the total vaporizing area of the sample, and the geometry of the sample as will be seen in the simple calculations below.[2] It is, however, independent of the pressure in the Knudsen cell, as long as α_c is independent of pressure. The vaporization coefficient α_v is a measure only of the probability of a molecule initially vaporizing from the solid. After a molecule is in the vapor inside a pore its chance of escaping depends on the number of collisions made with the pore wall and on the condensation coefficient. Thus if the condensation coefficient is unity, only those molecules which have a line of sight path out of a pore can escape. This means that the effective area has a minimum value equal to the area of the plane immediately above the sample when $\alpha_c = 1$. This minimum value is equal to the cross-sectional area of the cell, $A' = B$, when the sample completely covers the cell bottom.

The effective vaporizing area approaches a maximum value equal to the total vaporizing area of the sample, A, as the condensation coefficient approaches zero. This limit means that almost every molecule which vaporizes escapes because a molecule will not recondense until it has made a very large number of collisions with the surface. In practice this means that increasing the total vaporizing area of a substance with a very low condensation coefficient (on the order of 10^{-6} for example) increases the effective area proportionately. If the sample were a porous solid, a Langmuir evaporation rate which increased directly with the depth of sample in the crucible would be observed.

There is another limit on the effective area which is imposed by the thermodynamic condition that the mass flow in any plane in any direction cannot be greater than the mass flow corresponding to the equilibrium pressure.

$$u_2 \leq P_e/G \qquad [10]$$

$$u_2 B \leq B\, P_e/G \qquad [11]$$

The rate of evaporation from the sample is $P_e \alpha_v A'/G$. As some of the molecules traveling downward through plane 2 are reflected when $\alpha_c < 1$,

$$u_2 B \geqq P_e \alpha_v A'/G \qquad [12]$$

Combining [11] and [12] yields the condition

$$\alpha_v A' \leq B \qquad [13]$$

the equal sign holding only when $\alpha_v = \alpha_c = 1$.

[2] The effective vaporizing area could also have been defined in terms of the net rate of vaporization. The latter is directly accessible by experiment at all ambient pressures whereas the gross rate of vaporization is not. In those terms, the effective vaporizing area would be the area of plane sample surface which gives rise to the measured net rate of vaporization. It follows that the net rate of vaporization will always be equal to $\alpha_v^* A'(P_e - P)/G$. The coefficient α_v is that discussed in the preceding footnote. It can be shown that the effective area defined in such a manner is identical to the effective area described in the text.

In summary, the following limits exist for the effective area, A', of a homogeneous solid sample with total vaporizing area, A, which completely covers the bottom of a cell of cross-sectional area, B:

$$B \leq A' \leq \begin{cases} B/\alpha_v \\ \text{or} \\ A \end{cases} \quad \text{whichever is less} \qquad [14]$$

Some calculations of the effective area.—Vidale (13) has presented an interesting approximation to the effective area of a uniform, porous, powder sample by considering the problem to be one of diffusion through the powder. It was assumed that $\alpha_v = \alpha_c =$ constant. The powder sample can be considered to be infinitely deep when α_v is large enough and the sample is deep enough for the equilibrium pressure to be maintained at the bottom of the porous sample. Vidale's analysis for this case yields

$$A' = 1.55\, B\, (\epsilon/\alpha_c)^{1/2} \qquad [15]$$

where ϵ is the ratio of pore volume to total volume of the powder and the other symbols have the same meaning as before. When α_c becomes very small ($< 10^{-10}$) Vidale's equations give

$$A' = 6\,(1 - \epsilon)\, lB/d \qquad [16]$$

where d is average diameter of a powder particle and l is the depth of powder in the crucible. Thus when α_c is very small the effective area is directly proportional to the depth of the sample, or total vaporizing area, and independent of the value of α_c, as expected.

An attempt to treat the effective area problem has been made by Melville (14) who derived an equation for the rate of vaporization from a wedge-shaped crack. Unfortunately, in addition to mathematical errors, Melville appears to assume that when one follows a group of molecules which vaporize at a given time, the fraction of molecules escaping after each rebound from the walls of the crack is the same as the fraction which escaped on the initial vaporization. The problem of the effective vaporizing area of a pore in a substance with a low condensation coefficient is in many ways equivalent to the problem of the deviation from black-body radiation of the radiation emerging from various parts of a cylindrical cavity. This latter problem has been discussed by a number of authors (15-20), who used a variety of mathematical approximations to obtain numerical results.

Vaporization in a spherical cavity.—This section is concerned with the rate of molecular flow through an opening of plane area A_o when the total vaporizing area is A and no molecules return to the cavity through the opening A_o. The crucial assumption is that the number of molecules striking any elemental area of surface is the same as that striking any other elemental area, both initially and on all rebounds. This assumption is true for a spherical cavity containing a homogeneous vaporizing surface as a consequence of the cosine spatial distribution of the vaporizing and reflected molecules. The model serves also as an approximation to other

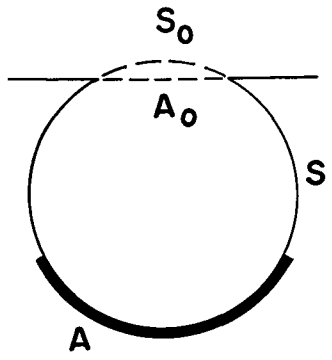

Fig. 2. Diagram of spherical vaporizing cavity

geometries where the area of the opening, A_o, is considerably smaller than the area of the wall containing the opening.

Consider the spherical cavity shown in Fig. 2. The opening has plane area, A_o, and area on the sphere, S_o. For the sake of generality only a portion of the spherical surface, A, is considered to consist of vaporizing sample. The remainder of the spherical surface is S. This could correspond, for example, to a different crystal face of the vaporizing material. Now follow a particular group of molecules which evaporate from A in unit time.

1. Of those that vaporize initially a fraction $S_o/(S_o + S + A)$ escape. $S/(S_o + S + A)$ hit the wall while $A/(S_o + S + A)$ hit the vaporizing surface again. Of those that strike the vaporizing surface a fraction α_c condense, so $(1 - \alpha_c)\ A/(S_o + S + A)$ make the first rebound. As all molecules hitting the wall rebound, the total fraction of the initially vaporizing molecules which make the first rebound is $[S + (1 - \alpha_c)A]/(S_o + S + A)$.

2. Of those that make the first rebound a fraction $S_o/(S_o + S + A)$ escape, that is, the fraction $S_o\ [S + (1 - \alpha_c)A]/(S_o + S + A)^2$ of the initially vaporizing molecules escape after the first rebound. The fraction $S\ [S + (1 - \alpha_c)A]/(S_o + S + A)^2$ rebound from the walls and $(1 - \alpha_c)A\ [S + (1 - \alpha_c)A]/(S_o + S + A)^2$ rebound from the sample surface. Thus the total fraction of the initially vaporizing molecules making the second rebound is $[S + (1 - \alpha_c)A]^2/(S_o + S + A)^2$.

3. The fraction which escape after the second rebound is then $S_o\ [S + (1 - \alpha_c)A]^2/(S_o + S + A)^3$.

4. The fraction of the initially vaporizing molecules which escape through the opening after the nth rebound is

$$\left[\frac{S + (1 - \alpha_c)A}{S_o + S + A}\right]^n \cdot \frac{S_o}{S_o + S + A}$$

Summing the fractions which escape on each of an infinite number of rebounds gives

$$\text{Total fraction escaping} = S_o/(S_o + \alpha_c A)$$

The rate of vaporization inside the cavity is $\alpha_v A P_e/G$. The rate of escape of molecules through the opening, which is the rate which is measured, is then

$$r = \frac{\alpha_v A P_e}{G} \cdot \frac{S_o}{S_o + \alpha_c A} \qquad [17]$$

The effective area, which has been defined by the equation $A' = rG/\alpha_v P_e$, is simply

$$A' = S_o A/(S_o + \alpha_c A) \qquad [18]$$

It can be shown that the plane area, A_o, is related to the spherical area, S_o, by $A_o = S_o(S + A)/(S_o + S + A)$. The effective vaporizing area of the cavity can then be expressed as

$$A' = \frac{1}{\alpha_c\left(\frac{1}{\alpha_c A} + \frac{1}{A_o} - \frac{1}{S + A}\right)} \qquad [19]$$

If the cavity were a spherical cavity in a homogenous sample, S would be zero.

$$A' = \frac{1}{\alpha_c\left(\frac{1}{\alpha_c A} + \frac{1}{A_o} - \frac{1}{A}\right)} \qquad [20]$$

Examination of this result shows the effective area to behave as expected. When the condensation coefficient, α_c, is very small the effective area, A', is equal to the total vaporizing area, A. When $\alpha_c = 1$, $A' = A_o$, the area of the opening.

It is interesting to consider this cavity as a Knudsen cell. If r in Eq. [17] is equated with q in Eq. [1] and the area A_o is designated as the orifice area, a, (with $W_a = 1$, $\alpha_v = \alpha_c = \alpha$, and $S = 0$) one obtains

$$\frac{P_e}{P_m} = 1 + \frac{a}{A}\left(\frac{1}{\alpha} - 1\right) \qquad [21]$$

which is identical with Motzfeldt's result, Eq. [2], when the resistance of the cell to flow is negligible ($W_B = 1$). The derivation of Eq. [21] shows that Motzfeldt's equation would be expected to be a good approximation to the vaporization of a nonporous solid which completely lines a Knudsen cell of total interior area A (when $a << A$), if the assumption $\alpha_v = \alpha_c =$ constant were correct. It should, perhaps, be pointed out that the spherical cavity also reduces to the same equation as derived by Motzfeldt's steady-state model when α_v is assumed different from α_c in both derivations.

Procedures to Obtain P_e and α

On the basis of Eq. [2], Motzfeldt (1) suggested that a plot of P_m against $P_m W_a a/B$ for a liquid sample would be a straight line with intercept P_e and slope $-(1/\alpha + 1/W_B - 2)$. The result of the general effective area case, Eq. [9], can be rearranged to

$$P_m = P_e - P_m W_a a\left(\frac{1}{\alpha A'} - \frac{2}{B} + \frac{1}{W_B B}\right) \qquad [22]$$

Equation [22] immediately points out two dangers in applying the suggested procedure to porous solids. If the ratio $W_a a/B$ were varied by changing the cell cross-sectional area, B, the intercept of the plot would not be P_e unless the effective vaporizing area had changed in direct proportion to B. Also, if the orifice area, a, were varied, P_m plotted against $P_m W_a a/B$, and a straight line obtained (this appears unlikely for reasons discussed below), the vaporization coefficient still could not be calculated from the slope of this plot. At best, the product $\alpha A'/B$ would be obtained where A' might be vastly different from B.

The discussion in the preceding paragraph implicitly accepts the assumptions made in the derivation of Eq. [2] and [9]. It is instructive to examine the effect on Eq. [9] of the removal or modification of these assumptions, and thus examine the effect of these assumptions on such procedures to obtain P_e and α as are implied by Eq. [9] and [22]. Equation [22] suggests that a plot of P_m against $P_m W_a a$ will be a straight line with intercept P_e when $a = 0$. It is intuitively clear that P_m must approach P_e as a approaches zero. Use of the Clausing factor, W_B, in the derivation ignores the radial dependence of the vapor density inside the cell, the nonuniform distribution of the molecules reflected from the top of the cell, and the possible departure from a cosine spatial distribution of the molecules vaporizing from a porous sample with a low condensation coefficient. Carlson's (11) and Balson's (12) analyses of the flow of vapor in a Knudsen cell show that the resistance to flow of the Knudsen cell varies as the orifice area is varied. This means that W_B in Eq. [9] is not a constant but, rather, a function of the orifice area, a. This being so, a plot of P_m against $P_m W_a a$ will deviate somewhat from a straight line.

Equation [2] has alternately been taken to indicate that a plot of $1/P_m$ against $W_a a$ will be a straight line with intercept $1/P_e$ and slope $(1/BP_e)(1/\alpha - 2 + 1/W_B)$. The hazards and uncertainties discussed herein are equally applicable to this latter procedure.

For substances which have very small vaporization coefficients the $\alpha A'$ term in Eq. [9] is much larger than the B and $W_B B$ terms so that these latter terms, and their uncertainties, can be neglected. This is the situation of primary interest in this paper. Usually when α_v is close to unity the orifice area can be made small enough so that the measured pressure is very close to the equilibrium pressure.

It was assumed in deriving Eq. [9] that the vaporization and condensation coefficients are independent of pressure and, therefore, that $\alpha_v = \alpha_c$ at all pressures. Neither theory nor experiment has yet given a description of the behavior of α_v and α_c for molecular substances. However, both theory and experiment indicate that α_v and α_c are not constants independent of pressure. Knacke, Schmolke, and Stranski (21) predict the vaporization coefficient of an ionic crystal to be a function of the undersaturation of the vapor and of the crystal face vaporizing. Jaeckel and Peperle (22) have measured Knudsen cell pressures of single crystal faces of NaCl, KI, Sb_2S_3, and sulfur with different cells and orifice areas. Their results show that the value of α calculated from Eq. [2] varies with the orifice size.

Herth and Pound (23) have considered the vaporization of perfect metal crystals to monatomic vapors. For such substances $\alpha_c = 1$. They calculate $\alpha_v = (2/3)(P/P_e) + 1/3$. Their result might be taken to suggest a function for molecular substances with low condensation coefficients such as

$$\alpha_v = (P/P_e)(1 - z)\,\alpha_c + z\alpha_c \qquad [23]$$

where α_c and z are constants (≤ 1) independent of P. This function has α_v vary from α_c at equilibrium to $z\alpha_c$ under Langmuir conditions.[3] The effective area model leading to Eq. [9] can be extended to include Eq. [23]. The solution is exactly the same as Eq. [9] with α replaced by the vacuum vaporization coefficient, $z\alpha_c$. The rate-determining step in the vaporization of a molecular substance with a low vaporization coefficient is expected to be very different from the rate step considered by Hirth and Pound, removing justification for an equation of the form of Eq. [23]. Indeed, Jaeckel and Peperle's results (22) indicate that $z\alpha_c$ in Eq. [23] is a function of P. As the actual variation of α_v and α_c with pressure is, at present, a matter of conjecture it cannot be assumed that a plot of P_m *vs.* $P_m W_a a$ will be a straight line even when the B and $W_B B$ terms are negligible.

This last conclusion contains a further warning. It is only possible to extrapolate to P_e with confidence after experiments with a number of orifices have defined the curvature of the plot used and when the measured pressures are reasonably close to the equilibrium pressure. If these conditions are not met, the resulting long extrapolation necessary to obtain P_e is hazardous.

An Empirical Equation

As has been seen there are many uncertainties in models of the type considered in this paper. This is particularly due to the lack of experimental information on the variation of α_v and α_c with pressure. It is therefore tempting to try to obtain helpful information from experiments which have been published. Brewer and Kane (4) report the results of Knudsen measurements on the vapor pressure of porous arsenic at 575°K. The vapor pressure was measured for seven different orifice sizes which differed by a factor of 10,000 while the other geometrical and experimental variables were held constant. Their results are illustrated in Fig. 3. If an attempt is made to treat these measurements by an equation such as [9], α is found to vary regularly and to a great degree.

However, Brewer and Kane's results can be rep-

[3] However, α_v^*, the vaporization coefficient defined in the first footnote, is a constant equal to $z\alpha_c$.

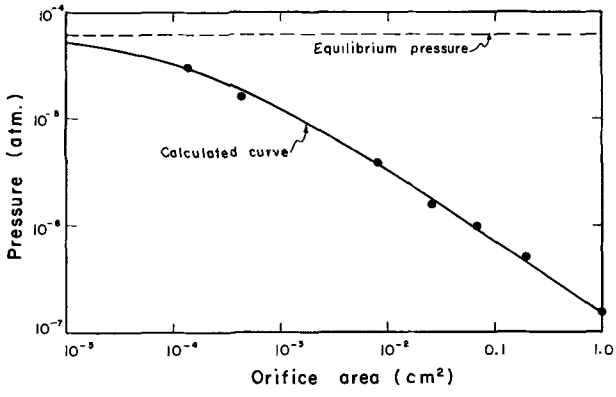

Fig. 3. Kundsen cell data for arsenic at 575°K. The experimental results and equilibrium pressure are from Brewer and Kane (4). The calculated curve represents the empirical equation, $P_e/P_m = 1 + (a/k)^{2/3}$, with $k = 1.3 \times 10^{-4}$. •, Experimental results.

resented within experimental error by a one-parameter, empirical equation

$$P_e/P_m = 1 + (a/k)^{2/3} \quad [25]$$

The curve drawn through the experimental results in Fig. 3 represents this equation. P_e, P_m, and a are taken directly from their paper. The value of k used to calculate the curve (1.3×10^{-4}) is the average of the k values calculated from the measurements. The fit of the seven experimental points to this simple equation is surprising considering the complexity of the situation inside the Knudsen cell and the large range of variables covered.

Comparing Eq. [25] with Eq. [9] suggests association of the empirical constant k with $\alpha A'$. The area a would be $W_a a$ if significant Clausing factors were involved. It might be interesting to determine if Eq. [25] applies to experimental results on other substances having low vaporization coefficients, when only the orifice area is varied while the other geometrical variables are held constant. One way to test the aptness of Eq. [25] would be a plot of $1/P_m$ *vs.* $(W_a a)^{2/3}$. It would, perhaps, be instructive to find a model for vaporization in a Knudsen cell which leads to an equation of the form of Eq. [25].

Conclusions

The model used to describe the vaporization of porous solids with low vaporization coefficients is subject to many uncertainties. A particular difficulty is the unknown variation of the vaporization and condensation coefficients with the undersaturation of the ambient vapor. The model does, however, focus attention on the effective vaporizing area of a solid sample and shows that vaporization coefficients for porous samples cannot be obtained from the slope of a plot of P_m against $P_m W_a a$. The model also demonstrates that attempts to vary the cell dimensions or the sample vaporizing area will not necessarily extrapolate to P_e.

Uncertainty regarding the behavior of α_v and α_c with pressure suggests that Knudsen measurements on substances with low vaporization coefficients can only be extrapolated to the equilibrium pressure reliably when experiments have been carried out with a number of orifice sizes and when the measured pressures are close to the equilibrium value. This very uncertainty also suggests that experimental data should be carefully examined to see what light they throw on this unknown behavior.

A simple equation empirically represents the variation with orifice area of Knudsen measurements on arsenic. It would be interesting to ascertain if this equation has more general validity.

Acknowledgments

The author wishes to thank Professor Leo Brewer for his helpful suggestions and interest. This work was supported by the U.S. Atomic Energy Commission.

Manuscript received Oct. 17, 1962. This paper was prepared for delivery before the Los Angeles Meeting, May 6-10, 1962.

Any discussion of this paper will appear in a Discussion Section to be published in the December 1963 JOURNAL.

SYMBOLS

- a, cross-sectional area of orifice of Knudsen cell.
- A, total vaporizing area.
- A', effective vaporizing area.
- B, cross-sectional area of Knudsen cell.
- $G = (2\pi RMT)^{1/2}$
- k, empirical constant.
- P_e, equilibrium pressure.
- P_m, measured pressure.
- q, number of moles of vapor effusing through orifice of Knudsen cell in unit time.
- r, gross number of moles vaporizing in unit time.
- W, Clausing factor for orifice (W_a) or cylindrical cell (W_B).
- α, condensation coefficient (α_c) and/or vaporization coefficient (α_v) when these are equivalent and constant.

REFERENCES

1. K. Motzfeldt, *J. Phys. Chem.*, **59**, 139 (1955).
2. P. Clausing, *Ann. Physik*, (5) **12**, 961 (1932).
3. I. N. Stranski and G. Wolff, *Research*, **4**, 15 (1951).
4. L. Brewer and J. S. Kane, *J. Phys, Chem.*, **59**, 105 (1955).
5. R. Littlewood and E. Rideal, *Trans. Faraday Soc.*, **52**, 1598 (1956).
6. C. I. Whitman, *J. Chem. Phys.*, **20**, 161 (1952).
7. R. Speiser and H. L. Johnston, *Trans. Am. Soc. Metals*, **42**, 283 (1950).
8. M. G. Rossman and J. Yarwood, *J. Chem. Phys.*, **21**, 1406 (1953).
9. G. W. Sears, *ibid.*, **22**, 1252 (1954).
10. W. L. Winterbottom and J. P. Hirth, *ibid.*, **37**, 784 (1962).
11. K. D. Carlson, U. S. At. Energy Comm. *ANL-6156* (April 1960).
12. E. W. Balson, *J. Phys. Chem.*, **65**, 1151 (1961).
13. G. L. Vidale, General Electric Missile and Space Vehicle Department Technical Information Series, Report No. *R60 SD 468* (October 1960).
14. H. W. Melville, *Trans. Faraday Soc.*, **32**, 1017 (1936).
15. H. Buckley, *Phil. Mag.*, **4**, 753 (1927); **6**, 447 (1928); **17**, 577 (1934).
16. J. C. DeVos, *Physica*, **20**, 669 (1954).
17. A. Gouffe, *Rev. opt.* **24**, 1 (1945).
18. G. Liebmann, *Z. tech. Physik*, **12**, 433 (1931).
19. G. Ribaud, "Traite de Pyrometrie Optique" (1931).
20. T. Yamuti, *Commission Int. des Poids et Mes., Proc. Verb*, **16**, 243 (1933).
21. O. Knacke, R. Schmolke, and I. N. Stranski, *Z. Krist.*, **109**, 184 (1957).
22. R. Jaeckel and W. Peperle, *Z. physik. Chem.*, **217**, 321 (1961).
23. J. P. Hirth and G. M. Pound, *J. Chem. Phys.*, **26**, 1216 (1957).

The Distribution of Potential at the Germanium Aqueous Electrolyte Interface

P. J. Boddy and W. H. Brattain

Bell Telephone Laboratories, Incorporated, Murray Hill, New Jersey

ABSTRACT

Measurement of the interfacial capacity of germanium electrodes in aqueous solutions of pH 4.5-11.5 permits the determination of the potential difference (p.d.) across the semiconductor space charge region (ψ_S). Hence, under changing conditions, changes in the p.d. across the Helmholtz region (V_H) may be deduced since

$$\Delta V_E = \Delta V_H - \Delta \psi_S$$

where V_E is the electrode potential on an arbitrary scale. The steady-state value of V_H depends on anodic current density. The values of V_H corresponding to a fixed current density vary by about 59 mv per decade of hydrogen ion concentration. This supports a recent view that a "dissociation double layer" is formed by the pH dependent ionization of surface hydroxyl groups. For solutions more acid than pH 4.5 and more alkaline than pH 11.5 the data indicate that considerable densities of fast surface states occur.

Recent measurements on germanium surfaces anodically polarized in aqueous solution (1, 2) have shown that the p.d. across the space-charge region in the semiconductor may be determined from the observed interfacial capacity, provided precautions are taken with regard to the purity of the solution [*i.e.*, Cu^{++} etc. $\lesssim 10^{-9}$M (8, 9)].

Consideration of the distribution of potential at the germanium-aqueous electrolyte interface (3, 4) indicates that p.d.'s may exist across three separate regions; the space-charge regions in the solution and the semiconductor, and the Helmholtz region a few Ångstroms either side of the interface. With sufficiently concentrated electrolyte ($\gtrsim$M/10) the space-charge region in the solution, for the purposes of the experiments described here, need not be considered.

We have previously shown that germanium electrodes, under moderate anodic polarization, rapidly applied, in nearly neutral aqueous solution obey the relationship (1)

$$\psi_S - (kT/e) \ln \lambda = V_E + K \qquad [1]$$

where ψ_S is the p.d. across the semiconductor space-charge region, V_E is the electrode potential on some arbitrary scale (in this case *vs.* SCE), and λ is p/n_i, p being the bulk hole concentration in the particular electrode, n_i the electron concentration in intrinsic germanium, and K is a constant. The equation indicates that instantaneous changes in $\psi_S - (kT/e) \ln \lambda$ and V_E are equal, and that at a given V_E the space-charge potential for variously doped electrodes varies by $(kT/e) \ln \lambda$.

Using the physical convention that bands bending up makes the space-charge potential more negative and the electrochemical convention that anodic bias (*i.e.*, bands bending up) makes the electrode potential more positive, Eq. [1] should be rewritten

$$\psi_S - (kT/e) \ln \lambda = - V_E + K \qquad [2]$$

The constant K contains all the p.d.'s in the system other than that across the semiconductor space-charge region. Extracting from K the p.d. across the Helmholtz region (V_H) and introducing another constant L we have

$$\psi_S - (kT/e) \ln \lambda = - V_E + V_H + L \qquad [3]$$

Where V_H is that part of the inner p.d. not occurring in the semiconductor space-charge region, measured on an arbitrary scale of potential with the same sign convention as V_E, L contains none of the p.d.'s in the semiconductor-solution interfacial region and hence is constant under all conditions in a properly conducted experiment.

Considering changes of potential, we have from Eq. [3]

$$\Delta V_E = \Delta V_H - \Delta \psi_S \qquad [4]$$

The value of ψ_S may be determined from capacity measurements and, since ΔV_E is directly observed, the behavior of the p.d. across the Helmholtz region can be examined.

Due to the relatively low bulk charge density in semiconductors, interfacial electric fields are generally small and the contribution to the p.d. across the Helmholtz region from this source is negligible. Dewald (3) gives a table of the approximate magnitude of this quantity in a variety of cases. Exceptions to this situation occur when there is a high density of charged surface states or ionized surface groups. Further contributions to changes in the p.d. across the Helmholtz region which may be of importance on semiconductors arise from changes in number or kind of covalently bonded surface groups and adsorbed dipoles.

Knowledge of the dry, etched germanium surface (5) indicates that the surface states may be classified as fast or slow according to their speed of equilibration with changing carrier densities in the

semiconductor space-charge region. Our previous work (1, 2) has indicated that there are no fast surface states within 200 mv of the center of the forbidden gap for an anodically polarized electrode in a nearly neutral solution that has been carefully purified.

The results of Bohnenkamp and Engell (6) suggest that the change in electrode potential with pH occurs at least partially across the Helmholtz region. We have carried out experiments to determine the detailed potential distribution over a range of pH and, in particular, to investigate the conditions under which changes in V_H may occur.

Experimental

The experimental arrangements, electrodes, materials, and methods have been described previously (1, 2). Only a brief description is given here.

The experiments were carried out in a cell containing aqueous M/10 K_2SO_4, adjusted to appropriate pH by H_2SO_4, KOH, phosphate or borate buffer. The solutions were purified by treating with germanium finely crushed *in situ*. The atmosphere in the cell was purified helium replenished by constant flow through a fritted disk in the solution.

Both simple and bridge electrodes were used. The simple electrodes were 42 ohm-cm n-type and 25.5 ohm-cm p-type germanium in the form of plane ended cylinders. The bridge electrode was 25.5 ohm-cm p-type. The plane faces were of (100) orientation. Before each experiment they were etched in CP4, washed, then anodized in the purified solution.

The bridge electrodes were used to measure surface conductivity and surface recombination velocity as previously described (1). Capacity measurements were made on both types of electrode by examination of the voltage response to short duration current pulses.

Polarization of the interface with respect to a large area platinum electrode in an auxiliary compartment was carried out with a constant current source. Electrode potentials were measured *vs.* a calomel electrode on a L&N millivoltmeter.

Results

A typical plot of interfacial capacity *vs.* V_E in a solution of pH 7.4 is shown in Fig. 1. We have shown

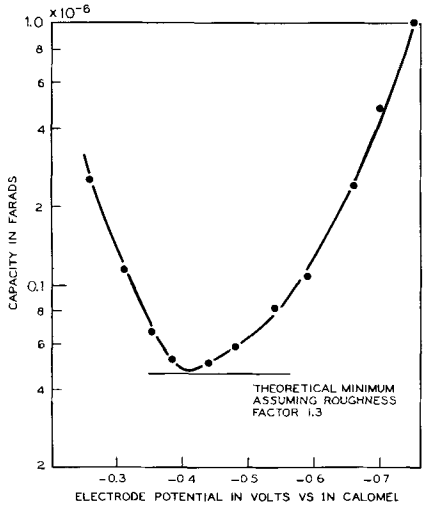

Fig. 1. Experimental capacity for 42.2 ohm-cm n-type (100) in M/10 K_2SO_4, phosphate buffered to pH 7.4.

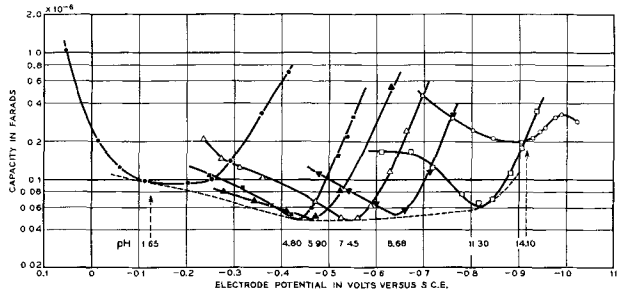

Fig. 2. Experimental capacity for 25.5 ohm-cm p-type (100) in several solutions of different pH. Pulsed polarization, zero current steady state.

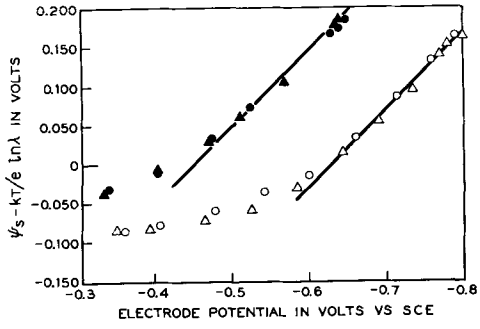

Fig. 3. Analysis of some data from Fig. 2: ○,●, 25.5 ohm-cm p-type (100); △,▲, 42.2 ohm-cm n-type (100); solid points pH 5.90; open points pH 8.68.

previously that such curves are most reasonably interpreted as the capacity of the space-charge region in the germanium with negligible extra capacity due to fast surface states. Under these circumstances the data may be analyzed to yield ψ_S by comparing the experimental and theoretical capacity *vs.* potential curves.

Figure 2 shows the data obtained for one electrode at a variety of pH values. It is clear that over the range of pH from *ca.* 4.5 to *ca.* 11.5, the curves are similar in general shape and minimum value, involving only a shift on the V_E scale and minor changes in shape. Over this range the data were analyzed by comparison with theory to yield plots of $\psi_S - (kT/e) \ln \lambda$ *vs.* V_E. Figure 3 shows typical examples at two pH values. The curvature of the plots at less negative potentials, *i.e.*, greater anodic polarization, (the extreme right-hand point in each case represents the condition of the unpolarized electrode at that pH) has been previously discussed (1) and will be further dealt with later in this paper. The slope of the linear portion of the curves is near to minus unity indicating a one-to-one relationship between changes in V_E and ψ_S. This is consistent with our view of a negligible density of fast surface states in this region of potential and also indicates that over this range of polarization there is no change in V_H from the original unpolarized value, *i.e.*, $\Delta V_E = -\Delta\psi_S$, $\Delta V_H = 0$ in Eq. [4].

For the data in the intermediate pH range we may choose some arbitrary value of $\psi_S - (kT/e) \ln \lambda$, determine the corresponding values of V_E lying on the linear portions of the $\psi_S - (kT/e) \ln \lambda$ *vs.* V_E curves and plot these *vs.* pH. Since the linear relations in Fig. 3 indicate that V_H has not changed from the rest condition due to polarization at each pH we are es-

sentially plotting the variation of V_H with pH, *i.e.*, $\Delta V_E = \Delta V_H$, $\Delta\psi_S = 0$ in Eq. [4]. It matters not at all which value of $\psi_S - (kT/e) \ln \lambda$ we prefer as a standard; for convenience we choose the value zero, *i.e.*, flat band on an intrinsic semiconductor. The linear portions of the $\psi_S - (kT/e) \ln \lambda$ *vs.* V_E curves must be extrapolated to this value, if necessary, to maintain the condition that ΔV_H (due to polarization) = 0. The data shown in Fig. 2 were in response to pulsed polarization. The parameters were measured as rapidly as possible (less than 1 sec) after the application of polarization, and the electrode was at zero net current density between polarization pulses.

We have previously mentioned the slow change in V_H which causes the nonlinear behavior of the curves in Fig. 3 and also the broadened capacity *vs.* V_E curves obtained by steady state rather than by pulse polarization. At a particular pH the steady-state value of V_H depends on the anodic current density. The attainment of the steady-state value however requires the passage of a certain amount of charge. Hence an established value of V_H is maintained for a more or less brief time when the current density is changed abruptly. For large changes in current density the time is faster than we are able to obtain the data, leading to the curvature in Fig. 3. It has been shown that the change in V_H with current density at constant pH reaches a plateau of about 180 mv for anodic current densities of approximately 10 μa cm^{-2}, and changes only a little at higher current densities for (100) 1*N* sulfate solutions of pH 7.45 (1).

Data similar to that previously described were taken from a steady-state condition of an anodic current of 50 μa cm^{-2}. This current was passed through the interface establishing particular values of V_E, V_H, and ψ_S, and pulsed polarizations made around this point. The cathodic polarizations did not exceed 50 μa cm^{-2} so that the net current density was never such as to make the electrode cathodic. The capacity curves obtained by this method are shown in Fig. 4. In form they are quite similar to those in Fig. 2, but displaced to more anodic potentials by virtue of the different values of V_H. An analysis for $\psi_S - (kT/e) \ln \lambda$ similar to that in Fig. 3 has been made for this case and appears in Fig. 5. The curvature due to change in V_H with polarization appears as we approach zero net current density, *i.e.*, as we approach the right-hand side of Fig. 5 (actually beyond the limit of the figure for pH 8.68), and the linear portion of the curve (left-hand side)

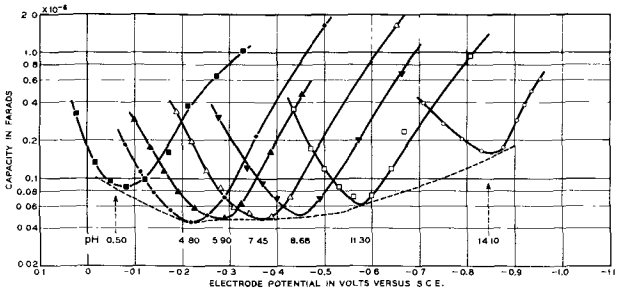

Fig. 4. Similar to Fig. 2, but pulsed polarization, 50 μa cm^{-2} anodic steady state.

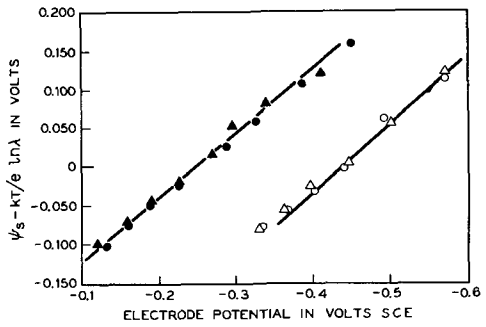

Fig. 5. Analysis of some data from Fig. 4. Symbols as in Fig. 3

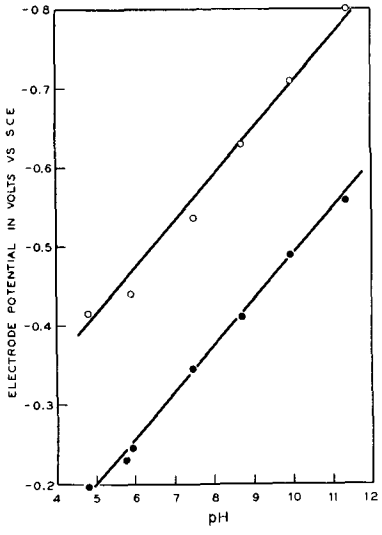

Fig. 6. V_E [for $\psi_S - (kT/e) \ln \lambda = 0$] *vs.* pH. ○,●, zero and 50 μa cm^{-2} anodic steady state, respectively. Each point is an average for n- and p-type of data similar to that in Fig. 3 and 5.

corresponds to the limiting value of V_H under 50 μa cm^{-2} anodic polarization. In both cases (0 and 50 μa cm^{-2}) the steady-state values of V_E and $\psi_S - (kT/e) \ln \lambda$ lie on the linear portion of the appropriate curves (Fig. 3 and 5, respectively).

The values of V_E at $\psi_S - (kT/e) \ln \lambda$ equal to zero for all the curves in the intermediate pH range in both cases are plotted *vs.* pH in Fig. 6. The lines are drawn with a slope of 59 mv per pH unit.

Before proceeding to discussion of these data we will describe some experiments dealing in more detail with the situation in strongly acid and alkaline solutions. It is clear from Fig. 2 that at the extremes of pH, assuming the same roughness factor, there is capacity in excess of that of the semiconductor space-charge region. These were the pH regions most extensively studied by Bohnenkamp and Engell (6). We are in agreement with them that in these ranges of pH the observed minima are several times larger than the theoretical values.

The data we will present were obtained in a separate experiment. The major problem was to determine ψ_S under conditions where the observed capacity is no longer solely that of the space-charge region. For this purpose we used a bridge electrode and measured changes in the surface conductivity. We have previously shown that the surface conductivity experiment does not behave as expected by simple theory (1), due probably to the combined

effects of parallel conductivity through the solution and distribution of potential along the thin arm of the electrode under polarization, as also considered by Harvey (7). It was shown, however, that the surface conductivity was a reproducible function of V_E and that it could be normalized to ψ_S derived from capacity or photovoltaic response (2) and subsequently used to determine ψ_S in the presence of fast surface states. This approach has been used to determine parameters of fast surface states resulting from the interaction with germanium surfaces of the ions Cu(II) (8), Ag(I), and Au(III) (9).

In the experiment under question we first made detailed measurements of capacity and surface conductivity in a purified solution of *p*H 7.4. When these data were established, a little concentrated sulfuric acid or potassium hydroxide solution, which had been purified in an auxiliary compartment by prolonged stirring with crushed germanium in a helium atmosphere, was transferred by helium pressure to the main cell. The final *p*H values were 1.4 and 12.9 in the two separate experiments. The capacity was first examined over a narrow range of pulsed polarization including the minimum value, which was found to be considerably increased over the case of neutral solution. Since very little current had crossed the interface as a result of the polarization, we assume no change in roughness factor for the electrode surface. Subsequent greater polarizations had little effect on the magnitude of the capacity at a given potential, hence we will assume the roughness factor to be constant throughout our measurements.

In Fig. 7 and 8 we show the total measured capacity plotted versus $\psi_S - (kT/e)$ ln λ determined from conductivity measurements. In Fig. 9 we show several $\psi_S - (kT/e)$ ln λ *vs.* V_E relationships determined by surface conductivity measurements in the alkaline solution. The relationship for acid solution was similar except that it was displaced by about 0.60v in the direction of more positive V_E.

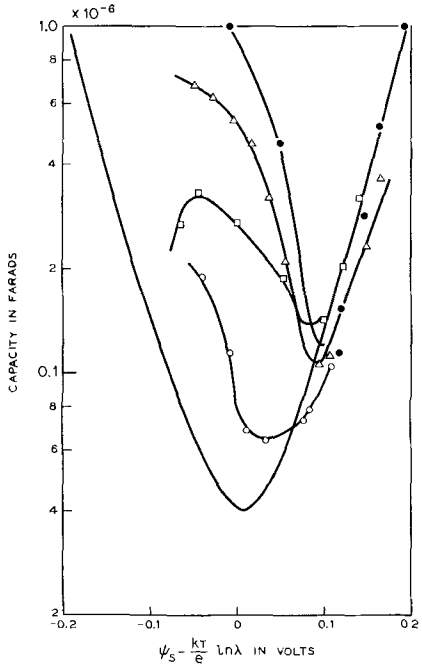

Fig. 7. Experimental capacity for 25.5 ohm-cm p-type (100), H_2SO_4 *p*H 1.4: ○, after 20 min; △, after 60 min; □, immediately after 500 μa cm^{-2} anodic for 1 min; ●, after further 60 min. The lower curve is theoretical (assuming no surface states).

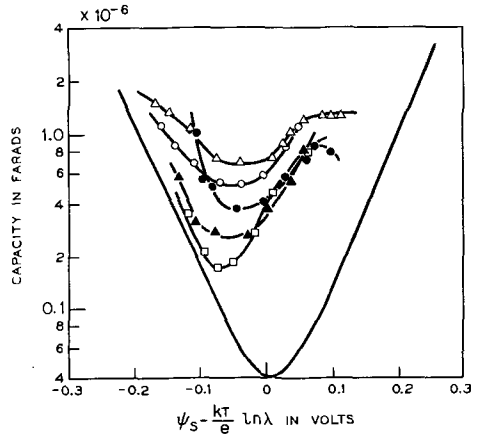

Fig. 8. Experimental capacity for 25.5 ohm-cm p-type (100), KOH *p*H 12.9: ○, after 10 min; △, after 20 min; ▲, immediately after 500 μa cm^{-2} anodic for 1 min; □, repeat of ▲; ●, after further 25 min. The lower curve is theoretical.

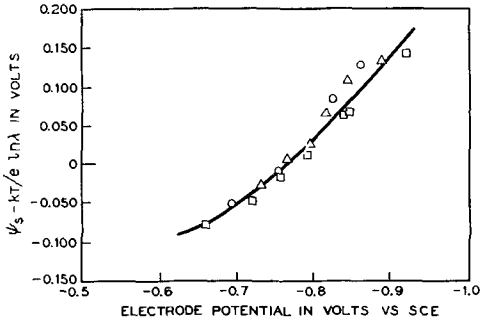

Fig. 9. Relationship between $\psi_S - (kT/e)$ ln λ and V_E deduced from conductivity at *p*H 12.9. The various symbols refer to some of the conditions in Fig. 8.

The additional capacity was determined by subtracting the theoretical curve [multiplied by 1.3 for roughness factor (1)] from the experimentally observed capacity. The results of this procedure are shown in Fig. 10 and 11. In each case the interfacial capacity was measured over a range of V_E at intervals of time. The electrode was then anodized (500 μa for 1 min) and remeasured at intervals. Note that even immediately after anodizing, the curve shows a greater minimum than that observed in neutral solutions. At the present time our data are insufficient to justify detailed analysis in terms of the conventional physical model of discrete surface states, although we hope to obtain more extensive data in future experiments.

Discussion

Figure 1 indicates that over the range of *p*H lying between 4.5 and 11.5, V_H changes by approximately 59 mv per decade of hydrogen ion concentration. It should be noted that this is true both in the case of zero current and 50 μa cm^{-2} anodic current as the steady-state condition of the electrode. As we have pointed out, the difference between these two conditions involves a relatively slow change in V_H (becoming more positive) on the passage of current

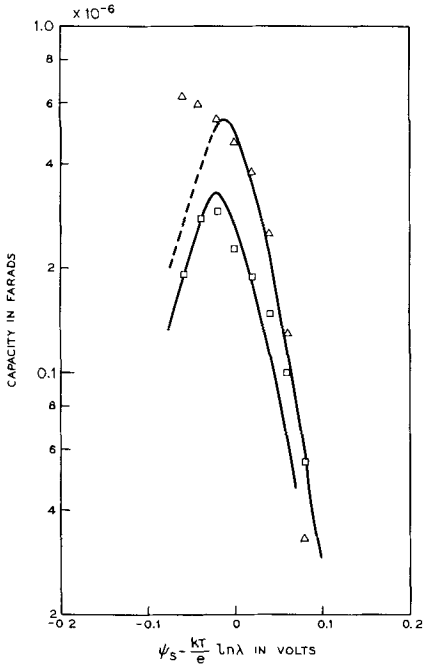

Fig. 10. Additional capacity from some data in Fig. 7. The curves are the theoretical capacities of surface states with parameters $\nu = 0.8\ kT/e$, $N_t = 1.7$ and 1.06×10^{11} cm^{-2}.

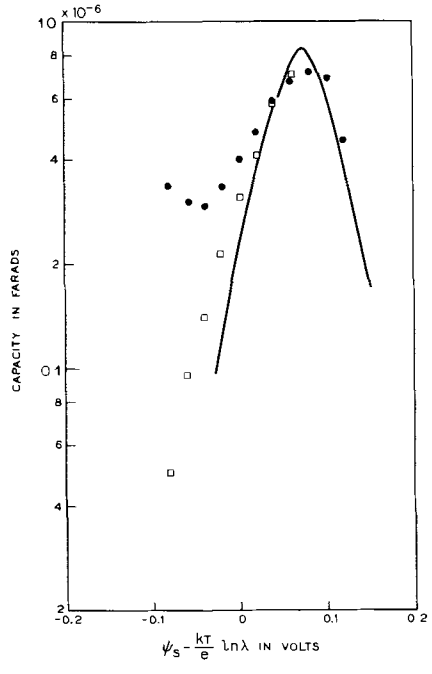

Fig. 11. Additional capacity from some data in Fig. 8. The curve is the theoretical capacity of a surface state with parameters $\nu = 2.7\ kT/e$, $N_t = 2.6 \times 10^{11}$ cm^{-2}.

through the interface, the limiting magnitude of the change being related to the current density up to $\sim 10\ \mu$a cm^{-2} anodic after which little further change occurs. It is evident that any meaningful measurement of the V_H *vs.* pH relationship must be made under conditions that the part of V_H depending on current density is kept constant. We feel that this is true for the pulsed polarization method over the range where the $\psi_S - (kT/e)\ \ln \lambda$ *vs.* V_E is linear with a slope of minus unity in Fig. 3 and 5.

Measurements of a nature similar to some of those described here have been published recently (10).

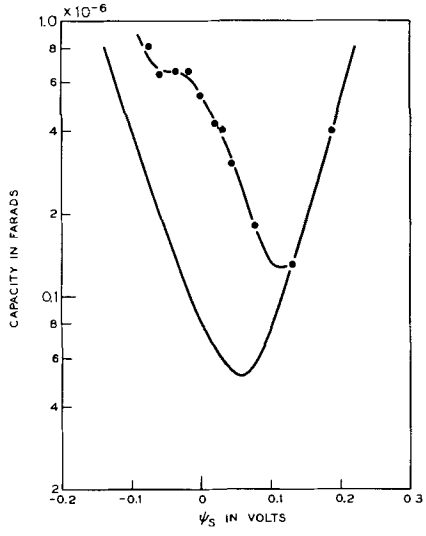

Fig. 12. Effect of 5 x 10^{-7}M Cu^{++} on experimental capacity for 25.5 ohm-cm p-type (100). The lower curve is theoretical.

These measurements differ in several respects from ours. The minimum capacities observed seem to be at least some three times those calculated for the theoretical minimum over the whole pH range. This is in conflict with our observation of *ca.* 1.3 times over the intermediate pH range. The effect of minute traces of impurity ions on the capacity observed in the neutral range is shown in Fig. 12. Such effects are increased considerably by cathodic polarization of the electrode (11) which these authors employed in order to obtain the complete curves. We have found that this is acceptable for small current densities if done on a pulsed basis (8, 9), but under the influence of direct current a germanium cathode is subject to marked changes in the electrical character of the surface (11). Effects of this kind were observed in ref. (10).

A further comment concerns the current density dependent part of V_H, which in our measurements is kept constant, but in ref. (10) may, in principle, vary depending on whether or not the arbitrarily chosen point on the total space charge plus surface states capacity curve always occurs at the same current density.

The disagreement between their quoted value for dV_H/dpH of -50 to -56 mv and our value of -59 mv is possibly due to a combination of the effects mentioned above, although inspection of their Fig. 5 shows that the data for solutions more alkaline than pH 5.0 are consistent with a value close to -59 mv. It is only in solutions more acid than pH 5.0 that the value becomes numerically smaller to an appreciable extent.

We are in agreement with these authors that the phenomena are best interpreted on the basis of a "dissociation double layer" due to a pH dependent equilibrium between ionized and un-ionized surface hydroxyl groups. On a (100) surface the first ionization equilibrium

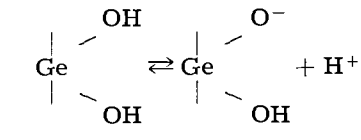

[5]

is considered, and the expression they derive for the p.d. across the dissociation double layer is equivalent to

$$dV_H/dpH = RT/F(1-d\ln(a_{GeOOH^-}/a_{Ge(OH)_2})/dpH) \quad [6]$$

Since the experiments show that $dV/dpH \approx -59$ mv for solutions more alkaline than pH 5.0 this implies that $d\ln(a_{GeOOH^-}/a_{Ge(OH)_2})/dpH$ is negligibly small. Assuming that the integral capacity of the region across which the ionization equilibrium occurs is approximately 30 x 10^{-6} farads cm^{-2} then since $\Delta Q = C.\Delta V$, we have between pH 5.0 and pH 11.0, $\Delta Q \approx 30 \times 10^{-6} \times 0.35 \approx 10^{-5}$ coulombs. This change in charge is produced by the ionization of a fraction α of the monolayer of surface hydroxyl groups, hence $\Delta Q = \alpha nq$, where n is the number of germanium atoms cm^{-2}, q is the electronic charge, and therefore $10^{-5} = \alpha.6 \times 10^{-14}.1.6 \times 10^{-19}$ whence $\alpha \approx 0.1$. This shows that the observed potential change requires the ionization of about one tenth of the surface hydroxyl groups, *i.e.*, considering only one ionizable group attached to each germanium atom. During this change in concentration of the surface species the quantity $d\ln(a_{GeOOH^-}/a_{Ge(OH)_2})/dpH$ must remain small since a slope of $-RT/F$ is observed. From this we may make a rough estimate of the degree of ionization of the surface groups. This may be done more simply by deriving an alternative expression for the ionization equilibrium. Consider the process as the adsorption of hydrogen ions onto a plane of $-O^-$ groups, then

$$\bar{\mu}_{H^+\,surface} = \bar{\mu}_{H^+\,solution} \quad [7]$$

$$\mu^O_{H^+\,surface} + RT \ln a_{H^+\,surface} + F.\phi_1 = \mu^O_{H^+\,solution} + RT \ln a_{H^+\,solution} + F.\phi_{solution} \quad [8]$$

where ϕ_1 is the plane of the $-O^-$ and $-OH$ groups (inner Helmholtz plane).

$$V_H = \phi_1 - \phi_{solution} = \text{constant} - (RT/F)pH - (RT/F)\ln a_{H^+\,surface} \quad [9]$$

$$dV_H/dpH = -RT/F(1+d\ln a_{H^+\,surface}/dpH) \quad [10]$$

It is required that $d \ln a_{H^+\,surface}/dpH$ is small compared to unity. We may place an upper limit on its value by assuming our experimental accuracy to be $\pm 10\%$, and that $a_{H^+\,surface} = \theta/1-\theta$ where θ is the fractional coverage of H^+ (*i.e.*, fractional coverage by un-ionized groups), then over the range from pH 5.0 to pH 11.0, since we have shown that $\alpha(=d\theta) \approx 0.1$

$$\{\ln(\theta-0.1)(\theta-1)/\theta(\theta-1.1)\}/6 < \pm 0.1$$

whence θ is 0.2-0.8.

The experimental results indicate an error of somewhat less than 10%, and the range of acceptable values for θ is less than that shown above. θ is probably close to 50% since we calculate a 6% variation of dV_H/dpH from RT/F for a change in θ from 0.45 to 0.55.

There is a further point of interest in the value of dV_H/dpH. For the case of specific adsorption of anions on mercury it is found that the variation of the potential of the ecm with logarithm of concentration of the ion in solution is numerically greater than $-RT/F$ (14), although on the assumptions that $\phi^M - \phi_1 = 0$ and $E^{ecm}_{ads} - E^{ecm}_O = \phi_1 - \phi^S$, it should equal $-RT/F$. The numerically greater values that are observed are ascribed to penetration of the field, set up due to the charge separation on adsorption, into the region between the metal surface and the inner Helmholtz plane, due to the discreteness of charge (15) in the inner Helmholtz plane. As a consequence, the adsorbing ion moves through only a part of the potential difference $E^{ecm}_{ads} - E^{ecm}_O$. The flat band potential ($\psi_S=0$) on germanium is analogous to the ecm. Both our data and those of Hoffmann-Perez and Gerisher show that for solutions more alkaline than pH 5.0, dV_H/dpH has its thermodynamically predicted value, and hence there is no penetration of the field into the region between the germanium surface and the inner Helmholtz plane. A possible explanation may be in a screening effect due to "smearing out" of the charges in the closely packed inner Helmholtz plane because of the rapid fluctuations in their locations, thus

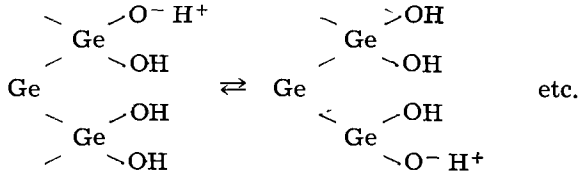

Another possible explanation would be that $d\ln a_{H^+\,surface}/dpH$ was not small compared to unity, but was almost exactly canceled by the discreteness of charge effect. This would be an unlikely coincidence.

In strongly acid and alkaline solutions as we have shown, it is not possible to deduce the change in V_H from capacity measurements due to the presence of surface states even in carefully decontaminated solutions. The flat band condition at the pH extremes may be deduced from the conductivity measurements, *e.g.*, Fig. 9. The points obtained relate to the zero current line in Fig. 6, but the data do not lie on that line. This is not too surprising since we know that there are considerable differences in the nature of the interface at the extremes of pH (as evidenced by the occurrence of fast surface states) compared with the near neutral region.

The relatively slow change in V_H on polarization at fixed pH, which is evidenced by the shift in the V_E *vs.* $\psi_S-(kT/e)\ln\lambda$ relationships in Fig. 3 and 5 under the two different steady-state conditions appears in the constant term in Eq. [2], which is constant only at a given steady current density or under experimental conditions where $\Delta V_E = \Delta(\psi_S-(kT/e)\ln\lambda)$. We may conclude that it is probably not due to a variation of the density of covalently bonded hydroxyl groups. If this were so, the limiting case for high anodic current would presumably be the complete absence of surface hydroxyl groups. The reasoning behind this statement is that since about 50% of ΔV_H (due to polarization) occurs for 2 μa cm^{-2}, we conclude that this current is already comparable with the spontaneous rate of re-establish-

ment of the dipole. Assuming that there is a simple competition between anodic dissolution and rate of replenishment, the steady state at high anodic current should be almost zero density of the species giving rise to the dipole. However, from the variation of V_H with pH at higher current densities (> 10 μa cm^{-2}) we know that there must still be a considerable surface density of hydroxyl groups present under these conditions, and that increase in current density above this figure (up to at least 200 μa cm^{-2}) does not change the density significantly, since little further change in V_H is observed. This is in accordance with the view that the attachment of hydroxyl groups to a germanium surface during anodic dissolution occurs rapidly (12).

We feel that it is more likely that the effect is due to an oriented layer of water molecules, hydrogen-bonded to the surface hydroxyl groups thus

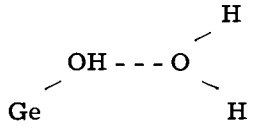

The passage of current will, by virtue of the removal of surface atoms and the diffusion of reactants and products through the solution side of the double layer, disrupt this oriented layer of molecules. It is assumed that at 10 μa cm^{-2} the layer becomes largely disoriented. The observed value for ΔV_H (due to polarization at a fixed pH) of *ca.* 180 mv is not unreasonably far from the experimentally measured values of the surface potential for water of 300-400 mv (13). The structure as written above is consistent with the fact that its removal will cause V_E to be more positive at a given ψ_S. However, we cannot rule out other possible explanations.

With regard to the additional capacity shown at the pH extremes in Fig. 10 and 11, we do not propose to make a complete analysis at the present time. One of the objects of this work was to determine if surface states could be observed on germanium even when none of the metal ion contaminants which have been observed to create surface states (8, 9) were present. This is apparently the case, and we conclude that the states observed are due to particular surface oxide structures at the extreme pH values.

In Fig. 10 and 11 we have included the theoretical curves for localized fast surface states of the given parameters as an indication of the approximate fit of the data to such a model. We hope to carry out further experiments to examine in detail the nature of these surface states.

Conclusions

The p.d. across the Helmholtz region between a germanium electrode and a concentrated aqueous electrolyte depends on both current density and pH. Over an intermediate range of pH the variation at constant current density is 59 mv per pH unit and suggests the presence of ionized surface hydroxyl groups.

At more extreme pH values fast surface states are observed even in solutions carefully purified from traces of noble metal ions. This indicates that surface states may be an intrinsic property of some structural features of the surface occurring in these ranges of pH.

Acknowledgments

The authors are indebted to Dr. W. W. Harvey of Lincoln Laboratory, Massachusetts Institute of Technology, for discussion and to Mr. W. J. Sundburg for technical assistance.

Manuscript received Aug. 28, 1962; revised manuscript received Dec. 6, 1962. This paper was presented at the Los Angeles Meeting, May 6-10, 1962.

Any discussion of this paper will appear in a Discussion Section to be published in the December 1963 JOURNAL.

REFERENCES

1. W. H. Brattain and P. J. Boddy, *This Journal*, **109**, 572 (1962).
2. P. J. Boddy and W. H. Brattain, *Ann. N.Y. Acad. Sci.*, **101**, 683 (1963).
3. J. F. Dewald in "Semiconductors," N. B. Hannay, Editor, Reinhold Publishing Co., New York (1959).
4. M. Green in "Modern Aspects of Electrochemistry," Vol. II, J. O'M. Bockris, Editor, Butterworths (1959).
5. Reviewed by A. R. Plummer in "Electrochemistry of Semiconductors," P. R. Holmes, Editor, Academic Press, New York (1962).
6. K. Bohnenkamp and H. J. Engell, *Z. Elektrochem.*, **61**, 1184 (1957).
7. W. W. Harvey, paper presented at the American Chemical Society Symposium on "Semiconductor Surfaces," Washington (1962).
8. P. J. Boddy and W. H. Brattain, *This Journal*, **109**, 812 (1962).
9. W. H. Brattain and P. J. Boddy, paper presented at the International Conference on Semiconductors, Exeter (1962).
10. M. Hoffmann-Perez and H. Gerisher, *Z. Elektrochem.*, **65**, 771 (1961).
11. W. H. Brattain and P. J. Boddy, Unpublished data.
12. H. Gerisher and F. Beck, *Z. Elektrochem.*, **63**, 500 (1959).
13. Summarized by R. Parsons in "Modern Aspects of Electrochemistry," Vol. I, J. O'M. Bockris, Editor, Butterworths (1954).
14. O. Esin and B. Markov, *Acta Physicochim. USSR*, **10**, 353 (1939).
15. O. Esin and V. Shikov, *Zhur. Fiz. Khim.*, **17**, 236 (1943).

Transport of Bicarbonate, Carbonate, and Chloride Ions through Ion Exchange Membranes

M. Block[1] and K. S. Spiegler[2]

Department of Chemistry, Technion-Israel Institute of Technology, Haifa, Israel

ABSTRACT

The integral transport numbers of chloride and bicarbonate ions in the commercial anion-exchange membranes "Permutit 3148," "AMF 101" (American Machine and Foundry Company) and "Asahi Anionic," and the concomitant water transport were determined. The cathode compartment contained mixed solutions of sodium bicarbonate and chloride in different proportions and of total normality 0.05. It was found that in all three membranes preferential transport of chloride takes place, that the electroosmotic transport of water with bicarbonate is higher than with chloride and that the electroosmotic water transport varies in the same order as the water content of the chloride forms of the membranes expressed in terms of moles H_2O per equivalent Cl^-. Competitive transport of carbonate and chloride in "AMF 101" was also measured. The preferential transport of chloride is even more pronounced in this case than in chloride-bicarbonate systems.

In the electrodialysis of waters containing bicarbonates and/or carbonates, scale formation is often encountered. Scale is caused by the local buildup of high concentrations of these ions on the side of the anion exchange membrane facing the concentrate stream (1-3). The resulting precipitation of calcium carbonate and/or magnesium hydroxide greatly decreases the efficiency of the electrodialysis process. The concentration polarization causing these phenomena is due to the difference of the ion transport numbers in solution and membrane, respectively.

It was therefore considered of interest to measure the transport number of bicarbonate in a number of commercial anion exchange membranes and in the presence of chloride ions. Previous field experience with these and other commercial membranes had indicated that chloride transport was favored over bicarbonate transport under some conditions (4, 5) but opposite effects had also been reported (6). In the present work we determined the transport numbers[3] of bicarbonate and chloride in three membranes in contact with mixed bicarbonate-chloride solutions, in which the total concentration was held constant, at 0.05*N* while the

[1] Present address: Department of Mining and Mineral Technology, Imperial College of Science and Technology, London, England.

[2] Present address: Willgoos Physical Chemistry Laboratory, Pratt and Whitney Aircraft, East Hartford, Connecticut.

[3] The transport numbers referred to are the "integral transport numbers" (6a) which are somewhat different from the "differential transport numbers" measured between solutions of almost identical composition (7).

Table I. Properties of anion exchange membranes (chloride form)

Name	Permutit No. 3148	AMF 101	Asahi Anionic*
Manufacturer	Pfaudler-Permutit Inc., New York, N. Y.	American Mach. and Foundry Co., Springdale, Conn.	Asahi Chemical Co., Yurakucho, Chiyoda-ku, Tokyo
Type	Heterogeneous, strengthened by inert plastic fiber	Homogeneous	Homogeneous
Capacity, meq/g dry resin	0.7	1.5-1.6	1.3-1.4
Thickness, mm	0.17	0.12	0.16
Electrical resistance, ohm cm^2			
in 0.1*N* NaCl 25°C	11.0		2.0-2.5
in 0.5*N* NaCl 25°C		9.0	
Water content, %	17	17	25
molecules per Cl^-	15-16	6-7	13-14
Electroosmotic water transport			
molecules H_2O per Cl^-	6.5	3	4 ± 0.5
molecules H_2O per HCO_3^-	9.5	5.7	6.5

* The membrane tested had the chemical characteristics of the material designated as DA-1, which is now in commercial production in sheets of 0.23 mm thickness.

bicarbonate: chloride concentration ratio was varied in different experiments. The water transport occurring at the same time as the ion transport was also measured, and so was the transport number of carbonate in the presence of chloride across one membrane. The results showed that chloride ion is transported in preference to bicarbonate and that bicarbonate carries more water than chloride.

Experimental

The membranes used and their relevant properties are listed in Table I. Duplicate membrane ion-exchange capacity determinations were performed by shaking weighed samples with successive portions of sodium chloride solution, followed by exhaustive displacement of Cl^- with 1*N* sodium nitrate. The combined nitrate washings were titrated for chloride. Membrane water content was determined by equilibration of duplicate samples in 0.05*N* NaCl solutions, rapid blotting and weighing, with subsequent drying to constant weight over phosphorus pentoxide.

The cell for the measurement of ion and water transport is an adaptation of a cell used by one of the authors (KSS) previously (7) and is shown in Fig. 1. It is made of "Plexiglas," has a flat bottom to allow magnetic stirring and a curved roof to facilitate the escape of gases formed in electrode reactions. (In the experiments reported here, no gas formation occurred.) Each half-cell contains an electrode, a thermometer, and a microburette, introduced through "Nylon" plugs, as well as a spare plug.

In our experiments the anion exchange membrane was clamped between the two half-cells and a constant current passed for a specified period by means of a thyratron-controlled power supply. The exposed membrane surface was 10 cm^2. Both electrodes were silver-silver chloride made from 20 mesh pure silver wire wound on a cylindrical Plexiglas support of diameter 3.9 cm and length 3.2 cm and conditioned before use by electrolysis in 0.1*N* HCl with periodic current reversal. At the start of each experiment the cathode compartment was filled with a mixed solution of NaCl and $NaHCO_3$ (or Na_2CO_3) of total concentration 0.05*N*. The anode compartment was filled with a 0.05*N* NaCl solution.

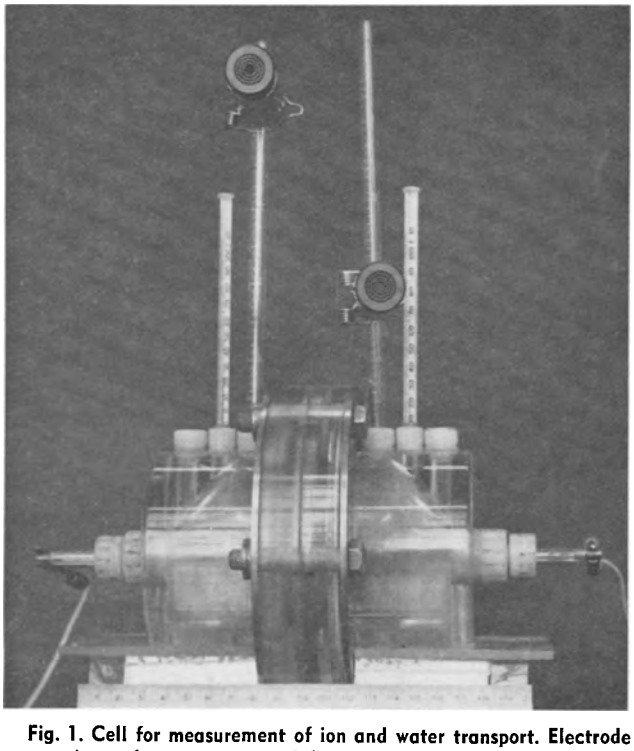

Fig. 1. Cell for measurement of ion and water transport. Electrode connections, thermometers, and burets with magnifiers are shown. Ruler is calibrated in centimeters.

As a result of the passage of the current, the concentrations in both compartments changed. From these changes the transport numbers of the anions were calculated. Material balances confirmed that polarization side reactions were almost negligible. The analyses of the solutions in the cell compartments were carried out potentiometrically with a Beckman "Zeromatic" *p*H meter: chloride by titration with 0.03*N* $AgNO_3$ solution, bicarbonate, carbonate, and hydroxide with 0.01*N* H_2SO_4 (8).

Electroosmotic water transport was calculated from the difference in anolyte volume at constant hydrostatic pressure before and after each run, corrected for electrode volume change and for molar volume change caused by solute transfer, as well as for thermal expansion.

All experiments were carried out at ambient room temperature. It is known that both ionic transport number and electroosmotic water transport per ion are affected only slightly by the prevailing temperature fluctuations.

The total charge passed was calculated from the volume of hydrogen-nitrogen mixture evolved from a hydrazine sulfate solution in a Page-Lingane coulometer in series with the transport cell (9). Current densities were kept low, and the solutions were vigorously agitated by magnetic stirrers to minimize polarization phenomena. The electrolysis period in these experiments was between 60 and 200 min, depending on current density and composition of the solutions.

The rate of interdiffusion of chloride and bicarbonate (or carbonate) between a 0.05*N* NaCl solution and a mixed chloride and bicarbonate (or carbonate) solution of total concentration 0.05*N* was also measured. These measurements were made in the absence of an external applied voltage and showed that the diffusion flux of the ions is considerably smaller than the flux induced by the electric field.

Results and Discussion

The bicarbonate transport number as a function of the average equivalent fraction of bicarbonate in the catholyte is shown in Fig. 2. "Average" refers here to the arithmetic mean of the bicarbonate fraction in the catholyte at the beginning and the end of the experiment. Only the bicarbonate transport numbers, $t_{HCO_3^-}$, are reported, since the chloride transport numbers, calculated independently from the argentometric titrations, were found to be equal to $1 - t_{HCO_3^-}$ within 1.5%. The estimated accuracy of the experiments is indicated by the size of the points on the graphs.

The interdiffusion experiments lasted 3 hr and are shown in Fig. 2. In electrodialysis at 4 ma/cm^2

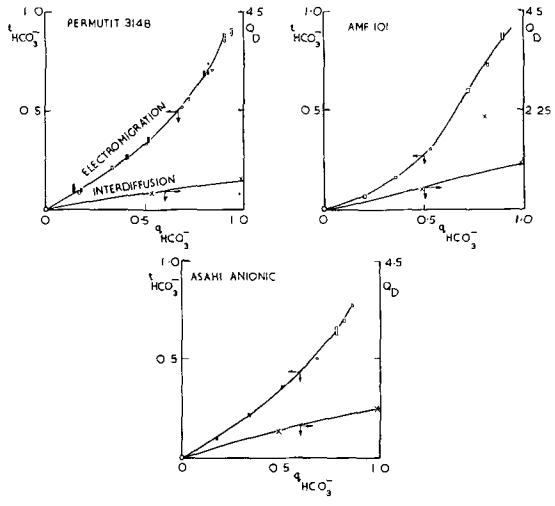

Fig. 2. Bicarbonate transport number and interdiffusion in the system: (anode) Ag/AgCl/ 0.5*N* NaCl / Anion-exchange membrane / Mixed solution o $NaHCO_3$ and NaCl / AgCl/Ag (cathode). Total normality of mixed solution is 0.05. $t_{HCO_3^-}$ = integral bicarbonate transport number; $q_{HCO_3^-}$ = mole fraction of bicarbonate in the anolyte; Q_D = meq HCO_3^- diffused through membrane from mixed solution of $NaHCO_3$ and NaCl into NaCl solution in 3 hr. Points marked solid rectangle and open rectangle refer to current densities of 4 and 8 ma/cm^2 membrane surface, respectively.

a charge of 4.5 m**F** would have passed in this period. To permit some comparison between electromigration and interdiffusion experiments, the scale chosen was such that interdiffusion values of 4.5 meq are opposite chloride transport number values of 1.0, respectively, and both scales start at a common zero line.

The results of these experiments show that in all three membranes chloride transport is favored over bicarbonate transport, because $t_{HCO_3^-}$ is smaller than $q_{HCO_3^-}$ over the whole range covered. This is true in spite of the fact that the bicarbonate concentration in the anolyte was lower than in the catholyte, so that driving forces were present for diffusion of bicarbonate ions in the same direction as electromigration and of chloride ions in the opposite direction. Had the transport number been measured in such a manner that the concentrations of the electrolytes on both sides were kept constant throughout the experiment, a still higher preference for chloride transport would no doubt have been found. A method for the measurement of transport numbers under such conditions has been described (7) using radioactive tracers. However, in practice such conditions are not encountered. Moreover, it was observed (*a*) that experiments conducted at 8 ma/cm^2 fell on the same curve as those at 4 ma/cm^2, although the duration of the runs varied by a factor of two, and (*b*) that changes in initial anolyte concentration had only a slight effect on the t_{Cl^-} found. Both these facts show that under the conditions of these experiments, transport is determined mainly by the applied electric force.

In Fig. 3 the transport number of carbonate ion in the AMF 101 anion exchange membrane is plotted against the average carbonate concentration in the catholyte. Interdiffusion is also shown. Because of the hydrolysis of sodium carbonate, hydroxyl

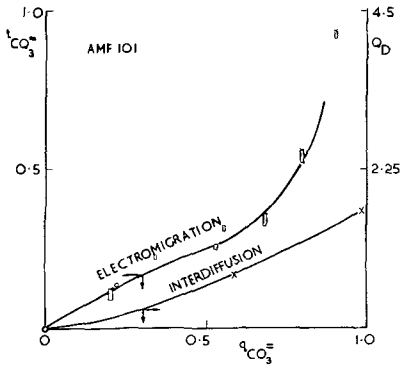

Fig. 3. Carbonate transport and interdiffusion conditions as in Fig. 2 except that carbonate was substituted for bicarbonate.

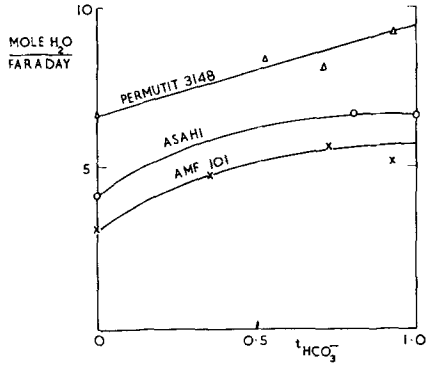

Fig. 4. Electroosmotic water transport in three membranes. Bicarbonate and chloride ions migrate through membrane from mixed solution of NaCl and $NaHCO_3$ of total normality of 0.05*N* into 0.05*N* NaCl solution. Water transport is plotted against integral transport number of bicarbonate.

ions are present and contribute to the flow of current through the membrane. This effect is most pronounced at the highest carbonate concentrations, (exceeding 0.03*N*) when the transport number of hydroxyl ions was found to be 0.03 ± 0.015%. At the lower carbonate concentrations, the sum of the transport numbers of chloride and carbonate ions was unity within the experimental error of the respective experiments, estimated at 1.5%. It is seen that the preferential transport of carbonate over chloride in this membrane is even more pronounced than the transport of bicarbonate.

The variation of electroosmotic water transport from chloride-bicarbonate solutions with bicarbonate transport numbers for the three membranes is plotted in Fig. 4. The curves show that more water is transported with the bicarbonate than with the chloride ion. Preliminary experiments showed the same tendency with carbonate ion, which carried even more water across the membranes. Moreover, the electroosmotic water transport increases in the same order as the number of water molecules per counterion (listed in Table I.) These trends are not surprising since previous experiments with cation exchangers have shown that high electroosmotic water transport is correlated with low electrical mobility of ions (10) and high water content of those resins (11). Theoretical considerations (12) also lead to these conclusions.

Manuscript received Sept. 4, 1962, This paper presents material from the thesis of M. Block submitted

in partial fulfillment of the M.Sc. requirements of Technion-Israel Institute of Technology.

Any discussion of this paper will appear in a Discussion Section to be published in the December 1963 JOURNAL.

REFERENCES

1. J. R. Wilson, Editor, "Demineralization by Electrodialysis," Butterworth, London (1960).
2. B. A. Cooke, *Electrochimi. Acta*, **3**, 307 (1961).
3. K. S. Spiegler, in "Saline Water Conversion 2," Advances in Chemistry Series, American Chemical Society, Washington, D. C. (1963).
4. E. H. Sieveka, *J. Am. Water Works Assoc.*, **52**, 556 (1960).
5. Y. Tsunoda, M. Seko, M. Watanabe, T. Misumi, Y. Yamagoshi, and S. Ogawa, Japanese Pat. 8515 (1958).
6. Ionics Inc., Office of Saline Water Res. and Dev. Rep. No. 11, U. S. Department of the Interior, Washington, D. C. 1956.

6a. F. Helfferich, "Ion Exchange," p. 408, McGraw-Hill Book Co., New York (1962).

7. J. G. McKelvey, K. S. Spiegler, and M. R. J. Wyllie, *This Journal*, **104**, 387 (1957).
8. I. M. Kolthoff and E. B. Sandell, "Textbook of Quantitative Inorganic Analysis," 3rd ed., p. 523, MacMillan Co., New York (1952).
9. J. J. Lingane, "Electroanalytical Chemistry," 2nd ed., p. 456, Interscience Publishers, Inc., New York (1958).
10. A. G. Winger, R. Ferguson, and R. Kunin, *J. Phys. Chem.*, **60**, 556 (1956).
11. R. J. Stewart and W. F. Graydon, *ibid.*, **61**, 164, (1957).
12. K. S. Spiegler, *Trans. Faraday Soc.*, **54**, 1408 (1958).

Technical Notes

The Effect of the Dielectric Constant of the Embedding Media on Electroluminescent Light Intensity

John Tanaka and Daniel Berg

Research Laboratories, Westinghouse Electric Corporation, Pittsburgh, Pennsylvania

The electrical properties of the dielectric greatly influence the operation of an electroluminescent lamp. The brightness of the lamp has been shown to be dependent on the dielectric constant of the dielectric, by Roberts (1) for polymers with dielectric constants up to 7 and by Katona (2) for various dielectric liquids with dielectric constants up to 1300.[1] Katona, following Roberts, gave an electrical analysis of the suspended phosphor-dielectric assuming spherical phosphor particle shape, and he took account of the loss tangent as well as the dielectric constant in calculating the field under which the phosphor particle is actually excited. For a dielectric constant of 2.5 or greater, the field across the phosphor particle is almost independent of tan δ up to tan $\delta = 0.25$. For practical electroluminescent cells where the dielectric constant of the embedding medium is about 10, the light intensity is not strongly dependent on tan δ since it is very difficult to obtain tan δ's of 0.25 with a material of dielectric constant equal to 10.

It should be mentioned also that the complex dielectric constant of the excited phosphor particle changes with the impressed field. This has never been taken into account, and the simple theory without this feature seems to apply fairly well.

In this paper, the effect of the dielectric constant of solid embedding materials on the brightness of electroluminescent lamps is described for dielectric constants up to 65. The theory Roberts used, for spheres embedded in a dielectric medium, is applied and successfully accounts for the variation of light intensity with dielectric constant.

[1] Katona's (2) measured value for ϵ' for acetone was 1300 with a tan δ of 25 at 1 kc; at 10 kc ϵ' was 23, and tan $\delta = 0.7$. The literature value of ϵ' for acetone is 20.7. The material used by him must have been sufficiently lossy to cause electrode polarization and equivalent capacitance. See Table of Dielectric Constants of Pure Liquids, National Bureau of Standards, Circular 514, 1951.

Experimental Method

Materials.—At first, liquids were considered as the dielectric medium because of the ready availability of a wide range of dielectric constants. However, the high losses of the higher dielectric constant liquids (even when purified) rendered measurements difficult. In view of this, solid dielectrics were chosen. Various dielectric constants were obtained by using mixtures of dielectric materials. Acetate rayon and cyanoethyl cellulose mixtures gave films with dielectric constants ranging between 6 and 15. Cyanoethyl cellulose and succinonitrile mixtures gave films with dielectric constants ranging between 15 for the pure cyanoethyl cellulose to 65 for the pure, waxy succinonitrile. A sulfone, which was prepared in this laboratory and which was most probably α-napthylphenyl sulfone, was also used. It is a waxy substance with a dielectric constant of 24.

The phosphor used in the different lamps was from the same batch of originally prepared material. Its concentration was kept close to 60% by weight in the solid mixture. The phosphor particles were irregular, angular particles approximately 10μ in diameter.

Dielectric constant.—Films of the embedding material were deposited on NESA glass (Trademark of Pittsburgh Plate Glass Company) which is a glass with a conducting, transparent tin oxide surface. The dielectric constant at 60 cycles was determined using the NESA coating as one electrode. For higher frequencies the NESA coating introduces errors because of its resistance. Since it was difficult

to determine film thicknesses to the accuracy desired, especially with softer films, the dielectric constant of the mixtures was calculated according to the empirical equation (3)

$$\log \epsilon'_x = V_1 \log \epsilon'_1 + V_2 \log \epsilon'_2 \qquad [1]$$

where ϵ'_x is the dielectric constant of the mixture, ϵ'_1, ϵ'_2 are dielectric constants of components 1 and 2, respectively, and V_1, V_2 are the volume fractions of components 1 and 2, respectively.

Succinonitrile tends to sublime easily, so that evaporated aluminum electrodes could not be applied by vacuum evaporation. Therefore, a mercury electrode was used as the second electrode as shown in Fig. 1.

Light output.—In order to determine comparative light outputs, a thickness of 1.5 mil for the phosphor-dielectric film was established as a standard of reference, for a lamp to be operated at 60 cps. Because a lamp of exactly this thickness was difficult to make, a series of lamps of varying thicknesses were prepared from each phosphor-dielectric mixture and their light outputs determined. The light output for a 1.5-mil thick lamp was then interpolated from these data.

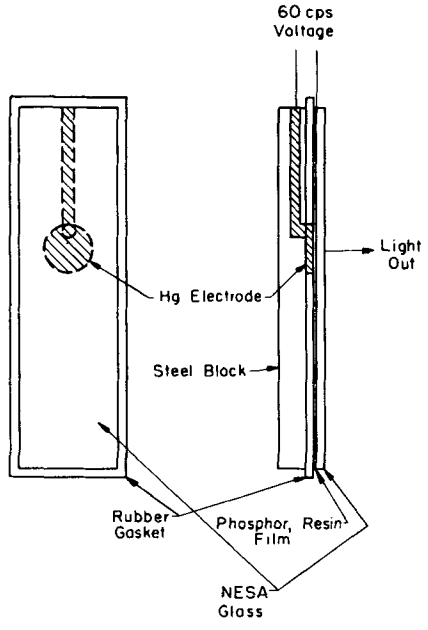

Fig. 1. Mercury electrode for EL cell measurements

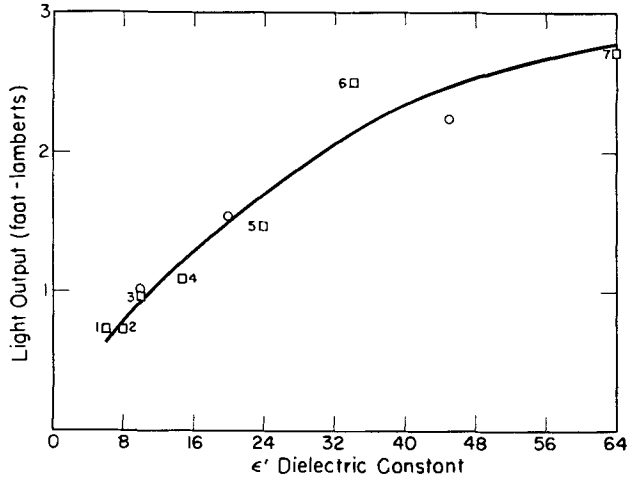

Fig. 2. Light output as a function of dielectric constant. ○, Theory (fitted for $\epsilon' = 5.9$; see text); □, experiment, 120v, 60 cps, 1.5 mil film; phosphor 60% by weight.

Results and Discussion

The relationship between light intensity and dielectric constant is shown in Fig. 2. The numbers refer to the embedding materials listed in Table I. Table I also gives the dielectric constant, and tan δ for these embedding materials. The points marked experimental are measured values. The points marked theoretical were computed. The field on the phosphor for an applied voltage of 120v was computed for the various dielectric constants of the embedding dielectric using the equation of Roberts (1)

$$\frac{E_2}{E_m} = \frac{3\epsilon_1}{2\epsilon_1 + \epsilon'_2 - V_2(\epsilon'_2 - \epsilon'_1)} \qquad [2]$$

where E_2 is the field on the phosphor particle, E_m the applied field (voltage divided by cell thickness), ϵ'_1 the dielectric constant of the dielectric, ϵ'_2 the dielectric constant of the phosphor (~ 10), and V_2 the volume fraction of the phosphor.

In order to convert the calculated values for the field on the phosphor particles embedded in the various media to brightness values, a lamp which was prepared with acetate rayon of dielectric constant 5.9 had its brightness determined as a function of 60-cycle voltage. The brightness values obtained when the voltage was sufficient to create the field calculated are plotted against the dielectric constant and are labeled "theory" in Fig. 2. These can then be compared with the actual light intensity for the lamps made with the specified dielectric constant and measured at 120v.

From the agreement between the calculated points and the experimental ones, one can draw several conclusions. Equation [2] seems to apply to nonspherical particles embedded in dielectric media. The data also are in agreement with the plot of Roberts which shows that the light intensity increases fourfold with an increase in dielectric constant of the suspending medium over the range of 4-65, for operation at a constant applied field of

Table I. Dielectric constants and tan δ for embedding materials

Point in Fig. 2	Dielectric	at 60 cps, 25°C	tan δ
1	Acetate rayon	5.9	~0.02
2	66.2% Acetate rayon + 33.8% CEC	7.9*	~0.02
3	35.3% Acetate rayon + 64.7% CEC	11*	~0.02
4	Cyanoethyl cellulose (CEC)	15	~0.02
5	α Naphthyl sulfone	24	~0.05
6	50.2% CEC** 49.8% Succinonitrile	34	~0.05
7	Succinonitrile	65	~0.1

* Calculated from Eq.[1] using the values for the pure components listed under 1, 4, and 7. Assuming the densities to be equal, weight fractions were substituted for the volume fractions of the components.

** This lamp unexplainedly darkened with time. The light intensity was measured before the darkening was apparent.

100 v/mil. Hence, it also can be concluded that the light output is not a strong function of dielectric constant for dielectric constants higher than 30 (in agreement with Katona's observation that light intensity is relatively independent of dielectric constants for values greater than 50).

Roberts has also shown that for very low fields the dielectric constant of the embedding material exerts a large effect on the light output of a lamp, because at low fields the light output is an exponential function of the field to the first power. At higher fields, the dependence of light output is an exponential function of the field to a power less than one. The field on the phosphor increases with increasing dielectric constant of the embedding dielectric, but in a diminishing manner for higher dielectric constants. Hence, for both these reasons, (the diminishing effect of dielectric constant on field, and of field on brightness), the incremental light output decreases rapidly with incremental dielectric constant. Therefore, an increase in dielectric constant of the embedding medium above 30 does not contribute to a sufficiently increased light output to justify development of new materials with higher dielectric constants.

Manuscript received Dec. 11, 1962; revised manuscript received Feb. 18, 1963.

Any discussion of this paper will appear in a Discussion Section to be published in the December 1963 JOURNAL.

REFERENCES

1. S. Roberts, *J. Opt. Soc. Amer.*, **42**, 850 (1952).
2. G. P. Katona, *This Journal*, **109**, 695 (1962).
3. Lichtenecker Logarithmic Mixing Formula, ASTM Standards on Electrical Insulating Materials, p. 178, ASTM, Philadelphia (1959).

The Growth of Crystals from Compounds with Volatile Components

G. R. Cronin, Morton E. Jones, and O. Wilson

Texas Instruments Incorporated, Dallas, Texas

Many compounds being studied for possible semiconductor device or thermoelectric application contain elements which have a significant vapor pressure at the melting point of the compound. Hence, crystal pulling equipment developed for nonvolatile silicon and germanium is not satisfactory for these compounds, and new apparatus must be developed.

The basic requirement for such a crystal puller is a chamber which can maintain an equilibrium pressure of the volatile component over the compound melt. This means that any part of the chamber in contact with the vapor must be heated to, or above, the condensation temperature of the vapor. Generally, the melt need not be stoichiometric to achieve good crystal growth, but it is desirable.

Several designs for such crystal pullers have been described. The Gremmelmaier method (1) involves magnetic coupling to impart spin and pull motion to the seed inside a sealed chamber. A syringe type puller described by Moody and Kolm (2) employs a close-fitting quartz piston to obtain motion of the seed while maintaining a closed chamber. Richards (3) describes a puller for gallium arsenide with a liquid gallium seal to close the chamber. Each of these methods emphasizes a pulling chamber which is as gas tight as possible to prevent loss of the volatile component whose pressure is then controlled by the temperature at the coldest part of the chamber.

Apparatus

The crystal puller described in this paper is based on the principle that a gas-tight system is not necessary when the volatile component has an equilibrium pressure of less than 1 atm at the melting point of the compound. The entire pulling chamber is kept above the condensation temperature of the vapor, and the proper atmosphere is maintained by balancing the chamber pressure against the external ambient and diluting the component vapor with an inert gas such as argon. Under these conditions the loss of vapor through leaks in the chamber occurs by diffusion and is sufficiently slow to allow the growth of large single crystals. Consequently the need for elaborate or precision ground quartz as well as an external magnetic pulling system has been eliminated.

A schematic of the apparatus is shown in Fig. 1. The central feature of this equipment is a quartz chamber, 25 cm high, 7.5 cm ID with 2 mm wall. The chamber is open at the top and fitted at the bottom

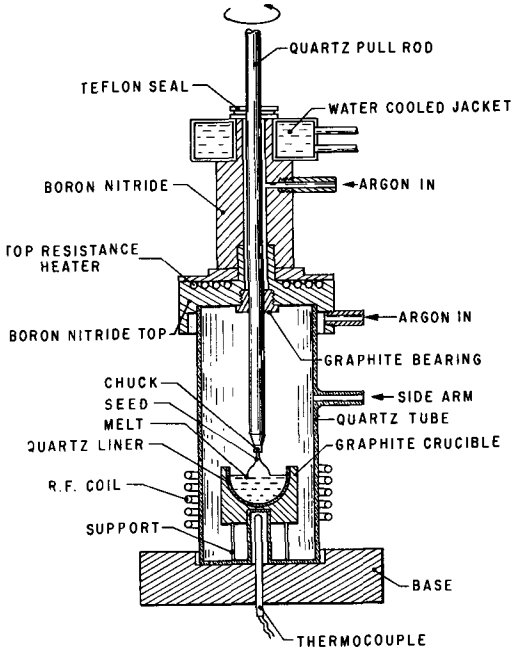

Fig. 1. Crystal growing apparatus for compounds with volatile components.

with a receptacle for a thermocouple. The lid for this chamber is made of boron nitride and contains a resistance heater so that its temperature can be maintained above the condensation temperature of the volatile component. An effective seal is maintained between the quartz pull rod and the boron nitride lid by means of a threaded graphite bearing at the bottom and a water-cooled Teflon bearing at the top. These two bearings also maintain the alignment of the pull rod. A spring-loaded pressure seal is made between the top of the quartz chamber, which has been lapped flat, and the bottom of the boron nitride lid. During crystal growth a small amount of the volatile component diffuses through the hot graphite bearing and condenses inside the boron nitride lid in a small enclosure provided for this purpose. The rate of this loss is the critical factor governing the amount of melt which can be grown into a single crystal. A slight positive pressure of argon is maintained in the space above the graphite bearing in the boron nitride lid throughout crystal growth and particularly during the cooling cycle to prevent intrusion of air. The pressure seal between the top of the quartz chamber and the bottom of the boron nitride lid is similarly protected by an envelope of dry argon. The effectiveness of this seal is demonstrated by the fact that the crystals maintain a clean, shiny, apparently unoxidized surface. A graphite crucible, centered in an induction coil, is fitted with a quartz liner and rests on a quartz pedestal inside the chamber. The seed is held in place at the lower end of the pull rod by a quartz pin which fits into a small notch sandblasted on one edge of a square sectioned seed. A thermocouple well in the bottom of the susceptor allows close temperature control of the melt.

A photograph of the equipment ready for operation is shown in Fig. 2. Quartz fiber batting is used to insulate the chamber wall. Heat radiated from the boron nitride lid and the glowing susceptor is sufficient to keep the chamber free from condensate when growing gallium arsenide, for example. An

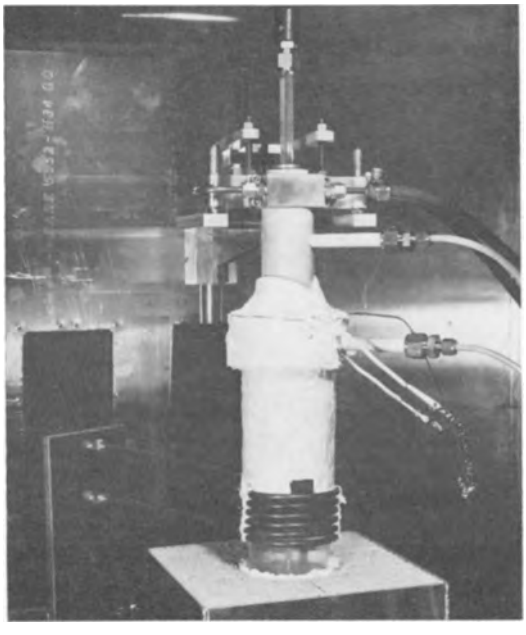

Fig. 2. Crystal puller ready for operation

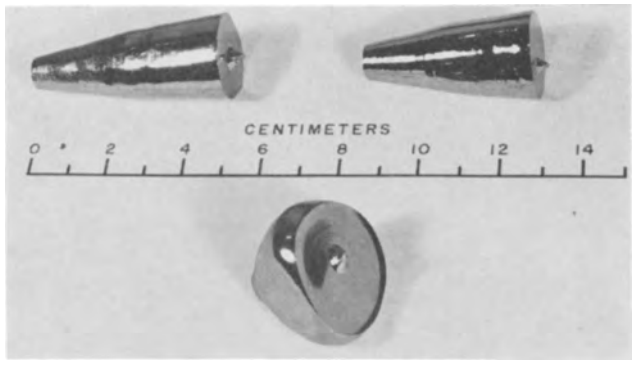

Fig. 3. Indium arsenide crystals

area of a few square centimeters on the chamber wall just above the level of the melt surface is left free of insulation for viewing purposes, and heat radiated from the susceptor will maintain this area sufficiently free from condensate.

Indium Arsenide

Indium arsenide can be compounded and pulled into a single crystal in one operation. Freshly etched indium is placed in the crucible. An amount of arsenic which is about 7-10% in excess of the stoichiometric amount is placed in the bottom of the chamber surrounding the crucible. The excess arsenic allows for the necessary atmosphere within the chamber as well as small losses which occur by diffusion through the graphite bearing. Typically 2 to 4 grams of arsenic are removed from the inner wall of the boron nitride lid after each run. The chamber is flushed with dry argon, and the boron nitride lid is placed in position with the spring load applied. The flushing side arm is removed with a hydrogen-oxygen torch and the crucible temperature raised slowly over about an hour to the maximum melting point. Heat radiated from the crucible vaporizes the arsenic which subsequently dissolves in the indium to form indium arsenide. The slow compounding is necessary to avoid rapid vaporization and excessive loss of arsenic. When all the arsenic has vaporized from the bottom of the chamber and the melt temperature has stabilized, the seed is dipped and the crystal pulled. Typical spin and pull conditions are 20 rpm at 3-4 cm/hr. The yield of single crystal indium arsenide is about 80% or greater based on a total charge weight of 100g (Fig. 3).

Electrical properties of a typical crystal compounded from six nines grade starting material are shown in Table I.

Gallium Arsenide

Usually gallium arsenide is grown by placing a precompounded charge in the crucible and additional arsenic for supplying the ambient in the bot-

Table I. Electrical data on indium arsenide and gallium arsenide crystals

	°K	ρ (ohm-cm)	μ ($cm^2\ v^{-1}\ sec^{-1}$)	n (cm^{-3})
InAs	300	1.33×10^{-2}	2.74×10^{4}	1.72×10^{16}
	77	6.81×10^{-3}	6.12×10^{4}	1.50×10^{16}
GaAs	300	2.40×10^{-2}	4.83×10^{3}	5.37×10^{16}
	77	2.81×10^{-2}	5.09×10^{3}	4.36×10^{16}

Fig. 4. Gallium arsenide crystals

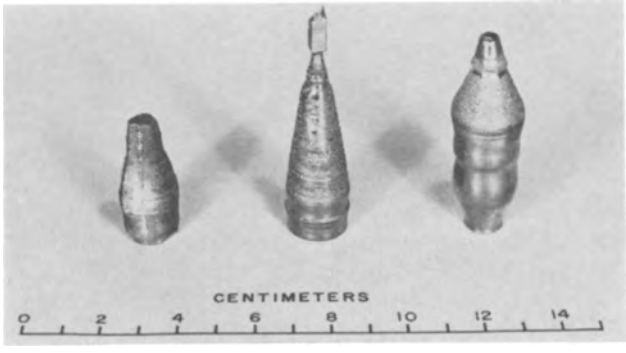

Fig. 5. Lead telluride crystals

tom of the chamber. After flushing with argon and sealing off the side arm, the crucible is heated to melt the charge. During this heating the excess arsenic vaporizes, flushing argon from the chamber and forming the desired ambient. After melting, the seed is lowered and the crystal grown under conditions similar to those described for indium arsenide. Crystals have been successfully grown along all major growth directions, although the [111] is generally used. Gallium arsenide can also be compounded and grown in one operation like indium arsenide.

Figure 4 is a photograph of typical gallium arsenide crystals grown in the apparatus, and Table I gives the electrical properties. The charge was precompounded from six nines grade gallium and arsenic. 58 mg of tin was added to the charge (122g) in the crystal puller. The dislocation density, measured by selective etching, was about 6000/cm^2.

Lead Telluride

Single crystals of lead telluride have been grown from the elements. Again, all major orientations have been successfully employed. Stoichiometric amounts of five nines grade lead and tellurium are placed in the crucible and the temperature slowly raised to the melting point of lead telluride where a single crystal is grown as previously described. It is possible to pull up to 90% of the original charge, growing crystals of about 75g (Fig. 5). Typical dislocation densities range from 6 x 10^4/cm^2 to 2 x 10^6/cm^2.

Stoichiometric melts invariably give p-type crystals, whereas if the melt is about 51 at. % lead, n-type portions of the crystals have been observed. Typical electrical data are shown in Table II.

Table II. Electrical data on lead telluride crystals

	Stoichiometric melt	Melt 51 at. % Pb
ρ(ohm-cm)	2.36×10^{-3}	3.04×10^{-3}
μ(cm^2 v^{-1} sec^{-1})	794	1440
n(cm^{-3})		1.42×10^{18}
p(cm^{-3})	3.92×10^{18}	

Conclusions

This pulling apparatus offers several advantages over other systems designed for volatile materials. The quartz work required for preparing chambers is simple and requires no precision grinding or fitting in contrast with piston-type pullers. The preparation and dismantling of the apparatus is rapid and uncomplicated and involves no liquid seals. The rotation of the seed is smooth and undisturbed, a characteristic not always achieved with magnetically coupled pullers. The apparatus is relatively inexpensive to operate since the quartz chamber, boron nitride lid, and pull rod, etc., can be used repeatedly for a number of runs.

On the other hand, the severest limitation of this equipment is its inability to cope with internal pressures above 1 atm. Also, because of the graphite bearing around the pull rod, the chamber cannot be completely evacuated. To circumvent this limitation, air is removed from the chamber at the beginning of each run by flushing with an inert gas such as argon.

The purity of the InAs described in Table I, even though prepared from as received starting materials, compares favorably with that reported elsewhere. Allred (4) reports pulled InAs with a mobility at 77°K of 70,000 cm^2/volt-sec while Effer (5) reports one sample of boat grown materials with a mobility of 75,700 cm^2/volt-sec at 77°K.

The mobility of undoped crystals of GaAs has in general not been as high as that reported elsewhere (4, 6). This is principally due to contamination from the quartz crucibles. Silicon free crucible materials such as aluminum nitride are currently under investigation.

Manuscript received Nov. 15, 1962; revised manuscript received Feb. 8, 1963.

Any discussion of this paper will appear in a Discussion Section to be published in the December 1963 JOURNAL.

REFERENCES

1. R. Gremmelmaier, *Z. Naturforsch*, **11a**, 511 (1958).
2. P. L. Moody and C. Kolm, *Rev. Sci. Instr.*, **29**, 1144 (1958).
3. J. L. Richards, *J. Sci. Instr.*, **34**, 289 (1957).
4. W. P. Allred, "Ultrapurification of Semiconductor Materials," M. S. Brooks and J. K. Kennedy, Editors, p. 562, The Macmillan Company, New York (1962).
5. D. Effer, *This Journal*, **108**, 357 (1961).
6. S. E. Bloom, *J. Appl. Phys.*, **33**, 2391 (1962).

The Chemical Polishing of Gallium Arsenide in Bromine-Methanol

M. V. Sullivan and G. A. Kolb

Bell Telepohne Laboratories, Incorporated, Murray Hill, New Jersey

The {111} (gallium rich) faces[1] of gallium arsenide have always been the most difficult to polish chemically. It is now possible to produce a high polish on these as well as on the other common faces of gallium arsenide by incorporating intensive stirring with a new etching composition.

The use of intensive stirring to improve the smoothness and flatness of electrochemically or chemically treated surfaces is not new. Sullivan *et al.* have described the electrochemical polishing of germanium and silicon, using intensive stirring (1-3). Young and Wilson have described a polishing apparatus and composition for the chemical polishing of single crystal copper (4).

One of the best chemical polishes available for gallium arsenide was reported by Cunnel, Edmond, and Harding (5). This polish is quite good for all of the common faces except the {111} on which it leaves a rough finish. Sullivan and Pompliano have used this polishing composition along with a new and simple method for intensive stirring which improved the smoothness and flatness (6). Stirring was obtained by placing slices of gallium arsenide between Teflon disks in the bottom of a rotating inclined beaker. The two Teflon disks had different diameters. This resulted in a different rotational velocity for each disk as it was driven by the rotation of the beaker. In this way, a better stirring action was produced than if the disks were of the same diameter. This method of obtaining intensive stirring requires very little equipment and, therefore, has application in research and development laboratories. It does not, however, produce surfaces as highly polished as the equipment described in the present paper.

[1] This notation is meant to include the (111), $(\bar{1}1\bar{1})$, $(1\bar{1}\bar{1})$ and $(\bar{1}\bar{1}\bar{1})$ faces. The opposite four faces are referred to as the $\{\bar{1}\bar{1}\bar{1}\}$.

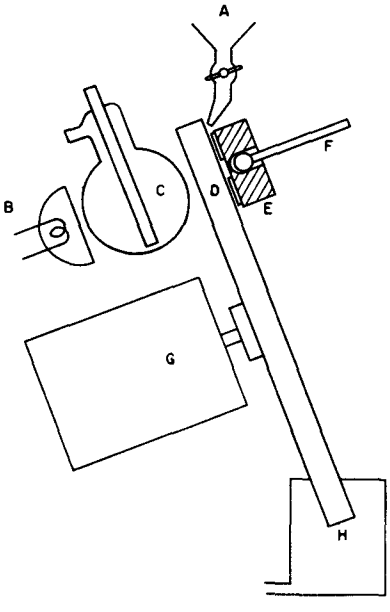

Fig. 1. Schematic arrangement of polishing equipment: A, dropping funnel containing etchant; B, light; C, heat absorber; D, cloth covered rotating disk; E, polishing block holding three or more specimens; F, support rod for polishing block; G, motor drive; H, drip pan.

The use of chlorine or bromine in methanol as a chemical polish for gallium arsenide was suggested by Fuller and Allison (7). The heat of reaction between chlorine and methanol was sufficient to ignite the methanol under certain circumstances; therefore, bromine was chosen for this investigation. Concentrations up to a few per cent of the bromine were very effective as a chemical polish without intensive stirring. With the addition of intensive stirring the etching rate for a given concentration of bromine was increased by more than an order of magnitude. The combination of this new etchant and intensive stirring has given the smoothest and flattest chemically polished gallium arsenide surface of any known technique.

Experimental

The equipment is shown schematically in Fig. 1. The polishing wheel was a plate-glass disk about 20 cm in diameter, 0.6 cm thick and covered with a sheet of Pellon[2] cloth. This cloth comes with an adhesive backing. After the cloth was attached to the wheel, the entire wheel was soaked overnight in a solution of 0.05 vol. % bromine in methanol. It was found that this treatment was necessary to maintain good control of the etching rate. If this treatment had not been given, the limited amount of bromine used in the polishing process would have been shared by the gallium arsenide and the polishing wheel in an uncontrolled manner. The wheel was then rotated at about 72 rpm and fed with the etchant at a rate of 15-20 cc/min.

The gallium arsenide material was mounted on the polishing block and hand-lapped for about a minute to bring all slices on the block into a common plane. The polishing block was then placed as indicated in Fig. 1 and chemically polished in the bromine-methanol system (reagent grade chemicals used throughout). The planetary rotation of the block which holds the gallium arsenide samples was similar to that obtained in conventional mechanical polishing machines. The addition of a bright lamp[3]

[2] PAN-W Pellon cloth may be obtained from The Geoscience Instruments Corporation, New York City.

[3] A Sylvania Sun Gun was operated at about three-fourths of its operating voltage and with forced-air cooling to increase bulb life.

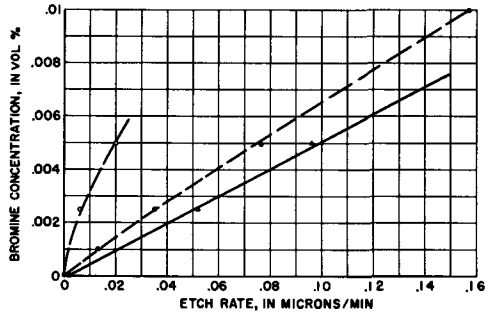

Fig. 2. Etch rate for gallium arsenide as a function of the concentration of bromine in methanol. The solid line is for the $\{\bar{1}\bar{1}\bar{1}\}$ faces and the two dashed lines are for the {111} faces. The upper dashed line is for a pressure of 83 g/cm^2 and the lower two lines are for 250 g/cm^2.

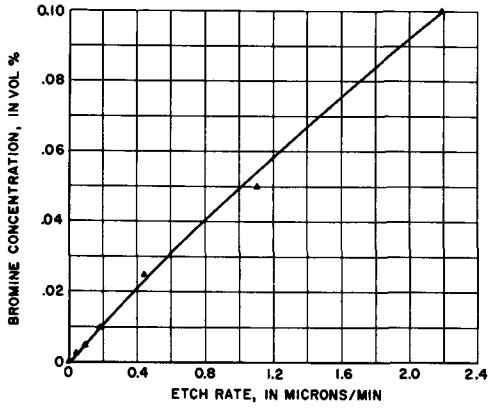

Fig. 3. Etch rate for the $\{\bar{1}\bar{1}\bar{1}\}$ faces of gallium arsenide as a function of bromine concentration. A constant pressure of 250 g/cm^2 was used with intensive stirring of the samples.

to illuminate the surface when the {111} faces were being polished was desirable but not absolutely necessary. It seemed to prevent the occasional formation of etch pits.

Results

Figure 2 is a graph showing the etch rate as a function of bromine concentration. The upper two (dashed) lines are for the {111} faces at two different pressures. The lower line is for the $\{\bar{1}\bar{1}\bar{1}\}$ faces. The $\{\bar{1}\bar{1}\bar{1}\}$ faces etch about 30% faster than the {111} faces at the 85 g/cm^2 pressure. The identification of these faces was made using the technique described by White and Roth (8).

The two upper lines of Fig. 2 are both for the same crystal face but polished under different pressures. The etching rate appears to be directly proportional to pressure in this range. Since polishing is usually a slow process, this acceleration due to pressure was desirable. The smoothness of the polished surface was also improved by the increased pressure. Pressures as high as 2000 g/cm^2 have been used, but difficulties were encountered with tearing of the polishing cloth at this level. In order to obtain several day's wear on each polishing cloth, a pressure of about 250 g/cm^2 is recommended for routine use.

Figure 3 gives the etching rate for the $\{\bar{1}\bar{1}\bar{1}\}$ faces of gallium arsenide as a function of bromine concentration up to 0.1% bromine. The recommended polishing composition for these faces as well as the {100} and the {110} faces is 0.05% bromine in methanol. A very good polish was obtained on all of these faces in 15-30 min starting from a surface which had been lapped with 1950 alumina (5μ particle size) or any finer abrasive. At bromine concentrations above 0.05%, the polishing action is significantly poorer.

The most difficult faces of gallium arsenide to polish are the {111}. However, a very high polish was also obtained on these faces if the bromine concentration was reduced to 0.0025%. The polishing rate is very low at this concentration and, therefore, a very short mechanical polish with Linde A (0.3μ particle size) is desirable before the chemical polish. In this manner, a polish equal to that found on the other faces can be achieved in 15-30 min.

Figures 4a and 4b are interference photographs of (111) and $(\bar{1}\bar{1}\bar{1})$ faces, respectively, of a slice of gallium arsenide. Both faces were lapped with 1950 alumina and then etched in a beaker with normal stirring at 80°C in the following composition (5): H_2SO_4 (98%), 60 vol. %; H_2O_2 (30%) 20 vol. %; H_2O 20 vol. %. Figures 4c and 4d are photographs of the same two faces after relapping and etching in the intensively stirred bromine methanol system (see Fig. 1) as described earlier in this section. As a further check on the comparison, the highly polished surfaces shown in 4c and 4d were then re-etched (without relapping) in the sulfuric acid-hydrogen peroxide system, and the resulting interference patterns were found to be indistinguishable from 4a and 4b. The average roughness of surfaces such as 4a and 4b were 2000 and 200Å, respectively. The average roughness of the intensively stirred surfaces was less than 25Å as measured on a Brush Surface Analyzer.

The edges of all of the polished surfaces show a significant rounding. The bromine methanol polished surfaces are flatter, however, than the conventionally polished surfaces. In Fig. 4c and 4d the center 70% of the area is flat to $\pm 1\mu$ (4 interference

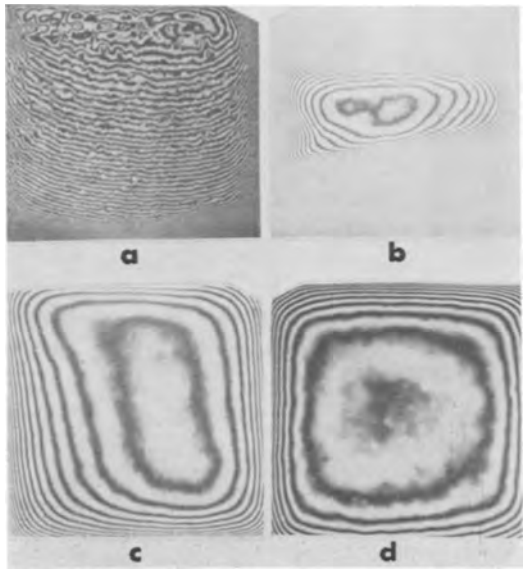

Fig. 4. A quarter inch square of gallium arsenide polished at 80°C in the Cunnel, Edmond and Harding etch (4a and 4b), and at room temperature in the bromine methanol etch (4c and 4d). The left-hand views (a and c) are the (111) face and the right-hand views (b and d) are the $(\bar{1}\bar{1}\bar{1})$ face.

fringes). A number of resistivities in the range of 10^{-3} to 10^{7} ohm-cm and both n- and p-type conductivities have been successfully polished.

Manuscript received Jan. 11, 1963. This paper was prepared for delivery before the Boston Meeting, Sept. 16-20, 1962.

Any discussion of this paper will appear in a Discussion Section to be published in the December 1963 JOURNAL.

REFERENCES

1. M. V. Sullivan and R. M. Finne, *This Journal*, **107**, 191C (1960) (Abstract of talk given at Houston meeting).
2. D. L. Klein, G. A. Kolb, L. A. Pompliano, and M. V. Sullivan, *ibid.*, **108**, 60C (1961) (Abstract of talk given at Indianapolis meeting).
3. M. V. Sullivan, D. L. Klein, R. M. Finne, L. A. Pompliano, and G. A. Kolb, *This Journal*, **110**, 412 (1963).
4. F. W. Young, Jr. and T. R. Wilson, *Rev. Sci. Instr.*, **32**, 559 (1961).
5. F. A. Cunnel, J. T. Edmond, and W. R. Harding, *Solid State Electronics*, **1**, 97 (1960).
6. M. V. Sullivan and L. A. Pompliano, *This Journal*, **108**, 60C (1961) (Abstract of talk given at Indianapolis meeting).
7. C. S. Fuller and H. W. Allison, *ibid.*, **109**, 880 (1962).
8. J. D. White and W. C. Roth, *J. Appl. Phys.*, **30**, 946 (1959).

Low-Temperature Thermal Expansion of the Group 4a Carbides

N. H. Krikorian, T. C. Wallace, and James L. Anderson[1]

Los Alamos Scientific Laboratory of the University of California, Los Alamos, New Mexico

References to an exhaustive survey on the thermal expansion measurements of refractory materials have been given by Wachtman, Scuderi, and Cleek (1). Linear coefficients of thermal expansion have been determined for carbides from room temperatures to high temperatures (2-5), but there are no reported lattice parameter measurements at liquid nitrogen temperatures. This note deals with determinations of linear coefficients of thermal expansion for TiC, ZrC, and HfC based on measurements at 26°C and −190° ± 1°C.

X-ray diffraction data were obtained using a 114.6 mm diameter Debye-Scherrer powder camera for the room temperature measurements and a diffractometer attachment designed by Pretzel and Petty (6) for the measurements at −190°C. Lattice parameters were computed with an IBM-704 program using the modified least squares extrapolation of Hess (7).

The TiC powder consisted of fragments of a Linde TiC single crystal. $ZrC_{0.97}$ was obtained from Union Carbide Metals Company. All the HfC samples and $ZrC_{0.95}$ and $ZrC_{0.80}$ were prepared by reacting the metal and spectroscopic grade graphite for 1 to 2 hr at about 2200°C in a vacuum of 10^{-5} to 10^{-6} Torr. Reactor grade zirconium metal and hafnium containing <200 ppm Zr were used as starting materials.

Since the group 4a transition metal carbides have a rather wide range of homogeneity, it is important to characterize the composition of the samples. The compositions listed in Table I were determined by chemical analyses for major metal, total carbon, and free carbon. The metal and total carbon were determined by combustion. Spectrographic analyses were also made on representative samples to determine trace metal impurities. In all cases metal impurities were present in concentrations lower than 300 ppm.

Table I also lists the calculated lattice constants, together with the standard deviation, the change in lattice constant, and the average linear coefficient of thermal expansion for the measured temperature range. In this temperature range, there appears to be an increase in α in the series TiC, ZrC, and HfC.

On comparing the lattice parameters of HfC and ZrC as a function of carbon content, it appears that $ZrC_{0.95}$ has a lattice constant higher than that of $ZrC_{0.97}$, while $HfC_{0.89}$ has a parameter similar to that of $HfC_{0.95}$. However, this result may be due to the presence of oxygen, since data obtained in this laboratory (8, 9) indicate that the lattice parameter is lowered appreciably by the presence of small amounts of oxygen in the carbide lattice. Unfortunately, at present, no reliable method for the determination of low concentrations of combined oxygen in these compounds has been developed. It is believed that the oxygen content of these samples was not great since precautions were taken to exclude oxygen during preparation. The presence of nitrogen would have a similar effect on the lattice constant, but to a much lesser degree (8, 9).

Manuscript received Nov. 26, 1962; revised manuscript received Feb. 14, 1963. Work on this paper was done under the auspices of the United States Atomic Energy Commission.

Any discussion of this paper will appear in a Discussion Section to be published in the December 1963 JOURNAL.

REFERENCES

1. J. B. Wachtman, Jr., T. G. Scuderi, and G. W. Cleek, *J. Am. Ceram. Soc.*, **45**, 319 (1962).
2. J. J. Gangler, *ibid.*, **33**, 367 (1950).

[1] Guest Scientist, Los Alamos Laboratory Summer Student Program.

Table I. Compositions of the samples

MC_x	a_o in Å, 26°C	a_o in Å, −190°C	Δa_o in Å	$\alpha \times 10^{-6}$, $C^{\circ-1}$
$TiC_{0.95}$	4.3292 ± 0.0002	4.3260 ± 0.0002	0.0032	3.4 ± 0.4
$ZrC_{0.97}$	4.6986 ± 0.0004	4.6951 ± 0.0001	0.0035	3.5 ± 0.4
$ZrC_{0.95}$	4.7025 ± 0.0006	4.6987 ± 0.0002	0.0038	3.7 ± 0.6
$ZrC_{0.80}$	4.6980 ± 0.0004	4.6961 ± 0.0004	0.0019	1.9 ± 0.8
$HfC_{0.97}$	4.6395 ± 0.0006	4.6354 ± 0.0003	0.0041	4.1 ± 0.7
$HfC_{0.95}$	4.6381 ± 0.0004	4.6338 ± 0.0001	0.0043	4.3 ± 0.4
$HfC_{0.89}$	4.6382 ± 0.0003	4.6347 ± 0.0002	0.0035	3.5 ± 0.4

3. K. Becker and H. Ewest, *Z. tech. Physik*, **11**, 216 (1930).
4. R. D. Elliott and C. P. Kempter, *J. Phys. Chem.*, **62**, 630 (1958).
5. S. J. Grisaffe, *J. Am. Ceram. Soc.*, **43**, 494 (1960).
6. F. E. Pretzel and R. L. Petty, *Phys. Rev.*, **127**, 777 (1962).
7. J. B. Hess, *Acta Cryst.*, **4**, 209 (1951).
8. J. D. Farr, Unpublished data on ZrC.
9. N. H. Krikorian, Unpublished data on HfC.

Brief Communications

Growth Rates of Epitaxial Gallium Arsenide

N. Goldsmith

Semiconductor and Materials Division, Radio Corporation of America, Somerville, New Jersey

An increasing number of reports have appeared dealing with the epitaxial growth of gallium arsenide from the vapor phase. These reports have presented conflicting evidence as to the relative growth rates of the (111) and ($\bar{1}\bar{1}\bar{1}$) planes (A and B surfaces) (1-5).

The over-all reaction for the iodine system (6) has been described as follows

$$3GaI + \tfrac{1}{2}\ As_4 \rightleftharpoons 2GaAs + GaI_3$$

The reaction for the corresponding chloride system is complicated by the stability of Ga_2Cl_4 at the temperatures normally used (7). The major variable in the methods reported thus far has been the manner in which the lower halide is produced within the system.

If these methods are arranged in order of increasing initial HX concentration as shown in Table I, and the reported ratios for A-to-B growth rates are compared, there is a clear trend toward decreasing ratios with increasing HX concentration. A possible explanation for the observed differences may be derived from consideration that a fundamental step in the growth process involves the following reaction

$$3GaX \rightleftharpoons 2Ga + GaX_3$$

This type of reaction has been shown to be base-catalyzed (8). Thus, the B surface having a pair of free electrons (9) is a basic surface, and higher growth rates are expected. If, however, the first step in the growth process is considered to be the formation of a layer of arsenic atoms on the A face, the resulting surface is much more basic than the B face because the arsenic is only singly bonded to the surface. In the presence of HCl, which is presumably a stronger acid than GaCl, the effect of this strongly basic surface is reduced as a result of interaction with the acid. At sufficiently high HCl concentrations, the difference between the two surfaces can be expected to disappear or to change in favor of the B face. This effect is particularly noticeable in an open tube system, where an appreciable HCl concentration will exist in the vapor over the growing layer.

This effect has been observed qualitatively. Because the growth-rate ratio can be expected to vary with both source and deposition temperature, as well as with variables of the system, the various results are not subject to quantitative comparison. However, it is felt that conflicting reports of growth rates on the A and B surfaces of vapor-grown gallium arsenide can be reconciled in this manner.

Manuscript received Jan. 29, 1963. The work described was performed in part under the sponsorship of the Electronic Technology Laboratory, Aeronautical Systems Division, Air Force Systems Command, United States Air Force.

Any discussion of this paper will appear in a Discussion Section to be published in the December 1963 JOURNAL.

REFERENCES

1. V. J. Lyons and V. J. Silvestri, *This Journal*, **108**, 177C (1961).
2. F. V. Williams and R. A. Ruerwein, *ibid.*, **108**, 177C (1961).
3. R. L. Newman and N. Goldsmith, *ibid.*, **108**, 1127 (1961).
4. F. W. Tausch and T. A. Longo, Paper No. 77 presented at Los Angeles Meeting of the Society, May 1962.
5. R. Moest and B. Shupp, *This Journal*, **109**, 1065 (1962).

Table I. Variation of GaAs epitaxial growth rates with growth procedure

Method	Initial HX pressure, Torr	Growth rate A/B	Reference
GaAs + I_2 (closed tube)	0	nonepitaxial on B face	(1)
GaAs + $GaCl_3$ + H_2 (open tube)	0	10:1	(3)
Ga + $GaCl_3$ + H_2 + As (open tube)	0	10:1	(10)
GaAs + HCl + H_2 (open tube)	1	2:1	(3)
GaAs + HCl + H_2 (open tube)	10	1.7:1	(2)
GaAs + HCl (closed tube)	50-200	1:1	(5)
$GaCl_3$ + $AsCl_3$ + H_2 (open tube)	~100	0.6:1	(4)

6. V. J. Silvestri and V. J. Lyons, *ibid.*, **109**, 963 (1962).
7. A. Glassner, The Thermochemical Properties of the Oxides, Fluorides and Chlorides to 2500°K, ANL-5750, Argonne National Laboratories.
8. D. Richman, Private communication.
9. H. C. Gatos and M. C. Lavine, *This Journal*, **107**, 427 (1960).
10. Unpublished work.

Condenser Pressure as an Explanation of Field Dependent Tafel Slopes of High Field Ionic Conduction of Anodic Tantalum Pentoxide Films

L. Young

British Columbia Research Council, University of British Columbia, Vancouver, British Columbia

According to the theory proposed by Bean, Fisher, and Vermilyea (1) the ionic conduction process in anodic oxide films on tantalum involves two processes in which ionic movement is assisted by the applied field. These processes are the production of Frenkel defects and the transport of the interstitial tantalum ions thus produced. Each of these processes has been supposed to depend on the field in the oxide according to expressions of the "high field" form

$$i = 2an\nu \exp\{-(W - qaE)/kT\} \qquad [1]$$

where i is rate, n concentration of ions, ν vibration frequency, W activation energy, q charge on ion, a activation distance, E field, k Boltzmann's constant, and T absolute temperature.

It is possible with tantalum to obtain sufficiently accurate results to be able to detect that the temperature and field dependence of $\partial E/\partial \log i$ for both these processes is anomalous, as was first shown in the case of the steady-state kinetics by Vermilyea. The accuracy of present techniques is not, however, so great that agreement exists about the precise form of the anomalies. Thus, although Vermilyea (2) in his second study of the steady-state kinetics reported that the activation distance for the production of Frenkel defects doubled over a certain range of field and that the pre-exponential factor varied in a rather complex fashion, the present author (3, 4) found that his experimental results for both steady-state and transient kinetics could be described adequately by adding a quadratic term in E to the expression of the form given by Eq. [1], *i.e.*,

$$i = i_0 \exp\{-(W - \alpha E + \beta E^2)/kT\} \qquad [2]$$

This modification could not be explained at the time. It was, in particular, not explained by the idea that a range or distribution of parameters is associated with an amorphous material.

The purpose of the present note is to point out a rather obvious physical explanation of the quadratic term in E. Thus, the pressure in the oxide due to the applied field is $P = E^2\epsilon/8\pi$ (E in e.s.u., pressure in dynes cm^{-2}). Using the zero field value of the dielectric constant $\epsilon = 27.6$, we obtain for the experimental range of field strength

E (10^6v cm^{-1})	4	5	6	7
P (atm)	190	300	430	590

Now the experimental data on the pre-exponential factor for the mobility of interstitial ions indicate a large positive entropy of activation, if the concentration of mobile ions is not to be excessively large. This is a common finding in low field ionic conduction, and the usual physical explanation (5) is that the activation energy for ionic movement decreases as the lattice expands with increasing temperature. One would expect, therefore, if the usual explanation holds for the present case, that, as with low field ionic conduction, the activation energy should increase with increase in pressure. A rule of thumb given by Jost is that, with materials such as AgCl, 100 atm are about equivalent to 1°C. If we assume a similar order of effect here, then the condenser pressures listed above would appear to be of the magnitude required to explain the amount of curvature observed in plots of log i *vs.* E. It should be noted that other anomalies exist in the behavior of these films (1). The effect deduced here must exist even if the identification with the experimental observation is incorrect. It may also occur at electrodes without oxide films at which the rate of an electrode process is controlled by the transfer of ions through the double layer.

Acknowledgment

This work was supported by the Defence Research Board of Canada and is published with their permission.

Manuscript received Feb. 14, 1963.

Any discussion of this paper will appear in a Discussion Section to be published in the December 1963 JOURNAL.

REFERENCES

1. L. Young, "Anodic Oxide Films," Academic Press, London and New York (1961).
2. D. A. Vermilyea, *This Journal*, **102**, 655 (1955).
3. L. Young, *Proc. Roy. Soc.*, **A258**, 496 (1960).
4. L. Young, *ibid.*, **A263**, 395 (1961).
5. W. Jost, "Diffusion in Solids, Liquids, Gases," pp. 149-153, Academic Press, London and New York (1952).

Discussion Section

This Discussion Section includes discussion of papers appearing in the JOURNAL of The Electrochemical Society, Vol. 109, No. 11 (November 1962). Discussion not available for this issue will appear in the Discussion Section of the December 1963 JOURNAL.

A Solid Electrolyte Fuel Cell

J. Weissbart and R. Ruka (pp. 723-726, Vol. 109, No. 8)

R. Littlewood[1]: The authors quote three factors which can result in a current-producing galvanic cell giving a lower voltage than the open-circuit voltage. There is however, an additional factor which needs to be considered. This is the possible occurrence of electronic conductance in the mixed oxide electrolyte which will give an "internal short-circuit" and lead to a low emf even on open ciruit.

Electronic conductance in ZrO_2-CaO mixtures can arise under highly reducing conditions, such as in highly purified hydrogen or in contact with a highly reducing metal, *e.g.*, calcium. Oxygen ions are removed from the lattice, giving oxygen vacancies and also free electrons, in accordance with an equation such as

$$2\,O^{2-} \rightarrow O_2(\text{gas}) + 2\,O\square + 4e \qquad [1]$$

Thus the electronic conductivity should be proportional to (oxygen pressure)$^{-1/4}$ and electronic conductance will become dominant over anionic conductance at very low oxygen partial pressures. When this occurs (at the anode) the emf of an oxygen concentration cell (for constant oxygen partial pressure at the cathode) will tail off. Ultimately, as the conditions at the anode are made even more reducing, the emf will begin to fall and may even become zero. Measurements, reported informally at a recent meeting by Steele and by Wagner[2], suggest that the limiting value of oxygen partial pressure is about 10^{-30} at 800°C and 10^{-24} atm at 1000°C, and will be higher for higher temperatures.

This effect will be a further factor limiting the emf obtainable (at constant value of oxygen partial pressure at the cathode) from an oxygen concentration cell with a mixed oxide electrolyte.

J. Weissbart[3] and R. Ruka: We agree with Dr. Littlewood that any electronic conductance in the mixed oxide electrolyte results in an open-circuit voltage lower than the theoretical maximum. However, the statement in question on p. 725, is intended to apply only to those cases where the open-circuit voltage decreases when current is drawn. While the voltage losses due to the general polarization phenomena listed increases with increasing current drawn from the cell, the loss due to electronic conductance in the electrolyte decreases, provided the chemical composition of the electrolyte remains invariant. This can readily be shown by considering the load resistance to be in parallel with the "electronic resistance" of the electrolyte. The analysis is similar to the equivalent circuit approach used by Jost[4] and Hoar and Price[5].

To check on the open-circuit voltage loss we could expect in the present cell we had earlier made another study which showed that the average electronic transference number in $(ZrO_2)_{0.85}(CaO)_{0.15}$ is small for the range of oxidizing and reducing conditions actually studied. This data was reported in a paper presented at the 1961 fall meeting of The Electrochemical Society[6]. As Dr. Littlewood points out, at lower effective oxygen partial pressures significant compositional changes can occur in the oxide electrolyte and electronic conductance then becomes important.

[1] The British Iron and Steel Research Association, 140 Battersea Park Rd., London, S. W. 11, England.

[2] B. C. H. Steele and C. Wagner, "Nuffield Group Spring Meeting," Imperial College, London, April 1962. (Unpublished).

[3] Present address: Materials Sciences Lab., Lockheed Missiles & Space Co., Palo Alto, Calif.

[4] W. Jost, "Diffusion und chemische Reaktion in festen Stoffen," p. 149, Verlag von Theodor Steinkopff, Dresden and Leipzig (1937).

[5] T. P. Hoar and L. E. Price, *Trans. Faraday Soc.*, 34, 867 (1938).

The Lithium Hydride Electrode

Maurice E. Indig and Richard N. Snyder (pp. 757-759, Vol. 109, No. 9)

A. K. M. Shamsul Huq[7]: You have given two reaction schemes in your paper: $LiH \rightarrow Li^+ + H^+ + 2e$ and $LiH \rightarrow Li^+ + \frac{1}{2}H_2 + e$. Are they electrode reactions or over-all reactions? If they are electrode reactions, what are the corresponding reactions at the counter electrode? If they are over-all reactions, what are the individual electrode reactions to make up the over-all reaction? Did you observe the discharge (plating out) of any alkali metal or metals at the cathode?

M. E. Indig and R. N. Snyder: The reactions listed, $LiH \rightarrow Li^+ + H^+ + 2e$ and $LiH \rightarrow Li^+ + \frac{1}{2}H_2 + e$ are single electrode reactions that occurred to varying degrees at the nickel anodes. The complete cell reaction that occurred on discharge of the lithium hydride was the decomposition of the compound, $LiH \rightarrow \frac{1}{2}H_2 + Li$. In the case of the two electron oxidation of the lithium hydride, the cathodic reaction proceeds concurrently as, $H^+ + 1e \rightarrow \frac{1}{2}H_2$ and $M^+ + 1e \rightarrow M^o$ (where M is Li or K). The fact that hydrogen was produced at the counter electrode was definitely shown in the experiments involving the V-tube assembly as illustrated in the paper (Fig. 6). In the one electron oxidation of lithium hydride, the reaction occurring on the counter electrode was simply $M^+ + 1e \rightarrow M^o$. After termination of a typical discharge, examination of the cell showed the presence of a ring of liquid, silvery metal floating on the surface of the electrolyte adjacent to the stainless steel counter cathode. The metal produced was lithium or potassium or some alloy of these, as lithium and potassium ions were the only reducible metal ions in the electrolyte.

Effects of Electrostatic Fields on the Surface Tension of Salt Solutions

G. M. Schmid, R. M. Hurd, and E. S. Snavely, Jr., (pp. 852-856, Vol. 109, No. 9)

E. P. Damm, Jr.[8]: I have read with interest the recent article by Schmid, Hurd, and Snavely. I would like to comment on a number of their assumptions and conclusions.

I have done extensive work on the attraction of liquids by divergent electric fields. It has been noticed that the transit time of polar liquids across air gaps is lower with negative air electrodes than with positive air electrodes. This decrease in transit time is evident whether positive or negative charged colloids are present in the test liquid. It is not attributed to a sub-

[6] J. Weissbart and R. Ruka, Electrochemical Society Meeting, Detroit, Oct. 2-5, 1961, Extended Abstract No. 44, Battery Div.

[7] Materials Research Lab., TYCO, Inc., Bear Hill Rd., Waltham, Mass.

[8] International Business Machines Corp., General Products Div., Development Lab., Endicott, N. Y.

stantial decrease in surface tension difference by negative air electrodes over positive air electrodes as might be inferred from the paper by Schmid *et al.* It has been presumed to be a prebreakdown phenomenon perhaps related to cathode emission. This would account for the phenomenon also noted by Horgan and Edwards.[9] I would like to point out also that Hakim and Higham[10] and Farazmand[11] using Schlieren Optics have noted rather large changes in the refractive index of liquids around negative points but not around positive points.

Incidentally, it should be noted that the experiment the authors used to correct for the rise in the liquid and effects due to the "position of the working edge of the float" were performed with a positive electrode. It should also be noted that since the liquid in the tray is an aqueous salt solution, it is difficult to believe that the authors really have a uniform field configuration. Field plots plus a few numerical calculations would probably reveal the field to be quite nonuniform at the edges of the air electrode. In fact the experimental data might even be reproducible without the presence of the bottom metal electrode, provided a ground connection is made to the liquid body.

However, if the liquid would effectively serve as the lower electrode in the authors' configuration, it would cast doubt on the absoluteness of the data obtained for the surface tension depression by the electric field.

This is because of the following reason:

(*A*) The assumptions made in developing their model are based on a uniform field configuration.

(*B*) Cutting out portions of the dielectric will certainly change the field if the liquid can be considered mathematically as a second conductor.

(*C*) Within the confines of the edges of the upper air electrode the field will be fairly uniform. Therefore when the dielectric is entirely within this region a change in the force on the balance arm would be expected merely on the basis of field geometry. This effect might even overshadow any expected change in surface tension because of reorientation of the surface molecules.

G. M. Schmid[12], R. M. Hurd, and E. S. Snavely, Jr.: We are pleased to have the interest and the comments of Mr. Damm.

It is true that the field at the edges of the air electrode is not uniform. This is indicated by the fact that the sudden drop in balance deflection does not occur when the front part of the mica float just enters the confines of the air electrode. Rather it occurs when the front part of the float is somewhere between shield and air electrode. However, apart from field distortion by the float itself, the field can reasonably be assumed to be uniform within the area covered by the air electrode.

It is difficult to see how a sudden change in balance deflection should be due to the fact that the float enters the confines of the air electrode. The field forces on the float should then be proportional to the area of the float and are accounted for by extrapolation.

Oxygen-Transport and Reaction Rates at an Air-Depolarized Copper Cathode

H. C. Weber, H. P. Meissner, and D. A. Sama (pp. 884-889, Vol. 109, No. 10)

A. K. M. Shamsul Huq[13]: Steel wool of apparent large area was used as the anode and it was tacitly assumed that the rate of the over-all cell reaction would be governed by this reaction rate at the cathode of much smaller area. This is only partially true. The cell reaction may very well be controlled by the reaction rate of the steel anode which may be passivated in alkaline solution[14]. Should this happen, one would observe a limiting current under apparently varying conditions at the cathode, *viz.*, area exposed above electrolyte level, oxygen pressure.

H. C. Weber, H. P. Meissner, and D. A. Sama: Two experimental observations[15] indicate that reaction rates at the steel wool anodes did not govern performance of these cells. First, the limiting current at a given copper cathode was found to remain constant when the steel wool anode area was doubled. Second, for any given anode, doubling the wetted perimeter of the partially submerged copper cathode doubled the limiting current.

Prior to use as a cell anode, the steel wool electrode was connected for a few minutes to a zinc wire coil submerged in the electrolyte. The hydrogen evolved within the steel wool electrode swept entrained oxygen out of the steel wool and probably removed any passive oxide film which might have been present at the outset. Steel wool electrodes, so treated, showed an unchanged performance even after several weeks of submergence and use. It will be noted that passivation occurred in the example from Kortum and Bockris only when the current density was raised to 8.3 ma/cm^2. The current densities on the wool cathode under discussion were at least 50-fold smaller than this.

Sodium Borohydride, an Interesting Anodic Fuel

M. E. Indig and R. N. Snyder, (pp. 1104-1106, Vol. 109, No. 11)

J. P. Elder[16]: The general characteristics of the anodic behavior of the borohydride ion at platinum electrodes in alkaline aqueous media have already been established.[17] An oscillographic investigation[18] has confirmed unequivocally that the sole electrochemical reaction is the ionization of hydrogen from the BH_4^- and similar type ionic groups. These charging curve studies also indicated that under certain conditions, this negative potential electrochemical oxidation may proceed at nickel surfaces. These latter observations pertain solely to smooth electrodes.

In order to set up a stable borohydride ion electrode system, two factors must be taken into consideration. Firstly, the electrode material must have the power of adsorbing the bound hydrogen and rendering it available for ionization on anodic polarization. Secondly, the molar ratio, $[OH^-]:[BH_4^-]$ must not be too high. At highly active surfaces, such as platinized platinum, this latter consideration is not of such great import. Thus, this negative potential may be sustained at a molar ratio of 20:1. However, when a smooth nickel electrode is employed, the molar ratio must always be less than unity. By using porous nickel, the importance of the molar ratio effect is reduced. The electrochemical features of the porous nickel-borohydride ion electrode are in excellent agreement with those characterizing the corresponding electrode system at platinum surfaces.

At a smooth nickel electrode immersed in a 0.1M potassium borohydride solution in potassium hydroxide at *p*H 12.5, *i.e.*, a molar ratio of 3.16:1, potential decay studies[18] indicated an open circuit potential of −0.95v on the hydrogen scale. Thus, the potential of the nickel-borohydride electrode is 0.21v more nega-

[9] J. D. Horgan and D. L. Edwards, *J. Appl. Phys.*, 32, [9], 1784 (1961).

[10] S. S. Hakim and J. B. Higham, *Nature*, 189, [4769], 996 (1961).

[11] B. Farazmand, *Brit. J. Appl. Phys.*, 12, 251 (1961).

[12] Present address: Dept. of Chemistry, University of Alberta, Edmonton, Alberta, Canada.

[13] Materials Research Lab., TYCO, Inc., Bear Hill, Waltham, Mass.

[14] G. Kortüm and J. O'M. Bockris, "Textbook of Electrochemistry," Vol. II, p. 463, Elsevier Publishing Co., New York (1951).

[15] D. A. Sama, Sc. D. Thesis, Massachusetts Institute of Technology, 1960.

[16] Chemical Engineering Div., Argonne National Laboratory, Argonne, Ill.

[17] J. P. Elder and A. Hickling, *Trans. Faraday Soc.*, 58, 1852 (1962).

[18] J. P. Elder, *Electrochimica Acta*, 7, 417, (1962).

tive than the reversible hydrogen potential in the same basic medium. This is in excellent agreement with the figure of 0.22v obtained by Drs. Indig and Snyder from galvanostatic measurements in a more concentrated solution with a molar ratio of 3:1. Their polarization data shows a limiting current density plateau commencing at a potential 0.4v more positive than the open circuit potential in qualitative agreement with the findings at platinized platinum.[17] At an active nickel surface, a reaction mechanism analogous to that proposed at a platinum electrode would appear to be operative. Thus, the static potential is characteristic of a fast two-electron partial hydrogen ionization from the parent ion, BH_4^-. On anodic polarization, further hydrogen ionization from the adsorbed BH_3OH^- ion occurs by an analogous process. The stoichiometry of the reaction at porous nickel is similar to that observed at smooth platinum, which has been accounted for by a competition between hydrolytic and ionization reactions following the initial electrochemical step. There is every indication that at high *p*H and a fairly large molar ratio, the main anodic process is the four-electron transfer cited by Drs. Indig and Snyder.

The borohydride ion has great potentialities as an anodic fuel. One is dealing with a simple electrolyte system and furthermore, the final reaction product in solution, the $H_2BO_3^-$ ion appears to have no deleterious effect. One of the disadvantages of employing a smooth platinum surface is that it "ages." A stable open circuit potential is never maintained. The potential slowly and steadily drifts to more positive values, ultimately reaching the oxygen evolution region. This is accompanied by a steady decrease in the rate of hydrogen evolution from the surface. At platinized platinum, the reaction rate is steady. When the molar ratio is greater than 3:1, a limiting current density is attained and hydrogen evolution ceases, this surface being sufficiently active to ionize the free hydrogen produced by hydrolysis. However, like smooth platinum, it is highly probable that nickel is not sufficiently active for this latter effect to be observed.

In concluding, I should like to congratulate Drs. Indig and Snyder on their work and inquire for what length of time will the porous nickel-borohydride ion electrode continue to operate without deactivation of the surface and subsequent rapid polarization to the oxygen evolution region?

M. E. Indig and R. N. Snyder: It is unfortunate that the publications cited by Dr. Elder were unavailable until after our publication was submitted. However, it is gratifying to see the points of agreement between the work of Drs. Elder and Hickling and that of ourselves. In response to the question concerning the deactivation of the nickel surface, we can only say that in the length of time of our galvanostatic discharges, which were no longer than five hours, rapid polarization did not occur until 86 to 98% of the four-electron oxidation was achieved. Also in the case of the lower coulombic efficiencies the potential gradually drifted upward, approaching open circuit values after the polarizing load was removed.

The Anodic Dissolution of Binary Alloys

R. F. Steigerwald and N. D. Greene, (pp. 1026-1034, Vol. 109, No. 11)

W. A. Mueller[19]: The experimental study of the anodic dissolution of alloys is certainly very useful for the clarification of the rate and mechanism of attack. Also the process by which components of lower dissolution rate accumulate on the surface may find interesting elucidation by the same study. Unfortunately the authors chose the short exposure time of 10 min. The accumulation of components of low solubility is often still in the initial stage after 10 min of exposure. Even after days the steady state of dissolution is not attained in extreme cases if the component of low solubility is present in low concentration. Hence the change from Eq. [5] to Eq. [9] as theoretically derived before is by no means generally finished after 10 min time of exposure. Actually the best test would have been to follow the dissolution curve with increased time of exposure, *e.g.*, by the multipoint-polarization-curve technique. For the same reason the correction factors for the dissolution of intermetallic compounds should have been calculated from current-density-time curves after attaining steady state. Moreover, the correction factor should be valid independent of the applicability of Eq. [5] or [9]. Some confusion is caused by the fact that displacement along the current axis is derived from the experimental data, but a shift along the potential axis is claimed in the summary.

R. F. Steigerwald and N. D. Greene: We thank Dr. Mueller for his comments. Apparently there has been some misunderstanding and we wish to re-emphasize several points of the published experimental procedure.

(*A*) "Prior to polarization, the specimens were exposed to the test solution for several hours to insure that a stable corrosion potential was attained."

(*B*) "At most potentials, the current reached steady-state values in a short time (less than 5 min) and these steady-state values are reported.

Only the passive currents were time-dependent, and these currents were recorded after ten min. We realized the difficulty in reporting the passive currents after so short a time and mentioned this as a possible source of error in the discussion of the differences between the experimental and calculated passive currents. It is important to note that our conclusions were not based on the time-dependent passive currents but rather, on the steady-state values and the over-all polarization behavior of the alloys.

We do not understand the confusion regarding the experimental results and our statements in the summary. Experimentally, we observed that the polarization curves of intermetallic compounds were frequently displaced along the current axis and stated in the summary: "—but stronger solid state interactions may shift their polarization curves along the current axis."

[19] Physical Chemistry Div., Pulp and Paper Research Institute of Canada, 3420 University St., Montreal 2, Canada.

Report on the Investigation of the Binary System CoS-In_2S_3

R. E. Johnson[1]

Department of Metallurgy, Pennsylvania State University, University Park, Pennsylvania

Hahn and co-workers (1) showed the existence of sulfide spinels, which were prepared by solid-state reactions $AS + B_2S_3 = AB_2S_4$. In these spinels the sulfur ions occupy a close-packed, face-centered cubic lattice, while the A and B cations are located on octahedral and tetrahedral sites. The situation seems to be analogous to oxide spinel systems, and it seemed profitable to study the defect structure and solid-state reactions in a way similar to that used for oxide spinel systems in several previous investigations (2, 3).

The work covered in this report is the preparation of CoS, In_2S_3, $CoIn_2S_4$, the study of the quasi-binary phase diagram CoS-In_2S_3, and the stability of $CoIn_2S_4$ at different sulfur partial pressures.

Phase diagrams of Co-S and In-S systems are given in ref. (4). Stubbles (5) gives further information on the sulfur partial pressure for $Co_{1-\delta}S$ at 1100°C. No data for sulfur partial pressures for equilibria involving indium sulfides and free energies of formation of indium-sulfides could be located in the literature.

Both the indium and the cobalt sulfide were prepared as follows: Stoichiometric amounts of high-purity metal and sulfur were placed in quartz tubes. These tubes were evacuated, sealed, and heated in an electric furnace. CoS formed from the elements at 900°C after about 24 hr; In_2S_3 required about 5 hr longer to prepare. The formation of the sulfide was assumed to be complete when no sulfur could be noted on the side of the quartz tube. About 2g of material was produced in each tube.

CoS and In_2S_3 were powdered and mixed thoroughly in appropriate amounts to cover the quasi-binary system CoS-In_2S_3, evacuated and sealed as before, and heated at temperatures of about 1000°C for one day. At the cooler end of the tubes In_2S_3 was deposited, if the tubes were not sufficiently small and the heating zone of the furnace not sufficiently uniform in temperature. On cooling molten CoS in the evacuated quartz tubes, these tubes always broke as the sulfide solidified.

After quenching the different annealed mixtures of CoS and In_2S_3, the (666)-reflection of x-rays for the spinel structure was studied as a function of the CoS/In_2S_3 ratio in order to get information on the phase boundaries. Figure 1 shows the results. Between 0 mole % CoS and 50 mole % CoS the lattice parameter changes continuously, while between 50 and 100 mole % CoS the spinel line is always present without a change in the lattice parameter. This indicates a one-phase region between 0 and 50% CoS and a two-phase region between 50 and 100% CoS. The one-phase region can be understood by the fact that In_2S_3 crystallizes in the γ-Al_2O_3 structure, which is quite similar to a spinel structure (both have close-packed cubic sulfur lattices) and by the fact that the lattice parameter of In_2S_3 ($= In_{2/3}In_2S_4$) is only about 2% greater than the lattice parameter of $CoIn_2S_4$ ($a = 10.55$). In the two-phase region the phases could be identified as $CoIn_2S_4$ and CoS by x-ray analysis.

In order to supplement the x-ray analysis, the liquidus of the system CoS-In_2S_3 was determined by thermal analysis. As before, appropriate amounts of CoS and In_2S_3 were placed in quartz tubes shown in Fig. 2, evacuated and sealed, then the samples

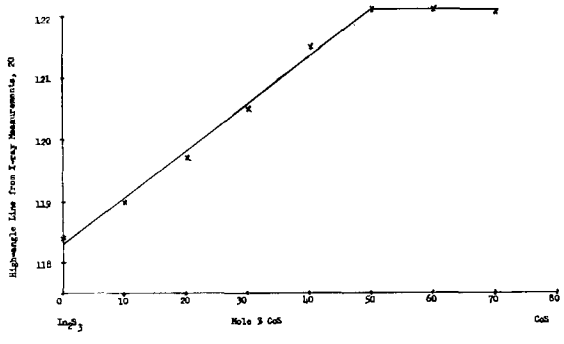

Fig. 1. X-ray measurement of line shift with composition in the In_2CoS system.

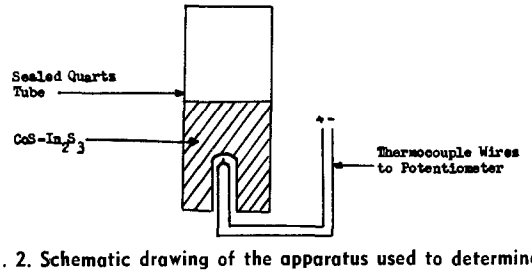

Fig. 2. Schematic drawing of the apparatus used to determine the CoS-In_2S_3 phase diagram.

[1] Mr. Johnson is the first recipient of the F. M. Becket Memorial Award of the Electrothermic and Metallurgy Division of the Society. See p. 135C of the May 1962 JOURNAL. The research was conducted at the Max-Planck-Institut für physikalische Chemie, Göttingen, under the guidance of Dr. H. Schmalzried and with the technical assistance of Mr. H. H. Hohmann.

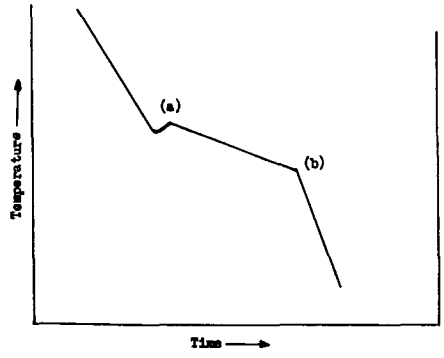

Fig. 3. Schematic figure of a cooling curve obtained by cooling a mixture of CoS-In_2S_3 from the liquid. The first slope change (a) is ascribed to the reaching of the liquidus; the slope change at (b) is ascribed to the reaching of the solidus. Supercooling effects cause the slight dip near (a).

(about 200 mg each) were heated above the melting point of the mixture (about 1100°C). After the furnace power was cut off, the temperature drop of the sample was measured by a Pt-PtRh thermocouple. In general, curves of the type as represented in Fig. 3 were obtained. The first change of the slope in the cooling curve was ascribed to reaching the liquidus. The temperature of the final change of the slope (Fig. 3) was ascribed to reaching the solidus. The melting point of In_2S_3 could be compared with literature data (4). Both values agreed quite well, indicating the consistency of the values between 0 and 50% CoS. Since the melting point of CoS is very sensitive to changes in the ratio Co/S, a similar proof as on the In_2S_3 side of the phase diagram was not possible. Figure 4 shows the results of the measurements.

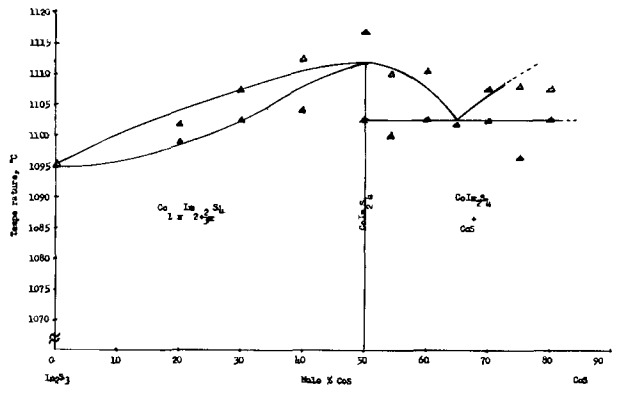

Fig. 4. Phase diagram of the In_2S_3-CoS system: △, liquidus; ▲, solidus.

Finally, the stability of the spinel with the stoichiometric composition $CoIn_2S_4$ at different sulfur partial pressures at 900°C was investigated. To this end, mixtures of H_2S and H_2 were fed into the furnace through calibrated capillaries. Various ratios H_2S/H_2 were tried and the range of stability determined by x-ray analysis. Preliminary results indicate that, at a temperature of 900°C, the spinel $CoIn_2S_4$ is stable in a sulfur pressure range of $10^{-4} - 10^{-2}$ atm.

REFERENCES

1. H. Hahn and W. Klingler, *Z. anorg. u. allgem. Chem.*, **263**, 177 (1950).
2. H. Schmalzried, *Z. physik. Chem., N.F.*, **33**, 111 (1962).
3. A. Morkel and H. Schmalzried, *Z. physik. Chem. N.F.*, **32**, 76 (1962).
4. M. Hansen and K. Anderko, "Constitution of Binary Alloys," McGraw-Hill Book Co., New York (1958).
5. J. Stubbles, Diffusion and other Kinetic Studies of the System Cobalt-Sulphur, Thesis, University of London, London, 1957.

A General Thermodynamic Theory of the Potential of Passive Electrodes and Its Influence on Passive Corrosion

K. J. Vetter

Fritz-Haber-Institut of the Max-Planck-Gesellschaft, Berlin-Dahlem, Germany

ABSTRACT

A theory of the electrode potential of nonstoichiometric electron conductive metal oxides MeO_n on a foreign metal is presented. When the oxygen ions of the oxide are in equilibrium with the electrolyte the oxide electrode potential is $\epsilon_h = (1/2F) \cdot d\Delta G(n)/dn - 0.059 \cdot pH$ with the free enthalpy $\Delta G(n)$ for the reaction $Me + nH_2O \rightarrow MeO_n + nH_2$ as a function of the degree of oxidation n. The oxide electrode potential for the case of an equilibrium of the metal ions between the oxide and the electrolyte is also derived. The condition of equilibrium between the oxide MeO_n and the electrolyte with dissolved z-valent metal ions ($z \neq 2n$) is given. The "equilibrium oxide" relative to its parent metal and the corresponding potential are discussed. The potential of a passive electrode depends only on the surface oxide in contact with the electrolyte and is independent of the construction of the passive layer.

The effect of the corrosion rate and of the current density on the passive potential and on the construction and composition of the inner layer are discussed. The establishment of a stationary layer is explained. The experimental pH dependence of the corrosion current density of equal surface oxides of Ni, Fe, and Cr are analyzed. For this reason passive potentials against the hydrogen electrode at the same pH value are compared.

In electrolytic solutions the passivity of metals is caused by a porefree (1) oxidic layer, which prevents the direct contact of the metal and the electrolyte. The behavior of the passive metal depends on the properties of this passive layer, especially on the thickness, chemical composition, rate of dissolution in the electrolyte, and the electronic and ionic conductivity. In most cases of clear[1] passivity the electronic conductivity is good. The rate of dissolution of the passive layer in the electrolyte is a function of the chemical composition at the interface passive layer/electrolyte. After a stationary state of this layer has been reached, the rate of dissolution is equal to the remaining corrosion rate of the metal in the passive state. Therefore the corrosion rate is one of the most important properties of the passive metal.

The chemical composition and thickness of the passive layer depend on the potential. The stationary thickness is regulated by the ionic current through the layer, which depends on the electrical field strength in the layer. The field strength and therefore the ionic current increase with increasing potential difference in the layer and decrease with increasing layer thickness. By changing the layer thickness the ionic current density can become equal to the corrosion current density. At this point, the stationary state of the layer will be reached. In this case the anodic rate of formation of passive oxide will be equal to the dissolution rate in the electrolyte.

In this paper the composition of a nonstoichiometric inhomogeneous passive layer shall be discussed according to Vetter (2) as a function of the potential, corrosion rate, pH-value, and electrolyte concentration of ions of the passive metal on the basis of thermodynamic considerations.

[1] The definition of passivity is very difficult. A definition which is satisfactory in all cases cannot be found as yet.

Potential of an Oxide Electrode with a Nonstoichiometric Oxide with Electronic Conductivity

Oxide on a Foreign Metal. Oxygen Ion Equilibrium Oxide/Electrolyte

Single-phase (homogeneous) oxide.—This problem will be worked out most simply for the case of an arbitrary nonstoichiometric oxide, oxyhydrate, or hydroxide $MeO_n \cdot mH_2O$ on a foreign metal other than the parent metal Me in the oxide. Later these considerations will be extended to the case of an oxide in contact with its parent metal Me. It may be assumed that the foreign metal is completely insoluble in the oxide. In this case the metal simply acts as an electron carrier. Figure 1 represents the phase scheme for this case. At the phase boundaries the equilibrium of the electrons $\beta(1,2)$ and of the oxygen ions $\beta(2,3)$ O^{2-}(oxide) + $2H^+$(electrolyte) $\leftrightharpoons$ H_2O(electrolyte) are established (straight lines). All other reactions are assumed to be completely inhibited (dotted lines). Later, this restriction will be

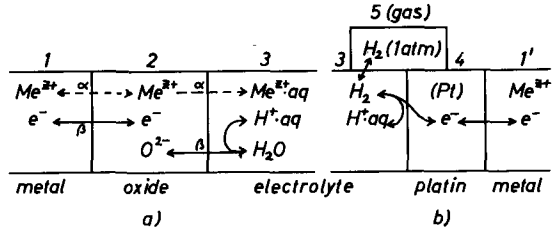

Fig. 1. (a) Phase scheme of an oxide electrode in contact with a foreign metal; (b) hydrogen reference electrode.

removed to a certain extent. Instead of reaction $\beta(2,3)$ the reaction $\beta'(2,3)$ O^{2-}(oxide) + H^+(electrolyte) $\leftrightharpoons$ OH^-(oxide) can occur. Both reactions are thermodynamically equivalent. Therefore only the first one $\beta(2,3)$ shall be discussed further.

By an anodic current O^{2-} ions will be taken up, and for each O^{2-} ion two electrons of the own metal ions will be delivered to the foreign metal. If the anodic current is so small that the equilibrium potential differences at the two phase boundaries 1,2 and 2,3 are not appreciably disturbed, both phase boundary reactions occur reversibly. Therefore, the total electrode process is a thermodynamically reversible absorption of oxygen atoms by the oxide MeO_n or $MeO_n \cdot mH_2O$.[2] Through this process the degree of oxidation n will be increased by a small amount. In the case $\beta'(2,3)$ protons H^+ will be emitted in a thermodynamically reversible manner. The assumption is that the phase width is large enough that no further oxide phase is formed. For ν moles MeO_n and $2F$ coulombs the reversible overall electrode reaction is

$$\nu MeO_n + H_2O \rightarrow \nu MeO_{n+1/\nu} + 2H^+ + 2e^- \quad [1]$$

Against a hydrogen electrode in the same electrolyte (same pH value, Fig. 1) the reversible cell reaction is

$$\nu MeO_n + H_2O \rightarrow \nu MeO_{n+1/\nu} + H_2\ \Delta G \quad [2]$$

with the electrode reaction valency 2 and the free enthalpy of the reaction[2*] ΔG. The reversible cell voltage becomes $\epsilon = +\Delta G/2F$.

This free enthalpy of the reaction ΔG can be calculated from the values of free enthalpies of formation $\Delta G(n)$ and $\Delta G(n+1/\nu)$ for the oxides MeO_n and $MeO_{n+1/\nu}$ according to

$$Me + nH_2O \rightarrow MeO_n + nH_2\ \Delta G(n) \quad [3]$$

$$Me + (n+1/\nu)H_2O \rightarrow MeO_{n+1/\nu} + (n+1/\nu)H_2\ \Delta G(n+1/\nu) \quad [4]$$

Therefore ΔG amounts to

$$\Delta G = \nu \cdot [\Delta G(n+1/\nu) - \Delta G(n)] = \frac{\Delta G(n+1/\nu) - \Delta G(n)}{1/\nu} \quad [5]$$

For the limiting case when $\Delta n = 1/\nu \rightarrow 0$ one gets

$$\lim_{\nu \rightarrow \infty} \Delta G = \lim_{\Delta n \rightarrow 0} \Delta G = \frac{d\Delta G(n)}{dn} \quad [6]$$

Therefore the reversible cell voltage against the hydrogen electrode of the same pH value can be expressed by the differential quotient of the free enthalpy of formation of the oxide MeO_n to the degree of oxidation n

$$E_o = +\frac{1}{2F} \cdot \frac{d\Delta G(n)}{dn} \quad [7]$$

Against the standard hydrogen electrode the potential ϵ_h of the oxide electrode on a foreign metal is (at 25°C)

$$\epsilon_h = \frac{1}{2F} \cdot \frac{d\Delta G(n)}{dn} - 0.059 \cdot pH \quad [8]$$

[2] Instead of $MeO_n \cdot mH_2O$ the abbreviated formula for the oxide MeO_n shall be used in the following part. The same treatment may also be applied to $MeO_n \cdot mH_2O$.

[2*] Change of Gibbs free energy ΔG.

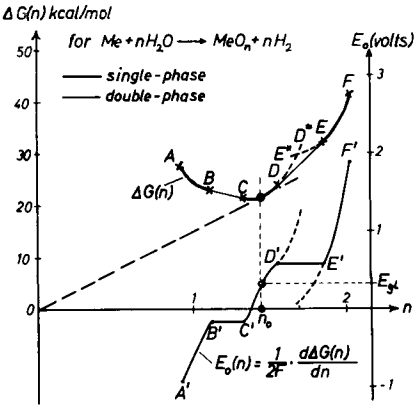

Fig. 2. Free reaction enthalpy $\Delta G(n)$ and the deviated oxide electrode potential E_o (Eq. [8]) as function of the degree of oxidation n (arbitrary assumed values).

If an oxide $MeO_n \cdot mH_2O$ is considered, the value of $\Delta G(n)$ corresponds to the reaction Me + $(n+m)$ $H_2O \leftrightharpoons MeO_n \cdot mH_2O + nH_2$. Equations [5] to [8] are likewise valid. However, the value of the potential ϵ_h depends on the content m of water, which can be a function $m = f(n)$ of n. In Fig. 2 $\Delta G(n)$ is represented as a function of the degree of oxidation n by assuming arbitrary values for $\Delta G(n)$. Equations [7] or [8] are first of all only applicable to one of the three ranges of homogeneous solid solution series of the oxide, which are assumed in Fig. 2.

For a nonhydrated ($m = 0$) oxide MeO_n Eq. [7] and [8] can also be formulated by using the standard free enthalpy of formation of the oxide from the elements $\Delta G_o(n)$ following the paper of Bell and Huber (3). From the relation

$$\Delta G(n) = \Delta G_o(n) - n \cdot \Delta G_o(H_2O)$$

with the free enthalpy of formation of water $\Delta G_o(H_2O)$ according to $H_2 + 1/2\ O_2 \rightarrow H_2O$, Eq. [7] transforms into

$$E_o = \frac{1}{2F} \cdot \frac{d\Delta G_o(n)}{dn} - \frac{1}{2F} \Delta G_o(H_2O) \quad [9]$$

The term $-(1/2F) \cdot \Delta G_o(H_2O) = +1.23$v is the potential of the reversible standard oxygen electrode.

For a hydrated oxide $MeO_n \cdot mH_2O$ with a water content $m = f(n)$ depending on the degree of oxidation n the relation

$$\Delta G(n) = \Delta G_o(n) - (n+m) \cdot \Delta G_o(H_2O) \quad [10]$$

is valid. Therefore the standard oxide potential E_o, according to the formulation of Bell and Huber (3), becomes

$$E_o = \frac{1}{2F} \cdot \frac{d\Delta G_o(n)}{dn} - (1 + dm/dn) \cdot \frac{1}{2F} \cdot \Delta G_o(H_2O) \quad [11]$$

Regarding $\Delta G_o(n,m)$ as a function of two independent variables n and m, $d\Delta G_o(n)/dn$ can be formulated as

$$\frac{d\Delta G_o(n,m)}{dn} = \frac{\partial \Delta G_o(n,m)}{\partial n} + \frac{\partial \Delta G_o(n,m)}{\partial m} \cdot \frac{dm}{dn}$$

Using this relation, Eq. [11] changes to

$$E_o = \frac{1}{2F} \cdot \frac{\partial \Delta G_o(n,m)}{\partial n}$$

$$+\frac{1}{2F}\cdot\left[\frac{\partial\Delta G_o(n,m)}{\partial m}-\Delta G_o(H_2O)\right]\cdot\frac{dm}{dn}$$

$$-\frac{1}{2F}\cdot\Delta G_o(H_2O) \quad [12]$$

The bracket in the second term represents the free enthalpy of association of the crystal water.

In the special case of the frequently observed oxide series $Me(OH)_2 \rightarrow MeO(OH) \rightarrow MeO_2$ which mostly form series of mixed crystals without miscibility gap, the water content m is $m = a - n$ (here $2 - n$). Because $m = 2 - n$ is $dm/dn = -1$ and Eq. [11] simplifies to

$$E_o = \frac{1}{2F}\cdot\frac{d\Delta G_o(n)}{dn} = \frac{1}{2F}\cdot\frac{d\Delta G(n)}{dn} \quad [11']$$

(for $m = a - n$)

In all cases the electrode potential ϵ_h against the standard hydrogen electrode is $\epsilon_h = E_o - 0.059 \cdot pH$.

Double-phase (heterogeneous) oxides.— During the oxidation of the oxide the upper limit n_1 (point D in Fig. 2 for example) of the phase range may be reached. Then, further oxidation causes a formation of a new phase of the lower limit n_2 (point E in Fig. 2), if the formation of crystal nuclei is fast enough. Then both phases are in equilibrium. When two phases are in equilibrium, the potential will not depend on the ratio of the quantities of the phases. The potential will remain constant during the oxidation until the first phase with the upper limit n_1 is consumed. By analogy the preceding evaluation, the potential is now defined by the quotient of differences instead of the differential quotient

$$\epsilon_h = \frac{1}{2F}\cdot\frac{\Delta G(n_2)-\Delta G(n_1)}{n_2 - n_1} - 0.059 \cdot pH \quad [13]$$

This equation is used for the two-phase ranges in Fig. 2. If in Fig. 2 the upper and the lower limits of two succeeding single-phase ranges are connected by straight lines, the first equation with the differential quotient can be used in the whole range of degrees of oxidation n. The curve A'F' in Fig. 2 represents the potential ϵ as a function of the degree of oxidation n according to Eq. [8] and [9] or also [13].

Oxide on a Foreign Metal. Metal Ion Equilibrium at the Phase Boundary Oxide/Electrolyte

Contrary to the foregoing discussion on oxide on a foreign metal the equilibrium $\alpha(2,3)$ of the metal ions at the phase boundary oxide/electrolyte Me^{z+} (oxide) $\leftrightharpoons$ Me^{z+} (electrolyte) shall be established. Moreover the equilibrium of the electrons $\beta(1,2)$ and a sufficiently high electronic conductivity shall be assumed again. This means that the reactions

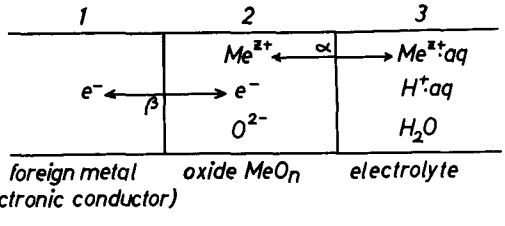

Fig. 3. Phase scheme of an oxide electrode in contact with a foreign metal. Equilibrium of the metal ions.

represented in Fig. 3 are in equilibrium, and all other reactions are essentially inhibited.

The valency z of the metal ion Me^{z+} in the electrolyte must not generally have the same value as the average valency $2n$ of the metal ions in the oxide. By an anodic current metal ions Me^{z+} will be transferred from the oxide into the electrolyte, and the remaining negative charge will be delivered as z electrons to the foreign metal. The total electrode process is a thermodynamically reversible transfer of a metal atom from the oxide and the formation of a metal ion Me^{z+} in the electrolyte. It is assumed that the current is so small that the equilibrium potential differences at the two phase boundaries 1,2 and 2,3 (Fig. 3) are not disturbed to any significant extent. The degree of oxidation n will be increased through this process by a small amount $\Delta n(=n/\nu)$. The quantity of oxygen ions in the oxide remains constant during this process. Therefore the reversible electrode reaction, for zF coulombs and considering a single phase range of sufficient width, is

$$(\nu + 1)\ MeO_n \rightarrow \nu MeO_{n+n/\nu} + Me^{z+}\cdot aq + z\cdot e^- \quad [14]$$

This reaction involves no hydrogen ions. Therefore the electrode potential will not depend on the pH value, and it will be suitable to choose the standard hydrogen electrode as counter electrode in a reversible galvanic cell. The reversible cell reaction is then

$$(\nu + 1)\ MeO_n + zH^+\ (a = 1) \rightarrow$$

$$\nu MeO_{n+1/\nu} + Me^{z+}\cdot aq + \frac{z}{2}H_2\ (1\ atm) \quad [15]$$

with the electrode reaction valency z. The reversible cell voltage ϵ_h results from the free enthalpy ΔG of reaction [15] according to $\epsilon_h = +\Delta G/zF$. ΔG results by using $\Delta G(n)$ of reaction $Me + nH_2O \rightarrow MeO_n + nH_2$ and ΔG_{Me} of reaction $Me + zH^+(a=1) \rightarrow Me^{z+}\cdot aq + (z/2)H_2$ according to the relation

$$\Delta G = \nu\,[\Delta G(n+n/\nu) - \Delta G(n)] - \Delta G(n) + \Delta G_{Me} \quad [16]$$

Since

$$\lim_{\nu\rightarrow\infty}\nu\cdot\left[\Delta G\left(n+\frac{n}{\nu}\right)-\Delta G(n)\right] = n\cdot\frac{d\Delta G(n)}{dn}$$

and $\Delta G_{Me} = zF\cdot\epsilon_{Me}$ where ϵ_{Me} is the reversible potential of a $Me/Me^{z+}\cdot aq$-electrode against the standard hydrogen electrode, the potential ϵ_h of the oxide electrode under consideration becomes

$$\epsilon_h = \epsilon_{Me} + \frac{n}{zF}\cdot\frac{d\Delta G(n)}{dn} - \frac{1}{zF}\cdot\Delta G(n) \quad [17]$$

with

$$\epsilon_{Me} = E_{o,Me} + \frac{RT}{zF}\cdot\ln a_{Me^{z+}}$$

$E_{o,Me}$ is the standard potential of the metal ions Me^{z+}. ϵ_{Me} is the reversible potential of the electrolyte in contact with the compact metal Me according to the Nernst equation, and the term $[n(\Delta G(n)/dn) - \Delta G(n)]/zF$ is the deviation of the oxide electrode potential from the reversible potential of the active Me/Me^{z+} electrode.

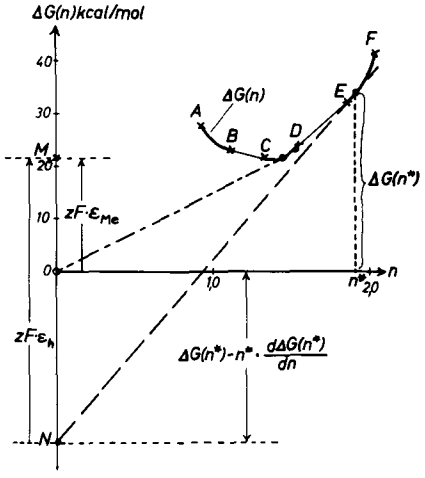

Fig. 4. Free reaction enthalpy $\Delta G(n)$ as function of the degree of oxidation n (arbitrary assumed values). Evaluation of the oxide potential for an equilibrium of the metal ions.

Here instead of $\Delta G(n)$ one can also use the free enthalpy of formation of the oxide $MeO_n \cdot mH_2O$ from the elements $\Delta G_o(n)$ according to the reaction

$$Me + \frac{n+m}{2} O_2 + mH_2 \rightarrow MeO_n \cdot mH_2O \quad \Delta G_o(n)$$

Then Eq. [10] and [11] are to be taken for $\Delta G(n)$ and $d\Delta G(n)/dn$. However, the formula received in this manner is not very clear.

Equation [17] is graphically interpreted in Fig. 4 and is for the time being only valid for a single-phase, homogeneous oxide with sufficient phase width. For a double-phase heterogeneous oxide MeO_{n1}/MeO_{n2} instead of the differential quotient $d\Delta G(n)/dn$ the quotient of differences $[\Delta G(n_2) - \Delta G(n_1)]/(n_2 - n_1)$ is to be used. It results that

$$\epsilon_h = \epsilon_{Me} + \frac{1}{zF} \frac{n_1 \Delta G(n_2) - n_2 \Delta G(n_1)}{n_2 - n_1} \qquad [18]$$

The establishment of the equilibrium of the metal ions Me^{z+} at the phase boundary oxide/electrolyte is only guaranteed if other electrochemical phase boundary reactions are either totally inhibited or in equilibrium. For example it may be possible, that for a nonstoichiometric oxide with $2n \neq z$, ions of the same metal but having another valency z^* can also be dissolved from the oxide in the electrolyte. Only if the electrolyte is saturated with these metal ions Me^{z*+} with respect to the oxide will the equilibrium of the Me^{z+} ions not be disturbed.[3] Between the Me^{z+} ions and the Me^{z*+} ions there exists a redox potential

$$\epsilon_{red} = E_{z/z^*} + \frac{RT}{(z^* - z)F} \cdot \ln \frac{a^*}{a} \qquad [19]$$

Because of the good electronic conductivity and according to Eq. [17] or [18] ϵ_h must be equal to ϵ_{red} (Eq. [19]). This relation defines a ratio a^*/a of the activities of the two dissolved metal ions of different valency. In many cases this ratio will be extremely small. Then the electrolyte can be saturated near the oxide surface through the dissolution of extremely small amounts of z^* valent metal ions. In this manner the conditions will not be appreciably disturbed. However, this circumstance had to be taken into consideration for an application of Eq. [17] or [18].

[3] For example, MnO_2 ($2n = 4$), Mn^{z+}-ions (z), and Mn^{3+}-ions (z^*).

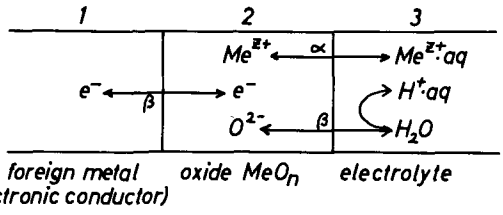

Fig. 5. Phase scheme of an oxide electrode in contact with a foreign metal. Equilibrium of the oxide with the electrolyte.

Oxide on a Foreign Metal in Equilibrium with the Electrolyte (Simultaneous Metal Ion and Oxygen Ion Equilibrium)

If all equilibria, the metal ion equilibrium $\alpha(2,3)$ Me^{z+} (oxide) $\leftrightarrow$ Me^{z+} (electrolyte), all other metal ion equilibria Me^{z*+} (oxide) $\leftrightarrow$ Me^{z*+} (electrolyte), and the oxygen ion equilibrium $\beta(2,3)$ O^{2-} (oxide) + $2H^+$ (electrolyte) $\leftrightharpoons$ H_2O (electrolyte) or O^{2-} (oxide) + H^+ (electrolyte) $\leftrightharpoons$ OH^- (oxide) are established (Fig. 5), the oxide is in a total solubility equilibrium with the electrolyte. This solubility equilibrium differs from the normally discussed equilibrium between a solid stoichiometric substance and a saturated solution only because of the different valency of the metal ions in the electrolyte (z) and in the oxide ($2n$). The normally used solubility product is defined for a solid substance of the same valency as the dissolved ions.

Now we shall discuss the fact that the condition $2n = z$ is not necessary. A solubility equilibrium can also exist when $2n \neq z$. For the evaluation of the equilibrium condition for this case the potentials according to Eq. [8] and [17] must be equal. From Eq. [8] and [17] it results that

$$\epsilon_h = \epsilon_H + \frac{1}{2F} \cdot \frac{d\Delta G(n)}{dn} = \epsilon_{Me} + \frac{n}{zF} \cdot \frac{d\Delta G(n)}{dn} - \frac{1}{zF} \cdot \Delta G(n) \qquad [20]$$

With the potential $\epsilon_H = (RT/F) \cdot \ln a_{H+}$ of the hydrogen electrode against the standard hydrogen electrode, and after transformation

$$(n - \frac{z}{2}) \cdot \frac{d\Delta G(n)}{dn} = \Delta G(n) - zF\,(\epsilon_{Me} - \epsilon_H) \qquad [21]$$

takes place for the equilibrium condition. The terms $zF(\epsilon_{Me} - \epsilon_H)$ and $z/2$ are fixed by the concentrations (activities) of the metal ions and of the hydrogen ions in the electrolyte. According to Eq. [21] the degree of oxidation n of the oxide is defined by the electrolyte. Only one oxide with a definite degree of oxidation n exists in equilibrium with a fixed electrolyte. The value n depends on the electrolyte according to Eq. [21].

Because of a constant value

$$\epsilon_{Me} - \epsilon_H = E_{o,Me} + \frac{RT}{zF} \ln a_{Me^{z+}} - \frac{RT}{F} \ln a_{H+} = \text{constant} \qquad [22]$$

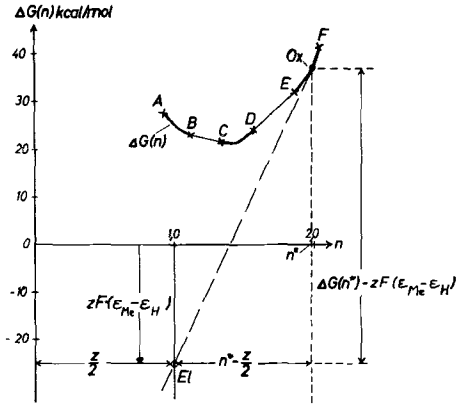

Fig. 6. Free reaction enthalpy $\Delta G(n)$ as function of the degree of oxidation n (arbitrary assumed values). Evaluation of the oxide potential and the degree of oxidation n^* for an equilibrium between oxide and electrolyte.

the degree of oxidation is defined and constant. A "solubility product" $[P(n,z)]$ follows from Eq. [22], thus

$$P(n,z) = a_{Me^{z+}} \cdot a^z_{OH^-} = P^z_{H_2O} \cdot \exp\left(-\frac{zFE_{o,Me}}{RT}\right) \cdot \exp\left(\frac{\Delta G(n) - (n-z/2) \cdot \Delta G(n)/dn}{RT}\right) \quad [23]$$

with the ionic product $P_{H_2O} = a_{H^+} \cdot a_{OH^-}$ of water. This solubility product depends on the function $\Delta G(n)$ and the valency z of the dissolved metal ions.

Equation [21] can be graphically interpreted in a similar manner as Eq. [8] and [17] in Fig. 2 or 4, respectively. The values of the abscissa and ordinate of point El in Fig. 6 are defined by the electrolyte. The coordinates of point El are $z/2$ (n-scale) and $zF \cdot (\epsilon_{Me} - \epsilon_H)$ in the energy scale ($\Delta G(n)$-scale). The tangent to the $\Delta G(n)$ curve from the point El results in the degree n^* of oxidation at the point of contact Ox. The slope of the tangent amounts to the reversible electrode potential

$$\epsilon_h = \frac{1}{2F} \cdot \frac{d\Delta G(n^*)}{dn} + \frac{RT}{F} \ln a_{H^+} \quad [8']$$

as calculated from Eq. [8]. For a defined electrolyte ($[Me^{z+}],[H^+]$) only one oxide MeO_{n^*} with a fixed potential ϵ_h (Eq. [8']) exists in the mentioned case of equilibria. Because of the assumed high electronic conductivity of the oxide the condition Eq. [19] $\epsilon_{red} = \epsilon_h$ must be fulfilled for all other possible valencies of the parent metal ions in the electrolyte. In many cases the necessary concentrations of these metal ions will be small or even extremely small. Then this mentioned condition can be easily verified in an experiment.

Oxide on Its Parent Metal (Equilibrium Oxide MeO_{n_o})

At passive metals the oxide layer $MeO_n \cdot mH_2O$ is on its own parent metal of the oxide and not on a foreign metal. Therefore the preceding consideration is to be expanded for a contact between the oxide and its own metal. Here the assumption that the metal is insoluble in the oxide is no longer valid.

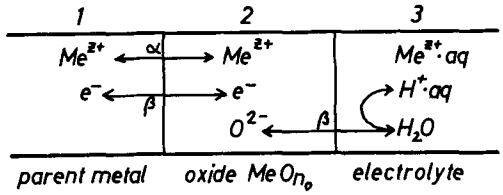

Fig. 7. Phase scheme of an oxide electrode in contact with the parent metal.

On the contrary the parent metal can only be in contact with one oxide, the "equilibrium oxide" MeO_{n_o} (or $MeO_{n_o} \cdot m_oH_2O$). The composition of this equilibrium oxide generally will depend on the temperature. However at a constant defined temperature only one oxide can exist in a thermodynamic equilibrium with the own metal. In this case, in addition to Fig. 1 the metal ion equilibrium at the phase boundary metal/oxide has also to be established. Figure 7 represents these conditions. In the anodic direction reactions $\alpha(1,2)$ and $\beta(2,3)$ result in the anodic formation of the equilibrium oxide according to

$$Me + n_oH_2O \rightarrow MeO_{n_o} + 2n_oH^+ \quad [24]$$

or against the hydrogen electrode in the same electrolyte

$$Me + n_oH_2O \rightarrow MeO_{n_o} + n_oH_2 \quad [25]$$

The free enthalpy of the reaction is $\Delta G(n_o)$ and therefore the reversible potential of the "equilibrium" oxide electrode is

$$\epsilon_{o,h} = +\frac{\Delta G(n_o)}{2n_oF} - 0.059 \cdot pH \quad [26]$$

Simultaneously the reaction sequences $\beta(1,2)$ and $\beta(2,3)$ of the case already discussed are in equilibrium so that the potential can also be calculated by using Eq. [8] with the differential quotient of $\Delta G(n)$. Therefore as to be seen in Fig. 2, the tangent of the $\Delta G(n)$ curve at the value n_o goes through the zero point. The tangent from the zero point to the $\Delta G(n)$ curve results in the value n_o at the point of contact.

Nonequilibrium Oxide MeO_n on an Intermediate Layer with Electronic Conductivity (Passive Layer)

For all previous considerations of the discussion on potential of oxide electrodes in this paper an electronic equilibrium between the metal and the oxide was supposed. This means that the electrochemical potential $\eta = \mu + zF \cdot \psi$[4] of the electrons from the oxide throughout all the phases up to the metal of the voltmeter wires (mostly copper) is constant. Therefore the potential difference $\psi_1 - \psi_2 = \psi_{1,2}$ results as

$$\psi_{1,2} = \psi_1 - \psi_2 = \frac{1}{F}(\mu_1 - \mu_2) \quad [27]$$

since $\eta = \mu_1 - F \cdot \psi_1 = \mu_2 - F \cdot \psi_2$. If another metal, for example the parent metal (phase 1a) or any electronic conductor, for example the equilibrium

[4] μ is the chemical potential, μ_e is the chemical potential of the electrons = Fermi potential, ψ is the Galvani potential.

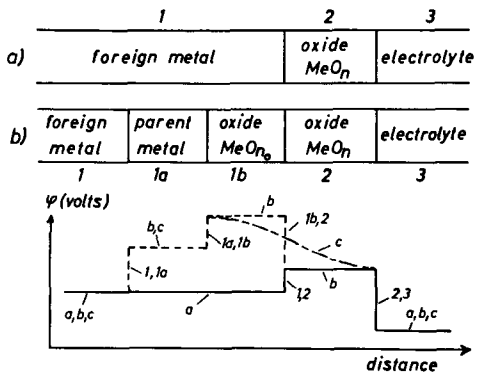

Fig. 8. (a and b). Change of the potential distribution by insertion of other electronic conductors (parent metal, equilibrium oxide MeO_{n_0}) between the foreign metal and the oxide of an oxide electrode; (c) without miscibility gap.

oxide (phase 1b) is inserted between the metal (phase 1) and the oxide (phase 2) as shown in Fig. 8, the cell voltage against the same reference electrode will not be changed. The potential difference $\psi_{1,2} = \psi_1 - \psi_2$ consists of $\psi_{1,2} = \psi_{1,1a} + \psi_{1a,1b} + \psi_{1b,2}$ (Fig. 8). Because of the relations

$$\psi_{1,1a} = \psi_1 - \psi_{1a} = \frac{1}{F} \cdot (\mu_1 - \mu_{1a})$$

$$\psi_{1a,1b} = \psi_{1a} - \psi_{1b} = \frac{1}{F} \cdot (\mu_{1a} - \mu_{1b})$$

$$\psi_{1b,2} = \psi_{1b} - \psi_2 = \frac{1}{F} \cdot (\mu_{1b} - \mu_2)$$

$$\psi_{1,2} = \psi_1 - \psi_2 = \frac{1}{F} \cdot (\mu_1 - \mu_2) \qquad [27a]$$

the value $\psi_{1,2}$ remains unchanged in the case when another or even some other electronic conductors are inserted between the metal and the oxide.

The thus inserted electronic conductors can be in the form of the equilibrium oxide MeO_{n_0} in contact with its own metal in phase 1, as represented in Fig. 8b. This is possible if a miscibility gap exists between the two oxides MeO_{n_0} and MeO_n, otherwise a continuous change of the degree of oxidation from n_0 to n will be established (curve c in Fig. 8). In all cases the very important result for all passivity phenomena is the fact that the electrode potential depends only on the thermodynamic properties of the oxide at the phase boundary 2,3 oxide/electrolyte. If the electronic equilibrium through the layer and also the ions equilibrium $\beta(2,3)$ or $\alpha(2,3)$ are established the potential of an oxide electrode cannot depend on the construction of the oxide layer. Therefore the potential of a passive electrode is only defined by the property and the composition of the surface oxide near the electrolyte. The layer thickness and the existence of intermediate layers cannot have any direct influence on the passive potential, may be by an indirect influence of these parameters on the degree of oxidation of the surface oxide. A fixed passive potential signifies a defined surface oxide. This statement must be used as the leading idea for all considerations about passivity.

If the pH value is changed, the potential of the passive electrode is

$$\epsilon_h = E_o(n) - 0.059 \cdot pH \qquad [28]$$

$E_o(n)$ is a definite function of the degree of oxidation of the surface oxide and is equal to E_o of Eq. [7] or [11], if the reaction $\beta(2,3)$ is potential determining.

Influence of a Corrosion Process on the Potential

The corrosion process of a passive metal covered with a pore-free oxide is represented by the reaction $\alpha(2,3)$ Me^{z+} (oxide) → $Me^{z+} \cdot aq$ (electrolyte). In the previous parts it was assumed that this reaction was either totally inhibited (Section on Oxide on a Foreign Metal. Oxygen Ion Equilibrium Oxide/Electrolyte) or in equilibrium (Section on Oxide on a Foreign Metal. Metal Ion Equilibrium at the Phase Boundary Oxide/Electrolyte). In most cases of passivity the reaction $\beta(2,3)$ O^{2-} (oxide) + $2H^+$ (electrolyte) ⇆ H_2O (electrolyte) determines the potential (Section on Oxide on a Foreign Metal. Oxygen Ion Equilibrium Oxide/Electrolyte) although the corrosion reaction $\alpha(2,3)$ is not totally inhibited. Therefore the influence of the rate of this corrosion process on the thermodynamically evaluated electrode potential is discussed here.

Current Equivalent to the Rate of Corrosion

If the corrosion reaction $\alpha(2,3)$ is not completely inhibited, the passive layer will be dissolved by a certain rate in the electrolyte. This loss of oxide can be compensated by an anodic formation of oxide. In the stationary state which is associated with a temporary constant layer thickness, the loss and the anodic formation of oxide must have exactly the same rate. Therefore the anodic current of the stationary state is equivalent to the corrosion rate, it is in fact the corrosion current density i_K. It may be remarked that this result is only valid in the absence of redox processes; therefore no electrons can cross the phase boundary oxide/electrolyte. In spite of the assumed good electronic conductivity no electronic current can then flow through the passive layer. The total current must be an ionic current.

The corrosion process can also be interpreted in another manner, and this may be the better one for regarding the elementary reactions. It was assumed that the electrolyte is not saturated by metal ions. Therefore there exists a thermodynamic tendency for a transfer of the metal ions of the oxide to the electrolyte. The rate of this process is the corrosion rate or the dissolution rate of the oxide. The rate of this metal ion transfer depends on the potential difference oxide/electrolyte and on the composition of the oxide, but it must be essentially independent of other parameters such as layer thickness, construction of the layer, etc. If the electrical field strength in the layer has such a value that the ionic current density is equivalent to the corrosion current density of the metal ions at the oxide/electrolyte boundary, the same amount of metal ions which reach[5] this boundary by ionic conductance will be transferred to the electrolyte by the corrosion process. A reaction O^2(oxide) + $2H^+ \cdot aq$ ⇆ H_2O (electrolyte) does not pass. It is to be recognized by this consideration

[5] Migrating oxygen ions in the electrical field have the same effect. In this case excess metal ions will remain at the phase boundary and will be transferred to the electrolyte with the corrosion rate. No distinction can be made between metal ion or oxygen ion migration.

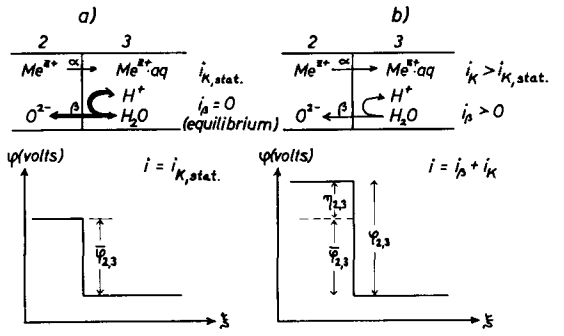

Fig. 9. Phase and potential scheme of the interface oxide/electrolyte. (a) Stationary state $i = i_{K,stat}$ (b) nonstationary state $i \neq i_{K,stat}$. $\eta_{2,3}$ = overvoltage.

that even the oxygen ions equilibrium has to be established if the stationary corrosion current density i_K flows. Therefore all thermodynamically evaluated relations referred to in the section on Potential of an Oxide Electrode assuming equilibrium $\beta(2,3)$ are valid for $i = i_K$. Figure 9a represents these conditions. $\bar{\psi}_{2,3}$ is the equilibrium potential difference.

No Current

In the currentless case an anodic partial current density i_K of metal ion dissolution $\alpha(2,3)$ continues and must be compensated by an equal cathodic partial current density of oxygen ion recombination with hydrogen ions to form water, reaction $\beta(2,3)$. The equilibrium potential difference $\psi_{2,3}$ of the reaction $\beta(2,3)$ must be cathodically polarized by a current density equal to $i_\alpha \approx i_K$. The electrode potential must differ from the equilibrium potentials Eq. [8], [11], or [13] by the cathodic overvoltage $\eta_{2,3}$ of the reaction $\beta(2,3)$. If the corrosion current density i_K is small compared to the exchange current density i_o of reaction $\beta(2,3)$ the overvoltage is small according

$$\eta = -\frac{RT}{2F} \cdot \frac{i_K}{i_o} \qquad [29]$$

For the nonstationary state the conclusions are also valid if i_K is the nonstationary corrosion current density.

Any Arbitrary Current Density i

If $i \neq i_K$, the layer is not in the stationary state. In absence of a redox process the current must be caused by an ionic migration through the layer in a high electrical field. However, this process is not to be discussed in connection with the problem of potential establishment if the electronic conductivity is good enough that the electrochemical potential $\eta = \mu + zF\psi$ of the electrons can be considered constant throughout the whole layer.

From this point of view the oxide electrode potential assumes a value which differs from the reversible potentials ϵ_h in Eq. [8], [11], or [13] by an overvoltage $\eta_{2,3}$ of the potential difference $\psi_{2,3}$ at the phase boundary oxide/electrolyte (Fig. 9b). This overvoltage is caused by the formation or dissolution of oxygen ions according O^{2-} (oxide) + $2H^+$ (electrolyte) $\leftrightharpoons$ H_2O (electrolyte) with a rate equivalent to the current density $i_\beta = i - i_K$. Primarily a variation of the current can only produce a change of the electrode potential $\Delta\epsilon = \Delta\eta = \eta_2 - \eta_1 = \eta(i_2 - i_{K,2}) - \eta(i_1 - i_{K,1})$. Very soon a variation of the degree of oxidation n of the surface oxide will follow by the reaction $\beta(2,3)$, and a further change of the potential will ensue. In all these considerations it is important that the corrosion current density i_K does not generally have the stationary value $i_{K,stat}$. The process $\alpha(2,3)$ Me^{z+} (oxide) $\rightarrow$ Me^{z+} (electrolyte) depends on the potential difference $\psi_{2,3}$, which changes with the overvoltage. Therefore $i_K(\eta)$ will be a function of the overvoltage η. Moreover $i_K(\eta)$ is a function of the degree of oxidation n. The thickness or the interior composition and construction of the layer cannot have any primary influence on the passive potential.

Influence of the Inner Layer Construction and Layer Thickness on the Ionic Current

The electrode potential depends only on the surface oxide (n) and the overvoltage $\eta_{2,3}$ of reaction $\beta(2,3)$; however, it does not depend on the construction of the layer. An ionic current can flow only if a gradient of the electrochemical potential of the ions (metal or oxygen ions) exists. Here an electrical field of 10^6 to 10^7 v/cm (4-11) has an important influence. The degree of oxidation n has to increase from the metal boundary to the electrolyte boundary. Only in such a layer can the migration of metal ions from the metal to the electrolyte side and the migration of oxygen ions in the opposite direction lead to an equalization of the different layer compositions at both sides, if this layer would be isolated.

The difference of the electrochemical and chemical potentials $\Delta\eta$ and $\Delta\mu$ of the Me^{2n+} and O^{2-} ions and also the electrical potential difference $\Delta\psi$ inside the layer is fixed by the electrode potential. This is the result of the former discussion. However, the ionic current density depends on the gradient $\partial\eta/\partial\xi$, $\partial\mu/\partial\xi$ and $\partial\psi/\partial\xi$ in the layer. Therefore the ionic current depends at the same potential on the layer thickness. The thicker the layer the smaller is the ionic current. The stationary layer thickness is then reached if at a pretended electrode potential, which defines the value $\Delta\eta = \Delta\mu + zF \cdot \Delta\psi$, the ionic current density is equal to the corrosion current density i_K. This stationary layer thickness δ_o can be reached from both sides, from $\delta < \delta_o$ by $i > i_K$ and from $\delta > \delta_o$ by $i < i_K$. The variation of the stationary layer thickness by changing the electrode potential depends on the variation of the corrosion current density.

Passive Electrodes with Equal Surface Oxides at Different pH Values

In the stationary case $i = i_K$ the overvoltage $\eta_{2,3}$ of the process $\beta(2,3)$ $O^{2-} + 2H^+ \leftrightharpoons H_2O$ must be zero. Therefore Eq. [8] and [13] must be exactly valid here. Then a stationary passive electrode has the same surface oxide in contact with the electrolyte if the passive potential against the hydrogen electrode in the same electrolyte (same pH value) is equal.

These considerations are necessary to comprehend the dependence of the corrosion current density on the potential and on the pH value. The reaction rate of $\alpha(2,3)$ Me^{z+} (oxide) $\rightarrow$ Me^{z+} (electrolyte) will

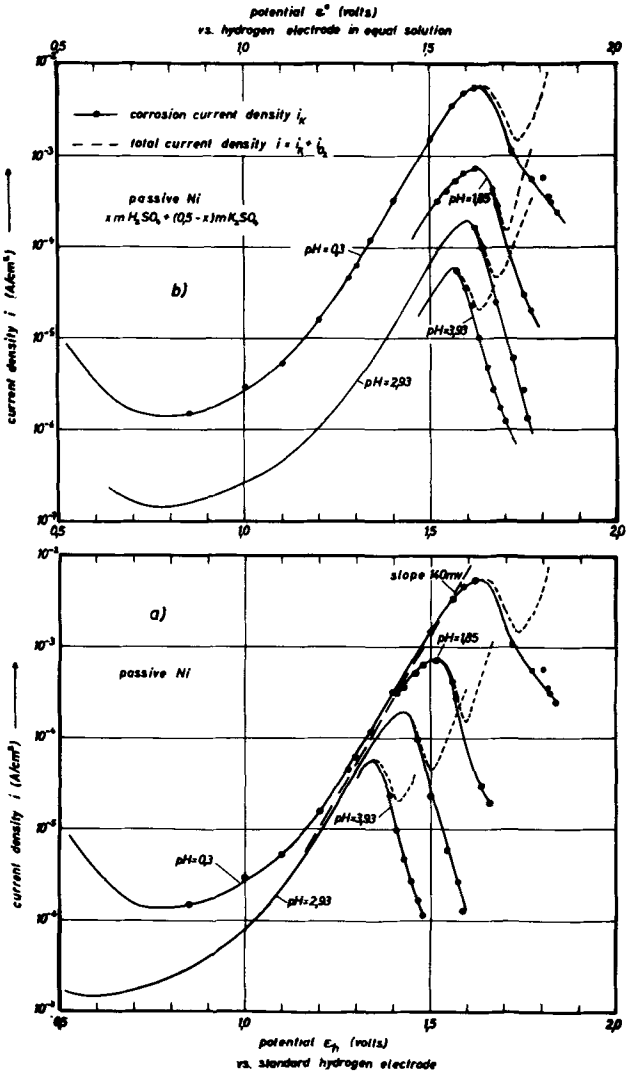

Fig. 10. Corrosion current density i_K of Ni at 25°C in dependence on the potential for different pH values: (a) potential against the standard hydrogen electrode; (b) against the hydrogen electrode of the same pH value.

depend on the potential difference $\psi_{2,3}$ and on the degree of oxidation n of the surface oxide. At the same pH value $\psi_{2,3}$ depends definitely on the value of n. A defined function $i_K(n)$ results. However, at constant n-value $\psi_{2,3}$ depends on the pH value according to

$$\psi_{2,3} = {}_0\psi_{2,3} - 0.059 \cdot \text{pH} \qquad [30]$$

At passive Ni, Fe, and Cr this conception may be applied in the following part.

Passive Nickel, pH-Dependence of Corrosion

Figure 10a represents the corrosion current density at passive nickel according to Vetter and Arnold (12). Similar curves were also found by Okamoto (13) and Osterwald, Uhlig, and Feller (14, 15). For all pH values the potential in Fig. 10a is referred to the standard hydrogen electrode. In certain potential range, in which moreover a Tafel line is valid, the corrosion current density seems to be independent of the pH value. It must be understood that this independence is only accidental. Here, two parameters work against each other and compensate almost completely. These two parameters are the change of

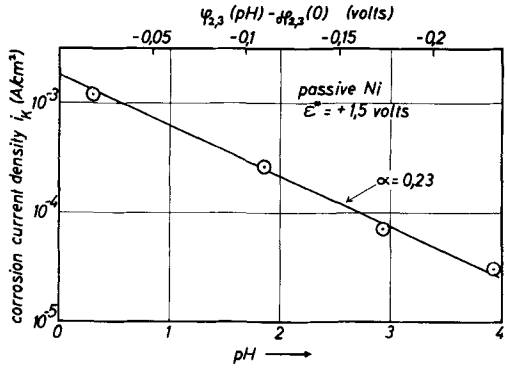

Fig. 11. Dependence of the corrosion current density i_K of Ni on the pH value at a fixed potential (1.5v) against the hydrogen electrode of the same pH value.

the composition of the oxide by the potential and the change of the potential difference at the phase boundary oxide/electrolyte by the pH value of the electrolyte. The states of the oxides which are compared at the same potential ϵ_h for different pH values are not the same ones as mentioned before. The states and compositions of the oxides are always equal for all pH values at the same potential against the hydrogen electrode of the same corresponding pH value. However, the corrosion current densities should be compared advantageously at different pH values with the same oxide of the same degree of oxidation. Therefore for this purpose the corrosion current density has to be drawn against the potential of the hydrogen electrode at the corresponding pH values in Fig. 10b.

In nearly the whole potential range, that is in nearly the whole range of degrees of oxidation, the dependence of the current densities on the pH values is equal in Fig. 10b. For the equivalent state of the oxide the corrosion current density depends on the pH value or on the potential difference oxide/electrolyte, respectively, according to a Tafel relation. This relation is represented in Fig. 11. The straight line corresponds to a transfer reaction of the nickel ion Ni^{2+} with a transfer coefficient $\alpha = 0.23$. The change of the corrosion current density by the potential ϵ is connected with the corresponding change of the degree of oxidation.

Passive Iron, pH Dependence of Corrosion

The corrosion current density of passive iron is in a wide potential range independent of the potential according to Franck and Weil (16, 1). The investigated potential range is above the Flade potential $\epsilon > \epsilon_F$ where a surface oxide of an approximate composition γFe_2O_3 is assumed (17-20). The degree of oxidation may change only to a very small extent in spite of the independence of i_K since the potential dependence is very strange and is not yet explained.[6] The pH dependence of i_K is found by Vetter (21) to be $\log i_K = a - 0.84 \cdot \text{pH}$ and would correspond to a transfer coefficient $\alpha = 0.28$ for trivalent iron ions Fe^{3+}.

Passive Chromium, pH Dependence of Corrosion

The corrosion current density of passive chromium is strongly dependent on the pH value and

[6] The explanation of Vetter (21) and Schottky (22) must be changed according to the new theory.

also on the potential. According to Heumann (23) and also to our measurements (24) in the range where a Tafel line is valid, the potential for a definite current density depends on the pH value and closely follows the relation $\epsilon_h = \epsilon_0(i) - 0.059 \cdot pH$. However, at a constant current density, these potentials correspond to a constant surface oxide as could be drawn from the previously presented theory and since the potential change is nearly 59 mv/pH unit. In a representation of the current density against the hydrogen electrode of the same pH value as that of the electrolyte the Tafel lines of different pH values coincide. This means that the corrosion current density, for an oxide of constant composition, is independent of the pH value.

Any discussion of this paper will appear in a Discussion Section to be published in the December 1963 JOURNAL.

REFERENCES

1. K. J. Vetter, *Z. Elektrochem.*, **55**, 274 (1951), special for passive iron.
2. K. J. Vetter, *ibid.*, **66**, 577 (1962).
3. G. S. Bell and R. Huber, *This Journal*, being reviewed.
4. K. J. Vetter, *Z. Elektrochem.*, **58**, 230 (1954).
5. K. J. Vetter, *Z. physik. Chem.*, **202**, 1 (1953).
6. K. J. Vetter, *Z. physik. Chem. N.F.*, **4**, 165 (1955).
7. A. Güntherschulze and H. Betz, *Z. Physik*, **91**, 70 (1934).
8. A. Güntherschulze and H. Betz, *ibid.*, **92**, 367 (1934).
9. D. A. Vermilyea, *Acta Met.*, **1**, 282 (1953).
10. D. A. Vermilyea, *ibid.*, **2**, 476 (1954).
11. D. A. Vermilyea, *This Journal*, **102**, 655 (1955).
12. K. J. Vetter and K. Arnold, *Z. Elektrochem.*, **64**, 244 (1960).
13. G. Okamoto, H. Kobayashi, M. Nagayama, and N. Sato, *ibid.*, **62**, 775 (1958).
14. J. Osterwald and H. H. Uhlig, *This Journal*, **108**, 515 (1961).
15. J. Osterwald and H. G. Feller, *ibid.*, **107**, 473 (1960).
16. U. F. Franck and K. G. Weil, *Z. Elektrochem.*, **56**, 814 (1952).
17. K. J. Vetter, *ibid.*, **62**, 642 (1958).
18. K. G. Weil and K. F. Bonhoeffer, *Z. physik. Chem. N.F.*, **4**, 175 (1955).
19. K. E. Heusler, K. G. Weil, and K. F. Bonhoeffer, *ibid.*, **15**, 149 (1958).
20. H. Göhr and E. Lange, *Naturwiss*, **43**, 12 (1956).
21. K. J. Vetter, *Z. Elektrochem.*, **59**, 67 (1955).
22. W. Schottky, *Halbleiterprobleme*, **2**, 233 (1955).
23. Th. Heumann and W. Rösener, *Z. Elektrochem.*, **59**, 722 (1955).
24. K. Vetter and W. Plieth, Unpublished paper.

Anodic Passivation of Nickel in Sulfuric Acid Solutions

Norio Sato and Go Okamoto

Physicochemical and Electrochemical Laboratory, Faculty of Engineering, Hokkaido University, Sapporo, Japan

ABSTRACT

The potential decay curve of a passive nickel electrode on open circuit was followed in solutions of pH ranging from 0.4 to 1.4. The three arrest potentials observed in the decay curve correspond to the equilibrium potentials for the NiO/Ni, Ni_3O_4/NiO, and the Ni_2O_3/Ni_3O_4 electrodes, respectively; the second potential is called the Flade potential, and the passivation occurs beyond this potential. A process for formation of the film is proposed that can be represented by the successive reactions, $Ni + OH^- \rightarrow NiOH^+ + 2e$, $3NiOH^+ + OH^- \rightarrow Ni_3O_4 + 4H^+ + 2e$. Then the critical potential beyond which the oxide formation takes place is calculated, under conditions when the solution in the vicinity of the surface becomes saturated with $NiOH^+$ corresponding to the solubility product of NiO, and is found to be equal to the Flade potential. The proposed mechanism can also explain the ability of the passive film to protect the metal against active dissolution due to breakdown of the film.

The mechanisms of dissolution of nickel in the passive and overpassive potential regions are discussed from measurements of the Tafel constant [$\tau = RT/F\ (\partial \ln i/\partial E)$] and the pH dependence of the dissolution rate ($\lambda = \partial \log i/\partial$ pH).

The results are summarized as follows: passive region; Ni^{2+} (oxide) + OH^- (aq.) → $NiOH^+$ (surface), $NiOH)^+$ (surface) → $NiOH^+$ (aq.): Overpassive region; Ni + H_2O (aq.) → NiOH (ads.) + $H^+ + e$, NiOH (ads.) → $NiOH^+$ (aq.) + e.

Since the day of Faraday many investigations have been performed on the passivity of metals, but the mechanism of anodic passivation is still to be clarified.

The present authors have made a series of experiments on the passive nickel to find the characteristic behavior on the passivation of this metal (1-12). The purpose of the present investigation is to elucidate the mechanism of anodic passivation of nickel and dissolution of passive nickel in sulfuric acid solutions.

Experimental

Electroplated (A) and rolled (B) nickel plates were used as specimens. The electroplated specimen was prepared in the following way. A pure nickel plate was welded with a platinum current lead which was sealed by a glass tube. The electroplating was performed in a nickel sulfate bath ($NiSO_4 \cdot 7H_2O$

Table I. Composition of specimens

Specimen	Co	Cr	Al	Mg	Mn	Ca	Zn	Ag	Cu	Sn	Pb	Fe	Ni
A	0.88	—	<0.04	<0.015	—	+	—	+	+	—	—	+	Balance
B	0.28	—	<0.04	—	<0.03	+	Trace	—	+	—	—	+	Balance

30g H_2BO_3 3.8g H_2O 100 cc) at a current density of 10 ma/cm^2 at 40°-50°C, the thickness of the film plated out being about 1 mm. In order to prepare specimen B, an electrolytic nickel plate was melted and cast into an ingot in a vacuum atmosphere; then it was cold rolled into a plate of 5 mm thickness and was annealed at 800°C for 10 min. The specimen of 15 x 10 mm with a small handle was cut out from the plate. After polishing the surface with 4/0 emery paper, a Pt current lead was soldered to the handle of the specimen and was sealed into a glass tube with an epoxy resin. The spectroscopic analysis of these specimens A and B gave the composition as in Table I where the sign (+) referred to detectable elements and (—) the undetectable.

Specimens were degreased by swabbing with benzene, etched with a mixed solution of 50% H_2SO_4 and 50% HNO_3 for about 1 min, followed by washing with a splash of distilled water.

Solutions of various hydrogen-ion concentrations were made from double-distilled water, sulfuric acid, sodium sulfate, and sodium hydroxide of A.R. grade reagents. In all cases the concentration of the sulfate ion was adjusted to a constant value of 0.5m SO_4^{2-}/l. A small amount of phosphate or acetate solution was added to this sulfate solution in order to increase the buffering capacity for hydrogen-ion when necessary.

The glass electrolytic cell, having a capacity of about 500 ml, consists of two compartments that contain the specimen and the auxiliary platinum electrode, respectively. These compartments are connected to each other with a sintered glass filter in order to avoid contamination of the specimen with hydrogen produced on the auxiliary electrode.

Dissolved oxygen and the other impurities in solution were carefully removed by pre-electrolysis with a platinum cathode of 10 cm^2 for several hours at a current density of about 5 ma/cm^2 and by bubbling pure nitrogen gas ($O_2 < 0.001\%$) for one day before the experiment. All the experiments were carried out in pure nitrogen gas at temperatures of 25° and 40°C.

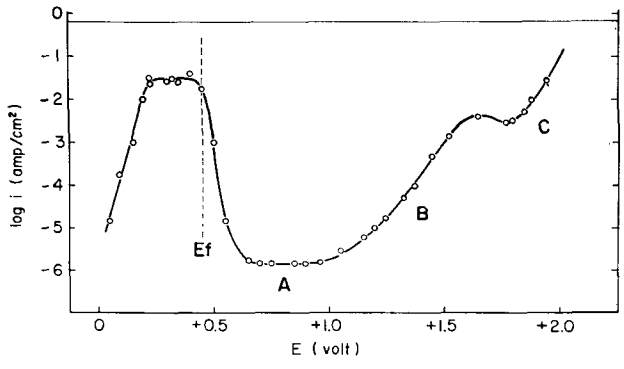

Fig. 1. Steady-state anodic polarization curve of nickel obtained by a potentiostatic method. Electrolyte: 1N H_2SO_4 saturated with pure nitrogen gas; temperature, 25°C.

Potentiostatic and galvanostatic methods were used for polarization measurements. The electronic potentiostat used has a current capacity of 150 ma in both anodic and cathodic directions, and the response-time for potential variation is about 10^{-2} sec/v.

Potential of the specimen was measured with reference to a saturated calomel electrode by a vacuum tube potentiometer and was converted to the standard hydrogen scale.

Results and Discussion

Flade potential.—Figure 1 shows the steady-state anodic polarization curve of nickel obtained by the potentiostatic method in 1N H_2SO_4 solution. The transition from the active to the passive state takes place in the range extending from +0.3 to +0.7v, and hence no clearly defined transition is observed. The dissolution current is almost constant in the passive potential region A, and it increases steeply with rising potential in the over-passive region B. The evolution of oxygen was observed in the potential region C. An oscillation of current is often observed in the transition region between B and C.

The dissolution rate of nickel and the rate of oxygen evolution were measured at various potentials and compared with the anodic current. It is found from the measurement (2, 4) that nickel dissolves into the solution in the form of divalent ion in both regions A and B and that it dissolves as trivalent ion in region C.

In the next experiment, the potential decay of passive nickel was followed after switching the anodic current off. The experiment was started from a fixed potential in region A. Two potential arrests E_2 and E_1 were observed in acid solutions as can be seen in Fig. 2. These potential arrests are longer and more clearly defined the longer is the time of polarization at the fixed potential.

When the potential of nickel was allowed to decay from a steady state in region C, an additional po-

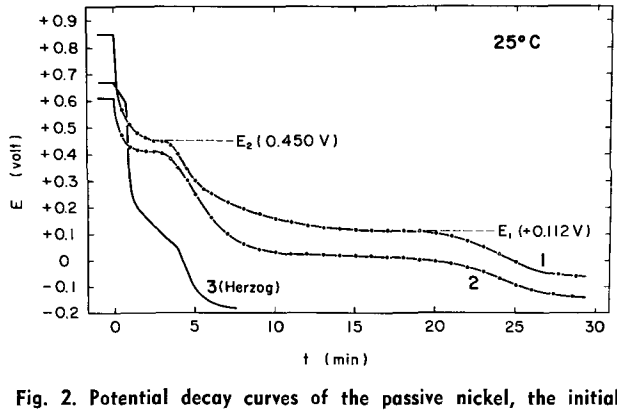

Fig. 2. Potential decay curves of the passive nickel, the initial potential being maintained at a constant potential in the passive region (A region) for about 30 hr: curve 1, 1N H_2SO_4; 2, 1M H_3PO_4, pH = 0.98; 3, 1N H_2SO_4 + 0.1N $NiSO_4$, measured by Herzog (14).

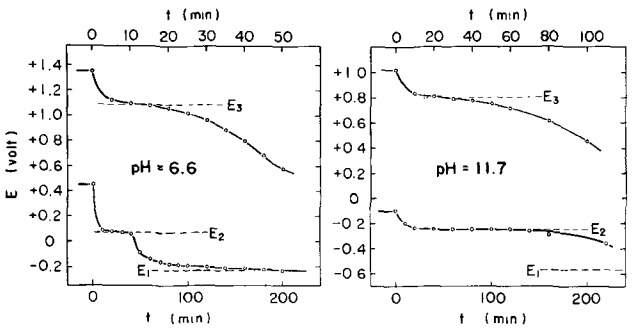

Fig. 3. Potential decay curves of nickel anode in neutral and alkaline solutions at 25°C, in the case of passive state (the curve in the less noble potential region) the initial potential being maintained at a constant potential for about 30 hr. Electrolyte: 0.5M Na_2SO_4 + 0.1M (KH_2PO_4 + K_2HPO_4), pH 6.6; 0.5M Na_2SO_4 + 0.01*N* NaOH, pH, 11.7.

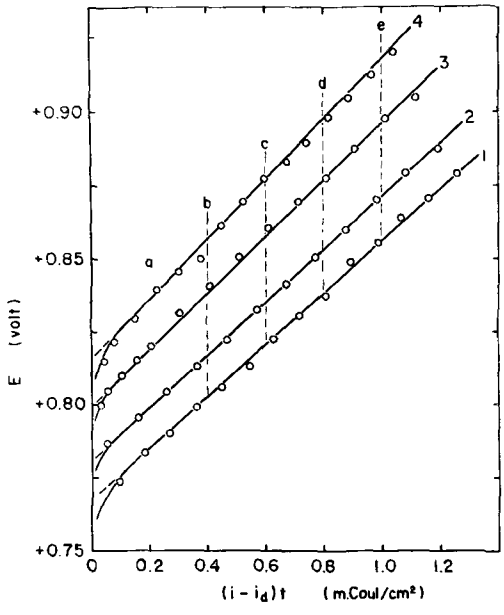

Fig. 4. Relation between potential and quantity of electricity accumulated in the passive oxide film at various anodic current densities. Initial potential, + 0.75v; equivalent dissolution current, i_d + 6.75 μa/cm^2; 40°C; 1N H_2SO_4. Curve 1, *i* 8.26 amp/cm^2 *K* 0.0870 v·cm^2/mcoul; curve 2, *i* 9.36 amp/cm^2, *K* 0.0900 v·cm^2/mcoul; curve 3. *i* 11.88 amp/cm^2, *k* 0.0950 v·cm^2/mcoul; curve 4, *i* 14.25 amp/cm^2, *K* 0.0995 v·cm^2/mcoul.

tential arrest appeared around the potential E_3 which was close to the transition potential from region B to region C. These potential arrests, E_1, E_2, and E_3, were also observed in neutral and in alkaline solutions,[1] two examples of which are shown in Fig. 3.

In order to confirm the value of the Flade potential E_f, the time variation of the polarization potential of passive nickel was measured at various anodic current densities in 1*N* H_2SO_4 (3, 9). The specimen was kept at a fixed potential in region A before the experiment. A linear relation was obtained between the polarization potential and the quantity of electricity accumulated in the passive film as is shown in Fig. 4. From this the spontaneous potential of passive nickel (the Flade potential) was estimated according to the following equation (3, 9, 13).

$$E - E_f = K\delta = K\,(i - i_d)t + \delta_o \qquad [1]$$

[1] Only the least noble potential E_1 tends to approach the final spontaneous potential with the decrease of hydrogen-ion concentration.

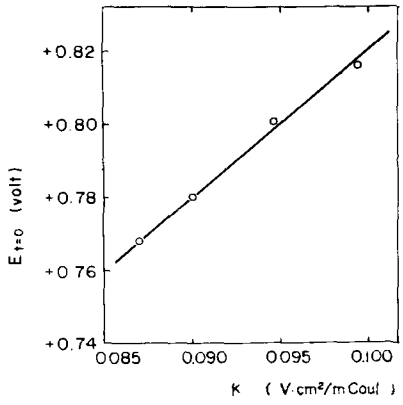

Fig. 5. Relation between estimated potential at t = 0 and the slope of the straight line in Fig. 4, which shows that extrapolation of all straight lines in Fig. 4 goes through one point from which the Flade potential E_f and the initial film thickness δ_o can be estimated. δ_o = 3.85 mcoul/cm^2.

	K v·cm^2/mcoul	Ef v
1	0.0870	+0.434
2	0.0800	+0.434
3	0.0948	+0.436
4	0.0995	+0.433

where E is the polarization potential applied at a current density i, E_f the Flade potential, i_d the potential-independent dissolution current in region A, t the time, δ_o the initial thickness of the passive film, and K a constant. The value of the Flade potential calculated from Eq. [1] which as indicated in Fig. 5 is close to the arrest potential E_2 observed in the decay curve of passive nickel. The arrest potential E_2 is very close to the transition potential for the passivation of nickel that is seen in the anodic polarization curve shown above in Fig. 1.

The arrest potentials E_1, E_2, and E_3 and the final spontaneous potential reached after the decay were estimated in sulfate solutions of various pH's extending from acid to alkaline regions. Results are shown in Fig. 6. The pH dependence of these potentials is expressed by

$$E_1 = +\,0.13 - 0.060\,\text{pH}\ (V) \qquad [2]$$

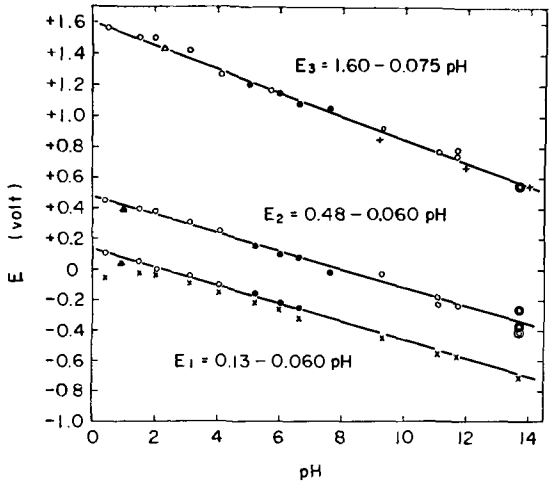

Fig. 6. Effect of pH on E_1, E_2, and E_3 at 25°C. x, spontaneous potential; ⊙, 0.5M SO_4^{2-}; •, 0.5M SO_4^{2-} + 0.1M (KH_2PO_4 + K_2HPO_4); △, 0.5M SO_4^{2-} + 0.1M (CH_3COOH + CH_3COOK); ▲, 1M H_3PO_4; ○, 1*N* KOH; +, values measured by Hickling and Spice (15).

$$E_2 = +0.48 - 0.060\,pH\ (V) \quad [3]$$

$$E_3 = +1.60 - 0.075\,pH\ (V) \quad [4]$$

The arrest potential E_1 seems to agree with the equilibrium potential for the formation of NiO

$$Ni + H_2O \rightleftharpoons NiO + 2H^+ + 2e \quad [5]$$

$$E_1(calc) = +0.108 - 0.059\,pH\ (V, 25°C) \quad [6]$$

It is therefore a reasonable assumption that E_1 is mainly due to the redox reaction given by Eq. [5].

It is quite natural to presume here that E_2 and E_3 correspond to the potential of the formation of higher oxides. The existence of two types of higher oxide, Ni_3O_4 and Ni_2O_3 have been shown by a number of workers, and the potential of the Ni_2O_3 electrode in an alkaline solution (15) appeared to be very close to the observed potential E_3.

The present authors assume here that the following reactions are directly related to E_2 (Flade potential) and E_3, respectively

$$3NiO + H_2O \rightleftharpoons Ni_3O_4 + 2H^+ + 2e \quad [7]$$
$$E_2 = E_2^\circ - 0.059\,pH\ (V, 25°C)$$

$$2Ni_3O_4 + H_2O \rightleftharpoons 3Ni_2O_3 + 2H^+ + 2e \quad [8]$$
$$E_3 = E_3^\circ - 0.059\,pH\ (V, 25°C)$$

When the concentration of divalent nickel ion in solution is comparatively large, another possibility of explaining the arrest potentials E_2 and E_3 arises. The reactions are

$$3NiOH^+ + H_2O \rightleftharpoons Ni_3O_4 + 5H^+ + 2e \quad [9]^2$$
$$E_2^1 = {}_oE_2^1 - 0.0885\,pH\ (V, 25°C)$$

$$2NiOH^+ + H_2O \rightleftharpoons Ni_2O_3 + 4H^+ + 2e \quad [10]^2$$
$$E_3^1 = {}_oE_3^1 - 0.118\,pH\ (V, 25°C)$$

In the case where the exchange rate of reaction [9] at the equilibrium potential is larger than that of reaction [7], the arrest potential E_2 will be determined by redox reaction (9). This situation could be expected if the concentration of nickel ion in solution is high, since the exchange rate of this reaction increases with nickel ion concentration (17). The discrepancy between the observed pH dependence of E_3 and that expected from reaction [8] may be caused by a side redox reaction involving nickel ion in solution which is produced as the result of the dissolution of nickel. The rate of this side reaction may be relatively large in acid solution.

It is concluded from the above that the Flade potential is not the formation potential of NiO but the transformation potential from NiO to the higher oxide Ni_3O_4 when the concentration of nickel ion in solution is small. The passive oxide film, therefore, will be either the single higher oxide Ni_3O_4 or the duplex oxide of NiO and Ni_3O_4. The potential of multiple-phase oxide electrode has been discussed in general from the point of view of thermodynamics and electrode kinetics (7).

Mechanism of anodic formation of passive film.— In this section, the authors will explain how the passivation of nickel in acid solution takes place at the Flade potential which is the transformation potential from NiO to Ni_3O_4.

Two possible processes have been proposed for the anodic formation of passive oxide film on metals (18, 21).

(*A*) "Precipitation" from supersaturated solution (process A).

$$\text{Metal} \xrightarrow[\text{dissolution}]{\text{(electrode reaction at the surface)}} \rightarrow$$

$$\text{Soluble metal ion} \xrightarrow[\text{precipitation}]{\text{(chemical reaction in the solution)}}$$

→ Oxide film deposition

(*B*) Direct reaction of metal with solution (process B).

$$\text{Metal} \xrightarrow[\text{formation of oxide film}]{\text{(electrode reaction at the surface)}}$$

→ Surface oxide film.

When the nickel electrode in sulfuric acid solution is polarized anodically in the active region, it dissolves into the solution in accordance with the reaction

$$\alpha : Ni + OH^- \rightarrow NiOH^+ + 2e \quad [11]$$

the equilibrium potential of which is given by

$$E_\alpha = E_\alpha^\circ + \frac{RT}{2F} \ln [NiOH^+]\,[H^+]$$

$$= +0.0278 - 0.0295\,pH + 0.0295 \log NiOH^+, (V, 25°C) \quad [12]$$

where E_α° denotes the standard redox potential, $[NiOH^+]$ and $[H^+]$ the concentration of $NiOH^+$ and H^+ ions, respectively.

The rate of anodic dissolution increases with rising potential as schematically shown in Fig. 7. According to electrode kinetics, the rate equation of this reaction could be formulated if the rate of backward reaction is negligible compared to that of the forward reaction. Thus

$$i_\alpha = k_\alpha [OH^-] \exp\{\tau_\alpha FE/RT\}$$
$$= i_\alpha^\circ \exp\{\tau_\alpha F(E - E_\alpha)/RT\} \quad [13]$$

where k_α is the rate constant, i_α° the exchange reaction rate at the equilibrium potential, and τ_α the Tafel constant. As the anodic dissolution proceeds, the concentration of nickel ion in the vicinity of surface will approach an equilibrium value. Thus

$$[NiOH^+]_{max} = \frac{1}{[H^+]} \exp\{2F(E - E_\alpha^\circ)/RT\} \quad [14]$$

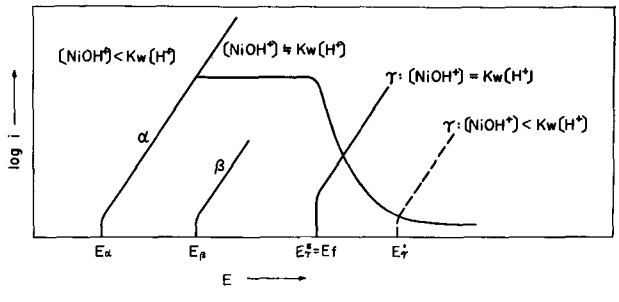

Fig. 7. Schematic potential-current curves of nickel for passivation in acid solution. α, dissolution in active state, $Ni + OH \rightarrow NiOH^+ + 2e$; γ, formation in active state, $3NiOH^+ + OH^- \rightarrow Ni_3O_4 + 4H^+ + 2e$; E_f, Flade potential; K_w, $[NiOH^+]/[NiO][H^+] = 10^{2.73}$.

[2] The existence of the divalent complex-ion $NiOH^+$ has been ascertained by several workers (16). The redox reactions involving trivalent nickel ion should also be considered.

When the concentration of $NiOH^+$ ion becomes larger than the saturated value which is determined by the solubility product of NiO, the precipitation of NiO occurs in the vicinity of the surface.

$$w : NiOH^+ \rightarrow NiO + H^+ \qquad [15]$$

The value of solubility product of NiO has been estimated as

$$K_w = [NiOH^+]_s/[H^+] = 10^{2.78} \qquad [16]$$

The critical potential above which this precipitation process occurs can be calculated from Eq. [14] and [16]

$$E_w = E_w^\circ + \frac{RT}{2F}\ln K_w + \frac{RT}{F}\ln [H^+]$$

$$= + 0.108 - 0.059\, pH \ (V, 25°C) \qquad [17]$$

This potential, of course, coincides with the equilibrium potential of the direct formation reaction of oxide on nickel.

$$\beta : Ni + OH^- \rightarrow NiO + H^+ + 2e \qquad [18]$$

$$E_\beta = E_\beta^\circ + \frac{RT}{F}\ln [H^+]$$

$$= + 0.108 - 0.059\, pH \ (V, 25°C) \qquad [19]$$

Thermodynamically, these two reactions [15] and [18] can occur in the potential region above E_w or E_β.

The oxide film deposited from the solution according to reaction [15] is expected to have a porous character. The limiting current of the active dissolution through pores would be calculated by the following equation if the rate of dissolution is controlled by the diffusion of $NiOH^+$ ion from the surface to the bulk of solution. Considering that the surface is saturated

$$i_{limit} \approx 2F\frac{D}{d}[NiOH^+]_s \qquad [20]$$

where D is the diffusion coefficient and d the thickness of the diffusion layer. The limiting dissolution rate increases with the decrease of pH in accordance

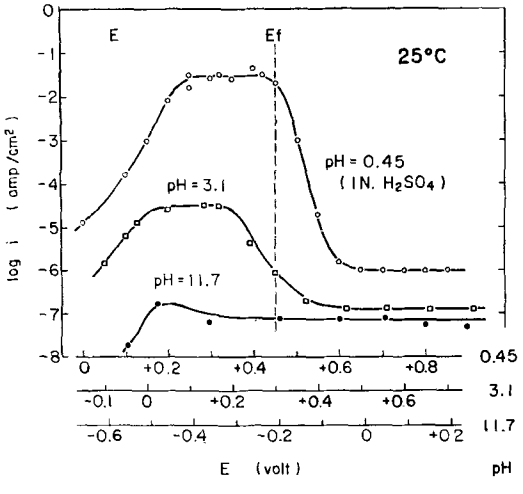

Fig. 8. Steady-state anodic polarization curves of nickel in sulfate solutions of acid and alkali measured by a potentiostatic method. Electrolyte, 0.5M SO_4^{2-}/1, saturated with N_2 gas; specimen, electrolytic nickel.

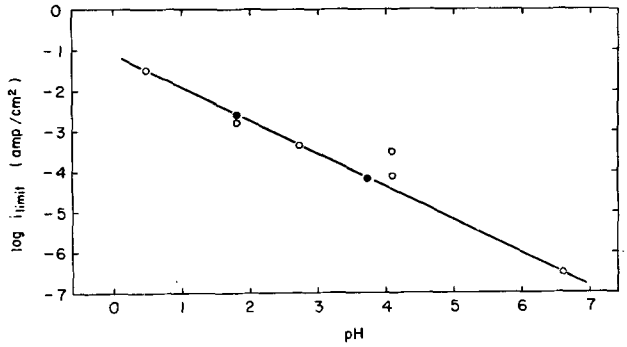

Fig. 9. Relation between pH and the limiting dissolution current of nickel in active state. Log i_{limit} = — 1.1 — 0.83 pH; 25°C; electrolyte, pH = 0.45 — 4.1, 0.5M SO_4^{2-}; pH = 6.6, 0.5M SO_4^{2-} + 0.1M (K_2HPO_4 + KH_2PO_4); ○, electrolytic nickel melted in vacuum; ●, commercial nickel.

with the change in the saturation concentration of $NiOH^+$. Thus, in acid solution the dissolution rate is so large that the existence of precipitated oxide NiO does not contribute to the passivation. Figure 8 shows the steady-state anodic polarization curves measured in acid and alkaline solutions. The limiting dissolution current observed in the active state is shown in Fig. 9; the pH dependence of it is close to that expected from Eq. [20].

If the oxide film of NiO is formed by the direct reaction of nickel and water, it would be pore-free and would render the specimen passive. However, it is not clear whether or not such a direct formation of oxide proceeds on the surface where rapid dissolution of nickel is taking place. The rate of the two reactions i_α and i_β is given as follows

$$i_\alpha = i_\alpha^\circ \exp\{\tau_\alpha F(E - E_\alpha)/RT\} \qquad [21]$$

$$i_\beta = i_\beta^\circ \exp\{\tau_\beta F(E - E_\beta)/RT\} \qquad [22]$$

where i_α° and i_β° denote the rate of the exchange reactions at equilibrium potentials E_α and E_β, τ_α and τ_β being the Tafel constant for both reactions. In acid solution, the potential current curve for the reaction α is usually in the less noble potential region compared to that for the oxide formation as can be seen in Fig. 7. In order to satisfy the condition $i_\beta > i_\alpha$, the potential of nickel electrode should be kept more noble than the potential E^x.

$$E^x = \frac{\tau_\beta E_\beta - \tau_\alpha E_\alpha}{\tau_\beta - \tau_\alpha} + \frac{RT}{\tau_\beta - \tau_\alpha}\ln\frac{i_\alpha^\circ}{i_\beta^\circ} \qquad [23]$$

Thus, the passivation of nickel due to the direct formation of oxide is expected to occur above the potential E^x. Accordingly, it is necessary to show that τ_β is unequal to τ_α so that the value of the potential E^x can be realized. However, no value of τ_β has been available, and its exact measurement cannot be made using available electrochemical technique. It seems also to be difficult in the direct formation mechanism to explain the coincidence of the passivation potential observed on the polarization curve with the Flade potential observed on the potential decay.

The present authors, then, proposed a new mechanism that is represented by the electrode reaction

producing a higher oxide film from the metal ion in solution.

$$\gamma: 3NiOH^+ + OH^- \rightarrow Ni_3O_4 + 4H^+ + 2e \quad [24]$$

$$E_\gamma = E_\gamma^\circ - \frac{3RT}{2F}\ln[NiOH^+] + \frac{5RT}{2F}\ln[H^+] = +0.725 - 0.1475\,pH - 0.0885\log NiOH^+, (V, 25°C) \quad [25]$$

The concentration of $NiOH^+$ in the vicinity of the surface will be maintained at about the saturated value of $[NiOH^+]_s$ in the potential region more noble than E_β, owing to the precipitation of the oxide NiO, so that the critical potential (equilibrium potential) for the formation of this oxide can be derived from Eq. [16] and [25].

$$E_\gamma^s = E_\gamma^\circ - \frac{3RT}{2F}\ln K_w + \frac{RT}{F}\ln[H^+) = +0.480 - 0.059\,pH\,(V, 25°C) \quad [26]$$

This is the passivation potential expected from this mechanism. The critical potential E_γ^s is the same as the equilibrium potential of the redox reaction between NiO and Ni_3O_4

$$f: 3NiO + OH^- \rightarrow Ni_3O_4 + H^+ + 2e \quad [27]$$

$$E_f = E_f^\circ + \frac{RT}{F}\ln[H^+] = +0.480 - 0.059\,pH\,(V, 25°C) \quad [28]$$

because the value of $\{E_\gamma^\circ - (3RT/2F)\ln K_w\}$ is calculated to be equal to E_f°.

Thus, the proposed mechanism interprets without ambiguity the important experimental fact that the passivation occurs beyond the Flade potential, *i.e.*, the transformation potential between NiO and Ni_3O_4.

According to the electrode kinetics, the rate of oxide formation γ is given by

$$i_\gamma = k_\gamma [NiOH^+][OH^-]\exp\{\tau_\gamma FE/RT\} = i_\gamma^\circ \exp\{\tau_\gamma(E-E)/RT\} \quad [29]$$

The current i_γ increases with the rise of potential and also with the increase of the concentration of $NiOH^+$ which is formed by the dissolution reaction α. Thus, pores in the passive film, if they happen to appear, will be repaired quickly according to the high concentration of $NiOH^+$ produced at the pores. In other words, the passive film of higher oxide Ni_3O_4 possesses the capacity of self-repairing which brings about more effective protection of the nickel electrode.

The anodic polarization curves of nickel in acid solution (Fig. 1 and 8) show that the specimen must be kept at somewhat more noble potential than the Flade potential in order to obtain the stable passive state. Differences between the Flade potential and the critical potential of the stable passive state have been reported on the anodic passivation of iron in acid and neutral solutions (22-24). According to the proposed mechanism γ, the anodic passivation of nickel in acid solution commences to occur around the Flade potential at which the saturated concentration of $NiOH^+$ ion and OH^- ion in the vicinity of surface and hence the rate i_γ of Eq. [29] begins to decrease because of the formation of Ni_3O_4 from these ions and the decrease of the area of bare metal surface. The change of the potential-current curve of reaction γ with the decrease of $NiOH^+$ concentration is schematically shown in Fig. 7. The decrease in the rate i_γ results in the decrease in the self-repairing capacity of the passive film. Accordingly, in order to obtain the stable passive state it is necessary to polarize the specimen at a somewhat more noble potential than the Flade potential, because the increase of the rate of reaction γ with the rise of potential is also expected.

The standard chemical potentials used are as follows

$\mu_{NiOH^+} = -55.41$ kcal/mole $\mu_{NiO} = -51.7$ (25), $\mu_{Ni_3O_4} = -189.7$ (5), $\mu_{H_2O} = -56.69$ (25), $\mu_{OH^-} = -37.595$ (25)

The value of μ_{NiOH^+} was calculated from the stability constant of the complex ion (16) given by $[NiOH^+][H^+]/[Ni^{2+}] = 10^{-9.4}$, and the value of $\mu_{Ni_3O_4}$ was calculated from the Flade potential measurement by the present authors.

Dissolution of passive nickel.—In the passive potential region A, the dissolution rate of passive nickel in sulfuric acid solution is independent of electrode potential as is seen in Fig. 1. The width of region A increases with decreasing pH and in alkaline solutions the active potential region disappears almost completely as can be seen in Fig. 10.

The dissolution current i_A was measured in sulfate solutions of various pH's, the result being shown in Fig. 11. In the acid region, i_A decreases with the increase of pH while in the alkaline region it increases with increasing pH. The relation between i_A and pH in the acid region is expressed by

$$\log i_A = k - 0.46\,pH \quad [30]$$

where k: 1.9 $\mu a/cm^2$ at 25°C and k: 10.9 $\mu a/cm^2$ at 40°C. No effect of the concentration of sulfate ion on the dissolution current i_A was observed in acid solutions. The concentration of divalent nickel ion did not affect the dissolution current i_A in acid solution when the concentration was not too large. This means that the rate of the backward reaction is negligibly small compared with that of the forward reaction when the concentration of nickel ion is small.

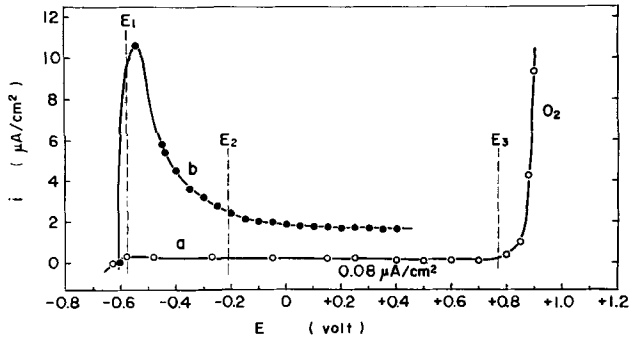

Fig. 10. Potential-current curves of nickel in alkaline solution under the nitrogen atmosphere. pH, 11.7, 25°C. Specimen, electrolytic nickel; electrolyte, 0.5M Na_2SO_4 + 0.01N NaOH; a, stationary state; b, transient state, the potential being changed with a rate of 0.02 v/min.

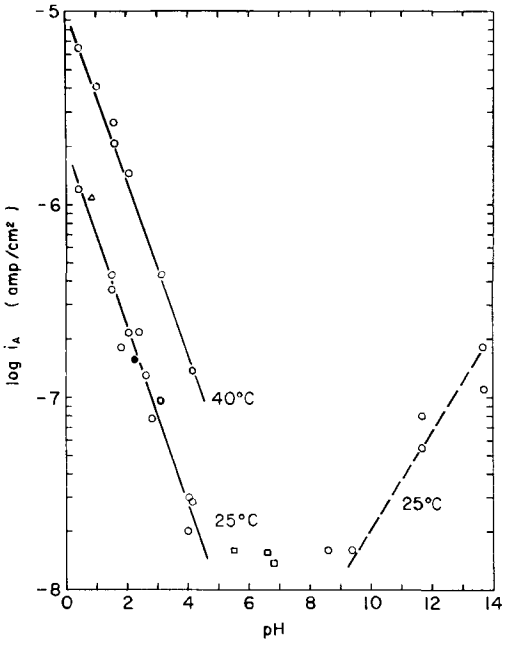

Fig. 11. Effect of pH on the dissolution current of passive nickel. log $i_A = k - 0.46$ pH. Specimen, electrolytic nickel. ○, 0.5M SO_4^{2-}; ●, 1M CH_3COOH; △, 1M H_3PO_4; □, 0.5M SO_4^{2-} + 0.1M CH_3COO^-.

When the specimen is in the passive region the formation and the dissolution of passive film proceed simultanously. The rates of these reactions are exactly the same at the steady state of polarization so as to keep thickness of the film constant. The dissolution reaction may be expressed by

$$(Ni^{2+},O^{2-}) + H^+ (aq.) \rightarrow Ni^{2+} (aq.) + OH^- (aq.) \quad [31]$$

The rate of this reaction is not affected by the electrode potential of nickel, but controlled only by the Galvani-potential difference across the oxide/solution interface.

Reaction [31] is a coupled reaction of the following two processes

$$a : O^{2-} (oxide) + H^+ (aq.) \rightarrow OH^- (aq.), \quad z = -2$$

$$b : Ni^{2+} (oxide) \rightarrow Ni^{2+} (aq.), \quad z = +2$$

where z is the charge of the ion passing across the interphase in the anodic direction. If the nickel ion dissolves as the complex ion $NiOH^+$, reaction b could be expressed as follows

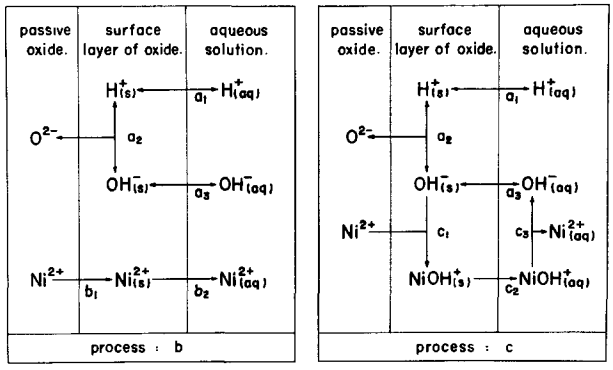

Fig. 12. Possible reaction steps at the phase boundary of oxide/solution in acidic region.

$$c : Ni^{2+} (oxide) + OH^- (aq.) \rightarrow NiOH^+ (aq.), \quad z = +2$$

In the same way, the reactions a, b, and c can be divided, respectively, into the following steps.

Process a.

$$a_1 : H^+ (aq.) \rightarrow H^+ (s), \quad z = -1$$

$$a_2 : O^{2-} (oxide) + H^+ (s) \rightarrow OH^- (s), \quad z = 0$$

$$a_3 : OH^- (s) \rightarrow OH^- (aq.) \quad z = -1$$

Process b.

$$b_1 : Ni^{2+} (oxide) \rightarrow Ni^{2+} (s), \quad z = 0$$

$$b_2 : Ni^{2+} (s) \rightarrow Ni^{2+} (aq.), \quad z = +2$$

Process c.

$$c_1 : Ni^{2+} (oxide) + OH^- (s) \rightarrow NiOH^+ (s), \quad z = 0$$

$$c_2 : NiOH^+ (s) \rightarrow NiOH^+ (aq.), \quad z = +1$$

$$c_3 : NiOH^+ (aq.) \rightarrow Ni^{2+} (aq.) + OH^- (aq.), \quad z = 0$$

Here, (s) denotes an ion located in the surface layer of the passive oxide. Figure 12 is the schematic representation of these processes.

Since processes a are in equilibrium, the Galvani-potential difference g between the passive oxide and the solution can be expressed as

$$\begin{aligned} g &= g_o + (RT/F) \ln [H^+ (aq.)]/[H^+ (s)] \\ &= g_o' + (RT/F) \ln [H^+ (aq.)]/[H^+ (s)] \\ &= g_o'' + (RT/F) \ln [O^{2-} (oxide)]/[OH^- (aq.)] \end{aligned} \quad [32]$$

where g decreases with the increase of pH. The rate equations can be formulated for process b and process c if the rate-determining step is assumed (26). The pH dependence of dissolution rate was estimated theoretically by assuming the symmetry factor of the rate determining step is 0.5. The results of the calculation shown in Table II were compared with

Table II. Theoretical pH dependence of the dissolution rate of passive nickel for possible reaction steps

Reaction step	z	$\partial \log i/\partial$ pH
$a_1 : H^+ (aq) \rightleftarrows H^+ (s)$	−1	
$a_2 : O^{2-} (oxide) + H^+ (s) \rightleftarrows OH^- (s)$	0	
$a_3 : OH^- (s) \rightleftarrows OH^- (aq)$	−1	
$b_1 : Ni^{2+} (oxide) \rightarrow Ni^{2+} (s)$	0	0
$b_2 : Ni^{2+} (s) \rightarrow Ni^{2+} (aq)$	+2	-2α
$c_1 : Ni^{2+} (oxide) + OH^- (s) \rightarrow NiOH^+ (s)$	0	0
$c_2 : NiOH^+ (s) \rightarrow NiOH^+ (aq)$	+1	$-\alpha$
$c_3\ NiOH^+ (aq) \rightarrow Ni^{2+} (aq) + OH^- (aq)$	0	−1
$d_1 : Ni^{2+} (oxide) + 2\ OH^- (s) \rightarrow NiO_2H^- (s) + H^+ (s)$	0	0
$d_2 : NiO_2H^- (s) \rightarrow NiO_2H^- (aq)$	−1	$+\alpha$

(s) designates the surface layer in the passive oxide; z is the number of the elemental charge of ion passing through the phase boundary of oxide/aqueous solution in the anodic direction; α is the symmetry factor of reaction step. In many electrode reactions, it has been known that $\alpha \approx 0.5$.

the pH-dependence of i_A ($\partial \log i_A/\partial$ pH = −0.46) observed for the sulfuric acid solutions, and it was concluded that the dissolution of passive film proceeds through process c in which step c_2 is rate-controlling. The following mechanism may be suggested for the dissolution of passive nickel in alkaline solutions

$$d_1 : Ni^{2+}(\text{oxide}) + 2OH^-(s) \rightarrow NiO_2H^-(s),\ z = 0$$
$$d_2 : NiO_2H^-(s) \rightarrow NiO_2H^-(aq.) \qquad z = 1$$

As can be seen in Table II, the pH-dependence of the dissolution rate is + 0.5 for the rate-determining step d_2. Here, the sign is reversed compared to that for the acidic solution. The experimental results obtained in the alkaline region agreed with this, even though the agreement was not perfect with respect to the number (Fig. 13).

Anodic dissolution in overpassive region.—The steady-state anodic polarization curves of nickel for the sulfuric acid solutions of various pH's were measured in the potential region extending from the passive to the overpassive region. The result is shown in Fig. 14. The anodic current observed in the overpassive region may be regarded as the sum of the dissolution current of passive film i_A and the

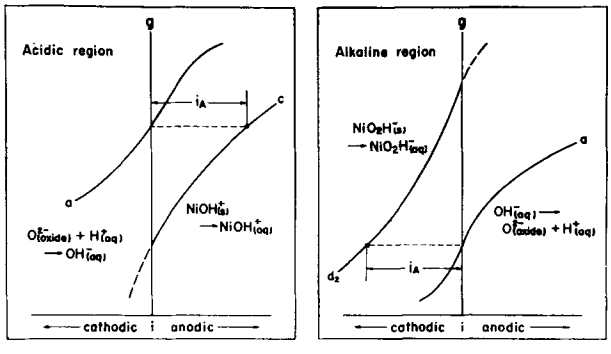

Fig. 13. Postulated Galvani potential-current diagram at the phase boundary of oxide/solution in acidic and alkaline region.

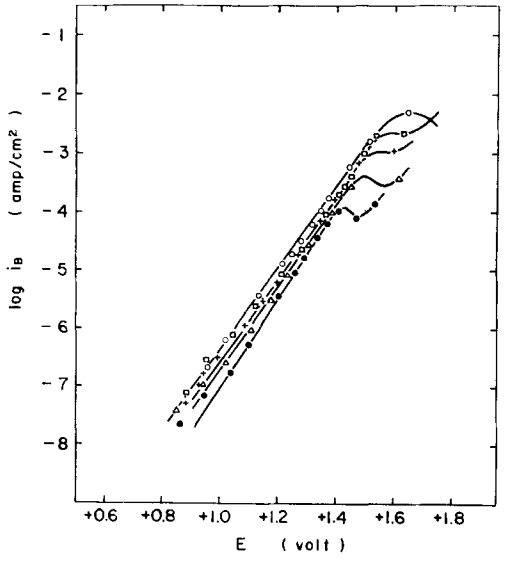

Fig. 14. Effect of pH on the steady-state anodic polarization curve of nickel in the passive and over passive region. Specimen, electrolytic nickel. 0.5 mole/l SO_4^{2-}, 25°C. ○, pH 0.45; □, pH 1.55; +, pH 1.80; △, pH 2.08; ●, pH 4.01.

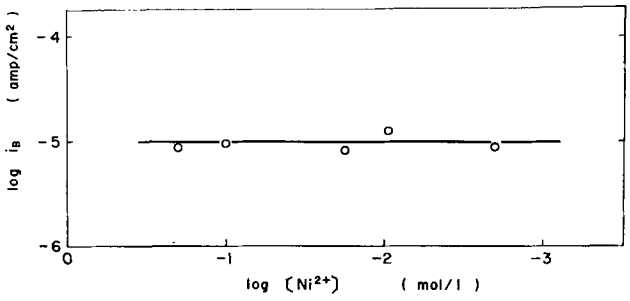

Fig. 15. Effect of pH on the potential-current curve for anodic dissolution of overpassive nickel in sulfate solution. $i_B = i - i_A$. pH, 1.55; 25°C; + 1.25v.

dissolution current of nickel i_B through the active patches in the passive film.

$$i_B = i - i_A \qquad [33]$$

It was found that the Tafel relation was observed between the potential and the current i_B and that it was scarcely affected by the hydrogen ion concentration in solution (Fig. 15). The results of the estimation of the Tafel constant are shown in Table III. The mean value amounts to about 0.5 which is close to that observed by Vetter and Arnold (27).

$$\tau = \frac{RT}{F}\left(\frac{\partial \ln i_B}{\partial E}\right) \approx 0.5 \qquad [34]$$

The concentration of sulfate ion and nickel ion, as well as that of hydrogen ion, does not affect the dissolution current i_B. However, the maximum value of i_B observed at the potential E_{BC} decreased with the increase of pH according to the equation

$$\log i_B{}^{max} = -2.13 - 0.46\ \text{pH},\ (\text{amp/cm}^2),\ 25°\text{C} \qquad [35]$$

The experimental results are shown in Fig. 16 and 17. The relation between the critical potential E_{BC} and pH can be expressed by the equation

$$E_{BC} \approx +1.68 - 0.08\ \text{pH (volt)} \qquad [36]$$

which is not affected by the temperature between 25° and 40°C. The value of this potential and its pH-dependence are in a good agreement with those of the arrest potential E_3 observed in the potential decay curve of anodized nickel electrode (*cf.* Fig. 6).

In Table IV are shown several possible reaction paths of the potential dependent dissolution of nickel together with the Tafel constant and the pH dependence of reaction rate estimated theoretically by assuming the symmetry factor of each step is 0.5.

Comparison between this and the result of experiment was made in the same way as described above,

Table III. Tafel constant of the dissolution of overpassive nickel measured in 0.5M SO_4^{2-}/l sulfate solutions with various pH values

Solution pH	Slope of Tafel line	Tafel constant $\tau = (RT/F)\partial \ln i_B/\partial E$
0.45	0.123	0.480
1.55	0.129	0.458
1.80	0.122	0.484
2.10	0.125	0.472
2.80	0.131	0.451
3.10	0.131	0.451
4.01	0.125	0.472
4.10	0.121	0.488

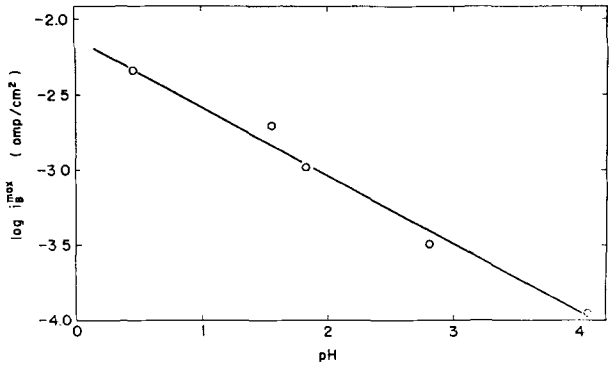

Fig. 16. Effect of pH on the maximum dissolution current of overpassive nickel in sulfate solution. 0.5M SO_4^{2-}, 25°C. log $i_B^{max} = -2.13 - 0.46$ pH.

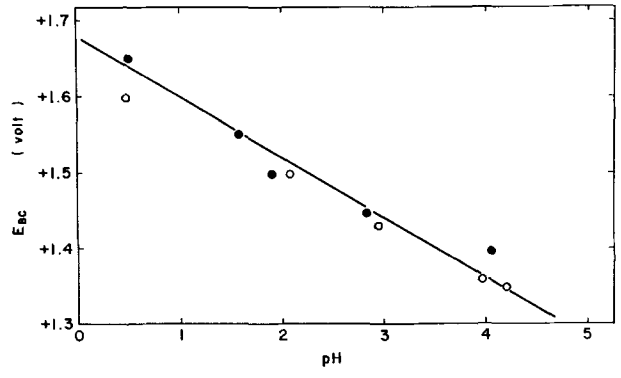

Fig. 17. Effect of pH on the critical potential where the maximum dissolution current i_B^{max} of overpassive nickel were observed. $E_{BC} = +1.68 - 0.080$ pH. 0.5M SO_4^{2-}; •, 25°C; ○, 40°C.

and it is concluded that the rate-determining step is reaction d or possibly reaction b where the whole surface of nickel is covered with NiOH. It has been concluded from a separate series of experiments (12) conducted by the authors that in the active potential region nickel dissolves through the reaction path (a + b) with the rate-determining step a; in other words the rate of step b is larger than that of step a. Therefore, if step b is rate controlling, the dissolution rate observed in the overpassive region should be larger than the dissolution rate of active nickel extrapolated to the same potential region because step a is rate determining in the active region. This is contrary to the experimental result.

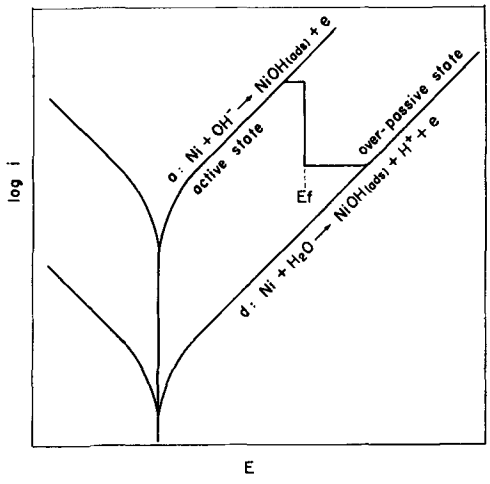

Fig. 18. Postrated potential-current curves of nickel in active and overpassive state.

Thus, step b is discarded. It is then clear that the dissolution reaction in the overpassive region proceeds through the consecutive reaction (d+b) in which step d is rate controlling.

The equilibrium potential of the dissolution reaction (d+b) in the overpassive region is equal to that of the dissolution reaction (a+b) in the active region, even though there is a difference between the rates of these reactions. Figure 18 shows the schematic interpretation for the proposed mechanisms of anodic dissolution in active region and in overpassive region.

Acknowledgment

The authors wish to express their thanks to Dr. M. Nagayama for his helpful discussion.

Any discussion of this paper will appear in a Discussion Section to be published in the December 1963 JOURNAL.

REFERENCES

1. G. Okamoto, H. Kobayashi, N. Sato, and M. Nagayama, *J. Electrochem. Soc. Japan*, **25**, 199 (1957), Overseas Ed., **25**, E45 (1957).
2. G. Okamoto, H. Kobayashi, M. Nagayama, and N. Sato, *Z. Elektrochem.*, **62**, 777 (1958).
3. G. Okamoto and N. Sato, *J. Electrochem. Soc. Japan*, **27**, 321 (1959); Overseas Ed., **27**, E128 (1959).
4. G. Okamoto and N. Sato, *J. Japan Inst. Metals*, **23**, 662 (1959); *Trans. Japan Inst. Metals*, **1**, 16 (1960).

Table IV. Tafel constant and pH dependence of reaction rate for various reaction steps

Reaction	Tafel constant $\tau = (RT/F) \cdot \partial \ln i_B/\partial E$	pH dependence $\lambda = \partial \log i_B/\partial pH$
w: Ni + OH^- (aq) → NiOH$^+$ (aq) + 2e	1	1
c: NiOH$^+$ (aq) → Ni^{2+} (aq) + OH^- (aq)	2	1
a: Ni + OH^- (aq) → NiOH (ads) + e	0.5	1
b: NiOH (ads) → NiOH$^+$ (aq) + e		
($x_{NiOH} \to 0$)	1.5	1
($x_{NiOH} \to 1$)	0.5	0
c: NiOH$^+$ (aq) → Ni^{+2} (aq) + OH^- (aq)	2	1
z: Ni + H_2O → NiOH$^+$ (aq) + 2e	1	0
c: NiOH$^+$ (aq) → Ni^{2+} (aq) + OH^- (aq)	2	0
d: Ni + H_2O → NiOH (ads) + H^+ + e	0.5	0
b: NiOH (ads) → NiOH$^+$ (aq) + e		
($x_{NiOH} \to 0$)	1.5	1
($x_{NiOH} \to 1$)	0.5	0
c: NiOH$^+$ (aq) → Ni^{2+} (aq) + OH^- (aq)	2	0

5. G. Okamoto and N. Sato, *J. Japan Inst. Metals*, **23**, 721 (1959).
6. G. Okamoto and N. Sato, *ibid.*, **23**, 725 (1959).
7. G. Okamoto and N. Sato, *ibid.*, **24**, 179, 183 (1960).
8. G. Okamoto and N. Sato, *ibid.*, **24**, 105 (1960).
9. G. Okamoto and N. Sato, *ibid.*, **24**, 130 (1960).
10. N. Sato and G. Okamoto, *ibid.*, **24**, 735 (1960).
11. N. Sato and G. Okamoto, *Trans. Japan Inst. Metals*, **2**, 113 (1961).
12. N. Sato, "Electrochemical Study on the Passive State of Nickel," Dissertation, Hokkaido Univ., Sapporo, Japan (1961).
13. K. G. Weil, *Z. Elektrochem.*, **59**, 711 (1955).
14. N. W. Herzog: Prom. Nr. 2671, Eidgenogssischen Techn. Hochschule Zurich (1957).
15. A. Hickling and J. E. Spice, *Trans. Faraday Soc.*, **43**, 762 (1947).
16. K. H. Gayer and L. Woontner, *J. Am. Chem. Soc.*, **74**, 1436 (1952); S. Chaberek, R. C. Courtney, and A. E. Martell, *ibid.*, **74**, 5057 (1952); "Stability Constant of Metal-Ion Complexes, Part II," The Chemical Society, Burlington House, London (1958).
17. J. O'M. Bockris, "Modern Aspect of Electrochemistry," Chap. IV, Academic Press, Inc., New York (1954).
18. W. J. Muller, *Z. Elektrochem.*, **30**, 401 (1924); **36**, 367 (1930); "Die Bedeckungstheorie der Passivität der Metalle," Berlin (1933).
19. E. Müller and K. Schwabe, *Z. Elektrochem.*, **39**, 414, 815 (1933).
20. W. A. Mueller, *This Journal*, **107**, 157 (1960).
21. H. Gerischer, *Agnew. Chem.*, **70**, 285 (1958).
22. U. F. Franck and K. G. Weil, *Z. Elektrochem.*, **56**, 814 (1952).
23. K. G. Weil and K. F. Bonhoeffer, *Z. Physik. Chem. N.F.*, **4**, 175 (1955).
24. K. E. Heusler, K. G. Weil, and K. F. Bonhoeffer, *ibid.*, **15**, 149 (1958).
25. W. M. Latimer, "The Oxidation Potentials," Prentice-Hall, New York (1952).
26. J. O'M. Bockris, "Modern Aspect of Electrochemistry I," Chap. IV, Academic Press Inc., New York (1954).
27. K. J. Vetter and K. Arnold, *Z. Elektrochem.*, **64**, 244 (1960).

The Initiation of Pores in Anodic Oxide Films Formed on Aluminum in Acid Solutions

T. P. Hoar and J. Yahalom

Department of Metallurgy, University of Cambridge, Cambridge, England

ABSTRACT

When pure aluminum is passivated at constant applied voltage in solutions ranging from pH 0-7, the current density representing film growth falls during the first few seconds in a manner that is qualitatively and nearly quantitatively the same for all solutions. The fall of current is succeeded by a rise to a constant value; the rise occurs the earlier, and is the greater, the lower the pH. The fall is interpreted as caused by barrier-layer formation, and the rise as caused by pore initiation when the field across the barrier layer has fallen low enough to allow the entry of protons into the film. Electron micrographs of the film surface show that very few pores are present on specimens that have not been anodized long enough for the initial current fall to halt, and that the pore system is fully established as soon as the succeeding rise is complete. A mechanism for pore formation is proposed.

When aluminum is made the anode in nearly neutral solutions such as those of ammonium borate or tartrate, with a voltage of *ca.* 4-400v across the cell, it quickly becomes passivated with an oxide film. This continues to thicken, at a decreasing rate, by ion migration under high-field conditions, forming a "barrier" layer; it substantially ceases to thicken when its thickness reaches about 14 Å/v of the cell voltage (1), because at the corresponding field strength, *ca.* 7 x 10^6 v/cm, the forming current density has fallen to a very small value. Quantitatively (2, 3)

$$i = A \exp(BE_F/y) \qquad [1]$$

where i amp/cm^2 is the current density, E_F v the p.d. between the metal and the solution, (the "forming voltage") and y cm the film thickness; A and B are constants, found by Charlesby (3) in work on substantial films formed at fairly high voltages to be 10^{-18} amp/cm^2 and 3.1 x 10^{-6} cm/v, respectively (3), although the earlier values found by Gunterschultze and Betz (2) and the more recent values of Johansen, Adams, and Van Rysselberghe (4) are somewhat different. The exponential current/field relationship arises from the high-field nature of the processes of ion transport either across the metal/film interface or through the film, either or both of which processes may control the over-all current density, according to Verwey (5), Cabrera and Mott (6), and Dewald (7).

When aluminum is made the anode in acid solutions such as 5-20% aqueous sulfuric or phosphoric acid, the current density (at a cell voltage of 10-20v) does not fall to a very small value and the film continues to thicken indefinitely. A barrier layer of thickness some 10 Å/v forms (8), but a very much thicker porous layer forms outside it, and part of the aluminum oxidized appears in the solution. Studies by electron-microscope (9-11), birefringence (12), and a.c.-impedance techniques (13, 14) have shown that the pores are long, nearly cylindrical tubes reaching from the outer surface to the barrier layer, and that they are arranged in a nearly regular hexagonal pattern with a center-to-center spacing of

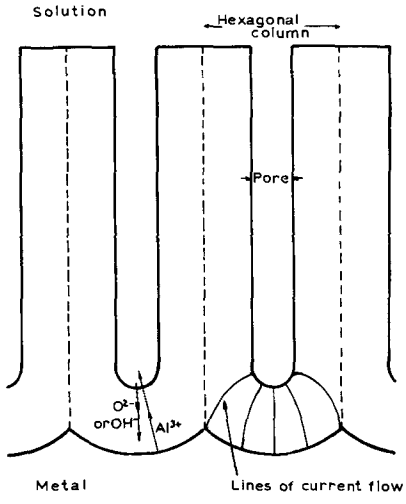

Fig. 1. Porous structure of acid formed anodic film, showing lines of current flow, pore-base structures and hexagonal columns.

about double the thickness of the barrier layer (Fig. 1). The continuing growth of the porous layer has been explained by Hoar and Mott (15) as caused by ion migration of Al^{3+} outward and OH^- inward through the film; oxygen movement inward and sideways from the pore end is necessary to build oxide ions into the hexagonal columns surrounding each pore (see Fig. 1). Migration of O^{2-} is considered (15) less likely than that of OH^-; this, having migrated through or partly through the growing solid, dissociates to O^{2-}, which stops, and H^+, which easily migrates back and fetches in more oxygen as OH^-. The total film thickness agrees very closely with that calculated for compact Al_2O_3 from the total charge passed; thus the Al^{3+} found in the solution must have dissolved, not from the surface of the porous film nor from the sides of the nearly cylindrical pores, but solely from the oxide at the base of the pores, and this dissolution is almost certainly field-assisted (15) rather than "thermal."

Franklin (16) from electron microscope studies has suggested that the pores initiate during the formation of the barrier layer, in the nearly hexagonal pattern; he has even suggested that this layer contains pore nuclei from the beginning. Nonetheless, no detailed mechanism for pore initiation, or explanation of the hexagonal pattern, has been given.

We have now studied the early stages of film formation in various acid solutions by measuring current-density transients at constant applied emf, by measuring the a-c impedance of thin formed films, and by electron microscopic examination of the film surface at different stages. The results indicate that the film in its earliest stages is of compact barrier nature, without pore nuclei, in every case. However, when the forming current density has fallen to a particular value, dependent on the anodizing solution and in particular on its *p*H, it increases considerably and, after passing through a maximum, finally reaches a steady value corresponding to the formation of the porous layer and the dissolution of Al^{3+} at the base of each pore. We interpret the rise in forming current density as caused by pore initiation, for which we suggest a mechanism. By electron microscopic examination of the film surface at different stages, we have confirmed that pores are indeed initiated during the period when the current density has ceased to decrease according to ideal barrier layer formation, and that the near-hexagonal pore pattern is fully established by the time that the final steady current density is reached.

Experimental Technique

Materials.—Superpure aluminium wire[1] specimens, 0.264 cm in diameter and 22 cm long, were used. They were stopped off at both ends to expose an area of *ca.* 3 cm^2 by the method of Hoar and Wood (14). The experimental surface was provided by a final chemical brightening in the following solution, used at 95°-100°C, in which the specimens were immersed with gentle movement for 45-75 sec: phosphoric acid (s.g. 1.75) 78% by volume; nitric acid (s.g. 1.42) 11% by volume; sulfuric acid (s.g. 1.84) 11% by volume; $FeSO_4 \cdot 7H_2O$ 0.8 g/l. Solutions were made from Analar chemicals and water condensed on Pyrex.

Apparatus.—A simple anodizing cell (Fig. 2), held at constant temperature to within ±0.2°C by conventional means, was used. Emf was provided from lead/acid batteries with suitable resistors in series, with simple switching. Current was recorded with a Honeywell Recorder (series 153 x 16, 0.25 sec pen speed) or with a Model 1049 Cossor Oscillograph with a Cossor Camera Model 1428 for the faster transients. The p.d. across the cell (and any compensating resistance, Fig. 2) was measured with an Avometer Model 8 or with a Solartron oscilloscope (CD 513). Impedance measurements were made with the bridge described by Wood, Cole, and Hoar (17), and electron micrographs were obtained on a Siemens Elmiskop I.

Procedure.—Before a particular anodizing, the specimen was degreased in methanol and acetone

[1] 99.99% Al, supplied by the Aluminum Development Association.

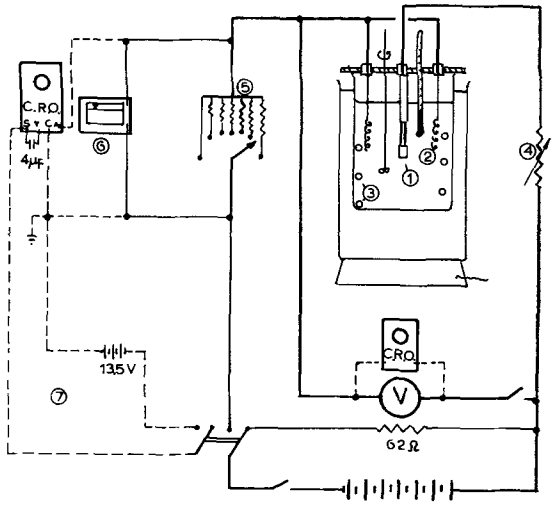

Fig. 2. Anodizing cell and circuit: (1) anode; (2) Pt cathodes; (3) cooling water coil; (4) compensating external resistance; (5) resistors to give a maximum of 10 mv potential drop for various current ranges; (6) pen recorder; (7) external beam-triggering circuit.

and dried. It was then chemically polished, rinsed in tap and distilled water, dipped in distilled water for 1 min, and dipped into the anodizing bath for 1 min before the current was switched on. The emf supply was kept permanently on circuit through a suitable resistor before switching over to the cell, so as to be as stable as possible. Thirty seconds after the current was switched off, the specimen was removed from the bath, rinsed in running distilled water, and dipped for 1 min in distilled water, before it was used for a-c impedance measurements or for producing a carbon replica.

The Honeywell recorder was arranged with shunting resistors to give full scale deflection of 10 mv for various current density ranges, as indicated in Fig. 2. When the current density transients were recorded oscillographically, two alternative methods were employed, the moving-film technique, and the time-base beam-triggering technique with the triggering circuit closed simultaneously with the anodizing circuit. One beam of the oscilloscope was connected across the resistors in the same way as the Honeywell recorder, while the second beam was used as a reference line and as a time control on the oscillogram, with a small 50 cps signal.

Impedance measurements on formed films were carried out at room temperature in a 3% solution of ammonium tartrate, with a cylindrical aluminum counter-electrode as described by Hoar and Wood (14).

Carbon replicas for electron microscopy were prepared on the dried specimens by graphite evaporation *in vacuo*. The carbon film on the specimen was carefully scratched into 2-mm squares, and the specimen was dipped for 2 sec in the chemical polishing solution at room temperature and immediately afterward into distilled water in a Petri dish, in which it was rotated slightly for a few seconds. The replicas then floated on the water surface. This method fulfilled the requirement that no gas, which may break the replica, should be evolved during the oxide dissolution; all the carbon film was stripped off in water, and there was no difficulty in mounting the replica on a 200-mesh electron microscope grid. Replicas were shadowed with gold-palladium alloy to improve contrast, and electron micrographs were taken at a magnification of 60,000X.

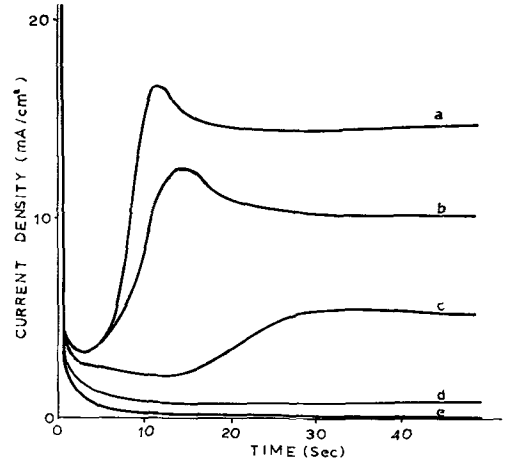

Fig. 3. Current transients for anodizing in various electrolytes at 14.4v, 25°C (pen recorded). a, 15% w/v sulfuric acid, pH 0.02; b, H_2SO_4 + $NaHSO_4$, pH 0.23; c, 183.6 g/l $NaHSO_4$, pH 0.36; d, $NaHSO_4$ + Na_2SO_4, pH 1.19; e, 3% ammonium tartrate, pH 7.30.

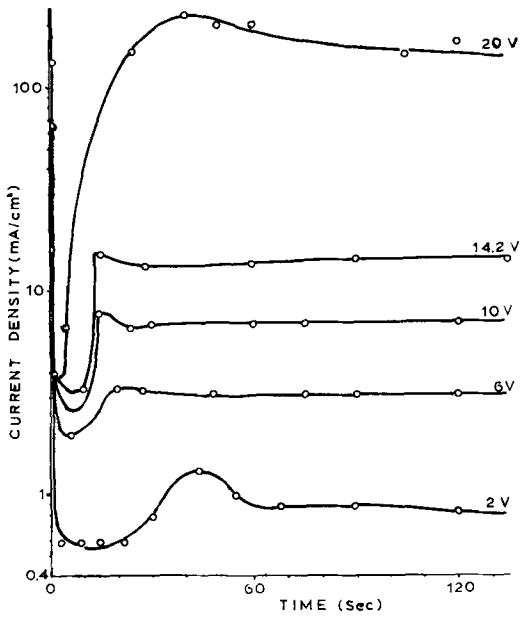

Fig. 4. Influence of cell voltage on current transients 15% w/v sulfuric acid at 25°C.

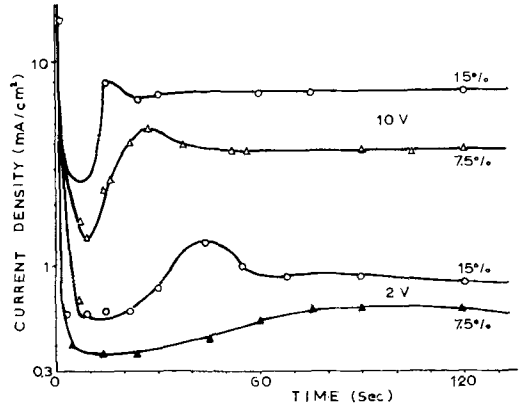

Fig. 5. Influence of sulfuric acid concentration on current transients at applied emf of 2v and 10v.

Results and Interpretation

Current-density/time relation.—Typical continuously recorded current density transients, for anodizing at 25° and 14.4v applied emf in several solutions, are shown in Fig. 3. It is evident that the initial parts of all the curves are very nearly identical. Also, the minimum c.d. and the final steady c.d. are higher and occur earlier, the lower the *p*H of the solution. The fall of c.d. to a minimum, and its subsequent rise to a final steady value, are well-known features of sulfuric acid anodizing giving porous films (18).

Influence of cell voltage.—Figure 4 shows some manually recorded current density transients for anodizing in 15% w/v sulfuric acid at 25°C at applied emf from 2 to 20v. The shape of all the curves is similar and the final steady c.d. is dependent on the applied voltage.

Influence of acid concentration.—Figure 5 shows the effect of diluting sulfuric acid from 15% to

Table I. Thickness of pore-base layer, shortly after the start of steady-state anodizing, and in later stages, showing influence of forming voltage

Solution	Temp, °C	Run	Steady state current density, i_s, ma/cm²	Forming voltage, E_F, v	Total charge passed, c/cm²	Balancing capacitance at 30 cps, μF/cm²	Thickness of pore-base layer, y, Å	$\frac{E_F}{y}$, v/cm × 10^7
H_2SO_4 (15% w/v)	17	1	1.53	7.4	2.7	1.13	66	1.13
		2	3.93	11.2	2.8	0.707	105	1.07
		3	7.73	15.3	2.8	0.525	142	1.08
		4	7.33	15.3	20.0	0.541	137	1.12
		5	43.3	21.4	19.9	0.421	177	1.21
H_2SO_4 (7.5% w/v)	25	6	0.55	3.5	2.8	2.77	27	1.30
		7	1.03	7.4	2.8	0.887	84	0.88
		8	3.70	11.3	2.8	0.707	105	1.08
		9	3.67	11.3	19.7	0.729	102	1.11
		10	6.47	15.3	19.7	0.537	138	1.11
		11	17.8	21.2	19.7	0.533	139	1.53
H_2SO_4 (15% w/v), pH 0.02	25	12	0.83	3.4	2.8	2.96	25	1.36
		13	1.77	5.3	2.8	1.63	46	1.15
		14	3.17	7.3	2.8	1.23	60	1.22
		15	—	*ca* 11.2	2.8	0.750	99	—
		16	7.0	11.2	19.7	0.752	99	1.13
		17	13.7	15.2	19.7	0.550	135	1.13
		18	127	21.1	19.7	0.450	165	1.28
H_2SO_4 + $NaHSO_4$,* pH 0.23	25	19	9.43	15.7	5.7	0.517	144	1.09
$NaHSO_4$ (18.36% w/v),* pH 0.36	25	20	4.65	15.8	2.8	0.509	146	1.08
$NaHSO_4$ + Na_2SO_4,* pH 1.19	25	21	1.43	15.8	0.9	0.467	159	0.99

* SO_4^{2-} concentration as in H_2SO_4 (15% w/v).

7.5%; it is similar to that obtained by changing to sulfate solutions of higher pH (Fig. 3).

Influence of temperature.—Reducing the bath temperature from 25° to 17°C had a marked influence on the final anodizing current density, Table I, but not on the general shape of the curves. These results are discussed later.

Initial part of the transients.—The initial parts of some of the transients were examined in more detail by photographically recording oscillograph traces. Figure 6a shows a typical trace for anodizing in 3% ammonium borate solution, Fig. 6b one for 15% sulfuric acid solution. These are not strictly comparable because of the much higher electrolytic resistance of the ammonium borate solution, which produced a considerable ohmic drop; Fig. 6c shows a typical trace for the 15% sulfuric acid solution with a 16.8 ohm compensating resistor in series, and the close qualitative resemblance of this trace to Fig. 6a is evident. Figure 6d is a typical trace for the 18.36% sodium dihydrogen sulfate solution, pH 0.36, also with a series resistor; it is almost identical with the trace of Fig. 6c. It is evident that the early part of the film formation is substantially the same for all solutions, and it seems very probable that the process is the formation of a barrier layer of Al_2O_3 (γ or amorphous) in every case.

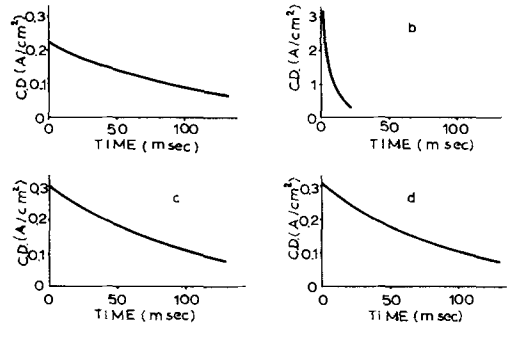

Fig. 6. Current transients for anodizing at 14.4v and 25°C in various solutions oscillographically recorded (a) 3% ammonium borate; (b) 15% w/v sulfuric acid; (c) 15% w/v sulfuric acid with 16.8 ohm in series; (d) $NaHSO_4$ (183.6 g/l) with 16.8 ohm in series.

We shall assume that an Al_2O_3 layer grows according to Eq. [1] with $A = 10^{-18}$ amp/cm², $B = 3.1 \times 10^{-6}$ cm/v. E_F, the forming voltage across the film between the metal and the solution, is given by

$$E_F = E_{app} + E_{int} - \eta_c - i\sigma(R_{sol} + R_{ext}) \qquad [2]$$

Here E_{app} v is the applied emf (Fig. 2). E_{int} v is the emf of the cell having as over-all reaction

$$2Al + 3H_2O \rightarrow Al_2O_3 + 3H_2$$

As pointed out by Vermilyea (19), such an "internal" emf must be included as part of the driving force in the anodizing circuit; from the free energy of formation data in the literature (20) we take it as 1.50v. η_c v is the overpotential at the cathode, measured in separate experiments. i amp/cm² is the current density at the anode and σ cm² its surface area, R_{sol} Ω is the resistance of the cell solution (measured with a bright platinum anode of the same geometry as the aluminum anodes at 10 kc/sec on an a-c bridge) and R_{ext} Ω is the external series resistance as shown in Fig. 2. Thus, substituting the value of E_F given by Eq. [2] in Eq. [1], we can estimate the

Table II. Anodic film thickness at earliest stages, estimated from charge passed (X) and from Eq. [1] (Y)

Applied emf: 14.4v. Temp, 25°C

Solution	Solution resistance, R_{sol}, ohm	Series resistance, R_{ext}, ohm	Area of specimen, σ, cm²	Time of anodizing, t, msec	Current density, i, ma/cm²	Cathode overpotential, η_c, v	Forming voltage, E_F	Charge passed, $\int_o^t i dt$, mc/cm²	Anodic film thickness from $\int_o^t i\,dt$, X, Å	Total film thickness from i and Eq. [1], Å	Anodic film thickness from i and Eq. [1], Y, Å	X/Y
H_2SO_4 (15% w/v)	0.3	16.8	2.59	0	300	0.8	1.8	0	0	13	0	—
				50	181	0.7	7.2	12.0	62	56	43	1.44
				100	108	0.6	10.5	19.2	99	83	70	1.41
$NaHSO_4$ (18.36% w/v)	0.5	16.8	2.56	0	313	0.5	1.5	0	0	11	0	—
				50	184	0.3	7.5	12.2	63	58	47	1.34
				100	107	0.3	10.9	19.4	100	86	75	1.33
Ammonium borate (3%w/v)	17.9	0	2.69	0	225	0.8	4.3	0	0	33	0	—
				50	140	0.8	8.4	8.8	46	66	33	1.39
				100	90	0.7	10.9	14.6	75	87	54	1.39
Ammonium tartrate (3% w/v)	5.5	6.0	2.68	0	330	0.9	4.8	0	0	37	0	—
				50	190	0.8	9.2	13.4	69	71	34	2.03
				100	119	0.7	11.5	21.6	111	91	54	2.05

film thickness y cm for any current density i. We can also estimate the thickness of film formed by anodizing from the charge passed at time t, $\int_o^t i dt$, and the density of Al_2O_3, taken as 3.42, assuming a roughness factor of unity and no film dissolution. Film thicknesses estimated by the two separate methods, for $t = 0$, 50, and 100 msec, for several solutions, are given in Table II, of which the salient features are:

(*A*) The initial film thickness, before the application of the anodizing emf, is small but significant: from the value in the borate (pH 8) solution, it is about what would be expected for the film left after chemical polishing. The smaller values found in the acid solutions may indicate some dissolution of the initial film, occurring before the anodizing emf was applied. These estimates assume, of course, that the film left after chemical polishing obeys Eq. [1] with the same values of A and B as those appropriate to Charlesby's anodic films.

(*B*) The agreement between the film thickness as obtained from the i/E_F relationship and from $\int_o^t i dt$ might be thought as good as could be expected, in view of the thinness of the films. However, the differences found are almost certainly significant. It is notable that the ratio

$$\frac{\text{Anodic film thickness estimated from charge passed}}{\text{Anodic film thickness estimated from Eq. [1]}}$$

is always in the range 1.33-2.05. It is probable that the small ratio arises mainly because the "roughness factor" is somewhat larger for our surfaces with very thin films than it was for the much thicker films from which A and B in Eq. [1] were determined by Charlesby (3); it is evident that the estimate of film thickness from charge passed diminishes in inverse proportion to the roughness factor, and it is easily shown that the estimate from Eq. [1] increases slightly with increase of roughness factor. The use of values for A and B given in the early work of Gunterschultze and Betz (2), 3.62×10^{-23} amp/cm² and 4.25×10^{-6} cm/v, respectively, merely alters the range of the above ratio to 1.2-1.9, without affecting the argument.

These quantitative results, experimentally scarcely distinguishable for the various solutions, are good confirmation that the initial process is the formation of a barrier layer almost independent of the solution.

The current density at which the i/t relationship for the film-forming begins to deviate from that for the nearly neutral solutions, i_p, the minimum current density, i_m, and the final steady current density, i_s, (Fig. 3, 4, 5, 7) depend on the solution, in particular on its pH and temperature. Decrease of pH and/or increase of temperature leads to larger values of i_p, i_m, and i_s; i_p is, of course, difficult to determine quantitatively. i_m, evidently governed by the overlap of transients representing different processes, Fig. 7, has qualitative relevance in that it occurs earlier, showing that the second process leading to the increase of i with time begins sooner, at lower pH values and higher temperatures.

These results are most easily interpreted by supposing that at i_p pores begin to form, and that by the time i_s is reached, the pore distribution is complete; the growing porous film subsequently offers very little resistance to its own growth, this resistance being almost completely provided by the steady-state pore-base layer. We note here particularly that

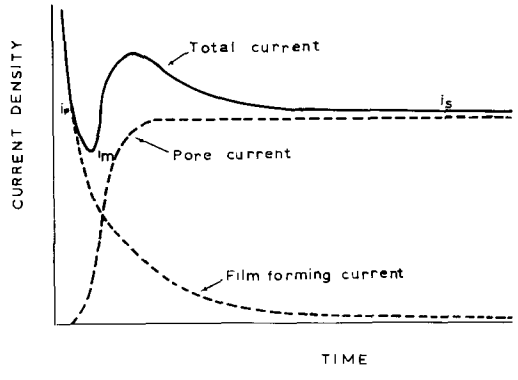

Fig. 7. Schematic illustration of "overlapping" processes leading to minimum in current transient.

the process leading to deviation from the initial barrier growth does not begin until i, and thus the field between the metal and the solution (Eq. [1]), is small enough. Since this process begins at higher values of E_F when the solution pH is lower and/or the temperature higher, we conclude that it is the thermal entry of protons from the solution into the barrier film against the field. We consider later a mechanism by which such a process may be expected to initiate pores.

Electron microscopic examination.—Figures 8a and b are electron micrographs of shadowed carbon replicas of the surface of anodic films formed at 25°C 14.4v respectively for 0.5 sec and 10 min in 3% ammonium tartrate solution. In Fig. 8a no pores are visible; the few singularities of irregular distribution are defects in the original pre-anodizing film or in the replica. In Fig. 8b there are distinct indications of a few pores, which may be supposed to have become initiated just as in the acid-formed films, but after the much longer time lapse. Figures 9a and b show similar replicas of the surface of anodic films formed in sulfuric acid at 14.4v, 25°C respectively for 0.25 sec and 5 sec. In Fig. 9a a substantial pore-free area is visible, although some pore initiation has already occurred; it was impossible to anodize for a short enough time and to remove the specimen before i_p was reached. In Fig. 9b the pore system may be seen to be fully established.

These results are in harmony with the interpretation of the current density transients, that pores are

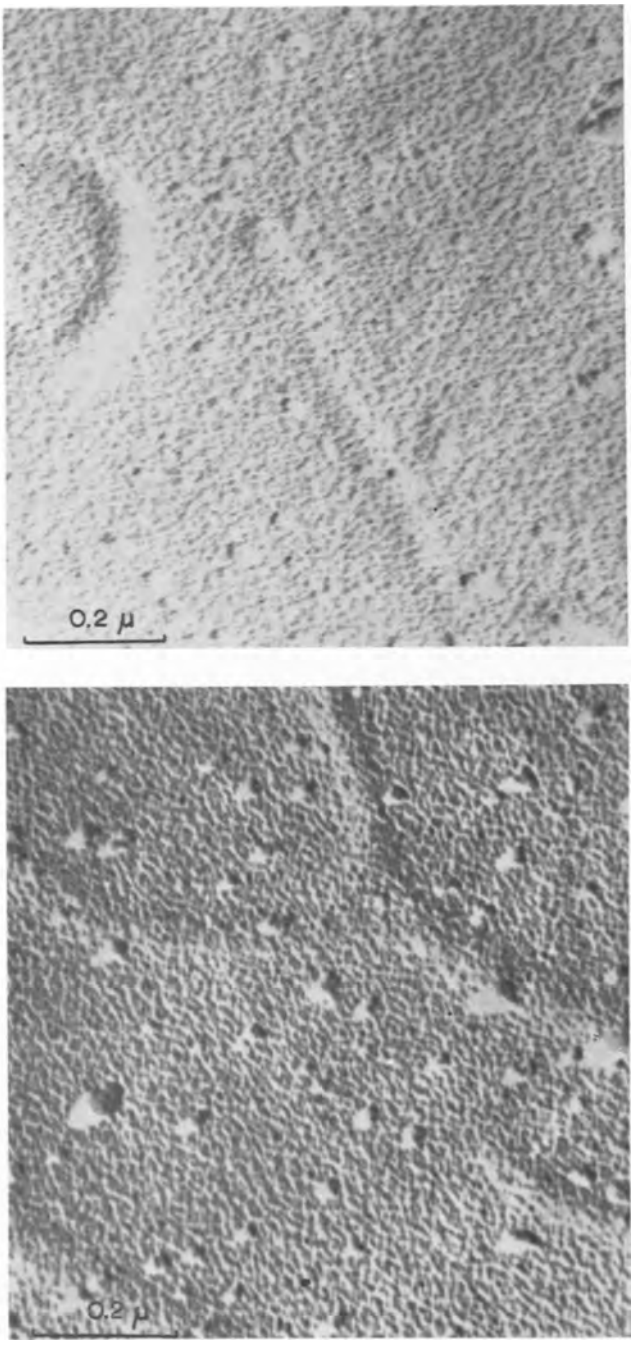

Fig. 8. Electron micrographs of oxide surface of specimens anodized in 3% ammonium tartrate at 14.4v 25°C (carbon replica, Au-Pd shadowed. (a) (top) anodizing for 0.5 sec; (b) (bottom) anodizing for 10 min.

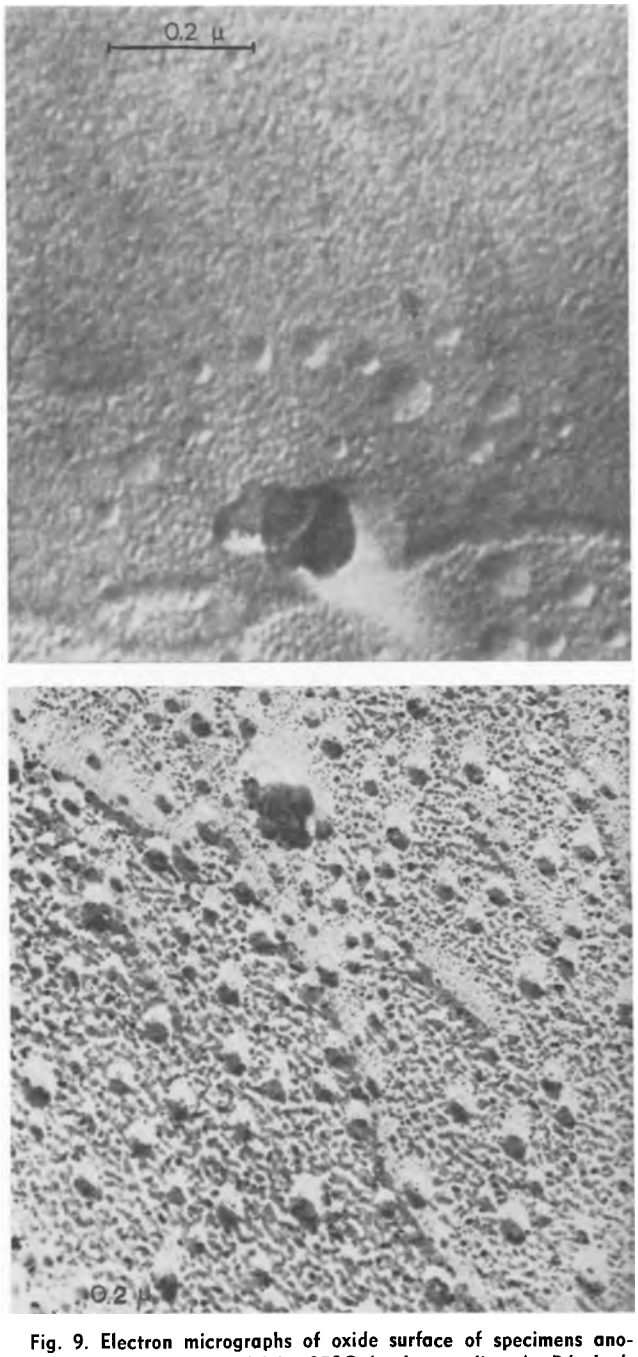

Fig. 9. Electron micrographs of oxide surface of specimens anodized in 15% H_2SO_4 at 14.4v, 25°C (carbon replica Au-Pd shadowed. (a) (top) anodizing for 0.26 sec; (b) (bottom) anodizing for 10 sec.

not initiated until the field across a first-formed barrier layer falls low enough, to a value that is lower for higher solution pH and lower temperature. It is significant that these are well-known conditions for the formation of less porous and nearly nonporous films.

Franklin's conclusion (16) that formed barrier-layer films may contain pores is also confirmed, but his suggestion that these pores originate in the earliest stages of formation formed is not supported by our results.

Later part of the transients.—Impedance measurements.—To confirm that the pore distribution is complete and a steady-state pore-base layer established by the time i_s is reached, the specific impedance of the electrode surface was measured with specimens anodized as far as i_s and after. The bridge method of Hoar and Wood (14) with an input of *ca.* 3 mv at 30 cps was used; as shown by Hoar and Wood, a balancing capacitance with series resistance gives the pore-base-layer capacitance very closely under these conditions, since the impedance is almost solely that of the pore-base-layer capacitance in series with the pore resistance of any porous layer. The pore-base-layer capacitance per unit area, together with the density 3.42 and dielectric constant 8.4 of Al_2O_3, then gives directly the pore-base-layer thickness, and even if wrong values of the parameters are used,[2] the results are comparable. That the outer conductor of the assumed "parallel plate" pore-base-layer capacitor consists of an hexagonal pattern of small pore-bases rather than a complete plate scarcely matters, as shown by Dekker and Urquhart (22).

Some results for sulfuric acid and sulfate solutions are given in Table I. It may be seen that barrier layers of thickness some 10 Å/v of forming voltage E_F are indeed present when i_s has been reached, and that they change very little with the total amount of film formation (runs 3,4; 8,9; 15,16). The slightly thicker pore-base layers found with the less acid solutions (runs 17, 19, 20, 21) are qualitatively in line with the smaller values of i_s.

Figure 10 is a plot of log i_s *vs.* E_F/y, the "mean" field across the pore-base layer of thickness y. There is no obvious correlation, even among groups of points representing different pore-base layers in the same solution. However, all the points lie fairly close to lines

$$\log i_s = \log A + \frac{BE_F}{2.303y}$$

the logarithmic form of Eq. [1], whether we take $A = 10^{-18}$ amp/cm², $B = 3.1 \times 10^{-6}$ cm/v following Charlesby (3) or $A = 3.62 \times 10^{-23}$ amp/cm², $B = 4.25 \times 10^{-6}$ cm/v from the earlier results of Gunterschultze and Betz (2), both obtained from relatively thick barrier layers formed at high forming voltages in various ammonium borate solutions. This is further evidence that the thin pore-base layer underlying the porous layer in sulfuric acid or sulfate solutions has electrical properties that are nearly quantitatively the same as those of the thick barrier layers formed in borate solutions.

[2] Hoar and Wood (14) used 10.0 for the dielectric constant; others have used 8.4. It is unlikely that the barrier layer material is in fact stoichiometric Al_2O_3; it may well contain protons and SO_4^{2-} ions in amounts depending on the conditions. Furthermore the dielectric "constant" ϵ no doubt increases at high frequencies (21). Within the range of our conditions, however, ϵ is probably very nearly constant.

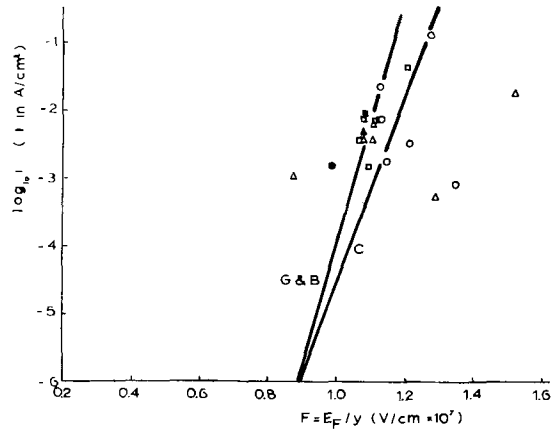

Fig. 10. Logarithm of current density vs. electric field across the pore base. □, H_2SO_4 (15% w/v), 17°C; △, H_2SO_4 (7.5% w/v), 25°C; ○, H_2SO_4 (15% w/v), 25°C; ■, H_2SO_4 + $NaHSO_4$ pH 0.23, 25°C; ▲, $NaHSO_4$ (183.6 g/l) pH 0.36, 25°C; ●, $NaHSO_4$ + Na_2SO_4 pH 1.19 25°C; G & B, line given by log i = log A + BF/2.303 using A = 3.62×10^{-23} amp/cm²; $B = 4.25 \times 10^{-6}$ cm/v according to Gunterschulze and Betz (2); C, similar line using $A = 10^{-18}$ amp/cm²; $B = 3.1 \times 10^{-6}$ cm/v, according to Charlesby (3).

Discussion

During the early stages of barrier-layer thickening, the cell voltage comprises potential drops across the metal/film interface, through the film, across the film/solution interface, through the solution, and at the cathode. As the (nonohmic) film resistance increases and the current density decreases, the potential drop through the film increases and all the other potential drops, including that across the film/solution interface, decrease. Thus pore initiation at the film/solution interface, so far from being field-assisted, appears to be field-inhibited; it occurs only when the field across the film/solution interface is sufficiently low. The only processes that could operate against the anodic field are the "thermal" passage of O^{2-} anions outward or that of H^+ cations inward. Either process would clearly be favored by an acid solution as compared with the nearly neutral solutions in which pores are not nearly so readily initiated. We think that proton passage into the film is much the more probable, because it leads to no loss of anions from the barrier layer, which becomes only very slightly thinner during the subsequent porous film formation.

If protons enter the barrier layer against the field, either statistically at random or at already welcoming positions such as a grain boundary, a vital consequence ensues. It is known that the hydrated oxides of aluminum have lower specific electrical resistance than the anhydrous oxides. It is thus very likely that quite a small degree of protonation gives an appreciable drop of specific resistance. Thus at a favorable protonated spot, the current density increases. Local Joule heating in the adjacent solution and in the film itself then still further favors the rate of proton uptake, and that of Al^{3+} dissolu-

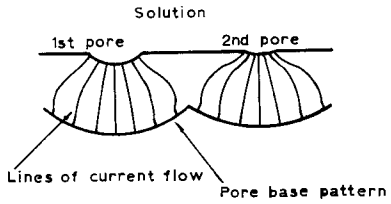

Fig. 11. Schematic picture demonstrating the spreading of pore nuclei on the surface of the initial barrier film.

tion. Thus a pore begins to form in depth, (any thinning caused by any O^{2-} dissolution further reducing the film resistance), and also to spread radially.

If the heating effect were the sole consequence of proton entry followed by pore initiation, the pore would spread radially until general film dissolution occurred, as indeed happens at forming voltages greater than 25v in 15% sulfuric acid. Otherwise put, the probability of initiation of a second pore is greatest at the edge of the first, where the heating effect is largest. We have to explain why the pore spreads to only a small degree (radius *ca.* 50-100Å) and why subsequent pores in fact nucleate at a distance from the first.

The possible charge carriers within the barrier layer are Al^{3+}, O^{2-}, OH^-, and H^+ ions, moving under high-field conditions. Considerably more Al^{3+} than the equivalent of O^{2-} or OH^- must be transported through the barrier layer, because some of the Al^{3+} dissolves into the solution in the pore. It is unlikely that the values of the various cation and anion mobilities are close to each other. If the Al^{3+} mobility is greater than that of O^{2-} and OH^-, in the steady state there will be a positive ionic space charge in the barrier layer in the neighborhood of the nucleated pore. Such a charge distribution will tend to inhibit further H^+ uptake from the solution into the barrier layer, the inhibiting effect being greatest nearest to the growing nucleus, and to discourage the further concentration of current near to the pore; thus the probability of initiation of a second pore will increase with the distance from the first.

The opposing effects set out above will lead to a maximum probability of further H^+ uptake at a particular distance from the center of the first nucleus; owing to the geometrical form of current distribution spreading in the barrier layer from the first nucleus (Fig. 11) this distance will be approximately twice the barrier layer thickness. As soon as a second nucleus has so developed on the circumference of such a circle around the first, a third nucleus may be expected at the intersection of the similar circles around the first and second; repetition of the process will, of course, produce the hexagonal pattern. This may be expected to spread over the surface from a relatively small number of primary nuclei, in the short period during which the mean total current density over the whole surface increases to the value characteristics of porous-film formation.

The electrical properties of the initial barrier layer and the steady-state pore-base layer that form in sulfuric acid and sulfate solutions are evidently closely similar to those of thin or thick barrier layers formed in nearly neutral borate or tartrate solutions. It is clear that all these films are, basically, nearly anhydrous, nearly amorphous alumina: the well-known incorporation of substantial amounts of sulfate, borate, etc., anions into the "lattice" has no very great effect on the electrical or mechanical properties, probably because one SO_4^{2-} replaces four O^{2-}, one BO_3^{3-}, three O^{2-} etc., a matter we shall discuss elsewhere. The entry of protons, however, gives the very marked effect that we suggest perhaps because of the great modification of the anion lattice consequent upon the production of OH^- and of hydrogen bonding.

Acknowledgments

The authors are grateful to the Aluminum Development Association for a maintenance allowance to one of them (J.Y.) for the period during which this work was carried out, and to Messrs. J. C. Bailey and F. C. Porter of the Association for very useful discussions and for arranging supplies of aluminum.

Any discussion of this paper will appear in a Discussion Section to be published in the December 1963 JOURNAL.

REFERENCES

1. G. Hass, *J. Am. Opt. Soc.*, **39**, 532 (1949).
2. A. Guntherschultze and H. Betz, *A. Physik*, **92**, 367 (1934).
3. A. Charlesby, *Proc. Phys. Soc.*, **66B**, 317 (1953).
4. H. A. Johansen, G. B. Adams, and P. Van Ryssel-berghe, *This Journal*, **104**, 339 (1957).
5. E. J. W. Verwey, *Physica*, **2**, 1059 (1935); *J. Chem. Phys.*, **3**, 592 (1935); *Z. Krist.*, **91**, 65, 317 (1935).
6. N. Cabrera and N. F. Mott, *Rep. Prog. Phys.*, **12**, 163 (1948).
7. J. F. Dewald, *This Journal*, **102**, 1 (1955).
8. M. S. Hunter and P. Fowle, *ibid.*, **101**, 481, 514 (1954).
9. F. Keller and A. H. Geisler, *Trans. AIME*, **156**, 82 (1944).
10. F. Keller, M. S. Hunter, and D. L. Robinson. *This Journal*, **100**, 411 (1953).
11. C. J. L. Booker, J. L. Wood, and A. Walsh, *Brit. J. Appl. Phys.*, **8**, 347 (1957).
12. K. Huber, *Z. Elektrochem.*, **62**, 675 (1958); *J. Colloid Sci.*, **3**, 197 (1948).
13. A. C. Jason and J. L. Wood, *Proc. Phys. Soc.*, **68B**, 1105 (1955).
14. T. P. Hoar and G. C. Wood, *Electrochim. Acta*, **7**, 333 (1962).
15. T. P. Hoar and N. F. Mott, *J. Phys. Chem. Solids*, **9**, 97 (1959).
16. R. W. Franklin, *Nature*, **180**, 1470 (1957).
17. G. C. Wood, M. Cole, and T. P. Hoar, *Electrochim. Acta*, **3**, 179 (1960).
18. R. B. Mason, *This Journal*, **102**, 671 (1955).
19. D. Vermilyea, *ibid.*, **101**, 389 (1954).
20. W. L. Latimer, "Oxidation Potentials," 2nd Ed., Prentice-Hall, (1959).
21. J. J. McMullen and M. J. Pryor, 1st Int. Congr. Met. Corrosion, Butterworths, London, p. 52 (1962).
22. A. J. Dekker and H. Urquhart, *Can. J. Res.*, **B28**, 541 (1950).

The Corrosion of 1100 Aluminum in Oxygen-Saturated Water at 70°C

J. E. Draley, Shiro Mori, and R. E. Loess

Argonne National Laboratory, Argonne, Illinois

ABSTRACT

In oxygen-saturated distilled water at 70°, the rate and amount of corrosion during short exposure are influenced by experimental conditions. One noteworthy effect is that contamination of the water by the reaction increases the corrosion rate. Subsequent to the first several days, the amount of corrosion varies with the logarithm of the exposure time. This behavior holds for at least 180 days; it is believed to hold for as long as tests have provided reasonable data, the longest being about 650 days. These results are interpreted in terms of local film rupture and growth. A method of averaging the over-all corrosion rate on the basis of cyclical local reactions is derived.

The corrosion of aluminum in nearly pure water has been under study in this laboratory for a number of years. Originally 1100 aluminum (then 2S) was chosen for study at temperatures below 100° because it was under consideration for use in water-cooled nuclear reactors. Subsequently, when the research objective became simply the determination of corrosion mechanisms, the same alloy was continued under study. Although this alloy contains a number of impurities, the major ones being iron, silicon, and copper, its behavior is reproducible, and the backlog of information previously obtained is helpful in interpreting more recent results and in testing hypothesized mechanisms.

A certain amount of research has also been done with pure aluminum in water. From the point of view of kinetic studies this material does not lend itself to relatively simple treatment because of the local penetrating attack which takes place at grain boundaries, and because of a sensitivity to the amount of impurities present.

In a previous publication (1), many of the features of the corrosion of 1100 aluminum in oxygen-saturated distilled water at 70° have been described. Of particular interest to the present investigation are: (*A*) No gross pitting occurs, although micropits of the order of 20μ in diameter form. These do not grow in size, but their number increases. Localized, self-stifling reaction is indicated. (*B*) After sufficiently extended exposure, bits of the corrosion product slough or flake off, leaving a metallic sheen. The corrosion product does not again grow thick in those places, and there is no observable increase in corrosion of the specimens. It is apparent that, at least at long exposure times, the protective oxide is thin and the bulk of the corrosion product coating is not significantly protective.

Also in the same publication, some aspects of the kinetics of the reaction were given. For the first several hours of exposure of wet-ground specimens the amount of corrosion varied as the logarithm of time; subsequently, an increase in rate occurred, followed by a period of diminishing corrosion rate. The shape of this part of the curve was not established.

In the present publication, some of the features of the initial period of corrosion are explored, the kinetics of the reaction during long exposure is determined, and for the latter there is derived a rate expression which seems to fit the known facts.

Experimental

Water.—High quality water was provided for all tests by passing laboratory steam condensate through ion exchange resins and then distilling. Occasional spectrographic analyses showed only a few metallic elements present above the limit of detection. Sodium, potassium, and magnesium contents varied from a few ppb (grams per 10^9g H_2O) up to 50 ppb.

This water was vigorously boiled in Pyrex carboys at room temperature (by pumping with a steam ejector) for degassing, and oxygen was bubbled through it for a period of time. Periodic measurement showed the water to have a *p*H of 6.5 ± 0.2 and specific resistance 1.4 ± 0.2 × 10^6 ohm-cm. No noticeable change in *p*H was caused by passage over the specimens; there was sometimes a slight increase in resistivity, indicating that the oxide-covered specimens had somewhat purified the water.

Method of exposure.—Eight (or fewer) specimens were suspended on Pyrex glass in the chamber shown in Fig. 1 (thermostatted to 70° ± 1°C). Fresh water from the carboy was added continuously through a regulating section of Pyrex capillary, and the excess water was discharged to the drain.

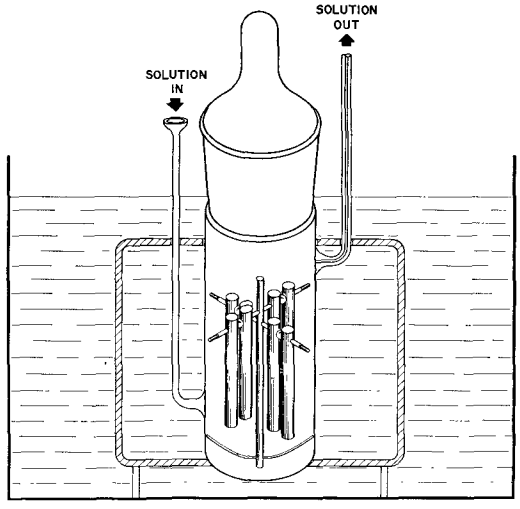

Fig. 1. Corrosion test chamber

The difference between the temperature and pressure in the test chamber and those in the storage carboy (2-4 psig O_2) caused continuous slow evolution of oxygen gas during the corrosion exposure. For the test of long duration, two chambers were used in series, with the refreshing water passing through each in turn; the rate was about 15 cc/min for the first 5 days and 7 cc/min thereafter.

Material and sample preparation.—The material source was one batch of commercially extruded 1100 aluminum rod. Analyses showed impurities to consist of: 0.54% Fe, 0.12% Cu, 0.07% Si, 0.017% Zn, 100-200 ppm Ti, 25-50 ppm Zr, 5 ppm Mo. Samples were prepared by careful machining to a size just slightly too large for use in the eddy current thickness gauge. They were then degreased and etched (10 cc conc. HNO_3, 1 cc 48% HF, 89 cc H_2O; about 60°C) until approximately 50μ had been removed. Specimens were rinsed and annealed (15 min at 360°C, slow cooled) before being weighed, measured in the thickness gauge, and corroded.

Determination of amount of corrosion.—Since the predominant corrosion product is an adherent oxide, specimen weight gain provides an approximate measure of the amount of corrosion. However, some of the oxide is lost to the water (dissolution, spallation, etc.), and the composition of the product changes with time as well as with exposure conditions. These features are illustrated in Fig. 2 where, for a single specimen, the gain in weight (G), the amount of metal corroded (L), determined by the eddy current gauge to be described, and the amount of aluminum lost from the specimen (ξ) during exposure to O_2-saturated water at 70°C are shown. The amount of metal lost was determined by chemical analyses of the effluent solution from the test chamber, after it had been concentrated by evaporation. It was necessary to correct these values for the amount of aluminum initially present in the water.

Using the approximation that the composition of the corrosion product is $Al(OH)_x$, the value of x is readily shown to be equal to $\frac{G+\xi}{L-\xi} \cdot \frac{27}{17}$. This ratio is observed to decrease with exposure time for the present experiment, although other types of change have sometimes been observed. It is typically not equal to 3.0, the stoichiometric composition of the oxide (bayerite) indicated by x-ray diffraction to comprise the bulk of the corrosion product.

There are two chemical methods available for determining directly the amount of unreacted metal at the end of an exposure. The metal can be dissolved in a solution of iodine in methanol (2), or the oxide can be dissolved from the surface (1). Both of these methods have been considered unsatisfactory for the present research. The errors for the specimens used range from about 0.1 mg (for the film removal method) to something several times this magnitude for the metal dissolution method. These errors are objectionably high and would make impossible a satisfactory determination of the kinetics of the reaction of 1100 aluminum with water after the first few months of exposure.

In addition to the inaccuracy of these two methods there is another problem. Different specimens characteristically corrode to a different extent, even though the corrosion rates in an individual test are generally identical, as well as can be measured, after extended exposure. Any method of determining the amount of corrosion which destroys the sample for subsequent exposure adds a kind of statistical scatter in the data which has made it impossible to determine curve shapes with reasonable confidence.

A specially developed eddy current thickness gauge is insensitive to the amount of oxide coating. For a few years it has been used in obtaining data which are believed reliable and of acceptable precision (± 25Å penetration). The change in the inductive properties of a coil are measured as a function of the thickness of metal placed within it. Details of this gauge are yet to be reported, although a first model (3) and a usable but less sensitive version have been described (4). The calibration curve, as used in the present investigation, is given in Fig. 3. The straight line drawn through the points for samples which were etched in HNO_3-HF solution continued linearly, beyond this figure, up through 200 mg of metal removed per sample. Since all specimens had the same surface area (29.19 ± 0.01 cm²), this calibration curve could readily be used to determine the amount of corrosion in mg/dm².

The solid points are for specimens which had been corroded in water; most of those showing more cor-

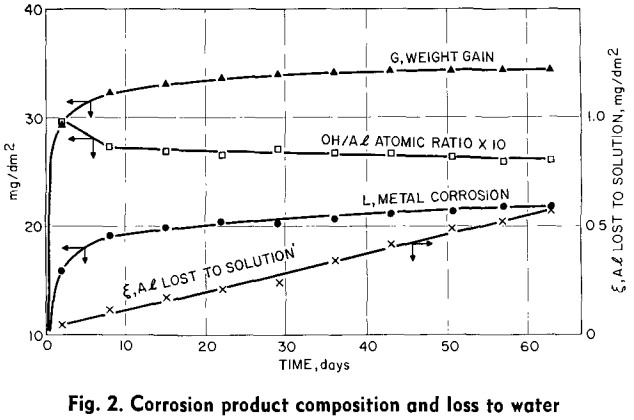

Fig. 2. Corrosion product composition and loss to water

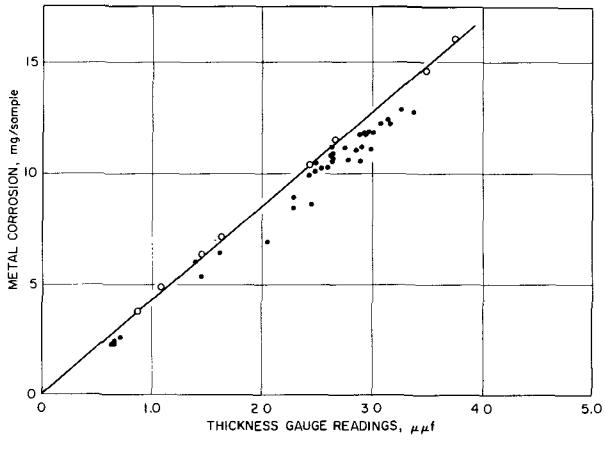

Fig. 3. Thickness gauge calibration curve; ○, etched HNO_3-HF; ●, corroded in H_2O.

rosion than 10 mg/sample were the ones used in determining the kinetics for extended exposure. In all such cases, the weight of metal corroded was obtained after removal of the corrosion product coating following exposure. It is noted that these points generally fall below the line. This is apparently a consequence of uneven corrosion of the specimens. During the early part of the exposure the specimens had less corrosion product near the ends than in the center, suggesting that less corrosion had taken place at the ends. As a consequence it is believed that data reported at present can be expected to apply to the central portion of the specimens only. The phenomenon is believed related to a water contamination effect during the initial stages of the corrosion reaction (see next section). For the longest exposure times, there is also another factor contributing to deviation of the points from the line. This will be described later.

Data and Results

Short time behavior.—In ref. (1) it was indicated that the amount of corrosion in water at 70° is proportional to the logarithm of time through about the first 7 hr of exposure. The characteristics of the corrosion kinetics in this stage have been investigated somewhat further. It is not considered suitable to discuss here all of the experimental parameters which influence the rate and amount of corrosion during early exposures. However, it is considered desirable to point out a few of the important observations for the purpose of adding perspective in the consideration of the longer time corrosion.

Effect of exposure interruption.—If it is desired to make a series of measurements of the amount of corrosion on the same sample, with further corrosion exposure between measurements, it is important to know whether the amount of corrosion has been influenced by removal from the test water and drying. Subsequent to the first several days of exposure, when reaction rates have become low, it has been demonstrated that there is no discernible effect of this interruption of the exposure.

For short exposures the situation is different. A series of 10 specimens was placed in one chamber and corroded together. These specimens were removed one at a time for exposures up through 48 hr, dried, and the amount of metal corroded determined with the eddy current thickness gauge. Each of these specimens was subsequently reinserted in the test for further exposure, up to a total of about 13 days. The points representing continuous exposure are connected by a solid line in Fig. 4. This line is quite similar in character to data previously reported (1). There is apparently a logarithmic corrosion behavior up to something less than half a day, followed by an increase in slope of the line on semilog coordinates.

Note that after initial exposures through 1 day all specimens corroded at much lower rates on reexposure to the water. The dependence of the rate on further exposure is not well determined, but there is a common break upward in the curves after a time of the order of 5 days. It is thus evident that removing the specimens and drying them causes a substantial reduction in subsequent corrosion rate and a delay of the upward break in the semilog plot.

Number of specimens.—There are a number of indications that during the initial stages, a product of the corrosion reaction contaminates the water and increases the amount of corrosion occurring. One of the indications of this is illustrated in Fig. 5. Two tests were run identically except that one chamber contained eight specimens and the other contained only one. It is characteristic that substantially more corrosion occurred per specimen in the chamber containing the greater area of corroding metal.

A number of other such comparative experiments have shown that the time of onset of the upward break in the semi-log plot and its magnitude are the most sensitive aspects of the corrosion reaction to this variable.

Refreshment rate.—When the number of specimens in the chamber was made the same but the rate of addition of refreshing water was changed from 5 to 16 ml/min similar results were obtained. Apparently the higher flow rate diluted the contaminant and reduced the magnitude of its corrosion-inducing effect.

Further illustration of this effect is shown in Fig. 6. Here the gain in weight of specimens corroded in identical fashion for 16 hr is plotted as a function of the rate of refreshment. It is indicated that for these particular conditions, something above 20 ml/min refreshment rate minimizes the effect of the

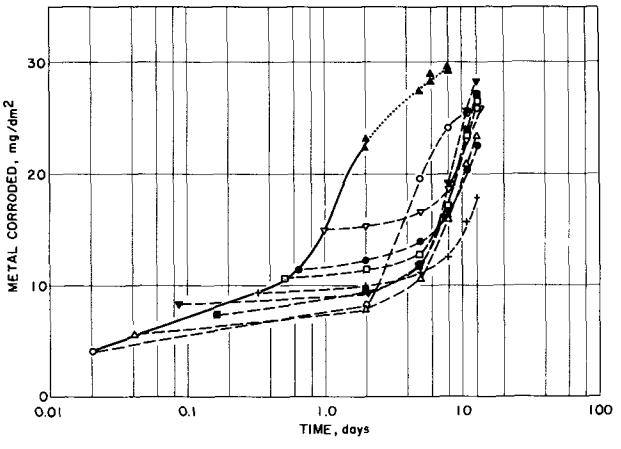

Fig. 4. Effect of exposure interruption

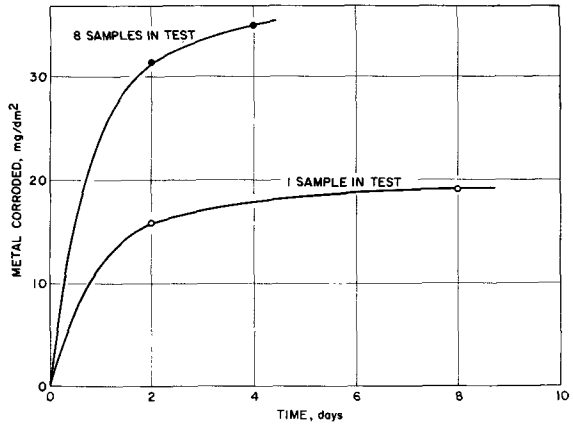

Fig. 5. Influence of number of specimens in test, refreshment rate 6 ml/min.

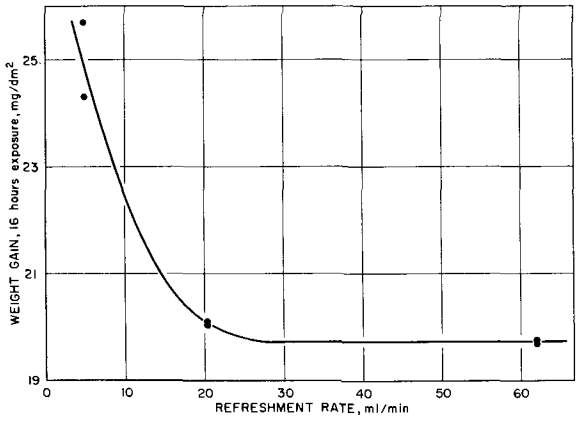

Fig. 6. Effect of rate of refreshment on amount of corrosion

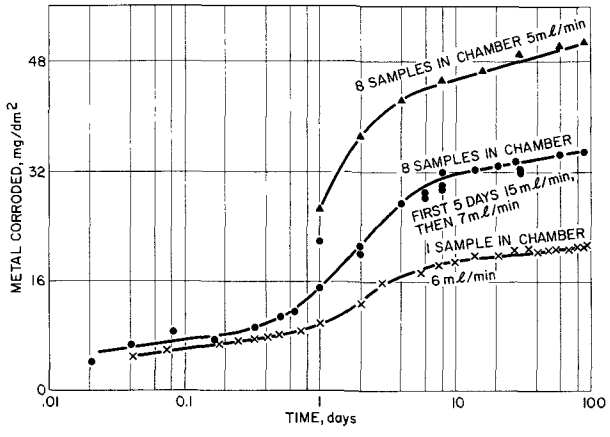

Fig. 7. Various effects of water contamination

contaminant, and that further increase in the refreshment has no further effect. The specimens in this series of experiments were wet-ground before exposure, but the results are believed to be indicative of the behavior of initially etched surfaces. The weight gain provides only an approximation of the amount of metal corroded, but the trend is evident.

In Fig. 7 are shown curves which seem to illustrate all of the three effects so far discussed: interruption, number of specimens, and refreshment rate. Comparison of the top two curves indicates that a high refreshment rate provides a smaller amount of corrosion (abetted by early interruption). Comparison of the middle and bottom curves shows that the effect of the number of specimens was greater than that of the refreshment rate. The middle curve was run at conditions which have now been taken as standard. For the earliest part of the exposure the flow rate was maintained high to minimize the effect of contamination; subsequently the refreshment rate was decreased for ease in performing the long time experiment.

Reproducibility.—For longer tests it is characteristically observed that different specimens in the same test show amounts of corrosion which differ by perhaps 10% although the rates of corrosion seem to be identical. This effect is a consequence of variable behavior of specimens during early exposure. The slopes of the logarithmic curves generally have been equal prior to the upward break: however the time at which the break occurs has varied over a

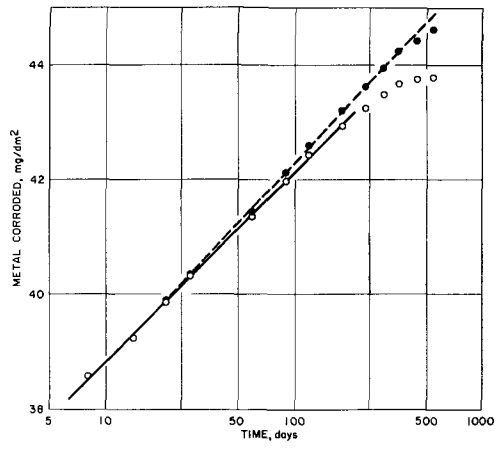

Fig. 8. Long term kinetic behavior; ○, uncorrected; ●, corrected

fairly wide range, and this has influenced the height of the final plateau.

Long Time Behavior

The results of one long test will be described here. As a precaution against possible metallurgical changes in the specimens which would influence the readings taken on the eddy current thickness gauge, three specimens were maintained in a helium environment. These were kept in the same constant temperature bath which was used for the corrosion exposure, and they were removed and replaced at the same times as the corroding specimens. Their apparent thicknesses, as determined by the gauge, were recorded periodically.

The changes in thickness gauge readings were significant, but very erratic. The general trend and all total changes were in the direction opposite to the change caused by corrosion, although there were irregular reversals, sometimes quite large. It was concluded that some metallurgical changes, influencing thickness gauge readings, were occurring at corrosion temperature. Aging was suspected as the primary change; its rate and even the rate law were not satisfactorily determined. It was clear that the change was minor for about the first 180 days of test.

For corroding specimens, plots of thickness gauge readings from 8 days onward showed that corrosion was logarithmic for 180 days exposure. Such data for one specimen (No. VI) are shown as the open circles in Fig. 8. A good straight line is formed, with relatively little scatter. Subsequent to 180 days, consistent deviation of the points from a straight line is observed. Only one reading, at one day, was taken for each specimen at times less than 8 days. This point was consistently far below the extrapolated long-time line. It is indicated that at that time the amount of corrosion had not yet reached the plateau following the upward short time break in the corrosion curve.

At 180 days, there remained six specimens in each chamber; two from each had been removed earlier to provide data for calibrating the thickness gauge. Data from these twelve were plotted (uncorrected) as in Fig. 9, and the basic constants of the logarithmic curves were determined for all except No. XV

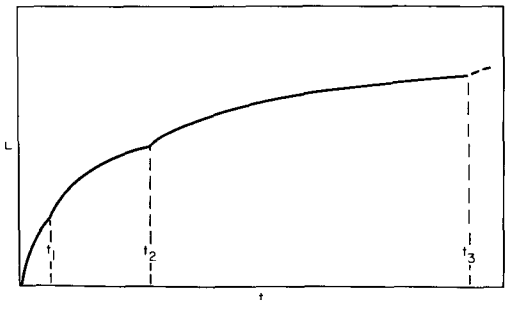

Fig. 9. Suggested corrosion at one point

(which unexplainably showed too much scatter to be used). The slopes and the extrapolated amounts of corrosion at one day (logarithmic "intercepts") are shown in Table I. The intercept values perhaps reflect the fact that the exposure was interrupted at 1 day and thus must be considered representative only of the particular experimental conditions employed.

Specimens II through VII were in the second chamber; their refreshing water was the effluent from the first chamber. The chamber containing specimens X through XIV received refreshing water directly from the storage carboy. Both the slopes and intercepts of the second chamber specimens were greater than those of the specimens in the first chamber (by about 17%).

It was clear that the available information was not sufficient to determine whether corrosion continued logarithmically to the end of the test at 547 days. In an effort to provide a reasonable estimate, corrections were calculated from the thickness gauge readings of the standard samples which had been aged in helium. It was assumed that the aging (or other metallurgical change) had occurred at a constant rate throughout the time they were kept at 70°, and that the average for the three standard specimens could legitimately be applied to each corrosion specimen. Accordingly the "least squares" slope of all of the thickness gauge changes of the standards (as a function of time) was determined and used to calculate "corrections" to be added to the basic data for the corrosion specimens. As illustrated in Fig. 8, the "corrected" points formed reasonably good straight lines on the semilog plots for the full test duration. There was also a slight increase in slope in going to corrected values, but in view of the uncertainties in the corrections it is not considered desirable to report the corrected slopes and intercepts.

Table I. Constants for logarithmic corrosion
1100 Aluminum, distilled water, 70°C, O_2-saturated

Specimen No.	Slope,* mg/dm²-cycle	L at 1 day,* mg/dm² (extrapolated)
II	3.15	35.36
III	3.22	36.70
IV	3.28	33.47
V	3.16	36.98
VI	3.26	35.61
VII	3.29	34.20
Average	3.23	35.59
X	2.62	30.20
XI	2.83	30.37
XII	2.91	30.15
XIII	2.77	30.95
XIV	2.78	29.32
Average	2.78	30.20

* Determined from uncorrected data.

Some years ago, before the thickness gauge had been perfected, a corrosion test was run, at the same nominal conditions as those for the present report, for a total exposure time of 940 days. The average gain in weight of all the specimens varied linearly with the logarithm of time from 18 through 650 days. Beyond that time, the weight gain showed some decrease and some erratic behavior, probably because of the sporadic sloughing of some of the corrosion product. Although the weight gain is not considered to be a truly reliable indication of the amount of corrosion, these observations tend to support the opinion that long-term corrosion remains logarithmic.

Discusison

The dependence of short time corrosion on many experimental parameters indicates the need of extensive investigation to understand the reactions. In particular, the nature of the water contamination by the corrosion reactions and how this influences corrosion rate should be studied. Some efforts to do this are being made in this laboratory. The variation of the *p*H of the water is being measured as a function of time and position, both along the surface and normal to it. Substantial *p*H changes do occur, particularly close to the corroding surface (0.1 mm).

It has seemed to be true that initial corrosion is logarithmic and is followed in turn by an increase in rate and by a subsequent extended period of logarithmic reaction. It has not been determined for how long this extended period endures. The rate law seems clearly to hold for at least 180 days; subsequently, it can only be guessed that to a total observation time of 650 days no change in kinetics occurs.

It is interesting to speculate as to the mechanism which is responsible for the long time, reproducible, logarithmic corrosion behavior. Previous observations, as pointed out in the introduction, have indicated that at any one time much of the corrosion reaction occurs at a small number of localized points, and that most of the corrosion product coating is not influential in determining corrosion rate. These observations suggest that previous derivations (5) are not sufficient to explain the corrosion behavior. The following development of a rate expression is based on the periodic logarithmic growth and breakdown of protective oxide.

It is assumed that at any point on the specimen surface corrosion follows logarithmic curves of the type indicated in Fig. 9. Subsequent to each time that breakdown of the protective film occurs the initial rate of reaction is less than at the preceding break. The total amount of corrosion occurring in each cycle is the same; consequently the duration of succeeding cycles is longer.

It is also assumed that at any time the various points on the corroding specimen are behaving as

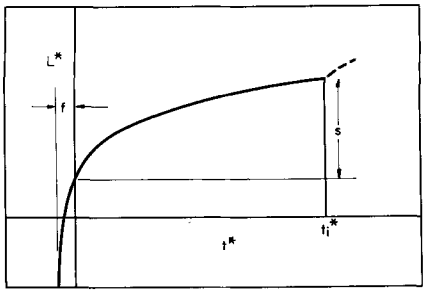

Fig. 10. Hypothetical rate curve for one time

though at random points along a characteristic logarithmic growth curve. Thus, corrosion rates of points on the specimen are equal to slopes of various portions of the following general equation from 0 to t_i^* (illustrated in Fig. 10)

$$L^* = a + b \ln (t^* + f) \qquad [1]$$

The value of f determines the initial slope. t_i^* is the end of the curve segment, and s is the (constant) amount of corrosion occurring in the cycle.

The average corrosion rate will be the average slope of this line from 0 to t_i^*. The value of this is

$$\frac{\overline{dL^*}}{dt^*} = \frac{s}{t_i^*} \qquad [2]$$

Now, realizing that s is equal to $L_i^* - L_o^*$, an expression for it can readily be obtained from Eq. [1]. Rearranging, by solving for t_i^*, gives Eq. [3]

$$t_i^* = f\,(e^{s/b} - 1) \qquad [3]$$

Substituting this into Eq. [2] gives Eq. [4], which is the average (over the surface) rate of corrosion for the specimen at any one time.

$$\frac{\overline{dL^*}}{dt^*} = \frac{s}{f\,(e^{s/b} - 1)} \qquad [4]$$

In order to decrease (with respect to time) the corrosion rate immediately following the various breaks in the local corrosion curve, it is now assumed that $f = ct$. Substituting this into Eq. [4] and dropping the *, since we are dealing with actual corrosion rather than a hypothetical curve for some particular time, the over-all rate expression in Eq. [5] is obtained.

$$\frac{dL}{dt} = \frac{s}{ct\,(e^{s/b} - 1)} \qquad [5]$$

Integrating, and using the boundary condition that $L = a$ when $t + ct = 1$, the expression given in Eq. [6] is obtained.

$$L = a + \frac{s}{c(e^{s/b} - 1)} \ln [t(c + 1)] \qquad [6]$$

This is observed to be a simple logarithmic equation of the form $L = K_1 + K_2 \ln t$.

It has not been possible to demonstrate that this derivation correctly explains the logarithmic dependence of the amount of corrosion on time. It does seem to fit the known observations. It is an attractive hypothesis in that the amount of corrosion for each cycle at any particular point on the specimen surface is constant. This suggests that the cause of the break is some direct effect of the total amount of corrosion which occurred during this cycle. At this time the part of the corrosion process which is preferred to explain this is the liberation of gaseous hydrogen beneath the protective oxide film. It is assumed that a fixed percentage of the corrosion product hydrogen is produced beneath the oxide film (6); that when the gas at any point reaches the amount required to generate pressure sufficient to rupture the oxide, the film is broken and the next cycle of the logarithmic growth is ready to begin. This analysis suggests that a given area is alternately cathodic and anodic (in accordance with surface appearance), and that the cathodic activity is largely responsible for activation and the change to active anodic corrosion.

There is nothing in the present research which offers an explanation for the apparent fact that local oxide growth is logarithmic. Evans (5) has derived such a rate expression in which it is assumed that there is healing or filling of internal cracks and voids in the (protective part of the) oxide film. On the basis of a number of observations, this explanation seems tenable, although the actual pore-filling mechanisms seem likely to be different from the simple one used by Evans.

It is believed that the present method of deriving an over-all rate expression for nonuniform corrosion is potentially applicable to many corrosion systems. A limitation to the value at the present time is that it appears to be quite difficult to determine experimentally the constants basic to the mechanism.

The work on this paper was performed under the auspices of the U. S. Atomic Energy Commission.

Any discussion of this paper will appear in a Discussion Section to be published in the December 1963 JOURNAL.

REFERENCES

1. J. E. Draley, "Aqueous Corrosion of 1100 Aluminum and of Aluminum-Nickel Alloys," Proceedings of AEC-Euratom Conference on Aqueous Corrosion of Reactor Materials, Brussels, Oct. 14-17, 1959; TID-7587 (U.S. Atomic Energy Commission), pp. 165-187.
2. M. J. Pryor and D. S. Keir, *This Journal*, **102**, 370 (1955).
3. W. B. Doe, "Eddy Current Type Diameter Gauge for Corrosion Measurements," ANL-5001 (Feb. 1, 1953) Argonne National Lab.
4. W. E. Ruther, *Corrosion*, **14**, 387t (1958).
5. U. R. Evans, "The Corrosion and Oxidation of Metals," pp. 829-30, 834-35, 837, Edward Arnold, Ltd., London (1960).
6. J. E. Draley and W. E. Ruther, *This Journal*, **104**, 329 (1957).

Contribution to the Electrochemical Behavior of Chromium and Iron-Chromium Alloys in the Transpassive Region

Th. Heumann and H. S. Panesar

Institut für Metallforschung der Universität Münster/Westf., West Germany

ABSTRACT

The polarization curves of Cr in electrolytic solutions containing different anions showed that these anions did not have any influence on the mechanism of dissolution of Cr in the transpassive region and that only OH^- ions take part. The current/potential curves of CrOOH and Cr_2O_3 demonstrated the possibility of the former compound being present in the passive layer. Measurements of the roughness factor of Cr after polarization in the active or the passive state indicated that the roughness of the surface remains constant within the accuracy of this method. The average roughness factor was 1.7. Further surface measurements were carried out on a Fe-Cr alloy (containing 27% Cr) which demonstrated an increase in the roughness of the surface after polarization of the alloy in the primary transpassive region.

During the past few years many investigations (1-9) of the electrochemical behavior of chromium and iron-chromium alloys have been carried out, which demonstrate their great tendency toward passivation. These experiments still do not give sufficient data to explain clearly the mechanisms of: 1, passivation; 2, dissolution in the transpassive region; and 3, activation and cathodic deposition. Almost all the investigations were carried out in sulfuric acid.

In order to discuss the most important mechanisms of passivation and dissolution in the transpassive state, we will consider current/potential curves which have been measured using the potentiostatic method. Figure 1 shows the current/potential curves of chromium in H_2SO_4 of different normalities. An anodic current density of 10^{-3} amp/cm^2 in 0.2*N* H_2SO_4, applied to a chromium specimen in the active state causes passivation. The passivation is complete at a potential value of —300 mv. As the potential is further increased, the sign of the current is reversed. Evolution of hydrogen takes place on the passive surface of the chromium. The next change in the current sign takes place at a potential which can vary over a wide range. The variations in this equilibrium rest potential are due to a small exchange current density. The smaller the amount of adsorbed hydrogen on the surface of the chromium, the greater is the value of the equilibrium rest potential.

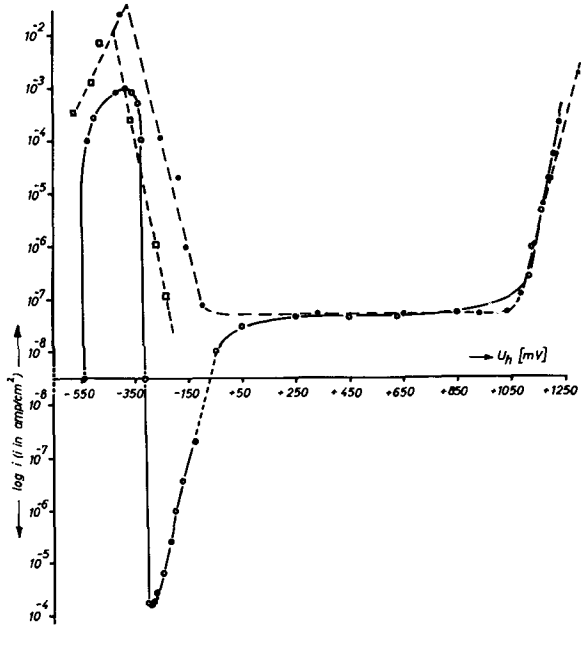

Fig. 1. Current density/potential curves of Cr in H_2SO_4 with different normalities measured potentiostatically; ○——○, 0.2*N* H_2SO_4 (3); □——□, 0.1*N* H_2SO_4 (Kolotyrkin) and ●——● 1*N* H_2SO_4 (Kolotyrkin) (7), analytically determined.

In the passive region, chromium dissolves as trivalent Cr^{3+}, and when the potential is raised to 1050 mv and above it goes into solution as chromate. The polarization curves for the dissolution of Cr as chromate, which are reproducible, are displaced toward higher potentials as the *p*H of the electrolytic solution decreases and are parallel to each other (1). It was assumed from these observations that the dissolution of Cr as chromate in the transpassive region required 2 OH^- ions.

In the case of Fe-Cr alloys (Cr above 11%) a double passivation is observed (4). In the primary transpassive region the polarization curves of Fe-Cr alloys coincide with that of pure Cr and in the secondary transpassive region with that of pure iron.

The further investigations described in this report were designed to test or measure: (i) the influence of anions on the mechanism of dissolution of pure Cr in the transpassive region; (ii) the behavior of the compounds CrOOH and Cr_2O_3 on anodic polarization, because the passive layer on chromium could be composed of one of these compounds; and (iii) the true surface area of the Cr and Fe-Cr specimens after different preliminary treatments.

The electrolytic chromium was reduced in a hydrogen atmosphere at about 1300°C. Microscopic examination showed afterwards an absence of oxide

inclusions. The material which had a larger grain size (1-2 mm) in comparison to the original one, was used for all further investigations.

The iron-chromium alloys were prepared by melting carbonyl iron and the purified chromium and annealed to homogenize before use.

Experimental details are given in the literature (1,2). All the investigations were carried out at 20°C.

Dissolution of Chromium in the Transpassive Region in the Presence of Different Electrolytes

The current/potential curves were measured in solutions of chromic, sulfuric, hydrochloric, nitric, and acetic acids. These acids contained the corresponding potassium salts to increase the conductivity and buffer action.

Figure 2 shows the results for hydrochloric acid. All the curves are parallel to each other and show the same potential/pH dependence as was observed in the previous investigations (1). The current/potential measurements in the remaining solutions gave identical results. When the potentials for a

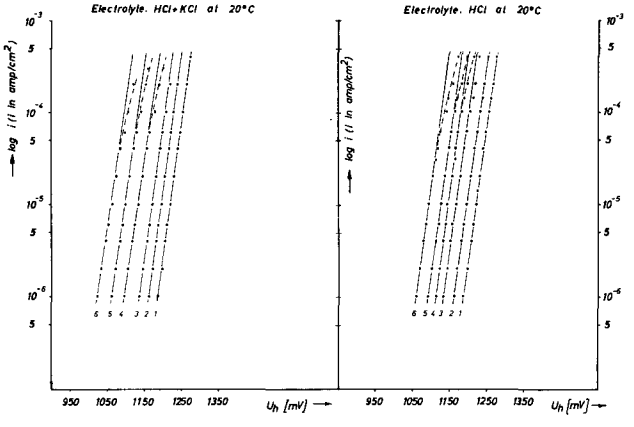

Fig. 2. Polarization curves of Cr with and without addition of KCl; left, pH, 1, 0.15; 2, 0.60; 3, 0.91; 4, 1.70; 5, 2.20; 6, 2.65; right pH, 1, 0.10; 2, 0.60; 3, 1.10; 4, 1.27; 5, 1.70; 6, 2.40.

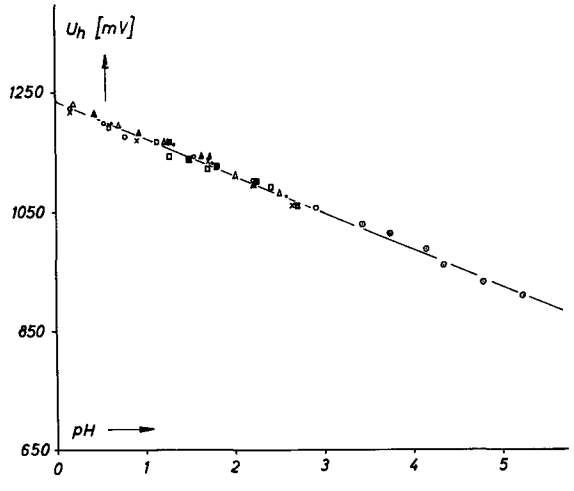

Fig. 3. Potential of Cr in different electrolytes in relation to the pH value with an anodic current density of 10^{-5} amp cm^{-2}. Solid circle, HNO_3; open triangle, 0.1M KNO_3 + HNO_3; open square with an x, H_2SO_4; open circle, 0.1M K_2SO_4 + H_2SO_4; x, HCl; open square, 0.1M KCl + HCl; open dotted triangle, chromic acid; open dotted circle, K-acetate + acetic acid.

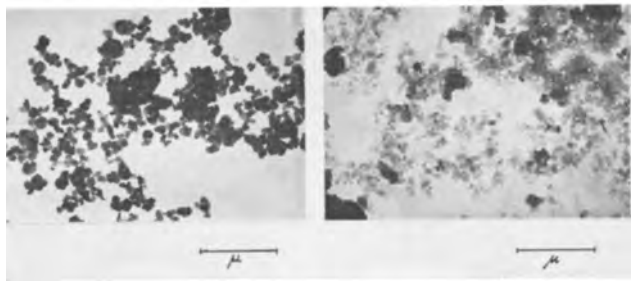

Fig. 4. Electron microscope photographs of CrOOH (right) and Cr_2O_3 (left) powder.

particular current density are taken from the curves for the different solutions and plotted against the corresponding pH a straight line with an inclination 65 mv/pH is obtained, as shown in Fig. 3. This shows clearly that the presence of different anions in the solution does not have any influence on the dissolution of chromium as chromate in the transpassive region and that only the OH^- ions are responsible. The transfer coefficients had the same value for the different electrolytes in the studied pH range. The Fe-Cr alloys show the same behavior as far as the primary transpassive region is concerned.

Polarization Curves of CrOOH and Cr_2O_3

These substances, in a very fine powder form,[1] were first examined with the aid of an electron microscope. Electron micrographs, in Fig. 4, show that their grains have almost the same size but different shapes.

Because of the low electrical conductivity of these materials it was not easy to study them electrochemically. The following treatment was successful, however.

The material, in a fine grained powder form, was suspended in a solution containing previously precipitated platinum. After stirring the solution for about 30 min it was possible to obtain a good homogeneous mixture. It was then filtered, washed with distilled water many times to get rid of Na^+ and Cl^- ions, and then dried. This mixture, containing an excess of platinum, was pressed into tablet form using a pressure of 150 kg/cm^2. The specimen so prepared possessed high conductivity and hardness. After imbedding in a special plastic material, they were abraded on 6/0 emery paper. These specimens then showed metallic luster. The ratio of the surface areas, oxide to Pt was 1:1.5 with corresponding weight ratios of 0.15:1.2g. The equilibrium rest potential values of the oxide electrodes in 0.1*N* H_2SO_4 were identical with those of Pt.

Before measuring current/potential curves on these electrodes by the galvanostatic method, they were cathodically polarized with a current density of 1 ma/cm^2, resulting in hydrogen evolution on the surface.

In order to investigate the influence of the Pt black in the electrode, a specimen consisting of a Pt-ring and a chromium disk was prepared. Figure 5 shows the Pt ring-Cr specimen. The polarization curves of this specimen are shown in Fig. 6. It is observed that the potential remains constant as the

[1] The authors are grateful to Dr. Hundt for supplying the pure compound CrOOH.

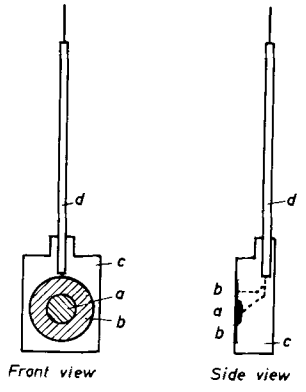

Fig. 5. Electrode composed of Pt ring and Cr disk; a, Cr; b, Pt ring; c, plastic material; d, isolated Cu wire.

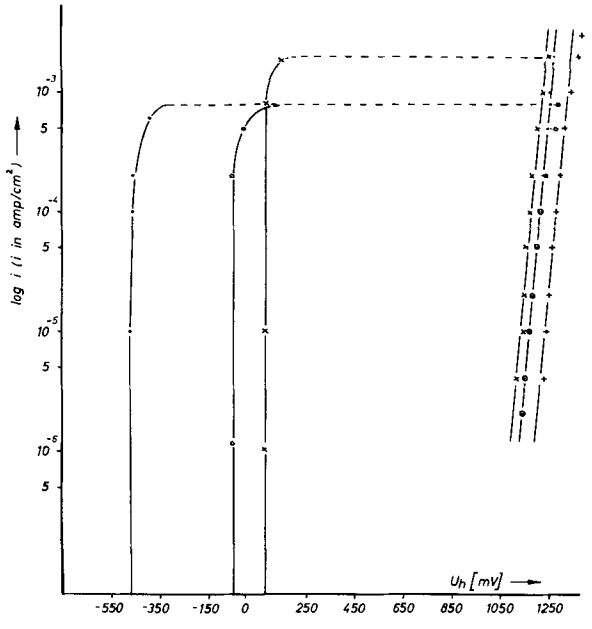

Fig. 6. Current density/potential curves of Cr, CrOOH, Cr_2O_3, and Cr-Pt ring electrodes. Electrolyte, 0.1N H_2SO_4 at 20°C; ○, Pt ring + Cr; •, Cr; ×, Pt black + CrOOH; +, Pt black + Cr_2O_3.

current density increases. When the current density reaches a value of 1 ma/cm², there is a sudden increase in potential, and simultaneously the yellow color due to the formation of chromate is seen.

This fact is observed not only on the platinum ring-chromium electrode, but also on CrOOH and Cr_2O_3 electrodes. For the sake of verification, the polarization curve of pure chromium is plotted in the same figure. It is seen that in the transpassive region the Pt-ring-Cr curve completely coincides with the current/potential curve of the pure chromium electrode. It is therefore assumed that the presence of platinum does not in any way influence the dissolution of CrOOH and Cr_2O_3 as chromate, but increases only their conductivity.

Further, Fig. 7 shows that the current/potential curves of CrOOH and Cr_2O_3 and passive Cr are parallel to each other. With reference to the Cr curve, the CrOOH curve is displaced by 35 mv to a lower potential, and the Cr_2O_3 curve is shifted by 80 mv to a higher potential.

The parallel displacement of the CrOOH curve is due to the greater surface area of fine powdered

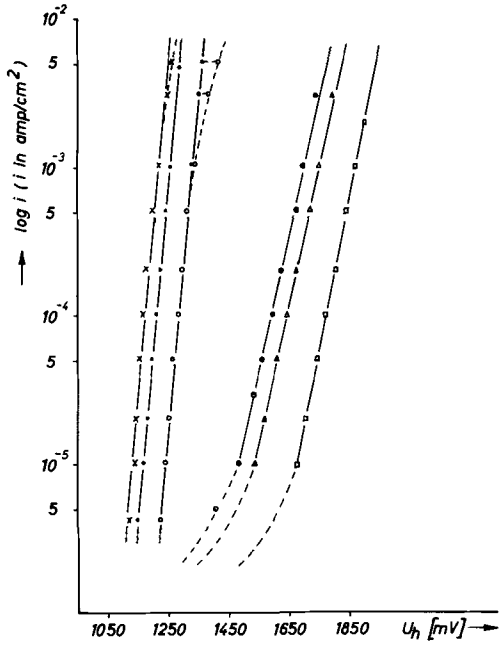

Fig. 7. Current density/potential curves on different electrodes in 0.1N H_2SO_4 at 20°C. ×, CrOOH; •, Cr; ○, Cr_2O_3; □, Pt; △, Pt black pressed; ⊙, Pt black deposited on Pt electrode.

CrOOH in comparison to that of chromium. The displacement of the curves to a lower potential, due to the increase in the surface area, can be explained by the results of the following investigation carried out on platinum.

Figure 7 shows the current/potential curve on platinum, platinum black in pressed form and platinum black deposited on a platinum electrode. They all run parallel to each other and are displaced in order of their surface areas to the lower potential values (surface areas: Pt black deposited > Pt black pressed > Pt). In the same figure the current/potential curves of oxide electrodes which were measured in a separate experiment, are plotted. Now because both the oxide materials have almost the same grain size (see Fig. 4) and therefore possibly the same areas and the same porosity when mixed and pressed with Pt black in the same proportion, the displacement of the Cr_2O_3 curve to the higher potential is not due to the smaller surface area but due to a higher overvoltage which is needed for the oxidation of trivalent Cr to hexavalent Cr. It can also be seen that if the Cr and the CrOOH specimen had the same surface areas, their current/potential curves would coincide.

It can therefore be said that the passive layer on Cr is possibly composed of CrOOH and not of the less probable Cr_2O_3. It is difficult, however, to come to unequivocal conclusion about the nature of the passive layer on the basis of these experiments. The question of how far the electrochemical properties of the thin oxide films differ from those of the compact materials must first be thoroughly studied before a specific decision is made.

Determination of the Roughness Factor (R.F.)

The quantitative evaluation of electrochemical investigations fail mostly because the true surface area of the specimen is not known. In calculations

of such results, one generally assumes a roughness factor of 2-3. In previous investigations using this R.F., the thickness of the passive layer on electrolytic chromium was found to be 1-2 atoms thick. It is important therefore to find a method for determining the true surface area, as far as possible. Furthermore, as most of the electrodes used possessed surface areas of about 1 cm^2, methods like B.E.T. or dye adsorption were excluded.

The method of Erbacher (10) for determining R.F. was found to be the most suitable for this purpose. By this electrochemical method, cations of a metal, more noble in potential than the substrate, are deposited by direct atom exchange from their solution, without using any external current on the surface of the metal electrode. According to Erbacher (10), the layer so deposited is only one atom thick. The amount of the element deposited, being very small, could only be determined with the help of a radioactive tracer. In our case, Bi^{212} isotope, occurring as a decay product in the radioactive thorium series, was used as tracer. For the accuracy of this method, it may be said that the results obtained are not completely exact, but enable us to draw valuable conclusions when used in the electrochemical calculations. This method, verification of its assumptions, and the obtained results are described below.

In the preliminary experiments, a passive chromium electrode was placed into $BiCl_3$ solution which contained an excess of 0.1*N* HCl. The change in equilibrium rest potential was noted with time. After about 2 hr, the equilibrium rest potential of chromium reached a constant value. This value corresponds to the one observed for a Bi electrode in the same solution, under similar conditions. Figure 8 shows the noted potential/time dependence.

The Bi^{212} isotope used as tracer was separated from the natural radioactive thorium in the following way. The emitted radon gas (Rn^{220}) was collected on a platinum foil. Rn^{220} isotope decays further into other isotopes, but the one with the longest half life, 10.6 hr, is Pb^{212}. The Pb^{212} isotope further decays into Bi^{212}, which subsequently decomposes into radioactive products with very short half life, finally producing inactive Pb^{208}. On the platinum foil were mainly Pb^{212} and Bi^{212} in equilibrium with each other.

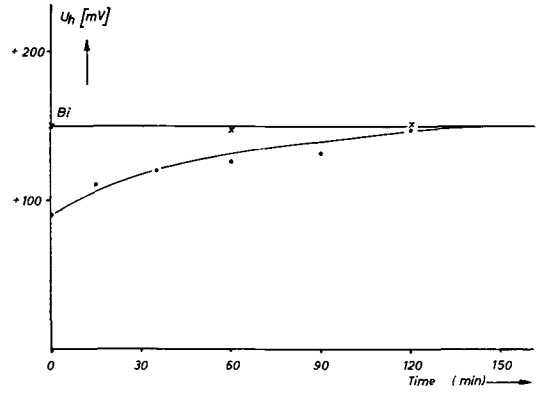

Fig. 8. Potential/time curves on Bi and Cr electrodes in $BiCl_3$ solution; conc., 1 mg Bi/l; electrolyte, $BiCl_3$ at 20°C; ×, Bi; •, Cr.

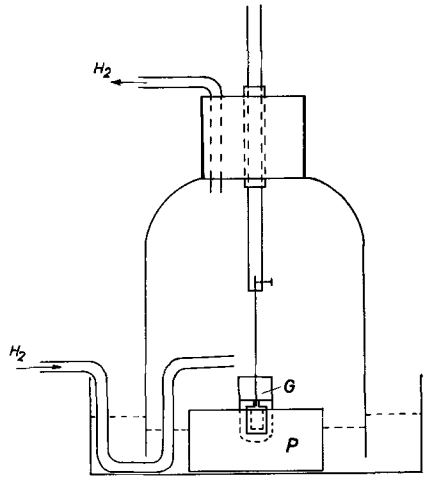

Fig. 9. Experimental arrangement for depositing Bi. G, small test tube; P, plastic material.

The platinum foil was kept in radioactive atmosphere of natural thorium for about 36 hr in order to get a large quantity of Pb^{212} isotope.

For the separation of B^{212} from the Pb^{212} isotope, the radioactive deposit was dissolved electrolytically from the platinum foil in 0.1*N* HCl. The hydrochloric acid used was air free and saturated with hydrogen. This solution was placed under the vessel shown in Fig. 9. The glass test tube G, containing about 40 ml of the solution, was fixed in a bored plastic material P, which was itself fitted in a glass base containing distilled water. Hydrogen was passed through the glass vessel during the whole experiment to prevent the entrance of oxygen from the atmosphere into the glass vessel. Oxygen or air redissolves the deposited bismuth in hydrochloric acid. A platinum foil, 1 cm^2 in area, was dipped in the radioactive solution and rotated in it. After about 90 min Bi isotope deposition was complete. In order to prevent the adsorption of even a small amount of lead isotope on the platinum foil, 1 mg of solid $PbCl_2$ was added to the original solution. The particles of inactive lead adsorbed on their surface the active Pb isotope. The deposition of Bi^{212} isotope on platinum foil under these conditions takes place preferentially because of its nobler potential against that of lead.

This separated Bi^{212} was electrolytically dissolved in 0.1*N* HCl, and by using a "Bohrloch crystal" its half life was determined. Figure 10 shows the intensity/time curve. The half life period determined in this way was in good agreement with the one stated in the literature.

For depositing bismuth on the surface of the chromium electrode, the same experimental apparatus was used as shown in Fig. 9.

To 1 ml of the active solution, 0.5 ml of inactive bismuth solution (conc. 1 mg Bi/liter) was added. This concentration is sufficient to cover the surface of the chromium with a bismuth layer of only one atom thickness.

The difference in the measured radioactive intensity before and after deposition enabled the determination of the absolute amount of bismuth deposited. The intensity measurements were carried out by means of a scintillation counter. In separate

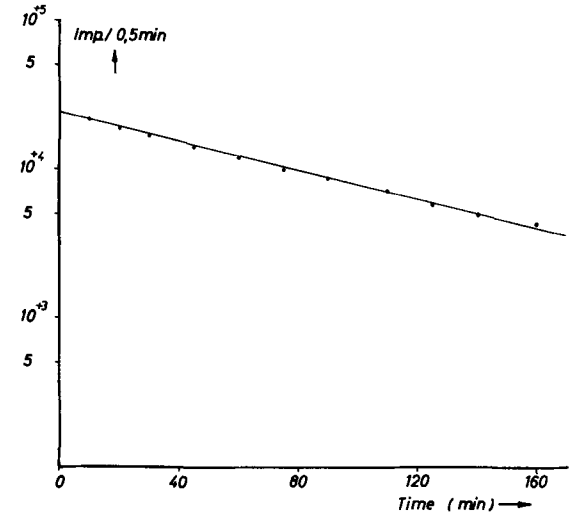

Fig. 10. Radioactive decay of experimentally separated Bi isotope. τ, 62.0 min; in literature, τ, 60.5 min.

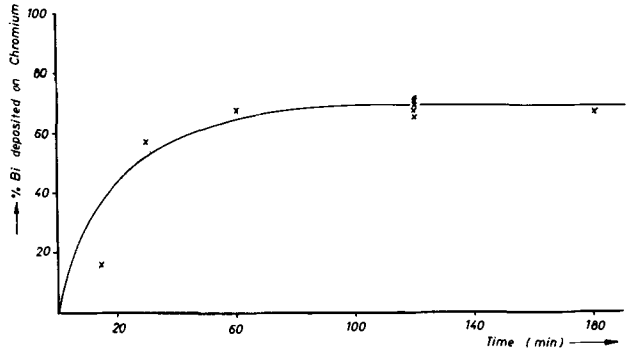

Fig. 11. Amount (%) of Bi, deposited on Cr, plotted against time. Geometrical surface area of Cr, 0.625 cm^2; concentration of Bi in solution before deposition, 1 mg/l.

experiments, the amount of bismuth adsorbed on the plastic material, in which the Cr and Fe-Cr electrodes were imbedded, was determined. It was found to be about 5% of the quantity of bismuth in solution. It was therefore always subtracted from the observed values of the bismuth deposition. In a close-packed layer of bismuth atoms the surface area occupied by a single bismuth atom according to Erbacher (10) is 6 r^2 tan 30°, where r is the radius of the bismuth atom. Figure 11 shows the amount in per cent of bismuth deposited, plotted against time. As seen from this figure, after about 100 min the whole surface of the electrode seems to be covered with bismuth atoms.

Varying the concentration of bismuth in solution between 3 x 10^{-6}g and 5 x 10^{-7}g bismuth per liter did not affect, within the accuracy of this method, the quantity of bismuth finally deposited on the electrode. It is therefore assumed that the amount of bismuth deposited is independent of the original bismuth concentration. This justified further the basis of this method.

All the specimens were abraded on 6/0 emery paper and given different preliminary treatments.

Table I presents the data from a series of measurements, and Table II gives all the results for the different roughness factor determinations.

Table I. Data from a series of measurements

No.	g Bi in solution	% Bi deposited	g Bi deposited	Surface area found, cm^2	Geometrical surface area, cm^2	R.F.
1	5×10^{-7}	71.10	3.55×10^{-7}			
2	5×10^{-7}	68.21	3.41×10^{-7}			
3	5×10^{-7}	71.13	3.55×10^{-7}	1.12	0.625	1.81
4	5×10^{-7}	68.04	3.40×10^{-7}			
5	5×10^{-7}	65.48	3.27×10^{-7}			
			3.43×10^{-7}			

Table II. Results for different roughness factor determinations

Specimen	Preliminary treatment	R.F.
Cr	Abraded on 6/0 emery paper	1.8
Cr	Abraded on (6/0) and polarized in the active state	1.6
Cr	Abraded on (6/0) and polarized in the passive state	1.7
Fe-Cr (27%)	Abraded on (6/0)	2.0
Fe-Cr (27%)	Abraded on (6/0) and polarized in the primary transpassive region	2.7

The values found for the R. F. seem to agree in order of magnitude with the one generally assumed in electrochemical calculations.

It is worth noting that the true surface area of the chromium remains practically constant after anodic dissolution in the transpassive region with an anodic current density of 5 x 10^{-4} amp/cm^2 or after polarization with a cathodic current density of -10^{-5} amp/cm^2 in the active state. This agrees with the fact that the polarization curves can be reproduced so well, pointing to an even dissolution of the chromium surface.

Using the quantity of current 1.4 millicoulombs/cm^2 required for passivation (3), and the average R.F. of 1.7, the thickness of the passive layer on chromium is found to be about 1.5 atoms thick.

In earlier investigations (2) for untreated electrolytic chromium the quantity of current necessary for passivation was found to be 2.3 millicoulombs/cm^2. It can therefore be concluded that the R.F. for this material is about 1.6 greater than the one found for hydrogen-treated chromium.

The R.F. for an Fe-Cr alloy (27% Cr) is increased after polarization in the primary transpassive region. This agrees with our supposition that the passive layer, on this alloy in the primary transpassive region, is almost identical with the passive layer on pure chromium. The mechanism of dissolution gives rise to a greater surface roughness, which remains constant on further polarization of the alloy.

Current investigations have shown that this "chromium passivity" is observed not only in case of Fe-Cr alloys but also for Ni/Cr, Co/Cr, and Mn/Cr alloys containing Cr in solid solution. They all show similar mechanisms of dissolution in the primary transpassive region. It can therefore be said that chromium, because of its outstanding property of passivity, confers it on all alloys containing at least 10% Cr.

It was not possible to strip off the passive layer from the Fe-Cr alloys by the known bromine-methanol technique (11), after passivating them in the primary transpassive region. The reason is obviously that the primary passive layer is only about 1-2 atoms thick. In contrast, the passive layer from the Fe-Cr alloy after passivating in the secondary transpassive region could be removed.

Absolute analytical results are hard to produce because a selective dissolution and a back adsorption, during the process of stripping, cannot be excluded. It is possible *e.g.*, to show that Cr was adsorbed by the passive layer from the bromine-methanol solution, which can simulate a higher concentration. Satisfactory results can only be obtained if a technique is found which can be used to analyze the passive layer while it remains on the surface of the alloy.

One of the authors wishes to thank the Deutscher Akad Emischer Austauschdienst, Bad Godesberg, West Germany for their financial support of this research.

Any discussion of this paper will appear in a Discussion Section to be published in the December 1963 JOURNAL.

REFERENCES

1. Th. Heumann and W. Rösener, *Z. Elektrochem.*, **59**, 722 (1955).
2. Th. Heumann and W. Diekötter, *ibid.*, **62**, 745 (1958).
3. Th. Heumann and W. Diekötter, To be published in *Z. Elektrochem.*
4. Th. Heumann and R. Schürmann, *Werkstoff und Korrosion*, **9**, 560 (1961).
5. M. Prazak and V. Prazak, *Z. Elektrochem.*, **62**, 739 (1958).
6. R. Olivier, Passivität von Fe und Fe-Cr Leg. Diss. Leiden, 58 ff (1955).
7. Y. M. Kolotyrkin, *Z. Elektrochem.*, **62**, 664 (1958).
8. H. Gerischer and M. Käppel, *Z. Phys. Chem. N.F.*, **8**, 258 (1956).
9. R. H. Roberts and Shutt, *Trans. Faraday Soc.*, **34**, 1455 (1938).
10. O. Erbacher, *Z. Phys. Chem.*, **A163**, 215 (1933); O. Erbacher, W. Herr, H. Babo, and M. Ebert, *Arch. Metallk.*, **12**, 409 (1949).
11. N. A. Nielsen, E. M. Mahla, and T. N. Rhodin, *Trans. Electrochem. Soc.*, **89**, 167 (1946).

The Passivity of Iron-Chromium Alloys

Gerald Aronowitz[1] and Norman Hackerman
Department of Chemistry, The University of Texas, Austin, Texas

ABSTRACT

Chronopotentiometry and differential capacity measurements were used to study the passive films formed by anodic polarization of a series of Fe-Cr alloys in dilute H_2SO_4. Steady-state conditions were established by electronic control of the electrode potential prior to making measurements.

Cathodic reduction studies indicated the presence of at least three types of surface materials. One is nonprotective in the case of Fe and several of the lower Cr alloys, but achieves considerable stability to reduction or dissolution at an alloy composition approaching 12% Cr. Another material is essential for passivity of Fe and the alloys with Cr content less than 12% and plays an important role in the electrical properties of the films on these alloys. A third type of surface material appears as a by-product of processes occurring in the transpassive region.

In the composition range 2.70-9.02% Cr, capacity-potential curves are quite similar and capacities follow a reciprocal relation with electrode potential over a range of potentials. Extrapolation of these data was used to obtain a relation between film thickness, dielectric constant, and charge equivalents involved in film reduction. Film dielectric constant values, calculated assuming the reduction of normal Fe_2O_3, varied from 29.1 to 87.5, depending on the reduction reaction assumed. At an alloy composition approaching 12% Cr, the passive film assumes optimum protective properties. Correspondingly, humps develop in the capacity-potential curves, and the curves shift in the direction of higher capacity values with increasing Cr content.

At present, two major points of view exist as to the cause of passivity: the adsorbed film theory and the bulk oxide theory. While the ultimate formation of an oxide having bulk properties on passive Fe, Ni, Cr, etc., is generally recognized, the problem is centered on the exact nature of these films in their early stages and on whether or not adsorption plays a role in passivity.

In this connection, a theory was put forth recently which attempts to reconcile these views by postulating a sequence consisting of adsorption, electron transfer to the adsorbate, and ultimate formation of bulk amorphous oxide *via* cation migration into the adsorbed array (1).

[1] Present address: American Oil Company, Research & Development Department, P. O. Box 431, Whiting, Indiana.

Iron which demonstrates the main features of the active-passive transition, has been studied probably more than any other metal. In recent years, however, considerable interest has been shown in the passivity of stainless steel and the iron-chromium alloys because of the wide range of corrosion resistance shown by these metals. In addition, the attainment of optimum corrosion resistance and ease of passivation at a critical alloy composition in the neighborhood of 12% Cr has raised further questions.

Chronopotentiometry was employed in this work to determine passive film charge equivalents. Anodic film formation techniques very often do not satisfy the requirement of known or 100% current efficiency because of simultaneous anodic dissolution. Cathodic film reduction studies can suffer from these

It was not possible to strip off the passive layer from the Fe-Cr alloys by the known bromine-methanol technique (11), after passivating them in the primary transpassive region. The reason is obviously that the primary passive layer is only about 1-2 atoms thick. In contrast, the passive layer from the Fe-Cr alloy after passivating in the secondary transpassive region could be removed.

Absolute analytical results are hard to produce because a selective dissolution and a back adsorption, during the process of stripping, cannot be excluded. It is possible *e.g.*, to show that Cr was adsorbed by the passive layer from the bromine-methanol solution, which can simulate a higher concentration. Satisfactory results can only be obtained if a technique is found which can be used to analyze the passive layer while it remains on the surface of the alloy.

One of the authors wishes to thank the Deutscher Akad Emischer Austauschdienst, Bad Godesberg, West Germany for their financial support of this research.

Any discussion of this paper will appear in a Discussion Section to be published in the December 1963 JOURNAL.

REFERENCES

1. Th. Heumann and W. Rösener, *Z. Elektrochem.*, **59**, 722 (1955).
2. Th. Heumann and W. Diekötter, *ibid.*, **62**, 745 (1958).
3. Th. Heumann and W. Diekötter, To be published in *Z. Elektrochem.*
4. Th. Heumann and R. Schürmann, *Werkstoff und Korrosion*, **9**, 560 (1961).
5. M. Prazak and V. Prazak, *Z. Elektrochem.*, **62**, 739 (1958).
6. R. Olivier, Passivität von Fe und Fe-Cr Leg. Diss. Leiden, 58 ff (1955).
7. Y. M. Kolotyrkin, *Z. Elektrochem.*, **62**, 664 (1958).
8. H. Gerischer and M. Käppel, *Z. Phys. Chem. N.F.*, **8**, 258 (1956).
9. R. H. Roberts and Shutt, *Trans. Faraday Soc.*, **34**, 1455 (1938).
10. O. Erbacher, *Z. Phys. Chem.*, **A163**, 215 (1933); O. Erbacher, W. Herr, H. Babo, and M. Ebert, *Arch. Metallk.*, **12**, 409 (1949).
11. N. A. Nielsen, E. M. Mahla, and T. N. Rhodin, *Trans. Electrochem. Soc.*, **89**, 167 (1946).

The Passivity of Iron-Chromium Alloys

Gerald Aronowitz[1] and Norman Hackerman
Department of Chemistry, The University of Texas, Austin, Texas

ABSTRACT

Chronopotentiometry and differential capacity measurements were used to study the passive films formed by anodic polarization of a series of Fe-Cr alloys in dilute H_2SO_4. Steady-state conditions were established by electronic control of the electrode potential prior to making measurements.

Cathodic reduction studies indicated the presence of at least three types of surface materials. One is nonprotective in the case of Fe and several of the lower Cr alloys, but achieves considerable stability to reduction or dissolution at an alloy composition approaching 12% Cr. Another material is essential for passivity of Fe and the alloys with Cr content less than 12% and plays an important role in the electrical properties of the films on these alloys. A third type of surface material appears as a by-product of processes occurring in the transpassive region.

In the composition range 2.70-9.02% Cr, capacity-potential curves are quite similar and capacities follow a reciprocal relation with electrode potential over a range of potentials. Extrapolation of these data was used to obtain a relation between film thickness, dielectric constant, and charge equivalents involved in film reduction. Film dielectric constant values, calculated assuming the reduction of normal Fe_2O_3, varied from 29.1 to 87.5, depending on the reduction reaction assumed. At an alloy composition approaching 12% Cr, the passive film assumes optimum protective properties. Correspondingly, humps develop in the capacity-potential curves, and the curves shift in the direction of higher capacity values with increasing Cr content.

At present, two major points of view exist as to the cause of passivity: the adsorbed film theory and the bulk oxide theory. While the ultimate formation of an oxide having bulk properties on passive Fe, Ni, Cr, etc., is generally recognized, the problem is centered on the exact nature of these films in their early stages and on whether or not adsorption plays a role in passivity.

In this connection, a theory was put forth recently which attempts to reconcile these views by postulating a sequence consisting of adsorption, electron transfer to the adsorbate, and ultimate formation of bulk amorphous oxide *via* cation migration into the adsorbed array (1).

[1] Present address: American Oil Company, Research & Development Department, P. O. Box 431, Whiting, Indiana.

Iron which demonstrates the main features of the active-passive transition, has been studied probably more than any other metal. In recent years, however, considerable interest has been shown in the passivity of stainless steel and the iron-chromium alloys because of the wide range of corrosion resistance shown by these metals. In addition, the attainment of optimum corrosion resistance and ease of passivation at a critical alloy composition in the neighborhood of 12% Cr has raised further questions.

Chronopotentiometry was employed in this work to determine passive film charge equivalents. Anodic film formation techniques very often do not satisfy the requirement of known or 100% current efficiency because of simultaneous anodic dissolution. Cathodic film reduction studies can suffer from these

disadvantages if the film breaks down spontaneously during the reduction, if solution components are simultaneously reduced, or if electrode roughening occurs. By suitable choice of experimental variables these difficulties may be avoided. In principle, the method should also differentiate between separate reduction steps and thus indicate the existence of more than one type of passive film component.

Differential capacity measurements have been used with some success in recent years in determining the thickness of anodic films formed on metals such as tantalum and aluminum (2). Recent studies on passive iron (3, 4) have shown that reciprocal capacity-potential relations exist to a degree of approximation, but that the electrical properties of the system are more complicated than for anodized tantalum or aluminum. Differential capacity studies were included to provide comparisons with the behavior of metals like anodized tantalum and clean surface metals such as platinum and mercury, and to see if electrical property changes in the passive film parallel property changes such as corrosion resistance and ease of passivation at some critical alloy composition.

Experimental Materials and Procedures

A series of Fe-Cr alloys ranging from 2.70 to 19.1 wt % Cr was obtained from the laboratories of Professor H. H. Uhlig. Their preparation is discussed elsewhere (5, 6). The iron used came from a stock of zone-refined iron, supplied by the Battelle Memorial Institute. Their analysis shows: carbon, 10 ppm; oxygen, 23 to 28 ppm; nitrogen, 2 ppm; hydrogen, 0.1 ppm. Cylindrical electrodes, approximately 2 cm long and 0.2 cm in diameter, were abraded with 4/0 emery paper, electropolished according to the method of Sewell *et al.* (7), and mounted in a Pyrex holder with polyethylene. Immediately before use, electrodes were electropolished briefly and then rinsed in conductivity water. Electrodes pretreated by mechanical abrasion only gave poor reproducibility.

The cell and pre-electrolysis vessel were constructed of Pyrex. The use of stopcock grease was avoided entirely. All solutions were 0.1M in Na_2SO_4 and were prepared from 3x recrystallized Na_2SO_4 and conductivity water of specific resistance $> 3 \times 10^6$ ohm cm. The range of solution *p*H used was from 0.6 to 13.6 and was adjusted with H_2SO_4 or NaOH. Freshly prepared solutions were subjected to pre-electrolysis for periods up to 120 hr at a c.d. of ~8 ma/cm^2. It was found that a 24-hr pre-electrolysis was sufficient to insure that difficulties due to solution impurities would be avoided. Bureau of Mines Grade A helium was bubbled through the test solution for 12 hr prior to beginning an experiment, and also during the experiment. All runs were made at 4.5° ± 0.2°C.

Chronopotentiometric studies were made in the usual way by recording the potential decay during constant current polarization and measuring the lengths of arrest regions in the traces. Capacities were measured as a function of anodization potential, using the constant current pulse method of Riney *et al.* (8) modified for square wave charging. A description of the electrical apparatus and circuit is available elsewhere (3). Electrode potentials were measured with respect to a $Hg/Hg_2SO_4(s)$ $Hg_2SO_4 + K_2SO_4$ (sat'd) half cell, which was allowed to assume the temperature of the laboratory atmosphere (25° ± 3.0°C). Connection was made to the cell through a salt bridge filled with test solution. Because of small but unknown thermal and concentration junction potentials and potential variations induced by the square wave signal, electrode potentials are reported only to the nearest 0.01v. All electrode potentials given were corrected to the normal hydrogen electrode (NHE).

Experimental Results

Preliminary studies were performed to determine the potential regions in which measurements could be made with a minimum of metal dissolution occurring, as significant changes in surface roughness and in the Cr content of the surface layers of the alloy were undesirable. For similar reasons cold 0.1M Na_2SO_4, adjusted to *p*H 2.2, was employed in most of this work. For the present purposes, this was sufficiently well buffered and assured relatively low coulomb and c.d. requirements for passivation of the alloys, and for maintenance of the passive state.

Anodic current densities.—The anodic c.d. in the passive potential region varied from 10^{-6} amp/cm^2 for the 2.70% Cr alloy to 10^{-7} amp/cm^2 for the 12.2% Cr alloy. For alloys with Cr content $\geqslant$9.02%, and at anodization potentials more noble than 1.05v, the anodic c.d. increased above these steady values to a peak at about 1.35v. This was followed by a decline just prior to reaching the O_2 evolution region. The peak values varied from 3.5 μa/cm^2 for the 9.02% Cr alloy to 22 μa/cm^2 for the 19% Cr alloy. Shifting the electrode potential in the opposite direction, from O_2 evolution to 1.05v, resulted in lower values of the anodic c.d. throughout this region. While these data are not too reproducible, the behavior noted has been observed previously and agrees qualitatively with observations made by other investigators, *e.g.* ref. (9).

At potentials more noble than 1.65v, the anodic c.d. for O_2 evolution followed a Tafel relation with electrode potential. Table I lists the *b* values of the potentiostatically obtained electrode potential-log c.d. plots for several of the alloys, corrected for resistance overvoltage.

Cathodic chronopotentiometry.—Examples of the time-potential behavior of a passive alloy under constant current cathodic polarization are shown in Fig. 1. Curve 1 is for 2.70% Cr and shows a potential arrest (B) at a more active potential than the Flade

Table I. *b* values of electrode potential-log c.d. plots for several alloys

Alloy	*b*, (pH 2.2)	*b*, (pH 13.6)
7.14% Cr	0.043	
9.02% Cr	0.042	
12.2% Cr		0.050
18.6% Cr	0.052	

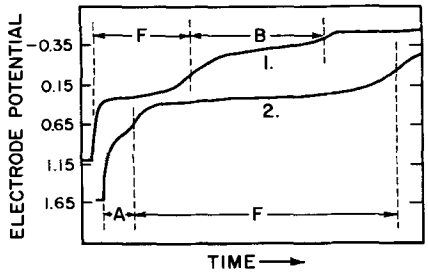

Fig. 1. Time-potential curves taken during constant current cathodic polarization of a pre-anodized electrode in oil M Na_2SO_4, pH 2.2, 5.0°C. Curve 1, 2.70% Cr alloy, c.d. 1173 $\mu a/cm^2$; curve 2, 12.2% Cr alloy, c.d. 17.5 $\mu a/cm^2$.

arrest (F). Curve 2 for 12.2% Cr shows still another arrest (A) at a more noble potential than the Flade arrest. These arrests were studied with respect to occurrence and growth as a function of anodization potential, E, chromium content, and pH. In addition, the effect of cathodic c.d., chromium content, and pH on the arrest potentials, V, was examined. Arrest lengths were estimated to be between points of inflection in the arrest break off regions of the traces. With these, specific charge values in units of μcoul/cm^2 (Q) were obtained from the traces. Time independent values of Q for a given E were usually attained within several minutes, but anodizations of 5-min duration were uniformly used. The experimental points in the Q-E curves for A and F were in most cases averaged over three separate runs with freshly prepared electrodes and fresh solution each time. Average deviations did not exceed 10% for more than 95% of the points. Q-E curves for B were plotted from the data of individual runs, but that for the 2.70% Cr alloy represents an average of three separate runs with average deviations not exceeding 6.0%.

For the alloys with Cr content $\geqslant$4.98%, A makes its initial appearance at 1.05v. Figure 2 shows the

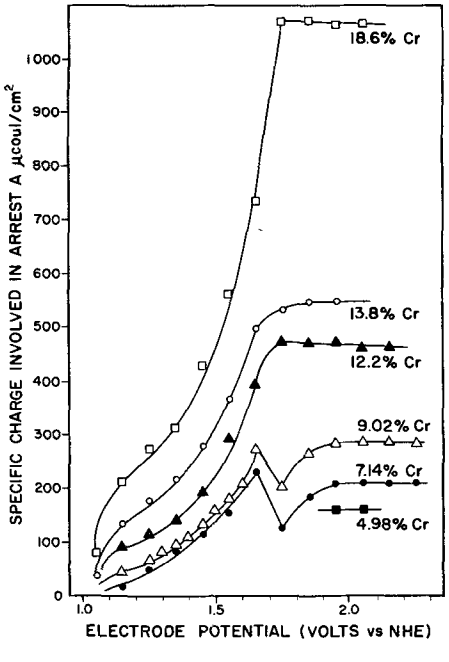

Fig. 2. Q(A)-E curves for alloys from 4.98 to 18.6% Cr in 0.1M Na_2SO_4, pH 2.2, 5.0°C.

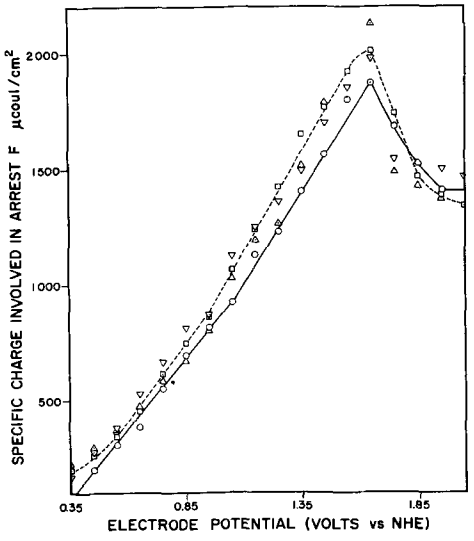

Fig. 3. Q(F)-E curves for the "lower" range alloys in 0.1M Na_2SO_4, pH 2.2, 5.0°C. Open dotted circle, 2.70% Cr; open dotted square, 4.98% Cr; inverted dotted triangle, 7.14% Cr; open dotted triangle, 9.02% Cr.

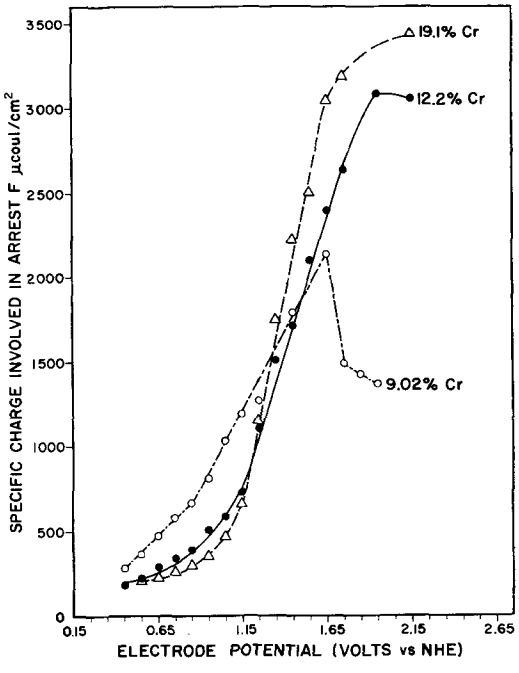

Fig. 4. Q(F)-E curves for alloys from 9.02 to 19.1% Cr in 0.1M Na_2SO_4, pH 2.2, 5.0°C. The curve for the 9.02% Cr alloy is presented for comparison and was replotted from Fig. 3.

variation in specific charge, Q(A), involved in A, with anodization potential. A shift to higher Q(A) values is found with increasing Cr content. In the O_2 evolution region, Q(A) is independent of E. If the latter Q(A) values are plotted as a function of the mole % Cr, the plot is nearly linear, at least up to 14.8 mole %.

Arrest F, which was observed here before (10, 11) on either open-circuit decay or forced decay of passive iron electrodes in acid solutions, can be seen for all the alloys investigated. The arrest region is not well defined for $E < 0.55$v, but the arrest potential, V(F), does not vary with E for E noble to 0.55v. The Q(F)-E curves shown in Fig. 3 and 4 indicate a change in form between the "lower" alloys (2.70

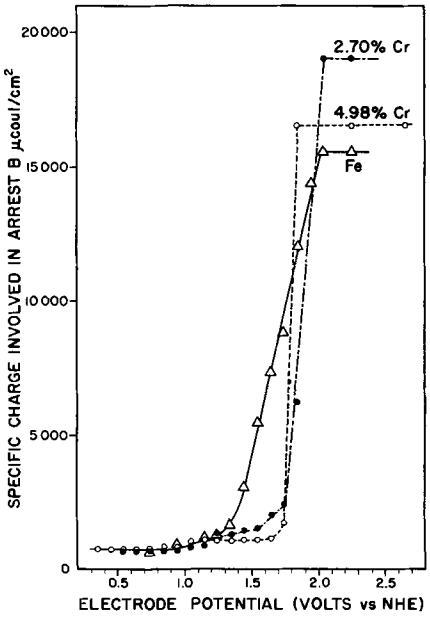

Fig. 5. Q(B)-E curves for Fe, a 2.70% Cr alloy, and a 4.98% Cr alloy in 0.1M Na_2SO_4, pH 2.2, 5.0°C.

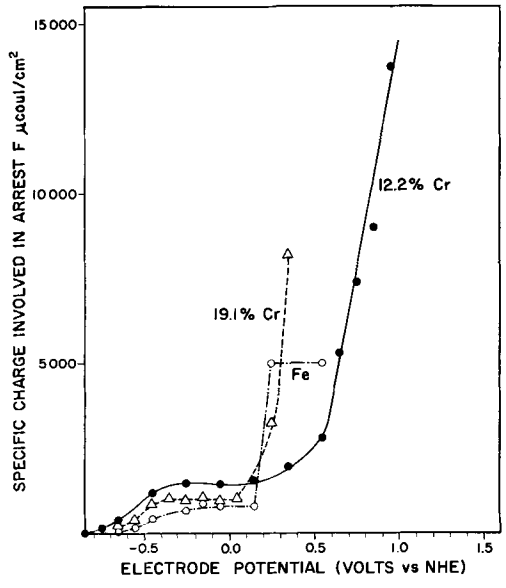

Fig. 6. Q(F)-E curves for Fe, a 12.2% Cr alloy, and a 19.1% Cr alloy in a 0.1M NaOH + 0.1M Na_2SO_4 at 5.0°C.

to 9.02% Cr) and the "higher" alloys (12.2 to 19.1% Cr).

Q(B)-E curves are shown in Fig. 5 for Fe, 2.70% Cr and 4.98% Cr alloys. V(B) shifted to more negative values with increasing Cr in the "lower" range, resulting in a poorly defined arrest for alloys with Cr content >4.98%. If cathodic polarization charging was interrupted after passing F, Q(B) decreased on subsequent cathodic treatment with time of open-circuit treatment. While 5-10 sec was sufficient to reduce Q(B) to zero for Fe, or a 2.70% alloy, arrest B could not be removed for alloys with Cr content $\geqslant$12.2% without a vigorous cathodization or repolishing of the electrode.

The potentials of the various arrests were taken to be at the point of minimum slope in the arrest region. These values varied linearly with solution pH from pH 0.6 to 13.6. The following relations were obtained from extrapolation of the V-pH plots

$$V(\mathrm{A}) = 0.89 - 0.066\ \mathrm{pH} \qquad [1]$$

$$V(\mathrm{F}) = 0.45 - 0.066\ \mathrm{pH} \qquad [2]$$

While V(A) did not vary with Cr content over the range studied, V(F) (calculated for pH = 0) varied from 0.55v for Fe to 0.45v for a 19.1% Cr alloy. V(B)-pH studies were not done here, but from data reported for Fe in a previous work (3), *e.g.*

$$V(\mathrm{B}) = 0.30 - 0.063\ \mathrm{pH} \qquad [3]$$

For a given value of E, Q(A) and Q(B) did not vary with cathodic c.d. for values >100 μa/cm². Q(F) was independent of c.d. between 4.0 μa/cm² and 10 ma/cm² for alloys in the "lower" range. In these cases c.d.'s from ~0.5 ma/cm² to ~1.5 ma/cm² were employed. For the "higher" alloy range, c.d.'s <50 μa/cm² were used as otherwise Q(F) decreased with increasing c.d. In addition, neither Q nor V was affected by solution stirring or replenishment.

If, after a normal anodization, E was changed and held at a more negative value, Q values normally found at E persisted for several hours upon cathodic polarization from the more negative potential. This hysteresis was not apparent from potentials within 0.1-0.2v noble of the arrest potentials. In summary, Q was metastable with respect to E, except for E values approaching V.

At pH values <2.2, the traces retained their form but Q values were lower. In alkaline solutions Q(A) decreased sharply with increasing pH, and A could not be observed in 1.0M NaOH. Figure 6 shows Q(F)-E curves for several alloys in 0.1M NaOH along with one for Fe taken from a previous work (3).

Anodic chronopotentiometry.—Figure 7 is a time-potential trace for constant current anodic polarization of an initially active 19.1% Cr alloy. The trace can be divided into three regions; 1, 2, and 3. The specific charge involved in region 1 was difficult to reproduce, but that for regions 2 and 3 could be reproduced to better than 10% if the electrode were briefly etched in warm 50% H_2SO_4 after electropolishing. In this case specific charge values for regions 2 and 3 were independent of anodic c.d. over the range of c.d. studied (~200 μa/cm² to ~5 ma/cm²). Region 3 appeared only for alloys with Cr content $\geqslant$9.02%. The charge involved in region 3 increased with increasing Cr content. Figure 8 shows

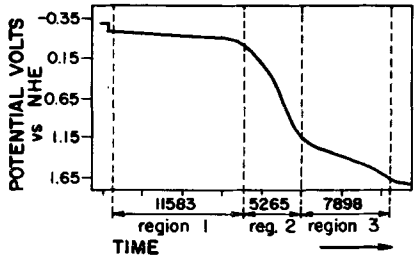

Fig. 7. Time-potential trace for anodic polarization of an initially active 19.1% Cr alloy. Anodic c.d. 1755 μa/cm², 2.0 sec/div. Specific charge values in μcoul/cm² involved in the various regions are noted below the trace.

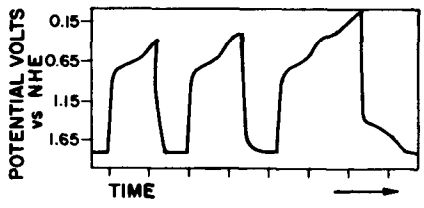

Fig. 8. Time-potential traces for alternate cathodic and anodic polarization of a 19.1% Cr alloy initially at an O_2 evolution potential. Anodic c.d. 3510 $\mu a/cm^2$, cathodic c.d. 567 $\mu a/cm^2$ 2.0 sec/div.

the results of alternate cathodic and anodic charging on a 19.1% Cr alloy initially at an O_2 evolution potential. Specific charge values involved in the anodizing and cathodizing portions respectively, agreed if only arrest A was passed as in the first two traces. In the third trace, F is passed as well and region 3 of Fig. 7 appears in the anodizing portion.

Differential capacity measurements.— Throughout the potential region studied, time independent values of the capacity, C, could usually be obtained in the order of seconds, although at least two readings, 5-10 min apart, at a given electrode potential, and agreeing to within 1.0%, were used for all of the plotted data. As the C-E curves showed hysteresis in terms of the direction of potential change, runs were begun by setting E at the extreme negative end of the passive potential region. It was then altered in the direction of more noble values in increments of 0.01v. At 1.75v, E was then changed in the opposite direction until the lower limits of stable passivity had been reached, or on to the approach of the H_2 evolution region. Capacities were not studied in the regions of H_2 or O_2 evolution. In the former, measurements drifted with time, while in the latter, the time-cell voltage trace showed considerable curvature and slopes were difficult to measure accurately.

Capacity values for an electrode on open circuit were measured immediately after immersion in the solution. Open-circuit potentials were −0.39 to −0.40v. Capacity measurements for a given alloy could be reproduced to better than 3.0% and values of 16.9 $\mu f/cm^2$ and 18.1 $\mu f/cm^2$ were obtained for a 2.70% Cr alloy and a 13.8% Cr alloy, respectively. These values averaged to 17.5 $\mu f/cm^2$.

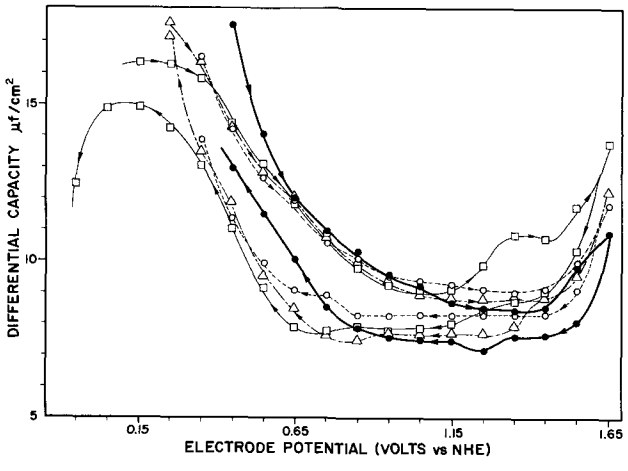

Fig. 9. C-E curves for the "lower" range alloys in 0.1M Na_2SO_4 pH 2.2, 5.0°C. •——•, 2.70% Cr; ○ - - - ○, 4.98% Cr; △ — - — △, 7.14% Cr; □——□, 9.02% Cr.

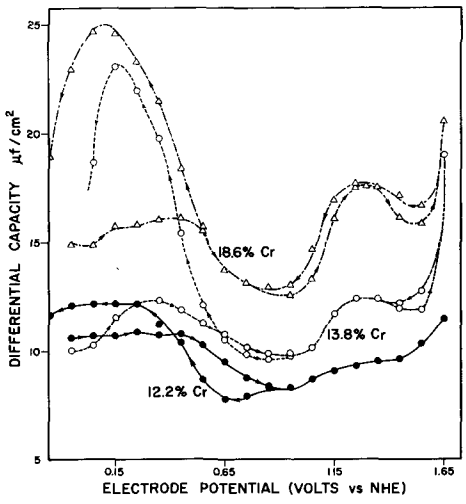

Fig. 10. C-E curves for the "higher" range alloys in 0.1M Na_2SO_4, pH 2.2, 5.0°C. •——•, 12.2% Cr; ○ - - - ○, 13.8% Cr; △ — - — △, 18.6% Cr.

Figures 9 and 10 show C-E plots for the alloys in pH 2.2 solution. The points on these plots represent values averaged from between two and four runs made with fresh solution and with freshly prepared electrodes each time. Average deviations were less than 6.0%.

Except for the small hump in the vicinity of 1.35v for the 9.02% Cr alloy, and several slightly high values for the 2.70% Cr alloy at the left of the curves, the curves for the alloys in the "lower" range (Fig. 9) are quite similar. Figure 11 is a plot of $1/C$ *vs.* E for the points of the curves in Fig. 9 taken in the direction of increasingly noble values, *i.e.*, the upper branches. Except for the two most negative potentials for the 2.70% Cr alloy, C appears to follow a reciprocal relation with E up to ~1.05v, *i.e.*

$$E = 13.4/C - 0.475$$

Figure 10 shows that important changes occur in going to the "higher" range alloys. The hysteresis is opposite to that found with the "lower" alloys (note arrowheads on curves).

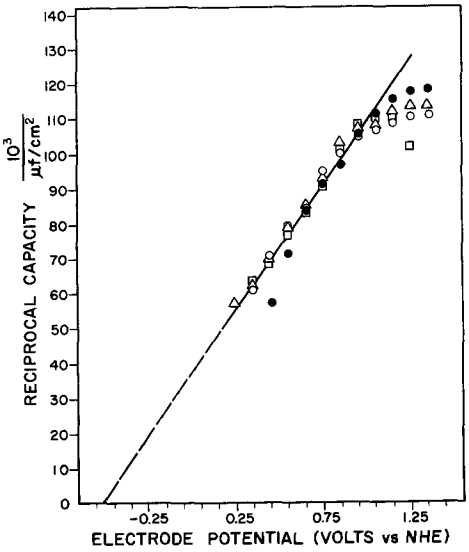

Fig. 11. $1/C$ *vs.* E plots of the upper branches of the curves in Fig. 7. •, 2.70% Cr; ○, 4.98% Cr; △, 7.14% Cr; □, 9.02% Cr.

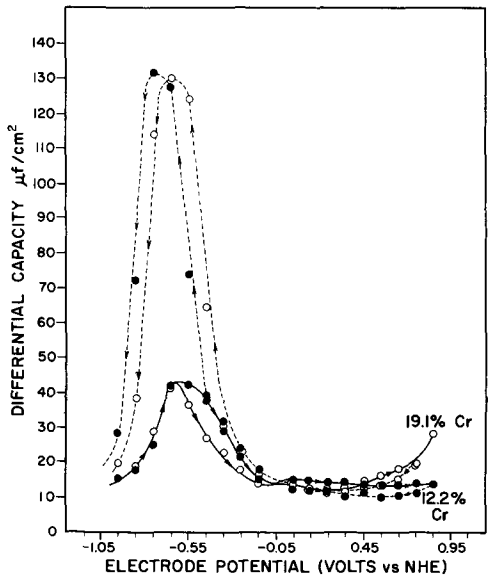

Fig. 12. *C-E* curves for a 12.2% Cr alloy and a 19.1% Cr alloy in 0.1M NaOH + 0.1M Na_2SO_4 at 5.0°C.

At the left of the curves a broad peak is found for the 13.8 and 18.6% Cr alloys with maximum values of *C* increasing, and shifting to more negative *E* with increasing Cr content. This region was examined further. Beginning with a freshly prepared specimen, *E* was adjusted to some value noble to the peak region. The potential was then altered in the negative direction and capacities were measured. Peak heights were found to increase as more noble potentials were reached. With vigorous cathodization after anodization at 1.65v, peak heights decreased with time of cathodic treatment. However, it was necessary to repolish the electrode to reproduce the original capacity values in the peak region (—0.05 to 0.45v).

Figure 12 shows *C-E* plots for the 12.2 and 19.1% Cr alloys in 0.1M NaOH + 0.1M Na_2SO_4. Although the plotted points represent individual runs, an additional run on the 19.1% Cr alloy indicated that reproducibility of better than 6.0% could be expected for all but a few of the points. The plots are characterized by a small hump in the negative potential region of the plots on going to more noble potentials and a general decrease in *C* in this direction. In the opposite direction, capacities increase gradually and then rise to a peak value in excess of 130 μcoul/cm^2 at the more negative potentials. The hysteresis behavior observed in this region is qualitatively similar to the results obtained for the higher alloys in acid solutions. The curves seen in Fig. 9 compare favorably to *C-E* curves reported for Fe in alkaline solution (3).

Discussion

A number of observations provided evidence that the potential arrests correspond to a *p*H dependent reduction of surface compounds. *Q* was independent of solution stirring rate, solution replenishment, or cathodic c.d. but not of *E*. Added to these were the *p*H dependences of the arrest potentials, the hysteresis behavior of the *Q-E* curves, and the *Q* values themselves. The latter were too great to be accounted for by such processes as reduction of solution impurities or buildup of concentration overvoltage for hydrogen evolution.

A comparison of the *Q-E* curves for arrests A, B, and F showing an absence of any obvious correlations, indicates that the form of the cathodic time-potential curves does not result from a sequence of reduction steps originating from a single reactant but involves the reduction of three individual surface materials; "A," "B," and "F."

Material "B" becomes increasingly stable with respect to both reduction and dissolution in the "higher" alloy range. Reduction of "A" and "F" fails to activate a 12.2% Cr alloy. That "B" can sustain passivity for alloys $\geqslant$12.2% Cr without the presence of "F," is also indicated by the discrepancy of several hundred millivolts between *V*(F) and the passivation potential of these alloys. Both the rapid growth of "B" with *E* in the O_2 evolution region and the strong time dependence of this growth at a given O_2 evolution potential suggests that material "B" grows in this region by diffusion of O_2 or some intermediate of O_2 evolution through the film.

While lower *Q*(F) values have been reported for Fe (11, 12), *V*(F) and the passivation potential do not change in going to a 2.70% Cr alloy. The observed *p*H variation of 0.066 mv/*p*H unit can be compared to the value 0.059 mv/*p*H unit reported for Fe (13). Since the "lower" range alloys behave almost identically with respect to both *Q*(F) and capacity, it seems reasonable to conclude that material "F" changes little in structure or composition between Fe and an alloy composition of 9.02% to 12.2% Cr.

Arrest A makes its appearance for alloys $\geqslant$ 4.98% Cr at $E > 1.05$v, *i.e.*, the potential of the onset of a region of secondary activity characteristic of the Fe-Cr alloys and Cr. It is attributable to chromate production on comparing the polarization curves of the alloys with that for chromium (14). The material reduced during the arrest may well be hexavalent chromium. This is suggested by the general increase in *Q*(A) with increasing Cr content of the alloy, and by the noble value of *V*(A). A Cr^{+3} containing species should be reduced at a more negative potential. While correlation between *V*(A), its *p*H coefficient, and the thermodynamic CrO_3/Cr_2O_3 or H_2CrO_4/Cr^{+3} potentials was not found, a comparison can be made with the thermodynamic potential of 0.90v at *p*H = 0 for the reaction $HCrO_4^- + 3H^+ + 3e^- = CrO_2^- + 2H_2O$. This was calculated using the reported standard potentials (15, 16) for the reactions: $2H_2O + Cr = CrO_2^- + 4H^+ + 3e$ and $HCrO_4^- + 7H^+ + 6e^- = 4H_2O + Cr$. The drop in *Q*(A) with increasing *p*H fits a previously reported observation that decreases in solution chromate uptake on a Cr surface occurs with increasing *p*H (17). This was explained as due to competitive adsorption by OH^-.

Region 3 of the anodic time-potential curve (Fig. 7) is a potential arrest occurring at ~ 1.35v *i.e.*, at the potential of the peak c.d. in the transpassive region. In addition, the range of alloy composition in which region 3 appears, *i.e.*, $\geqslant$ 9.02% Cr, parallels

the range in which the secondary activity is observed. Region 3 must then be connected with the production of the secondary passivity. Both the traces of Fig. 8 and the simultaneous appearance of arrest A with the onset of the secondary activity suggest that material "A" does not produce the secondary passivity but is probably a by-product of processes occurring in the transpassive region. Changes in "F," which prevent the continuous passage of chromium through the passive film, must be looked to.

Both the $Q(F)-E$ and $1/C$ *vs.* E plots are linear between ~ 0.35 and 1.05v for the "lower" alloys. In addition, both show hysteresis. It seems reasonable to connect these data. If material "F" were the dielectric of a parallel plate capacitor in this potential range, an equation relating thickness of F, d, $Q(F)$, and dielectric constant, k, can be obtained assuming a passive film-solution interfacial capacity, $C_{film\text{-}sol'n}$ in series with a film capacity, C_{film}, and that "B" makes no contribution to the measured capacity, C. From the linear portion of the curve of Fig. 11, the branch of the lower curve in Fig. 3 which lies at potentials less than about 1.05v, and the parallel plate capacitor formula:

$$E = 13.4\ (1/C_{film} + 1/C_{film\text{-}sol'n}) - 0.475 \quad [4]$$

$$E = 8.43 \times 10^{-4}\, Q(F) + 0.254 \quad [5]$$

$$C_{film} = k/0.113\, d \quad [6]$$

If [4] and [5] are combined with the condition that $1/C_{film} = 0$ when $Q(F) = 0$, a value for $C_{film\text{-}sol'n}$ can be obtained

$$C_{film\text{-}sol'n} = \frac{13.4}{0.475 + 0.254} = 18.4\ \mu f/cm^2$$

This value is comparable to the value of 17.5 $\mu f/cm^2$ obtained experimentally for an active electrode at ~ −0.40v. Combining Eq. [4], [5], and [6] with the value obtained for $C_{film\text{-}sol'n}$

$$Q(F) = 1.80 \times 10^3\, d/k \quad [7]$$

or

$$k = 1.80 \times 10^3\, d/Q(F)$$

If the reduction reaction, the density, and the molecular weight of "F" are known, a relation between $Q(F)$ and d can be obtained. Assuming the reaction is

$$3Fe_2O_3 + 2H^+ + 2e^- = 2Fe_3O_4 + H_2O$$

then

$$d/Q(F) = \frac{159.7 \times 10^8 \times 10^{-6}}{5.12 \times 2/3 \times 96{,}500} = 4.85 \times 10^{-2}$$

Combining this result with Eq. [7], a value for the apparent dielectric constant of "F" can be obtained

$$k = 1.80 \times 10^3 \times 4.85 \times 10^{-2} = 87.5$$

If the reaction of $Fe_2O_3 + 2H^+ + 2e^- = 2FeO + H_2O$ is assumed, a value of 29.2 obtains for k. Reduction to Fe can be ruled out since d less than the $O^=$ diameter would obtain for some values of E. Values reported for the dielectric constants of normal oxides of iron range from 7 to 20 (18-20).

For E more noble than 1.05v, $1/C$ *vs.* E relations fail, and a hump develops in the C-E curves for the "higher" range alloys. This can be contrasted with the behavior of Fe in dilute H_2SO_4, in which case C continues to decrease hyperbolically with increasing E (3,4). While for iron, small anodic current flow extends to the beginning of oxygen evolution, a potential of 1.05v marks the onset of the secondary activity region for the alloys in the *p*H 2.2 solution used. A connection can thus be established between the secondary activity and the observed change in electrical properties. Electrical changes in "F," perhaps caused by the continuous passage of chromium through the film, may be involved. Significant structural changes seem unlikely since $V(F)$ is independent of E.

The shift of the curves to higher C values between 12.2 and 18.6% Cr could be accounted for if either the dielectric constant or the electronic conductivity of the film increased. At 18.6% Cr, the C-E curve (except for the hump in the transpassive region) compares quite favorably with C-E data obtained for "clean" Pt in neutral Na_2SO_4 solutions (21).

Conclusion

While the alloys studied show some of the behavior found on phase oxide covered metals like Ta and Al, the fact that a $1/C$ *vs.* E relation holds only for the "lower" range alloys over a restricted range of anodization potential and only in acid solutions indicates that a classification with the latter group of metals is not appropriate. At the same time, a film consisting of monolayer quantities or less of a single type of adsorbate, *i.e.*, O, OH, O_2, cannot be reconciled with the results either. Indeed $Q(F)$ attains values too high for this to occur.

The results might be accounted for better by a model consisting of a monolayer of oxygen atoms adsorbed on the metal over which an amorphous mixture of metal ions and oxygen ions might form by metal ion movement through the adsorbed array. Some evidence can be presented to support this view. $Q(B)$ remains at ~ 0.7 mcoul/cm^2 over a range of E, *i.e.*, close to the value of 0.6 mcoul/cm^2 calculated for reduction of a monolayer of adsorbed oxygen atoms in 1:1 correspondence with the surface metal atoms. That "B" is nonprotective for Fe but achieves optimum protective properties at ~ 12% Cr fits an electron configuration theory of passivity which relates this critical composition to d-electron vacancies in the alloy components and the resulting ability of the alloy to chemisorb oxygen (22). Indeed, that "F" fails to grow as rapidly with E, at $E < 1.05$v for the "higher" range alloys as for the "lower" range suggests that strong adsorption forces inhibit the movement of metal ions through the adsorbed array for the former metals. The hysteresis behavior in the C-E curves for these alloys seems more reasonable on the basis of such a model.

The change in the form of the C-E curves for the "higher" range alloys parallels the attainment of optimum passive film stability with respect to both "F" and "B." Other investigators have observed this composition to mark the attainment of either optimum ease of passivation or maximum corrosion re-

sistance (5). The validity of the capacity data in studies like these is thus supported.

Acknowledgment

The authors are pleased to acknowledge the Robert A. Welch Foundation and the Office of Naval Research for Financial support. Appreciation is extended to the Battelle Memorial Institute for their gift of zone-refined iron and to Professor Herbert H. Uhlig for kindly providing the alloys used.

Any discussion of this paper will appear in a Discussion Section to be published in the December 1963 JOURNAL.

REFERENCES

1. Norman Hackerman, *Z. Elektrochem.*, **62,** 632 (1958).
2. L. Young, *Anodic Oxide Films,* Academic Press, Inc., New York (1961).
3. N. E. Wisdom and Norman Hackerman, To be published.
4. W. J. Engell and B. Illschner, *Z. Elektrochem.*, **59,** 716 (1955).
5. P. F. King and H. H. Uhlig, *J. Phys. Chem.*, **63,** 2026 (1959).
6. H. H. Uhlig and G. E. Woodside, *ibid.*, **57,** 280 (1953).
7. P. D. Sewell, C. D. Stockbridge, and M. Cohen, *Can. J. Chem.*, **37,** 1813 (1959).
8. J. S. Riney, G. M. Schmid, and Norman Hackerman, *Rev. Sci. Inst.*, **32,** 588 (1961).
9. M. Prazak *et al., Z. Elektrochem.*, **62,** 739 (1958).
10. E. S. Snavely and N. Hackerman, *Can. J. Chem.*, **37,** 268 (1959).
11. W. H. Wade and Norman Hackerman, *Trans. Faraday Soc.*, **53,** 1 (1957).
12. G. M. Schmid and Norman Hackerman, To be published.
13. K. J. Vetter, *Z. Elektrochem.*, **62,** 642 (1958).
14. W. A. Mueller, *Corrosion,* **18,** 73t (1962).
15. W. M. Latimer, "Oxidation Potentials," p. 248, Prentice Hall, Inc., New York (1952).
16. M. S. Udy, "Chromium," Vol. I, p. 134, Reinhold Publishing Corp., New York (1956).
17. N. Hackerman and R. A. Powers, *J. Phys. Chem.*, **57,** 139 (1953).
18. T. Takei, *J. Inst. Elec. Engrs. Japan,* **66,** 121 (1946).
19. F. Wagenknecht, *Kolloid-Z.,* **112,** 35 (1948).
20. A. W. Kohlschutter, *Z. Anorg. u. allgem. Chem.*, **278,** 270 (1951).
21. P. V. Popat and Norman Hackerman, *J. Phys. Chem.*, **62,** 1198 (1958).
22. H. H. Uhlig, *Z. Elektrochem.*, **61,** 700 (1958).

The Influence of Film Thickness on the Thermodynamic Properties of Thin Oxide Layers on Iron

K. G. Weil

Eduard Zintl Institut der Technischen Hochschule Darmstadt, Lehrstuhl für Physikalische Chemie, Darmstadt, West Germany

The properties of a passive metal are, in general, determined by the properties of the oxide films which cover the metal surface. Recently Vetter (1) showed how to calculate the equilibrium potential of such an oxide-covered electrode from the free energy of formation of the oxide. To use his formulae the free energy of formation of the oxide must be known as a function of the degree of oxidation. This information, however, can only be acquired by experiments which are usually done on bulk oxides. In this paper it will be shown that it may be risky to use results obtained for such bulk materials to calculate equilibrium properties of thin films.

In the first stage the free surface energy will be taken into account. In a system metal/oxide/solution there may be three interfaces, and therefore the free energy change of such a system at constant volume and temperature may be written as

$$dF = \sum_i \mu_i dn_i + \sum_j \left(\frac{\partial F}{\partial O_j} \right)_{V,T} dOj \qquad [1]$$

where the integer i denotes the different species involved in the oxide forming reaction and the integer $j = 1,2,3$ denotes the three different interfaces O_j. Introducing the extent of reaction λ according to de Donder we obtain

$$dn_i = \nu_i d\lambda$$

and

$$dO_j = \frac{dO_j}{d\lambda} d\lambda$$

and finally

$$dF = \left\{ \sum_i \mu_i \nu_i + \sum_j \left(\frac{\partial F}{\partial Oj} \right)_{V,T} \frac{dOj}{d\lambda} \right\} d\lambda \qquad [2]$$

When equilibrium is obtained the term in brackets must vanish, *i.e.*,

$$\sum_i \mu_i \nu_i + \sum_j \left(\frac{\partial F}{\partial Oj} \right)_{V,T} \frac{dOj}{d\lambda} = 0 \qquad [3]$$

Comparing Eq. [3] with the equilibrium condition for chemical reactions in bulk phases: $\sum_i \mu_i \nu_i = 0$, we find, that an influence of the free surface energy is to be expected in all cases in which $dOj/d\lambda \neq 0$. This is the case when the metal surface is not completely covered by the oxide, and the fraction of the surface covered varies during the reaction. It may also be the case when the oxide does not form a smooth film, but forms whiskers the height of which, and therefore also the oxide surface, varies during the reaction. In this case a change in the roughness factor will be related to the term $dOj/d\lambda$.

Under certain conditions another effect may be responsible for deviations in the free energy of formation of an oxide film from the value obtained by experiments done on bulk phases. Thermodynamically an oxide is defined by its chemical composition as well as by its crystallographic state, especially by the concentration and distribution of lattice defects and interstitials. These properties are very likely to be different in oxide layers grown on solid surfaces from those in bulk oxide phases. Especially when

the film thickness is of the same order of magnitude as the lattice constant of the oxide crystals forming the film, considerable deviations are to be expected.

In these cases a term depending on the film thickness is to be introduced into the equation for the free energy change

$$dF = \sum_i \mu_i dn_i + \left(\frac{\partial F}{\partial \xi}\right)_{V,T} d\xi \qquad [4]$$

(ξ is the film thickness). Assuming the growth of a smooth film with uniform density and chemical composition we have the following relation between $d\xi$ and the extent of reaction

$$d\xi = \frac{M}{\rho O} \nu_{\text{oxide}}\, d\lambda$$

(M is the molecular weight of the oxide, ρ its density, ν_{oxide} the stoichiometric number of the oxide in the oxide forming reaction, O the amount of surface.)

The equilibrium condition in this case reads

$$\sum_i \mu_i \nu_i + \left(\frac{\partial F}{\partial \xi}\right)_{V,T} \frac{M}{\rho O} \nu_{\text{oxide}} = 0 \qquad [5]$$

Evaluating the first term of Eq. [5] we get

$$\sum_i \mu_i \nu_i = \sum_i \mu_i^0 \nu_i + \sum_i RT \ln p_i^{\nu_i} = -RT \ln K_p^\infty + RT \sum_i \ln p_i^{\nu_i} \qquad [6]$$

with K_p^∞ = equilibrium constant of the oxide forming reaction for $\xi \to \infty$. Introducing Eq. [6] into [5] we obtain finally

$$\sum_i \ln p_i^{\nu_i} = \ln K_p^\infty - \left(\frac{\partial F}{\partial \xi}\right)_{V,T} \frac{M}{\rho O R T} \nu_{\text{oxide}} \qquad [7]$$

In cases in which the p_i can be measured as a function of ξ, $\left(\frac{\partial F}{\partial \xi}\right)_{V,T}$ can be obtained as a function of ξ, as will be shown for one typical case in the section on thin FeO films at high temperatures.

Application to the Theory of the Flade Potential

In the case of passive iron the Flade potential corresponds to the free energy of the reaction (2, 3)

$$2Fe_3O_4 + H_2O = 3\gamma Fe_2O_3 + H_2$$

According to the considerations in the preceding section it should depend on the thickness of the film formed during the reaction. Unfortunately it seems impossible to find experimental conditions under which the film is formed with definite known thicknesses. On the other hand, the film thickness does not decrease uniformly over the whole surface during the activation process so that one cannot associate with certainty the observed activation potentials to different film thicknesses.

Nevertheless, it can be shown that the properties of the passive film depend on its thickness, provided the film thickness is of the same order of magnitude as the lattice constant of its constituents. In a previous paper (4) it could be proved that the film thickness in the stationary state in acid solutions is over a wide range of potentials proportional to the potential-difference $U - U_f$ (U is the potential of the passive electrode, U_f the Flade potential measured against the same reference electrode). Using the figures given in that paper it is possible to plot the steady-state current of a passive iron electrode against the film thickness. Such a plot is shown in Fig. 1, using data reported by Herbsleb and Engell (5). [Similar data are reported by Bartlett and Ord (6) and by Osterwald (7).] It is very obvious from the figure that the properties of the passive iron are dependent on the film thickness between 0 and about 12Å and are completely independent at higher thicknesses. [The increase at ~ 1500 mv is caused by oxygen evolution.]

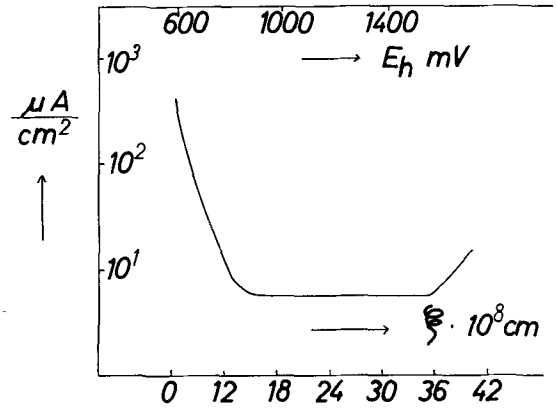

Fig. 1. Steady-state current vs. layer thickness. Iron in 1N H_2SO_4. Upper abscissa, potential against normal hydrogen electrode.

Herbsleb and Engell also showed that in the region between 600 and 850 mv, where the steady-state current is thickness-dependent, Fe^{++} ions are formed as corrosion product besides Fe^{+++} ions which are found in the whole range of passivity (8). They related the occurrence of the ferrous ions to the existence of fluctuating pores in the passive film within this potential range.

These findings fit very well the assumption that the properties of an extremely thin film differ from those of a thicker one. Generally the film thickness will not be uniform over a macroscopic region of a surface. This spatial fluctuation does not matter in cases when the film thickness is high enough to provide a free energy independent of film thickness ($\partial F/\partial \xi = 0$). If, however, ξ is so small that $\partial F/\partial \xi > 0$ then fluctuations in ξ will give rise to fluctuations in the free energy, and therefore a reaction is possible. As can be seen from Fig. 2 places with lower ξ are less stable with respect to those with higher ξ,

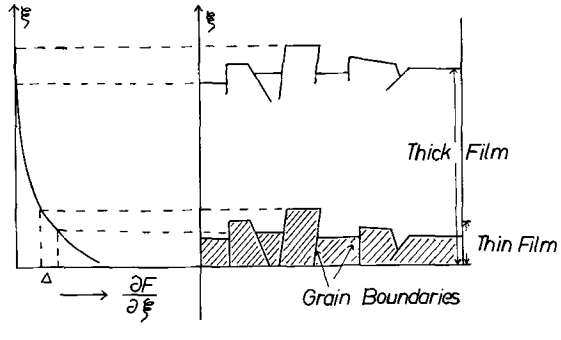

Fig. 2. Influence of fluctuations in thickness on free energy fluctuations for normal and extremely thin films.

and so the reaction leads to the formation of pores at those positions where spots of lower film thickness were situated originally. Whether the pores formed by this process will grow and cause total activation of the passive metal, or whether they will be closed by tangential growth of the film is merely a question of the capacity of the potentiostat used in the experiment.

Thin FeO Films at High Temperatures

The fact that it was possible to describe some properties of the passive film using the concept of a thickness-dependent free energy encouraged us to carry out some experiments to show the influence of film thickness on equilibrium properties in a more quantitative manner. The system Fe/H_2O_{vapor} was chosen, for the equilibrium constant of the reaction

$$Fe + H_2O = FeO + H_2 \qquad [9]$$

can easily be determined by simple measurements of the pressure if the partial pressure of the steam is kept constant during the experiments.

Experimental Design

The iron specimen consisted of "Magnetreineisen" of the Vakuumschmelze Hanau. Ten sheets with a total geometric surface of 100 cm^2 were mounted in a glass vessel which was fixed in the center of the coil of a high-frequency furnace. The glass vessel was cooled by running water supplied by a thermostat kept at a temperature of 18°C. The iron specimen was kept in its position by two thin wires of Pt and Pt/10 Rh which at the same time served as a thermocouple. The vessel could be connected with a container filled with a saturated $CaCl_2$ solution carefully thermostatted at 15°C to maintain the partial pressure of the steam at 5.1 Torr. The total pressure in the system was measured by a mercury manometer, the readings being taken by means of a cathetometer.

It is essential to keep the total volume of the reacting system as small as possible. This may be shown by the following considerations. In the initial state the iron surface is free of oxide ($\lambda = 0$) and the atmosphere consists only of steam at a given partial pressure. When reaction [9] occurs the hydrogen pressure increases in proportion to the extent of reaction

$$p_{H_2} = \frac{RT}{V}\lambda \qquad [10]$$

As the partial pressure of the steam is kept constant during the reaction, the pressure ratio also increases proportionally

$$p_{H_2}/p_{H_2O}{}^{\circ} = \frac{RT}{p_{H_2O}{}^{\circ} \cdot V}\lambda \qquad [11]$$

The reaction comes to an end when this pressure ratio equals the equilibrium constant of reaction [9]. This is illustrated schematically in Fig. 3. The unbroken curve represents the equilibrium constant as a function of λ as expected according to the considerations in the preceding sections. The two dotted lines show the increase of the pressure ratio with λ for two different values of the product $p_{H_2O}{}^{\circ} \cdot V$. It

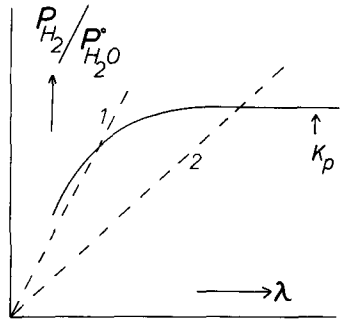

Fig. 3. K_p and $p_{H_2}/p_{H_2O}{}^{\circ}$ vs. extent of reaction for two different apparatus.

is obvious from Fig. 3 that an apparatus in which $p_{H_2O}{}^{\circ} \cdot V$ has the value used for the construction of curve 2 is useless for measurements of the dependence of K_p on λ. The apparatus used in the investigations reported here corresponded to curve 1 with $p_{H_2O}{}^{\circ} \cdot V \cong 10^3$ Torr cm^3 ($p_{H_2O}{}^{\circ} = 5.1$ Torr, $V = 187$ cm^3).

The necessity of working in such a small volume makes it impossible to use an apparatus according to the advice of Emmett (9). The measured equilibrium constants therefore may be erroneous due to any effect of thermal diffusion. But as is seen from Table I only the quotients $K_p{}^{\infty}/K_p$ are needed for the purposes of this paper, and therefore the error will be reduced remarkably. On the other hand, as long as there is no information about the true surface, the uncertainty which arises from the estimation of the roughness factor will be much larger than that arising from the thermal diffusion effect.

Experimental Procedure

All experiments were carried out with the temperature of the metal at 815°C. At the beginning of each experiment the iron specimen was annealed in a hydrogen atmosphere of 200 Torr for 2 hr. This was followed by a second annealing *in vacuo* for 2 hr. Finally, the specimen was annealed in a hydrogen atmosphere of 10 Torr to saturate the metal with hydrogen at about the same pressure as would be established in the oxidation reaction following.

The hydrogen in the gas phase was then removed very rapidly before opening the stopcock between the reaction vessel and the container with the $CaCl_2$ solution. From then on pressure readings were taken every minute until equilibrium was established.

Table I

n_{FeO}/cm^2, 10^8	K_p	$K_p{}^{\infty}/K_p$	ξ, A	$\left(\frac{\partial F}{\partial \xi}\right)_{V,T}$, kcal/cm
16.0	1.38	1.00	67.2	0
14.1	1.38	1.00	59.2	0
11.9	1.35	1.02	50.0	0.33
10.2	1.31	1.05	42.8	0.85
8.9	1.27	1.09	37.3	1.49
8.0	1.25	1.103	33.7	1.70
6.4	1.10	1.255	26.9	3.95
6.0	1.10	1.255	25.2	3.95
5.5	1.04	1.33	23.1	4.82
4.8	0.95	1.46	20.2	6.55
4.1	0.85	1.625	17.2	8.37

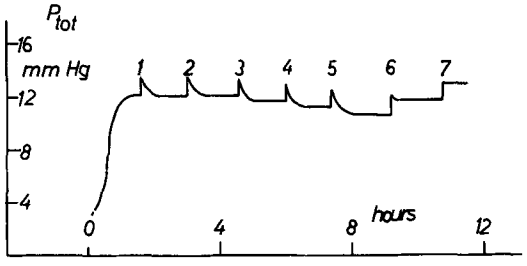

Fig. 4. Pressure readings in one set of experiments, showing the decrease in total pressure with decreasing amount of oxide.

The next steps of the process are easily described with help of Fig. 4. At various times, denoted with 1, 2, . . ., small amounts of hydrogen were added to the equilibrium mixture. (The amount of hydrogen added in each step was about 1/5 to 1/10 of the amount formed in the oxidation reaction at the beginning of the experiment.) This caused a sudden rise in the total pressure, followed by a slow decrease until the new equilibrium was established. Each equilibrium state corresponds to a different amount of oxide present on the iron surface. It can be seen from Fig. 4 that a remarkable decrease in equilibrium pressure is observed in the steps 3, 4, and 5 as the amount of oxide diminishes more and more. After the 6th addition of hydrogen all the oxide is reduced, and equilibrium is no longer reached.

To calculate the amount of oxide present at the various stages of the process it is necessary to know the amount of hydrogen formed or consumed at these stages. As the temperature is not uniform in the system the gas laws cannot be applied directly. We determined the average temperature in the following way. The whole system was kept at room temperature and hydrogen added up to a pressure $p(T_1)$. Then the iron specimen was heated to 815°C, and the pressure $p(T_2)$ was measured. During this experiment the $CaCl_2$ solution was covered with a film of silicon oil to prevent the formation of water vapor in the system. The average temperature can then be calculated

$$p(T_1)/p(T_2) = T_1/T_{\text{average}} \qquad [12]$$

This ratio proved to be pressure-independent in the range of pressures used in the experiments. The average temperature was calculated to be $T_{\text{average}} = 383°K$. All the experiments were repeated several times and showed a fairly good reproducibility.

Results

The results of the experiments are given in Table I. The figures in the first two columns are calculated directly from the experimental data without introducing any assumptions. To calculate the values of ξ from those obtained for n_{FeO} assumptions must be made for the density of the oxide and for the roughness factor. The density was taken as 5.7 g cm^{-3}, being the value for the bulk material at room temperature. The roughness factor was estimated to be 3, as the metal recrystallized during the annealing procedure, and showed a considerably rough surface after the experiments. To calculate the value of $(\partial F/\partial \xi)$ Eq. [7] was used. The density again was assumed to be 5.7 g cm^{-3}, for O the geometrical surface was taken. Figure 5 shows graphically the results for K_p as a function of the amount of oxide on the surface.

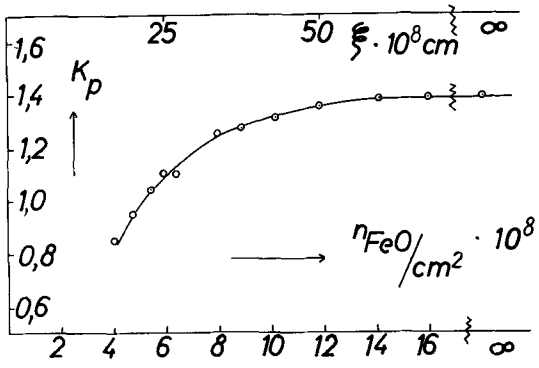

Fig. 5. K_p as a function of the amount of oxide on the metal. Upper abscissa, estimated film thickness (ξ).

It is striking to see from Fig. 5 that deviations from normal behavior become obvious at film thickness as high as ~50Å. It is very unlikely that a film of 50Å which consists of at least 15 atomic layers would show an abnormal equilibrium behavior. But these values of ξ are, of course, average values, and it is possible that a reasonable part of the surface is covered by a thinner film even if the average film thickness equals 50Å.

Conclusions

The experiments reported above gave evidence for the existence of thickness-dependent equilibrium properties of solid layers on solid materials. The experimental data, however, are not sufficient to suggest any detailed mechanism. The only conjecture that can be made is that it is very likely that mechanical stresses caused by the difference in lattice parameters of the base metal and the layer are responsible for this behavior. These stresses act on each atom in the interface in a different direction so that no yield processes are possible and the total energy of strain is stored in the interface and its surroundings.

It is to be noticed that thermodynamically this concept differs from that of a surface energy. The existence of a surface energy can only influence equilibria the establishing of which is connected with a change in surface. Nevertheless, the physical causes for the existence of a surface energy between two solids will be the same as those responsible for the existence of a thickness-dependent free energy in thin films.

Acknowledgments

The author wishes to thank Dr. H. Witte for his valuable advice as well as for his help and encouragement during the investigation.

Any discussion of this paper will appear in a Discussion Section to be published in the December 1963 JOURNAL.

REFERENCES

1. K. J. Vetter, *Z. Elektrochem.*, **66**, 577 (1962).
2. H. Göhr and E. Lange, *Naturwissenschaften*, **43**, 12 (1956).
3. K. J. Vetter, *Z. Elektrochem.*, **62**, 642 (1958).

4. K. G. Weil, *ibid.*, **59**, 711 (1955).
5. G. Herbsleb and H. J. Engell, *ibid.*, **65**, 881 (1961).
6. J. L. Ord and J. H. Bartlett, Technical Report No. 7, (1962).
7. J. Osterwald, *Z. Elektrochem.*, **66**, 401 (1962).
8. U. F. Franck and K. G. Weil, *ibid.*, **56**, 814 (1952).
9. P. H. Emmett and J. F. Shultz, *J. Am. Chem. Soc.*, **55**, 1376 (1933).

Ion-Exchange Properties of the Film on Passive Iron and Steel

G. H. Cartledge and Dieter H. Spahrbier[1]

Chemistry Division, Oak Ridge National Laboratory,[2] Oak Ridge, Tennessee

ABSTRACT

Measurements of ion exchange between the film on passive ferrous metals and aqueous ions have been made as a means of studying the chemical and electrochemical interactions of the film *in situ*. It is shown that the chromate ion, in particular, is held exchangeably in amounts approaching a monolayer. This exchanged slowly with alkaline or weakly acidic sulfate solutions, and the kinetics of the exchange has been studied. It was found that the rate equation contains both a linear depletion term and a term exponential in the extent of the replacement reaction. This is interpreted mathematically by an activation energy which increases linearly with the quantity exchanged. The similarity to the kinetics of adsorption of gases on metals in certain cases is pointed out.

The chemical state and electrochemical properties of the surface of a passive metal have been regarded in a variety of ways since Faraday ascribed its peculiar behavior to a film of oxygen fixed in some undetermined form. In recent years, the film on passive iron has been examined by a number of experimental techniques, but almost all the procedures used required the drying of the film or even its removal from the metallic substrate. Hence, the results do not necessarily disclose the nature of the film as it exists in contact with its aqueous environment. For the understanding of the relation of the properties of the film to electrochemical processes occurring at or through it, one needs to study the appropriate phenomena with the film *in situ*, and only a few experiments of this kind have been described.

Thus, it has been shown that the passive film on iron in nitric acid has a low electronic resistivity (1), and the capacity of passive metal surfaces has been measured in a few instances, although the results are not easily understood. It has been shown also (2, 3) that the film produced when iron is passivated in oxygenated inhibitor solutions exhibits the Flade potential when activated by added anions and hence has an electrochemical character similar to that of the film produced by anodic polarization in a strongly acidic solution. Cathodic reduction processes at passive surfaces on zirconium (4), stainless steel (5), and iron (6-9) have been reported recently from this laboratory. These measurements have shed some light on the behavior of the surface films with respect to transport of charge across the interface. They also disclosed marked acceleration of cathodic processes when $Os(OH)_4$ or $Tc(OH)_4$ was deposited over the passive iron film.

Although the film on iron is generally described as an oxide and electron diffraction of dry film reveals the structure of magnetite or γ-Fe_2O_3, there is some reason to believe that the material *in situ* is at least partially hydroxylated, perhaps as γ-FeOOH. Such data as exist show that this compound (or the α-form) has considerable stability under passivating conditions (10). Whatever the mechanistic source of the Flade potential may be, its dependence on the hydrogen-ion concentration and the rapid response of the potential of a passivated electrode to changes in acidity demonstrate that some kind of proton interaction is involved at the interface. In several instances, it has been shown (11-14) that partial oxidation of a solid $M(OH)_2$ consists of the mere loss of a proton and an electron without change of structure. These facts make it probable that protons need to be considered as essential components of the passive film and as participants in any electrochemical processes at the surface.

That anions, as well as protons, may interact with the passive surface is indicated by numerous studies in this laboratory (9, 15) as well as elsewhere. Further, measurements of effects related to zeta potentials have demonstrated definite and specific interactions between an "oxide" surface and dissolved ions (16). These effects are most readily understood as a kind of acid-base interaction.

Finally, it has been demonstrated by Kraus *et al.* (17) that several precipitated oxides or insoluble hydrous salts possess highly specific ion-exchange properties. Thus, it was shown that the chromate ion is firmly bound on certain of them but may be exchanged by anions such as the hydroxide ion. The same substrate failed to adsorb pertechnetate ions (TcO_4^-) in the same medium, in the experiments of these authors. They observed, further, that the exchange capacity diminished when the precipitates were sintered at only moderately elevated temperatures.

All these lines of investigation suggest a need for a more intimate knowledge of the chemistry of the passive film in its unique state while intervening between a metal and an aqueous environment. If it also

[1] Present address: Varta AG, Zentral Laboratorium, Frankfurt, Germany.

[2] Operated for the United States Atomic Energy Commission by the Union Carbide Corporation, Oak Ridge, Tennessee.

enters into specific exchange processes with neighboring ions, it can be treated no longer merely as an inert barrier to transport of charge (electrons, ions, or defects), because its composition, structure, and the gradient of potential through it will be dependent on the composition of the solution with which it is in contact. For these reasons, we have studied ion-exchange processes at the surface of passivated iron, steel, and stainless steel, in the hope that a comprehensive knowledge of the behavior of ions of different types may lead to a clearer understanding of the thin outer surface of the film, where the kinetics of corrosion and other electrochemical processes is so largely determined. The present paper describes the orienting experiments with several systems and gives an analysis of the kinetics of exchange for one particular system.

Experimental

In preliminary experiments, the metals used were carbonyl iron powder and carbon steel (0.1%C). The powder consisted of spheres without porosity; after brief treatment with 1*f* $HClO_4$, its surface area was determined by the B.E.T. method to be 0.4 m^2g^{-1}.[3] Sufficient powder (3-10g) was rinsed in 1*f* $HClO_4$ and then passivated for 3-5 da in aerated chromate or molybdate solutions adjusted to *p*H values as low as 3.5. Samples of this size provided a sufficiently large surface for spectrophotometric procedures to be used in analyzing the extracts subsequently made. In this way, it was possible not only to determine the amount of chromium or molybdenum recovered from the film, but also, in the case of chromium, to demonstrate that it was removed as the anion containing Cr(VI), rather than as some reduction product. Chromate ions were determined by use of diphenylcarbazide, which is not sensitive to Cr(III). Molybdenum was determined by the thiocyanate procedure.

The passivated powder was washed repeatedly on a suction filter with distilled water having the *p*H value of the passivating solution and then was extracted with successive portions of 3*f* NH_4OH at 24°. It was found that the seventh water wash contained a barely detectable amount of Cr(VI), whereas the first subsequent ammonia extract was sometimes visibly yellow. Thus, in a typical experiment, the total amount removed in four 10-min extractions with 3*f* NH_4OH at 24° was 1 x 10^{-8}g (Cr)cm^{-2}, and additional extractions with a more alkaline solution showed that all the Cr(VI) had not been removed. The results of several such experiments indicated that the total exchangeable Cr(VI) approached monolayer coverage, if the chromate ion is taken to cover 25A^2 [3.47 x 10^{-8}g(Cr)cm^{-2}]. Similar experiments with iron powder passivated in aerated molybdate solutions showed that molybdenum also is removed by ammonia.

Preliminary experiments were conducted also with the pertechnetate ion as passivating agent. The metal was either No. 36 iron wire ("for standardization") or 1 x 2 cm pieces of low-carbon steel. The passivating solutions were 1.5-5x10^{-4} *f*$KTcO_4$ at *p*H *ca* 6. No exchangeable TcO_4^- exceeding possibly a percent or so of a monolayer was detected by measuring the beta activity both of the extracts (after suitable treatment) and of the metal itself. This negative result would agree with the observations of Kraus *et al*.(17), but in view of subsequent experiments does not exclude the possibility that some exchange might be found if passivation could be effected at a lower *p*H and with a more highly concentrated pertechnetate solution. Further efforts in this direction will be made.

In a test for cation exchange, tracer Zn^{65} was used with steel sheet which was first passivated in oxygenated $10^{-2}f$ phthalate inhibitor at *p*H 5.87. In a typical experiment, subsequent exposure to Zn^{65} in the passivating medium for 15 hr gave a zinc content of 2.31 x 10^{-8}g(Zn)cm^{-2} on the rinsed specimen. The metal was then extracted with $10^{-2}f$ $Mg(NO_3)_2$ in $10^{-2}f$ phthalate at *p*H 6.88. In 5 extractions over a period of 3 hr, 1.18 x 10^{-8}g(Zn)cm^{-2} was removed. The total amount on the metal would correspond to only a few per cent of a monolayer of zinc ions if it were all confined to the surface.

Rate measurements.—Since the existence of anion exchange was demonstrated and shown to be a slow process, a study of the rate of exchange was undertaken. For this purpose, the chromate-sulfate-hydroxide system was selected, in view of the convenience and sensitivity of radiometric measurements with Cr^{51} of 27.8-day half-life.

For the preparation of the radioactive inhibitor solution, 4-6 mc of Cr^{51} as $CrCl_3$ was freed of chloride by precipitation of $Cr(OH)_3$ and converted to $Cr_2O_7^=$ in $10^{-2}f$ $K_2Cr_2O_7$ adjusted to *p*H 2.35. The freshly prepared passivating solutions had such specific activities as to give 1 count/min for about 2 x 10^{-11}g Cr, when using enough channels of a multichannel analyzer to cover the 0.32 mev peak of Cr^{51}. By measuring the loss due to absorption when thick metallic electrodes were used, it was possible to check the material balance at the end of an experiment.

Because of the slowness of the exchange, the first experiments were conducted at 40° with a concentrated solution as extractant, namely, 1*f* $(NH_4)_2SO_4$ in 6*f* NH_4OH. In later experiments, 0.5*f* K_2SO_4 buffered to *p*H 9.22 by a 0.1*f* carbonate mixture was used. For the quantitative rate measurements, type 347 stainless steel specimens were used in order that passivity might be maintained by air throughout the experiment. The specimens were either pieces of 3-4 cm^2 sheet or cylinders 1 cm in diameter by 2 cm long (*ca.* 7 cm^2 area, counting only one exposed circular section). They were prepared with surfaces of differing roughness by electropolishing, alternate activation in H_2SO_4 and passivation in HNO_3, etching in 6*N* HCl + H_2O_2, or abrading with 2/0 emery. In some instances, the specimens were prepassivated in 0.1*N* H_2SO_4 in air or by addition of a small amount of H_2O_2 to the acid. They were then passivated in the $10^{-2}f$ dichromate solution for periods of 16 hr to several days at 24°. Before extraction, the specimens were rinsed 30 sec under running distilled water, since it was known from work with the pertechnetate ion that this treatment effectively removes adhering solution.

[3] The authors are indebted to the Analytical Chemistry Division for this measurement.

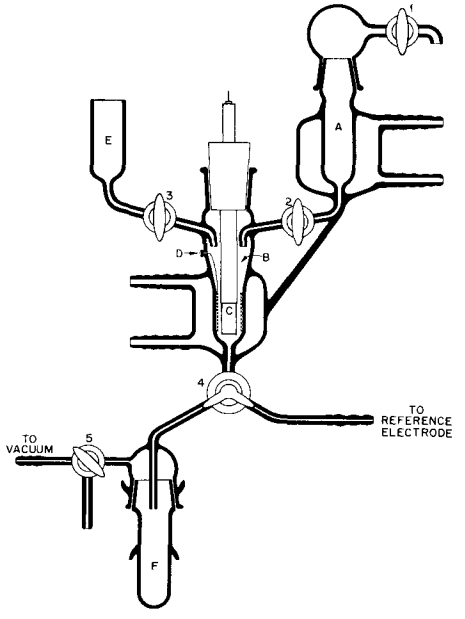

Fig. 1. Apparatus for ion exchange. A, Water-jacketed reservoir; B, jacketed extraction cell; C, specimen, held by a Teflon support having an axial stainless steel rod for electrical connection; D, contact for platinum gauze counter electrode; E, reservoir for rinsing; F, holder for counting tubes.

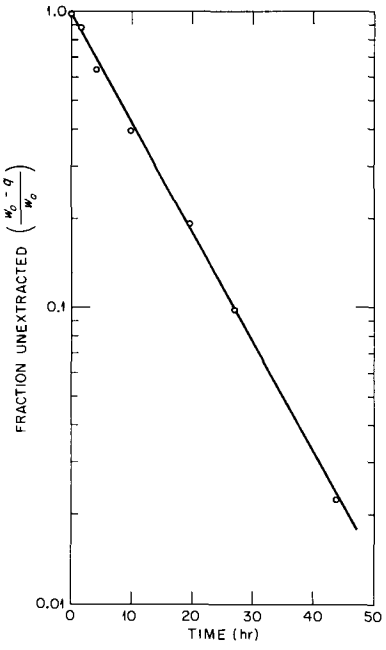

Fig. 2. First-order exchange of Cr^{51} on surface by aqueous $Cr_2{}^{52}O_7{}^{=}$; w_0 is the initial exchangeable chromate and q the amount exchanged at time t. The curve represents the slow exchange following a rapid initial removal of some Cr^{51}.

The extractions were conducted by exposing the specimens to successive 2 or 3 ml portions of solution for measured times, either in tubes which fitted into the well of the detector of the analyzer or in the apparatus shown in Fig. 1. In both instances, the extraction vessel was held at 40° by water circulating through a constant-temperature bath. To determine whether the kinetics was affected by agitation, a comparison was made in two experiments under identical conditions except that, in one, the solution was continuously agitated by a stream of oxygen, whereas there was no deliberate stirring in the other. The results were alike.

Figure 1 shows the details of the apparatus used when it was desired to follow or control the potential of the specimen during the extraction.

Two types of experiments were made in order to establish the correctness of the presumption that only surface chromium was being exchanged with significant rapidity. In the first type, two specimens were prepared with as nearly similar surface treatments as possible. One specimen was passivated in $10^{-2}f$, $K_2Cr_2{}^{52}O_7$ (at *p*H 2.35), while the other was passivated in a similar solution containing Cr^{51}. The two specimens were then extracted by successive portions of $1f$ $(NH_4)_2SO_4$ in $6f$ NH_4OH at 40° over a period of 22 hr. Then, without intervening treatments, both specimens were soaked for 1 hr at 24° in the Cr^{51} passivating solution and again carried through the extractions. Thus, one specimen contained Cr^{51} throughout its film, whereas the other could have contained it only so far as it might have penetrated into the pre-existing film in the 1 hr exposure. In the parallel extractions in two sets of experiments of this type, the two rate curves almost coincided during the first 5 hr, when depletion began to be indicated for the specimen having only superficial Cr^{51}. In the subsequent kinetic analysis of the data, it was found that they followed the same kinetics. The significance of a very slow residual extraction of Cr^{51} from the specimen initially passivated in $K_2Cr_2{}^{51}O_7$ will be considered at a later point.

In the second type of experiment, the kinetics of ion exchange of film Cr^{51} by aqueous Cr^{52} was determined. Having the aqueous $Cr_2{}^{52}O_7{}^{=}$ in large excess, one would expect the rate of exchange to be first order with respect to Cr^{51} remaining on the surface at time t if only a surface-exchange process were rate determining. This should not be true if diffusion from the interior of the film were the limiting factor. In each of three experiments, first-order kinetics was demonstrated, following a fast initial process which will be treated more fully in a subsequent paper. Figure 2 illustrates one of the series of measurements which was carried to about 98% completion in 43 hr. The excellent agreement with first-order kinetics thus demonstrates that the measurements are not significantly complicated by either diffusion or a reverse process.

Results

Since the measurements extended from 1 min to several days, as a rule, it was found convenient not to count the first extraction of 1 min duration in the kinetic analysis because of irregularities involved in the adjustment of temperature, wetting of the specimen, and response of the surface to the considerable difference in *p*H between passivating medium and the solution for extraction. From the type of kinetics followed by the system, it will become apparent that the mathematical analysis may be started at any point early in the experiment, the only difference being in the values of the constants. The amount of chromium found in the first extract has been counted, however, in the total quantity of chromium exchanged, W_0.

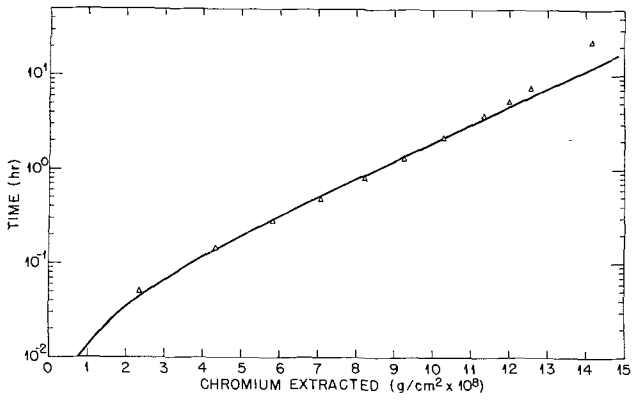

Fig. 3. Typical exchange-log time curve. Passivation in $10^{-2}f$ $K_2Cr_2O_7$ at pH 2.35; extraction at 40° by 1*f* $(NH_4)_2SO_4$ in 6*f* NH_4OH. Specimen etched and abraded. (Point 11 in Fig. 7.)

The points of Fig. 3 are from a typical measurement. One might have expected a first-order dependence of rate on chromium activity remaining on the surface, in view of the enormous excess of the extracting ion. The rate diminished initially much too rapidly for such a relationship, however, and it was found that a plot of q, the amount exchanged per square centimeter of projected area at time t against log t became almost linear after some minutes. The curve in Fig. 3 is a least-squares fit of the data to an equation of the form

$$q = m \log(nt + 1) \qquad [1]$$

the derivation of which will be given below. The q-log t relation held for several hours in measurements at 40°, until the rate became slower, evidently by depletion of the exchangeable chromium on the surface.

The log t relationship suggests an analogy to the Elovich equation, which applies to the rate of adsorption or desorption of a gas on a metal. As shown experimentally by Scholten and Zwietering (18), this type of kinetics arose in their system

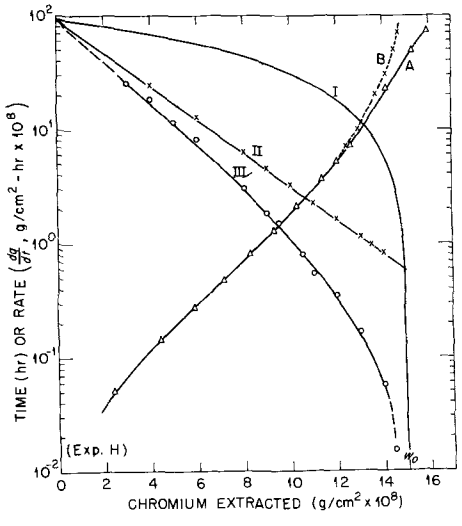

Fig. 4. Curve A, data of Fig. 3; Curve B, corrected by an "end-effect" factor. Analysis of experimental rate-q curve (III) into a first-order term (I) and a term exponential in q (II). Circles on III are taken from tangents to a linear plot of q (corrected) vs. t.

because of a linear variation of the activation energy with the extent of coverage, θ. A rate equation for the ion-exchange process was therefore developed from the Eyring absolute rate theory, under the provisional assumption that the activation energy increases linearly with the extent of exchange, as measured by q, that is

$$\Delta H_q^{\ddagger} = \Delta H_o^{\ddagger} + \frac{rq}{f} \qquad [2]$$

In order that the constant r may be referred to the true area available for ion exchange, the factor f was introduced to represent the ratio of this area to the projected area on which q is based. The factor r thus has the dimensions cal $mole^{-1}$ cm^2 g^{-1} based on the available area, when q is in g (Cr) cm^{-2} (projected). (Unlike a conventional roughness factor, f may readily be less than unity, since it refers only to sites that are both chemically and geometrically accessible to the exchange process.)

The complete rate equation then contains a linear depletion factor, w_o-q, where w_o is the amount of chromium exchanged from time zero to the limit, and an exponential term in q

$$\frac{dq}{dt} = S_o' [w_o - q] \exp\left[-\frac{rq}{fRT}\right] \qquad [3]$$

Here S_o' includes the usual kinetic factors, the constant concentration of the extracting species, exp $[-\Delta H_o^{\ddagger}/RT]$, and the entropy term, variation of which is assumed to be of minor importance. This equation may be explicitly integrated only over such a time as the exponential term is dominant. For this case, we obtain for a particular experiment

$$q = 2.3\frac{fRT}{r}\log\left[\frac{rS_o}{fRT}\cdot t + 1\right] \equiv 2.3\, m \log\left[\frac{S_o}{m}\cdot t + 1\right] \qquad [4]$$

S_o being the initial rate, $S_o'w_o$, $(q = 0)$. This is seen to be equivalent to Eq. [1], which closely describes the course of the exchange process for some hours at 40° (Fig. 3). All of the series of measurements followed this relationship for periods of time which varied according to the treatment given the specimens before exposure to the Cr^{51} passivating solution.

The applicability of Eq. [3] for longer times was tested in the following way. If the right side of the equation is multiplied by w_o/w_o, we may obtain Eq. [5]

$$\log\frac{dq}{dt} = \log S_o + \log\frac{w_o - q}{w_o} - \frac{rq}{2.3\, fRT} \qquad [5]$$

or

$$\log\left[\frac{dq}{dt}\cdot\frac{w_o}{w_o - q}\right] = \log S_o - \frac{rq}{2.3\, fRT} \qquad [6]$$

Rates were taken as tangents to linear plots of q *vs.* t. Log dq/dt was then plotted *vs.* q, as shown by curve III in Fig. 4. If Eq. [6] is valid, it should be possible

to find a value of w_o, consistent with the value approximately indicated by the experimental curve III, such that a graph of the left side of Eq. [6] against q is linear and extrapolates to a value of S_o at $q = 0$ that also is consistent with the experimental rate curve. Curve II in Fig. 4 is such a result, curve I being the rate that would have been observed for the first-order depletion process with constant activation energy. This type of analysis was made for 15 experiments in 10^{-2} to 1f sulfate at 40°, the solution being alkaline with NH_4OH in 11 cases, buffered at pH 9.22 with a 0.1f carbonate mixture in 2 cases, and at pH 4.82 in 2 cases.

In addition, one experiment was conducted at 0°. Even after 70 hr, the extraction was still following the simplified Eq. [4] so closely that an accurate estimate of w_o was not possible. In another experiment at 40°, the rate of extraction of chromium by distilled water was measured. This followed the same type of equation, but substitution of 0.5f K_2SO_4 + 0.1f[Na, H]$_2CO_3$ at pH 9.22 for water toward the end of the experiment showed the rate (for a 15-min extraction) to be about 25 times faster in the salt solution than it was in water.

When experiments were extended for some days at 40°, a complication appeared after the rate had diminished by something like 3 to 4 orders of magnitude from the initial value. It was apparent that the rate now decreased more slowly than was required by the depletion term. As was pointed out previously, depletion was approached closely when only the surface of the passive film contained Cr^{51}, whereas, after several hours, Cr^{51} in appreciable amounts continued to pass into the extracts when the entire film contained Cr^{51}. In the long-continued experiments (25-200 hr), it was therefore necessary to take this end effect into account as a minor correction, if it was desired to deduce values of w_o. The corrections became significant, however, only when the exchange rate had fallen to a few tenths of a percent of the initial rate, as seen in Fig. 6, for one example. Here Curve III-A gives the experimental rates and III-B the rates corrected for a constant "end effect" of 7 x 10^{-11}g (Cr)cm^{-2} hr^{-1}. It is seen that the experimental rate curve showed signs of

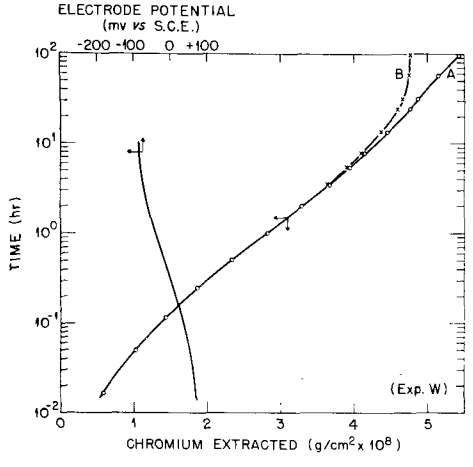

Fig. 5. Curve of q vs. log t showing variation in potential during exchange. Passivation in $10^{-2}f$ $K_2Cr_2O_7$ at pH 2.35. Extraction at 40° by 0.5f K_2SO_4 + 0.1f [Na,H]$_2CO_3$ at pH 9.22.

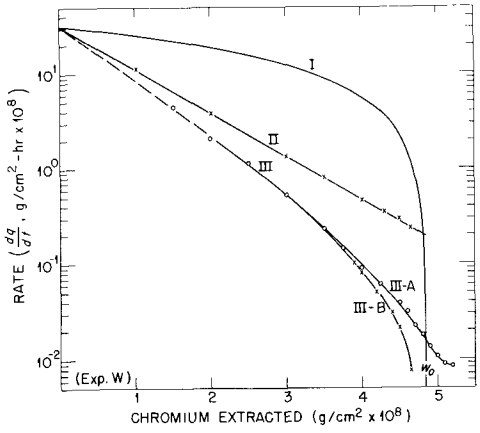

Fig. 6. Analysis of the data of Fig. 5

leveling off at some such value, the extractions having been continued for 95.5 hr.

It is not clear whether the end effect arises from a continuing corrosion process, a simple dissolution of film, diffusion of Cr(VI) from the interior of the film, or, possibly, a slow isotopic exchange whereby Cr^{51}(III) in the film passes into Cr^{51}(VI) and then into solution. The rate is probably of the right order of magnitude for the corrosion rate in the alkaline medium, but, in any case, is so low as not to disturb the conclusions regarding the kinetics over by far the greater part of the process. The correction was observed to be greater when a sulfate solution at pH 4.2 was used for the exchange.

Discussion

It appears that Eq. [3], containing the assumption of varying activation energy, applies to the exchange process under a variety of conditions and over a range of rates extending over something like four orders of magnitude. By treating the surface in a variety of ways before exposing it to Cr^{51}(VI), it was possible to begin the experiments with amounts of exchangeable chromium ranging between 2.3 and 20.3 x 10^{-8}g (Cr)cm^{-2} (projected). (These numbers are W_o and include the amounts remaining on the specimen after the 30-sec rinse with distilled water even though w_o, used in the calculation of rates, excludes the amount removed during the first minute.) To gain some information as to r, the rate at which the activation energy increases during exchange, the data were treated in the following way.

The values of W_o increased with the roughness of the surface, which was known qualitatively from the pretreatment given the specimens. Hence, the values of f/r given by curves like II in Fig. 4 and 6 were plotted against W_o. The points for the 15 experiments roughly indicated a linear relation $f/r = a + bW_o$. A least-squares line computed for this equation had an intercept on the f/r axis at −0.14, with $b = 2.44 \times 10^{-4}$. Within the statistical precision of the data, this intercept equals zero, which it should do for physical reasons, since the factor f is a measure of the relative surface area available for exchange and $W_o = 0$ when $f = 0$. Hence, a second least-squares line was computed with $a = 0$ in the equation above. This gave $b = 2.32 \times 10^{-4}$; the resulting curve is drawn in Fig. 7. It is seen that 10 of

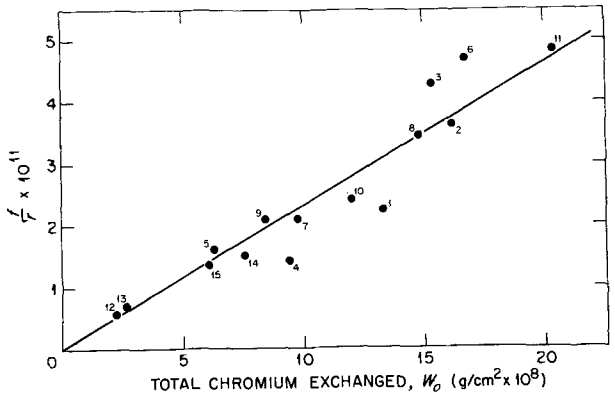

Fig. 7. Graph of f/r vs. W_0. The numerals merely identify the experiments in chronological sequence.

the points fall very close to the curve, with some scatter for the others.[4]

The least-squares value of $W_0 r/f$ given by Fig. 7 is 4.31 x 10^3 cal mole^{-1}, and this represents the amount by which the activation energy of the process increases upon exchange of the amount of chromium corresponding to a complete layer of ions. To evaluate r, it is necessary to determine W_0/f, which may be derived at least approximately by the following considerations.

The close approach to linearity in the relation between f/r and W_0 is strong evidence both for the constancy of r in these experiments and for the assumption that the total initial amount of exchangeable chromium is simply proportional to the available surface area, for the given conditions of passivation. If both of these conditions were not satisfied, it would then be necessary to assume that simultaneous variations in r and W_0 were just such as to give the observed linearity by compensating each other. This seems unlikely. It follows also that, in all the experiments, the initial fractional coverages must have been very approximately equal.

That the chromium is not initially derived in significant amounts from underlying parts of the film was demonstrated in the experiments described previously (see above, page 646). Hence, we can consider the sites for exchange to be on the more or less flat surface of the passive film. From the dimensions of the chromate ion in crystals, one may calculate that a tetrahedral face of the ion has an area of 25Å^2. If such ions were closely packed on a plane surface, complete ionic coverage would require 3.47 x 10^{-8}g (Cr) cm^{-2} (true area). The actual areas of the specimens are, of course, not known accurately. Specimens for experiments 12 and 13 were heavily electropolished, however, to a very bright finish; they also had the lowest values of f/r. Specimen 12 was polished somewhat more heavily than 13. No great error can therefore be introduced by assuming that the surface factor for chromate ions is essentially equal to unity for specimen 12, so far as geometry alone is concerned. (The value might be larger for smaller adsorbable entities.) On this assumption, the minimum value for complete coverage would be the observed W_0 for specimen 12, or 2.26 x 10^{-8}g cm^{-2}. This is 0.65 of the maximum value calculated from the dimensions of the ion. It is certainly a reasonable result, especially since close packing of anions without some means of diminishing the repulsive forces is hardly to be expected.[5] If we then take $f = 1$ and $W_0 = 2.26$ x 10^{-8}g cm^{-2} for experiment 12, we obtain $r = 1.91$ x 10^{11} cal mole^{-1} g^{-1} cm^2.

The magnitude of r accounts for the relative effects of the depletion factor $(w_0 - q)/w_0$ and the activation-energy term, exp $(-rq/fRT)$, in causing the rate dq/dt to decrease during the exchange process. For a typical experiment, 8, for example, the depletion factor alone reduces the rate by one order of magnitude at $q = 0.9\ w_0$, the exponential term alone by two orders, for an over-all reduction of the rate by three orders. This large effect of the exponential term accounts for the fact that the q *vs.* log t graphs become linear after a short time and remain so over a large portion of the extraction process.

The experiments thus give additional evidence for the chemical activity of the passive film towards the solution which bathes it. It is seen also that the ion-exchange process at the passive interface of a metallic substrate differs radically from a simple reversible chemical process. Until other systems have been examined quantitatively, it would be premature to draw conclusions as to the details of the electrochemical reasons for this difference. It is suggested, however, that the results emphasize the necessity to consider the passive film as a region in which energy levels or potential gradients are markedly influenced by the population of ions on its surface, in quite the same manner as Boudart has treated the adsorption of gaseous molecules on a metallic substrate (19). Otherwise, it would be difficult to understand why the kinetics of the exchange process should be so different when the radioactive film interacts with Cr^{52} chromate ions, in one case, and with sulfate or hydroxide ions, in the other.

The experiments are being continued with other systems and under other conditions.

Any discussion of this paper will appear in a Discussion Section to be published in the December 1963 JOURNAL.

REFERENCES

1. K. J. Vetter, *Z. Elektrochem,* **55,** 274 (1951).
2. G. H. Cartledge and R. F. Sympson, *J. Phys. Chem.,* **61,** 973 (1957).
3. H. H. Uhlig and P. F. King, *This Journal,* **106,** 1 (1959); see *ibid.,* p. 1074 for discussion of this paper.
4. R. E. Meyer, *ibid.,* **107,** 847 (1960).
5. Franz A. Posey, G. H. Cartledge, and R. P. Yaffe, *ibid.,* **106,** 582 (1959).
6. G. H. Cartledge, *J. Phys. Chem.,* **64,** 1877 (1960).
7. G. H. Cartledge, *ibid.,* **64,** 1882 (1960).
8. G. H. Cartledge, *ibid.,* **65,** 1009 (1961).
9. G. H. Cartledge, *ibid.,* **65,** 1361 (1961).

[4] Figure 7 includes experiments done early in the study, before the conditions for attaining highest accuracy in the values of W_0 had been established. The linear relationship is confirmed by measurements in other systems which will be published elsewhere.

[5] Also, it is not yet determined experimentally whether all the area geometrically available is also chemically suitable for exchange. There is some evidence that this depends somewhat on the acidity of the passivating solution. This point is being investigated further.

10. R. Fricke and W. Zerrweck, *Z. Elektrochem.*, **43,** 52 (1937); *cf.* J. D. Bernal, D. R. Dasgupta, and A. L. Mackay, *Nature,* **180,** 645 (1957).
11. W. Feitknecht and G. Keller, *Z. anorg. Chem.*, **262,** 61 (1950).
12. W. Feitknecht, H. R. Christen, and H. Studer, *ibid.*, **283,** 88 (1956).
13. G. W. D. Briggs and W. F. K. Wynne-Jones, *Trans. Faraday Soc.*, **52,** 1272 (1956).
14. W. Feitknecht and W. Marti, *Helv. Chim. Acta,* **28,** 129 (1945).
15. F. A. Posey and R. F. Sympson, *This Journal,* **109,** 716 (1962).
16. See, for example, P. J. Anderson, "Proceedings of the Second International Congress on Surface Activity," p. 67, Butterworth's Scientific Publications, London (1957); and *Trans. Faraday Soc.*, **54,** 130 (1958).
17. K. A. Kraus, H. O. Phillips, T. A. Carlson, and J. S. Johnson, "Second United Nations Conference on the Peaceful Uses of Atomic Energy," vol. 28, p. 3, (1958).
18. J. J. F. Scholten and P. Zwietering, *Trans. Faraday Soc.*, **53,** 1363 (1957).
19. M. Boudart, *J. Am. Chem. Soc.*, **74,** 1531, 3556 (1952).

Corrosion and Passivity of Molybdenum-Nickel Alloys in Hydrochloric Acid

H. H. Uhlig, P. Bond,[1] and H. Feller[2]

Corrosion Laboratory, Massachusetts Institute of Technology, Cambridge, Massachusetts

ABSTRACT

Data are presented on corrosion rates of 3-25% Mo-Ni alloys in 10% HCl at 25°, 70°C, and the boiling point. Data also include measurements of corrosion potentials, critical current densities for passivity, anodic polarization in the active potential region, and hydrogen overvoltage. Molybdenum-nickel alloys, like other passive metals, corrode under anodic control, but their corrosion potentials, unlike values for the passive chromium alloys, are more active than the corresponding Flade potentials at which a passive film is established. Corrosion resistance derives apparently from a sluggish anodic dissolution reaction, such as a low rate of ion hydration. Chemical properties of Mo are imparted to Ni or to Ni plus Fe alloys at critical ratios related to electron configuration of the component metals.

Chromium is outstandingly passive, and it confers this property on alloys of iron at a minimum concentration of about 12% Cr. The latter alloys make up the stainless steels. Chromium also confers passivity on other alloys, *e.g.*, of nickel, the minimum composition coming at about 14% Cr, and of cobalt, the minimum composition coming at about 8% Cr as measured by critical current densities for passivity in H_2SO_4 (1). Nearest to chromium in atomic electron configuration is molybdenum, which except for an extra closed shell of electrons, has the same outer configuration. It might be expected, therefore, that molybdenum similar to chromium would also impart passivity to its alloys, and, in fact, several commercially important corrosion resistant nickel-base alloys are produced.

But there are outstanding differences in chemical properties between Mo and Cr alloys. For example, the Mo alloys react readily with nitric acid and with many other oxidizing agents contrary to Cr and the passive chromium alloys. On the other hand, Mo and Mo alloys tend to be corrosion resistant to hydrochloric acid in which Cr alloys corrode at high rates. Also, Mo tarnishes in the atmosphere, whereas Cr is free of visible surface films and remains bright for a long time. These differences suggest that the electron configuration of Mo and Cr despite similarities of the atoms are not alike in the metallic state. It is of interest nevertheless to compare the passive properties of the two metals, and to compare the atomic percentages at which either metal confers optimum corrosion resistance and passivity on its alloys.

Experimental Procedure

Measurements were made of the potentials, polarization behavior, and corrosion rates of molybdenum-nickel alloys. These alloys exist in solid solution up to 20 wt % Mo. Passivity in the molybdenum-iron alloys is not as easy to study because a two-phase structure begins at 7 wt % Mo, limiting any possible interpretation of results within the passive composition range.

Relatively pure alloys were made up in a vacuum furnace using alumina crucibles. The melts were drawn into 7 mm quartz tubes in an atmosphere of helium purified by passing the gas over Ti sponge at 800°C, and the ingots were quenched in water. Carbonyl nickel and commercially pure molybdenum were used; a few alloys (3.1 and 5.6% Mo) were melted using spectroscopically pure Mo and hydrogen-decarburized carbonyl Ni (0.001% C, < 0.002% S) in order to check the effect of impurities. No essential differences in properties were found for the two sets of alloys. Ingots were homogenized at 1100°C for 12 hr. They were then rolled to 0.10 in.

[1] Present address: Ford Scientific Laboratory, Dearborn, Michigan.
[2] Present address: Institut für Metallkunde der Technischen Universität, Berlin, West Germany.

(0.25 cm) strip, heated for 15 min at 1000°C in He or A, and water quenched. Composition was determined by chemical analysis. Specimens measuring 0.5 to 1 cm wide, 3 cm long and 0.2 cm thick were cut from the strip. A hole was drilled at one end of each specimen from which it was suspended by a glass hook. Surface preparation was by abrasion, ending with No. 600 silicon carbide paper applied wet. Specimens were washed in water, degreased with boiling benzene, and pickled in warm 6*N* HNO_3.

Corrosion rate determinations in hydrochloric acid at 25°C were conducted in separate 2-liter glass vessels for each specimen. The vessels were placed in an air thermostat maintained at 25° ± 0.5°C. At 70°C, 1-liter glass vessels were located in a water thermostat, each vessel being fitted with an air-cooled reflux condenser. Air or nitrogen at 40 ml/min entered the acid through gas dispersion tubes, the acid being saturated with either gas several hours before each run. Nitrogen was purified by passing the gas over copper turnings at 450°C. Purified hydrogen was used to deaerate the acid at 25°C. Corrosion rates were determined both by weight loss of the specimen and by analysis of the acid for Ni^{++} using a standard colorimetric method employing dimethylglyoxime as indicator (2). Reported corrosion rates are steady-state values determined from slopes of metal loss *vs.* time (4-8 day tests at 25°C, 1-3 days at 70°C). From a few weight loss-time curves carried out at 70°C for alloys containing between 3 and 9% Mo, it was found that the initial rate is higher than the final rate and that the steady-state rate is achieved after about 1 hr. For boiling acid, only weight loss values were determined; these results, therefore, represent average corrosion rates including an induction time (1-2 day tests). Gases were not bubbled through the boiling acid, contrary to the lower temperature runs.

Polarization measurements were conducted at 25°C in an air thermostat using Ag-AgCl, 0.1*N* KCl as reference electrode. A constant current was supplied by 30 dry cells in series with a variable resistance. Critical current densities were determined by the method of Uhlig and Woodside (3) using deaerated acid. This method consisted of applying increasing increments of current and observing the steady-state potential. The lowest current which brought the specimen to the passive potential was taken as the critical value. To make certain that the applied current was or was not below the critical, polarization was continued in each instance until the potential changed less than 2 mv/min.

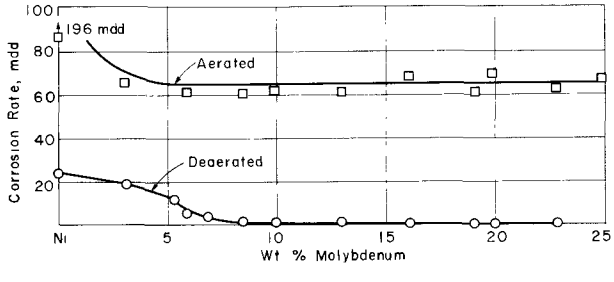

Fig. 1. Corrosion rates of nickel-molybdenum alloys in aerated and deaerated 10% HCl at 25°C (4-8 day exposure).

Results

Corrosion rates in aerated and deaerated 10% HCl at 25°, 70°, and 102°C (boiling) are shown in Fig. 1-4. At 25°C in aerated acid, the average corrosion rate of alloys at and above 3% Mo is 65 mdd; in deaerated acid the rates are lower becoming extremely small above 10% Mo, and zero within the experimental accuracy of the measurements at 19.1% Mo and above. At 70°C, rates in deaerated acid are also substantially lower than in aerated acid. In deaerated acid, a minimum rate is reached

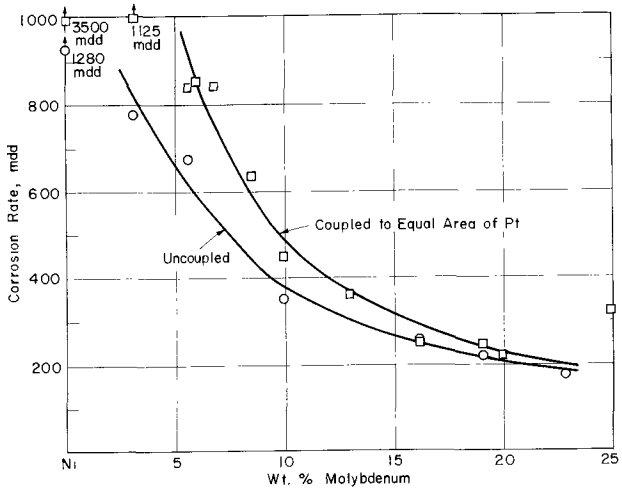

Fig. 2. Corrosion rates of nickel-molybdenum alloys in aerated 10% HCl at 70°C (1-3 day exposure).

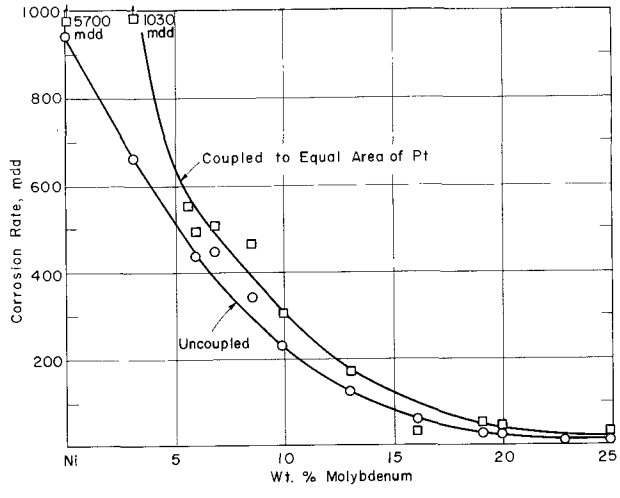

Fig. 3. Corrosion rates of nickel-molybdenum alloys in deaerated 10% HCl at 70°C (1-3 day exposure).

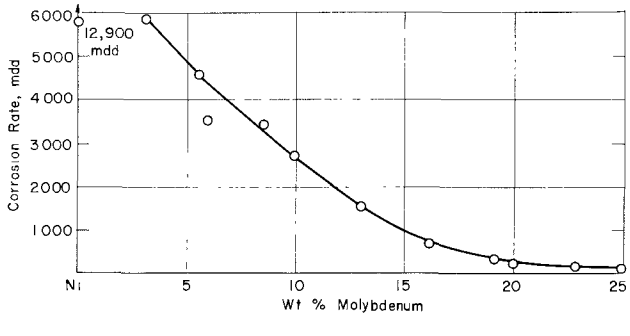

Fig. 4. Corrosion rates of nickel-molybdenum alloys in boiling 10% HCl (1-2 day exposure).

at or above 20% Mo; a similar minimum is also observed in boiling 10% HCl. The present results do not agree with earlier results of Field (4) who reported much higher corrosion rates in 10% HCl at 70°C for 5 and 10% Mo compositions. On the other hand, the present results are in reasonable accord with those of Grube and Schlecht (5) who obtained data in 4.3*N* HCl (15%) at 60°C. Their alloys were slowly cooled from 1280°C, and the specimens for corrosion tests were rotated at 500 rpm.

The present data show reproducible slight discontinuities in corrosion rate at about 7% Mo (Fig. 2 and 3). Although sufficient points are not available to reach a definite conclusion, it may be significant that the Curie temperature for these alloys also occurs at the same approximate composition, and hence a change in magnetic properties may account for the observed fluctuation in corrosion rate.

In order to determine the possible effect of cathodic impurities, and also whether the rate is anodically or cathodically controlled, parallel runs were conducted in 10% HCl at 70°C for alloys galvanically coupled to an equal area of platinum. Rates with Pt are somewhat higher in aerated acid, with the difference diminishing as Mo content of the alloys increases. In deaerated acid, the rates with or without Pt are not greatly different except for Ni and the 3% Mo-Ni alloy. Alloying, on the other hand, has an appreciable effect on the rate. In boiling 10% HCl, for example, the rate for 20% Mo-Ni alloy is only 1/50 the rate for Ni. The lowering of the corrosion rate which results from alloying additions of Mo is more pronounced in deaerated than in aerated acids. There was a tendency toward intergranular attack in a few of the low-Mo alloys for which the corrosion rate was highest. This tendency persisted even in the pure alloys prepared from spectroscopically pure Mo and decarburized Ni.

Corrosion potentials of all the alloys in H_2-saturated 5% H_2SO_4 at 25°C were within 2 mv of a hydrogen electrode in the same solution. Similar values for H_2-saturated 10% HCl are given in Table I.

Critical current densities for passivity in 0.01*N* H_2SO_4 at 25°C, deaerated with purified N_2, showed no definite trend with composition. The values ranged from 0.3 to 0.83 ma/cm^2. On the other hand, alloyed molybdenum had an appreciable effect on anodic polarization in the active potential region in contrast to the passive region. Values of potential at an anodic current density of 0.3 ma/cm^2 in deaerated 0.01*N* H_2SO_4 and in deaerated 0.01*N* $HClO_4$ are shown in Fig. 5. Polarization in each acid reaches a maximum beginning at about 15 wt % Mo (9.8 at. % Mo).

Hydrogen overvoltage measurements showed no trend with alloy composition. The overvoltage at 1 ma/cm^2 at 25°C in pre-electrolyzed 5% H_2SO_4 saturated with purified hydrogen was the same for

Table I. Corrosion potentials of Mo-Ni alloys (anode) in H_2-saturated 10% HCl, 25°C vs. H_2 electrode (cathode) in same solution

Wt % Mo	0.0	3.0	6.8	9.9	13.0	22.8
Potential, v	0.099	0.017	0.005	0.000	0.000	0.000

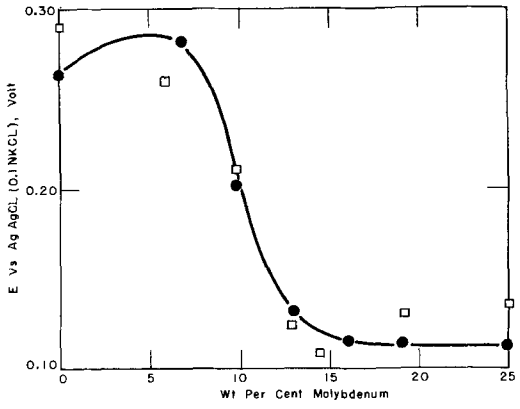

Fig. 5. Anodic polarization of nickel-molybdenum alloys at 0.3 ma/cm^2 in N_2-saturated H_2SO_4 or $HClO_4$ at 25°C. □, 0.01*N* $HClO_4$; •, 0.01*N* H_2SO_4.

all alloys including pure nickel, averaging 0.30 ± 0.08v. At 10 ma/cm^2, the value was 0.43 ± 0.05v. Lack of an effect may be real or may be caused by a similar composition surface for all alloys, brought about by selective etching. The latter possibility would not enter anodic polarization measurements to the same extent because of continuous removal of the alloy surface by anodic dissolution.

Discussion

It is apparent that the Mo-Ni alloys in 10% HCl, despite a low corrosion rate, are not passive in the same sense as are the stainless steels in dilute sulfuric acid. The Mo-Ni alloys, for example, corrode more rapidly in aerated than in deaerated acid, contrary to the behavior of passive chromium alloys. Also, the corrosion potentials in deaerated acid are not noble but are close to or equal to the potential of the hydrogen electrode (Table I). This behavior indicates marked polarization of anodic areas on the alloy surface and, furthermore, that the alloys corrode under anodic control. Although anodic control is typical of passive metals, corrosion potentials of the present alloys are more active than the corresponding Flade potentials, contrary to passive Cr alloys the corrosion potentials of which are more noble than their Flade potentials. Although hydrogen overvoltage values show no significant change with alloy composition, anodic polarization data, on the other hand, show an appreciable change, the maximum beginning at about 15% Mo in either 0.01*N* H_2SO_4 or $HClO_4$. Maximum polarization beginning at about 15% Mo was also reported by Masing and Roth (6) for alloys polarized as anode in 2*N* deaerated HCl. Similar anodic behavior in three different acids suggests that the critical alloy composition, although possibly resulting from an invisible reaction-product film which differs from the passive film forming at the Flade potential, more likely results from a high activation energy for dissolution of metal ions. The latter may be caused, for example, by a slow rate of ion hydration. Along these lines, the rate of dissolution of pure Mo in HCl and in H_2SO_4 is appreciably below that of Ni. A difference in activation energies can also account for the relative ease of electrodepositing Ni from solutions of its salts, compared to the difficulty or

impossibility of electrodepositing Mo. The electron configuration theory in agreement with results of anodic polarization predicts that the critical alloy content for imparting chemical properties of Mo to Ni lies at about 9.1 at. % or 14 wt % Mo (7).

The minimum corrosion rate in deaerated acid begins at the somewhat higher alloy composition of about 20% Mo rather than at 15% Mo. This is true of values at 70° and 102°C, and even at 25°C in deaerated acid, the rate decreases from 0.9 mdd at 9.9% Mo to 0.0 mdd at 19.1% Mo and higher Mo compositions. One possible reason for the difference is that the presence of hydrogen generated by corrosion tends to shift the critical composition to a higher molybdenum value. A similar effect of interstitial hydrogen has been observed in the Cr-Fe alloy system (8).

Aeration increases the corrosion rate by increasing the potential difference between anodic and cathodic areas, the potential of cathodic areas approaching but not attaining the potential of the oxygen electrode. Mixed control of the corrosion rate predominates in aerated acids except at 25°C, where it appears that the rate of oxygen reduction on the alloy surface is controlling. On pure Ni, for example, oxygen reduction proceeds at a higher rate and the corresponding corrosion rate is higher than for the alloys, all of which corrode at the same rate despite change in anodic polarization. Oxygen reduction, therefore, may be an activation-controlled reaction rather than diffusion controlled. The rate for all the Mo-Ni alloys (65 mdd) falls below the maximum rate of about 100 mdd calculated from the limiting diffusion current for oxygen reduction in air-saturated water at room temperature [0.039 ma/cm^2 (9)]. The calculated value should be reduced about 20% because of reduced solubility of O_2 in 10% HCl, but the corrected value is still larger than 65 mdd.

Corrosion resistance of commercial Mo-Ni-Fe alloys of about 30% Mo, 60% Ni, and 10% Fe composition probably also follow a mechanism paralleling that described above for the Mo-Ni alloys, and similarly their corrosion potentials lie at values more active than the corresponding Flade potentials at which a passive film forms. These alloys are used in practice to withstand relatively concentrated nonoxidizing acids such as HCl or H_2SO_4. Since they are active in potential and cannot set up passive-active cells as do the passive Cr alloys, they are not subject to pitting in the chemical media to which they are usually exposed. The maximum amount of Fe which can be tolerated in such solid solution alloys for optimum corrosion resistance corresponds in accord with the electron configuration theory to an atomic ratio Mo/Fe equal to or greater than 0.2 (10). Results of Schmidt and Wetternick (11) for corrosion of various Mo-Ni-Fe alloys in boiling 29.8% H_2SO_4 confirm that a ratio of this order is observed. This is similar to the ratio accounting for passivity beginning at about 12 wt % Cr (atomic ratio Cr/Fe = 0.15) in the Cr-Fe alloys. This ratio, it was found (12), is preserved in the solid solution ternary Cr-Fe-Ni alloys, being most pronounced in alloys below 50% Ni.

Hence, although passivity in the Mo alloys apparently derives from a sluggish anodic reaction in contrast to the Cr alloys which form a metastable passive film accompanied by a noble potential, the alloying proportions leading to optimum corrosion resistance are similar for both metals and can be related to their similar atomic configuration.

Acknowledgment

The authors are pleased to express appreciation for support of this investigation both to The Shell Oil Companies in the U.S. and to The Office of Naval Research on Contract No. Nonr 1841(09) NR 036-007. They are also indebted to N. Stolica for obtaining the anodic polarization data in perchloric acid.

Any discussion of this paper will appear in a Discussion Section to be published in the December 1963 JOURNAL.

REFERENCES

1. P. Bond and H. Uhlig, *This Journal*, **107**, 488 (1960).
2. E. B. Sandell, "Colorimetric Determinations of Traces of Metals," Interscience Publishers, Inc., New York (1944).
3. H. Uhlig and G. Woodside, *J. Phys. Chem.*, **57**, 280 (1953).
4. B. Field, *Trans. AIME*, **83**, 149 (1929).
5. G. Grube and H. Schlecht, *Z. Elektrochem.*, **44**, 413 (1938).
6. G. Masing and G. Roth, *Werkstoffe u. Korrosion*, **3**, 176, 253 (1952).
7. H. H. Uhlig, *Z. Elektrochem.*, **62**, 700 (1958).
8. H. Uhlig, N. Carr, and P. Schneider, *Trans. Electrochem. Soc.*, **79**, 111 (1941).
9. H. H. Uhlig, *This Journal*, **108**, 327 (1961).
10. "Corrosion Handbook," Fig. 4, p. 29, H. H. Uhlig, Editor, John Wiley & Sons, Inc., New York (1948).
11. M. Schmidt and L. Wetternick, *Korrosion u. Metallschutz*, **13**, 184 (1937).
12. H. Feller and H. Uhlig, *This Journal*, **107**, 864 (1960).

Optical Studies of the Formation and Breakdown of Passive Films Formed on Iron Single Crystal Surfaces in Inorganic Inhibitor Solutions

Jerome Kruger

National Bureau of Standards, Washington, D. C.

ABSTRACT

Polarized light was used to measure the thickness and optical properties of passive films as they were forming while simultaneous electrochemical measurements were being made. The film formation studies showed that a change in film thickness of 15-20Å was associated with the onset of a passive potential. A direct, logarithmic-type law governed the growth of a semiconductor film with crystallographic orientation of the substrate having little effect.

When iron surfaces prepared in an ultrahigh vacuum (a vacuum of the 10^{-9} Torr order of magnitude), were passivated a 20Å film formed instantaneously on the introduction of an air-saturated 0.1*N* $NaNO_2$. This film then dissolved and a new film commenced to grow. A passive potential coincided with a film 15Å thick. No such initial dissolution occurred when the solution contained only dissolved oxygen, the instantaneously formed film continuing to grow and a passive potential occurring after the growth of around 40Å. When the solution contained no dissolved gases, the instantaneous film did not form.

Film breakdown studies revealed that only the 20-30Å film next to the metal was responsible for passivity even if thicker films were initially present. Studies of the sites of film breakdown showed that the number of sites was highest for films on {110} iron surfaces and that these sites were not related to points where dislocations intersected the surface. These studies support the oxide film theory of passivity.

One of the great experimental obstacles to resolving the controversy that exists between the various schools of thought on the nature of the passivity of iron, which Faraday (1) referred to as "this very beautiful and important case of voltaic condition presented to us by the metal iron," is the great difficulty in being able to distinguish between an adsorbed film and a thin compound film. Even if this difficulty did not exist, there would still remain the problem, common to all surface studies, of how to be sure that there does not exist already on the surface a precursor to the passive film or a chemical species that drastically modifies the passivation process, giving rise to a false picture of the passivation process. Primarily because of these two experimental difficulties and because of theoretical ones, the controversy continues between those who favor an adsorbed oxygen film (2-4) and those who favor a three-dimensional oxide film (5-7). An intermediate group in the controversy (8, 9) says that the first step in the passivation process is the adsorption of an oxygen film which confers temporary passivity; this then becomes an oxide film by incorporation of a metal ion into the adsorbed oxygen.

This work describes experimental approaches that attempt to attack these difficulties by a technique that enables one to learn something about the nature of the passive film and the passivation processes while they are actually going on. This technique uses elliptically polarized light to measure the thickness of a film formed and to determine some of its optical properties. An advantage of this technique is that film thicknesses as low as 3-5Å can be measured simultaneously with the electrochemical potential to give an indication of the onset of passivity. This technique was pioneered over thirty years ago by Tronstad (10, 11).

This work differs from that of Tronstad in that greater attention has been paid to starting with clean, well-characterized surfaces. This has been made possible by the use of modern ultrahigh vacuum techniques (12) and single crystal surfaces. The use of ultrahigh vacuum techniques is especially important in such a study since one of the sources of contention is the existence of a monolayer film that is supposed to be responsible for passivity. Unless ultrahigh vacuum techniques are used such monolayer films can form on a surface at pressures of 10^{-6} Torr in times less than 1 sec (13). Hence, only by the use of such ultrahigh vacuum techniques can one start to cope with the question of the importance of a monolayer film of oxygen in conferring passivity to an iron surface.

In the studies described here, elliptically polarized light is used to follow both the formation and the breakdown of passive films produced in inorganic inhibitor solutions.

Because a complete description of passivation involves, in addition to a knowledge of the nature of

the passive film, an understanding of the role played by the atomistic structure of the metal surface, the influence of surface structure on formation kinetics and on the sites where breakdown of a passive film occurs was studied. The breakdown studies used optical and thin foil electron microscopy to examine surfaces treated by a technique which decorated the sites of breakdown of passive films. The crystallographic orientation of the metal surface and the presence of defects in it were related to breakdown sites using this approach.

Passive Film Formation

In all of the present studies concerned with following the formation of passive film with time, ellipsometry was used. A description of the ellipsometer and the method used to evaluate the results is given elsewhere (14). This technique was used to measure both the thickness of the films that existed on a surface at a given time and the optical properties of the film. A very comprehensive description of the theoretical and experimental aspects of the use of elliptically polarized light to study surfaces is given by Winterbottom (15).

To compare this ellipsometric method for studying passive film formation directly with another entirely different technique, the kinetics of passive film growth on iron in K_2CrO_4 solution was first studied. This system had been studied with a radiotracer technique by Brasher and Kingsbury (16). The iron specimen [240 ppm impurities and described by Moore (17)] was mechanically polished using a $\frac{1}{4}\mu$ diamond abrasive as the final polish and then chemically polished in a chemical polishing solution.[1] After rinsing the specimen in distilled water and spectrographic grade methanol, and taking a reading on the dried surface, the specimen was placed in a vessel containing 0.0025M K_2CrO_4 solution. Readings were then taken periodically by the ellipsometer on the surface so immersed in the inhibitor solution. The film thicknesses[2] measured on a {100} iron surface in 0.0025M K_2CrO_4 solution are plotted against log (t + 1) in Fig. 1. The thicknesses plotted in this figure are not absolute values, but increments of thickness over that of the initially present air-formed film. Other grains on the specimen used gave essentially the same readings as the {100} grain. A rate constant of 1.43Å was obtained, treating this data in the manner described by Kubaschewski and Brasher (18). This ellipsometric value compares reasonably well with that of 1.5Å obtained by the entirely different radiotracer technique (18).

Similar preliminary experiments were carried out using concentrated HNO_3 as the passivating solution. It was rather difficult to make precise enough measurements in this case to determine what sort of rate law governed the passivation process for a number of reasons. First, the refractive

[1] MirroFe, a chemical polishing solution for iron manufactured by MacDermi Corporation, containing an alcohol and phosphoric acid. Three parts of this were then mixed with 1 part of 30% H_2O_2 to produce the proper polishing bath.

[2] These were based on the approximation, used by Tronstad and Borgmann (11), for films less than 100Å that the mean thickness is proportional to the difference in the phase retardation values of the "film-free" and film-covered surface ($\bar{\Delta} - \Delta$), 1° corresponding approximately to 5Å.

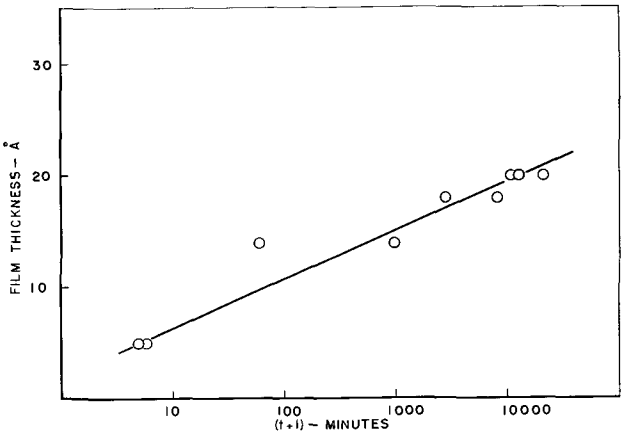

Fig. 1. Growth of a passive film on a (100) iron surface in an air-saturated 0.0025M K_2CrO_4 solution. Logarithmic plot.

index of the solution changed with time because of the slight decomposition of nitric acid that occurred. Second, the surface was somewhat roughened on introduction of the specimen into the acid during the short time interval before it became passive. Finally, thick films formed in a not too reproducible manner.

Usually a film approximately 60Å thick formed on the iron in a period of 1 hr. When the specimen was allowed to remain in the concentrated HNO_3 overnight, a film with a thickness greater than 100Å formed, and the specimen exhibited passivity to a copper sulfate solution. The thickness of the films formed on the large-grained iron specimen varied with the crystallographic orientation of the grains. This could be seen with the unaided eye, for different grains exhibited different colors.

For more controlled studies of passive film growth in inorganic inhibitor solutions, sodium nitrite solutions were selected because the complication of the introduction of other metallic elements into the film, such as chromium when chromates are used, is absent.

The apparatus used in this study is shown in Fig. 2. It was similar to the apparatus described elsewhere (19) in that no greased joints were used, the

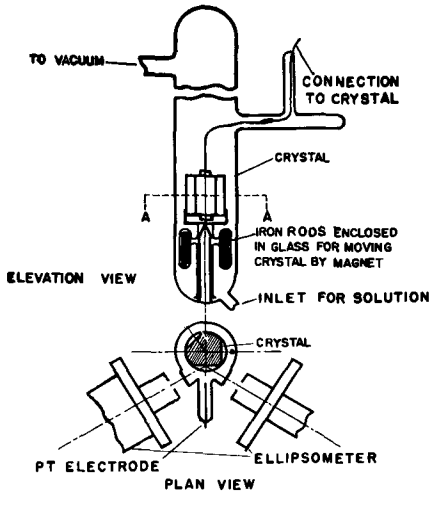

Fig. 2. Apparatus for studying the optical properties and the electrochemical potentials of an iron surface immersed in a passivating solution.

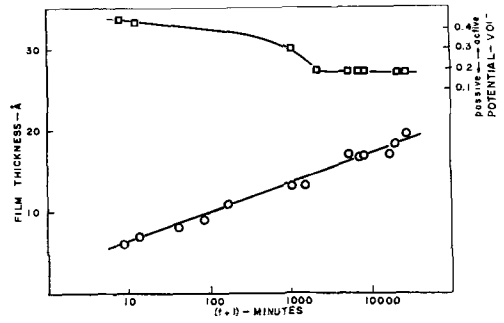

Fig. 3. Growth of a passive film on a (110) iron surface in an air-saturated 0.1*N* $NaNO_2$ solution. Logarithmic plot.

specimen being sealed in for each run and the solution introduced after the specimen had been annealed in purified hydrogen at 500°C. After this anneal and evacuation, readings were made on the "bare" surface, and solution was introduced. This apparatus differed from the previously described apparatus in that a platinum wire was sealed into the apparatus to permit measurement of the potential of the iron specimen with respect to the solution in which it was immersed.[3] The iron specimen used was of the same purity and had the same surface pretreatment described for the chromate experiments just given. It had two large grains having {110} and {211} orientations, and ellipsometric measurements could be made on each of these two grains. Runs were carried out in an atmosphere of pure oxygen or air.

Figure 3 shows the results obtained for a {110} surface in a 0.1*N* $NaNO_2$ solution saturated with air. The potential was measured at the same time as the film thickness and is shown on this curve. In this figure and in all the other figures to follow where potential is plotted, the initial rapidly changing values are not shown. It should be mentioned, however, that a change of around 0.8v occurred in the transition from an active to a passive iron surface. No great differences in behavior between the two different orientations, {110} and {211}, studied in this manner were observed, a difference of less than 4Å being observed after 40 days of exposure. The rate of growth appears to obey a direct logarithmic law. The fact that the line obtained does not extrapolate to zero thickness indicates either that there already existed a film at the beginning of the process or that the formation of the initial monolayers was nonlogarithmic.

Because a direct linear logarithmic relationship was observed for the growth of passive films on iron in both nitrite and chromate solutions, the theory of Hauffe and Ilschner (20) may be applicable. This theory suggests that for extremely thin films a direct logarithmic rate law is obeyed because electron movement rather than ion transport through the film is the rate-determining step. The growth

[3] Platinum was used rather than a more suitable reference electrode in order to avoid the introduction of anions other than those of the passivating salt and to enable the construction of a cell which could be heated to high temperatures. The potential measurements were thus made to determine the onset of passivity rather than to determine thermodynamically meaningful values. That the values of potential obtained by using a platinum electrode do correspond to the onset of passivity was verified in another cell where both a saturated calomel reference electrode and a platinum electrode were used to measure the potential of iron in an air-saturated 0.1*N* $NaNO_2$ solution. If oxygen were excluded from the solution, however, the platinum could not be reliably used to determine the onset of passivity.

Table I. Constants obtained from Hauffe-Ilschner theory

Passivating solution	Rate constant, l_o, Å	Height of potential barrier, Φ, ev
0.0025M K_2CrO_4	1.43	0.46
0.1M $NaNO_2$	1.00	0.95

law based on this theory was formulated by Kubaschewski and Brasher (18) as follows

$$l = l_o \ln (t + 1)$$

where l is the film thickness, t time and $l_o = h/4\pi\sqrt{2M\Phi}$ where h is Planck's constant, M mass of electron, and Φ the height of the potential barrier across the film. In Table I are listed the values of l_o, the rate constant, and Φ for the films formed in the solutions studied. The values of Φ are of the order of magnitude consistent with those found for semiconductors (21).

Since there was undoubtedly present on the iron surface at least a monolayer film under the conditions prevailing in the experiments just described it was necessary to go to the now well-known techniques (12) for working *in vacua* of the 10^{-8} Torr or better. By taking readings on surfaces prepared under such ultrahigh vacuum conditions one could be better assured that the starting point of the passivating process, before the introduction of an inhibiting solution, approached a "bare" surface. Such considerations are, of course, extremely pertinent in view of the importance ascribed to a monolayer film by the adsorption theory of passivity.

The final version of a number of different modifications of the apparatus used in these ultrahigh vacuum studies is shown in Fig. 4. In this version the specimen was screwed into place by opening the bottom of the cell and then sealing the glass bottom with a torch. Thick quartz windows (3 mm) were used to minimize thermal and mechanical strains which would affect the optical measurements.

The iron specimen,[4] mechanically polished using $\frac{1}{4}\mu$ diamond abrasive for the final polish, was

[4] In these experiments polycrystalline vacuum melted iron (Ferro-Vac) was used rather than the iron previously described because it was easier to outgas.

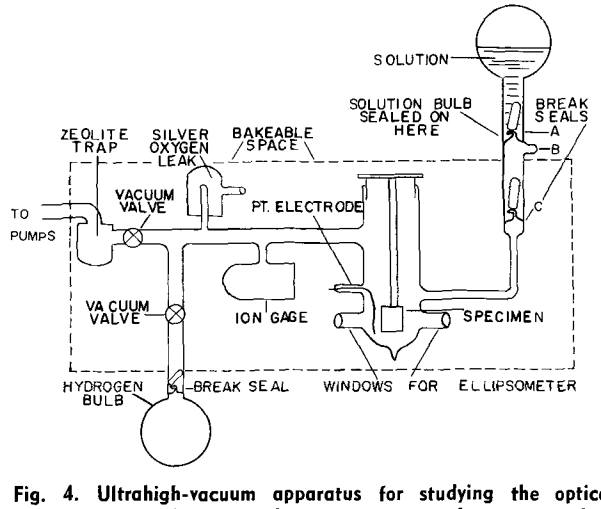

Fig. 4. Ultrahigh-vacuum apparatus for studying the optical properties of and the electrochemical potential of an iron surface immersed in a passivating solution.

etched for a second in dilute nitric acid and immediately rinsed in spectrographic grade methanol.

It was then out-gassed by vacuum annealing it in another vacuum apparatus at 900°C until the pressure in this system went down to approximately 10^{-6} Torr with the specimen still at temperature. After this outgassing, the specimen was sealed into the ultrahigh-vacuum system and annealed in hydrogen to remove the oxide film formed during the sealing-in procedure. The system was then baked at 430°C for 5-6 hr and a pressure of 10^{-9} Torr obtained. The specimen was heated to redness using an induction coil in assayed reagent grade hydrogen[5] admitted to a pressure of 1-2μ. At this pressure a glow discharge occurs in the field of the high-frequency induction coil so that the iron surface was thus bombarded by hydrogen atoms and ions. Readings were made with the ellipsometer after each step in the surface treatment, the values of the optical parameters, Δ, the relative phase retardation, and ψ, the amplitude reduction, changing in a direction indicating that the surface was becoming cleaner. This procedure was continued until no changes in Δ and ψ were observed with further hydrogen annealing. The specimen was then vacuum annealed and the system baked out again. No changes in Δ and ψ were again noted, and the values measured at this point were used as those for a clean surface.

In some experiments a solution open to the air and saturated with air was used to approximate the majority of passivity experiments in the literature.

In other experiments the solutions were prepared so that their dissolved gas content could be controlled. The solution in the bulb shown above break-seal C in Fig. 4 was degassed in another vacuum system by alternate freezing and thawing five times in vacuum and then introducing either assayed reagent grade oxygen or argon[6] (for experiments where oxygen was to be excluded). This bulb, in which the solution was in equilibrium with 0.5 atm of gas, was then sealed off from the solution preparation system and sealed onto the ultrahigh-vacuum system above break-seal C. The space between A and C was then pumped out by a zeolite sorption pump at B, the pump then being removed by sealing off at B. A run was started by breaking break-seal A and then C, the solution covering the specimen in less than 15 sec. Readings could then be made with the ellipsometer and potential measurements made of the iron surface *vs.* the platinum electrode.

The results obtained, using such an approach, differed from those obtained under less rigorous conditions (Fig. 1 and 3) in that at the beginning of the passivation process the relative phase retardation, Δ, increased rather than decreased with time. Such initial increases in Δ were found occasionally by Tronstad and Borgmann (11) for films formed in concentrated HNO_3. This is shown in Fig. 5, along with a simultaneous plot of the potential of the iron surface *vs.* platinum for an air saturated 0.1*N* $NaNO_2$ solution.

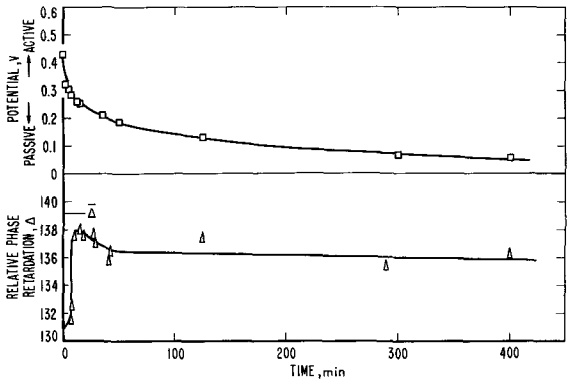

Fig. 5. Change in phase retardation with time for an iron surface immersed in air-saturated 0.1*N* $NaNO_2$ solution.

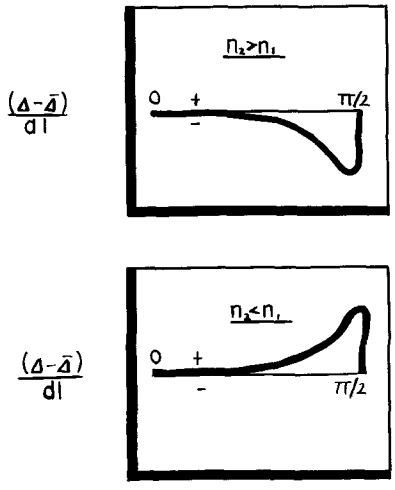

Fig. 6. Influence of the optical constants of the film and the medium on the variation of the phase retardation with thickness for different angles of incidence. [After Winterbottom (15) p. 46.]

Because the growth of oxide films is accompanied by a decrease in Δ (11), the increase found indicates that at the beginning of the passivation process something else was occurring. Figure 6 which is taken from Winterbottom (15) points to one possible reason for the increases. The curves show that for a metal surface such as iron the change in Δ with thickness $(\Delta - \bar{\Delta})/dl$ is negative if the refractive index of the film n_2 is less than that of the surrounding medium n_1 and is positive if $n_2 < n_1$. This implies that a rise in Δ could indicate that a film is forming with a refractive index less than 1.3349, the refractive index of 0.1*N* $NaNO_2$ solution for the wavelength of the light used in all of the studies reported here, 5461Å. None of the oxides of iron whose refractive indices are known or indeed any of the possible solids whose values are known which could constitute the film have a refractive index lower than that of the nitrite solution. On the other hand, an oxygen film (14) or an adsorbed nitrite film would probably have a refractive index lower than the solution.

This interpretation does not apply in this case, however, because although a rise in Δ-values was initially observed, Δ was always less than $\bar{\Delta}$, the value of the phase retardation for the film-free surface. This quantity (shown in Fig. 5) was obtained from a calculation of its value in nitrite solution

[5] This was specified to have no impurities as found by mass spectrographic analysis.

[6] Impurities in the oxygen were in mole per cents 0.0040 A, 0.02 H, 0.019 N, 0.0065 CO_2 and 0.00018 total hydrocarbons, and in the argon were none as indicated by mass spectrographic analysis.

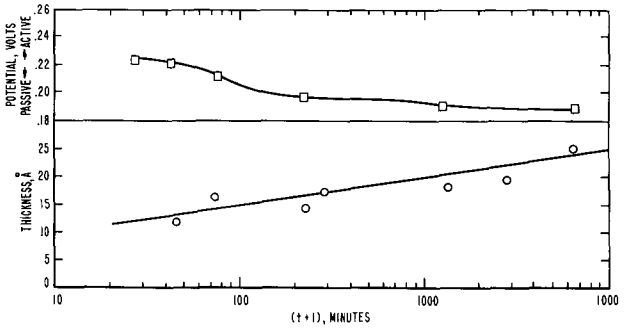

Fig. 7. Growth of a passive film on an iron surface in an air-saturated 0.1*N* $NaNO_2$ solution. Logarithmic plot.

based on the all-important measurements made in ultrahigh-vacuum. During the time when the solution was introduced into the cell containing the specimen, and a reading was made (in some cases less than 0.5 min), Δ had decreased 4°. This corresponds to the formation of a 20Å film, whose refractive index was higher than that of the solution, during the time of solution introduction. Thus the rise of Δ-values was due either to the adsorption of a low index film ($n_2 < n_1$) on top of the film formed almost instantaneously at the beginning of the process, or the dissolution of this initial film, where decreasing film thickness values cause an increase in Δ-values. The fact that Δ max. always approached $\bar{\Delta}$ closely, but never exceeded it argues for the film dissolution interpretation. If the instantaneously formed film was Fe_3O_4, as is quite likely (7) in the atmosphere of air and water vapor that existed between the time the system was opened to the solution and the solution covered the specimen, its dissolution in the air saturated nitrite solution (*p*H 5.8), based on Pourbaix's diagram for iron and water (22), is thermodynamically reasonable. In Fig. 7 the thickness and potential data obtained for an air-saturated solution are plotted logarithmically for times after the initial adsorption or dissolution processes had stopped (after about 45 min).

In order to see if initial film dissolution was occurring because of the low *p*H of the air-saturated solution due to the CO_2 present in it, outgassed solutions, prepared as described earlier, in equilibrium with 0.5 atm of high-purity oxygen were used. As can be seen from Fig. 8 the initial rise in Δ is completely absent, the instantaneously formed film instead continuing to increase (Δ decreasing) with

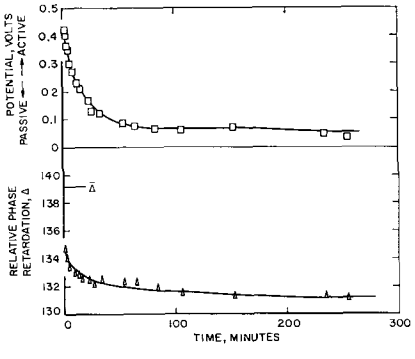

Fig. 8. Change in phase retardation with time for an iron surface immersed in 0.1*N* $NaNO_2$ solution in equilibrium with 0.5 atm of pure oxygen.

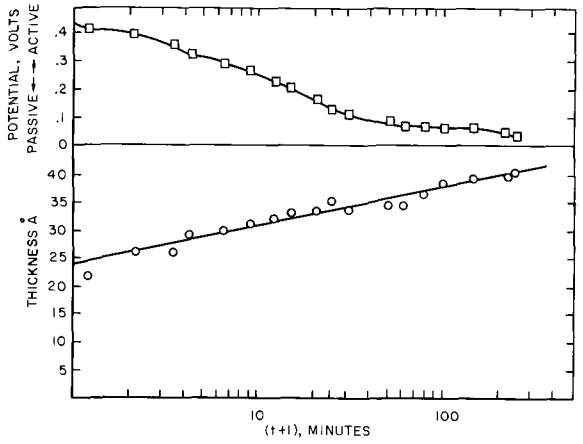

Fig. 9. Growth of a passive film on an iron surface in 0.1*N* $NaNO_2$ solution in equilibrium with 0.5 atm of pure oxygen. Logarithmic plot.

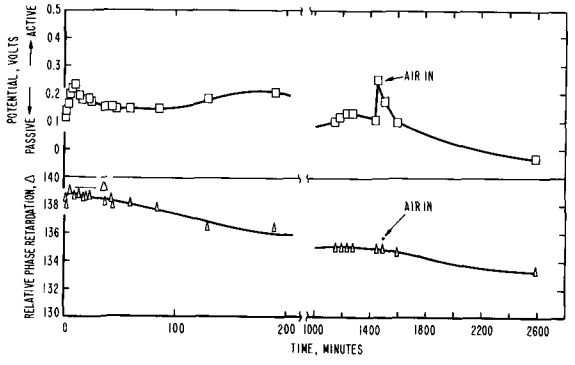

Fig. 10. Change in phase retardation with time for an iron surface immersed in a deaerated 0.1*N* $NaNO_2$ solution.

time. Thus it appears that the initial rise in Δ for air-saturated solutions was due to film dissolution rather than to the adsorption of a low index film on top of instantaneously formed film, for the condition for the latter possibility still existed when oxygen was the only gas present. Figure 9 shows a logarithmic plot of the thickness and potential data for the solution in equilibrium with pure oxygen.

To ascertain whether the instantaneously formed film was produced during the solution introduction interval by interaction with oxygen and water vapor, experiments were carried out using deaerated solutions and high-purity argon as the gas for pushing the solution in rapidly. As Fig. 10 shows, an extremely thin film (< 5Å) formed in the almost completely deoxygenated solution. An initial adsorption on top of or dissolution[7] of this film appeared to take place; it then started to grow. As mentioned before, the potential measurements using a platinum electrode in the absence of oxygen do not give a meaningful indication of the onset of passivity. After 1400 min air was introduced and, as Fig. 10 shows, the rate of film formation increased. The changes in potential that occurred after air was introduced probably suggest that the 20Å film that was present before the introduction of air was not yet a passive film. No dissolution occurred upon introducing air indicating that the film formed

[7] On the basis of Pourbaix's diagram for iron, low oxygen concentration would tend to have the same effect on the dissolution of Fe_3O_4 as low *p*H. Thus dissolution seems to be the more likely alternative here as it was for the air-saturated solution.

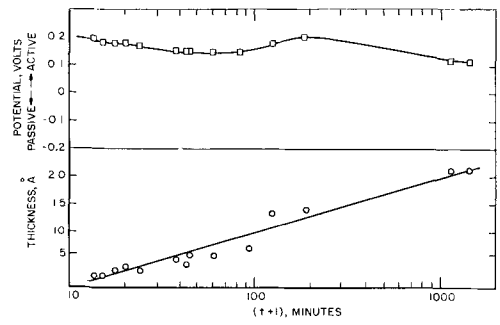

Fig. 11. Growth of a film on an iron surface in a deaerated 0.1*N* $NaNO_2$ solution. Logarithmic plot.

in the presence of the inhibitor differs from the film formed instantaneously during the solution introduction interval. Figure 11 is a logarithmic plot of the potential and thickness data for the deaerated solution. The fluctuations in film thickness probably mean nonuniform film formation not really amenable to analysis by the Hauffe-Ilschner theory. However, the constants calculated using this theory are compared in Table II for the deaerated solution along with the other solutions studied.

Passive Film Breakdown

These studies, qualitative in nature, were concerned with the changes in film thickness that occur when a passive film passes through the Flade potential.

In one set of experiments an iron specimen was rinsed in distilled water and then placed in a solution that would cause a decay in passivity in the same manner as described by Uhlig and King (23). Film thickness changes were measured with the ellipsometer during decay through the Flade potential. Activation was carried out in the acid, neutral, and alkaline regions of the *p*H scale.

Acid.—Here distilled water with a *p*H of approximately 3.5 (adjusted by the addition of HNO_3) was used to cause a decay in the passivity. For iron passivated in concentrated HNO_3 a change in film thickness of over 100Å was observed after passage through the Flade region. The time to go from − 0.22v to + 0.62v (vs. saturated calomel electrode) was less than 1 min. Measurements indicated that the iron surface was essentially bare after activation. Similar behavior was observed with iron passivated in 0.0025*M* $NaNO_2$, the film thickness change again indicating the dissolution of the entire passive film, 30Å thick in this case. The time to go from the passive to the active state was approximately 5 min.

Neutral.—0.2M Na_2SO_4 solution was used as the activating solution. Iron passivated in concentrated HNO_3 overnight took 35 min to pass through the Flade region. The change in film thickness accompanying the change from the passive to the active potential was 40Å. A film of greater than 100Å thickness remained on the iron surface after an active potential was reached.

Alkaline.—It was difficult to activate passivated surfaces in the alkaline region. KOH solutions having a *p*H of 9 and 0.2M Na_2SO_4 solutions whose *p*H was adjusted to 9 with KOH were used. For surfaces passivated in either concentrated HNO_3 or $NaNO_2$ activation was very slow and erratic. In those cases where the surfaces were rendered active in the alkaline solution, the change in film thickness observed was 10Å or less.

The behavior observed in the neutral and alkaline solutions would seem to bear out a suggestion of Pryor's (24) that erratic breakdown that occurs at high *p*H is due to exchange between oxide and hydroxyl ions which decreases ionic resistance so that an active potential may be measured without much dissolution of the film.

Besides the method of causing a decay of passive films just described, another method was employed for iron passivated in concentrated HNO_3. In these studies the decay of the passive film was brought about by the slow addition of water to the HNO_3. When the concentrated HNO_3, in which was immersed an iron surface bearing a film of greater than 100Å thickness, was diluted to less than 20 parts of acid to 1 part of water by the addition of water, the thickness of the film on the iron remained the same. If, however, the HNO_3 was diluted still further to, *e.g.*, 10 to 1, the film on the iron decreased to a thickness of 20-30Å, although the potential exhibited by the iron surface to the HNO_3 solution was still a passive one. Further additions of water caused periodic breakdowns of this 20-30Å film. These breakdowns coincided with the exhibition of momentarily active potentials as determined by the use of a recorder. Such a recorder trace is shown in Fig. 12. This breakdown and repair of the passive film continued at more frequent intervals as more water was added until complete breakdown occurred. This phenomenon could be followed by making ellipsometer and potential measurements simultaneously.

This sort of experiment shows that the thick films that form on iron in concentrated HNO_3 may be made up of two components, the outer layer not being responsible for passivity; for, when this was

Table II. Hauffe-Ilschner constants for 0.1*N* $NaNO_2$ solutions containing different gases

Passivating solution	Rate constant, l_o, Å	Height of potential barrier, Φ, ev
Air-saturated solution	2.13	0.21
Oxygenated solution	3.00	0.11
Deaerated solution	4.17	0.01

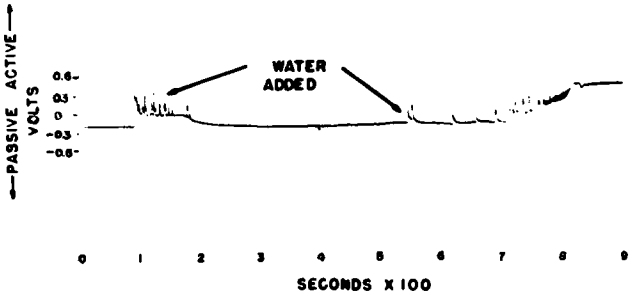

Fig. 12. Breakdown of a > 100Å passive film formed in concentrated HNO_3 by the addition of water. Film is 20-30Å thick after first addition of water shown on curve.

removed, the thin film remaining still rendered the surface passive. This thicker outer film was also responsible for the differences in film thicknesses observed on surfaces of different crystal orientations as mentioned above for iron passivated in concentrated HNO_3. No large orientation effect was observed when the thin passive film was present.

Sites of Film Breakdown

Other than electron diffraction studies [some of the most recent by Cohen (15)] little work has been done on the influence of the structure of the iron surface on the nature and properties of the passive film. This is so because the passive film is too thin to be observed even by using the electron microscope. Thus, an indirect approach was used which investigated the influence of the surface structure on the breakdown of the film, or actually the sites of breakdown, rather than the properties of the film itself.

A technique was used for decorating the sites where the passive film breakdown occurs. It involved placing the passivated iron surface in a solution containing copper ions and allowing it to remain there until the potential exhibited by iron started slowly to become active. The specimen was then quickly removed and rinsed before the whole surface became coated with copper. Examination by the optical microscope and by the electron microscope revealed the formation of discrete (some having definite geometric shapes) crystallites at many sites on the surface. The copper apparently precipitated at sites in the passive film where film breakdown had taken place first. An example of the results obtained with a polycrystalline specimen using a 0.01M solution of copper sulfate is shown in Fig. 13. This shows the difference in density of decorated sites on different orientations. There also appears to be a piling up of sites at one of the grain boundaries. The density of sites is seen to vary between the grains, and there also appears to be two distinct types of sites where decoration occurs.

In order to learn about the nature of the materials making up the sites and the influence any imperfections in the iron may play in initiating them, thin foil electron microscopy studies were carried out.

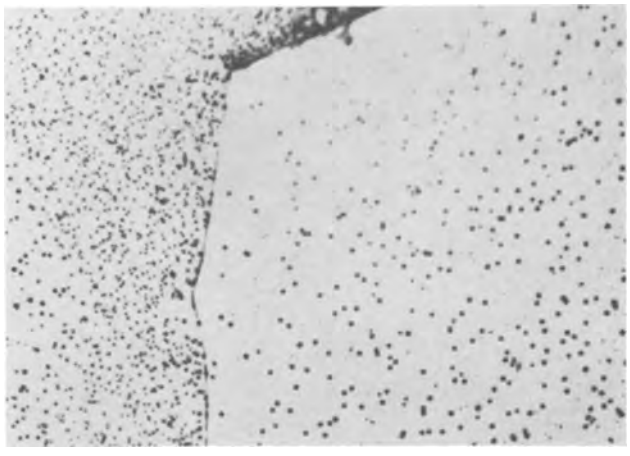

Fig. 13. Polycrystalline iron surface passivated in 0.1*N* $NaNO_2$ solution with sites of film breakdown decorated using 0.01M $CuSO_4$ as decorating solution. Magnification approximately 700X.

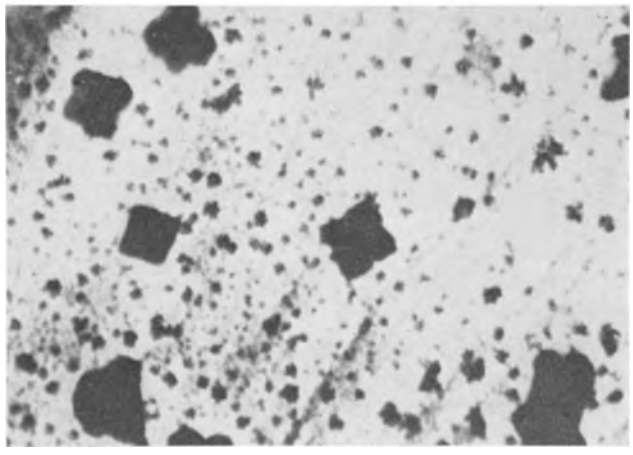

Fig. 14. Transmission electron micrograph of a thin foil treated as in Fig. 13. Magnification approximately 7000X.

A 0.05 mm thick foil of Armco iron 99.9% annealed in hydrogen at 950°C for 18 hr was placed in the chemical polishing solution mentioned earlier for 2 min. It was then placed in fresh polishing solution and allowed to remain there until the foil had thinned sufficiently so that it started to float on top of the solution. Usually portions of the foil had been dissolved away. At this point in the procedure the thinned foil was rapidly removed, rinsed in distilled water for one minute and then placed immediately in a passivating solution. After passivation and breakdown-decoration the foil was rinsed in spectrographic grade methanol. A small portion near the edge of a dissolved-away part of the foil was then cut out and mounted for study with the electron microscope. Such pieces were less than 1000Å in thickness.

The decorated sites were studied by looking at them in transmission with the electron microscope. Selected area diffraction patterns were made of the various decorated sites. Figure 14 shows an electron micrograph made from one of these foils. The diffraction patterns showed that the cubes were, as thought, copper, and the other material was

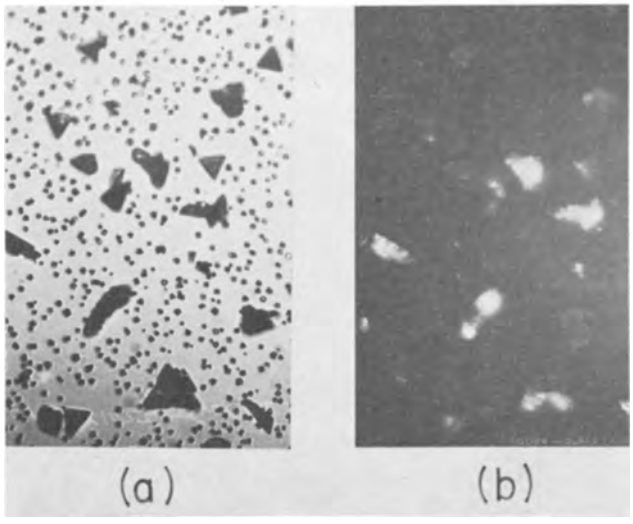

Fig. 15. Polycrystalline iron surface passivated in 0.1*N* $NaNO_2$ solution with the sites of film breakdown decorated by 0.015M $CuCl_2$ as decorating solution. Note two types of breakdown sites. (A) Bright field illumination; (B) polarized light illumination. Magnification approximately 700X.

Table III. Breakdown sites X 10^{-7}/cm^2

Orientation of surfaces	{110}	{100}	{210}	{211}	{111}
Cathodic sites	6.4	3.7	2.5	4.7	3.8
Anodic sites	0.28	0.16	—	—	—

γFeOOH. This agrees with the work of Mellors, Cohen, and Beck (26) who showed that in the breakdown of passive films γFeOOH forms as blisters at discrete spots.

Thus using the decoration technique one could decorate the cathodic sites where reduction takes place on the metal surface with copper and the anodic sites where Fe^{++} ions enter the solution with γFeOOH. Since γFeOOH is birefringent it could be picked out with polarized light. Figure 15 shows this for the case where 0.015M $CuCl_2$ was used as the decorating solution.

The effect of crystallographic orientation is shown in Table III where a comparison of the numbers of cathodic and anodic sites (determined from a large number of photographs) for different crystal orientations is presented.

With regard to these experiments the question arises as to whether the decorations are characteristic of the passive films or the metal substrate. To answer this, unpassivated surfaces were decorated. They gave a much higher concentration of anodic sites per unit area, and there was no one-to-one correspondence with the cathodic sites found when the same area was passivated and decorated. Thus, it appears that the phenomena observed on passivated surfaces depended on the properties of the film, this being affected, in turn, by the metal substrate, since surface orientation had an influence on the number of breakdown sites.

The fact that the closest packed plane for the body-centered-cubic structure, the {110}, exhibited the largest number of breakdown sites coincided with earlier studies on the pitting of iron in water (27) which found that this plane also exhibited the largest number of pits. The reason for the greater reactivity of the closest packed plane may be connected with the observation made by Germer, MacRae, and Hartman (28), using low energy electron diffraction, that in the face-centered-cubic system the less densely packed planes form a firmer bond with foreign atoms such as oxygen than the more densely packed planes. Perhaps this is also the case for the body-centered-cubic iron.

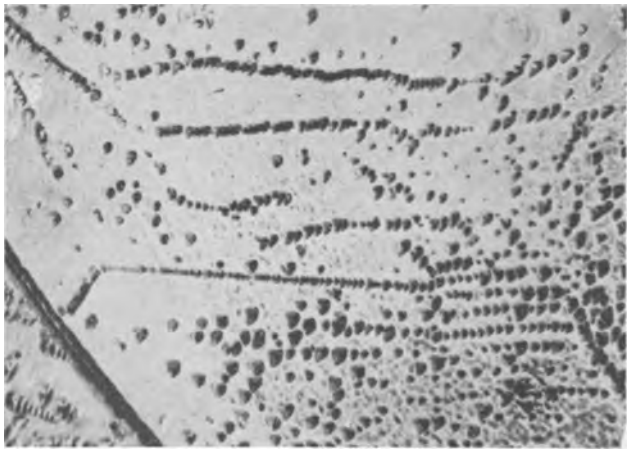

Fig. 16. Etch pits formed on iron using an etchant containing 10 parts HCl, 5 parts HNO_3, and 1 part HF. Magnification approximately 350X.

The question then arises as to the nature of breakdown sites. A brief study was carried out to determine whether they were related to sites where dislocation lines emerge from the iron surface. An etchant ($HCl:HNO_3:HF$ = 10:5:1) was developed that produced etch pits at sites that looked as if they were related to dislocations when compared with similar phenomena in the literature (see Fig. 16). At any rate, these etch pits could be obtained repeatedly at the same sites each time they were removed by repolishing. When this same surface was polished mechanically, chemically polished, passivated, and decorated, there was no relationship between the decorated sites and these etch pits. Thus it appears that the breakdown sites in the passive film were not related to dislocations (or the sites where the etch pits formed). Likewise, no connection between breakdown sites and dislocations was noted in the thin foil electron experiments.

This may indicate that the surface free energy change for breakdown is considerably higher than the differences that may exist between perfect and imperfect surface sites.

Discussion

The most significant results reported in this study are those obtained in the ultrahigh vacuum experiments. These experiments were aimed at fulfilling the need, so far unsatisfied (29), for a positive way for distinguishing between the adsorption and solid film theories of passivation. By using ellipsometry it is possible to determine whether the passivation process involves the adsorption of an oxygen film, the growth of a three dimensional oxide, or a combination of both, a transformation of an adsorbed film into an oxide. The theoretically derived variation of Δ with thickness for each of these three models is shown in Fig. 17.

The optical and potential measurements made on an iron surface passivated in nitrite solution containing only pure oxygen clearly indicated that oxide growth was present even before a passive potential was observed. Thus it should be emphasized that this film, formed almost instantaneously

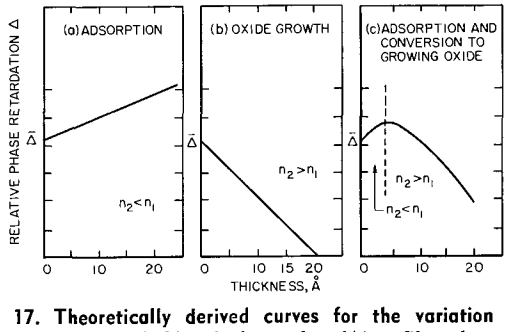

Fig. 17. Theoretically derived curves for the variation of the phase retardation with film thickness for: (A) a film whose refractive index is less than the solution ($n_2 < n_1$); (B) a film whose refractive index is greater than the solution ($n_2 > n_1$); (C) a film where initially $n_2 < n_1$, but later n_2 becomes greater than n_1.

while solution was being introduced, was not yet the passive film. Indeed, it took still further growth and/or alteration of this film before a passive potential was observed. However, when a passive potential was finally observed, a three dimensional film of > 30Å thickness was present on the iron surface. On the basis of the work of Vetter (6), Cohen (7), and others this oxide film which formed instantaneously by reacting with the moist oxygen atmosphere was Fe_3O_4, and during the passivation process the outer layer, at least, of the Fe_3O_4 was converted into γFe_2O_3. It is not possible by ellipsometry to establish positively this composition of the passive film. The optical studies do, however, indicate the formation of a film with a refractive index greater than that of the solution. In fact, calculations indicate that it is approximately the complex number, 2.5-0.3i, a value close to that found for the oxide film formed by oxidizing iron in air (30). The rate studies also indictae, if the Hauffe-Ilschner theory is correct, the formation of a film with a potential barrier reasonable for a semiconductor. Hence all indications point to the presence of a growing oxide film from the very moment that the oxygenated nitrite solution contacts the iron surface.

The possibility that the film observed in this case is an adsorbed oxygen film is completely ruled out for two reasons. First, the refractive index of an adsorbed oxygen film would probably be lower than 1.25, the value found for solid oxygen films on gold (14) and the variation in Δ with thickness would be as Fig. 17a rather than 17b. Second, even if the refractive index of the oxygen film were higher than that of the solution, the values of Δ would indicate adsorbed oxygen films around 40Å when the surface had become passive as judged by the potential measurements. Such a thick adsorbed oxygen film (10-15 monolayers) is very unlikely.

When the iron was passivated in air-saturated nitrite solution, the variation of Δ with time (or thickness) (see Fig. 5) appears to follow the model illustrated by Fig. 17c, the initial adsorption of an oxygen film followed by its conversion to an oxide. Were it not for the readings made on the iron surface in the ultrahigh-vacuum system, this conclusion would be reasonable. However, because these measurements were made on the essentially bare iron surface prior to the introduction of the solution, it could be seen that the Δ-values measured were always less than $\bar{\Delta}$. This means that there was always present on the surface an $n_2 > n_1$ film. As mentioned earlier the increase in Δ values initially observed could be either the adsorption of oxygen or nitrite ions on top of the instantaneously formed Fe_3O_4 film, or, more likely, the initial dissolution of this Fe_3O_4 and the subsequent formation of γFe_2O_3. The results obtained on the less rigorously prepared iron surface tend to bolster the latter interpretation. No initial increase in Δ values were observed for passivation in air-saturated nitrite solution here. Since the iron surfaces in these experiments were prepared in a system where the pressure was never lower than 10^{-6} Torr an oxide film undoubtedly existed on this surface, and according to Sewell, Stockbridge, and Cohen (31) this oxide formed in the dry conditions existing in the vacuum, was probably γFe_2O_3 at the oxide-gas interface. Apparently when this oxide is present in the beginning rather than Fe_3O_4 the initial dissolution process does not occur.

It therefore can be concluded that the experimental observations described for passive film formation strongly support the oxide film model. The film breakdown experiments, however, point to an area which still needs a great deal of study, the special properties of this oxide film. For instance the breakdown experiments in nitric acid showed that the special properties of the 20-30Å film next to the metal were responsible for passivity and not the rest of the thick film observed. Nielsen and Rhodin found essentially the same situation for oxidized stainless steels (34). The fact that no great differences in passive film thickness on substrates of different crystallographic orientation were observed also points to the special properties of the three-dimensional film, indicating an absence of the factors that affect rate differences between different crystallographic planes such as strain and the presence of grain boundaries. It is planned to go into the breakdown process in greater detail in future experiments where the optical properties of iron surfaces whose potentials will be fixed at various active, passive, and transpassive values with a potentiostat will be studied.

Acknowledgments

The author wishes to express his sincere thanks to J. P. Calvert and H. T. Yolken for their aid in carrying out some of the experiments. Grateful acknowledgment is also made to the Corrosion Research Council which partially supported this work.

Any discussion of this paper will appear in a Discussion Section to be published in the December 1963 JOURNAL.

REFERENCES

1. M. Faraday, "Experimental Researches in Electricity," Vol. 2, p. 250, London (1844).
2. B. W. Erschler, *Doklady Acad. Nauk*, **37**, 258, 262 (1942).
3. Y. M. Kolotyrkin, *Z. Elektrochem.*, **62**, 664 (1958).
4. H. H. Uhlig, *ibid.*, **62**, 626 (1958).
5. U. R. Evans, *ibid.*, **62**, 619 (1958).
6. K. J. Vetter, *ibid.*, **62**, 642 (1958).
7. M. Cohen, *Can. J. Chem.*, **37**, 286 (1959).
8. N. Hackerman, *Z. Elektrochem.*, **62**, 632 (1958).
9. L. V. Wanyukowa and B. N. Kabanov, *Zhur. Fiz. Khim.*, **28**, 1025 (1954).
10. L. Tronstad, "Optische Untersuchungen Zur Frage der Passivitat des Eisens und Stahls," Det Kgl Norske Videnskabers Selskabs Skrifter 1931, *1* F. Bruns Bokhandel, Trondheim (1931).
11. L. Tronstad and C. W. Borgmann, *Trans. Faraday Soc.*, **30**, 349 (1934).
12. D. Alpert, *J. Appl. Phys.*, **24**, 860 (1953).
13. T. A. Vanderslice, *Chem. and Eng. News*, **39**, [51], 86 (1961).
14. J. Kruger and W. J. Ambs, *J. Opt. Soc. Amer.*, **49**, 1195 (1959).
15. A. B. Winterbottom, "Optical Studies of Metal Surfaces," Det Kgl Norske Videnskabers Selskabs Skrifter 1955, *1*, F. Bruns Bokhandel, Trondheim (1955).
16. D. M. Brasher and A. H. Kingsbury, *Trans. Faraday Soc.*, **54**, 1214 (1958).
17. G. A. Moore, *J. Metals*, **5**, 1443 (1953).

18. O. Kubaschewski and D. M. Brasher, *Trans. Faraday Soc.*, **55**, 1200 (1959).
19. J. Kruger, *This Journal*, **108**, 504 (1961).
20. K. Hauffe and B. Ilschner, *Z. Elektrochem.*, **58**, 382 (1954).
21. A. J. Cornish, *This Journal*, **106**, 685 (1959).
22. M. Pourbaix, *Z. Elektrochem.*, **62**, 670 (1958).
23. H. H. Uhlig and P. F. King, *This Journal*, **106**, 1 (1959).
24. M. J. Pryor, *ibid.*, **106**, 557 (1959).
25. M. Cohen, *J. Phys. Chem.*, **56**, 451 (1952).
26. G. W. Mellors, M. Cohen and A. F. Beck, *This Journal*, **105**, 322 (1958).
27. J. Kruger, *ibid.*, **106**, 736 (1959).
28. L. H. Germer, A. V. MacRae, and C. D. Hartman, *J. Appl. Phys.*, **32**, 2432 (1961).
29. T. P. Hoar in "Modern Aspects of Electrochemistry," J. O'M. Bockris, Editor, Vol. 2, p. 280, Butterworths Scientific Publications, London (1959).
30. A. B. Winterbottom, *J. Iron Steel Inst.*, **165**, 9 (1950).
31. P. B. Sewell, C. D. Stockbridge, and M. Cohen, *This Journal*, **108**, 933 (1961).

Investigation into the Nature of Anodic Passive and Barrier Coatings

K. Schwabe[1]

Technische Hochschule, Dresden, East Germany

I. Effect of Cl on the Anodic Behavior of Iron in Alkaline Solutions

The rendering passive of many metals, especially nickel, is possible according to our investigations and in conformity with the ideas of Uhlig (1) and Kolotyrkin (2) by means of a chemisorbed oxygen film. Even if a given metal is coated with a bulk oxide, nevertheless the decisive effect on its passive behavior is exerted by the phase boundary between the metal and the oxide, which can also be regarded as an oxygen chemisorption layer. The removal of this layer can be achieved by having very adsorptive anions, *e.g.*, Cl^-, displace the chemisorbed oxygen, thus making the metal active. From the anodic behavior of nickel in alkaline solutions in the presence of Cl^- or Br^- it has been shown that the displacement of oxygen from the chemisorption layer by the halogen ions determines the potential curve up to the active region if a constant anodic current density is applied to the metal.

The frequently investigated effect of chloride ions on the anodic behavior of iron in alkaline solution was now assumed in principle to be based on the displacement of the oxygen by the Cl^-. In this case, however, we do not expect to find the same quantitative relationships because iron differs considerably from nickel in its exchange current density. Therefore its passivation current density under comparable conditions is about 1,000 times greater than that of nickel. Moreover the over-voltages of the electrode process and the adsorption behavior of anions on both metals is very different. At least the anodic products (nickel or ferric hydroxide) have different solubilities. This latter point was important inasmuch as no reproducible voltage-time curve at constant current density could be obtained for nickel at first on account of the precipitation of nickel hydroxide at the anode; only when the precipitation of the hydroxide was prevented by the addition of ammonia could the curves be reproduced reliably and interpreted quantitatively. In the case of iron it was not possible to avoid the precipitation of ferric hydroxide. The addition of complex forming anions was to be avoided because otherwise no clear statement could be made concerning the effect of the Cl^-. Consequently the anodic voltage time curves for iron at constant anodic current density have a less regular shape than those for nickel in the presence of ammonia. By intensive movement of the electrolyte in front of the electrode surface it was indeed possible to eliminate to a large extent the effect of the ferric hydroxide separating out; on the other hand the conditions with respect to the electrolyte composition at the anode were considerably altered compared with the investigations of nickel, a point which will have to be examined in greater detail.

Test Set-up and Procedure

As in the amperostatic investigations with nickel the rod-shaped anode of soft steel with traces of Cr, Cu, and As was situated in a ground section on the bottom of the electrolytic cell. However, the reference electrode was not situated in a capillary probe near the surface of the electrode; instead a

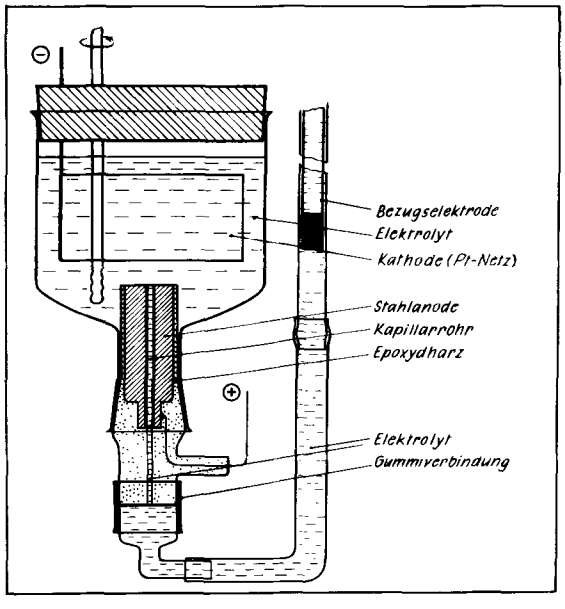

Fig. 1. Cell for measuring with Müller-Soller probe. The inserts top to bottom are: reference electrode; electrolyte; cathode (Pt gauze); steel anode; capillary tube; epoxy resin; electrolyte; rubber connection.

[1] Experiments of Chr. Voigt, Q. Nguyen, and M. Paul.

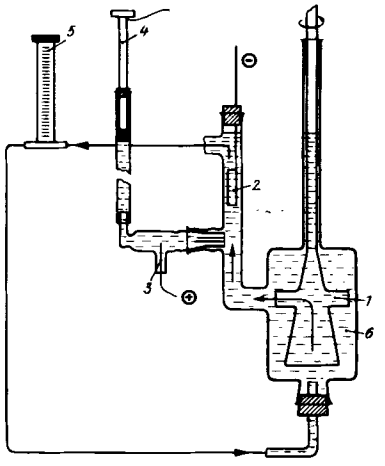

Fig. 2. Cell for flow experiments

1. Circulating pump
2. Pt cathode
3. Anode (cf. Fig. 1)
4. Calomel electrode
5. Flow meter
6. Electrolyte

Müller-Soller probe was used in which the steel cylinder was pierced and the capillary tube inserted into the hole projected into the lower part of the ground section which was filled with the electrolyte and which provided the liquid connection with the reference electrode (saturated calomel electrode) through a U tube (Fig. 1). A lead wire insulated from the electrolyte solutions and brought laterally from the ground section was soldered to the steel cyinder and connected to the positive terminal of the polarizing current source. The steel anode was coated up to its front face with an insulating compound (epoxy resin) so that the effective electrode surface was 0.6 cm^2. In order to remove rapidly the ferric hydroxide formed at the surface of the anode, a plastic wiper was rotated against the anode in some of the tests; in other tests the steel anode with Müller-Soller probe was inserted temporarily in a glass tube through which the electrolyte was pumped at high variable speed by means of a glass circulating pump (Fig. 2). The arrangement for producing a constant direct current and for measuring or recording the anode voltage with reference to the saturated calomel electrode was the same as that described previously (5).

Before each test the anode was ground [with graded sand paper (180 to 700)] and degreased. After insertion in the test cell and filling with electrolyte a certain time, generally 15 min, was allowed before switching on the polarizing current. Generally speaking the electrolytic solutions were not deaerated so that the effect of oxygen on the voltage behavior could be studied; however, tests were also carried out under nitrogen with solutions from which O_2 had been eliminated carefully. The KOH concentrations were varied from 10^{-3} to 2 moles/l, those of the KCl from 10^{-4} to 2.5 moles/l. Tests carried out in 3-4M KOH solutions showed no activation of the iron even at KCl saturation. Current densities were varied in a range from 0.1 to 35 ma/cm^2 (7).

Test Results

When the current is switched on the potential jumps to a positive value and then falls to negative

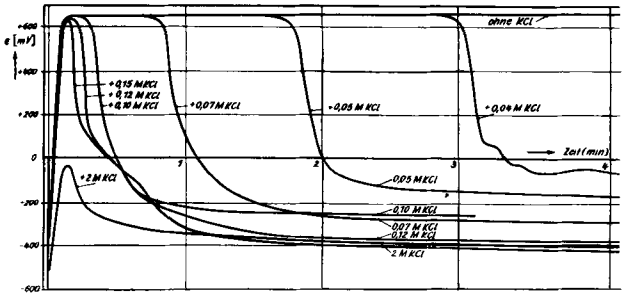

Fig. 3. Effect of KCl concentration at constant (0.1M) KOH and anode current density (j = 1 ma/cm^2). Air-saturated solutions. Waiting-time 15 min.

values (in the active region) the faster the higher the KCl concentration, but the voltage decrease does not occur so regularly as in the case of nickel (Fig. 3).

We must therefore distinguish between the following potential regions:

1. The potential region of rest before the current is switched on is always in the active region [—300 to —500 mv (SCE)].
2. The passive region after the current is switched on [approximately +650 mv (SCE)].
3. The potential drop to the active potential.
4. The active region accompanied by anodic formation of ferric hydroxide.

The time that it stays in the passive region (t_p) is determined by the composition of the electrolyte, by the time spent in the solution before switching on the current, and the oxygen content. In accordance with the considerations presented earlier and confirmed on nickel, the anode potential should vary exponentially with time according to the function

$$\epsilon_t = \epsilon_p - K \cdot (1 - e^{-K,t}) \qquad [1]$$

where ϵ_p is the potential of the passivation. For very brief times therefore the potential is at the passive value. The value of the constant is determined by the ratio of the KCl and KOH concentrations at the surface of the electrodes. At constant KOH concentrations (0.1M) t_p decreases exponentially with the concentration of KCl (c mole/l) according to Eq. [2]

$$t_p = 687 \cdot e^{-35.7 \cdot c} \qquad [2]$$

at 25°C in the concentration range 0.03-0.12 moles/l (Fig. 4). For every KOH concentration there is a minimum KCl concentration (c_{min}), which just barely suffices to bring about a decreasing potential in the active region. Generally speaking we may write

$$1/t_p = K_2 (c - c_{min}) \qquad [3]$$

where the constant K_2 depends on the KOH concentration, agitation or flow conditions, and all the time prior to polarization (Fig. 5). The time t_p in air or O_2 saturated solutions increases approximately proportionally to the waiting time; in oxygen free solutions it is almost independent of the waiting time. With increasing current densities the time remaining in the passive region, t_p, decreases approximately proportionally (in the range 0.1-20 ma/cm^2).

$$t_p = a \cdot j + b \qquad [4]$$

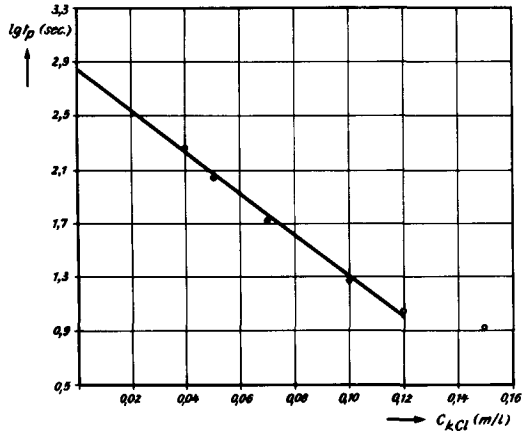

Fig. 4. Time in passive region (t_p) as function of KCl concentration.

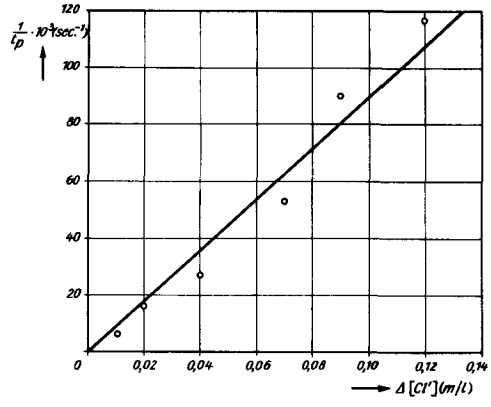

Fig. 5. tp as function of KCl concentration. $1/tp = K (C_{KCl} - C_{KCl,min})$.

where j is the current density in ma/cm^2, and a and b are constants depending on the composition of the electrolyte.

When the electrolyte flows past the anode, then where the KCl concentration is small in relation to the KOH concentration and the flow velocity is sufficiently high so that the electrode can be kept passive for an arbitrarily long time ($t_p \rightarrow \infty$); when the flow is stopped, a drop to the active region takes place and when the circulation pump is turned on again the anode gradually becomes passive once more (Fig. 6). At high KCl concentrations, however, t_p is decreased by the flow of the electrolyte.

When the variation of the potential (ϵ_m) after the time t_p is analyzed as a function of t, we find in the first seconds a relationship of the form

$$\epsilon_m = \epsilon_p - (t - t_p)^3 \cdot K_3 \qquad [5]$$

furthermore, K_3 increases approximately in proportion to the ratio c_{Cl^-}/c_{OH^-} (see Fig. 7a and b). Over

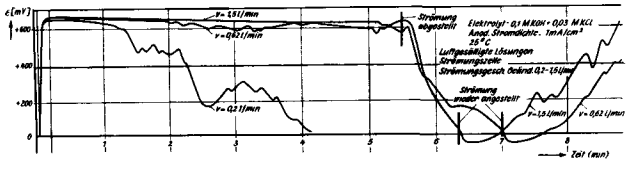

Fig. 6. Effect of electrolyte flow velocity (0.1 M KOH + 0.03 M KCl; j = (ma/cm^2).

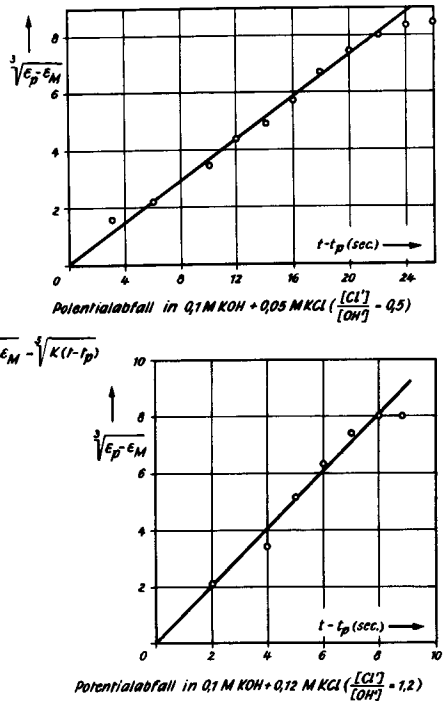

Fig. 7a, b. Potential fall after the time t_p

longer periods of time irregularities in the potential decrease appear (see Fig. 3 and 6) which do not permit the calculation of a function, but it can be assumed that in principle the potential follows an exponential function from the beginning of the flow of current to the active region, as we found earlier for the case of nickel.

In the active region the measured potentials correspond approximately with the process $Fe \rightarrow Fe^{\cdot\cdot} + 2\theta$.

Discussion

The results can be interpreted if we again assume, as in the case of nickel, that the iron is at first covered by chemisorbed oxygen, which is displaced by the Cl^-, and that this displacement leads to the activation of the iron. As already stated for nickel a greater ratio c_{Cl^-}/c_{OH^-} will prevail at the anode than in the solution owing to the current which accounts for discharge of OH^- in the passive state and the transference of Cl^-. Also for activation, therefore, the important consideration is not the ratio in solution but that at the electrode surface. Hence, a high concentration of KCl^- without polarization does not suffice to bring about for instance activation in 0.1M KOH; only at a ratio of more than twenty in the solution does the electrode become active practically immediately. The necessity of increasing the ratio c_{Cl^-}/c_{OH^-} as a condition for the activation also explains the decrease in the time t_p with the current density in accordance with Eq. [4]. During the time in the passive region the increase in the Cl^- concentration at the anode is proportional to the current density and according to [3] inversely proportional to the time t_p. If the electrode rests in the solution in the presence of oxygen, a small amount of corrosion occurs as the potential situation indicates and leads to a porous non-

Table I. Minimum KCl concentration with activating effect for $j = 1$ ma/cm² on iron as a function of the KOH content at 25°C

KOH (m/l):	10^{-3}	10^{-2}	0.05	0.10	0.15	0.20	0.50	1	2
KCl (m/l):	10^{-4}	10^{-3}	10^{-2}	0.03	0.07	0.1	0.33	0.75	2.5

On nickel

KOH (m/l):	0.035	0.070	0.14
KCl (m/l):	0.05	0.080	0.20

passivating coating. However, this coating prevents the arrival of the Cl^- partly in a mechanical way and partly perhaps by forming basic chlorides and thus delaying the concentration of Cl^- at the electrode surface; this expresses itself in prolonging the time spent in the passive region. When the electrolyte flows past the anode at high velocity, the required enrichment cannot occur at not too great concentrations, and thus the electrode remains passive, but when the flow is interrupted the required concentration takes place. The higher the current density, the more rapid will be the enrichment process. The increased rapidity of the transition to the active state at high Cl^- concentrations is perhaps due to the fact that, on account of the high Cl^- concentrations, corrosion even in the passive region is still so considerable that inhibiting coatings are formed which are removed by the flow. To interpret the change of potential after passage through the passive region it must first be noted that the attack on the iron, when occurring, always takes the form of pitting; thus the active part of the surface, f, is very small in relation to the total surface and even to the passive part (1-3% compared with $1-f$). When it is assumed therefore that the potential ϵ_m at a given time t can be calculated from the passive potential and the reversible potential of the iron dissolution ϵ_{Fe} according to

$$\epsilon_m = (1-f) \cdot \phi_p \epsilon_p + \phi_{Fe} f \cdot \epsilon_{Fe} \qquad [6]$$

and if at the same time the proportionality factors ϕ_p and ϕ_{Fe} are regarded as constant, the first term can be put approximately equal to $\phi_p \cdot \epsilon_p$ = constant.[2]

According to Engell and Stolica (8) the radius of pitting increases proportionally with the time, *i.e.*, $r = c_1 t$ (c_1 = constant) and so does the number of pits $z = c_2 \cdot t$ (c_2 = constant), from which follows that the fraction of the active surface by integration of $F = \int_o^z F_i \cdot dz$, where F_i is the area of a pit and O is the total electrode surface and the form $f = \frac{2\pi c_1^2 \cdot c_2 \cdot t^3}{3 \cdot O}$ or with $\frac{2\pi c_1^2 \cdot c_2}{3 \cdot O} = G$ then $F = G \cdot t^3$.

For ϵ_m we then have

$$\epsilon_m = \phi_p \cdot \epsilon_p + \phi_{Fe} \cdot G \cdot \epsilon_{Fe} t^3$$

If we count the time from the beginning of the decreasing potential, ϕ_p is approximately 1 and take into account ϵ_{Fe} is negative, we obtain in conformity with the experiments in the formula

$$\epsilon_m = \epsilon_p - K_3 (t - t_p)^3$$

[2] In reality these factors will be a function of the ratio of exchange current density and partial current density of the process involved. In each case it can be assumed that $\phi_p << \phi_{Fe}$. C.f. K. Bonhoeffer and W. Renneberg, *Z. phys. Chem.*, **118**, 389 (1941), who introduce a "critical threshold area."

Of course, since $(1-f) = 1$ was implied we can expect to find this curve only at the beginning of activation. As the process continues we must expect an exponential drop according to Eq. [1] derived earlier. It must be borne in mind of course that K and K_1 contain, in addition to the concentration of Cl^- and OH^-, also their adsorbtivities on the metal in question as well as the rate constants of adsorption, and that consequently these constants could assume quite different values. Moreover, in derivation [5] of this equation the coefficients ϕ_p and ϕ_{Me} are not taken into account, but actually it must be assumed that $\phi_{Fe} > \phi_{Ni}$ because with iron the reaction $Me \rightarrow Me^{\cdot\cdot} + 2\theta$ is much less inhibited than in the case of Ni. Because of this also the activation by Cl^- can follow a different course with the two metals; however, we can actually find no differences in principle between the behavior of nickel and that of iron in alkaline solutions in the presence of halogen ions. The time remaining in the passive region is considerably shorter for nickel than for iron which, as already stated, can be attributed to the differing adsorbtivities of the anions or to different exchange current densities, and also perhaps to the fact that in the case of nickel the phase oxide form has been kept in solution by the addition of NH_3. With nickel the potential decrease is slower than with iron, but it is much more strongly affected by Cl^- concentration, and the minimum Cl^- concentration required for activation is greater (Table I).

It can be concluded from the results that for iron and nickel (probably also for cobalt) the active anodic dissolution of metal in alkaline solutions containing halide does not take place until the halogen ions have displaced chemisorbed oxygen or adsorbed OH^-; in the course of this, intermediate products may occur in accordance with

$$(MeOH)_{ad} + X^- \rightarrow (MeOHX^-)_{ad} + n\,H_2O \quad \text{(i)}$$

and

$$(MeOH,X^-)_{ad} + m\,H_2O \rightarrow MeOH^{\cdot} + X^- + \theta \quad \text{(ii)}$$

as Frumkin (9) for example has assumed. If we suppose at the same time that the activating adsorption of halogen ions and the passivating adsorption of OH^- occur as competing simultaneous reactions (4), it

Table II. Change in dissolution potential for 2*N* KCl = constant and $j = 1$ ma/cm² with the KOH content (measured in each case after 3.5 min) at 25°C

KOH (m/l):	10^{-3}	10^{-2}	10^{-1}	1
(mv SCE):	−505	−450	−385	−265

Table III. Change of dissolution potential at 0.1*N* KOH = constant and j = 1 ma/cm² with the KCl — content (measured after 3.5 min in each case) at 25°C

KCl (m/l):	0.04	0.05	0.07	0.12	0.15
ϵ(mv, SCE):	−40	−150	−280	−390	−425

also becomes understandable that for constant Cl^- concentration with increasing OH^- concentration the potential becomes more positive $\frac{\partial \epsilon}{\partial \ln c_{OH^-}} > 0$ (Table II), whereas for the process

$$Fe + 2\,OH^- \rightarrow Fe(OH)_2 + 2\theta \qquad \text{(iii)}$$

a negative coefficient $\frac{\partial \epsilon}{\partial \ln c_{OH^-}} = -\frac{RT}{F}\,2.303$ would have to occur.

We have found, of course, similar to observations of Popowa and Kabanow (10) that at very small current densities (<0.5 ma/cm²) the gradient actually does become negative. Possibly the reaction always occurs to a slight extent and at small current densities where reactions (i) and (ii) are not required for the penetration of the charge, becomes the determining factor for the potential. The gradient $\frac{\partial \epsilon}{\partial \ln c_{Cl^-}}$ as expected is negative (~ −73 mv) (Table III).

On the other hand Heusler and Cartledge (11) have found that in acids containing halide for iron $\frac{\partial \epsilon}{\partial \ln c_{OH^-}} = -59$ mv and $\frac{\partial \epsilon}{\partial \ln c_{Cl^-}} = +53$ mv. Thus, for the anodic dissolution in acids containing halide still other factors must be decisive. For example the strong adsorbtivities of the halogen ions after removal of the passive film could prevent dissolution, just as it can of course, inhibit the H^+-discharge. The negative gradient $\frac{\partial \epsilon}{\partial \ln c_{OH^-}} = -59$ mv, which is attributive of course to the catalytic effect of the OH^- on the dissolution of the iron (12), is at first difficult to interpret (13). Theoretical investigations and experiments with tracer ions are at present in progress with regard to this question. It must not be overlooked that reliable quantitative statements are made much more difficult by the fact that the corrosion current densities and the form of the attack on the electrode surfaces depend very strongly on the prehistory and pretreatment of this surface, on the purity of the electrode metal (14), and on the voltage situation. As proof we may cite three micrographs of nickel electrodes from which, under completely similar conditions at different potentials, approximately the same quantity of nickel was brought anodically into solution in 5*N* H_2SO_4, whereas in the active range [~ + 50 mv (SCE) and at + 1400 mv (SCE)] a completely uniform surface attack takes place. At + 1700 mv a definite grain boundary corrosion occurs. These results are confirmed by many determinations (15).

REFERENCES

1. Compare H. H. Uhlig and P. F. King, *This Journal*, **106**, 1 (1959).
2. Y. M. Kolotyrkin and W. M. Knjashewa, *J. Phys. Chem., U.S.S.R.*, **30**, 9 (1956).
3. K. Schwabe and G. Dietz, *Z. Elektrochem.*, **62**, 751 (1958); K. Schwabe, *Wiss. Z. TH Dresden*, **8**, 240 (1958/59); *Z. physik. Chem., Leipzig*, **214**, 343 (1960).
4. Compare K. Schwabe, *Electrochim. Acta*, **3**, 186 (1960).
5. K. Schwabe and R. Radeglia, *Werkstoffe u. Korrosion*, **13**, 281 (1962).
6. Haber and Goldschmidt, *Z. Elektrochem.*, **12**, 62 (1906); B. Kabanow and D. Leikis, *Acta Physik. UdSSr*, **21**, 769 (1946); B. Kabanow and D. Leikis, *Ber. Akad. Wiss. UdSSR*, **58**, 1685 (1947); L. Wanjukowa and B. Kabanow, *Ber. Akad. Wiss. UdSSR*, **59**, 917 (1948); L. Wanjukowa and B. Kabanow, *J. Phys. Chem., U.S.S.R.*, **28**, 1025 (1954); I. Rosenfeldt and Maximtschuk, *ibid.*, **35**, 1832 (1961); I. Rosenfeldt and Maximtschuk, *Z. Phys. Chem.*, **215**, 25 (1961); T. Popowa and B. Kabanow, *J. Phys. Chem., U.S.S.R.*, **35**, 1295 (1961); B. Kabanow, R. Burstein, and A. Frumkin, *Discussion Faraday Soc.*, **1**, 259 (1947); G. Schmidt and N. Hackerman, *This Journal*, **108**, 741 (1961).
7. For closer values see Dipl.-Arbeit Chr. Voigt, TU Dresden 1962, Institut fur Electrochemie und phys. Chemie.
8. *Z. physik. Chem. N.F., Frankfurt*, **20**, 113 (1959).
9. B. Kabanow, R. Ch. Burstein, and A. Frumkin, *Discussions Faraday Soc.*, **1**, 259 (1947).
10. *J. Phys. Chem., U.S.S.R.*, **35**, 1295 (1961).
11. K. E. Heusler and G. H. Cartledge, *This Journal*, **108**, 732 (1961).
12. K. Heusler, *Z. Elektrochem.*, **62**, 582 (1958).
13. C.f., J. O'M. Bockris. D. Drazic, and A. R. Despic, *Electrochim. Acta*, **4**, 325 (1961).
14. J. O'M. Bockris and D. Drazic, *ibid.*, **7**, 293 (1962); G. Trumpler and W. Saxer, *Helv. Chim. Acta*, **36**, 1630 (1953).
15. Dissertation E. Kunze, T. U. Dresden, in preparation.

II. Investigations of Ion Conducting Barrier Layers with Anodic Polarization

Whereas in the case of metals with restricted passage reaction

$$Me \xrightarrow{+\,n\,H_2O} Me^{++} + 2\theta$$

e.g., for nickel, iron, and cobalt we regard a chemisorbed oxygen film formed by the competing reaction

$$Me + OH_2 \rightarrow Me - O_{ad} + 2H^+ + 2\theta$$

(see Part I), as sufficient for their passivation, for metals with unrestricted passage reaction such as Ag, Zn, Cd, and Al ion conducting barrier layers of salts or oxides can produce high anodic polarization.

On zinc salt barrier layers were investigated which in many respects show a behavior similar to the aluminum barrier layer (1), in saturated solutions of zinc sulfate and other salts. In particular very high positive potentials (up to greater than

10v) were measured even with the interrupted method. These were interpreted as condenser charges.

On mercury in chloride solutions using oscillographic switch off curves, we have found that the high anode potentials we were able to measure during polarization were made up of three components, an ohmic voltage drop (resistance polarization), a type of condenser charge, and the relatively slight chemical polarization which can be attributed primarily to the fact that after exceeding saturation, *i.e.*, at a certain supersaturation, solid salt must be formed from the metal directly on the surface of the electrode. If the voltage drop is plotted semilogarithmically against the time, three rectilinear curve segments are obtained which correspond to the three polarization effects. We now apply this method to zinc in a saturated sulfuric acid zinc sulfate solution. We shall not discuss here the details of the experimental procedure, especially the verification of the fact that this does involve a zinc sulfate layer which brings about the polarization. In any case it was again found that, after a steep drop which takes place in less than 10^{-3} sec and which in relation to the total polarization decreases with increasing anode potential during the flow of current, a potential drop occurs which goes according to a function $U = K \cdot e^{-t/\tau}$ and increases with increasing total polarization, and finally a relatively slow drop which is more or less independent of the total polarization (Fig. 1). Here, too, we interpret the first steep drop as a resistance polarization, the second as a condenser discharge, and the slow drop at the end as chemical polarization; of course, these three processes overlap to some extent.

When we compare the rate of the potential drop on zinc in NaOH with that in saturated zinc sulfate solution (3), we find that it takes place more slowly by several orders of magnitude with zinc oxide in NaOH than in sulfate. The rapid drop in sulfate and other salt solutions was long ago (4) attributed to the fact that the salt layer is dehydrated electroosmotically by the high potential gradient, and hence its insulation resistance is considerably increased. This would also explain the rectifying effect of such layers because with cathodic charging of electrodes with such layers the water is returned, and hence the barrier effect is practically eliminated. Several years ago Müller (5) expressed the view that the rectifier effect in the case of oxide coated aluminum is due essentially to such dehydration, to which it was subjected; however, (6) aluminum shows a rectifier effect even in nonaqueous sulfuric acid. We have now demonstrated that in the case of zinc in a saturated sulfate solution water is forced out of the barrier layer by an anodic field. For this purpose we connected a zinc electrode in saturated zinc solution, in which the water had been tagged with tritium, to the anode and polarized it until there was a drop in current density, *i.e.*, until the barrier layer had been formed; the current was then turned off and the electrode was removed from the radioactive solution, washed with dioxane to conserve the salt layer, and immersed in an inactive saturated $ZnSO_4$ solution. From this point on, by taking samples, the activity of this continuously stirred solution was measured with a liquid scintillator counter and a coincidence measuring position (7). After a certain time when isotope exchange equilibrium had become established at the surface, and thus the activity was constant, the electrode was connected to the anode, whereupon after a high initial value the current immediately decreased sharply. At the same time the activity of the solu-

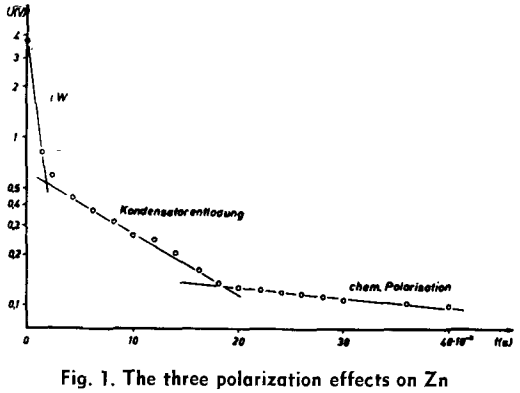

Fig. 1. The three polarization effects on Zn

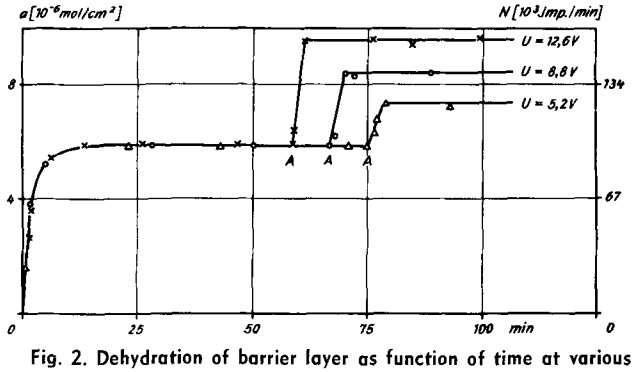

Fig. 2. Dehydration of barrier layer as function of time at various field strengths. (Zn in saturated $ZnSO_4$ solution). Aanodic potential applied at A.

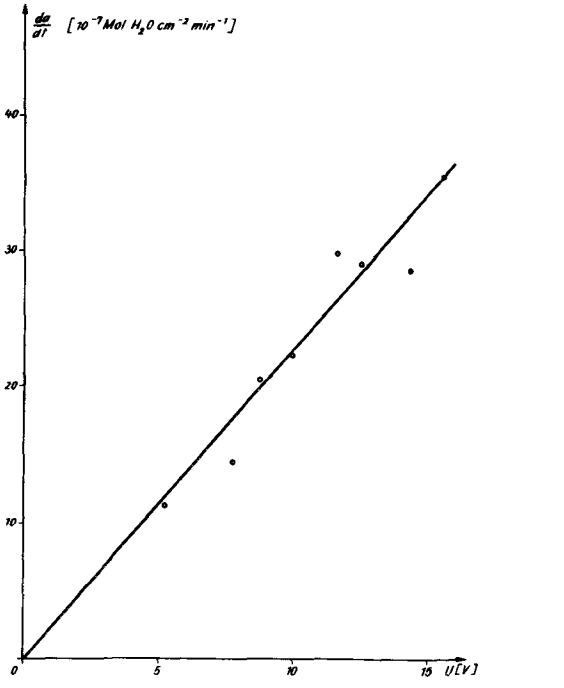

Fig. 3. The rate of water emergence as a function of anodic voltage (Zn in saturated $ZnSO_4$ solution).

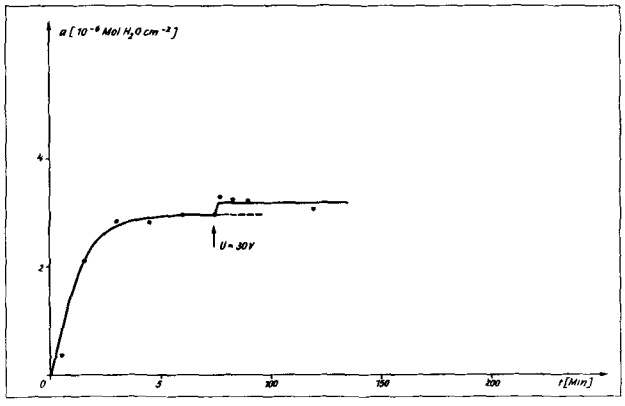

Fig. 4. Dehydration of Zn anode in 90% H_2SO_4 saturated with $ZnSO_4$.

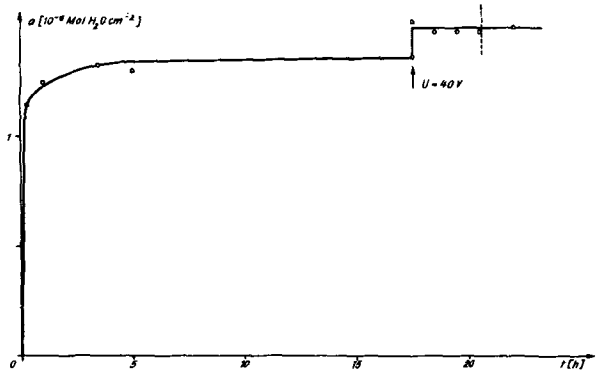

Fig. 5. Dehydration of Al anode in ammonium borate solution

tion was measured; it immediately showed a steep increase and then remained constant (Fig. 2). The rate of water emergence measured by the increase in the pulse rate is proportional to the applied voltage, as was to be expected in an electroosmotic dehydration process (Fig. 3). In 90% sulfuric acid saturated with zinc sulfate, the much smaller effect is just barely measurable at 30v applied voltage (Fig. 4). For aluminum we were also able to demonstrate such a dehydration effect in a similar way with T_2O tagged ammonium borate solution. The increase of pulse rate per cm^2 of course was very much smaller, probably because of the smaller coating thicknesses. For the electrode, therefore, we used a hollow aluminum cylinder with an inside surface area of about 250 cm^2 and placed it about 3 mm away from a solid aluminum cylinder as the cathode; the electrolyte volume was therefore very small (7). Otherwise the same procedure was followed as for zinc in zinc sulfate; however, the anode voltages were considerably larger. Figure 5 shows that when 40v are applied there is a sudden increase in the tritium activity which corresponds approximately to a water emergence of 1 to 1.5 · 10^{-7} mole H_2O/cm^2. Because of the much smaller effect here we could not establish a clear relationship between the water emergence rate and the applied voltage. Nevertheless for aluminum also Mueller's assumption that the rectifier effect is brought about or at least promoted by an electroosmotic dehydration is thereby given considerable support. The rectifier effect in nonaqueous sulfuric acid could then be explained by an electroosmotic ejection of H_2SO_4 from the barrier layer, especially when it is considered that the dielectric constant of H_2SO_4 (84) is decidedly greater than that of the Al_2O_3 barrier layer (7.5 for Al_2O_3). In order to clarify this question we carried out measurements in fuming sulfuric acid which had been tagged with S^{35}, after first establishing that a dehydration of the barrier layer by fairly long pretreatment in this acid does not influence the rectifier effect, the quotient; J_{Gl}/J_{eff} both before and after the treatment was 0.40-0.45.

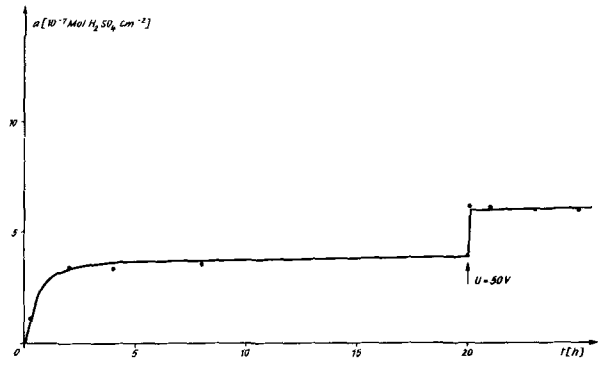

Fig. 6. H_2SO_4 emergence at an Al anode

After the aluminum electrode had been connected for a fairly long time to the anode in sulfuric acid tagged with $H_2S^{35}O_4$ the current was switched off and the cylinder was removed, washed, and put in inactive sulfuric acid. After the isotope equilibrium had been established various anode voltages were again applied. In all cases a rapid increase in the pulse rate in the inactive sulfuric acid took place; after a short time the activity became constant. Figure 6 shows the effect for an applied voltage of 50v; the establishment of isotope exchange equilibrium in the case of aluminum always requires a considerably longer time than for zinc even in aqueous solutions. As a result of the applied voltage about 2 · 10^{-7} mole H_2SO_4/cm^2 are given off. This is of the same order of magnitude as that for water.

This seems to us to prove that the barrier forming effect of aluminum oxide layers is determined to a large extent by electroosmotic effects, and thus a previous assumption, which was proposed by Fischer (8) is confirmed. Of course the cathodic electrode process also plays a part in saturated zinc sulfate solution. We do not observe any queer rectifier effect ($J_{Gl}/J_{eff} \cong 0.01$). In 90% H_2SO_4 saturated with $ZnSO_4$ an effect is present ($J_{Gl}/J_{eff} \cong 0.15$). In the first case there is deposition of zinc during the cathodic impulses, as is evident under the microscope, but the saturation at the anode is thereby eliminated, and thus passage for the current of the anodic impulse is made possible. In 90% H_2SO_4 because of the slight solubility of $ZnSO_4$ at the high hydrogen ion concentration no appreciable Zn deposition takes place, and therefore we observe a rectifying effect here. Our view is further supported by the fact that silver in chloride solution has no rectifier effect (9), whereas magnesium in magnesium sulfate does show such an effect, if only a slight one (10). In each case

of course it depends on the structure of the layer, and this is determined not only by the composition of the electrolyte but also by the method of its formation.

Any discussion of this paper will appear in a Discussion Section to be published in the December 1963 JOURNAL.

REFERENCES

1. K. Schwabe, Habilitationsschrift, TH Dresden, 1933; K. Schwabe and F. Lohmann, *Z. physik. Chem.*, **215**, 158 (1960).
2. *Electrochim. Acta*, **7**, 1 (1962).
3. B. K. Schwabe, *ibid.*, **3**, 47 (1960).
4. K. Schwabe, *Ber. Verhandl. sächs. Akad. Wiss. Leipzig*, **101**, 1 (1954).
5. W. J. Müller and K. Konopicky, *Z. physik. Chem.*, **A141**, 343 (1929).
6. A. Günther-Schulze, *ibid.*, **A143**, 62 (1929).
7. V. K. Schwabe, *Naturwiss.* **49**, 56 (1962). Einzelheiten der Versuchs- und Messtechnik werden in Kurze an anderer Stelle mitgeteilt.
8. *Z. physik. Chem.*, **48**, 211 (1904); *Z. Elektrochem.*, **10**, 877 (1904).
9. A. Günther-Schulze, *Ann. Physik*, **26**, 373 (1908).
10. A. Günther-Schulze, *ibid.*, **24**, 43 (1907).

The Anodic Oxidation of Iron in a Neutral Solution

II. Effect of Ferrous Ion and *p*H on the Behavior of Passive Iron

Masaichi Nagayama[1] **and Morris Cohen**

*Division of Applied Chemistry, National Research Council, Ottawa, Canada**

ABSTRACT

The anodic polarization curve, the static passive potential, and the behavior of the decay of the polarized passive potential of iron were examined in neutral boric acid/borate solutions with and without Fe^{++} ion addition. It was found that the passivation potential is a function of the $[Fe^{++}]$ and *p*H and corresponds to the equilibrium potential of the reaction of γ-$Fe_2O_3 + 6H^+ + 2e \leftrightharpoons 2Fe^{++} + 3H_2O$. The polarized passive potential in the steady state is related to a pseudoequilibrium potential that corresponds to a higher defect concentration in the oxide surface and to a lower $[Fe^{++}]$ at the oxide/solution interface. The potential gradient across the film appears to be very small. The decay of the polarized passive potential on open circuit is explained as due mainly to the change in the defect-concentration and consequently of the film composition at the oxide/solution interface either by the outward migration of iron through the film or by the reaction with Fe^{++} ion in solution when the latter had been added or supplied by a small amount of self-corrosion.

It was shown in the previous paper (1) that anodically passivated iron in a boric acid/borate buffer solution at a *p*H of 8.41 is covered with an oxide film (10-30Å) consisting of an inner Fe_3O_4 and an outer γ-Fe_2O_3 layer of which the outermost portion is a cation-deficient structure such as $Fe_x^{6+} \cdot Fe_{2-2x}^{3+} \cdot \square_x \cdot O_3$. The thickness of the layers and the concentration of defects were estimated as functions of the applied passive potential. The slope of the film-thickness/potential curve becomes smaller beyond the potential E_a^2 which is found between the passivation potential E_a^1 and the oxygen evolution potential E_a^3, whereas the concentration of defects begins to increase appreciably above this potential. It was also found in the previous investigation that the γ-Fe_2O_3 layer begins to be produced or to be reduced above and below the passivation potential E_a^1. The reduction occurs as the dissolution of Fe^{++} ion in the solution with almost 100% current efficiency.

The main purpose of this investigation is to interpret the significance of the characteristic potentials E_a^1 (the passivation potential) and E_a^2, and the role of defects in the mechanism of passivity.

[1] Postdoctorate Fellow; present address: Faculty of Engineering, Hokkaido University, Sapporo, Japan.
* N.R.C. No. 7436.

Experimental

Materials and their preparations were the same as those used in the previous investigation (1). Specimens were electropolished Ferrovac iron sheets. Electrolytes were a mixture of 0.15*N* boric acid and 0.15*N* sodium borate solution, saturated with purified nitrogen. Electrolytes of various *p*H's between 5 and 9 were prepared by changing the ratio of these solutions; the buffering capacity was fairly small below *p*H 7. An equivolume mixture at a *p*H of 8.41 was mainly used as a standard solution, and it was kept in the first storage vessel. The second storage vessel was filled with the standard solution or with a solution of different *p*H. Fe^{++} ion could be added by the anodic dissolution of an iron wire inserted into the vessel.

The electrolytic cell and the electrical circuits were the same as employed in the previous investigation. Anodic passivation of the specimen was always done in the standard solution by the potentiostatic method, by starting with a fresh iron surface from which all previous oxide film had been removed by cathodic treatment. In the experiments in which the effect of Fe^{++} ion and *p*H were examined, the solution was changed from the standard

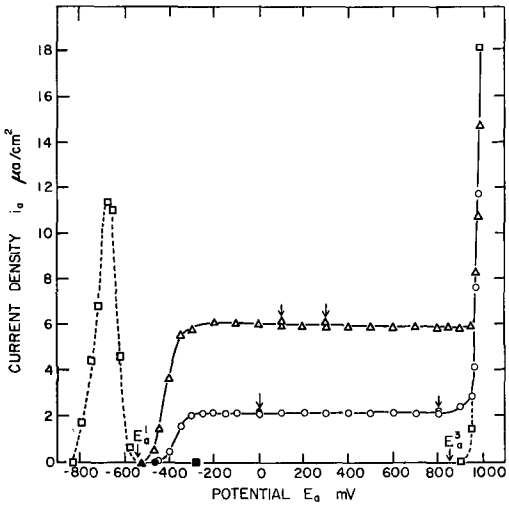

Fig. 1. Effect of ferrous ion concentration on the anodic polarization curve of passive iron; pH = 8.41. -△-, Fe^{++} = 5.81 x 10^{-4} mole/l; -○-, Fe^{++} = 2.06 x 10^{-4} mole/l; - - □ - -, no ferrous ion addition. Fe^{++} in the passive potential region is of the order of 10^{-7} mole/l; ▲,●,■, static passive potentials for above solutions, ↓ current was checked after renewal of the solution.

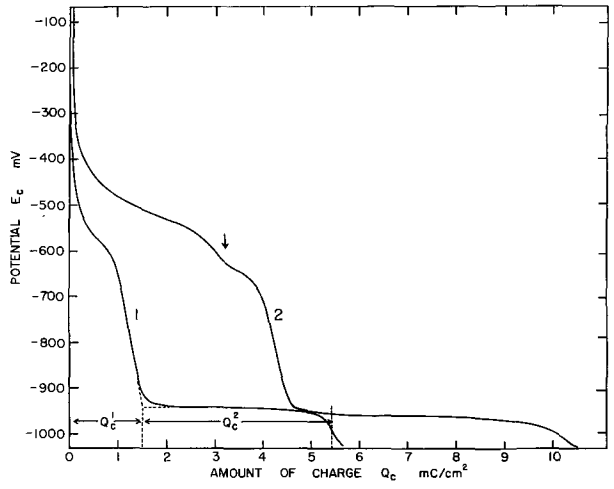

Fig. 2. Comparison of the cathodic reduction curves obtained for thin and thick passive films; standard solution, c.d. = μa/cm²; Expt. 1, cathodically pretreated iron was passivated at +850 mv for 1 hr in the standard solution. The amount of charge passed during anodic polarization is about Q_a = 6.80 mc/cm², Q_c^1 = 1.54 mc/cm², Q_c^2 = 3.92 mc/cm². Expt. 2, After repetition of Expt. 1, solution was changed for one containing about 1.8 x 10^{-4} mole/l Fe^{++} ion, and passivation was continued for half an hour. The amount of charge accumulated on the surface after the change of solution was Q_a = 3.82 mc/cm². [Q_c^1 = 4.55 mc/cm², Q_c^2 = 5.64 mc/cm²] Inflection of Curve 2 indicated by arrow is explained by the noncontinuous change between the primary and the secondary oxide films which are obtained before and after the change of solution.

solution to the solution of different pH and Fe^{++} ion content, without interrupting the anodic polarization. The cathodic reduction of the passive specimen was conducted only in the fresh standard solution by a galvanostatic method with a constant c.d. of 10 μa/cm². The amount of ferrous ion in solution was analyzed by the o-phenantroline method.

Experimental Results

Effect of ferrous ion on the polarization curve.— The steady-state potential/current relationship for the passive iron was measured in solutions (pH 8.41) to which Fe^{++} ion had been added at various concentrations. The result is shown in Fig. 1, together with the polarization curve obtained in a solution without Fe^{++} ion addition (the standard solution). The limiting current is observed to increase with the ferrous ion concentration in the passive potential region above —200 mv. The current gradually drops to zero as the potential is lowered to the region of the passivation potential, E_a^1. The results were the same when measured in the direction of either increasing or decreasing potential. It was determined by chemical analysis of the solution that the current observed roughly corresponds to the rate of oxidation of Fe^{++} ion to ferric oxide at the oxide/solution interface (Table I). Because of the gradual decrease of Fe^{++} ion concentration with time, the solution had to be changed twice during the measurement of the polarization curve. The value of the limiting current was finally checked by the renewal of the solution at the end of the measurement as is indicated by arrows in Fig. 1. Thus, if the anodic polarization is continued for a long period of time in the presence of Fe^{++} ion in solution, an oxide film of any thickness can be obtained in contrast to the maximum film thickness of about 30Å obtained in a solution originally free from Fe^{++} ion (cf. Fig. 9). The behavior on cathodic reduction of the thicker film, however, was quite similar to that of the thin passive film, even though the number of coulombs required to reduce the thick film is of course much greater (Fig. 2). This indicates that the oxide formed by the oxidation of Fe^{++} ion in solution is essentially the same as that formed by anodic oxidation of iron.

A straight line passing through the origin is obtained when the limiting current measured at +600 mv is plotted against the Fe^{++} ion concentration as is seen in Fig. 3. The pH of the solution seems to have no effect on the results. The limiting current

Table I. Comparison between the amount of charge passed and the amount of oxidation of Fe^{++} ion during anodic polarization in solutions with Fe^{++} ion addition (pH = 8.41)

No.	Pre-polarization E_a', mv	t_a', min	Polarization E_a, mv	t_a, min	Amount of charge passed Q_a^{obs}, mc	Initial amount of Fe^{++} ion W_1, μg	Final amount of Fe^{++} ion W_2, μg	$W_1 - W_2$, μg	*Calculated amount of charge Q_a^{cal}, mc	Q_a^{cal}/Q_a^{obs}
1	+590	40	+590	60	46.5	223.5	196.1	27.4	47.4	1.02
2	+400	80	+400	48	37.7	246.2	225.1	20.7	35.8	0.95
3	+600	120	—200	78	42.5	153.7	127.9	25.8	44.6	1.05
4	After Expt. No. 3		+100	60	15.6	76.2	65.6	10.6	18.3	1.17

* Calculated by assuming the reaction $Fe^{++} \rightarrow Fe^{+++} + e$.

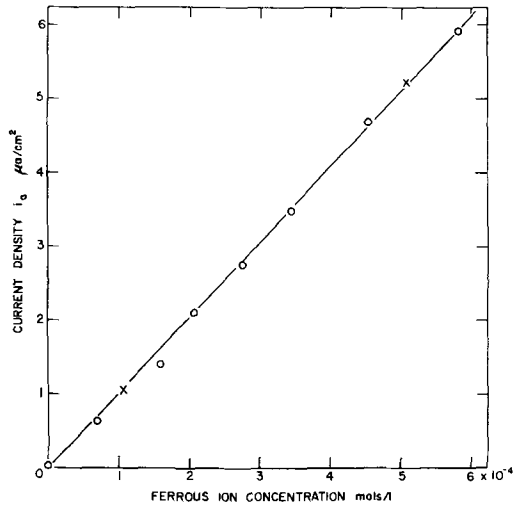

Fig. 3. Relation between ferrous ion concentration and the anodic current. $D_{Fe^{++}} \doteq 5.3 \times 10^{-6}$ cm^2 sec^{-1}. ○, + 600 mv, pH, 8.41; X, + 850 mv, pH, 7.31.

was markedly increased by stirring the solution. It is clear from these experimental facts that, in the potential region where the limiting current is observed, the reaction is controlled entirely by the rate of diffusion of ferrous ion from the bulk of solution to the oxide/solution interface where the ferrous ion concentration is considered to be very small. The diffusion coefficient of ferrous ion was estimated as $D = 5 \times 10^{-6}$ cm^2 sec^{-1} by using the simple diffusion equation

$$i_a = n\mathbf{F}DC/d \quad (n = 1)$$

where i_a (amp/cm^2) is the limiting current at a ferrous ion concentration of C (mole/cm^3), $\mathbf{F}$ is the Faraday, and the effective thickness of the diffusion layer d in a stagnant solution is assumed to be 5×10^{-2} cm. The value obtained seems to be reasonable.

Effect of [Fe^{++}] *and* pH *on the static passive potential.*—When the circuit is interrupted after applying anodic polarization the potential decays until a static passive potential is reached. The final steady potential, which is in the region of the passivation potential, is often called the Flade potential (2). The effect of ferrous ion concentration and pH of the solution on the static passive potential was examined in a series of experiments. The results obtained are summarized in Table II.[2]

The relation between the potential and the logarithm of the ferrous ion concentration at constant pH is a straight line having a slope of 60 mv per logarithmic unit (Fig. 4). A linear relationship is also found between the potential and pH at a constant ferrous ion concentration, the slope being 163 mv per pH unit (Fig. 5). It should be emphasized that the value of the measured static potential is not dependent on the previous history of the specimen, such as the applied anodic potential, the time of polarization or the film thickness, but is determined only by the existing Fe^{++} ion concentration

[2] During the experiment it was noticed that the static potential was normally maintained steadily for an indefinite time, although at high concentration of ferrous ion ($C = 3 \times 10^{-4}$ mole/l) the value sometimes fell off again after showing a plateau. In the latter case plateaus were not perfectly level but had a slight downwards slope; in such cases the potential values shown in Fig. 4 were taken just before the sharp drop at the end of the plateau.

Table II. Effect of pH and [Fe^{++}] on the static potential of passive iron (boric acid-sodium borate buffer solutions)

E_a, mv	t_a, hr	pH	[Fe++], mole/l	E_{stat}, mv
	2.5	9.21	3.63×10^{-6}	—444
	2.6	9.21	9.88×10^{-6}	—472
+850	11.0	9.21	4.23×10^{-5}	—513
	3.0	9.21	5.37×10^{-5}	—512
	5.0	9.21	1.04×10^{-4}	—538
	3.0	8.41	4.7×10^{-7}	—285
	—	8.41	2.15×10^{-6}	—328
	3.0	8.41	7.25×10^{-6}	—347
	3.0	8.41	9.52×10^{-6}	—352
	4.5	8.41	1.02×10^{-5}	—360
+850	2.5	8.41	1.85×10^{-5}	—370
	4.3	8.41	4.95×10^{-5}	—404
	3.0	8.41	5.80×10^{-5}	—410
	2.5	8.41	7.86×10^{-5}	—410
	5.0	8.41	1.66×10^{-4}	—430
	3.0	8.41	2.39×10^{-4}	—430
	2.7	8.41	5.75×10^{-4}	—460
	16.5	8.41	5.54×10^{-6}	—338
—100	2.0	8.41	1.93×10^{-5}	—381
	2.0	8.41	1.36×10^{-4}	—425
	16.0	8.41	2.72×10^{-4}	—432
	1.0	7.31	3.01×10^{-6}	—156
	1.0	7.31	7.85×10^{-6}	—189
+850	1.0	7.31	1.70×10^{-5}	—208
	3.0	7.31	9.78×10^{-5}	—255
	1.0	7.31	1.05×10^{-4}	—254
	3.0	7.33 (7.31)	5.09×10^{-4}	—295 (—293)†
	1.0	6.31	1.61×10^{-6}	+22
	3.0	6.31	4.90×10^{-6}	+1
	4.0	6.31	1.02×10^{-5}	—22
	5.5	6.34 (6.31)	3.21×10^{-5}	—62 (—57)†
+850	6.0	6.35 (6.31)	7.31×10^{-5}	—83 (—77)†
	12.5	6.38 (6.31)	1.09×10^{-4}	—102 (—91)†
	4.0	6.36 (6.31)	1.73×10^{-4}	—108 (—100)†
	5.5	6.44 (6.31)	3.62×10^{-4}	—144 (—123)†
	3.0	6.54 (6.31)	1.01×10^{-3}	—189 (—152)†
+850	3.4	5.78	9.14×10^{-5}	+34
+850	17.0	5.58	3.34×10^{-5}	+98
+850*	1.25	4.02	3.42×10^{-5}	+232
	6.0	4.02	9.39×10^{-4}	+151

* 0.15*N* sodium borate-acetic acid solutions.
† . . . Value of potential was corrected with the aid of the equation shown in section on Effect of [Fe++] and pH on the static passive potential.

and pH. The measured points indicated in Fig. 4 as circles are obtained for the specimen prepolarized at +850 mv for various periods of time ranging from 1 to 15 hr. The points indicated by triangles correspond to prepolarization at —100 mv, the times ranging from 2 to 16 hr. On the basis of this experiment, the static passive potential can be expressed as $E_{stat.} = 958 - 163$ pH $- 60 \log [Fe^{++}]$ mv (*vs.* N.H.E.).

Decay of the polarized potential and the effect of Fe^{++} *ion on it.*—The static potentials mentioned above were obtained after the decay of the polarized passive potential on open circuit. The characteristics of the decay of potential will now be described in this section. Curves 1, 2, and 3 in Fig. 6 were obtained in standard solution (pH 8.41) without the addition of ferrous ion. The specimens were prepolarized at +850 mv for various periods of

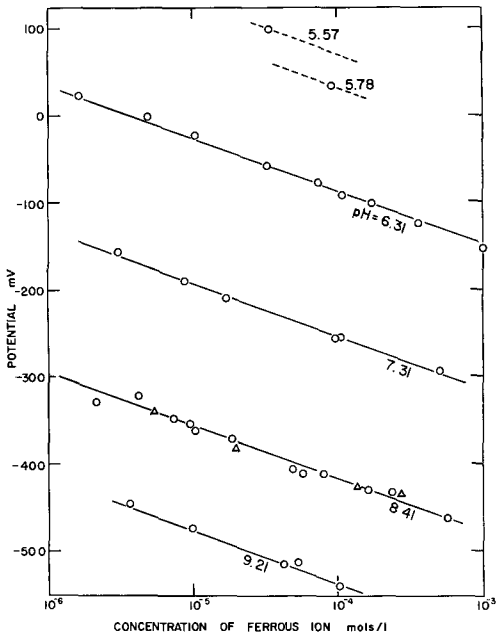

Fig. 4. Effect of ferrous ion concentration on the static potential of passive iron; ○, $E_a = +850$ mv; △, $E_a = -100$ mv; 0.15*N* boric acid-borate solutions.

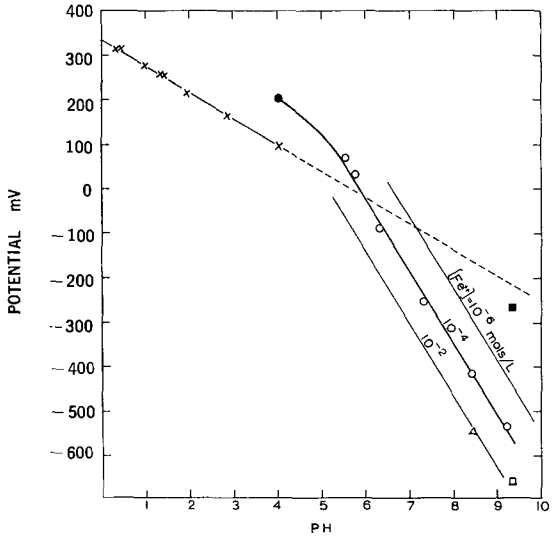

Fig. 5. Effect of pH on the static potential of passive iron. ○, 0.15*N* boric acid-borate solutions (pH, 5-9); ●, 0.15*N* acetic acid-borate solutions (pH, —4); X, results obtained by Franck for acid solutions; △, passivation potential E_a^1 appeared in the anodic polarization curve (standard solution at pH, 8.41); □, passivation potential E_a^1 and activation potential $E_a^{1'}$ which appeared in the anodic polarization curve and in the cathodic reduction curve, respectively, of Heusler, Weil, and Bonhoeffer for borate solution at a pH of 9.3.

time. It is seen that there is no sharp drop of potential on cutting the current and that the rate of decay is fairly slow and decreases with the time of prepolarization; the reproducibility of the curves becomes worse below about +300 mv. The amount of Fe^{++} ion dissolution during the decay was then followed by separate experiments. From the results indicated by the numbers on curve 2, it seems that Fe^{++} ion dissolution begins to occur below about the characteristic potential E_a^2 (0 mv) even though the amount detected was very small. No effect of

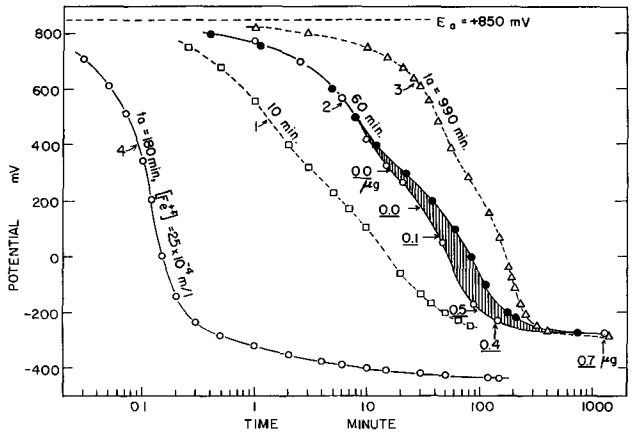

Fig. 6. Effect of time of anodic polarization and ferrous ion addition on the decay of the polarized potential. Numbers attached to curve 2 indicate the amount of Fe^{++} ion found in solution during the decay of potential.

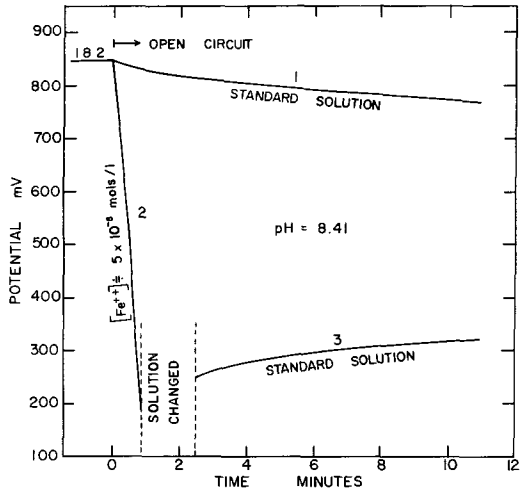

Fig. 7. Effect of the change of solution on the behavior of decay of potential. Expt. 1, the decay of potential was followed in the standard solution for a specimen prepolarized at +850 mv for 960 min in the same solution; Expt. 2, after Expt. 1, the specimen was polarized again at +850 mv for 60 min in the standard solution and the decay of potential was followed in another solution containing about 5 x 10^{-5} mole/1 ferrous ion; Expt. 3, after Expt. 2, cell and specimen were both quickly rinsed twice with standard solution and the change of potential with time was followed on open circuit in the standard solution.

stirring of the solution was observed in these experiments.

It was found that the addition of large amounts of Fe^{++} ion to the solution accelerated the decay quite remarkably. In this case the rate of decay was observed to increase sharply by stirring. Curve 4 in Fig. 6 was obtained for a Fe^{++} ion concentration of 2.5 × 10^{-4} mole/1 after 3-hr prepolarization in a solution without Fe^{++} ion addition. The final static potential obtained in this case is, of course, much lower compared to that shown in curves 1, 2, and 3, as would be expected from the much higher concentration of Fe^{++} ion in solution.

In the next experiment, after following the decay of potential for a short time in a solution containing a large amount of Fe^{++} ion, the cell and specimen were both quickly rinsed with the standard solution, and the change of potential with time was traced on open circuit in the standard solution (Fig.

7). As can be seen, a slow rise of potential was obtained instead of the continuation of the decay. The same sort of potential change was observed after interruption of a cathodic current which had been applied to the passive specimen for a short period of time.

Change of cathodic reduction curve during decay. —In order to obtain further knowledge of the mechanism of the decay of the polarization potential, two kinds of experiments were conducted in the standard solutions for specimens prepolarized at +850 mv for 1 hr: expt. 1, cathodic reduction curves were observed at different times during the decay without the addition of Fe^{++} ion to the solution; expt. 2, after draining the solution after passivation, dried specimens were exposed to a nitrogen atmosphere for different periods of time, and cathodic reduction curves were then measured.

The cathodic reduction curve obtained is always of a typical shape having three arrests or two waves as can be seen in Fig. 2. In general, the transition from the first to the second wave becomes sharper with the time of decay or of nitrogen exposure. The change in the number of coulombs Q_c^1 and Q_c^2 associated with the first and the second waves was followed in expt. 1 and 2; the results are shown in Tables III and IV, respectively. In the preceding investigation (1), the first and the second waves were shown to correspond to the reduction of the outer "γ-Fe_2O_3" layer to Fe^{++} ion in solution and to the reduction of the inner Fe_3O_4 layer to metallic iron, the current efficiency of these reactions being almost 100% and 40%, respectively. If it is assumed here that the over-all current efficiency of these reduction reactions does not change with the time of decay or of exposure, the change in the values of Q_c^1 and Q_c^2 would give a rough idea of the change of composition of the passive film with time.

Table III. Effect of the time of decay on the cathodic reduction curve

No.	Time of decay, min	Static potential after decay, mv	Q_c^1, mc/cm²	ΔQ_c^1, mc/cm²	Q_c^2, mc/cm²	ΔQ_c^2, mc/cm²
0	0	+850	1.540		3.92	
0′	0	+850	1.541	1.54	3.93	3.92
0″	0	+850	1.534			
1	18	+380	1.53	—0.07	3.91	—0.01
2	27	+330	1.51	—0.03	3.88	—0.04
3	58	+188	1.50	—0.04	4.01	+0.09
4	125	+20	1.48	—0.06	3.94	+0.02
5	289	—190	1.42	—0.12	4.16	+0.24
6	295	—233	1.40	—0.14	4.22	+0.30
7	1260	—270	1.36	—0.18	—	—
7′	1260	—	1.38	—0.18	4.32	+0.40

Table IV. Effect of the time of exposure to a nitrogen atmosphere on the cathodic reduction curve

No.	Time of exposure, min	Static potential after exposure, mv	Q_c^1, mc/cm²	ΔQ_c^1, mc/cm²	Q_c^2, mc/cm²	ΔQ_c^2, mc/cm²
0	0	+850	1.54	—	3.92	—
1	90	+250	1.48_5	-0.05_5	4.05	+0.13
2	960	+92	1.43	—0.11	4.25	+0.33
3	5280	—63	1.39	—0.15	4.83	+0.91

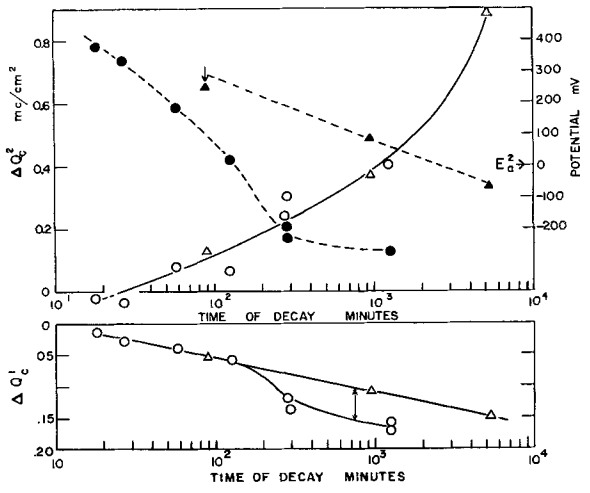

Fig. 8. Change in the amount of charge associated with the first and the second waves of the cathodic reduction curve during the decay of polarized potential. ○, Q_c^1 or Q_c^2 for Expt. 1; △, Q_c^1 or Q_c^2 for Expt. 2; ●,▲, potential of the specimen just before the cathodic reduction experiment; ↓, potential changing fairly rapidly.

As can be seen in the above tables, the results obtained in both experiments are quite similar; Q_c^1 decreasing and Q_c^2 increasing with time. This could be interpreted simply as a decrease in the amount of defects and γ-Fe_2O_3 and an increase of the amount of Fe_3O_4 with time. However, as can be seen in Fig. 8, $|\Delta Q_c^1|$ increases rapidly in the first type of experiment after about 100 min when the potential has fallen to the region of the characteristic potential E_a^2 of about 0 mv where the commencement of Fe^{++} ion dissolution is to be expected. The change of Q_c^2 with time on the other hand appears to be unaffected by the presence of the solution.

Discussion

Previous Theories on the Passivation Potential

The anodic passivation of iron is characterized by the existence of a passivation potential above which passivity becomes stable, so that, in order to discuss the mechanism of passivity, it is quite essential to understand the significance of this potential. It has been observed for iron in an acidic solution that the passivation potential observed in a potentiostatic polarization experiment has almost the same value as the Flade potential-arrest which is observed just before the spontaneous activation of the passive specimen occurs (3, 4). Franck (5) measured the effect of pH on the Flade potential by using several kinds of buffer solutions at values of pH from 0.3 to 4 and obtained the empirical equation

$$E = 580 - 59\,\mathrm{pH}\ \mathrm{mv}\ (vs.\ \mathrm{N.H.E.}) \qquad [1]$$

Most previous theories of passivation more or less attempt to explain Eq. [1]. However, attempts to interpret the Flade potential as corresponding to the equilibrium potential of formation of any known oxide from metallic iron have been unsuccessful because the theoretical values are always far lower (by about 660 mv) than the experimental values. In order to avoid this difficulty, Beinert and Bonhoeffer (6) first assumed an oxygen-rich iron oxide of unknown structure as the passive film. Pryor (7)

recently proposed a somewhat continuous change of defect structure with thickness in a single phase γ-Fe_2O_3 film, the inner and the outer part of the film being a metal excess and an oxygen excess type of oxide, respectively. He suggested that the structure of the outermost part of film controls the behavior of the Flade potential. Göhr and Lange (8, 9) and later Vetter (10) pictured the system as being $Fe/Fe_3O_4/\gamma$-Fe_2O_3/H_2O and explained the passivation potential as the equilibrium potential of the reaction

$$3\,\gamma\text{-}Fe_2O_3 + 2H^+ + 2e \rightleftharpoons 2Fe_3O_4 + H_2O \qquad [2]$$

They considered that the chemical potential of iron in the magnetite layer decreases with the distance outward from the metal surface in accordance with the inner potential difference across the film when the electrode $Fe/Fe_3O_4/H_2O$ is anodically polarized; at the distance where the potential lowering comes to a value ($\Delta\phi$ = 660 mv) corresponding to the change in the free energy of the reaction[3] $3Fe_3O_4 \rightarrow 4\ '\gamma\text{-}Fe_2O_3' + Fe$, the formation of γ-Fe_2O_3 occurs to give a duplex layer and resulting passivity. According to Vetter's concept, there is no further change of composition with thickness in the outer γ-Fe_2O_3 layer and growth of film occurs simply forced by the field strength set up across the layer. He also considered that, after the interruption of the circuit, once the outer γ-Fe_2O_3 was consumed by slow dissolution in an acid solution it was followed by an extremely rapid dissolution of the magnetite layer and resulting activation. Heusler, Weil, and Bonhoeffer (11, 12) observed that in neutral and alkaline solutions the values of passivation potentials were much more negative than that expected from Eq. [1]. They explained that the primary Fe_3O_4 film is sufficiently insoluble to produce "pseudopassivity," and that "real passivation" occurs when the potential is raised to the equilibrium potential of the formation of γ-Fe_2O_3 from Fe_3O_4. Cartledge (13) interpreted the passivation potential in a similar way as Lange and Vetter by postulating an electrode system of $Fe|'FeO'|Fe_2O_3|H_2O$.[4] In contrast to these workers Uhlig and King (14) have considered that the Flade potential is an equilibrium potential for the reduction of chemisorbed oxygen atoms and molecules on the surface of iron.

The data reported here show that the passivation potential and the static potential observed after the decay of the polarized anodic potential are essentially the same and is dependent on both $[Fe^{++}]$ and pH. Because the above considerations are inadequate for the explanation of these results a new mechanism is proposed for anodic passivity in neutral solutions.

Effect of Fe^{++} Ion on the Formation of the Passive Film

In the previous paper (1) it was observed that there was a region in the anodic passivation range (−550 mv to −200 mv) where Fe^{++} was found in solution after 1 hr of polarization. This is shown in Fig. 9. When ferrous ion is added to a solution in which iron with the passive film is being anodically polarized (Fig. 1) it is converted to Fe_2O_3 at a rate dependent on the concentration of Fe^{++} and the applied potential. At sufficiently high applied potentials the rate of oxidation to Fe_2O_3 is simply diffusion controlled (Fig. 3). In the absence of an applied current and at constant pH the static potential is dependent on $[Fe^{++}]$. It was also observed that the decay rate of the potential of films formed at higher oxidation potentials was increased by the addition of Fe^{++} ion to the solution.

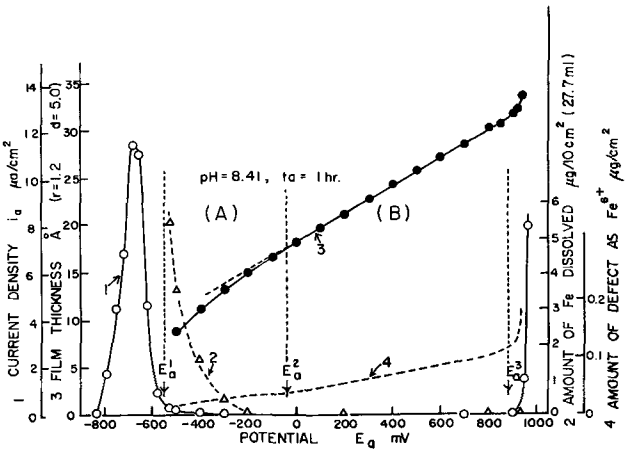

Fig. 9. Anodic polarization curve and effect of potential on the amount of Fe^{++} ion dissolution, film thickness, and on the amount of defects.

In the previous paper a characteristic potential (E_a^2) was observed at which there was an increase in the rate of formation of vacancies in the outer layer of oxide with potential (Fig. 9). On the basis of the above observation this potential would appear to correspond to a range in which the $[Fe^{++}]$ is so low that it cannot affect the rate of formation of vacancies by reaction with the outer layer of oxide. Thus, although E_a^2 is not a specific potential relating to a reaction, it is convenient to discuss the range of potentials in which passivity is obtained in two regions, "Region A" where Fe^{++} in solution is observed, and "Region B" where the $[Fe^{++}]$ is too low for analysis.

Behavior of Passive Iron in Region A

It is to be expected from the above that the defect concentration in the extreme surface of the oxide found previously (1) is maintained at almost zero in the potential region A because of the reaction of defects with Fe^{++} ion in the solution. If the defect is expressed as Fe^{6+} ion, the reaction will be

$$Fe^{6+} + 3Fe^{++} \rightarrow 4Fe^{+++}$$

The rate of the reaction is assumed to be very high due to the relatively high concentration of Fe^{++} ion in this potential region; the rate must be a function of the concentration of the surface defects and of the $[Fe^{++}]$ in solution.

The possible change in the final composition of the oxide film with distance from the metal is shown schematically as curve A in Fig. 10; the film will consist of γ-Fe_2O_3, with a more or less defect

[3] The value of the chemical potential of "oxide" is chosen so as to explain the Flade potential which was measured by Franck in acidic solutions.

[4] See footnote 3.

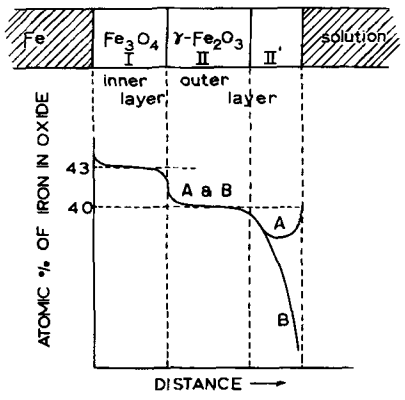

Fig. 10. Possible change of composition of the passive film with thickness: curve A, potential region A; curve B, potential region B.

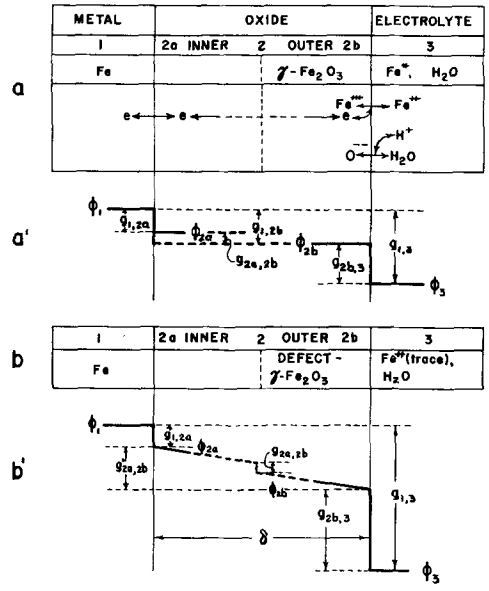

Fig. 11. Phase arrangement of the electrode system and the distribution of inner potential across the phases: a, a', potential region A; b, b', potential region B.

structure, and Fe_3O_4 layers, the latter being adjacent to the metal. In the initial period of passivation for a cathodically pretreated specimen the passive oxide film, whose change of composition with thickness is shown as curve B, is formed by the high potential gradient initially applied across the film. As Fe^{++} ions are accumulated in the solution with time, the composition of the extreme surface of the oxide changes toward that of stoichiometric γ-Fe_2O_3. However, since the rate of migration of defects from the interior part of the film is quite small, the defects in the interior cannot be eliminated within the ordinary time of the experiment. Hence even in region A after 1-hr polarization a small number of defects is observed by analysis (Fig. 9).

If we assume here that the interior part of the oxide film, whatever composition it has, behaves merely as an electronic conductor, the passive iron would behave basically as an electrode system of $Fe|\gamma\text{-}Fe_2O_3|Fe^{++}, H_2O$, irrespective of the existence of an inner oxide layer having a different composition.

Derivation of Potential in Region A

Figure 11(a) shows the schematic phase arrangement of the electrode system and the possible partial reactions at interfaces. In a pseudoequilibrium condition[5] of this electrode, the inner potential difference (g) across each interface can be expressed in terms of the chemical potential (μ) of the substances which participate in each partial reaction. Between the metal (phase 1) and the outer oxide (phase 2b), electron transfer reactions are

$$ {}_1e \leftrightharpoons {}_{2a}e \leftrightharpoons {}_2e \leftrightharpoons \ldots\ldots\ldots\ldots \leftrightharpoons {}_{2b}e $$

so that the inner potential difference between the metal and the outer oxide can be expressed as

$$ g_{1,2b} = \phi_1 - \phi_{2a} + \phi_{2a} - \phi_2 + \phi_2 - \ldots\ldots\ldots - \phi_{2b} $$
$$ = \phi_1 - \phi_{2b} = -({}_1\mu_e - {}_{2b}\mu_e)/-F \qquad [4] $$

where ϕ is the inner potential of a phase.

Thus, as far as the expression of $g_{1,2b}$ is concerned, the presence of the inner oxide layers having different compositions can be neglected.

At the oxide/solution interface

$$ \left.\begin{aligned} {}_{2b}Fe^{+++} + {}_{2b}e &\leftrightharpoons {}_3Fe^{++} \\ {}_{2b}O^{--} + 2{}_3H^+ &\leftrightharpoons {}_3H_2O \end{aligned}\right\} \text{double equilibrium reaction} $$

$$ \therefore g_{2b,3} = \phi_{2b} - \phi_3 = -({}_{2b}\mu_{Fe^{+++}} + {}_{2b}\mu_e - {}_3\mu_{Fe^{++}})/2F = -({}_3\mu_{H_2O} - {}_{2b}\mu_{O^{--}} - 2{}_3\mu_{H^+})/2F \qquad [5] $$

As can be seen in Eq. [5], the value of $g_{2b,3}$ is determined only by the chemical potential or the activity of H^+ ion in solution if the composition of the surface oxide is constant, since in this condition ${}_3\mu_{H_2O}$, ${}_{2b}\mu_{Fe^{+++}}$ and ${}_{2b}\mu_{O^{--}}$ are expected to be constant. The chemical potential of the electron, ${}_{2b}\mu_e$, is considered to be a function of the chemical potential or the activity of Fe^{++} ion in solution when the composition of the surface oxide and the activity of H^+ ion are constant, so that, if the activity of Fe^{++} ion is changed, $g_{1,2b}$ will be changed according to Eq. [4] because the value of ${}_1\mu_e$ is expected to be constant.

The electrode potential is the sum of the inner potential difference across the interfaces so that

$$ g_{1,3} = \phi_1 - \phi_3 = g_{1,2b} + g_{2b,3} = ({}_{2b}\mu_{\gamma\text{-}Fe_2O_3} + 6{}_3\mu_{H^+} + 2{}_1\mu_e - 2{}_3\mu_{Fe^{++}} - 3{}_3\mu_{H_2O})/2F $$

This corresponds to the equilibrium potential of the net reaction of

$$ \gamma\text{-}Fe_2O_3 + 6H^+ + 2e \leftrightharpoons 2Fe^{++} + 3H_2O \qquad [6] $$

If $g_{1,3}$ is measured against the normal hydrogen electrode as E_h, using the relation $\mu = \mu^\circ + RT \ln a$,

[5] Strictly speaking one cannot use the term equilibrium in a system of this type. Obviously in the thermodynamic sense, iron is essentially unstable when anodically polarized in a water solution due to such reactions as

$$ Fe \rightarrow Fe^{++} + 2e $$
$$ Fe + Fe_2O_3 \rightarrow Fe_3O_4 $$

However, in that it is observed that these reactions take place only extremely slowly in this system, one can use the term equilibrium while meaning "pseudoequilibrium."

the dependence of E_h on $[Fe^{++}]$ and pH can be expressed as

$$E_h = \{(\mu^\circ_{\gamma-Fe_2O_3} + 6\mu^\circ_{H+} - 2\mu^\circ_{Fe++} - 3\mu^\circ_{H_2O})/2F\} + (3RT/F) \ln a_{H+} - (RT/F) \ln a_{Fe++} = E_h^\circ - 177\,pH - 59 \log a_{Fe++}\ mv\ (25°C) \quad [7]$$

The equilibrium potential of the electrode is a function of only $[Fe^{++}]$ and pH, since the chemical potential of the outer γ-Fe_2O_3 is expected to be constant as far as it has constant stoichiometric composition. Thus, the change of the inner potential across the phases is shown schematically in Fig. 11a. Equation [7] is supported by the data shown in Fig. 4 and 5.

If passive iron in pseudoequilibrium at a constant pH is anodically polarized by ΔE in this potential region A, a flow of electrons across the film toward the metal/oxide interface occurs in accordance with the effective potential gradient $\Delta E/\delta$ [6] (δ: film thickness) set up in the film, being accompanied by the oxidation of Fe^{++} ion to γ-Fe_2O_3 at the oxide/solution interface. The consumption of Fe^{++} ion in solution is continued slowly until the change of $g_{1,2b}$ compensates the polarization ΔE. In other words, at equilibrium obtained after an infinite passage of time the applied polarization will be off-set by a change of the potential difference between the outer oxide and metal $g_{1,2b}$ (the concentration polarization of Fe^{++} ion), and there will be no gradients of potential in the body of the oxide, such gradients existing only during electron flow in the approach to equilibrium. During the nonsteady state of polarization, growth of the film due to the migration of iron ions outward from the metal is also possible under the influence of the potential gradient that exists in the film. It should be emphasized here that, in ordinary times of experiment, such a pseudoequilibrium state is not attained, even though the changeable potential difference ΔE (effective potential gradient $\Delta E/\delta$) across the film is very small compared to the total potential difference $g_{1,3}$.

Significance of the Passivation Potential

The effect of $[Fe^{++}]$ and pH on the static passive potential (Flade potential), which was described above, is in fairly good agreement with Eq. [7]. Accordingly the passivation potential observed in neutral borate solutions can be interpreted as corresponding to the equilibrium potential for the reaction between γ-Fe_2O_3 and Fe^{++} ion in solution. Thus, in region A, it seems quite likely that the passive film obtained in this experiment behaves simply as an $Fe|\gamma\text{-}Fe_2O_3|Fe^{++}, H_2O$ electrode in the presence of Fe^{++} ion in solution, even though the composition of the interior part of the film is different from the nearly stoichiometric γ-Fe_2O_3 that exists at the surface of oxide. This behavior is expected for the passive film which has been shown to be a duplex type of oxide electrode which, by ignoring complications due to the variation of defect concentration in the interior (cf. Fig. 9), can be simply expressed as

$$Fe|Fe_3O_4|\gamma\text{-}Fe_2O_3|Fe^{++}, H_2O$$
$$(1)\quad (2a)\quad (2b)\quad (3)$$

To get agreement in behavior it is necessary to assume that the oxide is a good electronic conductor and that the exchange rates of the partial reactions at the oxide/solution interface ($_{2b}Fe^{+++} + {}_{2b}e \leftrightharpoons {}_3Fe^{++}$ and $_{2b}O^{--} + 2_3H^+ \leftrightharpoons {}_3H_2O$) are much greater than that of the partial reaction at the oxide/oxide interface ($_{2a}Fe^{8/3+} \leftrightharpoons {}_{2b}Fe^{+++} + 1/3\ {}_2e$). The exchange current of the latter reaction which is accompanied by the movement and the rearrangement of iron ions and oxygen ions in the oxide phase must be extremely small. It was shown previously in the cathodic reduction experiment (1) that the reduction of γ-Fe_2O_3 to Fe^{++} ion in solution begins to occur with almost 100% current efficiency when the potential is lowered to the region of passivation potential E_a^1. It is seen, on the other hand, in the section on Effect of ferrous ion on the polarization curve, that the change of potential above E_a^1 causes the reaction from Fe^{++} to Fe_2O_3 to occur, again with almost 100% current efficiency. These experimental facts give clear evidence of the validity of the assumption that the oxide is a good electronic conductor and that the potential-determining reaction is the reaction at the oxide-solution interface.

Heusler, Weil, and Bonhoeffer (11) compared, in their measurements conducted in a borate solution (pH = 9.3), the value of the passivation potential E_a^1 obtained when active iron is anodically polarized by a stepwise potentiostatic method and that of the potential $E_a^{1'}$, at which a specimen completely passivated at relatively high potential begins to be reduced cathodically to the active state. As is indicated in Fig. 5 for purpose of comparison with the result of our static potential (Flade potential) measurements their potential E_a^1 is in the same region as ours, but $E_a^{1'}$ is much more positive (by about 500 mv) than E_a^1. Their explanation was that E_a^1 and $E_a^{1'}$ correspond to the potentials of the formation of Fe_3O_4 and Fe_2O_3 which produce "pseudo-" and "real-passivity," respectively; the pseudopassivity is expected only in neutral and alkaline solutions in which the rate of dissolution of Fe_3O_4 is sufficiently small to produce passivity (cf. section on Previous Theories on the Passivation Potential). However, their explanation does not fit our previous experimental result (1) which shows that the formation of a substantial amount of γ-Fe_2O_3 begins to occur at the passivation potential corresponding to their potential E_a^1, where they postulate the presence only of Fe_3O_4. The above disagreement between E_a^1 and $E_a^{1'}$ should be interpreted in terms of Fe^{++} ion concentration which is in equilibrium with γ-Fe_2O_3, the passive oxide. In precise terms, the potential they measured as E_a^1 will correspond to a fairly high concentration of Fe^{++} ion because an initially active specimen is gradually passivated; the potential $E_a^{1'}$, on the other hand, is considered to correspond to a much lower concentration of Fe^{++} and consequently higher concentration of defects in the surface of oxide (cf. section on Deriva-

[6] ΔE does not include the inner potential difference originally existing between different oxide phases.

tion of Potential in Region A) which is observed if the specimen has been maintained at a sufficiently high potential for a sufficient period of time.

As can be seen in Fig. 5, the results of our static potential measurements obtained over a pH range of 5-9 at various Fe^{++} ion concentrations on extrapolation to the acidic region do not agree with those obtained by Franck (5) for specimens passivated in acidic solutions. The cause of the disagreement is not clear at the moment. However, the nature of the passive film and the mechanism of passivity for iron in strongly acidic solution may be quite different, by judging from the fact that the addition of Fe^{++} ion to the solution and stirring of the solution do not change the size of anodic current i_a in the passive potential region (15).[7] It may be that, in view of the high rate of autoreduction in acid solutions, the decay potential observed is a highly polarized mixed potential.

Behavior of Passive Iron in Region B

As has been described above, the concentration of Fe^{++} in the vicinity of the oxide/solution interface is considered to be extremely small when the potential of the passive iron is held in the higher potential region B. In this case, the change in the composition of film with thickness is expressed by curve B in Fig. 10 and the passive iron is assumed to behave essentially as an electrode system of $Fe|$defect γ-$Fe_2O_3|Fe^{++}$ (very dilute), H_2O, the phase arrangement being shown in Fig. 11b. The partial reactions occurring at the interfaces are considered to be essentially the same as those assumed for the electrode system in the potential region A (Fig. 11a'), except for the additional effect of the defects, which appear in the surface of the oxide in this potential region, on the reaction at the oxide/solution interface. At the pseudoequilibrium condition of this electrode, the total potential difference $g_{1,3}$ is much larger than that in region A because of the unusually low activity of Fe^{+++} ion (or the correspondingly high activity of O^{--} ion) in the oxide phase as well as the extremely low concentration of Fe^{++} ion in solution. The appearance of surface defects in potential region B provides a second form of concentration overpotential because the concentration of defects, as well as H^+ ions in solution, can also change the value of $g_{2b,3}$.

When the specimen is anodically polarized in the potential region B, a potential gradient is set up across the film and defects begin to be produced by the removal of electrons from Fe^{+++} ions at the oxide surface, accompanied by the transfer of the corresponding excess amount of O^{--} ion from the solution ($_3H_2O \rightarrow {}_2O^{--} + 2_2H^+$). Simultaneously, growth of the film and a decrease of Fe^{++} ion in the vicinity of the oxide surface take place. However, since there is a tendency for migration of defects from the surface to the interior part of the film, it will take a very long time to attain a steady concentration of defects at the oxide surface under constant applied potential. At the pseudoequilibrium condition, the distribution of defects across the film (cf. Fig. 10, curve B), the surface concentration of defects, and also the surface concentration of Fe^{++} ion remain unchanged with time, and the changes in the values of $g_{1,2b}$ and $g_{2b.3}$ almost completely compensate the applied polarization for the $Fe|\gamma$-$Fe_2O_3|Fe^{++}$, H_2O electrode. For the intermediate stage before equilibrium, the effective potential gradient across the film

$$\Delta E/\delta = (g'_{2a,2b} - g_{2a,2b})/\delta$$

is shown schematically in Fig. 11b'.

As can be expected from the above, the potential gradient across the film ΔE would be much greater if the defects were not produced under the same applied potential. Thus, the role of defects in the mechanism of passivity is simply to decrease the effective potential gradient across the film, which will be the driving force for film growth by the migration of cations through the oxide film. The decrease in slope of the film thickness-potential curve observed above the potential E_a^2, that was described in the section on the Effect of Fe^{++} on the Formation of the Passive Film, can thus be explained as being due to the beginning of an increase in surface defect concentration with potential.

Mechanism of the Decay of the Polarized Potential

The characteristics of the decay of the polarized potential on open circuit in solutions initially free from ferrous ion can be explained in terms of the change in the pseudoequilibrium potential of the Fe defect γ-$Fe_2O_3|Fe^{++}$, H_2O electrode due to changes in both the concentration of defects and of Fe^{++} ion. As can be seen in Fig. 6 there is no major change in potential immediately after stopping the current. This observation is consistent with the view that the polarized potential is very close to the equilibrium potential of the defect oxide. The relatively slow decay of the potential to the static potential characteristic of γ-Fe_2O_3 is due to reactions, probably diffusion controlled, between the substrate metal and the oxide. The over-all reactions are as follows

$$Fe + 4Fe_2O_3 \rightarrow Fe_3O_4 \qquad (a)$$

$$xFe + Fe_{2-x}O_3 \rightarrow Fe_2O_3 \qquad (b)$$

$$Fe + Fe_2O_3 + 3H_2O \rightarrow 3Fe^{++} + 6\,OH^- \qquad (c)$$

Reaction (c) is only possible when the specimen is in contact with the solution. These reactions can be divided into the partial reactions

$_1Fe \rightarrow {}_3Fe^{++} + 2e \rightarrow {}_2Fe^{+++} + 3e$
(anodic reaction)
$_2Fe^{6+} + 3e \rightarrow {}_2Fe^{+++}$, $_2Fe^{+++} + e \rightarrow {}_3Fe^{++}$
(cathodic process)

In the absence of solution iron diffuses from the metal into the oxide to give both reactions (a) and (b) as can be seen from Fig. 8. There is an increase in the amount of magnetite and a decrease in the amount of Fe_2O_3. This reaction should take place by diffusion of ferrous ion and electrons and, if this is the only diffusion process taking place, the composition of the surface of the oxide, and hence the immersion potential, should not be changed until

[7] This has been partially confirmed in our experiment for a borate-acetic acid solution at pH of 4. However, the effect of Fe^{++} ion on the static passive potential is observed even in this solution (cf. Table II).

practically the whole of the oxide is changed to Fe_3O_4. Electron diffraction examination of the anodic oxide (1) gave patterns and spot sizes very similar to those observed previously (16). These patterns were interpreted to mean that the particle size in this highly oriented film is only 30-50Å, and hence there are a large number of grain boundaries. Grain boundary diffusion is much faster than bulk diffusion. One might therefore expect pipes of Fe_3O_4 at the grain boundaries which would allow more rapid access of Fe^{++} and electrons to the oxide surface. These would combine to reduce the concentration of defects at the surface and hence the immersion potential long before the body of the oxide is converted by simple bulk diffusion. This gradual conversion of the oxide to Fe_3O_4 was also noted in a previous study (16).

In the presence of solution the process of conversion of the surface of the oxide to stoichiometric oxide and finally the reductive dissolution of the γ-Fe_2O_3 is accelerated by reaction (c). Iron ions can be supplied both by diffusion through the magnetite pores and by reductive dissolution of any stoichiometric γ-Fe_2O_3. In region B any iron ion which gets into the solution will be consumed by reaction with nonstoichiometric oxide on the surface with a subsequent decrease in potential. When the potential reaches region A at about 0 mv (E_a^2), some iron should appear in the solution, and the potential will gradually approach the static potential for γ-Fe_2O_3 characteristic for this pH and $[Fe^{++}]$. As can be seen in Fig. 8, although the composition of the outer layer is changed more rapidly in the solution than in nitrogen, the rate of growth of magnetite is essentially the same. This indicates that bulk diffusion in both cases is equal. A considerable time will elapse before the steady state is attained because of the slow migration of defects from the interior to the surface of the oxide film. At a constant pH, the static potential is determined only by the existing Fe^{++} ion concentration whereas the potential during the decay is a function of the concentration of both defects and Fe^{++} ions. During the decay of potential in this region slight thinning of the film due to autoreduction is to be expected in spite of the thickening due to the migration of iron through the film. As a matter of fact, the amount of corrosion, 0.5 μg Fe^{++}/10 cm^2, estimated[8] from the deviation of the Q_c^1/time curve for Expt. 1 from that for Expt. 2 (Fig. 8) is of the same order of magnitude as that obtained by an analysis of the solution which is indicated in Fig. 6. It should be pointed out here that Fe^{++} ion dissolution was detected only when the potential came down to about 0 mv (E_a^2) whereas no change in the solution was observed above this potential (Fig. 8).

The above conclusion is supported by the fact that a marked potential decay occurs very rapidly when the specimen is put in contact with a large number of Fe^{++} ions in solution (Fig. 6). The rise of potential observed after changing the solution containing Fe^{++} ion to the standard solution (Fig. 7') constitutes strong evidence for the migration of defects from the interior to the surface of the oxide during the potential decay.

[8] For the purpose of the calculation, the reactions were assumed to be $Fe \rightarrow Fe^{++} + 2e$; γ-$Fe_2O_3 + 6H^+ + 2e \rightarrow 2Fe^{++} + 3H_2O$.

General Mechanism for Film Growth and Breakdown

On the basis of the above data and discussion it is now possible to propose a general mechanism for the formation, stability, and breakdown of the anodically formed oxide films (passive films) in neutral solutions.

When an anodic potential is first applied to a film-free iron specimen the iron is oxidized to form both a film of magnetite and ferrous ion in solution. When the applied anodic potential is above the range where γ-Fe_2O_3 is stable, γ-Fe_2O_3 is formed on top of the magnetite, and any excess ferrous ion in the solution over the equilibrium value is also oxidized at the oxide-solution interface to form γ-Fe_2O_3. In the initial stages the film is thin so that there is a high potential gradient across the film and thickening occurs rapidly. However as the potential gradient decreases with thickening the rate of migration also decreases and the anodic current drops. The second factor leading to a decrease in the film growth rate is a change in the composition of the outer layer of oxide. As the equilibrium concentration of Fe^{++} in the solution drops to a very low number (around E_a^2) it becomes possible to form an oxide with cation defects at the surface because of the strong oxidizing conditions. The higher equilibrium potential associated with this defect oxide leads to a further decrease in the potential gradient across the film which is finally almost independent of applied potential because of the combination of thicker films and increased cation vacancies (accompanied by a higher "equilibrium potential") at the higher applied anodic potential.

Only those films formed close to the passivation potential (E_a^1) will give equilibrium behavior with regard to $[Fe^{++}]$ and pH. Films formed at higher potentials tend to change to the equilibrium type film on cessation of anodic polarization. This decay of the potential can occur naturally by diffusion or autoreduction through "pores" and can be accelerated by the addition of ferrous ion to the solution or slight cathodic treatment. In the long run all of the oxide may be removed by autoreduction and the reaction of iron to give ferrous ion in solution will predominate. This latter condition, of course, is the active state.

Any discussion of this paper will appear in a Discussion Section to be published in the December 1963 JOURNAL.

REFERENCES

1. M. Nagayama and M. Cohen, *This Journal*, **109**, 781 (1962).
2. F. Flade, *Z. physik. Chem.*, **76**, 513 (1911).
3. U. F. Franck, *Z. Elektrochem.*, **55**, 154 (1951).
4. U. F. Franck and K. G. Weil, *ibid.*, **56**, 814 (1952).
5. U. F. Franck, *Z. Naturforsch.*, **4a**, 378 (1949).
6. H. Beinert and K. F. Bonhoeffer, *Z. Elektrochem.*, **47**, 536 (1941).
7. M. J. Pryor, *This Journal*, **106**, 557 (1959).

8. H. Göhr and E. Lange, *Naturwiss.*, **43**, 12 (1956).
9. H. Göhr and E. Lange, *Z. Elektrochem.*, **61**, 1291 (1957).
10. K. J. Vetter, *ibid.*, **62**, 642 (1958).
11. Heusler, K. G. Weil, and K. F. Bonhoeffer, *Z. physik Chem., N.F.*, **15**, 149 (1958).
12. K. G. Weil and K. F. Bonhoeffer, *ibid.*, **4**, 175 (1955).
13. G. H. Cartledge, *J. Phys. Chem.*, **60**, 1571 (1956).
14. H. H. Uhlig and P. F. King, *This Journal*, **106**, 1 (1959)
15. K. J. Vetter, "Passivierende Film und Deckschichten," p. 87, Springer-Verlag, Berlin (1956).
16. P. B. Sewell, C. D. Stockbridge, and M. Cohen, *This Journal*, **108**, 933 (1961).

Valency Changes in the Surface Oxide Films on Metals

H. S. Isaacs and J. S. Llewelyn Leach

Metallurgy Department, Imperial College of Science and Technology, London, England

ABSTRACT

Two methods are described by which a square current pulse may be used to measure the surface capacity and resistance of metal electrodes immersed in an electrolyte. The methods have been applied to the study of electrodes of aluminum, tantalum, and zirconium, and to electrodes of titanium, niobium, vanadium, and uranium. The first group shows surface capacities which vary with the hydrogen content of the oxide but which are always less than those of the double layers. The second group shows surface capacities greatly in excess of those associated with double layers, and these have been interpreted in terms of reversible reactions occurring within the oxide layers.

It has been suggested that hydrogen, formed as a corrosion product, may influence the physical or chemical properties of the protective oxide, and the resulting change may give rise to enhanced corrosion (1, 2). A change in the valency of the metal ion has also been suggested as a cause of change in the corrosion rate. However, considerable difficulties are involved in directly examining the properties of these oxide films without altering their characteristics.

Of the indirect techniques available, a-c measurements are one of the most sensitive for determining the properties of metal electrodes in solutions, and the use of these methods has contributed substantially to the understanding of the properties of and processes occurring at electrode surfaces (3, 4). The results of such measurements can be described in terms of the surface capacity and resistance of the electrode. The values of the capacity of oxide layers on the valve metals are usually less than 15 $\mu F/cm^2$, and the behavior of these oxides at anodic potentials is similar to that of the dielectric in a parallel plate condenser, the electrodes of which, in the case of the oxide layers, are formed by the metal on the one side and the solution on the other. Little is known about these oxide-covered electrodes at cathodic potentials besides the fact that electronic current flows producing rectification (5, 6).

Previous measurements on uranium (1) which rapidly forms an oxide layer, have shown high capacities (*ca.* 300 $\mu F/cm^2$) in a restricted potential range. A similar observation has been made on iron by Hackerman (7). This would not be expected if the oxide behaved as a dielectric, and it was therefore decided to test a series of oxide-covered metals in order to investigate this phenomenon.

Experimental Methods

In principle the technique used examines the voltage response of an electrode on which a square current wave is imposed. This voltage change has been examined in two ways. In the first method the behavior of the electrode is compared with that of an analogue circuit consisting of a capacitor and a resistor in parallel. In the second method the voltage response is recorded as a function of time and analyzed mathematically.

The apparatus used in the first method was developed by Denholm (1). The voltage developed by the current wave (*ca.* 10 mv) is measured by comparing the voltage of the specimen with that of a silver wire reference electrode. This method overcame some of the difficulties involved in the use of more conventional impedance bridges which include, in the measured impedance, the impedance of the anode and the resistance of the solution. As virtually no current flows through the silver reference electrode the voltage response is independent of its impedance.

The a-c voltage of the test electrode was compared with the voltage response of an analogue circuit, consisting of a variable capacitor and resistor in parallel, to which was applied a square current wave in phase with that through the test electrode. An electronic integrator circuit eliminated the need for several decades of capacity and resistance in the analogue circuit. The two voltage responses, after amplification, were applied respectively to the X and Y plates of an oscilloscope, a correct balance being indicated by a straight line at 45°, Fig. 1a.

The use of square wave excitation enables series resistance to be examined separately, as a parallelogram, with one pair of sides at 45° and the other pair

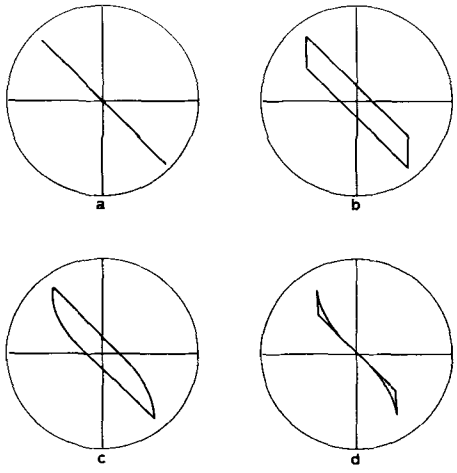

Fig. 1. Oscilloscope traces indicating (a) an ideal balance, (b) an ideal balance with uncompensated series resistance, (c) balance with distortion caused by a smaller time constant, (d) compensation for apparent series resistance in (c).

vertical, indicates the presence of series resistance associated with the test electrode (see Fig. 1b). Provision is made in the equipment to compensate for this series resistance which was shown to be associated, in most cases, with the resistance of the solution between the reference and test electrodes and was not measured. If, instead of a square wave, a sine wave of the same repeat frequency was used, values at balance were the same in both cases once all series resistance was compensated.

If the behavior of an electrode is more accurately represented by two analogue circuits with different time constants, one much smaller than the other, then the balance obtained which reflects the larger time constant is represented by a pseudoparallelogram with one pair of sides at 45°, but in this case the obtuse angles are rounded as in Fig. 1c. These curves are formed by the initial portion of the square wave (high frequencies) which, in the presence of two time constants, produces a more rapid voltage change in the circuit having the smaller value of time constant. When fully charged the voltage across this circuit is constant and the circuit behaves as a series resistance. The trace obtained on correcting for this as if for a series resistance is shown in Fig. 1d. As the difference between the two time constants decreases, the rounded portion occupies more of the trace and, under certain conditions, no balance can be obtained. As the time constants become more nearly the same the balance represents a mean value.

This equipment has limitations in that, although it is very sensitive to changes in parallel capacity, precise changes in parallel resistance are more difficult to determine. In addition, measurements at high repeat frequencies (>20 kc/sec) are complicated by the small signal and limitations of the amplifiers in the apparatus. The results appearing in Fig. 4-12 were obtained using this technique.

In the second method the voltage response of the test electrode to the square current wave is displayed directly on a measuring cathode-ray oscilloscope, as a function of time. The circuitry of the apparatus is shown in Fig. 2. The magnitude of the square current wave can be altered by varying the

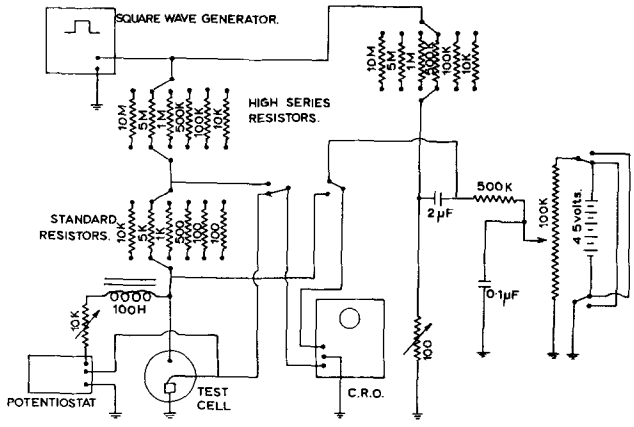

Fig. 2. Electrical circuit of apparatus for measuring the voltage response of a metal electrode to a square current wave.

values of the high series resistors or by changing the peak to peak value of the square wave voltage. The current is measured by displaying on the oscilloscope the potential developed across the standard resistors. This method also permits the shape of the current wave to be monitored. The rise time of the voltage wave (claimed to be 4×10^{-8} sec) could not be measured as the band width of the amplifiers of the oscilloscope is not sufficiently large. The minimum value of the band width which occurs at maximum gain (1 mv/cm) is of the order 0.5 Mc/sec. The apparatus thus enabled a voltage response at times greater than 2.10^{-6} sec to be observed. Compensation of the series resistance can be made and the d-c potential of the specimen can be measured in a manner similar to that adopted in the other equipment, *i.e.*, by use of a differential amplifier on the oscilloscope. As the potential of the silver electrode tended to vary with time, it was standardized against a saturated calomel electrode using a valve voltmeter.

Assuming that the electrode behavior can be represented by a resistor, R, and capacitor, C, in parallel, with a constant current, I, flowing through the circuit, then the voltage across the circuit is given by

$$V = IR(1 - e^{-t/CR})$$

Differentiating gives

$$\frac{dV}{dt} = \frac{I}{C} e^{-t/CR}$$

which can be expressed as

$$\log \frac{dV}{dt} = \log \frac{I}{C} - \frac{t}{CR} \cdot \frac{1}{2.3}$$

A plot of log dV/dt against t should give a slope $1/2.3CR$ and an intercept at $t = 0$ of log I/C. Alternatively the logarithmic scale may be normalized by plotting log $1/I\ dV/dt$ which allows direct comparison of results.

This analysis is correct for the case where the square current step is superimposed on steady-state conditions. In the present equipment the imposed current reverses periodically giving a zero net additional direct current. The frequency is such that in general steady-state conditions are not achieved

prior to each reversal, and the form of the voltage response is modified so that it is expressed

$$V = IR\left\{1 - \left(1 + \tanh\frac{T}{CR}\right)e^{-t/CR}\right\}$$

where $4T$ is the period of the square wave oscillation.

When T/CR is small $\tanh T/CR << 1$ and the equation reduces to that for a single step. The voltage response then indicates the value of the capacitor as nearly all the current flows into the capacitor and little leaks through the resistor. When T/CR is large (>10), $\tanh T/CR \doteq 1$. The capacitor can then reach a fully charged state and all the current flows through the resistor. Generally $(1 + \tanh T/CR)$ will be neither one nor two but will be between these two values. As in the first case (a single step) the plot of log dV/dt against t will give a slope $1/2.3CR$. However, the intercept at $t = 0$ is log I/C $(1 + \tanh T/CR)$ and this correction factor must be applied.

This method permits the calculation of the parallel capacity and resistance from the slope and intercept on the logarithmic axis when log dV/dt is plotted against t, as, for a single value of capacity and resistance, the plot is a straight line.

Where the measured values of C and R are a function of frequency, as is usually the case with oxide films, the relation between log dV/dt and t is not linear. The values of C and R for any frequency, f, can be derived by drawing the tangent to the curve at time t (where $t \times f = 1$). The behavior of the electrode may be approximated to any desired degree by a number of analogues in series, the components of each of which are frequency independent. This is done by taking the tangent to the curve at long times, giving the components of one analogue. The rate of voltage change arising from this analogue is then subtracted from the original curve and the remainder treated in the same way giving another set of components and so on. Figures 14 and 15 show results obtained by this method of analysis from data of the type given in Fig. 13.

Measurements of the electrode impedance were made at cathodic potentials, initially on changing the potential to more negative values and then with the potential increasing. The solutions, which were made

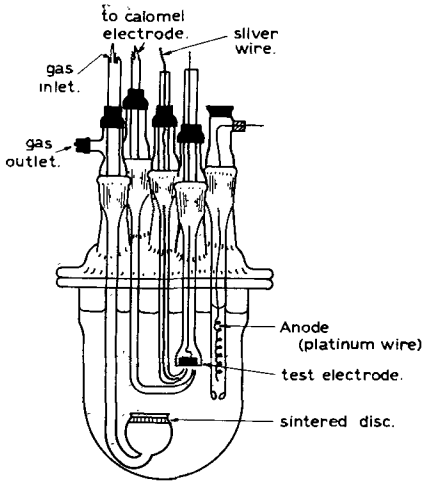

Fig. 3. Diagram of the cell

Table I. Metals tested

Metal	Percentage composition
Al	99.99 Al
Ta	99.8 Ta, 0.1 Nb, 0.01 C
Zr	99.9 Zr
Ti	99.9 Ti
Nb	99.5 Nb, 0.3 Ta, 0.05 Al, Fe, C, Si, O
V	99.7 V, 0.09 O, 0.05 C, Fe, N, Si
U	99.95 U, 0.009 Fe, O, N, C, Si, Al
Cr	99 Cr, 0.3 Fe, 0.2 Al, 0.1 Si, 0.06 C, Cu, S, P

from distilled water and Analar reagents, were a carbonate-bicarbonate buffer solution ($5/N$ $NaHCO_3$ + $5/N$ Na_2CO_3) having a pH of 9.7 and a normal solution of sodium sulfate the pH of which was adjusted with sodium hydroxide or sulfuric acid. The cell used is shown in Fig. 3. Oxygen-free nitrogen was bubbled into the solution prior to testing to reduce the oxygen concentration.

The metals tested were aluminum, tantalum, zirconium, niobium, titanium, vanadium, uranium, and chromium (see Table I). The electrodes were prepared by mounting samples in a cold setting plastic followed by grinding on emery paper down to 600 grade. The resulting surface was either used in that state or anodized in a boric acid solution, adjusted to pH 9-10 by additions of ammonium hydroxide. The more detailed tests on titanium electrodes involved surfaces prepared by chemical etching in a hydrofluoric acid and hydrogen peroxide mixture (10 cc 40% HF + 90 cc 20 vols H_2O_2). This preparation was found to give more reproducible values of capacity, although the values were not strictly comparable with those for abraded surfaces due to the differences in true surface area.

Results

The variation of the capacity with potential for an aluminum electrode both when abraded and when

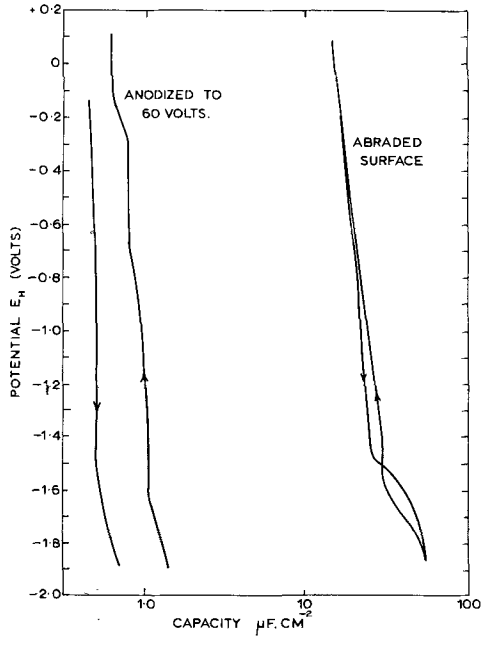

Fig. 4. Variation of the capacity of an anodized and an abraded electrode of aluminum with potential. Carbonate solution pH 9.7.

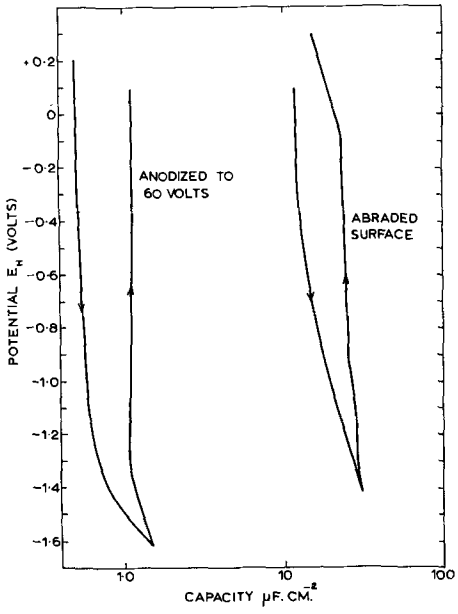

Fig. 5. Variation of the capacity of an anodized and an abraded electrode of tantalum with potential. Carbonate solution pH 9.7.

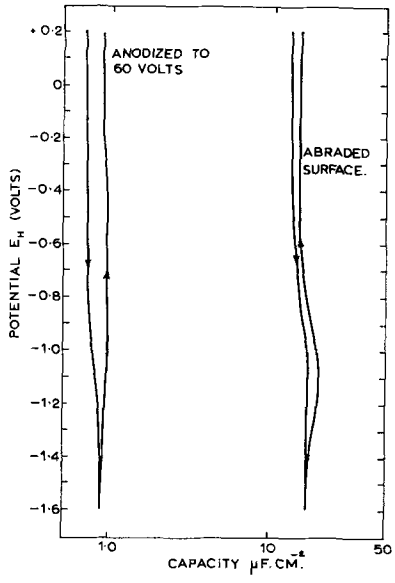

Fig. 6. Variation of the capacity of an anodized and an abraded electrode of zirconium with potential. Carbonate solution pH 9.7.

anodized to 60v is shown in Fig. 4. The results for similarly prepared specimens of tantalum, zirconium, niobium, and titanium are shown in Fig. 5, 6, 7, and 8, respectively.

From these results it can be seen that the capacities of the anodized specimens, measured prior to cathodic polarization, are lower than those for abraded surfaces. The subsequent behavior of niobium and titanium, which on decreasing the potential shows marked capacity maxima, differs significantly from that of aluminum, tantalum, and zirconium.

The capacities of vanadium, chromium, and uranium specimens, which had been abraded prior to testing, are shown in Fig. 9, 10, and 11. The vanadium specimen, on decreasing the potential, shows two capacity maxima. Chromium (Fig. 10) shows a capacity of the order of 25 $\mu F/cm^2$ and has no marked maximum. Figure 11 shows the results for uranium

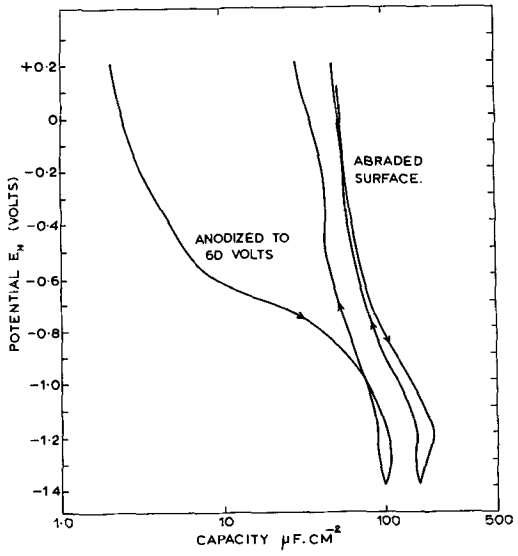

Fig. 7. Variation of the capacity of an anodized and an abraded electrode of niobium with potential. Carbonate solution pH 9.7.

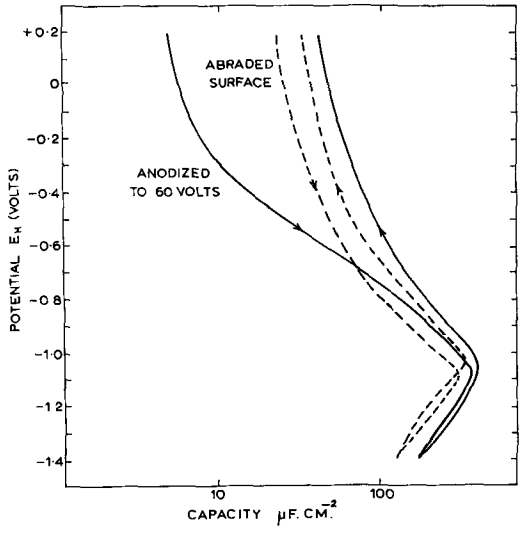

Fig. 8. Variation of the capacity of an anodized and an abraded electrode of titanium with potential. Carbonate solution pH 9.7.

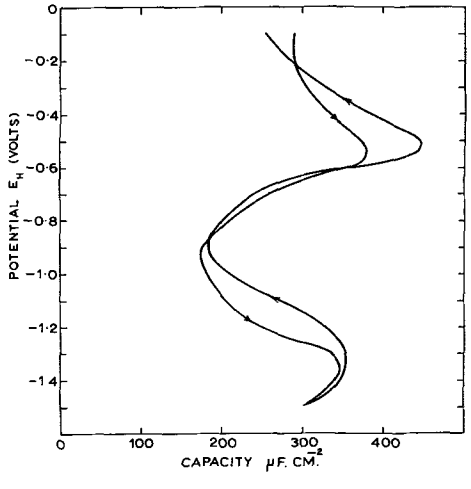

Fig. 9. Variation of the capacity of an abraded electrode of vanadium with potential. Carbonate solution pH 9.7.

in a sulfate solution of pH 9.8; the results are similar to those observed in a carbonate solution of similar pH (1).

Figure 12 shows, for a titanium electrode, the variation with *p*H of the potential of the capacity maximum in a sodium sulfate solution. The potential is independent of *p*H up to a value near 11 and then decreases by 0.06 v/*p*H unit. In the lower *p*H region below a *p*H of about 5, a second capacity maximum is present at a more positive potential than the one shown in Fig. 12 and appears to be dependent on *p*H but as yet has not been fully investigated.

Figure 13 shows the voltage response of an etched titanium electrode in the carbonate buffer solution

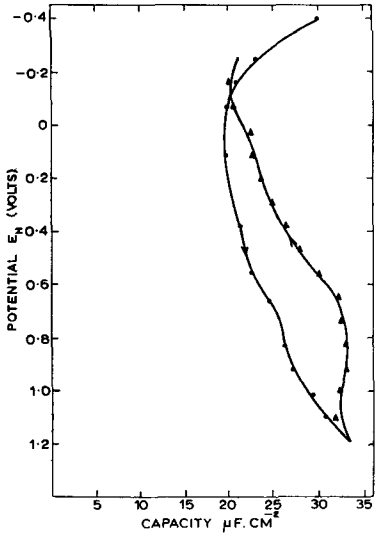

Fig. 10. Variation of the capacity of an abraded electrode of chromium with potential. Carbonate solution *p*H 9.7.

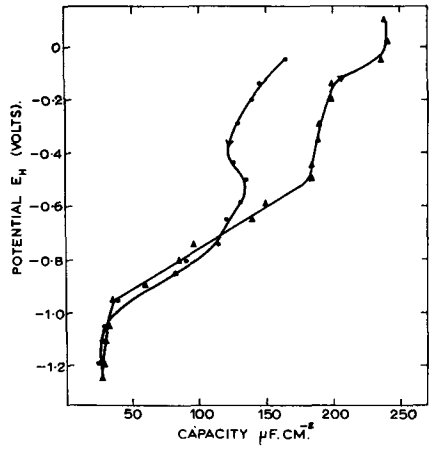

Fig. 11. Variation of the capacity of an abraded electrode of uranium with potential. Sulfate solution *p*H 9.8.

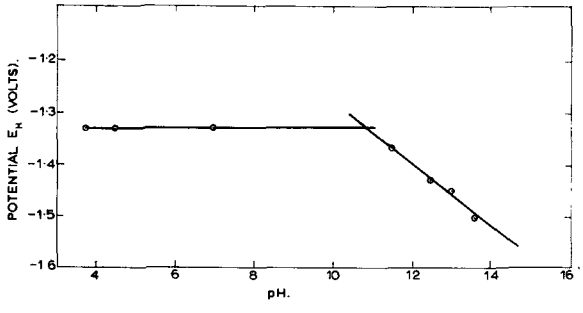

Fig. 12. Variation with *p*H of the potential of the capacity maximum for a titanium electrode. Sulfate solution.

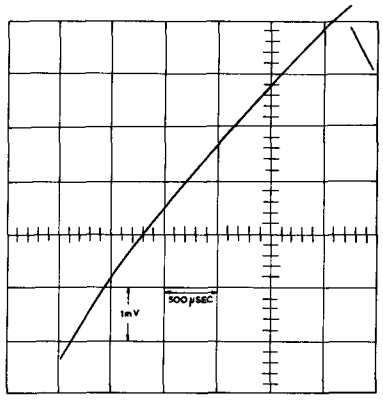

Fig. 13. Voltage response of an etched titanium electrode to a square current wave. Carbonate solution *p*H 9.7; electrode potential —0.03v SHE; area of electrode 0.33 cm^2.

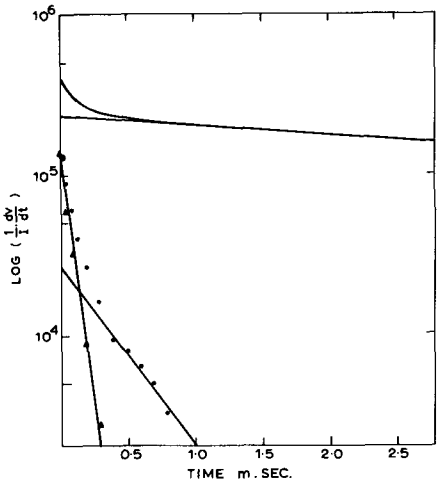

Fig. 14. Plot of log 1/*I* *dV/dt* vs. *t* for Fig. 13

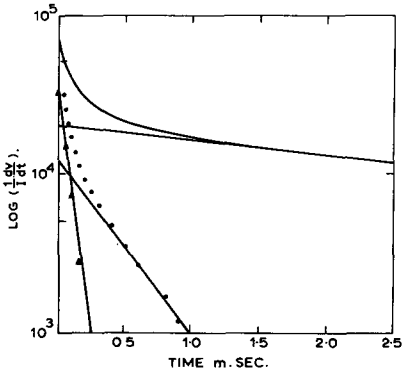

Fig. 15. Plot of log 1/*I* *dV/dt* vs. *t* for the titanium electrode at —1.055v SHE.

at a potential of —0.03v SHE. The repeat frequency was 200 c/sec, and the current was $\pm 12.10^{-6}$ amp for the curve shown. The graphically determined derivative of the curve is plotted logarithmically against time in Fig. 14. Figure 15 shows the same parameters for a titanium electrode at a potential of —1.055v SHE. The current pulse in this case was $\pm 58.1 \times 10^{-6}$ amp. Both measurements were made on decreasing the potential of the specimen.

Discussion

From an examination of the results it is possible to divide the oxide-covered metal electrodes into two

groups: the first consists of those metals the oxides of which behave as dielectrics, and the second group comprises those whose oxides show high capacity values, greater than the values usually accepted for the electrochemical double layer. Titanium shows both characteristics and, as a result, was studied in more detail than the other metals.

Normally oxide-covered metals would be expected to show capacities which correspond to the thickness of the oxide, decreasing with increased thickness as has been shown with the valve metals aluminum, tantalum, zirconium, and niobium, at anodic potentials.

The increase of capacity with decreasing potential for aluminum, tantalum, and zirconium could be attributed either to a thinning of the oxide, or, as appears more likely, to a change in the resistance of the oxide. If the oxide is considered to be composed of a series of layers, an increase in the conductivity of a layer could act as a shunt across that layer of oxide. This principle may be illustrated by considering the analogue shown in Fig. 16a. Reducing the high resistance in either of the parallel circuits to a low value will effectively short out the relevant capacitor and result in a larger measured value of capacity.

On increasing the potential, the values of the capacity and conductivity for the anodized specimens of aluminum, tantalum, and zirconium are larger than the values recorded on decreasing the potential. The magnitude of the increase (called hysteresis) appears to be dependent on the minimum potential reached. This has been the subject of a more detailed study which has confirmed the results shown here with other measurements on anodized zirconium (10) which had been subjected to more negative potentials. The hysteresis of the kind shown in that work has been reported previously (1, 5, 12) and in the present work has been observed on all the oxide-covered metals investigated. It was also shown in that work that the capacity decreased with time at 0v SHE (solution *p*H 9.7) to its original value. The capacities of the 60v oxide films, on aluminum, tantalum, and zirconium after hydrogen had been evolved from their surfaces, could be restored to a value approaching the original, prior to cathodic treatment, by anodizing to 10v. This treatment would not give rise to any oxide growth. These results suggest that hydrogen in the oxide increases its conductivity. The hydrogen can be introduced into the oxide by cathodic polarization accompanied by the evolution of hydrogen and removed by anodic polarization. These processes might provide a mechanism by which the rectification observed on these metals could occur. A similar mechanism has also been proposed by Schmidt (9).

The conductivity change does not appear to be uniform throughout the thick oxides as indicated by

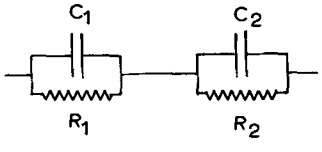

Fig. 16. Hypothetical analogue of an oxide composed of two layers

the value of the capacity change. A uniform decrease in the resistance of the oxide would not be accompanied by an apparent change in the capacity of the oxide unless its dielectric constant also increases.

These results are in many respects similar to those reported by Vermilyea (11) who found that the capacity of anodized films on tantalum increased after heating *in vacuo* above 300°C without any significant change in the interference colors of the films or their porosity. He attributed the increased capacity to an increase in the conductivity of the oxide resulting from loss of oxygen to the metal during vacuum heat treatment. Young (8) has interpreted his results on the variation of the impedance with frequency, as showing that the resistivity of the oxide on niobium varies with the depth below the oxide surface.

It should be stressed that, in all the effects so far discussed, the surface capacity of the electrodes of aluminum, tantalum, and zirconium at no time exceeded that corresponding to a clean surface, i.e., the capacity of the electrochemical double layer.

Considering the behavior of the capacity of titanium and niobium before and after cathodic polarization, it is seen that an increase in both the conductivity and capacity results from cathodically polarizing the anodized specimens, but to a very much greater extent than is found with the metals aluminum, tantalum, and zirconium. Subsequent anodic polarization to 10v restores the capacity to the original value prior to cathodic polarization (corresponding to a 60v film), indicating that little change in the thickness of the oxide occurred during cathodic treatment. The interference colors observed on the anodized specimens also remained apparently unchanged, supporting this interpretation.

The high values of the capacity obtained with titanium, vanadium, and niobium cannot be explained on the model of a parallel plate condenser as the value of the thickness of the oxide calculated on this basis would be less than 1Å at the potential of the capacity maximum.

Similar capacity maxima have been observed at the polarographic half-wave potential (3), where a species in the solution is depositing on the mercury surface, and by Breiter on platinum where adsorption processes are occurring (4). In the present work the solutions used for measuring contained no active species, other than those composing the water, which could be involved in an electrochemical reaction.

The basic requirement for a high Faradaic capacity is that the electrochemical reaction taking place must be reversible. The similarity between a reversible reaction and a capacitor has been drawn by Bryer and Gutmann (13). When the current is cathodic, deposition of a metal ion takes place, while on the reverse cycle dissolution occurs; the process thus involves the storage of charge, either metal ions in the solution or electrons by the metal to be released on the opposite half cycle of the current.

If a valency change occurred reversibly in the oxide, it could account for the high capacity values observed in the present work with the electrodes of titanium, niobium, and vanadium and those previously reported for uranium and iron. The capacity

Table II

Reaction	Potential		Remarks
	Calculated	Observed	
$V_2O_2 + H_2O = V_2O_3 + 2H^+ + 2e^-$	−1.393	−1.35	Carbonate soln.
$V_2O_3 + H_2O = V_2O_4 + 2H^+ + 2e^-$	−0.363	−0.5	pH 9.7 Ref. (14)
$NbO + H_2O = NbO_2 + 2H^+ + 2e^-$	−1.198	−1.21	Carbonate soln.
$2NbO_2 + H_2O = Nb_2O_5 + 2H^+ + 2e^-$	−0.862	NO	pH 9.7 Ref. (15)
$3Ti_2O_3 + H_2O = 2Ti_3O_5 + 2H^+ + 2e^-$	−1.063	−1.03	Carbonate soln. pH 9.7 Ref. (16, 18)
$3UO_2 + 2H_2O = U_3O_8 + 4H^+ + 4e^-$	−0.05	−0.5 to 0*	Sulfate and carbonate solns.
$U_3O_8 + H_2O = 3UO_3 + 2H^+ + 2e^-$	+0.32		pH 9.7 Ref. (17)

NO, no capacity maximum was observed around this potential.
* No sharp capacity maximum was observed although the values of the capacity were high (ca. 200 $\mu F/cm^2$).

maxima observed do occur in the vicinity of the potentials which may be calculated from thermodynamic data (see Table II). Aluminum, tantalum, and zirconium do not exhibit a change in valency, and no large capacities are observed with these metals.

The stability of trivalent chromium covers a large potential range, and no high capacity is observed within this range. If the high capacities resulted from an adsorption process, it would be expected that such a reaction would be seen with the chromium electrode, as the resistance of the oxide is relatively low and capacity relatively high.

The reaction occurring in the oxide is believed to be of the form

$$MO + H^+ + e^- \leftrightharpoons MOH$$

which only requires that protons and electrons are mobile species. The process therefore would depend on the concentration of hydrogen in the oxide, and this could explain the observed hysteresis in the capacity on potential cycling of titanium and vanadium. The presence of greater concentrations of protons would allow the reaction to proceed more rapidly, increase the value of the capacity measured, and move the potential of the capacity maxima to more positive values.

In order to get a clearer understanding of this phenomenon a more detailed study has been made of the behavior of a titanium electrode.

On the basis of a reaction such as $MO + H^+ + e^- \leftrightharpoons MOH$ it would be expected that the potential of the capacity maximum would depend on the pH of the solution, according to the equation

$$E = E_o - 0.059\ pH$$

where E_o is the reversible or equilibrium potential for the reaction. This variation with pH has been found to hold with titanium in a sodium sulfate solution above pH values of 11, as shown in Fig. 12. At lower pH values the potential of the capacity maximum is independent of pH.

There are two possible explanations for this behavior. The first is that the reaction occurring does not involve hydrogen ions and results from the change in valency of some ions most probably in solution, *e.g.*

$$Ti^{3+} + e^- = Ti^{2+}$$

The other possible explanation is that the pH at the interface between the oxide and solution is independent of the solution pH up to a value of about 11. This could be due to the hydrogen evolution reaction associated with the d-c polarization which results in a high concentration of hydroxyl ion at the electrode-solution interface.

The potential of the capacity maximum of the titanium electrode depends on the composition of the solution, as can be seen from the comparison of the potentials at which the maximum occurs in the sulfate (Fig. 12) and carbonate (Fig. 8) solutions.

From the measured values of the capacity of the electrodes an estimate can be made of the number of ions changing valency. For the case of titanium a surface capacity of 150 $\mu F/cm^2$ corresponds to 4.7×10^{12} titanium ions per cm^2 changing valency from Ti^{2+} to Ti^{3+}. This is about 5×10^{-3} of the number of atoms in the surface. From this it might be concluded that this phenomenon is confined to the oxide surface. However, preliminary results show that, under certain conditions, the capacity exhibited by both uranium and titanium increases with increasing oxide thickness. This phenomenon appears to be dependent on the pH and on the nature of the anion in the solution, and more work is required to elucidate the details. It is reasonable to ask why so few ions change valency, and it seems likely that the number is limited by the availability of hydrogen in the oxide which might be expected to be in the range $10^{-6} - 10^{-3}$ mole fraction. A preliminary examination of the behavior of these high capacities shows that the measured values are time dependent in a way which adds additional support to the suggestion that this is not a surface phenomenon, but involves the bulk of the oxide.

The deviation from linearity of the derivative of the voltage response, as shown in Fig. 14 and 15, indicates that the analogue of a parallel capacitor and resistor chosen to represent the titanium specimen is only approximately correct. There is a closer ap-

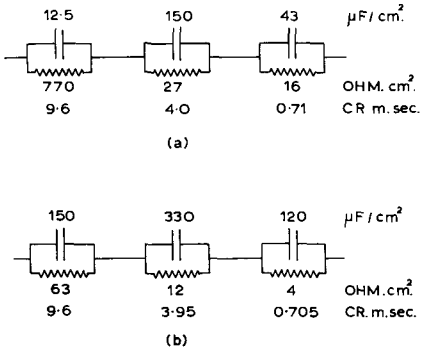

Fig. 17. Analogue circuit derived (a) from Fig. 14, (b) Fig. 15

proximation to a straight line when the oxide behaves as a dielectric (Fig. 14) than under those conditions where the oxide behaves as an electrolyte giving rise to an electrochemical reaction.

The deviation from linearity is larger with anodized specimens and on increasing the potential after hydrogen had been evolved from the oxide surface. These results suggest that the properties of the oxide are not homogeneous and that a high hydrogen activity does increase the heterogeneity of the oxide, which would account for the increased capacity.

As explained previously, by plotting the numerical values of the deviation from linearity in a manner similar to those of the derivative, two more time constants can be derived. The three series networks of capacitors and resistors in parallel equivalent to the three time constants, approximate closely to the voltage response of the electrode. Figure 17a shows such an analogue derived from Fig. 14 while Fig. 17b is derived from Fig. 15. At the present stage of development it is not possible to say whether such more complex analogues have any reality in a physical sense or whether this is merely a mathematical device for describing a frequency dependent process.

Conclusions

1. The surface capacity and conductivity of oxide-covered metal electrodes can be greatly changed by the presence of hydrogen.

2. The marked increase in capacity and conductivity observed on aluminum, tantalum, and zirconium electrodes after cathodic polarization has been explained in terms of a change in the oxide conductivity rather than in terms of mechanical damage to the oxide film. Nevertheless the oxide continues to behave like a dielectric, and the measured surface capacities do not exceed those corresponding to the double layer.

3. The behavior of the metals titanium, niobium, uranium, and vanadium which can show surface capacities greatly in excess of the double layer capacity cannot be explained in terms of a dielectric oxide without implying a large and variable increase in the dielectric constant. The phenomena are discussed in terms of a Faradaic capacity arising from a change of valency of cations in the oxide by a reaction such as

$$MO + H^+ + e^- \leftrightharpoons MOH$$

which only involves the movement of electrons and protons.

4. Further work is required to clarify the relations between the measured values of capacity and such variables as frequency of measurement, oxide thickness, and nature of the solution all of which have been shown to be important.

Acknowledgments

The authors wish to thank Professor J. G. Ball in whose department the work is proceeding, the Central Electricity Generating Board for financial support, and the South African Atomic Energy Board from whom one of us (H.S.I.) is seconded. The authors also wish to acknowledge Imperial Chemical Industries Ltd. for supplying some of the materials.

Any discussion of this paper will appear in a Discussion Section to be published in the December 1963 JOURNAL.

REFERENCES

1. J. S. L. Leach, *J. Inst. Metals*, **88**, 24 (1959-60).
2. J. E. Draley and W. E. Ruther, *This Journal*, **104**, 329 (1957).
3. P. Delahay, "New Instrumental Methods in Electrochemistry," Interscience Publishers, Inc., London and New York (1954).
4. "Transactions of the Symposium on Electrode Processes," E. Yeager, Editor, John Wiley & Son, Inc., New York (1961).
5. W. G. L. van Geel, and C. A. Pistorius, *Philips Research Rept.*, **14**, 23 (1959).
6. H. E. Haring, *This Journal*, **99**, 30 (1952).
7. P. V. Popat and N. Hackerman, *J. Phys. Chem.*, **65**, 1201 (1961).
8. L. Young, *Trans. Faraday Soc.*, **51**, 1250 (1955).
9. P. F. Schmidt, *J. Appl. Phys.*, **28**, 278 (1957).
10. G. Fawkes, Private communication.
11. D. Vermilyea, *Acta Met.*, **5**, 113 (1957).
12. H. S. Isaacs, D.I.C. Dissertation, Imperial College, London (1960).
13. B. Bryer and F. Gutmann, *Discussions Faraday Soc.*, **1**, 19, (1957).
14. Cebelcor Technical Report 29 (1956).
15. Cebelcor Technical Report 53 (1957).
16. Cebelcor Technical Report 4 (1953).
17. Cebelcor Technical Report 31 (1956).
18. B. D. Tomashov, R. M. Al'Tovskii, and M. Ya. Kushnerev, *Doklady Akad. Nauk S.S.S.R.*, **141**, 193 (1961).

The Growth of Thin Passivating Layers on Metallic Surfaces

M. Fleischmann and H. R. Thirsk

Department of Chemistry, King's College, Newcastle upon Tyne, England

The Nature of the "Passivating Material"

The main problem in interpreting the passivation of metals in terms of a theoretical model lies in the nature of the "passivating material." Discussion repeatedly returns to this question [see for example (1-3)], and the answer usually takes one of two extreme forms, the first: passivation is due to a three-dimensional film of a definite chemical phase; the second: passivation is due to a disordered monomolecular array of adsorbed ions or molecules. In the light of the discussion given in this paper we might well add a third form: passivation is due to an ordered monomolecular, two-dimensional film of a definite chemical phase.

In many instances there can be little doubt that the first answer is correct (4). A new phase is formed at a potential close to a well-defined reversible potential, discrete centers can be seen to grow by microscopy or electron microscopy, and the electrode is passivated some time after these centers coalesce. Any adsorbed layer formed before the three-dimensional film clearly has little passivating effect. The growth of the centers is in general controlled by at least two potential dependent rate constants, the nucleation rate constant A^1 (nuclei cm^{-2} sec^{-1}) and the crystal growth constant (moles cm^{-2} sec^{-1}) (5-7). If the formation of the new phase is examined under constant potential conditions, the current-time transients obtained can be analyzed and the rate constants deduced. The concentration and potential dependence of these rate constants can then in turn be investigated and the mechanism of lattice formation deduced by methods familiar in the general field of electrochemical kinetics (5-7). The principles involved are referred to briefly in the next section. There can again be little doubt that a three-dimensional film is passivating the surface in cases where the formation of similar growth centers in a parent phase (itself formed from the substrate metal) can be followed potentiostatically such as in the oxidation of lead sulfate (8) or of silver sulfate (9).

In a large number of cases, notably of iron and stainless steel, the simple explanation of the blocking of the electrode by three-dimensional growth centers is insufficient. Passivation is much faster and the essential step is usually masked by side reactions such as the "active dissolution" of the metal. The only well-defined electrochemical step which can be observed for example on iron (10) as well as on metals such as aluminum and tantalum (11, 12) is the thickening of the passivating material by high field conduction (13-15). A three-dimensional film can be stripped from the underlying metal for example with iron (16, 17) and stainless steel (18, 19), and the thickness can be measured in a variety of ways, for example by chemical estimation (20) or by measuring the change in rotation of plane polarized light (21). The thickness of the films has also been shown to depend on the applied potential, for example, on iron (22, 23). In view of these properties of the protected metal, passivation in these systems is also often attributed to the formation of a three-dimensional film. Many features of the passivation process are, however, more readily explained in terms of the effect of adsorbed layers on the metal (24, 25). The inhibition of corrosion by adsorption of carbon monoxide (26, 27), the oxygen uptake by stainless steel (28), and the effect of this adsorption on the dissolution of iron (29) and chromium and nickel (30) can all be explained in terms of such a model. The similarity of the passivation process to the inhibition of other reactions such as the ionization of hydrogen on platinum by the adsorption of anions (31) has also been taken to support the view that passivation is due to adsorption, particularly of hydroxyl ions (32).

A combination of the two views is sometimes advanced in specialized theories of adsorption followed by reaction leading to passivation (3, 33). It can be assumed for example that the "decision" for passivation may be taken at the monolayer adsorption stage (1). The relative role of adsorption and film formation in causing passivation is still uncertain, however. It has been suggested that the rapidity of the first adsorption stage precludes the formation of an ordered film and that passivation must be due to the formation of a random adsorbed layer (3). The purpose of this paper is to examine the initial stages of passivation in a number of systems by measurements of the kinetics at constant potential using potentiostats suitable for measurements at high frequencies (34) and to correlate the measurements with structural observations obtained by electron microscopy and electron diffraction. It will be shown that the problem can be treated, in favorable cases, as an example of the electrochemical kinetics of crystal growth.

Growth of Discrete Centers on Electrodes

Discrete centers can grow on electrodes in a number of ways (5-9). At constant potential the rate constants governing crystal growth are independent of time, and in general the current in amp/cm^2 into surface S will be given by

$$i = zFkS \qquad [1]$$

This equation also holds for centers which expand in one dimension only, *i.e.*, the current is independ-

ent of time. For centers growing in two or three dimensions the current may be expressed by using the linear dimensions of the particles, r

$$r = \frac{Mkt}{\rho} \qquad [2]$$

where M is the molecular weight and ρ is the density. For cylinders and hemispheres we therefore obtain, respectively

$$i = \frac{2zF\pi Mhk^2t}{\rho} \qquad [3]$$

and

$$i = \frac{2zF\pi M^2k^3t^2}{\rho^2} \qquad [4]$$

where h is the height of the cylinders. These equations for the growth of a single center must be linked with the appropriate law giving the time dependence of the number of nuclei, N. If

$$i = f_1(t) \qquad [5]$$

and

$$N = f_2(t) \qquad [6]$$

then in the initial stages where there is no limitation of the area of the growing centers by overlap

$$i = \int_o^t f_1(u)\left(\frac{df_2}{dt}\right)_{t=t-u} du \qquad [7]$$

If nucleation takes place at a number of preferred sites N_o on the substrate and the probability of forming a nucleus is uniform with time

$$N = N_o(1 - \exp - At) \qquad [8]$$

where A is in seconds^{-1}, Eq. [8] commonly reduces to two limiting forms: if A is large so that $At >> 1$ for the bulk of the period of growth

$$N \approx N_o \qquad [9]$$

i.e., the nuclei appear to be formed instantaneously; on the other hand if A is small so that $At << 1$ during the period of growth

$$N \approx AN_ot = A't \qquad [10]$$

where A' is nuclei cm^{-2} sec^{-1}. Equation [10] also applies if there are no preferred sites for nucleation. Combination of [8] or [10] with the appropriate law for the growth of a single center according to [7] gives the over-all current-time transient in the initial stages of growth. For example, for two-dimensional centers with instantaneous formation of nuclei

$$i = \frac{2zF\pi MhN_ok^2t}{\rho} \qquad [11]$$

and for progressive nucleation

$$i = \frac{zF\pi Mhk^2A't^2}{\rho} \qquad [12]$$

while for three-dimensional centers with progressive nucleation

$$i = \frac{2zF\pi M^2k^3A't^3}{3\rho^2} \qquad [13]$$

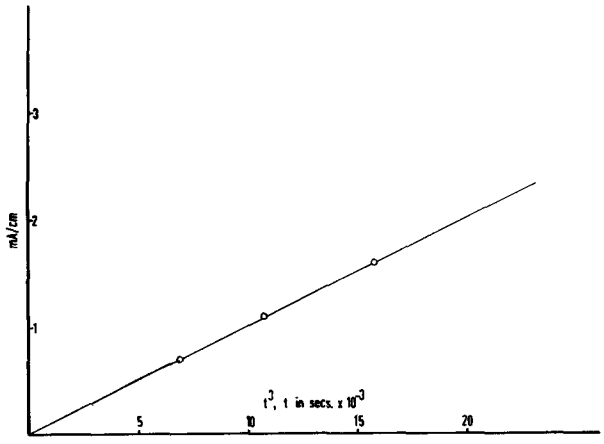

Fig. 1. Variation of current with cube of time for the electrodeposition of γ-manganese dioxide onto a platinum electrode at a potential E_h = 1320 mv. Solution composition: 0.01M $MnSO_4$, 1.0M Na_2SO_4, 0.25M H_2SO_4.

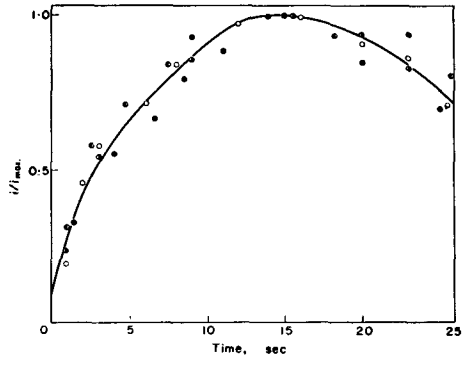

Fig. 2. Variation of (current/current at maximum) with the time for the oxidation of silver sulfate to argentic oxide in molal sulfuric acid at the following potentials with respect to the lead dioxide/lead sulfate electrode: solid circle + 0.325v, half opened circle, solid on right side + 0.350v, open circle + 0.0375v, half opened circle, solid on left side + 0.400v.

This equation is illustrated in Fig 1 by the initial stages of the electrodeposition of γ-manganese dioxide from manganous sulfate solutions onto platinum electrodes (35). It has also been found to apply for the electrodeposition of α- and β-lead dioxide (36, 5) as well as the oxidation of lead sulfate (8).

In the later stages of crystal growth the centers overlap, and the area available for electrodeposition becomes restricted. In the cases of interest in the context of this paper reaction must finally stop either when the electrode surface is "blocked" or when the parent phase has been completely converted into the new phase. The current must therefore pass through a maximum. This is illustrated in Fig. 2 by the oxidation of silver sulfate to silver oxide (9). In this system cylindrical centers grow from nuclei which are formed instantaneously, but it can be seen that the initial linear rise of the current with time is rapidly restricted by overlap. The extent of overlap of centers taken two at a time can be readily calculated for most growth geometries. In the present example the overlap area takes the particularly simple form

$$S_o = 4\pi N_o^2rh\int_o^{2r} a\cos^{-1}\frac{a}{2r}\cdot da = 4\pi^2N_o^2hr^3 \qquad [14]$$

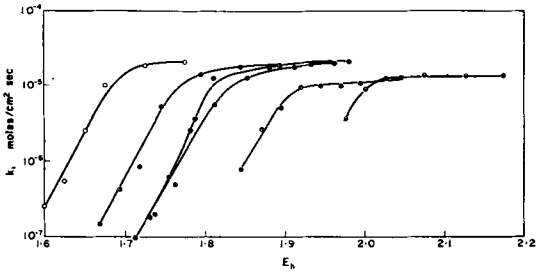

Fig. 3. Variation of the rate constant for the oxidation of silver sulfate with electrode potential and solution composition. Open circle, 0.001M sulfuric acid + M sodium sulfate; half open circle, solid on right side, 0.01M sulfuric acid + 0.99M sodium sulfate; solid circle, 0.1M sulfuric acid + 0.9M sodium sulfate; half opened circle, solid on left side, 0.1M sulfuric acid; half opened circle, solid on top, M sulfuric acid; half opened circle, solid on bottom, 5M sulfuric acid.

where a is the radius of an annular ring of thickness da surrounding the center of radius r. Combination with the freely growing area gives the current-time transient

$$i = \frac{2zF\pi MhN_0k^2t}{\rho}\left(1 - \frac{\pi N_0M^2k^2t^2}{\rho^2}\right) \quad [15]$$

Equation [15] has been shown to hold for the oxidation of silver sulfate illustrated in Fig. 2. In general the equations derived by allowing for overlap of centers have a similar form and predict a maximum in the current-time curve. The time and current at the maximum can be obtained by differentiation, and the rate constants k^nA' or k^nN_0 may be derived from the experimental values or from the slope of the appropriate power law plot in the initial stages of growth. In favorable cases the nucleation and growth constants can be separately determined by detailed analyses of the current-time transients (8). The nucleation rate can also be obtained by counting the number of growth centers on micrographs (9) or electron micrographs (35) or by forming a large number of nuclei by means of a preliminary polarization for a short time at a high potential and thereby changing the transient from that for progressive to that for instantaneous nucleation, *e.g.*, from Eq. [12] to Eq. [11] (36, 5, 7).

When the characteristics of the crystal growth processes have been found, the variation of the rate constants k and A' with solution composition and potential can be examined. This is again illustrated in Fig. 3 for the formation of silver oxide from silver sulfate (9). For this one electron oxidation the slope of the Tafel lines at low potentials is nearly 60 mv^{-1}, and the reaction is proportional to pH. At high potentials the rate constant is independent of potential and pH. These facts are all explained by a rate-determining formation of the lattice at the growth sites by a slow chemical reaction between argentous ions and adsorbed hydroxyl radicals formed by an electrochemical equilibrium

$$H_2O \rightleftharpoons OH_{ads} + H^+ + e$$

$$OH_{ads} + Ag^+ \xrightarrow{\text{slow}} AgO + H^+$$

In other examples which have been examined lattice formation has also been found to be the slow step in contrast to the assumptions frequently made in theories of crystal growth (see for example [7]).

Growth of Centers of Monomolecular Height

An important example of the kinetics of crystal growth is obtained if centers of monomolecular height grow two dimensionally on electrodes. If the new phase shows a definite orientation, the height of the growing centers is a definite spacing of the unit cell. If these centers are regarded as cylinders, Eq. [11] and [12] again apply for the initial stages of growth for instantaneous and progressive nucleation, respectively. If the nuclei are distributed over the surface in a completely random manner, it is possible in these cases to calculate the current-time transient completely, that is, to allow for all possible forms of overlap between growing centers (37-39, 7). If S is the area of substrate covered by the growth centers, $S_{1\,ex}$ is the extended area (37) of all the patches ignoring overlap then

$$S = 1 - \exp(-S_{1ex}) \quad [16]$$

Since the volume v of the new phase is given by

$$v = Sh \quad [17]$$

then

$$i = \frac{zF\rho}{M} \cdot \frac{dv}{dt} \quad [18]$$

The most important case is that of progressive nucleation according to Eq. [10]. Substituting in [16] and [18] one obtains

$$i = \frac{zF\pi Mhk^2A't^2}{\rho}\exp\left(-\frac{\pi M^2k^2A't^3}{3\rho^2}\right) \quad [19]$$

while for instantaneous nucleation

$$i = \frac{2zF\pi MhN_0k^2t}{\rho}\exp\left(-\frac{\pi N_0M^2k^2t^2}{\rho^2}\right) \quad [20]$$

If the growing centers are not circular, the area covered by a single center may be written

$$s = \frac{\sigma M^2k^2t^2}{\rho^2} \quad [21]$$

where σ is a shape factor (*e.g.*, $\sigma = 6\tan\pi/6$) in the case of regular hexagons (40). With the expression one obtains for example instead of [19] the equation

$$i = \frac{\sigma zFMhk^2A't^2}{\rho}\exp\left(-\frac{\sigma M^2k^2A't^3}{3\rho^2}\right) \quad [22]$$

These equations show that it is possible to distinguish the formation of crystallites of monomolecular height from adsorption by following the kinetics of the process. The equations are similar in form to those obtained by only considering the overlap of centers taken two at a time such as Eq. [15]. The approximate equation is in fact given by the first term of the expansion of the exponential. The current again has a maximum, but the value and position differ by a numerical factor from that derived from the appropriate approximate equation. At high times the predicted current however approaches zero asymptotically. These equations are also of interest as they express the current-time transient for the formation of a single layer ac-

cording to a mechanism similar to the classical mechanism of crystal growth (41-43). The differences lie in the assumption of growth from a large number of nuclei rather than from one nucleus, in the restriction of growth by the overlap of growth centers rather than by the boundaries of the substrate crystal plane, and in the slow stage being the lattice formation at the periphery of the growing centers rather than the diffusion of reacting entities to the points where the lattice is built up. A consequence of these changes in the assumptions is a complete change in the potential and concentration dependence of the rate of deposition in the event of the repeated deposition of monolayers (7). The classical mechanism of crystal growth demands the nucleation of growth centers which requires an appreciable supersaturation or the equivalent overpotential. It is to be noted that, since crystals will grow at low supersaturations, it has been suggested in recent years that the lattice is built up at the edges of self-perpetuating steps such as those produced by screw dislocations (44-46, 5), but it has been pointed out (5) that the rejection of the classical mechanism depends on an assumption of the frequency factor for nucleation which may not be justified.

Investigation of the Initial Stages of Passivation

Evidence for the formation of ordered crystals or for the validity of the classical mechanism of crystal growth has not been obtained in previous investigations. This has probably been due mainly to the use of solid substrate electrodes. Even for highly perfect single crystal faces it is likely that imperfections such as dislocations or even the presence of mosaic boundaries will lead to a lack of "synchronization" of the current-time transient between different parts of the surface so that the over-all current-time transient will be a superposition of transients of the type [19] and [20]. Even for the deposition of a single layer this superposition would give rise to a plateau on the current-time plot instead of a maximum. In the event of the deposition of several layers the observation of a plateau is still more likely, and this does not give any distinguishing feature as to the mechanism of formation of the layer. It is clear that it is important to avoid nucleation at preferred sites, and we have attempted this in the first place by measuring the kinetics of formation of layers on liquid mercury and amalgam electrodes. Although these surfaces are in no sense perfect we can regard them as perfectly random so that nucleation is likely to take place at a uniform rate over the whole surface. It is likely therefore that equations of the type [19] will apply for the formation of a single layer.

In all the kinetic measurements reported here the working electrode had the form of a segment of a sphere formed on the end of a wide bore capillary fed from a precision syringe controlled with a micrometer. The size of the electrode was set either by extruding a known volume or by adjusting the height while viewing through a cathetometer. The formation of the initial layers and the adsorption of anions preceding it have been found to be fast processes (38, 39), and potentiostats suitable for measurements at short times have been used (34) the cells being also designed so as to minimize the effect of stray capacities at high frequencies (34). The potential to be applied to the working electrode by the potentiostat was controlled by means of pulse generators of fast rise time and accurate amplitude stability, and all current-time transients were measured oscillographically.

Examples of the kinetics of adsorption and of layer formation are shown in Fig. 4-10. If the potential of the working electrode is pulsed from a potential negative to that for the formation of the new phase to a second potential which is either less negative to the reversible potential or actually at the reversible potential and if this second potential is positive to the electrocapillary maximum of the substrate, then there will be a specific adsorption of anions in most systems. The implication of the term "specific" is that this is to some extent an activated process so that it will cover an appreciable period of time. An example is given in Fig. 4 for a 300 mv pulse negative to the reversible calomel potential on mercury in 0.1*M* hydrochloric acid (47). It would be expected that the current-time transients due to adsorption would usually have this form. It is of interest that the process is appreciably retarded although the time scale is such that the retardation

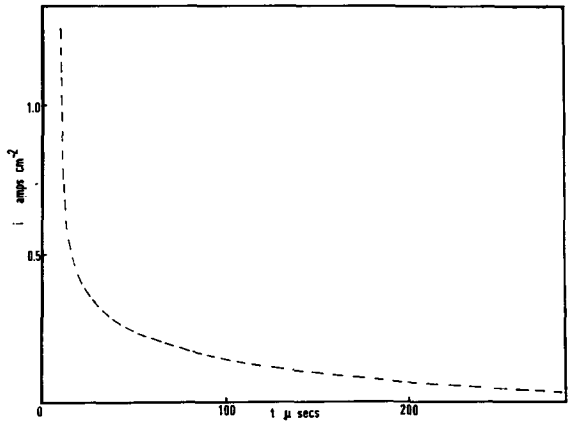

Fig. 4. Variation of current with time for the specific adsorption of chloride ions on mercury at the reversible calomel potential in 0.1M hydrochloric acid, 0 mv.

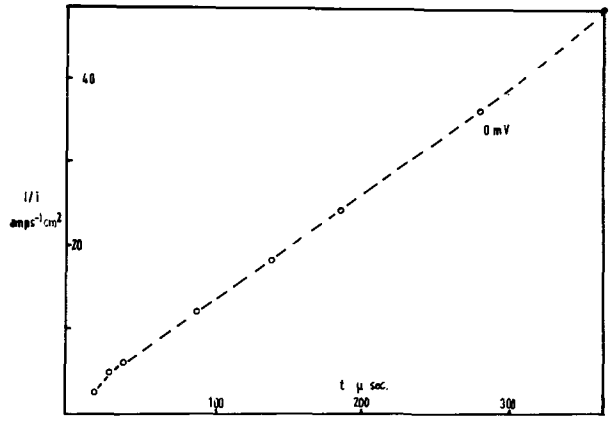

Fig. 5. Plot of 1/t against t for the specific adsorption of chloride ions on mercury at the reversible calomel potential in 0.01M hydrochloric acid.

would not normally be observed in measurements of the differential capacity (48). Estimates of the amount adsorbed agree with measurements derived from the differential capacity and indicate that the adsorption is following a Temkin isotherm. In consequence the time dependence of the adsorption follows the Elovich equation at low coverage which is best illustrated by a plot of $1/i$ against t, Fig. 5 (47). The adsorption of chloride ions on thallium amalgam is illustrated in Fig. 6 (50). At potentials more than 20 mv negative to the reversible thallous chloride potential the transient has the same form as for the adsorption of chloride ions on mercury, but at less negative potentials a plateau develops on the current-time curve. The significance of this plateau is discussed in the last section.

At potentials positive to the reversible potential the current-time curves in general develop a series of peaks (38). This is illustrated for calomel in Fig. 7. In this system up to seven maxima can be observed. It is natural to attribute the maxima to a successive deposition of layers on the surface according to the mechanism giving Eq. [19] for one layer. With increasing overpotential the amplitude of the peaks increases and the time scale contracts due to the increase of the rate constants. The area under each peak remains constant and approximates to a monomolecular layer of the {110} plane, the

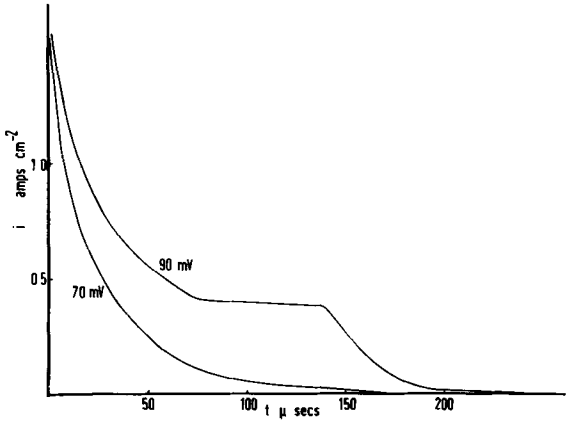

Fig. 6. Variation of current with time for the specific adsorption of chloride ions on thallium amalgam observed by applying a pulse of 70 mv and of 90 mv from an initial potential 100 mv negative to the thallium chloride potential.

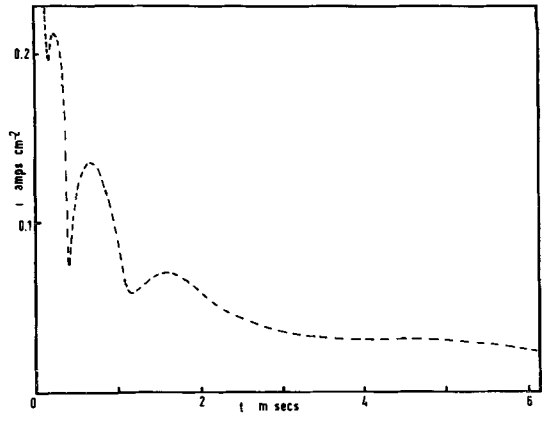

Fig. 7. Variation of current with time for the formation of calomel on mercury in 0.1M hydrochloric acid at an overpotential of 36 mv.

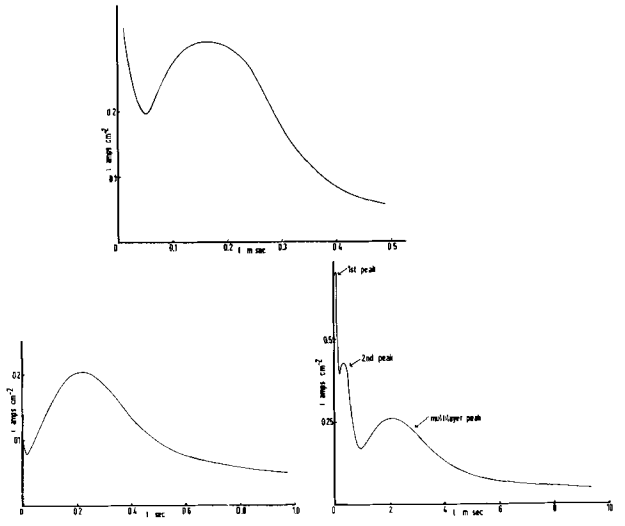

Fig. 8. Variation of current with time for the formation of thallous chloride on thallium amalgam in M hydrochloric acid: A (top) overpotential of 30 mv, first monolayer peak; B (bottom left) overpotential of 30 mv, multilayer peak; C (bottom right) overpotential of 75 mv, first and second monolayer and multilayer peaks.

adsorption transient being added to the first peak. The effect of the adsorption can obscure the first peak and can be largely eliminated by applying a first pulse up to the reversible potential and then a second pulse to a positive overpotential. The results in Fig. 7 and 8 have been taken in this way.

In the case of thallous chloride (50) two peaks are observed at low overpotentials, the first corresponding to the deposition of a single layer of the {100} plane parallel to the substrate (see next section), the second up to 100 layers, Fig. 8A, 8B. At higher overpotentials the second peak is split, and the formation of a second monomolecular layer can be detected. The quantity of electricity under the third multilayer peak decreases, about eight layers being deposited in the example shown. At still higher potentials the orientation changes, the prism face lying parallel to the substrate.

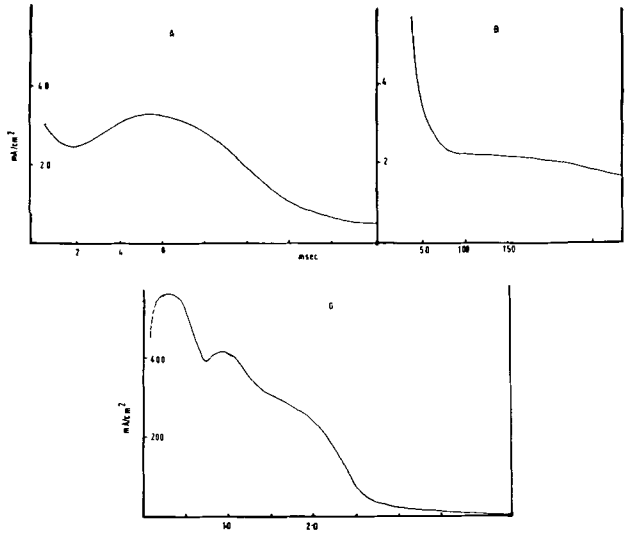

Fig. 9. Variation of current with time for the formation of cadmium hydroxide on cadmium amalgam in N sodium hydroxide: A, overpotential of 20 mv, first monolayer; B, overpotential of 20 mv, second monolayer; C, overpotential of 170 mv, first, second, and third monolayer.

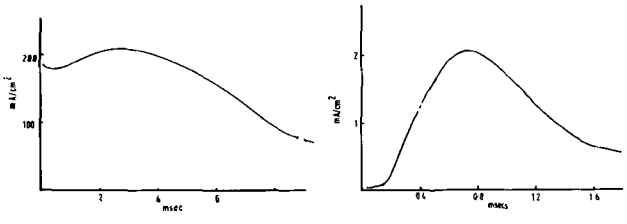

Fig. 10A (left) Variation of current with time for the formation of zinc oxide on zinc amalgam in 0.1*N* sodium hydroxide + 0.9*M* sodium nitrate at an overpotential of 185 mv; B (right) variation of current with time for the reduction of zinc oxide on zinc amalgam in borate buffer of *p*H 9.14 at an overpotential of 35 mv.

In the formation of cadmium hydroxide on cadmium amalgam (40) two peaks can be observed at low overpotentials which again occur at widely different times and which differ in amplitude, Fig. 9A and 9B. With increasing overpotential the second peak "catches up" on the first peak, and the amplitudes become nearly equal. At the same time a shoulder develops on the second peak. This may be attributed to the formation of a third layer since the total quantity of electricity used is somewhat in excess of that required for three layers of the {001} plane (see next section), whereas at low overpotentials the area under each peak approximates to one layer of this plane.

A final example is the formation of zinc oxide on zinc (51), Fig. 10A. In this case a single layer only is formed on the surface. The kinetics of reduction of this single layer are illustrated in Fig. 10B and can be seen to follow the same pattern as the formation of the layers, Fig. 7-10. This pattern must be attributed to the formation and growth of two-dimensional holes in the layer.

Investigation of the Structure of the Deposits

It is evident that for the analysis of the data in Fig. 7-10 the orientation and structure of the films must be determined. Since the layers are very thin this is best done by transmission electron microscopy and diffraction of films stripped from the surface. In the present investigation the following method was employed as a standard technique: the deposit was formed on a horizontal pool electrode fed from a syringe and connected in parallel to a second working electrode. The Luggin capillary was carried on a sleeve joint and after the formation of the film had been completed was placed opposite this second electrode. The solution level was lowered, the polarization interrupted, and the layer washed with water or alcohol and dried. The film was then coated with a drop of 0.1% Formvar in chloroform, and the composite layer was strengthened by the addition of a few drops of 2% collodion in ethyl acetate. At this stage the backed film could be removed in the form of a disk about 1 cm in diameter from the mercury or amalgam surface. Small areas near the center of the disk were cut out by means of a razor blade, and then pieces approximately 2 mm square were placed on E.M. grids using a drop of acetone to fix the films in position. The grids and attached films were placed in amylacetate vapor and then in the liquid for several hours to remove the collodion supporting film, and finally placed in chloroform to reduce the thickness of the Formvar film.

Specimens were then studied at minimum beam intensity in the electron microscope and at the same time selected area electron diffraction patterns taken with a 10μ diameter selection area at the specimen. Calibration of the diffraction patterns was conveniently carried out by placing a grid carrying an evaporated gold film adjacent to the grid carrying the film in the specimen carrier of the microscope. Values of spacings in a direction perpendicular to the film were ascertained by transferring the grid to a Finch-type electron diffraction camera and rotating the specimen round a horizontal axis some 30°-50°.

Cadmium hydroxide possesses a similar structure to cadmium iodide, that is a layer structure consisting of two plane hexagonal networks of hydroxide ions superimposed in such a way that the oxygen atoms of one rest on those of the other in alternate interstices with an hexagonal network of cadmium atoms separating the pair of layers of hydroxide ions but with the cadmium ion lying at the center of a line perpendicular to the layer plane and joining the center of a line perpendicular to the layer plane and joining the center of the triangles of hydroxide ions. The hexagonal layers of cadmium are arranged with the ions directly above those of the next lower layer.

The actual a_o,c_o axial spacings of the hexagonal unit cell vary quite widely in the literature. Reasons for this variation may probably be the inclusion of water molecules in the "OH" layer. Indeed under the wide variety of conditions of formation it would not be unreasonable to seek for a $CdCl_2$ type of structure and for abnormalities in the stacking of the hexagonal nets giving rise to a doubling of the c_o axis repetition unit corresponding to the suggestions made by Arnefelt (52). In this essentially kinetic investigation we have satisfied ourselves, by the methods described briefly below, that the structure of the hydroxides prepared are of the "normal" CdI_2 type, by using techniques which would disclose small changes in the a_o,c_o parameters but have not sought as yet for the presence of systematic changes in lattice spacings with preparative conditions.

Selected films, prepared as described above from the layers deposited in the kinetic experiments, were first examined by electron microscopy. Electron diffraction was then used to confirm the orientation; this was invariably one with the [0001] axis perpendicular to the mercury surface as shown in Fig. 11a and showing therefore hk,O diffractions only. Fig. 11b shows a composite pattern with the gold diffraction calibrating rings. A cube edge parameter of a_o = 4.0786Å (53) was used in the calibration of the $Cd(OH)_2$ spacings. Selected area diffraction permitted the calculation in many cases of the actual number of crystals present in the given area from the resolution of the diffraction spots in the rings. This number is in approximate agreement with the number of hexagonal crystallites which can be counted on the micrographs, Fig. 11c. It is likely therefore that these crystallites are the basic units growing on the surface. Rotation of the specimen

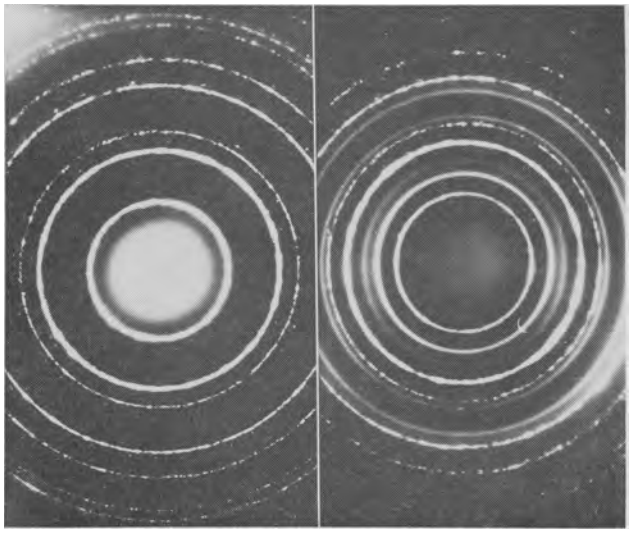

Fig. 11A (left) Electron diffraction pattern of cadmium hydroxide film formed on cadmium amalgam in 1*N* sodium hydroxide; beam || to <001> axes of crystallies; B (right) composite pattern with gold for calibration.

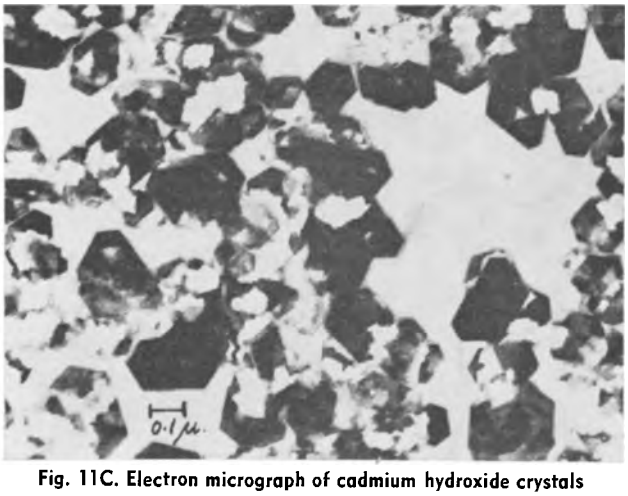

Fig. 11C. Electron micrograph of cadmium hydroxide crystals

in the electron beam gave rise to patterns similar to the example indexed in Fig. 12 where the {hk,l} hexagonal indices (written as {hkl} for convenience on the diagram) correspond to sharp and easily measured spots developing on the layer lines corresponding to a spacing of $\lambda L/c_o \cos\theta$ where λ is the wave length, L the camera length, and θ the extent of rotation of the film from the position with the c_o axis parallel to the beam.

The plane spacings can be internally calibrated from the a_o value calculated from the {hk,O} diffractions calibrated in turn with the gold. The axial ratio is then calculated by the expression

$$\frac{c_o}{a_o} = \frac{l}{\left[\frac{a_o^2}{d^2} - \frac{4}{3}(h^2 + k^2 + hk)\right]^{1/2}} \qquad [23]$$

Typical data for the cadmium hydroxide films produced through three kinetic runs with 1% cadmium amalgam concentration in 1*N* sodium hydroxide are for an overpotential $\eta = 70$ mv $a_o = 3.502$Å $c_o/a_o = 1.339$; $\eta = 120$ mv a_o 3.510Å $c_o/a_o = 1.323$ and $\eta = 220$ mv $a_o = 3.489$Å $c_o/a_o = 1.323$. These values should be compared with the A.S.T.M. index

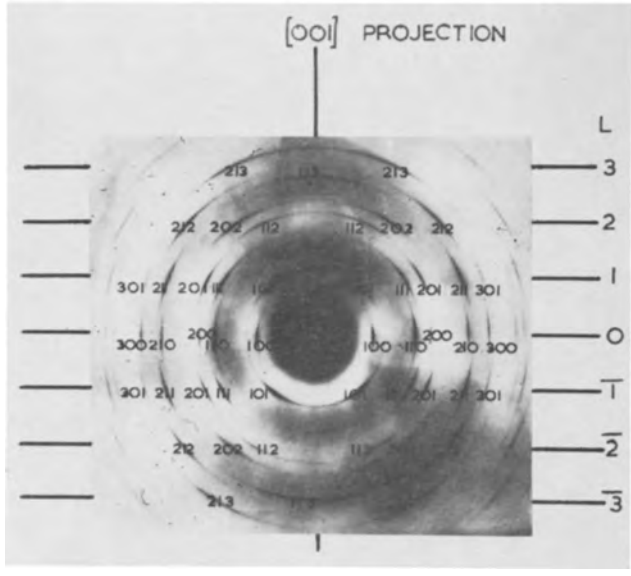

Fig. 12. Indexed electron diffraction pattern of cadmium hydroxide film tilted through 41° (hexagonal indices).

which gives for the unit cell $a_o = 3.580$ $c_o/a_o = 1.405$; $a_o = 3.475$ $c_o/a_o = 1.358$ (54); $a_o = 3.47$Å $c_o/a_o = 1.337$ (55).

A similar technique with mercurous chloride with the electron beam at an angle to the orientated plane parallel to the mercury surface yields patterns such as that shown in Fig. 13. The orientation with the c_o axis of the tetragonal cell together with the end face diagonal is invariably followed under any condition of deposition. The patterns are most readily indexed by substituting as unit cell one of $\sqrt{2}a_o$ and c_o as the parameters, this cell lying with the

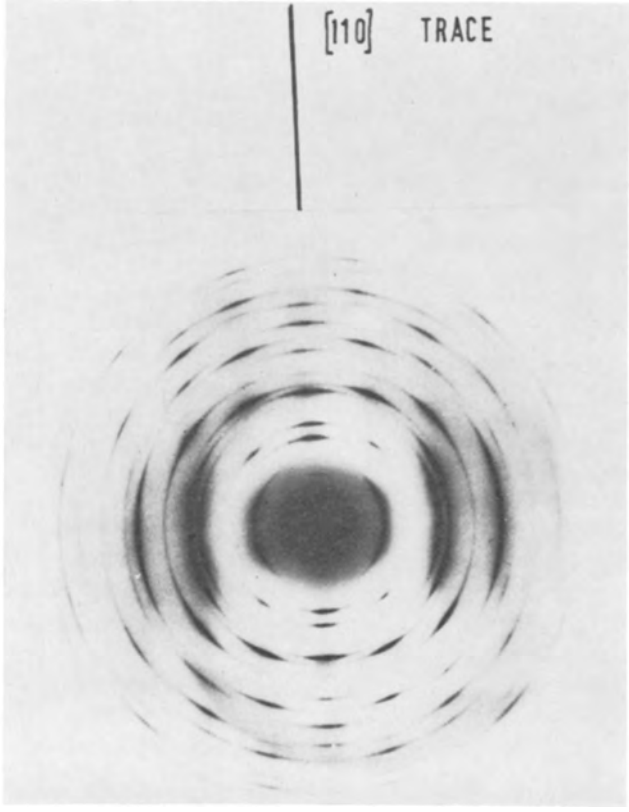

Fig. 13. Electron diffraction pattern of tilted calomel film

{100} face in the film and the layer lines developing from the $a_o\sqrt{2}$ plane spacings perpendicular to the film.

Thallous chloride (cesium chloride structure) crystallizes with spacings strictly in accordance with the massive material. At overpotentials up to about 80 mv the basal orientation is with a cube face parallel to the amalgam surface; at higher overpotentials a change in orientation is observed, and the larger crystals can be seen to have a {110} face parallel to the amalgam surface. This is clearly shown in Fig. 14A and B. With more finely crystalline material it is difficult to say if the {110} orientation is unique because there are no absent reflections as is the case with the finely crystalline material in the {100} orientation.

The confirmation of the structure of the extremely thin layers of zinc oxide has proved to be of considerable difficulty. Reasonably clear diffraction patterns were obtained with an Akashi Tronscope electron microscope after the removal of the pole pieces and on a Metropolitan Vickers type E.M.3. instrument. Attempts to use a Finch-type electron diffraction camera were without success. There was a close similarity between the patterns from the films which were clearly of very small particle size. Typical d spacings in Å are 2.821, 2.437, 1.623, 1.357 corresponding to diffractions from the {10,0}, {10,1}, {11,0}, and {20,1} planes of hexagonal zinc oxide. (The ASTM index gives 2.861, 2.476, 1.626, 1.354Å, respectively.) The {00,2} diffraction ring is completely missing as are the {10,2} and {10,3}. We consider that the evidence for a nearly unimolecular layer of finely crystalline zinc oxide with a predominantly basal orientation is thus quite strong.

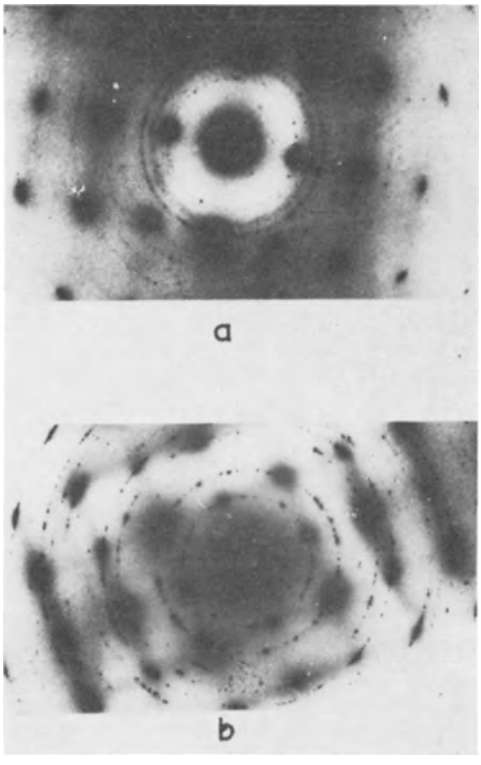

Fig. 14. Electron diffraction patterns of thallium chloride films formed on thallium amalgam in 1*N* hydrochloric acid. A, overpotential of 90 mv, [110] orientation; B, overpotential of 50 mv, [100] orientation.

Discussion of the Kinetics of the Initial Stages of Passivation

It has already been pointed out that the current-time transients obtained below the reversible potential can be explained by the slow adsorption of anions. In most systems the coverage at the reversible potential is already very high, of the order 0.5. At potentials above the reversible potential the shape of the current-time transient changes and this shape is clearly consistent with the mechanism of growth of two-dimensional centers. This mechanism is clearly favored by the highly condensed adsorbed layer which is formed at these potentials. In such a layer the formation of clusters leading to two-dimensional nucleation is very likely.

Detailed tests of the fit of the data to Eq. [19] can be carried out at low overpotentials where a single peak can be observed separately, for example, for cadmium hydroxide, Fig. 9A. For the reduction of the layer on zinc amalgam the initial part can be observed independently of other processes such as adsorption. In this region of time Eq. [19] reduces to Eq. [12]. A test of this equation is shown in Fig. 15. At longer times the exponential term, leading to a reduction in the current, must be taken into account. Equation [19] can be written

$$\ln\frac{i}{t^2} = \ln\frac{zF\pi Mhk^2A'}{\rho} - \frac{\pi M^2k^2A't^3}{3\rho^2} \qquad [24]$$

A test of this is shown in Fig. 16A. It can be seen that the fit is again good (40). On the other hand a similar test for the second layer, assuming this to grow on a uniform complete monolayer of the new phase, does not give a good fit, Fig. 16B. It is clear that layers after the first cannot be assumed to grow independently of each other. It is difficult to treat the problem of the deposition of a succession of monolayers algebraically, but it has been shown (38, 39) that transients of the kind in Fig. 7, 8c, and 9c can be obtained by direct simulation in a digital computer of the multilayer problem. It is possible in this way to obtain also a separate esti-

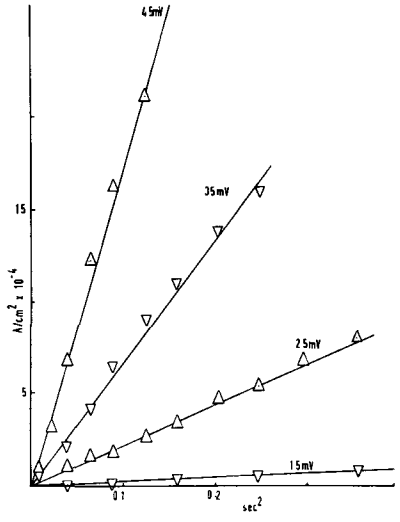

Fig. 15. Variation of the current with the square of time for the reduction of zinc oxide on zinc amalgam in borate buffer of *p*H 9.14 at the overpotentials shown (-ve values).

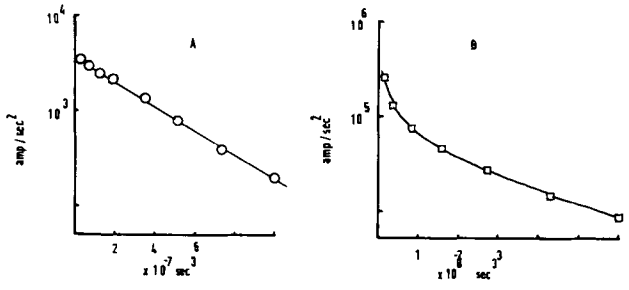

Fig. 16. Variation of log i/t^2 with the cube of time for the formation of cadmium hydroxide on cadmium amalgam in 5*N* sodium hydroxide. A, first monolayer at an overpotential of 30 mv; B, second monolayer at an overpotential of 80 mv.

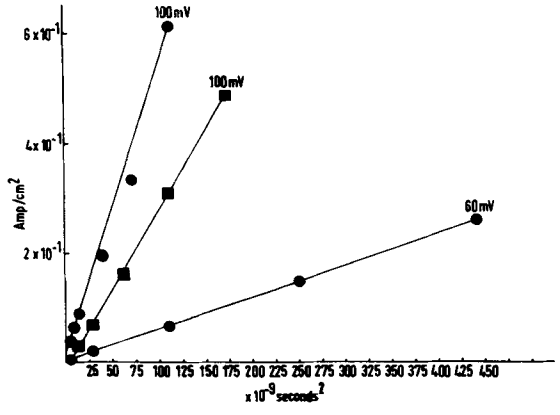

Fig. 17. Variation of the current with the square of time according to Eq. [25] for the growth of cadmium hydroxide on cadmium amalgam in *N* sodium hydroxide at the overpotentials shown: —●— first layer; —■— second layer.

mate of k and A^1. The assumption that the succeeding layers grow independently of each other is most likely to hold in the vicinity of the current maximum and the validity of the model can alternatively be tested in this region for all the layers (7, 39, 40). Expansion about the maximum gives for small time displacements $\pm u$ using the general Eq. [22] for randomly orientated centers

$$i_u + i_{-u} \approx 2i_m - \frac{3 \exp\left(\frac{4}{3}\right) M^2 i_m^3 u^2}{2z^2F^2h^2\rho^2} \qquad [25]$$

provided $u^2/t^2 >> u^4/t^4$. This equation can be tested in two ways. In the first place the current in the vicinity of the maximum should vary with the square of the displacement from the maximum. This is illustrated in Fig. 17 for the first and second peak observed during the formation of cadmium hydroxide. Second, the slope of these plots should be proportional to the cube of the current at the maximum, and this is illustrated in Fig. 18 again for the formation of cadmium hydroxide. The value of the intercept can be calculated furthermore from the observed orientation and gives the full line in Fig. 18. It can be seen that the agreement with this stringent test is reasonable and that there are no systematic differences between the first and second layers. The assumption that the first and second layers grow independently of each other in the vicinity of the current maximum is therefore justified (40). Similar agreement has been obtained for the first three layers of calomel growing on mercury (39) and the first two layers of thallium chloride on thallium amalgam (50).

The fit of the current-time transients to the model assuming the growth and overlap of two-dimensional centers leads to further conclusions and results. Since the equations of the type [19] and [22] are derived assuming a uniform rate of deposition (k moles $cm^{-2}sec^{-1}$) it follows that the overlap of the centers cannot lead to a retardation of growth as it would, for example, if the rate of mass transfer of ions to the centers were reduced by the interaction of the diffusion fields. The slow stage of crystal growth must therefore take place at the edges of the growing centers so that lattice formation by an electrochemical reaction is rate-determining in the same way as in the growth of three-dimensional centers (5, 6, 8, 9, 35). The composite rate constant k^2A' can therefore be deduced from the parameters of the peaks, preferably the current at the maximum. The potential and concentration dependence of the composite rate constant k^2A' can then be examined in the usual way. The example for the first two peaks of cadmium hydroxide shown in Fig. 19 is typical of the results obtained. At high overpotentials the rate constants for the two peaks are equal. It follows that k and A' must separately be equal for the two layers. At low overpotentials the value of k^2A' for the second peak is much smaller than that for the first peak, and this has been attributed to a decrease in the nucleation rate constant for the second succeeding layers (7, 38, 39) as compared to the first. Formulation of the nucleation rate constant for the first layer according to the classical theory gives

$$A_1' = Kk_0 \exp - \frac{N\pi h^2\sigma_1^2}{\left[\frac{h\rho zF\eta}{M} + (\sigma_3 - (\sigma_1 + \sigma_2))\right] RT} \qquad [26]$$

where σ_1, σ_2, and σ_3 are the surface energies between the nucleus and the solution, the nucleus and the

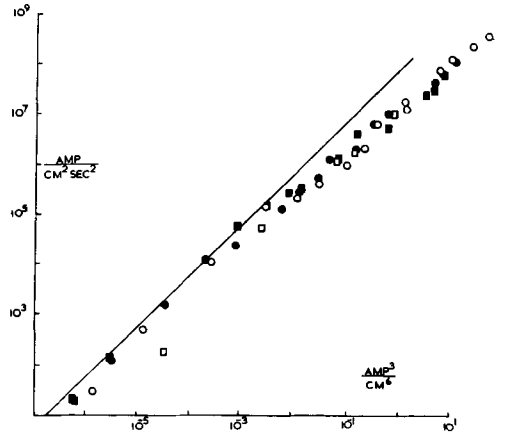

Fig. 18. Variation of the slope of plots such as those in Fig. 17 with the cube of the current at the maximum. The full line is drawn according to Eq. [25] with the crystallographic values of h and ρ. ○, first layer on 1% cadmium amalgam in 5*N* sodium hydroxide; □, second layer on 1% cadmium amalgam in 5*N* sodium hydroxide; ●, first layer on 1% cadmium amalgam in 1*N* sodium hydroxide; ■, second layer on 1% cadmium amalgam in 1*N* sodium hydroxide.

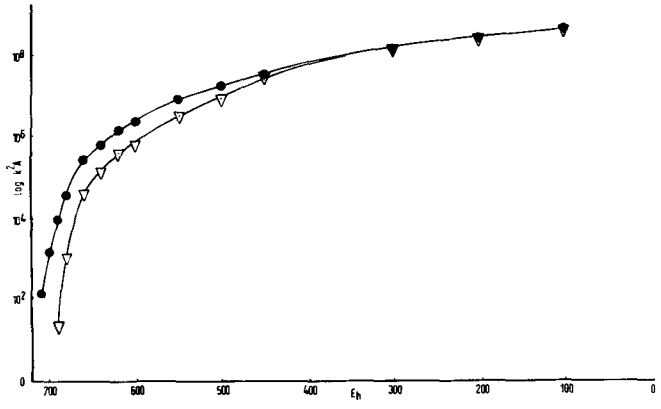

Fig. 19. Variation of rate constant k^2A with electrode potential for the growth of cadmium hydroxide on 1% cadmium amalgam in 1N sodium hydroxide. —●—, first layer; —▽—, second layer.

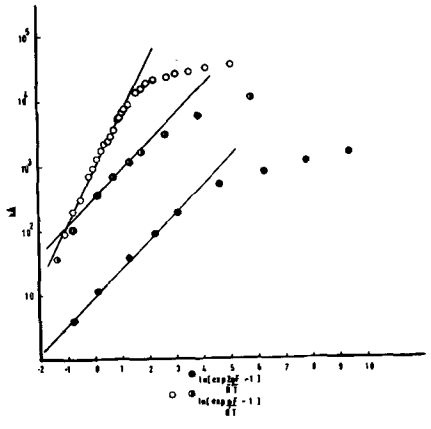

Fig. 20. Variation of the rate constant $k\sqrt{A}$ for the growth of the first monolayer of calomel, cadmium hydroxide, and thallous chloride with overpotential at low overpotentials. —●—, cadmium hydroxide; half opened circle, solid on right side, calomel; —○—, thallous chloride. The full lines are drawn with the theoretical slopes according to the mechanisms suggested in the text.

electrode, the electrode and the solution, k_o is the value of k at the reversible potential, and K is a constant containing the number of adsorbed species. For the second and succeeding layers it is likely that $\sigma_3 - (\sigma_1 + \sigma_2)$ is small so that the usual expression for two-dimensional nucleation is obtained.

$$A_2' = Kk_o \exp - \frac{NM\pi h\sigma_1^2}{\rho zF\eta RT} \qquad [27]$$

Since $\ln \frac{k^2A_2'}{k^2A_1'}$ can be shown to vary linearly with $1/\eta$ it has been suggested (39, 40, 50) that $\sigma_3 - (\sigma_1 + \sigma_2)$ is large for the first layer giving a nucleation rate nearly independent of potential (neglecting the variation of σ with ϕ). The large value of the surface energy between the metal and solution in fact drives the nucleation in the first layer and in favorable cases could lead to incipient crystal growth below the reversible potential. This behavior is analogous to the formation of condensed layers on adsorbents below the saturation vapor pressure and is the most likely explanation for the plateau developing on the current-time curves for the specific adsorption of chloride ions on thallium amalgam, Fig. 6.

With the assumption of a constant nucleation rate in the first layer the variation of k with composition and potential can be examined. In favorable cases (39) the nucleation rate can also be estimated giving absolute values of k and k_o. These are large, of the order $k_o = 4 \times 10^{-3}$ moles cm^{-2} sec^{-1} in the case of the crystal growth of calomel. These large values in the particular crystallographic directions along the plane undoubtedly again favor the classical mechanism of crystal growth. It is of interest that the values of k when corrected for the effects of the reverse reaction give simple Tafel slopes near the reversible potential, Fig. 20, which imply a rate-determining formation of the lattice from ions "discharged" onto the edge. From an examination of the potential and concentration dependence it has been suggested that in the case of calomel (39) this is the incorporation of a simple Hg^+ ion, for cadmium hydroxide a rate-determining rearrangement of two OH^- ions into the layer planes (40), and for thallous chloride a succession of two first order deposition steps (50) possibly analogous to the nucleation of kinks at steps (56) followed by growth at these kinks. It must be noted that since lattice growth is the slow stage, the results do not give any indication as to the mechanism of ion transport to the growth sites.

The systems which have been examined already show a wide variety of behavior. In the case of cadmium amalgam in alkaline solution and of mercury in chloride solutions passivation sets in after a defined number of monolayers have been formed. For thallium amalgam in chloride solutions a multimolecular layer succeeds the formation of two monolayers before the electrode is passivated, while for the case of zinc amalgam in alkaline solutions a single layer only is found. The results show that a monomolecular film of a definite chemical phase is formed from the adsorbed layer and that the processes of adsorption and lattice formation can be kinetically distinguished and examined structurally. It seems likely that the process of passivation will usually be easy when there is a favorable crystal type and habit such as a layer structure. In the examples so far studied it appears that the kinetics of the initial stages of passivation can be regarded as a problem in electrocrystallization, the process of crystal growth being sterically defined.

Any discussion of this paper will appear in a Discussion Section to be published in the December 1963 JOURNAL.

REFERENCES

1. U. R. Evans, *Z. Elektrochem.*, **62**, 619 (1958).
2. H. H. Uhlig, *ibid.*, **62**, 626 (1958).
3. N. Hackerman, *ibid.*, **62**, 632 (1958).
4. W. J. Müller, "Die Bedeckungstheorie der Passivität der Metalle und ihre experimentelle Begründung," Verlag Chemie, Berlin (1933).
5. M. Fleischmann and H. R. Thirsk, *Electrochim. Acta.*, **2**, 146 (1959).
6. M. Fleischmann and H. R. Thirsk, *ibid.*, **2**, 22 (1960).
7. M. Fleischmann and H. R. Thirsk, in "Advances in Electrochemistry," P. Delahay, Editor, Interscience, New York, To be published.
8. M. Fleischmann and H. R. Thirsk, *Trans. Faraday Soc.*, **51**, 71 (1955).
9. I. Dugdale, M. Fleischmann, and W. F. K. Wynne-Jones, *Electrochim. Acta.*, **5**, 229 (1961).

10. K. J. Vetter, *Z. Elektrochem.*, **58**, 230 (1954); **62**, 643 (1958).
11. A. Güntherschulze and H. Betz, *Z. Physik.*, **91**, 70 (1934); **92**, 367 (1934).
12. D. A. Vermilyea, *Acta Met.*, **1**, 282 (1953); **2**, 476, 482 (1954); **3**, 106, (1954). *This Journal*, **102**, 655 (1955).
13. E. J. W. Verwey, *Physica*, **2**, 1059 (1935).
14. N. Cabrera and N. F. Mott, *Rept. Progr. Phys.*, **12**, 163 (1949).
15. L. Young, "Anodic Oxide Films," Academic Press, London and New York (1961).
16. U. R. Evans, *J. Chem. Soc.*, **1927**, 1020.
17. J. E. O. Mayne and M. J. Pryor, *ibid.*, **1949**, 1831.
18. W. H. Vernon, F. Wormwell, and T. J. Nurse, *J. Iron Steel Inst.*, **150**, 281 (1944).
19. E. M. Mahla and N. A. Nielsen, *J. (and Trans.) Electrochem. Soc.*, **93**, 1 (1948).
20. W. Schwarz, *Z. Elektrochem.*, **55**, 170 (1951).
21. L. Tronstad and L. W. Borgmann, *Trans. Faraday Soc.*, **30**, 349 (1934); L. Tronstad, **29**, 502 (1933).
22. K. J. Vetter, *Z. Elektrochem.*, **58**, 230 (1954).
23. K. G. Weil, *ibid.*, **59**, 11 (1955); U. F. Franck and K. G. Weil, *ibid.*, **56**, 814 (1952).
24. I. Langmuir, *J. Am. Chem. Soc.*, **38**, 2267 (1946).
25. B. V. Ershler, *Doklady Akad. Nauk S.S.S.R.*, **37**, 258 (1946).
26. H. H. Uhlig, *Ind. Engng. Chem.*, **32**, 1490 (1940).
27. C V. King and E. Rau, *This Journal*, **103**, 331 (1956).
28. H. H. Uhlig and S. S. Lord, *ibid.*, **100**, 216 (1956).
29. R. Ch. Burshtein, N. A. Shumilova, and K. Golbert, *Acta Physicochim. U.R.S.S.*, **21**, 785 (1956); N. A. Shumilova and R. Ch. Burshtein, *Doklady Akad. Nauk. S.S.S.R.*, **41**, 475 (1948); R. Ch. Burshtein, *Z. Elektrochem.*, **62**, 655 (1958).
30. Y. M. Kolotyrkin and W. M. Knasheva, *Zhur. fiz. Khim.*, **30**, 1990, (1956).
31. E. A. Aykasjan and A. J. Fedorova, *Doklady Akad. Nauk. S.S.S.R.*, **86**, 1137 (1952); A. N. Frumkin and E. A. Aykasjan, *ibid.*, **100**, 315 (1955).
32. Y. M. Kolotyrkin, *Z. Elektrochem.*, **62**, 665 (1958).
33. L. V. Vanyukova and B. N. Kabanov, *Zhur. fiz. Khim.*, **28**, 1025 (1954).
34. A. Bewick, A. Bewick, M. Fleischmann, and M. Liler, *Electrochim. Acta*, **1**, 83 (1959); A. Bewick and M. Fleischmann, *ibid.*, **8**, 89 (1963).
35. M. Fleischmann, H. R. Thirsk, and I. Tordesillas, *Trans. Faraday Soc.*, **58**, 1865 (1962).
36. M. Fleischmann and M. Liler, *Trans. Faraday Soc.*, **54**, 1370 (1958).
37. M. Avrami, *J. Chem. Phys.*, **7**, 1103 (1939); **8**, 212 (1940); **9**, 177 (1941).
38. A. Bewick, Ph.D. Thesis, University of Durham (1961).
39. A. Bewick, M. Fleischmann, and H. R. Thirsk, *Trans. Faraday Soc.*, **58**, 2200 (1962).
40. M. Fleischmann, K. S. Rajagopalan, and H. R. Thirsk, *ibid.*, **59**, 741 (1963).
41. I. N. Stranski, *Z. phys. Chem.*, **136**, 259 (1928).
42. I. N. Stranski and R. Kaishev, *Physikal. Z.*, **36**, 393 (1935).
43. M. Volmer, "Die Kinetik der Phasenbildung," Steinkopf, Dresden und Leipzig (1939).
44. W. K. Burton, N. Carbrera, and F. C. Frank, *Phil. Trans.*, **A243**, 299 (1951).
45. W. Lorenz, *Z. Naturf.*, **9A**, 716 (1954); *Z. phys. Chem.*, **17**, 136 (1958).
46. D. A. Vermilyea, *J. Chem. Phys.*, **25**, 1254 (1956).
47. A. Bewick, M. Fleischmann, and H. R. Thirsk, To be published.
48. D. C. Grahame, *Chem. Revs.*, **41**, 441 (1947). R. Parsons, Chap. 3 in "Modern Aspects of Electrochemistry," J. O'M. Bockris, Editor, Butterworths, London (1954).
49. D. C. Grahame and R. Parsons, *J. Am. Chem. Soc.*, **83**, 1291 (1961).
50. M. Fleischmann, J. Pattison, and H. R. Thirsk, To be published.
51. M. Fleischmann, K. S. Rajagopalan, and H. R. Thirsk, To be published.
52. H. Arnefelt, *Arkiv. f. Mat. Astron. Fysik. B.*, **23**, No. 2 (1932).
53. H. E. Swanson and E. Tatge, N.B.S. Circular 539, I, 33 (1953).
54. Strukturberichte II 258.
55. Strukturberichte I 161.
56. R. Becker and W. Döring, *Ann. Phys.*, **24**, 719 (1935).

Throwing Power of the Current in Anodic and Cathodic Protection

W. A. Mueller

Pulp and Paper Research Institute of Canada, Montreal, Quebec, Canada

ABSTRACT

Based on Ohm's and Kirchhoff's laws, a differential equation is derived relating the changing potential slope in the length direction of a pipe to the current density at the inner pipe surface. The extension of the pipe that can be passivated or maintained in the passive state by supplying current with one cathode is formulated for linear as well as exponential types of polarization curves and for pipes of finite and infinite length. Completely passivated pipes can be kept in the passive state over a much greater distance from the cathode than partly passive pipes. Agreement is found with reported experimental data on the throwing power of anodic protection. The same basic equations are valid with respect to the throwing power of cathodic protection, which is much smaller than that of anodic protection at comparable corrosiveness. On the application of anodic protection redox reactions of substances produced on cathodes, anodes on corroding metals and alloys can strongly influence the behavior.

For the application of anodic protection (1-6) in any lengthy vessel the throwing power (4) of the current is of primary importance. Evidently passivity is reached very rapidly in a vessel when the current density on its whole surface surpasses the maximum value of the polarization curve. However, even at lower average current densities, formation and expension of passivity occur when the current density locally surpasses the maximum value of the polarization curve. After the area of best current

supply has been passivated, more distant areas receive an increasing fraction of current.

A study of this problem has been carried out by Edeleanu and Gibson (7). They developed an experimental arrangement for the derivation of the throwing power of anodic protection. To this end a wire fed into a glass tube which was filled with an electrolyte was used as anode. From the wire the current flowed through the electrolyte to the cathode which was attached to the opening of the glass tube. From the length of the passivated area in the glass tube and from the current supplied, conclusions were made about the length of a pipe (made of the same metal as the tested wire) that can be passivated by current supply from one end. In this paper the throwing power of the current in anodic and cathodic protection is derived theoretically from polarization curves without the requirement of any other experimental data.

For the practical application of anodic protection a rough estimation of the required current is often possible without extended calculation. The high current required for initial passivation is equal to, or smaller than the product of the exposed surface area and the maximum current density of the pertinent polarization curve. In a vessel of lengthy shape, stepwise passivation can reduce the necessary current to a fraction of the amount required for simultaneous passivation. Also passivation from properly distributed cathodes or from both ends of tubes reduces the required current. The reader who is interested in practical application only, may omit the study of the complicated derivations to find most practical suggestions in the discussion.

Basic Derivation

This derivation refers to a pipe filled with an electrolyte of the specific resistance ρ ohm x cm. For the sake of simplicity a constant cross section of the pipe and a clean inner surface are assumed. Irregularities in the metal composition and deposits of foreign material are excluded.

The potential slope in the length direction of the pipe is according to Ohm's law

$$\frac{dE}{dx} = -\rho I_L \qquad [1]$$

where E is the potential, x the length coordinate of the pipe, and I_L the current density in the length direction of the pipe.

Kirchoff's law may now be applied to calculate the change of the current in the length direction occurring when a fraction of it is branched off to the pipe surface. The current in the length direction of the pipe is $I_L \pi R^2$ where R is the radius of the pipe. The current exchange with the pipe surface between x and $x + dx$ amounts to $2\pi R I_S dx$, where I_S is the current density at the pipe surface. Hence

$$\frac{dI_L}{dx} = -\frac{2}{R} I_S \qquad [2]$$

dI_L/dx can be derived from Eq. [1]. Thus a differential equation of general validity is derived (8)

$$\frac{d^2E}{dx^2} = \frac{2\rho}{R} I_S \qquad [3]$$

Equation [3] can be used for the derivation of $E = f(x)$ if the polarization curve is known, *i.e.*, the current density I_S as a function of the potential difference between pipe surface and electrolyte. It serves to derive the throwing power of the current in anodic and cathodic protection. In the present derivation the throwing power of the current with respect to anodic protection is expressed in two different ways: (*a*) as the maximum length of a pipe that can be passivated by current supplied from one end of the pipe which was originally in the active state, and (*b*) the maximum length of an originally passive pipe which can be maintained passive by supplying current. With respect to cathodic protection, the throwing power of the current is the maximum length of the pipe within which the corrosion rate is substantially reduced by cathodic protection. The values of R, ρ, and of the length of the pipe are required for the calculation. Equation [3] can be applied to any form of the polarization curve. Winsel (9) treated a similar problem, the distribution of current in porous electrodes. He limited the derivation to exponential polarization curves only, whereas in this paper the cases of linear current-density-potential relation and of potential-independent current density are also discussed.

Application to an Exponential Polarization Curve in the Active State with Respect to Anodic Protection

Initially the whole pipe may be in the active state. It is then passivated by anodic protection up to a certain distance from the cathode. The active state is assumed to be stable as indicated by a positive current density at the maximum of the polarization curve (1, 3, 10). The passive state may be stable or unstable, but in any case the current density in the passive state should be negligibly low in comparison to the current density in the active state.

For example, the polarization curve may be of the form given in Fig. 1 (12). For the slope of the polarization curve in the active state the decline of the current density may follow approximately the equation (12).

$$I_S = 2I_{SM} \exp \beta(E - E_M) \qquad [4]$$

where I_{SM} is the maximum value of I_S, β the exponent (12) (volt^{-1}), and E_M the potential at which I_S is equal to I_{SM}. The numerical factor 2 in Eq. [4] is only an approximate value (12); it equals unity at $E = E_M$.

After substituting I_S from Eq. [4] into Eq. [3]

$$\frac{d^2E}{dx^2} = \frac{4\rho}{R} I_{SM} \exp \beta(E - E_M) \qquad [5]$$

which is valid for $E_M - E > 0$.

For $E = E_M$, $\exp \beta(E - E_M) = 1$ and therefore

$$\left(\frac{d^2E}{dx^2}\right)_{(E=E_M)} = \frac{4\rho}{R} I_{SM} \qquad [6]$$

The apparent deviation of Eq. [6] from Eq. [3] by the factor 2 is caused by the deviation of the

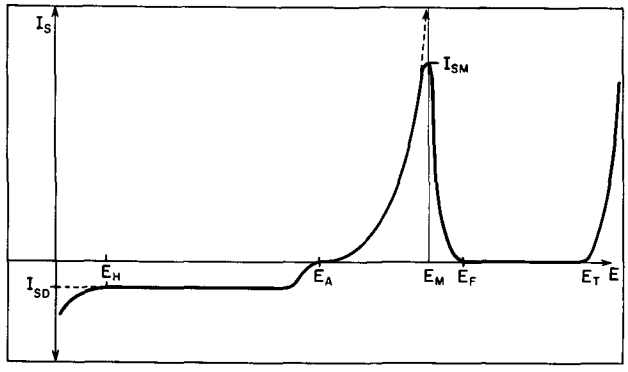

Fig. 1. Schematic diagram of a polarization curve composed of an exponential branch of the anodic dissolution current (10) leading to the constant very low current density in the passive state and of the diffusion current I_{SD} in the active state.

polarization curve from the exponential course when approaching I_{SM} (see definition of E_M).

It is easily shown that

$$\frac{dE}{dx} = -\left(\frac{4\rho}{R} I_{SM} \frac{2}{\beta} \exp \beta (E - E_M) + C\right)^{1/2} \quad [7]$$

is the solution of the differential Eq. [5], because Eq. [5] results from differentiation of Eq. [7]. It is understood from the derivation that Eq. [7] is valid for $E < E_M$. As the polarization curve reaches the maximum value of I_S at E_M, the deviation of dE/dx from Eq. [7] becomes very pronounced.

With respect to pipes of various lengths the value of C can be derived from the assumption $dE/dx = 0$ at the closed end of the pipe. Of course, the limits of the validity of Eq. [4] are to be considered. For a pipe of finite length

$$C = -\frac{8 \rho I_{SM}}{R \beta} \exp \beta (E_E - E_M) \quad [8]$$

where E_E is the potential reached at the closed end of the pipe.

After substitution into Eq. [1], I_L is derived by integration

$$I_L = \left(\frac{8 I_{SM}}{\rho R \beta}\right)^{1/2} \left((\exp \beta(E - E_M) - \exp \beta(E_E - E_M) \right)^{1/2} \quad [9]$$

For the potential $E = E_M$, Eq. [9] becomes

$$I_{LM} = \left(\frac{8 I_{SM}}{\rho R \beta}\right)^{1/2} (1 - \exp \beta (E_E - E_M))^{1/2} \quad [10]$$

I_{LM} is the current density flowing in the length direction of the pipe where the potential is E_M.

In an analogous manner the behavior in the range of the conversion from active to passive states can be derived, assuming an exponential decrease of the current density (10) according to

$$I_S = 2 I_{SM} \exp \gamma (E_M - E) \quad [11]$$

where γ is a constant. Close to $I_S = I_{SM}$ a deviation occurs as discussed with respect to Eq. [6] and [7].

The current density in the length direction is derived for the potential range between E_M and the Flade potential E_F

$$I_L = -\left(\frac{8 I_{SM}}{\rho R \gamma}\right)^{1/2} (+ \exp \gamma (E_M - E) - \exp \gamma (E_M - E_F))^{1/2} + I_{LF} \quad [12]$$

where I_{LF} is the current density flowing from the passive to the active range of the pipe.

Usually the term $\exp \gamma (E_M - E_F)$ can be neglected and I_{LM} is given by

$$I_{LM} = -\left(\frac{8 I_{SM}}{\rho R \gamma}\right)^{1/2} + I_{LF} \quad [13]$$

I_{LF} results from Eq. [10] and [13]

$$I_{LF} = \left(\frac{8 I_{SM}}{\rho R \gamma}\right)^{1/2} + \left(\frac{8 I_{SM}}{\rho R \beta}\right)^{1/2} (1 - \exp \beta (E_E - E_M))^{1/2} \quad [14]$$

Equation [14] is valid for a pipe in which the potential $E_E < E_M$ is reached at the end located distant from the current supply.

The density of the current which flows from the cathode to the active range of the pipe is I_{LF}. If I_S in the passive state can be neglected, I_L in the passive state equals I_{LF} and the slope of the potential in the passive range is ρI_{LF}. The current supplied to the cathode can be increased so as to reach the potential of the borderline E_T between passive and transpassive range at the pipe surface close to the cathode. Then in agreement with Edeleanu and Gibson (7) the passive length L_P of the pipe is derived from Eq. [1]

$$L_P = \frac{E_T - E_F}{I_{LF} \rho} \quad [15]$$

By substitution in Eq. [14] L_P is derived for a pipe of finite length

$$L_P = \frac{(E_T - E_F)}{\left(\frac{8 \rho I_{SM}}{R \gamma}\right)^{1/2} + \left(\frac{8 \rho I_{SM}}{R \beta}\right)^{1/2} (1 - \exp \beta (E_E - E_M))^{1/2}} \quad [16]$$

If the whole pipe is initially in the active state, the current density at the pipe surface close to the cathode may initially be greater than I_{SM}. Hence the potential of that area of the pipe shifts rapidly to the passive range. The increasing extension of the passive range can be calculated from Eq. [16] if the changing polarization curve is known with respect to a surface that is active before the passivating current is switched on. For a pipe of limited length the passive area becomes somewhat further extended than for a pipe of infinite length. If two cathodes of distance D apart are used, D can be chosen twice the length of a tube with closed ends that can be passivated by applying current at one point only. For the calculation of L_P the value of E_E in Eq. [16] is required.

Hence the change of the potential with the distance from the source of current is of interest. Across the passive region of the pipe, dE/dx equals

$-I_{LF}\rho$. As in the active range an increasing fraction of I_L passes to the pipe surface, dE/dx decreases with increased distance from the source of current. According to Eq. [7] and [8] the relation between potential and the distance $x - x_M$ from the point where $E = E_M$ is given by

$$x - x_M = -\left(\frac{R\beta}{8\rho I_{SM}}\right)^{1/2} \int_{E_M}^{E} \frac{dE}{\left(\exp\beta(E - E_M) - \exp\beta(E_E - E_M)\right)^{1/2}} \quad [17]$$

Equation [17] can be integrated by applying the standard integral

$$\int \frac{dx}{(a + \exp px)^{1/2}} = \frac{-2}{p\sqrt{-a}} \arcsin(-a)^{1/2} \exp -\frac{p}{2}x + C \quad [18]$$

to Eq. [17], giving

$$x - x_M = \left(\frac{R}{2\beta\rho I_{SM}}\right)^{1/2} \cdot \frac{\arcsin \exp\frac{\beta}{2}(E_E - E_M)\left(\exp -\frac{\beta}{2}(E - E_M) - 1\right)}{\exp\frac{\beta}{2}(E_E - E_M)} \quad [19]$$

Equation [19] represents the relation between the metal-electrolyte potential difference and the distance $(x - x_M)$ from the point where $E = E_M$. For the application of Eq. [19] $(x - x_M)$ might be calculated as a function of $(E - E_M)$ for a variety of $(E_E - E_M)$ values.

For a pipe of infinite length $\exp\frac{\beta}{2}(E_\infty - E_M)$ can be neglected. Hence the relation is considerably simplified and can be formulated

$$x - x_M = -\left(\frac{R}{2\beta\rho I_{SM}}\right)^{1/2} \left(\exp -\frac{\beta}{2}(E - E_M) - 1\right) \quad [20]$$

From Eq. [20] the potential difference $E - E_M$ is given by

$$E - E_M = -\frac{\beta}{2} \log\text{nat}\left[\frac{x_M - x}{\left(\frac{R}{2\beta\rho I_M}\right)^{1/2}} + 1\right] \quad [21]$$

The potential changes approximately proportionally to the logarithm of the distance from the point where $E = E_M$. These equations hold only in the potential range where anodic dissolution produces the main fraction of the current (Eq. [4]). For instance, the equations no longer apply when H_2 development causes the flow of current at an amount comparable to that caused by the dissolving metal.

The polarization curve does not always follow the model course assumed in the above derivation. For instance, it may follow a straight line from the maximum value I_M at E_M to the stable potential in the active state E_A (Fig. 2)

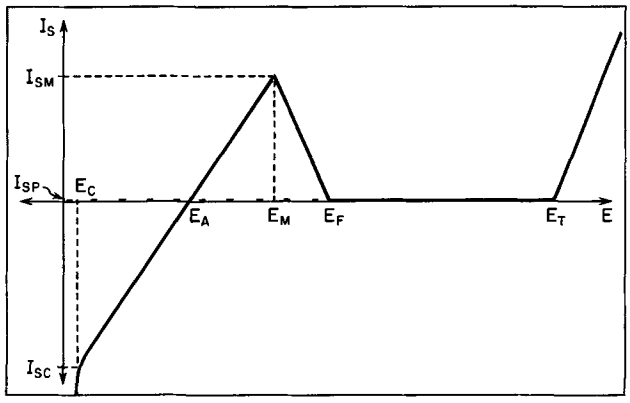

Fig. 2. Schematic diagram of a polarization curve composed of branches which change linearly with the potential.

$$I_S = I_{SM}\frac{E - E_A}{E_M - E_A} \quad [22]$$

According to Eq. [3] the corresponding differential equation is

$$\frac{d^2(E - E_A)}{dx^2} = \frac{2\rho I_{SM}}{R}\frac{E - E_A}{E_M - E_A} \quad [23]$$

In a manner analogous to the above derivation the potential-distance relation is derived to

$$\frac{E - E_A}{E_M - E_A} = \exp\sqrt{\frac{2\rho I_{SM}}{R(E_M - E_A)}}(x - x_M) \quad [24]$$

where $(x - x_M)$, the distance of the point of the potential E from that of the potential E_M, is zero or negative. This equation shows that the potential approaches the stable active potential with an exponential curve. It applies to the potential range $E_A \leqq E \leqq E_M$.

Application to the Conditions of the Passive State

It has been proven (4) that excellent throwing power is obtained with respect to anodic protection of a lengthy tube even if the current is supplied only at one open end. This is possible because the density of the anodic dissolution current in the demonstrated case is almost negligible. To investigate this effect, assumptions have to be made with respect to the current-density-potential relation. For the sake of simplicity a constant current density ($I_S = I_{SP}$) may be assumed. Equations [1] to [3] are the basis of any such derivation. Integration of Eq. [3] results in

$$\frac{dE}{dx} = \frac{2\rho}{R}\int I_{SP}\,dx \quad [25]$$

At the end of the pipe $dE/dx = 0$ and $(x - x_0)$ may be the distance from the closed end, hence

$$\frac{dE}{dx} = -\frac{2\rho}{R} I_{SP}(x - x_0) \quad [26]$$

The potential is derived by another integration

$$E - E_o = \frac{\rho I_{SP}}{R}(x - x_0)^2 \quad [27]$$

where E_o is the potential at $x = x_0$. If the potential of the pipe at the point which is closest to the cathode is E_T and the potential at the end of the Flade potential E_F, $(x - x_0) = L_M$, which is the maximum length that can be kept in the passive state by means one cathode, then

$$L_M = \left(\frac{(E_T - E_F)R}{\rho I_{SP}} \right)^{1/2} \quad [28]$$

Of course for safety reasons the total difference $(E_T - E_F)$ cannot be used; the potential at the end has to be higher than E_F to make sure no shift to the active state can occur even when conditions are changed temporarily.

Equation [28] may now be compared with the data given by Sudbury and co-workers (4) with respect to the passivation of a tube of 60 ft (1820 cm). The tube radius was ¾ in. (1.91 cm). The potential drop was 0.4v; the specific resistance of 67% by weight H_2SO_4 is about 1.54 ohm x cm at 75°F (13). The current density is therefore calculated to

$$I_{SP} = 0.15\ \mu a/cm^2 \quad [29]$$

if the current was supplied only from one end of the tube, and to

$$I_{SP} = 0.60\ \mu a/cm^2$$

if the current was supplied from both ends of the tube, *i.e.*, through the back flowing acid as well as through the acid entering the pipe.

Shock and others (5) found at 304 stainless steel immersed in 67% H_2SO_4 by weight a decreasing current density which attained 0.6 $\mu a/cm^2$ after 1-2 hr. On the other hand, it is known that the decrease of the current density continues for days and weeks (11), and the calculated value of 0.15 $\mu a/cm^2$ may have been reached during the operation of anodic protection. In any case, the calculations give the right order of magnitude.

Throwing Power of Cathodic Protection

The equations of general validity, *viz.*, Eq. [1]-[3], can also be applied to derive the throwing power of cathodic protection with respect to pipes. In this application the form of the polarization curve in the cathodic range is of decisive importance. If the negative current density in the cathodic range follows the same trends as the positive current density in the anodic range, the same equations apply to the current-density-potential-distance relation. For instance, the polarization curve may follow a straight line from the current density I_{SC} (Fig. 2) attained at the most cathodic potential to zero at the potential E_A. Then the current density I_S amounts to

$$I_S = I_{SC} \frac{E - E_A}{E_C - E_A} \quad [30]$$

Equation [30] is equal to Eq. [22] except for the constants. In an equation analogous to Eq. [24] the potential distance relation can be formulated

$$\frac{E - E_A}{E_C - E_A} = \exp \sqrt{\frac{2\rho I_{SC}}{R(E_C - E_A)}}\,(x - x_C) \quad [31]$$

where $x = x_C$ at the potential $E = E_C$. From Eq. [31] the corrosion rate in a pipe can be calculated as a function of the distance from the anode, provided the current-density-potential relation follows Eq. [30].

There is another group of polarization curves in which the negative current density maintains a constant level over an extended range. For instance, this type of polarization curve is formed when the total depolarization current is diffusion-controlled. Under these conditions Eq. [25]-[27] apply when I_{SP} is replaced by the diffusion current I_{SD} (Fig. 1) and E_O by E_A. Analogous to Eq. [27] the current density-potential-distance relation is formulated

$$E - E_A = \frac{\rho I_{SD}}{R}(x - x_C)^2 \quad [32]$$

If the part of the pipe which is closest to the anode is kept at the potential E_H at which the negative current begins to increase rapidly (because of H_2 development) the range covered by cathodic protection is

$$L_M = \left(\frac{(E_H - E_A)R}{\rho I_{SD}} \right)^{1/2} \quad [33]$$

I_{SD} is greater than or equal to the density of the corrosion current I_{corr}. Hence under the conditions of Eq. [33] the distance from the anode at which cathodic protection would begin to reduce the corrosion rate in a pipe is equal to, or lower than $\left(\frac{(E_H - E_A)R}{\rho I_{corr}} \right)^{1/2}$. For an effective protection of the pipe the distance from the anode should be considerably smaller. Equation [28] equals Eq. [33] except for the definition of the current densities. However, when the range protected by cathodic protection becomes large because of a very small value of I_{SD}, the corrosion rate found at that small value of I_{SD} which is reduced by cathodic protection is very small. But in anodic protection I_{SP} can be many orders of magnitude smaller than the corrosion current in the active state. Hence a high throwing power of the current in anodic protection can be attained even if the corrosion rate in the active state is high.

Discussion

The present derivation is based on the assumption that the actual polarization curve is known for the conditions under consideration. In addition to the polarization curve, only Ohm's and Kirchhoff's laws are used in Eq. [1]-[3]. Detailed equations are derived with respect to a polarization curve that can be formulated as a Tafel relation. For the application of the derived equations an exact knowledge of actual polarization curves is of fundamental importance. Swinging potentials and time-dependent polarization curves require particular attention. Also differences in the supply of chemicals to the metal surface may have a considerable influence. In this respect the strong influence of reagents produced by corrosion and by the applied current may be mentioned. The rapid dissolution of the metal in the boundary region between active and passive areas causes a rapidly increasing concentration of the produced metal ions. The partial current originating from redox reactions of these ions has to be con-

sidered in the calculations. For instance, if in an iron pipe the electrolyte flows from active to passive areas (14), bivalent iron ions formed in the active range would react with the passive fraction of the pipe to form trivalent iron ions. The anodic current caused by this redox reaction would decrease the current supplied to the active fraction of the pipe, thus strongly reducing the throwing power of anodic protection. In an analogous manner an electrolyte flowing from passive and transpassive to active areas might carry oxidizing reagents which would initiate a cathodic partial current in the active area thus reducing the total current density, *i.e.*, the throwing power of the current in anodic protection would be increased. On the other hand, reducing reagents produced at the cathode and carried by the flowing electrolyte would have the opposite effect. Evidently redox reactions and their dependency on the flow direction of the electrolyte can strongly influence the throwing power of anodic and cathodic protection. These conclusions suggest methods to improve the throwing power of electrochemical protection, and they may explain some important phenomena (14). No experiments have been carried out to corroborate the derived equations, which appear to be reliable because no arbitrary assumptions had to be made in the basic derivations of Eq. [1]-[3]. The comparison with the experimental data of Sudbury and co-workers shows a reasonable agreement.

A striking result of these derivations is the great difference between the excellent throwing power of the anodic current in a completely passivated system and its fairly limited throwing power in a pipe which is partly in the active state. This result can be expressed by the ratio L_M/L_{P_∞}, where L_{P_∞} is the length of the passivated fraction of the pipe of infinite length which is in the active state except for the passivated fraction close to the cathode. From Eq. [16] and [28] is derived

$$\frac{L_M}{L_{P_\infty}} = \left(\frac{I_{SM}}{I_{SP}}\right)^{1/2}\left(\frac{8}{E_T - E_F}\right)^{1/2}\left[\left(\frac{1}{\beta}\right)^{1/2} + \left(\frac{1}{\gamma}\right)^{1/2}\right] \quad [34]$$

The factor $\left(\frac{8}{E_T - E_F}\right)^{1/2}\left[\left(\frac{1}{\beta}\right)^{1/2} + \left(\frac{1}{\gamma}\right)^{1/2}\right]$ is usually close to unity. As the ratio I_{SM}/I_{SP} is in the range 10^4 to 10^8 in most cases, the protection in a completely passivated system covers about 10^2 to 10^4 times the length protected in a system which is partly in the active state. The initial passivation of an originally active pipe requires special methods to attain the extremely high throwing power known for completely passivated systems. The pipe might be passivated by filling with a passivating solution at low temperature (7, 15). Once passivity has been attained in the total length of the pipe, current is required only to maintain passivity when replacing the passivating solution by the solution to be conducted in the pipe. If the passive state is unstable, reactivation is caused by interruption of the current. With respect to a portion of a tube which is just being reactivated, the current required for repassivation is much less than the current required for the initial passivation.

Any discussion of this paper will appear in a Discussion Section to be published in the December 1963 JOURNAL.

REFERENCES

1. C. Edeleanu, *Nature*, **173**, 739 (1954); *Metallurgia*, **50**, 113 (1954); *Corrosion Technol.*, **2**, 204 (1955).
2. Milan Prazak, *Hutnické listy*, **11**, 644 (1956).
3. W. A. Mueller, *Can. J. Technol.*, **34**, 162 (1956); *Tappi*, **40**, [3], 129 (March 1957); *Pulp Paper Mag. Can.*, **60**, T3 (January 1959); *Tappi*, **42**, [3], 179 (March 1959).
4. J. D. Sudbury, O. L. Riggs Jr., and D. A. Shock, *Corrosion*, **16**, 91 (1960).
5. D. A. Shock, O. L. Riggs Jr., and J. D. Sudbury, *ibid.*, **16**, 99 (1960).
6. O. L. Riggs, Jr., Merle Hutchinson, and N. L. Conger, *ibid.*, **16**, 102 (1960).
7. C. Edeleanu and J. G. Gibson, *Chemistry and Industry*, **10**, 301 (March 1961).
8. W. A. Mueller, *Corrosion*, **18**, 359t (1962).
9. A. Winsel, *Z. Elektrochem.*, **66**, 287 (1962).
10. K. J. Vetter, in "Passivierende Filme und Deckschichten," H. Fischer, K. Hauffe, and W. Wiederholt, Springer Verlag (1956).
11. W. A. Mueller, *Corrosion*, **18**, 73t (1962).
12. W. A. Mueller, *This Journal*, **107**, 157 (1960).
13. A. N. Campbell, E. M. Kartzmark, D. Bisset, and M. E. Bednas, *Can. J. Chem.*, **31**, 303 (1953).
14. J. D. Sudbury and O. L. Riggs, Private communication.
15. W. A. Mueller, *Corrosion*, **17**, 557t (1961).

On the Passivity of Manganese in Acid Solutions

K. E. Heusler

Max-Planck-Institut für Metallforschung, Abteilung Sondermetalle, Stuttgart, Germany

A review of the literature concerning the anodic behavior of manganese gives some indication that manganese can be passivated. Passing sufficiently large anodic currents through a manganese electrode enobles the potential until oxygen is evolved and permanganate is formed (1). One would expect (2) the passive manganese to be covered by a thin, invisible, and electron conducting oxide layer similar to the layers known to exist on iron and chromium. However, in most of the earlier experiments with manganese passivity was accompanied with formation of a thick, visible deposit of manganese dioxide. The thick deposits could have been formed by oxidation of manganous ions or by decomposition of permanganate from the solution.

Detailed information on passive manganese is lacking. Polarization curves of passive manganese have not yet been measured, and it is an open ques-

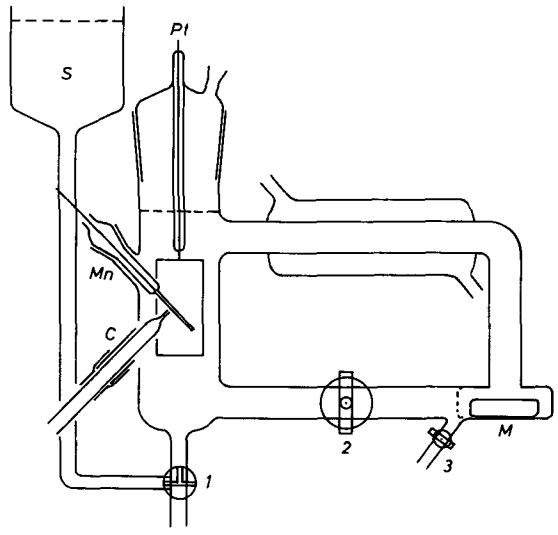

Fig. 1. Electrolytic cell with Mn, manganese electrode; Pt, platinum counter electrode; C, Haber-Luggin capillary; S, supply of electrolyte; M, magnetic stirrer. In order to renew the electrolyte, stopcock 2 was closed and stopcock 3 was opened. After removing from the cell about 2/3 of the electrolyte, stopcock 1 was opened to fill the cell.

tion whether an activation potential of the type first discovered by Flade (3) on iron can also be found on manganese. An attempt to clarify some of these problems is presented in this paper.

Experimental

Smooth manganese electrodes were produced by cathodic deposition of manganese on platinum wire electrodes from a solution of 1M $MnSO_4$ and 1M $(NH_4)_2$ SO_4 adjusted to pH = 2.2 by addition of H_2SO_4. The current density was 50 ma/cm^2. The solution was kept at about 22°C.

Most of the experiments were performed in 0.5M orthophosphoric acid solutions which had been partially neutralized by addition of sodium hydroxide until the desired pH value was reached. All solutions were prepared from Merck analytical grade chemicals and triple distilled water.

The cell (Fig. 1) was designed to allow for effective renewal of the solution, which could be circulated by a magnetic stirrer. Experiments were performed at about 22°C.

A Wenking potentiostat was used in the potentiostatic circuit. Currents could be measured by feeding the voltage drop across a precision resistor to the input of a Cary 32 vibrating reed amplifier connected to a Siemens Linecomp recorder. The vibrating reed amplifier also served to determine time dependences of the potential in galvanostatic experiments. Potentials were measured *vs.* a saturated calomel electrode (SCE).

Results

Passivation.—The manganese could be passivated in phosphoric acid solutions by applying an anodic current density of several hundred ma/cm^2. Passivation usually started from a certain point of the electrode apparently corresponding to the highest local current density and spreading from there over the rest of the electrode. During passivation a zone where permanganate and small bubbles of oxygen were produced moved across the electrode surface replacing the zone where active manganese dissolved with hydrogen evolution. After completion of the passivation the electrode was covered by a brown deposit which was easily swept away on renewing the solution. In the solution free of manganese ions the manganese was kept potentiostatically at a potential in the region between the potentials of oxygen evolution and of activation. The metallic appearance of the manganese was retained even after days.

Polarization curves.—A polarization curve measured under potentiostatic conditions in 0.5M orthophosphate solution at pH = 1.9 one day after passivation is shown in Fig. 2. The Tafel line at noble potentials corresponds to oxygen evolution. The region of formation of permanganate at very high potentials was avoided during the experiments. At more negative potentials the current density was almost potential independent. Such behavior is characteristic of passive metals (4). The current density corresponding to the corrosion rate of the passive metal increased at lower potentials, and the manganese finally became active.

The points on the polarization curve were taken by changing the potential stepwise and waiting for 1 to 2 hr until the current density became approximately independent of time. Immediately after shifting the potential in the negative direction a cathodic current or an anodic current smaller than the steady-state current flowed. If the potential was made more noble, the anodic current at first was larger than in the steady state. These observations indicate that after a shift of the potential certain electric charges, which are large compared to those expected for charging the double layer capacity, are stored in the electrode and serve to change the thickness or the state of oxidation of the passive layer.

The potential independent corrosion rate of the passive manganese was still decreasing slowly after

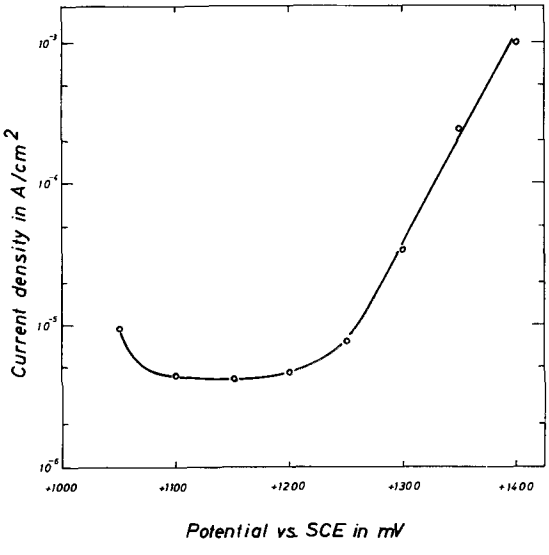

Fig. 2. Polarization curve of passive manganese in 0.5M sodium orthophosphate solution, pH = 1.9, measured after having maintained a potential of about E_{SCE} = + 1300 mv for one day after passivation.

several days. The corrosion current densities found after four days were about 1 $\mu a/cm^2$ at pH = 1.0 and about 0.1 $\mu a/cm^2$ at pH = 4 (5). These values taken in unstirred solutions at 22°C were three to four times lower than the corrosion current densities at 42°C.

It was difficult for two reasons to evaluate the corrosion current density quantitatively: In rapidly stirred solutions the current densities were a few tenths of a $\mu a/cm^2$ larger than in unstirred solutions. This pH-independent, additional current density apparently resulted from the oxidation of traces of manganous ions, phosphorous acid, or hydrogen diffusing to the electrode. Although the diffusion current density must be quite small in unstirred solutions, measurements of the corrosion current density were made uncertain at high pH values where the corrosion is very slow. Another difficulty arose at low pH values close to pH = 1, where only a minimum of the current density and no region of potential independent current density was observed. The reason for this effect is that the pH dependence of the potential of activation (see section on The Flade potential of Mn) is much larger than the pH dependence of the oxygen evolution reaction. The corrosion current density at about pH = 1 must be evaluated from the deviations from the Tafel line at low current densities.

The Flade potential of manganese.—To determine the Flade potential of manganese Flade's original method (3a) of self-activation was used. The manganese was kept passive for at least several hours at a fixed potential. The potentiostatic circuit then was interrupted and the time dependence of the potential was recorded (Fig. 3). At first the rate of decrease of the potential slows down, increasing again after a certain point of inflection has been passed. The point of inflection was taken as the Flade potential. The Flade potential is a function of the pH value of the solution, and it is not significantly influenced by the prehistory of the electrode. From Fig. 4, the pH dependence of the Flade potential of manganese (*vs.* S.H.E.) can be described by

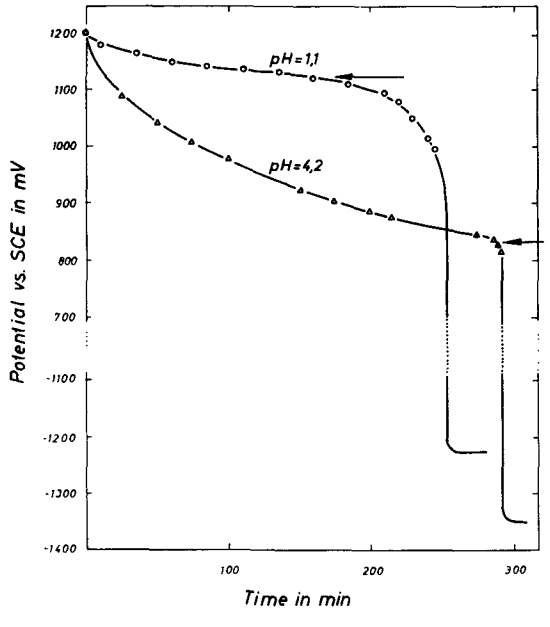

Fig. 3. Potential decay during self-activation of passive manganese in 0.5M sodium orthophosphoric acid solutions at different pH values.

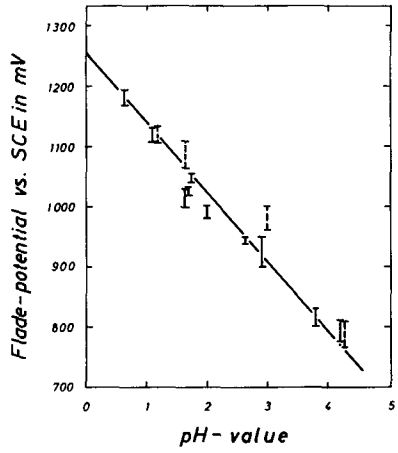

Fig. 4. Flade potential of manganese as a function of the pH value of sodium orthophosphoric acid solutions. (I) from potential decays; (I) from polarization curves.

$$E_{F(Mn)} = 1.50 - 0.118\,pH \qquad [1]$$

The Flade potential, as determined by the galvanostatic method of self-activation, must be expected to coincide with the potential corresponding to the first increase of the anodic current density when measuring the polarization curve under potentiostatic conditions from noble toward less noble potentials. In fact, within the experimental limits the same values of the Flade potential have been measured by both methods.

Factors influencing potential decay.—A manganese electrode covered by manganese dioxide obtained by keeping the manganese passive in a solution containing manganous ions, exhibited the same Flade potential as a passive manganese electrode of metallic appearance. The manganese dioxide slows down the potential decay, but it does not affect the value of the point of inflection corresponding to the Flade potential. In Fig. 3 the potential decay shown for pH = 1.1 is characteristic for an electrode covered with a visible deposit of manganese dioxide, whereas the potential decay shown for pH = 4.2 is characteristic for the normal case of a clean passive manganese electrode.

The time of activation, the interval from interrupting the potentiostatic circuit until the Flade potential is reached, increases with increasing pH of the solution and with ennobling of the potential at which the manganese had been kept potentiostatically.

The potential of the point of inflection and the time of activation are influenced by additions of manganous ions or ferrous ions to the solution, or by cathodic currents. The action of manganous and ferrous ions was tested in the following way: The potential decay was observed in a solution containing no manganese ions. When the potential approached the region close to the Flade potential the solution was replaced by an almost identical solution, but containing some manganous or ferrous salt. Figure 5 shows that the potential of the point

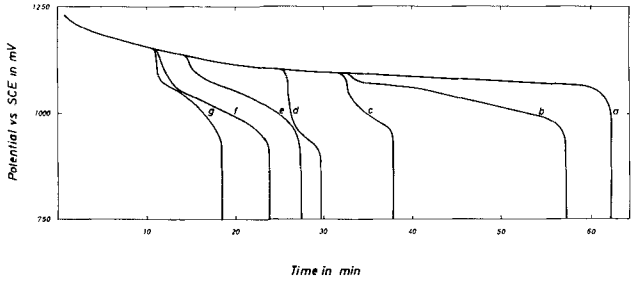

Fig. 5. Influence of reducing agents or cathodic currents on the potential decay during the activation of manganese in 0.5M orthophosphoric acid solution of pH = 1.95. a, normal potential decay; b, $c_{(Mn^{++})} = 10^{-5}$M; c, $c_{(Mn^{++})} = 10^{-4}$M; d, $c_{(Mn^{++})} = 10^{-3}$M; e, $j = -1.0$ μa/cm^2; f, $c_{(Mn^{++})} = 10^{-4}$M; g, $c_{(Fe^{++})} = 10^{-4}$M.

of inflection is made more negative than the Flade potential found in solutions free of Mn^{++} for concentrations $c_{(Mn++)} > 10^{-5}$M. The time of activation is markedly decreased.

Addition of Fe^{++} caused almost identical decay curves, if the Fe^{++} concentration was about one tenth of the Mn^{++} concentration. The same effects could be produced by applying cathodic currents. A current density of 1.0 μa/cm^2 corresponded to about $c_{(Mn++)} = 10^{-4}$M, a current density of 10 μa/cm^2 to about $c_{(Mn++)} = 10^{-3}$M.

Current impulses applied to the passive manganese during the potential decay should yield information on the state of oxidation of the passive layer. A linear relationship between the logarithm of the charge necessary to polarize the manganese to a given potential and the potential reached during the potential decay was observed (Fig. 6). If the potential decay had passed the Flade potential, the charge increased even more than exponentially. This is easily explained by the fact that the corrosion current density increases below the Flade potential. Only the difference of the applied current density to the corrosion current density can contribute to the charge stored in the passive layer.

If the pH value of the solution was suddenly changed during the potential decay, the potential

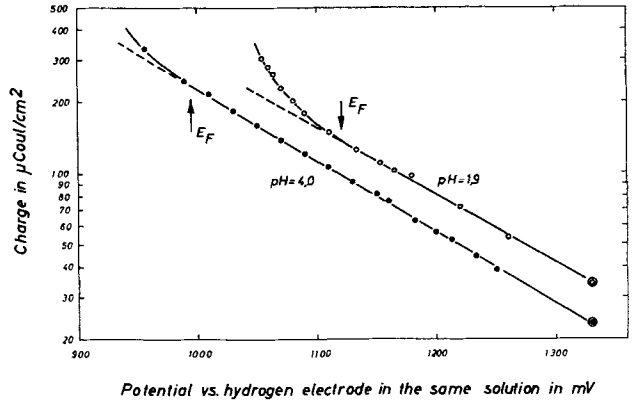

Fig. 6. Charge stored in the passive manganese as a function of the potential E_{HSS} vs. the hydrogen electrode in the same solution. By applying an anodic current density of 10 μa/cm^2 the potential was brought back to $E_{HSS} = +1330$ mv. Curves are corrected by adding a charge Q_o (dotted circle, circle within a circle) to the charges determined experimentally. Q_o is the charge which would be necessary to shift the potential of the passive manganese from $E_{HSS} = +1330$ mv further to $E \rightarrow +\infty$.

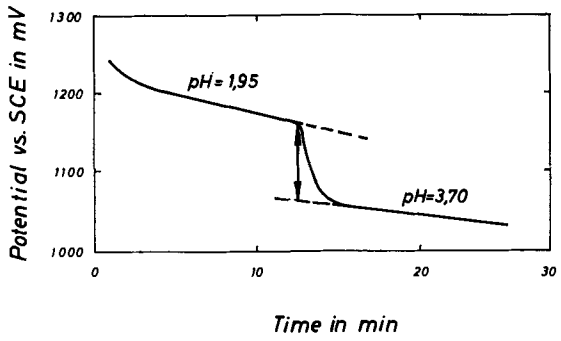

Fig. 7. Change of the potential of passive manganese in 0.5M orthophosphoric acid solution after replacing a solution of pH = 1.95 by a solution of pH = 3.70.

shifted by about $(\partial E/\partial pH) = -57$ (± 5) mv (Fig. 7).

Influence of anions on the passivity of manganese. —Some experiments conducted at various phosphate concentrations between 0.1 and 1.0M and in orthoarsenic acid solutions did not show any effect on the behavior of the passive manganese.

It was very difficult to passivate or keep the manganese passive in acid sulfate, perchlorate, or acetate solutions. This is connected, evidently, with the fact that the manganous salts of these anions are extremely soluble. Experiments by Agladze *et al.* (1) have demonstrated that manganese is more and more easily passivated in sulfuric acid solutions at concentrations from 10 to 22*N*, where the solubility of manganous sulfate is relatively low.

Discussion

The experiments described above are in accord with the assumption that a continuous oxide layer governs the electrochemical behavior of passive manganese in a way similar to that known for other passive metals. The Flade potential, in particular, is determined by properties of the oxide layer. Therefore it has to be decided whether the Flade potential is an equilibrium potential or whether it is determined by kinetic parameters.

The pH dependence of the Flade potential given by Eq. [1] cannot be explained as an equilibrium potential between two oxides or between an oxide and the metal:

$$MnO_x + y\,H_2O \leftrightarrow MnO_{x+y} + 2y\,H^+ + 2y\,e^- \quad x \gtrless 0 \quad [2]$$

All reactions of the type given by Eq. [2] have equilibrium potentials with the same pH dependence of 59 mv/pH as the reversible hydrogen electrode.

If the Flade potential corresponds to an equilibrium potential at all, the reaction must involve twice as many hydrogen ions as electrons and, consequently, manganese ions from the solution. The most probable reaction of that type is given by Eq. [3]

$$Mn^{++} + 2H_2O \leftrightarrow MnO_2 + 4H^+ + 2e^- \quad [3]$$

An equilibrium involving trivalent manganese ions in the solution is highly improbable, since this ion is unstable in orthophosphoric acid solutions. The standard potential of reaction [3] is $E_N = 1.23$v (6).

The Flade potential normalized to pH = 0 of E_F = 1.50v would be the reversible potential of reaction [3] at a manganous ion activity of $10^{-4.5}$M. The Flade potential should depend on the manganous ion activity by $\partial E/\partial \log a_{(Mn++)} = -29$ mv/decade. The effect found experimentally is about twice this value.

In addition, it is difficult to understand that the time of activation is considerably shortened by an increase of the manganous ion concentration. The manganous ions seem to act on the passive manganese as a reducing agent (7). This view is supported by the observation that the activation of passive manganese is affected by ferrous ions or by suitable cathodic currents in the same way as by manganous ions.

Very probably the Flade potential of manganese, as for iron, must be explained as resulting from the kinetics of dissolution of the passive oxide.

According to Vetter (2) the composition of an oxide at the oxide solution interface in solutions of different pH values is the same at equal potentials *vs.* the hydrogen electrode in the same solution. The conditions are that the oxide is a good electron conductor, and that the corrosion rate is small compared to the rate of exchange of oxygen ions between the oxide and the water of the solution. Both of these conditions are fulfilled: Oxygen evolution or any other redox reaction proceeds at normal overvoltages. Therefore the passive oxide must be a good electron conductor. Figure 7 shows that, on sudden change of the pH, the potential of the passive manganese responds by a potential change of about

$$(\partial E/\partial \mathrm{pH}) = -RT/F \qquad [4]$$

which is expected for an equilibrium between the oxygen ions in the oxide and in the water (2). No appreciable change of the state of oxidation can occur in the passive layer during this experiment.

Measured against the hydrogen electrode in the same solution the Flade potential of manganese is

$$E_{F(HSS)} = 1.50 - 0.059\ \mathrm{pH}\ (\mathrm{v}) \qquad [5]$$

Relation [5] means that at the Flade potential the passive oxide is in a lower state of oxidation at high pH values than at low pH values. The results given in Fig. 6 verify this conclusion. More charge must be stored in the passive layer at high pH values than at low ones in order to oxidize the layer existing at the Flade potential to a given state of oxidation. The proportionality between the logarithm of the charge and the potential reached during the potential decay indicates that the charge is stored by changing the state of oxidation of the passive oxide rather than the thickness. A change of thickness at constant composition of the oxide would yield a linear relation between charge and potential (8). The charge is only a measure of the amount of the reduced oxide reoxidized during the anodic pulse. Nothing is known about the distribution of the concentrations as a function of time and of the distance from the oxide-solution interface, nor about the activity coefficients as a function of the composition of the oxide. Therefore an explanation of the slope of the curve in Fig. 6 cannot be given without more experiments.

At the noble potentials where the manganese is passive, only some modification of manganese dioxide can exist thermodynamically. Since γ-MnO_2 can be reduced through a wide range of composition to α-MnOOH in a homogeneous phase (9), the reduced form of the oxide will be denoted as MnOOH and the oxidized form as MnO_2 without excluding other possibilities. It follows from thermodynamic considerations that

$$\partial E_{(HSS)}/\partial \log \left\{ \frac{a_{(MnOOH)}}{a_{(MnO_2)}} \right\} = -RT/F \qquad [6]$$

The ratio of the activities $a_{(MnOOH)}/a_{(MnO_2)}$ at the oxide solution interface should increase by one decade per pH at the Flade potential, as now can be concluded from Eq. [5]. Thus, the observed pH dependence of the Flade potential is caused by two effects, given by Eq. [4] and [6].

The kinetics of the dissolution of the passive oxide must be such that at noble potentials the oxide dissolves at a potential independent rate. If at less noble potentials a certain state of oxidation corresponding to the pH value of the solution is reached, the rate of dissolution increases as the potential is shifted into the negative direction. The mechanism of the reduction of manganese dioxide is not known sufficiently well. At potentials negative to the Flade potential of the manganese, a potential dependent reductive dissolution of manganese dioxide influenced by pH and composition of the oxide has been observed (9b, 10). This process may correspond to the increase of the corrosion rate of the manganese just below the Flade potential.

The activation of the passive manganese appears to be a process very similar to the activation of iron in neutral and alkaline solutions. The Flade potential, defined as the potential where the corrosion current density starts to increase when making the potential more negative, has a much greater pH dependence for iron in neutral and alkaline solutions than in acid solutions below pH = 4. The pH dependence of 59 mv/pH observed in acid solutions (3b) means that the Flade potential always corresponds to the same composition of the passive oxide. At pH > 4 the passive oxide on iron must be reduced more the higher the pH, in order to obtain a rate of the potential dependent, reductive dissolution exceeding the rate of the potential independent, nonreductive dissolution. In alkaline solutions at potentials negative to the Flade potential expected from the measurements in acid solutions, the passive layer has to be reduced from Fe_2O_3 to Fe_3O_4 almost completely before the actual Flade potential is reached at relatively negative potentials (11). Vetter and Klein (12) were able to detect the reduced form of the passive layer on iron in solutions of pH = 4 to pH = 7. At these low pH values the reduced form of the passive layer was found to dissolve very rapidly.

Acknowledgment

The author appreciates helpful discussions with Dr. H. Schurig of this Laboratory. Financial support

of the Arbeitsgememschaft Korrosion der Gesellschaft Deutscher Chemiker is gratefully acknowledged.

Any discussion of this paper will appear in a Discussion Section to be published in the December 1963 JOURNAL.

REFERENCES

1. a, W. J. Müller, *Z. Elektrochem.*, **10,** 518 (1904); b, G. Grube and H. Metzger, *ibid.*, **29,** 17 (1923); c, R. I. Agladze and G. M. Domanskaja, *Zhur. Priklad. Khim.*, **24,** 787, 915 (1951); d, R. I. Agladze and M. Ya. Gdzelishvili, *Elektrochim. Margantsa, Akad. Nauk Gruz. SSR,* **1,** 139 (1957); quoted in *C. A.*, **53,** 19625 (1959); e, R. I. Agladze and N. I. Khabaradze, *ibid.*, **1,** 235, 253, 279 (1957); quoted in *C. A.*, **54,** 100 (1960).
2. K. J. Vetter, *Z. Elektrochem.*, **66,** 577 (1962).
3. a, F. Flade, *Z. physik. Chem.*, **76,** 513 (1911); b, U. F. Franck, *Z. Naturforschung,* **4a,** 378 (1949).
4. K. J. Vetter, "Elektrochemische Kinetik," p. 608 ff, Springer (1961).
5. An analogous dependence has been observed on passive iron: K. J. Vetter, *Z. Elektrochem.*, **59,** 67 (1955).
6. K. H. Maxwell and H. R. Thirsk, *J. Chem. Soc.*, **1955,** 4054, 4057, with review of older literature.
7. A reaction of manganous ions with manganese dioxide was observed by J. M. Cowley and A. Walkley, *Nature,* **161,** 173 (1948).
8. a, D. A. Vermilyea, *Acta met.*, **1,** 282 (1953); b, K. J. Vetter, *Z. Elektrochem.*, **58,** 230 (1954); c, K. G. Weil, *ibid.*, **59,** 711 (1955).
9. a, H. Bode, A. Schmier, and D. Berndt, *Z. Elektrochem.*, **66,** 586 (1962), with review of older literature; b, J. Reynaud and J. Brenet, *Electrochim. Acta,* **6,** 1 (1962).
10. M. Fleischmann, H. R. Thirsk, and J. M. Tordesillas, *Trans. Faraday Soc.*, **58,** 1865 (1962).
11. K. E. Heusler, K. G. Weil, and K. F. Bonhoeffer, *Z. physik. Chem., N.F,* **15,** 149 (1958).
12. K. J. Vetter and G. Klein, *ibid.*, **31,** 405 (1962).

Dissolution of Brass in Sulfuric Acid Solutions

11. 95/5 Brass

T. J. Kagetsu[1] and W. F. Graydon

Department of Chemical Engineering and Applied Chemistry, University of Toronto, Toronto, Canada

ABSTRACT

Dissolution rates of 95/5 brass cylinders in dilute sulfuric acid solutions have been determined as a function of rotational speed, acid concentration, oxygen partial pressure, temperature, apparent surface area, and corroding solution volume. The dissolution of copper from 95/5 brass was found to be autocatalytic as in the case of pure copper and copper from 85/15 brass, and a similar mechanism was indicated. Deviations due to changes in the brass surface were observed. The slower copper rate for 95/5 brass as compared to pure copper indicated that zinc entered solution by a displacement mechanism. At long times, the rate of dissolution of copper from 95/5 brass became independent of cupric ion concentration and was controlled mainly by the diffusion of oxygen to the metal-solution interface.

Much of the early work on the corrosion of brass was concerned with the practical aspect of preventing dezincification, the lowering of zinc content in a corrosive environment. The weight loss data obtained to determine the effects of the different variables are not amenable to analysis by the methods of chemical kinetics.

In the present work, the rates of dissolution of 95/5 (95% Cu-5%Zn) brass in dilute sulfuric acid solutions were determined to investigate the mechanism of the dissolution process. Dissolution of 85/15 (1) and 95/5 brasses were investigated simultaneously as an extension of an earlier study on pure copper (2).

Experimental

The experimental procedure has been described elsewhere (1, 2). The annealed polycrystalline brass supplied by the Anaconda American Brass Limited analyzed 94.83% Cu, 5.10% Zn, 0.06% Sn, 0.01% Fe, and 0.005% Pb. In a standard experiment, a polished 1.9 cm diameter cylinder with 11 cm^2 surface area was rotated at 1410 rpm in 500 ml of air-saturated 0.26N H_2SO_4 at 35°C. Samples of the corroding solution were analyzed polarographically for copper and zinc (1, 3).

[1] Present address: Union Carbide Nuclear Company, Tuxedo, New York.

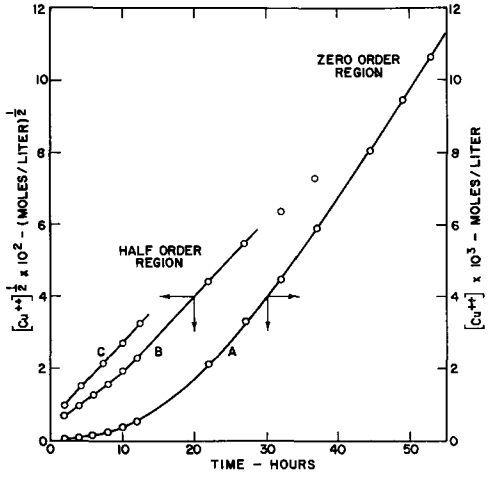

Fig. 1. Dissolution of copper from 95/5 brass under standard conditions. A, Zero order plot for a polished sample shows zero order region at long dissolution times; B, half order plot for a polished sample shows change in rate; C, half order plot for a corroded sample shows no change in rate.

Results and Discussion

The rate of dissolution of copper from 95/5 brass is given by the slope of the tangent to curve A in Fig. 1. The nonlinear portion of curve A indicates that the rate increases with time. As in the case for the autocatalytic dissolution of pure copper (2) and copper from 85/15 brass (1), the data were correlated on the basis of a half order rate dependence on cupric ion concentration. Since $\frac{d[Cu^{++}]}{dt} = k[Cu^{++}]^{1/2}$, the reaction rate constant, k, is equal to $\frac{2d[Cu^{++}]^{1/2}}{dt}$, *i.e.* twice the slope of the square root plots.

When a polished sample was used, initial deviations from this half order rate dependence were found. About 0.4 mg/cm^2 of copper was dissolved during this period which sometimes lasted as long as 15 hr. Even though the plots of cupric ion concentration *vs.* time were linear during this initial period, the faster rates obtained when cupric sulfate was added to the corroding solution indicate some rate dependence on cupric ion concentration. Since these initial deviations could be eliminated by using a brass sample that had been corroded to the half order region, it is concluded that a change of the brass surface altered the kinetics. With 85/15 brass (stage 1), dezincification of the surface was detected in this region. A similar behavior is assumed for 95/5 brass although the initial zinc concentrations were too low to establish this experimentally. The dissolution of the polished surface layer may also contribute to this initial deviation.

For the dissolution of a polished 95/5 brass sample, a change in rate was also observed in the half order region as shown by curve B, Fig. 1. Curve C shows that the faster rate could be obtained from

the start of the run by using a sample that had previously been corroded to give this faster rate. Since etching of the brass surface was observed during the first part of the half order region, the increase in rate was attributed to an increase in effective surface area.

The rates of dissolution of copper from 95/5 brass in the half order region were independent of the rotational speed of the sample, and of the acid concentration above 0.15N; they were half order with respect to the oxygen partial pressure of the gas saturating the corroding solution. The experimental data for the half order region are summarized by the following empirical rate equation

$$\frac{d[Cu^{++}]}{dt} = Ke^{-E/RT}\,[Cu^{++}]^{1/2}\,[p_{O_2}]^{1/2}\,A/V \quad [1]$$

where the rate is in moles/liter/hr. For the first part of the half order region, $K = 5.0 \times 10^5$ based on 61 plots and $E = 13{,}000$ cal/mole; for the second part of the half order region with the faster rate $K = 7.2 \times 10^3$ based on 48 plots and $E = 10{,}200$ cal/mole. The average deviation was less than 5%, the maximum deviation about 10%. The range over which the variables were investigated are as follows: T, absolute temperature (287°-318°K); p_{O_2}, partial pressure of oxygen (0.05-1.0 atm); A, brass surface area (5.6-11.6 cm^2); V, solution volume (0.25-0.75 liter); S, peripheral velocity (1700-20,-600 cm/min); and $[H_2SO_4]$, acid concentration (0.15-0.26N).

The difference in over-all Arrhenius activation energies can be attributed to the rate of increase of surface area at a given temperature. For a polished sample, the dissolution of about 1 to 1.5 mg/cm^2 of copper was required before the faster half order rate was obtained. Thus, at the higher temperatures, the rate of increase in surface area was faster and for the conditions under which the fastest rate was obtained (*i.e.*, oxygen, 45°C), only the faster half order rate was observed.

At long dissolution times, the plot of cupric ion concentration against time was linear (see curve A, Fig. 1). This zero order rate dependence on cupric ion concentration shows that there is a limit to the increase in the rate of dissolution of copper from 95/5 brass due to autocatalysis. The rate of dissolution of copper from 95/5 brass in this zero order region was proportional to the 0.62 power of the rotational speed and to the 0.69 power of the oxygen partial pressure of the gas phase. A first order dependence on oxygen concentration would be expected if the process was controlled completely by the diffusion of oxygen to the interface. The observed dependence indicates that the concentration of oxygen at the metal-solution interface is not zero, but varies with the gas composition and rotational speed used. In the transition from a chemically controlled process to one that is diffusion-controlled, a region of mixed control can be assumed. Hochberg and King (4) have reported a similar situation for the dissolution of copper in acetic acid solutions containing p-benzoquinone.

In the zero order region, the Arrhenius plot was not linear. The temperature coefficient between 15° and 25°C was 1.9, and between 35° and 45°C it was 1.3. This difference in temperature coefficients also indicates that the rate is not completely diffusion-controlled.

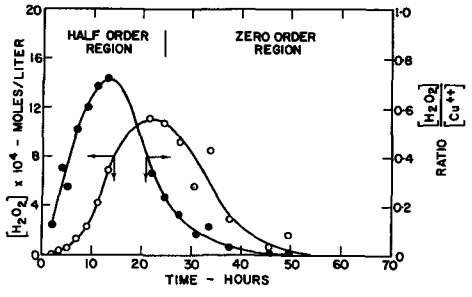

Fig. 2. Typical plot showing hydrogen peroxide formation and disappearance at 45°C.

The experimental data for the zero order region are summarized by the following empirical rate equation derived from 30 plots

$$\frac{d[Cu^{++}]}{dt} = 1.7 \times 10^{-7}\,(p_{O_2})^{0.69}\,(S)^{0.62}\,A/V \quad [2]$$

The range over which the variables were investigated are the same as for the half order region. However, Eq. [2] is only valid for a reaction temperature of 35°C.

Hydrogen peroxide was detected during the dissolution of 85/15 (1) and 95/5 brasses. The amount of hydrogen peroxide formed was much greater on a molar basis than the amount of zinc corroded from the brass. Thus most if not all of the hydrogen peroxide formed is associated with the dissolution of copper from 95/5 brass. A typical plot of hydrogen peroxide concentration as a function of time is shown in Fig. 2. The molar ratio of hydrogen peroxide to copper in solution increased during the first part of the half order region where surface changes were occurring. In some cases, the ratio of hydrogen peroxide to cupric ions formed over a short time interval approached unity. The rate of appearance of hydrogen peroxide in solution began to fall off during the latter part of the half order region even though the absolute amount of hydrogen peroxide in solution continued to increase with time. In the zero order region, the hydrogen peroxide concentration decreased with time. Qualitatively, higher maximum hydrogen peroxide concentrations were obtained when the zero order copper dissolution rate was faster and concentrations as high as 0.004M were observed.

The rate of dissolution of copper from a corroded 95/5 brass sample in a new batch of acid was the same as for the old solution containing hydrogen peroxide. Thus hydrogen peroxide at the concentrations obtained during dissolution had no noticeable effect on the rate. On the other hand, when a sufficient amount of hydrogen peroxide was added to the corroding solution initially, the surface effects normally found for a polished sample could be eliminated.

Delahay's (5) work on oxygen reduction on various metals including copper and zinc indicates that two- and four-electron processes can occur simultaneously to form hydrogen peroxide and water

Table I. Comparison of copper dissolution rates
(slower half order region)

Temperature, °C	Pure copper*	Copper from 95/5 brass	Copper from 85/15 brass**
	Calculated reaction rate constants, $k \times 10^3$		
15	0.99	0.68	0.45
25	2.25	1.47	0.85
35	4.87	2.99	1.52
45	10.0	5.82	2.63

Conditions: Polished sample, $p_{O_2} = 0.21$ atm, $A = 10.8$ cm², $V = 0.5$ l.

* Ref. (2), Eq., page 162.
** Ref. (1), Eq. [6].

respectively. Hydrogen peroxide appears to be stabilized in dilute sulfuric acid solutions (6), and the catalytic decomposition of hydrogen peroxide by cupric sulfate has been found to be slow (7). These factors can affect the hydrogen peroxide concentrations.

The rates of dissolution of pure copper and copper from 85/15 and 95/5 brasses have been determined under practically identical conditions. The results indicate that in all three cases, the dissolution of copper is occurring by the same mechanism which has been discussed in the other two papers (1, 2). The zinc content of the brass has a marked effect of the rate of dissolution of copper from brass as shown in Table I.

If the dissolution of zinc from brass occurs by a displacement mechanism, then cupric ions will be reduced to metallic copper. The effect of this decrease in cupric ion concentration will be magnified because of autocatalysis and will result in a slower copper dissolution rate. Also, the initial deviations from the half order dependence on cupric ion concentration can be attributed to this displacement process which results in the postulated dezincification of the surface.

The displacement of cupric ion by zinc metal in cupric sulfate solutions is not a simple reaction (8, 9). King and Burger (9) found the rate of chemical reaction for the displacement process to be fast when compared to a diffusional process. Since cupric ions are formed at the metal-solution interface, the dissolution of zinc from brass should not be a rate-controlling factor.

Thus, the rates of dissolution of 85/15 and 95/5 brasses are governed by the rates of dissolution of copper from these brasses and the exposed zinc reacts rapidly by a displacement mechanism. After the initial surface changes were completed, the ratio of copper and zinc in solution were found within analytical limits to be the same as in the brass. Since the reported rates of dissolution of pure copper (2) and copper from 85/15 brass (1) were slower than the rates calculated by Eq. [2], no zero order region was observed for these metals.

Acknowledgments

The authors are grateful to the International Nickel Company of Canada Limited for the Graduate Research Fellowship (three sessions 1954-1957) and to the Corrosion Subcommittee of the National Research Council of Canada for three summer grants awarded to T. J. K.

Manuscript received May 23, 1962; revised manuscript received Feb. 1, 1963.

Any discussion of this paper will appear in a Discussion Section to be published in the June 1964 JOURNAL.

REFERENCES

1. J. Bumbulis and W. F. Graydon, *This Journal*, **109**, 1130 (1962).
2. B. C.-Y. Lu and W. F. Graydon, *Can. J. Chem.*, **32**, 153 (1954).
3. I. M. Kolthoff and J. J. Lingane, "Polarography," 1st ed., Interscience Publishers Inc., New York (1946); I. M. Kolthoff and E. F. Orlemann, *J. Am. Chem. Soc.*, **63**, 2085 (1941); M. M. Dedesa and D. N. Hume, *Anal. Chem.*, **25**, 983 (1953).
4. H. Hochberg and C. V. King, *This Journal*, **97**, 191 (1950).
5. P. Delahay, *ibid.*, **97**, 198, 205 (1950).
6. W. C. Bray and R. S. Livingstone, *J. Am. Chem. Soc.*, **45**, 1251 (1923).
7. H. W. Rudel and M. M. Haring, *Ind. Eng. Chem.*, **22**, 1234 (1930); E. I. Shpitalskii and B. A. Konovalova, *J. Russ. Phys. Chem. Soc.*, **62**, 1033 (1930), *C. A.*, **25**, 3230 (1931); M. O. Kharmandaryan and E. A. Alekseeva, *J. Russ. Phys. Chem. Soc.*, **62**, 1677 (1930), *C. A.*, **25**, 3230 (1931).
8. M. Tzentnershver and Y. Drukker, *J. Russ. Phys. Chem. Soc.*, **47**, 528 (1915), *C. A.*, **9**, 2475 (1915); M. Tzentnershver and W. Heller, *Z. Physik. Chem.*, **A161**, 113 (1932); A. Galecki and J. Tomaszewski, *Roznicki Chem.*, **10**, 437, 601 (1930), *C. A.*, **25**, 2067 (1931); F. W. Van Straten and W. F. Ehret, *J. Am. Chem. Soc.*, **61**, 1798 (1939).
9. C. V. King and M. M. Burger, *Trans. Electrochem. Soc.*, **65**, 403 (1934).

The Bond in Heterogeneous Interfaces

B. Steverding

Physical Sciences Laboratory, United States Army Missile Command, Redstone Arsenal, Alabama

ABSTRACT

Evaporation characteristics of metallic films deposited on nonmetallic substrates are evaluated to determine the interfacial bonding energies and to elucidate the energy structure in the vicinity of the interface. This method also allows measurement of the range of the bonding forces and the determination of their temperature dependency. A small energy step in a distance of 400-500Å is observed in several metal-oxide systems.

The great possibilities of combining heterogeneous materials like metals and ceramics, organics and glasses, etc., to new composite materials with predictable property spectra depend to a large degree on the bond in the interface. Since the interface is the region where mechanical and thermal stresses obtain their maximal values, these effects may often overshadow the physicochemical interface phenomena if studied on a macroscopic scale. Therefore a method was sought which would permit the measurement of the physicochemical bond, independent of side-effects like the mechanical interlocking of rough surfaces, not matching coefficients of thermal expansion, etc. For homogeneous interfaces like grain boundaries, two new methods were recently developed, but there is no equivalent procedure available for heterogeneous interfaces of solids. Theoretically, it is possible to apply the present method to homogeneous interfaces, like grain boundaries, but because of their thermal instability this is difficult in practice. However, it may be reasonable to assume that certain characteristics of heterogeneous interfaces may be of value to interpret the structure of grain boundaries.

If it is the goal to investigate the energetical behavior of heterogeneous interfaces, methods which are concerned with the structure only do not give the final answer. Electron microscopy and x-ray investigations of all kinds can give valuable results and might even give some indirect clues about bonding energies, but they fail to describe the acting physicochemical forces, their range, magnitude, and dependency on temperature and other parameters.

Other, different attempts were made to obtain a deeper insight into the energy structure of solid interfaces. One method consists of measuring the heat of bonding in the initial state of vapor deposition by very sensitive thermocouples, but this method gave erratic results (1).

Another method is based on a theory of Frenkel (2) in which the critical condensation rate is related to the binding energy. Unfortunately, it is very difficult to determine critical evaporation rates and to distinguish between nucleation and growth of the depositing film in this early stage (3, 4). Only the formation of nuclei refers strictly to the binding energy, and it depends on the number of structural imperfections, impurities, etc., on the surface of the substrate.

In the present study a different method was employed. The decrease of the rate of evaporation of a metallic film in the vicinity of the interface is related to the binding energy. Since the integration of the evaporation rate, carried out over the time interval, is a measure for the thickness of the remaining film, the range and the potential of the interfacial forces can be determined within the same experiment also.

An advantage of the method is that the temperature dependency of the binding force is easily determinable. Since the binding energy of solid as well as liquid films can be studied, it is possible to compare the results with data obtained from other direct methods, *e.g.*, the sessile drop method, etc.

Description of the Apparatus

The apparatus consists of a vacuum tube furnace in which the specimen, a metal coated oxide plate, is suspended by means of a 100 cm long and 0.5 mil thick tungsten wire (Fig. 1). The wire is fastened to a thin titanium rod which enters the heated

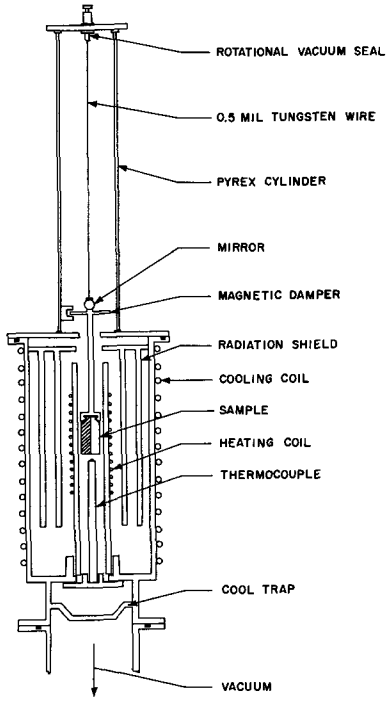

Fig. 1. Evaporation apparatus

zone of the furnace and adapts the specimen holder. One half side of the rectangular shaped oxide plate is coated with the metal film so that when heated the evaporating atoms of this film will exert an angular momentum in the suspension wire. The torsional spring constant of the wire was determined by measuring the period of the suspended system before and after adding a small magnesium disk of known moment of inertia. The torsional spring constant had a value of $5.23 \cdot 10^{-3}$ dyne cm. The sensitivity of this torsional system is high enough to measure vapor pressures in the range of 10^{-7}-10^{-8} mm Hg. The suspended system is magnetically dampened by a magnesium disk and a horseshoe magnet. The magnesium disk is engraved in degrees and serves to measure the angular deflection. Thin plates of alumina of highest purity and density were vapor coated with 2000Å thick layers of Cu and Al. Other samples were obtained by anodizing thin aluminum foils on one side so that an aluminum metal film remained on the other side.

The vapor coating was done at a pressure of 10^{-5} mm Hg. After the coating procedure the specimen remained in vacuum until it was inserted in the apparatus, so that the film was exposed to air for only a few minutes.

Method

The method used in this investigation is based on the following principle. Layers of film material are continuously removed until the vicinity of the interface is reached. The energy to remove these layers in various parts of the interval differs, and this energy change corresponds to the interfacial binding energy. The layer removal is achieved by evaporation.

A metal film of high purity and of sufficient thickness evaporates under isothermal conditions with a constant rate like the bulk material. But as the film becomes thinner and thinner in the course of further evaporation, the free surface of the metal film finally enters the range of the interfacial bonding force and the evaporation rate decreases. At this temperature the remaining metal of the film is removed at a much slower rate which may finally fall below the sensitivity limit of the instrument. If the temperature is then raised further, evaporation takes place until eventually the last traces of the film are removed.

There are obviously two prerequisites for a universal application of this method: (i) the vapor pressures of the film and the substrate must be of a different order of magnitude, (ii) film and substrate substances should not interdiffuse. If interdiffusion takes place, binding energies and force ranges may still be determined if the diffusion coefficient is known, but they depend on the history and the momentaneous mixture ratio of the adjacent substances. Also the definition of an interface will become somewhat confusing in this case.

The angular deflection θ, caused by the momentum of the evaporating atoms, is related to the vapor pressure p by the following equation

$$p = 4D\theta/a^2 l \qquad [1]$$

where D is the torsional spring constant, a the width of the film, and l the length of the film.

The free energy of binding ΔF may be expressed by the ratio of the vapor pressure of the bulk metal and the vapor pressure of the metal subjected to the interfacial bonding forces

$$\Delta F = -RT \log p/p_o = -RT \log \theta/\theta_o \qquad [2]$$

where p_o is the bulk vapor pressure, p the vapor pressure under the influence of bond, and R the gas constant.

Since p is obtained experimentally as a function of the time, ΔF can also be plotted against time. But it is possible to transform the time coordinate into a distance coordinate so that ΔF values may be determined as a function of the remaining film thickness. This may be done by the following consideration.

If the coated specimen is of the previously described rectangular shape, the momentum of the isothermally evaporating molecules exerted on the suspension system is

$$\theta D = \frac{dN}{dt} m\, l\, a^2/2(2kT/m\pi)^{1/2} \qquad [3]$$

where $\frac{dN}{dt}$ is the number of evaporating atoms per sec and cm^2, m the mass of the atoms, and k is Boltzmann's constant.

The following relation is easily verified

$$m \int_o^\tau \frac{dN}{dt}\, dt = (x_o - x)\rho$$

where the integration is carried out over the duration τ of the experiment and x_o is the initial film thickness, x the film thickness after the time τ, and ρ the density of the film.

Inserting this expression in Eq. [3] yields the following formula for the film thickness

$$x = x_o - 2D/la^2\rho(\pi m/2kT)^{1/2} \int_o^\tau \theta\, dt$$

The integration can be carried out graphically.

In these considerations it is assumed that the vapor is atomic. Recent mass spectroscopical studies revealed, however, that many metal vapors consist partly of binary molecules or larger molecular clusters (5). In almost all cases the concentration of polymolecular clusters is 1% or less; therefore, the error of the previous calculation will remain small.

Some other difficulties, however, must be eliminated to guarantee the validity of the conclusions which will be drawn from the experimental facts. Under the influence of vacuum and temperature, thin metal films may coagulate into droplet-like small particles with greatly increased surface area. The incubation time for this phenomenon is controlled by diffusion and is dependent on temperature, film thickness, nature of the substrate, and rate of evaporation. The vacuum apparently has a pronounced influence, because films of even noble metals like gold do not coagulate readily in air but will agglomerate in vacuum if the temperature exceeds

500°C for a long enough period. Somewhere around the recrystallization temperature, the mobility of the atoms increases to the point where internal stresses in the film can be released by a variety of mechanisms. For thin films, for example, one possibility is to transform the stored elastic energy resulting from unequal coefficients of expansion, etc., into surface energy. However, if oxide layers or even absorbed gas layers are bonded to the surface, the activation energy for this energy transformation is generally too high and film surfaces stay coherent and retain their high optical reflectivity. The stress affected zones of the surface may also be removed by evaporating the surface layer, and, if this is done fast enough, no coagulation will occur. It was observed that with relatively long heating times and small rates of evaporation the angular deflection may increase, even at a constant temperature, by about 15%, indicating that surface coagulation occurred. In such cases, the experiment was repeated with more rapid heating and higher rates of evaporation.

Despite the fact that film coatings on nonporous glass substrates yielded evaporation curves of the same general shape as shown in Fig. 2 and 3, the porosity of the substrate could influence the evaporation characteristics and affect the validity of the conclusions derived from the experiments. The porosity of the alumina plates used in the experiments was on the order of 3%, so that $(3/100)^{2/3}$, or about 10% of the surface, is covered with holes. In high density alumina, pores are rather shallow and not interconnected.

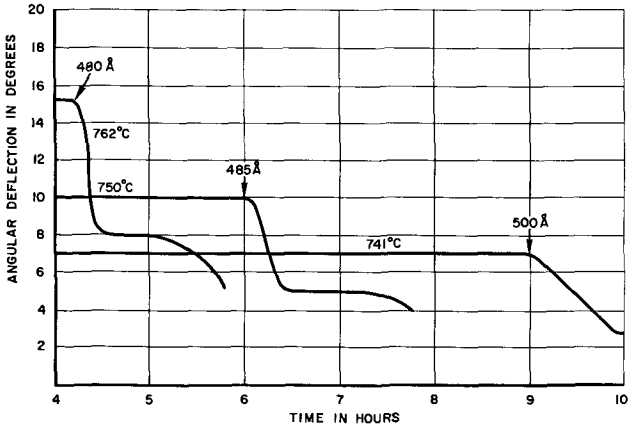

Fig. 2. Isothermal evaporation of Al films on Al_2O_3 substrates (initial film thickness, 2000Å).

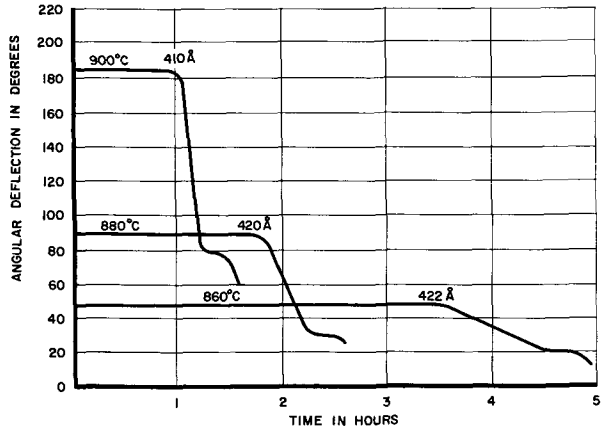

Fig. 3. Isothermal evaporation of Cu films on Al_2O_3 substrates (initial film thickness, 2000Å).

If metal evaporates from the bottom of a pore, two very different possibilities exist: (i) that only part of the evaporating metal will escape through the pore opening and contribute to the recoil, with the remainder forming a secondary metal film on the pore walls; (ii) that the bond between substrate and metal is not sufficiently strong to allow metal to be deposited on the hot walls of the pore, and either re-evaporation or reflection of the bombarding metal atoms will occur. It will be shown later that the secondary plating of the pore walls cannot occur under the conditions of the experiment. If this holds, evaporation from a pore will cause a slightly higher repulsive momentum than evaporation from a flat plate because the molecules are leaving under angles closer to 90°. In those rare cases where the pore opening is very small, the pore could be considered as a tiny Knudsen cell with all the atoms leaving nearly perpendicular to the plate surface. The step between the upper and lower level of the curve in Fig. 2 and 3 would not be affected, however, and the calculated values for the binding energy are the same if the surface is slightly porous or not. With the large pore openings which generally prevail, there is no prolonged after-effect, and evaporation from the pores will follow the evaporation from flat surfaces with only a slight delay.

There is also a possibility that wrong thickness determinations may be made if the substrate is porous because $\int \theta dt$ will be larger. A comparison of thickness determinations by x-ray spectroscopy and measurements made by evaporation techniques showed that the effect of a small porosity is negligible and within experimental errors (6).

It will now be shown that the pore walls are not plated by the re-evaporating metal within the pores. When an atomic beam impinges on a surface which is maintained at a constant temperature, a continuous deposit can be formed only when the rate of incidence of atoms is larger than a certain critical value. This critical beam density is determined by temperature of the substrate and the binding energy by the following relationship

$$n_c = A \cdot e^{-b/kT_1}$$

where n_c is the critical beam density, A a constant insensitive to temperature, b the binding energy, and T_1 the critical substrate temperature. If the critical beam densities are determined for two different substrate temperatures T_1 and T_2, b may be calculated by

$$b = k \frac{T_1 \quad T_2}{T_1 - T_2} \log \frac{n'_c}{n''_c} \qquad [4]$$

The first visible deposit of copper on the alumina furnace tube was observed at a spot where the wall temperature was 610°C and the beam density was $7 \cdot 10^{12}$.

Let us assume a pore which has only a very small opening so that equilibrium vapor pressure is main-

tained inside the pore. The testing temperature for the copper-alumina samples was around 870°C. The vapor pressure of copper at this temperature is about $7 \cdot 10^{-7}$ mm Hg, and the wall of the pore would be bombarded by around 7.10^{14} at./sec/cm^2, according to

$$n = \frac{N_L \cdot p}{(2\pi MRT)^{1/2}}$$

If it is assumed that $7 \cdot 10^{14}$ is the critical beam density, the binding energy may be calculated by the two sets of (n_c, T) values from Eq. [4]. A value of 36 kcal is obtained, which appears far too high for the interfacial bond of copper to alumina (7). If it is considered that most pores have large openings in which the equilibrium pressure cannot be maintained, even higher binding energies would be calculated. The assumption that vapor plating occurred at the testing temperatures must therefore be ruled out. The same arguments are true for the Al-Al_2O_3 experiments. A small degree of porosity will not affect the validity of the conclusions.

Discussion and Results

Isothermal evaporation rate curves for 2000Å thick aluminum films deposited on polycrystalline Al_2O_3 are shown in Fig. 2. In the indicated temperature range, the aluminum film evaporates like the bulk metal down to a distance of 480-500Å from the interface. At this point there is a fairly sudden decrease in the evaporation rate and, consequently, in the vapor pressure. After this transition zone with a thickness of about 100Å is passed, the evaporation rate remains constant for some time at the lower level and decreases only slowly hereafter. The free energy change between the two constant levels is seen from Table I. In the case of aluminum, the sensitivity of the apparatus was not high enough to study the solid-solid interface. At the test temperature, the aluminum film was already liquified.

Figure 3 shows the results of the studies on the system Cu-Al_2O_3. The 2000Å thick copper film evaporates with a constant rate down to a thickness of 410-422Å. At this threshold the free energy of bonding changes over a distance of about 100Å by about 1980 cal (see Table I). After this transition zone is passed, the evaporation rate becomes constant again and is only slightly decreased later. The free energy of the bond apparently does not change in the temperature range from 900°-860°C.

Table I. Free energy change

Temp, °C	θ	θ_o	ΔF, cal
	Al-Al_2O_3		
762	8	15.5	1360
750	5.2	10.5	1310
741	3.5	7.0	1295
	Cu-Al_2O_3		
901	81	186	1980
880	37	89	1990
860	19.5	47	1980

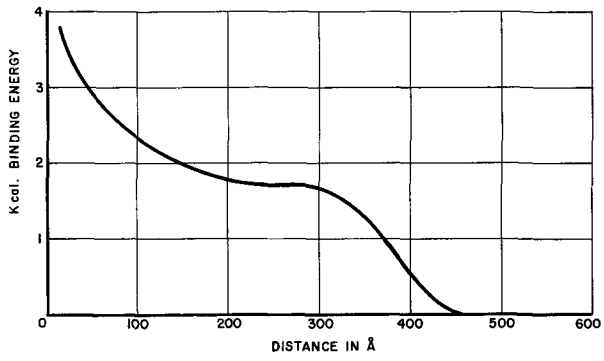

Fig. 4. Free binding energy increase in vicinity of metal-oxide interfaces.

It is interesting to note that the energy step occurs at almost the same film thickness in both solid and liquid states. This seems to rule out the theory that the force field of interfacial dislocations is responsible for this phenomenon.

This energy structure insinuates the idea that a distorted, almost amorphous atomic structure extends a few hundred Angstroms deep into the bulk of the film. The structural situation in liquids and solids would be similar. This structural independency suggests that the distorted range is not very temperature dependent. It would be very interesting to study this phenomenon with single crystal substrates under epitaxial conditions.

The Hall constants of some metal films have maxima in this thickness range of 400-500Å (8). Electric resistance curves for thin films have their smallest radii of curvature in this range. The thickness of the amorphitized layer between metallic grain boundaries, as determined by the line broadening of scattered x-rays, also falls within these limits (9).

This investigation was mainly concerned with the first energy step in a distance of 400-500Å, but measurements at higher temperatures in a closer vicinity to the interface suggest the energy structure schematically shown in Fig. 4. High values of the binding energy are reached at the close distance of several 10 atomic distances from the interface.

This range was not studied systematically because of the present temperature limitations of the furnace. It was hoped that the energy structure in the immediate vicinity of the interface could be studied better in the Zn-ZnO system, in which the metal can easily be evaporated at relatively low temperatures. Because of the high rate of interdiffusion in this system, the results in the range below 100Å were not consistent or reproducible. A further small energy step of about 2000 cal at approximately 400Å was observed in the Zn-ZnO system.

Manuscript received Aug. 17, 1962; revised manuscript received Dec. 21, 1963.

Any discussion of this paper will appear in a Discussion Section to be published in the June 1964 JOURNAL.

REFERENCES

1. T. A. Bennet, Structure and Properties of Thin Films, Conf. Proc., p. 58 (1959).
2. J. Frenkel, *Z. Physik.*, **26**, 117 (1924).
3. J. D. Cockroft, *Proc. Roy. Soc.*, **A119**, 293 (1928).

4. L. Yang, C. E. Birchenall, G. M. Pound, and M. T. Simanad, *Acta Met.*, **2**, 462 (1954).
5. J. Franzen and H. Hinterberger, *Z. Naturforsch.*, **16a**, 535 (1961).
6. B. Steverding, *Am. Rocket Soc.*, p. 294 (February 1962).
7. T. N. Rhodin, *Discussions Faraday Soc.*, **5**, 215 (1949).
8. A. Colombani and P. Huet, Structure and Properties of Thin Films, Conf. Proc., p. 253 (1959).
9. V. I. Arkharov *et al.*, *Phys Met. Metallogr.*, **10**, 53 (1961).

Mechanism of Electrodeposition from Aqueous Solutions of Square Planar Complexes

George W. Watt and James A. Cunningham

Department of Chemistry, The University of Texas, Austin, Texas

ABSTRACT

Cathode current efficiencies and/or cathode potentials have been measured for a variety of spin-paired square planar complexes of Pt(II), Pd(II), and Au(III) in aqueous solutions. It was found that the tendency toward electrodeposition depends on the bond strengths of the particular ligands about the central metal ion, and that the over-all charge of the complex influences current efficiency in the expected direction, *i.e.*, complexes with more negative over-all charges tend to deposit at lower efficiencies even though thermodynamically less stable. The mechanism of deposition has been shown not to involve dissociation; rather, experimental data show that deposition proceeds from the undissociated complex as a whole.

Earlier work (1) led to the proposal that cathode current efficiencies measured for the electrodeposition of nickel from liquid ammonia solutions of octahedral spin-free Ni(II) complexes were interpreted best in terms of an initial S_N2 substitution into the nickel complex by a competitive ligand. This was followed by a rate-controlling S_N1 dissociative-type mechanism similar to that proposed by Lyons (2) which would be influenced by the relative translabilizing power of the substituted ligand. More recently, current efficiency measurements for the deposition of cobalt from ammonia solutions of octahedral spin-paired Co(III) complexes were interpreted (3) by a similar translabilized dissociative mechanism. Only fair agreement was found between the trends in cathode current efficiencies exhibited by the complexes of these two metal ions and the increasing trans effect exhibited by Pt(II) complexes. This is not unexpected since the trans effect series is based only on qualitative observations; more important, there is little reason to assume that the same sequence would apply equally well to the cases of square planar and octahedral symmetry. Since the experimental evidences for the trans effect *per se* are limited largely to Pt(II) chemistry (4), it was of interest to investigate a series of Pt(II) complexes in order to provide further evidence and possible verification of the trans effect in electrodeposition. These studies were further of interest since efforts to study the deposition of platinum from aqueous solutions by polarographic methods have been unrewarding (5, 6).

Two complications at once arise. First, it is impractical to employ the same solvent as used in the earlier work since complexes of the type $[Pt(NH_3)_3X^-]^+$ react almost instantaneously with liquid ammonia to form $[Pt(NH_3)_4]^{2+}$. Accordingly, all of the present measurements employed aqueous solutions. Second, it would be reasonable to assume that square planar complexes in solution in a polar solvent might be expected to assume, and exhibit properties associated with, distorted octahedral symmetry. The results reported here however are not consistent with this assumption.

The initial experiments with platinum complexes indicated that the mechanism of electrodeposition did not involve dissociation; therefore, a trans effect could not be tested. Moreover, the combined data gathered in this laboratory by several workers indicate that there is a fundamental difference in the mechanism of deposition between octahedral and square planar complexes. Hence, electrodeposition from solutions of complexes of Pd(II) and Au(III) was also investigated in order to explore more broadly the behavior of square planar species.

Experimental

Equipment and Experimental Procedures

The cell.—Unless stated otherwise, both cathode current efficiencies and cathode potentials were measured using the cell shown in Fig. 1. The cell was designed so that 100 ml of solution could be introduced and removed easily, and the cathode holder was constructed to provide for easy removal of electrodes for direct weighing. Other details of the cell include: separated anode and cathode compartments, facilities for rapid stirring in the cathode chamber, and a means for purging the catholyte with any desired gas.

Cathode current efficiency measurements.—For current efficiency measurements, a series electrical circuit consisting of a milliammeter, silver coulometer, rheostat, 50v battery, and cell was employed. Efficiencies that were calculated either by measuring time and current or silver deposited were well within experimental error. Constant current was

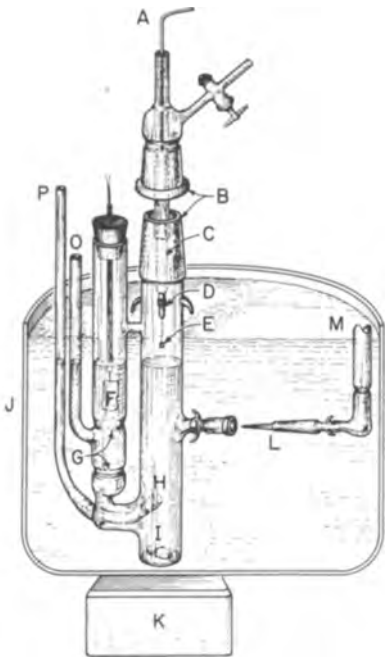

Fig. 1. Electrolysis cell. A, copper rod; B, standard taper 34/45 ground glass joints; C, 3/8-in. OD Teflon rod drilled to fit copper rod; D, gold plated chuck; E, platinum cathode; P, platinum anode; G, fine porosity glass frits; H, glass frit; I, Teflon stirring bar; J, constant temperature bath; K, stirring motor; L, Luggin capillary; M, to reference electrode; O, filling tube; P, gas inlet tube.

maintained by manually adjusting the rheostat as the run progressed. For platinum deposition, the cathodes were rinsed in distilled water and heated to redness before and after each run; a similar procedure was used for palladium and gold deposition, except that the drying temperature was *ca.* 200°C.

Determination of cathode potentials.—Cathode potentials for aqueous solutions of platinum complexes were measured with conventional equipment including: a Ag/AgCl, 0.1M KCl reference electrode; a Luggin capillary containing saturated KCl solution gelled with agar; and a potentiometer. For palladium, the reference electrode was Ag/AgX, 0.1M KX where X was either Cl^-, Br^-, or I^- depending on the particular palladium complex under investigation. In this case, the reference electrode made electrical contact with the working cathode by means of a bridge which contained 0.1M KX solution. The bridge held two fine-porosity glass frits which were separated by a distance of 15 cm and terminated at the working cathode in a Luggin capillary. A similar reference electrode was employed when anhydrous methanol was used as the electrolyte; the $E°$ value of the resulting Ag/AgCl, 0.1M NaCl (methanol) electrode was taken as 0.0228v at 35°C from the data of Harned (7). (The potentials of all reference electrodes used were taken from this source.)

All runs were made at constant current, and the catholyte was rapidly stirred; a platinum cathode was used in every case. When possible, differences in electrolyte concentrations between the reference electrode and the plating solution were kept at a minimum to avoid significant junction potentials.

Materials

Water.—Distilled water passed through "Deeminac" ion exchange resin was used to prepare all plating solutions and reference electrodes.

Supporting electrolytes.—Reagent grade electrolytes used to prepare the plating solutions and ref-

Table I. Analytical and x-ray diffraction data

Complex	Anal. for M[a], % Calcd.	Found	Ref.	*d*, A and I/I_o[b]
K_2PtCl_4	47.0	46.9	9	7.06, 3.18 (0.9), 2.51 (0.9)
K_2PtBr_4	32.9	32.3	10	7.56, 4.35 (0.7), 3.35 (0.7)
$K_2Pt(NO_2)_4$	42.7	42.6	11	6.55, 3.97 (0.6), 3.75 (0.8)
$K_2Pt(CN)_4$	51.8	51.8	12	7.95, 6.71 (0.5), 3.29 (0.7)
$K_2Pt(SCN)_4$	38.6	38.2	13	8.37, 5.53 (0.5), 4.00 (0.5)
$K[PtCl_3(NH_3)]$	54.6	54.6	14	6.39, 3.88 (0.6), 3.79 (0.6)
$[Pt(NH_3)_4]Cl_2$[c]	55.4	55.4	15, 16	7.36, 3.64 (1.0), 3.26 (1.0)
$[Pt(NH_3)_4]Br_2$[c]	44.8	44.8	—	7.56, 6.51 (0.5), 3.41 (0.9)
$[Pt(NH_3)_3Cl]Cl$	61.6	61.6	17	5.64, 5.94 (0.4), 3.53 (0.5)
$[Pt(NH_3)_3Br]Br$	48.2	48.4	31	5.91, 4.55 (0.9), 3.92 (0.9)
$[Pt(NH_3)_3NO_2]Cl$	59.6	59.0	18	4.35, 6.47 (0.9), 3.72 (0.9)
$[Pt(NH_3)_2Cl_2]$[d]	65.2	65.4	19	6.21, 7.30 (0.1), 3.40 (0.3)
$[Pt(NH_3)_2Br_2]$[d]	50.3	50.4	20	6.11, 7.48 (0.9), 3.27 (0.7)
$[Pt(NH_3)_2(NO_2)_2]$[d]	60.8	60.7	18	6.04, 3.25 (0.6), 2.28 (0.6)
K_2PdCl_4	32.5	32.8	21	7.06, 3.18 (0.9), 2.51 (0.9)
$K_2Pd(CN)_4$[c]	34.7	34.8	22	7.96, 3.30 (0.9), 3.19 (0.7)
$K_2Pd(NO_2)_4$	28.9	28.9	23	(Amorphous)
$K_2Pd(SCN)_4$	25.5	25.5	24	6.59, 3.95 (0.7), 3.75 (0.9)
$[Pd(NH_3)_4]Br_2$	31.9	31.5	25	3.86, 3.45 (0.9), 2.73 (0.8)
[Pd(dien)Br]Br[e]	28.9	29.1	26	3.86, 6.28 (0.5), 4.90 (0.6)
[Pd(dien)I]I	23.0	22.8	26	4.55, 4.44 (0.8), 3.88 (0.9)
$KAuCl_4$	52.2	52.0	27, 28	5.67, 6.14 (0.8), 3.53 (0.7)
$KAuBr_4$	35.5	35.6	29	7.58, 3.77 (0.9), 3.31 (0.6)
$KAu(CN)_4$[f]	56.4	56.8	30	4.24, 8.18 (0.9), 4.92 (0.9)

[a] M = Pt, Pd, Au. Where necessary, complexes were also analyzed for total halogen (8).

[b] X-ray powder diffraction patterns were obtained using CuK_α radiation, Ni filter, 35 kv tube voltage, 15 ma filament current, and exposure times of 8-24 hr. Relative intensities were estimated visually. The first *d*-spacing listed in each case corresponds to a relative intensity of 1.0. Only the three most intense lines are given here; more extensive data are available elsewhere (8).

[c] Monohydrate.
[d] cis-isomer.
[e] dien = diethylenetriammine.
[f] Hemihydrate.

erence electrodes were recrystallized once before use.

Complexes.—Most of the complexes of Pt(II), Pd(II), and Au(III) were prepared by known methods or by minor modifications thereof, the details of which are available elsewhere (8). Others were prepared by new or improved procedures as described below. The purity of all of these products was established by analysis and by x-ray diffraction data (Table I).

Tetrammineplatinum(II) bromide.—A solution of 6g of cis-$[Pt(NH_3)_2Br_2]$ in 300 ml of 28% aqueous ammonia was evaporated at 90° until the volume was reduced to *ca.* 50 ml. After 1 hr at 25° the mixture was filtered, the white solid was washed successively with acetone and ether, and dried in air at room temperature. The yield was 6g.

Bromotriammineplatinum(II) bromide.—As suggested by relevant work by Tschugaev (31), 13.22g of cis-$[Pt(NH_3)_2Br_2]$ was dissolved in 500 ml of boiling water, 2.64g of KOCN was added with stirring, and after 2 min 5 ml of 48% HBr was added cautiously. The solution was boiled for an additional 5 min, cooled to 0°, and unreacted solid was removed by filtration. A solution of 9g of K_2PtBr_4 in water was added to the filtrate; the resulting precipitate was collected, extracted with 300 ml of boiling water, and filtered hot. Green insoluble $[Pt(NH_3)_4]PtBr_4$ was thereby removed, and brown $[Pt(NH_3)_3Br]PtBr_4$ crystallized from the filtrate. The crystals were recrystallized once from 250 ml of boiling water and dried. This product (3.05g) and 1.0g of $[Pt(NH_3)_4]Br_2 \cdot H_2O$ were boiled in 10 ml of water for 5 min, cooled in an ice bath, filtered, and 1 ml of 48% HBr was added to the filtrate. Precipitation was effected by addition of 500 ml of acetone. After standing over night, the mixture was filtered and the cream-colored bromotriammine was washed successively with acetone and ether and dried at 65°; the yield was 1.5g.

Potassium trichloronitrosylplatinate (II).—Nitric oxide was bubbled for 2 hr through a stirred solution of 1.34g of KCl and 0.831g of K_2PtCl_4 at 25°. The color of the solution changed from red to yellow-green, precipitation of $[Pt(NO)_2Cl_2]$ did not occur, and addition of $[Pt(NH_3)_4]Cl_2$ to a portion of the solution gave only a red-brown precipitate of $[Pt(NH_3)_4][PtCl_3(NO)]_2$; these observations indicate that the tetrachloro complex was quantitatively converted to the trichloronitrosyl compound, which was not isolated.

Results

Preliminary Experiments

Effect of separation of anode and cathode compartments.—Early experiments were carried out in a cell similar to the one shown in Fig. 1, except that the anode and cathode compartments were not separated. It was observed that the cathode current efficiency drifted severely with time because of species generated at the anode [probably complexes of Pt(IV)]. The efficiency was independent of time if a cell with divided compartments was employed, and all subsequent runs were made in this type of cell (Fig. 1). The solutions in the anode and cathode compartments were of the same composition, unstirred solution was contained in the compartment between the two frits (Fig. 1) and run times were 15-30 min. These conditions were designed to minimize diffusion effects.

Effect of cathode surface pretreatments.—Electrodeposition from solutions of $[Pt(NH_3)_4]Cl_2$ gave essentially equal and reproducible current efficiencies when the cathode was given the following pretreatments: (*a*) the electrode was immersed in boiling 5% hydrazine solution for 30 min, rinsed with distilled water, and dried by heating to redness; (*b*) after a 1-min dip in boiling aqua regia, the electrode was rinsed with distilled water and heated to redness. This was followed by heating the cathode in a hydrogen atmosphere for 1 hr at 500°C and cooling in an atmosphere of helium.

Furthermore, electrodeposition from solutions of K_2PtCl_4 yielded equivalent current efficiencies (within experimental error) using cathodes of either bright "new" or dulled platinum (from previous deposits). Hence, it was concluded that the initial condition of the cathode surface was not a parameter which would influence cathode current efficiency measurements.

Effect of hydrolysis.—No effects were found which could be attributed to hydrolysis; *i.e.*, aged solutions gave essentially the same results as fresh solutions.

Quality of the deposits.—The quality of the deposits varied from very rough to bright and smooth, but in all cases the deposits were sufficiently adherent for good reproducibility. From the standpoint of both brightness and adherence, the best deposits usually occurred when the efficiency was 70% or less. One noteworthy exception was that mirror-bright platinum could be deposited at 100% efficiency from a 0.01M K_2PtCl, 0.1M KCl, deoxygenated solution at current densities of from 2 to 8 ma/cm^2 at 25°. Deposition of "platinum black" was not observed in any case. All cathodes were heated to redness prior to final weighing.

Cathode Current Efficiency Measurements

The effects of current density, complex concentration, dissolved gases, and temperature on cathode current efficiency were studied to establish optimum conditions for comparing the effects of specific ligands on current efficiency.

Effect of current density on current efficiency.—Figure 2 illustrates the effect of current density on current efficiency and also gives an indication of experimental reproducibility. It is apparent that the efficiency is independent of current density at least over the range from 1 to 3 ma/cm^2; therefore, subsequent runs were made in this region. These runs were made with air-saturated, 0.01M K_2PtCl_4 solutions without supporting electrolytes at a temperature of 71.0°C.

Effect of concentration on current efficiency.—Figure 3 illustrates the effect of concentration on current efficiency for solutions of three platinum complexes. The experiments were carried out using air-saturated solutions without supporting electrolytes; the current density was 1.5 ma/cm^2 and the

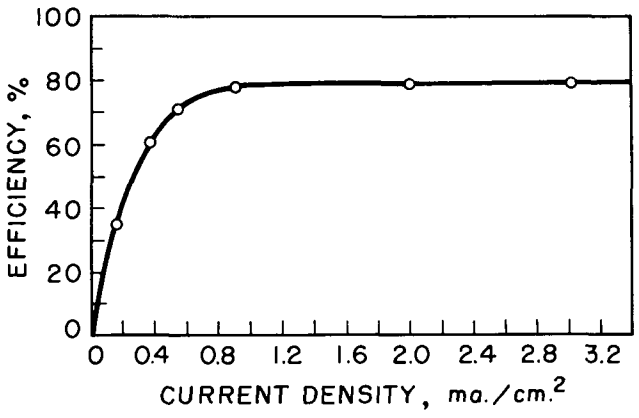

Fig. 2. Effect of current density on cathode current efficiency for K_2PtCl_4 solutions.

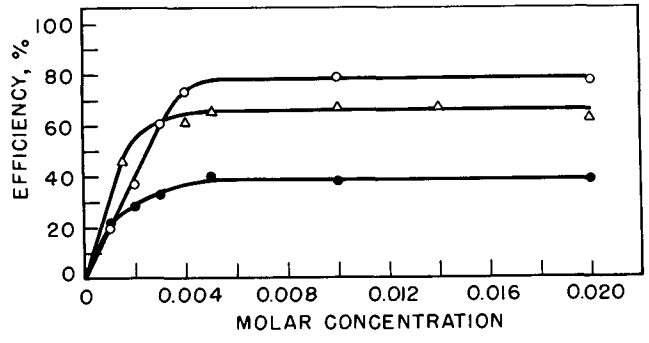

Fig. 3. Effect of concentration on cathode current efficiency. •, $[Pt(NH_3)_3NO_2]Cl$; △, $[Pt(NH_3)_3Cl]Cl$; ○, $K_2[PtCl_4]$.

temperature was 40°C. It was concluded that the efficiency is essentially independent of complex concentration above *ca.* 0.005M. Furthermore, for these solutions the efficiency was found to be temperature-independent (between 40°-70°C) if the concentration was above 0.005M; below this concentration increasing temperatures resulted in higher efficiencies.

Effect of specific ligands on current efficiency.— In general, depending on the composition of the plating solution, three reactions compete to varying degrees at the cathode, *i.e.*, metal deposition, oxygen reduction, and hydrogen evolution. The question of the effect of oxygen concentration was studied by either deoxygenating the plating solution with helium or by saturating the solution with oxygen. Thus, the following three types of solutions were studied:

1. Air-saturated solutions. The effect of specific ligands on current efficiency is shown in Table II. Supporting electrolytes were added to investigate the effect of suppressing possible hydrolysis or dissociation of the various complexes. These runs were made at a temperature of 40°C, and the current density was 1.5 ma/cm². The reproducibility was from 2 to 4%.

2. Oxygen-saturated solutions. The data shown in Table III illustrate the marked decrease in efficiency caused by dissolved oxygen (oxygen was bubbled through the solutions for 1 hr prior to deposition). In this case, it was noted that the tendency to electrodeposit was considerably less from solutions of K_2PtBr_4 than from solutions of K_2PtCl_4, whereas the efficiencies corresponding to these two complexes were quite close in air-saturated solutions. These runs were made at a temperature of 30°C, and the current density was 2.5 ma/cm².

3. Helium-saturated solutions. Electrodeposition from deoxygenated solutions resulted in the data shown in Table III, and it is clear that metal deposition was the only cathodic process occurring in the case of deposition from solutions of K_2PtCl_4, K_2PtBr_4, $K[PtCl_3(NH_3)]$, $[Pt(NH_3)_3Cl]Cl$, and $[Pt(NH_3)_3Br]Br$. The low efficiencies associated with $[Pt(NH_3)_3NO_2]Cl$ and $K[PtCl_3(NO)]$ are con-

Table II. Effect of ligands on cathode current efficiency (air-saturated solutions)

Complex	Conc, M	Added electrolyte	Conc, M	Efficiency, %
$[Pt(NH_3)_3NO_2]Cl$	0.01	None		38
		KNO_3	0.1	37
		NH_4NO_3	0.1	24
		KNO_2	0.1	21
	0.005	KNO_2	0.05	
		NH_4NO_3	0.05	19
$K[PtCl_3(NH_3)]$	0.01	None		100
		NH_4Cl	0.1	87
	0.01	None		68
$[Pt(NH_3)_3Cl]Cl$	0.005	None		66
		NH_4Cl	0.1	67
$[Pt(NH_3)_3Br]Br$	0.01	None		75
		NH_4Br	0.1	74
K_2PtCl_4	0.004	None		74
	0.01	None		79
	0.005	KCl	0.1	75
K_2PtBr_4	0.01	None		83
		KBr	0.1	80
$[Pt(NH_3)_4]Cl_2 \cdot H_2O$	0.01	None		2
$K_2Pt(NO_2)_4$	0.01	None		0
$K_2Pt(CN)_4$	0.01	None		0
$K_2Pt(SCN)_4$	0.01	None		0
K_2PdCl_4	0.01	None		100
		KCl	0.01	99
$K_2Pd(CN_4) \cdot H_2O$	0.01	None		0
$K_2Pd(SCN)_4$	0.01	None		93
		KSCN	0.01	100
$K_2Pd(NO_2)_4$	0.01	None		72
		KNO_2	0.01	66
$[Pd(NH_3)_4]Br_2$	0.01	None		84
		NH_4Br	0.01	84
$KAuCl_4$	0.01	None		100
		KCl	0.01	99
$KAuBr_4$	0.01	None		100
		KBr	0.01	97
$KAu(CN)_4 \cdot \frac{1}{2}H_2O$	0.01	None		71
		KCN	0.01	44

Table III. Cathode current efficiencies for oxygen-saturated and helium-saturated solutions

Complex, 0.01M	Added electrolyte, 0.1M	Current density, ma/cm²	Efficiency, % Oxygen-saturated	Helium-saturated
K_2PtCl_4	KCl	2.5	50	96
K_2PtBr_4	KBr	2.5	25	100
$K[PtCl_3(NH_3)]$	KCl	2.5	50	99
$[Pt(NH_3)_3Cl]Cl$	KCl	2.5	—	50
		1.25	—	99
$[Pt(NH_3)_3Br]Br$	KBr	1.25	—	100
$[Pt(NH_3)_3NO_2]Cl$	KCl	2.5	—	7
		1.25	—	16
$K[PtCl_3(NO)]$	KCl	1.25	—	20

sidered in the Discussion Section. These runs were made at 30°C.

Cathode Potentials

Cathode potential measurements were made to provide another criterion to aid in establishing trends for the effect of specific ligands on the tendency to electrodeposit.

During metal deposition, the current density range from about 0.5 to 5 ma/cm^2 gave potentials which were reproducible to about 0.02v. Measured potentials outside this range were less reproducible. Approximately 1 min after a current change, the drift in potential was less than experimental error.

Platinum (II) complexes.—The cathode potential-current density determinations for platinum complexes were made using deoxygenated solutions at 35°C (Fig. 4 and 5). These polarization curves clearly indicate that hydrogen evolution is not a reaction concurrent with metal deposition at low current densities.

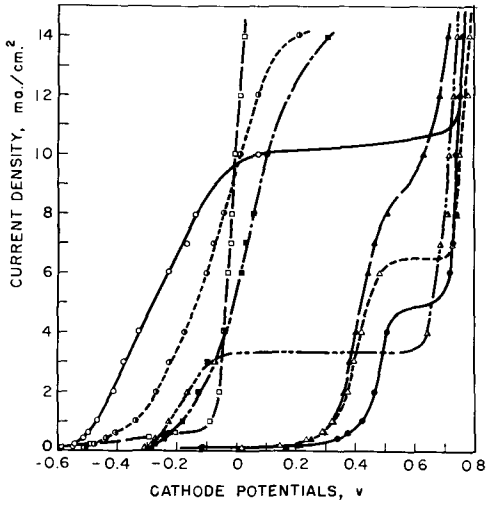

Fig. 4. Cathode potential-current density curves for platinum complexes and for oxygen. Open circle, $K_2[PtCl_4]$; half opened circle darkened on right side, $K_2[PtBr_4]$; open square, $K[PtCl_3NO]$; solid square, $K[PtCl_3NH_3]$; solid triangle, $[Pt(NH_3)_3Br]Br$; open triangle, $[Pt(NH_3)_3Cl]Cl$; solid circle, $[Pt(NH_3)_3NO_2]$ Cl; half opened triangle darkened on right side, saturated oxygen solution.

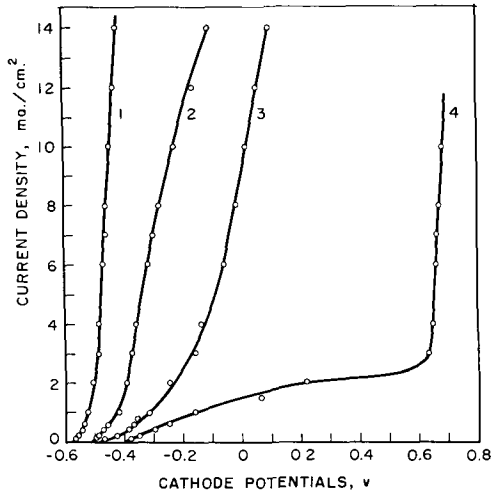

Fig. 5. Cathode potential-current density curves for K_2PtCl_4-KCl solutions. 1, 0.1M $K_2[PtCl_4]$, 0.1M KCl; 2, 0.01M $K_2[PtCl_4]$, 0.1M KCl; 3, 0.01M $K_2[PtCl_4]$, 1M KCl; 4, 0.001M $K_2[PtCl_4]$, 0.1M KCl.

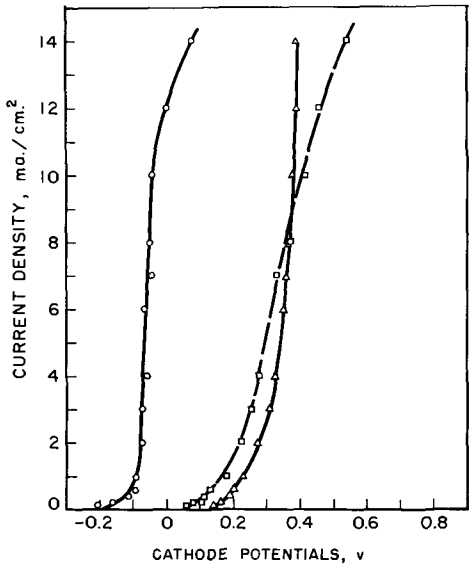

Fig. 6. Cathode potential-current density curves for [Pd(dien)X] X-KX solutions. ○, [Pd(dien)Cl]Cl; □, [Pd(dien)Br]Br; △, [Pd(dien)I]I.

Using dry methanol as a solvent, 0.01M solutions if $K_2Pt(SCN)_4$ and $K_2Pt(CN)_4$ were prepared, and cathode potential-current density measurements were attempted. Surprisingly, no deposition resulted in either case before the applied potential was sufficiently high to decompose the solvent; thus, it was concluded that the oxidation potentials of these two complexes are more positive than about 1.1v (the decomposition potential of methanol).

Palladium(II) complexes.—Figure 6 shows the results of similar cathode potential experiments (at 50°C) for three palladium complexes. The effect of the iodo, bromo, and chloro ligands in the coordination sphere of Pd(II) complexes is clear, *i.e.*, the tendency to electrodeposit decreases as $Cl^- > Br^- > I^-$.

Discussion

The complexes formed with Pt(II), Pd(II), and Au(III) have many properties in common: They all form square-planar complexes with very few exceptions; Pt(II), Pd(II), and Au(III) are isoelectronic d^8 systems; the thermodynamic stabilities of the halo complexes of these ions are known to stand in the same order, *i.e.*, $I^- > Br^- > Cl^- >> F^-$ (32); and there is considerable evidence (33-37) which indicates that the order of decreasing bond strengths is $CN^- > NO_2^- > NH_3 > SCN^- > I^- > Br^- > Cl^-$ for the complexes of these metals in the indicated oxidation states. Even comparable standard oxidation potentials are quite close.[1]

Since these complexes are so similar (and the experimental data presented here offer no contradictions to their general similarity), it is assumed that the mechanism of electrodeposition is probably the same for the three metals studied. Thus, the following discussion, generally concerned with platinum deposition, can be extended to include deposition from solutions of Pd(II) and Au(III) complexes.

Electrodeposition from the systems described

[1] The standard oxidation potentials for the reaction $M + 4X^- \rightarrow [MX_4]^{n-4} + ne$ for the chloro and bromo complexes of Pt(II), Pd(II), and Au(III) are given by de Bethune *et al.* (38).

yielded cathode current efficiencies and cathode potentials that are markedly dependent on the particular ligands coordinated about the central metal ion. Compared with this effect, the results show that the influences on deposition of the parameters of temperature, complex concentration, cathode surface conditions, and even current density (within limits) are negligible. With this in mind, four possible slow steps in the mechanism of electrodeposition can be considered: (I) Transfer or diffusion of ions to the cathode (concentration polarization). (II) Orientation or crystallization of metal atoms on the cathode (crystallization polarization). (III) Dissociation of the complex by loss of one or more coordinating groups (a type of concentration polarization). (IV) Complex ion discharge in the double layer (discharge or activation polarization).

Depending on which reaction step is rate-determining, it is possible to derive different equations for the relation between the polarization, η, and the current density, i,[2] and it appears theoretically possible to determine the mechanism of electrodeposition from the experimentally determined η *vs.* i relation. This method has had some successes with hydrogen evolutions but has been markedly unsuccessful for metal deposition, and the polarization data in the literature are often in poor agreement (39, 40). Many authors feel that the main experimental difficulty centers about the fact that the cathode surface changes area and properties as deposition proceeds. Glasstone has pointed out that at low current densities, the expression for crystallization polarization and activation polarization are the same (41). It is therefore not surprising that we were unable to correlate the present data with theoretical η *vs.* i curves.

I. *Concentration polarization.*—Figure 3 shows that the rate of diffusion of ions to the cathode probably becomes rate-controlling (at 1.5 ma/cm^2) if the concentration falls below about 0.005M; the temperature effect noted in this low concentration region supports this conclusion. Similarly, the cathode potential-current density curves show that limiting currents can be reached at quite low current densities (6-7 ma/cm^2) at complex concentrations of 0.0091M (see curve for K_2PtCl_4 in Fig. 4). These effects were observed even though all measurements were made in efficiently stirred solutions. Nevertheless, the following discussions of the rate-controlling process assume that concentrations are sufficiently high and current densities are adequately low to prevent any appreciable effects which could be attributable to concentration polarization.

II. *Crystallization polarization.*—Theoretical arguments (42) indicate that the rate of surface diffusion, or rate of orientation in the crystal lattice, of adsorbed atoms (adatoms) is probably not the rate-determining step for Ni(II), Fe(II), and Co (II) deposition [Ni(II) and Pt(II) are isoelectronic] and would be even more unlikely to influence platinum deposition because of its relatively higher sublimation energy (*ca.* 4.9 ev) (43). Furthermore, it seems unlikely that the energies necessary for deposition would be dependent only on the particular ligands coordinated about the central metal ion, as this work shows, if such a surface diffusion step were rate-controlling. However, surface diffusion of adsorbed adions to appropriate metal surface sites cannot be ruled out as a contributing factor in the over-all deposition mechanism.

III. *Dissociation of the complex.*—A dissociative type mechanism, as described by Lyons (2), in which the forward rate of a reaction of the type

$$M(X)_4 \rightleftharpoons M(X)_3 + X$$

taking place in the bulk solution is related to the rate-controlling step, is not compatible with the following experimental results:

(*a*) Figure 3 shows that efficiency is independent of complex concentration above about 0.005M.

(*b*) The addition of a plating solution of a supporting electrolyte which has ligands that are common to those in the metal complex should force reactions of the above type far to the left, and the current efficiency should greatly decrease, if such an S_N1 type mechanism were operative. Inspection of Table II shows that such a lowering effect was observed for the cases: $K[PtCl_3(NH_3)]$, $[Pt(NH_3)_3NO_2]Cl$, and $KAu(CN)_4 \cdot 1/2H_2O$; but no significant reductions in efficiency were observed for $[Pt(NH_3)_3Cl]Cl$, $[Pt(NH_3)_3Br]Br$, K_2PtBr_4, $KAuBr_4$, $KAuCl_4$, $K_2Pd(SCN)_4$, $[Pd(NH_3)_4]Br_2$, and $K_2Pd(NO_2)_4$. The reduction in efficiency found for $KAu(CN)_4 \cdot 1/2H_2O$, KCN solutions is due to the well-known dissolution of gold in KCN solution, and therefore is not comparable; the lowering effect associated with $[Pt(NH_3)_3NO_2]Cl$ also is not comparable as shown below.

The three triammines $[Pt(NH_3)_3NO_2]Cl$, $[Pt(NH_3)_3Br]Br$, and $[Pt(NH_3)_3Cl]Cl$ were prepared originally with the intention of testing a possible trans effect, *i.e.*, if bond breaking was occurring trans to the monosubstituted group, the efficiencies should be dependent on the relative translabilizing powers of the particular monosubstituted ligands. This, of course, is assuming that a dissociative type mechanism is operative. Chatt *et al.* (4) give $NO_2^- > Br^- > Cl^-$ for the order of decreasing translabilizing effects. Table II shows that the efficiencies in air-saturated solutions decrease in the order $[Pt(NH_3)_3Br]Br > [Pt(NH_3)_3Cl]Cl > [Pt(NH_3)_3NO_2]Cl$ (the triamminebromo and chloro cases are quite close), which is not the expected trend if the trans effect were operative. However, the results for these triammines are not comparable, unfortunately, because the reactions concurrent with platinum deposition were not the same in each case. The experimental results indicate that oxygen reduction was the only reaction occurring other than metal deposition for both triamminehalo complexes (the efficiencies were 100% in deoxygenated solutions as Table III indicates), but for the case of the triamminenitrito complex, NO_2^- was reduced also, since the efficiency was very low even in oxygen-free solutions. A similar situation occurred in the case of $K[PtCl_3NO]$, in that the nitrosyl ligand was reduced. This effect explains the anomalous cathode potential curve (Fig. 4) and the low efficiency

[2] For a review of the theory of polarization at electrodes see ref. (39).

which were exhibited by this complex in oxygen-free solutions.

The polarization curves in Fig. 4 show that hydrogen evolution did not occur during electrodeposition of platinum if the current density was sufficiently low, except perhaps for the case of $[Pt(NH_3)_3NO_2]Cl$, which was reduced close to potentials high enough for simultaneous hydrogen evolution.

(c) The classical expressions for concentration polarization lead to an approximate expression

$$i_{lim} = 25mZ$$

for the limiting current density i_{lim} in ma/cm^2, where m is the molar concentration of the reacting species, and Z is the electrochemical valence. This relation is for an unstirred solution at 20°C. Glasstone (44) estimates that for a well-stirred solution at 35°C, a fair approximation is

$$i_{lim} = 1700\,mZ$$

For a 0.001M K_2PtCl_4, 0.1M KCl solution at 35°C, assuming that the plating species is $(PtCl_4)^{2-}$, the above expression gives about 3 ma/cm^2 for i_{lim}. Figure 5 shows that the experimentally determined limiting current for such a solution is about what is predicted from theory. Assuming that the reacting species is Pt^{2+} ion, and the equilibrium constant for K_2PtCl_4 is about 10^{-16} (45), for a similar 0.001M K_2PtCl_4, 0.1M KCl solution, the above expression gives about 3 x 10^{-12} ma/cm^2 for the limiting current density. Furthermore, the equilibrium constant for the ligand substitution reaction

$$(PtCl_4)^{2-} + H_2O \rightleftharpoons [PtCl_3(H_2O)]^- + Cl^-$$

is known to be 0.021 at 30°C (46), and assuming deposition from $[PtCl_3(H_2O)]^-$, a similar calculation for a 0.01M K_2PtCl_4, 1M KCl solution gives about 0.7 ma/cm^2 as the limiting current density. Figure 5 shows that this agreement is quite poor also. Thus, the electrodeposition of these metals probably proceeds from the undissociated complex ion.

It is significant to note that limiting currents cannot be reduced by large excesses of ions common to those making up the complex (Fig. 5) but can be reduced easily by lowering the molar concentration of the reacting complex. The potential shifts noted here are attributed to changing junction potentials, changing $(PtCl_4)^{2-}$ activity, and increased adsorption of K^+ and Cl^- ions on the cathode surface when the KCl concentration is increased.

IV. *Activation polarization.*—The standard free energy change for the reaction

$$\text{Metal} + \text{solvent} \rightarrow \text{Metal}^{z+}\ (\text{solvated}) + Ze$$

is given approximately (entropy terms neglected) by

$$\Delta F = S + I - W - Z\phi$$

where S is the sublimation energy; I is the ionization energy of the metal in the vapor state; W is the solvation energy of the gaseous ion, or in this case, the coordination and solvation energies; and $Z\phi$ is the electronic work function of the metal.

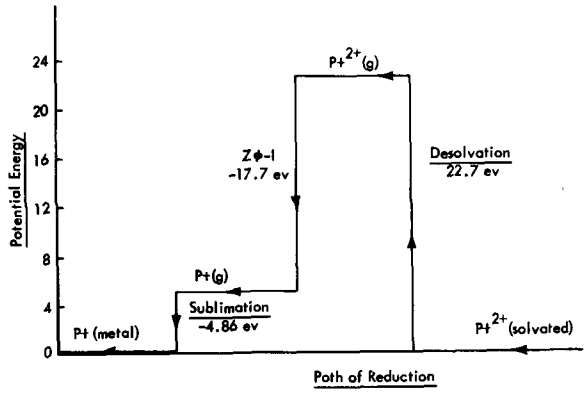

Fig. 7. A possible path for electrodeposition of platinum for solutions of Pt^{2+}.

For platinum, the values are: S = 4.86 ev (43), I = 28.3 ev (47), W = 22.7 ev,[3] $Z\phi$ = 10.64 ev (48).

A possible path of reduction could be pictured as shown in Fig. 7. This represents an adion type mechanism, which seems unlikely considering the height of the barrier presented by the desolvation energy. An easier path (lower energy barrier) would be an initial electron transfer to the central metal ion which would weaken the bonds with coordinated ligands. Thus, the rate-controlling step is probably dependent on the magnitude of the energy barrier presented by the complex for the over-all processes of stripping the complex of its coordinated ligands in the double layer, and transfer of electrons to the metal ion.

Regardless of the detailed mechanism, the tendency to electrodeposit is certainly dependent on the bond energies of the particular ligands coordinated about the central metal ion. The polarization curves give $K_2PtCl_4 > K_2PtBr_4 > K[PtCl_3(NH_3)] > [Pt(NH_3)_3Br]Br \sim [Pt(NH_3)_3Cl]Cl > K_2Pt(SCN)_4 \sim K_2Pt(CN)_4$ and $[Pd(dien)Cl]Cl > [Pd(dien)Br]Br > [Pd(dien)I]I$ as the orders of decreasing ease of reduction. Efficiency data give (using the data for oxygen-saturated solutions, Table III, for the first three) $K_2PtCl_4 \sim K[PtCl_3(NH_3)] > K_2PtBr_4$, and $[Pt(NH_3)_3Cl]Cl \sim [Pt(NH_3)_3Br]Br > [Pt(NH_3)_3NO_2]Cl > K_2Pt(SCN)_4 \sim [Pt(NH_3)_4]Cl_2 \cdot H_2O \sim K_2Pt(NO_2)_4 \sim K_2Pt(CN)_4$, and $K_2PdCl_4 > K_2Pd(SCN)_4 > [Pd(NH_3)_4]Br_2 > K_2Pd(NO_2)_4 >> K_2Pd(CN)_4 \cdot H_2O$, and $KAuCl_4 \sim KAuBr_4 > KAu(CN)_4 \cdot 1/2H_2O$ as the orders of decreasing ease of reduction. Recalling that the order of decreasing bond strengths for these complexes is $CN^- > NO_2^- > NH_3 > SCN^- > I^- > Br^- > Cl^-$, the correlation between bond strengths and these experimental data is evident.

The efficiencies found in air-saturated solutions (Table II) for the triammines and $K[PtCl_3(NH_3)]$ were surprisingly high, considering their positions on the polarization curves. The efficiency associated with $K[PtCl_3(NH_3)]$ (100%) is higher than that of K_2PtCl_4 (79%), even though K_2PtCl_4 is thermodynamically less stable than $K[PtCl_3(NH_3)]$. This implies that the over-all charge of the complex may

[3] Calculated from ligand field theory for the reaction $Pt^{2+}(g) \rightarrow Pt^{2+}(aq)$, which should be close to the value for an anionic complex of the type $(PtX_4)^{2-}$ because the extra solvation energy of the free anion compared with a neutral ligand compensates for the firmer bonding in the complex (47).

influence the rate of electrodeposition, *i.e.*, the more positive the charge, the greater the rate.

Acknowledgment

This work was supported by the U.S. Atomic Energy Commission, Contract AT-(40-1)-1639, and by the Robert A. Welch Foundation. One of us (JAC) is indebted to The Celanese Corporation of America for a Predoctoral Fellowship, 1959-1961.

Manuscript received Oct. 16, 1962.

Any discussion of this paper will appear in a Discussion Section to be published in the June 1964 JOURNAL.

REFERENCES

1. G. W. Watt and D. A. Hazlehurst, *This Journal*, **106**, 117 (1959).
2. E. H. Lyons, Jr., *ibid.*, **101**, 376 (1954).
3. G. W. Watt and J. W. Vaughn, *ibid.*, **108**, 351 (1961).
4. J. Chatt, L. A Duncanson, and L. M. Venanzi, *J. Chem. Soc.*, **1955**, 4456.
5. J. B. Willis, *J. Am. Chem. Soc.*, **67**, 547 (1945).
6. P. Kivalo and H. A. Laitinen, *ibid.*, **77**, 5205 (1955).
7. H. S. Harned, *ibid.*, **54**, 1350 (1932); **60**, 336, 2130 (1938).
8. J. A. Cunningham, Dissertation, The University of Texas, 1961.
9. M. Vezes, *Bull. soc. chim.*, **19**, 879 (1898); P. Klason, *Ber.*, **37**, 1360 (1904).
10. E. Biilmann and A. C. Anderson, *Ber.*, **36**, 1570 (1903).
11. J. Lang, *J. prakt. Chem.*, **83**, 415 (1861); L. F. Nilson, *Ber.*, **9**, 1722 (1876).
12. L. Gmelin, *Schev. J.*, **36**, 231 (1822).
13. G. B. Buckton, *Ann.*, **92**, 280 (1854); *Quart. J. Chem. Soc.*, **7**, 32 (1853).
14. T. S. Elleman, J. W. Reishus, and D. S. Martin, *J. Am. Chem. Soc.*, **80**, 536 (1958).
15. R. N. Kellor, "Inorganic Syntheses," Vol. 2, p. 250, McGraw-Hill Book Co., Inc., New York (1946).
16. J. Reiset, *Compt. rend.*, **11**, 711 (1840); **18**, 1100 (1844).
17. H. J. S. King, *J. Chem. Soc.*, **1948**, 1912.
18. L. A. Tshugaev and S. S. Kiltinovic, *ibid.*, **109**, 1286 (1916).
19. L. Ramberg, *Z. anorg. Chem.*, **83**, 33 (1913).
20. H. D. K. Drew, F. W. Pinkard, W. Wardlow, and E. G. Cox, *J. Chem. Soc.*, **1932**, 988.
21. J. J. Berzelius, *Svenska Akad. Handl.*, 45 (1828).
22. J. H. Bigelow, "Inorganic Syntheses," Vol. 2, p. 245, McGraw-Hill Book Co., Inc., New York (1946).
23. J. Lang, *J. prakt. Chem.* **83**, 421 (1861).
24. I. Bellucci, *Atti reale accad. Lincei*, **13**, 386 (1904).
25. H. Müller, *Lieb. Ann.*, **86**, 353 (1853).
26. F. Basolo, H. B. Gray, and R. G. Pearson, *J. Am. Chem. Soc.*, **82**, 4200 (1960).
27. A. Lanier, *Monatsh.*, **11**, 220 (1890).
28. E. G. Cox and K. C. Webster, *J. Chem. Soc.*, **1936**, 1636.
29. B. P. Block, "Inorganic Syntheses," Vol. 4, p. 14, McGraw-Hill Book Co., Inc., New York (1953).
30. C. Himby, *Lieb. Ann.*, **42**, 337 (1842).
31. L. A. Tschugaev, *J. Chem. Soc.*, **107**, 1247 (1915).
32. F. Basolo and R. G. Pearson, "Mechanisms of Inorganic Reactions," p. 23, John Wiley & Sons, Inc., New York (1958).
33. Ref. (32), p. 44.
34. J. Chatt, L. A. Duncanson, B. L. Shaw, and L. M. Venanzi, *Discussions Faraday Soc.*, **26**, 131 (1958).
35. F. Basolo, H. B. Gray, and R. G. Pearson, *J. Am. Chem. Soc.*, **82**, 4200 (1960).
36. S. Ahrland, J. Chatt, and N. Davies, *Quart. Rev.*, **12**, 265 (1958).
37. A. A. Grinberg and G. A. Shagisultanova, *Russ. J. Inorg. Chem.*, **5**, 134 (1960).
38. A. J. de Bethune, T. S. Light, and N. Svendeman, *This Journal*, **106**, 616 (1959).
39. E. Mattsson, *Trans. Roy. Inst. Tech., Stockholm*, **96**, 35 (1955).
40. G. Kortüm and J. O'M. Bockris, "Textbook of Electrochemistry," Vol. 2, p. 418, Elsevier Publishing Co., New York (1951).
41. S. Glasstone, "An Introduction to Electrochemistry," p. 463, D. Van Norstrand Co., Inc., New York (1942).
42. B. F. Conway and J. O'M. Bockris, *Proc. Roy. Soc. (London)*, **A248**, 394 (1958).
43. K. K. Kelly, "Heats of Fusion of Inorganic Compounds," *U. S. Bur. Mines Bull. 393* (1936).
44. Ref. (41), p. 451.
45. Ref. (32), p. 192.
46. L. F. Grantham, T. S. Elleman, and D. S. Martin, *J. Am. Chem. Soc.*, **77**, 2965 (1955).
47. Ref. (32), p. 67.
48. L. V. Whitney, *Phys. Rev.*, **50**, 1154 (1936).

Mechanism of Electrodeposition of Metals from Liquid Ammonia Solutions

George W. Watt and Joe W. Vaughn

Department of Chemistry, The University of Texas, Austin, Texas

ABSTRACT

Absorption spectra, x-ray diffraction, and cathode current efficiency data have been used to support a previously postulated mechanism for the generation of the electrochemically active species in the deposition of metals from liquid ammonia solutions of octahedral complexes. New data for certain copper(II) complexes are also presented. Deposition of metal did not occur from solutions of complexes of chromium(III), rhodium(III), and osmium(III).

Earlier work (1) has shown that deposition of cobalt from liquid ammonia solutions of octahedral spin-paired cobalt(III) complexes can be correlated with the operation of the trans effect. Thus, enhancement of cathode current efficiency for $[Co(NH_3)_5I]^{2+}$ as compared with $[Co(NH_3)_6]^{3+}$ is attributed to the translabilizing effect of the I^- ligand. Similarly, the increase in cathode current efficiency for $[Co(NH_3)_6]^{3+}$ + KSCN as compared with $[Co(NH_3)_6]^{3+}$ alone is explained by a bimolecular ligand substitution

$$[ML_6]^{n+} + X^- \rightleftharpoons [ML_5X^-]^{(n-1)+} + L$$

followed by a translabilization-induced dissociation process of the type proposed by Lyons (2)

$$[ML_5X^-]^{(n-1)+} \rightleftharpoons [ML_4X^-]^{(n-1)+} + L$$

thus giving rise to the electrochemically active species.

Although cathode current efficiency data for both spin-free (3) and spin-paired (1) octahedral complexes are in agreement with these ideas, it seemed worthwhile to secure independent evidence for the reality of the initial ligand substitution process. Such evidence is given below together with an extension of these studies to copper(II) complexes some of which are octahedral and some of which may be square planar.[1] Efforts to secure additional supporting evidence were unsuccessful since metal deposition did not occur from ammonia solutions of octahedral complexes of chromium(III), rhodium(III), and osmium(III).

Experimental

Materials.—The following complexes were prepared and purified by the procedures to which reference is made; the calculated and experimentally determined metal content, respectively, are given in brackets: Nitropentamminechromium(III) nitrate (5), [16.7, 16.9]; aquopentamminechromium(III) nitrate (5), [16.1, 15.8]; chloropentamminerhodium (III) nitrate (7), [34.9, 34.9]; bromopentammineosmium(III) bromide (8), [37.0, 37.3]. Copper(II) complexes were prepared as described below; x-ray diffraction data are given in Table I.

[Cu(dien)I]I.—To a solution of 8.5g (0.05 mole) of $CuCl_2 \cdot 2H_2O$ in 25 ml of water was added 5.3g (0.05 mole) of diethylenetriamine (dien) with stirring. The solution was added to 12.7g (0.76 mole) of KI dissolved in a minimum amount of water, whereupon the solution became black and viscous. Another 3 ml of dien was added to redissolve the precipitate; this was followed by excess solid KI which precipitated a dark green product. This was filtered, dissolved in a minimum amount of water, and reprecipitated by addition of solid KI. The product was filtered, washed with ethanol, ether, and air-dried. The final product was a green powder (15.0, 14.7).

$[Cu(dien)_2]I_2$.—To a solution of 8.5g (0.05 mole) of $CuCl_2 \cdot 2H_2O$ in 25 ml of water was added 10.6g (0.103 mole) of dien, with stirring. The resulting warm solution was cooled to room temperature and filtered; the filtrate was treated with excess solid KI whereupon a blue solid separated. This was filtered, washed with ethanol and ether, and dried over magnesium perchlorate [12.1, 12.2].

[Cu(dien)SCN]I.—To a solution of 8.5g (0.05 mole) of $CuCl_2 \cdot 2H_2O$ in 50 ml of water was added with stirring 5.3g (0.05 mole) of dien. Sufficient dilute HCl was added to destroy the blue color of the complex; the acid solution was treated with 5.3g dien followed by 19g (0.19 mole) KSCN in a small amount of water to provide a bright blue solid. This was filtered, dissolved in hot water, and treated with 8.5g (0.05 mole) of KI in a minimum amount of water. Blue-gray metallic plates precipitated and were recrystallized several times from hot water and KI, and air-dried [18.1, 17.5]. Treatment of an aqueous solution of this salt with Ag^+ results in the precipitation of only AgI.

[Cu(dien)SCN]SCN.—This compound was prepared as described above except that recrystallization was effected using KSCN rather than KI [22.5, 22.5].

$[Cu(en)_2]SO_4$.—This was prepared by the method of Gordon and Birdwhistle (9). Conversion to the iodide was accomplished by treating a concentrated aqueous solution of the sulfate with barium iodide; the product was recrystallized from water and air-dried [22.0, 22.4].

The potassium iodide, potassium thiocyanate, potassium nitrite, hexamminecobalt(III) nitrate, and nitritopentamminecobalt(III) nitrate were prepared and purified as described previously (1).

Spectra.—The cells employed to make absorption spectrum measurements on liquid ammonia solutions were fabricated from optical quartz (12 mm OD, 10 mm ID) obtained from the Lamp Division of The General Electric Co. Accurately weighed samples of the cobalt complexes sufficient to provide 10^{-4} and 10^{-3}M solutions in 7-9 ml of liquid ammonia were added to the cell which was then evacuated to *ca.* 10^{-3} mm and cooled in dry ice-acetone. Anhydrous gaseous ammonia was condensed in the cell, the dry ice-acetone was replaced by liquid nitrogen, and the cell was sealed. After the cell and contents had warmed to room temperature, the cell was transferred to the cell holder of a Beckman DU quartz spectrophotometer. The resulting data are

[1] For related studies concerned with deposition from aqueous solutions of spuare planar complexes see ref. (4).

Table I. X-ray diffraction data*

$[Cu(dien)_2]I_2$		[Cu(dien)I]I		[Cu(dien)SCN]I		[Cu(dien)SCN]SCN	
d, A	I/I_o	*d*, A	I/I_o	*d*, A	I/I_o	*d*, A	I/I_o
5.2	1.0	5.4	1.0	9.6	0.6	5.3	1.0
4.0	0.7	5.1	1.0	7.9	0.6	4.7	0.4
3.7	0.6	4.6	0.6	5.1	1.0	4.0	0.5
3.4	1.0	4.5	0.6	3.4	0.5	3.7	0.2
$[Cu(en)_2]I_2$		$[Co(NH_3)_6](NO_3)_3$		$[Co(NH_3)_5NO_2](NO_3)_2$		$[Co(NH_3)_6]$-$(NO_3)_3 + KNO_2$	
6.1	0.5	6.2	0.8	6.1	0.8	6.2	0.7
5.2	1.0	5.3	0.9	5.2	1.0	5.2	1.0
4.1	0.7	3.9	1.0	4.6	0.5	4.6	0.3
3.7	0.7	2.8	0.3	4.1	0.5	4.0	0.5

* CuK_α radiation, Ni filter, 40 kv tube voltage, 15 ma filament current, 7-8 hr exposure time. Relative intensities were estimated visually; only the four most intense lines are included here.

Table II. Absorption spectra of cobalt(III) complexes in liquid ammonia at 25°-27°

Complex	Optical density: Maxima	Optical density: Minimum
$[Co(NH_3)_6](NO_3)_3$	476-480, 340	390
$[Co(NH_3)_5NO_2](NO_3)_2$	466	400
$[Co(NH_3)_5NCS](NO_3)_2$*	476-480, 340	390
$[Co(NH_3)_6](NO_3)_3 + KNO_2$	476-480, 340† 472-474‡	

* At room temperature, ligand substitution occurred rapidly to form $[Co(NH_3)_6](NO_3)_3$.

† Readings taken as soon as cell came to room temperature.

‡ Readings remained constant after intervals of 18, 42, and 66 hr.

given in Table II. Where necessary for examination of residual solids, the cells were recooled in liquid nitrogen, opened, and the solvent allowed to evaporate.

Cathode current efficiency data.—The electrolysis cell, electrode holders, electrodes, and coulometer were the same as those described earlier (1). In all cases the total solution volume was 100 ml. The concentrations of the chromium(III), rhodium(III), and osmium(III) complexes were 2.0-3.7 x 10^{-3}M; that of the copper(II) complexes was 5.6-6.0 x 10^{-3}M; and the added potassium salts, 1-2 x 10^{-2}M.

At current densities that ranged from 0.4 to 1.0 ma/cm^2, metal deposition did not occur over periods of 2.5-4.0 hr from liquid ammonia solutions of $[Cr(NH_3)_5NO_2](NO_3)_2$, $[Cr(NH_3)_5H_2O](NO_3)_2$, $[Cr(NH_3)_5SCN](NO_3)_2$, and $[Rh(NH_3)_5Cl](NO_3)_2$. With $[Os(NH_3)_5Br]Br_2$, the apparent cathode current efficiency was 72-76%, but material removed from the cathode gave an x-ray diffraction pattern that did not correspond to either osmium metal or the original bromide. When, in a duplicate experiment, the cathode and deposit were dried *in vacuo* for 5 days before weighing, the apparent cathode current efficiency was decreased by 14%.

Data for the copper(II) complexes are given in Table III; all of these measurements were made at a constant current density to avoid variations in current efficiency that might be attributable to changes in current density. The nature of the deposited copper varied with the complex used, and from run to run for the same complex. However, all deposits were sufficiently adherent to permit weighing of the electrodes.

Discussion

On the basis of cathode current efficiency data it was proposed earlier (1) that electrodeposition of cobalt from, for example, the spin-paired complex $[Co(NH_3)_6](NO_3)_3$ in the presence of the competitive ligand NO_2^- would involve an initial dissociation

$$[Co(NH_3)_6]^{3+} \rightleftharpoons [Co(NH_3)_5]^{3+} + NH_3 \quad [1]$$

and introduction of an NO_2^- ligand

$$[Co(NH_3)_5]^{3+} + NO_2^- \rightleftharpoons [Co(NH_3)_5NO_2]^{2+} \quad [2]$$

resulting in translabilization leading to generation of the species that participates in the primary electrode process

$$[Co(NH_3)_5NO_2]^{2+} \rightleftharpoons [Co(NH_3)_4NO_2]^{2+} + NH_3 \quad [3]$$

by virtue of the availability of a bonding orbital resulting from [3]. The present work provides two additional kinds of evidence in support of the reality of the species postulated in [2]: The shift in the absorption maximum for $[Co(NH_3)_6](NO_3)_3 + KNO_2$ as compared with $[Co(NH_3)_6](NO_3)_3$ alone (Table II), even though small, is indicative of the *in situ* generation of $[Co(NH_3)_5NO_2]^{2+}$. Not to be neglected is the fact that the optical density of the nitrite-containing solution increased by *ca.* 0.02 unit during the first 18 hr; after this initial change the optical density remained constant, thus indicating an equilibrium situation. Still more convincing is the fact that, after evaporation of the solvent ammonia, the x-ray diffraction pattern for the residual solid provided an unequivocal identification of $[Co(NH_3)_5NO_2](NO_3)_2$ (Table I).

The effects produced by the competitive ligands in the case of the copper(II) complexes are in accord with those observed for cobalt(III) complexes, but the magnitude of the effect is considerably enhanced in the case of copper(II). Addition of KI to a liquid ammonia solution of $[Cu(dien)_2]I_2$ produces no change, but addition of KSCN results in an increase of 100% in the cathode current efficiency. This large increase is attributed to the formation of $[Cu(dien)SCN]^+$; however, conversion of $[Cu(dien)_2]^{2+}$ to $[Cu(dien)SCN]^+$ must be incomplete since the observed current efficiency is about 30% less than that found for $[Cu(dien)SCN]^+$ alone.

The data in Table III include other significant features. The $[Cu(dien)_2]^{2+}$ ion is more stable than the corresponding ethylenediamine complex, $[Cu(en)_2]^{2+}$. This is not too surprising in view of the ligand effect; however, in the case of $[Cu(dien)_2]^{2+}$ a forced configuration with considerable strain would be expected. Granted that $[Cu(en)_2]^{2+}$ probably exists in liquid ammonia solution as a distorted octahedron, this configuration nevertheless should be relatively strain free as compared with $[Cu(dien)_2]^{2+}$.

If the order of increasing cathode current efficiency can be considered to parallel the increase in trans effect of the ligand X in complexes of the type $[Cu(dien)X]^{n+}$, it is concluded that the thiocyanate ligand has a much greater trans effect than the iodide ligand. This result is in accord with previous work (1) on complexes of cobalt(III) and with the results of Palmer and Basolo (10) for square planar complexes of Pt(II). By use of the

Table III. Electrolysis of liquid ammonia solutions of copper(II) complexes at —34° and 1.5 ma/cm^2

Complex	Time, hr	Added salt	Cathode current efficiency, %
$[Cu(dien)_2]I_2$	2.0	—	21.0, 18.3
		KI	21.0, 16.0
		KSCN	40.0
$[Cu(dien)I]I$	2.5	—	25.2
	2.75	—	28.3
$[Cu(dien)SCN]I$	2.0	—	75.0, 70.0
$[Cu(dien)SCN]SCN$	2.0	—	73.3
	1.75	—	73.5
$[Cu(en)_2]I_2$	2.5	—	25.2, 25.8

present criteria it is possible to differentiate the relative trans effects of various ligands. Methods based on synthesis do not make this distinction; and in fact, the synthetic methods show that the thiocyanate and iodide ligands exhibit closely comparable trans effects.

As indicated above, complexes of chromium(III) and rhodium(III) were not reduced to the corresponding metals under the experimental conditions employed; the unusual stability of chromium(III) complexes in liquid ammonia has been observed previously by Booth and Merlub-Sobel (11). The results obtained using bromopentammineosmium(III) bromide suggest that the deposit on the cathode consisted of an ammoniated complex containing osmium in an oxidation state $<3^+$.

Acknowledgment

This work was supported by the Robert A. Welch Foundation and the U. S. Atomic Energy Commission, Contract AT-(40-1)-1639.

Manuscript received Oct. 25, 1962.

Any discussion of this paper will appear in a Discussion Section to be published in the June 1964 JOURNAL.

REFERENCES

1. G. W. Watt and J. W. Vaughn, *This Journal*, **108**, 351 (1961).
2. E. H. Lyons, Jr., *ibid*, **101**, 363, 376 (1954).
3. G. W. Watt and D. A. Hazlehurst, *ibid.*, **106**, 117 (1959).
4. G. W. Watt and J. A. Cunningham, *ibid.*, **110**, 716 (1963).
5. M. Mari, "Inorganic Syntheses," Vol. 5, p. 132, McGraw-Hill Book Co., Inc., New York (1957).
6. A. Werner, *Ber.*, **39**, 2669 (1906).
7. J. N. Friend, "Textbook of Inorganic Chemistry," Vol. 10, p. 204, Charles Griffin & Co., Ltd. (1928).
8. G. W. Watt and L. Vaska, *J. Inorg. Nucl. Chem.*, **5**, 304 (1958).
9. G. Gordon and R. Birdwhistle, *J. Am. Chem. Soc.*, **81**, 3567 (1959).
10. J. W. Palmer and F. Basolo, *J. Phys. Chem.*, **64**, 778 (1960).
11. H. S. Booth and M. Merlub-Sobel, *ibid.*, **35**, 3303 (1931).

Subsolidus Equilibria and Luminescence Data on Phases in the System MgO-GeO_2-SiO_2-TiO_2

J. F. Sarver[1] and F. A. Hummel

Department of Ceramic Technology, The Pennsylvania State University, University Park, Pennsylvania

ABSTRACT

As an aid to the understanding of the luminescence of manganese-activated magnesium germanates, silicates, and titanates, subsolidus compatibility relationships were determined for the systems MgO-GeO_2-SiO_2 and MgO-GeO_2-TiO_2. The new data on these systems, coupled with previous work on the systems MgO-GeO_2, MgO-SiO_2, MgO-TiO_2, and MgO-SiO_2-TiO_2, and the polymorphism of the compound $MgSiO_3$, permit an understanding of the host lattices responsible for luminescence and the influence of solid solution on the peak wavelength and brightness of these red-emitting phosphors under ultraviolet and cathode-ray excitation. Some interesting observations have been made on the red luminescence of manganese-activated spinel and olivine-type Mg_2GeO_4, Mg_2SiO_4 (olivine), the olivine solid solution series, $MgGeO_3$, $MgSiO_3$ and their intermediate solid solutions, but Mg_4GeO_6 remains as the only efficient red emitter with ultraviolet excitation.

The crystal chemical similarities between the germanates, silicates, and titanates of magnesium provided a basis for an investigation of the manganese emission of phosphors in portions of the system MgO-GeO_2-SiO_2-TiO_2.

The polymorphism of GeO_2 and the luminescence exhibited by the rutile-type modification of GeO_2 have been discussed previously (1, 2). Shafer and Roy (3), using both dry and hydrothermal quench techniques, established subsolidus relationships in the GeO_2-SiO_2 system. Solid solution of GeO_2 in α-quartz raises the inversion temperature from 573°C for pure SiO_2 to about 750°C for a solid solution containing about 30 mole % GeO_2. There is complete solubility between the β-quartz modifications of GeO_2 and SiO_2, but the rutile modification of GeO_2 will not take any SiO_2 in solid solution. This is understandable since Si^{4+} is rarely found in any oxygen coordination other than tetrahedral. A subsolidus diagram for the GeO_2-TiO_2 system was published by Sarver (4). There is partial solid solubility between the rutile modifications of the end members. According to DeVries, Roy, and Osborn (5), there is no solid solution formation in the SiO_2-TiO_2 system. This can be attributed to the differences in ionic radii and coordination preferences of Si^{4+} (0.39Å) and Ti^{4+} (0.64Å).

In the present investigation subsolidus equilibrium data for the MgO-GeO_2-SiO_2 and MgO-GeO_2-TiO_2 systems were used to establish compatibility relationships and extent of solid solution formation. Using these data, manganese-activated phosphors were prepared, and the effects of systematic variations in chemical composition on the emission char-

[1] Present address: Lamp Research and Development Organization, Lamp Division, General Electric Company, Nela Park, Cleveland, Ohio.

acteristics of the solid solution phosphors were considered.

Experimental Procedure

Starting materials.—Oxides, carbonates, or hydrates of the various components were used as starting materials. In some cases it was necessary to add small quantities of MgF_2 as a mineralizer to promote the attainment of equilibrium. Starting materials were as follows: basic magnesium carbonate, $3MgCO_3 \cdot Mg(OH)_2 \cdot 3H_2O$, Fisher Scientific C. P.; silicic acid, $SiO_2 \cdot xH_2O$, Mallinckrodt phosphor grade; germanium dioxide, GeO_2 (quartz-type), General Electric phosphor grade; titanium dioxide, TiO_2 (anatase), G.E. phosphor grade; manganous carbonate, $MnCO_3$, G.E. phosphor grade.

Apparatus.—Heat-treatment.—Solid-state reactions of gram-size batches were carried out in platinium crucibles in a Globar-type furnace which could be controlled to ±10°C for several days at temperatures up to 1300°C. For quenching experiments, a platinum-wound vertical tube furnace which could be controlled to ±1°C was used.

A limited number of reactions were carried out under hydrothermal conditions to enhance attainment of equilibrium at low temperatures. A silver-lined Morey bomb was used so that gram quantities of material could be reacted without danger of contamination. A test tube-type bomb with externally controlled pressure was used for higher temperature runs, but this method limits the amount of material preparation to milligram quantities.

Identifications of phases encountered were made by use of a Norelco x-ray diffractometer employing Ni-filtered CuK_α radiation and operating at 40 kv and 15 ma.

Emission measurements.—Ultraviolet excitation measurements were made with a 15w black light lamp for 3650Å radiation and a germicidal lamp for 2537Å excitation. For cathodoluminescence measurements the phosphor was coated on one side of a glass plate which was placed in a demountable cathode-ray tube. Minus 325 mesh material was screened by standard settling techniques to give a phosphor screen density of 4.0 mg/cm². The plates were dried for 20 min at 425°C.

Spectral energy distribution measurements were made on a G.E. recording spectroradiometer. Peak positions were obtained by measuring the width of peaks at 75% maximum intensity and calculating the wavelength falling midway between the limits of the band at this position.

Cathodoluminescence brightness readings were made with a Weston eye-corrected foot-lambert meter (Model 931) for specified anode voltages and beam current densities.

Experimental Results

Mn-*Activated Binary Compounds*

In Table I are summarized compositional, heat-treatment, and luminescence data for manganese-activated magnesium germanate and magnesium silicate compounds. Magnesium titanate phosphors were not prepared since it has been shown by Tiede and Villain (6) that the orthotitanate which has the inverse spinel structure is the only one which can be activated by manganese to produce a phosphor. Kröger (7) has demonstrated that the valence of manganese in this phosphor lies between three and four in air or oxygen firings.

The second Mg_4GeO_6 phosphor listed in Table I was prepared with 1 mole % of the magnesium added as MgF_2. Mg_2SiO_4 was prepared similarly, but the protoenstatite modification of $MgSiO_3$ was reacted with 2 mole % MgF_2. A portion of the protoenstatite phosphor was used for the preparation of the clinoenstatite phosphor by heating at 1450°C for 24 hr, quenching, reheating to 800°, and cooling to 400°C over a period of several days.

Attempts were made to prepare gram quantities of the spinel modification of Mg_2GeO_4 hydrothermally at 600°C in a silver-lined Morey bomb, but because of the large heat capacity of the bomb, it could not be cooled sufficiently rapidly from 600°C to prevent the formation of hydrated magnesium germanate phases which are stable below 520°C under hydrothermal conditions according to Roy and Roy (8).

Ternary Subsolidus Equilibrium Relationships

System MgO-GeO_2-SiO_2.—A complete series of solid solutions between Mg_2SiO_4 and the high-tem-

Table I. Summary of data for Mn-activated magnesium germanates and silicates

Host lattice	Crystalline modification	Mole % Mn	Firing temp, °C/24 hr	Excitation[1]	Emission peak, Å	Brightness
Mg_4GeO_6		0.25	1350	3650Å	6310, 6570	85% commercial[2]
Mg_4GeO_6		0.25	1350	3650Å	6310, 6570	90% commercial
Mg_2GeO_4	Spinel[3]	1.00	700	c.r.	Red	Weak
Mg_2GeO_4	Olivine	1.00	1300	2537Å	6550	Weak
				3650Å	6630	Weak
				c.r.	6510	10.8 ft-L
$MgGeO_3$	Enstatite	1.00	1200	2537Å	6800	Weak
				3650Å	6830	Weak
				c.r.	6780	5.9 ft-L
Mg_2SiO_4	Olivine	1.00	1300	c.r.	6390	14.0 ft-L
$MgSiO_3$	Protoenstatite	1.00	1300	c.r.	6610	8.0 ft-L
	Clinoenstatite[4]	1.00	1450	c.r.	6720	3.3 ft-L

[1] Cathode-ray excitation conditions: 16 kv, 2 μa/cm². NBS $Zn_3(PO_4)_2$ gave brightness of 43.8 ft-L with peak emission at 6380Å under similar conditions.
[2] No fluoride added.
[3] Prepared under pressure of 8000 psi in test tube-type bomb.
[4] 16 kv, 1 μa/cm².

perature olivine or forsterite modification of Mg_2GeO_4 was established by Ringwood (9). Dachille and Roy (10) have published high-pressure data on the solid solubility of Mg_2SiO_4 in the low-temperature spinel modification of Mg_2GeO_4.

In the present investigation ternary compositions were reacted in the temperature range from about 900° to 1350°C. Since none of the compositions were reacted at high pressures and lower temperatures, the spinel modification of Mg_2GeO_4 was not encountered.

The enstatite modification of $MgGeO_3$ is the stable polymorph below 1555°C, whereas that of $MgSiO_3$ is stable below 1042°C. It was found that enstatite solid solutions between these two compounds could be prepared. With increasing $MgSiO_3$ content, it became increasingly difficult to form these solid solutions without a mineralizer. Up to about 50% $MgSiO_3$, complete reactions occurred at 1300° for 24 hr, but for compositions between 50 and 100% $MgSiO_3$, it was necessary to use 2% by weight of LiF as a mineralizer. Figure 1 was constructed from quenching data given in Table II. The protoenstatite solid solutions which were found to exist at high temperatures by high-temperature x-ray diffraction experiments invert to clinoenstatite solid solutions during quenching. The two-phase region between enstatite solid solutions and protoenstatite solid solutions rises very rapidly with increasing amounts of $MgGeO_3$. If a protoenstatite modification of $MgGeO_3$ were stable above 1555°C, one could probably expect to find complete solubility between the protoenstatite modifications of the end members with rather simple ascendant t-x relationships; however, Robbins and Levin (11) did not observe a protoenstatite form of $MgGeO_3$. If a protoenstatite form of $MgGeO_3$ were a stable polymorph and if the relationships from Fig. 1 are considered, there would have to be either a maximum in the two-phase region or a miscibility gap between the two regions of

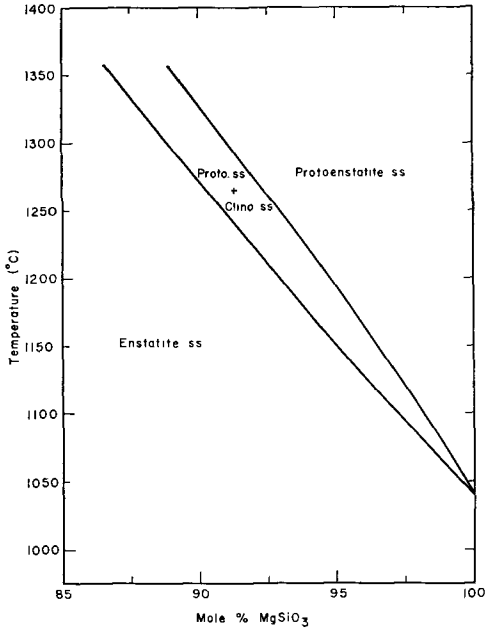

Fig. 1. Subsolidus equilibria in a portion of the system $MgGeO_3$-$MgSiO_3$.

Table II. Quench results for the system $MgGeO_3$-$MgSiO_3$

Mole % $MgSiO_3$	Temperature, °C	Time, hr	Phases at room temperature*
95	1152	24	Enstatite ss
	1158	19	Enst. ss + tr. clino. ss
	1172	23	Enst. ss + clino. ss
	1179	29	Enst. ss + clino. ss
	1189	24	Clino. ss + tr. enst. ss
	1204	25	Clinoenstatite ss
90	1266	24	Enstatite ss
	1279	6	Enst. ss + tr. clino. ss
	1300	7	Enst. ss + clino. ss
	1318	7	Enst. ss + clino. ss
	1329	5	Enst. ss + clino. ss
	1334	6	Clinoenstatite ss
	1361	5	Clinoenstatite ss
85	1335	5	Enstatite ss

* Tr.—trace.

Table III. Compositions, heat-treatments, and phase analyses of MgO-GeO_2-SiO_2 mixtures

MgO	Mole % GeO_2	SiO_2	Temp, °C	Time, days	Phase analysis
10	45	45	900	14	Enst. ss + quartz ss + cristobalite
20	40	40	900*	14	Enst. ss + quartz ss
60	20	20	1200	2	Enst. ss + forsterite ss
80	10	10	1300	2	Forst. ss + MgO + Mg_4GeO_6

* Reacted with 2% LiF to attain equilibrium.

protoenstatite solid solutions. It would seem more probable that no protoenstatite modification of $MgGeO_3$ exists, and that if sufficiently high temperatures could be attained without volatilization losses of GeO_2, a region of clinoenstatite solid solutions would be established on the $MgGeO_3$ side of the system.

Ternary equilibrium data given in Table III were used to construct the diagram shown in Fig. 2. Compositions containing MgO in excess of the ortho-ratio yield three-phase assemblages, namely MgO + Mg_4GeO_6 + forsterite solid solution, so that an infinite number of three-phase triangles exist, one of

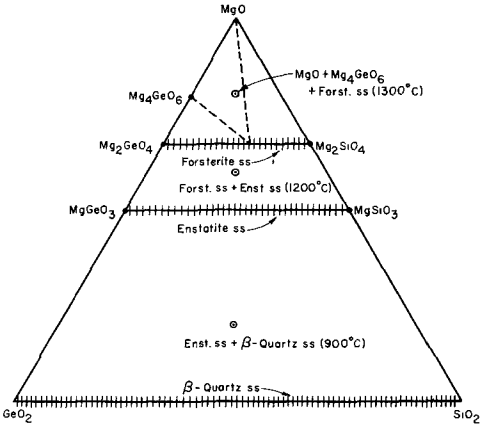

Fig. 2. Partial subsolidus relations in the system MgO-GeO_2-SiO_2

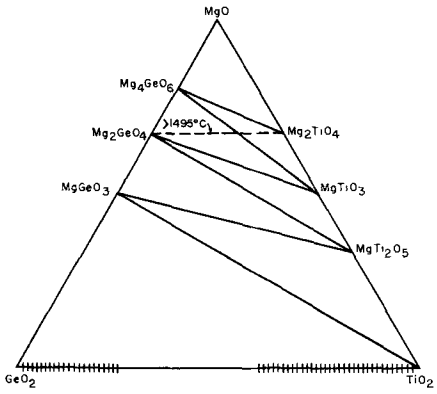

Fig. 3. Compatibility relations in the system MgO-GeO_2-TiO_2

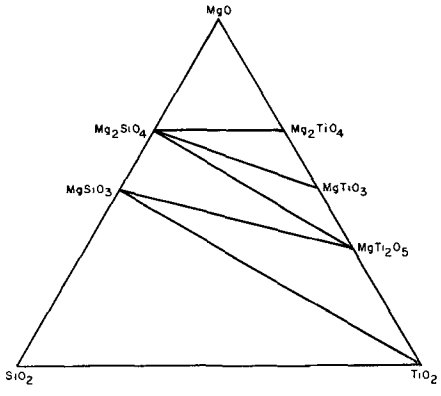

Fig. 4. Compatibility relations in the system MgO-SiO_2-TiO_2

which is represented by the dashed lines. An attempt was made to replace about 5% of the Ge^{4+} in Mg_4GeO_6 by Si^{4+}, but no solid solution could be detected, as evidenced by the appearance of MgO and a forsterite solid solution, and by the constancy of high-angle peak positions in the x-ray diffraction pattern of Mg_4GeO_6. The absence of Mg_4GeO_6 solid solutions may be due to octahedrally coordinated Ge^{4+}, recalling that Si^{4+} will not replace Ge^{4+} in the rutile modification of GeO_2.

System MgO-GeO_2-TiO_2.—The compatibility relations in this system are shown in Fig. 3 and were established by equilibrating several ternary compositions. Quenching data are summarized in Table IV. The incompatibility between Mg_2GeO_4 and Mg_2TiO_4 is surprising since Mg_2GeO_4 occurs in a spinel modification at temperatures below 810°C. The absence of solid solubility of Mg_2TiO_4 in the olivine modification of Mg_2GeO_4 is understandable on the basis of the octahedral coordination preference of Ti^{4+}. A composition midway between these two compounds, heated at 1542°C for 24 hr, yielded a mixture of Mg_2GeO_4 and Mg_2TiO_4, but no solid solution could be detected in either compound, as evidenced by the constancy of high-angle x-ray reflections. The same composition was heated in a test tube-type hydrothermal bomb at 750°C for 24 hr at 10,000 psi pressure. Instead of the olivine modification of Mg_2GeO_4, the spinel modification was compatible with Mg_4GeO_6 and $MgTiO_3$. The dashed line in Fig. 3 indicates the change in compatibility relations above 1495°C, the temperature at which Mg_4GeO_6 dissociates to MgO and Mg_2GeO_4. The joins Mg_4GeO_6-Mg_2TiO_4 and Mg_4GeO_6-$MgTiO_3$ cease to exist, and Mg_2GeO_4 and Mg_2TiO_4 become compatible. Due to the nonexistence of ternary solid solutions in this system, no phosphors were prepared.

Note that the presence of TiO_2 mineralizes the formation of Mg_4GeO_6 at 1100°. Mg_4GeO_6 will not crystallize at this temperature without a mineralizer.

System MgO-SiO_2-TiO_2.—The compatibility relations in this system, as determined by Massazza and Sirchia (12) and confirmed in this investigation, are shown in Fig. 4. They are similar to those in the MgO-GeO_2-TiO_2 system at temperatures above the dissociation temperature of Mg_4GeO_6. Again, the absence of ternary solid solution precluded the preparation of phosphors.

Mn-*Activated Ternary Compositions*

Olivine-type solid solutions.—In addition to the end members in the Mg_2GeO_4-Mg_2SiO_4 system, four intermediate compositions activated with 1 mole % manganese were fired at 1300°C for 24 hr, and the cathodoluminescence data for these compositions are given in Table V. The number of moles of MgF_2

Table IV. Compositions, heat treatments, and phase analyses of MgO-GeO_2-TiO_2 mixtures

Mole % MgO	Mole % GeO_2	Mole % TiO_2	Temp, °C	Time, hr	Phase assemblage
10.0	45.0	45.0	950	48	$MgGeO_3$ + GeO_2 ss + TiO_2 ss
33.3	33.3	33.3	1100	48	$MgGeO_3$ + TiO_2
50.0	25.0	25.0	1100	48	Mg_2GeO_4 + $MgGeO_3$ + $MgTi_2O_5$
66.6	16.7	16.7	1100	48	Mg_4GeO_6 + Mg_2GeO_4 + $MgTiO_3$
			1542	24	Mg_2GeO_4 + Mg_2TiO_4
80.0	10.0	10.0	1200	48	MgO + Mg_4GeO_6 + Mg_2TiO_4

Table V. Cathodoluminescence data for Mn-activated Mg_2GeO_4-Mg_2SiO_4 solid solutions

Mole % Mg_2SiO_4	Moles MgF_2	Peak position, Å	Brightness* (ft-L)
0	0.000	6510	10.8
20	0.002	6500	8.1
40	0.004	6480	6.8
60	0.006	6470	5.8
80	0.008	6430	7.3
100	0.010	6390	14.0

* 16 kv, 2 μa/cm² (NBS $Zn_3(PO_4)_2$:Mn, 43.8 ft-L).

Table VI. Cathodoluminescence data for Mn-activated $MgGeO_3$-$MgSiO_3$ enstatite solid solutions

Mole % $MgSiO_3$	Moles MgF_2	Peak position, Å	Brightness* (ft-L)
0	0.000	6780	5.9
20	0.005	6770	3.9
40	0.010	6760	2.2
60	0.015	6750	1.7
80	0.020	6740	1.1

* 16 kv, 2 μa/cm² (NBS $Zn_3(PO_4)_2$:Mn, 43.8 ft-L).

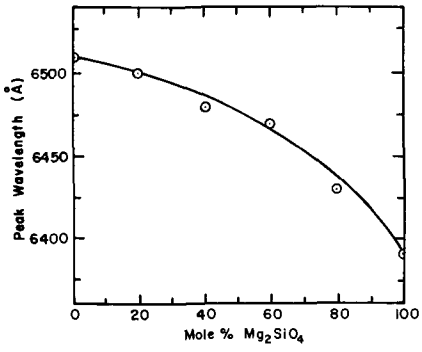

Fig. 5. Cathodoluminescence peak positions for Mn-activated Mg_2GeO_4-Mg_2SiO_4 solid solutions.

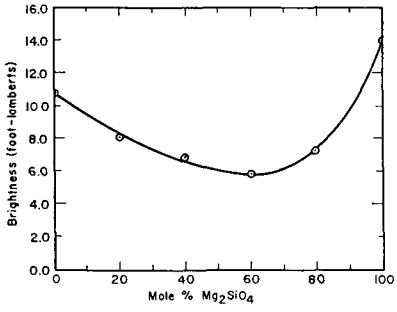

Fig. 6. Cathodoluminescence brightness values for Mn-activated Mg_2GeO_4-Mg_2SiO_4 solid solutions.

refer to the amount of this material added as a mineralizer per mole of solid solution.

In Fig. 5, peak positions are plotted as a function of composition, and Fig. 6 is a similar representation of corresponding brightness values.

Enstatite-type solid solutions.—Cathodoluminescence data for compositions in the $MgGeO_3$-$MgSiO_3$ system are given in Table VI. The compositions were fired at 1200°C for 24 hr, with small amounts of MgF_2 as a mineralizer. Since $MgSiO_3$ enstatite will not form with even 3% MgF_2, and since the presence of lithium from LiF additions tends to promote the oxidation of manganese, this phosphor was not prepared.

As shown in Fig. 7 and 8, the shift in the position of the peak wavelength of the emission to lower values with increasing Si^{4+} for Ge^{4+} substitution is observed as with the olivine solid solutions, whereas a continuous decrease in brightness extends to at least 80% $MgSiO_3$.

Discussion of Luminescence Data

Magnesium Germanates

Mg_4GeO_6.—Commercial Mn-activated magnesium germanate with 0.25% manganese substituted for magnesium responds efficiently to 3650Å excitation. It is prepared at about 1100°C in air with a portion of the magnesium added as MgF_2. X-ray powder patterns of the commercial phosphor indicated well-crystallized Mg_4GeO_6 on the basis of x-ray data given by Robbins and Levin (11). No other phases could be detected. It is known that some of the MgF_2 is converted to MgO by reaction with ambient water vapor during solid-state reactions.

In the present investigation, this phosphor was prepared at 1350°C for 24 hr in air. A sample prepared without MgF_2 was about 85% as bright as the commercial preparation. A sample prepared with 0.04 mole MgF_2 per mole of Mg_4GeO_6 was 90% as bright. With 3650Å excitation, no differences in peak positions could be detected in comparing the emission curves of these preparations with that of the commercial one shown in Fig. 9. The fine structure of the emission bands is not characteristic of Mn^{2+}. The emission is made up of several overlapping bands with two predominating peaks at about 6310 and 6570Å. According to Thorington (13), the

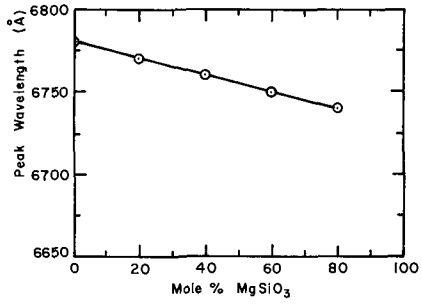

Fig. 7. Cathodoluminescence peak positions for Mn-activated $MgGeO_3$-$MgSiO_3$ enstatite solid solutions.

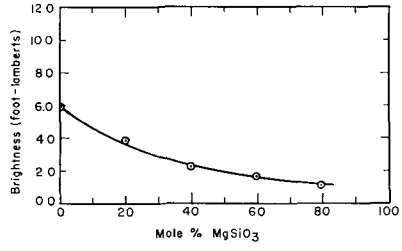

Fig. 8. Cathodoluminescence brightness values for Mn-activated $MgGeO_3$-$MgSiO_3$ enstatite solid solutions.

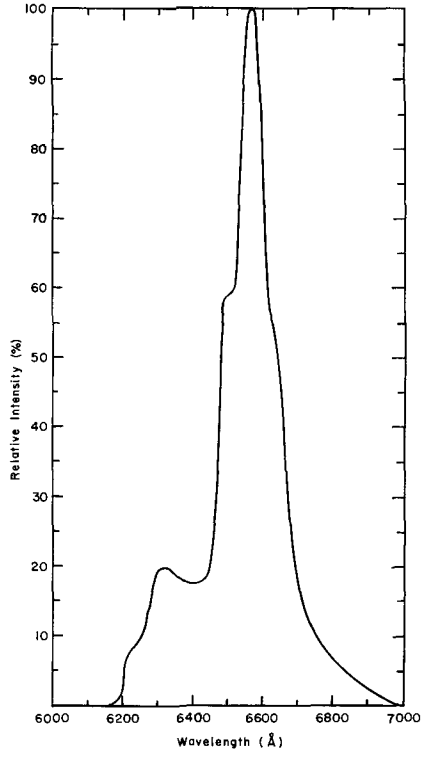

Fig. 9. Emission curve for Mg_4GeO_6:Mn, 3650Å excitation

emission consists of at least six extremely narrow line bands.

Kröger and van den Boomgaard (14) reacted a similar composition at 1100°C without MgF_2. It is highly improbable that the emission spectrum they observed for this composition was that of the 4:1 compound alone. In the absence of a mineralizer, temperatures in the vicinity of 1250°-1300°C are required to form well-crystallized, single phase Mg_4GeO_6 in a few hours. Lower temperature firings without a mineralizer invariably yield nonequilibrium mixtures of MgO and other magnesium germanate compounds. It is noteworthy, in this respect, that Koelmans and Verhagen (15) did not encounter Mg_4GeO_6 in their studies on the luminescence of binary and ternary germanates of the alkaline earth elements.

A detailed knowledge of the structural characteristics of Mg_4GeO_6 would probably be helpful in accounting for the peculiar manganese emission. The substitution of Mn^{4+} for Ge^{4+} might be justified from ionic radii considerations. As will be shown in a later publication, Zn^{2+} ($r = 0.83$Å) does not substitute for Mg^{2+} ($r = 0.78$Å) in Mg_4GeO_6. This might explain why Mn^{2+} ($r = 0.91$Å) would not replace Mg^{2+}. Although a Goldschmidt radius for Mn^{4+} has not been determined, the Pauling radius is 0.46Å as compared with a Pauling radius of 0.44Å for Ge^{4+}.

On the basis of the emission data for the composition prepared without the use of MgF_2, it is conceivable that the role of MgF_2 in commercial preparations is to mineralize the formation of well-crystallized Mn^{4+}-activated Mg_4GeO_6, rather than to take part structurally as a so-called magnesium fluorogermanate phosphor. It is likely that magnesium fluorogermanate compounds do exist between Mg_2GeO_4 and MgF_2, as in the case of silicates (chondrodite minerals), but from the data presented here it would be difficult to explain the observed luminescence on the basis of a magnesium fluorogermanate phase.

Magnesium orthogermanate.—The olivine modification of Mg_2GeO_4 has a broad emission band characteristic of the Mn^{2+} emission in other phosphors. Kröger and van den Boomgaard (14) reported that a similar composition fired at 1100°C did not respond to u.v. excitation but had a cathodoluminescence which peaked at 6600Å as compared to 6510Å found in the present investigation. Their value is apparently insignificant since they found that the x-ray diffraction pattern of their preparation did not correspond to that for Mg_2GeO_4. It is very probable that 1100°C is not sufficiently high to synthesize this compound without a mineralizer.

Magnesium Silicates

Magnesium orthosilicate.—Mg_2SiO_4 is isotypic with the olivine or forsterite modification of Mg_2GeO_4. Leverenz (16) reported a peak position of 6420Å for this phosphor with a manganese concentration of 1.2 mole %, the material being fired at 1600°C for 1 hr. The value for the peak emission of a phosphor activated with 1 mole % Mn was 6390Å in the present investigation. This slight difference in manganese concentration probably could not account for the 30Å difference in peak wavelength. As will be discussed later, Mg_2GeO_4 in solid solution in Mg_2SiO_4 causes the peak emission to shift toward longer wavelengths, but an addition of about 15 mole % Mg_2GeO_4 is necessary to shift the peak to 6420Å. It is interesting that Leverenz also cites a reference to a Mg_2SiO_4:Mn phosphor which peaked at 6400Å when fired at 1180°C in steam. This value is much closer to that obtained in the present investigation.

Magnesium metasilicate.—The results of the most recent investigation of the polymorphism of $MgSiO_3$ have been published by Sarver and Hummel (17). The stable high-temperature polymorph known as protoenstatite, activated with 1 mole % manganese, did not respond to u.v. excitation, but did exhibit a red cathodoluminescence with a peak position at 6610Å and a brightness of 8.0 ft-L. This agrees well with a value of 6600Å reported by Leverenz (16) for the same composition fired at 1180° in steam, although the identity of the product was not specified as protoenstatite.

Clinoenstatite is a metastable polymorph of $MgSiO_3$ which can be retained at room temperature indefinitely. It forms only from protoenstatite below 865°C via a metastable crystallographic transformation which is favored by large crystallite size of the original protoenstatite. The substitution of 1 mole % Mn^{2+} for Mg^{2+} in protoenstatite somewhat inhibits the conversion of protoenstatite to clinoenstatite on cooling (17). A portion of the protoenstatite phosphor was reheated to 1450°C for 24 hr to promote crystal growth. On air-quenching the phases present were protoenstatite and clinoenstatite. Reheating to 800°C and cooling very slowly to about 400° over a period of several days produced a mixture consisting of clinoenstatite with only a trace of protoenstatite remaining. The clinoenstatite phosphor responded only to cathode ray excitation, and the peak position of the emission was 6720Å, with a brightness of 3.3 ft-L (16 kv, 1 μa/cm^2). This agrees fairly well with a value of 6740Å reported by Leverenz (16) for a similar composition fired at 1600°C for 1 hr. The stable low-temperature polymorph of $MgSiO_3$ known as enstatite could be synthesized only with a LiF addition which promoted oxidation of the manganese in experiments carried out to produce an enstatite phosphor.

Ternary Compositions

Olivine-type solid solutions.—In the manganese-activated Mg_2GeO_4-Mg_2SiO_4 compositions, substitution of Si^{4+} ($r = 0.39$Å) for Ge^{4+} ($r = 0.53$Å) produces two antagonistic effects on the emission. The decrease in lattice parameters tends to decrease the Mn-O distances in MnO_6 octahedra. Considered alone, this would cause increased perturbation of the electronic clouds of the Mn^{2+} ions, favoring an increase in the peak wavelength of the emission. However, this effect is more than balanced by an opposite effect, namely decreasing the Mn-O interactions due to the greater field strength or polarizing power of the Si^{4+} ion. This more dominant effect leads to a continuous decrease in the peak wave-

length of the manganese emission as the Ge^{4+} is replaced by Si^{4+}.

The results of the brightness measurements were somewhat unexpected. One might expect a continuous increase or decrease in brightness in a series of solid solutions, rather than a minimum. In Mn^{2+}-activated phosphor systems, the position (peak wavelength) and the shape (half-width) of the emission band is determined by the environment of the luminescent centers. On the other hand, the intensity of the emission (relative peak height) is not predictable and depends on many factors. According to Kröger (7), the most important of these factors are the efficiency of the absorption of the excitation energy by the phosphor, the transfer of the absorbed energy to the centers, the efficiency of conversion of the excitation energy into luminescence in the centers, and the absorption of the emission as it leaves the centers and passes through the crystals. These effects are complicated still further by such factors as manganese concentration and the phosphor screen densities which were kept constant in the cathode ray excitation studies.

Enstatite-type solid solutions.—If the curve in Fig. 7 is extrapolated to 100% $MgSiO_3$, it is obvious that the position of the peak emission for $MgSiO_3$ enstatite should occur around 6730Å. This is not significantly different from the value of 6720Å measured for clinoenstatite in which the octahedral coordination of Mg^{2+} is similar to that of Mg^{2+} in enstatite. In protoenstatite, half of the magnesiums are octahedrally coordinated by two oxygens each at 2.0, 2.1, and 2.2Å. The remaining magnesiums are coordinated octahedrally also but by four oxygens at 2.1Å and two at 2.5Å according to Smith (18). It is possible that Mn^{2+} ions, which are larger than Mg^{2+}, preferentially occupy the more asymmetric sites since these sites have an effectively larger volume. This might account for the stabilizing effect in protoenstatite which is observed when 1 mole % Mn^{2+} is substituted for Mg^{2+}, as well as for the shorter wavelength emission of the manganese-activated cathodoluminescence which peaks at 6610Å. The higher energy of the Mn^{2+} emission in protoenstatite may therefore be the result of decreased perturbation of the electronic clouds of the Mn^{2+} ions associated with effectively longer Mn^{2+}-O^{2-} distances.

Summary

Of the three ternary systems which make up three of the faces of the quaternary system MgO-GeO_2-SiO_2-TiO_2, only the MgO-GeO_2-SiO_2 system contained regions of extensive solid solution. Neither Ge^{4+} for Ti^{4+} nor Si^{4+} for Ti^{4+} substitution occurs between binary compounds in the systems MgO-TiO_2-GeO_2 and MgO-SiO_2-TiO_2.

Si^{4+} for Ge^{4+} substitution in olivine-type solid solutions between Mg_2GeO_4 and Mg_2SiO_4 produced a gradual shift in the peak position of the cathodoluminescence from 6510 to 6390Å, the direction of the shift being explained by qualitative reasoning based on ionic radii and relative polarizing powers of Si^{4+} and Ge^{4+}. Similar substitution in the enstatite solid solution series between $MgGeO_3$ and $MgSiO_3$ also produced a shift in peak position of the cathodoluminescence to higher energies from 6780Å for $MgGeO_3$ to 6740Å for a composition containing 80 mole % $MgSiO_3$.

Si^{4+} does not substitute for Ge^{4+} in Mg_4GeO_6, suggesting the possibility of octahedral coordination of Ge^{4+} in this compound.

Acknowledgment

The authors are grateful to the Chemical Products Plant of the General Electric Company, Cleveland, Ohio, for financial support which made this work possible and to Marjorie Brines of the Chemical Products Plant for obtaining emission data.

Manuscript received Aug. 17, 1962; revised manuscript received Feb. 1, 1963. Contribution No. 61-64 from the College of Mineral Industries, The Pennsylvania State University, University Park, Pa.

Any discussion of this paper will appear in a Discussion Section to be published in the June 1964 JOURNAL.

REFERENCES

1. J. F. Sarver and F. A. Hummel, *J. Am. Ceram. Soc.*, **43**, 336 (1960).
2. J. F. Sarver and F. A. Hummel, *This Journal*, **108**, 195 (1961).
3. E. C. Shafer and R. Roy, "The System GeO_2-SiO_2", Tenth Technical Report on U.S. Army Signal Corps Contract DA36-039, SC63099, College of Mineral Industries, The Pennsylvania State University (1956).
4. J. F. Sarver, *Am. J. Sci.*, **259**, 709 (1961).
5. R. C. DeVries, R. Roy, and E. F. Osborn, *Trans. Brit. Ceram. Soc.*, **53**, 525 (1954).
6. E. Tiede and E. Villain, *Ber.*, **73**, 274 (1940).
7. F. A. Kröger, "Some Aspects of the Luminescence of Solids," Elsevier Publishing Co., Inc., New York (1948).
8. D. M. Roy and R. Roy, *Am. Min.*, **39**, Nos. 11 and 12, 957-975 (1954).
9. A. E. Ringwood, *Am. J. Sci.*, **254**, 707 (1956).
10. F. Dachille and R. Roy, *Am. J. Sci.*, **258**, 225 (1960).
11. C. R. Robbins and E. M. Levin, *Am. J. Sci.*, **257**, 63 (1959).
12. F. Massazza and E. Sirchia, *Chimica e industria*, **40**, 460 (1958).
13. L. Thorington, *J. Opt. Soc. Am.*, **40**, 579 (1950).
14. F. A. Kröger and J. van den Boomgaard, *This Journal*, **97**, 377 (1950).
15. H. Koelmans and C. M. C. Verhagen, *ibid.*, **106**, 677 (1959).
16. H. W. Leverenz, "An Introduction to Luminescence of Solids," John Wiley & Sons, Inc., New York (1950).
17. J. F. Sarver and F. A. Hummel, *J. Am. Ceram. Soc.*, **45**, 152 (1962).
18. J. V. Smith, *Acta. Cryst.*, **12**, Part 7, 515 (1959).

Electroluminescent Lines in ZnS Powder Particles

II. Models and Comparison with Experience

A. G. Fischer

RCA Laboratories, Radio Corporation of America, Princeton, New Jersey

ABSTRACT

Existing theories of ZnS-powder-EL are shown to be unable to explain the new findings of electroluminescent striations or lines described in Part I of this work. Several new hypotheses are discussed. Among these, a model seems to be likely which is based on simultaneous bipolar field-emission from opposite ends of conducting imperfection lines into the insulating crystallite, with trapping of injected holes in activator centers, and recombination with mobile electrons at field-reversal. This model, which is shown to be consistent with facts, is discussed in detail. A new impact ionization model is also described which is very similar to that of the field-emission model. At present, it is experimentally indistinguishable from the field-emission model.

Despite extensive research efforts, the theoretical situation about the now 26 year old Destriau effect is still in a state of confusion. The main reason for this is the inaccessibility of the individual active elements within the tiny powder particles to direct observation and measurement, so that models have to be more or less speculative. In the first models it was assumed that impact excitation throughout the volume of the particles was the cause of EL; later, depletion layers at the surfaces were assumed to be the site of impact ionization. At present, versions of these models, p-n junction theories, and Zener emission models are in circulation. Many of these models are incomplete, several are presented in a cryptic fashion, some are logically inconsistent, others go into highly mathematical details before the underlying concepts are clear. In addition, the number of purely empirical papers containing unexplained data is rapidly growing. In such a situation, a synthesis effort directed toward unification of the multiplicity seemed justified.

To make new starts toward theoretical interpretation, a firm experimental basis is the prime requirement. Measurements on directly contacted single crystals are not *a priori* suitable for this purpose, since a different mechanism may be active in embedded powder particles. Measurements on complete EL cells are not too informative since they do not reveal the properties of the individual emitting elements. By means of novel embedding media with matched refractive index, it has now become possible to observe and measure the light-emitting elements in single powder particles of 10μ average dimensions taken from typical, industrial EL powders. As described by Gillson and Darnell (1) for small single crystals, and further corroborated by Fischer (1a) for typical powder particles, light is emitted in the form of lines which extend through the bulk of the particles at slight angles to the field. The luminescent lines are associated with line-shaped crystal imperfections. The luminescent lines usually consist of two collinear halves which have the appearance of two comets fleeing each other. The halves light up alternately, whenever the adjacent cell electrode becomes positive. The time-integrated brightness of single lines follows approximately the same relation which holds for the complete cell, without apparent low-field threshold, but in some cases with a saturation range at very high applied fields.

It will be shown that existing models are not able to explain the new experimental facts so that a re-evaluation of the situation is necessary. In the course of a survey of all former and several new models, the final choice will be narrowed down by successive elimination to two models, which use elements of former models, plus new features (field-emission of electrons and holes, impact ionization by electrons moving toward internal precipitates) in new combinations.

Quantitative treatment of the very intricate situation is often impossible at this stage and would only add more confusion and complication. Therefore, prevalence of qualitative arguments is unavoidable, although this will, at first, disturb many readers. On deeper penetration one will recognize, however, that the two selected models are the simplest possible ones to cope with the set of given facts.

Survey of Models for AC-Excited EL of Embedded ZnS-Type Powders

Requirements for a consistent model.—A consistent analysis of an extremely complicated "molecular electronics device" such as an EL particle must contain all of the following features:

(*a*) Carrier generation mechanism: Since there is no external supply of charge, new carrier pairs to make up for radiative recombination losses have to be created within the particles by one of the following mechanisms: (i) Impact ionization of activator centers or of the lattice by accelerated electrons in barrier layers. Here it has to be demonstrated how the barrier layers are constituted, physically and chemically. (ii) Thermal generation in low-band-gap or metallic inclusions with subsequent injection into adjacent luminescent material. Here the chemical nature of the inclusions and the

physical properties of the injecting contacts have to be described. (iii) Tunneling or internal field emission from the valence band across the forbidden gap in one step, or *via* "trap ladders," or from quasi-continuous surface states, or from conducting inclusions. Here it has to be demonstrated how the local field strength can become high enough that these phenomena can occur.

Only where electrons are excited on internal ionic levels without ionization, is carrier re-generation unimportant.

(*b*) Carrier transport and recombination mechanism: Since pair generation according to one of the above mechanisms takes place either in non-luminescent regions of the crystal, or in high-field regions where electrons and holes are immediately separated once a pair has been created, it has to be shown where the carriers exist after generation. This includes transport and trapping processes.

(c) Consistency with the body of established facts, such as: (i) brightness-voltage-relation, (ii) brightness-frequency-relation, (iii) brightness waves, delayed emission, build-up and quenching phenomena, (iv) temperature dependence of brightness, (v) all observations pertaining to the chemistry of the preparation process, (vi) compliance with the new facts presented in ref. (1) and, Part I (1a). Compatibility of a model with the finding of long, alternately coruscating double lines is an especially important criterion for the validity of a model.

Since thermal regeneration across the bandgap of 3.7 ev is negligible, it is insufficient to postulate that electroluminescence is based on minority-carrier injection in forward-biased p-n junctions if one does not show how new carriers are created (2). Similarly, it does not suffice to postulate that the effect is due to "carrier accumulation" (3), if the information required under (*a*) and (c) above is not given.

Previous and new models.—To enable the reader to evaluate the models to be developed in this discussion in their proper context, it is necessary to give a simultaneous critical review of the most important, previously proposed hypotheses of the EL process. Such a synoptic treatment does not yet exist in the literature.

Impact ionization models.—Destriau (4) assumed that the externally applied fields of about 10^4 v/cm are sufficient to cause impact ionization throughout the volume of the particles, a view later supported by Curie (5). Theories of dielectric breakdown and of "hot" electrons (6) suggest, however, that fields in excess of 10^6 v/cm are necessary for pair creation by impact.

Piper and Williams (7) and Fischer (8) recognized that in n-type conducting, directly contacted crystals or sintered layers depletion regions with enhanced field-strength exist in front of the negative contact, in which impact ionization can take place. Light is mainly emitted when the electrons flow back at voltage reduction and reversal and reunite with previously ionized centers. Piper and Williams (9) put forth a quantitative model in which it is assumed that the crystal has shallow and deep donors. Depletion of shallow donors in front of the cathode creates a high-field region, until the field is high enough to empty the deep donors. The field-released primary electrons become accelerated and cause impact ionization. The number of primary electrons released per cycle is assumed to be about constant; however, the fraction which is able to cause collision ionization increases with the field. Alfrey and Taylor (9, 10) modified and improved the Piper-Williams model by incorporating the Seitz function (11) which states that the fraction of primary electrons which is accelerated to impact ionization energy increases as exp-const/F, F being the field strength. Further they introduced the relation $F \sim \sqrt{V}$ which connects the maximum field strength within a depletion layer with the externally applied voltage V (12). Thus the brightness voltage relation given by the theory becomes

$$I = A \exp - B\ V^{-1/2}$$

which fits measurements of most powder cells very well.

The obvious shortcoming of this theory is that it has to assume conducting crystals. Whereas there is no doubt that this type of impact-ionization EL in the cathodic depletion layer exists indeed in directly contacted conducting ZnS (7), ZnSe (13), ZnO (14), and GaP (15) crystals and in many semiconductors, even with d-c current excitation, it is also certain that efficient, Destriau-type powder particles do not fit into this model since they are insulating. This is demonstrated by high-frequency-loss measurements on powders with increasing copper content: Powders with equal concentrations of copper and co-activator are electrically compensated and have low losses, like insulators. If the copper (=acceptor) content exceeds the coactivator (=donor) content, localized, dark precipitations become visible and the losses go up. This is not due to p-type conductivity in the ZnS since removal of the external precipitates by cyanide washing reduces the losses. The losses are caused by the conducting precipitates, whereas the adjacent luminescent material remains insulating, in the order of 10^{14} ohm cm (16). Further, the Piper-Williams-model does not treat the case of embedded particles. It also cannot explain the existence of long electroluminescent lines extending throughout the bulk of the particle; to get the required field-intensification of 100 in one part of a crystal, the applied field has to relax to zero over 99% of the length of the crystal, and in this part, impact ionization is hardly possible.

Zalm, also claiming that electroluminescence occurs exclusively at the surfaces, modified the Piper-Williams model to explain the EL of embedded powder (17). He assumed that the particles are insulating, having equal amounts of donors and acceptors, with externally precipitated copper sulfide layers to serve as a reservoir of primary electrons. He first assumed that the conducting coating completely covers the particle, which is somewhat suspect (18), but Klasens showed (19) that the model works if we assume that there are non-contiguous

Cu_2S specks[1] which form blocking contacts for electron flow into the interior. At field application, starting at fine roughnesses at the Cu_2S-ZnS interface, electrons tunnel from the conducting speck into the ZnS. The conducting speck is assumed to be an unlimited reservoir, yielding primary electrons according to the field-emission function $A \exp - C\, V^{-1/2}$ (20). A fraction of the primary electrons proportional to the Seitz function (which has the same form) is capable of causing impact ionization. The electrons drift toward the positive end of the particle, whereas the excess holes remain trapped in front of the injecting spike, thus creating a positive space charge layer which enhances tunneling and impact ionization. Radiative recombination takes place at field reversal. Zalm completely neglects polarization, but polarization has an important influence: as soon as the displaced charge Q which is shifted from one end of the insulating crystal to the other has filled the capacitance C given by the particle dimensions, a polarization voltage $V = Q/C$ develops which cancels the voltage drop of the applied voltage over the particle. The integrated current must then change from $I = A \exp - B\, V^{-1/2}$ to $I = A'V$ (high voltage saturation) which, however, Zalm's measurements do not show. [In Part I (1a) and previously by Lehmann (21) it has been found that saturation does exist.] Similar difficulties exist in Zalm's interpretation of the brightness-frequency dependence.

To explain the electroluminescent double-lines, observed in Part I (1a), by the Zalm model, one could assume that the particle has Cu_2S specks on the front and back surface so that electrons created by impact in the cathodic depletion layer drift into the anodic layer which contains the holes created by impact ionization in the previous half cycle. This mechanism would yield the correct phase-relation of the light wave [Part I (1a)]. As in the Destriau-Curie model, it would have to be assumed, however, that impact ionization avalanches can extend from the surface far into the interior, where the field is low, to explain the observed lines. Another proposed explanation, which might be adaptable to explain the EL lines, assumes that holes can drift from the space charge layer where they were created, into the crystal, and recombine there with electrons coming from the other side of the particle (22). The objection to both proposals is that the shape of the EL lines should be the reverse of that which is observed, due to the diffusion-broadening of either the avalanche or the migrating hole-cloud (Fig. 1a, b). In the case of the migrating hole-cloud, emission should become concentrated near the surfaces at higher frequencies since not enough time is available for the diffusion into the center of the particle. In Part I (1a), the contrary was observed: The lines become sharper and brighter at high frequencies; surface emission prevails at low frequencies. However, the main objection against this model is that it can be easily proved by etching experiments that the surfaces of cyanide-washed EL particles do not possess any conducting Cu_2S coatings. One can reduce the size of EL particles to 1/10 by gradual dissolution in a stream of fresh acid and completely maintain EL properties (23). Besides, many EL lines start in the interior of particles and end in the interior, without ever reaching the surface. Some lines are crooked, even have zig-zag form where part of the line bends back against the field, which certainly cannot be accounted for by long impact ionization avalanches.

[1] There is no conclusive evidence published for the exact chemical composition of the conducting copper sulfide precipitates. Throughout this paper we will neglect this difficulty.

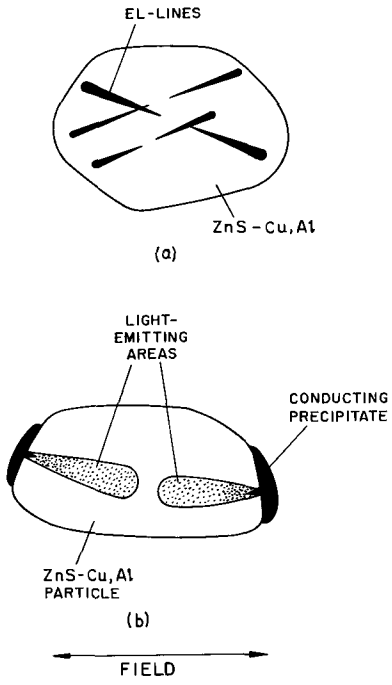

Fig. 1. (a) Observed EL lines; (b) broadening of impact avalanches or of trap-hopping hole clouds which extend from the surface into the interior, due to sideward diffusion. The shape of these EL lines is just the reverse as in Fig. 1a (exaggerated).

One can modify the Zalm model in the way suggested by Lehmann (16) and Ivey (24) and treated by Maeda (25), by assuming that impact ionization by electrons occurs alternatingly at the ends of internal, conducting, Cu-containing precipitates in which the applied field relaxes so that field intensification at the ends takes place (Fig. 2). The existence of such internal precipitations is long established and has often been associated with the mechanisms of EL (26) though in vague terms. In this model the primary electrons are field-released from the conducting inclusion and accelerated. The impact avalanches move away from the inclusion. Hence, the light pulses should be emitted at that end of a conducting line which is next to the cell

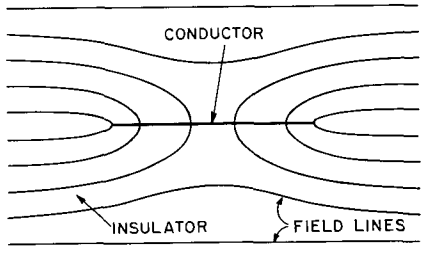

Fig. 2. Conducting needle embedded in insulator. A uniform electric field is applied parallel to the needle. Geometrical field-intensification at the ends.

electrode which is turning negative so that the excess electrons can flow back to and recombine with the previously ionized centers. The objection to this model is that this phase relation is 180° different from the observed one.

To prevent this shortcoming one can reverse Maeda's model and assume that the primary electrons are released from traps in the bulk of the insulator and move toward the line-shaped conducting inclusion at which the field is intensified. Impact ionization takes place in the high-field-region near the surface of the conducting line. The impact-generated holes are trapped there in activator centers, and the excess electrons flow into the conductor, from which they are field-emitted into the luminescent crystal at the other end of the line, where they recombine with holes trapped there since the previous half-cycle (main light peak). Other field-detrapped electrons do not get sucked up by the conductor but move through the bulk to recombine directly with trapped holes (secondary light peak). This model can explain all the findings, including the line-shape of EL emission. Compared to the bipolar field-emission model discussed in the main part of this paper, it may require higher fields (10^6 v/cm). This mechanism may, however, become contributing at higher applied voltages. It is illustrated in Fig. 3. We will come back to this model later.

In an attempt to find a mechanism by which impact ionization at low fields (10^4 v/cm) can be made plausible, a hypothesis was proposed (27) which makes use of the saw-toothed band-curvature associated with staggered stacking fault planes previously postulated to explain the higher-than-band-gap photovoltages in certain ZnS crystals (28). If a "warm" electron is field-driven over the crest of a saw-tooth, it finds itself suddenly 0.3 ev above the conduction band edge, like a "hot" electron (Fig. 4). At this energy, friction due to phonon interaction has been reduced so that unimpeded acceleration up to lattice ionization energy becomes possible, even in low fields. The objection to application of this concept to powder-EL is that in most published work electroluminescent striations are reported to run parallel to stacking faults, with the field parallel to the stacking faults (29), whereas the model postulates EL only if the field is perpendicular to the stacking fault planes. Besides, dotted rather than continuous lines would have to be expected, unless the dots are so close together that the microscope cannot resolve them.

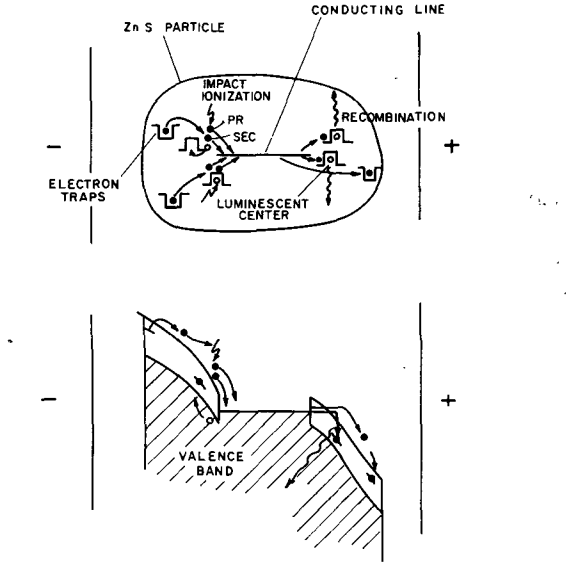

Fig. 3. Inverted Maeda model. Above, geometrical model; below: band model. For clarity, only a few electron and hole traps are shown. In reality, there is a uniform trap distribution throughout the volume. Electrons field-released from traps generate secondary electrons and holes by collision before entering the conducting line. At the other end, electrons are field-emitted from the line and recombine with holes which were generated there in the previous half-cycle.

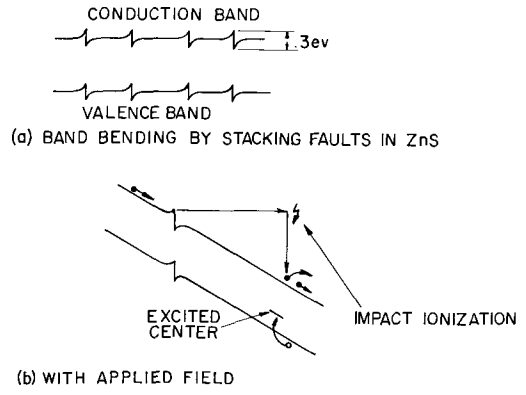

Fig. 4. (a) Band-curvature due to the pyroelectric charges at location of stacking fault planes; (b) with external field, "warm" carriers become "hot" carriers as they cross the stacking fault plane.

Injection in p-n junctions.—It has always been tempting to ascribe the Destriau effect to minority-carrier injection in p-n junctions. Yet, there are formidable obstacles to overcome for any consistent theory of this type. First, the problem of carrier regeneration has to be solved since thermal generation across the bandgap of ZnS is substantially zero. Further, due to the well-known property of ZnS of possessing deep-lying centers (electron traps 0.3 to 0.8 ev, hole traps 1.2 ev) and of favoring compensation of electrically active centers by creation of vacancies and by donor-acceptor pair formation during the firing process (30), the conductivity in ZnS, especially the p-type conductivity, is very low. Since the thickness of p-n junctions is proportional to the inverse of the square root of carrier density (31) which may be 10^{16}/cm^3 in ZnS (32), p-n junctions in ZnS become so broad that dotted EL lines should be visible under the microscope, which is not the case, even with the highest resolution. Besides, germanium-type p-n junctions with their forward-current dependence $I = A\ (\exp V/kT - 1)$ are very unlikely to exist in ZnS: A p-n junction in ZnS at room temperature resembles a p-n junction in silicon at liquid helium temperatures, as far as the electron population in traps is concerned. The latter case has been studied (33): Forward breakdown voltages, negative resistance, hysteresis have been reported. Such phenomena are not treated in conventional diode theory. They are describable by the theory of space-charge-limited, lifetime-modulated double injection currents in insulators (34).

Thornton (2) mentions that fine, metallic-conducting elements are needed to connect the stacked p-n junctions postulated by him. This implies that the metallic conductors make ohmic contacts to n-type ZnS at one end and to p-type at the other end. In view of the large bandgap of ZnS and the short distances from junction to junction (0.1μ, below the resolution of the microscope, otherwise the EL lines would appear dotted), this seems improbable.

A model where graded bandgap transitions from the conducting inclusions to the embedding luminescent insulator are postulated to make possible ohmic injection of both electrons and holes was proposed by the author (30). Whereas it can explain the line-shape and the observed phase relation, it fails to account for the brightness-voltage relation unless further assumptions are introduced, like impurity-ionization avalanches. Moreover, it was recognized later that graded-gap, quasi-homogeneous junctions between Cu_2S and ZnS are impossible because of the very limited solid solubility of these two compounds. Thus the concept of ohmic bipolar injection from Cu_2S into ZnS has to be dropped, which leaves only the approaches to be discussed in the main part of this paper.

Field emission.—Field-emission of primary electrons from traps, surface coatings or conducting, sharp-pointed inclusions has often been postulated in impact-ionization models (9, 17, 25). This is, however, not a suitable means for carrier-regeneration.

The often-discussed Zener-type field emission from the valence band to the conduction band (9, 35) is improbable in ZnS, since the required fields are so high that other phenomena would set in before Zener emission can occur. There are ways, however, by which the large forbidden gap could be divided up into smaller transitions which are more probable. Band-gap reduction due to the Franz-Keldysh effect (36) is not significant enough to become important, but field-emission via trap-ladders caused by gross lattice disturbances, either in the bulk or at the surface, is possibly important. These lattice disturbances would normally act as "killer" centers for excess carriers, but in high fields their action is reversed and they become "generating" centers (37), a common explanation for the reverse current in semiconductor p-n junctions (38). Since not only the forbidden energy distance, but also the density of emitting and receiving states enter into these calculations, field emission via isolated single trap levels is too slow to be significant. Quasi-continuous disturbed states, localized impurity bands, or low-band-gap inclusions are more effective. In these cases, less than half the bandgap has to be tunneled which is a significant alleviation for the tunneling process.

This draws attention to the important fact that in semiconductors not only electrons but also holes can be field-emitted. This is in contrast to the vacuum case, where there is no positron analog. In particular, it is possible in our case that electrons and holes are field-emitted from opposite ends of the conducting, needle-shaped inclusion, through

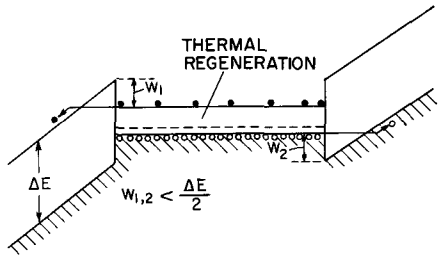

Fig. 5. Field-emission from semiconductor into insulator (simplified). Note that less than half of the insulator-bandgap has to be tunneled. The concept of field-emission of holes is new.

the high-field regions in front of the needle, into the embedding, near-insulating ZnS crystal (Fig. 5). New carrier pairs are thermally regenerated within the conducting inclusion, which is degenerate, intrinsic, semiconducting, or metallic conducting.

Since injected electrons and holes are separated, recombination and emission take place only after field reversal when the carriers can flow into each other. Due to the properties of ZnS-Cu, Cl (deep acceptors = luminescent centers, and shallow donors = electron traps), injected holes become firmly trapped, after only short travel, in luminescent centers (=excitation), whereas the injected electrons remain relatively free. Therefore, radiative recombination takes place at field reversal in form of a sheath around that half of a conducting line where holes were injected and trapped in the previous half cycle. The electrons which move to the trapped holes can either be field-emitted from the conducting needle (primary light peak), or they can flow back from the other end of the crystal where they were stored during the previous half cycle (secondary light peak). A preliminary illustration of the model is given in Fig. 6.

The fact that the field-emission current follows the Fowler-Nordheim equation (39) which is very similar to the Alfrey-Taylor equation

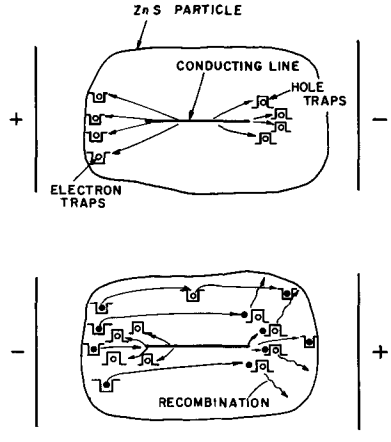

Fig. 6. Illustration of the basic principle of the field-emission model. Above, at field application, electrons and holes are field-emitted from opposite ends of the conducting inclusion, where the field is intensified, into the insulator. Holes are trapped after a short path. Electrons can travel farther. Below, at field reversal, trapped electrons flow back to recombine with trapped holes (light emission.) Other electrons are field-emitted into the trapped holes. New holes are field-emitted at the other end of the conducting line.

$I = A\,F^2 \exp - B/F$, (I current[2], A, B constants)

(if all complications due to space charge are neglected for the moment) immediately suggests that the brightness-voltage relation can be explained by the model. A more detailed discussion of this model will follow.

Various other possibilities excluded.—In Part I (1a) and in ref. (1) it was pointed out that some of the microscopically visible elongated black lines in ZnS crystals are hollow channels. This immediately brings to mind the rather heretic proposition that electrodeless gas discharges in voids might be the cause of electroluminescence (40). This can be countered by the argument that the channels are most probably lined with conducting Cu_2S which acts like Faraday cages for the included gas. Moreover, the large round cavities which are present in all EL particles [Part I (1a)], and the tiny spherical gas bubbles in the embedding medium which are easily visible [Part I (1a)], are definitely not the site of light emission, whereas they should be preferred sites of light emission if the above hypothesis were correct.

It has been suggested that light which is emitted by some unidentified mechanism somewhere in the crystal could be scattered by line-shaped optical nonhomogeneities (e.g., Al_2O_3 precipitates) in the crystal, or be conducted in "leaky" light pipes from local bright spots into the bulk so that the impression of EL striations is created (41). This can be discounted since at the sites where electroluminescent lines appear with field excitation, the embedded particles appear completely homogeneous under the microscope both with intense dark and bright field illumination.

Gillson and Darnell (1) suggest that excess electrons and holes created by impact ionization in unspecified hypothetical, reverse-biased p-n junctions, drift or diffuse to imperfection lines which act as preferential trapping and recombination sites. This concept can be discounted because microscopic examination reveals that with intense x-ray or u.v. excitation the luminescence is distributed homogeneously throughout the bulk of the crystals. Besides, it is unlikely that the imperfection lines act as especially efficient radiative recombination centers. Since they must be assumed to be decorated with precipitated Cu_2S, (a fact neglected by Gillson and Darnell), it is more likely that they are killer centers. Finally, one would like to know more about the hypothetical p-n junctions, and what they do at forward bias.

Detailed Discussion of Bipolar Field-Emission Model and of Inverted Impact Ionization Model

In the preceding paragraph the conclusion was drawn that the inverted model of Maeda (Fig. 3) and the bipolar field-emission model (Fig. 6), which are both new models though they contain features of former models, are suited to explain the finding of alternately coruscating double lines. All the other models fail in important details upon confrontation with known qualitative facts.

[2] I will be used interchangeably for current and EL brightness throughout this paper.

We will now attempt to compile more evidence for the correctness of these new models and try to eliminate one of them. It will be shown that the bipolar field-emission model has a high degree of probability. The inverted impact ionization scheme cannot be excluded and may be contributing. We will discuss the impact ionization model after the field emission model for didactic reasons: Most of the arguments fit both models but are easier to present and understand with the field emission model.

Bipolar field emission from conducting, line-shaped inclusions.—Main features.—In agreement with observations, the embedded particles are assumed to be insulating, compensated semiconductors with equal concentrations of activator (= acceptor) and co-activator (= donor) centers (10^{18} cm^{-3}). The donor electrons occupy acceptor centers. Due to the very similar lattice energies of the cubic and hexagonal modification of ZnS, the particles contain many imperfection lines [one-dimensional stacking faults (42), screw dislocations (1)] at which the excessive, insoluble copper, which was added before the firing process, precipitates during cooling in the form of conducting copper sulfide. Decorated imperfection lines have been observed in Si, CdS, and ZnS (43). Since copper diffuses rapidly, the decoration of the imperfection lines can also be achieved by reprocessing after the main firing step. The length of the decorated lines varies, some extending through the whole diameter of the particle. Their diameter is less than 0.05μ so that they are invisible under the microscope, both with dark and bright field illumination. Not only their thinness makes the lines invisible, but also the fact that Cu_2S is transparent in thin layers [Part I, (1a)] and has a refractive index similar to ZnS. Whereas the cyanide washing process removes the Cu_2S from the external surfaces of the particles, it does not reach the internally precipitated copper except possibly the copper in those imperfection lines which reach the surface.

If an external field is applied, it relaxes in those conducting lines which have a component parallel to the field, so that the conducting lines remain at equal potential. This gives rise to a field-intensification from the center of the line, where the field is zero, to the tips, where the field is much higher than the applied field (Fig. 2). The field-dependence along the line can be calculated, assuming that the line is prolate, conducting spheroid in a uniform field (44). According to Maeda (25), the field at the tips is proportional to $(L/d)^2$, where L is the length, d the diameter of the line.[3] To obtain a field-intensi-

[3] The derivation of this result is mathematically complicated. The correctness can be checked very easily: The uniform applied field F_0 induces in the conducting line (length L, thickness d) a dipole such that the dipole field cancels F_0 near the surface of the line at $L/2$, so that the center of the line is field-free. If we assume, for simplicity, that the dipole charges are concentrated at the tips of the line, then the size of the induced charges can be calculated from the condition

$$\frac{2Q}{4\pi\epsilon\epsilon_0 (L/2)^2} = F_0;\ Q = \frac{\pi\epsilon\epsilon_0 F_0 L^2}{2}$$

With this charge, the field F_{max} at the tips (radius of curvature $d/2$) is then

$$F_{max} = F_0\left(\frac{L}{d}\right)^2.$$

In reality, the charge is not all concentrated in the tips, hence this enhancement factor is somewhat too large.

fication of 100, a line of 10^{-4} cm length has to be 10^{-5} cm thick, which indicates that even much higher intensification factors are easily possible.

From the field-emission microscope (39) where the tip radius is much larger than in our case, in the order of 1000Å, it is known that appreciable currents (10^{-6} amp) can be drawn from alkali-covered tungsten tips at fields in excess of 10^6 v/cm.

In the case of decorated imperfection lines, the effective tip radius is much smaller, since it is very likely that the precipitations are rough so that a multitude of very fine tips are active with radii in the order of a few atom diameters.

Even if the conducting lines were smooth, their diameter must be much smaller than 1000Å because of their invisibility.[4] However, since these precipitations are formed by diffusion, it is much more likely that they are rough with countless small emitting tips, with a statistical distribution of tip radius and tip protrusion.

The height of the threshold to be tunneled between conducting inclusion and embedding luminescent crystal (similar to the work function in the vacuum case) is less than half the bandgap of ZnS, *i.e.*, about equal to the work function of cesium (see Fig. 5). In zinc sulfo-selenides with their lower bandgap, it is even less than that of cesium. The Fermi level of the conducting inclusion stays automatically in about the middle of the insulator bandgap for the following reason: The conducting line has to emit equal amounts of positive and negative charge from opposite ends in order to prevent excessive charging. If more charge of one sign is emitted than of the other, then the line charges up and its Fermi level shifts in a direction to make the work function of the stronger emitted charge type higher and to quench excessive emission. Simultaneously, emission of the other carrier type becomes easier.

These two effects, sharper tips and lower work function, make it plausible that the fields required to obtain noticeable tunnel emission are lower than 10^6 v/cm, possibly lower than 10^5 v/cm. Calculations to prove this point are less convincing than the above-mentioned comparison with the field-emission microscope.

The mechanism of field-emission of electrons and holes from opposite ends of a conducting inclusion, with thermal regeneration of carriers in the inclusion, has an additional unique feature: Since the inclusion can never charge up appreciably, it forms an unlimited, inexhaustible source of supply. If only one carrier type were emitted, as in the case of a fine, insulated wire suspended in a field in vacuum, only a very small amount of charge Q given by $Q = C\,V$, where C is the capacitance of the wire and V the potential drop across it, can be emitted. The same holds for a conducting precipitate in ZnS which emits only electrons.[5]

In the case of bipolar emission, the only limitation of the emitted charge is given by the polarization field which is created by charges which pile up at the ends of the crystallite where they are stopped by the embedding thermoplastic resin. This polarization field weakens the applied field and thus brings tunnel emission to a stop. The emitted charge is thus limited by particle capacitance and the potential drop across the particle.[6]

It may be mentioned in passing that the thermal regeneration of carriers in the conducting inclusion should produce a slight cooling effect which may partially compensate the heat which is generated by conduction losses.

The detailed structure of the contact between conducting inclusion and luminescent crystal is still open to speculation. We may have an abrupt transition from the conducting phase (which may be copper, cuprous, or cupric sulfide, polysulfide, or a special mixture which also contains zinc and coactivator) to the luminescent ZnS, as shown in Fig. 5. It is possible that the ZnS adjacent to the precipitate is rich in Cu which makes it slightly p-type (Fig. 7a-c), or that the crystal is strongly disturbed

[4] A platinum wire whose thickness had been determined with the electron microscope to be about 1000Å was visible under the Leitz Panphot light microscope, whereas the site of bright EL lines is indistinguishable from the bulk when external illumination is used.

[5] The capacitance of a prolate conducting spheroid of length L and thickness d is given by the relation (45)

$$C = \frac{\epsilon\epsilon_0 L}{\ln \frac{4d}{L}}.$$

For $L = 5.10^{-4}$ cm, $d = 10^{-6}$ cm, $\epsilon = 10$, $C \sim 10^{-17}$ Farad.

[6] The capacitance of an idealized cube-shaped particle of edge d is

$$C = \epsilon\epsilon_0 d.$$

With $d = 10^{-3}$ cm and $\epsilon = 10$, $C \sim 10^{-15}$ Farad.

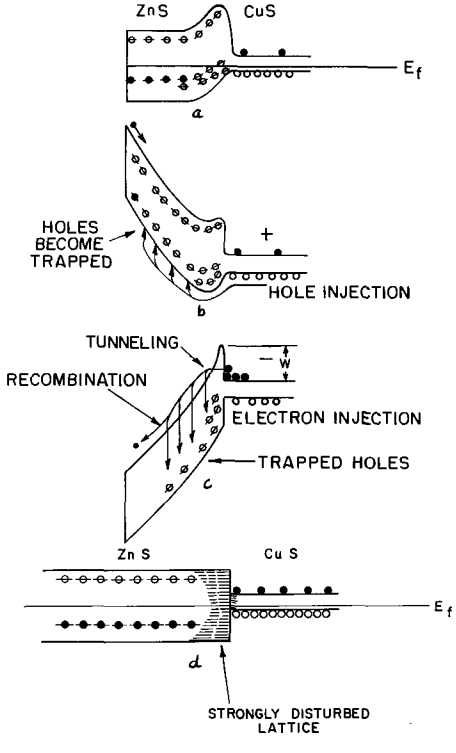

Fig. 7. (a-c) Bipolar injection at Cu_2S-ZnS contact. The injection of holes may be alleviated over the injection of electrons since the ZnS may be slightly p-type adjacent to the Cu_2S. (d) Another possibility of the Cu_2S-ZnS contact. Due to lattice mismatch or different thermal expansion there may be many dislocation levels in the junction.

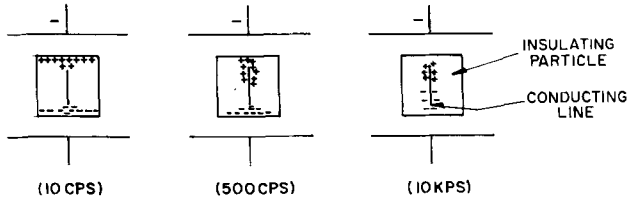

Fig. 8. Redistribution of injected charge due to drift (trap-hopping) in an applied field, in dependence of frequency. The effect leads to changes in the effective capacitance of the particle, and to changes in the appearance of EL lines (extremes: sharp lines, surface emission).

at the contact (Fig. 7d) so that emission of carriers proceeds via traps.

Such differences have no influence on the model because the Fowler-Nordheim equation is obeyed, at least approximately, in any case. Assume, for instance, that hole-injection is near-ohmic as illustrated in Fig. 7a, b. The electron-injection must be all the more non-ohmic and governed by tunnel-emission as shown in Fig. 7c. Since the resistance for electron-emission is much higher than for hole-emission, the electron-current also limits the hole current, which then also follows the Fowler-Nordheim equation, otherwise the inclusion would charge up as explained previously.

The injected electrons remain relatively free due to their high mobility ($\sim$ 200 cm^2/v sec) and because of the relatively shallow electron traps (0.3 ev). The injected holes, however, are efficiently captured by deep-lying levels (activator centers, 1.2 ev in ZnS) and become immobilized after a short distance of travel given by their mean free life time [10^{-10} — 10^{-12} sec (46)], forming a sheath of positive space charge around the line. Only at very high fields and/or low frequencies does the drift of trapped holes become noticeable, as demonstrated by a gradual fading of the electroluminescent lines in favor of emission near the particle boundaries (Fig. 8). The polarization field due to holes trapped in front of the positive end of the conducting line impedes not only further hole emission, but also electron emission from the negative end of the line.[7] The line, due to its small capacitance which is in the order of 10^{-17}**F**, charges up positively if more electrons than holes are injected from it. Whereas at low frequencies and high fields, where hole migration is possible, the particle capacitance, which is in the order of 10^{-15}**F**, forms the limit for the amount of charge emitted per half cycle, at high frequencies and/or low fields, where the holes have no time for migration by trap-hopping, the capacitance of the conductive line (10^{-17}**F**) forms the final limitation. [This is one reason for the decrease of light-output per cycle with increasing frequency. Another reason is that at higher frequencies not all injected carriers find time to recombine during one cycle so that a conductivity due to unrecombined charge develops which shields the conducting lines from the applied field and reduces the efficiency due to I^2R-losses. Photoconductivity, which is self-induced in blue-emitting EL powder, has the same harmful effect. Illumination of the lines with spots of ultraviolet quenches the EL (1). Another reason may be that at high frequencies, due to the finite conductivity of the copper-sulfide-decorated lines, the relaxation time of the field in the conducting line has the same order as the period of the applied field so that the field at the tips is lower.]

At field reversal, electrons are injected from the negative half of the conducting line into the positive space charge sheath of holes trapped in front of the emitting tips in the previous half cycle. This electron emission is, therefore, space-charge-enhanced until all of the trapped holes have recombined, which is accompanied by the typical recombination radiation (primary light peak). The secondary light peak which, with sine-wave excitation, can be observed separately from the primary light peak, may be caused by electrons which, on reduction of the applied field, return from the opposite end of the crystal through the bulk to recombine radiatively with trapped holes. During this current flow trapping and detrapping of electrons occur, hence the secondary peak should be more sensitive to temperature variations than the primary peak. This is in accordance with observations. Since the current flow connected with this secondary peak extends over wider distances and is driven by lower fields than the current of the primary peak, the secondary peak is also more susceptible to field-quenching by superimposed voltage pulses than the primary peak. This also agrees with experimental findings (47).

Since the luminescent transition in ZnS consists of a free electron in the conduction band dropping into an excited activator center, light is emitted only when electrons are moved into regions containing trapped holes. If holes are injected into regions containing trapped electrons, luminescence is field-quenched because the electrons which evaporate from traps into the conduction band are swept away faster than they can recombine with the holes. Thus, the model explains the observed fact that light is emitted from that half of a line which is next to the electrode becoming positive.[8]

The model also explains the observed fact of "delayed emission" (48) *i.e.*, that no light is emitted from a rested cell at first application of voltage, but only at removal or reversal of the voltage; also the observation that EL "spots" (in our picture: halves of EL lines) light up only once per cycle, finds a natural explanation. A more detailed illustration of the events during a full cycle is given in Fig. 9a-f.

At the instant of first field application (Fig. 9a), the applied field collapses within the conducting line in a time span given by its relaxation time. After this has happened, we have the field distribution of Fig. 9b, where the field is concentrated at the tips of the conductor. Electron and hole emission from sharp points set in. It is likely that the conducting lines have sharp points not only at their ends, but that they are rough ("barbed wire"), with

[7] Illumination of the line with fine spots of IR has been found to enhance the EL under certain conditions [Oranovskii *et al* (2)]. This can be interpreted as optical detrapping of captured holes, leading to a reduction of space-charge-quenching of injection.

[8] In phosphors which have not only deep hole traps but also deep electron traps (*e.g.*, In coactivator), brightness is severely quenched because electrons cannot travel, but experience the same space-charge limitations as holes. The active capacitance (Fig. 8) becomes that of the conducting line. The secondary peak, which is ascribed to back-flowing electrons, is suppressed.

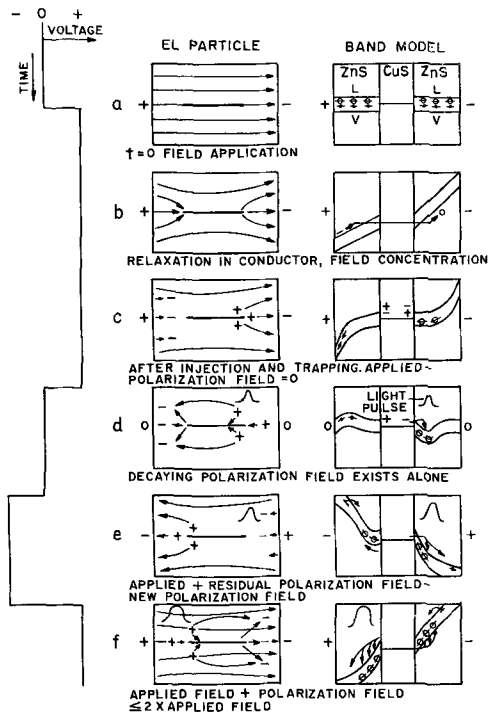

Fig. 9. (a-f) Events during full cycle of voltage applied to idealized particle. Explanation see text.

numerous emitting spots of various effective field strengths. For simplicity, we disregard this effect here and consider only the ends of the lines. Due consideration of multiple emission will be presented later.

Since the electrons are more mobile than the holes, the inhibiting space charge is that of holes trapped in front of the positive emitter and not that of trapped electrons. Current-flow comes to a stop as soon as the polarization field reduces the field strength at the positive emitter where further emission becomes negligible due to broadening of the barrier (Fig. 9c).

If the external field is removed, only the "frozen-in" polarization field between the positive space-charge region and the conducting line exists (Fig. 9d). This unbucked polarization field causes field-emission of electrons from the same point which previously emitted holes, giving rise to light emission. It also moves electrons back from the other end through the bulk of the crystal to recombine with trapped holes, giving rise to light emission. The light is emitted at the end of the line next to the electrode which was negative or which is becoming more positive.

If the time during which no external field is applied to the particle is short, a portion of the polarization field still exists at the moment the field is reversed. This polarization field adds to the applied field so that a stronger pulse of electrons is emitted than at the first application of the field. The field-emitted charge first neutralizes the residual trapped holes, giving rise to a light pulse, and then builds up a polarization field of the opposite polarity until again the field at the emitter is sufficiently weakened so that further emission practically ceases (Fig. 9e). We will come back to the utilization of this effect of space-charge-enhanced injection for the explanation of initial build-up of brightness.

If the field is reversed instantly, without a field-free period as before, the polarization field and the applied field are additive so that the effective field at the emitter is almost twice the applied field, with the corresponding emission of current proportional to $\exp - B/2F$. The space charge of the previous half cycle is neutralized by direct field emission into trapped charge and by electrons flowing back through the bulk (Fig. 9f). The positive end of the conducting line is likely to attract some of the loose electrons which gives rise to losses (Fig. 9e,f).

It can be seen that slowly changing fields like triangular or sine waves lead to a less pronounced increase in injection current since the polarization field has decayed before the field is reversed. The field-enhancement is strongest for excitation with square-waves with steep flanks. The increase in brightness for square-wave-excitation over sine and triangular-wave excitation with equal P-P voltage has been actually observed by Rajchman and co-workers (49) and was demonstrated to the author by Shrader (41) at low frequency (below 300 cps).

Detail Problems.—(*a*) Initial build-up of brightness.—The effect of space-charge-enhanced or space-charge-inhibited transient injection can be used to explain the build-up of brightness of a rested cell during the first few cycles of the applied voltage.

During the first half cycle, no trapped charge of opposite sign exists in front of the emitters, so injection is space-charge-quenched due to trapping of charge of the same sign. In the second half cycle, injection is at first space-charge-enhanced to compensate the trapped opposite charge. In addition to this charge needed for neutralization, a pulse of space-charge-quenched current is now injected, of the same magnitude as in the first half-cycle, so that a higher total of charge has been emitted. In the third half-cycle, this larger amount of charge is first compensated, and again an extra amount of charge is injected to bring about space-charge-quenching of further emission, and so on. In this way, the injected charge per half-cycle keeps increasing, until radiative recombination of opposite charge carriers, which increases with the square of carrier concentration, catches up with carrier injection, and until the finite time available for injection during one half-cycle sets a limit to further increase.

(*b*) Shape of EL lines.—Since the field strength is much higher at the tips of the conducting lines than at positions closer to the center, one would expect that light is emitted at the tips only, and not, as observed, in the form of the typical collinear double-comets [Part I (1a) and (1)]. The observed shape is the consequence of space-charge-quenching of hole-emission which sets in at the tips first, so that then emission from positions along the line which are remote from the tips can take place.

Though most of the lines are double-lines, one sometimes observes unpaired lines which do not fit into the general scheme discussed so far. The existence of unpaired lines can be explained in two ways: (i). A conducting line may be attached to

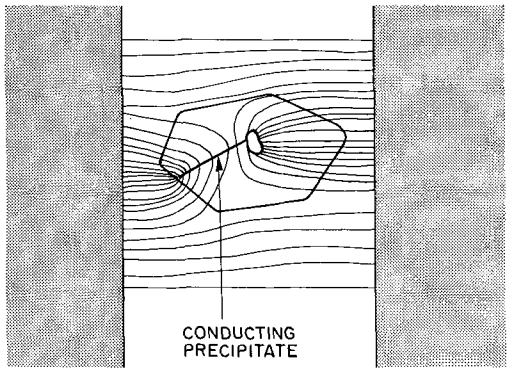

Fig. 10. Field-distribution in unpaired EL line. Only the left half is capable of field-emission.

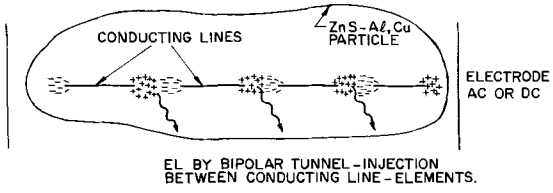

Fig. 11. Alternate explanation for unpaired EL lines. The length of the conducting elements and of the insulating interspaces may be submicroscopic.

the Cu_2S-coating of a void [Part I (1a)], which, by its lack of sharp edges and tips, is incapable of field-emission but acts as capacitance (Fig. 10). (ii). An unpaired line can consist of a series of submicroscopic collinearly stacked Cu_2S-lines, with insulating, luminescent ZnS filling the interspaces, into which double-field-injection with radiative recombination takes place (Fig. 11).

Unlike the case of stacked p-n junctions against which arguments were presented before, the stacked, conducting line-elements can be so short and so closely spaced that the microscope cannot resolve the light-emitting spots so that a continuous line is seen. Experimental evidence in powder particles supports case (i).

Sometimes, odd-shaped lines can be seen with zig-zag or whip form where part of the line bends back against the field or runs perpendicularly to the field. This can be easily accounted for because a conducting line in a field has a field component perpendicular to the surface at all points except at a short range where the potential of the field matches the constant potential of the line, regardless of the configuration of the line. As mentioned before, former impact ionization theories cannot explain these odd forms. Some of the lines perpendicular to the field are also explainable by assuming that the crystal contains not only decorated imperfection lines but also decorated conducting stacking fault sheets, at the edges of which alternate, bipolar field-emission takes place.

(c) Brightness-voltage relation.—The explanation of the brightness-voltage relation is an important test for the validity of an EL model. The bipolar field-emission model is not in disagreement with facts also in this respect. It offers two different, mutually nonexclusive ways to describe the measurements reported in Part I (1a).

(i). It is very likely that the conducting lines are rough on a submicroscopical level, with countless little spikes of varying sharpness from which field-emission takes place. Using this multiple-tip concept one can presume that each little emitter injects only one short burst of current per half cycle, which starts when the local field surpasses a critical value where field-emission becomes significant, and stops as soon as the local polarization field due to trapped holes reduces the field at the tip. This concept supplies one possible explanation for the brightness-voltage relation if it is postulated that the number of field-emitting spikes within one line increases exponentially with voltage. In Fig. 10 of Part I (1a) it has been shown that the number of lines which are perceptible above a given threshold of intensity, increases steeply with voltage in an exponential way. A similar relation may hold for the emission from submicroscopic roughnesses within a single line.

(ii). The brightness-voltage relation can be accounted for in another way which does not exclude the simultaneous existence of the above explanation. The momentary field-emission current through the contact Cu_2S-ZnS follows the well-known Fowler-Nordheim equation (39)

$$I = \frac{AF^2}{W^{3/2}} \exp - \frac{BW^{3/2}}{F} \text{ [amp/cm}^2\text{]} \qquad [1]$$

where A and B are constants, W = work function. This equation is very similar to the observed brightness-voltage relation, but, as Lehmann has pointed out (21), the pre-exponential term causes Eq. [1] to become infinite at high fields, whereas EL brightness shows saturation at high field strengths.

The time-integrated brightness of EL cells made of powders with "natural" particle size distribution is best described by the equation

$$I = A \exp - B/V^{1/2} \qquad [2]$$

Lehmann reported (21) that cells made of powders with uniform particle size, and also the brightness of single particles, fit better the equation

$$I = A \exp - B/V \qquad [3]$$

and that cells made with powder having a distribution function differing from the natural distribution function coming with a normally fired powder have brightness-voltage relations intermediate between Eq. [2] and [3]. Lehmann also showed that Eq. [2] can be obtained by summation of several functions of type [3] having different values of A and B. (This leads to the conclusion that it may be unnecessary to postulate depletion layers with F_{max} = const $V^{1/2}$ in front of the field-emitting junctions, which fits very well in our concept of insulating particles.) Our own measurements in Part I (1a) strongly support Lehmann's findings. Therefore, one should attempt to deduce Eq. [3] from the model.

For a strict proof that our model yields a brightness-voltage dependence of Eq. [3] we would have to integrate Eq. [1] with all necessary corrections, over half a cycle of the applied field, assuming that the light emission from one half of a line is propor-

tional to the charge emitted from that half into the crystal. This will be shown to be too difficult so that we shall limit ourselves to a semiquantitative plausibility argument for the present.

Several corrections would have to be applied to Eq. [1]: (i) The "image force" correction (39) which takes into account the effect of the bending down of the rims of the potential well of the conductor by the external field, causing a higher current to flow than predicted by Eq. [1]. (It is unknown to what extent this effect is significant for internal field-emission into insulators.) (ii) Space-charge limitation due to free carriers in front of the emitter at very high current densities, similar to the well-known case of the vacuum diode (Child equation) (50):

$$I = \frac{V^2}{d^3}$$

(The nonplanar geometry in our case allows d, the electrode spacing, to be only estimated.) (iii) Space-charge limitation due to traps. (Available one-carrier space-charge-limited current theories treat the stationary case, or describe only the transient case for the situation of conducting crystals with one ohmic and one blocking contact (50) which is different from our case. Besides, if the crystal region into which injection takes place contains trapped charge of the opposite sign, then injection is space-charge-enhanced until compensation is complete, and then becomes not only space-charge-limited but space-charge-quenched.) (iv) Quenching of charge-injection due to polarization of the particle. At high brightness this limitation due to the particle capacitance becomes indeed dominant, a fact that was evaded in former theories.)

These modifications of Eq. [1] make it very difficult to perform the necessary integration. Further, the quantum efficiency does not remain constant, since at very high fields it is likely that trapped holes can be released by the field and attracted by the conducting line so that the storage over half a cycle, which is necessary for the functioning of the model, becomes partially ineffective. The observed drop of efficiency at high operating voltage (51) may well be caused by this field-detrapping, and reabsorption by the conductor, of injected holes. These changes make it even more difficult to arrive at a strict solution.

As a substitute for a complete solution, the trends of the brightness-voltage and brightness-frequency dependence of single EL particles can be approximated by a circuit model (Fig. 12a, b), consisting of a resistor and a capacitor in series. The resistor, symbolizing the field-emitting junctions, is variable with a voltage dependence

$$R_r = \frac{V_r}{I} = \frac{V_r}{A\,F^2 \exp - B/F} \sim \frac{\exp B/V_r}{V_r\,A}$$

It is assumed that no depletion layers are present in front of the emitter, so that the relation $F \sim V_r$ can be used, where V_r is the voltage drop over the resistor. An a.c., rms voltage is applied, and the variables R_r, V_r, I, and F may all signify rms values.

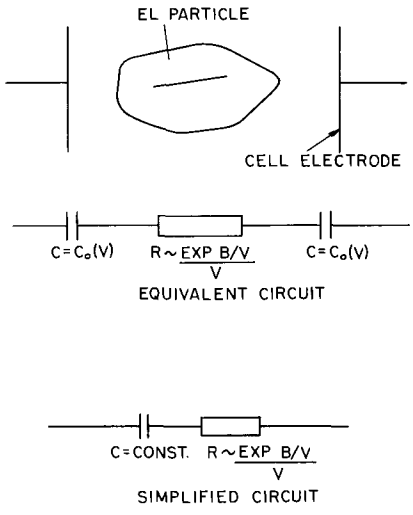

Fig. 12. Circuit model of EL line

The capacitor, which symbolizes the finite capacitance of the EL particle, is also voltage-dependent since, as discussed before, its value can shift from the capacitance of a conducting line at low voltage and/or high frequency, to the larger value given by the geometry of the particle, at high voltage and/or low frequency. To simplify the discussion, we shall assume that the capacitance is constant, thus $R_c = \frac{1}{j\,\omega\,C}$. Since the nonlinear resistor distorts the sinusoidal voltage, R_c may also signify an average value which takes into account higher harmonics. The total impedance is then

$$R = \sqrt{R_r^2 + R_c^2}$$

U is the total applied rms voltage which is divided, to an unknown voltage and frequency dependent extent, into the voltage across the capacitor, V_c, and the voltage across the nonlinear resistor, V_r, so that $U = V_c + V_r$.

If the resistor were constant, the rms current through the circuit would be

$$I = \frac{\omega C U}{\sqrt{\omega^2 C^2 R_r^2 + 1}}$$

Replacement by the variable resistance leads to

$$I = \frac{A\,\omega\,C U}{\sqrt{\left(\frac{\omega C \exp B/V_r}{V_r}\right)^2 + A^2}}$$

The expression $\left(\frac{\omega C \exp B/V_r}{V_r}\right)$ may be called P.

It is realized that this treatment is inaccurate due to the nonlinearities involved, but it is suitable to discuss the approximate trends.

Let us first discuss the trend of the voltage-dependence at constant frequency, (ω = constant). The constant A, which stems from the Fowler-Nordheim equation, is related to the (unknown) emitting area of the tips. It may be suitably adjusted so that at low voltage $P > A$. At low voltage the resistance is large and most of the applied voltage develops across the resistor, so that $U \sim V_r$. The brightness dependence is then

$$I = A\,U^2 \exp - B/U$$

which agrees in form with experimental findings. At high voltages, where $P < A$, we obtain

$$I \sim U \omega C$$

a linear voltage dependence, in accordance with our measurements on long, bright lines [Part I (1a)].

For the trend of brightness with increasing frequency at constant voltage U, we find a linear increase at low frequency where $P < A$, changing to a sublinear increase at intermediate frequencies where $P \sim A$, and a frequency-independence at high frequencies where $P > A$ and $U \sim V_r$. These trends agree with observed trends.

It must be noted that in this circuit model voltage and frequency dependence are interrelated in a much more pronounced way than is observed in El cells. (The stronger interdependence of the model is caused by neglecting the voltage-variable capacitance of the particle.) The high-voltage saturation of brightness sets in at lower voltage at low frequency than at high frequency, and the frequency-saturation of brightness sets in at lower frequencies at low voltage than at high voltage. Such effects are observed in EL cells (21). This interdependence explains the strange finding [Part I (1a) Fig. 11] that the brightness of long lines rises more steeply (but still sublinearly) with frequency than that of short lines: At the tips of long lines there is a higher field than at the tips of short ones so that $P_{long} < P_{short}$, hence the long lines show frequency saturation at higher frequencies than the short lines.

The almost linear increase of brightness with frequency to which much significance was attributed in former models is not observed for single EL lines. In large EL cells it is caused by an increase in the number of participating EL lines with frequency.[9]

(*d*) Effect of particle size.—It has been observed by several authors (51, 52) that the brightness of cells made of uniform small particles rises more steeply with voltage and reaches higher values than the brightness of comparable cells made with selected large particles. Goldberg (52) has analyzed these findings and concludes that one has to assume a constant number of "barriers" (of unspecified nature) per particle regardless of size. The voltage drop across each particle must be assumed to be proportional to the diameter of the particle. Since Goldberg concludes elsewhere that the particles are quite insulating (23), it is not clear how the "barriers" can be exposed, as assumed in his treatment, to a voltage proportional to the particle diameter. In our model, Goldberg's generalized theory immediately gains a very concrete meaning if we introduce the length L of conducting imperfection lines, which we assume to be proportional to the diameter of the particles. This assumption is plausible: Dislocation lines are stable only if they start and end at a surface. Besides, if a particle has both long and short conducting lines, then the long ones absorb most of the power and shield the short ones from the field, so that always the longest ones are active.

If one replots the published data on brightness-voltage curves in dependence of particle size, or the measurements of long and short EL lines [Part I(1a)], and uses as the abscissa, instead of the applied field, the actual field which is active at the tips of the conducting lines and which is proportional to the square of the length L of the lines (25)

$$F_{max} = \text{const } L^2 F_{appl}$$

then the Fowler-Nordheim equation becomes

$$I = A L^4 F^2 \exp - B/L^2 F \text{ or } I = A' F^2 \exp - B'/F$$

and the brightness-voltage curves for different particle sizes or line-lengths coincide.

(*e*) Maximum brightness of EL cells.—The low brightness of EL panels has always been a disappointment to those who had hoped for a new light source for room illumination. The following consideration permits the prediction that the maximum brightness level has about been reached and that order-of-magnitude improvements cannot be expected.

An EL cell with a phosphor-to-binder ratio of 1:2 by volume can be idealized as in Fig. 13. It may be operated at maximum field strength, 2.10^5 v/cm or 600v P-P.[10] If the dielectric constant and average dielectric loss factor of binder and phosphor are equal ($\epsilon = 10$), the voltage drop across the phosphor is 1/3 the applied voltage or 200v. The capacitance/square centimeter of the 10μ thick phosphor layer is 10^{-9} **F**/cm^2. At 200v, the maximum charge which can be displaced from one side of the layer to the other is given by $Q = C\ V$ as 2.10^{-7} coulomb/cm^2, or 1.2 x 10^{12} elementary charges/cm^2. It is assumed that each second charge carrier transported from one side to the other gives rise to the emission of one photon of 2.5 ev energy (50% quantum efficiency).[11] The light energy emitted per second and square-foot area if the applied frequency is 60 cps, is then 2.7 x 10^{-2} watts. For an energy-equivalent for ZnS-Cu green emission of 400 lumens/watt we obtain as maximum brightness a very realistic value of 11 ft-L. This brightness limitation is a sole consequence of the polarization field in insulated particles and does not exist for directly contacted layers of the type discussed in ref. (30). The brightness-limitation due to polarization also applies for models

[9] Certain ZnSe-Cu EL phosphors show a steeper than linear rise of brightness at low frequency, which can be explained in a completely different way: Due to much shallower activator centers, the trapped holes can be thermally released if enough time is available. At increasing frequency, less and less time is available for the trapped holes to escape and to be reattracted by the conducting line, so that the efficiency increases with frequency, giving rise to a superlinear increase of brightness with frequency.

[10] Above this field strength, safe operation is impossible because of breakdown.

[11] This value is reached by good ZnS phosphors with u.v. excitation.

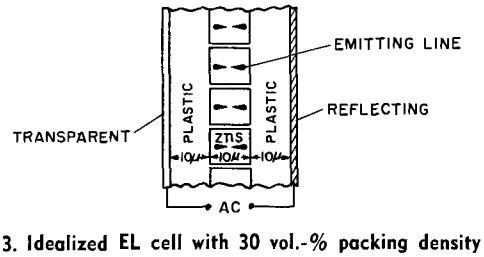

Fig. 13. Idealized EL cell with 30 vol.-% packing density of 10μ particles.

which postulate p-n junctions in embedded particles. It also holds for impact-ionization models, even if one primary electron is capable of producing more than one collision ionization event during its passage through the particle: each ionization gives rise to one extra mobile electron which moves to the boundary of the embedded crystal and contributes to the polarization.

(*f*) Efficiency.—The above-mentioned simple calculation for a layer which is one particle diameter thick also yields crude estimates for the efficiency. Since, at 50% quantum efficiency, every second elementary charge, upon passing the voltage drop across the particle (which is assumed to contain one emitting line), gives rise to the emission of one photon of 2.5 ev of energy, the efficiency is 2.5/(2 x voltage drop). Due to the build-up of the polarization field, the voltage drop across the particle is 200v only at the very beginning and decays in some exponential way (square-wave-excitation). Inserting an average voltage drop/electron/half-cycle of 100v, the efficiency is 1.2% or 4.8 lumen/watt. The other energy is converted into heat by the current oscillating within the conducting lines and by the currents flowing through the crystal.

Despite the fact that the model does not require impact-ionization or hot-carrier concepts, considerable energy is wasted because the carriers, after emerging from the tunnel are needlessly accelerated and braked down by lattice vibration until they settle down in traps.

An increase in brightness and efficiency can be achieved if, instead of one long line per particle, many collinearly stacked ones can be produced within one particle, so that each passing electron can give rise to many emitted photons. A similar effect can be obtained by dense packing of small particles having the same number of lines/particles as large particles. This brightness-and-efficiency-increase is an empirically known fact (51).

(*g*) Deterioration of EL cells.—EL cells deteriorate under operating conditions, even if moisture effects [which lead to darkening of the front and back faces of the particles due to electrolytical generation of free zinc (53)] are completely excluded.

The conducting-line-model offers a new and plausible deterioration mechanism which is similar to the one acting in the field-emission microscope: blunting of the tips. The tips of the copper-sulfide-decorated imperfection lines (not only the end tips but also the innumerable little roughnesses) can be blunted by outward drift of copper ions, or by attraction of ions from the adjacent host crystal, or, most likely, by sideward-drift of copper ions in front of the tips during their back-and-forth oscillation under the influence of the high a-c field in front of the tips. One may assume that a cloud of interstitial copper ions builds up which, since the ions are charged, masks the roughnesses and thus reduces the local field.[12]

[12] Displacement of this ion cloud with a resultant field-change at the tips, may be the explanation for the observed "memory effects" (41) if sharp pulses are superimposed on the exciting sine-wave, and for the recovery effects if an aged cell is rested for a while, or baked.

The ion cloud becomes thicker during prolonged operation until only the end-tips of the conducting line, where the local field is still high enough to produce field-emission, remain for light generation.

This change of an emitting double-comet-line into just two light-emitting points at the positions where the "heads" of the comets were before, and the corresponding disappearance of the comet "tails," has actually been observed under the microscope, using the matched-refractive-index embedding medium described in Part I(1a).

It is known that EL cells made with zinc sulfoselenide powders have a longer life than cells made of zinc sulfide (54). Aside from the possible explanation that the ion mobility may decrease with increasing selenium content of the crystals because the bigger selenium ions block diffusion more than do sulfur ions, one can assume that, due to the reduced work function at the emitting contacts caused by the lower band gap of ZnS-ZnSe, lower fields suffice to get the same amount of field emission. Lower fields mean less ion drift.

The deterioration mechanism seems to be photon-assisted. This follows from the fact that blue-emitting cells deteriorate faster than orange-emitting ones, with the same host material (55). One may assume that the Cu-ion cloud is actually generated by light quanta which are absorbed by the Cu_2S and knock off Cu-ions.

(*h*) Color shift with frequency.—Electroluminescent ZnS-Cu, Cl powders change their emission color from green to blue with increasing frequency.[13] Similar color shifts are observed in these phosphors with photoexcitation, where high temperature and/or low excitation density favor the green band emission, whereas low temperature and/or high excitation density promote emission of the blue band (56).

Microscopic observation of the color-shift in EL lines, using the low-melting As-S-Br-glass or the TlBr-TlCl mixture as matched embedding media [Part I (1a)] was not yet possible since the required heating of the powder, even if it lasts only a minute, destroys the color shift. The unmatched P-S-CH_2I_2 [Part I (1a)] had to be used. It could be established that all El lines turn from green to blue with increasing frequency, as opposed to the possible alternative that the green lines disappear and new blue lines emerge.

A possible explanation of the color shift is based on the plausible assumption that the ZnS adjacent to the copper-decorated lines is richer in copper than the bulk (see Fig. 7a-c). At high frequency, when the lines become sharp and concentrated (see Fig. 8) the blue emission of the copper-rich ZnS predominates. At low frequencies, where the lines are spread out, the green emission of the bulk ZnS predominates. Heating promotes the precipitation of excess copper to the line and thus quenches the color shift.

(*i*) Contact-electroluminescence.—Lehmann discovered that certain non-electroluminescent but photoluminescent powders (*e.g.*, ZnS, 3% MnS, fired with NaCl flux under exclusion of oxygen) become

[13] Some ZnS-ZnSe-Cu, Br phosphors show a similar color shift from yellow to green.

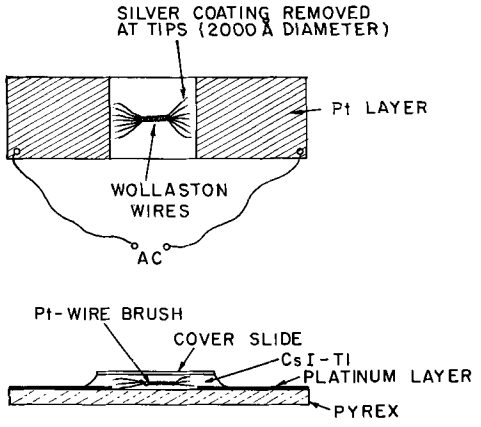

Fig. 14. Macroscopic analog of the model. A double-brush made of Wollaston wire is mounted on a gap cell. The silver coating of the tips is etched away, so that the invisibly fine platinum wire (2000Å) is exposed. The structure is covered with molten and recrystallized CsI-Tl. Light-emission at the tips is observed.

electroluminescent if they are mixed with sharp-edged, highly conducting powder particles (16). This finding has recently been disputed as being caused by gas discharge in the decomposing embedding medium (40), but Lehmann's results (57) were confirmed by the author.

The sharp-pointed, highly conducting particles which contact, or bridge, insulating luminescent particles, perform the same role as the conducting copper-sulfide-decorated imperfection lines within ZnS particles, only with reduced efficiency. In addition to Lehmann's experiment, a functioning macroscopic analog of the conducting line model has been prepared which consists of a gap-cell [see Part I (1a)] containing 2000Å thick Wollaston wires fused in luminescent, thallium-activated cesium iodide (mp 620°C) (Fig. 14).

Impact ionization electroluminescence according to the inverted Maeda model.—The discussion of this model, the main features of which were outlined before, can be brief because it is in many ways surprisingly similar to the field-emission model despite the fact that the carrier-generation mechanisms are quite different.

Again we assume that the ZnS powder particles are nearly compensated semiconductors (= insulating) with a uniform distribution of shallow donors and deep acceptors, and with conducting lines decorated with copper sulfide. At field application, a few electrons from donors which are not compensated are field-released from their traps as the local field strength surpasses a critical value. The field-release is aided by temperature. The released electrons are attracted by the conducting line which, by geometrical field enhancement, forms a sink of field lines at its one half, and a source at the other, with the field strength increasing towards the line (Fig. 2). The electrons become accelerated, and some of them impact-ionize the crystal lattice shortly before they fall into the conducting line, thereby creating a secondary electron, which also falls into the line, and a hole. The hole travels in the opposite direction, but becomes soon trapped in an activator center, thereby "activating" it. The positive space charge due to trapped holes locally weakens the field near the line.[14] Other positions along the conducting line now become active as the field increases further. The conducting line becomes increasingly negative due to the absorbed electrons and starts to field-emit electrons at the other end. These electrons become trapped at the other end of the crystal. At field reduction, some of these electrons flow back through the crystal and recombine radiatively with trapped holes. The conducting line, which still has some negative charge, field-emits electrons from the end which formerly attracted electrons, into the surrounding positive space charge due to the high local unbalanced polarization field. As the applied field is reversed, electrons are field-released from traps which previously had become filled (note: more primary electrons are available now!) and are attracted by the line, impact-creating secondaries and holes. The electrons which now are field-emitted from the opposite end of the line, find there trapped holes left from the previous half cycle, with which they can recombine. In the next cycles this build-up increases until an equilibrium between recombination and regeneration which is characteristic for the given field, frequency and temperature conditions, has been reached.

The field-distribution during a full cycle is the same as in the other model. The supply of primary electrons follows a relation of the type exp $-\Delta E/F$ (20), where ΔE is the (temperature-dependent) effective trap depth and F the local field. As soon as the charge displaced from one end of the particle to the other comes in the order of $Q = C\ V$, where C is the particle capacitance and V the potential drop across the particle, the polarization field weakens the applied field and the local field no longer increases proportional to the externally applied field.

The number of collision excitations per primary electron [Seitz function (11)] which starts with a very low fraction of one and can become almost one, also saturates as the particle capacitance becomes the limiting factor at high applied fields.

The arguments which were used to explain the observations and measurements on EL double lines [Part I(1a)] by the field-emission model, can with little change be used by the collision model. In one case, holes are field-injected, in the other case collision-generated, but the timing, the charge flow, and the recombination are exactly the same.

A distinction between the two models, for instance by means of predictable field or temperature dependences, is hardly possible because of too many factors which work in opposite directions.[15]

A combination with the other model seems possible where the accelerated electrons do not impact-ionize the ZnS-lattice before they enter the con-

[14] Therefore, the probability of impact ionization decreases. This effect of trapped holes is similar to the reduction of field-emission due to polarization caused by holes trapped in front of the emitter.

[15] It has been attempted to use the fact that ZnS-Cu,Cl,Mn shows electroluminescence with the characteristic manganese emission as evidence that the effect is based on the collision mechanism, assuming that the Mn fluorescence is excitable only by impact. If one accepts this, then it is of course logical to postulate that the impact ionization mechanism also applies if no Mn is present (58). Gumlich (59) has established, however, that the internal Mn luminescence can be excited by a free-carrier transition, consisting of an electron in a trap associated with the Mn center recombining with a free hole in the valence band. The recombination energy is resonance-transferred to the Mn-ion.

ducting line, but where their kinetic energy is transferred to holes at the surface of the conducting material, enabling them to overcome the barrier and move into the ZnS.

It is also possible that both mechanisms are active simultaneously, but in changing proportions depending on the conditions.

Acknowledgment

The author is deeply indebted to Dr. R. E. Shrader for discussions and for a critical review of the original manuscript. It is a pleasure to thank Dr. A. Rose for suggestions and valuable criticism. Gratitude is expressed to Dr. S. Larach for his continuing interest in this work. Clarifying comments on the content of this paper were supplied by several referees and the Editors of this Journal, and by several European colleagues. The research in this paper was sponsored by the Electronics Research Directorate, Air Force Cambridge Research Laboratories, Office of Aerospace Research, U.S. Air Force, under Contract AF19(604)-8018.

Manuscript received Aug. 16, 1962; revised manuscript received Jan. 28, 1963. This paper was presented at the Los Angeles Meeting, May 6-10, 1962, and at the German Physical Society Meeting, Stuttgart, September 1962.

Any discussion of this paper will appear in a Discussion Section to be published in the June 1964 JOURNAL.

REFERENCES

1. J. L. Gillson and F. J. Darnell, *Phys. Rev.*, **125,** 149 (1962).
1a. A. G. Fischer, *This Journal*, **109,** 1043 (1962).
2. V. F. Oranovskii and B. A. Khmelinin, *Optics and Spectroscopy*, **7,** 336 (1959); W. A. Thornton, *This Journal*, **108,** 636 (1961).
3. H. K. Henisch and B. R. Marathe, *Proc. Phys. Soc. (London)*, **76,** 782 (1960).
4. G. Destriau, *Phil. Mag.*, **7,** 700 (1947).
5. D. Curie, *J. phys. radium*, **14,** 135, 510, 672 (1953).
6. See, *e.g.*, W. Franz, in "Handbuch der Physik," Vol. 17, Springer Verlag, Berlin (1956).
7. W. W. Piper and F. E. Williams, *Phys. Rev.*, **81,** 151 (1952).
8. A. Fischer, *Z. Naturforsch.*, **8a,** 756 (1953); *Physik. Verhandl.*, **3,** 64 (1954).
9. W. W. Piper and F. E. Williams, *Brit. J. Appl. Phys., Suppl. No. 4*, S39 (1955).
10. G. F. Alfrey and J. B. Taylor, *Proc. Phys. Soc.*, **B78,** 775 (1955).
11. F. Seitz, *Phys. Rev.*, **76,** 1376 (1949).
12. H. K. Henisch, "Metal Rectifiers," p. 88, Clarendon Press, Oxford (1949).
13. A. G. Fischer and A. S. Mason, *Bull. Am. Phys. Soc.*, Ser. II, Vol. 8, p. 30, GA3, and to be published.
14. A. G. Fischer, *Z. Naturforsch.*, **8a,** 756 (1953).
15. G. A. Wolff, R. A. Hebert, and J. D. Broder, in "Halbleiter und Phosphore," p. 547, Proceedings of the Int. Conf. Garmisch-Partenkirchen, Friedr. Vieweg and Sohn, Braunschweig (1958). Also *Phys. Rev.*, **100,** 1144 (1955).
16. W. Lehmann, *This Journal*, **104,** 45 (1957).
17. P. Zalm, *Philips Research Repts.*, **11,** 353, 417 (1956).
18. M. Maeda, *Physica*, **25,** 721 (1959).
19. H. A. Klasens, in "Semiconductors and Phosphors," p. 247, Fr. Vieweg and Sons, Braunschweig (1958).
20. W. Franz, *Ann. Physik (Leipzig)*, **11,** 17 (1952).
21. W. Lehmann, *This Journal*, **107,** 20 (1960); **103,** 667 (1956).
22. M. V. Fock, *Soviet Physics Uspekhi*, **3,** 832 (1961) [transl. of *Uspekhi Fiz. Nauk*, **72,** 667 (1960)].
23. P. Goldberg and S. Faria, *This Journal*, **107,** 521 (1960), and own unpublished work.
24. H. F. Ivey, *Sci. American*, p. 40, (August 1957).
25. K. Maeda, *J. Phys. Soc. (Japan)*, **13,** 1351 (1958); **15,** 2051 (1960).
26. H. Homer, R. M. Rulon, and K. H. Butler, *This Journal*, **100,** 566 (1953).
27. A. G. Fischer and A. S. Mason, Contract AF19(604)-8018, report AFCRL 979 (1961).
28. W. J. Merz, Solid State Physics in "Electronics and Telecommunications," Vol. 2, part 2, p. 811, Brussels Conference, Academic Press Inc., New York (1960).
29. L. W. Strock, *Illum. Eng.*, **55,** 25 (1960); M. A. Short, E. G. Steward, and T. B. Tomlison, *Nature*, **177,** 240 (1956).
30. A. G. Fischer, *Solid State Electronics*, **2,** 232 (1961).
31. See, *e.g.*, G. Foudat and C. Meuleau, "Semiconductors," p. 222, McDonald and Evans Ltd., London (1957).
32. M. Aven, Los Angeles Meeting Electrochemical Society, May 1962, Electronics Division, Enlarged Abstract No. 40.
33. A. K. Jonscher, *Brit. J. Appl. Phys.*, **12,** 363 (1961).
34. M. A. Lampert, *Phys. Rev.*, **125,** 126 (1962).
35. A. N. Georgobiani, *Optics and Spectroscopy*, **11,** 231 (1961).
36. R. Williams, *Phys. Rev.*, **117,** 1487 (1960).
37. W. Shockley, "Electrons and Holes in Semiconductors," p. 345, D. Van Nostrand Co., Princeton, N. J. (1950).
38. M. Gershenzon and R. M. Mikulyak, *J. Appl. Phys.*, **32,** 1338 (1961).
39. E. W. Müller, in Ergeb. Ex. Naturwiss. 27, 290, Springer Verlag, Berlin (1953); R. H. Good and E. W. Müller, in Handbuch der Physik, Vol. 21, Springer Verlag, Berlin (1956).
40. A. Herwelly, *Acta Physica Austriaca*, **5,** 30 (1951); B. Morosin and F. A. Haak, *This Journal*, **108,** 477 (1961); **109,** 540 (1962).
41. R. E. Shrader, Private communication.
42. A. H. McKeag and E. G. Steward, *This Journal*, **104,** 41 (1957); D. W. Ballentyne, *J. Phys. Chem. Solids*, **10,** 242 (1959); *This Journal*, **107,** 807 (1960).
43. W. C. Dash, *J. Appl. Phys.*, **27,** 1193 (1959); J. Woods, *Brit. J. Appl. Phys.*, **11,** 296 (1960); P. Goldberg, *J. Appl. Phys.*, **32,** 1520 (1961).
44. J. F. Stratton, "Electromagnetic Theory," p. 209, McGraw-Hill Book Co., New York (1941).
45. K. Küpfmüller, "Einführung in die theor. Elektrotechnik," p. 39, 69, Springer Verlag, Berlin (1941).
46. H. S. Sommers, Jr., R. E. Berry, and I. Sochard, *Phys. Rev.*, **101,** 987 (1956).
47. M. V. Fock, *Soviet Physics Uspekhi*, 4, 759 (1962) [transl. of *Uspekhi Fiz. Nauk*, 75, 259 (1961)].
48. J. F. Waymouth and F. Bitter, *Phys. Rev.*, **95,** 941 (1954).
49. J. A. Rajchman, G. R. Briggs, and A. W. Lo, *Proc. IRE*, **46,** 1808 (1958).
50. M. A. Lampert, *RCA Rev.*, **29,** 682 (1959); W. Helfrich and P. Mark, *Z. Physik*, **166,** 370 (1962).
51. W. Lehmann, *This Journal*, **105,** 585 (1958).
52. P. Goldberg, *ibid.*, **106,** 34 (1959).
53. I. L. Smith, R. M. Potter, and M. Aven, Paper presented at Chicago Meeting Electrochem. Society, May 3, 1960.
54. W. A. Thornton, *This Journal*, **107,** 895 (1960).
55. P. M. Jaffe, *ibid.*, **108,** 711 (1961).
56. F. A. Kroeger, J. E. Hellingman, and N. W. Smit, *Physica*, **15,** 990 (1949); N. W. Smit, *ibid.*, **16,** 317 (1950); F. A. Kroeger and J. Dikhoff, *ibid.*, **16,** 297 (1950).

57. W. Lehmann, *This Journal*, **109**, 540 (1962).
58. D. A. Cusano, in "Luminescence of Organic and Inorganic Materials," p. 494, John Wiley and Sons, New York (1962).
59. H. Gobrecht and H. E. Gumlich, *J. Phys. radium*, **17**, 754 (1956); H. Gobrecht, H. E. Gumlich, H. Nelkowski, and D. Langer, *Z. Physik*, **149**, 504 (1957); H. Gobrecht, H. E. Gumlich, and J. zum Bruch, *Z. Physik*, **162**, 169 (1961); and private communication with H. E. Gumlich.

On the Emission of Electrons from Solids in Gas Discharges

II. Accelerating Field Emission

D. M. Speros and P. R. Buccilli

Lamp Research Laboratory, General Electric Company, Nela Park, Cleveland, Ohio

ABSTRACT

The behavior of practical cathodes in gas discharges under accelerating field conditions is examined.

Part I of this work (1) examined cathode emission in the vicinity of zero field. Part II is concerned with emission phenomena under accelerating field conditions.

The intrinsic behavior of cathodes in gas discharges is normally masked by variations in cathode temperature and state of activity caused by the discharge. This is especially true when the cathode is subjected to ionic bombardment due to an accelerating field.

In this study, cathode behavior is examined during the first few microseconds after the ignition of the discharge (1). The discharge is extinguished a few milliseconds later. The cathode is allowed to recover before a new measurement is made. The results thus obtained are reproducible and give an idea of (i) the capability of the cathode system while at a thermochemically definable equilibrium, and (ii) volt-ampere characteristics of the system cathode-discharge which are nearly independent of undeterminable variations in the cathode component.

The cathode-discharge system of interest here is that of fluorescent lamps. Since the voltage drop along the positive column and its variations is a separate subject, cathode-anode gaps of a few millimeters were used. The discharge tubes, Fig. 1, were made and degassed with all the care normally devoted to high vacuum diodes. The gettering arrangement and operation was such that the argon (2.5 mm Hg)-mercury atmosphere remained uncontaminated during the measurements. The cathodes were those of normal fluorescent lamps and consisted of a tungsten coiled-coil coated with oxides of the following composition by weight

$$BaO:SrO:CaO:ZrO_2 = 49:29:19:3$$

Five milligrams of this material were on each coated cathode. The tungsten coil was that used in standard 40w fluorescent lamps. The over-all diameter of the coil was 0.7 mm, the length between leads 14 mm, and the coated portion 12 mm.

Measurements were made both with uncoated (pure tungsten) and oxide-coated cathodes.

The results of the study of the current-voltage isotherms of these tubes are seen in Fig. 2 and 3 where the situation emerges remarkably uncomplicated in comparison to results of past work (2-3): for a significant range, the logarithm of the current is linearly[1] dependent on the voltage. This tends to

[1] This is tentative because the semilog nature of the plots and the range of the results do not allow a precise determination of the exponent of V.

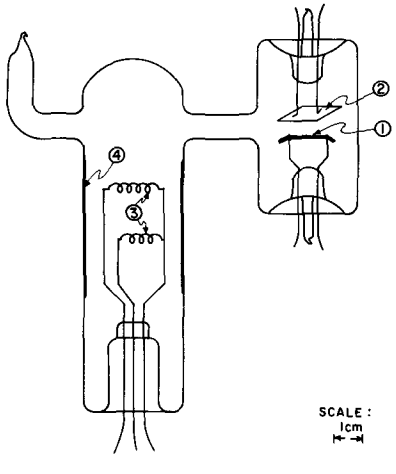

Fig. 1. Experimental discharge tubes: 1, cathode; 2, anode, 15 x 15 mm tantalum foil; 3, titanium heater-evaporator coils; 4, titanium film deposit continuously replenished by means of 3.

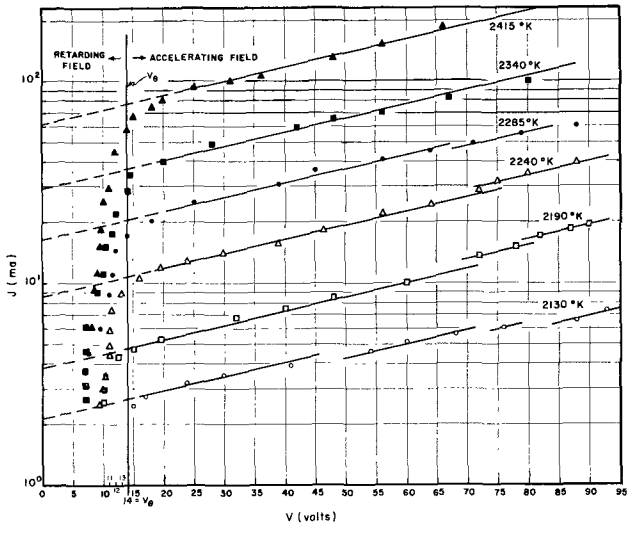

Fig. 2. Current-voltage interdependence for tungsten cathode. Value of $d \ln J/dV = 7.05 \times 10^{-3}\ V^{-1}$.

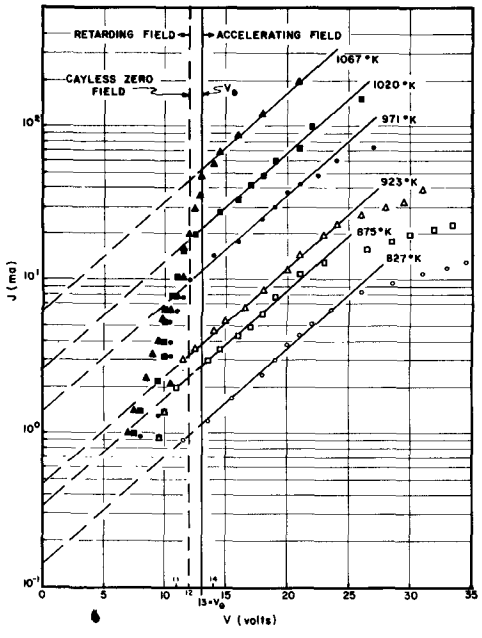

Fig. 3. Current voltage interdependence for oxide cathode. Value of $d \ln J/dV = 7.07 \times 10^{-2} V^{-1}$.

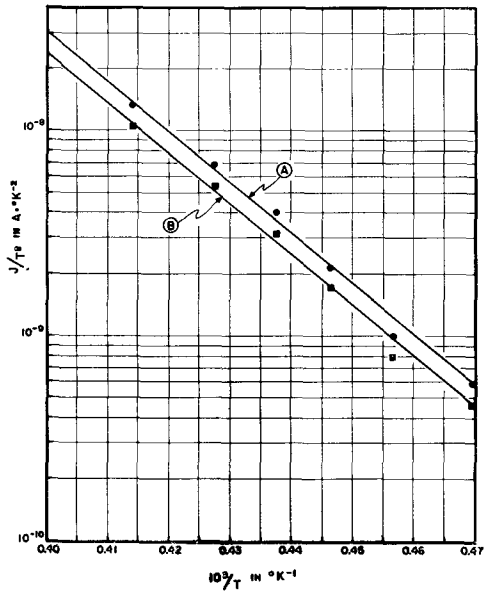

Fig. 4. Richardson-Dushman plots of A, points of intersection between the isotherms and $V = V_\theta$ of Fig. 2; and B, points of intersection between isotherms and ordinate at $V = 0$ of Fig. 2. Slopes = 4.87 ev.

occur above a certain voltage V_θ, the value of which is constant with temperature and which (see below) identifies the condition of "zero field." Hence the points of intersection of the isotherms with the V_θ line, when plotted on a Richardson-Dushman plot give a straight line, lines A in Fig. 4 and 5, with the appropriate slopes. Therefore the behavior of this cathode-discharge system of great practical importance can be expressed as

$$\ln J = \ln J_\theta + \frac{d \ln J}{dV}(V - V_\theta)$$

where J_θ is the "thermionic" contribution and $(d \ln J/dV) \cdot \Delta V$ is that due to the field. It is seen that, for these stable cathodes, $(d \ln J/dV) = K$ is

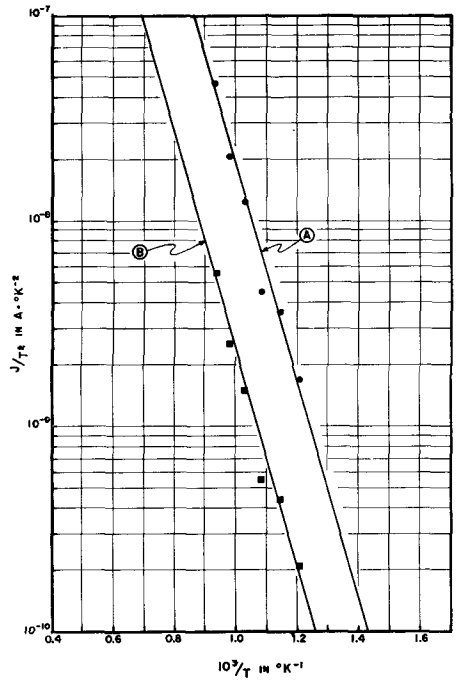

Fig. 5. Richardson-Dushman plots of A, points of intersection between the isotherms and $V = V_\theta$ of Fig. 3; and B, points of intersection between isotherms and ordinate at $V = 0$ of Fig. 3. Slopes = 1.05 ev.

constant and amounts to $7.07 \times 10^{-2} V^{-1}$ for the oxide cathode and $7.05 \times 10^{-3} V^{-1}$ for the tungsten cathode.[2] Accordingly the ability of these cathodes to emit electrons can be defined by the constant A_θ, ϕ, and K in

$$J = A_\theta T^2 e^{-e\phi/kT} \cdot e^{K(V - V_\theta)}$$

which are measured as already described here and in ref. (1).

The value of V_θ turns out to be the voltage at which plateau B of ref. (1) disappears, and this was shown to occur in the vicinity of zero field. The zero field identification according to the method of Cayless (2, 4) is also shown on Fig. 3 and is near V_θ. A glimpse of the physical significance of V_θ and also of the Cayless zero field voltage is obtained by noting that their values are, within correction for contact and residual potentials, near the values of the first excitation or ionization potentials of argon (11.5 and 15.7v, respectively). If so, they should vary with changes in the rare gas. Preliminary work indicates that they do.

Lines B in Fig. 4 and 5 show the Richardson-Dushman plots of the points of intersection between the extrapolated isotherms and the ordinate at $V = 0$. It remains to be seen whether this would correspond to the vacuum zero field behavior of these tubes. However, Cayless (5) in similar work found experimentally a similar correspondence between zero field vacuum and discharge emission as is found here by extrapolation.

In Fig. 10 of ref. (1) an emission hysteresis effect was shown as function of both cathode temperature and field. The effect of changing cathode activity because of the field at constant cathode tem-

[2] Unstable cathodes tend to give isotherms whose slopes increase with temperature, thus giving a fan shaped appearance to Fig. 3.

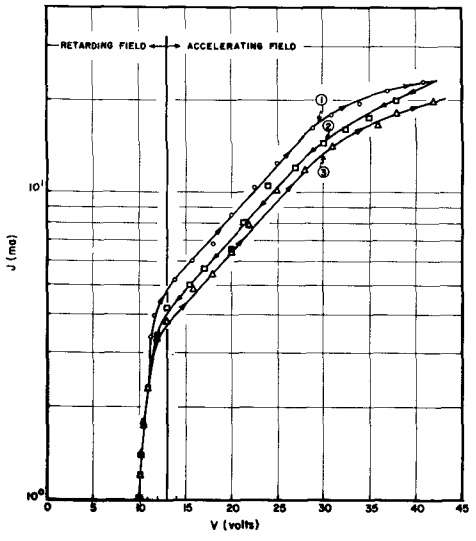

Fig. 6. Progressive emission hysteresis due to field at constant temperature for oxide cathode. Measurements followed the sequence shown by the numbers for each branch and the arrows within each branch.

perature is seen in Fig. 6: the current-voltage dependence is reproducible, in the oxide cathode, as long as the field remains small. For fields higher than V_θ by about 12v irreversible effects begin to occur. It is this kind of effect that causes the third line from the bottom of Fig. 3 to be out of place in comparison to the rest. This hysteresis becomes the more pronounced the higher the current until above about 100 ma, for these cathodes, emission slumps in a matter of microseconds if the field is higher than V_θ.

Further insight into the significance of the results reported here involves their intercomparison with results obtained using planar, unipotential cathodes (6).

Acknowledgments

Thanks are due to Drs. C. B. Collins, J. S. Saby, and J. E. White for their interest and critical discussions.

Manuscript received Jan. 28, 1963.

Any discussion of this paper will appear in a Discussion Section to be published in the June 1964 JOURNAL.

REFERENCES

1. D. M. Speros and P. R. Buccilli, *This Journal*, **109**, 940 (1962).
2. M. A. Cayless, *Brit. J. Appl. Phys.*, **8**, 331 (1957).
3. A. E. Pengelly and D. A. Wright, *ibid.*, **5**, 391 (1954).
4. A. D. Forster-Brown and M. A. Cayless, *ibid.*, **10**, 409 (1959).
5. Ref. (2) Fig. 7 and 8, p. 335.
6. Prepared for publication.

Field-Induced Luminescence of Powdered Phosphors

F. C. Palilla and M. Rinkevics

General Telephone & Electronics Laboratories, Inc., Bayside, New York

ABSTRACT

Luminescence has been observed in a variety of materials under the action of a-c and d-c fields. The materials include rare earth tungstates, Al_2O_3, and ZnO which have been self-activated or activated with Cr, Mn, or a rare earth element. Experiments in reduced pressures of a variety of atmospheres indicate that the luminescence observed is not the same as the electroluminescence of ZnS or of ZnO phosphors. This is further confirmed by differences in the frequency dependence of emission and by the analysis of the spectral components of the emission. Speculations as to the mechanism of the possible emission processes are discussed.

Investigations of the phenomenon of electroluminescence have been most extensive with materials based on zinc sulfide as the host and activated with copper alone or with copper and manganese. A search has nonetheless continued to provide families of materials characterized by greater stability, range of emission colors, and sensitivity to various modes of excitation than is currently available with ZnS. The recent activity in optical masers has directed attention to a variety of oxygen-dominated host lattices. Adams *et al.* have reported on the electrofluorescence of Al_2O_3 activated with rare earth and transition elements (1, 2). Van Uitert *et al.* have published extensively on the luminescent characteristics of rare earth-activated oxides including tungstates, molybdates, and vanadates (3). This investigation was therefore directed toward an evaluation of the electroluminescent capabilities of a variety of oxygen-dominated host lattices.

Materials

The materials studied include self-activated ZnO, ZrO_2, rare earth garnets, and rare earth tungstates as well as Cr, Mn, and rare earth activated Al_2O_3, rare earth tungstates, and alkali and alkaline earth metal tungstates.

In all cases, the sensitivity to an applied electric field was generated by incorporating in the synthesis a thermal treatment in air at a temperature above 1200°C or in an atmosphere of N_2 or Cl_2 at a temperature above 900°C. A brief description of the phosphor systems with examples follows:

ZnO:X where X = excess Zn. A synthesis involving conversion of ZnS to ZnO has been found to give

photo-, cathodo-, and electroluminescence response superior to that obtained by equivalent thermal treatment of the oxide. The emission color is green.

ZrO_2 is rendered luminescent by a thermal treatment in air above 1000°C with no intentionally added activators.

Al_2O_3:X where X = Cr, Mn, or a rare earth metal according to the method of Adams *et al.* (1). In no case has an electric field-induced luminescence been observed unless a thermal treatment in a Cl_2 atmosphere has been applied. Activation with Cr leads to green and/or red emission. Activation with Mn, Eu, or Sm leads to red emission, and Tb leads to green emission. With Mn or Tb activation, no visual photoluminescence is observed. The rare earths Er, Yb, Pr, Dy, Ho, Lu, Gd, and Tm give a purplish light at the negative electrode when a d-c field is used, but no emission either in an a-c field or under u.v. excitation. Nd or Ce likewise give no detectable emission under u.v. excitation, but do give a purple emission in a-c fields and at both electrodes in a d-c field.

An unusual effect is found in Al_2O_3:Cr. If the material is prepared with a lead-bearing flux, red emission is observed at the positive electrode, but a new green band is also present at the negative electrode when observed through transparent (conductive glass) electrodes. Red emission is normally observed at the negative electrode when Pb is absent in the synthesis. This fact, and spectroscopic observations of the light intensities at both electrodes, speak against two light-generating processes, one originating at the cathode and the other at the anode. These observations, together with the excitation spectrum and absorption characteristics of Al_2O_3:Cr indicate instead either (i) two field-induced emission processes originating at the cathode with preferential self-absorption by the phosphor of the green emission, or (ii) one field-induced emission (green) originating at the cathode followed by photoexcitation of the red emission by the green (cascade).

Rare earth garnets. These represent a family of materials derived from the formula type $M_3^{2+}R_2^{3+}X_3^{+4}O_{12}$ in which the di- and tetra-valent metals (M and X) are replaced by trivalent metals (R), one of which is a rare earth (4). In particular, $Y_3Al_5O_{12}$ activated with Cr or Eu yield red-emitting phosphors.

$R_2(WO_4)_3$ and $RR'(WO_4)_3$ where R and R′ are rare earth metals. Single and double rare earth tungstates have been prepared by direct reaction between the oxides and tungstic acid, with and without a $Na_2W_2O_7$ flux. The emission color depends on the combination and concentrations of rare earth metals used.

$M_{0.5}^{+}R_{0.5}^{3+}WO_4$ and $M_{(x)}^{+}M_{(1-2x)}^{2+}R_{(x)}^{3+}WO_4$ where M^+ is an alkali metal, M^{2+} is an alkaline earth metal, and R can represent one or more of the rare earth elements (6). Quantitative measurements of the effect of the host metal radius on the rare earth photoluminescence emission intensity and how this is involved in the mechanism of the absorption and emission processes has been described by Van Uitert and co-workers (6). The enhancement and quenching effects of one rare earth element on another in these matrices have also been investigated (7). Initial investigation of the Tb-Eu interaction in $Na_{0.5}Eu_{0.5-x}Tb_xWO_4$ has shown that Tb can enhance the Eu emission under 2537Å excitation with possibly a concomitant shift in emission color to shorter wavelengths. Concurrently, the response to 3600Å decreases, as well as the response to an electric field.

Experimental

It should be noted that absolute brightness readings are not reported in this article because such data may prove misleading. Due to the difficulty of making dry powder layers reproducibly, equal brightness does not always result when several cells are prepared with the same phosphor and excited by the same fields. However, with any given cell preparation, the observations made (*i.e.*, brightness dependence on reduced pressure, frequency, atmosphere, etc.) still apply.

Investigations have indicated that the emissions observed with the above-described phosphors in a-c and d-c fields are not of the intrinsic type associated with ZnS phosphors. Rather, the phenomena observed appear to be extrinsic, and furthermore of two distinct types: Type I, contact electroluminescence which among the phosphors investigated is peculiar to ZnO and which has previously been described (8), and Type II, which may tentatively be called electrical luminescence, which is less clearly defined, and appears to be common to the remaining phosphors investigated. In all cases, the electrical response was observed by applying the field (200-600v) to the phosphor pressed between two conductive plates (spaced 6 mils apart) at least one of which was transparent. The transparent electrode was generally a tin oxide coated glass although conductive mica has also been used. The other electrode was metallic and made of brass, aluminum, or stainless steel. With any combination, no difference in results were observed.

In $CaCl_2$-dried air, the Type II emission initially observed under an electric field increases in intensity as the ambient pressure is reduced. These experiments were performed in a bell-jar, and evacuation was achieved by a combination of a mechanical and an oil diffusion pump. The emission intensity reaches a maximum and then fades away when the pressure is reduced to a point just before a luminous discharge is observed. Below about 1μ of Hg, no emission is observed. In pure O_2, N_2, or A, even at pressures above 1μ, no luminescence is found. With traces of water vapor in these gases, however, strong luminescence occurs which follows the same sequence as that which occurs in air when the pressure is reduced. In sulfur hexafluoride, which is known not to be subject to discharge at atmospheric pressure, no emission occurs, and the addition of moisture does not result in luminescence. This is true even at partially reduced pressures. With the Type I emission in air, on the other hand, there is no increase in intensity on (*a*) reduction of the ambient pressure, or (*b*) on introduction of moisture. Due to the conductivity of ZnO, fields in excess of a few hundred volts lead to breakdown. Consequently, at the low voltages applied, there is little

probability for corona-type discharges to occur. In contrast to the oxygen-dominated phosphors, electroluminescent ZnS:Cu,Cl powders generally give no emission in a d-c field. With a-c fields, the dry powder gives an emission which is much weaker than that obtained when it is embedded in castor oil dielectric, but both emissions persist at reduced pressures of ambient. Furthermore, the Type II oxide phosphors give no observable emission under any circumstances when embedded in castor oil, although Type I does give an emission when so embedded. Both types also apparently require a continuous conductive path between both electrodes, but ZnS:Cu,Cl emits light even with an insulating layer between one electrode and the phosphor grains. Also, while emission occurs throughout the bulk of the ZnS:Cu,Cl powder, in the Type II oxide phosphors the emission originates in the vicinity of one of the electrodes while Type I does not show this dependence on polarity. In Type II the electrode at which the emission occurs depends on the previous history of the material. For example, with ZrO_2 the emission occurs at the negative electrode when the field response is generated by a thermal treatment in Cl_2 at 1000°C, but the emission occurs at the positive electrode when the field response is generated by a thermal treatment in air at 1400°C. In most cases studied here the emission originates at the cathode. Under a-c excitation, as is to be expected, the emission is of equal intensity at both electrodes.

A further difference between the oxygen-dominated phosphors and ZnS:Cu,Cl is in the frequency dependence of brightness. While the ZnS electroluminescence intensity increases appreciably with frequency, the oxygen-dominated phosphors are characterized by an emission intensity which decreases slightly, if at all, with increase in frequency up to 6000 cps. Generally, no decrease was observed, but in a few cases, the emission decreased by about 10% with a frequency increase of 100 times.

Still another difference observed among the three light processes involved here is that the ZnS and ZnO phosphors have no measurable u.v. component in their field-induced emissions while the remaining Type II phosphors show a strong u.v. component. In all such cases at least 20% of the response of a 1P22 photomultiplier tube was due to the u.v. component of the emission, as determined by appropriate filters. A tabulated summary of the above observations is given in Table I.

Discussion

The observations for ZnS and ZnO are consistent with the familiar theories postulated for the impact ionization mechanism of electroluminescence in ZnS and with the contact injection mechanism of electroluminescence in ZnO. It is clear that the light-generating process involved with the other phosphor systems differs considerably from either of these two mechanisms. The observations that certain species in the gaseous ambient are necessary for field excitation allow for the following speculations as to the mechanism of the excitation process or processes:

1. Photoexcitation associated with a corona type discharge occurring in the nonuniform field of a powder specimen in a gas-powder layer, or at the vicinity of the electrodes where high field barrier regions can be developed by migration of conductive ionic species away from the electrodes. The time required for the development of such regions can explain the negative, but small, frequency-dependence of brightness observed. The presence of a short wavelength component in the emission spectrum supports this discharge-photoexcitation mechanism. However, the apparent absence of photoluminescence in some materials which nevertheless show a field emission (*i.e.*, Al_2O_3:Tb and Al_2O_3:Mn) constitutes evidence against this mechanism. The enhancement of the emission by traces of moisture can be related to the ease with which negative ions are formed by the presence of hydrogenous impurities such as H_2O, and the efficient production of H_3O^+ (9, 10).

Thus, the sequence of events here involves (*a*) an initial continuous conductive path between both electrodes due to conductive ionic species on the surface of the phosphor grains which are in contact with each other or with the electrodes, (*b*) the migration of the conductive species on the phosphor surfaces away from one of the electrodes due to ion-ion repulsion (the electrode at which this occurs depending on the ionic species involved), (c) the distribution of the field predominantly across this now "nonconductive" region leading to a gaseous dis-

Table I. Summary of observations

	EL type		
	ZnS	Type I ZnO	Type II
Emission in a-c field	Yes	Yes	Some
Emission in d-c field	No	Yes	Yes
Emission in air dielectric	Little	Yes	Yes
Emission in castor oil dielectric	Yes > air	Yes = air	No
Intensity of emission with reduced pressure	Persists	—	Fades
Enhancement with moisture	No	No	Yes
Requirement for conduction between electrodes	No	Yes	Yes
Polarity dependence	—	None	Some
Ultraviolet component in emission	None	None	Yes
Frequency dependence	Yes	Little, if any	Little, if any

charge, and finally (*d*) a photoexcitation of the phosphor by the energetic, short wavelength components resulting from the discharge.

The effect described here is clearly not the phenomena observed by Morosin and Haak (11), Herwelly (12), or Thorington (13). While the emissions observed by Morosin and Haak and Thorington may well be due to photoluminescence induced by the u.v. light emitted by electrical discharges, the mechanisms by which these come about and the materials investigated differ considerably from those reported here. Morosin and Haak explain the results of "contact" electroluminescence as due to the presence of large field inhomogeneities generated by the presence of high conductivity particles admixed with the phosphor or by the incorporation in the embedment medium of materials with high dielectric constants. Neither of these two procedures have resulted in field emission with the phosphors reported herein. As mentioned previously, no emission was observed using a liquid embedment. This is true even with the further addition of metallic filings or inorganic salts. Herwelly suggested the occurrence of electrical discharges originating within internal voids of individual phosphor grains from gases in the embedding medium. This does not explain our observations that the emissions occur at the electrode vicinities and not in localized areas throughout the bulk of the layers, or the absence of any emission in liquid embedments which have not been degassed. Herwelly, furthermore, observes no emission in steady d-c fields and observes emission only when the field is changing, *i.e.*, in a-c fields or on the application and removal of the d-c field. The experiments described by Thorington likewise are not the same as those described here. He has described materials which are not electroluminescent under the usual experimental conditions, but which are made responsive simply by placing them in a vacuum. He, however, does not attribute the excitation to a field-induced gas breakdown since it is observed at very low pressures. He furthermore only observed this vacuum enhancement with ZnS type phosphors. This is not in conflict with our observations with ZnS:Cu,Cl which we have used here to indicate how the Type II phosphors differ.

2. Ionoluminescent processes, incidental to or associated with a gaseous discharge, involving energy transfer to the phosphor crystallites by fast moving gaseous ions. Here, gaseous ionic species can result from a gaseous type discharge as in 1 above or by direct ionization of the gas molecules at the electrodes. Thus, cathodo- or anodoluminescent processes can result depending on the ionic species generated and/or the electrode involved. The molecular ion so formed is subsequently accelerated by the field. On recombination of the molecular ions at or near the surfaces of the phosphor grains, energy is transferred to the phosphor grains, resulting in emission.

Except for the somewhat inconclusive evidence mentioned in 1 above with respect to the nonphotoluminescent materials which nevertheless show a field emission, both processes can explain all the observations made. Further experimentation would be required to establish the correct one.

Acknowledgments

It is a pleasure to express thanks to Drs. L. Bodi, A. K. Levine, and N. Wotherspoon for many helpful discussions and suggestions.

Manuscript received Jan. 9, 1963; revised manuscript received Feb. 26, 1963. This paper was presented at the Pittsburgh Meeting, April 15-19, 1963.

Any discussion of this paper will appear in a Discussion Section to be published in the June 1964 JOURNAL.

REFERENCES

1. I. Adams, T. R. AuCoin, and J. W. Mellichamp, *J. Appl. Phys.*, **33,** 245 (1962).
2. I. Adams and J. W. Mellichamp, *J. Chem. Phys.*, **36,** 2456 (1962).
3. L. G. Van Uitert, R. R. Soden, and R. C. Linares, *ibid.*, **36,** 1793 (1962).
4. R. C. Linares, *J. Am. Ceram. Soc.*, **45,** 119 (1962).
5. L. G. Van Uitert and R. R. Soden, *J. Appl. Phys.*, **31,** 328 (1960).
6. L. G. Van Uitert and R. R. Soden, *J. Chem. Phys.*, **36,** 517 (1962).
7. L. G. Van Uitert and R. R. Soden, *ibid.*, **36,** 1289 (1962).
8. G. Destriau and H. F. Ivey, *Proc. IRE,* **43,** 1911 (1955).
9. P. F. Knewstubb and A. W. Tickner, *J. Chem. Phys.*, **36,** 674 (1962).
10. P. F. Knewstubb and A. W. Tickner, *ibid.*, **36,** 684 (1962).
11. B. Morosin and F. A. Haak, *This Journal,* **108,** 477 (1961).
12. A. Herwelly, *Acta Phys. Austriaca,* **5,** 30 (1951).
13. L. Thorington, Paper presented at Electrochem. Society Meeting Philadelphia, 1952 (Abstract 52).

Emission Spectra of (Zn,Cd)S Phosphors

W. Lehmann[1]

Research Department, Westinghouse Electric Corporation, Bloomfield, New Jersey

ABSTRACT

Single emission bands of ZnS-type phosphors are represented as Gaussian curves and critically examined. The width (at half maximum amplitude) of the emission bands of almost all ZnS and (Zn,Cd)S phosphors activated by Cu or Ag and containing various coactivators is 0.36 ev. The colors of single emission bands, and of superpositions of the two main bands in case of copper activation, are represented in color diagrams. A red shift of the green copper emission band of ZnS phosphors with increasing high concentrations of activator and coactivator, as reported by Froelich for ZnS:Cu, Al, has also been observed in (Zn,Cd)S phosphors and with many different coactivators.

Zinc sulfide type phosphors are well known to display many different emission spectra depending on the phosphor matrix, the impurities, the conditions of excitation, etc.[2] With the exceptions of edge emissions, which ordinarily can be observed only at very low temperatures, and of the complex line spectra due to incorporated rare earths, all spectra consist of structureless broad bands of various widths and peak positions. Even a single activator, *e.g.*, copper in ZnS, may cause several emission bands to appear simultaneously, often with considerable overlap, so that an analysis of such spectra is not simple. However, zinc sulfide-type phosphors emitting only, or primarily, in a single emission band can be prepared, and these spectra are more accessible to a quantitative study. The work presented here was originally undertaken in an attempt to obtain a simple yet fairly accurate mathematical expression of the shape of a single emission band, and to compute CIE color coordinates and luminosity factors corresponding to these bands. However, the results appear to be of interest beyond the original scope. The experiments were limited mainly to photoluminescence of blue emitting ZnS:Ag, of blue or green ZnS:Cu, and of the corresponding emission bands of (Zn,Cd)S phosphors with various CdS concentrations. Some additional results on other phosphors indicate that the observed pattern has a rather general validity.

Experimental Procedure

The phosphors prepared in this work were made in conventional ways, *i.e.*, by firing intimate mixtures of luminescent grade ZnS, CdS, and the desired impurities[3] at temperatures ranging from 600° to 1200°C. Care was taken to avoid any element which might interfere with the properties of the phosphors, *e.g.*, chlorine was added only as $ZnCl_2$ (not as NaCl, etc.) and copper only as CuS. About 10g of the dry raw mixes were placed in closely fitting capped silica tubes [described by Wachtel (1)] of about 12 cm^3 capacity. Small amounts of purified sulfur were added which, at a relatively low temperature, evaporated and drove all air out of the tubes. The relatively large free headroom over the phosphor provided a sufficiently constant atmosphere surrounding the phosphor during firing and contained mainly sulfur vapor, volatile compounds originating from the phosphor (*e.g.*, $ZnCl_2$) and, probably, some nitrogen from the protective atmosphere surrounding the capped tubes during firing. After firing and cooling, all phosphors were washed in appropriate solutions in order to remove separated second phases (*e.g.*, unreacted free sulfur, zinc halides, copper sulfides) as well as possible.

Zinc sulfide is known to occur in two different modifications, hexagonal (high-temperature form) and cubic (low-temperature form). In general, the spectra of cubic ZnS phosphors peak at somewhat lower energies than those of corresponding hexagonal phosphors (2-4). Hence, it is imperative to determine the lattice structure wherever there is doubt. The structure is immediately obvious in some cases. For instance, (Zn, Cd)S phosphors containing appreciable amounts of CdS crystallize only in the hexagonal form under all ordinary circumstances. The lattice structures of all other samples were determined by x-ray analysis. A phosphor was considered to be 100% cubic if the [200] reflection line (d = 2.705Å) appeared, but the lines [100] (d = 3.309Å) and [101] (d = 2.925Å) were missing, and *vice versa*. The limit of detectibility of a cubic portion in an otherwise hexagonal phosphor, and *vice versa*, was about 1%.

The phosphors were excited to photoluminescence by shining 365 mμ radiation onto thin layers spread with a little nonluminescent binder on glass. Thick layers were avoided in order to minimize the danger of reabsorption which, since selective, may falsify the shape of an emission spectrum. This could be observed to occur in several cases of thick layers. However, separate measurements of emission and absorption spectra of thin phosphor layers used in these experiments indicate only negligible reabsorption.

The emission spectra were recorded either with a General Electric Recording Spectro-Radiometer or with a Perkin-Elmer Spectrometer (Model 13U) calibrated with a standard tungsten ribbon lamp supplied by the U. S. Bureau of Standards. The re-

[1] Present address: Westinghouse Research Laboratories, Pittsburgh, Pennsylvania.

[2] No attempt shall be made here to cover the complete literature on this often investigated topic.

[3] All concentrations expressed in per cent of gram atom per mole of the ZnS, CdS, etc.

sults from both instruments were identical within narrow limits and are believed to be fairly accurate. The recorded spectra were normalized, point by point, and constitute the figures presented here. All measurements were done at room temperature.

Results

Single emission bands of ZnS-type phosphors are of asymmetrical shape if presented in the conventional way by plotting the energy derivative, $\epsilon = dE/d\lambda$, as a function of the wavelength, λ. Typical examples are shown in Fig. 1. The curves extend more toward the long-wave than toward the short-wave side and are the wider the more the peak position is shifted toward longer wavelength (by variation of the ZnS/CdS ratio, for instance). It seems to be little known that this asymmetry disappears and that all curves very approximately have Gaussian shapes of constant width independent of the ZnS/CdS ratio if ϵ is plotted not as a function of λ but of $1/\lambda$.[4] Hence

$$\epsilon = \epsilon_0 \exp [-(\nu - \nu_0)^2/c^2] \qquad [1]$$

where $\nu = 1/\lambda$, and c = constant. Amplitude and position of this curve are denoted by ϵ_0 and by $\nu_0 = 1/\lambda_0$, respectively. A critical proof of the fit of this equation to experimental data can be obtained by a method proposed by Patterson and Klick (11), *i.e.*, by plotting $(\ln \epsilon_0/\epsilon)^{1/2}$ as a function of ν so that each side of a Gaussian becomes a straight line. The

[4] Although this method of representation has no obvious physical significance, it appears to provide a closer fit to experimental data than other, physically more meaningful descriptions proposed by various other workers (4-10).

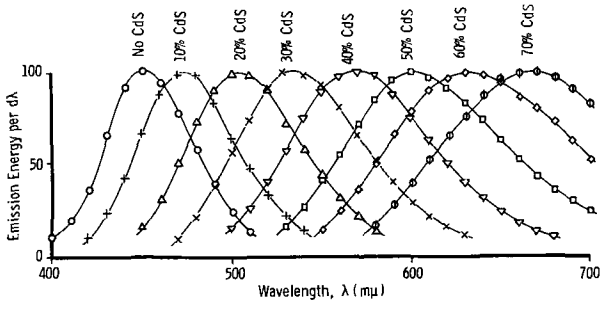

Fig. 1. Emission spectra of (Zn,Cd)S:Ag, Br phosphors excited by ultraviolet (365 mμ) at room temperature. The sample containing no CdS is cubic in structure; all others are hexagonal.

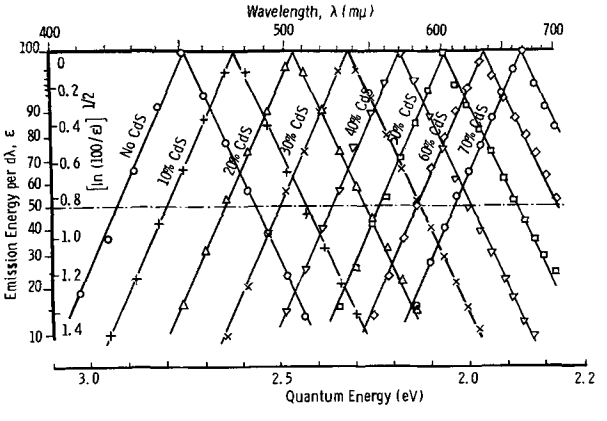

Fig. 2. Emission spectra of Fig. 1 redrawn as functions of $1/\lambda$. The ordinate scale is deformed so that each side of a normalized Gaussian becomes a straight line. The width of all bands is 0.36 ev.

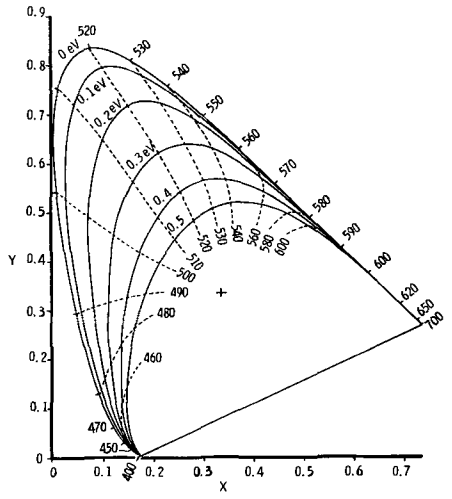

Fig. 3. CIE color coordinates of single emission bands as a function of width (in ev) and peak position (in mμ).

emission curves of Fig. 1 are replotted in this way in Fig. 2. The method requires that the spectra be essentially single bands. However, weak sub-bands, if present, can easily be detected in the tail of a main band. All curves in Fig. 2 have equal width which may be described by the distance between two points of the curve where $\epsilon = \epsilon_0/2$. This width is 0.36 ev independent of the CdS concentration.

The CIE color coordinates of single emission bands following Eq. [1] have been computed for different widths and different peak positions. The result is shown in Fig. 3. The color coordinates of single emission bands 0.36 ev wide, which are the rule in (Zn, Cd)S:Ag phosphors, are also described by the dashed curves in Fig. 6, 7, and 8; they agree with results reported by Crosnier and Curie (12). This dashed curve, in combination with the straight base line of the diagram, represents all possible colors which can be obtained with emission bands of 0.36 ev width. All colors must be either on the dashed curve (if one emission band) or within the area surrounded by it and the straight base line (if two or more emission bands are present, *e.g.*, in blends of several phosphors), but cannot be outside of it.

This relatively simple picture becomes much more complicated if silver is replaced by copper. Silver ordinarily creates only one emission band in these phosphors (*e.g.*, blue in ZnS) while copper produces two main bands (*e.g.*, blue and green in ZnS) depending mainly on the ratio of the copper to the coactivator.[5] The general behavior is shown in Fig. 4 for the case of ZnS:Cu, Cl. The blue copper emission band dominates at low chlorine/copper ratios. An increasing chlorine/copper ratio causes the blue band to disappear gradually in favor of the green band until the latter is practically isolated. Both bands are of constant peak positions within this range (samples A to F in Fig. 4).

If the concentrations of both copper and chlorine are increased to high values, the position of the green emission band is no longer constant but shifts to longer wavelengths (samples G to K in Fig. 4).

[5] The self-coactivated emission (yellow in ZnS:Ag and orange in ZnS:Cu) are not considered here.

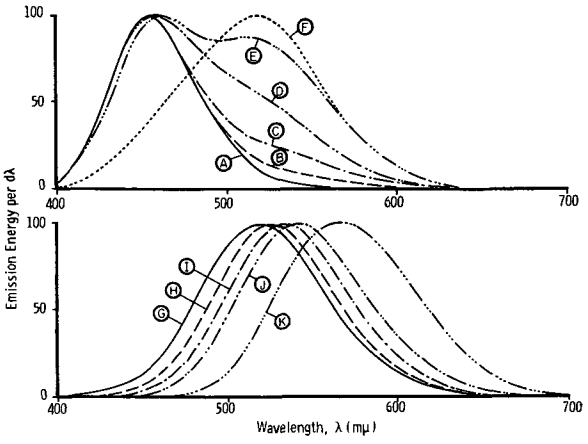

Fig. 4. Emission spectra of ZnS:Cu,Cl and ZnS:Cu,I excited by ultraviolet (365 mμ) at room temperature. (A) 0.5% Cu + 0.1% I, cubic; (B) 3% Cu + 0.03% Cl, cubic; (C) 0.3% Cu + 0.01% Cl, cubic; (D) 3% Cu + 0.1% Cl, cubic; (E) 0.1% Cu + 0.1% Cl, cubic; (F) 0.1% Cu + 1% Cl, mixed; (G) 0.3% Cu + 1% Cl, mixed; (H) 1% Cu + 1% Cl, cubic; (I) 3% Cu + 3% Cl, cubic; (J) 1% Cu + 10% Cl, cubic; (K) 3% Cu + 10% Cl, cubic. Concentrations given are those added before firing (950°C, 1 hr.)

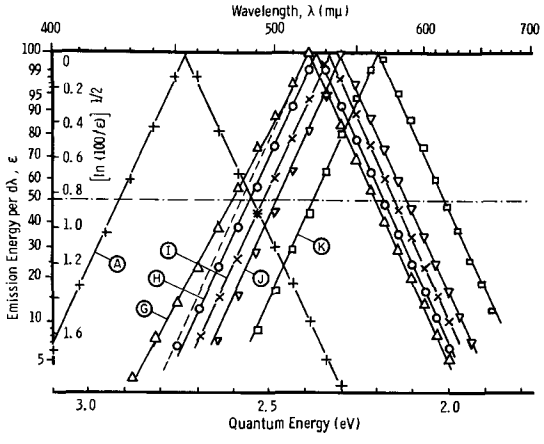

Fig. 5. The spectra (A) and (G) to (K) of Fig. 4 redrawn.

Figure 5 shows these spectra redrawn to demonstrate that they are still of Gaussian shape, if plotted as functions of $1/\lambda$, and that their widths remain constant (0.36 ev) over all this variation. The color locations of all spectra of Fig. 4 are given in Fig. 6.

A behavior completely similar to ZnS:Cu, Cl has been observed with ZnS:Cu, Br and with ZnS:Cu, Al phosphors [the latter in agreement with Froelich (13)]. Iodine behaves somewhat differently inasmuch as, possibly because of its larger ionic size, it apparently does not diffuse very easily into the ZnS lattice under usual conditions. However, green emitting ZnS:Cu, I phosphors can be prepared by firing in concentrated iodine atmosphere at low temperature, and the color shift of the green band toward yellow is qualitatively identical with that observed in ZnS:Cu, Cl. Gallium and indium coactivated ZnS:Cu phosphors again behave somewhat differently as they, even at comparatively low concentrations, tend to display an additional long-wave band (yellowish-green for Ga, orange for In) besides the regular copper emission (14-17).

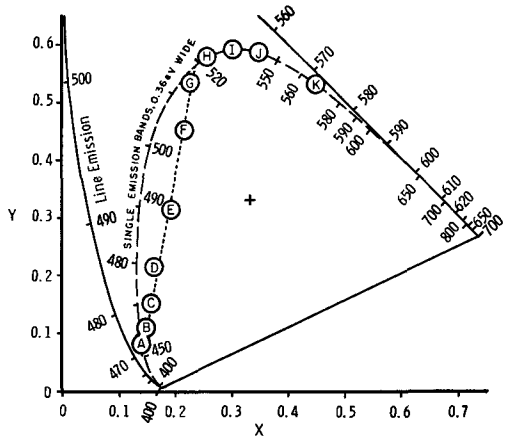

Fig. 6. CIE color coordinates of the emission of ZnS:Cu phosphors. The dashed curve indicates the colors of single emission bands, of 0.36 ev width, depending on their peak positions (in mμ). Possible emission colors of cubic ZnS:Cu, Cl phosphors extend along the dotted line from (A) to approximately (G) and from these along the dashed curve toward (K). The points (A) to (K) correspond to the spectra (A) to (K) in Fig. 4.

The emission spectra and colors of Fig. 4 to 6 refer only to zinc sulfide. Gradual replacement of the ZnS by CdS causes a shift of both emission bands, blue and green, toward longer wavelengths. This is expressed by a shift of both end points of the straight dotted line in Fig. 6 along the dashed curve towards the red. An example is shown in Fig. 7 for (Zn, Cd)S:Cu, Br containing 10 mole % CdS. As far as can be determined, the width of all these emission bands is 0.36 ev. Hence, since the shift of the peak positions of the emission bands with increasing CdS concentration is well known (examples are Fig. 1 and 2), one is able to compute the area in the CIE color diagram which, in principle, can be reached by a combination of the two main emission bands of copper activated (Zn, Cd)S phosphors, cubic or hexagonal, of any ZnS/CdS ratio, and with any intensity ratio of the two, 0.36 ev wide, emission bands. This area is shown in Fig. 8.

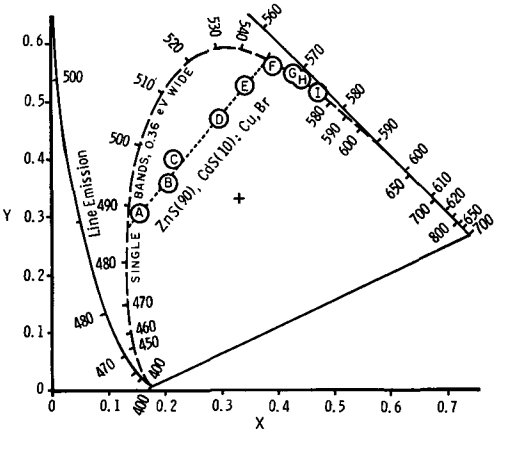

Fig. 7. CIE color coordinates of the emission of (Zn,Cd)S:Cu phosphors containing 10 mole % CdS. Excitation by ultraviolet (365 mμ) at room temperature. (A) 1% Cu + 0.1% I, cubic; (B) 1% Cu + 0.02% Br, cubic; (C) 1% Cu + 0.05% Br, cubic; (D) 1% Cu + 0.1% Br, cubic; (E) 1% Cu + 0.2% Br, cubic; (F) 1% Cu + 0.35% Br, cubic; (G) 1% Cu + 0.6% Br, mainly cubic; (H) 1% Cu + 0.9% Br, hexagonal; (I) 1% Cu + 1.5% Br, hexagonal. Concentrations given are those added before firing (720°C, 4 hr).

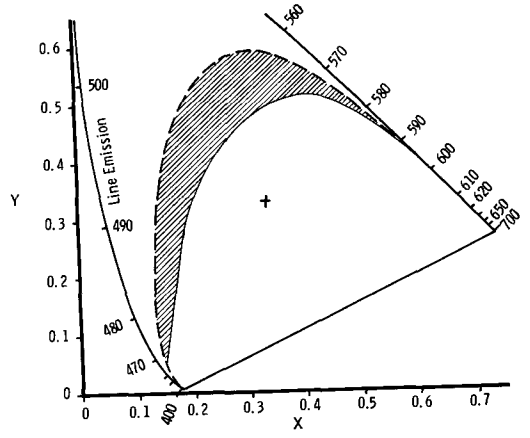

Fig. 8. CIE color diagram indicating the range of emission colors (shaded area) obtainable with single, copper-activated ZnS or (Zn,Cd)S phosphors emitting in one or both of the two main emission bands, each of 0.36 ev width.

So far, only very few deviations from the 0.36 ev width of Cu or Ag activated ZnS or (Zn, Cd)S phosphors have been observed. One such exception is shown in Fig. 9 for a set of (Zn, Cd)S:Cu, Ga phosphors containing 15 mole % of CdS.[6] The phosphors were prepared at 600°C in iodine vapor so that, besides gallium, some iodine is also certain to be present in all samples. The emission spectrum is independent of this presence of iodine in all samples except those of the very lowest gallium concentrations. The samples are cubic in structure up to about 0.1% gallium. The width of the emission bands, once again, is 0.36 ev within the range of the cubic structure, but only 0.32 ev for the predominantly or completely hexagonal phosphors (0.2% Ga and more).

Zinc selenide phosphors, on the other hand, emit in bands appreciably narrower than those observed in the sulfide phosphors. Examples of a ZnSe:Cu, Cl and a Zn(S, Se):Cu, Br phosphor containing 40 mole % ZnSe are given in Fig. 10 (curves E and F) where the widths are only 0.27 ev. A detailed in-

[6] Due to this CdS concentration, the "low-energy" emission band of gallium [yellow-green in ZnS:Cu,Ga (16, 17)] did not appear.

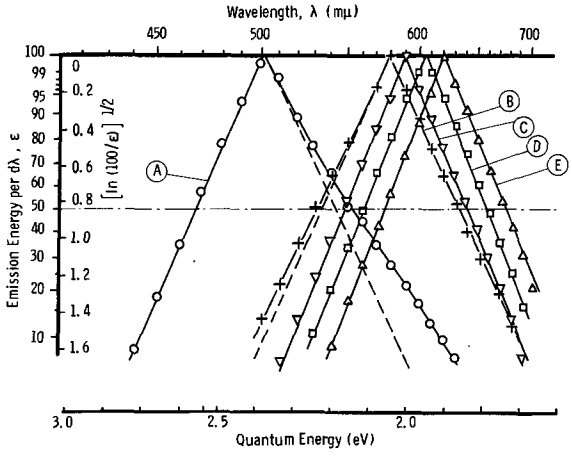

Fig. 9. Emission spectra of (Zn,Cd)S:Cu, Ga phosphors containing 15% CdS fired in iodine vapor at 600°C. (A) 1% Cu, no Ga, cubic, 0.36 ev; (B) 1.1% Cu + 0.1% Ga, cubic, 0.36 ev; (C) 1.2% Cu + 0.2% Ga, hexagonal, 0.32 ev; (D) 1.5 % Cu + 0.5% Ga, hexagonal, 0.32 ev; (E) 2.0% Cu + 1.0% Ga, hexagonal, 0.32 ev. Concentrations given are those added before firing.

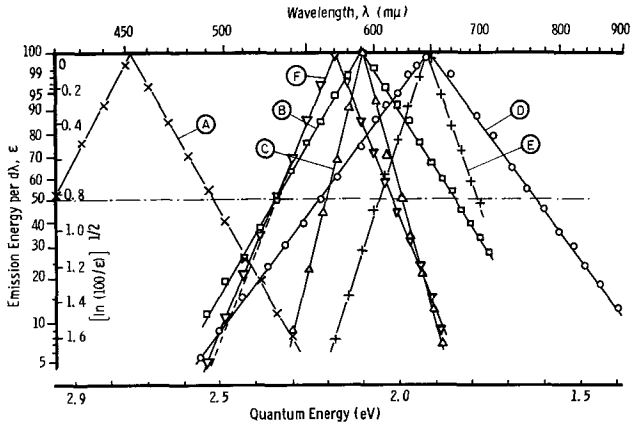

Fig. 10. Emission spectra of various ZnS type phosphors. Excitation by ultraviolet (365 mμ) at room temperature. (A) ZnS:Cl (self-activated), hexagonal, 0.44 ev; (B) ZnS:Li, hexagonal, 0.50 ev; (C) ZnS:Mn,Cu,Cl, cubic, 0.22 ev; (D) ZnS:Cu (self-coactivated), cubic, 0.60 ev; (E) ZnSe;Cu,Cl, cubic, 0.27 ev; (F) Zn(S,Se):Cu,Br (40% ZnSe), cubic, 0.27 ev.

vestigation of the emission spectra of the complete ZnS-ZnSe system, under similar precautions as described above for the ZnS-CdS system, is still missing, however. Also, the band widths of ZnS and (Zn, Cd)S phosphors due to other activators than Cu or Ag are different. Some examples are also given in Fig. 10.

Conclusions

The fact that single emission bands of ZnS type phosphors can be closely described by Gaussian curves if ϵ is plotted as a function of $1/\lambda$ probably is only an empirical approximation and has no obvious physical meaning. Hence, it does not directly contribute to new knowledge concerning the mechanism of emission in the phosphors. However, there are several other conclusions to be drawn from the results of this work.

1. The blue silver band and the blue and green copper emission bands of ZnS phosphors ordinarily are all 0.36 ev wide (width at half of peak intensity[7]). Replacement of more or less of the ZnS by CdS shifts the emission bands to longer wavelengths, but leaves the bandwidth unchanged at 0.36 ev. In contrast, even a partial replacement of the ZnS by ZnSe reduces the bandwidth to 0.27 ev. A qualitative understanding may be possible by the familiar model of copper or silver replacing zinc or cadmium in the lattice. The width of an emission band appears to be determined primarily by the activator and its nearest neighbors, *i.e.*, by sulfur or selenium, but little or not at all by the more distant zinc and cadmium atoms in the lattice.

2. At low concentrations of activator and coactivator, the emission of (Zn, Cd)S:Cu phosphors consists mainly of the two well-known bands corresponding to the blue and green bands of ZnS:Cu, Cl. Within this concentration range, the emission bands have fixed positions and their intensity ratio

[7] The fact should be emphasized that the width of an emission band depends little or not at all on the way the band is presented, *i.e.*, whether energies or quanta, wavelengths or wave numbers are the units of calibration in the diagram. An example may be found by comparing curve D of Fig. 10 with Fig. 4 of ref. (8). Both curves are presented in different ways, but apparently were obtained on phosphors displaying the same emission band. The two widths are 0.60 and 0.62 ev, respectively.

depends on the particular phosphor, the temperature, and the wavelength and intensity of the exciting ultraviolet. An increase of both activator and coactivator up to high concentrations first causes the short-wave band to disappear in favor of the long-wave band, and then the long-wave band to shift, as a whole, to still longer wavelengths. This shift was first described by Froelich for the case of ZnS:Cu, Al (13), but is now observed to occur also in ZnS:Cu, Cl,|ZnS:Cu, Br,|ZnS:Cu, I, and in corresponding (Zn, Cd)S phosphors. The latter phosphors also display a similar shift of the long-wave band (corresponding to the green Cu emission band in ZnS) with gallium and indium as coactivators. In all cases, the shape of the emission bands stays strongly Gaussian if ϵ is plotted as a function of $1/\lambda$, and the width in almost all cases, regardless of the amount of the shift, remains at 0.36 ev; only in a few rare cases so far has it been observed to be only 0.32 ev. Froelich tentatively assumed the shift to be simulated by a close superposition of a least three sub-bands of fixed positions but varying intensities. If this were the case, the sub-bands would have to be narrower than 0.36 ev (or even 0.32 ev), and one would expect a deviation from the Gaussian shape at least in some cases. The former may be possible although it is unlikely, since even the emission bands at low activator concentrations are 0.36 ev wide, and the latter could not be observed. Hence, the shift probably is not simulated by a superposition of narrow sub-bands, but is a real shift of a single band as a whole.

3. Care has to be taken in the determination of the peak positions of Cu-activated ZnS type phosphors. The blue emission of ZnS:Cu may contain a weak green band, or *vice versa*, which easily remains unnoticed but has an influence on the apparent peak position of the emission. Additionally, the green band may shift toward yellow, especially if one attempts to suppress the blue band completely. A sure means to determine the peak positions of the two main emission bands in the range of low activator concentrations appears to be the CIE color diagram where the positions are rigorously determined by the end points of a straight line through the color coordinates of the phosphors under consideration.

Acknowledgments

The writer wishes to thank Dr. C. K. Lui Wei for x-ray analysis, Mr. I. Meister for the determination of many emission spectra. Mr. D. Morgan for computing color coordinates, and Drs. H. F. Ivey and W. A. Thornton for reading and suggesting improvements in the original manuscript.

Manuscript received Dec. 21, 1962. This paper was presented at the Pittsburgh Meeting, April 15-18, 1963.

Any discussion of this paper will appear in a Discussion Section to be published in the June 1964 JOURNAL.

REFERENCES

1. A. Wachtel, *This Journal*, **107**, 602 (1960).
2. H. W. Leverenz, "Luminescence of Solids," John Wiley & Sons, Inc., New York (1950).
3. F. A. Kröger and J. E. Hellingman, *J. (and Trans.) Electrochem. Soc.*, **93**, 156 (1948).
4. M. H. Payen de la Garanderie, *J. phys. rad.*, **22**, 423 (1961).
5. S. T. Henderson, P. W. Ranby, and M. B. Halstead, in "Solid State Physics in Electronics and Telecommunications," M. Desirant and A. L. Michiels, Editors, Vol. 4, Part 2, p. 714, Academic Press, New York (1960).
6. S. T. Henderson, *Proc. Roy. Soc.*, **A173**, 323 (1939).
7. C. C. Vlam, Dissertation, Univ. of Groningen, 1953; *Brit. J. Appl. Phys.*, **5**, 443 (1954).
8. M. H. Aven and R. M. Potter, *This Journal*, **105**, 134 (1958).
9. F. E. Williams and M. H. Hebb, *Phys. Rev.*, **84**, 1181 (1951).
10. D. L. Dexter, *ibid.*, **96**, 615 (1954).
11. D. A. Paterson and C. C. Klick, *ibid.*, **105**, 401 (1957).
12. A. Crosnier and G. Curie, Internat. Conf. on Luminescence, New York University, New York (1961).
13. H. C. Froelich, *This Journal*, **100**, 496 (1953).
14. E. F. Apple, *ibid.*, **105**, 251 (1958).
15. E. F. Apple and F. E. Williams, *ibid.*, **106**, 224 (1959).
16. W. van Gool, A. P. Cleiren, and H. J. M. Heijligers, *Philips Res. Repts.*, **15**, 254 (1960).
17. F. A. Kröger and J. A. M. Dickhoff, *Physica*, **16**, 296 (1950).

Electroluminescent (Zn,Cd)S:Cu Phosphors

W. Lehmann[1]

Research Department, Westinghouse Electric Corporation, Bloomfield, New Jersey

ABSTRACT

Preparation conditions for ordinary electroluminescent ZnS:Cu phosphors are applied to (Zn,Cd)S:Cu. Modifications of the conditions permit extension of the range in which the lattice remains cubic in structure up to 15 mole % CdS, thus extending the range of obtainable emission colors from the blue and green of the ZnS:Cu into the yellow and orange. The electroluminescence of hexagonal (Zn,Cd)S:Cu phosphors, at higher CdS concentrations, can be considerably improved by a sulfurizing treatment at low temperatures. This extends the useful range of emission colors into the red and near-infrared. The observed dependence of the intensity of electroluminescence on the CdS concentration indicates a strong influence of deep electron traps, little or no influence of the depth of shallow electron traps, and little or no influence of the separation in energy of the activator centers from the conduction band.

Electroluminescent zinc sulfide and selenide phosphors activated by copper are well known. In striking contrast, zinc-cadmium sulfide phosphors containing more than a few per cent of CdS have been found to be only poorly, if at all, electroluminescent (1-4) despite the fact that they may be well photo- and cathodoluminescent. Two reasons for this behavior were observed. One is the appearance of a black Cd-Cu sulfide of somewhat undefined composition which precipitates out of (Zn,Cd)S:Cu,Cl phosphors as a separate phase and so disturbs the composition and the electrical properties of the remaining phosphor (2, 3). Later it was observed that (for still unknown reason) this peculiar sulfide does not appear, or does so to a much lesser degree, if chlorine is replaced by either bromine or iodine. Hence, it can relatively easily be avoided.

The other reason for the poor electroluminescence of (Zn,Cd)S:Cu phosphors containing more than a few per cent of CdS was explained by their tendency to crystallize only in the hexagonal modification (wurtzite). Microscopic observations indicated that the particles of such hexagonal phosphors were much more perfect in structure than the particles of cubic, and well electroluminescent, zinc sulfides and selenides (4). They ordinarily do not seem to contain many structural faults (stacking disorders, voids, Cu_2S segregations, etc.) which are believed to be a prerequisite for good electroluminescence (2, 4-11). This indicates two possible ways to improve the electroluminescence of (Zn,Cd)S:Cu phosphors of higher CdS concentrations. First, the preparation conditions may be modified to extend the range in which the phosphors are still cubic in structure to higher than the usual (roughly 5-10%) CdS concentrations. Second, means may be found to enhance the poor electroluminescence of hexagonal (Zn,Cd)S:Cu phosphors, *e.g.*, by artificially creating lattice faults. Both ways were investigated, have yielded the expected results, and will be reported separately here.

[1] Present address: Westinghouse Research Laboratories, Pittsburgh, Pennsylvania.

Methods of Preparation and Testing

The phosphors were prepared in essentially the same manner as that described by Wachtel (2) for the case of ZnS phosphors. Unfired zinc and cadmium sulfide (luminescent grade, low chlorine content) were dry ball milled in the desired ratio. The impurities Cu (as the acetate), Ga (as the nitrate), In (as the nitrate), and the halogens (as the zinc halides) were added in aqueous solutions, and the resulting slurry dried. Sulfur and iodine (wherever used) were added as the solid elements; they do not require special care regarding uniform distribution because of their high volatilities at elevated temperatures. The phosphors were fired in small capped silica tubes, usually surrounded by nitrogen. The amounts of phosphor (about 10g each) were measured so that they had some "headroom" in the capped tubes during firing. After completion of the firing schedule, which in many cases involved several steps, all phosphors were washed in a cyanide solution in order to remove excess copper sulfide from the particle surfaces, gently milled to break up agglomerates, washed in water, in alcohol, and dried.

The time-average of the emission intensity of electroluminescence was tested in an oil cell described elsewhere (12). The excitation conditions (*e.g.*, cell spacing, applied voltage) were kept under close control so that the emission intensities from sample to sample could be compared with an accuracy of about $\pm 10\%$. Designation of the emission intensity in terms of visible brightness has little physical meaning if, as is the case here, the emission colors may vary over a wide range and, in some cases, even extend into the infrared. Hence, the emission intensities were measured with a photoconducting PbS cell in close proximity to the phosphor. PbS is very approximately a quantum counter (13) so that the results can be considered to be fair indications of the emission intensities in terms of quanta per unit cell area and unit time. All measurements were made at room temperature.

The emission colors of electroluminescence were evaluated by comparison with the colors of photoluminescence of a set of (Zn,Cd)S:Ag phosphors whose single emission bands were separately determined (14) and denoted by their peak positions. As an example, the emission color of electroluminescence of 570 mμ means a color which closely approaches that of a single emission band of a (Zn,Cd)S:Ag phosphor peaking at 570 mμ. This method of color characterization is fairly accurate (except in the deep blue and the deep red) in all cases where the test sample emits only, or predominantly, in one band, but it is only an approximation if the test phosphor emits in two bands of comparable intensities. Fortunately, the latter was the exception rather than the rule in all phosphors tested in this work.

The lattice structures of the phosphors were determined by x-ray analysis by comparing the intensities of the reflection lines [100] or [101], which appear only in the hexagonal modification, with that of the [200] line which appears only in the cubic structure. The limit of detectibility for a cubic portion in an otherwise hexagonal lattice, and *vice versa*, was about 1%.

Cubic (Zn,Cd)S:Cu Phosphors

The transition temperature between the low-temperature cubic and the high-temperature hexagonal modification of pure ZnS has been reported to be about 1020°C (15), but it may be changed considerably by the presence of impurities such as copper, chlorine, oxygen, etc. (16-18). Quantitative data for zinc-cadmium sulfides are apparently not available in the literature, but one may reasonably expect a decreasing transition temperature with increasing cadmium concentration. This is confirmed by experimental results shown at the top of Fig. 1. The curves denoted by solid lines in Fig. 1 refer to phosphors which, for reasons to be described later, were fired in a rather unusual atmosphere, namely iodine. No other coactivator was added in these cases. The dashed curves refer to (Zn,Cd)S:Cu,Br phosphors containing 10% CdS, 1% Cu, and 0.3% Br[1] (added before firing) which were more conventionally fired, namely in sulfur vapor plus some nitrogen from the protecting atmosphere surrounding the capped silica tubes.

Bromine and iodine (chlorine is excluded for reasons mentioned earlier) have two different effects on ZnS and (Zn,Cd)S phosphors. They provide the coactivator necessary to dissolve enough copper activator in the lattice, and they serve as "flux" in the mechanism of the particle growth during firing, probably involving the reaction

$$(Zn,Cd)S + X_2 \rightleftarrows (Zn,Cd)X_2 + \frac{1}{2}S_2 \qquad [1]$$

where X stands for either Br or I. This defines a minimum firing temperature required to obtain particles of roughly 10μ mean size which, by experience, are necessary for good electroluminescence. On the other hand, the firing temperature should also be as low as possible in order to be able to use high CdS concentrations and yet to keep the lattice cubic. Figure 1 shows that iodine is superior to bromine in this respect, it permits firing temperatures as low as 600°-650°C and, hence, incorporation of about 15% CdS while the bromine-coactivated phosphors fired in sulfur + nitrogen require about 750°C to develop comparable particle sizes and, therefore, permit only about 10% CdS. Unfortunately, iodine tends to develop the short-wave emission band almost alone (16) which, even with 15% CdS, is only blue-green (comparable to the blue-green of ordinary ZnS:Cu,Cl). Hence, bromine probably represents the best combination of coactivation and particle growth promotion in one substance.

The electroluminescence emission intensity (time average) of a set of (Zn,Cd)S:Cu, (1%), Br (0.3%) as a function of the CdS concentration is shown in Fig. 2. These phosphors were fired 2 hr at 720°C. They were surrounded by sulfur vapor (due to the added free sulfur) at the beginning but more or less

[1] All concentrations in this report are expressed on a molar basis.

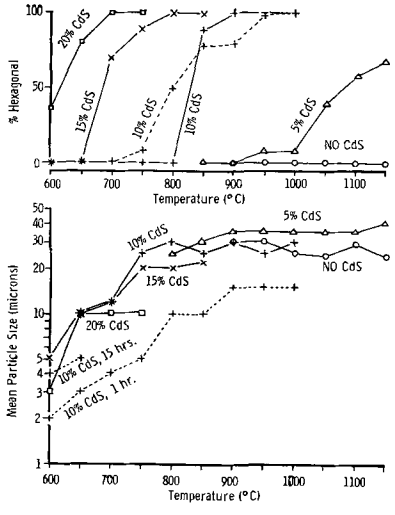

Fig. 1. Top, Estimated percentage of hexagonal crystal structure; bottom, mean particle sizes of (Zn,Cd)S:Cu (1%). Solid lines, fired 1 hr in iodine vapor, no other coactivator; dotted lines, 0.3% bromine added, fired 1 hr in sulfur plus nitrogen.

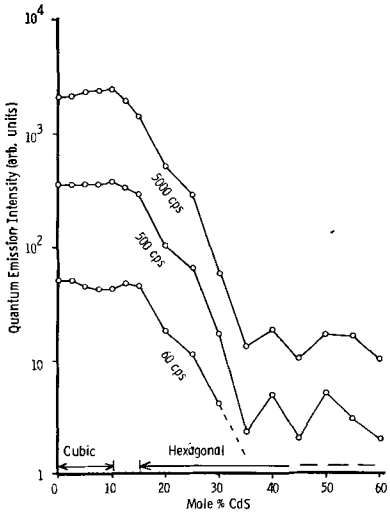

Fig. 2. Emission intensities of electroluminescence of (Zn,Cd)S:Cu (1%), Br (0.3%) phosphors as a function of the CdS concentration. The phosphors were fired 2 hr at 720°C in sulfur + nitrogen atmosphere.

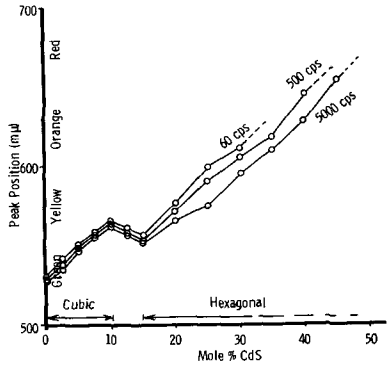

Fig. 3. Emission colors (in terms of apparent peak positions) of electroluminescence of the phosphors of Fig. 2 and 10.

by nitrogen (diffused from the protecting atmosphere into the tubes during firing) at the end of the firing time. The result is an almost constant emission intensity from zero to roughly 10% CdS and a sharp drop beyond, in qualitative agreement with previously published results (2, 4). The emission spectra of all samples consist predominantly of the long-wave band (corresponding to the green band of ZnS:Cu,Cl) so that their emission colors can well be described by their apparent peak positions. The result is shown in Fig. 3. The emission shifts at a rate of about 3.6 mμ/% CdS toward red within the cubic and within the hexagonal structure ranges, with a transition range in between characterized by an inverse color shift.

A variation of the bromine concentration added to cubic (Zn,Cd)S:Cu,Br phosphors containing 10% CdS reveals qualitatively the same interactions between the two emission bands as observed in case of cubic ZnS:Cu,Cl or ZnS:Cu,Br phosphors. Low bromine concentration develops almost only the short-wave band (peak at 485 mμ). Increasing bromine concentration first causes the long-wave band (peak at 550 mμ) to increase until it dominates, and then a shift of it to still longer wavelengths (14). In agreement with observations on ZnS:Cu,Cl and ZnS:Cu,Br phosphors, the emission intensity stays roughly constant as long as both emission bands appear simultaneously, but drops sharply at higher concentrations of bromine where the long-wave emission band begins to shift toward the red end of the spectrum. From this, the upper permissible limit of the concentration of bromine (added before firing in sulfur + nitrogen, as described above) of about 0.35% was derived. The corresponding phosphor emits almost entirely in the long-wave band depending somewhat on the frequency of excitation (Fig. 4). This is a greenish-yellow color corresponding closely to the maximum of the human eye sensitivity so that this phosphor appears to be about 20-30% brighter than a common, bluish-green emitting, ZnS:Cu,Cl phosphor of the same quantum yield.

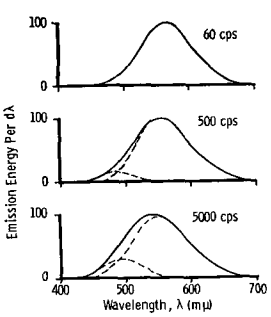

Fig. 4. Normalized emission spectra of electroluminescence of cubic ZnS (90%), CdS (10%): Cu (1%), Br(0.35%) at three different frequencies of excitation. The dashed resolutions into long-wave and short-wave bands are estimated.

A new way to prepare cubic (Zn,Cd)S:Cu phosphors of higher than 10% CdS concentrations and of yellow to orange emission colors opens up if the phosphors are fired in concentrated iodine vapor at the required low temperatures, and if an additional coactivator, such as Cl, Br, Al, Ga, or In, is used besides iodine. Various tests revealed the usefulness especially of gallium. In this combination, iodine acts mainly as particle growth promoter at the required low firing temperature but has little or no influence on the emission color, while gallium develops the desired long-wave emission band but has little or no influence on particle growth. The firing schedule to prepare such phosphor consists of several steps:

(*a*) Prefiring an intimate mixture of ZnS, CdS, Cu, and Ga (*i.e.*, no iodine) in an inert or sulfurizing atmosphere (*e.g.*, N_2, H_2S, or S_2 + N_2) at about 1000°C. This prefiring has the purpose of introducing the Cu and the Ga into the (Zn,Cd)S lattice and thus to improve the reproducibility of the next step. The phosphor resulting from this first step has very small and poorly developed particles, is completely hexagonal in structure, and may well be photoluminescent but is not electroluminescent.

(*b*) Firing the prefired material in closed containers in static iodine atmosphere for several hours at 600°C. It is sufficient for this procedure to add a few iodine crystals to the phosphor in the capped silica tubes and to surround the latter by a static protecting atmosphere. The iodine crystals evaporate rapidly and this creates a static iodine atmosphere surrounding the phosphor inside the silica tube during firing. This firing step develops the final phosphor particles. They grow completely cubic in structure even if the original material was hexagonal.

(c) Baking in a flow of an inert gas (*e.g.*, N_2), also at 600°C, to remove excess of iodine [probably present as (Zn,Cd)I_2] which otherwise would cause an extremely poor maintenance of electroluminescence of this phosphor.

Experimental results on a phosphor series containing 1% Cu and 0.1% Ga, prepared in this way, are given in Fig. 5 and 6. Gallium creates relatively deep traps in ZnS phosphors which become shallower in (Zn,Cd)S phosphors with increasing CdS concentrations (19). This is probably the reason for the poor performance of the ZnS:Cu,Ga but also for the rapid improvement if more and more of the ZnS is replaced by CdS. At low-frequency excitation (60 cps), the quantum yield of the sample con-

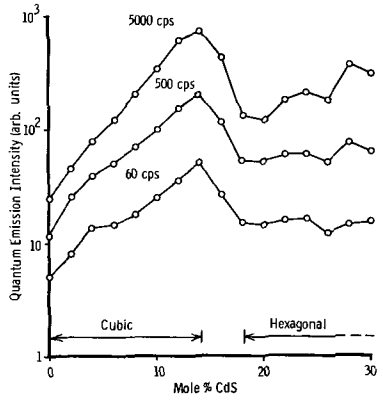

Fig. 5. Emission intensities of electroluminescence of (Zn,Cd)S:Cu (1%), Ga (0.1%) as a function of the CdS concentration. The phosphors were first fired at 1000°C in sulfur, then at 600°C in iodine, and finally at 600°C in nitrogen.

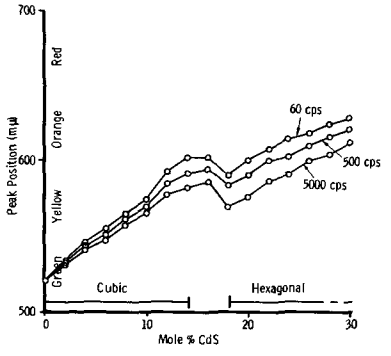

Fig. 6. Emission colors (in terms of apparent peak position) of electroluminescence of the phosphors of Fig. 5 and 11.

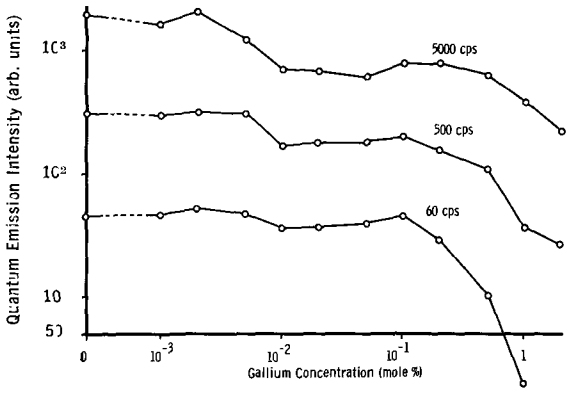

Fig. 7. Emission intensities of electroluminescence of cubic ZnS (85%), CdS (15%): Cu, Ga phosphors as a function of the added gallium concentration. The added concentration of copper was 1% in all samples. Firing procedure as in Fig. 5.

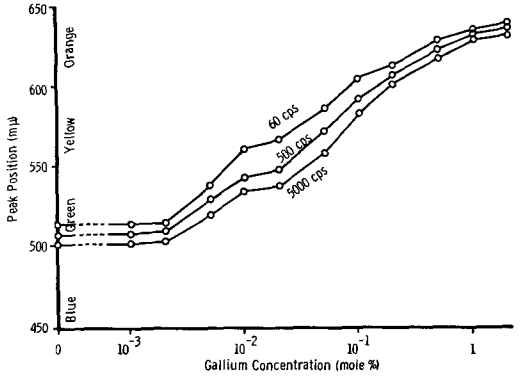

Fig. 8. Emission colors (in terms of apparent peak positions) of electroluminescence of the phosphors of Fig. 7.

taining 14% CdS (Fig. 5) is equal to that of a good green emitting ZnS:Cu,Cl phosphor, but its emission color is orange-yellow (resembling that of a cubic ZnS:Mn,Cu,Cl phosphor).

The influence of variation of gallium concentration on the electroluminescence of cubic (Zn,Cd)S:Cu,Ga containing 15% CdS and fired in iodine vapor at 600°C, as described above, is shown in Fig. 7 and 8. The quantum yield of electroluminescence is relatively little dependent on the gallium concentration from zero up to about 0.1% (Fig. 7). A study of the emission spectra (not shown here) reveals the same behavior of the two main emission bands as observed for chlorine and bromine coactivated ZnS:Cu and (Zn,Cd)S:Cu phosphors. Little or no gallium causes almost only the short-wave emission band (peak at 500 mμ) to develop. Increasing gallium concentration first causes the long-wave band (peak at 560 mμ) gradually to increase until it dominates, and then a shift of it to still longer wavelengths. This corresponds to a change of the emission colors, shown in Fig. 8, from bluish-green (no Ga) over orange-yellow (0.1% Ga) to orange-red (1% Ga).

Hexagonal (Zn,Cd)S:Cu Phosphors

Attempts were made to improve the ordinarily poor electroluminescence of hexagonal (Zn,Cd)S:Cu phosphors by gently ball milling, followed by annealing at various elevated temperatures. The procedure was based on the idea of creating more faults in the otherwise too perfect particles, and diffusing copper sulfide from the particle surfaces into the faults. All these experiments failed, however. The damage (Druckzerstörung) to the luminescence abilities of the phosphor due to mechanical treatment apparently dominates any improvement.

Another method became available with the discovery that iodine-coactivated hexagonal (Zn,Cd)S:Cu phosphors were much better electroluminescent than similar phosphors coactivated with either chlorine or bromine, and that the electroluminescence of all hexagonal (Zn,Cd)S:Cu phosphors, regardless of the original coactivator, could be considerably improved by baking in pure iodine vapor.[3] The procedure is simple. The prefired phosphors, and a small amount of elemental iodine, were placed in capped silica tubes which, in turn, were placed in a long silica firing tube which also contained some iodine crystals. The iodine, evaporating at elevated temperature, drives all other gases out of the tubes so that the phosphors were surrounded by a static iodine atmosphere during the bake. After baking and rapid cooling, the phosphors were washed in a cold cyanide solution in order to remove all excess of copper sulfide.

Iodine seems to have at least three different effects on electroluminescent (Zn,Cd)S:Cu phosphors

[3] This part of the work was supported by the Aeronautical Sytems Division, Air Force Systems Command, U.S. Air Force, Wright-Patterson Air Force Base, Ohio, under contract AF 33(616)-7350.

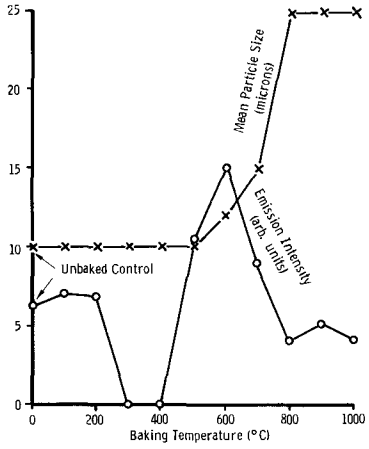

Fig. 9. Emission intensity of electroluminescence of hexagonal ZnS (70%), CdS (30%): Cu (0.5%), I (0.1%) as a function of iodine bake temperature. The phosphors were prefired in sulfur at 650°C, then baked in concentrated iodine vapor at the indicated temperatures.

depending on the bake temperature. They are demonstrated on Fig. 9.

(*A*) At low temperatures (*i.e.*, from room temperature to about 200°C), iodine reacts with the excess of black copper sulfide present in all electroluminescent sulfide phosphors after firing and converts it to colorless copper iodide

$$Cu_2S + I_2 \rightarrow 2CuI + S \qquad [2]$$

The photo- and electroluminescence of these phosphors (after the cyanide wash) are affected very little.

(*B*) At about 300°-400°C, the copper iodide seems to diffuse into the phosphor particles and so to enhance considerably the concentration of activator-coactivator pairs. As a consequence, these phosphors are not electroluminescent any more, and their photoluminescence is strongly shifted toward longer wavelengths (*e.g.*, from green to yellow), typical of phosphors to which very high activator and coactivator concentrations are added intentionally (14, 20). The existence of this harmful temperature range requires that all phosphors baked above this range be cooled very quickly in order to be in the harmful temperature range as short a time as possible.

(*C*) At about 500°C, iodine begins to attack the (Zn,Cd)S lattice

$$(Zn,Cd)S + I_2 \rightleftarrows (Zn,Cd)I_2 + \frac{1}{2}S_2 \qquad [3]$$

Copper iodide, present in the lattice as activator-coactivator pairs, diffuses out and reacts again with the free sulfur thus created to form black copper sulfide

$$2CuI + \frac{1}{2}S_2 \rightarrow Cu_2S + I_2 \qquad [4]$$

As a consequence, the body color of the phosphor turns dark, the color of the photoluminescence shifts back to where it was originally (*e.g.*, from yellow to green), and the phosphor again is electroluminescent and may now be many times better than before the iodine treatment. A bake temperature of

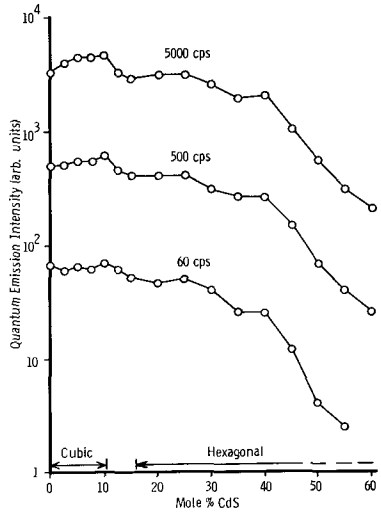

Fig. 10. Emission intensities of electroluminescence of (Zn,Cd)S: Cu (1%), Br (0.3%) as a function of the CdS concentration. The phosphors are identical to those of Fig. 2 except for an additional bake in iodine vapor at 550°C.

500°-600°C gives best results. This is also the temperature where the first indications of particle growth can be observed. Still higher temperatures cause too large particles and, probably for this reason, again a decrease of electroluminescence.

The intensity of electroluminescence of a series of (Zn,Cd)S:Cu,Br phosphors, fired in sulfur + nitrogen atmosphere at 720°C, then baked in iodine vapor at 550°C (30 min) and, finally cyanide washed as usual, is shown in Fig. 10 as a function of the CdS concentration. Comparison with Fig. 2, which shows the same on a similar phosphor without iodine bake, demonstrates the relatively small improvement in the cubic range but the tremendous enhancement in the hexagonal range of structure.

Figure 11 shows the dependence of electroluminescence on the CdS concentration of (Zn,Cd)S:Cu,Ga phosphors prepared identically to the series shown in Fig. 5 except that the bake in an inert gas at

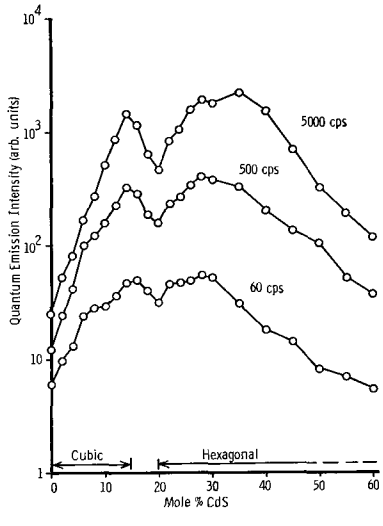

Fig. 11. Emission intensities of electroluminescence of (Zn,Cd)S: Cu (1%), Ga (0.1%) as a function of the CdS concentration. The phosphors were first fired at 1000°C in sulfur, then at 600°C in iodine, and, finally, at 550°C in iodine (*i.e.*, no firing in nitrogen, as in Fig. 5).

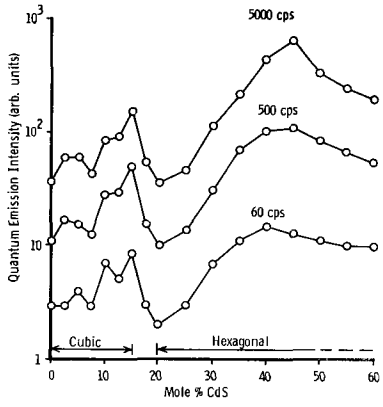

Fig. 12. Emission intensities of electroluminescence of (Zn,Cd)S: Cu (1%), In (0.1%) as a function of the CdS concentration. Firing procedure as in Fig. 11.

600°C is replaced by a bake in iodine at 550°C. Here again, there is little or no effect in the cubic range, but a considerable improvement in the hexagonal range so that, besides the "cubic" peak at about 15% CdS, another, and even higher, "hexagonal" peak appears at about 30% CdS. The behavior of a similar phosphor series where the gallium is replaced by indium is shown in Fig. 12. They are, in general, inferior to the corresponding gallium-coactivated phosphors except at CdS concentrations of about 50% and higher where even indium traps become sufficiently shallow.

An iodine bake at 550°C has little or no effect on the emission color of electroluminescence. Thus, the dependence of the emission color on the CdS concentration of the bromine-coactivated phosphors of Fig. 10 agrees closely with that of the nonbaked series of Fig. 3. Similarly, the colors of the iodine baked gallium-coactivated phosphors of Fig. 11 are also described by Fig. 8. An interesting example of color variation is shown in Fig. 13 for the case of (Zn,Cd)S:Cu,In. The samples containing little or no CdS emit strongly in the orange band characteristic of indium (21-23). This orange band predominates more at low than at high frequency of excitation so that these phosphors have a color shift with frequency which is just the opposite of that which occurs with ordinary phosphors, *e.g.*, with ZnS:Cu, Cu. The indium emission band disappears at about 10% CdS so that all samples from this toward higher CdS concentrations display an ordinary color shift.

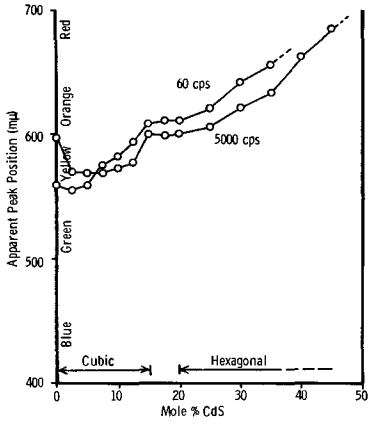

Fig. 13. Emission colors (in terms of apparent peak positions) of electroluminescence of the phosphors of Fig. 12.

It should be mentioned here that the iodine bake procedure, which so much improves the intensity of electroluminescence of hexagonal (Zn,Cd)S:Cu phosphors, also causes the phosphors to have a relatively poor maintenance. The effect is assumed to be due to an excess of iodine [perhaps as $(Zn,Cd)I_2$] remaining in the phosphor. It can be driven out easily by gentle heating in an inert atmosphere. That is the reason for the bake in nitrogen used in the case of cubic phosphor where it has little or no effect on the intensity of electroluminescence but considerably improves its maintenance. In hexagonal phosphors, however, any bake in an inert atmosphere at elevated temperatures also reduces the intensity of electroluminescence and, finally, brings it back to that before the iodine bake.

A way out of this situation was found with the discovery that a bake in sulfur may also considerably improve the intensity of electroluminescence of hexagonal (Zn,Cd)S:Cu phosphors, and that these phosphors (in contrast to corresponding iodine-baked samples) also show excellent maintenance. Some instability at elevated temperature remains, however. The sulfur bake is effective only if the phosphor is in direct contact with sulfur during all the time it is hot. Subsequent heating of the phosphor in an inert atmosphere (*e.g.*, in N_2) to a temperature exceeding the boiling point of sulfur (445°C) again reduces the intensity of electroluminescence to that before sulfur baking.

The dependence of the intensity of electroluminescence on the temperature of the sulfur bake is shown in Fig. 14 for a series of orange-yellow emitting hexagonal (Zn,Cd)S:Cu,Br phosphors containing 30% CdS. The phosphors were fired in sulfur at 800°C (2 hr) and then baked in sulfur (30 min) at the indicated temperatures. In the low-temperature range (up to 400°C), the phosphors were mechanically admixed with about 10-20% (by

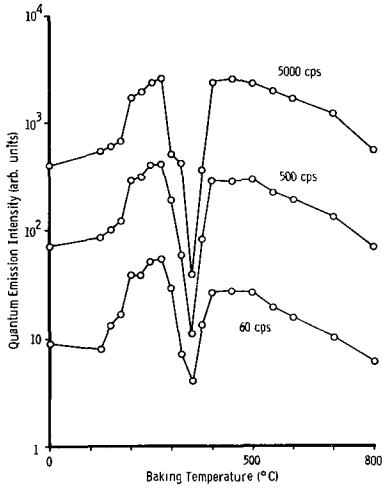

Fig. 14. Emission intensities of electroluminescence of hexagonal ZnS (70%), CdS (30%): Cu (1%), Br (0.3%) as a function of sulfur bake temperature. The phosphors were fired in sulfur at 800°C (2 hr) and then baked (30 min) in sulfur at the indicated temperatures.

weight) of elemental sulfur and then baked in open boats in nitrogen. Sulfur is only a liquid at these low temperatures and completely "soaks" the phosphor during the bake. In the high-temperature range (450°C and higher), the phosphors were baked in capped silica tubes containing, and surrounded by, an atmosphere of pure sulfur vapor (*i.e.*, no N_2). After the bake, as usual, all samples were washed in an aqueous solution of NaCN + NaOH which quickly dissolves all excess of Cu_2S and all remaining free sulfur. The very pronounced minimum of electroluminescence at a bake temperature of about 350°C (Fig. 14) corresponds to a "shift" of the emission color toward red (similar to the case of iodine bake at the same temperature, see Fig. 9). Its nature is not completely understood at present.

Conclusions

Good electroluminescent (Zn,Cd)S:Cu phosphors of cubic structure, containing up to 15 mole % CdS, can be prepared by a sufficient reduction of the firing temperature. The obtainable emission colors extend into the orange-yellow. Except for the different spectral emission distribution these cubic phosphors behave identically in all respects to ordinary electroluminescent ZnS:Cu phosphors.

The electroluminescence of hexagonal (Zn,Cd)S:Cu phosphors can be enhanced to the level of a corresponding cubic phosphor by a bake in a sulfurizing atmosphere. This may be provided either directly by sulfur or by a concentrated iodine atmosphere. The roughly identical dependences of electroluminescent intensity on the bake temperature in sulfur and in iodine indicate similar actions of both. Probably, the free sulfur is provided by the iodine bake according to reaction [3]. The reason why sulfurization enhances the electroluminescence of hexagonal, but not or to a much lesser degree of cubic, phosphors is unknown. Careful x-ray analysis indicated no noticeable change whatsoever of the lattice structure of hexagonal phosphors baked in sulfur at low temperature, nor would one expect a change at these low temperatures. Yet, the bake considerably enhanced the intensity of electroluminescence. A microscopic examination revealed the electroluminescence of hexagonal (Zn,Cd)S:Cu phosphors to be concentrated in tiny spots or lines inside the particles, just the same as observed in cubic ZnS:Cu phosphors (24, 25). The sizes and the intensities of these spots are the same for an unbaked and a baked hexagonal phosphor; the latter only contains many more emitting spots than the former. Hence, if this electroluminescence is due to some kind of lattice faults (which is likely because of the existence of emitting "spots"), the sulfurizing bake either creates new faults or causes previously inactive faults to become active. The complete lack of any change in the x-ray pattern due to low-temperature sulfur bake indicates the latter possibility to be the most probable, but more conclusions can hardly be drawn at present.

Since the enhancement effect of a sulfurizing bake on the electroluminescence of hexagonal (Zn,Cd)S:Cu phosphors is not understood, and at present is still relatively little investigated, no conclusions as to the mechanism of electroluminescence in these phosphors can be drawn from the experimentally observed dependences. However, the phosphors of the cubic range resemble so much in all points ordinary, and well investigated, cubic ZnS:Cu phosphors that three important conclusions can fairly safely be drawn.

(*A*) Deep electron traps clearly reduce the intensity of electroluminescence. This has been proposed already in a number of theories (26-30), and qualitatively it is immediately visible by a comparison between Fig. 10, 11, and 12 (corresponding to phosphors containing Br, Ga, and In, respectively). As long as the deep traps are dominant (*i.e.*, as long as they are not exhausted during one half of a cycle of the applied frequency of excitation), their influence on the intensity of electroluminescence, L, can reasonably be expected to be described by

$$L = A \exp(-BE) \qquad [5]$$

where A and B are constants and E is the trap depth. A first-order approximation between decreasing trap depth with increasing CdS concentration, [CdS], is a linear one, *i.e.*,

$$E = E_{ZnS} - C[CdS] \qquad [6]$$

where C is a constant and where E_{ZnS} is the trap depth in ZnS. This gives

$$L = A \exp(-BE_{ZnS}) \exp(BC[CdS]) \qquad [7]$$

which is the exponential increase of L with CdS concentration observed in the cubic range of Fig. 5 and 11.

(*B*) The intensity of electroluminescence is independent of the depth of shallow electron traps in the phosphor. This is demonstrated by those parts of the curves of Fig. 2 and 11 which correspond to the cubic range of structure. Bromine (in contrast to gallium and indium) causes relatively shallow traps in these phosphors. A decrease of the trap depth with increasing CdS concentration at a rate of 0.017 ev/% CdS has been reported (17). This corresponds to bromine traps in the samples containing 10% CdS which are about 0.17 ev shallower than corresponding traps in the samples containing no CdS. Yet this variation of the depth of electron traps has little or no effect on the intensity of electroluminescence. This absence of an effect can be understood fairly easily, although qualitatively, by complete exhaustion of the shallow bromine traps within the time of a half cycle of the applied frequency. Once the traps are shallow enough that they are substantially all emptied during a half cycle, then a further reduction of the trap depth does not affect the number of electrons which become available for recombination.

(*C*) The intensity of electroluminescence seems to be little dependent on the separation in energy of the activator centers from the conduction band. This is expressed by those parts of the curves of Fig. 2 and 11 which correspond to the cubic range of structure. Unfortunately, this range is rather narrow. A reasonable estimate of what could be ex-

pected in case of, *e.g.*, collision excitation from a reduced excitation energy due to a replacement of 10% of ZnS by CdS yields an increase of the emission intensity of roughly 25% (high applied voltage) to 100% (low voltage) under otherwise unchanged conditions. Such variation of the emission intensity with the CdS concentration is not discernible in Fig. 2 and 11, nor does it occur with the same phosphor series at lower excitation voltages (not shown in Fig. 2 and 11).[4] Nevertheless, the writer hesitates to draw the conclusion that the energy separation activator-conduction band really is unimportant in the excitation mechanism of the Destriau effect. If this would be the case, any model in which this energy separation is critically involved would have to be abandoned. Whether or not the one or the other kind of the proposed injection mechanisms (25, 31) is in better agreement with the experimental behavior is still open to question. Further experimental work will have to decide.

Acknowledgments

The writer wishes to thank Dr. C. K. Lui Wei for x-ray analysis of many phosphor samples, and Drs. W. A. Thornton and H. F. Ivey for helpful discussions and for reading and suggesting improvements in the original manuscript.

Manuscript received Dec. 21, 1962. This paper was presented before the Pittsburgh Meeting, April 15-18, 1963.

Any discussion of this paper will appear in a Discussion Section to be published in the June 1964 JOURNAL.

REFERENCES

1. P. Zalm, *Philips Research Repts.*, **11**, 11 (1956).
2. A. Wachtel, *This Journal*, **107**, 602 (1960).
3. A. B. Dreeben, Extended Abstract No. 70, Electrochem. Society Meeting. Chicago, May 1960.
4. W. Lehmann, *This Journal*, **108**, 607 (1961).
5. G. Diemer, *Philips Research Repts.*, **10**, 194 (1955).
6. E. E. Loebner and H. Freund, *Phys. Rev.*, **98**, 1545 (1955).
7. W. Lehmann, *This Journal*, **104**, 45 (1957).
8. A. Lempicki, D. R. Frankl, and V. A. Brophy, *Phys. Rev.*, **107**, 1238 (1957).
9. M. A. Short, E. G. Steward, and T. B. Tomlinson, *Nature*, **177**, 240 (1956).
10. A. Kremheller, *This Journal*, **107**, 8 (1960).
11. L. W. Strock, *Illum. Eng.*, **55**, 24 (1960).
12. W. Lehmann, *This Journal*, **103**, 24 (1956).
13. T. S. Moss, *Proc. IRE*, **43**, 1869 (1955).
14. W. Lehmann, *This Journal*, **110**, 754 (1963).
15. E. T. Allen and J. L. Crenshaw, *Z. anorg. Chem.*, **79**, 130 (1913).
16. S. Larach and E. Shrader, *RCA Rev.*, **20**, 532 (1959).
17. M. Aven and J. A. Parodi, *J. Phys. Chem. Solids*, **13**, 56 (1960).
18. J. W. Nickerson, P. Goldberg, and D. H. Baird, Extended Abstract No. 30, Electrochem. Society Meeting, Indianapolis, May 1961.
19. W. H. Hoogenstraaten, *Philips Research Repts.*, **13**, 515 (1958).
20. H. C. Froelich, *This Journal*, **100**, 496 (1953).
21. E. F. Apple, *ibid.*, **105**, 251 (1958).
22. E. F. Apple and F. E. Williams, *ibid.*, **106**, 224 (1959).
23. W. van Gool, A. P. Cleiren, and H. J. M. Heijligers, *Philips Research Repts.*, **15**, 254 (1960).
24. W. Lehmann, *This Journal*, **107**, 657 (1960).
25. A. G. Fischer, *ibid.*, **109**, 1043 (1962).
26. P. Zalm, *Philips Research Repts.*, **11**, 417 (1956).
27. W. Lehmann, *J. Opt. Soc. Am.*, **48**, 647 (1958).
28. D. Curie, *J. Phys. Radium*, **13**, 317 (1952); **14**, 135, 510, 672 (1953).
29. W. A. Thornton, M.I.T. Physical Electronics Conf., Cambridge, Mass., March 1961.
30. C. H. Haake, *J. Opt. Soc. Am.*, **47**, 881 (1957).
31. W. A. Thornton, *This Journal*, **108**, 636 (1961).

[4] Similar independences of the emission intensity on the energy separation from the activator to the conduction band are to be observed between the blue and the green copper emission band of ZnS:Cu,Cl and within the series of Zn(S,Se):Cu,Cl phosphors of varying ZnSe concentrations, for instance.

New Ternary Semiconducting Compounds, $Cd_4(P,As)_2(Cl,Br,I)_3$

Lawrence Suchow and Norman R. Stemple

International Business Machines Corporation, Thomas J. Watson Research Center, Yorktown Heights, New York

ABSTRACT

Five new ternary semiconducting compounds have been synthesized: $Cd_4P_2Cl_3$, $Cd_4P_2Br_3$, $Cd_4P_2I_3$, $Cd_4As_2Br_3$, and $Cd_4As_2I_3$. These compounds are all cubic (space group Pa3) and isomorphous with each other. Their lattice constants vary with sizes of the component atoms. The structure appears to be based on a nearly face-centered cubic arrangement of cadmium atoms in a pseudocell having half the edge of the true primitive cell. All the new compounds are deeply colored. Estimates of their energy band gaps have been made from optical and electrical measurements.

In a further effort to synthesize semiconducting compounds with an antichalcopyrite structure,[1] attempts were made to prepare Cd_2YX, where Y is P or As, and X is Cl, Br, or I. Such compounds were not found, nor were compounds with zincblende structure corresponding to Zn_3PI_3 and Zn_3AsI_3, which were found in related work with zinc compounds (1). However, five new ternary semiconducting compounds were found which are outside the pseudobinary Cd_3Y_2-CdX_2 cut through the ternary system.

[1] For a fuller discussion, see ref. (1).

Preparation and X-Ray Crystallography

Because of the viewpoint from which this work was initiated, preparations were first made by re-

Table I. Chemical analysis of $Cd_4P_2Br_3$ crystals

%	Found	Calculated for $Cd_4P_2Br_3$
Cd	60.0	59.85
P	8.24	8.25
Br	31.8	31.91

action of either Cd_3P_2 or Cd_3As_2 with $CdCl_2$, $CdBr_2$, or CdI_2. The Cd_3P_2 and Cd_3As_2 for use as starting materials were synthesized by reaction of stoichiometric quantities of extremely pure powders of the constituent elements in evacuated sealed quartz tubes. The powder mixtures were brought up to temperature gradually and kept at the maximum for several hours; the maximum for Cd_3P_2 was 750°C and for Cd_3As_2 700°C. These temperatures were determined empirically, with x-ray diffraction used to analyze the products. The cadmium halides used were the best laboratory grades commercially available.

When equimolar quantities of Cd_3As_2 or Cd_3P_2 and cadmium dihalide were heated together in evacuated sealed quartz tubes at about 500°-550°C, new compounds formed, but, as it will now be shown, they were not pure at this composition. Taking the Cd_3P_2-$CdBr_2$ system as an example, it was found that single crystals forming from the vapor phase in cooler portions of the tube had an x-ray diffraction powder pattern like that of the bulk of the product in powder form, but was free of several additional lines in the pattern of the powder. These additional lines proved to be due to cadmium, and changes in intensity of some lines common to the new compound and Cd_3P_2 indicated that there was probably also excess Cd_3P_2 present in the powder. Chemical analysis of the single crystals (see Table I) indicated that the composition was not Cd_2PBr, but rather $Cd_4P_2Br_3$. This compound is therefore not along a pseudobinary cut Cd_3P_2-$CdBr_2$ in the ternary phase diagram. Figure 1 illustrates the positions in the ternary diagram of the new compound and of hypothetical compounds along the pseudobinary cut, including one with a formula corresponding to that

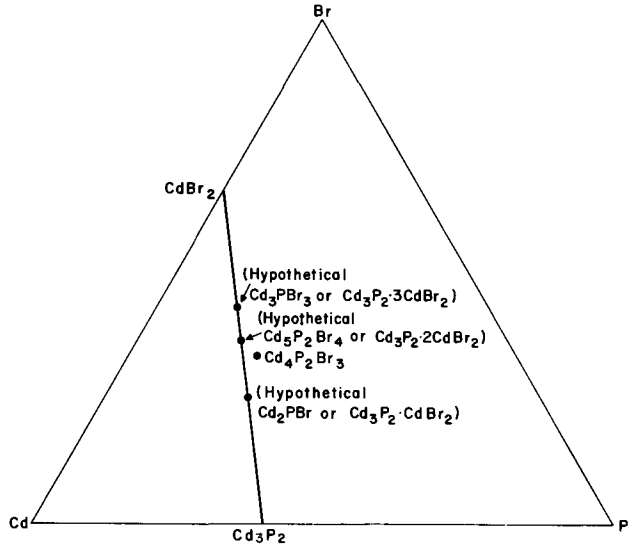

Fig. 1. Location of $Cd_4P_2Br_3$ in the ternary system Cd-P-Br

Table II. Lattice constants of the new compounds

All are cubic, with space group Pa3.

Compound	Lattice constant, A
$Cd_4P_2Cl_3$	12.15_6
$Cd_4P_2Br_3$	12.33_2
$Cd_4P_2I_3$	12.73_6
$Cd_4As_2Br_3$	12.64_0
$Cd_4As_2I_3$	13.02_0

of an antichalcopyrite phase and one corresponding to the disordered defect zincblende structure compounds Zn_3PI_3 and Zn_3AsI_3 (1). None of these hypothetical compounds was found to form.

Following establishment by chemical analysis of the true formula of the compound, synthesis was effected using stoichiometric quantities. That is, the reaction carried out was

$$5Cd_3P_2 + 9CdBr_2 + 2P \rightarrow 6Cd_4P_2Br_3$$

With single crystals of this compound in a Weissenberg x-ray diffraction camera it was determined that the structure was cubic with space group Pa3, and the lattice constant was obtained.

It was then found possible also to synthesize in similar fashion the corresponding compounds $Cd_4P_2Cl_3$, $Cd_4P_2I_3$, $Cd_4As_2Br_3$, and $Cd_4As_2I_3$. The formulae of these compounds were established by the finding that all were isomorphous with $Cd_4P_2Br_3$. This was done by indexing the x-ray diffraction powder pattern of $Cd_4P_2Br_3$ on the basis of information obtained from the single crystal and then indexing the powder patterns of the four other new compounds by comparison. The lattice constants of the five new compounds are given in Table II. The qualitative relationship between anionic size and lattice constant is quite apparent. A reaction intended to yield $Cd_4As_2Cl_3$ appeared to produce a new compound, but it was not isomorphous with the others in the group, and no effort has been made to establish its true composition. Its physical properties are considerably different from those of the other compounds. The failure of this compound to form isostructurally with the others is probably due to the large difference in ionic radii of Cl^- and As^{3-}. This difference is greater than for any other pair in the group and is therefore probably beyond the tolerance for this structure type. Compounds along the pseudobinary cuts Cd_3Y_2-CdX_2 were sought in all the systems studied, but as in the Cd_3P_2-$CdBr_2$ system, none was found to form.

Inspection of the x-ray diffraction powder pattern of $Cd_4P_2Cl_3$ revealed a group of strong lines within the indexed pattern which correspond to a face-centered cubic cell with a cell edge half that of the larger primitive cell. Since the strongest scatterers in this compound are the cadmium atoms, it appears likely that the large primitive cell is composed of eight pseudocells with cadmium atoms in or near face-centered cubic positions in the smaller cells. When heavier atoms are substituted for phosphorus and chlorine, the strong subpattern due to the pseudocell weakens and finally does not stand out at all from the total pattern. Thus, it is weaker

but plainly visible in $Cd_4P_2Br_3$ and only slightly evident in $Cd_4As_2Br_3$. In $Cd_4As_2I_3$ it is nearly gone, and in $Cd_4P_2I_3$ it is not at all evident. However, these compounds are all still isomorphous. There are, therefore, 32 cadmium atoms in the true unit cell. It is likely that the 16 phosphorus and 24 chlorine atoms can then be placed in or near allowable positions of the 32 octahedral holes and the 64 tetrahedral holes formed by the cadmium sublattice in such a way that the larger cell will be primitive. The average phosphorus valence of −2.5, a value not known to have been reported heretofore, indicates that there is more than one type of phosphorus present. All of these observations are consistent with the space group; further work is required to determine the complete structure.

The density of $Cd_4P_2Br_3$ has been measured by displacement of distilled water by a powder sample in a 2-ml specific gravity bottle. The determined value of 5.29 g/ml corresponds to 7.95 formula weights of $Cd_4P_2Br_3$ per unit cell. This compares extremely well with the value of 8 which is indicated by the x-ray evidence described above. (Another way of stating this is that the measured density is 5.29 and the x-ray density is 5.32.) Such close agreement is good confirmation of the unusual chemical formulae of the new compounds.

Single crystals of some of the compounds have been grown in evacuated sealed quartz tubes 3 in. in length; these were kept in thermal gradients in a tube furnace for several days in such a way that the reactants were confined to the hot end at 550°C, while the empty cool end was at about 528°C. Crystals thus grown from the vapor phase at the cool end have been either chunky ones up to about 2 mm in size or needles up to about 4-5 mm long. Because larger crystals were not obtained, measurements reported below were made on powders.

The new compounds appear to melt incongruently below 600°C. $Cd_4P_2Br_3$ is not attacked by either water or benzene at room temperature, and this is probably true of all the compounds.

Electrical and Optical Properties

Electrical and optical measurements were made on powders. As shown in Table III, all the compounds were deeply colored because the absorption edges fall in the visible portion of the spectrum. It was noted qualitatively that the colors shift to considerably longer wavelengths on heating. The absorption edges were determined with a Beckman DU Spectrophotometer with diffuse reflectance attachment. Results are given in Fig. 2. The optical band gaps were derived from these curves by choosing as the absorption edge the mid-point of the region in which reflectance is changing most rapidly.

Table III. Electrical and optical properties of the new compounds

Compound	Color at 24°C	Absorption edge, Å, at 24°C	Optical band gap, ev, at 24°C	Electrical band gap, ev
$Cd_4P_2Cl_3$	Orange	5725	2.17	2.24
$Cd_4P_2Br_3$	Orange	5650	2.19	1.80
$Cd_4P_2I_3$	Orange	5725	2.17	1.76
$Cd_4As_2Br_3$	Dark red	6950	1.78	1.88
$Cd_4As_2I_3$	Red	6550	1.89	2.30

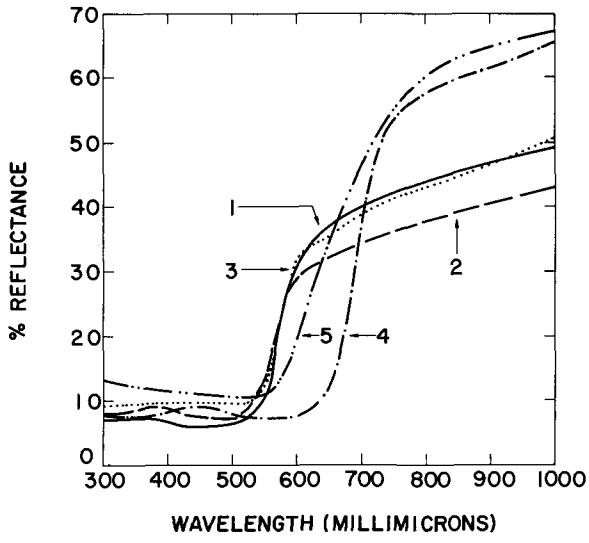

Fig. 2. Diffuse reflectance spectra of the new compounds: curve 1, $Cd_4P_2Cl_3$; 2, $Cd_4P_2Br_3$; 3, $Cd_4P_2I_3$; 4, $Cd_4As_2Br_3$; 5, $Cd_4As_2I_3$.

Electrical conductivity was measured on ¼ in. diameter cylindrical pellets formed by pressing powder at 40,000 lb/in². Silver paste electrodes were applied to the two flat surfaces of the pellet which was then placed between ½ in. diameter disks of platinum foil. This assembly was next placed between plates in a gold-plated brass cell. Pressure contact was maintained by means of a metal spring and an adjustable screw forcing the plates together. Insulation between electrodes was achieved with high resistance ceramic and with quartz. The cell was fitted so that dry nitrogen

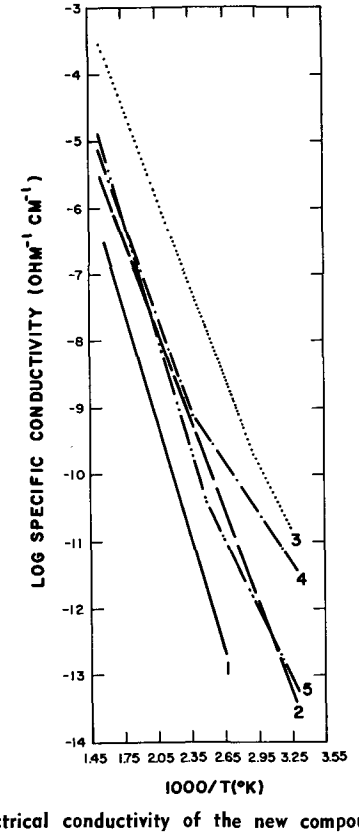

Fig. 3. Electrical conductivity of the new compounds: curve 1, $Cd_4P_2Cl_3$; 2, $Cd_4P_2Br_3$; 3, $Cd_4P_2I_3$; 4, $Cd_4As_2Br_3$; 5, $Cd_4As_2I_3$.

could be led through it while measurements were being made. The entire cell was then placed in a tube furnace whose temperature could be varied as required, and d-c conductivity was measured from about 24° to 350°C and then back down again, using a Keithley Electrometer, Model 610A, as an ohmmeter. In no case was reversal of polarity found to cause any change in conductivity. A plot of log specific conductivity *vs.* reciprocal temperature for the five new compounds is given in Fig. 3. Since measurements at very low conductivity levels are relatively inaccurate, the slopes (or the absence of change of slope) at lower temperatures may not be meaningful. However, the upper parts of the plots are reproducible on temperature cycling and with different samples and are therefore considered significant. These upper portions are taken to represent intrinsic conductivity so that the energy band gaps are derived by doubling the activation energies determined from the slopes. The band gaps found in this way are listed in Table III. It will be seen that some of the determined values are very close to the optical values while others are off by about 20%. Dember effect measurements (2) at room temperature have shown all the new compounds to be n-type conductors. The possibility of some ionic conductivity superimposed upon the electronic conductivity is not thus ruled out, but this has not been studied.

Acknowledgments

This study has been carried out with the able assistance of Mr. John J. Minchak. Chemical analyses were performed by Mr. Bert L. Olson.

Manuscript received Feb. 15, 1963. This paper was presented at the Pittsburgh Meeting, April 15-18, 1963.

Any discussion of this paper will appear in a Discussion Section to be published in the June 1964 JOURNAL.

REFERENCES

1. L. Suchow, M. B. Witzen, and N. R. Stemple, *Inorg. Chem.*, in press.
2. These measurements were made by F. F. Morehead and W. Hammer using the technique described in the paper by F. F. Morehead and A. B. Fowler, *This Journal*, **109**, 688 (1962).

Conductivity and Thermoelectric Potential Measurements on Perylene:Metal Halide Complexes

Martin S. Frant[1] and Roger Eiss

AMP Incorporated, Harrisburg, Pennsylvania

ABSTRACT

The conductivities and Seebeck coefficients of a series of perylene complexes with metal halides from groups IIB, IIIA, IVA, VA, VB, VIB, VIIA, and VIII of the periodic table have been studied to determine possible dependence of these properties on the nature of the halide. No direct correlation was found between conductivity and position on the periodic table. The complexes having a conductivity of $>10^{-5}$ mho/cm ($InCl_3$, PCl_3, $FeCl_3$, ICl, $SbCl_5$, I_2) were black in color; none of the others were black. Activation energies were measured for materials having a conductivity $>10^{-11}$ mho/cm and were 0.60 ev or lower. There was an approximate straight line relationship between the log conductivity and the activation energy, indicating that conductivity for the series is determined primarily by the number of thermally activated carriers rather than by the reservoir of available carriers in lower energy states. As a rule the most conductive materials had the lowest Seebeck coefficients. It was found that perylene:$FeCl_3$ could be prepared as either p- or n-type depending on the initial reactant ratio, with the perylene-rich material showing p-type properties.

The unexpectedly high electrical conductivity shown by the complexes formed by the reaction of polycyclic hydrocarbons with halogens was first reported in 1956 by Akamatu (1). The properties of one of the most interesting members of this group, perylene:iodine, were reported by Labes (2), Kommandeur (3), and Uchida and Akamatu (4) who found that the electrical conductivity of the molecular complex was at least 10-12 orders of magnitude higher than the constituent compounds. This behavior has also been shown by the complex of perylene with antimony pentachloride (5).

In order to gain some understanding of the generality of this behavior, and to determine whether there is an obvious relationship between the semiconductive behavior of the complex and the chemical or physical properties of the constituents, we have prepared a large number of complexes with perylene as the standard donor. The acceptors are all metallic halides, almost all are chlorides, and eight different groups in the periodic table are represented. Of those reported below only the iodine, ferric chloride, stannic chloride, and antimony pentachloride complexes have ever been isolated from the solution, and most have not been previously reported. The complexes prepared in this investigation were isolated as dry, crystalline precipitates. It was felt that by working with a family of closely

[1] Present address: Prototech Incorporated, Cambridge, Massachusetts.

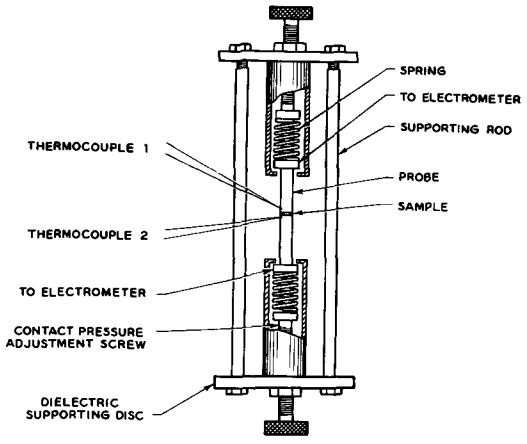

Fig. 1. Sample holder for electrical conductivity measurements. The assembly shown is placed in a heavy water-jacketed copper cannister equipped to maintain a positive dry argon pressure and with Teflon seals for the electrical leads.

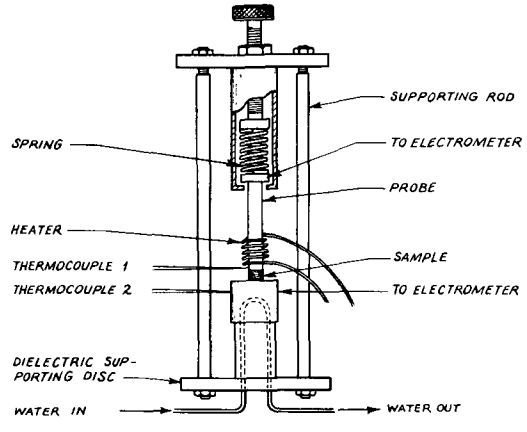

Fig. 2. Sample holder for thermoelectric potential measurements. The assembly is placed in a similar copper jacket to that described in Fig. 1.

related complexes, all prepared under similar conditions and measured under identical circumstances, relationships would be found which might otherwise remain obscure.

Experimental

Apparatus.—A sample support for conductivity measurements was constructed as shown in Fig. 1 and electrically shielded by a heavy copper cylinder. The sample, a pressed pellet, was placed between two gold plated copper probes. About 500-700g contact pressure was maintained by adjustable springs exerting force on each probe. In the case of thermoelectric potential measurements a modified holder, shown in Fig. 2, was used. The lower probe was much larger, and water was pumped through it at constant temperature to provide an infinite heat sink. A coil of resistance heating wire was wound around the upper probe (but not in contact with the probe) to heat the upper portion of the sample preferentially.

The temperature at the upper and lower faces of the sample was measured by iron-constantan thermocouples to the probes. The thermocouple potentials were measured and recorded using a Sanborn Model 150 amplifier and Model 152 recorder. In order to evaluate the accuracy of the temperature measurements, a run was made after attaching an additional thermocouple directly to each of the electrodes. This run was limited to a comparison of temperatures indicated by the electrically insulated thermocouples with those indicated by the thermocouples in direct thermal contact with the probes, and demonstrated that thermal conduction through the electrical insulation was sufficient to permit temperature readings accurate within $\pm 0.1°C$. A Keithley Electrometer Model 610A was used to measure the sample resistance or the potential across the sample. Over-all temperature of the system was controlled by a constant temperature water bath; complete electrical shielding of the supports and of all leads to the supports was found to be essential for acceptable results.

Materials.—Perylene was prepared in a number of small batches using the method of Hansgirg and Zinke (6), which uses β-naphthol as the starting material. This route was selected in order to reduce contamination by higher polycyclic hydrocarbons, but suffered from the drawback that it could not be scaled up to give yields per run in excess of 5-10g. The metal halides, where commercially available, were analytical reagent grade. The complexes were synthesized by adding an excess of the metal halide dissolved in an appropriate solvent (such as benzene, alcohol, or ether) to a hot solution of perylene in benzene. The only exception was in the preparation of p-type perylene:ferric chloride, when a 1.3:1 excess of perylene was used. Dried solvents were employed throughout, and in some instances the entire preparation was made under specially dried nitrogen.

The powdered complexes were pressed at 2900 kg/cm^2 into cylindrical pellets having a basal diameter of 0.635 cm. These pellets were placed between the probes of the sample holder and a dry argon atmosphere introduced about 1 hr before readings were taken. Preheating was found experimentally not to be required if the sample had been pressed from carefully dried powder. The resistance runs reported below were made by cooling to about 7°C and raising the temperature to about 40°C over an 8-hr period. No significant difference between successive preparations of the same complex was observed, provided only that precautions to exclude moisture had been taken during the preparation of the complex and its subsequent handling. The Seebeck coefficient measurements were made using a ΔT of at least 8° at approximately 35°C. Similar measurements over the temperature range 7°-40° showed no significant variation.

Results and Discussion

Conductivities.—Figure 3 shows the conductivity *vs.* reciprocal temperature relationship for two typical perylene complexes, in order to show the extent to which the data may be fitted to a straight line. All the complexes whose conductivity as a function of temperature could be measured by our equipment (10^{-11} mho/cm) showed similar behavior. The activation energies are calculated by measuring the slope of the fitted line, according to the well-known relationship:

$$\sigma = \sigma_0 e^{-\epsilon/KT}$$

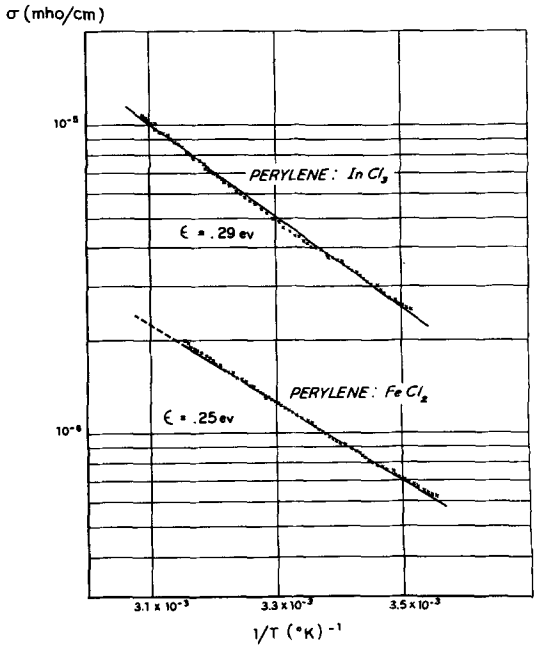

Fig. 3. Log electrical conductivity vs. reciprocal temperature for 2 perylene complexes. The fit of the data is typical of those observed for the complexes shown in Fig. 4.

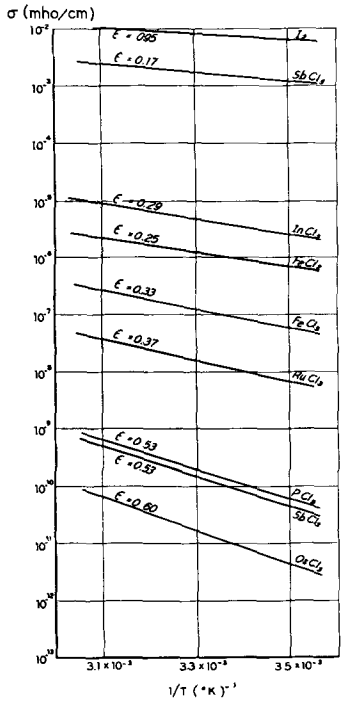

Fig. 4. Semilog plot of the electrical resistivity vs. reciprocal temperature for all the perylene complexes whose conductivity was on the order of 10^{-11} mhos or greater.

The results on the complexes with conductivities greater than about 10^{-11} mho/cm are summarized in Fig. 4, and the room temperature conductivities for the remaining materials are listed in Table I. In each group there was a tendency for higher atomic weight metal halides to show increasing conductivity, with only the series Fe^{III}, Ru^{III}, Os^{III} running counter to this trend. The sequence $CdCl_2$, $InCl_3$, $SnCl_4$, $SbCl_5$ did not give conductivities in the same order.

Table I. Room temperature conductivity of other perylene complexes

Complex	σ 298°K, mho/cm
Perylene: ICl	10^{-5}
Perylene: $PtCl_4$	10^{-7}
Perylene: $NiCl_2$	$>10^{-11}$
Perylene: $AsCl_3$	10^{-12}
Perylene: CdI_2	10^{-12}
Perylene: $MoCl_5$	10^{-13}
Perylene: $CdCl_2$	10^{-13}
Perylene: $AlCl_3$	10^{-13}
Perylene: PCl_3	10^{-13}
Perylene: tetracyanoethylene	10^{-14}
Perylene (uncomplexed)	10^{-14}

The changes in electronic structure resulting from complex formation are known to result in the formation of absorption bands in the visible spectra (7). In the perylene:metal halide series, for the materials with a conductivity above 10^{-5} mho/cm, the absorption is so strong that the solid materials appear black in color.

Activation energies.—In Fig. 4 it will be observed that there seems to be a tendency for the activation energy to increase with decreasing conductivity of the complexes. In order to ascertain the nature of this relationship the data were plotted as shown in Fig. 5. A plot of the activation energy *vs.* the log of the conductivity at room temperature shows an essentially straight line relationship, with the exception of the indium chloride complex and the two materials which had the highest conductivity. This suggests that the conductivity for the series is determined primarily by the number of thermally activated carriers rather than by the reservoir of available carriers in lower energy states. Singer and Kommandeur (8) have reported that for this type of donor-acceptor complex electron spin resonance studies have shown the number of charge carriers to be the only temperature dependent factor at temperatures about 200°K, and that the mobilities are temperature-independent. This conclusion is further substantiated by the data in Table II in which the σ_0 values have been calculated for the same complexes. Although the complexes represent a range in conductivity of six orders of magnitude

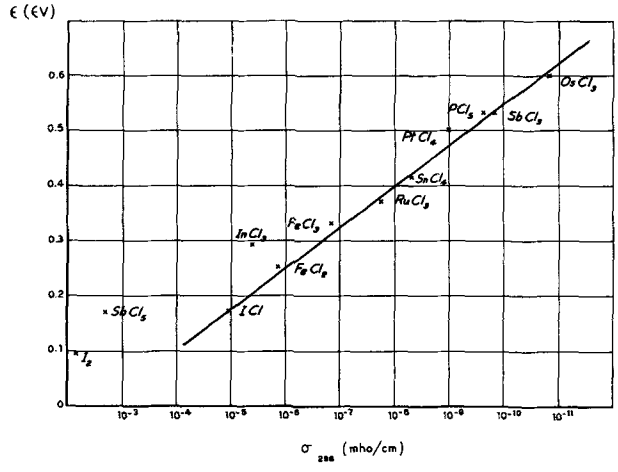

Fig. 5. Activation energy vs. log conductivity for the complexes shown in Fig. 4.

Table II. Room temperature conductivity, activation energy, and σ_0 for the more conductive complexes

	Complex	σ_{298}, mho/cm	ϵ, ev	σ_0, mho/cm
1.	Perylene: I_2	8×10^{-3}	0.095	0.32
2.	Perylene: $SbCl_5$	1.6×10^{-3}	0.17	1.2
3.	Perylene: $InCl_3$	5.1×10^{-5}	0.29	4.1
4.	Perylene: ICl	1.1×10^{-5}	0.17	0.0083
5.	Perylene: $FeCl_2$	1.3×10^{-6}	0.25	0.022
6.	Perylene: $FeCl_3$	1.2×10^{-7}	0.33	0.046
7.	Perylene: $RuCl_3$	1.6×10^{-8}	0.35	0.013
8.	Perylene: $SnCl_4$	3.1×10^{-8}	0.42	0.39
9.	Perylene: $PtCl_4$	1.0×10^{-9}	0.50	0.29
10.	Perylene: PCl_5	2.3×10^{-10}	0.53	0.21
11.	Perylene: $SbCl_3$	2.8×10^{-10}	0.53	0.26
12.	Perylene: $OsCl_3$	1.7×10^{-11}	0.60	0.24

Standard deviation of σ_0 = 0.14 for items 4-12.

the σ_0's are found to have an average value of 0.16 mho/cm with a standard deviation of only 0.14. It should be noted that the materials which do not fall on the line in the activation energy *vs.* conductivity plot appear to have larger σ_0 values than the rest of the group. In the case of these most highly conductive complexes there seem to be additional carriers available from some other conduction mechanism, or from increased mobility of the carriers. Other charge transfer complexes such as phenylenediamine: chloranil (2), Na 3,4 benzoquinoline (2), or haemaglobin (9) do not lie on this same line, nor do the more classic inorganic semiconductors such as iodine, germanium, or silicon. It would appear that the reservoir of available carriers is fixed for the series described in this paper, but can vary considerably for other materials. It is also apparent further study is needed to explain the relationship between the nature of the metal halide acceptor and the activation energy of the complex, and other factors, such as the dielectric constant of the material, ought to be considered.

Thermovoltaic properties.—Additional useful information on the nature of the charge carriers can be obtained from the measurement of the Seebeck coefficient and its sign. Table III lists the Seebeck coefficients which were measured and indicates the predominate type of carrier which was observed. First of all, those materials having higher resistivity generally showed higher Seebeck coefficients. Since the usefulness of the material for thermovoltaic purposes is defined by the figure of merit which is usually expressed as

Table III. Seebeck coefficient of some perylene complexes

Complex	S, mv/°C	Type
Perylene: $RuCl_3$ (as prepared)	0.12	p
Perylene: $RuCl_3$*	0.06	p
Perylene: $PtCl_4$	0.04	p
Perylene: $FeCl_3$ (excess acceptor)	—0.46	n
Perylene: $FeCl_3$ (excess donor)	0.1	p
Perylene: I_2	0.035	p
Perylene: ICl	0.015	p

* After prolonged heating in vacuum.

$$z = \frac{S^2\sigma}{k}$$

where S is the thermoelectric power in volts per degree, σ the specific electrical conductivity in mho/cm, and k the thermal conductivity in watts per degree per cm, it will be seen that the trend in these materials is not a desirable one.

Second, the unusual behavior of perylene: ferric chloride is not fully understood and is still under investigation. Thus far, it would appear that if the complex is prepared with an excess of the acceptor molecule, conductivity is predominately by a positive carrier. We have found that p-type perylene: ferric chloride complex could be converted to n-type by prolonged heating under vacuum. It is believed that this is due to removal of excess perylene. It is not clear whether two or more distinct compounds are formed, or whether one is dealing with an impurity effect.

Conclusions

1. Within the limits of the work done thus far, it is not possible to correlate the conductivity of the complex with any of the obvious properties of the metal halide donor.

2. Except for the most highly conductive members of the series, the product of the number of available charge carriers and their mobilities appears to be constant; the conductivity is determined primarily by the activation energy required to free the charge carriers.

3. Seebeck coefficients are generally lower for the more conductive materials.

4. It has been found possible to prepare perylene: ferric chloride within either p- or n-type carriers predominating.

It is believed that the study of closely related families of complexes is a useful technique in attempting to understand the relationship between chemical and electrical properties.

Acknowledgment

The assistance of H. A. Fox, Jr., in the synthesis of the perylene and in the preparation of the complexes is greatly appreciated.

Manuscript received Nov. 19, 1962; revised manuscript received Feb. 8, 1963.

Any discussion of this paper will appear in a Discussion Section to be published in the June 1964 JOURNAL.

REFERENCES

1. H. Akamatu, H. Inokuchi, and Y. Matsungaga, *Bull. Chem. Soc. Japan*, **29**, 213 (1956).
2. M. M. Labes, R. Sehr, and M. Bose, *J. Chem. Phys.*, **33**, 868 (1960).
3. J. Kommandeur and F. R. Hall, *ibid.*, **34**, 129 (1961).
4. T. Uchida and H. Akamatu, *Bull. Chem. Soc. Japan*, **34**, 1015 (1961).
5. G. E. Blomgren and J. Kommandeur, *J. Chem. Phys.*, **35**, 1636 (1961).
6. F. Hansgirg and A. Zinke, *Montash.*, **40**, 403 (1919).
7. R. M. Keefer and L. J. Andrews, *J. Am. Chem. Soc.*, **74**, 4500 (1952).
8. L. S. Singer and J. Kommandeur, *J. Chem. Phys.*, **34**, 133 (1961).
9. M. H. Cardew and D. D. Eley, *Discussions Faraday Soc.*, **27**, 115 (1959).

Microhardness of Single Crystals of BeO and Other Wurtzite Compounds

Carl F. Cline and J. S. Kahn

Lawrence Radiation Laboratory, University of California, Livermore, California

ABSTRACT

The microhardness of single crystals of BeO, ZnS, AlN, CdS, ZnO, and CdSe has been measured as a function of crystallographic orientation and the results correlated with bond distance, melting point, and band gap.

Thirty-six binary compounds of the elements in Group IV, Groups III/V, Groups II/VI, and Groups I/VII in the periodic table are reported to have structures of the wurtzite type or zincblende type. Of these compounds six show only the wurtzite structure and five are dimorphous with respect to the zincblende form. The 11 compounds are listed in Table I along with some physical properties of interest in this study; included also are two compounds, MnS and MnSe, which have a close relationship to the II/VI compounds.

The wurtzite structure is hexagonal with the space group $P6_3mc$. It is illustrated in Fig. 1 and can be described in several ways. For the purposes of this discussion it is probably clearest to describe the structure as two identical and interpenetrating hexagonal close-packed lattices. The two arrays are shifted with respect to each other so that points of each lattice lie in the center of the tetrahedral interstices of the other lattice. This shift (z parameter) is equal to 0.375 times the c-axis. The cations occupy the points of one lattice and the anions the other lattice. All the atoms then have tetrahedral coordination, with the tetrahedra of one type all pointing in the same direction along the c-axis. The sphalerite structure can be described in a related manner, except that the lattices are cubic close-packed.

The ideal c_0/a_0 ratio (1, 2, 3) for a hexagonal close-packed lattice is 1.633 (*i.e.*, $2\sqrt{2}/\sqrt{3}$). Most of the wurtzite type compounds show some deviation from this ideal value. This deviation requires a distortion of the "ideal" regular coordination tetrahedra. However, this ratio does not give any indication of the magnitude of the shift of the two close-packed lattices. The bond distances listed in Table I have been calculated assuming the shift to be 0.375 for all compounds. It has been shown (3, 4) that for BeO, with $c_0/a_0 = 1.622$, and AlN, with $c_0/a_0 = 1.600$, the shifts are 0.379 and 0.385, respectively. Whether this pattern is the same in other wurtzite compounds remains to be proved. For the purposes of this paper the bond distances in Table I will be adequate.

Table I. Properties of wurtzite structures

Compound	c/a	Observed bond distance, A[a]	Optical band gap, ev	Melting point, °C
AlN	1.600	1.86, 1.90	~5.6	2200 (2 atm)
GaN	1.625	1.94, 1.94	3.3	800
InN	1.611	2.13, 2.16	2.4	
BeO	1.623	1.64, 1.65	~15.0	2570
ZnO	1.602	1.95, 1.98	3.14	1970
MgTe	1.622	2.75, 2.76		
CdS[b]	1.622	2.51, 2.53	2.50	1750 (100 atm)
ZnS[b]	1.635	2.33, 2.33	3.5	1850
CdSe[b]	1.630	2.63, 2.64	1.74	—
AgI[b]	1.635	2.81, 2.80		
SiC	1.641	1.89, 1.88	~2.85	
MnS[c]	1.62	2.41, 2.44		
MnSe[c]	1.63	2.52, 2.52		

[a] Calculated from the unit cell dimensions assuming the difference in the z-parameter for the cation and anion is 0.375.
[b] Dimorphous with zincblende structure.
[c] Trimorphous with metastable NaCl structure.

To understand the processes taking place in crystalline compounds it is necessary to consider various properties of these materials (electrical, physicochemical, mechanical, etc.). Knowledge of such properties should give the distribution of particles in a substance, the nature of these particles, and the way they are bound together, *i.e.*, the electron density distribution or the type of chemical bond.

The hardness of covalent and ionic crystals is one of the properties related in a general way to the type of chemical bond (5, 6). Goldschmidt (7) suggested that the hardness H of a given structure follows the equation $H = \text{constant} \times r^{-m}$, where r is the bond distance and m is an empirical constant related to the type of bonding. Wolff *et al.* (8) have related the hardness of the elements and zincblende III/V compounds to the bond distance using the Goldschmidt formula. They found that the constant

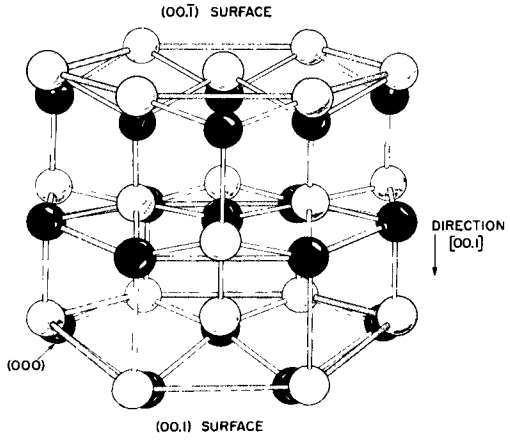

Fig. 1. Wurtzite structure

Table II. Knoop hardness[a] of wurtzite compounds

Compound	Plane indented	Indentation direction	Hardness, kg/mm²	Remarks
BeO	(00.1)	[10.0], [11.0]	1300	No orientation dependence
	(00.$\bar{1}$)	[10.0], [11.0]	1100	No orientation dependence
	(10.0)	[00.1]	1175	
	(10.0)	[10.0]	917	
ZnO	(00.1)	[10.0], [11.0]	274	No orientation dependence
	(00.$\bar{1}$)	[10.0], [11.0]	238	No orientation dependence
	(10.0)	[00.1]	241	
	(10.0)	[10.0]	170	
CdS	(00.1)	[10.0], [11.0]	118	No orientation dependence
	(10.0)	[00.1]	91	No orientation dependence
	(10.0)	[10.0]	53	
CdSe	(00.1)	[10.0], [11.0]	83	
	(11.0)	[11.0]	63	
	(11.0)	[00.1]	49	
ZnS	(00.1)	[10.0], [11.0]	246	No orientation dependence
	(11.0)	[11.0]	158	
	(11.0)	[00.1]	—	
AlN	(00.1)	[10.0], [11.0]	1187	No orientation dependence

[a] 100g load.

m assumes the approximate value 5 and 9 for the elements and III/V compounds, respectively.

Wolff has recently found the same relationship to hold for II/VI compounds as well (9).

Experimental Results

The microhardness of the single crystals of BeO, AlN, ZnO, CdS, and CdSe was determined as a function of orientation using a Leitz Durimet hardness tester with a Knoop diamond. The crystals were either mounted in Bakelite mounds and polished before testing, or tested in the as-grown state. Indentations on each specimen were made independently by the authors and the results compared and averaged. The latter represent at least 25 measurements. All indentations were examined at 1600X magnification. Those associated with cracks of any sort were not included in the study. No evidence of twinning was observed. The indentation load was varied between 15 and 200g; no load dependence was found. The rate of indentation was also varied between 1 sec and 10 min; no rate dependence was apparent. However, the incidence of cracking was related to the rate of loading. The faster the loading, the greater the incidence of cracking. With respect to BeO, the cracking incidence was also associated with the surface environment of the crystal. Cracking was essentially eliminated when an organic solvent such as kerosene was applied to the crystal prior to indenting it. The experimental data are tabulated in Table II. In Fig. 2, 3, and 4, the hardness is graphically related to bond distance, band gap, and melting point; it can be seen that a logarithmic relation exists.

The band gaps for most of the compounds were obtained from Bube and others (10-12). The gap

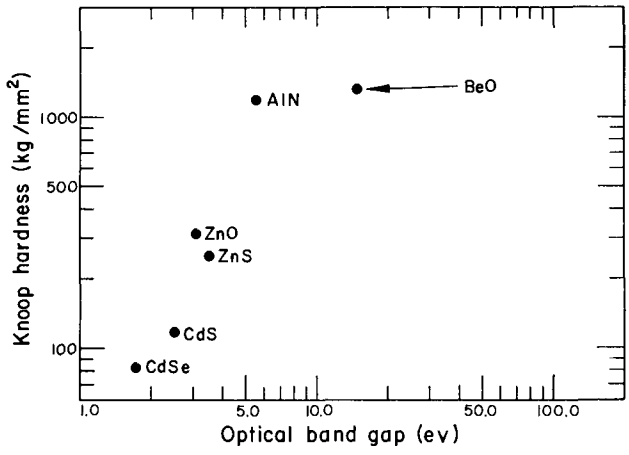

Fig. 2. Knoop hardness as a function of optical band gap. Basal plane (0001).

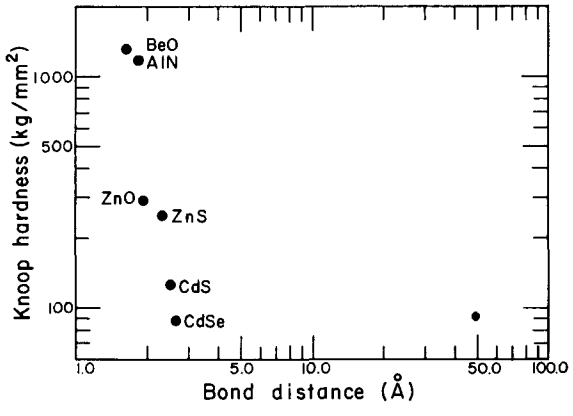

Fig. 3. Microhardness of wurtzite compounds on basal plane as a function of bond distance. (Knoop, 100g load).

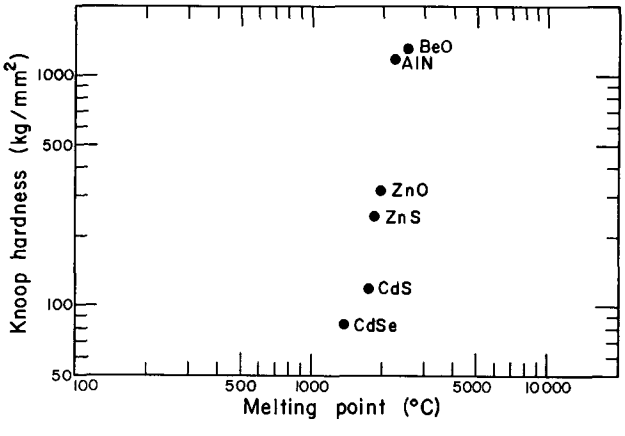

Fig. 4. Relation between Knoop hardness and melting point

for BeO was obtained in our laboratories using a vacuum ultraviolet spectrograph where the fundamental absorption occurred at approximately 800Å, indicating a very large band gap.

Discussion of Results

The hardness measurements for CdS, CdSe, and ZnO agree with data by Wolff (9), while the hardness data for BeO and AlN disagree with reported data. The absence of any studies on the slip crystallography of the wurtzite compounds precludes any discussion of its relationship to hardness. However, current studies at this laboratory are aimed at elucidating this relationship.

BeO is reported (13, 14) to have a Mohs hardness of 9, which would correspond to a Knoop hardness of approximately 2000 kg/mm^2. It can be seen from our data that its true hardness is closer to 8 than 9. In view of the correlations obtained with bond distance, band gap, etc., it is felt that hardness reflects a measure of the bonding energy of the compounds.

The anisotropy of the hardness measurements for the wurtzite compounds is felt to be a true reflection of the differential bonding. Hardness values are lower on the $(10\bar{1}0)$ than on the basal plane where the hardness is isotropic. On the $(10\bar{1}0)$ surface the highest hardness parallels the (0001) face. The lower hardness parallels the prismatic cleavages (15-18).

The explanation presumably lies in the fact that basal cleavage, with the breaking of one bond per unit cell area, leaves the two halves oppositely charged, while breaking the same number of bonds along $(10\bar{1}0)$ and $(11\bar{2}0)$ leaves both halves neutral. In order to leave both cleaved basal planes neutral it would be necessary to break two bonds per unit cell.

The differential hardness on the (0001) and $(000\bar{1})$ as found on BeO and ZnO is at this time difficult to explain, but it is felt that either dislocation density or strain is responsible for the difference.

Summary

The microhardness of BeO, ZnO, AlN, CdS, ZnS, and CdSe have been measured as a function of orientation and compared with the literature. Their hardness can be correlated with band gaps, bond distance, and melting point.

It is felt that the orientation dependence of the hardness can be explained by the crystal structure.

Acknowledgments

The authors would like to acknowledge the advice and assistance of Dr. Gunther Wolff of Harshaw Chemical Company, Cleveland, Ohio; Dr. Herbert W. Newkirk for growing the crystals of BeO and ZnO; and Mr. L. M. Foster who furnished the crystals of AlN. Discussions with Dr. D. K. Smith have also been very helpful. This work was performed under the auspices of the U.S. Atomic Energy Commission.

Manuscript received Dec. 11, 1962; revised manuscript received Feb. 18, 1963. This paper was presented at the Boston Meeting, Sept. 16-20, 1962.

Any discussion of this paper will appear in a Discussion Section to be published in the June 1963 JOURNAL.

REFERENCES

1. H. Ott, *Z. Physik*, **22**, 201 (1924).
2. W. Zachariasen, *Z. physik. Chem.*, **119**, 201 (1926).
3. G. Jeffrey *et. al.*, *J. Chem. Phys.*, **25**, 1024 (1956).
4. D. K. Smith, H. W. Newkirk, and J. S. Kahn, *This Journal*, Being reviewed.
5. J. J. Gilman, Paper presented at American Ceramic Society Meeting, April 29, 1962, New York.
6. J. Westbrook and J. J. Gilman, G. E. Report 62-RL-2972M, March 1962.
7. V. M. Goldschmidt, *Norske Vod. Akad. i. Oslo Skr., Mat.—Nat. Kl.*, **8**, 102 (1926).
8. G. A. Wolff, L. Tolman, N. J. Field, and J. C. Clark, "Semiconductors and Phosphors," Interscience Publishers, Inc., New York (1958).
9. G. A. Wolff, Personal communication.
10. R. Bube, "Photoconductivity of Solids," John Wiley & Sons, Inc., New York (1960).
11. N. B. Hannay, "Semiconductors," Reinhold Publishing Corp., New York (1959).
12. G. A. Wolff, Private communication.
13. F. H. Norton, "Refractories," McGraw-Hill Book Co., Inc., New York (1949).
14. F. H. Norton, *J. Am. Ceram. Soc.*, **30**, 242 (1947).
15. J. D. Dana, "The Systems of Mineralogy," John Wiley & Sons, Inc., New York (1944).
16. L. Helmholtz, *J. Chem. Phys.*, **3**, 740 (1935).
17. C. F. Cline, V. D. Frechette, and J. S. Kahn, Abstract of paper presented at the British Ceramic Society Meeting on Mechanical Properties of Nonmetallic Crystals and Polycrystals, Hasting, England, October 1962.
18. G. A. Wolff and J. D. Broder, *Am. Mineral.*, **45**, 1230 (1960).

Gaseous Equilibria in the Germanium Iodine System

R. F. Lever

International Business Machines Corporation, Thomas J. Watson Research Center, Yorktown Heights, New York

ABSTRACT

Measurements on the thermal dissociation of gaseous GeI_4 and the reaction of gaseous GeI_4 with excess germanium have been made by observing the dependence of the total pressure on temperature for the corresponding closed systems at constant volume. The dependence of equilibrium constant on temperature is given for the reactions

$$Ge_{(s)} + GeI_{4(g)} = 2GeI_{2(g)}$$

and

$$GeI_{4(g)} = GeI_{2(g)} + I_{2(g)}$$

Average heats of reaction and entropy changes are deduced for the temperature range 600°-1200°K.

The equilibria determining the composition of the gas phase in the germanium-iodine system are of interest for their practical application to germanium crystal growth (1, 2). Jolly and Latimer (3) have measured the disproportionation of solid GeI_2 in the range 540°-640°K. In the course of their measurements they obtained rather approximate values for the vapor pressure of solid GeI_2 so that some estimate of the equilibrium

$$2GeI_{2(g)} = Ge_{(s)} + GeI_{4(g)} \qquad [1]$$

may be obtained. Estimates of the free energy of formation of GeI_4 may be obtained from the heat of formation of solid GeI_4 obtained by Evans and Richards (4) and entropy values given by Rolsten (5). Although the information thus available is sufficient to make the general behavior of the germanium-iodine system reasonably clear, further observations are necessary in order to obtain the composition of the gas phase with reasonable accuracy.

In this investigation the total pressure at constant volume has been measured as a function of temperature for two systems: 1, GeI_4 with slight excess iodine; 2, germanium iodides in the presence of excess germanium. In system 1 both the germanium and iodine contents of the gas phase are fixed, and a pressure rise with increase in temperature is observed due to the dissociation of GeI_4 into GeI_2 and elemental iodine. In system 2, the germanium content of the gas phase is variable, and a pressure rise with increase in temperature is observed due to the operation of reaction 1. The pressures observed may be interpreted unambiguously by assuming that the only species present in the gas phase in measurable amounts are GeI_4, GeI_2, I_2, and I and values of the heats of formation and entropies of GeI_4 and GeI_2 in the gaseous state deduced therefrom.

Experimental

The total pressure in the constant volume system was measured using a quartz "spoon gauge" as a null indicator in conjunction with a conventional gas handling system and a Wallace and Tiernan dial gauge as pressure measuring instrument. The spoon was sealed to a cylindrical quartz reaction chamber having a volume of the order of 30 cc and surrounded by a nichrome wound furnace powered by a constant voltage transformer and a variac. The temperature was measured by means of a Pt-Pt-10%Rh thermocouple. The chemical components were added separately as elemental germanium and iodine in all runs.

The procedure for loading the reaction chamber was identical to that described by Silvestri and Lyons (6), except that in the measurements on system 2, the iodine was not weighed. In the germanium-iodine system, reaction does not take place between germanium and iodine at temperatures below 180°C, so that it is also possible to obtain the iodine content from the observed pressure of unreacted iodine. The null point was observed on system 2 by viewing the position of the end of a quartz pointer attached to the spoon relative to the position of the end window. It was found possible in measurements on system 1 to use a less sensitive, and hence more robust, spoon by using a direct optical lever technique. An optically polished quartz disk, with the back surface ground to avoid double reflections, was attached to the end of the spoon and used as a mirror to view a light source by means of a viewing telescope. A second light source was viewed by reflection from the front quartz window. This provided a fiducial mark, automatically avoiding error due to any movement of the system. In both cases, readings could be reproducibly made to ±1 mm. The dial gauge was checked against a barometer at atmospheric pressure and found correct. Errors due to reading the pressure can be considered negligible compared with errors from other sources.

Theory

In interpreting the total pressure observations, two assumptions are made: (i) The species present in the gas phase are limited GeI_4, GeI_2, I_2, and I. (ii) All gaseous species may be treated as ideal.

The concentration of a component or species will be denoted by n moles/liter and the corresponding partial pressure by p. The actual species or component involved will be denoted by a suffix as follows. The species GeI_4, GeI_2, I_2, and I will be denoted by suffixes 4, 2, 1, and 0, respectively. The components iodine and germanium will be denoted by suffixes I and Ge, respectively. N and P without suffixes will denote the total molar density of all species and the total pressure, respectively.

System 1.—There are no condensed phases, hence the total densities of germanium and iodine in the gas phase are fixed experimentally, being given by

$$n_I = 4n_4 + 2n_2 + 2n_1 + n_0 \quad [2]$$

and

$$n_{Ge} = n_4 + n_2 \quad [3]$$

In addition, the reaction (7)

$$2I = I_2$$

gives us the relation

$$n_1 = Kn_0^2 \quad [4]$$

where K is known from the literature.

The measurements on system 1 give

$$\frac{P}{RT} = N = n_4 + n_2 + n_1 + n_0 \quad [5]$$

Hence, from [3], [4], and [5]

$$N - n_{Ge} = n_1 + n_0 = n_0 + Kn_0^2$$

which may be solved to give n_1 and n_0. Equations [2] and [5] then yield the values of n_2 and n_4. Hence the equilibrium constant for the reaction

$$GeI_4 = GeI_2 + I_2$$

is readily calculated. This equilibrium, being entirely between gas phase species, holds in all germanium-iodine systems, irrespective of whether solid germanium is present or not.

System 2.—Again, n_I is fixed, but excess germanium is present. This, of course, is a system of practical interest for vapor growth. The interpretation of the measurements is greatly simplified by the fact that, under the conditions of our experiments, the values of n_1 and n_0 are negligibly small giving us simply

$$n_I = 2n_2 + 4n_4 \quad [6]$$

$$N = n_2 + n_4 \quad [7]$$

hence

$$n_2 = 2N - \tfrac{1}{2}n_I$$

$$n_4 = \tfrac{1}{2}n_I - N$$

Hence, the equilibrium constant for reaction 1 is obtained directly.

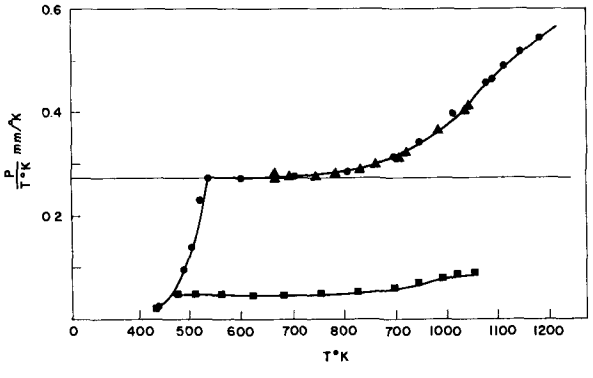

Fig. 1. *P/T* vs. temperature for system 1. Triangles and dots denote two runs at the same iodine content. Squares denote a run at lower iodine content.

These reactions then enable us to completely characterize a germanium-iodine system given the temperature and iodine content.

Results

System 1.—Two runs were made. In each case, the amount of iodine used was slightly in excess of stoichiometry. A measurement of the total pressure of the system before and after reaction of the germanium and iodine gave values of n_{Ge} and n_I in agreement with the values obtained by weighing but having somewhat greater precision. Figure 1 shows the results in the form of a plot of P/T against T°K.

Two runs were made on a system containing iodine at a level of 0.534 mm/°K before reaction and one run on a system containing 0.090 mm/°K before reaction. It is seen that after following its vapor pressure curve, GeI_4 expands substantially as an ideal gas between 520° and 650°K after which the value of P/T rises due to dissociation. The equilibrium constant for the reaction $GeI_4 = GeI_2 + I_2$ has been deduced from the experimental data using Eq. [2]-[5] and is plotted in Fig. 2.

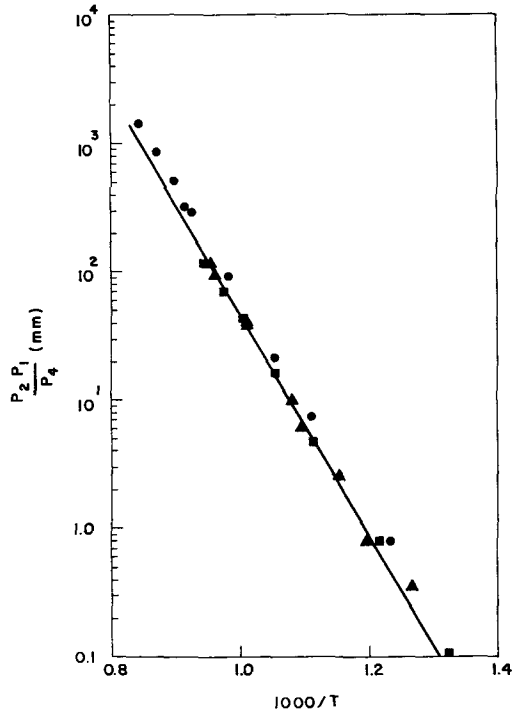

Fig. 2. Equilibrium constant vs. 1000/*T* for system 1

System 2.—Two runs were made in the presence of excess solid germanium. In this case, I_2 and I are present in negligible amounts at the temperatures and pressures that were employed. Figure 3 shows a plot of P/T against T for one run. In this system the behavior at low temperatures is complicated by the existence of condensed iodides in imperfect equilibrium with the excess germanium, and so only that portion of the curve corresponding to a two phase system solid germanium-gas is shown. It is seen that as the gas composition approaches pure GeI_2, the P/T increase with temperature levels off as P tends to the value $\frac{1}{2}n_IRT$ corresponding to a P/T value of approximately 0.195. At low temperature, P would approach the value $\frac{1}{4}n_IRT$ as the gas tended to become pure GeI_4, except that GeI_2 condenses out giving us a three phase system.

In these runs the iodine was not weighed. In both runs of system 2 it was found, after reaction had taken place, that the n_I values obtained from the total iodine pressure before reaction could not be relied on with high accuracy due to movement of the apparatus during the warm up[1] (as observed by a small shift in the zero portion after completion of the run). The value of n_I was, therefore, obtained by assuming that at the maximum temperature observed, the concentrations of GeI_4, I_2, and I in the gas phase were negligible so that $(P/T)_{max} = \frac{1}{2}n_I/R$, (point *B* in Fig. 3). The procedure and assumptions were checked by taking values of n_I corresponding to values 2% higher and lower than the estimated value (points C and A respectively) and calculating the equilibrium constant for all three cases.

Using Eq. [6] and [7], including the estimated values of n_I, values of the equilibrium constant for the reaction under consideration were deduced. This resulted in three plots of log *K* vs. $1/T$ (Fig. 4). Above 840°C the plots corresponding to ±2% deviations of n_I gave noticeable departures from linearity. (The points shown are taken at 20° intervals from the smooth curve drawn through the experimental points in Fig. 3.) The curves A, B, and C correspond to the analogous levels of $\frac{1}{2}n_I/R$ marked on Fig. 3. It is seen that picking level A instead of B

[1] This difficulty did not occur during the measurements on system 1 which were actually performed at a later date than the measurements on system 2.

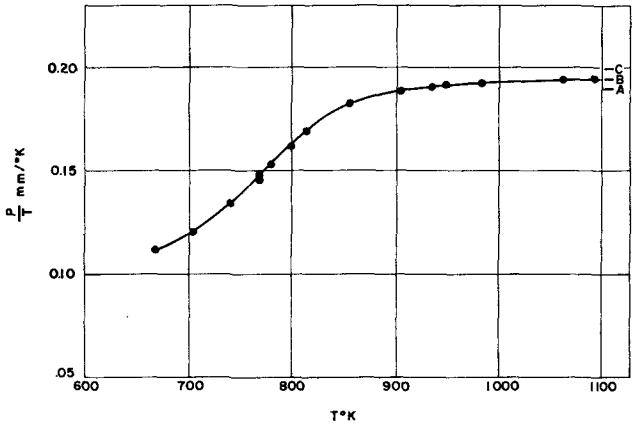

Fig. 3. *P/T* vs. temperature for system 2, low pressure run

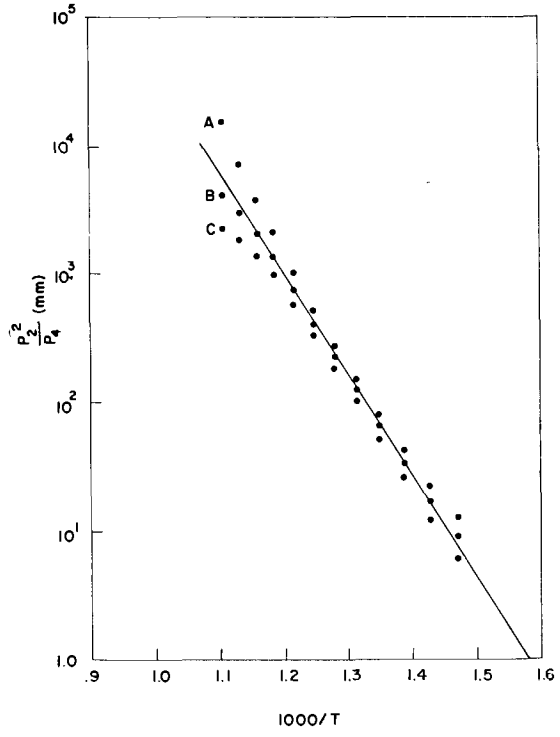

Fig. 4. Equilibrium constant vs. 1000/T for system 2. Low pressure run showing the effect of varying the assumed iodine content.

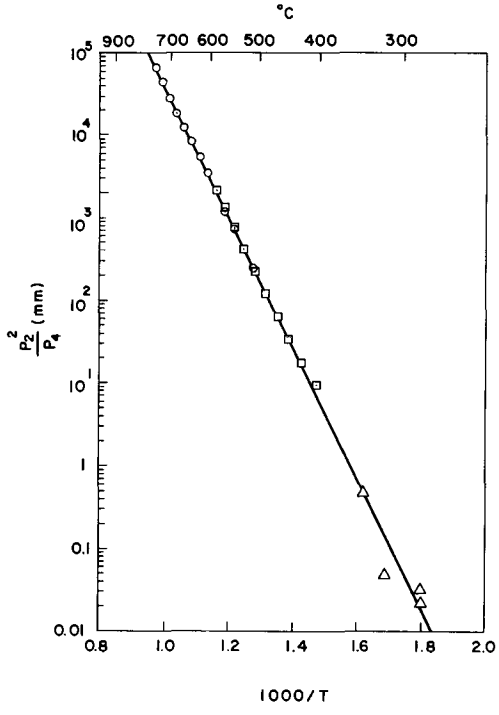

Fig. 5. Equilibrium constant vs. 1000/T, system 2: open dotted circle, first run; open dotted square, second run; open triangle, Jolly and Latimer (3).

results in a displacement of the log K vs. $1/T$ curve equivalent to a temperature displacement of about 8°C or a displacement on the log K direction corresponding to a factor of 1.3. This would lead to an error in the entropy of reaction of approximately 0.5 cal mole^{-1} deg^{-1}. Hence the choice of point B leads to very reasonable results. If the other points had been chosen the errors would not have been great. It is felt that the probable error due to this procedure for evaluating n_I is likely to be ±0.1 cal mole^{-1} deg^{-1}. A second run which employed an iodine content approximately three times higher gave results consistent with the previous run. Figure 5 shows a composite curve of the equilibrium constant, derived from the two runs, in which the points are calculated from values taken at 20° intervals from the smoothed P/T curves. Data from the measurements of Jolly and Latimer are also included.

Discussion

It is appropriate at this point to consider the probable validity of the assumption that only the species GeI_2, GeI_4, I_2, and I exist in the systems. We may note that in both systems 1 and 2 good straight line plots of log K vs. T^{-1} are obtained. In system 1, good agreement is obtained between runs operated at iodine contents giving values of P/T before reaction of the iodine with germanium of 0.534 and 0.090 mm/°K, respectively. In system 2, agreement is obtained between two runs operated at iodine contents corresponding to P/T values before reaction of 0.694 and 0.196 mm/°K, respectively. These agreements strongly suggest that the model used is appropriate for the pressures and temperatures employed in the measurements, *i.e.*, that other species are most unlikely to be present as major constituents. In considering the effect of errors in n_I on the log K vs. $1/T$ plot for system 2, it was demonstrated that errors in n_I even as high as 3% would not give grossly incorrect results. It would seem to follow that small quantities of other species, perhaps as high as 5% mole fraction, could not be detected by our measurements as a noticeable inconsistency in our model.

In deriving the data, no attempt has been made to estimate specific heat differences between the various reactants and products involved. The thermochemical data quoted are derived by drawing straight lines through the experimental $\log_{10} K$ vs. $1000/T$ plots and fitting to the equation $4.574 \log_{10} K = \Delta S - \Delta H/T$. For the purposes of this calculation, the K's are expressed relative to a standard state of 1 atm. The ΔH and ΔS values are average values over the range 600°-1200°K, not the values at 298°K.

Errors in the quoted values will occur due to inaccuracies in (a) the pressure measurements, (b) the temperature measurements, (c) the ideal gas assumption, (d) for system 2, the method described for estimation n_I. The temperature accuracy is estimated at ±5°C, and this is considered to be the major source of error. A uniform temperature error of 5°C would give rise to an error of approximately 1 kcal mole^{-1} in the ΔH values and approximately 0.5 cal mole^{-1} deg^{-1} in the ΔS values. We. therefore, quote the results as follows

System 1.—Reaction $GeI_{4(g)} = GeI_{2(g)} + I_{2(g)}$

$$\log_{10}(p_1 p_2/p_4) = 7.23 - 8370/T$$

where $p_1 p_2/p_4$ is measured in atm and all species are in the gaseous state. This gives us

$$\Delta H = 38.3 \pm 1.0 \text{ cal mole}^{-1}$$
$$\Delta S = 33.1 \pm 0.5 \text{ cal mole}^{-1} \text{ deg}^{-1}$$

System 2.—Reaction $Ge_{(s)} + GeI_{4(g)} = 2GeI_{2(g)}$

$$\log_{10}(p_2^2/p_4) = 9.68 - 7936/T$$

where p_2^2/p_4 is measured in atm, the iodides are in the gaseous state and the Ge is solid. This gives us

$$\Delta H = 36.3 \pm 1.0 \text{ kcal mole}^{-1}$$

$$\Delta S = 44.3 \pm 0.5 \text{ cal mole}^{-1} \text{ deg}^{-1}$$

Examination of Fig. 5 suggests that these values also describe the system reasonably well in the temperature range investigated by Jolly and Latimer (1). Substituting into their formula at 600°K, we obtain for their reaction

$$2GeI_{2(s)} = GeI_{4(g)} + Ge_{(s)}$$

$$\Delta H = 27.7 \text{ kcal mole}^{-1} \quad \Delta S = 35.4 \text{ cal mole}^{-1} \text{ deg}^{-1}$$

Hence we obtain for the heat and entropy of sublimation of GeI_2 at 600°K, the values

$$\Delta H = 32.0 \text{ kcal mole}^{-1} \quad \Delta S = 39.8 \text{ cal mole}^{-1} \text{ deg}^{-1}$$

These results may, of course, be stated in the form of the reactions

$$Ge_{(s)} + 2I_{2(g)} = GeI_{4(g)}$$

$$Ge_{(s)} + I_{2(g)} = GeI_{2(g)}$$

For the first reaction, we obtain $\Delta H = 40.3$ kcal mole^{-1} and $\Delta S = -21.9$ cal mole^{-1} deg^{-1} as the average enthalpy and entropy of formation of gaseous GeI_4 from solid germanium and gaseous iodine over the temperature range 600°-1200°K. If we take the published entropies and heat content data for Ge, I_2, and GeI_4 (7, 8), we then obtain for GeI_4 [2]

$$\Delta H_{298} = -41.1 \text{ kcal mole}^{-1}$$

$$S_{298} = 108.6 \text{ cal mole}^{-1} \text{ deg}^{-1}$$

While the former is in good agreement with Evans and Richards (4) the entropy value seems somewhat high compared with published values (3, 5).

For the second reaction, we obtain the corresponding quantities:

$$\Delta H = 2.0 \text{ kcal mole}^{-1}$$

and

$$\Delta S = +11.2 \text{ cal mole}^{-1} \text{ deg}^{-1}$$

If specific heat differences are neglected, this gives us for GeI_2 [2]

$$\Delta H_{298} = -2.0 \text{ kcal mole}^{-1}$$

$$\Delta S_{298} = 80.9 \text{ cal mole}^{-1} \text{ deg}^{-1}$$

Acknowledgment

The author is greatly indebted to J. Regh, who did most of the experimental work, and also benefited from discussion with S. P. Keller, R. W. Keyes, and V. J. Lyons.

Manuscript received Dec. 5, 1962; revised manuscript received Feb. 15, 1963. This paper was delivered before the Los Angeles Meeting, May 6-10, 1962.

Any discussion of this paper will appear in a Discussion Section to be published in the June 1963 JOURNAL.

REFERENCES

1. R. P. Ruth, J. C. Marinace, and W. C. Dunlap, *J. Appl. Phys.*, **31**, 995 (1960).
2. J. C. Marinace, IBMJ, **4**, 248 (1960).
3. W. L. Jolly and W. M. Latimer, *J. Am. Chem. Soc.*, **74**, 5754 (1952).
4. D. F. Evans and R. E. Richards, *J. Chem. Soc.*, **1952**, 1292.
5. R. F. Rolsten, "Iodide Metals and Metal Iodides," p. 296, John Wiley & Sons, New York (1961).
6. V. J. Silvestri and V. J. Lyons, *This Journal*, **109**, 963 (1962).
7. Nat. Bur. Standards, "Selected Values of Chemical Thermodynamic Properties," Series III.
8. K. K. Kelley, *Bur. Mines Bull.* 584 (1960).

[2] In both of the above cases, the ΔH_{298} values refer to the enthalpy of formation of the gaseous compound from solid germanium and gaseous iodine.

Photoconductivities of α and β Forms of Metal-Free Phthalocyanine

C. Y. Liang and E. G. Scalco

Exploratory Research Laboratory, American Viscose Corporation, Marcus Hook, Pennsylvania

ABSTRACT

Some experimental results on the photoconductivities of α and β forms of metal-free phthalocyanine are presented and discussed. It is found that the photocurrent threshold energy is lower for the α sample than that for the β sample. The activation energies for dark conduction are about 1.9 ev for the β sample and 1.4 ev for the α sample, while the activation energies for photoconduction are about 0.34 ev for the β and 0.42 ev for the α. All these differences are interpreted as due to the disordered structure of the α sample.

The phthalocyanines are known to exist in several polymorphic crystalline forms. Susich (1) reported the x-ray diffraction patterns of α, β, and γ forms of metal-free phthalocyanine. Karasek and Decius (2) reported the x-ray study of metal-free phthalocyanine and discussed the sublimation pressures for obtaining the α and β forms. The infrared spectra of the α and β forms of metal-free phthalocyanine and a number of metal phthalocyanines were reported by Ebert and Gottlieb (3), Sidorov and Kotlyar (4), and Kendall (5). The detailed crystal structure of the β phthalocyanine was deter-

mined by Robertson (6). A possible crystal structure of the α phthalocyanine was proposed by Tarantino and his co-workers (7). It may be noted that Tarantino and Kendall used a different nomenclature. In this report, Susich's nomenclature is adopted and the stable crystalline form studied by Robertson is called the β form.

The electrical conductivities of phthalocyanines and related compounds were reported by a number of investigators (8-18). Eley and Parfitt (9) using an a-c method found that at 150°C the resistance of the β form phthalocyanine is about ten times higher than that of the α form. Wihksne and Newkirk (16) reported the conductivity of the α form phthalocyanine to be more nearly 10^5 times greater than that of the β form at temperatures near 180°C. They also found that the activation energy was 0.5 ev for the α form and 1.8 ev for the β form.

In the present study some results on the photoconductivities of the α and β forms of metal-free phthalocyanine are reported. It is hoped that investigations of this kind will lead to a better understanding of the relation between electrical properties and crystal structure of organic semiconductors.

Experimental

The metal-free phthalocyanine prepared in our laboratory was in the β form. The material is crystalline and is believed to have a high purity. The α form was prepared as follows: The β form phthalocyanine was dissolved in concentrated H_2SO_4, precipitated in large quantity of water, washed and dried at 120°C for several hours. X-ray diffraction patterns of the α and β samples are shown in Fig. 1. Sample pellets of half inch in diameter and a few millimeters thick were prepared by subjecting the powdered material to pressures to about 4000 psi. Two Al foil electrodes were attached to the same side of the pellet by silver paint. The separation of electrodes was about 1 mm. Conductivities at various temperatures were measured by placing the sample in a metal container which was evacuated to about 10^{-4} mm Hg during measurement.

The monochromatic light source was obtained from a tungsten lamp with a Perkin-Elmer Model 12B infrared spectrometer equipped with a quartz prism. The plain mirror behind the exit slit of the spectrometer was replaced by a flat quartz plate which reflects a small percentage of the light to the spherical mirror which in turn focuses the light on the spectrometer thermocouple detector.The transmitted light from the quartz plate was then condensed by a quartz lens onto the sample. The relative intensity of the tungsten light source was controlled by a variac and was measured from the small reflected portion by the thermocouple detector.

The conductivities of the samples were measured using a General Radio Electrometer. A bias potential was connected to the ground terminal and was used to balance the dark current in order to make the photocurrent measurement in a sensitive scale (18).

Results

The temperature dependences of dark conductivities of the α and β samples are shown in Fig. 2. The results can be fitted into the well-known equation

$$R = R_0 \exp(\Delta E/2kT) \qquad [1]$$

where R_0 is a constant and ΔE is the activation energy for dark conduction. The activation energy for the α sample is 1.4 ev while that for the β sample is 1.9 ev. These values are generally in agreement with those reported in the literature. However, different investigators did report different values for the activation energy within the range of 0.5-2 ev. The difference could arise from different methods for sample and cell preparations.

The resistance at room temperature of the β sample is about 1000 times higher than that of the α sample. The smaller resistance for the α sample implies that the charge carrier concentration in this sample could be much higher than that in the β sample at room temperature. It was found that the density of the α sample is 1.478 g/cc, while that of the β sample is 1.459 g/cc. (The density of a needle-shaped single crystal is 1.446 g/cc). The slightly higher density of the α sample would also be in

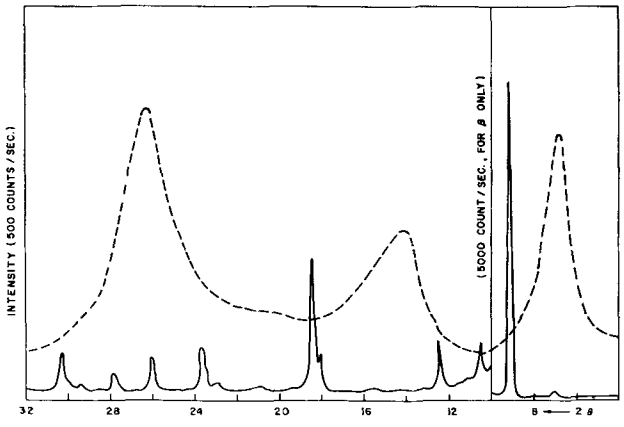

Fig. 1. X-ray diffraction patterns of α and β phthalocyanines: ———, α; ———, β.

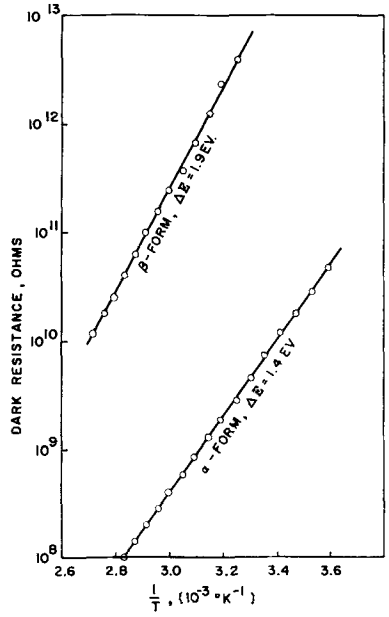

Fig. 2. Resistance of α and β phthalocyanines vs. reciprocal of absolute temperature.

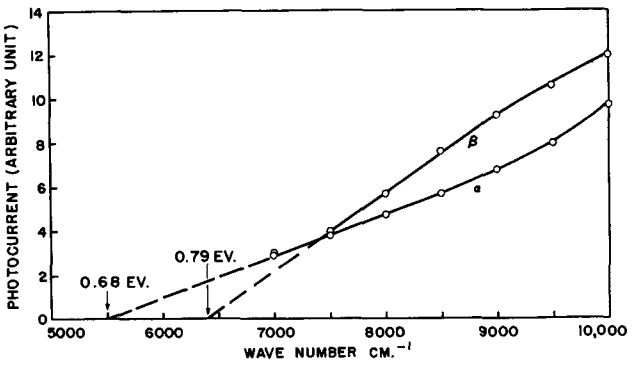

Fig. 3. Wavelength dependence of photocurrents and threshold energies of α and β phthalocyanines.

line with a lower resistance for this sample in comparison with the β sample.

The photoconductivities for the α and β phthalocyanine samples were measured with monochromatic light. It has been noted that the spectral responses for these two samples are somewhat different. The photocurrents between 5000 and 10,000 cm^{-1} calibrated to constant intensity of illumination are shown in Fig. 3. It is found that the photocurrent threshold for the α sample is 0.68 ev while that for the β sample is 0.79 ev.

The intensity dependence of photoconductivities of α and β phthalocyanine samples are shown in Fig. 4. A monochromatic light source was set at the wavelength near the highly photosensitive region for each sample (about 12,500 cm^{-1} for the α and 9,700 cm^{-1} for the β). Each photocurrent was recorded for 5 sec of exposure, when the current was over 80% of the steady-state photocurrent for extended illumination. In the intensity region studied, the photocurrent is proportional to the intensity for the β sample. This may be explained by a simple model of two photon process (exciton-exciton interaction): $dN/dt = AN^2_{ex} - BN^2 - CNN_{tr}$, where N, N_{ex}, and N_{tr} are, respectively, the concentrations of charge carrier, exciton, and trapping center. A is a constant and B and C are, respectively, the coefficients of recombination and trapping. In the steady state we have $dN/dt = 0$. Assuming $BN >> CN_{tr}$, then N is proportional to N_{ex} or the steady state photocurrent is proportional to the light intensity.

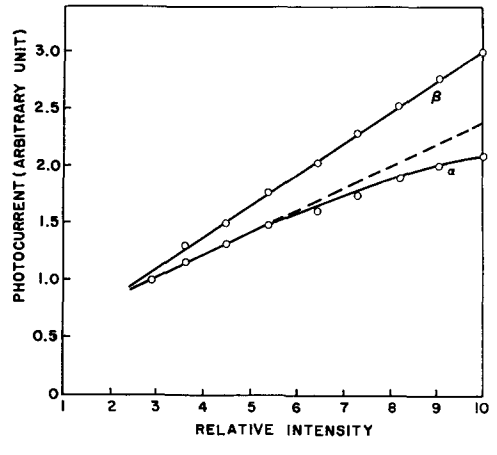

Fig. 4. Intensity dependence of photocurrent of α and β phthalocyanines.

In the case of the α sample, the photocurrent tends to deviate from the linear behavior at higher intensity of illumination. This may be explained by the one photon process: $dN/dt = AN_{ex} - BN^2 - CNN_{tr}$. At lower intensity, we may assume $BN << CN_{tr}$. Then, in the steady state, N is proportional to N_{ex} or the photocurrent is proportional to the light intensity. At higher intensity, we may assume $BN >> CN_{tr}$, the steady-state photocurrent is now proportional to the square root of the light intensity.

The photocurrent-voltage plots at five different temperatures for the α and β phthalocyanine samples are shown respectively in Fig. 5 and 6. In the temperature and voltage regions studied, the β sample exhibits essentially ohmic behavior, while deviation for the ohmic behavior may be noted for the α sample. In order to deduce the temperature dependence of photoconductivity, the photocurrents at 90v for the samples at various temperatures obtained from Fig. 5 and 6 were plotted *vs.* inverse absolute tem-

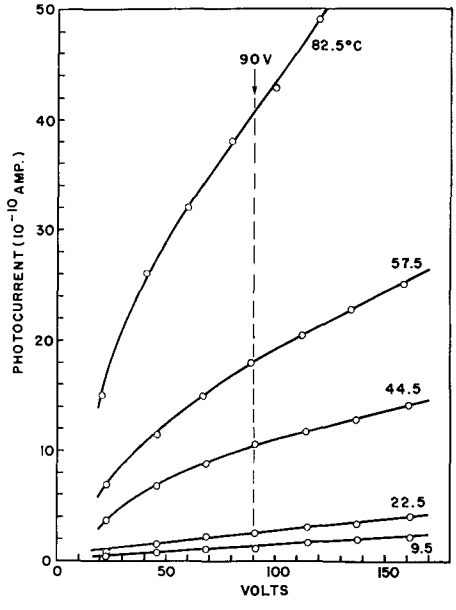

Fig. 5. Photocurrent *vs.* voltage for α phthalocyanine at various temperatures.

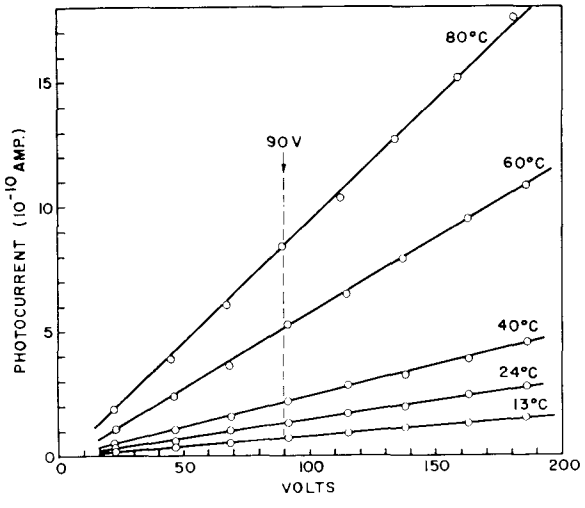

Fig. 6. Photocurrent *vs.* voltage for β phthalocyanine at various temperatures.

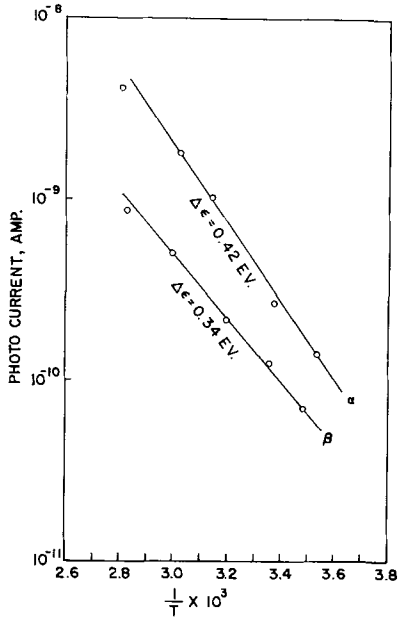

Fig. 7. Photocurrents of α and β phthalocyanines vs. inverse absolute temperature.

perature shown in Fig. 7. The five points for each of the samples lie approximately on a straight line. One may therefore assume that the photocurrent follows the equation

$$i = i_0 \exp(-\Delta\epsilon/k/T) \quad [2]$$

where i_0 is a constant and $\Delta\epsilon$ is the activation energy for photoconduction. The activation energies were estimated to be about 0.42 ev for the α and 0.34 ev for the β.

Discussion

Mechanisms of electronic conduction for organic materials have been discussed by a number of authors (19). Because of the shortage of knowledge of the intermolecular interaction in organic solids, the mechanisms proposed have been mainly qualitative and speculative. It is perhaps a tentative conclusion that the semiconduction of phthalocyanine involves the excitation of π-electrons to the conduction state and at the same time the formation of holes, and the electrons and holes so formed can transfer in the organic solids in an applied field. For dark conduction, mobile electrons (or holes) are generated thermally and then move from one part of a molecule to the other part of the same molecule, from molecule to molecule, from crystal to crystal (for polycrystalline sample), and from crystal to electrode. For a molecule of conjugated chains or ring systems the barrier hindering the electron transport within a molecule would be very small. The barrier between the boundary of an organic semiconductor and the attached electrode would depend on the character of the organic compound and the work function of the electrode material. When ohmic contact is made, this barrier would be eliminated. The activation energy for dark conduction may thus be considered as due partly to the energy E_N required for charge carrier generation and partly to the energy E_μ required to overcome the barriers for charge carrier transport. The temperature dependence of dark conductivity can be expressed as

$$\sigma = eN\mu = eN_0\mu_0 \exp[-(E_N + E_\mu)/2kT] \quad [3]$$

where μ is the carrier mobility and N_0 and μ_0 are constants. From Eq. [1] and [3], we have

$$\Delta E = E_N + E_\mu \quad [4]$$

It may be noted that E_N (not ΔE) would be considered as the "band gap" if such a concept could be adopted to the case of phthalocyanine.

The temperature dependence of photoconductivity for organic solids have been discussed by a number of authors (17, 20, 21). The difference in activation energies for photoconduction observed for the α and β phthalocyanine samples would rule out the application of the triplet theory (21). Such a theory, which was based on the molecular electronic states, would predict essentially the same activation energy for photoconduction for both α and β samples, since the absorption spectra in the ultraviolet and visible region for the samples were observed to be almost identical. In the present case the postulate proposed by Kommandeur and his co-workers (20) is adopted. The temperature dependence of photoconductivity may then be written as

$$\Delta\sigma = e\mu\Delta N = e\mu_0\Delta N \exp(-E_\mu/2kT) \quad [5]$$

assuming the increase in charge carrier concentration by light excitation, ΔN, to be independent of the temperature. Comparing Eq. [2] and [5], we have $E_\mu = 2\Delta\epsilon$. E_μ is calculated to be 0.68 ev for the β and 0.84 ev for the α. The higher barrier for the α sample compared to the β sample implies that the α sample is likely to be in the disordered state since structural imperfections would serve as traps or additional barriers hindering charge carrier transport.

Equation [4] may be written as $E_N = \Delta E - 2\Delta\epsilon$. From this equation, E_N is calculated to be about 0.6 ev for the α and 1.2 ev for the β. The higher value of E_N for the β form signifies that there exists a wider "band gap" for this form when compared to the α form. This result is in line with the disordered state of the α sample. Structural imperfections would introduce isolated energy levels in the "band gap" and hence the photocurrent threshold is lowered.

Acknowledgment

The authors wish to express their appreciation to R. W. Waite and M. J. Danzig of their laboratory for the preparation of the β form metal-free phthalocyanine.

Manuscript received Sept. 6, 1962; revised manuscript received Feb. 8, 1963. This paper was delivered before the Pittsburgh Meeting, April 15-18, 1963.

Any discussion of this paper will appear in a Discussion Section to be published in the June 1964 JOURNAL.

REFERENCES

1. G. Susich, *Anal. Chem.*, **22**, 425 (1950).
2. F. W. Karasek and J. C. Decius, *J. Am. Chem. Soc.*, **74**, 4716 (1952).
3. A. A. Ebert, Jr. and H. B. Gottlieb, *ibid.*, **74**, 2806 (1952).
4. A. N. Sidorov and I. P. Kotlyar, *Optics & Spectroscopy*, **11**, 92 (1961).
5. D. N. Kendall, *Anal. Chem.*, **25**, 332 (1953).

6. J. M. Robertson, *J. Chem. Soc.*, 615 (1935); 1195 (1936).
7. F. R. Tarantino, D. H. Stubbs, T. F. Cookes, and L. A. Melsheimer, *Am. Ink Maker*, **29**, 35 (1951).
8. A. S. Vartanyan, *J. Phys. Chem. U.S.S.R.*, **22**, 769 (1948); *C. A.*, **43**, 1272g (1949).
9. D. D. Eley, G. D. Parfitt, M. J. Perry, and D. H. Taysum, *Trans. Faraday Soc.*, **49**, 79 (1953).
10. D. D. Eley and G. D. Parfitt, *ibid.*, **51**, 1529 (1955).
11. P. E. Fielding and F. Gutman, *J. Chem. Phys.*, **26**, 411 (1957).
12. W. Felmayer and I. Wolf, *This Journal*, **105**, 141 (1958).
13. G. Tollins, D. R. Kearns, and M. Calvin, *J. Chem. Phys.*, **32**, 1013, 1020 (1960).
14. A. Many, E. Harnik, and D. Gerlich, *ibid.*, **23**, 1733 (1955).
15. G. H. Heilmeier, G. Warfield, and S. E. Harrison, *Phys. Rev. L.*, **8**, 309 (1962).
16. K. Wihksne and A. E. Newkirk, *J. Chem. Phys.*, **34**, 2184 (1961).
17. M. J. Danzig, C. Y. Liang, and E. Passaglia, *J. Am. Chem. Soc.*, **85**, 668 (1963).
18. C. Y. Liang, E. G. Scalco, and G. Oneal, Jr., *J. Chem. Phys.*, **37**, 459 (1962).
19. See for example: C. G. B. Garrett, "Semiconductors," N. B. Hannay, Editor, Reinhold Publishing Co., New York (1959); and "Symposium on Electrical Conductivity in Organic Solids," H. Kallmann and M. Silver, Editors, Interscience Publishers, New York (1960).
20. J. Kommandeur, G. J. Korinek, and W. G. Schneider, *Can. J. Chem.*, **35**, 998 (1957).
21. B. Rosenberg, *J. Chem. Phys.*, **29**, 1108 (1958).

Reactions Between Refractory Oxides and Graphite

K. L. Komarek, A. Coucoulas,[1] and N. Klinger[2]

Department of Metallurgy and Materials Sciences, College of Engineering, New York University, New York, New York

ABSTRACT

Reactions between alumina, magnesia, spinel, beryllia, and graphite have been studied in vacuum by measuring the amount of carbon monoxide formed. Two types of reactions were observed: a diffusion-controlled reaction with alumina, beryllia, and thoria, and a phase boundary-controlled reaction with magnesia, beryllia, spinel, and titania. The following activation energies were obtained: 316 kcal for Al_2O_3, 40 kcal for BeO below 1700°C (parabolic rate law), 61.3 kcal for BeO above 1700°C (linear rate law), 59.8 kcal for MgO, 59.5 kcal for spinel, and 59 kcal for TiO_2. The relative reactivities of these oxides with graphite increase in the following order: BeO, spinel, MgO, ThO_2, Al_2O_3, TiO_2. For the reactions following a linear rate law a mechanism is proposed. It was concluded that the reaction proceeds over the gas phase by dissociation of the oxide into atomic oxygen and that the desorption of carbon monoxide from the graphite surface is the rate-determining step.

In spite of great efforts our knowledge of the nature and the mechanism of most heterogeneous reactions is limited. Specifically, our understanding of the reaction between oxides and graphite is largely empirical and qualitative. This reaction has been studied on a selected group of refractory oxides to find by comparison common characteristics. An attempt has been made to explain some of the features of the reaction by analogy with other better known reactions.

Kroll and Schlechten (1) have conducted a qualitative investigation of the reaction of metal oxides and carbon in vacuum. Johnson (2) has determined temperatures for the beginning of the reaction of refractory oxides and graphite in vacuum. Nadler and Kempter (3) have found that yttria, urania, and thoria reacted with carbon at atmospheric pressure at 1540°, 1500°, and 1650°C, respectively. Pavlov (4) has studied the beginning of the reaction between various oxides and graphite with radioactive carbon and has suggested a linear relationship between the melting point of the oxides and the temperature of noticeable reaction.

[1] Present address: Air Reduction Co., Murray Hill, New Jersey.
[2] Present address: Bettis Plant, Westinghouse Electric Company, Pittsburgh, Pennsylvania.

Experimental

The reaction was studied in a high vacuum furnace shown in Fig. 1. The stainless steel shell (8⅝ in. OD, 11 in. high, ½ in. wall thickness) and the top and bottom plates (2 in. thick) are water-cooled and electrically insulated from each other. The graphite heating element (1 in. ID, 12 in. long, 3/16 in. wall) is fitted into copper contacts, and its outside diameter is reduced by ⅛ in. over a length of 5½ in. in the center to provide a uniform heating zone. A temperature of 2200°C can be attained easily with 1000 amp and 6v. On thermal expansion the element can slide along the contact cone of the upper plate. The element has two slits near the top so that the gas evolved can quickly establish equilibrium with the rest of the system. The radiation shields consist of four concentric 0.005 in. W and Mo cylinders. Molybdenum shields also cover the top and bottom of the cylindrical arrangement. A 1 in. Vycor window on top serves for visual observation and temperature measurement. It is protected by an iron shutter which can be shifted magnetically. The graphite sample container (⅝ in. ID, 1 in. long) is designed to approach black body conditions and can be magnetically lifted and lowered. The crucible lid

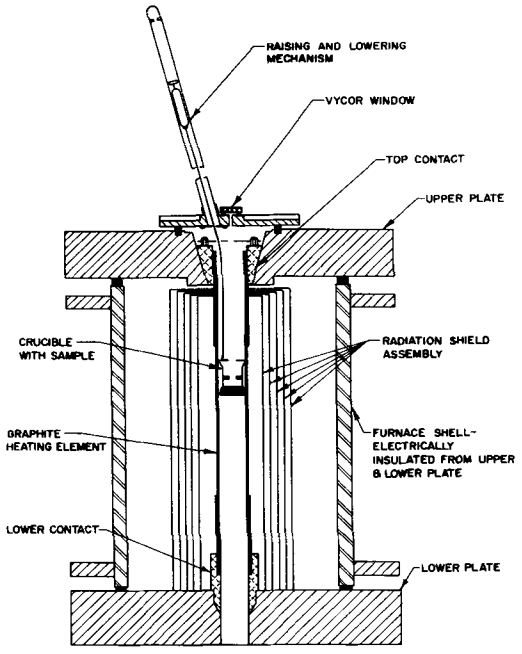

Fig. 1. High temperature furnace for measuring reactions between refractory oxides and graphite.

has a ⅛ in. hole at the top. The temperature is kept constant by a Pt/Pt-10% Rh thermocouple connected to a Celectray temperature controller which can divert a fraction of the current to a resistor if the temperature rises above a preset value. Temperature fluctuations are thus limited to 3°-5°C. The temperature of the sample is measured by an optical pyrometer (L&N, Type 8622-C) calibrated under experimental conditions against a Pt/Pt-10% Rh thermocouple with the junction covered by graphite. The linear relationship between the temperature of the thermocouple and that of the pyrometer in the range of 900°-1500°C was extended by extrapolation. The system is evacuated by an oil diffusion pump and a mechanical vacuum pump. A water-cooled baffle and a high vacuum valve above the diffusion pump prevent oil vapors from condensing in the furnace. The pressure is measured by an alphatron gauge (National Research Corporation, Type 520) and an ionization gauge (Consolidated Electrodynamics Corporation, Type VG-1A) which are directly attached to the upper plate of the furnace. The alphatron gauge has a range from 1×10^{4} to 1×10^{-4} mm Hg and the ionization gauge of 1×10^{-4} mm and below. A glass system with a calibrated flask and a McLeod gauge with a range between 2×10^{-1} and 5×10^{-6} mm Hg is connected to the upper plate.

Materials.—The graphite powder (325 mesh) had an average total ash content of less than 30 ppm (United Carbon Products Company, Bay City, Michigan). Beryllia was obtained in the form of hot-pressed compacts of 96+% theoretical density (courtesy of the Brush Beryllium Company, Cleveland, Ohio) which were prepared from UOX Grade powder. Alumina, purchased as a synthetic sapphire single crystal boule and as powder of −100 mesh (Linde Company, Boston, Massachusetts), had an impurity content of less than 10 ppm. Spinel in the form of a single crystal boule (Linde Company) had the chemical formula $MgO \cdot 3.3Al_2O_3$ with the following impurities (in weight per cent, w/o): 0.15 NiO, 0.05 TiO_2, 0.05 V_2O_5. Magnesia (courtesy of General Electric Company, Pittsfield, Massachusetts) was in the form of large fused crystals with an impurity content of 100 ppm. Titania was in the form of 99.9+% powder (Baker Analyzed Reagent Grade). Thoria powder of 99.9% purity (Heavy Minerals Company, Chattanooga, Tennessee) was cold pressed at a pressure of 54,000 psi and the compacts sintered in oxygen at 1650°C for 2 hr.

The oxides were comminuted to powder, and the fraction between 100 and 140 mesh was collected. Excess graphite was added at the same oxide to graphite ratio for each mixture. The total weight of the samples varied from 0.1 to 1g, but variations within this range had no effect on the results. With approximately 50 graphite particles per oxide particle there was in the average no contact and therefore no sintering of oxide particles.

Procedure.—The powders were weighed on a semimicrobalance, thoroughly mixed in the graphite crucible, covered with a layer of graphite powder, and placed in the furnace. The furnace was evacuated for 18 hr at room temperature, then heated and held for 5 hr about 100°C above the reaction temperature to degas the system. During this period the sample remained in the cooler zone of the heating element (900°-1000°C). The high vacuum valve was then closed and the leak rate was measured. Values lower than 0.1μ Hg/30 sec were acceptable. If the leak rate was too high, the degassing was repeated. The crucible was then raised to the hot zone and the pressure was measured as a function of time by the alphatron gauge. The temperature of the sample was recorded at regular intervals with the optical pyrometer. The runs lasted for 15-60 min depending on the rate of reaction at a given temperature. Rates were in the range of 0.5-5μ/30 sec. At the end of the run the sample was lowered to the cold zone, and the leak rate was again measured with the gas still in the system.

The reactions were followed only to a few per cent reduction to keep the total pressure within one scale of the alphatron gauge and to limit the time of one run to 1 hr, since temperature control at high temperatures was difficult. This also made it unnecessary to correct for changes in particle size during the reaction. The total pressure was usually kept below 100μ to eliminate problems arising from diffusion in the gas phase and to stay well below the equilibrium pressure. Since at high temperatures and low pressures the amount of CO_2 in the gas is negligible, the pressure after calibration can be expressed in moles of CO. To convert the pressure readings into mm Hg the alphatron gauge was calibrated against the McLeod gauge at various pressures with the furnace at temperature. For further conversion of pressures into moles CO the volume of the glass system was determined with helium at room temperature with a glass flask of known volume previously calibrated by the National Bureau of Standards. By expanding a known quantity of CO into the furnace kept at the reaction temperature a

pressure relationship was obtained which allowed the experimental results to be expressed in moles CO per oxide particle or per unit area.

Results

In preliminary experiments the reaction between CO and molybdenum was checked. A molybdenum sheet was heated to the reaction temperature in pure CO of 50μ. There was no noticeable pressure change over a 30-min period. Nevertheless, as a precautionary measure the furnace was preconditioned by heating in CO atmosphere. To determine the effect of degassing, a graphite crucible with 0.5g graphite powder was placed in the cold zone (at about 800°C) while the furnace was degassed at 1300°C for 5 hr. The high pressure valve was then closed and the crucible was raised to the hot zone. For the first 90 sec there was an increase in pressure to about 0.5μ, but after this period the degassing effect was smaller than the leak rate. The procedure was repeated with 0.5g of each oxide in a molybdenum crucible, and about the same initial increase in pressure was found for the same length of time.

Alumina.—Alumina from the single crystal boule was studied in the range of 1307°-1450°C with a weight ratio of 0.944 alumina to graphite. Two runs, at 1439° and 1450°C, were carried out to 2% completion, the others to 1% or less. After the reaction at 1401°C had progressed for a short time, a drop in temperature was recorded, but there were enough data for the initial stage to be included in the results. The reaction seems to follow a parabolic rate law, as can be seen from the plot of moles CO x 10^8/10,000 particles *vs* $\sqrt{t}$ (Fig. 2). The parabolic rate equation has been derived from $dn_{(CO)}/dt = k_p/n_{(CO)}$ which on integration gives $n^2_{(CO)} = 2k_pt$ where $n_{(CO)}$ is the moles of CO evolved, t is the time in seconds, and k_p is the parabolic rate constant. The plot of $n_{(CO)}$ *vs.* $\sqrt{t}$ gives straight lines and from the slope, $\sqrt{2k_p}$, the parabolic rate constant can be obtained. Figure 3 is a plot of log k_p *vs.* $1/T$. The method of least squares gives a value of 316 kcal for the activation energy (curve I) from the relation $E = 4.575\ \Delta\log\ k_p/\Delta(1/T)$. Less accurate short-time experiments with

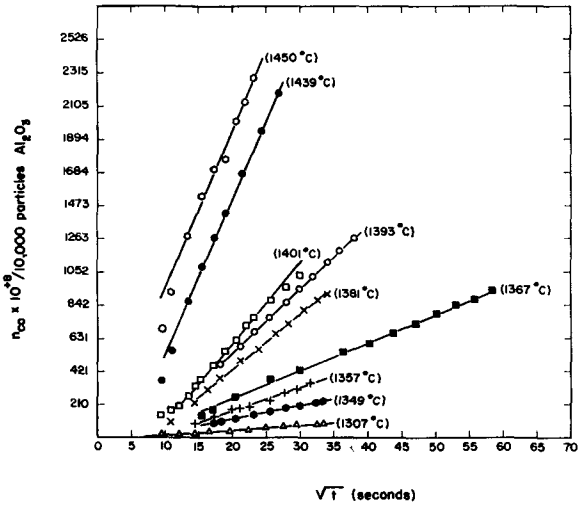

Fig. 2. Normalized concentration of liberated CO as a function of time at various temperatures for the reaction alumina-graphite.

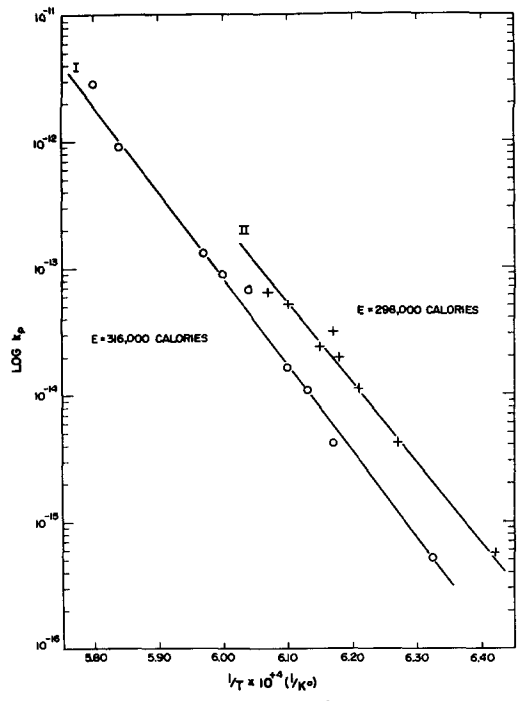

Fig. 3. Parabolic rate constant as a function of reciprocal temperature for the reaction alumina-graphite.

alumina powder and graphite of mesh size −100 gave similar results. Log k_p *vs.* $1/T$ is shown as curve II in Fig. 3. The two curves are almost parallel, but curve II is shifted to the right indicating a higher rate at the same temperature for oxide of smaller particle size. No deposits were observed on the colder parts of the furnace.

Magnesia.—Magnesia was studied in the range of 1352°-1558°C. A weight ratio of 0.872 magnesia to graphite was used; results are shown in Fig. 4. During the reaction at 1450°C the temperature changed and a second curve at 1462°C was drawn for the same run. The run at 1388°C had progressed for some time before the temperature became constant. A run at 1352°C and one at 1432°C are not shown in Fig. 4, but are included in Fig. 5. For all experiments a linear time law is eventually attained. The linear rate relation is obtained by integrating $dn_{(CO)}/dt = k_L$ which lead to $n_{(CO)} = k_Lt$ where k_L is the linear rate constant. An activation energy of

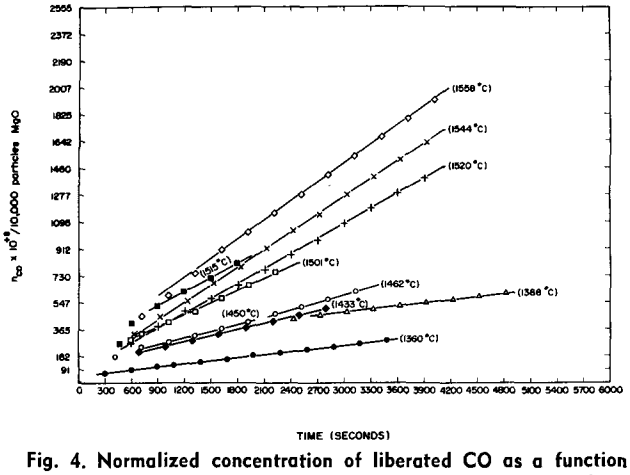

Fig. 4. Normalized concentration of liberated CO as a function of time at various temperatures for the reaction magnesia-graphite.

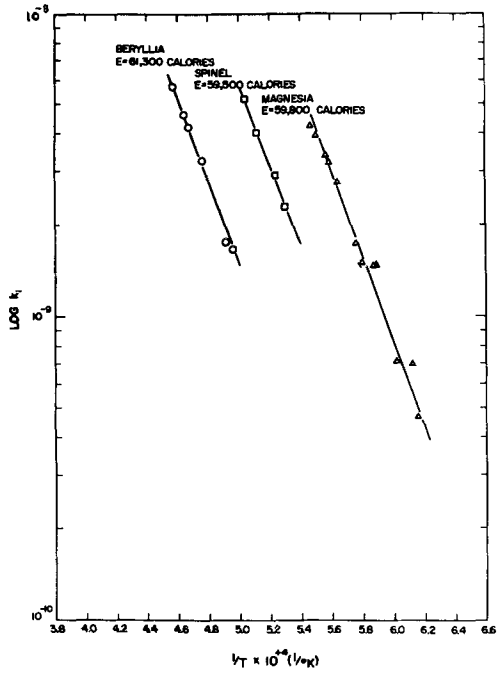

Fig. 5. Linear rate constant as a function of reciprocal temperature for the reaction magnesia-graphite, spinel-graphite, and beryllia-graphite.

59.8 kcal was calculated from the slope of the plot log k_L *vs.* $1/T$ (Fig. 5). Some magnesium condensed on the colder parts of the furnace. Since it could react with CO to form MgO and C which would reduce the CO pressure in the system, an attempt was made to determine the extent of this back reaction. A nickel container with nickel filings was placed above the crucible to absorb the magnesium vapor by alloy formation before it had a chance to condense and to react with CO. Although the pressure readings were not higher than those for the other magnesia runs, a slight negative leak rate (about $-0.1\mu/30$ sec) after completion of all the runs indicated some back reaction. This leak rate was small and was approximately the same for all the experiments so that at higher reaction rates the effect of the back reaction on the experimental results was slight.

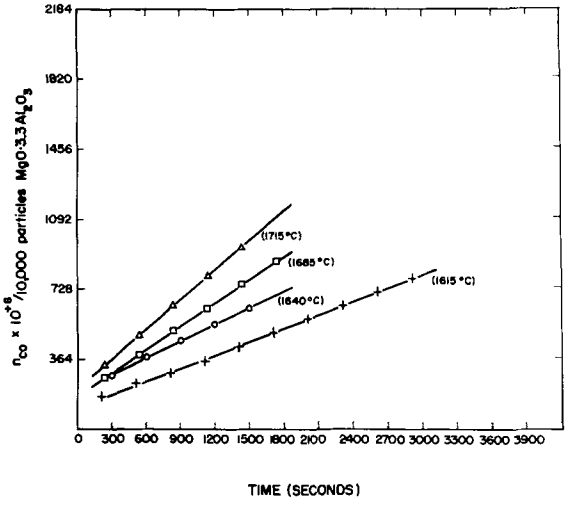

Fig. 6. Normalized concentration of liberated CO as a function of time at various temperatures for the reaction spinel-graphite.

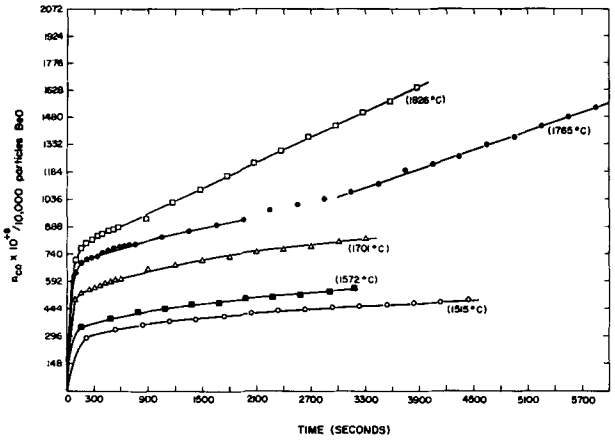

Fig. 7. Normalized concentration of liberated CO as a function of time at various temperatures for the reaction beryllia-graphite in the parabolic range.

Spinel.—Spinel was selected as an example of the reactivity of a binary compound. It had an approximate composition of 23.2 mole % MgO which according to the phase diagram (5) should be just inside the two-phase region between Al_2O_3 and the solid solution of Al_2O_3 in spinel. Since the sample was a single crystal it was probably supersaturated with Al_2O_3. Experiments were carried out from 1615° to 1715°C with a weight ratio of 0.880 spinel to graphite. The $n_{(CO)}$ *vs.* time plot (Fig. 6) is linear with an activation energy of 59.5 kcal (Fig. 5). Small deposits similar to those in the magnesia runs were found. Negative leak rates (about $-0.1\mu/30$ sec) after the completion of the reaction indicated some back reaction.

Beryllia.—Beryllia was studied from 1515° to 1913°C with a weight ratio of 0.680 beryllia to graphite. Results are shown in Fig. 7 and 8. At lower temperatures (between 1515° and 1765°C) the reaction follows initially an apparently parabolic rate law which can best be seen in a $\sqrt{t}$ plot with an activation energy of approximately 40 kcal. This value could not be determined more accurately due to low reaction rates and a large pressure increase at

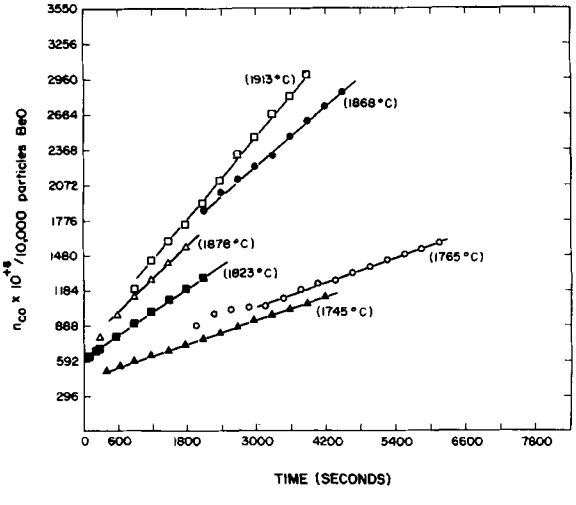

Fig. 8. Normalized concentration of liberated CO as a function of time at various temperatures for the reaction beryllia-graphite in the linear range.

Table I. Standard free energies of oxide-graphite reactions

Reaction	$\Delta G°_T$, in cal/g-mole CO	References
$2Al_2O_{3(s)} + 9C_{(s)} = Al_4C_{3(s)} + 6CO_{(g)}$	$+98{,}400-44.9T$	(7), (8)
$MgO_{(s)} + C_{(s)} = Mg_{(g)} + CO_{(g)}$	$+149{,}300-70.8T$	(7)
$MgO\cdot 3.3Al_2O_{3(s)} + 15.85C_{(s)} = Mg_{(g)} + 1.65Al_4C_{3(s)} + 10.9CO_{(g)}$	$+103{,}500-47.0T$	(9-12)
$2BeO_{(s)} + 3C_{(s)} = Be_2C_{(s)} + 2CO_{(g)}$	$+100{,}900-40.7T$	(13), (14)
$BeO_{(s)} + C_{(s)} = Be_{(g)} + CO_{(g)}$	$+188{,}100-70.8T$	(7), (8)
$ThO_{2(s)} + 4C_{(s)} = ThC_{2(s)} + 2CO_{(g)}$	$+97{,}100-42.7T$	(7), (11)

the beginning of each reaction. The apparent parabolic stage is followed by an increase in the rate of reduction which eventually becomes constant, *i.e.*, linear. Six successful experiments were carried out in the linear range between 1745° and 1913°C. All samples with the exception of that at 1868°C had been preheated and kept in a dessicator prior to the runs. The run at 1868°C showed a slightly higher initial pressure increase than the others, but the rate of reaction was not affected. A plot of log k_L *vs.* $1/T$ (Fig. 5) gave an activation energy of 61.3 kcal for the linear reaction. In all experiments above 1745°C a small deposit was found on the colder regions of the furnace.

Titania and thoria.—Two short runs at 929° and 959°C were made with titania with a particle size of −100 mesh. The weight ratio of titania to graphite was 2.07. The reaction followed a linear rate law, and from the two points an activation energy of 58.5 kcal was obtained. Thoria reacted in the temperature range 1430°-1550°C. A weight ratio of thoria to graphite of 2.14 was used. Plots of $n_{(CO)}$ *vs.* time follow a parabolic rate law, and plots of $n_{(CO)}$ *vs.* $\sqrt{t}$ are straight lines. The scatter in the data, however, was too great to evaluate an activation energy.

Discussion

The size of the oxide particles in all experiments was the same. Their shape when viewed under the microscope was similar and roughly spherical. While the actual surface roughness and the surface and contact area of the reactants were not known, it could be assumed that these parameters were approximately the same for all experiments. The observed specific rates will differ from the absolute specific rates by an unknown but constant factor, but the activation energies will be the same as for samples with well-defined contact areas. Furthermore, the ratio between experimental specific rates will be the same as between absolute specific rates. The oxide powders were made from single crystals or highly sintered compacts to obtain smooth surfaces with a minimum of adsorbed gases. The pressure of CO during the experiments was always much lower than the equilibrium pressures as calculated from the standard free energy equations computed from published data (Table I). Any back reaction between the products can therefore be neglected, especially since it was observed that in similar systems (15) the rate of the back reaction is much slower than that of the forward reaction. The primary gaseous product of the reaction is most probably CO since Eyring and co-workers (16, 17) have found that in the oxidation of graphite CO and not CO_2 is formed. Thermodynamic calculations show that CO will not undergo conversion to CO_2 to any measurable extent under the conditions of our experiments.

Alumina.—The reaction between alumina and graphite follows a parabolic rate law, with k_p given in Table II. The rate-controlling step is probably the diffusion of one or more ion species through an intermediate layer of one or more carbide phases. Aluminum forms two stable oxycarbides, Al_4O_4C, and Al_2OC, and the stable carbide Al_4C_3 (18). Prescott and Hincke (19) have measured the CO equilibrium pressure between 1700° and 2020°C by assuming the formation of Al_4C_3. Their results show excellent agreement at 1600°C with data calculated from heats of formation and entropies (13), but with increasing temperature the two values diverged. At the lower temperatures apparently no substantial amounts of oxycarbides were formed, and the measured CO pressures were therefore consistent with the equation in Table I. At higher temperatures the deviation was caused by loss of aluminum by vaporization as Al or Al_2O, as shown by a cream-colored deposit, and the formation of oxycarbides. Incidentally, at very high temperatures Al_4C_3 decomposes into gaseous Al and solid C (20). Our experiments were carried out much below 1700°C, and no deposit was observed. It was therefore concluded that the reaction proceeded according to the equation in Table I and that the intermediary layer formed was Al_4C_3. A high activation energy is not uncommon for diffusion-controlled processes in aluminum compounds. From sintering studies of Al_2O_3 in vacuum, Kuczynski (21) has obtained an activation energy for diffusion of oxygen of 230 kcal. It is therefore not impossible that the diffusion of ions through the intermediate carbide layer may have the high activation energy

Table II. Specific rates of reactions between oxides and graphite

Oxide	Temperature range, °K	Experimental specific rate constants
MgO	1625-1831	$k_L = 6.34 \times 10^{-2} \exp(-59{,}800/RT)$
Spinel	1888-1988	$k_L = 1.82 \times 10^{-2} \exp(-59{,}500/RT)$
BeO	2018-2186	$k_L = 7.64 \times 10^{-3} \exp(-61{,}300/RT)$
Al_2O_3	1580-1723	$k_p = 2.42 \times 10^{28} \exp(-316{,}000/RT)$
BeO	1788-2018	$k_p = 1.01 \times 10^{-10} \exp(-40{,}000/RT)$

calculated. A further clarification of the mechanism will have to wait for additional experiments, especially the measurement of the movement of inert markers and the determination of the chemical constitution of the intermediate layer.

Magnesia.—The reaction between magnesia and graphite is the basis of the Hansgirg process for the carbothermic production of magnesium (22). Since the two magnesium carbides, MgC_2 and Mg_2C_3, are thermodynamically unstable over the whole temperature range (13), the reaction will proceed according to the equation in Table I. The reaction follows a linear rate law, and from analogy with oxidation the reaction can be said to be phase boundary controlled. The k_L values are given in Table II. The reaction was studied by Russian investigators (23) by weight loss measurements. At the optimum reaction rate they obtained an activation energy of 53 kcal which agrees reasonably well with ours. They concluded that the reduction is primarily due to intermediate reactions in the gas phase involving carbon oxides and not due to the reduction of MgO vapors or the dissociation of MgO into Mg and O and subsequent reaction with C. Our results indicate that the reaction most probably proceeds by dissociation of MgO.

Spinel.—The data indicate that at least the initial reaction is phase boundary controlled with the same activation energy as for MgO, namely 59.5 kcal. The k_L value is given in Table II. The ratio of the specific rates of MgO and spinel is $k_{MgO}/k_{spinel} = 3.48$ or $k_{spinel} = 0.288\ k_{MgO}$. Therefore at all temperatures magnesia is 3.5 times as reactive as spinel. As a probably fortuitous coincidence k_L of spinel is approximately equal to k_L of MgO multiplied by the mole fraction of MgO in spinel (nominal composition $N_{MgO} = 0.232$). Although the mechanism of the reaction is obscure, two possible explanations are given. Since the activation energy is the same as for magnesia and since a deposit was formed on the walls, the reaction proceeded according to the equation in Table I and the rate-determining step was the same as for magnesia. The lower rate is then simply a consequence of the lower magnesia content. In view of the rate of the alumina reaction this explanation is not very satisfactory. As a more plausible explanation one could assume that at the higher temperatures of the spinel reaction alumina will react with graphite to form CO and gaseous aluminum and that this reaction will obey the same general linear rate law as exemplified by the magnesia reaction. The spinel reaction would then obviously follow the same pattern. Unfortunately the deposit was too small to allow for an analysis of the relative amounts of magnesium and aluminum.

Beryllia.—Beryllium forms only one stable carbide, Be_2C, which dissociates without melting above 2150°C (24) and vaporizes predominantly to the elements (20). Since BeO reacts with graphite and melts at about 2300°C to form an unidentified compound, the existence of condensed oxycarbides is not excluded. However, in the absence of further information the reaction below 1700°C is treated as leading to Be_2C and above 1700°C to gaseous beryllium (Table I). The reaction is somewhat complex and resembles strongly the oxidation of a metal, *e.g.*, tantalum (25), where an initial protective stage obeying a parabolic rate law is followed by an increase in the oxidation rate which eventually becomes constant (linear or breakaway oxidation). The curve of $n_{(CO)}$ *vs.* time can be divided into three distinct sections. At the beginning there is a sudden rise in pressure which is only moderately well reproducible. Part of this pressure rise is due to degassing and/or dehydrating of the oxide but the effect could not be eliminated by preheating the oxide powder for 30 min at 1800°C in vacuum. It is quite possible that the BeO contained a small amount of an easily reducible oxide, visible as gray regions in the sintered compacts, which was picked up during compacting and hot pressing and which was reduced in the first stage. Although the curves were shifted due to this reaction, the shapes of the subsequent parabolic and/or linear sections were not affected.

The second parabolic stage with an activation energy of 40 kcal is clearly observed only at low or intermediate temperatures. It is assumed that an intermediate layer of Be_2C is formed and that the rate is controlled by diffusion of one or more species (ions) through the layer. The nature of the diffusing ions was not established. The parabolic region is followed by a third linear stage in which the reaction is phase boundary controlled with an activation energy of 61.3 kcal. The incubation period for the onset of the linear rate becomes shorter with increasing temperature. Above 1830°C the incubation period becomes too short to be observed clearly with the experimental technique employed. The change from the parabolic to the linear rate law can be explained by assuming that after a certain thickness growth stresses will induce cracks and fissures in the Be_2C layer. The break-up can also be caused by the dissociation of Be_2C which will increase rapidly in this temperature range. At high enough temperatures the stability of Be_2C will be so low that the reaction will proceed without the formation of an intermediate carbide layer and the products will be gaseous beryllium and CO. The experiments at the highest temperatures corroborate this explanation since only the linear rate law is observed with an activation energy close to that of the magnesia reaction and a deposit is formed at the colder parts of the furnace. Table II gives the k_L and k_p values.

Titania and thoria.—The initial reaction with TiO_2 follows a linear rate law with an approximate activation energy of 59 kcal. Due to the unspecified particle size k_L could not be calculated. TiO_2 loses oxygen on heating, and recent investigations of weight changes of TiO_2 in a vacuum of 10^{-6} mm Hg indicate that the decomposition commences above 875°C (26). Since in our experiments the temperature and the pressure were of the same order, the reaction proceeded probably over the gas phase by decomposition of TiO_2 without the formation of TiC. The oxygen reacted with graphite to form CO. The rate-determining step was probably the rate of oxidation of graphite, since the rate of decomposition of TiO_2 should depend on the diffusion of ox-

ygen ions in the rutile lattice and the reaction would then follow a parabolic rate law.

Thorium forms with certainty two carbides, ThC and ThC_2, but no oxycarbides have been reported. Although the first investigation (15) of the reaction between ThO_2 and carbon was based on the equation in Table I, the most probable product is a mixture of ThC_2 and ThC (27). Our results show that the reaction follows a parabolic rate law. The rate-determining step is the diffusion of unidentified ions through a thorium carbide layer.

Reactivity

The relative reactivities of oxides following the linear rate law can be simply expressed in terms of the apparent specific rates given in Table II. Since for these oxides the exponential term is the same within the limits of experimental error, the ratio of the apparent rates will be equal to that of the absolute rates and will be independent of temperature. Relating all the rates to that of BeO we obtain $k_{MgO} : k_{spinel} : k_{BeO} = 8.28 : 2.38 : 1$ which are also the ratios of the reactivities of these oxides with graphite, the reactivity of BeO taken as unity. The reactivities of all oxides increase in the following order: BeO, spinel, MgO, ThO_2, Al_2O_3, TiO_2.

Beryllia is the most stable oxide in contact with graphite. However, as shown by spinel, it is quite possible that a binary compound of beryllia with some other oxide has an even greater stability. A closer scrutiny reveals no quantitative relationship between the reaction temperature and the melting points of the oxides or the thermodynamic stability as suggested by Pavlov (4).

The results of previous investigators are given in the same order with the lowest temperature of reaction in °C in parenthesis:

ThO_2 (1380°), Al_2O_3 (1350°), MgO (1350°), BeO (1315°), TiO_2 (1100°) (1).

BeO (2300°), ThO_2 (2000°), MgO (1800°) (2).

ThO_2 (1650°-1730°), UO_2 (1500°-1620°), Y_2O_3 (1540°-1590°) (3).

With the exception of the reactivity of BeO observed by Kroll and Schlechten (1), the qualitative agreement is good. The reaction temperatures, however, vary widely depending on the experimental conditions.

Kinetics and Mechanism

The oxides investigated react with graphite either according to a linear rate law (MgO, spinel, BeO, TiO_2) or according to a parabolic rate law (Al_2O_3, BeO, ThO_2). The common feature of the latter reaction will be the formation of a carbide or oxycarbide layer, and the rate will be controlled by diffusion of one or more ion species through the layer. Since the nature of the ions and of the layer will be different in each individual case, the activation energies will not be the same. In the reactions following a linear rate law a carbide layer is not formed at all or the carbide layer does not determine the rate of the reaction. Since the activation energy for all oxides obeying the linear rate law is the same within the experimental error, *i.e.*, about 60 kcal, the same elementary process seems to be rate-determining, and a general common explanation can be derived. Experimental and theoretical evidence suggests that the linear reaction proceeds by decomposition and/or evaporation of the oxide and subsequent reaction of the gas with graphite, and not in the solid state.

The decomposition pressures (p_O and p_{O_2}) have been calculated from thermodynamic data (7, 28), based on the equations $2MeO_{(s)} = 2Me_{(g)} + O_{(g)}$, $2MeO_{(s)} = 2Me_{(g)} + 2O_{(g)}$, and $p_{Me} = p_O + 2p_{O_2}$. Although vapor pressures of MgO and BeO have been measured (29, 30), only total vapor pressures can be obtained from these data. According to Brewer and Porter (31) solid MgO vaporizes mainly as MgO gas, and the partial pressures of Mg, O, and O_2 contribute only slightly to the total vapor pressure. This result is at variance with data obtained by Porter *et al.* (32) who found at 1950°K the following species in decreasing pressure order: Mg, O, MgO. The ratio Mg/MgO was greater than 1000. It was observed that the total pressure over $MgO_{(s)}$ might be high because of generation of Mg gas by reduction of $MgO_{(s)}$ as indicated by the fact that $Mg >> O_2$. The composition of the vapor above $BeO_{(s)}$ at 2242°K was investigated by Chupka *et al.* (33). The species observed in decreasing pressure order were (in atm) : Be(5.0×10^{-7}), O(5.0×10^{-7}), $(BeO)_3$ (1.0×10^{-7}), $(BeO)_4$ (4.4×10^{-8}), O_2(2.0×10^{-8}), and several other BeO-polymers.

For the weight loss of the oxide one can use as a first approximation Langmuir's equation with accommodation coefficient unity

$$W = \frac{p}{17.14}\sqrt{\frac{M}{T}}$$

where W is the rate of evaporation in g/cm²-sec, p the vapor pressure of the material in mm Hg, M the molecular weight of the material in the gas phase, and T the temperature in °K. The application of Langmuir's equation seems to be justified since in our experiments the pressure was at the most 100μ and the distance between oxide and graphite particles was much smaller than the mean free path. Any molecule leaving the surface of an oxide particle would therefore strike a graphite particle before colliding with another gas molecule. Since an oxide particle was completely surrounded by graphite particles, the probability was small that a molecule, evaporated from the surface of an oxide particle, would strike the surface of another oxide particle.

The experimental rates of weight loss, $W_{exp.}$, were compared with calculated theoretical rates, $W_{theor.}$. Experimental weight losses were calculated from k_L values (Table II). For example, k_L for MgO at 1625°K is 5.64×10^{-10} $n_{(CO)}$/10,000 particles/second ($n_{(CO)} = n_{(O)} = 2n_{(O_2)} = n_{(MeO)} = xn_{(MeO)x}$). The number of moles were converted into grams by multiplying by the molecular weight: $g_{(CO)} = 28n_{(CO)}$; $g_{(O)} = 16n_{(CO)}$; $g_{(O_2)} = 32n_{(O_2)} = 16n_{(CO)}$; $g_{(MeO)} = MeO \cdot n_{(CO)}$; $g_{(MeO)x} = X \cdot MeO \cdot n_{(MeO)x} = MeO \cdot n_{(CO)}$. Assuming spherical shape, the surface area of 10,000 particles is about 5.1 cm². We obtain $W_{exp.}$/cm²/sec as 3.1×10^{-9} $g_{(CO)}$, 1.8×10^{-9} $g_{(O)}$

Table III. Rates of weight loss of MgO and BeO

T, °K	$W_{exp.}$ $g_{(O)}/cm^2 \cdot sec$	$g_{(MgO)}/cm^2 \cdot sec$	$g_{(O)}/cm^2 \cdot sec$	$W_{theor.}$ $g_{(O_2)}/cm^2 \cdot sec$	$g_{(MgO)}/cm^2 \cdot sec$
		MgO			
1625	1.8×10^{-9}	4.5×10^{-9}	3.4×10^{-9}	1.0×10^{-8}	1.8×10^{-7}
1793	9.8×10^{-9}	2.5×10^{-8}	1.0×10^{-7}	3.0×10^{-7}	6.3×10^{-6}
1880	2.1×10^{-8}	5.4×10^{-8}	4.6×10^{-7}	1.3×10^{-6}	2.8×10^{-5}
T, °K	$W_{exp.}$ $g_{(O)}/cm^2 \cdot sec$	$g_{(BeO)}/cm^2 \cdot sec$	$g_{(O)}/cm^2 \cdot sec$	$W_{theor.}$ $g_{(O_2)}/cm^2 \cdot sec$	$g_{(BeO)_x}/cm^2 \cdot sec$
		BeO			
1625	1.3×10^{-10}	2.1×10^{-10}	1.9×10^{-11}	3.5×10^{-13}	1.1×10^{-12}
1880	1.8×10^{-9}	2.8×10^{-9}	5.8×10^{-9}	1.8×10^{-10}	9.9×10^{-10}
2000	4.8×10^{-9}	7.5×10^{-9}	4.9×10^{-8}	1.6×10^{-9}	1.4×10^{-8}
			Ratio W_{MgO}/W_{BeO}		
T, °K	Exp, (O)	Exp. (MeO)	Theor. (O)	Theor. (O_2)	Theor. (MeO)
1625	1.4×10^{1}	2.1×10^{1}	1.8×10^{2}	2.9×10^{4}	1.6×10^{5}
1880	1.2×10^{1}	1.9×10^{1}	8×10^{1}	7.2×10^{3}	2.8×10^{4}

(or $g_{(O_2)}$), or 4:5 x 10^{-9} $g_{(MeO)}$ (or $g_{(MeO)x}$). Since the surface area of the oxide particles will be larger than 5.1 cm^2/10,000 particles, $W_{exp.}$ as calculated will be the maximum value. In Table III experimental and theoretical rates are listed for several temperatures. Theoretical rates for atomic oxygen (column 4) and molecular oxygen (column 5) were calculated from thermodynamic data (7, 28). Rates for gaseous MgO (column 6) were obtained from the data by Brewer (31). For gaseous BeO the combined rates for $(BeO)_3$ and $(BeO)_4$ are given (33).

The theoretically calculated rates for MgO exceed in the experimental temperature range the observed rates for all evaporation processes. Due to the difference in the temperature coefficients, the theoretical weight losses decrease much faster with decreasing temperature than $W_{exp.}$ so that $W_{exp.}$ will eventually exceed $W_{theor.}$. Therefore at some lower temperature the evaporation process of the oxide may become the rate determining step and the reaction rate will become negligible. For weight losses based on atomic oxygen, $W_{exp.}$ and $W_{theor.}$ will be equal at 1575°K. It should be noted that at 1625°K the CO pressures were already so small that they could be measured only with difficulty. The data for BeO show that the extrapolated rates for atomic oxygen will be equal at 1780°K. At this temperature $W_{exp.}$ for BeO will be the same as $W_{exp.}$ for MgO at 1575°K. The relative reactivity as expressed by the ratio of the experimental weight losses (Table III) is of the order of 10 and varies but little with temperature. Although the ratios of the theoretical values for each evaporation process are larger and show a greater change with temperature, the data for atomic oxygen are much closer to the experimental values. The data indicate that the decomposition pressures of MgO and BeO are high enough to account for a reaction over the gas phase. There is strong evidence that the species entering the reaction is atomic oxygen and not gaseous oxide. The linear reaction will start when the partial pressure of atomic oxygen exceeds a certain value, but the rate of decomposition of the oxide does not seem to be the rate-controlling step of the linear reaction.

The final step in the reaction sequence will be the formation of an adsorbed oxygen atom at the graphite surface and the desorption of CO. These steps should bear a close relation to the oxidation of graphite by oxygen, water vapor, or carbon dioxide. According to Binford and Eyring (16) the reaction between water vapor and graphite is of zero-order with an activation energy of 60.3 kcal/mole in the 900°-1100°C range. In the 1200°-1300°C range it changed to a first order process with an activation energy of 42.9 kcal/mole. They assumed that there are two types of active sites on the graphite surface which are important in oxidation processes. At lower temperatures the rate-determining step is the desorption of CO from the first kind of active sites, and at higher temperatures it is the adsorption of H_2O at active sites of the second kind. In a more recent investigation the same authors (34) concluded that the rate-determining steps are the desorption of H_2O with an activation energy of 35.6 kcal and the desorption of H_2 with an activation energy of 75 kcal. In a study of the reaction between oxygen and graphite, Blyholder and Eyring (17) observed that with very thin samples the surface reaction is zero order with an activation energy of about 80 kcal/mole. On thicker samples, the diffusion of oxygen into the pores in the graphite resulted in an observed one-half order reaction with an activation energy of 42 kcal/mole. A general kinetic theory of the oxidation of carbonized filaments was developed (6), and for very high temperatures a zero-order reaction with an activation energy of about 80 kcal/mole was proposed with desorption of CO as the rate-determining step. The gasification of various grades of carbon and graphite by CO_2 in a fluidized bed was studied by Ergun (35). The author deduced that the rate-determining step is the desorption of CO. From the product of the specific rate of desorption and the total number of active sites the same activation energy, 59 kcal/mole, was obtained for all grades

of graphite. The results suggested that in the 700°-1400°C range the number of reaction sites is independent of temperature.

The perfect agreement between the activation energies obtained in this investigation and that for the reaction between CO_2 and graphite (35) suggests that for the linear reaction the desorption of CO from the graphite surface is the rate-determining step. Since the specific rate will be the same for all reactions, any difference in the reaction rates has to be explained by a difference in the number of active sites on the graphite surface. Our results could be explained by the assumption that metal atoms will also become adsorbed at the graphite surface and will therefore reduce the number of active sites available for oxygen atoms. The number of graphite atoms thus de-activated will be a function of the bond strength between a metal and a graphite atom. An indication of the strength of this bond is the thermodynamic stability of the metal carbides. Since magnesium carbides are unstable and beryllium carbide is stable up to high temperatures, more active sites on the graphite surface are covered by beryllium atoms than by magnesium atoms. The rate of reaction between BeO and graphite will therefore be lower than that between MgO and graphite. A similar explanation can be proposed for spinel, since an Al-C bond is stronger than an Mg-C bond. The desorption of CO as the rate-determining step also explains the admittedly very sketchy results for TiO_2 with an activation energy of 59 kcal. Even if a different mechanism is operative for MgO and BeO, it is quite possible that at the beginning of the reaction between TiO_2 and graphite, the desorption of CO is the rate-determining step.

In conclusion we can say that present evidence suggests that the rate-determining step of the reaction between oxides and graphite obeying a linear rate law is the desorption of CO from the graphite surface. Since the decomposition pressures of the oxides are high enough and the theoretical and experimental weight losses are the same at the beginning of the linear reaction for MgO and BeO, the reaction proceeds probably over the gas phase by dissociation of the oxide into atomic oxygen.

Acknowledgment

The work presented in this paper is based on research sponsored by Aeronautical Research Laboratory, Wright Air Development Division, Office of Aerospace Research, on Contract No. AF 33(616)-6082. The authors wish to acknowledge the helpful interest of Captain H. Rizzo, project engineer, and permission to publish the results.

Manuscript received Sept. 13, 1962; revised manuscript received March 7, 1963. This paper was delivered at the Los Angeles Meeting, May 7-10, 1962.

Any discussion of this paper will appear in a Discussion Section to be published in the June 1964 JOURNAL.

REFERENCES

1. W. J. Kroll and A. W. Schlechten, *J. (and Trans.) Electrochem. Soc.*, **93**, 247 (1948).
2. P. Johnson, *J. Am. Ceram. Soc.*, **33**, 168 (1958).
3. M. R. Nadler and C. P. Kempter, *Rev. Sci. Inst.*, **32**, 43 (1961).
4. Y. A. Pavlov *et al.*, "Primenenie Radioktiv. Izotopov v Met. Sbornik," **34**, 48 (1955).
5. E. M. Levin, H. F. McMurdie, and F. P. Hall, "Phase Diagrams for Ceramists," Amer. Ceram. Soc., Inc., Columbus (1956).
6. G. Blyholder, J. S. Binford, and H. Eyring, *J. Phys. Chem.*, **62**, 263 (1958).
7. J. P. Coughlin, *U.S. Bur. Mines Bull. 542*, XII, (1954).
8. J. F. Elliott and M. Gleiser, "Thermochemistry for Steelmaking," Vol. 1, American Iron Steel Inst. (1960).
9. F. D. Richardson *et al.*, *J. Iron Steel Inst.*, 213 (1950).
10. E. G. King, *J. Phys. Chem.*, **59**, 218 (1955).
11. O. Kubaschewski and E. LL. Evans, "Metallurgical Thermochemistry," Pergammon Press, New York (1958).
12. K. K. Kelley, *U.S. Bur. Mines Bull. 584*, XIII, (1960).
13. C. W. Beckett *et al.*, *U.S. Nat. Bur. Standards Report 6645* (1960).
14. R. Hultgren *et al.*, "Selected Values for the Thermodynamic Properties of Metals and Alloys," Minerals Research Laboratory (1960).
15. C. H. Prescott and W. B. Hincke, *J. Am. Chem. Soc.*, **49**, 2744 (1927).
16. J. S. Binford and H. Eyring, *J. Phys. Chem.*, **60**, 486 (1956).
17. G. Blyholder and H. Eyring, *ibid.*, **61**, 682 (1957).
18. L. M. Foster, G. Long, and M. S. Hunter, *J. Am. Ceram. Soc.*, **39**, 1 (1956).
19. C. H. Prescott and W. B. Hincke, *J. Am. Chem. Soc.*, **49**, 2753 (1927).
20. W. A. Chupka *et al.*, *J. Phys. Chem.*, **62**, 611 (1958).
21. G. C. Kuczynski, L. Abernethy, and J. M. Allan, "Kinetics of High-Temperature Processes," p. 163, John Wiley & Sons, New York (1959).
22. F. J. Hansgirg, *Iron Age*, **152**, 56 (1943).
23. B. S. Gulyanitzkii and D. M. Chizhikov, *Izvest. Akad. Nauk. S.S.S.R., Otdel. Tekh. Nauk.*, **11**, 13 (1955) as quoted in *C. A.*, 5441g (1956).
24. J. F. Quirk, AEC-TIS Reactor Handbook, Vol. 3, (1955).
25. P. Kofstad, *J. Inst. Metals*, **90**, 253 (1962).
26. A. W. Czanderna and J. M. Honig, *J. Phys. Chem.*, **63**, 620 (1959).
27. O. C. Dean and J. M. Chandler, *Nuclear Sci. & Eng.*, **2**, 57 (1957).
28. J. L. Margrave, in "Physico-Chemical Measurements at High Temperatures," p. 353, Academic Press Inc., New York (1959).
29. J. F. Wygant and W. D. Kingery, *Am. Ceram. Soc. Bull.*, **31**, 7, 251 (1952).
30. N. D. Erway and R. L. Seifert, *This Journal*, **98**, 83 (1951).
31. L. Brewer and R. F. Porter, *J. Chem. Phys.*, **22**, 1867 (1954).
32. R. F. Porter, W. A. Chupka, and M. G. Inghram, *ibid.*, **23**, 1347 (1955).
33. W. A. Chupka, J. Berkowitz, and C. Giese, *ibid.*, **30**, 827 (1959).
34. G. Blyholder and H. Eyring, *J. Phys. Chem.*, **63**, 693 (1959).
35. S. Ergun, *ibid.*, **60**, 480 (1956).

Thermodynamic Properties of the Manganese-Lead-Bismuth System

Martin Weinstein[1] **and John F. Elliott**

Department of Metallurgy, Massachusetts Institute of Technology, Cambridge, Massachusetts

ABSTRACT

The thermodynamic properties in the liquid region of the Mn-Pb-Bi system from 700° to 1000°C are reported. They were obtained from the reversible potentials of the cell:

$$\mathrm{Mn(s)} \;\big|\; \begin{matrix}\mathrm{Mn^{++}} \\ \mathrm{KCl, NaCl}\end{matrix} \;\big|\; \begin{matrix}\mathrm{Mn} \\ \text{(in Pb-Mn-Bi sol'n)}\end{matrix}$$

The liquidus surface for the ternary system was also obtained for this temperature interval.

To gain more detailed information on the thermodynamic behavior of components at dilute concentrations in liquid metallic solutions, several studies have been underway in this laboratory for a number of years. One of the aims of the work, experimentally, was to improve the quality of measurements by the reversible emf cell method using chloride electrolytes and the chemically more active metals for measurements above 950°C (1). Another has been to explore the behavior of a dilute component as the character of the solvent is varied by substituting one element for another in a ternary system. A third purpose was to validate the available methods for estimating the activity of a solute component in the dilute region. Accordingly, study of the Mn-Pb-Bi system with the reversible cell

$$\mathrm{Mn(solid)} \;\big|\; \begin{matrix}\mathrm{Mn^{++}}\text{ (in molten KCl} \\ \text{+ NaCl)}\end{matrix} \;\big|\; \begin{matrix}\mathrm{Mn\ in\ Pb} \\ \mathrm{Mn\ in\ Bi} \quad \text{(liq)} \\ \mathrm{Mn\ in\ Pb\text{-}Bi}\end{matrix}$$

was undertaken. The virtual cell reaction is

$$\mathrm{Mn\ (Pure\ solid,}\ \alpha \text{ or } \beta) \rightarrow \mathrm{Mn\ (in\ liquid\ alloy}(\quad [1]$$

with a transfer of two Faradays in the external circuit per gram atom of manganese converted from the pure state to it dissolved in the solution. The solubility of solid manganese in Bi-Pb solutions is relatively low so that reliable potential readings could be made at quite low manganese concentrations. This in turn provides data which are useful in revealing the adherence to, or deviation from, Henry's law by manganese at low concentrations. Studies on other systems exhibiting several types of miscibility gaps will be reported in the near future.

The relationships between the potential of the cell and the properties of manganese in the solution are

$$\overline{F}_{Mn} - F^{\circ}_{Mn} = F^{M}_{Mn} = -2\mathbf{F}E \qquad [2]$$

$$\overline{S}_{Mn} - S^{\circ}_{Mn} = S^{M}_{Al} = 2\mathbf{F}\left[\frac{\partial E}{\partial T}\right]_{X_{Mn},P} \qquad [3]$$

and

$$RT \ln a_{Mn} = -2\mathbf{F}E \qquad [4]$$

[1] Present address: Tyco Laboratories, Inc., Waltham, Massachusetts.

The related excess properties are more convenient for use in calculations

$$F^{E}_{Mn} = F^{M}_{Mn} - RT \ln X_{Mn} = -2\mathbf{F}E - RT \ln X_{Mn} \qquad [1a]$$

$$S^{E}_{Mn} = S^{M}_{Mn} + R \ln X_{Mn} = +2\mathbf{F}(\partial E/\partial T)_{X_{Mn},P} + R \ln X_{Mn} \qquad [2a]$$

Also

$$RT \ln \gamma_{Mn} = -2\mathbf{F}E - RT \ln X_{Mn} \qquad [3a]$$

and

$$H^{E}_{Mn} = H_{Mn} = 2\mathbf{F}\left[T\frac{\partial E}{\partial T} - E\right]_{X_{Mn},P} \qquad [4]$$

The terms are those customarily used in thermodynamics. **F** is Faraday's constant, 23,063 cal/v eq. The reference state for each component is the pure component in the state normally stable at the temperature of interest, *i.e.*, α or β-manganese, and pure liquid lead and bismuth. Accordingly, the standard state in each case is also the normally stable state at 1 atm pressure.

Experimental Procedure

The design of the cell is shown in Fig. 1. Two reference electrodes of solid manganese were suspended by their tungsten lead wires (0.9 mm diameter) within the electrolyte. Four liquid alloy electrodes were contained within small doubly recrystallized alumina crucibles resting within the electrolyte. Tungsten lead wires were immersed in the alloy electrodes. The electrode crucibles and electrolyte were contained in a high-quality porcelain crucible. The tungsten leads were encased in close-fitting alumina tubing down to the electrode surfaces. A Vycor-sheathed chromel-alumel thermocouple was positioned on the centerline of the cell with its tip at the salt-metal line of the cathode electrodes. A dummy crucible having properly located holes for the leads and thermocouple sheath was fitted tightly on top of the cell crucible. It served as a thermal shield, a retainer for the leads, and as a reflux condenser to minimize the loss of the electrolyte by volatilization at high temperatures. The whole assembly was contained in a closed-end Vycor tube that was sealed with a water-cooled brass cap. Appropriate seals in the cap permitted entry of the

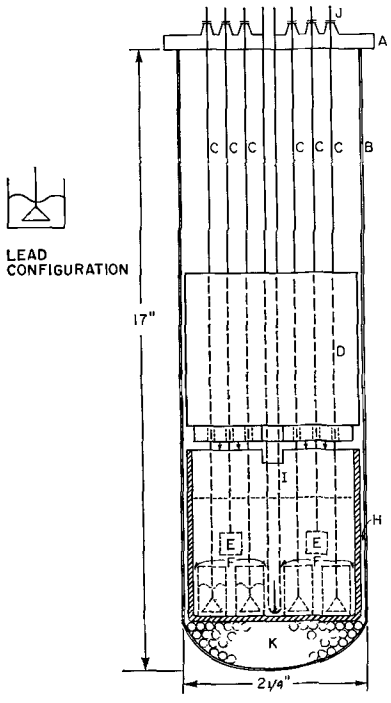

Fig. 1. Cell design: A, water-cooled brass furnace head; B, Vycor furnace tube; C, tungsten lead with alumina protection tube; D, porcelain positioning crucible; E, pure manganese buttons; F, alumina electrode crucibles (⅝ in. ID x 1 in.); H, large alumina crucible (2 in. OD x 3 in.); I, Vycor thermocouple protection tube (7 mm); J, rubber tube seal with pinch clamp; K, alumina beads. Electrolyte (KCl-$NaCl$-$MnCl_2$).

leads, thermocouple sheath, and gas tubes. After assembly, and while the system was cold, the cell tube was sealed and then evacuated by a mechanical pump. It was then filled with purified argon and maintained at a pressure slightly greater than atmospheric throughout the operation of the cell. The cell tube was positioned vertically in a hot resistance-heated tube furnace for the duration of an experiment.

The electrolyte.—The electrolyte was 42% by weight sodium chloride and 53% potassium chloride with 5% manganese chloride added thereto. Reagent grade materials were used in the charge for each cell. Two hundred grams of the mixed powders were placed in a sealed Vycor tube. The tube was connected to a mechanical vacuum pump and evacuated for 24 hr. During this time, the mixture was brought to 700°C and fused. This technique invariably yielded a clear amber solution that gave satisfactory results in all the cells.

Electrodes.—Manganese buttons for the anodes were formed by fusing 4g of electrolytic manganese under argon in a small doubly recrystallized alumina crucible. Heat to melt the button was obtained from an induction heated molybdenum susceptor. The tip of the tungsten lead was immersed in the liquid manganese and the metal was kept molten for 10 min to insure good contact between the lead and the manganese electrode. The electrode was cooled slowly to prevent cracking. After use, several electrodes were broken open, and it was found that the contact between the manganese and tungsten was sound and there was no evidence of solution of the lead.

Table I. Analysis of metals (lot analyses)*

Impurity	Mn (99.9 + %)	Pb (99.99 + %)	Bi (99.999 + %)
Bi	—	0.0008	—
C	0.007	—	—
Cu	—	0.0003	0.0001
Fe	0.01 or less	0.0002	0.0001
Si	0.004	—	—
Ag	—	—	0.0004

* All values in weight per cent.

The alloy electrodes which weighed approximately 10g each were prepared by weighing to 0.1 mg the required amounts of the pure metals. The pieces were placed in the anode crucibles and fusion occurred as the cell was brought to temperature. Analyses of the pure metals used are shown in Table I. A series of alloys for each of the following binary and pseudobinary systems were prepared; Mn-Bi, Mn-Pb/Bi = 0.504, Mn-Pb/Bi = 2.01 and Mn-Pb.

Cell assembly.—All components (except electrodes) of the cell were cleaned successively in nitric acid, distilled water, and acetone. They then were held at 140°C overnight in a drying oven. The complete cell was assembled outside the Vycor cell tube with the leads and electrodes properly positioned. The purified electrolyte was transferred by a pipette from the purification tube to the cell crucible. It solidified very rapidly on being added to the crucible and held the parts of the cell firmly in position. Within a minute, the cell assembly was placed in the cell tube. The tube was then sealed, evacuated, and flooded with argon. The cell was placed in the furnace which was at 700°C. When the electrolyte and alloy electrodes were molten, the tungsten leads were lowered to place their tips ⅛ in. from the bottom of the crucibles. The appropriate leads were connected to the measuring circuit, and the cell was held at 700°C overnight to equilibrate. Measurements were started the next morning and continued for two to three days.

Cell operation.—Potential readings were obtained between 700° and 1000°C, or between the liquidus temperature and 1000°C with Mn-Pb and Mn-Pb-Bi alloys. However, with the Mn-Pb system, slight variations in the potentials were observed above 900°C. Hence, in this system, readings were accepted between 680° and 850°C, or between the liquidus temperature and 850°C. The temperature sequence for a cell was arranged so that the early readings were distributed along the range, and any drift of the potentials from the expected linear plot of E *vs.* T could be detected. Readings at 8 to 3 temperatures were obtained with the fewer number being possible with an alloy having its liquidus temperature close to the maximum experimental temperature as indicated above.

Sources of Error

Reversibility.—The primary requisites in a study using electrode potential measurements for determining thermodynamic properties of metallic solutions are (i) the cell operates reversibly with respect to the reaction being studied, and (ii) no side reactions occur at an appreciable rate in the cell. In this

Table II. Analysis of electrodes

Alloy Mn-Pb-Bi	Wt % Mn		Wt % Pb	
	Charged	Analyzed	Charged	Analyzed
14	2.80	2.60	32.1	31.8
15	6.16	6.07	31.2	31.1
16	10.13	10.12	30.00	29.30
17	14.70	15.35	28.20	27.80

work, the behavior of the experimental cells indicated that these conditions were attained. Reproducible potentials were obtained regardless of the direction of approach to the equilibrium temperature and also regardless of the direction of approach to the reversible potential by the potentiometer. There was no significant exchange of manganese from the electrolyte to the alloys as it was observed that (*a*) the potentials were very constant with time, (*b*) a potential at a given temperature could be reproduced even though the cell had been at a different temperature for a number of hours, and (*c*) analyses of the electrodes after a run indicated that no compositional changes had occurred (see Table II). The absence of lead or bismuth in the electrolyte and the absence of any chemical attack on the refractories eliminated further the possibility of side reactions.

Wagner's method (2) has been used to estimate the possible error because of the displacement of manganese in the electrolyte by lead, or bismuth, from the alloy electrodes

$$Mn^{++} + \underline{Pb} = \underline{Mn} + Pb^{++}$$

With the Mn-Bi or Mn-Pb pairs, the difference in the standard free energies of formation of the two chlorides must be approximately 7 kcal per equivalent, or greater, if the error in the measured activity of Mn is to be kept under 1% when $X_{Mn} = 0.01$. The actual difference is approximately 27 kcal per equivalent at 1000°K (3). Hence it may be assumed that the exchange reaction is not a significant source of error in the experiment.

General.—The potential difference between a pair of standard electrodes (pure solid β-Mn) in a cell was less than 0.15 mv below about 800°C and 0.05 mv near 900°C. The potential reading selected for an alloy was for the reference electrode giving the highest potential. It is to be noted, however, that this uncertainty was negligible in all cases as it is equivalent to but a few calories in $F^M{}_{Mn}$.

No temperature gradient was observed when the thermocouple was moved slowly from the bottom of the crucible to the top of the electrolyte. Taking into consideration the normal uncertainties in the means for calibrating the thermocouples and measuring their potentials with a good quality potentiometer, the temperature reported is probably within 1°C of the true temperature of the cell.

A specific statement of the accuracy of each of the final results is difficult to make. The following statements should be used as guides in the use of Table IV and Fig. 3 through 12. Free energy values are accurate to three significant figures from the left.

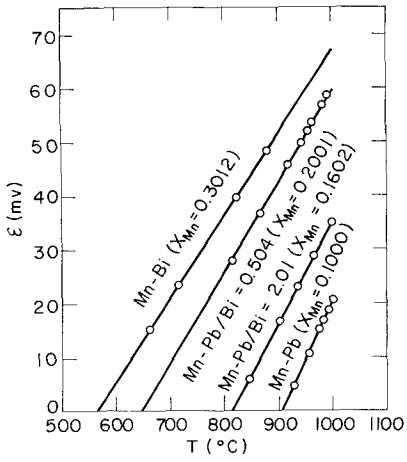

Fig. 2. Typical emf *vs.* temperature plots (raw experimental data).

Enthalpy values are accurate to two significant figures, reading from the left. Where fewer digits are given, the accuracy is limited to the number of figures reported. In a number of cases the values are carried out to one additional figure beyond that indicated above. This is necessary to obtain consistency with all properties tabulated. The accuracy of the values for activity and activity coefficient should be judged according to the above statement concerning the free energy values.

Experimental Results and Discussion

The potentials of all cells varied linearly with temperature (see Fig. 2). All experimental data

Table III. Potentials of experimental cells for liquid Mn-Pb, Mn-Bi and Mn-Pb-Bi systems

Electrode composition, X_{Mn}	*E*, volts		$(\partial E/\partial T)_{x_{Mn}}$ P, volts/°C × 10^6
	800°C	1000°C	
	Mn-Pb System		
0.0141	0.05745	0.1266	348
0.0199	0.04140	0.1062	336
0.0402	0.01070	0.06770	285.3
0.0601	sat.**	0.04540	257.5
0.0801	sat.	0.03120	243.8
0.0999	sat.	0.02070	232.6
0.1198	sat.	0.01260	210.9
0.1399	sat.	0.00635	200.9
	Mn-Bi System*		
0.095	0.09415	0.1398	229.1
0.2016	0.05920	0.09625	185.8
0.3012	0.03640	0.06800	157.4
0.4005	0.01725	0.04050	115.7
0.500	sat.	0.00970	69.76
	Mn-Pb-Bi System: X_{Pb}/X_{Bi} = 0.504/1		
0.0985	0.06020	0.1015	207.1
0.2001	0.02600	0.05950	168.1
0.3002	0.00375	0.03275	144.9
0.4105	sat.	0.00840	120.0
	Mn-Pb-Bi System: X_{Pb}/X_{Bi} = 2.01/1		
0.0461	0.05110	0.1017	252.5
0.1199	0.0100	0.0510	204.8
0.1602	sat.	0.0355	190.2
0.2100	sat.	0.0215	168.6

* Data at 1000°C obtained by extrapolation of lines of *E vs. T*.
** Alloy saturated with Mn (solid).

were plotted on 18 x 24 in. diagrams of this type, and the potentials and values of dE/dT used in calculating the thermodynamic properties were taken from these plots. Values are shown in Table III. The data were then correlated by means of the alpha and beta functions for 980°C in Fig. 3 and 4. The functions and the related experimentally determined properties are

$$\alpha_{Mn} = \frac{\ln \gamma_{Mn}}{(1 - X_{Mn})^2} = \frac{-2FE/RT - \ln X_{Mn}}{(1 - X_{Mn})^2} \quad [5]$$

$$\beta_{Mn} = \frac{H^M_{Mn}}{(1 - X_{Mn})^2} = \frac{-2F[E - T(\partial E/\partial T)]}{(1 - X_{Mn})^2} \quad [6]$$

The values of these two functions at saturation with manganese in the two binary and two pseudobinary systems were fixed by the actual compositions at saturation obtained in this study and which will be discussed later (see Fig. 13, 14, and 15.) At saturation where $a_{Mn} = 1$, the limiting value of α can be calculated. The curves in Fig. 3 were drawn to terminate at these points. Each curve of β in Fig. 4 was simply extended to the saturation composition.

Calculations.—The thermodynamic properties of lead and bismuth in the ternary system were obtained from the α and β functions of manganese by Darken's method (5, 6) for the Duhem integration. The integration constants for the determination of the molar properties F^E and H^M are these properties for the Pb-Bi system. The constants were obtained for the appropriate ratios of Pb/Bi of the pseudo-

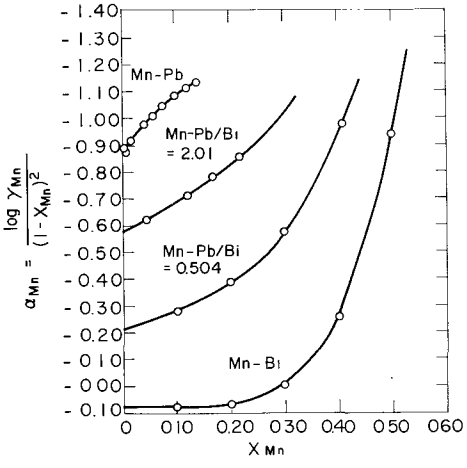

Fig. 3. Alpha function (α_{Mn}) for the Mn-Pb, Mn-Bi, and Mn-Pb-Bi systems at 980°C.

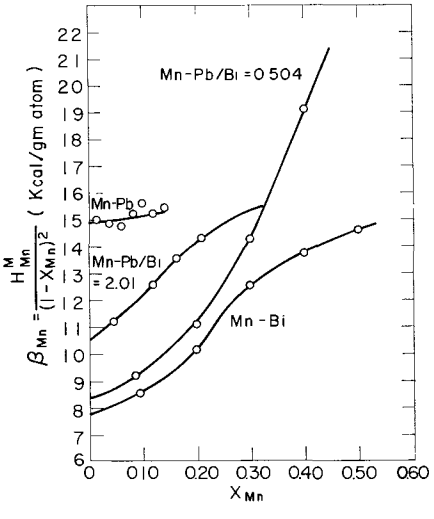

Fig. 4. Beta function (β_{Mn}) for the Mn-Pb, Mn-Bi, and Mn-Pb-Bi systems at 980°C.

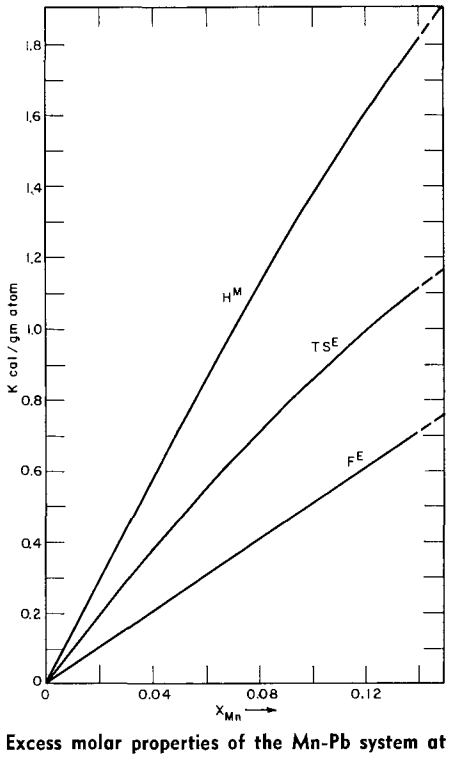

Fig. 5. Excess molar properties of the Mn-Pb system at 980°C.

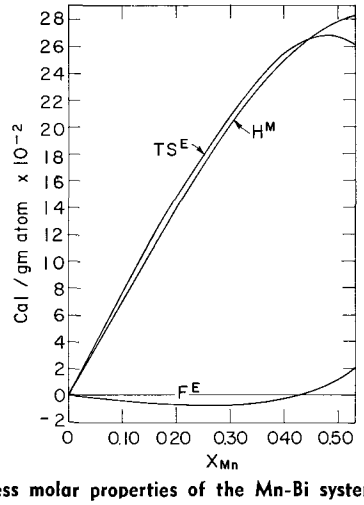

Fig. 6. Excess molar properties of the Mn-Bi system at 980°C

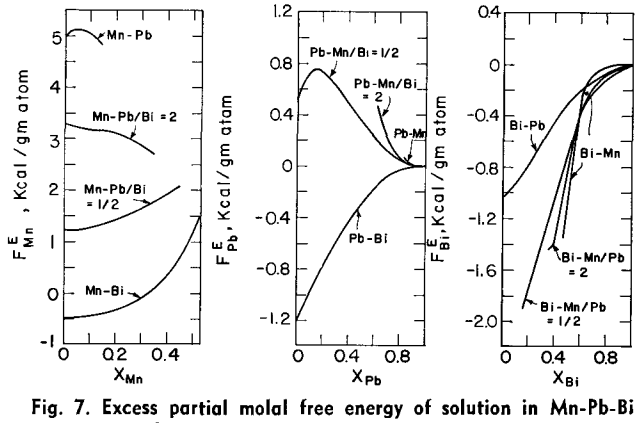

Fig. 7. Excess partial molal free energy of solution in Mn-Pb-Bi solutions at 980°C.

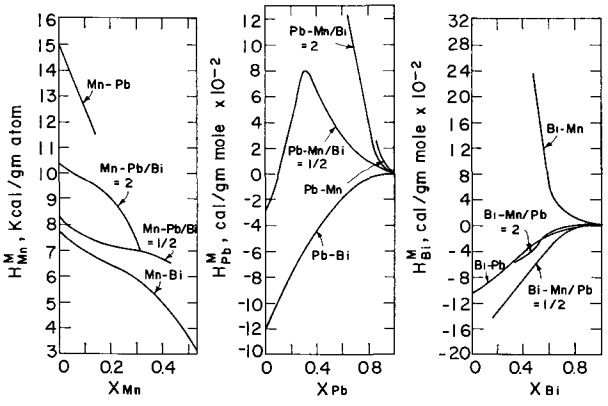

Fig. 8. Partial molar heat of solution in Mn-Pb-Bi solutions at 980°C.

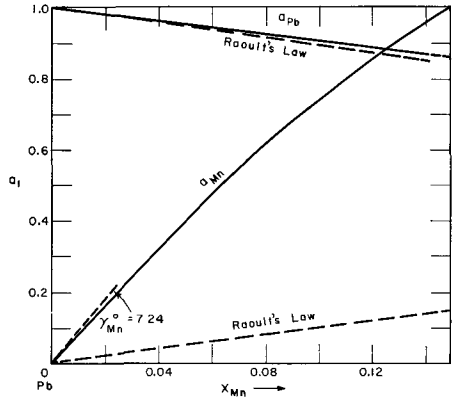

Fig. 9. Activity of Mn and Pb in the Mn-Pb system at 980°C

binary lines of this study from Elliott and Chipman's (6) results on the Pb-Bi system. The results of the calculations are contained in Table IV and pertinent curves are shown in Fig. 5 through 12.

If it is desired to convert the values obtained from the diagrams to the standard state of pure liquid manganese at 1 atm pressure, the values of ΔF°_m (+700 cal/mole) and ΔH°_m (4280 cal/g atom) for the melting of β-manganese (7) at 980°C should be subtracted from the corresponding partial molar properties

$$F^E_{Mn}[Mn(l)\,s.s.] = F^E_{Mn}[Mn(\beta)\,s.s.] - 700 \text{ cal/g atom}$$

$$H^M_{Mn}[Mn(l)\,s.s.] = H^M_{Mn}[Mn(\beta)\,s.s.] - 4280 \text{ cal/g atom}$$

The terms in brackets specify the standard states for manganese. The molar properties also may be converted from the standard states of pure β-manganese and liquid lead and bismuth to that of pure liquid Mn, Pb, and Bi according to the following

$$F^E\,[Mn(l)\,s.s.] = F^E\,[Mn(\beta)\,s.s.] + \Delta F^\circ_m \times X_{Mn}, \text{ cal/mole}$$

$$H^M\,[Mn(l)\,s.s.] = H^M\,[Mn(l)\,s.s.] + \Delta H^\circ_m \times X_{Mn}, \text{ cal/mole}$$

Table IV. Thermodynamic Properties of the Manganese-Lead-Bismuth System at 980°C

X_{Mn}	a_{Mn}	a_{Pb}	γ_{Mn}	γ_{Pb}	F^E_{Mn}	F^E_{Pb}	F^E	H^M_{Mn}	H^M_{Pb}	H^M	TS^E
A. Manganese-lead											
0.000	0.00	1.00	7.24	1.00	4,930	0.0	0	14,800	0.0	0	0
0.0141	0.109	0.986	7.58	0.9987	5,043	—1.0	70	14,580	2.5	208	137
0.0199	0.152	0.974	7.70	0.9994	5,083	—1.6	100	14,430	5.3	292	193
0.0402	0.317	0.958	7.89	0.9986	5,143	—3.6	203	13,910	31	579	376
0.0601	0.474	0.939	7.87	0.9988	5,135	—2.9	305	13,410	47	849	544
0.0801	0.613	0.920	7.66	1.001	5,057	1.7	408	12,920	98	1,120	717
0.0999	0.742	0.904	7.43	1.004	4,992	10.0	507	12,430	134	1,360	854
0.1198	0.856	0.888	7.14	1.009	4,894	22.4	606	11,950	194	1,600	995
0.1399	0.957	0.897	6.84	1.021	4,787	52.7	714	11,470	265	1,830	1,120
B. Manganese-bismuth											
X_{Mn}	a_{Mn}	a_{Bi}	γ_{Mn}	γ_{Pb}	F^E_{Mn}	F^E_{Bi}	F^E	H^M_{Mn}	H^M_{Bi}	H^M	TS^E
0.00	0.00	1.000	0.824	1.000	—487	0.0	0	7,800	0	0	0
0.095	0.082	0.903	0.859	0.998	—378	—5.3	—41	7,000	3.3	700	740
0.2016	0.180	0.792	0.894	0.992	—279	—20	—72	6,470	104	1,400	1,460
0.3012	0.304	0.617	0.01	0.953	—24	—120	—82	6,130	210	2,000	2,080
0.4005	0.492	0.510	1.23	0.851	513	—400	—35	4,920	880	2,500	2,530
0.500	0.858	0.322	1.71	0.644	1,340	—1,100	+123	3,650	1,920	2,790	2,660
0.530	1.00	0.273	1.9	0.582	1,580	—1,350	+203	3,280	2,320	2,830	2,620
C. Manganese-lead-bismuth											
1, X_{Pb}/X_{Bi} = 0.504/1											
X_{Mn}		a_{Mn}	γ_{Mn}		F^E_{Mn}	F^E		H^M_{Mn}	H^M		TS^E
0.000		0.00	1.61		1,190	—270		8,400	—270		0
0.098		0.164	1.67		1,270	—124		7,470	+530		656
0.200		0.353	1.76		1,410	+39		7,120	1,290		1,250
0.300		0.576	1.92		1,620	+222		7,000	2,010		1,780
0.411		0.894	2.18		1,940	+447		6,660	2,770		2,320
0.442		(0.99)	2.23		2,000	+543		6,500	3,010		2,460
2, X_{Pb}/X_{Bi} = 2.01/1											
0.000		0.00	3.73		3,280	—265		10,520	—265		0
0.046		0.168	3.64		3,220	—103		10,150	+224		326
0.120		0.442	3.52		3,130	+152		9,690	+973		821
0.160		0.563	3.51		3,130	+289		9,560	1,370		1,060
0.210		0.716	3.41		3,050	+456		8,910	1,830		1,380
0.328		(1.00)	3.05		2,780	+824		7,000	2,610		1,780

* All values of free energy, enthalpy, and TS^E are in cal/g atom.

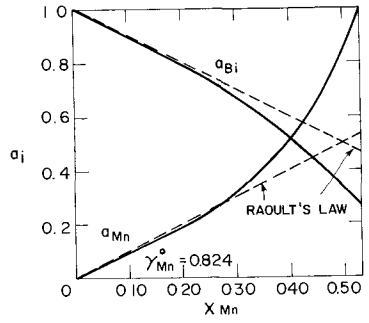

Fig. 10. Activity of Mn and Bi in the Mn-Bi system at 980°C

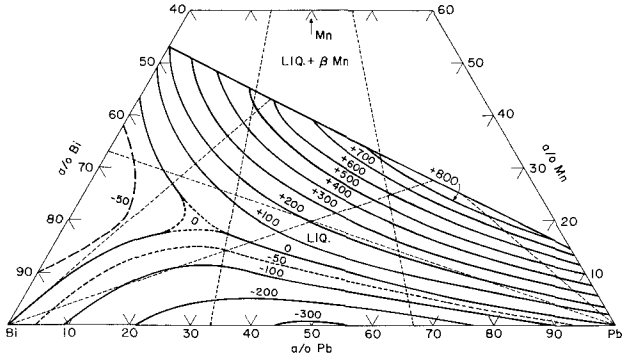

Fig. 11. Molar excess free energy of solution (F^E) of the Mn-Pb-Bi system at 980°C, cal/g atom.

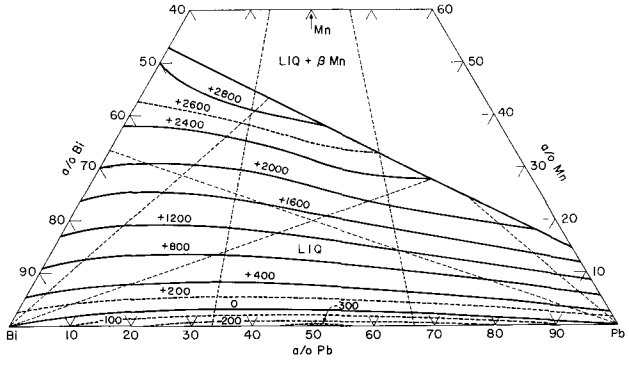

Fig. 12. Molar heat of solution (H^M) of the Mn-Pb-Bi system at 980°C cal/g atom.

The activity of manganese relative to the pure liquid is 1.32 times its activity relative to β-manganese at 980°C.

The interaction coefficient for the solute components at the lead and bismuth corners of the liquid ternary system are contained in Table V.

Phase diagrams.—The position of the liquidus line in the phase diagrams of the Mn-Pb, Mn-Bi and for the two pseudobinary lines in the Mn-Pb-Bi systems were obtained from the plots of E *vs.* T (Fig. 2), and from extrapolation of the lines of a_{Mn} *vs.* composition. The temperature of saturation with manganese for each alloy composition is the intercept where $E = 0$. This assumes that the stable phase of pure manganese ($\alpha_{Mn} = 1$) at that temperature is in equilibrium with the liquid alloy. It appears that there is essentially no solubility of lead or bismuth in solid manganese between 550° and 1000°C; consequently it may be assumed that $a_{Mn} = 1$ in the equilibrium solid phase. However, as the cell was cooled below the saturation temperature, a small negative potential of approximately 1 mv developed. A separate study, which will be reported later, has indicated that a metastable phase precipitates from the liquid which probably is γ-manganese.

The slope of the line of E *vs.* T should change below 727°C where α-manganese is the stable form. The effect is small and could not be detected experimentally because measurements could not be obtained below 680°C. A correction of the liquidus based on thermal data is not warranted in view of the precision of the experimental measurements.

Table V. Interaction coefficients

$$\epsilon_i^j = \left(\partial \ln \gamma_i / \partial X_j\right)_{X_i \to 0,\, X_j \to 0}$$

Solvent

Coefficient	Pb	Bi
ϵ^{Bi}_{Mn}	−2	—
ϵ^{Bi}_{Mn}	−2	—
ϵ^{Mn}_{Pb}	—	+8
ϵ^{Pb}_{Mn}	—	+5

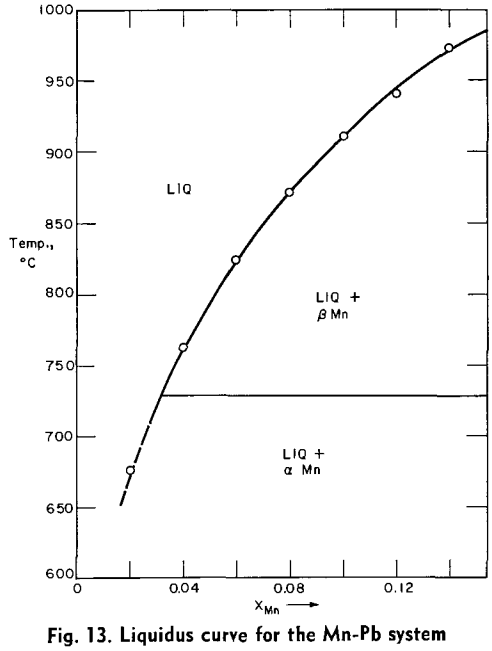

Fig. 13. Liquidus curve for the Mn-Pb system

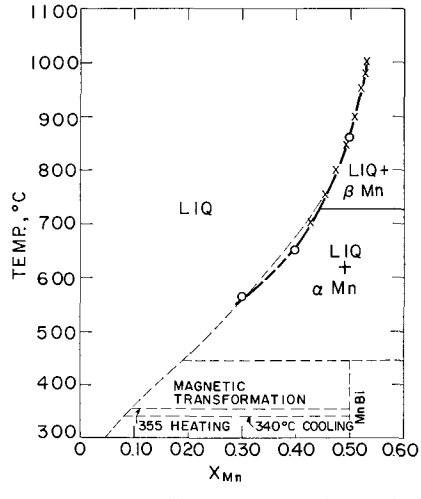

Fig. 14. Liquidus of the Mn-Bi system. This study: x, a_{Mn} *vs.* X_{Mn} intercepts; O, E *vs.* T°C intercepts. — — —, Seybolt *et al.* (9).

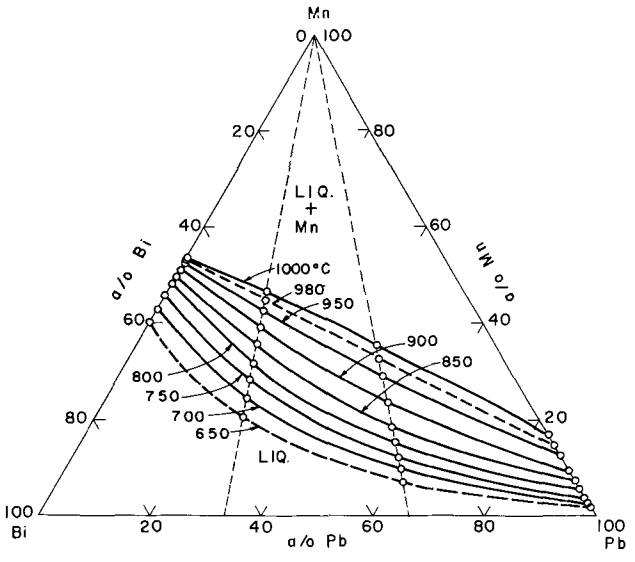

Fig. 15. Liquidus surface of the Mn-Pb-Bi system

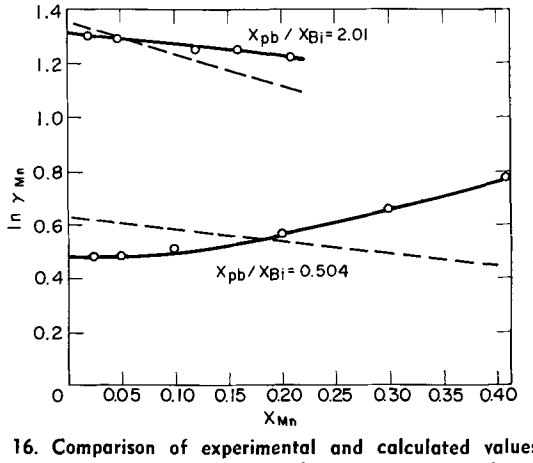

Fig. 16. Comparison of experimental and calculated values of ln γ_{Mn} in the two pseudobinaries studied: O, experimental; — —, calculated, using Eq. [7].

For example, the liquidus line 100°C below the equilibrium transformation temperature should be corrected by approximately 0.01 X_{Mn} as a result of $\Delta F^\circ_{900^\circ\alpha \rightarrow \beta}$ being 51 cal (7).

The liquidus lines for the Mn-Pb and Mn-Bi systems are shown in Fig. 13 and 14. The liquidus surface for the Mn-Pb-Bi system which was interpolated from the curves for the binary and pseudobinary systems is shown in Fig. 15. The only previous results on the Mn-Pb line was reported by Williams (8) in 1907 who estimated the liquidus to be approximately 4 a/o Mn higher at 850° than that shown here. Seybolt and co-workers' data (9) on the Mn-Bi system are in reasonable agreement with the results reported here. Siebe's (10) results on which Hansen (11) relied for the liquidus of the diagram between 600° and 1000°C, is in surprisingly good agreement with the present results at 600° but not at 800° and 1000°C. It is to be noted that Siebe worked with relatively impure manganese.

Estimation of ternary properties.—Alcock and Richardson (12) have developed a simple model for metallic solutions based on the quasichemical approximation. Their equation is

$$[\ln \gamma_{Mn}]_{Pb/Bi} = X_{Pb}\,[\ln \gamma_{Mn}\,(X_{Pb} = 1)] + X_{Bi}\,[\ln \gamma_{Mn}\,(X_{Bi} = 1)] - [F^E/RT]_{Pb/Bi} \quad [7]$$

The equation is applicable at $X_{Mn} << 1$. The activity coefficient on the left is that of manganese in the ternary solution, and those on the right are for the two appropriate binary solutions at infinite dilution of manganese. The term F^E is the excess free energy of mixing in the Pb-Bi binary at the ratio of Pb to Bi present in the ternary solution. Wagner (13) has noted that the Alcock-Richardson equation is applicable only if the binary system (in this case Pb-Bi) is strictly regular in behavior. Essentially this is so (6).

Figure 16 shows that there is fair agreement between the measured values of ln γ_{Mn} and those calculated by Eq. [7]. The agreement is not improved by using the values for ln γ_{Mn} in the binary system at the manganese concentration of the ternary solution.

Summary

The activity of manganese in the liquid Mn-Pb, Mn-Bi, and Mn-Pb-Bi systems has been measured in the temperature range of 600° to 1000°C with a reversible emf cell using a fused chloride electrolyte. The thermodynamic properties of bismuth and lead have been computed from the data.

The results have also been used to establish the liquidus surface in the ternary system between 700° and 1000°C.

Acknowledgments

The authors wish to express their sincere appreciation to the United States Atomic Energy Commission for their financial support of this study under Contract No. AT(30-1)-1888 and to Donald L. Guernsey and William T. Martin, Jr., for their analyses of the electrodes.

Manuscript received Dec. 12, 1962. This paper was delivered at the Boston Meeting, Sept. 15-19, 1962. This paper is based on a thesis submitted by M. Weinstein in partial fulfillment for the requirements for the M.Sc. at MIT, 1959.

Any discussion of this paper will appear in a Discussion Section to be published in the June 1964 JOURNAL.

REFERENCES

1. R. A. Oriani, *This Journal*, **103**, 184 (1956); J. Chipman, J. F. Elliott, and B. L. Averbach, NPL Symposium No. 9, HMSO, paper 18 (1959).
2. C. Wagner, "The Role of Displacement Reactions in Electromotive Force Measurements," Unpublished, (1957).
3. O. Kubaschewski and E. L. Evans, "Metallurgical Thermodynamics," 3rd. ed., p. 139, 336, Pergamon Press, Ltd., London (1958).
4. C. Wagner, "Thermodynamics of Alloys," Addison-Wesley Press, Inc., North Reading, Mass. (1952).
5. L. S. Darken, *J. Am. Chem. Soc.*, **72**, 2909 (1950).
6. J. F. Elliott and J. Chipman, *ibid.*, **73**, 2682 (1951).
7. A. H. Sully, "Metallurgy of the Rarer Metals, Manganese," Academic Press Inc., N. Y., and Butterworthe Scientific Publications, London (1955).
8. R. S. Williams, *Z. Anorg. Chem.*, **53**, 31 (1907).
9. A. U. Seybolt, H. Hansen, B. W. Roberts, and P. Yurcisin, *Trans. AIME*, **206**, 606 (1959).
10. P. Siebe, *Z. Anorg. Chem.*, **108**, 161 (1919).
11. M. Hansen and K. Anderko, "Constitution of Binary Alloys," McGraw Hill Book Co., New York (1958).
12. C. B. Alcock and F. D. Richardson, *Acta Met.*, **6** 385 (1958).
13. C. Wagner, Private communication.

The Diffusion Coefficients for Hydrogen in β-Zirconium

V. L. Gelezunas and P. K. Conn

Nuclear Materials and Propulsion Operation, General Electric Company, Cincinnati, Ohio

and R. H. Price

Department of Chemistry, University of Cincinnati, Cincinnati, Ohio

ABSTRACT

The diffusion coefficients of hydrogen in β-zirconium were calculated from experimental hydrogen sorption curves. The results were D (cm²/sec) = 5.32 x 10^{-3} exp (—8320/RT), (760°-1010°C). This relationship was independent of hydrogen concentrations (to 41 a/o H) and oxygen concentrations (to 4.2 a/o O) in β-zirconium. Oxygen in solid solution with zirconium and surface films on the zirconium reduced the rate of hydrogen sorption by zirconium. The effect of oxygen in solid solution with zirconium was observed to be related to the α to β transformation, while the effect of surface films was related to the hydrogen concentration at the film-zirconium interface.

Early efforts to measure the diffusion coefficients of hydrogen in the zirconium-hydrogen system were confined to a relatively low-temperature range (1), and the work was done on relatively impure zirconium.

In the more recent diffusion work, in which high-purity, relatively hafnium-free zirconium was used, the diffusion coefficients of hydrogen have been determined in α- (2, 5), δ- (3), and β-phases (4, 5) of the zirconium-hydrogen system. The results are in fair agreement for the α-phase, while a large discrepancy exists for the β-phase. The activation energy for diffusion of hydrogen in β-zirconium has been reported as 45,900 cal/mole (4) and 8540 cal/mole (5).

Previous work (6, 7) has also shown that oxygen when contacted with zirconium prior to hydrogen sorption can influence the rate of hydrogen sorption at a relatively low temperature (150°C), but that small quantities of nitrogen and oxygen in solid solution have only a small effect on the rate of hydrogen sorbed at 150°C. However, the investigation was limited to low hydrogen concentrations, and the reaction was not followed to equilibrium.

This investigation was confined to determining the diffusion coefficients of hydrogen in β-zirconium as a function of temperature by measuring the amount of hydrogen sorbed as a function of time. The effect of hydrogen concentration on the diffusion coefficient was evaluated over a significant range of hydrogen concentrations in the β-phase. The diffusion coefficients were measured from near the low temperature limit of the existence of the β-phase to the materials temperature limit of the experimental apparatus. The sorption rate of hydrogen by zirconium was studied at temperatures up to 960°C using zirconium samples with surface films. Also, the diffusion coefficient of hydrogen was determined in the temperature range of 750°-1000°C on zirconium samples which contained various quantities of oxygen in solid solution.

Experimental

In general, the solubility of hydrogen in metals which are classed as exothermic occluders (8) is relatively large. This fact has resulted in either failure to follow the reaction of hydrogen with the metal to equilibrium (9), or to the experimental expediency of using very large hydrogen reservoirs which undergo a small and potentially significant pressure drop as hydrogen is delivered from the reservoir (10). The experimental techniques used in this investigation were capable of following the sorption of hydrogen to equilibrium at a constant temperature and hydrogen pressure.

Experimental apparatus.—The experimental apparatus used to measure the sorption of hydrogen by zirconium as a function of time at constant temperature and hydrogen pressure is shown schematically in Fig. 1. The main features of the apparatus were: (i) the hydrogen reservoir which was capable of delivering approximately 4000 cm³ of hydrogen (STP), (ii) the system used to measure the quantity of hydrogen delivered from the reservoir which was based on the resistance change of a Pt:Pt-10% Rh wire loop suspended in the mercury used to displace the hydrogen, and (iii) the system used to control the pressure of hydrogen over the zirconium to better than ±0.2 mm Hg which consisted of pulsating solenoid valves (A) and (D) actuated by a change in hydrogen pressure over the zirconium.

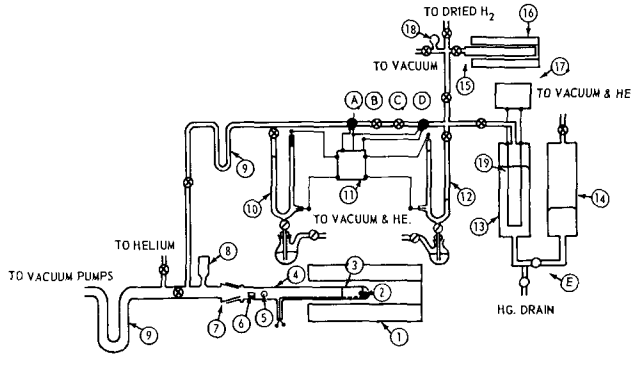

Fig. 1. Schematic diagram of experimental apparatus. 1, Marshall furnace; 2, Pt-Pt-10% Rh thermocouple; 3, Mo-foil; 4, silica muffle; 5, zirconium sample; 6, magnetic pusher; 7, 29/42 standard taper joint; 8, VGIA ionization gauge; 9, liquid nitrogen traps; 10, system manometer; 11, relays, pulse time, and lights; 12, reservoir manometer; 13, hydrogen reservoir; 14, reservoir pressure adjustment; 15, UH_3 reservoir; 16, UH_3 furnace; 17, emf measurement; 18, vacuum pressure gauge; 19, 0.012 cm diameter Pt-Pt-10% Rh wire loop; ∅, stopcock; x in a circle, bellows-type valves; •, solenoid valves; ○, needle valves; •-, electrical connections; A, B, C, D, see text.

The weight of hydrogen delivered to the zirconium was known to ±0.3%. A major part of this uncertainty resulted from the ±0.5°C temperature fluctuations of the hydrogen reservoir. The temperature of the zirconium was known to ±2°C within 30 sec after the start of an experiment.

A high-purity molybdenum foil shaped into a split cylinder and located in the quartz muffle was used as a sample holder to prevent the zirconium from directly contacting the hot quartz muffle during an experiment. There was no evidence of alloying between the Mo and Zr during the course of the experiments. The quartz muffle was declined about 5° from the horizontal to provide gravity contact between the zirconium sample and the calibrated Pt:Pt-10% Rh thermocouple; the foil also acted as a spring to hold the thermocouple fixed in position (see Fig. 1). The quartz muffle was connected to the vacuum system with an air-cooled Apiezon W wax seal.

In order to get a reproducible zirconium surface, the following procedure was established: the zirconium was cleaned by degreasing in boiling trichloroethylene vapor, rinsed in a hot alkaline cleaner and chemically etched in an ultrasonically vibrated, 1 w/o (weight per cent) solution of HF. After a rinse in deionized water and drying in flowing argon, a sample was weighed and transferred into the muffle. The entire procedure exposed the zirconium to air for an estimated 30 sec. This cleaning process left a chemical film (see Results and Discussion Section) on the sample surfaces; the film was solubilized by a high-temperature treatment in the apparatus before the sorption studies were made which led to the hydrogen diffusion coefficients.

To minimize contamination of the zirconium from the outgassing of the apparatus the muffle was evacuated to a pressure of less than 1×10^{-6} mm Hg at room temperature for at least 24 hr, and the part of the silica muffle to be heated during an experiment was out-gassed for at least 48 hr at 960°C at a pressure of less than 0.3×10^{-6} mm Hg with the zirconium sample located in the cold zone. Blank experiments showed that this procedure limited the pressure rise in the muffle volume to less than 2 μ/hr at 960°C. After outgassing, the quartz tube was cooled, and the zirconium was worked from the cold zone into the Mo sample holder and against the thermocouple by means of the magnetic pusher and an external magnet. The furnace was replaced over the muffle and the sample was heated to 960°C in a vacuum for an hour to solubilize the surface film. The temperature was set at the run temperature, one-half hour was allowed for thermal equilibrium, and then the valve to the vacuum pumps was closed and hydrogen was admitted to the system. Satisfactory temperature and hydrogen pressure control was obtained in approximately 30 sec. During this time interval, the temperature of the sample would rise approximately 30°C above the original set temperature due to the increased convection and the heat of solution of hydrogen in zirconium. Although this phenomenon made the experimental technique more difficult, it should not affect the experimental results since the thermal diffusivity of zirconium is several orders of magnitude greater than the diffusivity of hydrogen in zirconium. The temperature rise was compensated by manually increasing the power to the furnace at a time which had been experimentally predetermined.

The quantity of hydrogen delivered to the muffle was determined at various intervals of time, and equilibrium was defined as occurring 20 min after no further hydrogen transfer to the muffle was detected. The quantity of hydrogen in the muffle necessary to establish dynamic equilibrium with the zirconium was determined by calibration.

Oxygen or nitrogen for forming surface films or solid solutions was delivered to the muffle from a second reservoir at ambient temperature and of known volume. The pressure in this volume was measured by a mercury manometer or a thermocouple type vacuum gauge. The Mo foil was moved to the cold zone prior to the admittance of oxygen or nitrogen to the muffle. For the formation of zirconium-oxygen solid solutions, oxygen was added in small increments from the reservoir of known volume to the zirconium sample at 960°C. After the desired amount of oxygen was added and the pressure had dropped to less than 0.005 mm Hg, the pressure over the sample was lowered and maintained at less than 0.5×10^{-5} mm Hg at 960°C prior to and also between hydrogen sorption experiments.

Materials.—(*a*) Hydrogen: Commercial grade, cylinder hydrogen was first dried and then reacted with uranium. Purified hydrogen was then obtained as required by the thermal decomposition of uranium hydride. (*b*) Oxygen: USP grade oxygen was passed through a liquid nitrogen trap to remove condensable vapor prior to its use. (c) Nitrogen: USP grade nitrogen was used after passing through a liquid nitrogen trap. (*d*) Zirconium: Arc-melted, iodide zirconium rods were machined into cylinders (a = 0.624, L = 1.244 cm) and spheres (a = 0.764 and 1.029 cm). Results of the spectrographic and vacuum fusion analysis of the spheres are given in Table I. The diameter of the zirconium rod, from

Table I. Results of spectrographic and vacuum fusion analysis of iodide zirconium

Element	Analysis, ppm*	Analysis, ppm**
Fe		400
Hf		<100
Cr		60
Ni		50
Ar		40
Si		37
Cu		32
Mo		<20
Ca		<20
Pb		<20
Mn		<20
Mg		<10
B		0.9
O†	1800	600
H†		33
N†	80	20

† Results by vacuum fusion.
* Results for sphere (a = 0.764 cm) and cylinder (a = 0.624, L = 1.244 cm) after hot swaging and machining. Analyses were not obtained for balance of elements in table.
** Results for a sphere (a = 1.029 cm).

which the smaller spheres ($a = 0.764$ cm) and the cylinders were machined, was reduced by hot swaging prior to machining. This hot working resulted in an increased nitrogen and oxygen content as shown in Table I.

Theoretical hydrogen sorption equation and calculation of diffusion coefficient.—The use of a gas-solid system to measure the diffusion coefficients of hydrogen in the zirconium-hydrogen system requires that the transfer of hydrogen from the gas phase to the bulk of the zirconium be controlled by diffusion of hydrogen into zirconium and not by absorption and subsequent solution of hydrogen into the zirconium.

One test of whether the diffusion of hydrogen in a metal is rate controlling is to compare the experimental sorption curves to the theoretical curves obtained by assuming that diffusion of hydrogen in the metal is the rate-controlling step (10). With the assumption that the bulk diffusion of hydrogen is the rate limiting step, the sorption of hydrogen, expressed as the fraction of the total sorbed at equilibrium, as a function of time is given theoretically for a sphere by (11)

$$\frac{w - w_o}{w_\infty - w_o} = 1 - \frac{6}{\pi^2} \sum_{n=1}^{\infty} \frac{1}{n^2} e^{-\lambda n t} \qquad [1]$$

where: w is the weight of hydrogen in the zirconium at time t, g mole; w_o the initial weight of hydrogen in Zr, g mole; w_∞ the equilibrium weight of hydrogen in Zr, g mole; λ_n the separation constant, $n^2\pi^2 D/a^2$, sec^{-1}, a the radius of sphere, cm; D the diffusion coefficient, cm^2/sec; and t time, sec.

The diffusion coefficient (D) was calculated from the slope (λ_1) of the linear asymptote of the sorption curves (the logarithm of the fraction of hydrogen remaining to be sorbed *vs.* time curve) and the radius of the sphere (a) from the following relation

$$D = \frac{\lambda_1 a^2}{\pi^2}$$

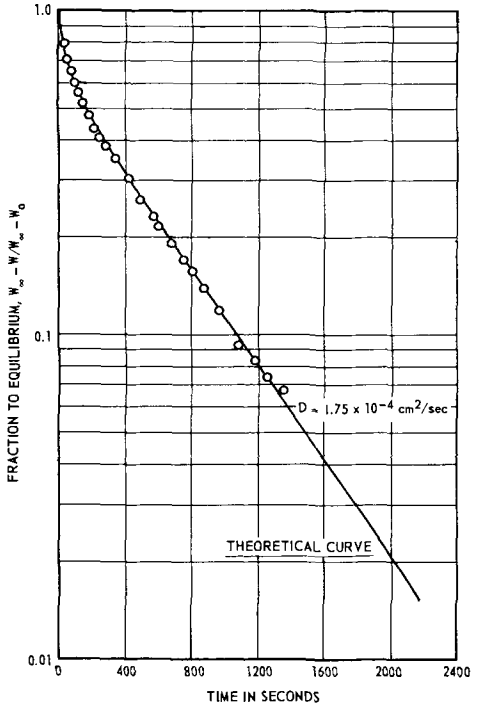

Fig. 2. Hydrogen sorption by a zirconium sphere (radius = 1.029 cm) at 963°C.

Results and Discussion

Diffusion of Hydrogen in Zirconium

A typical experimental hydrogen sorption curve, expressed as the fraction of the equilibrium quantity of hydrogen which remained to be sorbed *vs.* time, at a given temperature and hydrogen pressure is presented graphically in Fig. 2. The parameters which were varied were temperature, pressure, and initial hydrogen concentration. Good agreement was obtained for similar experiments on the same sample and between duplicate samples. Good agreement was also obtained between the experimental sorption curve obtained from the vacuum-heat-treated samples and the theoretical curve, if a time lag of the order of 30 sec were allowed. The time lag is clearly seen in run 4 of Fig. 4. This time lag was the result of the temperature rise associated with the heat of solution of hydrogen in zirconium, and the finite time required to establish and maintain a set hydrogen pressure over the zirconium. The greater the surface to volume ratio of the zirconium, the larger was the temperature rise for a given geometry. This also explained the larger scatter of the sorption data which was observed for cylinders and the small spheres of zirconium when compared to the larger spheres, since for a larger temperature rise, the control of the sample temperature was more difficult. All of the cyclic deviations which occurred in the sorption curves could be correlated with deviations in the sample temperatures from the set temperature.

No effect was observed on the hydrogen diffusion rates in a large zirconium sphere as a result of varying the equilibrium hydrogen pressure at a given temperature in experiments at temperatures of 793°, 910°, and 960°C. The sorption curves at each temperature were identical within experimental limits, and the over-all concentration range in the experiments was 0-41 a/o (atomic per cent) H. Therefore, it was concluded that the diffusion coefficient was independent of hydrogen concentration in this range. The results at 793°C also demonstrated that the α- to β-transformation had no measurable effect on the sorption curves, since at this temperature the zirconium existed initially in the α phase. It is important to note that this conclusion was drawn for zirconium which contained 0.3 a/o oxygen.

The diffusion coefficients of hydrogen which were calculated from the hydrogen sorption curves are presented as a function of temperature in Fig. 3. The diffusion coefficients as determined from the sorption curves for the cylindrical samples, and the small spheres, exhibited the largest deviations from the line representing the large sphere data, as would be expected. The results from two other investigators (4, 5) are also included in Fig. 3.

The data shown in Fig. 3 are summarized in Table II for all three investigations. The diffusion coefficients shown for this work have been corrected to account for the small volume change due to thermal

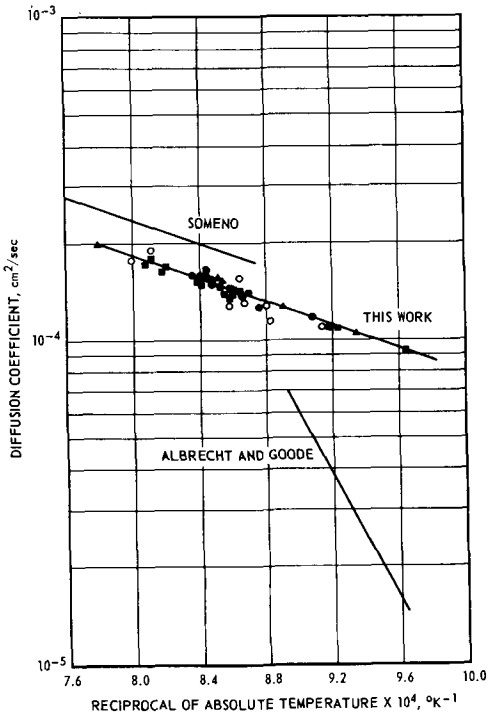

Fig. 3. Diffusion coefficients for the beta phase of the zirconium-hydrogen system. ▲, ■, sphere, a = 1.029 cm; ●, sphere, a = 0.764 cm; ○, cylinder, a = 0.624, L = 1.244 cm.

expansion and hydrogen sorption. This correction factor was 1.03. Included in Table II are the standard deviations of the diffusion equation parameters. Since Someno (5) did not report the standard deviations, it was necessary to calculate the values reported here.

On the basis of the statistical analysis, there was no significant difference between the results of Someno and the present investigation, and the difference which does exist is probably a result of the errors in the different experimental techniques used. Since the precision of this work appears to be greater, the results of the present investigation seem to represent more nearly the true diffusion coefficient.

The large and significant difference between the results of Albrecht and Goode, who used the permeation technique, and those of the two other investigations could be the result of surface contamination by oxide or metallic films, as a result of the experimental techniques used in the former investigation. Surface contaminations of this type on zirconium were found in the early stages of the present investigation.

Table II. Summary of the reported diffusion coefficient data for hydrogen in β-zirconium presented as the parameters in the equation $D = D_0 e^{-Q/RT}$

Investigator	D_0, cm²/sec	Q, cal/mole	Temperature range, °C
Someno (5)	$7.37\ ^{+3.82}_{-2.50} \times 10^{-3}$	8540 ± 1050	870-1110
Albrecht and Goode (4)	6.14×10^4	43900	650-850
This work	$5.32\ ^{+0.41}_{-0.37} \times 10^{-3}$	8320 ± 170	760-1010

Effect of Surface Barrier

The effects of zirconium surface films on the sorption of hydrogen were studied using surface films produced in three different ways: (i) by chemical etching of the zirconium in an ultrasonically vibrated 1.0 w/o HF solution, hereafter referred to as the chemical film; (ii) by exposing the zirconium to oxygen in the experimental system at three different temperatures for various times producing an oxide film, although at the highest temperature an oxygen solid solution layer might be more descriptive; and (iii) by exposing the zirconium to nitrogen at the same temperatures as used for oxygen. The effects of nitrogen and oxygen were determined with separate samples. At room temperature and 300°C the quantities of oxygen and nitrogen sorbed by the zirconium were not measured, but the oxide films were produced by exposing zirconium to oxygen at a pressure of 250 mm Hg for 48 hr at 23°C, and to oxygen at 1 mm Hg for 30 min at 300°C. The chemical film, initially on the zirconium, was solubilized by a 2-hr vacuum treatment at 960°C prior to exposure with oxygen or nitrogen gas.

The effect on the sorption curves of sequential runs on the same sample with an initial chemical film is shown graphically in Fig. 4. Temperatures listed in Fig. 4 are the actual run temperatures. Run 1 was obtained after quickly bringing the α-zirconium to 750°C, but with the admittance of hydrogen to the muffle and the subsequent temperature rise the actual run temperature was 774°C. Run 2 (not shown in Fig. 4 for sake of clarity) was made at the same temperature but at a higher pressure and was in agreement with the theoretical sorption curve; the β-zirconium initially contained the equilibrium hydrogen concentration from run 1. Run 3 was carried out under conditions similar to run 1 after the zirconium had been vacuum outgassed at 750°C sufficiently long to insure that the zirconium again existed in the α phase (12, 13). Run 4, which was made after the zirconium had been vacuum outgassed at 927°C for 90 min, and cooled to the run temperature, was also in agreement with the theoretical sorption curve.

The sigmoid curve shapes observed for runs 1 and 3 were attributed to the chemical film which limited

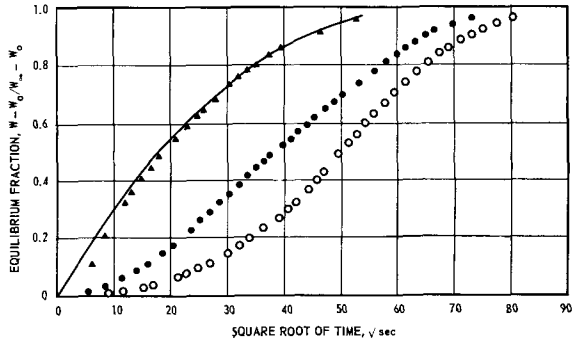

Fig. 4. Hydrogen sorption by a zirconium sphere (radius = 1.029 cm) showing the effects of a surface film. ○, Run 1, 774°C; ●, run 3, 777°C; ▲, run 4, 793°C; —, theoretical curve, D = 1.0 x 10^{-4} cm²/sec.

the hydrogen concentration at the surface of the zirconium, rather than the α- to β-phase transformation *per se* which occurred early in the sorption experiments at these temperatures. The experimental sorption curve which resulted from run 1 (Fig. 4) could be fitted for up to 60% hydrogen sorbed to a theoretical equation based on Fick's second law in which the surface hydrogen concentration was assumed to vary linearly with respect to time. This indicated that the character of the film did not change abruptly due to the α- to β-transformation at the film-zirconium interface, as would be expected if the change was primarily a result of this transformation. Further, as already noted, there was no apparent effect on the sorption curve shape at this temperature due to the bulk α- to β-phase transformation in zirconium which did not have the surface film. It can be shown that the negligible effect of the bulk phase transformation *per se* under these experimental conditions has a theoretical basis (14).

The experiments on the same sample which followed run 1 yielded an insight into the character of the chemical film. Run 2 (not shown in Fig. 4), as indicated by the sorption curves, showed no evidence of the film, while run 3 did. This suggested that the film was present during run 2, but was discontinuous and did not significantly reduce the rate of hydrogen sorption. The discontinuous film was probably caused by a combination of the following: (i) expansion of the zirconium due to hydrogen sorption (15), (ii) mismatch between the crystallites of the film and the zirconium surface which was brought about by the α- to β-transformation in zirconium due to sorption of hydrogen, and (iii) mismatch as a result of grain growth of the zirconium which occurred fairly rapidly in the β-phase (16).

The increased hydrogen sorption rate during run 3 over that during run 1 indicates that the character of the film (thickness, crystallite size, defect content, and phase transformations) has changed. It was observed in other experiments that 90 min at 927°C was sufficient to remove the effects of a chemical film on the sorption curve. We suggest that some of the reduction in the resistance of the film to hydrogen permeation in run 3 was due to oxygen diffusion from the film into the sample during the time interval (7 hr) at 780°C between the start of run 1 and the start of run 3 leaving empty interstitial sites in the zirconium lattice for hydrogen penetration.

The effect on the sorption curves of a film produced by exposing zirconium to oxygen at various temperatures is shown in Fig. 5. The sorption curves shown were determined at 891°C, however, experiments were made in the range of 760°-960°C. The sorption curve for the sample containing the room temperature oxide film also exhibited a sigmoid characteristic. The film formed at 300°C offered only a slight resistance, while the film formed at 880°C offered no discernible resistance as inferred from the hydrogen sorption curves. In the latter case, 7 x 10^{-6}g mole of O_2 was sorbed by the zirconium in approximately 5 min. Since oxygen mobility increases with temperature, the temperature for formation of a surface film and the amount of oxygen

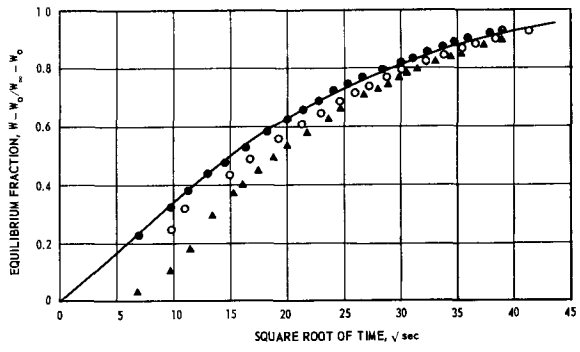

Fig. 5. Hydrogen sorption by a zirconium sphere (radius = 1.029 cm) at 891°C preceded by oxygen contact at various temperatures: ▲, oxygen at room temperature; ○, oxygen at 300°C; •, oxygen at 880°C; ———, theoretical curve, D = 1.40 x 10^{-4} cm²/sec.

sorbed apparently determines the character of the film (*i.e.*, number of vacant interstitial sites) and its resistance to hydrogen permeation.

The effect of the room temperature oxide film was reproducible and independent of the time during which the zirconium was in contact with oxygen for times of up to 96 hr.

Different results were obtained from similar experiments at 774°C on the room temperature oxide and chemical films. After the initial sorption of hydrogen, the effect of the oxide film could no longer be detected in subsequent runs at 774°C contrary to the results obtained with the chemical film. Also, the film formed by chemical etching offered a considerably greater resistance to hydrogen permeation at comparable temperatures. We suggest that the different results are due primarily to different effective film thicknesses. When the results could be compared, this investigation was in agreement with the sorption work by Gulbransen and Andrew (6, 7) which was carried out in the α-δ phase region (150°C, 24 mm Hg) of the zirconium-hydrogen system.

Similar experiments were carried out with nitrogen. At the highest temperature used for nitrogen absorption, 880°C, 7 x 10^{-6}g moles of nitrogen was readily sorbed by the zirconium in approximately 10 min. No effect on the sorption curves was observed regardless of the temperature of contact of nitrogen with zirconium. This appears reasonable, since the rate of attack of nitrogen with zirconium is less than that of oxygen (16), and apparently the rate of attack at room temperature for the times involved was negligible.

Based on these experiments, a surface barrier can significantly affect the sorption of hydrogen by zirconium if it is formed by chemical etching or low temperature oxidation. However, the effects of these films can be removed by a proper high-temperature treatment.

Effect of Oxygen in Solid Solution

The effects on the hydrogen sorption curves of various concentrations of oxygen in solid solution with zirconium were investigated and typical data are shown in Fig. 6. The sorption curves were made at a hydrogen pressure of 39.5 mm Hg and in the temperature range of 871°-902°C on the same sample. Values listed for oxygen concentrations were

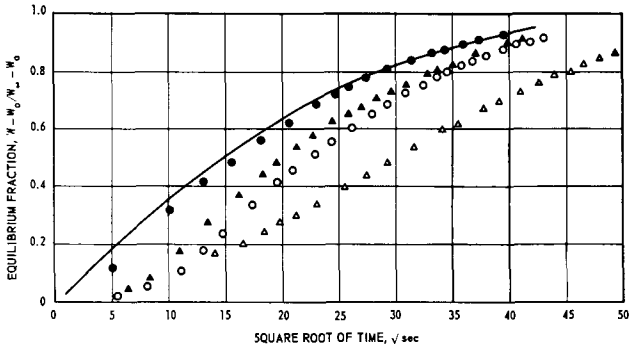

Fig. 6. Hydrogen sorption in the temperature range 871°-902°C by a zirconium sphere (radius = 1.029 cm) containing oxygen in solid solution: •, 0.3 a/o oxygen; ▲, 1.0 a/o oxygen; ○, 2.1 a/o oxygen; △, 4.2 a/o oxygen; ———, theoretical curve, D = 1.50 x 10^{-4} cm^2/sec.

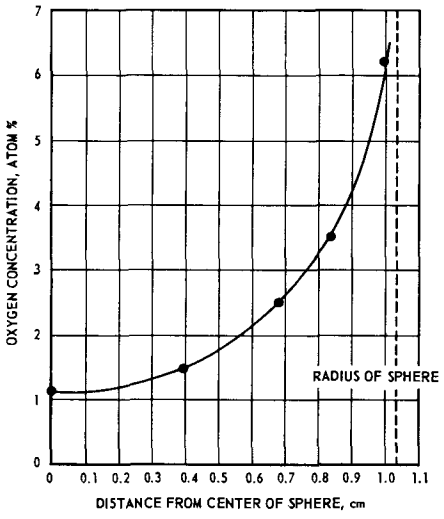

Fig. 7. Oxygen distribution in a zirconium sphere (radius = 1.029 cm) held at 960°C.

based on values calculated from the quantity of oxygen added to the zirconium, assuming the oxygen was uniformly distributed throughout the zirconium.

The displacement seen in Fig. 6 for the hydrogen sorption curve along the square root of time axis for zirconium containing 1.0 a/o oxygen and greater was also observed in the sorption curves for the zirconium cylinders and small spheres. These samples contained an initial oxygen concentration of 1.0 a/o in the as-machined condition as already noted. The displacement effect observed in samples containing 1.0 a/o oxygen and greater was a very sensitive function of small changes in the initial hydrogen concentration in the samples which could be controlled by varying the hydrogen outgassing time and temperature. The sorption curves were reproducible at comparable temperatures, and the displacement along the square root of time axis appeared to be only a function of the initial hydrogen concentration. A considerably higher initial hydrogen concentration was required to eliminate the displacement on the square root of time axis for the samples with oxygen levels of 2.1 and 4.2 a/o. Sorption experiments with zirconium containing 4.2 a/o oxygen and a relatively large initial hydrogen concentration resulted in data which were identical, within experimental limits, to sorption data obtained for zirconium containing 0.3 a/o oxygen at corresponding temperatures. Therefore, it appears that the diffusion coefficient of hydrogen in β-zirconium is independent of the oxygen content in the range 0.3-4.2 a/o oxygen.

Sorption curves were measured 24, 48, and 72 hr after a given oxygen addition and the results agreed within experimental error.

When the sorption experiments were completed, it was found that the oxygen was not uniformly distributed even after approximately 90 hr at 960°C after the last oxygen addition (calculated 4.2 a/o). The oxygen gradient which existed was determined by vacuum fusion analysis and is shown in Fig. 7. The fact that an oxygen concentration gradient existed in the zirconium suggests that the diffusion coefficient would not be significantly affected by an even higher oxygen concentration.

We interpret the preceding experimental observations as follows: Oxygen is known to have a profound influence on the α- to β-transformation in zirconium. Generally speaking, the primary effect is that the α-phase is retained to a higher temperature as the oxygen level in zirconium is increased. However, the temperature at which the transformation is initiated is only slightly raised for low oxygen concentrations (17). These facts indicated that the sorption curves were determined for zirconium initially in the two-phase α-β region for these particular experimental conditions and the percentage of α-phase present increased with increased oxygen content. It can be shown that under these conditions, the experimental sorption curves are in qualitative agreement with what would be predicted based on the case of a single phase region (β) advancing by diffusion into a two-phase region ($\alpha + \beta$) (14).

Effect of Repeated Sorptions and Desorptions of Hydrogen

A total of thirty hydrogen sorption experiments to concentrations of 20-35 a/o H followed by the same number of desorptions of hydrogen were made on one zirconium sphere at various temperatures. No effects of the repeated sorptions on the hydrogen sorption curves were detected, which was in disagreement with the "rift" theory (8).

The surface of the zirconium was observed to have roughened considerably, although the over-all diameter measured at room temperature, remained unchanged to within ±0.003 cm. Metallographic examination of this sample after the repeated runs revealed a very large grain size, greater than ASTM-1. This grain growth occurred over the course of the experiments. Since the sorption curves at comparable temperatures remained unchanged over the course of the experiments, intercrystalline diffusion of hydrogen in zirconium was negligible as compared to intracrystalline diffusion in the temperature range of the experiments as expected.

Conclusions

1. The isothermal sorption of pure hydrogen as a function of time by high-purity zirconium at a constant hydrogen pressure was adequately described by an equation based on Fick's second law and de-

rived on the assumption that bulk diffusion was the rate-controlling step.

2. The diffusion coefficients of hydrogen in β-zirconium were found to be independent of the hydrogen and oxygen concentrations in β-zirconium for hydrogen concentrations of up to 41 a/o H, and oxygen concentrations of up to 4.2 a/o oxygen. In addition, results showed that intercrystalline diffusion was negligible as compared to intracrystalline diffusion of hydrogen in β-zirconium.

3. Depending on the initial hydrogen concentration, oxygen in solid solution with the zirconium was found to reduce the rate of hydrogen sorption by zirconium when compared to the theoretical rate for β-zirconium. This phenomena could be related to the effect of oxygen on the α- to β-transformation in zirconium.

4. Surface films on zirconium were also effective in reducing the rate of hydrogen sorption by zirconium. The film formed during chemical etching was the most resistant to hydrogen permeation of the films studied. The resistance of oxide films on the zirconium surface to hydrogen permeation was a function of the temperature at which the films were formed. The effect of the films could be eliminated by a high-temperature, vacuum treatment. No apparent resistance to hydrogen permeation was exhibited by the surface of zirconium contacted with nitrogen prior to hydrogen permeation.

Acknowledgments

Thanks are due to the General Electric Company, Aircraft Nuclear Propulsion Department and Flight Propulsion Laboratory Department, Nuclear Materials and Propulsion Operation, for the use of laboratory facilities and for the generous fellowship which made this work possible. The two departments were operating under AEC and/or Air Force contracts AEC-AT(11-1)-171; Air Force-AF33 (038)-21102, AF33(600)-38062; and AEC-AT(40-1)-2847, respectively.

Manuscript received Aug. 27, 1962; revised manuscript received March 12, 1963. This manuscript was based in part on a dissertation submitted (by V. L. G.) to the Graduate School of the University of Cincinnati in partial fulfillment of the Ph.D. degree.

Any discussion of this paper will appear in a Discussion Section to be published in the June 1964 JOURNAL.

REFERENCES

1. C. M. Schwartz and M. W. Mallet, *Trans. Am. Soc. Metals*, **46**, 640 (1954).
2. M. W. Mallet and W. M. Albrecht, *This Journal*, **104**, 142 (1957).
3. W. M. Albrecht and W. D. Goode, "The Diffusion of Hydrogen in Zirconium Hydride," Report No. 1426, Battelle Memorial Institute, March 3, 1960.
4. W. M. Albrecht and W. D. Goode, "The Diffusion of Hydrogen in Beta Zirconium," Report No. 1373, Battelle Memorial Institute, August 25, 1959.
5. M. Someno, *Nippon Kinzoku Gakkaishi*, **24**, 249 (1960).
6. E. A. Gulbransen and K. Andrew, *This Journal*, **101**, 348 (1954).
7. E. A. Gulbransen and K. Andrew, "Nature and Properties of the Thin Oxide Film Formed on Zirconium and Zirconium and Zircaloy, Reactive Metals," W. R. Clough, Editor, Metallurgical Society Conference, Vol. 2, Interscience Publishers, New York (1959).
8. D. P. Smith, "Hydrogen in Metals," University of Chicago Press, Chicago (1948).
9. R. J. Wasilewski and G. L. Kehl, *Metallurgia*, **50**, 225 (1954).
10. W. Jost, "Diffusion in Solids, Liquids, Gases," Academic Press, Inc., New York (1960).
11. J. Crank, "Mathematics of Diffusion," Clarendon Press, Oxford (1956).
12. G. Libowitz, "The Zirconium-Hydrogen System at High Hydrogen Contents," USAEC Report NAA-SR-5015, Atomic International, June 30, 1960.
13. C. Ells and A. McQuillan, *J. Inst. Metals*, **85**, 89 (1956).
14. C. Wagner, in W. Jost's "Diffusion in Solids, Liquids, Gases," Academic Press, Inc., New York (1960).
15. D. S. Parker and C. L. Huffine, "Properties of Hydrided Zirconium," USAEC Report APEX-561, General Electric Company, Aircraft Nuclear Propulsion Dept., December 1959.
16. B. Lustman and F. Kerze, "The Metallurgy of Zirconium," McGraw-Hill Book Co., New York (1955).
17. J. H. de Boer and J. D. Fast, *Rec. trav. chem.*, **55**, 459 (1936).

The Activated Sintering of Tungsten with Group VIII Elements

H. W. Hayden and J. H. Brophy

Department of Metallurgy, Massachusetts Institute of Technology, Cambridge, Massachusetts

ABSTRACT

Small additions of Group VIII transition elements permit the densification of tungsten powder compacts at temperatures well below those employed for sintering commercial purity tungsten powder. The mechanism of this process has been examined using the model concepts of current general sintering theories. The added solid element accelerates mass transport along its interface with a tungsten particle. This process, together with sintering in the presence of a liquid phase or a volatile component, comprises the three types of carrier phase sintering in which one of several possible pure component solid-state sintering mechanisms is selectively accelerated.

A comprehensive examination has been made in the Metals Processing Laboratory at M.I.T. (1-5) into the fundamental mechanism behind the striking increase in tungsten sintering rates when Group VIII elements are present at temperatures far below the equilibrium melting point of the respective alloy systems involved (6, 7). This investigation has led to the concept of a carrier phase sintering mech-

anism. At present this mechanism appears to include liquid phase sintering and possibly the other types of empirically observed cases in which a modification of sintering mechanism is effected beyond that which would be expected for a pure solid component.

On the basis of the time, nickel-concentration, and particle size dependencies of linear shrinkage it was concluded that for the particular case of nickel-tungsten sintering the mechanism is a kinetic intermediate between solid and liquid phase sintering (1). Comparison of observed sintering kinetics with the predictions of simple models led to the conclusion that sintering rate is controlled by the separation of tungsten atoms from a particle into a nickel-rich layer at points of interparticle contact. It is perhaps coincidental that the critical amount of nickel for full "activation" of the sintering process would be just that necessary to form a monolayer on tungsten of the particle size employed.

The final stage of densification in nickel-tungsten compacts is accompanied by grain growth. In more recent work it was shown that the rate of densification is still indicative of control by "solution" of tungsten into a nickel-rich grain boundary layer (3). The evidence for nickel remaining on the surface of tungsten particles during the early stage of sintering and at grain boundaries during the final stage is based on several observations:

1. During the final stage, grain size after a given sintering treatment was inversely proportional to the square root of nickel content, indicating that diffusion of tungsten across a nickel layer is a barrier to grain growth (3). If nickel was lost into the tungsten grain, the grain size should have been considerably larger than was found experimentally at lower nickel contents. Since nickel was located at the grain boundary late in the process, it must have been there from the start. In this way nickel continued to serve as an activating agent to promote tungsten densification after prolonged sintering times.

2. Approximately equivalent results have been obtained by aqueous deposition of nickel on tungsten powder (1) and by co-reduction of nickel nitrate and tungstic oxide (4, 7).

3. It has been found (4) that the mechanical strength of sintered nickel-tungsten varies in a manner consistent with the proposed sintering model.

4. An estimate of diffusion rates indicates that the diffusion of nickel in tungsten is very low at the temperatures involved. Although an experimental value for the diffusion coefficient for nickel volume diffusion into tungsten is not available, using a typical D_o value ranging from 1.0 to 100.0 cm^2/sec and a Q value of 135 kcal/mole, the depth at which nickel content would be 0.001 of the surface nickel solubility has been calculated to lie between 4 and 40Å after sintering 100 hr at 1100°C. Since the tungsten grain size for compacts originally containing 0.25 weight per cent (w/o) nickel after such a treatment would be 50μ and the nickel solubility in tungsten is at most 0.3 w/o, it appears that nickel volume diffusion into tungsten is probably negligible.

5. Chemical analysis revealed no total nickel loss during the sintering treatment.

At this point a number of issues remain unsettled in the analysis of carrier phase sintering. It was the purpose of the investigation described in the following sections to examine the kinetics of tungsten sintering in the presence of the chemical relatives of nickel in Group VIII of the periodic table. The primary objectives were a description of the over-all mass transport process beyond the solution step dominating the behavior of nickel- tungsten and insight into the characteristics required of an element to serve as an "activator" for tungsten diffusion and sintering.

Experimental Procedure

The tungsten employed in this investigation was hydrogen-reduced powder of 0.56μ BET average particle diameter purchased from the Wah Chang Corporation. Nickel was obtained in the form of reagent grade nitrate. Palladium, rhodium, ruthenium, and platinum as chlorides were supplied initially through the courtesy of the International Nickel Company and purchased subsequently from Engelhardt Industries.

The activator compounds were weighed to yield the desired amount of the element, dissolved in water, and mixed with the necessary amount of tungsten powder. After overnight evaporation in air at 150°C, the resulting powder cake was broken manually and pre-reduced in hydrogen at 800°C for 1 hr. Rectangular specimens 2 in. by ⅛ in. by ⅛ in. were pressed in an unlubricated steel die at 26,000 psi. Each specimen was weighed and measured in linear dimensions.

Sintering was accomplished by rapidly inserting an alundum boat containing the sample into a wire-wound Vycor tube furnace at the desired temperature. After the required sintering time, the sample was similarly withdrawn from the furnace and cooled to room temperature. At all times the sample was under prepurified hydrogen when above room temperature. It was found that about 1 min was needed for each sample to reach furnace temperature, and, after sintering, about 1 min passed for the sample to cool to 600°C. These intervals were recognized when reporting sintering times.

After sintering, linear dimensions were again recorded, and occasional density measurements were made. It was found that completely reproducible results were obtained using either individual samples for each sintering condition, or accumulated sintering times on a continuous sample. The latter technique was used in the bulk of the cases.

Experimental Results and Discussion

The previous analysis of nickel-tungsten sintering employed linear shrinkage as a function of time and nickel content with particle size and temperature as parameters (1). The postulate of solution or phase boundary control was based on a time exponent of ½ and independence of nickel content as would be indicated from the data shown in Table I.

Table I. Densification relations in carrier phase sintering of tungsten (1)

$$\frac{\Delta L}{L_o} = (\text{constants})\ c^p\, r^q\, t^s$$

Process	p	q	s
Tungsten solution in the carrier phase layer	0	—1	1/2
Tungsten diffusion controlled:			
1. Radially at interparticle flats	—1/2	—1	1/2
2. Circumferentially in carrier layer	1/3	—4/3	1/3
3. Circumferentially in interface between carrier layer and massive tungsten	0	—4/3	1/3
4. Radially over entire particle surface	—1/3	—1	1/3

This general technique served as an analytical outline for the data of this investigation.

Palladium-tungsten compacts were sintered at temperatures ranging from 850° to 1100°C. The time dependence of linear shrinkage is shown in Fig. 1 and the composition dependence in Fig. 2. The density of samples sintered 30 min and 16 hr at 1100°C was 93.5 and 99.5%, respectively. A comparison to the nickel-tungsten results of 92 and 98% shows that palladium actually led to more rapid densification than did nickel with tungsten. From Fig. 1 and 2 it has been concluded that palladium tungsten linear shrinkage depends on the cube root of time and is essentially independent of palladium content in the range from 0.25 to 4.0 w/o. Reference to Table I suggests that this is indicative of a transport process controlled by tungsten diffusion circumferentially in the interface between the palladium-rich layer and massive tungsten. The apparent activation energy computed from Fig. 1 was 86,000 cal/mole.

Ruthenium-tungsten compacts were sintered in the temperature range 950° to 1100°C. Figure 3 shows the time dependence and Fig. 4 shows the composition dependence of linear shrinkage. The slope of the curves in Fig. 3 is 0.39, indicating that linear shrinkage varies with time to a power slightly greater than 1/3. This experimental time exponent is closer to that predicted for the dependence of linear shrinkage when volume diffusion is rate controlling

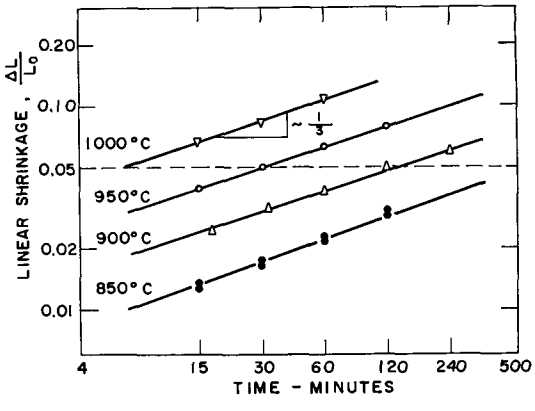

Fig. 1. Time dependence of linear shrinkage in palladium-tungsten; tungsten + 2 w/o palladium.

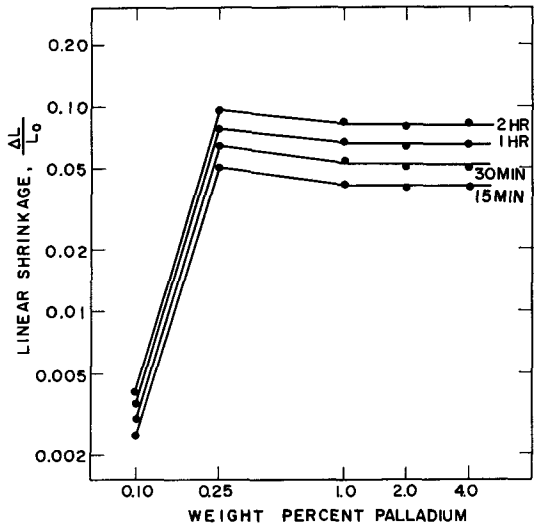

Fig. 2. Composition dependence of linear shrinkage in palladium-tungsten, temperature, 950°C.

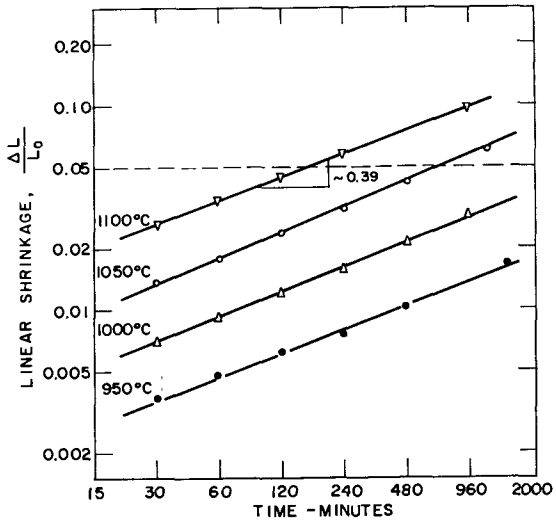

Fig. 3. Time dependence of linear shrinkage in ruthenium-tungsten; tungsten + w/o ruthenium.

(8), but it seems that ruthenium could hardly accelerate the volume diffusion of tungsten and that the discrepancy of the experimental time exponent of 0.39 with the predicted value of 1/3 might be attributed to the difficulty in measuring the low shrinkage values observed in the case of ruthenium-tungsten sintering. The view that ruthenium-tungsten shrinkage is controlled by the diffusion of tungsten through the interface of a ruthenium-rich layer and massive tungsten is supported by the data in Fig. 4 which shows that shrinkage is independent of ruthenium content beyond 0.5 w/o. The activation energy computed from Fig. 3 was 114,000 cal/mole.

Platinum-tungsten compacts were sintered at temperatures from 1000° to 1150°C. Figure 5 shows that linear shrinkage varies with the cube root of time with an activation energy of 92,000 cal/mole. Figure 6 shows that linear shrinkage is independent of platinum content above 0.5 w/o. These data indicate that platinum-tungsten sintering is also controlled by the interface diffusion process.

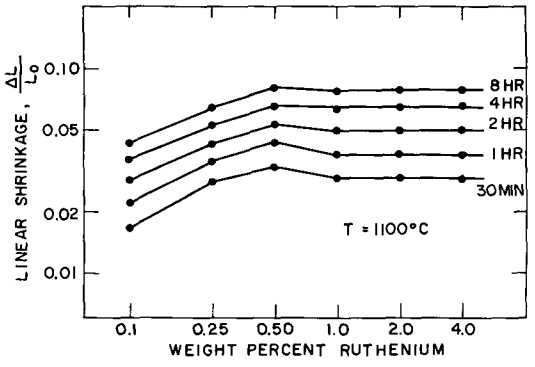

Fig. 4. Composition dependence of linear shrinkage in ruthenium-tungsten.

The preceding four cases were apparently controlled either by the solution step or interface diffusion step in the tungsten transport process. With a single added element, the rate-controlling step was the same over the entire range of sintering conditions employed. In the two alloy systems which follow, the rate-controlling step apparently changed with sintering temperature in one case and with the amount of shrinkage in the other.

Recent results on the linear shrinkage of molybdenum sintered with nickel indicated dependence on the square root of time at 950°C and the cube root at 1000°-1100°C (5). These results were independent of nickel content from 0.25 to 4.0 w/o at 1100°C. The activation energy between 1000° and 1100°C was 77,000 cal/mole. For this case it appears that the solution step is rate controlling at low temperatures, while interface diffusion prevails at higher temperatures.

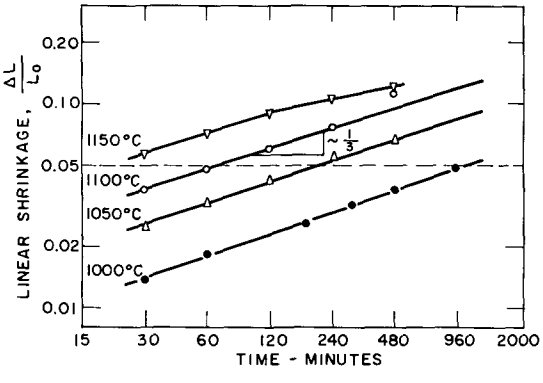

Fig. 5. Time dependence of linear shrinkage in platinum-tungsten; tungsten + 2 w/o platinum.

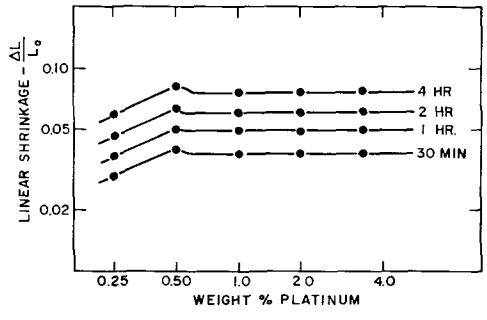

Fig. 6. Composition dependence of linear shrinkage in platinum-tungsten, temperature, 1100°C.

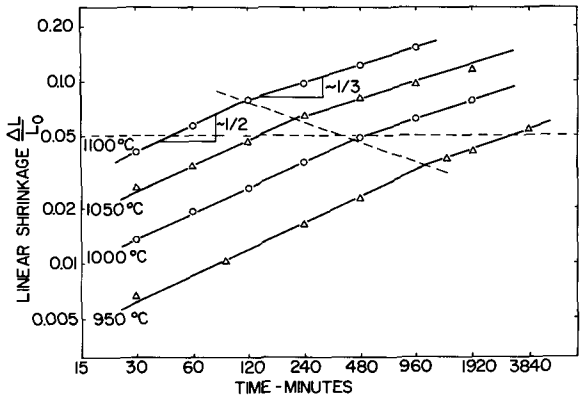

Fig. 7. Time dependence of linear shrinkage in rhodium-tungsten; tungsten + 1 w/o rhodium.

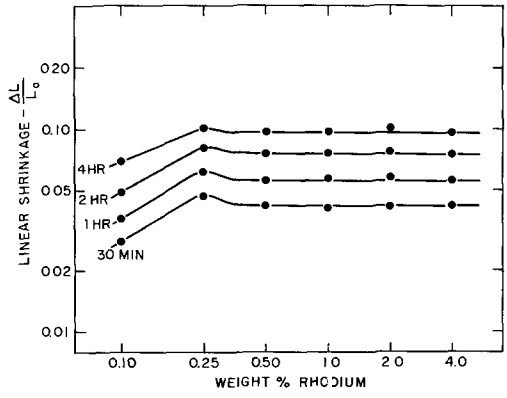

Fig. 8. Composition dependence of linear shrinkage in rhodium-tungsten, temperature, 1100°C.

Rhodium-tungsten compacts were sintered at temperatures from 950° to 1100°C. Figure 7 shows the time dependence of linear shrinkage, and Fig. 8 the rhodium content dependence. At all temperatures, linear shrinkage initially increases with the square root of time, but at higher values of linear shrinkage the curves shift toward a cube root of time dependence. Figure 8 shows that shrinkage is independent of rhodium content above 0.25 w/o. This behavior is consistent with a process in which the solution step controls the rate when linear shrinkage (and interparticle flat area) is small, and interface diffusion controls when shrinkage (and interparticle flat area) is large.

Table II summarizes the experimental results discussed in the previous paragraphs. Figure 9 shows a compilation of Arrhenius' plots for tungsten sintering with small amounts of Group VIII transition elements. These curves were determined by plotting the logarithm of the time necessary for 5% linear shrinkage *vs.* the reciprocal of the absolute sintering temperature. The change in slope of the nickel-tungsten curve is due to the presence of an intermetallic compound at temperatures below approximately 950°C. The apparent activation energies included in Table II were obtained from Fig. 9. The values for the interfacial diffusion path lie in the range 86,000 to 114,000 cal/mole. These values straddle the published activation energy of 90,000 cal/mole for grain boundary diffusion of thorium in tungsten (9), which is believed to be comparable to the activation energy for grain boundary self-

Table II. Summary of carrier phase sintering results with tungsten and molybdenum

$$\frac{\Delta L}{L_0} \propto c^p t^s$$

System	p	s	Control	Activation energy, cal/mole	Reference
W-Ni	0	1/2	Solution	68,000	(1)
W-Pd	0	1/3	Diffusion	86,000	
W-Ru	0	1/3	Diffusion	114,000	
W-Pt	0	1/3	Diffusion	92,000	
Mo-Ni					
Low temperature	–	1/2	Solution	—	(5)
High temperature	0	1/3	Diffusion	77,000	
W-Rh					
Low shrinkage	0	1/2	Solution	85,000	
High shrinkage	0	1/3	Diffusion	98,000	

diffusion in tungsten. Consequently the influence of the Group VIII element is largely a modification of the interfacial transport of tungsten atoms.

The activation energies for the solution-controlled processes with nickel and rhodium on tungsten are in general lower than those observed for diffusion control.

Figure 9 also permits a comparison of the relative effectiveness of each of the added elements in enhancing the densification of tungsten. At a given temperature, palladium led to the most rapid densification, followed in order by nickel, rhodium, platinum, and ruthenium.

The results of this investigation and of previously published work suggest a possible mechanism for what has previously been called "activated sintering" of tungsten. It appears that tungsten atoms move by a sequence of steps: first, separation from the tungsten particle by a "solution" process and, second, by diffusion in the interface between the "activating" element and the tungsten particle. Both of these steps occur in series, and under a given set of conditions the slower of the two determines the rate of sintering. Whether the solution step or diffusion step controls the rate, depends on the identity of the activating element and, in some cases, is determined by increasing transport path length through densification, or by the differing influence of temperature on the rates of the two steps. In either step the over-all driving force is the reduction of surface free energy, which increases the tungsten activity in the carrier phase interface at the points of particle contact.

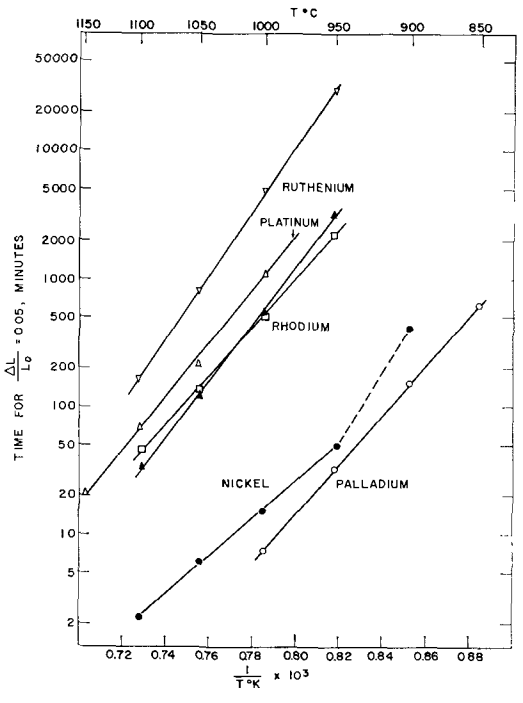

Fig. 9. Summary of Arrhenius' plots of data from carrier phase sintering of tungsten. Added element and activation energy, cal/mole: ○, palladium, 86,000 diff.; ●, nickel, 68,000 soln.; □, rhodium, 85,000 soln; ▲, rhodium, 98,000 diff.; △, platinum, 92,000 diff.; ▽, ruthenium, 114,000 diff.

The reason that Group VIII transition elements are particularly effective as activators in tungsten sintering has not been established as yet. It may prove to be associated with the fact that they all dissolve 10-20% tungsten, but are soluble in tungsten only to a very limited extent at the temperature employed in sintering. The fuller implications of this factor remain to be studied.

Conclusions

The densification rate in sintering tungsten powder can be significantly increased by small additions of Group VIII transition elements. Of the added elements explored to date, palladium appears to have the greatest effect, followed in order by nickel, rhodium, platinum, and ruthenium. With 0.25 w/o palladium densities of 93.5 and 99.5% of theoretical were obtained after sintering 30 min and 16 hr, respectively, at 1100°C in hydrogen. In the absence of such an added element, tungsten powder can only be presintered at 1100°C.

A mechanism for this increased densification rate has been proposed. The activating element appears on the tungsten particle surface forming a "carrier phase" layer. Tungsten dissolves preferentially into the layer at points of particle contact and diffuses outward in the interface between the carrier phase layer and the particle itself. The result is a decrease in distance between adjacent particle centers and over-all shrinkage of the powder compact. The rate of the process is significant at temperatures well below the minimum melting points in the binary alloy systems between the added elements and tungsten, and below the temperatures ordinarily required to sinter tungsten powder of commercial purity.

The carrier phase sintering process is an example of the selective acceleration of one of the possible mass transport mechanisms previously proposed for sintering pure solid components. This analysis suggests that liquid phase sintering, formerly considered to be distinct from sintering in the solid state, is one of the special cases of carrier phase sintering. Under a given set of experimental conditions one of the mass transport processes may be observed to control sintering rate of a pure component. The identity of the rate-controlling process may change with changing experimental conditions. This has been demonstrated with changing particle size and sin-

tering temperature, and with the presence of foreign phases which are gaseous, liquid, or solid.

Acknowledgments

The authors would like to acknowledge the counsel and suggestions of Professor John Wulff and the financial support of this investigation from the U.S. Navy, Bureau of Naval Weapons, under contract Number NOw-61-0326-d.

Manuscript received July 23, 1962; revised manuscript received Feb. 6, 1963. This paper was presented at the Detroit Meeting, Oct. 1-5, 1961.

Any discussion of this paper will appear in a Discussion Section to be published in the June 1964 JOURNAL.

REFERENCES

1. J. H. Brophy, L. A. Shepard, and J. Wulff, "Nickel Activated Sintering of Tungsten," in "Powder Metallurgy," W. Leszynski, Editor, p. 113, AIME, MPI, Interscience, New York (1961).
2. H. W. Hayden, Nickel Activated Sintering of Tungsten, S. B. Thesis, Metallurgy Department, M.I.T. (1960).
3. J. H. Brophy, H. W. Hayden, and J. Wulff, *Trans. AIME*, **224**, 797 (1962).
4. J. H. Brophy, H. W. Hayden, and J. Wulff, *ibid.*, **221**, 1225 (1961).
5. J. R. Buta, Nickel Activated Sintering of Molybdenum, S. B. Thesis, Mechanical Engineering Department, M.I.T. (1962).
6. F. H. Driggs and W. H. Lenz, Contact Alloys, *U.S.P.*, 2, 227, 446, (February 13, 1939).
7. J. Vacek, On Influencing the Sintering Behavior of Tungsten, *Planseebericht fur Pulvermetallurgie*, **7**, 6 (1959).
8. W. D. Kingery and M. Berg, *J. Appl. Phys.*, **26**, 1205 (1955).
9. I. Langmuir, *J. Franklin Inst.*, **217**, 543 (1934).

Transference Numbers in Pure Molten Sodium Nitrate

Roger J. Labrie and Vernon A. Lamb

Metallurgy Division, National Bureau of Standards, Washington, D. C.

ABSTRACT

Transference numbers of the ions of pure molten sodium nitrate were measured in cells equipped with legs of sodium-ion conductive porcelain in the form of cylindrical membranes. The membranes served as sodium "electrodes" for selectively introducing sodium ions into the anode compartment and removing them from the cathode compartment of the cell during passage of current. Porous diaphragms of Pyrex, porcelain, and alundum were used to separate the anode and cathode compartments of the cell.

Transference numbers for about a dozen pure[1] molten salts have been reported in the last seven years. Cells with a porous diaphragm to separate anode and cathode compartments have been used for all measurements for pure salts. Either the change in volume of the liquid in the compartments or the change in concentration of a radioactive isotope must be measured. The volume change has in some cases been determined with the bubble cross-arm introduced by Duke (1) and in some cases by measuring the relative rise and fall of molten salt in vertical capillary tubes connected to the two arms of the cell (2). Cells of both the bubble cross-arm and vertical capillary types were used in the present work.

Lack of suitable electrodes has posed a problem on design of cells for some kinds of salts. Salts of metals such as silver, lead, or cadmium have presented no problem because these metals can be used as electrodes. Measurements of transference numbers of alkali halides and nitrates have also been made, even though ideal electrodes were not available. As expedients, lead or silver electrodes were used for alkali halides (3) and a liquid junction with $Ag/AgNO_3$ electrodes for alkali nitrates (4). While it is probable that the results thus obtained are reliable, an electrode system that would not introduce any foreign ion into the cell is desirable, since the chance of error due to volume or conductance effects of the foreign ion would then be absent.

[1] The word "pure" in this context infers a single salt instead of a mixture.

In the work described here, this problem of providing a suitable electrode was solved for sodium nitrate by the use of a sodium-ion-conductive porcelain membrane (5). Details of the preparation of the porcelain will be given in a future paper.

Apparatus, Materials, and Procedure

Cells used for the measurements were of two types. Earlier work was done with cells of the bubble cross-arm type. In this type of cell, change of volume in the two compartments due to transport of salt is determined by measuring the travel of a small air bubble trapped in the cross-arm. Later measurements were made with cells like that shown in Fig. 1, in which the change of volume is determined from the change in levels of salt in the vertical capillaries.

The legs of both types of cells were made of sodium-ion-conductive porcelain tubes, sealed to the cells as shown. Each tube dipped into a cup of sodium nitrate. Silver electrodes made contact with the sodium nitrate in the external cups, except for cell No. 17 for which gold or platinum was used. The chemical composition of the porcelain is approximately: Na_2O, 10%; SiO_2, 54%; Al_2O_3, 36%. Data previously reported show that this porcelain, when in contact with a molten sodium salt, conducts solely by transfer of sodium ions, and not by transfer of electrons or other ions (5). Its conductivity is approximately 100 times that of glass.

After the transference measurements were in progress, we found that silver ions will exchange

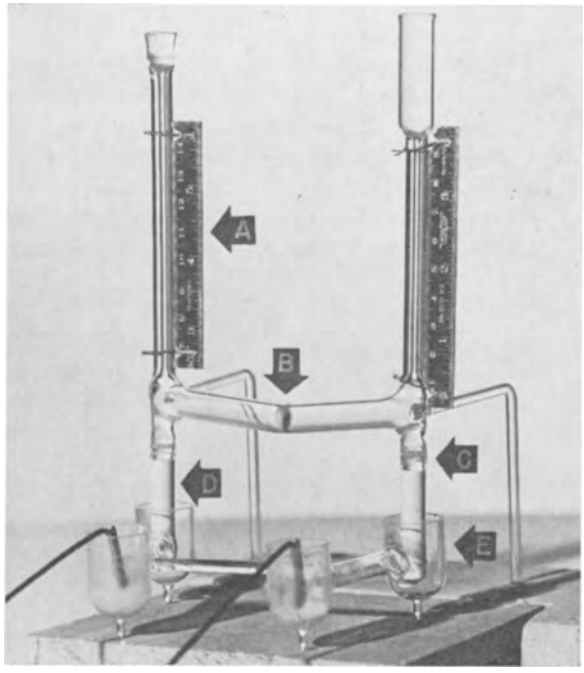

Fig. 1. Vertical arm cell. A, Steel rule attached to capillary arm; B, diaphragm; C, graded seal between Pyrex and porcelain; D, porcelain leg; E, cup to contain $NaNO_3$.

with sodium ions in this porcelain. Such exchange could be a source of error since silver ions are produced in the anodic cup during a run. However, it was shown by two experiments that, under the conditions of the transference measurements, silver did not enter the cell and thus interfere with the determination. In the first experiment, the salt in the cell, after cooling following a run, was dissolved in water and tested for the presence of silver by adding chloride ion. Cloudiness of the solution due to a precipitate of silver chloride was never found. The other experiment consisted of performing an extended dummy run with an H-shaped cell with porcelain legs like a transference cell, and with the same electrode arrangements, but minus the separator diaphragm and bubble cross-arm. It was filled with molten sodium nitrate and a current of 100 ma was passed in alternating directions corresponding to 20 transference measurements. At the end of the experiment, no silver was present in the cell, and the weight of the contents, initially 7.3802g, was practically unchanged, 7.3799g. The cell itself lost 1.1 mg due to slight etching of one leg.

The internal diameters of the capillaries in both types of cell were calibrated with mercury. For cross-arm cells, capillary tubes with an ID of 1.4-1.8 mm, selected for uniformity, were used. A capillary diameter of 1.0 mm was too small, resulting in sticking of bubbles. For vertical-arm cells, precision bore capillary tubing, 1.75 mm diameter (procured from Fish-Schurman Corporation) was used. Observation through a cross-hair telescope of a well-lighted meniscus against a piece of steel rule rigidly wired to the capillary allowed quick measurements of meniscus location accurate to 0.01 cm. Dimensions of the capillary and steel rule were corrected for temperature change. Both cross-arm and vertical-arm cells were constructed symmetrically about the diaphragm to minimize the effects of small temperature fluctuations and of resistance heating within the cell.

Three different materials were used for the porous diaphragms that separated the anode and cathode compartments of the cells: fritted Pyrex (Corning Glass Works), porous porcelain, a material composed of alumina, silica, 1.7% by weight of potassium, and containing less than 0.1% of sodium (Selas Corporation of America), and porous alundum (Norton Company RA84). Pore dimensions are given in Table I. Each kind of diaphragm was sealed into the cross-arm with a glass having an appropriate coefficient of thermal expansion: Corning No. 3320 for the Selas porcelain, and Corning No. 7052 for the Norton alundum.

Reagent grade sodium nitrate was used for these measurements without further purification. Cells were filled while they were hot by dropping solid sodium nitrate directly into them.

Bubble-cross-arm cells were heated in a vertical tube furnace, 16 in. long, in which the temperature was uniform through most of its length. The level of the cross-arm was adjusted so that the bubble remained stationary for at least 20 min. A measurement in a cross-arm cell was carried out by determining the number of coulombs required to shift the bubble a measured distance of 0.5-1.0 cm in the

Table I. Transference data for molten sodium nitrate

Cell No.	Type of cell	Diaphragm material	Max. pore diameter, μ	Back-flow, cm/min/cm of head	Temp. of furnace, °C	$t_{NO_3^-}$**	Standard deviation	No. of runs
1	Bubble	Pyrex	5.5	—	352-423*	0.298	0.026	18
7	Bubble	Pyrex	1.4	—	397-414*	0.305	0.003	10
14	Vertical capillary	Pyrex	1.4	0.006	372-401	0.302	0.001	8
17	Vertical capillary	Pyrex	1.4	0.006	345-348	0.286	0.003	4
					338-342	0.261†	0.003	3
3	Bubble	Porcelain	2.8	—	334-364*	0.236	0.013	10
4	Bubble	Porcelain	2.8	—	354-379*	0.261	0.018	10
		(same disk as No. 3)						
5	Bubble	Porcelain	6.0	—	347*	0.263	0.005	10
15	Vertical capillary	Porcelain	1.2	0.030	339	0.239	0.005	6
18	Vertical capillary	Porcelain	1.2	0.004	320-3	0.278	0.001	4
16	Vertical capillary	Alundum	0.1	0.025	367	0.281	0.002	4

* Temperature measured near the diaphragm. Range indicates differing temperature in different runs.
** Individual values are the mean of the number of runs shown.
† This value was obtained after refilling cell No. 17.

cross-arm. Coulombs were measured with a gas coulometer similar to that described by Lingane (6). For all runs a constant current of 100 ma was passed through the cell before the measuring period to establish thermal equilibrium before the bubble reached the measured interval, and continued through the run. Runs were made in pairs, one in each direction of bubble travel, to minimize systematic errors. From the density of the salt at the temperature of the cell, measured at the cross-arm (7), and the volume swept out by the bubble, the number of equivalents of sodium nitrate displaced was calculated. The transference number of the nitrate ion is equal to this value divided by the corresponding number of faradays.

Vertical-arm cells were heated in a large muffle furnace maintained constant in temperature to within ±1°C with a time-proportioning controller which regulated about one-fourth of the total power used. The controller proportioned a 5-sec time cycle into on and off parts so that temperature fluctuations were of short period compared to the duration of a run. The current passing through the cell was maintained constant manually, at 100 ma, within 0.2% It was measured with a calibrated milliammeter. In a typical run, current was passed until thermal equilibrium was established and a difference of level between the melt in the arms of 1.5 to 2 cm was produced. The current was then reversed and the run continued for a period of about 60 min, which produced an opposite displacement of 1.5-2 cm. The levels of salt in the capillaries were measured at 1-min intervals.

From these measurements the head between the two arms was calculated, using as a zero-point the equilibrium level with no current. The values of head, plotted against time on 16 x 24 in. graph paper, formed a smooth slightly curved line. The departure of this line from linearity represented back-flow through the diaphragm due to the pressure difference. The slope of the tangent to the curve at the point of zero head is equal to twice the rate of transport of salt through the diaphragm due to current, corrected for back-flow. This tangent was obtained by adding a correction factor at several points distributed over the curve of head *vs.* time, and drawing a straight line through the corrected points. The correction for a given point is equal to kA where k equals the separately measured back-flow per cm of head per minute, and A is the area under the transference curve (head *vs.* time), between the limits of zero head and that at which the correction is applied. In all cases, the resulting points fell on the zero-point tangent to the curve, within 0.02-0.03 cm of head, which shows that the graphical computation adequately corrects for back-flow. Total amount of back-flow during a run, except for cells 15 and 16, amounted to no more than 10% of the salt displaced. Transference numbers were computed with the formula

$$t_- = \frac{SA\,d\,\mathbf{F}}{2MI}$$

where I is the current, S is the slope of the zero-point tangent in cm/sec, A is the average cross section of the arms in cm^2, d is the density of the salt, $\mathbf{F}$ is the faraday, and M is the formula weight of the salt in grams. Runs were made in pairs, with the current reversed in the second run of the pair.

Experiments were carried out aimed at detecting the streaming potential which must exist as a necessary consequence of the occurrence of transport due to an applied voltage. Cells similar in form to the transference cells were used. The arms were modified so that air or oxygen could be applied to force a flow of molten sodium nitrate through fritted Pyrex (maximum pore diameter 0.9-1.4μ) or Selas porous porcelain (maximum pore diameter 0.60 and 1.4μ), respectively. A sodium nitrate-silver nitrate melt (1:1 mole ratio) was used in the cups into which the porcelain legs of the cell dipped. A silver electrode in each cup completed a cell which was in essence the same as those described in ref. (5).

A pressure differential of about 20 psi was applied across the diaphragm of the cell by reducing the pressure of one arm and applying gas pressure to the other. This pressure resulted in a flow of ½-1 ml/min. The pressure and vacuum were periodically reversed with valves while potential measurements were made with a potentiometer.

Results and Discussion

Results of the measurements are given in Tables I and II. Duke and Owens (4) reported a value of 0.29 ± 0.01 for the transference number of the nitrate ion, determined in cells containing a Pyrex separator. With the exception of one value (second determination in cell No. 17), the data we obtained in cells with a Pyrex separator agree closely with their result.

Values for the transference numbers of most of the salts reported in the literature were obtained from measurements made with cells that contained

Table II. Effect of temperature on the transference numbers of molten sodium nitrate

Cell No	Type of cell	Diaphragm material	Max. pore diameter, μ	Back-flow, cm/min/cm of head	Temp of furnace, °C*	$t_{NO_3^-}$	Standard deviation	No. of runs
18	Vertical capillary	Porcelain	1.2	0.004	320-3	0.278	0.001	4
					355	0.281	0.001	4
					320-3	0.277	0.003	2
					403-13	0.277	0.002	4
					324	0.276	0.003	2

* Temperature was cycled in the order shown.

only one kind of diaphragm. However, Duke and Laity showed that the transference numbers of the ions of lead chloride are independent of the diaphragm material for Pyrex, porcelain, and asbestos (8). They also showed that a porous Pyrex diaphragm did not affect the activation energy of conductivity for several salts, and therefore should not be expected to affect the measured transference numbers (9).

In general, we obtained higher values for the transference number of the nitrate ion with Pyrex diaphragms than with porcelain diaphragms. Our value with an alundum diaphragm is intermediate. Since we know of no source of accidental error that would account for the observed differences and since the deviations between runs for a given cell are small, it seems likely that the differences obtained are real.

Two specific diaphragm effects are considered as possible causes of the observed differences. The first is the sodium ion conductivity of the diaphragm material. The conductivity of Pyrex is too small to be significant. The same would be expected to be true for alundum. The porcelain diaphragm material was analyzed and found to contain 1.7% by weight of potassium. This potassium content might make it slightly conductive to sodium ion, the effect of which would be to diminish the measured transference number of the nitrate ion.

The above factor cannot explain the results obtained from cells 3 and 4 or from cell 17. The same disk was used as a diaphragm in both cells 3 and 4. After runs were completed in cell 3, all salt was dissolved out of the diaphragm, it was cut out from cell 3 and sealed into cell 4. In the case of cell 17, after the first group of runs was completed, it was cooled and washed clean, all salt being dissolved out of the diaphragm. It was then reheated, refilled, and the second group of runs made. We suggest that in the case of cells 3 and 4 re-sealing of the diaphragm may have altered the surface characteristics of the pores of the diaphragm so as to influence the apparent value of the transference number. This explanation implies that the diaphragm introduces an electroosmotic effect. Our experiment aimed at measuring a streaming potential yielded inconclusive results. Due to slight temperature fluctuations, the cell potential varied within a range of ± 0.05 mv, hence, any streaming potential less than 0.05 mv was undetected. The relationship $(E/P)_{I=0} = (V/I)_{P=0}$, discussed by Mazur and Overbeek (10) applies here. E is the electrical streaming potential corresponding to a pressure difference P where no current flows, and V is the flow corresponding to the current I in a corresponding electroosmotic experiment, when no pressure difference exists. This equation also applies to a transference experiment as well as an electroosmotic experiment, as was shown by the general derivation, making use of general thermodynamic relationships and irreversible thermodynamics, carried out by Mazur and Overbeek. For a flow corresponding to a transference number, $t_{NO_3^-} = 0.28$, and a pressure difference of 20 psi in the streaming potential experiment, one obtains from the above relation a value of E of 0.018 mv resulting from total transport.[2] Since the electroosmotic portion of the transport, if an electroosmotic effect were present, would correspond to only a fraction of 0.018 mv, it is apparent that our experiment was not sufficiently sensitive to detect an electroosmotic effect.

Small differences in the concentration of water in the molten sodium nitrate may have occurred and might account for some of the variability in the results. Frame and co-workers (11) have shown that water has a slight but reversible solubility in molten sodium nitrate.

Considerable uncertainty exists in the true temperature at which measurements were made because of resistance heating of the diaphragm, and no attempt was made to make local temperature measurements within it. The average temperature of the salt in the cell usually rose about 4°C, in some cases a maximum of 12°C, due to ohmic heating of the entire cell and melt. It is likely that temperatures in the diaphragms rose somewhat more than this, but not substantially more in view of the small wattages dissipated within them. In no case was voltage across the cell greater than 50v for a current of 0.1 amp and generally, it was 20-30v. Allowing for about 1w dissipated in the porcelain legs and melt, a maximum of 4w was dissipated within the diaphragm. Further indication that ohmic heating was not large is the lack of decomposition of the melt as evidenced by the complete absence of gas formation, even at the highest operating temperatures.

The effect of temperature on the transference numbers was determined with measurements with cell 18 over a range of 90°C. Results are given in Table II. It is seen that within this range of temperature, the transference number is essentially constant. The other cells, shown in Table I, also showed no significant temperature effect over smaller ranges of temperature. Similar negligible effect of temperature has been reported previously (8, 9). Since a change in ambient temperature of 90°C did not significantly effect the transference numbers, the uncertainty in diaphragm temperature referred to is not important. Volume changes caused by ohmic heating did not cause error in measured values of the transference numbers, because the cell was pre-electrolyzed to obtain temperature equilibrium before a run was started.

The sodium-ion-conductive porcelain membranes, used as sodium "electrodes" to pass sodium ions into and out of the transference cell, performed this function satisfactorily.

Acknowledgment

This research was supported financially by the Atomic Energy Commission, Division of Research, Chemistry Branch.

[2] If $t_{NO_3^-}$ is taken as 0.28, then in a transference experiment 0.28 equivalents is seen to be the flow per faraday, or 12.8 cm³. Then, from the above relation, $E = \frac{(12.8)}{F}\frac{(20)}{14.7}(102) = .018$ mv, where F is taken as 96,500 coulombs, 20/14.7 is the pressure difference in atmospheres, and 102 embodies conversion from joules to cc-atm and v to mv.

Manuscript received Nov. 16, 1962; revised manuscript received Jan. 23, 1963. This paper was delivered at the Detroit Meeting, Oct. 1-5, 1961.

Any discussion of this paper will appear in a Discussion Section to be published in the June 1964 JOURNAL.

REFERENCES

1. F. R. Duke and R. W. Laity, *J. Am. Chem. Soc.*, **76**, 4046 (1954).
2. F. R. Duke, R. W. Laity, and B. Owens, *This Journal*, **104**, 299 (1957).
3. F. R. Duke and A. L. Bowman, *ibid.*, **106**, 626 (1959).
4. F. R. Duke and B. Owens, *ibid.*, **105**, 548 (1958).
5. R. J. Labrie and V. A. Lamb, *ibid.*, **106**, 895 (1959).
6. J. J. Lingane, "Electroanalytical Chemistry," 2nd ed., Interscience Publishers, New York (1958).
7. International Critical Tables, Vol. 4, p. 443, E. W. Washburn, Editor, McGraw-Hill Book Co., New York (1928).
8. F. R. Duke and R. W. Laity, *J. Phys. Chem.*, **59**, 549 (1955).
9. R. W. Laity and F. R. Duke, *This Journal*, **105**, 97 (1958).
10. P. Mazur and J. Overbeek, *Rec. trav. chim.*, **70**, 83 (1951).
11. J. P. Frame, E. Rhodes, and A. R. Ubbelohde, *Trans. Faraday Soc.*, **57**, 1075 (1961).

An Electrochemical Investigation of the Reduction of Nitrate in $NaNO_3$-KNO_3 Eutectic at 250°C

H. S. Swofford, Jr.,[1] and H. A. Laitinen

Noyes Chemical Laboratory, University of Illinois, Urbana, Illinois

ABSTRACT

Molten $NaNO_3$-KNO_3 eutectic is well suited for use as a high-temperature solvent having a 2.5v range of potentials [+1.2 to −1.3v *vs.* Ag/Ag(I) (0.07*M*)] available for observation of oxidation-reduction reactions involving solutes of fundamental electrochemical interest.

Studies carried out at 250°C demonstrate that the peak phenomenon observed at approximately −1.65v in cathodic polarization curves using various solid microelectrodes and dropping mercury may be identified with the beginning of the irreversible reduction of NO_3^-, limited by the precipitation of Na_2O at the electrode surfaces. It appears that the after-peak current limiting process is the rate of dissolution of the Na_2O film, which determines the rate of reduction necessary to sustain a steady state. The anodic and cathodic limits of potential are observed to represent the evolution of NO_2 gas (+1.2v) and reduction of alkali metal (−2.8v); subsequent reaction of deposited alkali metal with NO_3^- produces a colorless, odorless gas, and oxide ion in amounts indicating N_2 as the reduction product.

The alkali nitrates represent a class of nonaqueous solvent systems having the desirable characteristics of low vapor pressure, low viscosity, and high electrical conductivity; furthermore, a low melting point facilitates application of conventional aqueous electrochemical techniques.

Among the first work carried out in fused nitrate media was that of Steinberg and Nachtrieb (1, 2) who obtained well-defined and reproducible reduction waves for Ni(II), Pb(II), Cd(II), and Zn(II) in the molten ternary eutectic $LiNO_3$-$NaNO_3$-KNO_3 at 160°C using a dropping mercury electrode. Lyalikov *et al.* (3, 4) and Flengas (5) have employed a solid, gas-flushed, platinum needle electrode in current-voltage investigations and solubility studies, respectively, in fused alkali nitrate media, while Delimarskii and co-workers (6, 7) have used a stationary platinum microelectrode to investigate the current-voltage behavior of a large number of metal ions dissolved in both KNO_3 and $NaNO_3$.

The first comprehensive electrochemical investigations carried out on the base electrolyte $NaNO_3$-KNO_3 eutectic void of any dissolved ions was that of Hills and Johnson (8). Current-voltage curves for this mixture recorded by these authors using stationary platinum microelectrodes displayed a low linear residual current in the range 0.0 to −1.5v *vs.* a massive platinum anode reference. However, the authors reported that the steeply rising current observed at approximately −1.5v (depending somewhat on solvent and temperature), recorded by previous workers (1-7) as being due to the reduction of alkali metal cation, was actually the beginning of a process which produced a maximum in the current (*i.e.*, peak). Hills and Johnson observed that the peak and small after-peak steady-state current (3 ma/cm^2) were markedly temperature dependent, the latter having an activation energy of 11 kcal·mole^{-1}. Final reduction of the solvent occurred at −2.9v. It was proposed that the process observed at −1.5v was in fact the beginning of the irreversible reduction of NO_3^- and not reduction of an alkali metal as originally supposed.

The identity of the reduction products and the nature of the origin of the peak and after-peak currents are the subjects of this paper.

Experimental

Equipment and material.—The electrolytic cell used in these studies consisted of a 200 ml, three-

[1] Present address: Department of Chemistry, University of Minnesota, Minneapolis, Minnesota.

necked, round bottom flask. Because of the danger involved in using ordinary rubber in conjunction with a highly oxidizing medium, silicone rubber stoppers (No. 5) were used to provide pressure-tight seals for the melt container. The stoppers were bored with a variety of holes to admit necessary apparatus (electrodes, compartments, etc.). Medium-porosity sintered-glass sealing tubes (12 mm OD) were used to separate the melt into compartments. All metal or glass parts which came into contact with the melt were cleaned in boiling HNO_3, washed with demineralized water, and oven dried at 130°C.

A movable piece of glass tubing made it possible to bubble dried and oxygen-free nitrogen gas through the melt for purposes of stirring, purging the melt of other gases or to maintain a moderate positive pressure of the gas above the melt during the course of the electrochemical investigations. The gas was purified of oxygen and moisture by passage through an activated copper column heated to 300°C followed by a $Mg(ClO_4)_2$ drying tube.

A standard 200 ml Glas-Col heating mantle (Glas-Col Apparatus Company, Terre Haute, Indiana) in series with a Variac transformer (Standard Electric Product Company, Dayton, Ohio) and Wheelco Capacitrol, Model 241P (Wheelco Instrument Company, Chicago, Illinois) temperature regulator, provided a means of fusing and controlling the temperature of the melt (±3°). Connected to the temperature regulator was an iron-constantan thermocouple enclosed in a glass sheath immersed in the fused eutectic.

Instruments sensitive to line voltage fluctuations were connected through a General Radio, Type No. 1570AL (General Radio Company, Cambridge, Massachusetts) automatic voltage regulator.

Potential measurements were made with either a L&N student potentiometer when high sensitivity was required or a high input-impedance vacuum-tube voltmeter when rapid measurement was desired. Constant current was obtained from either a Sargent coulometric current source, Model IV (E. H. Sargent and Company, Chicago), or from a constant voltage source through a large resistor in the usual manner.

Current-voltage curves were recorded with a L&N Electrochemograph, Type E. Alternatively, a Sargent, Model XV, Polarograph was used. Chronopotentiograms were obtained using a Sargent M.R. recorder; the equipment used to supply the small constant current necessary along with its construction is described elsewhere (9).

All glassware which came into contact with the melt was Pyrex or Vycor unless otherwise specified.

Electrodes.—The solid microelectrodes (areas ~ 10^{-3} cm^2) used in this work were prepared by sealing the appropriate metal wires in glass where possible. Alternatively they were prepared by plating the desired metal on a base platinum microelectrode. Following their preparation the electrodes were polished and examined under a high-powered optical microscope before use. For further details the reader is referred to the original thesis (10).

Massive working electrodes (areas ~ 1.5 cm^2) were prepared in the usual manner by spot-welding a piece of platinum foil to platinum wire sealed in soft glass. The dropping mercury electrode used for current-voltage investigations was of the conventional type.

Earlier workers (11, 12) established by concentration cell measurements that an Ag/Ag(I) couple follows the predicted Nernst behavior in fused nitrate media. This electrode was used by later investigators (13-15) as a point of reference in electrochemical studies; hence, its use in the present work seemed appropriate. The reference electrode was prepared by placing a piece of silver wire (20 gauge, B.&S.) in a sintered-glass sealing tube, previously filled by immersion in the $NaNO_3$-KNO_3 eutectic melt, and passing anodic current 20 ma, 600 sec); a massive platinum electrode in a second compartment served as the counter cathode. From the previously determined density of the melt at 250°C (1.96 ± 0.04 g ml^{-1}) (10), and the weight of the reference compartment, the concentration of silver ion (usually approximately 0.07*M*) could be calculated.

Reagents.—Reagent grade chemicals, oven dried and stored in a desiccator until needed, were used in all cases.

Preparation and purification of eutectic.—Reagent grade KNO_3 and $NaNO_3$ (J. T. Baker Chemical Company) were taken directly from the reagent bottles and mixed in the correct eutectic proportions (45 mole % $NaNO_3$ and 55 mole % KNO_3). The mixture (270g) was pulverized with the aid of a mortar and pestle and placed in a drying oven for 24 hr and then introduced into a specially prepared fusion and filtration column [for details of column construction and operation see original work (10)]. Fusion of the solid mixture in the column was accomplished by adjusting the Variac controlled input to the column heater windings to such a value that the final temperature obtained would be approximately 250°C. After allowing the fused eutectic to stand in the column for 45 min (time allowed for oxidation of organic impurities), the melt was filtered into the electrolytic cell previously heated to 250°C. Following filtration the melt was purged with purified nitrogen gas for 3 hr, which was kept above the melt as an atmosphere at all times during the course of the investigations. Each melt was prepared immediately prior to its use and filtered directly into the cell used in the experiment. This treatment in preparation usually gave a pure melt; the criterion for purity was a residual current of less than 0.5 μa at an applied potential of −0.8v *vs.* Ag/Ag(I) (0.07*M*) using a platinum microelectrode (area = 10^{-3} cm^2).

Techniques.—The procedures necessary for carrying out potential measurements and current voltage studies were of a conventional nature and need no explanation. In current-voltage measurements using a dropping mercury electrode, a cold trap (acetone dry ice) was attached to the gas exit of the electrolytic cell to trap any mercury vapor.

The chronopotentiometric technique was conveniently applied using the usual three electrode sys-

tem (all electrodes in separate compartments). The indicating electrode was a platinum microelectrode (area = 8 x 10^{-3} cm^2) used in conjunction with a large platinum working electrode and the usual Ag/Ag(I) (0.07*M*) reference. Since the electrolysis resistance between the indicator electrode and counter electrode was only of the order of 30 ohms, no complications due to iR drop arose.

Electrolyses of the $NaNO_3$-KNO_3 eutectic melt were carried out using a simple potential divider to impose a voltage across the working cathode and anode (areas = 1.5 cm^2) which were isolated from each other in the melt. By adjusting the voltage across the cell, it was possible to control the potential of either electrode *vs.* the silver reference electrode in a third compartment. A silver coulometer provided a value for the total coulombs passed during the course of a controlled potential electrolysis experiment. Chemical analysis of the cathode compartments following electrolysis experiments enabled identification of the reduction products of nitrate.

Results and Discussion

The present work was the first reported instance in which a Ag/Ag(I) reference electrode was subjected to polarization studies in this solvent; hence, a more critical evaluation of its reversibility was necessary. Silver(I) was generated *in situ* rather than by the usual addition as silver nitrate. The Ag(I) concentration cell, with liquid junction, used in these investigations was prepared by anodizing silver in separate compartments. After an equilibrium potential was reached, following the generation of a particular increment of Ag(I), current pulses of varying intensity and duration were applied to one of the silver electrodes and its rate of reattainment of equilibrium was followed as a function of time with respect to the second (see Table I). Following the completion of the electrochemical studies, the Ag(I) in each compartment was determined gravimetrically as silver chloride in order to verify that Ag(I) was generated at 100% current efficiency.

It is evident from Fig. 1 that a plot of E *vs.* log $t_{(sec)}$ (the time of generation is a linear function of concentration) is a straight line with slope 0.104v, as compared to the theoretical value 2.3 RT/F of 0.103v, which is consistent with previously published work. From Table I it is clear that equilibrium is reached and maintained even when the Ag/Ag(I) reference electrode is subjected to extreme conditions of passage of current.

The shape of a typical current voltage profile obtained in the present work (see Fig. 2) using a solid

Table I. Equilibrium potential-current pulse studies

Current intensity and duration	% Total coul present	Initial potential *vs.* reference, v	Time for equilibrium, sec	Final potential *vs.* reference, v
50 μa for 10 sec	0.0043	0.0590	0	0.0590
50 μa for 100 sec	0.043	0.0589	0	0.0589
400 μa for 20 sec	0.069	0.0590	0	0.0585
			15	0.0587
			30	0.0589

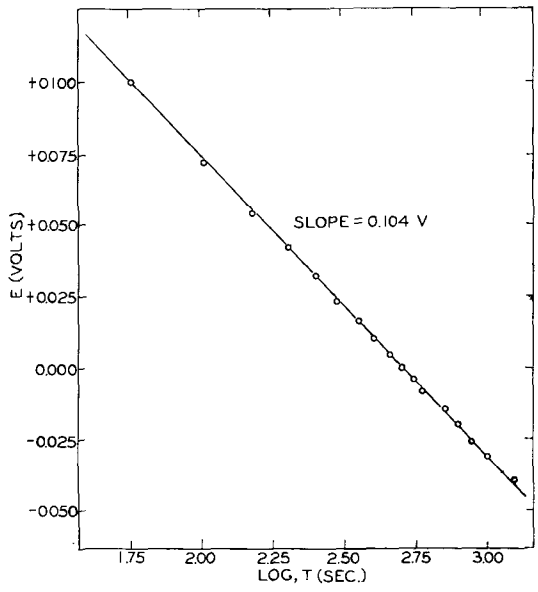

Fig. 1. Potential of silver concentration cell *vs.* log $t_{(sec)}$

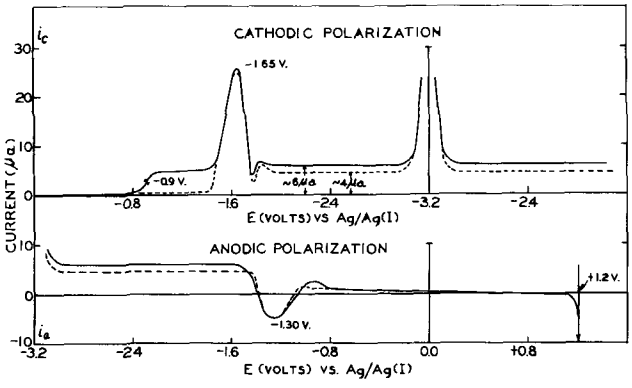

Fig. 2. Residual current-voltage curves of KNO_3-$NaNO_3$ eutectic at 250°C using a platinum microelectrode (A≃1 × 10^{-3} cm^2); ———, not degassed; - - - N_2 (dried) passed for 2 hr.

platinum microelectrode is in complete agreement with that reported by Hills and Johnson (8), a slight shift in potential due to a different choice of reference being the only difference. The anodic dip (—1.30v) observed on anodically polarizing a cathodized platinum microelectrode may be attributed to the irreversible oxidation of products formed during the prior cathodic cycle. It appears in the first instance that the peak (peak maximum at —1.65v) is part of a process which begins at —0.9v; however, closer examination of a current-voltage curve shows an inequality in the current flowing before and after the peak, suggesting that they arise from two separate reduction processes. It was found that the prepeak wave can be removed by purging the melt with purified nitrogen gas; further investigation indicated that this reduction process may be affected directly or indirectly by water present as a contaminant in the melt. An appreciable solubility of water in nitrate melts has previously been reported (16, 17). Since the peak and after-peak currents are not lowered by an amount corresponding to the prepeak current, it is probable that the first reduction process is blocked by the onset of the second.

Table II. Summary of residual current-voltage curves for various solid metal microelectrodes in KNO_3-$NaNO_3$ eutectic at 250°C

(Cathodic polarization 0.0 → −3.0v; anodic polarization −3.0 → 0.0v)

Type	*E* (cathodic peak), v	*E* (anodic peak or dip), v	Comments
Pt	−1.65	−1.30	Small anodic dip
Pt-Pt	−1.56	−1.28	Sharp anodic peak
Au	−1.56	−1.33	Rough plate; sharp anodic peak
Au	−1.62	−1.32	Smooth plate; small anodic dip
Ag	−1.62	−1.30	Very small anodic dip, did not cross zero current axis
Ni	−1.65	None	Chemical attack; erratic trace on anodic polarization
Cu	−1.66	−1.25	Chemical attack; erratic trace on anodic polarization
Hg*	−1.66	None	Limit of cathodic polarization −2.4v; second cathodic peak seen on anodic polarization (−1.65v)
W	−1.61	None	Second cathodic peak seen on anodic polarization (−1.33v)

* Mercury plated on gold.

The results presented in Table II indicate that the peak and after-peak phenomena are characteristic of a bulk property of the melt, the peak maximum occurring at nearly the same potential on all metal surfaces (see column 2). However, with any given metal the potential of the peak is dictated to a certain extent by the roughness of the metal surface.

Manual current-voltage profiles obtained with a Sargent, Model III, Polarograph established that the peak was not an artifact of the automatic recording of the current-voltage curves.

The activation energy 11 kcal·mole^{-1} reported by previous workers (8) and confirmed in this work is approximately three times that expected for any process ascribed to diffusion. Since stirring of the melt also has little effect, a kinetic or surface controlled reduction of nitrate is suggested.

The reduction products of NO_3^-, resulting from controlled-potential experiments, were quantitatively identified as NO_2^- and $O^=$ (Table III). It is noticed immediately in the electrolysis of a nitrate eutectic melt that a precipitate forms on the surface of the platinum foil cathode. If its potential is controlled at a point approximately one third of the way up the peak (−1.50v), no gas is observed. The precipitate, following its formation, is observed to dissolve in the melt at open circuit. Any reduction reaction written for nitrate in this medium involves the elimination of oxide and produces a lower oxidation state of nitrogen; nitrite was assumed *a priori* to be the most reasonable reduction product of nitrogen. The compartment analyzed for oxide was dissolved in aqueous solution and titrated with standard 0.01*M* HNO_3, while that to be analyzed for nitrite was dissolved in a standard solution of 0.01*N* $KMnO_4$ and back-titrated with a solution of 0.01*N* Fe(II). The results shown in Table III indeed correspond to a reduction having the stoichiometry

$$NO_3^- + 2e \rightarrow NO_2^- + O^= \qquad [1]$$

Further investigation established that $NaNO_2$ was soluble in all proportions in the eutectic melt and ruled it out as taking part in the precipitate formation; hence oxide ion must be involved. A current-voltage curve of pure KNO_3 at 350°C using a platinum microelectrode (area, 1 x 10^{-3} cm^2) and the usual reference prepared in the eutectic mixture displayed a low linear residual current between 0.0 and −1.35v; the current is observed to increase without bound at potentials more negative than −1.35v. Addition of 10% $NaNO_3$ by weight produced the same residual behavior; however, a peak was observed with maximum at −1.40v. It was found that it is possible to precipitate Na_2O from pure KNO_3 saturated with calcium oxide by adding $NaNO_3$. Similar results were obtained using decomposed Na_2O_2 as a source of oxide and sodium ion. It is reasonable to conclude that the peak observed in current-voltage curves using solid microelectrodes originates as a result of the gross inhibition of the reduction of NO_3^- by the precipitation of Na_2O on the surface of the cathode.

Current-voltage curves obtained using a dropping mercury electrode and recorded as a function of the height of the mercury column (Fig. 3) are consistent with precipitated Na_2O as an inhibitor in the reduction of NO_3^-. The peak (maximum at −1.75 on dropping mercury) is observed to appear and disappear as the mercury column height is raised and lowered. The final reduction of the supporting electrolyte (deposition of alkali metal) is observed at −2.1v which is expected since the reduction product is soluble in mercury. A slope of 0.81 for a plot of the log of the heights of mercury

Table III. Results of analysis of the cathode compartments in the controlled potential electrolysis of KNO_3-$NaNO_3$ eutectic

Equiv. of elect. passed	Theor. moles of nitrogen as NO_2^-	Theor. moles of $O^=$	Moles NO_2^- found	Moles $O^=$ found
1.20×10^{-4}		6.00×10^{-5}		5.70×10^{-5}
1.17×10^{-4}	5.85×10^{-5}		5.50×10^{-5}	

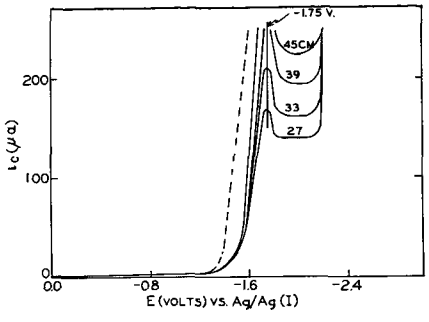

Fig. 3. Residual current-voltage curves using a D.M.E. in KNO_3-$NaNO_3$ eutectic at 250°C as a function of height of mercury. - - -, 76 cm, 68 cm, 61 cm, 52 cm.

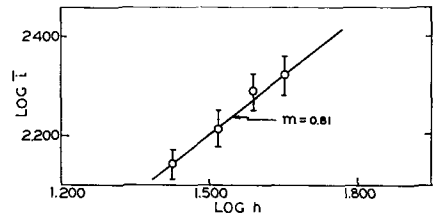

Fig. 4. Log i vs. log h for average after peak currents observed at D.M.E.

column (corrected for back pressure) *vs.* the log of the corresponding after-peak steady-state currents is expected for a surface-controlled process with a convective or mass transport component (see Fig. 4). A plot of the log of the current on the rising portion of the curve before the peak *vs.* potential produces a straight line with a slope of 0.100v, corresponding to an activation-controlled cathodic process without concentration polarization with $n\alpha$ = 0.97. The linear dependence of log current on potential, for the reduction of NO_3^- in the eutectic mixture, will be obeyed until a potential is reached such that the cathode surface becomes inhibited with Na_2O. Comparing the potential at which this deviation takes place (Fig. 5) with a current-voltage curve (Fig. 3) it is observed to correspond to a point approximately one-third of the way up the rising portion of the curve. Instantaneous current-time curves as a function of applied potential, shown in Fig. 6, indicate a shift in the reduction process from diffusion (normal current-time behavior) to surface control (maximum in current during single drop life). This shift in the reduction-controlling process explains the appearance and disappearance of the peak as a function of the height of the mercury column (Fig. 5). Although the onset of the change in the rate-controlling process is noted in Fig. 5 at approximately —1.5v, the process remains primarily diffusion controlled as long as the rate of drop growth is fast enough to prevent serious inhibition by Na_2O ($h > 52$ cm); however, when drop growth

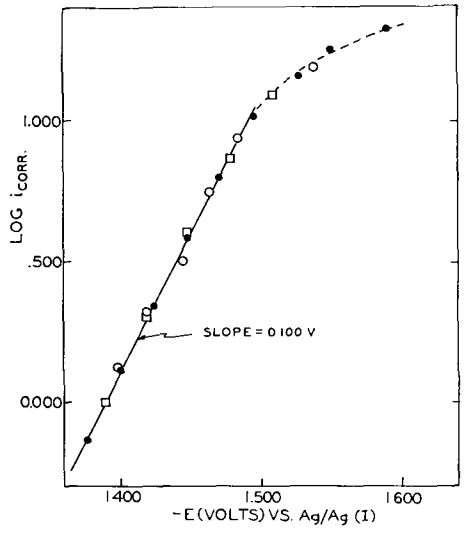

Fig. 5. Log $i_{corr.}$ *vs.* E (v) for rising part of peak using data from residual current-voltage curves taken with a D.M.E. in KNO_3-$NaNO_3$ eutectic at 250°C. ○, h = 69 cm; ●, h = 62 cm; □, h = 52 cm.

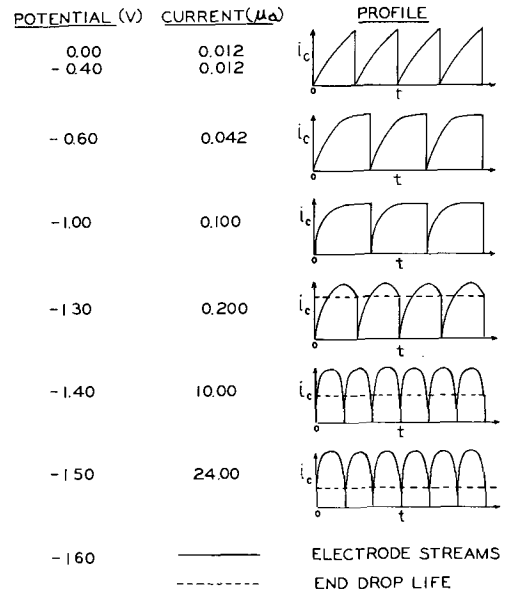

Fig. 6. Variation of mercury drop profiles with constant applied potential in KNO_3-$NaNO_3$ eutectic at 250°C (h=28 cm).

becomes sufficiently slow ($h < 45$ cm), Na_2O can collect in quantities large enough to inhibit the reduction process and surface control takes over. From the magnitude of the currents observed it is obvious that monolayer amounts are not involved.

A value of —1.10v for the e.c.m. determined in this work is in good agreement with that of Randles and White (—1.12v *vs.* $Hg/HgSO_4$) (18). Because mercury is oxidized near 0v *vs.* Ag/Ag(I), the points of reference are very close.

Chronopotentiometric investigations carried out in connection with this work complemented the current-voltage investigation. A typical chronopotentiogram, shown in Fig. 7, has $E_{1/4}$'s of —1.68v (τ_c) and —1.30v (τ_a) corresponding to cathodic and anodic processes which are in excellent agreement

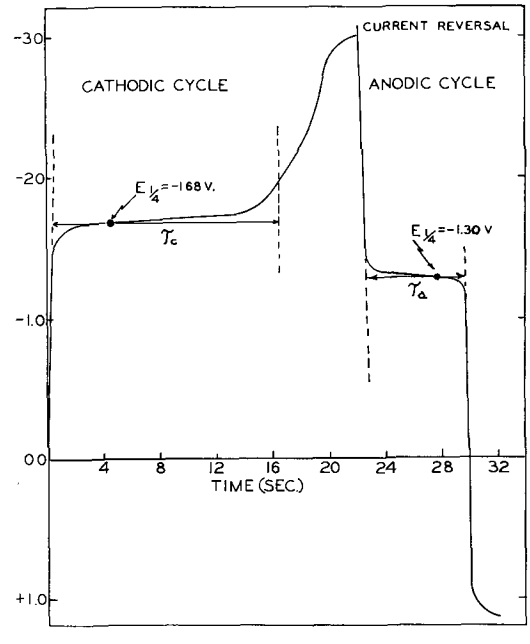

Fig. 7. Typical chronopotentiogram using a platinum microelectrode (i/A = 19 ma cm^{-2}) in KNO_3-$NaNO_3$ eutectic at 250°C.

with the potentials of the cathodic peak (—1.65v) and anodic dip (—1.30v) observed in the current-voltage work.

The data presented in Table IV represent the results of two separate series of experiments involving cathodic and anodic transition times observed as a function of the time a cathodized platinum microelectrode (*i.e.*, only cathodic chronopotentiometric cycles run at a constant current density of 12.3 ma/cm^2) stood in the melt at open circuit. The reappearance of τ_c and disappearance of τ_a indicates that one of the reduction products (Na_2O) must be a solid material, physically attached to the electrode surface, and dissolving with time. Since precipitated Na_2O controls the availability of both of the reduction products at the electrode surface (NO_2^- trapped in it), the products will be present to undergo reoxidation. Stirring the melt (Table V) tends to increase τ_c and to decrease τ_a of the precipitate, as expected.

Observations of cathodic and anodic transition times as a function of applied current density (Table VI) and as a function of the time of current interruption during a cathodic cycle at a constant current density (Table VII) were also consistent with these conclusions. For oxidation-reduction reactions involving an oxidant and reductant both soluble and free to diffuse in solution, the ratio of τ_c/τ_a should be 3, while it should be unity for a totally insoluble reductant (19). From Table VI, it

Table IV. τ_c and τ_a At constant current density (12.3 ma/cm^2) as a function of the time a cathodized platinum microelectrode stands in the eutectic mixture at open circuit

Time, sec	τ_c, sec	τ_a, sec
0	0	15.3*
100	0.1	13.2
200	0.4	12.4
225	5.5	9.5
250	11.3	8.1
300	12.0	5.0
400	17.0	3.2
750	19.4	1.5
800	20.0	0.5
—	22.4*	—

* τ_c and τ_a in normal cathodic and anodic cycles.

Table V. Transition times as a function of stirring the melt

I, ma/cm^2	Melt	τ_c, sec	τ_a, sec
12.3	Unstirred	25.0	15.1
12.3	Stirred	32.7	13.2

Table VI. Transition times as a function of current density in molten nitrate eutectic, 250°C

I, ma·cm^{-2}	τ_c, sec	τ_a, sec	τ_c/τ_a	$I\tau_c$, 10^2	$I\tau_a$, 10^2
18.8	16.5	6.7	2.46	3.10	1.26
25.0	10.0	4.4	2.27	2.50	1.10
31.3	6.5	3.3	1.96	2.04	1.04
37.5	4.0	2.8	1.60	1.50	1.05
43.8	2.6	2.3	1.13	1.14	1.01
50.0	2.2	2.1	1.05	1.10	1.05

Table VII. t_c/τ_a At constant current density (12.3 ma · cm^{-2}) as a function of current reversal at different times during cathodic cycle

t_c, sec	τ_a, sec	t_c/τ_a
22.7	15.0	1.51
24.0	12.0	2.00
25.2	12.6	2.00
25.4	10.0	2.54
19.6	7.5	2.61
16.1	6.1	2.63
9.5	3.0	2.70

is apparent the τ_c/τ_a varies from a value of 2.46 at low current density to 1.05 at high current density when the current reversal took place at the instant of reaching the end of the cathodic transition time. Likewise, at a constant applied current density, the ratio of t_c/τ_a varied from 2.70 for reversal early in the cathodic cycle to 1.51 for reversal late in the cathodic cycle, when a precipitate was present.

The variability of anodic dips (*i.e.*, peaks) with surface roughness indicates that a roughened surface favors retention of insoluble reduction products formed during the cathodic polarization cycle. Prolonged use of a platinum microelectrode in chronopotentiometric studies caused a gradual increase of surface area and of transition times. Repolishing of the electrode surface restored its original condition.

To determine whether a kinetically controlled reduction of NO_2^+ present at a small equilibrium concentration in the melt occurred (20), attempts were made to shift the equilibrium

$$NO_3^- \rightleftharpoons NO_2^+ + O^= \qquad [2]$$

Neither the addition of $K_2S_2O_7$ as an acid nor K_2CO_3 or Na_2CO_3 as a base affected the current-voltage curves. It appears that the current-limiting process is the rate of dissolution of the Na_2O film, which determines the rate of reduction necessary to sustain a steady state and that the equilibrium in Eq. [2] is not involved.

Preparative electrolyses were carried out to establish the reactions taking place at the extreme anodic and cathodic ends of the potential range available. The anode is depolarized at a potential of +1.2v *vs.* Ag/Ag(I) with the evolution of NO_2 gas. This observation is in agreement with anodic depolarization of microelectrodes both in the current-voltage and chronopotentiometric studies (see Fig. 2 and 7). The cathode is depolarized at —2.8v *vs.* Ag/Ag(I); this reaction appears to be a very complicated process. A blue liquid, reported in previous work by Hittorf (21), is first seen to form on the electrode surface; approximately 45 sec later, a subsequent reaction of this liquid with nitrate produces a colorless, odorless gas. The most probable explanation for this phenomenon is a formation of a metastable solution of alkali metal which then reacts with NO_3^-, reducing it to N_2. Analysis of cathode compartments for controlled-potential electrolyses carried out by holding the potential of the cathode at —3.5v *vs.* Ag/Ag(I) indicated oxide present in an amount roughly equivalent to that expected if NO_3^- were reduced to N_2 gas.

A final comment[2] of a practical nature may be of interest. Molten nitrate baths used for the heat treatment of aluminum sheets deteriorate over a period of time and form "stains" of sodium aluminate on the sheets. The baths may be rejuvenated with sodium dichromate, which presumably reacts with oxide to form sodium chromate. These observations are consistent with the findings of the present work.

Acknowledgment

One of the authors (H. S. S.) would like to express his gratitude to the National Science Foundation for support supplied through summer and cooperative fellowships. Thanks are also due to the Socony-Mobil Oil Company and finally to the State of Illinois for financial aid in the form of teaching assistantships.

Manuscript received Nov. 2, 1962; revised manuscript received Feb. 10, 1963. This paper was delivered at the Los Angeles Meeting, May 6-10, 1962.

Any discussion of this paper will appear in a Discussion Section to be published in the June 1964 JOURNAL.

REFERENCES

1. M. Steinberg and N. Nachtrieb, *J. Am. Chem. Soc.*, **72**, 3558 (1950).
2. N. Nachtrieb and M. Steinberg, *ibid.*, **70**, 2613 (1948).
3. Y. Lyalikov and V. Karmazin, *Zavodskaya Lab.*, **14**, 144 (1948).
4. Y. Lyalikov, *Zhur. Anal. Khim.*, **8**, 38 (1953).
5. S. N. Flengas, *J. Chem. Soc.*, **109**, 534 (1956)
6 K. Delimarskii and I. Panchenko, *Doklady Akad. Nauk.*, **91**, 115 (1953).
7. K. Delimarskii and I. Panchenko, *Ukrain. Khim. Zhur.*, **19**, 47 (1953).
8. G. J. Hills and K. E. Johnson, Proceedings of The 2nd International Congress on Polarography, Cambridge (1959), p. 974, Pergamon Press, London (1961).
9. D. R. Rhodes, Ph.D. Thesis, University of Illinois (1961).
10. H. S. Swofford, Jr., Ph.D. Thesis, University of Illinois (1962).
11. Richards and Gordon, *Z. physik. Chem.*, **28**, 302 (1899).
12. S. N. Flengas and E. Rideal, *Proc. Roy. Soc.*, **A233**, 443 (1956).
13. D. Inman and J. O'M. Bockris, *Trans. Faraday Soc.*, **57**, 2308 (1961).
14. F. R. Duke and H. M. Garfinkel, *J. Phys. Chem.*, **65**, 461 (1961).
15. J. Braunstein, M. Blander, and R. Lindgren, *J. Am. Chem. Soc.*, **84**, 1529 (1962).
16. J. Frame and E. Rhodes, *Trans. Faraday Soc.*, **57**, 1075 (1961).
17. W. T. Carnall, D. M. Gruen, and R. L. McBeth, *J. Phys. Chem.*, in press.
18. J. E. Randles and W. White, *Z. Elektrochem.*, **59**, 666 (1955).
19. W. H. Reinmuth, *Anal. Chem.*, **32**, 1514 (1960).
20. F. R. Duke and S. Yamamoto, *J. Am. Chem. Soc.*, **81**, 6378, (1959).
21. W. Hittorf, *Poggendorfs Ann. Phys.*, **72**, 481 (1847).

[2] Kindly supplied by Dr. T. R. Ingraham.

Interferometric Study of $Zn/ZnSO_4/Zn$ System

I. Relative Position of Electrodes and Convective Effects

R. N. O'Brien, W. F. Yakymyshyn, and J. Leja

Department of Chemistry, University of Alberta, Edmonton, Alberta, Canada

ABSTRACT

Concentration gradients at the $Zn/ZnSO_4$ electrodes, studied by Fizeau fringes, were found to depend markedly on the relative positions of the narrow-faced electrodes. Positions investigated were: shallow vertical, deep vertical, horizontal cathode above anode, and horizontal anode above cathode. Gravitation effects, parallel or vertical to the electrode face, cause different convection flows which affect the fringe patterns. Onset of convection was studied in relation to electrode positions, current density, and electrode concentration.

The interferometric investigation of the system $Zn/ZnSO_4/Zn$ was carried out in a specially constructed microcell (containing less than 1 ml of electrolyte between the electrodes) with the objective of obtaining the contour of concentration changes between the electrodes. The work of Ibl (1, 2) has shown that certain perturbations of the fringe pattern can be corelated with free convective flow. Eisenberg (3) and co-workers also showed that the orientation of the cell in the earth's gravitational field profoundly affects the transport phenomena in the cell. Such convection and orientation effects across the whole layer of electrolyte between the electrodes in the cell are qualitatively demonstrated in this paper; quantitative treatment is reserved for later papers in the series.

The concentration changes in the electrolyte contained between two working electrodes have been sought since the beginning of systematic investigation in electrochemical systems. The techniques used were based either on external measurements (such as current density and voltage measurements) or internal measurements on the electrolyte itself. Direct sampling techniques of considerable value and ingenuity have been developed, *e.g.*, quick freezing a layer of electrolyte (4) onto a cylindrical electrode and then machining off successive layers for analysis sampling by syringe (5) through a pinhole in a plane

electrode through which a sample could be withdrawn, etc. In addition, optical methods using colored electrolytes, pH indicators, or schlieren techniques were tried out to give concentration changes. However, it appears that interferometry holds the most promise of all the optical techniques.

It was early predicted by many workers [and given a good theoretical treatment by Levich (6)] that three types of transport phenomena (mass transfer) should exist in any electrodeposition cell: diffusion, electromigration and convection. Tobias and co-workers (7) discussed further the effects of activity coefficients and the variation of diffusion coefficient with concentration of electrolyte, on the over-all mass transfer phenomena. The theory of mass transfer in electrolysis was tested by Ibl (1) in a classic series of experiments, using a Jamin type of interferometer (which is of a split-beam type and therefore cannot conveniently give a complete concentration contour between the two electrodes). Ibl (2) showed the role played by convection and correlated his interferometric results with long exposure photographs showing movement of suspended collophonium in copper sulphate. The work of Ibl is hereby extended to show the interferometric patterns across the whole distance from anode to cathode in our cell, and for various positions of electrodes with respect to earth's gravitational field.

Apparatus

The electrodeposition cell, which is also an interferometer, is shown in a cut-away drawing (Fig. 1). A schematic drawing of the optical train (Fig. 2)

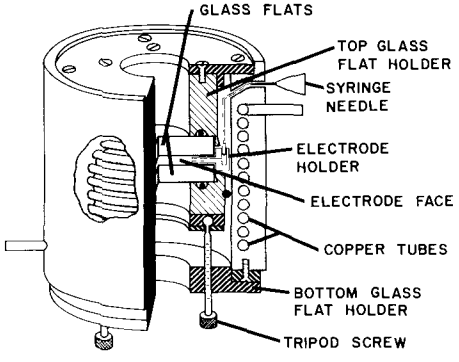

Fig. 1. Details of the electrodeposition cell assembly used for studying interferometric patterns drawn to scale.

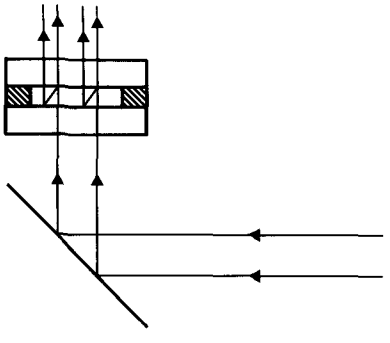

Fig. 2. Schematic diagram of the light path for the shallow vertical position showing the division of amplitude of the light beam. For the other positions suitable reorientation of components is easily visualized.

shows the light path. Collimated monochromatic sodium vapor light is reflected up into the cell by a first-surface mirror. It first encounters a glass flat with a 90% reflecting coating at the glass-electrolyte interface. The transmitted 10% of the light traverses the thickness of the cell through the electrolyte encountering a 70% reflecting coating at the electrolyte-glass interface of the top flat. Thus, approximately 7% of the original light beam is reflected back through the electrolyte to the bottom flat and 90% of this is again reflected back to the top flat, etc. The transmitted and reflected parts of the light (and of course the contribution of further reflections and transmissions) constitute superimposed coherent beams with different optical paths and hence interfere to produce a fringe pattern. Because the relative widths of the light and dark fringes are about 2:1, the effective average number of reflections appears to be about two (this can also be calculated roughly from the known reflectivity of the glass flat coatings). The spacing between successive light (or dark) fringes is governed by the wedge angle between the flats. A camera is focused on the fringe pattern (which appears localized in the cell) in such a way as to keep the electrode edges in sharp focus.

Four sets of Zn electrodes were prepared from 99.999% Zn (obtained from Consolidated Mining and Smelting Company Limited, Trail, British Columbia). Sets No. 2 and 3 were machined from castings remelted under argon in copper molds coated with carbon black. Set No. 3 was, in addition, lightly cold-worked and annealed. The as-cast electrodes had columnar grain structure of about 40 grains/cm^2, and No. 3 set had an equiaxed grain structure of about 70 grains/cm^2.

The electrodes were held in a heat-cured epoxy resin holder which positioned the electrodes and accommodated the hypodermic needle for introducing and withdrawing solution.

The electrolyte between the working faces of each electrode was normally limited to a volume of dimensions 0.2 x 3 x 0.3 cm, or about 0.18 cm^3. The working face of each electrode was approximately 0.2 x 3 cm, the usual separation of electrodes was approximately 0.3 cm.

The electrical circuit (Fig. 3) consisted of an ordinary 6 v lead-acid storage cell kept just above ½ charge for stability, a 10,000 ohm decade resistance box calibrated against a standard resistance supplied by the National Research Council, Ottawa, Ontario, a variable resistance, and the cell itself. The potential across the cell was measured using a Tins-

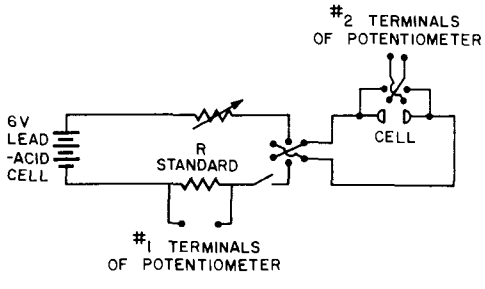

Fig. 3. Electrical circuit

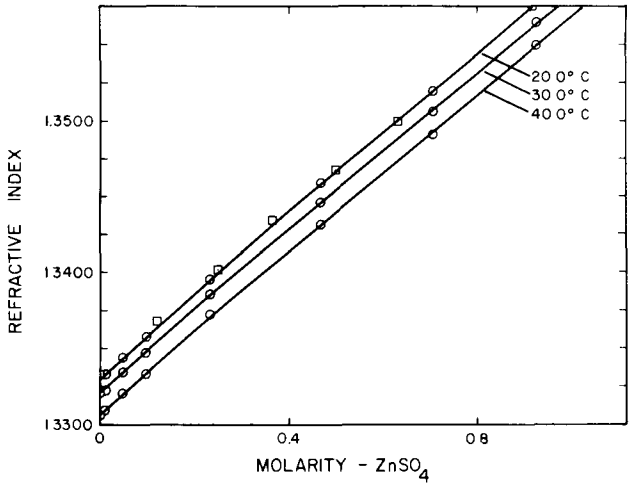

Fig. 4. Dependence of refractive index on concentration for $ZnSO_4$ at 20°, 30°, and 40°C (compared with values from Landolt-Bornstein Tables for 17.5°C, open dotted square).

ley Portable Potentiometer (calibrated against a National Research Council potentiometer). The current passing through the cell was calculated from the potential across the high standard resistance.

Experimental Procedures

Interferometric information can be related to concentration only when the dependence of refractive index on concentration is accurately known. A Pulfrich Refractometer was used to establish the refractive indices for $ZnSO_4$ solutions. As can be seen in Fig. 4, the dependence of refractive indices upon molar concentration is almost linear. The $ZnSO_4$ solutions were made up from doubly distilled and freshly boiled water (pH 6.8 and 1.5 x 10^{-6} mhos conductivity) an Analar grade $ZnSO_4 \cdot 7H_2O$. A stock solution approximately 1M was made up and titrated with E.D.T.A.

The electrodes were prepared for an electrolysis run by polishing the working faces on 600 grit emery paper, and etching in dilute H_2SO_4 solution until the grain structure was just visible. During electrolysis the electrolyte slowly advanced into the very thin gap between the electrode and glass. A white deposit, soluble in acid solution [presumably $Zn(OH)_2$] was formed in the electrolyte within this gap and, with continued electrolysis, somewhat obscured the edges of the electrode. To avoid this, the nonworking surfaces of electrodes were coated with a catalyzed two-component polyurethane (obtained from Plastiglo Industries Ltd., Edmonton, Alberta), which could be put on thinly enough to nearly fill the space and yet resist any chemical or electrochemical action.

On injection of the electrolyte into the assembled cell, a potential difference of 1-15 mv was usually found to exist between the two electrodes. This potential was found to disappear if a low current was passed in one direction for a few minutes, then reversed for ½ this time, each successive reversal (usually only one was necessary) being for ½ the time of the previous. An application of an a-c current at 1v and 60 cycles for 5 min was found to be equally effective. The electrolyte used in this process was then withdrawn by syringe and fresh electrolyte injected.

The time necessary for a stable fringe pattern to be established varied considerably depending on the orientation of the electrodes with respect to the gravitational field. When the fringe pattern was stabilized, the voltage and current density measurements were made as quickly as possible and a photograph (interferogram) of the pattern taken.

Polarization curves were found to be very complicated and will be presented later in the series from data obtained by an oscilloscope synchronized with a cine-camera. The conductivity of the cell goes through a minimum and a maximum then decreases very slowly with time. The current density and voltages for the interferograms reproduced here were taken as soon as the potentiometer could be balanced, *i.e.* within 5-10 sec of the photograph.

The interference fringes formed in the cell are of the Fizeau type of multiple beam fringes (8). Each fringe constitutes a refractive index contour since along the total length of any fringe the difference in path length is constant. The optical path is the physical distance traversed multiplied by the refractive index of the medium. Therefore the exact location of any fringe may be established from the formula $n\lambda = 2\mu t \cos \phi$, where λ is the wavelength of the monochromatic light, μ is the refractive index, t is the thickness of the cell, and ϕ is the angle of incidence, measured from the perpendicular. In all experiments ϕ was kept as close to zero as possible, hence $\cos \phi = 1$. In order to get a fringe spacing convenient for photographing, *i.e.*, about 3 fringes/mm, a wedge angle of about 1 min of arc was used.

The orientations studied have been designated as follows, (Fig. 5): shallow vertical, deep vertical, horizontal cathode above anode, and horizontal anode above cathode. One electrode was drilled to allow circulation of refrigerated alcohol through it; a temperature gradient thus established allowed the direction of fringe bending during subsequent electrolysis to be interpreted as a negative or a positive refractive index change. Figure 6 shows the results of this experiment. Since on cooling, the refractive index is increased and the fringes have bent toward the top of the page, the apex of the wedge of electrolyte must be toward the top of the page; and a similarly oriented bend at the anode must mean increased concentration. The two interferograms also show the very dissimilar characteristics of tem-

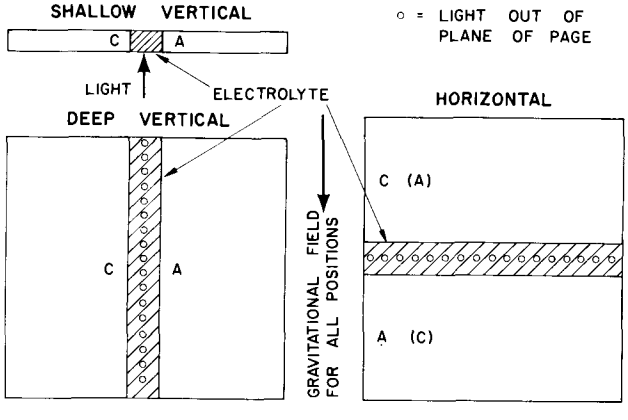

Fig. 5. Nomenclature given to the four orientations showing the direction of the passage of light.

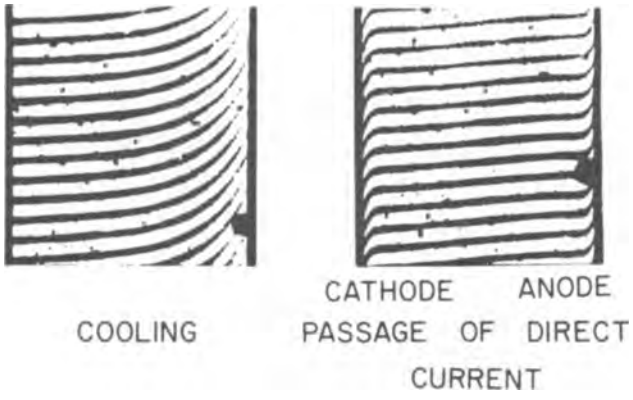

Fig. 6. Interferometric patterns showing the effect of cooling one electrode compared with electrolysis (to obtain the direction of the wedge angle).

perature and concentration differences and constitute an effective argument that the effects observed on electrolysis are not thermal in nature.

Figure 7 is a schematic diagram of a typical fringe pattern encountered with electrodes in the shallow vertical position indicating the nomenclature tentatively adopted to describe the perturbations. The first region of concentration change, which corresponds to the diffusion layer, is called the "first wave," the second (which Ibl called the "anomalous maximum at the cathode") is here called the second wave since it appears both at the anode and the cathode. The third wave which is the next reversal does not occur except at very high current densities (apparently only in the shallow vertical position) and is presumed to be also the consequence of convection. In all interferograms which follow, the apex of the wedge angle is upward in vertical positions and to the right in horizontal position.

The rates and modes of build-up of the typical fringe patterns for the four positions are very different and will be discussed later.

Results

The effect of increasing current density on the fringe system of 0.1M $ZnSO_4$ solution for the shallow vertical position is shown in Fig. 8 (all interferograms were taken after 3 min of electrolysis at 25°C, *i.e.*, when the fringes become stable). A current density of about 2.5 ma/cm² is necessary to produce a distinct second wave; at 9 ma/cm², the fringes in the diffusion layer become unresolvable by the instrument. The third wave can be faintly detected at 22.56 ma/cm².

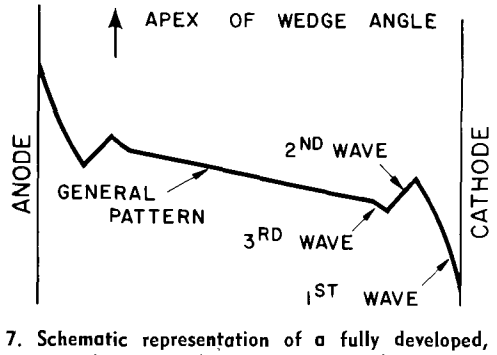

Fig. 7. Schematic representation of a fully developed, typical fringe pattern found in the shallow vertical position at high current densities.

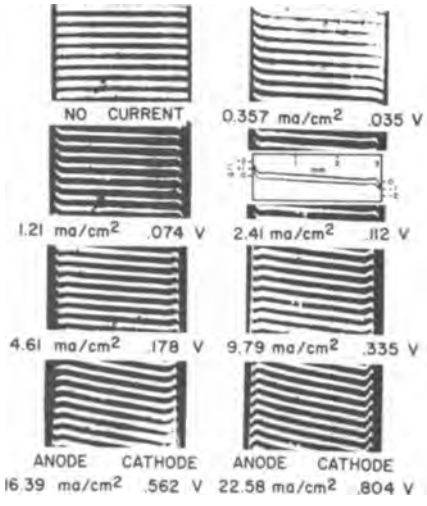

Fig. 8. Effect of current density on the fringe pattern in the shallow vertical position, for 0.1M $ZnSO_4$ at 25°C after 3 min of electrolysis. A concentration scale has been inserted which is the same for all interferograms except those in Fig. 13.

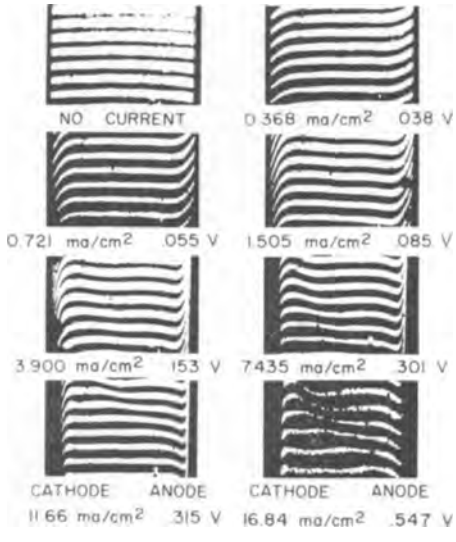

Fig. 9. Effect of current density on the fringe pattern in the shallow vertical position for 0.1M $ZnSO_4$ at 25°C after 5 min of electrolysis.

Figure 9 is a series of interferograms at increasing current densities with the electrodes in the deep vertical position, taken after 5 min of electrolysis at a preset potential. The most noticeable difference between shallow vertical and deep vertical positions is that the first wave or "diffusion layer" has increased in thickness from about 0.15 mm to about 0.33 mm or roughly by a factor of two for an increase in the height by a factor of 15. Obviously if diffusion were the only factor responsible for the change of electrolyte concentration in this layer, it should retain its thickness regardless of the height of electrodes. These differences in the "diffusion layer" thickness have been predicted by Levich, Tobias, Keulegan and their co-workers, and experimentally found by Ibl for the cathode and anode region in cells of much larger capacity than ours. The spreading out of the first wave away from the electrode face allowed resolution of the fringes at a

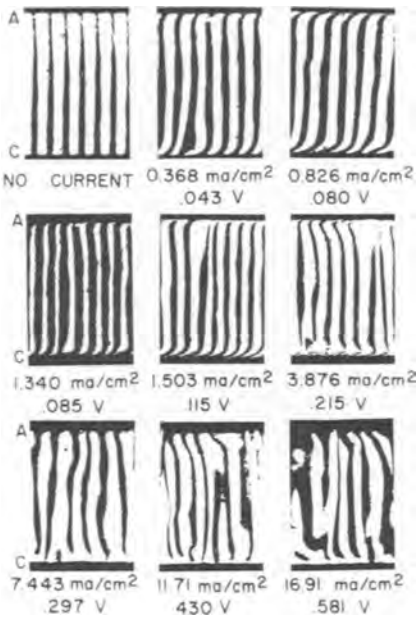

Fig. 10. Effect of current density on the fringe pattern in the horizontal anode over cathode position for 0.1M $ZnSO_4$ at 25°C after 3 min of electrolysis.

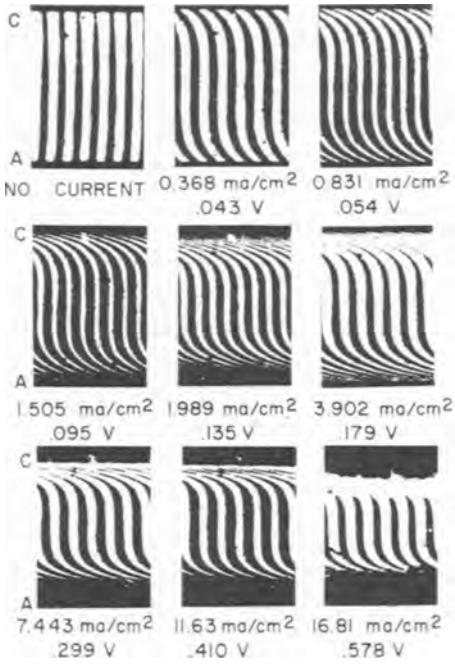

Fig. 11. Effect of current density on the fringe pattern in the horizontal cathode over anode position for 0.1M $ZnSO_4$ at 25°C after 3 min of electrolysis.

higher current density, *i.e.* over 12 ma/cm², compared to about 9 ma/cm² for shallow vertical position. It is also apparent that the second wave has spread outward and become much less sharp. In the last interferogram, at 16.84 ma/cm², a stable pattern over the whole cell has not yet been established; the two fringe patterns originating at the two electrodes are still in motion relative to each other. No third wave was obtained in the deep vertical position.

As can be seen from the voltages impressed across the cell, the deep vertical position has a much greater conductivity at the higher current densities.

The horizontal positions should and do produce very different patterns to those obtained in the vertical positions because in the anode over cathode position nearly all ionic transport should occur by convection, and in the cathode over anode position, it should all be due to diffusion and ion migration. Figure 10 taken after 3 min of electrolysis shows the concentration contour in the horizontal anode over cathode position. At very low current densities, the density changes at the electrodes are small and the convective processes have laminar flow patterns, although the solution moving downward from the anode must be meeting and passing (with some mixing) lighter solution rising from the cathode. The more active areas on the electrode show some turbulence, which appears at the anode near the middle of the interferogram (shown as a broadened fringe) at 1.5 ma/cm². At this low current density, the existence of a first wave indicates that diffusion is still an important mode of mass transfer at least over a portion of electrolyte near the solid. The first wave is of about the same thickness as that in the deep vertical position at low current density. At about 4 ma/cm², general turbulent convection has begun. The first wave becomes progressively less evident but it is still recognizable even at nearly 17 ma/cm². The conductivity is generally lower than that in the deep vertical configuration but higher than in the shallow vertical orientation.

Figure 11 shows the fringes in the horizontal cathode over anode orientation. In this configuration, there should be no convection since a denser solution exists at the anode, at the bottom of the cell, and a less dense at the top near the cathode. The smooth fringe pattern confirms this deduction. The first wave is now spread over 0.85 mm distance from the electrode (or six times that in the shallow vertical and three times greater than in the other positions). In this position, the conductivity measurements are of doubtful significance because of the deposition of a loosely held, needlelike zinc deposit on the cathode which grows rapidly out into the solution and effectively changes the distance between the electrodes. In all other positions, the metal is deposited as a fairly smooth and adherent coating on the cathode.

To study the motion of electrolyte between the electrodes, tiny particles of insoluble solids were introduced into the cell and viewed through the lens of the camera during the electrolysis at various positions of the cell. The patterns of their motion are drawn in Fig. 12. The two vertical positions ex-

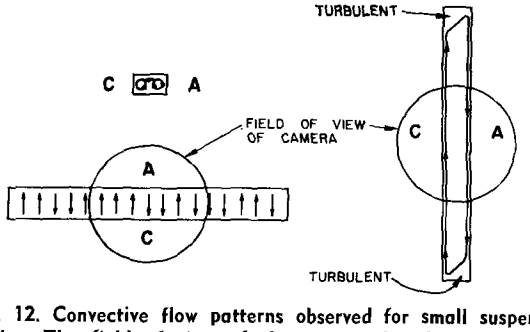

Fig. 12. Convective flow patterns observed for small suspended particles. The field of view of the camera has been drawn in, but not all of the field is reproduced in the interferograms.

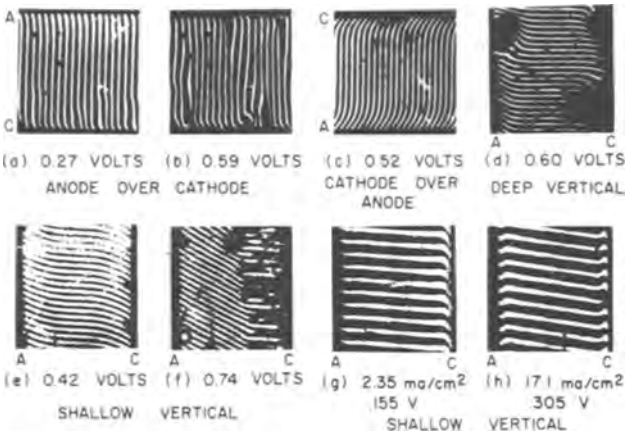

Fig. 13. Fringe patterns obtained with thin (0.19 mm) electrodes in the four orientations and the effect of a stronger electrolyte used in the shallow vertical position (last two interferograms). All interferograms were taken after 3 min of electrolysis at 25°C in 0.1M $ZnSO_4$ except the last two which were 0.1M $Zn(ClO_4)_2$.

hibit similar patterns, but there appears to be a depth-width ratio at which two separate closed patterns of circulation can form. In the shallow vertical position, two loops occur with some carry-over between them. The deep vertical position exhibited one closed loop of circulation, although locally turbulent regions (marked "turbulent") existed and fringes became distorted like those in the horizontal anode over cathode position. For this reason all interferograms were taken in the middle regions of electrode length and are typical of the main bulk of the electrolyte.

To test whether there is a limit to a visible convection effect a very thin cell was constructed using Zn foil of 0.19 mm thickness. The results are shown in Fig. 13. The usual but attenuated patterns developed in all cases with the exception of the shallow vertical position where the second wave did not form. This suggests that with very thin cells in this position the normal convection pattern must be absent. The pattern obtained at 0.74v with 0.19 mm thick electrodes in shallow vertical position shows the Zn deposit nearly half-way across the cell. The porosity of the structure is shown by the interference fringes between the needles of zinc. The black patches at the electrodes in the vertical positions are due to gas bubbles.

The fringe pattern obtained with $Zn(ClO_4)_2$, an electrolyte stronger than the moderately associated $ZnSO_4$, shows that, contrary to previous belief (9), ion pairs have little or no effect on the development of second wave in the system.

Therefore, we feel that natural or free convection can be detected by interferometric patterns which show the effect of convection on the concentration boundary layer. In solutions of electrolytes, the solute usually has a density far greater than the solvent (about 2.5 or more) and hence a concentration change will affect both the density and the refractive index of a solution at the same time. For these reasons, we believe that the second wave is an evidence of a smooth laminar convective flow in the vertical positions, and that the nonuniform fringe system in the horizontal anode over cathode position indicates a turbulent, free convection.

Acknowledgment

The authors wish to thank the National Research Council of Canada for partial support of this work.

Manuscript received Sept. 4, 1962; revised manuscript received Feb. 16, 1963. The paper was delivered before the Los Angeles Meeting, May 6-10, 1962.

Any discussion of this paper will appear in a Discussion Section to be published in the June 1964 JOURNAL.

REFERENCES

1. N. Ibl and R. Muller, *Z. Elektrochem.*, **59**, 671 (1955).
2. N. Ibl and R. Muller, *This Journal*, **105**, 346 (1958).
3. M. Eisenberg, H. F. Bauman, and D. M. Brettner, *ibid.*, **108**, 909 (1961).
4. A. Brenner, Proceedings of the 29th Convention of the American Electroplaters' Society, p. 28 (1941).
5. A. K. Graham, S. Heiman, and H. J. Read, *Proc. Am. Electroplaters' Soc.*, p. 95, (June 1939).
6. B. Levich, *Acta Physicochim. U.R.S.S.*, **17**, 257 (1942).
7. C. W. Tobias, M. Eisenberg, and C. R. Wilke, *This Journal*, **99**, 359C (1952).
8. S. Tolansky, "Multiple Beam Interferometry," p. 1, Oxford University Press (1948).
9. R. N. O'Brien and C. Rosenfield, *Nature*, **187**, 935 (1960).

Formation and Dissolution of Platinum Oxide Film: Mechanism and Kinetics

S. W. Feldberg,[1] C. G. Enke, and C. E. Bricker[2]

Frick Chemical Laboratory, Princeton, New Jersey

ABSTRACT

Oxide film formation on a smooth platinum electrode in perchloric acid solution has been studied as a function of potential, current, time, and electrode history, using constant current and controlled potential techniques. Anodic film formation proceeds through two, single electron steps: a slow step followed by a fast (reversible) one. During film reduction the fast step occurs first, followed by the slow step. In the case of constant current reduction the slow step does not occur, and the film is exactly half-reduced. Complete reduction requires several hours at a controlled potential. Three electrode states are thus clearly defined: oxidized, half-reduced (active), and completely reduced or clean. A single kinetic equation quantitatively relates the current, potential, and time parameters, predicts the initial rate of open-circuit potential decay following film formation, and strongly suggests that the oxide is a chemisorbed film.

The formation and dissolution of an oxide film on platinum are phenomena well known to electrochemists (1-13). The oxide film may be formed chemically (1-5) or electrochemically (1, 4, 6-12) and may be formed or removed either chemically (1-3, 13) or electrochemically (1, 3, 6-8, 10, 11, 13). Young (14) has thoroughly reviewed the literature on this subject. In the present literature there is considerable disagreement regarding the nature of the oxidized state and the formation and dissolution reactions. The chronopotentiograms (constant current charging curves) for the oxide formation and dissolution reactions are quite different in shape implying a high degree of irreversibility (10, 15-17). The cathodic curve is a shorter (10) and more typically shaped chronopotentiometric curve. The irreversibility is further demonstrated by a large hysteresis observed in the curve relating the quantity of oxide to the electrode potential (9, 11). The surface state of a platinum electrode has a marked effect on the reversibility of oxidation-reduction processes occurring at the electrode (18-23). Experimenters often produce an "active" electrode surface by oxidation and subsequent reduction of the electrode. This active state is different in character from either the reduced or oxidized state. Anson (24) attributes its properties to a light platinization of the electrode surface.

The results of this investigation indicate that the anodic film formation reaction proceeds through two, single electron steps: a very slow step followed by a much faster one. The film reduction reaction is simply the reverse of the formation reaction, the rapid step being followed by the slow one. The irreversibility of the over-all reaction is due to the slow step. The apparent difference in the anodic and cathodic reactions arises because the slow step controls the rate of the anodic reaction while the reduction reaction proceeds quickly through the first step, the second step being so slow it is not normally observed. Thus, the anodic film, after cathodic stripping, is only half reduced. The partially reduced surface is "active," *i.e.*, the reversibility of certain redox processes is enhanced. This proposed mechanism permits an exact description of the three states of the platinum electrode observed by Anson (24).

A kinetic equation is presented which quantitatively correlates current, potential, and time parameters for the oxide formation and dissolution processes. The equation clearly distinguishes between the oxide formation and oxygen evolution processes. An equation based on the theory of double layer discharge through the faradaic process (oxide deposition in this case) quantitatively explains open-circuit potential decay.

Apparatus

Electrodes.—Electrochemical measurements were made with a three electrode system composed of a platinum test electrode, a hydrogen reference electrode (with Luggin capillary contacting the working electrode), and a platinum counter electrode. These electrodes were used in the cell shown in Fig. 1.

The hydrogen reference electrode was inserted in an unfused Vycor[3] test tube which had been presoaked several days in 0.80M perchloric acid. Nitrogen gas passing through the scrubber cells removed hydrogen gas from the solution thereby preventing hydrogen from diffusing into the cell. Carbon dioxide was used to deaerate the cell and blanket the solution.

The counter electrode was constructed from an 11 x 2.5 cm piece of 1 mil smooth platinum foil spot welded into a cylinder 3.3 cm in diameter and spot welded to a 6 in. length of 0.0125 in. diameter platinum wire. The cylinder fit snugly in the cell.

[1] Present address: Brookhaven National Laboratory, Upton, New York.

[2] Present address: University of Kansas, Lawrence, Kansas.

[3] Corning Glass, Corning, N. Y.

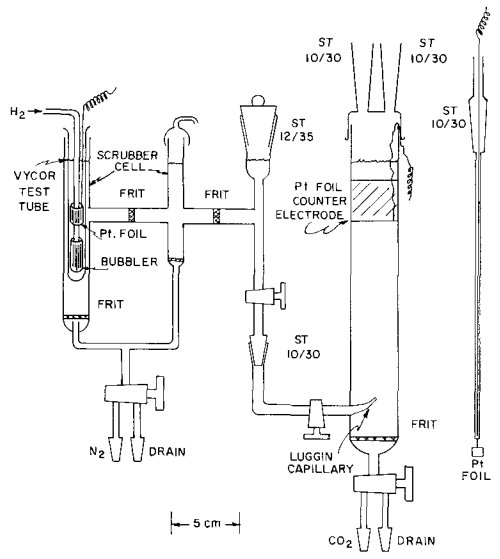

Fig. 1. Cell construction

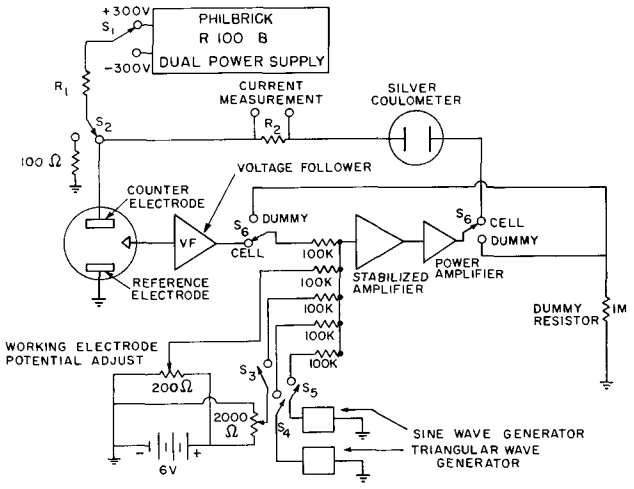

Fig. 2. Measurement apparatus

Approximately square, foil electrodes ranging from 0.5 cm^2 to 3.3 cm^2 geometric area were constructed from 10 mil platinum foil.

Solutions and preparation.—The electrolyte used was 0.8M perchloric acid. Baker and Adamson 70% concentrated perchloric acid was purified by combining 150 ml of concentrated $HClO_4$ with 50 ml of concentrated HNO_3 and boiling the mixture down to a volume of 100 ml. Impurities such as halides and organics were oxidized by the boiling nitric acid. At the completion of the procedure the nitric acid had been completely boiled away.

Laboratory distilled water was purified by redistilling from a basic permanganate solution in an all-glass distilling apparatus.

The same electrolyte was used in the reference electrode, scrubber cells, and in the cell containing the working and counter electrodes. Liquid junction potentials were thus eliminated. Since the *p*H dependence of the reversible hydrogen electrode is the same as the *p*H dependence of the phenomena occurring at the platinum electrode (10), the potentials observed are thus independent of the acid concentration common to both the platinum and the reversible hydrogen electrode.

The nitrogen gas and carbon dioxide gas were washed with 0.80M perchloric acid. The cell was cleaned by washing with hot perchloric acid, and the electrodes were cleaned by dipping them into boiling concentrated perchloric acid for 15-30 sec. The Luggin capillary section was filled with deaerated electrolyte from the cell compartment.

Electronic apparatus.—The electronic apparatus was designed to provide constant cathodic or anodic current, control the potential of the test electrode at a constant value or vary the potential in a prescribed manner, and permit observation and recording of the voltage, current, and time parameters. The complete electronic measurement and control system is shown in Fig. 2.

The constant current was obtained by placing a high resistance R_1 in series with the highly regulated plus or minus 300v output of a Philbrick R100B Power Supply. Switch S_2 directs the current through the cell or through a dummy load. The potential of the test electrode was measured with a voltage follower amplifier connected to a Tektronix 502 Dual Beam Oscilloscope. The voltage follower amplifier has unity gain, but has an input impedance in excess of 100 megohms. The follower was constructed from a Philbrick USA-4 operational amplifier.

The test electrode potential was electronically controlled with a stabilized operational amplifier. The amplifier consisted of a Philbrick K2-X operational amplifier and a K2-P stabilizing amplifier. The operational amplifier acts through the counter electrode to keep the cell potential equal to the algebraic sum of the control potentials (25). In addition to controlling at a constant potential, various potential wave forms could be imposed on the working electrode, *e.g.*, sinusoidal or triangular. A Hewlett Packard Model 200CD oscillator or a Heathkit Model AG-10 generator were used for the sine wave source. The triangular wave generator was constructed in this laboratory (26). Switch S_6 put the potentiostat in and out of the cell circuit. For certain experiments requiring fast switching from controlled potential to constant current or open circuit, the stabilized amplifier could not be used. An unstabilized potentiostat using only the K2-X and a simplified circuit was used in such cases. To increase the current output capability of the stabilized potentiostat to about 200 ma, a transistor power amplifier was used.

A silver-silver chloride coulometer (27) in series with the counter electrode was used in several experiments as a current integrator. The electrolyte in this coulometer was 0.1M KCl with a few drops of acetic acid. The electrodes were both silver: a 1 cm^2, silver foil coated with AgCl, and a small, uncoated silver wire. For integration of anodic currents, the silver wire side of the coulometer was connected directly to the counter electrode. During the integration AgCl formed on the Ag wire. The coulometer was then removed from the circuit, and stripped with a current equal to that used to strip the test electrode. The time required to reach the potential break which occurs when the silver chloride is com-

pletely removed from the silver wire is a direct measure of the anodic coulombs.

Experimental

Anodic to cathodic charge ratio.—Vetter and Berndt (10) using constant current techniques observed that the ratio of anodic coulombs Q_a to cathodic coulombs Q_c (for the oxide formation and dissolution processes) was approximately 2:1. Will and Knorr (11) and Bold and Breiter (12) rapidly oxidized and reduced the surface film by controlled potential techniques and noted a ratio of 1:1. In this study of the ratio, both constant current and controlled potential techniques of anodization were used to evaluate the relationship between ratio and electrode history.

Controlled potential anodization.—A 3.30 cm^2 platinum test electrode was anodized at a controlled potential of 1.40v for 2 min. The electrode and coulometer were each stripped at a current of 122 μa and the ratio of anodic coulombs to cathodic coulombs (Q_a/Q_c) was noted. The ratio in several runs varied from about 1.9:1 to 1.4:1, the highest value being obtained on the first measurement, with subsequent measurements yielding decreasing ratios.

An electrode was anodized at 1.40v (E_a) for 2 min, stripped at constant current to 0.50v, and then held at 0.70v (E_w) for a given time (t_w). After time t_w, the electrode was again anodized at E_a for 2 min and then reduced at constant current. The electrode was then held at 0.70v for a longer t_w. A graph of the ratio Q_a/Q_c *vs* t_w (Fig. 3) shows the gradual approach to a maximum ratio of very close to 2.0:1 at long t_w. A similar curve was obtained when E_w was 0.60v. Leaving the electrode at open circuit after stripping effected only a slight ratio change after 10 hr. The rate of ratio change is very sensitive to solution impurities which might reduce the oxide film. None of these curves was exactly reproducible except for the maximum ratio value of 2.0:1 which occurs when $E_w = 0.60$v or 0.70v.

When E_w was 0.50v the ratio increased to as high as 3:1 after periods of an hour. A series of anodic chronopotentiograms (Fig. 4) clearly shows the development of a potential holdup when the electrode was held at $E_w = 0.50$v for increasingly longer t_w. This potential holdup was not observed when $E_w =$ 0.60v, 0.70v, or at open circuit. The holdup indicates

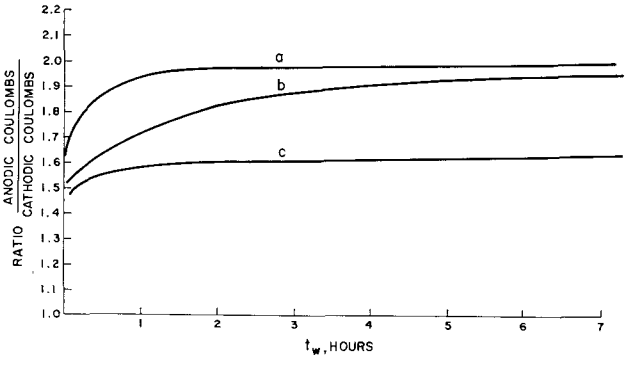

Fig. 3. Anodic to cathodic charge ratio as a function of pretreatment time, t_w, at several potentials, E_w. Curve a, E_w, 0.6v; curve b, E_w, 0.7v; curve c, E_w, open circuit.

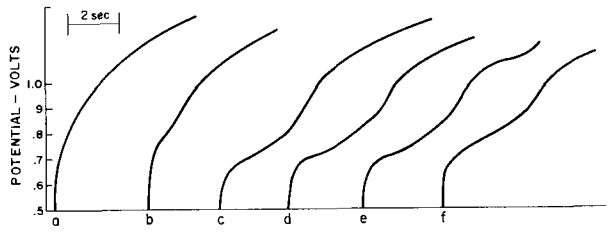

Fig. 4. Anodic charging curves for pretreatment at $E_w = 0.50$v, after various lengths of pretreatment time, t_w: a, t_w = 0 min; b, 1/3 min; c, 2 min; d, 4 min; e, 10 min; f, 20 min; anodizing current = 68 $\mu a/cm^2$.

that the ratios greater than 2:1 are due to the oxidation of some species formed at 0.50v.

For anodization at a given E_a, Q_c is essentially constant, independent of t_w. Thus Q_a is approximately proportional to the ratio.

Further ratio measurements were made in which the electrode was anodized at 1.10, 1.20, and 1.30v and which also show maximum ratios of nearly 2.0:1. As in the case of anodization at 1.40v the ratio Q_a/Q_c remained constant at about 2.0 after t_w of 3 hr at $E_w = 0.6$v or 10 hr at 0.7v.

Constant current anodization.—The electrode was held at 0.60v for 3 hr with the unstabilized potentiostat. A 2.0:1 ratio of Q_a/Q_c could be obtained by anodizing at a constant current of 68 $\mu a/cm^2$ to 1.40v, reversing the current and cathodizing at the same constant current (Fig. 5a). Continual manual reversing of the current so that the potential varied from 0.50 to 1.40 to 0.50v, etc., caused the ratio to shift gradually (during 10 or 20 cycles) from the 2.0:1 ratio (Fig. 5a) to a value approaching 1:1 (Fig. 5b). Equally interesting is the fact that oxidation when $Q_a/Q_c = 1$ begins at a lower potential than when $Q_a/Q_c = 2$. On anodization to a given potential E_a, a decrease in current density causes an increase in Q_a, Q_c, or both. When a higher current density was used, fewer anodic-cathodic cycles were required to achieve the minimum ratio of 1:1, and the final ratio value was closer to 1.0:1. As the current density was increased and the time for the anodic-cathodic cycle became less than about 1 sec, the experiment became impossible to perform manually.

A minimum ratio of approximately 1:1 occurred at E_a between 1.00 and 1.40v of anodization (Table I). Ratios were measured using a synchronized clock and a stopwatch to measure the cathodic and anodic times.

Many mechanisms for the oxidation and reduction reactions were tested for compatability with the

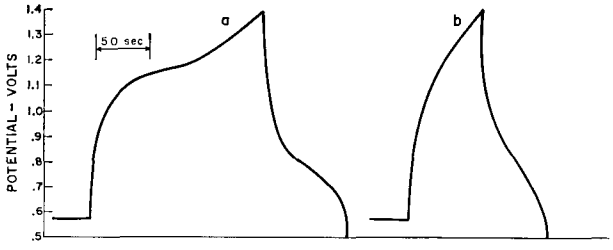

Fig. 5. Alternating anodic-cathodic charging curves at i = 68 $\mu a/cm^2$. a, After pretreatment at 0.60v for 3 hr; b, after 10-20 consecutive anodic-cathodic cycles.

Table I. Minimum ratio, Q_a/Q_c at various potentials $i = 34\ \mu a/cm^2$ alternately anodic and cathodic

Anodization potential, v	Minimum ratio
1.00	1.05
1.10	1.07
1.20	1.11
1.30	1.17
1.40	1.17

following observed phenomena: (*a*) the maximum ratio Q_a/Q_c was 2.0:1 at all anodization potentials and therefore 2.0:1 for varying quantities of oxide; (*b*) pretreatment for a long period of time was necessary for attainment of the 2.0:1 ratio and elimination of pretreatment gave ratios between 1.0:1 and 2.0:1; (c) repeated anodic-cathodic cycling resulted in Q_a/Q_c ratio of 1.0 and lowered the potential at which oxidation began; (*d*) cathodic coulombs were nearly constant for anodization at a given potential, despite variations in t_w and ratio; (*e*) cathodic coulombs were independent of the stripping current density (9).

The simplest mechanism satisfying these criteria is

$O_1)$ $Pt + xH_2O \rightarrow Pt(OH)_x + xH^+ + xe^-$ slow
$O_2)$ $Pt(OH)_x \rightarrow Pt(O)_x + xH^+ + xe^-$ fast
$R_1)$ $Pt(O)_x + xH^+ + xe^- \rightarrow Pt(OH)_x$ fast
$R_2)$ $Pt(OH)_x + xH^+ + xe^- \rightarrow Pt + xH_2O$ slow

The symbols $Pt(O)_x$ and $Pt(OH)_x$ represent the substances O and OH chemisorbed on the platinum surface. The subscript x is not necessarily an integer, but rather represents the ratio of chemisorbed O or OH to surface platinum atoms. Ershler (29) also noted that repeated anodic-cathodic cycling caused the oxide formation to occur at lower potentials. He attributed this to stronger adsorption of atomic oxygen caused by a change in the surface state. The above mechanism explains this phenomenon and requires no such change in the surface state.

According to this mechanism, constant current stripping (the measurement of Q_c) is the best way to evaluate the quantity of oxide on the electrode surface Q_s. The quantity $Q_s = 2Q_c$ after any anodization, but $Q_s = Q_a$ only when the anodized surface had all forms of the oxide previously removed.

Sinusoidal controlled potential oscillation.—The stabilized potentiostat with power amplifier was used to control the potential of the test electrode in a sinusoidal wave.

The area of each small Pt foil test electrode was determined by comparing its double layer capacitance with that of a larger foil electrode which was identically pretreated. The true area of the large electrode was assumed to be 1.12 times the geometric area (9).

A sinusoidal potential variation was applied to the test electrode so that the maximum value of the potential was the desired anodization potential (E_a) and the lowest potential was 0.50v. The electrode potential and current were each observed on separate traces of the dual beam oscilloscope (Fig. 6).

The variable experimental parameters were maximum anodization potential (E_a) and frequency of

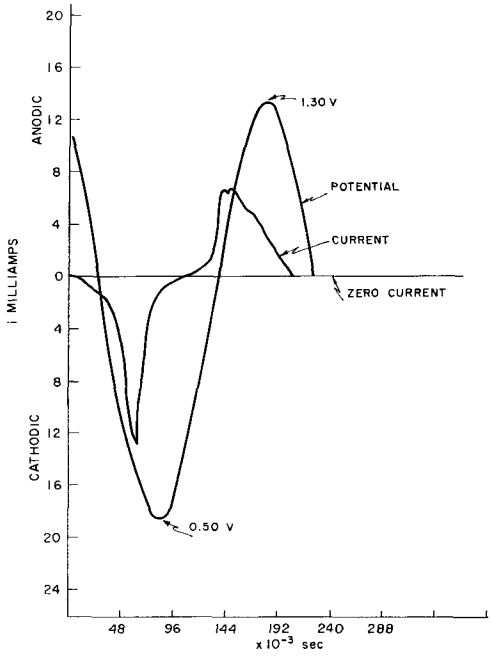

Fig. 6. Example of current-time curve for sinusoidally varying potential; frequency is 5 cps.

oscillation. The minimum potential was always 0.50v. The results are tabulated in Table II.

The ratio Q_a/Q_c was very close to 1.0:1. This could be expected from the discussion of previous data (Table I) when successive anodic-cathodic cycles were run manually at constant current. A plot of Q_a as a function of $1/f$ (Fig. 7) shows that the quantity of oxide formed at a given anodization potential increases with increasing time of anodization. The actual time of anodization t_a, is at most 1/2 the total time of one cycle, $1/f$.

Q_a did not decrease markedly until the frequency was greater than 20 cps ($t_a \approx 25$ ms). Laitinen and Enke (9) performed an analogous experiment by anodizing the electrode at a given potential for various times. The quantity of oxide deposited was

Table II. Relationship of potential, coulombs, ratio Q_a/Q_c, and frequency of potential oscillation

Electrode area = 0.65 cm² E_a, v	f (cps)	Q_a/Q_c	Q_a (mc/cm²)
1.20	5.0	0.92	0.33
	10.0	0.91	0.33
	20.0	1.03	0.35
	50.0	0.93	0.29
	100.0	0.99	0.26
	200.0	0.96	0.19
	400.0	0.98	0.13
	800.0	0.95	0.08
1.30	5.0	0.99	0.47
	10.0	0.99	0.47
	20.0	0.93	0.43
	50.0	0.98	0.39
	100.0	0.97	0.35
	200.0	0.88	0.26
1.40	5.0	0.94	0.59
	10.0	0.97	0.59
	20.0	0.95	0.51
	50.0	0.93	0.48
	100.0	0.97	0.41
	150.0	0.93	0.34

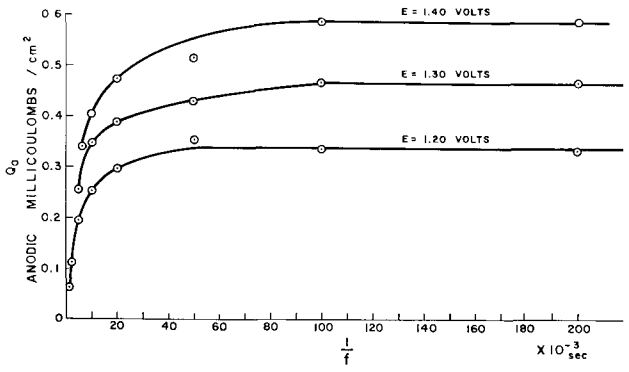

Fig. 7. Anodic coulombs, Q_a, for sinusoidally varying potential as a function of frequency. Peak potentials are 1.20, 1.30, and 1.40v.

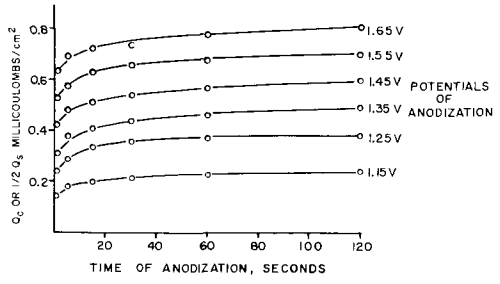

Fig. 8. Cathodic coulombs, Q_c, as a function of the time of anodization at several controlled potentials. Q_c was determined by constant current reduction [from Laitinen and Enke (9)].

determined by constant current stripping (Fig. 8). The quantity of oxide measured (Q_c) decreases at anodization times less than 10 sec. The rate of the anodic reaction observed by Laitinen and Enke is thus about 10/0.025, or 400 times slower than the reaction rate observed in these experiments. The quantity of oxide deposited by the oscillating potential technique (see mechanism, step O_2) is the same as the quantity of oxide stripped by Laitinen and Enke (see mechanism, step R_1) for a given E_a (Table III).

The agreement between the two techniques is to be expected since they both represent quantities which are equal to half the total surface oxide, Q_s.

Three surface states defined.—Three distinct surface states of the platinum anode can be defined from the proposed mechanism. They are the reduced or "clean" state (Pt), the oxidized state ($Pt(O)_x$), and the half-reduced state ($Pt(OH)_x$). A clean electrode is obtained by holding the electrode potential at 0.7v for 10 hr or 0.6v for 3 hr. A clean electrode exhibits a ratio Q_a/Q_c of 2:1. An electrode is oxidized at potentials over 1.0v. The half-reduced state is formed by stripping an oxidized electrode with a constant current to 0.5v, or with a constant potential of 0.6-0.7v for 1 sec or less. A half-reduced electrode exhibits a ratio of Q_a/Q_c of 1:1. These three states may also be obtained by use of chemical oxidants and reductants.

Table III. Comparison of coulombs of oxide deposited by potentiostatic and oscillating potential techniques

E_a =	1.20v	1.30v	1.40v
Q_a (From Fig. 7 at t_a = 0.05 sec)	0.33 mc	0.47 mc	0.59 mc
Q_a (From Fig. 8 at t_a = 120 sec)	0.32 mc	0.44 mc	0.56 mc

Measurement of electrode impedance as a function of potential.—A triangular wave was applied to the electrode with the potentiostat, power amplifier, and triangular wave generator so that the electrode potential varied linearly with time between 0.50 and 1.30v at a constant frequency of 1.15 cps. Superimposed on this wave was a 20 mv sign wave whose frequency was varied from 50 to 2000 cps. The a-c current was measured as the vertical thickness of the current time curve. The impedance, Z, at any potential could be calculated from the a-c voltage-current ratio.

The electrical model of the electrode-solution interface is usually considered to be the double layer capacitance, C_{dl} in parallel with the reaction or faradaic impedance. The reaction impedance can be represented by a series combination of the reaction resistance and the reaction capacitance (30,31). The impedance Z of this network is the total electrode impedance. At potentials where an electrode reaction occurs, the electrode impedance will be lowered by conduction through the reaction path. Because of the reaction resistance, the double layer capacitance presents the least impedance at high frequencies so the electrode impedance is simply $Z = 1/(2\pi f C_{dl})$.

The term $1/(2\pi fZ)$ was plotted vs. electrode potential as though the total impedance were simple capacitance. The result is a series of six curves for the six different frequencies used (Fig. 9). The data obtained indicate that at 2000 cps the impedance is due only to the double layer capacitance of the electrode. The electrode double-layer capacitance is 50 $\mu f/cm^2$, the same value found by Laitinen and Enke for an oxidized surface. During these experiments, the electrode is never in the clean state. Minute quantities of $Pt(OH)_x$ lost during the cathodic half cycle are regenerated on the subsequent cycle. Thus $Pt(OH)_x$ as well as $Pt(O)_x$

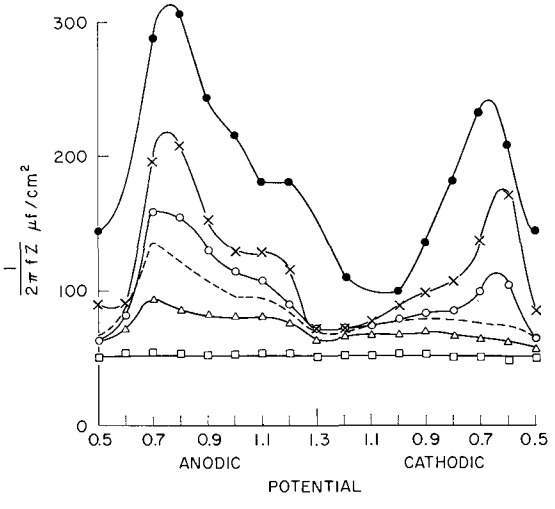

Fig. 9. The term $1/(2\pi fZ)$ as a function of potential during linear anodic-cathodic potential sweeps from 0.50 to 1.30v. □, 2000 cps; △, 1000 cps; - - -, 500 cps; ○, 250 cps; x, 100 cps; •, 50 cps.

change the double layer capacitance from that of a clean electrode (20 μf/cm^2).

The maxima observed at lower frequencies indicate a decrease in the electrode impedance which may be attributed to a faradaic process occurring at the electrode surface. The maximum on the anodic cycle occurs at a potential of 0.70v while the maximum on the cathodic cycle occurs at a potential of 0.60v. The potential difference of only 0.10v is indicative of a process far more reversible than that indicated by the hysteresis noted by Laitinen and Enke (Fig. 11). A certain similarity between the anodic and cathodic portions of the curves in Fig. 9 indicates that anodic and cathodic mechanisms are the same.

The experimental evidence obtained by the impedance technique substantiates the proposed mechanism.

Effect of surface on oxygen potential.—A simple experiment was performed to demonstrate that a clean electrode surface is different from a half-reduced electrode surface in its response to an electroactive species. Oxygen gas was used because of the ease of addition and removal from the electrolyte.

Two electrodes, A and B, each 3.30 cm^2 (geometric area) were pretreated by controlling the potential at 0.70v for 10 hr. A L&N electrometer (*p*H meter) was connected to the electrodes so that the open-circuit potential of either one could be observed. Electrode A was kept in the clean state. Electrode B was anodized at 1.40v for 1 min and then stripped to 0.50v with constant current, thus creating the half-reduced state. The open-circuit potential of the two electrodes was alternately observed with the electrometer. Carbon dioxide was continuously passed through the cell. When the electrode potentials had stopped drifting the open-circuit potential of (A) was 0.79v and the open-circuit potential of (B) was 0.81v. The bubbling of CO_2 was stopped and the solution saturated with O_2 by bubbling. The electrode potential was noted at 1 min intervals after oxygenation had started. When the open-circuit potentials reached a steady value, the solution was deoxygenated with carbon dioxide. The open-circuit potentials were observed at 1 min intervals after deoxygenation had started. Results are shown in Fig. 10.

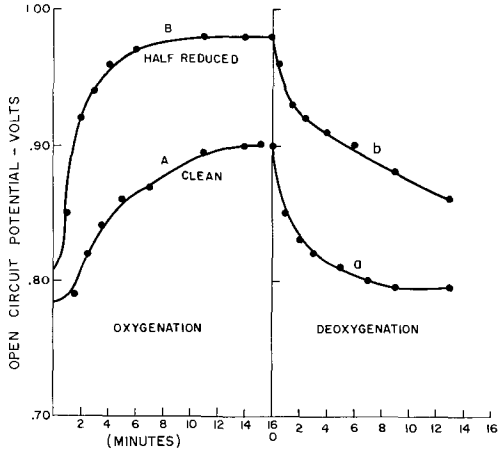

Fig. 10. Potential responses of clean and half reduced platinum electrodes to dissolved oxygen.

Clearly, there is a difference between a pretreated electrode and a stripped electrode, which difference can manifest itself by affecting the electrode response to an electroactive couple. Two electrodes, one "clean," the other half-reduced, simultaneously exhibited different open-circuit potentials in oxygen-stirred solution even after long periods of time. Thus, the composition of the electrode surface must be affecting its response to an electroactive species.

Kinetics

The inexact knowledge of the structure of the oxide film precludes a rigorous derivation of a kinetic expression. The relationships among anodic current, coulombs of oxide deposited, and time, have been carefully noted (9, 11), and a simple modification of the conventional electrochemical rate equation can relate these parameters mathematically.

The rate equation.—The mechanism for the oxide formation and reduction has been established. The conventional electrochemical rate equation (30) may be written

$$i = n'\mathbf{F}AC_R k^o_{bh} \exp\left((1-\alpha)\frac{n\mathbf{F}}{RT} E \right) \qquad [1]$$

where $\mathbf{F}$, A, C_R, α, $\mathbf{F}$, R, and T, have their usual significance; i is the anodic current, n' the number of electrons in the over-all process, n the number of electrons in the rate-controlling step, E the electrode potential *vs.* the reversible hydrogen electrode, and k^o_{bh} the rate constant for the anodic reaction.

At potentials where measurable quantities of oxide are deposited the rates of the anodic reactions O_1 and O_2 are much greater than the rate of the cathodic reaction R_1. Thus $i_{anodic} >> i_{cathodic}$, and $i = i_{anodic}$. The cathodic term has been omitted from Eq. [1], and the sign of the anodic current will be considered positive for convenience.

The linearity of the Q *vs.* E curve may be expressed by assuming that the rate constant k^o_{bh} diminishes with an increase in the quantity of surface oxide, Q_s, in the following way (recalling that $Q_s = Q_a/n'$)

$$k^o_{bh} = k_{bh} \exp -\left(\phi(1-\alpha)\frac{2zQ_a}{n'A} \right) \qquad [2]$$

Thus

$$i = n'\mathbf{F}AC_R k_{bh} \exp\left[(1-\alpha)\phi\left(E - \frac{2zQ_a}{n'A} \right) \right] = \frac{dQ_a}{dt} \qquad [3]$$

where ϕ equals $n\mathbf{F}/RT$, z, a proportionality constant, and Q_a anodic coulombs for deposition of the oxide. Note that the term $(E-2zQ_a/n'A)$ in the exponent expresses the linear relationship between Q_a and E observed in Fig. 8 and 11. Implicit in this equation is the assumption that the properties of the surface oxide are not dependent on how that oxide was deposited, *i.e.*, by anodization at the clean platinum surface or by anodization of the half reduced surface, but depend only on the quantity of oxide on the surface, Q_s. The term $2Q_a/n'$ is equal to Q_s whether n' is 1 or 2.

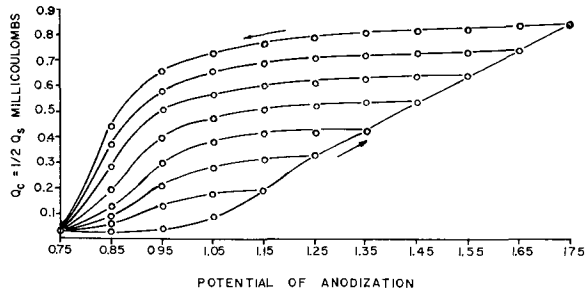

Fig. 11. Cathodic coulombs, Q_c, as a function of anodization potential [from Laitinen and Enke (9)].

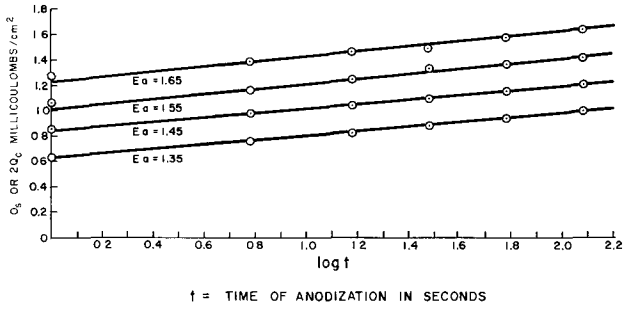

Fig. 12. Coulombs of surface oxide, Q_s, *vs.* log *t*, the anodization time, at a given potential (data from Fig. 8).

This empirical equation may be shown to quantitatively correlate much of the experimental data.

Evaluation of equation parameters.—Rearranging and integrating both sides of Eq. [3] gives

$$\frac{n'A}{2(1-\alpha)\phi z}\exp\left[2zQ_a(1-\alpha)\phi n'A\right] = n'\mathbf{F}AC_R k_{bh} t \exp\left[(1-\alpha)\phi E\right] + U \quad [4]$$

The integration constant, U, may be evaluated by assuming the boundary condition that at $t = 0$, $Q_a = 0$:

$$U = \frac{n'A}{2(1-\alpha)\phi z} \quad [5]$$

Substituting in Eq. [4] and taking the logarithm

$$\ln\frac{n'A}{2(1-\alpha)\phi z} + \frac{2(1-\alpha)\phi z Q_a}{n'A} = \ln\left[n'\mathbf{F}AC_R k_{bh} t \exp[(1-\alpha)\phi E] + \frac{n'A}{2(1-\alpha)\phi z}\right] \quad [6]$$

To evaluate the constant z, differentiate Eq. [6] with respect to E

$$\frac{2(1-\alpha)\phi z}{n'A}\frac{dQ_a}{dE} = \frac{n'\mathbf{F}AC_R k_{bh} t\,(1-\alpha)\phi \exp\left[(1-\alpha)\phi E\right]}{n'\mathbf{F}AC_R k_{bh} t \exp\left[(1-\alpha)\phi E\right] + \dfrac{n'A}{2(1-\alpha)\phi z}} \quad [7]$$

If the assumption is made that $\dfrac{n'A}{2(1-\alpha)\phi z}$ is much smaller than $n'\mathbf{F}AC_R k_{bh} t \exp\left[(1-\alpha)\phi E\right]$, then Eq. [7] reduces to

$$z = \frac{n'A}{2\left(\dfrac{dQ_a}{dE}\right)} \quad [8]$$

The conditions under which this assumption is valid will be clarified after the parameters are evaluated. The value dQ_a/dE may be calculated from the Q *vs.* E curve of Laitinen and Enke (Fig. 11)

$$z = 1/(2.05 \times 10^{-3}) = 4.9 \times 10^2 \text{ (volt cm}^2\text{)/coulomb}$$

Evaluation of α.—To evaluate the transfer coefficient, α, Eq. [6] is simplified by assuming again that the integration constant is negligible

$$\ln\frac{n'A}{2(1-\alpha)\phi z} + \frac{2(1-\alpha)\phi z Q_a}{n'A} = \ln n'\mathbf{F}AC_R k_{bh} t + \left[(1-\alpha)\phi E\right] \quad [9]$$

Inspection of this equation shows that a plot of Q *vs.* ln t at constant E, gives a straight line with a slope

$$dQ_a/d\log t = \frac{2.303\,n'A}{2(1-\alpha)\phi z} \quad [10]$$

A graph (Fig. 12) of Q_a *vs.* log t was plotted from the data of Laitinen and Enke in Fig. 8. The expected linear plots had nearly identical and constant slopes, implying that the assumption made in neglecting the integration constant was valid. The average value for the slopes is 0.196×10^{-3} coul/log t. Substituting this value in Eq. [10] one can evaluate: $(1-\alpha)n = 0.62$. From the proposed mechanism, $n = 1$. Thus, $\alpha = 0.38$.

Evalution of rate term $C_R k_{bh}$.—The constant term $k_{bh}C_R$ may be evaluated from Eq. [9]. Twenty points from the graph of Q_c *vs.* t (Fig. 8) for potentials from 1.35 to 1.65, and times from 6 to 120 sec gave twenty values of $k_{bh}C_R$ averaging $5 \pm 1 \times 10^{-21}$ sec^{-1} cm^{-2}. Thus, the equation appears to be of the proper form to describe the observed phenomena. The values determined for the parameters z, α, and k_{bh} may be used to check the assumption that

$$n'\mathbf{F}AC_R k_{bh} t \exp\left[(1-\alpha)\phi E\right] >> \frac{n'A}{2(1-\alpha)\phi z}$$

The assumption is valid to 1% at $E > 1.25$v when t is greater than 10^{-1} sec. All the data of Laitinen and Enke were measured at times considerably longer than this lower limit.

Derivation of the current-time relationship for anodization at constant potential.—A current time relationship is easily derived by differentiating Eq. [6] with respect to time and again neglecting the integration constant. Simplifying the resulting equation gives

$$i = \frac{n'A}{2(1-\alpha)\phi z t} \quad [11]$$

The final expression for the current as a function of time is potential independent and independent of the rate term $k_{bh}C_R$. Laitinen and Enke observed experimentally that the anodizing current at controlled potential was essentially potential independent.

Derivation of the current-time relationship for continuously varying potential.—The point has been emphasized that the expression for current dependence on time is independent of the constant term $k_{bh}C_R$. This suggests that the oxidation of the half-reduced oxide to the oxide could be described by an equation of the same form. Neglecting the integra-

tion constant is even more valid in this case since the heterogeneous rate constant for this reaction is larger by a factor of more than 400. When a sinusoidally varying potential was applied to the electrode, a surface covered with half-oxide was developed, and the ratio of anodic coulombs to cathodic coulombs became 1.0:1. An equation predicting the peak heights is easily derived. Equation [3] is modified for the oxidation of the half-reduced oxide.

$$i = n'\mathbf{F}AC_R'k_{bh}' \exp\left[(1-\alpha')\phi\left(E-\frac{2zQ_a}{n'A}\right)\right] \quad [12]$$

where k_{bh}' is the rate constant for oxidation of the half-reduced oxide; C_R', the reactant, half-reduced oxide); α', the transfer coefficient for the half-reduced oxide; and n' equals 1, since the half-reduced oxide is being reoxidized. Differentiating i in Eq. [12] with respect to t and setting equal to zero gives the relationship between Q_a and E at i_{max}.

$$0 = \frac{di}{dt} = n'\mathbf{F}AC_R'k_{bh}' \exp\left[(1-\alpha')\phi\left(E-\frac{2zQ_a}{n'A'}\right)\right]\left[\frac{dE}{dt}-\frac{2z}{An'}\frac{dQ_a}{dt}\right] \quad [13]$$

$$\frac{dE}{dt} = \frac{2z}{An'}\frac{dQ_a}{dt} \quad [14]$$

and since

$$\frac{dQ_a}{dt} = i_{max} \quad [15]$$

then

$$i_{max} = \frac{dE}{dt}\cdot\frac{An'}{2z} \quad [16]$$

Equation [16] can predict current peak heights at frequencies of 5 and 10 cps when the maximum potential of the sinusoidal variation was 1.30 and 1.40v (the minimum potential was always 0.50v). The term dE/dt may be evaluated from the equation

$$dE/dt = 2\pi fB\cos\theta \quad [17]$$

where B is the amplitude of the sine wave, in volts and θ is the phase angle of the potential sine wave at i_{max} (Table IV).

Derivation of an equation describing the rate of open circuit overpotential decay for the oxide formation process.—When a clean platinum electrode was anodized at a given potential, and the electrode then disconnected from the potentiostat, the electrode potential immediately decayed. The initial rate of potential decay was observed to depend on the time of previous anodization. The longer the time of anodization the slower the rate of potential decay.

Armstrong and Butler (32) have explained overpotential decay as the discharge of the double layer capacitance through a faradaic process. In the case of the formation of the platinum oxide film, the double layer capacitance decays through the oxide formation process. The rate of capacitive potential decay may be expressed as

$$dE/dt = i/C_{dl} \quad [18]$$

where i is the current and C_{dl} is the double layer capacitance (50 μf/cm^2 for an oxidized platinum electrode).

At the beginning of the potential decay, the discharge current of the double layer capacitor is exactly equal to the anodic current immediately prior to cessation of anodization. This current may be evaluated from the equation

$$i = \frac{An'}{2(1-\alpha)\phi z t_a} \quad [11]$$

where t_a is the time of anodization at constant potential and n' equals 2. Substituting this expression for i into Eq. [18] one obtains an expression for the initial rate of open circuit potential decay as a function of prior anodization time (t_a) at constant potential on a clean platinum electrode.

$$\frac{dE}{dt} = \frac{n'A}{2C_{dl}(1-\alpha)\phi z t_a} \quad [19]$$

Initial rates of potential decay at different potentials of anodization were noted and may be compared to some calculated values (Table V). The initial potential decay rates were essentially independent of anodization potential if the potential was in the linear portion of Laitinen and Enke's Q_c *vs.* E curve, *i.e.*, E_a greater than 1.30v. The potentials used to obtain the experimental values were all below that potential (1.45v) where oxygen evolution becomes significant.

Discussion and Conclusions

Nature of the Oxide Film

The electrokinetic equation quantitatively relates a wide range of experimental data without postulating discrete platinum oxides of the types $Pt(O)_n$, n = 1,2 . . ., etc. It is highly unlikely that the oxide film involves discrete platinum oxides. This is substantiated by noting that many of

Table IV. Comparison of the theoretical and experimental current peaks when a continuously varying potential is applied to the electrode

Electrode area = 0.65 cm² (except where noted)

Frequency, f, cps	Maximum anodization potential, E, v	θ	Calculated, i_p, ma	Experimental, i_p, ma
5	1.30	40°	6.4	6.6
10	1.30	24°	15.3	13.0
5	1.40	31°	8.1	8.4
10	1.40	14°	18.2	16.5
From triangular wave			A = 0.73 cm²	
1.15	1.30		0.93	1.0

Table V. Comparison of calculated initial rates of potential decay with observed rates

t_a, sec	E_a, v	Experimental (dE/dt), v/s	(dE/dt), v/s, Calculated from Eq. [19]
20	1.30	80×10^{-3}	
	1.35	88×10^{-3}	84×10^{-3}
	1.40	88×10^{-3}	
30	1.30	43×10^{-3}	
	1.35	47×10^{-3}	56×10^{-3}
	1.40	50×10^{-3}	
120	1.30	10×10^{-3}	14×10^{-3}

the phenomena described by the equation are not peculiar to the platinum electrode. Remarkably similiar behavior has been noted for iridium, rhodium, palladium, and gold. Will and Knorr (11) obtained nearly identical dQ/dE values for platinum, iridium, and rhodium, while Laitinen and Enke (9) and Laitinen and Chao (33) using identical techniques obtained nearly identical dQ/dE values for platinum and gold, respectively. The similarity of the anodic behavior of different metals is more easily understood if the anodic process is considered to be the oxidation of water rather than the oxidation of the surface metal atoms. In other words, a water molecule, on giving up an electron, is oxidized, and at this point the (OH) may become chemisorbed to the platinum surface. Further oxidation occurs when another electron is transferred from the oxygen atom to the bulk platinum metal. The surface oxide is then better thought of as discrete oxidation states of water bonded to the platinum surface than as discrete oxides of surface platinum atoms. Inspection of anodic-cathodic charging curves on gold indicates that the oxide is completely removed by cathodic stripping rather than half-reduced.

Activation of the Platinum Electrode

The mechanism discussed in the experimental section clearly establishes the nature of three electrode states: (i) the oxidized state, $Pt(O)_x$; (ii) the half-reduced oxide state, $Pt(OH)_x$; and (iii) the reduced state, Pt. A platinum electrode is "activated" by strong oxidation and subsequent reduction producing the half-reduced oxide. This film can enhance electron transfer in oxidation-reduction reactions. Reduction of IO_3^- (21), O_2 and Vanadium V (34) on platinum is enhanced by simultaneous reduction of the oxide film. The data of Laitinen and Chao indicate that the gold oxide film is completely removed by cathodic stripping, and no half-reduced oxide is formed. No enhancement of the IO_3^-, O_2, or V (V) reduction would be expected on gold. This conclusion has been verified for the IO_3^- and O_2 (23).

Acknowledgment

The authors gratefully acknowledge the Air Force Office of Scientific Research for their support of this project. The cooperation of Brookhaven National Laboratories during the preparation of this manuscript is also greatly appreciated.

Manuscript received June 18, 1962; revised manuscript received Jan. 25, 1963. This paper was presented in part before the Los Angeles Meeting, May 6-10, 1962.

Any discussion of this paper will appear in a Discussion Section to be published in the June 1964 JOURNAL.

REFERENCES

1. F. C. Anson and J. J. Lingane, *J. Am. Chem. Soc.*, **79**, 4901 (1957).
2. B. B. Baker and W. H. MacNevin, *ibid.*, **75**, 1476 (1953).
3. F. P. Bowden, *Proc. Roy. Soc.*, **A125** (1929).
4. M. Breiter, C. A. Knorr, and W. Volkl, *Z. Elektrochem.*, **59**, 681 (1955).
5. J. K. Lee, R. N. Adams, and C. E. Bricker, *Anal. Chim. Acta*, **17**, 321 (1957).
6. J. Giner, *Z. Elektrochem.*, **63**, 386 (1959).
7. J. Giner, *ibid.*, **64**, 491 (1960).
8. A. Hickling and W. H. Wilson, *This Journal*, **98**, 425 (1951).
9. H. A. Laitinen and C. G. Enke, *ibid.*, **107**, 773 (1960).
10. K. J. Vetter and D. Berndt, *Z. Elektrochem.*, **62**, 378 (1958).
11. F. G. Will and C. A. Knorr, *ibid.*, **64**, 258 (1960).
12. W. Bold and M. Breiter, *Electrochimica Acta*, **5**, 145 (1961).
13. J. A. V. Butler and G. Armstrong, *J. Chem. Soc.*, **1934**, 743.
14. L. Young, "Anodic Oxide Films," Academic Press, London and New York (1961).
15. J. A. V. Butler and G. Armstrong, *Proc. Roy. Soc.*, **A137**, 604 (1932).
16. A. Hickling, *Trans. Faraday Soc.*, **41**, 333 (1945).
17. T. I. Zalkind and B. V. Ershler, *Zhur. Fiz. Khim*, **25**, 565 (1951).
18. D. G. Davis, *Talanta*, **3**, 335 (1960).
19. J. Giner, *Electrochimica Acta*, **4**, 42 (1961).
20. J. J. Lingane, *J. Electroanal. Chem.*, **1**, 379 (1960).
21. F. C. Anson, *J. Am. Chem. Soc.*, **81**, 1554 (1959).
22. J. J. Lingane, *J. Electroanal. Chem.*, **2**, 296 (1961).
23. D. T. Sawyer and L. V. Interrante, *ibid.*, **2**, 310 (1961).
24. F. C. Anson, *Anal. Chem.*, **33**, 934 (1961).
25. H. V. Malmstadt, C. G. Enke, and E. C. Toren, "Electronics for Scientists," W. A. Benjamin, Inc., New York (1962).
26. S. W. Feldberg, Ph.D. Thesis, Princeton University, Princeton, N. J.
27. C. G. Enke and J. H. Griest, Jr., Paper in preparation.
28. W. Bold and Breiter, *Z. Elektrochem.*, **64**, 897 (1960).
29. B. Ershler, *Discussions Faraday Soc.*, **1**, 269 (1947).
30. P. Delahay, "New Instrumental Methods in Electrochemistry," Interscience Publishers, Inc., New York (1954).
31. D. C. Grahame, *Chem. Revs.*, **41**, 441 (1947).
32. G. Armstrong and J. A. V. Butler, *Trans. Faraday Soc.*, **A143**, 89 (1934).
33. H. A. Laitinen and M. S. Chao, *This Journal*, **108**, 726 (1961).
34. C. W. Oatley, *Proc. Phys. Soc.*, **51**, 318 (1939).

Electrostatic Interaction in the Double Layer

Paul Rüetschi

Carl F. Norberg Research Center, The Electric Storage Battery Company, Yardley, Pennsylvania

ABSTRACT

The fundamental difference between the electrostatic potential of a unit charge and its average electrostatic energy content, in a medium containing a number of similar, statistically equivalent, charges, is clarified. The expression $Z_i e_0 \psi_i$, where Z_i is the valence, e_0 the electronic charge, and ψ_i the electrostatic potential at its location, does not represent the average electrostatic energy content of a charged particle i; proper consideration of the mutual electrostatic interaction terms leads to the introduction of a factor of ½ into this expression. The summation over all the energy terms involved when the particles are transferred individually from infinity into the considered system is shown to be equivalent to the charging procedure used by Debye or Guntelberg, leading to the factor of ½. The factor of ½ enters the expression for the activation energy of electrochemical reactions and is identified as the dominant part of the "transfer coefficient α." The dependence of the structure of the double layer on potential is shown to be related to the deviations of α from the constant value of ½. As examples, the hydrogen and oxygen evolution reactions are discussed in the light of this treatment.

Any attempt to calculate the rates of electrode reactions on the basis of theoretical models involves the question: What is the energy content, in particular the free energy (or its logarithm, the activity), of a reacting particle at an electrode surface? Because of the high electric fields in the interface the particles are subject to strong electrostatic forces. The task to calculate accurately the interaction energy with the other ions in the double layer, and with the charged particles of the solid surface, is a very difficult one. We shall resort to the general interaction theory of point-charge systems, and discuss its relation to the treatment of Debye and Huckel for calculating the electrostatic interaction energy and the activity.

Electrostatically, we can treat both the ions on the solution side of the interface of the double layer and the charges on the metal surface as point-charges $e_i = Z_i e_0$, or equivalent smoothed charges $\rho_i d\tau_i$ where ρ_i is the charge density in the chosen volume element of $d\tau_i$. Figure 1 shows a model of the double layer between electrode and electrolyte. There is a distance of closest approach for undischarged hydrated ions. (In order to simplify the picture, oriented adsorbed water dipoles and specifically adsorbed other charged species, such as surface-active anions and cations, are not shown.) An ion in the interface is surrounded by a relatively compact layer of charge on the electrode and by a more diffuse charge layer in the electrolyte. The diffusivity is due to thermal motion. For most electrolytes of practical importance, concentrations are above 0.1 m/l, and the charge layer on the solution side is only a few angstroms thick.

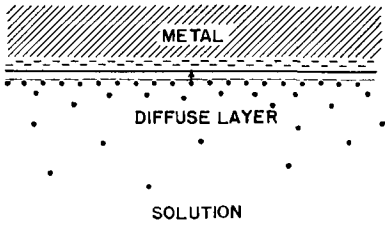

Fig. 1. Schematic diagram of an electrochemical double layer

The potential energy of the charged particles in the double layer (ions in solution and charged atoms on the electrode) is composed of coulombic long-range electrostatic interaction, operative over distances considerably greater than the molecular diameter of the ions, and short-range chemical interaction of the homeopolar type with next neighbors, *e.g.*, solvent molecules in the electrolyte and atoms of the electrode materials. This chemical interaction would still be present if the charges of all ions were miraculously removed and did not produce electrical dipoles of any kind.

As in the theory of Debye and Huckel (1) we shall first separately consider the electrostatic interaction, which, as will be shown, is related to the macroscopic measurable electrode potential. Debye and Huckel used the model of a central fixed ion α or charged volume element $d\tau_\alpha$, surrounded by a spherical space-charge cloud of opposite sign (Fig. 2). The charge of the ionic atmosphere is thought to be smeared out uniformly around the central ion.

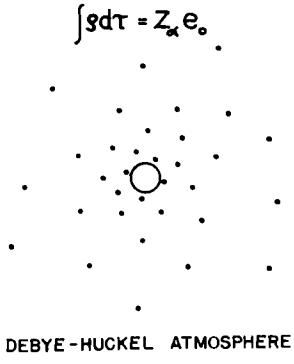

Fig. 2. Debye-Huckel ionic atmosphere spherically surrounding the central ion with charge $Z_\alpha e_0 = \int \rho d\tau$.

For an ion, or charged volume element, located in an electrochemical interface the space charge surrounding it is no longer spherically symmetrical. It consists of two-dimensional charge sheets parallel to the electrode surface. For either spherical or nonspherical space charges around an arbitrarily chosen central ion or element of charge, the total space charge surrounding it must be equal in magnitude and opposite in sign, since the total system must be electrically neutral. The electrostatic energy content of any arbitrarily selected element is determined by (i) the geometry of its space charge, and (ii) the absolute value of its charge. As in any condenser, the geometry is a measure for the capacity. To evaluate the electrostatic energy content one must therefore charge a condenser having the geometry of the space charge. In the theory of Debye and Huckel the space charge is a sphere and the electrostatic energy thus equal to the energy required to charge this sphere.

Principles of the Debye and Huckel Theory

For a clear presentation of the theory of interaction to be presented below, it appears necessary to contrast it with the theory of Debye and Huckel. The first step in evaluating the electrostatic interaction energy is, according to Debye and Huckel, to determine the "electrostatic potential" ψ at the location of the ion under consideration. The "electrostatic potential" ψ of Debye and Huckel is composed of (*a*) the self-potential of the ion ψ_α and (*b*) the potential due to the atmosphere (that is the surroundings) ψ_s of the ion; this latter part alone is of revelance to the electrostatic interaction energy, and is thus determining the activity of the ion, or the energy difference between a state of infinite separation and the actual configuration. Each ion with charge $Z_i e_0$ produces at the distance r the potential $Z_i e_0/Dr$, where D is the dielectric constant. Thus

$$\psi = \psi_\alpha + \psi_s$$
$$= Z_\alpha e_0/Dr + \sum_{i \neq \alpha} Z_i e_0/Dr \qquad [1]$$
$$= Z_\alpha e_0/Dr + \int \rho \, d\tau/Dr$$

The replacement of the sum by the integral over the space charge density ρ corresponds to the smoothed charge model and the law of linear superposition, which can be derived from Green's theorem (2). With the help of the latter it can also be shown that the discreteness of charge can have no effect on the energy of an actual ionic point charge if the point charges forming its atmosphere or surroundings have charges statistically equivalent to the one of the ion under consideration. The smoothed charge density model follows naturally from the probability of finding an ion in a given volume element $d\tau$, somewhat analogous to the conception of an electronic orbital around a nucleus.

Spherical space charge.—The derivation of the Debye-Huckel theory, familiar to everyone, is based on the use of the Boltzmann formula for the probability of occurrence of an ion β in a volume element $d\tau$ in the vicinity of the central ion α

$$N_{\alpha\beta} = \exp\left[-W_{\alpha\beta}/kT\right] d\tau/V \qquad [2]$$

where V is the total volume of the system. The exact meaning of $W_{\alpha\beta}$ has been discussed by Fowler and Guggenheim (3); it is the potential energy whose gradient gives the average force between α and β particles. This equation is coupled with the fundamental equation between charge density ρ and electrostatic potential ψ

$$\nabla^2 \psi = 4\pi\rho/D = 4\pi \sum N_{\alpha\beta} Z_\beta e_0/D \qquad [3]$$

where D is the dielectric constant and $Z_\beta e_0$ the charge on the β particles.

The un-obvious assumption introduced by Debye and Huckel is

$$W_{\alpha\beta} = Z_\beta e_0 \psi \qquad [4]$$

The validity and limitation of this approximation have been discussed by Onsager (4) and Kirkwood (5). Without entering here into a discussion of Debye's approximation[1] it will simply be pointed out that this approach leads to the general differential equation

$$\nabla^2\psi = \kappa^2\psi \qquad [5]$$

and the following solution

$$\psi = \psi_\alpha + \psi_s = (A/r) \exp(-\kappa r) \qquad [6]$$

with

$$\kappa^2 = 4\pi \sum_i N_i Z_i^2 e_0^2/VD\,kT \qquad [7]$$

The final result for ψ_s becomes

$$\psi_s = -(Z_\alpha e_0/D)\,\kappa = -(Z_\alpha e_0/D)\,1/\overline{r} \qquad [8]$$

The quantity $1/\kappa = \overline{r}$ has the meaning of the capacity of a charged sphere *vs.* an infinitely diluted counter charge, which means that the counter charge is in effect at infinity, or zero potential. Thus $\overline{r}$ is the effective radius of the ionic atmosphere.

Generalization to nonspherical ionic atmospheres.—The above solution applies if no geometric restrictions are imposed by short-range chemical interaction to the charge distribution around the central ion. If access to certain parts of the total volume is restricted for some, or all, ions of the atmosphere, *e.g.*, by conditions of closest approach between ions or by orientation of charge layers along macroscopic phase boundaries, κ is no longer given by Eq. [7], but is replaced by a term dependent on the geometry of the atmosphere. The solution for ψ_s will then have the general form

$$\psi_s = -(Z_\alpha e_0/D)\,K \qquad [9]$$

where K is a quantity describing the geometry of the space charge; $1/K$ is the capacity of the ionic atmosphere with regard to an infinitely diluted counter charge. Introducing for instance a distance of closest approach "a" between ions one obtains

$$K = \kappa/(1 + \nu a) \qquad [10]$$

[1] The physical meaning of ψ remains unclear since one is concerned always with the energy of particles of finite charge $Z_i e_0$, and not of infinitesimally small charge. The charge of an ion cannot act on itself and the introduction of ψ_α therefore physically is not meaningful in determining the energy of the central ion α. However, Debye and Huckel make, in their final result, only use of ψ_s, a quantity which is physically unambiguous.

In general $K = f(T, V, N_i, G)$ is a function of temperature T, volume V, number of particles N_i, and geometry G of the space charge. The potential ψ_s exerted by the surroundings on the central ion α is proportional to the charge of the central ion (which is equal to the negative charge of the atmosphere) and inversely proportional to the capacity of the atmosphere.

Electrostatic energy content of a particle.—In order to obtain the electrostatic energy per particle (using now the subscript i instead of α for an arbitrary particle), defined by

$$\mu_i^{el} = \partial F^{el}/\partial N_i \qquad [11]$$

where F^{el} is the total electrostatic energy content of the system, and N_i the number of particles of type i, a charging process is employed. Debye and Huckel proceed to integrate over the charge of all ions of the system simultaneously to obtain

$$F^{el} = \int \sum_i \psi_s \, e_0 \, dZ_i = \int_0^1 \sum_i \psi_s \, (\lambda) \, e_0 \, Z_i \, d\lambda$$

$$= -\sum_i N_i \, Z_i^2 \, e_0^2 \, \kappa/3D$$

From this, the energy per particle is determined by differentiation with respect to N_i, whereby one must consider that κ depends on N_i according to [7].

$$\mu_i^{el} = \partial F^{el}/\partial N_i = (Z_i^2 \, e_0^2/2D) \, \kappa$$

$$= -\psi_s \, Z_i \, e_0/2 \qquad [12]$$

Guntelberg (6) uses the simpler procedure to integrate over the charging of one individual ion only

$$\mu_i^{el} = \int_0^1 \psi_s \, (\lambda) \, e_0 \, Z_i \, d\lambda = (Z_i^2 \, e_0^2/2D) \, \kappa \qquad [13]$$
$$= -\psi_s \, Z_i \, e_0/2$$

Both processes lead to the same solution for μ_i^{el} if $Z_i \, e_0$ is proportional to ψ_i, and κ or K constant during the charging process; this is required for self-consistency.

The electrostatic energy of a particle is thus not equal to the product of its charge and the electrostatic potential at its location. Rather, the electrostatic part of the free energy μ_i^{el} is the product of the charge of the particle and the potential ψ_s produced at its location by the combined action of all other charges of the systems, divided by two.

General Theory of Electrostatic Interaction of Charged Elements

We shall now contrast the foregoing treatment with some general considerations on point-charge systems (2).

In a system with only two point charges, or two charged volume elements, the electrostatic energy resulting from the coulomb force is

$$-F_{12}^{el} = e_1 \, e_2/Dr_{12} \qquad [14]$$

where e_1 and e_2 are the two charges in electrostatic units (equivalent to $\rho_1 \, d\tau_1$ and $\rho_2 \, d\tau_2$), D the effective dielectric constant relative to vacuum, and r_{12} the effective distance between the two charged elements in centimeters. With more than two charged elements present, one can start again with charge 1 and then transfer charge 2 from infinity to the distance r_{12}; further charge 3 from infinity into the vicinity of charge 1 and 2, namely to distances r_{13} and r_{23}, and so on. The total energy required to introduce all the charged elements becomes

$$-F^{el} = e_1e_2/Dr_{12} + e_1e_3/Dr_{13} + e_1e_4/Dr_{14} \ldots$$
$$+ e_2e_3/Dr_{23} + e_2e_4/D_{24} \ldots$$
$$+ e_3e_4/D_{34} \ldots$$

or

$$-F^{el} = (1/2) \sum_i{}' \sum_k{}' e_i e_k/Dr_{ik} \qquad [15]$$

The factor 1/2 appears because in the double summation each combination of i and k appears twice. The prime at the sum signs indicates that all combinations of i = k are to be excluded from the summation, since a charge cannot act on itself. The result of [15] can be rewritten in a simpler form if one considers that the sum

$$\sum_i{}' \, e_i/Dr_{ik}$$

has just the meaning of the electrostatic potential ψ_k due to the combined action of all the charges except k, at the location of the charge k. Therefore, [15] becomes

$$F^{el} = -(1/2) \sum_{k=1}^{k=N} \psi_k e_k \qquad [16]$$

This result can readily be adapted to systems with continuous charge distributions. Each charge e_k can then be treated as a volume element $d\tau_k$ carrying the charge density ρ_k thus $e_k = \rho_k \, d\tau_k$. This can be also written in the form

$$e_k = \rho_k \, \tau_k \, dk$$

where τ_k is the volume element associated with the charge e_k and k is a counting parameter. The expression for the total electrostatic interaction energy of a system then becomes

$$F^{el} = -(1/2) \int_{k=0}^{k=N} \psi_k \, \rho_k \, \tau_k \, dk \qquad [17]$$

It is of great importance to consider that all charges of a given type k which are electrostatically equivalent must be subject to the same potential ψ_k. For instance, all positive ions in a 1:1 electrolyte or a 1:1 ionic lattice are at the same potential $\psi_k = \psi_+$ and all negative ions at the same potential $\psi_k = \psi_-$. Symmetry requires: $Z_+e_0 = -Z_-e_0$ and $\psi_+ = -\psi_-$ because of the opposite sign of the space charge. Thus, all the N terms in [16] are of the same magnitude and one obtains for F^{el}

$$F^{el} = -(1/2) \sum_1^N \psi_+ e_+ = -(1/2) \, N \, \psi_+ e_+$$
$$= -(1/2) \, N \, \psi_+ Z_+ e_0$$

The total electrostatic energy can then be divided equally among all charged elements N, and the energy per element becomes

$$\partial F^{el}/\partial N = \mu^{el} = -\psi_+ Z_+ e_0/2 \qquad [18]$$

More generally, one can obtain the energy for an individual charge k by differentiating [17] with respect to the upper limit of the integral, which yields

$$\mu_k^{el} = \partial F^{el}/\partial N = -(1/2) \psi_k \rho_k \tau_k$$
$$= -(1/2) \, \psi_k e_k = -\psi_k Z_k e_0/2 \qquad [19]$$

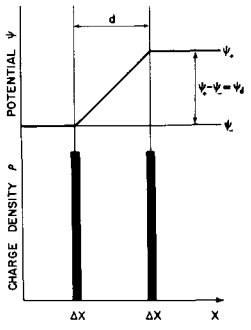

Fig. 3. Illustration of an ideal double layer.

where ψ_k and e_k are potential and charge of the charged element k.

Equations [18] and [19] can be compared immediately with the Debye-Huckel equation [12]. The expressions are identical, with ψ_+ or ψ_k equal ψ_s. The summation over all interaction terms as performed above is therefore equivalent to the Debye charging process.

This general treatment of electrostatic interaction confirms the result that the electrostatic energy of a charged element, in a medium containing other similar charged elements, is equal to one half of the product of its charge and the electric potential at its location produced by all the other charged elements.

Particles in Double Layers

A very simple system involving opposite layers of charge is illustrated in Fig. 3. The two layers of charge, each of infinitesimal thickness Δx are separated by the effective distance d, whereby $d >> \Delta x$. Each charged sheet can be considered as planar array of N rectangular volume elements with thickness Δx and basis cross sectional area a^2. Each volume element is uniformly filled with the charge density $\pm \rho$ and carries thus a charge $e_\pm = \pm \rho_k \Delta x\, a^2$. All positive charges e_+ are at the same potential ψ_+ and the negative charges at the potential ψ_-. With Eq. [17] the total energy of the system becomes

$$F^{el} = -(1/2) \int_0^{N_+} \psi_+ \rho_+ \Delta x\, a^2\, dk - (1/2) \int_0^{N_-} \psi_- \rho_- \Delta x\, a^2\, dk$$

Since $\rho_+ = -\rho_- =$ constant over the total surface, and $N_+ = N_-$

$$F^{el} = -(1/2)(\psi_+ - \psi_-)\, \rho_+ \Delta x\, a^2 \int_0^{N_+} dk$$

It is convenient to write

$$(\psi_+ - \psi_-) = \psi_d$$

since ψ_d would be the experimentally measurable total potential difference across the double layer. This is equivalent of setting the potential in the negative charge sheet at zero and considering only the positive charges. After summation over the total surface one obtains

$$F^{el} = -(1/2)\, \psi_d\, \rho_+ \Delta x\, a^2\, N_+ = -(1/2)\, \psi_d\, Q_+ \quad [20]$$

where Q_+ is the sum of all the charges e_+ in the positive charge sheet, and N_+ their total number.

This result is equal to the negative electrostatic charging energy of a condenser with capacity C, a result readily obtained by the procedure:

$$U^{el} = -F^{el} = \int_0^{\psi_d} \psi_d\, dQ_+ = \int_0^{\psi_d} \psi_d\, C\, d\psi_d = C\, \psi_d^2/2 = Q_+^2/2C = (1/2)\, \psi_d\, Q_+$$

This again demonstrates the equivalence of the summation process and the charging process.

What is now the energy of a small fraction of the considered system, consisting just of one pair of charges $e_+ = \rho_+ \Delta x\, a^2$ and $e_- = \rho_- \Delta x\, a^2$? It is quite obvious that the total electrostatic energy must be distributed uniformly among all the equivalent charge pairs e_+ and e_-, and since $Q_+ = N_+ e_+$ one obtains from [20]

$$\mu^{el} = (\partial F^{el}/\partial N_+)_{\psi_d} = -\psi_d\, e_+/2 \quad [21]$$

The differentiation with respect to N_+ must be performed at constant ψ_d in order to obtain the average energy per charged dipole pair.

If instead the energy of the condenser is differentiated with respect to N_+ or Q_+ at constant C, then one would obtain

$$(\partial F^{el}/\partial N_+)_C = -\psi_d\, e_+$$

However, this expression is not equal to the average electrostatic energy per charge pair; rather it represents the energy associated with the addition of the last charge pair e_+ and e_- to the condenser if the charging process is done at constant C; then different additions of the same charge involve different energies, depending on the particular voltage at the time. The expression $\psi_d\, e_+$ is thus not equal to the mean energy of interaction per charge pair. It happens to be the particular energy required to add the Nth charge pair, whereby the energy required to add the identical $(N-1)$th charge pair would have been different. At constant C, the energy involved in adding one charge pair of a given kind, with fixed charge e_+ and e_-, keeps changing with increasing total number of charges already present at the time of the addition.

This short discussion shows the importance of the "constant energy step procedure" for building up a point charge system from charged elements initially at infinity. Each hypothetical step must involve the same constant energy in order that the energy of any step becomes equal to the average interaction energy per element.

The double layer of actual electrochemical interfaces is more complicated than the arrangement shown in Fig. 3. Charges on the metal electrode surfaces in general form a fairly compact layer of charge which can, in many cases, be treated as infinitely thin. (In contrast, for certain semiconductors space charges might be quite diffuse.) The charge layer on the solution side is composed of a complicated arrangement of adsorbed charged species, water dipoles, more or less dehydrated anions and cations, and a diffuse layer of hydrated ions towards the electrolyte.

In calculating the energy of such a system per unit charge, it is important to consider that these

various charges will have different average distances from the hypothetical surface, *e.g.*, adsorbed dehydrated anions will be closer to the surface than hydrated anions or hydrated cations. The relative average positions of the various species are determined by the equilibrium between short-range chemical forces and coulombic long-range attraction or repulsion. In this manner, the different chemical species are "graded" by the various forces with respect to the distance from the surface.

For treating such an interface, one preferably applies the smoothed-out charge model, with all charges smeared out uniformly in sheets parallel to the electrode surface; the equipotential surfaces are parallel to the hypothetical phase boundary. Charge densities of positive and negative charge are superimposed and subtracted from each other when occurring at the same location.

It is of course understood that, electrostatically, no difference must be made between the various kinds of charges, *e.g.*, charges on ions in solutions or charges on atoms of the solid surface. Coulomb's law is the sole basis of the interaction and it applies equally to any kind of electrical charges. Moreover, since we are only concerned with the experimentally measurable potential differences across the total double layer, we can again set the potential on one side, *e.g.*, in the metal phase, equal to zero.

The total electrostatic energy content of such a system is again given by [16] or [17]. The question remains how to evaluate the energy of an individual charge pair. Apparently, we again must try to build up the system in steps of equal energy. The difficulty is that a quantity of charge added to, *e.g.*, the outer region of the diffuse double layer, will cause a different differential voltage increase than the same quantity of charge added at a position very close to the hypothetical interface, and accordingly, different electrostatic energies will be involved in these steps.

Let us consider thin layers of space of thickness dx, oriented parallel to the surface (Fig. 4) All the points in a thin layer at distance x are then effectively at the same potential ψ_x and can thus be treated as equivalent species. Each layer will contain substantially the particular type of charged species for which, at this location, the long-range electrostatic forces are exactly balanced by the short-range chemical forces. The whole interface can then be considered as a superposition of a series of flat-plate condensers of the type shown in Fig. 3, each with a different distance between the charge layers. The linear superposition of electric fields is a principle always assumed valid in electrostatic calculations of this type. Any one of these condensers consists of two charged sheets containing equal amounts of positive or negative charge. The various condensers have different effective distances from each other and contain different charges. Each condenser contributes an amount of electrostatic energy according to Eq. [20]. The superposition of the condensers results in the over-all charge and voltage distribution illustrated in Fig. 4. The total electrostatic energy of the interface thus becomes, according to [16]

$$F^{el} = -(1/2)\,\Sigma \qquad N_k e_k \psi_k \qquad [22]$$

where ψ_k and N_k are the potential and number of charges in the *kth* layer. In order to obtain the electrostatic energy content due to a charge e_i in the *i*th layer we write

$$F^{el} = -(1/2) N_i e_i \psi_i - \Sigma' \; 1/2\, N_k e_k \psi_k$$

whereby the prime at the sum sign means that in the summation the term k = i is to be excluded.

The energy for one species i with the charge e_i then becomes

$$\mu_i^{el} = \partial F^{el}/\partial N_i = -\psi_i e_i/2$$

or, with $e_i = Z_i\, e_0$ where Z_i is the valence and e_0 the electronic charge

$$\mu_i^{el} = -\psi_i\, Z_i\, e_0/2 \qquad [23]$$

This equation is again identical to the expression [12] of the Debye-Huckel theory and to Eq. [18] and [19].

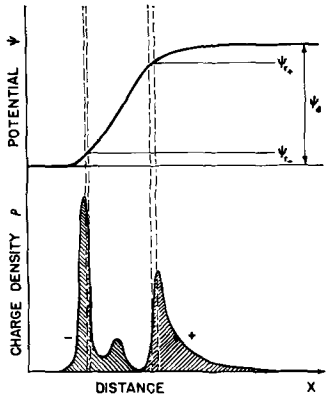

Fig. 4. Voltage and charge distribution in a hypothetical electrochemical interface. The integrals over the charge density $\int \rho dx$ for positive and negative charge are equal and opposite in sign. The potential $\Psi = \int E dx$ is determined from the field through $\int \rho dx = E/4\pi$.

Application to the Treatment of Electrochemical Reaction Rates

In order to obtain the energy of the reacting species in the double layer we consider once more thin layers, parallel to the surface, as in Fig. 4. One such layer is placed corresponding to the average location of the reacting ions on the solution side, *e.g.*, protons for the hydrogen evolution reaction; the potential at this location shall be ψ_{r+}. Another such layer may be placed at the effective location of the opposite reactants, *e.g.*, the negative charge layer in the electrode surface at a potential ψ_{r-}. Since in the charge transfer reaction the same amount of electricity $Z_r e_0$ is removed from the negative charge sheet and added to the positive charge sheet, we obtain for the average electrostatic energy of one pair of the reactants in the interface according to [23]

$$\mu_r^{el} = -Z_r\, e_0\, (\psi_{r+} - \psi_{r-})/2 \qquad [24]$$

The "effective" positions of the two charge sheets and thus of ψ_{r+} and ψ_{r-} must be chosen such that expression [24] gives the average electrostatic en-

ergy characteristic for the state prior to the electron transfer step. It is convenient to write

$$\Delta(\psi_{r+} - \psi_{r-}) = (1 - \gamma)\Delta\psi_d$$

where Δ stands for a variation and γ is often found to be a small fraction. Only a change in the total voltage $\Delta\psi_d$ across the interface, not the absolute value, is experimentally measurable. If a voltage change is brought about solely by accumulation of reacting species in the two corresponding charge layers of Fig. 4, and if the charge distribution of all foreign species outside of these layers remains constant, then the electric field and the electrostatic energy contribution due to these foreign species is also constant; therefore

$$\Delta(\psi_{r+} - \psi_{r-}) = \Delta\psi_d$$

and

$$\Delta\mu_r^{el} = - Z_r e_0 \Delta\psi_d/2$$

This case is always realized with the ideal double layer of Fig. 3. If, however, upon a change of the over-all voltage ψ_d across the double layer, also the charge distribution of the foreign ions undergoes a change, then

$$\Delta\mu_r^{el} = - Z_r e_0 \Delta\psi_d (1 - \gamma)/2 \qquad [25]$$

This shows that $(1 - \gamma)$ can be considered as that fraction of the over-all voltage change which affects the energy of the reacting ions. The voltage change due to foreign ions which do not influence the electric field around the reacting charges is given by the expression $\gamma \cdot \Delta\psi_d$. Thus $\gamma\Delta\psi_d$ has a somewhat broader meaning than the ψ_1 potential of Frumkin (8). It does not refer specifically to the absolute voltage drop in the diffuse double layer, or any one particular other geometric portion of the potential-distance diagram. It refers to that fraction of a voltage change resulting from the change in the charge distribution at those locations in the interface which do not have a direct influence on the field around the reacting species.

The manner in which the factor $(1 - \gamma)$ determines the energetic state of the reacting species in an electrochemical interface becomes also transparent by considering the electric field in the double layer. The electrostatic energy density (energy/cm^3) stored in an electric field is given by

$$u = DE^2/8\pi \qquad [26]$$

Let us define a column of space of cross sectional area a^2 (corresponding roughly to the area occupied by one pair of reacting species), intersecting the charge layers vertically as shown in Fig. 5. The electrostatic energy stored in this column of space is

$$\mu^{el} = - \int_{-\infty}^{+\infty} (1/8\pi)\, DE^2 a^2 dx \qquad [27]$$

This expression is equivalent to

$$\mu^{el} = - \int_{-\infty}^{+\infty} (1/2)\, \psi_x \rho_x a^2 dx \qquad [28]$$

derived by application of [17].

The field E and the potential ψ_x are, in general, complicated functions of the distance x. If the distance and voltage between the two boundary layers indicated in Fig. 5 are d, and $(\psi_{r+} - \psi_{r-})$, respectively, and if the average effective field between them is $\bar{E}$, the energy stored in the shaded area of Fig. 5, which we can consider as the reacting complex with regard to the electrostatic interaction, becomes

$$\mu_r^{el} = -(1/8\pi)\, D\bar{E}^2 a^2 d$$

Considering that the field is related to the charge density ρ by

$$\int_{\pm\infty}^{x} \rho dx = e_r/a^2 = D\bar{E}/4\pi \qquad [29]$$

and the field is determined by the voltage according to

$$E = (\psi_{r+} - \psi_{r-})/d$$

One obtains immediately for the electrostatic energy of the reacting complex

$$\mu_r^{el} = - e_r (\psi_{r+} - \psi_{r-})/2 \qquad [30]$$

and

$$\Delta\mu_r^{el} = - \Delta[e_r (\psi_{r+} - \psi_{r-})]/2$$

where e_r is the charge which creates the field between the two layers indicated in Fig. 5. If the cross-sectional area of the column of space is selected such that e_r becomes equal to the charge of the tranfer reaction $Z_r e_0$ one recovers immediately [25]. However, one could have selected instead a column of space of larger cross section a^2 with charge $e_r \neq Z_r e_0$, (for example $e_r = Z_r e_0 + \Sigma e_i$, where e_i are charges due to foreign species) but chosen in turn a smaller value of d or $(\psi_{r+} - \psi_{r-})$ to arrive at the same value for μ_r^{el}. This shows that the factor $(1 - \gamma)$ in [25] relates in fact to the product of effective voltage and effective charge of the reacting complex represented by the shaded area of Fig. 5. The exact definition of $(1 - \gamma)$ thus is given by the equation

$$\Delta[e_r(\psi_{r+} - \psi_{r-})]/2 = (1 - \gamma)\, Z_r e_0 \Delta\psi_d/2 \qquad [31]$$

If a change in over-all voltage $\Delta\psi_d$ is brought about by accumulation of reacting species at the same positions from the surface, the boundary layers of the reacting complex can be set at these positions and it is obvious from Fig. 5 that in this case

$$\Delta(\psi_{r+} - \psi_{r-}) = \Delta\psi_d$$

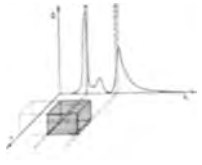

Fig. 5. The "electrostatic reacting complex" for an electrode reaction.

This condition always holds for the ideal double layer of Fig. 3; the factor $(1 - \gamma)$ becomes equal to one.

If, on the other hand, the voltage change is produced by incorporation of foreign ions into the double layer in such a manner that they do not influence the field between the reacting ions, then this voltage change would have no influence on the rate of the reaction and $(1 - \gamma)$ would be equal to zero. Theoretically, γ could assume values between $-\infty$ and $+\infty$, but in general will be small fraction close to zero; it is an electrostatic screening constant describing the influence of the foreign ions (10). The factor $(1 - \gamma)$ is related to the structure of the double layer; changes in double layer capacity, *e.g.*, caused by incorporation of new foreign species, will change the factor $(1 - \gamma)$.

In order to obtain the total energy content of one reacting charge pair in the interface, the coulombic interaction energy given by [25] must be added to the short range chemical interaction energy. A change in the total average potential energy of one reacting charge pair thus can be expressed as:

$$\Delta\mu_r = \Delta\mu_r^{el} + \Delta\mu_r^{chem}$$

The particles in the interface are subject to thermal motion. For certain relatively improbable configurations requiring high local energy, electron transfer to the reacting ions becomes possible and reaction takes place. The immediate long-range electrostatic interaction and the short-range chemical homeopolar electronic interaction can be separated entirely from the relatively slow thermal motion in accordance with the principle of Born and Oppenheimer. For the configuration corresponding to the state of the reacting particles prior to the electron transfer step, the electrostatic potential energy depends on the electrode potential according to $- Z_r e_0 \Delta\psi_d (1 - \gamma)/2$. This energy change correspondingly influences the probability for a pair of reactants to acquire the critical energy for reaction.

Using the picture of an energy barrier (Fig. 6) the energetic state of the reacting species in the interface is shifted towards lower levels by the presence of the electrostatic field, which leads to a decrease in the over-all activation energy.

Introducing a chemical short-range activation energy $\Delta\mu_r^{chem*}$ and applying the statistical treatment for reaction rates to the reacting particles in the double layer one obtains with [25] readily the probability of a reacting particle to acquire the critical energy for reaction. Multiplying this probability with a frequency factor A one recovers immediately the Volmer equation [7] for electrode reactions

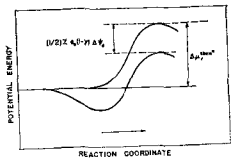

Fig. 6. Schematic diagram of the potential energy diagram of an electrochemical reaction.

$$i = A \exp \{-[\Delta\mu_r^{chem*} - Z_r e_0 \Delta\psi_d (1 - \gamma)/2]/kT\} \quad [32]$$

between current i and electrode potential variations $\Delta\psi_d$. The factor

$$(1 - \gamma)/2 = \alpha \quad [33]$$

is equivalent to the "transfer coefficient α." The present derivation of the transfer coefficient is physically more meaningful and realistic than the old derivation based on hypothetical symmetrical activation energy barriers. The present theory derives the factor ½, found so frequently for many electrode reactions, without any speculative assumptions on the distance between the activated complex and the surface. In addition, it properly accounts for electrostatic interaction between charged species in the interface (9, 10) which was not considered previously.

Predictions Concerning Electrochemical Reaction Rates

What are the implications of this treatment to the interpretation of electrochemical reaction rates? On the basis of the derivations given above a number of predictions can be advanced, which, substantiated, in turn prove the effectiveness of this treatment. The predictions are:

1. Changes in double layer capacity are related to the slope of the Tafel plot; a change in double layer capacity should be reflected by a change in Tafel slope (γ changes its value).

2. In voltage regions where the Tafel plots are straight, the double layer capacity can be expected to be constant. (γ is constant.)

3. The value of $\alpha = (1 - \gamma)/2 = 1/2$ can be expected when a variation in voltage is due only to accumulation of reacting species in the same adsorption state in the double layer (γ is equal to zero).

4. Adsorption of foreign inert ions of opposite charge to the reacting ions can decrease the overvoltage for evolution of hydrogen or oxygen by electrostatic screening. (γ is negative), however chemical short-range interaction can obscure this effect.

5. Hydrogen or oxygen overvoltage are increased in the presence of adsorbed foreign ions of the same sign, cations or anions respectively, in the absence of opposite short-range chemical effects (γ is positive).

Experimental verification.—Experimental verification of these predictions for the hydrogen and oxygen evolution can be found as follows:

Direct measurements of the double layer capacity in the region of hydrogen and oxygen overvoltage is possible with pulse techniques. The a-c techniques are not well suited because of the superimposed large Faradaic d-c currents.

In Fig. 7 the double layer capacity of various hydrogen evolving electrodes is plotted against overvoltage for regions where the Tafel plots are straight. It is clearly seen that in every instance the double layer capacity is practically constant over the potential region where straight Tafel lines

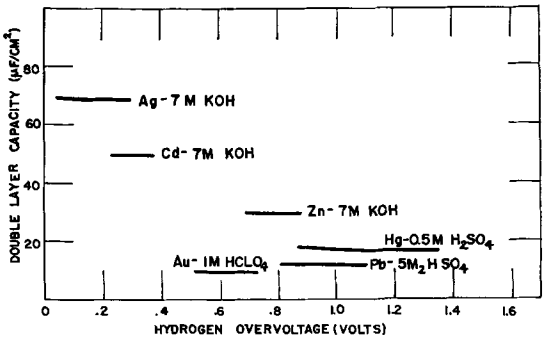

Fig. 7. Double layer capacity in the region of hydrogen evolution. Data from the following references: H_2 evolution on Hg in 1*N* H_2SO_4 (11); H_2 evolution on Pb in 10*N* H_2SO_4 (12); H_2 evolution on Ag 7*N* KOH (13); H_2 evolution on Cd in 7*N* KOH (13); H_2 evolution on Zn in 7*N* KOH (13).

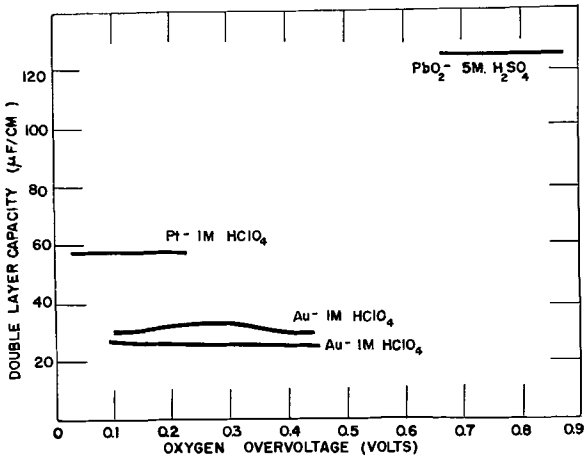

Fig. 8. Double layer capacity in the region of oxygen evolution. Data from the following references: O_2 evolution on gold 1*N* perchloric acid (14); O_2 evolution on gold in 1*N* perchloric acid (15); O_2 evolution on platinum in 1*N* perchloric acid (16); O_2 evolution on lead dioxide in 10*N* H_2SO_4 (12).

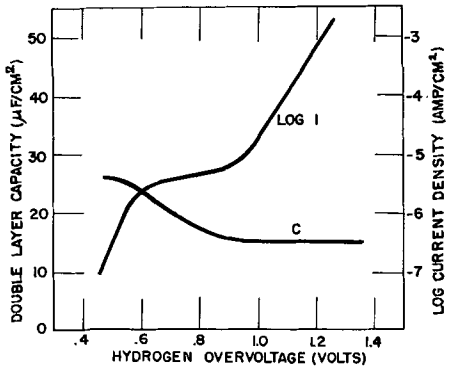

Fig. 9. Double layer capacity and log of current density as function of electrode potential for hydrogen evolution on lead in 1*N* H_2SO_4 (17).

are observed. It is also of interest to note that high overvoltage materials have in general low double layer capacities, and vice versa. The absolute values of the capacities are somewhat in doubt because of the uncertainty relating to the true surface areas of solid electrodes. All the data shown in Fig. 6 relate to measurements where the surface area was known to a reasonable degree, *e.g.*, by BET area measurements, or where the electrode surfaces were absolutely smooth.

Similar data are shown in Fig. 7 for oxygen overvoltage. Also here, the double layer capacities are constant within the potential regions where the Tafel lines are straight. These data constitute direct confirmation of the theory outlined in this paper. Moreover, there is considerable experimental evidence which proves that the double layer capacity starts to change at the same potential where the Tafel plot deviates from linearity.

Figure 8 shows an example relating to hydrogen overvoltage on lead in H_2SO_4 from the work of Kolotyrkin and Bune. The double layer capacity is constant in the Tafel region. At the point where sulfate ion adsorption sets in, the double layer capacity increases and the hydrogen overvoltage decreases abruptly (Fig. 9). This is a particularly good example for the influence of the factor $(1-\gamma)$, describing the action of foreign ions in the double layer. The sulfate ions decrease the effects of the accumulation of the hydrogen ions and oppose both, charge and voltage due to latter, which clearly depicts $(1-\gamma)$ as an electrostatic screening constant.

The most significant result of the present analysis is that the value of 1/2 for the "transfer coefficient" appears naturally, without introduction of any hypothesis on the symmetry of the activation energy barrier, as a result of electrostatic interaction (9, 10). Deviations from the value of 1/2 are due to the variation in the amount of foreign ions present in the double layer (18, 19).

In 1943 Frumkin pointed out (8) that for hydrogen evolution on mercury "none of the theories proposed can explain the astonishing fact that α retains a constant value very close to 0.5 within the remarkable range of current densities from 10^{-8} to 10^{+1} amp/cm^2." As shown in the present paper, this phenomenon is explained as a consequence of electrostatic interaction in the interface, which changes the energetic state of all charged particles (including the charges on the solid surface) subject to the field of the double layer.

Manuscript received May 31, 1962. This paper was delivered before the Los Angeles Meeting, May 6-10, 1962.

Any discussion of this paper will appear in a Discussion Section to be published in the June 1964 JOURNAL.

REFERENCES

1. P. Debye and E. Huckel, *Physik. Z.*, **24**, 185 (1923).
2. G. Joos, "Lehrbuch der Theoretischen Physik," p. 240, Akademische Verlagsgesellschaft, Leipzig (1945).
3. R. Fowler and E. A. Guggenheim, "Statistical Thermodynamics," p. 261, Cambridge University Press (1956).
4. L. Onsager, *Chem. Rev.*, **13**, 73 (1933).
5. J. Kirkwood, *J. Chem. Phys.*, 2, 767 (1934).
6. E. Guntelberg, *Z. physik. Chem.*, **123**, 199 (1926).
7. T. Erdey Gruz and M. Volmer, *Z. phys. Chem.*, **150**, 203 (1930).
8. A. Frumkin, *Z. physik. Chem.*, **164**, 121 (1933), *Acta Physicochimica USSR*, **18**, 23 (1943).
9. P. Rüetschi, *This Journal*, **106**, 819 (1959).
10. P. Rüetschi, *ibid.*, **108**, 600 (1961).
11. V. E. Past and Z. A. Iofa, *Zhur. Fiz. Khim.*, **33**, 913 (1959).
12. P. Rüetschi, J. B. Ockerman, and R. Amlie, *This*

Journal, **107**, 325 (1960); B. D. Cahan, and P. Rüetschi, *ibid.*, **109**, 543 (1962).
13. R. F. Amlie, J. B. Ockerman, and P. Rüetschi, *ibid.*, **108**, 377 (1961).
14. G. M. Schmid and N. Hackerman, *ibid.*, **109**, 243 (1962).
15. H. A. Laitinen and M. S. Chao, *ibid.*, **108**, 726 (1961).
16. H. A. Laitinen and C. G. Enke, *ibid.*, **107**, 773 (1960).
17. Data from N. Y. Bune and Y. M. Kolotyrkin, *Doklady Akad. Nauk. USSR.*, **100**, 295 (1955); Y. M. Kolotyrkin and N. Y. Bune, *Zhur. Fiz. Khim.*, **29**, 435 (1955).
18. P. Rüetschi, Papers presented at Meetings of The Electrochemical Society, New York, 1958, Philadelphia, 1959, and San Francisco, 1962.
19. P. Rüetschi, Lecture given at the Symposium in Commemoration of Dr. David Grahame, Division of Colloid Chemistry and Physical Chemistry of the American Chemical Society, New York, September, 1960.

Technical Notes

Electrophoretic Deposition of Metals

F. Pearlstein, R. Wick, and A. Gallaccio

Research and Development Group, Pitman-Dunn Laboratories, Frankford Arsenal, Philadelphia, Pennsylvania

Electroplating, which is usually the simplest and most economical method for producing high-quality metal coatings, cannot be readily used to deposit many metals including aluminum, titanium, zirconium, and tungsten.

The present investigation was undertaken to determine whether electrophoresis could be used to produce deposits of metal powders which might subsequently be fused or alloyed with the substrate metal. Aluminum was selected for the preliminary investigation because of its availability in various powder forms, its low density, and its low fusion temperature. This report covers the work accomplished to determine suitable suspending media and some of the more important parameters affecting electrophoretic deposition of aluminum. Also described is electrophoretic deposition of titanium and tungsten as well as some preliminary work on fusion of electrophoretic deposits.

Procedure

Aluminum flake of less than 44μ was used. The stearic acid normally on the flake was removed by separate washings with pure acetone. Removal of stearate was not completely accomplished by this technique. The various organic liquids used as suspending media were distilled after drying for one week over anhydrous sodium sulfate.

Test suspensions of aluminum flake were prepared by shaking 1g of the flake with 50 ml of the organic liquid in glass stoppered graduates.

Electrophoretic deposition was carried out within the graduates, after thoroughly mixing the contents. The electrodes were made of ⅛ in. diameter Monel metal rods plated with 2 mils of gold. The rods were spaced 0.175 in. apart by means of a Plexiglas holder. A Teflon sheet was used to prevent contact of the organic liquids with the Plexiglas. The electrodes extended to about one inch of the bottom of the graduates.

Results and Discussion

Electrophoretic deposits were made at applied potentials of 20, 40 80, 160 and 320v. Deposits could be produced from suspensions of aliphatic alcohols of chain length greater than three carbon atoms from most hydrocarbons but not from ketones, esters or ethers. Deposits were produced with as little as 20v applied from suspension of aluminum flake in chloroform, sec-butyl alcohol, butyraldehyde, tert-amyl alcohol, n-hexane, n-heptane, cyclohexane, ethylbenzene, toluene, xylene, monochlorobenzene, n-butylamine, or ethylene dichloride. The deposition rate increases, and there is greater likelihood of deposition when the applied voltage is increased.

Deposits of aluminum flake from suspension in pure liquids were obtained at the cathode with the exception of the butylamine suspension from which anodic deposits were produced. In all cases, the deposits were very viscous slurries, and in many instances sagging or run-off occurred on removal of the electrodes from the suspensions. Deposits which were allowed to dry had very little physical strength as determined by very light pressure causing the deposit to powder and fall away. The deposits from the butylamine suspension had somewhat better physical strength than the others.

The suspending media with the highest dielectric constants (acetone, nitrobenzene, methanol, ethanol) produced flocculating suspensions incapable of electrophoretic deposition under the test conditions. This is unfortunate since maximum deposition rates are theoretically possible when liquids of greatest dielectric constant are used as the suspending media (1).

Table I. Effect of butylamine addition on sediment volumes and deposits of aluminum flake

Suspending medium	Sediment volume, ml, after 24 hr	Deposit thickness, mils Front	Back	Electrode deposited on
Methyl acetate	5.0	0	0	—
	3.5*	18	12	Anode
Acetone	5.1	0	0	—
	2.3*	39	17	Anode
sec-Butyl alcohol	3.2	13	2	Cathode
	4.8*	7	1	Anode
Nitromethane	10.0	0	0	—
	11.0*	0	0	—
Ethylene dichloride	—	9	2	Cathode
	3.6*	10	2	Cathode
Chloroform	2.8	4	1	Cathode
	2.3*	14	1	Cathode
Isopropyl ether	3.3	0	0	—
	3.8*	4	1	Anode
Toluene	3.6	2.5	2.5	Cathode
	3.4*	0	0	—
Heptane	3.5	1	1	Anode and cathode
	3.5*	0	0	—
Nitrobenzene	7.0	0	0	—
	8.0*	0	0	—

* 0.5 ml Butylamine added to 50 ml of suspension.

The greatest deposition rate and most coherent deposits were produced when butylamine was used as the suspending medium for aluminum flake. Because of this, it was decided to investigate the effect of addition of this material to aluminum flake suspensions in various other selected solvents. A half milliliter of butylamine was added to a suspension of 1g of aluminum flake in 50 ml of solvent. A settling time of 24 hr was found sufficient to show up differences in sediment volumes owing to the presence of butylamine. Deposits were produced by applying 80v across the electrodes for 3 min. The deposit thickness was determined at points nearest to and farthest from the opposite electrode. Such data give information as to the throwing power of the suspension (see Table I). It was found that when butylamine was added to the suspension in acetone, stability of the suspension was markedly improved [as shown by the decreased sediment volume (2)] and very rapid anodic deposition was achieved. Without butylamine, deposits were not produced. Addition of butylamine to suspensions with cholorform resulted in a heavier deposit at the cathode than is normally the case. The deposits also were more coherent. The addition of butylamine to methyl acetate gave rather rapid deposition in combination with good throwing power.

These three suspensions were selected from the group shown in Table I for further study. The effect of applied voltage and aluminum flake concentration on deposition rate was determined using 250 ml of suspension. Deposit thicknesses were measured at locations along the electrode nearest the facing electrode. Here the field strength and deposit thickness are at a maximum.

A straight line relationship was obtained between flake concentration and deposit thickness at a given voltage for the suspension in chloroform-

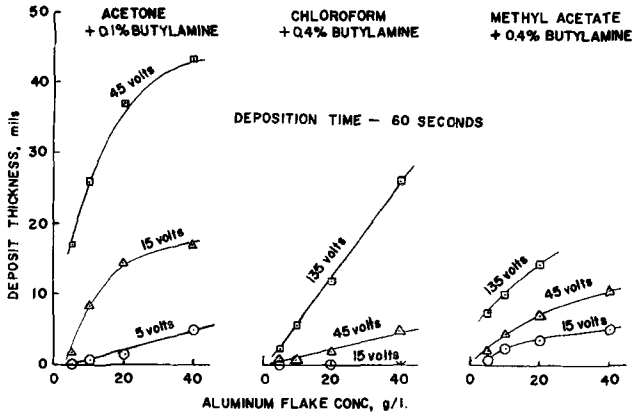

Fig. 1. Effect of aluminum flake concentration on electrophoretic deposit thickness.

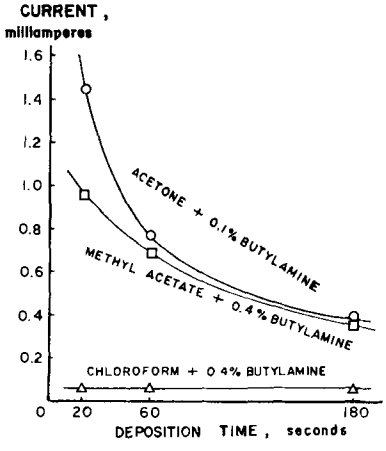

Fig. 2. Effect of deposition time (deposit build-up) on current flow; 40 g/l aluminum flake, 45v applied.

butylamine (Fig. 1) as consistent with electrophoresis theory. The deviation from linearity for the other suspensions is assumed to result because the deposits in these systems offer greater electrical resistance than the suspension. This is substantiated by the decrease in current observed with deposit build-up for suspensions with acetone or methyl acetate (Fig. 2). Thus, although the applied potential is maintained constant during deposition, the voltage drop through the deposit steadily increases, thereby decreasing the field strength through the suspension which is the driving force for electrophoresis (1). The deposits formed from suspension in chloroform apparently offer no added resistance to the system and deposition continues at a constant rate.

The effect of deposit thickness on throwing power is shown in Fig. 3. The throwing power is expressed as the ratio of deposit thickness on the back of the electrode to that on the front, the front being that portion closest to the opposite electrode. The throwing power of the suspension with methyl acetate increases rapidly with deposit thickness while the suspension with chloroform achieves little increase in throwing power with deposit build-up.

Deposits from all three suspensions were easily damaged by handling, although the deposits from chloroform were noticeably superior in particle co-

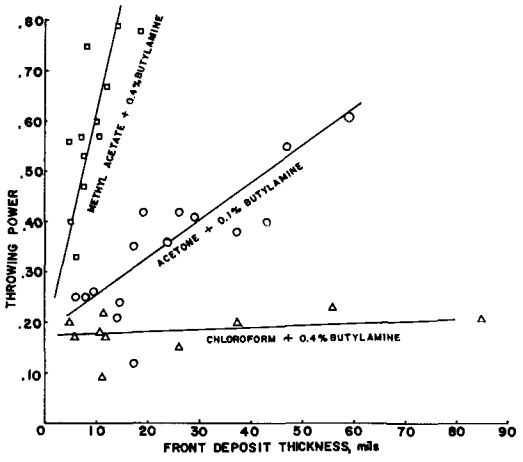

Fig. 3. Effect of electrophoretic deposit thickness of aluminum flake on throwing power.

hesion. Certain binder materials can be added to suspensions to improve cohesion of the deposits, *e.g.*, ethyl cellulose (3) or rosin.

Attempts to deposit electrophoretically aluminum spherical powder of less than 44μ particle diameter from suspension in acetone-butylamine were unsuccessful. The method of production of aluminum spherical powder, unlike the flake, does not involve the use of stearates. Since the residual stearate film on the flake may play an important role in the properties of suspensions, a stearate film was applied to the aluminum spherical powder by exposing for 24 hr to a solution of acetone saturated with stearic acid. The liquid was decanted. The residue was washed with fresh acetone and decanted to remove most of the stearic acid. Addition of butylamine to suspension of the treated spherical powder with acetone now resulted in anodic deposits being produced with 200v applied between the electrodes. The stearate treatment described above may also be applicable to other powders normally difficult to deposit electrophoretically.

It was found that tungsten powder was capable of anodic electrophoretic deposition with about 400v applied when suspended in pure acetone. Titanium powder deposits could be obtained from suspension in acetone when butylamine was added.

Fusion and Diffusion of Electrophoretic Deposits

Some preliminary tests were conducted on the fusion and diffusion of electrophoretic deposits on steel.

An 8-mil electrophoretic deposit of aluminum flake on a steel wire was heated under argon to 790°C for 2½ hr. There was no evidence of fusion of the deposit, but when the specimen was brushed with a wire wheel to remove loosely adhering particles, the surface was found to be quite hard, indicating a diffusion layer consisting of intermetallic compounds. Such specimens were found to be resistant to attack by 50% nitric acid and high-temperature air oxidation. Figure 4 shows a longitudinal cross section of the steel wire of which part had been coated with the aluminum flake and given the diffusion treatment described above. The specimen was then heated to dull red heat over a gas burner

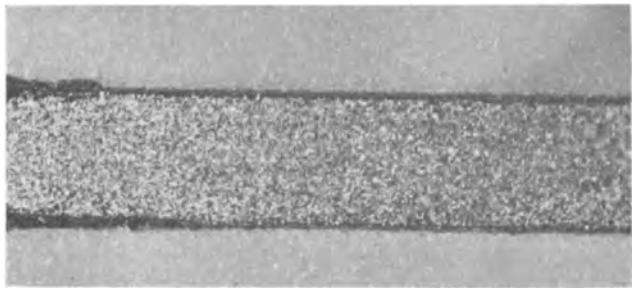

Fig. 4. Protective effect of diffused aluminum film on steel wire to high-temperature air oxidation.

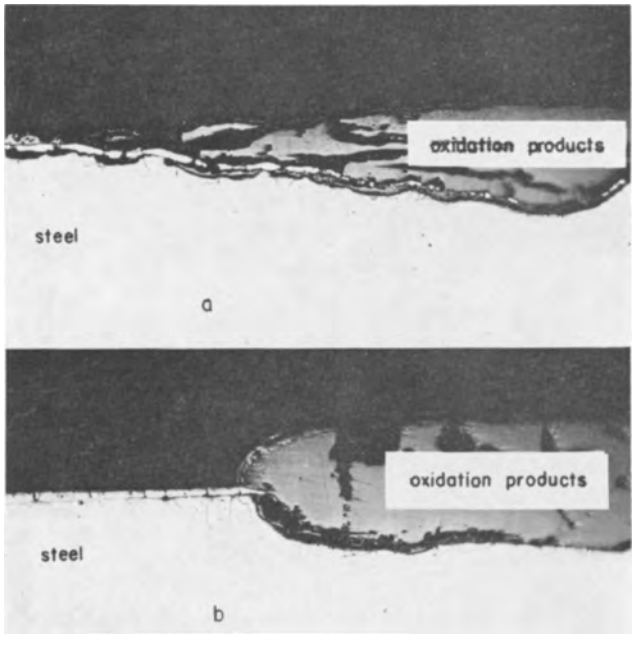

Fig. 5. Protective effect of hot pressed deposits on steel to high-temperature air oxidation: a, aluminum flake deposit; b, spherical aluminum powder deposit.

for 2½ hr. The oxidation produced on the left side, which had not been coated with aluminum flake, is evident.

Fusion of the deposit and diffusion into the basis metal should be enhanced by the intimate contact provided by placing the deposit under pressure. Steel panels, electrophoretically coated with aluminum flake or aluminum spherical powder, were compacted with 1 ton/in.^{2} pressure while heated to 650°C under inert atmosphere (4). The spherical powder deposit was more nearly fused than the flake. The pressed deposits were approximately 3 mils thick. In order to test the oxidation resistance of the deposits, the specimens were heated in air to red heat over a gas flame 8 hr each day for a total of 4 days. The flame was directed at the bottom of the specimens. Photographs of specimens that were cross-sectioned and mounted are shown in Fig. 5. The powder deposit offered much more complete resistance to oxidation than did the flake.

Steel panels were coated with titanium and tungsten powder and heated in inert atmosphere to 1090°C while under 1 ton/in.^{2} pressure. Some fusion of the titanium was observed but none with tungsten powder. Slight diffusion of both metals into the steel was observed.

Acknowledgment

The authors wish to thank the U.S. Army Munitions Command for permission to publish this article.

Manuscript received Sept. 18, 1962; revised manuscript received Dec. 3, 1962. This paper was delivered at the Houston Meeting, Oct. 9-13, 1960.

Any discussion of this paper will appear in a Discussion Section to be published in the June 1964 JOURNAL.

REFERENCES

1. S. Glasstone, "An Introduction to Electrochemistry," p. 533, D. Van Nostrand Co., Inc., New York (1942).
2. H. R. Kruyt, "Colloid Science," Vol. 1, p. 86, Elsevier Publishing Co., New York (1952).
3. J. J. Shyne, H. H. Barr, W. D. Fletcher, and H. G. Scheible, *Plating*, **42**, 1255 (1955).
4. W. McNeill, J. E. Chrostowski, and T. J. Mackus, *This Journal*, **108**, 763 (1961).

P-N Junction Photovoltaic Effect in Anodically Formed Oxide Films of Titanium

Franz Huber

Paul Moore Research & Development Center, Republic Aviation Corporation, Farmingdale, New York

It has been over 100 years since Becquerel (1) in 1839 first discovered that a photovoltage was developed between two electrodes immersed into an electrolyte when one of these electrodes was illuminated with light. Later Lifschitz and Reggiani (2), Rosenthal (3), Baer (4), Walkenhorst (5), Young (6), Schmidt *et al.* (7), Sasaky (8), and Rupprecht (9) investigated photoeffect and photoconduction on anodically formed oxide films of Al, Ta, Nb, and Ti in the system metal-metal oxide-electrolyte. In some of his investigations Van Geel *et al.* (10) replaced the electrolyte with a partially transparent layer of Cu or CuI, deposited directly onto the metal oxide film.

Van Geel (10) attributes the appearance of the photo emf generated across the oxide film to the difference of the work functions between Ta-Ta_2O_5 and Ta_2O_5-electrolyte or to the difference of the work functions between Ta-Ta_2O_5 and Ta_2O_5-Cu. It is claimed, *e.g.*, that the work function Ta-Ta_2O_5 is less than the work function Ta_2O_5-electrolyte. Sasaki (8) explains the photoeffect in the system Ta-Ta_2O_5-electrolyte in terms of a p-i-n junction model. Schmidt *et al.* (7) found that the open-circuit photoeffect in the system metal-metal oxide-electrolyte disappears after slight etching of the oxide film, *i.e.*, after removal of a surface barrier. In a more recent paper Lucovsky *et al.* (11) discussed photoelectric effects in thin films of anodically formed Al_2O_3 and Ta_2O_5, sandwiched between two metal films. These authors found good agreement of their experimental results with the hypothesis of internal photoelectric emission over the potential barrier at a metal-insulator interface.

According to our results, as reported here, the photo emf in anodically formed oxide films of titanium seems rather to arise from the existence of a p-n junction within the oxide film than from the difference in work functions at the interfaces. Excess of metal atoms at the interface metal-metal oxide and deficiency of metal atoms or excess of oxygen in the surface layer of the oxide film might be responsible for the formation of the n- and p-layers, respectively. We had been able to show that thin films of anodically formed titanium oxide, sandwiched between two metals (Ti-titanium oxide Pd), exhibit rectification properties (12) similar to germanium p-n junction diodes and show a voltage dependence of the capacitance like that of a graded p-n junction (13). The photovoltaic effect of titanium oxide films, as reported here, is considered as further support for the assumption of a p-n junction within anodically formed oxide films of titanium.

The experiments on the photovoltaic effect were performed on evaporated titanium films. Titanium was evaporated in a vacuum system at a pressure of about 10^{-5} Torr by resistive heating and deposited as a metal film, about 3000Å thick. Glass slides were used as substrates. The surface of the titanium film was then converted into titanium oxide by anodic oxidation. The electrolyte consisted of a mixture of equal parts of ethylene glycol and aqueous solution of oxalic acid. According to our measurements the oxide film is about 300Å thick and in good agreement with a rate of growth of 22 Å/v as reported by Hass (14). Contact electrodes of palladium were deposited onto the oxide film as shown in the schematic Fig. 1. The contact to the oxide layer should cover as little as possible of the photosensitive surface. In order to achieve this re-

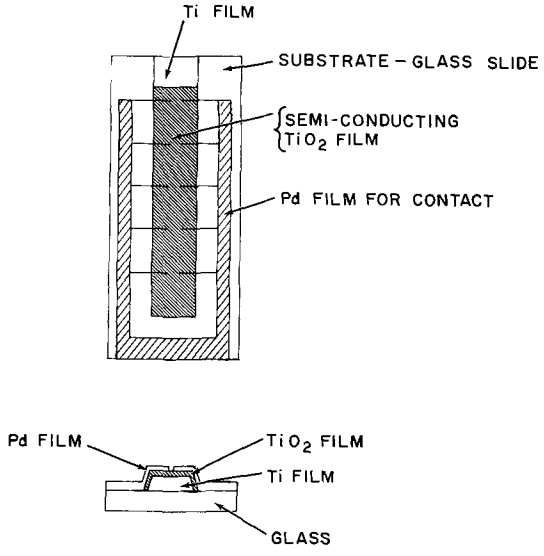

Fig. 1. Schematic drawing of titanium oxide cell

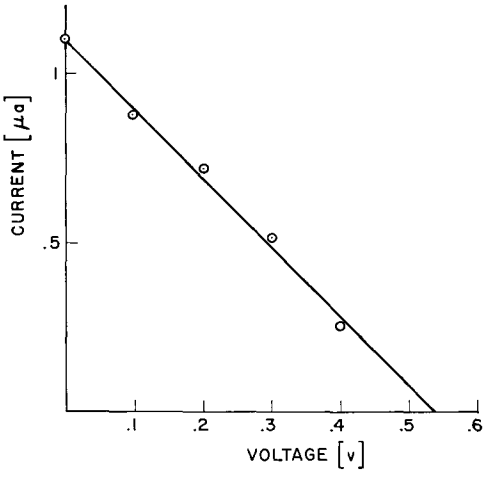

Fig. 2. Current-voltage characteristic for titanium oxide films obtained by illumination with mercury lamp.

sult, narrow lines of palladium, 5-10 mils wide, were deposited. Palladium films were used to obtain ohmic contact to the titanium oxide film as in the case of the thin-film titanium oxide diodes (12).

When the titanium oxide film is irradiated with ultraviolet light from a Hg lamp a photo emf is built up with the Ti electrode as the negative pole. The measurements of the photovoltage between the Ti and Pd electrodes were made with a vacuum tube volt meter, whose input impedance is greater than 10^{12} ohms. Photocurrents produced without the application of an auxiliary voltage were measured with a low-resistance ampere meter. Figure 2 shows the current-voltage characteristic. The fact that the curve is nearly linear implies the existence of a large internal resistance.

Similar I-V characteristics were obtained with samples in which the Pd contact areas were shielded against illumination. This result rules out a photo emf obtained possibly by the difference of work functions at the interfaces, as claimed, *e.g.*, by van Geel (10). Illumination of the titanium oxide film with green light (mercury lamp and 5460Å filter) does not affect the maximum photovoltage of 0.53v. This value agrees well with the measurements on Ti-TiO_2-electrolyte, as reported by Rupprecht (9).

Acknowledgment

Grateful acknowledgment is made to Dr. A. Bramley for helpful discussions.

Manuscript received Sept. 13, 1962; revised manuscript received Feb. 27, 1963.

Any discussion of this paper will appear in a Discussion Section to be published in the June 1964 JOURNAL.

REFERENCES

1. E. Becquerel, *Compt. rend.*, **9**, 561 (1839).
2. J. Lifschitz and M. Reggiani, *Z. physik. Chem.*, **A155**, 431 (1931).
3. G. Rosenthal, *Z. Physik*, **99**, 607 (1936).
4. W. Baer, *ibid.*, **115**, 658 (1940).
5. W. Walkenhorst, *Z. tech. Physik*, **22**, 14 (1941).
6. L. Young, *Trans. Faraday Soc.*, **50**, 164 (1954).
7. P. F. Schmidt, F. Huber, and R. F. Schwarz, *J. Phys. Chem. Solids*, **15**, 270 (1960).
8. Y. Sasaky, *ibid.*, **13**, 177 (1960).
9. J. Rupprecht, *Naturwiss.*, **47**, 127 (1960).
10. W. Ch. van Geel, C. A. Pistorius, and P. Winkel, *Philips Research Repts.*, **13**, 265 (1958).
11. G. Lucovsky, C. J. Repper, and M. E. Lasser, Am. Phys. Soc. Meeting, Evanston, June 1962.
12. F. Huber, *J. Solid-State Electr.*, **5**, 410 (1962).
13. F. Huber and M. Rottersman, *J. Appl. Phys.*, **33**, 3385 (1962).
14. G. Hass, *Vacuum*, **2**, 331 (1952).

Tungsten, Titanium, and Tantalum Carbides and Titanium Nitrides as Electrodes in Redox Systems

F. Mazza and S. Trassatti

Laboratory of Electrochemistry and Metallurgy, University of Milan, Milan, Italy

Boron carbide (B_4C) has been proposed as a solid electrode, particularly as an anode, for polarographic determinations (1). The advantage of such an electrode, compared with the usual platinum or gold electrodes, is that its surface remains unoxidized and the electrode may, therefore, be used in studies of electrode processes without the hindrance of oxide films. The boron carbide electrode can be used as an anode for potentials approaching that required for oxygen discharge. It may also be used as a cathode for potentials equal to or exceeding that required for hydrogen discharge. Recent information on the application of such an electrode for oxygen reduction indicates that the electrode is entirely inert and serves merely as an electronic conductor (2). It can be obtained in rod-like form, but the working and the assembly of the electrode present some difficulty. TiB_2, ZrB_2, and $MoSi_2$ have also been studied; their behavior as electrodes has been found to be inferior to B_4C, however.

The study of the electrochemical behavior of compounds, such as carbides, borides, silicides, nitrides, etc., is also of interest, since, owing to their good electrical conductivity, corrosion resistance, and eventual catalytic activity, these compounds are applicable as electrodes in electrolytic cells. For example, it has been reported (3) that titanium carbide has been applied, without adverse effects from the sulfuric acid or the sulfate, in the electrolytic oxidation of manganese sulfate to MnO_2 at current densities exceeding 100 amp/ft^2. In addition to formation by sintering, these electrodes may be prepared in some cases by high-temperature diffusion (carburizing, nitriding, etc.) and cementation in

various shapes or in thin sections not possible by a sintering process on a laboratory scale.

This note deals with an electrochemical study of the behavior of tungsten, tantalum, and titanium carbides and of titanium nitride obtained by high-temperature cementation. The electrodes were prepared in disk form 25 mm in diameter and 5-12μ in thickness. The methods chosen were found to yield surfaces which were free of contamination of foreign substances.

Tungsten and tantalum carbides were prepared by direct carburization by putting carbon black on the surface of tungsten or tantalum and heating in a furnace at 1200°C for 2 hr under a stream of spectroscopically pure argon. For each electrode two successive carburizations were made; this was necessary since x-ray structural analysis showed incomplete carburization and the presence of the lower carbides (W_2C and Ta_2C) in the surface after only one carburization. After two successive carburizations x-ray structural analysis showed that the respective surfaces consisted of nearly pure tungsten or tantalum carbide (WC or TaC).

Titanium carbide electrodes were prepared by passing carbon monoxide gas over titanium metal for 5 min at 900°C. Before and after this treatment the electrode was warmed and cooled in a stream of spectroscopically pure argon. X-ray structural analysis revealed the presence of titanium and traces of the lower carbide in the bulk carbide, TiC, produced on the titanium surface.

Titanium nitride electrodes were prepared by directly nitriding the surface of titanium with 99.999% nitrogen at 1200°C for 5 hr. X-ray structural analysis showed that the surface consisted of compact layers of pure titanium nitride (TiN). X-ray analysis also showed that the nitriding was incomplete if the process was attempted in a shorter period of time (less than 5 hr).

The above methods were found to yield not only uniform and compact layers of carbides or nitrides on metallic bases but ones which adhered well. Coatings with the following thicknesses were obtained: WC, 9μ; TaC, 5μ; TiC, 5μ; TiN, 12μ.

The electrochemical behaviors of these electrodes were determined by polarization curves in different solutions and under prolonged hydrogen or oxygen discharge on their surfaces in acid solutions.

Using a potentiostatic method anodic and cathodic polarizations were studied in acid (0.5M H_2SO_4), neutral (0.5M Na_2SO_4 + 0.5M H_3BO_3), and alkaline (0.1M NaOH + 0.5M Na_2SO_4) solutions containing one of the following

O_2 (P_{O_2} = 1 atm)

10^{-2}M H_2O_2

10^{-1}M $K_3Fe(CN)_6$

10^{-1}M $K_4Fe(CN)_6$.

All experiments were conducted at 25°C in a glass cell previously described (4). All potentials reported here are with reference to the normal hydrogen electrode.

The data presented in Fig. 1 show that tungsten carbide, titanium carbide, and titanium nitride behave similarly for the oxidation of $K_4Fe(CN)_6$ in acid solutions whereas tantalum carbide requires higher potentials. Similar results were obtained in neutral or alkaline solutions except for WC which corrodes in alkaline solutions. The dotted line in this figure indicates the potential for the reversible discharge of OH^- ions.

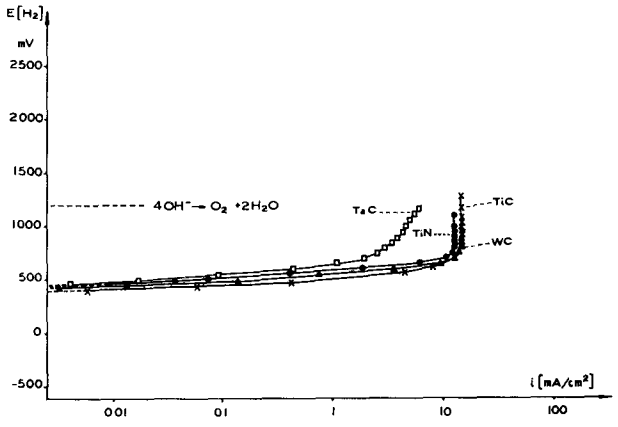

Fig. 1. Anodic polarization curves for $K_4Fe(CN)_6$ oxidation on TaC, TiC, WC, and TiN electrodes; acid solution.

In Fig. 2 the behaviors of the various electrodes in acid solutions containing hydrogen peroxide are shown. Only WC represents an efficient anode and then only if the discharge potential for oxygen is not exceeded, in which case the WC surface is rapidly corroded. On the other hand, the other electrodes (TiN, TaC, and TiC) are all corroded even at potentials below that required for the discharge of oxygen. The dotted line in this figure indicates the potential for the reversible discharge of OH^-.

The data of Fig. 3 shows that WC and TiN electrodes behave similarly in the cathodic reduction of $K_3Fe(CN)_6$ in acid solutions whereas TiC and TaC electrodes require more cathodic potentials. The dotted line in this figure indicates the potential for the reversible discharge of H^+ ions. Analogous results were obtained in neutral and alkaline solutions except for WC which, as stated above, corrodes in alkaline solutions.

In the case of the cathodic reduction of oxygen, WC electrodes are superior to the others as is evident from the data presented in Fig. 4. These electrodes sustain hydrogen discharge from acid so-

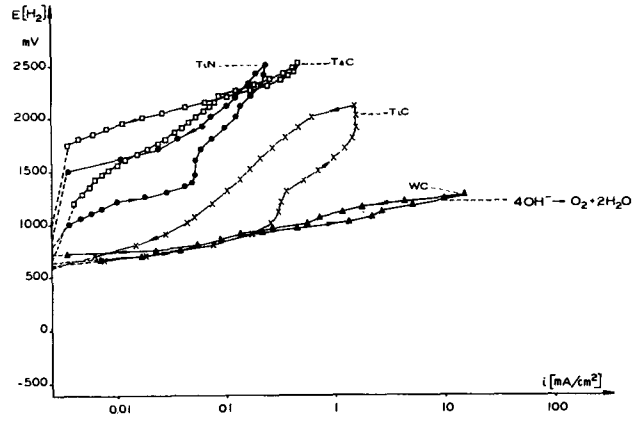

Fig. 2. Anodic polarization curves for H_2O_2 oxidation on TaC, TiC, WC and TiN electrodes; acid solution.

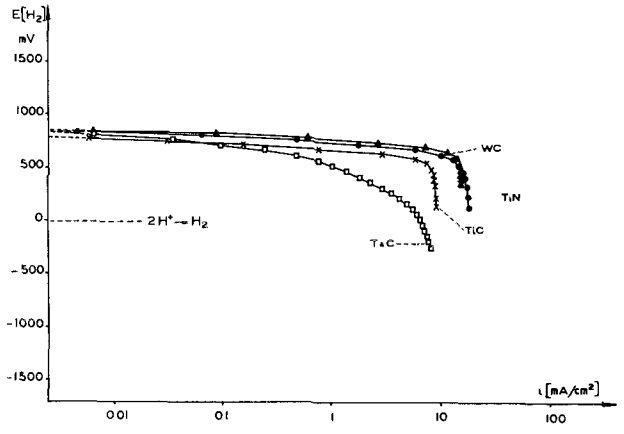

Fig. 3. Cathodic polarization curves for $K_3Fe(CN)_6$ reduction on TaC, TiC, WC, and TiN electrodes; acid solution.

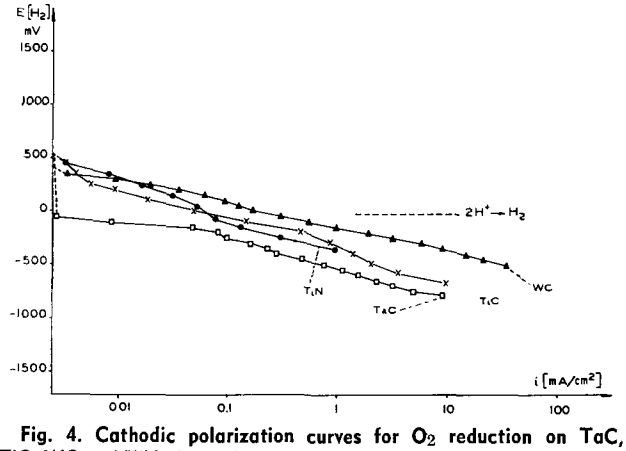

Fig. 4. Cathodic polarization curves for O_2 reduction on TaC, TiC, WC and TiN electrodes; acid solution.

lutions for more than 100 hr at a current density of 4 ma/cm^2 and at a steady potential of −0.25v. The dotted line in this figure indicates the potential for the reversible discharge of H^+ ions.

In summary then WC electrodes are superior electrodes for studies in acid solutions at potentials below that required for oxygen evolution. They cannot be used in alkaline solutions, however, since they then corrode rapidly. TiN electrodes behave similarly to WC electrodes for intermediate potentials.

This note has shown that WC and TiN electrodes may be used successfully in studying redox systems as well as B_4C electrodes which have been previously recommended for such purposes. WC and TiN electrodes, even on a laboratory scale, may be readily prepared in desired shapes by high-temperature cementation although such small pieces are not readily prepared by machining of sintered blanks. Of the electrodes studied WC is the best for acid solutions, TiN for alkaline solutions. WC electrodes may be used in acid solutions below the potentials required for oxygen discharge but erode in alkaline medium. TiN electrodes may be used at potentials intermediate to hydrogen and oxygen discharge and in alkaline solutions. TiC and TaC electrodes give less satisfactory results.

Manuscript received Jan. 29, 1963; revised manuscript received March 9, 1963. This research was sponsored by Consiglio Nazionale delle Ricerche, Roma.

Any discussion of this paper will appear in a Discussion Section to be published in the June 1964 JOURNAL.

REFERENCES

1. T. R. Mueller, L. L. Olson, and R. N. Adams, "Voltammetry at Boron Carbide and Carbon Paste Electrodes; Advances in Polarography," Vol. 1, p. 198, London (1960).
2. D. T. Sawyer and E. T. Seo, *J. Electroanalit., Chem.*, **3**, 410 (1962); T. R. Mueller and R. N. Adams, *Anal. Chem. Acta*, **23**, 467 (1960).
3. U. S. Pat. No. 2,636,856, Feb. 28, 1953.
4. R. Piontelli, U. Bertocci, G. Bianchi, C. Guerci, and G. Poli, *Z. Elektrochem.*, **58**, 86 (1954).

The Use of α-Spectroscopy for Studying Anodic Oxidation

J. A. Davies[1] and B. Domeij

Nobel Institute of Physics and Royal Institute of Technology, Stockholm, Sweden

The techniques of nuclear spectroscopy now available make it possible to measure the depth of a radioactive tracer beneath the surface of a solid. In the most favorable cases, a precision of ±5 atom layers can be attained. Such techniques provide a sensitive, nondestructive method for observing the location of a suitable tracer atom within an oxide layer at various stages during anodic oxidation. In this way, useful information about the mechanism of oxide film growth, and particularly about the relative mobilities of the oxygen and metal ions within the growing oxide, can be obtained. If oxidation takes place by metal ion migration, then the fresh oxide would be laid down outside the previously tagged layer, provided, of course, that the injected marker atom itself does not move appreciably under the high potential gradient of the anodizing field. If, on the other hand, the oxygen ion moves during oxidation, then the fresh oxide would be formed beneath the existing tagged layer.

The use of a high precision β-spectrometer for following the location of an inert gas isotope (Xe^{125}) during the anodic oxidation of Al and Ta has already been described (1). The results were somewhat unexpected. With Ta, the Xe^{125} atoms after oxidation were located somewhere near the middle of the oxide layer, thereby indicating that in this case both metal and oxygen migration are contributing to film growth. With Al, on the other hand, after anodizing at 0.1 ma/cm^2, it was found that the Xe^{125} atoms remained in the outermost layers of oxide. This was interpreted as evidence that the oxide film on Al grows by oxygen migration alone, a conclusion that is valid only if the oxide forms a homogeneous layer. There is some evidence (2) to

[1] On leave of absence from Atomic Energy of Canada Limited, Chalk River, Ontario.

Table I. Burying of inert gas atoms during anodic oxidation

Target	Current density, ma/cm²	Oxide thickness, μg/cm²	Mean depth of tracer beneath surface, μg/cm² Xe^{125} [a]	Mean depth of tracer beneath surface, μg/cm² Rn^{222}	Half-width of α-peak, kev
Al unanodized	—	1.0	3.2	2.0	22.2 ± 1.0
Al anodized to 200v	20.0	95	35 ± 5	27 ± 2	24.6 ± 1.0
Ta unanodized	—	—	7	6.1	23.5 ± 1.0
Ta anodized to 200v	2.0	280	90 ± 25	74 ± 6	25.6 ± 1.0

[a] Data obtained at Chalk River (1, 3).

suggest that at low current density the outermost layer of aluminum oxide develops pores, even in a buffered electrolyte such as dibasic ammonium citrate, and that subsequent film growth occurs underneath this porous region. If this is the case, then the Xe^{125} atoms located just beneath the target surface would soon become trapped in "dead" oxide, and would not provide information about the mechanism of oxide growth in the underlying barrier layer. Some support for this explanation is found in recent work at Chalk River (3) using Xe^{125}, in which the behavior in Al was found to vary markedly with the current density. At higher current densities (1-20 ma/cm²), where pore formation is supposedly negligible, the behavior of Al is similar to Ta in that the Xe atoms become deeply buried within the oxide.

There is one important question that the β-spectrometer method fails to answer. Due to the wide-angle scattering of electrons, the energy attenuation of an individual electron leaving the target at normal incidence is not a simple function of the depth of the Xe^{125} atom beneath the target surface. Consequently, although the method gives the mean depth of the Xe^{125} atoms beneath the oxide surface, it does not provide information on the depth distribution of the individual atoms about the mean value. When the Xe^{125} atoms remain close to the oxide surface, as for Al anodized at low current density, this limitation is not serious. But when the Xe^{125} atoms become deeply buried in the growing oxide, as in the case of Ta or of Al at high current density, it is necessary to establish that the Xe^{125} atoms have retained their original sharp distribution and have not become dispersed throughout the oxide layer.

In order to overcome this particular limitation of β-spectroscopy, we have developed an alternative technique, using an α-emitting isotope such as Rn^{222} instead of Xe^{125}. Since α-particles lose their energy almost continuously and without undergoing significant wide-angle scattering, the energy loss sufferred by each particle is determined only by the distance between the surface and the parent Rn^{222} atom. Consequently, by measuring accurately the position and shape of the energy spectrum of the emitted α-particles, it is possible to deduce both the mean depth of the embedded Rn^{222} atoms and the distribution of individual atoms about the mean. The position of the peak in the energy spectrum provides directly the mean absorber thickness; the shape of the peak gives information about the distribution.

Experimental

This paper reports some preliminary experiments in which α-spectroscopy has been used to study the anodic oxidation of Al and Ta under those conditions in which, from previous Xe^{125} work, a significant burying is known to occur. The development of a sufficiently precise α-spectrometer has already been described (4) in conjunction with a separate investigation of the range of accelerated atomic particles in metals. It consists of a solid-state detector of the surface-barrier type and a multichannel pulse-height analyzer. The technique is somewhat less sensitive than β-spectroscopy: *viz.*, ±8 atom layers of Ta and ±25 atom layers of Al. A similar method was developed independently by Anderson (5) for measuring the thickness of thin plastic films.

In the present experiments, a beam of Rn^{222} ions accelerated to 2-6 kev energy was injected into the flat face of an Al or Ta target (2.0 x 1.0 x 0.1 cm) by means of an electromagnetic isotope separator. The total integrated beam current striking each target was less than 10^{12} atoms/cm², and so introduces a negligible concentration of Rn into the surface layer of the metal. From other work in this laboratory (6), it is known that the mean penetration depth of a 6 kev Rn^{222} beam is quite small: 2.0μg cm^{-2} in Al, and 6.1 μg cm^{-2} in W. The value in Ta is assumed similar to that in W.

After measuring the energy spectrum of the 5.486 Mev α-particles, the targets were anodized at constant current (see Table I) to 200v, using a 3% solution of dibasic ammonium citrate in water as electrolyte, and the energy spectrum of the particles remeasured. With Al, the current density was sufficiently high that the electrolysis was completed in less than 30 sec; under such conditions, pore formation in the oxide should not occur (2).

Unlike electrons, the attenuation (dE/dx) of α-particles is sufficiently well understood as a function of energy and of the atomic number of the absorber that no calibration is required. Values of (dE/dx) for 5.486 Mev α-particles in any absorbing material can be calculated from Whaling's tabulation of stopping powers (7), with an estimated error of about 8%. Values of 0.59 kev/μg cm^{-2} for Al_2O_3 and 0.31 kev/μg cm^{-2} for Ta_2O_5 were obtained in this way.

The results of the anodic oxidation are illustrated in Fig. 1 and 2. It is evident that, although the shape of the α-spectrum remains virtually unchanged, the position of the peak in each case is shifted to a considerably lower energy, indicating

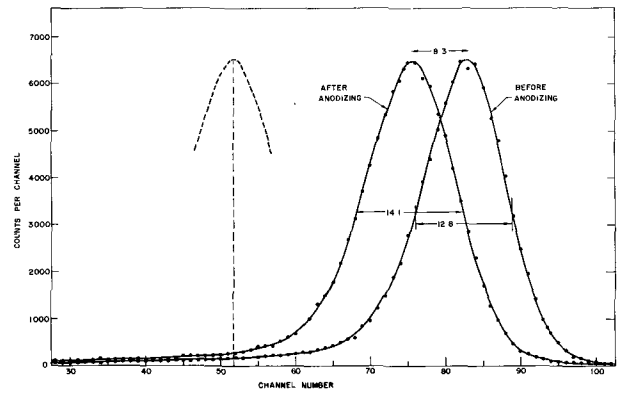

Fig. 1. The α-spectrum of Rn^{222} in aluminum before and after formation of a 200v oxide layer by anodic oxidation at high current density (20 ma/cm²). The dotted line is the spectrum that would have resulted if the Rn^{222} atoms were located at the metal-oxide interface. One channel is equivalent to 1.74 kev.

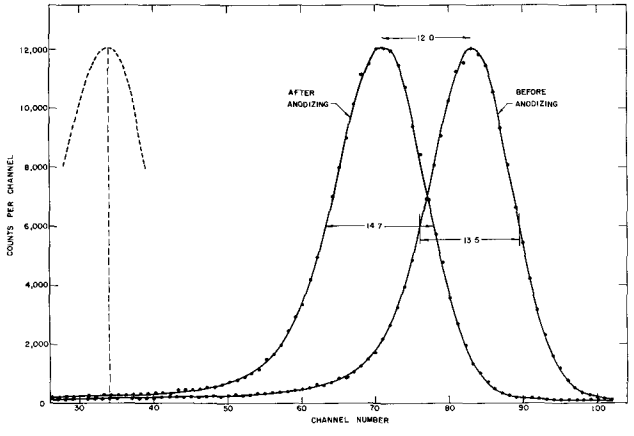

Fig. 2. The α-spectrum of Rn^{222} in tantalum before and after the formation of a 200v oxide layer by anodic oxidation at 2.0 ma/cm². The dotted line is the spectrum that would have resulted if the Rn^{222} atoms were located at the metal-oxide interface. One channel is equivalent to 1.74 kev.

that the Rn^{222} atoms have become deeply buried within the oxide layer. From the observed decrease in energy, and the known stopping power of Al_2O_3 and Ta_2O_5, the mean depth of the embedded tracer atoms can be readily calculated. In Table I, the values thus obtained for the burying of Rn^{222} during anodic oxidation are compared with those observed previously (1, 3) for Xe^{125}, using β-spectroscopy. The agreement between the two methods is well within the estimated errors of the respective calibrations. Evidently both anion and cation migration contribute to film growth in the anodic oxidation of Ta and also in the oxidation of Al at higher current densities.

The observation that the α-spectrum does not broaden appreciably during anodic oxidation confirms the validity of our earlier assumption (1) that the inert gas atoms are not dispersed throughout the oxide layer, but retain a fairly sharp distribution. It can also be seen from Fig. 1 and 2 that a negligible amount (< 1%) of the Rn is trapped at the metal-oxide interface.

The last column of Table I indicates that in each case, a slight increase (about 10%) in peak width does occur as a result of the oxidation. There are two main factors involved which might produce such an effect: (*a*) a small straggling in the energy-loss process itself; and (*b*) a broadening of the Rn^{222} distribution during the oxidation.

The first factor is not negligible and could possibly account for all of the observed increase. Experimental data on the energy straggling of α-particles traversing such thin layers of absorber are unfortunately not available; however, a fairly reliable estimate of the straggling may be obtained from the proton straggling measurements of Madsen (8) with appropriate corrections. From this analysis, the estimated half-widths due to energy straggling, for α-particles traversing 27 μg cm^{-2} of Al_2O_3 and 74 μg cm^{-2} of Ta_2O_5, are 6.5 and 8 kev, respectively. Adding these widths quadratically to the experimental widths of the unanodized targets, we obtain a combined width of 23.2 kev for the Al_2O_3 and 24.8 kev for the Ta_2O_5 targets. These values are still somewhat less than the observed peak widths of the anodized targets in Table I, but the discrepancy is within the estimated experimental error. Consequently, there is no evidence to suggest that any appreciable broadening of the Rn^{222} distribution has occurred.

A small broadening of the Rn^{222} distribution is in fact inevitable during the early stages of oxidation, due to the conversion to oxide (with a consequent increase in total mass) of the surface region into which the Rn atoms were originally injected. But this effect introduces a half-width term of only 1-2 kev, and so has a negligible influence when combined with the observed widths of the unanodized targets.

Conclusions

The present work shows that embedded inert gas atoms such as Rn^{222} retain a sharp distribution within the growing oxide film, as would be expected if they are truly inert tracers.

The observed "burying" of Rn^{222} atoms during the anodic oxidation of Ta agrees within experimental error with an earlier result using Xe^{125} (1), and supports the previous conclusion that both oxygen and metal ion migration contribute to oxide film growth.

In Al, anodized at high current density (20 ma/cm²), the Rn^{222} atoms undergo a comparable degree of burying to that observed in Ta, thereby suggesting that the mechanism of oxidation in the two metals is quite similar. At low current density (0.1 ma/cm²), the lack of burying, observed previously (1) for Xe^{125} in Al, implies either a change of mechanism with current density, or more probably a significant amount of pore formation in the earlier study.

Acknowledgments

It is a pleasure to acknowledge the encouragement and assistance of Dr. I. Bergström in developing the experimental technique. The authors are also indebted to J. P. S. Pringle for valuable discussions on the interpretation of the results and to G. C. Hanna for assistance in computing the energy straggling of α-particles.

Manuscript received Feb. 4, 1963; revised manuscript received April 4, 1963.

Any discussion of this paper will appear in a Discussion Section to be published in the June 1964 JOURNAL.

REFERENCES

1. J. A. Davies, J. P. S. Pringle, R. L. Graham, and F. Brown, *This Journal*, **109**, 999 (1962).
2. T. A. Renshaw, *ibid.*, **108**, 185 (1961).
3. J. P. S. Pringle, Private communication, and in a paper to be presented at the Pittsburgh meeting of the Electrochem. Soc. (April, 1963).
4. B. Domeij, I. Bergström, J. A. Davies, and J. Uhler, *Arkiv för fysik*, **24**, 399 (1963).
5. H. L. Anderson, *Nuclear Instr. and Meth.*, **12**, 111 (1961).
6. I. Bergström, J. A. Davies, B. Domeij, and J. Uhler *Arkiv för fysik*, **24**, 389 (1963).
7. W. Whaling, *Handbuch der Physik*, **34**, 193 (1958).
8. C. B. Madsen and P. Venkateswarlu, *Phys. Rev.*, **74**, 1782 (1948).

Anodic Film Growth by Anion Deposition in Aluminate, Tungstate, and Phosphate Solutions

William McNeill and Leonard L. Gruss

Pitman-Dunn Laboratories, Frankford Arsenal, Philadelphia, Pennsylvania

ABSTRACT

Films were obtained by anodic treatment of Al, Mg, Ni, Fe, Zn, Bi, Cd, Co, and Cu in 0.1*N* $NaAlO_2$ and Al, Bi, Cd, Cu, and Zn in 0.1*N* Na_2WO_4. A formation voltage of 30v was applied for 10 min in all cases except Al in $NaAlO_2$ where the maximum formation voltage was 100v. The anodic films were studied by electron diffraction and chemical analyses. Films obtained in $NaAlO_2$ solution appeared to be β-$Al_2O_3 \cdot 3H_2O$, and those obtained in Na_2WO_4 solution were oxides of the anode metal, or mixtures of the anode metal oxide with WO_3. The incorporation of phosphorus compounds in anodic films formed on Al in 0.1*N* Na_2HPO_4 solutions was also observed. The mechanism of anion deposition and film growth in these solutions is discussed.

In a previous paper (1) there were described a number of anodic spark reactions and products in solutions of $NaAlO_2$, Na_2WO_4, and Na_2SiO_3. The occurrence of these reactions showed that a high-voltage barrier film is present on the anode, but the composition and properties of the barrier below the spark potential were not investigated. This paper is concerned with the composition, thickness, and structure of the anodic films which form below the spark potential on a variety of metals in solutions of $NaAlO_2$ and Na_2WO_4. Formation of anodic films on Al in Na_2HPO_4 solution was also investigated.

Experimental

The materials and apparatus employed in this investigation were the same as those in the previous paper (1), with the addition of reagent grade Na_2HPO_4 and 99% pure H_3PO_4 which had been prepared at the Oak Ridge National Laboratory and contained a high level of radioactive phosphorus-32.

Anode geometry for the study of anodic film growth on Ni in $NaAlO_2$ solution and for the study of $HPO_4^=$ incorporation in anodic films on Al was also the same as in the previous paper. Anodes on which films were grown for electron diffraction study were made with the end to be anodized machined to form a flat plate which could be detached and mounted in the electron diffraction sample holder. Anode cleaning procedures were in all cases as described previously.

Electron diffraction patterns were obtained for films grown on various anodes in 0.1*N* $NaAlO_2$ and 0.1*N* Na_2WO_4. The anodic coatings were formed at a maximum current density of 0.016 amp/cm^2 up to a formation voltage of 30v, with the exception of the coating on the aluminum anode which was formed at 100v. The coated anodes were washed in distilled water, dried, and then inserted in the electron diffraction sample holder. An RCA 100 kv Model EMU 3D electron diffraction unit was employed for these exposures.[1] The diffraction patterns were measured on a Model-A circular film measuring instrument made by the Chas. Supper Company.

Information as to the film thickness and quantity of the anion constituent deposited in the water insoluble anodic films was obtained by two methods employing (*a*) nickel anodes in $NaAlO_2$ solution, and (*b*) aluminum alloy anodes in radioactive Na_2HPO_4 solution.

Nickel anodes having apparent surface areas of either 7.9 or 2.85 cm^2 were anodized in 0.1*N* $NaAlO_2$ for periods of 10 min with final formation voltages of 10, 30, and100v. With each anode the voltage was raised from zero to the final value by manual adjustment of the power supply at a rate sufficiently slow to maintain the current density below 0.04 amp/cm^2. After anodizing, the anodes were washed in distilled water and then soaked in 1-1 HCl to dissolve the anodic coating. Resulting solutions contained aluminum chloride together with small amounts of nickel chloride. The aluminum content was determined gravimetrically following precipitation with 8-hydroxy-quinoline. The nickel in the sample was complexed with tartaric acid to prevent its precipitation. Similar analyses were conducted with blanks prepared from nickel rods which were not anodized but which were soaked in distilled water, 1-1 HCl, or 0.1*N* $NaAlO_2$. In order to calculate the thickness of the aluminum containing portion of the anodic film, it was assumed that the aluminum compounds had a density of 2.5 g/cm^3 which is the value for β-$Al_2O_3 \cdot 3H_2O$.

The amount of phosphate incorporated in anodic films on 7075 alloy aluminum anodes was measured using an 0.1*N* NaH_2PO_4 solution which contained radioactive P-32. This experiment was similar to one reported by Plumb (2).

The anodes for measurement of phosphate incorporation in anodic films consisted of round 11 mm 7075 alloy aluminum rods. Disks, having one anodized flat surface, were cut from these rods, and counts were made on the disks with a Tracerlab Model SC-18A scaler counter which monitored the

[1] The electron diffraction patterns were prepared at the Aeronautical Materials Laboratory, Naval Air Materials Center, Philadelphia, Pennsylvania.

output of a 2.5 mg/cm² end window Geiger-Mueller tube to a precision of 1.5% probable error.

The activity of the electrolyte was determined from aliquots and was also determined for specimens anodized 10 min at a maximum current density of 0.016 amp/cm² to final voltages of 5, 15, 30, and 108v. In each case the voltage was increased to the desired value and then maintained constant, with current density being allowed to decrease. In order to correct the amount of the activity picked up by the anodes due to adsorption, counts were also made on a sample which was anodized at 30v in a nonradioactive Na_2HPO_4 solution and then soaked in the radioactive solution for 10 min. The number of counts for this sample was taken as the measure of radioactivity increase due to absorption or exchange of phosphate. It amounted to 6.7% of the total counts for samples anodized at 30v in the radioactive electrolyte.

Results and Discussion

Coating Structure and Composition

The data in Table I are for the most part the results of electron diffraction measurements of coated anode surfaces, and therefore it should be noted that the compounds listed are those found in the outer portion of the anode coating. No attempt was made to obtain complete information on the inner portion of the anode coating, which probably contained compounds produced by oxidation of the anode. X-ray diffraction and chemical analyses were also employed in the study of the films on Ni, Co, and Al anodes. It is true that any electron diffraction measurement represents only a very small portion of the sample surface and may be difficult to interpret. Nevertheless, the evidence appears conclusive that coatings of either hydrated or anhydrous Al_2O_3 are formed on anode surfaces in $NaAlO_2$ solution. The results of x-ray diffraction and chemical analyses which showed the presence of substantial quantities of aluminum in the coatings on Ni anodes provide strong support of this conclusion. There is some confusion as to the particular Al_2O_3 phases which are formed. This is not surprising in view of the complexity of the Al_2O_3 and Al_2O_3-H_2O systems and the similarity of several of the anhydrous Al_2O_3 phases (3).

Table I. Electron and x-ray diffraction analyses of unsparked anodic coatings formed in sodium aluminate and sodium tungstate solutions

Anode	Electrolyte	
	0.1*N* $NaAlO_2$	0.1*N* Na_2WO_4
Cd	Amorphous	WO_3
Mg	β-$Al_2O_3 \cdot 3H_2O$ + MgO	—
Bi	β-$Al_2O_3 \cdot 3H_2O$ + γBi_2O_3	Crystalline, not identified
Cu	β-$Al_2O_3 \cdot 3H_2O$ + CuO	Cu_2O*
Zn	β-$Al_2O_3 \cdot 3H_2O$ + ZnO	H_2WO_4
Fe	θ-Al_2O_3	—
Al	β-$Al_2O_3 \cdot 3H_2O$ appears after formng 24 hr at 100v.	δ or θ Al_2O_3
Ni, Co	Amorphous, hydrated Al_2O_3 Crystallizes at 600°C to γ, θ, or δ Al_2O_3	— —

* Inner coating layer.

The appearance of H_2WO_4 or its dehydration product, WO_3, on anodes coated in Na_2WO_4 solution is analogous to the appearance of hydrated and anhydrous Al_2O_3 phases on anodes coated in $NaAlO_2$ solution. In both cases the anion constituent of the electrolyte is deposited on the anode.

The Fe, Ni, Co, and Cu anodes coated in $NaAlO_2$ solution were covered with thick white outer coatings of aluminum compounds which were deposited over thinner coating layers which were in direct contact with the anode metal. With these anodes the transition from the outer to the inner layer of anodic coating was sharp, and the bonding between the two layers was so weak that large flakes of the outer coating could be detached readily.

The Bi, Al, and Mg anodes coated at 30v in $NaAlO_2$ solution were covered with transparent or slightly cloudy films in which no sharp division between inner and outer layers could be observed. The film on the Al anode coated at 30v yielded no electron diffraction pattern. Anodization for 24 hr at 100v produced an adherent opaque white layer of β-$Al_2O_3 \cdot 3H_2O$ on the Al anode.

The Cd and Zn anodes coated in $NaAlO_2$ solution were covered with opaque, white, powdery material in which no sharp division between inner and outer layers could be observed. Thus, in those cases where it was possible to distinguish more than one layer in the coating, the constituents derived from the electrolyte formed the outer coating layer as might be expected.

The thickness of the anion deposition layer obtained on Ni anodized in 0.1*N* $NaAlO_2$ solution was investigated, and results are shown in Table II. The thickness-voltage ratio decreases from 2.9 x 10^3 Å/v at 10v to 1.4 x 10^3 Å/v at 100v. These values are based on the assumption of a nonporous coating having a density of 2.5 g/cm³ which is the density of β-$Al_2O_3 \cdot 3H_2O$. It is possible that the β-$Al_2O_3 \cdot 3H_2O$ layer contained some porosity, and if that were the case, the actual thickness values would be larger than those shown in Table II.

Evidence was obtained indicating that phase transformations may occur in the deposit on Ni anodes in $NaAlO_2$ solution. In Table I, the coating formed for 10 min at 30v on Ni anodes is listed as amorphous; crystallizing to δ or θAl_2O_3 on heating at 600°C for 2 hr. This result showed that the initial anion deposition layer was some form of hydrated or anhydrous Al_2O_3. The moisture loss of the amorphous material was determined gravimetrically as 40.5% which is slightly more than that calculated for

Table II. Thickness of anodic coatings formed on nickel in 0.1*N* $NaAlO_2$

Anode formation voltage, v	Coating thickness, cm
0	Negligible
10	2.9×10^{-4}
30	6.4×10^{-4}
100	1.4×10^{-3}

β-$Al_2O_3 \cdot 3H_2O$ (34.6%). When a Ni anode was allowed to form at 30v for 17 hr in 0.1*N* $NaAlO_2$, the anion deposition layer was shown, by powder x-ray diffraction, to contain crystalline β-$Al_2O_3 \cdot 3H_2O$. Thus it was apparent that either a phase transformation occurred in the anodic film or the character of the anion deposition process changed. Either of these two effects might have occurred, although there is some precedence for the former, in the electric field induced nucleation of crystal growth in anodic films, as observed by Vermilyea (4, 5).

The experiments described above and in previous work (1) show that anions such as AlO_2^-, $WO_4^=$, and $SiO_3^=$ (or their decomposition products) are incorporated in anodic films grown in solutions containing them. In fact, with these electrolytes, anodic barrier films containing only material derived from the electrolyte can be formed on anodes such as Au and Pt.

For comparison purposes, we conducted one further series of measurements to determine the extent of anion incorporation in anodic films grown on Al in 0.1*N* Na_2HPO_4 solution. This system was selected because it had been shown (6) that the anodic films obtained with it were nonporous, and because of the possibility of employing radiotracer techniques for the determination of phosphate in the anodic coatings. The results are in approximate agreement with those of Plumb (2) for the films formed at 108v, but films formed at lower voltages contained a much larger percentage of phosphate than those prepared by Plumb, and at 5v the weight per cent of phosphate in the coating was determined as 46%. The reason for this discrepancy was not obvious, and further experiments of this type are being conducted. However, our results and those of Plumb both show that anodic films grown on Al in neutral or alkaline phosphate solution contain substantial quantities of phosphorus.

Film Growth Mechanism

The compositions of the anodic films formed in $NaAlO_2$ and Na_2WO_4 solutions can be accounted for by a film growth mechanism which includes the following steps: (*a*) accumulation and precipitation of the anion constituent on the anode surface; (*b*) dehydration or crystallization or both occurring in the anion deposition layer. This is not, of course, the only process going on at the anode. There may be simultaneous formation of a film of oxide of the anode metals as in the case of Al and Ta anodes, or dissolution of the anode as in the case of Mn in $NaAlO_2$ solution (1). When a highly insulating barrier forms due to oxidation of the anode, *e.g.*, on Al anodes, the anion deposition layer still forms, but more slowly. Conversely, the formation of the anion deposition layer may be entirely prevented if the anode is readily soluble in the electrolyte.

It is probably significant that the solutions in which there is observed a strong tendency to form anodic films by deposition of the anion constituent are also solutions in which the anions tend to form polymeric species.

Anion Deposition

The formation of anodic barrier films containing both anode oxidation products and material deposited from the electrolyte has been discussed by several authors. For example, Godsey (7), in an early paper, proposed that anodic barrier films are double layers formed in part by deposition of adsorbed liquid from the electrolyte. Mason (8) showed that anodic oxide coatings formed on Al in H_2SO_4 solution contained sulfate, and Plumb (2) showed that phosphate is similarly deposited from phosphate solution. Vermilyea (9) described duplex anodic films on Ta formed in H_2O-H_2SO_4 electrolytes and showed that the outer portions of these films had optical and solubility properties which were dependent on the electrolyte composition.

In general, investigation of the effect of the electrolyte on the nature of anodic barrier films has been limited to anodes such as Al and Ta which exhibit strong tendencies to form anodic barrier films in most electrolytes. In contrast, it is apparent that with electrolytes such as $NaAlO_2$ and Na_2WO_4 the anion constituent can be deposited to form a film which acts as a barrier to the passage of electric current. Whether the barrier effect arises solely from the anion deposition film or from interaction of this film with the products of anode oxidation is a question which needs further investigation. However, it has been observed that Au and Pt anodes, which have virtually no tendency to form anodic barrier films in other electrolytes, become covered with films which can sustain voltages in excess of 150v without spark breakdown, when anodized in $NaAlO_2$ solution.

It is appropriate therefore to distinguish anion deposition from other anodic phenomena such as polarization or growth of a film of anode metal oxide, in order to focus attention on this process as an aspect to be considered in the study of anodic film growth and as an electrochemical process of possible practical value. At the present time, there is not sufficient understanding of anion deposition to enable us to speculate on the types of anions that can be deposited, or on the parameters which control the physical properties and adhesion of the deposits.

Acknowledgment

The authors wish to thank Mr. John Danovich of The Naval Air Materials Center, Philadelphia, and Mrs. Mary Schuler of Frankford Arsenal for the preparation and measurement of electron diffraction patterns. They also wish to thank Drs. R. E. Salomon, L. Teitell, and H. Gisser for helpful discussions and review of this manuscript.

Manuscript received Nov. 2, 1962; revised manuscript received Feb. 28, 1963.

Any discussion of this paper will appear in a Discussion Section to be published in the June 1964 JOURNAL.

REFERENCES

1. L. Gruss and W. McNeill, *Electrochem. Technol.*, To be published.
2. R. C. Plumb, *This Journal*, **105**, 498 (1958).
3. H. C. Stumpf, A. S. Russell, J. W. Newsome, and C. M. Tucker, *Ind. Eng. Chem.*, **42**, 1398 (1950).
4. D. A. Vermilyea, *This Journal*, **102**, 207 (1955).
5. D. A. Vermilyea, *ibid.*, **104**, 542 (1957).
6. J. D. Edwards and F. Keller, *Trans. AIME*, **156**, 288 (1944).
7. F. N. Godsey, Jr., *Trans. Electrochem. Soc.*, **61**, 515 (1932).
8. R. B. Mason, *This Journal*, **102**, 671 (1955).
9. D. A. Vermilyea, *Acta. Met.*, **2**, 482 (1954).

Influence of Environment on the Corrosion of Zirconium and Its Alloys in High-Temperature Steam

J. N. Wanklyn, C. F. Britton, D. R. Silvester, and N. J. M. Wilkins
Atomic Energy Research Establishment, Harwell, Berkshire, England

ABSTRACT

Measurements of weight gains and film capacities of zirconium and zirconium alloys in steam and oxygen at atmospheric and high pressures are reported. At best, the behavior of resistant alloys and of Van Arkel zirconium in steam inhibited with boric acid is comparable to that of Van Arkel zirconium in oxygen. It is concluded that in steam, but not in oxygen, the pressure drop due to the flow of gas through porous oxide is a significant factor in the effects observed. Alloying elements, and also boric acid inhibition, decrease the film cracking or porosity which, with unalloyed zirconium, leads to very rapid corrosion in high-pressure steam. With some more resistant materials there appears to be a compensation effect whereby films formed in high-pressure steam are less porous than those formed at atmospheric pressure.

Detailed topographical studies of the early stages of film growth and breakdown on Van Arkel zirconium in steam and in oxygen are described. In addition to uniform film growth, at rates varying with grain orientation, rapid localized attack is found in steam. Such attack is accelerated by an increase of pressure and appears to be diminished by additions of copper and by boric acid inhibition. This localized corrosion is considered to be due to the same type of film failure as is responsible for cracking or porosity in thicker, more uniform, films at a later stage of corrosion. The implications of the findings for the development of steam-resistant alloys are considered.

Earlier publications have considered the influence of alloying elements on the corrosion of zirconium alloys (1) and the uptake of corrosion-produced hydrogen by alloys and by unalloyed zirconium (2). This paper describes attempts to elucidate the mechanisms of oxide film growth and breakdown by varying the corrosive environment. Most of the experiments were conducted at the same temperature, 500°C, and comparisons were made of behavior in steam and in dry oxygen, and of the influence of pressure in these two media. For some purposes experiments started in one condition and then transferred to another were found informative. Detailed topographical studies of the early stages of oxidation of unalloyed zirconium under various conditions were made to identify modes of film breakdown in the various media.

Materials

The analyses and methods of preparation of the alloys and Van Arkel zirconium have been reported previously (1-3). Some of the earlier Van Arkel zirconium specimens, tested as rolled, contained defects formed during the rolling which caused enhanced local corrosion, and later material was annealed for 30 min at 750°C, a treatment which, combined with multiple annealing between successive rollings, not only reduced the tendency for the formation of surface defects, but also reduced the overall weight gains in some tests (3). For the topographical studies Van Arkel material of large grain size was prepared, either by further α-annealing or by the method of Langeron and Lehr (5). Using the latter it was found possible, with four or five 1-week cycles, to grow crystals up to 3-4 cm^2 in size in material 1 mm thick.

Apparatus and Procedures

Earlier publications have described the autoclaves and other apparatus used for tests in steam at atmospheric pressure and at high pressure (1, 2) and also the stainless steel tubes used to attain conditions of high temperature and pressure in short (<7 min) times (3). Apparatus similar to that used for atmospheric pressure steam was used for oxygen at 1 atm pressure. Tests in high-pressure oxygen were conducted in static gas using the same autoclaves as used for steam, or in flowing gas in a modified autoclave. The latter was connected to an oxygen cylinder (British Oxygen Company breathing quality containing ~20 vpm water vapor) and to a "Grove" back-pressure regulator which maintained the desired pressure while allowing a flow of about 50 ml/min (at 1000 psi, 500°C) of oxygen. A further modification of this apparatus, in which a second autoclave containing water was connected to the pipe supplying the high-pressure gas, permitted experiments in low-pressure steam + high-pressure gas. In these experiments the gas was either argon or oxygen, and the composition of the corrosion medium was determined by condensing and freezing the water, downstream from the regulator valve, and determining the gas flow at atmospheric pressure, with a Rotameter (Fig. 1). In experiments with oxygen/steam mixtures the apparatus was flushed and pressurized with argon during heating and cooling periods.

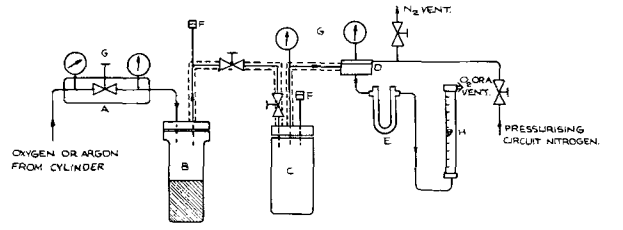

Fig. 1. Pressure apparatus for argon/steam or oxygen/steam: A, high-pressure regulator; B, water reservoir (~100°C); C, autoclave containing specimens; D, back pressure regulator; E, U-tube for estimation of water carry-over (~ —40°C); F, bursting disks; G, pressure gauges; H, rotameter; connections with trace heating.

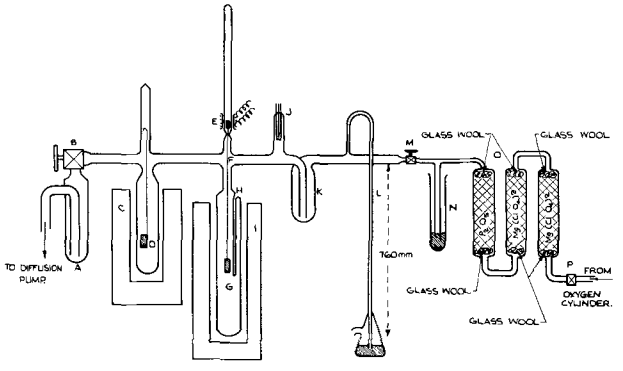

Fig. 2. Apparatus for exposure of zirconium to purified oxygen at atmospheric pressure; A, liquid N_2 trap; B, 1 in. metal valve; C, "getter" furnace (~550°C); D, Zr alloy "getter"; E, lifting solenoid; F, fine Pt wire; G, specimen; H, thermocouple pocket; I, furnace (500°C); J, ion gauge; K, solid $CO_2/CHCl_3$ trap (~ —40°C); L, mercury manometer; M, greaseless tap (P.T.F.E. seat); N, mercury filled vent; O, drying train; P, needle valve.

Another apparatus used for oxygen at atmospheric pressure is shown in Fig. 2. The specimens were lowered into the furnace after the gas had been dried by phosphorus pentoxide and freezing and had been exposed to a fresh Zr-1% Ni or Zr-1% Cu alloy, overnight at 550°C. This exposure to alloys of high hydrogen uptake was intended to "getter" reactive impurities in the gas (12). No rubber seals or greased taps were used in the apparatus. Contamination from the air, which might affect the results, was eliminated by the use of a fully sealed system.

Film capacity measurements to determine the degree of cracking or porosity were performed as described elsewhere (1, 6). Anodic films were prepared on Van Arkel zirconium, and the relation between weight gain and color (or interference minima, measured on a spectrophotometer) were determined (4). Corrosion films were estimated by comparison of colors (from photographic transparencies taken at 50-100X magnification) or, on large crystals, by spectrophotometric measurements, assuming the properties of the anodic and thermal films to be similar.

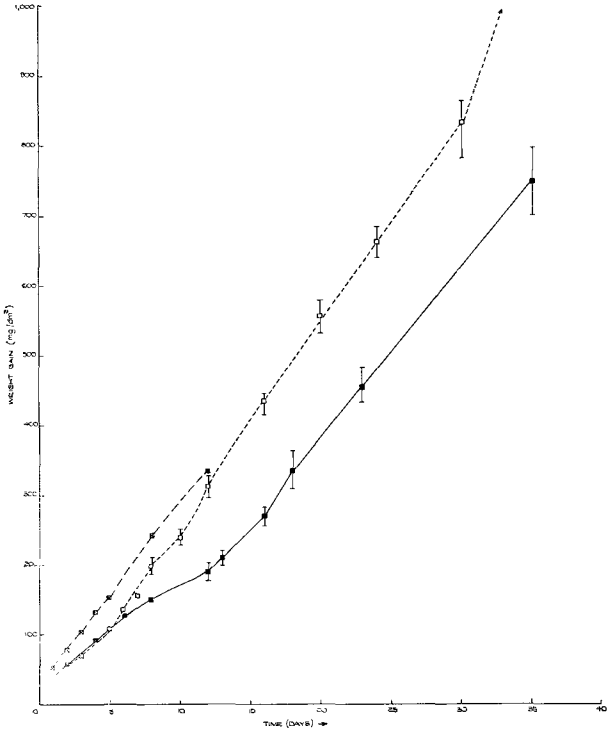

Fig. 3. Weight gain vs. time for Zircaloy 2 (Z105 as rolled) in steam at 1 atm, 1250 and 1500 psi, 500°C; □, 1 atm, flowing; ⊠, 1250 psi, flowing; ■, 1500 psi, static.

Results

Influence of pressure.—There was a general tendency for corrosion in steam at high and low pressures to become more similar as the resistance of the alloy improved. This is illustrated by Table I. For one of the two batches of Zircaloy 2, weight gain results at 1 atm and 1250 psi were similar (Fig. 3 and 4); but, in spite of this, film porosities at the higher

Table I. Effect of steam pressure on corrosion of alloys at 500°C

	1 Atm			1500 psi		
Alloy, wt %	Heat treatment	Wt gain, mg/dm²	Time, days	Heat treatment	Wt gain, mg/dm²	Time, days
Van Arkel Zr (11B)	α	37	1	α	3,000-5,000	1
Kroll stock (ZL 9015)	α	326	28	α	Flaking	3
0.1 Cu	(α + β)	417	49	(α + β)	4,000	7
0.3 Cu	β (Full quench)	98	10	(α + β)	180*	10
0.3 Cu	(α + β)	133	20	(α + β)	200*	20
1.0 Cu	(α + β)	306	68	(α + β)	440 (Interpolated)	68
0.3 Fe	β (Full quench)	720-908	75	(α + β)	600 (Interpolated)	75
0.3 W	α	305	48	α	Completely oxidized	3
0.5 Cu 0.5 W	α	122	34	α	120 (Interpolated)	34
0.5 Cu 0.5 W	α	151	54	α	145 (Interpolated)	54

* Nonuniform corrosion.

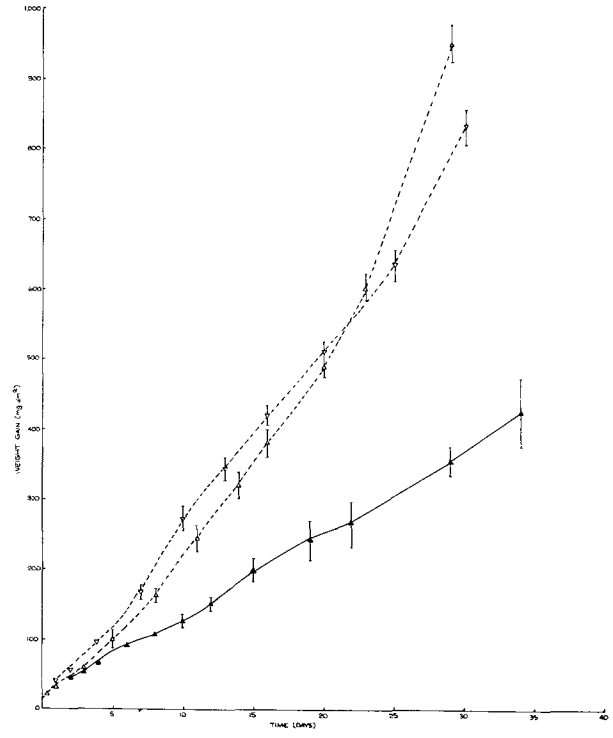

Fig. 4. Weight gain vs. time of Zircaloy 2 (Z8006) in steam at 1 atm and 1500 psi, 500°C: ▽, 1 atm, flowing (specimens quenched from 1000°C); △, 1 atm, flowing (specimens as rolled); ▲, 1500 psi, static (specimens as rolled).

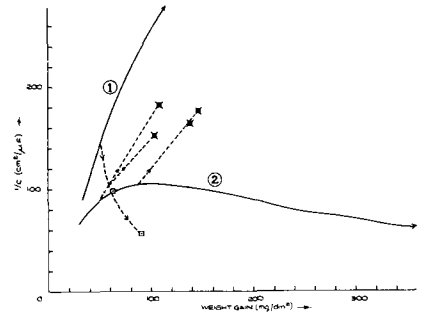

Fig. 6. 1/C vs. weight gain for Zircaloy 2 (Z105 as rolled), transferred high ⇌ low pressure steam at 500°C; curve 1, behavior at high pressure; curve 2, behavior at low pressure; ⊠, transferred from 1 atm to 1250 psi steam; ⊡, transferred from 1250 psi to 1 atm steam; dotted lines drawn from estimated 1/C at observed weight gain at time of transfer.

pressure were significantly lower, as shown by the capacity values of Fig. 5. The latter shows the reciprocal capacity, because this quantity is proportional to the "capacity thickness" of uncracked oxide (1, 6). It was further found that, when specimens of Zircaloy 2 were corroded initially in high-pressure steam and then transferred to low pressure, their capacity values changed toward values characteristic of the new conditions, and a reverse effect was found on transferring from low to high pressure. Since the capacity measurement is destructive, it was necessary to estimate the values before transfer, using the observed weight gain and the already established relations between reciprocal capacity and weight gain. However, as Fig. 6 shows, the pressure-transfers produced changes large compared with the uncertainties of this estimate. In agreement with the suggestion that less porous films form in high-pressure steam, the weight-gain rates also changed on making a transfer, upward with an increase of pressure and downward for a downward pressure change, as shown in Fig. 7.

Van Arkel zirconium, which is much less resistant to steam, showed a greater enhancement of corrosion with increase of pressure, Fig. 8, and with this material capacity measurements indicated that high-pressure films were more porous than those formed in low-pressure steam (Fig. 9).

For comparison with the large effect of steam pressure on the corrosion of Van Arkel zirconium,

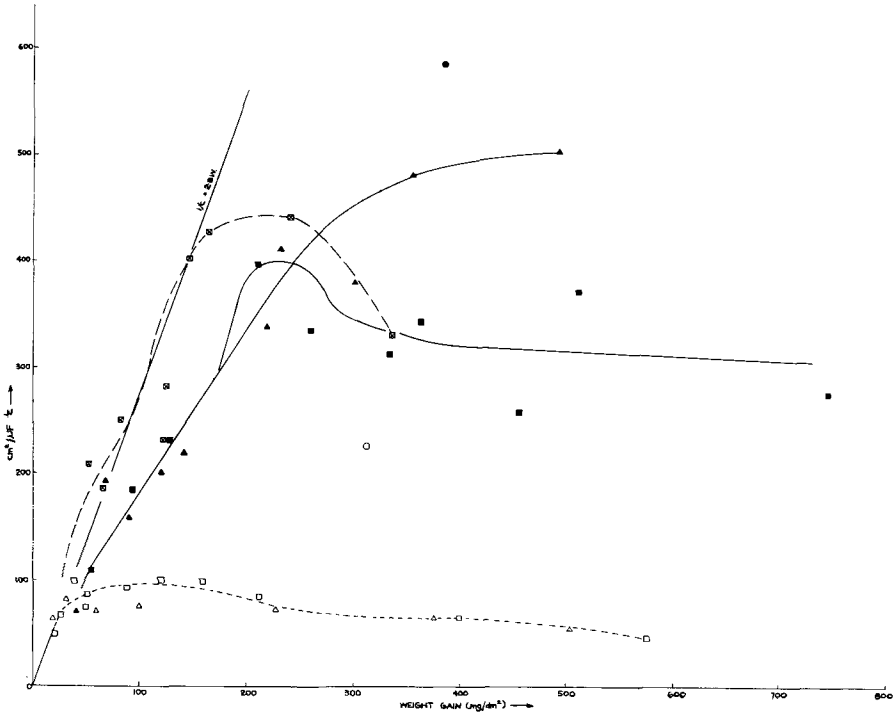

Fig. 5. 1/C vs. weight gain for Zircaloy 2 (as rolled) and Zr/1% Cu in 1 atm and high-pressure steam at 500°C: □, Z105 1 atm, flowing; ⊠, Z105, 1250 psi, flowing; ■, Z105, 1500 psi, static; △, Z8006 1 atm, flowing; ▲, Z8006, 1500 psi, static; ○, Zr/1% Cu 1 atm, flowing; ●, Zr/1% Cu, 1500 psi, static.

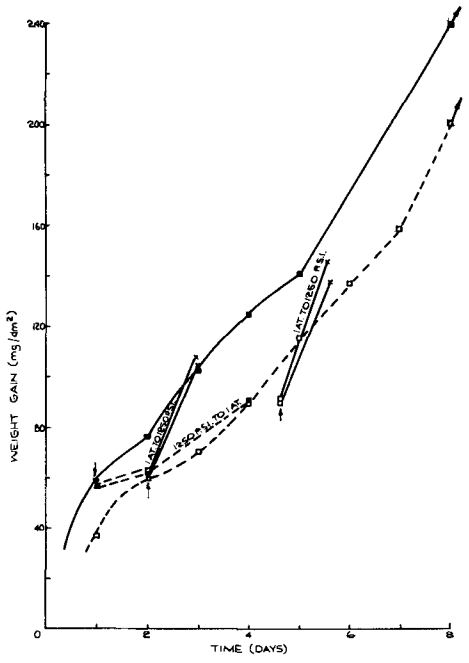

Fig. 7. Weight gain vs. time for Zircaloy 2 (Z105 as rolled) "cross-over" experiment, (transferred between 1250 psi and 1 atm steam at 500°C); ⊠, 1250 psi; □, 1 atm; ↑ □-X, transferred from 1 atm to 1250 psi; ↓ ⊠-⊡, transferred from 1250 psi to 1 atm.

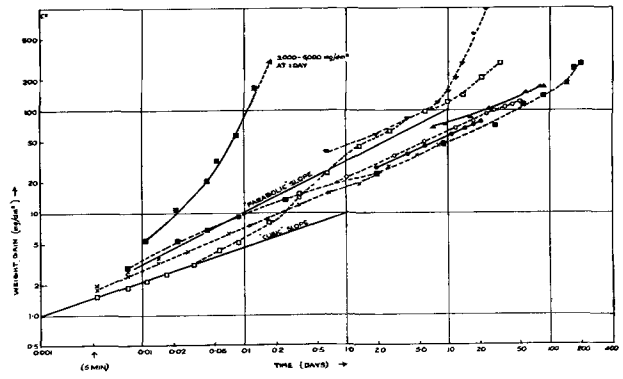

Fig. 8. Weight gain vs. time (log/log plot) for annealed Van Arkel zirconium in oxygen and steam at 1 atm and 1000 psi for as-rolled Van Arkel zirconium in steam at 1 atm, and for 0.5% Cu, 0.5% W alloy in steam at 1500 psi, 500°C: ■, steam 1000 psi, static; □, steam 1 atm, flowing; ○, O_2 1 atm, dried, flowing; X, O_2 1 atm, dried, static; •, O_2 1000 psi direct from cylinder; ⊠, steam 1000 psi + H_3BO_3 (static); ▽, steam 1 atm, flowing, (as-rolled zirconium); ▲, steam 1500 psi static (annealed Zr, 0.5% Cu; 0.5% W).

tests in oxygen were performed and showed very little difference between oxidation rates in 1 atm and 1000 psi oxygen (Fig. 8, 10). The variations of moisture content in the different experiments had only small effects. In agreement, the 1/C values for these experiments were close to the values for uncracked films, Fig. 9. Furthermore, as might be anticipated from the capacity data, transfer from low- to high-pressure oxygen and vice-versa had little effect on kinetics or capacity values (Fig. 9, 11).

Experiments in gas mixtures.—In an attempt to elucidate the "compensation" effect of steam pressure on the porosity of films on Zircaloy 2, experiments were performed in which steam at low pressure was mixed with argon or oxygen at a high pressure. Weight gain results for these experiments are given in Fig. 12. As shown in Fig. 13, the former mixture gave films with reciprocal capacities typical of low-pressure steam. Transfer experiments, from the gas mixture to high-pressure steam gave concordant results for both capacity (Fig. 13) and weight gain behavior (Fig. 14). In both respects the argon-steam films behaved as low-pressure films. A rather similar result was obtained in an oxygen/steam mixture (Fig. 13), although one point, at 143 mg/dm², suggested a possible approach to "high-pressure steam" behavior.

Topographical studies.—To identify the modes of film breakdown in different media, and in particular to compare behavior in steam and in oxygen, topographical studies of the early stages of the corro-

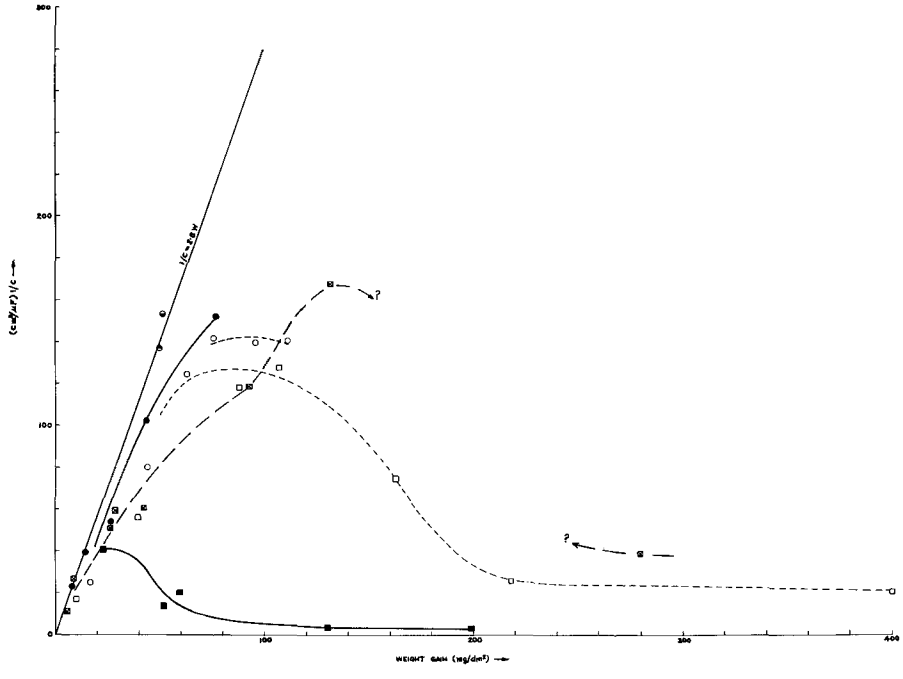

Fig. 9. 1/C vs. weight gain for annealed Van Arkel zirconium in steam and oxygen at 500°C: ○, 1 atm O_2 (dried P_2O_5), flowing; •, 1000 psi O_2, flowing; ○, 1 atm O_2 transferred to 1000 psi O_2; ○, 1000 psi O_2 transferred to 1 atm O_2; □, 1 atm steam, flowing; ■, 1000 psi steam, static; ⊠, 1000 psi steam + H_3BO_3, static.

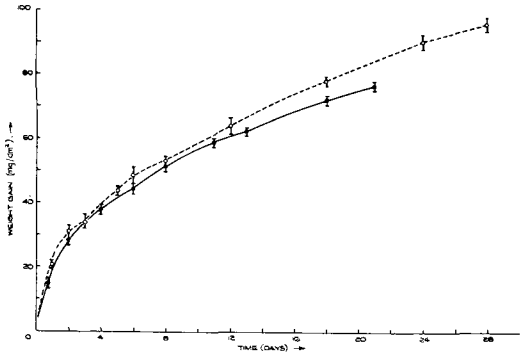

Fig. 10. Weight gain vs. time for annealed Van Arkel zirconium in oxygen at 1 atm and 1000 psi 500°C: ○, 1 atm (dried P_2O_5), flowing; •, 1000 psi, static or flowing direct from cylinder.

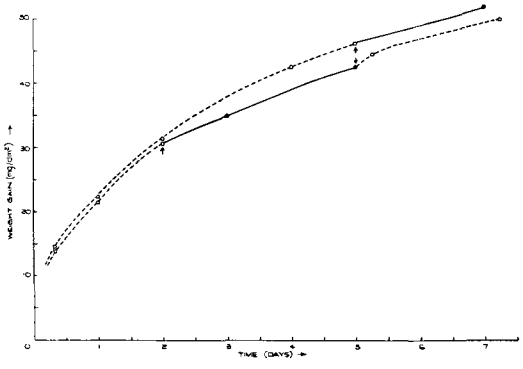

Fig. 11. Weight gain vs. time for annealed Van Arkel zirconium transferred between 1 atm and 1000 psi oxygen at 500°C; ○, 1 atm O_2 (dried P_2O_5), flowing; •, 1000 psi O_2, flowing; ↑ transferred to high pressure; ↓ transferred to low pressure.

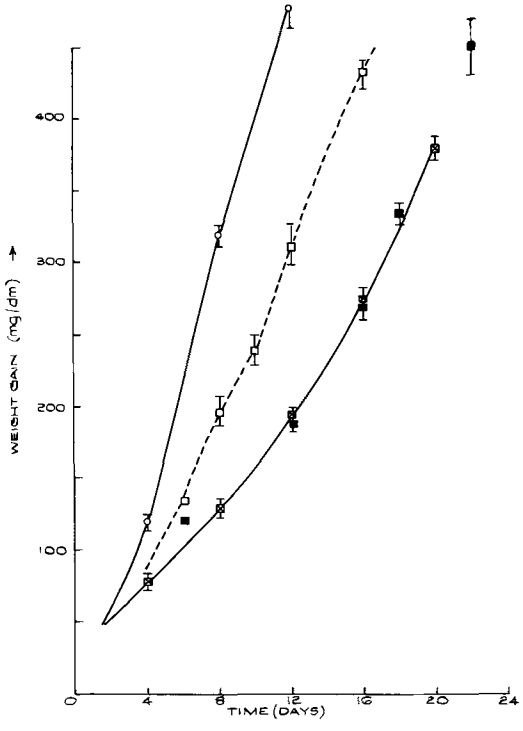

Fig. 12. Weight gain vs. time for as rolled Zircaloy 2 (Z105) in argon/steam and oxygen/steam at 500°C: ○, 6 atm steam + 1000 psi oxygen; ⊠, 6 atm steam + 1000 psi argon; □, 1 atm steam; ■, 1500 psi steam, static.

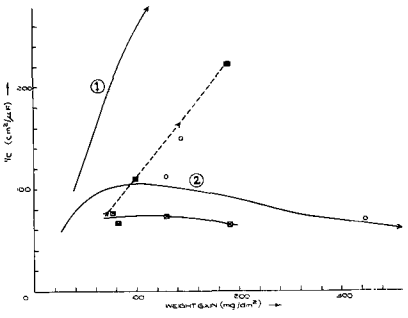

Fig. 13. 1/C vs. weight gain for as-rolled Zircaloy (Z105) in argon/steam and oxygen steam, and after transfer from argon/steam to 1000 psi steam at 500°C; curve 1, behavior in high-pressure steam; curve 2, behavior in low-pressure steam; ○, 6 atm steam + 1000 psi O_2; ⊠, 6 atm steam + 1000 psi argon; ■, transferred from 6 atm steam + 1000 psi argon to 1000 psi steam; dotted line drawn from estimated 1/C at observed weight gain at time of transfer.

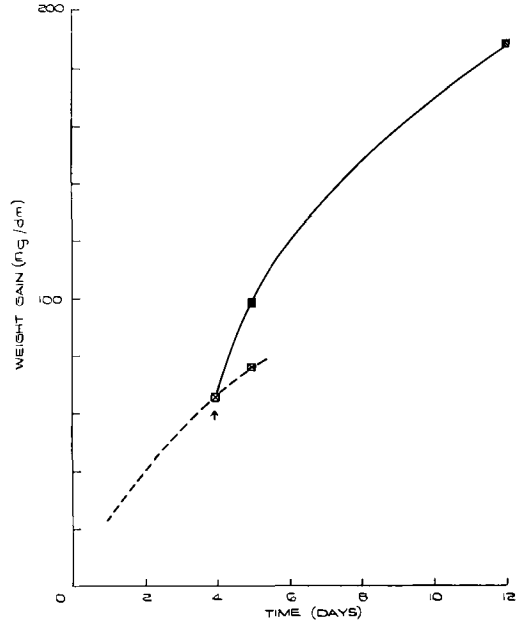

Fig. 14. Weight gain vs. time for as-rolled Zircaloy 2 (Z105) in argon/steam transferred to 1000 psi steam at 500°C; ⊠, 6 atm steam + 1000 psi argon; ■, 1000 psi steam; ↑ transferred from argon/steam to 1000 psi steam.

sion of Van Arkel zirconium were made. Successive examinations after exposure to steam at atmospheric pressure showed three distinct phenomena, illustrated in Fig. 15 and 16:

1. Uniform film growth, at different rates on different grains, as already reported by Pemsler (10). The dependence of rate on orientation was not determined in the present work, but two groups of twelve randomly selected grains were each found to contain two types, "fast" and "slow." The former showed at thickness/time relation between cubic and parabolic, the latter a relation having a rate-law index of about 3. Values for a group of nine grains are plotted in Fig. 17.

2. A uniform gray coloration succeeded the sequence of interference colors, at an estimated weight gain of between 5 and 8 mg/dm^2. This state was

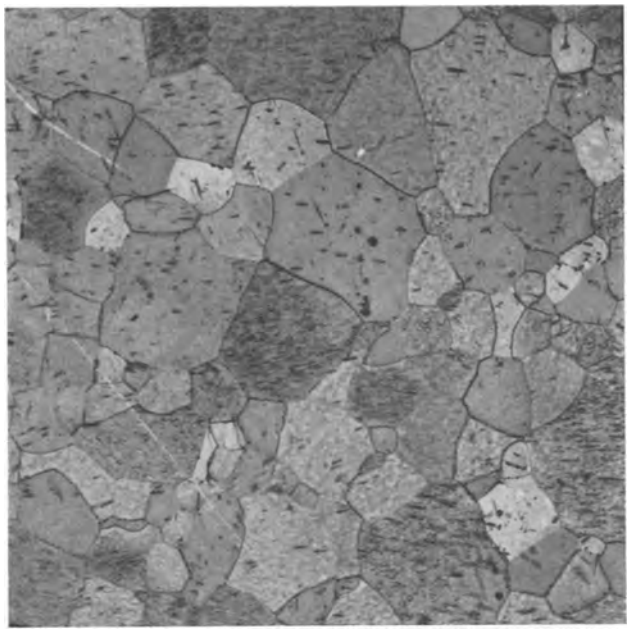

Fig. 15. Annealed Van Arkel zirconium in 1 atm steam at 500°C, 500 min. Magnification 80X.

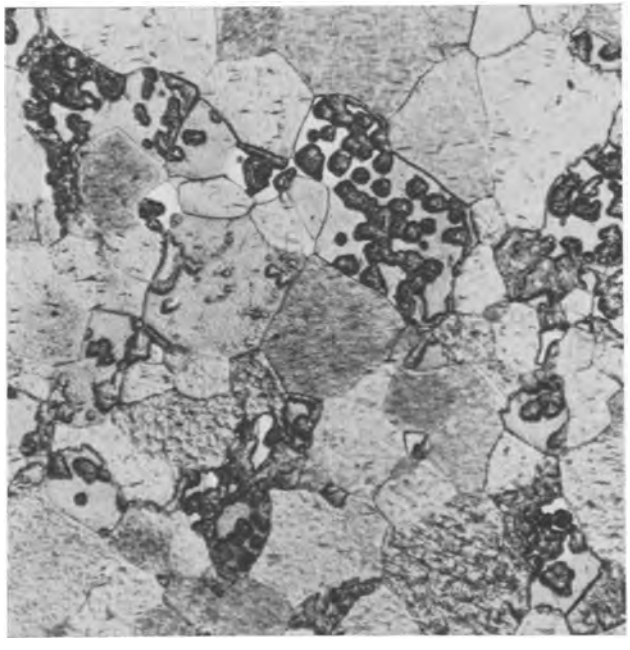

Fig. 16. Annealed Van Arkel zirconium in 1 atm steam at 500°C, 42 hr. Magnification approximately 80X.

reached by "fast" films in 1-4 hr, whereas "slow" films retained their colors to at least 60 hr, when they were entirely covered by "pustules" (3 below).

3. Local formation of thick mounds or pustules of oxide, visible in Fig. 16 and shown at successive stages in Fig. 18, 19, and 20. These appeared white under polarized light and were, accordingly, considered to contain numerous microcracks.

No simple rate law described the growth of colored films, and a comparison with the oxide-dissolution data of Pemsler (10) suggested that, at least with the slow films significant amounts of oxygen (~10% of the weight gain) could be dissolved in the metal during corrosion.

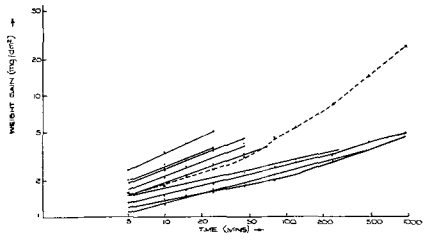

Fig. 17. Weight gain *vs.* time (log/log plot) for individual grains of Van Arkel zirconium in steam at 1 atm 500°C; ———, estimated from interference colors; - - - - - -, over-all weight gain, by weighing.

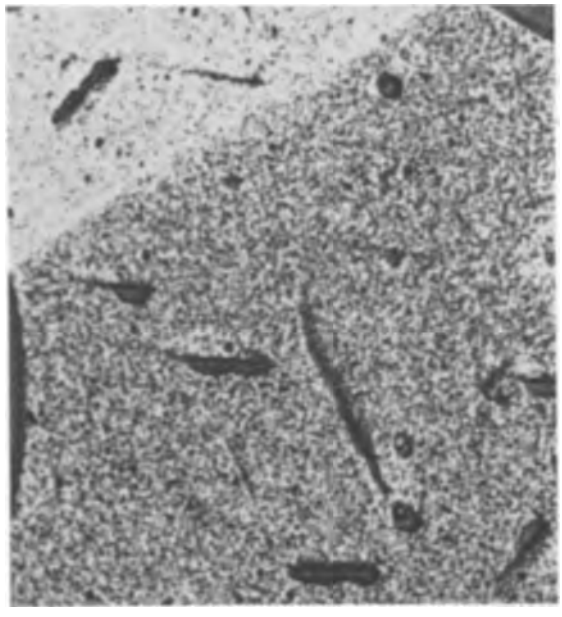

Fig. 18. Enlarged view of part of area shown in Fig. 15, 16 after 500 min in steam at 1 atm 500°C. Magnification approximately 680X.

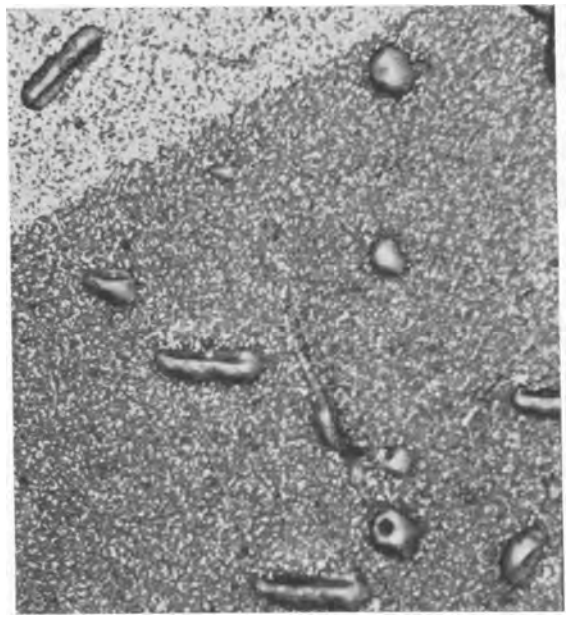

Fig. 19. Same area as Fig. 18 after 800 min in steam at 1 atm, 500°C. Magnification approximately 680X.

It was noteworthy that pustules hardly ever began on grains carrying fast growing films, even though these contained suitable nuclei (see Fig. 16).

Fig. 20. Same area as Fig. 18 after 24 hr in steam at 1 atm, 500°C. Magnification approximately 680X.

In specimens which contained a significant amount of hydride and had been rather heavily etched before corrosion, pustules began predominantly along the grooves formed by etching-out hydride platelets, but, when these features were less numerous, pustules occurred at grain boundaries. Pustules also started from other features, such as twins and slip lines, and from unidentified inclusions in the metal surface. These observations gave the general impression that the conditions for their production were primarily geometrical, *i.e.*, that surface features providing sharp curvatures provoked film cracking and breakdown.

Fig. 21. Surface of Van Arkel zirconium after 17 hr at 1 atm and 1 hr at 500 psi in steam at 500°C. Magnification approximately 500X.

Fig. 22. Surface of Van Arkel zirconium after 14 hr at 1 atm and 4 hr at 500 psi in steam at 500°C. Magnification approximately 500X.

Experiments at high pressure were also conducted in a recirculating steam apparatus (2) in which specimens were exposed initially at 1 atm, the pressure being raised to a high value for appropriate periods. This procedure was adopted because the apparatus could change the pressure quickly, but could only make slow changes of temperature. The results indicated no significant effect on the growth of color films, but showed a considerable enhancement of pustule growth at high pressures, as illustrated in Fig. 21 and 22.

A few observations of a 1% Cu alloy in atmospheric pressure steam suggested that pustule growth was much less serious than on unalloyed zirconium.

Topographical studies were also made of Van Arkel zirconium exposed to dry oxygen. Film growth

Fig. 23. Surface of Van Arkel zirconium after 24 hr in oxygen at 1 atm, 500°C showing general cracking (Formvar/carbon replica, shadowed Pd/Au). Magnification approximately 4000X.

Fig. 24. Surface of Van Arkel zirconium, after 10 min in dry oxygen at 1 atm, 500°C showing "fronts" of thicker oxide. Magnification approximately 100X.

Fig. 25. Surface of Van Arkel zirconium after 10 hr in steam at 1 atm, 500°C, showing pustule (Formvar/carbon replica, shadowed Pd/Au). Magnification approximately 4000X.

was different from that in atmospheric pressure steam in two significant respects:

1. Rapid localized breakdown did not occur, although the longer exposures did produce film cracking of a more general type, Fig. 23.

2. Instead of the uniform colors on each grain, as in 1 atm steam, variations within the grains were found. In short exposures these took the form of an enhanced rate of color growth which started at points within grains or at their boundaries and swept across the grain, so that the thickness changed steeply at a "front" of closely spaced colors (Fig. 24). These fronts also crossed boundaries and affected neighboring grains. Although such growth enhancement sometimes had an obvious starting point, such as hydride or other precipitate, or a grain boundary, there was nothing to show how the influence spread to adjoining oxide.

A further observation, whose implications cannot yet be assessed, was that the colors formed in oxygen were much less bright than those formed in 1 atm steam, and had a pasty, subdued tint. It seems possible that difference of light absorption could be responsible.

Discussion

Influence of Pressure: Zircaloy 2

Table I indicates a general tendency for the sensitivity of corrosion to steam pressure to increase as resistant character of the alloy diminishes. As discussed earlier (1), at the weight gains involved here, corrosion is probably controlled by the extent to which the oxide films crack, rather than by processes within the oxide lattice. In agreement with this the effect of pressure, although only approximately indicated by Table I, is clearly more considerable than the fractional-power relationship appropriate to ionic processes.

Under these circumstances it seems reasonable to attribute enhanced corrosion at higher pressures to an increased flow of steam through fine cracks in the oxide. Approximate calculations, based on Poiseuille flow, indicate that at a rate corresponding to corrosion at 5000 mdd, a pressure drop of several hundred psi would be supported by cracks 10Å wide and spaced 0.2μ apart in a film 10μ thick. Evidently, a streamline flow equation cannot be applied to such fine pores, which are of a size appropriate to activated diffusion (7), and, qualitatively, the latter involves a higher pressure drop at a given corrosion rate, *i.e.*, the rate is even more likely to be pressure-sensitive.

In this connection the capacity values for Zircaloy 2 (Fig. 5) were particularly interesting because they suggested that, in higher pressure steam, less porous films were formed. The higher values of 1/C indicate a greater "mean protective thickness" of film (6). Moreover the kinetic data of Fig. 3 show that, either fortuitously or for more fundamental, unexplained reasons, the variation of porosity was just sufficient in one case (Z105) to offset the influence of pressure, and so to produce very similar corrosion rates in the two media. The reality of the effect is confirmed by Fig. 6 and 7. When specimens were transferred from one pressure to the other, their capacities changed toward values appropriate to the new conditions, and their weight gain behavior immediately after transfer was consistent with the films formed initially in low-pressure steam being more porous than those started at high pressure. A single pair of capacity values for a 1% Cu alloy (Fig. 5) suggested that the same might be true for this more resistant material.

Influence of Pressure: Van Arkel Zirconium

The response of Van Arkel zirconium, a material of low resistance to steam, to an increase of pressure was quite different from that of more resistant alloys. As Fig. 8 shows, corrosion at high pressure was much more severe than at 1 atm, and the capacity data of Fig. 9 show the high-pressure films to be more cracked than those formed at low pressure. There is, in fact, no sign of the "compensation" effect found with more resistant alloys and due presumably to an effect of the beneficial elements which the latter contains. The higher rate of steam flow which is possible at high pressure results in a greater rate of corrosion, which in turn apparently further enhances film degradation.

In contrast, the reaction of Van Arkel zirconium with oxygen was similar at high and low pressures (Fig. 10), and in both media reciprocal capacities were high (Fig. 9), indicating low porosity. Moreover, transfer from low to high pressure gave no sharp changes of oxidation kinetics (Fig. 11), and the reciprocal capacities of specimens which had undergone such transfers were similar to (or possibly even slightly higher than) those of the other oxygen exposed specimens.

These facts all indicate that the formation of pores and the flow of gas through them plays a negligible part in the reaction of unalloyed zirconium with oxygen, at least at the weight gains examined here. This is a sharp contrast with behavior in steam and suggests that some feature of the latter, probably related to the presence of hydrogen, plays an important part in film degradation.

Corrosion of Zircaloy 2 in Gas/Steam Mixtures

The observations discussed above may be rationalized in the suggestion that corrosion in steam is controlled by a thin "protective layer" of oxide at the base of the film, adjacent to the metal. However, this layer, in which material transport is ionic in character, is not itself rate-determining because cracking or some other form of degradation is steadily advancing into it. The corrosion rate, and the (constant) thickness of the protective layer, thus depend on a balance between film growth (represented by conversion of metal to oxide) and film degradation (cracking, probably related to stresses accumulating in the oxide film).

Experiments with Zircaloy 2 suggested that, in high-pressure steam, this balance was displaced in such a way as to compensate the influence of pressure on steam flow through the porous part of the film, and attempts were made to influence the balance by other means, with a view to establishing its mechanism. The first attempt was based on the consideration that a high pressure may, purely mechanically, aid the elimination of closed porosity from a solid (8). If such porosity were a precursor to the open cracking postulated in the corrosion mechanism (open porosity would of course be unaffected by external pressure), a high pressure of inert gas, added to steam at low pressure, should reproduce the film porosity characteristic of high-pressure steam. Figure 13 shows that such a result was not obtained in 1000 psi argon + 6 atm steam, the film capacities being typical of low-pressure steam. Further confirmation of the films' "low pressure" character was provided by transfer to high-pressure steam, which produced a sharp increase in the rate of weight gain and an increase in 1/C (Fig. 13, 14).

It seemed possible that the growth/degradation balance might respond to a more chemical influence, a possible example of which was the oxidizing character of the medium. This could play a part if the change from substoichiometric to stoichiometric ZrO_2 were involved in the behavior of the protective part of the film. An attempt was made to simulate such an influence by exposing specimens in 1000 psi oxygen and 6 atm steam. Again, the capacity values were near to those appropriate to low-pressure films, but the rather high 1/C value at 143 mg/dm^2 (Fig. 13) suggested that there might be some approach to high-pressure behavior and more work along these lines seems worthwhile.

Inhibition of Corrosion by Boric Acid

As a further example of the influence of environment, brief mention may be made of the very considerable inhibition of the corrosion of Van Arkel zirconium in high-temperature steam when about 3 wt % of boric acid is dissolved in the latter (3). The weight gain values of Van Arkel zirconium in inhibited steam, reproduced in Fig. 8, are lower than almost all those obtained with even the best alloys. The effectiveness of the inhibition may be due to the protective element, being in solution in the steam, being readily supplied to all parts of the oxide film which require it.

Practical Implications

From the practical viewpoint it is worth noting that the best values for resistant alloys (and also for boron-inhibited zirconium) approach, but do not surpass, those for Van Arkel material in dry oxygen, Fig. 8. This suggests that at best alloying merely offsets the film degradation peculiar to steam, and that if such protection would be consolidated by further work one might hope to obtain, in steam, behavior similar to that in oxygen, *viz.*, Fig. 8, 10. The latter shows a weight gain rate of about 1 mdd at 20 days, so that to achieve the 0.25-0.5 mdd or less at 500°C which is desirable in a high-temperature alloy, it will be necessary to defer film degradation and the consequent transition to much longer times. So far only the boric acid/Van Arkel results and a few values from one batch of the 0.5 Cu 0.5 W alloy (1) show any sign of possibly achieving this. The only further method of improvement would be a modification of the lattice diffusion process itself, so that oxidation rates in oxygen were also reduced. Existing data (9) on binary zirconium alloys in oxygen is not particularly hopeful in this respect. A more subtle use of ternary additions, combined with a prevention of film degradation, might be beneficial.

Topographic Studies of Van Arkel Zirconium: Steam

The balance, which has been described above, between film growth and degradation is essentially a property of fairly thick films. In steam the weight gains have to attain about 50 mg/dm^2 before the corrosion of most alloys becomes more or less linear (1). One may imagine that at this weight gain a film of reasonably uniform thickness is set up in a "steady state" in which, if conditions are not altered, film growth and degradation rates are equal and determine the corrosion rate. (At this stage, it should be noted, the thickness of the protective layer does not control, but is established by, these other processes.) Although these phenomena relate essentially to thick films, it was thought that examination of the initial stages of film growth might throw

light on the breakdown processes which, since they proceed deep within the thick films, cannot be observed directly. It was for this reason that the topographical studies described above were carried out.

From the viewpoint of long term corrosion, the oxide pustules were the most interesting finding. Visual examination suggested that they would rapidly become the major part of the weight gain of the whole specimen, and this is confirmed by Fig. 17 which shows that shortly after their appearance the over-all rate of weight gain increased, became linear, and diverged from the plot corresponding to colored films. These observations show, incidentally, how inappropriate it may be to apply rate law considerations, which refer implicitly to uniform film growth, to surfaces on which several processes are occurring simultaneously.

It seems likely that the rapid growth of the pustules is due to film breakdown or degradation of the type considered earlier in connection with film capacity measurements. In agreement with this, an increase of pressure, applied after pustules had developed in atmospheric pressure steam, greatly accelerated their growth, Fig. 21 and 22, without apparently greatly changing the growth of colored films.

In agreement with the important role assigned to the breakdown which leads to pustules, it is this form of failure which is eliminated when steam corrosion is inhibited with boric acid (3). Moreover, examination of a 1% Cu alloy after exposure to 1 atm steam for 100 hr suggested that similar reduction of pustule breakdown was the major effect of the copper addition.

The marked absence of pustules on fast growing grains may be due to the fact that films on such grains quickly attain large thicknesses, and so smooth out geometrical irregularities. As an example of this, a single crystal, after formation of a fast-growing oxide in 1 atm steam, survived 24 hr in steam at 1000 psi 500°C, although heavily attacked at the edges. The film thickness, estimated optically, was equivalent to 15 mg/dm^2 weight gain. Polycrystalline material shows 3000-5000 mg/dm^2 in similar high-pressure exposure.

It is not yet clear how far into the "gray" region fast-growing films can be measured. It is, however, possible to use optical methods beyond the point at which visible colors disappear. The single crystal referred to above, carrying a gray film, was examined on the spectrophotometer and found still to show interference minima. These fitted a long extrapolation of the color/weight gain relations, and indicated a weight gain of about 15 mg/dm^2. This observation suggests that the gray color may not be due, as was first thought, to excessive light absorption, but to the fact that, at large thicknesses, interference produces many minima. Accordingly the light returning from the surface consists of a number of colors, fairly evenly spread across the spectrum: this the eye sees as gray. The growth-rate of these gray films requires further study, because a few thickness measurements, made on microsections, suggested that some of them may grow more rapidly than the colored films which precede them.

Such enhanced growth could be due to a type of breakdown, more uniform and on a smaller scale than that responsible for pustules. Electron microscope replicas, Fig. 25, showed no evidence of breakdown smaller than the obvious cracks around pustules and elsewhere, down to the limit of resolution. However, the uniformity of attack on alloys, on which pustules probably do not occur, but which do eventually show more or less linear rates of weight gain, suggests that more subtle forms of degradation may exist. Such degradation might also be responsible for the reported increase by irradiation of post-transition corrosion (11).

Topographical Studies of Van Arkel Zirconium: Oxygen

In oxygen, the absence of pustule formation resulted in long-time weight gains being lower than in steam, but the growth of colored films, apparently as a result of the spreading phenomenon described above, was rather faster than in steam. Up to about 6 hr the over-all weight gain in oxygen was greater than in steam, until pustule growth in the latter became appreciable. This supports the view that it is the occurrence or nonoccurrence of rapid film degradation rather than rates of transport within the oxide lattice which is important for corrosion resistance.

However, cracking of a more general type was seen after long exposure to oxygen, Fig. 23 [such cracking was also seen on specimens whose steam corrosion was inhibited by boric acid (3)], and the low corrosion rates of such specimens suggest that cracking of this type is of a secondary nature and therefore to be distinguished from the more damaging degradation which occurs at sites of pustules. Thus the visual observation of cracks in the outer surface of films does not necessarily give information about their protective character.

It is interesting to note that the reaction with oxygen, according to the log/log plot of Fig. 8, retains a rate law of constant index, between cubic and parabolic, over nearly 4 orders of magnitude in time, in spite of the variation of film thickness from point to point on the surface. This further illustrates the danger of making deductions from the linearity of such plots without regard to topographical aspects.

Influence of Mode of Application of Steam Pressure

As described above, the specimens in the high-pressure topographical experiments (*e.g.*, Fig. 22) were first exposed at 1 atm, the pressure being raised to a high value for appropriate periods. More recent experiments with specimens brought quickly [$<$ 7 min, using small stainless steel capsules (3)] to a high temperature and pressure have provided an interesting contrast. Their films showed the variations within grains previously only seen in oxygen; moreover, their colors were more advanced at a given time than films formed in 1 atm steam or those started in 1 atm steam and subsequently exposed at high pressure. With these specimens, of course, in-

itial film growth occurred with both temperature and pressure varying, and it is not clear to what extent this was responsible for the observations. These suggest, however, that it may in future be necessary to pay attention to the mode of starting a high-pressure test, a factor to which zirconium has hitherto been thought insensitive. Effects of this kind have been reported with aluminum (13) and mild steel (14).

Conclusions

1. The corrosion of zirconium alloys in steam at 500°C shows a dependence on pressure, between 1 atm at 1500 psi, which decreases as the resistance of the alloy increases.

2. The pressure dependence is probably related to the pressure drop accompanying the flow of steam through cracks or pores in the oxide film, rather than to ionic processes within the latter. These pores are likely to be extremely small, of the order of a few tens of angstroms in width.

3. The corrosion of alloys is interpreted in terms of a balance between film thickening by ionic processes within the oxide lattice and film "degradation," which produces cracking or porosity and in which stress and the presence of hydrogen play a part. The ultimate controlling process is film degradation, the corrosion rate and the thickness of the inner protective layer of oxide being determined by the film growth/degradation balance.

4. With Zircaloy 2, capacity measurements indicate that, above weight gains of about 50 mg/dm^2, films formed in high-pressure steam are less porous than those formed at 1 atm pressure. The behavior of weight gains and capacities of specimens transferred during corrosion from one pressure to the other supports this view. As a result of this compensating effect, corrosion rates at high and low pressures are not greatly different.

5. A few values for the more resistant 1% Cu alloy show a similar tendency.

6. Zircaloy 2 films formed in low-pressure steam + 1000 psi argon have the characteristics of "low pressure" films, as do films formed in low-pressure steam + 1000 psi oxygen. The latter, however, show indications of approaching high pressure behavior in some cases.

7. No such effects are found with Van Arkel zirconium in steam, corrosion at high pressure being very much more rapid than that at atmospheric pressure. Capacity values indicate high-pressure films to be much less protective than those formed at low pressure.

8. In oxygen, however, the oxidation of Van Arkel zirconium shows no pressure dependence, nor is the effect of transferring from one pressure to another significant. Up to about 100 mg/dm^2, capacity values approximate to those of uncracked films. It is concluded that, under the conditions studied, pressure drops due to gas flow in pores are not involved in the reaction of Van Arkel zirconium with oxygen.

9. The best results with good alloys (and those obtained with Van Arkel zirconium in inhibited steam) are comparable to the behavior of Van Arkel zirconium in oxygen. It is concluded that alloying and inhibition are primarily effective against the film degradation which is peculiar to steam, and that if further improvements are to be made it will be necessary, in addition, to find alloying elements which influence ionic transport within the oxide lattice.

10. Microscopical studies of the initial behavior of Van Arkel zirconium in steam show that, in addition to the growth of uniform films which pass through a sequence of colors and eventually become gray, local film breakdown leads to heavy pustules of oxide, beneath which penetration is very rapid. Growth of the pustules, but not of color films, appears to be accelerated by an increase of pressure.

11. Although local breakdown can be seen on Van Arkel zirconium exposed to oxygen, it is not nearly so rapid as in steam.

12. It is suggested that the film degradation which occurs during the linear corrosion of an alloy, at a rate depending on the latter's resistant character, is of the same type as that responsible for pustule growth.

13. There are indications that some uniform (*i.e.*, without pustules) films on Van Arkel zirconium in steam may, when they reach the gray stage, also undergo a form of breakdown leading to increased growth rates. The behavior of such films may also depend on starting conditions of the test.

Acknowledgments

The authors wish to thank Messrs. J. Isaacs, P. Lawrence, and J. V. Arthurs for assistance with some of the experiments, and Drs. J. S. Llewelyn Leach and G. F. Hewitt for stimulating discussions.

Manuscript received Nov. 7, 1962; revised manuscript received March 4, 1963.

Any discussion of this paper will appear in a Discussion Section to be published in the June 1964 JOURNAL.

REFERENCES

1. J. N. Wanklyn, J. T. Demant, and D. Jones, UKAEA Report AERE—R 3655 (1961).
2. J. N. Wanklyn, D. R. Silvester, J. Dalton, and N. J. M. Wilkins, UKAEA Report AERE—R 3768 (1961).
3. C. F. Britton and J. N. Wanklyn, *J. Nucl. Mater.*, **5** [3], 326 (1962).
4. N. J. M. Wilkins, *This Journal*, **109**, 998 (1962).
5. J. R. Langeron and P. Lehr, *Rev. Met.*, **55** (10), 901 (1958).
6. J. N. Wanklyn and D. R. Silvester, *This Journal*, **105** (11) 647 (1958).
7. P. C. Carman, "Flow of Gases in Porous Media," p. 129, Butterworth, London (1956).
8. Ya. E. Geguzin, *Soviet Phys.—Doklady*, **5** [6], 1338 (1961).
9. H. A. Porte, J. G. Schnizlein, R. C. Vogel, and D. F. Fischer, USAEC Report ANL 6046 (1960); *This Journal*, **107**, 506 (1960).
10. J. P. Pemsler, *This Journal*, **105**, 315 (1958).
11. R. C. Asher and B. Cox, IAEA Conference on Corrosion of Reactor Materials, Salzburg, 1962.
12. J. E. Castle, S. J. Gregg, J. E. Antill, and W. B. Jepson, *J. Nucl. Mater.*, **5**, 254 (1962).
13. J. E. Draley, W. E. Ruther, and S. Greenberg, USAEC Report ANL 6207 (1961).
14. W. E. Ruther, USAEC Report ANL 6516, 169 (1961).

A Study of Embrittlement of High Strength Steels by Hydrogen Isotopes

I. Testing of Steel Rings as Specimens, a Comparison of Hydrogen and Deuterium Embrittlement, and Permeation Studies

Gwendolyn B. Wood

Metallurgy Division, National Bureau of Standards, Washington, D. C.

ABSTRACT

Embrittlement of steel produced from electrolytic charging in H_2O- and D_2O-solutions is discussed. A comparison of the retention of embrittlement with retained gas content in uncoated steel is given. The separation factor for the electrodeposition of hydrogen and deuterium on SAE 4130 steel was found to be 5.9. Permeation of the mixture of these isotopes through steel results in further enrichment with respect to hydrogen. The diffusion coefficients and permeation rates for hydrogen and deuterium in steel are compared.

Studies of hydrogen embrittlement are of practical as well as theoretical interest. The practical interest has arisen in attempting to prevent the embrittlement of steel that results from the various methods of finishing and fabricating steel parts and from the use of steel in corrosive environments, in welded structure, etc. For example, embrittlement results from pickling of and the electroplating on new high strength steels. It may also result from the use of steels in corrosive environments or from the retention of hydrogen by massive parts following melting of steel or from the welding of steel structures. On the academic side, a thorough understanding of the mechanism of hydrogen embrittlement is needed. The role of gases in metals is not well understood, and studies of hydrogen embrittlement add to the knowledge of gases in metal.

The literature dealing with hydrogen embrittlement of steels is extensive. Summaries of this literature have been written by other authors (1-3). Hydrogen embrittlement is believed to involve the redistribution of hydrogen by diffusion from a uniform to nonuniform state (4-7). As far as is known, no experiment has been devised to demonstrate that a driving force exists which will cause the hydrogen to redistribute itself throughout the steel in such a fashion as to influence the fracture process. They (4-7) postulate that hydrogen contributes to the energy involved in the growth of cracks during the time the steel is being stressed. We must conclude that the mechanism is not definitely known. To add to the uncertainty, the mechanism by which hydrogen enters the steel or the state of hydrogen in steel at temperatures at which hydrogen embrittlement occurs have not been firmly established.

Knowledge concerning the effect of gas content on the ductility and strength of steel may be helpful in the understanding of the actual mechanism of the embrittlement process. Studies were undertaken to determine whether a correlation exists between the charging variables, gas content, and the resulting embrittlement.

The hydrogen, electrolytically introduced into steel, can be determined, if the hydrogen content of an uncharged sample is not significant or is constant enough to be subtracted for correction. The amount of hydrogen usually found in blank specimens is variable and may be considerably more than the amount of electrolytic gas found in some specimens of steel. Thus, the determination of the electrolytic hydrogen content of the steel in many instances may not be accurate. The use of deuterium as the charging gas permits a more accurate determination of the electrolytically introduced gas, because it can be differentiated from the hydrogen initially present in the steel or present as surface moisture. The hydrogen from sources other than electrolytic charging will be referred to as "extraneous hydrogen."

Equipment

Choice of steel and specimen.—The detrimental effect of hydrogen embrittlement is particularly severe with high strength steels. SAE 4130 steel was chosen as representative of this group of steels for these studies.

Since the main objective of the present investigation was to determine the gas content of steel instead of primarily detecting hydrogen embrittlement or studying its effects on the mechanical properties of steel, a simple type of test specimen was used. Many types of specimen have been employed by those investigating hydrogen embrittlement. The main requirements in choosing the test specimen were that it be (*a*) inexpensive and easy to prepare, and (*b*) of a small size so that it could be charged

in a small volume of solution and easily introduced into the vacuum-fusion apparatus. The ring type of specimen, which was first used by Noble (8), met these requirements and was used.

The design and selection of the test specimen was based on exploratory tests with rings, 0.9 cm long, that were cut from SAE 4130 seamless tubing of various diameters, 1.25, 1.88, and 2.5 cm, and wall thickness, 0.08, 0.16, and 0.24 cm. In these exploratory tests the specimens were embrittled by cadmium plating and evaluated by crushing tests. The specimen selected for most of the experiments consisted of a ring with 2.5 cm (1 in.) OD, 0.78 mm (1/32 in.) wall, and 0.9 cm (0.35 in.) length. During these early experiments the embrittled rings, when crushed, broke in different manners; slightly embrittled specimens broke at 90° from the platens of the press, and severely embrittled specimens broke at the point of contact of the platens. To increase the reproducibility of the place of failure of the rings and thus improve the reproducibility of the crushing test, the rings were provided with two axial 60° notches, 5 mils deep, and 180° apart, cut with a sharp tool. These grooved specimens were used for most of the studies. Toward the end of the investigation it was found that somewhat better reproducibility was obtained if the grooves were made by grinding (9).

Crushing Equipment.—The equipment used for determining embrittlement by dynamic crushing to failure incorporated a laundry scale as the load indicating device, a screw press for crushing a ring against the platform of the scale, and a dial micrometer to permit the collection of deflection data. The load scale reads from zero to 300 lb, is equipped with a maximum load indicator, and can be read with an accuracy of ¼ lb. Embrittlement was determined by stressing the rings at a constant rate to failure and determining the differences between breaking loads and amounts of deformation at breaking for charged and uncharged specimens. The load to failure was found to be much more reproducible than the deformation, but the changes in deformation were highly sensitive to the amount of electrolytically charged gas in the steel. The reproducibility of these two types of measurements differed by about the same ratio for both unembrittled and embrittled rings: 10-15% for deformation at failure and 2-7% for the reduction in load to failure. The size specimen chosen gave the optimum combination of sensitivity to embrittlement.

In an effort to find a more sensitive test method for detecting embrittlement, a delayed failure test was tried in which the time to failure at 90 percent of the breaking load was measured. For these tests a lever-device was used. The reproducibility of the sustained load test was found to be too erratic to be used extensively in these studies and a dynamic test method, which proved to be a more sensitive test method, was developed by slowing down the rate of crushing of specimens. In most of the investigations reported herein a rate of crushing specimens of 0.1 in./min was employed. For a more sensitive test, speeds of 0.05, 0.02, 0.01 and 0.005 in./min were used. Experiments employing these slower speeds are discussed in Part II of this paper (9).

Electrolytic cells.—Three different types of electrolytic cells were designed for these studies and are shown in Fig. 6 and 7 in the Appendix. They all contain concentric outside anodes and a central anode. Soluble anodes were used in the cadmium, copper, and nickel plating solutions; lead anodes in the chromium plating solutions; and platinum anodes in the electrolytic charging solutions containing sulfuric acid or sodium hydroxide. The cells differ mainly in the method of mounting the cathode and in provisions for heating or cooling the solution.

Method of analyzing steel for gas content.—The gas content of the steel specimens was determined by first extracting the gas by means of the tin-fusion method (10) in a vacuum fusion equipment discussed in the appendix. The gas was then subjected to analysis by a mass spectrograph. The mass spectrograph was used since it would differentiate between hydrogen and deuterium and, if desired, permit determination of other gases, such as carbon monoxide, nitrogen, oxygen, and hydrocarbons. Since this instrument gives only the relative proportions of the constituents of a gaseous mixture, a calibration was required to convert the ratios to actual quantities of gas. This was done by introducing a known amount of argon into the gas collected from the steel before it was removed from the vacuum system for analysis. The argon was introduced into the vacuum-fusion apparatus by means of the microburet shown in Fig. 10 in the Appendix. This method of analysis is unique for determining the gas content of metals, because it requires the measurement of only one pressure, that of the argon introduced into the system.

Experimental Procedure

Preparation of steel rings.—To obtain reproducible results, each step in the preparation of the steel rings from the first polishing procedures to the analysis had to be treated as a critical step. The inside and outside surfaces of the as-received steel tubing were mechanically polished to remove oxidation products, carburization, or decarburization and to minimize any surface scratches or pits. To prevent any oxidation or decarburization of the surface during heat treatment, the steel was heat treated and tempered in fused salt baths. To assure more reproducible results freshly opened C.P. chemicals were used instead of proprietary mixtures for making these baths. For heat treating, a 20/25/55 mixture by weight of NaCl, KCl, and $BaCl_2$ was used; for tempering, a 45/55 mixture by weight of $NaNO_2$ and KNO_3 was used. These baths were kept neutral by the addition of TiO_2. The steel tubing, cut in about 10 cm lengths, was heat treated at 846° ± 35°C for 2 to 8 min, rapidly quenching in oil, and tempered at 270° ± 15°C for 8 to 12 min.

To check the uniformity of lots which were heat treated at different times, samples from ten different heat treatments were chosen for hardness measurements. The hardness of all of the specimens was

between 47 and 48 Rockwell "C," indicating satisfactory uniformity of the heat-treated steel. These hardness values correspond to a strength of 16,100 to 16,450 kg/cm^2 (229,000 to 234,000 lb/in.^{2}).

After heat treatment, the steel was again polished to a bright finish, oiled to prevent surface oxidation, and stored in a desiccator. To prepare the test specimens, two grooves were cut in the tube. They were parallel to the longitudinal axis of the tube and were diametrically opposite. The grooves were a 60° notch, 0.13 mm (5 mils) deep. The 10 cm (4 in.) length of tubing was then cut into small bands or rings, 0.9 cm (0.35 in.) long.

Uncharged specimens with grooves were tested for reproducibility of breaking load and deformation to failure. Results of both of these types of measurements deviated from the average as much as ±7%. The reproducibility for embrittled steel rings charged for 1 hr at 3 amp/dm^2 in 10% NaOH in H_2O was about ± 2% for breaking load and ±9% for deformation.

These data show the difficulty in obtaining closely reproducible results in embrittlement studies, even when all of the specimens come from the same pieces of tubing. Similar embrittlement studies made after several years have elapsed do not duplicate results closely either. These variations in measurements are apparently due to uncontrollable variables having to do with the steel or the embrittling process. Even though the over-all reproducibility was not high, the relative magnitudes of embrittlement produced by various embrittling procedures were reproducible.

Use of inert atmosphere chamber.—In some of the initial experiments with heavy water, the electrolyses were performed in covered cells. The solution, anodes, and the steel rings to be charged were exposed often to the moisture of the air. Some of these solutions were analyzed by a spectroscopic method (11) to determine whether H_2O had been picked up by the D_2O solutions. Results indicated that several per cent H_2O had been absorbed by these solutions used in the atmosphere. It was necessary to confine the handling, pouring, and electrolysis of all D_2O solutions to an inert atmosphere chamber containing a dry atmosphere of helium. This increased the time required to perform experiments, but insured the collection of more accurate data.

Electrolytic solutions were also made in this chamber. The NaOD was made by reacting Na and D_2O. D_2SO_4 was made from SO_3 and D_2O. Plating baths were made from anhydrous salts and D_2O.

Analysis of D_2O-Plating Solutions for H_2O Content.—Small amounts of H_2O picked up by the D_2O solutions would lead to a mixture of the hydrogen isotopes as the electrolytic gas. The embrittlement caused by each could not be separated. Because of the variations in the extraneous hydrogen content, analysis of the charged steel by the tin-fusion method would not indicate whether the steel was free from electrolytic hydrogen. It was therefore decided to determine how much H_2O is picked up by the D_2O charging solutions handled only in the inert atmosphere chamber. Essentially, no pick-up of H_2O by these solutions would provide deuterium embrittlement studies free from superimposed hydrogen embrittlement. Small amounts of the plating baths to be analyzed were distilled in an H_2O-free atmosphere. Infrared analysis (12) showed that the pick-up of H_2O by the D_2O baths handled only in the inert atmosphere chamber had been small, ranging from 0.18 to 0.27%.

Cleaning procedure for steel specimen.—Poor adhesion of electrodeposits to steel was obtained if the surface of the steel was cleaned and dried before introduction into the inert atmosphere chamber for plating. Hence, a procedure of cleaning steel was sought which could be performed in the chamber just prior to plating. The following anodic cleaning solutions were investigated at current densities ranging from 0.5 to 20 amp/dm^2: 70% H_2SO_4; 4*M* NaCN; 1.5*M* $K_4P_2O_7$ at 70°C with the *p*H adjusted to 7 or 10 with $H_4P_2O_7$; 6.7*M* NaOH with versene; 9.6*M* NaOH from room temperature to 100°C; and 1.6*M* $(NH_4)_2HC_6H_5O_7$ (ammonium citrate) at *p*H 5.

The best adhesion of cadmium to steel was obtained after anodic treatment of steel in either sodium hydroxide or sulfuric acid. To avoid chemical attack of the steel by acid, the alkaline solution, 9.6*M* NaOD in D_2O was preferred. Cleaning was conducted at 15 to 20 amp/dm^2 for 6 to 15 min.

Steel to be plated in alkaline baths (Cd, Cu, etc.) was transferred directly from the alkaline cleaning solution to the plating solution without a rinse. Steel to be plated in acid baths (Cr, Ni, etc.) was rinsed before being introduced into acid solutions. For studies involving deuterium embrittlement, D_2O was used as the solvent for the anodic cleaning solution, the prerinse, and the charging or plating solution.

Charging and storing steel rings.—The specimens, after anodic cleaning, were immersed in the charging or plating baths with the circuit closed, charged or plated for some predetermined period of time, and placed for periods up to 2 hr in liquid nitrogen until used for the crushing test, which was made just prior to analysis by the tin-fusion method.

To improve the reproducibility of the experiments without greatly increasing the number of gas analyses, the following procedure was adopted. Triplicate rings were crushed to measure embrittlement. For the gas analysis, one-half of each of the three rings were simultaneously melted. In this manner the variations in the experiments were averaged to some extent.

Operation of the vacuum fusion apparatus.—Immediately after the embrittlement was measured, the plated-ring (or one-half of each of three rings) was placed in the antechamber, which was then evacuated to permit the passage of the specimen through the gate valve into the evacuated furnace assembly. When desired, unplated specimen can be passed more quickly through the mercury float valve into a preevacuated antechamber.

The pressure in the system was reduced to 10^{-4} mm, and the furnace area and gas collection areas were isolated from the pumping area of the system. The specimen was dropped into the molten tin at 1060°C. The gases liberated from the melted steel

were pumped into the collection area by means of a mercury diffusion pump. This required about 20 min. The collection area was then isolated from the furnace assembly and the mercury diffusion pump allowed to cool for 15 min. A known amount of argon was then added to the gases from the specimen and this gas mixture removed to a sample bottle by means of a Toepler pump. The ratio of hydrogen and deuterium to argon was determined with a mass spectrograph.

Experimental Results

Comparison of embrittling effect of deuterium and hydrogen on ungrooved rings.—Because of the similarity of the many properies of hydrogen and deuterium, it seemed reasonable to predict that deuterium would embrittle steel. A few of the initial comparisons of hydrogen and deuterium embrittlement are reported herein. A cadmium plating bath was made from H-free compounds and D_2O as solvent. Steel rings, which were not grooved, were plated with cadmium from this heavy water bath and from ordinary water baths. The magnitude of the embrittlement produced is shown in Fig. 1 and 2. The embrittlement resulting to steel was less for charging in the D_2O solution than in the H_2O solution. Hence, it may be concluded that deuterium embrittles steel less than hydrogen. Because the D_2O solutions contained moisture (H_2O) picked up from the atmosphere, some of the embrittlement resulting from electrolysis in this solution may be attributed partly to hydrogen. Experiments, discussed in Part II (9) of these investigations, employ careful controls against moisture pick-up by the D_2O solutions and demonstrate more clearly that deuterium embrittles steel.

Determination of extraneous hydrogen.—Before extensive analyses were made for the amount of electrolytic hydrogen in embrittled steel, the amount of "extraneous" hydrogen was determined. This hydrogen may have originated in the course of the manufacture of the steel or as moisture adsorbed on the surface of the test specimen. To determine the extraneous hydrogen from the latter source, steel control specimens were immersed in D_2O, then dried or wiped by different techniques, and introduced into the vacuum fusion apparatus. Some data are given

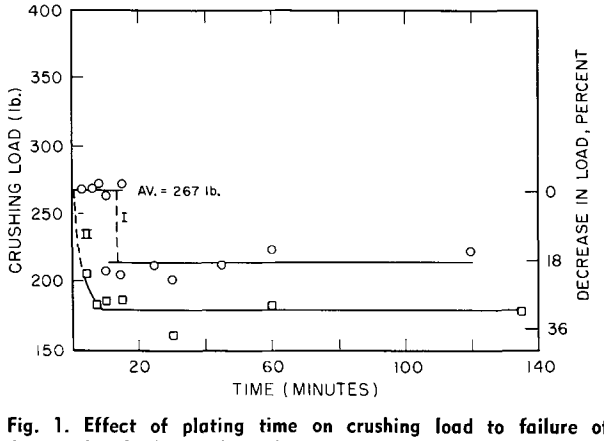

Fig. 1. Effect of plating time on crushing load to failure of cadmium-plated SAE 4130 steel rings. Curve I solvent, D_2O; curve II solvent, H_2O.

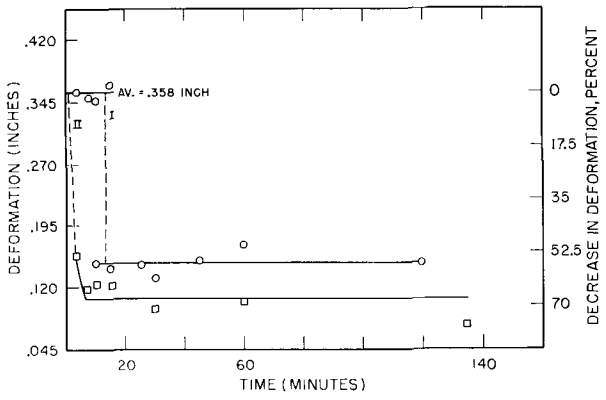

Fig. 2. Effect of ploting time on deformation to failure of cadmium-plated SAE 4130 steel rings. Curve I solvent, D_2O; curve II solvent, H_2O.

in Table I. The amount of adsorbed moisture is indicated by the amount of deuterium remaining on the steel. The amount of deuterium found was not significant compared to the extraneous hydrogen from other sources. The latter shows a large variation among the steel blanks analyzed and indicates that a correction for extraneous hydrogen may be very inaccurate. In the present work analyses of blanks or the as-received steel gave an average of 17 mm^3 hydrogen/g of steel for extraneous hydrogen with a variation of ± 14 mm^3 hydrogen/g of steel. The variation in extraneous hydrogen explains the difficulty in determining accurately the quantity of electrolytic hydrogen introduced into steel. The pre-

Table I. Contribution of moisture adsorbed on the surface of steel to extraneous hydrogen

Steel blank No.	Last liquid rinse	Duration of dip, min	Rubbed to dry	Gas analysis D_2, mm^3/1 g steel	Gas analysis H_2, mm^3/1 g steel
1	D_2O	20	Yes[x]	0.52	12.4
2	D_2O	1	No[y]	0.29	7.9
3	D_2O	1	Yes[x]	0.11	9.04
4	Acetone	1	Yes[z]	None	17.03

[x] Rubbed with paper that had been stored in dry-box for 5 days to remove adsorbed H_2O.
[y] Steel ring under vacuum in antechamber for 22 hr before analysis.
[z] Rubbed with gauze in the air after removal from acetone.

Table II. Hydrogen isotopes extracted from steel rings embrittled in heavy water

Period of extraction, min	Specimen 1 D mm^3/g of steel[x]	Specimen 1 H mm^3/g of steel[x]	Specimen 2 D mm^3/g of steel[x]	Specimen 2 H mm^3/g of steel[x]
10*	—	—	0.2	0.05
10-1000*	5.4	0.8	9.5	1.5
15 (melted steel)**	0.1	15.0	0.01	3.0

[x] Corrected to include H or D in HD.
* At room temperature.
** At 1100°C.

cision, based on pressure readings of the McLeod gauge, was better than ±0.5 mm³ hydrogen/g of steel.

Differences in behavior of electrolytic deuterium and extraneous hydrogen in steel.—Specimens of steel were charged with deuterium in a 10% solution of NaOD in D_2O. Each specimen, immediately after charging, was placed in a high vacuum system and the rate of escape of deuterium measured over several intervals of time. Analysis of the gas showed that it was mainly the isotope deuterium without any appreciable proportion of extraneous hydrogen. The gas contents of the aged steel specimens were then determined by vacuum fusion and found to consist mainly of extraneous hydrogen and virtually no deuterium (see Table II). These experiments show (*a*) very little of the extraneous hydrogen undergoes isotopic exchange with electrolytically introduced deuterium; (*b*) the extraneous hydrogen must be either trapped as molecular hydrogen or more tightly bound in the steel (perhaps as a compound) than the electrolytically introduced deuterium.

Retention of electrolytic deuterium or hydrogen by steel at liquid nitrogen temperature.—In some of the initial experiments, embrittled but uncoated steel specimens were aged in liquid nitrogen. Their embrittlements were measured by crushing immediately after they were warmed to room temperature. Experiments were designed to determine whether hydrogen diffused from these uncoated steel rings during storage at liquid nitrogen temperature. The new procedure provided that all steps requiring the steel to be held at room temperature for several minutes be eliminated or the time be reduced to a minimum.

The mercury float valve shown in Fig. 10 was devised for quickly introducing 1-in. OD rings into the high vacuum system. The crushing test was eliminated. The specimens were charged, stored (if desired) at liquid nitrogen temperature, and analyzed. With these changes, the steel was at room temperature for only 4 to 7 min from the time the charging was completed until collection of gas from the specimen was started.

Two different types of solutions were used for these studies. The first was a strongly basic and the second a strongly acidic medium. Results of the experiments are given in Fig. 3 and 4. For the steel charged in the basic solution, all of the gas appeared to be liberated from the steel in 3 hr at room temperature. A maximum of 28.5 mm³ hydrogen/g of steel was collected when the steel was not aged (curve A, Fig. 3). Two other specimens aged at liquid nitrogen temperature for 2 hr (curve B) and 40 hr (curve C) showed reductions of the amount of hydrogen given off of 4 and 2 mm³/g of steel, respectively. The steel charged in the acidic medium was heated in the high vacuum system to 310°C to accelerate the liberation of the electrolytic gas. A total of 107 mm³ hydrogen/g of steel was collected from steel which was not aged at liquid nitrogen

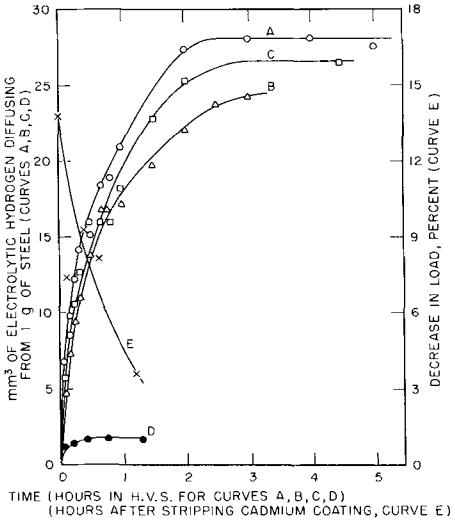

Fig. 3. Quantity of electrolytic hydrogen escaping from uncoated steel after cathodic charging in basic medium compared with the retention of embrittlement by steel after stripping of cadmium coating.

Curve	Method, In H_2O soln.	Electrolytically charged Time, hr	CD, amp/dm²	Time steel at R.T. from charging to H.V.S., min	Time steel stored at —196°C after being charged, hr
A	10% NaOH	2.5	3.3	4.25	None
B	10% NaOH	2.5	3.3	6.50	2
C	10% NaOH	2.5	3.3	4.25	40
D	Uncharged specimen	—	—	—	—
E	Cd-CN	0.5	3.5	—	—

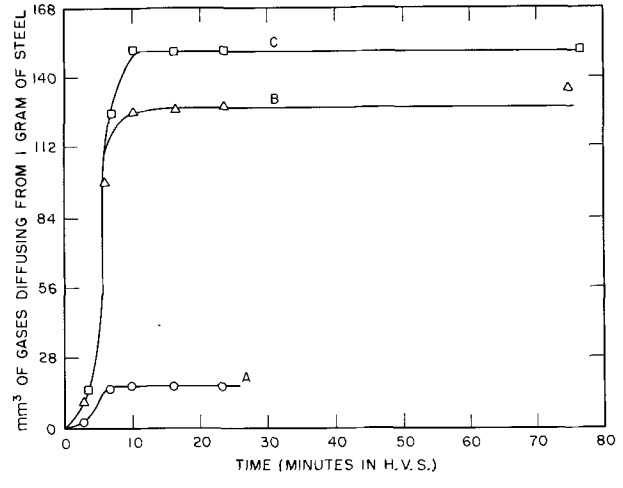

Fig. 4. Quantity of gas which diffused from uncoated steel held at 310°C after cathodic charging in acid medium. Gas collected was mainly hydrogen; SAE 4130 steel ring (5g); Electrolytically charged for 10 min at 3.3 amp/dm² in 4% H_2SO_4; Poison was P in CS_2(4 g/20 ml) added as 4 drops/50 ml of acid.

Curve	Time steel at R. T. from charging to H.V.S., min	Time steel stored at —196°C after being charged	Poison
A	5	None	None
B	7-1/3	None	Yes
C	6	16 hr	Yes

Table III. Study of effect of changes of H/D ratio in liquid on H/D ratio in gases liberated at steel cathode and gases permeating steel tube as a result of electrolytic charging in alkaline solution*

$(H/D)_{Liq}$	$(H/D)_{G_{El}}$	$(H/D)_{G_P}$	$\frac{(H/D)_{G_{El}}}{(H/D)_{Liq}}$	$\frac{(H/D)_{G_P}}{(H/D)_{Liq}}$	Permeation rate** P, × 10^7, cc/sec/cm²/0.78 mm†
0.005	0.030	0.036	6.0	7.2	4.1[x]
0.022	0.132	0.19	6.0	8.6	4.1[x]
0.050	0.3	0.46	6.0	9.2	2.5
0.115	0.67	—	5.9	—	—
0.148	0.87	1.2	5.9	8.1	2.8
0.173	1.0	1.3	5.8	7.5	4.2
1.0	5.9	7.3	5.9	7.3	—
		Average	5.9	8.0	

G_{El}, cathodic gas; G_P, gas which permeated steel: Liq, solution electrolyzed.

* Outside surface of SAE 4130 steel cylinder charged in 10% NaOX in X_2O (where X is H or D) at 10 amp/dm².

** P, determined between 4 and 5 hr of electrolytic charging.

† 0.78 mm is the thickness of the steel rings.

[x] Poison in solution (sodium arsenite).

Table IV. Effect of previous electrolytic charging on the permeation of a mixture of deuterium and hydrogen through a steel tube*

Order** of charging	Time required for gases† to permeate steel, min	Total time of electrolysis, min	Temp, °C	Permeation rate P, × 10^7, at end of charging, cc/sec/cm²/0.78 mm
1	40	172	35	—
2	34	319	35	2.7
3	32	310	35	3.6
4	20	284	55	6.8
5	30	300	35	3.1

* Cathodic charging at 10 amp/dm² in 20% NaOX in X_2O, where X is H or D and the $(H/D)_{Liq} = 0.010$.

** Time between successive experiments at least 16 hr.

† Time for gas to appear on inside of cylinder.

temperature (curve B, Fig. 4), while a total of 115 mm³ hydrogen/g of steel was collected from a specimen aged at liquid nitrogen temperature for 16 hr. These experiments indicate that very little electrolytic gas diffused from the steel at liquid nitrogen temperature.

Rate of escape of electrolytic hydrogen from unplated steel vs. the retention of embrittlement.— Steel specimens, which were cadmium plated for 30 min at 3.5 amp/dm², were stripped of the cadmium coating, allowed to stand at room temperature for different lengths of time, and then the embrittlement determined by crushing. Embrittlement was retained by the stripped steel for over 76 min. Analyses were not performed on these specimens. The loss of embrittlement (curve E, Fig. 3) was compared with the loss of gas from uncoated steel charged in an alkaline medium (curves A, B, and C, Fig. 3). Even though the charging procedures were different and may not be directly comparable, these experiments indicate that the loss of embrittlement and loss of gas are roughly parallel.

Comparison of the permeation of hydrogen and deuterium through SAE 4130 steel.—A comparison of the amounts of hydrogen and deuterium which are electrolytically discharged on the surfaces of steel from heavy water solutions contaminated with ordinary water and a comparison of the permeation of hydrogen and deuterium through SAE 4130 steel were made. These studies were felt to be necessary since both deuterium and hydrogen embrittlement were to be studied, and such information would help in the interpretation of data. Steel cylinders were used for the study of the relative rates of permeation of hydrogen and deuterium. Each cylinder was 2.5 cm (1 in.) in diameter, 10 cm (4 in.) long, and had a wall thickness of 0.08 cm (1/32 in). One end was closed with a soldered steel cap. The open end of the cylinder was sealed to a piece of glass tubing with wax. This assembly was attached to a vacuum system which included a McLeod gauge, to permit measurement of the pressure rise in the interior of the cylinder.

The charging solution included various mixtures of a 10% solution of NaOD in D_2O with a 10% solution of NaOH in H_2O. The data collected from these experiments are given in Tables III, IV, and V, and observations drawn from them are informative. The conclusions are:

Table V. Permeation rates and diffusion constants for hydrogen and deuterium in SAE 4130 Steel

Temp, °C	C.D., amp/dm²	P_H, × 10^7 cc/sec/cm²/0.78 mm	P_D, × 10^7 cc/sec/cm²/0.78 mm	P_H/P_D	D_H, × 10^7, cm²/sec	L, min	D_D, × 10^7, cm²/sec	L, min	D_H/D_D
35	6.8	4.8*	—	—	1.20	146	—	—	—
35	10	7.2*	3.1**	2.3	1.25	140	1.1	151	1.14
35[x]	10	—	4.1**	—	—	—	1.34	130	—
55	10	10.6*	5.4**	2.0	3.8	46	3.0	58	1.27

P_H and P_D = permeation rates for hydrogen and deuterium determined after 4 hr of electrolytic charging.
D_H and D_D = diffusion constants for hydrogen and deuterium calculated by the time-lag method (13,14), where $D = 0.0062$ cm²/6L (sec). L is the point where the tangent to curve for steady state of flow crosses time axis of pressure *vs.* time plot (pressure on outgoing side of steel).

[x] Poison in solution (sodium arsenite).

* Steady state of flow for 1 hr.

** Steady state of flow for 2 hr.

(*A*) Addition of a poison, sodium arsenite, to the charging solution caused an increase in the rate of permeation of the hydrogen isotopes through steel (see Table III).

(*B*) Slight increases in temperature of the solution increased the rate of permeation and reduced the time required for hydrogen and deuterium to appear inside the tube (see Tables IV and V).

(*C*) The limited data dealing with variations in current density indicated that increasing the current density increased the rate of permeation of the hydrogen isotopes (see Table V).

(*D*) The ratio of hydrogen to deuterium in the electrolytic gas produced at the surface of SAE 4130 steel was 5.9 times larger than the corresponding ratio in the electrolyte (see Table III).

(*E*) The ratio of hydrogen to deuterium in the gases which permeated the cylinder was about 8 times larger than that for the electrolyte (see Table III).

(*F*) The diffusion constant calculated for a given set of conditions was larger for hydrogen than deuterium. The D_H/D_D ratio was 1.14 and 1.27 (see Table V). The diffusion constants were determined by the time-lag method discussed by Barrer (13) and by Jost (14).

(*G*) A slightly shorter time was required for the gases to permeate a steel tube on each successive permeation. Sufficient time (as much as 16 hr to 4 days) was allowed between permeations to permit the penetrating gases to diffuse out at room temperature. Successive permeations of the same piece of steel yielded nearly the same permeation rate. The rate was affected most by changes in temperature (see Table IV).

(*H*) The permeation rates for hydrogen and deuterium determined after 4 hr of electrolytic charging are given in Table V. The average P_H/P_D ratio was about 2.1.

Comparison of electrolytic hydrogen contents in steel charged by different procedures.—These electrolytic studies with hydrogen have indicated on analysis a range of total hydrogen content present in the steel from 20 to 167 mm^3 hydrogen/g of steel. When electrolytic conditions were used that introduced a small quantity of hydrogen, the gas contents due to electrolysis could not be determined with a high degree of accuracy. As the total quantity of hydrogen became larger, the analysis became easier and more accurate. Table VI summarizes some electrolytic hydrogen contents found in steel as a result of the listed charging processes. These gas contents were the result of one analysis per charged steel specimen, and they show the small electrolytic hydrogen content introduced into steel by various electrolytic processes. Sulfuric acid containing a poison (P in CS_2) appears to be the only process listed, which introduces hydrogen rapidly into steel during a 10-min charging period.

Effect of solvent on hydrogen embrittlement of steel.—A few studies were made to determine if water was necessary to the entry mechanism for the introduction of hydrogen into steel and, hence, influence the hydrogen embrittlement of steel. The ethereal hydride-aluminum bath (15) was the first nonaqueous plating bath investigated. The quantity of hydrogen discharged during the deposition was small. The cathode current efficiency of deposition of aluminum from this bath is about 95%, with the remainder of the current producing hydrogen. The steel rings did not become embrittled when plated with aluminum for 30 min at a current density of 2 amp/dm^2.

Analysis of the gas produced in the anode compartment during electrolysis of the hydride-aluminum bath indicated only hydrogen was liberated. Whether the hydrogen is a primary product of electrolysis or a secondary decomposition of hydrides was not established. The severe embrittlement of the steel rings which resulted when they were made anodic in this ethereal solution is shown in Fig. 5. The experiments indicate that the presence of water as a solvent is not necessary to the entry mechanism, for the maximum embrittlement obtained was greater from ethereal than from aqueous solution.

Table VI. Electrolytic hydrogen content of SAE 4130 steel rings charged by different processes

Experiment	Electrolytic charging process Solvent = H_2O	Time, min	Current, amp/specimen	Electrolytic hydrogen* mm^3/specimen	Electrolytic hydrogen* mm^3/g steel
A	CN^--Cd Plating	15	0.5	100	20
B	CN^--Cu Plating	15	0.28	225	45
C	$SO_4^=$-Cr Plating	15	2.5	65	15
D	NaOH (10%)	10	0.5	60	12
E	NaOH (10%)	15	0.5	70	14
F	NaOH (10%)	150	0.5	140	28
G	H_2SO_4 (4%)	10	0.5	70	14
H	H_2SO_4 (4% + poison)	10	0.5	750	150
I	Steel blank (avg)	—	—	85	17
	(variation)	—	—	15-155	3-31

* Corrected for average hydrogen content of blank I.

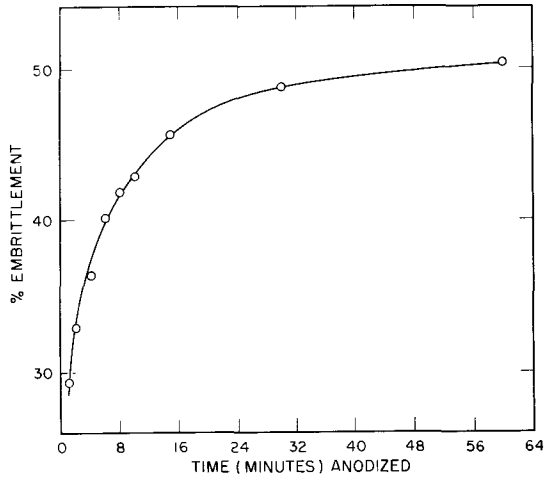

Fig. 5. Anodic charging of SAE 4130 steel in an ethereal hydride aluminum bath.

To examine further the embrittling effect of hydrogen discharged from a nonaqueous medium, specimens were made cathodic in solutions of alcohol, propylene glycol, ethylene diamine, and dimethyl formamide which were made conducting by the addition of lithium chloride. Although the investigations of these solutions are not complete, the evidence indicates that no embrittlement occurred on cathodic treatment of steel.

Discussion

Johnson, Morlet, and Troiano (16) have stated that they were unable to detect the presence of electrolytically introduced hydrogen in steel by conventional vacuum-fusion techniques, with a precision of ± 2 mm^3 hydrogen/g of steel. Their embrittling procedure included a 5-min charge in a 4% H_2SO_4 solution at 0.31 amp/dm^2, followed by cadmium plating from a cyanide bath for 25 min at 2.2 amp/dm^2.

At the higher current densities used in the present studies hydrogen could be detected either by permitting it to diffuse from uncoated steel in a high vacuum system or by melting the steel. The precision of the whole analytical method was ± 0.5 mm^3 hydrogen/g of steel. Enough electrolytic hydrogen was introduced into the steel so hydrogen over and above the extraneous hydrogen could be detected. Even so, the content of extraneous hydrogen in steel is too variable to permit an accurate determination by the tin fusion method of the electrolytic hydrogen introduced into steel by most of the embrittling procedures. The use of electrolytic deuterium permitted the distinguishing of extraneous and electrolytic gas. Analyses of the heavy water plating solutions for ordinary water picked up from the atmosphere and the permeation studies indicate that the heavy water solutions used for the study of deuterium embrittlement must be handled in an atmosphere free from ordinary water to give good assurance that deuterium embrittlement is studied free from hydrogen embrittlement.

During the course of these experiments there was some doubt as to the retention of the hydrogen isotopes in steel at liquid nitrogen temperature. Embrittlement was retained after several days' storage at this temperature. Yet in some analyses, electrolytic hydrogen or deuterium was not found in the steel some 40 min after the crushing test was performed. Various experiments reported herein have shown that the analyses of uncoated steel must be made within minutes after the steel has been warmed to room temperature or a large portion of the electrolytic gas introduced by alkaline charging is lost. Thus, the age of the specimen after charging is very critical in the determination of the magnitude of embrittlement and gas content of uncoated steel. This one factor may be the main reason for the scatter of data reported by the many investigators of the phenomenon of hydrogen embrittlement. Experiments have indicated that the embrittlement disappears as the hydrogen diffuses from the steel. Also, the use of long period sustained loading test on uncoated steel as a measure of embrittlement appears to be very impractical.

The various types of charging procedures appear to introduce different maximum quantities of gas into the steel (see Table VI). The maximum amount of gas introduced into a given specimen of steel is probably dependent on the driving force of the charging procedure. Steel rings charged at 3.6 amp/dm^2 for 4 hr in 10% NaOH in H_2O contained 144 mm^3 of electrolytic hydrogen (29 mm^3/g of steel). Several experiments indicated that this is nearly the maximum quantity of electrolytic hydrogen that can be introduced into the steel specimens by this charging procedure. This value was determined by analyses of charged steel rings. It was confirmed by the permeation studies listed in Table V, in which the time to establish a steady state of flow was about 4 hr and the rate of permeation for hydrogen through steel at a steady state of flow was 7.2 cc/sec/cm^2/0.78 cm. This rate would be 0.6 mm^3/min/14 cm^2/0.78 cm for charging a steel ring specimen for 1 min. If most of the gas which enters the steel ring during this first 240 min of charging is retained by the steel until it becomes saturated with hydrogen, the saturation value would be about 144 mm^3 of electrolytic hydrogen. For steel charged in a solution containing sulfuric acid and poison, the equilibrium quantity of gas introduced into the steel was much larger, for 750 mm^3 of hydrogen (150 mm^3/g of steel) were introduced into the steel rings during only 10 min of charging.

The permeation studies showed that the rate of permeation increased with an increase in the rate of discharge of the gas, for example, with elevation of the current density or with lowering of the cathode current efficiency. The rate of permeation also increased with elevation of temperature and with the introduction of the poison, sodium arsenite, into the electrolyte. These latter two factors may operate through retarding the combination of hydrogen atoms to form molecules at the surface of the steel. The factors which affect these permeation experiments in steels and are discussed in Part II of these studies (9).

Frank, Lee, and Williams (17) have reported relative permeation rates and diffusion coefficients for hydrogen and deuterium in SAE 1010 steel. Instead of electrolytic charging they introduced the gases into the steel by abrasion in a mixture of normal and heavy water. The ratio of diffusion coefficients, D_H/D_D, determined by them was not too different from that reported here. Their value for SAE 1010 steel was 1.37 ± 0.02, and the value reported here for SAE 4130 steel was about 1.2. Thus, the rate of diffusion of these isotopes within the two steels appears to be of the same order of magnitude. The ratio of permeation rates, P_H/P_D, for the two steels was quite different. The values for SAE 1010 steel ranged from 4.4 to 10.7 for temperatures ranging from 26° to 86°C. The limited data shown in Table V indicate that this value for SAE 4130 steel for temperatures ranging from 35° to 55°C and determined for gases liberated in a vacuum is only about 2.1. This difference may be due to the differences in the nature of the steels, in the surface of the steels, in the environment on the exit side of steel, in the driving forces of the two experiments, etc.

Conclusions

1. The embrittlement produced by hydrogen is larger than that produced by deuterium for a given condition of electrolysis.

2. Electrolytically introduced deuterium diffuses out of uncoated steel in a few hours at room temperature, but more slowly than electrolytically introduced hydrogen. In contrast, metallurgically introduced hydrogen remains in steel for years or indefinitely at room temperature.

3. Isotopic exchange between metallurgically introduced hydrogen and electrolytically introduced deuterium was not indicated at room temperature. The hydrogen introduced during the making of the steel is more tightly bound than that introduced electrolytically.

4. The rate of escape of electrolytic gas roughly paralleled the disappearance of embrittlement in the steel.

5. The separation factor for hydrogen and deuterium electrolytically evolved from alkaline solution on SAE 4130 steel was 5.9.

6. The ratio of hydrogen to deuterium which permeated a steel cylinder was about eight times larger than their ratio in the alkaline electrolyte.

7. The ratio of diffusion coefficients (D_H/D_D) was about 1.2.

8. The ratio of permeation rates (P_H/P_D) determined after 4 hr of electrolytic charging in alkaline solution was about 2.1.

9. The rate of permeation of hydrogen and deuterium increased with the current density, with elevation of the temperature of electrolytic solution, and with the presence of a poison, sodium arsenite, in the alkaline electrolyte.

10. The entry of hydrogen into steel takes place in the presence of diethyl ether as well as in the presence of water as solvent for the charging medium.

Manuscript received Sept. 18, 1962; revised manuscript received March 29, 1963. This paper was delivered before the Columbus Meeting, Oct. 18-22, 1959.

Any discussion of this paper will appear in a Discussion Section to be published in the June 1964 JOURNAL.

REFERENCES

1. R. W. Buzzard and H. E. Cleaves, "Hydrogen Embrittlement of Steel, Review of the Literature," NBS Circular 511, Sept. 1951.
2. Harold J. Read, "Hydrogen Embrittlement in Metal Finishing," Reinhold Publishing Corp., New York (1961).
3. P. Cotterill, *Progr. Materials Sci.*, **9**, [4], 201 (1961).
4. J. G. Morlet, H. H. Johnson, and A. R. Troiano, *J. Iron Steel Inst.*, **189**, 37 (1958).
5. F. deKazinczy, *ibid.*, **177**, 85 (1954).
6. N. J. Petch and P. Stables, *Nature*, **169**, 842 (1952).
7. P. Bastien and P. Azou, *Rev. Met.*, **49**, 837 (1952).
8. H. J. Noble, *Iron Age*, **148**, 45 (1941).
9. G. B. Wood, *This Journal*, **110**, 877 (1963).
10. D. J. Carney, J. Chipman, and N. J. Grant, *Trans. AIME*, **188**, 397 (1950).
11. H. P. Broida, H. J. Morowitz, and M. Selgin, *J. Research Natl. Bureau Standards*, **52**, 293 (1954).
12. J. Gaunt, *Analyst*, **79**, 580 (1954).
13. R. M. Barrer, "Diffusion in and Through Solids," Cambridge University Press (1941).
14. W. Jost, "Diffusion in Solids, Liquids, Gases," New York Academic Press, Inc. (1952).
15. D. Couch and A. Brenner, *This Journal*, **99**, 234 (1952).
16. H. H. Johnson, J. G. Morlet, and A. R. Troiano, *Trans. AIME*, **212**, 528 (1958).
17. R. C. Frank, R. W. Lee, and R. L. Williams, *J. Appl. Phys.*, **29** [6], 898 (1958).

APPENDIX

Electrolytic Cells

The main feature of Cell I (Fig. 6) is a hollow, water-cooled anode which served to keep the temperature of the plating bath from rising during operation. Cell II (Fig. 7) has a hollow glass tube connected to the bottom of the glass vessel at the center to provide for a thermocouple and anode connections in the tube without disturbing the bath or the electrodes. A heater jacket fits around the vessel and acts as a stand for Cell II.

Components of the High Vacuum System

A high vacuum system was built to permit the tin fusion of steel. In several features, the equipment was improved in comparison with similar apparatus described previously in the literature (10). For example, it provided a higher pumping rate, provided greater ease of recharging the furnace with tin, permitted the introduction of 1-in. diameter steel specimen, and provided for the collection of the extracted gas for analysis. Several innovations are described below.

A schematic drawing of the furnace assembly is shown in Fig. 8. The major points of interest are as

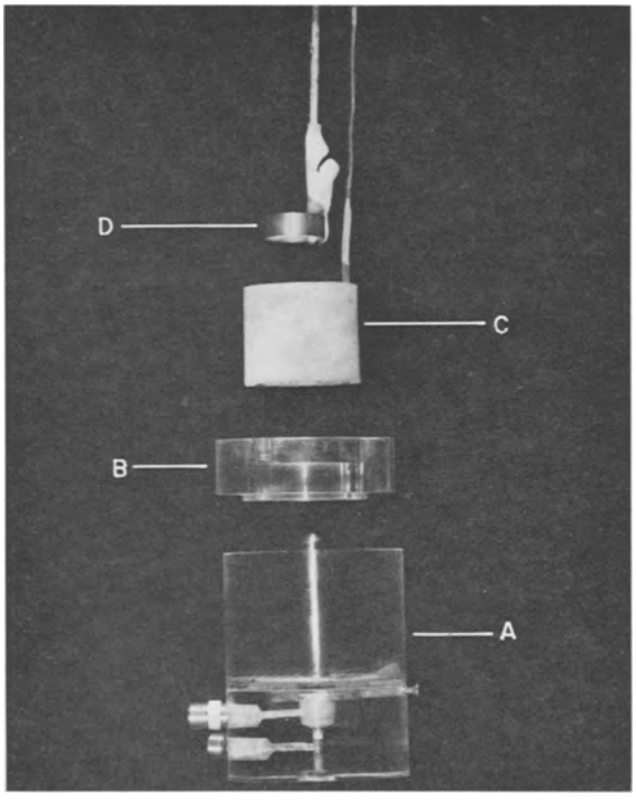

Fig. 6. Water-cooled electrolytic cell. Parts of the electrolytic cell, from the bottom upward are: A, Lucite container and water-cooled anode assembly (Cd-plated); B, cover for cell; C, cadmium outside anode; D, steel ring cathode, contact made by clip, which is mostly plastic coated.

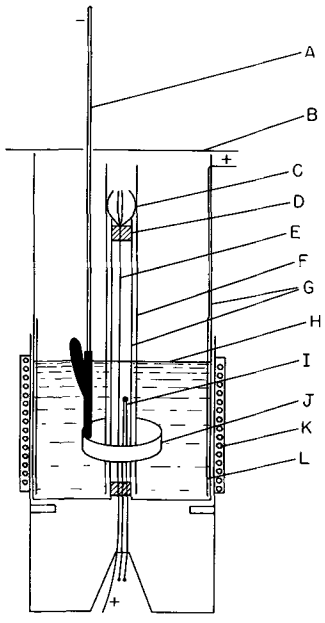

Fig. 7. Electrolytic cell equipped with heater: A, cathode lead; B, removable top; C, phosphorus bronze contacts to control anode; D, epoxy resin; E, anode lead; F, central cylindrical anode; G, Pyrex tube sealed to bottom of vessel; H, electrolyte; I, thermocouple or thermistor; J, steel specimen; K, heater (110v); L, outside cylindrical anode.

follows: (*A*) Vycor instead of Pyrex was used for the outside container to eliminate blow-ins in the heated area. (*B*) The standard taper joint is sealed by an "O" ring instead of wax and is above rather than below the heated zone. This seal is tight enough and eliminates the contamination of the furnace area with

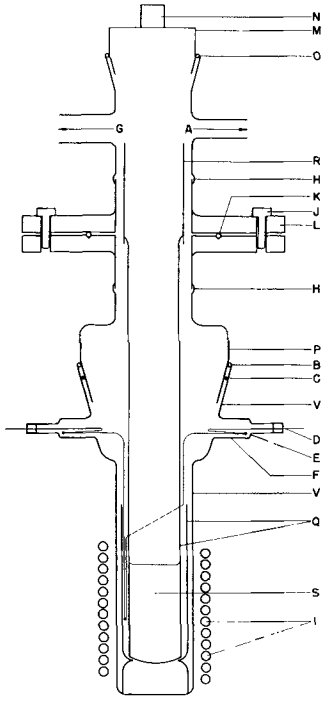

Fig. 8. Furnace assembly of high vacuum system for tin fusion method of gas analysis: A, to high vacuum system; B, wax seal (optional); C, O-ring standard taper joint; D, thermocouple wire soldered to brass plug which is soldered to Kovar; E, Kovar to Pyrex seal; F, Pyrex to Vycor seal; G, to antechamber; H, Kovar to Pyrex seal; I, induction furnace coils; J, screws; K, rubber O-ring; L, metal flange; M, optical glass; N, prism (90°); O, Apiezon wax; P, Pyrex; Q, fused silica; R, Pyrex shield; S, tin.

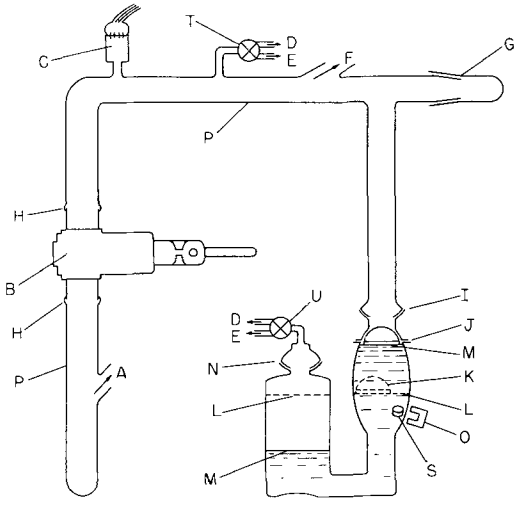

Fig. 9. Antechamber and mercury air lock for introducing steel specimen into high vacuum system: A, to furnace and tin bath; B, gate valve; C, thermocouple gauge; D, to vacuum pump; E, to atmosphere; F, to oil diffusion pump; G, standard taper joint; H, copper to Pyrex seal; I, ball joint; J, ground flange (coated with graphite); K, glass float (coated with graphite); L, mercury level when valve is open; M, mercury level when valve is closed; N, ball joint; O, magnet; P, Pyrex; S, steel specimen in transit through open mercury lift; T, stopcock; U, stopcock.

wax. (*C*) A metal flange, L, sealed by an "O" ring was installed to increase the ease of dismantling the furnace area for recharging with fresh tin. The top of this flange was mounted permanently, and the rest of the furnace hung from it. (*D*) The silica tube, which holds the tin inside the furnace, was made long enough to reach the lower part of the flange. This permitted easy removal of the tin-containing tube, provided a cold surface on which most of the tin and cadmium vapors could condense, and guided the steel specimen's fall into the melt. (*E*) Both "O" ring seals were kept cool by an air blower. (*F*) A thermocouple was installed to make the heat control of the furnace automatic.

An antechamber provided with a gate valve to close it from the system was installed in the vacuum-fusion system. A schematic drawing may be seen in Fig. 9. The gate valve permitted the steel specimen to be introduced into the antechamber at atmospheric pressure while the rest of the system was under vacuum. About 10 min elapsed from the time the specimen was placed in the antechamber to the time it was dropped into the molten tin. This lapse of time was not serious for electroplated steel because the coating keeps the hydrogen from escaping. For a charged, unplated specimen this delay plus the time from the completion of cathodic charging until introduction into the antechamber may be very critical. The unplated specimen can be introduced into the vacuum system more expeditiously through a mercury float valve as shown in Fig. 9. The time elapse from charging bath to molten tin was 2 min.

Attached to the gas collection area was the gas microburet, already referred to, for adding known quantities of argon to the gases collected from the steel. A schematic drawing may be seen in Fig. 10. The argon is added after the gases from the steel have been isolated in the gas collection area and the mercury diffusion pump has been cooled. The operation of the microburet is discussed below.

Procedure for Using Gas Microburet

The microburet shown in Fig. 10 is operated as follows: The copper tubing to the argon tank, which is tightly closed, is evacuated by means of mechanical pump (D) and the vacuum relieved with argon. This is repeated several times. The mercury in bulb (G) is lowered to point (P) by adjusting the height of bulb (K). The mercury in capillary tubing (I) is lowered by 76 cm. Clamp (N) is closed before raising

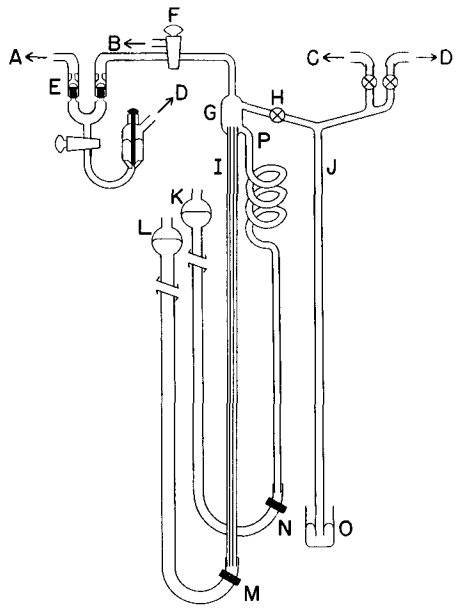

Fig. 10. Gas microburet for metering known quantities of argon into the high vacuum system. The gas microburet consists of a mercury valve (E) connected to the vacuum system (A); a three-way stopcock (F) which opens to the atmosphere at (B); a gas trapping bulb (G); a calibrated capillary (I); leveling bulb (L) which is connected to (I) through Tygon tubing; leveling bulb (K) which is connected to (G) through Tygon tubing and a 76-cm length of 5 mm capillary tubing with a glass spiral at the upper end for flexibility; a two-way stopcock (H); a manometer (J); a stopcock with copper tubing connected to an argon tank (C); and a stopcock with rubber vacuum tubing to a mechanical vacuum pump (D).

bulb (K) to the level of point (P). Stopcock (H) is opened to bring bulb (G) to atmospheric pressure and to fill it with argon. The mercury in capillary (I) is lowered or raised so that the quantity of argon to be added to the unknown gas in the vacuum system remains above the mercury in the capillary tubing. The diameter of the capillary was 0.502 mm and a 1-cm length would contain 0.002 cc of gas at atmospheric pressure. The volume of the gas collection area of the vacuum-fusion equipment was 2.14l. If a 50-cm length of the capillary was filled with argon, this quantity of gas when expanded into the gas collection area would produce a pressure of 0.035 mm. During all of the above operation, argon was flowing from the argon tank through (J) and out at (O). The argon flow is now stopped. Bulb (K) was then raised so that the mercury rises in (G) from point (P) to 1 cm above the top of (I). This is accomplished by adjusting clamp (N). Clamp (N) should now be closed. By slightly lowering bulb (L) the trapped gas in capillary (I) moved to the bottom of the capillary where the diameter of the tubing is larger. Bulb (L) is raised until the downward flow of mercury nearly stops. This can be judged by watching the formation of mercury drops at the gas pocket at the bottom of (I). A small length of the mercury column in the capillary (I) then is frozen. Bulb (G) is evacuated through (D) and then stopcock (H) closed. Bulb (K) is raised above stopcock (F). Clamp (N) is opened to permit the mercury to fill bulb (G). Any trapped gas and some mercury is flushed to the atmosphere at (B). Bulb (K) is lowered so as to permit about one-half of the mercury to flow from bulb (G). The mercury in the small capillary is allowed to warm. The gas trapped at the bottom of the capillary now rises into bulb (G). Bulb (K) is raised above stopcock (F) ready to force this gas into the high vacuum system. Stopcock (F) is carefully opened to permit the gas to expand through (A). Stopcock (F) is then closed. The pressure in the gas collection area is determined before and after the argon is added so that the exact quantity of argon added is known.

A Study of Embrittlement of High Strength Steels by Hydrogen Isotopes

II. A Comparison of Gas Contents and Hydrogen or Deuterium Embrittlement Resulting from Electroplating Processes

Gwendolyn B. Wood

Metallurgy Division, National Bureau of Standards, Washington, D. C.

ABSTRACT

Plating processes introduce more deuterium into steel from heavy water solutions than hydrogen from ordinary water solutions, yet hydrogen embrittles steel more than deuterium. No simple relation between the total gas content and embrittlement was found. Embrittlement appears to be dependent on factors other than the total gas content. The present work does not preferentially support any one of the mechanisms which have been proposed for hydrogen embrittlement. The difference in the chemical affinity of steel for hydrogen and deuterium is discussed.

There are only limited published data (1-4) dealing with the hydrogen content of embrittled steels. There are no published correlations between gas content and the embrittlement resulting from plating processes and their related variables. Knowledge of the gas content of embrittled steels would permit such correlations to be made, if they exist.

In hydrogen embrittlement studies the loss of the electrolytically introduced hydrogen must be prevented until the steel is ready for analysis. Since

Table I. Electroplating conditions

	Cadmium cyanide bath		Copper cyanide bath		Chromic bath		Alkali bath	
Bath composition, g/l	CdO NaCN $NiSO_4$	44.4 122.0 0.5	CuCN NaCN Na_2CO_3	22.5 34.0 15.0	CrO_3 Na_2SO_4	250 3.7	Na	57.6
Solvent	D_2O or H_2O		D_2O or H_2O		D_2O or H_2O		D_2O or H_2O	
Temperature	R. T.*		40° ± 2.5°C		50° ± 2.5°C		R. T.*	
Current density, amp/dm²	3.5		1.9 or 3.8		16.6		3.5	
amp/specimen	0.5		0.28 or 0.56		2.5		0.5	

* Room temperature.

metal coatings deposited on the surface of the steel act as a barrier to the diffusion of gases from the steel at room temperature, plating processes were studied because they lend themselves better to a study of the gas content of steel than electrolytic charging procedures in alkaline and acid solutions.

In an earlier communication (1) on hydrogen embrittlement studies of high strength steels, the embrittlement of steel by deuterium and by hydrogen was demonstrated to be different. The desirability of using deuterium as the charging or embrittling gas was illustrated, for it permitted differentiation from the "extraneous hydrogen" present in the steel.[1] Permeation studies established the differences in diffusion and permeation rates for hydrogen and deuterium in unstressed SAE 4130 steel.

The same equipment and general experimental procedures used in this earlier communication (1) also apply in the studies reported here. Rings were again used as steel specimens.[2] All experiments involving plating from baths with D_2O as solvent were performed in the inert-dry atmosphere chamber.

Experimental Results

Gas Contents and Embrittlement Resulting from Electrodeposition of Cd, Cu, and Cr

In these experiments the steel was electroplated with cadmium or copper from a cyanide bath or with chromium from a conventional type of chromic acid plating bath. The compositions of the baths and the plating conditions are given in Table I. The graphs in Fig. 1 indicate the embrittlement obtained as determined by the decreases in crushing load or by the decrease in the deformation of crushed specimen. The graphs show that for the same period of electroplating, or indirectly for the same thickness of deposit, the embrittlement caused by deuterium was less than that caused by hydrogen. Most of the studies included plating periods from 1 to 15 min. During this plating period the embrittlement caused by deuterium, as indicated by the crushing load, was in most cases no more than 6%, which value is close to the 3% reproducibility of the crushing load of control specimens. However, the decrease in deformation was from 15 to 20%, which was above the range of fluctuation of the controls.

[1] Hydrogen from sources other than electrolytic charging.

[2] The rings had 2.5 cm (1 in.) OD, 0.08 cm (1/32 in.) wall, and 0.9 cm (0.35 in.) length and were made from SAE 4130 steel heat treated to 47 or 48 Rockwell "C" hardness.

The magnitudes of both hydrogen and deuterium embrittlements accompanying cadmium plating were found to be much larger for the ungrooved rings discussed in Part I (1) of these researches than for

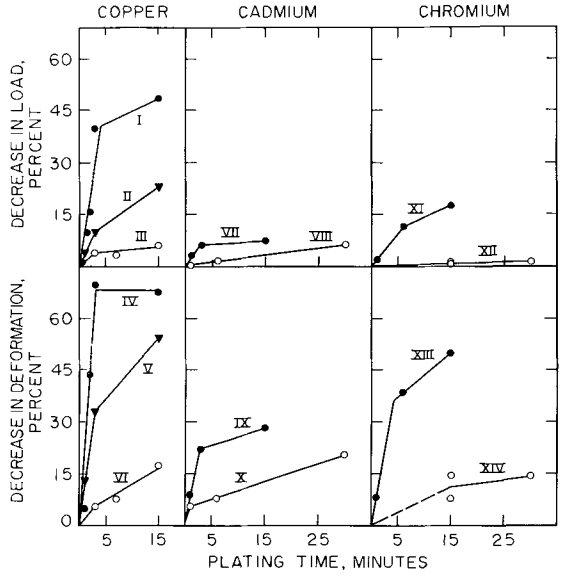

Fig. 1. Effect of plating time on load or deformation at failure for rings plated with copper or cadmium in a cyanide bath or with chromium in a conventional chromic acid bath. Copper, curves I, IV, 3.8 amp/dm², II, III, V, VI, 1.9 amp/dm²; cadmuim, curves VII, VIII, IX, X, 3.5 amp/dm²; chromium, curves XI, XII, XIII, XIV, 16.6 amp/dm²; ○, D_2O solvent; ●, ▼, H_2O solvent.

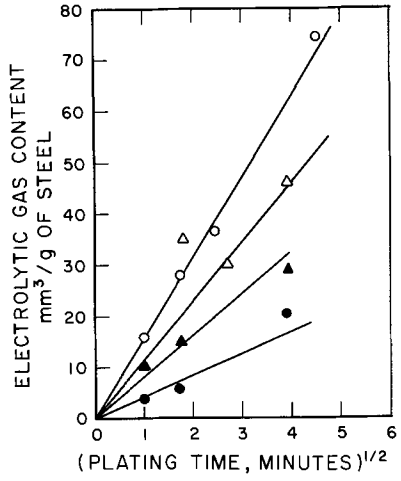

Fig. 2. Effect of plating time on the electrolytic gas content of the steel. Gas: H_2, ● plated with Cd, ▲ plated with Cu; D_2, ○ plated with Cd, △ plated with Cu.

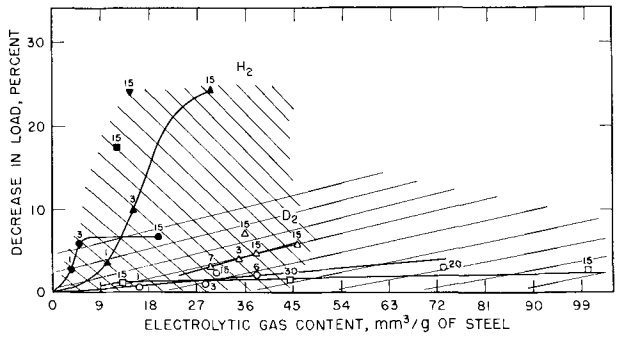

Fig. 3. Relation between the electrolytic deuterium or hydrogen content of plated-steel and the per cent embrittlement determined by decrease in load at failure. Arabic numerals on graph represent plating time in minutes. Specimens were plated with cadmium or copper from a cyanide bath, or with chromium from a chromic acid bath.

Gas H_2, D_2	Plated with	Current, amp/specimen
●, ○	Cd	0.5
▲, △	Cu	0.28
■, □	Cr	2.5
▼	Cu	0.56

the grooved rings discussed herein. The hydrogen embrittlement produced during 15 min of plating was 32% (by load) or 72% (by deformation) for rings not grooved compared with 7% (by load) or 28% (by deformation) for grooved rings. This difference is attributed mainly to the method of failure of the rings due to the presence of the groove.

A comparison has been made between the quantity of electrolytic deuterium and/or hydrogen found in the steel after electroplating and the resulting embrittlement. The gas contents of specimens embrittled by cadmium and by copper plating and crushed before analysis are shown in Fig. 2 for periods of plating time up to 15 min. The results are surprising, since for a given period of plating the specimens took up a larger amount of deuterium than of hydrogen. This result seems inconsistent since the larger embrittlement was sustained by the hydrogen-containing specimens. The relationship between embrittlement and gas content is different for deuterium and hydrogen (see Fig. 3). The points on the graph in Fig. 3 were not always reproduced since some scatter is found in this type of data. The diagonal line drawn on the graph suggests the area to which most of the data obtained in these studies fall.

Even more unexpected results were obtained as a result of chromium or nickel plating. Chromium plating from H_2O baths produced from 2 to 18% embrittlement in rings which contained only 1-12 mm^3 of electrolytic hydrogen/g of steel, but plating from D_2O baths produced only from 1 to 3% embrittlement in rings which contained as much as 100 mm^3 of electrolytic deuterium/g of steel. No embrittlement was detected in rings nickel plated from D_2O baths even though the rings contained as much as 70 mm^3 of electrolytic deuterium/g of steel.

Effect of Plating Variables on Hydrogen Embrittlement

The variations in electrolytic gas content in steel accompanying increases in current density from 3.8 to 21.4 amp/dm^2 during cadmium plating from a cyanide bath are given in Table II. A statistical study would be necessary to determine accurately the effect of current density of plating on gas content. It would appear from these limited data that large changes in gas content resulting from cadmium plating cause only small changes in embrittlement at the current densities that were used.

Table II. Effect of current density on the hydrogen embrittlement of steel caused by cadmium plating

Plating time min	C.D., amp/dm^2	Hydrogen embrittlement: Load reduction, %	Hydrogen embrittlement: Deformation reduction, %	Electrolytic hydrogen, mm^3/g steel
1	3.8	3.0	8.7	3.7
3	3.8	6.2	22.3	5.6
15	3.8	6.7	27.9	20.6
6	10.7	2.8	14.1	3.6
15	10.7	3.2	17.2	58.4
6	21.4	7.4	20	—

The magnitude of embrittlement increases much more rapidly with increase in current density for copper plating than for cadmium plating due to the lower current efficiency and greater availability of electrolytic gas during the initial plating period. Figure 1, curves I through VI, illustrates the effect of current density on embrittlement during copper plating.

Because of the small volumes of the copper and cadmium plating baths, consideration was given to changes in "free cyanide" content of the baths. Analyses showed that free cyanide concentration in the copper plating baths changes rapidly and that it influences the magnitude of the embrittlement. The embrittlement of steel produced by copper plating decreased as the free cyanide content of the bath decreased and the deposits became inferior in quality (see Fig. 4). Control of the free cyanide concentration was necessary to obtain reproducible embrittlement, and its concentration was determined prior to each experiment.

The free cyanide concentration in the cadmium cyanide bath was essentially constant with use and varied only from 2.3 to 2.1*N*. Special procedures to control the cyanide concentration in the cadmium plating baths were therefore unnecessary.

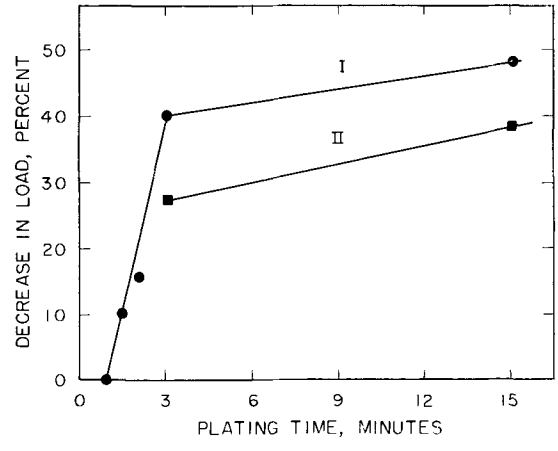

Fig. 4. Effect of plating time at different cyanide concentrations on load at failure for copper plated rings. Free [CN^-] in H_2O baths, ● 7-10 g/l; ■ 3.4 g/l.

Comparison of Loss of Gas from Rupture Surface and External Surface of Steel

Determination of gas loss through rupture surfaces.—Most of the theories (5-8) that attempt to describe the mechanism of hydrogen embrittlement imply that hydrogen migrates while the steel is being stressed to voids, dislocations, or points of triaxial stress and causes lowered strength levels. The difference in the magnitude of hydrogen and deuterium embrittlement and the quantity of hydrogen and deuterium found in steel on analysis of plated rings could be explained if hydrogen was found in the gases given off during fracture of the specimen. Some preliminary experiments tabulated in Table III indicated that either a large amount of electrolytic hydrogen was lost as the result of the crushing of cadmium-coated steel rings (specimen a, h, b, and g) or the hydrogen content varied greatly from specimen to specimen. No loss of electrolytic deuterium was indicated during the crushing test (specimen c, d, and j).

The probability that a large amount of gas would be lost through the rupture surface seemed small. However, since many of the analyses in this program had been run on crushed specimen, it was desirable to know whether enough gas could have been lost during the crushing process to account for the observed variations in hydrogen content. To permit the crushing of rings in the high vacuum system the crushing device shown in Fig. 5 was built and installed in the antechamber, so that measurement of the gas liberated from the steel during crushing could be made.

Cadmium plated rings plated for 15 min at 3.8 amp/dm^2 in an H_2O bath were crushed in this equipment. Embrittlement in the range of 20% was indicated by the amount of deformation of the rings. There was no measurable sudden rise in pressure. This experiment indicated that no more than 0.18 mm^3 hydrogen/g of steel was lost through the rupture surface during the crushing process, which required about 4 min. A high vacuum system which maintains a much lower background rise would be necessary to confirm or disprove the idea that gas is lost spontaneously during the crushing operation. Nevertheless, the amount of gas lost through the rupture surface even in 1 hr did not account for the normal variation in hydrogen content of steel found in Table III, experiments a, h, b, and g. The result also shows that the loss in gas from unplated steel, discussed in a previous communication (1), does not occur due to the crushing process, but must occur through the surface of the ring during the time of handling the ring at room temperature before analysis.

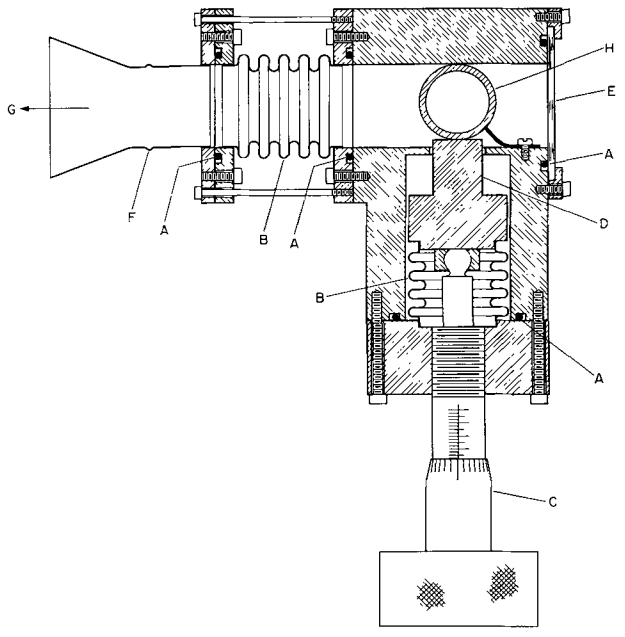

Fig. 5. Top view of cross section of crushing equipment installed in high vacuum system. A, "O" ring; B, bellows, stainless steel; C, micrometer; D, ram; E, Pyrex window; F, Pyrex to copper seal; G, to high vacuum system; H, steel specimen.

Escape of electrolytic gas from steel after stripping of cadmium plate.—Different thicknesses of cadmium were deposited from a D_2O bath on four steel rings, and the resulting deuterium embrittlement was measured. Three of the specimens were analyzed with the coating intact. Half of the fourth specimen, after crushing, was stripped of its cadmium coating in aqueous ammonium nitrate solution and then analyzed. Results are given in Table IV. The embrittlement by deuterium and the deuterium content of specimens 1, 2, and 3 did not increase greatly with the thickness of deposits greater than 8μ. Specimen 4, which had been stripped 25 min prior to analysis, had a low content of only 1.8 mm^3 of deuterium/g of steel. The deuterium could have been lost because it was contained in the cadmium deposit or because it diffused from the steel during stripping or before analysis.

Table III. Effect of crushing on the hydrogen or deuterium content of cadmium-coated steel rings

Specimen	Bath solvent	Ring crushed	Gas collected H	Gas collected D	Electrolytic H*	Electrolytic D	Embrittlement Load reduction, %	Embrittlement Deformation reduction, %
			mm^3/g steel		mm^3/g steel			
e	Steel blank	yes	25.8	—	—	—	—	—
c	D_2O	no	34.3	19.2	1.8	19.2	—	—
d	D_2O	no	31.6	21.5	0	21.5	—	—
j	D_2O	yes†	31.7	20.4	0	20.4	5.6	10.6
a	H_2O	no	86.2	—	53.7	—	—	—
h	H_2O	no	75.8	—	43.3	—	—	—
b	H_2O	yes**	58.9	—	26.4	—	1.0	6.3
g	H_2O	yes†	22.3	—	—	—	4.4	19.6

* Electrolytic H = Total H collected—H blank (32.5 mm^3/g steel determined from specimens c, d, and j).
** Ring broke during crushing at only one notch, ○-, and then analyzed.
† Ring deliberately broken at both notches before analysis, -○-.

Table IV. Effect of stripping of cadmium plate on deuterium content of steel

Steel specimen No.	Cadmium deposit Estimated thickness, μ	Cadmium deposit Estimated weight, g	Embrittlement* Load reduction, %	Embrittlement* Deformation reduction, %	Total hydrogen isotopes extracted from steel D, mm³/g steel	Total hydrogen isotopes extracted from steel H, mm³/g steel‡
1	7.6	0.055	None	None	17.8**	21.6
2	15.2	0.11	6.6	31.5	18.5**	34.1
3	22.8	0.165	9.6	40.2	12.5**	15.6
4	15.2	0.11	8.0	30.7	1.8†	22.0

* Cadmium coatings intact during all crushing tests.
** Analysis of cadmium coated steel.
† Specimen crushed to failure and broken into two halves; cadmium plate from one half was stripped in concentrated solution of NH_4NO_3, the steel dried, and analyzed 25 min after stripping.
‡ This is metallurgical hydrogen and is of no significance to the embrittlement study.

The possibility of the loss of deuterium due to solubility in the cadmium coating was examined first. The deuterium content of cadmium coatings, which had been mechanically peeled from different basis metals, was determined by the tin fusion method. The data in Table V show that the deuterium content of the cadmium coatings was small enough to be ignored in the determination of the gas content of the steel.

The loss of deuterium during the time required to introduce the specimen into the furnace area of the high vacuum system was next considered. For comparison the release of hydrogen from steel in a vacuum at room temperature after electrolytic charging in an alkaline solution is illustrated in curve A, Fig. 5 of Part I (1) of these investigations. This experiment showed that about 20 min is required for the release of 50% of the electrolytic hydrogen from this steel, and the rate of release of hydrogen from steel in a vacuum obeys a first order rate mechanism which is not fast enough to account for the nearly 90% loss of gas from specimen 4, Table IV, in 25 min.

During the stripping process some or all of the surface of the steel was exposed for a time to the aqueous stripping solution. Hudson, Norris, and Stragand (9) have shown that moisture on the surface of steel speeds up the rate of removal of hydrogen from steel in comparison to that for a dry surface in a vacuum. In their experiments, the first 50% of the electrolytic hydrogen contained in a steel specimen was lost six times faster when the steel was immersed in water than when it had a dry surface. They showed that the release mechanism for hydrogen on a wet surface obeyed a second order rate law and that the corresponding surface reaction markedly accelerated the release of hydrogen (see Table VI). In view of the possibility that removal of hydrogen from steel is accelerated by water, the accelerated release of electrolytic gas from specimen 4, Table IV, is explained. The stripping of coatings from steel before gas analysis was avoided in further experiments.

Table V. Deuterium content of cadmium electroplated from D_2O bath

No.	Basis metal	Weight of cadmium, g	Deuterium in cadmium plate, mm³/0.11g Cd*
1	Brass	0.20	—
2	Shim steel	1.02	0.053
3	SAE 4130	0.70	0.383

* 0.11g is the weight of a 20-min cadmium plate deposited at 3.5 amp/dm² from a conventional cadmium cyanide plating bath with D_2O as solvent. The current density was uniform over all of the surface of the specimen.

An Attempt to Obtain Higher Precision in Testing for Embrittlement of Plated Rings

Use of more accurately made rings.—A discussion concerning the production of ring specimens may be found in Part I (1) of this paper. Irregularities in the specimens had been noted that were believed to be undesirable from the standpoint of reproducibility of test results. For example, the radius of curvature of the notch, a major factor in the sensitivity of the crushing test, varied from 0.005 to 0.015 in.; wall thickness varied by as much as 1.5 mil. Therefore, specimens with more closely controlled dimensions were deemed desirable. The following tolerances were achieved by machining the rings from tubing stock and by grinding the groove with a ceramic wheel: thickness of ring below groove, 0.0253 ± 0.003 in.; radius of curvature of groove, 0.005 ± 0.005 in. Roundness and wall thickness were also closely controlled.

Table VI. Rate constants for removal of hydrogen from steel

Charging medium	Environment during release	Total hydrogen in steel, mm³/g	Temp, °C	t 1/2, hr	k_1,* sec^{-1} × 10^5	k_2,** g/cc/sec × 10^5	Reference
2N H_2SO_4	Vacuum, 3 mm Hg	127 (est)	38	6	3.4	—	(5)
2N H_2SO_4	In H_2O	127 (est)	38	1	—	205	(5)
10% NaOH	Vacuum	28	20	1/3	0.41	—	Fig. 4(1)
Cu plated	Vacuum	49	310	1/10	140.0	—	Fig. 8
Cd stripped	In H_2O	16.3	20	1/20†	—	—	Table IV

* First-order rate constant from semilog plot of 1/c *vs.* t.
** Second-order rate constant from plot of 1/c *vs.* t, where c is the concentration of electrolytic hydrogen in steel at time t.
† Estimated.

Table VII. Average deuterium contents of steel accompanying the electrodeposition of cadmium, copper chromium, and nickel during 15 min of plating and embrittlement measured at different crushing speeds

Type deposit	amp-hr†	C.E., %	Deposit weight, g	Deposit thickness, mil	D in deposit, g/plate × 10^5	D found in coating and steel specimen by vacuum fusion, mm³/spec.*	g/spec. × 10^5	Estimated quantity of D in steel, g/spec. × 10^5	Embrittlement Crushing rate ≅ 0.05-0.1 in./min Load reduction, %*	Deformation reduction, %*	Crushing rate ≅ 0.005-0.02 in./min Load reduction, %*	Deformation reduction, %*
Cd	0.125	92	0.241	0.8	0	^{2}150	2.7	2.7	^{10}3.0	^{10}13.2	^{2}5.5	^{2}20.4
Cu	0.07	60	0.100	0.3	0‡	^{5}180	3.2	3.2	^{16}6.5	^{16}17.2	^{1}9.8	^{1}33.2
Cr	0.625	18	0.036	0.14	3.4**	^{5}500	8.5	5.1	^{5}3.7	^{5}25	^{5}15	^{5}44
Ni	0.125	99	0.137	0.44	2.0**	^{3}350	6.3	4.3	—^{6}1.95	^{2}2.4	—	—

† Plating time was 15 min.
* Superscripts are the number of specimen averaged.
** Quantity of deuterium estimated [on basis of analysis for hydrogen in Cr and Ni plate given by Brenner, Burkhead, and Jennings (19)].
‡ Assumption.

A higher precision of testing was obtained with the new specimens. Embrittling tests by plating could be reproduced within 2 or 3% while previously the variation was from 2 to 7%. Hence, any radical scatter in results with the new specimens must be attributed to such things as the nature of the steel, nature of the embrittling process, variations in the plating procedures, speed of testing, etc. These new specimens were used for the study of the effect of crushing speed, discussed below.

Use of slower crushing speeds.—Some results obtained with chromium-plated specimens indicated that low precision might result from the use of a too-rapid crushing speed. That is, the deuterium embrittlement accompanying chromium plating was unexpectedly low, only 3.7% (determined by load) while the deuterium content of the specimen was not low, but 100 mm³/g of steel (see Table VII). This low embrittlement could conceivably result from too fast a test rate, if the rate-controlling step leading to embrittlement is dependent on the rate of diffusion of gas within the steel.

In order to define crushing conditions which establish the best reproducibility for embrittlement tests several crushing speeds were investigated. The rate of crushing specimens in most of the studies reported herein was 0.1 in./min. Slower speeds, determined at the time the specimens broke, were investigated and included the following rates: 0.05, 0.02, 0.01, and 0.005 in./min. The embrittling techniques included chromium, copper, and cadmium plating from D_2O baths. The average values of several experiments are shown in Table VII, and a graph of some of the results are shown in Fig. 6.

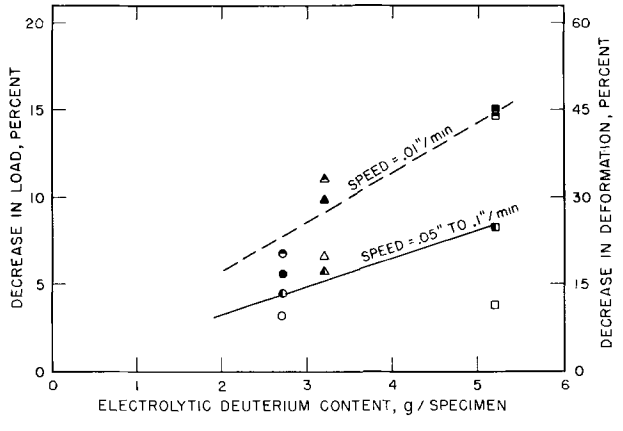

Fig. 6. Effect of different dynamic crushing speeds on the measured embrittlement. Plating conditions given in Table VII.

Type of Plate	Embrittlement measured by Load	Deformation
Cd	○, ●	◐, ◓
Cu	△, ▲	◭, △
Cr	□, ■	◧, ◨

Chromium showed the largest variation in magnitude of embrittlement with crushing speed. The deuterium embrittlement was 3.7% (by load) and 25% (by deformation) for both crushing speeds of 0.1 and 0.05 in./min; however, when the crushing speeds were slowed to 0.02 or 0.01 in./min, the embrittlement was 15% (by load) and 44% (by deformation). Similarly, the hydrogen embrittlement was changed from 27% (by load) and 57.3% (by deformation) for a crushing speed of 0.07 in./min to 35% (by load) and 63.8% (by deformation) for a speed of 0.01 in./min.

The data indicate that the change in the magnitude of the measured embrittlement with the speed of crushing may be a function of the quantity of gas present in the steel. The rate of crushing changes the measured embrittlement more drastically in the case of chromium plating than it does in the cases of cadmium and copper plating (Fig. 6).The significance of the abrupt change in measured deuterium embrittlement at a change in crushing rate from 0.02 to 0.05 in./min is not understood.

Effect of Aging or Heat Treatment on Retention of Embrittlement and of Gas in Steel

The current theories of hydrogen embrittlement assume that the recovery of an embrittled specimen with aging or heat treatment is a result of the escape of the hydrogen. Similarly, the preservation of the embrittlement of a cathodically charged specimen of steel by storage at −196°C is attributed to the negligible escape of gas at low temperature, which is illustrated in Fig. 7.

Experiments by Probert and Rollinson (10) have shown that hydrogen embrittlement of steel plated with 0.45 mil of cadmium can be reduced and possibly eliminated by heat treatment at 190°C for 5 or 6 hr. Federal specifications (11) recommend not less than 3 hr of heat treatment at 190° ± 14°C for steel plated with 0.5 mil of cadmium.

Experiments were started to ascertain whether the electrolytic gas actually diffuses through the

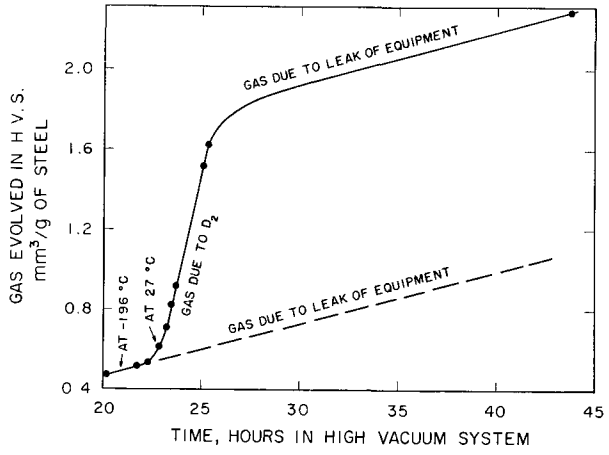

Fig. 7. Deuterium evolved from ring in high vacuum system. Ring was: (*a*) cathodically charged in 10% NaOD in D_2O at 3.5 amp/dm² for 150 min; (*b*) held at room temperature for 39 min while being transferred into high vacuum system; (*c*) stored in H.V.S. at —196°C for 22.5 hr; (*d*) coolant removed and steel gradually warmed to room temperature; in 3.5 hr, 1.8 mm³ deuterium/g of steel was liberated, after which no more gas was evolved.

coating and escapes or whether it diffuses throughout the steel and remains in the form of a dilute solution with no concentration gradient. Knowledge of the gas content of the heat-treated steel would help answer this question.

Cadmium-plated steel rings, coated to a thickness of 3.8 mils in a D_2O bath, were heat treated at 190°C in an oil bath, crushed, and analyzed for the retention of deuterium. The steel retained both embrittlement and deuterium after 6 hr at 190°C. Experiments are being continued to determine whether deuterium can be eliminated completely from the steel through fairly thick as well as thin cadmium coatings. Data obtained to date indicate that a longer period of heat treatment (in an oil environment) is required to relieve cadmium-coated steel of deuterium embrittlement than of hydrogen embrittlement.

Heat Treating at 350°-500°C in High Vacuum as a Method of Analysis for Electrolytic Deuterium Content of Steel without Melting the Steel

All of the analyses in this present paper were performed by the tin fusion method. This requires that each specimen of steel be melted by alloying with tin at 1100°C. This method has a definite advantage in that all of the gases in the steel are liberated rapidly for analysis. The main disadvantage involves the frequent recharging of the furnace with tin.

Uncoated steel when heated to 310° for 10 min releases all of the electrolytic gas [see Fig. 6 of Part I (1)]. At this or higher temperatures some of the metallurgical hydrogen (12) is liberated along with the electrolytic hydrogen, and, as in the tin fusion method, a differentiation between the source of hydrogen cannot be made. In the present work, the liberation of all of the electrolytically charged deuterium is all that is required. If the method liberates metallurgical hydrogen, the mass spectrograph can be used to determine the quantity of each isotope present.

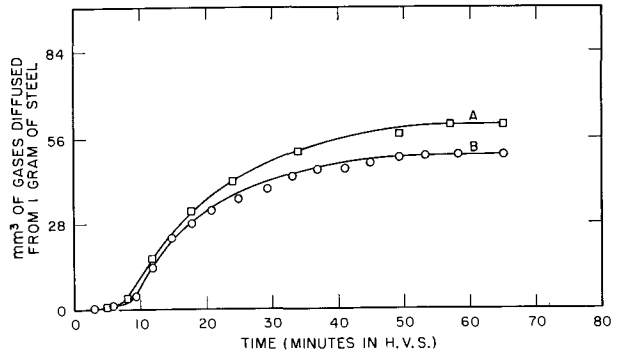

Fig. 8. Quantity of gases which diffused from copper-coated steel held at 500°C. SAE 4130 steel ring (5g), Cu-coated in cyanide bath for 15 min at 1.85 amp/dm². Curve A, not covered with Cu evenly under contact clip. Curve B, even coating of Cu; total gas collected, analyzed, and found to contain 64.3% of deuterium (equivalent to 25.6 mm³ of deuterium/g of steel at room temperature).

A simple method of releasing the gas for analysis would be quite desirable; therefore, the finding of conditions for heating coated steel easily in a Pyrex vessel was undertaken. As an initial experiment, copper-plated steel was heated to 500°C in a Pyrex tube connected to the high vacuum system, and the gases were collected and analyzed. The rate of liberation of electrolytic deuterium is shown in Fig. 8. The gas liberated during a 65-min heating period contained 25.6 mm³ of deuterium/g of steel. The copper-plated steel was then melted, and any gases remaining in the steel were collected and analyzed. Nearly all of the deuterium had diffused through the copper in 1 hr at 500°, because only 1 mm³ of deuterium/g of steel was found in the melted steel. A slightly longer period of heating most probably would have liberated the remainder. Thus, the heating of plated steel in a vacuum at 500°C appears to be an adequate method of extracting electrolytic deuterium for analysis. The period of heating would vary with the particular coating. A lower extraction temperature would be adequate for some coatings, for example, cadmium (mp 320.9°C).

Determination of Depth of Penetration of Deuterium in Steel with Time

One experiment was performed to determine the depth of penetration into steel of electrolytic deuterium introduced by cadmium plating. Other authors (10, 13) have indicated that hydrogen remains close to the surface. A steel ring was plated with cadmium on its edges and inside surface in a bath made with H_2O. After heat treatment to eliminate any electrolytic hydrogen, the ring was plated on its outside surface with cadmium in a bath made with D_2O. Electrolytic deuterium entered the steel from only one surface, and cadmium coatings acted as a barrier to its exit from the other surfaces. The ring was immediately cooled to liquid nitrogen temperature. The cadmium coating on the outside surface and steel to the depth of 0.005 in. were machined from the ring while it was held at liquid nitrogen temperature. Only 10.0 mm³ deuterium/specimen was found in the portion of the ring and cadmium left after the outer surface had been machined off. Unmachined rings, which had been cadmium coated

in the same fashion, contained 75 mm^3 deuterium/specimen. This preliminary experiment indicates that most of the electrolytic deuterium introduced during plating is still near the surface of the steel immediately following the plating operation.

Discussion and Results

The plating processes discussed herein involve the codeposition of a metal and hydrogen or deuterium atoms. The surface reaction involving hydrogen may or may not be complicated by the change of the composition of the metallic surface from steel to that of the codeposited metal. The solubility of hydrogen and deuterium in cadmium and copper coatings is practically nil. Yet, during the first 15 min of plating the electrolytic gas content of the plated specimens increases according to the following relationship as shown in Fig. 2: $C = k\sqrt{t}$, where C is the absorbed volume, k is a constant, and t is the time of plating. This would suggest that the charging process on the plated surface is diffusive in character. In the case of chromium and nickel plating the charging process appears to be more complicated, probably due to the solubility of the electrolytic gas in the plated coating on the steel.

These studies have shown that the presence of coatings of cadmium, copper, or chromium on steel does not prevent the entrance of atomic hydrogen or deuterium during the first 30 min of plating. Nevertheless, the degree of hydrogen embrittlement does not increase linearly with this constant increase in hydrogen content. Instead, a maximum embrittlement is approached. Results of plating chromium, copper, and cadmium to thicknesses of 0.14, 0.3, and 0.8 mils, respectively, (deposits produced in 15 min of plating) indicated that no maximum embrittlement was attained with increasing quantities of deuterium. More deuterium than hydrogen is required to attain comparable embrittlements.

With the limited experiments in this study, a general correlation between the degree of embrittlement and the electrolytic gas content of plated steel specimens was not found. Yet, a strong correlation was found when the gas contents were corrected for the solubility of gas in the chromium coatings as indicated in Table VII. A plot of per cent deuterium embrittlement *vs.* the average deuterium content introduced into steel by different plating processes during a 15 min plating period was made in Fig. 6. It showed that the embrittlement increased as the electrolytic deuterium content in the steel increased. Apparently, different quantities of atomic deuterium entered the steel due to the differences in the amount of gas evolved during the different plating processes. These experiments indicate that the embrittlement is dependent more on the amount of deuterium which actually entered the steel than on the type of plating process.

The per cent embrittlement measured was found to be dependent not only on the amount of gas present in the steel but on the speed with which the rings were crushed as shown in Fig. 6. Uncharged rings from similarly heat-treated steel stock failed at similar breaking loads for the crushing speeds investigated. Thus, the mechanism of embrittlement appears to be dependent on the time permitted for the gas to diffuse within the steel to the point of failure.

During the course of these studies many cases of lack of parallelism between embrittlement and total gas content were encountered. For example, although the curves in Fig. 3 representing deuterium embrittlement produced by different plating processes did not fall on top of each other, all of these curves could be averaged with a variation of no more than $\pm 2\%$ after correction is made for the gas content of the chromium coatings. This may be the limit of accuracy of this type of embrittlement test, or the embrittlement measured in the steel may not be solely dependent on the electrolytic gas content and the speed of crushing test. Other explanations are not readily available.

From the data presented in Parts I (1) and II of this study it appears reasonable to conclude that deuterium embrittles steel. The analyses (1) of plating solutions discussed in Part II gave a range for $(H/D)_{liq}$ from 0.005 to 0.007. If it is assumed that the gases which enter the steel during plating are equivalent to the gases which permeated steel in electrolytic charging unaccompanied by metal deposition, then the enrichment with respect to hydrogen would be eightfold (1). The $(H/D)_{Gp}$ ratio pertaining to the gases which entered the steel would then range from 0.041 to 0.056. The maximum quantity of hydrogen entering the steel during plating would have been 2.5 mm^3 hydrogen/g of steel accompanying 45 mm^3 deuterium/g of steel. This amount of hydrogen would produce no more than 1.5% embrittlement (by load) as seen in Fig. 3. This would not account for the 6% or larger embrittlement found in steel resulting from plating in D_2O solutions.

Hydrogen and deuterium both affect the plastic properties of steel, but to different degrees. Figure 3 shows that smaller amounts of hydrogen than deuterium cause larger embrittlements. This conclusion is reliable because some of the data are the averages of a large number of fairly closely reproduced replicates. An example of this average data is given in Table VII.

Steel, electroplated with a metal from a given type of bath, absorbs larger quantities of electrolytic gas when the bath is operated under conditions that decrease its cathode efficiency. For example, increase in the concentration of the free cyanide in a copper bath increases the amount of absorption of hydrogen by a steel cathode.

In comparing the cyanide-type baths, the data indicate that copper plating causes more severe embrittlement of steel than does cadmium plating under the conditions studied. These baths are alike in character and can be further compared. During a given period of plating, *e.g.*, 15 min, a thicker deposit of cadmium is produced (~0.8 mils at 0.5 amp/spec.) than of copper (~0.3 mils at 0.28 amp/spec.) (see Table VIII). Cadmium plating produces less hydrogen embrittlement of steel than does copper plating. This may be due to either the faster build up of cadmium deposit or to the lesser permeability of cadmium to hydrogen. Other authors (14)

have indicated that the cyanide ion catalyzes hydrogen embrittlement of steel charged in alkaline solution. If this were the sole factor controlling embrittlement during plating from cyanide-type baths, cadmium would be expected to embrittle steel more than copper, since the free cyanide concentration is much higher in the cadmium plating bath. Thus, it can be concluded that the quantity of gas which enters steel during plating must be dependent on factors in addition to cyanide ion concentration.

Permeation studies (1) have shown the diffusion coefficients for hydrogen and deuterium in steel to be $D_H = 1.25 \times 10^{-7}$ cm^2/sec and $D_D = 1.1 \times 10^{-7}$ cm^2/sec. The magnitudes of embrittlement produced by hydrogen and deuterium are quite different even though they diffuse within the steel at about the same rate. Electroplating processes have been shown to introduce more deuterium than hydrogen into steel, yet hydrogen embrittles steel more than deuterium. Diffusion studies in unstrained steel present no apparent explanation for the differences in the magnitude of hydrogen and deuterium embrittlement.

The differences between the action of hydrogen and deuterium during the brittle fracture of steel most probably are due to the differences in the physical and chemical properties of the isotopes. Pertinent to the present discussion is the work of Sidhu (15). This author has shown that metals which readily form hydrides have different chemical affinities for hydrogen and for deuterium and that deuterium causes more shrinkage of the metal lattice than does hydrogen. Similar differences can be expected for hydrogen and deuterium in steel even though the solubility of either gas is small in the body-centered cubic lattice of iron probably due to the size of the spacings within the lattice structure (16). Such differences would help to explain the variation in embrittlement caused by the two isotopes. The precise way in which hydrogen is distributed within the lattice and voids during the straining of steel has not been explained. Nevertheless, the present data indicate that deuterium changes the plastic properties of steel less than hydrogen.

Conclusions

1. Electrolytically introduced hydrogen or deuterium does not appear to be trapped in internal cracks as molecular gas, which cannot readily diffuse at room temperature from the steel.

2. Deuterium appears to cause embrittlement of SAE 4130 steel but to a smaller degree than does hydrogen. On the other hand, plating processes introduce more deuterium into steel from heavy water solutions than hydrogen from ordinary water solutions.

3. The quantity of electrolytic gas introduced into steel gives some correlation with the degree of embrittlement of the steel, but it is not the sole factor determining the magnitude of embrittlement measured.

4. The present work does not preferentially support any one of the mechanisms (5-8, 17, 18) which have been proposed for hydrogen embrittlement. Deuterium would be expected to diffuse more slowly than hydrogen into voids or within the lattice due to the greater expected chemical affinity of steel for deuterium than hydrogen. The difference in the behavior of the hydrogen isotopes has not explained the way hydrogen is distributed between the so-called voids, dislocations, or interstitial sites during the straining of steel.

5. The plating processes studied introduce larger quantities of electrolytic gas into steel than does electrolytic charging, in either a 10% solution of sodium hydroxide or a 4% solution of sulfuric acid. If a poison such as carbon disulfide is present in the sulfuric acid, comparable or larger quantities of hydrogen are introduced into steel (even during short charging times) than by the plating processes studied.

Acknowledgment

The author expresses her sincere appreciation to Dr. A. Brenner, National Bureau of Standards, for his advice and guidance during the course of this investigation and to the National Aeronautics and Space Administration and to the Metallurgy and Ceramics Research Branch, Aeronautical Research Laboratory, United States Air Force, for their financial support during part of this investigation.

Manuscript received Sept. 18, 1962; revised manuscript received Mar. 29, 1963. This paper was presented at the Columbus Meeting, Oct. 18-22, 1959.

Any discussion of this paper will appear in a Discussion Section to be published in the June 1964 JOURNAL.

REFERENCES

1. G. B. Wood, *This Journal*, **110**, 867 (1963).
2. L. S. Darkin and R. P. Smith, *Corrosion*, **5**, 1 (1949).
3. J. B. Seabrook, N. J. Grant, and Dennis Carney, *Trans. AIME*, **188**, 1317 (1950).
4. Taiji Toh and W. M. Baldwin, Jr., "Ductility of Steels with Different Amounts of Hydrogen," ONR Contract N6-ONR-273/I, Jan. 1955.
5. F. deKazinczy, *J. Iron Steel Inst.*, **177**, 85 (1954).
6. N. J. Petch and P. Stables, *Nature*, **169**, 843 (1952).
7. E. A. Steigerwald, F. W. Schaller, and A. R. Troiano, *Trans. AIME*, **251**, 1048 (1959).
8. J. G. Morlet, H. H. Johnson, and A. R. Troiano, *J. Iron Steel Inst.*, **189**, 37 (1958).
9. R. M. Hudson, W. G. Norris, and G. L. Stragand, *Ind. Eng. Chem.*, **51**, 319 (1959).
10. L. E. Probert and J. J. Rollinson, *Electroplating and Metal Finishing*, **14**, 396 (1961).
11. Federal Specification, "Plating, Cadmium (Electrodeposited)," QQ-P-416a, Dec. 11, 1956.
12. C. E. Sims, G. A. Moore, and D. W. Williams, *AIME Met. Tech.*, Oct. 1948, TP 2454.
13. R. P. Frohmberg, W. J. Barnett, and A. R. Troiano, *ASM Trans.*, **47**, 892 (1955).
14. W. Beck and E. J. Jankowsky, *Tech Proc. Am. Electroplaters' Soc.*, **1960**, 152.
15. S. S. Sidhu, L. Heaton, and M. H. Mueller, *Proc. 2nd Intern. Conf. Peaceful Uses At. Energy*, Geneva, 1958 **14**, 212.
16. W. Hume-Rothery and G. V. Raynor, "The Structure of Metals and Alloys," pp. 216-218, Institute of Metals (1954).
17. C. A. Zapffe and C. E. Sims, *Trans. AIME*, **145**, 225 (1941).
18. A. S. Tetelman Thesis, The School of Engineering of Yale University, 1960.
19. A. Brenner, P. Burkhead, and C. Jennings, *J. Research Natl. Bur. Standards*, **40**, 37 (1948).

A Technique for the Evaluation of Hydrogen Embrittlement Characteristics of Electroplating Baths

M. A. V. Devanathan and Z. Stachurski
Electrochemistry Laboratory, University of Pennsylvania, Philadelphia, Pennsylvania
and W. Beck
Aeronautical Materials Laboratory, Naval Air Engineering Center, Philadelphia, Pennsylvania

ABSTRACT

A simple electrochemical technique is described for measuring the quantity of hydrogen permeating a thin membrane of iron or steel during cathodic charging or electroplating. For cadmium electroplating, the quantity is small when this metal is deposited from a fluoborate or a DL-α-amino-n-butyrate bath, but comparatively high when a cyanide bath is used. The mechanism which governs hydrogen permeation in alkaline solutions containing capillary active anionic species is discussed, and the remarkable similarity between hydrogen permeation and hydrogen induced brittle fracture of high strength steel is demonstrated.

As an unavoidable electrode reaction proceeding simultaneously with electroplating, hydrogen ions or water molecules are discharged. The product of this discharge is atomic hydrogen which can either recombine and evolve as molecular hydrogen or diffuse into the interior of the metal. Atomic hydrogen, when introduced into and subsequently absorbed in high strength steel parts, may cause reduction in ductility or delayed brittle cracking of notched tensile specimens subjected to sustained static loading.

A simple and precise electrochemical procedure is described, suitable for the determination of the quantity of hydrogen penetrating through thin membranes of iron or steel during any type of cathodic treatment. Because of the results of this study, it is believed that this method will appropriately serve as a basis for a standard test from which useful information can be obtained about the hydrogen embrittlement characteristics of a plating bath.

Principle of the Procedure

Thin iron or steel membranes are used for the measurements. One side of the membrane, the cathode side, is subjected to the cathodic treatment, and a small fraction of the simultaneously formed hydrogen atoms introduced into the membrane reaches the opposite side, in contact with a 0.2*N* NaOH solution.

This side is called the anode side because the hydrogen atoms arriving at the metal solution interface are almost quantitatively ionized by an applied anodic potential. Thus, diffusion of hydrogen takes place under conditions resembling those of polarographic measurements with the membrane as the diffusion layer and with a concentration gradient of the hydrogen through the membrane.

Electrolytic Cell and Electrical Circuit

Two carefully polished glass tube flanges (Fig. 1), coupled with the membrane, are bolted together and a water tight seal produced by using Teflon washers. The polarizing electrodes consist of platinum covered with platinum black, and the surface of the membrane facing the anode compartment is in contact with a Luggin capillary, coupled to a saturated calomel electrode (1). During the measurements, high-purity nitrogen was continually bubbled

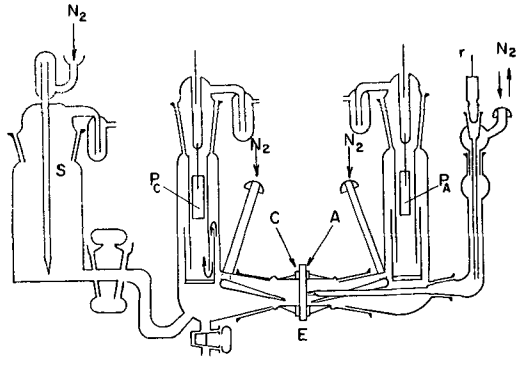

Fig. 1. Electrolytic cell: E, iron or steel membrane; C, cathodically treated side of membrane; A, anodically polarized side of membrane; P_C, P_A, polarizing electrodes; r, saturated calomel reference electrode; s, container with experimental solution.

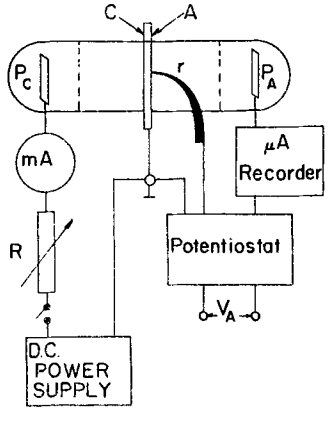

Fig. 2. Galvanostatic circuit: R, power decade resistor; other symbols as in Fig. 1.

through all solutions. The temperature was kept constant at 25° ± 1°C.

For both cathodic charging and plating, a simple galvanostatic device was used as shown in Fig. 2. The anodic polarization circuit consisted of a Wenking potentiostat with a sensitive current recorder in series. A Sargent polarograph, with the bridge set at zero, having the required sensitivity and a sufficiently wide measuring range, was used as the recorder.

Operation of the Electrolytic Cell

The cell was operated as follows. The anode compartment was filled with a 0.2*N* NaOH solution, containing 10^{-5} mole/liter palladium nitrite complex and a very thin layer of palladium electrodeposited, which prevents anodic dissolution or passivation of iron without materially decreasing the permeation rate of the hydrogen atoms. After completion of plating, a potential maintained at —0.600v (SCS) is applied, and the hydrogen leaving the presaturated membrane is removed by oxidation until the current in this anode circuit becomes very small and constant. Finally, the cathode compartment is filled with the experimental solution and cathodic polarization begun, using a galvanostatically controlled current density of 8.1 ma/cm^2. The hydrogen, permeating the membrane and the palladium film, is ionized by an applied anodic potential. The hydrogen permeation current produced in this manner is monitored by the recorder, and from the recorded charts the quantity of hydrogen which permeates the membrane can be calculated.

Pretreatment of Membranes

Membranes of Armco iron, tempered as rolled, 0.77 mm thick, after heating for 2 hr at 600°C, and cooling to room temperature in a streaming hydrogen atmosphere, were used (2).

This pretreatment, not applicable to the high strength steel with a tempering temperature of about 400°F, was, therefore, replaced by a cathodic treatment in 0.1*N* H_2SO_4, using a current density of 10 ma/cm^2 which was maintained for a period of 6 hr. The high strength steel specimens were polished after this treatment with fine emery paper to a smooth finish. Presaturation with hydrogen is indispensable for the attainment of uniform permeation during any type of cathodic treatment.

After completion of the above described procedures, all membranes were etched for 20 sec in a solution consisting of a milliliter of conc. H_2SO_4 in 100 cc of methyl alcohol and, prior to drying, carefully rinsed with distilled water. By this treatment, not only the adherence of the electrodeposits is improved, but also the reproducibility of the permeation measurements which were started shortly after rinsing.

Results

Typical permeation curves are plotted in Fig. 3 to 6. As can be seen from curve 2 in Fig. 3, addition of NaCN to the NaOH solution brings about a tremendous increase in the hydrogen permeation. The trend of curve 3, obtained for the amino butyrate solution is more complex than that for the CN$^-$-containing solution because the steep initial rise is followed by a rather rapid fall and, on account of that, the steady-state permeation is considerably below that resulting in the CN-containing solution.

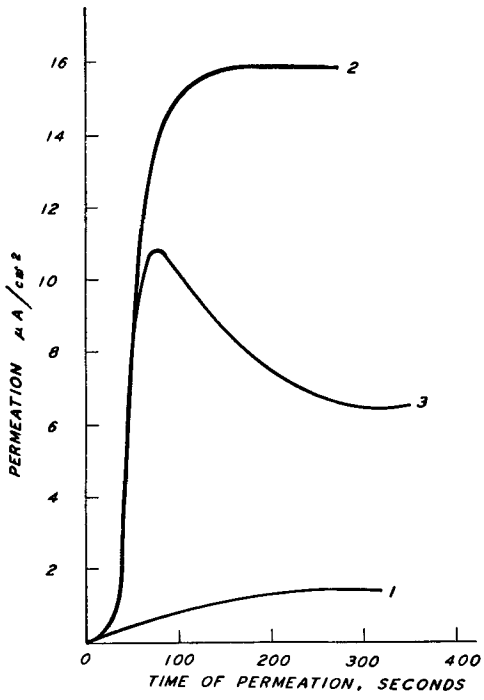

Fig. 3. Dependency of permeation on time of cathodic charging. Armco iron membrane, 0.77 mm thick; cathodic current density 8.1 ma/cm^2. Curve 1, NaOH solution; 2, NaOH + NaCN solution; 3, amino butyrate solution.

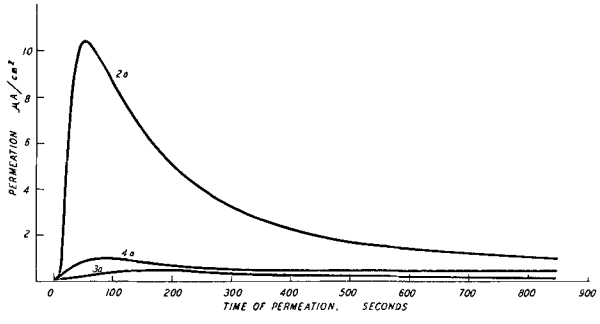

Fig. 4. Dependency of permeation on cadmium plating time. Armco iron membrane, 0.77 mm thick; plating current density 8.1 ma/cm^2. Curve 2a, standard cyanide bath; 3a, amino butyrate bath; 4a, fluoborate bath.

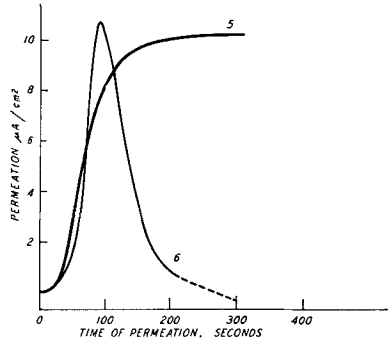

Fig. 5. Dependency of permeation on time without and with iron plating. Armco iron membrane, 1.04 mm thick; cathodic current density 8.1 ma/cm^2. Curve 5, acetate buffer; 6, ferrous sulfate-sodium sulfate iron plating bath.

Still more complex is the trend of the curve obtained from the saturated ammonium fluoborate solution which, therefore, is not plotted. The steady-state permeation in this solution is again rather low and only about 4.0 μa/cm^2.

As demonstrated in Fig. 4, the trends of the curves are markedly changed when the permeation measurements are made in conjunction with electrodeposition. During plating from the cyanide bath (curve 2a), initially, the permeation current recorded in the anode circuit rises rapidly, whereas the permeation throughout a following period drops gradually until it becomes insignificant.

Similar features, although much less marked, can be distinguished on the curves based on measurements on specimens plated from the other two cadmium baths (curves 3a and 4a).

The trend of curve 6 in Fig. 5, which depicts results obtained with plating iron on iron, deviates from the other plating curves insofar as the initial steep rise is abruptly followed by a fall which is just as rapid and finally results in a permeation of a negligible order. In contrast, on curve 5 obtained from measurements in the acetate buffer, a rather high steady-state permeation can be distinguished.

In Fig. 6, measurements are plotted, which were obtained from high strength 4340 steel. The permeation through both plated and unplated steel is much slower than through Armco iron. Again, in the presence of a cadmium layer, the permeation is depressed to values almost as low as those obtained from a pure NaOH solution.

The total quantity of hydrogen permeating the membrane during cadmium plating is obtained by integration of the i-t curves, presented in Fig. 4, and results are compiled in Table I.

These values again demonstrate impressively that the quantity of hydrogen permeating the membrane during cyanide cadmium plating exceeds by far that produced during electroplating from the other two baths.

Discussion

In this section, several variables are considered which are involved in the mechanism that controls hydrogen permeation through thin membranes of iron or steel during electroplating. The discussion is partially based on the results obtained from charging experiments in solutions with a composition similar

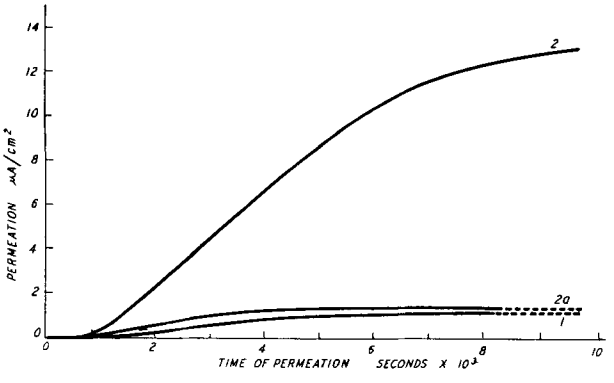

Fig. 6. Dependency of permeation on time without and with cadmium plating. High strength 4340 steel membrane, 1 mm thick; cathodic current density 8.1 ma/cm^2. Curve 1, NaOH solution; 2a, standard cyanide plating bath; 2, NaOH + NaCN solution.

Table I. Quantity of hydrogen in moles 10^{-9} per 1 cm^2 permeating Armco iron membranes during electrodeposition of cadmium from different baths

		Temperature 25° ± 1°C H-permeation after:		
No. of curve in Fig. 4	Designation of bath	400 sec, a	following 400 sec, b	total a + b
2a	Cyanide	21.46	5.92	27.38
4a	Fluoborate	2.66	1.77	4.43
3a	Amino butyrate	1.29	0.71	2.00

to the plating baths but without the presence of the metallic complex. In addition, a comparison is made between hydrogen induced brittle fracture of cadmium plated high strength steel and hydrogen permeation through Armco iron membranes during plating from identical baths.

As discussed elsewhere, the rate of hydrogen permeation through a thin iron membrane is proportional to the concentration of hydrogen atoms covering the metal surface when subjected to cathodic polarization (2). The steady state permeation in curve 1 in Fig. 3 reached after an initial sigmoid shaped rise, is considered an indication of the attainment of a constant hydrogen coverage. The same is true for cathodic polarization in the other alkaline and acidic solutions, as shown by curves 2, 3, in Fig. 3 and curve 5 in Fig. 5. A comprehensive theoretical analysis of curves of type 1 in Fig. 3 has recently been presented elsewhere (1).

An experimental study and theoretical analysis (3) has disclosed that CN^-, which is strongly chemisorbed during cathodic polarization of a steel surface, effectively retards the recombination rate of simultaneously adsorbed hydrogen atoms. The chemisorption increases rapidly with polarization time, and this results in a rise in the hydrogen coverage and creation of a steep hydrogen concentration gradient at the steel surface.

This mechanism explains the rapid initial rise of permeation in the CN^--containing charging solution and the relatively high steady-state hydrogen coverage. If in the strongly alkaline solution, the amino butyrate anion is also chemisorbed, essentially the same mechanism applies as found appropriate for cyanide. However, in the amino butyrate solution (curve 3, Fig. 3), the generally considerably lower permeation current apparently indicates a higher hydrogen recombination rate than in solutions containing CN anions.

Hydrogen coverage in acidic solutions appreciably exceeds that in alkaline solutions (3) which is reflected in the much higher steady-state permeation in the acetate buffer than in the pure NaOH solution (Fig. 5 and 3).

Regarding the permeation in conjunction with electrodeposition, it is suggested that the following facts be taken into consideration. If the electrodeposited metal has a lower permeability than the basis metal, it would be expected that within a rather short initial period of electrodeposition, resulting in an extremely thin plated layer, the rate of hydrogen permeation would be determined primarily by the permeability of the iron itself. However, throughout a second phase of the process of electrodeposition,

the permeation predominantly would be controlled by variables such as hydrogen coverage, permeability, and barrier effectiveness of the electrodeposited coating. Cadmium has a lower permeability than iron, and the curves presented in Fig. 4 and 6 will now be discussed in the light of the just mentioned variables.

The limited barrier effectiveness of the very thin cadmium film and the relatively low hydrogen coverage are considered the reasons for the fact that the ascending branch of curve 2a in Fig. 4 is something below that of curve 2 in Fig. 3. The descending branch of curve 2a reflects primarily the barrier effectiveness of the plated layer which is enhanced with rising thickness.

As compared with the permeation during cyanide cadmium plating, that during electrodeposition from the amino butyrate bath, particularly throughout the initial period, is much lower. This is probably the result of the action of the cadmium barrier as well as the higher recombination rate of the hydrogen atoms (compare curves 2 and 3 in Fig. 3). Likewise, an explanation of the low permeation during plating from the fluoborate bath would consider, besides the barrier action of the electrodeposit, the low steady-state hydrogen coverage.

The remarkable effectiveness of the iron layer (curve 5, Fig. 6) in rapidly inhibiting hydrogen permeation, might be on account of an immobilization of hydrogen atoms by the formation of iron-hydrogen compounds.

The results obtained on high strength 4340 steel are plotted in Fig. 6. The permeability of this steel is similar to that of Armco iron and, therefore, it is concluded that on both materials, unplated and cadmium plated, the hydrogen permeation is controlled by the same variables. However, there are great differences between the hydrogen diffusion constants for Armco iron and the hardened steel alloy. The following values were calculated:

$$D'_{25°\pm1°C} = 8.3 \times 10^{-5}\ cm^2\ sec^{-1}$$
$$D''_{25°\pm1°C} = 2.0 \times 10^{-7}\ cm^2\ sec^{-1}$$

D′ signifies Armco iron and D″ AISI 4340 Steel (UTS = 260-280 ksi).

The differences in the diffusion coefficients could be caused by differences in the hydrogen solubility. If similar coverage is anticipated, the hydrogen solubility in the high strength steel would then be about 400 times greater than in Armco iron. Differences in hydrogen solubility in pure iron and steel alloys, respectively, have been attributed to various causes (4).

It is of interest to compare the diffusion constants derived from the electrochemical measurements with those from more orthodox methods. The diffusion constant for SAE 4130 steel, heat treated to a strength level similar to that of the steel used in this study, was determined to be 1.25 x 10^{-7} cm^2 sec^{-1} at 25°C (5), which compares favorably with that given above for 4340 steel. Calculation of the diffusion constant from the measurements on pure α iron by Geller and Sun (4) yields 2 x 10^{-5} cm^2 sec^{-1}, which is in fair agreement with the value for Armco iron obtained in this study.

Finally, the question arises of whether correlation exists between embrittlement induced by hydrogen during plating of steel with the total quantity of hydrogen permeating the Armco iron membrane during plating under comparable conditions.

The available number of appropriate embrittlement measurements on high strength 4340 steel cadmium plated from the three baths used in this study is too limited to permit a statistical correlation with the permeation data. So far, it appears possible only to make a comparison between these measurements. In the literature (6, 7) are reported reduction in area measurements and fracture values on bend test specimens, deflected in compression. Also available are measurements of times to failure at various applied stresses on notched tensile specimens subjected to sustained loading and average survival times (8) of the same type of specimens stressed to 75% of the unplated notched tensile strength, which broke in less than 100 hr of sustained loading.

Bend fractures, reductions in area, and strengths of specimens under sustained loading, employed for the evaluations to be described below, are the averages of 3 determinations. Calculation of the average survival time for specimens plated with cyanide cadmium are based on measurements on 9 tensile bars and, for those plated with amino butyrate cadmium, on measurements on 18 bars. Thickness of the cadmium layer electrodeposited from the amino butyrate bath, measured on the unnotched sections, was approximately 0.0007 and from the other baths, approximately 0.0005 in.

The values plotted in the histogram, Fig. 7, were obtained as follows. In Section I, the total quantity of hydrogen permeating the Armco iron membrane during cyanide cadmium plating was set equal to 100, and the calculation of the plotted percent permeation during plating from the other two baths was based on this value. In Section II, the difference between deflection at fracture of the unplated specimens and that of the cyanide cadmium plated bend specimens is again set equal to 100 and the calculation of the plotted per cent reduction in fracture deflection of the fluoborate plated specimens is based on this relationship. Similar calculations were made with reduction in area measurements.

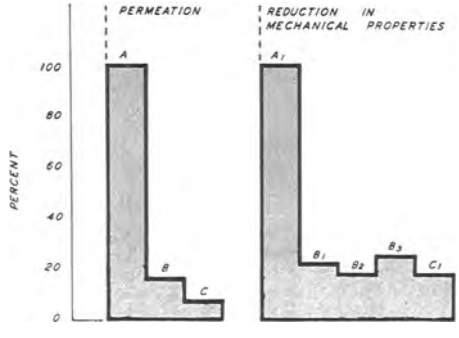

Fig. 7. Histogram: Letters without index designate Armco Iron Membranes; those with index, specimens of AISI 4340 Steel, 260-280 ksi: A, A_1, cyanide cadmium plated specimens; B, B_1, B_2, B_3, ammonium fluoborate cadmium plated specimens; C, C_1, aminobutyrate cadmium plated specimens; A_1, all mechanical tests; B_1, deflection at fracture; B_2, reduction in area; B_3, notched tensile strength after 1000 hr of sustained loading; C_1, deflection at fracture.

Likewise, the per cent reduction in strength due to fluoborate plating is based on the notched tensile strengths of the unplated specimens and the strengths of the fluoborate cadmium plated specimens after 1000 hr of sustained loading.

The histogram, Fig. 7, indicates clearly the close relationship between the total quantity of hydrogen permeating the Armco iron membrane during plating with cadmium from the 3 different baths with the hydrogen induced brittle fracture of the high strength steel. The same is true for the average survival time which is increased 200 times when specimens are plated from the butyrate instead of from the cyanide bath.

Acknowledgments

The authors are much indebted to Dr. J. O'M. Bockris, Professor of Chemistry, University of Pennsylvania, Mr. Sam Goldberg, Bureau of Naval Weapons, and Mr. F. S. Williams, Superintendent, Metallurgical Division, Aeronautical Materials Laboratory, Naval Air Engineering Center, for the keen interest they have taken in this investigation. The financial support of the work at the University of Pennsylvania by the Naval Air Engineering Center, Philadelphia, is gratefully acknowledged.

Manuscript received Jan. 31, 1963.

Any discussion of this paper will appear in a Discussion Section to be published in the June 1964 JOURNAL.

REFERENCES

1. M. A. V. Devanathan and Z. Stachurski, *Proc. Roy. Soc.*, **A270**, 90 (1962).
2. M. A. V. Devanathan and Z. Stachurski, To be published.
3. W. Beck, A. Glass, and E. Taylor, To be published.
4. W. Geller and T. H. Sun, *Archiv. Eisenhuttenwesen*, **51**, 430 (1950).
5. G. Wood, Private communication.
6. W. Beck and E. J. Jankowsky, Report No. NAMC-AML-1059, Aeronautical Materials Laboratory, issued 10 June 1958.
7. W. Beck and E. J. Jankowsky, *Proc. Am. Electroplaters' Soc.*, **47**, 152 (1960).
8. P. N. Vlannes and S. W. Strauss, *Plating*, **46**, 1051 (1959).

APPENDIX

Charging and Plating Solutions

I. *Charging solutions.*—1, 0.1*N* NaOH solution; 2, 0.1*N* NaOH + 0.1*N* NaCN solution; 3, saturated (200 g/l) ammonium fluoborate solution, *p*H = 3.1; 4, DL-α-amino-n-butyric acid solution; amino acid 2M + 350 ml/l conc. NH_4OH solution, *p*H = 9.50; 5, acetate buffer *p*H = 3.6.

II. *Cadmium plating baths.*— 1, Standard cyanide bath *p*H = 12.5 with Udylite brightener; 2, fluoborate bath: cadmium fluoborate [$Cd(BF_4)_2$], 240 g/l; Cd 94 g/l; ammonium fluoborate, 60 g/l; with licorice addition, *p*H = 3-3.4(7); 3, DL-α-amino-n-butyrate bath (8); amino acid 2M, Cd 1M, + 350 ml/l conc. NH_4OH solution, *p*H = 9.50.

III. Iron plating bath.—1*N* $FeSO_4$ + 1*N* Na_2SO_4 with H_2SO_4 to *p*H = 3.50. All solutions used at 25° ± 1°C.

Radiochemical Studies of Thiourea in the Electroless Deposition Process

J. S. Sallo, J. Kivel, and F. C. Albers

Honeywell Research Center, Hopkins, Minnesota

ABSTRACT

The effect of thiourea on the electroless nickel deposition reaction has been studied by the use of sulfur-35 and carbon-14 labeled thiourea. The amount of sulfur in the deposit was found to be much greater than the amount of carbon, thereby indicating cleavage. The effect of thiourea on the rate of nickel deposition has been shown to be due to two different mechanisms depending on the thiourea concentration. It is proposed that the catalytic substrate acts as a Raney nickel-type surface. Kinetics studies have been carried out correlating the rate of sulfur inclusion in the deposit with rate of nickel deposition. Mechanisms have been postulated to explain the observed results.

The effect of certain addition agents on the nickel electroless deposition process has been reported by Talmey and Gutzeit (1) and by deMinjer and Brenner (2). It was observed that thiourea, and to a lesser extent, thiocyanate, increased the rate of nickel deposition when present in very small concentration. An increase in bath stability was noted when thiourea was present. Larger concentrations inhibited the reaction. Evidence for depletion of thiourea during the course of the reaction was presented (2).

Radiotracer techniques have been used previously to study addition agent effects in electrodeposition systems. Beacom and Riley (3, 4), in studies of the effect of sodium allyl sulfonate on electrodeposited nickel, have shown selective adsorption of the addition agent at the high points of the deposit. They also reported cleavage of the addition agent and suggested that the deposit contained nickel sulfide. Rogers *et al.* (5) studied S^{35}-thiourea as an addition agent, reporting more sulfur at the high points of the deposit and more sulfur build-up at lower cur-

rent density. However, since only S^{35}-thiourea was used, conclusions could not be drawn concerning cleavage of the addition agent.

In the present work S^{35}-thiourea and C^{14}-thiourea have been used to study the electroless deposition process. The labeling of different parts of the molecule enables determination of the amount of cleavage. Since thiourea concentration controls the rate of the reaction, there may be a correlation between the C^{14} or S^{35} content of the deposit and the plating rate. A comparison of addition agent effects in electrodeposition and electroless deposition is also of interest.

Experimental

The following system was studied: $NiCl_2 \cdot 6H_2O$, 30 g/l; $NaH_2PO_2 \cdot H_2O$, 10 g/l; $NaC_2H_3O_2 \cdot H_2O$, 3 g/l; thiourea, 0.15-1.5 mg/l; H_2O to 500 ml total volume. The initial *p*H of this system was 6.0.

The temperature was maintained at 85° ± 1°C by means of an electric heating mantle. The substrates used in this investigation were 1 x ½ in. nickel metal strips. The substrates were sensitized by previously described techniques (6).

In each experiment, a 1-hr deposit and a series of successive 10-min deposits were prepared. In addition, deposits were prepared for 1, 2, and 5 min intervals throughout the reaction.

Agitation of the system was accomplished by mechanical stirring or by bubbling nitrogen through a sintered glass sealing tube. Measurements of *p*H were carried out for all experiments using high-temperature calomel and glass electrodes.

In each experiment the desired amount of thiourea-S^{35} (initial specific activity, 2.0 mc/mm) was added to the system. The amount of activity remaining in solution was determined by removing aliquots of solution at definite time intervals throughout each experiment, evaporating the samples to dryness in a small oven maintained at 102°C, and counting. All samples were counted in a gas flow counter having a thin aluminized mylar window of 0.9 mg/cm^2. The samples were compared to standards prepared from the original thiourea solutions which were, in turn, calibrated against absolute sulfur and carbon standards.

All samples were corrected for self-absorption of radiation. In the experiments incorporating sulfur-35 labeled thiourea, corrections were made for radioactive decay. All samples were counted to a minimum of 10,000 counts. Most samples containing S^{35} were counted for over 100,000 total counts.

Experiments to determine if reaction occurred between hypophosphite ion and thiourea were carried out in the following concentrated system: $NiCl_2 \cdot 6H_2O$, 10 g/l; $NaH_2PO_2 \cdot H_2O$, 100 g/l; thiourea, 20 g/l. All results are reported as the average of several experimental runs.

Results

The results obtained when a series of 10-min deposits were prepared from a fresh bath containing sulfur-35 labeled thiourea are shown in Fig. 1 for four different thiourea concentrations. The amount of sulfur in the deposit is plotted against deposition time. The nitrogen flow rate in this system was maintained at 200 ml/min. The data were converted from activity (cts/min) to micromoles of sulfur in the deposit by assuming uniform distribution within each 10-min deposit. A similar series of 10-min deposits using carbon-14 labeled thiourea was prepared; the results obtained for this system are presented in Fig. 2. Uniform distribution within each 10-min deposit was also assumed for the carbon-14 experiment.

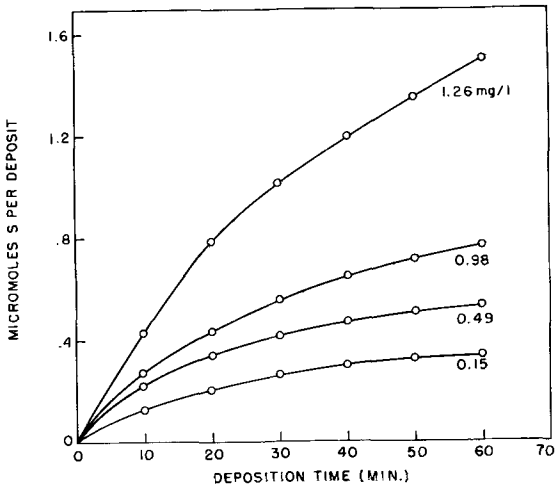

Fig. 1. Buildup of sulfur in the deposit at several thiourea concentrations.

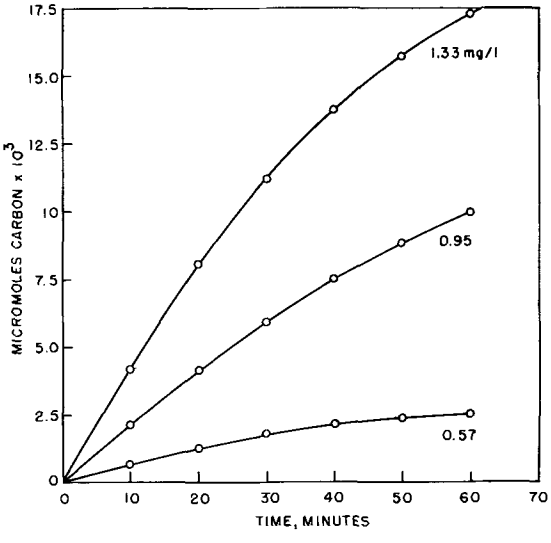

Fig. 2. Buildup of carbon in the deposit at several thiourea concentrations.

Corrections for uniform distribution were made by assuming the validity of the expression: $I = I_o e^{-\mu x}$, where μ is the absorption coefficient in cm^2/mg, and I and I_o are the observed and corrected counting rates at a point x mg/cm^2 distant from the surface. Upon integration over the entire thickness of the deposit, the expression $I/I_o = 1/\mu t \ (1 - e^{-\mu t})$ was obtained for a deposit of t mg/cm^2 thickness. This expression was used to calculate the self-absorption. Absorption studies of sulfur and carbon in chemically deposited nickel were made by depositing varying thicknesses of electroless nickel over sulfur-35 and carbon-14 sources. Using a density of 7.85 g/cm^3 (7), the values obtained for the absorp-

tion coefficients were 0.25 and 0.27 cm^2/mg for S^{35} and C^{14}, respectively.

Although corrections for self-absorption were made assuming uniform distribution, evidence, based on comparison of the deposits plated for different lengths of time, indicated that the sulfur is distributed nonuniformly in the deposit. From the series of 1, 2, and 5 min deposits it was found that the rate of sulfur incorporation into the deposit increased rapidly, reaching a maximum and then dropping rapidly and leveling off, all within the first 10 min of the deposition reaction. The maximum in the sulfur inclusion rate was, to some extent, dependent on the initial thiourea concentration. Beyond the first several minutes of the deposition reaction the decrease in sulfur inclusion became more gradual. Results of this investigation are still in an early experimental stage and are included only since they pertain to the present data.

The deposits studied in this investigation were quite thin. The total amount of nickel deposited in 10 min on each substrate was 5-10 mg depending on the plating rate. The difference between the actual distribution and the assumed uniform distribution was small and could be neglected, especially for deposits prepared after the first 10 min.

It has previously been shown (6, 8), that the rate of nickel deposition is affected by agitation. The effect of agitation by nitrogen bubbling on the incorporation of sulfur into the deposit has been studied and is shown in Table I for a solution containing 0.49 mg/l thiourea.

In all the experiments using thiourea -C^{14} as the tracer, the sum of the activity in the deposits and the solution was equal to the initial activity within experimental error. The sulfur-35 experiments in the nonagitated system yielded the same results. However, on agitation by nitrogen bubbling, a portion of the S^{35} was lost. These results indicate that a sulfur-containing fragment is produced, which is soluble but volatile and is swept out by nitrogen bubbling. The carbon fragment is nonvolatile. The results of an experiment in which hydrochloric acid was added to a solution containing thiourea-S^{35} that had been agitated by nitrogen bubbling during deposition showed that further loss of S^{35} did not occur, indicating that only nonvolatile sulfur, presumably as thiourea, remained in solution. Hence, only in the agitated system could the activity in solution be correlatable with thiourea concentration.

Table I. Sulfur incorporation in agitated[a] and nonagitated systems at 0.49 mg/l thiourea

Initial thiourea activity = 2.0 millicuries/millimole

Deposition time, min	Agitated		Nonagitated	
	Corrected CPM[b]	Micromoles S per deposit	Corrected CPM[b]	Micromoles S per deposit
0-10	77.6×10^3	0.228	76.5×10^3	0.224
10-20	32.0	0.094	31.7	0.092
20-30	28.6	0.084	25.8	0.076
30-40	17.4	0.051	14.7	0.043
40-50	13.5	0.040	10.6	0.031
50-60	10.9	0.032	7.2	0.021

[a] Agitation supplied by nitrogen bubbling at 200 ml/hr.
[b] Counts corrected for self-absorption and resolution losses

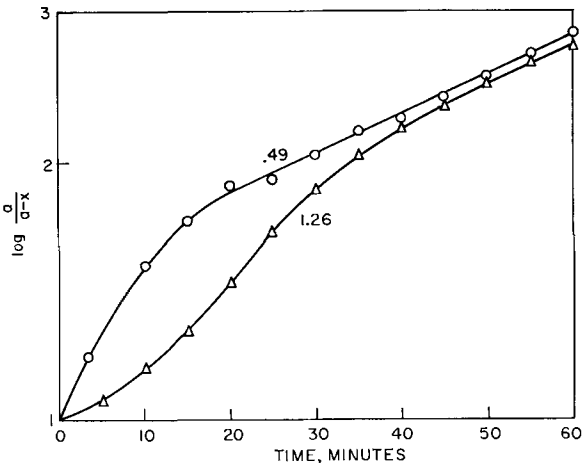

Fig. 3. Rate of depletion of thiourea from solution

Depletion of S^{35} labeled thiourea from this agitated system has been studied. The results obtained for 0.49 and 1.26 mg/l thiourea concentrations are plotted in Fig. 3 as a function of initial and remaining thiourea *vs.* time.

Discussion

The present studies were undertaken in a nonbuffered or Brenner-type system. Other work (2) on the effect of the thiourea addition agent on rate was carried out in a similar system, and direct comparison of results is possible. Brenner (2) has reported an increased plating rate at low thiourea concentration, but a decreased plating rate above 0.5 mg/l of thiourea. This implies a change in mechanism for the effect of thiourea on the rate of nickel deposition.

The data obtained for sulfur and carbon inclusion in the deposit (Fig. 1 and 2) indicate that cleavage of the thiourea molecule is the predominant source of sulfur in the deposit. The sulfur to carbon ratios in the deposits are typically 100 to 1. During a typical 1-hr reaction about 35% of the initial thiourea is consumed. In order for the thiourea to produce the large effect observed on the rate and be consumed, it must be selectively adsorbed at the reacting surface. Adsorption of thiourea at the electrode has been proposed as a mechanism for thiourea action in electrodeposition (5, 9-11).

The carbon found in the deposit is probably due to adsorption and occlusion of entire thiourea molecules. However, the amount of sulfur deposited by occlusion is small compared to the total amount of sulfur in the deposit. The majority of the sulfur is entering the deposit by means of a separate mechanism involving cleavage and reduction of thiourea.

The electrode is an active nickel surface covered with hydrogen gas, and an analogy may exist between this surface and a Raney nickel surface. Raney nickel is commonly used for the removal of sulfur from organic molecules (12). Reaction of thiourea with Raney nickel under mild conditions has been shown to yield formamidine (13). The sulfur is incorporated into the catalyst as nickel sulfide. In addition, Raney nickel reacts with sodium hypo-

phosphite to produce hydrogen and phosphite (14). This Raney nickel-type surface may be responsible for the cleavage reaction which leads to the bulk of the sulfur incorporation into the deposit.

The rate of nickel deposition in this system is diffusion controlled and can be influenced by agitation. An increase in rate of agitation yields an increase in nickel deposition rate. The effect of agitation (Table I) reflects the dependence of S inclusion on the rate of nickel deposition. The results show that in the early stages of the deposition the amount of sulfur in the deposit is the same in either still or agitated systems. Beyond 20 min the amount of sulfur in the deposit is greater in the agitated system. This indicates that sulfur inclusion in the deposit is independent of the rate of nickel deposition during the initial stages of deposition from a system containing 0.49 mg/l thiourea, but becomes dependent upon the rate of nickel deposition after about 20 min. This change in the mechanism of S inclusion may be due to either the *p*H change or to the depletion of the thiourea or to both of these factors.

Results comparing the agitated and still systems indicate the formation of sulfide ion in solution. As discussed previously, the sulfide ion is removed from solution in the agitated system. Since in the nonagitated system sulfide ion will contribute to the total of the counts in solution, kinetic studies on the rate of disappearance of thiourea can be carried out only in an agitated system. Kinetic studies were carried out in a system where all other rate-controlling parameters such as *p*H and hypophosphite ion concentration had constant initial values. The results of this kinetic study (Fig. 3) show the rate of thiourea[1] disappearance from solution to be first order in thiourea concentration in the low thiourea concentration region. Due to the constancy of the other rate-controlling variables, the data really show pseudo-first order dependence. First order kinetics are obtained beyond 15 min for the 0.49 mg/l initial thiourea concentration. This is in agreement with the time at which the rate of sulfur incorporation into the deposit becomes dependent on the rate of nickel deposition. For an initial thiourea concentration of 1.26 mg/l, first order kinetics are not reached until 40 min have elapsed. In both systems, the initial *p*H was 6.0 and decreased to about 4.0 after 60 min of deposition. Since the *p*H change is similar for the two thiourea concentrations this result shows that the change in mechanism is dependent on thiourea concentration and not on *p*H.

Figure 4 shows Brenner's data (2) for rate of nickel deposition in microns/hour *vs.* thiourea concentration and shows a plot of micromoles of sulfur in the deposit *vs.* thiourea concentration. This curve is a replot of the data in Fig. 1 for 1-hr deposits. Figure 4 has been divided into regions A, B, and C.

In region A the rate of nickel deposition has been shown to increase with increasing thiourea concentration. In this region the rate of sulfur incorporation in the deposit is dependent on the rate of nickel deposition, and the rate of thiourea disappearance from solution is first order in thiourea concentration. In region C the rate of nickel deposition decreases with increasing thiourea concentration, and eventually nickel deposition ceases. In this region the rate of sulfur deposition increases rapidly with increasing thiourea concentration and is not dependent on the rate of nickel deposition. The rate of disappearance of thiourea from solution is no longer first order in thiourea, but is more complex. Region B represents a transition between the two mechanisms of thiourea action. The inflection points of both curves occur in region B at about 0.5 mg/l of thiourea. Clearly two mechanisms are involved, and the data found for sulfur inclusion correlate with Brenner's data on rate of deposition.

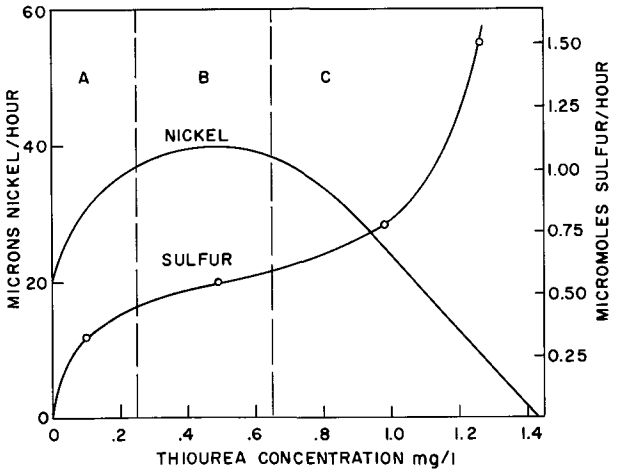

Fig. 4. Comparison of rate of nickel deposition and rate of sulfur buildup in the deposit.

It is assumed that in region A, thiourea, or more likely a nickel ion thiourea complex, is adsorbed at the active surface. This complex is more easily reduced than is the hydrated nickel ion (9, 10). The complex is reduced by hypophosphite or by some reactive species derived from the decomposition of hypophosphite at the active surface. If the reduction of the nickel ion is the rate-controlling step for nickel deposition, the rate will be increased by the lowering of the reduction (redox) potential due to complexation. The thiourea molecule can act as a bridge for the reaction; after the nickel ion in the complex is reduced, a new nickel ion is complexed by the thiourea molecule. The thiourea complex is in dynamic equilibrium on the active surface, although on occasion a thiourea molecule fails to act as a bridging complex and undergoes its normal transformation on the Raney nickel surface. This leads to a molecule of nickel sulfide in the deposit and to an organic fragment. This cleavage of a thiourea molecule probably occurs on a statistical basis relative to the number of nickel ions transferred to the surface. For this reason the sulfur buildup in the deposit is dependent on the rate of nickel deposition. The entire process is probably controlled by the diffusion of thiourea into the active surface. This is a necessary assumption to explain the first order kinetics. On rarer occasions a thiourea molecule is plated into the surface, resulting in carbon and sulfur appearing in the deposit by an inclusion mechanism.

The Raney nickel analogy fails to account for the occurrence of sulfide ion in solution. The *p*H at

[1] The data really show the rate of S^{35} disappearance from solution to be first order in S^{35} remaining in solution. It is assumed throughout that all soluble, nonvolatile S^{35} is thiourea.

the interface is probably very low, due to the formation of hydrogen ion as a reaction product. It is possible that in region A sulfide is formed by hydrolysis of nickel sulfide already formed at the deposit surface. In further support of the hydrolysis mechanism the kinetic data indicate that in region A sulfur in the deposit and sulfide ion in solution arise from the same mechanism.

In region C the mechanism must be entirely different. In this region a much higher thiourea concentration exists at the active surface. It is suggested that in this region a direct attack by hypophosphite takes place on the adsorbed thiourea to yield sulfide. This competition for the reducing agent between thiourea and nickel ion leads to a decreased plating rate and, ultimately, to a poisoning of the surface. As the reaction proceeds the thiourea is depleted rapidly and the entire process moves into region A. This is shown clearly in the kinetic data for 1.26 mg/l of thiourea (Fig. 3).

In concentrated systems such as are described in the experimental section, nickel ion is reduced spontaneously by hypophosphite ion to produce nickel metal. Subsequently hypophosphite reacts at the nickel surface to produce hydrogen gas and phosphite ion. When thiourea is present in such a system, the precipitation of nickel occurs much more slowly, the resulting particles are more numerous and much smaller, and hydrogen gas is not evolved. During the course of the reaction, hydrogen sulfide is produced along with ammonia. Even if the thiourea is added after all of the nickel ion has been reduced by hypophosphite, the thiourea is reduced to hydrogen sulfide and ammonia at the nickel surface. These results further support direct attack of hypophosphite ion on thiourea at a nickel surface.

These experiments show that at high thiourea concentration, hypophosphite will reduce thiourea directly at an active surface. The failure of hydrogen gas to evolve and the failure of nickel particles to grow further implies that a competition between thiourea and nickel ion does occur at the active interface.

Stabilization of electroless nickel systems by thiourea was observed by Gutzeit (1) and by Brenner (2) and has also been noted in this work. The experiments in concentrated systems also show stabilization. The question of whether this stabilization is due to thiourea or to sulfide ion was raised by Brenner (2). The tracer experiments show that in an agitated system only trace amounts, if any, of sulfide remain. Since stabilization occurs in such a system, it is suggested that thiourea may be the stabilizer in this case rather than sulfide ion. The mechanism of stabilization is probably the same as that already given for region C.

Radioautographs of the deposits containing active S were made. In the case of scratched substrates the greatest buildup of activity was noted on the peaks of the deposit. This finding is in agreement with results obtained by Beacom and Riley for electrodeposits (4). Further analogy with electrodeposition may exist. A Raney nickel mechanism has been proposed for nickel electrodeposition by Edwards (11). Similar mechanisms may apply to iron (15), cobalt (16), and even copper (17). Raney nickel is known to remove sulfur from sulfonic acids (18) with resultant products in general agreement with the findings and theory of Beacom and Riley for allylsulfonic acid (3).

The Raney nickel analogy predicts that the organic fragment resulting from thiourea should be formamidine or resulting breakdown products such as formamide or formic acid. Radiochemical studies directed toward the identification of this fragment are currently in progress.

Conclusions

It has been concluded that the primary source of thiourea depletion in this system is a cleavage reaction. Two mechanisms for the thiourea action have been found depending on the thiourea concentration. It is suggested that at low thiourea concentrations thiourea lowers the redox potential and facilitates chemical reduction of nickel. Cleavage of thiourea occurs through a Raney nickel-type mechanism, and sulfide ion is formed through hydrolysis of nickel sulfide at the interface. In the higher thiourea concentration system an attack of hypophosphite on thiourea adsorbed at the Raney nickel like surface is proposed. Thus thiourea competes for the reducing agent and slows the rate of nickel deposition. Thiourea itself, rather than by-product sulfide ion, is believed to act as a system stabilizer.

Acknowledgments

The authors wish to acknowledge the assistance of Mr. L. L. Egan and Mr. D. C. Prem.

Manuscript received Nov. 26, 1962; revised manuscript received March 8, 1963. This paper was delivered before the Boston Meeting, Sept. 16-20, 1962.

Any discussion of this paper will appear in a Discussion Section to be published in the June 1964 JOURNAL.

REFERENCES

1. P. Talmey and G. Gutzeit, U.S. Pat. 2,762,723.
2. C. H. deMinjer and A. Brenner, *Plating*, **44**, 1297 (1957).
3. S. E. Beacom and B. J. Riley, *This Journal*, **108**, 758 (1961).
4. S. E. Beacom and B. J. Riley, *Nucleonics*, **18** [5], 82 (1960).
5. G. T. Rogers, M. J. Ware, and R. V. Fellows, *This Journal*, **109**, 389 (1962).
6. J. S. Sallo, J. I. Swenson, and J. M. Carr, *ibid.*, **109**, 389 (1962).
7. A. W. Goldenstein, W. Rostoker, F. Schlossberger, and G. Gutzeit, *ibid.*, **104**, 104 (1957).
8. G. Gutzeit, *ibid.*, **109**, 1219 (1962).
9. J. S. Sallo and R. D. Fisher, *ibid.*, **107**, 277 (1960).
10. R. D. DeMars, *ibid.*, **108**, 779 (1961).
11. J. Edwards, *Trans. Inst. Met. Finishing*, **39**, 45 (1962).
12. H. Hauptmann and W. F. Walter, *Chem. Rev.*, **62**, 347 (1962).
13. D. J. Brown, *J. Appl. Chem.*, **2**, 202 (1952).
14. J. Bougault, E. Cattlelain, and P. Chabrier, *Bull. soc. chim. France*, **5**, 1699 (1938).
15. R. Paul and G. Hilly, *ibid.*, **6**, 218 (1939).
16. G. Dupont and P. Pigceniol, *ibid.*, **6**, 322 (1939).
17. L. Faucounau, *ibid.*, **4**, 58 (1937).
18. E. Schwenk, D. Papa, B. Whitman, and H. Ginsberg, *J. Org. Chem.*, **9**, 1 (1944).

Electrode Kinetic Parameters for Copper Deposition on Clean and Soiled Copper Cathodes

Leonard Karasyk[1] **and Henry B. Linford**

Department of Chemical Engineering, Columbia University, New York, New York

ABSTRACT

A galvanostatic method for measuring the overpotentials and obtaining the charging curves for the deposition of copper was developed. The copper was plated from an acid copper sulfate bath, on flat plate copper cathodes. Rigorous standards of solution and electrode purity were maintained, and the results of runs using clean electrodes are in excellent agreement with those reported by other investigators for spherical electrodes of pure copper. Values of α_c and i_o for the clean cathodes were 0.57 and 11.0 ma/cm^2, respectively. The techniques developed are easily applied to study the effects of surface treatments on deposition kinetics. Hence some cleaned cathodes were soiled with stearic acid and with mineral oil by means of the evaporation technique, and charging curves were obtained for these cathodes. In addition, sequences of charging curves were obtained for the soiled electrodes as deposition proceeded. The soils when present in quantities equivalent to a monolayer greatly increase activation overpotential and decrease the value of α_c, as determined from the slope of the Tafel line, to about 0.3. The exchange currents for the cathodes on which the equivalent of a monolayer of stearic acid is freshly deposited are higher than those for similar clean electrodes. An explanation is suggested for this observation based on the assumption that the freshly applied stearic acid is preferentially deposited at sites other than those active for electrodeposition. Cathodes soiled with paraffin oil and oriented stearic acid in quantities equal in thickness to a monolayer of stearic acid have exchange currents which are close to those for clean electrodes.

The presence of these trace contaminants causes a reduction in the double layer capacity, and consequently the charging curves for the soiled electrodes are much steeper than those for cleaned ones. Sequential charging curves reveal that as plating proceeds the electrode contaminants are eventually covered by the freshly deposited copper, and, therefore, the charging curves tend to approach in shape and magnitude those of clean electrodes. Cathodes soiled with the equivalent of 0.5 monolayer of freshly applied stearic acid have charging curves which are similar to those of cleaned electrodes, and the values of α_c and i_o as determined from the Tafel line are not appreciably different. The implication is made that organic contaminants similar to stearic acid present in quantities less than about 0.5 monolayer will not have an appreciable effect on the mechanism and hence the kinetic parameters of the electrodeposition.

Although the presence of some adsorbed organic films on electrodes was generally known to affect the overpotential and the kinetics of electrodeposition, the question of how clean the metal surface needed to be for kinetic measurements was unanswered. Many of the "standard" procedures for cleaning electrodes prior to plating or before obtaining kinetic data, as reported in the literature, can remove large quantities of organic contaminants, but they are ineffective in removing the last traces of these soils, *i.e.*, in the monolayer or fraction of a monolayer range. The questions of how clean the electrode must be for kinetic measurements and of how these contaminants affect the mechanism of the electrodeposition on these electrodes are therefore quite important.

An investigation of the effects of minute quantities of organic contaminants, stearic acid and paraffin oils, was therefore undertaken. The plating of copper on copper cathodes from an acid copper sulfate bath was the reaction chosen for study. In addition to having extensive commercial application, this system was a good one for analysis because there was negligible complexing of the copper ions, and the potential of the deposition process was such that the simultaneous liberation of hydrogen was insignificant. Although pure stearic acid and pure paraffin oil hardly ever appear as contaminants on commercial electrodes, they are typical of the classes of organic soils which may be found on electrodes. The stearic acid is a hydrophobic material which, when allowed to remain on a metal surface, forms an oriented and strongly chemisorbed film; stearates and related compounds are found in many industrial

[1] Present address: Allied Chemical Corporation, Morristown, New Jersey.

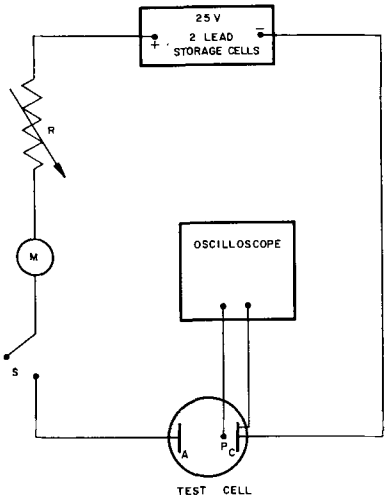

Fig. 1. Schematic diagram of the circuit for measuring overpotential: A, anode of test cell; C, cathode of test cell; M, ammeter; P, reference probe of test cell; R, variable resistance box; S, high speed switch, Western Electric Mercury Contact Relay D 171 584.

lubricants and are picked up by parts to be plated during the buffing and machining operations. Paraffin oil is a hydrophobic contaminant which easily spreads over the surface and exists as an unoriented, weakly held film.

Experimental

The apparatus for these experiments consisted of a measuring circuit for obtaining the charging curves, devices for the purification and cleaning of the electrodes and the solutions, and a dry box containing a purified helium atmosphere in which cleaned electrodes could be stored and soiled and where the test cell could be assembled and sealed before being removed and connected into the measuring circuit.

Measuring circuit.—The measuring circuit is shown in Fig. 1. It consisted of two 12.5v, 200 amp-hr batteries connected in series with a variable resistance, by means of which the current flowing through the test cell could be varied. The switch S was a mercury relay[2] which was tested and found, when used with one pole free, to establish full electrical contact in less than 10^{-6} sec. An oscilloscope[3] was used in conjunction with a preamplifier[4] which allowed for a wide range of sensitivity and high-frequency responses (D.C. to 350 kc at 1 mv/cm sensitivity increasing to 2 mc at 50 v/cm). The oscilloscope was equipped with a single-sweep feature so that only one trace (the charging curve) would appear on the screen where it could be immediately photographed with a Polaroid camera. The oscilloscope was so connected that it was triggered when the switch was thrown and current flowed through the test cell. The controls could be adjusted so that the oscilloscope triggered when the potential between the probe and the cathode changed very slightly. A direct reading of the activation overpotential *vs.* time was obtained and photographed. All of the components of the measuring circuit were electrostatically shielded, and the shielding was connected to a common ground. The test cell was immersed in a constant temperature bath at 25°C whose temperature was easily maintained constant within ±0.5°C.

Test cell.—The test cell was constructed entirely of Pyrex glass and could be sealed gas tight. Five copper plated leads were sealed into the glass and suspended from the upper half of the cell. Two electrode holders directly facing one another were suspended from the top, each directly under a lead, and a glass tube with a capillary tip designed to hold the copper reference electrode was attached to one of the holders with the tip of the tube spaced about 0.5 cm from the glass electrode holder. The copper electrodes were placed in the glass holders and a glass block was inserted behind the copper, pressing the electrode against the wall of the holder containing a circular window. Through this opening the electrode and solution made contact. The cell was designed so that electrodes, glass blocks, and clips connecting the leads to the electrodes could be handled and put into place by means of forceps, the tips of which were previously made atomizer clean. The copper connecting clips were plated with copper to coat the phosphor bronze springs.

Reference electrode.—The reference electrode consisted of a small piece of the same purified, cleaned copper which was used for the other electrodes. This strip of copper was inserted in a small bent tube with a capillary tip which, as a permanent fixture in the test cell, faced the cathode. The use of a copper reference electrode was desirable since it could not contaminate the system as other reference electrodes would. When the test cell was filled, the reference electrode tube was also filled with solution of the same composition.

Because of the high input impedence of the oscilloscope, the currents flowing through the reference electrode were quite small and appreciably below the exchange current for clean copper.

Dry box and gas purification system.—The test cell was assembled within a dry box equipped with a vacuum entry port. The gas purification system was the same one used by Linford and Feder (1). Helium leaving the dry box was first mixed with a slow steady stream of makeup helium (to compensate for leakage out of the purification system) and passed through a bed of hot copper turnings maintained at 500°-600°C to remove all but traces of oxygen. The gas stream was further purified by passing through an alumina drier, a tank of molecular sieve, and a cloth filter to remove suspended particles. The entire dry box and gas purification system was operated at a slight positive pressure of about 0.2 cm of oil. The gas recirculation rate was about 10 ft^3/min.

Vacuum system.—A vacuum system was required for the preparation of the electrodes and the outgassing of the plating solutions. It contained a mechanical pump in series with an oil diffusion pump and could produce vacuums of the order of 3×10^{-5} mm Hg.

Procedure

Electrode preparation.—The electrodes were prepared from ultrapure copper, 99.999+% pure,

[2] Western Electric type 275B Mercury Relay, No. D171584.
[3] Tektronix type 532-S7 oscilloscope.
[4] Tektronix type-D plug-in preamplifier.

which was cold-rolled into strips 0.030 in. thick and was virtually oxygen free.[5] These strips were next anodically etched in 5% H_2SO_4 until the average thickness was decreased to 0.025 in. The copper was then electropolished in an orthophosphoric acid bath (sp gr = 1.35) for 1 min and from these polished copper strips the electrodes were cut using a Diacro cutter to minimize burrs along the cut edges. On the cathodes a circular area with a diameter of 20 mm was outlined by a scratch and was so placed that the center of the 12.5 mm diameter circular window of the electrode holder coincided with the center of the scribed area. This larger scribed area was the portion of the cathode that was soiled in the stearic acid runs.

The electrodes were then mounted on a frame of copper wire and separated from one another by copper beads. On this frame the electrodes were cleaned by means of the following steps in the order listed.

1. Carbon tetrachloride, soak and dip.
2. Alkaline cleaning, 30-min boil in solution containing 6.5 g/l sodium carbonate and 40 g/l sodium silicate.
3. Overflow of the alkaline cleaning solution to remove upper layers of the solution which contained the organics previously removed from the copper.
4. A 30-min boil in a solution containing 3% by volume of 30% H_2O_2 in distilled water.
5. Overflow of the H_2O_2 solution by addition of distilled water.
6. Tap water rinse.
7. Three rinses with about 200 ml deionized water (R = 4 meg ohm-cm).
8. Two 5-min soaks in deionized water.

This treatment invariably produced atomizer clean electrodes.[6] With the aid of clean forceps, the electrodes were then placed in a heating tube which was previously cleaned. Care was taken during the handling to avoid contact of the electrodes with any nonclean surfaces. The heating tube was connected to the vacuum system and evacuated to about 50μ. Prepurified hydrogen was then passed into the tube to bring its pressure up to 1 atm, and it was heated up to 500°C. Several treatments of this sort removed oxides from the electrode surface. Following this step, the pumps were turned on again and the electrodes were outgassed at 500°C till the ionization gauge read a pressure of about 3 x 10^{-5} mm Hg. The heating tube was then closed off, disconnected from the system, and allowed to cool down rapidly to room temperature. When the heating tube had cooled down, it was placed in the vacuum entry port which was then evacuated to 50μ. Helium from the cylinder was then passed into the port to raise its pressure to slightly above atmospheric pressure. After circulating the tank helium through the purification system and entry port for 5 min, the sealed tube was admitted to the dry box. Here the heating tube was disassembled and the electrodes carefully removed from the tube and the supporting frame by means of cleaned forceps and cleaned wire cutters. The electrodes were stored in cleaned glass jars covered with ungreased ground glass stopper-tops. Under these conditions, the electrodes would remain atomizer clean for periods longer than 2 weeks. The atomizer clean cathodes could then be placed in the cell, as they were for "clean" runs or they could be soiled by the evaporation technique. In the latter case, the large scribed area was covered with a solution of known concentration of stearic acid[7] or paraffin oil[8] and the solvent was allowed to evaporate. Analytical grade carbon tetrachloride was a satisfactory solvent for the soiling solution since it did not leave an organic residue on evaporation as many other solvents do and it had no appreciable effect on the charging curve for the electrode.

Both the front and back of the "tongue" of the electrode were soiled for the paraffin oil runs. This drastic step was necessary since the charging curves for electrodes where only the scribed areas were soiled with paraffin oil were quite erratic. This effect was believed to be due to the rapid random spreading of the oil, and indeed, the results were more consistent when both sides of the electrode were soiled with the oil.

Electrodes containing the equivalent of 0.5 and 1.0 monolayer of stearic acid[9] and a film of paraffin oil as thick as 1.0 monolayer of stearic acid[10] were the soiled cathodes examined.

The soiled cathode was then carefully placed in the electrode holder of the test cell along with the reference electrode and the anode, and connections were made to the proper leads. The cell was sealed and was ready for the introduction of the purified solution by means of a specially designed filling bottle. Solution was pumped into the cell up to a level slightly higher than the top of the windows in the test cell. Sufficient solution was presented to cover known areas of exposed cathode and anode, and to contact the pure copper of the reference electrode with the solution. Following this step, the sealed test cell was withdrawn from the dry box and connected into the circuit. The time between the soiling of the cathode and the obtaining of the experimental data varied between 17 and 28 min for the case of the "freshly applied" stearic acid runs and the paraffin oil runs. Some additional experiments were made with cathodes in which the time between soiling with stearic acid and the measurements was 24 hr. The solution was in contact with the electrodes in all cases for times of the order of 7 min prior to the measurements.

Solution preparation.—Analytical grade copper sulfate was recrystallized three times, once from distilled water and twice from deionized water (R $\geq$ 4 megohm-cm). The purified copper sulfate

[5] Spectroscopic grade copper prepared by American Smelting and Refining Company.

[6] The atomizer test developed by Linford and Saubestre (2, 3) is one of the most sensitive tests for determining the cleanliness (absence of hydrophobic contaminants) of a metal surface. The test consists of spraying a fine mist of water on the surface. If a uniform film is formed with very little water after several seconds of spraying, the surface is atomizer clean. If it is dirty, spray forms many droplets on the metal. The test can detect as little as 0.2 monolayer of stearic acid on steel.

[7] USP stearic acid.

[8] Fisher USP paraffin oil, sp gr 0.876, viscosity 335/350.

[9] 1.1 x 10^{-7} g/cm^2 and 2.2 x 10^{-7} g/cm^2 stearic acid are equivalent to 0.5 and 1.0 monolayers, respectively.

[10] 2.3 x 10^{-7} g/cm^2 paraffin oil is equal in thickness to 1.0 monolayer of stearic acid.

and reagent grade sulfuric acid were dissolved in the deionized water to prepare a plating bath whose composition was 1.5*N* $CuSO_4$ and 0.45*N* H_2SO_4. This solution was then placed in a cleaned Teflon beaker and covered first with a watch glass and then a bell jar. In the Teflon beaker, the plating solution was pre-electrolyzed for 63-65 hr at a current density of about 1 ma/cm^2. Atomizer clean, purified copper pre-electrolysis electrodes were used. Approximately 25 cm^2 of area of each electrode was exposed to solution. Agitation was provided by means of a Teflon covered magnetic stirring bar.

Following pre-electrolysis, the solution was poured into the filling bottle and frozen in a dry-ice acetone bath. The filling jar was connected to the vacuum system where it was outgassed to 200μ. The solution was then thawed out, allowing dissolved gases to bubble out of the liquid phase. Two more purges down to 200μ were performed to outgas the solution sufficiently. The filling bottle was sealed off and removed from the vacuum system. After this, it was ready for introduction into the dry box to fill the test cell. A tapered glass joint on the filling bottle mated with the solution entry port and made possible the liquid transfer to the cell without contaminating the dry box atmosphere. In all the experiments performed the solution was never allowed to come in contact with greased joints or organic materials other than the Teflon beaker or the Teflon stopcock in the filling bottle. Atomizer clean copper electrodes in contact with the solution were found to remain atomizer clean before and after plating from the solution.

All the glasswear, the test cell, the filling jar, the electrode heating tube, were rigorously cleaned before being used. The procedure included soaking in hot chromic acid solution, rinsing with tap water, deionized water, acetone, and analytical grade CCl_4. Between experiments these glass vessels were filled with deionized water and covered.

Results

The types of charging curves obtained in these investigations are illustrated by the typical examples shown in Fig. 2. The ohmic overpotentials, as Bockris and Mattsson (4) have demonstrated, are shown as vertical gaps in the charging curves, and the activation overpotential as a function of time is shown as the continuous curve. Since the concentration of copper ions in the solution was high and the time sweep was rapid, the "steady-state" activation overpotential appeared as a well-defined plateau in the charging curve without the added interference of concentration polarization. Very obvious differences appear in the charging curves for atomizer clean cathodes and soiled ones. In all cases, the overpotentials for the soiled surfaces are considerably higher than those for cleaned ones, and the slope of the curve for soiled surfaces is very much steeper, *i.e.*, the rise time for soiled cathodes is much less than that for clean cathodes.

A plot of ohmic overpotential shows the expected linear relation with total current strength. The line passes through the origin, and its slope is equal to the electrical resistance of the experimental system between the terminals of the oscilloscope, including the resistance of the solution between the probe tip and the cathode. Slightly different values of this slope are shown with different electrodes because of the nature of the cell construction and the clip-type contacts. Variations in distance between the electrode surface and probe tip and differences in the contact area and contact pressure of the clips caused differences in resistance.

Using the data from the charging curves, plots of activation overpotential against log i can be drawn, and very noticeable differences can be seen in the Tafel lines for cleaned and soiled cathodes. Figure 3 is a composite plot of the Tafel lines for the cathodes studied in this investigation.

The presence of stearic acid and mineral oil on copper cathodes has a very noticeable effect on the

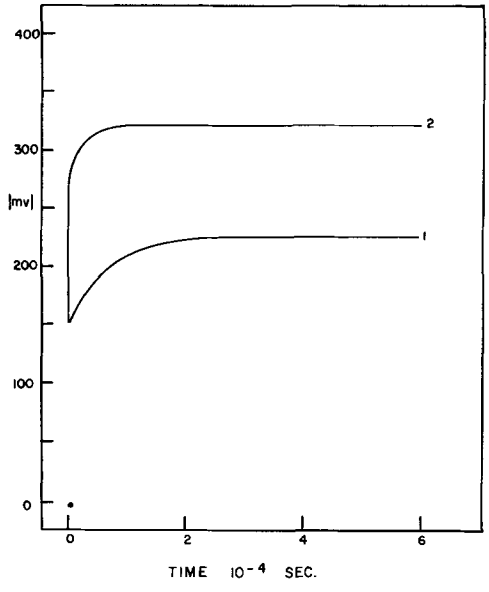

Fig. 2. Typical charging curves i = 89 ma/cm^2. Curve, 1, atomizer clean cathode; 2, cathode covered with 2.2 x 10^{-7} g/cm^2 stearic acid, freshly applied.

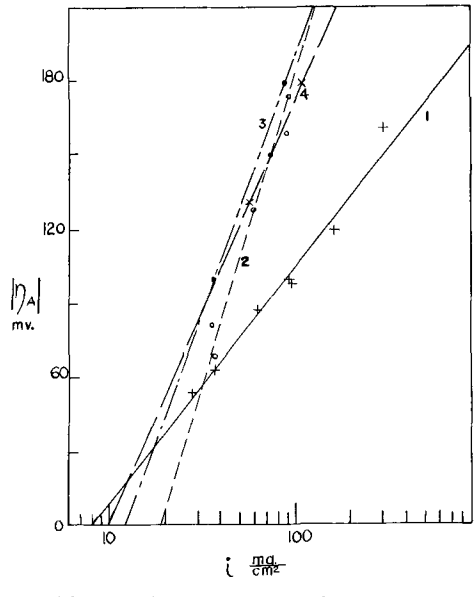

Fig. 3. Tafel lines for various cathode treatments. Curve 1, atomizer clean cathode; 2, cathodes with 2.2 x 10^{-7} g/cm^2 stearic acid, freshly applied; 3, cathodes with 2.2 x 10^{-7} g/cm^2 stearic acid, applied 24 hr before plating; 4, cathodes freshly soiled with 2.3 x 10^{-7} g/cm^2 paraffin oil.

Table I. Parameters for deposition of copper from an acid copper sulfate plating bath on copper electrodes as determined from Tafel lines

Bath composition, 1.5*N* $CuSO_4$, 0.45*N* H_2SO_4; electrodes, spectro grade copper

A. Atomizer clean cathodes

Run	i_o, ma/cm²	α_c
1	11.5	0.57
4	15.8	0.54
5	10.3	0.59
6	8.1	0.58
Mean	11.4	0.57
Standard deviation	±3.2	±0.02

B. Cathodes soiled with the equivalent of 1 monolayer stearic acid (2.2×10^{-7} g/cm² freshly applied, 20 min)

Run	i_o, ma/cm²	α_c
2, 7, 8, 9	20.5	0.23
18, 19	15.0	0.29
Mean	18.7	0.25
Standard deviation	±3.9	±0.04
composite of 2, 7, 8, 9, 18, 19	19.0	0.23

C. Cathodes soiled with the equivalent of 1 monolayer stearic acid which has been allowed to remain on the electrode for 24 hr

Run	i_o, ma/cm²	α_c
14, 15	11.0	0.31

D. Cathodes soiled with a film of paraffin oil equivalent in thickness to that of 1 monolayer of stearic acid (2.6×10^{-7} cm)

Run	i_o	α_c
16, 17	9.8	0.335

parameters for copper deposition. The parameter α_c of the transfer coefficient is significantly reduced for the contaminated surfaces. The values of α_c for cathodes soiled with the equivalent of 1 monolayer of stearic acid or with a film of mineral oil equivalent in thickness to that of one monolayer of stearic acid are of the order of 0.3 whereas atomizer clean cathodes have values of α_c in the vicinity of 0.57.[11] The exchange current i_o is not appreciably different for cathodes which are atomizer clean or soiled with mineral oil or stearic acid which has been on the electrode for 24 hr. Values of i_o for these conditions are of the order of 11 ma/cm². Freshly applied stearic acid, however, has the unexpected effect of slightly increasing i_o.[12] These results are tabulated in Table I. It is interesting to note that the values listed for clean cathodes are in excellent agreement with those reported by other investigators (4, 5).

The parameters listed in Table II were computed from the Tafel lines drawn from the data. The parameters for the soiled electrodes were determined from at least two separate measurements each on a different electrode, since during each measurement, the soiled surface becomes partially coated with a deposit of copper thereby masking some of the contaminant. Successive measurements on the same soiled electrode therefore could not be used for determining α_c and i_o. As a result, the parameter for the soiled electrodes as determined by the Tafel lines were subjected to an additional source of variation, namely, a different electrode with the same apparent aggregate soil density on the surface. Equations developed by the authors (6) may be used to obtain estimates of the parameters from one charging curve, but the trial and error calculations involved are extremely tedious for hand computation.

Despite the variations introduced by different electrodes, the activation overpotential of all the electrodes which were freshly soiled with 2.2×10^{-7} g/cm² stearic acid fall very nicely on a straight line when ploted against the logarithm of the current density, as shown in Fig. 2.

The differences in slope of the charging curves for the soiled electrodes and those which are atomizer clean are principally due to a reduction in the double layer capacity. The basic differential equation describing the growth of activation overpotential for the model of the rate-determining step characterized as a resistance and capacitance in parallel is

$$\frac{d\eta_A}{dt} = -\frac{1}{C_A}[i - i_F] \qquad [1]$$

where i_F is the Faradaic current.

At low overpotentials, during the initial portions of the charging, the slope of the charging curve is approximated by

$$\frac{d\eta_A}{dt} \approx -\frac{i}{C_A} \qquad [2]$$

Obviously as C_A is decreased, $d\eta_A/dt$ is increased. That the presence of some organic contaminants reduces the double layer capacity has been shown experimentally in the past (7). This phenomenon occurs because the adsorbed organic film of lower dielectric constant replaces the aqueous adsorbed film of higher dielectric constant. Typical values of the double layer capacitance as determined by means of Eq. [2] are about 50-60 μf/cm² for clean electrodes compared with about 7-26 μf/cm² for soiled electrodes.

As electrodeposition proceeds, the soiled cathode becomes coated with copper and the electrode surface changes. A sequence of charging curves for a soiled electrode reveals that as plating proceeds the charging curves become lower and less steep, approaching the shape of a curve for a similar cleaned electrode at the same current density. No such variation is however observed for electrodes which are initially atomizer clean. Figure 4 shows a sequence of charging curves for a cathode which was initially soiled. This type of behavior was observed with all of the electrodes soiled with 2.2×10^{-7} g/cm² stearic acid and with 2.3×10^{-7} g/cm² paraffin oil.

From the sequences of charging curves, plots of the steady-state overpotential *vs.* the coulombs/cm² deposited can be constructed. Figure 5 illustrates this decline in activation overpotential as plating proceeds on soiled cathodes.

From the curves of η_A *vs.* coulombs/cm² previous deposition, Tafel lines can be constructed as function of the amount of previous plating, and the kinetic parameters α_c and i_o can be determined. Results are shown graphically in Fig. 6, 7, and 8.

[11] The hypothesis that $\alpha_{c(\text{clean electrode})} \leq \alpha_{c(\text{electrode freshly soiled with stearic acid})}$ is accepted at the 5% significance level by a means of a "t" test. This statement means if the transfer coefficients were really equal but differed in this case only because of random error, the probability that such a large random difference could exist is less than 5%.

[12] A "t" test of the hypothesis

$$i_{o\ \text{electrode freshly soiled with stearic acid}} > i_{o\ \text{clean}}$$

is accepted as the 10% significance level.

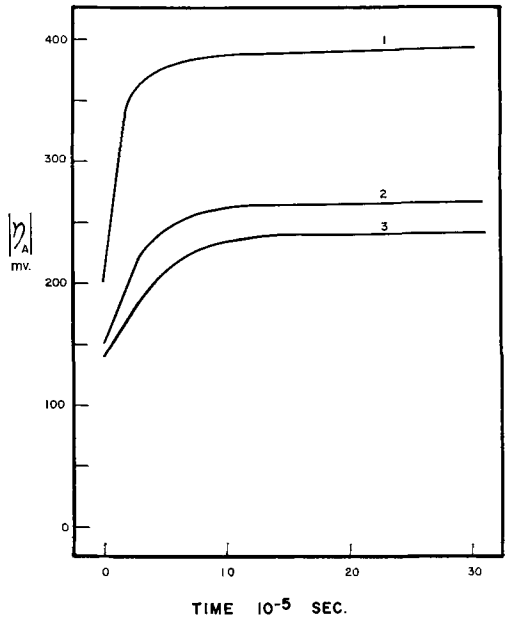

Fig. 4. Charging curves for cathodes soiled with 2.2 x 10^{-7} g/cm^2 stearic acid 24 hr before plating: 1, 0 coulombs/cm^2; 2, 0.178 coulombs/cm^2; 3, 1.96 coulombs/cm^2.

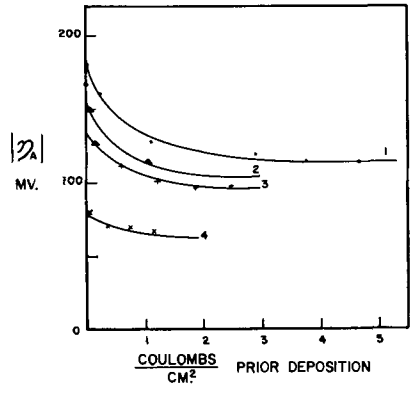

Fig. 5. Overpotential as a function of prior plating on a cathode freshly soiled with 2.2 x 10^{-7} g/cm^2 stearic acid. Curve 1, i = 89 ma/cm^2; 2, i = 73 ma/cm^2; 3, i = 61 ma/cm^2; 4, i = 37.7 ma/cm^2.

Some runs were made with 0.5 monolayer of freshly applied stearic acid, and the values of α_c and i_o found from the Tafel line are 0.54 and 10 ma/cm^2. These are essentially the same as those for a surface which is atomizer clean.

A series of experiments to test the cleanliness of soiled and cleaned electrodes after plating and to determine the degree of cleanliness of the experimental methods was undertaken, and the results are summarized in Table II. The last entry in Table II was extremely interesting in that the cathode showed two zones with different degrees of cleanliness. The area of the cathode exposed to the solution was almost atomizer clean, that is, the film of water sprayed in this area was almost continuous, whereas the area around the exposed zone which had been soiled but not electroplated was spotted with many droplets of water. Thus considerable cleaning of the surface had occurred during the deposition. Also, the values of α_c and i_o for this electrode had become

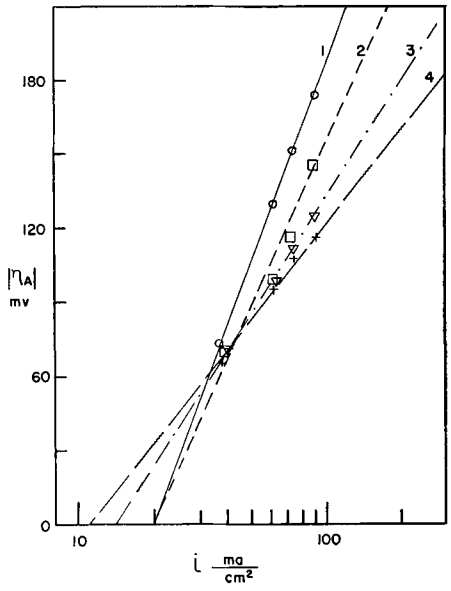

Fig. 6. Sequence of Tafel lines for cathodes freshly soiled with 2.2 x 10^{-7} g/cm^2 stearic acid. Curve 1, 0 coulombs/cm^2; 2, 0.5 coulombs/cm^2; 3, 1.5 coulombs/cm^2; 4, 3.5 coulombs/cm^2.

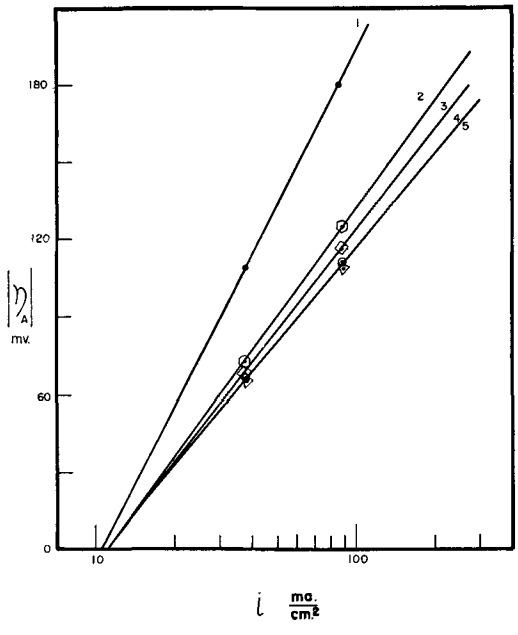

Fig. 7. Sequence of Tafel lines for cathodes soiled with 2.2 x 10^{-7} g/cm^2 stearic acid applied 24 hr before plating. Curve 1, 0 coulombs/cm^2; 2, 0.25 coulombs/cm^2; 3, 0.5 coulombs/cm^2; 4, 0.75 coulombs/cm^2; 5, 1.0 coulombs/cm^2.

that of cleaned electrodes at the time the atomizer test was performed, *i.e.*, 0.56 and 9.8 ma/cm^2. From this evidence, it appears that, if less than 1.1 x 10^{-7} g/cm^2 stearic acid (equivalent in weight to 0.5 monolayer) is present on the cathode, the parameters determined from the Tafel line will be, within the limits of experimental error, identical to those for atomizer clean electrodes.

Discussion

The values of the kinetic parameters for cleaned electrodes determined by the experiments described above are in excellent agreement with those reported by Mattsson and Bockris (4) for the same acid copper sulfate system. The techniques used in these ex-

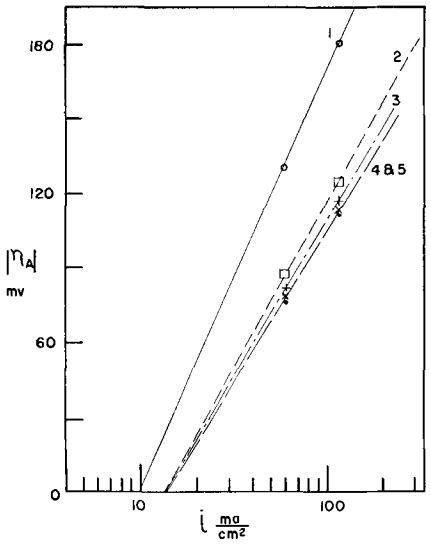

Fig. 8. Sequence of Tafel lines for cathodes soiled with 2.3 x 10^{-7} g/cm^2 paraffin oil. Curve 1, 0 coulombs/cm^2; 2, 0.2 coulombs/cm^2; 3, 0.4 coulombs/cm^2; 4, 0.8 coulombs/cm^2; 5, 2.0 coulombs/cm^2.

periments, however, are more amenable to practical situations since flat plate electrodes were employed making the study of the effects of deposited surface contaminants on the values of α_c and i_o possible.

A fact which is apparent from the results of these investigations is that rather small quantities of organic materials like stearic acid can affect the mechanism and hence the kinetic parameters for the deposition of copper. The critical amount of stearic acid beyond which the values of the parameters change lies somewhere between quantities equivalent in weight to 0.5 and 1.0 monolayer. Recently, Linford and Grunwald (8), in studies of metal plating adhesion as a function of cathode cleanliness have found that adhesion of the deposit is not affected appreciably until the surface density of stearic acid soil exceeds a value equivalent to about 0.8 monolayer. This work suggests that the mechanism of the deposition may have a relationship to the adhesion of the deposit. Furthermore, the fact that soil quantities equivalent to a large fraction of a monolayer are needed for a noticeable change in kinetic parameters confirms the idea that the final step occurs principally at certain active sites which are distributed over the surface. A high degree of surface coverage is required before a large enough fraction of these active zones are covered up or affected by the soil. This fact indicates that the soil (freshly applied stearic acid) when placed on the electrode surface may be preferentially deposited at places other than these special sites.

Table II. Summary of results

Initial condition of cathode	Extent of deposition, coulombs/cm^2	Cathode cleanliness after removal from cell
Atomizer clean	0	Atomizer clean
Atomizer clean	1.57	Atomizer clean
2.2×10^{-7} g/cm^2 Freshly applied stearic acid	3.03	Soil concentration near the limit of detectability of the atomizer test

During the electrodeposition, the soiled cathode behaves as if it were being cleaned, that is, the kinetic parameters approach those of clean surfaces as electrodeposition proceeds. Therefore, considerable deposition eventually occurs over the soil. Oriented stearic acid and paraffin oil behave in a similar fashion although the effect of the oriented stearic acid is masked more rapidly. This is probably due to the spreading of the paraffin oil from the area of the cathode which was soiled but was not exposed to the solution. About 1 coulomb/cm^2 of coverage is needed before the values of α_c and i_o level off for the surface in contact with 2.2 x 10^{-7} g/cm^2 stearic acid for 24 hr. Thus a deposit of about 3710Å average thickness completely masks the effect of the organic contaminant. A deposit of about 900Å average thickness ($\approx$ 300 Cu atoms thick if the deposit were uniform) causes a significant increase in α_c, from 0.31 to 0.42. The thickness of the oriented monolayer of stearic acid is about 30Å, another indication that deposition may occur preferentially at the active spots leaving the other areas relatively bare of fresh copper for a longer time.

Mattsson and Bockris have shown that, for clean copper electrodes in the plating solution studied, ion transfer was the rate-determining step at the current densities studied here and postulated the following transfer reactions

$$e^- + Cu^{++} \xrightarrow{\text{slow}} Cu^+ \qquad (I)$$

$$Cu^+ + e^- \xrightarrow{\text{fast}} Cu \qquad (II)$$

For soiled electrodes, the postulation of a rate-determining mechanism is somewhat more difficult. It is possible that transfer is not rate determining, although the charging curves for these electrodes are consistent with the model of a resistance and capacitance in parallel. A theoretical discussion starting with the assumption that a single rate-determining process other than transfer exists is presented below to show that the value of α_c as determined from the Tafel slope under this stipulation should be less than 0.5. Consequently, the converse, namely, that if $\alpha_c \leq 0.5$, the rate-determining step is not a transfer process, is plausible. One of the processes following transfer may therefore be the rate-determining step, *e.g.*, surface diffusion of adions or incorporation into the lattice.

Consider a cupric ion in the process of deposition. It is initially in the region adjacent to the cathode or moves there by means of diffusion and migration. From this region it crosses the double layer; it is transferred. Bockris and Conway (9) have presented theoretical arguments that transfer should involve the neutralization of only one positive charge since the calculated values of the energy barrier for neutralization of two positive charges is much higher. The fraction of depositing ions possessing sufficient energy for this direct transformation is very low.

The transferred cuprous ion is then at the cathode surface or is adsorbed on it, *i.e.*, it is an adion. The

deposition process continues with a gradual neutralization of the single positive charge and a loss of the remnants of its hydration sheath until definite and final incorporation of the neutral copper atom into the lattice occurs.

The sequence of steps in the deposition process can be represented by the general equations shown below.

$Cu^{++} + e^- \rightleftarrows Cu^+$ (III) transfer to electrode surface

$pCu^+ + e^- \rightleftarrows pCu^{q+}$ (IV)

$mCu^{s+} + e^- \rightarrow mCu^{u+}$ (V) rate-determining step

$Cu^{s+} + \left(\frac{1}{m}\right) e^- \rightarrow Cu^{u+}$ (Va)

All of the steps following transfer occur on the electrode surface. The coefficients p, ... , m must be ≥ 1 since at most only one positive charge remains to be neutralized. The charge coefficients q, ... , s,u must of course lie between zero and one for the same reason.

The process can be characterized by considering only the energy barrier of the rate-determining step and the changes in potential relative to the active state in the rate-determining step.

At equilibrium, the energies of activation for the deposition and dissolution reactions are $\Delta G_{1\,rev}$ and $\Delta G_{2\,rev}$, respectively. The overpotential which builds up when the deposition occurs at a finite rate is used to decrease the energy barrier for deposition while increasing it for dissolution. A fraction of this overpotential, β, decreases the activation energy for deposition, and the remaining fraction $(1-\beta)$ raises the energy barrier for dissolution.

The activation energy for the rate-determining deposition step at an overpotential η_A is

$$\Delta G_{1\,rev} - \beta|\eta_A|\mathbf{F}\ (1/m) \qquad [3]$$

while that for the dissolution is

$$\Delta G_{2\,rev} + (1-\beta)|\eta_A|\mathbf{F}(1/m) \qquad [4]$$

The deposition and dissolution currents can then be written as

$$\overleftarrow{i} = (\text{constant})_1 \exp\left[\frac{-\Delta G_{1rev} + \beta|\eta_A|\mathbf{F}(1/m)}{RT}\right] \qquad [5]$$

and

$$\overrightarrow{i} = (\text{constant})_2 \exp\left[\frac{-\Delta G_{2\,rev} - (1-\beta)|\eta_A|\mathbf{F}(1/m)}{RT}\right] \qquad [6]$$

respectively. At high cathodic overpotentials where the Tafel equation is valid, the dissolution current is negligible compared to the deposition current, and the net current may be reasonably approximated by the deposition current. Hence

$$i = \overleftarrow{i} = (\text{constant})_1 \exp\left[\frac{-\Delta G_{1\,rev} + \beta|\eta_A|\mathbf{F}\ (1/m)}{RT}\right] \qquad [7]$$

Taking the logarithm of Eq. [7] and differentiating $|\eta_A|$ with respect to ln i yields

$$\frac{\partial|\eta_A|}{\partial \ln i} = \frac{RT}{\beta\mathbf{F}(1/m)} \qquad [8]$$

Equation [8] also represents the slope of the Tafel equation which is

$$|\eta_A| = \left| \frac{RT}{\alpha_c\mathbf{F}} \ln i_o - \frac{RT}{\alpha_c\mathbf{F}} \ln i \right| \qquad [9]$$

or

$$\frac{\partial|\eta_A|}{\partial \ln i} = \frac{RT}{\alpha_c\mathbf{F}} \qquad [10]$$

Comparing Eq. [8] and [9] shows that

$$\alpha_c = \beta(1/m) \qquad [11]$$

which is identical with the equation developed by Bockris and Potter (10) in which they use λ in place of $1/m$.

Considerable evidence exists for supposing that the energy barrier is at least nearly symmetrical and that $\beta = 0.5$ (4, 9, 11-14). However, since $m \geq 1$, $(1/m)$ must be ≤ 1 or α_c can be limited by

$$\alpha_c \leq 0.5 \qquad [12]$$

Hence, if $\alpha_c \leq 0.5$, the conclusion that transfer is not the rate-controlling step is plausible.

For a rate-controlling mechanism different from that of cleaned electrodes, there must be a relatively higher energy barrier for the rate-controlling step of the soiled electrodes than the energy required for an ion transfer step for this system. An examination of the exchange currents for soiled electrodes indicates that these are of the same order of magnitude as those for clean electrodes, and that in the case of freshly applied stearic acid, the exchange current is even higher. These seemingly anomalous observations can be explained by the fact that organic material at the electrode solution interface lowers the capacity of the double layer as was observed experimentally. This lowering of the capacity probably facilitates transfer by making "leakage" of charged ions through the capacitance easier. The rate-determining step for the soiled electrode is then another process which has a higher energy barrier than that required for transfer across the double layer of reduced capacity. The fact that freshly applied stearic acid (2.2×10^{-7} g/cm^2) in an uneven deposit[13] raises the exchange current is perhaps another indication that preferential adsorption of stearic acid occurs at sites which are not identical to those required for deposition. Consequently, the copper adions are less likely to be "side-tracked" on the surface, but are effectively forced to the active sites for deposition since the other zones are occupied with stearic acid.

Hillson (15) in investigating the mechanism of the reaction at a Cu-Cu^{++} electrode found that the reaction initially occurred on only a small fraction of the electrode surface. He also observed that surface active materials that were present on the electrode were first adsorbed on the quiescent parts of

[13] The work of Linford and Grunwald (8) has shown that the method of soiling employed here left surfaces with uneven deposits of stearic acid.

the metal and merely served to block the mobility of the freshly deposited adatoms. Only when surface coverage with the contaminant was nearly complete, were active sites covered.

Similarly, Samartsev (16) made a microscopic study of silver deposition at low current densities. From especially pure solutions, crystal growth occurred only at certain active nuclei and continued to grow until the solution adjacent to these nuclei became so depleted of silver ions that the concentration polarization required for continued crystal growth exceeded the overpotential needed to form a fresh nucleus. In the presence of traces of impurities, certain faces of the crystal suddenly went passive and growth proceeded from the active nucleus in a threadlike way.

These earlier studies support the view that contaminants such as stearic acid which are deposited on the electrode are first adsorbed preferentially on sites which are not necessarily the ones at which final metal deposition occurs.

As the stearic acid becomes oriented and is sufficient to cover much of the surface, the other, less preferred sites (such as those needed for deposition) become covered, and the exchange current for the deposition does not decrease as coverage with fresh copper increases. The difference in activation energies between rate-controlling steps for deposition on a cathode freshly soiled with 2.2 x 10^{-7} g/cm^2 stearic acid and a clean one can be computed directly from the ratio of the exchange currents, if the assumption that the constants and the activities in the rate equations shown below are identical. Thus

$$i_{o_c} = (\text{const})\ a_{Cu++} \exp\left[\frac{-\Delta G_{c\,rev}}{RT}\right] \quad [13]$$

$$i_{o_s} = (\text{const})\ a_{Cu++} \exp\left[\frac{-\Delta G_{s\,rev}}{RT}\right] \quad [14]$$

where the subscripts c and s refer to cleaned and soiled surfaces, respectively.

Using the values of 20.5 ma/cm^2 and 11.0 ma/cm^2 for soiled and cleaned surfaces, respectively, and dividing Eq. [14] by Eq. [13] gives

$$\Delta G_{c\,rev} - \Delta G_{s\,rev} = 0.365 \text{ kcal/g mole}$$

This difference in activation energy is quite small and indicates that the contribution which the freshly applied stearic acid makes to increasing the reaction rate is also small. This fact is in agreement with the picture of the freshly deposited stearic acid aiding the deposition by preferentially covering up those sites which are not active for deposition.

Recently, Turner and Johnson (5) studied the effect of certain addition agents on the kinetics of copper electrodeposition from a sulfate solution and found that the Tafel exchange current increased with the addition of small amounts of thiourea or 1(−) cystine. For instance, with thiourea, the exchange current with 4 x 10^{-6} and 4 x 10^{-5} mole/l of addition agent was of the order of 10 ma/cm^2 whereas, in the absence of this addition agent, the experimental exchange current was about 3 ma/cm^2. Turner and Johnson concluded that the presence of small quantities of thiourea or 1(−) cystine, both sulfur compounds, resulted in the formation of copper sulfide in the deposit. This surface impurity, they argue, caused the mechanism of copper electrodeposition to be limited by surface diffusion of adatoms even at high current densities where normally, for clean electrodes, ion transfer would be limiting. Turner and Johnson also observed a decrease in α_c similar to that observed in this research when low concentrations of the organic addition agents were present. The reduction in α_c for copper deposition appears to be characteristic of surface diffusion as a limiting step and is in agreement with arguments presented previously.

Conclusions

1. Flat plate electrodes can be utilized to yield good, reproducible kinetic data when rigorous standards of solution and electrode purity are maintained. The values of the kinetic parameters determined for clean electrodes are in excellent agreement with those values obtained by other investigators using spherical electrodes. The use of flat plate electrodes has, however, the added advantage of being more amenable to studies of surface treatments.
2. Organic soils such as stearic acid and paraffin oil when present in quantities equivalent to about 1 monolayer affect overpotential measurements and values of the kinetic parameters.
3. For copper plating on copper electrodes, if the quantity of organic soil is present in less than an amount equivalent to about 0.5 monolayer, its effect on the overpotential and kinetic parameters is negligible.
4. Ion transfer is probably not the rate-controlling step for electrodes soiled with the equivalent of about 1 monolayer of stearic acid or paraffin oil. Instead the rate-determining step occurs on the surface of the electrode and is possibly surface diffusion.

Acknowledgment

The authors are indebted to the American Electroplaters' Society for the financial support and the encouragement they provided for this research under A. E. S. Project 12. The authors are especially grateful for the technical assistance given by the Project Subcommittee composed of Mr. E. T. Candee, Dr. E. A. Parker, Dr. E. B. Saubestre, and Dr. D. O. Feder.

Manuscript received Nov. 29, 1962; revised manuscript received Feb. 25, 1963.

Any discussion of this paper will appear in a Discussion Section to be published in the June 1964 JOURNAL.

REFERENCES

1. H. B. Linford and D. O. Feder, *Plating*, **45**, 349 (1958).
2. H. B. Linford and E. Saubestre, *ibid.*, **37**, 1265 (1950); *ibid.*, **38**, 60, 158, 367, 713, 847, 1157, 1263 (1951); *ibid.*, **39**, 55 (1952); *ibid.*, **40**, 379, 489, 632 (1953).
3. H. B. Linford and E. Saubestre, "A New Degreasing Evaluation Test," ASTM Bull. No. 190 (TP 73) May, 1953.
4. J. O'M. Bockris and E. Mattsson, *Trans. Faraday Soc.*, **55**, part 9, 1586 (1959).
5. D. R. Turner and G. R. Johnson, *This Journal*, **109**, 798 (1962).
6. H. B. Linford and L. Karasyk, "Some exact and approximate solutions to the differential equations

describing activation overpotential as a function of time," (Unpublished). A.E.S. Project 12 (1960).
7. M. Proskurnin and A. Frumkin, *Trans. Faraday Soc.*, **31**, 110 (1935).
8. H. B. Linford and J. Grunwald, *Plating*, **46**, 1039 (1959).
9. J. O'M. Bockris and B. E. Conway, *Proc. Roy. Soc.*, **248**, 394 (1958).
10. J. O'M. Bockris and Potter, *J. Electrochem. Society*, **99**, 169 (1952).
11. J. O'M. Bockris, *Z. Physik Chem. (Leipsig)*, **215**, 1 (1960).
12. J. O'M. Bockris, *Electrochim Acta*, **3**, 340 (1961).
13. J. O'M. Bockris, *Electrochemical Constants*, National Bureau of Standards, (1953). No. 524, Chapt. 23.
14. J. O'M. Bockris, and Mehl, *Can. J. Chem.*, **37**, 190 (1959).
15. P. J. Hillson, *Trans. Faraday Soc.*, **50**, 385 (1954).
16. Samartsev, *Acta Pysiochim.*, **16**, 206 (1942).

The Uniformity of the Wetting and Dissolution of Germanium by Molten Indium

A. A. Bergh and L. H. Holschwandner

Bell Telephone Laboratories, Incorporated, Allentown, Pennsylvania

ABSTRACT

The two methods generally applied to evaluate wetting have been used to examine the wetting of germanium by indium, and it is shown that in order to get reliable information they both have to be used simultaneously. A process yielding uniform wetting is achieved by subjecting the indium and germanium separately to a high-temperature (600°C) hydrogen treatment prior to alloying and bringing them into contact in the same reducing atmosphere at elevated temperatures (300°-350°C). The effect of the different factors influencing wetting is evaluated by introducing them one by one into this process. Wetting can be inhibited by trapped gas bubbles on the germanium-indium interface and by the presence of germanium and indium oxides at the interface. The effects of the oxides are found to be most pronounced. It is shown finally that the reproducibility of the reverse junction characteristics is greatly influenced by the uniformity of wetting.

In the preparation of pnp alloy transistors, spheres or disks of indium are placed on the opposite sides of a <111> oriented n-type germanium wafer and heated to allow the indium to melt. The molten indium wets the germanium surface and dissolves part way into the wafer. As the molten alloy is cooled the dissolved germanium recrystallizes at the liquid-solid interface of the wafer which acts as a single-crystal seed. Since the recrystallized germanium contains indium in solid solution, a p-n junction forms between the original and recrystallized materials. Many difficulties in this process have been attributed to nonuniform wetting and dissolution of germanium by the molten indium, resulting in irregular junctions. The purpose of this investigation was to determine the effect of different factors on wetting and to collect information about the relationship between electrical characteristics and the uniformity of wetting. To accomplish this first a reliable evaluation method was needed, *i.e.*, the limitations of methods used at present had to be evaluated.

Evaluation of Wetting

Two widely accepted techniques (1, 2) to evaluate the uniformity of wetting and dissolution are (i) the removal of indium by chemical etching (concentrated HCl) after alloying followed by a microscopic examination of the regrown germanium surface, and (ii) the preparation of linear cross sections orthogonal to the alloyed area. While the information about wetting by the first method is obtained indirectly, *i.e.*, by assuming that the regrown germanium surface closely resembles the shape of the junction, the second method is limited to an arbitrary cross section. Since the above assumption is not always valid as shown below in detail, it proved to be necessary to use both methods simultaneously to arrive at reliable conclusions.

Examination of many samples revealed three types of irregularities based on the kinetics of their formations: (i) No wetting or dissolution and no regrowth at certain spots (Fig. 1). A "barrier" has

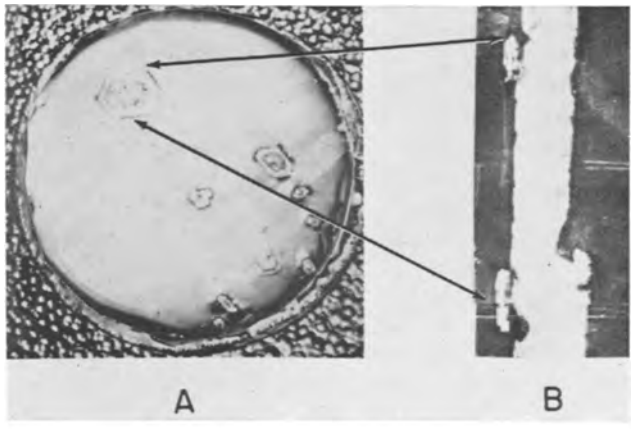

Fig. 1. No wetting or dissolution and no regrowth. A, regrown germanium surface; B, vertical cross section of the unwetted area.

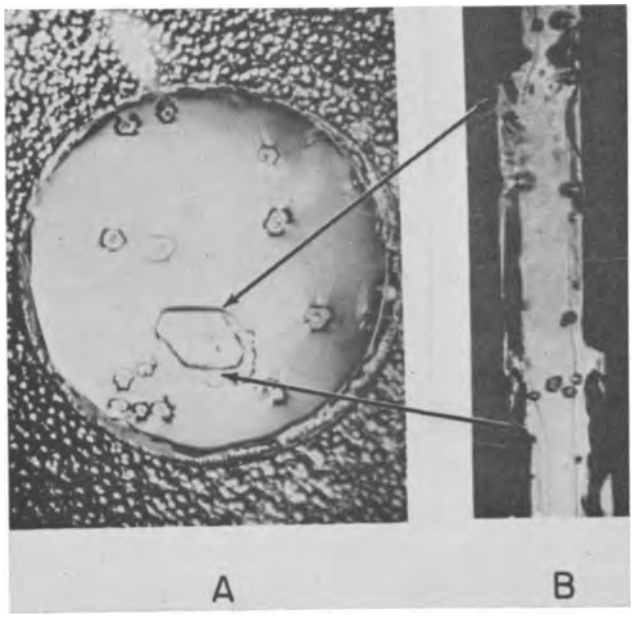

Fig. 2. No wetting or dissolution but the unwetted area partially hidden by the regrowth. A, regrown germanium surface; B, vertical cross section of the unwetted spot.

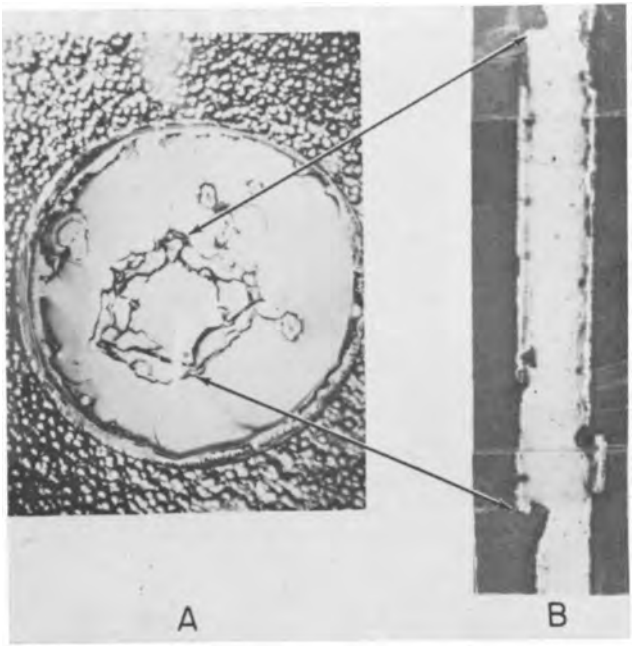

Fig. 3. Limited dissolution but uniform wetting and regrowth, revealed by the elevated junction on the vertical cross section (B): A, regrown germanium surface.

separated the germanium from the indium during the entire alloying process. The original germanium surface is revealed unchanged and probe test shows it still to be n-type. (ii) No wetting or dissolution, but the unwetted spot partially or fully hidden by the regrowth (Fig. 2). Here the shape of the recrystallized germanium surface yields misleading information about the position of the junction. (iii) Uniform wetting, limited dissolution and regular regrowth (Fig. 3). The "barrier" separating the germanium from the molten alloy has been removed only during the dissolution process reducing the time for dissolution. In all three cases a barrier of some kind has separated the germanium surface from the melt during all or a part of the dissolution process. Since there are several factors which might act as barriers all of which may be present in a manufacturing process, their individual effects could be studied only by introducing them one by one into an alloying process yielding uniform wetting and dissolution.

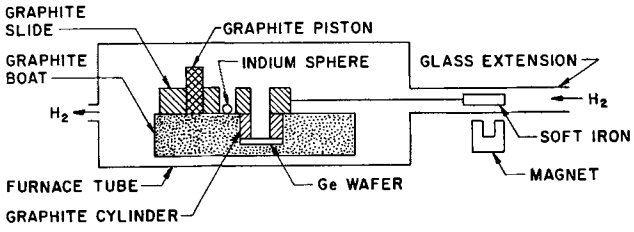

Fig. 4. Schematic cross section of the alloying apparatus

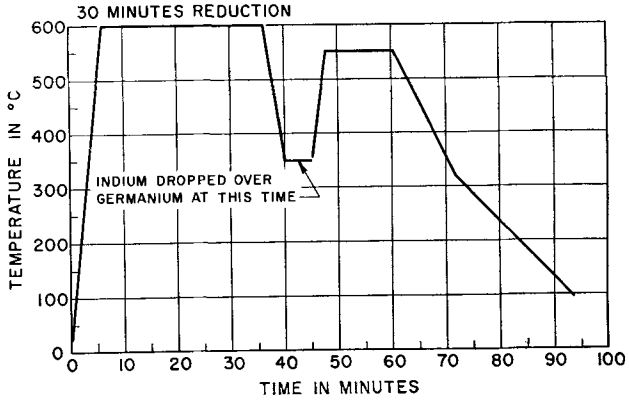

Fig. 5. Temperature cycle for alloying molten indium over germanium.

Experimental Techniques

A schematic cross section of the alloying apparatus is shown in Fig. 4. The square shaped germanium wafer 6.25 mm on one side, 0.125 mm thick, and cut parallel to the (111) plane was placed in a graphite boat and partially covered by a graphite cylinder. A graphite slide contained the indium sphere, 1.52 mm in diameter, and a graphite piston which could be successively dropped over the germanium wafer by moving the slide with the help of a magnet from the outside. After closing the furnace, dry and oxygen free hydrogen was introduced and the gas flushing (3.5 l/min) continued over the entire process. The temperature was raised to 600°C and kept there for 30 min to remove the surface oxides from the alloying components. After reduction the temperature was lowered to 300°C, and the indium and graphite piston were dropped over the germanium. Alloying was carried out at 550°C during a temperature cycle represented in Fig. 5. After cooling the furnace below 50°C the hydrogen flush was replaced by a nitrogen flush for about 5 min, the furnace opened, and the alloyed units removed.

Effect of the Different Factors Influencing Wetting

As a result of the above process, uniform wetting could be achieved reproducibly on germanium wafers with dislocation densities ranging from zero to 10,000/cm^2. The effect of the different factors on wetting could be evaluated now by introducing them one by one into this process.

The factors receiving most consideration as possible barriers separating the germanium surface from the molten indium are: (i) gas bubbles trapped on the germanium-indium interface; (ii) indium oxide having a higher melting point than that of indium; (iii) oxide film on the germanium surface. Their effect on the uniformity of wetting will be examined in turn.

Gas bubbles.—An indication that gas bubbles might prevent wetting is found in the circular appearance of many unwetted areas (3). Concerning the possible sources for bubble formation the following factors were evaluated: (i) mechanically trapped gas from the furnace atmosphere, (ii) gas products of the reduction of germanium and/or indium oxides if alloying in a reducing atmosphere.

In the previously described alloying process (referred to herein as the "standard" process) the spherical molten indium is dropped over the germanium surface and is forced to spread out symmetrically to a circular disk shape. In the course of spreading the gas is forced from the pits on the germanium surface thus preventing the trapping of gas from the furnace atmosphere as indicated by the lack of any unwetted spots. On the other hand if a previously deformed circular indium disk is placed over the germanium surface as shown in Fig. 6 it will first melt at the outside periphery trapping the gas between the interfaces and enabling it to escape only through the bulk of the indium. Figure 7 shows the recrystallized germanium surfaces of two such alloys. The element on picture A was alloyed at 450°C, and the large circular unwetted area in the center of the regrowth indicates a complete separation of the indium and germanium during the whole process. The flat, but elevated center portion on picture B indicates that the gas bubble escaped during the dissolution process leaving time only for a limited amount of dissolution. This in turn resulted in an elevated base and thus an elevated region. The magnitude of this elevation can be used to determine the approximate temperature at which the gas bubble escapes. No correlation could be established between the parameters of the germanium (*e.g.*, dislocation density from 0 to 10,000/cm^2) and the temperature at which the bubbles escape. The generalization can be made, however, that they are largely eliminated between 450° and 500°C. Similar to the purposely introduced cavities there are a great number of small cavities due to surface roughnesses on both the indium and germanium surfaces whenever an indium disk is applied. The resulting elevations in the junction are generally small in size, are covered by the regrowth, and have no appreciable effect on the reverse junction characteristics.

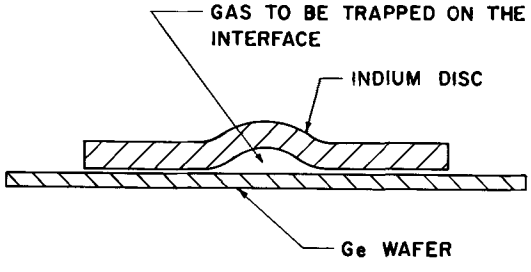

Fig. 6. Schematic cross section of the indium disk deformed in order to trap a gas bubble on the indium-germanium interface.

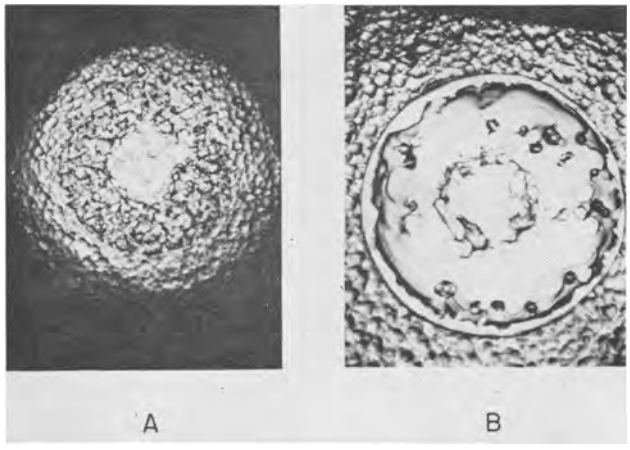

Fig. 7. Effect of gas bubbles trapped on the indium-germanium interfaces. Regrown germanium surfaces after alloying at 450°C (A) and 550°C (B).

Another possible source of bubble formation is the gaseous products of the reduction of the germanium and indium oxides. Examining however the mechanism of the wetting in connection with the reduction of the oxide films, it becomes apparent that the probability of any gas trapping is extremely slight during this process. When an indium disk, previously exposed to air at 100°C for 1 hr is placed on a germanium surface previously rinsed in dilute HCl, it retains its shape even above the melting point (156°C) and is restrained from wetting by the continuous oxide film. At higher temperatures when the hydrogen becomes effective in reducing the oxide film, the thickness and mechanical strength of the film is reduced, thus yielding to the forces extended by the restrained melt. Once the oxide shell is broken the molten and oxide free indium flows out of its enclosure and wets the germanium surface. The above mechanism is clearly illustrated in Fig. 8. In picture A the oxide shell was broken at 200°C by applying pressure on the indium disk. The light circle shows the area where the indium wetted the germanium surface and the dark central portion is still completely protected by the remaining oxide film. Picture B shows the regrowth from which the

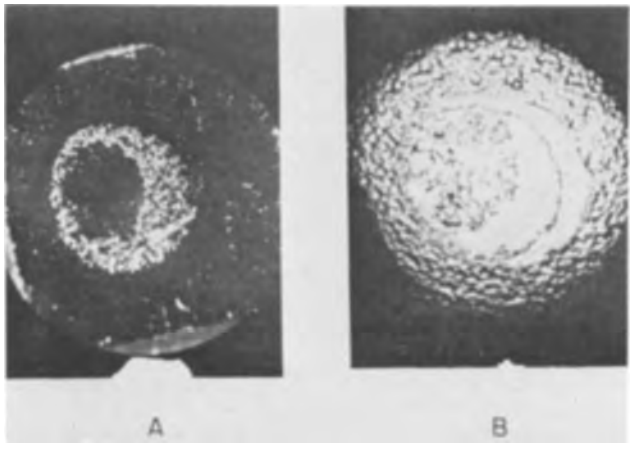

Fig. 8. Effect of indium oxides on wetting. Regrown germanium surfaces after alloying at 200°C (A) and 550°C (B).

indium has been removed after alloying at 550°C. The nearly circular area covered with unwetted spots is surrounded by two circular portions both having very smooth, regular appearances. It is interesting to note also that the unwetted spots are irregular in shape in contrast to the circular shape of those due to gas bubbles. Once the oxide film is surrounded by the melt, further reduction can occur only if the hydrogen can penetrate to the germanium-indium interfaces. The possibility of such a penetration is shown to be very unlikely by the results of the following experiment.

After reducing both the indium and germanium surfaces, the indium sphere was dropped over the germanium at 300°C, cooled to room temperature, and removed from the furnace. Following this operation, the element was exposed to air at 100°C for 2 hr and alloyed in a slightly oxidizing atmosphere at 550°C. After removing the indium, no unwetted spots were revealed on the regrown germanium indicating that once the indium is tacked to the germanium surface the interfaces are completely protected from oxidation and, most probably, from any gas penetration, thus ruling out any reduction by hydrogen at the interfaces. The conclusion can be drawn therefore that the only important source for bubble formation is mechanically trapped gases from the furnace atmosphere, the amount of which is greatly affected by the geometry of the alloying components.

Indium and germanium oxides.—The inhibiting affect of both indium and germanium oxides on wetting has been previously acknowledged (3, 4) and the necessity of reducing both components prior to alloying in order to achieve uniform wetting established. No attempt was made however to study their influence separately by keeping the oxide thickness constant on one component while varying it on the other. This information is necessary however to establish ideal alloying condition in case the indium and germanium cannot be prefired in hydrogen in the alloying furnace.

Flat, circular indium disks, 4.32 mm in diameter and 0.26 mm thick, were alloyed on germanium wafers similar to those reported in the previous experiments. Both components were used with three different oxide films prepared by: (i) reduction in hydrogen at 600°C for 30 min with the alloying furnace (oxide free), (ii) rinsing the indium pellet and the germanium wafer in dilute hydrochloric acid prior to alloying (etched), (iii) keeping the indium at 100°C and the germanium at 200°C for 1 hr in air having a relative humidity of 35% at 25°C (oxidized). All experiments were repeated several times using the alloying conditions described under "Experimental Techniques." Their sequence with the corresponding representative picture is summarized below.

No.	Preparation of germanium	Preparation of indium	Corresponding figure
1	Oxidized	Etched	9A
2	Etched	Etched	9B
3	Oxide free	Etched	9C
4	Etched	Oxidized	8B center
5	Etched	Oxide free	8B periphery

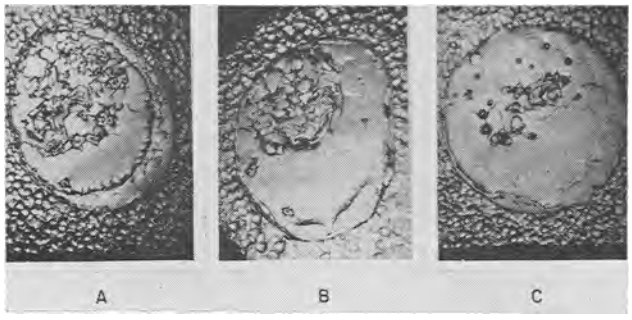

Fig. 9. Effect of germanium oxides on wetting. Indium rinsed in dil. HCl was alloyed on oxidized (A), etched (B) and oxide free (C) germanium.

The oxide thickness was kept constant on the indium pellet while that of the germanium was varied on the alloyed units shown in Fig. 9. In picture A a large unwetted area is surrounded by a uniform regrowth. The size of the unwetted area is reduced in picture B while the area of uniform wetting increases. In picture C finally only a few small unwetted spots, some of them probably due to trapped gases, indicate the effect of the indium oxide. Since the results of experiments 4 and 5 are very similar to those of 1 and 3, respectively, no pictures of these experiments are shown. The reader is referred instead to Fig. 8B where the conditions of these experiments are essentially duplicated. The uniform unwetted area in the center is due to the indium oxide and the periphery shows the uniform regrowth after alloying oxide free indium over etched germanium. Comparing the results of experiment 2 (both components etched) with those of 3 and 5 (one component etched, the other oxide free), a much greater reduction in the size of the unwetted areas can be detected than that expected from the experimental conditions. In experiment 2 both components are covered by a light oxide layer which is removed from one of the components in the following two cases. If the unwetted area were proportional to the total amount of oxides present, the sum of the unwetted areas in experiments 3 and 5 should be approximately equal to that found in experiment 2.

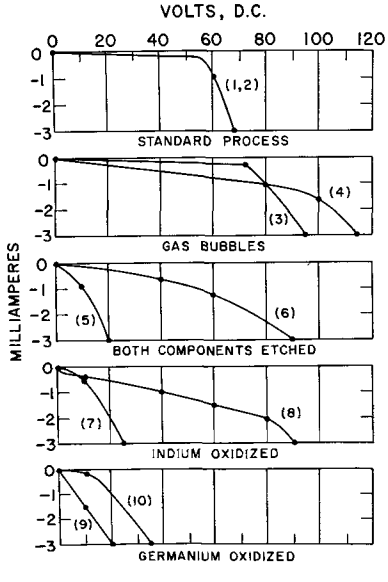

Fig. 10. Effect of wetting on the reverse junction characteristics

Instead, ten repeated experiments showed that the sum of the unwetted areas from experiments 3 and 5 was much less than the unwetted area for experiment 2. In several cases there was no unwetted area in experiment 5. This indicates that (i) the unwetted area is not linearly proportional to the sum of the oxides and that a certain amount of germanium oxide might be removed by oxide free indium, (ii) a certain minimum amount of oxide is necessary to result in unwetted spots. The results of experiments 1 through 5 indicate that nonwetting can be caused by oxides on the indium, the germanium, or both.

Effect of Wetting on the Reverse Current Characteristics

The uniformity of wetting has always been considered one of the most important factors contributing to high reverse currents in transistor manufacturing. An attempt was made therefore to establish correlations between reverse characteristics and wetting. Diodes from the previously discussed materials were prepared under different conditions, ten to twenty of each, and the reverse characteristics measured. With the exception of our standard process the results were found to be erratic and showed great variations between the two limiting values represented in Fig. 10.

A summary of the experimental conditions is given below:

No. of test	Preparation of germanium	Preparation of indium	Introduced gas bubbles
1, 2	Oxide free	Oxide free	None
3, 4	Oxide free	Oxide free	Some
7, 8	Oxide free	Oxidized	None
9, 10	Oxidized	Oxide free	None
5, 6	Etched	Etched	None

On examining the regrown germanium surfaces no direct correlation could be established between the reverse characteristics and the number and shape of the unwetted areas. All factors resulting in nonuniform wetting decrease the reproducibility of the reverse junction characteristics with the greatest effect being probably from the germanium oxides.

Manuscript received Aug. 8, 1962; revised manuscript received Nov. 29, 1962. This paper was presented at the Houston Meeting, Oct. 9-13, 1960.

Any discussion of this paper will appear in a Discussion Section to be published in the June 1964 JOURNAL.

REFERENCES

1. J. I. Pankove, *J. Appl. Phys.*, **28** (1957).
2. D. Baker, *Proc. Inst. Elec. Engrs. (London)*, **106**, 442 (1959).
3. Arnold Rose, *R.C.A. Rev.*, **19**, 423 (1958).
4. J. W. Peterson, J. McGlasson, and W. C. Hittinger, *J. Metals*, **9**, 823 (1957).

The Spreading of Molten Indium Over Germanium

A. A. Bergh

Bell Telephone Laboratories, Incorporated, Allentown, Pennsylvania

ABSTRACT

The control over the spreading of molten metals over semiconductor surfaces presents many difficulties in the manufacture of alloy junction transistors. The spreading of molten indium over germanium surfaces has been investigated to gain better understanding about the effect of different factors influencing spreading. The effect of various imperfections in the germanium crystal, rate of temperature rise, size of the indium sphere, preparation of the germanium surface, gaseous ambient, and oxides of the alloying components were evaluated *vs.* an arbitrarily chosen standard procedure. The most favorable conditions for spreading were obtained by using germanium crystals free of imperfections, slow temperature rise, inert atmosphere, a small amount of germanium oxide, and oxide free indium.

Current theories are inadequate to explain our experimental results; their deficiencies are shown in detail. Comparing the results with those of spreading liquid metals over solid metals it is concluded that the anisotropy of the single crystal germanium toward the dissolution in molten indium and the surface roughness influence primarily the geometry of the wetted area, and the most important single factor contributing to spreading is the reduction of germanium oxides by indium probably enhanced by surface migration.

The control over the spreading of liquid metals over semiconductor surfaces presents many difficulties in the preparation of semiconductor devices and especially in the manufacture of alloy junction transistors. While the spreading of liquid metals over solid metals has been the subject of many previous investigations (1) very little information is available concerning the spreading of liquid metals over semiconductor surfaces. Liquid indium-germanium is one of the most frequently investigated systems (2-6), however, the conclusions reached are partly contradictory and partly restricted to a few special experimental conditions. An attempt was made therefore to determine the effect of many different factors influencing the spreading of liquid indium over germanium surfaces and to examine

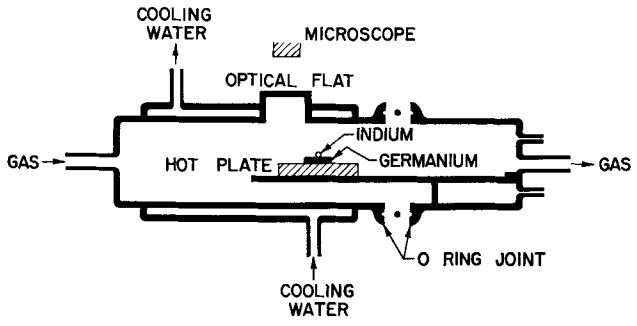

Fig. 1. Schematic diagram of the alloying apparatus

the current theories explaining this process in the light of our experimental results.

Experimental

Our experimental technique was basically the same as that used for the preparation of alloy junction transistors (7). A schematic diagram of the alloying apparatus is shown in Fig. 1; it consists of two 40 mm ID Pyrex tubes connected by an O-ring joint. The first tube terminates in a 6 mm ID inlet tube for gas flushing, and it is surrounded by a water-cooling jacket except for a short tube, 16 mm OD, which is covered by an optical flat. This window served to observe the behavior of the indium during alloying through a 40 power stereo microscope. The second tube has extensions for the gas outlet and for the electrical wiring connected to the heating element and the thermocouple probe. All gases were dried in a Baker Deoxo Puridryer (moisture content <4 ppm) and flow rate of 2.5 l/min was maintained during all experiments. The alloying cycle was programmed to maintain a linear temperature rise between 100° and 600°C. The temperature was automatically recorded by a Brown Strip Chart Instrument.

Materials.—The different size indium spheres were supplied by Alpha Metals Inc. from 99.999% purity material. All germanium wafers were cut from 2-5 ohm-cm n-type material parallel to the (111) plane. The shape of the wafers was square or circular having a side or diameter of 6.35 mm, respectively, and a thickness of 0.15-0.25 mm.

Before cutting the wafers all the germanium slices were carefully examined for both the number and shape of etch pits by exposing them to CP-4. Several investigators have reported the occurrence of three different types of etch pits (usually designated as A, B, and C pits) on CP-4 etched germanium surfaces (9-14). The A pits have a terraced conical shape and correspond to dislocations as shown by Vogel *et al.* (8). The triangular B and the round, smooth, shallow C pits are probably due to some contamination, such as SiO_2 precipitate (12, 14) in the germanium crystal lattice. All experiments reported in this paper were carried out on materials exhibiting only A type pits. The behavior of the germanium showing B and C type pits will be the subject of a forthcoming publication. It can be stated in general, however, that smaller wetted areas were observed on materials showing B- and C-type pits than on those reported here.

Results.—A set of conditions have been selected as our standard procedure as follows: Lapped germanium wafers were etched in "superoxol,"[1] rinsed in

[1] 1:1:3 by volume of H_2O_2 (30%), HF (48%), and water.

Table I. Summary of the effect of the different factors on spreading

Variable	Conditions	Shape of wetted area	Spreading ratio
Rate of temp rise	125°C/min	C	1.6
	33°C/min	C-H	2.0
	8.3°C/min	H	3.0 SP
Diameter of In sphere	0.175 mm	T	2.9
	0.450 mm	T	3.2
	0.600 mm	H	3.0 SP
Preparation of the germanium surface	"Superoxol" etch	H	2.9 SP
	Sand blasted	C	3.0
	CP-4 A etch	C-H	3.2
	Electropolished	C-H	3.3
Etch pit count/cm^2	50-100 sand blasted	C	3.8
	5-8 $\times$ 10^3 sand blasted	C	3.1
	50-100 etched	H	3.6
	5-8 $\times$ 10^3 etched	H	3.0 SP
Gaseous ambient	Hydrogen	C	2.4
	Nitrogen	H	3.0 SP
	Nitrogen + 1% oxygen	C	0.8
Germanium reduced in	Hydrogen at 600°C	H	2.4
Oxidized in room air	225°C for 5 min	H	3.2
	400°C for 5 min	C-H	1.7
	600°C for 120 min	C	0.9
Indium exposed to room air at	25°C for 5 min	H	2.9 SP
	225°C for 5 min	H	2.5
	350°C for 5 min	C	1.4

C, circular; H, hexagonal; T, triangular; SP, standard procedure.

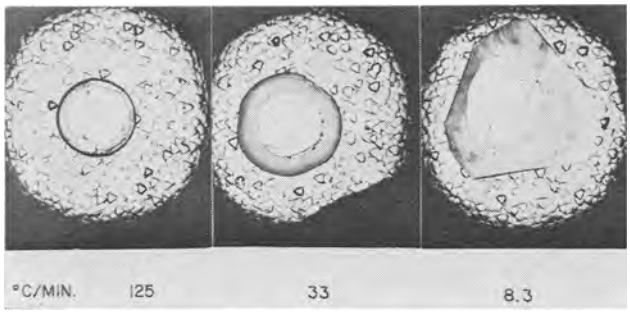

Fig. 2. Effect of the rate of temperature rise (°C/min) on spreading.

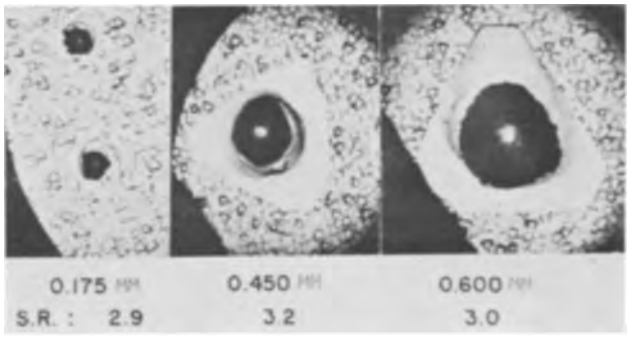

Fig. 3. Effect of the size of the indium sphere (mm) on spreading.

deionized water, and dried at room temperature in a forced air current. Indium spheres of 0.6 mm in diameter were degreased in trichloroethylene and acetone, rinsed in dilute hydrochloric acid, and dried. The temperature cycle consisted of an 8.3°C/min temperature rise from 100° to 600°C, a 5-min plateau at 600°C, and an 8.3°C/min temperature drop from 600° to 100°C. The system was flushed by dry nitrogen containing a few tenth of a per cent hydrogen at a flow rate of 2.5 l/min during alloying. The above conditions were varied one by one and the changes evaluated with respect to the standard procedure. The extent of spreading is described by the spreading ratio, a term introduced by Pensak (2). It is defined as the diameter of the wetted area (if not circular then the diameter of a circle of equal area), divided by the diameter of the indium sphere. An account of our experiments is given below, Table I summarizing all the results.

Effect of Rate of Temperature Rise on Spreading

The effect of the rate of the temperature rise is shown in Fig. 2. All three experiments were performed on the same wafer, the first two (125°C/min and 33°C/min temperature rise) representing the change in the size of the wetted area due to a faster temperature rise than that applied in the standard procedure (8.3°C/min). The results agree with Mueller's data (3) and confirm that spreading is a slow, time-consuming process. The rate of the temperature rise also affects the geometry of the wetted area. The second experiment represents a transition between the circular shape of the faster and the hexagonal shape of the slower rise.

Effect of indium size on spreading.—Since the control over spreading is most difficult in the preparation of small area alloy junction devices, wetted areas were produced with indium spheres of different diameters. Results are shown in Fig. 3. Indium spheres of 0.175-0.600 mm in diameter were placed on the same germanium wafer and alloyed with our standard procedure. The spreading ratios were found to be all within our experimental error indicating no influence on the part of the size of the indium on spreading in the tested range of diameters.

Effect of Preparation of Germanium Surfaces and Etch Pit Count on Spreading

Lapped germanium surfaces in the previously described experiments were etched in "superoxol" to remove about 0.05 mm of material from both sides of the wafer. This etching results in a pitted, rough surface, the pits being triangular in shape, lined up toward certain crystal orientations and bearing no relationship to the crystal imperfections (15). In order to examine the effect of the preparation of the germanium surfaces on spreading two changes were made in the above procedure. First, since surface roughness is believed to influence contact angles and thus spreading (16, 17), smooth surfaces were produced on several wafers by applying CP-4A[2] etch and electropolishing, respectively. To maintain the chemical identity of the surfaces, alloying was preceded by a short (30 sec) superoxol etch. The obtained spreading ratios and the geometry of the wetted areas are listed in Table I. Spreading was slightly enhanced in both cases, and the anisotropy of the germanium, *i.e.*, the tendency to form a triangular wetted area, was substantially reduced. The second change in the surface preparation of germanium was introduced to examine the effect of the anisotropy of the germanium crystal on spreading. The rate of the dissolution of germanium in molten indium was shown to be a function of the crystal orientation (4) explaining the triangular or hexagonal shape of the wetted area. Surface treatments disturbing the crystal structure can be expected therefore to diminish this effect. In order to accomplish this, one half of several wafers previously etched in superoxol were sand-blasted and indium spheres alloyed on both parts simultaneously. No change in the spreading ratios could be observed, but the wetted areas on the damaged surfaces become circular in shape as listed in Table I and shown in Fig. 4.

Dislocations have been reported to inhibit spreading (3-5). Our experiments confirmed this statement as shown in Table I, provided that only A-type pits were present on the germanium.

Effect of Gaseous Ambient on Spreading

The effect of the gaseous ambient on spreading is shown in Fig. 5. The inert atmosphere (nitrogen, 2nd picture) used in the standard procedure was changed to a reducing (hydrogen, 1st picture) and to an oxidizing atmosphere (nitrogen +1% oxygen, 3rd picture), respectively. Both alloying components were exposed to air prior to alloying and thus covered by thin films of oxides. While these films were not affected by the inert atmosphere of the standard procedure they were both reduced in the dry hydrogen ambient at about 420°-450°C (18, 19), and the

[2] CP-4 without bromine.

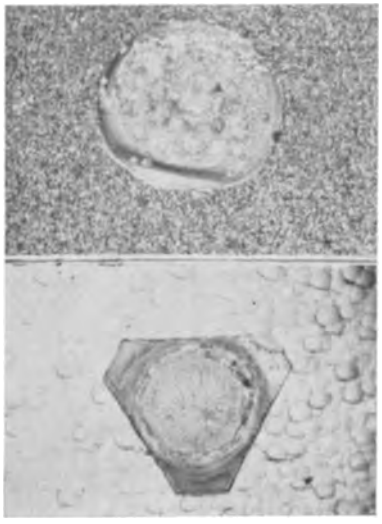

Fig. 4. Effect of the preparation of the germanium surface on spreading. Top, sand-blasted, 50-100 etch pit count (cm^2); bottom, etched in superoxol, 50-100 etch pit count (cm^2).

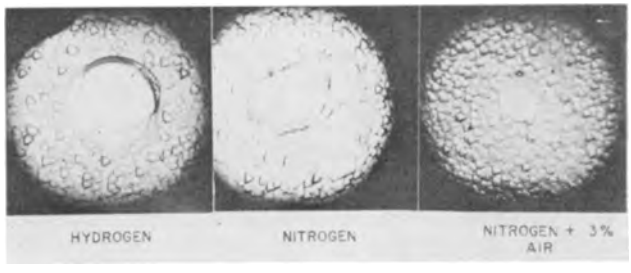

Fig. 5. Effect of the gaseous ambient on spreading

thickness of both oxides were increased in the nitrogen ambient containing 1% oxygen. Both the removal of the oxides and the increase of the oxide thicknesses restricted spreading indicating that a thin film of germanium and/or indium oxide promotes spreading. The relative importance of the two oxides is revealed in the following two experiments.

Effect of Germanium and Indium Oxides on Spreading

First, indium spheres cleaned in dilute hydrochloric acid were placed on germanium wafers containing different amounts of oxides. Some wafers were reduced in hydrogen at 600°C, others were oxidized in room air (34% relative humidity at 25°C) at different temperatures. Some of the results are collected in Table I. The size of the wetted area first increases with increasing germanium oxide thicknesses up to a certain point beyond which further oxidation of the germanium has the opposite effect. Oxidation at 650°C for 2 hr restricted spreading to an area smaller in diameter than that of the indium sphere.

In the second series of experiments indium spheres covered with different oxide thicknesses were placed on a germanium wafer prepared according to the standard procedure. After alloying the largest wetted areas resulted invariably from indium spheres containing the least amount of oxide, the areas gradually decreasing with increasing oxide thicknesses.

As a conclusion of all the above experiments, the most favorable conditions for spreading can be summarized as follows: (*a*) slow temperature rise during alloying; (*b*) highly polished germanium surfaces; (*c*) dislocation free germanium (especially free of C-type pits); (*d*) inert atmosphere during alloying; (*e*) oxide free indium; and (*f*) a thin film of germanium oxide. It can be concluded furthermore that the surface roughness of the germanium has a more pronounced effect on the geometry than on the size of the wetted area, a damaged surface yielding circular spreading. Finally, cross sections perpendicular to the wetted areas revealed that the penetration of indium parallel to the (111) crystal plane is larger by a factor of 100 to 150 than that toward the bulk for spreading ratios of about 3.

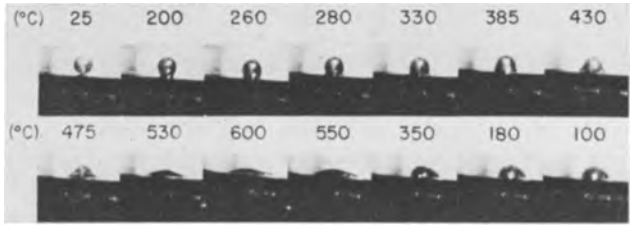

Fig. 6. Spreading and contraction of indium on germanium during a 1-hr alloying cycle (side view).

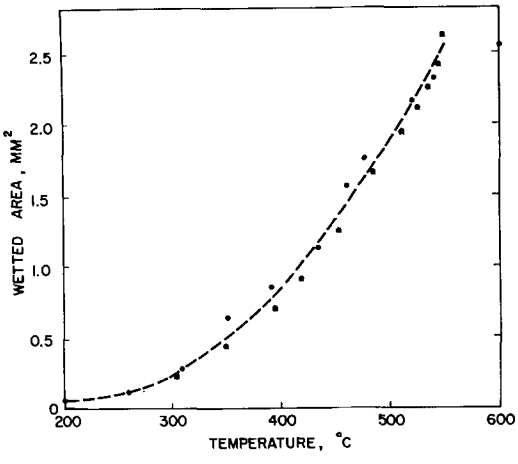

Fig. 7. Increase of the wetted area as a function of temperature during alloying (8.3°C/min temperature rise, 0.6 mm diameter indium sphere).

Kinetics of Wetting Germanium by Molten Indium

The design of the alloying apparatus made it possible to observe the change in the shape of the indium during alloying and to measure the diameter of the wetted area with the eyepiece-micrometer of a stereo microscope. Figure 6 shows a sequence of pictures taken during alloying while Fig. 7 represents the increase of the wetted area as a function of temperature during a linear temperature rise of 8.3°C/min. The pictures in Fig. 6 are side views of the indium and show its changing shape during the alloying cycle. At 200°C the indium already wets the germanium over a small area, nearly retaining its spherical shape. The diameter of the wetted area becomes about equal to the diameter of the sphere (spreading ratio = 1) between 310° and 350°C while the indium assumes a hemisphere-like shape. Up to this point the increase in the wetted area is relatively slow, and nearly equilibrium condition is maintained as indicated by the convex profile of the

indium. Further increase in temperature results in faster spreading and equilibrium is no longer maintained until about 560°-590°C. The profile during this period distinctively shows the effect of the two opposite forces acting on the indium, *i.e.*, the surface tension of the indium tends to retain the smallest possible surface area as indicated by the convex contour of the top section, while an opposite force causing spreading pulls it along the germanium surface resulting in a concave outline near the periphery.

Contraction usually occurs at the plateau or during the cooling part of the temperature cycle, although it has been observed occasionally to alternate with spreading during the temperature rise. This phenomena is greatly inconsistent from wafer to wafer, the two extremes being no contraction at all or a pull back of the indium to its original shape. Although the former case is more frequent at smaller wetted areas (spreading ratio <2) there is no sharp dividing line between the two cases. Despite this inconsistency all observed contractions have two features in common: (i) contractions occur in sudden steps at unpredictable time intervals, and (ii) they never start over the whole circumference of the wetted area, but only at a small portion of it (in the case of triangular shape at a corner) and progress step by step toward the opposite side of the wetted area. The increase of the wetted area during a 1-hr linear temperature rise from 100° to 600° is shown in Fig. 7. Since the temperature was continuously changed and equilibrium has never been established the data collected here cannot be used for thermodynamic calculations.

About the Current Theories Explaining the Spreading of Molten Indium over Germanium

There are basically two approaches in the current literature to explain the mechanism of spreading molten indium over germanium surfaces. One neglects chemical interactions between the alloying components while the other takes only bulk properties into consideration. Let us examine them in turn.

Spreading under equilibrium conditions can be described as the result of several interacting forces as expressed by the Gibbs equation (20)

$$\gamma_{GS} - \gamma_{LS} = \gamma_{GL} \cos \theta$$

where θ is the contact angle, γ_{GS} is the specific free energy of the solid-gas interface, and γ_{LS} and γ_{GL} are the specific free energies of the liquid-solid and the gas-liquid interfaces, respectively. The contact angle (θ) can be used to describe the size of the wetted area, 180° corresponding to a spherical shape of the liquid and thus no wetting. As the value of θ decreases the wetted area increases and the entire solid surface becomes covered by the liquid at $\theta = 0°$.

It has been suggested (5) that spreading can be explained by the decrease in the value of γ_{GL} due to the increase in temperature, and that contraction is caused by the opposite effect of the dissolved germanium on the surface tension of the melt (assuming the value of $\gamma_{GS} - \gamma_{LS}$ to be constant over the whole alloying process). Besides the fact that present experimental conditions are not applicable for above

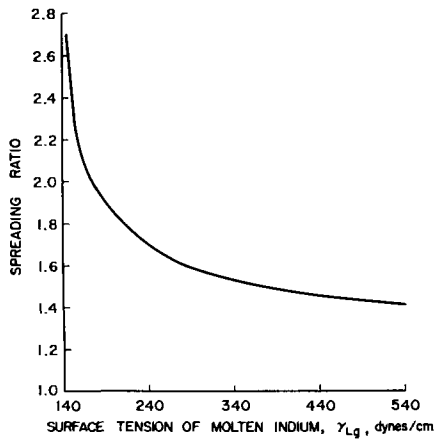

Fig. 8. Spreading ratio vs. the surface tension of molten indium, $\gamma_{sg} - \gamma_{sI}$ = constant.

equation (20) as it was proven useless in many investigations for systems exhibiting chemical interactions (1), three additional arguments can be raised against this explanation. (*A*) The profile of the indium indicates that no equilibrium is established during spreading during an 8.3°C/min or faster temperature rise. (*B*) Assuming that ($\gamma_{GS} - \gamma_{LS}$) is constant and that the shape of the indium is that of a section of a sphere the spreading ratio can be plotted as a function of γ_{LG} (Fig. 8). The most commonly observed spreading ratio of 3 corresponds here to a drop in the value of γ_{LG} of about 400 dynes/cm, which is far greater than the measured decrease of 25 dynes/cm (21). (*C*) As for the effect of the dissolved germanium on the surface tension of molten indium, our measurements (22) showed no change in the value of γ_{LG} up to 16.98 at. % dissolved germanium at 600°C within a measuring error of ±5 dynes/cm. It can be concluded therefore that the above theory can by no means be applied to this system.

The second explanation is based on the anisotropic behavior of germanium toward the dissolution in molten indium (23). Goldstein (4) has measured the relative dissolution rates of the principal crystal planes of germanium as a function of temperature and the germanium content of indium. The differences among the relative rates were found to increase at the lower temperatures and with the increasing germanium content of the melt. The greatest relative dissolution rates observed for the fastest (110) and slowest (111) crystal orientations (in molten indium 75% saturated with germanium at 347°C) was 5 to 1 corresponding to a ten times larger diameter of the wetted area than the penetration toward the (111) plane. This is much smaller than the observed ratios of 100 to 150 in our experiments. The deficiency of this theory also becomes apparent when the spreading on a damaged and thus isotropic surface is considered. Our experiments showed that the anisotropy of the crystal affects only the shape of the wetted area (Fig. 4). It can be concluded therefore that, although the anisotropy of the single crystal germanium has probably an important role in the formation of the triangular wetted areas, bulk dissolution rates are inadequate to explain the mechanism of spreading.

Evaluation of Results

The above discussion about current theories points strongly to surface effects as the most decisive contribution to spreading. The lack of quantitative data on the migration of indium over germanium surfaces, on the reaction between pure indium and germanium oxides, and on the surface energies of the different oxides prevents, however, the development of a quantitative theory. On the other hand comparison with other systems can help to perform reasonable estimates and to establish an over-all quantitative picture.

Our most important observations (see conclusions *a-f* in Effect of Germanium and Indium Oxides on Spreading) point toward surface effects. In view of the theories explaining the spreading of liquid metals over solid metals this can mean: (i) the deposition of indium or its oxides on the germanium surface during alloying (1), (ii) the surface migration of the indium over the germanium probably enhanced by a thin film of oxide (24), and finally (iii) a surface reaction between the clean indium and the germanium oxides. While thermodynamic considerations rule out the first possibility (equilibrium vapor pressures of indium and all of its oxides are very low at the alloying temperatures) they substantiate the third one. Indium oxide, In_2O_3, has a lower standard free energy of formation than that of the germanium oxide, GeO_2 (25), and although actual rates are not available it is reasonable to assume that a reaction takes place according to the general formula

$$3GeO_2 + 4In = 3Ge + 2In_2O_3$$

If GeO_2 and pure indium are heated at 600°C in a closed and evacuated quartz tube, the formation of small germanium crystals can indeed be detected. The effect of this reaction on the germanium surface would be threefold. It involves heat, it removes oxides from the germanium surface, and finally it forms oxides over the surface of the molten indium. Let us examine this effect in turn.

Since the heat of reaction (~64 kcal/mole) evolves at the front of spreading, it can be expected to increase the rate of reduction and to enhance the surface migration of the indium. In order to examine the effect of the surface oxides on spreading let us refer again to Gibb's equation (which although not strictly applicable to the present system is probably a contributing factor)

$$\cos\theta = \frac{\gamma_{GS} - \gamma_{LS}}{\gamma_{GL}}$$

where γ_{GS}, γ_{LS}, and γ_{GL} are interfacial free energies between the gas-solid, liquid-solid, and gas-liquid interfaces, respectively, and a decrease in the contact angle, θ, corresponds to a greater wetted area, i.e., to enhanced spreading. γ_{LS} is not affected by the surface properties of the alloying components and can be assumed constant at a given temperature. Any increase in the value of γ_{GS} or any decrease in that of γ_{GL} results in a lower contact angle and thus spreading. Liney and Murray's review article (26) describes the influence of oxides on the surface energies of solid and liquid metals in detail. In oxides containing cations of high polarizing power such as In^{3+} and Ge^{4+}, polarization of the oxygen anions and surface screening of the cations invariably produce low-energy surfaces. Although no experimental data are available for indium and germanium the values for similar high valence cations are shown in Table II.

Table II. Values for high valence cations

Metal	Temp, °C	γ_{GL}, dynes/cm	Ref.	Oxide	Temp, °C	γ_{GL}, dynes/cm	Ref.
Al	700	840	(27)	Al_2O_3	2050	580	(29)
Si	1420	720	(28)	SiO_2	1400	200-260	(30)

Similar decrease in the surface free energies can be expected on both germanium and indium as a result of oxide-formation. In other words both the removal of the germanium oxides (increased γ_{GS}) and the formation of indium oxides (decreased γ_{GL}) should contribute to larger wetted areas and thus spreading.

The experiments have demonstrated the influence of the different bulk dissolution rates and surface roughness on the geometry of the wetted area. The circular spreading on damaged (sand-blasted) surfaces clearly indicates the importance of the anisotropic properties of the single crystal on the geometry of the wetted area. No clear cut explanation can be offered for the effect of the dislocation density (etch pit count); it is conceivable, however, that it has an influence on the formation of surface oxides while also reducing the anisotropy of the crystal.

A more quantitative theory requires further investigation and a thorough evaluation of several, presently unknown kinetic and thermodynamic data.

Acknowledgment

The author wishes to acknowledge the help of Mr. L. H. Holschwandner in carrying out the alloying experiments.

Manuscript received Sept. 18, 1962; revised manuscript received Nov. 30, 1962. This paper was delivered before the Detroit Meeting, Oct. 1-5, 1961.

Any discussion of this paper will appear in a Discussion Section to be published in the June 1964 JOURNAL.

REFERENCES

1. See, *e.g.*, the references in Bondi's review article: A. Bondi, *Chem. Revs.*, **52**, 417 (1953).
2. Pensak, Transistors I. RCA Laboratories, pp. 112-120 (1956).
3. C. W. Mueller, *RCA Rev.*, **18**, 205 (1957).
4. B. Goldstein, *ibid.*, **18**, 213 (1957).
5. J. I. Pankove, *J. Appl. Phys.*, **28**, 1054 (1957).
6. A. S. Rose, *RCA Rev.*, **19**, 423 (1958).
7. F. J. Biondi, Editor, "Transistor Technology," Vol. III, p. 175, Van Nostrand Publishing Co., New York (1958).
8. F. L. Vogel, W. G. Pfann, H. E. Covey, and E. E. Thomas, *Phys. Rev.*, **90**, 489 (1953).
9. A. G. Tweet, *J. Appl. Phys.*, **30**, 2002 (1959).
10. Muraoka, *Toshiba Rev.*, **15**, 580 (1960).
11. J. R. Dale and J. C. Brice, *Solid-State Electronics*, (Pergamon Press) **3**, 105 (1961).
12. W. Kaiser and C. D. Thurmond, *J. Appl. Phys.*, **33**, 115 (1961).
13. T. Abe and T. Dhashi, *Acta Met.*, **9**, 1072 (1961).

14. H. Kato, H. Muraoka, and T. Abe, *Toshiba Rev.*, **16**, 24 (1961).
15. B. W. Batterman, *J. Appl. Phys.*, **28**, 1236 (1957).
16. N. K. Adam, "The Physics and Chemistry of Surfaces," 3rd ed., Oxford University Press, London (1941).
17. R. Shuttleworth and G. L. J. Bailey, *Discussions Faraday Soc.*, **3**, 16 (1948).
18. M. I. Stubbs, J. A. Schufle, and A. J. Thompson, *J. Am. Chem. Soc.*, **74**, 620 (1952).
19. H. Baba, *Bull. Chem. Soc. Japan*, **29**, 789 (1956).
20. J. W. Gibbs, Collected Works, "Thermodynamics," vol. I, pp. 55 ff, Longmans Green, New York (1928).
21. D. A. Melford and T. P. Hoar, *J. Inst. Metals*, **85**, 197 (1957).
22. A. A. Bergh, *This Journal*, **110**, 904 (1963).
23. J. Bloem and J. C. van Vessem, Paper presented at the Houston Meeting of the Society, 1960.
24. G. L. J. Bailey and H. C. Watkins, *J. Inst. Metals*, **80** [2], 57 (1951/52).
25. A. Glassner, "The Thermochemical Properties of the Oxides, Fluorides, and Chlorides to 2500°K," Atomic Energy Commission, Report ANL-5107 (1959).
26. D. T. Livey and P. Murray, *J. Am. Ceram. Soc.*, **39**, 363 (1956).
27. Handbook of Chemistry and Physics, 39th ed., 2022 (1957-58).
28. S. N. Zadumkin, *Soviet Phys. Solid State*, **1** [4], 416 (1959).
29. H. von Warttenberg *et al.*, *Nachr. Ges. Wiss Gottingen*, **2**, 65 (1936).
30. P. Kozakavitch, *Rev. Met.*, **46**, 505 (1949).

The Anodic Formation of Germanium Oxidic Films

Robert D. Wales

Materials Sciences Laboratory, Research & Engineering, Lockheed Missiles & Space Company, Sunnyvale, California

ABSTRACT

Good results were obtained for the anodic oxidation of germanium in acetic anhydride containing 0.6 mM $LiNO_3$, 0.105M HAc, 0.278M H_2O, and 0.011 mM GeO_2. Films can be formed in this solution to about 7000Å thickness with a differential field strength of 2.1 ± 0.3 × 10^6 v/cm and a current efficiency of 78 ± 7%. The normalized slope of the voltage-time relationship is 118 ± 10 v/amp-sec. The breakdown voltage at 250 $\mu a/cm^2$ is about 150v and about 180v at 100 $\mu a/cm^2$.

The presence of oxidic films on semiconductors is useful (*a*) in the study and understanding of the surface properties of these semiconductors, (*b*) in the study and understanding of new devices, and (*c*) for providing insulation. Use of electrochemical techniques permits the formation of oxidic films at room temperature so that the characteristics of the substrate are unaltered. Furthermore, this technique readily gives pertinent information concerning the film, such as differential field strength, thickness, and resistivity. Finally, the rate of film growth may be readily controlled; thus thick, amorphous films are easily obtained.

The anodic oxidation of germanium has been studied in both acid and alkaline aqueous solutions (1). In alkaline solutions, GeO_2 may be deposited when the solution becomes supersaturated (2). At high current densities in 0.1*N* H_2SO_4 or at not too high an OH^- concentration, an orange deposit is formed which is thought to be GeO (2, 3).

The solubility of the germanium oxide produced by anodization apparently makes it impossible to produce such films in aqueous solutions except under extreme conditions. Thus, it seems more likely that germanium oxidic films can be formed in nonaqueous systems. Generally, all of these nonaqueous systems contain a small amount of water or some other oxygen-containing material in which the oxygen is easily available. This is probably a point often overlooked by workers in this field.

Zwerdling and Sheff (4) have studied the anodic formation of germanium oxidic films in an electrolyte of anhydrous sodium acetate in glacial acetic acid. Using currents between 66 and 240 $\mu a/cm^2$, they obtained films with thicknesses ranging from 220 to 1240Å. A comparison of results on the {111}, {110}, and {100} faces showed no variations for n- and p-type material greater than the experimental uncertainty. Current efficiencies of 10-20% and field strengths in the range of 0.7 to 3.5 x 10^6 v/cm were obtained.

Experimental

Apparatus.—The experiments were performed at room temperature in a cell similar to that designed by Sheff, Gatos, and Zwerdling (5). The electrode was supported against a hole in the side of the cell of such a size that the electrode area was 0.600 cm^2. The cathode was a large sheet of tantalum. The current was measured with a Greibach Instruments Corporation, DC microammeter, Model 500. The data are for constant current operation, and the cell voltage, measured with a Model 610 Keithley Electrometer, was used for the voltage-time relationships.

Germanium.—Pieces of intrinsic polycrystalline germanium measuring 1/4 x 1/16 x 2 in. were obtained from Eagle-Picher and were used without further machining. The pieces used for the study of the effects of water, acetic acid, and combinations of these were chemically polished in CP-4 etchant

(6),[1] rinsed with distilled water, then with acetone, air dried, and used immediately. An orange-peel surface was obtained on all samples. All other pieces were polished to a mirror finish, first on a "Lap-Master" using 10μ grit; then on a silk cloth using distilled water and Linde A, 0.3μ, high-purity alumina abrasive.

Lithium nitrate.—Mallinckrodt Analytical Reagent vacuum dried 15 hr at 82°C was used.

Acetic anhydride.—"Baker-Analyzed" Reagent, 99.9%, was used as received and distilled. The center cut was retained.

Acetic acid.—DuPont Reagent was used after it had been refluxed with 10% acetic anhydride for several hours and then distilled. The center cut was retained.

Germanium dioxide.—Eagle-Picher germanium dioxide, 99.999%, was vacuum dried about 15 hr at 82°C before use.

Results and Discussion

Effect of electrolyte composition.—Water.—Solutions of water and lithium nitrate in acetic anhydride were prepared by dissolving the lithium nitrate in water in concentrations such that the acetic anhydride solution contained 0.4 mM lithium nitrate.[2] The results are indicated in Fig. 1. Too little water resulted in poor voltage-time relationships and a low breakdown voltage. Too much water gave poor voltage-time relationships, probably because of the solubility of the film. At about 0.233M water, a good voltage-time relationship was obtained at 100 μa/cm^2, while breakdown occurred at about 85v at 500 μa/cm^2. At 0.461M and 0.694M water, a small "step" was obtained in the voltage-time relationship at 500 μa/cm^2.

Acetic acid.—Solutions of acetic acid and lithium nitrate in acetic anhydride prepared as above gave voltage-time curves as indicated in Fig. 2. These curves are nonlinear at both 100 and 250 μa/cm^2.

Acetic acid and water.—The voltage-time relationships for various concentrations of acetic acid and water in acetic anhydride with 0.6 mM lithium nitrate are indicated in Fig. 3. With 0.58M acetic acid, 0.183M water gives a linear relationship at 100 μa/cm^2, while breakdown is indicated at about 60v at 250 μa/cm^2. Although the relationship for 0.366M water does not indicate breakdown at the same voltage at 250 μa/cm^2, it does indicate an anomaly in the μa/cm^2 relationship. With 0.145 acetic acid, the data indicate a falloff of the voltage-time relationship for 0.183M water at both 100 and 250 μa/cm^2.

With 0.273M water and between 0.017 and 0.190M acetic acid, the data indicated little change in the voltage-time relationship at 250 μa/cm^2, while at 100 μa/cm^2, the voltage-time relationship falls off at 0.190M acetic acid and is greater for 0.105M acetic acid than for 0.017M acetic acid.

[1] 15 cc acetic acid, 25 cc cencentrated HNO_3, 15 cc 48% HF, and 0.3 cc bromine.

[2] The reaction of water and acetic anhydride is fairly slow, decreasing as the water concentration is decreased or as the acetic acid concentration is increased (7).

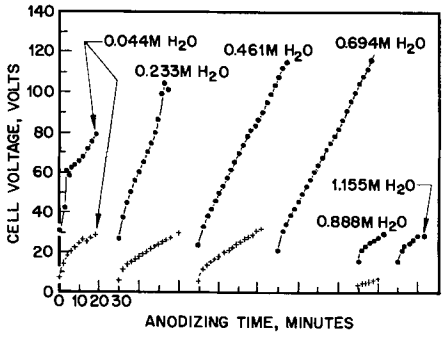

Fig. 1. Anodic oxidation of polycrystalline germanium in acetic anhydride containing 0.4 mM $LiNO_3$. Effect of water at current densities of 100 μa/cm^2 (+) and 500 μa/cm^2 (o) (curves offset on time scale for clarity). Anode area, 0.600 cm^2; temperature, 26°C.

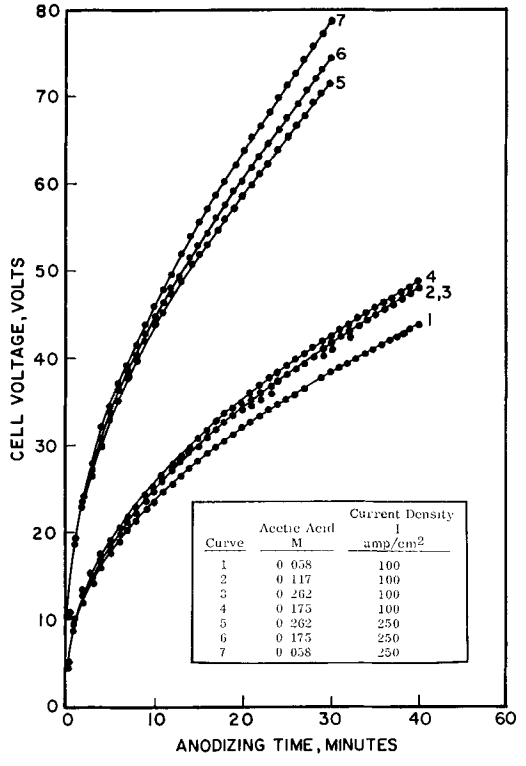

Fig. 2. Anodic oxidation of polycrystalline germanium in acetic anhydride containing 0.7 mM $LiNO_3$. Effect of acetic acid. Anode area, 0.600 cm^2; temperature, 26°C.

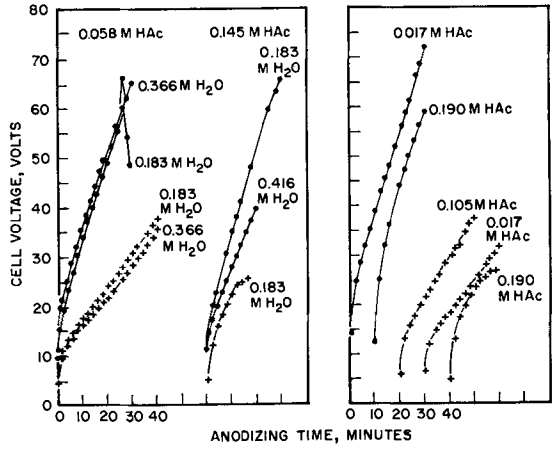

Fig. 3. Anodic oxidation of polycrystalline germanium in acetic anhydride containing 0.6 mM $LiNO_3$, acetic acid and water at current densities of 100 μa/cm^2 (+) and 250 μa/cm^2 (o) (curves offset on time scale for clarity). Anode area, 0.600 cm^2; temperature, 26°C. a. (left) Effect of water in solutions containing 0.058M and 0.145M acetic acid; b. (right) effect of acetic acid in solutions containing 0.278M H_2O.

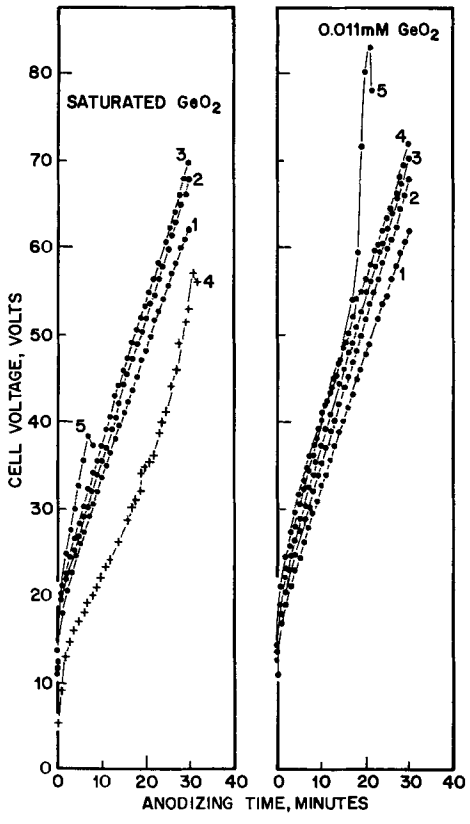

Fig. 4. Anodic oxidation of polycrystalline germanium in acetic anhydride containing 0.6 mM $LiNO_3$, 0.105M acetic acid, 0.278M water and GeO_2. Effect of GeO_2 in the electrolyte solution at current densities of 100 $\mu a/cm^2$ (+) and 250 $\mu a/cm^2$ (o). Anode area 0.600 cm^2, temperature 26°C. Runs made consecutively in each solution as numbered.

Germanium dioxide.—The voltage-time relationship for consecutive runs on acetic anhydride solutions containing 0.6 mM lithium nitrate, 0.105M acetic acid, and 0.278M water with 0.011 mM GeO_2 and when saturated with GeO_2 are indicated in Fig. 4. While the voltage-time relationships for the first two or three runs are similar, the saturated GeO_2 solution gave poor results. The saturated solution turned milky, and a soft, nonadherent film was obtained.

Anodization parameters.—Efficiency, thickness, and differential field strength.—The amount of germanium in the film was determined using a modification (4) of the method of Newcombe *et al.* (8). The back and edges of the electrodes were painted with GC Electronics Polystyrene Q-Dope No. 37-2 and air dried. The film was dissolved in 5 ml of 0.01*N* NaOH by immersion for 15 sec; the solution was then made acid by addition of 2 ml of 0.05*N* H_2SO_4 and diluted up to about 10 ml. The other reagents were then added as indicated by Newcombe *et al.* and allowed to stand 1 hr before diluting to 25 ml and running in the Beckman Model B spectrophotometer at 540 mμ.[3]

The current in all runs was controlled to about 1% and the voltage was within about 2%.

[3] Contrary to the results of Newcombe *et al.*, the oxidized hematoxylin prepared in the Lockheed Materials Sciences laboratory was not stable with time, and the solution could not be used after standing one week. Thus, it was necessary to prepare standard GeO_2 solutions for each series of determinations.

The differential field strength E_d at any thickness is defined as

$$E_d = \frac{dV}{ds} = \frac{dV}{\beta\epsilon\, Idt}$$

where $s = s_0 + \beta\epsilon\, It$; s_0 is thickness prior to electrolysis (taken as zero in this work), ϵ the efficiency, I the current density (amp/cm^2), t anodizing time (sec), β thickness of film (cm) formed per amp-sec/cm^2 of the charge passed leading to film formation. Assuming the density of amorphous germanium dioxide to be 3.637 g/cm^3 (9), the value of β is 7.426 x 10^{-5} cm^3 (amp-sec)$^{-1}$. The normalized slope of the voltage-time relationship is dV/Idt.

The efficiency, normalized slope, thickness, and differential field strengths are given for 12 runs in Table I. The data are for current densities of 25, 100, and 250 $\mu a/cm^2$. The data indicate an average efficiency of 78 ± 7% and an average differential field strength of 2.1 ± 0.3 x 10^6 v/cm. The average normalized slope of the voltage-time relationship, dV/Idt, is 118 ± 10v (amp-sec)$^{-1}$.

Zwerdling and Sheff (7) used the density of bulk hexagonal GeO_2 as the density of amorphous GeO_2. Their value of β was thus 6.35 x 10^{-5} cm^3/amp-sec. Their reported values of E_d covered the range from 0.7 to 3.5 x 10^6 v/cm. When the density reported for amorphous GeO_2 was used (9), their values ranged from 0.6 to 3.0 x 10^6 v/cm, while the results reported in this work ranged from 1.4 to 3.0 x 10^6 v/cm.

Effect of anodization time and age of solution.—No more than one or two satisfactory runs could be made in the same solution unless GeO_2 was present in the solution, in which case, several satisfactory runs could be made in the same solution. No satisfactory run could be made on a solution kept overnight unless water was added. Figure 5 indicates the effect of anodization time and age of the solution on the voltage-time relationships when solutions of acetic anhydride containing 0.6 mM $LiNO_3$, 0.105M acetic acid, 0.278M water, and 0.011 mM GeO_2 were used. A later series of runs gave normalized slopes

Table I. Anodic oxidation of polycrystalline germanium in acetic anhydride containing 0.6 mM $LiNO_3$, 0.105M acetic acid, 0.278M water, and 0.011 mM GeO_2 (anode area 0.600 cm^2, temperature 26°C)

	Electrochemical parameters					
Run No.	Anodization time, t, min	Current density, I, $\mu a/cm^2$	Efficiency, ϵ, %	Normalized slope, dV/Idt, v/amp-sec	Differential field strength, E_d, v/cm x 10^{-6}	Thickness, s, Å
144	20	100	78	121	2.1	700
149	20	100	79	124	2.1	710
142	30	100	59	131	3.0	790
141	30	100	74	121	2.2	990
148	30	100	77	108	1.9	1040
143	30	100	80	139	2.3	1070
152	132	25	82	114	1.9	1200
147	40	100	90	93	1.4	1600
139	30	250	61	114	2.5	2030
145	50	100	94	131	1.9	2080
138	30	250	77	112	2.0	2580
137	30	250	87	108	1.7	2890
Average:			78 ± 7	118 ± 10	2.1 ± 0.3	

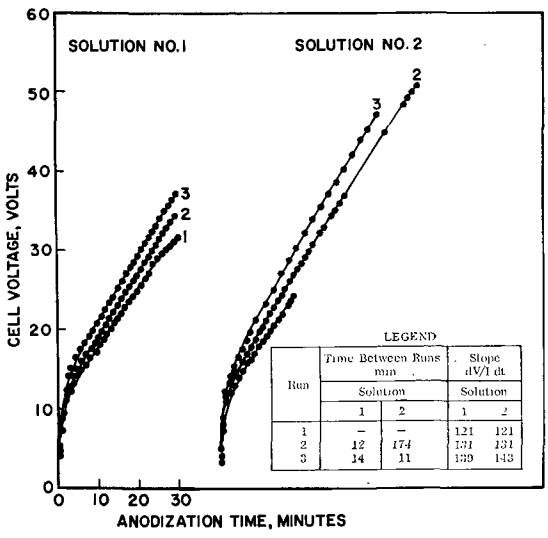

Fig. 5. Anodic oxidation of polycrystalline germanium in acetic anhydride containing 0.6 mM $LiNO_3$, 0.105M acetic acid, 0.278M water, and 0.011 mM GeO_2. Effect of anodization time and age of solution. Anode area, 0.600 cm^2; current density, 100 $\mu a/cm^2$; temperature, 26°C.

of 119, 131, and 132 v/amp-sec, respectively, and as indicated by the normalized slopes in Table I, the values obtained at 250 $\mu a/cm^2$ were somewhat lower and not much different. The results indicate that one solution can be used at least four times in one day and cannot be kept more than one day.

Breakdown voltage.—At current densities of 250 $\mu a/cm^2$, breakdown occurs at about 150v in the "normal" manner, with a 10-20v fluctuation but no continual rise of voltage. At 100 $\mu a/cm^2$ breakdown occurs at about 180v, but the voltage begins to rise linearly with time at a much faster rate. It is postulated that at the lower current densities, the current is low enough with respect to the various rates to allow the continued formation of crystalline GeO_2 on the surface, whereas at the higher current densities, the current is great enough with respect to the various rates so that the crystalline GeO_2 film breaks down. For example, the film could break down because of local heating.

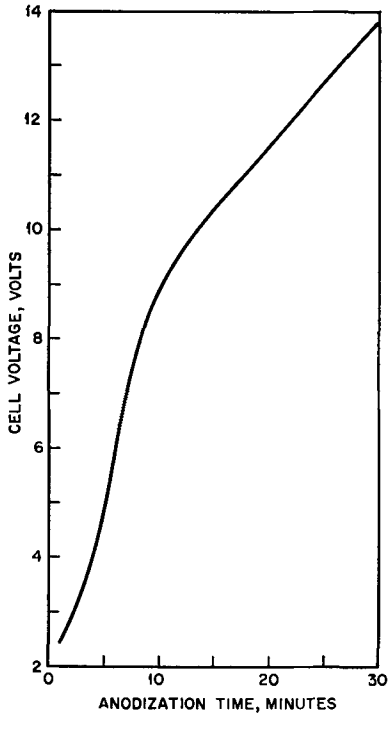

Fig. 6. Anodic oxidation of polycrystalline germanium in acetic anhydride containing 0.6 mM $LiNO_3$, 0.105M acetic acid, 0.278M water, and 0.011 mM GeO_2. Anomaly at beginning of anodization. Anode area, 0.600 cm^2; temperature, 25°C; current density 25 $\mu a/cm^2$.

Anomalies.—The voltage-time relationship is not linear down to zero time. As indicated in all the figures, there is an initial rapid rise of voltage with time. In Fig. 6, this is strikingly evident for a run at a current density of 25 $\mu a/cm^2$, which, assuming the same efficiency, is equivalent to a film thickness of about 90Å before the voltage-time relationship is linear. Although Zwerdling and Sheff (4) present several possibilities, the significance of this initial anomaly is not understood at present.

The film.—The crystalline material formed when the germanium is anodized to the breakdown voltage was found by x-ray analysis to be GeO_2. Infrared transmission data have indicated strongly bound water and no acetate ion in the amorphous film. There is a moderately sharp GeO_2 (4) transmittance minimum at 869 cm^{-1} which may be usable for determination of film thickness.

Films ranging in thickness from approximately 90 to 7000Å have been formed with the expected interference color changes. As indicated by Vasícek (10), the extremely thin films are clear, turning a

Table II. Interference colors obtained on polycrystalline germanium anodized in acetic anhydride containing 0.6 mM $LiNO_3$, 0.105M acetic acid, 0.278M water, and 0.011 mM GeO_2

Films produced in this work		Film colors as calculated from data of Vasicek (10) using a refractive index of 1.607 (11)	
Thickness, Å	Color	Thickness, Å	Color
87 ± 8	Clear (white)	—	—
174 ± 15	Faint brown-yellow	—	—
261 ± 23	Darker brown-yellow	—	—
348 ± 31	Brown-yellow	—	—
522 ± 47	Violet	—	—
—	—	653	Brown-yellow
696 ± 62	Dark blue	—	—
—	—	784	Purple
—	—	871	Violet
872 ± 78	Light blue	—	—
1043 ± 93	Blue white	—	—
—	—	1108	Blue
1221 ± 109	Blue green	—	—
—	—	1282	Bluish white
—	—	1431	Greenish blue
1461 ± 131	Yellow	—	—
1566 ± 140	Orange (brown-yellow)	—	—
—	—	1593	Yellowish white
1739 ± 156	Red	—	—
—	—	1756	Yellow
—	—	2048	Brownish yellow
2088 ± 187	Blue	—	—
—	—	2400	Purplish red
2540 ± 228	Dark blue	—	—
—	—	2700	Blue
4385 ± 383	Red white	—	—

brown-yellow as the thickness is increased, then traversing the regular order of interference colors. In Table II the colors of some of the anodic films produced on germanium are presented along with the colors given by Vasícek (10) for thickness determined using a refractive index of 1.607 (11) for amorphous GeO_2. A perfect comparison cannot be expected since Vasícek did his work with films on glass in perpendicular white daylight. The films obtained in this work were on germanium, and their colors were determined in fluorescent light at an angle slightly off the perpendicular. Also, the true area was assumed to be equal to the apparent area.

Conclusions

A good solution for the anodic oxidation of germanium consists of acetic anhydride containing 0.6 mM $LiNO_3$, 0.105M acetic acid, 0.278M water, and 0.011 mM GeO_2. Films can be formed in this solution to about 7000Å thickness with a current efficiency of about 78% at current densities ranging from 25 to 250 $\mu a/cm^2$. The differential field strength of these films is about 2.1×10^6 v/cm, with a breakdown voltage of about 150v at 250 $\mu a/cm^2$ and about 180v at 100 $\mu a/cm^2$.

It is suggested that the continued formation of a crystalline film after reaching the breakdown voltage of the amorphous film at low current densities occurs because the current is low enough with respect to the various rates to allow the continued formation of crystalline GeO_2 on the surface.

Manuscript received Jan. 21, 1963; revised manuscript received March 18, 1963.

Any discussion of this paper will appear in a Discussion Section to be published in the June 1964 JOURNAL.

REFERENCES

1. L. Young, "Anodic Oxide Films," p. 329, Academic Press, New York (1961).
2. F. Jirsa, *Z. anorg. u. allgem. Chem.*, **268**, 84 (1952).
3. F. Beck and H. Gerischer, *Z. Elektrochem.*, **63**, 500 (1959).
4. S. Zwerdling and S. Sheff, *This Journal*, **107**, 338 (1960).
5. S. Sheff, H. C. Gatos, and S. Zwerdling, *Rev. Sci. Instr.*, **29**, 531 (1958).
6. J. F. Law, *J. Phys. Chem.*, **23**, 543 (1955).
7. E. K. Plyler and E. S. Barr, *J. Chem. Phys.*, **3**, 679 (1935).
8. H. Newcombe, W. A. E. McBryde, J. Bartlett, and F. E. Beamish, *Anal. Chem.*, **23** [7], 1023 (1951).
9. P. J. Holmes, "The Electrochemistry of Semiconductors," p. 216, Academic Press, New York (1962).
10. A. Vasícek, "Optics of Thin Films," p. 137, Interscience Publishers, Inc., New York (1960).
11. E. Kordes, "Optische Datenzen Bestimmung anorganisher Substanzer," Verlag Chemie, p. 35, Weinheim/Bergstr (1960).

The Electrolytic Reduction of Dicyandiamide

An Experimental Approach to the Difference inTwo Courses of Electrolytic Reduction

Kiichiro Sugino, Keijiro Odo, and Eiichi Ichikawa

Department of Applied Electrochemistry, Tokyo Institute of Technology, Tokyo, Japan

ABSTRACT

Dicyandiamide was found to undergo a four electron reduction at a mercury cathode at —1.05v (S.C.E.) although no distinct polarographic wave was obtained. At a palladium black cathode, dicyandiamide was reduced at —0.10v (S.C.E.) with 100% current efficiency to give the dihydro compound. This difference in products is believed to be caused by direct electron transfer in the former case and reduction by chemisorbed hydrogen in the latter.

The electrolytic reduction of dicyandiamide in aqueous acid at mercury and lead cathodes has been shown to produce aminomethyleneguanidine (1) which is stable only in cold acidic solution. When electrolysis was continued until the catholyte was basic, the compound hydrolyzed to give guanidine, ammonia and formaldehyde.[1]

Dicyandiamide does not give a cathodic wave at the dropping mercury electrode under these conditions and is similar to cyanamide in this behavior.

In the present study, the reduction of dicyandiamide has been reinvestigated to determine whether a slow rate of reduction is responsible for this discrepancy as is observed with cyanamide (2).

[1] A part of the compound was further reduced to guanidine and methylamine.

Experimental

The apparatus has been previously described (3). A 150 ml beaker served as the cell and a magnetic stirrer was used to stir the catholyte. The solid cathode area was 68 cm^2; the Hg cathode area was 34 cm^2; the anode was platinum. The purity of the lead, cadmium, tin, zinc, and copper electrodes was better than 99.9% while that of the nickel cathode was above 99.8%. The mercury was purified by distillation. The electrodes were prepared by polishing the surface with sandpaper, immersing in 10% HCl or HNO_3 (for lead), and washing with water. Blank electrolyses were carried out in 5% H_2SO_4 using the electrode as the cathode.

The palladium black electrode was prepared by electrolytic deposition of palladium on palladium or

platinum from a solution composed of 20 ml of 1% palladium chloride and 100 ml of 1*N* HCl. The electrolysis was continued 1 hr at 3 amp/dm^2 using a palladium anode with a purity of 98.5%. Following electrolysis the electrode was washed with water and stored under water. Blank electrolysis was carried out in 5% H_2SO_4 using the palladium black electrode as cathode until 100% hydrogen evolution was obtained.

The catholyte consisted of 100 ml of 5% H_2SO_4, KCl, and HCl (*p*H less than 2), acetic acid and sodium acetate (*p*H 3-5), or KH_2PO_4 and NaOH (*p*H 6-7). The solutions except 5% H_2SO_4 contained, in addition, 3g of ammonium sulfate. The anolyte consisted of 40 ml of 5% H_2SO_4

Electrolysis.—After 100% hydrogen evolution was confirmed at the cathode, 4.2g of dicyandiamide was added to the catholyte. The dicyandiamide dissolved slowly as the electrolysis proceeded. The electrolysis was conducted so as to permit the catholyte to remain acidic. The temperature of the electrolysis was 10 ~ 15°C. Measurement of hydrogen evolution was carried out at definite intervals to determine current efficiency.

Following the electrolysis a saturated solution of sodium picrate was added to the catholyte. In electrolyses using lead or mercury cathodes, aminomethyleneguanidine dipicrate precipitated first and was followed by guanidine picrate. The net result was partial separation of the picrates. The catholyte obtained using a palladium black cathode gave a mixture of formylguanidine picrate and guanidine picrate.

The crude samples of aminomethyleneguanidine dipicrate (purification is very difficult) obtained from the mercury and lead cathode electrolyses, decomposed in the range 200°-230°C. [the melting points are indistinct, see ref. (1)] and were 88% and 96% pure, respectively, as determined by the amount of formaldehyde obtained upon hydrolysis.

The crude mixed picrate obtained from the palladium black electrolysis was a light yellow powder (mp 180°-208°C) which turned brown on contact with air. This mixed picrate, from the amount of formic acid formed on hydrolysis, contained about 60% formylguanidine picrate. The mixed picrates were treated with large amounts of water to remove the guanidine picrate. The remaining formylguanidine picrate melted at 216°C, and a mixture with an authentic sample (5) showed no depression of the melting point.

Table I. Yields of products from the reduction of dicyandiamide at various cathodes

Cathode	Faradays/ mole	Dicyandiamide converted, %	Formylguanidine picrate, %*	Aminomethylene guanidine picrate, %*	Guanidine picrate, %*
Hg	4.04	62	0	47	45
Pb	8.08	42	0	43	63
Pd-black	2.02	85	56	0	36**
Cd, Zn, Sn, Ni, and Cu	2.02	Current efficiency less than 3%			

* Based on converted dicyanidiamide.
** Calculated from amount of formylguanidine picrate formed.

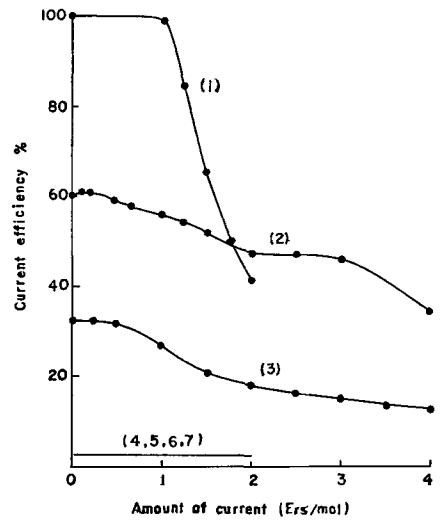

Fig. 1. Current efficiency at various cathodes: 1, Pd-black; 2, Hg; 3, Pb; 4, Cd; 5, Sn; 6, Cu; 7, Ni.

The filtrate from the picrate precipitation was acidified with dilute HNO_3, and the unconverted dicyandiamide was precipitated as the dicyandiamide-silver picrate on addition of 5% silver nitrate solution. The complex was filtered, dried at 110°C, and weighed. The filtrate was made basic, and the gases formed were directed through an aqueous hydrochloric acid trap. The solution in the trap was evaporated and the residue extracted with butanol in order to separate the ammonium chloride from the methylammonium chloride. No methylammonium chloride was found.

At potentials greater than —0.4v aminomethyleneguanidine was also formed at the palladium black cathode.

When the electrolysis at mercury and lead was carried out with only 2 Faradays per mole, no formylguanidine was found. Similarly electrolysis at the palladium black cathode with 4 Faradays per mole produced no aminomethyleneguanidine.

Results

The results[2] obtained at a current density of 5 amp/dm^2 are shown in Table I.

The current efficiency at various cathodes was determined by measuring the hydrogen evolution using a current density of 5 amp/dm^2 and is given in Fig. 1.

The influence of *p*H on current efficiency was studied at the mercury cathode. At a current density of 1 amp/dm^2, low enough so as not to affect the *p*H greatly, the efficiency was found to drop almost linearly from 60% at *p*H 0 to zero at *p*H 4. All reductions were run, therefore, in 5% H_2SO_4.

Polarograms of dicyandiamide in a KCl-HCl buffer (*p*H 2.0) with concentrations varying from 4 x $10^{-4}M$ to 5 x $10^{-2}M$ showed no reduction wave. The hydrogen discharge wave shifted to more positive potentials with increasing concentration from *p*H 2 to 6. This shift increased with decreasing *p*H.

Controlled potential reductions were carried out at mercury, lead, and palladium black cathodes in

[2] The detailed descriptions of organic parts of this study appeared in a separate paper (6).

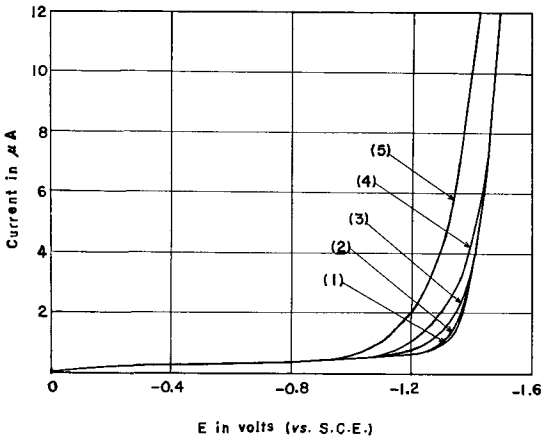

Fig. 2. Polarograms of dicyandiamide. Concentration of dicyandiamide: 1, O (supporting electrolyte); 2, 4 x 10^{-4} mole/l; 3, 2 x 10^{-3} mole/l; 4, 1 x 10^{-2} mole/l; 5, 5 x 10^{-2} mole/l. Supporting electrolyte: KCl-HCl buffer solution (pH 2.0); sensitivity of galvanometer: 0.1 μa/mm; dropping mercury electrode; $m^{2/3} t^{1/6} = 1.36$. $h = 45$ cm.

order to determine the reduction potential of dicyandiamide. Current *vs.* potential plots are shown in Fig. 3.

Constant potential reductions were carried out at palladium black and mercury cathodes at —0.30 and —1.175v, respectively. The current *vs.* time plots are shown in Fig. 4 and 5.

The area under the current-time curve for the mercury cathode after subtraction of the current due to hydrogen discharge (shaded area) was 2.63 amp-hr which corresponds to 4 Faradays per mole.

The area under the current-time curve for the palladium black cathode was 1.27 amp-hr which corresponds to 2 Faradays per mole.

Discussion

The fact that the reduction of dicyandiamide at mercury occurs at —1.05v to produce aminomethyleneguanidine, and that the reduction at

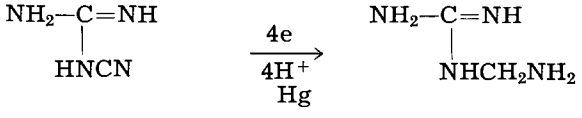

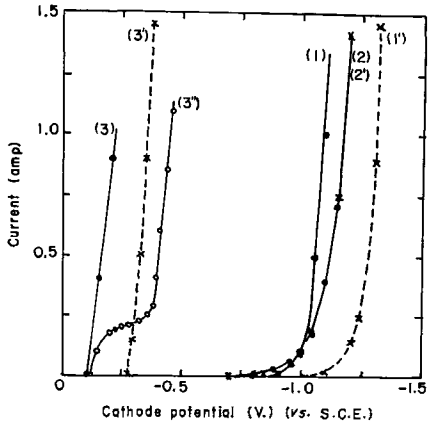

Fig. 3. Current *vs.* potential curves for the reduction of dicyandiamide. 1 and 1', Hg cathode; 2 and 2', Pb cathode; 3, 3', and 3", Pd-black cathode. •, 2.1g dicyandiamide in 100 cc 5% H_2SO_4; ○, 0.21g dicyandiamide in 100 cc 5% H_2SO_4; x, 100 cc 5% H_2SO_4.

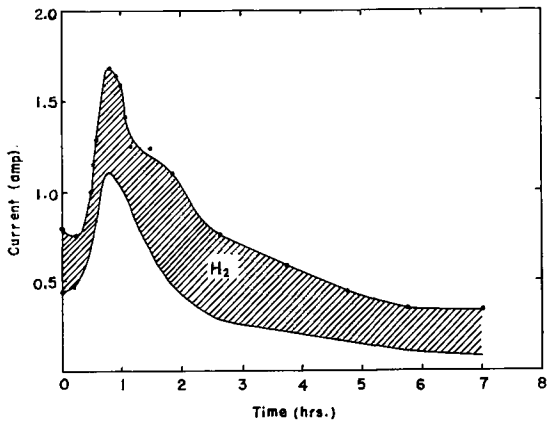

Fig. 4. Constant potential reduction of dicyandiamide at a Hg cathode (—1.175v) in 5% H_2SO_4. Catholyte: 2.1g of dicyandiamide in 100 ml 5% H_2SO_4; anolyte: 40 ml of 5% H_2SO_4.

palladium black at —0.10v produces formylguanidine, indicates that the mechanism of the reductions are completely different. The proposed intermediate guanylformamidine has been prepared as the hydrochloride (mp 126°-127°C) by catalytic reduction of dicyandiamide in methanolic HCl with a palladium on carbon catalyst (4). Since the reduction at palladium black is considered to be reduction by chemisorbed hydrogen, the reduction at mercury should be reduction by direct electron transfer,

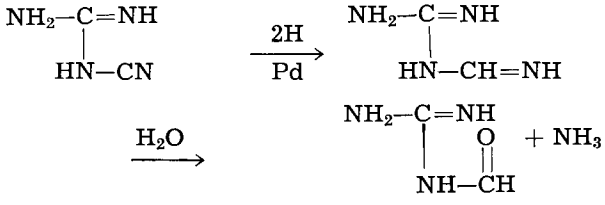

although there is some uncertainty as to the reduction potential in the case of the dicyandiamide reduction.

Since aminomethyleneguanidine is formed at the palladium black cathode at voltages greater than —0.40v, the second step reduction of dicyandiamide may be voltage controlled and affected by the type of cathode used. Metals with a high hydrogen overvoltage would cause this reduction as has been observed in the reduction of cyanamide to formami-

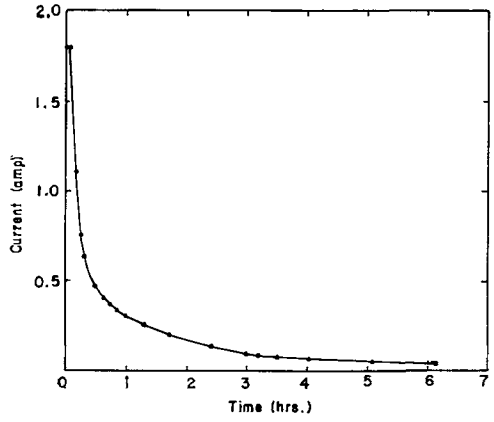

Fig. 5. Constant potential reduction of dicyandiamide at a palladium black cathode (—0.30v) in 5% H_2SO_4; same concentrations as in Fig. 4.

dine. In this work the formation of guanylformamidine could not be verified because of its instability in aqueous solution.

The discrepancy in the behavior of dicyandiamide at the dropping mercury electrode and on a macro scale at a mercury cathode may be caused by a slow rate of reduction of the dicyandiamide.

Acknowledgment

The aid of a grant for fundamental scientific research from the Ministry of Education of Japan is gratefully acknowledged.

Manuscript received Oct. 2, 1961; revised manuscript received Jan. 28, 1963. This paper was presented at the Second Seminar on Electrochemistry held at the Central Electrochemical Research Institute, Karaikudi, India, Dec. 17-20, 1960, at the annual meeting of the Electrochemical Society of Japan held at Tokyo, April 24-25, 1961, and at the meeting of the Electrochemical Society at Detroit, Oct. 1-5, 1961.

Any discussion of this paper will appear in a Discussion Section to be published in the June 1964 JOURNAL.

REFERENCES

1. K. Sugino, *J. Chem. Soc. Japan*, **60**, 111 (1939); *C. A.*, **34**, 2795 (1940); *Bull. Chem. Soc. Japan*, **27**, 358 (1954).
2. K. Odo, E. Ichikawa, K. Shimogai, and K. Sugino, *This Journal*, **105**, 598 (1958).
3. K. Odo and K. Sugino, *ibid.*, **104**, 160 (1957).
4. E. Ichikawa and K. Odo, Unpublished work.
5. W. Traube, *Ber.*, **43**, 3586 (1910).
6. K. Odo and E. Ichikawa, *J. Electrochem. Soc. Japan*, **30**, 559 (1962).

Oxidation of Boron Carbide by Air, Water, and Air-Water Mixtures at Elevated Temperatures

Lawrence M. Litz and R. A. Mercuri

Research Laboratory, National Carbon Company, Division of Union Carbide Corporation, Parma, Ohio

ABSTRACT

A study of the oxidation of boron carbide powder has shown measurable reaction at temperatures as low as 250°C with water vapor and 450°C in dry air. Removal of the B_2O_3 oxidation product by water vapor occurs at a rate in excess of the oxidation rate below 550°-600°C. The presence of B_2O_3 on the B_4C surface was found to inhibit the oxidation by H_2O but not by air. Linear dependence of rate on the partial pressure of water was observed. The activation energy for the water-B_4C reaction was 11 kcal/mole-°C, while that for the air-B_4C reaction was 45 kcal/mole. Oxidation by dry air occurs at a lower rate than with water vapor until approximately 700°C (for 235 mm water partial pressure).

Boron carbide has found considerable usage as a stable, high-temperature source of boron in various nuclear applications. In some of these, the reaction of the boron carbide with air or with water vapor at elevated temperatures becomes an important consideration. The meager information on the corrosion behavior of boron carbide in such environments is summarized by Hoyt (1). No systematic study of the mechanism or kinetics appears to have been carried out to date.

Of particular current interest is the system involving boron carbide incorporated in graphite (2). In order to establish a foundation for the understanding of the reactions which boron carbide in such materials might undergo, studies of the reaction of boron carbide powder with water vapor and/or air were initiated.

Experimental

The reactions were followed by automatically recording the weight changes utilizing a Mauer thermogravimetric balance (3). A sketch of the system is shown in Fig. 1, and it is photographed in Fig. 2. A standard analytical balance is employed with the specimen suspended from the bottom of one of the pans. Environmental control was maintained within a 50 mm diameter quartz furnace tube through which dried argon or air or either of these gases saturated with water at various dew points could be passed. The specimen hung in a fixed position approximately ¼ in. above a thermocouple which provided a continuous record of its temperature. The furnace involved had a flat temperature gradient, uniform within 2°; for a distance of approximately 2 in. above and below the sample proper. The temperature control on the furnace maintained the desired temperature within ±5°C.

Weight changes in the sample were sensed by the motion of a light beam reflected from a mirror fastened to the center of the balance arm of the analytical balance by a type 920 split phototube. This motion was translated electronically into a restoring force in the proper direction applied by a solenoid to the opposite side of the balance. The response was so rapid that no motion of the balance pointer was apparent even on dropping a 500 mg weight on either balance pan. The current in this solenoid was linearly related to the force exerted on the balance and was directly read in milligrams on a recorder. The sensitivity of the system was such as to easily permit the reading of a change of ±1 mg.

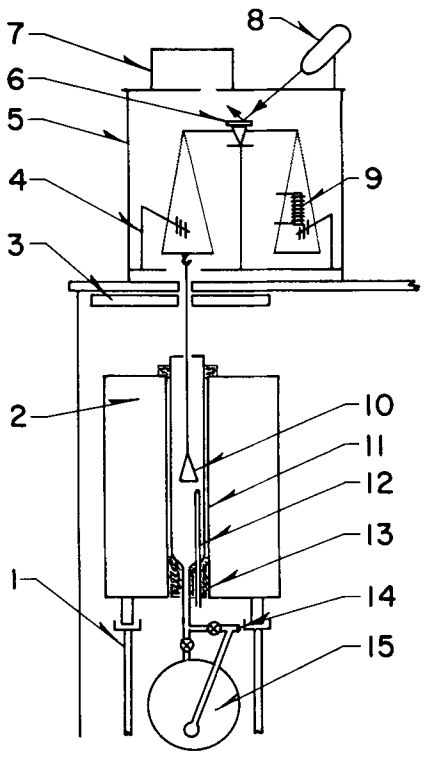

Fig. 1. Thermogravimetric apparatus: 1, guide rails and rollers; 2, globar furnace; 3, water-cooled heat shield; 4, weight drop device; 5, analytical balance; 6, mirror; 7, photo tube, type 920; 8, light source; 9, electromagnet and core; 10, sample holder; 11, quartz envelope; 12, thermocouple well; 13, insulation; 14, gas inlet to boiler; 15, water flask and heating jacket.

Gas flow rates were metered with an integrating American Meter Company dry gas meter for the dry streams and with a Precision wet-test meter for those gas streams containing moisture. The instantaneous flows were also monitored using conventional flow meters. Saturation of the gases with water was accomplished after metering by passing them through a fritted disk immersed in a constant temperature, constant level water bath. Water pickup by the gas stream was checked by measurement of the consumption of water over periods of from 8 to 24 hr.

The boron carbide used in these studies was a granular material obtained from the Carborundum Company. The −150, +200 mesh screen fraction was utilized for most of the work reported below. The BET surface area of this fraction was 0.44 m^2/g. Its chemical analysis was 81.08% boron, 18.08% carbon, and 0.20 w/o oxygen. Spectroscopic analysis showed approximately 0.3% Fe, 0.2% Si, 0.1% Al, and 0.04% Ca.

Each run was made with a fresh charge of the B_4C powder. To minimize effects of varying depth and area of powdered sample, 0.500g was used for most of the runs. It was uniformly distributed over the bottom of a flat platinum dish 2.5 cm in diameter and 0.5 cm high. The powder depth was approximately 1 mm. This dish was suspended from the balance with a platinum and quartz suspension. The gases were fed into the bottom of the furnace tube through a heated line to prevent moisture condensation.

The procedure for each run involved preweighing the boron carbide sample and distributing it on the platinum dish in its holder. With the furnace at temperature and the furnace tube flushed with argon, the system was assembled, and the necessary balancing and zero adjustments were made. The desired gas was then fed into this system at a fixed flow rate. Automatic recorders provided the information relative to the weight change *vs.* time and the temperature of both the sample and the furnace control point. The latter was outside the quartz furnace tube. Transcribed plots of the records of a number of typical runs are shown in Fig. 3, 4, and 5.

Results

As may be seen from Fig. 3 and 4, oxidation of the B_4C powder proceeds in a similar fashion in both the argon-water and air-water atmospheres over the temperature range studied (200°-750°C). In both systems, at temperatures up to approximately 600°C, a linear weight loss is obtained as a function of time. At higher temperatures, there is an initial weight increase followed by a weight decrease. As the reaction proceeds under these latter conditions, the rate of weight change becomes constant, and a straight line weight loss curve is obtained. In a number of experiments at these higher

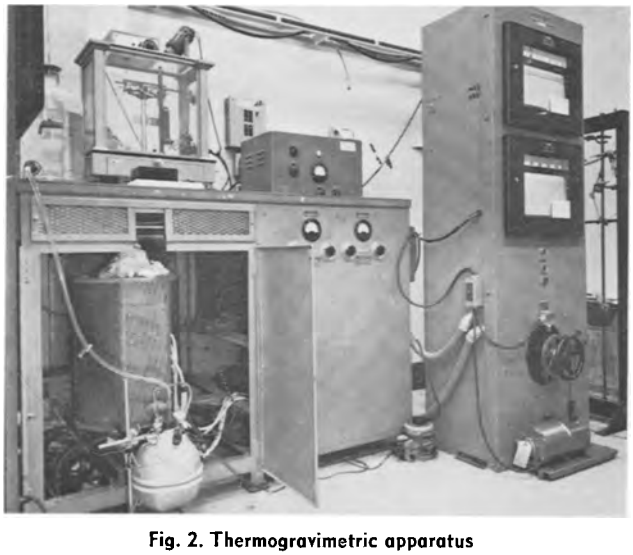

Fig. 2. Thermogravimetric apparatus

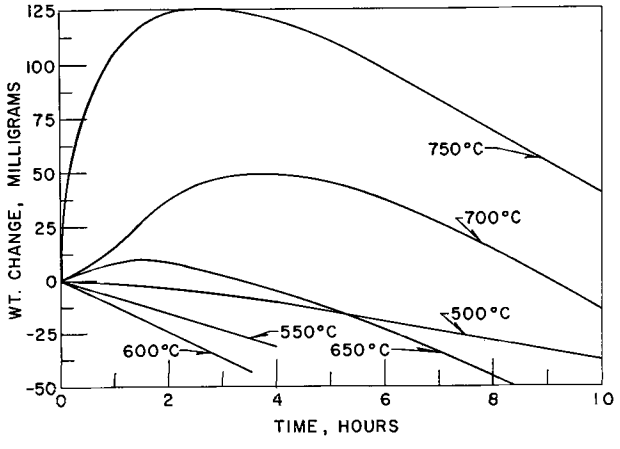

Fig. 3. Thermogravimetric curves of B_4C oxidation in argon-water vapor. B_4C powder: weight, 0.500 g; mesh size, 150, + 200; surface area, 0.44 M^2/g. Argon: flow rate, 4 CFH; dew point, 70°C; P_{H_2O}, 235 mm.

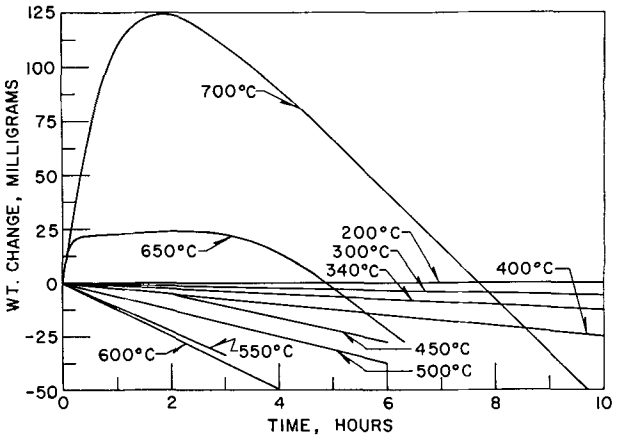

Fig. 4. Thermogravimetric curves of B_4C oxidation in air-water vapor. B_4C powder: weight, 0.500g; mesh size, —150, +200; surface area, 0.44 M^2/g. Air: flow rate, 5 CFH; dew point, 70°C; P_{H_2O}, 235 mm.

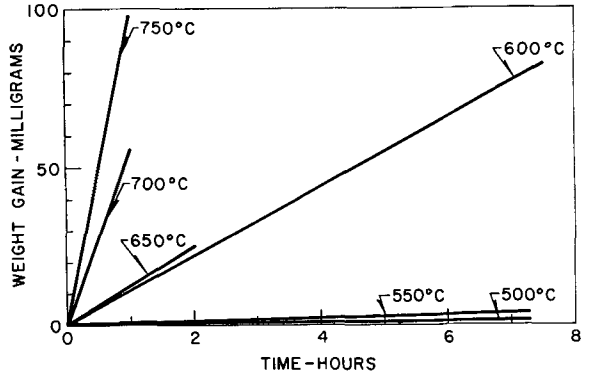

Fig. 5. Thermogravimetric curves of B_4C oxidation in dry air. B_4C powder: weight, 0.500g; mesh size, —150, +200; surface area, 0.44 M^2/g. Air (dried): flow rate, 5 CFH.

temperatures, the weight loss was measured to a point where the weight of the material had dropped to one-half the original weight, and the rate of change was still constant. In the air-water oxidation studies, at 200° and 70°C dew point, the weight change was less than the 1 mg detectable level in a period of 70 hr.

The thermogravimetric curves of the oxidation of the —150, + 200 mesh boron carbide powder in dry air, depicted in Fig. 5, showed a linear increase in weight at all temperatures studied through a weight change corresponding to reaction of at least 10% of the B_4C. At fairly high per cent reaction, the deviation from linearity due to changing surface area was observed. At 450°C, the 0.500g sample changed less than 1 mg in weight in 100 hr.

Examination of the carbide remaining after the various experiments showed that those which had exhibited a weight gain, whether oxidized in dry air or in the water-containing gases, were covered with a clear glassy material which was subsequently determined to be B_2O_3. On the other hand, in those cases where only a continuing weight loss was observed, as in the lower temperature runs in the water-containing systems, no B_2O_3 covering was seen, and the particles were loose in the dish. Determination of the boron content of the products' water soluble phase confirmed these observations. Chemical analysis of a number of the residues, involving the determination of the water soluble boron and the boron and carbon content of the insoluble phase, led to the following conclusions:

1. Oxidation of boron carbide in dry air, in the temperature range studied, results in complete loss of the carbon with the boron remaining on the unreacted B_4C as B_2O_3.

2. Oxidation in air-water systems under conditions where no initial weight gain is obtained results in complete loss to the gas phase of both the boron and carbon of the oxidized B_4C.

3. Oxidation in the air-water systems under conditions where an initial weight gain is observed results in a fraction of the B_2O_3 remaining with the unreacted B_4C and in some of the carbon remaining behind, probably as free carbon. The analysis of the gaseous reaction products from the water systems showed hydrogen and CO_2 to be formed.

4. In the argon-water systems, a varying fraction of the carbon remains with the solid phase at all temperatures.

Reaction Mechanism

The weight changes and the product analyses are consistent with the following reactions:

Air oxidation

$$B_4C + 4\,O_2 \rightarrow 2B_2O_3(l) + CO_2 \qquad [1]$$

Water oxidation

$$B_4C + 8H_2O \rightarrow 2B_2O_3(l) + CO_2 + 8H_2 \quad \text{and/or} \quad [2a]$$

$$B_4C + 6H_2O \rightarrow 2B_2O_3(l) + C + 6H_2 \qquad [2b]$$

B_2O_3 transport

$$B_2O_3 + H_2O \rightarrow 2HBO_2(g) \quad [\text{or possibly } H_3BO_3(g)] \qquad [3]$$

As long as the equivalent rate of transport of HBO_2(gas), by Eq. [3] exceeds the rate of formation of B_2O_3 by either reactions [1] or [2a], the weight loss curves directly depict the oxidation rate. However, when the oxidation rate exceeds the rate of removal of B_2O_3, a film of the oxide will build up on the surface, and a net weight gain may result. As the thickness of the oxide film increases, the oxidation by H_2O is inhibited, and the rate of oxidation will decrease until a point is reached where the film thickness is constant due to equivalent rates of formation and transport of B_2O_3.

Once the oxidation rate becomes fixed by the constant thickness of the B_2O_3 film, the system will again lose weight in a linear fashion. Apparently because of the particle shape and surface roughness, the expected deviations from linearity resulting from reduction in surface area as the B_4C is consumed does not become evident until a substantial fraction of the charge is consumed.

The inference drawn from this steady-state condition is that the transport of water through the oxide film is equal to the rate of oxidation of the boron carbide by the water. Therefore, given an adequate measure of the oxide film thickness and the rate information, one should be able to determine the diffusion coefficient for water through

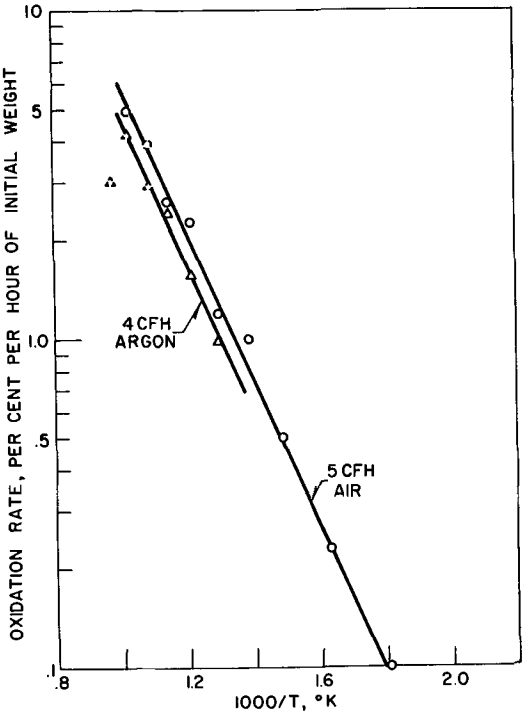

Fig. 6. Arrhenius plot of air-water and argon-water oxidation rates. B_4C powder: weight, 0.5g; mesh size, —150, +200; surface area, 0.44 M^2/g. Water: dew point, 70°C; partial pressure, 235 mm.

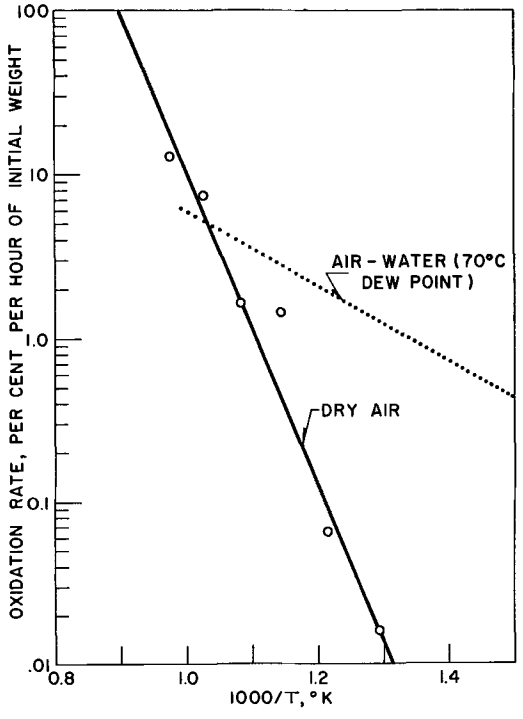

Fig. 7. Arrhenius plot of dry air oxidation rates. B_4C powder: weight, 0.500 g; mesh size, —150, +200; surface area, 0.44 M^2/g. Air (dried): flow rate, 5 CFH.

the B_2O_3 at these temperatures. The linear rate observed in the dry air oxidation runs indicates that the rate of transport of oxygen through the B_2O_3 is greater than the oxidation rate.

Reaction Kinetics

The oxidation rate data obtained in these studies provide a good fit to typical Arrhenius rate equations. Figure 6 is such a plot of the data obtained from the oxidation of the —150, +200 B_4C powder with argon-water and air-water mixtures having a dew point of 70°C. These points were obtained from those experiments in which the B_2O_3 oxidation product was completely removed from the B_4C by the water. Thus, the oxidation rate could be directly calculated from the weight loss line, assuming that all of the carbon was removed as CO_2 in accord with reaction [2a]. It is quite apparent that, in the temperature range depicted, from approximately 200° to approximately 600°C, the presence of air is not a significant factor in the rate of oxidation of the B_4C.

The small difference in oxidation rate between the air and the argon systems is not related to the difference in flow rate used for the two sets of series of experiments. Since some of the carbon of the B_4C is left behind in the solid product and is not lost with CO_2, the apparent oxidation rate with argon as calculated here, is lower than if the argon rate numbers are corrected for the per cent of carbon remaining behind in the sample. If this correction is made, the argon-water points lie rather well along the line obtained in the air-water system.

A number of experiments were run in which the air flows were as much as doubled for a given dew point and the observed rates lay within the normal scatter, indicating the independence on air flow in the rate range utilized here. In all of these experiments the amount of water consumed in the reaction proper was only a few per cent of that actually in the gas phase.

Figure 7 is the Arrhenius plot obtained from the series of experiments in which the oxidation of the B_4C powder was carried out in dry air. Here again, a good fit was obtained over approximately three orders of magnitude in the oxidation rate. The rates plotted in Fig. 7 were obtained from the slopes of the lines of Fig. 5 multiplied by the appropriate factor to convert the observed weight gain into per cent oxidation of the B_4C powder.

The dotted line of Fig. 7 is that obtained from the 70°C dew point air-water experiments. The large contrast in the relative rates of oxidation in these two systems is quite apparent. The air-water system at this vapor pressure of water, approximately 235 mm, reacts with B_4C at a greater rate than that obtained with dry air at temperatures below 700°C. The activation energy for the air-water reaction is approximately 11 kcal/mole as contrasted to approximately 45 kcal/mole for the dry air system.

The variation of oxidation rate with the partial pressure of water is apparent from the data plotted in Fig. 8. The points give the measured oxidation rate at water partial pressures of 25, 90, 235 and 525 mm, respectively. The lines drawn in this graph are those which correspond to the equation

$$\text{Oxidation rate} = 6.17 \times 10^{-2}\, p_{H_2O}\, e^{-10{,}650/RT}$$

g/g-mm H_2O-hr

A linear relation was found between the observed weight change per unit time and the amount of sample used in the experiment, indicating a linear dependence of rate on the available surface area. If it is assumed that the area available for reaction in these systems is that measured for this powder by

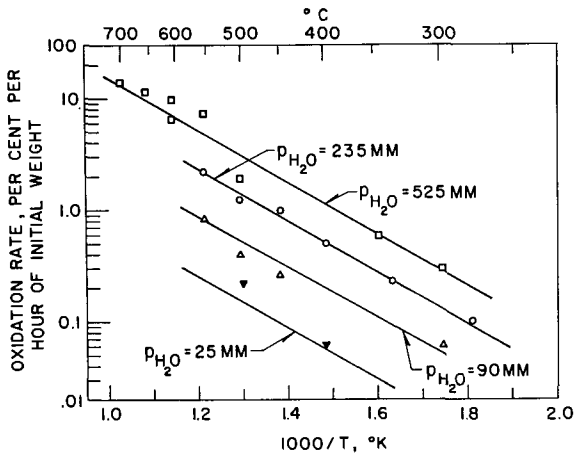

Fig. 8. Dependence of B_4C oxidation rate on water vapor pressure

the BET nitrogen absorption method, 0.44 meter²/g, then the following rate equations express the oxidation rate of the boron carbide powder under the conditions described in this study:

Dry air

$$\text{Rate} = 1.36 \times 10^9 \, Ae^{-45/RT} \text{ g/m}^2\text{-hr}$$

Wet air

$$\text{Rate} = 0.14 \, p_{H_2O} \, Ae^{-11/RT} \text{ g/m}^2\text{-hr-mm } H_2O$$

where the activation energies are expressed in kcal/mole.

Although the above equations describe fairly accurately the reaction kinetics of the particular boron carbide material used for these studies, identical equations may not apply to other specimens. For one, it is generally recognized that, in heterogeneous reactions, the character of the surface may play a significant part in determining the reaction kinetics. Further, with a material such as boron carbide, it would be anticipated that various impurities may either retard or accelerate its oxidation.

The assumption that the BET surface area represents the true reaction area may also be open to question. The measured area is roughly a factor of 30 greater than the area calculated for small, theoretically dense spheres of the diameter determined by the mesh size of the screens used. The particles actually used in the experiment, as viewed under a microscope, are actually quite angular with fairly flat cleavage surfaces. These surfaces are not smooth, but are quite grainy in character at a submicron level and possibly indicate the presence of submicron pores. It is expected that the long linear portion of the oxidation curves occur because the surface area changes very slowly with per cent oxidation due to these geometric characteristics of these particles.

Conclusions

The significant findings of this study may be summarized as follows:

1. Water vapor can react with boron carbide at temperatures as low as 250°C. The reaction with dry air is detectable at temperatures of the order of 450°C.

2. Water vapor oxidizes boron carbide at a faster rate than air in the lower temperature ranges. Utilizing the above rate equations, the temperatures at which equivalent rates of oxidation for air and water would occur would be at approximately 550°, 650°, 700°, and 750°C for water vapor pressures of 10, 100, 235, and 500 mm, respectively.

3. Water vapor will react with the B_2O_3 reaction product to form a gaseous boric acid molecule and thereby remove the B_2O_3 as it is being formed. Depending somewhat on the water vapor pressure, the water may remove the oxide as fast as it is formed and thereby maintain a clean boron carbide surface. This was found to occur at temperatures up to the order of 550°-600°C at dew points ranging from 25° to 70°C and as high as 650° at a dew point of 88°C. At temperatures above these, the B_2O_3 forms faster than it is being removed and accumulates on the surface of the oxidizing carbide.

4. When a layer of B_2O_3 exists over the B_4C, inhibition of the water reaction rate occurs. The presence of B_2O_3 does not inhibit the oxidation rate by oxygen.

5. The oxidation rate is linearly dependent on the water pressure as well as the area of the carbide.

Manuscript received Dec. 26, 1962. This paper was presented at the Boston Meeting, Sept. 16-20, 1962.

Any discussion of this paper will appear in a Discussion Section to be published in the June 1964 JOURNAL.

REFERENCES

1. E. W. Hoyt, GEAP-3680, "Information on the Use of Boron Carbide as a Nuclear Control and Poison Material," Vallecitos Atomic Lab., General Electric Co., Pleasanton, Calif., Mar. 15, 1961.
2. W. P. Eatherly and J. T. Meers, "Some Recent Advances in Graphite Technology," Paper presented at the ANS Topical Meeting on High Temperature Materials for Nuclear Applications at San Diego, April 11-13, 1962.
3. F. A. Mauer, *Rev. Sci. Instr.*, **25**, 598 (1954).

Integration of Single-Sweep Oscillopolarograms

I. Determination of Reactant Adsorption and Oxide Film Reduction at Platinum Electrodes

R. A. Osteryoung, G. Lauer, and F. C. Anson[1]

North American Aviation Science Center, Canoga Park, California

ABSTRACT

Integration of the equation for the current-time relationship when a linear potential sweep is applied to an electrode has led to an equation for the number of coulombs passed, $Q = kCA/\nu^{1/2}$, where k is a constant dependent on the potential interval over which the integration is carried out, but independent of sweep rate, C the concentration of the species undergoing reaction, A the electrode area, and ν the time rate of change of the linear potential sweep. A procedure to distinguish between coulombs due to diffusing and nondiffusing reactants is given. The derived relationships are verified experimentally. Separation of the coulombs due to the reduction of ferric iron and platinum oxide under conditions where both reactions take place concomitantly is described. In the iodide-iodine-triiodide system, it is concluded that iodine, rather than triiodide, is the adsorbed species.

In a recent preliminary communication, we outlined a new method for the study of reactant adsorption on electrode surfaces (1). Experimental verification of the previously derived relationships and application of the method to the study of adsorption from triiodide solutions are the subjects of this paper. The experimental technique involves the determination of the coulombs passed during a potentiostatically applied linear potential sweep over a chosen potential range.

For a reversible electrode reaction, where reactant and product are both soluble species, with mass transfer controlled by semi-infinite linear diffusion, the current-potential relationship observed during a potential sweep experiment may be written as

$$i = n^{3/2}\mathbf{F}^{3/2}AD^{1/2}c\nu^{1/2}(RT)^{-1/2}P(\nu t) \qquad [1]$$

where n, $\mathbf{F}$, R, T, A, D, have their usual significance, ν is the time rate of change of potential of the electrode, which is constant during any single experiment, and P is a function of νt (2).

During any single sweep, the coulombs, Q, consumed will be given by

$$Q = \int_0^t i\,dt = n^{3/2}\mathbf{F}^{3/2}AD^{1/2}c\nu^{1/2}(RT)^{-1/2}\int_0^t P(\nu t)\,dt \qquad [2]$$

The potential of the electrode at time t will be given by

$$E = E_i + \nu t \qquad [3]$$

where E_i is the initial potential of the electrode, and since ν is constant

$$dE = \nu dt \qquad [4]$$

and

$$P(\nu t) = P(E - E_i) \qquad [5]$$

Equation [2] may thus be rewritten in terms of E

$$Q = kC/\nu^{1/2} \qquad [6]$$

where

$$k = n^{3/2}\mathbf{F}^{3/2}AD^{1/2}(RT)^{-1/2}\int_{E_i}^{E} P(E - E_i)\,dE \qquad [7]$$

The value of k will depend on the potential interval $E_i - E$ through which the integration is performed. However, since k is not dependent on ν, the product of the number of coulombs passed in a given potential interval and the square root of the sweep rate will be a constant for a given concentration of reactant.

The equations given above are written for the case where the only species reacting at the electrode are supplied by linear diffusion and, it should again be noted, are strictly valid only for a reversible reaction. Additional coulombs due to double layer charging, oxide film formation or removal, or reaction of adsorbed material may also contribute to the coulombs measured; these additional coulombs in the simplest cases will be independent of the coulombs resulting from diffusing reactant. Thus,

$$Q_{\text{total}} = kC/\nu^{1/2} + (Q_{\text{adsorbed}} + Q_{\text{double layer}} + Q_{\text{film}}) \qquad [8]$$

Since coulombs due to any of the quantities inside the brackets should not depend on sweep rate (with certain limitations which will be discussed), plots of Q *vs.* $\nu^{-1/2}$ should be linear with a slope dependent on the concentration of the diffusing species, but with a positive intercept which corresponds to coulombs due to processes indicated inside the brackets. Just such behavior is observed in the experiments to be described.

Experimental

A block diagram of the electronic apparatus is given in Fig. 1. While discussing the apparatus it may be instructive at the same time to describe how it is used in the actual experiment.

A linear voltage sweep is applied through a potentiostat to an indicator electrode. The sweep generator, consisting of a Philbrick UPA-2 operational amplifier connected as an integrator with a variable input voltage, is connected so its output is fed into

[1] Permanent address: Division of Chemistry and Chemical Engineering, California Institute of Technology, Pasadena, California.

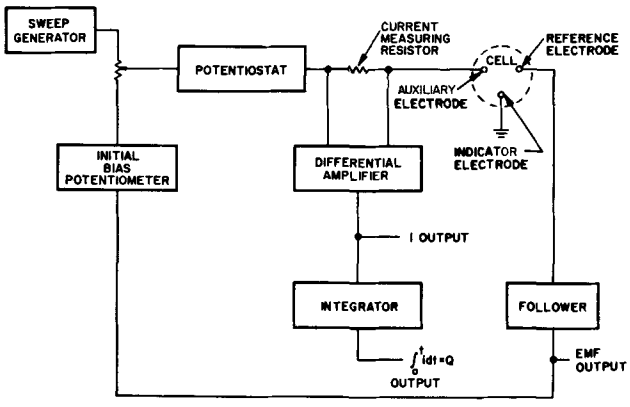

Fig. 1. Schematic diagram of electronic apparatus

another UPA-2 operational amplifier connected as a potentiostat with a current booster amplifier in the output (3-5). The potentiostat supplies the current that is passed between the auxiliary electrode and the indicator electrode, which is grounded. The potential of the indicator electrode was measured with respect to a reference electrode through a high impedance follower amplifier. (A Philbrick P-2 solid state amplifier was used as the follower amplifier.) The output of this amplifier was applied to a recorder or oscilloscope. The initial bias potentiometers permitted the indicator electrode to be held at any desired potential prior to the initiation of the potential sweep. The electronics causes the indicator electrode to follow the linearly increasing input voltage so the process is designated as a potentiostatic potential sweep in spite of the obvious contradiction.

Sweep rates from *ca.* 0.5 to 200v/sec were employed. Integration of the current-potential curves to give coulombs was carried out electronically. The current was measured by means of a differential amplifier across a standard resistor in series with the cell. The differential amplifier, consisting of two Philbrick P-65 amplifiers and a Philbrick P-2 amplifier connected as an electrometer, had its output fed into a Philbrick UPA-2 amplifier connected to operate as an integrator. The output of the integrator was observed on a Tektronix 561 oscilloscope or other voltage measuring equipment.

Alternatively the output of the differential amplifier was fed into a Vidar Voltage to Frequency converter and the output of the converter fed into a Computer Measurement Corporation Scalar. Auxiliary electronic equipment served to operate two electronic gates, via a Schmitt trigger, which could be set to activate and deactivate the scalar at predetermined potentials. Thus, an integral could be obtained across any desired potential region during the potential sweep. If the output of the potential measuring follower amplifier was applied to the X-axis and the integrator output applied to the Y-axis of the CRO, a potential-coulomb plot resulted. The integrator output was sometimes read without the aid of the cut-off gates by adjusting the oscilloscope so that the center graticule corresponded to the potential at which it was desired to terminate the integral. The point at which the trace crossed the center line was observed visually and recorded.

When a solution initially contained both members of a reversible redox couple, such as the triiodide-iodide, the sweep was initiated from the equilibrium potential of the indicator electrode. The reference electrode in this case usually consisted of a separate nonpolarized platinum electrode, and the equilibrium potential was zero volts. Results using such a reference were identical to those using a calomel reference electrode in which cases the initial bias potential applied to the potentiostat was adjusted to the equilibrium potential of the indicator and calomel electrode pair. Adjustment to the equilibrium potential was carried out while the solution was stirred, by adjusting the bias potentiometers so that the integrator output became stationary, except for random noise. As values of the integral in the microcoulomb range could readily be detected it is estimated that less than 0.5 μa could have flowed undetected. When only one half of the redox couple was initially present, the sweep was initiated from a selected initial potential. In this case, particularly when the initial potential was more positive than 1v *vs.* S.C.E. the integrator drift was not zero due, at least in part, to the gradual formation of an oxide film on the electrode. The error involved in such cases was negligible except at extremely slow sweep rates.

Various types of cells were used during the course of the experiments. Best results were obtained with the indicator and reference electrodes positioned as close together as possible to minimize ohmic potential drops. The auxiliary electrode consisted of a platinum foil or wire while the reference was either a Beckman saturated calomel electrode or, in the case of a well-poised system, a platinum flag. Indicator electrodes were either Beckman platinum button electrodes, of approximately 0.2 cm^2 area, or platinum flag electrodes, which were spot welded to platinum wires. The flag electrodes were not sealed into glass. Solutions were degassed with prepurified argon.

In determining the amount of oxide on the electrode surface, the number of coulombs of oxide found was independent of whether or not gas was passed through the solution during a sweep experiment, so long as the electrode was not potentiostated above +1.4v *vs.* S.C.E. where significant amounts of oxygen were evolved. After potentiostating at potentials above +1.4v *vs.* S.C.E. the electrode was potentiostated briefly at +1.2v with bubbling before the sweep was initiated. All chemicals were of reagent grade and were used without further purification.

Results and Discussion

Ferric iron-platinum oxide system.—In order to verify the theory, particularly with regard to the behavior of adsorbed species, it was felt that a "known" system would be desirable. Since Eq. [8] indicated that coulombs arising from platinum oxide reduction, for example, would display the same sweep rate independence as those arising from adsorbed reactant, it was decided to investigate the behavior of a diffusing species which was reduced at the same potential as the platinum oxide layer on the surface of the electrode. Such a system could be ex-

pected to mimic the behavior of a system in which true reactant adsorption occurred, but with the advantage that the amount of oxide film on the electrode could be measured independently. The reduction of ferric iron in sulfuric acid has been shown to take place at essentially the same potential as platinum oxide reduction in chronopotentiometric experiments (6). Therefore, potential-sweep experiments were performed in which the coulombs due to the reduction of both ferric iron and platinum oxide were measured as a function of sweep rate with oxidized platinum electrodes. Assuming coulombs due to double layer charging and adsorbed material to be negligible, Eq. [8] becomes:

$$Q_{total} = Q_{diffusing} + Q_{oxide} = kC/\nu^{1/2} + Q_{oxide} \quad [8']$$

Reproducible amounts of platinum oxide were formed on a platinum button electrode in iron-free sulfuric acid by potentiostating at +0.6, 1.2, and 1.4v against the S.C.E. The amount of oxide formed at each potential was determined by integration of a subsequent cathodic potential sweep. The integration was halted at +0.15v, but the sweep continued out to −0.2v *vs.* S.C.E. In carrying out the experiments at 1.2 and 0.6v, the electrode was potentiostated for 30 sec prior to the initiation of the cathodic sweep. For experiments at 1.4v, the electrode was potentiostated at 1.4v for 15 sec with argon bubbling, then at 1.2v for 15 sec without argon bubbling to eliminate any possible interference from the oxygen which may have been evolved at 1.4v. The cathodic sweep was then initiated. With a sweep rate variation of 0.6-12 v/sec, cathodic coulombs, in the absence of iron, varied only slightly with sweep rate (<10%); the variation appears due to the fact that there is a small shift of the platinum oxide reduction peak to more cathodic potentials as the sweep rate increases. After potentiostating at 1.4, 1.2, and 0.6v the microcoulombs arising from oxide reduction were 330, 280, and 25, respectively.

The experiment was then repeated in a 1F H_2SO_4 solution containing 4 mM Fe(III), and the results are shown in Fig. 2 and Table I. The units on the abscissa in the figures are arbitrary; sweep rates in volts per second are indicated at the top of all figures. The intercepts of the plots of Q *vs.* $\nu^{-1/2}$ in

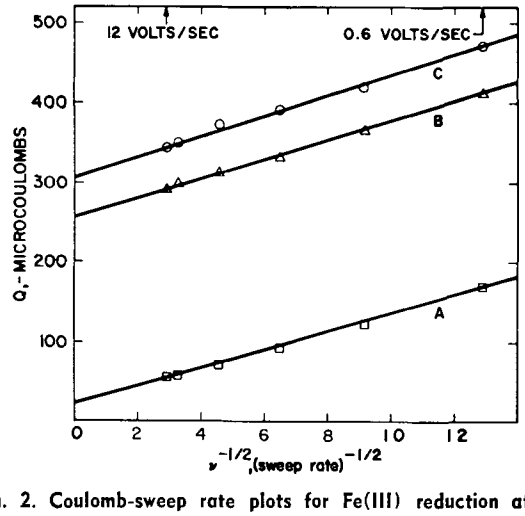

Fig. 2. Coulomb-sweep rate plots for Fe(III) reduction at oxidized platinum electrodes.

Table I. Reduction of ferric iron in the presence of platinum oxide

ml Fe(III) *	$E_{initial}$, v *vs.* S.C.E.	Q_{oxide}** μcoulombs	Intercept	Slope† $\left(\frac{\partial Q}{\partial \nu^{-1/2}}\right)_C$	$\left(\frac{\partial Q}{\partial \nu^{-1/2}}\right)_C \cdot \frac{1}{C}$
1	+0.6	25	24	112	
	1.2	280	260	121	
	1.4	330	310	123	
				119 avg.	119
2	+0.6	25	24	242	
	1.2	280	260	234	
	1.4	330	300	255	
				243 avg.	121
4	+0.6	25	12	480	
	1.2	280	220	460	
	1.4	330	260	472	
				471 avg.	119

* Fe(III) stock solution *ca.* 0.3F.
** Pt button microelectrode, area 0.2 cm².
† Corrected for dilution.

Fig. 2 are 310, 260, and 24 microcoulombs for 1.4, 1.2, and 0.6v, respectively. These values are seen to agree quite well with the coulombs of oxide found in the absence of the ferric iron. Note that if the small number of coulombs arising from the known amount of oxide produced at 0.6v *vs.* S.C.E. were subtracted from the total coulombs observed at each sweep rate, a straight line through the origin would result. This confirms the assumption that no appreciable contributions from adsorbed Fe(III) or double layer charging are involved. (If the double layer capacity were taken as 20 $\mu f/cm^2$, then the contribution expected due to double layer charging at the button electrode would be about 4 μcoulombs for a 1v change in potential.) Table I gives data for three different concentrations of iron. At the higher concentration the value of the intercept is seen to decrease somewhat, but this is very likely the result of the chemical reduction of some of the platinum oxide by the ferrous iron formed at the electrode surface. The reality of such a reaction has been established by reverse current chronopotentiometric experiments (7). Column 5 in Table I gives the slopes of the Q-$\nu^{-1/2}$ plots from Fig. 2 and from similar figures for the other concentrations of iron. Note that the experimental slopes for each concentration of iron appear to be reasonably independent of the initial potential. Column 6 indicates the constancy of the slope divided by the concentration, a further verification of Eq. [7]. The rather good agreement between the theory and the experimental system indicates that the method is capable in principle of differentiating between coulombs arising from diffusing reactants and from reactants initially present on the electrode surface. The data in Table I show that a linear relation is obtained between coulombs and concentration which suggests possible analytical utility.

Iodide-iodine-triiodide system.—The results with Fe(III) indicated that the presence of adsorbed reactant should be detected by this technique with our apparatus. It was therefore decided to apply the technique to a system where reactant adsorption

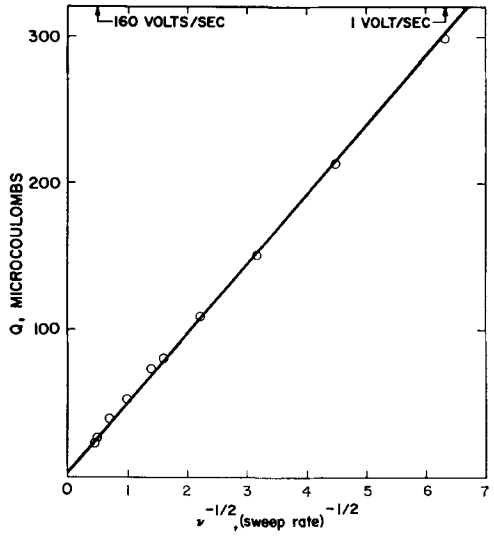

Fig. 3. Coulomb-sweep rate plots for oxidation of 5 mM iodide in 1F H_2SO_4.

might occur. Lorenz (8) has presented chronopotentiometric data for the reduction of iodine at heavily platinized electrodes which he interpreted in terms of extensive iodine adsorption. Further, his work indicated that the double layer capacity was quite small in iodide solutions, as did our own rough charging curve experiments. Thus, triiodide solutions appeared attractive for application of the integration technique to the detection and study of adsorption. Solutions investigated included dilute (0.2-5 mM) iodine in 0.1M iodide, in which case the iodine existed mainly as triiodide; solutions dilute in iodide, and free of iodine; and solutions dilute in both iodide and iodine, in which both iodide oxidation and iodine + triiodide reduction could be investigated in the same solution.

Figure 3 shows a plot of Q *vs.* $\nu^{-1/2}$ for iodide oxidation at a platinum button electrode in 1M sulfuric acid; integration was from +0.3 to 0.8v *vs.* S.C.E. Linearity is observed, and the line, within the experimental error, appears to pass through the origin.

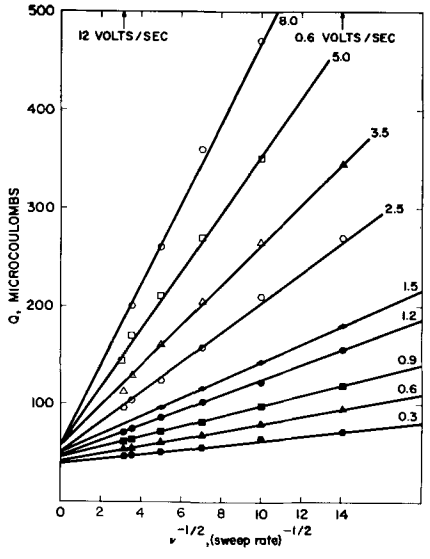

Fig. 4. Coulomb-sweep rate plots for reduction of iodine in 1F H_2SO_4 containing 1F KI. The numbers on the curves multiplied by 8×10^{-4} give the molarity of iodine.

Table II. Slope and intercept of I_3^- reduction: effect of concentration of I_3^-

Concentration, ml IO_3^-*	Slope $\left(\frac{\partial Q}{\partial \nu^{-1/2}}\right)_C$	$\left(\frac{\partial Q}{\partial \nu^{-1/2}}\right)_C \cdot \frac{1}{C}$	Q_o, intercept, μcoulombs
0.3	23	77	39
0.6	38	63	42
0.9	52	59	46
1.2	77	65	47
1.5	92	62	50
2.5	152	63	51
3.5	205	62	57
5	294	63	58
8	409	57	58

* Multiply by 8×10^{-4} for formal concentration of iodine.

This again serves to indicate the validity of the previously developed equations, and also indicates that if any iodide is adsorbed, it gives rise to less than ca. 6 μcoulombs on the 0.2 cm^2 electrode. Note that potential sweeps of up to 200 v/sec were used, indicating the validity of the procedure to rather high sweep rates.

Values of Q *vs.* $\nu^{-1/2}$ for cathodic potential sweeps in a series of triiodide solutions in 1F H_2SO_4 are shown in Fig. 4. The solution was 0.1F in iodide, and iodine was produced by adding measured aliquots of a 0.02F KIO_3 solution. The linearity of the plots indicates that Eq. [7] is obeyed, and the concentration dependent intercepts apparently correspond to adsorbed iodine which is reduced in the 150 mv interval over which the integration was carried out. The second column in Table II contains the slopes of the plots in Fig. 4 at the various triiodide concentrations while the third column indicates the constancy of the slopes divided by the concentration, *i.e.*, since $Q = kC/\nu^{1/2}$, $(\partial Q/\partial \nu^{-1/2})_C C^{-1} = k$. Column 4 contains the intercept on the Q axis. An apparent isotherm may be obtained by a plot of the intercept, corresponding to coulombs due to adsorbed iodine, against concentration. (However, see below for a complication involving the dependence of the intercepts on the magnitude of the potential range over which the integration is performed.)

Effect of electrode area.—Experiments were performed with a single triiodide solution in which the lightly platinized platinum flag electrode was successively diminished in area by cutting sections from the flag. Q *vs.* $\nu^{-1/2}$ plots for this electrode gave slopes and intercepts which were directly related to the area, as shown by the data in Table III.

Effect of platinization.—The absolute values of the intercepts of plots similar to Fig. 4 are highly de-

Table III. Slope and intercept of I_3^- reduction: effect of electrode area

Relative area	Relative slope	Relative intercept
1*	1	1
0.77	0.74	0.80
0.37	0.38	0.29

* Area 3.7 cm^2.

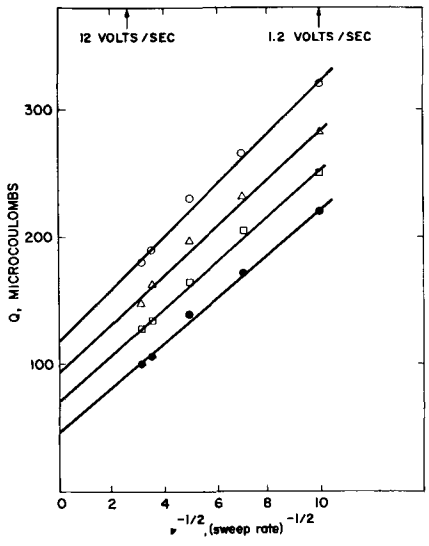

Fig. 5. Coulomb-sweep rate plots for reduction of 1.6 mM iodine in 0.1F KI at increasingly platinized electrode. Platinization times for the plots in ascending order were 0, 5, 12.5, and 24.5 min.

pendent on electrode surface pretreatment. The electrode used to obtain the data in Fig. 4 had been very lightly platinized by being cycled between +1.6 and −0.2v *vs.* S.C.E. for 5 min at 30 cps (9); the electrode appeared to the eye as a bright platinum surface. If the surface were more heavily platinized, one would expect the amount of adsorption to increase with the extent of platinization. However, one would not necessarily expect the effective "diffusional" area to increase provided that the surface roughness remained small compared to the diffusion layer thickness. The results of a series of experiments designed to test these expectations are indicated in Fig. 5 and Table IV. The plots of Q *vs.* $\nu^{-1/2}$ in Fig. 5 were all obtained in the same triiodide solution, but with increasing periods of electrode platinization preceding each experiment. Platinization was carried out by removing the electrode from the iodide solution and immersing it in a 1F H_2SO_4 solution where it was potentiostatically cycled between −0.2 and +1.6v *vs.* S.C.E. at 30 cps for increasing periods of time. Figure 5 and Table IV show that there is a pronounced increase in the intercepts of the Q *vs.* $\nu^{-1/2}$ plots as the electrode platinization increases. The slopes also increase, but to a much smaller extent than the intercept. The increase in the intercept is interpreted as reflecting the greater quantity of iodine adsorbed at the more platinized electrode. The increase in slope presumably stems from the increase in effective diffusional area of the electrode from the platinization. (After 25 min of platinization, the electrode surface appeared quite black.) The fact that the intercepts increase more rapidly than the slopes means that only a portion of the area contributing to the increased adsorption contributes to the effective diffusional area.

Table IV. Slope and intercept of I_3^- reduction: effect of electrode platinization

Platinization time, min	Slope $\left(\frac{\partial Q}{\partial \nu^{-1/2}}\right)_\sigma$	Intercept, μcoulombs
0	173	47
5	181	71
12.5	189	94
24.5	203	118

Similar experiments performed with dilute solutions of iodide did not give rise to the marked increases in intercepts noted with the triiodide. The iodide intercept at both lightly and moderately platinized electrodes remained very near the origin.

To determine if iodine or triiodide was the adsorbed species, experiments were carried out in which separate anodic and cathodic potential sweeps were applied to an electrode in a solution containing iodide, triiodide, and iodine. The resulting Q *vs.* $\nu^{-1/2}$ plots give positive intercepts for the cathodic sweeps in which iodine and triiodide are reduced, but not for the anodic sweeps in which iodide and triiodide are oxidized to iodine. This would appear to support the contention that I_2 (or I atoms) but not I_3^- is adsorbed. Further evidence for this contention was obtained by observing the effect on the slope and intercept obtained for cathodic Q *vs.* $\nu^{-1/2}$ plots in iodine-triiodide solutions to which increasing quantities of iodide were added. As shown in Fig. 6, the slope was not affected, but the intercept decreased, as would be expected if I_2 were the adsorbing entity since the concentration of I_2 is decreased by the addition of I^-.

In an effort to determine the potential region in which the adsorbed iodine was reduced integrations of cathodic and anodic sweeps were carried out over potential intervals of 50-500 mv from the equilibrium potential of a solution 4 x 10^{-3}F in KI and 2.4 x 10^{-3}F in I_2. Results are shown in Fig. 7, where the upper plots are for integration of cathodic sweeps and the lower plots for integration of anodic sweeps. The anodic plots are observed to pass through the origin for all integration ranges in agreement with the previous conclusion that I^- and I_3^- are not adsorbed. A similar set of experiments was performed in a solution 6 x 10^{-3}F in KI and 3.6 x 10^{-3}F in I_2. Table V indicates that for corresponding potential intervals the ratios of the slopes of the Q *vs.* $\nu^{-1/2}$

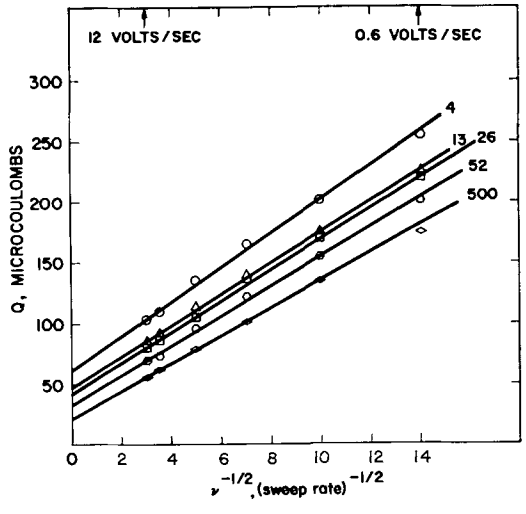

Fig. 6. Coulomb-sweep rate plots for iodine reduction at various iodide concentrations in 1F H_2SO_4. Numbers on the curves give the concentration of iodide in millimoles per liter. Concentration of iodine is 1.6 mM.

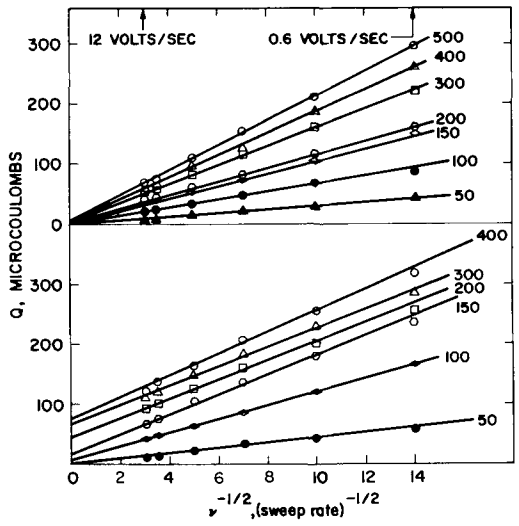

Fig. 7. Coulomb-sweep rate plots for various intervals of integration. Solution composition is given in text. Upper plots are for iodide oxidation, lower for iodine reduction. Numbers on the lines are the potential interval in millivolts, over which the integration was carried out.

plots for both solutions are constant, as required by Eq. [6].

The iodine-triiodide reduction appears more complex than iodide oxidation. Figure 8 shows a plot of the intercepts, Q_o, of the lower plots in Fig. 7 *vs.* the interval of integration ΔE. Even at potentials 200 mv more negative than the equilibrium potential some adsorbed I_2 appears to remain unreduced. This behavior is not consistent with expectations based on the Nernst equation. On the other hand, the fact that the Q *vs.* $\nu^{-1/2}$ plots for anodic iodide oxidation behave quite reasonably and display no dependence of the intercept on the potential interval of the integration argues against an experimental artifact being responsible for the anomalous behavior of the cathodic Q *vs.* $\nu^{-1/2}$ plots. This behavior is under study and will be discussed in a subsequent communication. It must be pointed out, however, that the isotherms calculated from the intercepts of Q *vs.* $\nu^{-1/2}$ plots at various triiodide concentrations will not be independent of the integration interval, unless the interval is sufficiently great to correspond to the plateau indicated in Fig. 8.

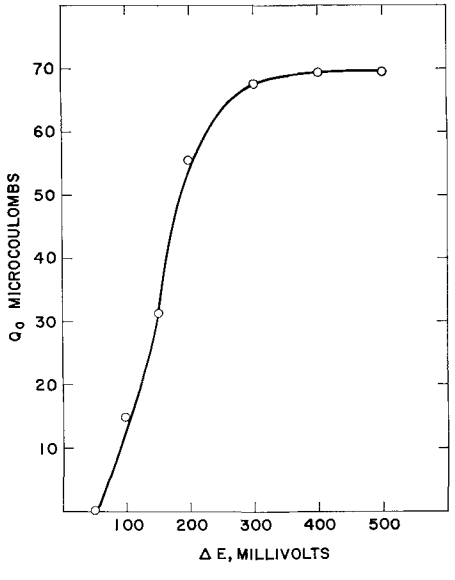

Fig. 8. Dependence of the intercepts of the Q-$\nu^{-1/2}$ plots for iodine reduction on the potential interval over which the integration was carried out.

Table V. Effect of integration interval on iodide oxidation

Integration interval, mv	$\left(\frac{\partial Q}{\partial \nu^{-1/2}}\right)_{C_1}$	$\left(\frac{\partial Q}{\partial \nu^{-1/2}}\right)_{C_2=1.5C_1}$	$\frac{\left(\frac{\partial Q}{\partial \nu^{-1/2}}\right)_{C_2=1.5C_1}}{\left(\frac{\partial Q}{\partial \nu^{-1/2}}\right)_{C_1}}$
50	20	30	1.50
100	49	64	1.31
150	68	104	1.53
200	83	114	1.38
300	109	157	1.44
400	129	181	1.41
500	149	210	1.41
			1.41 avg.

Conclusion

Extrapolation of plots of the integral of current-potential curves against the reciprocal of the square root of the potential sweep rate appears to have significant advantages over most previously used or advocated techniques for the study of adsorption at electrodes. Breiter and Gilman have carried out integration of current-potential curves at various sweep rates, in a study of the adsorption of methanol at platinum electrodes (10). However, they plotted coulombs against the logarithm of the sweep rate and found an apparent independence of Q on ν at high sweep rates. Such behavior is not to be expected for a reversible system (Eq. [6] and [7]).

Considerable attention has been given to chronopotentiometry as a method for the determination of reactant adsorption (8, 10, 11). However, a major drawback is inherent in the chronopotentiometric technique because it is rarely known with any certainty how the constant current that is passed through the electrode divides between adsorbed and diffusing reactants. It is necessary to assume models for the current distribution in order to interpret the data, and the models that lead to tractable mathematics are not those which are most intuitively appealing.

Interpretation of data resulting from the integration of current-potential curves does not require any artificial models in order to be interpreted. Because the potential, rather than the current, is controlled, as little or as much current is supplied as is necessary for the reaction of both adsorbed and diffusing reactants at all potentials, and this should be true whether the diffusing and adsorbed reactants react concomitantly or seriatim. This might not be true if adsorbed reactant interfered with the reaction of some diffusing reactant, but the presence of this sort of complication probably could be discerned from the shape of the current-potential curves (13).

Measurement of double layer capacity by a-c bridge technique has been widely used to study ad-

sorption at mercury electrodes (14). This technique is much less useful with platinum electrodes because of the unexplained frequency dependence of the measured capacitance. Furthermore it is necessary to make an assumption regarding the relationship between double layer capacitance and the surface excess on the electrode in order to interpret the data. Because the current-potential curve integration technique measures adsorbed reactant directly, no such assumption is required.

Further investigations of this technique and its application to the study of reactant adsorption are in progress.

Acknowledgment

The helpful comments, criticisms, and data supplied by Mr. Joe Christie are acknowledged with pleasure.

Manuscript received Sept. 26, 1962; revised manuscript received Mar. 8, 1963.

Any discussion of this paper will appear in a Discussion Section to be published in the June 1964 JOURNAL.

REFERENCES

1. R. A. Osteryoung, G. Lauer, and F. C. Anson, *Anal. Chem.*, **34**, 1833 (1962).
2. P. Delahay, "New Instrumental Methods in Electrochemistry," p. 118, Interscience Publishers, Inc., New York (1954).
3. M. T. Kelly, A. C. Jones, and D. J. Fisher, *Anal. Chem.*, **31**, 1475 (1959).
4. D. DeFord, paper presented American Chemical Society Meeting, San Francisco, April, 1958.
5. Philbrick Operations Manual, George A. Philbrick Researches, Inc. Boston 16, Mass.
6. F. C. Anson, *Anal. Chem.*, **33**, 934 (1961).
7. R. A. Osteryoung, G. Lauer, and F. Anson, Unpublished experiments.
8. W. Lorenz, *Z. Elektrochem.*, **59**, 730 (1955); W. Lorenz and H. Muhlberg, *ibid.*, **59**, 737 (1955).
9. F. C. Anson and D. M. King, *Anal. Chem.* **34**, 362 (1962).
10. M. Breiter and S. Gilman, *This Journal.*, **109**, 622 (1962).
11. H. A. Laitinen, *Anal. Chem.* **33**, 1458 (1961).
12. W. H. Reinmuth, *ibid.*, **33**, 322 (1961).
13. S. Gilman, General Electric Research Labs., Interim Report No. 1 to U.S. Army, Fort Belvoir, Va., Jan. 24, 1962.
14. P. Delahay and I. Trachtenberg, *J. Am. Chem. Soc.*, **79**, 2355 (1957).

Porous Carbon Gas Diffusion Electrodes

R. R. Paxton and J. F. Demendi

Pure Carbon Company, St. Marys, Pennsylvania

and G. J. Young and R. B. Rozelle

Surface Processes Research and Development Corporation, Dallas, Pennsylvania

ABSTRACT

Porous carbon materials of widely differing properties were evaluated as gas diffusion fuel electrodes. The fuel gases were hydrogen, ethane, propane, and isobutane. Graphitized electrodes performed as well as nongraphitized electrodes. Performance of carbons with larger pore diameters could be improved as much as tenfold by wetproofing or by operating at high enough gas pressure to cause bubbling; however, the ultimate concentration polarization limitations appeared related only to the micropore structure. A simple method of measuring the micropore volume was developed. Limiting current densities with hydrocarbons were substantially less than with hydrogen under identical cell conditions. Chemical attack, including electrochemical oxidation of some of the carbons was observed.

In much of the work on low-temperature fuel cells, gas diffusion electrodes fabricated from porous carbons have been employed. The basic performance characteristics sought in such electrode structures are: (i) rapid diffusion of reactants to the electrode-electrolyte interface; (ii) maximum effective catalytic surface; (iii) a stable electrode/electrolyte/gas interface; (iv) ready diffusion of products and nonreactive diluents from the interface without limiting transport of reactants; (v) conduction of electrical current with a minimum of ohmic polarization.

Optimization of an electrode system requires detailed information on the relationship between the requirements listed above and certain physical characteristics of the electrode.

Experimental and theoretical studies on the relation between electrochemical performance and physical properties of electrode materials have been reported by Yeager (1-3), Rusinko (4), Austin (5, 6), Urbach (7), and others. However, there still exists an urgent need for a considerable extension of knowledge in this area.

The present paper seeks to furnish additional insight into the problem through correlating a number of important physical parameters of carbon electrode materials with their polarization behavior as gas

diffusion electrodes. No activation of the carbon electrode structures was attempted since our purpose was not to seek the maximum current densities possible but rather to compare various structural properties.

Porous Carbons

Porous carbons used in this investigation were especially prepared to cover a wide range of porosities and surface areas. Calcined petroleum coke, synthetic (Acheson) graphite, natural flake graphite, pitch-treated lampblack, and activated coconut charcoal in varying proportions were used as filler materials. Coal tar pitch and phenolic resin were used as binders. The mixes were molded into plates at pressures ranging from 1000 to 30,000 lb/in^2. The resulting plates were baked to carbonize the binder, and a neutral or reducing atmosphere was maintained around the carbon throughout the baking cycle. Weight losses during baking ranged from 3 to 12%, and linear shrinkages up to 8% were observed.

Four of the carbons were then "graphitized" at 2700°-2800°C. A further weight loss due to volatilization of the ash occurred during graphitization; also some further shrinkage was measured.

Table I lists physical properties of the ten carbons investigated. The carbons are arranged in order of increasing median pore diameters of the macropores.

Pore sizes.—Pore volume measurements were made with an Aminco-Winslow Porosimeter (8). A critical discussion of this method of measuring pore diameters can be found in Emmett (9).

The data obtained with the porosimeter are plotted in Fig. 1 as cumulative macropore volume *vs.* pore diameter. The pore diameter corresponding to the mid point of the void volume is called the "Median Pore Diameter." Graphitized grades are shown as broken lines.

All of the grades used in this study have a steep rise beginning the volume *vs.* diameter curve. This homogeneous macropore structure was deliberately sought to aid gas distribution and minimize flooding and wetting problems.

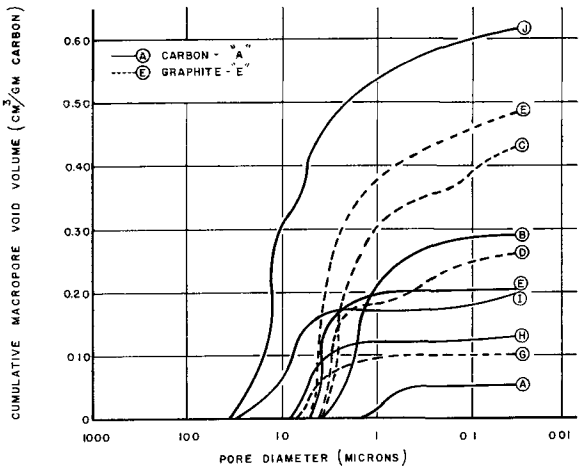

Fig. 1. Cumulative void volume in pores above 0.035μ in diameter, electrodes A through J.

The largest pore size indicated in any of the ten grades was 40μ. However, visual inspection of electrodes in several of the grades seemed to indicate many pores in the 100-1000μ range. To determine whether this was actual porosity, a modified porosimeter was built to measure void volumes in this pore size range. In every carbon tested, this special porosimeter showed a negligible percentage of volume in "pores" over 100μ. Thus, it was concluded that what appeared to be large pores in these electrodes were in reality shallow surface cavities. These cavities may have been caused by machining, or may have come from cutting an hour-glass shaped pore at its wide dimension. In this connection it should be noted that the porosimeter diameters are minimum diameters since the mercury is stopped at the first restriction in the pore.

The standard 5000 psi Aminco-Winslow Porosimeter is suitable for obtaining the void volume in pores having diameters down to 0.035μ (350Å). These are often referred to as macropores.

Micropore volume.—In addition to the void volume in macropores, there is often considerable void volume in smaller micropores. This was measured by

Table I. Physical properties of carbons

Electrode carbon	A	B	C	D	E	F	G	H	I	J
Median pore diameter, μ (Macropores)	0.8	1.7	2.0	2.9	3.0	4.1	4.5	5.4	6.9	11
Macropore volume, cm^3/g	0.05	0.29	0.43	0.26	0.49	0.20	0.11	0.13	0.20	0.61
Micropore volume, cm^3/g	0.01	0.33	0.14	0.01	0.07	0.01	0.00	0.01	0.03	0.31
Total pore volume, cm^3/g	0.06	0.62	0.57	0.27	0.56	0.21	0.11	0.14	0.23	0.92
Porosity, vol %	20	56	51	36	50	30	18	21	31	64
Flow resistance, mm Hg/cm	370	14	6	6	—	4	20	7	0.5	0.1
Surface area, M^2/g	0.3	300	9	3	7	0.5	0.2	0.4	2	560
Average density, g/cm^3	1.70	0.90	0.90	1.32	0.90	1.45	1.62	1.49	1.35	0.70
Scleroscope hardness	90	50	15	40	25	35	65	90	60	20
Transverse strength, psi	10,000	1,000	500	2,000	1,000	3,500	6,500	8,000	4,000	300
Volumetric resistance, ohm cm	0.005	0.03	0.005	0.006	0.004	0.003	0.003	0.005	0.008	0.10
Sulfur, %	1.8	0.001	0.05	—	0.01	0.21	0.01	0.21	0.12	0.24
Ash, %	4.7	10	0.1	0.2	0.1	0.5	0.1	0.2	0.2	6
Spectrographic analysis on ash, selected elements, %										
SiO_2	50+	50+	2	3.0	2	5.0	50+	50+	7.0	50+
Al_2O_3	30	10	0.5	5.0	0.5	0.5	10	1	3.0	2
Fe_2O_3	3	10	5	50+	5	50+	20	10	50+	10
CaO	3	1	1	20	1	0.5	1	0.05	0.1	1
MgO	2	0.8	0.1	0.25	0.1	0.25	1	0.3	2.0	0.5
TiO_2	1	0.2	50+	0.5	50+	0.15	0.5	0.2	0.05	0.8
Na_2O	0.2	8	0.1	—	0.1	0.1	3	1	0.5	2
K_2O	—	—	0.1	—	0.1	0.1	—	0.3	—	5

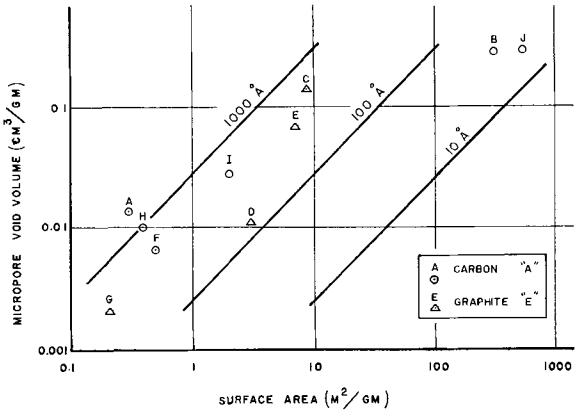

Fig. 2. Surface area and micropore volume, electrodes A through J. Solid lines represent the expected surface for those micropore diameters indicated.

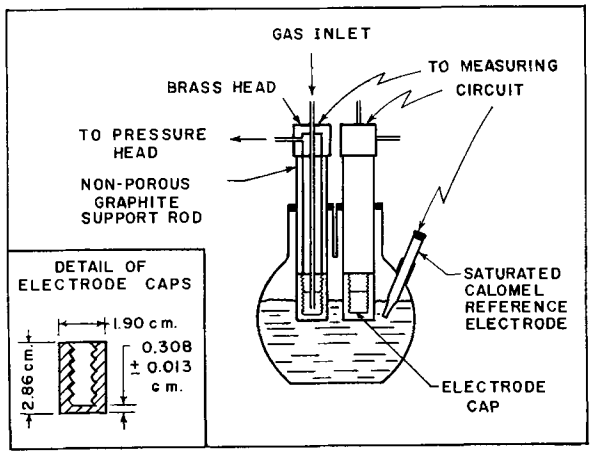

Fig. 3. Cell electrode assembly

evacuating the carbon and then flooding it with distilled water. The carbon, still covered with water, was then subjected to a minimum of 100 psi. (Pressure was used to decrease the amount of time required for filling the pores.) It was then superficially dried and quickly weighed to determine the amount of water in the pores.

Impregnation pressures from 100 to 5000 psi, and specimen thicknesses from ⅛ to 1 in. were explored. In no case was additional water forced into the carbon by pressures above 100 psi; also the water content of the impregnated carbon was independent of sample thickness in this range.

"Micropore void volume" (Table I) is taken as the increase in void volume obtained with water at 100 psi over that obtained with mercury at 5000 psi. It is the void volume in open pores smaller than 350Å diameter.

Surface areas.—Surface areas were determined by conventional BET methods (10) using N_2. Samples were outgassed overnight at 10^{-6} mm Hg and 250°C before measurement. Nearly all of the surface area of porous carbons is associated with the fine micropore structure. The relation between surface area and pore volume for the carbons investigated is illustrated in Fig. 2. Also shown in Fig. 2, by the broken lines, are correlations between void volume and surface area calculated by assuming all pores are smooth walled cylinders having the diameter specified. It is seen that for high surface area samples, the majority of the surface area is contributed by the micropore structure.

Total porosity.—Total porosity is taken as the sum of macropore and micropore void volume. Table I shows total porosity both as cm^3/g carbon and as volume per cent. The skeleton density of the carbon electrode may be calculated by dividing the average density by (100 vol % porosity)1/100. It is interesting to note that in every case the skeleton density was well below 2.26 g/cc, the theoretical density for carbon(graphite). This implies that these structures contained 5-15% of closed pores and pores inaccessible by the techniques employed.

Flow resistance.—This was measured by forcing N_2 at room temperature through the carbon at a measured rate of 1 cm^3/cm^2 min and noting the pressure gradient required. (This value for gas flow approximates H_2 flow rates needed to produce a current density of 140 ma/cm^2.) The pressure gradient, mm Hg/cm carbon thickness was independent of carbon thickness between 0.02 cm and 1.0 cm. Comparative measurements with hydrogen and nitrogen showed the gradient required was proportional to gas viscosity.

Flow resistance values may be converted into Darcies by dividing into 0.22. Thus

$$\text{Permeability, Darcies} = \frac{0.22}{\text{Flow Resistance, mm Hg/cm}}$$

Average density, transverse strength, scleroscope hardness, volumetric resistance.—These are physical properties conventionally used to characterize carbons. Average density is calculated from the dimension of the carbon and its weight. Transverse (or flexural) strength is an indicator of the length to thickness ratio that can be used in electrode structures without excessive breakage. Hardness is an indication of machinability, with carbide tools generally required to handle material in the 70-90 range, metal working tools for the 30-70 range, and wood working tools usually suitable below 30. Volumetric electrical resistance, like the other three properties, was measured using the standard NEMA/AIEE (11) method.

Electrode Preparation and Evaluation

The electrodes were machined from the molded porous carbon plates described previously. Dimensions of these electrode caps are given in Fig. 3. In use, much of the electrode was coated with Silastic RTV 502, a silicone resin, so that only 1 cm^2 of the bottom of the cap was exposed to the electrolyte.

Catalyst deposition.—After the electrodes were machined, they were washed thoroughly with deionized water by vacuum impregnation and dried. Care was taken to keep the electrode free from contaminants which might alter the wetting characteristics. Subsequently, the electrodes were impregnated with a 10% solution of platinum tetrachloride and again dried. The platinum tetrachloride impregnated electrodes were then reduced in hydrogen at 450°C for 4 hr. The amount of platinum in each electrode was determined by weighings before and after impregnation and reduction. The catalyst surface area was

determined by hydrogen chemisorption using known techniques (12, 13).

Measurements.—The electrode assembly used in the electrochemical evaluations is illustrated in Fig. 3. After the catalyst was deposited in the electrode and silicone resin coated on the exterior to define the active electrode area, the caps were threaded onto the nonporous graphite support rods. The fuel gas was admitted to the electrode via the internal inlet tube. The pressure differential across the active area of the electrode was maintained at approximately 18 mm Hg. The electrolyte employed was generally 12M KOH except for those experiments involving hydrocarbon fuel gases where it was 6M H_2SO_4.

Electrolytic hydrogen was purified before entering the electrode by a deoxo unit. Other gases were research grades and used directly without further purification.

Saturated calomel reference electrodes at the temperatures of the runs were employed in obtaining the polarization data. A platinum catalyzed carbon-oxygen electrode was used as a working cathode. Potentials and currents were measured with properly adapted high impedance vacuum tube voltmeters. Particular care was exercised to ensure that all measurements represented steady-stage conditions. The ohmic polarization was removed from the polarization curves by a current interrupting technique using a modified Kordesch-Marko bridge circuit.

Results and Discussion

Polarization curves for hydrogen electrodes, prepared from each of the ten carbons investigated, are given in Fig. 4. A number of determinations, ranging from three to ten or more, were made on different electrodes from the same material. The ohmic polarization has been subtracted from these curves. In no case was the internal resistance of the experimental cells in excess of 0.5 ohm.

Effect of catalyst content.—In order to assess clearly the influence of carbon structure on electrode polarization, it was necessary to establish an amount of catalyst required in the electrode to reduce activation polarization to a minimum. Thus, polarization curves for each electrode were determined with varying amounts of platinum impregnated into the carbons. For most of the experiments a vacuum impregnation technique was used. On certain electrodes, however, a high-pressure impregnation technique also was employed to deposit the catalyst. Typical data are given in Table II for the weight per cent catalyst deposited by the different methods. Approximately four times as much platinum was introduced into the electrode under high pressure.

Table II. Variation of catalyst content with impregnation method

Electrode No.	Wt % catalyst by vacuum impregnation	Wt % catalyst by high-pressure impregnation
J	3	10.4
E	0.5	5
F	0.3	1
A	0.1	0.4

Only one electrode showed an increase in performance with increased amount of catalyst. This was electrode A, a material with a very small average macropore diameter. The polarization behavior relative to the open-circuit potential of electrode A, as illustrated in Fig. 5, improved at the lower current densities where principally activation polarization was present. As might be expected, the limiting current density of about 11 ma/cm^2 was not altered.

Data on the platinum catalyst, deposited in electrodes used in obtaining the polarization curves in Fig. 4, are given in Table III. The surface area of the platinum is reported as square meters per gram of deposited platinum and also on the basis of square meters of catalyst per square centimeter of geometric electrode area (0.125 in. thick). The weight of catalyst is based on the weight deposited in a square centimeter of geometric electrode area (0.125 in. thick). It is noted from Table III that there is no correlation between platinum content and platinum surface area. Also, a careful check was made (by impregnating various amounts of catalyst in the carbons) to insure that electrochemical performance was not a function only of catalyst content.

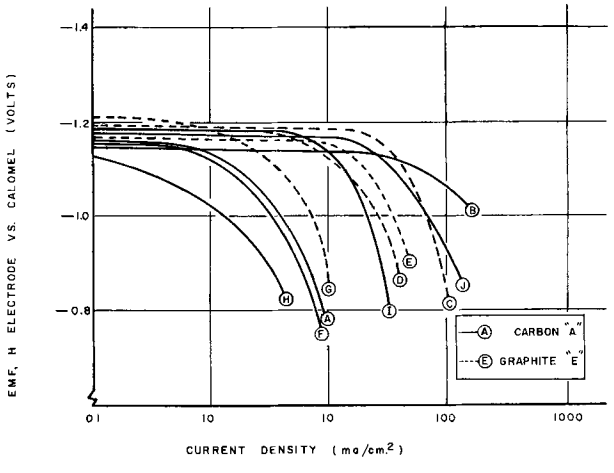

Fig. 4. Anodic polarization curves with hydrogen vs. geometric current densities. Solid lines graphitized; dashed lines, gas baked; calomel reference at test temperature. Temperature, 70°C; electrolyte, 12M KOH; catalyst, Pt; fuel, H_2.

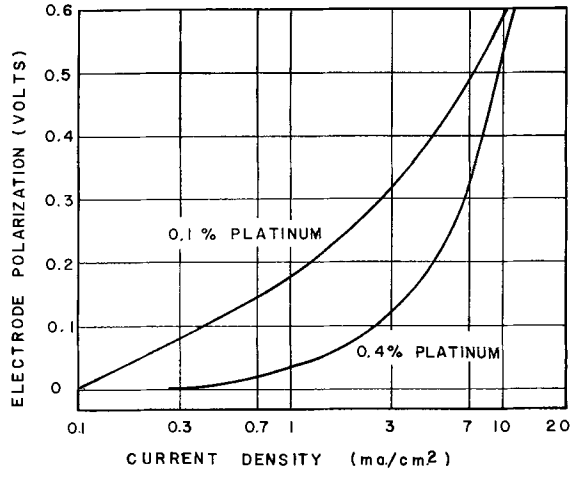

Fig. 5. Effect of catalyst content on anodic polarization of electrode A at various geometric current densities. Lower curve corresponds to A curve in Fig. 4. Temperature, 70°C; electrolyte, 12M KOH; catalyst, Pt; electrode, A; fuel gas, hydrogen.

Table III. Electrode catalyst data

Electrode	Catalyst surface area M^2/g Pt	Catalyst surface area M^2/cm^2 electrode	Weight of catalyst Wt %	Weight of catalyst mg/cm^2
A	170	0.07	0.1	0.41
B	470	0.60	1.3	1.27
C	75	0.23	2.4	3.06
D	—	—	0.6	—
E	68	0.08	0.5	1.17
F	15	0.02	0.3	1.17
G	58	0.02	1.0	0.41
H	185	0.11	1.3	0.59
I	—	—	0.9	—
J	765	1.02	3	1.33

Graphites vs. carbons.—The fact that an electrode material was a carbon or a graphite *per se*, appeared to have no direct bearing on the polarization. In Fig. 4, it is seen that both graphitized (broken lines) and nongraphitized electrodes fall in all ranges of performance. These results are in direct contradiction to those of other investigators (4) who concluded that graphites were poor electrodes. Graphitization sharply reduces micropore void and surface area, and this, of course, affects performance. However, for materials with similar structural characteristics, the results of this study lends no support to contentions that graphite electrodes are unsatisfactory.

Gas permeability.—Calculations from gas permeability measurements indicated that carbon A was the only electrode in which the current density would be limited to low values by gas transport through the macropore structure of the carbon. A limiting current density of 20 ma/cm^2 is calculated for carbon A assuming that all of the pore volume is available for transport of hydrogen to the sites electrochemical reaction. This value may be compared to the experimental limiting current density of about 11 ma/cm^2. Carbon G has the next highest flow resistance; however, the calculated limited current density due to this cause is over 500 ma/cm^2. If all of the macropore structure were available for gas transport in the other electrodes, gas diffusion could only limit the electrochemical reaction at very high current densities. However, the data in Fig. 4 indicate that three electrodes, (F, G, and H), besides A, are diffusion polarized at current densities which are less than 15 ma/cm^2. With these three electrodes, flooding of the pore structure by the electrolyte appears responsible for the poor performance. Electrodes F, G, and H gave excellent performance when wetproofed or when the fuel gas was bubbled through the pores.

Pore sizes, pore volume, and surface area.—The major parameter correlating with polarization behavior of the electrodes was the total micropore void volume. The order of decreasing micropore volume in the carbons is B>J>C>E>I>D>F,H,A>G. The electrochemical performance of the electrodes is roughly in the same order. The electrodes may be placed in three categories, (i) carbons with a micropore volume greater than 0.10 cc/g and limiting current densities greater than 100 ma/cm^2 (B, J, C); (ii) carbons with a micropore volume between 0.01 and 0.10 cc/g and limiting current densities between 15 ma/cm^2 and 100 ma/cm (I, D, E); and (iii) carbons with a very small micropore volume and limiting current densities less than 15 ma/cm^2 (F, G, H, A). In this categorizing, it is recognized that the smaller macropores also may contribute to the electrochemical performance.

Since the performance of all electrodes may be improved by wetproofing or bubbling, the correlation with micropore volume reflects at least partial operation under diffusion limitations arising from electrolyte penetration into the pore structure. Apparently, the presence of an extensive micropore structure enhances operation under these conditions, presumably by providing more paths for diffusion of electrolyte species.

Figure 2 illustrated that a rough empirical correlation exists between the surface area of a carbon and its micropore volume. Hence, surface area also roughly correlated with the observed electrochemical behavior of the carbons as electrodes, although some discrepancies are found.

Macropore volume in the carbons did not appear to be a significant variable in determining the polarization behavior of the hydrogen fueled electrode. Total pore volume was of interest only to the extent that it reflected the amount of micropore volume.

Results on wetproofed electrodes.—The electrochemical behavior of a catalyzed carbon electrode may be varied considerably when the carbon is treated with a hydrophobic agent. Figure 6 illustrates polarization curves relative to the open-circuit potential for electrode G in an acid electrolyte. The upper curve represents the polarization for an untreated carbon. A limiting current density of 10-12 ma/cm^2 was observed with the general shape of the curve being similar to that obtained in the 12M KOH electrolyte (Fig. 4). No greater difference in the polarization was observed on different electrodes in the same electrolyte. When the electrode was subjected to a hydrocarbon pretreatment, however, the discharge curve showed little polarization (lower line) to a current density of 100 ma/cm^2 and only 50 mv at a current density of 300 ma/cm^2 (not including ohmic polarization). Since it was desired to demonstrate the effect of various physical parameters of porous carbon electrodes, no attempt was made to

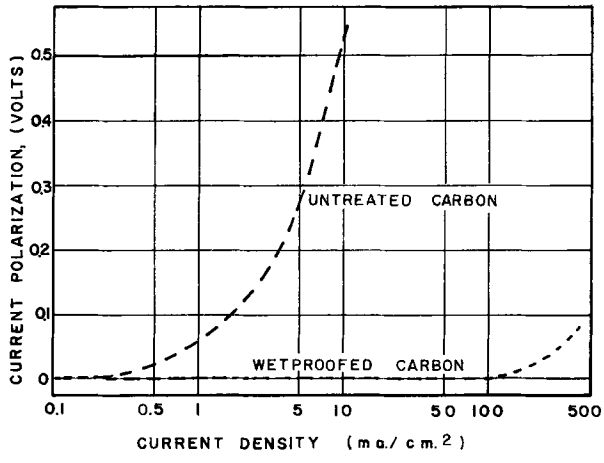

Fig. 6. Effect of wetproofing on anodic electrode polarization, vs. open-circuit voltage. Electrode G; electrolyte 3M H_2SO_4; temperature, 70°C; catalyst, Pt; fuel gas, hydrogen.

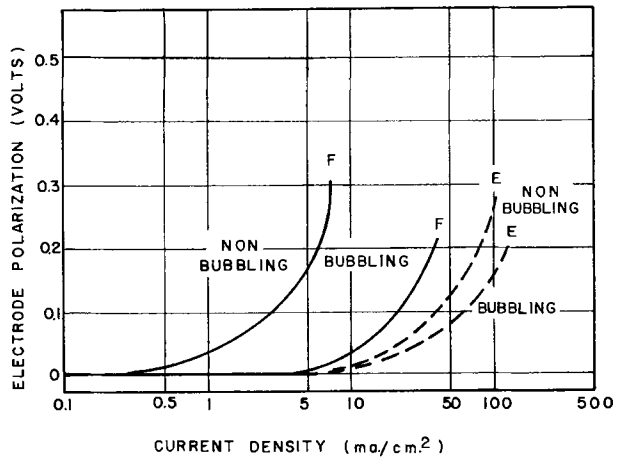

Fig. 7. Effect of bubbling on anodic electrode polarization, vs. open-circuit voltage. Electrodes E and F; temperature, 70°C; electrolyte, 12M KOH; catalyst, Pt; fuel, hydrogen.

compare all electrode performances under optimum individual operating conditions.

Results on bubbling electrodes.—Figure 7 demonstrates the difference in polarization curves (relative to the open-circuit potentials) of electrodes when the gas was bubbled or forced through the carbon pores in the electrochemically active area, compared to the nonbubbling electrodes.

Apparently, individual reaction sites are capable of sustaining appreciable current densities with hydrogen in the absence of concentration polarization (*e.g.*, carbon G, Fig. 6, and carbon F, Fig. 7). In a simple case where the product enters the electrolyte, it would seem that electrolyte diffusion problems could be overcome by wetproofing, bubbling, or by providing a sufficient number of diffusion paths (*i.e.*, micropore structure). However, with other fuel gases where activation polarization is more pronounced, a large number of reaction sites are also required for good performance.

Results on other fuel gases.—Polarization curves for the electrochemical oxidation of ethane, propane, and isobutane are given in Fig. 8 for a 6M H_2SO_4 electrolyte at 90°C. Bubbling graphite electrodes (C) were employed with all the fuels. Little polarization of the hydrogen electrode is observed in the current density range shown. However, the hydrocarbon electrodes are polarized extensively. After a high initial activation polarization, the performance of the electrodes appears to be limited by concentration polarization. Presumably, this arises due to restrictions on gas diffusion. The limiting current density with ethane on this electrode was 22 ma/cm^2, whereas that for propane and isobutane was 12 ma/cm^2. It is interesting that the electrode polarization increased with the size of the reacting molecule.

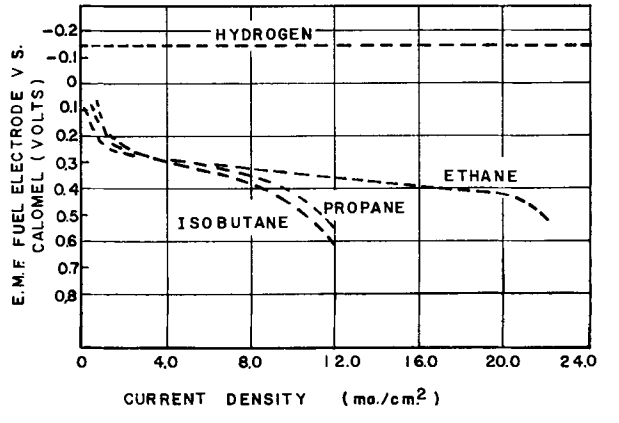

Fig. 8. Comparison of anodic polarization curves for hydrogen, ethane, propane, and isobutane fuels at 90°C vs. calomel reference. Electrolyte, 6M H_2SO_4; temperature 90°C; catalyst, Pt; carbon, No. C.

Reactivity of carbon electrodes.—All of the carbon electrodes employed in this study are susceptible to electrochemical oxidation in both acid and alkaline electrolytes, some more than others. Also, certain of the electrodes were subject to physical deterioration and swelling as a result of constant contact with the acid and alkaline electrolytes. X-ray diffraction patterns run on these electrodes, however, failed to show any change in the La, Lc or d spacing, indicating that the basic crystallites were not attacked in the time of exposure and implying that the binder was involved.

Summary and Conclusion

A series of porous carbons were evaluated as diffusion anodes in a H_2/O_2 fuel cell. Performance with partial electrolyte penetration into the pore structure ranged from 3 to 200 ma/cm^2 at 0.2v polarization. Under these operating conditions, the micropore void volume appeared to be an index of the limiting current density. Graphitization *per se*, macropore volume, macropore diameter, and platinum content (above a minimum amount) all had little apparent effect on performance.

With partial electrolyte penetration into the pore structure of the electrode, all anodes exhibited diffusion polarized at modest current densities. However, when wetproofed or operated as bubbling electrodes, performance was greatly enhanced and limiting current densities extended. Apparently the micropores can play a significant role in the transport of electrolyte species.

Electrochemical oxidation and, in some cases, severe chemical attack of the carbon by the electrolyte was observed. X-ray diffraction studies indicated that no changes in crystallite dimensions had occurred; hence, it is assumed that only the binder was involved.

Direct electrochemical oxidation of low molecular weight hydrocarbons appeared to parallel the performance with hydrogen. However, in the former case there is indication that concentration polarization may result from limitations on diffusion of the fuel gas.

Porous carbons, because of their inherent properties as relatively inert, low cost, electrically conducting catalyst supports, are attractive as fuel cell electrodes. Further development is required, however, to obtain a carbon that is permanently hydrophobic and is completely inert to chemical and electrochemical attack under all cell conditions. This study indicates the carbon should also have a uniformly fine pore structure with a large void volume in pores smaller than 0.3μ.

Manuscript received June 19, 1962; revised manuscript received March 12, 1963. This paper was presented at the Boston Meeting, Sept. 16-20, 1962.

Any discussion of this paper will appear in a Discussion Section to be published in the June 1964 JOURNAL.

REFERENCES

1. E. Yeager *et al.*, "Fuel Cells: Basic Considerations," Proc. 12th annual Battery Research and Development Conference, pp. 2-8 (1958).
2. E. Yeager, "The Oxygen Electrode in Aqueous Fuel Cells," Tech. Report 12, Contract Nonr. 2391 (00) OTS Report PB 150008 (Aug., 1960).
3. E. Yeager, K. V. Rao, A. Kozawa, and F. Hovorka, Fuel Cell Symposium, Electrochemical Society Meeting, Detroit (Oct. 1961).
4. F. Rusinko, R. W. Marek, and W. E. Parker, *Proc. 15th Annual Power Sources Conf.*, pp. 9-12 (1961).
5. L. G. Austin, "Fuel Cells," G. J. Young, Editor, pp. 34-50, Reinhold Publishing Co., New York (1960).
6. L. G. Austin, "Fuel Cells," vol. II, G. J. Young, Editor, pp. 95-112, Reinhold Publishing Co., New York (1963).
7. H. B. Urbach, "Fuel Cells," vol. II, G. J. Young, Editor, pp. 77-94, Reinhold Publishing Co., New York (1962).
8. N. M. Winslow and J. J. Shapiro, ASTM Bulletin No. 236 February 1959.
9. P. H. Emmett, "Catalysis," vol. I, Reinhold Publishing Co., New York (1954).
10. S. Brunauer, "The Adsorption of Gases and Vapors," Princeton University Press, Princeton, N. J. (1945).
11. Joint Subcommittee on Carbon Brushes, "Test Code for Carbon Brushes," AIEE No. 504, Amer. Inst. of Electrical Engineers, New York (1958).
12. L. Spenadel, "Dispersion of Platinum on Supported Catalysts," Petroleum Div. 135th A.C.S. Meeting, Boston, Mass. (1955).
13. B. M. W. Trapnell, "Chemisorption," Butterworth, London (1955).

Technical Notes

Residual Tritiated Water in Anodized Tantalum Films

G. M. Krembs

Philco Scientific Laboratory, Blue Bell, Pennsylvania

In anodized films it has been speculated that the space charge due to excess tantalum cations and excess oxygen anions in the oxide lattice can cause a-c rectification. In addition to this inherent space charge, other lattice defects in the insulating layer may control electrical characteristics. Alkahori (1) showed that anodized aluminum films prepared in oxalic acid are microporous in structure, having a barrier layer as thin as 50Å, and he postulated that the pores were filled with residual electrolyte. Sulfate ions from the anodizing bath have been measured in anodized films (2), but no data have been published on the concentration of residual water occluded in or adsorbed on anodized films prepared in aqueous electrolytes. In this study, the concentration of the radioisotope tritium was measured in anodized Ta films and monitored during subsequent room air exposure and thermal bake-out cycles.

Experimental

To detect trace quantities of water, the radiotracer method was selected instead of absorption spectroscopy, the Karl Fisher reagent or other analytical methods, because it is a very sensitive and nondestructive technique. Franklin (3) has used this approach in a study of anodized aluminum, but no details were reported about his experimental results.

Tantalum anodes were prepared by cathodic sputtering onto glass substrates and had a surface area of 1.5 cm^2. The surfaces were cleaned in a dichromate bath, rinsed in deionized water, and blown dry in a nitrogen gas stream just prior to anodization. The anodizing solution contained 0.5g oxalic acid dihydrate, 1.35 ml ethylene glycol, and 1.00 ml tritiated water. Bath temperature was held at 25°C, and Pt wire served as the cathode. Tritiated water having a specific activity of 1 curie per ml was obtained from Tracerlab, Inc. in a sealed vial. Although higher specific activity water could have been utilized, this hydrogen-tritium ratio proved to be adequate for the counting method finally employed.

Samples were inserted into the anodizing bath within the glove box, and the voltage across the cell slowly increased without exceeding 100 $\mu a/cm^2$ until a forming voltage of 90v. Current was allowed to decay back to 2 $\mu a/cm^2$, after which the voltage was cut off and the sample removed immediately. The sample was dipped in a nonradioactive water bath to remove droplets and other weakly sorbed water, then dried in dry nitrogen gas. The anode contact was removed before counting by scribing and breaking the glass substrate. The final surface area was 0.8 cm^2.

Several experimental methods were compared in their relative counting efficiency for adsorbed tritium. A vibrating reed electrometer could not detect any activity above background unless the tritium compound was thermally desorbed from the solid surface into the gas phase within the ion chambers. Liquid scintillation also proved inefficient be-

cause, even when the activity was chemically removed from the solid surface, the etchant used for the removal quenched the phosphor, as noted in the change of background spectrum. With several types of etchants, no improvement was observed in the counting efficiency of liquid scintillation as applied to this particular experiment.

The most efficient and convenient counting method was windowless gas flow, with the tube voltage established in the Geiger region of the gas mixture of 98.7% helium, 1.3% butane. Operation in the proportional region with a proportional gas of 90% argon, 10% methane, gave a lower count rate, as expected, since the dead time of the counting tube was much less than the mean-time-to-decay of the tested sample. Since the samples were placed on a planchet, activity due to tritium adsorbed on the glass back surface did not contribute to the counting rate.

Results

Two experiments have been performed, and the data are presented in Fig. 1. Sample No. 1 was anodized in the tritiated solution, and the activity was counted at successive time intervals after emergence from the solution, while being stored at room temperature in room ambient. Sample No. 2 was anodized in the same manner, but in a nontritiated solution. It was then immersed in the same tritiated anodizing bath of the same activity for the same amount of time required to anodize the other sample, rinsed in deionized water, and blown dry in a nitrogen gas stream. The count rate was observed to decrease rapidly during the first day on both samples and then reach a constant value. The results show that tritium occluded in the film during growth either existed in higher concentration within the film, or was more tightly bound within the film than the tritium which was adsorbed in the dipping experiment after anodization. More accurate and reproducible data are required of the rapid decrease during the first day before this question can be resolved.

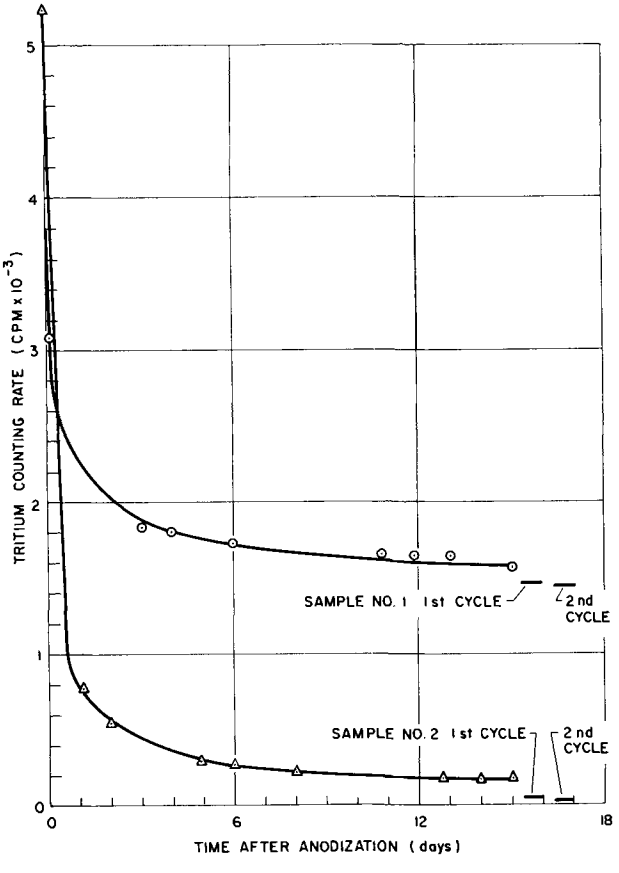

Fig. 1. Tritium activity on anodized Ta film. ⊙, Sample No. 1; △, sample No. 2.

Samples 1 and 2, after reaching a constant counting rate, were placed into an oven at 170°C with a circulated room-air atmosphere (50% relative humidity) for 1 hr. After the anodized films cooled to room temperature, the activity was counted and the bake-out cycle repeated. Sample No. 2 showed a drop in counting rate from 178 to 56 cpm after correction for background (~20 cpm). The tantalum film which was anodized in the tritiated bath lost about the same absolute number of counts per minute, but a much smaller percentage of the total activity. This result illustrates the difficulty of correlating changes in capacitor electrical data, such as working voltage or dissipation factor, with the chemical changes produced within the anodized film by thermal heating.

Discussion

Since these experiments are preliminary, their main importance is in the demonstration that tritiated water having a specific activity of 1 curie/ml provided adequate counting rates to study the water contamination of anodized thin films. One might also conclude from the data that the observed fast initial loss of activity is caused by evaporation of physically adsorbed water not removed from the surface in the stream of nitrogen gas. However, part of the decrease may result from exchange of moisture in the air with a part of the tritiated water molecule chemisorbed on the surface, and not entirely due to evaporation. The experiment conducted with Sample No. 2 proved that not all the measured tritium reacts in the same manner to thermal cycling. Since burn-out temperatures as high as 500°C have been employed by manufacturers of anodized capacitors, further tests at these higher temperatures are being planned.

An approximate estimate of the hydrogen concentration in or on the anodized films can be obtained from the data. For a specific activity of 1 curie/ml, there are 3200 hydrogen atoms per tritium atom. Since tritium has a half-life of 12.46 years,

$$\frac{dN}{dt} = \frac{1}{\epsilon}[R_c] = \frac{0.693N}{T^{1/2}} \qquad [1]$$

where dN/dt is the disintegration rate, ϵ is the counting efficiency including backscattering and absorption factors, R_c is the measured count rate, and N is the total number of tritium atoms. Because the counting efficiency ϵ for the weak beta emitted by tritium was about 5%, a count rate of 1000 cpm is equivalent to 18.6×10^{10} tritium atoms or 6×10^{14} hydrogen atoms. If all tritium existed in the molecular form of chemisorbed water, our results could be interpreted as one monolayer of surface coverage. However, if all tritium had diffused into the bulk

lattice during thermal bake-out, the hydrogen or proton concentration in the lattice would be 4.15 x 10^{19} at./cm^3 for a forming voltage of 90v (20Å/v). Of course, both cases are extremes, and the actual chemical nature of the sorbed tritium is probably due to both types.

A detailed interpretation of these results requires a study of the isotope effect and solution exchange. Isotope effect is the change in reaction rates due to the increased atomic mass of the heavier isotope. In this particular experiment, all measured data converted to tritium concentration in the anodized thin film are less than the value that would be found if the hydrogen concentration had been measured directly. For guidance on the magnitude of error, reaction ratios for many tritium/hydrogen isotope effects have been measured in other scientific fields such as biochemistry (4). Typically, tritium concentrations have been found to be one to two orders of magnitude less than the true hydrogen concentration.

Solution exchange rates are a measure of the replacement of a hydrogen atom in the other molecules or in the electrolyte ions with the tritium that was added in the form of tritiated water. In the experiments described previously, some of the tritium could have replaced the hydrogen on the oxalic acid or ethylene glycol molecules. In analyzing the above results, some of the tritium activity measured in the film may be in a chemical form other than water. Data on solution exchange rates are necessary to completely identify the chemical species.

Conclusion

Tritiated water was used to detect the hydrogen concentration on or in anodized tantalum films. Residual hydrogen may be present in more than one form, as evidenced by the different thermal behavior of activity sorbed during and after growth, although the exact nature of the chemical species is unknown. The calculated concentration of hydrogen was found to be in the range to influence the electrical properties of dielectric thin films; further studies are needed to identify its relative importance along with other impurities and defects in anodized films.

Acknowledgment

The author is indebted to F. M. Acampora for a large part of the experimental work.

Manuscript received Feb. 28, 1963; revised manuscript received May 6, 1963.

Any discussion of this paper will appear in a Discussion Section to be published in the June 1964 JOURNAL.

REFERENCES

1. H. Alkahori, *J. Electronmicroscopy*, **10**, 175 (1961).
2. J. E. Lewis and R. C. Plumb, *This Journal*, **105**, 496 (1958).
3. L. Young, "Anodic Oxide Films," p. 214, Academic Press, New York (1961).
4. L. Melander, "Isotope Effects on Reaction Rates," Ronald Press, New York (1960).

Dendritic Growth of InSb

H. Nicholson and J. W. Faust, Jr.

Metallurgy Department, Westinghouse Electric Corporation, Pittsburgh, Pennsylvania

Long ribbons of germanium can be pulled under controlled conditions from supercooled melts (1-3). The ribbons are quite uniform and have flat faces that approximate {111} planes (4). It has been shown that at least two twin planes parallel to and midway between the flat faces are necessary for continuous ribbon growth (2, 5). Furthermore, it has been shown that ribbons grow in three main stages: (*a*) a rapid lengthwise extension, called the core, which proceeds by means of re-entrant edges formed at the twin planes; (*b*) a somewhat less rapid lateral extension which proceeds independently of the twin structure by means of re-entrant edges formed at the intersection of the side facets giving the I-beam structure, and (*c*) the material between the arms of the I-beam solidifying to form the complete cross section (3). A fourth step may, under certain conditions, take place; this step involves a layered overgrowth on the two main flat faces (4). The crystal perfection of these ribbons has been reported (6, 7). When dislocations were present, they were shown to be in one or all of 3 main areas while a microsegregation of impurities, and under adverse conditions a macrosegregation of impurities, was present in a characteristic pattern.

It has been reported that the growth and perfection of InSb (8) and GaAs (9) ingots grown by the Czochralski technique are strongly affected by the polarity of the seed crystal. The group V face is reported to yield good single crystals while the group III face yields polycrystalline ingots. If such is the case, considerable doubt would be placed on the possibility of growing ribbons of the III-V intermetallic compounds or at least on the quality of their main faces.

It is the purpose of this note to report on dendrites of InSb and to present evidence that gives insight into the growth mechanism.

Experimental Procedures

Primitive InSb dendrites were obtained by dipping a single crystal seed into a supercooled stoichiometric melt and pulling it rapidly from the melt. Most of the primitive dendrites were found to contain an even number of twin planes; the explanation of this has been given elsewhere (2). Seeds were

lattice during thermal bake-out, the hydrogen or proton concentration in the lattice would be 4.15 x 10^{19} at./cm^3 for a forming voltage of 90v (20Å/v). Of course, both cases are extremes, and the actual chemical nature of the sorbed tritium is probably due to both types.

A detailed interpretation of these results requires a study of the isotope effect and solution exchange. Isotope effect is the change in reaction rates due to the increased atomic mass of the heavier isotope. In this particular experiment, all measured data converted to tritium concentration in the anodized thin film are less than the value that would be found if the hydrogen concentration had been measured directly. For guidance on the magnitude of error, reaction ratios for many tritium/hydrogen isotope effects have been measured in other scientific fields such as biochemistry (4). Typically, tritium concentrations have been found to be one to two orders of magnitude less than the true hydrogen concentration.

Solution exchange rates are a measure of the replacement of a hydrogen atom in the other molecules or in the electrolyte ions with the tritium that was added in the form of tritiated water. In the experiments described previously, some of the tritium could have replaced the hydrogen on the oxalic acid or ethylene glycol molecules. In analyzing the above results, some of the tritium activity measured in the film may be in a chemical form other than water. Data on solution exchange rates are necessary to completely identify the chemical species.

Conclusion

Tritiated water was used to detect the hydrogen concentration on or in anodized tantalum films. Residual hydrogen may be present in more than one form, as evidenced by the different thermal behavior of activity sorbed during and after growth, although the exact nature of the chemical species is unknown. The calculated concentration of hydrogen was found to be in the range to influence the electrical properties of dielectric thin films; further studies are needed to identify its relative importance along with other impurities and defects in anodized films.

Acknowledgment

The author is indebted to F. M. Acampora for a large part of the experimental work.

Manuscript received Feb. 28, 1963; revised manuscript received May 6, 1963.

Any discussion of this paper will appear in a Discussion Section to be published in the June 1964 JOURNAL.

REFERENCES

1. H. Alkahori, *J. Electronmicroscopy*, **10**, 175 (1961).
2. J. E. Lewis and R. C. Plumb, *This Journal*, **105**, 496 (1958).
3. L. Young, "Anodic Oxide Films," p. 214, Academic Press, New York (1961).
4. L. Melander, "Isotope Effects on Reaction Rates," Ronald Press, New York (1960).

Dendritic Growth of InSb

H. Nicholson and J. W. Faust, Jr.

Metallurgy Department, Westinghouse Electric Corporation, Pittsburgh, Pennsylvania

Long ribbons of germanium can be pulled under controlled conditions from supercooled melts (1-3). The ribbons are quite uniform and have flat faces that approximate {111} planes (4). It has been shown that at least two twin planes parallel to and midway between the flat faces are necessary for continuous ribbon growth (2, 5). Furthermore, it has been shown that ribbons grow in three main stages: (*a*) a rapid lengthwise extension, called the core, which proceeds by means of re-entrant edges formed at the twin planes; (*b*) a somewhat less rapid lateral extension which proceeds independently of the twin structure by means of re-entrant edges formed at the intersection of the side facets giving the I-beam structure, and (*c*) the material between the arms of the I-beam solidifying to form the complete cross section (3). A fourth step may, under certain conditions, take place; this step involves a layered overgrowth on the two main flat faces (4). The crystal perfection of these ribbons has been reported (6, 7). When dislocations were present, they were shown to be in one or all of 3 main areas while a microsegregation of impurities, and under adverse conditions a macrosegregation of impurities, was present in a characteristic pattern.

It has been reported that the growth and perfection of InSb (8) and GaAs (9) ingots grown by the Czochralski technique are strongly affected by the polarity of the seed crystal. The group V face is reported to yield good single crystals while the group III face yields polycrystalline ingots. If such is the case, considerable doubt would be placed on the possibility of growing ribbons of the III-V intermetallic compounds or at least on the quality of their main faces.

It is the purpose of this note to report on dendrites of InSb and to present evidence that gives insight into the growth mechanism.

Experimental Procedures

Primitive InSb dendrites were obtained by dipping a single crystal seed into a supercooled stoichiometric melt and pulling it rapidly from the melt. Most of the primitive dendrites were found to contain an even number of twin planes; the explanation of this has been given elsewhere (2). Seeds were

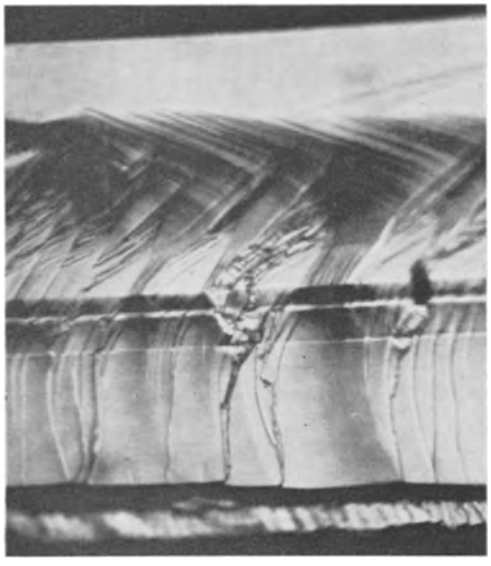

Fig. 1. Fractured cross section of InSb showing 5 twin planes. Magnification approximately 200X.

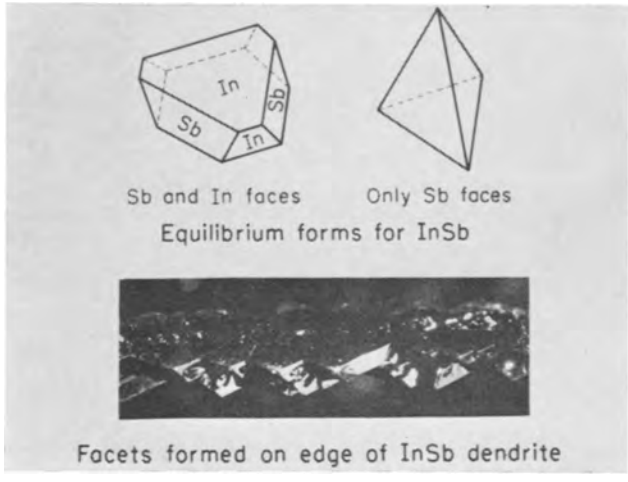

Fig. 2. InSb dendrite showing In and Sb facets on the serrated edges. The two drawings represent the equilibrium forms for (a) both In and Sb facets and (b) only Sb facets.

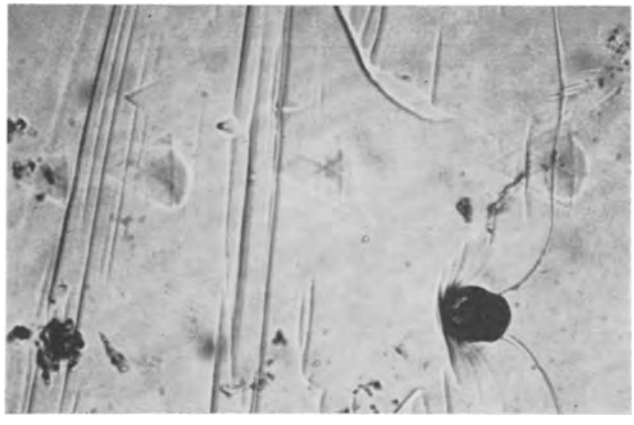

Fig. 3. Growth steps and slip patterns on natural faces of InSb. Magnification approximately 100X.

chosen from these primitive dendrites and used to grow more dendritic material under controlled conditions. The dendrites were examined unetched to study their morphology and any slip patterns. The twin structures were examined by:

(*A*) Fracturing (10). Although the primary cleavage plane of the III-V intermetallic compounds is the {110} plane, cleavage can be "forced" along the secondary {111} cleavage plane. When this is done, one often gets cleavage steps marring the surface; however, the twin planes are still clearly distinguishable as can be seen in Fig. 1.

(*B*) Etching polished cross-sections for 10 sec with HNO_3:HCl:H_2O (1:1:2). The etching anomaly reported on opposite {211} faces of germanium was not found on InSb.

(*C*) Staining polished cross sections with concentrated HNO_3. It was found that $\{\bar{2}11\}$ and the $\{2\bar{1}\bar{1}\}$ planes react differently to the concentrated HNO_3. For dendrites with an even number of twin planes, the material on either side of the twin lamellae will have the same appearance; for dendrites with an odd number of twin planes, the material on one side of the twin lamellae will be stained while that on the other side will not.

The crystal perfection of the dendrites on the group III face and on the cross sections was studied by etching with either the HNO_3:HCl:H_2O etch or with the CP4 and on the group V face by etching with $FeCl_3$:HCl.

Experimental Results

General appearance.—Examination of dendrites showed them to be identical in appearance to those of germanium. The main faces were {111} planes, the edges were serrated, and the growth direction was <211>. The dendrites contained at least two twin planes. For germanium whose {111} planes are all equivalent, the twinning operation may be considered either as a mirror image across the twin composition plane, the {111} planes, or as a 180° rotation about the twinning axis, the <111> directions. The {111} planes of InSb, however, are not all equivalent, and the twinning operation must be considered as a 180° rotation about the twinning axis. Such an operation means that one face always contains In atoms while the opposite face contains Sb atoms regardless of the number of twin planes. This was indeed born out experimentally.

Studies of the serrated edges of the dendrites showed them to be faceted by {111} planes. Both main faces and the facets on the serrated edges were unusually flat. If, for example, the In facets yielded polycrystalline growth as reported for Czochralski crystals, this face would be in the best case rough and only Sb facets would show up on the serrated edges. That both In and Sb facets are present is evident from Fig. 2. In this figure one drawing shows the equilibrium form containing both In and Sb facets while the other drawing contains only Sb facets. Comparison with the faceted edge of the InSb dendrite shows that both types of facets are present. Since both In and Sb facets grew apparently with equal ease, it seems that the polar axis does not affect the growth of the different {111} planes for dendritic growth.

Microscopic examination of the main faces showed them to contain shallow growth steps.[1] Slip patterns running down the center of both main faces were found on many of the dendrites. These slip patterns

[1] These will be reported in detail elsewhere (13).

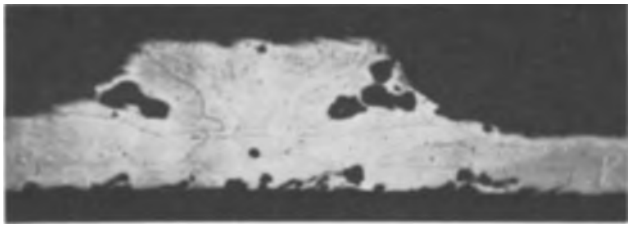

Fig. 4. Cross section of InSb dendrite showing macrosegregation and faint microsegregation. Magnification approximately 100X.

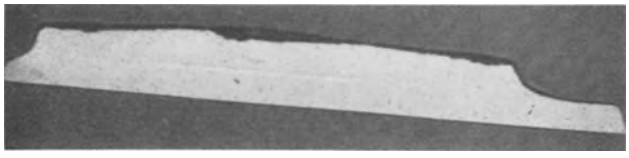

Fig. 5. Polished and stained cross section of an InSb dendrite showing a degenerate two twin plane lamella. Magnification approximately 50X.

have the familiar triangular pattern found in germanium dendrites (6); this can be seen in Fig. 3 along with growth steps.

Studies of cross sections.—Numerous dendrites were cross-sectioned and studied for their twin structure. With the exception of the twin spacing, the results were not too far different for those of germanium. No dopants were added purposely, thus no microresistivity striations could be revealed to show the growth stages either on the cross sections or on the main faces; however, two dendrites had enough microsegregation of residual impurities to faintly outline the main I-beam structure although not enough to show the core. This can be seen in Fig. 4 along with some macrosegregation. The regions in which the macrosegregation are found give further evidence for the I-beam growth mechanism.

In some cases the twin planes were continuous across the entire cross section while, in other cases, pairs of twin planes were degenerate as shown by the stained cross section on Fig. 5. When there was a pronounced difference in the width of the main faces on dendrites with an odd number of twin planes, it was found that the single twin plane that was not degenerate jogged toward the narrow face; this has been explained in the case of germanium dendrites (3).

The range of twin spacings was not too different from that found in germanium although it was observed that InSb dendrites could grow with a much larger twin spacing than in germanium; however, not enough dendrites were examined to determine the preferred twin spacing.[2] Often it was difficult to determine the exact number of twin planes because two or more were too close together to be resolved. When such was the case, the staining technique proved invaluable in determining whether an odd or even number of twin planes was present.

Crystal perfection.—The crystal perfection of the dendrites varied greatly, from essentially dislocation free to very highly dislocated. The dislocations were limited to the three general areas given for germanium dendrites (6). The central stripe of slip patterns were shown to be highly dislocated patches

[2] Further observations on the twin spacing and its effect on the growth of InSb dendrites has been recently reported (14).

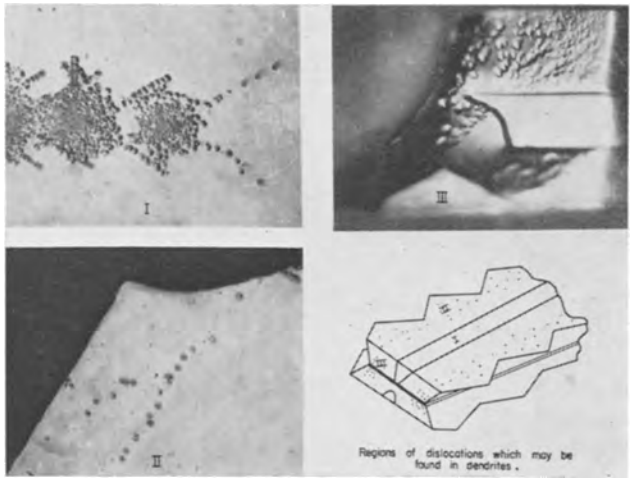

Fig. 6. The three areas of dislocations in dendrites illustrated by InSb. Area I, central stripe; area II, edges of main faces; area III, internal. Magnification approximately 70X.

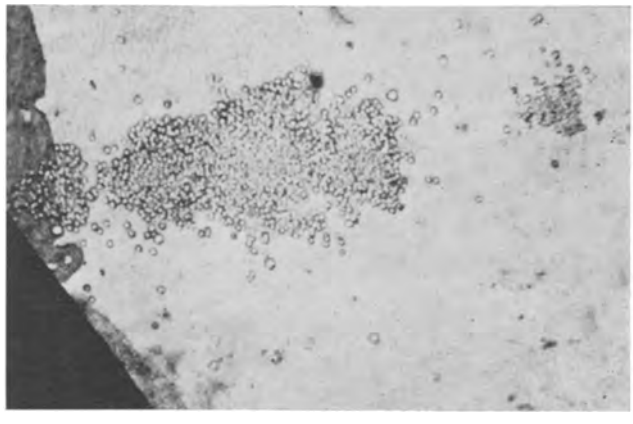

Fig. 7. Dislocations in area I on the Sb face. Magnification approximately 200X.

with the typical star pattern (area I in Fig. 6). Random dislocations were found along one or both edges of the main faces (area II in Fig. 6). Pockets of dislocations were found on the cross sections running parallel to the twin lamellae near one or both edges (area III in Fig. 6).

Photomicrographs of these areas on an InSb dendrite are also shown in Fig. 6. On the patterns in area I, the arms of the stars can be seen to consist of both single lines of dislocations and double lines as found in germanium (6). It has not been determined whether the single lines represent only one side of the dislocations half loops or are dislocations along a conventional slip line. Thus there is conflicting evidence on the ability of the etch to reveal both α and β dislocations. Figure 7 shows the dislocation in area I on the Sb. On cross sections no dislocations were found within the twin lamellae, see Fig. 6, not even within the thick lamellae.

Discussion

The presence of both In and Sb main faces of equal excellence and the presence of the {111} side facets of both In and Sb strongly suggest that the effect of the polar axis on the growth of {111} planes is not as drastic as has been reported (8, 9).

Although we have no direct evidence of the growth sequence, the following findings could only

be produced by a growth sequence similar to that given for germanium (2, 3, 11).

1. The striking similarity between the InSb and germanium dendrites (*i.e.*, growth direction, main faces, serrated edges, etc.).

2. Isolated slip patterns running down the center of the main faces of the dendrites and the general dislocation pattern.

3. The continued growth of InSb dendrites with two twin planes when the twin lamellae is degenerate and only covers a small part of the cross section.

4. The patterns of macrosegregation and the main traces of the microsegregation pattern outlining an I-beam structure.

Although the polar axis does not drastically effect the growth of InSb dendrites, it does presumably play a role in the growth mechanism. Bolling and Tiller (11) have proposed the formation of tetrahedra at {100} poles near the tip of the dendrite core and their subsequent growth to produce the I-beam structure. Presumably the tetrahedra would form at {110} poles according to the nucleation and growth sequence proposed by Faust and John (12) for III-V intermetallic compounds. This, however, should make no difference in the over-all growth mechanism.

Acknowledgments

The authors wish to thank Drs. R. Moss, A. I. Bennett, and S. O'Hara for making available InSb dendrites grown by them and to thank Mrs. H. Larsen and Mrs. S. Hillbeck for valuable assistance.

Manuscript received Mar. 20, 1963. This paper was presented at the Chicago Meeting, May 1-5, 1960.

Any discussion of this paper will appear in a Discussion Section to be published in the June 1964 JOURNAL.

REFERENCES

1. A. I. Bennett and R. L. Longini, *Phys. Rev.*, **116**, 53 (1959).
2. J. W. Faust, Jr., and H. F. John, *This Journal*, **108**, 855 (1961).
3. J. W. Faust, Jr., and H. F. John, *ibid.*, **108**, 860 (1961).
4. R. L. Longini, A. I. Bennett, and W. J. Smith, *J. Appl. Phys.*, **31**, 1204 (1960).
5. D. R. Hamilton and R. Seidensticker, *ibid.*, **31**, 1165 (1960).
6. J. W. Faust, Jr., and H. F. John, *This Journal*, **108**, 864 (1961).
7. S. O'Hara, "Metallurgy of Elemental and Compound Semiconductors," R. O. Grubel, Editor, p. 149, Interscience Publishers, New York (1961).
8. H. C. Gatos, P. L. Moody, and M. C. Lavine, *J. Appl. Phys.*, **31**, 212 (1960).
9. P. L. Moody, H. C. Gatos, and M. C. Lavine, *ibid.*, **31**, 1696 (1960).
10. J. W. Faust, Jr., and H. F. John, *This Journal*, **107**, 562 (1960).
11. G. F. Bolling and W. A. Tiller, "Metallurgy of Elemental and Compound Semiconductors," R. O. Grubel, Editor, p. 97, Interscience Publishers, New York (1961).
12. J. W. Faust, Jr., and H. F. John, *J. Phys. Chem. Solids*, **23**, 1119 (1962).
13. G. R. Booker, To be published.
14. N. Albon and A. E. Owen, Electrochem. Soc., Electronics Div. Abstracts, **10**, 95 (1961).

The Diffusion of Oxygen in Hafnium

G. R. Wallwork[1]

School of Metallurgy, University of New South Wales, Kensington, Australia

and W. W. Smeltzer

Department of Metallurgy and Metallurgical Engineering, McMaster University, Hamilton, Ontario, Canada

In an earlier paper (1) Wallwork and Jenkins reported that the oxygen gradients in titanium, zirconium, and hafnium attain steady-state profiles with respect to the oxide/metal interface upon onset of linear oxidation kinetics. More recently, Akram and Smeltzer (2) have shown that an analysis carried out by Tiller *et al.* (3) and Wagner (4) for diffusion in a phase where the boundary migrates at a constant rate may be applied to the data for this stage of the oxidation reaction to evaluate oxygen diffusion constants. Values of these constants for titanium and zirconium calculated from oxidation data were found to agree with those values determined from diffusion anneal experiments. This paper reports determinations of the oxygen diffusion constants in hafnium at 800° and 950°C from measurements of the steady-state oxygen profile in the metal and reported linear oxidation data (5).

[1] Visiting Research Professor, McMaster University, Hamilton, Ontario, Canada.

The appropriate steady-state solution for the oxygen gradient in the metal phase measured from the oxide/metal interface during linear oxidation is (2)

$$C(x) = (C_o^I - C_o') \exp -\frac{K_L}{D}x + C_o' \qquad [1]$$

Here, $C(x)$ and C_o^I are the oxygen concentrations in the metal at distance x and at the metal interface, K_L is the linear rate constant, and D is the diffusion constant of oxygen. This exponential equation is the unique solution of Fick's diffusion equations for a steady-state concentration profile at a boundary moving at constant rate (3, 4). In the case of linear oxidation kinetics, the rate of migration of the metal interface is given by the linear rate constant. Also, the initial oxygen concentration in the metal C_o', must equal the atmospheric oxygen concentration for this steady state to exist. Fortunately these quantities are sufficiently small to be set equal to zero,

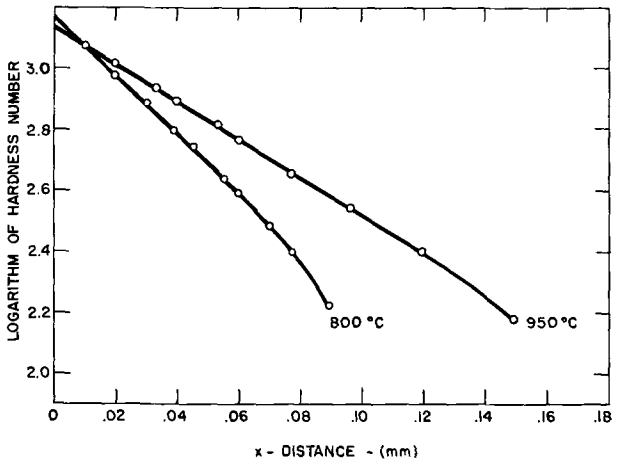

Fig. 1. Microhardness determinations plotted according to Eq. [1] of hafnium specimens oxidized for 96 and 24 hr in oxygen at 760 mm. Hg pressure at 800° and 950°C. In this figure, the microhardness number is H_x-H_0, where H_0 = 50 for the annealed as-received metal.

thus obtaining effective equality. For example, the atmospheric oxygen concentration at 1 atm pressure and 800°C of 3.6 x 10^{-4} g/cc corresponds to an oxygen content in the metal of only 0.004 wt %.

The hafnium metal used in the oxidation experiments, the analysis of which has been reported (5), contained a major impurity of 5.0% zirconium. Specimens 0.025 in. thick were exposed in oxygen at 1 atm pressure at 800° and 950°C for 96 and 24 hr, respectively. Hardness measurements were employed as a measure of the oxygen concentration in the metal substrate (1). Utilizing a Leitz microhardness instrument with a 50g load, indentation measurements were made at known distances adjacent to the oxide/metal interface. Five hardness scans, reproducible within ± 10%, were determined and the arithmetical averages taken for the determinations.

The hardness determinations are plotted according to Eq. [1] in Fig. 1 under the assumption that the hardness of the metal is directly proportional to its oxygen concentration as has been reported for titanium (6) and zirconium (7). This assumption may be questioned by the hardness measurements made on hafnium-oxygen alloys containing 2.2% zirconium by Rudy and Stecker (8) who report a nonlinear relationship over the range of oxygen solid solubility but with hardness numbers from only 270-650 DPN. However, our results show this range to be 50-1220 DPN. Under these circumstances, a constant proportionality between hardness and concentration is assumed, and the curves in Fig. 1 then

Table I. Diffusion constants of oxygen in hafnium

Temp, °C	K_L/D, 1/cm	K_L, cm/sec	D (oxidation), cm²/sec	D (diffusion anneal) (9), cm²/sec
800	222	3.2×10^{-9}	1.4×10^{-11}	3.8×10^{-11}
950	141	1.4×10^{-8}	1.0×10^{-10}	7.6×10^{-10}

demonstrate that the exponential relationship represents the oxygen penetration data to a first approximation. Consequently, the slopes of these curves give values of the ratio K_L/D.

One may therefore evaluate the oxygen diffusion constants from the previously reported weight-gain kinetics of hafnium (5). To convert the oxidation constants from g/cm² sec to cm/sec, the value of 10.22 g/cm³ was employed for the density of hafnia (9). Values of the diffusion constants at 800° and 950°C are recorded in Table I.

These determinations of the diffusion constants may be compared to estimates calculated from the results reported by Pemsler (9) from diffusion anneal experiments in the temperature range 500°-620°C, by extrapolating the Arrhenius equation of the results reported under the assumption that the oxygen saturation concentration in hafnium was 20 at. %. This value has been recently reported as the saturation cencentration over the temperature range of interest (8). These values are also recorded in Table I.

It is to be noted that the recorded values of the diffusion constants at 800° and 950°C are of the same order of magnitude, but those from this investigation are smaller than the estimates from the lower temperature results. Because this difference would be larger if the relationship between hardness and concentration decreased with increasing oxygen concentration (8), the present findings suggest that the discrepancy between the determinations from oxidation and diffusion anneal experiments at lower temperatures is associated with the Arrhenius type extrapolation over a broad temperature range or the impure polycrystalline hafnium specimens.

Acknowledgments

This work was supported by the Australian Atomic Energy Commission and the U.S. Air Force Office of Scientific Research, Office of Aerospace Research.

Manuscript received Feb. 11, 1963; revised manuscript received April 22, 1963.

Any discussion of this paper will appear in a Discussion Section to be published in the June 1964 JOURNAL.

REFERENCES

1. G. R. Wallwork and A. E. Jenkins, *This Journal*, **106**, 10 (1959).
2. K. H. Akram and W. W. Smeltzer, *Can. Met. Quart.*, **1**, 41 (1962).
3. W. A. Tiller, K. A. Jackson, J. W. Rutter, and B. Chalmers, *Acta Met.*, **1**, 428 (1953).
4. C. Wagner, *J. Metals*, **6**, 154 (1954).
5. W. W. Smeltzer and M. T. Simnad, *Acta Met.*, **5**, 328 (1957).
6. W. P. Roe, H. R. Palmer, and W. R. Opie, *Trans. Am. Soc. Metals*, **52**, 191 (1960).
7. R. M. Treco, "Zirconium and Zirconium Alloys," p. 254, American Society for Metals (1953).
8. E. Rudy and P. Stecher, *J. Less Common Metals*, **5**, 78 (1963).
9. J. P. Pemsler, *This Journal*, **106**, 1067 (1959).

Brief Communications

The Recovery from Polarization of α- and β-PbO_2 in H_2SO_4 Electrolyte

Harry B. Mark, Jr.

Division of Chemistry and Chemical Engineering, California Institute of Technology, Pasadena, California

The potential-time curves obtained when the two crystallographic modifications of PbO_2 (1, 2), α-PbO_2(rhombic) and the more common β-PbO_2 (tetragonal), recover from polarization in acid electrolyte have been re-examined using more sensitive recording conditions (3) than employed in previously reported work (4, 5). Cylindrical platinum electrodes (surface area equal approximately 5 cm^2), plated with either α- or β-PbO_2, were discharged by passing a constant cathodic current until a steady-state or slowly changing closed circuit potential was obtained. At this point, the current was interrupted and the electrode allowed to recover to a steady-state open circuit potential. The recovery was recorded. The electrodes were in contact with a stirred 0.1*M* H_2SO_4 electrolyte saturated with $PbSO_4$. Details of the experimental conditions, apparatus, and procedure were identical to those described previously (3-5).

Typical experimental recovery curves are shown in Fig. 1. The potential-time curve for β-PbO_2 was found to pass through a distinct potential maximum before a steady-state open circuit potential was obtained, as shown by curve 1. This potential maximum was also observed in each recovery of an electrode from a series of successive polarizations.

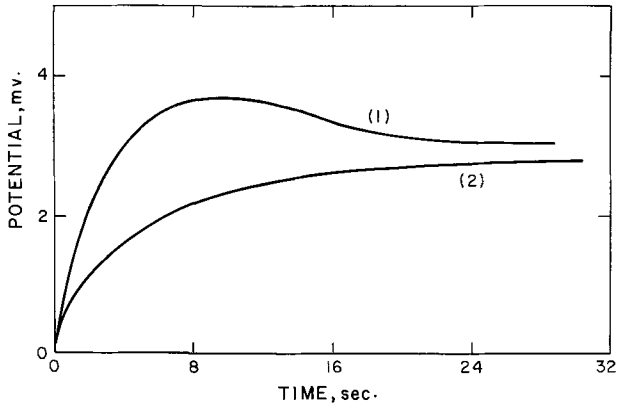

Fig. 1. Potential-time curves observed for PbO_2 electrodes on recovery from polarization in 0.1*M* H_2SO_4 (sat. $PbSO_4$) electrolyte: difference between open-circuit and steady-state closed-circuit potentials *vs.* time after opening the circuit. Curve 1, β-PbO_2 electrode (polarization current was 0.013 ma/cm^2); curve 2, α-PbO_2 electrode (polarization current was 0.04 ma/cm^2).

This maximum was not observed previously (4, 5). The potential-time curve for the recovery of α-PbO_2 from polarization did not, however, exhibit a potential maximum under any condition. See curve 2 of Fig. 1 for a typical α-PbO_2 recovery curve.

These experimental observations are consistent with the previously proposed theory that the crystal lattice of β-PbO_2 undergoes a considerable expansion as the lower oxide reduction product is formed on and within the electrode surface, but the α-PbO_2 lattice does not undergo appreciable expansion (4, 5). As the β-PbO_2 electrode recovers from polarization, the lower oxide is removed from the surface and from within the electrode lattice, which raises the potential of the system. However, as the lower oxide product is removed, the crystal lattice recovers to approximately its initial dimensions. This process results in a decrease in the energy of the system. Thus, the potential summation of these two processes, one an increase and the other a decrease in potential, results in a potential maximum. A similar combination of the reverse of the above two processes having opposite potential changes has been proposed as the explanation of the potential minimum observed in the growth of polarization during discharge of γ-MnO_2 (6), Tl_2O_3, and β-PbO_2 (4, 5).

The fact that α-PbO_2 does not exhibit a potential minimum on discharge (4, 5) leads to the postulation that α-PbO_2 does not undergo a similar lattice expansion.

These experiments also explain why the results of previous x-ray experiments failed to show the lattice expansion for a partially discharged β-PbO_2 electrode (5). In the previous work, x-ray powder diffraction patterns were made of the electrode material both prior to the electroreduction and after the electrode had recovered to an open circuit steady-state potential after the discharge. If the explanation of the potential maximum observed on recovery is correct, then the crystal lattice of the electrode material had returned to approximately its initial dimensions before the x-ray patterns were made.

A detailed study of the depolarization potential-time curves of α- and β-PbO_2 under varying conditions of applied discharge current density, nature

of the supporting electrolyte, and conditions of electrodeposition of the oxide film is in progress. As Tl_2O_3 and γ-MnO_2 electrodes exhibit potential minima during the growth of polarization similar to β-PbO_2 (4), their recovery potential-time curves are being studied to see if a similar potential maximum can be observed on their recovery. X-ray and electron diffraction studies of α- and β-PbO_2 films during the course of electroreduction are planned for the immediate future. The electrolyte will be chosen such that the lower oxide reduction products are not removed (or dissolved) from the electrode by the electrolyte. Thus, the expanded lattice should be stable enough to permit its study, as was the case of γ-MnO_2 in basic electrolyte (7-9).

Manuscript received Mar. 27, 1963. Contribution No. 2960 of the Gates and Crellin Laboratories of Chemistry.

Any discussion of this paper will appear in a Discussion Section to be published in the June 1964 JOURNAL.

REFERENCES

1. A. I. Zaslavskii, Yu. D. Kondrashov, and S. S. Tolkachev, *Doklady Akad. Nauk S.S.S.R.*, **75**, 559 (1950).
2. H. Bode and E. Voss, *Z. Elektrochem.*, **60**, 1053 (1956).
3. H. B. Mark, Jr., and F. C. Anson, *Anal. Chem.*, **35**, 722 (1963).
4. H. B. Mark, Jr., and W. C. Vosburgh, *This Journal*, **108**, 615 (1961).
5. H. B. Mark, Jr., *ibid.*, **109**, 634 (1962).
6. S. Yoshizawa and W. C. Vosburgh, *ibid.*, **104**, 399 (1957).
7. J. P. Brenet, *Proc. Intern. Comm. Electrochem. Thermodynam. and Kinetics*, 8th Meeting, Madrid, 1956, pp. 394-401.
8. S. Ghosh and J. P. Brenet, *Electrochim. Acta*, **7**, 449 (1962).
9. K. Neumann and W. Fink, *Z. Elektrochem.*, **62**, 114 (1958).

Power Supply for Currents of 200 Microamperes or Less

Robert D. Wales

Materials Sciences Laboratory, Lockheed Missiles and Space Company, Palo Alto, California

A constant current power supply for use in anodic oxidation or other applications in which the load varies from zero to several megohms is diagramed in Fig. 1. This power supply consists of a 931A photomultiplier tube with 15 Eveready No. 490 90V batteries, one between each dynode, one between the anode and the first dynode, and 6 between the last dynode and the plate. A 470 k ohm resistor was connected across the 6 batteries to the plate to help stabilize the voltage on these batteries. The photomultiplier tube was activated with two GE No. 51 lamps and the current in the load controlled by the intensity of the No. 51 lamps.

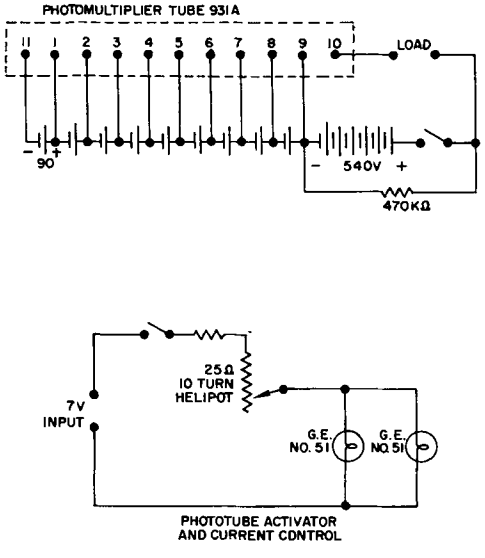

Fig. 1. Phototube constant current power supply

The stability and operating characteristics for this power supply were very good. The current drift, after about a 1-hr warm-up period, was about 3μa/hr at 60 μa. The current change was less than 5% at 100 μa for a load change from zero to about 2 megohms.

Acknowledgment

The idea was suggested by Leo Davis of the LMSC Electronics Sciences Laboratory and the power supply was assembled by Bob Cross of the Electronics Shop.

Manuscript received March 29, 1963.

Any discussion of this paper will appear in a Discussion Section to be published in the June 1964 JOURNAL.

Electrochemical Corrosion of Iridium in Hydrochloric Acid Solutions

J. Llopis and L. Jorge

Instituto de Química Física "Rocasolano," C.S.I.C., Madrid, Spain

ABSTRACT

Iridium is anodically dissolved by electrolysis in HCl solutions as $IrCl_6^{\equiv}$ and $IrCl_6^{=}$. The attack is enhanced by increasing the HCl concentration and the temperature. Superimposition of an alternating current increases the corrosion rate, the effect being most pronounced at low frequencies. As in the case of Pt, at any direct current there is no corrosion up to a value of $i_{ac} >> i_{dc}$. For any set of experimental conditions Ir is more resistant to corrosion than Pt. Finally, the mechanisms of dissolution and passivation of Ir electrodes in solutions containing Cl^- ions are discussed.

In aqueous solutions $IrCl_6^{=}$ and $IrCl_6^{\equiv}$ established a redox potential (1, 2) corresponding to the equilibrium

$$IrCl_6^{=} + e \rightleftharpoons IrCl_6^{\equiv} \qquad [1]$$

The standard potential at 25°C is $E_o = 0.97$v according to Terrey and Baker (3), and $E_o = 1.026_4$v according to Woo (4), *vs.* the standard hydrogen electrode. Since this potential is less positive than that of the system Cl_2/Cl^- ($E_o = 1.369$v), $IrCl_6^{\equiv}$ oxidizes completely to $IrCl_6^{=}$ in aqueous solutions containing Cl_2 at a pressure of 1 atm.

Among the metals of the platinum group, Ir is closest in its behavior to Rh and Pt. The anodic behavior of Ir has been studied little as compared with the great number of publications on Pt. However, generally speaking, it can be said that Ir is characterized by a great resistance to corrosion when used as anode. Although the metal shows a great resistance to corrosion, even in solutions with high concentrations of Cl^- ions, it can be dissolved at the anode as $IrCl_6^{\equiv}$ and $IrCl_6^{=}$ during electrolysis in such solutions (5, 6). Of the three metals Ir, Rh, and Pt, Pt corrodes most rapidly, and its corrosion rate increases with the concentration of HCl, the temperature, and the partial pressure of air (7). The corrosion of these metals is increased also by the superposition of an a-c current (8). The effect of an alternating current is smaller with Ir than with Pt in all the electrolytes studied (9).

The lack of data about the anodic behavior of Ir in general, and mainly about its corrosion when used as anode, are the reasons which have convinced us to study the anodic behavior of this metal in the electrolysis of concentrated solutions of HCl. In this way it has been possible to establish that Ir is more resistant to corrosion than Pt, in the case of electrolysis with either direct or alternating currents.

Study of the Polarization Curves

The polarization curves obtained by Luther and Brislee (10) and Chang and Wick (11) actually correspond to the formation of Cl_2 on passive anodes of Ir. To obtain information about the anodic corrosion of this metal, the polarization curves have to be obtained at lower current densities. As in the case of Pt (12), the passivation of Ir in HCl solutions is shown by a shift of potential in the galvanostatic curves. The first part of these curves corresponds to the anodic corrosion of the metal and the second to evolution of Cl_2 on the passivated anode. For low concentrations the electrode becomes passive even for very low current densities. Corrosion starts at a certain value of the halide concentration, which depends on the nature of both the metal and the halide ions (13). An increase in the concentration of the halide ion shifts the passivation knee toward higher current densities.

The polarization curves give information about the best conditions under which corrosion can be studied. In the present paper the corrosion rate was measured by the loss of weight of the Ir electrode during each experiment and is expressed as mg cm^{-2} h^{-1} (geometric area). In the discussion of the results it is assumed that Ir can be dissolved at the anode as Ir^{III} and Ir^{IV}.

The experimental technique used in this work was similar to that described previously when dealing with Pt (8, 12). In the cell shown in Fig. 1 the

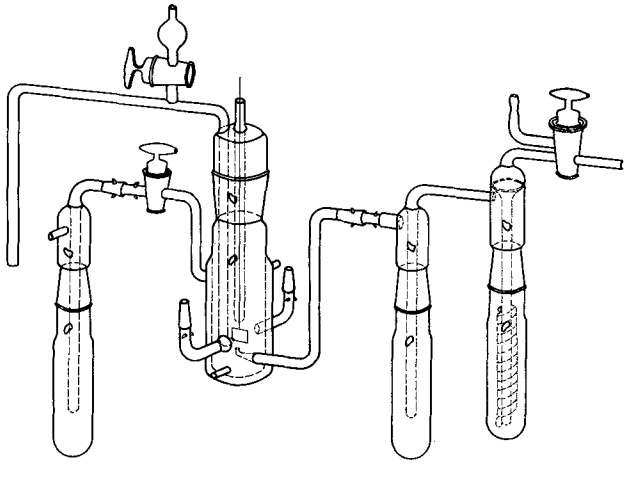

Fig. 1. Electrolytic cell

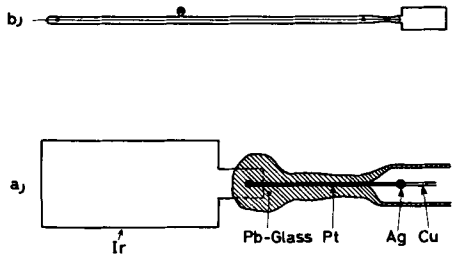

Fig. 2. Setting up of the electrodes

anodic and cathodic compartments are separated by a sintered glass disk. The electrolyte is thermostated by circulating water from a thermostat through the double wall of the cell. N_2 could be bubbled through the electrolyte. Graphite rods were used as auxiliary electrodes. The electrode used in these experiments (denoted by "A") is a plate of pure Ir, 3.2 x 1.5 cm, from "Semp" (Madrid), mechanically attached to a Pt wire. The latter is welded with silver to a copper wire which acts as conductor. The set up of these electrodes can be seen in Fig. 2. The Ir electrode made in this way can be weighed easily with a precision of 0.2 mg. Experiments were carried out in all cases with the electrode surfaces strongly corroded. The roughness factor was about 20, as deduced from the study of the charging curves in 2*N* $HClO_4$ and 2*N* HCl. This study of the anodic and cathodic charging curves will be published elsewhere. The electrode potentials are referred in all cases to the S.C.E., and the reported current densities are based on geometric area (apparent current densities).

The d-c and a-c circuits were described in a previous paper (8). The a-c current sources were sine waves (50-400 cps) and square waves (10 cps) from electronic oscillators, and the current was introduced to the electrolysis circuit through a Roselson (ULT 34) transformer.

The polarization curves obtained with only direct current, using HCl solutions of increasing concentrations and keeping the temperature constant (20°C), show that for 3*N* HCl the Ir electrode is passive even for the lower current densities and the potentials correspond to anodic evolution of Cl_2. For concentrations of HCl higher than 4*N* the polarization curves show a knee of passivation. The current densities at which the potential shift appears are higher as the HCl concentration and temperature increase, but in any case they are lower than those observed with Pt electrodes in similar conditions. The poor reproducibility observed in these curves is probably due to a more or less active initial state of the electrode surface.

When an alternating current is superimposed a depolarizing effect appears, which is more important as the frequency decreases and the alternating current density i_{ac} increases (14). Both in the case of Pt and Ir the passivation knee appears for a direct current density i_{dc} which is higher as the amplitude of the superimposed a.c. increases and/or its frequency decreases. This can be seen in Fig. 3, where the polarization curves obtained using 6*N* HCl as electrolyte, at 19°C and different values of alternating current, i_{ac}, (μ = 50 cps), are shown. If the

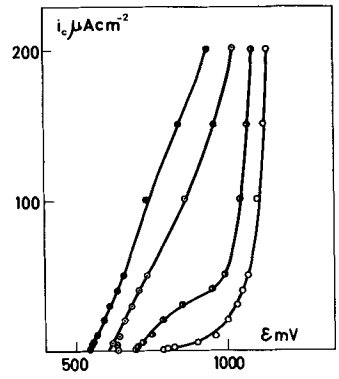

Fig. 3. Effect of the a.c. on the polarization curves: open circle, i_{ac} = 5 ma cm^{-2}; half opened circle, i_{ac} = 10 ma cm^{-2}; dotted circle, i_{ac} = 15 ma cm^{-2}; solid circle, i_{ac} = 20 ma cm^{-2}. HCl 6*N*, temperature 19°C, ν = 50 cps.

superimposed value of i_{ac} is higher than 15 ma/cm^{-2}, the electrode behaves as active even for high values of the direct current, i_{dc}. Similarly, an increase of temperature or higher concentration of HCl favor the active part of the polarization curves when an alternating current is superimposed.

Quantitative Study of Anodic Corrosion

Experiments carried out with direct current.—Table I summarizes the anodic corrosion rates observed at various d.c. currents in 12*N* HCl solution, at 50°C. The electrode was previously activated by cathodic prepolarization (1 ma/cm^2 for 1 hr) while bubbling pure N_2. During these experiments it was observed that the potential drifted toward more positive values, indicating a tendency to passivation.

Since it is necessary to work at very low current densities and during long times (in the order of 3-4 days) to obtain measurable corrosions, the scatter of the results is considerable. This makes it difficult to determine the valence state of Ir dissolved under these conditions. However, from the results obtained with superimposed currents, shown below, it seems that in the experiments carried out with only direct current Ir^{III}, Ir^{IV}, and Cl_2 are formed at the anode. The formation of Ir^{III} tends to be more important at less positive potentials (greater activity of the electrode or lower current densities), but in all of the experiments here described the formation of Ir^{IV} is more important. As the current density increases Ir^{IV} tends to be formed, with an increasing proportion of Cl_2.

Experiments carried out with superimposed currents.—In all these experiments a 6*N* HCl solution was used as electrolyte and the temperature was 19° and 50°C. Figure 4 shows the corrosion rates δ(mg cm^{-2} h^{-1}), as a function of the alternat-

Table I. Anodic corrosion of iridium by direct current. Electrode "A"; electrolyte 12*N* HCl solution; temperature 50°C

i_{dc}, μa cm^{-2}	ϵ, mv	δ, μg cm^{-2} h^{-1}
7	590	6.0
10	560	23.4
10	560	13.2
20	600	30.0
30	650	36.6

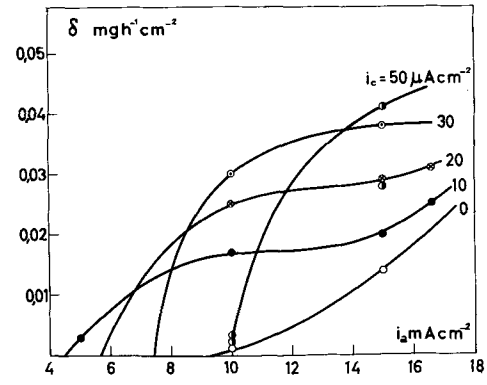

Fig. 4. Effect on corrosion of square wave a.c., 10 cps, superimposed to given values of i_{dc}. HCl 6*N*, temperature 19°C; ν = 10 cps.

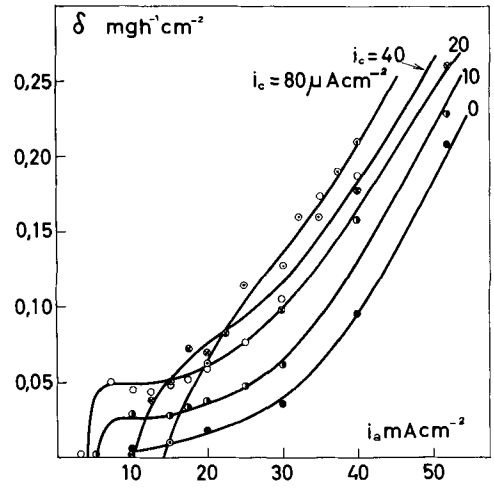

Fig. 5. Effect on corrosion of a sine wave 50 cps a.c. HCl 6*N*, temperature 19°C, ν = 50 cps.

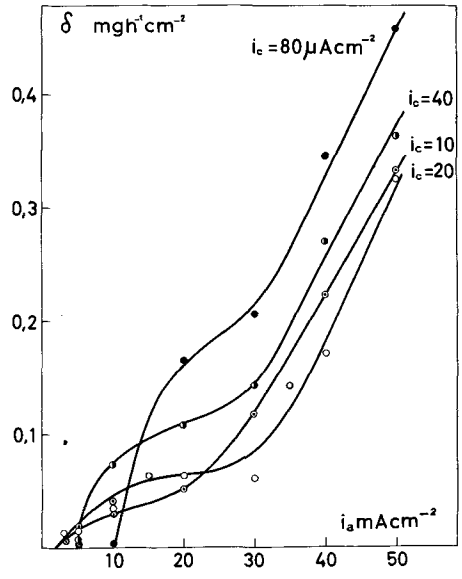

Fig. 6. Effect on corrosion of a sine wave 50 cps a.c., HCl 6*N*, temperature 50°C.

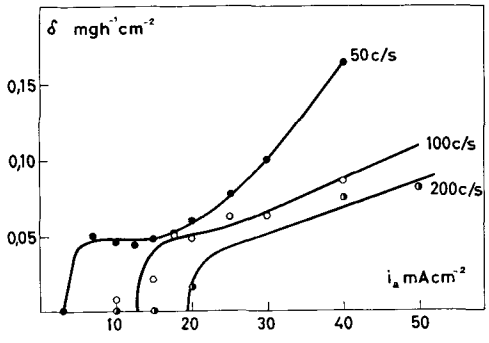

Fig. 7. Influence of frequency on corrosion by superimposed alternating currents. HCl 6*N*, temperature 19°C, i_c = 20 μa/cm².

ing current densities, i_{ac}(ma/cm²), for each value of the direct current density i_{dc}(μa/cm²). The superimposed a-c signal was a square wave of 10 cps frequency. It should be pointed out that this series of experiments was carried out with a plate of pure Ir from a different supplier, "Degusa" (Francfurt), which shows a higher resistance to corrosion that could not be explained by a smaller roughness factor ($\simeq 11$). This electrode was denoted "B."

As in the case of Pt, Fig. 4 shows that for any value of i_{dc} there is no evident corrosion, that is, the electrode remains passive, up to a certain value of $i_{ac} >> i_{dc}$. This "threshold" value of i_{ac}, below which there is no corrosion, depends on the i_{dc} value. Above the "threshold" value of i_{ac} the corrosion passes from nil to a certain value, nearly independent of i_{ac} in a certain range of alternating current density. The corrosion rate in this range of i_{ac} corresponds to a dissolution process controlled mainly by the i_{dc} value imposed.

The same behavior is observed in the results shown in Fig. 5 obtained with a frequency of 50 cps and a temperature of 19°C. Results shown in Fig. 6 correspond to a series of experiments carried out under the same conditions (electrode "A") but at 50°C. It appears that the corrosion rate increases with temperature, the other conditions being constant.

The influence of frequency is shown in the curves plotted in Fig. 7. As expected, if the frequency is increased, a higher value of i_{ac} has to be superimposed to depassivate the electrode and to make its anodic dissolution possible.

Table II summarizes the "threshold" values of i_{ac} for the same conditions of electrolyte and temperature, but at different values of i_{dc} and of the

Table II. Anodic corrosion of iridium by superimposed currents. "Threshold" values of alternating current density i_{ac}^m for different values of i_{dc} and frequency ν. Electrolyte 6*N* HCl and temperature 19°C

Electrode	ν, cps	i_{ac}^m, μa cm⁻²	i_{dc}, μa cm⁻²	Ratio i_{ac}^m/i_{dc}
B	10	5×10^3	10	500
B	10	6×10^3	20	300
B	10	8×10^3	30	266
B	10	10×10^3	50	200
A	50	5×10^3	10	500
A	50	5×10^3	20	250
A	50	10×10^3	40	250
A	50	14×10^3	80	175
A	100	14×10^3	20	700
A	200	20×10^3	20	1000

Table III. Study of the state of valence of the dissolved iridium. Electrolyte 6*N* HCl; temperature 20°C; frequency of the superimposed alternating current 50 cps; electrode "A"

i_{dc}, μa	i_{ac}, ma	ϵ, mv	Ir^{IV}, %	Ir^{III}, %
200	200	400	97	3
200	50	380	100	0
200	10	760	—	—
100	50	320	63	37
50	50	270	44	56
10	50	280	50	50

frequency of the superimposed a.c. Two electrodes ("A" and "B") of different behavior have been used, as indicated in Table II.

State of Valence of Dissolved Iridium

The anodic solution of Ir proceeds with formation of Ir^{III} and Ir^{IV} and in some cases with simultaneous evolution of Cl_2. To confirm this point a series of experiments was carried out with different values of the direct and alternating current densities. The amount of Ir^{IV} in the solution was determined by analysis.

The analytical method, due to Woo and Yost (15), consists of an iodometric determination of Ir^{IV}. It requires a previous elimination of the Cl_2 and a complete absence in the solution of other ions of the platinum group. The total amount of dissolved Ir was measured as before by the loss of weight of the electrode. The amount of Ir^{III} is determined by subtracting from this total the amount of Ir^{IV} obtained by titration.

Table III summarizes the results of a series of experiments that confirm the assumption made before. A 6*N* HCl solution was used as electrolyte, the temperature was 20°C, and a 50 cps a.c. was superimposed. The proportion of Ir^{III} diminishes as the potential becomes more positive, and it is enhanced as i_{dc} decreases and/or as the ratio i_{ac}/i_{dc} increases.

Discussion

Mechanism of the Anodic Solution Process

The influence of the adsorption of electrolytes on the anodic dissolution kinetics of metals and amalgams has been shown in the last few years. In a recent paper by Kolotyrkin (13) a general theory on these effects is described.

According to these ideas, in the presence of halide ions X^-, and for a given value of *p*H, the anodic dissolution of a metal can be expressed as

$$i = k[X^-]^\gamma \exp\left(\frac{\beta F}{RT}\epsilon\right) \qquad [2]$$

where $[X^-]$ is the concentration of the halide ions, ϵ is the electrode potential, and γ and β are parameters whose physical meaning it is not necessary to discuss here.

The activating effect of X^- ions on the anodic corrosion of some metals can be explained as a sequence of successive reactions. The halide ions are specifically adsorbed at the metal surface, frequently even at rather negative potentials.

$$Me + \delta X^- \rightarrow (Me \ldots X_\gamma)^{-\gamma} \qquad [3]$$

There is a correlation between the ability of the anions to be adsorbed on a metal and their capacity to form complexes with its cations. The formation of these complexes at the metal surface leads to a weakening of the bonds between the surface atoms and the lattice of the metal. On the other hand, the formation of complexes implies also a variation in the energetic state of the reacting particles at the side of the solution (16).

Consequently, on a basis of elemental considerations, it can be expected that a specific adsorption of this nature leads to a diminution of the free energy barrier which controls the rate of the anodic dissolution process of the metal. When the potential becomes more positive, the metallic ions will pass to the solution forming complexes with the halide ions. This second step is represented by the reaction

$$(Me \ldots X_\gamma)^{-\gamma} \rightarrow [Me\,X_\gamma]^{n-\gamma} + ne \qquad [4]$$

In the case of Ir, its anodic corrosion in HCl solutions is due to the possibility of forming the complex ions $IrCl_6^{\equiv}$ and $IrCl_6^{=}$. The formation of Ir^{IV} generally prevails, but the proportion of Ir^{III} increases at lower potentials. This process of anodic corrosion is more irreversible in the case of Ir than with Pt, and this irreversibility leads to a passivation of the former metal, even at very low current densities.

The adequacy of an expression like [2] for the first part of the polarization curves, which corresponds to the anodic corrosion of the metal, implies a linear relationship between log i and the potential ϵ, for a given concentration of HCl. However, the fact that Ir passivates at such low current densities, even for high HCl concentrations and temperatures, makes it difficult to confirm this logarithmic relationship. In the case of Pt an expression of this type was found (17).

Mechanism of the Passivation Process

In the simplest case, *i.e.*, if only the interaction of water molecules with the surface atoms of the metal were considered, the anodic dissolution of the metal could be represented as follows.

$$Me + m\,H_2O \rightarrow \underset{I}{\rightarrow} Me(H_2O)_m + ze \qquad [5]$$

$$Me\ldots(H_2O)_m \underset{II}{\rightarrow} (Me \ldots O_\gamma) + 2\gamma H^+ + 2\gamma e \qquad [6]$$

If process I requires a high overpotential, as is the case with Ir, process II takes place and the metal becomes passive.

In acid solutions containing Cl^- ions, the anodic corrosion of Ir proceeds according to reactions [3] and [4] through the formation of the complexes of Ir^{III} and Ir^{IV}. However, process [4] requires a high overpotential and the electrode passivates easily, with evolution of O_2 and Cl_2.

In a general way, adsorbed anions participate in the process of anodic corrosion of a metal (18); for example, in the case of Pt the adsorption of anions and oxygen hinder each other (19, 20). If the po-

tential is not very positive, the halide ions can remove the chemisorbed oxygen (21, 22), this being an important factor in accounting for the depassivating effect of the halide ions (13). This competition depends, among other factors, on the concentration of halide ions and the acidity of the electrolyte, although with Pt it has not yet been established if at rather positive potentials chemisorbed oxygen displaces the halide ions from the electrode surface.

It has been found that passivity sets in on platinum metals at a potential where the anodic formation of a chemisorbed layer of oxygen occurs (22). This phenomenon of surface oxidation has been studied recently on Ir electrodes by Knorr, Breiter *et al.*, (23-27). On the other hand, it was found by Ershler (28, 29) that a small surface coverage by chemisorbed oxygen reduces considerably the rate of anodic dissolution of Pt in HCl solutions. The study of the charging and discharging curves with Ir electrodes, using HCl solutions as electrolyte, shows that the effect of the surface oxidation, leading to the passivation of the electrode, is apparent at low HCl concentrations. As this concentration increases the oxidized surface fraction for a given value of potential decreases, tending to be minimum when concentrated solutions of HCl are used as electrolytes (30).

On this line of ideas, concerning the passivation of the platinum metals by chemisorbed oxygen, arises the question of how the dissolution process of the metal is actually hindered. On this point Krasillshikov (31) has proposed the idea that such a chemisorption diminishes the number of electrons at metal surface (Tam quantum states of the surface). The activation energy of the dissolution process increases linearly with this diminution of electrons in the surface states, and consequently the dissolution rate diminishes exponentially with the chemisorption of oxygen.

Effect of Alternating Currents

It follows from the above that with Ir electrodes the anodic corrosion process is hindered by the chemisorption of oxygen at their surfaces. In this case the effects of the alternating currents are due mainly to the successive passivating and depassivating processes taking place during each cycle of the a.c. In this sense, for cases where the electrochemical behavior is determined by the oxidation state of the electrode surface, it has been established that this oxidation increases as the polarizing i_{dc} increases and decreases when an alternating current i_{ac} is superimposed.

During a cycle of a.c. the potential changes from that corresponding to the formation of Cl_2 on a passive electrode to that of evolution of H_2. The corrosion of Ir can occur between those extreme processes, mainly in the presence of Cl^- ions. However, the fact that in this case the dissolution of the metal requires a higher overpotential than in the case of Pt determines a higher resistance of Ir to corrosion, even when this is due to superimposition of an a.c.

Manuscript received Jan. 8, 1963; revised manuscript received April 25, 1963.

Any discussion of this paper will appear in a Discussion Section to be published in the June 1964 JOURNAL.

REFERENCES

1. E. Ogawa, *J. Chem. Soc. Japan*, **50**, 123 (1929).
2. "Gmelins Handbuch der anorganischen Chemie" (Iridium), 94, Verlag Chemie, Berlin (1939).
3. H. Terrey and H. C. Baker, *J. Chem. Soc.*, **1930**, 2593.
4. S. C. Woo, *J. Am. Chem. Soc.*, **53**, 469 (1931).
5. W. M. Latimer, "The Oxidation States of the Elements and Their Potentials in Aqueous Solutions," 205,206 New York (1938).
6. E. Newbery, *J. Chem. Soc.*, **119**, 477 (1921).
7. V. G. Tronev, *Doklady Akad. Nauk SSSR*, **15**, 555 (1937).
8. J. Llopis and A. Sancho, *This Journal*, **108**, 720 (1961).
9. E. Raub and G. Buss, *Z. Elektrochem.*, **46**, 195 (1940).
10. R. Luther and F. I. Brislee, *Z. phys. Chem.*, **45**, 217 (1903).
11. F. T. Chang and H. Wick, *ibid.* **A172**, 448 (1935).
12. A. Rius, J. Llopis, and I. M. Tordesillas, *Anal. real soc. españ. fís. y quím.*, **48B**, 23 (1952).
13. Ya. M. Kolotyrkin, *This Journal*, **108**, 209 (1961).
14. J. Llopis and F. Colom, *Anal. real soc. españ. fís. y quím.*, **51B**, 11 (1955).
15. S. C. Woo and D. M. Yost, *J. Am. Chem. Soc.*, **53**, 884 (1931).
16. Ya. M. Kolotyrkin, *Izv. Kazan Akad. Nauk. SSSR*, (Khim. Ser.) **5**, 9 (1959).
17. A. Rius, J. Llopis, and I. M. Tordesillas, *Anal. real soc. españ. fís. y quím.*, **48B**, 639 (1952).
18. K. Schwabe, K. Wagner, and Ch. Weismantel, *Z. phys. Chem.*, **206**, 309 (1957).
19. N. H. Balashova, *ibid.*, **207**, 340 (1957).
20. N. H. Balashova, *Electrochim. Acta*, **7**, 559 (1962).
21. N. H. Balashova, *Zhur. Fiz. Khim.*, **32**, 2266 (1958).
22. J. Giner, *Z. Elektrochem.*, **63**, 386 (1959).
23. M. Breiter, C. A. Knorr, and W. Völkl, *ibid.*, **59**, 631 (1955).
24. M. Breiter, K. Hoffmann, and C. A. Knorr, *ibid.*, **61**, 1168 (1957).
25. K. Frauke, C. A. Knorr, and M. Breiter, *ibid.*, **63**, 226 (1959).
26. F. G. Will and C. A. Knorr, *ibid.*, **64**, 270 (1960).
27. W. Böld and M. Breiter, *Electrochim, Acta*, **5**, 169 (1961).
28. B. V. Ershler, *Zhur. Fiz. Khim.*, **14**, 357 (1940).
29. B. V. Ershler, *ibid.*, **18**, 131 (1944).
30. J. Llopis and L. Jorge, *Electrochim. Acta*, to be published.
31. A. I. Krasillshikov, *Zhur. Fiz. Khim.*, **35**, 2524 (1961).

Oxidation of Molybdenum 550° to 1700°C

E. A. Gulbransen, K. F. Andrew, and F. A. Brassart

Physical Chemistry Department, Westinghouse Electric Corporation, Pittsburgh, Pennsylvania

ABSTRACT

Weight change and oxygen consumption measurements were used to study the oxidation of molybdenum from 550° to 1704°C for pressures of 5 to 76 Torr. For temperatures of 550°-700°C two processes occurred simultaneously, oxide scale formation and molybdenum trioxide volatility. Above 800°C at pressures up to 76 Torr molybdenum trioxide volatilized as fast as it formed. At 900°C and 76 Torr using 1.2 cm^2 samples the primary chemical reaction gave a rate of about 10^{18} at. molybdenum/cm^2/sec. Above this temperature for 1.2 cm^2 specimens the reaction was limited by gaseous diffusion of oxygen. Little change was found in the rate of oxidation to 1615°C. Pressure had only a small effect on the rate of reaction for these reaction conditions. However, in the chemically controlled region pressure had an important effect on the rate of oxidation. To extend the temperature region where the primary chemical reaction was rate controlling, samples of small area were used. A sample having a total area of 0.12 cm^2 gave a reaction rate of 8 x 10^{18} at./cm^2/sec at 1410°C. For these very fast reactions, appreciable temperature rises occurred, and the actual sample temperature had to be estimated. A log K *vs.* $1/T$ plot of the primary chemical reaction data gave an energy of activation of 19.7 kcal/mole. Reaction conditions where gaseous diffusion processes are rate controlling were determined. All of the earlier studies were made for these reaction conditions. The activated state theory of surface reactions was applied to the primary chemical reaction in the oxidation of molybdenum. A mechanism of mobile adsorption was found to be the primary chemical reaction. This adsorption process probably occurred on a surface already covered with a layer of adsorbed oxygen atoms since MoO_3 was volatilized.

Molybdenum and its alloys have many useful high-temperature mechanical properties. However, its resistance to oxidation is poor. Although many studies have been made, the mechanisms of oxidation have not been established.

The reaction of molybdenum with oxygen is complex and involves several types of oxidation processes. The oxide volatilizes partially at 600° and 76 Torr oxygen pressure and melts at 795°C. Except for oxidation below 450°C, experimental results are somewhat conflicting. Results appear to depend on the individual reaction system, specimen size, and gas flow. In most studies, the primary chemical reaction has been masked by transport processes of oxygen through volatilized molybdenum trioxide to the metal surface.

The present work has several objectives: (*a*) to determine the nature of the oxidation mechanism between 550° and 800°C where both oxide films are formed and where oxide volatility occurs; (*b*) to separate experimentally the primary chemical reaction from the diffusion region of reaction; (*c*) to determine the nature of the primary chemical reaction; (*d*) to define the transition between chemical control and diffusion control of oxidation; and (*e*) to determine the factors affecting oxidation in the diffusion controlled region of the reaction.

Several reviews of earlier work have been made (1-3). Gulbransen and Wysong (1) and Gorbounova and Arslambékov (4) found adherent oxide films formed when the metal was oxidized below 400°C. The data were fitted to the parabolic rate law, and an energy of activation of about 36.0 kcal/mole was calculated. Above 400°C deviations from the parabolic rate law occurred. Volatilization of molybdenum trioxide occurred at 475°C under vacuum conditions (1).

Between 500° and 1000°C several studies have been made (5-7). Simnad and Spilners (5) found the data could be fitted by the parabolic rate law at 500°C and by the linear rate law above 500°C. Vaporization of MoO_3 occurred at 650°C in 1 atm of oxygen. Catastrophic oxidation took place at 725°C.

Jones, Mosher, Speiser, and Spretnak (2) oxidized molybdenum in still air between 701° and 983°C. At 938°C $(MoO_3)_3$ volatilized as fast as it was formed. The actual rate was less than that found at 816°C. Lustman (6) also found a nearly constant rate of oxidation above 795°C. Peterson and Fassel (7) studied the oxidation reaction as a function of pressure. The rate of oxidation followed a nearly linear rate law at all temperatures and pressures indicating a nonprotective oxide was formed. MoO_3 was the only oxide observed in the scale.

Three studies have been made for conditions above 1000°C. Semmel (8) studied the reaction in free flowing air between 982° and 1371°C. A linear rate law was found. The reaction was insensitive to the flow rate and to the reaction temperature. Bartlett and Williams (9) studied the reaction in air between 760° and 1204°C using a flow system. The rate of oxidation increased slowly with temperature and flow rate.

Modisette and Schryer (10) investigated the role of gaseous diffusion in the oxidation of molybdenum

for the temperature range of 1063°-1626°C and for flow velocities of 36-195 cm/sec. The oxidation rate increased slowly with temperature, flow velocity, and diffusivity.

Since the volatility of solid and liquid MoO_3 is directly involved in the oxidation of molybdenum, we have reviewed the literature and presented a study of the vapor pressure of solid MoO_3 (11) in a separate paper.

Experimental

Since oxygen reacts with molybdenum under certain conditions to form both oxide scale and a volatile molybdenum trioxide, it is essential to follow the reaction by both oxygen consumption and weight change methods (12, 13). A gold plated Invar beam balance enclosed in the reaction system was used (14). The balance had a period of less than 2 sec and a sensitivity of 66 μg/0.001 cm deflection at 7.25 cm using a sample weight of 0.872g. The oxygen pressure was controlled by leaking in oxygen from a calibrated volume to maintain constant pressure in the reaction system. The pressure in the auxiliary volume was accurately read and the oxygen used was calculated. An 8-mil platinum wire was used to support the specimen in the hot zone of the furnace.

The furnace tubes were high-purity vacuum-tight alumina. Temperatures up to 1600°C were obtained by use of a special Kanthal-Super furnace (12, 15). Calibrated Pt—Pt+10% Rh thermocouples were used to measure the temperature inside the furnace tube and adjacent to the samples.

Specimens were machined from pure molybdenum rod and polished through 4/0 polishing paper. Samples were then cleaned in petroleum ether and alcohol.

The standard specimen was a cylinder with hemispherical ends, 0.316 cm in diameter, 1.5 cm long, weighing about 0.872g and having a surface area of about 1.220 cm^2. Smaller specimens having surface areas of about 0.610, 0.304, and 0.12 cm^2 were used to determine the effect of surface area on the reaction rate. A spectroscopic analysis showed the following impurities in parts per million: Cu 10, Cr 45, Mn 5, Al 40, Fe 200, Ca 10, Ni 70, Sn 10, Mg 5, Si 50, and B 1. The elements Ba, Sr, Pb, Co, Ag, Cd, V, Nb, and Ti were not detected.

Thermochemical Calculations

Thermochemical data have been determined for the two oxides MoO_2 and MoO_3 (16). A recent review of the vapor pressure data has been made (11). Table I shows five reactions of interest in this work. Values of the standard free energies of reaction and equilibrium pressures are listed.

The equilibrium data show that both MoO_3 and MoO_2 are stable to direct decomposition. MoO_3 can dissociate to MoO_2 in high vacuum above its melting point, 795°C (11). MoO_3 is reduced at all temperatures by Mo to form MoO_2. MoO_3 has an appreciable vapor pressure above 500°C (1, 11). At 600°C the vapor pressure of $(MoO_3)_n$ is 6.08 x 10^{-6} atm, while at 700°C the vapor pressure is 4.69 x 10^{-4} (11). At the mp of 795°C the vapor pressure is 0.1 atm (11); the bp is 1155°C.

Table I. Thermochemical data; oxides of molybdenum

1. $Mo(s) + O_2(g) \rightleftarrows MoO_2(s)$ $\Delta F°$ kcal/mole
2. $Mo(s) + 3/2\ O_2(g) \rightleftarrows 2MoO_3(s,l)$ $\Delta F°$ kcal/mole
3. $2MoO_3(s,l) \rightleftarrows 2MoO_2(s,l) + O_2(g)$ P_{O_2} atm
4. $3MoO_2(s) \rightleftarrows 2MoO_3(s,l) + Mo(s)$ $\Delta F°$ kcal
5. $n\ MoO_3(s) \rightleftarrows (MoO_3)_n(g)$ at 600°C, $n = 3.24$

Temp, °K	1 $\Delta F°$, kcal/mole	2 $\Delta F°$, kcal/mole	3 P_{O_2}, atm	4 $\Delta F°$, kcal
298	—127.45	—159.7	5.38×10^{-48}	+63.0
400	—122.9	—153.45	4.44×10^{-34}	+61.85
600	—114.1	—141.35	1.42×10^{-20}	+59.6
800	—105.55	—129.6	7.23×10^{-14}	+57.45
1000	—97.15	—118.1	7.10×10^{-10}	+55.3
1200	—88.95	—112.7	9.51×10^{-8}	+50.4
1400	—80.95	—108.25	1.56×10^{-6}	+43.7
1600	—73.05	—99.55	—	—
1800	—65.35	—	—	—
2000	—58.0	—	—	—

Results

The experimental work was planned around three objectives. First, it was essential to determine the nature of the reaction between 550° and 1500°C. Second, the kinetics of oxidation was studied over a wide pressure and temperature range to determine the primary chemical reaction. Third, it was essential to determine the transition zone between chemical and transport controlled oxidation. Here it was necessary to introduce the surface area as a new variable.

Oxidation processes at 600°C and 76 Torr pressure.—Curves A and B of Fig. 1 show oxygen consumption and weight change measurements. Both measurements are in units of milligrams per square centimeter. The oxygen consumption data show a nearly linear rate law after an initial period of fast reaction. The weight change data show a slow initial reaction followed by a period of increasing rate of reaction.

Equation [1] relates the oxygen used to the formation of solid, liquid, or gaseous molybdenum trioxide.

$$Mo(s) + 3/2\ O_2 \rightleftarrows MoO_3(s,l,g) \qquad [1]$$

The weight change given by the balance readings indicates the difference between the oxide formed and molybdenum lost as volatilized oxide according to the equation

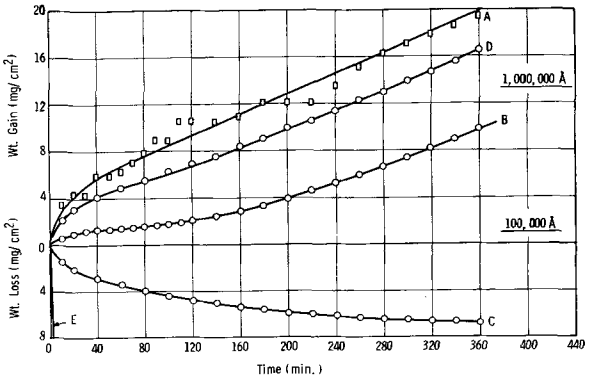

Fig. 1. Oxidation of molybdenum, 600°C, 76 Torr: curve A, O_2 consumed; B, weight change; C, molybdenum lost; D, O_2 in oxide scale; E, volatility of MoO_3 in vacuum.

$$3MoO_3(s,l) \rightleftarrows (MoO_3)_3(g) \quad [2]$$

From Eq. [1] and [2] and the laws of stoichiometry we set down the following equations:

$$W_O = xW_O + (1-x)W_O \quad [3]$$

$$W_B = xW_O - W_{Mo} \quad [4]$$

Here W_O is the weight of oxygen consumed, W_B the weight change of the balance, W_{Mo} the weight of molybdenum volatilized, and x and $1-x$ the fraction of oxygen used to form oxide scale and volatile oxide following Eq. [1] and [2]. From the atom weights of Mo and O in MoO_3 we have

$$W_{Mo} = 2(1-x)W_O \quad [5]$$

Subtracting [4] and [3] and substituting [5] we have

$$W_O - W_B = 3(1-x) \quad [6]$$

$$W_{Mo} = 2/3\ (W_O - W_B) \quad [7]$$

Using Eq. [7] we calculate the weight of molybdenum lost. This is shown as curve C of Fig. 1. Using Eq. [4] and [7] we calculate the weight of oxygen forming oxide scale. This is shown in Curve D of Fig. 1. Curve E is the volatility curve for molybdenum trioxide in vacuum (11).

To relate curve D to oxide thickness in angstroms a factor of 66,500 is used (1). Thickness markers are placed on Fig. 1. This evaluation assumes MoO_3 as the oxide, a surface roughness ratio of unity and the oxide is not porous or full of cracks.

The total weight of molybdenum reacting can be calculated from curve A using the stoichiometric ratio of $Mo/\frac{3}{2}O_2$ of 2.00 while the surface recession in angstroms can be calculated from curve A using the stoichiometric ratio of 2.00 and the density of 10.2. A factor of 19,600 is evaluated.

Figure 1 shows several interesting facts for the 600°C, 76 Torr reaction conditions. Both oxide scale formation and oxide volatility occur. Eighty per cent of the oxygen used goes to oxide scale formation. A nearly linear rate of oxidation is observed. Loss of molybdenum occurs very rapidly during the initial period of reaction. This rate decreases as oxidation proceeds. A study of Fig. 1 shows the inadequacy of using weight change methods alone to describe the reaction in this temperature range.

Figure 2A and B shows photographs of the unreacted and oxidized specimens. The oxidized specimen shows a poor quality oxide scale was formed.

Oxidation studies at 650° and 700°C at 76 Torr oxygen pressure show similar phenomena to that observed at 600°C. The percentage of oxygen forming oxide decreases as the temperature is raised. At 700°C only 30% of the oxygen used forms oxide scale. At 800°C all of the oxygen used forms volatile molybdenum trioxide. At 795°C the vapor pressure of molybdenum trioxide is 11.7 Torr.

Oxidation processes at 1000°C and 76 Torr pressure.—At 1000°C all of the oxygen used forms volatile molybdenum trioxide. Curves A and B of Fig. 3 show the oxygen consumption and weight change

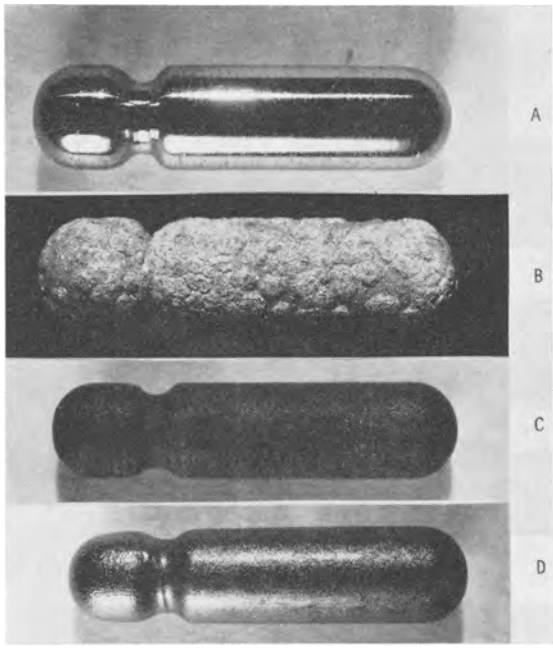

Fig. 2. Photographs of molybdenum specimens: A, unreacted; B, 600°C; 76 Torr, 420 min; C, 1200°C, 76 Torr, 8½ min; D, 1600°C, 76 Torr, 7 min. Magnification, approximately 5X.

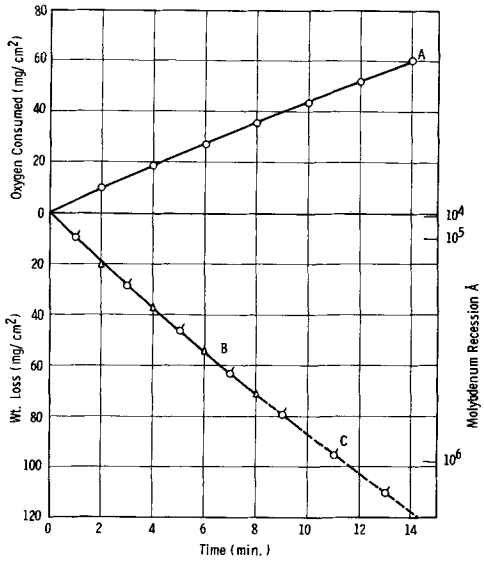

Fig. 3. Oxidation of molybdenum, 1000°C (1047), 76 Torr: A, oxygen consumption; B, weight loss △—△; C, calculated from A, O - - O.

measurements. Nearly linear rates of reaction are found. The small decrease in slopes can be related to the decrease in specimen area during reaction.

Using the stoichiometric ratio of $Mo/\frac{3}{2}O_2$, curve A can be used to calculate the expected weight loss of molydenum assuming all oxygen forms volatile molybdenum trioxide. Good agreement is found which confirms the nature of the reaction. The recession of molybdenum can be calculated using the relation 1 mg/cm² = 19,600Å.

Many units are used in presenting reaction rates. We prefer the unit of atoms of Mo per cm² per sec. The initial rate of reaction of the 1000°C oxidation

at 76 Torr is 1.08 x 10^{18} at./cm²/sec. This is a very rapid reaction.

For these high rates of reaction it is essential to have a more realistic value for the surface temperature. The surface temperature during reaction can be estimated. We assume (*a*) that radiation is the major source of loss of heat, (*b*) the emissivity of the surface and walls is 0.5 and the heat source is the sum of the heat of formation of MoO_3(s,l) (16) and the heat of vaporization of the oxide (11). For the conditions of the present experiment at 1000°C, we estimate a sample surface temperature of 1047°C. In all of our tables and figures we list both the furnace temperature and the calculated temperature.

We conclude that between 600° and 800°C both oxide scale formation and oxide volatility occur. Above 800°C only volatile molybdenum trioxide is formed. We will next present the effect of temperature on the oxidation reaction.

Effect of temperature.—Figures 4 and 5 and Table II show the effect of temperature on the oxidation of molybdenum at 76 Torr oxygen pressure. The weight change in mg/cm² is plotted against time in minutes. Figure 4 shows experiments for the temperature range 550°-1000°C. Oxide scale formation

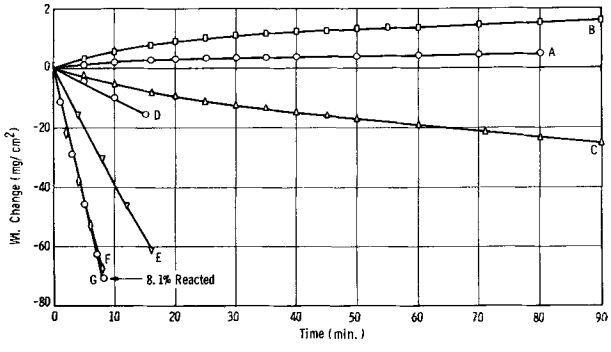

Fig. 4. Effect of temperature on oxidation of molybdenum 550°-1000°C, 76 Torr O_2: A, 550°C; B, 600°C; C, 650°C; D, 700°C; E, 800°C (829); F, 900°C (957); G, 1000°C (1047).

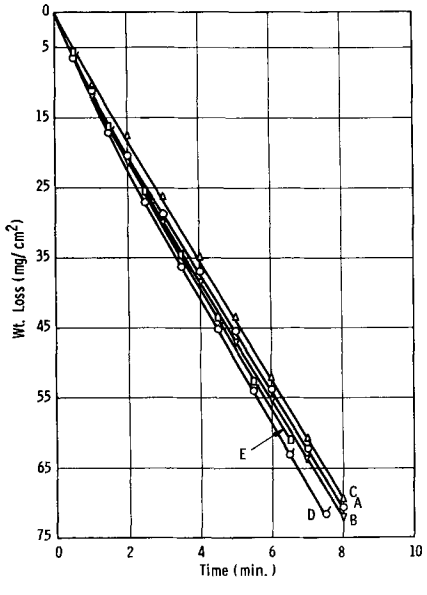

Fig. 5. Effect of temperature on oxidation of molybdenum, 1000°-1600°C, 76 Torr O_2: A, 1000°C (1047); B, 1100°C (1135); C, 1200°C (1227); D, 1400°C (1418); E, 1600°C (1614).

Table II. Effect of temperature on initial rates of oxidation
P = 76 Torr; surface area = 1.215 cm²

Furnace temp, °C	Calculated temp, °C	dn/dt, atoms/cm²/sec	log dn/dt
700	—	1.493 × 10^{17}	17.17
800	829	4.30 × 10^{17}	17.63
900	957	1.124 × 10^{18}	18.05
1000	1047	1.080 × 10^{18}	18.03
1100	1135	1.099 × 10^{18}	18.04
1200	1227	1.049 × 10^{18}	18.02
1400	1418	1.280 × 10^{18}	18.11
1600	1614	1.112 × 10^{18}	18.05

and oxide evaporation occur during oxidation at temperatures between 550° and 700°C. Table II shows the initial rates of total reaction calculated on the basis of oxygen used in the reaction and the calculated reaction temperatures. The rates of reaction are given in units of atoms of molybdenum reacting per cm² per sec. Figure 4 illustrates the transition in oxidation phenomena between oxide scale formation and oxide evaporation.

Figure 5 shows the results for the temperature range of 1000° to 1600°C. The calculated temperatures are given in brackets. The curves show a small decrease in rate of reaction due to the change in surface area. On the basis of these results alone we would conclude that temperature has little effect on the rate of oxidation. This would be predicted for oxidation reactions where the rate of reaction is limited by gaseous diffusion of oxygen (10). We will show later that these conclusions are incomplete.

Figure 2C and D show photographs of the oxidized specimens after reaction at 1200° and 1600°C.

Effect of pressure.—Table III shows a summary of the data using the 1.215 cm² area samples. The effect of pressure at three temperatures was studied. The initial rates of reaction are tabulated in mg/cm²/sec and in atoms of molybdenum reacting/cm²/sec. At 800°C the effect of pressure on the rate of reaction is large and the rate follows the 1.5 power of the pressure. While at 1600°C the effect of pressure is small and follows the 0.14 power of the pressure.

Classification of oxidation phenomena.—A classification scheme of the phenomena found during the oxidation of molybdenum is shown in Table IV.

Table III. Effect of pressure on initial rates of oxidation
surface area = 1.215 cm²

Furnace temp, °C	Calculated temp, °C	Pressure, Torr	dw/dt, mg/cm²/sec	dn/dt, at./cm²/sec	log dn/dt
800	829	76	0.0684	4.30 × 10^{17}	17.63
800	808	38	0.0180	1.13 × 10^{17}	17.05
800	803	19	0.00733	4.60 × 10^{16}	16.66
800	801	5	0.00327	2.05 × 10^{16}	16.31
1200	1227	76	0.167	1.049 × 10^{18}	18.02
1200	1224	38	0.150	9.42 × 10^{17}	17.97
1200	1219	19	0.116	7.28 × 10^{17}	17.86
1200	1207	5	0.044	2.76 × 10^{17}	17.44
1600	1614	76	0.177	1.112 × 10^{18}	18.05
1600	1612	38	0.156	9.80 × 10^{17}	17.99
1600	1611	19	0.141	8.85 × 10^{17}	17.95
1600	1610	5	0.127	7.98 × 10^{17}	17.90

Table IV. Classification scheme; oxidation of molybdenum

Class	Reaction conditions	Oxidation phenomena	Rate-controlling process
1	Below 450°C	Adherent oxide films or scales form.	Wagner type diffusion of metal or oxygen through oxide.
2	500°-700°C	Oxide scales form also oxide volatilizes, low pressure favors volatility of oxide.	Oxide scales not protective. Probably chemical-type processes on metal interface.
3	801°C to transition temperature	Liquid oxide can form, volatilizes as soon as oxide forms.	Chemical processes on metal interface
4	Above transition temperature	Oxide volatilizes as fast as it forms.	Transport of oxygen to metal interface. Turbulence in gas phase important.

Four temperature regions are proposed. Pressure can change the temperature limits of the several regions with low pressures favoring volatility of the oxide. Three types of rate-controlling processes are given in Table IV: (*a*) A Wagner type of diffusion of metal or oxygen through the oxide; here an energy of activation of 36 kcal has been found (1, 4). (*b*) In the intermediate temperature range where oxides are not present a surface type of chemical reaction is rate controlling. These processes are adsorption, chemical reaction, and desorption. (*c*) Above a certain transition temperature a complex type of transport process is found. Simple diffusion of oxygen through a stagnant layer as proposed by Modisette and Schryer (10) is not adequate. This type of reaction will be discussed further in a later section.

Study of the transition between chemical control and transport control of oxidation of molybdenum.—Gas flow methods have been used to study the mechanism of oxidation (8-10). Unfortunately, the gas flow was not varied over a sufficient range to change the mechanism of reaction. If transport of oxygen to the surface and reaction products away from the surface to a cold zone is controlling the rate of oxidation, the important factor is the total amount of reaction occurring per second. The rate of oxidation per unit area, dn/dt, can be varied by changing the surface area over a wide range.

Table V. Effect of sample area on initial rates of oxidation
$P = 76$ Torr

Furnace temp, °C	Calculated temp, °C	Sample area, cm²	dn/dt, at./cm²/sec	log dn/dt
1000	1047	1.215	1.08×10^{18}	18.03
1000	1124	0.604	2.22×10^{18}	18.35
1000	1159	0.304	3.49×10^{18}	18.54
1200	1227	1.213	1.05×10^{18}	18.02
1200	1262	0.605	2.46×10^{18}	18.39
1200	1296	0.301	3.90×10^{18}	18.59
1200	1410	0.121	7.92×10^{18}	18.90
1400	1418	1.216	1.28×10^{18}	18.11
1400	1451	0.605	2.95×10^{18}	18.47
1400	1509	0.304	6.59×10^{18}	18.82
1600	1614	1.218	1.11×10^{18}	18.05
1600	1634	0.608	2.73×10^{18}	18.44
1600	1660	0.303	4.94×10^{18}	18.69
1650	1704	0.302	4.84×10^{18}	18.68

Figure 5 and Table II show the rate of oxidation to be nearly independent of temperature above 800°C using a sample area of 1.2 cm². Samples were next prepared having areas of about 0.605, 0.304, and 0.12 cm². Table V shows a summary of the data. The rate of oxidation is nearly inversely proportional to the area, *i.e.*,

$$dn/dt \cdot A = K(p,T) \qquad [8]$$

Here dn/dt is the rate of oxidation, A is the sample area, and $K(p,T)$ is a constant depending on the pressure and temperature of oxygen.

Figure 6 shows a log dn/dt *vs.* $1/T$ plot of the data at 76 Torr pressure. The calculated surface temperatures are used. Part of the data fall along a straight line AB. We interpret oxidations along AB as being under chemical control with an activation energy of 19.7 kcal/mole. Rate constants falling to the right of the line AB we interpret as being in the region of transport process control. Smaller values for dn/dt at a given temperature are found.

The rate data for the several sample areas lie on curves C, D, and E. Point F is that for a 0.1 cm² sample area. A reaction rate of nearly 10^{19} at./cm²/sec was found. Since this point lies on the line AB we state that the reaction is limited by chemical control.

The reaction rate of 10^{19} at./cm²/sec is the highest reaction we have seen recorded for an oxidation re-

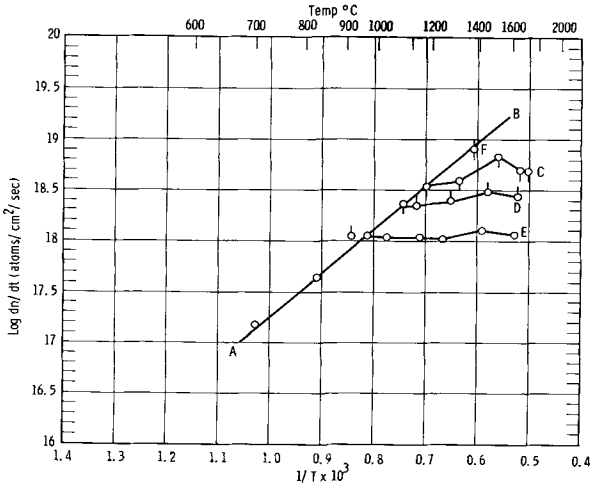

Fig. 6. Log dn/dt *vs.* $1/T$, oxidation of molybdenum, 600°-1704°C, 76 Torr O_2: line A-B, chemical control ($\triangle H_{AB} = 19.7$ kcal/mole); area to right of A-B, diffusion control; areas of samples: C, 0.304 cm²; D, 0.604 cm²; E, 1.215 cm²; F, 0.12 cm².

action. Using a flow system with air at 1371°C Semmel (8) found a reaction rate of 1.98 x 10^{18} at./cm^2/sec. Modisette and Schryer (10) using a flow system and a 21.5% oxygen-helium mixture found a value of 1.09 x 10^{18} at./cm^2/sec. Both values lie close to line E of Fig. 6.

Figure 6 also shows evidence that a maximum is reached in the oxidation reaction at a temperature of 1400°-1500°C. Above this temperature the rate decreases. This effect may be related to the dissociation of the $(MoO_3)_n$ complex.

We conclude that variation of sample area makes possible a study of the transition in mechanisms of oxidation of molybdenum. Also very high reaction rates can be measured using small specimens.

Capability of a reaction system for measurement of fast reactions.—The results of the previous section have shown that transport processes limit the measurement of fast reactions in a reaction system, where volatile reaction products are formed. We define the capability as the maximum observed total reaction rate in units of atoms per second. Equation [8] gives the relationship between capability $K(p,T)$, dn/dt and surface area. For molybdenum oxidized at 76 Torr pressure and 1400°C, our system had a value of $K(p,T)$ of 1.55 to 2.0 x 10^{18} at. of molybdenum reacting per second. Larger values would be found at higher pressures. Temperature also has an effect as can be determined from the data in Table V. If a sample area of 0.1 cm^2 is used, a reaction rate of about 2 x 10^{19} at./cm^2/sec could be measured. A capability of 2 x 10^{18} at./sec allows one to measure the primary chemical reaction over a temperature range of 600°-1400°C.

Calculations on Semmel's (8) and Modisette's and Schryer's (10) system using a flow system and oxygen at about 150 Torr and 1371°C showed capability constants, $K(p,T)$, of 7.2 x 10^{18} and 6.2 x 10^{18}, respectively. Modisette and Schryer used samples of about 6.3 cm^2. It was not possible to estimate the values for Semmel's system.

Considering the pressure factor in the capability number we conclude that the use of gas flow by Modisette and Schryer (10) increased the system capability by a factor of 2 to 3.

Discussion

Summary of kinetic work.—In the previous sections the primary chemical reaction of pure molybdenum was studied using cylindrical specimens of several sizes. Above 800°C and at pressures up to 76 Torr the oxygen consumption and weight change curves showed no evidence of an initial pickup of oxygen to form an oxide film. All of the oxygen reacted to form volatile molybdenum trioxide. The observed weight loss and oxygen consumption curves were nearly linear with time. For a short period of reaction the data could be fitted to the equation $W = At$, where W is the weight loss in mg/cm^2, A is a constant, and t is the time. For longer periods of time, surface area changes occurred which decreased the rate of weight loss.

The initial rate constant dn/dt could be fitted to an exponential equation $dn/dt = Ze^{-\Delta H/RT}$. A heat of activation of 19.7 kcal/mole was found, while the frequency factor has the units of atoms of molybdenum reacting per cm^2 per sec.

The effect of pressure on the oxidation of molybdenum was studied at 800°, 1200°, and 1600°C. At 800°C the results followed the 1.5 power of the pressure while at 1600°C the results followed the 0.14 power of the pressure.

Providing small samples were used, the reaction of molybdenum with oxygen could be studied in the chemical controlled region to 1400°C.

Mechanism of reaction.—A surface reaction may be separated into at least five distinct processes, the slowest of which determines the rate of reaction: (*a*) transport of oxygen gas to the surface; (*b*) chemisorption of the oxygen; (c) chemical reaction at the surface; (*d*) desorption; (*e*) transport of reaction products away. Process (*a*) and (*e*) are transport processes and, if rate controlling, the temperature dependence of the reaction rate may vary as $T^{1/2}$ where T is the absolute temperature. Chemical reactions (*b*), (c), and (*d*) usually have high activation energies and are usually distinguished by this factor from diffusion processes.

Predictions of absolute reaction rate theory.—This theory assumes the formation of a complex between the reacting gas and the surface, the chemisorbed gas and the surface, and the chemisorbed reaction product and the surface. The rate of any one of these surface reactions may be considered in terms of reaction complexes passing from one region of configuration space to another. According to Eyring and co-workers (17, 18), the number of reaction complexes crossing the energy barrier is given by the product of the number of complexes in the initial state at time t, the probability that the reaction complex crosses the barrier in any one attempt, and the frequency with which the complexes cross the energy barrier.

Adsorption.—Eyring and co-workers (17, 18) have given the following expressions for the several types of adsorption processes.

1. Immobile adsorption, adsorption of molecule, rate-determining

$$v_1 = C_g C_s \frac{\sigma}{\sigma\ddagger} \frac{h^4}{8\pi^2 I (2\pi mkT)^{3/2}} e^{-\epsilon_1/kT} \quad [9]$$

2. Immobile adsorption, dissociation is rate-controlling process

$$v_1 = C_g^{1/2} C_s kT \frac{h^{3/2}}{(2\pi mkT)^{3/4} (8\pi^2 IkT)^{1/2}} e^{-\epsilon_1/kT} \quad [10]$$

3. Mobile adsorption

$$v_1 = C_g \frac{kT}{h} \frac{h}{(2\pi mkT)^{1/2}} e^{-\epsilon_1/kT} \quad [11]$$

4. Mobile adsorption, no activation energy

$$v_1 = \frac{p}{(2\pi mkT)^{1/2}} \quad [12]$$

Here the symbols have the following definitions: C_g, concentration of molecules per cubic centimeter in the gas phase; C_s, concentration of adsorption sites per square centimeter; σ, symmetry number of the gas molecule; $\sigma\ddagger$, symmetry number of the acti-

vated complex; h, Planck's constant; I, moment of inertia; k, Boltzmann's constant; m, mass of molecule; T, absolute temperature; and ϵ, energy of activation.

Rate of desorption.—Desorption from an immobile layer may be regarded as involving an activated state in which a molecule attached to an adsorbing center acquires the necessary configuration and activation energy to permit it to escape from the surface. In the following rate expressions given by Eyring and co-workers (17, 18) both activated complexes and adsorbed molecules are considered immobile.

$$v_2 = C_a \frac{kT}{h} e^{-\epsilon_2/kT} \qquad [13]$$

Here v_2 represents the rate of desorption in molecules per square centimeter per second, C_a represents the concentration of adsorbed molecules per square centimeter, and ϵ_2 is the energy of activation.

Chemical reaction.—Let us assume the reaction involves one molecule of oxygen and the active surface site, S. This active site is assumed to consist of a site on which oxygen has been previously adsorbed. The activated complex consists of an adsorbed molecule which has acquired the appropriate amount of energy and the proper configuration.

First-Order Kinetics.—Consider the case when the active sites already have an oxygen atom attached to the molybdenum atoms. If the surface is covered with Mo atoms having one oxygen atom adsorbed per molybdenum atom, the concentration of sites C_s is nearly constant and identical with the number of sites for a bare surface. Under these conditions the rate of the reaction is proportional to the concentration of the molecules in the gas phase C_g and the reaction is of first order.

The rate expression is

$$v = C_g C_s \frac{\sigma}{\sigma\ddagger} \times \frac{\frac{1}{2}sh^4}{8\pi^2 I (2\pi mkT)^{3/2}} e^{-\epsilon_3/kT} \qquad [14]$$

where s is the total number of possible sites adjacent to any reaction center, σ and $\sigma\ddagger$ are the symmetry numbers of the molecules of reactant and activated complex, respectively, and ϵ_3 is the energy of activation for this type of reaction.

Zero-Order Kinetics.—Let us assume the active site already has an oxygen atom attached and that these sites are covered by adsorbed molecules to an appreciable extent. The value of C_s varies with the pressure of the gas. If the surface is nearly covered by adsorbed molecules, C_s is nearly constant, and the rate of reaction is nearly independent of the pressure. The following equation treats the reaction from the viewpoint of the adsorbed molecules, with the surface activation energy being the difference in energy between the activated state and the adsorbed reactants, or $\epsilon_0 + \epsilon$

$$v_2 = C_a \frac{kT}{h} e^{-E/RT} \qquad [15]$$

where E is the observed activation energy, ϵ is the heat of adsorption, and ϵ_0 is the difference in energy between the activated state and the initial gaseous reactant.

Comparison of theory with experiment.—Table VI shows a comparison of the rates of the various processes at 900°C and 76 Torr oxygen pressure as predicted from the absolute reaction rate theory with the experimentally determined rate of reaction. The calculations were based on an experimental heat of activation of 19.7 kcal/mole. The fact that several processes occur with a theoretical rate slower than the experimental value means the heat of activation was too high for this particular process. The comparison was significant only for those processes which give reasonable agreement.

The only feasible mechanism according to Table VI is mobile adsorption of oxygen molecules on a molybdenum surface already covered with a surface layer of oxygen.

Table VI. Correlation of predictions of absolute reaction rate theory with experimental rate of oxidation of molybdenum at 900°C, 76 Torr pressure of oxygen

Mechanism	Equation	Rate dn/dt, $t = 0$, atoms of Mo, cm² sec: Theory	Experiment
Immobile adsorption, adsorption of molecule, rate controlling	$v = C_g C_s \frac{\sigma}{\sigma\ddagger} \frac{h^4}{8\pi^2 I (2\pi mkT)^{3/2}} e^{-\epsilon/kT}$	1.054×10^{12}	1.08×10^{18}
Immobile adsorption, dissociation, rate controlling	$v = C_g^{1/2} C_s \frac{kT}{h} \frac{h^{3/2}}{(2\pi mkT)^{3/4}(1.5)^{1/2}(8\pi^2 IkT)^{1/2}} e^{-\epsilon/kT}$	9.54×10^{15}	1.08×10^{18}
Mobile adsorption	$v = C_g \frac{kT}{h} \frac{h}{(2\pi mkT)^{1/2}} e^{-\epsilon/kT}$	3.6×10^{17}	1.08×10^{18}
Mobile adsorption, no activation energy	$v = \frac{p}{(2\pi mkT)^{1/2}}$	1.38×10^{22}	1.08×10^{18}
Desorption	$v = C_a \frac{kT}{h} e^{-\epsilon_1/kT}$	1.29×10^{24}	1.08×10^{18}
Chemical reaction, first order kinetics	$v = C_g C_s \frac{\sigma}{\sigma\ddagger} \frac{\frac{1}{2}sh^4}{8\pi^2 I (2\pi mkT)^{3/2}} e^{-\epsilon/kT}$	4.216×10^{12}	1.08×10^{18}
Chemical reaction, zero order kinetics	$v = C_a \frac{kT}{h} e^{-\epsilon/kT}$	1.29×10^{24}	1.08×10^{18}

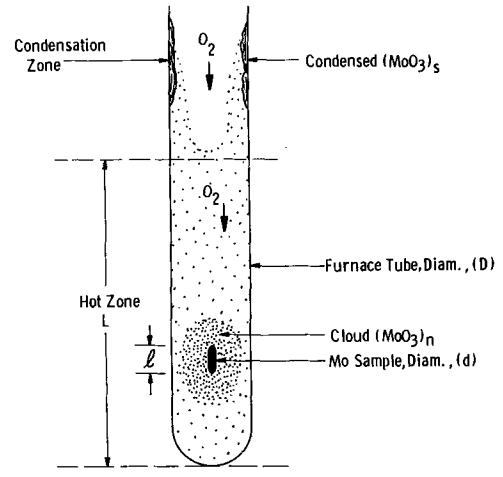

Fig. 7. Schematic picture of reaction system

In Table VI we assumed that all of the gas was involved in mobile adsorption with an activation energy of 19.7 kcal/mole. Actually we postulate a monolayer of oxygen is preliminarily adsorbed with a much lower activation energy. The reaction mechanism is

$$Mo \cdot Mo{-}O + O_2 \rightarrow Mo \cdot Mo{<}^{O}_{O}$$

mobile adsorption of O_2 on Mo—O monolayer

This complex undergoes chemical reaction

$$Mo \cdot Mo{<}^{O}_{O} \rightarrow Mo{-}MoO_3$$

and desorption to form gaseous molybdenum trioxide

$$n\,Mo{-}MoO_3 \rightleftarrows n\,Mo + (MoO_3)_n$$

The experimental value in Table VI of 1.08×10^{18} at. Mo/cm^2/sec should be reduced by 1/3 to 7.2×10^{17} to account for oxygen preliminarily adsorbed in the monolayer. The agreement of theory and experiment is within a factor of 2.

Interpretation of transport phenomena.—Equation [8] relates the observed rate of oxidation to specimen area. Values of dn/dt are always less than the values for chemical control $(dn/dt)_C$. A schematic drawing of the reaction system is shown in Fig. 7. During reaction the specimen is surrounded by a zone of $(MoO_3)_3$ vapor. From the equation

$$3Mo + 9/2\ O_2 \rightarrow (MoO_3)_3(g)$$

a change in volume of 3½ is observed. Oxygen gas is accelerated toward the sample due to the volume change and to the reaction. Localized heating occurs and large amounts of MoO_3 are formed. We visualize the reaction zone as very turbulent. As long as the ratios of L/l and D/d (see Fig. 7) are large, oxygen diffuses to the inner turbulent reaction zone. Under reaction conditions the transport of oxygen to the reaction zone equals the total rate of reaction. The relation of area A and dn/dt breaks down as dn/dt approaches $(dn/dt)_C$. In the turbulent region and for large values of L/l and D/d, the specimen reacts with all oxygen in the reaction zone.

Manuscript received Jan. 28, 1963; revised manuscript received April 1, 1963. This paper has been scheduled for presentation at the New York Meeting, Sept. 29-Oct. 3, 1963.

Any discussion of this paper will appear in a Discussion Section to be published in the June 1964 JOURNAL.

REFERENCES

1. E. A. Gulbransen and W. S. Wysong, *Trans. AIME (Metals Div.)*, **175**, 628 (1948).
2. E. S. Jones, J. F. Mosher, R. Speiser, and J. W. Spretnak, *Corrosion*, **14**, 2t (1958).
3. J. W. Semmel, Jr., "Refractory Metals and Alloys," Vol. 11, p. 119-68, Interscience Publishers, New York (1961).
4. K. M. Gorbounova and V. A. Arslambekov, 6e Reunion De La Societe De Chimie Physique, May 29-June 1, 1956, Paris, France.
5. M. Simnad and A. Spilners, *Trans. AIME*, **203**, 1011 (1955).
6. B. Lustman, *Met. Prog.*, **57**, 629 (1950).
7. R. C. Peterson and W. M. Fassel, Jr., Technical Report VI, Army Ordnance Contract DA-04-495 ORD-237, Sept. 1, 1954.
8. J. W. Semmel, Jr., "High Temperature Materials," p. 510-19, J. Wiley & Sons, Inc., New York (1959).
9. E. S. Bartlett and D. N. Williams, *Trans. AIME*, **212**, 280 (1958).
10. J. L. Modisette and D. R. Schryer, NASA-TN-D-222, March 1960.
11. E. A. Gulbransen, K. F. Andrew, and F. A. Brassart, *This Journal*, **110**, 242 (1963).
12. E. A. Gulbransen, K. F. Andrew, and F. A. Brassart, Kinetics of Oxidation of Pure Tungsten, 1150°C-1615°C, Westinghouse Research Lab. Scientific Paper 62-123-121-Pl, April 2, 1962.
13. E. A. Gulbransen, K. F. Andrew, and F. A. Brassart, *This Journal* **110**, 476 (1963).
14. E. A. Gulbransen and K. F. Andrew, "Vacuum Microbalance Techniques," Vol. 2, p. 129, Plenum Press, Inc., New York (1962).
15. E. A. Gulbransen, K. F. Andrew and F. A. Brassart, "Vacuum Microbalance Techniques," Vol. III, Plenum Press Inc., New York 1963, To be published.
16. E. G. King, W. W. Weller, and A. U. Christensen, U. S. Dept. of Int., Bureau of Mines, RI, 5664 (1960).
17. S. Glasstone, K. J. Laidler, and H. Eyring, "Theory of Rate Processes," McGraw-Hill Book Co., New York (1941).
18. K. J. Laidler, S. Glasstone, and H. Eyring, *J. Chem. Phys.*, **8**, 659 (1940).

Oxidation of Zirconium and Zirconium Alloys in Liquid Sodium

T. L. Mackay

Atomics International, A Division of North American Aviation, Inc., Canoga Park, California

ABSTRACT

The oxidation of zirconium and several zirconium alloys was investigated in the temperature range 400°-635°C in a static liquid sodium system with oxygen concentration approximately 10 ppm. A transition from a parabolic to a linear rate of oxidation was observed in the temperature region 400°-500°C for all of the zirconium alloys except Zircaloy-2. Above 500°C the transition was not observed, and a protective film continued to form. Using the parabolic rate equation to describe the kinetics of oxidation, activation energies of 52.9 ± 0.5 kcal/mole for unalloyed Zr and 45.3 ± 1.5 kcal/mole for zirconium alloys were found.

The use of zirconium and its alloys for nuclear applications would be benefited by a better understanding of corrosion behavior. From a kinetic standpoint, the important process in corrosion is the transfer of oxygen through the zirconium dioxide layer and into the metal. The broad objective of this investigation was to study the transfer processes involved in the oxidation of zirconium and zirconium alloys in contact with liquid sodium.

The reaction of zirconium with oxygen has been studied by several investigators (1-7). There has been disagreement as to whether the cubic or parabolic rate law best describes the reaction kinetics. It has been shown that pressure has little or no effect on the reaction of zirconium with oxygen (1, 4, 5, 10). Additives to the zirconium alloys have usually been found to increase oxidation rates (8-10).

The oxidation of zirconium in liquid sodium has been studied by Eichelberger (11), who found parabolic rates which were independent of the oxygen concentration in the sodium, above 20 ppm.

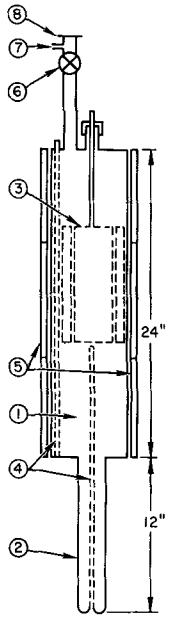

Fig. 1. Static sodium corrosion apparatus: 1, sodium pot; 2, cold trap; 3. specimen rack; 4, thermocouple wells; 5, heaters; 6, gate valve; 7, gas inlet; 8, "O" ring flange.

A disadvantage of zirconium and its alloys is their low strengths at temperatures above 900°F. Several zirconium alloys developed at Atomics International containing aluminum, tin, and molybdenum showed significantly higher strengths at elevated temperatures, and a preliminary investigation indicated that their corrosion resistance in sodium at 1000°F compared favorably with that of unalloyed zirconium. A more detailed study of the oxidation behavior of these alloys in sodium has been the subject of this investigation.

Experimental Procedure

Apparatus.—Liquid sodium exposure tests of zirconium alloys were conducted in a static, natural convection system. A schematic representation is shown in Fig. 1. The sodium pot consisted of a 5-in. stainless steel tube 2 ft long with welded end-plates. The sodium was heated by several Hevi-duty Nichrome resistance heating units; the temperature was controlled to ±2°C by a Wheelco controller. Tank argon was used as the cover gas.

The nominal oxygen concentration was maintained at 10 ppm by a cold trap operated at 150°C or at the selected temperatures at the bottom of the sodium pot. To ensure that the oxygen in the sodium would not be depleted, 5g of sodium peroxide was added to the sodium, and the system was held at 500°C for one week so that equilibrium conditions might be established.

The specimen rack was mounted so that it could be rotated and several specimen holders could be loaded into the apparatus at the same time. The specimen rack could also be adjusted up or down so that all of the specimens would be in a constant temperature zone.

Materials.—Zirconium and zirconium alloy test specimens were made from strips of metal ⅛ in. thick. These alloys had been prepared by double arc-melting, hot-rolling, and vacuum annealing. Table I shows nominal composition of alloys used in this study. A more complete description of alloy preparation and chemical composition has been reported elsewhere (12).

Table I. Zirconium base alloys, nominal composition

Alloy	Aluminum	Tin	(wt %) Molybdenum	Zirconium
1	—	—	—	100
2	1.5	—	—	98.5
3	1.5	1.5	—	97.0
4	1.5	3.0	—	95.5
5	1.5	—	1.5	97.0
6	1.5	1.0	1.0	96.5
7	3.0	—	—	97.0
8	3.0	1.5	—	95.5
9	—	1.5	(0.12 Fe, 0.1 Cr, 0.05 Ni)	Zircaloy-2

Sample preparation.—Parallelepiped specimens approximately 1 by ½ by ⅛ in. were used in this study. The surfaces were mechanically polished by machine sanding and wet polishing, starting with 180-grit and finishing with 600-grit silicon carbide paper. The specimens were then chemically polished for 2 min in an etching solution consisting of 15 parts hydrofluoric acid (48%), 80 parts nitric acid (conc.), and 80 parts water. The chemical polish removed 1-2 mils from each surface.

Prior to exposure, each specimen was carefully weighed to ±0.03 mg. Dimensions were measured to the nearest 0.001 in. in order to calculate surface areas. The specimens were degreased in n-heptane and rinsed in methyl alcohol and acetone. Then these specimens were suspended in liquid sodium for predetermined periods of time, after which they were washed in butyl alcohol, rinsed in methyl alcohol and acetone, dried, and reweighed.

Results and Discussion

Several experiments using duplicate samples were conducted to determine the effect of oxygen concentration on the rate of oxidation of Zircaloy-2 in liquid sodium. Oxygen concentrations were obtained from literature values (13) of the oxygen solubility in liquid sodium at the cold trap temperatures. Since no analytical determinations were made to determine actual oxygen determinations, these literature values are referred to as nominal concentrations. The exposure time was 145 hr at 595°C for all of these experiments. Weight gains are shown in Table II.

It would appear from these results that the rate of oxidation of Zircaloy-2 in liquid sodium is independent of the nominal oxygen concentration above

Table II. Effect of oxygen concentration on oxidation of Zircaloy-2 in liquid sodium at 595°C (145 hr exposure)

Cold trap temp, °C	Calculated oxygen concentrations, ppm	ΔW, weight gain, mg/cm²
160	10	0.45
160	10	0.45
340	200	0.45
340	200	0.50
418	500	0.46
418	500	0.45
340	200	0.52*
340	200	0.46*

* 5g of Na_2O_2 were added to the system.

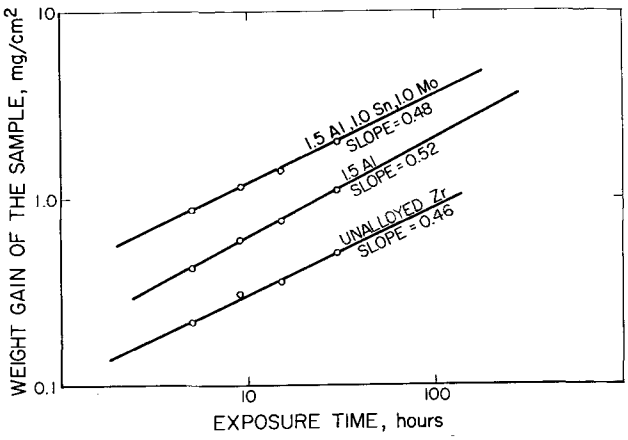

Fig. 2. Isothermal weight gain of zirconium and zirconium alloys exposed to liquid sodium. Sample temperature 635°C, cold trap temperature 15°C.

10 ppm, which is in agreement with Eichelberger's finding for pure zirconium (although see below the comparison with rates in gaseous oxygen).

The weight gain can be expresed by the general rate equation

$$\Delta W^n = kt \qquad [1]$$

where W is the weight gain, mg/cm², k is the rate constant, $(mg/cm^2)^n hr^{-1}$, n is a constant, and t is the time in hr.

A log-log plot of ΔW against t should give a straight line whose slope is $1/n$.

Samples of pure zirconium and various alloys were exposed in the sodium pot with a cold trap temperature of 150°C for a series of time intervals.

Typical plots are shown in Fig. 2, each point representing a different sample. Table III shows values of the slopes for all the alloys at 635°, 595°, and 555°C. In this temperature range the slope varied between 0.4 and 0.5, and in the majority of cases the slope was close to 0.5, indicating agreement with the parabolic equation. Table IV shows the parabolic rate constants, and it may be seen that except for Zircaloy-2, the alloys oxidize at substantially higher rates than does pure zirconium. The parabolic rate constants for pure zirconium are about one-tenth as large as those reported in the literature (1-10) for the oxidation of zirconium in oxygen, air, steam or carbon dioxide, a result which is an indication of either a different mechanism or of a much lower oxygen activity in liquid sodium compared with these gases. It may be that the finding of no dependence on oxygen concentration in sodium, men-

Table III. Slopes of log (weight gain) vs. log (time)

Alloy	Composition of zirconium base alloys	Temperatures 555°C	595°C	635°C
1	Unalloyed Zr	0.45	0.45	0.46
2	1.5 Al	0.41	0.46	0.52
3	1.5 Al, 1.5 Sn	0.50	0.50	0.50
4	1.5 Al, 3.0 Sn	0.42	0.46	0.50
5	1.5 Al, 1.5 Mo	0.41	0.45	0.49
6	1.5 Al, 1.0 Sn, 1.0 Mo	0.45	0.45	0.48
7	3.0 Al	0.41	0.48	0.46
8	3.0 Al, 1.5 Sn	0.40	0.45	0.50
9	Zircaloy-2	0.41	0.46	0.50

Table IV. Parabolic rate constants for the reaction of zirconium with oxygen in liquid sodium

Alloy	Composition of Zr-base alloys	Rate constant, k, $\times 10^3$ in (mg cm^{-2})^2 hr^{-1} at: 635°C	595°C	555°C	502°C	457°C	408°C
1	Unalloyed Zr	8.45	1.65	0.40	0.0505	0.00566	0.00050
2	1.5 Al	29	7.1	1.77	—	—	—
3	1.5 Al, 1.5 Sn	57.5	14.4	4.9	—	—	—
4	1.5 Al, 3.0 Sn	78.5	24.3	6.18	—	—	—
5	1.5 Al, 1.5 Mo	73.0	25.6	6.4	—	—	—
6	1.5 Al, 1.0 Sn, 1.0 Mo	168	44	13.4	—	—	—
7	3.0 Al	16.9	4.5	1.04	—	—	—
8	3.0 Al, 1.5 Sn	57.5	17.1	4.9	—	—	—
9	Zircaloy-2	8.1	2.0	0.42	0.0593	0.0183	0.0040

tioned above, is because the sensitivity of measurement was insufficient to detect the small differences that may have actually occurred over the relatively narrow range of oxygen activity of the experiments.

The rate constants for zirconium and Zircaloy-2 were determined over the temperature range 408°-635°C, and plots of the logarithm of the parabolic rate constants *vs.* $1/T$°K for zirconium and Zircaloy-2 are shown in Fig. 3 and 4, respectively. The activation energies as determined from the slope of the least squares straight line are 52.9 ± 0.5 kcal/mole for zirconium and 45.3 ± 1.5 kcal/mole for Zircaloy-2. The activation energies for the other alloys as determined from the rate constants listed in Table IV were approximately the same as for Zircaloy-2 (see Fig. 4). The activation energy obtained by Eichelberger (11) for the oxidation of chemically polished specimens of zirconium in liquid sodium containing 10 ppm of oxygen was 37.4 ± 9.5 kcal/mole, which was obtained by the least square method applied to his data (see Fig. 3).

When the exponent, n, of Eq. [1] is less than unity, the oxidation rate decreases with time and is described as protective. Tables III and IV show that this was the case during the initial period for all

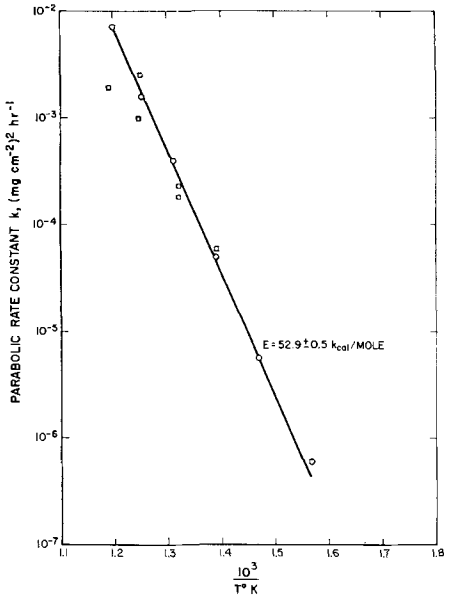

Fig. 3. Variation of reaction rate constant of zirconium in liquid sodium with temperature. □, Data of Eichelberger (11); ○, data of present work. Note: the solid line is drawn on the basis of the data of the present work.

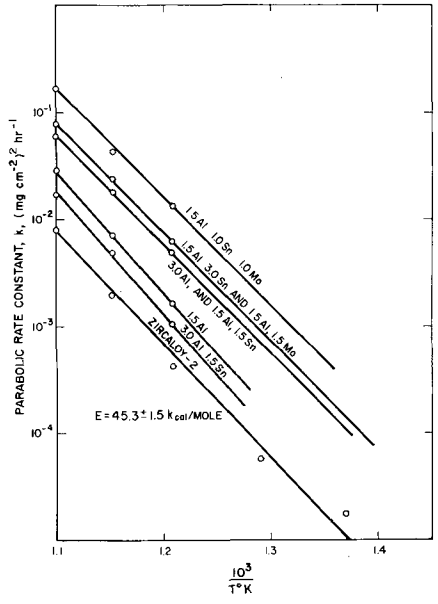

Fig. 4. Variation of reaction rate constant of zirconium alloys in liquid sodium with temperature.

the alloys and temperatures investigated. However, at temperatures of 500°C and below, transitions from protective rates to linear rates occurred for several alloys after oxidation periods of 25-200 hr, depending on temperature and alloy composition. The period of exposure at which rate transitions occurred increased for all the alloys as the temperature was lowered. The linear rates found are shown in Table V.

This type of rate transition is not new to the investigators of metal oxidation, who observed such transitions in the oxidation of zirconium alloys exposed to high-temperature steam (14) and to air

Table V. Linear rate constants of zirconium alloys after rate transition

Alloy	Composition of zirconium base alloys	Rate constant, k', $\times 10^2$ in (mg cm^{-2}) hr^{-1} at: 502°C	457°C	446°C	417°C
2	1.5 Al	2.24	—	1.33	—
3	1.5 Al, 1.5 Sn	9.0	6.2	3.83	1.86
4	1.5 Al, 3.0 Sn	5.6	—	3.93	2.17
5	1.5 Al, 1.5 Mo	5.6	—	3.93	1.12
6	1.5 Al, 1.0 Mo, 1.0 Sn	8.6	5.1	2.4	1.86
7	3 Al	—	0.453	—	—
8	3 Al, 1.5 Sn	—	0.915	—	—

(6, 15) as well as oxygen (6, 8-10). However, a unique aspect of the present work is that the rate transitions were not observed for temperatures above 500°C.

Several mechanisms have been proposed to account for the rate transition from parabolic (or cubic) to linear rate. The volume ratio of zirconium dioxide to zirconium is approximately 1.5; therefore, the oxide grows under compressive strain. Electron diffraction studies (10, 16-18) on thin films have shown evidences that the zirconium oxide film is cubic or tetragonal. On this basis it has been proposed that the kinetic deviation is due to a phase transformation (16, 18) from the cubic or tetragonal to the monoclinic structure of oxide and that the phase transformation is caused by compressive strains in the oxide film. However, x-ray studies of thicker films formed on zirconium alloys above 555°C in this work have confirmed the presence of oriented monoclinic ZrO_2. Notwithstanding the existence of the monoclinic phase, the rate transition did not occur in these thick films. Thus this phase transformation does not appear to be an important cause for the rate transition.

Cox (19) observed that in 300°C steam the oxidation mechanism of zirconium metal was not the same as that of Zircaloy-2. For zirconium metal, he found that a thin oxide film was formed initially. The film exhibited interference colors that became dark, first along the grain boundaries, and then over the whole oxide film in an inhomogeneous manner as the film thickened. He also observed that the rate transition occurred when the film started to become dark along the grain boundaries. In the case of Zircaloy-2, however, Cox observed a different phenomenon. The initially formed thin oxide film became uniformly dark throughout the oxide film rather than along the grain boundaries, and no rate transition occurred when the film started to become dark. However, when the film became fairly thick (and, of course, completely dark), the rate transition occurred.

Cox proposed the following mechanisms to explain the different oxidation behavior of the above two materials. In the case of zirconium metal oxidation, oxygen diffused along preferred paths created by grain boundaries and formed a much thicker film at or near the grain boundary than that on the central zone of the grain. Because the film was thick near the grain boundary, it cracked, thereby destroying the protective value of the oxide film, and the relation between weight gain and oxidation time became linear. In the case of Zircaloy-2, Cox assumed that, in addition to grain boundary paths, the existing intermetallic compounds throughout a grain also provided preferred paths to oxygen, and that these paths allowed the oxide film to grow fairly uniformly over the Zircaloy-2 surface. As the film grew thicker the rate transition, according to Cox, was initiated by a progressive increase of the number of fresh crystal nuclei.

None of the above mechanisms would predict that the rate transition could be suppressed by raising the temperature.

In the present work, the rate transition did not occur at any particular thickness of the oxide layer. The film thickness at the rate transition was found to be in the range of approximately 1-5μ. The thickness of the oxide film at the rate transition increased as the temperature was raised. This leads us to the conclusion that, in addition to the mechanisms proposed by various workers, the rate transition is controlled by a temperature-dependent parameter which relieves the compressive strain in the oxide film as the temperature is raised. It has been mentioned previously that the rate transition did not occur when the temperature was raised above 500°C. It is postulated that at high temperatures the compressive strain of the film due to large volume ratio of ZrO_2 to Zr is relieved by plastic flow while the film is growing. Thus, above 500°C the oxide film formed is sufficiently free from strain and no rate transition is observed. This may be the most important factor responsible for suppressing such rate transition.

Another possible contributing factor is that the oxygen deficiency in the oxide layer increases with increase in temperature. From the phase diagram for the zirconium-oxygen system by Domagala and McPherson (20), the O/Zr ratio varied from 1.95 to 1.93 in the temperature range 400°-500°C. This should cause a contraction of the lattice parameter in the oxide phase, relieving some of the compressive strains.

The compressive strain in oxide films above 500°C for zirconium alloys is probably relieved by a combination of these two processes: (*a*) increase in the plasticity of the metal as the temperature is raised, and (*b*) a contraction of the lattice parameter due to a decrease in oxygen in the oxide with increasing temperature.

Zirconium and Zircaloy-2 did not show any rate transition in this study. This might be attributed to the fact that considerably thinner films were formed on these materials. The thicknesses of oxide films on zirconium which had been oxidized in liquid sodium were estimated in the following manner.

$$\text{Thickness in Å} = \frac{(W_{\text{total}} - W_D) M_{ZrO_2} \times 10^5}{\rho_{ZrO_2} M_{O_2}} \quad [3]$$

where W_{total} is the total oxygen weight gain in mg/cm^2, W_D is the oxygen diffused from the oxide layer to the base metal in mg/cm^2 [calculated from Pemsler's diffusion data (21)], ρ_{ZrO_2} is the density of zirconium dioxide in g/cm^3, M_{ZrO_2} is the molecular weight of zirconium dioxide, and M_{O_2} is the molecular weight oxygen. The thicknesses calculated by Eq. [3] were compared with those determined by an interference color method (22, 23) standardized during the present work. At 408°C and an exposure time of 500 hr the thickness for zirconium was 540Å calculated by Eq. [3] compared with a range of 630-450Å by the interference color method. The thicknesses of oxide films calculated by Eq. [3] thus appeared to be approximately correct.

For zirconium and Zircaloy-2 the amount of oxygen diffusing into the metal (W_D in Eq. [3]) was approximately one-half of the total weight gain.

For these thinner films the compressive strain was relieved sufficiently to prevent oxide cracking, and hence, a rate transition was not observed for zirconium and Zircaloy-2 in the temperature range of this study.

Conclusion

The kinetics of oxidation in static (natural convection) liquid sodium for zirconium and zirconium alloys, was determined in the temperature region 400°-635°C.

The rate of oxidation for Zircaloy-2 was found to be independent of the nominal oxygen concentration above 10 ppm. In this investigation the rate of oxidation is best described by a parabolic rate law. A plot of the parabolic rate constants *vs.* $1/T$°K gave activation energies of 52.9 ± 0.5 kcal/mole for zirconium and 45.3 ± 1.5 kcal/mole for Zircaloy-2. The activation energies of the other alloys studied in the temperature region 635°-555°C were approximately the same as for Zircaloy-2.

In the temperature region 400°-500°C, most of the zirconium alloys exhibited rate transitions (from parabolic to linear); however, this transition was not observed for unalloyed zirconium or Zircaloy-2. The film thickness at which the transition occurred varied from 1 to 5μ, and the thickness of the oxide film at the rate transition increased as the temperature was raised for all of the alloys exhibiting a transition. Up to 500°C, the rate transition for zirconium alloys was controlled by a temperature-dependent parameter which relieved the compressive strain in the oxide film as the temperature was raised. Above 500°C, the rate transition was suppressed and a protective film continued to form. For zirconium and Zircaloy-2 the oxide films were considerably thinner, and the compressive stress was relieved sufficiently to prevent oxide cracking over the entire temperature range of this study.

Acknowledgments

The author wishes to thank Dr. Guy Ervin, Jr. for his valuable suggestions. Work on this paper was performed under the auspices of the U. S. Atomic Energy Commission Contract AT(11-1)-GEN-8.

Manuscript received Jan. 9, 1963; revised manuscript received April 15, 1963. This was presented at the New York Meeting, Sept. 29-Oct. 3, 1963.

Any discussion of this paper will appear in a Discussion Section to be published in the June 1964 JOURNAL.

REFERENCES

1. E. A. Gulbransen and K. F. Andrew, *J. Metals*, **1**, 515 (1949).
2. J. Belle and M. W. Mallett, *This Journal*, **101**, 339 (1954).
3. E. A. Gulbransen and K. F. Andrew, *J. Metals*, **9**, 394 (1957).
4. D. Cubicciotti, *J. Am. Chem. Soc.*, **72**, 4138 (1950).
5. M. W. Fassell, USAEC, NP-4246 (1952).
6. D. J. Garibotti, H. M. Green, and W. M. Baldwin, USAEC, AECU-3013 (1955).
7. P. Kofstad, *Acta Chem. Scand.*, **12**, 701 (1958).
8. M. W. Mallett and W. M. Albrecht, *This Journal*, **102**, 407 (1955).
9. E. A. Gulbransen and K. F. Andrew, *Trans. AIME*, **212**, 281 (1958).
10. H. A. Porte, J. G. Schnizlein, R. C. Vogel, and D. F. Fischer, *This Journal*, **107**, 506 (1960).
11. R. L. Eichelberger, to be published, J. Nuclear Materials.
12. R. K. Wagner and H. E. Kline, NAA-SR-3481 (1959).
13. O. N. Salmon and T. J. Cashman, USAEC, KAPL-1653 (1956).
14. B. Lustman and F. Kerze, "Metallurgy of Zirconium," McGraw-Hill Co., Inc., New York (1955).
15. L. F. Kendall, R. B. Wheeler, and S. H. Bush, *Nucl. Sci. and Eng.*, **3**, 171 (1958).
16. C. M. Schwartz, D. A. Vaughan, and G. C. Cocks, USAEC, BMI-793 (1952).
17. I. S. Kerr, Thesis, Imperial College, London (1955).
18. I. I. Korobkov, D. V. Ignatov, A. I. Evstyukhin, and V. S. Emel'yanov, *2nd Intern. Atomic Energy Conf.*, Geneva (1958) Paper P/2054.
19. B. Cox, *This Journal*, **108**, 24 (1961).
20. R. F. Domagala and D. J. McPherson, *J. Metals*, **6**, 238 (1954).
21. J. P. Pemsler, *This Journal*, **105**, 315 (1958).
22. J. J. Polling and A. Charlesby, *Proc. Phys. Soc.*, **67B**, 201 (1954).
23. R. D. Misch, *Acta Met.*, **5**, 179 (1957).

Corrosion of Carbon Steel by High-Temperature Liquid Mercury

A. H. Fleitman, A. J. Romano, and C. J. Klamut

Brookhaven National Laboratory, Upton, New York

ABSTRACT

All liquid Hg thermal convection loop experiments have been carried out at a temperature differential of 400°F (1000°-600°F) for 8000 hr in carbon steel systems. The effect of Ti and Zr additions in inhibiting corrosion was evaluated. Results of these experiments show that no adherent deposits were formed on the loop walls, and the presence of Zr and Ti resulted in less over-all corrosion. A comparison of the amount of iron residue filtered from the loops indicates Zr is a more effective inhibitor than Ti.

A study of corrosion in liquid metals intended for use as heat transfer and working fluids in compact reactor turbogenerator systems is in progress. One phase involves the study of the corrosive behavior of liquid Hg from 600°-1000°F. This study is concerned primarily with the long term corrosion resistance of low-carbon steels to mercury at high-temperature differentials and the relative merits of very small titanium or zirconium additions to mercury in retarding corrosive attack.

Background.—Data on the solubility in Hg of the elements in engineering alloys are incomplete. In-

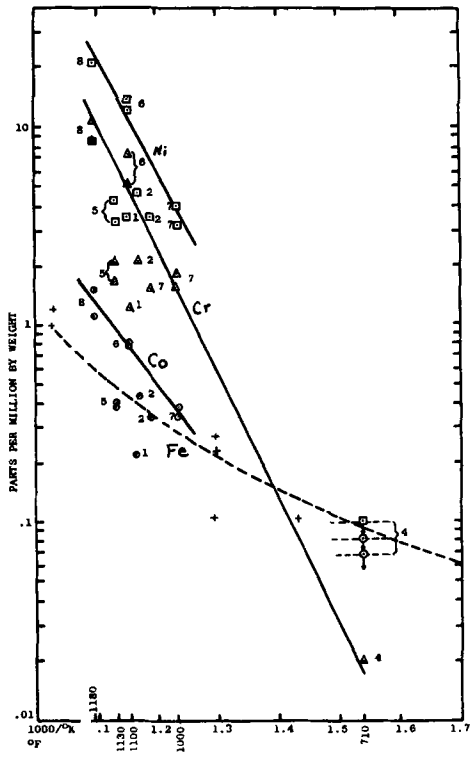

Fig. 1. Concentration of Co, Cr, and Ni in Hg after contacting with Haynes 25 alloy for 16 hr. The Hg-Fe liquidus after Norton, Epstein, and Marshall is shown for comparison. Figures refer to run numbers. Dotted circle, Co; dotted square, Ni; dotted triangle, Cr; two lines with an arrow facing down, detected but less than quantitative limit, plus sign, data on Fe in Hg (Marshall and Epstein); broken lines, curve derived from this data.

vestigation of the Hg-Fe liquidus by Marshall, Epstein, and Norton (1) showed that at 1000°F the iron solubility in Hg was 0.30 ppm. An experiment performed by Parkman (2) consisted of contacting Haynes 25 alloy (52% Co, 20% Cr, 15% W, 10% Ni, 3% Fe) with Hg at 1000°, 1100°, and 1180°F for 16 hr. Analysis of unfiltered samples showed that the Ni concentration was the greatest followed by Cr and Co with Fe and W undetectable. Figure 1 illustrates the results of this experiment and the Fe-Hg liquidus as determined by Marshall, Epstein, and Norton (1). Since the solubility of Fe is lower than that of the elements shown, a greater corrosion resistance might be anticipated in low-carbon or low-alloy steels than in other common engineering alloys.

Steels, especially low-alloy, or plain carbon steels, have been shown to have improved resistance to Hg attack when small quantities of certain metal additives are present in the Hg. Previous work on mercury systems by Nerad and his associates (3) at the General Electric Company had indicated that Zr, Cr, Ni, Al, and especially Ti were effective inhibitors of Hg attack on ferrous alloys. They also found that the addition of Mg or Na was beneficial. These latter two additives act as wetting agents by reducing oxides on steel surfaces and reacting with free oxygen, nitrogen, and water vapor in the Hg, thereby preventing the inhibitor from reaction with these elements.

Table I. Composition of carbon steel

	%
C	0.25
Mn	0.57
Si	0.18
S	0.035
P	0.10

Experiments at Brookhaven National Laboratory (4) in studying bismuth corrosion of steels indicated that low-alloy and plain carbon steels were more resistant to liquid bismuth corrosion with the addition of 100-250 ppm of Zr to the bismuth. ZrN and ZrC films formed on the steel surface were the principal mechanism of protection against liquid Bi attack.

An experiment performed by Miller (5) at Brookhaven showed that a microscopically visible film could be formed on an AISI 1020 steel after 120 hr contact with Hg containing Ti at 1365°F. X-ray diffraction of the steel surface indicated the presence of both TiC and TiN compounds.

Experimental Procedure

Three all-liquid Hg thermal convection loops were fabricated from coextruded ½ in. schedule 40 pipe having 1¼% Cr-½% Mo steel on the outside, and ASTM A106 silicon-killed, carbon steel on the inside. Each steel comprised half the wall thickness. The composition of the carbon steel and a diagram of a loop are shown in Table I and Fig. 2, respectively. The inside surface of each loop was sandblasted and degreased to remove all foreign material prior to welding. After welding the entire loop was stress relieved at 1292°F in a He atmosphere. The inhibited loops had inserts of Ti and Zr tubing wedged in the loop cold point. Placing "excess" inhibitor at the loop cold point limits the concentration of Ti or Zr dissolved to the solubility at the cold point temperature and insures a continuous supply of inhibitor. The loops then were filled with triple distilled Hg and pressurized with tank helium to

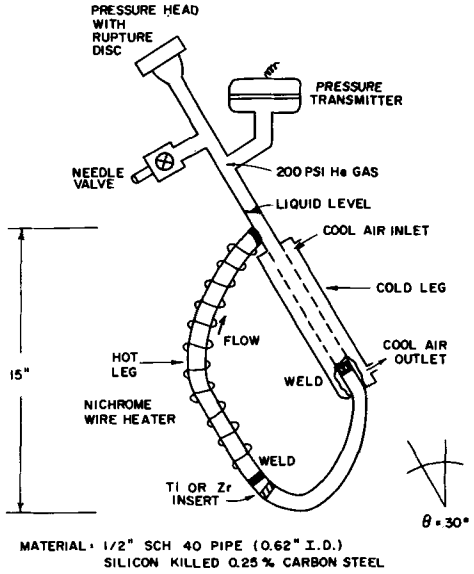

Fig. 2. Schematic of all-liquid Hg thermal convection loops

Table II. Operating characteristics of loop experiments

Loop No.	Hours of operation	Avg. Temp, °F Hot point	Cold point
124	8401	967° ± 20°	605° ± 20°
125	8663	960° ± 27°	536° ± 22°
131	7946	1019° ± 21°	597° ± 18°

Table III. Chemical analysis of loop experiments

Loop	Hg, g	Mg, g	Fe	Ti	Zr
125—Added	2700	0.0675	—	—	—
Filtrate	2673	0.013	7 ppm	—	—
Residue	26.9	0.007	2.39g	Trace	—
124—Added	2850	0.142	—	2.24	—
Filtrate	2843	0.134	1.21 ppm	—	—
Residue	7.3	0.008	0.80g	0.034g	—
131—Added	2800	0.140	—	—	>2g
Filtrate		0.076	1.6 ppm	—	—
Residue	N.D.*	0.022	<0.3081**	—	N.D.*

* Not determined.
** Dry residue Hg free.

prevent boiling. The Hg contained less than 0.1 ppm Ag and 0.1 ppm Cu with no other metals detected. Fifty ppm of Mg metal were added to the Hg of the inhibited loops and 25 ppm to the uninhibited loop to promote wetting and act as a deoxidizer.

The loops were operated with a nominal maximum temperature of 1000°F in the hot leg and 600°F in the cold leg for about 8000 hr. Small variations in the line voltage caused fluctuations in the day to day temperatures on each loop. Operating characteristics for each loop are shown in Table II. The actual flow velocity in thermal convection loops cannot be calculated, but measurements on Bi loops of similar design and geometry indicated that flow rates in these experiments were of the order of 0.05 ft/sec.

Fig. 3. Intergranular hot leg corrosion of uninhibited loop. Magnification 170X.

Fig. 4. Intergranular hot leg corrosion of Ti inhibited loop. Magnification 170X.

Fig. 5. Transgranular attack in Zr inhibited loop. Magnification 250X.

After completion of each run, the Hg in each loop was drained and filtered under inert atmosphere at room temperature. The entire loop then was cut transversely into small pieces, sectioned longitudinally, and prepared for metallographic examination.

Experimental Results

No adherent deposits were found in any of the loops. Filtered residues weighing 2.4, 0.8, and 0.3g (after vacuum distillation of adherent Hg) were found in the uninhibited, Ti inhibited and Zr inhibited loops, respectively. X-ray diffraction indicated that these residues were essentially Fe, and subsequent chemical analysis showed iron with

traces of Mg and the inhibitors, when present. Results of chemical analysis of the residue and filtrate of each loop are shown in Table III.

Shallow corrosion primarily intergranular, was found in the hot areas of the uninhibited and Ti-inhibited loops (see Fig. 3 and 4), and slight predominantly transgranular pitting corrosion was found over the entire Zr-inhibited loop (see Fig. 5). Corrosion-temperature "profiles" of each loop are shown in detail in Fig. 6, 7, and 8. Maximum penetration in the Zr-inhibited and the uninhibited loop was less than one mil. The Ti-inhibited loop showed one pit of about three mils (see Fig. 9), but otherwise showed less than 1 mil attack.

Examination of the Ti and Zr inserts in the inhibited loops showed that there was substantially greater dissolution of the Zr insert than of the Ti insert.

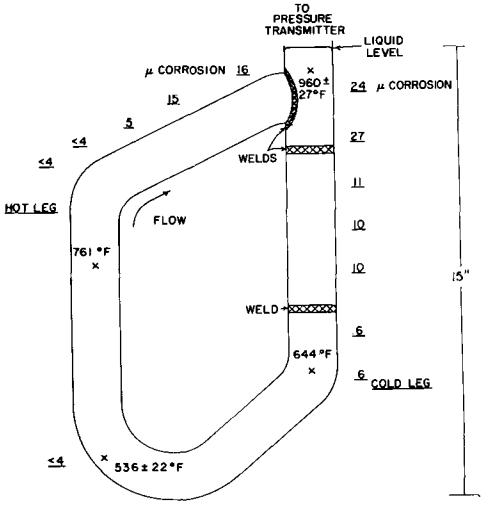

Fig. 6. Corrosion-temperature profile-uninhibited loop. Loop No. 125, carbon steel all liquid, uninhibited Hg loop; operating time 8663 hr; liquid velocity 0.05 ft/sec; additives, 25 ppm Mg; no inhibitor.

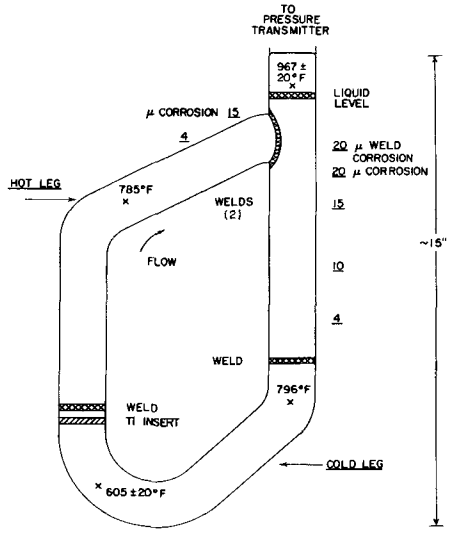

Fig. 7. Corrosion-temperature profile-Ti inhibited loop. Loop No. 124, carbon steel all liquid, Ti inhibited Hg loop; operating time 8401 hr; liquid velocity 0.05 ft/sec; additives, 50 ppm Mg; Ti inhibitor.

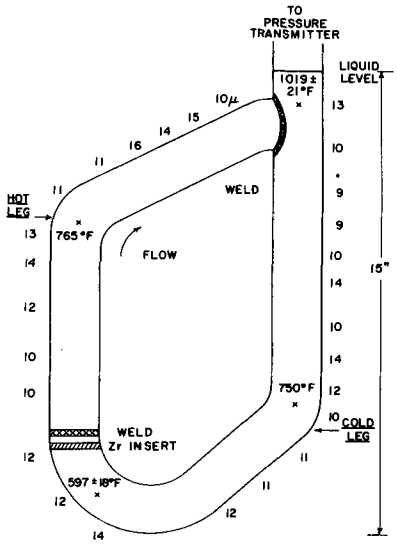

Fig. 8. Corrosion-temperature profile-Zr inhibited loop. Loop No. 131, carbon steel all liquid, Zr inhibited Hg loop; operating time 7946 hr; liquid velocity 0.05 ft/sec; additives, 50 ppm Mg; Zr inhibitor; residue 0.308g.

Fig. 9. Corrosion pit in Ti inhibited loop. Magnification 170X

Discussion of Results

Examination of the results of these experiments indicate that under the experimental conditions, 1000°F maximum and 600°F minimum Hg temperature and a flow rate of the order of 0.05 ft/sec, only slight corrosion was noted in a period of almost one year. The addition of either a Ti or Zr metal insert at the loop cold point reduced the amount of material corroded from the pipe walls. On this basis the Zr addition was a more effective inhibitor than the titanium addition.

Study of Hg corrosion of mild steel by Nerad and co-workers (3) indicated that in an uninhibited system at a maximum loop temperature of 1000°F, a corrosion rate of 0.18 g/cm^2/yr could be expected, corresponding to an average penetration of 9 mils/yr. In the presence of 10 ppm Ti dissolved in the Hg

the rate of attack on ferrous metals at 650°C (1200°F) was reported to be negligible. Most of Nerad's tests were carried out at a 10°C (18°F) temperature difference between the hot and cold zone and a mercury flow rate reported to be 0.1 ft/sec. Results at Brookhaven National Laboratory on liquid Bi in carbon steel show that the corrosion rate increases when the cold zone temperature is reduced at constant hot zone temperature (4). Thus, one might expect less attack in Nerad's experiments, since his conditions were less severe than the condition of the present experiments in which the temperature differential was about 400°F.

A review of the theory and derivation of mass transfer equations was performed by Bircumshaw and Riddiford (6) in 1952. Epstein (7) in 1957 applied the experimental results of Nerad on Hg corrosion of steel in uninhibited systems using the heat transport relationship. He found that the experimental corrosion rates were significantly higher than those predicted by this theory. Application of this relationship to the present work (see appendix) predicts a corrosion rate of 0.15 g/cm²/yr, corresponding to average penetration of 8 mils/year.

Corrosion mass transfer in the uninhibited loop may have been reduced by the lack of adherent deposition of precipitating crystallites of Fe in the cold region of the loop. Rather than sticking securely to the wall these Fe particles are carried into the hot zone. Because of their small size and high specific area these particles dissolve at a rate faster than that of the pipe surface. If complete dissolution of the precipitated particles occurred, the hot leg wall of the loop would be protected when steady state hot leg saturation of the Hg is achieved, and no further corrosion would occur during operation of the experiment. Since at a hot leg temperature of 1000°F only 0.75 mg of Fe would saturate the entire volume of Hg, and the Fe residue weight varied from 0.3 to 2.4g, it must be surmised that only partial dissolution occurs, assuming that the solids are circulated in suspension. It is not certain whether the particulate iron in the Hg stream was continually recirculating or floating to the free liquid surface in the "T" of the loop. Steady-state operation may have consisted of precipitation of nonadherent Fe crystallites in the cold leg, partial dissolution in the hot leg, and floating of the undissolved particulate Fe to the free liquid surface.

The presence of excess Ti and Zr at the loop cold point provided a continuous source of these elements for film formation. The greater attack on the Zr insert is borne out by the solubility studies of Zr (8, 9) and Ti (10, 11) in Hg. These studies show that at 350°C (662°F), Ti has less than 0.6 ppm solubility while the Zr solubility is reported to be 5 ppm. Film formation probably occurred in the Zr inhibited loop as this loop showed the predominantly transgranular corrosion associated with inhibition in Bi systems. Although intergranular corrosion was found in the Ti-inhibited loop, some film protection must have resulted because only 0.8g of Fe was corroded from the loop while 2.4g of Fe were corroded from the uninhibited loop. Corrosion in the cold leg of the Zr inhibited loop is puzzling and cannot be accounted for adequately. The attack appears to be independent of position and hence temperature, in the loop.

Conclusions

1. Corrosion in the uninhibited loop in one year was about 1 mil maximum at a 1000°F hot leg, 600°F cold leg Hg temperature. The observed corrosion was much less than that calculated by diffusion-controlled dissolution theory. It appears that the lack of adherent deposition of Fe crystals to the pipe wall in the cold zone of the loop may have resulted in partial "self-inhibition" and thus reduced corrosion.

2. The presence of either Ti or Zr metal at the loop cold point reduced the weight of Fe corroded, but Zr was more effective than Ti.

3. Addition of Zr to Hg resulted in a change of corrosion from the predominantly intergranular attack found in the Ti and uninhibited loop to a transgranular attack.

Acknowledgments

The authors express their appreciation to all their co-workers. Special thanks are due J. Brandon who set up and operated the experiments, O. Kammerer and J. Sadofsky who were responsible for the metallographic and x-ray results and R. Stoener and H. Finston for the chemical analyses. This work was performed under the auspices of the United States Atomic Energy Commission.

Manuscript received Jan. 21, 1963. This paper was presented at the Boston Meeting, Sept. 16-20, 1962.

Any discussion of this paper will appear in a Discussion Section to be published in the June 1964 JOURNAL.

APPENDIX

A. *Mass transfer equation for diffusion-limited corrosion in nonisothermal dynamic liquid systems.*—The empirical heat flow equation (6) is given by

$$\mathrm{Nu} = 0.023\ (\mathrm{Re})^{0.8} (\mathrm{Pr})^{0.4}$$

where Nu is Nusselt modulus, Re, Reynolds number, and Pr, Prandtl number.

The mass transfer analogue is given by the equation

$$(rd/D\Delta S) = 0.023\ (Vd/\nu)^{0.8}\ (\nu/D)^{0.4}$$

or

$$r = 0.023\, d^{-0.2}\, V^{0.8}\, D^{0.6}\, \nu^{-0.4}\, \Delta S$$

where r is the corrosion rate/unit area/sec = g/cm²/sec, d the diameter of pipe in cm, D the diffusion coefficient of solute in liquid, ΔS the equilibrium solubility difference at maximum and minimum temperatures in g/cm³, V the velocity in cm/sec, and ν the kinematic viscosity of liquid in cm²/sec, and all values are calculated at the maximum temperature in the system.

B. *Application of mass transfer equation to case of low-carbon steel, Loop No. 125 in mercury.*—Conditions corresponding approximately to those found in Loop No. 125 are: d = 1.58 cm, V = 1.52 cm/sec, ν = 6.83 x 10^{-4} cm²/sec, T_{max} = 1000°F, T_{min} = 600°F, ΔS = 0.28 ppm or 3.5 x 10^{-6} g/cm³, D = 5 x 10^{-5} cm²/sec for Fe atom diffusion in Hg at 1000°F, where D is estimated using the Stokes-Einstein relationship.

Substituting these values in the mass transfer equation yields

$$r = 4.75 \times 10^{-9}\ \mathrm{g/cm^2/sec}$$

or a corrosion rate of 0.15 g/cm²/yr, which is equivalent to an average penetration of 8 mils/yr.

REFERENCES

1. M. F. Parkman, "Summary of Work at Aerojet-General Nucleonics on Liquid Metal Corrosion," NASA-AEC Liquid Metal Corrosion Meeting, TID-7626 (Pt. 1) Dec. 14, 15, 1961.
2. A. L. Marshall, J. F. Epstein, and F. J. Norton, *J. Am. Chem. Soc.*, **72**, 3514 (1950).
3. L. F. Epstein, Compilation and discussion of unpublished data of A. J. Nerad and associates at the General Electric Company. "Liquid Metals Handbook," pp. 167-168, 2nd ed. (1954).
4. J. R. Weeks and C. J. Klamut, *Nuc. Sci. and Eng.*, **8**, 133-147 (1960).
5. W. E. Miller and J. R. Weeks, BNL-2913, USAEC, 1956.
6. L. L. Bircumshaw and A. C. Riddiford, *Quart. Rev. Chem. Soc.*, Vol. 6 (1952).
7. L. F. Epstein, Chemical Engineering Progress Symposium Series No. 20, Vol. 53, pp. 67-81.
8. L. R. Kelman, W. D. Wilkinson, and F. L. Yaggee, "Resistance of Materials to Attack by Liquid Metals," Argonne National Laboratory, 4417, July 1950.
9. M. Hansen and K. Anderko, "Constitution of Binary Alloys," McGraw-Hill Book Company Inc., New York (1958).
10. H. A. Liebhafsky, "The Solubilities of Certain Metals in Mercury," General Electric Co. Report, Data Folder 55868, April 5, 1939.
11. R. C. Reid, "Mercury Boiler Treatment With Titanium and Magnesium Metals," Unpublished. Technical Paper No. 51-5-13 presented at the 1951 spring meeting of the ASME.

The Epitaxial Vapor Deposition of Perovskite Materials

Egon K. Müller, Basil J. Nicholson, and Gerard L'E. Turner

Philco Scientific Laboratory, Blue Bell, Pennsylvania

ABSTRACT

A number of materials with a perovskite-like structure such as titanates, stannates, niobates, and cerates have been vapor deposited by a grain-by-grain evaporation technique. Also tungsten trioxide has been evaporated, being directly sublimed from a hot source. Analysis by electron diffraction showed that deposition onto heated LiF (100) or Au (100) surfaces can yield single crystal films of these materials. Corresponding planes and azimuthal directions of the cubic substrate and vapor deposited substance were found to be equal except for $CaTiO_3$ where a (110) plane was parallel to the LiF (100). The (100) planes of NaF yielded films with two azimuthal orientations. Other single crystal substrates such as Ge, Si, NaCl, CaF_2, PbS, MgO, and mica rendered the films polycrystalline, partly with preferred orientations. With the exception of WO_3 the structure of the epitaxed films was identical with that of the bulk material.

Extensive studies of epitaxy have been undertaken in recent years. Epitaxial vapor deposition, however, has until now been concerned only with congruently evaporating materials such as elements, halides, sulfides, and other simple compounds that form undissociated vapor molecules of the same composition as the solid or liquid evaporant (1).

There is considerable interest in the feasibility of preparing single crystal films of the double oxides of the perovskite structure which comprise materials of ferroelectric, antiferroelectric, ferromagnetic, and antiferromagnetic properties. Their refractoriness and the formation of dissociated vapor species with differing volatilities on heating make evaporation and vapor deposition of these substances difficult. Previous efforts were exclusively directed toward the preparation of barium titanate films. Polycrystalline films were achieved by Feldman (2) by a combination of direct evaporation and subsequent heat treatment at about 1200°C in air, which was necessary to react the dissociated components BaO and TiO_2 that had been deposited in sequence according to their volatility. A grain-by-grain evaporation technique in which a stream of grains of the evaporant is continuously vaporized from a hot boat was used by Müller, Nicholson, and Francombe (3) to deposit crystalline $BaTiO_3$ films *in situ* on substrates held at a temperature of about 500°C. In a short note (4), it has been reported that this method was successfully applied to the epitaxing of $BaTiO_3$ on LiF.

Moll (5), who first used the grain-by-grain evaporation technique for barium-strontium titanate, claimed to have vapor-deposited single crystal films onto Pt, mica, and NaF at a temperature of 200°, under the influence of an electric field. These claims were refuted by Roder (6). We found it impossible to verify Moll's results under the given experimental conditions. Single crystal films have indeed been prepared by different methods such as growth from solution (7), chemical etching (8), and a wetting technique (9). The minimum achievable thickness and the usable areas, however, are very restricted. The epitaxial vapor deposition of barium titanate and similar compounds can close this gap.

Experimental

Sample preparation.—$BaTiO_3$, $SrTiO_3$, $CaTiO_3$, $NaNbO_3$, and $BaSnO_3$ of commercial purity were used. The powders were dry pressed to a pellet in a die with a pressure of 8 tons/cm^2 and heat treated at 1300°C in air between 1 and 10 hr in a Pt crucible. It was confirmed that the weight loss was less than 1%. The sintered material was crushed into grains which were sieved to the required grain size, usually 100/200 mesh. The compounds $BaCeO_3$ and $SrSnO_3$

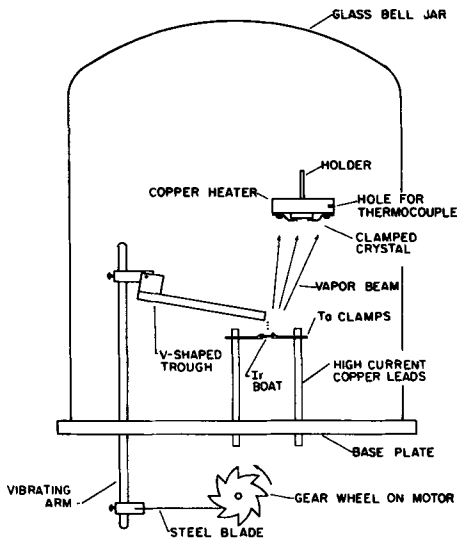

Fig. 1. Schematic view of the evaporation system

were first prepared from $BaCO_3$, $SrCO_3$, and the respective oxides by mixing the powders in the desired proportion, pressing to pellets and reacting at 1000°C, then repressed, sintered and sieved as described above. WO_3 was used as commercial powder.

The evaporation method.—The grain-by-grain evaporation method has been described in detail earlier (3). It has been pointed out that two procedures are possible, "flash evaporation" and "liquid-pool-evaporation." The latter procedure is not easily performable for materials with components of very different vapor pressures. Therefore, the first approach was used in the present work. The principal operation can be seen in Fig. 1.

By the action of a vibrator the evaporant grains traveled singly down a V-shaped trough, their speed being adjustable. From the trough each grain falls separately on to a resistively heated iridium boat (at around 2200°C), evaporating successively ("flash evaporation"), and forming a film on the heated substrate. In direct over-all evaporation the more volatile oxide constituent or other dissociating vapor is driven off first, and the more refractory parts later, thus making the deposited film layered in composition. In grain-by-grain evaporation each grain contributes an average increment of film thickness of less than a lattice constant. Thus no macroscopic layers of different composition can arise, the films as deposited are homogeneous. In our experiments we generally used a distance between boat and substrate of 8 cm and a grain size of 100/200 mesh; however, the use of a mesh size up to 40/60 did not change the results.

Some of the materials used, such as the alkali niobates and the stannates, develop a considerable vapor pressure below the melting point. In this case the grains falling on to the hot boat rebounce violently on initial contact before they can liquefy and wet the boat. This spitting effect is reduced by using a larger grain size or by enclosing the space between boat and substrate by a tube (*e.g.*, of Ta). Possible compositional alteration of the film deposit is thus avoided. The boat temperature also is adjusted as low as possible to give complete evaporation of the grains in a reasonable time. Film growth rates of 1-3 Å/sec were normal.

The boat consisted of a resistively heated iridium strip 5 mils thick with a free surface of about 20 mm^2. It was held by Ta clamps which were screened from the substrate because of possible reactions of Ta with scattered evaporant. The evaporation process and boat temperature were observed through an optical pyrometer. The temperatures used, corrected for an emissivity of 0.3 of Ir, varied from 2050° to 2300°C for different substances (see Table I). Iridium impurities from 0.1 to 5% due to its vapor pressure can be correspondingly expected; this was confirmed by spectroscopical analysis. The vapor pressure within the bell jar of the vacuum system could be kept at 2×10^{-5} Torr by means of a liquid nitrogen trap.

The use of an Ir boat does not allow the evaporation of some very refractory perovskite oxides such as zirconates, thorates, tantalates, aluminates. Other boat materials such as W and Ta incorporate large impurities and a high oxygen deficiency in the films (3).

Tungsten trioxide is the only perovskite-like material that evaporates practically congruently (10, 15). A direct sublimation of the powder from a Pt wire basket, onto which it was applied as a water paste, was therefore sufficient.

Film deposition.—To form substrates cleaved crystal plates of LiF, NaCl, NaF, CaF_2, MgO, PbS, about 10 x 5 x 1 mm in size, or cleaved mica sheets were used. Also tried were single crystals of Ge, and Si, which were etched and checked for surface perfection by electron diffraction before use. In a few experiments single crystal Au films grown on NaCl, LiF, and mica were used. These films, however, tend to peel off after deposition of a second oxide film, especially along the cleavage steps.

The substrates were rigidly fastened to a copper block heatable up to 700°C (Fig. 1). Its temperature was measured by a thermocouple. All substrate temperature values in this paper refer to this copper heater. The true temperature of the substrate surface might be lower by as much as 50°. At the temperatures of 500°-700°C found for epitaxing, the thermal etching effect upon LiF, NaF, or NaCl by vaporization is already strong enough to make cleaving just before use unnecessary.

The thickness of the deposited films was calculated from the weight increase per unit area of a

Table I. Evaporation temperature and lattice constants of epitaxed materials

Evaporated substance	Evaporation temp, °C	Lattice constant, Å Literature (11, 12)	Epitaxed on LiF
$BaTiO_3$	2200	(3.992, 4.035) *	4.00
$SrTiO_3$	2250	3.905	3.90
$CaTiO_3$	2270	(3.819, 3.815, 3.819, 90°40′) *	3.85
$BaSnO_3$	2060	4.116	4.13
$SrSnO_3$	2130	4.033	4.02
$BaCeO_3$	2130	4.377	4.38
$NaNbO_3$	2150	(3.916, 3.880, 3.916, 90°40′) *	3.90
WO_3	(1400)	(3.637, 3.756, 3.824, 89°56′) *	4.10

* Referring to the pseudo perovskite unit cell (room temperature).

thin metal foil placed beside the substrate using density values obtained from the crystallographic data (11).

Film analysis.—The deposited films were examined in a Siemens Elmiscope I by reflection electron diffraction, employing the Siemens manipulator in place of the projector lens. Single crystal films resulted in a streak or spot pattern. The path of the electron beam scanning the film surface was visible in the case of LiF by fluorescence. Diffraction patterns arise from areas with a length of substrate dimension up to 0.5 cm and the width of the electron beam. By scanning along the surface, the whole film could be investigated. Sometimes the single crystal pattern was accompanied by a weak ring pattern, independently of film thickness. These rings are probably due to imperfections at the crystal edges and cleavage steps. Electrical charging of the highly insulating films made it difficult in some cases to obtain sharp patterns even when a decharging gun was used. The LiF pattern was used for calibration.

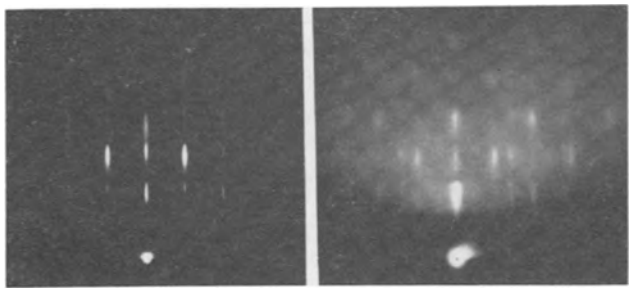

Fig. 2. Electron diffraction patterns of $BaTiO_3$ films; a (left) 920Å thick, deposited on LiF at 600°C, azimuth [100]; b (right) 850Å thick, deposited on NaF at 600°C, azimuth [100].

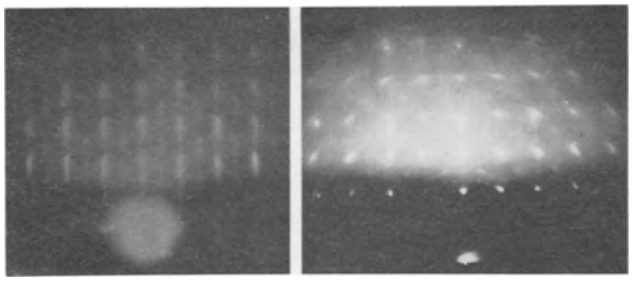

Fig. 3. Electron diffraction patterns of $NaNbO_3$ films: a (left) 380Å thick, deposited on LiF at 600°C, azimuth [100]; b (left) 370Å thick, deposited on LiF at 500°C, azimuth [100].

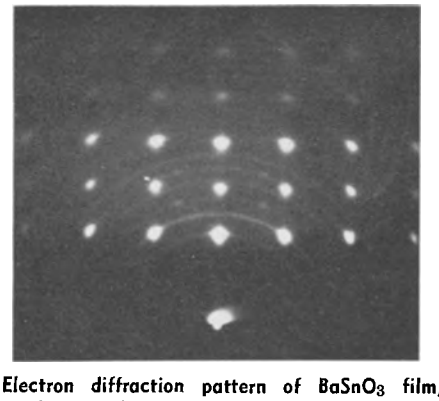

Fig. 4. Electron diffraction pattern of $BaSnO_3$ film, 1840Å thick, deposited at 550°C on LiF; azimuth [110].

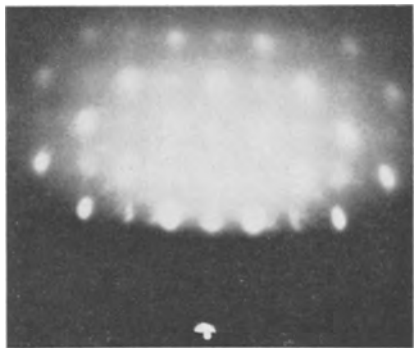

Fig. 5. Electron diffraction pattern of $BaCeO_3$ film, 1080Å thick, deposited at 600°C on LiF; azimuth [100].

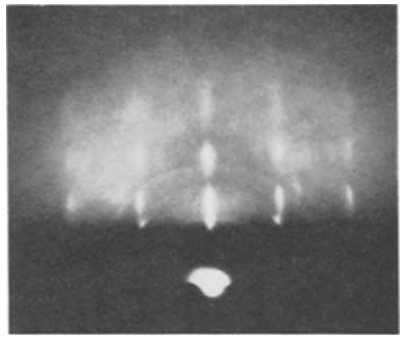

Fig. 6. Electron diffraction pattern of $SrTiO_3$ film, 650Å thick, deposited at 600°C on LiF; azimuth [110].

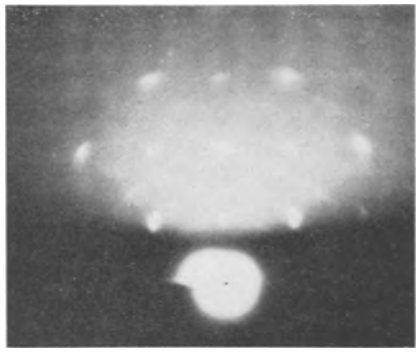

Fig. 7. Electron diffraction pattern of $CaTiO_3$ film, 570Å thick, deposited at 550°C on LiF; azimuth [100]. (LiF spots visible).

Results

Table I presents the substances investigated, together with the necessary evaporation temperatures. Other materials such as $LaCrO_3$, $LaAlO_3$, and $NaTaO_3$ proved to be too refractory for evaporation from an Ir source (melting point 2454°C). Apart from $CaTiO_3$ the substances all epitaxed on LiF in cube parallel orientation, *viz.*, (100)//(100) LiF, [001]//[001] LiF (Fig. 2-6). $CaTiO_3$ (Fig. 7) was found to epitax (110)//(100) LiF, [001]//[001] LiF. The diffraction pattern of WO_3 (Fig. 8a) indicates that the unit cell in the deposited film has double the dimensions of the pseudocubic cell, in agreement with the literature (12). However, the lattice constant appeared about 10% larger (see Table I). Starting the deposition process with black, oxygen deficient WO_3 (as obtained by heating in

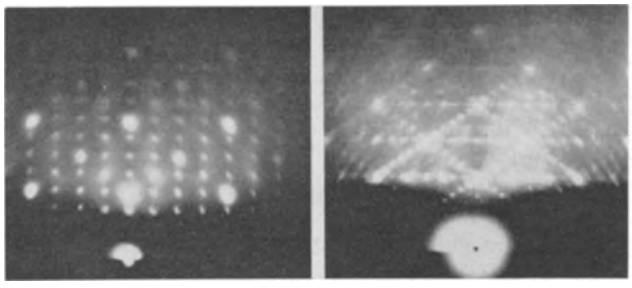

Fig. 8. Electron diffraction pattern of WO_3 films: a (left) 1850Å thick, deposited at 500°C on LiF, azimuth 110; b (right) 1850Å thick, (with oxygen deficiency), deposited at 450°C on LiF, azimuth [110].

vacuum) one obtains interesting variations of the diffraction pattern (Fig. 8b).

$BaTiO_3$, $CaTiO_3$, $NaNbO_3$, and WO_3 can have a pseudocubic structure (12). The differences from cubicity are so slight that our examination would not reveal them. From the pattern of $NaNbO_3$ (Fig. 3a) however, there is evidence for a larger pseudotetragonal unit cell in accordance with Vousden (13) with parameters $a = 5.5$Å and $c = 3.9$Å.

The spot intensities to be expected for $BaTiO_3$ are such that there are no absences. In the case of atoms close in atomic number as in $BaSnO_3$, $BaCeO_3$, and $CaTiO_3$, however, spots with mixed indices of odd sum are so weak as to be unobservable or very faint and may not reproduce in the figures. This gives for the [001] azimuthal direction a pattern that appears to have originated from a body-centered cubic structure.

It is interesting to note that $SrTiO_3$ epitaxes on LiF with a lattice constant of 4.1 (instead of 3.9) when evaporated from a tungsten boat. The tungsten is oxidized on contact and the oxide evaporates introducing a large amount of impurities (~20%) and rendering the film oxygen deficient. This explains the lattice distortion.

Besides LiF, sodium fluoride proved to be a substrate allowing epitaxy as shown for $BaTiO_3$ (Fig. 2b). The azimuthal orientation, however, is twofold

(a) $BaTiO_3$ [100]//NaF [100]

(b) $BaTiO_3$ [110]//NaF [100]

The misfit in the first case is −13%, in the second one +23%.

No epitaxy of these materials on NaCl (100), mica (001), or MgO (100) has been found at substrate temperatures of 500° and 600°C. Barium titanate rendered partly oriented films on Ge (100), Ge (110), Ge (111), Si (111), and on Au (111) films, prepared on a mica surface. However, complete epitaxy was found on Au (100) films prepared on a LiF surface, using 630°C substrate temperature. Both films had to be kept thin enough to prevent peeling (each about 200Å).

The lower limit of the temperature to yield crystalline $BaTiO_3$ films instead of amorphous ones is about 500° for the substances used. Of the substrates tried, LiF was the only one to have a lower temperature limit for epitaxy of $BaTiO_3$ as low as 400°C, giving a perfect streak pattern even at that temperature. No upper limit has been found. A practical limit of 700°C is given by the volatility of LiF. For the other materials the lower temperature limit of epitaxy was not investigated extensively. It seems that evaporant materials that give off much vapor before reaching boat temperature, such as stannates, require higher epitaxy temperatures. Figure 3b shows the diffraction pattern of a $NaNbO_3$ film deposited at 500°C; the spots are extended as arcs, different from the streak pattern of the film deposited at 600°C.

No thickness limit in the epitaxy of these perovskite materials on LiF has been found. Most films were prepared with a thickness of about 1000Å. In the case of $BaTiO_3$ the thickness of epitaxed films varied from 200 to 11,000Å. It is likely that the very thin films are not continuous, but consist of islands of equal orientation, grown around the nuclei.

As indicated above, deposition onto an unheated LiF crystal gives an amorphous film. Such an amorphous film of barium titanate was heat treated in air at 500°C for 20 hr. By the influence of the substrate the film crystallized in a slightly oriented way, showing an arched ring pattern. Epitaxy was, however, not achieved.

Discussion

Of the investigated materials, all of those which have the ideal cubic perovskite structure ($\alpha = 90°$) at the deposition temperature epitaxed on LiF with completely parallel orientation and with a lattice constant fully agreeing with that of the bulk. Of the materials with a distorted cubic unit cell even at high temperature, $CaTiO_3$ epitaxed in a different orientation, while WO_3 preserved parallel orientation, but assumed a lattice constant about 10% larger.

The fact that LiF has superior qualities to other single-crystal substrates in the epitaxy of materials with the perovskite structure might partly be based on the good match of the lattice constants (LiF 4.01Å). This is, however, not a primary factor. $BaCeO_3$ for instance, one of the perovskite materials with a very large lattice constant (4.36Å), would match the lattice of MgO ($a = 4.21$) better than that of LiF ($a = 4.01$), but epitaxy occurs only on the latter. The relatively low epitaxial temperature for these refractory materials suggests that part of the kinetic energy of the oncoming vapor molecules is effective for overcoming the necessary potential walls for epitaxy.

The possibility of epitaxial vapor deposition of single crystal films *in situ* suggests the following qualitative analysis of the grain-by-grain and deposition process. In the case of $BaTiO_3$ the grains heated up in vacuum by the boat start to lose oxygen at 760°C, according to Chebkasov (14), which renders the material black and semiconducting. The oxygen reaching the substrate recompensates any oxygen deficiency left on the previously formed layers of the film. At about 2100°C the oxygen deficient liquefied grain starts to evaporate from the boat, forming at first mainly BaO and then TiO_2 molecules together with the corresponding suboxides and dissociated metals and oxygen. This can be inferred from the evaporation characteristics of the BaO and TiO_2 phases (15). The vapor species, which impinge

the surface with different temperatures, are adsorbed in less than a monolayer thickness and put into the right structural positions. Both kinetic energy of the incoming molecules and the heat of the substrate seem to be effective. From the high resistivity of the films (3) and the transparency we can conclude that indeed practically all dissociated oxygen has been reabsorbed by the lattice. Stoichiometry of the film is thus preserved in the finished film. For the other compound oxides a similar evaporation mechanism can be expected.

Deposition on conductive surfaces, such as a Au (100), would provide a convenient means to determine the electrical properties of such compounds, many of which have only been investigated as polycrystalline materials. Continuous thin single crystal Au films, however, could not be used for this purpose because of the disruptive and peeling effects during deposition. Bulk metal single crystals should be more appropriate.

The successful epitaxy of a variety of materials with a perovskite structure by the method of grain-by-grain evaporation makes it likely that this technique is feasible for the preparation of single crystal films of alloys, dissociating oxides, complex compounds, or mixtures between them.

Acknowledgments

The authors are indebted to Mr. James Perry for technical assistance, to Mr. Alexander Noreika for electron microscope work, and to Dr. M. Lasser for his steady interest and support of this work.

Mansucript received Feb. 6, 1963; revised manuscript received April 22, 1963.

Any discussion of this paper will appear in a Discussion Section to be published in the June 1964 JOURNAL.

REFERENCES

1. For a survey of epitaxy see D. W. Pashley, *Advances in Physics*, **5**, 173 (1956); H. M. Abbott, Epitaxial Growth (Annotated Bibliography), March 1962; AD 275 588, July 1961; AD 253 404, Armed Services Technical Information Agency, Arlington, Va.
2. Charles Feldman, *Rev. Sci. Instr.*, **26**, 463 (1955).
3. E. K. Müller, B. J. Nicholson, and M. H. Francombe, *Electrochemical Technology*, **1** [5-6], 158 (1963).
4. E. K. Müller, B. J. Nicholson, and G. L'E. Turner, *Brit. J. Appl. Phys.*, **13**, 486 (1962).
5. Alexander Moll, *Z. angew. Phys.*, **10**, 410 (1958).
6. Oskar Roder, *ibid.*, **12**, 323 (1960).
7. R. C. DeVries, *J. Am. Ceram. Soc.*, **45**, 225 (1962).
8. J. T. Last, *Rev. Sci. Instr.*, **28**, 720 (1957).
9. E. V. Bursian and V. P. Smirnova, *Fiz. Tverd. Tela*, **4**, 1675 (1962).
10. L. Holland, "Vacuum Deposition of Thin Films," J. Wiley & Sons, Inc., New York (1958).
11. R. W. G. Wyckoff, "Crystal Structures," Interscience Publishers, Inc., New York (1961).
12. H. D. Megaw, "Ferroelectricity in Crystals," Methuen & Co. Ltd., London (1957).
13. P. Vousden, *Acta Cryst.*, **4**, 545 (1951).
14. A. V. Chebkasov, "Some Physical Properties of Vacuum Annealed Polycrystalline Barium Titanate," *Bull. acad. Sci. URSS*, Physical Series, **24**, 1259 (1960).
15. R. J. Ackerman and R. J. Thorn, "Vaporization of Oxides," in "Progress in Ceramic Science," Vol. 1, Pergamon Press, New York (1961).

Trace Impurity Effects on Growth Hillocks during Epitaxial Electrodeposition from Copper Perchlorate Solutions

D. Shanefield and P. E. Lighty

ITT Federal Laboratories, Nutley, New Jersey

ABSTRACT

Growth hillocks ordinarily cover the surface of copper electrodeposits from reagent grade solutions. A 75% decrease in the number of hillocks was observed when the plating baths were purified by pre-electrolysis and oxidation. When gelatin or Pb^{++} were added in parts per million or parts per billion concentration to the purified solutions, the surfaces of new electrodeposits were then completely covered with growth hillocks. It is concluded that the formation of surface features during electrodeposition from reagent grade solutions is affected by the presence of trace impurities.

The growth by electrodeposition of copper single crystals with regular flat facets was first reported by von Schwarz (1) in 1915. Much of the recent work on the electrolytic growth of copper single crystals has been concentrated on the growth habits of copper as deposited in thin layers onto electropolished copper substrates. Special attention has been given to electrodeposition growth spirals in connection with dislocation theories of crystal growth (2) and to the other shapes of growth hillocks formed under various electrodeposition conditions (3). However, the microscopic appearance of the facet surfaces on the electrodeposited crystals is somewhat unusual, and the surface features consist of rows of regular geometrically shaped growth hillocks and steps (3). The usual less-geometric steps or growth layers which are apparent on many other types of crystals can also be seen, and it has been suggested that these small steps coalesce by the so-called bunching (4) mechanism to form the

geometric growth hillocks on electrodeposits (5).

The bunching mechanism was used previously to explain certain details of crystal growth by nonelectrolytic means. In accordance with the theory that adatoms are most likely to settle in the kinks on monomolecular surface steps, thus promoting growth by lateral enlargement of the steps, these steps have been observed to sweep across the growing crystal. The bunching theory deals with the coalescing of steps to form larger surface features.

Very low steps, one or a few molecules high, have been observed occasionally with the electron microscope, both with (6) and without (7) a spiral configuration. Many examples have also been noted in visible light studies where the growth steps were high enough to be seen with an ordinary or a phase microscope. These steps could be observed to grow laterally, and their velocities were measured. It was noted most often that the steps of lowest height moved fastest (8, 9), although exceptions were noted also (10). A theoretical explanation for this difference in lateral velocities was suggested by Cabrera and Vermilyea (11a).

In the majority of observable cases, the moving steps are thousands of molecules high (12). If an imperfection in the substrate or a loosely adsorbed impurity should slow the motion of a low step enough for another step to catch up and thus form a new step of double height, then the new one, since it moves more slowly, will automatically absorb the succeeding low steps, and a large, slow moving wall will be formed (11a). This process has also been treated by a statistical approach (13) in the same manner as the waves of automobiles on crowded highways have been mathematically described (14). For both electrolytic (5) and other types (9) of crystal growth, the visibly large steps have indeed been observed to grow higher as they progress along the surface, presumably because they were absorbing invisibly small steps. The steps also have been observed to appear as regular geometric figures as the lateral motion progresses both in electrolytic (5) and in other types (9) of growth. The risers of the steps generally become low index faces.

Imperfections or impurities might be expected to impede the small steps mechanically, initiating the bunching action (11), or a high concentration of impurities might, by preferential adsorption, stabilize the facets which comprise the riser or the tread of the step (13). The impurities have been observed to increase the step height (2, 15), and, in another case, to decrease it (9). The edges or risers of the growth steps sometimes are arranged in geometric shapes during nonelectrolytic crystal formation, giving an appearance similar to that of the growth hillocks on electrodeposited copper. In one reported example of nonelectrolytic growth, the regular geometric arrangement of step edges was normally absent, but could be brought about by the addition of a certain impurity to the solution (9). In another case, imperfections in the substrate were shown to be uncorrelated with growth pyramids on a vapor-grown Ge deposit (16).

The growth of metal crystals by electrodeposition is extremely sensitive to contamination effects. The impurities present in reagent grade chemicals are too concentrated for reproducible single crystal growth by this method (17) and must be removed by special treatment. An extensive catalog of growth hillock shapes is now available from the literature on electrodeposition from specially purified solutions under various conditions of current density, etc. However, it is possible that those growth hillock shapes are not specific to the reported conditions, but are specific to the combination of reported conditions and the unknown impurities. In order to investigate this point, attempts at further purifications were made during the present study.

Since the anion in a plating bath is well known to affect the electrodeposit and to interact with impurities, it was desired that the anion in the present study be as nearly inert as possible with respect to adsorption on the crystal surface. Perchlorate ion, being strongly ionic, could be expected to be weak in its covalent and adsorption properties. While there have been cases of covalent properties (18a) and electroplating occlusion (18b) reported with perchlorate ion, the ion and its components generally are not found to be occluded into electroplates as much as are other anions in commercial plating baths. In addition, adsorption onto steel electrodes has been shown to be less with ClO_4^- than with other common anions (19). The copper was therefore electrodeposited from $Cu(ClO_4)_2$ solutions in the present study.

In several previous electrodeposition studies (2, 5, 20), removal of surface-active impurities, especially organics, has been effected by the use of activated charcoal. However, in the present study it was found that traces of acid-soluble materials which absorb visible and u.v. light could continuously be leached out of various types of charcoal, even after long extraction.

Since oxidation has been shown to remove contaminants from electrodeposition baths where charcoal had failed (2, 21, 22), it was decided that the perchlorate ion itself should be used as an oxidative purifier to replace the commonly reported charcoal treatment.

Cationic impurities were removed by pre-electrolysis in a long column (23), whereby the solution would come in contact with a fresh electrode surface as it moved along the column. Heavy deposits of fine copper powder in the pre-electrolysis column will presumably act to adsorb and occlude impurities.

Experimental

Electrodepositions were carried out on substrates cut from zone refined copper single crystals grown by the Bridgman method. Purity was reported by the supplier[1] to be 99.999+%. Spectrochemical analysis revealed less than 10 ppm of identifiable impurities, chiefly lead and tin.

After cutting with a diamond-grit wheel to expose a (100) face and then degreasing, the substrate crystal was electropolished in a rotating cathode apparatus (23). All electrodepositions were on faces cut to within 3° of the (100) plane. After electro-

[1] Obtained from the Virginia Institute for Scientific Research, Richmond, Va.

polishing in 50% v/v orthophosphoric acid, the substrates were rinsed in 10% orthophosphoric acid, then in perchloric acid, and then twice in portions of the purified electrodeposition bath, which portions were then discarded. No plastic masking was used on the substrates. Immersed areas included the half-inch diameter face and a small part of the sides of the cylindrical crystals.

Anodes during electrodeposition were graphite rods ordinarily used as spectrographic electrodes. These were used instead of soluble copper anodes in order to avoid the introduction of contaminants, since the copper anodes could not be purified as thoroughly as could the plating solutions.

The $Cu(ClO_4)_2$ solutions were made from spectrographically pure copper oxide[2] dissolved in triple distilled water and double vacuum distilled perchloric acid.[3] The solution was approximately half molar in $Cu(ClO_4)_2$ and one molar in $HClO_4$ after pre-electrolysis.

The containing vessels for refluxing, pre-electrolysis, and electrodeposition were all constructed of fused silica. Before use, each vessel and graphite electrode was rinsed in hot or boiling 72% $HClO_4$.

Before use, the electrodeposition solution was refluxed for 1 hr so that the excess perchloric acid would oxidize organic impurities. There was some danger that the $Cu(ClO_4)_2$ might crystallize on the walls of the apparatus. Dry copper perchlorate can be dangerous when heated (24). Therefore the refluxing apparatus was of one piece, with no joints where solids might collect. It consisted of a vertical quartz tube with a bulb blown on the lower end and a water jacket around the upper end. Heating of 30 cc batches was done on a sand bath, behind a heavy metal shield.

Removal of cationic impurities was then done by pre-electrolysis in an 18 in. long column. Each electrode consisted of several graphite rods, normally used as spectrographic arc electrodes, laid end to end in a horizontal quartz tube. The solution was passed slowly through the apparatus and about half of its copper content was removed electrolytically at a current of several amperes. About 500 coulombs were passed through each 90 cc of solution. The first and last portions of the solution were discarded.

The electrodeposition of single crystals took place in a 100 cc quartz beaker containing 30 cc of solution. The Bridgman-grown copper substrate was suspended with its electropolished face immersed, and the graphite anode was immersed nearby. The electrodeposition and also the previous electrolytic purification and substrate washings were performed in a glove box being continuously swept with filtered nitrogen. This was to protect against dust or other airborne contaminants that have been noted to affect the sensitive electrodeposition process (21, 25). All electrodepositions were at room temperature and 10 ma/cm^2.

Impurities to be added were weighed and then dissolved in water in volumetric flasks. Further dilution was done by pipetting samples into successive flasks of water, and 0.1 cc of the diluted solution was then pipetted into the electrodeposition bath.

[2] Obtained from Jarrell-Ash Company, Newtonville, Mass.

[3] Distilled and shipped in Vycor, under vacuum. Prepared and distilled by G. F. Smith Chemical Co., Columbus, Ohio.

Results

Unpurified $Cu(ClO_4)_2$ solutions gave electrodeposits which varied somewhat but generally appeared under the microscope to be similar to those reported previously for $Cu(ClO_4)_2$ solutions (3) and $CuSO_4$ solutions (5).

Electrodepositions from solutions which had been purified by boiling and pre-electrolysis had some areas in which microscopic appearance was the same as that of deposits from unpurified solutions. This is shown in Fig. 1. The geometric growth hillocks are pyramids, some of which have truncated square tops.

In five runs with purification, an average 75% of the deposit surface was smooth, with few geometric surface features at 460 diameters magnification. An example of this appearance is illustrated in Fig. 2. Some portions of the smoother 75% of the surface had an irregular ridge structure, as illus-

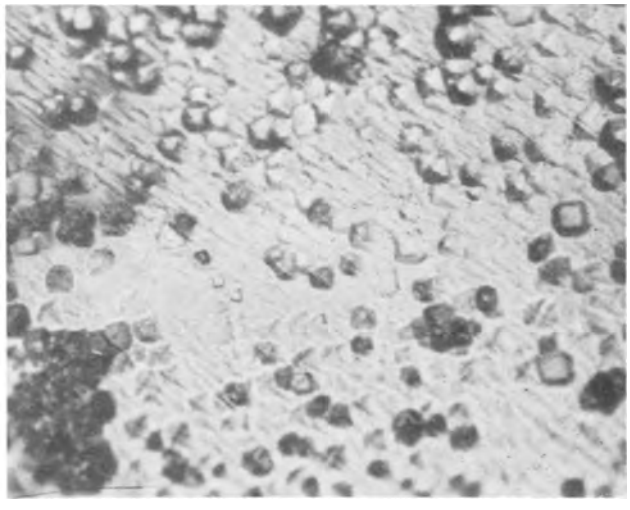

Fig. 1. Photomicrograph of part of the surface of a single crystal copper electrodeposit from a purified solution. It can be seen that this small part of the surface is completely covered by growth hillocks. Deposit is about 6μ thick. Magnification approximately 360X.

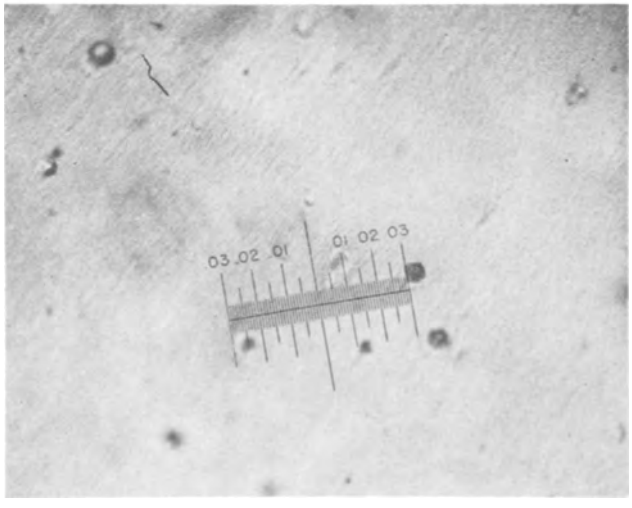

Fig. 2. A different part of the same surface that is shown in Fig. 1. Surface is not quite as smooth as that of the original electropolished substrate. Magnification approximately 360X.

trated in Fig. 3. At higher magnification, finer surface markings are visible, as in Fig. 4, while the original electropolished surfaces had appeared perfectly smooth at the highest magnification with visible light. Deposit thicknesses were approximately 6μ. Laue back-reflection photographs showed

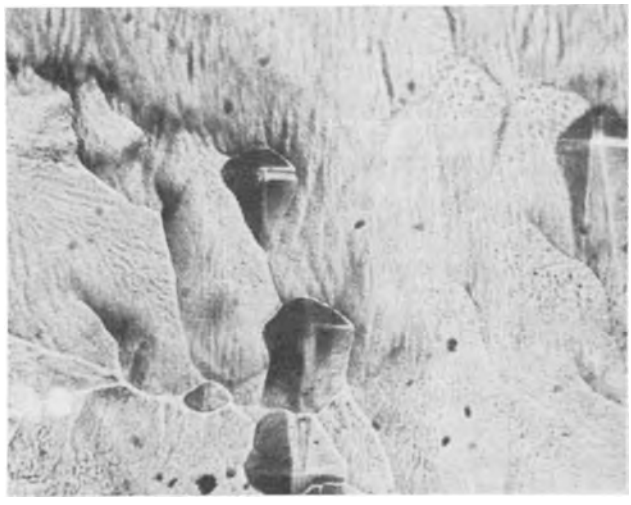

Fig. 3. A different part of the same surface that is shown in Fig. 1 and 2. Magnification approximately 360X.

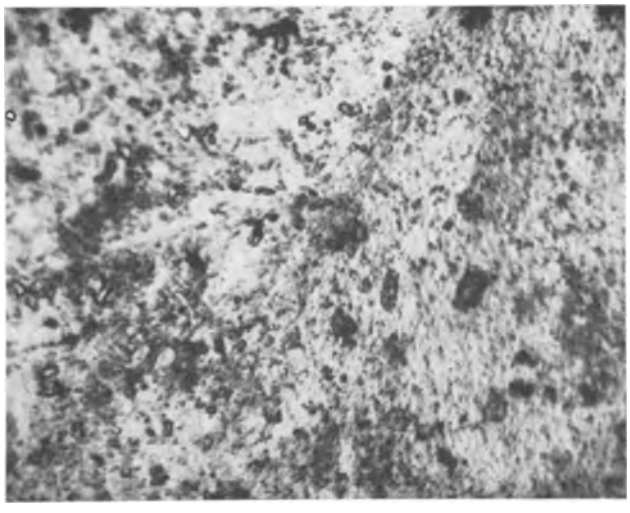

Fig. 4. The same view as shown in Fig. 2 but at higher magnification (approximately 1040X). The appearance of the area in Fig. 3 at the higher magnification is similar.

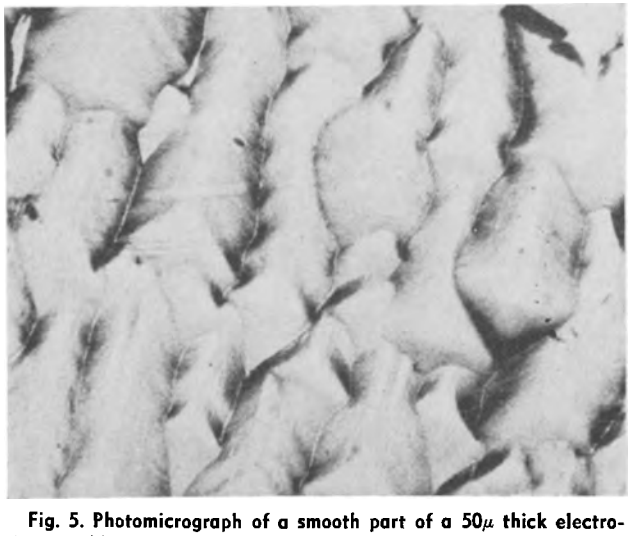

Fig. 5. Photomicrograph of a smooth part of a 50μ thick electrodeposit. Magnification approximately 360X.

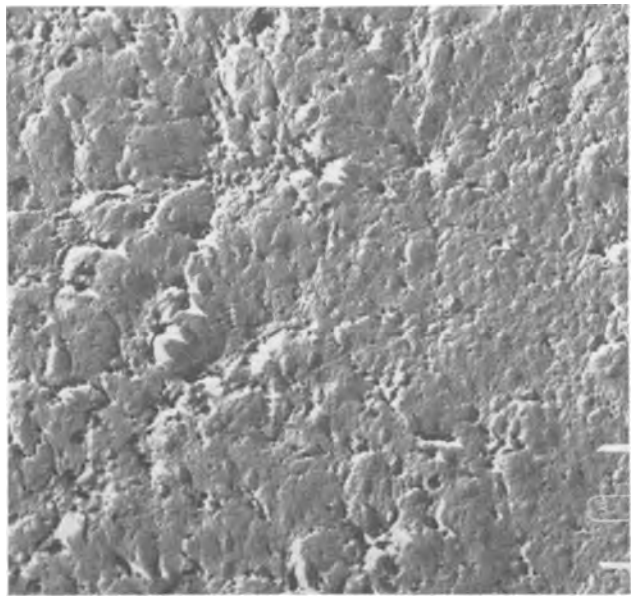

Fig. 6. Electron micrograph of a small portion of the area near the center of Fig. 2. Magnification approximately 12,500X.

that the deposits were single crystals and epitaxial with the substrate.

Deposits which were about 50μ thick had a similar appearance, but with deeper ridges, as shown in Fig. 5. This structure is closely similar to the results reported by the group at the University of Birmingham for lower current density deposits from charcoal-purified $CuSO_4$ baths (26). Laue back-reflection photographs showed that the 50μ deposits were also single crystals. At this thickness, the deposit is responsible for essentially all of the reflected x-rays (27).

Substrates weighed before and after deposition showed cathode efficiencies of approximately 100%, in agreement with previous work with epitaxial copper deposition at low current densities (3b).

With the purified solutions, electron micrographs[4] of the smooth area of the deposit surfaces showed no discrete steps and no discernible geometric shapes. Expectations that very low steps might be visible

[4] Electron micrographs were taken by Ernest F. Fullam, Inc., Schenectady, N. Y.

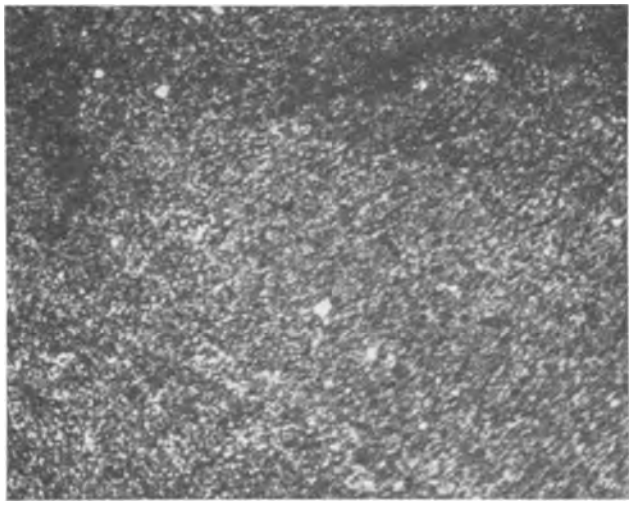

Fig. 7. Micrograph of electrodeposit from a purified bath to which 1 ppm of gelatin had been added. Magnification approximately 360X.

were not fulfilled. A typical electron micrograph, as shown in Fig. 6, is similar to published photographs of electroplated polycrystalline nickel (28).

USP gelatin (from Eli Lilly pharmaceutical capsules) was added to the purified $Cu(ClO_4)_2$ solutions in decades of concentration, and electrodeposits were then made. Freshly electropolished substrates were used for each deposition, since microscopic examination was found to allow contamination of the surface (a second plating was often polycrystalline). When the bath contained 1 ppm of gelatin, the surface appearance of a 6μ electrodeposit was as shown in Fig. 7. A Laue photograph, Fig. 8, indicates polycrystallinity. The solution was boiled for 1 hr, and the active components of the gelatin were thus destroyed. Subsequent electrodeposition on a freshly electropolished surface gave a deposit which was about 75% free of growth pyramids, as shown in Fig. 9. The Laue pattern indicates a single crystal, as in Fig. 10.

Gelatin at 0.1 ppm produced pyramid-covered deposits, similar to the results with unpurified $Cu(ClO_4)_2$ solutions (Fig. 1). At 0.01 ppm gelatin concentration, about 40% of the electrodeposit was free of growth pyramids, as in Fig. 11. At 0.001 ppm, the deposit appeared the same as with no gelatin added (Fig. 1, 2).

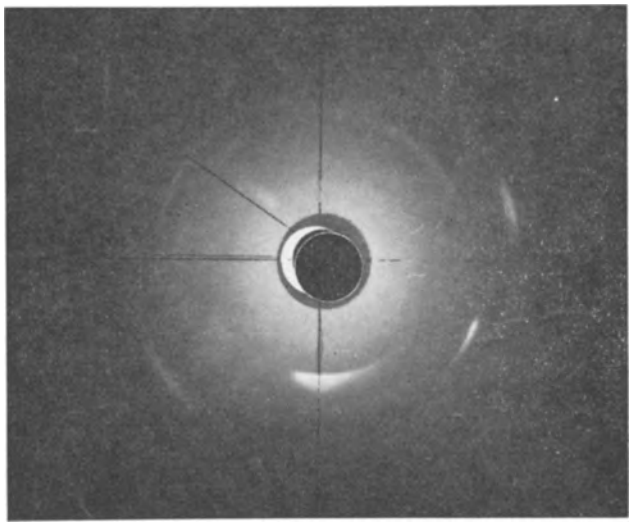

Fig. 8. Laue back-reflection x-ray photo of deposit shown in Fig. 7.

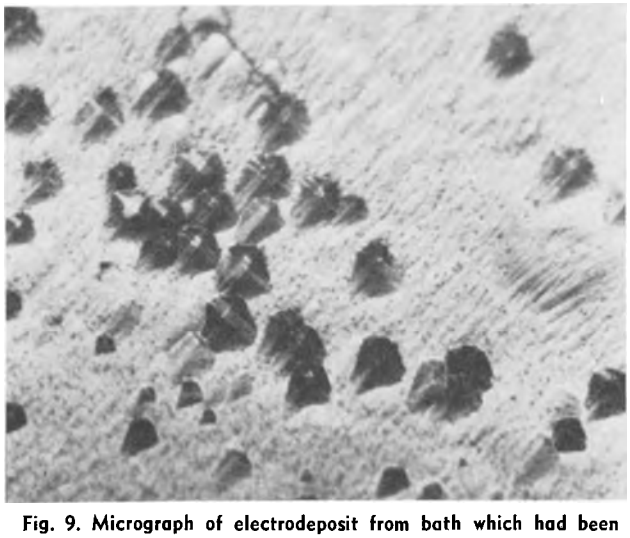

Fig. 9. Micrograph of electrodeposit from bath which had been boiled after the addition of the gelatin. Magnification approximately 360X.

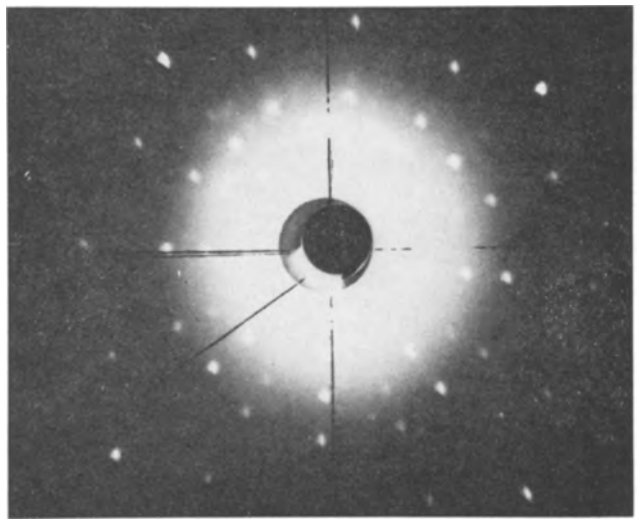

Fig. 10. Laue back-reflection x-ray photo of deposit shown in Fig. 9.

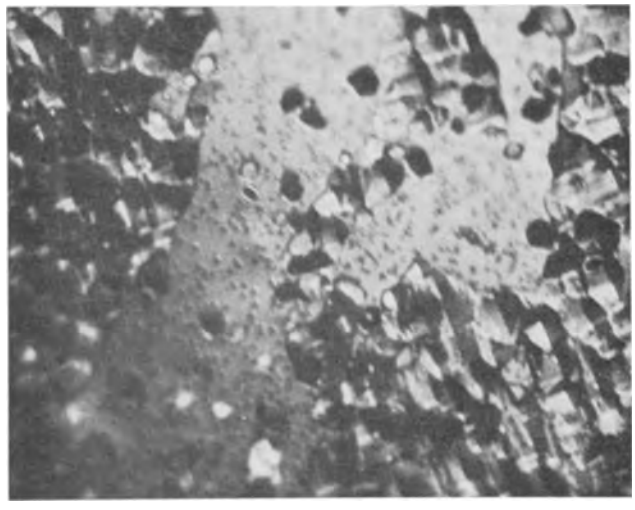

Fig. 11. Micrograph of electrodeposit from a purified bath to which 0.01 ppm of gelatin had been added. Magnification approximately 360X.

The above concentrations are calculated from the dilutions of the gelatin solutions added. However, the actual concentrations in the baths might be different from the calculated values due to such factors as gelatin adsorption onto the vessel walls.

$Pb(ClO_4)_2$ was added (as $PbCO_3$) to give a concentration of 4 ppm in a boiled and pre-electrolyzed $Cu(ClO_4)_2$ solution. The subsequent electrodeposit had the appearance of deposits from purified solutions, except that small growth hillocks were also visible, as in Fig. 12. The electrodeposition solution was then pre-electrolyzed again, removing approximately half of the remaining copper, but subsequent electrodeposits were not as free of growth hillocks as were the deposits shown in Fig. 2 and 3. They were, however, smoother than the deposits made before the second pre-electrolysis.

A boiled and pre-electrolyzed $Cu(ClO_4)_2$ solution from which flat surfaces had been electrodeposited was stored in a covered Pyrex beaker in the glove box overnight. An electrodeposit from this solu-

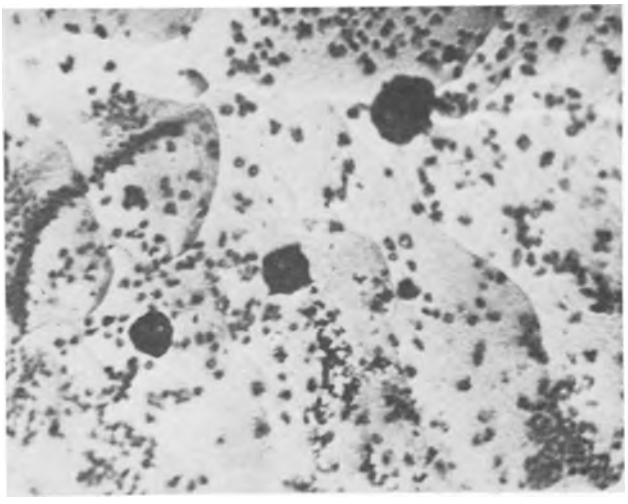

Fig. 12. Electrodeposit from a purified bath to which 4 ppm of Pb^{++} had been added. Magnification approximately 360X.

tion showed a large degree of coverage with growth hillocks. This solution was further boiled and pre-electrolyzed, and flat electrodeposits similar to those shown in Fig. 2 and 3 were electrodeposited from the solution.

Discussion

Pre-electrolysis and perchlorate oxidation treatments change the solution so as to decrease the surface density of growth hillocks. The opposite effect occurs when impurities are added. Therefore, it is probable that pre-electrolysis and oxidation are purifying the solution.

However, it is also possible that an impurity is inadvertently added during the attempts at purification, and that this impurity is one whose effect is to inhibit bunching. The spectrographic grade graphite anodes are unlikely to introduce significant inorganic impurities, but a residue of ungraphitized tar binder could possibly contaminate the solution in the parts per billion range of organic impurities. Mere contact of a solution with a piece of plastic has been shown to affect the kinetics of subsequent electrodeposition (29). Although the same type of anodes are used in both the pre-electrolysis and the deposition cells, there is more total bubbling during the pre-electrolysis than during the plating, and more impurities might be dislodged.

Evidence in favor of the purification hypothesis is that contamination with gelatin has the same effect as allowing the solution to stand overnight. It seems more likely that standing would introduce impurities than that it would allow impurities from purification attempts to disintegrate.

There will be some uncertainty on these points until the agents which are removed (or added) by the purification attempts can be analyzed at these low levels of concentration. The electron micrographs show that there are other types of surface features present, and possibly there are different growth mechanisms and impurities involved, in different orders of magnitude. These appearances can be misleading: sputtered micropolycrystalline copper sometimes forms flat-topped hillocks and steps (32) which appear very similar to the electrodeposited single crystal copper hillocks in Fig. 4 of Barnes' paper (3a) (from perchlorate solutions). It must be noted, in perspective, that hillock-free single crystals of nickel have been electrodeposited from ordinary reagent grade solutions (30), although the same workers produced only hillock-covered crystals under similar conditions (31).

Conclusions

Under the conditions reported here, electrodeposits from $Cu(ClO_4)_2$ solutions of ordinary reagent purity normally are covered with growth hillocks which presumably nucleate, take shape, and merge continuously during the growth of the electrodeposit.

The surface concentration of growth hillocks is significantly decreased when the solution is treated by oxidation and pre-electrolysis.

Since this effect is the opposite of the effects of impurity addition and of overnight storage, it is probable that the hillock decrease is due to the removal of unidentified impurities.

The hillock-free surfaces are not smooth on the scale of electron microscope observations.

Acknowledgment

The authors wish to thank Mr. E. J. Gelb for his painstaking assistance in the laboratory and Mr. E. W. Currier for the spectrographic analyses. This work was partially supported by the Air Force Office of Aerospace Research.

Manuscript received Nov. 28, 1963; revised manuscript received March 14, 1963.

Any discussion of this paper will appear in a Discussion Section to be published in the June 1964 JOURNAL.

REFERENCES

1. M. von Schwarz, *Intern. Z. Metallog.*, **7**, 125 (1915).
2. H. Seiter, H. Fischer, and L. Albert, *Electrochim. Acta*, **2**, 97 (1960).
3a. S. C. Barnes, *ibid.*, **5**, 79 (1961); R. Piontelli, G. Poli, and G. Serravalle, "Transactions of the Symposium of Electrode Processes," E. Yeager, Editor, p. 67, John Wiley & Sons, Inc., New York (1961).
3b. T. B. Vaughan and H. J. Pick, *Electrochim. Acta*, **2**, 179 (1960); I. Giron and F. Ogburn, *This Journal*, **108**, 842 (1961).
4. F. C. Frank, *Disc. Faraday Soc.*, **5**, 53 (1949).
5. H. J. Pick, G. G. Storey, and T. B. Vaughan, *Electrochim. Acta*, **2**, 165 (1960).
6. A. R. Verma, "Crystal Growth and Dislocations," p. 54, Butterworth's Scientific Publications, London (1953).
7. R. Marcelin, *Ann. phys.*, **10**, 185 (1918); L. Kowarski, *J. chim. phys.*, **32**, 303, 395, 469 (1935); R. W. G. Wykoff, *Acta Crist.*, **1**, 277 (1948); C. W. Bunn, "Chemical Crystallography," 2nd Ed., Plate II (opposite p. 19), Oxford University Press, Oxford (1961).
8. M. Volmer, *Z. physik. Chem.*, **A102**, 269 (1922); L. Kowarski, *op. cit.*
9. C. W. Bunn and H. Emmett, *Disc. Faraday Soc.*, **5**, 119 (1949).
10. W. J. Dunning and N. Albon, "Growth and Perfection of Crystals," R. H. Doremus *et al.*, Editors, pp. 439, 446, John Wiley & Sons, Inc., New York (1958).
11a. N. Cabrera and D. A. Vermilyea, *ibid.*, p. 393.
11b. J. V. Laukonis and R. V. Coleman, *J. Appl. Phys.*, **32**, 242, Fig. 6 (1961).

12. H. E. Buckley, "Crystal Growth," p. 206, John Wiley & Sons, Inc., New York (1951).
13. F. C. Frank, "Growth and Perfection of Crystals," *op. cit.*, pp. 411, 418.
14. M. J. Lighthill and G. B. Whitman, *Proc. Roy. Soc., London*, **A229**, 281, 317 (1955).
15. W. J. Dunning and N. Albon, "Growth and Perfection of Crystals," *op. cit.*, p. 439; G. Wranglen, *Electrochim. Acta*, **2**, 130 (1960).
16. H. S. Ingham *et al.*, "Metallurgy of Elemental and Compound Semiconductors," R. O. Grubel, Editor, p. 395, Interscience Publishers, New York (1961).
17. J. M. Keen and J. P. G. Farr, *This Journal*, **109**, 668 (1962).
18a. N. T. Barker, C. M. Harris, and E. D. McKenzie, *Proc. Chem. Soc.*, 335 (Sept. 1961).
18b. F. C. Mathers, Paper presented at The Electrochemical Society Detroit Meeting 1961; see Extended Abstracts of the Electrodeposition Division, p. 38.
19. F. A. Posey and R. F. Sympson, *This Journal*, **109**, 718 (1962).
20. B. Ke *et al.*, *ibid.*, **106**, 382 (1959).
21. D. A. Vermilyea, *ibid.*, **105**, 286 (1958).
22. Aften neglected in discussions of plating brighteners and electrode poisons is the electron pair theory as developed by Hackerman and Makrides in connection with catalyst poisons and corrosion inhibitors. This work points out that many inhibitors become inactive when mildly oxidized. See N. Hackerman and A. C. Makrides, *Indust. Eng. Chem.*, **46**, 523 (1954); p. 85 of Final Report, Contract DA-30-069-ORD-1680 (ASTIA TAB 6141 p. 102).
23. P. E. Lighty, D. Shanefield, S. Weissmann, and A. Shrier, To be published.
24. J. C. Schumacher, "Perchlorates," p. 215, Reinhold Publishing Co., New York (1960).
25. P. A. van der Meulen and H. V. Lindstron, *This Journal*, **103**, 390 (1956).
26. S. C. Barnes, G. G. Storey, and H. J. Pick, *Electrochim. Acta*, **2**, 195, Fig. 3a (1960).
27. C. S. Barrett, "Structure of Metals," p. 56, McGraw-Hill Book Co., Inc., New York (1952).
28. R. Weil and H. C. Cook, *This Journal*, **109**, 295 (1962); B. C. Bannerjee and P. L. Walker, *ibid.*, **109**, 436 (1962).
29. J. O. Bockris, "Annual Reviews of Physical Chemistry," G. K. Rollefson, Editor, p. 495, Annual Reviews, Inc., Stanford, Calif. (1954).
30. H. Leidheiser and A. T. Gwathmey, *This Journal*, **98**, 225 (1951).
31. H. Leidheiser and A. T. Gwathmey, *Trans. Electrochem. Soc.*, **91**, 95 (1947).
32. G. D. Magnusun, B. B. Meckel, and P. A. Harkins, *J. Appl. Phys.*, **32**, 371, Fig. 4 (1961).

Electroluminescent (Zn,Mg)S:Cu, Halide Phosphors

P. M. Jaffe

Research Department, Lamp Division, Westinghouse Electric Corporation, Bloomfield, New Jersey

ABSTRACT

Electroluminescent ZnS:Cu, halide phosphors can be prepared with up to 20 mole % MgS substituting for ZnS. MgS substitutions above 5% in the cubic Cl or Br coactivated ZnS phosphor result in a shift of the emission to shorter wavelengths, a change to the hexagonal modification, a decrease in brightness and an expansion of the unit cell. The iodine coactivated phosphors show similar but more complex changes. An unexpected effect of specific structural variations, *i.e.*, variations of the unit cell dimensions, on the EL characteristics of the (Zn,Mg)S:Cu phosphors was found in the iodine coactivated samples.

Alternating current electroluminescent (EL) ZnS phosphors activated by Cu have been extensively studied during the last few years. Partial replacement of Zn by Cd and/or Hg also results in EL phosphors (1-3). The present investigation is primarily concerned with EL ZnS:Cu phosphors produced by partial replacement of Zn by Mg.

Smith has investigated the cathodoluminescence of (Zn,Mg)S phosphors activated by Cu, Mn or Ag (4). He found that MgS is soluble in ZnS to about 20 to 25%,[1] with an associated lattice contraction. The emission of the Ag or Cu activated phosphors shifted to shorter wavelengths with increasing Mg additions. He also found that solid solutions of (Zn,Mg)S can be handled in a manner similar to that of pure ZnS, *i.e.*, no decomposition is observed on exposure to water.

Preparation of Materials and Experimental Techniques

Because MgS is very readily hydrolyzed, special methods for its preparation are necessary. The method that the writer found to be very satisfactory is one first discovered by Sarge (5) and further developed by Russo (6). This method involves the preparation of hydrated $Mg(NH_4)Cl_3$ and its subsequent conversion to the sulfide.

The hydrated $Mg(NH_4)Cl_3$ was prepared as follows: Mallinckrodt's SL grade MgO (or $MgCO_3$) was added to concentrated reagent grade HCl; the concentrations were so adjusted that there was a slight excess of HCl. A saturated solution of Mallinckrodt's SL NH_4Cl was added to the $MgCl_2$ solution and the mixed solution evaporated just to crystallization. The solution was allowed to cool overnight and the resultant crystals were filtered off and rejected. The filtrate was boiled down until crystallization commenced and allowed to cool overnight. The crystals were filtered off and washed several times with small additions of distilled alcohol and then dried at 120°C.

The double salt, $Mg(NH_4)Cl_3 \cdot XH_2O$, was converted to MgS by first converting it to anhydrous $MgCl_2$ by firing in dry HCl, and then firing it in puri-

[1] All concentrations are in mole or atom per cent unless specified otherwise.

Table I. Firing schedule for conversion of $Mg(NH_4)Cl_3 \cdot xH_2O$ to MgS

Temperature, °C	Total elapsed firing time, hr	Atmosphere
25-600	0-1.5	HCl
600	1.5-3	HCl
600	3-4.5	H_2S*
600-700	4.5-5.25	H_2S
700-1050	5.25-6.75	H_2S
1050	6.75-8.25	H_2S
1050-25	8.25-9.25	H_2S

* Before switching to H_2S at this point, the weight of $MgCl_2$ is determined in order to calculate the expected theoretical weight of MgS as explained in the text.

fied H_2S according to the schedule shown in Table I. The firing was done in silica tubes which were closed at one end and had gas inlet and outlet tubes at the other end. The double salt was contained in a silica boat. The conversion should be stopped after the formation of anhydrous $MgCl_2$ in order to determine the composition of the double salt so that the expected theoretical weight of the MgS can be calculated.[2] This need be done only once for a given batch of hydrated $Mg(NH_4)Cl_3$ if the unused portion of the double salt is kept in tightly closed containers. Succeeding conversions can be switched over directly from HCl to H_2S while the $MgCl_2$ is still in the furnace. The finished MgS should be stored in a desiccator over a good desiccant.

Phosphors were prepared from RCA ZnS (33-Z-19). The appropriate amounts of Cl, Br, or I (as the ammonium salts) and Cu (as the acetate) were added from stock solutions and mixed as a slurry. After drying at 120°C, 5 wt % S (7, 8) and the necessary amount of MgS were added and the entire raw mix thoroughly mixed;[3] these latter operations were carried out in a dry box. The samples were fired in loosely capped silica tubes which were contained in a larger silica tube closed at one end and having gas inlet and outlet tubes at the other end. Crystallization was carried out by firing at 950°C in a flowing N_2 atmosphere. The cooled samples were crushed, mixed with 5 wt % S and refired. The refired samples were washed in an NaCN-NaOH solution followed by several washings in H_2O and in distilled alcohol and then dried at 120°C in a vacuum oven. Samples were prepared with the composition $(100-x)$ ZnS·xMgS:0.6Cu,0.3 halide (Cl, Br or I) and x = 0,2,5,8,10,15, and 20.

The EL was measured in an EL cell with castor oil as the dielectric; sinusoidal excitation was used in all the measurements. Brightness measurements were made with a "Spectra" Brightness Spot Meter.[4] Brightness waveforms were observed on a dual beam oscilloscope.

[2] The theoretical weight of MgS obtained from each batch of $Mg(NH_4)Cl_3 \cdot XH_2O$ must be calculated. If the actual weight differed by more than approximately 1% from the theoretical value the batch was rejected. Generally, if the batch was off, it was below the theoretical weight due to the presence of oxide. With the firing schedule used here this rarely happened.

[3] The sulfur aids in removing vacancies which are detrimental to phosphor maintenance (9).

[4] Manufactured by Photo Research Corporation, Hollywood, California.

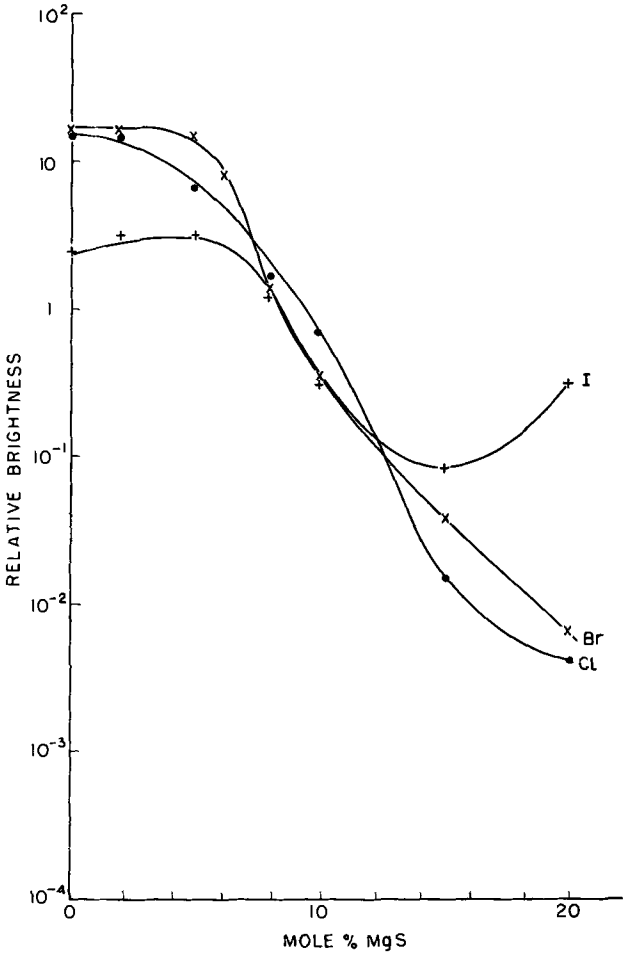

Fig. 1. Effect of increasing Mg content on the EL brightness of (Zn,Mg)S:Cu, halide phosphors. (100 — x)ZnS · xMgS: 0.6 Cu, 0.3 halide.

Experimental Results

Effect of MgS *on Brightness.*—Figure 1 shows the effect of increasing substitutions of MgS for ZnS on the EL brightness. For MgS additions up to 5% there is a little brightness variation. Above 5% MgS, there is a rapid decrease in brightness. The iodine coactivated phosphors, however, show a brightness minimum at 15% MgS; the brightness of the 20% MgS sample is similar to that of the 10% sample.

The decrease in brightness with increasing MgS above 5% is partly due to a change in emission color and partly due to a change in crystal structure (see below).

Influence of MgS *on the emission color.*—The effect of increasing additions of MgS on the EL emission color was determined by the ratio of the emission intensities measured through the blue and green filters of the Spectra Meter. The data are shown in Fig. 2; also shown are the corresponding data for 3650Å excitation.[5] The behavior of the Cl and Br coactivated samples is similar for both modes of excitation: For MgS additions up to 5% there is little variation of the emission color (EL or u-v excitation). With further additions of MgS, the behavior under u-v and EL excitation differs. Field excitation of the 8 to 10% MgS samples results in a shift toward the blue; the emission of the 15 and

[5] 100 watt high pressure Hg lamp with a Corning No. 9863 filter.

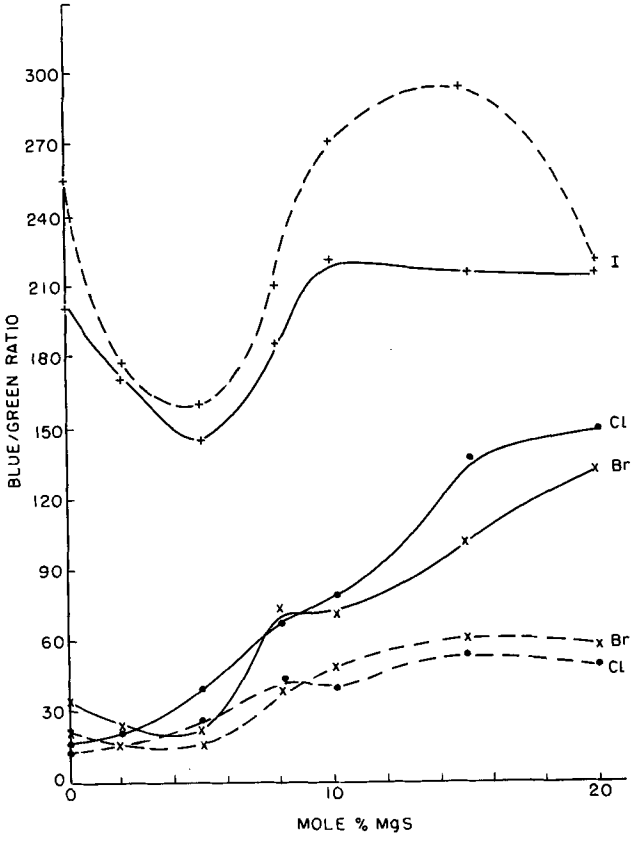

Fig. 2. Effect of increasing Mg content on the blue/green ratio of the luminescence of (Zn,Mg)S:Cu, halide phosphors. ----, Electroluminescence; ———, photoluminescence.

20% MgS samples is essentially the same and slightly bluer than that of the 10% MgS sample. For excitation by 3650Å, increasing additions of MgS over the range of 8 to 20% MgS result in the phosphors becoming progressively bluer. The addition of up to 5% MgS to the I coactivated phosphors produces a progressive shift of the emission (photoluminescence or EL) toward the green region of the spectrum. A further increase of MgS up to 10% results in a shift back toward the blue. Above 10% MgS the effect of further MgS additions varies with the mode of excitation. With 3650Å excitation the emission remains essentially unchanged. However, the EL is shifted further toward the blue for the 15% sample, but shifts back toward the green on addition of 20% MgS. This behavior of the I coactivated (Zn,Mg)S phosphors was very unexpected. Repeat preparations showed it to be qualitatively reproducible.

The I coactivated 90ZnS·10MgS, 85ZnS·15MgS, and 80ZnS·20MgS samples were analyzed for their residual Mg content using an EDTA titration after solution of the samples in an HNO_3-HCl mixture and separation of the Zn (10). No loss of Mg was found so that the change in the EL emission color as a function of the MgS content over this concentration range is real and not due to loss of MgS.

Voltage dependence of brightness.—The voltage dependence of the brightness of all (Zn,Mg)S phosphors followed the relationship $B = A \exp [-(V_0/V)^{1/2}]$. The influence of increasing MgS on the slope of the B-V curves varied, depending on the

Table II. V_0 values of (100-x) ZnS · xMgS:0.6Cu,0.3 halide (Cl, Br, or I) from the equation $B = A \exp [-(V_0/V)^{1/2}]$

% Mg	V_0 (×10⁴), volt Cl	Br	I
0	4.2	3.2	1.2
2	4.3	3.1	1.2
5	4.4	3.2	1.1
8	2.8	2.7	1.0
10	3.3	3.4	1.4
15	3.2	3.6	1.6
20	3.2	3.8	1.5

particular halogen coactivator, as shown in Table II.[6] With Cl coactivation the slopes of the B-V curves were similar for samples containing up to 5% MgS. The slopes of the curves for samples containing 10 to 20% MgS were also similar but less steep. The slope of the 8% MgS sample, however, was the lowest. The situation is similar for the Br coactivated phosphors except that the slopes of the 10 to 20% MgS phosphors are greater than that of the 0-5% MgS samples. The B-V slopes of the I coactivated 0 to 5% MgS samples were similar, as were those from the 10 to 20% MgS samples; the slopes of the latter samples were greater. The slope of the 8% MgS sample was similar to that of the 0-5% MgS samples. However, the 8% MgS sample had a greater percentage of cubic structure than the corresponding Cl or Br coactivator phosphors (see below).

Frequency dependence of brightness.—The frequency dependence of the brightness of the (Zn,Mg)S phosphors was examined over the frequency range of 60-10^4 cps. The brightness, B, increased with frequency, f, according to the same power law ($B \sim f^n$) to approximately 4000 cps and then started to approach saturation. The values of n were essentially constant (~0.6-0.8) and independent of the coactivator.

Brightness waveforms.—The brightness waveforms are essentially the same for Cl, Br, or I coactivation. The waveforms do vary as a function of the MgS content, as shown in Fig. 3. With MgS concentrations up to 8%, the waveforms consist of

[6] The values of V_0 are given in Table I since the slope is proportional to 0.435 $V_0^{1/2}$.

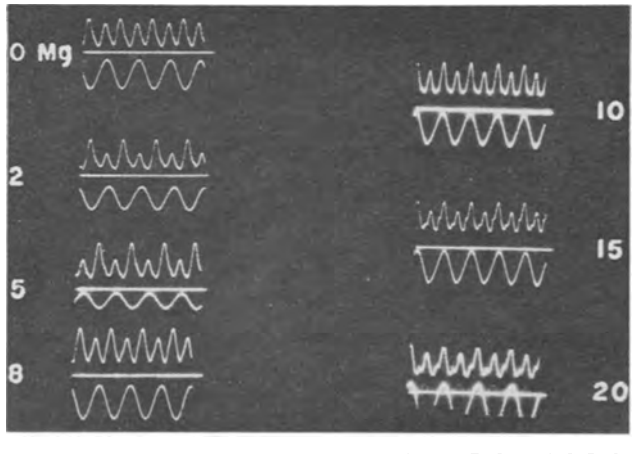

Fig. 3. Brightness waveforms from (100-x)ZnS · xMgS:Cu,I phosphors. Data taken at 400 cps.

a pronounced primary peak and a weaker secondary peak (shoulder) on the descending side of the primary wave. All the samples have a d-c component; the influence of MgS on this component was not investigated. The secondary brightness waves of the 10, 15, and 20% MgS samples become resolved into sharp peaks located between the primaries; the amplitude of the secondary peaks relative to the primary ones varies slightly, increasing with increasing MgS.

Structure studies.—ZnS exists in two structural modifications, the cubic or low temperature form and the hexagonal or high temperature form. The transition temperature is around 1020°C, but it is strongly affected by the preparative conditions. ZnS phosphors can be made having either structure. The "pure" ZnS phosphors prepared here were cubic. Addition of up to 5% MgS had no effect on the structure but caused a slight lattice expansion, Fig. 4. For MgS concentrations of 10% and above the structure was pure hexagonal. Samples containing 8% MgS had a mixed cubic-hexagonal structure.[7] Samples with hexagonal structure and coactivation by Cl, Br, or I showed an approximately uniform expansion of the unit cell along the a_h axis with increasing MgS; Cl and Br coactivated samples also showed an expansion along the c_h axis but there was a slight negative deviation from linearity. The I coactivated phosphors showed unexpected behavior: while there is also an expansion along c_h, it has a maximum at 15% MgS (Fig. 4).

The fact that, for MgS concentrations of 10% and above, the structure is hexagonal, means that either the presence of MgS in this concentration range causes a lowering of the transition temperature of the cubic to the hexagonal modifications or that in this concentration range only hexagonal (Zn,Mg)S can exist. The possible lowering of the transition temperature was investigated by preparing samples at 800°, 850°, and 900°C. The lowest temperature used was 800°C since there were indications of incomplete solid solubility, *i.e.*, evolution of H_2S on washing in water. All the samples prepared at these lower temperatures were hexagonal. Therefore, it would appear that over the concentration range of 10 to 20% MgS only the hexagonal modification is stable.

[7] The hexagonal content of the 8% MgS phosphors was too low to determine the hexagonal lattice constants accurately; hence the latter are not shown in Fig. 4.

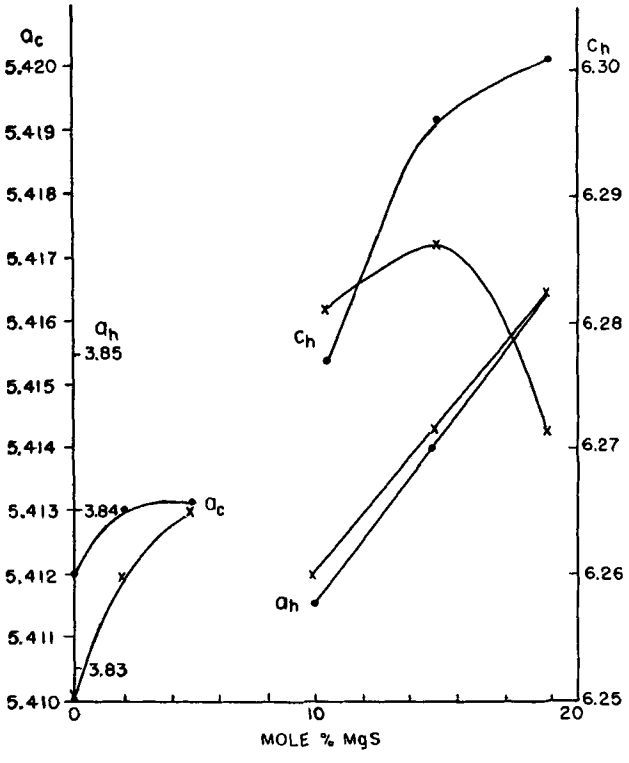

Fig. 4. Unit cell dimensions (in Angstroms) of cubic and hexagonal (Zn,Mg)S:Cu, halide phosphors as a function of increasing Mg content. •, Cl or Br; x, I.

Expansion of the ZnS lattice due to the incorporation of MgS was rather unexpected in the light of Smith's work on the (Zn,Mg)S system (4). He found that increasing MgS substitution results in a lattice contraction. The reason for the difference between Smith's and the present work is not known unless it is that here we actually have a three component matrix while Smith's was two component, *viz.*, ZnS-MgS-Cu_2S and ZnS-MgS, respectively.

Conclusions and Discussion

The most significant result of this study is the specific effect of structural variations on the EL characteristics of the phosphors. Previous studies had shown that the conversion of cubic to hexagonal ZnS (12) or (Zn,Cd)S (1-3, 11) was detrimental to the EL. The present study shows that it may not be the hexagonal structure *per se* which is detrimental but rather changes along specific crystallographic directions. This is indicated by examination of the data in Fig. 1, 2, and 4 for the I coactivated phosphors. Both the blue/green ratio and the brightness follow variations of the unit cell along the [001] direction, *i.e.*, the c_h axis. There is an indication that the Cl coactivated phosphors also show this effect but it is not very pronounced. Why the photoluminescence of the I coactivated phosphors is not affected by the variations along c_h is not known nor are the reasons for these variations of c_h. There might be a correlation with the observation that in single crystals of hexagonal ZnS:Cu the EL appears as streaks perpendicular to the c_h axis (13).

Acknowledgment

The writer would like to thank Mr. G. Scanlon for his aid in various phases of this work, Dr. C. K. Lui Wei for the x-ray measurements and Dr. H. F. Ivey for reading the manuscript and making several valuable suggestions.

Manuscript received Feb. 20, 1963. This paper was delivered before the Chicago Meeting, May 1-5, 1960.

Any discussion of this paper will appear in a Discussion Section to be published in the June 1964 JOURNAL.

REFERENCES

1. A. Wachtel, *This Journal*, **107**, 602 (1960).
2. A. Wachtel, *ibid.*, **107**, 682 (1960).
3. A. B. Dreeben, Abstract No. 70, Spring Meeting, Electrochemical Society, Chicago, Ill., May 1-5, 1960.
4. A. L. Smith, *This Journal*, **99**, 155 (1952).
5. T. W. Sarge, U. S. Pat. No. 2,358,661, Sept. 19, 1944.
6. E. Banks, V. Russo, and R. Ward, *J. Am. Chem. Soc.*, **72**, 3175 (1950).

7. A. Wachtel, U. S. Pat. No. 2,874,128, Feb. 17, 1959.
8. W. Lehmann, Canadian Pat. No. 579,685, July 14, 1959.
9. P. M. Jaffe, *This Journal*, **108**, 711 (1961).
10. A. Amin and M. Farah, *Chemist-Analyst*, **44**, 62, 65 (1955).
11. W. Lehmann, "Electroluminescent (Zn,Cd)S:Cu Phosphors," Spring Meeting, Electrochemical Society, Pittsburgh, Pa., April 15-18, 1963.
12. A. McKeag and E. Steward, *This Journal*, **104**, 416 (1957).
13. P. Zalm, *Philips Research Repts.*, **11**, 353 (1956).

An Investigation of the Optical Properties and the Growth of Oxide Films on Silicon

B. H. Claussen and M. Flower[1]

Standard Telecommunication Laboratories Limited, Harlow, Essex, England

ABSTRACT

A polarization spectrometer has been used to investigate the optical properties of oxide films on silicon. Good agreement has been obtained between the experimental results and data calculated from the exact theory of reflection. This has enabled accurate measurements to be made of the refractive indices and thicknesses of films prepared in various ways. In addition, oxidation rates have been determined for films grown thermally at 1200°C.

The use of polarization spectrometry or ellipsometry in the study of isotropic films on absorbing substrates has been limited in the past by the difficulty of obtaining numerical data from the exact theory of reflection. Nevertheless, the method has found some application in the study of oxide film growth. Thus Winterbottom (1, 2) has obtained graphical solutions of the exact equations and attempted to interpret the experimental data of Tronsted and Hoverstad (3) for aluminum oxide. Archer (4), on the other hand, has investigated the oxidation of silicon and germanium under normal laboratory conditions, using approximations originally derived by Drude (5) to evaluate the results. These approximations are only valid when the film thickness is much less than the wavelength of light.

The advent of modern computing techniques has, however, removed the limitations inherent in these procedures so that solutions of the exact equations can be obtained in a form suitable for the accurate determination of both the optical constants and thickness of the film. Using data computed in this manner, Archer (6) recently carried out a detailed investigation of film growth on silicon while Menard (7) used a similar approach in a study of the oxidation of titanium.

This paper describes an investigation of the optical properties of silica films on silicon. The films were prepared both by sputtering and by the thermal and anodic oxidation of silicon itself. [The conditions of preparation are somewhat different from those reported by Archer (6)]. In addition oxidation rates have been determined for the thermally grown oxide films.

Theory

In considering reflection from a film covered surface, it is most convenient to express the results in terms of the complex Fresnel coefficients for the two plane wave components having their electric field vectors vibrating parallel ($\hat{r}_p$) and perpendicular ($\hat{r}_s$) to the plane of incidence. If the film is isotropic, it may be shown that the ratio of the reflectances for the two components is given by the equation (8)

$$\frac{\hat{R}_p}{\hat{R}_s} = \frac{\hat{r}_{12p} + \hat{r}_{23p}\,\epsilon^{-2i\hat{\delta}}}{1 + \hat{r}_{12p}\,\hat{r}_{23p}\,\epsilon^{-2i\hat{\delta}}} \cdot \frac{1 + \hat{r}_{12s}\,\hat{r}_{23s}\,\epsilon^{-2i\hat{\delta}}}{\hat{r}_{12s} + \hat{r}_{23s}\,\epsilon^{-2i\hat{\delta}}}$$

where the subscripts 1, 2, and 3 refer to the surrounding medium, film, and substrate, respectively.

The Fresnel coefficients are defined as follows

$$\hat{r}_{\alpha\beta p} = \frac{\hat{n}_\beta \cos\hat{\phi}_\alpha - \hat{n}_\alpha \cos\hat{\phi}_\beta}{\hat{n}_\alpha \cos\hat{\phi}_\beta + \hat{n}_\beta \cos\hat{\phi}_\alpha}$$

$$\hat{r}_{\alpha\beta s} = \frac{\hat{n}_\alpha \cos\hat{\phi}_\alpha - \hat{n}_\beta \cos\hat{\phi}_\beta}{\hat{n}_\alpha \cos\hat{\phi}_\alpha + \hat{n}_\beta \cos\hat{\phi}_\beta}$$

$\alpha = 1$ or 2 $\qquad$ $\beta =$ 2 or 3

The refractive indices, $\hat{n}$, are in general complex and may be expressed in the form

$$\hat{n} = n - ik$$

k is related to the absorption coefficient, α in cm^{-1}, by the equation $\alpha = 4\pi k/\lambda$. The $\hat{\phi}_s$, which are also complex, are the angles of propagation in the respective media. $\hat{\delta}$ is a function of the film thickness and is given by the equation

$$\hat{\delta} = 2\pi d/\lambda \cdot \hat{n}_2 \cos\hat{\phi}_2$$

d is the film thickness measured in the same units as the wavelength of the light.

The ratio $\hat{R}_p/\hat{R}_s$ is also a complex number and may be written in the form $\tan\psi\epsilon^{i\Delta}$ where $\tan\psi$ represents the change in the amplitude ratio of the two

[1] Present address: Department of Electronic Computing, Leeds University.

plane wave components on reflection and Δ is the phase shift between them. The quantities ψ and Δ are those normally measured in an ellipsometer experiment.

In studying film growth it is necessary to know the optical constants of the substrate. These may be determined from measurements of Δ and ψ for a film-free surface. In accordance with Archer (9), n and k are then calculated from the relations

$$n^2-k^2=\tan^2\phi\sin^2\phi\frac{(\cos^2 2\psi-\sin^2 2\psi\sin^2\Delta)}{(1+\sin 2\psi\cos\Delta)^2}+\sin^2\phi$$

$$2nk=\tan^2\phi\sin^2\phi\frac{\sin 4\psi\sin\Delta}{(1+\sin 2\psi\cos\Delta)^2}$$

where ϕ is the angle of incidence with air as the ambient medium. Measurements of Δ and ψ are then made on surfaces covered with films of varying thickness, and the values of $\tan\psi\epsilon^{i\Delta}$ are plotted in the complex plane. The curve so obtained is compared with a series of theoretical curves, computed using the appropriate values for the optical constants of the substrate and assuming various values for the refractive index and absorption coefficient of the film. For the case of an absorbing film on an absorbing substrate, the curves spiral inwards ending at the point corresponding to reflection from a film infinite thickness. If the film is nonabsorbing, the curves are closed figures which repeat periodically and do not, in most practical cases, overlap or intersect each other. A good fit between the experimental curve and one of the theoretical curves indicates that the optical constants of the film are those of the theoretical curve, For a nonabsorbing film, it should of course, be possible to determine the refractive index and the thickness of the film from a single measurement. However, considerable inaccuracies will result from such a determination when the experimental point lies near the origin of the thickness scale, since in this region the curves for different refractive indices are almost coincident.

Experimental Technique

The optical measurements were carried out on an ellipsometer constructed in these laboratories. A diagram of the apparatus is shown in Fig. 1. Monochromatic light from a low pressure mercury vapor lamp in series with a mercury green filter ($\lambda=$ 5461Å) is collimated and passed successively through a polarizer, Faraday cell having a strain-free glass core, and quarter wave plate. The latter is fixed in a rotatable circle so that its fast axis can be set at a given angle to the plane of incidence. The light then strikes the specimen which is mounted on a spectrometer table. Iris diaphragms accurately aligned along the axis of the instrument ensure that the incident beam is parallel. The specimen holder is constructed so that the specimen can be moved in the horizontal and vertical planes. On reflection, the light passes through further iris diaphragms and thence to the analyzer which forms part of the movable arm of the instrument. Both the polarizer and analyzer consist of Nicol prisms mounted in graduated rotatable circles. The radiation transmitted by the analyzer is detected by a photomultiplier having an over-all gain of 200 amp/lumen.

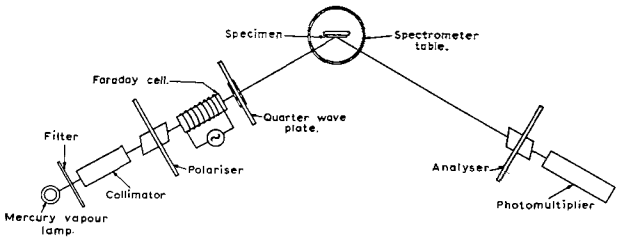

Fig. 1. Schematic diagram of ellipsometer

With this instrument the incident beam will, in general, be elliptically polarized, the ellipticity depending on the relative orientations of the polarizer and quarter-wave plate. These may be altered so that the phase change on reflection, Δ, is just compensated by the incident ellipticity. The reflected light will then be plane polarized, the analyzer reading at extinction being a measure of the amplitude ratio $\tan\psi$.

The procedure used to determine Δ and χ is similar to that described by Menard (7). The quarter-wave plate is set with its fast axis at 45° to the plane of incidence and, with a suitable angle of incidence, the specimen holder is adjusted until the beam as viewed through the analyzer, is centered on the specimen. Measurements are then made of the orientations P and A of the polarizer and analyzer at extinction. Finally the polarizer is rotated through 90° and a second extinction position determined, corresponding to an analyzer reading A'. The angles P, A, and A' are measured with respect to the plane of incidence as zero axis and are considered to be positive if, on looking along the direction of propagation, a clockwise rotation has occurred. It may then be shown that if δ is the actual retardation of the quarter-wave plate

$$\begin{aligned}\tan\Delta &= \sin\delta\cot 2P\\ \cos 2L &= -\cos\delta\cos 2P\\ \tan\psi &= -\cot L\tan A=\tan L\tan A'\\ \tan^2\psi &= -\tan A\tan A'\end{aligned}$$

where $\tan L$ is the ratio of the parallel and perpendicular amplitudes in the incident beam at the first extinction position. Values of Δ and χ determined in this manner can be checked by setting the slow axis of the quarter-wave plate at +45° to the plane of incidence when a similar set of equations can be shown to apply.

Using a microammeter to record the photomultiplier current, polarizer and analyzer settings at extinction can be read to within ±0.05°. If the ellipticity of the incident beam is made to oscillate by applying an a-c field to the Faraday cell, the photomultiplier signal can be observed on an oscilloscope. This enables polarizer settings to be made with an accuracy of ±0.01°.

The experiments were carried out on (111) slices of crucible-grown p-type silicon in the resistivity range 1-20 ohm-cm. For the thermal oxidations, the slices were mechanically polished using 0.25μ alumina as the final abrasive and then degreased in hot redistilled acetone. Prior to insertion in the furnace,

the specimens were boiled briefly in concentrated sulphuric acid to destroy organic matter and then rinsed in deionized water. The oxidations were carried out at 1200°C in a 3 cm diameter open ended quartz tube. The atmospheres used were: (i) oxygen containing less than 10 ppm of water, (ii) oxygen saturated with water at 28° and 85°C, (iii) argon saturated with water at 28° and 85°C, and (iv) steam. Except in the case of steam, a gas flow rate of 1 liter/min was maintained during the oxidation. Thermally grown layers were also prepared on slices which had been chemically polished in a solution consisting of 10 parts of concentrated nitric acid to 1 part of 40% hydrofluoric acid to 6 parts of glacial acetic acid, and on previously used slices from which the oxide layer had been removed by rinsing in 40% hydrofluoric acid.

The anodic films[2] were formed on mechanically polished slices that had been etched for 3 min in a solution containing 5 parts of concentrated nitric acid to 3 parts of 40% hydrofluoric acid and 3 parts of glacial acetic acid, and then rinsed in deionized water. The electrolyte was a dilute solution of potassium nitrate in N-methyl acetamide, both anhydrous and containing some 6-8% of water. Contact to the specimen was made either by alloying an aluminum wire to the back face or via a pool of mercury in a specially designed jig. With a platinum wire cathode, a constant current density of 10 ma cm^{-2} was maintained during the anodization.

The sputtered silica films[3] were also deposited on silicon slices that had been polished to a mirror finish. The sputtering itself was carried out in an atmosphere of dry oxygen at a pressure of 5×10^{-2} Torr using a water-cooled cathode of polycrystalline p-type silicon.

Results

As stated above, a prerequisite for a study of film growth is that optical constants of the substrate be known. Ellipsometer experiments suggest that it is possible to obtain a virtually oxide-free surface on etched silicon by annealing for half an hour at 1200°C in an atmosphere of hydrogen purified by passage through a palladium tube. This has been confirmed by reflection electron diffraction measurements at glancing angle incidence ($\theta \simeq 0.2°$) (10). The diffraction patterns obtained consist of strong Kikuchi lines and spots from the single crystal silicon, together with a few diffuse halos corresponding to amorphous silica. The intensity of the spot pattern indicates that the thickness of the residual oxide layer, if it assumed to be continuous and uniform is not more than 3Å.

Measurements of Δ and ψ were therefore made on such a surface and the values obtained were corrected for the presence of the residual (3Å) oxide layer (Δ is much more sensitively dependent on film thickness than ψ). The corrections were calculated from equations derived by Archer (4) assuming that the refractive index of the oxide is similar to that of bulk silica. On inserting the values of Δ and ψ so determined in the appropriate equations for n and k, the complex refractive index of silicon was found to be 4.05 — 0.03i at 5461Å. This is in good agreement with the figure obtained by Archer (6), where the imaginary part was calculated from the absorption data of Dash and Newman (10).

Using this figure, values of the ratio $\hat{R}_p/\hat{R}_s$ for a particular angle of incidence ϕ, were calculated as a function of the thickness, d, and refractive index of the oxide film, n_2. There calculations, which are normally extremely laborious, were carried out with the aid of a Stantec Zebra computer. For a nonabsorbing silica film, periodic curves are obtained on plotting the data in the complex plane. Figure 2 shows a typical set of curves with $\phi = 61.26°$ and n_2 varying between 1.2 and 2. The shape and position of the curves, at least within the limits of experimental error, are not affected by the possible inaccuracies in the optical constants of silicon (± 0.01 for both n and k).

The refractive indices of the oxide films are determined by fitting experimental values of tan $\psi e^{i\Delta}$ to a particular theoretical curve. This is illustrated in Fig. 3 in which ellipsometer data are plotted for

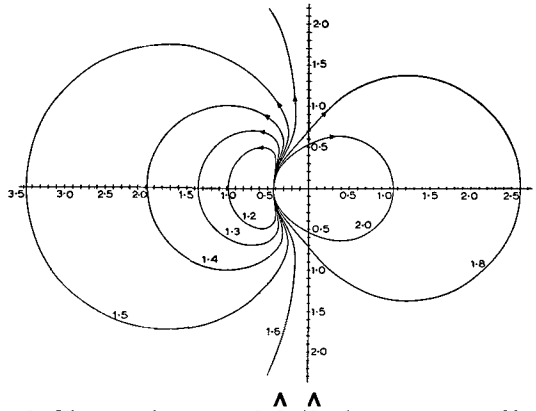

Fig. 2. Theoretical curves of $\hat{R}_p/\hat{R}_s$ for transparent films on silicon with $\phi = 61.26°$ and $\lambda = 5461$Å. The refractive index of the film is marked on each curve, the arrow showing the direction of increasing thickness.

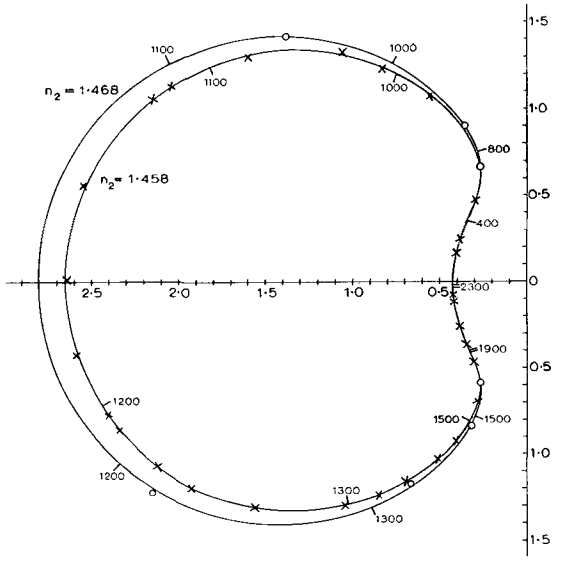

Fig. 3. Experimental results for silica films prepared by (⊙) anodization in a 0.0025N solution of KNO_3 in anhydrous N-methyl acetamide, (X) thermal oxidation at 1200°C in oxygen saturated with water at 28°C. Film thicknesses in angstroms (1st cycle only) are marked on each curve.

[2] Prepared by the Transistor Division of Standard Telephones & Cables.

[3] Prepared by the Capacitor Division of Standard Telephones & Cables.

Table I. Data for various silica films

Method of preparation	Refractive index of film	Dissolution rate, Å/sec (NH_4F/HF mixture at 18°C)
1. Thermal oxidation at 1200°C in		
(i) Dry oxygen	1.458	6.8
(ii) Oxygen saturated with water at (a) 28°C	1.458	6.7
(b) 85°C	1.455	7.1
(iii) Steam	1.452	7.3
(iv) Argon saturated with water at (a) 28°C	1.458	6.8
(b) 85°C	1.455	7.1
2. Anodic oxidation in		
(i) 0.0025N solution of KNO_3 in anhydrous N-methyl acetamide	1.468	49
(ii) 0.04N solution of KNO_3 in N-methyl acetamide containing 6-8% of water	1.417	>55
3. Sputtering	1.458	8.1

films prepared by two different methods (i) anodic oxidation in a 0.0025N solution of KNO_3 in anhydrous N-methyl acetamide, and (ii) thermal oxidation in an atmosphere of oxygen saturated with water at 28°C. The results cover a thickness range of about 2000Å for the anodic oxidations and 5500Å or just over two cycles for the thermal oxidations. Similar plots are also obtained for the other oxide films. The good agreement between experiment and theory permits accurate measurements to be made of the refractive indices and incidentally confirms that the correct values were used for the optical constants of silicon. However, the scatter of the experimental points is such as to make it impossible to resolve differences in the refractive indices of less than 0.003. In Table I, data obtained in this manner for the various silica films are given, together with the corresponding dissolution rates in a 12:1 mixture of a 12N solution of ammonium fluoride and 40% hydrofluoric acid.

To check the figures in Table I some measurements have also been carried out at other angles of incidence and with the fast axis of the quarter-wave plate set at −45° to the plane of incidence.

The thicknesses of individual films are determined directly from the appropriate refractive index curve,

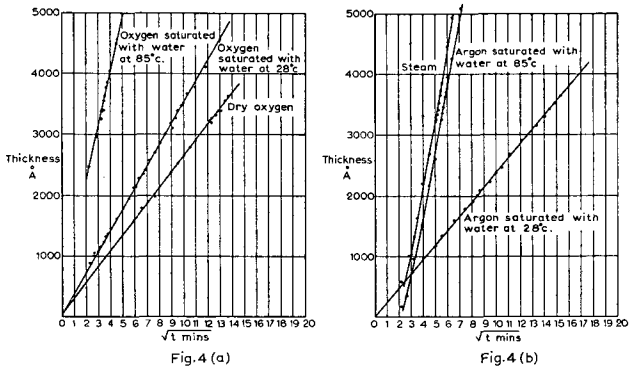

Fig. 4. Rate curves for silicon oxidations at 1200°C in (a) atmospheres having a high oxygen content, and (b) atmospheres having a low oxygen content.

Table II. Rate constants for oxidizing atmospheres

Atmosphere	Rate constant, Å²/min
(i) Dry oxygen	7.6×10^4
(ii) Oxygen saturated with water at	
(a) 28°C	12.2×10^4
(b) 85°C	87.0×10^4
(iii) Steam	130.0×10^4
(iv) Argon saturated with water at	
(a) 28°C	5.8×10^4
(b) 85°C	121.0×10^4

the variation in the thickness scale due to uncertainties in the optical constants of silicon being much less than the experimental error. Provided the order of the film is known, it is possible to measure its thickness with an accuracy of ±5Å. Using data obtained in this manner, rate curves are plotted in Fig. 4 for the various methods of thermal oxidation. In every case a parabolic rate law of the form $d = kt^{1/2}$ is obeyed over most of the thickness range studied. However in atmospheres containing little or no oxygen and a high concentration of water vapor (Fig. 4b) the films initially grow at a much slower rate. This behavior is not observed when the partial pressure of water vapor is sufficiently low. In Table II the rate constants at 1200°C are given for the various oxidizing atmospheres. Where measurements have been made under comparable conditions, the results are in reasonably good agreement with those of Deal (11).

Some investigations have also been made of the effect of surface preparation on the oxidation rate. In general there is little difference between the behavior of the surfaces investigated. However, it appears that in dry oxygen etched surfaces tend to oxidize faster than mechanically polished surfaces. Further experiments are being undertaken to clarify this situation.

Discussion

For each method of oxidation, the ellipsometer data can be fitted to a single $\hat{R}_P/\hat{R}_S$ curve computed with a particular value for the refractive index of the film. Over the thickness range studied (100-10,000Å) there is no indication that the refractive index changes with increasing film thickness. The scatter of the experimental points about a given curve is less than that reported by Archer (6), in spite of the greater uncertainty in determining the analyzer reading at extinction. This suggests that the films are more uniform than Archer's and that there is less variation in the refractive index from film to film.

The refractive indices of the thermally grown oxides are very similar, though somewhat lower values are obtained when the water concentration in the oxidizing atmosphere is high. This may be correlated with an increase in the water content of the film c.f. opaline silica ($SiO_2 \cdot XH_2O$) which has a refractive index lying between 1.40 and 1.46 that increases with decreasing hydration. It would therefore seem unlikely that the figure of 1.475 obtained by Archer (6) for films grown in high pressure steam are due simply to the presence of dissolved

water. In addition the value reported here for films grown in dry oxygen (1.458) is close to that of bulk vitreous silica (1.460) and distinctly higher than Archer's value (1.450). No explanation can be offered for this discrepancy, although the oxidation was carried out at slightly different temperatures.

With the electrolytically prepared oxides, the refractive index apparently decreases as the water content of the anodizing solution increases. The decrease is accompanied by an increase in the thickness at a given voltage. These findings are not in agreement with the results of Schmidt and Michel (13) who did not observe any effect on the thickness voltage relationship on dehydrating the solvent. There is some evidence to suggest, however, that the high value of refractive index obtained with the anhydrous solution is in part due to the low solute concentration.

The dissolution rates of the anodic oxides are considerably greater than those of the thermally grown oxides. Archer (6) explains similar results obtained on films prepared by anodization in aqueous borate solution by suggesting that the oxide is porous. Transmission electron micrographs obtained in this laboratory indicate that the films grown in anhydrous N-methyl acetamide are relatively porous in disagreement with the observations of Politycki and Fuchs (14). However the pore distribution is such as to suggest that the imperfections in the oxide are probably caused by dirt particles on the substrate surface. The presence of pores would be expected to lower the refractive index as well as increasing the etching rate, so that to account for the high value of refractive index obtained with the anhydrous solvent either the structure or the composition of the oxide must be different from that of the thermally grown oxide.

The sputtered films appear to be very similar to those prepared by thermal oxidation, though they have a slightly higher dissolution rate. All three oxides give electron diffraction patterns in which no trace of crystalline structure can be distinguished. This suggests that the anomalous behavior of the anodic films is more likely to result from a difference in composition.

As discussed by Flint (15), the thermal oxidation process can be thought of as occurring in three stages: (i) adsorption of the oxidizing gas at the oxide surface, (ii) diffusion of the oxidizing species through the oxide layer, and (iii) reaction of the oxidizing species at the $Si-SiO_2$ interface. Since a parabolic rate law applies over most of the thickness range studied, diffusion is presumably the rate-limiting step. The initial period of slow oxide growth in atmospheres largely free from oxygen may be explained by assuming that the oxide reacts with steam to form a volatile component, the reaction rate being dependent on the concentration of water vapor. The removal of the oxide, which would be inhibited by the presence of oxygen, ceases once a certain thickness is reached. Since silica itself reacts only slightly with steam, even at high pressures and temperatures (16), the cessation may be due to a change in composition of the oxide from SiO_x to SiO_2. (In atmospheres free from oxygen, silicon and silica react together at 1200°C to form silicon monoxide.)

Conclusions

The optical properties of various silica films on silicon have been studied by means of an ellipsometer. Good agreement has been obtained between the experimental data and curves of $\hat{R}_P/\hat{R}_S$ computed from the exact theory of reflection.

The refractive indices of the thermally grown oxides, like that of the sputtered films, are similar to that of bulk silica (1.460) though somewhat lower values are obtained when the concentration of water vapor in the oxidizing atmosphere is high. With the anodically formed oxides, the refractive indices differ quite markedly from that of bulk silica. Here again, an increase in the water content of the anodizing solution can be correlated with a reduction in the refractive index of the film.

The oxidation process has been found to follow a parabolic rate law over most of the thickness range studied. However, in atmospheres virtually free from oxygen and containing a high concentration of water vapor, the oxide initially grows at a much slower rate. This is tentatively explained on the basis of a reaction between the steam and the oxide to form a volatile component. Where the parabolic law is obeyed, the oxidation rates at 1200°C are similar to those found by other workers.

Acknowledgments

The authors are grateful to Standard Telecommunication Laboratories for permission to publish this paper and to Mrs. P. R. Gander for carrying out much of the experimental work. Thanks are also due to Mr. J. Peters for preparing the anodic films and to Mr. S. G. Ayling for depositing the sputtered silica layers.

Manuscript received Jan. 7, 1963.

Any discussion of this paper will appear in a Discussion Section to be published in the June 1964 JOURNAL.

REFERENCES

1. A. B. Winterbottom, *Kgl. Norske Videnskab., Skrifter* 1 (1955).
2. A. B. Winterbottom, *J. Optical Soc. Am.*, **38**, 1074 (1948).
3. L. Tronsted and T. Hoverstad, *Trans. Faraday Soc.*, **30**, 349 (1934).
4. R. J. Archer, *This Journal*, **30**, 349 (1957).
5. P. Drude, *Wied. Ann.*, **43**, 126 (1891).
6. R. J. Archer, *J. Optical Soc. Am.*, **52**, 970 (1962).
7. R. C. Menard, *ibid.*, **52**, 427 (1962).
8. O. S. Heavens, "Optical Properties of Thin Solid Films," p. 55, Butterworth's Scientific Publications (1955).
9. R. J. Archer, *Phys. Rev.*, **110**, 354 (1958).
10. H. Wilman and J. N. King, Private communication.
11. W. C. Dash and R. Newman, *Phys. Rev.*, **99**, 1151 (1955).
12. B. E. Deal, Electrochemical Society, Spring Meeting, Electronics Division Abstracts Vol. 11, pp. 224 (1962).
13. P. F. Schmidt and W. Michel, *This Journal*, **104**, 230 (1957).
14. A. Politycki and E. Fuchs, *Z. Naturforsch.*, **14a**, 272 (1959).
15. P. S. Flint, Electrochemical Society Spring Meeting Electronics Division Abstracts Vol. 11, p. 222 (1962).
16. E. L. Brady, *J. Phys. Chem.*, **57**, 706 (1953).

Crystallographic and Electrical Properties of Epitaxial Germanium

A. B. Kuper and H. Christensen

Bell Telephone Laboratories, Incorporated, Murray Hill, New Jersey

ABSTRACT

Germanium [111] epitaxial films deposited in an undoped flow system from H_2-$GeCl_4$ at about 850°C are known to be high resistivity p-type suitable for device manufacture. This paper describes further investigation of the quality of such films. Electron transmission micrographs showed no difference in general between these films and thin sections of germanium grown from the melt. A decrease in room temperature film conductivity as a function of annealing time at 550°C suggested that the principal impurity was copper which was precipitating at a slow rate characteristic of germanium with less than 10^3 dislocations/cm^2. The temperature dependence of carrier concentration at low temperature was characteristic of compensation by about 10^{13} cm^{-3} donors. The most sensitive test of the quality of these films was provided by the low-temperature Hall mobility which was 5.6 x 10^4 cm^2/v-sec at 33°K and agreed within approximately 10% with mobility in conventional p-type germanium with 10^{14} impurities/cm^3.

Germanium [111] epitaxial films deposited in an undoped flow system (1) from H_2-$GeCl_4$ at about 850°C can be high resistivity p-type suitable for device manufacture (2). In this work, crystallographic studies by electron transmission and Hall mobility measurements on epitaxially grown germanium films give further evidence of crystal quality comparable to that of melt-grown crystals. Measurements of room-temperature conductivity of the films as a function of annealing heat treatment suggest that copper is the principal impurity in our films. The slow precipitation of copper implies a low dislocation density.

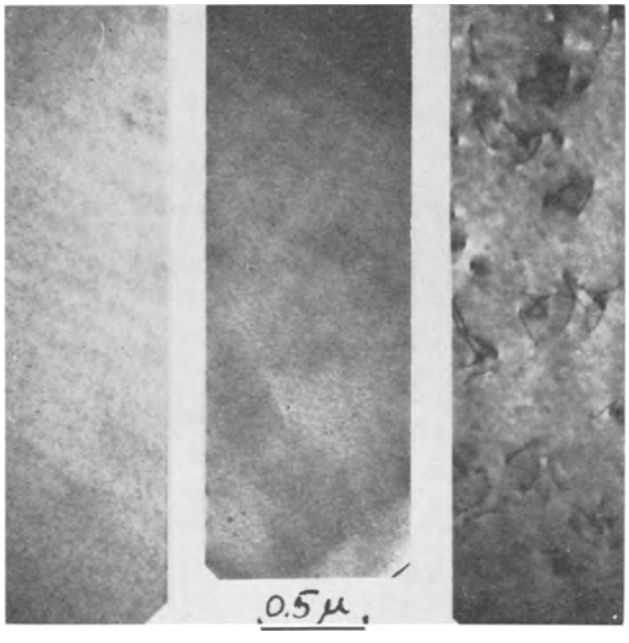

Fig. 1. Electron transmission micrographs of thin germanium sections. Left, conventional germanium; center, epitaxial film; right, evaporated film. Magnification is the same for each film.

The films were deposited at a rate of about 0.1 μ/min on [111] faces of germanium seeds by the hydrogen reduction of $GeCl_4$ at 850°C. Deposition was done using a flow system and a horizontal tube furnace. Oxygen and water vapor were removed by palladinized alundum and a liquid nitrogen trap containing Linde molecular sieve.

Crystallographic Properties

To examine crystal perfection, electron transmission was done using the technique of Riesz and Bjorling (3). Jet etching of the substrate was used to obtain a section of the film of about 40 μ^2 area and about 500Å thick measured from the film surface through to the etched dimple. Examination over the bottom of two dimples showed no appreciable difference between the epitaxial and the melt-grown germanium. Figure 1 shows electron transmission micrographs of epitaxial and melt-grown germanium measured the same way. Also shown for comparison is a similar micrograph of a single crystal germanium film evaporated[1] on a hot germanium substrate (4). This latter film shows considerable structure and electrically is not of device quality.

Using the same samples, electron transmission diffraction photographs were made. Figure 2 shows such a result on an epitaxial film. The diffraction spots and Kikuchi lines are the same on these films as on bulk samples.

Electrical Measurements

To measure net acceptor concentrations routinely in films deposited on p^+ seeds, junction capacity of n^+pp^+ junctions (made by diffusing Sb into the films for 16 hr at 600°C) was measured. A constant slope of log capacity *vs.* log junction reverse potential was found (Fig. 3) indicating a uniform distribution of acceptors except near the seed. The net

[1] We are indebted to R. P. Riesz for this micrograph.

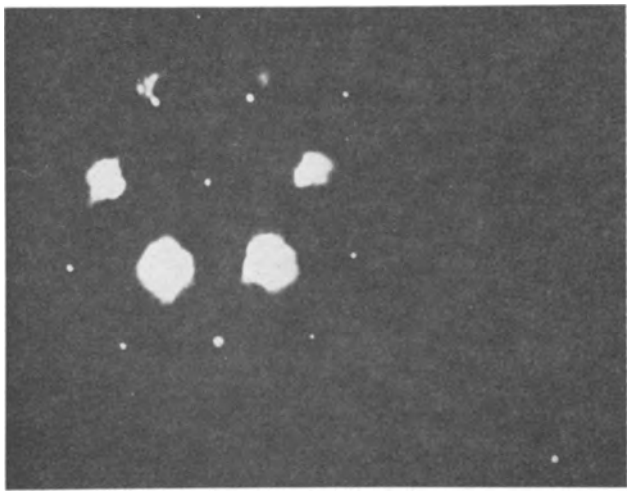

Fig. 2. Electron transmission diffraction photograph of thin section of an epitaxial germanium film.

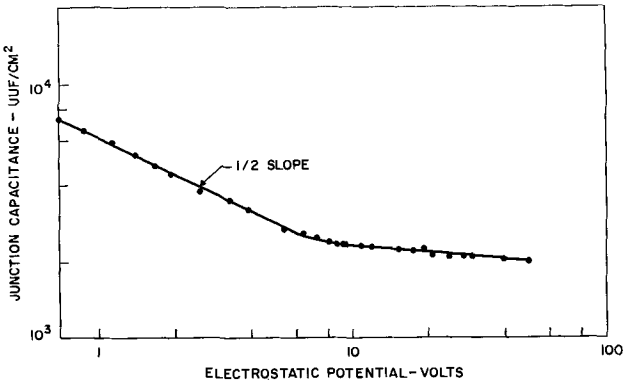

Fig. 3. Junction capacitance vs. total potential of an $n^+ pp^+$ diode formed by diffusion into a thin p-type epitaxial germanium film on a p^+ seed. The barrier layer reaches the heavily doped region at about 8v. Epitaxial layer thickness, 9.3μ; breakdown voltage, 60v.

acceptor concentration obtained was 2-6 $10^{14}/cm^3$ after 600°C with heavily or lightly doped p-type seeds. It was reasoned that the impurity was copper, commonly present in heat-treated germanium, which has a maximum solid solubility (5) of 3 x $10^{14}/cm^3$ at 600°C and has three acceptor levels which would be ionized within the space charge. Copper may come into the system in the gas flow, from the vessel walls, or on the samples. Careful cleaning of the seeds in a 10% aqueous KCN solution before deposition did not reduce the doping.

To check on the presence of copper an annealing experiment was performed to see if the acceptor would precipitate at a temperature less than 600°C where the germanium would be supersaturated with Cu. A thick film was deposited on an intrinsic seed of [111] orientation 2.44 mils thick. Analysis[2] of the crystal from which the seed slice was cut gave a maximum concentration of any one impurity to be 2 x $10^{12}/cm^3$; the impurities likely to be present being Cu, Sb, and As. In 6 hr at 850°C approximately 4 mils of film was grown. This added thickness as determined by weight gain was checked by a micrometer dial gauge measurement.

[2] We are indebted to L. P. Adda for this information.

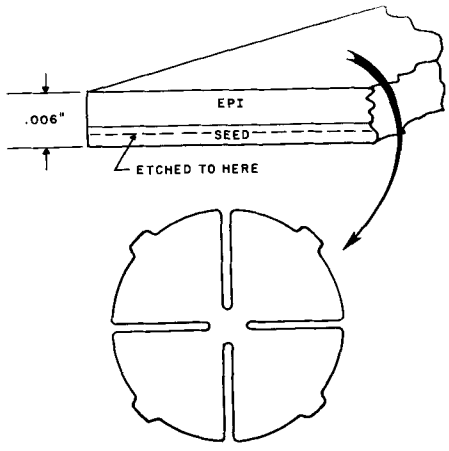

Fig. 4. Preparation of thick film for conductivity and Hall measurements.

The surface of the film was smooth except for a few isolated growth flaws (*e.g.*, tilted platelets), and probed p-type. The back of the sample was etched (Fig. 4) until approximately 0.8 mil of seed remained as measured by a Leitz light section microscope comparison with masked portions. Although this was not intended, it can be shown that the presence of this intrinsic sheet does not substantially change our conclusions. Sheet resistance gave a resistivity of about 10 ohm-cm which is typical of germanium films grown at low deposition rates in an uncontaminated system of this type.

The sample was then annealed in hydrogen 250 hr at 550°C. Probe resistivity was measured at intervals of time. In Fig. 5 are shown the results of room temperature conductivity *vs.* time at 550°C. The vertical lines indicate the spread of data over the sample. It is seen that the acceptor concentration decreases with time and the resistivity approaches 40 ohm-cm.

The precipitation rate of copper from a supersaturated solid solution in germanium has been shown by Tweet (6) to be a function of dislocation density. From the data in Fig. 5 we find a decay time of 60 hr which implies a density of the dislocations involved in precipitation of less than $10^3/cm^2$. The seed crystal had a dislocation density of $10^3/cm^2$ determined by etch pit count. It has been our experience that the etch pit counts in these films are of the order of, or less than, those in the seed. Large amounts of oxygen have also been shown (7) to accelerate the precipitation of copper in Ge. If oxygen were present at a concentration of the order

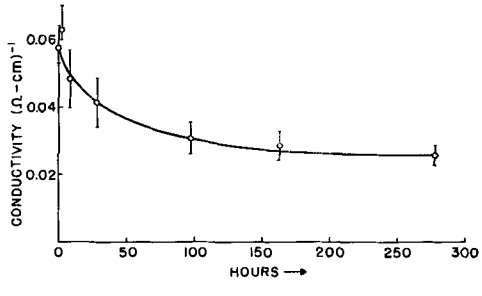

Fig. 5. Room temperature conductivity of thick film vs. time at 550°C.

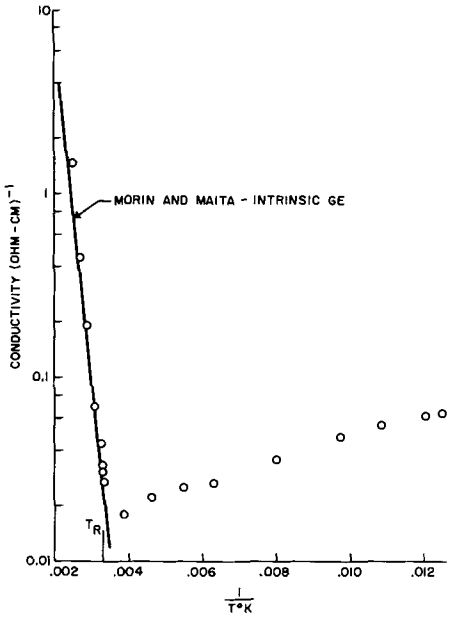

Fig. 6. Conductivity of annealed film *vs.* reciprocal absolute temperature. Solid line is data from melt-grown Ge (8).

of 10^{14} cm^{-3}, those experiments suggest it would have a small effect on copper precipitation at 550°C.

Conductivity and Hall mobility *vs.* temperature were next measured on this annealed film. A cloverleaf bridge was cut from the sample for resistivity and Hall measurements (Fig. 4). Contacts were electroless nickel plated and tin-lead soldered. The center of the bridge was 4.7 mils thick. Measurements were made from 30° to 400°K.

Results and Discussion

Conductivity *vs.* reciprocal temperature is shown in Fig. 6. The sample is seen to go intrinsic at about room temperature. For comparison, data (8) on bulk intrinsic germanium are also shown. It can be seen that our data above room temperature agree very closely with the result for melt-grown germanium.

Hole concentration (p) obtained from Hall and conductivity data is shown plotted *vs.* reciprocal temperature in Fig. 7 for temperatures below 200°K where the sample is extrinsic. Drift mobility (9) and $\mu_H/\mu_D \cong 1.2$ were used in the calculation of p. Although the low temperature data are not sufficient to determine the acceptor, we assume it is copper because of the annealing results. As a result of the long anneal at 550°C, the copper concentration (5) is expected to be $N_A = 5.6 \times 10^{13}$ cm^{-3}, and when the 0.04 ev level of copper is exhausted we expect to see $p = N_A$. This is shown by the solid line in Fig. 7. Since the exhaustion which we observe occurs at 1.3×10^{13} cm^{-3}, it is tentatively suggested that the film contains about 4×10^{13} cm^{-3} compensating donors.

The plot of Hall mobility *vs.* temperature in the extrinsic range shown in Fig. 8 supports this model. The solid lines are data on gallium doped germanium from Woodbury and Tyler (5). The mobility is consistent with scattering by about 10^{14} ionized impurities (N_D^+ and N_A^- are assumed to scatter the same) (10) from 80° to 125°K although the number of holes is $1.2\text{-}1.5 \times 10^{13}$ in this temperature

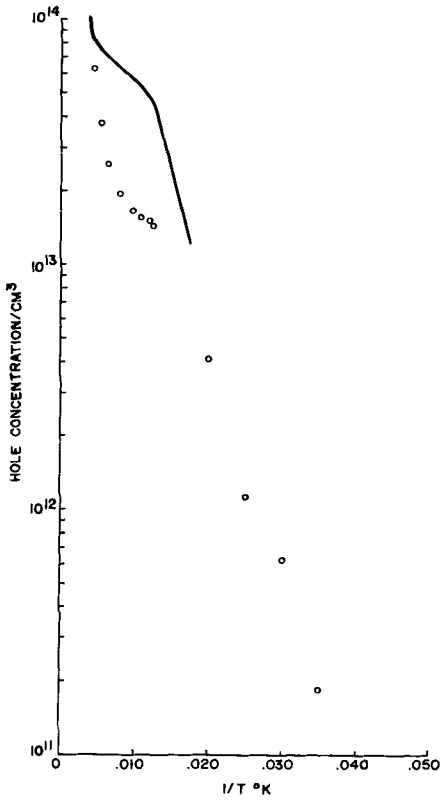

Fig. 7. Hole concentration in annealed film *vs.* reciprocal absolute temperature. The solid line denotes the expected copper acceptor exhaustion in the absence of compensation.

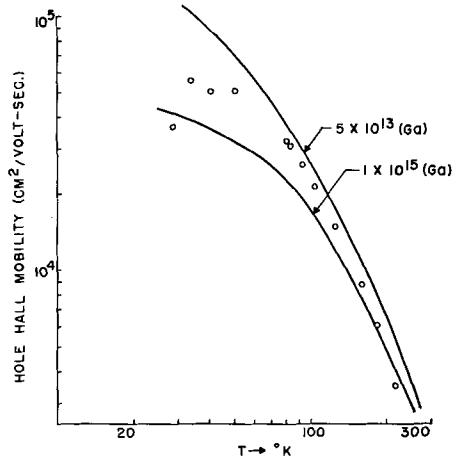

Fig. 8. Hole mobility in annealed film *vs.* temperature. Solid lines are published data for conventional doped germanium (5).

range. If compensating donors were present there would be $5.6 + \approx 4 \cong 10$ ionized impurities for 1.3 holes. Mobility is seen to drop further at the higher temperatures presumably due to copper becoming doubly ionized.

The possibility of donors is particularly interesting since N-type films result at high deposition rates with the present method. Donors were found by Ruth *et al.* (11) in germanium single crystal films obtained at 400°C by decomposition of germanium iodide. The donor level was 0.2 ev below the conduction band and was attributed to interstitials. Fuller and Doleiden suggested the level was due to oxygen (12).

The high values of mobility (Fig. 8) especially at low temperature are considered to be our most sensitive test of the high quality of the present films. In contrast are the low mobilities which have been reported in evaporated (4, 13) and sputtered (14) germanium single crystal films. The annealed films of Ruth *et al.* also do not show ideal lattice scattered mobility.

Conclusion

A germanium film grown from the vapor by the hydrogen reduction of $GeCl_4$ has been shown by electron transmission microscopy to be of crystal quality comparable to melt-grown germanium and to be near intrinsic at room temperature after annealing at 550°C for 250 hr.

Conductivity and Hall measurements are interpreted as showing conventional lattice scattered mobility and the presence near room temperature of about 10^{14} cm^{-3} total ionized impurities. The results are consistent with the presence of 5.6×10^{13} cm^{-3} copper as expected from the annealing and $\approx 4 \times 10^{13}$ cm^{-3} donors.

The experiment indicates that transport in germanium devices made from such annealed films doped 10^{15} cm^{-3} or more will be substantially the same as in conventional germanium.

Acknowledgment

The authors wish to thank B. G. Cohen and R. L. Johnston for their generous cooperation in making the Hall measurements. They would also like to thank R. A. Logan for making several preliminary Hall measurements, J. T. Nelson, B. Schwartz, J. Godfrey, and J. M. Whelan for helpful discussion, and O. H. A. Haase and Mrs. M. H. Read for their aid in obtaining the electron micrographs and diffraction patterns

Manuscript received Feb. 11, 1963; revised manuscript received April 11, 1963. This paper was delivered at the Detroit Meeting, Oct. 1-5, 1961.

Any discussion of this paper will appear in a Discussion Section to be published in the June 1964 JOURNAL.

REFERENCES

1. H. C. Theuerer and H. Christensen, *This Journal*, **107**, 268C (1960).
2. H. C. Theuerer, J. J. Kleimack, H. H. Loar, and H. Christensen, *Proc. IRE*, **48**, 1642 (1960).
3. R. P. Riesz and C. G. Bjorling, *Rev. Sci. Instr.*, **32**, 889 (1961).
4. R. P. Riesz and L. V. Sharp, *Trans. IRE*, ED-8, 430 (1961).
5. H. A. Woodbury and W. W. Tyler, *Phys. Rev.*, **105**, 84 (1957).
6. A. G. Tweet, *ibid.*, **106**, 221 (1957).
7. F. H. Doleiden, Private communication.
8. F. J. Morin and J. P. Maita, *Phys. Rev.*, **94**, 1525 (1954).
9. F. J. Morin, *ibid.*, **93**, 62 (1954).
10. E. Conwell and V. F. Weiskopf, *ibid.*, **77**, 388 (1950).
11. R. P. Ruth, J. C. Marinace, and W. C. Dunlap, *J. Appl. Phys.*, **31**, 995 (1960).
12. C. S. Fuller and F. H. Doleiden, *Physics. and Chem. Solids*, **19**, 251 (1961).
13. G. A. Kurov, S. A. Semiletov, and Z. G. Pinsker, *Kristallografiya*, **2**, 59 (1957). [Translated in *Soviet Physics—Crystallography*, **2**, 53].
14. F. Reizman, Proc. of AIMME Conference on Metallurgy of Elemental and Compound Semiconductors, August 1961, to be published.

The Preparation and Properties of Vapor-Grown GaAs-GaP Alloys

San-Mei Ku

General Telephone & Electronics Laboratories Inc., Bayside, New York

ABSTRACT

A method for the preparation and doping of various composition of single-crystal GaAs-GaP is described. By measuring the optical energy gap and the lattice parameter of the synthesized mixed crystal the iodine vapor epitaxial growth technique is found to give a one-to-one ratio of transport of GaAs and GaP from source to substrate. The variation of Hall mobility with composition from 5 to 50% of GaP mixture has been investigated. The edge emission peak of diodes made with alloys or less than 50% GaP varies linearly between the direct energy gap of GaAs and GaP.

The original report on the mixing of two semiconductors is that of Stöhr and Klemm (1), who investigated the phase diagram of Ge-Si by a powder annealing technique. Following this initial work, further investigations were made by many authors (2-4) on this type of alloy. It was shown that continuous solid solubility and variation of energy gap exists over the entire range of composition from pure Ge to pure Si. Work on semiconductor alloys has been expanded to mixtures of the III-V compounds for further extension of the range of available energy gap (5-9). Recent progress in developing high-efficiency infrared-emitting GaAs diodes has stimulated further interest in obtaining a high-efficiency light source in the visible region and thus prompted additional studies on mixing a higher-band-gap material such as GaP ($E_g = 2.2$ ev) with GaAs. The initial results on the GaAs-GaP system have already been published (5, 10, 18). It was found that continuous solution was obtained throughout the entire alloy range. Folberth (5) measured the variation of energy gap with composition between 50 and 100% of GaP for this system, and more recently Pizzarello (11) measured the lat-

tice parameter and energy gap for various compositions.

This paper describes the preparation of uniform single-crystal GaAs-GaP[1] by the epitaxial growth technique at a relatively low temperature. The influence of various types of dopants in the mixed alloys are discussed. Some electrical and optical properties of various compositions of GaAs-GaP are also reported.

Preparation

Previous works have proven the feasibility of both the closed and the open systems of growing individual GaAs or GaP by chemical reaction of the halides of the constituents or by other vapor-deposition techniques. The closed system used in this investigation to synthesize mixed binary crystals is similar to the one described by Hagenlocher (12) for the epitaxial growth of GaAs. This method was chosen because it allows uniform epitaxial growth of a mixed single crystal at relatively low temperature (as low as 650°C) and simultaneously permits doping during growth.

Transport and crystal growth of GaAs-GaP alloys of various composition was carried out via a vapor-phase reaction from a high-temperature source zone to a lower temperature substrate zone using iodine as the transport agent. The proposed chemical reactions at the source end of the tube are:

$$2x\,GaAs(s) + 2(1-x)\,GaP(s) + I_2(g) \xrightarrow{k_1} \frac{1}{2}x\,As_4(g) + \frac{1}{2}(1-x)\,P_4(g) + 2GaI(g)$$

and the competing reaction

$$3GaI(g) + \frac{1}{2}x\,As_4(g) + \frac{1}{2}(1-x)\,P_4(g) \xrightarrow{k_2} GaI_3 + 2x\,GaAs(s) + 2(1-x)\,GaP(s)$$

and at the substrate end

$$x\,As_4(g) + (1-x)\,P_4(g) + 4GaI(g) \xrightarrow{k_3} 4GaAs_xP_{(1-x)}(s) + 2I_2(g)$$

Experimentally, the reactions are carried out in a sealed, evacuated quartz tube of 2 in. in diameter and 8 in. in length, placed in a two-zone furnace. A typical thermal distribution profile and sample tube placement for the furnace are shown schematically in Fig. 1.

The source material consists of the calculated mole per cent of GaAs and GaP[2] (of same particle size) and measured amount of dopant (such as Te, Se, and Sn). The source materials are cleaned by etchants prior to being placed in the reaction tube. A small vacuum-sealed ampoule containing a measured amount of iodine is also inserted into the reaction tube at the source end.

[1] The epitaxially grown $Ga(As_xP_{1-x})$ layer has less than 0.002 in. variation in thickness over 80% of the total surface area. Uniformity of composition was confirmed by electrical and optical measurements. Less than 8% lateral variation of free carrier concentration was found on the epitaxial layer of 0.010 in. thick and 0.750 in. in diameter. Edge emission peak on diodes of 0.003 in.-diffusion from either surfaces of the same epitaxially grown layer of these mixed crystals have identical values. Therefore, the grown layer is not only uniform in composition across the wafer surface but also uniform throughout the thickness.

[2] Commercially available highest purity GaAs and GaP.

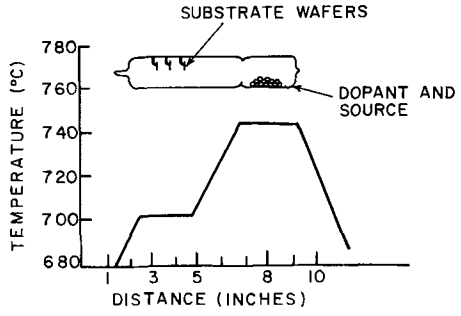

Fig. 1. Furnace temperature profile for epitaxial growth and relative position of the reaction tube in the furnace.

The substrate material used in this experiment is either GaAs or GaP, depending upon the percentage of the alloy composition; for alloys with 0.5 or larger mole fraction of GaP, pure GaP is used as substrate, otherwise, GaAs is used as substrate. The substrate wafers are polished to ¼μ finish and chemically etched in a mixture of H_2SO_4 and H_2O_2 solution, and rinsed in deionized water and then in methanol. These wafers are suspended in the center of the quartz capsule by quartz hooks. The entire capsule is baked at 150°C for 12 hr under vacuum (10^{-5} Torr). The iodine is then released from the ampoule by a magnetic hammer and the entire capsule is backfilled with a few tenths of an atmosphere of hydrogen and sealed off. Just prior to growth the substrate is further cleaned by reverse deposition for a few minutes, *i.e.*, by transporting the substrate to the source region. After growth for a period of time, the capsule is pushed out of the furnace and allowed to cool to room temperature. Generally, the source temperature is about 50°-80°C above the substrate temperature. In addition, it was found that uniform crystalline epitaxial growth is influenced not only by the substrate surface preparation, but also by the orientation of the substrate and the growth rate.

Results and Discussion

As one would have expected, the growth rate was found to be influenced by the orientation of the substrate surface. Epitaxial GaAs-GaP layers of 250μ to 630μ have been obtained on substrates of several low index orientations (100), (110), (111), and (112). In contrast to the hydrogen chloride transporting system reported by Moest and Shupp (13) for GaAs or GaP, no growth was observed on the As or P face of the $(\bar{1}\bar{1}\bar{1})$ direction. However, our results are in agreement with the epitaxial growth of GaAs reported by Pizzarello (14) using iodine as the transporting agent. Growth on the (111) planes was invariably found to contain triangular pyramids. The (110) direction was found to be the fastest growing orientation among the four principal crystallographic directions examined. The (100) plane was found to be the slowest, and the (112) plane gave the most uniform surface and growth pattern, as shown in Table I.

Except for an initial period of 15-20 min required to establish the steady-state condition of the reaction, the growth rate was found to be independent of time for a fixed set of variables (source temperature, pressure, orientation, geometry of the reaction

Table I. Epitaxial growth rate of GaAs-GaP crystals at 742°C source temperature and 680°C substrate temperature

Orientation of growth direction	Growth rate (μ/hr)
100	1.8-2.4
110	7.2-8.5
111	5.1-6.0
$\bar{1}\bar{1}\bar{1}$	zero
112	5.4-5.9

tube, etc.) until the source material is exhausted. No detectable amount of iodine was found to be incorporated within the epitaxial layer; therefore it is reasonable to assume that only a small amount of iodine is needed to transport a comparatively large amount of reactants. This may also explain the independence of growth rate with respect to time.

A series of experiments were made to determine the growth rate *vs.* initial pressure, source temperature, and substrate temperatures with a fixed substrate orientation (100). As expected, we have found that the geometry of the tube and the position of the substrate in the tube have a large effect on the uniformity of the deposit layer, since the transport of GaAs-GaP from the source to the substrate is controlled by convection as well as by diffusion. It was also noted that the growth rate was relatively insensitive to the substrate temperature. However, for simple GaAs-GaP transport, the substrate temperatures can be as low as 550°C, but to achieve uniform crystalline growth and preserve the desired composition, the substrate temperature should be slightly below the effective disproportionation-temperature. For a fixed source temperature of 742°C, and an initial iodine pressure of 210 Torr, a variation of substrate temperature from 600° to 700°C caused the growth rate to vary by less than 0.1%. Figure 2 shows that, at a fixed source temperature of 742°C, and an iodine pressure in the range of 80 to 250 Torr, the rate of growth increases with decreasing initial iodine pressure where the total pressure of the system remained constant. This result again substantiates the finding that iodine

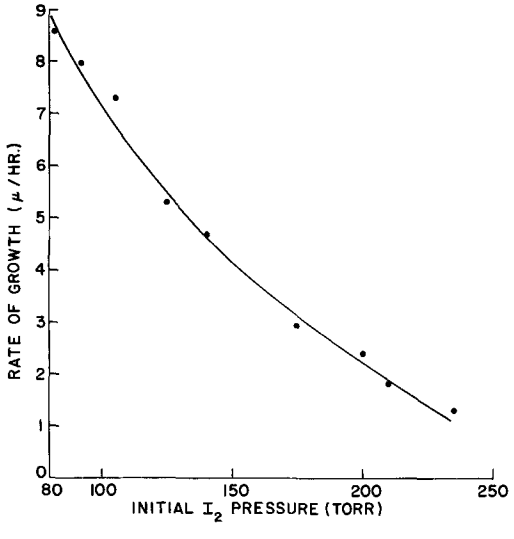

Fig. 2. Rate of growth *vs.* initial I_2 pressure at source temperature 742°C for (100) substrates.

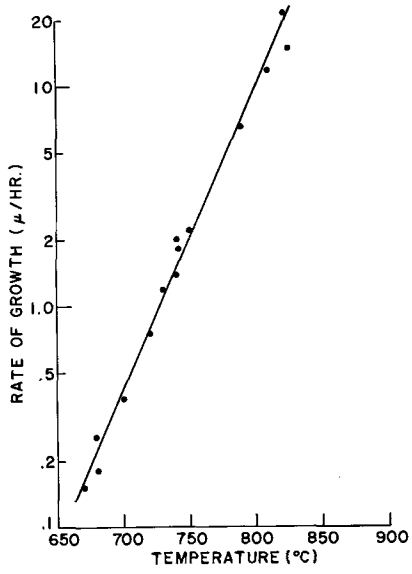

Fig. 3. Rate of growth *vs.* source temperature at initial I_2 pressure of 210 mm Hg for (100) substrates.

acts only as a transport agent in this process, and that it does not enter the epitaxial layer. Figure 3 shows that the growth rate increases with increasing source temperature at a constant initial iodine pressure of 210 Torr. Evidently several reactions are competing at the source, where high source temperature and low iodine pressure will favor k_1 over k_2.

The composition of the mixed alloys was determined by two methods: (i) Assuming that Vegard's law of solid solutions holds for this GaAs-GaP system, thereby measuring the lattice constant of these alloys, it will in turn determine the composition. (ii) From the energy gap *vs.* composition data of the mixed alloys obtained by previous authors (Fig. 4), composition can be determined by measuring the optical energy gap, E_g, values. The lattice constants of GaAs-GaP alloys made by the method mentioned above were measured at room temperature by the Laué back-reflection technique. The results are

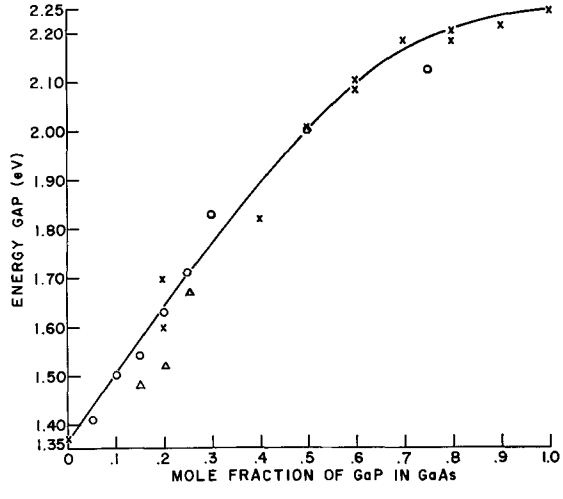

Fig. 4. Variation of energy gap *vs.* composition of GaAs-GaP alloys at 300°K. ○, 300°K transmittance *vs.* λ data; X, 300°K Folberth, Pizzarello and other published data; △, 300°K emission peak *vs.* λ data.

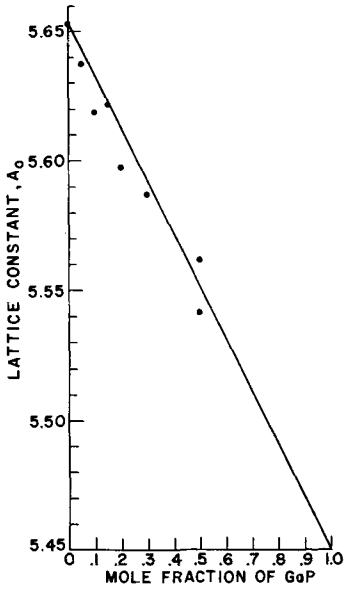

Fig. 5. Lattice constant vs. various composition range in the GaP-GaAs.

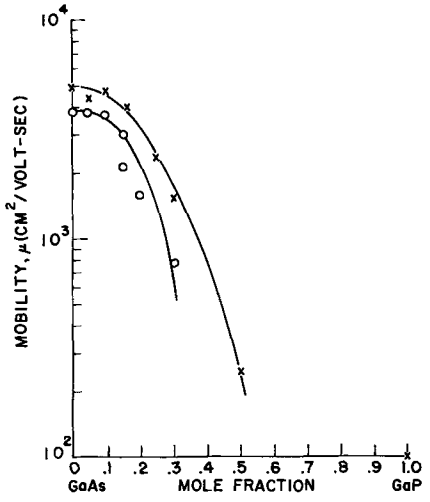

Fig. 6. Mobility vs. composition of GaP in GaAs. X, carrier concentration ~ 1.5×10^{17}/cm^3; ○, carrier concentration ~ 6×10^{17}/cm^3.

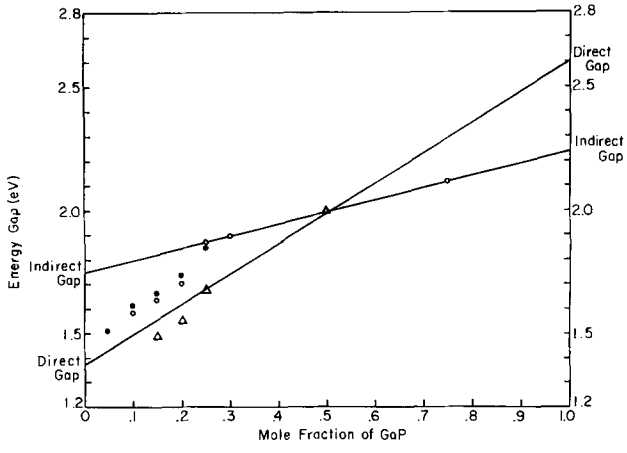

Fig. 7 Variations of edge emission peak of GaAs-GaP diodes with composition at 300° and 77°K. ○, 300°K transmittance data; △, 300°K edge emission data; •, 77°K edge emission data.

shown in Fig. 5. The decrease in lattice constant with increase of mole fraction of GaP is found to be in good agreement with Vegard's law of solid solutions; also the sharpness of the Laué back-reflection peak further indicates a high degree of perfection for these alloys. The energy gap values were determined by the linear extrapolation of the absorption edge in the transmittance *vs.* wavelength measurement. The compositions of these alloys determined from the E_g value *vs.* composition curve (Fig. 4) varied less than 2% with the predetermined source composition for the epitaxial growth. From the results of composition determination, by the above two methods, it seems that there is a one-to-one ratio of transport of GaAs and GaP from source to substrate.

All the synthesized alloys were doped with either selenium, tellurium, or tin. Each of these elements is an n-type dopant for the mixed crystals. Using the data from Hall-effect measurements, it was found that the highest free-carrier concentration produced for these alloys was obtained by doping with selenium (3×10^{19} carriers/cc). With tellurium as a dopant, the highest carrier concentration obtainable was about 7.8×10^{18}/cc, and 5×10^{18}/cc was the highest impurity concentration achieved with tin doping. The lower free-carrier concentration in tin-doped alloys may be attributed to the relatively large size of the interatomic radii of tin (1.40Å) in comparison to the other two types of dopants mentioned (selenium—1.14Å; tellurium—1.32Å) (15). Another plausible explanation for this result is that the tin atoms can be introduced into the GaAs-GaP alloys both as p- and n-type impurities.

From the room-temperature Hall effect and resistivity measurements, the simple Hall mobility calculated from the $\mu_H = \sigma R_H$ relation, is plotted against the mole fraction of GaP in Fig. 6. In contrast to other quasi-binary alloys such as InSb-GaSb (8) system, the mobility in GaAs-GaP alloy does not fall off rapidly from the value of pure GaAs of equivalent carrier concentration; instead, it remains fairly constant up to 15% of GaP, and then decreases steeply between 25-50% GaP.

It has been shown from the published absorption data (5, 11) and the transmittance *vs.* wavelength measurement of this experiment (Fig. 4) that the energy gap of $Ga(As_xP_{1-x})$ does not vary linearly over the entire composition range. This was further confirmed by the edge emission *vs.* wavelength measurement obtained on the forward-biased, zinc-diffused diodes made from tin-doped alloys of 10, 15, 20, 25, and 50% GaP compositions (17, 19). At room temperature, the edge emission peak of diodes made with alloys of less than 50% GaP follows the linear variation between the direct energy gap of GaAs (1.37 ev) and GaP (2.6 ev) (Fig. 7). As expected, at liquid nitrogen temperature the edge emission peak shifts to a shorter wavelength, but the increase in energy gap is found to be in good agreement with the estimated $\partial E/\partial T$ values for these alloys (assume that the $\partial E/\partial T$ for the alloys is somewhere between -5.4×10^{-4} ev/°K for GaP and -4.9×10^{-4} ev/°K for GaAs) (16).

Acknowledgment

The author gratefully acknowledges the assistance of A. Marx in the preparation of the material and

P. Lublin for making the lattice constant measurement on these alloys. The author is specially indebted to J. Black for many helpful discussions and to Dr. S. Mayburg for his guidance in all phases of this work.

Manuscript received Feb. 12, 1963; revised manuscript received April 19, 1963.

Any discussion of this paper will appear in a Discussion Section to be published in the June 1964 JOURNAL.

REFERENCES

1. H. Stohr and W. Klemm, Z. *anorg. Chem.*, **241**, 305 (1939).
2. A. Levitas, C. C. Wang, and B. H. Alexander, *Phys. Rev.*, **95**, 846 (1954).
3. M. Glicksman, *ibid.*, **102**, 1496 (1956).
4. F. Herman, M. Glicksman, and R. H. Parmenter, "Progress in Semiconductors" (1957).
5. O. G. Folberth, Z. *Naturforsch.*, **10a**, 502 (1955).
6. W. Koster and B. Thoma, Z. *Metallkunde*, **46**, 293 (1955).
7. J. C. Woolley, B. A. Smith, and D. G. Lee, *Proc. Phys. Soc.*, **B69**, 1339 (1956).
8. J. C. Woolley and C. M. Gillett, *J. Phys. Chem. of Solids*, **17**, 34-43 (1960).
9. F. A. Trumbore, P. E. Freeland, and A. D. Mills, *This Journal*, **109**, 645 (1962).
10. G. R. Antell, *ibid.*, **106**, 509 (1959).
11. F. A. Pizzarello, *ibid.*, **109**, 226 (1962).
12. A. Hagenlocher, *ibid.*, **108**, 213C (1961).
13. R. R. Moest and B. R. Shupp, *ibid.*, **109**, 1061 (1962).
14. F. A. Pizzarello, The Electrochemical Society Los Angeles Meeting, Electronics Division Abstracts, **11**, [1] 166 (1962).
15. L. Pauling, "Nature of the Chemical Bond," p. 179, Cornell Univ. Press.
16. H. Welker, "Solid-State Physics," **3**, 51, Academic Press Inc. (1956).
17. H. Lockwood, S. M. Ku, and J. Black, "Visible Injection Electroluminescence from GaAs-GaP Diodes," Bulletin of A.P.S. Series II, **7**, No. 8, 537 (Nov. 23, 1962).
18. N. Holonyak, Jr., D. C. Jillson, and S. F. Bevacqua, "Halogen Vapor Transport and Growth of Epitaxial Layers of Intermetallic Compounds and Compound Mixtures," "Metallurgy of Semiconductor Materials," J. B. Schroeder, Editor, Interscience Publishers, Aug. 30-Sept. 1, 1961.
19. S. M. Ku and J. F. Black, "Injection Electroluminescence in GaAs-GaP Diodes," To be published.

Effect of Electrolyte and Solvent on Polarographic Reductions of Nitrobenzene Derivatives

Donald J. Pietrzyk,[1] R. F. Breese,[2] and L. B. Rogers[3]

Department of Chemistry and Laboratory for Nuclear Science, Massachusetts Institute of Technology, Cambridge, Massachusetts

ABSTRACT

Anodic shifts of half-wave potentials for nitrobenzene derivatives on addition of calcium ion are usually greatest for substances having the most negative reductions on the negative side of the electrocapillary maximum. However, a small anodic shift has also been detected for reductions on the positive side of the electrocapillary maximum. An increase in pH or in percentage of methanol leads to a greater shift in all cases, probably as the result of greater interaction between calcium ion and the carbanion intermediate.

Irreversible polarographic reactions are frequently sensitive to the presence of surface-active agents and the cation of the "inert" background electrolyte (1-6). Calcium ion has been reported to shift anodically the alkaline reduction of p-dinitrobenzene which falls on the negative side of the electrocapillary maximum (2). A similar shift for the first wave, which falls on the positive side of the maximum, has now been studied as a function of pH and concentrations of methanol, and the survey has been extended to other nitro aromatics.

Experimental

Except for p-nitrotrimethylanilinium chloride which we prepared (7), the nitro compounds were Eastman Kodak Company products that had been further purified by distillation or crystallization. Lithium chloride was prepared from lithium carbonate and hydrochloric acid; all other inorganic compounds were commercially available analytical reagents.

Moderate concentrations of hydrochloric acid and sodium hydroxide were used for small and large pH values, respectively. Intermediate values were maintained using buffers, 0.01M in ionized form, which were prepared from ammonia or pyridine mixed with hydrochloric acid.

Polarographic solutions usually contained 1.00 x $10^{-4}M$ nitrobody and 0.005% freshly prepared gelatin.

The apparatus and procedure has been described (2, 3). Measurements were made at 25°C using a capillary with a 0.03 mm bore, which had a drop time of 5 sec and a value of $m^{2/3}t^{1/6}$ at − 0.5 v (*vs.* S.C.E) of 1.477 $mg^{2/3}$ $sec^{-1/2}$. Data for half-wave potentials usually had a spread of less than ± 3 mv when run in triplicate runs on each of two solutions.

[1] Present address: Chemistry Department, State University of Iowa, Iowa City, Iowa.

[2] Present address: Chicago, Rock Island and Pacific Railroad, Research and Development Laboratory, Chicago 9, Illinois.

[3] Present address: Chemistry Department, Purdue University, Lafayette, Indiana.

Table I. Effect of the presence of 0.2M calcium chloride on the half-wave potential for the first reduction of p-dinitrobenzene in varying percentages of methyl alcohol. Background: 0.01M sodium hydroxide, 1.0M lithium chloride, 0.005% gelatin

Per cent methyl alcohol	$-E_{E.C.M.}$	$-E_{1/2}$*	$\Delta E_{1/2}$
20	0.46	0.331	16 mv
40	0.44	0.345	18 mv
60	0.40	0.372	21 mv
80	0.38	0.395	36 mv

* In the absence of calcium.

Results

Dinitrobenzenes.—p-Dinitrobenzene in alkaline solution gives two waves. The first corresponds to a two-electron change with formation of a relatively stable divalent ion; the second, to the formation of p-hydroxylaminoaniline (8). A 56 mv shift of the second wave on addition of calcium ion has been reported (2) for a solution containing 40% methanol. Table I shows that a similar but smaller shift also occurs in the first wave, and that a larger per cent of methanol increases the shift. The unusual feature about this situation is that the shift is being induced by a capillary-inactive positive ion on the positive side of the electrocapillary maximum.

Changes in the concentration of lithium chloride had little effect on the half-wave potential. Furthermore, changes in junction potential were ruled out by observing that the half-wave potential of thallium (I) remained constant when calcium ion was added to the same background electrolyte.

o-Dinitrobenzene, which has half-wave potentials at — 0.39 and — 0.79v in 20% methanol, and — 0.47 and — 0.88v in 80% methanol exhibits similar but smaller shifts for both waves. This suggests that the shifts for both the ortho and para compounds are real.

Mononitro aromatics.—Unfortunately, mononitro aromatics do not reduce on the positive side of the electrocapillary maximum so they cannot be used to study that feature of the calcium induced shift. However, it was of interest to examine the effects of charge and structure of the aromatic species on the calcium-induced shift for the reaction on the negative side of the E.C.M.

When nitrobenzene in 80% methanol was used to examine the effect of apparent pH on the shift at pH values of 11.2, 9.2 4.2, and 2.0, anodic shifts of 75, 48, 8, and 0 mv, respectively, were observed. (The smaller calcium shift at lower values of pH was also confirmed for the dinitro compounds.) Such a result is reasonable because higher concentrations of protons would compete more successfully with the calcium ions for the carbanion produced by electron transfer.

The anodic shift caused by 0.02*M* calcium chloride was observed for several other substituted nitro aromatic compounds in 80% methanol-1.0*M* lithium chloride-0.01*M* sodium hydroxide-0.005% gelatin. Examining first the half-wave potentials, one can see in Table II that the values reflect the

Table II. Anodic changes in half-wave potentials for 1.0×10^{-4}M solutions of nitrocompounds due to the presence of 0.2M calcium chloride. Background: 1M lithium chloride, 0.01M sodium hydroxide, 0.005% gelatin, 80% methyl alcohol

Compound	$-E_{1/2}$,** v	$\Delta E_{1/2}$, mv
p-Nitrophenyltrimethylammonium chloride	0.634	42
Nitrobenzene	0.776	75
o-Nitrotoluene	0.852	77
p-Nitroanisole	0.861	77
p-Nitroaniline	0.918	79
1,3-Dimethyl-2-nitrobenzene*	0.95, 1.05	60, 190
p-Nitrophenol*	1.06, 1.26	90, 180

* Two waves; values rounded to closest 0.01v due to poor separation of waves.
** In the absence of calcium.

type of substituent on the aromatic ring. Using nitrobenzene as a reference, the inductive effect of the substituted ammonium ion results in a less cathodic value whereas the resonance stabilization of the $-OCH_3$, $-NH_2$, and —OH derivatives result in more cathodic values. A steric effect is illustrated in the case of the 1,3-dimethyl compound.

Examination of the effect of calcium shows that, on going from the positively charged tetraalkylammonium ion to the negatively charged phenolate ion, the shift becomes larger. Qualitatively, this is what one would expect if the shift were due to stabilization of a carbanion intermediate by calcium ion.

p-Nitrophenol (9, 10) and compounds similar to 1,3-dimethyl-2-nitrobenzene (11) give two waves in basic solution. As the pH increases above 9, the second becomes larger and the first wave smaller. In the presence of calcium ion, the anodic shifts of the second wave are so great that the two waves fuse into one. Thus, the transfer of one or more additional electrons is greatly aided. Figure 1 illus-

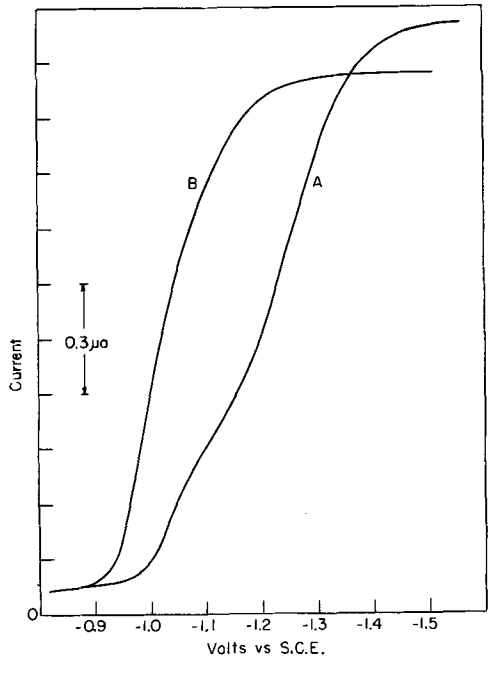

Fig. 1. Effect of 0.2M calcium chloride on the polarogram for p-nitrophenolate: A, 1M lithium chloride, 0.01M sodium hydroxide, 0.005% gelatin, and 80% methyl alcohol; B, 0.02M calcium chloride also present.

trates the shift for p-nitrophenol and the nearly symmetrical wave that resulted in the presence of calcium ion. Symmetry would undoubtedly have improved if more calcium had been added.

It is interesting to note that o-nitrotoluene (and p-nitrotoluene) shows no significant effect of hindrance (or induction). The reported half-wave potentials for both toluene derivatives are usually within 40 mv of nitrobenzene (12). Hence, one would expect the effect of calcium to be the same as for nitrobenzene, and this was found to be the case.

Discussion

Recent work by Piette *et al.* (13) indicates that a number of nitroaromatic compounds give detectable amounts of anion intermediates in aqueous media. Hence, formation of an ion-pair at the electrode surface should be possible, and it should be more extensive in lower dielectric media, as found in the present study.

An alternative explanation might be based on ion-dipole interactions prior to reduction. However, an extension of an earlier attempt to detect such an interaction on addition of calcium ion by differential spectrophotometry using nitrobenzene and p-nitroaniline, by solubility (of nitrobenzene), by potentiometric titration (of calcium with ethylenedinitrilotetraacetic acid in the presence of p-nitroaniline), and by conductivity measurements of calcium ion (upon addition of nitrobenzene) all failed to indicate any interaction. Hence, the calcium effect does not appear to be the result of a prior interaction.

Acknowledgment

This work was supported in part by the United States Atomic Energy Commission under Contract AT(30-1)905.

Manuscript received Aug. 14, 1961; revised manuscript received April 30, 1962.

Any discussion of this paper will appear in a Discussion Section to be published in the June 1964 JOURNAL.

REFERENCES

1. M. Ashworth, *Collection Czechoslov. Chem. Communs.*, **13**, 229 (1948).
2. L. E. I. Hummelstedt and L. B. Rogers, *This Journal*, **106**, 248 (1959).
3. J. J. Lothe and L. B. Rogers, *ibid.*, **101**, 258 (1954).
4. P. J. Elving, J. C. Komyathy, R. E. van Atta, C. S. Tang, and I. Rosenthal, *Anal. Chem.*, **23**, 1218 (1951).
5. R. W. Schmid and C. N. Reilley, *J. Am. Chem. Soc.*, **80**, 2087 (1958).
6. R. W. Schmid and C. N. Reilley, *ibid.*, **80**, 2101 (1958).
7. A. Zaki and H. Fahim, *J. Chem. Soc.*, **1942**, 270.
8. L. Holleck and H. J. Exner, *Z. Elektrochem.*, **56**, 677 (1952).
9. J. E. Page, J. W. Smith, and J. G. Waller, *J. Phys. & Colloid Chem.*, **53**, 545 (1949).
10. J. Pearson, *Trans. Faraday Soc.*, **44**, 692 (1948).
11. M. Fields, C. Valle, and M. Kane, *J. Am. Chem. Soc.*, **71**, 421 (1949).
12. I. M. Kolthoff and J. J. Lingane, "Polarography," 2nd ed., p. 751, Interscience, New York (1952).
13. L. H. Piette, P. Ludwig, and R. N. Adams, 140th Meeting of the American Chemical Society, Chicago, September 1961.

The Evaporation of Iron-Chromium Alloys Containing 5 and 25 Per Cent Chromium in the Temperature Range 900°-1080°C

L. A. Morris and W. W. Smeltzer

Department of Metallurgy and Metallurgical Engineering, McMaster University, Hamilton, Ontario, Canada

ABSTRACT

An investigation is reported on the evaporation and thermal etching of iron alloys containing 5 and 25% chromium in the temperature range 900°-1080°C under a vacuum of 10^{-6} mm Hg. Evaporation proceeded by constant rates for exposures extending several hours; the activation energies were 94.3 and 93.7 kcal/g f w for the austenitic 5% and ferritic 25% alloy, respectively. Thermal etching gave rise to both faceted and specular surfaces.

The evaporation and thermal etching of iron-chromium alloys have not been extensively investigated. Vapor pressure measurements of the solid alloys at temperatures higher than 1200°C have been employed by McCabe *et al.* (1) and Kubaschewski and Heymer (2) for activity determinations. More recently, Gulbransen and Andrew (3) studied the influence of metal volatility on the oxidation behavior of heat resistant alloys containing iron, chromium, and aluminum by measuring vapor pressures of binary and ternary alloys in the lower temperature range 900°-1100°C. Because such evaporation plays an essential role in high-temperature surface reactions, an investigation is reported on evaporation of alloys containing 5 and 25% chromium for relatively long exposures in the temperature range 900°-1080°C. To augment the results of this kinetics study, the surface morphologies developed during evaporation have been examined microscopically.

Experimental

The experiments carried out in the temperature range 900°-1080°C illustrate evaporation characteristics of austenitic and ferritic alloys containing 5 and 25% chromium, respectively. Alloy analyses

Table I. Analyses (weight per cent) of iron-chromium alloys

Element	Fe-5% Cr alloy, %	Fe-25% Cr alloy, %
Cr	5.0	25.0
C	0.00	0.00
Mn	0.04	0.20
P	0.005	0.017
Si	0.019	0.053
S	0.007	0.015
Fe	balance	balance

are presented in Table I. Square plate specimens, 0.1 cm thick with surface areas of approximately 3.5 cm^2, were employed for the evaporation tests. Surface preparation involved abrasion to 4/0 grade silicon carbide paper and washing in acetone.

The high-vacuum glass system containing the evaporation tube consisted of a mechanical pump, a two-stage oil diffusion pump, and a McLeod gauge. This gauge was isolated from the system during evaporation runs. The furnace surrounding the evaporation tube was controlled to ± 2°C.

The assembly employed for the evaporation measurements, with the exception of those on the Fe-5% Cr alloy at 1000°C, is illustrated in Fig. 1. The 3 cm diameter quartz evaporation tube was protected from the atmosphere by the outer mullite furnace tube which was maintained at a vacuum of 10^{-2} mm Hg. Specimens were lowered into the evaporation tube by the windlass. For positioning of specimens in the evaporation zone, a 1 in. triangular support of 1 mm quartz rod was attached to the platinum suspension wire. Two specimens were hung vertically from this support. The distance separating the faces of the plates was 1 cm.

For the evaporation tests on the Fe-5% Cr alloy at 1000°C, the evaporation assembly consisted of a 5 cm diameter unprotected mullite tube equipped with a windlass. Two or three specimens were hung vertically from the quartz support with the faces of the plates separated 2 or 1 cm, respectively. This simple assembly was abandoned after the experiments at 1000°C as two tubes developed leaks during the period of experimentation.

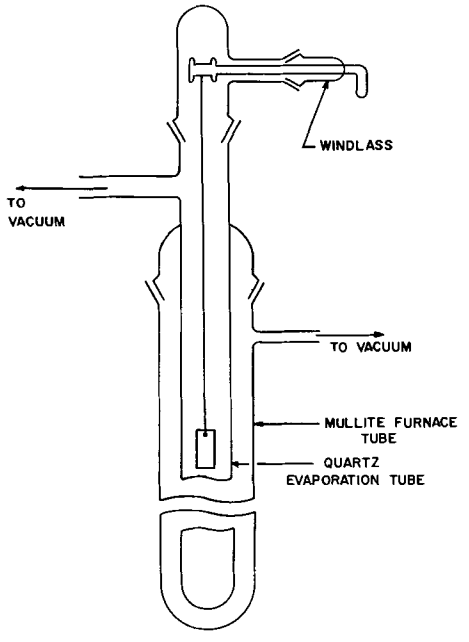

Fig. 1. Free evaporation cell

Evaporation kinetics were determined from weight losses of the specimens; newly prepared abraded specimens were used for each exposure test. Upon suspension of either two or three of these specimens on the quartz support, the system was evacuated to 10^{-6} mm Hg. After the temperature of the furnace had been established at 800°C, the specimens were lowered by the windlass into the evaporation tube and annealed for 2 hr. The furnace was then adjusted to the evaporation test temperature. After exposure for a specified time, the specimens were raised from the evaporation zone and removed from the support with forceps. The weight losses were determined with a Mettler Micro Gram-atic balance to an accuracy of ± 2 μg. A weight loss of 1 mg/cm^2 was equivalent to an evaporated layer 1.3 μ thick.

Results

The results for the evaporation kinetics are presented in conjunction with photomicrographs of the surfaces. There was deposition of a solid exhibiting the green coloration of chromium oxide on the wall of the evaporation tube indicating that evaporated metal gettered residual oxygen. Evaporation from the alloys was not detected at 800°C.

The evaporation determinations for the Fe-5% Cr alloy are presented by the plots, weight loss of metal, mg/cm^2, *vs.* time in hours in Fig. 2. Evaporation proceeded at constant rates under isothermal conditions. In the experiments at 1000°C, six of the eight exposures were completed with three specimens suspended 1 cm apart in the hot zone of the mullite evaporating tube. Two specimens suspended 2 cm apart were exposed in each of the other two exposures of 2 and 33 hr. Thus, 22 abraded specimens were exposed in this experimental series. The data represented in the plot of Fig. 2 demonstrated that the magnitude of this evaporation rate was independent of the experimental spacings between the plates and tube wall within the reproducibility of the measurements.

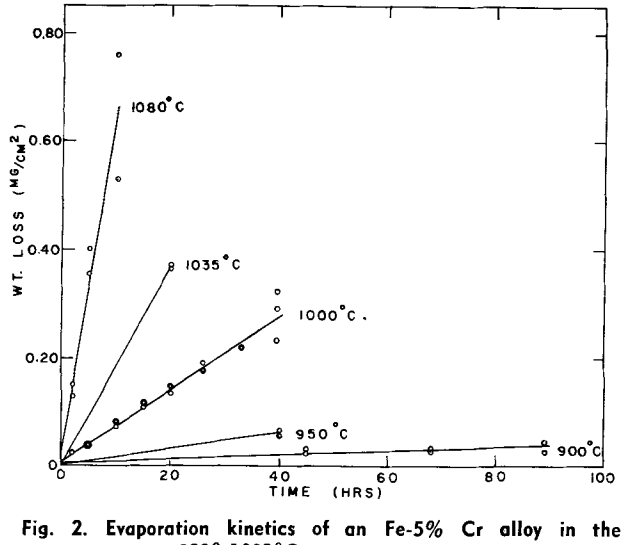

Fig. 2. Evaporation kinetics of an Fe-5% Cr alloy in the temperature range 900°-1080°C.

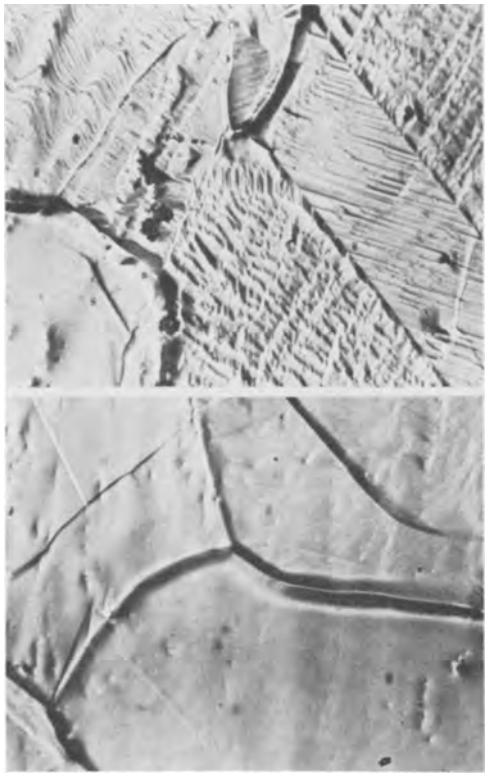

Fig. 3. Photomicrographs of surfaces on Fe-5% Cr alloy: top, exposure of 68 hr at 900°C; bottom, exposure of 10 hr at 1080°C. Magnification aproximately 865X.

Surface morphologies developed during evaporation of this alloy are shown in the photomicrographs of Fig. 3. The surfaces exhibited facets with orientations dependent on grain orientations, the degree of which was dependent on grain orientation and temperature. The twinned surface area of a specimen exposed at 900°C (top photomicrograph) illustrates that the degree of faceting was dependent on grain orientation. As illustrated by the surface of a specimen exposed at 1080°C (bottom photomicrograph) the degree of faceting decreased with increasing temperature. The large degree of grain boundary grooving found at all temperatures is also shown in these photomicrographs.

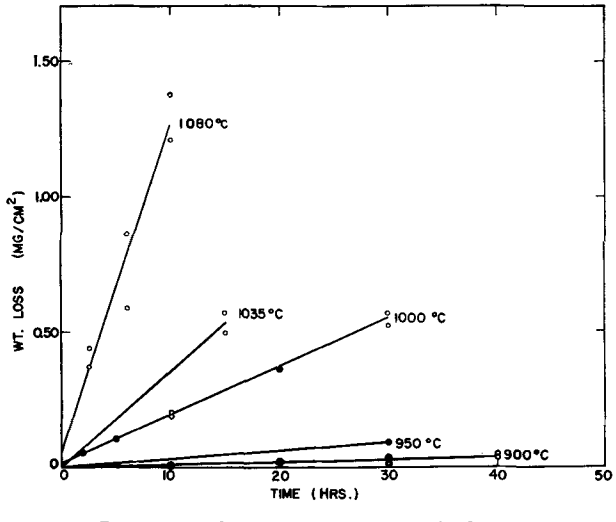

Fig. 4. Evaporation kinetics of an Fe-25% Cr alloy in the temperature range 900°-1080°C.

The evaporation determinations for the Fe-25% Cr alloy are presented in Fig. 4. As before, evaporation proceeded at constant rates under isothermal conditions. These rates are approximately twice as large as those for the 5% Cr alloy.

As shown by the photomicrographs in Fig. 5, the surfaces on this alloy were mainly specular at all temperatures. Although there was a small degree of pitting, the surfaces did not exhibit facets with orientation dependent on grain orientation. An interferogram of a specimen exposed at 1080°C, Fig. 6, illustrated that grain boundaries were grooved to a depth of 2μ and that its surface was smooth to dimensions not exceeding 500Å.

Discussion

In this section, the evaporation kinetics are correlated with determinations of vapor pressures and

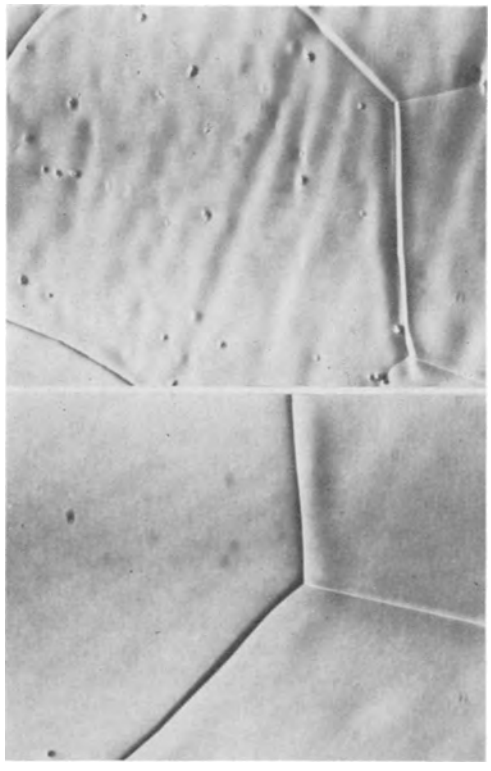

Fig. 5. Photomicrographs of surfaces on Fe-25% Cr alloy: top, exposure of 40 hr at 900°C; bottom, exposure of 10 hr at 1080°C. Magnification approximately 865X.

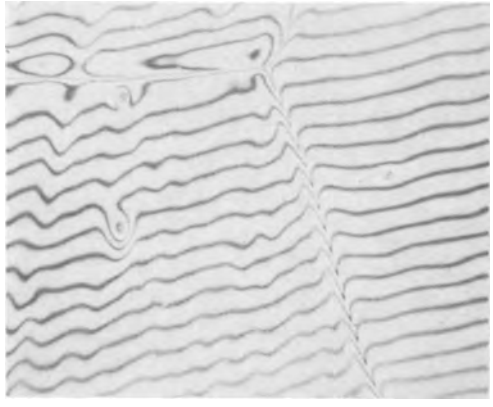

Fig. 6. Interference micrograph of surface on iron-25% chromium alloy after evaporation at 1080°C for 10 hr. Magnification approximately 450X.

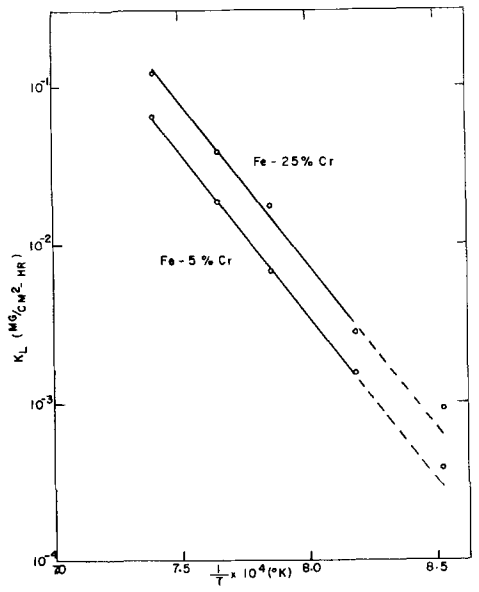

Fig. 7. Arrhenius plots of evaporation rates for the Fe-5% Cr and Fe-25% Cr alloy.

thermal etching properties of iron-chromium alloys.

In order to evaluate activation energies, the rates of evaporation may be expressed according to the Arrhenius relation. Such plots determined by the method of least squares from the values for the upper four investigated temperatures are presented in Fig. 7. The results at 900°C were not taken into account for these calculations since the small weight losses were equivalent to evaporated layers less than 0.1μ thick from abraded surfaces. The energies of activation are 94.3 and 93.7 kcal/g f w to an accuracy of ± 5.0 kcal for the 5 and 25% Cr alloy, respectively. In this temperature range, the heats of evaporation for iron and chromium are 96.2 and 94.2 kcal/g f w to an accuracy of ± 1.0 kcal, respectively (4). Hence, the temperature coefficients of alloy evaporation rates approximated closely to those of the pure metals.

Residual gas in the vacuum of 10^{-6} mm Hg influenced surface morphological development: evaporation of the alloy containing 25% Cr was influenced to a smaller degree by gas adsorption since facets only developed on the 5% Cr alloy (Fig. 3 and 5). Moreover, evaporation was determined by surface processes for escape of metal because activation energies were of the same magnitude as the heats of evaporation for the alloy components. Since evaporating metal sufficiently gettered residual oxygen and oxidizing gases preventing the formation of a surface oxide, the surface features were consistent with findings of Benard *et al.* (5, 6) for Fe-Cr alloys exposed in hydrogen-water atmospheres. They have shown that a critical oxygen pressure dependent on temperature and alloy composition must be exceeded to transform a specular to a faceted surface at pressures less than the dissociation pressure of chromium oxide. This effect was attributed to stabilization of preferred crystallographic faces by minimization of the total surface energy at a critical degree of oxygen adsorption. In the case of the evaporation of the 25% Cr alloy, the pressure of oxidizing gases was reduced to the stability range of a specular surface by the more rapid rate of chromium evaporation. The amount of adsorbed oxygen would also be decreased by its higher dissolution rate into the metal substrate due to its tenfold larger diffusion constant for a ferritic structured alloy (7). This explanation, however, must be tentatively accepted because adsorption of both oxidizing and hydrocarbon gases could possibly influence the migration of monatomic surface ledges and their pile-up to form facets during evaporation.

Although the temperature coefficients of evaporation approximate to those of the alloy components, one may show that the evaporation rates are smaller than values for free evaporation. The good agreement of vapor pressure determinations for iron and chromium at temperatures greater than 1200°C by either the Langmuir free evaporation or Knudsen effusion methods (1, 2) has shown that the condensation coefficients are unity. Accordingly, vapor pressures were determined from the results of this investigation by employing the Langmuir equation in the form

$$P = \frac{1}{\alpha}\frac{dw}{dt}\left(\frac{M}{2\pi RT}\right)^{-1/2} \qquad [1]$$

with the assumptions that $\alpha = 1$ and $M = (M_{Cr} + M_{Fe})/2$. Iron and chromium have similar atomic weights so this latter assumption does not introduce a significant error. As shown in Table II, the ratios of these pressures to the ideal pressures are less than unity being 0.4 and 0.5 for the 5 and 25% Cr alloys. The ideal pressures calculated from thermochemical data for iron and chromium (4) are good approximations to equilibrium vapor pressures because these alloys exhibit nearly ideal behavior at high temperatures (1).

The question therefore arises as to whether surface depletion of chromium during evaporation gave rise to low vapor pressure determinations. To test this possibility, the surface concentrations of chromium were calculated from equations for evaporation of a component from a plate (8) for the extreme exposure of 10 hr at 1080°C. The values for the chromium diffusion constants given by Heumann and Böhmer (9) were employed in these calculations, and it was assumed that the fractions of chromium in the evaporating metal were those to be expected for an ideal iron-chromium solid solution. The depletion of chromium from 25 to 24% for this hypothetical condition was not of sufficient magnitude to introduce a serious error in the evaluation of the pressures for the high chromium alloy. On the other hand, this calculation showed that chromium may be surface depleted from 5 to 3%

Table II. Ratios of vapor pressures calculated by the Langmuir equation to ideal vapor pressures

Temp, °C	Fe-5% Cr alloy	Fe-25% Cr alloy
950	0.42	0.43
1000	0.31	0.58
1035	0.45	0.49
1080	0.31	0.45
Average value	0.37 ± 0.08	0.49 ± 0.09

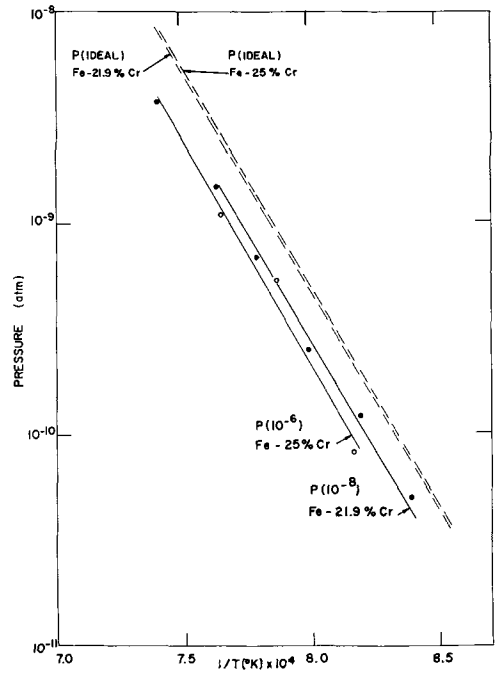

Fig. 8. Plots of the ideal and experimentally determined vapor pressures for iron alloys containing 21.9 and 25% chromium.

for this extreme exposure. Although this approximate calculation does not account for iron evaporation, it indicates that the lower evaluations for the pressure ratio of the Fe-5% Cr alloy (Table II) may be partially caused by chromium depletion from the evaporating surface.

Apparently the magnitudes of the evaporation rates are dependent on the exposure conditions. As substantiating evidence for this viewpoint, the estimated vapor pressures for the 25% Cr alloy are compared to determinations from an alloy containing 21.9% Cr in Fig. 8. These pressures for the latter alloy were determined by Gulbransen and Andrew (3) utilizing the evaporation kinetic method for abraded specimens exposed in an externally heated evaporation tube under a vacuum of 10^{-8} mm Hg. Although these pressures are larger than those for the 25% Cr alloy, the values are only 0.6-0.7 of the ideal vapor pressures.

One may not directly attribute, however, the low evaluations of vapor pressures in these two series of experiments to the different vacuum conditions. The data now available for evaporation in the temperature range 900°-1100°C have been obtained from weight losses of specimens suspended in a hot zone of an externally heated tube. Any back flux of metal to a specimen would then lead to low evaluations of the pressures when calculated by the Langmuir equation. A distinction could not be made in this investigation between the flux of metal bombarding the specimen from one another or the tube wall. As the degree of metal removal by reaction with residual gas and the tube wall is unknown, an attempt is not made to evaluate a correction to the evaporating flux. The findings in this investigation also do not necessarily support the conclusion that pressures determined from evaporation kinetics by assuming that the condensation coefficient is unity would be equal to vapor pressures if exposure conditions met requirements of free evaporation: Hirth and Pound (10) have demonstrated that the condensation coefficient for a polycrystalline metal may vary from one-third to unity depending on the sources and migration of surface ledges.

Conclusions

In the temperature range 900°-1080°C, iron alloys containing 5 and 25% Cr evaporated by constant rates for exposures of several hours in a vacuum of 10^{-6} mm Hg. Surfaces of the 5% Cr alloy exhibited faceting, the degree of which was dependent on grain orientation and temperature. The surfaces of the 25% Cr alloy remained specular. Both alloys exhibited grain boundary grooving. The formation of facets was consistent with the view that adsorption of oxygen from residual oxidizing gases stabilized surfaces consisting of preferred crystallographic faces. Activation energies for evaporation of 94.3 and 93.7 kcal/g f w were of the same order of magnitude as the heats of evaporation for the alloy components. An analysis demonstrated that results of evaporation kinetics in this investigation lead to low evaluations of vapor pressures.

Acknowledgments

This contribution is based on a thesis submitted by L. A. Morris to the School of Graduate Studies, McMaster University, in partial fulfillment of the requirements for the M.Sc. degree. He wishes to acknowledge the award of a University Scholarship. The authors appreciated discussions with M. B. Ives, J. S. Kirkaldy and R. G. Ward; they were indebted to W. E. Boggs, U. S. Steel Research Laboratories, and J. H. Kelly, Steel Company of Canada, for alloy samples and analyses, respectively.

This work forms part of a research project sponsored by the U. S. Air Force Office of Scientific Research, Office of Aerospace Research, and the Defense Research Board, Ottawa, Canada.

Manuscript received Dec. 17, 1962; revised manuscript received April 5, 1963. This paper was delivered before the Boston Meeting, Sept. 16-20, 1962.

Any discussion of this paper will appear in a Discussion Section to be published in the June 1964 JOURNAL.

REFERENCES

1. C. L. McCabe, R. G. Hudson, and H. W. Paxton, *Trans. AIME*, **212**, 102 (1958).
2. O. Kubaschewski and G. Heymer, *Acta Met.*, **8**, 416 (1960).
3. E. A. Gulbransen and K. F. Andrew, *Trans. AIME*, **221**, 1247 (1961).
4. J. F. Elliot and M. Gleiser, "Thermochemistry for Steelmaking," Addison-Wesley Publishing Co. (1960).
5. J. Benard, J. Moreau, and J. Plateau, *Z. Elektrochem.*, **61**, 59 (1957).
6. J. Moreau and J. Benard, *J. Chim. Phys. Fr.*, **53**, 787 (1956).
7. H. Schenck, E. Schmidtmann, and H. Müller, *Arch. Eisenhüttenw.*, **31**, 121 (1960).
8. J. Crank, "The Mathematics of Diffusion," p. 56, Oxford (1956).
9. U. T. Heumann and H. Böhmer, *Arch. Eisenhüttenw.*, **31**, 749 (1960).
10. J. P. Hirth and G. M. Pound, *J. Chem. Phys.*, **26**, 1216 (1957).

Application of Cyclic Voltammetry to the Kinetic Study of Electro-Oxidation of Organic Compounds

Andre L. Juliard and Harold Shalit

Houdry Process and Chemical Company, Marcus Hook, Pennsylvania

ABSTRACT

Information concerning the kinetics of electro-oxidation of methanol and formic acid in acid solution at a stationary platinum electrode can be obtained from the study of cyclic voltamgrams. The voltamgrams are obtained by recording the current density of the working electrode while its potential is scanned back and forth at constant rate between adequate potentials. The analysis of the shape of cyclic voltamgrams and of the effect of the rate of scanning on this shape sustains the hypothesis that the electro-oxidation of organic compounds to carbon dioxide and water is limited by the rate of formation of some intermediate platinum-carboxo surface compound. The thermodynamic yield of the electrode reaction seems to be limited by the stability of this intermediate compound.

The understanding of the mechanism of electro-oxidation of organic compounds at a stationary solid electrode has been retarded by the fact that the nature of the electrode surface changes progressively as the reaction proceeds from one steady state to another. For instance, as a result of this change, the chronopotentiometric transition times of a slow reaction at a solid electrode depend not only on the current density and the prepolarization potential, but also on the duration of the prepolarization and, furthermore, on the whole history of the electrode since the time of its last "cleaning."

This drawback is eliminated in cyclic voltammetry. Indeed, by scanning the polarization potential of a working electrode back and forth at constant rate between adequate potentials the same state of the surface can be re-established at the different points of the cycle. Therefore, perfectly repeatable complicated voltamgrams can be obtained with solid electrodes by cyclic voltammetry (1), from which meaningful chronopotentiometric measurements can be derived (2).

On the other hand, a cyclic voltamgram can be considered as a plane projection of a peculiar three dimensional surface in a current-voltage-time space. Therefore an analysis of the shape of a cyclic voltamgram and of the effect of the rate of scanning on this shape gives information concerning the kinetics of an electrochemical process and suggestions about the phenomena which perturb this process.

Cyclic voltammetry has been applied recently by Breiter (3) for the study of the oxidation of amyl alcohol in perchloric acid solution at a platinized electrode between 0 and +1.6v *vs.* H. The author concludes from his measurements that amyl alcohol undergoes an anodic oxidation in the potential region above +0.8v where an oxygen layer is formed simultaneously at the surface of the electrode, but that the oxidation occurs on the oxygen-free surface exclusively. Breiter concludes also that the alcohol molecules are adsorbed before their oxidation and that the oxidation current peak observed around +0.6v during the cathodic sweep, which is the sweep directed toward more negative potential, is due to the oxidation of an intermediate product formed during the preceding anodic sweep. Voltamgrams similar to that of Breiter were obtained in the cyclic voltammetry study of oxidation of methanol, formaldehyde, and formic acid by Buck, Griffith, MacDonald, and Schlatter (4). These authors show that the platinum oxide formation has a detrimental effect on the oxidation of these compounds. Besides, a retardation effect due to the accumulation of intermediate products has been suggested by Bogdanovskii and Shlygin (5) to explain the shape of simple voltammetric curves observed during the oxidation of ethyl alcohol. No systematic study of the shape of cyclic voltamgrams has been done at polarization potentials below +0.80v, where a platinum oxide layer would apparently not be formed at the surface of the electrode.

This work is part of a research directed to pinpoint the factors which limit the yield of electro-oxidation of carbonaceous compounds. It deals more specifically with the study of the oxidation of formic acid and methanol at platinized electrodes.

Experimental Technique

A schematic drawing of the electrical circuit is given in Fig. 1. This circuit is characterized by the low resistance values of its components. The voltage is scanned at different rates by means of a continuous rotated centered-tap potentiometer, ac-

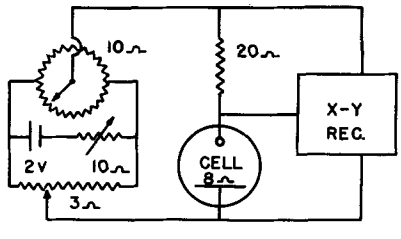

Fig. 1. Electrical circuit

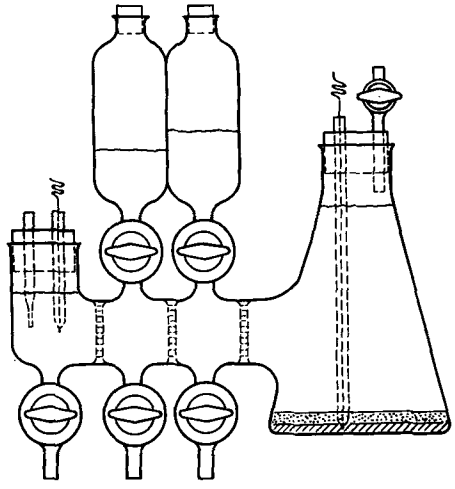

Fig. 2. Electrolytic cell

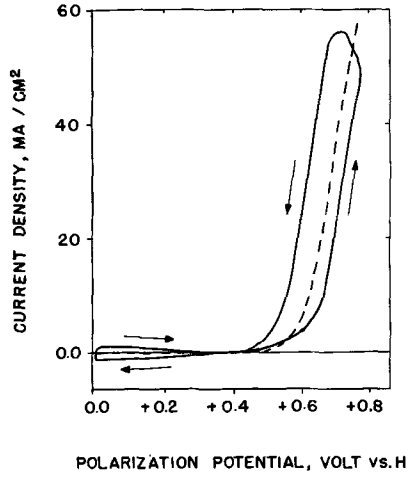

Fig. 3. Platinized platinum in 2.5M methanol-3.0M sulfuric acid solution. ——— Cyclic polarogram with scanning rate of 0.8 v/min; - - - stepwise scanned polarogram with increment of 0.1 v/min.

tivated by a synchronous motor. The current-polarization curves were recorded by an X-Y recorder with a 400 kilo-ohm input resistance on the voltage measuring scale. The cell, shown in Fig. 2, is of the H type with greaseless Teflon plugged stopcocks. It has an electrolytic bridge of 6 cm in length and 2 cm in diameter, segmented in two compartments by three coarse fritted glass diaphragms. The bridge was filled with fresh electrolyte at the beginning of a series of experiments and replaced after 2 hr of experiments to avoid the contamination of the fuel and the comparison electrode from cross diffusion of the electrolytes. The comparison electrode was a 30 cm^2 mercury pool in contact with a paste of mercurous sulfate. Most experiments were conducted in 3.7M sulfuric acid solution at 25°C. Under these conditions the potential of the comparison electrode was +0.61v *vs.* the equilibrium hydrogen electrode placed in the working compartment containing 4.0M sulfuric acid solution. The potentials reported in this paper are expressed *vs.* the potential of this hydrogen electrode. The resistance of the cell was 9.0 ohms when measured with an a-c bridge between the comparison electrode and an hydrogen electrode having the same apparent surfaces as the working electrode and placed in the working compartment. The working electrode was a platinum wire 2.5 mm in length and 0.5 mm in diameter protruding at the end of a glass tube, covered by a deposit of platinum approximately 2 mg/cm^2 obtained by the electrolysis of a chloroplatinic acid solution.

The sulfuric acid used in our experiments was duPont A.C.S. Reagent Grade containing less than 7×10^{-11} mole of arsenic and 4×10^{-9} mole of iron per liter. Methanol was a Baker and Adamson A.C.S. Reagent Grade, acetone-free product.

The usual precautions taken in conventional polarography were applied in the measurements. Traces of impurities do not affect markedly the cyclic voltammetric results since preliminary experiments have shown that practically identical voltamgrams were obtained by using simply distilled water instead of distilled and demineralized or conductivity water as solvent; or by pre-electrolyzing the sulfuric acid solution with a black platinum electrode; or by using the acetone-free reagent grade methanol as received or the heart cut of a careful distillation fraction of this sample. Oxygen was stripped out of the sulfuric acid solution by bubbling oxygen-free nitrogen through it for 15 min before each series of experiments. The bubbling was continued for a few minutes after addition of the organic compound. Experiments with pure acid solution were performed while nitrogen was bubbling through the solution. No measurable shift in the shape of the voltamgram was observed when the experiment was repeated without bubbling and under a nitrogen blanket.

Results and Discussion

A typical cyclic voltamgram obtained with a platinized electrode dipped in a concentrated methanol-sulfuric acid solution is shown in Fig. 3. The current-polarization curve shows a double loop with an inversion of the direction of the current in the vicinity of +0.40v, while the normal redox potential calculated from the free energy of oxidation of methanol to carbon dioxide is equal to +0.05v. The dashed curve represents the value obtained by stepwise polarization at 0.1v increments per minute. The same curve is obtained approximately whether the direction of scanning is anodic or cathodic.

The meaning of the loop between 0 and +0.35v is more easily understood after an analysis of the voltamgram obtained under the same conditions without methanol in the solution, as shown by the full curve of Fig. 4. This voltamgram, with its two pairs of symmetrical peaks, coincides practically with the voltamgram obtained in the same condition with a bright platinum electrode instead of the platinized one, as shown by the dotted curve of Fig. 4, provided that the rate of scanning of the two electrodes is adjusted to a ratio inversely proportional to the active surface of the two electrodes.

It was proved by Will and Knorr (6) that the scanned current observed with a bright platinum electrode in acid solution between 0 and +0.40v is generated by the building and the subsequent oxidation of a platinum-hydrogen surface complex.

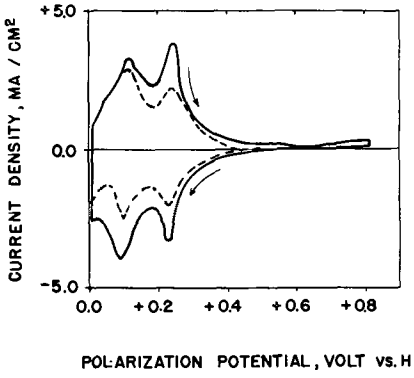

Fig. 4. Platinum in 3.0M sulfuric acid solution. ——— Platinized electrode with scanning rate of 0.8 v/min; - - - smooth platinum wire with scanning rate of 60 v/min.

Furthermore, the quantity of electricity, $\int idt$, corresponding to the anodic sweep of the current-polarization curve in this bracket of potential was used by these authors to measure the effective surface of the bright platinum electrode. The similarity of the two voltamgrams of Fig. 4 suggests that the same method can be used to measure the active surface of a platinized electrode. As expected, this surface varies largely with the plating procedure. The active area of the platinized electrode shown in Fig. 4 corresponds to 49.5 mcoulombs/cm^2 of apparent surface, a value which agrees quite well with the 45.0 mcoulombs/cm^2 measured by chronopotentiometry. This quantity of electricity would correspond to an effective surface of 200 cm^2/cm^2, if one accepts that 0.215 mcoulombs are required to cover 1 cm^2 of perfectly flat platinum surface, assuming that one atom of hydrogen is anchored by each atom of platinum (2, 6).

It is worthwhile to notice that the scanned current generated by the formation or the destruction of the platinum-hydrogen surface compound drops rapidly to zero when the scanning is stopped. The scanned current is also reversed instantaneously when the direction of the voltage scan is reversed. These facts mean that the coverage of the electrode by hydrogen is determined by the potential of the electrode and vice-versa in a reciprocal relationship and that the change in the coverage with the polarization potential proceeds at a relatively high rate, *e.g.* with a specific rate higher than 45.0/30 = 1.5 sec^{-1}.

The progressive addition of methanol to the sulfuric acid solution modifies profoundly the shape of the voltamgram between 0.0 and 0.8v, as shown by Fig. 5 and 6. The amount of hydrogen anchored on the electrode, measured by $\int idt$ of the oxidation current between 0.0 and 0.4v, decreases almost linearly with the concentration of methanol up to about 1 mole per liter, then remains approximately constant up to 3 moles per liter.

The amount of hydrogen attached to the platinum surface in concentrated methanol solution at 0.05v varies largely with the procedure of preparation of the electrode. The activity of the electrode bears a curious relation with this amount of hydrogen attached to the electrode in the absence and in the

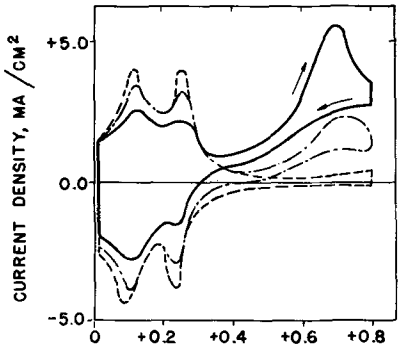

Fig. 5. Effect of concentration of methanol in 1.5M sulfuric acid solution. Platinized electrode polarized with scanning rate of 0.8 v/min. - - - - - No methanol; —·—·—·—·— 0.05 vol. % (0.015M); ——— 0.40 vol. % (0.12M).

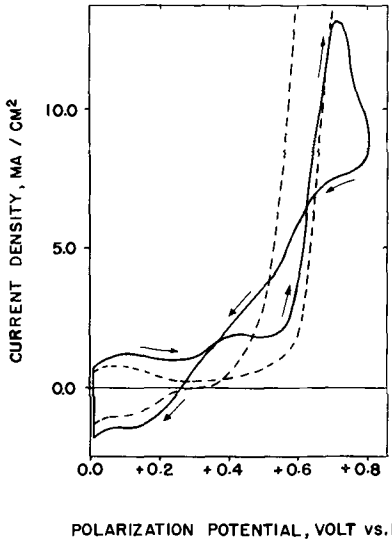

Fig. 6. Effect of concentration of methanol in 1.5M sulfuric acid solution. Platinized electrode polarized with scanning rate of 0.8 v/min. ——— 1.60 vol. % (0.05M); - - - - 10.0 vol. % (3.0M).

presence of methanol. More specifically, as shown in Table I, the activity of the electrode, A, measured by the steady state current of oxidation at 0.70v, is related to this value by the following equation

$$A = k\frac{(T-R)^2}{R} \qquad [1]$$

where T is amount of hydrogen attached to the electrode in the sulfuric acid solution at 0.0v in mcoulomb cm^{-2}; R, amount of hydrogen attached

Table I. Relation between the activity of platinized electrodes and their hydrogen active surface

Electrode No.	Activity in ma/cm² @ 0.70v A	Hydrogen active surface, mcoulomb/cm² 4.0M H_2SO_4 T	4.0M H_2SO_4 + 3M CH_3OH R	Rate constant k, in sec^{-1} $\frac{AR}{(T-R)^2}$
I	41	35	2.9	0.11
II	35	54	5.8	0.09
III	45	85	14	0.13
				Average 0.11 ±0.013

to the electrode in the methanol-sulfuric acid solution at 0.0v in mcoulomb cm^{-2}; k, rate constant in sec^{-1}.

It appears from Table I that the rate constant, k, calculated from Eq. [1] fluctuates around 10% of its average value even when T and R vary at random between 35 and 85, and 3 and 14 mcoulomb/cm^2, respectively. The validity of the relation expressed by Eq. [1] suggests that methanol is oxidized only at sites where two methanol absorbing platinum sites are adjacent, the probability of finding two adjacent platinum atoms at which a methanol molecule could be adsorbed being then inversely proportional to the concentration of platinum atoms at which methanol is not adsorbed below +0.40v. This hypothesis is consistent with the hypothesis of Muller and Takegami (7) and of Tanaka (8) who postulate a two-point hydrogen adsorption in the case of electro-oxidation of ethanol to explain the product distribution at moderately active electrodes.

The loop above 0.40v shown in Fig. 3 is due to the oxidation of methanol. However, the shape of this loop suggests that a product which depresses the activity of the electrode is formed and accumulated at low overvoltage and is progressively eliminated, probably by further oxidation, at higher overvoltage. The "poisoning" product can be an intermediate product of oxidation of methanol. In this case, the current of oxidation will remain below the steady state current during the last portion of the anodic sweep if the rate of scanning is greater than the rate of cleaning of the electrode. On the other hand, the current will be greater than the steady state current in the last portion of the cathodic sweep if the rate of scanning is greater than the rate of obstruction of the electrode with the "poisoning" product.

These hypotheses are in line with the complicated effect of the rate of scanning on the shape of the voltamgram, as shown in Fig. 7. These voltamgrams were obtained by scanning the polarization with increasing rate in the ratio of 1:4:16. In these experiments the anodic polarization scan was extended above +0.8v to assure a more thorough cleaning of the electrode, since previous experiments had shown that the active surface of a bright platinum electrode can be restored to its original value after being polarized between +1.2 and +1.4v in the methanol-sulfuric acid solution for a few seconds.

The shape of the loop between +0.35 and +0.80v of the slowest scanned voltamgram of Fig. 7 is similar to that of Fig. 3 obtained with a scanning rate two times greater but within a polarization span which prevents the formation of platinum oxide. The rate of poisoning of the electrode at different potentials is relatively slow and can be computed from the shift of the descending branch of the cathodic sweep toward negative potential with the increase in the rate of scanning. The progressive poisoning at a certain potential can also be computed by the change in the shape of the current-polarization curve during the anodic sweep between +0.35 and +0.80v. Indeed, the current of oxidation at low overvoltage increases with the rate of scanning because the time of sojourn of the electrode at the low potentials becomes then too short to allow the poisoning product to reach its equilibrium coverage during the cathodic sweep.

The triple loop observed with medium concentrated methanol solution when the anodic polarization reaches only 0.8v, as shown by Fig. 6, can be explained in the same way when one assumes that the desorption of methanol accompanying the formation of the surface platinum oxide starts at 0.7v when the surface is not beforehand saturated with methanol.

Similar phenomena are observed during the oxidation of formic acid, as shown by Fig. 8. The comparison of this voltamgram with that obtained with methanol shows: (*a*) that the formation of the poisoning product occurs at a slower rate with formic acid than with methanol, as translated by the higher current of oxidation and by the smaller

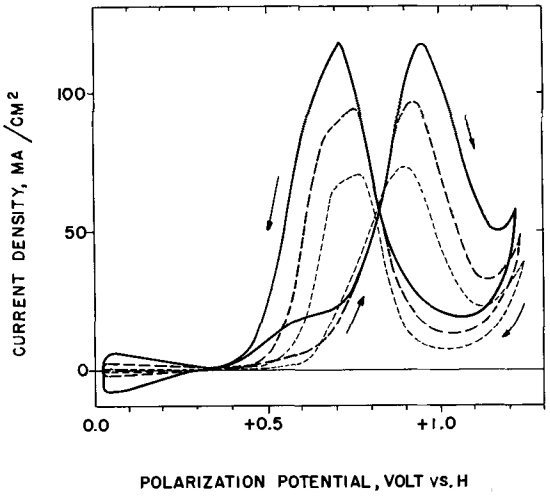

Fig. 7. Effect of rate of scanning with methanol. Platinized electrode in 3.0M methanol-3.7M sulfuric acid solution. - - - - 0.31 v/min; — — — 1.25 v/min; ——— 5.00 v/min.

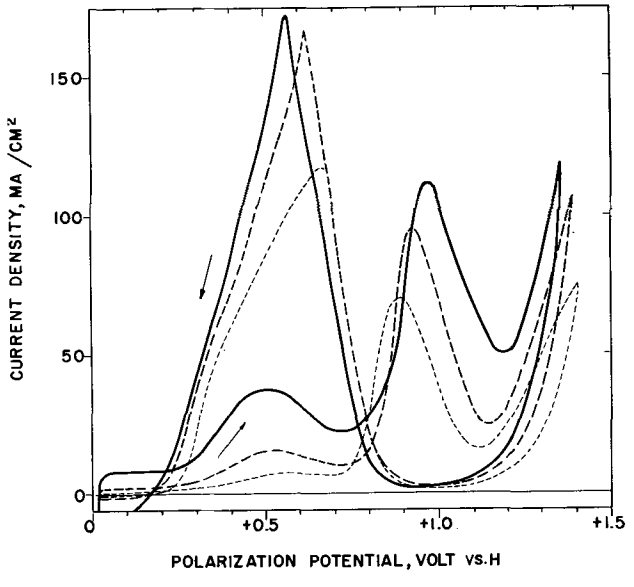

Fig. 8. Effect of rate of scanning with formic acid. Platinized electrode in 3.0M formic acid-3.7M sulfuric acid solution. - - - - 0.35 v/min; — — — 1.40 v/min; ——— 5.60 v/min.

effect of the rate of scanning on this current during the cathodic sweep, and (*b*) that the rate of oxidation of formic acid is smaller than that of methanol when the electrode is obstructed by the poisoning product, as shown by the smaller current observed during the anodic sweep between 0.3 and 0.8v at low scanning rate.

From these considerations, one can conclude that the rate of oxidation of formic acid and of methanol to carbon dioxide and water below +0.8v is determined by the rate of oxidation of an intermediate product whose rate of formation and rate of oxidation increases with the anodic potential. The potential dependence of these two rates is different, such that at low potential the rate of accumulation is greater than the rate of oxidation while at high potential the reverse is true.

x

x x

It is easier to speculate about the nature of this troublesome reaction in the case of formic acid than that of methanol, since the electro-oxidation of a molecule of formic acid proceeds in two steps at the maximum, while that of methanol may occur in six steps and requires, furthermore, the interaction of a molecule of water.

The first step of oxidation of formic acid at a bare platinum site could be

$$Pt^{o} + HCO_2H \rightarrow PtCO_2H + H^{+} + e \qquad (A)$$

where Pt^{o} represents an active platinum atom.

The second step would then be

$$PtCO_2H \rightarrow Pt^{o} + CO_2 + H^{+} + e \qquad (B)$$

which regenerates the active platinum Pt^{o}.

If this is the mechanism of the reaction, the surface compound $PtCO_2H$ will be stabilized by an amount of energy equal to the difference between the free energy of formation of the intermediate surface compound and one-half of the free energy for direct oxidation of formic acid

$$H_2CO_2 + 1/2\ O_2 \rightarrow CO_2 + H_2O \qquad (C)$$

The further oxidation of the intermediate compound $PtCO_2H$ to carbon dioxide will then liberate a quantity of free energy less than one-half of the free energy associated with reaction (C). Therefore, the normal potential of oxidation of formic acid *vs.* the normal potential of hydrogen, ΔE, will be smaller than the theoretical value

$$\Delta E_T = \frac{\Delta F^{\circ}}{2F}$$

calculated from the free energy of reaction (C). This seems to be the case, for instance, when platinum is used as a catalyst in the electro-oxidation of formic acid, formaldehyde, and methanol in acid solution at room temperature.

The suggested mechanism, assuming the formation of a relatively stable metal-carboxo intermediate compound, has furthermore the advantage of focusing attention on the importance of the nature of the compound formed at the surface of the electrode on the rate of the electrode process.

Acknowledgment

The authors wish to thank the Houdry Process and Chemical Company and the Northern Natural Gas Company for permission to publish the results of this research.

This work was supported in part by the Northern Natural Gas Company.

Manuscript received Sept. 14, 1962; revised manuscript received March 29, 1963. This paper was presented before an American Chemical Society Meeting, Atlantic City, September 1962.

Any discussion of this paper will appear in a Discussion Section to be published in the June 1964 JOURNAL.

REFERENCES

1. A. L. Juliard, *J. Electroanal. Chem.*, **1**, 101 (1959-60); *Nature*, **183**, 1049 (1959).
2. M. W. Breiter and S. Gilman, *This Journal*, **109**, 622 (1962).
3. M. W. Breiter, *ibid.*, **109**, 42 (1962).
4. R. P. Buck, L. R. Griffith, R. T. MacDonald, and M. Y. Schlatter, Armed Service Technical Information Agency, Arlington, Virginia, Report AD-254,312.
5. G. A. Bogdanovskii and A. I. Shlygin, *Zhur. fiz. Khim.*, **34**, 26 (1960).
6. F. G. Will and C. A. Knorr, *Z. Elektrochem.*, **64**, 258 (1960).
7. E. Muller and S. Takegami, *ibid.*, **34**, 704 (1928).
8. S. Tanaka, *ibid.*, **35**, 38 (1929).
9. M. W. Breiter and B. Kennel, *ibid.*, **64**, 1180 (1960).

The Electrochemistry of Nickel

II. Anodic Polarization of Nickel

M. L. Kronenberg,[1] J. C. Banter,[2] E. Yeager, and F. Hovorka

Department of Chemistry, Western Reserve University, Cleveland, Ohio

ABSTRACT

The anodic dissolution of nickel has been studied in acidified chloride, sulfate, and perchlorate solutions under a variety of nonpassivating conditions. The Tafel slopes at 45°C are approximately 0.085, 0.115, and 0.12, respectively. The lower value of the Tafel slope in chloride solutions is attributed to specific adsorption. The potential of the nickel anode is independent of Ni^{+2} concentration under conditions for which the back reaction is negligible, and no pH dependence has been found for pH of 1-2.5. The temperature dependence of the polarization yields an approximate value of 15 kcal/mole for the heat of activation in the chloride solution.

The electrodeposition of nickel has been the subject of many experimental investigations. With the exception of studies of anodic passivation, however, relatively little fundamental research effort has been directed toward an understanding of the anodic dissolution reaction. Where data are available, much of it is not conducive to fundamental analysis and interpretation. Of particular interest is the work cited in ref. (1-9).

The purpose of the present work has been to obtain information concerning the mechanism of the anodic dissolution of nickel. The anodic polarization has been measured as a function of current density, temperature, pH, concentration of nickel ion, nature and concentration of supporting electrolyte, and the source and crystallographic orientation of the nickel anode.

Apparatus

The indirect method has been used for the polarization measurements. This method was favored because it avoids some of the difficulties associated with the use of a Luggin capillary and because of the availability of equipment at Western Reserve University.

A block diagram of the electronic interrupter and its associated equipment is shown in Fig. 1. The current from the polarizing source is interrupted when repetitive rectangular negative pulses from the pulse generator are applied to the grids of parallel-connected triodes (6SN7) or beam power pentodes (6L6), driving them to cut off (10). For most of the results reported here the current was off for 50 μsec and on for 1300 μsec. These times, which represent a 96% duty cycle, were sufficient to permit buildup of the potential to a steady-state value prior to interruption.

[1] Present address: Research Laboratory, Union Carbide Corporation, Parma, Ohio.

[2] Present address: Oak Ridge National Laboratory, Oak Ridge, Tennessee.

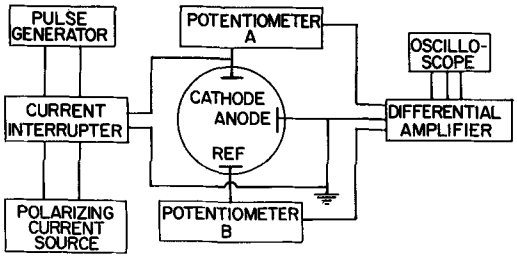

Fig. 1. Block diagram of electronic interrupter and associated equipment.

By means of the differential amplifier, the anode-reference, cathode-anode, and cathode-reference potential could be viewed on the oscilloscope (Tektronic type 512). The potential difference associated with any portion of the buildup or decay curve could be measured to ± 1 mv or ± 0.1% (whichever is larger) by adjusting potentiometers A and B (Fig. 1) so as to bring that portion of the trace on the oscilloscope screen to the zero deflection position. Switching transients were such that the potential could be measured within 1-3 μsec following interruption of the current. A complete circuit diagram is given elsewhere (10). A L&N K-2 potentiometer was used to measure the potentials between the reference electrodes involved in this work.

The glass polarization cell is similar to that described in the first paper (11) in this series. Provisions are made for various reference and preelectrolysis electrodes in addition to the anode and cathode involved in the polarization measurements. The cell provides for a controlled relatively high speed flow of the solution past the anode at rates up to 60 cm/sec in the bulk of the solution adjacent to the anode. The voltage from an electric tachometer was used as a relative measure of the solution velocity. The tachometer was calibrated in terms of flow rates under experimental conditions by means of a pitot tube as described earlier (11). The cell was mounted in a thermostatic bath which controlled the temperature to ± 0.05°C in the range 25°-45°C.

The hydrogen gas used for saturating the solution was passed through a purification train consisting of the following components: (*a*) De-Oxo unit for catalytic oxygen removal (Baker Company Inc., Newark, N. J.); (*b*) magnesium perchlorate for

drying; (c) Hopcalite for oxidation of trace CO (Mine Safety Appliance Company, Pittsburgh, Pa.); (d) soda lime for removal of CO_2 and H_2O; and (e) three liquid nitrogen cooled traps for the adsorption of impurities with the first filled with silica gel, the second with active carbon, and the third with glass wool.

Experimental Procedure

Several anode designs and sources of nickel were compared in preliminary experiments. The anodes were designed to provide a reasonably uniform current density over the surface of the electrode. The first electrodes used were 14-gauge (B. and S.) nickel wire of 99% purity and Johnson-Matthey nickel rod which was machined down to 3 mm in diameter. Both types were sealed in 8-mm OD soft glass and were rounded at the end to essentially the same radius of curvature as the cylindrical portion.

Efficiency measurements were obtained using an anode consisting of Johnson-Matthey nickel rod cut down to 3 mm in diameter. One end of the rod was drilled and tapped to fit the threaded end of the 14-gauge nickel wire which was sealed in soft glass. This permitted the direct weighing of the anode used in efficiency measurements. The design is shown in Fig. 2a. For current densities above 0.3 ma/cm^2 efficiencies could be measured with a precision of ± 2%.

The electrode design adopted for single crystal electrodes is shown in Fig. 2b. This design permitted polarization measurements at a particular face of a single crystal without introducing any plastics or organic sealers into the electrolyte. One face of the cylindrical nickel electrode was drilled and tapped and a threaded contact was made with nickel wire. The other face was kept even with the glass tubing so that only the desired face was exposed to the electrolyte. Hydrogen gas from the purification train flowed between the metal and glass to prevent the solution from flowing up the tube. The hole in the top of the glass through which the nickel wire passes was sealed with melted polyethylene. The ground glass joint facilitated removal and preparation of the anode.

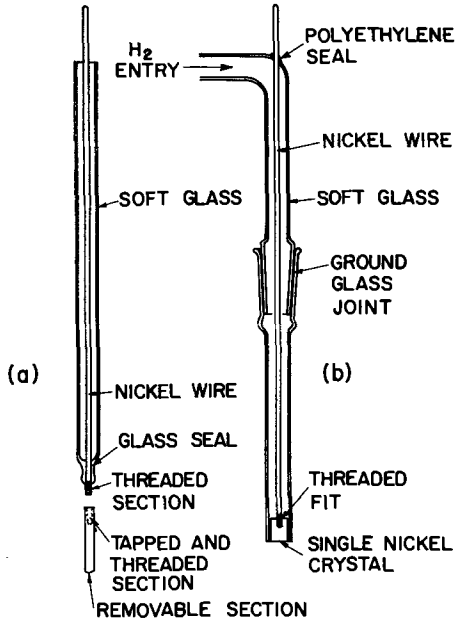

Fig. 2. Special electrode designs

The various nickel anodes all gave substantially the same results for the polarization when differences in the ratio of true to apparent area are taken into account. In the present work, the differences in the differential capacity between various electrodes at a given potential have been used as a criterion of relative changes in electrode area. The differential capacity c has been calculated from the initial rate of decay of the polarization following interruption of the polarizing current by means of the equation

$$c = i/(dE/dt)_o \qquad [1]$$

where i is the current and $(dE/dt)_o$ is the initial rate of decay of the potential.

Individual measurements of differential capacity were limited to an accuracy of ±10% because of difficulties associated with the determination of the slope from the oscilloscope trace. A small amount of 60-cycle pick-up, amounting to 0.7 mv, also was evident on the oscilloscope and limited the accuracy of the capacitance measurements.

The source of the nickel made a difference in the ease of obtaining reproducible polarization data. Nickel electrodeposited from a bath containing carefully purified nickel chloride and nickel sulfate exhibited the most rapid area changes on dissolution. This made it difficult to obtain reproducible polarization data. The measurements with such electrodes had to be made quickly and even then were restricted to low current densities. The 14-gauge nickel wire and Johnson Matthey nickel dissolved anodically with relatively minor area changes during short polarization runs. The Johnson-Matthey electrodes gave the most reproducible results. Unless otherwise indicated. Johnson-Matthey nickel electrodes were used for all the data presented in this paper.

The cathode used for the pre-electrolysis and polarization measurements consisted of a square piece of platinum foil 2.5 cm on an edge and 0.01 cm thick, attached to a platinum wire sealed in soft glass tubing. The pre-electrolysis anode also was platinum and of similar construction. Platinum was used for the pre-electrolysis anode to eliminate the possible introduction of impurities that might have resulted from a dissolving nickel pre-electrolysis anode.

Two types of reference electrodes were used for the polarization runs. A platinized Pt electrode was used as a working reference electrode within the cell. It was prepared by sealing platinum wire in soft glass and platinizing it in a 1% solution of platinic chloride (without any additives) at 100 ma/cm^2 for approximately 2 hr with periodic reversal of the current every 5 min (12). After platinizing, the electrodes were stored in slightly acidified conductivity water which was saturated with hydrogen.

A saturated calomel reference was used with chloride and perchlorate solutions, and a mercury-mercurous sulfate, saturated potassium sulfate reference was used with the sulfate solutions to check

the working reference electrode before and after each polarization run. To avoid the introduction of any contaminants into the electrolyte from the external reference electrode, a solution bridge filled with the same solution as in the cell was used between the cell and an intermediate vessel (test tube) containing the same solution as in the cell. The external reference electrode was connected to this intermediate vessel by a second solution bridge. The reference electrode and intermediate vessel were immersed in the same water bath as the cell.

Polarization measurements, with the exception of those in the sodium perchlorate solutions, were obtained in solutions prepared from Fisher certified reagent-grade salts which were further purified by double recrystallization from conductivity water. Sodium perchlorate solutions were prepared from reagent grade chemicals and conductivity water.

The anode was prepared for polarization measurements by polishing with progressively finer grades of emery paper down to 000 grade. It was then immersed in ethyl alcohol and rinsed in distilled water. In most instances the anode was then electropolished for 20 min at 150 ma/cm^2 in an electropolishing solution containing 15% H_2SO_4, 63% H_3PO_4, and 22% H_2O (13). The nickel anode was rinsed copiously in distilled and conductivity water before being placed in the polarization cell. Unless otherwise indicated, all polarization curves presented in this paper were obtained with electropolished electrodes.

The platinum pre-electrolysis anode was placed in the anode compartment during pre-electrolysis and removed entirely from the electrolyte when pre-electrolysis was completed. During pre-electrolysis the platinum anode was in the main flow stream, and stirring was maintained throughout the pre-electrolysis period. Pre-electrolysis was carried out at 20 μa/cm^2. This low current density did not produce appreciable pH changes during the pre-electrolysis period and was below the limiting current density for the oxidation of molecular hydrogen. During the pre-electrolysis the platinum anode was usually at a potential of $+0.1 \pm 0.03$v relative to the standard hydrogen electrode. The potential of the pre-electrolysis anode never approached that for the oxygen evolution reaction. The effectiveness of pre-electrolysis under these conditions is far from certain. This procedure, however, did lead to reproducible results.

In preparation for polarization measurements the cell was rinsed several times, first with distilled and conductivity water and finally with the solution to be investigated. The cell was filled with solution, and the electrodes were introduced into the solution after appropriate rinsings. Hydrogen gas was then bubbled into the solution, the stirrer was turned on, and the system was allowed to come to equilibrium. The pH was adjusted by addition of the appropriate acid and was determined by measuring the potential between the platinized Pt reference electrode within the cell and the external reference electrodes. The accuracy of the pH measurements is open to question because of the unknown liquid-junction potential. Pre-electrolysis was then begun. The solutions were pre-electrolyzed in the cell for 40 hr to remove trace impurities or at least to reduce their concentration to a reproducible minimum. A polarization run was then made and the pre-electrolysis was resumed for 6 to 8 hr. A polarization run was made again after this second pre-electrolysis period and, if both runs agreed within several millivolts, pre-electrolysis was regarded as complete.

After pre-electrolysis the working nickel electrode was anodically dissolved at 0.5 ma/cm^2 for 5 min prior to the beginning of polarization measurements. Polarization measurements were taken by adjusting the current and quickly measuring the anode potential relative to the internal working reference electrode after the potential had reached a reasonably constant value. This usually required less than 30 sec. Between polarization measurements while the current through the electronic equipment was being adjusted to a new value, the electrodes were disconnected from the circuit to minimize anode area changes.

Efficiency measurements were made by direct weighing of the anode using the detachable anode assembly described earlier. The coulombs passed were determined with a coulometer or from the time and IR drop across a precision resistor which was connected in series with the commutator circuit. Efficiency measurements were made at constant potential under conditions analogous to a polarization run. The time for each efficiency run was at least 1 hr.

Experimental Results

Anode efficiencies for nickel dissolution in chloride solutions of pH 2.0-3.0 were within a few per cent of 100% in the potential range which corresponded to current densities of 0.3 to 15 ma/cm^2. Efficiencies in perchlorate and sulfate solutions of pH 2.0-3.0 were difficult to determine because of a tendency toward passivation upon prolonged anodic dissolution even at moderate current densities. In several instances where the anode did not passivate, the efficiencies were less than 50% at potentials corresponding to current densities less than approximately 0.6 ma/cm^2. This indicates that hydrogen dissolution predominates under these conditions. For pH of 0.9-1.0, nickel dissolution efficiencies in perchlorate and sulfate solutions were virtually 100% over the range 0.3 to 5 ma/cm^2 in instances where the anode did not passivate.

The differential capacitance has been found to be strongly dependent on the method of preparation of the nickel anode. Nickel anodes prepared by electropolishing normally had a differential capacitance of 20 μF/cm^2 of apparent area in the 0.5M $NiCl_2$ solution. This value was substantially independent of potential over the range 0 to +0.15v relative to the standard hydrogen electrode. Nickel electrodes only finished by hand polishing with successively finer grades of emery paper down to 000 grade had differential capacitances of approximately 35 μF/cm^2 of apparent area over the same range of potentials. The differential capacitance depended also on the source of the nickel. For example, electropolished nickel wire and also electrodeposited nickel with no surface treatment after deposition had higher val-

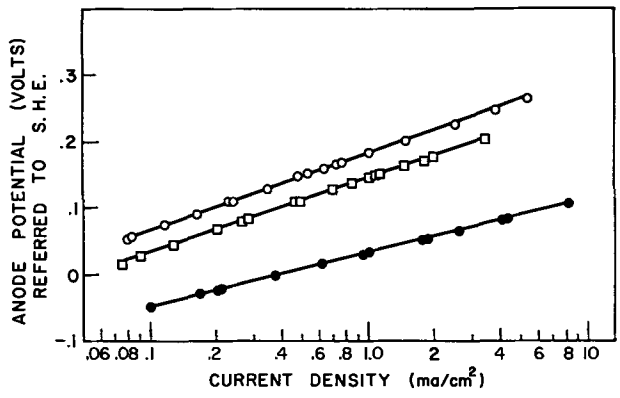

Fig. 3. Potential dependence on nature of electrolyte: ○, 1*N* $NaClO_4$, *p*H 0.9; □, 1*N* $NiSO_4$, *p*H 1.0; ●, 1*N* KCl, *p*H 2.5; temperature 45°C.

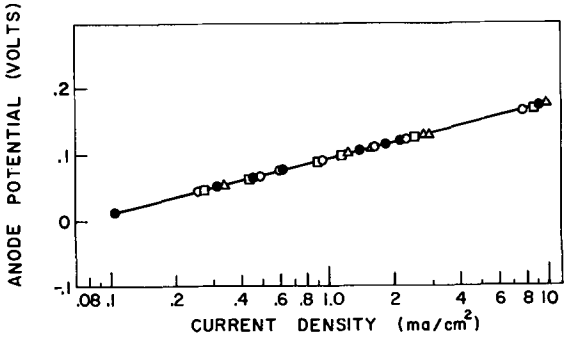

Fig. 4. Dependence on addition of $NiCl_2$ to 1.0M KCl: △, 1M KCl + 0.01M $NiCl_2$; □, 1M KCl + 0.05M $NiCl_2$; ●, 1M KCl + 0.1M $NiCl_2$; ○, 1M KCl; temperature 25°C; *p*H 2.6.

ues than electropolished pure Johnson-Matthey nickel.

The differential capacitance usually increased slowly during the anodic dissolution. This area change normally was less than 10% during the course of a single polarization run because the electrodes were disconnected between measurements to limit progressive area changes during dissolution.

The anode potential-current density curves for several electrolytes are compared in Fig. 3. The potentials are given relative to the standard hydrogen electrode, and the current densities are based on apparent areas. These curves show that a Tafel relationship exists for nickel in the various electrolytes and that the anode potential at a given current density is dependent on the type of electrolyte. The polarization in the chloride solution is substantially lower than in the perchlorate or sulfate solutions. The current efficiency for the metal dissolution was close to 100% for all three curves in Fig. 3. It was necessary to reduce the *p*H to 1.0 for the perchlorate and sulfate solutions, however, to accomplish this.

In the linear Tafel region, the back reaction should be negligible and the polarization should not depend on Ni^{+2} concentration provided double layer properties remain constant. This appears to be true from the data in Fig. 4. Identical polarization data have been obtained with and without Ni^{+2} present up to 0.1*M* Ni^{+2} provided an excess of a supporting electrolyte was present. Most of the subsequent measurements have been made without Ni^{+2} present. This avoids the necessity of purifying nickel salts, which are ordinarily difficult to purify because of problems associated with crystallization.

The differences in the anodic potentials at a given current density in Fig. 3 are not due principally to the presence or absence of Ni^{+2}. Differences in the double layer and in particular anion adsorption are probably the main factors responsible for the differences evident in this figure. Variations in liquid-junction potential also are involved, but probably are a minor factor.

The absence of Ni^{+2} in the solution does cause some awkwardness regarding absolute polarization values and the calculation of exchange current densities because of undefined reversible conditions. The apparent exchange current density depends on the Ni^{+2} concentration, which influences the reversible potential. In the present work the equivalent of an exchange current density has been obtained even in the absence of Ni^{+2} by extrapolating the linear Tafel curves to a potential corresponding to the standard electrode potential. This value obtained by extrapolation will be referred to as the standard exchange current density in this paper. It represents the exchange current density which would be found experimentally for a solution containing Ni^{+2} at unit activity if the transfer coefficients and double layer properties remained unchanged over a range of potentials extending from the linear Tafel region to the reversible value.

The dependence of the potential on concentration at a given current density is very slight in sodium perchlorate solutions in the absence of Ni^{+2} over the concentration range 0.25-1.0*M* on the basis of the data in Fig. 5. The linear range for nickel dissolution at *p*H 2.5 in the perchlorate solutions is quite limited because of the competing hydrogen oxidation reaction at low current densities and passivation at higher current densities. Unfortunately efficiency data were not available for the perchlorate system. The section of the curve below the inflection point, however, is associated primarily with H_2 anodic dissolution. An attempt has been made to construct the individual polarization curves for nickel and hydrogen dissolution in Fig. 5. The assumption has been made that the Tafel slope for the nickel dissolution curve does not change over the entire range of the plot. The procedure used in obtaining the

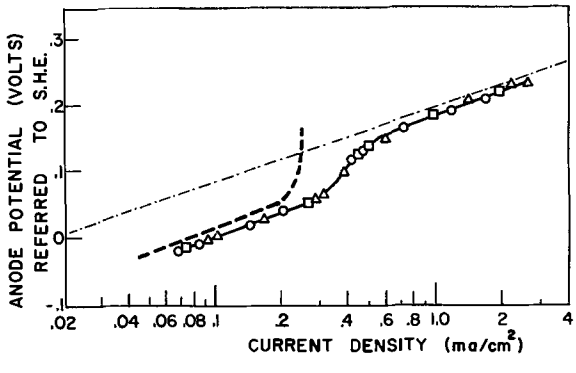

Fig. 5. Potential dependence on concentration of $NaClO_4$. For discussion of the three curves, see text. □, 0.25M $NaClO_4$; △, 0.50M $NaClO_4$; ○, 1.0M $NaClO_4$; temperature 45°C; *p*H 2.5. — · — · — Ni dissolution; — — — — H_2 dissolution.

component polarization curves in Fig. 5 involved first making an estimate of the limiting current density for H_2 oxidation. This value was then subtracted from the total current density for the upper portion of the over-all polarization curve and the component polarization curve for nickel dissolution constructed. The extension of this curve for nickel to current densities below the inflection point in the over-all polarization curve permitted the evaluation of the curve for H_2 oxidation. If the limiting current density indicated by this curve differed significantly from the original estimate, the complete process was repeated with a new estimate for the limiting current density for H_2 oxidation.

The procedure just described is not a very satisfactory substitute for current efficiency data in evaluating the H_2 oxidation curve, and the authors hope to undertake a study in which such data are obtained in the future. To the best knowledge of the authors, the polarization curve for H_2 oxidation represents the first time that such data have been available in acid media even on a provisional basis. The slope is 0.13 over the limited linear range represented in Fig. 5. This slope should not be interpreted as the ordinary Tafel slope because of the proximity of the limiting current density to the short range over which the apparent slope of 0.13 v/decade is exhibited.

A polarization curve similar to that in Fig. 5 has been obtained for a 0.5*M* $NiSO_4$ at *p*H 2.5 and 45°C. The apparent Tafel slope for H_2 oxidation in the $NiSO_4$ electrolyte is 0.11 v/decade.

The polarization curves in Fig. 6 indicate the effect of a 10 and 100 fold change in KCl concentration in the absence of Ni^{+2}. The efficiency for nickel dissolution has been found to be substantially 100% for all points in this figure. The decrease in polarization with increasing KCl concentration appears reasonable in terms of the concentration dependence which various workers (14-16) have estimated for the potential drop across the diffuse ionic layer. A quantitative comparison, however, is seriously complicated by specific adsorption, close proximity to the zero point of charge, and the liquid-junction potentials involved in the comparison of the internal hydrogen reference electrode with the external saturated calomel reference electrode (necessary for the calculation of the potentials of the polarized anode relative to the standard hydrogen electrode).

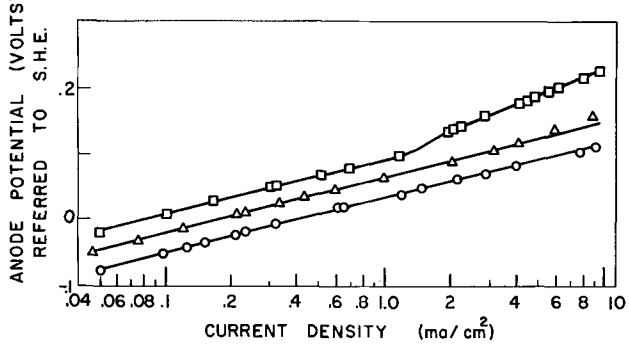

Fig. 6. Potential dependence on concentration of KCl: ○, 1M KCl, *p*H 2.6; △, 0.1M KCl, *p*H 2.5; □, 0.01M KCl, *p*H 2.5; temperature 45°C.

The increase in Tafel slope in 0.01*M* KCl at current densities greater than 2 ma/cm² was observed each of several times the experiment was repeated. The explanation is open to speculation. One possibility is that the nickel concentration in the solution in the immediate vicinity of the electrode surface became appreciable compared to the concentration of KCl in the dilute KCl solution, and a change in double layer properties occurred. A significant portion of the nickel would probably be involved in a chloride complex.

The dependence of anode potential on temperature in KCl, $NaClO_4$, and $NiCl_2$ solutions is shown in Fig. 7-9. In all cases, the anode potential decreases 2.7 ± 0.3 mv/°C increase in temperature for a given apparent current density, relative to the S.H.E. at the same temperature.

The results shown in Fig. 10 indicate that no appreciable change occurs in the anodic polarization over the *p*H range 2-3 in 1.0*M* KCl at 45°C under conditions where the efficiency for nickel dissolution

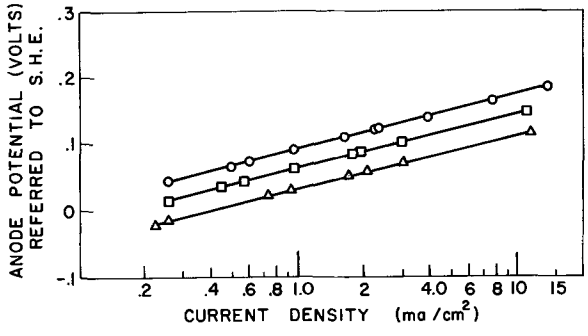

Fig. 7. Potential dependence on temperature in 1.0M KCl, *p*H 2.6: ○, 25°C; □, 35°C; △, 45°C.

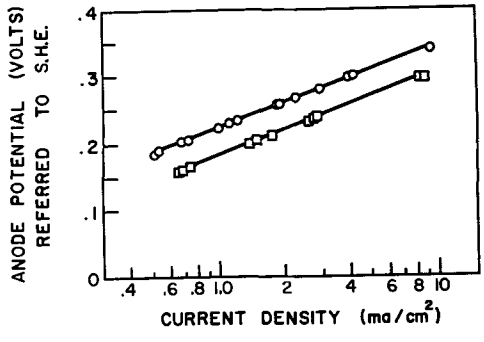

Fig. 8. Potential dependence on temperature in 1.0M $NaClO_4$, *p*H 0.9: ○, 27°C; □, 44°C.

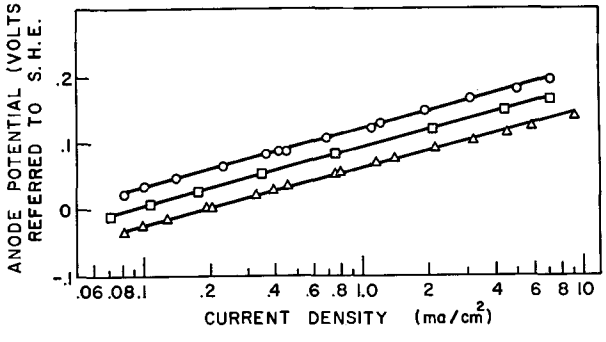

Fig. 9. Potential dependence on temperature in 0.5M $NiCl_2$, *p*H 2.5: ○, 25°C; □, 35°C; △, 45°C.

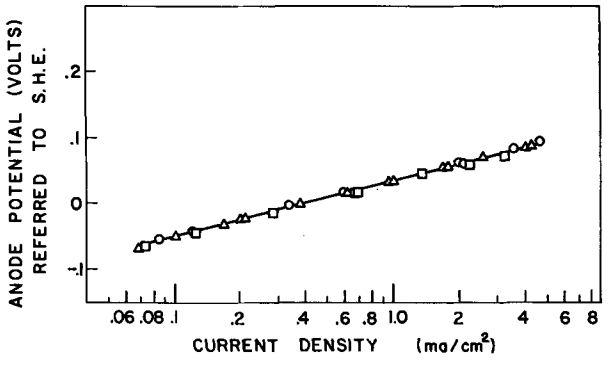

Fig. 10. Potential dependence of pH in 1.0M KCl, 45°C: ○, pH 2.0; △, pH 2.5; □, pH 3.0.

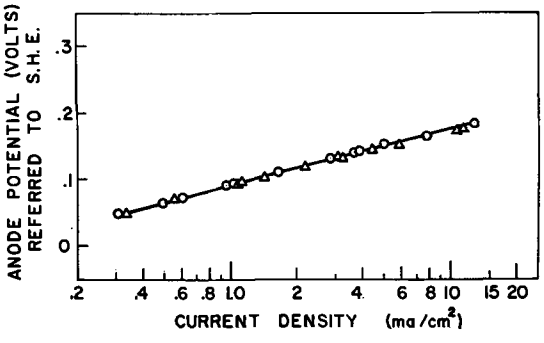

Fig. 11. Comparison of polycrystalline and single crystal nickel in 1.0M KCl, temperature 25°C, pH 2.6: ○, polycrystalline Johnson-Matthey nickel; △, 110 oriented single crystal.

is substantially 100%. The anodic polarization also has been found to be independent of pH in the range 1-2.5 in 0.5*M* $NiSO_4$ over the current density range 0.8-4.0 ma/cm² where the efficiency for the nickel dissolution process is virtually 100%.

Hollnagel and Landsberg (8) report finding a pH dependence for the anodic dissolution of nickel in both chloride and sulfate solutions in measurements of nonsteady-state polarization with a galvanostatic method involving rectangular current pulses. Their findings, however, may be somewhat misleading since the concentration of the supporting electrolyte was not large compared to the concentration of the acid added in adjusting the hydrogen ion concentration.

Polarization measurements have also been made with electropolished single crystal nickel anodes. The results are essentially the same as obtained with polycrystalline nickel. Figure 11 compares the polarization obtained on a surface parallel to the 110 plane with that for a polycrystalline anode of Johnson-Matthey nickel. The orientation of a particular crystallographic plane parallel to the electrode surface does not ensure that other crystallographic planes are not exposed to the electrolyte, *i.e.*, the micro-orientation of the surface need not and in most cases probably does not correspond to the macro orientation.

The Tafel slopes and standard exchange current densities based on apparent areas are listed in Table I. All of the data in this table were obtained under conditions for which the efficiency of the nickel dissolution process was substantially 100%. In most instances the Tafel linearity has been observed over

Table I. Tafel slopes and standard exchange current densities for anodic oxidation of nickel

Electrolyte	pH	Temp, °C	Tafel slope	Current density range for Tafel slope, ma/cm²	Standard* exchange current density, ma/cm²
1.0*M* KCl	2.6	25	0.084	0.25-13.0	1.4×10^{-7}
1.0*M* KCl	2.6	35	0.082	0.25-11.0	1.8×10^{-7}
1.0*M* KCl	2.6	45	0.080	0.22-12.0	2.8×10^{-7}
0.1*M* KCl	2.5	45	0.084	0.05-4.0	1.8×10^{-7}
0.01*M* KCl	2.5	45	0.084	0.05-1.2	1.0×10^{-7}
1.0*M* $NaClO_4$	0.9	27	0.125	0.5-9.0	2.3×10^{-7}
1.0*M* $NaClO_4$	0.9	44	0.13	0.6-9.0	5.0×10^{-7}
0.25*M* $NaClO_4$	2.5	45	0.11	0.55-3.0	3.0×10^{-7}
1.0*M* $NaClO_4$	2.5	45	0.11	0.55-3.0	3.0×10^{-7}
0.5*M* $NiCl_2$	2.5	25	0.090	0.08-7.0	1.35×10^{-7}
0.5*M* $NiCl_2$	2.5	35	0.085	0.07-7.0	1.27×10^{-7}
0.5*M* $NiCl_2$	2.5	45	0.090	0.08-9.0	3.1×10^{-7}
0.5*M* $NiSO_4$	1.0	45	0.115	0.07-4.0	3.6×10^{-7}

* See text for definition; based on apparent area.

a current density range of at least 1½ decades and in many instances 2 decades. The standard exchange current densities have been determined by extrapolating the linear Tafel plots to the standard electrode potential of nickel. The latter have been evaluated at the various temperatures by the same procedure used in the first paper in this series (11). The values calculated by this means are probably accurate to ±10 mv. The accuracy of the values for the standard exchange current densities, however, is limited more by the accuracy of the Tafel slope and the surface roughness than the accuracy of the values for the standard electrode potential.

Discussion of Experimental Results

From Table I it is evident that the Tafel slope at 45°C is 0.11-0.12 in both sulfate and perchlorate solutions. The Tafel linearity and the value of the Tafel slope provide evidence favoring a charge transfer step as rate determining. For a Tafel slope of 0.12, the corresponding value of αz is 0.52, where α is the transfer coefficient and z the charge of the species transferred over the potential energy barrier associated with the rate-determining step. The lower Tafel slope of 0.08-0.09 found for the chloride solutions probably reflects the specific adsorption of chloride ions on the electrode surface and the associated changes in the over-all double layer structure [see, for example, ref. (16)]. The adsorption of Cl^- on the anode surface is anticipated to favor the transfer of nickel from the metallic state to a position in the Helmholtz plane as an adsorbed ionic species.

In the earlier study of nickel electrodeposition the Tafel slope in a 0.5*M* nickel sulfate solution was found to be 0.091 at 45°C. A comparison of the Tafel slopes for the anodic and cathodic processes would prove interesting if it were not that the point of zero charge (pzc) is very likely interposed between the two sets of polarization measurements. For the sulfate and perchlorate solutions the pzc is estimated to be −0.1 to −0.2v relative to the standard hydrogen electrode on the basis that the differ-

ence in the pzc for nickel and mercury in a given electrolyte is the same as the difference in the work function (17, 18). Thus it is not surprising that the anodic and cathodic Tafel slopes are not complementary (19) for any reasonable (integer) value of the stoichiometric number.

The heat of activation $\Delta H\ddagger$ at the reversible potential may be calculated by the equation

$$d \ln i_0/d(1/T) = \Delta H\ddagger/R \qquad [2]$$

where T is the absolute temperature, i_0 the exchange current density, and R the gas constant. An attempt has been made to use this equation with the data for the $NiCl_2$ solution in Fig. 9. To determine the temperature dependence of ln i_0, it is necessary to extrapolate the linear Tafel plots over five decades to the reversible potentials. Even a slight error in the relative values for the Tafel slopes produces a large error in the derivative. If the Tafel plots for 25° and 45°C in Fig. 9 are extrapolated independently to the reversible potential, the resulting value for $\Delta H\ddagger$ is 8 kcal/mole. The reversible potentials at 25° and 45°C have been calculated by the same procedure as used in the earlier paper (11) with the temperature dependence of the ionic activity coefficient for nickel assumed to be negligible.

An alternate procedure is to assume that the transfer coefficient does not vary significantly with temperature. The Tafel slopes for 25° and 45°C then should be in the same ratio as the absolute temperatures. If the extrapolation of the curves for 25° and 45°C in Fig. 9 is done with the Tafel slope at 45°C taken as (20/298) x 100% or 6.7% greater than that at 25°C, the resulting value for $\Delta H\ddagger$ is 15 kcal/mole. This higher value for $\Delta H\ddagger$ is believed to be more reliable than the lower value despite the assumption concerning the constancy of the transfer coefficient. An additional assumption is that the ratio of true to apparent surface area is independent of temperature. The value found for the heat of activation for the reverse nickel electrodeposition process in the earlier paper (11) was 21 kcal/mole.

The limiting current density for the hydrogen oxidation in Fig. 5 appears low for diffusion control and may represent kinetic control. Any attempt at explaining the H_2 oxidation curve in Fig. 5, however, is premature at this time in view of the very restricted current density range of the curve and the assumptions involved in the construction of the curve from the over-all anodic polarization curve.

Summary

In summary, the following has been demonstrated in the present work:

1. The polarization curves for nickel dissolution have been shown to follow Tafel linearity over at least 1.5 decades and in some instances 2 decades in acidified chloride, sulfate, and perchlorate solutions with the apparent Tafel slopes in sulfate and perchlorate solutions equal to 0.12 ± 0.01 and in chloride solutions equal to 0.085 ± 0.005 at 45°C.

2. With proper buffering of the ionic double layer with a supporting electrolyte, the polarization has been shown to be independent of pH over a limited range.

3. The potential is independent of Ni^{+2} concentration over the range of potentials where the back reaction is negligible.

4. The energy of activation for the anodic dissolution process is approximately 15 kcal/mole if the transfer coefficient and the surface roughness are assumed to be independent of temperature for a dissolving nickel anode.

5. Anodic polarization measurements on single crystal (110 orientation) and polycrystalline nickel have not been found to differ significantly.

6. Hydrogen dissolution can occur simultaneously with nickel dissolution with the apparent Tafel slope of the polarization curve for the H_2 oxidation equal to 0.13.

Acknowledgment

The authors wish to express their appreciation to the Harshaw Chemical Company for the support of fellowships to two of the authors (M. K. and J. B.) and also to the U. S. Office of Naval Research for their partial support of this research.

Manuscript received Dec. 26, 1962; revised manuscript received March 29, 1963. This paper was delivered before the Houston Meeting, Oct. 9-13, 1960.

Any discussion of this paper will appear in a Discussion Section to be published in the June 1964 JOURNAL.

REFERENCES

1. N. Murphy and B. Oza, *Bull. Va. Polytech. Inst.*, **51** [7] (1958).
2. F. Salt, *Discussions Faraday Soc.*, **1**, 169 (1947).
3. D. Turner, *This Journal*, **98**, 434 (1951).
4. R. Piontelli and G. Serravalle, *Z. Elektrochem.*, **62**, 759 (1958).
5. J. Higgins, *This Journal*, **106**, 999 (1959).
6. E. Raub and A. Besam, *Metalloberfläche*, **13**, 308 (1959).
7. W. Wesley, *Trans. Inst. Metal Finishing*, **33**, 452 (1956).
8. M. Hollnagel and R. Landsberg, *Z. physik. Chem. (Leipzig)*, **212**, 94 (1959).
9. C. Chang, V. Krautsov, and Y. Durdin, *Zhur. Fiz. Khim.*, **34**, 2041 (1960); V. Krautsov and C. Chang, *ibid.*, **34**, 2205 (1960).
10. E. Yeager, T. Oey, and F. Hovorka, Tech. Report 6, ONR Contract Nonr 47002, Western Reserve University, June 1952.
11. J. Yeager, J. Cels, E. Yeager, and F. Hovorka, *This Journal*, **106**, 328 (1959).
12. J. O'M. Bockri Private communication.
13. C. Faust and H. Pray, *Proc. Am. Electroplaters' Soc.*, **1941**, 104.
14. A. Frumkin *et al.*, "Kinetics of Electrode Processes," Moscow University Publishers, Moscow, 1952.
15. M. Breiter, M. Kleinerman, and P. Delahay, *J. Am. Chem. Soc.*, **80**, 5111 (1958).
16. R. Parsons in "Advances in Electrochemistry and Electrochemical Engineering," P. Delahay, Editor, Vol. 1, Chap. 1, Interscience Publishers, New York (1961).
17. A. Frumkin, *Colloid. Symp. Annual*, **7**, 89 (1930).
18. See also R. Parsons in "Modern Aspects of Electrochemistry," J. O'M. Bockris, Editor, Vol. 1, Chap. 3, p. 170, Academic Press, New York (1954).
19. See for example J. Bockris, *loc. cit.*, pp. 187, 188.

Technical Notes

Oxidation Rates of Pure and Less Pure Nickel

W. L. Phillips, Jr.

Engineering Research Laboratory, E. I. du Pont de Nemours & Company, Inc., Experimental Station, Wilmington, Delaware

Nickel oxidizes according to the parabolic scaling rate law in the temperature range 500°-1300°C. Scaling constants reported by numerous investigators (1-18) have been plotted on log K (parabolic scaling constant) *vs.* $1/T$ (absolute temperature) coordinates in Fig. 1. All of the data except those of the four latest studies (16-19) cluster within the dashed lines shown in Fig. 1. Kubaschewski and Hopkins (20) have attributed the variation within the dashed lines to purity. Horn (21) has shown that most of the common alloying elements increase the oxidation rate of relatively impure nickel. One could rationalize the observed difference between (17, 18, 19) and (1-15) as due to experimental procedure. In the present investigation, pure and less pure nickel was tested in the same apparatus after the same pretreatment.

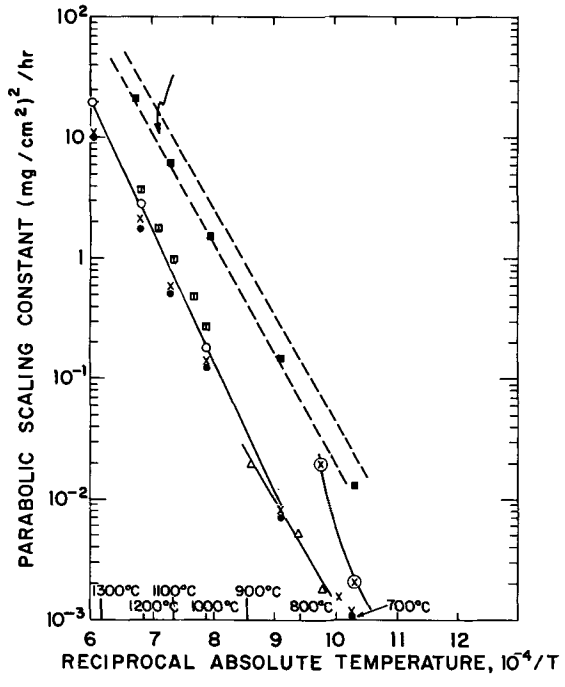

Fig. 1. Relationship between the parabolic scaling constant and reciprocal temperature for nickel. Data for (1-15) falls with the dashed lines (arrow). Circled X, Gulbransen and Andrew (16); open circle, Frederick and Cornet (17); open triangle, Moore and Lee (18): divided square, Sartell and Li (19). Present investigation: X, carbonyl nickel; solid square, wrought nickel; solid circle, electrolytic nickel.

The vendor's analyses of the nickel used in the present investigation and the analyses reported by previous (4, 16-19) investigators are given in Table I. The electrolytic and carbonyl powders used in the present investigation were compacted at 120 ton/cm² into billets 2.5 cm in diameter and 2.5 cm long. The billets were vacuum encased in nickel cans and extruded into 0.6 cm diameter rods at 880°C. Oxidation samples approximately 1.5 cm long x 0.5 cm diameter were machined from the extruded rods and the wrought nickel rod. The machine specimens were annealed for 5 hr at 900°C in H_2. The initial grain size in all samples was approximately 0.05 mm. A periodic Ainsworth milligram analytical balance was modified to accommodate a 12 in. long sapphire rod supporting a zircon crucible in a mul-

Table I. Spectrographic analysis of nickel in per cent,

	Gulbransen & Andrews (16) (electrolytic Ni)	Frederick & Cornet (17) (carbonyl Ni)	Pilling & Bedworth (3) (electrolytic Ni)	Moore & Lee (18) (carbonyl Ni)
Cu	0.001	0.0005	—	0.008
Ag	<0.0002	—	—	—
Mg	0.0002	0.0001	—	0.0025
Si	0.005	0.0001	0.04	—
Fe	0.0002	0.0003	0.25	0.015
Mn	—	<0.002	trace	none
Co	none	—	—	—
Ca	—	—	—	—
Al	none	—	—	—
Cr	—	<0.001	—	—
Pb	—	—	—	0.001

	Present investigation (electrolytic) *	Present investigation (carbonyl) *	Present investigation (wrought) *	Sartell & Li (19)
Cu	<0.0001	0.0010	—	0.0001
Ag	none	—	—	0.0001
Mg	0.00005	0.0001	—	0.0001
Si	0.0001	0.0001	0.14	0.0007
Fe	<0.0005	0.0005	0.48	0.0005
Mn	none	<0.002	0.15	—
Co	none	—	—	—
Ca	<0.0001	—	—	0.0001
Al	0.001	—	—	0.0002
Cr	none	0.001	—	—

* Electrolytic, purchased from Johnson, Matthey & Co., Ltd.; carbonyl, purchased from International Nickel Co.; wrought, (Nickel A) purchased from International Nickel Co.

lite combustion tube. Temperature was maintained with ± 5°C. Weight changes were transmitted to a transducer and reflected in millivolts on a recorder. The balance had a sensitivity of 0.1 mg; a range of 5g, and a capacity of 20g. Tests were run in moving air for periods of 100 hr.

The parabolic scaling rate law was obeyed for all nickel materials at all temperatures used in the present investigation. At low temperatures, below 1000°C two consecutive parabolic relationships were observed; above 1000°C only one relationship was observed. This has been observed previously (16-19). An Arrhenius plot, Fig. 1, shows that the data for the present materials give straight lines.

The present results lead to four conclusions. First, the difference observed in the scaling rate of very pure nickel of the same composition as a function of oxygen pressure is not as great as the difference which can be attributed to composition. This is demonstrated by the small difference between the present results in air (PO_2 = 152 mm Hg) and those of Gulbransen and Andrews (16) in O_2 at 0.1 atm (P = 76 mm Hg). By Wagner's theory (22), the scaling rate would be expected to increase with only the one-fifth power of the partial pressure of oxygen. Second, the present results confirm previous results (16-17) that the oxidation rate of either very pure electrolytic or carbonyl nickel at low temperatures (700°-800°C) is lower than that of less pure nickel (1-15). Third, the present results confirm the results of Frederick and Cornett (17) and Sartell and Li (19) over the temperature range 950°-1200°C and extend the data on pure nickel from 700°-1300°C. Fourth, the present results demonstrate that very pure nickel (99.9%) at elevated temperatures (700°-1300°C) has ten times the scaling resistance of nickel of 99.7% purity. Evans *et al.* (23) had postulated that this effect of purity would not be valid at high temperatures. This was based on the observation by Gulbransen and Andrews (16) that the oxidation resistance of very pure nickel at 750°C was approximately the same as less pure nickel. The present results do not confirm the data at 750°C of Gulbransen and Andrews (16). The results verify Horn's (21) observations that small amounts of impurities increase the oxidation rate significantly. The activation energy for pure and less pure samples is the same within experimental error, approximately 38,000 cal/mole. Moore and Lee (18) used less pure but preoxidized samples. The preoxidation treatment of their specimens may have affected their results.

Manuscript received March 25, 1963; revised manuscript received June 6, 1963.

Any discussion of this paper will appear in a Discussion Section to be published in the June 1964 JOURNAL.

REFERENCES

1. C. Wagner and K. W. Zimens, *Acta Chem. Scand.*, **1**, 547 (1947).
2. O. Kubaschewski and O. von Goldbeck, *Z. Metallk.*, **39**, 158 (1948).
3. N. B. Pilling and R. E. Bedworth, *J. Inst. Metals*, **29**, 529 (1923).
4. Y. Matsunaga, *Japan Nickel Rev.*, **1**, 347 (1943).
5. A. Preece and G. Lucas, *J. Inst. Metals*, **81**, 219 (1952).
6. P. Chevenaud and Y. Wache, *Rev. Met.*, **45**, 121 (1948).
7. A. Krupoioski and J. Jaszurowski, *ibid.*, **33**, 646 (1936).
8. H. von Baumback and C. Wagner, *Z. physik. Chem.*, **132**, 391 (1925).
9. Y. Utida and M. Saito, *Sci. Rpts., Tokoku Univ.*, **13**, 391 (1925).
10. W. H. Hatfield, *J. Iron Steel Inst.*, **115**, 483 (1927).
11. W. Bauloh and P. Funke, *Korrosion u. Metallschutz*, **18**, 126 (1942).
12. H. N. Terem, *Bull Soc. Chim.*, **6**, 664 (1939).
13. H. Pfeiffer and K. Hauffe, *Z. Metallk.*, **43**, 364 (1952).
14. G. Chauvenet and G. Valensi, *Compt. rend.*, **205**, 32 (1937).
15. P. Chevenard, X. Wache, and R. De la Tullaye, *Bull Soc. Chem.*, **11**, 11 (1944).
16. E. A. Gulbransen and K. F. Andrews, *This Journal*, **101**, 128 (1954).
17. S. F. Frederick and I. Cornet, *ibid.*, **102**, 285 (1955).
18. W. J. Moore and J. K. Lee, *Trans. Faraday Soc.*, **48**, 916 (1952).
19. J. A. Sartell and C. H. Li, *J. Inst. Metals*, **90**, 62 (1961).
20. O. Kubaschewski and B. E. Hopkins, "Oxidation of Metals and Alloys," p. 69, Academic Press Inc., London (1953).
21. L. Horn, *Z. Metallk.*, **40**, 73 (1949).
22. C. Wagner and K. E. Zimens, *Acta Chem. Scand.*, **1**, 547 (1947).
23. E. B. Evans, C. A. Phalnikar, and W. M. Baldwin, *This Journal*, **103**, 367 (1956).

A Graphical Method for Determining the Broad-Band Dielectric Behavior of Materials

James J. Whalen

Carlyle Barton Laboratory, The Johns Hopkins University, Baltimore, Maryland

A method of graphical analysis is developed by which the real part of the complex dielectric constant of a material may be determined in the microwave region. This method of analysis is especially useful if an approximate value of the dielectric constant is not known; then it is neither possible to cut a sample of material to a length that is approximately a quarter-wavelength (which is usually the optimum length) nor possible to solve the transcendental equation which often occurs in microwave dielectric constant measurements for a unique root. Although there are methods (1, 2) by which the value of the dielectric constant may be determined uniquely, it is difficult to obtain accurate results by these methods if the value of dielectric constant is greater than ten. These difficulties may

be avoided and the dielectric behavior of the material over a wide band of frequencies may be determined by comparing experimental data (microwave slotted line data) to a set of theoretical curves. This method of analysis is used in the investigation of resonant absorption of electromagnetic energy in the frequency band 26.5-38.0 kMc in crystals of lead nitrate, $Pb(NO_3)_2$, and thallium nitrate $TlNO_3$. In order to obtain crystals of these nitrates large enough for the microwave slotted line experiment, it was necessary to grow them from an aqueous solution in the presence of methylene blue (3). Although this alters the habit of the crystal, it is thought that it does not influence significantly the dielectric data obtained for these crystals.

These crystals have been investigated in the frequency band 26.5-38.0 kMc as part of a program the purpose of which is to determine the nonmagnetic absorption spectra of several salts having unresolved fine structure in the infrared (4). The absorption spectra are being investigated from the microwave frequency region to the very far infrared frequency region.

If the dielectric loss of a material in a static electric field is negligible, the absorption of energy by the material in a time varying field may be analyzed conveniently by assuming the medium has a complex dielectric constant ($\epsilon^* = \epsilon' - i\epsilon''$). The imaginary part of the dielectric constant is proportional to the energy loss (absorption). If the dependence of ϵ'/ϵ_o on the frequency is known over the entire frequency spectrum, the dependence of ϵ''/ϵ_o on the frequency can be determined from integral transforms (5). Although the resonant frequencies of an ionic crystal and the exact forms of the curves $\epsilon'(f)$ *vs.* f and $\epsilon''(f)$ *vs.* f (where f is the frequency) are not known, the general forms of these curves are known. In particular, it is known that $\epsilon'(f)$ varies considerably in a frequency band which is near a frequency at which resonant absorption occurs. Therefore, instead of measuring resonant absorption directly, the dispersion of the real part of the dielectric constant is investigated.

Graphical Method of Data Analysis

The complex dielectric constant of a medium may be determined if the intrinsic impedance and the propagation constant of the medium are known. The propagation constant in a rectangular waveguide completely filled with a homogeneous material may be determined from two input impedance measurements. One input impedance measurement is made with a short placed at the rear interface of the sample (6), and the other is made with the short placed a quarter-wavelength from the rear interface of the sample (1, 2). In each case the voltage standing wave ratio, (Γ), and the position of voltage minimum are measured. The position of the voltage minimum with the sample in the waveguide is designated by the letter D; the position of the voltage minimum without the sample in the waveguide is designated by the letter D_r; the length of the sample is d (see Fig. 1).

For a rectangular waveguide completely filled with a homogeneous, nonmagnetic material of complex permittivity ϵ^*, the propagation constant γ, and the wave impedance Z_H are (7)

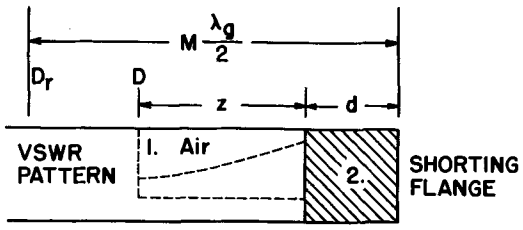

Fig. 1. Short circuit method of measuring dielectric constant

$$\gamma = j2\pi/\lambda_o\,[\epsilon^*/\epsilon_o - (\lambda_o/\lambda_c)^2]^{1/2}$$

$$Z_H = j\omega\,\mu_o/\gamma$$

where λ_o is the free-space wavelength, ϵ_o is the permittivity of free space, μ_o is the permeability of free space, and λ_c is the cut-off wavelength.

It is well known that the field equations for the TE_{01} mode may be expressed in a form that corresponds to that of the transmission line equations (8). The propagation constant, γ, of the transmission line has the same value as that of the waveguide, and the characteristic impedance of the transmission line, Z, is equal to the wave impedance Z_H.

The impedance at any plane in the waveguide can be written as (9)

$$Z/Z_o = (Z_L + Z_o \tanh\gamma z)/(Z_o + Z_L \tanh\gamma z)$$

where z is measured from the load impedance, Z_L, toward the generator. If Z_L is located at a voltage minimum, then, since $\Gamma = Z_o/Z_L$

$$Z/Z_o = (1 + \Gamma \tanh\gamma z)/(\Gamma + \tanh\gamma z)$$

The boundary conditions at the front interface of the sample require that the tangential component of the electric intensity and the tangential component of the magnetic intensity be continuous. Therefore, the impedance which is proportional to the ratio of these tangential components also is continuous at the interface. Application of the boundary condition to the waveguide circuit in Fig. 1 gives

$$Z_{10}(1 - \Gamma \tanh\gamma_1 z)/(\Gamma - \tanh\gamma_1 z) = Z_{20} \tanh\gamma_2 d \quad [1]$$

Z_{10} and Z_{20} are the characteristic wave impedances in air and in the dielectric, respectively; Γ is the voltage standing wave ratio in Eq. [1]; and γ_1 and γ_2 are the complex propagation constants in air and in the dielectric, respectively. If the dielectric is lossless and if losses in the walls of the waveguide are neglected, then γ equals $j2\pi/\lambda_g$ where λ_g equals $\lambda_o/(\epsilon'/\epsilon_o - (\lambda_o/\lambda_c)^2)^{1/2}$. If the permeability of the sample does not differ from the permeability of free space, then $\gamma_1 Z_{10}$ equals $\gamma_2 Z_{20}$, and Eq. [1] may be rearranged

$$\lambda_{g1} \tan(2\pi z/\lambda_{g1}) = -\lambda_{g2} \tan(2\pi d/\lambda_{g2}) \quad [2]$$

A parameter, Δ, is defined as being equal to $D_r - D + d$ where $D_r - D$ is the nodal shift caused by the insertion of the sample into the waveguide. From Fig. 1 it is apparent that $\Delta + z$ equals $m\lambda_g/2$.

$$\lambda_{g1} \tan(B_1\Delta) = \lambda_{g2} \tan(B_2 d) \quad [3]$$

If v equals λ_o/λ_c, and ϵ equals ϵ'/ϵ_o (ϵ is the relative dielectric constant of the material), Eq. [3] may be solved for Δ/λ_{g1}

$$\frac{\Delta}{\lambda_{g1}} = \frac{1}{2\pi} \text{arc tan} \left[\left(\frac{1 - v^2}{\epsilon - v^2} \right)^{1/2} \tan \frac{2\pi}{v} \left(\frac{d}{\lambda_c} \right) (\epsilon - v^2)^{1/2} \right] \quad [4]$$

Values of Δ/λ_{g1} are calculated from Eq. [4] for a fixed value of d/λ_c and successive values of ϵ from 1-20; these values of Δ/λ_{g1} are plotted *vs.* λ_{g1}/λ_c (Fig. 2 and 3). By measuring the nodal shift as a function of frequency, experimental values of Δ/λ_{g1} and λ_{g1}/λ_c may be obtained. The experimental curve of Δ/λ_{g1} *vs.* λ_{g1}/λ_c may be compared to the theoretical curves, and if ϵ is a constant independent of frequency, the value of ϵ may be determined. If the dielectric constant varies with frequency, the experimental curve of Δ/λ_{g1} *vs.* λ_{g1}/λ_c will intersect several of the theoretical curves of Δ/λ_{g1} *vs.* λ_{g1}/λ_c. If the derivative $d\epsilon/df$ is small, it is possible to determine the curve of ϵ *vs.* λ_{g1}/λ_c from these intersections. If $d\epsilon/df$ is not small, it is not possible to determine ϵ; however, the information that ϵ is varying rapidly indicates that absorption occurs at a frequency very near the frequency band in which the measurements are made.

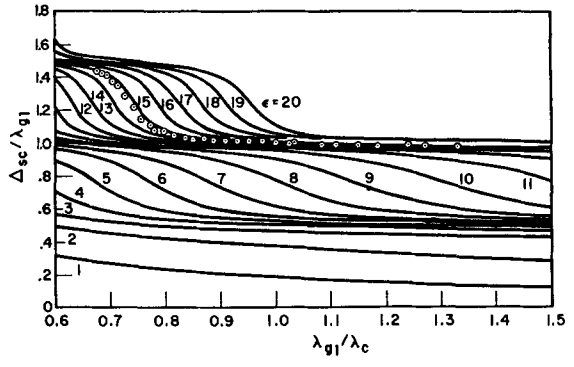

Fig. 2. Theoretical values of Δ_{sc}/λ_{g1} *vs.* λ_{g1}/λ_c for several values of ϵ for $d/\lambda_c = 0.195$. ⊙, experimental values for 0.278 cm sample of lead nitrate.

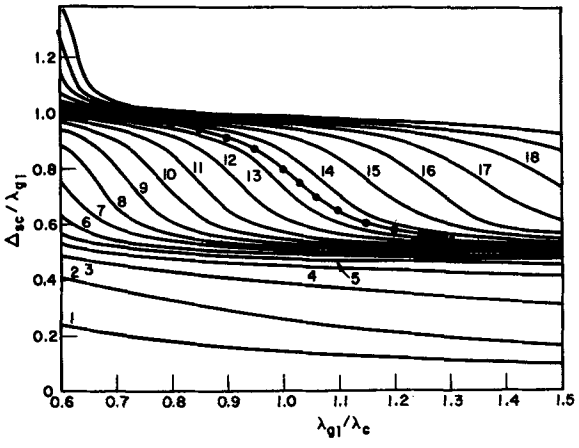

Fig. 3. Theoretical values of Δ_{sc}/λ_{g1} *vs.* λ_{g1}/λ_c for values of dielectric constant 1-20, for $d/\lambda_c = 0.150$. ⊙, experimental values for 0.213 cm sample of thallium nitrate.

Experimental Results

The short circuit data for lead nitrate and for thallium nitrate are plotted in Fig. 2 and 3. An arbitrary value of $n/2$ (where n is a positive integer) may be added to all experimental values of Δ_{sc}/λ_{g1} because the number of half-wavelengths in the sample is unknown. However, if the experimental values of Δ_{sc}/λ_{g1} *vs.* λ_{g1}/λ_c are plotted on Fig. 2 or 3 on which curves of theoretical values of Δ_{sc}/λ_{g1} *vs.* λ_{g1}/λ_c are plotted, it is apparent that n should be two. With this method of analyzing the data one may quickly determine the value of the dielectric constant of a material over a wide frequency band for the case in which an approximate value of dielectric constant is not known. It is important to remember that this method is valid only for low-loss materials.

A method of measurement similar to the one just discussed is the open circuit method in which the short is placed a quarter-wavelength from the rear interface of the sample. From the boundary condition that the impedance across the front interface is continuous and by assuming that the sample is lossless it follows that

$$\cot(B_2 d)/B_2 d = -(\lambda_{g1}/2\pi d) \tan(2\pi\Delta_{oc}/\lambda_{g1}) \quad [5]$$

Equation [5] may be solved for Δ_{oc}/λ_{g1} where Δ_{oc} equals $D_r - D + d$. The values of Δ_{oc}/λ_{g1} now may be calculated for a fixed value of d/λ_c and successive values of ϵ and plotted *vs.* λ_{g1}/λ_c. Then the experimental curve of Δ_{oc}/λ_{g1} *vs.* λ_{g1}/λ_c could be compared to the theoretical curves of Δ_{oc}/λ_{g1} *vs.* λ_{g1}/λ_c; thus, the open circuit data could be treated in the same manner as the short circuit data. However, this procedure was not actually carried out, but instead values of dielectric constant were calculated from the open circuit data for lead nitrate in the frequency band 27-33 kMc by a well-known procedure (1, 2). These values of dielectric constant (near 14.4) are slightly lower than the values (near 14.8) determined by the graphical method from the short circuit data in the frequency band 33-38 kMc.

Discussion

A graphical method has been described for determining the dielectric constant of a low-loss material over a wide frequency band for the case in which an approximate value of dielectric constant is not known. The method has been applied to determine the dielectric constant of lead nitrate and thallium nitrate. The dielectric constants of three crystals of lead nitrate (lengths —1.91, 2.78, and 3.66 mm) have been measured. The dielectric constant in the frequency band 29-35 kMc of the 1.91 mm crystal is 14.3 ± 0.1; the dielectric constant in the frequency band 33-38 kMc of the 2.78 mm crystal is 14.8 ± 0.1, and the dielectric constant in the frequency band 36-38 kMc of the 3.66 mm crystal is 14.1 ± 0.1. This variation of dielectric constant indicates the lack of uniformity of these crystals. The dielectric constant of thallium nitrate in the frequency band 27-37 kMc determined for one crystal of length 2.13 mm is 13.5 ± 0.1. These values for dielectric constant may be compared to the values 16.8 and 16.5 for lead nitrate and thallium

nitrate, respectively, determined by Eucken and Buchner (10) at 3.0 Mc with pulverized crystals.

Dielectric data at other frequencies are required in order to interpret completely the existing dielectric data. However, since the dielectric constant of any one crystal of lead nitrate or thallium nitrate does not vary significantly in the frequency band 28-36 kMc, it is concluded that neither lead nitrate nor thallium nitrate exhibit resonant absorption in this frequency band.

Manuscript received Nov. 13, 1962; revised manuscript received May 1, 1963. This research was supported by the Air Force Systems Command, United States Air Force.

Any discussion of this paper will appear in a Discussion Section to be published in the June 1964 JOURNAL.

REFERENCES

1. W. B. Westphal, "Technique of Measuring the Permittivity and the Permeability of Liquids and Solids in the Frequency Range 3 c/s to 50 kmc/s," Lab. for Insulation Research, M.I.T., Cambridge, Mass., pp. 38-56, 82-89, 92-93, 130-142 (1950).
2. M. Wind and H. Rapaport, "Handbook of Microwave Measurements," Vol. 1 and 2, Section X, Edwards Brothers, Inc., Ann Arbor, Mich. (1955).
3. H. E. Buckley, "Crystal Growth," p. 543, John Wiley & Sons, Inc., New York (1951).
4. R. Newman and R. S. Halford, *J. Chem. Phys.*, **18**, 1276 (1950).
5. D. E. Kerr, "Propagation of Short Radio Waves," p. 642, McGraw-Hill Book Co., New York (1951).
6. S. Robert and A. Von Hippel, *J. Appl. Phys.*, **17**, 610 (1946).
7. W. B. Westphal, pp. 130-142.
8. Montgomery, Dicke, and Purcell, "Principles of Microwave Circuits," pp. 30-38, McGraw-Hill Book Co., New York (1948).
9. *Ibid.*, pp. 67, 79-81.
10. A. Eucken and A. Buchner, *Z. Physik. Chem.*, **B27**, 321 (1934).

Junction Delineation in Gallium Arsenide

T. H. Yeh and A. E. Blakeslee

Components Division, International Business Machines Corporation, Poughkeepsie, New York

The purpose of this note is to describe a chemical staining method which can easily be used to delineate p-n diffused junctions or epitaxially grown junctions in GaAs. Many other chemical solutions which can also be used for junction delineation in GaAs have been reported by various authors (1-4), but with all of them the results are quite technique dependent. Staining time and amount and concentration of nitric acid used, for instance, are critical for the HF/HNO_3 solution (1, 2). Light intensity is critical for gold (3) or silver (4) chemiplating. The HF/HNO_3 staining method is further complicated on occasion by an inversion effect, whereby the n-type side of the junction is stained instead of the p-type. The chemical solution reported here consists of only a dilute solution of nitric acid in water, and its application to stain the p-layer is simple and straightforward.

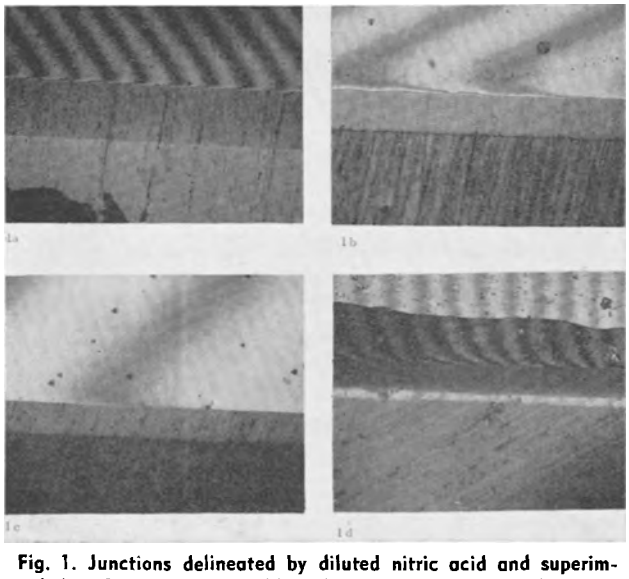

Fig. 1. Junctions delineated by diluted nitric acid and superimposed interference fringes. Magnification 150X (reduced to approximately 75X).

Samples are beveled at a small angle, using an appropriate jig. Beveled surfaces polished with Linde B abrasive over a flat glass plate have been found quite satisfactory. The sample is then immersed in the diluted nitric acid (10% by volume), and the development of the stain over the p-region can be observed with the unaided eye. This staining reaction is fairly slow; 10-15 minutes is the typical staining time. Furthermore, if this stain does not give satisfactory contrast between the dark and light regions adjacent to the junctions, one can immerse the sample again into the acid solution for 2 to 5 min to sharpen the contrast. This staining reaction is similar to that of the acid stain for silicon p-n junctions, which is believed to be a selective oxidation of the p-side to form a visible insoluble film.

Results for delineated junctions are best shown in Fig. 1. Figure 1a shows a p-n junction produced by zinc diffusion. Figures 1b and 1c show n-p junctions produced by the diffusion of sulfur and selenium, respectively, according to a special process to be detailed elsewhere (5). Figure 1d is a p-n-p double diffused structure consisting of two junctions produced by sulfur and zinc diffusion.

In addition to delineation of p-n junctions, this method has also been successfully applied in locating the substrate-film interface in the epitaxial growth of n-on-n GaAs, as shown in Fig. 2a. The interface is revealed as a line of etch figures when a very small drop of the solution is placed astride it and left quiescent for a minute or so. The geometry of these etch figures is very intriguing and deserves some comment. They occur as raised pyramids surrounded by troughs, but they differ from

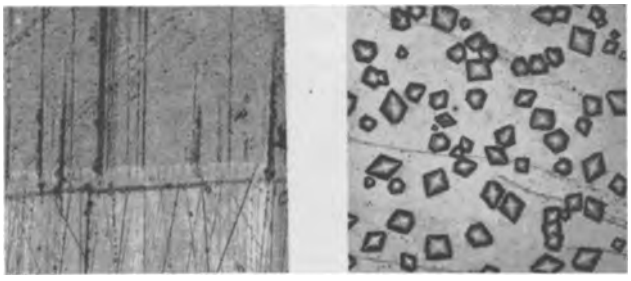

Fig. 2. Etch figures on GaAs: a (left), at substrate-film interface; b (right), cluster of pyramids after prolonged etching.

the arrays of etch pits or pyramids usually observed in semiconductors in that individual adjacent members bear little orientational resemblance to each other. Many different polygonal shapes can be found among the figures, the most prevalent being that of a diamond. Even though the matrix GaAs is definitely monocrystalline, the orientation of prominent lines or facets on these pyramids appears to be completely random. A typical cluster of them is shown in Fig. 2b. They can be generated not only at epitaxial interfaces but apparently on any polished surface of GaAs, the same randomly oriented clusters having been produced on at least half a dozen different crystals, with the effect being independent of orientation, doping, or conductivity type.

Manuscript received April 19, 1963.

Any discussion of this paper will appear in a Discussion Section to be published in the June 1964 JOURNAL.

REFERENCES

1. F. A. Cunnell, J. T. Edmond, and W. R. Harding, *Solid State Electronics*, **1**, 105 (1960).
2. L. A. D'Asaro, Recent News Paper, Electrochemical Society Los Angeles Meeting, May 6-10, 1962.
3. J. T. Edmond, *J. Appl. Phys.*, **31** [8], 1429 (1960).
4. R. W. Haisty, *This Journal*, **108**, 790 (1961).
5. T. H. Yeh, To be published.

The Normal Oxygen Potential on Bright Platinum

James P. Hoare

Research Laboratories, General Motors Corporation, Warren, Michigan

It is generally agreed that the oxidation and reduction of molecular oxygen in acid solution at inert noble-metal electrodes is quite irreversible. In the recent literature (1) it has been shown that under certain conditions of electrode preparation a reproducible rest potential may be obtained at a clean, bright platinum electrode in oxygen-saturated sulfuric acid solutions. It was suggested that this potential is a mixed potential (2) composed of the O_2/H_2O reaction

$$O_2 + 4H^+ + 4e \rightleftharpoons 2H_2O \qquad [1]$$

and the Pt/Pt-O reaction

$$Pt\text{-}O + 2H^+ + 2e \rightleftharpoons Pt + H_2O \qquad [2]$$

It was further suggested that the reversible oxygen potential of 1.23v cannot be observed in this system because the platinum is not truly inert to oxygen. Unless one can obtain an electronically conducting surface that is inert to oxygen, one should not expect to observe the 1.23-v potential.

Vetter (3) describes the various successes other researchers have had in observing this rest potential on inert electrodes in oxygen-saturated solutions. The best observations were made by Bockris and Huq (4), but they could maintain their potential of 1.24 ± 0.03v for no longer than 1 hr.

In this report, it will be shown that, when the platinum surface is covered by a complete film of chemisorbed oxygen at least a monolayer thick, a potential of 1225 ± 10 mv may be observed for extended periods of time, up to 24 hr or longer. Since these chemisorbed layers are good electronic conductors (1, 5), and since they do not thicken with continued anodization (1, 6, 7), one may say that the surface has been passivated with respect to its reaction with oxygen. This complete oxygen layer is obtained by passivating small platinum beads in concentrated nitric acid.

Experimental

Small platinum beads (0.1-0.15 cm in diameter) were melted on the end of platinum (99.99% pure) wires. These beads were then cleaned by flaming to white heat in a hydrogen flame followed by quenching in concentrated nitric acid. This process was repeated about 15 times. Teflon spaghetti was slipped over the platinum wires. Then, three beads as checks were mounted in a Teflon cell filled with concentrated nitric acid and allowed to soak for 75 to 100 hr in the acid. At the end of this time the acid was removed from the cell, and the platinum beads were washed several times in water triply distilled from an all-quartz still.

In a second Teflon cell, similar to the one described before (1), which had been soaking in triply distilled water for at least 48 hr with frequent changes of water, a palladium bead was mounted in the left-side compartment to be used as an alpha-palladium-hydrogen reference electrode (8, 9). This cell was filled with $2N$ H_2SO_4 solution and pre-electrolyzed for at least 24 hr against an auxiliary platinum-wire electrode that could be removed at the end of the pre-electrolysis procedure.

After pre-electrolysis, hydrogen gas, which had been purified in a multistage purification train, was bubbled into the left side of the cell until the palladium bead had registered 50 mv against a Pt/H_2 electrode in the same solution for at least 2 hr. Then, H_2 was bubbled into the right side of the cell for 20 min to destroy any peroxides produced by the pre-electrolysis procedure, since it was shown that the

presence of peroxides lowers the rest potential in the Pt/O_2 system (1). Stirring with H_2 was replaced by stirring with purified oxygen for at least 20 min to saturate the acid solution with oxygen.

Finally, the platinum bead test-electrodes were removed from the first Teflon cell and placed in the right side of the second cell in the O_2-saturated $2N$ H_2SO_4 solution. The cell was sealed up with molten polyethylene, and measurements were taken immediately with a General Radio electrometer, type 1230-A, with oxygen bubbling through the right side of the cell.

The partial pressure of oxygen was varied by diluting the oxygen with nitrogen, and its value was estimated from the two readings on the rotameters as described before (1). The *p*H was varied by diluting the $2N$ H_2SO_4 solution with $2N$ Na_2SO_4 solution to keep the ionic strength constant. At the end of a run, H_2 was bubbled through the cell, and the potential of a saturated calomel electrode (SCE) against a Pt/H_2 electrode was determined. The potential difference was 245 mv. If one takes a value of 242 mv as the potential of SCE against the normal hydrogen electrode (NHE), and since the α-Pd-H is 50 mv more noble than Pt/H_2 in the same solution, the experimentally observed potentials may be converted to the NHE scale by adding 47 mv. All potentials are recorded on the NHE scale unless otherwise stated. Also, at the end of a run while the hydrogen was bubbling through the right side of the cell and before the SCE was inserted, the purity of the system was checked by observing the large pseudocapacitance (1) at the platinum beads when cathodized by an electronic current interrupter. The temperature at which these experiments were carried out was 24° ± 1°C. All solutions were prepared with triply distilled water. The potential could be determined with a precision of one part in a thousand.

Results

In Table I are presented the data of a typical run. Such data have been repeated many times in this laboratory. The time in hours and minutes is recorded in the first column; the potential *vs.* α-Pd-H, in the second; the value of the notated independent variable, in the third; and applicable remarks, in the fourth. When the partial pressure was varied, the potential came to the new steady value within 45 sec. The bead was cathodized by varying the input impedance of the electrometer. The apparent current density was estimated from the measured potential, the exposed geometric area of the test-electrode, and the approximate value of the input impedance. It is assumed as before (1) that the observed polarization occurs only at the test-electrode at these minute current densities. The potential came to a steady value within about 100 sec after the current density had been changed.

An attempt was made to passivate Au, Pd, Rh, and Ir beads in nitric acid. Only limited success was obtained with one, Rh, while the others did not exhibit the normal oxygen potential. A potential of 1225 ± 3 mv was observed on a Rh bead for about 2 hr after which the potential slowly decayed.

Table I. Rest potential of Pt in O_2-saturated $2N$ H_2SO_4 solution

Time, hr:min	Potential *vs.* α-Pd-H, mv	Rotameter readings O_2	Rotameter readings N_2	P_{O_2}, atm	Remarks
0:00	1190				O_2 flow = 290 cc/min
0:02	1180				
1:30	1180				
2:30	1180				
3:30	1170				
					Vary P_{O_2} by diluting O_2 with N_2
3:35	1170	6.2	0	1	
3:36	—	6.4	4.1	0.61	Changed N_2 flow
3:37	1168	6.4	4.1	0.61	
3:39	1168	6.4	4.1	0.61	
3:40	—	6.4	8.3	0.43	Changed N_2 flow
3:41	1165	6.4	8.3	0.43	
3:43	1165	6.4	8.3	0.43	
3:44	—	3.7	8.4	0.31	Changed O_2 flow
3:45	1162	3.7	8.4	0.31	
3:47	1162	3.7	8.4	0.31	
3:48	—	6.0	8.3	0.42	Changed O_2 flow
3:49	1165	6.0	8.3	0.42	
3:51	1165	6.0	8.3	0.42	
3:52	—	6.0	4.0	0.60	Changed N_2 flow
3:53	1168	6.0	4.0	0.60	
3:55	1168	6.0	4.0	0.60	
3:56	—	6.0	0	1	Changed N_2 flow
4:00	1170	6.0	0	1	
5:00	1170	6.0	0	1	
					Sealed up cell and left on open circuit overnight. No O_2 flow.
21:00	1170				Started O_2 flow at 22 hr, 45 min.
22:45	1170				O_2 flow = 340 cc/min
24:00	1170				
		Apparent current density, $\mu a/cm^2$			Pt bead is cathodized by varying input impedance of electrometer.
24:10	1170	Open circuit			
	1170	0.00073			
	1170	0.0073			
	1165	0.073			
	1170	Open circuit			
	1165	0.073			
	1162	0.73			O_2 flow = 340 cc/min
	1150	7.2			
	1160	0.73			
	1163	0.073			
	1170	Open circuit			
	1165	0.073			
	1161	0.73			
	1150	7.2			
	1160	0.73			
24:45	1170	Open circuit			
26:30	1170				Left on open circuit with O_2 flowing
28:30	1170				
52:00	1010				O_2 flow = 50 cc/min
72:00	1020				Concluded experiment

A pH effect on the rest potential with respect to α-Pd-H was not observed which indicated that the Pt/O_2 electrode depends on hydrogen ion concentration in the same way as does the α-Pd-H electrode (11).

After a period of about 40 hr, the potential of 1225 ± 10 mv falls slowly to a steady value of 1060 ± 10 mv which may be maintained indefinitely.

Discussion

It is suggested that prolonged contact of platinum with concentrated nitric acid produced, on the Pt surface, a film of electronically conducting chemisorbed oxygen which is complete and is at least a monolayer thick. Such a surface is inert to oxygen and the O_2/H_2O reaction, Eq. [1], is established on this surface. Supporting evidence for this are the facts that a steady potential of 1225 ± 10 mv is maintained over extended periods of time, that the potential is dependent on the partial pressure of oxygen, that the potential has the same pH dependence as a hydrogen electrode in the same solution, that an estimate of the number of electrons transferred in the over-all potential-determining reaction from the Nernst relationship and the P_{O_2} data is close to 4 as shown in Fig. 1, and that, if the Pt/O_2 electrode is cathodized at low current densities, the potential returns to the value of 1225 ± 10 mv on open circuit.

However, it appears from Table I that in sulfuric acid solution a complete film is unstable and begins to dissolve chemically. This exposes platinum sites, and a mixed potential resulting from Eq. [1] and [2] is set up. The steady state is reached, as suggested before (1), when the potential reaches a value of 1060 ± 10 mv.

When hydrogen was bubbled at a rate of about 300 cc/min over a Pt/O_2 electrode that exhibited a potential of 1225 ± 10 mv, it required between 2000 and 3000 sec to bring the potential to the hydrogen potential (—50 mv *vs.* α-Pd-H). This time for the reduction of the oxygen layer on platinum is much longer than that observed before (1). This indicates that the oxygen layers formed on Pt in contact with HNO_3 are much different from those formed by exposure of Pt to oxygen-saturated acid solution, to dry oxygen in the gas phase, or to anodization in acid solution. The observed long reduction times may be a result of one or more of the following situations. Although the beads remain bright and smooth, the oxygen layers may be greater than a monolayer; or, instead of an adsorbed layer of oxygen atoms, a layer of definite oxide, such as PtO_2 is produced; or such a passivated surface is much less reactive with hydrogen. The data presented here cannot answer these questions, but they do show that the film produced on platinum by treatment in nitric acid (*a*) is electronically conducting, (*b*) is inert to oxygen, and (c) gives support to the contention expressed earlier (1) that the reversible oxygen potential could be observed on an electronically conducting surface that is inert to oxygen.

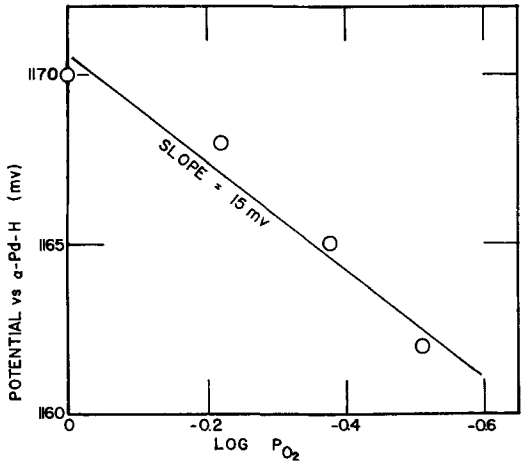

Fig. 1. A plot of the potential as a function of the logarithm of the partial pressure of oxygen. The points are experimentally determined. A line with a slope of 15 mv was drawn in to show that the data favor a 4-electron process.

It is interesting to note that Vetter (12) observed a potential of about 1.28v when oxygen was bubbled over a platinum electrode in a solution composed of HNO_3 and HNO_2. However, these solutions were very strong (7 to 14.5*N* in HNO_3), and since, in the present work, the Pt electrodes were thoroughly washed in triply distilled water, the effect of the NO_2/NO couple is negligible. Besides, after a Pt electrode which exhibited a potential of 1225 ± 10 mv was treated with H_2 stirring, the potential rose from — 50 mv to a steady value of 1060 ± 10 mv when H_2 stirring was replaced with O_2 stirring. If the NO_2/NO couple was important, one would have expected the potential to return to 1225 ± 10 mv with O_2 stirring which did not happen in any case. The mixed potential reported before (1) is always observed.

Also interesting is the fact that, if the platinum is soaked in HNO_3 for periods of time less than about 48 hr, erratic results are obtained. This is an indication that the formation of this film is very slow and most likely involves slow atomic and molecular rearrangements.

Manuscript received Jan. 25, 1963; revised manuscript received May 2, 1963. This paper was presented at the Pittsburgh Meeting, April 15-18, 1963.

Any discussion of this paper will appear in a Discussion Section to be published in the June 1964 JOURNAL.

REFERENCES

1. J. P. Hoare, *This Journal*, **109**, 858 (1962).
2. C. Wagner and W. Traud, *Z. Elektrochem.*, **44**, 391 (1938).
3. K. J. Vetter, "Elektrochemische Kinetik," p. 497, Springer Verlag, Berlin (1961).
4. J. O'M. Bockris and A. K. M. S. Huq, *Proc. Roy. Soc.*, **A237**, 277 (1956).
5. H. A. Laitinen and C. G. Enke, *This Journal*, **107**, 773 (1960).
6. K. J. Vetter and D. Berndt, *Z. Elektrochem.*, **62**, 378 (1958).
7. W. Bold and M. Breiter, *Electrochim. Acta*, **5**, 145 (1961).
8. D. J. G. Ives and G. J. Janz, "Reference Electrodes," p. 112, Academic Press, New York (1961).
9. J. P. Hoare, *G. M. Eng. J.*, **9** [1], 14 (1962).
10. D. C. Grahame, *Chem. Rev.*, **41**, 441 (1947).
11. S. Schuldiner, G. W. Castellan, and J. P. Hoare, *J. Chem. Phys.*, **28**, 16 (1958).
12. K. J. Vetter, *Z. anorg. Chem.*, **260**, 242 (1949).

Current Efficiencies for the Anodic Oxidation of Ammonia in Potassium Hydroxide Solution

T. Katan and R. J. Galiotto

Materials Sciences Laboratory, Lockheed Missiles & Space Company, Sunnyvale, California

Muller and Spitzer (1) have electrolyzed aqueous ammonia solutions which contained dissolved sodium hydroxide, and the anode products were found to be mixtures of nitrogen, sodium nitrate, and sodium nitrite in varying amounts.

$$2NH_3 + 6\,OH^- = N_2 + 6H_2O + 6e^- \quad [1]$$

$$NH_3 + 7\,OH^- = NO_2^- + 5H_2O + 6e^- \quad [2]$$

$$NH_3 + 9\,OH^- = NO_3^- + 6H_2O + 8e^- \quad [3]$$

Anodes of smooth platinum and other metals were tried (1, 2), but nitrogen was never produced in quantities which corresponded to complete stoichiometric consumption of ammonia with respect to Eq. [1]; substantial quantities of nitrate and lesser quantities of nitrite ions were always formed.

As part of a study on an aqueous fuel cell system using ammonia as an anodic reactant, an effort was made to synthesize nitrogen from aqueous ammonia solutions with near 100% yields. This study was undertaken to find the effect of the highly active electrode catalyst, platinum black, on the course of the over-all anode reaction in potassium hydroxide electrolyte of "maximum conductivity" concentration, 6.9M at 18°C (3).

Experimental

Electrolysis was carried out at 23°C in the cell

$$Pt(black),\ NH_3(3M),\ KOH(6.9M)/Cellophane/KOH(6.9M),\ Ni$$

The anode consisted of 0.2g of precipitated black platinum (4) evenly distributed and clamped between two 1 x 1 in. sintered nickel Clevite plates, 0.032 in. thick, which were connected to an electrical contact tab. A 1/32 in. diameter capillary leading to the anode face was connected to an Hg-HgO, 6.9M KOH reference cell. Electrolyte was pumped from a 2-liter reservoir through the anode at 6.8 cm/min and then recycled. A gas-liquid separator permitted the complete separation of the anode gas from the flowing electrolyte, and the gas volume was measured by standard gasometric techniques after scrubbing in 10% HCl solution to remove the ammonia.

The cathode chamber was static and connected to a eudiometer for the collection and measurement of the hydrogen volume. During a run, the current was kept constant, the time of the run was recorded, and the gases from the anode and cathode were collected simultaneously and measured. A typical run lasted 3 hr, and about 30 ml of anode gas were collected.

Ideal gas behavior was assumed throughout the calculations. Corrections were made for the vapor pressure of water over 6.9M KOH and 10% HCl.

The anode gas was analyzed with a gas chromatograph and found to be 100 ± 2% nitrogen. No hydrogen was present.

Results and Discussion

Results are summarized in Table I. The cathode gas collection provides an internal gas coulometer to check the time-at-constant-current coulombic measurement and also establishes the accuracy of the experiment. The average current efficiency with respect to hydrogen production is found to be 100.5% with an average deviation of ±1.7%.

Also from Table I, it is seen that the average current efficiency of nitrogen production with respect to reaction [1] is 99.7%, with an average deviation of ±1.8%. A current efficiency other than 100% would indicate that one or more additional reactions occur concurrently with nitrogen evolution.

Table I. Current efficiencies in the electrolysis of an aqueous 6.9M KOH — 3M NH_3 solution at 23°C

Current density, ma cm^{-2}	Calculated H_2 volume, STP, ml	Observed H_2 volume, STP, ml	Current efficiency, H_2, %	Calculated N_2 volume, STP, ml	Observed N_2 volume, STP, ml	Current efficiency, N_2, %	Polarized anode potential, v *vs.* SHE*
10	86.7	85.2	98.3	—	—	—	—0.31- —0.28
10	58.1	57.6	99.2	19.4	20.0	103	—0.28- —0.27
10	74.7	75.9	102	24.9	25.3	102	—0.26- —0.25
24	—	—	—	47.2	48.0	102	—0.31- —0.30
24	84.8	83.9	98.1	—	—	—	—0.07-0.16
24	86.0	85.2	98.9	—	—	—	0.03-0.13
24	84.6	84.3	99.7	28.2	27.8	98.6	—0.02-0.06
24	—	—	—	34.8	34.1	98.1	—0.11- —0.01
48	86.7	88.5	102	28.9	28.6	99.2	—0.04- —0.03
48	68.0	70.5	104	22.7	22.6	99.7	0.00-0.03
100	84.0	84.7	101	27.9	26.6	95.2	—0.13-0.05
100	82.3	84.0	102	27.4	27.2	99.2	—0.11-0.15

* Typical open circuit potential values were close to −0.6v *vs.* a SHE.

Reaction [1] is thus established as the only reaction occurring to within the experimental accuracy.

Acknowledgments

The authors wish to acknowledge the financial support of this research by the United States Army Transportation Corps under the research contract DA 44-177-TC-634.

Manuscript received April 5, 1963.

Any discussion of this paper will appear in a Discussion Section to be published in the June 1964 JOURNAL.

REFERENCES

1. E. Muller and F. Spitzer, *Z. Elektrochem.*, **11**, 917 (1905).
2. V. O. Reitlinger, *ibid.*, **20**, 268 (1914).
3. F. Kohlrausch and L. Holborn, "Das Leitvermogen der Electrolyte," 2nd ed., p. 159, Leipzig-Berlin (1916).
4. O. Loew, *Ber.*, **23**, 289 (1890).

Vibrational Frequencies of the Mercuric Halides

William Klemperer

Department of Chemistry, Harvard University, Cambridge, Massachusetts

In a recent article Janz and McIntyre discussed the fundamental vibration frequencies of the mercury halides (1). Their assignment of frequencies differ considerably from a body of earlier work (2-6). It is the purpose of this note to review the problem and show that, at least in this author's opinion, a great body of evidence favors the earlier vibrational assignment.

The discussion is concerned with the vibrational frequencies of the gaseous molecules. Since almost all of the arguments of Janz and McIntyre depend on spectral observations in condensed phases we will frequently have recourse to observations not made on gaseous systems. It is emphasized that our point of disagreement with Janz and McIntyre is concerned with the fundamental vibration frequencies of the isolated molecular species.

There is no controversy concerning the equilibrium nuclear configuration of the mercury dihalides. The accepted structure is linear, centrosymmetric, namely, point group $D_{\infty h}$. This structure has three normal modes of vibration: namely, two nondegenerate parallel (to the internuclear axis) vibrations, and one doubly degenerate perpendicular vibration.

There is no disagreement as to the frequency of the antisymmetric bond stretching vibration, ν_3. This vibration is infrared active and has been observed (6) in the vapor at 413 cm^{-1} for $HgCl_2$, 293 cm^{-1} for $HgBr_2$, and 237 cm^{-1} for HgI_2.

The second parallel vibration of this system is the symmetric bond stretching vibration ν_1 which is active in the Raman spectrum. Since there is some disagreement as to the proper value of this frequency we shall discuss the observations and interpretations in some detail.

Braune and Engelbrecht in 1932 (2) observed the Raman spectrum of the mercury halides in the vapor (P_{HgCl_2} = 1160 mm, P_{HgBr_2} = 1140 mm, and P_{HgI_2} = 910 mm), in the melt, and in solutions of either ethyl acetate or ethyl alcohol. Braune and Engelbrecht found the values of ν_1 in the vapor to be $HgCl_2$ = 355 cm^{-1}, $HgBr_2$ = 220 cm^{-1}, and HgI_2 = 155 cm^{-1}. For the melt they found $HgCl_2$ = 314 cm^{-1} and $HgBr_2$ = 195 cm^{-1} in good agreement with other work done subsequently.

In 1941 Rao observed the vibration ν_1 in gaseous $HgCl_2$ to be at 310 cm^{-1}, but was in perfect agreement with Braune and Engelbrecht on the value of ν_1 in molten $HgCl_2$. This discrepancy in gas phase measurements together with the size of the shift in going from gas to liquid lead Janz and McIntyre to remark that "there is need for additional work to resolve this." We believe that this work is already in existence. In 1938 Wherli (4) photographed the vacuum ultraviolet band system of the mercuric halides. Both he and Sponer and Teller (5) discussed the analysis of these molecules. In fact the latter authors remark in their review "The mercury halides offer the only examples for completely analyzed spectra of linear molecules." Their analysis gives for ν_1 $HgCl_2$ = 365 cm^{-1}, $HgBr_2$ = 229 cm^{-1}, and HgI_2 = 156 cm^{-1}. This certainly is in excellent agreement with the work of Braune and Engelbrecht (2). Sponer and Teller make no mention in their article of the work of Braune and Engelbrecht. Thus we do not agree with Janz and McIntyre that there is any room for doubt as to the value of ν_1 of the gaseous mercury halides.

The last vibration to be discussed, the perpendicular oscillation ν_2, is changed drastically in the new assignment of Janz and McIntyre. These authors assign the frequently observed weak Raman line of 377-381 cm^{-1} of the $HgCl_2$ to $2\nu_2$. This line, while not observed in the vapor, is observed in both crystal and melt. It should be noted however, that Plyler (8) observed this line (377 cm^{-1}) as the one band in the infrared spectrum of solid $HgCl_2$ not in the Raman as listed by Janz and McIntyre. A second argument of Janz and McIntyre for the assignment of ν_2 = 179 in $HgCl_2$ and 136 cm^{-1} in $HgBr_2$ is the observation of Delwaulle (9) in 1938 that the solution Raman spectra of equimolar mixtures of $HgCl_2$ and $HgBr_2$ show three lines not found in the spectra either of the individual components. These lines at 232 cm^{-1}, 347 cm^{-1}, and 139 cm^{-1} are assigned to the species Cl Hg Br. Janz and McIntyre assign the weak line at 139 cm^{-1} to ν_2 of Cl Hg Br. In a later paper by Francois and Delwaulle (10) in discussing the Raman spectra of the same species only the lines at 232 and 345 cm^{-1} are listed. We feel that the evidence that $2\nu_2$ as observed in the Raman spectra of melts and crystals of $HgCl_2$ is very weak in view of Plyler's observation of a band at the identical frequency in the infrared spectrum of crystalline $HgCl_2$, indicating that ν_3 of $HgCl_2$ in the melt and

Table I. Vibrational frequencies of the gaseous mercuric halides

	ν_1[a]	ν_2[b]	ν_3[c]
$HgCl_2$	360	70	413
$HgBr_2$	225	41	293
HgI_2	156	33	237

[a] Average value of the frequencies Raman and electronic spectra.
[b] Value of frequency from electronic spectra.
[c] Value of frequency from infrared spectra.

crystal is shifted appreciably from the gas phase frequency of 413 cm^{-1}

The early evidence of Delwaulle is less easily dismissed except to note that previous to the invention of the low-pressure Toronto arc weak Raman lines were frequently unreliable.

Evidence for the earlier assignment of ν_2 as 70 cm^{-1} in $HgCl_2$, 41 cm^{-1} in $HgBr_2$, and 33 cm^{-1} in HgI_2 is very strong. In a series of papers Braune, Knoke, and Engelbrecht reported the following:

1. The Raman spectra of the gaseous mercuric halides, determining ν_1. ν_3 was calculated using a simple valence force field (2).

2. The equilibrium constant of the gas reaction $HgX_2 = Hg + X_2$ over a range of temperature (11).

3. A determination of the structure and moment of inertia of HgX_2 by electron diffraction (3).

These authors fitted the entropy factors of the reaction $HgX_2 = Hg + X_2$ by adjustment of the frequency of ν_2. (It should be noted that the contribution to the entropy of ν_2 is large). They listed the values $HgCl_2 = 70$ cm^{-1}, $HgBr_2 = 64$ cm^{-1}, and $HgI_2 = 50$ cm^{-1}.

In the analysis of the vacuum ultraviolet bands of the mercuric halides, Sponer and Teller showed that progressions in $2V_2$ were expected and fitted the spectra, which were well resolved vibrationally, with ν_2 values of $HgCl_2 = 70$ cm^{-1}, $HgBr_2 = 41$ cm^{-1}, and $HgI_2 = 33$ cm^{-1}. These values are in excellent agreement with the values deduced previously by statistical thermodynamics. As noted earlier, Sponer and Teller were apparently unaware of the earlier work by Braune, Knoke, and Engelbrecht.

We feel that the evidence is overwhelmingly in favor of the vibrational assignment listed in Table I. The work of Braune, Engelbrecht, and Knoke in the early thirties and that of Wherli and Sponer and Teller in 1938-1940 represents a classic example of a detailed study of molecular structure. All the measurements were on gaseous molecules, and the theory necessary to reduce the observations is certainly adequate. The later work discussed by Janz and McIntyre is derived entirely from condensed phase measurements. The theory necessary to go with certainty from condensed phase measurements to isolated molecule constants is by no means quantitative at present. We feel that the condensed phase spectra show large "solvent" shifts and a relaxation of isolated molecule selection rules in condensed phases.

It should be noted that since this article was submitted, Janz and James (12) have published a discussion of the vibrational spectra of the mercuric halides in agreement with the present assignment.

Manuscript received Nov. 8, 1962; revised manuscript received April 10, 1963.

Any discussion of this paper will appear in a Discussion Section to be published in the June 1964 JOURNAL.

REFERENCES

1. G. E. Janz and J. D. E. McIntyre, *This Journal*, **109**, 842 (1962).
2. H. Braune and G. Engelbrecht, *Z. Physik. Chem.*, **B19**, 303 (1932).
3. H. Braune and S. Knoke, *ibid.*, **B23**, 163 (1933).
4. M. Wherli, *Helv. Phys. Acta*, **11**, 339 (1938); **13**, 153 (1940).
5. H. Sponer and E. Teller, *Rev. Mod. Phys.*, **13**, 75 (1941).
6. W. Klemperer and L. Lindeman, *J. Chem. Phys.*, **25**, 397,1066 (1956).
7. K. V. Krishna Rao, *Proc. Indian Acad. Sci.*, **14A**, 521 (1941).
8. J. Duchesne and L. Burnelle, *J. Chem. Phys.*, **19**, 1191 (1951) report the work of E. K. Plyler on the infrared absorption spectrum of solid mercuric chloride.
9. M. L. Delwaulle, *Compt. rend.*, **206**, 1965 (1938).
10. F. Francois and M. L. Delwaulle, *J. Chim. Phys.*, **46**, 80 (1949).
11. H. Braune and S. Knoke, *Z. Physik. Chem.*, **A152**, 409 (1931).
12. G. J. Janz and D. W. James, *J. Chem. Phys.*, **38**, 902 (1963).

Thermodynamics of Hydrocarbon Fuel Cells

E. J. Cairns, A. D. Tevebaugh, and G. J. Holm

Research Laboratory, General Electric Company, Schenectady, New York

ABSTRACT

Recently, there has been a great increase in activity in the field of hydrocarbon fuel cells. A rather neglected area has been that of the thermodynamics of the reactions in the anode compartment. The conditions under which a fuel cell must be operated in order to prevent carbon deposition have been calculated for the CHO system at 500°K under two important sets of conditions. Two literature methods for the calculation of the complex gas phase equilibria were evaluated, and an improved method extending one of these methods is presented. The calculations show that unexpectedly high and constant emf values are possible. Appreciable amounts (*ca.* 1%) of hydrogen were found to be present at equilibrium over a wide range of fuel compositions at 500°K. The levels of CO partial pressures at equilibrium were found to be about 10^{-5} atm.

In recent years, there has been a great upsurge of interest and activity in the field of hydrocarbon fuel cells. A great deal of effort has been expended in the search for optimum combinations of anode electrocatalysts, fuels, and electrolytes. A rather neglected area has been that of the thermodynamics of the reactions which take place or may take place in the anode compartment of a fuel cell using a hydrocarbon or a modified hydrocarbon (*e.g.*, CH_3OH) as the fuel. It is in this important area that the present work has been concentrated.

There are several areas relating to the theory and operation of hydrocarbon fuel cells where thermodynamics can make a contribution. The theoretical open-circuit voltage of a fuel cell at thermodynamic equilibrium may be calculated only if the composition of the anode gas is known. Usually, the assumption is made that the open-circuit voltage should correspond to that calculated by applying the Nernst equation to the inlet fuel composition. Hardly ever can this method be expected to yield an accurate result since the inlet fuel composition can be significantly different from the gas phase composition which would exist at chemical equilibrium. The maximum voltage attainable in a fuel cell during the process of oxidation, or during the procession of the fuel gas through a series of fuel cells (during which it is being oxidized) may be calculated, providing the composition of the gas is known as a function of the degree of oxidation. An important consideration, especially for fuel cells which are required to operate for extended periods of time, is whether or not it is thermodynamically possible for carbon to deposit from the fuel gas in the anode compartment during any stage of its oxidation. The deposition of carbon has been found to be a particularly troublesome problem to some fuel cell investigators (1-6). All of these problems and some others have been considered and are reported on here.

Making use of our recent results on the carbon deposition boundaries in the CHO system (7), it is now possible to calculate precisely the conditions under which carbon deposition at equilibrium can be avoided for any CH or CHO fuel system. These computations provide a starting point for the determination of the gas phase compositions and the maximum theoretical emf values for fuel cell operation outside the carbon deposition region. The two practical methods for avoiding carbon deposition are mixing water with the fuel and recycling the combustion products (CO_2 and H_2O) with the fuel. These general methods will be discussed for the case where methane is used as the fuel.

The calculation of the equilibria among the several important species in the anode compartment of a hydrocarbon fuel cell is not a simple task even using the so-called simplified methods. Because of the complexity of these calculations, it is desirable to discuss methods by which they may be carried out and the disadvantages of some procedures.

Thermodynamic Methods

Thermodynamic considerations may be used to determine the important chemical species which must be considered in calculating the equilibria of interest to fuel cell operation. The species most likely to be present in the greatest amounts are determined by their equilibrium constants of formation and the equilibria among these species under the conditions of interest. In the system containing the elements carbon, hydrogen, and oxygen at a pressure of 1 atm, the most important species are carbon, hydrogen, water, carbon dioxide, carbon monoxide, and methane, with other species such as ethane, methanol, and some of the other hydrocarbons being present in very much smaller amounts in the temperature range of 298°-1500°K. Details of the method establishing the above mentioned species as the only important ones have been given in an earlier paper (8).

Various simplified computational methods which have been applied to the CHO system containing only those species mentioned above are available in the literature (9-14). Some of these methods are largely graphical (9, 11, 12), while others are algebraic (10, 13, 14). These simple methods can be justified only when a limited number of results are

necessary, or when limited accuracy is desired. More sophisticated mathematical approaches, using computer methods (15, 16), are highly recommended where a large volume of high precision results is required.

Mayland and Hays (9) have presented a graphical method for determining the equilibrium gas phase composition for the CHO system in the absence of solid carbon. The preparation of a plot of log (CH_4/CO) *vs.* log (CO_2/CO) for various values of (H_2/CO) was described in detail. The procedure for the calculation of the amounts of H_2O and the various partial pressures was also described. Given this plot, it is necessary to perform subsequent calculations in order to obtain results applicable to a specific fuel cell system. These calculations will be described below.

Case I.—Prevention of carbon deposition by recycling oxidation products with methane as the fuel. The gas phase composition and the theoretical maximum emf are to be calculated for operation of a methane fuel cell at 500°K and 1 atm absolute pressure.

First, it is necessary to establish those conditions under which carbon cannot be present at equilibrium. Figure 1 shows some data selected from our recent work (8) which are pertinent to this example. Above the carbon deposition boundary, carbon will be present; below this boundary, all of the carbon is combined and is in the gas phase. The point representing CH_4 is shown on the H-C axis of Fig. 1. A straight line joining the CH_4 point to the 0 vertex shows the path of the over-all composition of the system during the oxidation process. The equilibrium gas phase composition during oxidation follows a path along the carbon deposition boundary until point a is reached. On further oxidation from point a, along the path aO to point b, carbon is no longer present at equilibrium. Point b (on the line joining CO_2 and H_2O) represents complete oxidation of the fuel mixture. It is along the path ab that the fuel cell will operate free of carbon at equilibrium (500°K, 1 atm total pressure).

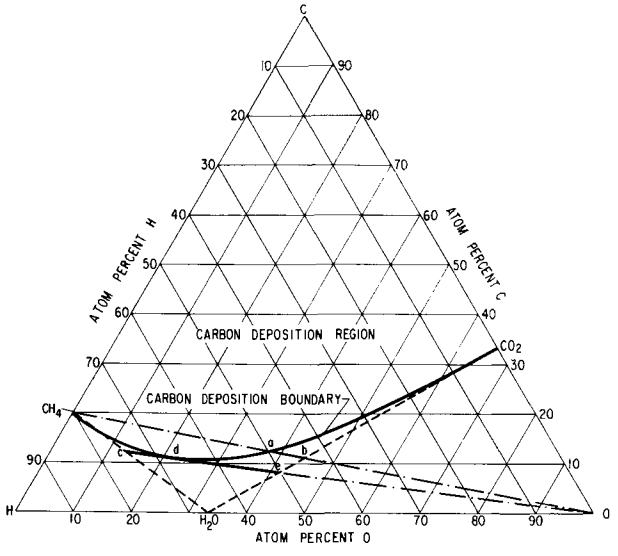

Fig. 1. Graphical determination of CH_4 fuel mixture compositions which will not deposit carbon at equilibrium (500°K, 1 atm).

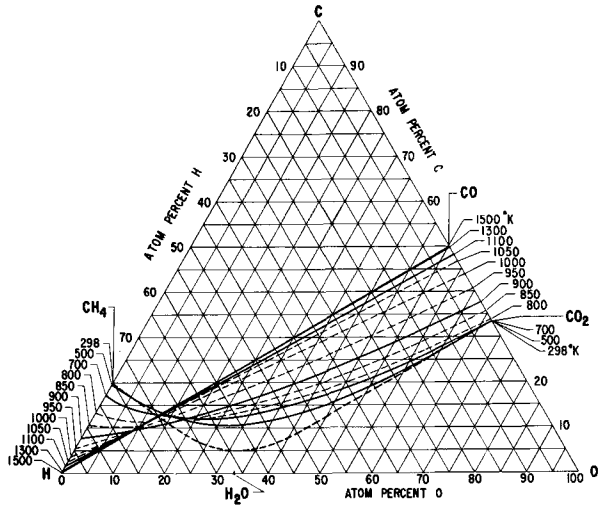

Fig. 2. Carbon deposition boundaries for the CHO system at 1 atm.

Point a in Fig. 1 determines the number of moles of oxidation products (1 CO_2 + 2H_2O) to be recycled with 1 mole of the methane fuel. This amount was calculated from Eq. [1] and the C:H:O ratio at point a.

$$\text{Point a} = 1\ (CH_4) + x(CO_2 + 2H_2O)$$

$$x = \frac{4 - 5f_{(H)}}{9f_{(H)} - 4} = \frac{4 - 5(0.5)}{9(0.5) - 4} = 3 \quad [1]$$

where $f_{(H)}$ = the hydrogen atom fraction at point a, Fig. 1. Thus, recycling three moles of the oxidation product mixture (1CO_2 + 2H_2O) with each mole of methane entering a fuel cell will (at equilibrium, 500°K, and 1 atm pressure) permit complete oxidation of the methane without the deposition of solid carbon.

The carbon deposition boundaries over the temperature range 298°-1500°K for 1 atm pressure are shown in Fig. 2 (7). The conditions under which a fuel cell may be operated outside the carbon deposition region at any temperature may be calculated by the use of this figure.

The calculation of the gas phase compositions along the fuel cell operating line ab (Fig. 1) was performed by an extension of the graphical method of Mayland and Hays (9). By comparison of the range of the C:H:O gas phase ratios for line ab with Fig. 1 of Mayland and Hays (9), it was found that the range of interest was not covered. Following their methods, the solid lines of Fig. 3 were then prepared to cover the desired range. Since the H_2/CO ratio is an important parameter in the use of Fig. 3, it was necessary to devise a method for determining H_2/CO along the line ab of Fig. 1.

Since all points along the line joining CH_4 to the 0 vertex in Fig. 1 have a constant H/C ratio equal to 4.00, this value of H/C is an important parameter in these calculations and was used to determine the path of the operating line ab when transferred to Fig. 3. Since the locus of all points of H/C = 4.00 in Fig. 3 corresponds to line ab of Fig. 1 it was necessary to locate the line on Fig. 3 corresponding to H/C = 4.00. In order to accomplish this, a crossplot of H/C *vs.* CH_4/CO from Fig. 3 was prepared

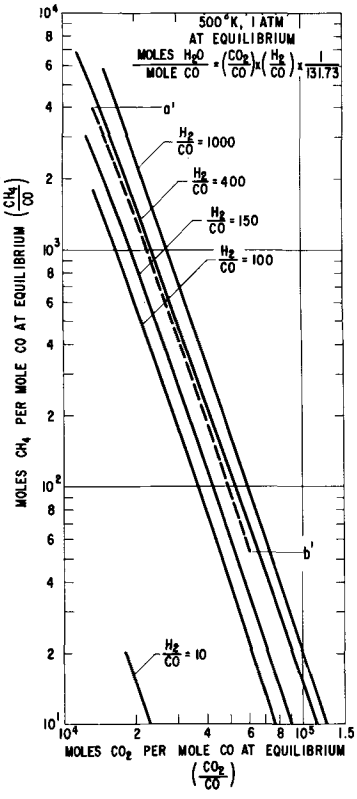

Fig. 3. Equilibrium gas compositions at 500°K and 1 atm for the CHO system.

for various constant values of CO_2/CO. The intersections of these lines with the line H/C = 4.00 then allowed the line a'b' to be plotted on Fig. 3. In order to determine the gas phase compositions from line a'b', it was necessary to know how H_2/CO varied along this line. This was accomplished by using a crossplot of H_2/CO *vs.* CH_4/CO for constant CO_2/CO values from the solid lines of Fig. 3. The CH_4/CO values from line a'b' were then used with this crossplot to determine H_2/CO at the various CO_2/CO values along line a'b'. Along the line a'b', H_2/CO was found to vary from 263 at a' to 261 at b'.

Using line a'b' and the values of H_2/CO, the relative partial pressures of H_2, CH_4, CO_2, and CO were known, and from Eq. [2]

$$K_1 = \frac{[H_2][CO_2]}{[CO][H_2O]}$$

$$\therefore [H_2O] = \frac{[H_2][CO_2]}{K_1[CO]} \qquad [2]$$

the relative H_2O partial pressure could be calculated. The true partial pressure of each species could then be calculated knowing that the total pressure was 1 atm.

Consistent with the previous discussion, point a of Fig. 1 was defined as the composition representing 0% combustion in the fuel cell, and corresponds to point a' of Fig. 3. The composition of the fuel mixture in the anode compartment during oxidation proceeds from a to b in Fig. 1 and from a' toward b' in Fig. 3. Various points along a'b' in Fig. 3 were chosen, and the gas phase compositions, cell potentials (from the Nernst equation), and per cents oxidation were calculated. The results will be discussed in detail in the next section.

Although this graphical method is straightforward, it was found necessary to prepare very large-scale plots and crossplots. In addition, it was required that the values obtained from the graphs be refined by trial and error calculation in order to maintain an error of less than 1%. These disadvantages cause the method to be very cumbersome and time consuming.

Case II.—Prevention of carbon deposition by mixing water with the methane fuel. The gas phase composition and the theoretical maximum emf are to be calculated for the operation of a methane fuel cell at 500°K and 1 atm absolute pressure.

The conditions under which carbon cannot be present at equilibrium were determined in a manner similar to that for case I. All mixtures of CH_4 and H_2O lie along the line joining the points CH_4 and H_2O in Fig. 1. In order to determine the fuel composition which is richest in CH_4, yet avoids carbon deposition during oxidation, a line is constructed from the O vertex such that it intersects the CH_4-H_2O line and is tangent to the 500°K carbon deposition boundary. The line cdeO was located in this manner. Point c represents a methane-water mixture, which can be oxidized completely (to point e) without carbon deposition at equilibrium. The water-methane mole ratio corresponding to point c, Fig. 1 was calculated (see case I) to be 1.039.

Due to the disadvantages encountered in the method of Mayland and Hays (cited in case I), the algebraic method of Montgomery *et al.* (10) appeared attractive. It was found that their equation 10b would not yield a correct solution for this case, although it was stated their equations applied to ". . . the general case with completely arbitrary feed ratios . . .". It was found, however, that equation 10b of Montgomery *et al.* (10) did yield correct results for H/C = 4.0, and that their material balance equations [13b] and [14b] were also correct. It was therefore decided to combine the equation

$$CH_s + nO_2 \rightarrow xCH_4 + aH_2O + \left(\frac{s}{2} - a - 2x\right)H_2 + (b - x)CO + (1 - b)CO_2 \qquad [3]$$

and their material balance equations

$$b = K_8\left[\frac{K_1}{r}\left(\frac{s}{2} - 2x + rx\right) - 1\right] \qquad (10)\ [13b]$$

$$a = (1 - b)\frac{r}{K_1} \qquad (10)\ [14b]$$

where

$$r = \frac{[H_2]}{[CO]} \text{ at equilibrium}$$

$$K_1 = \frac{[CO_2][H_2]}{[CO][H_2O]}$$

and

$$K_8 = \left[\frac{[CO_2][H_2]}{[CO][H_2O]} - 1\right]^{-1}$$

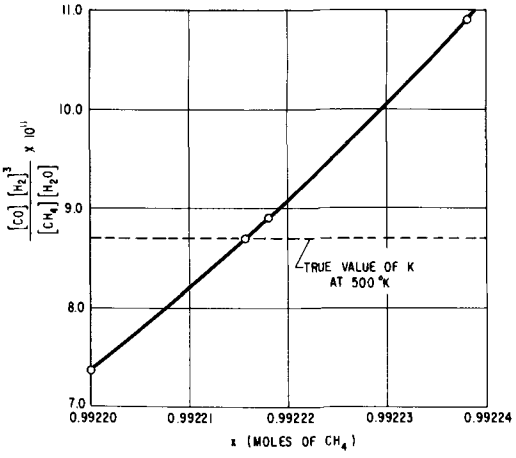

Fig. 4. Graphical solution for the equilibrium partial pressure of methane.

with a graphical method, plotting x *vs.* the deviation of the calculated equilibrium constants from the true values (see Fig. 4). As a guide in these calculations, the values of $[H_2]/[CO]$ at 0 and 100% oxidation were desired. These values for $[H_2]/[CO]$ were readily calculated. At 100% oxidation, the gas phase is primarily $CO_2 + H_2O$, and from material balance constraints and the equilibrium

$$CO + H_2O \rightleftharpoons CO_2 + H_2 \qquad K_1 \quad [4]$$

the $[H_2]/[CO]$ ratio can be calculated as follows:

$$\frac{\text{moles of } H_2O \text{ at 100\% oxidation}}{\text{moles of } CO_2 \text{ at 100\% oxidation}} = \frac{1.039 + 2.000}{1.000} = 3.039$$

$$K_1 = 131.73 = \frac{[CO_2]}{[H_2O]} \times \frac{[H_2]}{[CO]}$$

from which

$$\frac{[H_2]}{[CO]} = 400.3$$

The calculation of $[H_2]/[CO]$ at 0% oxidation is somewhat more involved than in the example above. As a first approximation, the problem can be approached in a manner similar to that above if one assumes that the methane and water do not react with each other; this yields a $[H_2]/[CO]$ ratio of

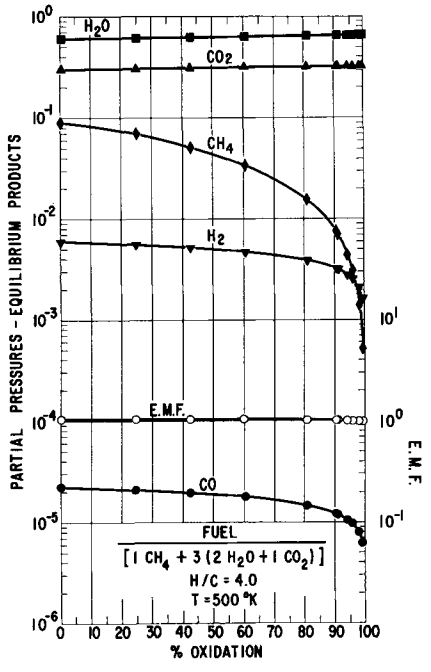

Fig. 5. Equilibrium gas compositions and cell potential as a function of per cent oxidation for a ($1CH_4 + 2H_2O + 1CO_2$) fuel, 500°K, 1 atm.

1,547 which can be used as a rough guide in the calculations from 100% oxidation to about 5% oxidation. When gas phase composition data have been calculated for approximately 5% oxidation, a more reliable boundary value for $[H_2]/[CO]$ at 0% oxidation can then be calculated. For example, using our results for 5.72% oxidation, material balance constraints, and the equilibrium constant equation K_1, the ratio of $[H_2]/[CO]$, as an upper limit, was calculated to be 17,030 for 0% oxidation of the fuel. The value 17,000 was used in the calculations and it was found that this value would correspond to a negative 0.47% oxidation; hence the true value of $[H_2]/[CO]$ for 0% oxidation is less than 17,000.

The combined algebraic and graphical method described above was found to be more rapid and simpler than the solution of the fourth order equation 10b of Montgomery *et al.*, and was very much faster than the all graphical method described for case I. A complete solution of the combined graphical and algebraic method for one set of conditions could be obtained on a desk calculator in 3 to 4 hr,

Table I. Case I: $1CH_4 + 2H_2O + 1CO_2$, 500°K, 1 atm

% Oxidation	Partial pressures, atm					Emf, v
	CH_4	H_2	CO	H_2O	CO_2	
0.069	9.01×10^{-2}	5.92×10^{-3}	2.27×10^{-5}	6.01×10^{-1}	3.03×10^{-1}	1.0355
24.6	7.03×10^{-2}	5.60×10^{-3}	2.14×10^{-5}	6.14×10^{-1}	3.10×10^{-1}	1.0338
42.5	5.17×10^{-2}	5.21×10^{-3}	1.99×10^{-5}	6.27×10^{-1}	3.16×10^{-1}	1.0319
60.2	3.45×10^{-2}	4.74×10^{-3}	1.81×10^{-5}	6.39×10^{-1}	3.21×10^{-1}	1.0294
80.6	1.60×10^{-2}	3.93×10^{-3}	1.50×10^{-5}	6.52×10^{-1}	3.27×10^{-1}	1.0252
90.4	7.86×10^{-3}	3.30×10^{-3}	1.26×10^{-5}	6.58×10^{-1}	3.30×10^{-1}	1.0210
90.8	7.19×10^{-3}	3.23×10^{-3}	1.23×10^{-5}	6.59×10^{-1}	3.31×10^{-1}	1.0204
94.0	4.58×10^{-3}	2.88×10^{-3}	1.10×10^{-5}	6.61×10^{-1}	3.31×10^{-1}	1.0180
95.8	3.18×10^{-3}	2.63×10^{-3}	1.00×10^{-5}	6.62×10^{-1}	3.32×10^{-1}	1.0160
97.9	1.46×10^{-3}	2.17×10^{-3}	8.26×10^{-6}	6.64×10^{-1}	3.32×10^{-1}	1.0118
99.0	5.29×10^{-4}	1.68×10^{-3}	6.40×10^{-6}	6.65×10^{-1}	3.33×10^{-1}	1.0063

Table II. Case II: 1 CH_4 + 1.039 H_2O, 500°K, 1 atm

% Oxidation	Partial pressures, atm					Emf, v
	CH_4	H_2	CO	H_2O	CO_2	
−0.47	4.83×10^{-1}	2.43×10^{-2}	1.43×10^{-6}	4.89×10^{-1}	3.79×10^{-3}	1.0708
5.72	4.31×10^{-1}	1.46×10^{-2}	6.34×10^{-6}	5.24×10^{-1}	3.00×10^{-2}	1.0579
10.0	3.96×10^{-1}	1.29×10^{-2}	8.63×10^{-6}	5.43×10^{-1}	4.77×10^{-2}	1.0545
13.5	3.69×10^{-1}	1.21×10^{-2}	1.09×10^{-5}	5.57×10^{-1}	6.12×10^{-2}	1.0525
21.3	3.15×10^{-1}	1.09×10^{-2}	1.25×10^{-5}	5.86×10^{-1}	8.87×10^{-2}	1.0492
39.0	2.13×10^{-1}	9.18×10^{-3}	1.53×10^{-5}	6.38×10^{-1}	1.40×10^{-1}	1.0437
55.8	1.38×10^{-1}	8.00×10^{-3}	1.60×10^{-5}	6.76×10^{-1}	1.78×10^{-1}	1.0398
71.1	8.16×10^{-2}	6.89×10^{-3}	1.53×10^{-5}	7.05×10^{-1}	2.06×10^{-1}	1.0353
91.2	2.15×10^{-2}	4.87×10^{-3}	1.19×10^{-5}	7.37×10^{-1}	2.37×10^{-1}	1.0269
94.7	1.24×10^{-2}	4.24×10^{-3}	1.05×10^{-5}	7.42×10^{-1}	2.41×10^{-1}	1.0238
97.9	4.42×10^{-3}	3.28×10^{-3}	8.17×10^{-6}	7.47×10^{-1}	2.45×10^{-1}	1.0181
99.8	1.45×10^{-4}	1.40×10^{-3}	3.49×10^{-6}	7.51×10^{-1}	2.48×10^{-1}	0.9999

with an accuracy of 3 or more significant figures in the calculated equilibrium constants.

Results and Discussion

Case I.—The results of the all-graphical method discussed above as applied to the case where carbon deposition was prevented by recycling the oxidation products with methane as the fuel (at 500°K) are presented in Table I and are plotted in Fig. 5. One of the most interesting aspects of Fig. 5 is that the emf remains surprisingly constant throughout nearly the full oxidation range, varying from 1.036v at 0.0% oxidation to 1.006v at 99.0% oxidation. Of course, the voltage must decrease very rapidly as 100% oxidation is very closely approached. The partial pressure of H_2 at equilibrium is sufficiently high in the above methane fuel mixture that the fuel cell performance on this fuel should be nearly equivalent to the performance on hydrogen alone if chemical equilibrium can be maintained, and if there are no gas phase mass transport limitations. Figure 5 also shows that the CO partial pressure is low enough at equilibrium that electrodes sensitive to its presence (*e.g.*, Pt) should not be "poisoned."

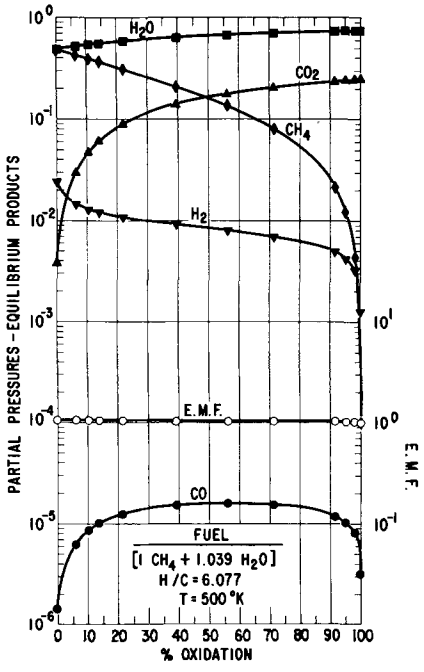

Fig. 6. Equilibrium gas compositions and cell potential as a function of per cent oxidation for a (1CH_4 + 1.039 H_2O) fuel, 500°K, 1 atm.

Case II.—The results of the combined algebraic and graphical method discussed earlier as applied to the case where carbon deposition was prevented by mixing water with the methane fuel (at 500°K) are presented in Table II and Fig. 6.

As in case I, it was found that the emf remained quite constant over nearly the full combustion range, varying from 1.0697v at 0.0% to 1.0135v at 99.0% oxidation. Again, the partial pressure of hydrogen is sufficiently high that the fuel cell performance might be expected to be considerably enhanced by its presence. On the average, the H_2 partial pressure for case II is about 1.7 times higher than for case I. An unexpected result was that the CO partial pressure showed a maximum, about an order of magnitude higher than its value at 0% oxidation. The general level of CO partial pressure is however very low from the standpoint of possible electrode "poisoning." In contrast to case I, CO_2 increases in partial pressure by about two orders of magnitude as the oxidation proceeds. This large change in CO_2 partial pressure is due to the fact that the fuel mixture of case I initially contained much more (combined) oxygen than was present in case II.

Theoretical Fuel Cell Potentials

The comparison of the emf values calculated for cases I and II as a function of per cent oxidation is shown in Fig. 7. These theoretical cell potentials were calculated from the equilibrium gas phase

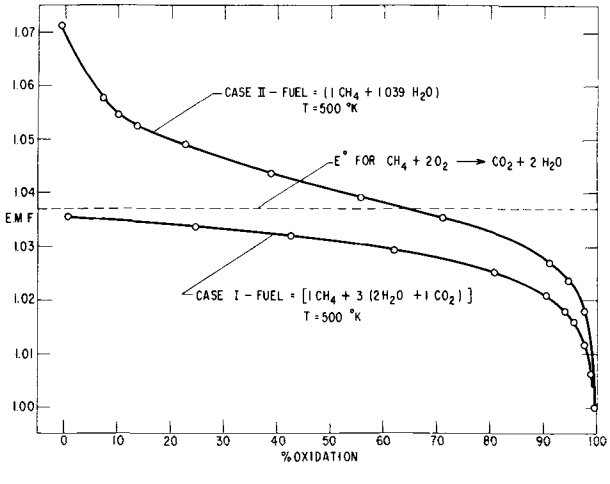

Fig. 7. Theoretical cell potentials for two fuel mixtures as a function of per cent oxidation (carbon free at equilibrium) at 500°K.

composition and the Nernst equation for a cell operating with 1 atm of oxygen at the cathode. As a reference, the dotted line in Fig. 7 shows the E° value at 500°K for the reaction

$$CH_4 + 2\,O_2 \rightarrow CO_2 + 2H_2O \qquad [4]$$

For case II, where water alone was added to the methane fuel, the theoretical cell potential lies above the E° value for reaction [4] up to 64.5% oxidation.

Summary and Conclusions

The conditions under which a fuel cell must be operated in order to prevent carbon deposition were calculated from our recent carbon deposition data for the CHO system. Two literature methods for calculations of CHO gas phase compositions in the absence of carbon were evaluated. An improved method based partially on one of the above methods was developed and illustrated. Examples of the two important methods for avoiding carbon deposition in a methane fuel cell at 500°K were calculated and compared in detail.

The conclusions drawn from the calculation are

1. Unexpectedly high and constant emf values (over a wide per cent oxidation range) were found for both of the methods of avoiding carbon deposition.

2. Appreciable (*ca.* 1%) amounts of hydrogen were present at equilibrium over essentially the full oxidation range. This could greatly enhance fuel cell performance on methane.

3. The levels of CO partial pressures at equilibrium were found to be very low ($\sim 10^{-5}$ atm) for all conditions considered, hence CO "poisoning" of fuel cell electrodes should not be a matter of concern so long as equilibrium is maintained.

Acknowledgments

The authors wish to thank H. A. Liebhafsky for his encouragement and support in this work. This work was supported in part by the Advanced Research Projects Agency (Order No. 247-61) through the United States Army Engineer Research and Development Laboratories, Ft. Belvoir, Va., under Contract No. DA-44-009-ENG-4853.

Manuscript received March 14, 1963; revised manuscript received May 10, 1963. This paper was presented at the Pittsburgh Meeting, April 15-18, 1963.

Any discussion of this paper will appear in a Discussion Section to be published in the June 1964 JOURNAL.

REFERENCES

1. V. S. Daniel-Bek, M. Z. Mints, V. V. Sysoeva, and M. V. Tikhonova, *Zhur. Priklad. Khim.*, **32**, 649 (1959).
2. C. G. Conway and H. H. Chambers, Proceedings from the International Symposium on Batteries, Christchurch, Hants, England (Oct. 1958).
3. G. H. J. Broers, Dissertation, Univ. of Amsterdam (1958).
4. H. H. Chambers and A. D. S. Tantram, Paper presented at Am. Chem. Soc. Meeting, Atlantic City (Sept. 1959).
5. D. L. Douglas, *Ind. Eng. Chem.*, **52**, 308 (1960).
6. E. B. Shultz, Jr., K. S. Vorres, L. G. Marianowski, and H. R. Linden, Paper presented at Am. Chem. Soc. Meeting, Chicago (Sept. 1961).
7. E. J. Cairns and A. D. Tevebaugh, Submitted to *J. Chem. Phys.*
8. E. J. Cairns and A. D. Tevebaugh, *ibid.*
9. B. J. Mayland and G. E. Hays, *Chem. Eng. Progr.*, **45**, 452 (1949).
10. C. W. Montgomery, E. B. Weinberger, and D. S. Hoffman, *Ind. Eng. Chem.*, **40**, 601 (1948).
11. R. E. Reitmeier, K. Atwood, H. A. Bennett, Jr., and H. M. Baugh, *ibid.*, **40**, 620 (1948).
12. K. Muraosa, *Kogyo Kagaku Zasshi*, **64**, 1782 (1961).
13. M. Greyson, J. J. Demeter, M. D. Schlesinger, G. E. Johnson, J. Jonakin, and J. W. Myers, Bur. of Mines Report 5137 (1955).
14. British Gas Research Board Communications, Vols. 11-20 (1944-1948).
15. S. R. Brinkley, Jr., and B. Lewis, Bur. of Mines Report 4806 (1952).
16. L. M. Naphtali, *J. Chem. Phys.*, **31**, 263 (1959).

On the Theory of Simultaneous Discharge of Metal Ions in Real Conjugated Systems

A. T. Vagramyan and T. A. Fatueva

Institute of Physical Chemistry, Academy of Sciences of the U.S.S.R., Moscow, U.S.S.R.

ABSTRACT

A differentiation is made in the theory of codischarge of ions in unconjugated and conjugated electrochemical reactions. It is shown that during simultaneous discharge of metal ions mutual effect takes place due to change in the state of ions in solution, change in concentration of discharged ions in the double layer, change in the substrate nature and the state of the electrode surface. As a result of these changes the reduction rates during simultaneous discharge of metal ions are different from those of separate discharge. An example of the electrodeposition of nickel and cobalt, nickel and iron showed that the reactions of coreduction of these ions are conjugated, and the usual theory of unconjugated systems is not applicable to them.

Simultaneous Discharge of Ions in Unconjugated Systems

According to the existing laws of electrode processes (1), the necessary condition for the simultaneous discharge of several types of ions is the equality of their potentials of reduction[1]

$$\psi_1^\circ + \frac{RT}{n\mathbf{F}} \ln a_1 - \eta_1 = \psi_2^\circ + \frac{RT}{n\mathbf{F}} \ln a_2 - \eta_2 \qquad [1]$$

where ψ_1^0, ψ_2^0, a_1, a_2, η_1, η_2 are, respectively, normal potentials, activities, and overvoltage for the first and second types of metal ions.[2] If it is assumed that the speed of the electrochemical reaction i [3] changes due to electrode potential (ψ) as follows $i = kce^{-\frac{\alpha\psi F}{RT}}$, then with a given electrode potential, it is possible to find the rate ratio of discharge of metal ions (2).

$$\frac{i_1}{i_2} = \frac{k_1 c_1 e^{-\frac{\alpha_1 \psi F}{RT}}}{k_2 c_2 e^{-\frac{\alpha_2 \psi F}{RT}}} \qquad [2]$$

Here it is assumed that the character of rate dependence of individual electrode reactions on the electrode potential remains the same, whether the ions are reduced separately or simultaneously.

Simultaneous Discharge of Ions in Conjugated Systems

As experimental results (3-5) indicate, during simultaneous discharge of metal ions under real conditions of electrolysis their mutual influence should be taken into consideration, since during codeposition changes take place in the substrate nature, the concentration of each ion in the double layer, and the state of ions in the solution.

Effect of Substrate Nature and the State of Electrode Surface on Speed of Ion Reduction

The effect of the nature of the substrate of the electrode on the reduction of metal ions may be of two kinds: (*a*) decrease in the potential of the electrode during simultaneous discharge in comparison with the equilibrium potential, owing to the alloy formation (depolarization) (6);[4] (*b*) increase in the electrode potential in comparison with the equilibrium potential due to the retardation of the electrochemical reaction (polarization).

In the case of the best known process of reduction of hydrogen ions, the rate of the electrochemical reaction, which depends on the electrode potential, changes in accordance with equation $i = ke^{-\frac{\alpha\psi F}{RT}}$; if we replace $k = e^{-a/6}$ and transform the equation, we get the well-known Tafel equation (8)

$$\psi - \psi^0 = \eta = a + b \ln i$$

where a shows the degree of retardation of the electrochemical reaction and depends on the substrate nature and the state of the metal surface; for instance, at 1 ma/cm^2 a varies from 1.56v for lead to 0.1 — 0.03v for the platinum group (9). Hence, it follows that a changes drastically depending on the nature of the metal.

It is obvious that constant a depends also on the state of the electrode surface. In some cases the reduction of the metal ions on the electrode surface adsorbed by foreign particles or on an oxidized surface is so difficult that metal practically does not deposit (10). For instance, the reduction of chromate ions on an oxidized surface in a solution of chromic acid is very difficult, and therefore it is the discharge of hydrogen ions that essentially takes place, in spite of the fact that the reduction potential is more negative. When the electrode surface is effectively scraped during the electrolysis cathode polarization decreases drastically and instead of the reduction of hydrogen ions a reaction $Cr^{6+} \rightarrow Cr^{3+}$ occurs. If the electrode that had been scraped off is left for some time in the electrolyte without current, it becomes passivated again, and the reduction of the chromate ion is retarded even when the electrode is polarized considerably higher. The effect of the electrode surface state on the electrode process during codeposition of nickel and molybdenum has been studied by Krasovsky (7). The important influence of the electrode surface state on the reduction rate of metal ions is also evident when studying electrodeposition of silver (10), nickel (11), manganese (12), alloys, etc.

Since, during codischarge of metals, the nature and surface state of the electrode differ from those which take place during deposition of separate components, it is necessary to substitute values (η_1) and (η_2) in Eq. [1] by the corresponding values of overvoltage on the alloy (η_1 alloy) and (η_2 alloy).

Change is Concentration of Ions Discharged in Double Layer

The rate of reduction of ions depends on their concentration in the double layer, but not on the concentration in the solution. As is well known, the ion concentration in the double layer (C_s) related to the concentration in the solution (C_v) for the simplest case by the following equation (8)

$$C_s = C_v e^{-\frac{F\psi}{RT}}$$

When the electrode polarization is constant, the concentration of each ion type in the double layer during codischarge of ions is less than during separate reductions, due to partial replacement of some ions by others. The degree of replacement of one type of ions in the double layer by ions of another type depends on the ion nature (radius, valency of ions, degree of ion hydration-factor α). It is evident that $\epsilon\alpha_i = 1$. As a result of this replacement the concentration of each type of discharging ion in the double layer decreases at a given overvoltage. This results in lowering the reduction rate of each type of metal ion during simultaneous discharge in comparison with separate reduction.

Figure 1 shows the dependence of nickel ion reduction rate on concentration of cobalt sulfate additions. The curves were obtained potentiostatically at 650 mv (*vs.* NHE) in 1*N* solution of nickel sulfate with *p*H 1.9 and with a different concentration of cobalt sulfate.

Curve 1 shows the change in the current used to discharge the ions with the addition of cobalt sulfate.

[1] It is obvious that this condition is not applicable when interaction of the reduced ions in the solution or of metal atoms in the deposit takes place.

[2] Hereafter ion concentration is given instead of ion activity.

[3] Reaction speed in the kinetics of the electrode processes is characterized by current density, *i*.

[4] A record of the depolarization action of the substrate during simultaneous discharge was proposed by Krasovsky (7).

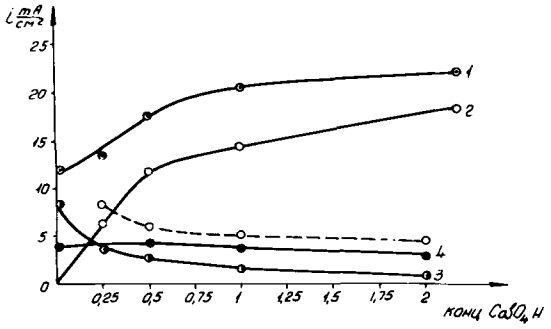

Fig. 1. Change of current for discharging Ni^{2+}, Co^{2+} and H^+ ions, depending on concentration of $CoSO_4$ added to solution of $NiSO_4$ during electrolytic codeposition. ψ_{const} 650 mv (NHE), pH 1.9, temperature 25°: curve 1, over-all curve; 2, discharge of Co^{2+} ions; 3, discharge of Ni^{2+} ions; 4, discharge of H^+ ions; dotted curve, calculated values.

Curves 2, 3, and 4 show the current used to discharge cobalt, nickel, and hydrogen, respectively. The rate of hydrogen reduction practically does not depend on the concentration of the salt additions (curve 4). When cobalt salts are added to the electrolyte in the amount of, say, 0.5N, the total current density increases from 12.2 to 17.5 ma/cm². However, the current used to reduce nickel decreases from 8.3 to 2.5 ma/cm² which is 3.3 times lower.

A similar retardation is observed in the course of a potentiostatic study of the reduction rate of the cobalt ions caused by the addition of nickel sulfate (Fig. 2). As can be seen from these curves, the addition of nickel salts sharply decreases the total current (curve 1) as well as that part of the current which is used to discharge the cobalt ions (curve 2), although the total concentration of ions in the electrolysis not only does not decrease, but even increases. The lowering in rate of cobalt ions reduction in this case can be accounted for only by the fact that part of the cobalt ions in the double layer are replaced by nickel ions, the reduction of which requires higher activation energy than the reduction of cobalt ions.

If we assume that with the concentration being equal the probability of nickel and cobalt ions getting into the double electrical layer is the same, it

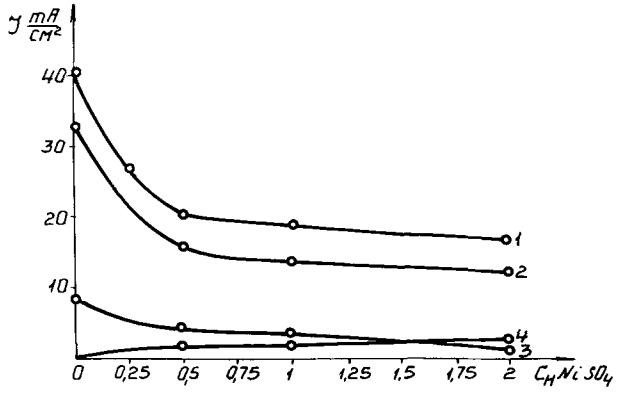

Fig. 2. Change of current for discharging Co^{2+}, Ni^{2+}, and H^+ ions, depending on concentration of $NiSO_4$ added to 1N solution $CoSO_4$ during electrolytic codeposition. ψ_{const} 606 mv (NHE), pH 1.9, temperature, 25°: curve 1, over-all curve; 2, discharge of Co^{2+} ions; 3, discharge of H^+ ions; 4, discharge of Ni^{2+} ions.

is possible to calculate the partial polarization of each ion type during codeposition. It is evident that it will be proportional to their concentration ratio in the electrolyte, if the rate of the electrochemical process is not limited by diffusion of the ions. The decrease in polarization of one ion type with the entry of another ion type into the double electric layer, taking into consideration penetration factor α, will amount to

$$\frac{RT}{n\mathbf{F}} \ln C_1 - \frac{RT}{n\mathbf{F}} \ln \frac{\epsilon\alpha_i C_i}{\alpha_1 C_1} = \frac{RT}{n\mathbf{F}} \ln \frac{\alpha_1 C_1}{\epsilon\alpha_i C_i} C_1$$

It is evident that in accordance with the decrease in this partial potential the reduction rate of a given ion type will decrease, if the total potential is maintained strictly constant.

If we assume that $\alpha_{Ni} = \alpha_{Co}$ and that the substrate nature does not substantially effect the deposition rate of cobalt and nickel ions, *i.e.*, that no depolarization takes place, it is possible to calculate the decrease of reduction rate of one ion type when co-discharged with other ions. The dotted line on Fig. 1 corresponds to this calculated value. It can be seen from Fig. 1 that the calculated value (dotted line), although considerably different from the experimental data, yields the same general character of relationship.[5] In view of the fact that the reduction rates of metal ions when codischarged differ from those that are discharged separately, due to the changes of ion concentration in the double layer, it is necessary to substitute $RT/n\mathbf{F}$ ln C in Eq. [1] by

$$\frac{RT}{n\mathbf{F}} \ln \frac{\alpha_1 C_1}{\epsilon\alpha_i C_i} C_1.$$

Galvanostatic studies of the speed of simultaneous and separate discharge of cobalt and nickel ions (Fig. 3) have shown that not only is the rate of nickel reduction decreased, but the character of dependence of the discharge speed on the potential also changes in comparison with the separate reduction of nickel. For instance, when $\psi = -650$ mv (Fig. 3), the rate of nickel discharge is reduced 10.5 times when codeposited with cobalt; at a potential of 550 mv the discharge speed of cobalt is decreased 16 times; at higher potentials the speed of cobalt discharge from a 2N solution is considerably higher and is incommensurable with the conjugated curve, as can be seen on Fig. 3. The change in rate correlation of the reduction of nickel and cobalt ions and the electrode potential shows that the delay in the process depends not only on the change in the ion concentration near the electrode layer, but on the change of the substrate nature as well. The discrepancy between experimental and calculated data (Fig. 1) also indicates that the change in the substrate nature affects the reduction rate of the metal ions.

In view of the above it would be correct, instead of using Eq. [1], to use the following expression which characterizes the condition for codischarge of ions in real conjugated systems (5):

[5] This discrepancy may be partially due to the fact that the calculation did not take into account the concentration of hydrogen ions.

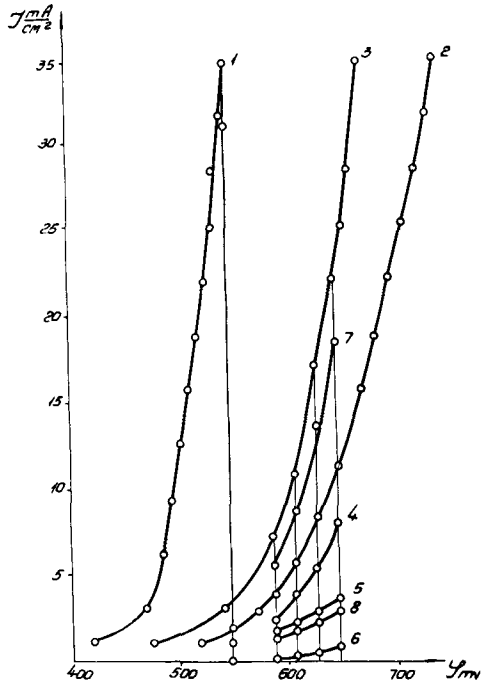

Fig. 3. Variation in current with electrode potential used to discharge Co^{2+}, Ni^{2+}, and H^+ ions in their simultaneous and separate deposition: curve 1, curve for the discharge of Co^{2+} from 2N $CoSO_4$; 2, over-all curve for the discharge of Ni^{2+} and H^+ from 1N $NiSO_4$; 3, over-all curve for the discharge of Ni^{2+}, Co^{2+}, and H^+ from 1N $NiSO_4$ + 1N $CoSO_4$; 4, partial curve for the discharge of Ni^{2+} from 1N $NiSO_4$; 5, partial curve for the discharge of H^+ from 1N $NiSO_4$; 6, partial curve for the discharge of Ni^{2+} from 1N $NiSO_4$ and 2N $CoSO_4$; 7, partial curve of the discharge of Co^{2+} from 1N $NiSO_4$ and 2N $CoSO_4$; 8, partial curve for the discharge of H^+ from 1N $NiSO_4$ and 2N $CoSO_4$

$$\psi_1^\circ + \frac{RT}{n\mathbf{F}} \ln \frac{\alpha_1 C_1}{\epsilon \alpha_i C_i} \cdot C_1 - \eta_1 \text{ alloy} = \psi_2^\circ + \frac{RT}{n\mathbf{F}} \ln \frac{\alpha_2 C_2}{\epsilon \alpha_i C_i} \cdot C_2 - \eta_2 \text{ alloy} \quad [3]$$

Since, during simultaneous discharge, overvoltage may either increase or decrease, depending on the changes in the substrate nature, the following cases are possible in real conditions of codeposition of metals:

1. When

$$\eta_1 \text{ alloy} + \eta_2 \text{ alloy} << \psi_1^\circ + \frac{RT}{n\mathbf{F}} \ln \frac{\alpha_1 C_1}{\epsilon \alpha_i C_i} \cdot C_1 + \psi_2^\circ + \frac{RT}{n\mathbf{F}} \ln \frac{\alpha_2 C_2}{\epsilon \alpha_i C_i} \cdot C_2$$

the rate of discharge of more electropositive metal ions is higher than the speed of discharge of more electronegative ions.

2. When

$$\eta_1 \text{ alloy} + \eta_2 \text{ alloy} >> \psi_1^\circ + \frac{RT}{n\mathbf{F}} \ln \frac{\alpha_1 C_1}{\epsilon \alpha_i C_i} \cdot C_1 + \psi_2^\circ + \frac{RT}{n\mathbf{F}} \ln \frac{\alpha_2 C_2}{\epsilon \alpha_i C_i} C_2 \text{ and } \eta_1 \text{ alloy} > \eta_2 \text{ alloy}$$

the rate of discharge of more electronegative metal ions is higher than the rate of more electropositive ions.

Thus, in real conjugated systems, as a result of the influence of the substrate nature on the overvoltage, a change in the reduction speed of both more positive and more electronegative metal ions over a wide range is possible.

Indeed, as has been observed by Glasstone, Symes, and others (13, 14), when nickel and iron are codeposited, the iron concentration in the alloy is much higher than that of nickel, although the reduction potential of the nickel ion, when deposited separately, is more positive than when iron ions are reduced.

In order to compare the reduction rate of nickel and iron during simultaneous and separate reduction, we have studied the dependence of the speed of these reactions on the electrode potential. Results of separate deposition of nickel (curve 1) and iron (curve 3) as well as of their codischarge (curve 2) are shown in Fig. 4.

Figure 4 shows that the discharge rate of iron ions when codeposited with nickel (curve 6) is considerably higher than that of nickel (curve 7). According to Eq. [1] there should be an inverse relationship between the deposition rates of nickel and iron.

From the data given in Table I it can be seen that at a cathode potential of $\psi = -730$ mv (with reference to the hydrogen electrode) the rate of discharge of iron ions determined by the current density corresponds to 4.5 ma/cm² during separate reduction and to 13.6 during coreduction. Thus, when iron is

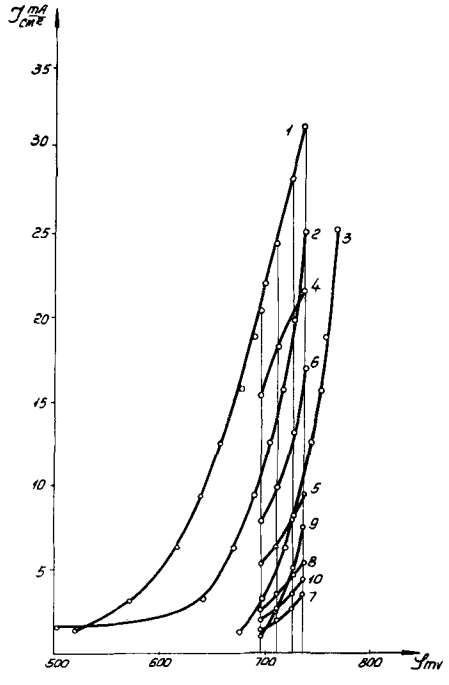

Fig. 4. Dependence of speed of reduction of ions of iron and nickel on electrode potential, pH 1.9, temperature, 25°: curve 1, over-all curve for discharge of Ni^{++} and H^+ ions from 1N $NiSO_4$; curve 2, over-all curve for discharge of Fe^{++}, Ni^{++}, and H^+ ions from solution 1N in $FeSO_4$ and 1N in $NiSO_4$; 3, over-all curve for discharge of Fe^{++} and H^+ ions from 1N $FeSO_4$; 4, partial curve of discharge of Ni^{++}: ions from 1N $NiSO_4$; 5, partial curve for discharge of H^{++} ions from 1N $NiSO_4$; 6, partial curve for discharge of Fe^{++} ions from 1N $FeSO_4$ and 1N $NiSO_4$; 7, partial curve for discharge of Ni^{++} ions from 1N $NiSO_4$ and 1N $FeSO_4$; 8, partial curve for discharge of H^+ ions from 1N $NiSO_4$ + 1N $FeSO_4$; 9, partial curve for discharge of Fe^{+++} ions from 1N $FeSO_4$; 10, partial curve for discharge of H^+ ions from 1N $FeSO_4$.

Table I. Distribution of current between separate reactions when electrodeposition of iron and nickel is carried out both separately and together

(cathode potential, —730mv)

Type of electrodeposition	Speed of ion reduction, ma/cm² Fe^{2+}	H^+	Ni^{2+}	Total speed of electro-deposition, ma/cm²
Iron without nickel	4.5	4.4	—	8.9
Nickel without iron	—	7.9	20.8	28.7
Iron with nickel	13.6	4.5	2.6	20.7

reduced together with nickel, the rate of reduction of iron ions becomes three times as high and the rate of discharge of nickel ions decreases at this potential from 20.8 to 2.6 ma/cm² which is approximately eight times as low. The rate of discharge of hydrogen ions with simultaneous reduction of nickel is 7.9 ma/cm², and that of reduction of hydrogen with iron 4.4 ma/cm²; in the case of codischarge of the ions of nickel and iron it is 4.5 ma/cm². From these data it is evident that hydrogen with nickel is reduced at a much higher rate than with iron. During the simultaneous reduction of iron and nickel ions, the reduction rate of the hydrogen ions is far less than in the case of nickel and somewhat higher than in the case of iron.

The results of codeposition of nickel and iron show the "anomalous" retardation of the discharge speed of nickel ions and the "facilitation" of the discharge of iron ions. This anomaly depends on the various degrees of retardation of the discharge of metal ions during codeposition. Therefore, when conditions allow the decrease of overvoltage during reduction, it may be expected that this anomaly will be eliminated.

High overvoltage during the reduction of metal of the iron group, as was shown in a number of papers (10, 15), depends on the inhibiting action of foreign substances (hydroxide, hydrogen) adsorbed on the electrode surface, which influence the reduction rate of the metal ions. With an increase in temperature, the irreversible adsorption of hydrogen (16) and hydroxides is drastically decreased; hence the inhibiting action of foreign particles and overvoltage (17) is also decreased. Therefore, when co-

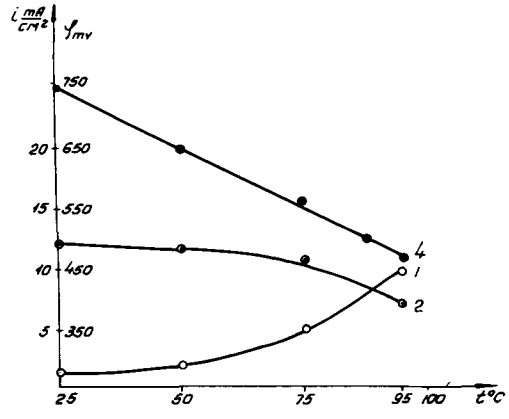

Fig. 5. Dependence of speed of reduction of Ni^{2+} ions (curve 1) and Fe^{2+} (curve 2) during codischarge upon temperature and change of electrode potential ψ (curve 4) in solution 1N $NiSO_4$, 1N $FeSO_4$. 30 g/l H_3BO_3, pH 1.9.

depositing nickel with iron at a low voltage, the anomaly referred to may be eliminated, *i.e.*, the alloy will contain more nickel than iron (5).

As can be seen from Fig. 5, with the temperature increase the potential of alloy deposition decreases and the discharge of the nickel ions is facilitated. Therefore, when the electrolyte temperature is about 100° at a current density of 20 ma/cm², the alloy contains more nickel than iron.

Thus the "anomalous" reduction rates of iron and nickel ions in accordance with Eq. [3] depend on the change of the overvoltage during codischarge. The overvoltage in this case depends on the state of the electrode surface during electrolysis, but not on the retarding effect on the change of metastable to stable nickel with the result that the further deposition of this metal is inhibited (13). Therefore, any addition agent which is not reduced on the electrode, but affects the state of the electrode surface and the overvoltage, may change the metal relationship in the alloy.

The above experimental results show that the theory of real conjugated systems makes a better allowance for the regularity of codischarge of metal ions.

Summary

1. It has been shown that when nickel and cobalt are codeposited the rate of each electrochemical reaction is retarded compared with the separate reduction of each ion.

2. It has been established that, for a given overall electrode polarization during codischarge, retardation of the separate reactions depends on the decrease of the ion concentration in the double layer.

3. It has been shown that the anomalous correlation of rates during codeposition of nickel and iron depends on causes which produce high overvoltage of the discharge of ions. During electrolysis, when the overvoltage is sharply reduced, this anomaly is eliminated.

4. An equation has been proposed which makes a better allowance for the conditions of metal deposits in real conjugated systems.

Manuscript received June 29, 1962; revised manuscript received April 30, 1963. This paper was presented before the Boston Meeting, Sept. 16-20, 1962.

Any discussion of this paper will appear in a Discussion Section to be published in the June 1964 JOURNAL.

REFERENCES

1. S. Glasstone, "An Introduction to Electrochemistry," D. Van Nostrand Company, Inc., New York (1942); C. L. Faust, "Modern Electroplating," p. 64 A. G. Gray, Editor, John Wiley & Sons, Inc., New York (1953); R. Kremann and R. Muller, "Elektromotorische Krafte Elektrolyse und Polarisation," Part 2, Akademische Verlagsges m.b.H., Leipsig (1931); V. V. Skorshelletti, "Teoreticheskaya Elektrokhimiya," (Theoretical Electrochemistry), Gosudarst. Nauch. Tekhn. Izdatel. Khim. Lit., Leningrad (1959).
2. O. A. Esin, *Z. Fiz. Khim.*, **6**, 795, (1935); **7**, 1071 (1936); **8**, 326 (1937); V. L. Kheifetz and A. L. Rotinyan, *Proc. Institute "Gipronikel,"* (1958).
3. A. T. Vagramyan and A. T. Fatueva, *Zhur. Neorg. Khimii*, **4**, 1281 (1959).
4. A. A. Fatueva and A. T. Vagramyan, *Doklady Akad. Nauk SSSR*, **128**, 773 (1959); A. T. Vagramyan

and T. A. Fatueva, *Z. physik Chem.* (Leipzig), **216**, 163 (1961).
5. A. T. Vagramyan and T. A. Fatueva, *Doklady Akad. Nauk SSSR*, **135**, 1413 (1960).
6. Haber and Sack, *Z. Elektrochem.*, **8**, 251 (1902); Bredig and Haber, *Ber.*, **31**, 2741 (1898).
7. A. I. Krasovsky, Proc. Fourth Conference on Electrochemistry, Izdat Akad. Nauk SSSR, 530 (1959).
8. Tafel, *Z. phys. chem.*, **50**, 641 (1905).
9. A. N. Frumkin, B. S. Bagotsky, Z. A. Ioffe, and B. N. Kabanov, "Kinetics of Electrode Processes," Izdat. MGU (1952).
10. A. T. Vagramyan and L. A. Uvarov, *Trans. Inst. Met. Finishing*, **39**, 56 (1962); A. T. Vagramyan, *Z. Fiz. Khim.*, **19**, 305 (1945); A. B. Price and D. A. Vermilyea, *J. Chem. Phys.*, **28**, 720 (1958).
11. A. I. Krasovsky, G. I. Kobosnidze, and A. T. Vagramyan, *Z. Fiz. Khim.*, **36**, 714 (1962).
12. A. T. Vagramyan, A. I. Krasovsky, Y. S. Petrova, and Z. A. Solovieva, *ibid.*, **34**, 1255 (1960).
13. S. Glasstone and T. E. Symes, *Trans. Faraday Soc.*, **23**, 213 (1927); **24**, 370 (1928).
14. R. Kremann and R. Maas, *Monatshefte f. Chemic.*, **35**, 731 (1914); H. W. Toepffer, *Z. Elektrochem.*, **6**, 324 (1899); F. W. Kuester, *ibid.*, **7**, 257 (1900).
15. A. T. Vagramyan and L. A. Uvarov, *Doklady Akad. Nauk SSSR*, **146**, 635 (1962).
16. N. Kavtaradze, *Z. Fiz. Khim.*, **32**, 909, 1214 (1958).
17. A. T. Vagramyan and Yu. S. Petrova, "Physico-Mechanical Properties of Electrodeposits" (in Russian), Izdat. Akad. Nauk SSSR, Moscow (1960). English translation, Consultants Bureau, New York (1962); A. T. Vagramyan and Z. A. Solovieva, "Technology of Electrodeposition," p. 398, Robert Draper Ltd., Teddington (1961).

The Kinetics of the Electrodeposition and Dissolution of Metal Monolayers as a Function of Dislocation Density

A. Damjanovic and J. O'M. Bockris

The Electrochemistry Laboratory, The University of Pennsylvania, Philadelphia, Pennsylvania

ABSTRACT

The mechanism and the kinetics of the short time metal deposition and dissolution has been analyzed on the basis of a model which includes transfer of ions across the double layer, diffusion of adions over the metal surface, and incorporation of ions into the lattice at steps one atom high. It is shown that it is possible to obtain data on the exchange current density of the reaction and on the equilibrium adion concentration from the initial portion of the potentiostatic transients. Steady-state current density is analyzed. Conditions necessary for the surface diffusion of adions or for the transfer of ions across the double layer to be the rate-controlling step in the over-all reaction are formulated and discussed. Current density at each potential depends on distances between the steps suitable for the incorporation of adions into the lattice, which distances are related in turn to the dislocation density. On an ideal surface, without nucleation, the steady-state current density should be zero. Conditions for two-dimensional nucleation are analyzed and discussed.

Some attention has been given recently to the problem of determining the path and rate-controlling step in mechanisms of electrochemical metal dissolution and deposition from solutions.

Concepts, *e.g.*, surface diffusion, growth steps (1-4), and dislocation densities (5) previously used in the theory of the growth of metals from the vapor (6-8), have been introduced into the electrode kinetics associated with metal deposition and dissolution. Lorenz (2) obtained a relation between current density and distance between growth steps for steady-state deposition, under surface diffusion control. Mehl and Bockris (1) analyzed deposition mechanisms under galvanostatic transient and steady-state conditions, near the reversible potential, and showed that (for Ag in $AgClO_4$ + $HClO_4$ solutions) rise times of the potential much greater than those to be expected for rate-determining charge transfer are consistent with rate-determining surface diffusion. They deduced for the first time the concentration of adions on the electrode surface. At high current densities, charge transfer was found to become rate-controlling. Independently, and with a different mathematical treatment, Gerischer (4) also suggested the same rate-controlling step for low current densities. Despic and Bockris (3) showed that, with a constant potential on the electrode surface, the local current density at steady state changes with position in respect to a step and can be much higher near growth steps than elsewhere. Kita, Enyo, and Bockris (5) related the number of growth steps to the dislocation density and showed that depending on the overpotential not all the steps may be active [cf. Cabrera and Burton (7)].

Fleischmann and Thirsk (9) considered transient and steady-state kinetics with rate-controlling surface diffusion and developed an expression for the steady-state deposition velocity as a function of the distance between spiral arms. Mott and Watts-Tobin (10) deduced conditions under which surface diffusion will occur [cf. Mehl and Bockris (1)]; they confirmed the conclusion of Despic and Bockris (3) concerning the concentration of current close to growth steps under surface diffusion control, but considered that deposition could occur directly from

the Helmholtz layer onto a kink site [cf. Conway and Bockris (11)]. Vermilyea (12) showed that on a dislocation free surface no deposition should occur below a critical overvoltage, and established this point experimentally using copper whiskers (13). Many examinations have been made of electrochemical crystal growth (the steps following those considered in this paper), but little progress has been made in the determination of molecular mechanisms of this process [cf. Seiter, Fischer, and Albert (14) and Pick, Storey, and Vaughan (18)].

A number of problems remain unsolved from these recent investigations of the kinetics of the formation of "monolayers." The effect of dislocation density on the kinetics is unexplored (5). Conditions for the onset of nucleation have not been worked out. The current-time transient as a function of dislocation density has not been developed. The transition from surface diffusion control to transfer control remains unexplained. Utilizing the model of Despic and Bockris these problems are here analyzed.

Transient Potentiostatic Polarization

Basic equation for the rate of charge transfer as a function of time and position.—Initially, after the commencement of polarization, the surface adion concentration is near to equilibrium. If, however, the rate constant for surface diffusion is much less than i_o, a change of adion concentration between growth steps with time will occur. In this section, the variations of the adion concentration with time and distance from the growth steps are analyzed. The cathodic partial current density (between growth steps) is considered independent of the distance from a growth step for low coverages with adions; the anodic partial current density is, however, proportional to the adion concentration, and thus is a function of time and the position between growth steps [cf. Despic and Bockris (3)]. Hence, the net, Faradaic current density also changes with time and the distance from a growth step. The variation of adion concentration with time t and at position x (see Fig. 1) is equal to the sum of the net charge transfer rate and of the divergence of the adion flux at the same position (2, 3, 9)

$$\frac{\partial c(x,t)}{\partial t} = \frac{i(x,t)}{zF} + D\frac{\partial^2 c(x,t)}{\partial x^2} \qquad [1]$$

The diffusion coefficient, D, is taken independent of adion concentration, $c(x,t)$. The net current density of charge transfer, $i(x,t)$ is, for the conditions stated above, given by (3, 9)

$$i(x,t) = i_o\left\{\exp\left(\frac{-\beta zF\eta}{RT}\right) - \frac{c(x,t)}{c_o}\exp\left[(1-\beta)\frac{zF\eta}{RT}\right]\right\} \qquad [2]$$

where β, z, F, R, and T have their usual meaning, η is the constant overpotential, and c_o is the equilibrium adion concentration.

It is assumed that the adion concentration at steps does not change with time and is always at the equilibrium concentration, which is tantamount to the assumption that the incorporation of adions into the lattice at steps is very fast. If the origin of the coordinate system is chosen at the mid-point between two growth steps, at distance $2x_o$ apart (Fig. 1), then the initial and boundary conditions for the differential Eq. [1] are

$$c(x,o) = c_o,$$
$$c(\pm x_o,t) = c_o, \text{ and}$$
$$\left[\frac{\partial c(x,t)}{\partial x}\right]_{x=0} = 0 \qquad [2a]$$

The third boundary condition states that at $x = 0$ the adion concentration reaches a maximum (in the cathodic area) or a minimum value (in the anodic case). With these, the solution of Eq. [1] is (see Appendix)

$$c(x,t) = A + B\cosh(mx) + \frac{2B'm^2x_o^2}{\pi}\sum_{o}^{\infty}\frac{(-1)^n\cos[(n+1/2)\pi x/x_o]}{(n+1/2)[(n+1/2)^2\pi^2+m^2x_o^2]}\cdot\exp\left[\left(-\frac{(n+1/2)^2\pi^2D}{x_o^2}-p\right)t\right] \qquad [3]$$

where

$$A = c_o\exp\left(-\frac{zF\eta}{RT}\right)$$
$$B = \frac{c_o\left[1-\exp\left(-\frac{zF\eta}{RT}\right)\right]}{\cosh(mx_o)}$$
$$B' = c_o\left[1-\exp\left(-\frac{zF\eta}{RT}\right)\right]$$
$$p = \frac{i_o}{zFc_o}\exp\left[(1-\beta)\frac{zF\eta}{RT}\right]$$

and

$$m = \sqrt{\frac{p}{D}} \qquad [3a]$$

Equation [3] gives the change of adion concentration with time at any point between growth steps.

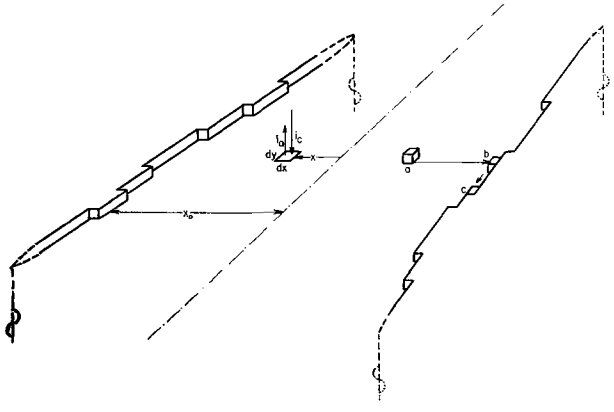

Fig. 1. Illustration of the model for electrodeposition. At the element of the electrode surface dxdy, number of arriving ions, represented as i_c, is greater than the number of ions escaping back to the solution, represented as i_a. The net charge transfer across the double layer at the point x on the surface is given by the difference $i_c - i_a$. Adions (a), diffuse to the step (a to b) formed between two screw dislocations of opposite sign, and along the step to the kink site (b to c) where they become incorporated into the lattice.

Since short time polarization only is considered, the surface structure will not be altered appreciably (see section on Rise time under potentiostatic conditions, below). The distance between growth steps, $2x_o$, can then be simply related to the density of dislocations. A surface is intersected by a number of dislocations with screw component perpendicular to it, and steps are produced between two emerging screw dislocations of opposite sign. In order to minimize the surface energy, the steps should tend to become straight when an electrode surface remains in contact with a solution, in the absence of net current. Straightening of a step in solution should be fast [~ order of minutes (12)] particularly if the exchange current, i_o, is high. Assuming a random distribution of dislocations the average distance between straight steps may then be related to the number of dislocations per square centimeter, N, terminating on the surface and producing growth steps.[1] Thus, to a first approximation

$$x_o = \frac{1}{2\sqrt{N}} \qquad [4]$$

By replacing x_o with $\frac{1}{2\sqrt{N}}$ and rearranging, Eq. [3] transforms to

$$c(x,t) = A + B\cos(mx) + \frac{2B'p}{\pi} \cdot \sum_{n=0}^{\infty} \frac{(-1)^n \cos[(2n+1)\pi x\sqrt{N}]}{(n+1/2)[(2n+1)^2\pi^2 ND + p]} \cdot \exp\{-[(2n+1)^2\pi^2 ND + p]t\} \qquad [5]$$

The net current density as a function of time and position, $i(x,t)$, is obtained from [2] and [5] as

$$i(x,t) = zF\left\{-Bp\cos(mx) - \frac{2B'p^2}{\pi} \cdot \sum_{n=0}^{\infty} \frac{(-1)^n \cos[(2n+1)\pi x\sqrt{N}]}{(n+1/2)[(2n+1)^2\pi^2 ND + p]} \cdot \exp\{-[(2n+1)^2\pi^2 ND + p]t\}\right\} \qquad [6]$$

At a sufficiently early time after application of a constant potential, [6] reduces in the limit $t \to 0$, to[2]

$$i(x,o^+) = i_o\left\{\exp\left(-\frac{\beta zF\eta}{RT}\right) - \exp\left[\left(1-\beta\right)\frac{zF\eta}{RT}\right]\right\} \qquad [7]$$

where o^+ represents the time just after the cessation of double layer charging. (The time necessary to charge the double layer can be made less than 1 μsec.) Thus, at this time, transfer across the double layer is the rate-controlling step, and the local charge transfer rate is independent of the distance from the growth step. With increasing time, the local current density at steps (in the sense of rate of charge transfer), as obtained by replacing x with x_o in Eq. [6], remains constant and is given by the right hand side of Eq. [7]. At the midpoints between growth steps, the current density changes with time and is given by

$$i(o,t) = zF\left\{-Bp - \frac{2B'p^2}{\pi}\sum_{n=0}^{\infty} \frac{(-1)^n \exp\{-[(2n+1)^2\pi^2 ND + p]t\}}{(n+1/2)[(2n+1)^2\pi^2 ND + p]}\right\} \qquad [8]$$

This equation shows that the net rate of charge transfer at midpoints between steps decreases with time toward the steady-state value both during deposition and dissolution. The ratio of the current densities at $x = 0$ and $x = x_o$

$$\frac{i(o,t)}{i(x_o,t)} = \operatorname{sech}\sqrt{\frac{p}{4ND}} + \frac{2p}{\pi}\sum_{n=0}^{\infty} \frac{(-1)^n \exp\{-[(2n+1)^2\pi^2 ND + p]t\}}{(n+1/2)[(2n+1)^2\pi^2 ND + p]} \qquad [9]$$

is less than unity and similarly decreases with time. The current density at the midpoint between two growth steps depends on the values of N, D, and of overpotential, and can reach very low values.

In Fig. 2, $c(x,t)$ and $i(x,t)$ are plotted *vs.* x for two values of ND and for η values + 30 mv and − 30 mv. These results are discussed later.

Average rate of charge transfer as a function of time.—The average rate of charge transfer over the whole surface (per square centimeter) as a function of time, $i(t)$, can be obtained by integrating [6] from 0 to x_o and dividing by x_o

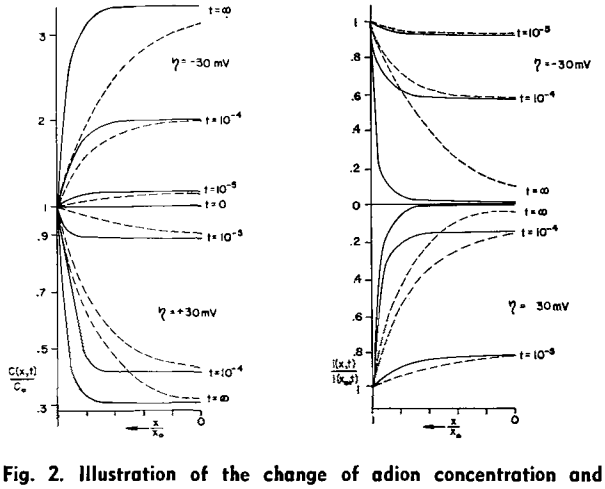

Fig. 2. Illustration of the change of adion concentration and current density with time (in seconds) and with the distance from the growth steps for two values of ND and overpotential of ± 30 mv. The current density close to steps is controlled by transfer reaction. Full lines are for $ND = 1$ sec^{-1}, dashed lines for $ND = 10^2$ sec^{-1}. i_o is taken as 100 ma/cm^{-2} and c_o as 10^{-10} mole/cm^2.

[1] N will be less than the density of dislocation, probably by an order of magnitude, since only a fraction of dislocations emerging on the surface produce steps suitable for growth. The objective here is to calculate the change of adion concentration with dislocation density under the nonequilibrium conditions. At equilibrium, the adion concentration is taken as independent of the dislocation density. In this treatment, all the steps are considered available for growth and hence are "active," or in other words, no potential dependence of the "activity" of growth steps is considered [*e.g.*, Kita, Enyo, and Bockris (5)]. The effect of the potential on the "activity" of growth steps is important only in the detailed interpretation of phenomena at low overpotentials and for high dislocation densities, and need not, therefore, be taken into account here.

[2] It can be shown that:

$$1 - \frac{\cosh(mx)}{\cosh(mx_o)} = \frac{2p}{\pi}\sum_{n=0} \frac{(-1)^n \cos[(2n+1)\pi x\sqrt{N}]}{(n+1/2)[(2n+1)^2\pi^2 ND + p]}$$

$$i(t) = -2zFB'\sqrt{NDp}\tanh\sqrt{\frac{p}{4ND}} - \frac{2zFB'p^2}{\pi^2} \sum_{n=0}^{\infty} \frac{\exp\{-[(2n+1)^2\pi^2ND+p]t\}}{(n+1/2)^2[(2n+1)^2\pi^2ND+p]} \quad [10]$$

During potentiostatic transients two processes may be distinguished: (*a*) the adion concentration will change; and (*b*) the adions will diffuse to steps and will become incorporated into the lattice, if deposition is considered; or, atoms in the steps will leave the lattice to form adions, if dissolution is considered. The average rate at which the adion concentration builds up or decreases is expressed in terms of current density as

$$i_{ad,t} = -\frac{2zFB'p}{\pi^2} \sum_{n=0}^{\infty} \frac{\exp\{-[(2n+1)^2\pi^2ND+p]t\}}{(n+1/2)^2} \quad [11]$$

Correspondingly, the rate at which adions diffuse to, or away from, steps is given by

$$i_{lat,t} = 2LzFD\left[\frac{\partial c(x,t)}{\partial x}\right]_{x=-x_0} \quad [12]$$

Here, L is the total length of steps per cm², and to a first approximation can be related to the distance between steps, $2x_0$, by the equation

$$L \cdot 2x_0 = 1 \quad [13]$$

Differentiating [5] with respect to x, and using [13], Eq. [12] becomes

$$i_{lat,t} = -2zFB'\sqrt{NDp}\tanh\sqrt{\frac{p}{4ND}} + 8zFB'NDp \sum_{n=0}^{\infty} \frac{\exp\{-[(2n+1)^2\pi^2ND+p]t\}}{(2n+1)^2\pi^2ND+p} \quad [12a]$$

For the first instant ($t = 0^+$) after application of a constant overpotential, the right hand side of Eq. [12a] reduces to zero,[4] and Eq. [10] and [11] reduce to Eq. [7], meaning that, at this time, transfer across the double layer is rate controlling (see above), and all the current is used to change the adion concentration. With increasing time, $i_{ad,t}$ (Eq. [11]), and the second term in Eq. [12a] diminish, attaining zero value at steady-state. Thus, no further build up of adions occurs, and the rate of the process is controlled by the rate of adion diffusion to, or away from, the steps.

Therefore, it may be concluded that whenever surface diffusion of adions is a slow process in comparison with the transfer of ions across the double layer, the rate of deposition or dissolution process during the potentiostatic transients will be controlled at the beginning by the transfer of ions across the double layer, and later on by surface diffusion of adions. Conditions under which surface diffusion will be the fast process are discussed in the section on Anodic polarization, below.

[3] Fleischmann and Thirsk (9) arrived at an expression superficially similar to [10], but the model considered involved the assumption of the presence of steps due to spirals.

[4] Relevant relationships for transformation can be found in ref. (15).

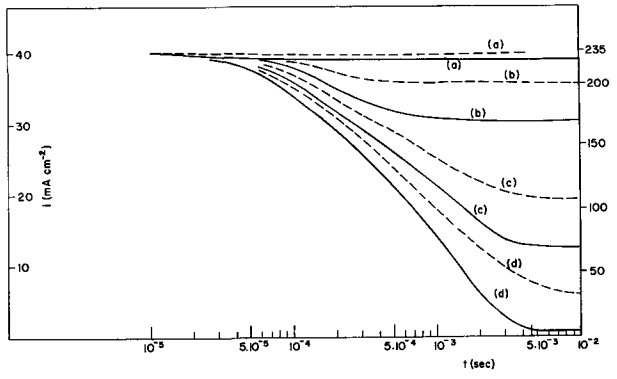

Fig. 3. Potentiostatic transient representing the calculated dependence of the average current density on time. Full lines, η = — 10 mv, current plotted on the left-hand scale; dashed lines, η = — 50 mv, current plotted on the right-hand scale. Curves a, b, c, and d are for $ND = 10^4$, 10^3, 10^2, and 10 sec^{-1}, respectively. i_0 is taken as 100 ma cm^{-2}, and c_0 as 10^{-10} mole/cm².

In Fig. 3, the average current densities for two overpotentials and various ND values are plotted against time. With decreasing density of dislocations, $i(t)$ decreases considerably; this is discussed further below.

Exchange current density and equilibrium adion concentration.—The usual method of determining the exchange current density, i_0, from the steady-state data by extrapolation of the linear part of log i—η curve to η=0, although sufficiently accurate for most purposes, may be subject to certain inaccuracy when surface diffusion of adions and the structure of the electrode surface are expected to be still important factors in determining the rate of the reaction even at higher (~50 mv) overpotentials (see Eq. [20]). This possible inaccuracy may be avoided if the nonsteady-state data of potentiostatic transients are considered. The current density at the first instant after application of a constant potential, ($i_{t=0+}$), since independent of the structure of the electrode surface, and on the surface-diffusion of adions, and determined only by the transfer rate in the over-all reaction (Eq. [7]), may be more suitable for obtaining the exchange current density than is the steady-state current density.

Also, the equilibrium value of the adion concentration, c_0, can be obtained from the potentiostatic transient. At a sufficiently early time after application of a constant potential, the slope on the i_t—t curve is given from [10] by

$$\left[\frac{di(t)}{dt}\right]_{t=0+} = \frac{[i(t)_{t=0+}]^2}{2zFc_0\sinh\left(\frac{zF\eta}{2RT}\right)} \exp\left(\frac{zF\eta}{2RT}\right) \quad [14]$$

from which c_0 can be evaluated.

Rise time under potentiostatic conditions.—The time necessary to reach the steady state when constant overpotential is applied across the electrode can be obtained from the second, nonsteady state part of Eq. [10]. Terms under the summation sign rapidly decrease when the time is near to, or larger than

$$\tau = \frac{2}{\pi^2 ND + p} \qquad [15]$$

When $t = \tau$, the second term ($n = 1$) in Eq. [10] can be neglected, since it is at least 10 times smaller than the first ($n = 0$), which itself is already at τ small (less than 10%) compared with the steady-state current density. Thus, τ represents the rise time. When, in the steady state, surface diffusion of adions is rate controlling, and $\pi^2 ND$ is less than p (see section on Average current density for cathodic polarization, below), the rise time depends on p, and therefore on the exchange current density, i_o. The reverse also holds, *i.e.*, when transfer is rate controlling in the steady state, τ depends on the rate of surface diffusion. Thus, in potentiostatic transients the rise time depends on the rate of the faster reaction.

In order to compare the rise time of the potentiostatic transients with that of galvanostatic transients, the nonlinear distribution of adions should be considered in both cases. However the expression for the galvanostatic rise time with the nonlinear distribution of adions has not yet been obtained. With the linear distribution of adions (Mehl and Bockris' model), the galvanostatic rise time, when surface diffusion is rate controlling, is given by (1)

$$\tau_g = \frac{c_o}{2v_o} \qquad [16]$$

where v_o, the surface diffusion flux, is equal to Dc_o/x_o^2 and, with $x_o = \frac{1}{2\sqrt{N}}$, to $4NDc_o$. Thus, contrary to the potentiostatic case, the rise time for the galvanostatic transient, when surface diffusion is rate controlling, depends on the rate of surface diffusion. Hence one can compare the galvanostatic rise time with that for the corresponding potentiostatic case, *i.e.*, that obtained from a linear distribution of adions with distance between the growth steps. It can easily be shown to be

$$\tau_p = \frac{2}{8ND + p} = \frac{2c_o}{2v_o + pc_o} \qquad [17a]$$

or, for low overpotentials

$$(\tau_p)_{\eta \to o} = \frac{2c_o}{2v_o + i_o/zF} \qquad [17b]$$

It is interesting to notice that there is no significant difference between the expressions for the potentiostatic rise time obtained with the linear and nonlinear adion distributions. The ratio between rise times for galvanostatic and potentiostatic transients for linear distribution of adions is therefore

$$\left(\frac{\tau_g}{\tau_p}\right)_{\eta \to o} = 1 + \frac{i_o}{2zFv_o} \qquad [18]$$

and is expected not to differ significantly from the ratio which would be obtained with nonlinear distribution of adions. Here, 90% rise time ($\tau = c_o/v_o$) is considered. Thus, it offers a possibility for establishing the rate-determining step in a given system by measuring the rise time under galvanostatic and potentiostatic conditions. When surface diffusion is the rate-determining step, $i_o/2zFv_o$ is greater than 1, and τ_g/τ_p should be reasonably greater than 2. Also, the value of i_o/v_o may be obtained directly from the above ratio.

The total number of atoms which diffuse to the steps and become incorporated into the lattice during the cathodic rise time, for instance, can be obtained by integration of the Eq. [12a] from $t = 0$ to $t = \tau$. The analysis shows that during the rise time the number of atoms incorporated into the lattice is only a fraction of the total number of atoms which have crossed the double layer. It can be shown that the number of adions which diffuse to steps and become incorporated into the lattice during the rise time is greater for galvanostatic than for potentiostatic case, and, therefore, to reach the same steady-state conditions, more ions have to cross the double layer in galvanostatic than in potentiostatic case. Even during the galvanostatic transient, the total number of ions crossing the double layer is equivalent to only a fraction of a monolayer (1,3), and only a part of these will diffuse to steps to be incorporated there into the lattice. During the potentiostatic transient the advance of steps therefore will not be significant, *i.e.*, the present approach allows a study of the kinetics of the build up and decay of monolayers to be made under conditions in which a difficult experimental feature of metal deposition kinetics, the change of electrode surface with time, is avoided.

Steady State

Steady-state distribution of current density.—In the steady state, the distribution of the net charge transfer rate between growth steps can be obtained by suitable transformation from the first, steady-state part of Eq. [6]

$$i(x) = -zFBp\cosh(mx) = i_o \left\{\exp\left(-\frac{\beta zF\eta}{RT}\right) - \exp\left[(1-\beta)\frac{zF\eta}{RT}\right]\right\} \frac{\cosh(mx)}{\cosh\sqrt{\frac{p}{4ND}}} \qquad [19]$$

The dependence of this net charge transfer rate on the distance between growth steps, $2x_o$, in the steady state, has already been treated by Despic and Bockris (3), who derived an essentially similar equation. In Fig. 4, the current density distribution between two steps is given for various overpotentials and ND values. When surface diffusion is the rate-controlling step, that is, at all anodic current densities and at sufficiently low cathodic current densities, the rate of charge transfer at midpoints between growth steps is small compared to that at the growth steps themselves, *i.e.*, a large part of the current is confined to the near vicinity of growth steps. This does not, however, imply that deposition, for instance, occurs predominantly directly from solution to kink sites at the steps, not only because the collisional probability is small, but because the required activation energy for trans-

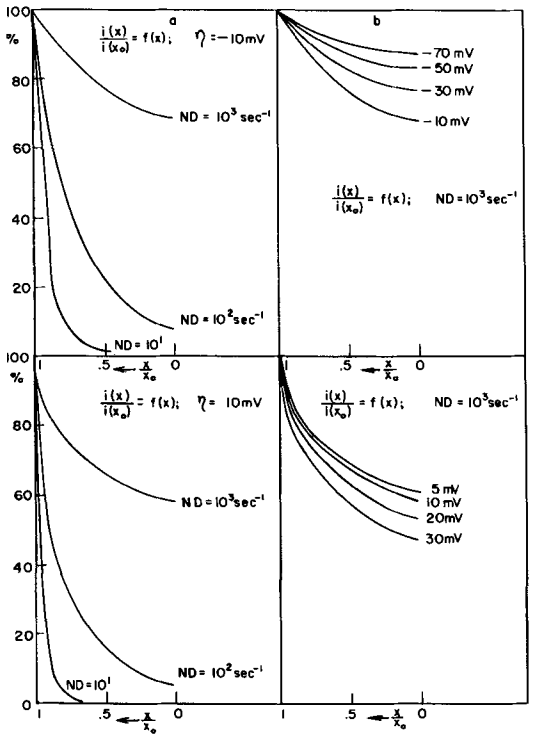

Fig. 4. Variation of the current density with the distance from the growth step: a, for various values of ND and $\eta = \pm$ 10mv; b, for $ND = 10^4$ sec^{-1} and various values of overpotentials, both cathodic and anodic.

fer directly to a kink site is prohibitively large (11, 16). The local rate of charge transfer can never be greater than that given by transfer as a rate-controlling step for the given overpotential. Were deposition to occur directly onto kink sites (10), the local rate of charge transfer would be by some orders of magnitude greater than that allowed for charge transfer [*cf.* also the identity of the current densities for liquid and solid electrodes in the rate-controlling charge transfer region (17).

Average current density for cathodic polarization.—The average current density, i, both for deposition and dissolution, can be obtained by integrating [19] from 0 to x_0 and dividing by x_0. It is

$$i = i_0 \left\{ \exp\left(-\frac{\beta z F \eta}{RT}\right) - \exp\left[(1-\beta)\frac{zF\eta}{RT}\right] \right\} \sqrt{\frac{4ND}{p}} \tanh \sqrt{\frac{p}{4ND}} \quad [20]$$

For $ND \geq p$, $\sqrt{\frac{4ND}{p}} \tanh \sqrt{\frac{p}{4ND}} \simeq 1$, and Eq. [20] reduces to

$$i = i_0 \left\{ \exp\left(-\frac{\beta z F \eta}{RT}\right) - \exp\left[(1-\beta)\frac{zF\eta}{RT}\right] \right\} \quad [20a]$$

This accounts for the gradual transition from rate-controlling surface diffusion at low cathodic overpotentials (p large) to rate-controlling transfer step at more cathodic overpotentials (p small), observed by Mehl and Bockris (1). As the overpotential becomes increasingly negative, the adion concentration increases, so that $\left|\frac{dc}{dx}\right|_{x=\pm x_0}$ increases and, hence, the surface diffusion rate increases to a nonrate-controlling value. The overpotential at which transition from rate-controlling surface diffusion to rate-controlling transfer during deposition occurs, depends on N and D. At more perfect crystal surfaces (N is small) the transition will occur at more negative overpotentials. For surface diffusion to be the rate-controlling step, it is necessary that (*cf.* Eq. [20])

$$ND < p = \frac{i_0}{zFc_0} \exp\left[(1-\beta)\frac{zF\eta}{RT}\right] \quad [21]$$

or, at low overpotentials

$$ND < \frac{i_0}{zFc_0}$$

Thus, for silver electrodes in a solution of 0.2N $AgClO_4$, for instance, with $i_0 = 0.1$ amp/cm^2, and $c_0 = 10^{-10}$ mole/cm^2, surface diffusion will be rate controlling if ND is less than 10^4 sec^{-1}. In fact, from Fig. 5 it can be seen that, for $ND = 10^4$ sec^{-1} and $\eta = -10$ mv, the steady-state currents are only a few per cent smaller than they would be if transfer were the rate-controlling step. It is possible to estimate the value of the diffusion coefficient of silver adions, for instance, in the system used by Mehl and Bockris (1). The best fit with their experimental data (see Fig. 6) can be obtained if in Eq. [20] ND is $3.4 \cdot 10^3$ sec^{-1}. A reasonable value of N for their electrodes can be taken as 10^9 cm^{-2}, and then D is approximately equal to $5 \cdot 10^{-6}$ cm^2 sec^{-1}. The accuracy with which the value of D can be obtained depends also on the accuracy with which c_0 is determined. Here, c_0 is taken as 10^{-10} mole/cm^2. With decreasing N values, surface diffusion will tend increasingly to become rate controlling. In Fig. 5, as an illustration, a family of $i - \eta$ curves is given for various ND values, $i_0 = 100$ ma/cm^2, and $c_0 = 10^{-10}$ mole/cm^2. In Fig. 6 the experimental results of Mehl and Bockris (1) on silver are plotted together with the theoretical curve obtained with Eq. [20].

Anodic polarization.—When surface diffusion is rate controlling, Eq. [20] indicates that the disso-

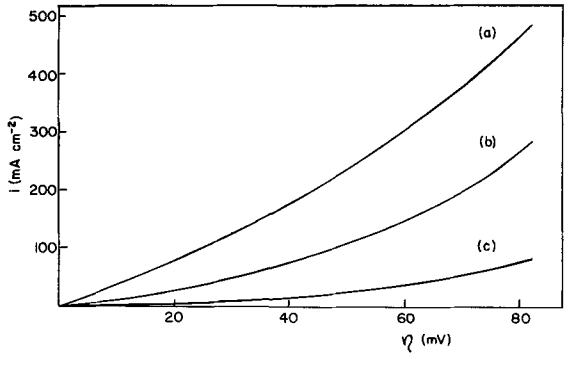

Fig. 5. Calculated average current density at the steady-state deposition as function of overpotential. Curves a, b, and c correspond to $ND = 10^4$, 10^2, and 10 sec^{-1}, respectively; $i_0 = 100$ ma cm^{-2} and $c_0 = 10^{-10}$ mole/cm^2.

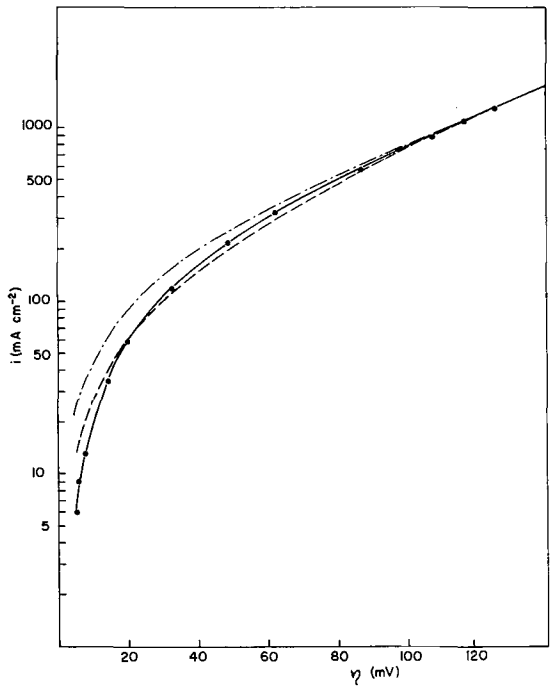

Fig. 6. Log i — η plot of experimental results of Mehl and Bockris full line. Dashed line, surface diffusion-controlled current according to the present analysis with i_o = 120 ma/cm², c_o = 10^{-10} mole/cm², and ND = 3.4 x 10^3 sec^{-1}v. Dashed and dotted line is the closest fit for transfer control.

lution current density is not symmetrical with that of deposition, and i_{cath} is greater than i_{an}. It should be pointed out that Despic and Bockris (3) observed a dissymmetry in the i — η curves at low overpotentials ($|\eta|$ < 20 mv) in the sense that the currents on the anodic side, for a nonactivated electrode became less than those on the cathodic side. Furthermore, the condition for surface diffusion $ND < p$ implies that surface diffusion will stay rate controlling for higher anodic overpotentials if it is rate controlling at low overpotentials. Moreover, Eq. [20] shows that, contrary to the deposition case, rate-controlling transfer at low overpotentials eventually should be replaced by surface diffusion rate controlling at higher overpotentials. There is, however, evidence (3) that, at higher anodic overpotentials, the log i — η relation on the anodic side has a gradient equal to that on the cathodic. This inconsistency may perhaps be interpreted by reference to the fact that at higher anodic overpotentials with surface diffusion control the adion concentration between the growth steps will decrease considerably (cf. Eq. [22]). The path of the reaction may then change so that the origin of the adions is no longer the growth steps only but the planes themselves. New growth steps will be thus created at numerous points, and this would effectively increase N in Eq. [20] and transfer will become rate controlling.

It may be pointed out that the process of formation of new steps by dissolving atoms in the surface can occur at relatively low overpotentials. Vermilyea (13) observed pitting in the extreme case of copper whiskers (N very low) and sudden rise in the dissolution current already at 20 mv. This would agree with a model in which the initial difficulty in dissolution from plane surface is relieved by the introduction of new growth steps. For activated electrodes, symmetry of the cathodic and anodic lines is observed (3), and this is consistent with transfer control on these electrodes, for anodic as well as cathodic currents, as will occur from [20] if N is large. Despic and Bockris' electrodes were activated by anodic dissolution which may have caused the creation of steps also at the edges of the crystals.

Adion concentration in the steady state.—The concentration of adions at the midpoints between two growth steps is given by (see Eq. [3])

$$c_{x=o} = c_o\left\{\exp\left(-\frac{zF\eta}{RT}\right) + \left[1-\exp\left(-\frac{zF\eta}{RT}\right)\right]\frac{1}{\cosh(mx_o)}\right\} \quad [22]$$

For the same overpotential, the concentration of adions varies with N. Thus, for the cathodic case, with η = — 50 mv, and D = 5.10^{-6} cm²/sec, ratio $c_{x=o}/c_o$ changes from approximately 1 to 7 when N changes from 10^{10} to 10^6 cm^{-2}. On surfaces with high dislocation densities, when growth steps are close to each other, no appreciable change of adion concentration occurs during deposition or dissolution above or below that of the equilibrium concentration even at the midpoints between two growth steps. On more perfect crystal faces, however, the increase of adion concentration during deposition may be so large that a new process, two-dimensional nucleation, may be expected at higher overpotentials. The variation of adion concentration with the distance between growth steps for various values of ND and overpotentials is illustrated in Fig. 7.

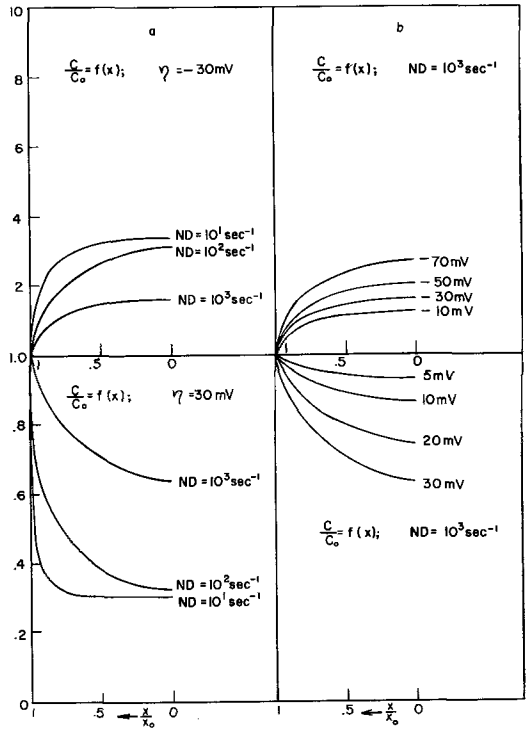

Fig. 7. Variation of adion concentration with the distance from the growth step; a, for various values of ND and η = ± 10 mv; b, for various overpotentials, both cathodic and anodic, and ND = 10^3 sec^{-1}.

Two-Dimensional Nucleation During Deposition

Free energy change in the formation of a two-dimensional nucleus and its critical radius.—During deposition, the adion concentration, particularly at the midpoints between steps, and if the density of growth steps is below a certain level, may reach a value at which nucleation will commence. The effect of the nucleation will be to form new growth steps, and this in turn will reduce x_o, and hence decrease the adion concentration and increase the rate of surface diffusion (see Eq. [12a] and [13]).

Adion clusters, or embryos, are in equilibrium with adions. An embryo may either disappear or grow. When it reaches a critical size, it becomes a nucleus. The free energy change for the formation of an embryo from adions is made up of two terms, one due to "condensation" of adions into the inner part of the embryo (edge ions are excepted), and the other due to the formation of the edge of the embryo. The first term decreases the free energy with respect to that of the number of adions concerned and is proportional to the number of ions in the embryo (except for those in the edge) and hence to the area of the embryo diminished by the edge contribution; the second increases the free energy change and is proportional to the number of ions in the periphery of the embryo

$$\Delta F = \left(\frac{2\pi r^2}{\sqrt{3}\, d^2} - \frac{2r - d}{d} \pi \right) \Delta F_1 + \frac{2r - d}{d} \pi \Delta F_2 \quad [23]$$

Here, ΔF_1, (< 0), is the free energy of the ion in the embryo diminished by that of an adion; and ΔF_2, (> 0), is the free energy of the ion in the edge diminished by that of an adion, d is the interatomic distance in the embryo, and r is the radius of the embryo. The factor $2/\sqrt{3}$ in the first term accounts for the close packing of atoms in the embryo on the (111) plane of fcc metals. A stable nucleus will be formed if the radius of an embryo exceeds a critical size. From the condition $\frac{d\Delta F}{dr} = 0$, the critical radius of the nucleus is obtained

$$r_c = -\frac{\sqrt{3} d (\Delta F_2 - \Delta F_1)}{2 \Delta F_1} = -\frac{\sqrt{3} d}{2} \cdot \frac{\Delta F_3}{\Delta F_1} \quad [24]$$

where ΔF_3 is free energy of an ion in the edge diminished by that in the nucleus.

To a first approximation, assuming in the calculation of the heat content part that the binding energies (of first nearest neighbors only) are additive and considering the entropy of mixing only, expressions for the free energy changes per atom may be written in the form

$$\Delta F_1 = -\frac{L}{2} - kT \ln \frac{n}{N - n} + \Delta F_4 \quad [25a]$$

and

$$\Delta F_3 = \frac{2.5}{12} L + \Delta F_5 \quad [25b]$$

where L is the heat of sublimation of the metal, n the number of adions/cm^2, N the number of available sites/cm^2 ($\sim 1.5 \times 10^{15}$), ΔF_4 is the free energy of hydration of an ion in the nucleus diminished by that of an adion, and ΔF_5 is the free energy of hydration of an ion in the edge diminished by that in the nucleus. On the (111) plane, the number of neighbors of an ion in the edge of the nucleus is either six or seven, and of an ion in the nucleus itself 9. In ΔF_3, the factor 2.5 is the difference $9 - 6.5$, as average.

Possible modes of hydration at various sites on the surface have been considered by Conway and Bockris (16), and their estimates for hydration of adions as well as of ions in the edge of the nucleus and in the plane itself can be used for numerical evaluations of the free energy changes.

At equilibrium ($n = n_o$), the free energy change ΔF_1 is equal to zero, and with this condition Eq. [25a] reduces to

$$\Delta F_1 = -kT \ln \frac{n(N - n_o)}{n_o(N - n)} \quad [26]$$

where n_o is the number of adions/cm^2 at equilibrium. Assuming $N >> n > n_o$, and with $n/n_o = c/c_o$, where c and c_o are adion concentrations at a given overpotential and at the zero overpotential, respectively, the radius of the critical nucleus becomes

$$r_c = \frac{\sqrt{3}}{2} \frac{d^2 \gamma}{kT \ln c/c_o} \quad [27]$$

where γ, the edge energy in ergs per centimeter of the circumference of the nucleus, is defined as

$$\gamma = \frac{\Delta F_3}{d} \quad [28]$$

and can be obtained numerically, providing the hydration energy term, ΔF_5, in Eq. [25b] can be estimated.

Frequency of nucleation.—An embryo having the critical radius, r_c, may become a stable nucleus after the elapse of time necessary for a further adion to join it. This is

$$\frac{1}{2\pi r_c v\, n} \quad [29]$$

where v is the average velocity of adions in a given direction. If 1 cm^2 of the surface contains N_c embryos of critical radius in equilibrium with n adions, all of them will become nuclei in $(2\pi r_c v\, n)^{-1}$ sec. Hence, in 1 sec, the number of embryos per cm^2 which become nuclei is

$$R = N_c \left(\frac{1}{2\pi r_c v\, n} \right)^{-1} = 2\pi r_c N_c n \cdot \sqrt{\frac{kT}{2\pi m}} \quad [30]$$

which is the rate of nucleation in nuclei per cm^2 sec^{-1}. Here, v is taken equal to $\sqrt{\frac{kT}{2\pi m}}$. Thus, as

$$N_c = n \cdot \exp\left[-\frac{\Delta F_c}{kT} \right] \quad [31]$$

where ΔF_c is the free energy change for the formation of a critical nucleus, the rate of nucleation becomes

$$R = 2\pi r_c n^2 \cdot \sqrt{\frac{kT}{2\pi m}} \cdot \exp\left[-\frac{\Delta F_c}{kT} \right] \quad [32]$$

The term ΔF_c, obtained from Eq. [23] when r is replaced by r_c, is equal to

$$\Delta F_c = \pi \Delta F_3 \left[\frac{r_c}{d} - 1 \right] \quad [33]$$

In addition, allowance has to be made for the energy of activation for surface migration E, so that, just after nucleation begins,

$$R = 2\pi r_c n^2 \sqrt{\frac{kT}{2\pi m}} \cdot \exp\left[-\frac{\Delta F_c + E}{kT} \right] \quad [34]$$

where both r_c and ΔF_c are dependent on the adion concentration which is a potential dependent quantity (cf. Eq. [22]). The rate of nucleation is thus strongly dependent on overpotential and, for a given overpotential, on the dislocation density.

Deposition on a step-free surface after the nucleation has commenced.—After application of a constant overpotential across a crystallographically flat surface ($N = 0$), net ion flow across the double layer will take place, but only until the adion concentration has reached the value (cf. Eq. [22])

$$c = c_0 \exp\left(-\frac{zF\eta}{RT} \right) \quad [35]$$

At this point, unless the conditions for nucleation are created, no further net flow will occur. Analysis of the equation for the rate of the nucleation (Eq. [34]) shows that significant nucleation may be expected in the case of silver, for instance, if the overpotential is of the order of 80-100 mv (cf. Fig. 8). Experimentally, it is found that with copper whiskers there is no deposition current unless overpotentials of the order of 100 mv are reached [cf. Vermilyea (13)]. The current density which would be observed just after the commencement of nucleation is not, however, that obtainable from R (Eq. [34]). It is governed by surface diffusion-control and can now reach significant values as the nucleation has provided the steps to which ions can diffuse. The problem of calculating the current density after nucleation has commenced, however, is complex, not only because the nuclei grow, coalesce, and spread across the surface and thus change the distance between "steps," but also because, once nucleation has started, the adion concentration will change and moreover, due to small diameters of nuclei (~20Å), the adion concentration at "steps" of the nuclei cannot be taken as the equilibrium adion concentration, c_0. Further, the rate of nucleation itself decreases after commencement because adion concentration decreases. It is therefore possible to obtain only an approximate upper limit for the rate of deposition just after the first nuclei are formed. This is

$$i = i_0 \left\{ \exp\left(-\frac{\beta zF\eta}{RT} \right) - \exp\left[(1-\beta)\frac{zF\eta}{RT} \right] \right\} \frac{2\sqrt{N_c}\tanh\left(\frac{m}{2\sqrt{N_c}} \right)}{m} \quad [36]$$

and is obtained from Eq. [20] when N is replaced by N_c, where N_c is the number of critical nuclei per cm^2.

Deposition on stepped surface after nucleation has commenced.—The possibility of nucleation on stepped surfaces is much less than on the crystallographically flat surface, as adion concentration even at the midpoint between steps is less than that at a step-free surface, under the same conditions (cf. Eq. [22]). Analysis of the rate of nucleation (Eq. [34]) shows that on a surface with high density of dislocation ($N \sim 10^{10}$ cm^{-2}), no nucleation is possible unless the overpotentials are over 150 mv. In Fig. 8 the rates of nucleation are plotted for various ND values. Due to nucleation, the net rate of charge transfer across the double layer will increase over that given by the steady-state equation (Eq. [20]), because of the effective decrease of adion concentration following nucleation. However, it is difficult to calculate this change, as the appearance of the first nuclei will make the kinetics of deposition complex for the reasons stated in the last section above. Nevertheless, a very rough estimate of the change of charge transfer rate across the double layer after nucleation has started can be made by assuming that the distances between the growth steps are effectively halved, as the nuclei will preferentially be formed at midpoints between steps.

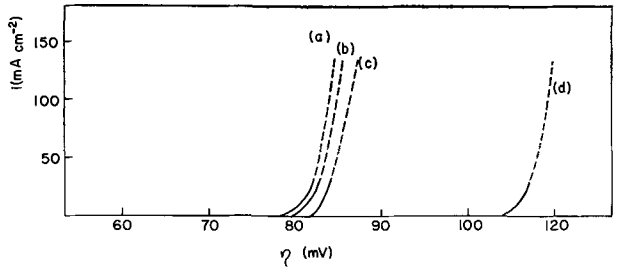

Fig. 8. Current density expected at the first instant after nucleation has commenced as function of overpotential. Curves a, b, c, and d correspond to ideally flat surface, $ND = 10$ sec^{-1}, $ND = 10^2$ sec^{-1}, and $ND = 10^3$ sec^{-1}, respectively.

Summary

The kinetics of the formation and decay of metal monolayers by electrochemical processes is considered for metal surfaces with steps due to emerging screw dislocations. The rate of ion transfer at low overpotentials across the double layer, integrated over the whole surface, varies considerably with the density of dislocations for the same overpotential, as does the rise time. Just after application of constant overpotential, the current density is independent of the fine structure of the substrate and the transfer reaction is always rate controlling. This enables a direct determination of the exchange current density to be made from measurements of the current-time transient immediately after double layer charging. The equilibrium adion concentration can be obtained from $(di/dt)_{t\to 0,\eta}$.

Contrary to the galvanostatic case, when transfer is rate controlling in the steady state, the rise time for potentiostatic charging is governed by the rate of diffusion of adions to growth sites and *vice versa*. A comparison of the rise times obtained in the po-

tentiostatic and galvanostatic transients allows distinction between the rate-controlling transfer and surface diffusion and the evaluation of the relative rate constants for transfer and surface diffusion. At low overpotentials, the steady-state cathodic current density under surface diffusion control is greater than the corresponding anodic value.

The steady-state current density, expressed in terms of a model which allows for the nonlinear distribution of adions with distance between the growth sites, gives rise to an interpretation of the observed gradual transition from surface diffusion control at low overpotentials, to transfer control at high overpotentials in deposition, and predicts diffusion to be rate controlling at all potentials in dissolution if it is controlling at low overpotentials, providing no dissolution from crystallographically flat surfaces or from edges of crystals occurs.

On surfaces with a high density of dislocations, diffusion of adions is relatively unimportant to rate control, since ions reaching the surface will diffuse quickly to the steps. The net rate of charge transfer is then the same all over the surface. At more perfect surfaces, when surface diffusion is rate controlling, the net current is confined to the near vicinity of growth steps, particularly at low current densities. Correspondingly, it is unlikely that deposition occurs directly from solution to kink sites.

Expressions are deduced for the rate of nucleation as a function of dislocation density and overpotential. On surface with a high dislocation density (say 10^{10} cm^{-2}), nucleation is improbable until an overpotential of the order of 100 mv is reached.

Acknowledgment

The authors wish to thank the National Science Foundation for the financial support of this work.

Manuscript received Nov. 28, 1962; revised manuscript received March 29, 1963.

Any discussion of this paper will appear in a Discussion Section to be published in the June 1964 JOURNAL.

REFERENCES

1. W. Mehl and J. O'M. Bockris, *Can. J. Chem.*, **37**, 190 (1959); *J. Chem. Phys.*, **27**, 818 (1957).
2. W. Lorenz, Z. *Elektrochem.*, **57**, 382 (1953); Z. *Naturforsch.*, **9a**, 716 (1954).
3. A. R. Despic and J. O'M. Bockris, *J. Chem. Phys.*, **32**, 389 (1960).
4. H. Gerischer, *Z. Elektrochem.*, **62**, 256 (1958).
5. H. Kita, M. Enyo, and J. O'M. Bockris, *Can. J. Chem.*, **39**, 1670 (1961).
6. F. C. Frank, *Discussion Faraday Soc.*, **5**, 48 (1949); W. R. Burton and N. Cabrera, *ibid.*, **5**, 33 (1949); W. R. Burton, N. Cabrera, and F. C. Frank, *Phil. Trans. Roy. Soc., London*, **A243**, 299 (1951).
7. N. Cabrera and W. K. Burton, *Discussion Faraday Soc.*, **5**, 40 (1949).
8. A. R. Verma, "Crystal Growth and Dislocations," Butterworths, London (1953).
9. M. Fleischmann and H. R. Thirsk, *Electrochim. Acta*, **2**, 22 (1960).
10. N. F. Mott and R. J. Watts-Tobin, *ibid.*, **4**, 79 (1961).
11. B. E. Conway and J. O'M. Bockris, *Proc. Roy. Soc.*, **A248**, 394 (1958).
12. D. A. Vermilyea, *J. Chem. Phys.*, **25**, 1254 (1956).
13. D. A. Vermilyea, *ibid.*, **27**, 814 (1957).
14. H. Seiter, H. Fischer, and L. Albert, *Electrochim. Acta*, **2**, 97 (1960).
15. E. T. Whittaker and G. N. Watson, "A Course of Modern Analysis," p. 136, Cambridge University Press (1920).
16. B. E. Conway and J. O'M. Bockris, *Electrochim. Acta*, **3**, 340 (1961).
17. J. O'M. Bockris and M. Enyo, *This Journal*, **109**, 48 (1962).
18. H. J. Pick, G. G. Storey, and T. B. Vaughan, *Electrochim. Acta*, **2**, 165 (1960).

APPENDIX

After introducing $i(xt)$ from Eq. [2] into [1], and setting

$$u(xt) = [c_\infty - c(xt)] \cdot e^{pt} \qquad [A\text{-}1]$$

Eq. [1] reduces to

$$\frac{\partial u}{\partial t} = D\frac{\partial^2 u}{\partial x^2} \qquad [A\text{-}2]$$

c_∞ is the steady-state distribution of adion concentration and is easily and directly obtainable from [1] and [2] when $\partial c/\partial t$ is placed equal to zero, and second and third condition of [2a] are used. Solution for c_∞ is then

$$c_\infty = A + B\cosh(mx) \qquad [A\text{-}3]$$

where A, B and m, and also p in [A-1] are given by [3a].

For the solution of [A-2], the initial and boundary conditions [2a] transform to

$$u(x,o) = c_\infty - c_o \qquad [A\text{-}4]$$

$$u(\pm x_o,t) = 0 \qquad [A\text{-}5]$$

and

$$\frac{\partial u(o,t)}{\partial x} = 0 \qquad [A\text{-}6]$$

By separation of variables and expanding in Fourier series, the general solution of [A-2] is

$$u(xt) = \sum_\alpha e^{-\alpha t}\left[a\cos\sqrt{\frac{\alpha}{D}}x + b\sin\sqrt{\frac{\alpha}{D}}x\right] \qquad [A\text{-}7]$$

Condition [A-6] requires that

$$b = 0$$

and [A-5] that

$$\sqrt{\frac{\alpha}{D}} = \frac{(n+1/2)\pi}{x_o}$$

Hence, at $t = 0$

$$u(x,o) = \sum_{n=0}^{\infty} a_n\cos\left[(n+1/2)\pi\frac{x}{x_o}\right] \qquad [A\text{-}8]$$

where a_n is given by

$$a_n = \frac{2}{x_o}\int_o^{x_o} u(x,o)\cos\left[\frac{(n+1/2)\pi x}{x_o}\right]dx$$

$$= -\frac{2(-1)^n B' m^2 x_o^2}{\pi(n+1/2)[(n+1/2)^2\pi^2 + m^2x_o^2]} \qquad [A\text{-}9]$$

Combining [A-1, 3, 7, and 9], solution [3] is obtained.

Effect of CdS on the Electroluminescence of ZnS:Cu, Halide Phosphors

Arthur Dreeben

RCA Laboratories, Radio Corporation of America, Princeton, New Jersey

ABSTRACT

The effect of CdS on the electroluminescence of ZnS:Cu phosphors coactivated with Cl, Br, or I has been determined. In each case, brightness is sensitive to the presence of CdS, and there is an apparent relationship between intensity and crystal structure. Maximum brightness is associated with the cubic modification. In iodide coactivated phosphors prepared at 700°C, the cubic phase persists up to 10 mole % CdS, and a decrease in power dissipation leads to improved efficiency. CdS also causes a variation in the amount of retained copper which is explained by postulating the formation of a new phase involving (Cu,Cd) (S,Halide).

Zinc cadmium sulfide solid solutions, activated with copper, are well-known and useful photo- and cathodoluminescent phosphors. It was felt, therefore, that they should also be examined more completely for electroluminescence (hereafter referred to as EL). An earlier finding in this laboratory (1) indicated that the addition of small amounts of cadmium sulfide to EL zinc sulfide phosphors significantly diminished their brightness. Other work describing a similar effect is limited to phosphors coactivated either with chloride (2) or with Group III elements (3). The present study, comparing iodide with chloride and bromide in EL(Zn, Cd)S:Cu, has shown that the effect of cadmium sulfide varies with the particular halide coactivator used.

Unique characteristics of the solid solutions coactivated with iodide and containing up to 10 mole % cadmium sulfide include (*a*) the stabilization of a single cubic phase, whereas the hexagonal modification is usual with as little as 2 or 3 mole % cadmium sulfide in chloride coactivated phosphors fired at 850°-900°C (4, 5); and (*b*) a remarkable decrease in power dissipation with only a slight decrease in brightness.

Experimental

The phosphors were prepared by intimately mixing dried slurries of the component sulfides (RCA Luminescent Grades) containing the activator (as the acetate) and the ammonium salt of the desired coactivator. In the firing process, use was made of the sulfur effect (2, 6, 7) by mixing 10 weight per cent (w/o) of purified sulfur with the unfired mix to facilitate development of EL at a lower firing temperature. For iodide coactivation, some results using this procedure are contrasted with a higher firing temperature in the absence of sulfur.

Firing tubes containing the mixes in covered quartz vials were preflushed with purified, dry nitrogen, but a static atmosphere was maintained during a 1-hr firing time. The gas exit tube was connected through a silicone-oil seal to prevent back diffusion of air. Products were cooled in a stream of the nitrogen.

After cooling, the products were digested in an alkaline solution of sodium cyanide to remove excess, unincorporated copper. In all cases, this treatment lightened the dark body color of the fired products. Finally, samples were washed free of cyanide with water. Brightness of the cells was determined with a McBeth Illuminometer, and power dissipation was measured with a VAW electronic wattmeter.

Results

Analyses confirmed that no copper was lost during synthesis, but that some was dissolved by the cyanide wash. The amount of copper retained in iodide coactivated samples depended on the firing temperature, but not on the proportion of CdS. For example, in phosphors containing up to 20 mole % CdS, and prepared with 0.15 mole % Cu and 10 w/o of ammonium iodide, 39% of the copper was finally retained in samples admixed with sulfur and fired at 700°C, and 28% was retained when the firing was accomplished at 1075°C in the absence of sulfur.[1]

In bromide and chloride coactivated samples, the proportion of CdS influenced the amount of retained copper which first increased and then decreased with greater proportions of CdS as shown in Table I. A progressively darker body color (after the cyanide wash) accompanied this increase in retained

[1] The amount of NH_4I was chosen to compensate for losses through volatilization on firing (9).

Table I. Retention of copper in Cl and Br coactivated (Zn,Cd)S phosphors

Mole % CdS	% Cu retained	
	Cl coactivated	Br coactivated
0	16	47
3	16	49
5	17	—
6	—	56
7	44	—
8	—	61
10	30	67
15	22	64

Mole % Cu originally added: Cl coactivated, 0.62; Br coactivated, 0.51. Both series fired at 950°C.

Table II. Crystal structure of (Zn,Cd)S:Cu, halide phosphors

Mole % CdS	Cl	Br	% Cubic phase I-700°C	I-1075°C
0	100	50	100	50
1	100	—	100	—
2	—	—	—	35
3	90	40	100	—
5	70	—	100	—
6	—	20	—	25
7	25	—	100	—
10	10	0-5	100	5-10
15	0-5	0-5	5	5
20	0-5	—	—	—

* Note: In a predominantly cubic phase, less than 1% hexagonal is detectable, but in a predominantly hexagonal phase, less than 5% cubic cannot be resolved.

copper particularly with chloride coactivation. There was also an increase in the phosphorescence observed after irradiation with 3650Å uv contrary to the typical effect of both increasing Cu and increasing CdS (5). These findings suggested the formation of a new cyanide insoluble phase involving (Cu, Cd) (S, halide). After similar observations, Wachtel (2) prepared a black, hexagonal material thought to be a (Cd,Cu)S compound. Bartels and Wasserman (8) suggested the formation of a copper-rich phase in photoconducting CdS:Cu,Cl powders to account for variations in dark conductivity. The present observation that the formation of such a phase is sensitive to the particular halide used in the phosphor suggests that the halide itself is a part of the complex affecting its stability and equilibrium in the system.

X-ray diffraction examination of representative samples from each of the series showed the presence in some samples of a single phase of either cubic or hexagonal structure, or coexistence of both phases in other phosphors. The proportion of cubic phase is given in Table II. The unit cell of the cubic phase expands linearly with increase in CdS, but the expansion of the hexagonal phase departs from linearity. This is attributed to interference from the cyanide insoluble complex phase described above and is consistent with the observation that the onset of the increase in retained copper, indicative of the formation of the complex phase, coincides approximately with the appearance of the hexagonal phase in chloride and bromide coactivated phosphors. Other effects related to crystal structure will be described later.

Spectral distribution of emission.—Spectral distributions of EL emission for samples with no CdS are shown in Fig. 1. Qualitative features of spectral position and dependence on excitation frequency for the chloride, bromide, and high-temperature iodide coactivated phosphors are in general agreement with similar data reported by Hegyi *et al.* (9). The low-temperature iodide coactivated material, however, has a broader emission band with an apparent peak in the blue at a somewhat longer wavelength than the high-temperature sample.

Representative curves for one (Zn,Cd)S composition from each series are shown in Fig. 2. Samples

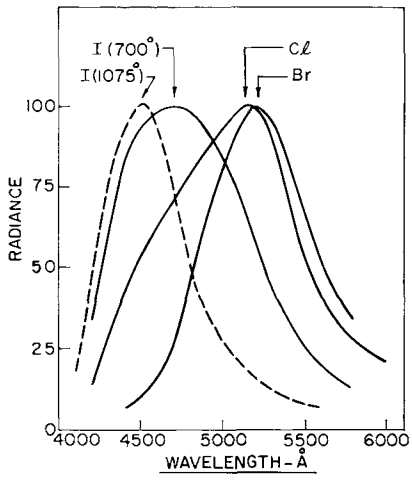

Fig. 1. Spectral distribution of EL emission of ZnS:Cu, halide phosphors, 200v, 200 cps (peaks normalized).

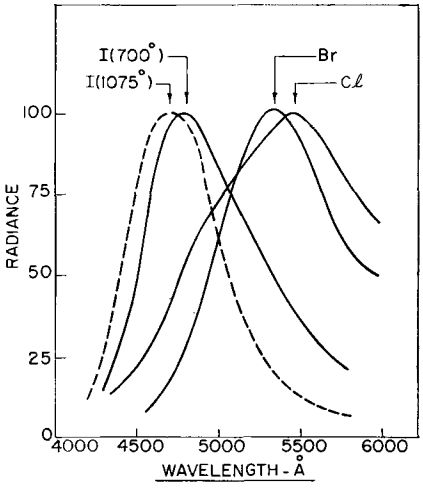

Fig. 2. Spectral distribution of EL emission of (Zn,Cd)S:Cu, halide phosphors; chloride and iodide—7 mole % CdS; bromide—8 mole % CdS; 200v, 200 cps (peaks normalized).

within each series with a given coactivator showed the expected shift to longer wavelengths with increasing proportion of CdS and a shift to shorter wavelengths with increasing excitation frequency. The magnitude of these shifts was somewhat dependent on the particular coactivator.

Brightness, power, and efficiency.—The relative brightness, power dissipation per cell unit area, and efficiency for bromide and chloride coactivation are shown as a function of CdS concentration in Fig. 3a, b, and c respectively.[2] These values all diminish rapidly when CdS is in excess of several mole per cent. Corresponding data for the high-temperature iodide coactivated phosphor are shown in Fig. 4a, b, and c. Here, brightness exhibits an immediate sensitivity to the presence of CdS and begins to decrease at once, but the power dissipation declines at an even faster rate. As a result, maximum efficiency occurs at 6 mole % CdS, but at this point the brightness has suffered a severe loss from its initial value.

2 Changes in EL emission color for the compositions of interest here were slight. Therefore, by considering luminance rather than total quanta, only a small error is introduced without affecting the trends.

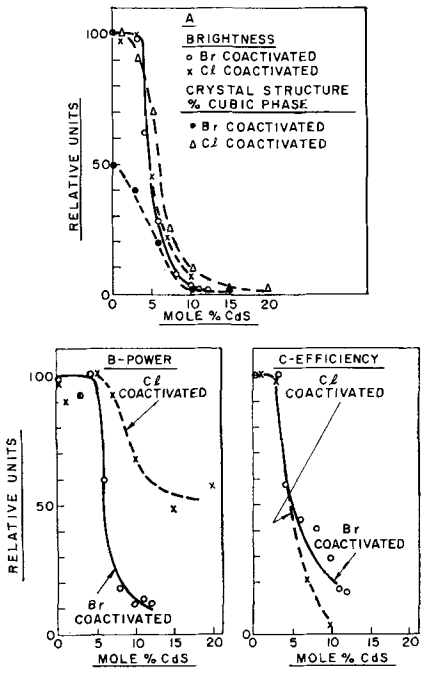

Fig. 3. Crystal structure, relative brightness, power, and efficiency for (Zn,Cd)S:Cu, Br, or Cl as a function of CdS concentration, 200v, 200 cps.

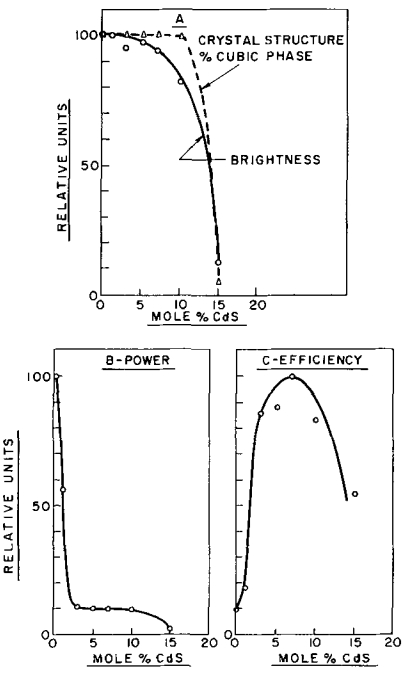

Fig. 5. Crystal structure, relative brightness, power, and efficiency as a function of CdS concentration for (Zn,Cd)S:Cu,I fired at 700°C with sulfur, 200v, 200 cps.

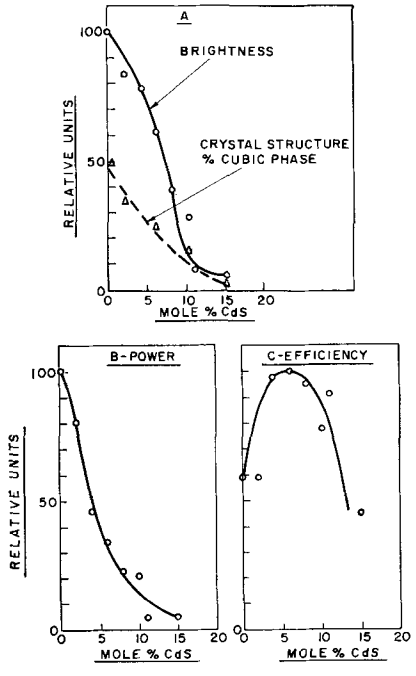

Fig. 4. Crystal structure, relative brightness, power, and efficiency as a function of CdS concentration for (Zn,Cd)S:Cu,I fired at 1075°C, 200v, 200 cps.

The most interesting behavior occurred in the iodide coactivated samples fired at 700°C with sulfur. In this series the phosphor with no CdS was considerably brighter than the corresponding high-temperature preparation, and the brightness of the former, shown in Fig. 5a, was diminished only slightly by the addition of as much as 7 mole % CdS, and even 10 mole % effected only a relatively moderate reduction. The power dissipation (Fig. 5b) was initially the highest in any of the series, but with increasing amount of CdS, a remarkable decrease occurred so that with 3 mole % CdS, the power is only 10% of its initial value. Efficiency, shown in Fig. 5c, reaches a maximum with 7 mole % CdS, but in this instance the improvement is not accompanied by the appreciable brightness loss noted with the high-temperature material.

Discussion

In the present study, phosphors with the highest brightness in a given series are associated with cubic or faulted structures. In the low-temperature iodide coactivated samples, the single cubic phase persists with a higher proportion of CdS (10 mole %) than in any of the other series (Fig. 5a). However, a slight decrease in brightness noticeable for the cubic compositions with 7 and 10 mole % CdS may be an indication of the incipient formation of the hexagonal structure. The different firing temperatures for the two iodide coactivated series account for structural differences in samples with equivalent ZnS-CdS ratios (compare Fig. 4a and 5a). The chloride and bromide coactivated samples, however, were fired at the same temperature (950°C) and it is probable that in their case structural differences (Fig. 3a) for equivalent compositions reflect a different influence of the respective coactivators. Similar effects on structure have been described by Shrader and Larach (11).

Conclusions

The data presented support the conclusion of an increasing number of investigators, (2, 3, 11-13) that cubic or complex faulted structures of ZnS are the most suitable for attaining maximum EL. This has been attributed to the absence in the cubic structure of deep traps found in the hexagonal modification (3, 11). The EL properties are simul-

taneously influenced by interrelated effects from phase relationships involving the segregation of copper, crystal structure, and trapping states. The relative importance of each of these separately cannot be decided at present.

Acknowledgment

The problem was suggested by R. E. Shrader with whom the author had valuable discussions. The gracious aid of S. M. Thomsen in making some measurements and his good advice are appreciated. Spectral distributions were recorded by H. E. MacDonald, x-ray diffraction data were obtained by W. C. Roth, and M. C. Gardels performed the chemical analyses for copper.

Manuscript received April 24, 1963. This paper was presented at the Chicago Meeting, May 1-5, 1960.

Any discussion of this paper will appear in a Discussion Section to be published in the June 1964 JOURNAL.

REFERENCES

1. R. E. Shrader and S. Larach, Unpublished data (1958).
2. A. Wachtel, *This Journal*, **107**, 602 (1960).
3. P. Zalm, *Philips Research Repts.*, **11**, 353 (1956).
4. S. Asano, *Science of Light*, **4**, 32 (1955).
5. G. R. Fonda, *Trans. Electrochem. Soc.*, **87**, 339 (1945).
6. S. Larach and R. E. Shrader, Brussels International Conference on Solid State Physics, p. 41, 1958.
7. A. Wachtel, U. S. Pat. 2,874,128 (1959).
8. B. E. Bartels and M. S. Wasserman, New York Meeting, Electrochem. Soc., April 1958, Abstract 31.
9. I. J. Hegyi, S. Larach, and R. E. Shrader, *This Journal*, **104**, 717 (1957).
10. S. Larach and R. E. Shrader, *RCA Review*, **20**, 532 (1959).
11. D. W. G. Ballentyne, *This Journal*, **107**, 807 (1960).
12. A. H. McKeag and E. G. Steward, *ibid.*, **104**, 41 (1957).
13. F. C. Palilla and D. H. Baird, *ibid.*, **109**, 1162 (1962).

An X-Ray Study of Pyrochlore Fluoantimonates of Calcium, Cadmium, and Manganese

M. A. Aia,[1] R. W. Mooney, and C. W. W. Hoffman

Chemical and Metallurgical Division, Sylvania Electric Products Inc., Towanda, Pennsylvania

ABSTRACT

Pyrochlore fluoantimonates of divalent metals have the general formula $M^{II}_{1+a+b/2}Sb_2O_6(O'_a + F_b)$ and can demonstrate both cation and anion defects. Fluoantimonates of Ca, Cd, and Mn having the pyrochlore structure were prepared and indexed as face-centered cubic from x-ray powder patterns. The cell edge of all binary combinations decreased linearly from Ca (10.30Å) to Cd (10.27Å) to Mn (10.14Å) fluoantimonate. Calcium fluoantimonate crystallized as a defect pyrochlore, with both Ca and F deficiencies. The structure of $Ca_{1.56}Sb_2O_{6.37}F_{0.44}$ was determined by the method of least squares from powder patterns. The value of the variable oxygen parameter x was 0.28_7. Fluoride is much less stable in the antimonates of Cd and Mn, but as little as 0.2% fluoride can be sufficient to cause these antimonates to crystallize in the pyrochlore structure.

Cubic compounds of the pyrochlore structure class have been studied with renewed interest since the discovery of ferro-electricity in cadmium niobate, $Cd_2Nb_2O_7$, by Cook and Jaffe (1). Pyrochlores have the idealized formula $A_2B_2O_6X$, where $A^{I,II,III}$ and $B^{IV,V,VI}$ are suitable cations of the proper valences, and X is O, OH, and F. Jona, Shirane, and Pepinsky (2) give an excellent description of the pyrochlore structure in their paper on $Cd_2Nb_2O_7$ and related compounds. Another synthetic compound with the pyrochlore structure, calcium fluoantimonate or fluoromeite, has recently been found to exhibit both fluorescence (3) and phosphorescence (4), thus introducing this structure class to the family of self-activated phosphors.

The first complete structural analysis for antimonate compounds of the type studied herein was given in 1932 by Zedlitz (5). In his study of the mineral romeite, with generalized formula $(Ca,Mn,Na)_2Sb_2O_6$ (O,OH,F), Zedlitz found that fluoride was essential to the formation of the pyrochlore structure, and that a continuous, three-dimensional array of SbO_6 octahedra held the structure together in a framework of composition $(Sb_2O_6)_\infty$. The Ca, F, and excess O ions occupied holes in the framework at special fixed positions. In 1944, Byström (6) reported a complete structural analysis of $Ca_2Sb_2O_7$, $Cd_2Sb_2O_7$, and $Sr_2Sb_2O_7$ and found that they had a structure not like pyrochlore, but instead like weberite, in which all seven oxygen atoms are co-ordinated to antimony atoms resulting in orthorhombic instead of cubic symmetry.

In 1950, Butler and co-workers (7) reported on studies of calcium antimonates as related to the formation of calcium halophosphate phosphors. Some of the x-ray work of Byström (6) and Magnéli (8) was confirmed, as was the contention of Zedlitz that fluoride ion was essential to the forma-

[1] Present address: General Telephone and Electronics Laboratories, Inc., Bayside, New York.

tion of calcium romeite, *i.e.*, calcium antimonate with the pyrochlore structure. However, in an attempt to explain the stoichiometry of calcium fluoantimonate, Butler and co-workers concluded that both trivalent and pentavalent antimony were present. They proposed the formula, $Ca_4Sb_2^{III}Sb_2^{V}O_{11}F_2$, which would invalidate the structure obtained by Zedlitz.

The present work was undertaken to resolve the differences in the literature by means of a structural analysis of cubic calcium fluoantimonate, and to extend the results to cover analogous compounds of manganese and cadmium. Since most calcium halophosphate phosphors now manufactured contain small amounts of cadmium (9), as well as manganese and antimony, the results could also be useful in a study of intermediates formed during the synthesis of such phosphors.

Experimental

Preparation of samples.—The cubic calcium fluoantimonate whose structure was analyzed was prepared by the method of Butler and co-workers (7) from $CaCO_3$, CaF_2, and $(Sb_2O_4)_{0.75}\cdot(Sb_2O_3)_{0.25}$, of luminescent grade purity. The $(Sb_2O_4)_{0.75}\cdot(Sb_2O_3)_{0.25}$ was prepared while attempting to prepare Sb_2O_4 by heating a 1-in. layer of cubic Sb_2O_3 for 10 hr at 400°-650°C in air; about 25% Sb_2O_3 was detected by x-ray diffraction after this treatment. One mole of each ingredient was pebble milled together, fired 1 hr at 980°C in a quartz crucible, ground, refired 1 hr at 1175°C, and reground. The blue-white calcium antimonate was suspended 3 times in 10% HNO_3 to leach out the excess CaF_2. Analysis of the dried product gave 15.0% Ca, 58.5% Sb, and 2.3% F, which corresponds to the formula $Ca_{1.56}Sb_2O_{6.37}F_{0.44}$. The experimental density was 5.02 g-cm^{-3}. If other compounds were present, they could not be found by x-ray diffraction, contrary to the results of Chevalier and co-workers (4) who found $CaSb_2O_6$ and $Ca_2Sb_2O_7$ in a similar preparation.

Cadmium fluoantimonate was best prepared by mixing one mole each of CdO_2 (10), CdF_2, and $(Sb_2O_4)_{0.75}(Sb_2O_3)_{0.25}$. A soft, uniformly reacted material was obtained by firing 1 hr at 845°C in a covered crucible. When CdO or $CdCO_3$ was used in place of CdO_2, the firing product was much less homogeneous. The olive-green cadmium antimonate was leached with 10% HNO_3 to remove the excess cadmium, which was present mostly as CdO after firing. Typical analyses were 38.8% Cd, 42.0%Sb, and 0.2% F, which corresponds to the formula $Cd_{2.0}Sb_2O_{6.9}F_{0.1}$. The experimental density varied from 6.76 to 6.86 g-cm^{-3}. No other compounds were found by x-ray diffraction.

A series was made in which a variable amount of CdF_2 was mixed with CdO and Sb_2O_3, keeping a constant atomic ratio of 2.05 Cd per 2 Sb. Static firing of the mixtures showed that, in the absence of fluoride, the orthorhombic $Cd_2Sb_2O_7$ formed at 430°C after 18 hr, and much faster at higher temperatures. The cubic cadmium fluoantimonate was formed by firing between 480° and 540°C for 75 min, when at least 0.4 atom F per mole Sb_2O_3 was present; samples fired at 720°C showed either the orthorhombic antimonate, or a mixture of this with the cubic fluoantimonate. Presumably, the composition moves across a phase boundary upon the loss of the small quantity of fluoride required to stabilize the pyrochlore structure.

Manganese fluoantimonates, and all the binary mixed antimonates were prepared by combining 2.0 moles of MO (MO was $CaCO_3$, CdO_2, $MnCO_3$, or any binary mixture), 1.0 mole of Sb_2O_3, and 1.2 moles of $NH_4F\cdot HF$. The mixtures were blended by pebble milling overnight in acetone. After drying, the powders were heated in covered porcelain crucibles at 550°C, mortared, reheated from 800° to 1150°C, and reground. The final firing schedule was varied, depending on the composition, to minimize sintering and inhomogeneity; the higher the Mn content, the darker the color, and the lower the firing temperature. Analyses on a manganese fluoantimonate reheated 2 hr at 850°C were 26.8% Mn, 49.7% Sb, and 0.35% F. Impurities (Mn_2O_3 and $MnSb_2O_6$) were found by x-ray diffraction, and it was not meaningful to estimate the stoichiometry of the manganese fluoantimonate prepared. In all samples, metallic impurities detectable by spectrographic analysis were less than 0.1%.

X-ray diffraction methods.—X-ray diffraction patterns were taken on a Philips-Norelco unit, using nickel-filtered CuKα radiation (1.5418Å). Long exposures were made on 114.6 mm Debye-Scherrer cameras to determine impurities. Intensity and 2θ values were taken from diffractometer tracings made at a scanning speed of ¼°/min. The diffractometer was calibrated with Si and checked with W, assuming values given by the National Bureau of Standards. The observed intensities were measured on the diffractometer tracing by graphical integration. The resulting values were corrected for changes in slit width, giving the I_o values, scaled to a maximum value of 1000, shown in Tables I and III. The reflections used to calculate the cubic-cell parameter were 662, 666 (1022), 840, 844, 1062, and 884 (1200). These reflections at high values of 2θ were selected because they were fairly intense and showed less interference from other reflections. Virtually no correction was indicated by calibration.

Chemical analyses.—**Antimony:** The sample was digested overnight with H_2SO_4 and K_2SO_4. Filter paper and more H_2SO_4 were added and the solution heated until clear. Antimony was then determined by titration with $KMnO_4$ (11). **Fluorine:** The sample was fused with Na_2O_2 and Na_2CO_3 then dissolved. Fluorine was distilled off as hydrofluosilicic acid and titrated with thorium nitrate solution (11). **Calcium:** Antimony was fumed off with HBr, then calcium was precipitated and weighed as the oxalate. **Cadmium:** Antimony was fumed off with HBr, then cadmium was precipitated from strongly acid solution and weighed as CdS. **Manganese:** Antimony was fumed off with HBr, then manganese was determined by flame photometry. The presence of calcium or cadmium did not interfere. **Oxygen:** Attempts to determine oxygen as H_2O by heating samples in a stream of hydrogen were unsuccessful, so oxygen was calculated by difference.

Table I. Indexed powder patterns and cell sizes of cubic fluoantimonates of calcium, cadmium, and manganese

hkl	$Ca_{1.56}Sb_2O_{6.37}F_{0.44}$ d (A)	I_o	$Cd_{2.0}Sb_2O_{6.9}F_{0.1}$ d (A)	I_o	Mn fluoantimonate (0.35% F) d (A)	I_o
111	5.94	549	5.92	16	5.85	210
311	3.104	381	3.093	10	3.058	210
222	2.973	1000	2.965	1000	2.927	1000
400	2.573	226	2.567	363	2.536	225
331	2.363	30	2.356	14	—	—
511, 333	1.9819	122	1.9762	20	1.9516	75
440	1.8204	503	1.8149	472	1.7928	385
531	1.7409	98	—	—	1.7142	75
533	1.5706	67	—	—	1.5457	60
622	1.5529	402	1.5478	440	1.5283	375
444	1.4866	95	1.4816	109	1.4636	115
711, 551	1.4422	73	—	—	1.4205	60
731, 553	1.3410	88	—	—	1.3201	100
800	1.2875	55	1.2834	56	1.2680	85
751, 555	1.1895	38	—	—	—	—
662	1.1816	140	1.1779	145	1.1633	150
840	1.1517	119	1.1480	129	1.1335	125
911, 753	1.1307	36	—	—	1.1134	30
931	1.0797	24	—	—	1.0626	35
844	1.0513	108	1.0483	113	1.0348	125
933, 771, 755	1.0352	24	—	—	1.0193	30
951, 773	0.9958	38	—	—	0.9796	35
1022, 666	0.9910	109	0.9883	131	0.9760	145
953	0.9606	20	—	—	0.9459	35
1111, 775	0.9289	23	—	—	0.9140	10
880	0.9105	41	0.9077	48	0.8961	70
1131, 971, 955	0.9000	50	—	—	0.8863	45
1133, 973	0.8737	49	—	—	0.8603	45
1062	0.8706	187	0.8680	200	0.8571	205
1200, 884	0.8585	137	0.8559	146	0.8451	145
1151, 777	0.8496	26	—	—	0.8367	40
1153, 975	0.8274	49	—	—	0.8148	80
1240	0.8144	135	0.8120	145	0.8019	95
1311, 1171, 1155, 993	0.7878	113	—	—		
1066	0.7855	195	0.7831	215		
1244	0.7766	213				
Cell size, a_o (Å)	10.300 ± 0.002		10.269 ± 0.003		10.141 ± 0.003	

X-ray Powder Patterns

X-ray powder patterns, indexed as face-centered cubic, are given in Table I for the fluoantimonates of calcium, cadmium, and manganese described above. Four lines due to Mn_2O_3 and $MnSb_2O_6$ impurities were discounted in the indexing of the manganese fluoantimonate. The cell sizes followed the expected progression and decreased from calcium to cadmium to manganese fluoantimonate. All three compounds were deficient in fluoride, and only the cadmium fluoantimonate contained the expected 2 atoms of divalent metal per two atoms of antimony. The apparent stoichiometry of cubic cadmium fluoantimonate was confirmed by chemical analysis of several other preparations and will be discussed later. However, no special significance need be ascribed to the specific ratios of atoms since they reflect, in part, the particular methods of preparation, the results of chemical analytical procedures, and the peculiarities of the pyrochlore structure.

Structure Determination

The diffraction pattern of $Ca_{1.56}Sb_2O_{6.37}F_{0.44}$, calcium fluoantimonate with the romeite or pyrochlore structure, contained 36 lines, all of which were readily indexed as cubic (Table I). The systematic absence of all hkl reflections for which h + k, k + l, and l + h $\neq$ 2n, and all Okl type reflections for which k + l $\neq$ 4n was consistent with the space group of pyrochlore, Fd3m-O^7_h. The density calculated for 8 molecules of $Ca_{1.56}Sb_2O_{6.37}F_{0.44}$ per unit cell is 5.06, which agrees within 0.8% of the experimental density of 5.02 g-cm^{-3}. The density calculated for $Ca_2Sb_2O_6F$ is 5.33. In 1932, Zedlitz (5) placed the atoms of the mineral romeite in the following special positions of space group Fd3m-O^7_h, with origin at 43m, and 8 molecules of $Ca_2Sb_2O_6(O', F)$, where O′ is the oxygen in excess of 6 atoms per 2 Sb:

16 Sb in 16d: ⅝, ⅝, ⅝; ⅝, ⅞, ⅞; ⅞, ⅝, ⅞; ⅞, ⅞, ⅝.
16 Ca in 16c: ⅛, ⅛, ⅛; ⅛, ⅜, ⅜; ⅜, ⅛, ⅜; ⅜, ⅜, ⅛.
8(O′ + F) in 8a: 0, 0, 0; ¼, ¼, ¼.
48 O in 48f: x, 0, 0; $\bar{x}$, 0, 0; ¼ + x, ¼, ¼; ¼ − x, ¼, ¼; 0, x, 0; 0, $\bar{x}$, 0; ¼, ¼ + x, ¼; ¼, ¼ − x, ¼; 0, 0, x; 0, 0, $\bar{x}$; ¼, ¼, ¼ + x; ¼, ¼, ¼ − x.

Further information is given in the International Tables (12). The only undetermined atomic parameter in the structure was x. As a first approximation, a value of 0.25 was chosen and relative intensities were calculated, with F and O′ atoms in the 8a special positions, from the well-known relation

Table II. Final values of oxygen parameter x for $Ca_{1.56}Sb_2O_{6.37}F_{0.44}$ (x and σ are expressed as fractions of the unit-cell parameter)

F and O′ positions	x	Std. dev., σ	$R = \Sigma\|I_o - I_c\|/\Sigma I_o$
8a	0.287	0.0022	0.101
8b	0.263	0.0051	0.234

$$I_c = k\,p\,|F_{hkl}|^2 \frac{(1+\cos^2 2\theta)}{(\sin^2\theta\cos\theta)}$$

where p is the multiplicity; F_{hkl} is the structure amplitude; f (θ) is the usual Lorentz polarization term; and k is a factor for scaling I_c to I_o by setting $\Sigma I_c = \Sigma I_o$. Values of atomic scattering factors were taken from James and Brindley (13). For the formula $Ca_{1.56}Sb_2O_{6.37}F_{0.44}$, the scattering factor, f, for the (F+O′) sites was taken as the mean between f_O and f_F because of their nearly equal occupancy of these sites (0.44 F + 0.37 O′), and because of their nearly equivalent atomic numbers. Completely randomized location of F and O′ ions in the special positions was thus assumed. The variable parameter x was refined by the method of least squares (14) to minimize $\Sigma w(I_o - I_c)^2$ and determine the probable error in x. The weighting factor, w, was assigned a value of unity throughout. A small temperature correction factor, $B = 0.5\text{Å}^{-2}$, was applied to the total structure during the iteration. This treatment refined the value of x to 0.287 and decreased R $(\Sigma|I_o - I_c|/\Sigma I_o)$ to 0.10. Calculations were then carried out for the F and O′ atoms in special positions 8b, which are also spatially possible. Results are summarized in Table II.

It is obvious that the best fit of calculated to observed intensities is given with the F and excess O atoms in the 8a positions. The 8b positions of F and O′ atoms yield a significantly larger R factor. The large effect of the seemingly small contribution of these atoms to the structure factor, $F^2 = \Sigma A^2 + \Sigma B^2$, occurs because the contribution of these atoms to A and B, the real and imaginary components of the structure factor, undergoes a phase change which reverses sign for all reflections with odd indices. This reversal in sign effects the summed values of A and B, as reflected in Table II. The calculations were not repeated for the formula $Ca_2Sb_2O_6(F,O')$ because the compound with 2Ca per 2Sb atoms would only be a special case of the general family of compounds, $Ca_{1+a+b/2}Sb_2O_6(O'_a + F_b)$, which is suggested by the structure. Furthermore, a formula such as $Ca_2Sb_2O_6F$ is unlikely since it is unbalanced by one electrical unit, and $Ca_2Sb_2O_7$ is not a pyrochlore. Table III gives values of observed intensity and calculated intensity for x = 0.287 (8a positions). The observed intensities were scaled so that the strongest reflection (222) had a value of 1000.

Table III. Values of I_o and I_c for the final value $x = 0.287$ for the compound $Ca_{1.56}Sb_2O_{6.37}F_{0.44}$

hkl	d	I_o	I_c	hkl	d	I_o	I_c
111	5.94	549	552	1020, 862	—	—	2
220	—	—	6				
311	3.104	381	398	951, 773	0.9958	38	30
222	2.973	1000	1018				
400	2.573	226	205	1022, 666	0.9910	109	122
331	2.363	30	41				
422	—	—	8	953	0.9606	20	21
511, 333	1.9819	122	110	1042	—	—	1
440	1.8204	503	551	1111, 775	0.9289	23	23
531	1.7409	98	101	880	0.9105	41	50
620	—	—	1	1131			
533	1.5706	67	48	971	0.9000	50	40
622	1.5529	402	376	955			
444	1.4866	95	66	1060, 866	—	—	2
711, 551	1.4422	73	61				
642	—	—	0	1133, 973	0.8737	49	41
731, 553	1.3410	88	87	1062	0.8706	187	190
800	1.2875	55	48	1200, 884	0.8585	137	112
733	—	—	3	1151, 777	0.8496	26	21
822, 660	—	—	3	1222, 1064	—	—	5
751, 555	1.1895	38	30	1153, 975	0.8274	49	46
662	1.1816	140	136				
840	1.1517	119	91	1240	0.8144	135	149
911, 753	1.1307	36	28	991	—	—	19
				1082	—	—	0
664	—	—	0	1311			
931	1.0797	24	20	1155	0.7878	113	104
844	1.0513	108	122	1171, 993			
933, 771, 755	1.0352	24	20	1066	0.7855	195	215
				1244	0.7766	213	290

The bond distances calculated from the structure are listed in Table IV. The bond distances found

Table IV. Bond distances for compounds related to calcium fluoromeite, and of the general formula $A_xB_2O_yF_z$ (all values in Angstroms)

Bond	Present work, $Ca_{1.56}Sb_2O_{6.37}F_{0.44}$	Zedlitz $(Ca,Mn,Na)_2Sb_2(O,OH,F)_7$	Byström $Cd_2Ta_2O_7$ (pyrochlore)	Byström $Ca_2Sb_2O_7$ (weberite)	Magnéli $PbSb_2O_6$	Pauling (calculated)
A — O	2.47	2.55	2.50 and 2.25	2.32-2.62	2.52	2.39
A — F	2.23	2.23	—	—	—	2.35
B — O	2.04	1.97	2.04	1.95-2.00	2.00	2.02
F — O	2.95	3.08	—	—	—	2.76
O — O	2.63-3.11	2.67-2.90	2.66-?	2.60-?	2.60-?	2.80
O — O (c axis)	4.39	—	—	—	—	—
Error:	±0.02	—	—	—	—	—

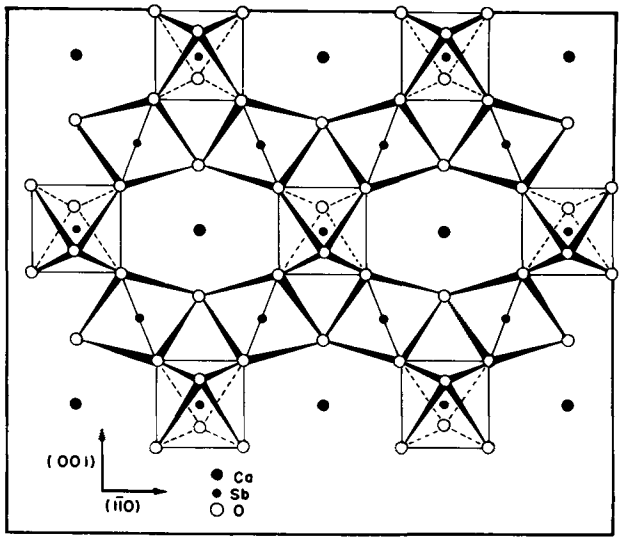

Fig. 1. Configuration of SbO_6 octahedra in calcium fluoantimonate, with pyrochlore structure, projected on (110). Not shown are the Ca ions which overlap the Sb ions at (⅛, ⅛), etc., and the excess oxygens and fluorines, located above and below the Ca ions. Adapted from Jona and co-workers (2).

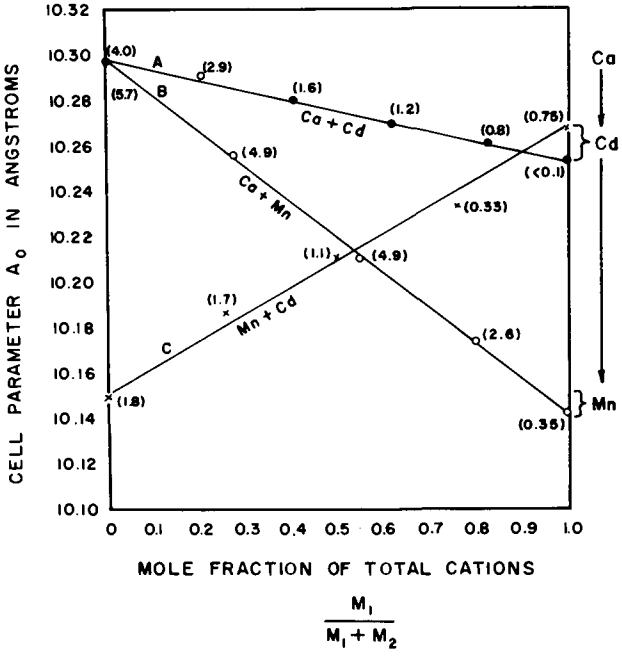

Fig. 2. Cell size *vs.* composition of pyrochlore fluoantimonates of Ca, Cd, and Mn. Weight per cent fluoride found by analysis is given in parentheses. Brackets indicate where cell size varied with fluoride content of antimonates containing only Cd or only Mn.

in $Ca_{1.56}Sb_2O_{6.37}F_{0.44}$ are in good agreement with those found in similar compounds, and with values predicted from Pauling's ionic radii. The agreement is especially good for the B-O, *i.e.*, Sb-O, bond distance. This is expected since the structures of all of the compounds are dependent on a continuous network of BO_6 octahedra for their rigidity.

Figure 1 shows the configuration of SbO_6 octahedra in calcium fluoantimonate, or for that matter, any pyrochlore antimonate. It is easily seen that calcium deficiencies can occur without damaging the integrity of the structure, which is held together by the octahedra, since the calcium ions actually occupy large holes in the network. The same is true of the fluorine and excess oxygen ions, which are located above and below the calcium ions, but are not shown on Fig. 1.

Solid Solution Studies

Binary mixtures of fluoantimonates of Ca, Cd, and Mn were prepared and studied by x-ray diffraction. The compounds showed a linear decrease in cell size as the cation was varied from Ca to Cd to Mn, indicating continuous solid solutions were formed. Variations in cell parameter and fluoride content with composition are shown on Fig. 2. It is evident that fluoride content also varied with composition, and that the cell parameter varied with fluoride content (shown as weight per cent). Much less fluoride than one F per two Sb atoms needs to be incorporated to obtain pyrochlore antimonates of Ca, Cd, or Mn. The fluoride content of five samples of cubic cadmium fluoantimonate ranged from <0.03 to a high of only 0.23 atom F per 2 atoms Sb. The instability of fluoride in cadmium fluoantimonate is discussed further below.

Discussion

Stoichiometry.—The cubic fluoantimonate of cadmium was not cation deficient like that of calcium. This can be explained by the fact that fluoride is not thermally stable in cadmium fluoantimonate, hence cadmium atoms do not have to be removed to compensate for the charge difference between incorporated F and O atoms. The lower thermal stability of fluoride in cadmium fluoantimonate *vs.* the high stability in calcium fluoantimonate is analogous to the relative stabilities of CaF_2 and CdF_2 and can be attributed to the much lower electropositive nature of Cd, which results in lower binding strength with fluorine. A comparison of the estimated partial charges on the atoms in the fluoantimonates and fluorides of calcium and of cadmium is given in Table V. The method of calculation, developed by Sanderson (15), is based on the electronegativities of the elements. The results indicate that the electrostatic attraction between Ca or Cd atoms and F atoms in the fluoride is very similar to the attraction in the fluoantimonates.

As reported above (p. 1050), the calculated and observed densities of $Ca_{1.56}Sb_2O_{6.37}F_{0.44}$ agree within 0.8%. For $Cd_{2.0}Sb_2O_{6.9}F_{0.1}$, the formula suggested by chemical analyses, the density calculated for the same structure is 7.11, which is 3.6% higher than the observed density of 6.86 g-cm^{-3}. The presence of a small amount of impurity such as $Cd_2Sb_2O_7$ cannot be ruled out and may be responsible for the density discrepancy with cadmium fluoantimonate. If all the antimony is assumed to be pentavalent, and the other atoms are assigned their

Table V. Comparison of partial charges on atoms in fluorides and fluoantimonates of calcium or cadmium

Compound	Partial Charge Ca or Cd	F
CaF_2	+0.94	−0.47
$Ca_{1.56}Sb_7O_{6.37}F_{0.44}$	+1.11	−0.38
CdF_2	+0.54	−0.27
$Cd_{2.0}Sb_2O_{6.9}F_{0.1}$	+0.49	−0.30

usual charges, the charges balance to within −0.06 unit in $Ca_{1.56}Sb_2O_{6.37}F_{0.44}$, and to within +0.1 unit in $Cd_{2.0}Sb_2O_{6.9}F_{0.1}$. Thus, it appears that an earlier formulation showing both trivalent and pentavalent antimony in calcium fluoromeite (7) is unnecessarily complicated and does not allow for cation and anion defects. The present structure determination shows that the cation and anion defects in the stoichiometry arise naturally from the peculiarities of the pyrochlore structure and the location of Ca and F ions therein. The general formula for the fluoantimonates studied in this work may be written as $M^{II}_{1+a+b/2}Sb_2O_6(O'_a+F_b)$.

Structure.—The structure found for calcium fluoantimonate agrees well with that found by Zedlitz (5) for the mineral romeite, and may be placed in the general class with pyrochlore. The Ca and F ions occupy holes in an infinite network of SbO_6 octahedra in face-centered cubic symmetry. Cadmium and manganese appear to form analogous fluoantimonates, as would be predicted by the geometric criteria established by Isupov (16) and Aleshin and Roy (17). These criteria and our experimental results indicate that Mn^{2+} is just barely a large enough cation to form a pyrochlore antimonate, and hence it is more difficult to prepare cubic manganese fluoantimonate free of other antimonates, especially $MnSb_2O_6$. While it is well known that fluorine can replace oxygen up to whole atom amounts in pyrochlores (5, 17, 18), it has not been previously reported that quantities of fluoride as low as 0.2% F can be sufficient to stabilize the pyrochlore structure for calcium and cadmium antimonates, which otherwise would have the weberite structure (6). Among the best discussions of the effect of variable oxygen content in pyrochlores is the one by Pyatenko (19).

Importance in calcium halophosphate phosphors.—It was reported in 1950 (7) that at 875°C, during the synthesis of antimony-activated calcium halophosphate phosphors from the usual raw materials, practically all of the original antimony is converted into the cubic calcium fluoantimonate (romeite) before diffusing into the halophosphate lattice. Later work (20) showed that from 875° to 1140°C nearly all the insoluble (pentavalent) antimony was present as the metaantimonate, $CaSb_2O_6$, and not as fluoromeite, but no results at temperatures below 875°C were given. It has recently been found that a small amount of Cd, in partial substitution for Ca, produces brighter halophosphate phosphors under ultraviolet excitation (9). Absorption of 2537Å is increased with about 6 at. % Cd substituted for Ca. Because there is an optimum amount of cadmium substitution in halophosphates, there must be an important interaction with the host lattice, or the activator ions. The nature of the interaction is still unresolved. A large effect on the lattice parameters would not be expected with incorporation of 6 at. % Cd because of the similarity of the ionic radii of Cd^{2+} and Ca^{2+}. The improvement may be due to the formation of $Cd^+ - Mn^{2+}$ pairs, and the resultant resonance exchange, as postulated by Ropp (21) in his study of Mn-activated cadmium pyrophosphate and cadmium chlorophosphate (22) phosphors. In qualitative agreement, we have found that calcium or strontium halophosphates without Mn present are not improved by cadmium. Apple (23) recently reported that Cd substitution in Ca halophosphate reduces color-center formation due to short-wave ultraviolet radiation, and leads to improved maintenance of brightness in Sb-and Mn-activated phosphors exposed to 1850Å radiation. However, Apple's observations do not explain why Mn is also required to obtain improved lamp performance at 0 or 100 hr. Another possibility lies in the phosphor synthesis since the fluoantimonate of cadmium forms at lower temperatures (around 480°C) than that of calcium (around 800°C). During halophosphate synthesis, the pentavalent antimony may be combined with cadmium in preference to calcium. This could reduce the amount of $CaSb_2O_6$ formed and alter the mechanism by which antimony diffuses into the halophosphate lattice. Antimonates of cadmium should be more easily incorporated than antimonates of calcium because of higher vapor pressures and greater possibility of vapor-phase reaction with the matrix at halophosphate firing temperatures. For example, in a furnace used to prepare cadmium-modified calcium halophosphate phosphors, we have found large quantities of cubic cadmium fluoantimonate deposited on the walls of the furnace. A study of the phosphor synthesis indicated that cadmium and antimony were volatilized during phosphor formation, at least in part, as the insoluble pyrochlore fluoantimonate, $Cd_2Sb_2O_7(F)$.

Acknowledgment

The authors wish to thank G. L. Meisenhelter, H. D. Wilcox, and J. E. Mathers who performed the chemical analyses.

Manuscript received March 4, 1963. This paper was presented at the Pittsburgh Meeting, April 15-18, 1963.

Any discussion of this paper will appear in a Discussion Section to be published in the June 1964 JOURNAL.

REFERENCES

1. W. R. Cook, Jr., and H. Jaffe, *Phys. Rev.*, **88**, 1426 (1952).
2. F. Jona, G. Shirane, and R. Pepinsky, *ibid.*, **98**, 903 (1955).
3. F. Gaume, R. Bernard, P. DuPont, and J. Janin, *Compt. rend*, **252**, 544-546 (1961).
4. N. Chevalier, F. Gaume-Mahn, J. Janin, and J. Oviol, *ibid.*, **255**, 1096 (1962).
5. O. Zedlitz, *Z. Krist.*, **81**, 253 (1932).
6. A. Byström, *Arkiv Kemi, Mineral. Geol.*, **18A**, 1 (1944).
7. K. H. Butler, M. J. Bergin, and V. M. B. Hannaford, *This Journal*, **97**, 117 (1950).
8. A. Magnéli, *Arkiv Kemi, Mineral. Geol.*, **15B**, 1 (1941).
9. M. A. Aia and S. M. Poss, U. S. Patent 2,965,786 (1960).
10. C. W. W. Hoffman, R. C. Ropp, and R. W. Mooney, *J. Am. Chem. Soc.*, **81**, 3830 (1959).
11. W. F. Hillebrand, G. E. F. Lundell, "Applied Inorganic Analysis," 2nd Ed., pp. 280 and 742, John Wiley and Sons, Inc., New York (1953).
12. N. F. M. Henry and K. Lonsdale, Editors, "International Tables for X-Ray Crystallography, Vol. I. Symmetry Groups," p. 340, The Kynoch Press, Birmingham, England (1952).

13. R. W. James and G. W. Brindley, *Z. Krist.*, **78**, 470 (1931).
14. D. P. Shoemaker, J. Donohue, V. Schomaker, and R. B. Corey, *J. Am. Chem. Soc.*, **72**, 2328 (1950).
15. R. T. Sanderson, "Chemical Periodicity," pp. 38-44, Reinhold Publishing Corp., New York (1960).
16. V. A. Isupov, *Kristallografiya*, **3**, 96 (1958).
17. E. Aleshin and R. Roy, *J. Am. Ceram. Soc.*, **45**, 18 (1962).
18. R. Mazelsky and R. Ward, *J. Inorg. Nucl. Chem.*, **20**, 39 (1961).
19. Yu. A. Pyatenko, *Kristallografiya*, **4**, 204 (1959).
20. W. L. Wanmaker, A. H. Hoekstra, and M. G. A. Tak, *Philips Research Repts.*, **10**, 11-38 (1955).
21. R. C. Ropp, *This Journal*, **109**, 569 (1962).
22. R. C. Ropp, *ibid.*, **110**, 113 (1963).
23. E. F. Apple, *ibid.*, **110**, 374 (1963).

Behavior of Germanium Electrodes in a Ziegler Electrolyte

R. J. Flannery,[1] J. E. Thomas, Jr.,[2] and Dan Trivich

Department of Chemistry, Wayne State University, Detroit, Michigan

ABSTRACT

The behavior of n- and p-type germanium electrodes, particularly under anodic condition, was studied in a Ziegler electrolyte composed of triethyl aluminum and sodium fluoride in a 2 to 1 mole ratio. Germanium did not dissolve anodically but rather the anode products consisted of principally ethane and ethylene together with some butane and an immiscible liquid. Limiting currents were observed for n-type germanium and silicon but not for the p-type materials. This result, together with the observation that the anodic saturation current increased directly with increase in light intensity on n-type electrodes, indicates that the anode reaction consumes holes. The cathode product, metallic aluminum, formed a rectifying junction on n-Ge or p-Si.

In recent years, studies have been made of the electrochemical behavior of germanium electrodes in relation to their semiconducting properties. Several reviews of this work have appeared (1-3). It has been established for semiconductor electrodes that, in addition to the various current limiting processes which can occur in the electrolyte phase, current-limiting processes can also occur within the electrode and that these can be studied under suitable experimental conditions.

Brattain and Garrett (4) and Turner (5) studied the anodic dissolution of germanium electrodes in aqueous potassium hydroxide solutions. They found that current limitation from within the electrode occurs for n-type germanium but not for p-type germanium. They concluded that holes are consumed in the rate-determining step of the electrochemical process and that the current is controlled by the rate of generation of carriers in the germanium when the supply of holes at the surface becomes depleted by the electrochemical reaction. They demonstrated that when the rate of generation of carriers was increased by illuminating the electrode, the limiting current increased in a predictable manner.

Thus in an anodic process which shows such a preference for reaction with holes, the chemical oxidation occurring on the surface of the electrode involves a transfer of electrons to the valence band of the semiconductor. In an n-type semiconductor, in which holes are the minority carrier, this results in depletion of holes from the surface region of the semiconductor. Application of larger anodic bias does not result in an increase in the concentration of holes at the surface but rather widens the space charge region extending inward from the surface. The anodic process then becomes limited by the rate at which holes are generated by thermal means, light, etc., in the space charge region and in the bulk of the semiconductor within a diffusion length of the edge of the space charge region. Thus all of the holes that diffuse into the space charge region are caught by the field and are driven to the surface.

Gerischer and Beck (6) showed, for many redox couples in aqueous solution at germanium electrodes, that oxidation preferentially occurs by transfer of electrons to the valence band and usually reduction preferentially consumes electrons from the conduction band. Current limitation from within the electrodes occurs for oxidation on n-type germanium or for reduction on p-type germanium.

In the experiments reported in this article it was intended to discern whether the anodic electrochemical process in the chosen nonaqueous electrolyte would be controlled by transfer of electrons to the conduction band or to the valence band as in the aqueous systems. The electrolyte used for these studies is free of oxygen and water, and it is possible that surface oxide films normally present on germanium are removed by electrolytic treatment in this electrolyte. If the preferences for transfer of electrons to the valence or conduction band exhibited by germanium electrodes in aqueous solutions are influenced by the existence of a surface oxide film, the behavior of the electrodes in this medium might be noticeably different from the aqueous case.

The electrolyte used was first reported by Ziegler and Lehmkuhl (7). These workers discovered that two moles of triethyl aluminum react with one mole of sodium fluoride to form a complex,

[1] Present address: Research and Development Department, American Oil Company, P. O. Box 431, Whiting, Indiana.

[2] Present address: IBM Components Division, P. O. Box 110, Poughkeepsie, New York.

$Na(AlEt_3)_2F$, having a high electrolytic conductivity. The complex is liquid at room temperature because it supercools readily. Its melting point is 35°C. It is a clear liquid, slightly more viscous than water. The specific conductivity (8, cf. 7) is 2×10^{-2} $(ohm\text{-}cm)^{-1}$, which is about the same as that of a 5% aqueous solution of sodium sulfate. The electrolyte complex has a high affinity for oxygen. Ethers are stable in its presence but alcohols, water, and oxygen gas react violently with it. For this reason experiments must be conducted in an environment free of active oxygen.

Electrolytic decomposition of the electrolyte produces very pure aluminum at the cathode and products characteristic of ethyl radicals as intermediate products at the anode. This is illustrated by the fact that lead anodes dissolve to produce tetraethyl lead (9). According to Ziegler (9) germanium alkyls can be prepared by anodic dissolution of germanium in this electrolyte. Our results showed that, in contrast to the behavior of lead, and contrary to the reported work of Ziegler, germanium does not dissolve anodically to produce tetraethyl germane, but is inert. The germanium used by Ziegler was probably not single crystal material. Based on the work of Ziegler it was expected that the germanium would etch to produce a truly oxide-free surface. It was found in this study that the germanium electrodes had to be conditioned by alternate heavy anodic and cathodic polarization before reproducible results could be obtained. This result suggests that reduction of the surface oxide occurred at least in part and was perhaps necessary for proper response of the electrodes.

Experimental Details

Electrolyte.—The electrolyte was prepared in an all-glass apparatus under an inert atmosphere of purified nitrogen. The inert atmosphere was required because of the spontaneous flammability in air of both triethyl aluminum and the electrolyte complex. The triethyl aluminum was freed of hydrides by overnight treatment with metallic sodium. The electrolyte was prepared by reacting anhydrous sodium fluoride with an excess of the purified triethyl aluminum at about 80°C. Minor impurities other than hydride in the triethyl aluminum remain in the unused portion. The electrolyte complex is immiscible with triethyl aluminum and more dense. It separates readily to form a layer beneath the unused triethyl aluminum. The spontaneously flammable liquids were moved about through the purification, preparation, storage, and electrolysis system by means of siphons operated by a positive pressure of nitrogen.

Electrodes.—The germanium and silicon electrodes were of single crystal material. They were cut roughly to shape with a diamond saw, polished to size with alundum powders, and etched smooth with CP4 etchant. They were again briefly etched in CP4 just before use. The electrodes were 1 cm wide by 1.5-2.5 cm long with thicknesses up to 2 mm. A collection of other metal electrodes was made for a survey of their properties in this electrolyte. These metal electrodes were cut or cast from the purest materials at hand.

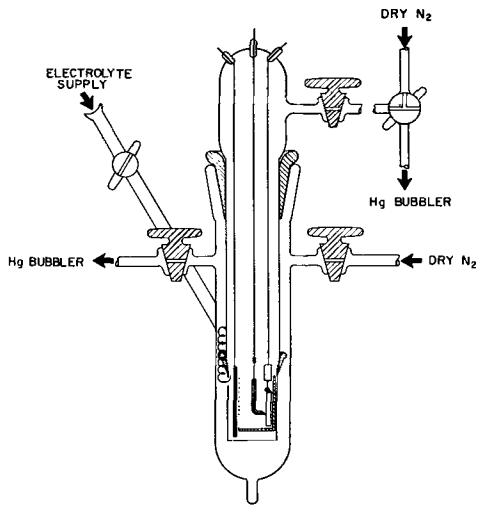

Fig. 1. Electrolysis cell. Flow of N_2 prevents ignition of the electrolyte when the electrodes are removed.

Electrolysis Cell.—A diagram of the cell used for the electrolysis studies is shown in Fig. 1. The cell, made of Pyrex glass, consisted of two parts, an electrolysis vessel containing the electrolyte and an insert carrying the electrodes. The electrolyte was introduced through a tube at the bottom of the vessel.

A N_2 gas-lock was used to prevent access of air to the electrolyte when adjustments or exchanges of electrodes were made. The gas-lock was operated by allowing the nitrogen to flow into the vessel and into the insert simultaneously. When the cell was opened, nitrogen flowed out of the top of the vessel, protecting the electrolyte from the air while, at the same time, nitrogen flowed out of the insert tip, keeping air away from the wet electrodes.

Two different electrode-bearing inserts were used. One insert was used for electrical measurements. The tip of this insert is shown in Fig. 2. The germanium electrodes were shaped to fit exactly at the back wall of a rectangular glass box, which thus served as an anode shield. The box consisted of a Beckman DU spectrophotometer cell (Pyrex), with one window cut off and the frosted sides

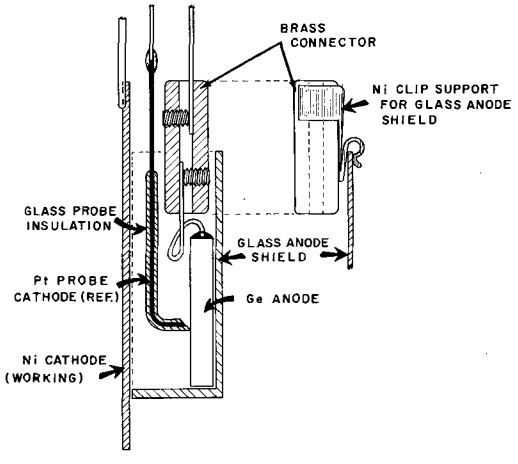

Fig. 2. Details of electrode assembly for germanium anode studies

polished clear. An aluminum-plated nickel counter-electrode was positioned so as to cover the open wall of the cell. A platinum probe electrode, glass coated except at the tip for insulation from the electrolyte, and bevel tipped for constant spacing from the working electrode, was used as a reference electrode for the germanium anode studies. The exploratory studies of other metal electrodes were made without reference electrode or anode shielding.

The other insert was used for collection of products. It contained the germanium electrode under the flared end of a narrow tube. The counter electrode was positioned along the inner surface of the vessel, well away from the flared tube. The opening of the flared tube extended beneath the surface of the electrolyte so that it confined gaseous and floating-liquid products. These were pulled up into the narrow tube and withdrawn from the cell for sampling.

Electrical measurements.—The current for the d-c measurements was supplied from a 22½v dry cell or from a small rectifier in series with a Simpson Model 260 VOM as ammeter and several small potentiometers. Voltage measurements were made with a Heathkit Model V6 vacuum tube voltmeter.

The a-c current-voltage curves were traced on a DuMont Type 250 oscillograph. The current was supplied by a Hewlett-Packard Model 202A low-frequency function generator in series with a 30 ohm resistance. The current signal was taken as a voltage drop across the 30 ohm resistance and was applied to the vertical d-c amplifier. The voltage of the electrode with respect to the platinum reference electrode was applied to the horizontal a-c amplifier. The d-c bias was supplied by a 67½v dry cell in series with 0.3 megohms across the cell.

Illumination of germanium electrodes.—Known multiples of an arbitrary value of light intensity were obtained by means of a small microscope illuminator lamp mounted on a meter-stick track in a horizontal line 45° from the normal to the center of the germanium electrodes. The light thus passed through the walls of the cell and the anode shield and through the electrolyte onto the front face of the electrode. Fixed stops were used to provide 2, 3, 4, and 8 times an arbitrary value of light intensity. A large infrared heat-lamp was used for intense illumination.

Results and Discussion

Results were obtained for: (I) exploratory studies of various metals, (II) detailed studies of germanium and silicon electrodes, and (III) chemical studies of products.

Exploratory studies of metal electrodes.—The current-voltage curves for electrolysis of the Ziegler electrolyte on various metal electrodes are shown in Fig. 3. The d-c anodic behavior of these electrodes was found to be of four characteristic types. Anodic dissolution as the only process was found for Pb, Cd, Bi, Sn, and Sb over the range of current densities studied. Pt, Ni, p-Ge, and p-Si were not etched and the only process observed to occur was the decomposition of the electrolyte. Zn, Al, Ag, and Cu were etched at low current densities but reached

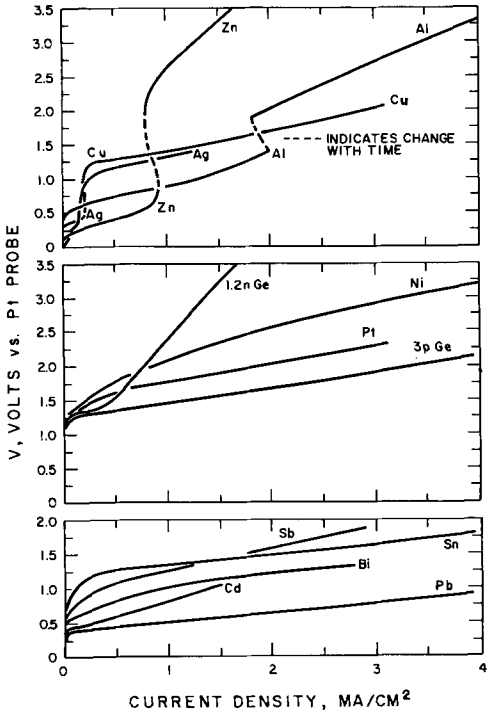

Fig. 3. Current voltage curves showing the anodic behavior of metals in the $Na(AlEt_3)_2F$ electrolyte. Lower block, metal electrode dissolves; middle block, electrolyte decomposes; upper block, metal dissolves at low current density, electrolyte also decomposes at higher current density.

initial limiting current densities at various values less than 2 ma/cm². At the limiting C.D. there was in each case a rapid shift in potential to values near 1.2-1.5v and the generation of gaseous and liquid products commenced. These initial limiting currents apparently correspond to rate controlling processes in the electrolyte or at the electrode surface. The n-Ge and n-Si electrodes also showed limiting current effects. The limiting current occurred at potentials at and above those at which the electrolyte decomposition was known to occur from the other results, including those for p-type Ge and Si. In this case the current-limiting process occurred not in the solution but within the electrodes as discussed below.

Detailed studies of germanium and silicon electrodes.—The preliminary studies of germanium anodes showed a current-limiting process at small current densities for n-type but not for p-type material. Further d-c studies were made with five different germanium electrodes using the anode shield and the insulated platinum probe electrode (cf. Fig. 2). The following germanium electrodes were studied: 0.1, 1, and 10 ohm-cm n-type and 2.5 and 10 ohm-cm p-type. Results are shown in Fig. 4. Current saturation occurs for n- but not for p-type electrodes. The saturation current is smaller for 1 ohm-cm n-type than for 10 ohm-cm n-type. These results indicate that holes are involved in the electrode process and that the limiting current effect exhibited by the n-type electrodes corresponds to diffusion control of the electrode process dependent on the supply of holes within the n-Ge rather than on ions within the solution.

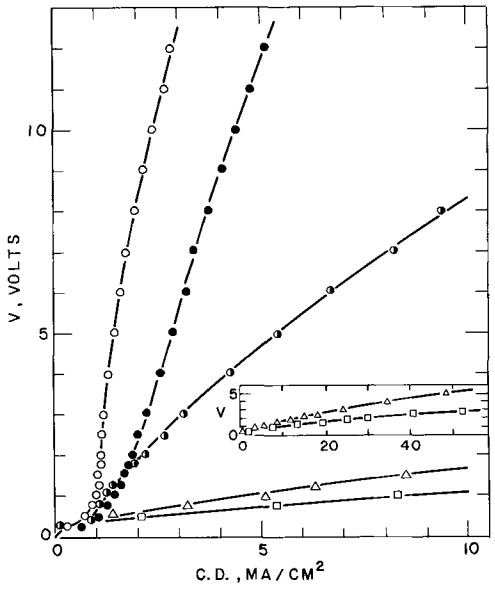

Fig. 4. Current-voltage curves for five different germanium anodes in the $Na(AlEt_3)_2F$ electrolyte. Open circle, 1 ohm-cm n-type; solid circle, 10 ohm-cm n-type; half open circle, 0.1 ohm-cm n-type; triangle, 10 ohm-cm p-type; and open square, 2.5 ohm-cm p-type. The current saturates for the n-type electrodes.

The 0.1 ohm-cm n-type germanium electrode might have been expected to give lower anodic currents than the 1.0 and 10 ohm-cm electrodes, and at low voltage there appeared to be a tendency in that direction, as Fig. 4 shows. However, over most of the voltage range, the currents were highest for the 0.1 ohm-cm sample. This presumably implies that the electric field just inside the semiconductor surface was high enough, in that case, to cause an increase in the supply of holes through some process of impact ionization.

The relatively small shifts in potential with current on the p-type electrodes apparently are due to activation polarization arising from some slow steps in the chemical and electrochemical processes on the surface of the electrode.

The effect of light was investigated to further test whether the current-limiting process on the germanium anodes involved the rate of supply of holes to the electrode surface. Figure 5 shows typical results for the effect of light of various intensities on the d-c anodic behavior of 10 ohm-cm n-type germanium. Similar results were obtained for the 1 and 0.1 ohm-cm electrodes. Light was applied as multiples of an arbitrary amount by moving the light source closer to the electrode through a series of fixed distances from the electrode surface. The saturation current density increased directly with the light intensity. The current density is limited to about 1 ma/cm² in the dark but reaches 50 ma/cm² in intense light. This kind of behavior is characteristic of the generation of holes by light for a hole-limited process. Typical results at 5v and 1v for 10, 1, and 0.1 ohm-cm n-type electrodes for the various light intensities are given in Table I. Additional evidence of the dependence of the anodic rate on the supply of holes to the germanium surface was obtained by means of a-c measurements. Current-voltage oscillograms resulting from appli-

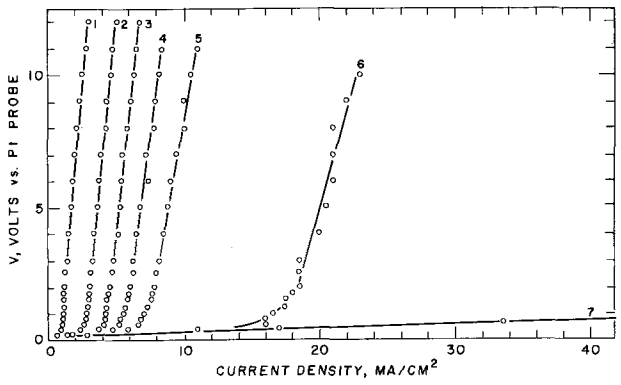

Fig. 5. Current-voltage curves showing the effect of light on the behavior of a 10 ohm-cm n-type germanium anode in the $Na(AlEt_3)_2F$ electrolyte. Curve 1 is the dark curve; curves 2, 3, 4, 5, and 6 result from illumination of the electrode with 1, 2, 3, 4, and 8 times, respectively, an arbitrary value of light intensity; curve 7 results from intense illumination with a heat lamp.

cation of 1000 cps a-c square-wave voltages, with and without d-c bias showed light-dependent current saturation effects with germanium and silicon electrodes. Without d-c bias and with small anodic bias the results were qualitatively similar to the d-c results.

A cathodic bias puts an aluminum film of variable thickness on the electrodes. The effectiveness of light in increasing the saturation current in n-type germanium electrodes was found to decrease as the aluminum film thickness increased. Very thick aluminum films eliminated the light effect as expected. Apparently the aluminum coating formed the familiar metal-to-n-type-germanium rectifier, with the current limiting mechanism still being the supply of holes from the bulk of the semiconductor.

An interesting difference in the behavior of silicon was found. Under anodic bias or no bias, the behavior of silicon in the a-c experiments was similar to germanium. However, when a thin film of aluminum was present on silicon, saturation occurred for p-type but not for n-type material. This is the opposite of the behavior of the germanium electrodes with aluminum coatings. This indicates that aluminum plated onto p-type silicon in this

Table I. Saturation current density at 1v and 5v for various values of light intensity at 10, 1, and 0.1 ohm-cm n-type germanium anodes

Light intensity, multiples of an arbitrary value, L	C.D., ma/cm² at 1v *vs.* Pt probe		
	10 ohm-cm	1 ohm-cm	0.1 ohm-cm
Dark	1.10	0.90	1.20
1 L	2.85	2.45	2.85
2 L	4.20	3.90	4.05
3 L	5.55	5.50	5.25
4 L	7.05	6.80	6.15
8 L	16.5	12.0	12.6
	C.D., ma/cm² at 5v *vs.* Pt probe		
Dark	1.70	1.50	4.05
1 L	3.60	3.40	5.85
2 L	5.30	5.25	7.20
3 L	6.80	7.10	8.40
4 L	8.75	8.80	10.2
8 L	20.5	16.5	21.0

electrolyte forms a rectifying barrier. Rectification by aluminum broad area contacts on p-type silicon has also been reported by Wurst and Borneman (10).

Chemical products.—The products of the electrochemical decomposition of the electrolyte at nonetching electrodes were studied qualitatively. Cathodic treatment produced a coating of metallic aluminum. Anodic treatment at inert germanium electrodes produced gaseous and liquid products. The gaseous anode product was a mixture consisting of ethane, ethylene, and n-butane, as determined by a gas chromatographic method. A 5-ft silica-gel column was used for the separation of ethane and ethylene. A 30-ft tricresyl phosphate on firebrick column was used for butane analyses. Less ethylene than ethane was found. Simple disproportionation of ethyl radicals should produce equal amounts of ethane and ethylene. The smaller than expected yield of ethylene may have occurred because of reaction of some of the product ethylene with triethyl aluminum in the electrolyte to form butyl or longer substituents by Ziegler-type ethylene polymerization catalysis. The liquid product which separated as an immiscible floating layer, consisted mainly of alkyl aluminum compounds. The liquid is believed to be largely triethyl aluminum since the electrolyte was made up to be saturated with $AlEt_3$. The $AlEt_2F$ presumed to be formed may be soluble in the electrolyte. The hydrolysis gas from the liquid product contained ethane, ethylene, and n-butane, but no longer-chained constituents. Diethyl aluminum fluoride was apparently not a prominent constituent of the liquid product since only a small amount of fluoride relative to the aluminum content was found.

Summary and Conclusions

The results show that, for germanium anodes in the $Na(AlEt_3)_2F$ electrolyte, n-type germanium anodes exhibit current-limiting processes which are not obtained for the p-type electrodes. The magnitude of the limiting current is increased by light. This indicates that the mechanism of the anodic electrode process involves a reaction of the electrolyte species with holes from the semiconductor, that is, that the process involves transfer of electrons from some entity in the electrolyte to the valence band of the semiconductor. In the case of the n-type germanium anodes, the rate of supply of holes from the bulk of the semiconductor to the surface of the electrode becomes the rate-controlling step. Product analyses suggest that ethyl radicals are formed as intermediates in the anodic process. The cathodic process involves a reduction of some entity in the electrolyte to form metallic aluminum.

The following proposed mechanism is in conformity with the results obtained:

Anodic reaction:

$$(AlEt_3)_2F^- + e^+ \rightarrow Et\cdot + \text{aluminum alkyl fluoride compounds} \quad (I)$$

$$2\,Et\cdot \rightarrow CH_3CH_3 + CH_2 = CH_2$$
$$\rightarrow CH_3CH_2CH_2CH_3$$

Cathodic reaction:

$$(AlEt_3)_2F^- + 3e^- \rightarrow Al + \text{aluminum alkyl fluoride compounds} \quad (II)$$

For (I), one could postulate the reaction products to be $AlEt_3 + AlEt_2F$. For (II), one could postulate that the reaction products are combined with $3AlEt_3$ to form $AlEt_3F^- + 3AlEt_4^-$. All of these postulated products are known and could exist in this system.

Acknowledgments

The aid of the Kettering Foundation in support of this work, in the form of a fellowship held by one of us (R.J.F.), is gratefully acknowledged. Thanks are due to the Ethyl Corporation which donated the triethyl aluminum used in the work and rendered much assistance in the form of procedures for the purification and handling of the compound. Thanks are also due to the Philco Corporation and to Texas Instruments Company for the donation of the semiconductor materials.

Manuscript received March 7, 1963; revised manuscript received May 6, 1963. This paper was presented at the Columbus Meeting, Oct. 18-22, 1959.

Any discussion of this paper will appear in a Discussion Section to be published in the June 1964 JOURNAL.

REFERENCES

1. J. F. Dewald, in "Semiconductors," N. B. Hannay, Editor, pp. 727-751, Reinhold Publishing Corp., New York (1959).
2. H. Gerischer, in "The Surface Chemistry of Metals and Semiconductors," H. C. Gatos, Editor, pp. 177-202, John Wiley and Sons, Inc., New York (1960).
3. D. R. Turner, in "The Electrochemistry of Semiconductors," P. J. Holmes, Editor, pp. 155-204 Academic Press, New York (1962).
4. W. H. Brattain and C. G. B. Garrett, *Bell System Tech. J.*, **34**, 129 (1955).
5. D. R. Turner, *This Journal*, **103**, 252 (1956).
6. H. Gerischer and F. Beck, *Z. Elektrochem.*, **63**, 943 (1959).
7. K. Ziegler and H. Lehmkuhl, *Z. anorg. allgem. Chem.*, **283**, 414 (1956).
8. G. E. Coates, "Organo-Metallic Compounds," 2nd Edition, p. 138, John Wiley and Sons, Inc., New York (1960).
9. K. Ziegler, Belgium Pat. 543,128, November 26, 1955.
10. E. C. Wurst, Jr., and E. H. Borneman, *J. Appl. Phys.*, **28**, 235 (1957).

Chemical Transport and Epitaxial Deposition of Gallium Arsenide

Frank A. Pizzarello

Semiconductor Division, Development Laboratory,
Hughes Aircraft Company, Newport Beach, California

ABSTRACT

A study of the nature of growth of gallium arsenide on substrates of various crystallographic orientations was conducted in a closed tube system. It is concluded that the dominant growth direction is in the (111) direction. Growth rate studies were conducted at various temperatures and pressures. It was found that the transport of matter is not dependent on a single mechanism, but rather on a combination of diffusion, convective and laminar flow, each contributing to greater or lesser extent depending on the conditions of growth.

The method of chemical mass transport has been used for many years as a method of preparing many materials in a pure state (1). Usually, the materials transported were polycrystalline masses deposited on substrates of no particular relationship to the transported solid. Recently (2, 3) the method of chemical mass transport was combined with the technique of epitaxy to devise the process generally referred to as epitaxial growth. In this method, material difficult to evaporate is transported by means of a chemical equilibrium reaction to a single-crystal substrate of the proper characteristics allowing the deposition of a single-crystal layer. With the advent of this method, a twofold problem arose. One, by what mechanisms is the reaction mass transported to the substrate? Two, what are the relationships of the growth on the substrate to the transport mechanism of material and to the nature of the substrate? In this paper, these questions are studied and some answers are submitted for examination.

Experimental

A schematic view of the apparatus used in these experiments is shown in Fig. 1. The furnace used was constructed with three separate heating elements, each individually controlled. It was found that heating elements arranged in this fashion yield the desired linear thermal gradients. A typical thermal distribution obtained and used for these experiments is shown in Fig. 1. This figure also shows a view of the reaction vessel used in these experiments. The reaction vessel was constructed of quartz tubing, 1.60 cm ID and 15 cm long. Since, as it will be shown later, the geometry of the reaction tube is critical, all dimensions during construction were maintained to a precision of 10%. Also, since temperature fluctuation may cause spurious results during epitaxial growth, temperature control was maintained to 2%.

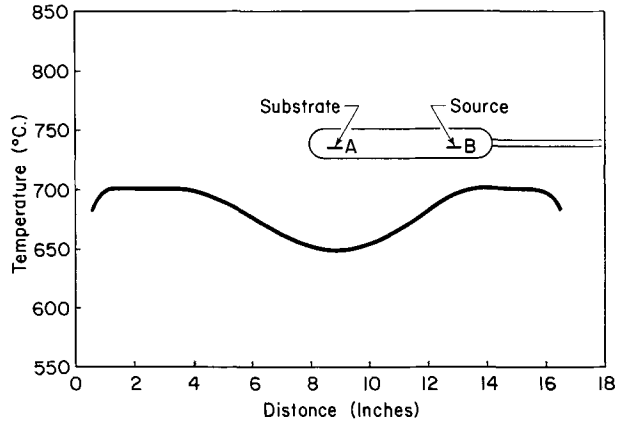

Fig. 1. View of the thermal gradient and the position of the reaction tube during growth.

To maintain optimum experimental control and obtain reproducible results, samples were prepared in the following manner: A wafer of GaAs (usually N-type 10^{17}/cc) was electropolished (4), weighed and placed in the substrate region of the reaction tube. After etching in 1-3-2 solution (1 part HF, 3 parts HNO_3, and 2 parts H_2O) a weighed quantity of polycrystalline GaAs is placed in the source position of the reaction tube. Twenty-five grams of high-purity iodine is placed in the reaction tube. This assembly is sealed on a vacuum system and pumped to 10^{-4} mm Hg. During evacuation the sample region of the reaction tube is kept at liquid N_2 temperature to avoid loss of iodine. After 30 min under vacuum, 20 cm of Hg of pure hydrogen is introduced to the system. The reaction tube is then sealed containing the hydrogen. The tube is placed in the furnace so as to locate the source and the substrate on opposite sides of the temperature dip. In this position, etching of the substrate surface occurs. This step is used to clean the substrate further, and proceed for 10 mins. At the end of this time, the tube is adjusted by means of the attached rod to a position in the thermal gradient where the substrate is located at the low-temperature region of the furnace. In this position growth occurs. The tube is maintained in this position for 24 hr. Using the procedure outlined above, an interface is obtained which has a minimum of structural defects. It was found during the course of experimentation that chemical etching or any mechanical treatment of the surface, such as polishing, leaves sufficient

damage on the surface to yield poor quality interface upon growth of an epitaxial layer.

Growth Habit of Epitaxial Layers

The substrates used in this study were oriented by the Laué back reflection method. Using this method, the orientation of the substrate and its angular relationship with other crystallographic direction was determined. Any growth structure occurring on these oriented surfaces could then be easily transposed to a standard stereographic projection where Miller indices could be assigned. The crystallographic orientation was determined with a precision of one degree.

The growth planes developed were measured by the use of a light figure apparatus with a precision of 1%. Epitaxial growth on substrates oriented in the (100), (110), (111)A, (111)B, (112), and (113) planes were studied. The epitaxial layers studied were grown in a 24-hr period and ranged in thickness from 0.020 to 0.030 in. Figures 2, 3, and 4, show the planes developed on the (100), (110), and (111)A planes, respectively. Note that the angular displacement of the growth figures from the basal plane is greatest for growth on the (100) plane, less for growth on the (110) plane, and least for the

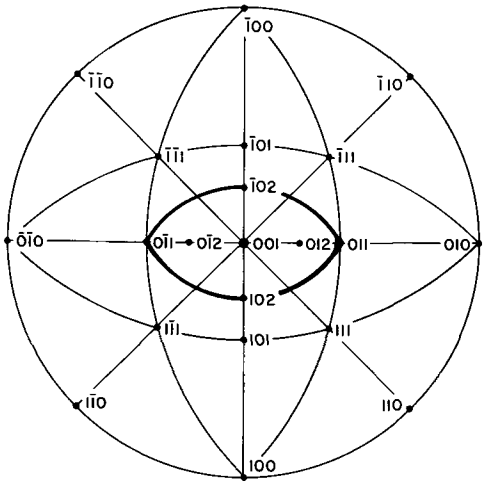

Fig. 2. Stereographic projection of growth occurring on the (001) plane. Series of planes developed during growth lie within region defined by heavy line.

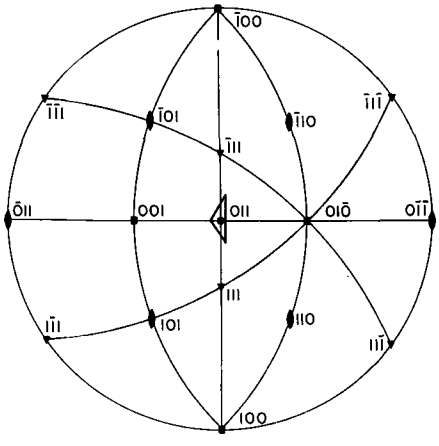

Fig. 3. Stereographic projection of growth occurring on the (011) plane. Series of planes developed during growth lie within region defined by heavy line.

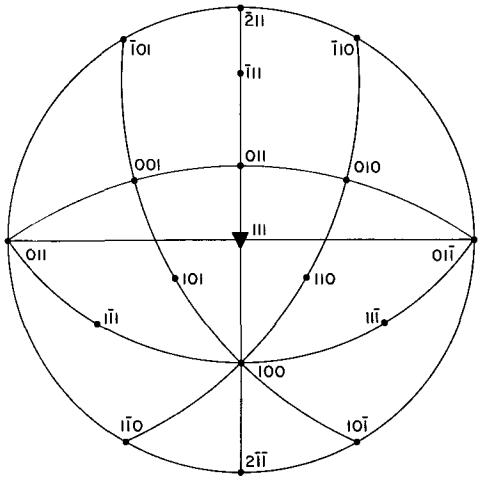

Fig. 4. Stereographic projection of growth occurring on the (111)A plane. Vicinal plane development with maximum angular deviation from the basal plane is 3°.

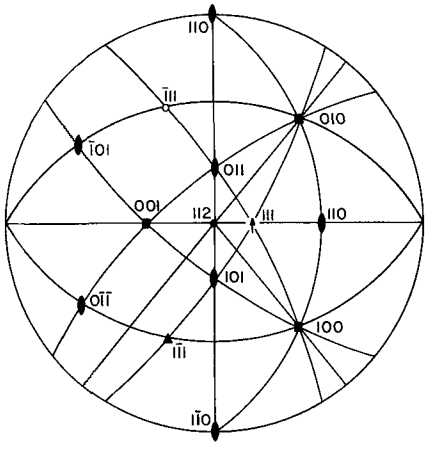

Fig. 5. Stereographic projection of (112) plane. Principal plane developed during growth is the (111)A plane.

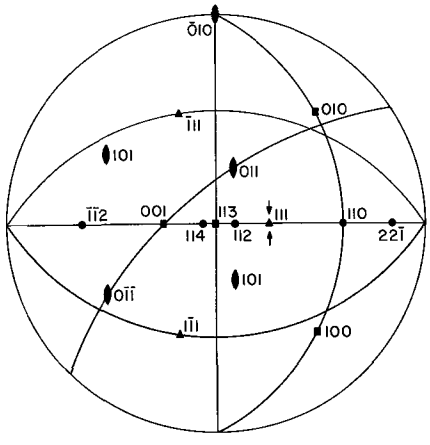

Fig. 6. Stereographic projection of the (113) plane. Principal plane developed during growth is the (111)A plane.

(111) plane. Figures 5 and 6 are stereographic projections of growth on the (112) and (113) planes, respectively. As is shown, only (111) planes are developed.

From the data presented it is seen that the crystallographic planes most readily developed are the (110) and (111) planes. These are planes of high reticular density [where the reticular density of

(100) < (110) < (111) planes]. It is further noted that the range of angular displacement of planes developed decreases with increasing reticular density until only vicinal planes are developed, as on the (111) plane. In the case of the (112) and (113) planes, these are planes of such low reticular density that uninhabited growth can readily occur in the [111] direction forming (111)A faces.

In the case of growth on the (111)A plane a maximum angular displacement of the growth planes is 3°. The vicinal plane developed noted on the (111)A plane is an unexpected result if growth on this plane is conceived to proceed as a sequence of layers forming one on another. It is tempting in view of this data to hypothesize that the vicinal planes developed during growth give rise to a surface containing many corners and edges such as is expounded in the theories of Kossel and Stranski (5) to lower the free energy of a particle on the surface and thus increase the rate of growth. Expanding on this view further, an atomistic model of growth can be developed. Consider a (111)A plane at the beginning of growth; the surface consists predominately of gallium atoms; to this surface an arsenic molecule can readily be absorbed from the gas phase. The arsenic molecule absorbed on this surface provides edges to which additional arsenic molecules may attach, thus forming on the Ga atom surface a small island of arsenic atom which expands in size. Simultaneously with this expansion, molecules of GaI are absorbed on the arsenic island forming a bond with arsenic atoms and liberating GaI_3 to the gas phase. The Ga thus adsorbed expands across the arsenic surface, simultaneously new arsenic molecules absorb on the new Ga surface, and the process repeats itself. With this kind of process occurring, it can readily be seen that in a short time a highly stepped surface will occur if many islands form on the same atomic plane simultaneously and proceed to add layers as described. This theory is verified to some extent by the fact that, when growth proceeds on crystallographic planes not oriented in the (111) direction, a wide angular displacement occurs with a tendency to grow to the (111) plane. An additional fact that also supports these ideas of growth mechanism is that little or no difference in the rate of growth over a 24-hr period seems to exist regardless of the crystallographic orientation used, indicating that growth proceeds in a [111] direction. However, this does not exclude the possibility that the growth rate initially may be drastically different for different crystallographic orientations. Figure 7 shows typical epitaxial growth on the (100), (111), and (113) oriented substrates.

Attempts to grow epitaxially on the $(\bar{1}\bar{1}\bar{1})$B plane resulted in every case in polycrystalline layers when iodine was used as the carrier. On the other hand, when chlorine was used the resultant layer was a single crystalline layer of high quality. An explanation for this effect is possible by noting that the $(\bar{1}\bar{1}\bar{1})$B plane is highly an electronegative (6) surface. Thus the gallium iodide molecule which has a large negative charge distribution on the iodine atom is readily repelled from the $(\bar{1}\bar{1}\bar{1})$B surface.

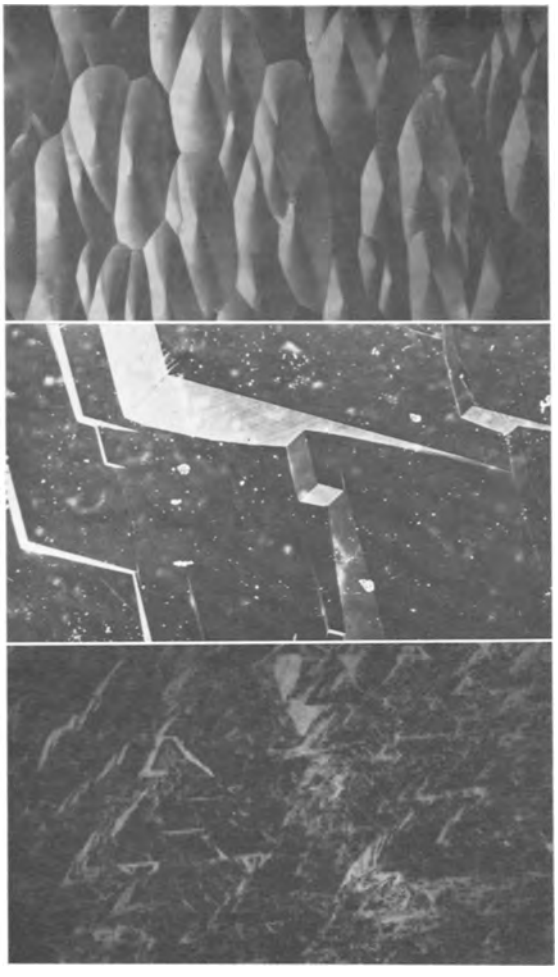

Fig. 7. Photographic views of epitaxial growth on a (top), (100); b (center), (111); and c (bottom), (113) planes. Magnification 45x.

On the other hand, a gallium chloride molecule has smaller negative charge distribution resulting in no significant repulsion from the surface.

Rate of Growth Experiments

To approach the problem of chemical mass transport even on a crude quantitative level the equilibrium reaction taking place and the associated values of free energy must be known. Work by Lyons and Silvestri (7) shows that the predominate equilibrium reaction occurring is

$$2GaI_3(g) + 4GaAs(s) = 6GaI(g) + As_4(g) \quad [1]$$

As the reaction is written the concentration in the gas phase of the products increases with increasing temperature. Consequently, under conditions of a thermal gradient the reaction products transported to the cooler region of the thermal gradient offset the equilibrium partial pressures sufficiently to support the deposition of GaAs. One can visualize this transport as a steady-state process where the GaAs is dissolved by GaI_3 at the higher temperatures to form a gas phase of a specific concentration of the reactants and products. The GaI and As_4 formed are transported through a concentration gradient established in the thermal gradient to the cooler temperature region. At the cooler temperature the

equilibrium concentrations are maintained by the deposition of GaAs and the liberation of GaI_3. The GaI_3 liberated flows back to the higher temperature region through the established concentration gradient and reacts with more GaAs to repeat the cycle. To relate this mechanism into mathematical terms the equilibrium constant

$$K = \frac{P^6_{GaI} P_{As4}}{P^2_{GaI3}}$$

where P_{GaI}, P_{As4}, and P_{GaI3} are the partial pressures of the gaseous constituent of the reaction as noted by the subscripts, must be known. Defining α as the fraction of the products formed (fraction of reaction) the following relations can be derived

$$P_{GaI} = 3\alpha n_{GaI3} \frac{RT}{V} \quad [2]$$

$$P_{As4} = \frac{\alpha}{2} n_{GaI3} \frac{RT}{V} \quad [3]$$

$$P_{GaI3} = (1-\alpha) n_{GaI3} \frac{RT}{V} \quad [4]$$

where V is the volume of the system, n_{GaI3} the number of moles of GaI_3 initially introduced, and T is the absolute temperature. Using these expressions K can be expressed as

$$K = \frac{3^6}{2} \left[n_{GaI3} \frac{RT}{V} \right]^5 \frac{\alpha^7}{(1-\alpha)^2} \quad [5]$$

Treating the reaction tube lying in the thermal gradient as consisting of three chambers V_1, V_2, and V_3, where V_1 is the volume in the high-temperature region T_1, V_2 is the volume in the low temperature region T_2, and V_3 the region in the thermal gradient, the following expressions for material transport can be used

$$n_{GaI} = D\,\alpha\,t \frac{dC_{GaI}}{dx} + aC_{GaI}\,v\,t \quad [6]$$

$$n_{GaI3} = D\,\alpha\,t \frac{dC_{GaI3}}{dx} + aC_{GaI3}\,v\,t \quad [7]$$

The terms in expressions [2] and [3] are defined as: D, diffusion coefficient for the gas, cm^2/sec mixture; a, cross-sectional area of the cm^2 reaction tube; t, time process is continued, sec; dC_{GaI3}/dx, concentration gradient of GaI_3; dC_{GaI}/dx, concentration gradient of GaI; v, mass flow velocity, cm/sec. Assuming $v=0$ in [2] and [3] noting that $3dC_{GaI}/dx = dC_{GaI3}/dx$ and $3n_{GaI} = n_{GaI3}$, the expression

$$n = Dat\, dC_{GaI}/dx \quad [8]$$

is derived. Assuming a linear concentration gradient $(C_1-C_2)/L$ exists between the volumes V_1 and V_2 expression [8] is reduced to

$$n_{GaI} = \frac{Dat}{L} (C_1-C_2) \quad [9]$$

where C_1 is the concentration of GaI at T_1, C_2 is the concentration of GaI at T_2, and L is the length of the

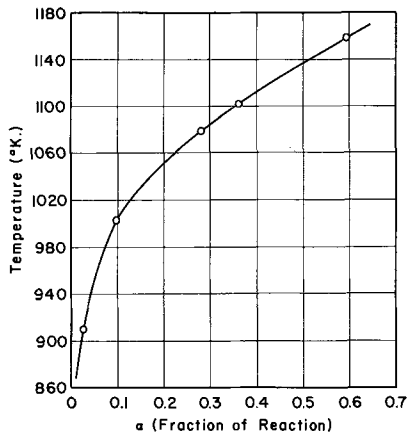

Fig. 8. Temperature of reaction mixture vs. α, the fraction of products GaI and As_4 formed.

concentration gradient. Using the expression for the concentration of GaI at T_1 and T_2 as

$$\frac{\alpha_1 n_{GaI3}}{V_1}, \frac{\alpha_2 n_{GaI3}}{V_2}$$

respectively, and noting that $V_1 = V_2 = V_{1,2}$ the equation

$$n_{GaI} = \frac{Dat}{LV_{1,2}} n_{GaI3} (\alpha_1-\alpha_2) \quad [10]$$

is obtained. Assuming all the GaI transported reacts to deposit GaAs the equation for the weight of deposition of GaAs in milligrams is given by

$$W = 96.42 \frac{Dat}{V_{1,2}L} n_{GaI3} (\alpha_1-\alpha_2) \times 10^3 \quad [11]$$

Using the free energy data of Silvestri and Lyons (7), values of α were calculated at various temperatures. A plot of this data is given in Fig. 8. Since α is seen to increase with temperature it is predictable from Eq. [11] that the weight transported is temperature dependent and should increase with increasing temperature differences. To verify the degree of applicability of this expression and to obtain an estimate of the diffusion coefficient D, a

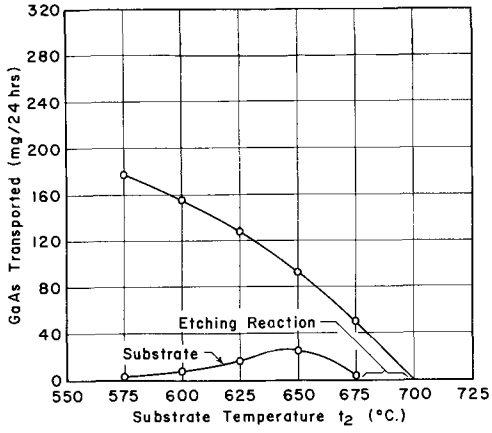

Fig. 9. Weight of GaAs transported in a 24-hr period vs. the temperature of the substrate chamber. The temperature of the source chamber is held fixed at 700°C. The substrate curve is weight gain of the substrate wafer in a 24-hr period. The source curve is the weight lost in a 24-hr period.

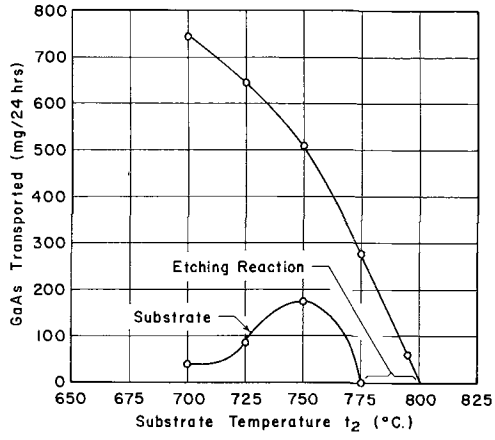

Fig. 10. Weight of GaAs transported in a 24-hr period vs. the temperature of the substrate chamber. The temperature of the source chamber held fixed at 800°C. The substrate curve is the weight gain of the substrate wafer in a 24-hr period. The source is the weight lost in a 24-hr period.

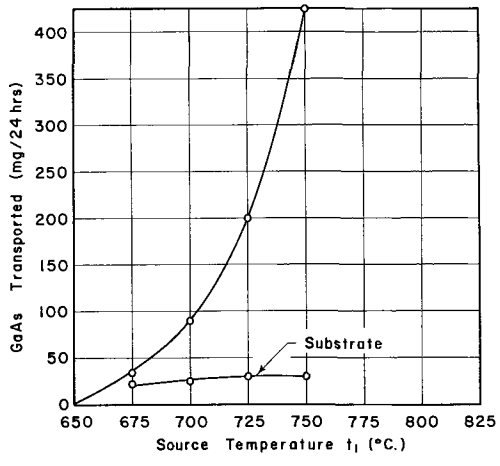

Fig. 11. Weight of GaAs transported in a 24-hr period when the substrate chamber temperature is held fixed at 650°C vs. source chamber temperature.

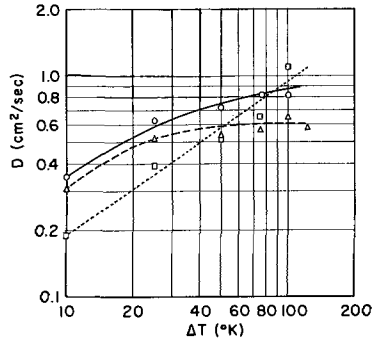

Fig. 12. Gaseous diffusion coefficient vs. the temperature difference between the source and substrate. -○-, source 1073°C, substrate varied; -△-, source 973°C, substrate varied; --□--, substrate 923°C, source varied; curve a, - - - -; curve b, ———; curve c, ...

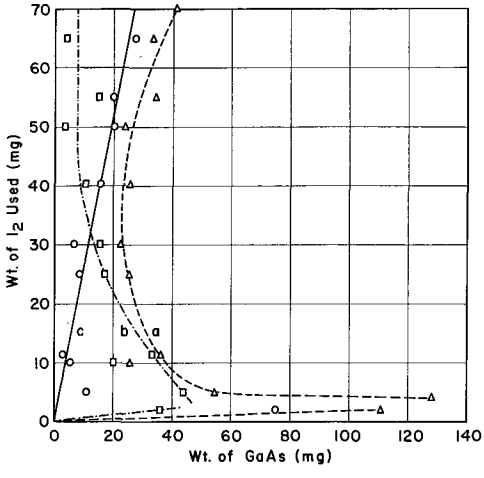

Fig. 13. Rate of growth with source temperature held at 700°C and substrate temperature held at 650°C, while the weight of I_2 used as a transporting media is varied. Curve a is the actual weight loss of the source in a 24-hr period; curve b is the substrate weight gain in a 24-hr period; curve c is the equivalent weight of GaAs in the gas phase.

series of experiments were performed in which in case 1, the source temperature was held fixed at 800°C and the substrate temperature was varied; in case 2, the source temperature was held fixed at 650°C and the source temperature was varied; and in case 3, the substrate temperature was held fixed at 650°C and the source temperature was varied.

The results of these experiments are given in Fig. 9, 10, and 11. Using Eq. [11], D is calculated for a number of points along each curve. In the calculation of D the numerical values $n_{GaI_3} = 1.30 \times 10^{-5}$ moles, $a = 2.01$ cm², $t = 8.65 \times 10^4$ sec, $V_{1,2} = 10.05$ cc, and $L = 5$ cm were used. The results of these calculations are given in Fig. 12 where ΔT, the difference in temperature between the source and the substrate, is plotted against the diffusion coefficient. It is seen in curves a and b that the diffusion coefficient quickly rises to a steady value. Since in these experiments the source is held fixed at 973° and 1073°K, respectively, and the substrate is varied downward to lower temperatures, the average temperature ($T_1 + T_2/2$) is decreasing, whereas the diffusion coefficient is increasing. This is an anomolous behavior and cannot be explained on the basis of simple gaseous diffusion. An important fact demonstrated by these curves, however, is that the source temperature has a predominate effect on the diffusion coefficient, and the effective temperature in the system is not simply the average temperature. Curve c shows where the substrate temperature is fixed at 923°K, and the source temperature is varied upward. The result in this case is consistent qualitatively with the kinetics theory of gaseous diffusion (8). This theory predicts $D \propto T^n/P$ where n lies in the range of 1 to 2. A value of $n = 20$ was computed from the data of curve c Fig. 12. This value of n precludes the mechanism based on simple gaseous diffusion and indicates the transport process to have perhaps a strong convective flow component (9).

Since the diffusion coefficient is not only temperature dependent, but also pressure dependent, experiments were performed where the total reactant pressure was changed by varying the amount of iodine used initially at a fixed source, substrate temperature difference. Results of these experiments are given in Fig. 13. Curve a of Fig. 13 is the total mass loss of the source material. Curve b is the actual weight gain of GaAs on substrate. Curve c

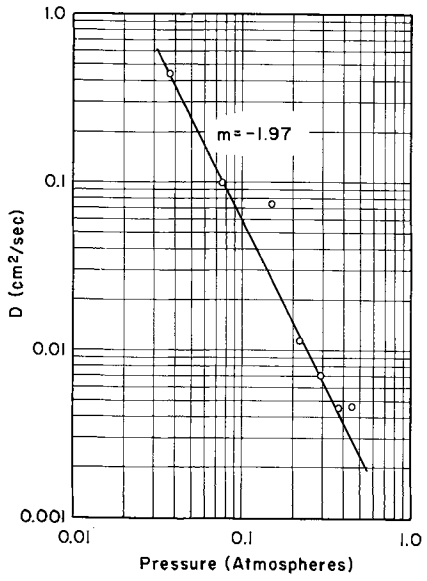

Fig. 14. Gaseous diffusion coefficient vs. the average total pressure of the system.

is the quantity of GaAs dissolved in the gas phase determined by assuming the chemical reaction

$$4GaAs(s) = 6I_2(g) = 4GaI_3(g) + As_4(g)$$

is complete and the chemical reaction

$$2GaI_3(g) + 4GaAs(s) = 6GaI(g) + As_4(g)$$

is 0.04% complete. The circular data points shown are obtained by subtracting the weight loss of the source from the weight gain of the substrate. Since these points lie very close to the theoretical curve c, an independent check of the accuracy of α is obtained. These data also show that very small losses of I_2 are encountered by the loading procedure used. At higher iodine weights it was observed that all material transported deposited on the substrate. At low iodine weights, deposition also occurred on the walls adjacent to the substrate. Using Eq. [11], D was calculated at various values of iodine weight used. A plot of D *vs.* total gas pressure is given in Fig. 14. The total gas pressure was calculated by using the equation $P = 2/3\ (1 + \alpha_n) \dfrac{Wt_{I_2}}{253.8} \dfrac{RT_{av}}{V}$.

In comparing the slope of the curve 1.9 of Fig. 14 with the expression $D \propto P^{-1}$ a difference is observed which indicates a departure of the transport process from a pure diffusion mechanism.

Substrate Growth

Returning to Fig. 10 and 11, the substrate weight gain is given under the experimental conditions of case I and case II. At small temperature differences an actual weight loss of the substrate occurs (region designated as etching reaction). The etching reaction operating under these circumstances is that given by Eq. [1]. The principal cause for this effect is a combination of slow diffusion of reactant, gases, and small local temperature gradients which act as sites of deposition of GaAs. At larger temperature differences between source and substrate an increase in the quantity depositing takes place until a maximum is obtained. The growth rate on this part of the curve is limited by the competition of the etching reaction rate and mass transport rate. The decreasing rate of deposition at very large temperature differences is attributed to the change in the rate of chemical deposition with temperature. Thus, this part of the growth rate curve is chemical deposition rate limited. To support this view the substrate curve of Fig. 12 is given. Under conditions of growth case III, the substrate temperature is held fixed; consequently, no change in the chemical deposition rate is expected. It is seen under these conditions of growth that the curve moves rapidly from the transport limited process to a saturation value limited by the chemical deposition rate. All the rate studies were performed with wafers of constant area (0.5 cm^2). However, in view of the quantity of GaAs depositing on the walls adjacent to the wafer, it is believed that the wafer area would have little or no effect on the quantity of mass transported.

Conclusion

Through the bulk of this paper an idealized model was applied to the problem of mass transport in a closed tube system. The dependence of the diffusion coefficient on temperature and pressure was given. It was found in both cases that no single mechanism of transport is attributable to results obtained. However, of interest is the marked effect high temperature and an optimum average pressure has on the transport process.

Up to this point very little has been said about the effects of geometry and thermal gradients on the mass transport rate. Preliminary experiments have shown that tubes of larger cross-sectional area and shorter length yield a greater mass transport rate, a result which is at least in qualitative agreement with theory. During the course of experimentation, thermal gradients with a significant radial nonuniformity were formed. As expected, the growth rate was altered drastically, and in some cases GaAs was removed from the substrate and deposited on the cooler walls. Thus it was found to assure uniformally reproducible results in growth rate, great care must be exercised in controlling the uniformity of the thermal gradient used.

Acknowledgments

The author wishes to thank Dr. George Dorosheski for his assistance in the mathematical computations needed, and Mr. Joseph Vuoto and Mr. Alan VanCouvering for the experimental work performed.

Manuscript received Nov. 26, 1962; revised manuscript received May 27, 1963. This paper was presented before the Los Angeles Meeting, May 6-10, 1962.

Any discussion of this paper will appear in a Discussion Section to be published in the June 1964 JOURNAL.

REFERENCES

1. R. I. Rolsten, "Iodide Metals and Metal Iodides," John Wiley & Son, Inc., New York (1961).
2. E. S. Wajda, B. W. Kippenhan, and W. H. White, *I.B.M. Journal*, **4**, 288 (1960).
3. J. C. Marimace, *ibid.*, **4**, 280 (1960).
4. J. G. Harper and M. S. Astor, Enlarged Abstracts,

Electronics Div., Electrochemical Society Philadelphia Meeting, May 1959.
5. H. E. Buckley, "Crystal Growth," John Wiley & Son, Inc., New York (1951).
6. H. C. Gatos and M. C. Lavine, *This Journal*, **107**, 427 (1960).
7. O. J. Lyons and V. J. Silvestri, *ibid.*, **109**, 963 (1962).
8. W. Jost, "Diffusion In Solids, Liquids, Gases," chap. X, p. 425, Academic Press, New York, (1960).
9. R. Nitsche, H. U. Bösterli, and M. Lichtensteiger, *J. Phys. Chem. Solids*, **21** [3/4], 199 (1961).

A Kinetic Theory for Autodoping for Vapor Phase Epitaxial Growth of Germanium

J. J. Grossman[1]

Hughes Research Laboratories, Malibu, California

ABSTRACT

A kinetic theory has been derived for the origin of autodoping in epitaxial vapor grown films based on the transient behavior of a general reaction mechanism. This mechanism is the series combination of an etching and growth reaction. A particular case is solved explicitly in closed form, and the behavior of more general cases is indicated.

Autodoping in epitaxial vapor grown germanium (1) and silicon (2) films was first reported at the October 1961 meeting of the Electrochemical Society by Matovich and Andres (1) and by Kahng, Manz, Atalla, and Thomas (2). The significant experimental observation is that impurities initially present in the substrate redistribute in the growing layer as growth proceeds. They redistribute at an ever decreasing concentration, while the externally added impurity builds up and finally takes control of the grown film doping. Two theoretical approaches are possible for examining autodoping (1, 2).

First, one can be purely phenomenological as were Kahng *et al.* (2, 3) and postulate a countercurrent or distillation type enrichment without regard for the detailed microscopic mechanism. In this theory one postulates three processes, etching, mixing, and growth, which occur repetitiously in that order.

On the other hand, one may derive kinetically an explicit time dependence for the reaction rate and thereby show details of the origin of the redistributed substrate impurity.[2] The observed logarithmic redistribution in the regrowth is then easily found in differential form since the adsorbed, liberated surface impurity C reincorporates into the substrate film in proportion to the growth rate R, the distribution coefficient between the solid and adsorbed phase k, and a loss factor due to impurity diffusion away from the surface A. The net change in adsorbed surface impurity per unit time dC/dt is given by

$$-\frac{dC}{dt}\,dt = AkCR\,dt = akC\,dz \qquad [1]$$

where a is a factor which depends on growth rate R and loss by diffusion. Integration during steady-state growth gives the impurity profile in the grown film with distance z, which is proportional to the adsorbed surface impurity $C(z)$

$$N = N^{\circ}\exp(-akz) \qquad [2]$$

where N° is the initial regrowth concentration of impurity which depends on the distribution coefficient and the total amount of impurity initially liberated from the substrate.

A comparison of the two methods shows that if the repetitive etching-mixing-growth step approaches zero in the Kahng (2)-Thomas (3) treatment, the expression becomes equivalent to Eq. [2]. However, strict adherence to a physical interpretation is no longer feasible. This can be shown in the following way.

In a typical case the substrate concentration is 10^{18} and regrowth starts at 10^{16}, decreasing to 10^{14} in 5μ. If the solid-gas phase distribution coefficient is assumed to be 10^{-2}, then a surface layer $k\overline{\Delta z}$ ($1\mu \cong \overline{\Delta z}$ = the average probable thickness of the autodoped regrowth layer) $10^{-2} \times 1\mu = 100$Å thick of the original solid substrate represents, approximately, the active surface volume from which the impurities are liberated and subsequently redistributed. Since it seems unlikely that at any given time an active surface volume 20 atoms deep is engaged in reaction, it is reasonable to suppose that impurities are first liberated from this volume by etching once, and then reincorporate logarithmically as suggested above.

On the other hand, the mathematical device of repetitive etching, mixing, and growth (3) with a cycle step less than 20 atoms deep is meaningless, since sufficient dopant could not be liberated from the surface. Nevertheless, if taken in perspective, the mathematical form presented by Thomas *et al.* (3) is still very useful.

The purpose of this paper is to demonstrate that the single etch-back mechanism is a natural consequence of the transient behavior involved in initiating a steady-state growth reaction.[3]

[1] Present address: Douglas Aircraft Company, AMT Unit 18, Santa Monica, California.

[2] Here we consider as trivial impurity liberation due to preprocessing the substrate. The combination of diffusion at a rate faster than growth is also ruled out since the two processes, autodoping and diffusion, are differentiated by the excellent capacitive impurity distribution measurements reported by Thomas *et al.* (3).

[3] This mechanism was first reported at The Electrochemical Society meeting by Matovich and Andres (1) with this author's permission.

Prototype Reaction Mechanism

The main assumption made about hydrogen reduction of $GeCl_4$ in an open tube epitaxial growth reactor is that $GeCl_4$ is reduced step-wise to $GeCl_2$ and then by H_2 to Ge. Furthermore, it can be assumed that $GeCl_4$ etches the substrate by means of the well known disproportionation reaction

$$GeCl_4 + Ge \underset{k_1^*}{\overset{k_1}{\rightleftharpoons}} 2GeCl_2 \qquad [3]$$

with

$$GeCl_2 + H_2 \underset{}{\overset{k_2}{\rightleftharpoons}} Ge + 2HCl \qquad [4]$$

acting as the hydrogen reduction step.

These two simplified equations provide a prototype reaction mechanism which contains the two main elements of the reaction, etching and growth, and which is a simplified, representative, mathematically tractable model of the real reaction. After the transient behavior of this simplified reaction mechanism is studied, the modified behavior of more complex mechanisms (more closely approximating the real system) will be examined.

The reaction system is imagined to comprise three phases (Fig. 1): the bulk gas phase, a boundary gas film through which reactants and products diffuse, and the gas-solid interface. The bulk gas phase is composed of hydrogen and germanium tetrachloride with concentrations $[H_2^\circ]$ and C_4° respectively. At the gas-solid interface the gas phase concentrations of these two components are $[H_2]$ and C_4 respectively. If the boundary film is idealized to have an effective thickness z°, the reactants will diffuse to the surface with a rate given by

$$(\text{Diffusion Rate})_i = \frac{\mathcal{D}_i}{z^\circ} C = \frac{\mathcal{D}_i}{z^\circ} (C_i^\circ - C_i) = D_i(C_i^\circ - C_i) \qquad [5]$$

where $\mathcal{D}_i$ is the diffusion constant of the i^{th} component and $D_i = (\mathcal{D}_i/x)$. Similarly, the reaction products $GeCl_2$ and HCl have gas-solid interface concentrations C_2 and [HCl], respectively, and diffuse out across the boundary film into the bulk gas phase, where their concentrations are assumed to remain zero since the products are carried away by the steady reactant gas stream.

The following simplifying assumptions are made: I, the reaction mechanism is represented by one etching reaction and one growth reaction, Eq. [3] and [4]; II, the reverse reaction of Eq. [4] is considered negligible; III, the concentration of $GeCl_4$ at the interface instantaneously becomes C_4, its steady-state value; IV, the concentration of H_2 at the interface is equal to its gas phase value H_2°; V, the component adsorption isotherms are linear and rapid.

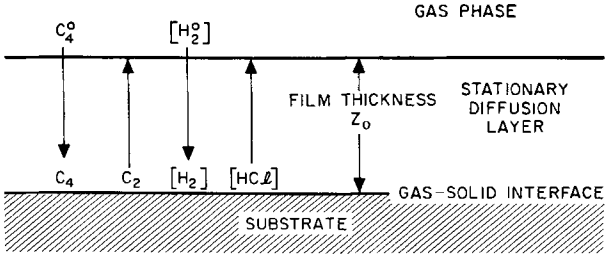

Fig. 1. Schematic representation of epitaxial growth in vapor phase deposition by hydrogen reduction of a gaseous halide.

With these assumptions and the mechanism proposed in Eq. [3] and [4], the time rate of change in concentration of these components C_2 and C_4 is given by the mass action relations at the gas-solid interface

$$-\frac{dC_4}{dt} = 0 = k_1C_4 - k_1^*C_2^2 - D_4(C_4^\circ - C_4) \qquad [6]$$

$$-\frac{dC_2}{dt} = 2k_1^*C_2^2 - 2k_1C_4 + k_2[H_2^\circ]C_2 + D_2C_2 \qquad [7]$$

and the germanium growth rate is

$$\frac{d[Ge]}{dt} = k_1^*C_2^2 + k_2[H_2^\circ]C_2 - k_1C_4 \qquad [8]$$

Since $dC_4/dt = 0$ in Eq. [6] by assumption III

$$C_4 = \frac{D_4C_4^\circ + k_1^*C_2^2}{D_4 + k_1} \qquad [9]$$

Substitution of C_4 from Eq. [9] converts Eq. [7] into a first order differential equation in the single variable $C_2 = C_2(t)$

$$-\frac{dC_2}{dt} = \left(\frac{2k_1^*D_4}{D_4 + k_1}\right)C_2^2 + (k_2[H_2^\circ] + D_2)C_2 - \frac{2k_1D_4C_4^\circ}{k_1 + D_4} \qquad [10]$$

This equation has as its standard solution the form

$$-qt = \ln\left[\frac{2\gamma C_2 + \beta - q}{2\gamma C_2 + \beta + q}\right] \cdot \left[\frac{\beta + q}{\beta - q}\right] \qquad [11]$$

where

$$q^2 = \beta^2 + 4\alpha\gamma$$
$$\alpha = \frac{2k_1D_4C_4^\circ}{k_1 + D_4}$$
$$\beta = k_2[H_2^\circ] + D_2$$
$$\gamma = \frac{2k_1^*D_4}{D_4 + k_1} \qquad [12]$$

When $t = \infty$,

$$C_2^\infty = \frac{q - \beta}{2\gamma} \qquad [13]$$

and Eq. [11] can be rearranged to the form

$$C_2 = \frac{C_2^\infty(1 - e^{-qt})}{\left(1 + \left(\frac{q - \beta}{q + \beta}\right)e^{-qt}\right)} \qquad [14]$$

Only two cases of Eq. [14] need be considered. These are the extremes when the $(q - \beta)$ term in the denominator is zero or one.

Case I. $$C_2 = C_2^\infty(1 - e^{-qt}) \qquad [15]$$

Case II. $$C_2 = \frac{C_2^\infty(1 - e^{-qt})}{1 + e^{-qt}} \qquad [16]$$

Normalized plots of these two functions in Fig. 2 show that they do not differ appreciably over the

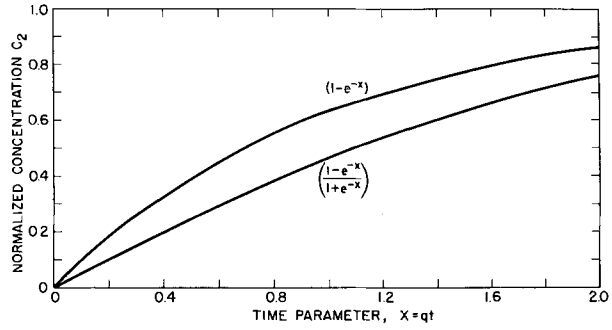

Fig. 2. Normalized plots of the two extremes of the dichloride concentration function variation with time.

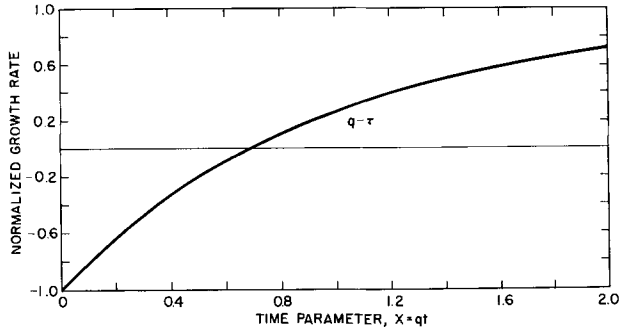

Fig. 3. Normalized growth rate as a function of time showing transient substrate etching during the initiation of the steady-state growth reaction.

entire range of the time parameter x. Therefore we need examine only the simpler case, Case I, to understand the general case as well. The germanium growth rate (Eq. [10]) becomes

$$\frac{d[\mathrm{Ge}]}{dt} = \frac{k_1^* D_4}{(k_1 + D_4)} C_2^{\infty 2}(1-e^{-qt})^2 + k_2[\mathrm{H_i}]\, C_2^{\infty}(1-e^{-qt}) - \frac{k_1 D_4}{k_1 + D_4} C_4^{\circ} \qquad [17]$$

A particular case of this function at low C_4° concentrations, where the assumptions made are most valid, has the form

$$\frac{d[\mathrm{Ge}]}{dt} = R\,[1 - 2(1-e^{-qt})] \qquad [18]$$

and is shown in Fig. 3. The initial etching period followed by growth is in all cases easily understood by referring to Eq. [8] modified by substituting Eq. [9] for C_4

$$\frac{d[\mathrm{Ge}]}{dt} = \frac{k_1^* D_4 C_2^2}{(k_1 + D_4)} + k_2[\mathrm{H_2^\circ}]C_2 - \frac{k_1 D_4}{(k_1 + D_4)} C_4^{\circ} \qquad [19]$$

Since the last term in C_4° has a fixed negative value and C_2 builds up from zero to its steady-state value C_2^∞, the growth rate is negative until C_2 becomes sufficiently large. The initial time interval, during which the growth rate is negative until it becomes zero, is defined as the induction period. Setting the growth rate $d[\mathrm{Ge}]/dt = 0$, the dichloride concentration $C_2(\tau)$ at a time equal to the induction period τ is given by

$$C_2(\tau) = \frac{k_2(D_4 + k_1)}{2k_1^* D_4} \cdot$$

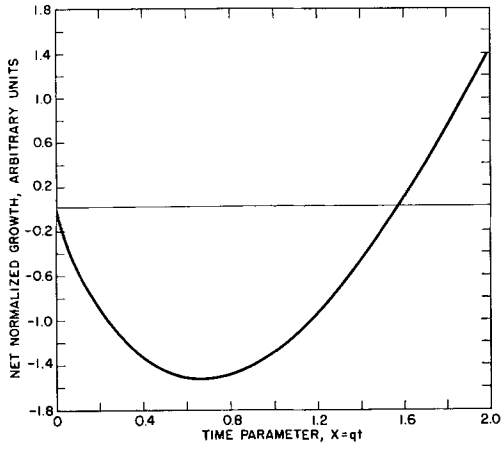

Fig. 4. Substrate growth as a function of time showing the etchback and subsequent steady-state growth.

$$\left[-1 + \sqrt{1 + \left[\frac{2D_4}{k_1 + D_4}\right]^2 \frac{k_1 k_1^* C_4^\circ}{k_2^2[\mathrm{H_2^\circ}]^2}}\right] \qquad [20]$$

By substituting this value for $C_2(\tau)$ into Eq. [14] one can in principle solve explicitly for the induction period t.

The growth rate can be integrated to give the height of the surface z from its initial position z_0

$$z - z_0 = \frac{(MW)}{d} \int_0^t \left(\frac{d[\mathrm{Ge}]}{dt}\right) dt \qquad [21]$$

This function is exemplified by the integral of Eq. [18] shown in Fig. 4.

Discussion

In a real system the tetrachloride concentration C_4 does not start at its equilibrium value but by diffusion builds up to its equilibrium value from zero. Therefore, instead of starting with a finite maximum negative value, the growth rate starts at zero, increases to a maximum negative value, decreases to zero, and then becomes positive. As a result, the etchback distance is not as great as would be expected by the equations derived herein. The differential equation for this case is a second order nonlinear differential equation in the form

$$\frac{d^2C_2}{dt^2} + (\bar{\alpha} + \bar{\beta})\frac{dC_2}{dt} + \bar{\alpha}\bar{\beta}C_2 + \bar{\gamma} + \delta\left(\frac{dC_2^2}{dt} + \epsilon C_2^2\right) = 0 \qquad [22]$$

which can be solved numerically. One can show that the growth rate at $t = 0$ is zero and that the slope of $d[\mathrm{Ge}]/dt$ *vs.* C_4° first becomes negative. Qualitatively, C_2 builds up almost as rapidly as C_4, whereas the induction period is comparable. Therefore the difference between the etching and growth rate is always less than in the first case, and the integrated etchback distance is less.

The etching-growth behavior is easily understood in terms of the reaction mechanism proposed. The reduction of the tetrahalide to subhalide C_2 etches the surface until C_2 builds up to a sufficiently high concentration to cause growth. In this reaction, diffusion of C_2 away from the surface limits the growth rate.

When the reverse of the growth reaction Eq. [4], or HCl etching is included, it also inhibits the

growth rate. In fact, it leads to substrate etching as the C_4^o concentration is increased beyond a critical value.[4]

Acknowledgment

The author thanks R. J. Andres, E. Matovich, and C. O. Thomas for fruitful and illuminating discussions on the subject material.

Manuscript received Jan. 21, 1963; revised manuscript received May 9, 1963.

Any discussion of this paper will appear in a Discussion Section to be published in the June 1964 JOURNAL.

REFERENCES

1. E. Matovich and R. J. Andres, Detroit Meeting, Electrochemical Society, October 1961, Abstract No. 137.
2. D. Kahng, R. C. Manz, M. M. Atalla, and C. O. Thomas, *ibid.*, Abstract No. 135.
3. C. O. Thomas, D. Kahng, and R. C. Manz, *This Journal*, **109**, 1055 (1962).

LIST OF SYMBOLS

a,A	loss factor due to impurity diffusing away from the surface defined in Eq. [1].
C	adsorbed impurity as measured by its gas phase concentration next to the solid-gas interface.
C_4	concentration of $GeCl_4$ at solid-gas interface.
C_2	concentration of $GeCl_2$ at solid-gas interface.
$[H_2]$	concentration of H_2 at solid-gas interface.
$[HCl]$	concentration of HCl at solid-gas interface.
C_4^o	concentration of $GeCl_4$ in the bulk gas phase.
$[H_2^o]$	concentration of H_2 in the bulk gas phase.
C_2^∞	see Eq. [13].
$\mathcal{D}_i$	diffusion coefficient of i^{th} species.
D_i	$\mathcal{D}_i/z_o$.
k	impurity distribution coefficient between the solid and gas phases during growth.
k_i	forward rate constant for reaction i.
k_i^*	reverse rate constant for reaction i.
N	impurity concentration in the solid phase.
q^2	$\beta^2 + 4\alpha\gamma$.
R	substrate growth rate.
z	distance measured normal to the surface from time zero.
z_o	effective thickness of stationary gas diffusion layer.
$\overline{\Delta z}$	average probable thickness of autodoped regrowth layer $= \int_o^\infty z\,N(z)\,dz / \int_o^\infty N(z)\,dz$
α,β,γ	see Eq. [12].
$\alpha,\beta,\gamma,\delta,\epsilon$	constants in Eq. [22].
τ	induction period — total time for transient substrate etching.

[4] This question is dealt with in greater detail in a companion paper on steady-state growth rates to be submitted to this Journal.

Vapor Growth of Germanium-Silicon Alloy Films on Germanium Substrates

R. C. Newman[1] and J. Wakefield

Research Laboratory, Associated Electrical Industries, Aldermaston Court, Aldermaston, Berkshire, England

ABSTRACT

Silicon has been transported from a source at 1100°C onto germanium single crystal substrates at 700°-900°C in a sealed system by the disproportionation of the iodide. Deposits thus formed are found to be germanium silicon alloys of variable composition. These structures have been examined by etching techniques, electron microbeam x-ray analysis, and by electron diffraction. During deposition, plastic deformation of the germanium occurs resulting in dislocation densities of up to $5 \times 10^7/cm^2$, and appreciable cavity formation is found in monocrystalline deposits formed at high substrate temperatures.

Epitaxial films of silicon are almost invariably prepared by the decomposition of trichlorosilane (1) or the hydrogen reduction of silicon tetrachloride (2); both these processes require a silicon substrate temperature of about 1200°C. A process less extensively studied is that described by Wajda *et al.* (3), who prepared monocrystalline films on silicon substrates by the disproportionation of silicon di-iodide. Silicon is transported from a source at a high temperature to the substrate at a lower temperature in a sealed tube by the reversible reaction

$$2SiI_2(g) \overset{\text{cold}}{\underset{\text{hot}}{\rightleftharpoons}} Si(S) + SiI_4(g) \qquad [1]$$

Wajda *et al.* gave source and substrate temperatures as 1100° and 900°C, respectively, but did not state the pressures used, which are controlled by the quantity of iodine introduced. The transport of silicon resulting from reactions with iodine has also been studied by Schäfer and Morcher (4), who found that the direction of transport along a temperature gradient depended on the pressure. At low pressures the reaction is

$$Si(S) + 4I(g) \rightleftharpoons SiI_4(g) \qquad [2]$$

and silicon is transported from a low-temperature region to a higher temperature region. At pressures greater than some value between 62-96 mm Hg of silicon tetra-iodide, however, reaction [1] was found to predominate with source and deposition zones at 1150° and 950°C, respectively.

In this paper the above iodide process for silicon deposition is investigated further, and in particular the deposition on germanium substrates has been examined, since it has been shown previously that germanium may be grown epitaxially on silicon using an iodide process (5).

Experimental Technique

The experimental system consisted of a closed quartz tube about 30 cm long and 2.2 cm bore,

[1] Present address: A.E.I. Research Laboratory, Rugby, Warwickshire, England.

similar to that used by Waja *et al.* (3). Slices of silicon or germanium about 1.5 cm diameter and 1 mm thick were hung from hooks on the end of a quartz rod which is sealed into one end of the tube. The silicon source material together with the iodine was also placed in the tube which was then drawn out at the open end and evacuated to a pressure of about 10^{-4} mm Hg. Sublimed iodine was introduced in an evacuated quartz capsule with break-tip seal, enabling the tube to be thoroughly outgassed before it was sealed. The vapor phase reaction was carried out in a vertical furnace with two temperature zones. The source silicon was held in the lower region at a temperature of approximately 1100°C while the temperature in the substrate zone was about 900°C; lower temperatures were however investigated with germanium substrates. Immediately before insertion, the substrates were chemically polished; silicon was etched in a 50/50 mixture of hydrofluoric and nitric acids, and germanium was etched in CP4.

Deposits on Silicon Substrates

The substrate was held at 900°C and the effect of gas pressure on the transport of silicon was investigated by varying the amount of iodine in the tube. When the calculated pressure of silicon tetra-iodide was less than about 100 mm Hg, etching of the substrates occurred indicating the transfer of silicon to the higher temperature end of the tube. At higher pressures, the direction of transport of the silicon was reversed, in qualitative agreement with the findings of Schäfer and Morcher (4). The deposits described in more detail below were obtained with a pressure of about 5 atm, and the growth rate, determined by sectioning, was about 15 μ/hr.

Growths on [111] substrates at 900°C were examined by reflection electron diffraction and found to be monocrystalline. The surfaces of such films were subsequently ground, etched in a mixture of 50% HF and 50% nitric acid and then Dash etched[2] to reveal the crystal structure. The features observed were: (i) a high dislocation density of approximately 2.10^6 cm^{-2}, (ii) a high density of stacking faults lying on <111> planes and up to 100μ in length, in some cases forming closed triangles, and (iii) polycrystalline inclusions about 100-200μ across. To examine the growth in depth and also the interface between the substrate and the film, a vertical section through the film was ground and etched as above. It was found that the interface between the substrate and film etched very rapidly, suggesting that this was a highly strained or dislocated region. The stacking faults could be traced back to the interface, and the regions of polycrystalline growth also appeared to nucleate here but were eventually covered by the surrounding monocrystalline growth. In addition, the dislocation density decreased with increasing distance from the interface.

Although large area single crystal growth was obtained on some [100] surfaces, it was found that randomly oriented particles, again nucleated at the interface, tended to grow preferentially and eventually predominated with increasing film thickness. The dislocation density in single crystal areas was approximately 2 x 10^5 cm^{-2} and was thus lower than that obtained for films grown on a [111] substrate; in addition, no etching features, characteristic of stacking faults, were observed on the [100] surfaces.

The poor crystal structure was almost certainly a consequence of an oxide or carbide layer (6) being formed on the surface of the substrate prior to the onset of deposition. Attempts to clean the substrate surface in situ by reversing the direction of reaction [1] were not satisfactory due to uneven attack of the substrate by the iodine and the formation of large etch pits. Thus it appears to be more difficult to achieve good crystal perfection in the deposits prepared by this iodide process compared with that obtainable from the chloride processes (1, 2).

Deposits on Germanium Substrates

An oriented overgrowth occurred readily on both [111] and [100] substrates at 900°C (see Fig. 1 and 2) without any special precautions being taken to remove spurious contamination from the reaction tube. The surface layer had the visual appearance of silicon and reflection electron diffraction showed that the lattice spacing of this layer was that of silicon within the experimental error of 0.5%.

Fig. 1. Oriented growth on a (111) germanium surface after 16 hr at 885°C. Magnification approximately 40x.

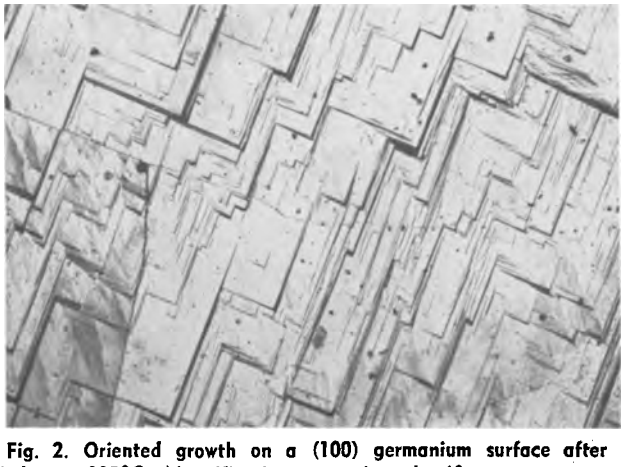

Fig. 2. Oriented growth on a (100) germanium surface after 16 hr at 885°C. Magnification approximately 40x.

[2] HF-HNO_3-acetic acid in ratio 1:3:8.

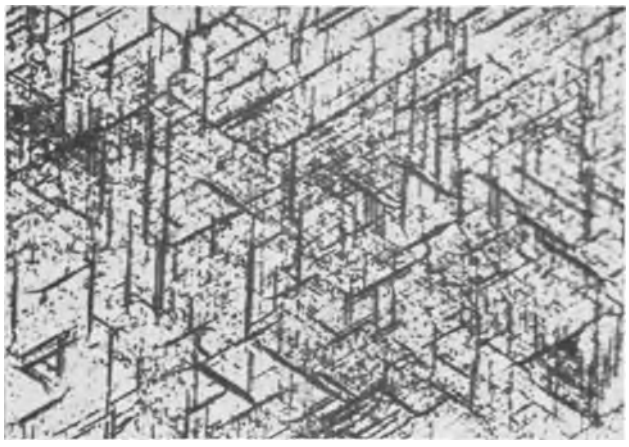

Fig. 3. Etched (111) growth showing a high density of stacking faults and dislocations. Magnification approximately 400x.

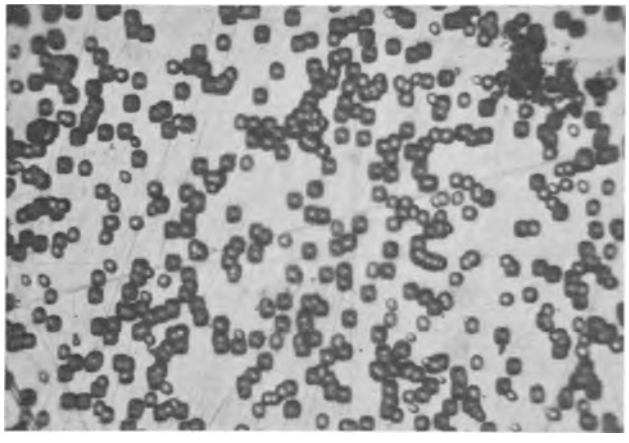

Fig. 4. Etched (100) growth showing only dislocations with a density of 10^7 lines/cm^2. Magnification approximately 1100x.

Chemical etching of these surfaces revealed similar features to those described for deposits on silicon substrates, *i.e.*, stacking faults and slip traces were evident on (111) surfaces but not on (100) surfaces, as shown in Fig. 3 and 4. The samples were then sectioned and polished. The thickness of the surface layer was found to be about 15-30μ, beneath which there was a second layer containing large cavities as shown in Fig. 5. The thickness of this cavitated layer increased with increasing time of reaction, until after 64 hr a germanium substrate originally 1 mm in thickness was no longer identifiable.

To determine the relative concentrations of germanium and silicon in these layers, such sections were scanned in a microbeam x-ray analyzer (7). The germanium content at the surface was about 2-5 a/o, which is consistent with the determination of the lattice parameter of this layer. The germanium concentration increased only slowly with increasing penetration until the interface between the cavitated layer and the germanium was approached; no discontinuity was found between the surface layer and the cavitated layer. The distribution of germanium about the second interface is shown in Fig. 6 for various substrate temperatures. It may be noted that, although this interface appears quite sharp on micrographs of samples reacted at all temperatures, the concentration gradient of the germanium increases with decreasing temperature. The distribution of silicon was likewise determined, but the results could not be interpreted accurately because the absorption coefficient for the characteristic x-rays from the silicon in the germanium-silicon alloy was not known. Qualitatively, however, the results indicated that the sum of the germanium and silicon concentrations was close to unity. Back-reflection Laue photographs showed that the cavitated layers were monocrystalline throughout, and lattice parameters intermediate between germanium and silicon were measured in agreement with the microanalysis.

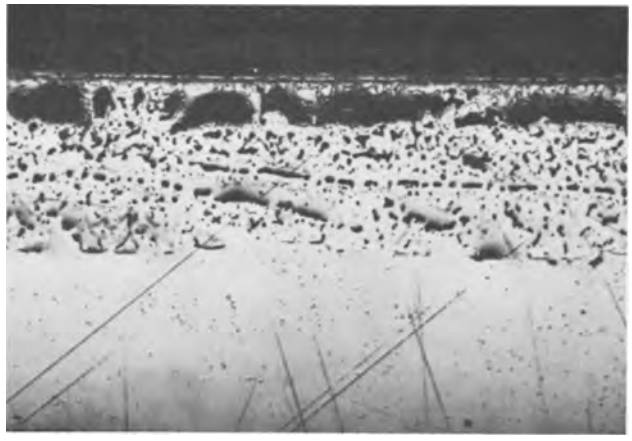

Fig. 5. Sectioned (111) sample showing cavitated layer below the thin coherent surface skin. Treatment 3½ hr at 870°C. Magnification approximately 70x.

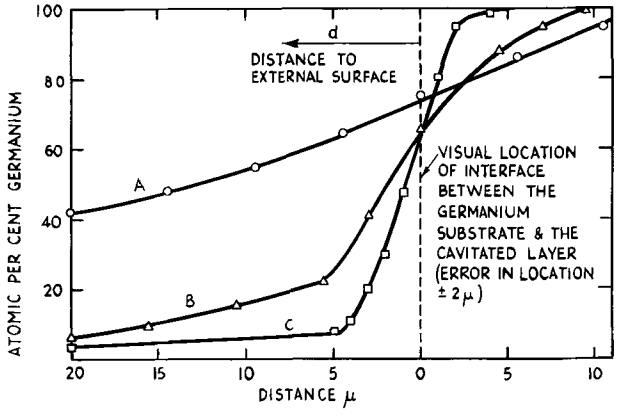

Fig. 6. Concentration of germanium in atomic per cent as a function of distance. The interface between the germanium substrate and the cavitated layer (see Fig. 5) is used as a reference line. Curve A, $T = 885$°C, $d = 410\mu$; curve B, $T = 800$°C, $d = 130\mu$; curve C, $T = 660$°C, $d = 20\mu$. The time of heating in each case was 17 hr and d is the distance from the reference line to the external surface.

The weight of the sample after the reaction was less than the weight of the original germanium substrate, but the thickness was considerably increased. Thus, as silicon is deposited, germanium must be transferred to the gas phase, and in fact, yellow germanous iodide was observed in the reaction tube on removal from the furnace.

This is consistent with the calculated values of the free energy ΔG of -20 kcal/mole and -27 kcal/mole, respectively for the reactions

$$Ge(S) + SiI_2(g) + \Delta G \rightleftharpoons GeI_2(g) + Si(S)$$

and

$$2Ge(S) + SiI_4(g) + \Delta G \rightleftharpoons 2GeI_2(g) + Si(S)$$

at a temperature of 1200°K; values of the free energy for silicon di-iodide and germanium di-iodide were obtained from previously published data (4, 8).

To elucidate the mechanism of the germanium transport through the silicon some further experiments were carried out. A sample was reacted in the usual way for a sufficient time to form a silicon coating on its surface, and then the iodine was condensed by the application of liquid air to a cold finger (at high temperature during the first part of the heating) after which heating of the sample was continued for several hours. Sections of the samples showed a structure appropriate to the short time of deposition, indicating that no appreciable diffusion occurred during the subsequent anneal. In fact, no change in the germanium concentration profile could be detected in a similar sample heated in an evacuated silica tube for 600 hr at 918°C. It therefore appears that the germanium is transported through the pores in the cavitated region (see Fig. 5) by a gas phase reaction involving iodine, although this was not detected by the microanalysis. This is not unexpected, since any condensed germanium or silicon iodides would be hydrolized in the atmosphere, thus allowing the iodine to escape; the concentration of iodine in solid solution is expected to be small in view of the results of Baker and Compton (9).

A possible mechanism for the formation of the cavities is now discussed. There is a continuous charge in lattice parameter from the surface of the deposits to the germanium substrate and dislocations must be generated to accommodate this change. In fact, etching revealed that the dislocation density in the germanium substrate increased during the reaction from about 10^4 cm^{-2} up to 5×10^7 cm^{-2}, thus giving positive evidence for the occurrence of plastic deformation. Vacancies generated by the nonconservative motion of jogs on such moving dislocations (10) may subsequently aggregate to form cavities which are likely to be stabilized by the presence of germanium di-iodide gas. The possibility that the pores arise from a Kirkendall effect (11) is thought to be unlikely, due to the observed negligible interdiffusion in the absence of iodine.

Oriented growths were obtained on [111] substrates at temperatures down to 650°C. At the lower temperatures, the rate of silicon deposition on the specimen was much reduced (see Fig. 6) and a film of silicon was deposited on the wall of the reaction tube in a zone at about 800°C. Oriented growths could not be obtained on [100] substrates at temperatures below 800°C. Twinning occurred on all {111} planes as determined by electron diffraction and these twinned crystallites were found to have large planar {111} facets similar to the structure observed on germanium deposits prepared by a similar iodide process (12).

Conclusions

It has been shown that silicon can be deposited onto germanium single crystal substrates to give epitaxial layers consisting of a germanium silicon alloy. The most interesting feature is that a single crystal structure can be maintained throughout the whole range of composition of germanium-silicon alloys in contrast to alloys prepared by the pulling technique (13). These results are thus complementary to those of Millar and Grieco (14) who obtained single crystal germanium-silicon alloy films by means of the chloride process.

Acknowledgments

Thanks are due to J. H. Neave for experimental assistance and to Dr. T. E. Allibone, C.B.E., F.R.S., Director of the Laboratory, for permission to publish this paper.

Manuscript received Feb. 28, 1963; revised manuscript received May 20, 1963. This paper was presented at the Boston Meeting, Sept. 16-20, 1962.

Any discussion of this paper will appear in a Discussion Section to be published in the June 1964 JOURNAL.

REFERENCES

1. R. Glang and E. S. Wajda, "Metallurgy of Semiconductor Materials," (AIME Los Angeles Conf., 1961), J. B. Schroeder, Editor, **15**, 27 (1962), Interscience Publishing Co., New York.
2. H. C. Theuerer, *This Journal*, **108**, 649 (1961).
3. E. S. Wajda, B. W. Kippenham, and W. H. White, *I.B.M. J. Res. Develop.*, **4**, 288 (1960).
4. H. Schäfer and B. Morcher, *Z. anorg. allgem. Chem.*, **290**, 279 (1957).
5. R. P. Ruth, J. C. Marinace, and W. C. Dunlap, Jr., *J. Appl. Phys.*, **31**, 995 (1960).
6. R. C. Newman and J. Wakefield, "Solid State Physics and Telecommunications," Brussels, 1958, Vol. 1, p. 318, Academic Press, New York (1960).
7. T. Mulvey, *J. Sci. Instruments*, **36**, 350 (1959).
8. W. C. Jolly and W. M. Latimer, *J. Am. Chem. Soc.*, **74**, 5752 (1952).
9. W. E. Baker and D. M. J. Compton, *I.B.M. J. Res. Develop.*, **4**, 269 (1960).
10. W. C. Dash, *J. Appl. Phys.*, **29**, 705 (1958).
11. A. D. Smigelskas and E. O. Kirkendall, *Trans. AIME*, **171**, 130 (1947).
12. R. C. Newman and J. Wakefield, "Solid State Physics and Telecommunications," Brussels, 1958, Vol. 1, p. 160, Academic Press, New York (1960).
13. E. R. Johnson and S. M. Christian, *Phys. Rev.*, **95**, 560 (1954).
14. K. J. Miller and M. J. Greico, *This Journal*, **109**, 70 (1962).

The Gettering Properties of Tantalum

E. G. Zubler

Lamp Research Laboratory, General Electric Company, Nela Park, Cleveland, Ohio

ABSTRACT

The reaction of tantalum with the gases, O_2, N_2, CO_2, CO, and H_2 at low pressures (0-200μ) was studied in the range 200°-2000°C. Measurable reaction rates which were independent of pressure were observed for O_2 at 350°-650°C, N_2 at 780°-940°C, CO_2 at 500°-1500°C, and CO at 950°-1500°C. H_2 was reversibly absorbed at 200°-730°C and was the only gas released after sorption below 1600°C.

As part of a general investigation of getters, a study has been made of the kinetics of reactions between tantalum and various gases. Tantalum and other bulk getters have been used in lamps and electron devices to remove detrimental gaseous impurities such as H_2, O_2, CO_2, CO, H_2O, and hydrocarbons. In order to use these getters effectively, a knowledge of sorption and desorption processes as a function of temperature and pressure is necessary.

While a comprehensive survey of gas sorption by metals (1) and recent bibliographies (2, 3) on getters are available, studies of the reactions between tantalum and the gases of interest (4-13, 17, 18) do not cover the low gas pressure (micron) region adequately. Consequently, this investigation of the gettering properties of tantalum as a function of temperature (200°-2000°C) and pressure (0-200μ) was initiated.

Experimental

The tantalum was obtained from Fansteel Metallurgical Corporation in 0.003 x 5/16 in. strips and was specified as 99.9+% purity with C and Fe each at a maximum level of 0.03%. The tantalum was formed into a 1.0 in. diameter ring with an approximate weight of 0.80g. The surface of the tantalum was smooth, and the surface area was calculated from the geometric dimensions.

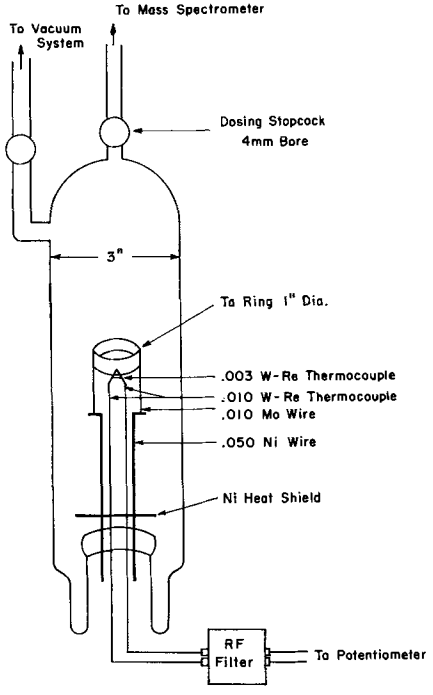

Fig. 1. Getter chamber

The gases with 99.5-99.99% purity were obtained in small cylinders or glass flasks, and further purification was not attempted except when possible the gas was passed slowly through a liquid nitrogen trap packed with glass beads to remove any possible water vapor.

A glass, high vacuum system using a mercury diffusion pump was constructed. The gas pressure for the gettering experiments was measured by a Consolidated Electrodynamics Corporation, Model 23-105, micromanometer. An ion resonance mass spectrometer was used to analyze the gas in the getter chamber.

A diagram of the getter chamber which is similar to one used by other investigators (14) is shown in Fig. 1. The tantalum ring was heated by a radio-frequency induction unit while the temperature was measured by the rhenium-tungsten thermocouple for which a calibration curve to 2100°C was available (15). Tungsten electrodes were used for all spot welding operations. A nickel heat shield was located between the hot and cold junctions of the thermocouple. The bottom section of the getter chamber was immersed in a water bath at room temperature which was taken as the cold junction temperature.

After the getter chamber was sealed to the glass vacuum system and pumped down, the volume of the chamber was determined by a calibrated volume and gas expansion technique. The getter chamber was then baked out at 350°C for 2 hr using heating tape. After bake out, the tantalum ring was slowly heated to 1800°-2000°C and held there until the pressure was less than 10^{-5} mm. Except for the evolution of adsorbed gas and sorbed hydrogen at relatively low temperatures, other gases were evolved only at temperatures greater than 1600°C.

After degassing, the tantalum was allowed to return to room temperature, and the gas under consideration was admitted at a pressure measured by the micromanometer. The tantalum ring was then heated to the desired temperature which was attained in 20-30 sec, and the pressure was then measured at 30 or 60 sec intervals.

As the gas pressure in the system decreased, there was a slight increase in the temperature of the tan-

Table I. Summary of data for the reaction of tantalum with oxygen, nitrogen, and carbon monoxide

Gas	Temp, °C	Time, min	Initial pressure, μ	Rate constant: Parabolic μ·l/cm²·sec^1/2	Rate constant: Linear μ·l/cm²·sec
O_2	360	10	62		1.06×10^{-3}
	390	8	48		1.69×10^{-3}
	410	14	169		2.14×10^{-3}
	430	12	86		2.98×10^{-3}
	460	15	153		5.26×10^{-3}
	460	13	132		5.14×10^{-3}
	485	15	174		9.08×10^{-3}
	500	15	196	0.76	
	515	10	186	0.90	
	535	16	190	0.83	
	550	12	118	0.85	
	555	8	88	0.95	
	590	6	105	1.65	
	635	5	95	2.87	
N_2	780	15	119		7.6×10^{-4}
	810	15	108		1.65×10^{-3}
	860	10	95		3.5×10^{-3}
	940	10	178		1.63×10^{-2}
CO	1200	20	142		7.9×10^{-3}
	1215	10	195		7.4×10^{-3}
	1265	10	170		1.05×10^{-2}
	1315	8	145		1.27×10^{-2}
	1350	10	180		1.70×10^{-2}
	1430	10	130		1.95×10^{-2}
	1535	10	75	0.49	
	1600	8	38	0.52	

talum ring which was corrected manually during the run by using a fine adjustment on the power control of the induction heater. With this technique, the temperature could be held constant to within 5°-10°C during a typical run.

After the run, the getter chamber was pumped down to 10^{-6} mm, and the tantalum ring was degassed at 1600°-2000°C. A new tantalum ring was used for each gas, and the amount of gas sorbed during a series of runs was considerably less than that required for saturation.

Results

The results of the reactions between a degassed tantalum ring and oxygen, nitrogen, and carbon monoxide are summarized in Table I. Below a certain temperature which depended on the gas, the gas pressure above the tantalum decreased linearly with time while above this temperature the pressure decreased linearly with the square root of time. The linear and parabolic relations for these temperature regions persisted even when large quantities of gas had been sorbed.

For oxygen, a linear pressure-time relation was observed at 350°-490°C while a parabolic relation was observed at 520°-650°C as shown in Fig. 2 and 3, respectively. In the linear region, the rate constant for a degassed tantalum sample at constant temperature was independent of initial pressure. Identical slopes were obtained for 3 pressure-time plots with initial pressures in the range 82-169μ. In the transition region, 490°-520°C, a linear rate law was obeyed for a degassed sample, and a parabolic rate law was obeyed if some sorption

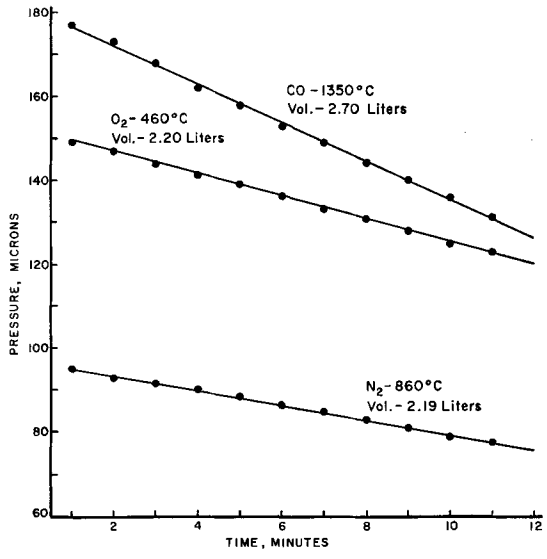

Fig. 2. Linear variation of pressure with time for oxygen, nitrogen, and carbon monoxide.

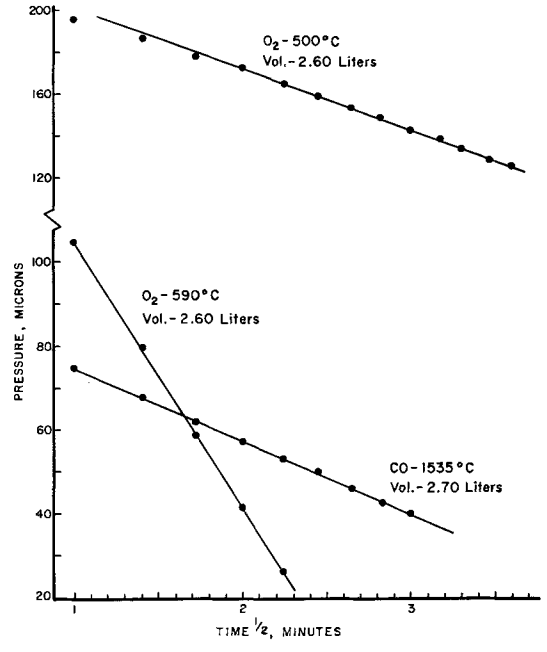

Fig. 3. Parabolic variation of pressure with time for oxygen and carbon monoxide.

had occurred previously. The run at 500°C in Fig. 3 shows a linear behavior followed initially by a transition to parabolic behavior.

Generally, there was no visible change in the tantalum during a run. However, in one experiment, the tantalum sorbed sufficient oxygen at 600°C to result in a visible darkening of the surface. A cross section of the tantalum showed that the product layer was approximately 0.0005 in. thick, and x-ray diffraction analysis identified the layer as β-Ta_2O_5.

For carbon monoxide, a linear rate law was obeyed at 950°-1500°C and a parabolic rate law at 1500°-1600°C for a degassed tantalum sample. However, a run at 1010°C which obeyed a linear rate law for several minutes became parabolic when the temperature was increased to 1180°C. When the tantalum was degassed and the reaction again observed at 1180°C, a linear rate law was obeyed for

14 min. In general for 1000°-1300°C, it was found that, if the temperature during a run was increased more than 70°-80°C, the pressure-time relation changed from linear to parabolic. If the temperature change were less, the reaction continued to follow a linear rate law.

At these low gas pressures and temperatures above 1500°C, there was a tendency for the RF field to produce a discharge in the getter chamber, and this limited the data in this region.

For nitrogen, the pressure-time relation was linear at 780°-940°C. At 940°C, there was a tendency for the pressure-time plot to become parabolic. At higher temperatures the reaction rate was too fast for the techniques employed so that actual parabolic plots were not obtained.

For oxygen, nitrogen, and carbon monoxide, plots of the logarithms of the linear reaction rates *vs.* reciprocal temperature and the activation energies calculated from the Arrhenius equation are shown in Fig. 4. A similar plot for oxygen at 530°-650°C where the reaction follows a parabolic rate law gives E_a = 22 kcal/mole. Insufficient data were available for the parabolic region of carbon monoxide to permit a calculation of E_a.

For carbon dioxide, the decrease in pressure with time was linear at 950°-1200°C and parabolic at 1230°-1440°C. A mass spectrometric analysis of the gas in the getter chamber during a run indicated that a reaction producing carbon monoxide occured at 500°-700°. The decrease of carbon dioxide as indicated by the mass 44 peak was linear with time in this temperature region. At higher temperatures, carbon monoxide was also sorbed, and the system behaved similar to that of pure carbon monoxide except that the transition from linear to parabolic behavior occurred at a lower temperature.

Hydrogen was sorbed reversibly at 200°-730°C. At 200°-500°C the reaction obeyed a parabolic rate law while at higher temperatures the reaction was too rapid to measure. For a degassed tantalum ring, the minimum temperature at which sorption was observed was 370°C. However, if the ring had sorbed some hydrogen at a higher temperature, *e.g.*, 500°-600°C, sorption was observed at 200°C. At any temperature, a plot of the solubility in cubic centimeters at STP per gram of tantalum *vs.* the square root of pressure was a straight line, indicating that atomic hydrogen was involved in the sorption process. The equilibrium pressure at a given temperature and concentration of sorbed gas was the same whether it was obtained by sorption or evolution indicating that the sorption process involved solution rather than compound formation. The temperature dependency of the solubility and the calculated heat of solution per mole of H_2 are given in Fig. 5.

Discussion

The linear and parabolic pressure-time relations observed in different temperature regions for oxygen, carbon monoxide, and indicated for nitrogen suggest different rate-controlling processes. At the lower temperatures where a linear rate law was obeyed, strong adsorption of the gas resulting in nearly complete surface coverage of the tantalum is postulated. Since, for nearly complete surface coverage, the concentration of adsorbed molecules is nearly independent of gas pressure, the reaction rate is pressure independent, and a linear rate law would be observed. At higher temperatures where a parabolic rate law was observed, a rate-controlling diffusion process is indicated. At these temperatures, a fast reaction results in the rapid formation of a product layer, and further reaction involves diffusion through this surface layer, resulting in a parabolic rate law. A product layer has been identified here for oxygen at 600°C. The relation between diffusion constants and parabolic rate constants for similar gas-metal system has been considered (7, 8, 10, 16).

For the gas pressure range considered here, the initial reaction might be expected to follow a linear rate law for degassed tantalum at any temperature. At high temperatures, the product layer is formed rapidly, and the linear region is not observed. At low temperatures, the product layer does not develop sufficiently in the time allowed to become rate controlling. At intermediate temperatures, the linear rate law may be obeyed initially followed by a transition to parabolic behavior. This type of be-

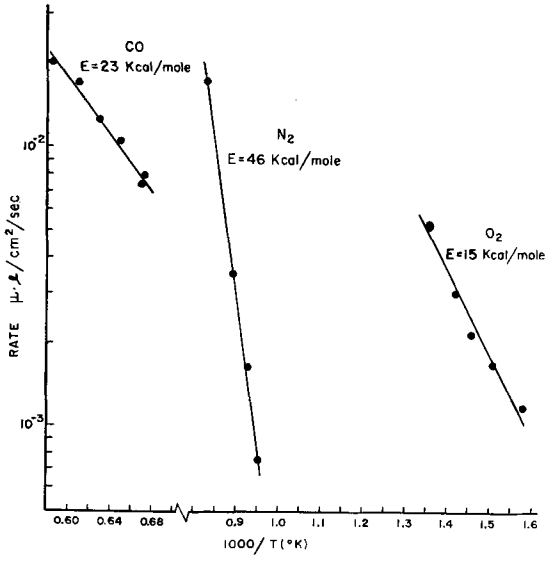

Fig. 4. Temperature dependence of linear sorption rates for oxygen, nitrogen, and carbon monoxide.

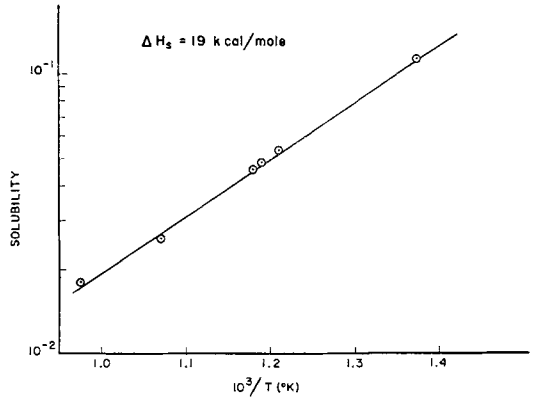

Fig. 5. Temperature dependence of solubility of hydrogen in cubic centimeters at STP per gram of tantalum.

havior was observed for oxygen at 500°C as shown in Fig. 3.

In previous studies, the oxidation reaction has been reported as linear (10, 13), parabolic (7), cubic (17), and logarithmic (9, 11, 12) for comparable temperatures but generally higher pressures and longer times than considered here. The higher pressures and longer reaction times would tend to mask the linear behavior observed in this study. At slightly higher pressures (1.5-16 mm) and longer reaction times (0-120 min), Gulbransen and Andrews reported parabolic behavior for oxygen at 250°-450°C and for nitrogen at 500°-850°C. They calculated E_a = 27.4 kcal/mole for the oxidation reaction compared to the 22 kcal/mole calculated in this study for the parabolic region (520°-650°C). For the diffusion of oxygen through tantalum Ang (19) reported E_a = 27.3 kcal while Albrecht *et al.* reported 22.9 kcal/mole. At much higher pressures (0.2-1.0 atm), Albrecht *et al.* observed linear behavior for oxygen at 400°-600°C with E_a = 60 kcal/mole compared to the 15 kcal/mole found in this study. They also observed that nitrogen obeyed a cubic rate law at 400°-700°C and a parabolic rate law at 800°-1475°C.

Acknowledgments

The assistance of R. Wyland in the laboratory, the x-ray diffraction and microscopy work of Miss J. Cooper, and the valuable suggestions and discussions of Miss A. Easley and Dr. L. V. McCarty are gratefully acknowledged.

Manuscript received Jan. 14, 1963; revised manuscript received May 7, 1963.

Any discussion of this paper will appear in a Discussion Section to be published in the June 1964 JOURNAL.

REFERENCES

1. S. Dushman, "Scientific Foundations of Vacuum Techniques," John Wiley & Sons, Inc., New York (1949).
2. C. J. Wensrich, UCRL-6514, University of California (1961).
3. N. M. Morris, Bell Tel. Lab., Bibl. No. 22, July 1958.
4. D. A. Wright, *Nature*, **142**, 794 (1938).
5. M. R. Andrews, *J. Am. Chem. Soc.*, **54**, 1845 (1932).
6. R. Myers, *Metallurgia*, **41**, 30 (1950).
7. E. Gulbransen and K. Andrews, *Trans. AIME*, **185**, 515 (1949); **185**, 741 (1949); **188**, 586 (1950).
8. E. Gulbransen and K. Andrews, *This Journal*, **96**, 364 (1949).
9. D. A. Vermilyea, *Acta Met.*, **6**, 166 (1958).
10. W. Albrecht, W. Klopp, B. Koehl, and R. Jaffee, *Trans. AIME*, **221**, 110 (1961).
11. H. Basseches, *This Journal*, **109**, 475 (1962).
12. J. T. Waber, G. E. Sturdy, E. Wise, and C. R. Tipton, Jr., *ibid.*, **99**, 121 (1952).
13. R. C. Peterson, W. M. Fassell, and M. E. Wadsworth, *Trans. AIME*, **200**, 1038 (1954).
14. V. Stout and M. Gibbons, *J. Appl. Phys.*, **26**, 1488 (1955).
15. J. C. Lachman, *Instr. & Contr. Syst.*, **32**, 1030 (1959).
16. N. F. Mott, *Trans. Faraday Soc.*, **36**, 472 (1940).
17. J. T. Waber, *J. Chem. Phys.*, **20**, 734 (1952).
18. A. Sieverts and H. Bruning, *Z. phys. chem.*, **A174**, 365 (1935).
19. C. Y. Ang, *Acta. Met.*, **1**, 123 (1953).

The Adsorption of Aromatic Hydrocarbons at the Gold Electrolyte Interface

Harold Dahms[1] and Mino Green[2]

The Electrochemistry Laboratory, The University of Pennsylvania, Philadelphia, Pennsylvania

ABSTRACT

The potential and concentration dependent adsorption of benzene, naphthalene, and phenanthrene at the gold/electrolyte interface has been investigated using a ^{14}C-radio tracer technique. For a fixed concentration of organic material the adsorption peak was found at about +500 mv (NHE) and the potential-adsorption curve was bell shaped, adsorption decreasing with potential on either side of the peak. An analysis of the adsorption isotherms for naphthalene leads to the conclusion that naphthalene lies flat on the electrode surface. Comparison of the extent of adsorption of the aromatic hydrocarbons with cyclohexane, n-octanoic acid, and n-decanoic acid (no detectable adsorption) indicates that aromatic compounds have a higher binding energy with metals than the corresponding aliphatic compounds. The added binding energy for aromatic molecules is attributed to their π-electron systems. Finally a comparison of mercury with gold points to the stronger binding energy of water to gold than to mercury.

Studies of the adsorption of organic molecules at the metal/electrolyte interface have been mainly confined to mercury. Knowledge of the adsorption at solid metals, however, is important to a number of electrochemical problems, *e.g.*, structure of the double layer, corrosion inhibition, and electrochemical oxidation of fuels. Simple aromatic compounds were chosen for this investigation because these substances were expected to give rise to relatively simple systems.

Studies of the adsorption of organic molecules at solid electrodes have been mainly carried out using

[1] Present address: Thomas J. Watson Research Center, International Business Machine Corporation, Yorktown Heights, New York.

[2] Present address: 45 Radley House, Gloucester Place, London, England.

capacity measurements (1), the direct determination of concentration changes in the solution (2), or radioactive tracer techniques. The determination of adsorption from capacity data is, however, not unambiguous because of the implied nonthermodynamic assumptions and the complication of the frequency dependence of the capacity. The direct study of adsorption by determination of the concentration change in the solution is limited to extremely dilute solutions and large area electrodes.

Radiotracer methods have been used by numerous workers. Most of these techniques require a separation of the labelled solution phase from the adsorbed species thereby causing possible sources of error. Various methods have, however, been developed to determine the extent of adsorption without disturbing the equilibrium at the interface. The precursor to the present method was developed by Joliot (3). This technique was modified by several workers: Power and Heyd (4) adopted it for α-emitting species. Kafalos and Gatos (5) presented a technique using hard β- and γ-emitters. Weissmantel (6) determined the adsorption of β-labelled species by measuring their radiation passing through thin films of various metals. Likewise Cook (7) and Blomgren and Bockris (8) measured the β-radiation through thin metal films. The latter workers used a mechanical method to separate the solution background from the total radiation. The mechanical separation in no way interfered with adsorption equilibrium. This last mentioned technique was used by Wroblowa and Green (9) to study the potential dependent adsorption of thiourea on gold.

The work described here was carried out using a similar technique, but with a different method to separate the radiation of the adsorbed species from that of the solution background.

Experimental

Arrangement and procedure.—A schematic diagram of the cell and counting arrangement is shown in Fig. 1. The cell is essentially the same as that described by Wroblowa and Green (9) modified only to permit continuous electromagnetical stirring.

The gold electrode, a foil of 2.10^4Å thickness, was fixed on the window of a gas-flow proportional counter. The electrode potential of the gold electrode was controlled by means of a potentiostat. The compartments for the reference electrode (saturated calomel electrode) and the working electrode were separated by stopcocks. Purified hydrogen or nitrogen (cleaned by passing the gas over heated platinum-asbestos, charcoal, and through liquid nitrogen cooled traps) was passed through the cell. The cell was isolated from the atmosphere by means of a water-seal. The labelled organic solution was added from a calibrated burette. The cell was placed on a microscopic drive to adjust it vertically in its position to the counter. The whole arrangement was operated in an air-thermostat.

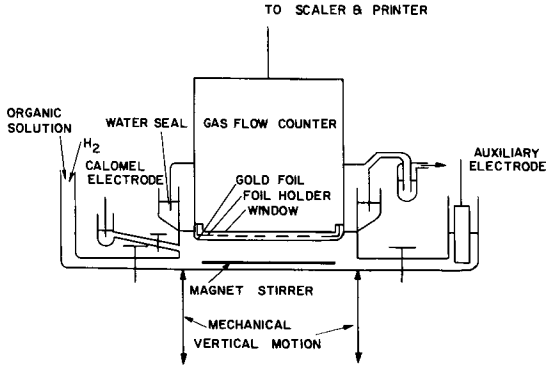

Fig. 1. Diagram of the experimental arrangement

The gold foil (purity 99.99% as given by the manufacturer) was first cleaned by extraction in ethanol and acetone. The foil holder was then covered with a thin layer of a high vacuum grease, and one side of the foil was fixed onto it. The gold electrode covered the foil holder and the lower part of the counter so that any contact of the grease with the outer side of the gold foil or with the solution was strictly avoided. Finally the gold electrode was cleaned by alternate anodic-cathodic pulsing in 1*N* H_2SO_4 (going from oxygen evolution to hydrogen evolution), terminating on cathodic polarization (hydrogen evolution for 1 min). The evolved hydrogen and oxygen were removed from solution by sweeping with nitrogen. After this treatment the electrode was perfectly wetted by water. Different cleaning procedures of the gold electrode (heating to about 300°C) did not influence the adsorption behavior.

The electrolyte in the cell was 1*N* H_2SO_4 prepared from pure concentrated sulfuric acid and conductivity water. After the dissolved gases had been swept out, the labelled organic solution was added. Then only a minimum amount of purified nitrogen was passed through the adsorption compartment to maintain a controlled atmosphere and yet minimize evaporation. The electrolysis current never exceeded 10^{-5} amp/cm^{-2} over the entire range of potential investigated and dropped during the experiment to values of 10^{-7} amp/cm^{-2}. Variation in current between had no apparent influence on the extent of adsorption. The count rate of the radiation counter was recorded automatically as a function of time and electrical potential.

Determination of the amount adsorbed.—Without any adsorption a certain amount of the radiation from the labelled solution will reach the counter, the resulting count rate will be given by

$$\mathrm{cps_{sol}} = k\ 3.7\ 10^{10}\ Ac\ \alpha \int_0^\infty e^{-\mu x}\,dx = k\ 3.7\ 10^{10}\ Ac\ \alpha \frac{1}{\mu} \qquad [1]$$

where $\mathrm{cps_{sol}}$ is the count rate from solution (sec^{-1}); k is the counting efficiency; A, the area of the electrode exposed to the counter (cm^2); c, the concentration of the organic material in solution (mole cm^{-3}); α, the specific activity of the organic material (curie mole^{-1}); μ, absorption coefficient of ^{14}C radiation in water [314 cm^{-1} (11)].

If adsorption occurs, the additional count rate is given by

$$\mathrm{cps_{ads}} = k\ 3.7\ 10^{10} \Gamma\ A\alpha \qquad [2]$$

where $\mathrm{cps_{ads}}$ is counts from the adsorbed material (sec^{-1}); and Γ is the amount of adsorbed material (mole cm^{-2}).

The total recorded count rate from [1] and [2] above is

$$cps_{sol} + cps_{ads} = k\, 3.7\, 10^{10}\, A\alpha \left(\frac{c}{\mu} + \Gamma \right) \quad [3]$$

In order to determine Γ from Eq. [3] we have to count under identical experimental conditions a solution of known specific activity in which adsorption is negligible ($\Gamma << c/\mu$). A 10^{-2}M $Na_2{}^{14}CO_3$ solution was used for this calibration after every experiment. Adsorption of CO_3'' does not influence this calibration technique, since the condition $\Gamma << c/\mu$ would still be fulfilled in a 10^{-2}M solution.

The specific activities of the $Na_2{}^{14}CO_3$ solution and the solutions of the organic compounds were determined in a liquid-scintillation counter with a standard deviation of several runs less than ±2%. The labelled organic material was supplied by Chemtrac Corporation, Boston. It was purified and analyzed by gas chromatography directly before delivery. The carbonate solution (Nuclear Chicago) was checked against a NBS standard solution.

The reproducibility of determinations of the adsorbed amount was found to be from 5 to 10% in the concentration range 2.10^{-7} to 10^{-4}M. The reproducibility was checked for every compound at all concentrations and potentials.

Results

Aromatic compounds.—

(*A*) The surface coverage as a function of potential at constant solution concentration is given in Fig. 2 to 4. The surface coverage θ is given by

$$\theta = \frac{\Gamma}{\Gamma_{max} \cdot R} \quad [4]$$

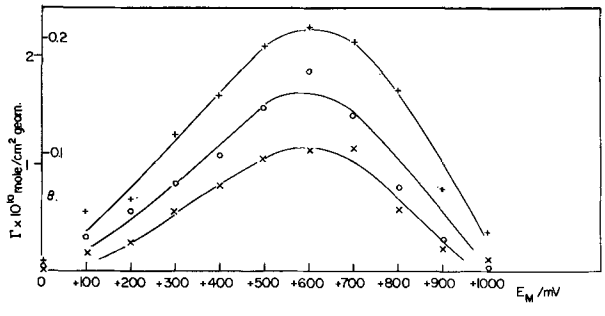

Fig. 2. Adsorption of benzene on gold from aqueous solution as a function of potential. $C_{H_2SO_4}$ = 0.5M. —×—, 2.10^{-4}M benzene; —O—, 5.10^{-4}M benzene; —+—, 10^{-3}M benzene.

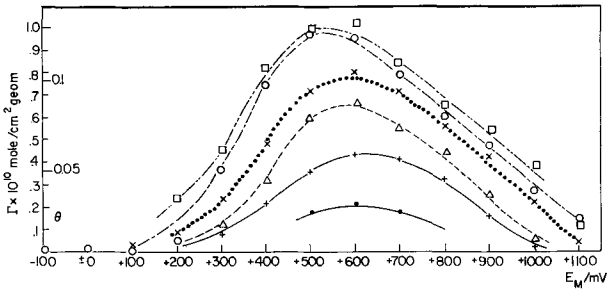

Fig. 3. Adsorption of naphthalene on gold from aqueous solution as a function of potential. $C_{H_2SO_4}$ = 0.5M, temperature, 25°C. —●—, 1.10^{-7}M naphthalene; —+—, 2.10^{-7}M naphthalene; ——△——, 5.10^{-7}M naphthalene; ●●●×●●●, 10^{-6}M naphthalene; ——O——, 5.10^{-5}M naphthalene; ——□——, 10^{-4}M naphthalene.

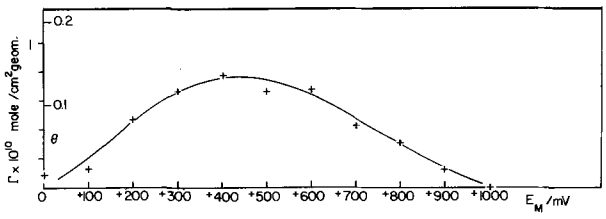

Fig. 4. Adsorption of phenanthrene on gold from aqueous solution as a function of potential. $C_{H_2SO_4}$ = 0.5M; $C_{phen.}$ = 10^{-6}M.

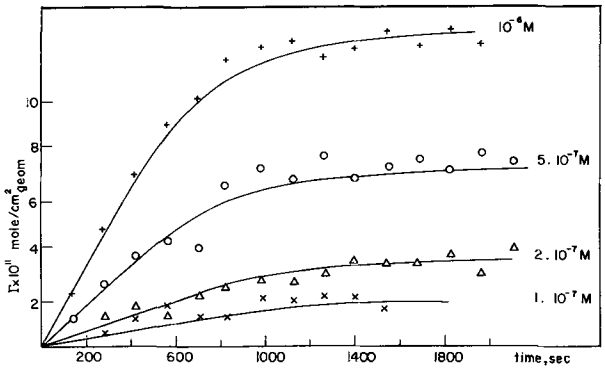

Fig. 5. Time dependence of naphthalene adsorption at +500 mv (NHE) for various concentrations of naphthalene (solution stirred at 60 rp).

where Γ is the amount adsorbed per apparent unit area; Γ_{max} is the maximal adsorbed amount in 1 monolayer (calculation as shown below); and R is the roughness factor of the electrode, determined by the BET method to be 2.2 ± 0.2.

(*B*) Time effects. The adsorption in more dilute solutions showed a considerable time-dependence (Fig. 5). The solution was stirred at 60 rpm. The equilibrium value at each potential was constant for hours after equilibrium had been established.

(*C*) Temperature effects. The temperature-dependence of adsorption was checked for the adsorption of naphthalene at 25° and 5°C. The change of the maximal adsorption at E = +500 mv was less than 5%.

(*D*) The surface coverage for naphthalene as a function of the solution concentration is plotted in Fig. 6 over the concentration range 10^{-7} to 10^{-6}M. For the other aromatic compounds (benzene

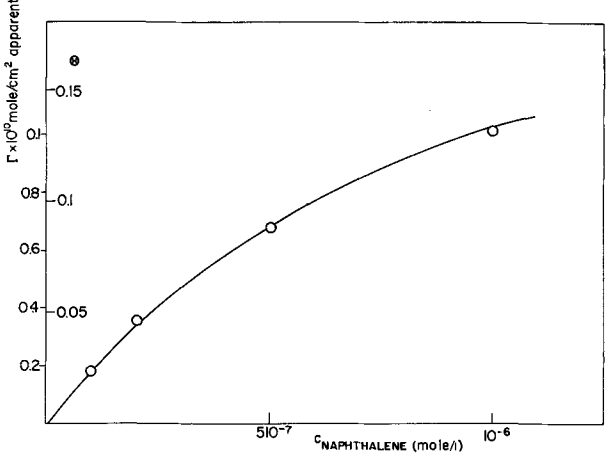

Fig. 6. Adsorption isotherm for naphthalene at +500 mv (NHE)

Table I. Limit of detectible adsorption of cyclohexane n-octanoic acid and n-decanoic acid

Compound	Solution concentration, mole/l	Sensitivity (adsorption must be lower than)
Cyclohexane	5.10^{-5}	θ^* <0.02
	10^{-5}	<0.01
	10^{-6}	<0.01
n-octanoic acid	10^{-5}	<0.005
n-decanoic acid	2.10^{-5}	<0.03
	10^{-4}	<0.06

* θ calculated using Eq. [4] [$\Gamma_{max} = 2.10^{-10}$ mole/cm² for cyclohexane; $\Gamma_{max} = 8.10^{-10}$ mole/cm² for the aliphatic chains as experimentally observed by Blomgren, Bockris, and Jesch (10) and Hansen *et al.* (1)].

and phenanthrene) the concentration dependence could not be studied over a sufficient concentration range because the specific activity available for benzene was too small and the solubility of the phenanthrene is too low.

Aliphatic compounds.—There was no measurable adsorption of the aliphatic compounds, cyclohexane, n-octanoic acid, and n-decanoic acid. Table I gives the sensitivity of the experimental arrangement. The sensitivity depends on the background of the solution and the available specific activity of the labelled compound.

Discussion

Adsorption Isotherm

The competitive adsorption of two species from a liquid phase has been treated by numerous authors, *e.g.*, (12-15), by means of the Langmuir isotherm. Recently, a Temkin isotherm was applied to the adsorption of neutral molecules on electrodes (16).

The isotherms, however, have to be modified if the two species in competition do not cover an equal molecular area at the surface. For the general case of different size of the species a relation based on the Langmuir isotherm will be given here. The competitive adsorption of species with different size has been treated recently for adsorption from the gas phase (17) and from nonelectrolyte solutions (18). The adsorption on electrodes will be derived here in terms of surface coverage.

The reaction leading to adsorption can be formulated as

$$n[\text{Water}_{ads}] + [\text{Organ}_{sol}] = n[\text{Water}_{sol}] + [\text{Organ}_{ad}] \quad [5]$$

n is the number of molecules of water which occupy the same surface area as one molecule of the organic compound. n is given by

$$n = \frac{\Gamma_{max,\,water}}{\Gamma_{max,\,organic}} \quad [6]$$

where Γ_{max} (mole/cm²) is the amount forming a monolayer of water and organic species, respectively.

Under ideal conditions (negligible interaction between the adsorbed particles, activity coefficients = 1) the electrochemical potential of the adsorbed organic entity in Eq. [5] may be written

$$\bar{\mu}_{org,ad} = \bar{\mu}^{o}_{org,ad} + RT \ln \theta \quad [7]$$

where $\bar{\mu}_{org,ad}$ is the electrochemical potential of the adsorbed organic species, $\bar{\mu}^{o}_{org,ad}$ is the standard electrochemical potential referred to the standard state of complete coverage with the organic compound. θ is the surface fraction covered by the organic species as defined by

$$\theta = \frac{\Gamma_{org}}{\Gamma_{max,org}} \quad [8]$$

For the adsorbed water the electrochemical potential is given by

$$\bar{\mu}_{w,ad} = \bar{\mu}^{o}_{w,ad} + RT \ln (1-\theta) \quad [9]$$

The electrochemical potentials of the species in solution are written in the usual way, *viz.*

$$\bar{\mu}_{org,s} = \bar{\mu}^{o}_{org,s} + RT \ln X_{org,s} \quad [10]$$

and

$$\bar{\mu}_{w,s} = \bar{\mu}^{o}_{w,s} + RT \ln X_{w,s} \quad [11]$$

where $X_{org,s}$ and $X_{w,s}$ are the mole fractions of organic and water, respectively.

For equilibrium according to Eq. [5]

$$\bar{\mu}_{org,s} + n\bar{\mu}_{w,ad} = \bar{\mu}_{org,ad} + n\bar{\mu}_{w,s} \quad [12]$$

Taking Eq. [7] and [9]-[11] for the electrochemical potentials and expressing the difference in standard free energy as

$$\Delta\bar{G}^{o} = \bar{\mu}^{o}_{org,ads} - \bar{\mu}^{o}_{org,s} - n(\bar{\mu}^{o}_{w,ads} - \bar{\mu}^{o}_{w,s}) \quad [13]$$

the isotherm is given by,

$$\frac{\theta \cdot X_{w,s}^{\,n}}{(1-\theta)^n \cdot X_{org,s}} = e^{-\frac{\Delta\bar{G}^{o}}{RT}} \quad [14]$$

In dilute solutions of the organic species in water $X_{w,s}$ becomes constant = 1 and [14] is then

$$\frac{\theta}{(1-\theta)^n} = e^{-\frac{\Delta\bar{G}^{o}}{RT}} \cdot X_{org,s} = K_a \cdot X_{org,s} \quad [15]$$

Equation [15] differs from the Langmuir equation by the power factor n.

The change of the ideal isotherms with n is plotted in Fig. 7 against an arbitrary concentration scale. For better comparison the concentration scale is chosen so that θ values of 0.25 coincide. It is evident that the value of n has a strong influence on the isotherm. For higher n-values the gradient of the curve decreases significantly even at low coverages.

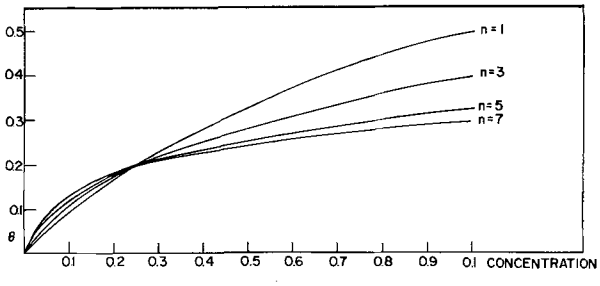

Fig. 7. Theoretical adsorption isotherms for competitive adsorption for molecules of various size ratios (n).

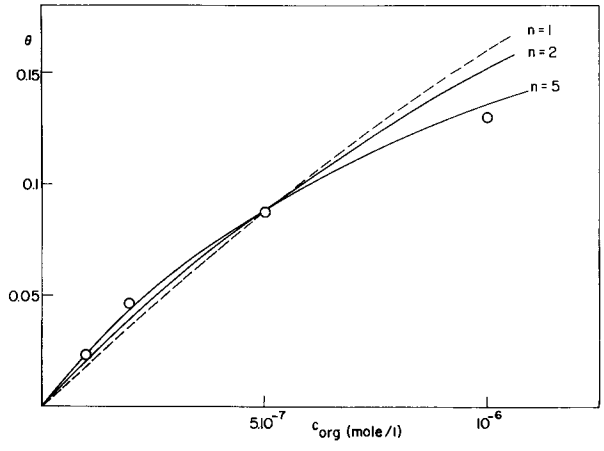

Fig. 8. Experimental values (○) of naphthalene adsorption at +500 mv (NHE) and calculated isotherms (Eq. [15]) for a planar position of naphthalene on the electrode ($n = 5$), a perpendicular position ($n = 2$), and equal size of the adsorbing species ($n = 1$).

This behavior is in good agreement with our experimental data for naphthalene (Fig. 8) for which $n = 5$ in planar configuration (Table III).

Free Energy of Adsorption of Aromatic and Aliphatic Compounds

The fact that only the aromatic compounds are adsorbed while the aliphatic compounds showed no detectable adsorption indicates the interaction of the aromatic π-electrons with the metal.

The solubilities of the investigated aliphatic compounds in aqueous solutions are similar to those of the aromatic entities (Table II).

For quantitative considerations the free energy of adsorption can be calculated from Eq. [15] for the more intensively studied systems (Table II). The adsorption values are taken at a potential near the maximum of adsorption, *i.e.*, $E_H = +500$ mv.

Table II. Adsorption and solubility of various organic compounds at the gold electrolyte interface

Compound	Solubility, mole/l	Adsorption at solution concentration $\frac{1}{10}$ saturated
Benzene	$1.1\ 10^{-2}$	$\theta = 0.2$
Naphthalene	$2\ 10^{-4}$	$\theta = 0.12$
Phenanthrene	$\sim 4\ 10^{-6}$	$\theta = 0.1$
Cyclohexane	$2.\ 10^{-4}$	Not detectable ($\theta < 0.01$)
n-Octanoic acid	$5.\ 10^{-3}$	Not detectable ($\theta < 0.005$)
n-Decanoic acid	$1.7\ 10^{-4}$	Not detectable ($\theta < 0.003$)

Table III. Geometrical areas of various molecules adsorbed on gold

Compound	Molecular area calculated from Fisher-Taylor-Hirshfelder models		Monolayer calculated $\times 10^{10}$ mole cm^{-2}		Experimental observed maximum adsorption $\times 10^{10}$ mole cm^{-2}
	Planar	Perpendicular	Planar	Perpendicular	
Benzene	34Å^2	18Å^2	5.0	9.5	2.3
Naphthalene	49Å^2	22Å^2	3.5	7.7	1.0
Phenanthrene	65Å^2	30Å^2	2.6	5.7	0.8
Cyclohexane	36Å^2	20Å^2	4.6	8.3	<0.05
(Water)	10Å^2		~ 17		

The free energy of adsorption as calculated from Eq. [15] and defined by Eq. [13] still contains contributions from organic compound-solvent interactions and the organic compound in its pure form. In order to compare the adsorption energy of the different compounds these contributions have to be excluded. This is done by replacing the mole fraction of the organic compound in the solution $X_{org,sol}$ in Eq. [15] by the activity and referring the activities of the organic compound in solution to a standard state in the gas phase.

In a saturated solution the vapor pressure of the organic is the same over the saturated solution and over the pure organic compound. So we can write

$$a_{org,sol} = p\frac{X_{org}}{X_{org\ sat}} \qquad [16]$$

where p is the vapor pressure of the organic compound at 25°C, X_{org} the mole fraction of the organic in solution, and $X_{org\ sat}$ is the mole fraction of the organic compound in the saturated solution.

In order to compare different compounds expression [16] has to be employed for both, so that the difference in their energy of interaction with the solution is then given by

$$\Delta\mu_{interaction} = RT \ln \frac{a_{1,org\ sol}}{a_{2,org\ sol}} = RT \ln \frac{p_1 \cdot X_{1\ org} \cdot X_{2,org\ sat}}{p_2 \cdot X_{2\ org} \cdot X_{1,org\ sat}} \qquad [17]$$

Adding this $\Delta\mu$ term to the free energy of adsorption $\overset{\circ}{\Delta G}$ (Eq. [14]) we obtain free energies which are comparable (Table IV).

It can be seen from the last column in Table IV that there is a considerable difference in the free energy (more than 3 kcal mole^{-1}) between comparable aliphatic compounds and aromatic compounds. This difference is attributed to π-bond/metal interaction. This comparison is possible because cyclohexane has about equal size and vapor pressure as benzene and has a solubility similar to that of naphthalene. The same comparison holds qualitatively for the other aliphatic compounds, n-octanoic acid and n-decanoic acid.

On the mercury-electrolyte interface aromatic and aliphatic compounds are adsorbed (10), while on the gold-electrolyte interface no detectable adsorption of aliphatics was found from solutions of equivalent concentration. This result can be interpreted that the bonding between gold and water is stronger than between mercury and water. Hence only the bonding aromatic compound-gold can overcome the increased bonding gold-water while the

Table IV. Comparison of free energies of adsorption of organic compounds at the gold electrolyte interface

	$\overset{\circ}{\Delta G}$ (Eq. [14]), kcal mole^{-1}	$P_{25°C}$, atm	Solubility, $X_{org\ sat}$	$\overset{\circ}{\Delta G} - \Delta\mu_{interaction}$, kcal mole^{-1}
Benzene	—6.1	0.125	$4.1\ 10^{-4}$	—6.1
Naphthalene	—0.7	$0.40.10^{-4}$	$4.8.10^{-6}$	—8.0
Cyclohexane	$<$—5.8	0.130	$3.6.10^{-6}$	$<$—2.8

Vapor pressures and solubilities were taken from ref. (19-21).

aliphatic compounds do not have the necessary energies. Unfortunately, no reliable data on the adsorption energy of water on gold are available.

Orientation of the Adsorbed Species

The experimentally observed maximum adsorption is considerably smaller than the calculated maximum values for a monolayer either in planar or in perpendicular orientation to the surface (Table III). Therefore no conclusion on the question of orientation can be drawn from the observed upper limit of coverage.

Evidence for the planar position (which would seem to favor π-bond interaction) is provided by the shape of the adsorption isotherm (Fig. 8).

It can be seen from Fig. 8 that the experimental values are fitted best by an isotherm calculated with Eq. [15] assuming a planar position of naphthalene on the electrode ($n = 5$). The isotherms calculated under the assumption of a perpendicular position ($n = 2$) or of equal size ($n = 1$) do not fit the results.

Influence of Electrical Field on Adsorption

The potential dependence of the adsorption of neutral molecules on electrodes can be due to one or more of the following factors:

1. The coverage of the electrode with hydrogen or oxide layers at cathodic or anodic potentials, respectively.

2. The specific adsorption of ions of the electrolyte solution and the adsorption of counter ions at the charged electrode.

3. The change of the free energy of adsorption of the water and the organic compound with the electrical potential.

In the case of gold in 1*N* H_2SO_4 the coverage with hydrogen or oxygen is negligible in the investigated potential region [hydrogen coverage less than 4% at $E_H = 0$ mv (22); oxygen coverage less than 10% at $E_H = +1100$ mv (23)].

The specific adsorption of ions seems not to play an important role in this system since the effects of the potential in the Gouy layer could be interpreted only under the assumption of no specific adsorption (28). The change in the free energy of adsorption of water and an organic species with the applied electrical field was treated by Frumkin (24), Butler (25), and Bockris, Devanathan, and Müller (26). These electrical contributions to the free energy of adsorption are different for water and the organic species. If the dipole moment of the organic species in the double layer (in our case = 0) is negligible compared with the effective dipole moment of water, the water plays the dominant role. [Differences in the polarizabilities between the organic and the water have no significant influence (26).] The theory (24-26) predicts, in this case, a maximum of adsorption near the point of zero charge of the metal with monotonically decreasing adsorption to negative and positive potentials.

This general picture is in agreement with our observations on gold. The point of zero charge of gold was determined by Pfuetzenreuther and Masing (27) to be at $E_H = +300$ to $+400$ mv. Our recent determination of the zero charge point (28) is in agreement with these data ($E_H = +300 \pm 50$ mv). The maximum of adsorption (Fig. 2-4) was observed to be at potentials of $E_H = +500$ to $+600$ mv. This fact has to be considered as a partial confirmation of the predominant role of water in determining the shape of the adsorption *vs.* potential curves on gold.

Acknowledgments

The authors are grateful to Professor J. O'M Bockris for the encouragement of this work. They wish to thank Mr. D. A. Swinkels of this laboratory for carrying out BET measurements on our gold electrodes and also for numerous stimulating discussions of this work. It is also a pleasure to thank the United States Steel Corporation for generous support of this research.

Manuscript received Nov. 27, 1962; revised manuscript received April 22, 1963. This paper was presented at the Pittsburgh Meeting, April 15-18, 1963.

Any discussion of this paper will appear in a Discussion Section to be published in the June 1964 JOURNAL.

REFERENCES

1. *E.g.*, R. Hansen and B. Clampitt, *J. Phys. Chem.*, **58**, 908 (1954); R. Hansen, R. Minturn, and D. Hickson, *ibid.*, **60**, 1185 (1956).
2. B. E. Conway and R. G. Barradas, Transact. Phila. Symp. Electrode Proc., Philadelphia 1959, p. 299, John Wiley & Son, Inc., New York (1961); B. E. Conway, R. G. Barradas, and T. Zawidski, *J. Phys. Chem.*, **62**, 676 (1958).
3. F. Joliot, *J. Chem. Phys.*, **27**, 119 (1930).
4. W. H. Power and J. W. Heyd, *Anal. Chem.*, **28**, 523 (1956).
5. I. A. Kafalas and H. C. Gatos, *Rev. Sci. Instr.*, **29**, 47 (1958).
6. Ch. Weissmantel, Thesis, Dresden, Germany (1958).
7. H. D. Cook, *Rev. Sci. Instr.*, **27**, 1081 (1956).
8. E. Blomgren and J. O'M. Bockris, *Nature*, **186**, 305 (1960).
9. H. Wroblowa and M. Green, To be published.
10. E. Blomgren, J. O'M. Bockris, and C. Jesch, *J. Phys. Chem.*, **65**, 2000 (1961).
11. W. F. Libby, *Phys. Rev.*, **103**, 1900 (1956).
12. A. Frumkin, *Z. physik. Chem.*, **116**, 466 (1925).
13. For comprehensive bibliography see J. J. Kipling, *Quart. Rev.*, **5**, 60 (1951).
14. E. Blomgren and J. O'M. Bockris, *J. Phys. Chem.*, **63**, 1425 (1959).
15. R. G. Barradas and B. E. Conway, *Electrochim. Acta*, **5**, 349 (1961).
16. P. Delahay and D. M. Mohilner, *J. Am. Chem. Soc.*, **84**, 4247 (1962).
17. S. Yu. Elovich and O. G. Larionow, *Izvest. Akad. Nauk USSR, Otdel. khim. Nauk*, **1962**, 531.
18. S. Yu. Elovich and O. G. Larionow, *ibid.*, **1962**, 209.
19. R. L. Bohen and W. F. Claussen, *J. Am. Chem. Soc.*, **73**, 1572 (1951).
20. "Handbook of Chemistry and Physics" The Chemical Rubber Publishing Co., Cleveland, Ohio, 1960.
21. A. Timmermanns, " Physico Chemical Constants," Elsevier Publishing Co., New York (1950).
22. M. Breiter, C. A. Knorr, and W. Völkl, *Z. Elektrochem.*, **59**, 681 (1955).
23. H. Dahms, J. O'M. Bockris, To be published.
24. A. Frumkin, *Z. Physik*, **35**, 792 (1926).
25. J. Butler, *Proc. Roy. Soc. (London)*, **A122**, 399 (1929).
26. J. O'M. Bockris, M. Devanathan, and K. Müller, Paper presented at CITCE Meeting Rome, 1962.
27. A. Pfuetzenreuther and G. Masing, *Z. Metallk.*, **42**, 361 (1951).
28. M. Green and H. Dahms, *This Journal*, **110**, 466 (1963).

Technical Notes

The Semiconducting Nature of Stannic Oxide

L. D. Loch

Research Branch, Research and Development Division, The Carborundum Company, Niagara Falls, New York

The research reported here is part of a broad study of SnO_2-based compositions as semiconductors. The electronic configurations of the outer shells of the Sn and O atoms are $5s^25p^2$ and $2s^22p^4$, respectively. Therefore, in forming solid SnO_2 the 5s and 5p electrons of the Sn atom are transferred to O atoms. Each O atom can accept two electrons in its 2p orbital to form a stable octet. On this basis a simple picture of the band structure of SnO_2 consists of a 5s conduction band and a 2p valence band, separated by a forbidden gap. As the 5s band is a broad band, we expect broad-band semiconduction.

The purpose of this particular phase of research was to determine whether SnO_2 actually does show broad-band behavior.

The literature contains many references to the properties of SnO_2 films and coatings as these have been commercial products for many years. Very few detailed studies can be found, however, on polycrystalline bodies or single crystals. Marley (1) and Reed (2) both have grown single crystals, but have not reported on their properties as yet.

A recent paper by Kohnke (3) on the electrical and optical properties of natural SnO_2 crystals is of interest. Kohnke found a value of 0.72 ev for the conductivity activation energy, compared to 0.77 ev calculated from the data of Foex (4) on polycrystalline specimens. Two of Kohnke's crystals were fairly pure, with indicated carrier densities of only 4×10^{14} and 8×10^{14} cm^{-3}, respectively. These crystals had Hall mobilities of approximately 50 cm^2-v^{-1}-sec^{-1} at 200°C. Above 150°C, the variation of Hall mobility with temperature was not far different from the $T^{-1.5}$ dependence for simple lattice scattering. On the basis of his observed mobilities and activation energy and of an effective mass less than one, Kohnke concludes that SnO_2 behaves as a normal broad-band semiconductor in the extrinsic conductivity region above room temperature.

In our experiments σ and S were measured for four different values of the electron concentration which spanned nearly three decades of concentration. The electron concentration was controlled by adding Sb to the lattice. The outer electron configuration of Sb is $5s^25p^3$ so that each atom of Sb adds one electron to the conduction band of SnO_2.

Experimental

The measurements of σ and S were made simultaneously at temperatures between 100° and 900°C in vacuum and in air. Specimens were polycrystalline bars 0.5 x 0.5 x 5 cm. They were held in a lava jig placed inside a Vycor tube, which could be evacuated to 10^{-6} mm Hg. All contacts were spring loaded pressure contacts. They consisted of Pt sheet for the current leads at either end and of two Pt-Pt 100 Rh thermocouples mounted on one side and spaced approximately 2 cm apart. The thermocouples served as potential probes for a four-terminal measurement of σ and to measure the temperature drop ΔT.

All of the conductivity measurements were, in effect, made with d.c. However, the direction of current flow was reversed at a frequency of 12 cpm, producing square wave patterns for the voltage drops across the specimen and across a standard resistor. The furnace was moved by small increments along the axis of the specimen to vary ΔT between 5° and 20°C. The resistive voltage drop V_{IR} across the specimen was obtained from the amplitude of the square wave, while the thermoelectric voltage V_T was obtained from the position of the square wave with respect to zero. The current was calculated, of course, from the voltage drop through the standard resistor.

Specimens were prepared from "Certified" reagent grade SnO_2 and Sb_2O_3 obtained from Fisher Scientific Company. The chief impurities in the SnO_2, as determined by spectrographic and wet analysis, were 0.10% Cu and 0.07% Pb. Neither of these impurities seemed to be electronically active. The ingredients were mixed in an acetone slurry and mixing was continued while the acetone evaporated. The essentially dry powder then was cold pressed at 8000 psi and sintered at 1400°C in air.

Results and Discussion

At the outset of this research the electronic measurements were made in air and in vacuum. It was found that the measurements in air were not very reproducible, while those in vacuum were. Also, the specimens behaved in air as though the Sb were coming out of solution at the lower temperatures. This is shown in Fig. 1, where the conductivities of highly doped (0.1 mole % Sb_2O_3) specimens in air and in vacuum are compared. It was not possible to prove conclusively our suspicion that the Sb was coming out of solution by means of x-ray diffraction. The shift in the x-ray lines as a result of solution of Sb in the SnO_2 lattice is too small to detect with assurance. However, in order to

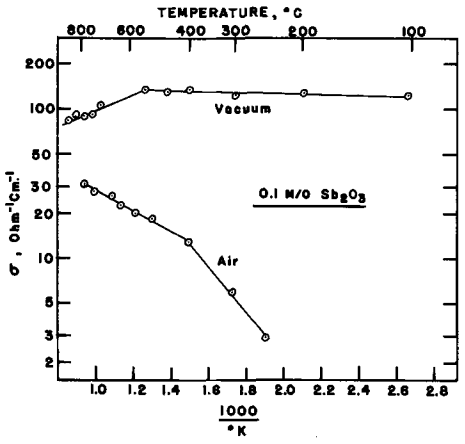

Fig. 1. σ for heavily doped SnO_2 in vacuum and in air

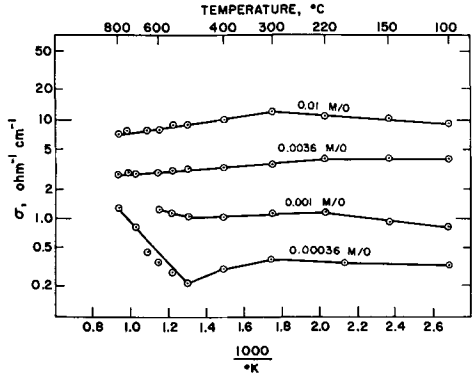

Fig. 2. σ vs. temperature for four doping levels

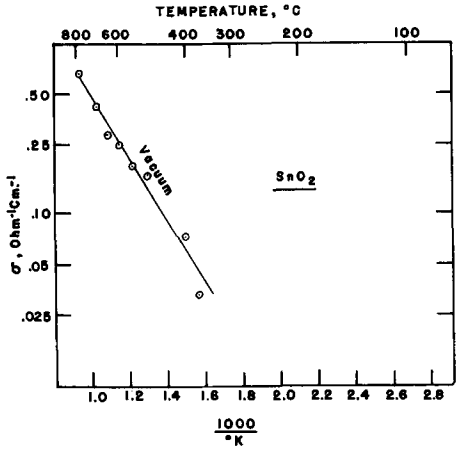

Fig. 3. σ for undoped SnO_2 in vacuum

obtain reproducible results and to insure that the Sb remained in solution, most of the experiments were conducted in vacuum.

Values of σ *vs.* temperature for four doping levels are shown in Fig. 2. These curves are typical of saturated extrinsic conduction as they show very little dependence on temperature; that is, the donors are completely ionized at and above room temperature. This agrees with the observation by Imai (5) that the donor levels in Sb-doped SnO_2 are already fully ionized at liquid nitrogen temperature.

To be certain that the majority of the conduction electrons were supplied by the Sb dopant and not by defects, σ of the undoped Fisher SnO_2 was measured in vacuum at temperatures up to 800°C. Comparison of the resulting data, shown in Fig. 3, with those in Fig. 2 suggests that the number of free electrons arising from defects is negligible compared to those supplied by the Sb donor levels, except at the very highest temperatures and the lowest Sb concentrations. The steeply rising conductivity of the 0.00036 mole % Sb specimen above 500°C in Fig. 2 is evidence that defect carriers are becoming important in this instance.

Plots of σ *vs.* N_d at constant temperature, where N_d is the concentration of Sb donor atoms, are quite linear. By means of the usual equation: $\mu = \sigma/ne$, and our observation that ionization of donors is complete, so that $n = N_d$, values for the electron mobility μ of 10.9 to 12.0 cm^2-v^{-1}-sec^{-1} were calculated for the temperature range 100°-500°C. Although at any one temperature the maximum deviation of μ from the average is 10% or less, there is no perceptible dependence of mobility on temperature.

One would expect to have contributions to electron scattering from both lattice vibrations and ionized impurities. As lattice scattering would cause a decrease in μ with increasing temperature while impurity scattering would have the opposite effect, the two types of scattering might tend to compensate each other over the temperature range of interest, thus accounting for the small change with temperature. However, final conclusions about the variation of μ with temperature should not be attempted on the basis of data obtained on polycrystalline semiconductors where the influence of particle size and chemical changes can be appreciable. The good agreement obtained here among the mobilities calculated for four different doping levels is about the most one can expect when working with polycrystalline materials.

The above range for μ compares favorably with the Hall mobilities of 17-32 cm^2-v^{-1}-sec^{-1} measured on SnO_2 films by Ishiguro *et al.* (6). Finally, Kohnke's value of 50 cm^2-v^{-1}-sec^{-1} is in reasonable agreement with our data, as one expects higher values of μ in single crystals than in polycrystalline compacts.

Comparison of the above values for μ with those for other oxides, both broad-band and narrow-band, shows rather conclusively that SnO_2 is a broad-band semiconductor. For example, room temperature Hall mobilities for the known broad-band oxide ZnO have been reported to be 60 cm^2-v^{-1}-sec^{-1} for sintered material (7) and 200 cm^2-v^{-1}-sec^{-1} for single crystals (8). On the other hand, two oxides of Ti, which almost certainly exhibit 3d narrow-band conduction have shown mobilities of 0.1-1.0 cm^2-v^{-1}-sec^{-1} for TiO_2 single crystals (9) and 0.36 cm^2-v^{-1}-sec^{-1} for polycrystalline TiO (10, 11). These values for μ are one to two orders of magnitude lower than those for SnO_2.

Our values of S up to about 900°C for the four doping levels are shown in Fig. 4. All of the values are negative, and they become numerically smaller as n increases. At the lower temperatures, there is a rapid increase in S with increasing temperature.

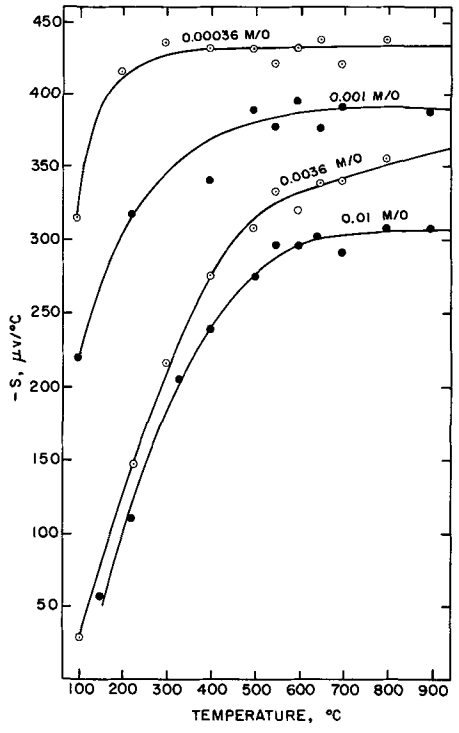

Fig. 4. S vs. temperature for four doping levels

The data of Fig. 4 were analyzed using the customary equations from classical statistics for nondegenerate broad-band semiconductors: $n = N_c \exp(E_F/kT)$ and $eST = E_F - 2kT$, where N_c is the effective density of states in the conduction band and E_F is the Fermi energy level with respect to the conduction band edge, *i.e.*, $E_F = \epsilon_F - \epsilon_c$. On combining these equations one obtains $eS/k = 2.303 \log (n/N_c) - 2$. As N_c is constant at a given temperature, the quantity eS/k should be a linear function of log n. That this is the case is shown in Fig. 5, in which eS/k is plotted against log n at four different temperatures. This agreement is further evidence that SnO_2 is a broad-band semiconductor.

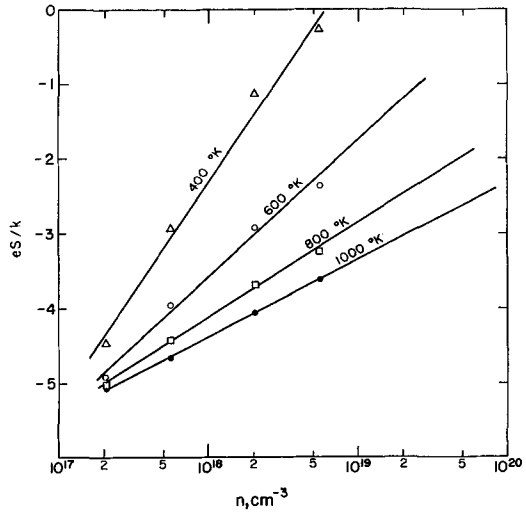

Fig. 5. eS/K vs. n for four temperatures

Summary

On the basis of electron mobilities calculated from the conductivities of Sb-doped polycrystalline specimens and the behavior of the Seebeck coefficient of such specimens, it is concluded that SnO_2 is a broad-band semiconductor. This agrees with Kohnke's conclusion, which was based on the Hall mobility and donor activation energy in natural single crystals. SnO_2 showed n-type behavior throughout.

Acknowledgment

The author wishes to acknowledge the fine assistance of Mr. W. H. Kaufmann in the experimental portion of this research.

Manuscript received April 2, 1963; revised manuscript received June 25, 1963. This paper was presented at the Boston Meeting, Sept. 16-20, 1963.

Any discussion of this paper will appear in a Discussion Section to be published in the June 1964 JOURNAL.

REFERENCES

1. J. A. Marley and T. C. MacAvoy, *J. Appl. Phys.*, **32**, 2504 (1961).
2. T. B. Reed, J. T. Roddy, and A. N. Mariano, *ibid.*, **33**, 1014 (1962).
3. E. E. Kohnke, *J. Phys. Chem. Solids*, **23**, 1557 (1962).
4. M. Foex, *Bull. soc. chim. France*, **11**, 6 (1944).
5. I. Imai, *J. Phys. Soc. Japan*, **15**, 937 (1960).
6. K. Ishiguro, T. Sasaki, T. Arai, and I. Imai, *ibid.*, **13**, 296 (1958).
7. S. E. Harrison, *Phys. Rev.*, **93**, 52 (1954).
8. A. R. Hutson, *ibid.*, **108**, 222 (1957).
9. R. G. Breckenridge and W. R. Hosler, *ibid.*, **91**, 793 (1953).
10. A. D. Pearson, *J. Phys. Chem. Solids*, **5**, 316 (1958).
11. F. J. Morin, "Semiconductors," Chap. 14, N. E. Hannay, Editor, Reinhold Publishing Corp., New York (1959).

X-Ray Diffraction Study of Evaporated CdS Films

Arthur J. Behringer and Lester Corrsin

Fundamental and Applied Research Laboratories, Xerox Corporation, Rochester, New York

An x-ray diffraction study was made of the structure of CdS films deposited on amorphous substrates as a function of substrate temperature. A marked decrease in condensate was observed with increase in substrate temperature. Modifications of the films' crystallinity and preferred orientation with changing deposition temperature were observed. Pyrolytic treatment of films in contact with $CdCl_2$ containing CdS powder resulted in modifying the orientation from preferred to random.

Optical and electrical measurements on evaporated cadmium sulfide films have been reported extensively in the literature (1-9). However, only a few publications describe the structure of such

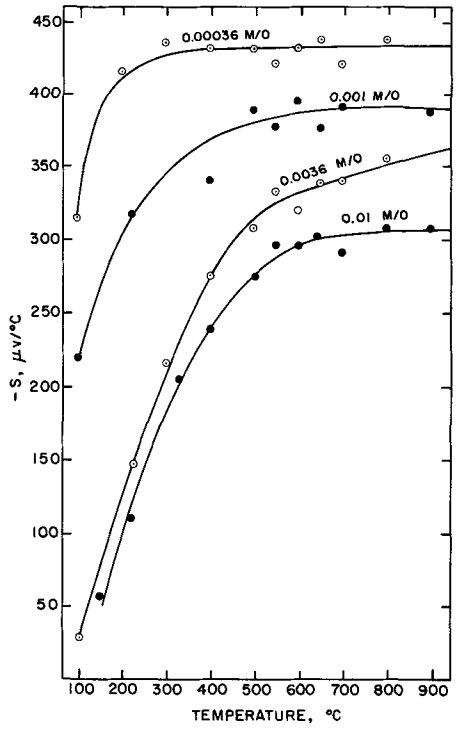

Fig. 4. S vs. temperature for four doping levels

The data of Fig. 4 were analyzed using the customary equations from classical statistics for nondegenerate broad-band semiconductors: $n = N_c \exp(E_F/kT)$ and $eST = E_F - 2kT$, where N_c is the effective density of states in the conduction band and E_F is the Fermi energy level with respect to the conduction band edge, *i.e.*, $E_F = \epsilon_F - \epsilon_c$. On combining these equations one obtains $eS/k = 2.303 \log (n/N_c) - 2$. As N_c is constant at a given temperature, the quantity eS/k should be a linear function of log n. That this is the case is shown in Fig. 5, in which eS/k is plotted against log n at four different temperatures. This agreement is further evidence that SnO_2 is a broad-band semiconductor.

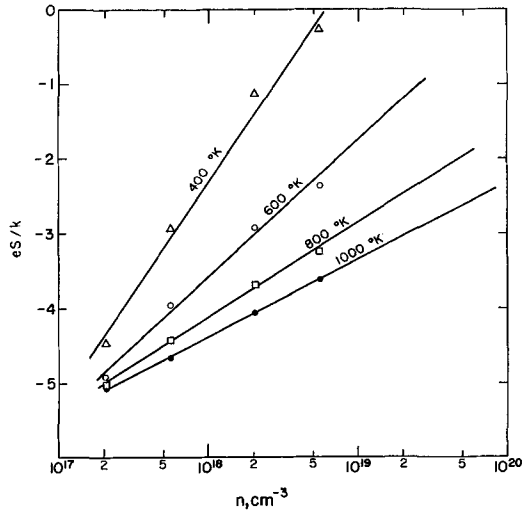

Fig. 5. eS/K vs. n for four temperatures

Summary

On the basis of electron mobilities calculated from the conductivities of Sb-doped polycrystalline specimens and the behavior of the Seebeck coefficient of such specimens, it is concluded that SnO_2 is a broad-band semiconductor. This agrees with Kohnke's conclusion, which was based on the Hall mobility and donor activation energy in natural single crystals. SnO_2 showed n-type behavior throughout.

Acknowledgment

The author wishes to acknowledge the fine assistance of Mr. W. H. Kaufmann in the experimental portion of this research.

Manuscript received April 2, 1963; revised manuscript received June 25, 1963. This paper was presented at the Boston Meeting, Sept. 16-20, 1963.

Any discussion of this paper will appear in a Discussion Section to be published in the June 1964 JOURNAL.

REFERENCES

1. J. A. Marley and T. C. MacAvoy, *J. Appl. Phys.*, **32**, 2504 (1961).
2. T. B. Reed, J. T. Roddy, and A. N. Mariano, *ibid.*, **33**, 1014 (1962).
3. E. E. Kohnke, *J. Phys. Chem. Solids*, **23**, 1557 (1962).
4. M. Foex, *Bull. soc. chim. France*, **11**, 6 (1944).
5. I. Imai, *J. Phys. Soc. Japan*, **15**, 937 (1960).
6. K. Ishiguro, T. Sasaki, T. Arai, and I. Imai, *ibid.*, **13**, 296 (1958).
7. S. E. Harrison, *Phys. Rev.*, **93**, 52 (1954).
8. A. R. Hutson, *ibid.*, **108**, 222 (1957).
9. R. G. Breckenridge and W. R. Hosler, *ibid.*, **91**, 793 (1953).
10. A. D. Pearson, *J. Phys. Chem. Solids*, **5**, 316 (1958).
11. F. J. Morin, "Semiconductors," Chap. 14, N. E. Hannay, Editor, Reinhold Publishing Corp., New York (1959).

X-Ray Diffraction Study of Evaporated CdS Films

Arthur J. Behringer and Lester Corrsin

Fundamental and Applied Research Laboratories, Xerox Corporation, Rochester, New York

An x-ray diffraction study was made of the structure of CdS films deposited on amorphous substrates as a function of substrate temperature. A marked decrease in condensate was observed with increase in substrate temperature. Modifications of the films' crystallinity and preferred orientation with changing deposition temperature were observed. Pyrolytic treatment of films in contact with $CdCl_2$ containing CdS powder resulted in modifying the orientation from preferred to random.

Optical and electrical measurements on evaporated cadmium sulfide films have been reported extensively in the literature (1-9). However, only a few publications describe the structure of such

films (10, 11). In one of these, Gilles and Van Cakenberghe (11), using x-ray diffraction studies, conclude that cadmium sulfide evaporated on heated amorphous glass substrates forms principally hexagonal crystallites with the C-axis normal to the substrate surface.

Film Preparation

General Electric EL grade CdS pellets were evaporated from molybdenum source, 800° ± 10°C, on preheated tin oxide coated borosilicate glass substrates at a pressure of about 4 x 10^{-5} Torr. The deposition temperatures ranged between 70° and 445°C. For the same quantity of starting material, the film thicknesses, measured with a profilometer, varied markedly according to deposition temperature. Thicknesses ranged from less than 1μ to 15μ at deposition temperatures of 445° and 250°C, respectively; thicknesses recorded for films deposited at 350° and 400°C were about 3μ.

Analysis of Films

Film crystallinity was examined with nickel-filtered copper radiation, using a General Electric XRD-5 Diffractometer Unit. In agreement with the findings of Gilles and Van Cakenberghe, the OOOL series of reflections appeared in all the diffractometer patterns, indicating preferred orientation with the C-axis normal to the substrate. In addition, the crystallites in the films were frequently found to be oriented with either or both the $10\bar{1}3$ and $10\bar{1}5$ lattice planes positioned parallel to the substrate. Considerable broadness in these later reflections was observed in patterns for films deposited at substrate temperatures between 70° and 250°C; this is presumably due to stacking faults, a condition described in some detail for cobalt by Edwards and Lipson (12). In the diffractometer patterns of the films deposited at the higher substrate temperatures, the reflections appeared sharp, indicating an enhancement of crystalline perfection attributable to the higher deposition temperatures. The presence of well-formed hexagonal crystallites in these films was confirmed on inspection of x-ray photograms of evaporated films stripped from their substrates and reduced to a fine powder.

Two methods used to enhance the photoconductivity in evaporated CdS films were studied to determine their effects on the crystallinity of films deposited on a substrate preheated to 350°C. One method, direct air-baking of film at 480°C for 1 hr, was found to have virtually no effect in altering the preferred orientation (Fig. 1a). This result is in agreement with the findings of Gilles and Van Cakenberghe (11). In the other method a similar film was heat-treated for the same duration at 480°C in contact with a copper-chlorine-doped cadmium sulfide powder containing an estimated 0.5% $CdCl_2$; the orientation of the crystallites was altered from preferred to random (Fig. 1b). The powder used in this heat treatment is hexagonal, as indicated in Fig. 1c. A random orientation also results if the film is similarly heat-treated in contact with a chlorine-doped CdS powder containing approximately 0.5% $CdCl_2$ and essentially free of copper; however, unactivated, $CdCl_2$-free CdS powder has virtually no effect on altering the orientation. These results indicate that the trace amount of $CdCl_2$ in the CdS powder is the influential factor. The presence of the chloride at the film surface probably initiates recrystallization at the surface by chemical exchange, resulting in crystal growth with the crystallites randomly oriented.

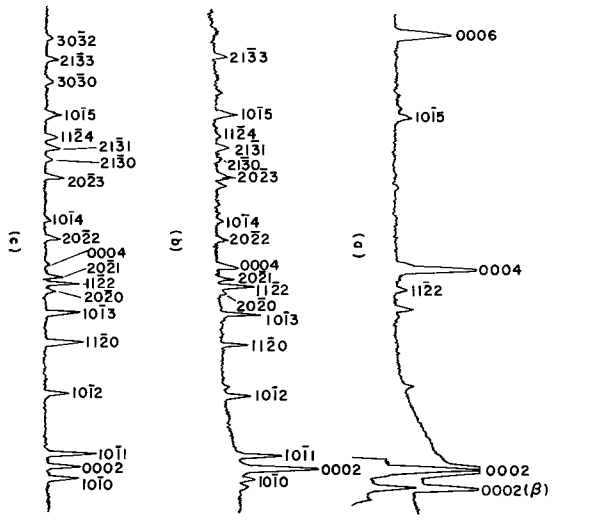

Fig. 1. X-ray diffractometer patterns, demonstrating the effect of heating evaporated CdS films previously deposited at 350°C: (a) at a temperature of 480°C for 1 hr in air; (b) in contact with Cu-Cl doped hexagonal CdS powder containing 0.5% $CdCl_2$; (c) pattern for the cadmium sulfide powder referred to in (b). The ordinate scale in each pattern is logarithmic.

Remarks

The details of the observed relationship between the quantity of condensate and the deposition temperature are not understood at this time; presumably a thorough investigation of the vapor phase composition will solve this problem. The aforementioned technique to obtain random orientation in evaporated CdS films may well be extended to evaporated films of other materials.

Acknowledgments

Appreciation is expressed to Drs. John C. Schottmiller, Paul Cherin, and Michael Smith for their helpful discussions and suggestions, to Keith Johnson for obtaining the x-ray diffraction data and to R. Moore who prepared the evaporated films. This work was supported by the Department of the Navy, Bureau of Naval Weapons under Contract No. NOas 59-6166-c.

Manuscript received March 27, 1963; revised manuscript received July 8, 1963.

Any discussion of this paper will appear in a Discussion Section to be published in the June 1964 JOURNAL.

REFERENCES

1. K. Weiss, German Pat. 837,424 (Apr. 28, 1952).
2. J. Gottesman and W. F. C. Ferguson, *J. Opt. Soc. Am.*, **44**, 368 (1954).
3. J. F. Hall and W. F. C. Ferguson, *ibid.*, **45**, 714 (1955).
4. A. B. Bramley, *Phys. Rev.*, **98**, 246 (1955).

5. A. Carlson, WADC Tech. Rept. 56-62, ASTIA 132274.
6. R. Lawrence, *Brit. J. Appl. Phys.*, **10**, 298 (1959).
7. H. I. Moss, *RCA Rev. XXII*, No. 1, 29 (1961).
8. K. V. Shalimova, T. S. Travina, and L. L. Golik, *Soviet Phys. Doklady*, **6** [5], 396 (1961).
9. K. V. Shalimova, T. S. Travina, and R. R. Rezby, *ibid.*, **6** [5], 404 (1961).
10. J. Dresner and F. V. Shallcross, *Solid State Electronics*, **5**, 205 (1962).
11. J. M. Gilles and J. Van Cakenberghe, "Solid State Physics in Electronics and Telecommunications," Vol. 2, Part 2, 900-906, Academic Press, Inc., New York (1960).
12. O. S. Edwards and H. Lipson, *Proc. Roy. Soc. (London)*, **A180**, 268 (1942).

Polarography of π-Complexes of Cobalt, Chromium, and Titanium in Formamide and Dimethylformamide

Hsiao-shu Hsiung[1] and Glenn H. Brown[2]

Department of Chemistry, University of Cincinnati, Cincinnati, Ohio

Few polarographic measurements appear to have been made on π-complexes. The work of Page and Wilkinson (1) showed the polarographic behavior of ferricinium, cobalticinium, and ruthenicinium ions in water. Pauson and Wilkinson (2) determined the half-wave potential for the solution of bis-indenylcobalt (III) ion while Wilkinson and Birmingham (3) reported polarographic data for the bis-cyclopentadienyl complexes of titanium (IV), vanadium (IV), and niobium (V) ions. With the exception of the niobium (V) complex all of these ions were found to give well-defined and reversible waves. The rhodicinium ion (4) shows a cathodic wave corresponding to the formation of neutral $Rh(C_5H_5)_2$. Kuwana *et al.* (5) studied the chronopotentiometric oxidation of a number of metal cyclopentadienyls and their derivatives in acetonitrile. They found ferrocene and its derivatives undergo a one-electron change, ruthenocene and its derivatives a two-electron change, while osmocene and its derivatives show a two-stage oxidation, involving one electron each in each stage.

Polarographic measurements have been made on a few π-complexes formed with compounds containing six-membered rings. Furlani and Fisher (6) were the first to investigate the $Cr(C_6H_6)_2$-$Cr(C_6H_6)_2^+$ transition. Furlani and Sartori (7) made polarographic measurements on compounds of the type $Ar_2Cr^+I^-$, where Ar is benzene, toluene, mesitylene, or pseudocumene; also, bis-cyclohexylphenylchromium iodide has been studied polarographically (8).

This paper reports the polarographic behavior of some aromatic complexes of cobalt, chromium, and titanium in two nonaqueous solvents, formamide and dimethylformamide.

Experimental

Formamide was purified as described previously (9) and N,N'-dimethylformamide obtained from the Matheson Company was purified by a method similar to that used by Wawzonek *et al.* (10). All polarographic measurements were made at a temperature of 25.0° ± 0.5°C and were taken in the same manner as reported in previous papers (9, 11).

[1] Present address: Department of Chemistry, Alton Center, Southern Illinois University, Alton, Illinois.

[2] Present address: Department of Chemistry, Kent State University, Kent, Ohio.

Cobalticinium triiodide, $(C_5H_5)_2CoI_3$, bis-indenylcobalt (III) perchlorate, $(C_9H_7)_2CoClO_4$, and bis-cyclopentadienyltitanium (IV) bromide, $(C_5H_5)_2TiBr_2$ were prepared according to Wilkinson (12), Pauson and Wilkinson (2), and Wilkinson and Birmingham (3), respectively. Bis-diphenylchromium (I) iodide, $(C_6H_5 \cdot C_6H_5)_2CrI$ and bis-benzenechromium (I) iodide, $(C_6H_6)_2CrI$, were contributed by H. H. Zeiss of the Monsanto Chemical Company.

Anhydrous sodium perchlorate was used as the supporting electrolyte for the study of the π-complexes of cobalt and chromium in both solvents. It was of "reagent grade" quality and was purchased from the G. Frederick Smith Chemical Company; it was used without further purification. Tetraethylammonium perchlorate, prepared according to the directions of Kolthoff and Coetzee (13), was used as the supporting electrolyte in formamide for the π-complex salt of titanium.

Results and Discussion

Of the π-complexes studied only the bis-cyclopentadienyltitanium (IV) bromide did not give a well-defined reduction wave. The polarographic characteristics of five different π-complexes are recorded in Table I. Our value of −0.81v *vs.* S.C.E. for the bis-benzenechromium cation in dimethylformamide compares favorably with the value obtained by Furlani and Fischer (6) who investigated its behavior in the mixture, 80% methanol-20%

Table I. Polarographic characteristics of some π-complexes of cobalt, chromium, and titanium
(supporting electrolyte 0.2M $NaClO_4$)

Compound	Conc. mM/l	−(E1/2), v *vs.* S.C.E.	I_d	D cm² × 10⁵, sec	0.059/n
Formamide as the solvent					
$(C_6H_6)_2CrI$	2.0	1.04	0.85	0.194	0.062
$(C_6H_5 \cdot C_6H_5)_2CrI$	2.0	0.89	0.85	0.194	0.057
$(C_5H_5)_2CoI_3$	4.0	1.11	0.30	0.025	0.059
$(C_9H_7)_2CoClO_4$	2.0	0.71	0.81	0.177	0.072
$(C_5H_5)_2TiBr_2$*	2.0	0.62	0.57	0.088	—
N,N'-dimethylformamide as the solvent					
$(C_6H_6)_2CrI$	2.0	0.81	0.88	0.200	0.063
$(C_6H_5 \cdot C_6H_5)CrI$	2.0	0.75	0.57	0.088	0.063
$(C_9H_7)_2CoClO_4$	0.74	0.53	1.18	0.375	0.071

* Supporting electrolyte is Et_4NClO_4.

benzene (by volume). From the data presented it can be seen that bis-diphenylchromium (I) iodide reduces more readily than bis-benzenechromium (I) iodide in both solvents.

The value of n established from diffusion current data and results of others (6-8) show that the reduction of the π-complexes of chromium is a one-electron step and that the complexes have a rather high stability to reduction. Even though bis-indenylcobalt (III) perchlorate gives well-defined reduction waves in formamide and dimethylformamide, the reduction is not reversible if one electron is involved in the process. As expected the diffusion current constants for the π-complexes reported here are smaller than those of the simple metal ions in the same solvent (9) and in water (14).

The composition of the ligand has an influence on the half-wave potential of π-complexes. Considering polarographic data on π-complexes published by others (1-3, 6-9) along with those obtained in this study, one finds that the bonding of a ring-type compound to a metal ion generally causes a marked decrease in the reduction potential of the ion when compared to the simple metal ion in the same solvent. Increased aromaticity around the metal ion increases the ease of reduction [*e.g.*, compare $(C_6H_6)_2CrI$ and $(C_6H_5 \cdot C_6H_5)_2CrI$ in the two solvents used]. A trend is noted in that substitution of a group on the parent compound (*e.g.*, cyclopentadiene) compared to indene causes the half-wave potential to shift, the direction of the shift depending on whether the substituent is an electron donating group or an electron withdrawing group. It is observed from this study and others (5, 7, 8) that the electron donating group causes the potential to shift to a more negative value than that of the parent compound, and an electron withdrawing group causes the potential to shift in a more positive direction.

Acknowledgment

The authors wish to express their thanks to Dr. H. H. Zeiss of the Monsanto Chemical Company for supplying samples of bis-diphenylchromium (I) iodide and bis-benzenechromium (I) iodide.

Manuscript received Feb. 18, 1963; revised manuscript received June 18, 1963.

Any discussion of this paper will appear in a Discussion Section to be published in the June 1964 JOURNAL.

REFERENCES

1. J. A. Page and G. Wilkinson, *J. Am. Chem. Soc.*, **74**, 6149 (1952).
2. P. L. Pauson and G. Wilkinson, *ibid.*, **76**, 2024 (1954).
3. G. Wilkinson and J. M. Birmingham, *ibid.*, **76**, 4281 (1954).
4. F. A. Cotton. R. O. Whipple, and G. Wilkinson, *ibid.*, **75**, 3586 (1953).
5. D. E. Bublitz, G. Hoh, and T. Kuwana, *Chem. and Ind. (London)*, **1959**, 635.
6. C. Furlani and E. V. Fischer, *Z. Elektrochem.*, **61**, 481 (1957).
7. C. Furlani and G. Sartori, *Ricerca Sci.*, **28**, 973 (1958); *C.A.*, **52**, 19606 (1958).
8. I. A. Korshunov, L. N. Vertylina, G. A. Razuvaev, Y. A. Sorokin, and G. A. Domrachev, *Doklady, Akad. Nauk. (USSR)*, **122**, 1029 (1958); *C.A.* **53**, 1959 (1959).
9. G. H. Brown and H. S. Hsiung, *This Journal*, **107**, 57 (1960).
10. S. Wawzonek, E. Blaha, R. Berkey, and M. E. Runner, *ibid.*, **102**, 235 (1955).
11. G. H. Brown and R. Al-urfali, *J. Am. Chem. Soc.*, **80**, 2113 (1958).
12. G. Wilkinson, *ibid.*, **74**, 6148 (1952).
13. I. M. Kolthoff and J. F. Coetzee, *ibid.*, **79**, 870 (1957).
14. L. Meites, "Polarographic Techniques," p. 247 ff, Interscience Publishers, Inc., New York (1955).

Brief Communications

A High Performance Saturated Hydrocarbon Fuel Cell

W. T. Grubb and L. W. Niedrach

Research Laboratory, General Electric Company, Schenectady, New York

A key technical problem in fuel cells is the achievement of high electrochemical oxidation rates using cheap fuels. Among such fuels the saturated hydrocarbons represent a class of major importance. Heretofore the saturated hydrocarbons have not displayed significantly high rates of electrochemical oxidation directly at fuel cell anodes below the fused salt temperature region or about 500°C.

It has now been found that propane can be oxidized rapidly at a platinum catalyzed fuel cell anode at 150°C. A polarization curve (voltage *vs.* current density curve) obtained from a propane-oxygen fuel cell containing platinum catalyzed electrodes and 14.6M phosphoric acid electrolyte is shown in Fig. 1. A cross-section diagram of the cell

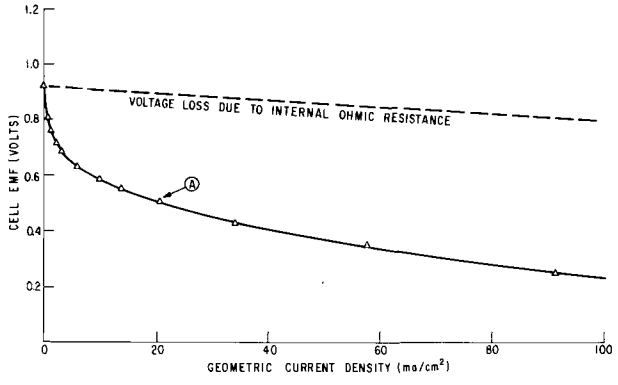

Fig. 1. Polarization curve for propane-oxygen fuel cell at 150°C; electrodes-platinum; electrolyte 14.6M phosphoric acid.

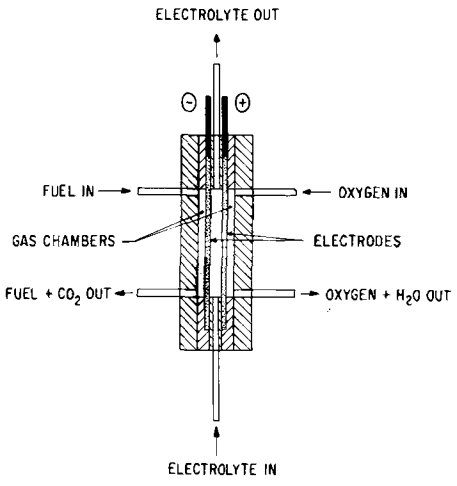

Fig. 2. Test cell cross section

used in the experimental work appears in Fig. 2. Two key features of this cell are (i) the employment of a new porous, gas electrode structure due to Niedrach and Alford (1) which preserves the catalytic (electrocatalytic) properties of platinum, and (ii) the employment of phosphoric acid electrolyte at a suitable temperature and concentration.

Practical implications of the results depend not only on obtaining high performance, but also on achieving complete oxidation of the fuel. The yield of CO_2 from the cell operating at point A of Fig. 1 was measured by a gas chromatographic method and found to be 98% ± 4% of that required by the reaction for complete anodic oxidation of propane

$$C_3H_8 + 6H_2O \rightarrow 3CO_2 + 20H^+ + 20e^-$$

The absence of a limiting current in the polarization curve is also of importance. This results from the thin structure of the new electrodes. Eight to ten mils thick, they are free from the long pores which tend to limit mass transport at relatively low current densities when the thicker "gas diffusion" electrodes of the literature are operated in the presence of inert gases (the CO_2 product in the present case). Similar freedom from limiting currents is seen when the new electrodes are operated on air to current densities of several hundred milliamperes per square centimeter.

Details of this work and further experiments up to 200°C will be reported later.

Acknowledgment

It is a pleasure to thank Miss Carol J. Michalske for carrying out the experimental work. This work was supported in part by the Advanced Research Projects Agency through the United States Army Engineer Research and Development Laboratories, Fort Belvoir, Virginia under Contract No. DA-44-009-ENG-4909.

Manuscript received April 15, 1963. Detailed paper was presented at the New York Meeting, Sept. 29-Oct. 3, 1963.

Any discussion of this paper will appear in a Discussion Section to be published in the June 1964 JOURNAL.

REFERENCE

1. L. W. Niedrach and H. R. Alford, To be published.

The Relative Corrosion Rates of Nickel Electrodeposits Having Different Textures

A. K. N. Reddy

The Electrochemistry Laboratory, University of Pennsylvania, Philadelphia, Pennsylvania

The author recently proposed (1, 2) a mechanism for the development of preferred orientations, with special reference to nickel electrodeposits. It was argued that textures result from two growth processes: (i) the preferential formation of facets of a particular crystallographic type, and (ii) the alignment of these facets normal to the substrate surface. The zone-axis of these "Wilman" facets becomes the texture axis.

The theory is applied, in this short communication, to some recent work (3) wherein it was observed that nickel electrodeposits having different preferred orientations confer different extents of protection against corrosion in dilute hydrochloric acid. Deposits with <210> orientation provide the best corrosion protection, and those with <110> orientation give less protection.

From the standpoint of the theory, deposits acquire a <210> texture by the formation of {211} facets on the free surface, and deposits with a <110> texture have octahedral facets. When {211} facets (in contrast to {111} facets) are exposed to the solution, not only can we consider the heat of hydrogen adsorption to be higher (4), and hence also the hydrogen overpotential (4, 5), but the dissolution of {211} facets can also be considered to be smaller [due to the reciprocity of growth and dissolution (6)].

The anodic dissolution reaction and the cathodic hydrogen evolution reaction are both hindered more on {211} facets than on {111} facets. Hence, the corrosion of deposits with {211} facets (*i.e.*, <210> texture) should be less than those with {111} facets (*i.e.*, <110> texture). This conclusion is in agreement with experiment.

Manuscript received Jan. 28, 1963; revised manuscript received June 24, 1963.

Any discussion of this paper will appear in a Discussion Section to be published in the June 1964 JOURNAL.

REFERENCES

1. A. K. N. Reddy, *J. Electroanal. Chem.*, **5** (1963).
2. A. K. N. Reddy and S. R. Rajagopalan, *ibid.*, **5** (1963).
3. B. C. Banerjee, *This Journal*, **107**, 80 (1960).
4. G. Okamoto, J. Horiuti, and K. Hirota, *Sci. Papers Inst. Phys. Chem. Res. Tokyo*, **29**, 223 (1936).
5. L. P. Bicelli and A. La Vecchia, *WADD Technical Note 60-270*, February 1961.
6. H. E. Buckley, "Crystal Growth," p. 304, John Wiley & Sons, Inc., New York (1951).

The Adsorption of Iron during Etching of Lithium Fluoride Crystals

G. Rosenblatt and M. B. Ives

Department of Metallurgy and Metallurgical Engineering, McMaster University, Hamilton, Ontario, Canada

The action of cation inhibitors in aqueous solutions on the etch morphology of cleavage surfaces of lithium fluoride has been exhaustively studied by Gilman, Johnston, and Sears (1). Of some thirty cations investigated only two, iron and aluminum, produced etchants that would form regular square dislocation etch pits. Gilman *et al.* concluded that the inhibitor ions, which need only be present in concentrations of the order of one part in 10^6, must be (*a*) within 25% of the size of the Li^+ ion, (*b*) have a stable fluoride salt with low solubility, and (*c*) form a stable fluoride complex. These criteria suggest that such ions will adsorb readily at cation sites on the crystal surfaces and thereby modify the dissolution conditions. That so few ions are necessary in solution to modify the etch morphologies profoundly suggests that they adsorb preferentially at the primary dissolution sources, *viz.*, kinks in crystal ledges (1, 2).

The present experiments were undertaken to investigate this possibility by relating the spatial distribution of adsorbed ferric ions to the etch morphologies. Etching of freshly cleaved {100} surfaces of lithium fluoride was carried out in dilute aqueous solutions of ferric chloride containing radioisotope Fe^{59} of known activity. After washing, the etched surfaces were placed on nuclear photographic emulsions and the distribution of radioactivity deduced by track-autoradiography. Preliminary experiments established that the washing procedures after etching produced a reproducible activity independent of washing time.

An early observation demonstrated that there is no (detectable) dependence of ferric ion adsorption on dislocation etch pit density, manifest as a constant track density over the whole of a given crystal surface. (Exceptions include large adsorption at gross defects, such as high cleavage steps, etc.) Any variations in track density with location of surface area measured are included in the statistical deviations of the mean results of track-counting fifteen areas per surface.

Using a ferric chloride stock solution of known specific activity of iron, a series of etchants was prepared of varying iron content and two lithium fluoride samples etched for 2 min in each. There is no observable change in adsorption for etching time greater than 3 sec. The ferric ion adsorption, measured as track densities (corrected for background) and converted to ions per square centimeter, is represented by the adsorption isotherm of Fig. 1. The isotherm is seen to exhibit a definite inflection corresponding to a mean iron coverage of about 3.5 x 10^{13} ions/cm^2, and occurring in the range of iron concentration in the bulk solution of from 0.2 to 2.0 x 10^{-6} parts by weight.

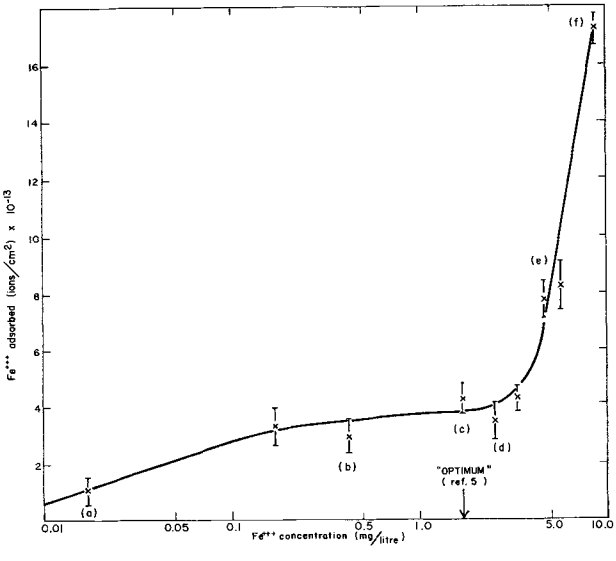

Fig. 1. Adsorption isotherm for ferric ions on a {100} cleavage surface of lithium fluoride at 22°C. (a), (b), (c), etc., refer to the bulk iron concentrations to which the micrographs of Fig. 2 correspond.

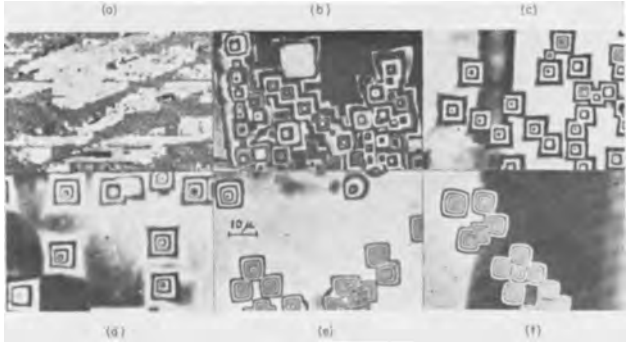

Fig. 2. Interference micrographs of dislocation etch pits on lithium fluoride surfaces etched in aqueous solutions of ferric chloride containing (a) 0.017; (b) 0.42; (c) 1.7; (d) 2.5; (e) 4.6; (f) 8.4 mg Fe^{+++}/liter.

Observation of dislocation etch pit morphology as a function of iron concentration followed the form first pointed out by Gilman *et al.* (1) and is demonstrated by the interference micrographs of Fig. 2. Correlation with the isotherm shows that the optimum etchant concentration (to produce square-based dislocation etch pits) corresponds closely to the point of inflection of the isotherm. At larger ferric ion concentrations, when adsorption increases, rounded pits are observed. At lower concentrations, terraced shallow pits correspond to less iron adsorption. These results are consistent with recent theoretical ideas on the effect of inhibitor on kink motion (2).

It should be realized that the whole surface of an ionic crystal is not available to an adsorbing cation (3). Assuming such an adsorbate to form a monolayer when all cation surface sites are filled, it is found that for the {100} surfaces of lithium fluoride, monolayer adsorption exists at 1.23×10^{15} ions/cm^2. On this scale, the adsorption inflection of Fig. 1 occurs at 1/35 of a monolayer of ferric ions.

Employing the established concepts of adsorption theory, this inflection may correspond to the complete filling of a particularly favorable type of adsorption site on a heterogeneous surface. It is attractive to suppose that these more favorable sites for the ferric ions are the kink-sites proposed by Gilman *et al.* (1). The inflection then corresponds to "monokink" adsorption. This suggests that in the ranges of optimum etchant concentration of iron, there will be, on the average, only three kinks in every hundred possible surface sites, the remainder comprising close-packed surface and straight ledges. This low density of kinks will cause the crystal surface to appear macroscopically composed of only ledge-surface {Okl} (2). This is observed in the form of flat-faced {Okl} pyramidal etch pits at points of dislocation emergence. Furthermore, for a uniform coverage of 1/35 of a monolayer, the absorbed ions will be about six sites apart in a square array, and this is approximately the spacing between monomolecular ledges on etch pit sides. This correlation suggests that dissolution morphologies are subject to part-poison, part-diffusion control (4) wherein the latter exists by the interaction of hemispherical diffusion fields centered on the dissolving kink-sites. The hemispheres can then interact both between kinks in the same ledge and between kinks in adjacent ledges. Also, since uniform iron coverage is observed, it is proposed that the whole crystal surface is composed, during dissolution, of {Okl} facets inclined to the close packed {100} plane at the same angle as the faces of etch pits. These other "surface" facets are not resolvable, however, since they are never able to attain sufficient size, due to the lack of a constant dissolution source. In many instances there is a suggestion of a surface mottle which could represent such facets.

Application of the Gibbs adsorption isotherm equation (5) to the results of this investigation allows for an estimate of the mean kink free energy, as follows. One form of the Gibbs equation may be written as

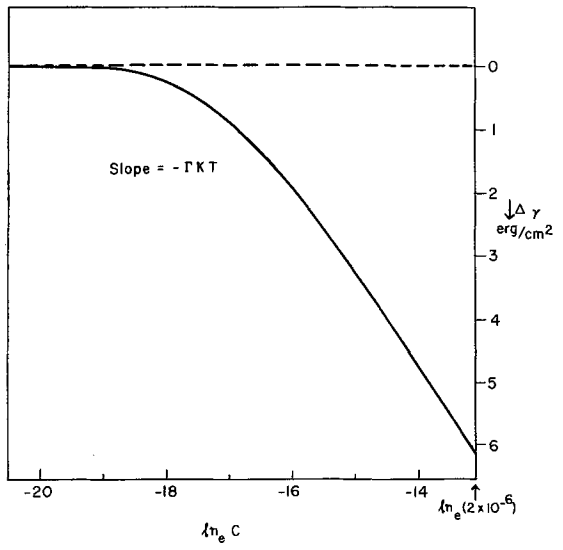

Fig. 3. Surface free energy of lithium fluoride surface as a function of the natural logarithm of the bulk solution concentration of ferric ions. Constructed geometrically.

$$\frac{d\gamma}{d(\ln c)} = -\Gamma kT$$

relating the rate of change of surface free energy γ with the natural logarithm of the bulk concentration of adsorbate, c, to the surface excess, Γ. Thus a curve of surface energy plotted against (ln c) will have instantaneous slope $-\Gamma kT$. Since we know Γ as a function of c, from the isotherm, we can therefore construct such a curve. This was done geometrically, and the result is reproduced in Fig. 3. Arbitrarily taking a bulk concentration of 2×10^{-6} for monokink adsorption, we obtain a measure of $\Delta\gamma$, the change in surface free energy due to the adsorption, as 6.1 erg/cm^2. Although the surface energy of a kink is not reduced completely to zero when it is filled with adsorbate, it can be assumed that a large fraction of its energy is reduced in this process, and the value obtained can be taken as a lower limit to the energy of kink-site in a lithium fluoride surface. These results give such a kink energy as 1.56×10^{-13} erg/kink, which appears to be of the correct order of magnitude, since it predicts a surface energy of a high index surface (maximum kink density) of approximately 200 ergs/cm^2. This compares favorably with the value of interfacial free energy of a {100} lithium fluoride surface in water of $\gamma_{LiF\text{-}H_2O} = 177$ erg/cm^2, used in a previous study (4).

In order to delineate further the kinetics of inhibitor adsorption in this system, it is necessary to deduce isotherms at other temperatures and undersaturations, and this work is in preparation. A complication feature of the system is its dynamic nature, in that the surface is continuously dissolving at a rate which, on the atomic scale, is considerable.

Acknowledgment

This work was performed under the sponsorship of the National Research Council of Canada and the U. S. Office of Naval Research.

Manuscript received March 25, 1963. This paper was presented at the Pittsburgh Meeting, April 15-18, 1963.

Any discussion of this paper will appear in a Discussion Section to be published in the June 1964 JOURNAL.

REFERENCES

1. J. J. Gilman, W. G. Johnston, and G. W. Sears, *J. Appl. Phys.*, **29**, 747 (1958).
2. M. B. Ives, *J. Phys. Chem. Solids*, **24**, 275 (1963).
3. W. C. Walker and A. C. Zettlemoyer, *J. Phys. Chem.*, **57**, 182 (1953).
4. M. B. Ives and J. P. Hirth, *J. Chem. Phys.*, **33**, 517 (1960).
5. See, for example, S. Brunauer, "The Adsorption of Gases and Vapors," Vol. 1, Princeton University Press, Princeton, N. J. (1945).

Impedance of Leclanche Cells and Batteries

Ralph J. Brodd[1] and Harold J. DeWane

National Bureau of Standards, Washington, D. C.

ABSTRACT

The impedance, open-circuit voltage, short-circuit current, performance on standard tests, and the pulse resistance were determined for a number of different size Leclanché cells produced by various manufacturers. The interpretation of the impedance in the light of modern relaxation theory indicated the existence of one process at the negative zinc electrode and two processes at the positive manganese dioxide electrode for all Leclanché cells assuming ideal behavior for each electrode process. The magnitude of the contributions to the total impedance and the relaxation time for each of the electrode processes in the cell were determined. The effect of varying manganese dioxide to carbon black weight ratios on the impedance of laboratory-prepared cells was determined. Also, the impedance of fresh cells and batteries was determined at several stages during discharges on various standard tests, and, in some cases, after shelf stands of up to two years. The extrapolated value of the impedance at infinite frequency, R_∞, was used to estimate the residual capacity of cells after shelf stands of one and two years. R_∞ was found to be identical with the internal resistance of the cell determined by pulse techniques.

The increasing demands of technology on the performance of dry cells and batteries have led to developments which have increased the capacity of the old primary cell systems, as well as to the development of new electrochemical systems for producing electrical power. It is of great importance both in improving the performance of the old-type cells and in designing new-type cells to have available a knowledge of all the properties of the many primary cell systems. Since the function of primary cell systems is to furnish electrical energy, it is especially important to have a detailed knowledge of the electrical properties of the various cell systems. It is well known that alternating current techniques may be employed to investigate the characteristics of reactions in electrochemical systems (1). Recently, a new interpretation has been given to the electrical properties of electrode systems (2).

Theoretical Representation

A brief summary will be given of the properties of electrode systems deduced from the application of relaxation theory to electrode systems (2). The impedance, z, is given by

$$Z = R - jX_c \qquad [1]$$

where R is the real component of the impedance or the resistance, $j = \sqrt{-1}$, and X_c is the imaginary component of the impedance or the capacitative reactance, $1/\omega C$, with ω the angular frequency and C the capacitance. It can be shown that the impedance of an electrode system is given by

$$Z = R_\infty + \sum_a \frac{R_a}{1 + j(\omega\tau_a)^{(1-h)}} \qquad [2]$$

where R_∞ is the impedance at infinite frequencies, R_a is the resistance associated with the electrode reaction, τ_a is a constant with dimensions of time, and h is a constant. The relaxation time of the electrode process, τ_a, is related directly to the rate constants of the electrode process by the kinetic equations describing the process. The constant h is associated with the distribution of relaxation time values about a mean value. It will be assumed arbitrarily that $h = 0$ for the electrode processes considered in this paper. That is, it will be assumed that τ_a is single valued. This assumption will greatly simplify Eq. [2], and, as a result, the interpretation of the observed behavior of the impedance will be facilitated.

It can be shown from Eq. [1] and [2] with $h = 0$ that

$$R = R_\infty + \sum_a \frac{R_a}{1 + (\omega\tau_a)^2} \qquad [3]$$

and

$$X_c = \sum_a \frac{R_a(\omega\tau_a)}{1 + (\omega\tau_a)^2} \qquad [4]$$

Two methods of representing the experimental data are used below. One representation is a plot of X_c *vs.* log ω. This representation is of particular value in the determination of the magnitude and frequency of the maximum value of X_c. From Eq. [4] the maximum value of X_c is $R_a/2$, while the relaxation time is found from the frequency of the maximum, ω_{max}

$$\tau_a = 1/\omega_{max} \qquad [5]$$

If more than one process is occurring simultaneously, the relaxation time and resistance associated with each process may be found using Eq. [2], [3], and [4]. The other form of data representation to be used is the Argand diagram. This method of data representation has the advantage of revealing both R and X_c simultaneously (2, 3). Each point on the Argand diagram describes R and X_c at a given frequency. The vector drawn from the origin to the

[1] Present address: Research Laboratory, Union Carbide Consumer Products Company, Division of Union Carbide Corporation, Parma, Ohio.

point on the curve describes the impedance at that frequency. The length of the vector is the numerical value of the impedance, and the angle the vector makes with the real axis is the phase angle for that frequency.

The resistance associated with the electrode process, R_a, is related directly to the rate of the electrode reaction at equilibrium by

$$I_o = \frac{RT}{FA\,R_a\,\lambda} \qquad [6]$$

where λ is the number of charges transferred in the process, I_o is the exchange current density for the process, A is the area of the electrochemically active surface, R is the gas constant, T is the absolute temperature, and F is Faraday's constant (1, 2).

Experimental

Impedance measurements.—The resistance and capacitance of Leclanché cells were determined by a substitution method using a series resistance-capacitance bridge (4). The ratio arms were 1000 ohm standard a-c resistors; the fixed arm of the bridge was composed of a series combination of a 100 ohm standard a-c resistor, and a 1.0 μF standard capacitor. The variable arm of the bridge was a calibrated resistor variable in steps of 0.01 ohm in series with two parallel calibrated capacitors, continuously variable from 50 pF to 1.1 μF. The detector was a tunable amplifier with a maximum sensitivity of 5 μv for a 10% deflection of full scale. The oscillator was coupled to the bridge by means of an isolation transformer.

In operation, the bridge was balanced initially with a short copper bar; then the cell under investigation was substituted for the copper bar, and the bridge was rebalanced. This procedure was repeated at each of ten frequencies between 50 cps and 50 kps. The values of the resistance and reactance for each frequency were calculated using the equations

$$R = R_i - R_c \qquad [7]$$

and

$$X_c = \frac{1}{\omega}\left[\frac{1}{C_i} - \frac{1}{C_c}\right] \qquad [8]$$

where the subscripts i and c denote the dial readings of the variable resistor and capacitor for the initial and final balances, respectively. The internal resistance of the cells was also determined using the pulse method (5).

Leclanché cell composition.—Commercially available Leclanché cells and batteries from several manufacturers as well as Leclanché cells specially constructed in the laboratory were included in this investigation. The laboratory cells were constructed with variations primarily in the manganese dioxide to carbon black weight ratio.

The black mix for all laboratory cells was prepared as described below. African manganese dioxide ore, Shawinigan acetylene black, and ammonium chloride were weighed out in the desired proportion and dry mixed for 2 min in a Pony mixer. The approximate amount of electrolyte (24 parts zinc chloride, 40 parts ammonium chloride, and 100 parts water by weight) was added to the mix. The mixing was continued for 10 min. The wetness of the black mix was then tested by compression. The desired wetness was obtained when 400 psi just forced electrolyte from the mix.

If the wetness test did not indicate sufficient electrolyte in the mix, more electrolyte was added and mixing was continued for 1 min. The mix was tested for proper wetness again. If more than 5 min mixing time was required to adjust the wetness, the mix was discarded. If the initial wetness test indicated too much electrolyte, the mix was discarded. This procedure was used in preparation of the wet mix for all desired manganese dioxide to carbon black weight ratios. The same per cent by weight of ammonium chloride was used in all mixes. In a typical mix with an 8:1 ratio of African ore to carbon black, 1400g of ore, 175g of acetylene black, and 217g of ammonium chloride were combined with 570 ml of electrolyte. This batch furnished mix for approximately 35 D-size Leclanché cells.

A paste composed of 7.15g of wheat flour, 14.30g of cornstarch, 22.7g of ammonium chloride, 10 ml of 45° Baumé zinc chloride solution, and 41 ml of water was used as the separator wall in all the laboratory cells. All of the laboratory cells were assembled in identical fashion. The wet mix was molded at 400 psi into bobbins with a brass capped carbon rod. A wax-impregnated cardboard star washer and sufficient paste just to fill the space between the bobbin and the zinc can were placed in a D-size zinc can. The bobbin was carefully inserted so that the paste was forced up evenly around the bobbin to form a continuous layer between the zinc can and the bobbin. The cell was then placed in a 72°C water bath for 2 min to gelatinize the flour and starch. A wax-impregnated cardboard spacing washer was placed ¼ in. from the top of the zinc can. The cell was sealed with molten bituminous pitch. After the cell was cooled to room temperature, the upper edge of the can was heated with a torch to insure a good seal.

Test procedure.—The Leclanché cells were discharged on the heavy industrial flashlight cell test (HIF), the light industrial flashlight cell test (LIF), the general purpose 4-ohm intermittent test (4-ohm), and the general purpose 2.25-ohm intermittent test (2.25-ohm). These tests were conducted according to the standard test procedure (6). The open-circuit voltage (OCV) of the cells was determined. A critically damped ammeter with a resistance including the leads of 0.01 ohm was used to measure the short-circuit current (SCC) of the cell. Some of the cells were removed periodically from the test racks during the open-circuit stand, and the impedance of the cells was determined as rapidly as possible. The cells were returned to the test racks and the discharge continued until the completion of the test. Cells were stored as prescribed for the standard tests (6).

Results and Discussion

Impedance of Leclanché cells.—The impedance of a typical laboratory cell constructed with an 8:1 African ore to carbon black weight ratio is shown

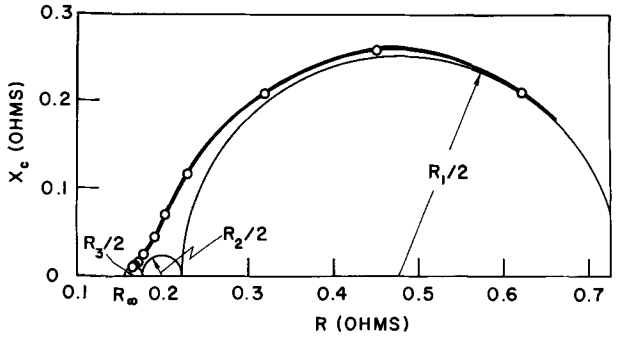

Fig. 1a. Argand diagram of the impedance of a Leclanché cell

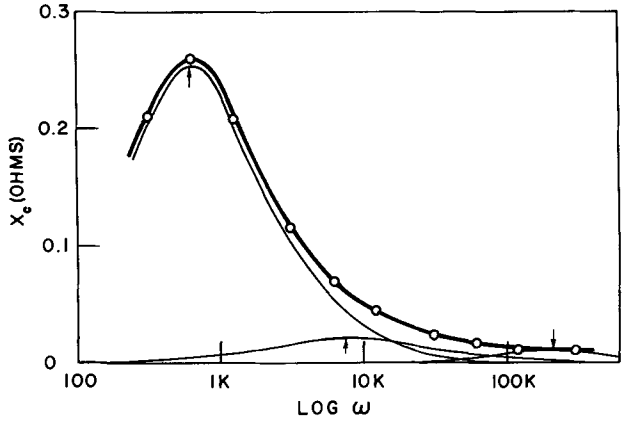

Fig. 1b. Dependence of X_c on frequency for a Leclanché cell in Fig. 1a.

in Fig. 1a. The impedance vector drawn from the origin to a point on the curve may be considered to be composed of two parts: a vector drawn from the origin to R_∞, and a vector drawn from R_∞ to the point on the curve. The vector from the origin to R_∞ represents the portion of the impedance that has the characteristics of a resistive element. It is composed of the resistance of the zinc can, the carbon rod, the carbon-manganese oxide matrix, and the electrolyte. The pulse method of determining the internal resistance of dry cells measures this portion of the cell impedance.

The vector drawn from R_∞ to the point on the curve represents the contribution of the electrode processes to the cell impedance for the frequency at that point. The effects of electrode polarization are found in this portion of the cell impedance. The frequency dependence of the contribution of the electrode processes to the cell impedance is given by Eq. [2]. The three semicircles lightly drawn in Fig. 1a represent the contribution of the cell impedance of three electrode processes occurring in the cell. The frequency and magnitude of the maximum of each of these three processes were located using Eq. [4] and the reactance-log ω plot shown in Fig. 1b.

For all Leclanché cells, both laboratory and commercial, graphic trial-and-error plots showed that it was necessary to assume the presence of three processes with their corresponding absorption-dispersion regions in order to fit the experimental curve. Each of the three absorption-dispersion regions correspond to the existence of an electrochemical process in the cell. It will be assumed that these processes are associated with the electrode reactions in the cells, as the solutions used in the preparation of the cells do not have processes which lead to absorption-dispersion regions in the frequency range of this investigation.

The value of R_∞ for each cell was determined by extrapolation of the Argand diagram to very high frequencies using Eq. [2] after the frequency and magnitude of each absorption-dispersion region had been established. The value of R_∞ determined in this fashion was always in excellent agreement (± 0.01 ohm or better) with the internal resistance of the cell determined by the pulse method.

Commercial Leclanché cells had the same general impedance characteristics as the laboratory cells. Since each manufacturer uses different techniques in the construction of cells, there was a variation of the cell parameters (R_∞, R_a, and τ_a in Eq. [2]) for the cells of various manufacturers. The most notable difference among commercially available cells was the resistance of the process occurring at low frequency, tentatively identified as the reaction at the zinc electrode. Apparently, there is a noticeable variation in the electrolyte at the zinc electrode in cell construction (7). The average impedance of D-size, C-size, and AA-size cells is shown in Fig. 2, 3, and 4, respectively. Information concerning the specific variation between manufacturers is given elsewhere (8).

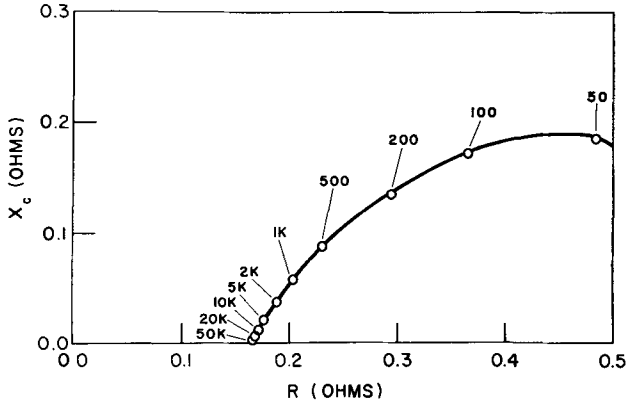

Fig. 2. Argand diagram of the average impedance of general purpose D-size Leclanché cells from 8 manufacturers. Nine cells from each manufacturer were used to construct the diagram.

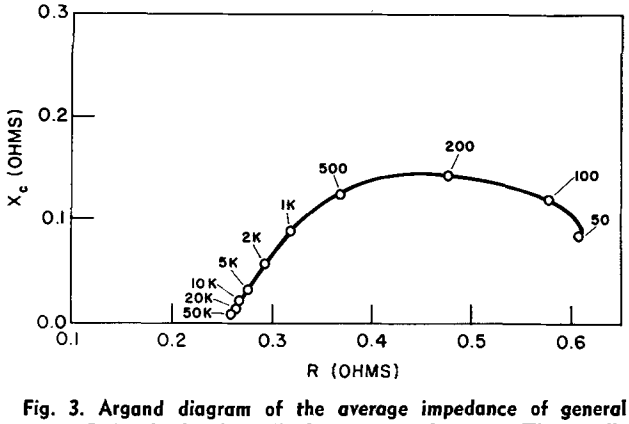

Fig. 3. Argand diagram of the average impedance of general purpose C-size Leclanché cells from 4 manufacturers. Three cells from each manufacturer were used to construct the diagram.

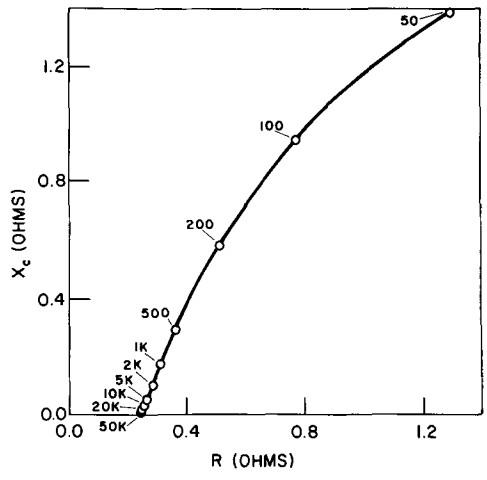

Fig. 4. Argand diagram of the average impedance of general purpose AA-size Leclanché cells from 5 manufacturers. Three cells from each manufacturer were used to construct the diagram.

It is possible to identify tentatively the reactions which correspond to the three absorption-dispersion regions of the cell impedance reported previously (2). The impedance of the zinc electrode in dry cell electrolyte reported by Euler and Tvarusko and confirmed by the authors corresponds to the process with $\omega_{max} = 400$ cps (3, 7). The impedance of the zinc electrode did not show any other absorption-dispersion regions. Therefore, the processes with $\omega_{max} = 3300$ cps and $\omega_{max} = 150$ kps are assumed to be associated with reactions at the positive electrode.

Unfortunately, there is no agreement in the literature concerning the reactions at the positive electrode (9, 10). The reaction scheme proposed by Vosburgh will be used for the purpose of illustration (10).

$$MnO_2 + H^+ + e \underset{k_2}{\overset{k_1}{\rightleftarrows}} MnOOH \qquad [9]$$

$$MnOOH + H^+ + e \underset{k_4}{\overset{k_3}{\rightleftarrows}} Mn(OH)_2 \qquad [10]$$

If the rate constants, k_3 and k_4 for reaction [10] are assumed to be much larger than the rate constants k_1 and k_2, for reaction [9], the process with $\omega_{max} = 3300$ cps corresponds to reaction [9] and the process with $\omega_{max} = 150$ kps corresponds to reaction [10]. Before a positive identification of the processes responsible for the observed absorption-dispersion regions is possible, more detailed study of the reactions and impedance of the positive electrode system is needed. It is very possible that reactions other than [9] and [10], such as a two-electron transfer reaction or ammonium ion reduction, may be responsible for the observed behavior (9). Also, the assumption that $h = 0$ in Eq. [2] may not be valid (11).

Variation of positive electrode composition in laboratory cells.—Since it has been demonstrated that the characteristic parameters of electrode reactions in the Leclanché cell can be separated and evaluated by the use of the techniques developed above, it is now possible to use the cell as a whole to study the effect of composition and construction on the individual electrode reaction parameters.

Table I. Impedance parameters for Leclanché cells of various mix compositions

Ore: black, weight	R_1, ohms	$1/\tau_1$, sec^{-1}	R_2, ohms	$1/\tau_2$, sec^{-1}	R_3, ohms	$1/\tau_3$, sec^{-1}	R_∞, ohms
4:1	0.510	390	0.050	3300	0.006	220K	0.111
5:1	0.410	470	0.050	3300	0.012	94K	0.121
8:1	0.476	604	0.054	6900	0.017	210K	0.159
11:1	0.476	490	0.074	4300	0.032	200K	0.200
14:1	0.480	500	0.084	3900	0.048	160K	0.321

The effect of varying the composition of the bobbin on the impedance of the laboratory cells is given in Table I. As the amount of manganese dioxide in the bobbin is increased, the manganese dioxide particles of higher resistivity and lower surface area are substituted for the carbon black particles. As a result, the resistance of the bobbin should increase, and the total positive electrode surface area (carbon black plus manganese dioxide) should decrease. Equation [6] shows that as the area of an electrode decreases the resistance associated with the electrode is increased. Thus, the increase in manganese dioxide content should reflect directly on the impedance as an increase in R_∞, and R_2 and R_3 the resistances associated with the processes at the positive electrode. This is confirmed by the results in Table I. Both the decrease in electrode capacitance and the increase in reaction resistances, as the ore content was increased, indicate that the electrochemically active surface area has decreased. It must be noted that these facts do not rule out the possibility that one of the reactions identified may involve a surface reaction on the carbon black in which manganese oxides are not involved.

It should be emphasized that changes in the exchange current and in the resistance of the electrode process (Eq. [6]) do not necessarily reflect a change in cell performance on a given test. The kinetic parameters of the electrode processes are directly related to the instantaneous ability of a cell to furnish electric current. Kinetic parameters do not reveal the total amount of reactants available for reaction. A low reaction resistance with a corresponding high exchange current for the battery electrode reaction does not guarantee satisfactory performance on all the standard tests. For instance, a hypothetical cell constructed with an extremely small ratio of African ore to carbon black weight (see Table I) will have low values associated with R_2 and R_3. These low reaction resistances and corresponding large exchange currents indicate a small polarization during current flow and a large SCC. The low resistances do not have any relationship to the total available manganese dioxide or total current-producing ability of the cell. The hypothetical cell does not contain as much active ore as a normal cell with a larger ore-to-black ratio of about 8:1, and, as a result, the hypothetical cell will not perform as satisfactorily as a normal cell on the general purpose tests. However, the hypothetical cell should prove very satisfactory as a photoflash cell

where large currents of momentary duration are required and long sustained current drains are not normally encountered in service.

Changes in exchange current and reaction resistances of a cell do affect the instantaneous polarization characteristics of a cell. When furnishing current, a cell which has small reaction resistances for the electrode processes will have a smaller polarization than a cell which has large reaction resistances. It was possible to predict the short-term characteristics of the cells used in this investigation from the impedance measurements.

Short circuit current calculations.—In the derivation of Eq. [2] it was assumed that the total polarization was a linear combination of the various polarizations. If this assumption is valid, the SCC of a Leclanché cell can be calculated from a knowledge of the impedance of the cell and Eq. [6]. When a cell is connected through an ammeter, the sum of all the emfs in the circuit is equal to the open-circuit voltage (OCV) of the cell. That is

$$\text{OCV} = E_{\text{external}} + E_{\text{internal}} + E_p \qquad [11]$$

The polarization voltage, E_p, is assumed to follow the Tafel equation with $b = 0.12$

$$E_p = 0.12 \log (\text{SCC}/i_o) \qquad [12]$$

where $i_o = I_o A$ is the exchange current calculated using Eq. [6] and the resistance of the electrode process deduced from the analysis of the impedance.

Now Eq. [11] can be written as

$$\text{OCV} = 0.01\ (\text{SCC}) + R_\infty\ (\text{SCC}) + \sum_{a=1}^{3} 0.12 \log (\text{SCC}/i_{oa}) \qquad [13]$$

In the first term on the right 0.01 is the resistance of the critically damped ammeter used to measure SCC. The value of SCC which satisfies Eq. [13] is easily found. A summary of the results of the calculations for D-size cells given in Table II includes three laboratory, two commercial cells, and a discharged commercial cell. It should be noted that the time of measurement of the SCC is much longer than the relaxation time of all electrode processes in the Leclanché cell. The agreement between the calculated and the experimental SCC was very satisfactory for all cells in this study.

Discharge of Leclanché cells.—At various intervals during the standard tests, cells were removed from the test racks and the impedances of the cells were determined. The impedance of a commercial cell discharged at various stages on the HIF test shown in Fig. 5 is typical of all cells discharged on any of the standard tests. After the first 4-min discharge data analysis revealed that R_∞ and the resistances of the positive electrode processes had not changed. The resistance of the zinc electrode process, however, had decreased, presumably as a result of the increase in zinc ion concentration produced by the electrode reaction and/or a change in the surface condition, including increased roughness of the zinc. As the discharge continued, both the resistances of the positive electrode processes and R_∞ increased steadily while the resistance of the zinc electrode process decreased to a very small value. The resistance of the zinc electrode process remained at a very small value until the end of the test.

Table II. Comparison of short circuit current derived from impedance analysis for D-size cells with direct measurement

	Laboratory cells			Commercial cells		Discharged cell
Calc'd SCC, amp	7.5	6.6	7.9	7.6	5.6	0.76
Direct SCC, amp	7.2	6.5	8.2	7.5	5.5	0.79

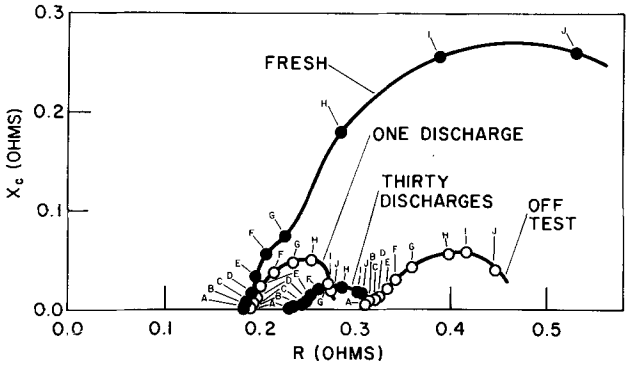

Fig. 5. Impedance of a D-size Leclanché cell after discharge on the HIF test for 1 discharge, 30 discharges, and at the end of the test. a, 50K; b, 20K; c, 10K; d, 5K; e, 2K; f, 1K; g, 500; h, 200; i, 100; j, 50.

The observed increase in R_∞ and the resistances of the positive electrode processes may be a result of the accumulation of reaction debris from the discharge reaction. The surface of the manganese dioxide particle becomes coated with lower valence high-resistance oxide during discharge, thus effectively removing a part of the surface from participating in the electrode reaction. The decrease in the effective surface area of the positive electrode will cause the resistance associated with the electrode process to increase (see Eq. [6]). The presence of the high-resistance material in the bobbin will increase the resistance of the bobbin matrix and, thus, R_∞.

The impedance of the various cells discharged on the standard tests followed the same pattern as was found for the HIF test. R_∞ and the resistances of the positive electrode processes always increased steadily as the test progressed. The resistance of the zinc electrode process decreased to a very small value during the initial parts of the test and remained at a very small value as the test continued. In a few cases, toward the end of the longer general purpose tests the resistance of the zinc electrode process began to increase from its very low value. Examination of the cell showed that the zinc container had perforated. It was found that R_∞ increased more during the longer general purpose tests than during the shorter industrial tests.

Examination of Fig. 5 illustrates the danger of drawing conclusions using impedance measurements at only one frequency. If a low frequency, say 50 cps, is selected as the experimental standard, the impedance first decreased then increased slowly as the test continued. However, if a high frequency, say

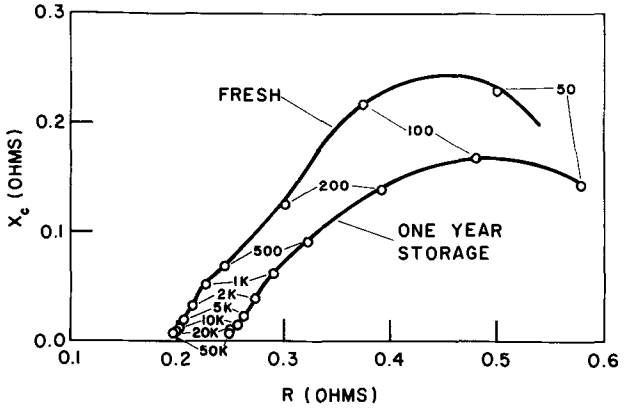

Fig. 6. Impedance of a Leclanché cell as received and after 1-yr storage.

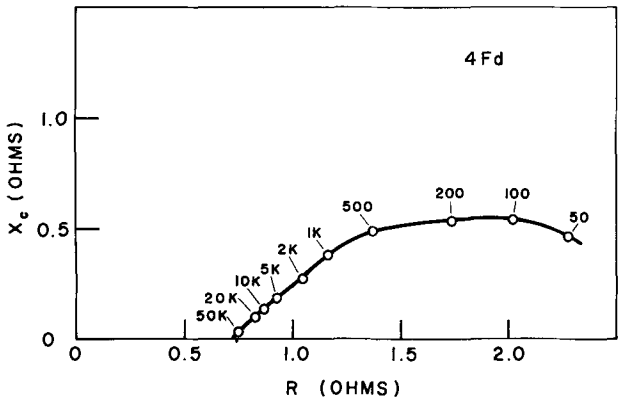

Fig. 7. Argand diagram of the impedance of a 1.5v A-battery (F4d).

5 kps, was selected as the experimental standard, the impedance increased during the entire discharge. It should be noted that Eq. [2] requires that the frequency be varied over at least two decades of frequency in order to establish the parameters of an electrode process.

Aging of Leclanché cells.—The effects of aging on the impedance of a D-size cell are shown in Fig. 6. Analysis of the impedance data revealed that after the one-year delay R_∞ increased, the resistances of the positive electrode processes increased slightly, and the resistance of the zinc electrode reaction decreased slightly. After the two-year delay, R_∞ had increased much more than during the first year, the resistances of the positive electrode processes had continued to increase, and the resistance of the zinc electrode process had increased. An examination of the cells after the first year showed that the cells were apparently unaffected by the storage. After the second year storage the cells had lost appreciable amounts of water, the zinc cans had perforated, and the OCV had decreased slightly. The aging effects in Leclanché cells are very complex and have been discussed elsewhere (12, 13).

An attempt was made to use the change in R_∞ on storage to estimate the residual capacity of the cells. A graph of R_∞ *vs.* discharge time prepared from the results of the discharge of the fresh cells was used to estimate cell performance at later dates (5). At the end of the first year the estimated and actual test performances on the LIF test were 505 min and 620 min, respectively. At the end of the second year the estimated and actual test performance were zero for each. Since this method of estimating cell performance relies solely on R_∞, factors such as the loss of water will affect R_∞, but may not alter appreciably the actual performance of the cell. The test performance of AA-size cells was estimated more successfully for the one-year delay tests. Their average performance was estimated to be 65 min, while actual result was 61 min showing a relationship between R_∞ and performance noted previously (5).

Leclanché batteries.—The affect of combining Leclanché cells into parallel (F4d) and series (4Fd) combination on the measured impedance is shown in Fig. 7 and 8. One of each type of the batteries was

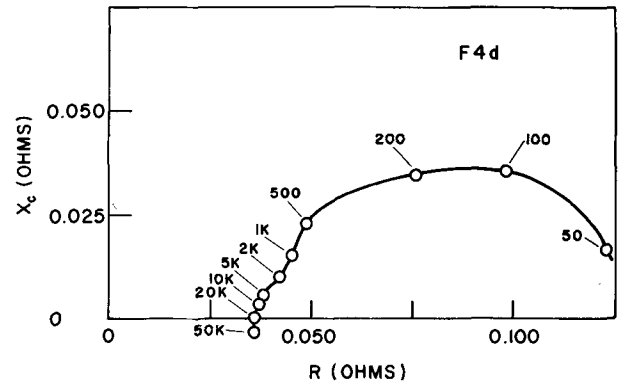

Fig. 8. Argand diagram of the impedance of a 6.0v (4Fd) lantern battery.

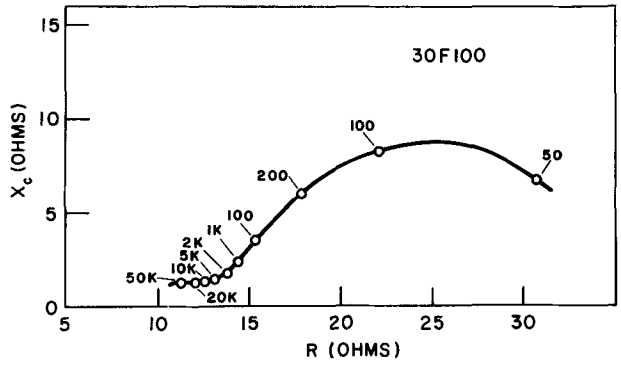

Fig. 9. Argand diagram of the impedance of a 45v B-battery (30F100).

disassembled, and the impedance of each cell of the battery was determined. The battery impedance was found to be the correct combination of the impedances of the individual cells composing the battery within the experimental limitations of measurement. The characteristics of the impedance during discharge of the batteries were very similar to that reported for the discharge of the single cells. R_∞ always increased during discharge, and the reaction parameters of the other electrode reactions varied as previously noted for the single cells.

The impedance of a 45v B battery (30F100) is shown in Fig. 9. The impedance of the other size 45v flat cell B batteries from any one manufacturer was

roughly inversely proportional to the physical size of the battery. The impedance of the B batteries during discharge and aging had the same characteristics as was found for single cells. There was considerable variation (about 200%) in the impedance of the same size battery from various manufacturers.

Acknowledgment

The authors wish to acknowledge the discussions with many members of the staff of the National Bureau of Standards during the course of this investigation, especially Drs. Ralph Kotter, John Lauritzen, J. D. Hoffman, and W. J. Hamer. The authors also thank William Vadnais for his help in constructing the laboratory cells and in conducting the standard tests.

Manuscript received March 11 1963; revised manuscript received June 27, 1963. This paper was delivered at the Columbus Meeting, Oct. 18-22, 1959.

Any discussion of this paper will appear in a Discussion Section to be published in the June 1964 JOURNAL.

REFERENCES

1. B. V. Ershler, *Zhur. Fiz. Khim.*, **22**, 683 (1940); H. Gerischer, *Z. Physik. Chem.*, **198**, 286 (1951); D. C. Grahame, *This Journal*, **99**, 370C (1952); J. E. B. Randles, *Discussion Faraday Soc.*, **1**, 11 (1947).
2. R. J. Brodd, *J. Research Nat. Bur. Standards*, **65A**, 275 (1961).
3. J. Euler and K. Dahmelt, *Z. Elektrochem.*, **61**, 1200 (1957).
4. G. W. Vinal, "Storage Batteries," 4th ed., p. 328, John Wiley & Sons, New York (1955).
5. R. J. Brodd, *This Journal*, **106**, 471 (1959).
6. National Bureau of Standards, "Specification for Dry Cells and Batteries," Handbook 71 (1959).
7. A. Tvarusko, *This Journal*, **109**, 881 (1962).
8. R. J. Brodd and H. J. DeWane, Technical Note, National Bureau of Standards (1963).
9. N. C. Cahoon, R. S. Johnson, and M. P. Korver, *This Journal*, **105**, 296 (1958).
10. W. C. Vosburgh, *ibid.*, **106**, 839 (1959).
11. J. Euler, *Electrochim. Acta.*, **3**, 134 (1960).
12. G. Vinal, "Primary Batteries," Ch. 4, John Wiley & Sons, New York (1950).
13. M. P. Korver, R. S. Johnson, and N. C. Cahoon, *This Journal*, **107**, 587 (1960).

The Thermally Regenerative Liquid-Metal Cell

B. Agruss

Allison Division, General Motors Corporation, Indianapolis, Indiana

ABSTRACT

The theory of a new, thermally regenerative, direct-conversion device is described. The device depends on the reaction of two liquid metals to furnish energy, with subsequent thermal decomposition of the product into the original reactants. As an example, the emf of cells composed of Na/glass/$Na_{(x)}Sn$ varied from 0.45-0.38v at temperatures between 500° and 702°C and at mole fractions of Na in the alloy between 0.136 and 0.40. Experiments confirmed theoretical predictions that Na can be distilled from NaSn alloys at temperatures of 1000°-1100°C yielding a relatively pure Na vapor and an approximately 3% (wt) alloy residue.

In fuel cell literature, there is very little work on regenerative systems. Yeager (1) suggested that thermal and electrochemical regenerative systems should be studied. A survey of the literature (2) revealed only about 20 inorganic compounds suitable for a thermally regenerative system, based on more or less practical criteria. Another evaluation (3), based on thermodynamic and reaction kinetic data, produced only three suitable reactions among the inorganic compounds, one of which, LiH, was already being studied (4). The other two reactions were not considered further because of the complicated equilibria involved. Also, liquid metal systems seemed to offer simpler equilibria and improved efficiency.

General thermodynamic descriptions of thermally regenerative electrochemical systems have been presented (5-7) and these systems have been shown to be Carnot limited. Thus, the over-all thermal efficiency depends on the temperature limits imposed on the system.

However, a general systems analysis (8) showed that the greatest improvement in the efficiency of regenerative systems could be accomplished by reductions in polarization and electrolyte resistance losses at any fixed temperature limits. It is known that the electrode reaction rates at liquid metal electrodes in contact with fused salts are extremely rapid (9), as exemplified by very large exchange currents. Also, the conductivity of fused salts is possibly 2-5 times greater than the conductivity of the best aqueous electrolytes. This paper presents the theoretical foundations for liquid-metal systems amenable to both thermal and electrochemical regeneration and some of the preliminary experimental work done to confirm theoretical predictions.

Electrochemical Theory

When metals react to form alloys, solutions, and compounds, an exchange of energy takes place which may manifest itself in the form of heat or useful work. These reactions can be analyzed by standard thermodynamic principles (10).

The free energies involved can be measured in galvanic cells in which the anode is formed of the more electrochemically active metal, and the cath-

ode is formed of the alloy. The cation of the electrolyte is the ionized form of the anode metal. The cell is represented schematically as

$$A_{a_0}|A^+|A_{a_2}(B) \qquad (S)$$

The above galvanic cell (S) is a special case of a concentration cell, which is represented by

$$A_{a_1}(B)|A^+|A_{a_2}(B) \qquad (G)$$

in which A and B may be a wide variety of metals and a_1 and a_2 are the activities of metal A in each electrode. The free energy change associated with scheme (G) can be expressed as

$$-\Delta\bar{G} = nFE = -RT \ln \frac{a_2}{a_1} \qquad [1]$$

where $\Delta\bar{G}$ is the change in partial molar free energy of species A. In all the following discussion the standard state corresponds to actual pure component A. The free energy change for cell (S) is expressed by Eq. [1] also, but, in this case, the activity, a_1 by definition is unity; therefore, the cell potential is

$$E = -\frac{RT}{nF} \ln a_2 \qquad [2]$$

The activity is defined by

$$a = \gamma N_A \qquad [3]$$

where the activity, a, can never be greater than unity, γ is the activity coefficient, and N_A is the mole fraction of species A.

When compounds are formed, however, the activity of A in the alloy is influenced also by the free energy of formation of the compound. For instance, for the reaction

$$xA + yB = A_xB_y \qquad [4]$$

the equilibrium constant is expressed by

$$K = \frac{a_{A_xB_y}}{a_A{}^x \cdot a_B{}^y} \qquad [5]$$

and

$$\Delta G^\circ \text{ (formation)} = -RT \ln K \qquad [6]$$

Since it is desired that the activity of the free A metal in the alloy be low to maintain a high potential, the free energy of formation should be large.

In addition, there will be a composition range wherein the change in activity of A will be small over a relatively large concentration change, resulting in a high, relatively steady voltage.

In a practical cell, however, constructed as in (S) comprising two liquid metal electrodes and a molten salt electrolyte, the operating voltage will be governed by

$$V = E_o - E_p - IR$$

Where E_o is the open-circuit voltage given by Eq. [2], R is the cell resistance, I the current, and E_p comprises both activation and concentration polarization factors.

Activation polarization has been shown to be negligible (9). Also, since a single-cation fused salt is used and not a solution of a salt in a solvent, it is hard to visualize any concentration polarization in the electrolyte. There can be some concentration polarization at the alloy electrode-electrolyte interface at high current densities where metal A can be discharged faster than diffusion can remove it, resulting in a thin, high alloy concentration layer. Because of the usually rapid diffusion rates at high temperatures in liquid metals this polarization should occur only at high current densities, but here the *IR* drop would greatly overshadow the small polarization effect. Hence, the only significant voltage loss in a liquid-metal cell of this type should be *IR* loss in the electrolyte.

These *IR* losses, also, are minimal and much lower than those encountered in aqueous systems, because molten salts have conductivities of the order of 2-5 mhos/cm while the best aqueous electrolyte conductivities are in the range of 0.5-0.9 mhos/cm.

Thus, the distinct advantages sought for regenerative systems, *viz.*, negligible polarization and low electrolyte resistance, have been deduced from the above for the liquid-metal cell (11) and in some cases found.

Regeneration Theory

Electrochemical regeneration requires nothing more than reversing the current through the cell depicted in either (S) or (G) (12). Many liquid metal electrodes in molten salts are strictly reversible and the negligible polarization limits the energy losses of the charge-discharge cycle to the resistive losses of the electrolyte. Incidentally, because of this characteristic, these cells can be fairly good storage batteries or energy storage devices for many applications. The solubility of the metal in its fused salt may, however, restrict the practical application because of reduced coulombic efficiency.

For thermal regeneration, the metals A and B must be chosen so that they have an appreciable difference in their boiling points or vapor pressures. In addition, one metal must exhibit an appreciable vapor pressure at the maximum temperature of the heat source. If these conditions are met, then thermal regeneration involves heating the alloy, A(B), or the compound A_xB_y, which has been discharged from the electrochemical cell, to a sufficiently high temperature, at which A exhibits a substantial vapor pressure. It is advantageous that B have only a minute vapor pressure at this boiling temperature of the alloy to avoid tranfer of B into the anode metal A. Continuing, gaseous A is condensed, collected, and returned to the cell along with the stripped alloy via their separate channels.

The vapor pressure of A also depends on the concentration of A in the alloy and, in the ideal case, follows Raoult's law. For these ideal or close to ideal solutions, the vapor will always contain some fraction of B, necessitating the use of a fractionating column to effect satisfactory separation.

For the electrochemical reasons mentioned, it is best to employ metal combinations which form marked intermetallic compounds, and in these cases the solutions depart substantially from ideality. Now it may be possible to separate the two components in a simple boiler, because at certain temperature and

concentration ranges the activity or vapor pressure of one component will be low, as compared to the other; hence practically one component is boiled over and condensed.

In a solution, the practical definition of a is p/Po where p is the partial pressure of A over the solution and Po the vapor pressure of pure A at temperature T. For most pure metals, Po is given in the literature (13), hence, the partial pressure of A can be determined from Eq. [2] if E or $\Delta\overline{G}$ is known or measured, *viz.*

$$E = -\frac{RT}{nF}\ln\frac{p}{Po} = -\frac{\Delta\overline{G}}{nF} \qquad [7]$$

Thus, Eq. [7] may be used to predict the ease of separating the two metals.

The driving force of the boiling or regeneration step is the difference in partial pressures of A over the alloys at the regeneration and electrochemical cell temperatures, respectively.

The composition of the stripped alloy issuing from the boiler is fixed by the difference in the two operating temperatures. This stripped alloy will have a composition wherein the partial pressure of A at the regeneration temperature equals the partial pressure of A at the electrochemical cell operating temperature. For a particular alloy composition the lowest regenerator temperature is similarly fixed.

The rate at which metal A is vaporized depends on the equilibrium between the rate at which heat can be supplied at the regeneration temperature, the partial pressure of metal A in the alloy at this temperature, the nature of metals A and B, the frictional pressure drop of the vapors in flowing from the hot zone to the cold zone, the vapor pressure of metal A at the cold zone, and the rate at which heat can be rejected at the cold zone temperature. These conditions are beyond the scope of this paper, but can be evaluated by the usual heat transfer measurements.

Experimental Results

Na/Sn *system-emf vs. composition and temperature.*—EMF vs. composition data were found only for 500°C (14). In order to predict vapor compositions, emf data were required for higher temperatures (as close as possible to regeneration temperatures) so that some confidence could be expected from data extrapolated to those temperatures where emf measurements are too difficult to make. Also the data would show the operating characteristics of a cell. These characteristics are necessary for systems and engineering analysis.

Four separate cells were used for the emf measurements. Each cell contained a different alloy composition and the four compositions were sufficient to cover the operating range of the projected electrochemical cell. Each cell consisted of two concentric Pyrex tubes as shown in Fig. 1 held apart by a neoprene rubber stopper. About a 5 cm depth of Na was placed in the inner tube and 6 cm of alloy in the outer tube. Hence, the inner glass tube container wall acted as the cell electrolyte. This technique has been thoroughly tested by Delamarski and others (15). A stainless steel cylinder 2.5 cm ID x 6 cm long was placed around the bottom of the cell in order to minimize deformation at temperatures approaching 700°C. The inner tube was closed also with a neoprene rubber stopper through which protruded the thermocouple sheath and the glass tube connected by rubber tubing to a N_2 manifold which furnished an inert atmosphere for both halves of the cell. All four cells were immersed together about 6 cm inside a Cenco-Cooley, electric furnace,[1] whose inside temperature was thermostatically controlled to ±1°C.

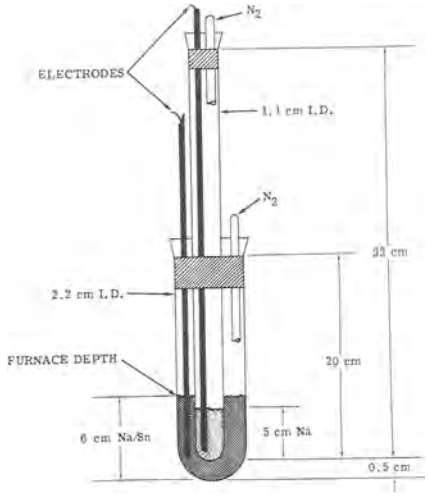

Fig. 1. Na/Sn emf cell

The temperature of each cell was measured by means of a stainless steel sheathed thermocouple immersed in the Na and which served also as the external lead from the Na. The cell temperature varied no more than ±0.5°C with time at any set point. The lead to the alloy pool was a tungsten wire.

The cell temperature was changed in 20°-25° steps and at each temperature the voltage was allowed to stabilize indicating temperature equilibrium before readings were taken. At this time, the voltage remained constant within ±1.0 mv for periods of 45 min to 1 hr. Recordings were made both on ascending and descending temperatures between 475° and 600°C. The potentials at ascending temperatures, only, were used between 600° and 700°C, because there appeared to be a slight attack of Na on the glass between 650° and 700°C. Delamarski (15) showed that a Pyrex-type glass is unattacked up to 500°C, and this work has found this to be true up to 600°C. Other materials in contact with either liquid metal were not attacked.

All voltages were read on a model 803 Fluke meter.[2] This is a precision AC/DC differential voltmeter electronically balanced, and is capable of being used on external impedances of 1-10 megohms.

The arithmetic average potentials at each composition and temperature are shown in Table I and the activity as calculated by Eq. [2].

Below 500°C the Fluke meter appeared to operate sluggishly and the spread between readings was wide. Apparently, the impedance became too high.

[1] Cenco catalog No. 13627, 700 watt.

[2] John Fluke Manufacturing Company, Seattle, Washington.

Table I. EMF and activity vs. temperature and composition

	Composition (mole fraction)							
	0.136		0.225		0.263		0.40	
Temp, °C	emf	Activity ($\times 10^3$)	emf	Activity ($\times 10^3$)	emf	Activity ($\times 10^3$)	emf	Activity ($\times 10^2$)
470	0.443	—	0.411	—	0.375	—	0.322	—
472	0.438	—	0.408	—	0.373	—	0.318	—
478	0.427	—	0.391	—	0.360	—	0.310	—
505	0.427	1.72	0.387	3.12	0.358	4.82	0.295	1.23
524	0.427	2.00	0.385	3.69	0.356	5.59	0.286	1.55
542	0.431	2.15	0.383	4.27	0.357	6.24	0.285	1.73
550	0.428	2.40	0.382	4.58	0.354	6.77	0.275	2.06
571	0.431	2.68	0.380	5.35	0.354	7.69	0.280	2.13
575	0.430	2.78	0.379	5.00	0.353	7.96	0.280	2.16
608	0.431	3.41	0.378	6.91	0.351	9.81	0.274	2.73
607	0.437	3.16	0.381	6.01	0.355	9.34	0.277	2.59
625	0.435	3.62	0.378	7.57	0.353	10.52	0.280	2.70
653	0.437	4.18	0.376	8.94	0.351	12.30	0.278	3.07
675	0.439	4.61	0.377	9.94	0.351	13.61	0.278	3.33
702	0.443	5.10	0.378	11.10	0.353	15.01	0.278	3.62

				550°	565°	600°
$\Delta E/\Delta T$	$+0.22 \times 10^{-4}$	-1.04×10^{-4}	-0.76×10^{-4}	−1.46	−1.16	-0.18×10^{-4}
$\Delta\bar{S}$Na	+0.53	−2.40	−1.75	−3.36	−2.67	−0.41
$\Delta\bar{S}$Na (Lit)	−1.56	−1.59	−1.57	−2.68 (500°)		

Since only data at higher temperatures were of interest here, only the results above 500°C were used. Except for the 0.40 mole fraction curve, all the other constant composition points could possibly be connected linearly in an emf *vs.* temperature plot not shown here for sake of brevity. In all cases, above 575°C, the curves appeared to be linear.

The slope of the straight line portion for each composition is given at the bottom of Table I as $\Delta E/\Delta T$. In the case of 0.40 mole fraction, the slope of tangents at three temperatures was taken. From the calculated slopes for these compositions, the $\Delta\bar{S}_{Na}$ was calculated and compared with the literature value (14) at 500°C. Agreement was within 50% at 0.225 mole fraction Na and 10% at 0.263, but a large divergence appeared at the lowest concentration. The reason for this is not known, but it appears certain the discrepancy is not experimental error. A positive $\Delta E/\Delta T$ has been obtained at approximately this composition in four separate measurements using other cell designs.

The discrepancy at 0.40 mole fraction Na may be due to a phase change. The solid-liquid phase diagram (14) shows a high melting intermetallic compound at about this composition which starts to separate out at about 500°C. Thus, the entropy should show an uncertainty at this composition. The marked departure from linearity of the emf-temperature curve at this composition in contrast to the others indicates this. Also Fig. 6 shows a change in mechanism at about 540°C, the intersection of the two straight line portions of the log a *vs.* $1/T$ plot for 0.40 mole fraction Na. The other compositions yield linear plots over the whole temperature range used.

In Fig. 2, the experimentally determined potentials are compared with the best literature data (14) at 500°C which is the only temperature reported for the NaSn system in the literature. Because the agreement appears good here it is felt that the new emf data up to 700°C should be reliable (also see Fig. 6).

These data show that an electrochemical cell containing a Na anode and a Na-Sn alloy cathode can be operated between the cathode alloy composition limits of 15-30 mole % Na at an open circuit voltage of 0.42-0.36v at 500°C and 0.43-0.33v at 700°C.

Cell studies using a fused salt electrolyte reported in a separate paper (16) have confirmed the above emfs, theoretical predictions of negligible polarization losses, and showed that all losses were resistive.

Regeneration

Distillation of Na from Sn was accomplished in the apparatus shown in Fig. 3. Approximately 150g of molten alloy was forced, under argon, into the boiler section through the inlet tube, after which it was welded shut. The whole system was placed in a furnace and completely evacuated. The regenerator was shut off from the vacuum system and tested for

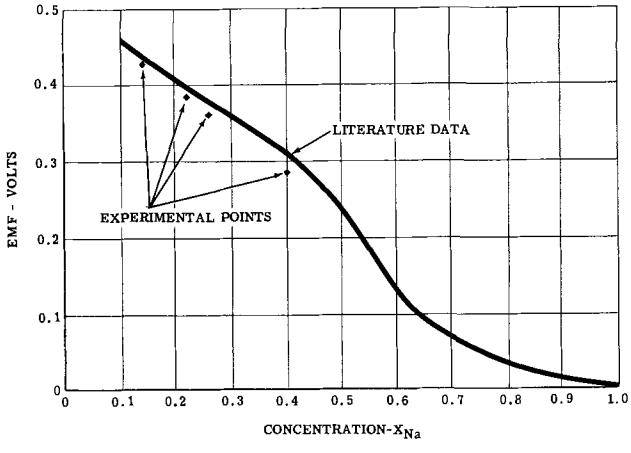

Fig. 2. Emf *vs.* concentration at 500°C. Literature data from ref. (14).

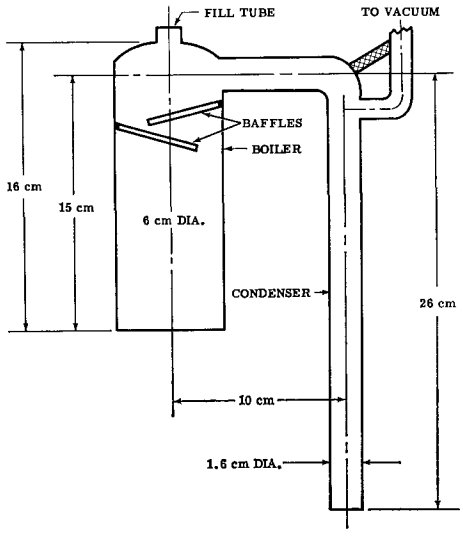

Fig. 3. Experimental still

leaks. If no leaks were present the furnace was turned on. The two halves of the furnace were controlled separately so that the boiler temperature was maintained at the desired point and the condenser tube at the contemplated cell operating temperature of 650°C.

When the operating temperatures were reached, x-ray photographs were made of the condenser tube through a slit provided in the furnace, first at 5 min intervals and then 10 min as the rate slowed down toward the end of the distillation. The height of the sodium in the condenser tube was measured in the x-ray photograph and from the dimensions of the tube, the volume and weight of the collected sodium were calculated.

The results of these distillations are shown in Fig. 4 and Table II. For all practical purposes the distillation was stopped after 90 min since the distillation rate was so slow as to cause but very little change in the composition of the remaining alloy. The 1038°C run was terminated at 75 min by a puncture of the boiler. The Na collected (column 2)

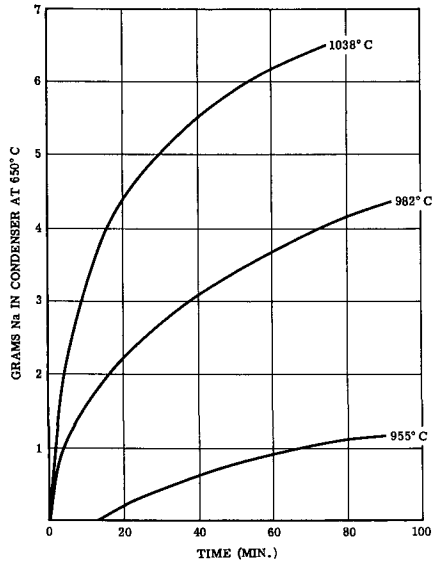

Fig. 4. Na distilled from 8% (wt) or 31% (mole) alloy; 150g alloy in still at start.

Table II. Na distillation results

Analysis of products after 90 min distillation; original alloy, analysis, 8% by weight; 0.31 mole fraction; condenser temperature, 650°C

Still temp, °C	Wt Na collected, g	Analysis, wt %	Final comp in still, % Na Wt	Mole	Calculated comp from Na loss to condenser, % Na Wt	Mole
955	1.6		7.16	28.4	7.0	28.0
982	4.5	0.13% Sn	5.64	23.5	5.20	22.1
1038*	6.1	0.20% Sn	3.30	15.0	4.0	17.8

Note: No Na collected in ½ hr at 900°C.
* 75 min run.

was subtracted from the 150g sample and also from the original 12g (150 x 0.08) Na contained in the alloy. On the basis of the remaining Na content and sample weight, the compositions in the last column of Table II were calculated. These data show that Na can be effectively separated from Sn in an 8% (wt) 31% (mole) Na/Sn alloy at temperatures above 955°C. At approximately 1000°C an alloy of approximately 3.3% (wt) 15% (mole) remained in the boiler. This means that the operating range of the electrochemical cell is limited to some extent, since this would be the cathode alloy returned to the cell during regenerative operation. However, at distillation temperatures of approximately 1100°C or above, alloys below 3% (wt) Na will be obtained from the still, greatly enhancing the cell operating range. This places the Na/Sn system in a high temperature operating range.

Experimental Regenerative Cell

Figure 5 shows a drawing from an x-ray negative of a regenerative Na/Sn cell which ran regeneratively for a short while before the metal to ceramic seals were corroded away by the hot Na vapor. This drawing shows the level of the 8% (wt) Na/Sn alloy right before the run. At this stage no Na was in the inner cup. The inner cup also acted as electrolyte and was made of porous alumina impregnated with a NaCl-NaI eutectic melting at 575°C. The cell to the right was maintained at 625°-650°C in a furnace and the regenerator to the left at 1000°C.

During the first 5-10 min no power was obtained until enough Na boiled over and condensed into the

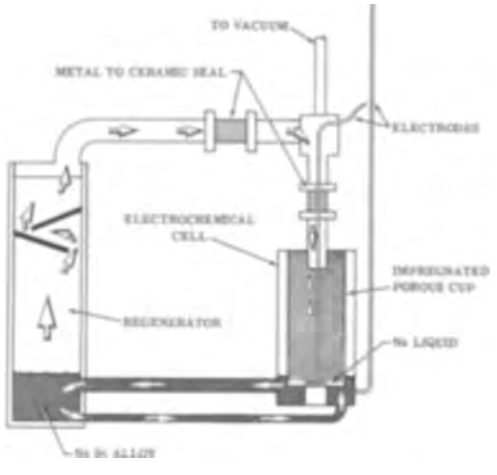

Fig. 5. Thermally regenerative cell system

cup to contact the electrode lead. Power was drawn for about 15 min at 0.3v and 0.1 amp until the seals failed. The cell was sectioned and examined after the run and about a 0.5 cm depth of Na was found in the cup indicating that Na distilled over into the cup allowing the cell to operate regeneratively.

Discussion of Results

In Fig. 6, the data of Table I are plotted as log activity of Na *vs.* the reciprocal of absolute temperature. Activity values were calculated from Eq. [2].

The obvious linearity of the points at constant composition lent credence to the reliability of the data and appear to indicate a continuance of the same reaction mechanism at increasing temperatures. Thus, the extrapolation to higher temperatures in order to obtain partial pressure data appears safe and reasonable. As pointed out previously, a change in reaction mechanism occurred at 540°C for the 0.40 composition. In this case, only the linear portion above 540°C was used for extrapolation.

The partial pressure of Na above the various alloys was calculated using the data of Fig. 6 and the definition of activity ($a = p/Po$). At any composition and temperature the activity was read from Fig. 6. The vapor pressure of pure Na at that temperature was obtained from ref. (13). The product of activity and pure Na vapor pressure gives the vapor pressures of Na above the alloy listed in Table III. In spite of the extrapolation, it was surprising how closely the regeneration data could be predicted. The vapor pressure of Na had to exceed 53 mm Hg (vapor pressure of pure Na in the condenser) (13) in order for any distillation to occur. Table III shows that a temperature of about 1000°C was necessary as was shown in the experimental distillation data.

Further confirmation was obtained by using the compositions of the alloys which remained in the still (Table II column 4). These alloys (repeated in column 2 Table IV) should exhibit a Na partial pressure equal to that of pure Na at the condenser temperature. In column 3 of Table IV the calculated condenser temperatures are given corresponding to the Na partial pressures of these alloys. These temperatures were calculated as follows: (i) the activity of Na at the still temperature was read from Fig. 6 by interpolating between the composition curves; (ii) the partial pressure of Na was obtained as the product of activity and vapor pressure of pure Na at the still temperature; (iii) the condenser temperature was obtained from ref. 13 and corresponded to the temperature at which the vapor pressure of pure Na equalled the calculated partial pressure of step (ii).

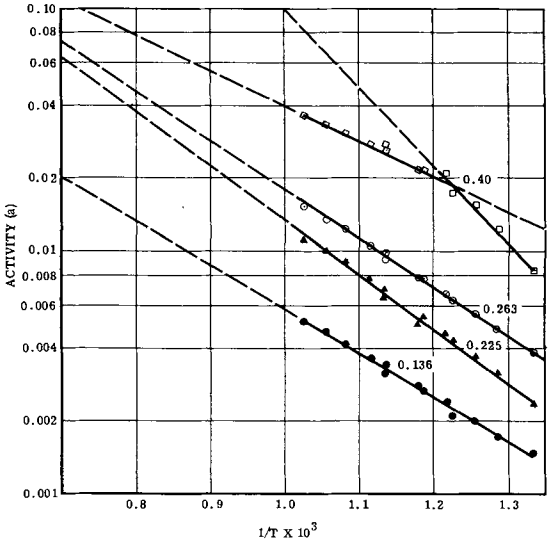

Fig. 6. Activity of Na *vs.* temperature at indicated mole fraction Na in alloy.

Table III. Calculated vapor pressure of Na

Vapor pressure (mm Hg) at composition (mole fraction)

Temp, °C	0.136	0.225	0.263	0.40
700	0.54	1.197	1.65	3.73
800	2.58	6.37	8.34	16.68
900	9.50	25.08	31.68	57.2
1000	28.12	79.20	97.02	160.38
1100	70.2	214.5	249.6	382.2

Vapor pressure pure Na at 650°C (average condenser temperature) is 53 mm.

Table IV. Distillation data

Comparison of calculated with experimental; 150g-0.31 mole fraction Na; condenser temperature 650°C

Temp still, °C	Na content, residue in still, mole fraction	Calculated condenser temperature	Na content, calculated from emf data
955	0.284	668	0.244
982	0.235	670	0.20
1038	0.150	650	0.15

These temperatures compare favorably with the actual 650°C temperature used. Conversely, in the last column the calculated compositions of the still residues are given corresponding to a pure Na vapor pressure of 53 mm Hg at 650°C. The still residue composition was calculated as follows: (i) the activity was calculated as the ratio of 53 to the vapor pressure of pure Na at the still temperature (13); (ii) the composition was read from Fig. 6 at the intersection of this activity with the still temperature by interpolating between the composition curves. The agreement with experiment (columns 2 and 4) is quite good considering the extrapolation errors and the fact that equilibrium most certainly was not completely established as shown by the small remaining curvature of the curves in Fig. 4 at the completion of the experiment.

These results indicate that for Na/Sn at least the data follow predictions and that emf data can be used to project distillation data. By these means operating data for other liquid metal systems should be predictable.

It is beyond the scope of this paper to present a detailed electrochemical engineering systems analysis. Such an analysis (17) has been made, however, based on the cell described in ref. 16. Conductivity and thermodynamic data in the literature and the cell data described herein and in ref. 16 were used. It was found that the over-all efficiency (thermal to electrical energy) was about 16% compared to a

Carnot efficiency of 32%. The cell operated at 0.32 w/cm^2, at which point it had a specific power rating of about 140 w/kg.

Conclusions

It has been shown, both theoretically and experimentally, using a Na/Sn alloy as an example, that the operation of a thermally regenerative liquid-metal power system is feasible.

For Na/Sn alloys, at least, theoretical predictions were confirmed by experiment.

Emf data for the Na/Sn system was extended from 500° to 700°C. Extrapolation to higher temperatures seemed reasonable since the extrapolation checked with distillation data. However, the extrapolated emf's should be confirmed by actual measurement if experimental difficulties can be overcome.

No doubt other practical or feasible alloy systems are possible. However, the scarcity of applicable emf and vapor liquid data seriously hamper the search. Further research is needed in these areas.

Acknowledgments

The author is indebted to H. R. Karas for much of the emf measurements and to D. L. Austermiller for the distillation measurements. He wishes to thank the management of the General Motors Corporation for permission to publish this investigation.

Manuscript received Jan. 11, 1962; revised manuscript received July 1, 1963. This paper was presented at the Boston Meeting, Sept. 16-20, 1962.

Any discussion of this paper will appear in a Discussion Section to be published in the June 1964 JOURNAL.

REFERENCES

1. E. Yeager, Proceedings 12th Annual Battery Research and Development Conference, Asbury Park, N. J., 1958, pp. 2-4.
2. W. G. Caple and E. L. Shriver, "Thermally Decomposable Inorganic Compounds," ACS #1, Allison Div., General Motors Corporation, Indianapolis, Ind., 1960.
3. James King, Jr., F. A. Ludwig, and J. J. Rowlette, "Energy Conversion for Space Power," pp. 387-410, Academic Press, New York (1961).
4. R. E. Shearer, *et al.*, Proceedings 14th Annual Power Sources Conference, p. 76, 1960.
5. H. A. Liebhafsky, *This Journal*, **106**, 1068 (1959).
6. J. B. Friauf, *J. Appl. Phys.*, **32**, 616 (1961).
7. A. J. deBethune, *This Journal*, **107**, 937 (1960).
8. R. E. Henderson, B. Agruss, and W. G. Caple, "Energy Conversion for Space Power," p. 411-423, Academic Press, New York (1961).
9. H. A. Laitinen, R. P. Tischer, and D. K. Roe, *This Journal*, **107**, 546 (1960).
10. O. Kubaschewski and E. LL. Evans, "Metallurgical Thermochemistry," pp. 6-72, Pergamon Press, New York (1958).
11. Iu. K. Delimarskii and B. F. Markov, "Electrochemistry of Fused Salts," p. 271, The Sigma Press, Washington, D. C. (1961).
12. Iu. K. Delimarskii, *ibid.*, p. 251.
13. C. J. Smithells, "Metals Reference Book," vol. II, p. 613, Interscience Publishers Inc., New York (1955).
14. Selected Values for the Thermodynamic Properties of Metals and Alloys, Minerals Research Lab., Institute of Engineering Research, University of California, Berkeley, Calif., 1959.
15. Iu. K. Delimarskii, *op. cit.*, p. 159.
16. R. D. Weaver, S. W. Smith, and N. L. Willmann, *This Journal*, **109**, 653 (1962).
17. S. W. Smith and R. D. Weaver, Report No. 4337-E Delco-Remy Division, General Motors Corp., March 1962.

Oxidation Kinetics of $ZrBe_{13}$ and $NbBe_{12}$

Guy Ervin, Jr., and Mark M. Nakata

Atomics International, A Division of North American Aviation, Canoga Park, California

ABSTRACT

Oxidation rates of the intermetallic compounds $ZrBe_{13}$ and $NbBe_{12}$ between 700° and 1500°C have been measured in oxygen by a volumetric method, using granular metal samples of known surface areas determined by a gas adsorption method. Oxidation of $ZrBe_{13}$ between 900° and 1500°C produced a BeO layer; the thickening of the oxide layer with time followed a parabolic law and showed activation energies similar to those for beryllium metal oxidation. At 600°-700°C, $ZrBe_{13}$ oxidized at an accelerating rate accompanied by disintegration of the metal phase, and this behavior was similar to beryllium metal oxidation at 700°-750°C. $NbBe_{12}$ did not show disintegrative oxidation, but showed other complexities. The relation of the parabolic oxidation constants to self-diffusion and to the defect structure of BeO is discussed. A tentative conclusion is that transport through the BeO layer depends chiefly on diffusion of Be^{+2} vacancies formed at the oxide-oxygen interface.

Refractory metal beryllides have been under study (1, 2) in recent years as potential lightweight structural materials with good oxidation resistance at temperatures from 1000° to 1500°C. However, it is now known that beryllides sometimes show what is called "pest" oxidation (3), a form of catastrophic oxidation occurring at intermediate temperature, below 1000°C, and shown by other intermetallic compounds such as silicides and aluminides.

The present report covers an experimental study of the oxidation behavior of two beryllides, $ZrBe_{13}$ and $NbBe_{12}$, principally at temperatures above 1000°C where more normal protective oxidation is found. Oxidation of beryllides holds added interest

by virtue of the fact that the oxide film which grows on the beryllide surface is principally BeO, and for this reason, oxidation of beryllides has similarities to the oxidation of beryllium metal. Comparison of intermetallic oxidation behavior with that of the pure metal yields new information about the fundamentals of the oxidation process. Furthermore, since oxidation involves transport of defect species through the oxide layer, beryllides permit studying transport processes through BeO at temperatures higher than the melting point of beryllium metal.

Kinetic data on beryllium metal oxidation (4-6) have been fitted to the parabolic law. However, several reports of recent work (7-10) have shown that this protective behavior occurs only during an initial period of varying length, after which acceleration and catastrophic failure occur, similar to the behavior of the beryllides.

Experimental Information

Apparatus.—Oxygen absorption by the beryllide samples was measured by a volumetric method which incorporated some novel features necessitated by the requirement of operation at a temperature of 1500°C or higher. To reach these temperatures, the furnace had to be located inside a gastight chamber. Because the volume change during a run had to be only that due to oxygen absorption by the sample, the heating element had to be inert to oxygen, and the average temperature of the entire chamber had to be constant during a run.

These requirements were met by the apparatus shown in Fig. 1, consisting of a tube furnace wound with Pt-20% Rh wire, the entire furnace being mounted inside an enclosure consisting of a silica tube which was connected to a mercury-filled burette. To keep the greased joint cool and to maintain volume constancy, the silica tube, including the joint, was immersed in a constant-temperature water bath kept at about 20°C by water cooling. The sample was contained in an alumina crucible 1¼ in. long and ¼ in. OD, fastened to the end of a Pt-20% Rh vs. Pt-40% Rh thermocouple. The furnace was insulated with mullite fiber (Fiberfrax) and by an evacuated silica jacket. Furnace and sample together were suspended from the removable cap, through which the furnace winding leads and thermocouple passed to the outside, using glass-to-metal seals. The shape of the silica tube was designed to give a convectional circulation of gas past the sample.

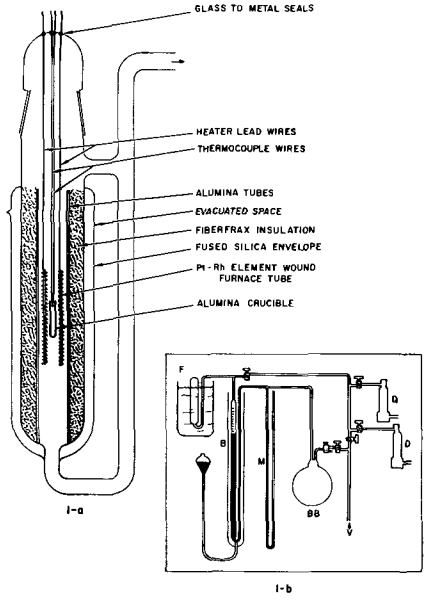

Fig. 1. Volumetric apparatus for studying oxidation kinetics to 1600°C.

For gas volume measurement a burette U-tube was attached, the calibrated arm leading to the furnace and the opposite arm to a ballast bulb filled with gas at the operating pressure. The furnace space was kept at constant pressure during a run by balancing the mercury columns in the burette with the leveling bulb and at the same time measuring the height of the mercury columns (using a cathetometer not shown in the figure). The change in height corresponded to a volume of oxygen absorbed by the sample, a volume measured at the temperature of the burette. Actual readings during a run were made most conveniently by setting the leveling bulb at a point such that the right column of mercury was slightly higher, then noting the time at which the upward moving left column reached the same level.

It was possible to make one or two runs a day, with oxidation periods per run of 2-4 hr. Precision in the measurement of the volume of oxygen absorbed was ±0.05 mg oxygen at 0.1 atm, which was of the order of ±1 $\mu g/cm^2$ of sample surface. However, a much larger error was introduced by fluctuations in specific surface area due to sampling, and this was the probable cause of most of the over-all deviation of ±10% (see Fig. 4).

The Pt-20% Rh *vs.* Pt-40% Rh thermocouple was calibrated prior to its use and again near the end of the oxidation runs. During operation, the thermocouple and sample were symmetrically placed with respect to the midpoint of the furnace; hence both were expected to be at nearly the same temperature. By actual measurement, the sample position was found to be 8°C hotter than the thermocouple at 1300°C. On this basis, an 8°C positive correction was applied to all temperatures reported.

The question of possible reaction of oxygen with platinum and rhodium deserves mention although this caused no difficulty. Actually, oxygen does react with platinum above 1000°C to give a volatile oxide, but this decomposes on a cooler surface and reforms Pt and O_2 with no net oxygen absorption. The absence of this or any other absorption effect was shown by several blank runs in which the volume change was followed while heating an empty crucible. The total change corresponded to about 0.2 mg of oxygen.

Each run was ended by shutting off the power to the furnace, which then cooled quickly, and at the same time, the remaining oxygen was pumped out. The weight of sample after completion of the run provided an independent measure of oxygen absorbed. The weight figure was always higher than the volume figure by 1-3 mg, depending on the temperature, and it was shown that this weight gain occurred in the first minute. The discrepancies may

Table I. Spectrographic analysis of $ZrBe_{13}$ and $NbBe_{12}$

Constituent	$ZrBe_{13}$, ppm	$NbBe_{12}$, ppm
Al	225	2100
Ca	125	75
Fe	300	450
Si	300	675
C*	650	460

* Determined by chemical analysis.

have been due to brief temperature excursions lasting only a few seconds during the first minute, and caused by heat of reaction. This would have resulted in high oxygen absorption and weight gain prior to the first volume measurement of the run.

Other volumetric and manometric procedures for studying metal oxidation have been summarized by Evans (10), and a recent elegant apparatus is described by Porte *et al.* (11), but none of these is suitable for temperatures above 1000°C.

Materials.—Both $ZrBe_{13}$ and $NbBe_{12}$ are definite intermetallic compounds of known crystal structure and are made commercially by heating mixtures of the elements in vacuum. Granular $ZrBe_{13}$ and $NbBe_{12}$ were purchased from Brush Beryllium Company, designated 20 to 100 mesh. Oxygen content was stated to be in the neighborhood of 1.5% expressed as BeO. Principal impurities found spectrographically are shown in Table I.

In order to use a material with more reproducible size and surface area for the series of runs, each material was screened further, and the 30-60 mesh portion was used. The surface areas of these samples were measured by krypton adsorption [an adaptation by Smith (12) of the conventional BET gas adsorption method], finding 200 ± 20 cm^2/g for $ZrBe_{13}$ and 450 ± 50 cm^2/g for $NbBe_{12}$.

Use of granular samples instead of solid bars has several advantages: a much higher sensitivity is achieved because of the relatively large specific surface area, a true surface area is measured, and no surface preparation is required.

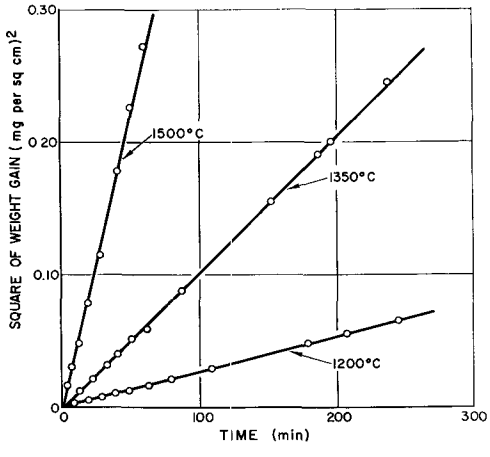

Fig. 2. Parabolic plot of $ZrBe_{13}$ oxidation in 0.1 atm oxygen; $W^2 = K_p t$.

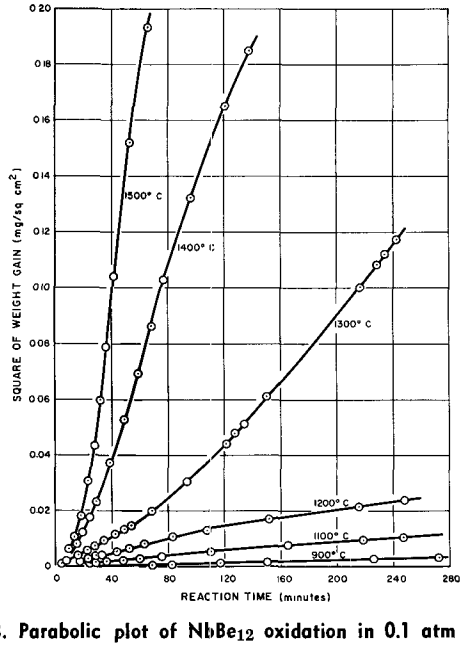

Fig. 3. Parabolic plot of $NbBe_{12}$ oxidation in 0.1 atm oxygen

Results

Oxidation rates.—For the most part the data fitted a parabolic law for $ZrBe_{13}$ between 900° and 1500°C and for $NbBe_{12}$ between 900° and 1300°C, but there were deviations during the first few minutes and breaks in the $NbBe_{12}$ oxidation curves after about 100 min. The agreement of the present data with a parabolic law may be judged from the straight lines shown in Fig. 2 and 3 where the square of the weight gain is plotted against time. At 1400° and 1500°C, $NbBe_{12}$ gave S-shaped curves instead of straight lines on this type of plot. The rate constants taken from the curves of Fig. 2 and 3 are given in Table II.

Data for a series of runs on $ZrBe_{13}$ at 1300°C are shown in Fig. 4 as an indication of reproducibility. The spread is probably due mostly to sampling error, as mentioned previously.

Curves showing the temperature dependence of these parabolic rate constants (*i.e.*, the data of Table II) are given in Fig. 5 for $ZrBe_{13}$ and in Fig. 6 for $NbBe_{12}$. These are Arrhenius-type plots, *i.e*, log

Table II. Parabolic oxidation rate constants for $ZrBe_{13}$ and $NbBe_{12}$ in 0.1 atm of dry oxygen

Material*	Temp, °C	Rate constant ($g^2\ cm^{-4}\ min^{-1}$) × 10^{10}
$ZrBe_{13}$	908	0.41
$ZrBe_{13}$	1008	0.65
$ZrBe_{13}$	1108	0.93
$ZrBe_{13}$	1208	2.0
$ZrBe_{13}$	1258	3.15
$ZrBe_{13}$	1308	5.7
$ZrBe_{13}$	1308	7.4
$ZrBe_{13}$	1308	6.6
$ZrBe_{13}$	1308	6.25
$ZrBe_{13}$	1350	8.7
$ZrBe_{13}$	1400	18.8
$ZrBe_{13}$	1500	40.0
$NbBe_{12}$	908	0.13
$NbBe_{12}$	1108	0.45
$NbBe_{12}$	1208	1.3
$NbBe_{12}$	1308	2.0

* Granular samples, screened through 30 mesh on 60 mesh.

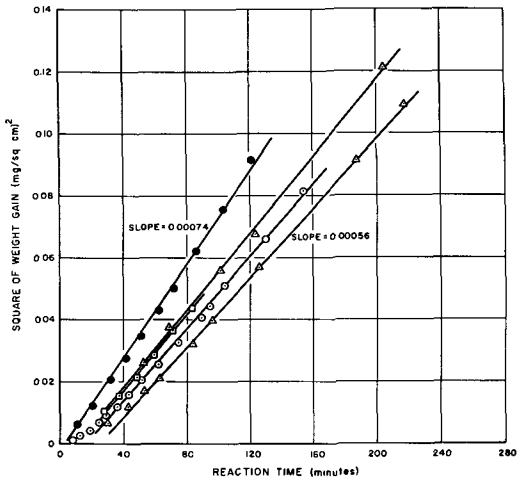

Fig. 4. Reproducibility of oxidation of $ZrBe_{13}$ at 1300°C in 0.1 atm oxygen.

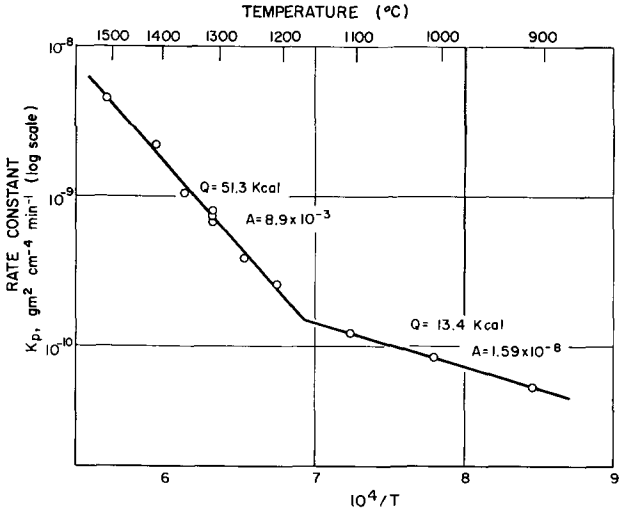

Fig. 5. Arrhenius plot of $ZrBe_{13}$ oxidation in 0.1 atm oxygen; $K_p = Ae^{-Q/RT}$.

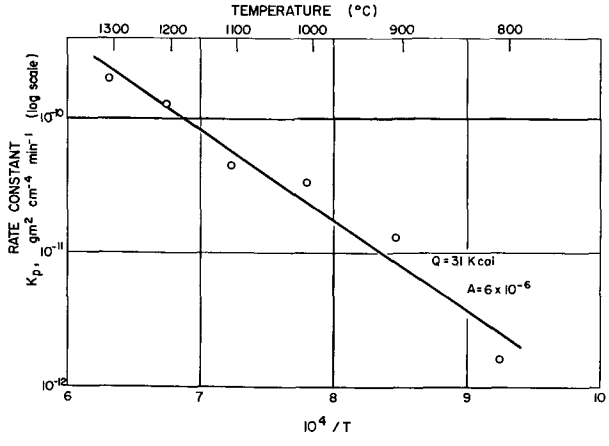

Fig. 6. Arrhenius plot of $NbBe_{12}$ oxidation in 0.1 atm oxygen; $K_p = Ae^{-Q/RT}$.

k *vs.* $1/T$, and from the slopes a value for Q is obtained, according to the equation

$$k = A\, e^{-Q/RT} \qquad [1]$$

The value of Q is considered to be an activation energy for the rate-controlling process. For $NbBe_{12}$, protective oxidation prevailed over a temperature range extending as low as 700°C.

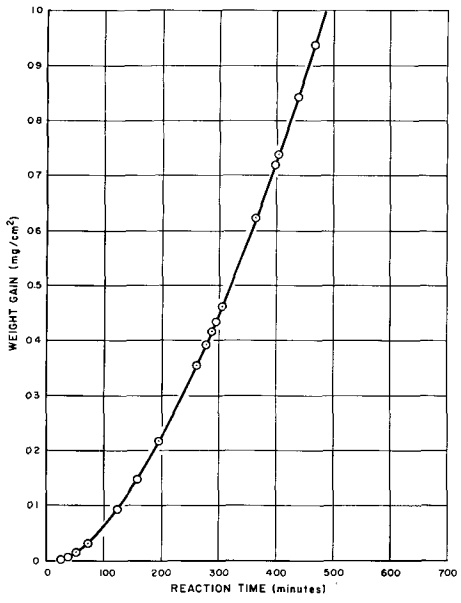

Fig. 7. Low-temperature accelerating oxidation of $ZrBe_{13}$ in 0.1 atm oxygen.

At 600°-700°C, the oxidation rate of $ZrBe_{13}$ accelerated as shown in Fig. 7. The direct cause of the acceleration in rate was fracture and disintegration of the metal phase causing a continual increase in the exposed metal surface area. In other experiments, even massive chunks of $ZrBe_{13}$ heated in oxygen at 700°C were completely oxidized in 2 or 3 days and reduced to a powder. In the early stages of oxidation, the powder consisted of metal particles surrounded by oxide. The completely oxidized powder was an intimate intergrowth of BeO and cubic ZrO_2.

For $ZrBe_{13}$ at 800°C, the oxidation rate was parabolic but much faster than at 900° and about equal to that at 1200°C. Perhaps fracture of the surface occurred at first, and the subsequent parabolic rate was thus higher than normal because of the higher surface generated in the early stages.

Subsequent to the completion of this work, low-temperature disintegration of $ZrBe_{13}$ has been reported by Paine *et al.* (13) and by Perkins (14), and similar behavior of a number of intermetallic compounds has been reported by others (3). The phenomenon is similar to "$MoSi_2$ pest," which has been known for several years.

Data on beryllide oxidation have been reported by Chubb and Dickerson (15) who give only percentage weight gain after an hours' heating at successively higher temperatures using solid chunks of $NbBe_{12}$ and $ZrBe_{13}$. These data cannot be translated quantitatively into rates per unit surface area but are not far from the present results, although on the high side. For $ZrBe_{13}$ at 700°C, these authors found the same disintegration as reported here for $ZrBe_{13}$ although they concluded erroneously that this would also take place at any higher temperature.

More extensive data on many beryllides have been reported by Paine, Stonehouse, and Beaver (1). While their data are in all cases higher, most of the differences can be attributed to the actual surface areas of their samples being appreciably higher than

Table III. Comparison of the oxidation rate constants for solid bars with those for granular samples

Temp, °C	Parabolic rate constants, $g^2\ cm^{-4}\ min^{-1} \times 10^{10}$ Solid bars	Granular (from Fig. 4)
1350	43	9.0
1490	60	35
1540	190	53

Table IV. Variation of oxidation rate with pressure

O_2 pressure, atm	Parabolic rate constant $(g^2\ cm^{-4}\ min^{-1}) \times 10^{10}$
0.00013	1.2
0.014	3.6
0.05	6.8
0.10	6.8, 7.3, 8.0
0.50	8.5, 9.7

the geometrical areas they assumed. More recent work by these authors on $ZrBe_{13}$ oxidation at 1260° and at 1372°C for 100-hr periods gave slopes of 1/3 and less on a log-log plot (13), indicating that oxidation approximated a cubic law rather than parabolic. One possibility is that the surface roughness is gradually smoothed out during the long oxidation period, which would be an additional factor causing the rate to slow down.

Oxidation of solid bars.—Some experiments on oxidation of polished bars of $ZrBe_{13}$ provide further information on the nature of the process. Measurement of oxidation rate using a thermogravimetric balance confirmed the parabolic behavior and showed rate constants 2-5 times as high as those found on granular materials (Table III).

The differences might be accounted for by surface roughness of the polished samples. The data on granular samples take into account surface imperfections by using the BET surface areas.

The oxidation runs on solid bars above 1500°C showed a type of breakaway behavior which was probably caused by breakdown of the oxide coating, but the new rate was again parabolic with a higher constant. Not enough runs were made to indicate reproducibility of this behavior, but in one case it occurred at about 1 mg/cm^2 weight gain or an oxide thickness of about 5μ.

One possibility is that strains caused by the high oxide-metal volume ratio (about 1.5) was responsible for the breakaway. A further indication of strain was the spalling of the oxide coat on cooling. This was more pronounced for rough-surfaced specimens than for highly polished ones, presumably because a rough surface produces more oxide per unit geometric surface area. However, other explanations for spalling should be considered, such as the formation of sublayers of a new intermetallic phase beneath the oxide.

A polished section across the oxide layer on a $ZrBe_{13}$ bar oxidized for 5 hr at 1320°C is shown in Fig. 8, and the photomicrograph reveals that besides the main oxide layer there are two thin sublayers, one metallic and one oxidic. By examination of spalled-off oxide, the outer layer, about 20μ thick, was identified by x-ray as BeO, with no other phases showing up. The photomicrograph shows another oxide layer of about 5μ thickness under the top BeO

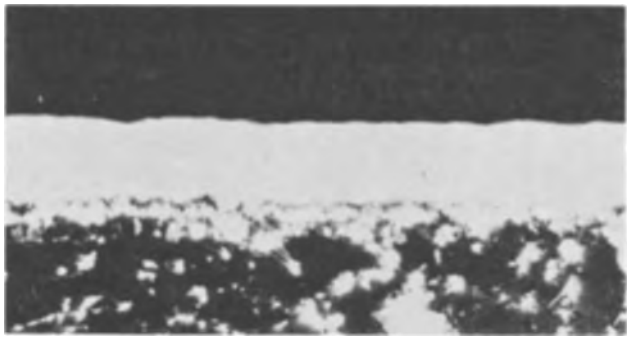

Fig. 8. Photomicrograph of polished cross section of surface layers on oxidized $ZrBe_{13}$. Crossed Nicols. Three layers are distinguishable above the original $ZrBe_{13}$ metal phase, which have been identified as Zr_2Be_{17}, cubic ZrO_2, and BeO. The BeO layer, the thick white one on top, is about 20μ thick. Magnification 500X.

layer, and under this 5μ thick layer, an anisotropic metallic layer of about the same thickness. Since x-ray of the coated surface showed cubic ZrO_2 and Zr_2Be_{17} in addition to BeO and $ZrBe_{13}$, it is indicated that these layers are cubic ZrO_2 and Zr_2Be_{17}, respectively.

Effect of water vapor.—Because BeO is known to react with H_2O at high temperatures to form gaseous beryllium hydroxide, it seems probable that in moist oxygen the rate of oxidation would be increased because of a tendency to remove the protective BeO film. Oxidation of $ZrBe_{13}$ at 1400° and 1500°C with oxygen at 0.1 atm saturated with water at room temperature gave parabolic rates showing that a protective oxide film was formed in spite of the water vapor. The rate was 40% higher at 1400°C and 20% higher at 1500°C than the corresponding rates in dry oxygen. Furthermore, the weight gain of the 1400°C sample was slightly less than the weight of oxygen absorbed, and the weight gain of the 1500° sample was only 60% of the weight of oxygen absorbed, thus consistent with loss of BeO as hydroxide. These experiments were under static conditions and it is probable that in flowing gas the BeO loss would be much greater. Another limitation of the static system for this experiment is that if H_2O is actually consumed by the reaction, it would be gettered to a low value early in the run, due to the large surface area of the granular beryllide relative to the volume of gas in the system.

Effect of oxygen pressure.—Rate constants for $ZeBe_{13}$ oxidation at various oxygen pressures at 1300°C are shown in Table IV.

A log-log plot of these data is shown in Fig. 9, which indicates a slope of one-fourth, meaning that the oxidation rate depends on the one-fourth power of the pressure. Also shown on this graph is the curve for the oxidation rate proportional to the one-sixth power of the oxygen pressure. It will be shown that the latter is consistent with an oxidation mechanism involving formation of cation vacancies at the oxide-oxygen interface. In other work, a similar pressure dependence was found for beryllium oxidation.

Discussion

Oxidation Mechanism

In deriving a theoretical expression for the parabolic rate constant, Wagner (16), Mott, and others

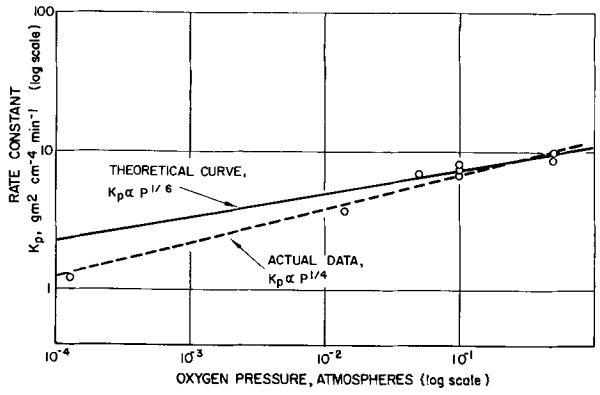

Fig. 9. Effect of oxygen pressure on oxidation rate constant; pressure dependence of oxidation of $ZrBe_{13}$ in oxygen at 1300°C.

(17) considered metal oxidation to depend on the flow of some type of solid state defect (*i.e.*, an interstitial or a vacancy) through the oxide film. Defects are generated at one of the oxide interfaces and annihilated at the other, the concentration of defects at the point of generation being related to the free energy change in the oxidation reaction. The concentration gradient of defects across the film is simply the concentration at the interface (where they are generated) divided by the film thickness, assuming that the gradient is linear and that the concentration at the opposite face is very small.

In BeO it is to be expected that cation mobility will be much greater than anion mobility, because Be^{+2} ion is much smaller than O^{-2} ion, and this expectation has been confirmed by Austerman's measurements (18) of self-diffusion of beryllium and of oxygen in BeO, which show beryllium diffusion to be orders of magnitude greater than oxygen diffusion. Therefore, we shall assume that during beryllide oxidation beryllium ions move outward through a fixed oxygen lattice and that the defects whose flow controls the oxidation rate are cation defects. However, these may be either interstitial Be^{+2} ions or cation vacancies. Interstitial Be^{+2} ions, together with electrons, would be generated at the Be/BeO interface and move outward, while cation vacancies would be generated at the BeO/O_2 interface, plus two electron holes for each vacancy, and these defects would move inward, still with the same result of a net flow of beryllium outward. An indication of which of these mechanisms is the important one in beryllide oxidation may be had from the dependence of oxidation rate on oxygen pressure, as shown by the equations derived below.

A recent derivation given by Jepson (19), when applied to oxidation controlled by diffusion through a BeO film, leads to the following equations showing the relation of rate constant to diffusion coefficient, defect concentration, free energy of reaction, and oxygen pressure:

assuming interstitials,

$$k'_p = 6D_i \left[\frac{n_i}{N}\right] [1 - e^{\Delta F^\circ/6RT} p^{-1/6}] \qquad [2]$$

assuming vacancies,

$$k'_p = 6D_v \left[\frac{n^\circ_v}{N}\right] p^{1/6} [1 - e^{\Delta F^\circ/6RT} p^{1/6}] \qquad [3]$$

where k'_p is the parabolic rate constant in cm^2/sec, D_i the diffusion coefficient for interstitials, D_v the diffusion coefficient for vacancies, $[n_i/N]$ fraction of interstitial Be^{+2} ions present, $[n^\circ_v/N]$ fraction of Be^{+2} vacancies present at 1 atm oxygen, ΔF° the standard free energy change for the oxidation reaction, and p oxygen pressure in atmospheres.

Examining these equations, it should be noted that the exponential part of the expression in brackets is very small because of the large negative value of ΔF° (essentially the free energy of formation of BeO) so that pressure has no significant effect on this term. Hence, the equation for interstitials is independent of pressure, and the equation for vacancies has a 1/6th power dependence on pressure. Qualitatively, the reason for this is that vacancies are generated at the oxygen surface and their concentration depends on oxygen pressure, while interstitials are generated at the Be/BeO interface, unaffected by oxygen pressure. The reason for the exponent of 1/6 is that each O_2 molecule adsorbed on the BeO surface generates two cation vacancies and four electron holes. The data of Table IV and Figure 9 show that the rate varies with the ¼th power of the oxygen pressure, and this may be interpreted as agreement within experimental error, or the deviation may indicate partial dissociation of cation vacancies and electron holes. In either case, the pressure dependence supports the cation vacancy mechanism, and our work on beryllium oxidation now shows a similar pressure dependence which confirms this mechanism for transport through BeO. It will now be shown that the lower activation energy found for $ZrBe_{13}$ oxidation in the low-temperature region is also consistent with the cation vacancy mechanism.

Table V. Comparison of oxidation rate data for $ZrBe_{13}$ with two sets of data for beryllium oxidation

Temperature range, °C	$ZrBe_{13}$ oxidation		Be oxidation (Ervin & Mackay)		Be oxidation (Gulbransen)	
	Activation energy, kcal	*Rate constant, k_p	Activation energy, kcal	*Rate constant, k_p	Activation energy, kcal	*Rate constant, k_p
1170-1550	51.3	10^{-10} to 10^{-8}				
900-1170	13.4	10^{-10}				
700-950			28.7	10^{-13} to 10^{-12}	50.3	10^{-13} to 10^{-11}
500-700			28.7	10^{-14} to 10^{-13}	8.5	10^{-13}
900	‡(51.3)	‡(10^{-12})		10^{-12}		10^{-11}

* Units of k_p are $(g/cm^2)^2/min$.
‡ Extrapolated from the high-temperature branch of Fig. 6.

The break at 1200°C in the Arrhenius plot of $ZrBe_{13}$ oxidation (Fig. 5) is the same kind of break that has often been reported for self-diffusion and for electrical conductivity in oxides and alkali halides and has been attributed to impurities or to short circuiting diffusion paths such as grain boundaries. The occurrence of such a break for $ZrBe_{13}$ oxidation fits well with the impurity hypothesis, the impurity in this case being Zr^{+4} ion substituting for Be^{+2} ion in the BeO lattice, causing an increase in cation vacancy concentration.

Comparison with beryllium oxidation.—Because the oxide film on the surface of oxidizing $ZrBe_{13}$ is essentially BeO just as it is on the surface of oxidizing Be metal, it is pertinent to compare the rates with those for Be metal. An extrapolation of the high-temperature branch of the $ZrBe_{13}$ curve down to the temperatures of Be oxidation shows good agreement with the data of Ervin and Mackay (20) at about 900°C, the upper limit of the Be data. Table V shows this comparison, and in addition, shows data by Gulbransen and Andrew (4) on Be oxidation which agree with those of Ervin and Mackay at about 700°C but show higher rate constants at both higher and lower temperatures.

No interpretation is offered for the various activation energies shown in Table V, other than the comment that the explanation probably lies in the widely varying impurity content among the various samples.

Comparison with Self-Diffusion in BeO

A simple relation between oxidation rate constant for beryllides (or beryllium) and the self-diffusion coefficients in BeO is to be expected if the processes are controlled by similar mechanisms; for example, the activation energies should be similar. Austerman (18) has made measurements of self-diffusion of both beryllium and oxygen in BeO, which indicate that the behavior is quite complex, such that no valid comparisons can be made. Austerman's data were obtained at 1550°C and above, while the data on beryllide oxidation were measured at 1550°C and below. The most that can be said at present is that at 1550°C the self-diffusion coefficients for beryllium are about the same order of magnitude as the oxidation rate constants.

Low-Temperature Catastrophic Oxidation

The occurrence of accelerating rates for $ZrBe_{13}$ has been described and is illustrated in Fig. 7. Since this behavior is an example of "pest" oxidation of intermetallic compounds which is now being widely investigated, some comments on possible mechanisms are appropriate.

Acceleration was due to fracture of the metal phase, exposing increased surface to the reaction, and the oxidation product was an intergrowth of BeO and ZrO_2. The occurrence of this intergrowth at low temperature in contrast with a pure BeO film at higher temperatures suggests that diffusion in the metal phase is so limited at 700°C that Zr and Be oxidize together *in situ*. Fracture of the metal phase occurs because of its brittleness and because of stresses built up by the increase in volume in converting metal to oxide. These effects may be enhanced by preferential growth of oxide in metal grain boundaries.

Work in this laboratory on beryllium oxidation (20) has shown that during the protective stage, pits are formed in the metal under the oxide film and that these pits later cause fracture of the metal phase. Similar pits have been found in $ZrBe_{13}$ after 700°C oxidation, but the many inclusions in the original material obscure the surface features, and it is not yet clear whether the observed pitting leads to fracture.

No disintegration was shown by $NbBe_{12}$ in our experiments. However, Perkins (14) has reported disintegration of $NbBe_{12}$ and Nb_2Be_{17} during oxidation at about 1000°C and reported a variety of observations which indicate that oxidation of these beryllides is quite complex between 700° and 1000°C; and to the extent that they can be compared, our results on $ZrBe_{13}$ are in agreement.

Conclusions

A volumetric method, using a furnace with an internal Pt-Rh heating element, has proved to be very convenient for measuring oxidation rates of granular metal samples at temperatures up to 1500°C.

At 900°C and above, $ZrBe_{13}$ and $NbBe_{12}$ oxidized at diffusion-controlled rates, and the oxide film was essentially BeO, a feature which makes beryllide oxidation similar to beryllium metal oxidation. Analysis of the temperature and pressure dependence of the rates led to the postulate that transport through the BeO layer is due to diffusion of Be^{+2} vacancies formed at the oxide-oxygen interface.

Acknowledgment

This paper is based on studies conducted for the Atomic Energy Commission under Contract AT(11-1), Gen-8.

Manuscript received Jan. 24, 1963; revised manuscript received June 10, 1963. This paper was presented at the Detroit Meeting, Oct. 1-5, 1961.

Any discussion of this paper will appear in a Discussion Section to be published in the June 1964 JOURNAL.

REFERENCES

1. R. M. Paine, A. J. Stonehouse, and W. W. Beaver, WADC-TR-59-29, Parts I and II (February 1959).
2. J. R. Lewis, *J. Metals*, **13** [5], 829 (1961).
3. J. J. Rausch, ARF 2981-4, 8/31/62.
4. E. A. Gulbransen and K. F. Andrews, *This Journal*, **97**, 383 (1950).
5. D. Cubicciotti, *J. Am. Chem. Soc.*, **72**, 2984 (May (1950).
6. M. M. Nakata, NAA-SR-4737 (November 1960).
7. D. W. Aylmore, S. J. Gregg, and W. B. Jepson, *J. Nuclear Mat.*, **2** [2], 169 (1960).
8. W. Bradshaw and E. S. Wright, LMSD 288232, Jan. 1960.
9. J. K. Higgins and J. E. Antill, *J. Nuclear Mat.*, **5** [1], 67 (1962).
10. U. R. Evans, "Corrosion and Oxidation of Metals," Edward Arnold Ltd., London (1960).

11. H. A. Porte, J. G. Schnizlein, R. C. Vogel, and D. F. Fischer, *This Journal*, **107**, 506 (1960).
12. T. Smith, NAA-SR-5319 (Oct. 1, 1960).
13. J. Booker, R. M. Paine, and A. J. Stonehouse, WADD-TR-60-889, April 1961, and WADD-TR-209-222, April 15, 1961.
14. F. C. Perkins, DRI-2031, 3/8/62.
15. W. Chubb and R. F. Dickerson, BMI-1327 (March 3, 1959).
16. C. Wagner, Chapter in "Atom Movements," A Symposium of the American Society for Metals (1951).
17. W. E. Garner, "Chemistry of the Solid State," Butterworth's Scientific Publications, London (1955).
18. S. B. Austerman, NAA-SR-5893, May 1961 and NAA-SR-6427, September 1961.
19. W. B. Jepson, *This Journal*, **107**, 53 (1960).
20. G. Ervin, Jr. and T. L. Mackay, 11th Annual AEC Corrosion Symposium, Brookhaven National Laboratory, May 1962.

The Effect of Dissolved Oxygen on the Oxidation of Zircaloy-2 by Steam

B. Cox and B. R. Harder

Chemistry Division, United Kingdom Atomic Energy Authority,
Atomic Energy Research Establishment, Harwell, Berkshire, England

ABSTRACT

Predetermined amounts of oxygen were added to Zircaloy-2 by three methods which were expected to give widely different distributions of the oxygen in the metal. Subsequent oxidation of these specimens in steam showed that increases in the oxidation rate could be ascribed largely to the inhomogeneous distribution of the oxygen. The closer a homogeneous oxygen distribution was approached, the closer the oxidation rate approached that of low-oxygen material. If the oxygen distribution in the surface was uniform, the presence of an oxygen gradient through the specimens did not result in an increase in the oxidation rate.

During the oxidation of many zirconium alloys in oxygen, steam, or carbon dioxide, a transition occurs from an approximately cubic rate law to a more rapid linear relationship. This transition is apparently due to the breakdown of the protective oxide film formed during the pretransition period, but the causes of this breakdown remain obscure.

It has been suggested that, in carbon dioxide, the transition occurs at the time when the dissolved oxygen diffusing from each face of the specimen reaches the center (or some critical gradient) and that the presence of oxygen uniformly distributed in the metal reduces the time to transition (1). A similar association of the transition point in steam with some feature of oxygen diffusing into the metal has been suggested.

Consideration of the situation which prevails during the oxidation of zirconium alloys shows that the time taken for the diffusion gradients to meet during oxidation in steam is very much longer than the observed times to transition. Since the metal immediately under the oxide film must be saturated in oxygen at all times, no other point occurs during the diffusion of oxygen into the metal at which a discontinuous change in the oxidation rate might be expected. The experimental results (1), which were used as evidence for the dependence of the time to transition on oxygen content, must be explained differently, therefore.

A possible explanation of these observations is that the method used for preparing the oxygen-containing alloys gave an inhomogeneous distribution of the oxygen in the metal. In earlier reports (2-4) we have shown that both inhomogeneous regions in the metal and precipitated particles can provide sites for localized diffusion through the overlying oxide. If these regions are relatively large and widely spaced, they may give rise to nonuniform oxide growth and thus lead to failure of the film due to the stresses produced.

Previous studies of oxygen containing Zircaloy-2 (5, 6) have only examined alloys with oxygen contents up to 0.6% by weight [although an unreferenced comment on the effect of 1 w/o (weight per cent) oxygen additions in zirconium is included by Lustman and Kerze (7)]. In both these studies heat treatment was found to play a major part in determining the size of the effect observed, thus lending further support to the suggestion that the distribution of the oxygen in the metal is critical in determining its behavior.

Accordingly we prepared specimens of Zircaloy-2, containing various concentrations of oxygen, by three different methods. These methods were expected to give widely different distributions of the oxygen in the specimens. By comparing the oxidation of these specimens we have been able to separate effects due merely to the presence of dissolved oxygen from effects due to its distribution.

Since the completion of this work, a study of the effect of oxygen additions on the oxidation behavior of unalloyed zirconium has been reported (8). This study showed a generally similar effect of oxygen content on oxidation to that reported here, but did

Table I. Analysis of Zircaloy-2 billets

	Sn	Fe	Cr	Ni	O	H	N	Hf	Al	Ti	Pb
	%							ppm			
Billet Z8006	1.55	0.172	0.138	0.057	1050	30	120	700	175	75	20
Billet ZL9012	1.70	0.100	0.082	0.0385	1150	11	100	410	74	110	—

Table II. Analysis of oxygen containing alloys

Nominal w/o \ Actual	0.030 in. Sheet homogenized at 1000°C	0.100 in. Sheet homogenized at 1000°C	Billet ZL9012 remelted	Sheet annealed at 800°C
0.5	0.7	0.3	0.4	—
1.0	1.1	0.6	1.0	—
1.5	—	1.45	—	—
2.0	1.5	2.2	1.8	—
2.15	—	—	—	1.3
3.0	1.2	2.0	2.3	—

not examine the relation between the microdistribution of the oxygen in the metal and the oxidation behavior.

Experimental

The methods employed for the preparation of the oxygen-containing alloys were: (i) annealing of Zircaloy-2 specimens (sealed in silica ampoules containing a measured quantity of oxygen) at 1000°C for times ranging from 1-8 days; (ii) a similar treatment of specimens at 800°C for the time calculated to give oxygen diffusion gradients meeting in the center (7 days for 0.030 in. thick specimens), and ½, 2, and 4 times this figure; and (iii) re-casting of Zircaloy-2 (in a tungsten arc-melting furnace) with the calculated quantity of oxygen added as powdered ZrO_2.

In specimens prepared by methods (i) and (iii) the oxygen levels chosen were ½, 1, 2, and 3% by weight. In specimens prepared by method (ii) the calculated oxygen content (at the point of meeting of the diffusion gradients) of 2.15% by weight was added.

Specimens were ground on emery paper to 3/0 grade and polished by an attack-polishing technique after the oxygen pretreatment. Specimens prepared by methods (i) and (ii) were from billet Z8006 and were 1.5 x 1 cm and 0.030 in. thick. A duplicate set of specimens was prepared by method (i) from 0.100 in. thick sheet. Specimens prepared by method (iii) were cast as ½ in. diameter cylindrical buttons (using billet ZL9012 as a base) and were machined or cut with an abrasive wheel to give disks ½ in. diameter x 0.040 in. thick. Analyses of billets Z8006 and ZL9012 are given in Table I; the final oxygen contents were determined by vacuum fusion analysis and are given in Table II. Analyses were carried out on duplicate specimens prepared in the same manner as the oxidized samples. Thus the low oxygen contents of the specimens with oxygen gradients probably result from the removal of some of the outer layers of high oxygen content during abrasion.

All specimens were oxidized in flowing steam at 450°C and 1 atm pressure and were weighed periodically. Specimens which showed evidence of spalling of the oxide were transferred to silica pots (with platinum lids) and the oxidation was continued. Each curve on Fig. 1-4 was obtained as the mean of results on duplicate specimens.

Results

Specimens prepared by annealing at 1000°C.— Following annealing at 1000°C it was expected that the oxygen would have achieved its equilibrium distribution in the metal. In this state it was expected to show considerable segregation at grain boundaries, and to be far from homogeneously distributed. This situation was confirmed metallographically on the 0.030 in. thick specimens. The specimens containing more than ½% oxygen showed large α-Zr grains with bands of very hard material (presumably containing a high percentage of oxygen) along the grain boundaries. They also showed many microcracks in the hard regions, the density of these increasing considerably with increasing oxygen content.

During oxidation these regions of high oxygen content oxidized preferentially and soon gave bands of white oxide on the surface. The specimens containing ½ w/o oxygen (which did not show bands of inhomogeneous material or contain microcracks) had pretransition weight gains similar to low-oxygen Zircaloy-2, but showed slightly shorter times to transition (Fig. 1). The effect of the inhomogeneities, resulting from higher oxygen contents, was to

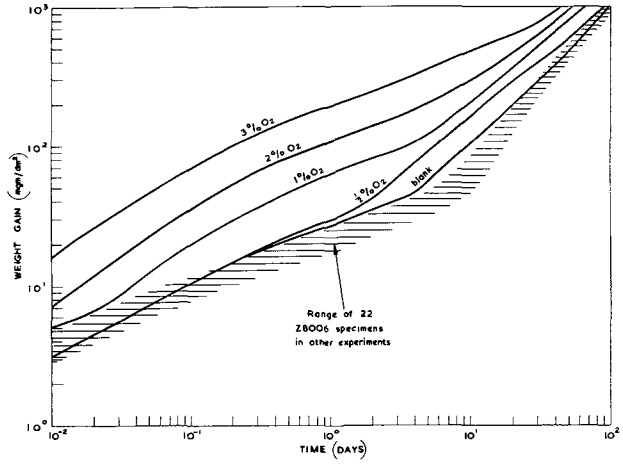

Fig. 1. Oxidation of 0.030 in. thick Zircaloy-2 containing oxygen added by annealing for 24 hr at 1000°C.

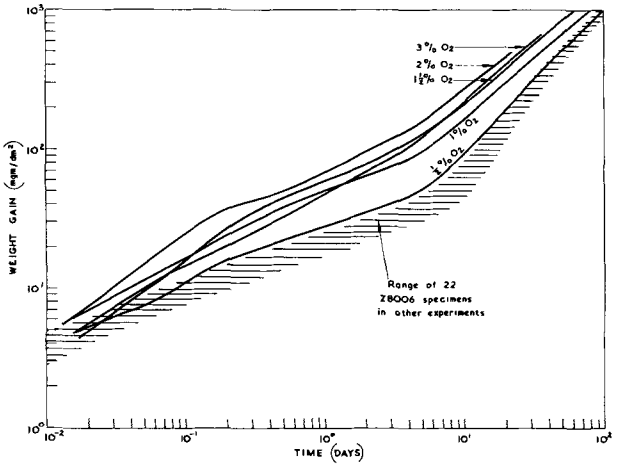

Fig. 2. Oxidation of 0.100 in. thick Zircaloy-2 containing oxygen added by annealing for 8 days at 1000°C.

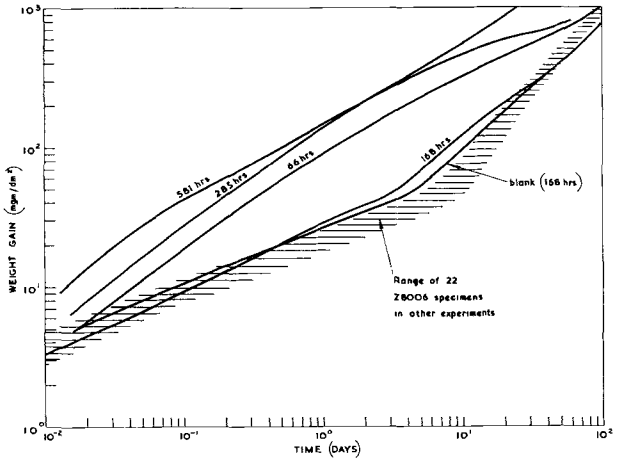

Fig. 3. Oxidation of Zircaloy-2 containing 2.15 w/o oxygen added by annealing at 800°C for various times.

increase the pretransition weight gain, but not to decrease markedly the time to transition. At the highest oxygen levels no transition was detected.

Since much of the increased oxide formation was thought to be associated with the presence of microcracks in the high oxygen regions, further specimens were prepared from 0.100 in. thick sheet. It was hoped that the depth of the microcracks would not be more than a few thousandths of an inch and that by abrading away about 0.025 in. from all faces (*i.e.*, about ½ the thickness of the specimen) they would be eliminated. Polishing of these specimens after abrading showed that the density of microcracks had been much reduced, but not completely eliminated.

Oxidation of this second set of specimens showed that elimination of the severely cracked surfaces reduced the rate of corrosion considerably (Fig. 2). An obvious transition point was now observed in the oxidation curve at all oxygen levels and the time at which this occurred showed little dependence on the oxygen content. In general the time to transition of the oxygen-containing specimens was slightly shorter than for low-oxygen Zircaloy-2, and the pretransition weight gain increased with increasing oxygen content, although not as steeply as for the previous group of specimens. This increase in pretransition oxidation rate with increasing oxygen content is ascribed to the effect of segregation of oxygen at grain boundaries. White oxide was usually observed first at these positions.

Specimens containing an oxygen gradient.—By preparing specimens with an oxygen concentration gradient in them it was expected that the oxygen would be distributed homogeneously across the surface, up to the point at which the diffusion gradients met in the center of the specimen. At longer times than this it was expected that some migration of oxygen to grain boundaries would occur. Oxidation of these specimens showed that the ones homogenized for the time calculated to give gradients meeting in the middle showed little difference in oxidation rate from low-oxygen Zircaloy-2 (Fig. 3). All the others rapidly formed loose white oxide along the edges of the specimen and gave high weight gains. This effect is thought to have resulted from some reaction with the silica ampoule, since these specimens were inadvertently treated without wrapping in platinum foil, and it was not thought to be related to the introduction of the oxygen gradient as such.

Specimens remelted with ZrO_2 additions.—This method of preparing specimens was expected to give a fine dispersion of ZrO_2 particles in the metal. Since the buttons were only melted once it was hoped that the oxide particles would not have had time to dissolve. Metallographic studies confirmed this.

In accordance with previous work (2-4) it was expected that the presence of precipitate particles in the metal would leave the pretransition oxidation rate unaffected, but (by providing nuclei for oxide film failure) that the time to transition would be reduced. Results obtained with these specimens (Fig. 4) showed this effect with the ½ and 1% oxygen alloys. The alloys with higher oxygen contents showed very much shorter times to transition but, as far as could be determined, their pretransition oxidation rates were also increased.

Discussion

It has been shown in earlier reports that the presence of inhomogeneous regions in the metal may give rise to early breakdown of the oxide film if

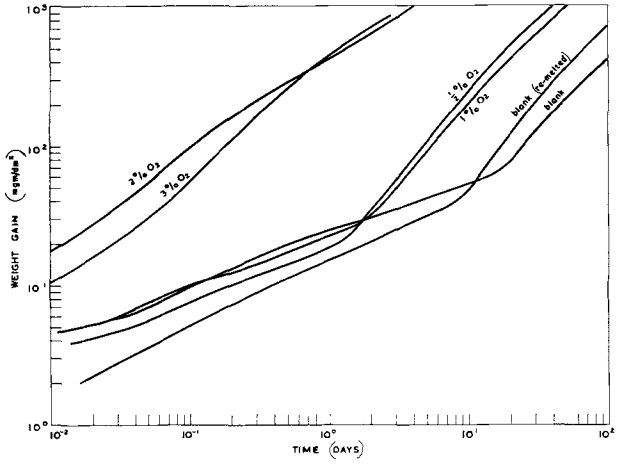

Fig. 4. Oxidation of Zircaloy-2 containing oxygen added by remelting with ZrO_2 additions.

the distribution of these regions is unsatisfactory (2-4). From the present work the specimens in which the oxygen was most inhomogeneously distributed were those containing a fine distribution of ZrO_2 particles and these showed similar pretransition rates to those of low-oxygen material (up to 1 w/o oxygen) but with the time to transition decreasing as expected, with increasing oxygen content.

The high weight gains of some of the specimens annealed at 1000°C (in both the pretransition and posttransition periods) were due to the segregation of some of the oxygen at the grain boundaries, as a result of the method of preparation. With improving surface finish (by elimination of microcracks) the oxidation rates approached those of low-oxygen material. However, it was only in specimens in which the oxygen at the surface was uniformly distributed (prepared by annealing at 800°C) that the oxidation rate was indistinguishable from that of low-oxygen Zircaloy-2.

Thus the breakdown of the oxide film on Zircaloy-2 is not affected by the presence of oxygen uniformly distributed in the metal, or present as a concentration gradient through the metal. It is affected by the inhomogeneous distribution of oxygen in the surface, and particularly by the limiting case of this where the oxygen is present as particles of ZrO_2 in the metal.

No examination of the microdistribution of the oxygen was made by Osthagen and Kofstad in their study of the effect of dissolved oxygen on oxidation of unalloyed zirconium (8). It appears from the work reported here that the distribution of the oxygen, on a microscale, is the most critical factor in determining the behavior of the resulting alloy. Thus, in the absence of information about the distribution of the oxygen in Osthagen and Kofstad's specimens, their conclusion about the effect of dissolved oxygen on oxidation and the mechanistic significance of this must be treated with reserve.

Acknowledgments

The authors are indebted to Mr. A. Symonds, Metallurgy Division, for preparation of the specimens containing ZrO_2 powder.

Manuscript received Oct. 12, 1962; revised manuscript received May 31, 1963.

Any discussion of this paper will appear in a Discussion Section to be published in the June 1964 JOURNAL.

REFERENCES

1. W. G. O'Driscoll, C. Tyzack, and T. Raine, 2nd Conference on Peaceful Uses of Atomic Energy, Geneva, 1958, p. 1450.
2. B. Cox, AERE-R-2874; *Corrosion*, **16**, 380t (1960).
3. B. Cox, AERE-R2931; *This Journal*, **108**, 23 (1961).
4. B. Cox, "Progress in Nuclear Energy," Series IV, Vol. IV. p. 166. Pergamon, London (1961).
5. M. D. Carver and E. T. Hayes, USBM-U-52, October 1955.
6. L. S. Rubenstein, J. G. Goodwin, and F. L. Shubert, *Trans. Am. Soc. Metals*, **54**, 20 (1961).
7. B. Lustman and F. Kerze, "Metallurgy of Zirconium," p. 618, McGraw Hill Publishing Co., New York (1955).
8. K. Osthagen and P. Kofstad, *This Journal*, **109**, 204 (1962).

Magnesium as a Passive Metal

Peter F. King

The Dow Metal Products Company, Division of the Dow Chemical Company, Metallurgical Laboratory, Midland, Michigan

ABSTRACT

Magnesium is normally in either the passive or transpassive state in aqueous environments. If in the transpassive state, its corrosion rate can be decreased by lowering its potential into the passive region. When high-purity magnesium is polarized in the negative direction to the region of its reversible potential, a considerable weight loss is observed which might be due to the incipient breakdown of passivity.

According to one of the accepted definitions of passivity, "a metal active in the emf series, or an alloy composed of such metals, is considered to be passive when its electrochemical behavior becomes that of an appreciably less active or more noble metal" (1). By this definition it can be argued that magnesium is characteristically passive or transpassive in aqueous environments, even when it corrodes at a very high rate. Thus the corrosion potential is usually a volt or more passive to the standard potential. Furthermore, since it has about the same standard potential as sodium, the violent reaction of the latter with water might be expected to be the corrosion behavior of magnesium in its active state. When compared to these thermodynamic expectations, magnesium usually behaves as if it is "an appreciably more noble metal" albeit rarely as a "noble metal."

However, even if magnesium is considered passive according to the above definition, it does show widely variable behavior. Thus, in distilled water and its solutions with alkali and alkaline earth hydroxides, silicates, fluorides, borates, sulfites, and carbonates (2), for example, the corrosion rate is extremely small near room temperature and, where tested, the potential is subject to further substantial ennoblement on the imposition of rather small anodic current densities. Let us restrict the word

"passivity" in this paper to this condition to differentiate it from the situation where the environment contains appreciable quantities of anions such as Cl^-, Br^-, $SO_4^=$, or ClO_4^- where the corrosion rate may be substantial while the potential is subject to little further ennoblement until the anodic current density becomes very high. This latter condition, which is the basis for the considerable utility of magnesium alloy anodes for cathodic protection and in power sources, will hereinafter be called "pseudo-activity."

This paper describes a brief exploration of the phenomenology of these states and the transitions between them. Of particular interest to the investigation was the relationship of the passive phenomenology to that of other metals since this could indicate routes to improved corrosion resistance.

Procedure

Experiments were carried out with sublimed and recast magnesium of the following spectroscopically determined compositions:

Parts per million

Lot	Al	Ca	Cu	Fe	Mn	Ni	Pb	Si	Sn	Zn
A	13	<100	<10	<10	<10	<5	<10	<30	<10	60
B	<10	<100	<10	<10	<5	<10	<10	60	<10	<10
C	<10	<100	<10	<5	<10	<5	<20	<10	<100	240
D	<10	<100	<10	6	<10	<5	<20	<100	<100	<30

Lot B was extruded into ⅜ in. rod after casting, while the other lots were used in the as-cast condition. Electrodes were cut in the form of cylinders 2.5 cm long x 0.75 cm in diameter, from which [after assembly with glass tube, weld rod lead, and Teflon gaskets as described in Stern (3)] 0.003 cm per side were removed by pickling in "acetic-nitrate" pickle (188 cc glacial acetic acid, 94.5g $NaNO_3$ and 950 cc water). For corrosion rate determination rectangular samples 2.5 x 5 x 1 cm were usually used. Exposure was by the "alternate immersion" test (4), (30 sec out of every 2½ min in solution, at 35°C).

Reagent grade chemicals and laboratory distilled water were used throughout.

Galvanostatic polarization measurements were made using the system described previously (5). Potentiostatic work was carried out in a 4-neck round bottom flask equipped with a platinum electrode, a Luggin capillary probe with associated commercial saturated calomel electrode, a thermometer, and the magnesium electrode. Constant potentials were applied using a 25-ohm, 25w potentiometer with 4½v across it, and by adjusting the potentiometer to keep the magnesium-calomel potential at the chosen value manually. An electronic *p*H meter was used to determine the potential.

A high speed recording oscillograph was used to record transient potentials at constant currents.

The potentials are reported according to the IUPAC convention, *e.g.*, potentials more noble than the standard hydrogen electrode are positive and those more active are negative.

Experimental Results

Upon the potentiostatic polarization of high-purity magnesium in 1*N* NaOH at 25°C, a relatively symmetrical steady-state current-potential curve is obtained as shown in Fig. 1, if one waits long enough for the steady state to establish itself. It seems to take several hundred minutes for the film to adjust itself to the new environment on immersion in caustic with an applied current. The arrows on Fig. 1 and Fig. 3 and 7 represent weight losses or currents which are too small to be resolved by our measurements.

Although the anode efficiency (defined as the applied current times one hundred divided by the anodic current calculated from the observed weight loss by Faraday's law) increases with increasing potential, so does the corrosion current (Fig. 2). In

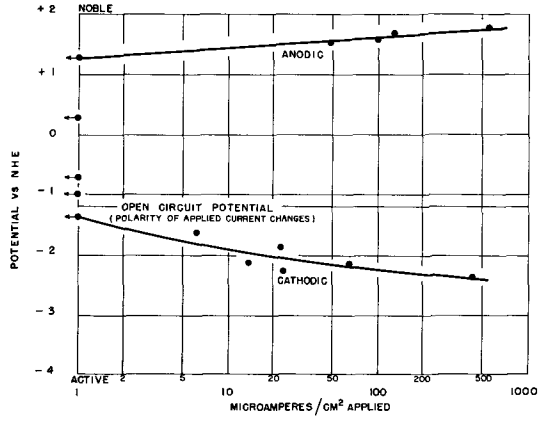

Fig. 1. Potentiostatic polarization curve for high purity magnesium (Lot C) in 1 N NaOH at 25°C. Arrows represent currents smaller than the resolution of our measurements.

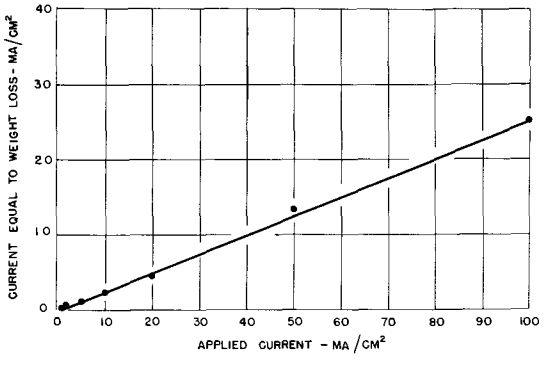

Fig. 2. Corrosion rate as a function of potential, anodically polarized high purity magnesium (Lot D) in 1 N NaOH, 25C.

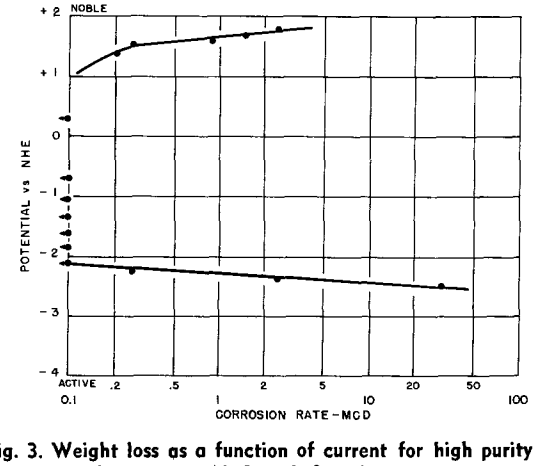

Fig. 3. Weight loss as a function of current for high purity magnesium (Lot C) in 1 N NaOH, 25°C. Arrows represent weight losses smaller than the resolution of our measurements.

this case a limiting efficiency of 400% appears to have been reached.

A complete polarization curve for high-purity magnesium (Fig. 3) at room temperature (showing the rate of magnesium dissolution as a function of potential) shows a rather long passive region. The open-circuit potential lies near the middle of this region, *e.g.*, it centers at about —1.1v, but drifts widely. There is increasing attack at both highly positive and highly negative potentials.

The transition from the passive to the transpassive state for magnesium in 1*N* NaOH resembles the conventional active-passive transitions in that a critical current for the transition can be deduced from the relation

$$\frac{1}{t_p} = k(I - I_c)$$

Here t_p is the time to reach the arbitrary transpassive potential, I is the applied current, and I_c the critical current below which the transition is not complete. The critical current at 25°C is 3 μa/cm^2, as shown in the determination shown in Fig. 4.

If a current greater than the above critical current is chosen and NaCl is added to the NaOH solution, several observations can be made:

1. Low chloride levels have no gross effect on the ennoblement of potential.

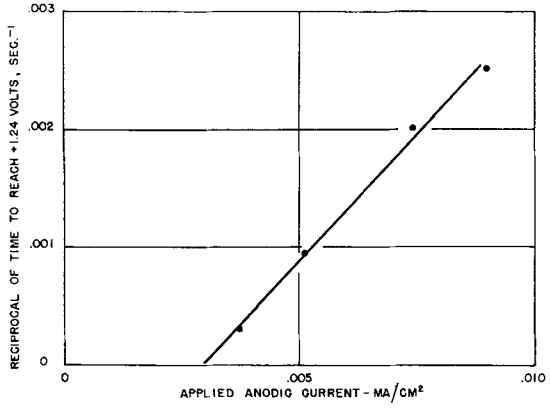

Fig. 4. Determination of critical current for passivity of high purity magnesium in 1N NaOH.

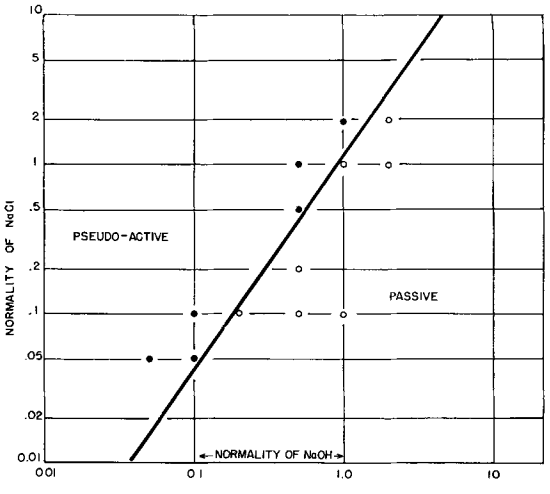

Fig. 5. Domains of passive and pseudoactive behavior of high purity magnesium (Lot B) in NaOH-NaCl mixtures, 25°C. O Potential recovered. • Potential did not recover.

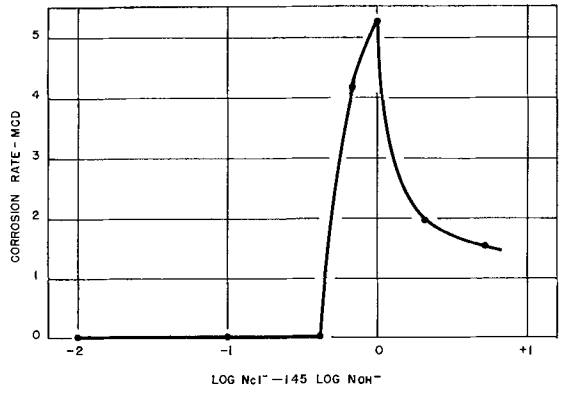

Fig. 6. Corrosion rate of high purity magnesium (Lot A) in NaOH-NaCl mixtures at 35°C, alternate immersion test, one week.

2. At higher chloride levels, the ennoblement is still observed, but it is followed by an irregular reactivation of potential with the result that it returns eventually to a value in the neighborhood of that observed on open circuit. The concentrations at which this reactivation occurs are relatively reproducible and can be used to define the domains of passive and pseudoactive behavior shown in Fig. 5. The straight line can be expressed by:

$$\log N_{\mathrm{NaCl}} - 1.45 \log N_{\mathrm{NaOH}} = 0$$

3. These concentration fields reflect themselves in the corrosion behavior of high-purity magnesium in NaOH-NaCl mixtures as illustrated by Fig. 6, in which the results of alternate immersion corrosion tests in mixtures of varying NaOH to NaCl ratios are reported. A marked increase in corrosion rate can be observed with increasing OH^- added to NaCl. This rate reaches a maximum at the concentrations where $\log N_{\mathrm{NaCl}} = 1.45 \log N_{\mathrm{NaOH}}$.

The attack in these tests, and also on cathodic polarization below —2.25v *vs.* NHE, is by the mechanism of "layered" attack. In this attack the metal is corroded preferentially along the basal plane to leave unattacked layers spaced at about 100μ intervals. This attack has been described previously (6). This is in contrast to the intergranular attack previously observed by Hoey and Cohen (7) on the cathodic polarization of magnesium in basic dilute NaCl solution.

In the case of high-purity magnesium in 1*N* NaOH, the open-circuit corrosion rate is too low to permit the determination in a test of reasonable duration whether or not cathodic protection is achieved at potentials more noble than those at which cathodic attack is observed. When a less corrosion resistant Mg-0.03% Fe alloy is exposed to the more agressive, 1*N* NaCl solution, it is observed that cathodic protection can be achieved over a range of currents as shown in Fig. 7. Again, at the higher cathodic currents the above discussed layered attack sets in.

Discussion

The work herein presented suggests that magnesium is naturally a passive metal whose Flade potential must lie very close to its very negative reversible potential (—2.4v *vs.* normal hydrogen electrode). At potentials more noble than about +1.2v

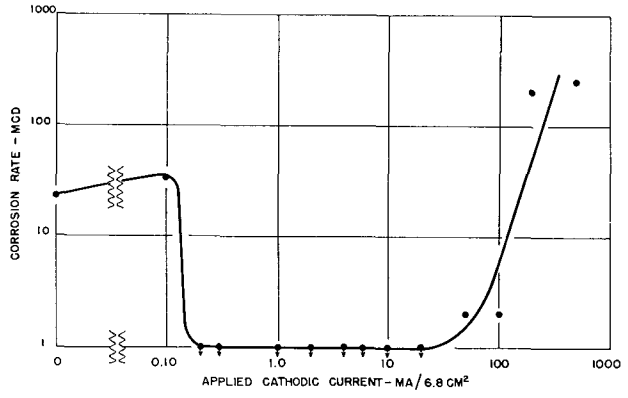

Fig. 7. Corrosion rate of Mg-.03% Fe binary in 1 N NaCl at 21°C as a function of applied cathodic current density. Arrows represent weight losses smaller than the resolution of our measurements.

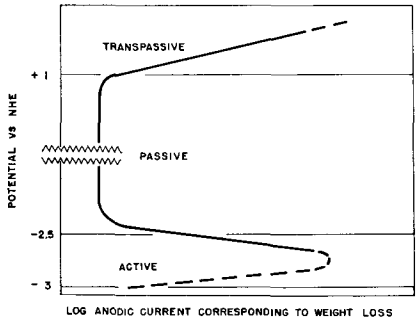

Fig. 8. Generalized anodic polarization curve for magnesium, deduced from our results.

vs. NHE (in 1*N* NaOH), the transpassive region has apparently been entered with high-purity magnesium because the weight loss begins increasing with increasing potential. If the potential of the specimen is forced in the negative direction, hydrogen is naturally evolved, but in addition, below about −2.25v there is evidence that the magnesium begins to activate in that weight losses are observed at the magnesium cathode.

Thus, taking a generalized anodic polarization curve similar to that given by Stern (8) (Fig. 8), we have investigated the solid portions. We speculate that the dotted portions representing the active portion of the curve are forced far to the active side, in keeping with the highly negative reversible potential of magnesium, so that the cathodic curves of most available cathodic reactions cut the anodic curve of high-purity magnesium in 1*N* NaOH in the passive region. In addition, this leaves the Flade potential for magnesium so negative that, as it is approached, the decomposition of water on the magnesium cathode becomes so fast that potential measurements become questionable.

If this reasoning is followed in the case of the Mg-0.03%Fe alloy in 1*N* NaCl, the alloy must already be in the transpassive region even though its potential is about −1.4v. The cathodic protection that was observed on cathodic polarization would then stem from the movement of the potential back toward the passive region.

In both cases, the cathodic attack observed on overprotection could be rationalized as movement out of the passive region in the negative direction.

While the behavior of magnesium as described here does appear to conform to the active-passive-transpassive phenomenology of other metals, it should be borne in mind that the apparent breakdown in passivity, if we judge from the distribution of attack in most instances, is a highly localized rather than a general process. Thus, it cannot be stated with complete certainty that the observed cathodic attack is not due merely to conditions varying locally from the mean behavior of the cathode as deduced from measured potential and weight loss.

Manuscript received Jan. 24, 1963; revised manuscript received June 21, 1963. This paper was presented at the New York Meeting, Sept. 29-Oct. 3, 1963.

Any discussion of this paper will appear in a Discussion Section to be published in the June 1964 JOURNAL.

REFERENCES

1. Corrosion Handbook, H. H. Uhlig, Editor, P. 27, John Wiley & Sons, New York (1947).
2. H. A. Robinson, *This Journal*, **90**, 499 (1946).
3. M. Stern, *ibid.*, **105**, 638 (1958).
4. J. D. Hanawalt, C. E. Nelson, and J. A. Peloubet, *Trans. AIME*, **147**, 273 (1942).
5. J. L. Robinson and P. F. King, *This Journal*, **108**, 37 (1961).
6. E. Schiebold and G. Siebel, *Z. Physik*, **69**, 459 (1931).
7. G. R. Hoey and M. Cohen, *This Journal*, **105**, 249 (1958).
8. M. Stern, *ibid.*, **102**, 609 (1955).

The Difference Effect on Magnesium Dissolving in Acids

W. J. James, M. E. Straumanis, B. K. Bhatia,[1] and J. W. Johnson[2]

University of Missouri, School of Mines and Metallurgy,

Departments of Chemical Engineering and Chemistry and of Metallurgical Engineering, Rolla, Missouri

ABSTRACT

The difference (Δ) effect on Mg metal was measured in HCl, $HClO_4$, and H_2SO_4 of concentrations between 0.05 and 0.50*N* at 25°C. Generally the effect was positive, but the usual linear relationship between Δ and I existed only at low current densities and high acid concentrations. In H_2SO_4 and HCl, the positive effect changed to negative at increased current densities and low acid concentration. Attempts to attribute the Δ effect to the anodic expulsion of uncommon valency Mg ions result in unrealistic values of cationic charges for positive values of Δ. The difference effect is explained on the basis of anodic polarization, film disruption, and disintegration of the magnesium anode, *i.e.* "chunk effect."

In the past sixty years considerable work has been done to arrive at a mechanism for the anodic dissolution of magnesium metal in aqueous solutions. It has been found that magnesium anode consumption measured in terms of hydrogen evolution is very much greater than predicted by Faraday's law for divalent magnesium ion formation. To account for this, Kleinberg and co-workers (1-3) have proposed that the metal enters solution as a univalent ion subsequently reacting with water to produce hydrogen. Others (4-7) propose that the anodic dissolution is film controlled, and as such the behavior of magnesium can be explained without the need of uncommon valency ions. More recently the "chunk effect" (8) has been advanced as a third possibility.

Accordingly a study of the difference effect exhibited by magnesium while dissolving in various acids was undertaken in order to arrive at a mechanism which best explains the experimental results.

Experimental

The difference effect on magnesium metal of 99.995% purity (as given by Dr. R. Gadeau of L'Aluminium Francais) was measured in hydrochloric, perchloric, and sulfuric acids at 25° ± 0.10°C. The concentration of the acids employed varied from 0.05 to 0.50*N*.

The apparatus and procedure used have been thoroughly described previously (9).

Three hundred milliliters of acid of known concentration were poured into the reaction flask and the system allowed to come to the desired temperature. The electrodes were then immersed (with external circuit switch open) in the acid, the stirring mechanism turned on, and the volume of gas recorded for definite time intervals until the rate became constant. At this time, the external circuit was closed and two consecutive volume readings were taken at equal time intervals together with the average milliammeter reading. Then, two consecutive volume readings were made with the circuit open. The above procedure of taking two volume readings without an external current and two with an external current flowing was repeated at several current densities.

Results

The difference effect is defined as the difference between hydrogen evolution rate V_1, from an electrode without current flowing and hydrogen evolution rate V_2 from the same electrode with current flowing, i.e.

$$\Delta = V_1 - V_2$$

Usually the two rates are not equal, and a positive or negative effect arises. The difference effect Δ expressed in $mm^3cm^{-2}min^{-1}$ is obtained from the experimentally available values of V_1 and V_t (the total hydrogen rate from both anode and cathode) through the following equation

$$\Delta = V_1 - (V_t - 6.97\,I)$$

where the factor 6.97 converts milliamperes of current flowing through the electrodes for 1 min into cubic millimeters of hydrogen at standard conditions.

Values of V_1 and V_t were plotted against the corresponding anodic current densities, I (ma/cm^2) and

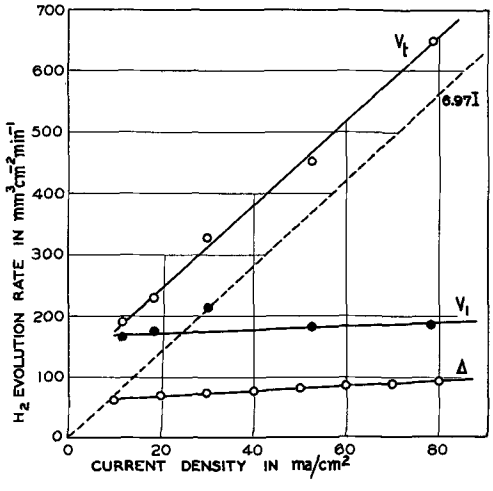

Fig. 1. Plot of V_t, V_1, and Δ vs. I for anodic dissolution of magnesium in 0.05*N* perchloric acid at 25°C.

[1] Present address: Monsanto Chemical Company, St. Louis, Missouri.

[2] Present address: Chemistry Department, University of Pennsylvania, Philadelphia, Pennsylvania.

curves were drawn through these points to obtain average values of V_1 and V_t. In general the open circuit rate V_1 was nearly constant over the time periods involved and the effects of acid depletion were so small as to be neglected in most instances. A plot of V_1 and V_t *vs.* current density, representative of the several plots made, is shown in Fig. 1.

From these smoothed-out data, Δ values were obtained using the above equation. The results are presented graphically in Fig. 2-4.

As can be seen from the figures a linear relationship between Δ and I exists only at low current densities. The deviation from linearity becomes more pronounced with increasing current density and decreasing acid concentration. In major part, the effect is positive over a considerable range of current densities, *i.e.*, the hydrogen evolution rate on the anode is decreased during passage of current.

In 0.10N sulfuric acid, Fig. 2, the relation between Δ and I is nonlinear over the entire range. Above 84 ma/cm^{-2} a negative Δ is observed, *i.e.*, the anodic hydrogen evolution increases upon passage of current. At an even lower concentration (0.05N) the negative effect occurs at a lower current density (22.5 ma/cm^{-2}). Thus, there is a change from the positive to the negative effect with increasing current density and decreasing sulfuric acid concentration. Similar results are obtained in hydrochloric acid (Fig. 1). However, in perchloric acid only a positive effect is observed within the range of acid concentration and current density covered. As the hydrogen ion activities of these two latter acids are about equal, an influence of the anions is suggested.

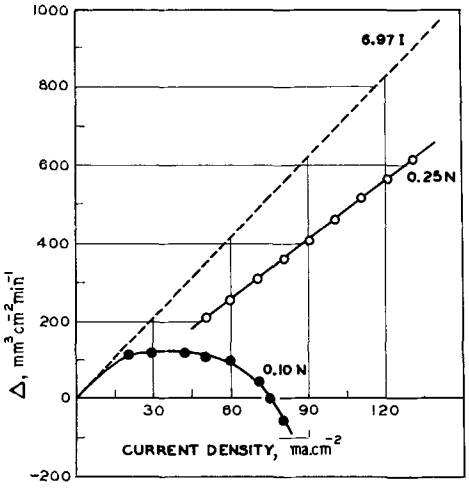

Fig. 2. Effect of current density on Δ for anodic dissolution of magnesium in hydrochloric acid at 25°C.

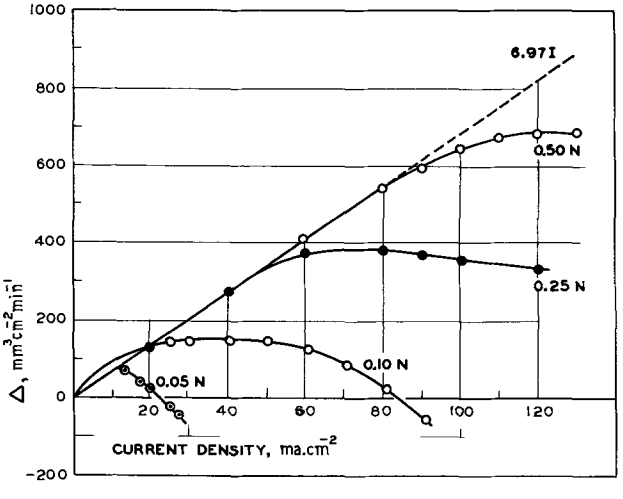

Fig. 3. Effect of current density on Δ for anodic dissolution of magnesium in sulfuric acid at 25°C.

Discussion

If the difference effects observed arise as a consequence of the expulsion of unusual valency ions from the magnesium anode, calculations of these valencies on the basis of Faraday's law can be made as follows. Using the values of Δ and I obtained from Fig. 2-4, the apparent cationic charge c^+ on magnesium during anodic dissolution is calculated from the equation (9)

$$c^+ = n_m \frac{11{,}207\, I}{1{,}608\,(V_t - V_1)}$$

where n_m = normal cationic charge of +2 for magnesium. It is assumed in this equation that the self-dissolution rate V_1 does not change during anodic dissolution, *i.e.*, the Δ effect is a consequence only of uncommon valency ions entering solution at the anode. In general, under such conditions, the cationic charge varies from infinity to approximately the normal cationic charge of +2 in the region of the positive difference effect, Fig. 4-6.

In the region where the negative difference effect is observed values less than +2 are obtained.

When a metal dissolves anodically in an aqueous solution at applied anodic currents or even at zero applied current (current arising as result of local action), the self-dissolution or freely corroding rate may be increased or decreased depending on the corrosive medium. In most aqueous salt solutions the self-dissolution rate is found to increase with current density giving rise to the experimentally observable negative difference effect. This effect has been ascribed to the disruption of a protective surface film during application of an anodic current, thus leading to increased local cell action (11, 12).

In most acid solutions the self-dissolution rate is observed to decrease thereby resulting in a positive difference effect. This decrease in self-dissolution rate has been attributed to anodic polarization

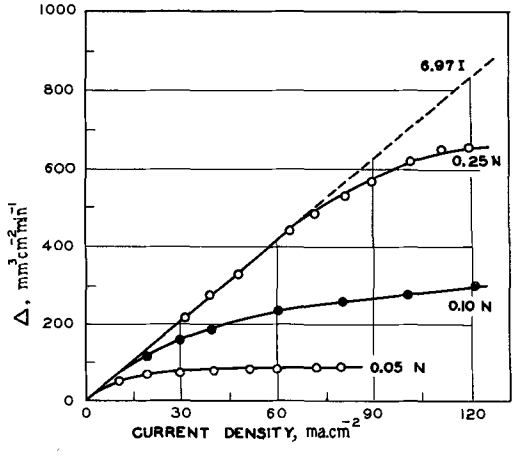

Fig. 4. Effect of current density on Δ for anodic dissolution of magnesium in perchloric acid at 25°C.

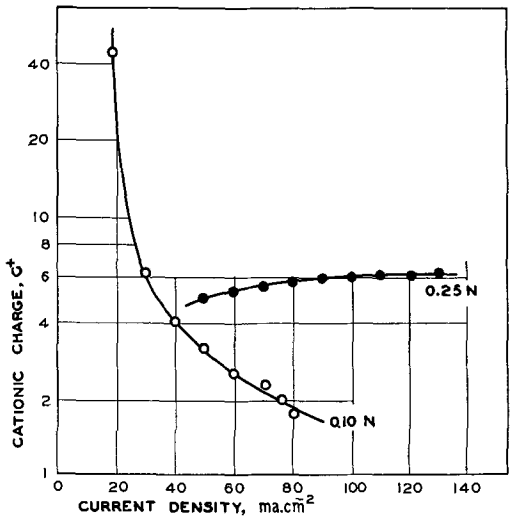

Fig. 5. Cationic charge as a function of current density for anodic dissolution of magnesium in hydrochloric acid at 25°C assuming no Δ effect exists.

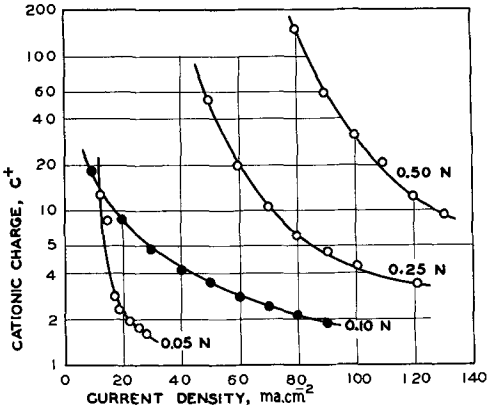

Fig. 6. Cationic charge as a function of current density for the anodic dissolution of magnesium in sulfuric acid at 25°C assuming no Δ effect exists.

(12). This arises if there is interference with (i) delivery of electrons to the local cathodes, or (ii) ejection of ions into the corrosive medium. Thus with increasing anodic current, applied or originating in local cells, the increased polarization reduces local cell action and gives rise to what is termed the positive difference effect. For both effects it has been found, that in general, Δ is linear over the smaller ranges of I ($\Delta = KI$). This suggests that K may be of fundamental significance as regards the mechanism of the anodic dissolution (11).

The results of present studies on magnesium in acids confirm that the positive effect is observed in general but that at lower acid concentration and high current density, negative values of Δ can result. If the difference effect is due solely to the expulsion by the anode of uncommon valency ions, one cannot justify the extremely high values of cationic charges in the positive region. Furthermore, there is no reason to expect that the cationic charge should vary as the current density. Although charges of less than +2 in the negative region are in accord with the findings of other investigators (1-3) it would appear more reasonable to search for an explanation covering the entire region of the observed effect and to assume that the self-dissolution rate

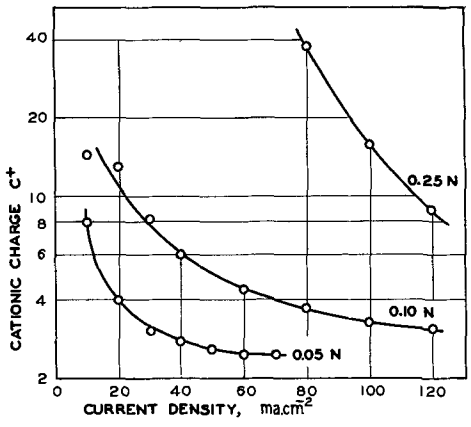

Fig. 7. Cationic charge as a function of current density for anodic dissolution of magnesium in perchloric acid at 25°C assuming no Δ effect exists.

due to local cell action does change under conditions of anodic polarization. It is necessary, however, to keep in mind that the above argument is based on the assumption that the Δ effect is caused only by the expulsion of uncommon valency ions at the anode. It is, of course, possible that uncommon valency ions could be present and that the change in the self-dissolution rate would be attributable only in part to this effect. However, as a result of these and other studies (13), it is more likely that these apparent valencies arise, in the case of magnesium, as a consequence of the disintegration of the anode to be discussed later.

Difference effect studies on other metals like titanium and aluminum (9, 12) have shown that Δ is directly proportional to I and nearly independent of acid concentration. It was further shown that the positive difference effect was caused by the polarization of local anodes, the extent of which is given by K and by I. As such the extent of polarization of the metal is constant in the absence of complications. As regards magnesium, if one considers the extent of polarization to remain constant, the deviation from linearity between Δ and I must be caused by some other mechanism. A reasonable and likely explanation is the formation or the presence of a surface film, doubtless an oxide. The positive effect can then be attributed to the presence of a film which at lower applied current densities inhibits the expulsion of magnesium ions into solution but with increasing current density is disrupted, accelerating corrosion due to local action and thus lowering the positive effect.

Another factor of possibly even greater influence is the dispersion of the magnesium anode in the form of microscopic chunks. Electrolysis experiments on magnesium dissolving in dilute hydrochloric acid (0.05N) revealed that during anodic dissolution magnesium developed a dark coating which broke off from the anode at high current densities (about 200 ma/cm^{-2}) and quickly turned white.

The dark flakes were made up in the most part of small aggregates of magnesium metal embedded in the oxide or hydroxide layer (14). When the external current was cut off, the flakes dissolved rapidly with hydrogen evolution. Hoey and Cohen

(15) and Higgins (5) found magnesium metal particles while anodically dissolving the metal in NaCl and several investigators have reported anodic disintegration for other metals (16, 17). From the observations of Mg electrolyzed in HCl, it appears that at higher current densities, dark flakes containing metallic magnesium are formed on the anode, separate from it and quickly dissolve in the adjacent anolyte. The dislodgement of metallic particles is probably caused by both the high current density and increased dissolution rate at the grain boundaries where impurities usually aggregate. Thus in the positive region as long as Δ is linear with I, the extent of polarization of local anodes (caused by a passivating film) remains constant. It is suggested that when this passivating film is disrupted, the self-dissolution rate V_2 increases slightly, but not in proportion to I. At higher current densities where K begins to approach zero, the dissolution of the anode through disintegration becomes effective, thereby rapidly increasing V_2 which, however, is still less than V_1, resulting in a positive effect. As the current density increases to still higher values, more and more particles leave the anode and dissolve outside the circuit until V_2 becomes equal to V_1 as observed at the lowest acid concentrations (Fig. 1 and 2) where $\Delta = 0$. Above this current density the dissolution by disintegration is so pronounced as to give values of V_2 greater than V_1 and accordingly, a negative difference effect.

This mechanism is basically in accord with that given for anodic dissolution of steel in aqueous solutions by Marsh and Schaschl (8). They conclude that the "chunk effect" and anodic polarization occur on the same piece of corroding metal and either the positive or negative difference effect is observed depending on the corrosive agent. However, in their study on steel the concept of film disruption was not postulated to explain their results.

This "chunk effect" or disintegration of the anode also explains in part or in whole the apparent valencies of less than +2 observed for Mg in the region of the negative effect as well as the low efficiency of Mg anodes used in cathodic protection. In the studies of Kleinberg and co-workers the valency of the anodic ion is obtained from a simultaneous measure of the weight loss of the anode and the amount of Faradaic current delivered. If particles of metal are ejected, as has been strikingly shown for beryllium (13), the dissolution of these metal particles takes place outside the circuit and accordingly valencies less than normal are calculated. It should be noted that in these measurements the total amount of hydrogen delivered is stoichiometrically in accord with the normal or stable state of the ion.

In summary it is proposed that for magnesium dissolving in acids, the difference effects result from (i) the change in electrochemical conditions at the interface (polarization of local elements) while an anodic current is flowing, (ii) the ease with which a protective surface film is formed or disrupted, and (iii) the rate at which metallic particles separate from the anode surface.

Acknowledgment

Appreciation is expressed for research support of the A.E.C. under Contract No. AT(11-1)-1047.

Manuscript received Oct. 18, 1962; revised manuscript received June 24, 1963. This paper was presented at the Boston Meeting, Sept. 16-20, 1962.

Any discussion of this paper will appear in a Discussion Section to be published in the June 1964 JOURNAL.

REFERENCES

1. R. L. Petty, A. W. Davidson, and J. Kleinberg, *J. Am. Chem. Soc.*, **76**, 363 (1954).
2. M. S. Rausch, W. E. McEwen, and J. Kleinberg, *ibid.*, **76**, 3622 (1954).
3. M. D. Rausch, W. E. McEwen, and J. Kleinberg, *ibid.*, **77**, 2093 (1955).
4. B. Roald and W. Beck, *This Journal*, **98**, 277 (1951).
5. W. E. Higgins, *ibid.*, **105**, 757 (1958).
6. J. L. Robinson and P. F. King, *ibid.*, **108**, 36 (1961).
7. J. H. Greenblatt, *Corrosion*, **18**, 125t (1962).
8. G. A. Marsh and E. Schaschl, *This Journal*, **107**, 960 (1960).
9. M. E. Straumanis and P. C. Chen, *ibid.*, **98**, 351 (1951).
10. M. E. Straumanis, *ibid.*, **108**, 1087 (1961).
11. W. J. Miller, *Trans. Electrochem. Soc.*, **76**, 107 (1939).
12. M. E. Straumanis and Y. N. Wang, *This Journal*, **102**, 304 (1955).
13. M. E. Straumanis and D. C. Mathis, *ibid.*, **109**, 434 (1962).
14. M. E. Straumanis and B. K. Bhatia, *Metall.*, **16**, 535 (1962).
15. G. R. Hoey and M. Cohen, *This Journal*, **105**, 245 (1958).
16. B. Roald and M. A. Streicher, *ibid.*, **97**, 283 (1950).
17. D. A. Vermilyea, *ibid.*, **105**, 547 (1958).

The Role of Cementite in the Acidic Corrosion of Steel

D. N. Staicopolus

Engineering Research Laboratory, Engineering Department,
E. I. du Pont de Nemours & Co., Wilmington, Delaware

ABSTRACT

Iron carbide (cementite) was isolated from specially prepared carbon-iron alloys by a selective (chemical) dissolution of ferrite in alcoholic HCl. Cathodic polarization studies on cementite electrodes have shown that this compound is an active cathodic site in corrosion of steel in that it does not polarize at low current densities. At high current densities, however, cementite rapidly polarizes to the potential which is characteristic of iron under similar current density conditions. This is considered the result of the chemical decomposition of cementite to iron and a variety of hydrocarbons under the influence of the cathodically evolved hydrogen. A number of hydrocarbons (predominantly methane) and carbon monoxide mixed with the evolved hydrogen have been identified by mass spectrometry.

The corrosion of a metal in contact with an electrolyte is a process involving at least one electrochemical step and one or more purely chemical steps. Active metals will react continuously with the electrolyte if this spontaneous process is not blocked either by dense product formation, by concentration polarization, or by electrical polarization. For a spontaneous reaction of an electrochemical nature to proceed, it is necessary to provide sites on the surface of the metal where a cathodic reaction will take place concurrently with an electrochemically equivalent anodic reaction which brings about the corrosion of the metal.

In the case of a pure iron specimen, the corrosion rate is slow, since both anodic and cathodic sites consist of iron. In steel, however, the presence of two phases, *i.e.*, cementite (Fe_3C) and ferrite (α-Fe), can accelerate the corrosion rate since it is possible for cementite to assume the role of a cathodic site while ferrite corrodes.

The over-all corrosion of low carbon steels and cast irons has been the subject of numerous investigations (1), none of which, however, have dealt specifically with the role of Fe_3C in the over-all process.

The oxidation of iron under anodic conditions has been studied (2), and information on the stability and complexing characteristics of the various products of oxidation can be extracted from the study of potential-pH diagrams contributed by Deltombe and Roubaix (3).

The behavior of cementite under cathodic polarization, however, has not been disclosed, presumably because of the difficulties encountered in the isolation of this metastable compound. It was therefore the purpose of this study to prepare Fe_3C and to study its behavior under cathodic polarization conditions in neutral and in acidic solutions.

Experimental

Preparation of cementite.—Cementite was extracted from specially prepared carbon/iron alloys. The latter were prepared at high temperature in an alumina crucible suspended in a vertical, 2-in. diameter Vycor pipe in an argon atmosphere. Pure iron (250 ppm impurity) and spectroscopic grade graphite were introduced into the crucible and gradually melted by induction. The melt was maintained in this condition for 30 min, then the crucible was released and allowed to drop into a container of chilled brine. Alloys containing approximately 1.8 and 6.7% carbon were prepared by this method and were used as sources for cementite.

The isolation of cementite was accomplished by selective dissolution of the ferrite phase in alcoholic HCl (1 part conc HCl, 1 part water, 1 part ethyl alcohol). The specimen was magnetically suspended near the surface of the solution. Platelets of cementite, when released, were attracted by the magnet and remained in the upper layers of the solution. The cementite, still attached to the specimen in the form of a loose network, was carefully removed by scraping and all the product was subsequently crushed to a fine powder. This product showed, under x-ray examination, neither the presence of free iron nor of graphite.[1] Cementite electrodes suitable for electrochemical investigation were formed by compressing the powder hydrostatically at room temperature to form a compact cylinder. Electrical contact was made via a small platinum wire surrounding the compact or embedded in it. The electrode was then molded in "Koldweld" cement.

The known, apparent area of the compact was exposed to the solution by grinding the plastic mounting. After each run, a new area of cementite was exposed by further grinding.

Electrochemical characteristics.—Current-potential relationships were obtained under constant-potential as well as under constant-current techniques. A specially arranged Luggin capillary was used. It was formed by heat-drawing the end of a Pyrex tube to a size that was small, compared to the size of the test electrode (about 0.3 mm OD). The Pyrex tube was then filled with the test solution, and a standard calomel electrode (Beckman type) was

[1] The electrochemical (anodic) selective dissolution of ferrite and, thus, the isolation of the carbide as described by Gurry *et al.* (4) was not attempted since the chemical separation here described was found effective and less time-consuming.

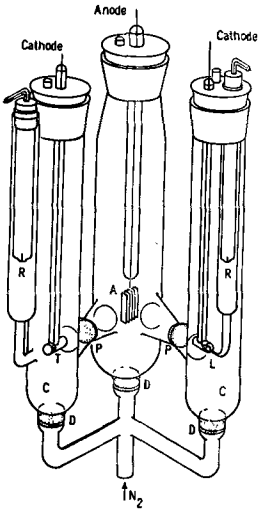

Fig. 1. Electrolytic cell for cathodic polarization studies

immersed in its upper section. This simple arrangement (L in Fig. 1) permits easy reforming of the tip and prevents contamination of the test solution (at the vicinity of the cathode) with chlorides or nitrates, an unavoidable circumstance with "conventional" agar-agar bridges.

For the amperostatic measurements, both the direct and the interrupter methods were employed and gave similar data. For the interrupter method, an electronic unit similar to the one described in an earlier publication (6) was used. With this method, no Luggin capillary was necessary, the reference electrode being in a side compartment (R) as shown in Fig. 1. The cell was designed so as to permit both methods of measurement. Each of two cathode compartments (C) was separated from a common anode compartment (A) by sintered glass plugs (P). Purified nitrogen was saturated with water vapor by bubbling through a bubbler containing a large quantity of the test solution before it was introduced through the fritted glass disks (D) into the main compartments, (A) and (C). Runs made by the interrupter method (current "off," 100 μsec; current "on," 1900 μsec) showed the polarization on cementite electrodes did not appreciably decay during the "off" period.

Solutions.—A 3% aqueous sodium chloride solution was the principal electrolyte. To this were added inorganic salts and some organic compounds, all being in one way or another classified as corrosion "inhibitors." A solution of 1*N* $FeSO_4$ acidified with H_2SO_4 to a *p*H of 0.7 and another solution of H_2SO_4 (*p*H 0.7) were also used in these cathodic polarization studies.

Discussion of Results

Shown in the accompanying figures are representative potential *vs.* logarithmic current density curves obtained on cementite. Figure 2 represents such data in acid (H_2SO_4 at *p*H 0.7, curve I) and in 1*N* $FeSO_4$ acidified with H_2SO_4 to *p*H 0.7 (curve II). The cathodic polarization on iron in the $FeSO_4$/H_2SO_4 solution is also shown (curve IV).

It is observed that at low current densities the polarization on cementite is low (Tafel slope 0.028),

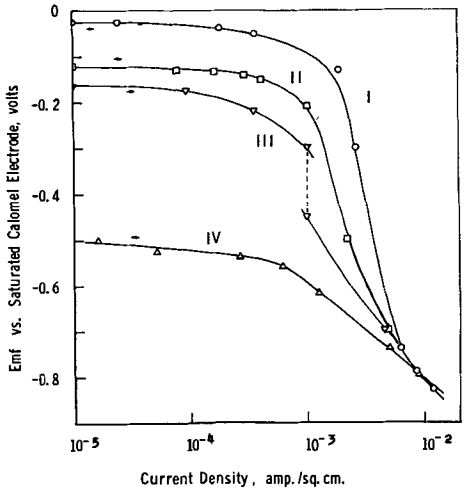

Fig. 2. Cathodic polarization *vs.* current density, iron and iron carbide in $FeSO_4/H_2SO_4$, *p*H 0.7. ○ Iron carbide in H_2SO_4, *p*H 0.7; □ iron carbide in 1*N* $FeSO_4$ + H_2SO_4, *p*H 0.7 (ascending current density); ▽ iron carbide in 1*N* $FeSO_4$ + H_2SO_4, *p*H 0.7 (descending current density); △ iron in 1*N* $FeSO_4$ + H_2SO_4, *p*H 0.7.

indicating that an atomic recombination process is the rate-controlling step in the electrodeposition of hydrogen. In this respect, cementite resembles platinum, providing an effective cathodic site for the deposition of hydrogen. This resemblance would be more complete if cementite were shown to possess high energy of adsorption for hydrogen, also, as does platinum. As a matter of fact, some evidence will be presented in the latter part of this discussion suggesting that this is probably true.

At higher current densities (*ca.* 10^{-3} amp/cm^2) rapid polarization of cementite begins but, beyond 10^{-2} amp/cm^2, the slope diminishes and becomes approximately equal to that of iron in the same solution (Tafel slope *ca.* 0.15) (7).

It is of interest to note that a prepolarized electrode of cementite will show a certain degree of hysteresis in the *E vs.* log *i* plot if such is obtained with descending values of *i* (current density).

Hysteresis may be very short as in acid media, as shown by curve III, Fig. 2, or very persistent as in neutral solutions, as shown in Fig. 3, curve II, and in Fig. 4, curves II and IV.

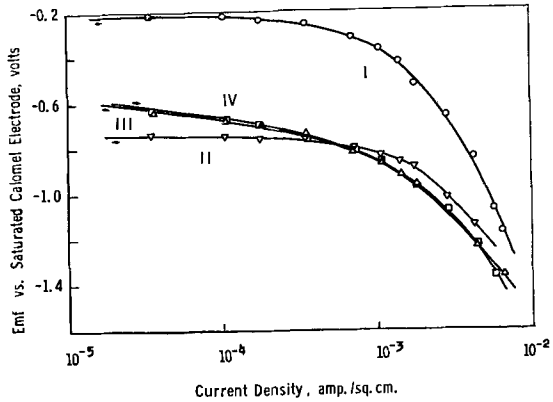

Fig. 3. Cathodic polarization *vs.* current density, iron and iron carbide in 3% NaCl + 0.1M $Na_2Cr_2O_7$.

Iron	Cementite	Current density
△	○	Increasing
□	▽	Decreasing

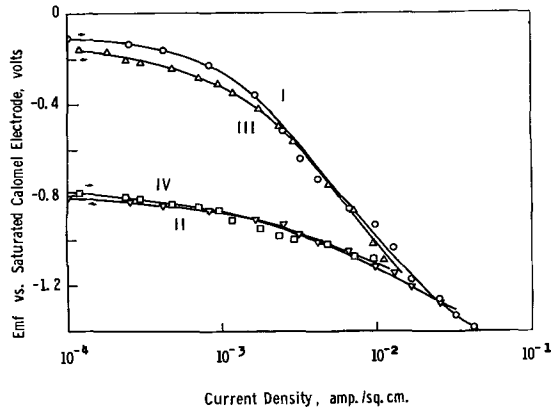

Fig. 4. Cathodic polarization *vs.* current density, iron carbide in 3% NaCl (neutral) and in 3% NaCl (neutral) + 0.1*N* $NaNO_2$. Fe_3Cl in 3% NaCl (neutral): △ ascending current density; □ descending current density. Fe_3Cl in 3% NaCl (neutral) + 0.1*N* $NaNO_2$: ○ ascending current density; ▽ descending current density.

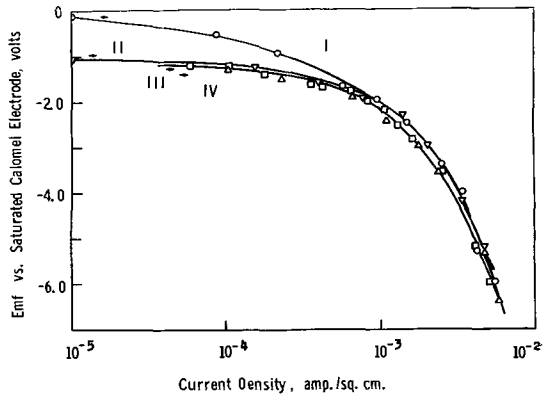

Fig. 5. Cathodic polarization *vs.* current density, iron and iron carbide in 3% NaCl containing 0.3 mole fraction glycerine.

Iron carbide	Iron	Current density
I	III	Ascending
II	IV	Descending

Information thus far obtained indicates that cementite possesses the following properties: (i) platinum-type cathodic behavior at low current densities; (ii) high affinity for hydrogen (as is required for a platinum-type behavior); (iii) rapid polarization in a narrow current-density region; (iv) change in Tafel slope at current densities greater than 10^{-2} amp/cm^2 to that of iron in the same solution; (v) hysteresis in overpotential *vs.* log *i* which is dependent on the pH (neutral or acidic) of the solution used. These facts permit the consideration of the following mechanism concerning the behavior of cementite in the corrosion of steels. At low current densities, cementite acts as an effective cathodic site offering least resistance to the electrochemical dissolution of ferrite. At higher current densities, adsorbed hydrogen on cementite becomes chemisorbed and, eventually, the following reaction can occur

$$Fe_3C + H_2 \xrightarrow[\text{cathode}]{} 3Fe + (-CH_2-)$$

The consequences of such a reaction are as follows: (i) iron carbide is reduced to iron (in the current density region of 10^{-3}-10^{-2} amp/cm^2; (ii) cathodic polarization characteristics are now those of an iron surface; (iii) iron surface characteristics are retained when the current density is reduced, if the electrolyte is neutral; but (iv) iron carbide characteristics are resumed in acid media, probably because of chemical dissolution of the surface (iron) in the electrolyte; (v) hydrocarbons are produced at the cathode either during cathodic polarization of cementite or during the chemical action of an acid on steels, since the evolution of hydrogen in the latter case, also, takes place on cementite (cathode sites).

Production of hydrocarbons on cementite.—It is known that a variety of hydrocarbons are produced during the dissolution of steels and cast irons in strong acids, but a detailed analysis of these products has not been disclosed. An attempt was therefore made to collect and analyze these products by mass spectrometric techniques.

The following substances were identified: H_2, 87.8%; CH_4, 4.5%; CO, 3.2%; C_3H_8 and C_4H_8 (each), less than 1.0%; C_2H_2, C_2H_6, C_4H_{10}, and H_2O (each) less than 0.5%; and CO_2, trace. It is very surprising that an appreciable percentage (3.2%) of CO was detected. This is not fully understood, but is tentatively attributed to the high affinity of cementite (or possibly an intermediate hydrocarbon residue) for hydrogen which is abstracted from a water molecule as indicated by the following equations

$$2Fe_3C + H_2O \rightarrow 6Fe + (-CH_2-) + CO$$

or

$$Fe_3C + (-CH_2-) + H_2O \rightarrow 3Fe + CH_4 + CO$$

Corrosion inhibitors.—The mechanism of action of a corrosion inhibitor cannot be generalized. Most probably, however, the inhibitor or a by-product can block either the anodic or the cathodic reaction by interference in the electrochemical step or in the chemical step. Additions of dichromate ions and nitrite ions in the NaCl solution used for the cathodic polarization studies on cementite (Fig. 3 and 4) show very little effect, if any. This is to be expected if these inhibitors act on the anodic sites (ferrite), as it is generally accepted, and not on the cathodic sites (cementite).

It was also of interest to study the effect of additions of glycerine and ethyl alcohol to the NaCl solution on the cathodic behavior of cementite, since it has been observed (8) that the rate of corrosion of steels in NaCl solutions containing these compounds is reduced. Jenkins has interpreted the data by assuming that in the presence of glycerine the activity of water at the surface of the specimen is drastically reduced. He has concluded that, since water is a participant in the over-all corrosion process, a reduction of its activity would reduce the corrosion rate.

Figure 5 of this study shows hydrogen overpotential *vs.* logarithmic current density plots obtained in 3% NaCl solution containing glycerine.[2] It is observed that a rapid polarization of cementite is brought about at low current densities (curve I) and

[2] Similar behavior has been observed in solutions containing ethyl alcohol instead of glycerine.

that the over-all polarization characteristics (after the initial polarization) resemble those of iron (curve II resembles curves III and IV). The role of glycerine or of ethyl alcohol is not yet fully understood, but from the electrochemical data, however, (Fig. 5) one might conclude that a reduction in the corrosion rate in glycerine/NaCl (aq.) solution is probably due to the rapid irreversible conversion of cementite to ferrite (iron), thereby reducing the potential difference between local anodes and cathodes.

Manuscript received Sept. 1, 1961; revised manuscript received May 16, 1963. This paper was presented at the Los Angeles Meeting, May 6-10, 1962.

Any discussion of this paper will appear in a Discussion Section to be published in the June 1964 JOURNAL.

REFERENCES

1. Among other treatises on this subject, the following is listed as a typical example: U. R. Evans, "The Corrosion and Oxidaion of Metals," St. Martins' Press, Inc., New York (1960).
2. T. P. Hoar, *Trans. Faraday Soc.*, **45**, 683 (1949).
3. E. Deltombe and M. Pourbaix, CEBELCOR RT7 (1954), CITCE VI, Butterworths, London (1954).
4. R. W. Gurry, T. Christakos, and C. D. Stricker, *Trans. Am. Soc. Metals*, **50**, 105 (1958).
5. D. N. Staicopolus, *Rev. Sci. Instr.*, **32**, 176 (1961).
6. D. N. Staicopolus, E. G. Yeager, and F. Hovorka, *This Journal*, **98**, 68 (1951).
7. International Critical Tables and J. O'M. Bockris, "Electrochemical Constants," Nat. Bur. Stand., No. 524, p. 243 (1953).
8. F. Jenkins, To be published.

Antireflection Films on GaAs Electroluminescent Diodes

O. A. Weinreich

General Telephone & Electronic Laboratories, Inc., Bayside, New York

ABSTRACT

The change of electroluminescent radiation of GaAs diodes during SiO evaporation was investigated. It is shown that a GaAs diode, when a.c. operated during evaporation, can be used to monitor its film thickness. At room temperature, the light output increases about 35% for quarter wavelength films of SiO. Monitoring GaAs diodes are also used to improve the transmittance of GaAs filters from 44% to 85% at wavelengths of about 0.9μ near the band gap.

Considerable transmission losses of radiation generated in dielectrics such as GaAs are due to their high refractive indices. For GaAs with $n = 3.55$ (1), total reflection at the GaAs-air discontinuity occurs at an angle of incidence of about 16°. The reflectivity for this interface at perpendicular incidence is $R = (n_3 - n_1/n_3 + n_1)^2 = 0.314$ with $n_1 = 1$ for air and $n_3 = 3.55$ for GaAs. By using the same value of R for all rays incident within the critical angle, the error is less than 10%. The theoretical increase in radiation by reducing the reflectivity to zero by means of an optimum single-layer antireflection coating amounts then to approximately 46%.

Internal reflection losses can be reduced by making use of the properties of a homogeneous dielectric film between the two media. The optimum conditions for reducing the internal reflectivity require that (i) the refractive index of the film be $n_2 = \sqrt{n_1 n_3}$; (ii) the film thickness be $t = \lambda/4n_2$ or an odd multiple of this value, where λ is the wavelength in air at which reflection reduction is to be obtained.

The reflectivity due to a homogeneous transparent dielectric film with index of refraction n_2 and thickness t is (2)

$$R = \frac{r_{32}^2 + r_{21}^2 + 2r_{32}\, r_{21} \cos 2\beta}{1 + r_{32}^2\, r_{21}^2 + 2r_{32}\, r_{21} \cos 2\beta} \qquad [1]$$

where r_{ij} is the reflection coefficient for interface ij as shown in Fig. 1, and $\beta = (1/\lambda)2\pi n_2 t \cos\theta_2$. For the work described here, $\cos\theta_1 = \cos\theta_2 = \cos\theta_3 = 1$.

Figure 2 shows a plot of R *vs.* k, where k is $n_2 t/\lambda$, for various values of n_2 with $n_3 = 3.55$ (GaAs) and $n_1 = 1$ (air). For $k = 0.25$ or $t = \lambda/4n_2 = \lambda_0/4$, R goes through a minimum, and for $n_2 = 1.9$ it is essentially zero.

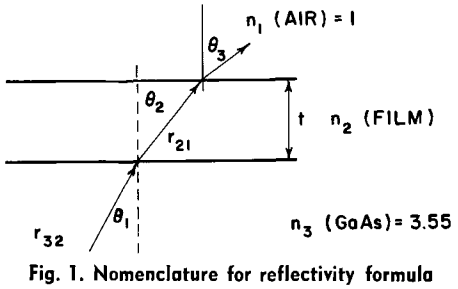

Fig. 1. Nomenclature for reflectivity formula

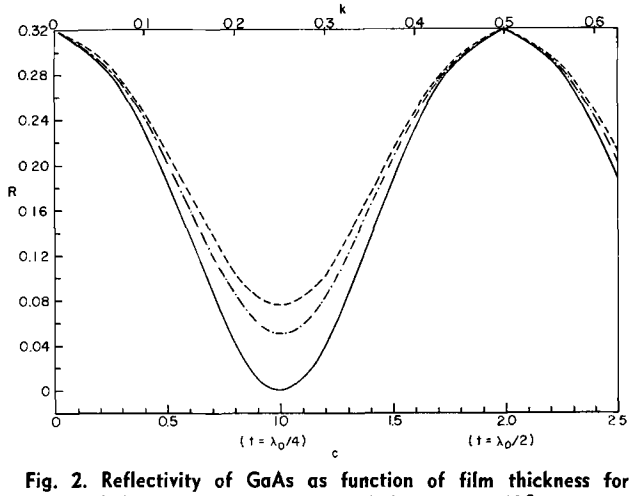

Fig. 2. Reflectivity of GaAs as function of film thickness for different dielectrics. .—.—., n_2 = 1.5, $\lambda_0/4$ = 1500Å; ———, n_2 = 1.9; $\lambda_0/4$ = 1185Å; — — — — n_2 = 2.5, $\lambda_0/4$ = 900Å.

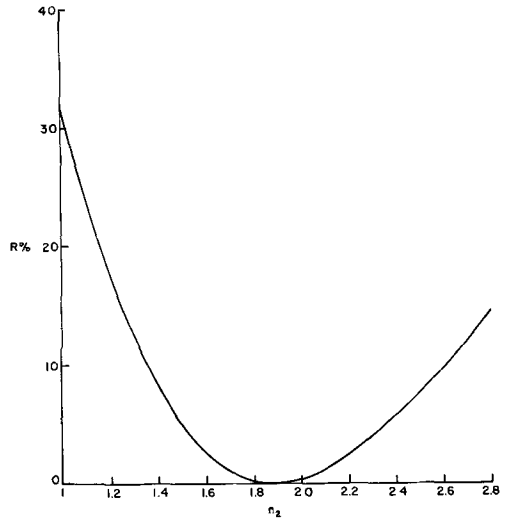

Fig. 3. Reduction of GaAs reflectivity at $\lambda_0/4$ film thickness vs. refractive index of the film.

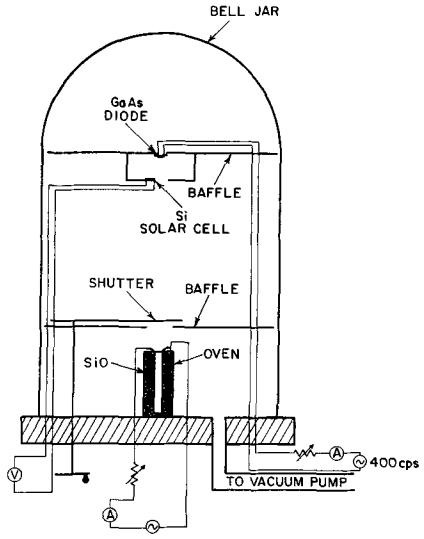

Fig. 4. Evaporation arrangement (schematic)

The abscissa of Fig. 2 also shows c, the fractional multiplier of $\lambda_0/4$, with a range from 0 to 2.0 corresponding to the range in k from 0 to 0.5. For a given reflectivity on one of the curves, the required thickness of the film is just $t = c(\lambda_0/4)$. Note that when films of refractive index different from the optimum value of 1.9μ are applied, the reduction in reflectivity is still relatively large. Figure 3 shows how the reflectivity is affected by the index of refraction of the quarter wavelength film. The refractive index of SiO (1.9) approaches the theoretical optimum value for elimination of the GaAs-air internal reflection within the critical angle.

Experimental

Films of SiO were evaporated onto polished GaAs injection luminescence diodes. The evaporation was carried out in a bell jar at a vacuum of 10^{-5} to 10^{-6} mm Hg. Reproducible rates of evaporation were obtained by using an oven as described by Drumheller (3). The physical properties of vacuum-evaporated SiO films depend strongly on source temperature and partial vapor pressure of oxygen in the evaporation chamber. For instance, the refractive index varies from 2 to 1.75 with a partial oxygen pressure change from 10^{-7} to 10^{-4} mm Hg (4). The color of a 2700Å film under these conditions changes from brown to green to transparent. The films reported here were yellow-brown and the refractive index was estimated to be 1.9.

In GaAs room temperature injection luminescence, light with a maximum intensity at approximately 0.9μ is generated inside a dielectric. This allows one to use a unique monitoring system for film thickness control. During the SiO evaporation the GaAs diode is operated and the change in light output due to the dielectric film is measured with an Si solar cell. During the evaporation, light from the evaporation source also reaches the detector either by reflection from the evaporation chamber or by reflection from the GaAs diode. This undesired contribution to the measured photovoltage of the Si solar cell is avoided by driving the GaAs diode with an a-c (400 cycle) voltage. The modulated light output generates a modulated photovoltage which is measured by an a-c voltmeter or oscilloscope. The arrangement is shown schematically in Fig. 4.

Results

To investigate reflectivity changes during SiO evaporation, GaAs diodes were made with emitting surfaces 0.125 x 0.125 in. The p-n junctions were made by Zn diffusion into 0.012 ohm-cm Sn-doped base material, and the light emission was measured from the n-type side.

When the SiO evaporation was interrupted at the first maximum of light output, the increase amounted to about 35%. Neglecting multiple internal reflections within the GaAs, the calculated increase is 46%. A smaller increase is expected if one assumes multiple reflections. Figure 5 shows a typical curve of the per cent increase in light output *vs.* time of evaporation. Films of SiO whose thicknesses were monitored by a GaAs diode were also deposited on GaAs filters in order to improve their transmission characteristics. For this purpose the GaAs filters were held in the evaporation chamber adjacent to the GaAs diode. The filters were

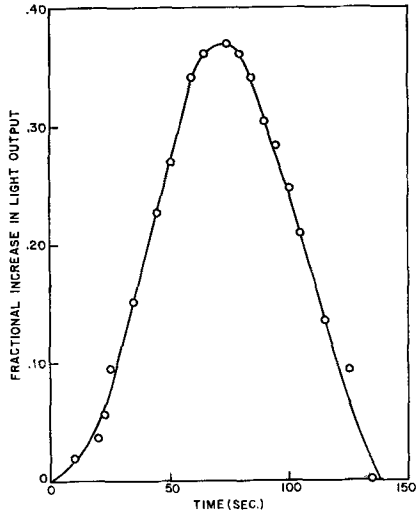

Fig. 5. Fractional increase of light output vs. time of evaporation.

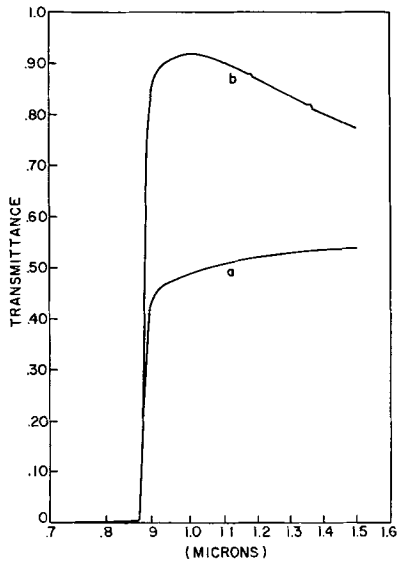

Fig. 6. Transmission curves for 0.010 in. thick GaAs filter: (a) uncoated; (b) SiO film $\lambda_0/4$ thick for $\lambda = 0.9\mu$.

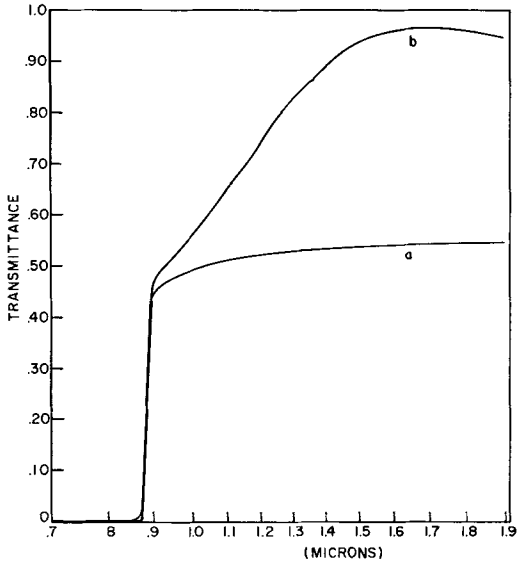

Fig. 7. Transmission curve of 20 mils thick GaAs filter: (a) uncoated; (b) SiO film $\lambda_0/2$ thick for $\lambda = 0.9\mu$.

prepared from lightly doped n-type material ($\sim 2 \times 10^{15}$/cc). If absorption is negligible, the transmission should be about 52%. Figure 6a is a transmission curve of a 0.010 in. thick filter, both sides of which were optically polished. At wavelengths beyond the absorption edge the transmission is 55%. At $\lambda = 0.9\mu$ the transmission is found to be 44%. The absorption coefficient calculated for this transmission is about 5 cm^{-1}. This is in reasonable agreement with the published values of absorption coefficients for GaAs (5).

After coating both sides of this sample with an SiO film of quarter wavelength thickness for $\lambda = 0.9\mu$ the transmission curve Fig. 6b is obtained where the transmission at 0.9μ is increased to 85%. From Fig. 2 we see that the reflectivity around its minimum value changes only slowly with film thickness. This explains the appearance of a maximum at $\lambda = 1.0\mu$ in the transmission curve of Fig. 6b. When the evaporation onto an uncoated sample is continued until the light output from the controlling GaAs diode has passed its first maximum and decreases to its initial value, the thickness then is $\lambda_0/2$ for 0.9μ. This corresponds to a quarter wavelength film at 1.8μ. The effect of this film thickness on the transmission of a 0.020 in. thick sample is shown in Fig. 7. At 1.8μ the transmission increased from 55% for the uncoated sample to 96% after coating.

The film thickness for quarter wavelength was checked by placing a glass plate next to the GaAs diode and measuring the film thickness with an interferometer. The quarter wavelength thickness calculated with $\lambda = 0.9\mu$ and $n_2 = 1.9$ was typically within minus 10% of the interferometer measurement. This difference is partly due to the fact that the RI^2 losses of the GaAs diode increase the junction temperature causing wavelength shifts to about 0.93μ. Also the assumed refractive index of 1.9 may be too high.

It should be mentioned that a symmetrical spread of the emission band around 0.9μ will not influence the optimum thickness. However, the transmission will be affected by the bandwidth. The room temperature bandwidth of GaAs is about 300Å or 3%. As one can see from Fig. 2 this spread decreases the transmitted intensity by an insignificant amount.

Conclusion

Under the experimental conditions described, the light emission of GaAs diodes at room temperature can be increased about 35% by antireflection SiO films. Because of the relatively large percentage decrease in reflectivity of GaAs for quarter-wavelength films of varying refractive indices, the described monitoring system may be also used to control the film thickness of other dielectrics on different substrates.

Acknowledgment

The author wishes to acknowledge many helpful suggestions in numerous discussions with H. F. Lockwood of the laboratory. Thanks are due to S. Barton for programming the machine calculations and to J. Alonzo for assistance in making the measurements.

Manuscript received June 20, 1963.

Any discussion of this paper will appear in a Discussion Section to be published in the June 1964 JOURNAL.

REFERENCES

1. Frank Stern, Am. Phys. Soc. Meeting, March 1963.
2. M. Born and E. Wolf, "Principles of Optics," p. 61, Pergamon Press, New York (1959).
3. C. E. Drumheller, "Vacuum Technology Transactions," Proc. 7th Natl. Symp. 306, 1960. Pergamon Press, New York (1960).
4. J. Priest and H. L. Caswell, "Vacuum Technology Transactions," Proc. 8th Natl. Symp. 1962, Vol. 2, 947, Pergamon Press, New York (1962).
5. W. G. Spitzer and J. M. Whelan, *Phys. Rev.*, **114**, 59 (1959).

The Phase Diagram for the Pseudo-binary System $CdTe-In_2Te_3$

Lars Thomassen, Donald R. Mason, Gerald D. Rose,[1] John C. Sarace,[2] and Gerald A. Schmitt

Department of Chemical and Metallurgical Engineering, The University of Michigan, Ann Arbor, Michigan

ABSTRACT

The phase diagram for the binary system $CdTe-In_2Te_3$ has been obtained by correlating information from differential thermal analysis measurements, microscopic studies, and x-ray powder patterns. In establishing the terminal points for this diagram, the melting point for In_2Te_3 was found to be 667° ±1°C. For CdTe, a melting point of 1092° ± 2°C was indicated. In going across the diagram, four peritectic transformations are apparent. The first (β, $CdIn_2Te_4$) is at 785°C and 50% In_2Te_3 in CdTe; the second (γ, $CdIn_8Te_{13}$) is at about 702°C and 80% In_2Te_3 in CdTe; the third (δ, $CdIn_{30}Te_{46}$) is at 695°C and about 94% In_2Te_3 in CdTe; and the fourth (ϵ, In_2Te_3) occurs at 678°C and about 98% In_2Te_3 in CdTe. There is a large retrograde solubility of $CdIn_2Te_4$ in CdTe. The ϵ-phase transforms to an ϵ'-phase at 550°C in an apparent order-disorder transition. Electrical measurements on some peritectic compositions from this diagram are reported elsewhere.

This work was undertaken to ascertain the phase diagram of the pseudo-binary system $CdTe-In_2Te_3$ which produced a typical chalcopyrite-like ternary compound, $CdIn_2Te_4$. It was obtained by correlating information from differential thermal analysis measurements, microscopic studies, and x-ray powder patterns. This system is of interest since all compounds formed by mixing CdTe and In_2Te_3 are semiconductors (1).

The compounds formed in this manner actually would lie on a plane in the ternary Cd-In-Te system. Since the In-Te and Cd-Te systems both contain compounds which have congruent melting points, the complex ternary system of the elements can be simplified by finding the existence of pseudo-binary planes which should extend between the congruently melting elements and compounds. Not all planes extending between any two congruently melting constituents are pseudo-binary planes (2), but the plane described in this work is such a plane.

In checking the terminal points for this diagram, the melting point for CdTe was found to be 1098° ±3°C (1, 3), which represents a considerable deviation from the widely reported value of 1045°C (4). More recent measurements indicate that a better value is 1092° ± 2°C. The variation can be attributed to the differences in purity of the tellurium which was available to Kobayashi in 1910 (mp 437°C), and that which is available today (mp 450°C), as well as to differences in experimental techniques. Lawson, Nielsen, Putley, and Young (5) have recently reported the melting point of CdTe as 1106°C, and deNobel has reported a melting point of 1090°C (6, 7).

The melting point of In_2Te_3 has been measured by Klemm and Vogel (8) and reported to be 667°C. Hahn (9), Inuzuke and Sugaike (10), Woolley, Pamplin, and Holmes (11), and Zaslavskii and Sergeyeva (12) have characterized a structure of In_2Te_3 which forms from the zinc blende structure after long annealing, which would indicate the presence of a transition somewhere below the melting point. Gasson, Holmes, Jennings, Parrott, and Penn (13) have reported a transition at 617° ± 5°C. Zhuze, Sergeyeva, and Shelykh (14) have reported an order-disorder transition in In_2Te_3 at 600°C. Grochowski and Mason (15) have found a new phase in the indium-tellurium system of composition In_4Te_7 (which on further examination may prove to be In_3Te_5) which has most of the attributes of "ordered In_2Te_3," and decomposes peritectically to liquid and disordered In_2Te_3 at 625°C. Another new compound was found at composition In_3Te_4, which decomposes peritectically at 650°C. The presence of these two compounds very close to the In_2Te_3 composition can help to explain many of the anomalies which have been reported in the properties and structures of In_2Te_3 (15).

Hahn *et al.* (16) have made lattice parameter measurements on this system and investigated the crystal structures of the $CdIn_2Te_4$ phase. Woolley and Ray (17) have also made lattice parameter measurements in this system.

Experimental

The experimental work reported in the paper can be conveniently classified into three categories: the preparation of the compounds, the determinations of the solid-liquid equilibria, and the determination of the solid-solid equilibria. Electrical measurements of some of the peritectic compositions in this system are reported in another paper (22).

Sample preparation.—All compounds used in the study were made by direct fusion from commercially available high-purity elements. Indium of 99.999+% purity was obtained from the Indium Corporation of America. Cadmium of 99.99+% purity and tellurium of 99.999+% purity were obtained from the American Smelting and Refining Company. Stoichiometric amounts of the elements were weighed into clear fused silica ampoules, evacuated to a pressure below 10^{4-} mm Hg, and sealed. The fusions

[1] Present address: Westinghouse Research Center, Pittsburgh, Pennsylvania.

[2] Present address: Bell Telephone Laboratories, Inc., Murray Hill, New Jersey.

were carried out using a programmed nonlinear heating cycle (18) over a period of several hours in such a way that the heat of reaction was evolved gradually so as not to break the ampoules by any sudden increases in the vapor pressures. The content of each ampoule was homogenized by maintaining it above its liquidus temperature in a rotating, agitating furnace. The samples used in the x-ray studies were quenched in water. After fusion each DTA sample was removed from its original container, crushed, and transferred to a new fused silica tube containing a deep thermocouple well concentric with the tube axis. Each sample was annealed for at least 24 hr below the lowest transition temperature to equilibrate and homogenize the samples before the differential thermal analysis measurements.

Solid-liquid equilibria by differential thermal analysis.—The solid-liquid equilibrium temperatures have been determined primarily from DTA measurements. The apparatus used in this work has been described by Barnes and Mason (19).

The samples were heated and cooled inside a nickel block using a liquid indium standard, at a rate of 2.5°C/min from room temperature to a maximum temperature well above that of the highest transition, and back to room temperature. The sample and thermocouple arrangement is shown in Fig. 1. The furnace is purged with dry nitrogen in order to prevent corrosion of the nickel sample holder. Although the DTA sample tubes sometimes cracked at low temperature as the sample contracted around the thermocouple well, they were not wet significantly by the sample and no apparent oxidation occurred. In the absence of any obvious chemical reactions, all the emf differentials are attributed to latent heat transformations.

Over 50 samples covering the composition range from pure CdTe to pure In_2Te_3 were prepared in this system and representative results from differential thermal analysis measurements are shown in Fig. 2. Differential emf is plotted against sample temperature for several different compositions.

In analyzing the results from the DTA experiments, the heating and cooling curves must be interpreted differently, depending on the type of transition which is being observed. The peritectic and congruent melting transitions are relatively easy to recognize, since the point of maximum deviation on the heating cycle usually corresponds closely to the onset of a deviation during the cooling cycle. In dilute solutions, time lags may occur because of supercooling or because the exponential decay of the differential emf following large transitions may mask the smaller transitions. Liquidus and solidus temperatures which vary with both temperature and composition are the most difficult to determine accurately.

During the heating portions of the cycle, the solidus lines were obtained by choosing the point where the first deviation in the differential emf occurred. The liquidus point is generally chosen as the point where the differential emf returns to the base line. The presence of chunks and large crystals in many samples can give rise to erratic deviations in the re-

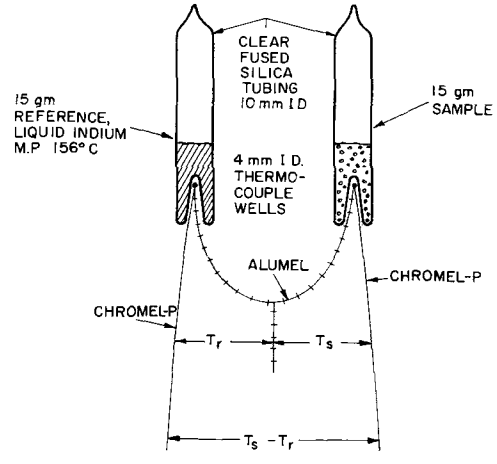

Fig. 1. Arrangement of differential thermal analysis sample and reference.

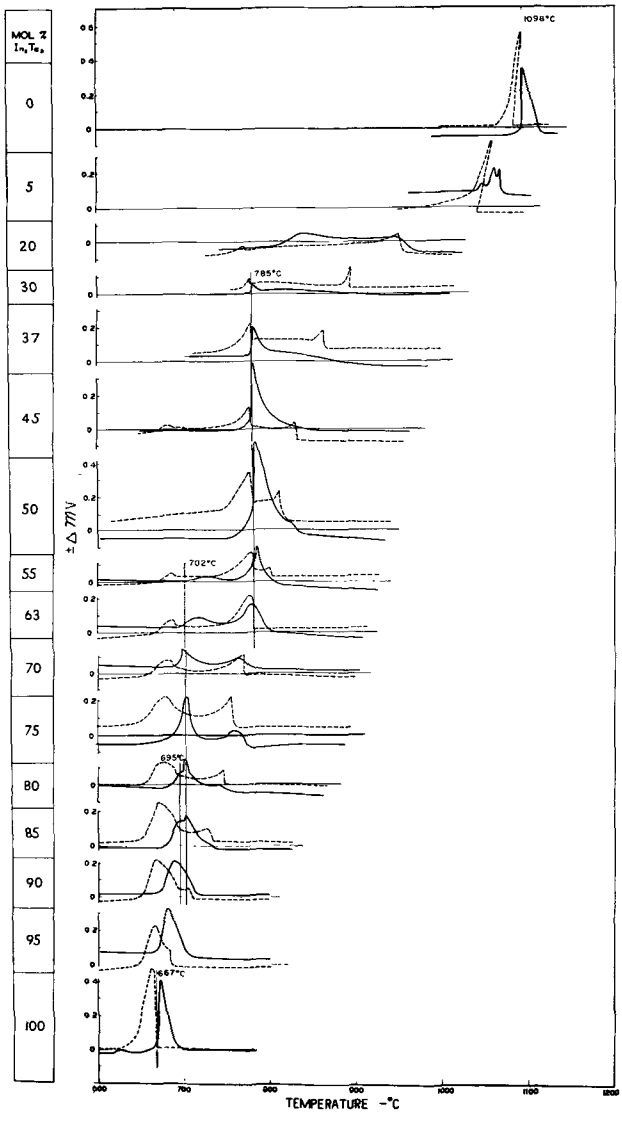

Fig. 2. Differential thermal analysis curves in the CdTe-In_2Te_3 pseudo-binary system, showing Δ emf as function of sample temperature for several representative compositions. The 15g samples were sealed in fused silica tubes under vacuum, measured inside a nickel block at heating and cooling rates of 2.5°C/min; samples were measured inside a nickel block, liquid indium being used as standard. Solid lines are heating curves and dashed lines are cooling curves.

gion of the liquidus so that it may be relatively difficult to establish with certainty.

During the cooling portion of the cycle, an initial differential deviation indicates the initial nucleation of the solid. If this initial deviation is moderate (producing less than 0.1 mv of differential emf), it usually presents a good indication of the position of the liquidus line. On the other hand, considerable supercooling has been observed on some samples, so that the released latent heat has been absorbed as sensible heat in the sample with an accompanying large increase in the sample temperature. This effect is particularly noticeable in the high-cadmium region in Fig. 2. In these instances, considerable judgment enters into the selection of the points which will actually be chosen to represent the data points, and it is highly desirable to have the differential curves for both the heating and cooling cycles. The ambiguity in interpreting the liquidus line from DTA results was particularly large over the range from 0 to 63 mole % In_2Te_3 in CdTe. The peritectic transformation at 785°C agreed well on both heating and cooling. From Fig. 2 other important transition points are apparent at 702° and 695°C. Note also the transition in the pure indium telluride (In_2Te_3) extending from 600° to 625°C. Work by Grochowski *et al.* (15) showed that the compound commonly identified as In_2Te_3 actually exists at 59.7 atomic per cent (a/o) Te ($In_{27}Te_{40}$) and the In_2Te_3 order-disorder temperature is between 550° and 600°C. The transformation shown for In_2Te_3 in Fig. 2 actually is a combination of the In_2Te_3 transformation and the In_4Te_7 (or In_3Te_5) peritectic.

Solid-solid equilibria from x-ray powder pattern studies.—The DTA runs gave erratic results below about 600°C and could not be relied on to clarify the exact location of phase boundaries at the high indium end of the phase diagram. Therefore, it was necessary to use x-ray powder pattern studies and microscopic examinations. The powder pattern analyses were made in 114.6 mm diameter cameras using Cu-K_α radiation through a nickel filter to eliminate the Cu-K_β radiation. The x-ray film was covered with an aluminum foil to reduce spurious radiation effects which arise from scattering.

The study of this system using x-ray powder patterns presents many problems, and the current literature is confusing. The variation in the lattice parameter over half of the composition range is confined to the third significant figure, increasing from 6.171Å for disordered In_2Te_3 to 6.24Å for the $CdIn_2Te_4$ phase. Furthermore, the works of Hahn *et al.* (16) and Woolley and Ray (17) both fail to identify the existence of our γ-phase, $CdIn_8Te_{13}$, and our δ-phase, $CdIn_{30}Te_{46}$. Therefore, the x-ray techniques were refined, and a very careful study was made on samples ranging in composition from 45 mole % In_2Te_3 in CdTe to 100% In_2Te_3. The samples were annealed for more than three months at 600°C. Just before the x-ray measurements were made a small amount of Si or Ge was added to each powder sample to provide internal calibration standards in the x-ray films. The powder patterns were then taken in a back reflection camera with a 120.0 mm diameter.

Results of these lattice parameter determinations are plotted in Fig. 3, along with the results of measurements that have been made by Hahn *et al.* (16) and Woolley and Ray (17). Woolley's technique of considering the Te lattice as the fixed entity, with varying amounts of Cd and In in the tetrahedral interstices, is used here, so that the two components then become Cd_3Te_3 and In_2Te_3. The lattice parameters then vary in a linear manner according to Vegard's law. An auxiliary nonlinear scale indicates the relationship between this viewpoint and molar mixtures of CdTe and In_2Te_3.

The data points clearly indicate that the lattice parameter becomes constant and equal to 6.195Å between 88.5 mol % In_2Te_3 in Cd_3Te_3 (72% In_2Te_3 in CdTe) and 92.5% (80%). At 92.5% In_2Te_3 in Cd_3Te_3 (80%) there is an abrupt discontinuity in the lattice parameter indicating a narrow solubility region for the $CdIn_8Te_{13}$ compound. The lower lattice parameter remains constant at 6.180Å until the composition exceeds 98 mol % In_2Te_3 in Cd_3Te_3 (94%). At this composition, there is another abrupt decrease in the lattice parameter to 6.172Å, whereupon it remains independent of composition over to the 100% In_2Te_3 point which is characteristic of the disordered ϵ-phase.

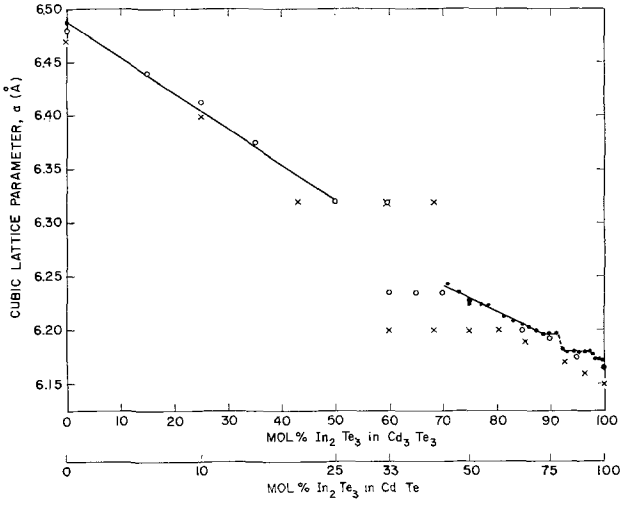

Fig. 3. Variation of cubic lattice parameter in the Cd_3Te_3-In_2Te_3 pseudo-binary system. X, Hahn *et al.*; O, Woolley and Ray; •, this work.

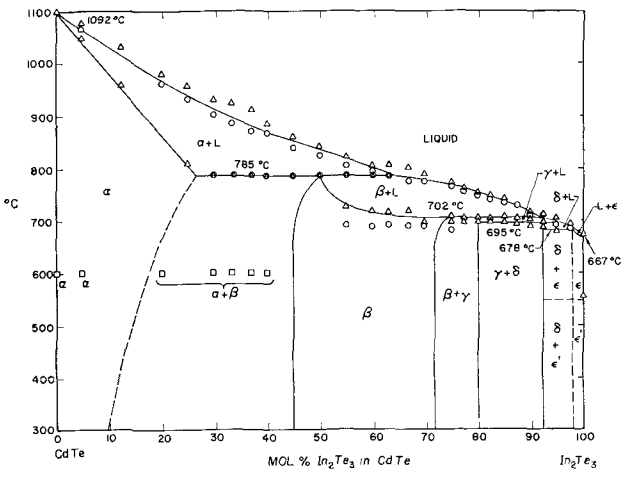

Fig. 4. Phase diagram for the pseudo-binary system CdTe-In_2Te_3

The phase diagram.—With these data, it is possible to determine the transition temperatures and composition ranges in the phase diagram. The results are plotted in Fig. 4. Both the heating and cooling liquidus points are plotted as discussed above. This diagram shows that cadmium telluride (CdTe = α) and indium telluride ($In_2Te_3 = \epsilon$) melt congruently. Although the actual In_2Te_3 composition deviates slightly from this composition the width of the pseudo-binary plane is apparently great enough to accommodate this slight difference in the central region of the phase diagram. DTA measurements on samples with compositions varying a few per cent on either side of this plane showed response curves considerably different from those shown in Fig. 2, indicating ternary behavior. In addition there are four peritectic points and a transformation in the In_2Te_3 structure from ϵ to ϵ'. The peritectic compounds occur at about 50% In_2Te_3 ($CdIn_2Te_4 = \beta$) and 785°C, at about 80% In_2Te_3 ($CdIn_8Te_{13} = \gamma$) and 702°C, and at about 93¾% In_2Te_3 ($CdIn_{30}Te_{46} = \delta$) and 695°C. As CdTe is added to In_2Te_3, a peritectic is formed at about 678°C and 98+% In_2Te_3. No congruently melting compounds form along this particular plane in the ternary system cadmium-indium-tellurium.

The retrograde solubility of $CdIn_2Te_4$ in CdTe was established by annealing samples in the α and ($\alpha + \beta$) range at 600°C and observing a Widmanstätten structure in microscopic examinations. The pure β-crystallites show up as single phase material, whereas the α-crystallites contain small platelets of precipitated β-phase. The relative amount of the α-phase observed in the photomicrographs decreased as the percentage of In_2Te_3 in the composition of the sample was increased towards the 50 mole % point. The solubility of In_2Te_3 in CdTe at the 785°C peritectic is over 25 mol %.

Crystal Structure Results

All the phases in the system were carefully analyzed by x-ray powder techniques. The diffraction patterns of the β, γ, and δ compounds all contain the zinc blende lines characteristic of the α and ϵ phases. However, the distribution and intensity of the additional weaker lines are distinctive, and it requires very careful measurements to separate them.

The structure studies in this system have been based solely on x-ray powder patterns. It is almost impossible to distinguish the atom positions from x-ray intensity measurements alone, since Cd, In, and Te have atomic numbers 48, 49, and 52, respectively, and therefore have almost identical x-ray scattering factors. However, since all these structures seem to be derived from the basic zinc blende structure, we have adopted the assumption of Hahn *et al.* (16) that the tellurium atoms alone form a face-centered cubic lattice, with the metallic atoms disposed in the tetrahedral interstices. Results of the measurements on each phase are discussed below.

The CdTe (α) *phase.*—The α-phase, cadmium telluride, has a zinc blende structure with lattice constant $a = 6.488 \pm 0.002$Å. Zachariasen (20) reported that $a = 6.477$ KX which is in good agreement with our work. As In_2Te_3 is added in solid solution to the CdTe, the lattice parameter is decreased.

The $CdIn_2Te_4$ (β) *phase.*—The first peritectic compound ($CdIn_2Te_4$) has been characterized by Hahn *et al.* (16) as a tetragonal, chalcopyrite-like structure with space group S_4^2 or $I\bar{4}$ and c/a = 2.00. Our x-ray results agree with those reported by Hahn, and we have accepted his structure designation without repeating the intensity calculations. Our results shown in Fig. 3 indicate that the lattice parameter actually varies with the composition of the β-phase from 6.24 to 6.197Å over the composition range from 45% In_2Te_3 in CdTe to 72% In_2Te_3 in CdTe. This curve is sufficiently accurate so that it can be used as an analytical technique for determining the composition of a material quite precisely.

The $CdIn_8Te_{13}$ (γ) *phase.*—The second peritectic ($CdIn_8Te_{13}$) or γ-phase exists at 80% In_2Te_3 in CdTe and seems to be a cubic chalcopyrite-like structure. The lattice parameter varies sharply from 6.197 to 6.180Å, and the existence of this phase was established only after careful lattice parameter measurements were made at a series of closely spaced compositions. Hence it is not surprising that Hahn *et al.* (16) and Woolley and Ray (17) have not defined the existence of the γ-phase, since their survey relied only on a relatively small number of x-ray analyses, and other means of phase diagram analysis such as DTA were not used.

The $CdIn_{30}Te_{46}$ (δ) *phase.*—The third peritectic ($CdIn_{30}Te_{46}$) or δ-phase exists at about 94% In_2Te_3 in CdTe and also seems to have a cubic chalcopyrite-like structure. The lattice parameter varies sharply from 6.180 to 6.172Å, and its existence could not be established by the data of Woolley and Ray (17).

The In_2Te_3 (ϵ) *phase.*—The ϵ-phase has a peritectic transformation at about 678°C and extends from 98% In_2Te_3 to pure In_2Te_3. It shows again the zinc blende structure, with some metal positions randomly vacant. At the pure In_2Te_3 side of the phase field we have found that $a = 6.171$Å, whereas Hahn and Klinger (21) reported $a = 6.146$Å, and Woolley and Pamplin and Holmes (11) report $a = 6.158$Å. Since our value is high, it has been carefully rechecked and is reproducible if quenching is carried out rapidly into ice water.

The ϵ-phase apparently transforms to an ordered ϵ' structure between 550° and 600°C. Inuzuke and Sugaike (10) report the ordered structure to be $F\bar{4}3$ m with $a = 18.40 \pm 0.04$Å, which corresponds to a basic cell dimension of 6.133Å. Woolley, Pamplin, and Holmes (11) have also considered the structure of low-temperature modification of In_2Te_3. Holmes suggests a tetragonal structure of P 4_2 m c m or P 4_2 n m, comprising basically nine cubic unit cells of a fluorite lattice with about two-thirds of the fluorite sites vacant. Woolley and Pamplin on the other hand suggest an orthorhombic structure, Imm2, derived from the zinc blende configuration with selected vacancies. The basic cell dimension measured by these workers is $a = 6.165$Å, which agrees exactly with our measurements.

Discussion

Although the presence of both the γ-phase and the δ-phase is indicated in our DTA data, the x-ray results of Hahn *et al.* (16) and by Woolley and Ray

(17) failed to show the existence of this phase. Therefore, the detailed and exhaustive x-ray measurements presented in Fig. 3 were made, where the data of the other workers are also presented.

The constancy of the lattice parameter in the two-phase region also warrants discussion. Between the α and β phases, lattice parameters characteristic of both phases were obtained in x-ray studies. When the β and γ phases are in equilibrium with one another it is presumed that each compound is created from a close packed Te lattice with identical lattice parameters, but the saturation cation ratio of In to Cd is different for the two phases. As this cation ratio increases in the γ-phase the lattice parameter decreases rapidly until a new phase (δ) forms from the same type of close packed Te lattice, and a constant lattice parameter is obtained in the two phase region.

After allowing for the conversion from KX values to angstrom units in Hahn's work, all his results are still low. Our agreement with Woolley and Ray is surprisingly good, and had they taken sufficient data they also should have found the γ-phase and the δ-phase. The zone refining experiment described by Woolley and Ray separates the α-phase from some β-phase material, but our DTA work clearly shows the peritectic behavior of the system, and clearly indicates that no eutectic is present in the system.

Acknowledgments

The authors would like to thank the many students who assisted in the preparation of the samples, and to acknowledge fruitful discussions with Professor J. C. Woolley, Dr. P. J. Holmes, and Dr. J. E. Parrott. This paper is Contribution No. 1 from the Semiconductor Materials Research Laboratory, College of Engineering, the University of Michigan, Ann Arbor, Michigan. This work was supported in part by Project MICHIGAN, under Department of the Army Contract (DA-36-039-SC-78801), administered by the U. S. Electronics Command, in part by grants from the National Science Foundation, and in part by the Institute of Science and Technology, at the University of Michigan.

Manuscript received Dec. 27, 1962; revised manuscript received June 10, 1963. This paper was presented at the Columbus Meeting, Oct. 18-22, 1959.

Any discussion of this paper will appear in a Discussion Section to be published in the June 1964 JOURNAL.

REFERENCES

1. D. R. Mason and D. F. O'Kane, "Proceedings of the International Conference on Semiconductor Physics, Prague, 1960," p. 1025, Czechoslovak Academy of Sciences, Prague (1961).
2. F. N. Rhines, "Phase Diagrams in Metallurgy," p. 193, McGraw-Hill Book Co., Inc., New York (1956).
3. D. R. Mason and B. M. Kulwicki, Electrochemical Society Chicago Meeting, Electronics Division Abstracts, 9, 192 (1960).
4. M. Kobayashi, *Z. anorg. u. allgem. Chem.*, **69**, 1 (1911).
5. W. D. Lawson, S. Nielsen, E. H. Putley, and A. S. Young, *J. Phys. Chem. Solids*, **9**, 325 (1959).
6. D. deNobel, *Philips Research Repts.*, **14**, 361 (1959).
7. D. deNobel, Ph.D. Thesis, University of Leiden (1958).
8. W. Klemm and H. U. v. Vogel, *Z. anorg. Chem.*, **219**, 45 (1934).
9. H. Hahn, *Angew. Chem.*, **64**, 203 (1952).
10. H. Inuzuke and S. Sugaike, *Proc. Japan Acad.*, **30**, 383 (1954).
11. J. C. Woolley, B. R. Pamplin and P. J. Holmes, *J. Less Common Metals*, **1**, 362 (1959).
12. A. I. Zaslavskii and V. M. Sergeyeva, *Solid State Physics (Russian)*, **2**, 2872 (1960).
13. D. B. Gasson, P. J. Holmes, J. E. Parrott, I. C. Jennings, and A. W. Penn, "Proceedings of the International Conference on Semiconductor Physics, Prague, 1960," p. 1032, Czechoslovak Academy of Sciences, Prague (1961).
14. V. P. Zhuze, V. M. Sergeyeva and A. I. Shelykh, *Solid State Physics (Russian)*, **2**, 2858 (1960).
15. E. G. Grochowski and D. R. Mason, Electrochemical Society Indianapolis Meeting, Electronics Division Abstracts, **10**, 100 (1961). (In_3Te_4 not shown).
16. H. Hahn, G. Frank, W. Klinger, A. D. Storger, and G. Storger, *Z. anorg. allgem. Chem.*, **279**, 241 (1955).
17. J. C. Woolley and B. Ray, *J. Phys. Chem. Solids* **15**, 27 (1960).
18. N. L. Hozak, J. S. Cook, and D. R. Mason, *This Journal*, **108**, 105 (1961).
19. C. E. Barnes and D. R. Mason, Electrochemical Society Chicago Meeting, Electronics Division Abstracts, **9**, 8 (1960).
20. W. Zachariasen, *Z. Phys. Chem.*, **124**, 277 (1926).
21. H. Hahn and W. Klinger, *Z. anorg. Chem.*, **260**, 97 (1949).
22. D. F. O'Kane and D. R. Mason, *This Journal*, **110**, 1132 (1963).

Semiconducting Properties of Peritectic Compounds from the Pseudo-binary System of $CdTe$-In_2Te_3

Daniel F. O'Kane and Donald R. Mason

The Department of Chemical and Metallurgical Engineering, The University of Michigan, Ann Arbor, Michigan

ABSTRACT

Single phase polycrystalline samples of three peritectic compounds from the pseudo-binary system of CdTe and In_2Te_3 were prepared by zone refining and zone leveling techniques. The compounds are 45 mole % CdTe-55 mole % In_2Te_3 ($CdIn_2Te_4$, β-phase), 20 mole % CdTe-80 mole % In_2Te_3 ($CdIn_8Te_{13}$, γ-phase), and 6 mole % CdTe-94 mole % In_2Te_3 ($CdIn_{30}Te_{46}$, δ-phase). The energy gap values obtained from electrical conductivity and Hall effect measurements show that $E_g = 1.38$ ev for the β-phase; $E_g = 1.02$ ev for the γ-phase; and $E_g = 1.17$ ev for the δ-phase. The addition of CdTe to In_2Te_3 or of In_2Te_3 to CdTe lowers the energy gaps of the resulting compounds.

The phase diagram for the CdTe-In_2Te_3 pseudo-binary system has been worked out by Mason and co-workers (1) using differential thermal analysis, x-ray measurements, and microscopic examinations, and is reported in the preceding paper. The semiconducting properties of three peritectic compositions in the pseudo-binary CdTe-In_2Te_3 system are reported in this work.

The pseudo-binary system of CdTe and In_2Te_3 was first investigated by Hahn *et al.* (2), who established the crystal structure for selected compositions in the system. Woolley and Ray (3) have reported x-ray analysis results, and Thomassen and Mason (4, 5) have given incomplete preliminary results of their work which is somewhat different from the final phase diagram reported in the preceding paper. The semiconducting properties of $CdIn_2Te_4$ have been investigated by Busch *et. al.* (6), who report an energy gap of 0.9 ev based on conductivity measurements over a temperature range. Optical measurements by Edwards and O'Kane (7) indicated an energy gap of 1.08 ev at room temperature, for indirect transitions. The energy gap for direct transitions is slightly greater.

In this work electrical conductivity and thermal conductivity measurements were made on the β-phase $CdIn_2Te_4$ material. Electrical conductivity, Hall effect, and Seebeck coefficient measurements were made on the γ-phase, $CdIn_8Te_{13}$, and the δ-phase, $CdIn_{30}Te_{46}$, materials. Zone refining and zone leveling techniques were used to obtain polycrystalline samples of the three peritectic compositions. The compositions of the single phase materials were established by x-ray analysis and comparison of the lattice parameter measurements throughout the phase diagram with the calibration reported in the previous paper (1).

Experimental Procedures

The samples for zone refining were prepared by fusing the stoichiometric quantities of the elements (99.999% purity tellurium and indium, and 99.99% purity cadmium) in sealed, evacuated fused silica tubes (8). Zone leveling techniques described by Mason and Cook (9) were used to separate two of the compounds, and zone refining was used to prepare the third compound. Hall effect and electrical conductivity measurements were made with direct current and a magnetic field of 2100 gauss in a hydrogen atmosphere. A dynamic calorimeter designed by La Botz (10) was used for the thermal conductivity measurements.

Results

The β-phase material was separated by zone leveling an ingot with an initial composition of 47 mole % CdTe and 53 mole % In_2Te_3. The resulting single phase, polycrystalline β-phase material in sections A and B of ingot number 137 with lattice parameter of 6.218Å, was identified as approximately 45 mole % CdTe and 55 mole % In_2Te_3 from the x-ray calibration curve determined in the preceding paper (1). Electrical conductivity measurements are shown in Fig. 1 for the two sections. Below 100°C, measurements of the Seebeck coefficient indicated that the samples are p-type. Electrical

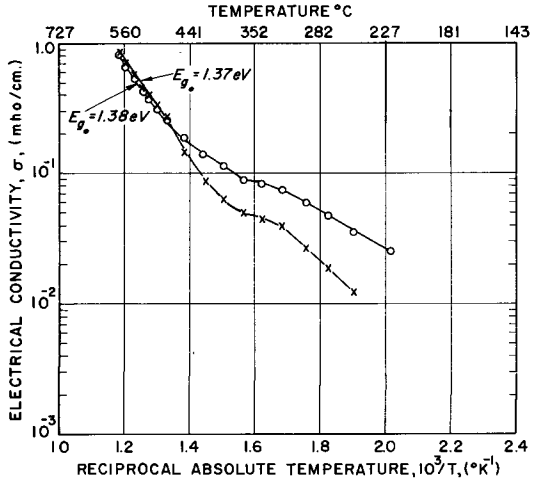

Fig. 1. Logarithm of electrical conductivity vs. reciprocal absolute temperature for β-phase material, sample No. 137, from the CdTe-In_2Te_3 system: X, section A; O, section B.

conductivity measurements in the extrinsic region indicated that there was an impurity gradient in the ingot, and the low-temperature Hall measurements were not reliable. Above 440°C, the Hall coefficient was too small to be measured.

Above 474°C, the electrical conductivity data in the intrinsic conductivity region indicated an energy gap of 1.37 ev for section A and 1.38 ev for section B. When considered in conjunction with the optical measurements of Edwards and O'Kane (7), these results indicate the variation of energy gap with temperature. The result is $(dE_g/dT) = -0.001$ ev/°K.

Thermal conductivity measurements on a section of sample No. 137 resulted in values of about 11 mw/cm°C between 60° and 300°C. The thermal conductivity sample contained some second phase material, but it should give a reasonable indication of the actual thermal conductivity of the β-phase material.

The γ-phase material is approximately 20 mole % CdTe-80 mole % In_2Te_3, $CdIn_8Te_{13}$. This composition was obtained from regions of two zone leveled ingots which had an initial composition of 10 mole % CdTe-90 mole % In_2Te_3. X-ray results on these regions, section 4 of sample No. 150 and section 4 of No. 151, showed a zinc blende-type structure with a lattice parameter, a_0, equal to 6.185Å for both samples. Normal zone refining of ingot No. 169, which had an initial composition of 17 mole % CdTe-83 mole % In_2Te_3, also produced some γ-phase material (section 2) with a lattice parameter, a_0, of 6.194Å and some weak diffraction lines which were not characteristic of a cubic structure. The difference in lattice parameter values between 169 {2} and the two exactly identical samples, numbers 150 {4} and 151 {4}, may be accounted for by a slight difference in composition of less than 1% and by ordering.

The electrical conductivity, σ, is plotted against the reciprocal of the absolute temperature, $1/T$, in Fig. 2 for the γ-phase samples, 150 {4}, 151 {4}, and 169 {2}. The energy gaps obtained from the slope of log σ *vs.* $1/T$ are: 0.98 ev for 150 {4}; 1.02 ev for 151 {4}; and 1.09 ev for 169 {2}. Both 150 {4} and 151 {4} are intrinsic before 280°C, whereas 169 {2} has a high impurity level as evidenced by the characteristics of the conductivity data. At low temperatures, 169 {2} is p-type, and, in the region of 250°C, it is n-type. Intrinsic conduction does not appear below about 440°C for this sample. A plot of the logarithm of the Hall coefficient times absolute temperature to the 3/2 power, $R_HT^{3/2}$, *vs.* the reciprocal of the absolute temperature, $1/T$, is given in Fig. 3 for samples 150 {4} and 151 {4}. The energy gaps calculated from the slope of $R_HT^{3/2}$ *vs.* $1/T$ are 0.98 ev for 150 {4} and 1.10 ev for 151 {4}.

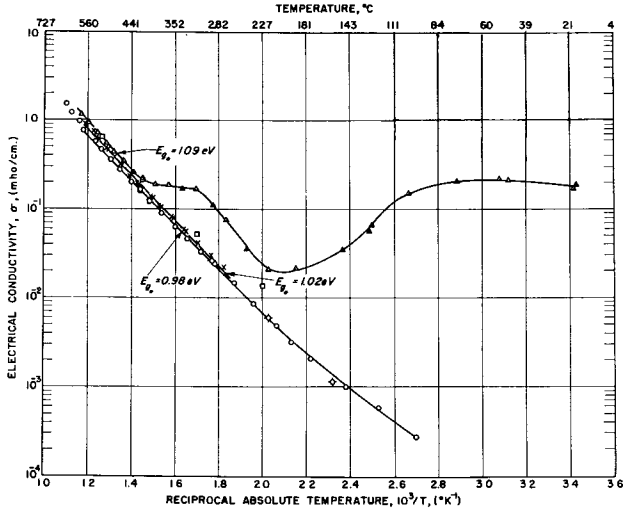

Fig. 2. Logarithm of electrical conductivity vs. reciprocal absolute temperature for the γ-phase material, sample No. 150 {4}, 151 {4}, and 169 {2}, from the CdTe-In_2Te_3 system. Circle, first heating cycle 150 {4}; Circle with four extensions, second heating cycle 150 {4}; X, heating cycle 151 {4}; square, cooling cycle 151 {4}; triangle, heating cycle 169 {2}.

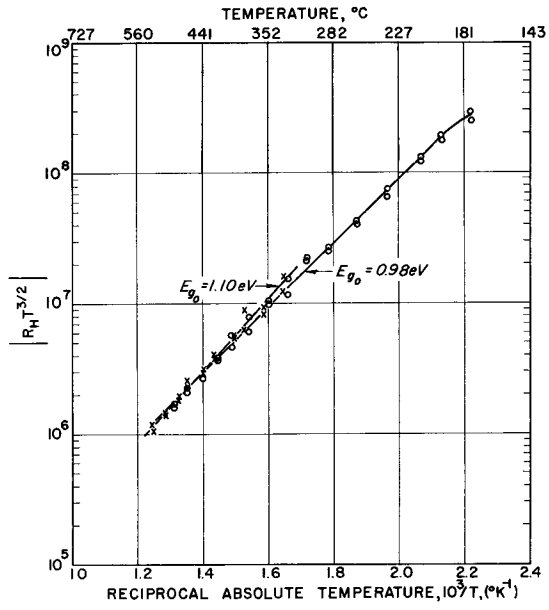

Fig. 3. Logarithm of $|R_HT^{3/2}|$ vs. reciprocal absolute temperature for the γ-phase material, sample No. 150 {4}, and 151 {4}, from the CdTe-In_2Te_3 system: O, No. 150 {4}; X, No. 151 {4}.

From the relationship for an intrinsic semiconductor

$$R_{H,i}\,\sigma_i = \beta(\mu_n - \mu_p)$$

where β is the ratio of the Hall mobility to the drift mobility, it can be seen that a plot of $R_H\sigma$ in the intrinsic range can give a minimum value for the electron mobility and a scattering exponent. A plot of this Hall mobility as a function of log T is given in Fig. 4 for the γ-phase samples 150 {4} and 151 {4}. The temperature dependence of $R_H\sigma$ is $T^{-1.7}$ for sample 150 {4} and $T^{-2.1}$ for sample 151 {4}. If the Hall mobility data can be extrapolated to 300°K, then the mobility of the γ-phase is 140 cm²/volt-sec for 150 {4} and 240 cm²/volt-sec for 151 {4}. The Seebeck coefficient, α, for the γ-phase material is shown as a function of absolute temperature in Fig. 5. Both samples are intrinsic above 250°C. The Seebeck data were plotted *vs.* reciprocal absolute temperature in an effort to ascertain the mobility ratio, but negative values were obtained. Apparently the measurements are too imprecise or else this material does not conform to the theory for a simple two band semiconductor.

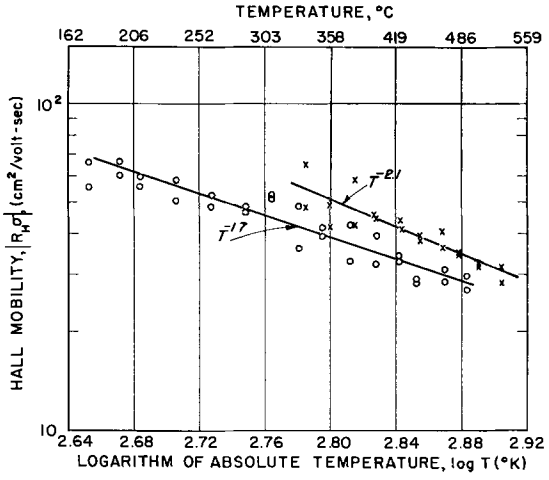

Fig. 4. Logarithm of Hall mobility *vs.* logarithm of absolute temperature for the γ-phase material, sample No. 150 {4} and 151 {4}, from the CdTe-In_2Te_3 system: ○, No. 150 {4}; X, No. 151 {4}.

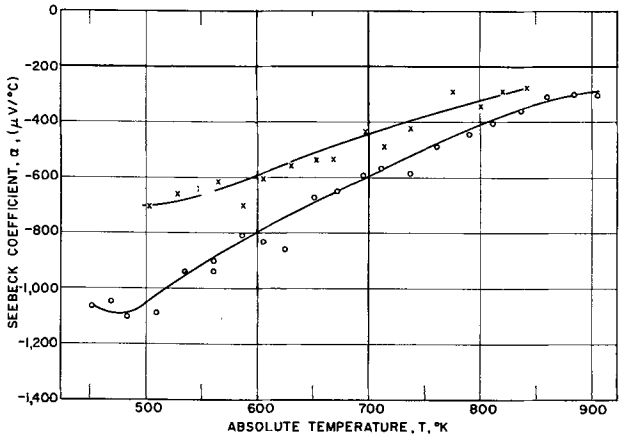

Fig. 5. Seebeck coefficient *vs.* absolute temperature for the γ-phase material, sample No. 150 {4} and 151 {4}, from the CdTe-In_2Te_3 system: ○, No. 150 {4}; X, No. 151 {4}.

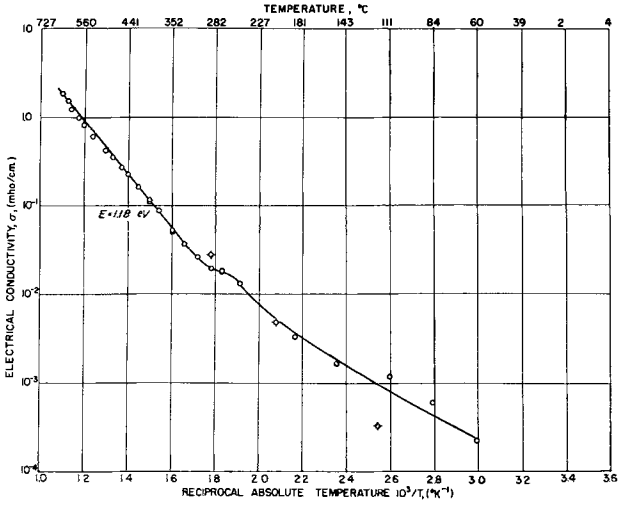

Fig. 6. Logarithm of electrical conductivity *vs.* reciprocal absolute temperature for the δ-phase material, sample No. 169 {3}, from the CdTe-In_2Te_3 system: circle, first heating cycle No. 169 {3}; circle with four extensions, second heating cycle No. 169 {3}.

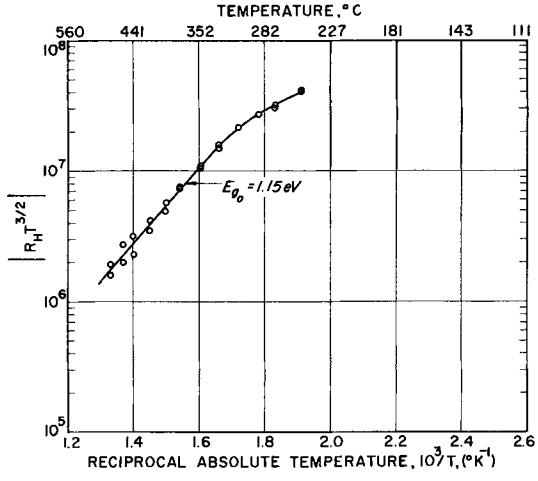

Fig. 7. Logarithm of $|R_H T^{3/2}|$ *vs.* reciprocal absolute temperature for the δ-phase material, sample No. 169 {3}, from the CdTe-In_2Te_3 system.

The δ-phase material was obtained from section 3 of the zone refined ingot, number 169, which had a lattice parameter, a_o, of 6.177Å, which is between the values of 6.172 and 6.180Å defining the limits of existence of this phase. This phase has a zinc blende-type cubic structure. Electrical conductivity results on this sample are shown in Fig. 6. The energy gap obtained from the log σ *vs.* $1/T$ data in the intrinsic region above 330°C is 1.18 ev. Figure 7 contains the Hall coefficient data on the δ-phase sample. The energy gap calculated from the slope of log $R_H T^{3/2}$ *vs.* $1/T$ is 1.15 ev. $R_H\sigma$ as a function of log T is given in Fig. 8. The Hall mobility is proportional to the temperature raised to the −1.1 power. By extrapolation, the Hall mobility at 300°K is 80 cm²/volt-sec. Seebeck coefficient data for this sample are contained in Fig. 9. Again, analyses of these data indicate a negative value for the mobility ratio, which cannot be interpreted intelligibly.

The electrical properties of the three peritectic materials from the CdTe-In_2Te_3 system are summarized in Table I.

Table I. Electrical properties of peritectic materials from the CdTe-In_2Te_3 system

Sample No.	Composition	Lattice parameter, a_o, Å	Energy gap, log σ *vs.* $10^3/T$ E_{g_0}, ev	Temp range of data, °C	Energy gap, log $R_H T^{3/2}$ *vs.* $10^3/T$ E_{g_0}, ev	Temp range of data, °C	Temperature dependence of Hall mobility $\mu_{H,n} = \mu_{300}(T/300)^{\gamma}$ μ_{300}	γ	Temp range of data, °C
137A	β-phase, $CdIn_2Te_4$	6.218	1.37	474 to 567					
137B	β-phase, $CdIn_2Te_4$	6.218	1.38	475 to 568					
169{2}	γ-phase, $CdIn_8Te_{13}$	6.194	1.09	437 to 581					
150{4}	γ-phase, $CdIn_8Te_{13}$	6.185	0.98	234 to 565	0.98	196 to 491	140	−1.7	177 to 491
151{4}	γ-phase, $CdIn_8Te_{13}$	6.185	1.02	276 to 567	1.10	335 to 529	240	−2.1	335 to 529
169{3}	δ-phase, $CdIn_{30}Te_{46}$	6.177	1.18	331 to 641	1.15	331 to 479	80	−1.1	250 to 479

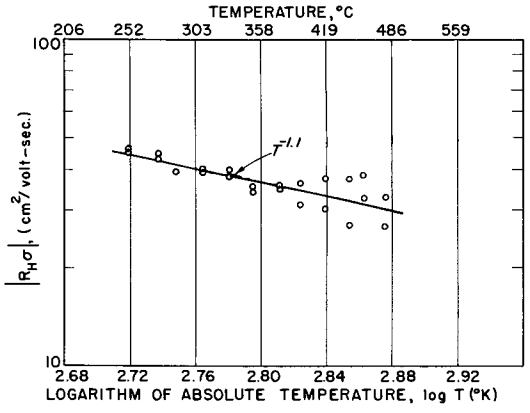

Fig. 8. Logarithm of Hall mobility vs. logarithm of absolute temperature for the δ-phase material, sample No. 169 {3}, from the CdTe-In_2Te_3 System.

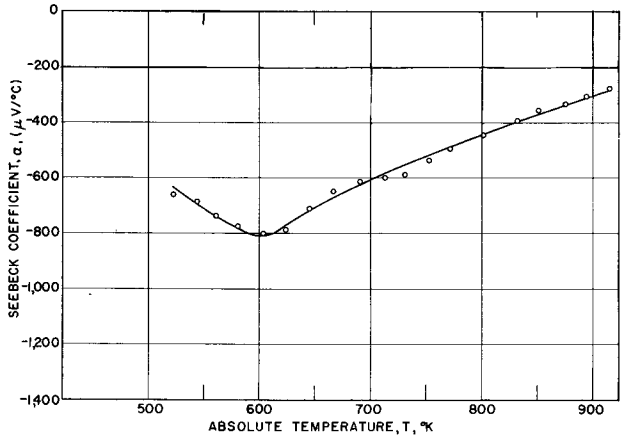

Fig. 9. Seebeck coefficient vs. absolute temperature for the δ-phase material, sample No. 169 {3}, from the CdTe-In_2Te_3 system.

Discussion

The energy gap of CdTe has been established as being equal to about 1.50 ev on the basis of electrical conductivity measurements (11), and 1.56 ev on the basis of optical measurements (11, 12). However there is considerable discrepancy in the reported values for the energy gap of disordered In_2Te_3. Although Zhuze *et al.* (13) report an energy gap of 1.12 ev for disordered In_2Te_3, and Gasson *et al.* (14) report that $E_g = 1.02$ ev, Woolley and Pamplin (15) report that $E_g = 1.55 \pm 0.05$ ev, and Appel (16) reports that E_g for disordered In_2Te_3 is equal to 2.4 ± 0.1 ev. These latter results along with preliminary unpublished work in our laboratory suggest that Zhuze *et al.* (13), Gasson *et al.* (14), and perhaps even Woolley and Pamplin (15) were not observing an energy gap characteristic of pure, uncontaminated disordered In_2Te_3.

In this case, it then appears as though the addition of In_2Te_3 to CdTe, or the addition of CdTe to In_2Te_3 reduces the energy gap of the resulting materials. The minimum value for the energy gap in this system occurs in the γ-phase compound and is in the neighborhood of 1.0 ev.

As the In_2Te_3 fraction increases the concentration of metal vacancies also increases since 3Cd atoms in Cd_3Te_3 are replaced by 2In atoms and a vacancy in In_2Te_3. It might seem that the observed decrease in the energy gap is associated with increasing vacancy concentration. However the evaluation of the energy gap data on In_2Te_3 given above would not support this conclusion since the vacancy concentration and energy gap variation diverge as the pure In_2Te_3 is approached.

Zhuze *et al.* report the Hall mobility for disordered In_2Te_3 to be between 5 and 70 cm²/volt-sec which is lower than the values observed in the γ- and δ-phases in this work.

The room temperature thermal conductivity, 11 mw/cm°C, of ordered In_2Te_3 (17) is identical to that found for the β-phase in this work. On the other hand, Gasson *et al.* (14) report the thermal conductivity of In_2Te_3 as 0.008 w/cm°C while Woolley and Pamplin (15) report a value of 0.014 w/cm °C. It is apparent that definitive work remains to be done on In_2Te_3. By way of further comparison CdTe, which has a zinc blende structure, has a thermal conductivity of 63 mw/cm°C (17) at room temperature. These materials do not appear to be particularly promising as thermoelectric materials because of their low mobilities and peritectic nature.

Acknowledgments

The authors wish to express their appreciation for assistance given by Messrs. P. W. Chiang, G. A. Schmitt, E. K. Parrott, P. H. Smith, and J. Q. Steigelman. Contribution No. 12 from the Semiconductor Materials Research Laboratory, College of Engineering, University of Michigan, Ann Arbor, Michigan. This work has been supported by Texas Instruments, Inc., Dallas, Texas.

Manuscript received Dec. 27, 1962; revised manuscript received June 10, 1963. This paper was presented at the Boston Meeting, Sept. 16-20, 1962.

Any discussion of this paper will appear in a Discussion Section to be published in the June 1964 JOURNAL.

REFERENCES

1. L. Thomassen, D. R. Mason, G. D. Rose, J. C. Sarace and G. A. Schmitt, *This Journal*, **110**, 1127 (1963).
2. H. Hahn, G. Frank, W. Klinger, A. D. Storger, and G. Storger, *Z. anorg. u. allgem. Chem.*, **279**, 241 (1955).
3. J. C. Woolley and B. Ray, *J. Phys. Chem. Solids*, **15**, 27 (1960).
4. L. Thomassen and D. R. Mason, *This Journal*, **106**, 206C (Abstract) (1959).
5. D. R. Mason and D. F. O'Kane, "Proceedings of the International Conference on Semiconductor Physics, Prague, 1960," pp. 1125-1131, Czechoslovak Academy of Sciences, Prague (1961).
6. G. Busch, E. Mooser, and W. Pearson, *Helv. Phys. Acta*, **29**, 192 (1956).
7. D. F. Edwards and D. F. O'Kane, Bull. Am. Phys. Soc., Series II, **5**, 78 (1960).
8. N. L. Hozak, J. S. Cook, and D. R. Mason, *This Journal*, **108**, 105 (1961).
9. D. R. Mason and J. S. Cook, *J. Appl. Phys.*, **32**, 475 (1961).
10. R. J. La Botz and D. R. Mason, *This Journal*, **110**, 121 (1963).
11. D. deNobel, *Phillips Res. Reports*, **14**, 361 (1959).
12. P. Davis and T. Shilliday, *Phys. Rev.*, **118**, 1020 (1960).
13. V. P. Zhuze, V. M. Sergeeva, and A. I. Shelykh, *Soviet Physics Solid State*, **2**, 2545 (1961).

14. D. B. Gasson, P. J. Holmes, I. C. Jennings, J. E. Parrott, and A. W. Penn, "Proceedings of the International Conference on Semiconductor Physics, Prague, 1960," pp. 1032-1038 Czechoslovak Academy of Sciences, Prague (1961).
15. J. C. Woolley and B. R. Pamplin, *This Journal*, **108**, 874 (1961).
16. J. Appel, *Z. Naturforschung*, **9a**, 265 (1953).
17. A. I. Zaslavskii, V. M. Sergeeva, and I. A. Smirnov, *Soviet Physics-Solid State*, **2**, 2565 (1961).

Galvanostalametry: A New Technique, Based on the Negative Pressure of Liquids, for Investigating Electrochemical Phenomena at an Electrode

John L. Sligh and Abner Brenner

Electrolysis and Metal Deposition Section, Metallurgy Division, National Bureau of Standards, Washington, D. C.

ABSTRACT

A procedure based on the negative pressure of water has been used as a sensitive indicator for the study of electrochemical phenomena. The apparatus consisted of a vertical glass tube, closed at the upper end, which was evacuated and filled with an electrolyte. The latter remained suspended in the column in a metastable state of tension. The column of electrolyte was dropped by producing a minute amount of electrolysis between an indicator electrode sealed in the top of the column and a companion electrode which could also be at the top or in the reservoir at the bottom of the column. The time or current required to drop the column was used for making the following experiments and/or observations: (*A*) The decomposition potential of water was determined by observing the lowest applied voltage required to drop the column. (*B*) The time required to drop the column (on passage of a constant current) was proportional to the concentration of iodide ion in the electrolyte. (*C*) The current required to drop the column was proportional to the area of the indicator electrode, regardless of the irregularity of its shape. (*D*) The formation of the gas required to drop the column occurred in less than 15 μsec after closing the circuit.

That a column of liquid can sustain a considerable negative pressure before rupturing is a scientific fact which is not commonly known, although the phenomenon was observed many years ago. A column of water, for example, can sustain a negative pressure of more than 200 atm (1). Briggs (2) was the first to utilize the negative pressure of water in an electrochemical experiment. He showed that a column of water, suspended under negative pressure, dropped on passage of an electrical discharge between two electrodes which had been placed in the liquid at the top of the column. He was chiefly interested in measuring the negative pressure of liquids and did not pursue further the electrochemical aspects of the phenomenon.

The electrical discharge causes the column of water under negative pressure to drop because a small amount of gas is generated at the electrodes; this acts as a nucleus for disrupting the column. Briggs showed that the minimum amount of gas that caused rupture was of the order of a monomolecular layer on either anode or cathode.

Since dropping of the metastable column of suspended water is extremely sensitive to minute traces of gas, the phenomenon can be used as an indicator of the first discharge of gas in an electrochemical reaction. We have given the name Galvanostalametry to this technique; the term is derived from "galvano," meaning current, and "stalao" a Greek word meaning to drop.

The objective of this initial exposition is to describe the technique and to discuss some of its practical applications. At this stage of the investigation no attempt was made to accumulate a large mass of data or to develop a high precision in the measurements. The experiments described in this paper show that the technique can be used for such varied applications as measuring hydrogen and oxygen overvoltage, determining the concentration of a salt in a solution, determining the area of an electrode, and obtaining information on the reaction time of the deposition or discharge of ions at an electrode.

Apparatus

A typical cell is shown in Fig. 1. It consists of a glass tube about 100 cm long and 1.3 cm in diameter terminating at its lower end in a reservoir of about 1 liter capacity. The orifice at the bottom of the vertical tube, shown in Fig. 1 and 2, permitted the introduction of electrodes or a salt bridge. In Fig. 3 are shown several types of closures and electrodes used at the top of the column. The spherical bulbs at the top of two of the columns were adopted because they improved the adhesion of the liquid to the top of the vessels. The demountable upper electrode assembly shown in Fig. 1 permitted rapid

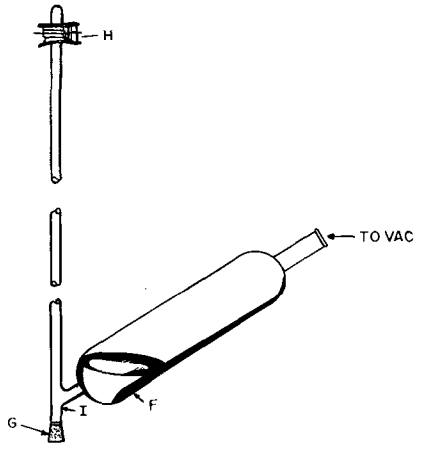

Fig. 1. Typical experimental cell, details of a similar one are shown in Fig. 2.

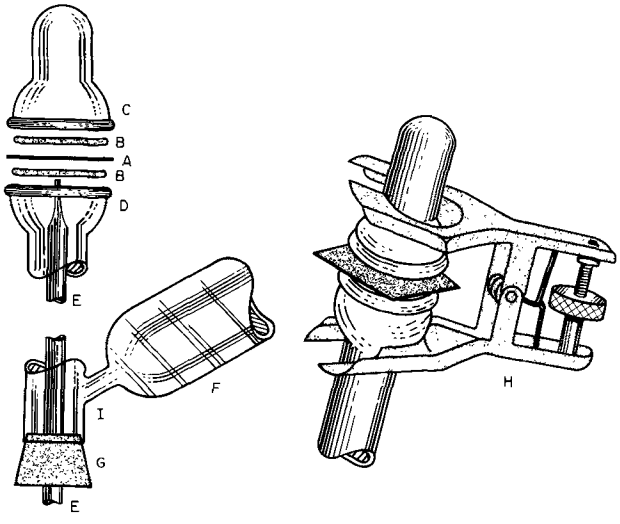

Fig. 2. Detailed view of the experimental cell: A, indicator electrode; B, O-ring; C, upper connector; D, lower connector; E, salt bridge or electrode probe; F, reservoir; G, rubber stopper; H, adjustable clamp; I, bottom of column.

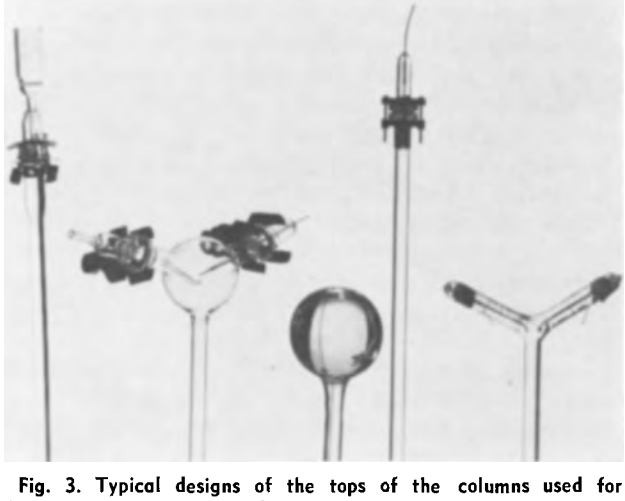

Fig. 3. Typical designs of the tops of the columns used for obtaining various galvanostalametric quantities.

removal and replacement of electrodes. Details of the design of the connectors are shown in Fig. 2. The connecting faces of the flanges contained O-ring grooves. Sufficient pressure could be applied to the joint with the adjustable clamp to provide a vacuum-tight seal.

The indicator or working electrodes at the top of the columns were smooth or platinized platinum (except as otherwise noted) ranging in geometrical area from 5 x 10^{-4} mm^2 to 300 mm^2. Electrodes having an area less than 0.01 mm^2 were made by sealing small platinum wires in glass tubing. The ends of the tubes were then cut at right angles to their axis and ground flat to expose only the cross section of the wire. The opposing platinum electrode is referred to in this paper as the counterelectrode. The counterelectrode may be located near the indicator electrode at the top of the column, but in most instances, it was placed in the reservoir, thus preventing it from influencing the dropping of the column. A potentiometer and suitable ammeter were used for measuring voltage and current, respectively.

A saturated calomel reference electrode was used for measurements of electrode potentials. A salt bridge extended from the reference half cell to a Luggin capillary, which was inserted through the orifice at the bottom of the column and terminated in the immediate vicinity of the electrode under study. The gel used in the salt bridge was made by adding to a 1*N* KCl solution approximately 140 g/l of acrylamide and about 8 g/l of N, N^1 Methylene bisacrylamide. The congealing of this solution was catalyzed by the addition of 10 ml/l each of 1% (weight) ammonium persulfate and 1% (weight) ferrous sulfate. This gel proved superior to agar, which allowed air to enter the cell, thus causing the column to fall prematurely.

The source of electricity was varied in accordance with the type of measurement. For example, a 6v battery was adequate if the process involved a steady current, as in the overvoltage study. On the other hand, when using condenser discharges, a 110v d-c line or a 3000v d-c source was used in conjunction with a voltage divider. The choice of voltage supply was dictated by the area of the indicator electrode and the capacity of the condenser. A larger potential was applied to the condenser in each successive experiment, until the minimum voltage which would drop the column was found.

For all experiments, an auxiliary a-c supply, in addition to the primary power supply, was required for immediate restoration of the electrode to a reproducible condition between successive measurements. The need for this procedure is clarified later in this paper.

Experimental Method

The solutions studied were heated to boiling, under reflux. This procedure removed most of the dissolved gases and thus provided a more stable suspended column. The hot solution was immediately transferred to the cell through the mouth of the reservoir, which was then attached to a vacuum pump by means of a rubber stopper and rubber vacuum tubing fitted with a screw-type pinch clamp. The screw clamp was continuously adjusted upon evacuating so that a steady but not violent ebullition was maintained until the solution was about room temperature. The clamp was then closed and the cell removed from the vacuum system.

To suspend the column, the cell was inverted slowly so that the solution did not slap against the top of the cell. This precaution was essential; otherwise microscopic bubbles formed and prevented suspension of the column. With the cell inverted, any trapped gas bubbles were allowed to ride up the column and escape into the reservoir; the column was returned to the upright position. The liquid was then under negative pressure and when a charge sufficient to create about a monolayer of gas on the indicator electrode was passed through the cell, the column of electrolyte dropped abruptly.

In the following discussion, the term galvanostalametry will be used to refer to all experiments or measurements made by this technique. In galvanostalametry, the quantities of interest are the current, voltage, charge, or time which prevails at the instant the column drops. Since these are obtained by gradually increasing the value of the current or voltage, sometimes in successive trials, it is obvious that the galvanostalametric quantities are the smallest values that will cause the column to drop.

In contrast to an adsorbed film, the galvanostalametric gas film is a transient one. Our studies confirmed Briggs' observation (2) that the electrolyzed gas film existed for a short period before dissolving in the electrolyte. This effect was not wholly cumulative since two discharges, each of which was about 62% of the critical value, failed to drop the column when applied in rapid succession. This indicated that much of the gas film disappeared rapidly. However, when a quantity of charge slightly less than the galvanostalametric charge was followed by a similar one, the column dropped, showing that a residuum of gas remained. If the column was allowed to remain suspended for several hours between measurements, the residuum of gas on the electrode disappeared, and reproducibilities of the original galvanostalametric charge approaching 1% were observed. One method of quickly restoring the electrode surface to a reproducible condition after each experiment was to apply an alternating current for a few seconds between successive measurements. A current density of approximately 7 ma (rms)/cm^2 at a frequency of 1000 cps resulted in reproduction of the initial film to within about 6.5%, which was considered adequate for a preliminary study.

It is convenient to mention here other factors which have an influence on the stability of the column or on the galvanostalametric charge required to drop it. According to Briggs (2, 3) the thickness of the gas film, and hence the charge required to drop a column of solution suspended under negative pressure, decreases as the height of the column increases. He showed that a decrease in the length of the column of water of 10 cm increased the critical film thickness by approximately 4%. We found that the variation in the film thickness or galvanostalametric charge is minor for a 1 or 2 cm change in column height and posed no problem in a qualitative study. In making precise measurements, care must be exercised to prevent leakage of air into the reservoir, since this has the effect of changing the head (or negative pressure) of the column.

The usual small changes in ambient temperature produced no noticeable effect on galvanostalametric values and were ignored in normal measurements, since the column remained suspended indefinitely at room temperature. The effect of increasing the temperature was illustrated by raising the temperature of the column to about 55°C with a heating tape, which caused the column to fall in several minutes.

Table I. Relationship between the electrode area and the galvanostalametric film thickness of hydrogen

Area,* mm^2	Qm	Qd	Number of monolayers, Qd/Qm
285	1.2×10^{-3}	7.2×10^{-4}	0.6
140	5.3×10^{-4}	4×10^{-5}	0.75
5×10^{-2}	1.82×10^{-7}	1.65×10^{-7}	0.91
5×10^{-4}	1.82×10^{-9}	9×10^{-9}	4.95
1.3×10^{-4}	5×10^{-10}	2.8×10^{-9}	5.6

Qm, coulombs theoretically required to yield a monolayer; Qd, coulombs required to drop the column; area of H_2 molecule (Van der Waals'), 7.62×10^{-14} mm^2; all electrodes consisted of platinum except for a tungsten electrode used in the last experiment.
* A roughness factor of 1 is assumed.

Experimental Results and Discussion

Relationship between critical film thickness and electrode area.—In harmony with Briggs' (2) results, our experiments showed that the quantity of charge required to drop a column of 0.2M H_2SO_4 corresponded to less than a monolayer of gas. An exception to this occurred if the area was less than 10^{-2} mm^2; in this case, a polymolecular gas film was required to drop the column. Some data on critical film thickness are given in Table 1.

If one selects a platinum indicator electrode whose area is greater than the minimum cited above, it is clear that the size of the electrode area can be approximately measured within the limits of the reproducibility of the critical thickness of the electrolytic gas film. The following experiment further shows that the technique is applicable to the measurement of the area of irregular surfaces. A planar platinum electrode having an area of 140 mm^2 was made the test electrode in an experimental cell which contained 0.2M H_2SO_4, and the critical charge was determined. The experimental electrode was removed, rolled into a coil of three loose turns, and the critical charge was again ascertained. The following data were obtained: planar electrode, 4.32×10^{-4} coulombs; coiled electrode, 4.08×10^{-4} coulombs. The 6% difference in the galvanostalametric charges are within the reproducibility of the measurements. The explanation of these data is similar to that given for the good covering power of anodizing. The deposition of a molecule of gas at a given site on the surface increases the energy required for another molecule to settle at that point. Consequently, a subsequent molecule locates on a bare site, which has a lower energy threshhold. This mechanism results in coverage of a surface with a monolayer before discharge occurs opposite an already covered site.

Minimum bubble-volume required to initiate column rupture.—The experiments with electrodes formed by exposing the cross section of small wires provided two interesting measurements. First, (as mentioned above) they showed that microelectrodes require a film thickness of several monolayers to drop the column. Second, they provided an indication of the size of the smallest gas bubble that can cause rupture of the column. As recorded in Table I, a charge of the order of 3×10^{-9} coulombs triggered the drop of the column. This quantity of electricity compares with that detectable by a suspended coil galvanometer. The hydrogen liberated by the above charge would have a volume of roughly 6×10^{-10} cm^3 at S.T.P. This amount is equivalent to a spherical bubble having a diameter of about 8μ, but we do not wish to imply that a single bubble was formed. This calculation demonstrates that a disturbance of microscopic magnitude is sufficient to upset a metastable system causing it to go to a more stable equilibrium state.

Effect of electrode material on the galvanostalametric charge.—All of the previously described experiments were performed with platinum electrodes. The investigation was extended to determine whether the electrode material affected the galvanostalametric film thickness. Exploratory experiments were performed with electrodes of copper, silver, gold, and lead in 0.2M H_2SO_4 solution. The electrodes were polished with a fine abrasive cloth, scrubbed with pumice, and sealed into the top of the cell by use of the O-ring method. The geometrical electrode area, about 300 mm^2, was governed by the diameter of the O-ring. In these experiments, capacitor discharges were chosen to drop the column since their use made it unnecessary to measure times of the order of a fraction of a second. However, as described in the following section, when an alkaline electrolyte buffered at *p*H 9 was used in place of the 0.2M H_2SO_4 solution, a steady current was conveniently employed. Results of the experiments in acid solution, shown in Table II, indicate that the critical film thickness is reasonably independent of the electrode material.

Measurement of the thickness of an oxide layer.—Another interesting application of galvanostalametry was the measurement of the thickness of an oxide layer. Our observations showed that a column of liquid under negative pressure required a larger cathodic charge than usual if the indicator electrode was anodically polarized immediately preceding its determination. The additional cathodic charge was about equivalent to the anodic charge that had been used.

Table II. Thickness of galvanostalametric gas films on various metals in 0.2M H_2SO_4 solution

Electrode	Volts	Fraction monolayer
Pt	30	0.6
Cu	25	0.48
Ag	20	0.40
Au	25	0.48
Pb	Reacts	

In all the experiments, the current source consisted of a 24-mfd condenser charged to the voltage shown in the table. All electrodes had an area of about 3 cm^2.

Table III. Effect of anodic oxidation of copper in increasing the time required to drop the column

Oxidation time, sec	Time to drop the column, sec	Δt, sec
0	12	12
30	42.2	12.2
30	42	12
180	194	14
180	190	10

The anodic and cathodic currents were 1 ma; the area of the electrode was 3 cm^2; Δt = column 2 − column 1.

For this experiment, a copper electrode was sealed in the top of the cell by the O-ring method, and the charge required to drop the column was ascertained. The average time for a cathodic current of 1 ma to drop the column was about 12 sec at an unoxidized copper electrode. The column was resuspended and permitted to stand for a sufficient period to allow the electrode to return to its original condition. The copper electrode was then electrolytically oxidized with a known number of coulombs. The anodic treatment was immediately followed by a redetermination of the critical cathodic charge. The current used throughout these measurements was 1 ma and the electrolyte was 1N sodium sulfate buffered at *p*H 9 to prevent the dissolution of copper oxide which occurred in acidic solution. The results of these experiments are given in Table III. These data showed, within the limits of experimental precision, that the column dropped only after passage of a quantity of current sufficient to reduce the oxide film and form a galvanostalametric film on the electrode. The approximate constancy of the third column in the table emphasizes the reversibility of the anode and cathode reactions since 12 sec is the time required for 1 ma to drop the column when the indicator electrode is made the cathode in the absence of prior anodic treatment.

The application of the new technique as a means for measuring the thickness of an oxide film was extended to include the film formed on copper by heating in air. The procedure for this experiment involved weighing the indicator electrode on a microgram balance before and after heating to determine the weight of oxygen. The oxidized copper electrode was then made the cathode in the galvanostalametric experiment. The quantity of charge required to deposit a monolayer of hydrogen was small with respect to that required to reduce the copper oxide present. Thus, the charge required to drop the column was taken as a measure of the amount of copper oxide. The following shows the results of the experiments: coulombs required to drop column, 1.13; weight of oxygen on surface (g), 9.7×10^{-5}; coulombs required by calculation to reduce 9.7×10^{-5}g oxygen, 1.16. The close agreement between the experimental and calculated charges shows that the method could be used to measure thickness of an oxide film.

Many electrochemical techniques have been employed for measuring the thickness of films on metals; some of these have been reviewed and evaluated in a paper by Lambert and Trevoy (4). They proposed an improvement for determining coulometrically the thickness of an oxide layer and other films on copper. Their procedure involved the removal of dissolved oxygen and ions from the test solution by pre-electrolysis in a cyclic process requiring a complex experimental cell. The purification technique suggested by these authors is well founded since any precise coulometric procedure for measuring the thickness of an oxide layer requires the elimination of interfering ions or reducible species. The galvanostalametric method has the advantage over other techniques in that it provides a sharper end-point than the inflection in a potential-time plot commonly used in the coulometric oxide thickness measurements to indicate complete reduction of the oxide layer.

Discharge of iodide ion at the anode; relation between current and time in dropping of the column. —In electrolysis of a solution containing an electrochemically oxidizable or reducible ion (at current densities below the limiting current density), the system reaches a steady state with respect to current and voltage in about a minute or two. If current densities larger than the limiting value are used, the concentration of the reactive ion at the cathode-solution interface is reduced to zero in much less time than this, and hydrogen or oxygen then begins to discharge, depending on whether the reaction occurs at the cathode or anode. The moment at which the concentration at the cathode-solution interface reaches zero is usually ascertained by plotting the curve of current density or potential as a function of time. The curve shows a bend or knee at the point where the gas evolution begins. Direct observation of the evolution of gas is seldom used because it is too inexact. However, the point of gas evolution can be determined sharply by galvanostalametry, because the column of liquid drops as soon as an infinitesimal gas discharge occurs.

Sand (5) was the first to demonstrate the simple relation between the current density, i, and the time, t, required to reduce the concentration of the reactive ion to zero at the cathode. $i\sqrt{t}$ = a constant for a given electrolyte. For this relation, the values of i should be at least twice the limiting current density. Sand used a copper sulfate solution and determined t by the decrease in current. Burt-Gerrans (6) made similar measurements with a rotating cathode and determined t from the voltage-time curve obtained with an oscillograph.

Our measurements were made with solutions of potassium iodide which were approximately 0.2M in sulfuric acid. A platinum indicator anode was placed at the top of the column and the counter-electrode in the reservoir. A constant current was passed, and the time required for the column to drop was noted with a stop watch. The amount of charge required actually to generate oxygen for dropping the column, after the concentration of iodide ion at the anode-solution interface was reduced to zero, amounted to 1% or less of the number of coulombs required to discharge the iodide ion. Since the charge required for gas discharge was less than our precision of measurement, it was disregarded.

Table IV. Relation between the galvanostalametric time and current in the electrolysis of 0.01M and 0.05M KI in 0.2M H_2SO_4 solution

Time, sec		Current, ma		$i\sqrt{t}$	
0.01M	0.05M	0.01M	0.05M	0.01M	0.05M
0.70	4.2	88	84	74	172
0.15	5.3	73	74	78	170
1.3	7.4	63	62	72	168
1.8	11	52	50	70	165
3.5	18	37	40	69	170
7	31	22	30	58.5	166
16		14		56.5	

Figure 4 shows curves A and B which were obtained with 0.01N and 0.05N solutions of potassium iodide, respectively. Table IV shows that each curve approximately fits the equation $i\sqrt{t} = K$, a constant.

For a given current, the time required to drop the column was approximately proportional to the concentration of iodide ion. This relation is derived from the ordinates to curves A and B of Fig. 4. The ratio of the iodide concentrations represented by curves B and A was 5. At currents of 40, 60, and 80 ma, the ratios of the ordinates of curves B to A were 6.0, 5.3, and 5.3, respectively. This proportionality between time and concentration does not follow simple diffusion theory which predicts that a direct proportionality should exist between the current and the concentration, whereas the time should vary with the square of the concentration.

The direct variation of the concentration of iodide ion with the time required to drop the column indicates that, with further development, galvanostalametry might be used for analytical purposes.

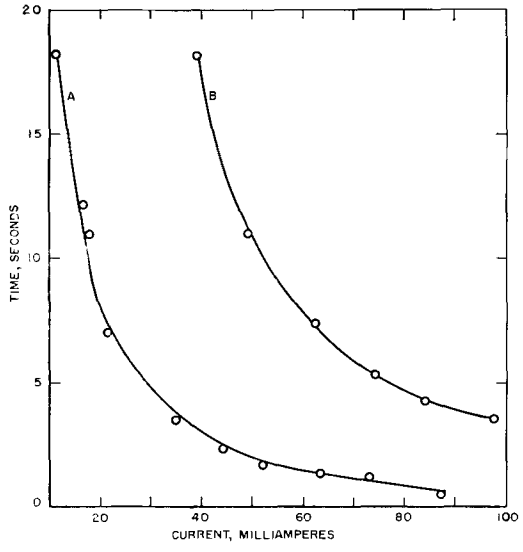

Fig. 4. Relation between time and current for anodic oxidation of KI in a supporting electrolyte of 0.2M H_2SO_4: A, 0.01M KI; B, 0.05M KI.

Minimum hydrogen and oxygen bubble overvoltage.—The measurements of the minimum overvoltage for discharge of gases at electrodes depend on bubble formation as an indication of gas evolution. The values obtained are usually called bubble overvoltages. These have not been commonly measured because of the difficulty in detecting the initial appearance of gas. The sensitivity of galvanostalametry to microscopic quantities of gas ideally suits it for such a determination.

The method for making bubble overvoltage measurements was by conventional means with the aid of the new technique as an indicator of gas discharge. The galvanostalametric electrode potentials at which hydrogen or oxygen was liberated at a platinized platinum indicator electrode was measured with a potentiometer with respect to a saturated calomel electrode. The bubble overvoltage was obtained by subtracting the theoretical reversible potential from the observed electrode potential. The theoretical reversible potential was calculated by inserting the *p*H in the Nernst equation. The overvoltage measurements were made at room temperature in a neutral electrolyte of 1*N* Na_2SO_4, whose *p*H was adjusted with NaOH or H_2SO_4 and buffered by standard buffer systems recommended by Lingane (7). In the case of the overvoltage study in unbuffered solutions the *p*H of the 1*N* Na_2SO_4 was adjusted by addition of suitable amounts of H_2SO_4 and NaOH to achieve the desired *p*H.

The study of hydrogen bubble overvoltage by galvanostalametry illustrated that the overvoltage attending hydrogen evolution was practically independent of *p*H. As shown in Fig. 5 and 6, respectively, the hydrogen bubble overvoltage was approximately 50 mv throughout the experimental *p*H range and essentially paralleled the theoretical reversible potential.

The hydrogen bubble overvoltage corresponding to the *p*H of an unbuffered solution cannot be measured because the passage of current causes the *p*H at the electrode-solution interface to change. Thus, the result of the galvanostalametric measurement is not an overvoltage but mostly a shift of potential owing to an increase in the *p*H. The apparent overvoltage shown in Fig. 5 for the unbuffered solution shows that the effect is large in solutions having a *p*H between 3 and 10. An explanation for the

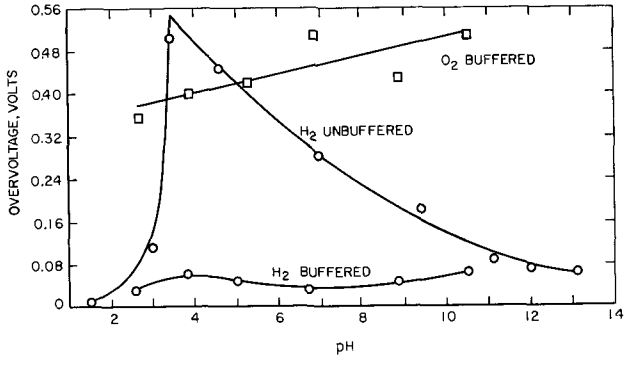

Fig. 5. Variation of hydrogen and oxygen overvoltages on a platinized platinum electrode in a supporting electrolyte of 1*N* Na_2SO_4 adjusted to the desired *p*H values with NaOH or H_2SO_4.

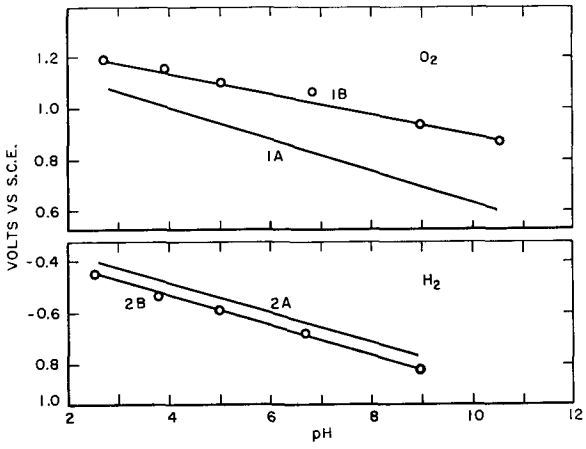

Fig. 6. Potential required to drop the column as a function of *p*H for the discharge of hydrogen and oxygen at a platinized platinum electrode in a supporting electrolyte of 1*N* Na_2SO_4. The "A" curves show the change of the theoretical reversible potential with *p*H and the "B" curves show the change of the experimentally observed potential with *p*H.

large shifts of potential is that current passing across the cathode-solution interface reduces dissolved oxygen to hydroxyl ions, which considerably increases the *p*H of the unbuffered solution.

The investigation of oxygen bubble overvoltage was confined to buffered solutions in view of the results with its hydrogen counterpart. The same procedure as that for hydrogen bubble overvoltage was employed except that a 1000 cps current was used for a few seconds between successive readings to obtain a reproducible electrode surface. The need for this treatment is explained earlier in this paper and was used in the anodic overvoltage experiment because the oxygen gas film maintained its influence on the subsequent galvanostalametric potential for a longer time than the hydrogen gas film.

Oxygen overvoltages resulting from these measurements were much less reproducible than those obtained for hydrogen as can be seen from the upward trend of the curve in Fig. 5. In general, deviations of 0.04v were observed about a mean of 0.46v in the *p*H range of 5-11. In addition, the study showed that the anode potential was influenced more by the previous history of the electrode than was the potential of the cathode. Figure 6 shows the relation between the experimental and theoretical reversible potentials for the formation of oxygen as a function of *p*H. From this plot one can see that the difference along the ordinate, between either set of curves, is a measure of the overvoltage at the *p*H which corresponds to the measurement.

Elementary reaction time for formation of hydrogen and oxygen.—Galvanostalametry provides a means for establishing an upper time limit for the initial formation of hydrogen or oxygen at an electrode. For example, we showed that a column of 1% H_2SO_4 could be dropped by an alternating current if one alternation contained a sufficient number of coulombs to produce a monolayer of gas on the test electrode. Further, it was observed that if the frequency of the current was increased, the column no longer dropped unless the amplitude was increased to compensate for the decrease in half cycle dura-

tion. These observations suggested that the drop was triggered by a single alternation and, hence, the electrode reaction occurred in the period of one-half cycle. Since the alternating current was continuous, one might surmise that the dropping of the column was the result of an accumulation of gas over several cycles and therefore not an instantaneous response.

In order to establish whether or not the formation of hydrogen and oxygen were immediate, some experiments with single pulses were performed. Conducting such experiments required pulses of microsecond duration possessing adequate charge to produce a critical film of gas on an electrode. These demands necessitated a compromise in electrode size in order to obtain compatibility with the capacity of the available pulse generator. An electrode of suitable size was prepared by sealing a platinum wire, 0.25 mm in diameter, in a long glass tube, as described under apparatus, giving a cross-sectional area of about 5×10^{-2} mm^2. This microelectrode was inserted through the tubulure at the bottom of the vessel and terminated at the top of the tube. The platinum counterelectrode was placed in the reservoir. The shortest cathodic pulse which dropped a column of 0.2M H_2SO_4 solution under these conditions was 10 μsec. The fall of the column induced by a 10 μsec pulse is not conclusive evidence that the electrode reaction is completed within that interval, since it is conceivable that the chemical reaction is slower than the charging process.

To obtain evidence on this question, a more sophisticated experiment was devised in which an initial critical pulse was followed instantly by a second critical pulse of opposite polarity. The application of such a composite waveform was effective in dropping the column. The duration of the positive and negative pulses were 10 and 5 μsec, respectively, indicating that the entire reaction was completed within a maximum of 15 μsec.

In this experiment the electrodes were about a centimeter apart which greatly decreased the resistance, thus increasing the current per pulse. The current, measured from an oscilloscope trace, represented a quantity of coulombs corresponding roughly to a monolayer of gas. Although we have not established a transition time for hydrogen and hydroxyl ions to form molecular hydrogen and oxygen, the above result indicates the possibility that there is no time lag between the passage of current and the completion of the reaction.

Acknowledgment

The authors wish to acknowledge the assistance of William Roberts who performed some of the initial experiments in this investigation and to thank the Aeronautical Systems Division, Air Force Systems Command, United States Air Force, for financially supporting this work.

Manuscript received Dec. 20, 1962; revised manuscript received June 17, 1963. This paper was presented at the Los Angeles Meeting, May 6-10, 1962.

Any discussion of this paper will appear in a Discussion Section to be published in the June 1964 JOURNAL.

REFERENCES

1. L. J. Briggs, *J. Appl. Phys.*, **21**, 721 (1950).
2. L. J. Briggs, *J. Chem. Phys.*, **21** [5], 779 (1953).
3. L. J. Briggs, *ibid.*, **23** [2], 261 (1955).
4. R. H. Lambert and D. J. Trevoy, *This Journal*, **105**, 18 (1958).
5. H. J. Sands, *Phil. Mag., London*, **6**, 45 (1901).
6. J. T. Burt-Gerrans, *J. Phy. Chem.*, **30**, 396 (1926).
7. J. J. Lingane, "Electroanalytical Chemistry," 2nd ed., p. 78 (1958).

The Pt/O_2 Electrode in Sulfuric Acid Solution

Sigmund Schuldiner and Robert M. Roe

U. S. Naval Research Laboratory, Washington, D. C.

ABSTRACT

Experimental results indicate that on a platinum electrode in sulfuric acid solutions of pH 0-0.75 the potential-determining equilibrium is $O_2 + H^+ + e^- = HO_2$. As the pH of the solution is increased a second potential-determining equilibrium $O_2 + 2H^+ + 2e^- = H_2O_2$ becomes of increasing importance. Rest potentials on platinum electrodes in helium-saturated solutions which are virtually free of oxygen indicate that these same reactions could also play an important role.

The purpose of this work was to determine the open-circuit potential behavior of platinum in helium-stirred sulfuric acid solutions which were virtually free of oxygen and then to observe the effects of additions of small amounts of oxygen to the helium stream. Even though considerable work has been done concerning the rest potentials of platinum, *e.g.*, Hoare (1), we felt that small traces of oxygen could have overriding effects on the measured potentials of this metal.

Experimental

The cell (Fig. 1), gas purification system (with an added palladium dispersed-on-alumina column), and general method were essentially the same as previously described (2). The test electrodes were originally a Pt (99.99%) bead electrode of 0.177 cm^2 true area (2), a 90% Pt-10% Rh gauze (80 mesh) electrode in the form of a cylinder about 5.7 cm high and 4.7 cm in diameter, the top and bottom of the cylinder being supported by rings made of 0.0127

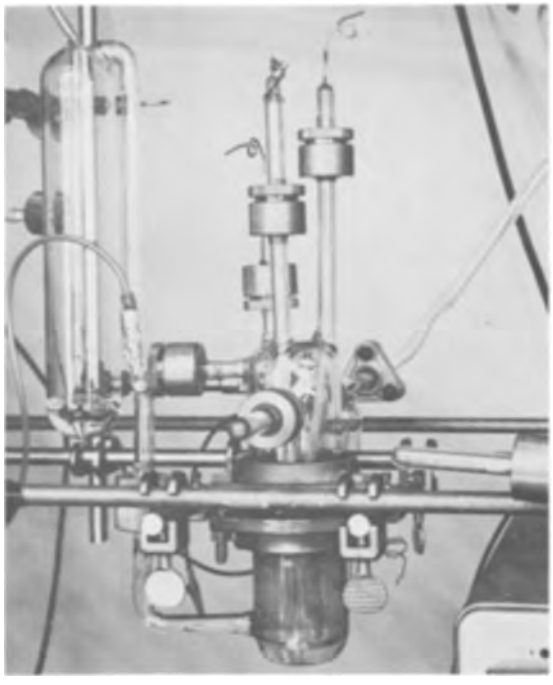

Fig. 1. Electrolytic cell

cm thick perforated Pt (99.99%) sheet, a Pd (99.97%) bead electrode of about 0.1 cm^2 area, and a L&N miniature glass electrode which was mounted in a side arm attached to the main compartment of the cell. In later experiments a Pt (99.99%) wire spiral electrode in which the wire was 0.0254 cm in diameter and 40 cm long was substituted for the Pt bead electrode and a Pd (99.97%) wire electrode 0.0127 cm in diameter and 2 cm long was added to the cell. In some experiments both palladium electrodes were removed from the cell. This established that the presence of palladium electrodes in the cell did not affect the behavior of the platinum electrodes.

The solutions used were 2.45, 1.08, 0.38, 0.17, 0.06, and 0.03*N* sulfuric acid. The *p*H values of these solutions were determined with a *p*H meter at the close of each series of runs. The temperature was 25° ±1°C.

A typical run was conducted in the following way. The solution was pre-electrolyzed by making the test platinum electrodes anodic relative to a platinum cathode, which was then removed from the cell. Purified hydrogen gas was bubbled into the cell at a rate of about 250 ml/min until the potential between the Pt/H_2 electrodes was zero and the potentials between Pt/H_2 and the Pd electrodes were 50 mv or less. The potential between the glass electrode and the equilibrium Pt/H_2 electrode was then determined (−0.665 ± 0.002v). Since the glass electrode was the reference electrode, the potential between this electrode and the Pt/H_2 electrode in the same solution (1 atm H_2) was used to convert all potentials measured with the glass electrode to the scale of the hydrogen electrode in the same solution. A *p*H correction was then made to convert all measurements to the normal hydrogen scale (N.H.E.). The glass reference electrode on rechecking with Pt/H_2 at the end of a run invariably gave the same value as was initially found.

The hydrogen flow was then replaced with a flow of purified helium flowing at a rate of 180 ml/min. It was important to completely disconnect the hydrogen line from the gas distribution system. Merely closing several valves did not suffice because very small but significant amounts of hydrogen did leak through the needle valves used in the system. Open-circuit potential changes with time on the platinum electrodes were determined against the glass reference electrode with a Keithley 610A Electrometer. Electrometer connections to determine potentials were made only for the period that potentials were measured (a few minutes). Continuous records of potential-time relations were not taken when long-time runs with pure helium flow were made.

When oxygen was added to the helium stream it was done by electrolysis of a sulfuric acid solution in a partitioned electrolysis cell in the helium gas purification train (2). Potential measurements of the effects of the partial pressures of oxygen were recorded continuously until steady-state potentials were achieved. The partial pressure of oxygen introduced into the helium gas stream was controlled by the current flow in the electrolysis cell. Checks of higher oxygen partial pressures were occasionally made with a Beckman magnetic susceptibility oxygen analyzer.

Platinum Rest Potentials in Helium Saturated Solutions

The course of a typical run in pH zero solution is demonstrated in Fig. 2. At zero hour the flow of hydrogen was replaced with helium. The change in potential with time in the hydrogen-free and virtually oxygen-free solution up to 260 hr is shown on both the Pt bead and Pt-Rh electrodes. Roughly three plateaus can be seen. These arrests correspond to the regions for the removal of hydrogen which is both chemisorbed on the metal surface and dissolved in the skin of the metal (2, 3).

The fact that the rest potential at the end of 260 hr was below 0.3v demonstrates several things: (*a*) the oxygen concentration in solution must be at an exceedingly low level; (*b*) platinum does not react spontaneously with sulfuric acid or water to form platinum ions, adsorbed oxygen, or an oxide because the calculated activities of these species are too

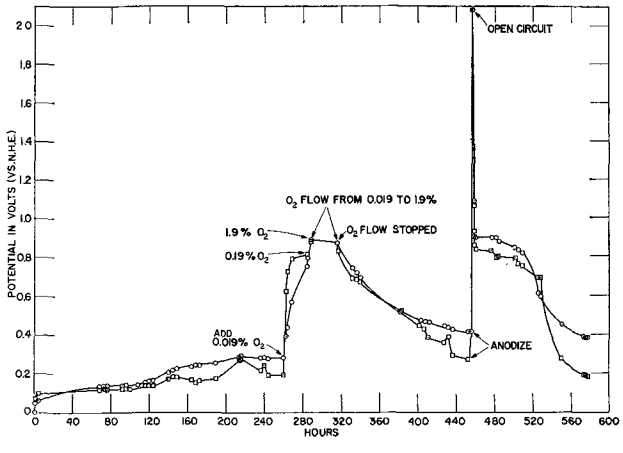

Fig. 2. Potential *vs.* time behavior of platinum and Pt/Rh in 2.45*N* H_2SO_4. Open circle with dot, Pt bead; open square with dot, 90% Pt-10% Rh gauze.

small; (c) a very small residue of hydrogen may still be associated with the platinum. It also seems reasonable that the bulk of the hydrogen is removed from the electrodes by reaction with the minute amount of oxygen which undoubtedly leaks into the system.

On the 260th hour 0.019% oxygen was added to the stream of helium flowing into the cell. This caused a sharp rise in potential. The rest potential was a function of the oxygen partial pressure. This point is discussed in more detail later.

When the oxygen flow was stopped, the rest potential on the platinum electrodes slowly decayed to the vicinity of 0.3-0.4v. This decay in potential demonstrates that (a) the solution is virtually free of oxygen, and (b) adsorbed oxygen or other oxygen bearing species react or are spontaneously desorbed from the platinum surface.

On the 456th hour the platinum electrodes were coupled together and anodized at 130 ma for 30 min. The circuit was then opened and the potential allowed to decay. Figure 2 shows this decay and demonstrates an arrest in the vicinity of 0.8-0.9v followed by a decay to 0.2 or 0.4v depending on the electrode. These results again show that the solution is almost free of oxygen and further demonstrate that platinum oxide and adsorbed oxygen atoms formed during anodic polarization are not stable and are spontaneously removed from the platinum surfaces. It is believed that this oxygen may be removed by reaction of oxide with sulfuric acid and by adsorbed oxygen dissolving in the bulk of the platinum metal rather than by eventual combination of oxygen atoms to molecules. This course is preferred because the high heat of adsorption of oxygen atoms on platinum makes their easy removal by displacement or combination improbable.

A similar time-potential relationship for a Pt spiral and Pt-Rh gauze electrode in 0.38*N* sulfuric acid solution is shown in Fig. 3. Although the rates of potential change may be different and although the final rest potentials do vary somewhat they are analogous to those found in Fig. 2 for 2.45*N* sulfuric acid. Other runs gave similar results.

In Fig. 2 and 3, the sharp rise in potential within the first few hours after the helium flow started indicated that adsorbed hydrogen atoms that are in rapid equilibrium with hydrogen ions as well as hydrogen gas are removed relatively rapidly as the partial pressure of hydrogen gas is decreased due to mixing with helium. At a potential of about 0.1v positive to the reversible hydrogen potential at 1 atm H_2 pressure in the same solution, there is an arrest in the time-potential curves. At such a potential (2) only about 30% of the total number of hydrogen atoms associated with the platinum at zero time are removed. This indicates that only a fraction of the total amount of hydrogen associated with the surface at zero time is in rapid equilibrium with hydrogen gas. Tests indicate that even if oxygen is added to the solution (0.019-1.9%) immediately after the hydrogen flow is replaced with helium there is a very slow removal of hydrogen from the Pt wire and Pt-Rh gauze electrodes which takes 24 hr or longer. Thus an appreciable amount of hydrogen also must be dissolved in the platinum which can only be removed by its migration to the surface and reaction with oxygen.

Effects of Oxygen on Platinum

For the run shown in Fig. 2 oxygen was added to the helium stream in the interval between the 260th and 316th hour. The relationship between the partial pressure of oxygen and the resulting rest potentials on the Pt-Rh gauze electrode are shown in Fig. 4, zero *p*H curve. As can be seen there is a reasonable semilog relation with a slope of 0.06v per decade of oxygen partial pressure. The points shown in Fig. 4 include values for both increasing and decreasing oxygen partial pressures. No significant hysteresis was found. Included are the results of Hoare (1) for a Pt bead electrode in 2*N* sulfuric acid solution with a partial pressure of 1 atm of oxygen. (The results given by Hoare were the rest potentials after an exposure of 20 hr or more.) The potentials measured on our Pt bead electrode responded very slowly to a change in oxygen partial pressure. However, if the electrode remained exposed to the same partial pres-

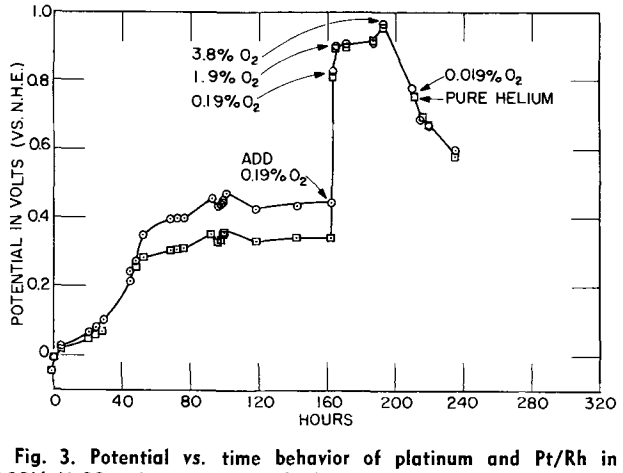

Fig. 3. Potential vs. time behavior of platinum and Pt/Rh in 0.38*N* H_2SO_4. Open circle with dot, Pt spiral; open square with dot, 90% Pt-10% Rh gauze.

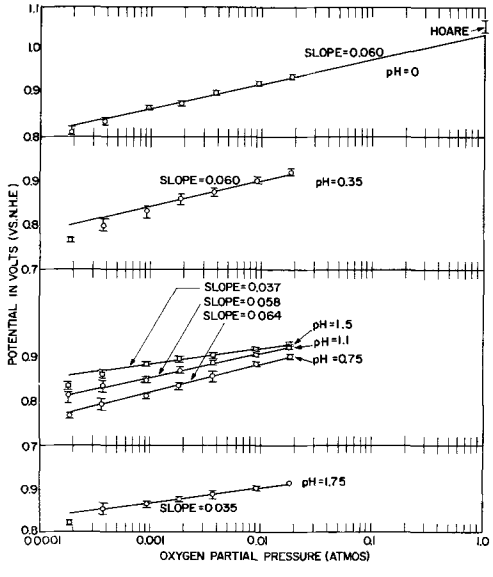

Fig. 4. Effect of oxygen partial pressure. Open circle with dot, average values, I range of values.

sure of oxygen for about 24 hr it did give essentially the same potential as did the large Pt-Rh gauze electrode. Because of this slow response only a few points were checked with the Pt bead. The Pt-Rh gauze electrode gave the results shown in the zero pH curve in Fig. 4. This electrode usually gave steady-state readings in from 30 to 60 min.

Samples of solution were removed from the cell during oxygen additions and tested for hydrogen peroxide or other oxidizing agents by both the titanium sulfate and iodide-starch tests. Negative results were always obtained for solutions of all pH values.

The linearity of the top curve in Fig. 4 and the slope of 0.06 indicate that the platinum was behaving as an equilibrium oxygen electrode in which there was a one-electron transfer. Latimer (4) lists a possible reaction

$$O_2 + H^+ + e^- = HO_2 \qquad [1]$$

where at 25°C

$$E = -0.13 - 0.059\,pH + 0.059 \log [P_{O_2}/a_{HO_2}] \qquad [2]$$

If such an equilibrium exists, then the calculated activity of perhydroxyl free radical, HO_2, is about 10^{-20} moles/liter. Because of the instability of HO_2 (5) one would not expect it to exist in any significant quantity in solution. The very low calculated concentration of this free radical shows that there is, in fact, virtually none of it in solution. However, it is possible that perhydroxyl radical does exist in significant numbers chemisorbed on the platinum electrode surface and that these radicals could be in equilibrium with a few such particles in solution.

If this assumption is correct then a pH dependence according to Eq. [2] should be found. This test was made with similarly pretreated electrodes in sulfuric acid solutions of higher pH and the results are shown in Fig. 4. These curves show potential *vs.* log oxygen partial pressure relations for pH values of 0, 0.35, 0.75, 1.1, 1.5, and 1.75 (all pure sulfuric acid solutions). The pH 0.35 to 1.75 curves in Fig. 4 are the data for the Pt spiral, which was substituted for the Pt bead, as well as the Pt-Rh gauze electrodes. The Pt spiral electrode gave potentials which were, within the ranges indicated in Fig. 4, the same as the Pt-Rh electrode. Hence as long as the area of the electrode is large there is essentially the same response time and potential for both the Pt spiral and Pt-Rh gauze electrodes.

In the range from pH 0 to 0.75 the pH *vs.* potential relation (Fig. 5) does essentially give the required 0.059 slope. Thus the data shown in Fig. 4 and 5 in a pH range of zero to 0.75 indicate that the equilibrium reaction shown in Eq. [1] is potential-determining. The fact that for pH values greater than 1.1, the slope of the potential *vs.* log oxygen pressure curves (Fig. 4) decreases indicates that a new potential-determining reaction is coming into play. Since the slope decreases to about 0.03v per decade of oxygen partial pressure, it also indicates that the potential-determining reaction in this pH range is influenced by a two-electron process. Figure 5 confirms this transition from the one- to two-electron process as the pH increases. Because of both

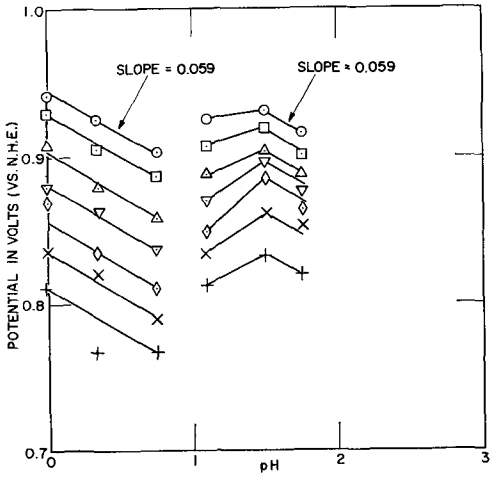

Fig. 5. pH effect. Open circle with dot, 0.0184; open square with dot, 0.0092; open triangle with dot, 0.00374; inverted triangle with dot, 0.00187; open diamond with dot, 0.00094; ×, 0.000374; +, 0.000187; atmos. O_2.

the two-electron change and the potential *vs.* pH slope of 0.059 between pH values of 1.5 and 1.75 it is indicated that the potential-determining reaction in this range is most likely the oxygen/hydrogen peroxide equilibrium, that is,

$$O_2 + 2H^+ + 2e^- = H_2O_2 \qquad [3]$$

$$E = 0.68 - 0.059\,pH + 0.03 \log [P_{O_2}/a_{H_2O_2}] \qquad [4]$$

The data in Fig. 4 and 5 therefore indicate that in the pH range 0-0.75 the potential is determined by the O_2/HO_2 equilibrium. At pH values above 0.75 the O_2/H_2O_2 equilibrium causes the potentials to become more positive, and in the pH range above 0.75-1.5 the potential is determined by both the O_2/HO_2 and O_2/H_2O_2 reactions. At pH values of 1.5 and above the O_2/H_2O_2 equilibrium predominates, and the correct potential *vs.* pH dependence of 0.059 is found. The fact that the potential *vs.* oxygen partial pressure slopes are somewhat above 0.03 indicates that the O_2/HO_2 reaction is playing a minor role in this range.

The calculated $a_{H_2O_2}$ in the 1.5-1.75 pH range is about 10^{-13} moles/liter. Thus negative chemical tests for H_2O_2 with $TiSO_4$ and KI are expected.

Equations [2] and [4] and Fig. 4 and 5 show that a_{HO_2} and $a_{H_2O_2}$ must remain independent of P_{O_2} and pH. This could be possible if all the active centers on the electrode are saturated with these species in their respective pH ranges.

The data further indicate that the potential-determining reactions for the steady-state rest potentials in the more acid solutions that are virtually free of oxygen as shown in Fig. 2 and 3 may also be largely due to the oxygen-perhydroxyl exchange. Since the HO_2 activity is in the order of 10^{-20} moles/liter, the calculated partial pressure of oxygen at 0.4v rest potential would be in the order of 10^{-11} atm. Whether or not such a calculation is valid under these conditions is, of course, questionable. However, it does indicate that the rest potential in the "oxygen-free" solutions may be influenced both by the very low oxygen partial pressure and the existence of some perhydroxyl radical on the platinum surfaces. In the

less acid solutions the oxygen-hydrogen peroxide exchange would similarly influence rest potentials.

The potential-determining equilibrium indicated in Eq. [1] can be depicted as follows on a platinum surface

$$Pt + O_2 = Pt - O_2 \quad [5]$$

$$Pt - O_2 + e^- = Pt - O_2^- \quad [6]$$

$$Pt - O_2^- + H^+ = Pt - HO_2 \quad [7]$$

$$Pt - HO_2 = Pt + HO_2 \quad [8]$$

where Pt— indicates a chemisorbed species on the platinum surface.

If the potential-determining equilibrium indicated in Eq. [3] were considered as a second electron transfer step following Eq. [7], a sharp transition from a 0.059 to 0.03 slope in the curves of Fig. 4 should be found. This is because the electron transfer steps would be in series, and the over-all equilibrium would depend only on the activities of oxygen and hydrogen peroxide. The fact that the experimental results show a gradual transition from the 0.059 to 0.03 slopes and that the potential *vs.* pH relation shown in Fig. 5 does show a range of indeterminate slope indicates that the O_2/H_2O_2 reaction involves a two-electron step rather than two separate one-electron steps. Hence, the O_2/H_2O_2 exchange on platinum

$$Pt - O_2 + 2e^- = Pt - O_2^{--} \quad [9]$$

$$Pt - O_2^{--} + 2H^+ = Pt - H_2O_2 \quad [10]$$

$$Pt - H_2O_2 = Pt + H_2O_2 \quad [11]$$

may likely occur in parallel with the O_2/HO_2 reaction.

The question as to why the two-electron step does not occur in solutions with a pH of 0-0.75 is intriguing and unanswered. Berl (6) and others have shown that the oxygen/peroxide equilibrium also occurs in alkaline solutions. Our feeling is that in the strong acid solution the configuration of the double layer may somehow retard the two-electron step. Our results indicate that the chemisorbed oxygen which exchanges with peroxide is somehow differently associated with the electrode surface than is the chemisorbed oxygen which exchanges with perhydroxyl radical. Effects of other adsorbed species should be of interest.

Acknowledgments

The authors are indebted to Dr. J. C. White of the Naval Research Laboratory, Professor P. H. Emmett of Johns Hopkins University, and Dr. A. C. Riddiford of Southampton University for helpful discussions concerning this work.

Manuscript received Oct. 31, 1962; revised manuscript received March 21, 1963. This paper was presented at the Pittsburgh Meeting, April 15-18, 1963.

Any discussion of this paper will appear in a Discussion Section to be published in the June 1964 JOURNAL.

REFERENCES

1. J. P. Hoare, *This Journal*, **109**, 858 (1962).
2. S. Schuldiner and R. M. Roe, *ibid.*, **110**, 332 (1963).
3. C. H. Presbrey, Jr., and S. Schuldiner, *ibid.*, **108**, 985 (1961).
4. W. M. Latimer, "The Oxidation States of the Elements and Their Potentials in Aqueous Solutions," 2nd ed., pp. 46-48, Prentice-Hall, New York (1952).
5. P. Gray, *Trans. Faraday Soc.*, **55**, 408 (1959).
6. W. G. Berl, *Trans. Electrochem. Soc.*, **83**, 253 (1943).

Technical Notes

Mechanism of the Oxidation of a Uranium-One Weight Per Cent Copper Alloy

J. E. Antill and K. A. Peakall

Metallurgy Division, Atomic Energy Research Establishment, Harwell, Didcot, Berkshire, England

Previous kinetic data (1) have shown that the addition of copper to uranium increases the oxidation resistance of the metal in carbon dioxide at 680°-1000°C, but has no effect at 500°C. Some improvement has also been reported in oxygen at 625°C(2). In carbon dioxide above 500°C uranium normally oxidizes by a linear rate law to produce uranium dioxide in the form of a nonadherent powder, although at 1000°C an adherent scale may be formed and the reaction rate slowly decrease with time. A thorough study of the mechanism leading to the beneficial effect of copper was not undertaken in the previous work with carbon dioxide, but it was inferred from particle size analyses of the product that copper improved the plasticity and sintering properties of the oxide, thereby leading to a more adherent protective oxide layer. As it was thought possible that the mechanism might also be applicable to compounds of uranium, *e.g.*, uranium carbide, a more detailed study was undertaken, and this is reported in the present note. The work consisted essentially of microscopic examination of sections of the oxidized samples and sintering experiments.

Table I. Summary of oxidation data for uranium and a U-1 w/o Cu alloy in carbon dioxide

Material	Temp, °C	Reaction rate, mg wt gain/cm²/hr	Particle size of product, percentage in various size ranges		
			>211μ	211-44μ	<44μ
U	500	0.1-0.3	—	—	—
U-1% Cu	500	0.16	—	—	—
U	680	3-10	90	8	1.5
U-1% Cu	680	1.2	96	3.3	0.5
U	800	250-330	80	19	1.4
U-1% Cu	800	5.9	100	0.01	Nil
U	1000	≤100	98	1.7	0.3
U-1% Cu	1000	12.2	100	Nil	Nil

The previous kinetic data and particle size analyses for alloys containing 1 weight per cent (w/o) copper are summarized and compared with those for uranium in Table 1. The specimens were oxidized in a thermal balance in gas flowing at 1 atm and 500 cc/min. The gas was obtained by volatilizing solid carbon dioxide and was dried by magnesium perchlorate to < 20 ppm (by volume) H_2O. The residual impurities were mainly oxygen and nitrogen, the approximate concentrations being 100 and 300 ppm, respectively.

The microscopic study revealed that at the high temperatures at which the beneficial effect of copper was apparent a layer of the intermetallic compound UCu_5, or of copper containing uranium oxide formed at the metal/oxide interface. Unfortunately it was not possible to obtain good photomicrographs revealing all the points of interest in both the oxide and metal because of the different polishing characteristics of the various phases, but diagrammatic representations of the samples oxidized at 500°, 680°, and 800°C are shown in Fig. 1, 2, and 3. In the unoxidized metal the copper was distributed as small cuboids of UCu_5, there being some evidence for the particles being arranged in a grain boundary type network. At 500°C the intermetallic particles were incorporated initially into the uranium dioxide film without change, but were later oxidized in the outer parts of the film. The particles act as markers and demonstrate that the formation of the nonflaking layer of oxide proceeds either by diffusion of oxygen ions through the uranium dioxide lattice or by the diffusion of carbon dioxide molecules down fine pores in the oxide followed by reaction near the oxide/metal interface.

The 680° and 800°C specimens had a bright copper-colored layer at the oxide/metal interface and

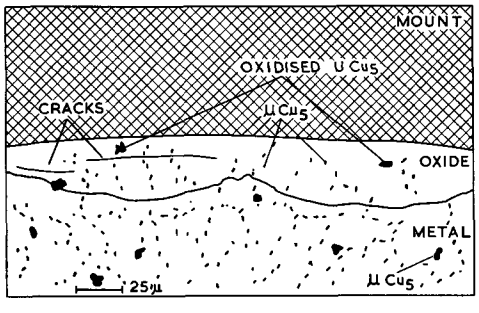

Fig. 1. Section of a U-1% Cu alloy oxidized in CO_2 at 500°C for 100 hr.

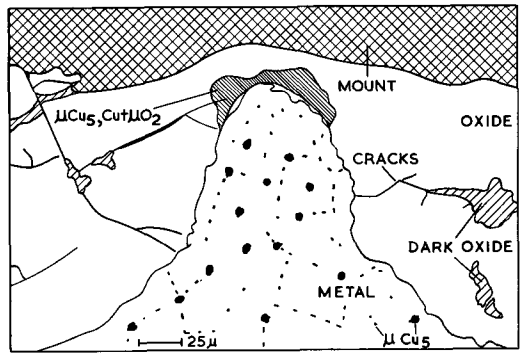

Fig. 2. Section of a U-1% Cu alloy oxidized in CO_2 at 680°C for 50 hr.

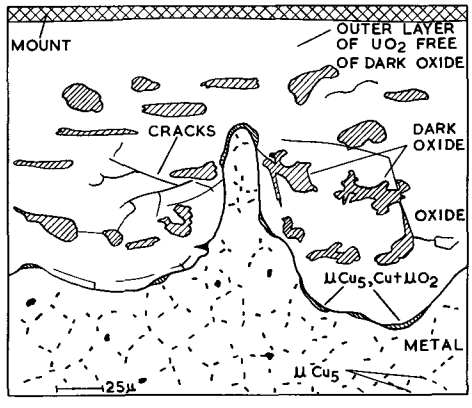

Fig. 3. Section of a U-1% Cu alloy oxidized in CO_2 at 800°C for 25 hr.

a second dark oxide phase embedded in the light gray uranium dioxide. The metallic layer resembled in some places the UCu_5 particles and in others copper-containing UO_2. Electron probe analysis gave the uranium content of the layer as ≈50 w/o which is consistent with UCu_5, or the intermetallic compound oxidized with the uranium dispersed as UO_2 in copper. The slightly higher figure than the theoretical value of 43% for UCu_5 is probably due to spreading of the electron beam. The layer was not continuous, and the oxide penetrated into the metal comparatively quickly at points where it was absent, demonstrating that the layer provided considerable protection. Although the area of the interface covered by a thick layer was small, electron probe analysis showed that the concentration of copper was high, and that a thin layer of UCu_5 probably provided some protection in the remaining areas. The areas of dark oxide were thought to be parts of the intermetallic layer which had become incorporated into the product and subsequently oxidized. It was not possible to obtain a similar metallographic section for the specimen oxidized at 1000°C, but examination of the dense scale also showed the presence of the dark oxide phase. The concentration of this phase at both 800° and 1000°C was approximately 30-40 vol %, indicating that it was a mixed oxide of copper and uranium consisting primarily of uranium oxide.

In order to confirm the protective role of the copper-colored layer, specimens of the intermetallic compound were prepared by arc melting and ox-

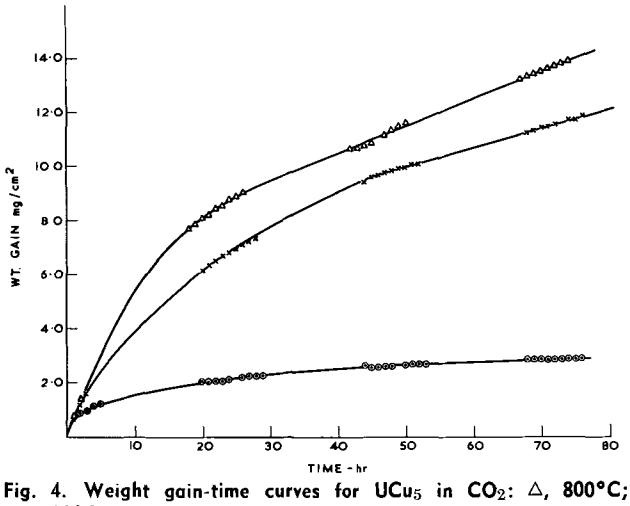

Fig. 4. Weight gain-time curves for UCu_5 in CO_2: △, 800°C; ×, 680°C; ⊙, 500°C.

idized in the thermal balance reaction chamber. The weight gain-time curves are given in Fig. 4 and show that the attack of the compound was approximately one tenth of that of the alloy. Microscopic examination of sections revealed that the attack proceeded by internal oxidation, resulting mainly in a fine distribution of oxide and copper although a layer (4μ thick at 680°C) of apparently pure bright copper was formed on the surface of the specimens.

To determine whether the copper achieved any increase in oxidation resistance by increasing the plasticity of the oxide, sintering experiments were done on cold pressed compacts of uranium dioxide powder (<300 mesh) mixed with 1 w/o cuprous oxide powder. Uranium dioxide may take into solid solution appreciable amounts of excess oxygen, and experiments were done on two compositions, $UO_{2.12}$ and $UO_{2.17}$. The compacts, together with reference samples not containing cuprous oxide, were sintered in flowing carbon dioxide for 24 hr at 750°, 850°, and 1000°C. The copper-containing compacts sintered to a higher density, but the cuprous oxide was reduced to give a dispersion of metallic copper particles. The results were therefore inconclusive as the experiments did not reproduce the structure of the scales. The available thermodynamic data for the oxides of copper (3) and uranium (4) show that pure cuprous oxide has a similar oxygen activity to the U_4O_9 phase at 680° and 800°C and $UO_{2.18}$ at 1000°C. Cuprous oxide can, therefore, only avoid reduction to the metal by having its activity lowered by the formation of a mixed oxide. The composition of the oxide scale formed at 800°C was analyzed as $UO_{2.00}$-$UO_{2.03}$ by determining the weight gain on heating in air at 600°C; the final products were assumed to be U_3O_8 and CuO. The activity of cuprous oxide has to be reduced from 1 to $<10^{-2}$ to be in equilibrium with this oxide, and it is noteworthy that the large reduction is consistent with the large uranium content of the mixed oxide deduced from the metallographic evidence. The reason why the mixed oxide formed more readily in the oxidation than in the sintering experiments is not clear.

The work has therefore shown that at least part or all of the protection is due to the formation of a layer of UCu_5 or copper containing uranium oxide at the metal/oxide interface. The layer appears to be formed by the diffusion of copper atoms into the metal away from the oxide resulting in a sweeping up of the intermetallic UCu_5 particles in the alloy. The lower oxidation rate resulting from this unusual mechanism would allow more time for stresses in the oxide to be relieved by deformation rather than cracking and would therefore explain the increase in particle size of the product. No conclusion can be drawn regarding a possible change in the plasticity of the oxide.

Manuscript received June 5, 1963.

Any discussion of this paper will appear in a Discussion Section to be published in the June 1964 JOURNAL.

REFERENCES

1. J. E. Antill and K. A. Peakall, *J. Less Common Metals*, **3**, 239 (1961).
2. L. Baker *et al.*, ANL 6596, p. 182.
3. O. Kubaschewski and E. Evans, "Metallurgical Thermochemistry," 3rd ed, p. 338, Pergamon Press (1958).
4. M. H. Rand and O. Kubaschewski, "The Thermochemical Properties of Uranium Compounds," p. 34, Oliver and Boyd (1963).

Relation of Partial (110) Pole Figures to Thickness and Microstructure of Electrodeposited Copper

Fielding Ogburn and Clarence Newton

National Bureau of Standards, Washington, D. C.

In the course of a general investigation of crystal growth by electrodeposition, the authors observed the occurrence of preferred orientation or fiber texture in electrodeposits. Some sixty literature references, most of which are dated before 1950, were consulted on the subject. These references definitely established the existence of such fiber texture and the fact that it is to be observed in most or in all of the commonly electrodeposited metals.

Very little of this earlier work, however, was quantitative, and not one of the references gave any data that might be considered as constituting a pole figure, that is the angular distribution of the degree of preferred orientation about the normal to the surface of the electrodeposit. It was with the desire to establish this quantitative and geometrical specification of the texture in the electrodeposited copper and, if possible, to relate it to other parameters of

Fig. 1. Cross section of copper electrodeposit, 1700μ thick, showing growth twins. Substrate at bottom. Etching reagent: ammonium hydroxide and hydrogen peroxide.

the electrodeposition process, that the authors entered the present study.

The distribution of crystal orientations within two copper electrodeposits differing in thickness only was determined. The deposits were prepared by electrodeposition from a solution of 250 g/l of $CuSO_4 \cdot 5H_2O$ and 50 g/l of H_2SO_4 at room temperature with mild agitation and at 10 ma/cm^2 average current density. The cathode was an 11½ x 11½ cm panel of cold-rolled low-carbon steel which had been plated with a thin layer of copper from a cyanide type solution. A rectangular Lucite box, 11½ x 11½ x 28 cm ID, was used as the plating tank with electrodes at either end and a mechanical stirrer just in front of the bagged anode. Reagent grade chemicals were used without any purification other than incidental electrolyses of the solution.

The two deposits were 14 and 1700μ thick. A cross section of the thicker deposit is shown in Fig. 1, after polishing and etching. For x-ray measurements, a coupon about 1.6 x 2 cm, was cut from the center of each where the thickness uniformity had been confirmed with a Magnegage. These were mounted in Bakelite so that the surfaces of the deposits could be easily polished and etched. The thicker specimen was polished on 600 grit paper just enough to give a flat smooth finish and then on a cloth wheel with Linde B to remove the 600 grit scratches. Both specimens were etched 20 sec in solution of ammonium hydroxide and hydrogen peroxide.

The x-ray measurements were made, using cobalt Kα radiation, with the x-ray source, proportional counter, and specimen set so that (220) diffracted radiation was counted, this diffraction owing to grain orientation being substantially more intense than (200), (111), or any other. The position of the specimen was indicated by the angle ψ[1] between the normal to the specimen surface and the normal to those planes that were contributing to the measured diffracted intensity. Thus, when $\psi = 0°$, one measured the relative area of {110} planes near to and parallel

[1] ψ was set with a vernier scale to 0.1°.

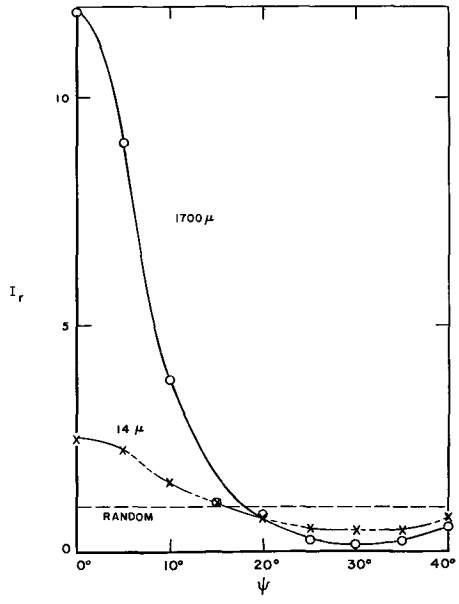

Fig. 2. Distribution of (110) poles near to the surface of two copper electrodeposits, 14 and 1700μ thick. 0° is normal to surface of polished deposit.

to the surface. Measurements were made on each specimen at 5° intervals between 0° and 40°.

The construction of the diffractometer was such that measurements for different values of ψ are not comparable and must be corrected for absorption. This was done by making similar measurements for a specimen of copper having a random distribution of crystal orientation.[2] Thus, measurements at two different angles are comparable after dividing by the corresponding values for the randomly oriented specimen. The corrected values are plotted in Fig. 2.

The curves of Fig. 2 are equivalent to conventional pole figures if the crystal orientations can be assumed to be symmetrical about the fiber axis. This would seem to be a safe assumption for the thin deposit, but questionable for the thicker one. Asymmetry would be expected for deposits with large grains since there might not be enough large grains contributing to the measurements to give representative values.

The increase in intensity as ψ approaches 0° indicates a strong preference for [110] axis in the direction of growth. This is in agreement with the fiber texture reported by Yang (1) and by Finch, Wilman, and Yang (2) for copper deposited from an acid sulfate solution. That the intensities increase as ψ increases from 30° simply reflects the geometry of a face-centered cubic crystal where (110) poles are 60° and 90° apart.

That the thicker specimen shows a greater degree of orientation than the thiner one is in line with the idea that the fiber structure is a result of grain growth. Figure 1 shows a corresponding growth in grain size between 14 and 1700μ. The substrate for both deposits was a layer of fine grained copper which according to diffractometer measurements was virtually randomly oriented and may have had a preference for other than the [110] direction.

[2] Disk of copper powder compressed at about 10,000 psi, below recrystallization temperature.

Also of interest are the very straight and near vertical boundaries in the cross section shown in Fig. 1. These are probably due to twinning which occurs along {111} planes. Since there are {111} planes parallel to the [110] direction, the orientation of these boundaries should be closely related to the corresponding pole figure as appears to be the case.

The frequency of these twinned planes leads one to speculate that the copper grains most favored for growth are those that are twinned with the twinning plane near a vertical position. The twinned plane or a combination of such planes may provide a self-perpetuating discontinuity at the crystal surface which facilitates layer growth or layer nucleation (3).

Acknowledgment

The authors are indebted to Virginia Dare Hill for preparation and mounting of the electrodeposits and to the Advanced Research Projects Agency, Department of Defense, which helped support the work described.

Manuscript received July 8, 1963.

Any discussion of this paper will appear in a Discussion Section to be published in the June 1964 JOURNAL.

REFERENCES

1. L. Yang, *This Journal*, **101**, 456 (1954).
2. G. I. Finch, H. Wilman, and L. Yang, *Discussions Faraday Soc.*, Electrode Processes, **1**, 144 (1947).
3. J. W. Faust, Jr. and H. F. John, *This Journal*, **108**, 109 (1961); **110**, 463 (1963).

A New Method of GaP Growth

J. D. Broder[1] and G. A. Wolff[2]

The Harshaw Chemical Company, Cleveland, Ohio

Several methods have been used to prepare single crystals of gallium phosphide. The variety and type of growth methods are limited and determined by the nature of the phase diagram, pressure-composition and temperature-pressure curves for the system Ga-P (Fig. 1). Corresponding data were reported by Folberth (1), Gershenzon *et al.* (6), and Rubinstein (5).

The most obvious method would appear to be that of pulling a crystal from the melt at temperatures of about 1465°C and under phosphorous pressures of about 20-50 atm. Good single crystals have been grown by this method in rather elaborate high temperature, high pressure equipment (2). If this method is attempted at lower pressures the resulting material is polycrystalline.

Another method which would not require temperatures quite so high and practically no pressure, would be to grow the crystals from a Ga rich melt (3). This process is diffusion controlled and yields strain-free single crystal platelets. Temperatures as low as 1100°C have been used and platelets of appreciable size have been prepared.

The new method proposed is an extension of the above method of solution growth (4). A single crystal seed is placed at the bottom of a suitable container of the size and diameter of the ingot to be grown. Among the materials that may be used for containers are alundum, graphite, sapphire, quartz, boron nitride, and aluminum nitride. A small column of gallium about 0.6 to 1.2 cm in height is placed above and in contact with the seed. The remainder of the tube then is filled to about 75% of its total volume with either a mixture of crushed GaP in gallium, crushed and powdered GaP, or a sintered or pressed rod of GaP. The gallium column then is heated either by direct coupling to an induction heater or in the case of the graphite crucible by radi-

[1] Present address: NASA, Lewis Research Center, Cleveland, Ohio.
[2] Present address: Erie Technological Products, Inc., Erie, Pennsylvania.

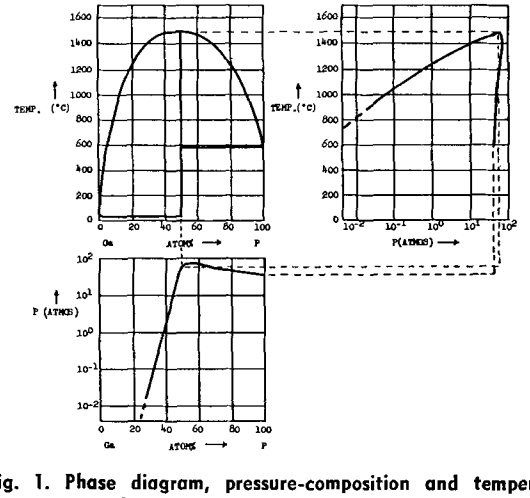

Fig. 1. Phase diagram, pressure-composition and temperature-pressure curves for Ga-P system, schematic.

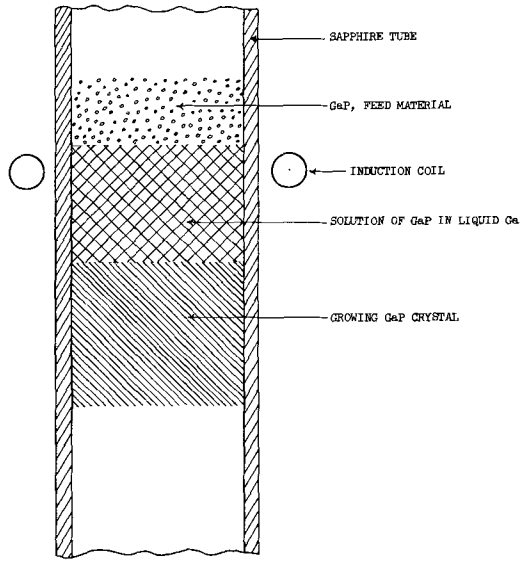

Fig. 2. Schematic of experimental arrangement to produce GaP ingots from powdered GaP. Zone measurement and interface (stability) controlled by rf or resistance heater.

Fig. 3. Ingot of GaP produced by solvent method, with large single crystal sections.

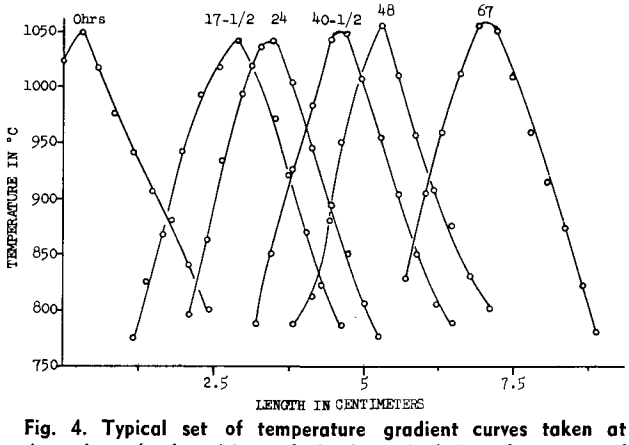

Fig. 4. Typical set of temperature gradient curves taken at various times (and positions of the heater) during the course of a run (pyrometric measurements), too fast a zone movement causing ingot rippling.

ation heating, the graphite coupling to the induction heater coil. The hot gallium zone then is made to move upward through the GaP feed material. As this occurs, GaP dissolves at the hot interface, diffuses through the gallium and deposits on the cooler single crystal seed. Figure 2 shows a schematic of the experimental arrangement. The hot interface temperature ranges from about 1000° to 1100°C and the movement of the induction heater coil should be less than 0.6 cm every 24 hr. Figure 3 shows one of the ingots produced during preliminary experiments.

Among the critical parameters is the temperature gradient along the crucible. Figure 4 shows a set of temperature gradient curves for a representative run.

One difficulty that was encountered in some of our growth runs was the rippling of the ingots, *i.e.*, the ingots grew in two or more separate sections, separated by thin columns or ripples of gallium. This might possibly be explained as follows: as the hot zone moves upward, GaP dissolves from the pressed GaP-Ga upper column. The dissolved GaP then diffuses through the gallium, deposits on the growing ingot and thus increases the volume of gallium. Thus the rate of deposition is slower than the rate of the coil movement. This increases the length of the liquid solvent column to the point where the diffusion path is now so long as to prevent further deposition on the ingot. After the interruption of the GaP deposition, the concentration of GaP in solution then increases, and eventually reaches the proper supersaturation for nucleation and crystallization to occur again. This crystallization will occur at some point away from the last GaP growth front, thus cutting off the liquid gallium below. A new liquid gallium diffusion path is established, and another ingot section then starts to grow. Apparently, a method of eliminating this effect would be to work with powdered GaP and a minimum of gallium, or eliminate the gallium from the GaP feed material entirely.

In the following, a model is presented which may serve to evaluate and establish the proper conditions for optimum ingot growth. The two conditions to be taken into account are the heat flow and the material flow. The material flow is given by the diffusion equation

$$J = -D\frac{dc}{dx} \qquad [1]$$

where J is the quantity of material deposited per square centimeter per second, D the diffusion constant, c the concentration, and x the diffusion path length. For a given concentration gradient, this equation gives the maximum rate of movement of the hot zone. The amount of GaP in solution at any temperature can be found from the information obtained by Rubinstein (5) on the solubility of GaP in Ga. Using this information and our growth rates, we have been able to calculate an approximate diffusion constant for GaP in Ga of 5×10^{-4} cm^2/sec.

The heat flow for any phase n of the system is given by the equation

$$\theta_n'' - H_n^2\,\theta_n = 0 \qquad [2]$$

where

$$\theta_n = T_n - T_r$$

$$H_n^2 = \frac{h_n}{K_n^2} = \frac{h_n}{l_n}\frac{p}{f}$$

T_n is the temperature of phase n in °K, T_r the room temperature in °K, h_n the radiation constant of phase n, l_n the coefficient of heat conductivity of phase n, p the circumference of ingot, f the cross section of ingot.

The first term of Eq. [2] is the heat conduction term and second term gives the heat loss by radiation from the surface. The general solution of Eq. [2] is of the form

$$\theta_n = c_1 e^{H_n X_n} + c_2 e^{-H_n X_n}$$

At $X_n = X_{n_0} = 0$ and $X_n = X_{nE}$ this becomes

$$\theta_{n_0} = c_1 + c_2$$

and

$$\theta_{nE} = c_1 e^{H_n X_{nE}} + c_2 e^{-H_n X_{nE}}$$

respectively it follows

$$\theta_n = \frac{\theta_{nE}\sinh(H_n X_n) + \theta_{no}\sinh[H_n(X_{nE} - X_n)]}{\sinh H_n X_{nE}} \qquad [3]$$

This equation exists for n = 1 and n = 2 for the two different phases. The boundary conditions for the system require that θ_{10} be kept constant, that the temperature at the interface, GaP-Ga mixture —GaP crystal, be the same and that the heat flow is constant across the interface. The temperature at the

growth interface (θ_I) is then given by the following expression

$$\theta_I \equiv \theta_{1E} = \theta_{20} = \frac{\frac{\sqrt{h_2 l_2}\,\theta_{2E}}{\sinh H_2 X_{2E}} + \frac{\sqrt{h_1 l_1}\,\theta_{10}}{\sinh H_1 X_{1E}}}{\sqrt{h_1 l_1}\coth H_1 X_{1E} + \sqrt{h_2 l_2}\coth H_2 X_{2E}} \quad [4]$$

where 10, 20, and 1E, 2E represent the beginning (0), and end (E) of respective phases [1], [2]. This equation gives the interface temperature as a function of the temperature at the end of the growing ingot θ_{2E}, and the length of the ingot, X_{2E}. If the condition that all the heat at the end of the ingot is lost by radiation is taken into consideration, then the interface temperature is given by the following expression

$$\theta_I = \frac{\sqrt{h_1 l_1}\,\theta_{10}}{\sqrt{h_2 l_2}\sinh H_1 X_{1E}\left[\sqrt{\frac{h_1 l_1}{h_2 l_2}}\coth H_1 X_{1E} + \coth H_2 X_{2E} + \frac{1}{\sinh H_2 X_{2E}\left(\sqrt{\frac{h_2 f}{l_2 p}}\sinh H_2 X_{2E} - \cosh H_2 X_{2E}\right)}\right]} \quad [5]$$

This shows the dependence of θ_I on X_{2E}, the length of the growing ingot. Since X_{2E} is continuously increasing, θ_{2E} will also change, which would in turn change θ_1 (Eq. [4]). This condition is a result of moving the heating element and keeping the crucible fixed. In this case, to maintain θ_I constant, θ_{2E} must be programmed according to the following relationship

$$\theta_{2E} = \frac{\sqrt{h_1 l_1}\,\theta_{10}}{\sqrt{h_2 l_2}\sinh H_1 X_{1E}\left[\left(\sqrt{\frac{h_1 l_1}{h_2 l_2}}\coth H_1 X_{1E} + \coth H_2 X_{2E}\right)\left(\cosh H_2 X_{2E} - \sqrt{\frac{h_2 f}{l_2 p}}\sinh H_2 X_{2E}\right) - \frac{1}{\sinh H_2 X_{2E}}\right]} \quad [6]$$

If the crucible is moved down and the coil is kept fixed in place, then a constant temperature bath at temperature θ_{2E} may be placed at a given X_{2E}, as determined by Eq. [5] and [6].

If radiation losses from the end of the crucible can be neglected, which may be accomplished by use of an extended crucible simulating the heat conductivity of GaP, then the expression for the interface temperature reduces to

$$\theta_I = \sqrt{\frac{h_1 l_1}{h_2 l_2}}\,\frac{\theta_{10}}{\sinh H_1 X_{1E}\left(\sqrt{\frac{h_1 l_1}{h_2 l_2}}\coth H_1 X_{1E} + 1\right)} \quad [7]$$

Knowledge of θ_{10} (the maximum temperature of the system) gives the solubility of GaP in Ga at that temperature. Assuming that the concentration does not change from this value at the growth interface and if a certain supersaturation is desired at the growth interface, then that supersaturation determines the temperature θ_I. By choosing a certain zone length (X_{1E}) and a θ_{10}, then Eq. [4] and [6] determine what must be done to θ_{2E} to maintain θ_I at a constant value. Experiments are under way to test these relationships and the influence of those variables which have been neglected, *e.g.*, heat conduction of the crucible wall.

This method has been successfully applied also to the growth of uniform mixed crystal ingots, for example $Ga(P_x,As_{1-x})$. By making use of the three dimensional phase diagram for the system Ga, GaP, GaAs (Fig. 5a,b), *i.e.*, by the proper choice of the starting mixture, a crystal with the desired ratio of GaP to GaAs can be produced. The addition of liquid Ga to molten Ga $P_{1-l}As_l$ forms a solution in which the ratio of P to As, or the value l, obviously remains unchanged. Should, upon the addition of Ga, the value l also remain unchanged when the liquid phase is in equilibrium with the solid solution of composition $GaP_{1-s}As_s$ (with $l > s =$ constant), the following conditions then hold (see Fig. 5). The dissolving $GaP_{1-s_1}As_{s_1}$ feed material, indicated at S_1 in Fig. 5b, of composition s_1, is in equilibrium with the liquid at A of composition l_1.

Point B corresponds to the liquid of composition l_2 at the interface with the growing crystal of composition s_2. The compositions l_1 and l_2 of both liquids at points A and B are in this figure arbitrarily assumed to be different due to the difference in the diffusion rate of As and P in the solution. In addition to the diffusion rates the dissolution and growth

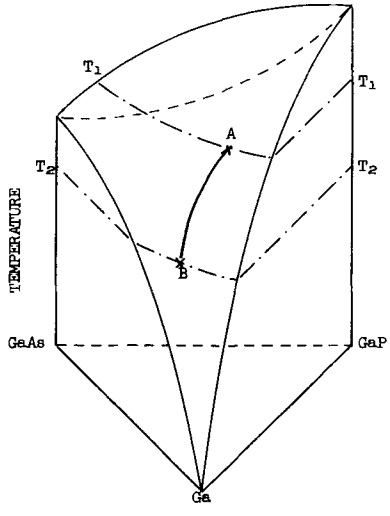

Fig. 5a. Ternary phase diagram of the GaP-GaAs-Ga system

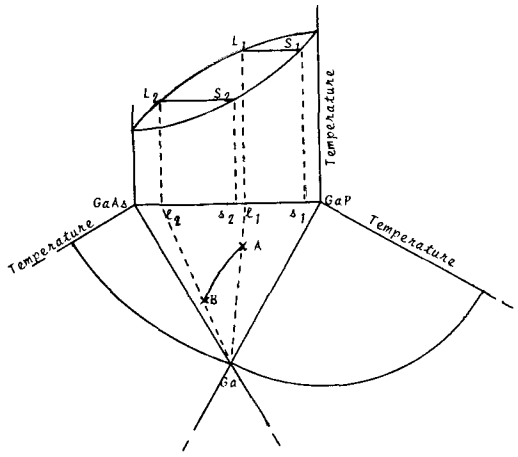

Fig. 5b. Unfolded phase diagram showing the top view of the ternary system and the side view of the three binary systems, schematic.

rates will change the position of B. Near-equilibrium conditions will prevail at both interfaces when the diffusion is rate-controlling. The compositions of both liquids l_1 and l_2 at point A and B will aways be different at the start of the growth run, and only when steady state conditions have not yet been established. When steady state has been established both liquids will only assume identical, off-equilibrium composition l_1 when the diffusion path X_{1E} is very small. The growing crystal will then be identical in composition (s_1) with the feed material. Thus B will lie on the line l_1A in Fig. 5b. It should be pointed out that the temperatures at the dissolving and growing interfaces, *i.e.*, at points A and B, respectively, are not identical with the temperatures corresponding to the points L_1, S_1 and L_2, S_2, respectively. Since in this investigation small D/X_{1E} values render the process diffusion controlled, the GaP: GaAs ratios of the dissolving and the growing ingot are equal and at steady-state-near-equilibrium conditions with their respective liquid boundary layers; as opposed to the floating zone method where uniformity in composition of the Ga(P,As) ingot would be difficult to achieve due to the interference of undesirable material transport via the vapor phase. In the latter case the vapor phase composition and pressure could only be in equilibrium with one or two sections of limited temperature range of the crystal ingot.

The application of this method of an induced solution zone movement can be extended to include many other materials (especially those having a volatile component; for example InP, InAs, GaAs and also ternary compounds, *e.g.*, $CuGaSe_2$, and other mixed crystal systems). The solvent is not necessarily limited to one of the components of the material in question, but may be any in which there is an appreciable solubility.

Manuscript received April 5, 1963; revised manuscript received June 4, 1963. This paper was presented at the Boston Meeting, Sept. 16-20, 1962.

Any discussion of this paper will appear in a Discussion Section to be published in the June 1964 JOURNAL.

REFERENCES

1. O. G. Folberth, *J. Phys. Chem. Solids*, **7**, 295 (1958); See also "Compound Semiconductors," Willardson and Goering, Vol. I, pp. 475-476, Reinhold Publishing Company, New York (1962).
2. C. J. Frosch and L. Derik, *This Journal*, **108**, 251 (1961).
3. G. A. Wolff, P. H. Keck, and J. D. Broder, *Phys. Rev.*, **94**, 753 (1954); See also G. A. Wolff, R. A. Hebert, and J. D. Broder, "Proceedings International Colloquium on Semiconductors and Phosphors, Garmisch, 1956," Interscience Publishers, Inc., New York.
4. G. A. Wolff, Proposal submitted by The Harshaw Chemical Company on "High Temperature Semiconductors Utilizing III-V Compounds & Derivatives" to WADD, Exploratory Materials Research Section, Solid State Dept., Sept. 20, 1960.
5. M. Rubinstein, Paper presented at Los Angeles Meeting, Electrochemical Society, Electronics Division Abstracts, **11**, No. 1, 129 (1962).
6. C. J. Frosch, M. Gershenzon, and D. F. Gibbs, Paper presented at Chicago Meeting, Electrochemical Society, Electronics Division Abstracts, **9**, No. 1, 212 (1960).

Diffused Junctions in GaAs Injection Lasers

J. C. Marinace

Thomas J. Watson Research Center, International Business Machines Corporation, Yorktown Heights, New York

In GaAs injection lasers at the present time, junctions formed by diffusion are more useful than junctions formed by any other means.

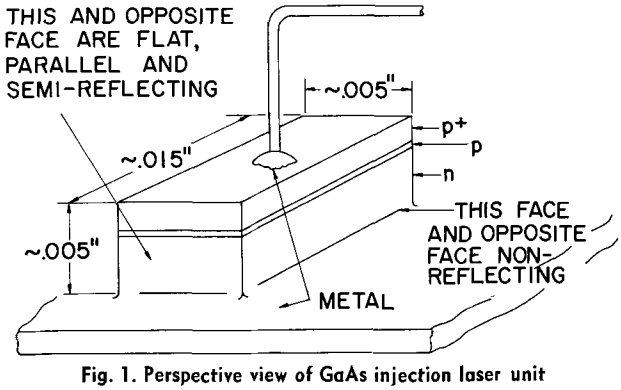

Fig. 1. Perspective view of GaAs injection laser unit

The position of the junction in a common injection laser structure is shown in Fig. 1. The dimensions shown are typical, and can be varied considerably. The p+ layer of the diffused region is often 0.001-0.002 in. thick; this seemingly excessive thickness affords the following advantages: (i) the junction is in the region where optical flatness is not disturbed by crumbling at the upper edge if the face is cleaved, or by rounding if the face is polished; (ii) fabrication of an ohmic, low-resistance contact is facilitated; and (iii) the resistivity of $10^{20}/cm^3$ p-type is approximately one-half of that of 10^{18} n-type, thereby reducing the series resistance.

The construction shown in Fig. 1 is of the Fabry-Perot kind. The directional beam of coherent light emanates from the flat, semi-reflecting ends.

In general, diffusion in GaAs is much more difficult to understand and control than it is in Ge or Si. Not only is GaAs more susceptible to damage and to reactions between the diffusant and crystal, but there is a much greater tendency for diffused junctions to be nonplanar or nonflat. Such nonflatness can have a profound effect on laser characteristics. Referring again to Fig. 1, it is seen that if there be a ripple in the highly absorbent p+ layer such that the reflected light had to pass through an appreciable fraction of it, then threshold currents would be appreciably increased. In most cases, directional lasing might not occur at all.

It has been our experience that all GaAs has a tendency to produce nonflat diffused junctions, and this tendency is more pronounced in some crystals than in others. This tendency is due to several causes, some of which are reasonably well understood; others are not understood at all. Nonflatness and its causes are the topic of this paper.

Zn, Cd, Mg, Ca, Hg diffusants have been tried. Zn, because of its anomalously rapid diffusion characteristic (1, 2), allows a useful junction depth to be reached before nonflatness occurs; therefore, it appears to be the most suitable of all the acceptor diffusants. Cd is second best, and the remainder do not seem yet to have any advantage at all. This paper, then, deals almost exclusively with Zn diffusion into n-type GaAs.

Diffusion Procedure

Substrates.—GaAs crystals, either Czochralski-pulled or boat-grown, with $N_d - N_a$ in the range from 6 x 10^{15} to 8 x 10^{18}/cm^3 are sawed into slices ~0.030 in. thick with the faces of the slices in the {100} plane. These are then lapped and chemically polished (rotating beaker, 30 min, 3:1:1::H_2SO_4:H_2O_2:H_2O) until the final thickness is ~0.020 in. In some cases, mechanical polishing is used, followed by 30 sec in the etch mentioned above.

The kind of donor element has not so far appeared to be critical. To a first approximation, no differences are easily discernible between crystals doped with Se, Te, C, Si, Ge, or Sn. Lowest threshold currents are observed when junctions are flat and $N_d - N_a$ is in the high 10^{17} or low 10^{18}/cm^3 range, regardless of the kind of donor.

Diffusant.—Zn in various forms has been used as a diffusant. Mostly, $ZnAs_2$ charges of 0.1-10 mg have been used. To a lesser extent, Zn and Zn plus As have been used as a diffusant source.

Tube.—General Electric silica tubes have been used in the experiments described in this paper. 11 mm ID tubes with the GaAs slices and diffusant have been pumped to ~10^{-6} mm Hg and then sealed off ~75 mm from the end of the tube. The resulting volume is ~7 cm^3, neglecting the volume of the contents.

Diffusion temperatures.—Diffusion temperatures ranged from 750° to 1020°C. However, most diffusions were carried out at 850°C.

Diffusion time.—For normal laser runs, 2-3 hours at 850°C will give junction depths of 25-50μ. Of course, junction depth depends also on Zn vapor pressure, doping level in the substrate, etc.

Demarcation of Junctions

To section the diffused slices, two different methods were used. First, an edge of the slice was cleaved on a {110} plane, the plane of easy cleavage in GaAs. No polishing was then required. Second, diffused slices were wax-mounted on angle blocks (5° 43′ to give a slope of 0.1) and the edges beveled by first lapping with 3μ alundum slurry and then with a Linde A polishing slurry on Pellon paper. After cleaving or polishing, etching is performed to demarcate the junction.

Two kinds of etching have been used. First, on cleaved edges electrolytic etching at high currents for approximately 1 sec in a 5% KOH aqueous solution reveals the junction clearly.[1] Second, on either a cleaved edge or a polished bevel surface, a drop of H_2O:HF:H_2O_2::10:1:1 is placed for ~15 sec under illumination by a strong white light. This white light can be supplied by the collimated beam from a General Electric No. 1493 lamp at rated voltage. The samples shown in the photomicrographs of this paper were treated in either of these two ways. This latter etch treatment not only demarcates the junction, but it also renders visible impurity stratification in n-type substrates of the kind presumably induced by constitutional supercooling.

An etching variation which is useful in enhancing contrast is as follows: a drop of gold chloride solution (0.66g of $HAuCl_4 \cdot 3H_2O$ in a liter of water) is placed on the beveled surface and given the strong white light illumination for ~1 min. The solution then is rinsed away, and the wafer is etched in the 10:1:1 solution for ~15 sec, with or without the light.

Example of Nonflatness in Diffused Junctions

To determine whether some nonflatness could be caused by local damage on the substrate surface, a {100} substrate was scratched by a tungsten carbide scribe with varying force. One set of scratches were made in <110> directions; the other set of scratches at 45° to the <110>. Results are shown in Fig. 2. Al-

[1] This electrolytic etching technique has been used to reveal junction position by R. F. Rutz of this Laboratory.

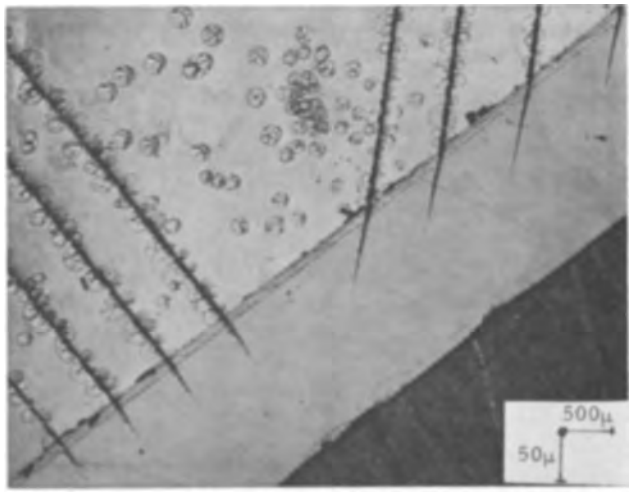

Fig. 2. Beveled section and upper surface of n-type GaAs which had been deliberately scratched with a tungsten carbide probe and then diffused at 850°C for 8 hr with 9 mg of Cd_3As_2 in the tube. Bevel slope is 0.1; X_j = 7μ. Actual gouged portion of scratches not more than ~ 1μ in depth.

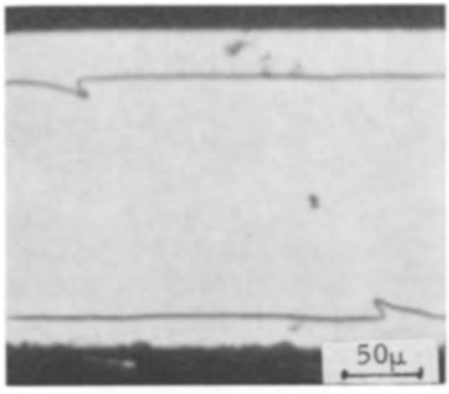

Fig. 3. Cleaved, electrolytically etched {110} edge of an n-type GaAs slice diffused with $ZnAs_2$ at 850°C for 2.5 hr with 8 mg of $ZnAs_2$ in the tube. $X_j = 30\mu$. The slice faces are in {100} planes.

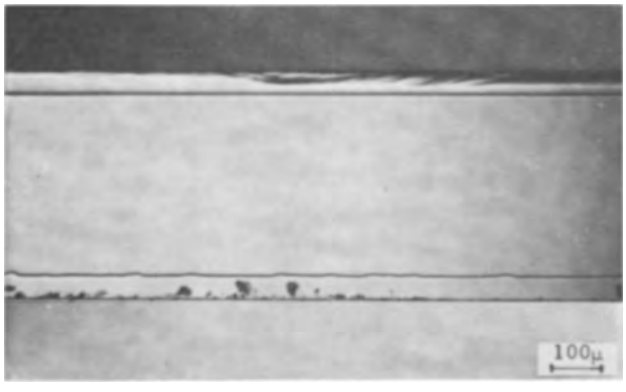

Fig. 4. Cleaved and electrolytically etched {110} edge of slice diffused with $ZnAs_2$ at 850°C for 8 hr. Slice faces in {111} plane; upper face optically polished then etched; lower face lapped slightly. $X_j = 40\mu$.

though Cd happened to be the diffusant in this particular example, similar results were observed in all cases of Zn diffusants at various temperatures and times. Note that the junction is fairly flat between the scratched regions. Figure 2 shows that scratches at the surface can affect junction flatness.

Figure 3 depicts a kind of departure from flatness sometimes seen in various substrates, and especially those which had been subjected to ultrasonic cutting, as was this sample. The photograph is of a cleaved edge which had been electrolytically etched after cleaving.

Figure 4 is another cleaved {110} edge which had been electrolytically etched. The slice faces were in {111} planes; the upper face happens to be the "A" face and the lower the "B" face, but this is not significant. The upper face was optically polished with Linde B abrasive, and then given a slight etch; the lower face was lapped slightly with 1900 mesh alundum, with some saw damage probably remaining. It can be seen that the junction nearer the upper face is flatter than the other junction, but in many similar cases no difference in flatness could be detected between junctions diffused from polished faces and from lapped faces. However, the point to be made is that, while surface damage can cause nonflatness, it can be avoided with relative ease. To be more specific, if the slices are sawed and lapped with reasonable care, and then chemically polished so that 0.005 in. or more of material is etched away,

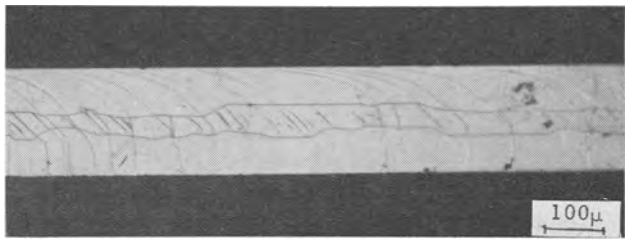

Fig. 5. Cleaved and electrolytically etched {110} edge of a slice of 0.0073 in. total thickness. Both faces had been optically polished and lightly etched. $ZnAs_2$ diffused at 850°C for 25 hr. These junctions represent extreme case of nonflatness.

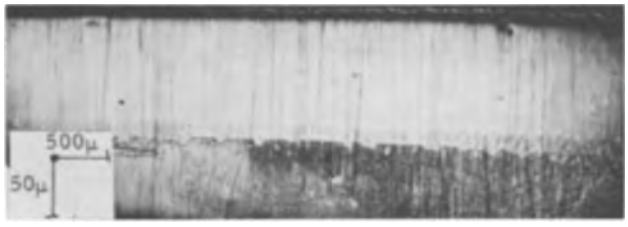

Fig. 6. Bevel-polished, gold plated lightly, and etched in 10:1:1::H_2O:H_2O_2:HF for 15 sec. $ZnAs_2$ diffused at 850°C for 16 hr. $X_j = 108\mu$; $X_j' = 95\mu$. Note difference of nonflatness between outer and inner portions of the slice. Bevel slope = 0.1.

one can be confident that any nonflatness which might occur is not due to surface damage.

However, nonflatness depends also on causes other than surface damage, as can be shown in Fig. 5, a photograph of a cleaved and electrolytically etched {110} edge of a slice 0.0073 in. thick, which had been diffused with a $ZnAs_2$ source at 850°C for 25 hr. Both surfaces had been optically polished and lightly etched.

Another extreme case of nonflatness is shown in Fig. 6. This sample was bevel-polished and then etched with a drop of 10:1:1::H_2O:H_2O_2:HF for ~15 sec in a strong light, as described earlier. To be noted first is that nonflatness is more pronounced near the original surfaces of the pulled crystal than near the axis. This has been a general observation in a large number of cases. Next to be noted is that the junction proper is the lower, more pronounced demarcation; this was determined by thermoelectric probing. The less distinct line above the junction is very often seen in Zn diffusions (less often in Cd diffusions), and was believed to be a demarcation between a p+ and a p-region. This was subsequently established by Dr. H. Rupprecht of this Laboratory, who used four-point probe measurements which determined the Zn diffusion profile.

In accordance with the conventional designation of junction distance as X_j, this extra line has been designated X_j'. Widths have varied from ~1 to 10μ, with wider $X_j - X_j'$ regions being found in substrates with lower $N_d - N_a$ values. By infrared photography (4), it has been demonstrated that the region of injection-recombination and stimulated emission lies on the p-side of the junction.

Lines other than this X_j' line have sometimes been observed, although much less often, on either side of the junction. Although they seem to depend somehow on illumination during etching, their nature is elusive, and they will not be discussed further in this paper.

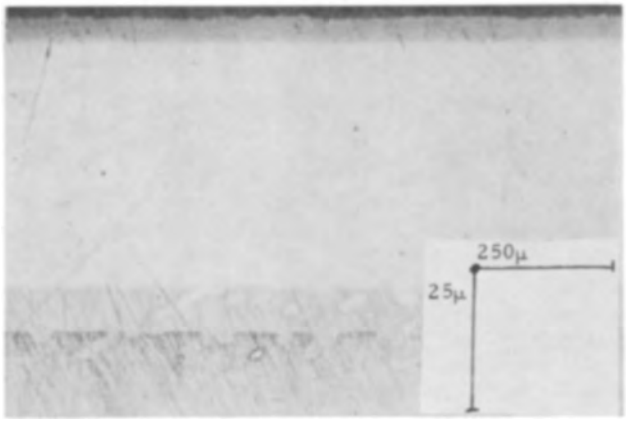

Fig. 7. Bevel-polished and etched under illumination. $ZnAs_2$ diffused at 950°C for 1.25 hr. $X_j = 53\mu$; $X_j' = 47\mu$. Note jogs in X_j' and corresponding jogs in X_j. Bevel slope = 0.1.

The existence of the X_j' line and its apparent concentration-dependence points out that there are really two ways in which junction nonflatness can occur: (i) an irregular diffusion front; and (ii) nonuniform doping in the substrate.

Figure 7 illustrates nonflatness of the first case. This is a beveled and stained sample which had been diffused at 950°C for 1.25 hr. Note that some of the jogs in X_j' have corresponding jogs in X_j, which are probably due to "diffusion pipes." The insular regions below X_j probably are due to the fact that this is a beveled section.

Figure 8 is a photograph of a cleaved {110} edge (which was then etched under illumination) of a sample which had $ZnAs_2$ diffused at 850°C for 14 hr. Again, note the jogs in X_j' and the corresponding jogs in X_j, without the distortion due to beveling, which is present in Fig. 7.

Because absorption of the stimulated radiation is higher in p+ GaAs than in other GaAs, this case of junction nonflatness, wherein jogs of p+ material extend in the "active" layer where the stimulated emission occurs, very likely causes higher threshold currents.

Junction nonflatness of the second case is shown in Fig. 9. $ZnAs_2$ was diffused at 850°C for 3 hr; the sample was then bevel-polished and etched under illumination. Impurity stratification in the substrate is evident as are the consequent jogs into the "active" layer. This stratification probably is due to constitutional supercooling during melt-growth.[2]

[2] Junction nonflatness due to impurity stratification in the substrate had been demonstrated earlier by C. Z. LeMay of this Laboratory.

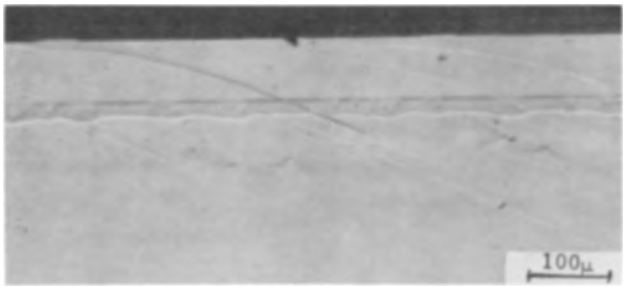

Fig. 8. Cleaved {110} edge, etched under illumination. $ZnAs_2$ diffused at 850°C for 14 hr. $X_j = 87\mu$; $X_j' = 75\mu$. Note jogs in X_j' and corresponding jogs in X_j.

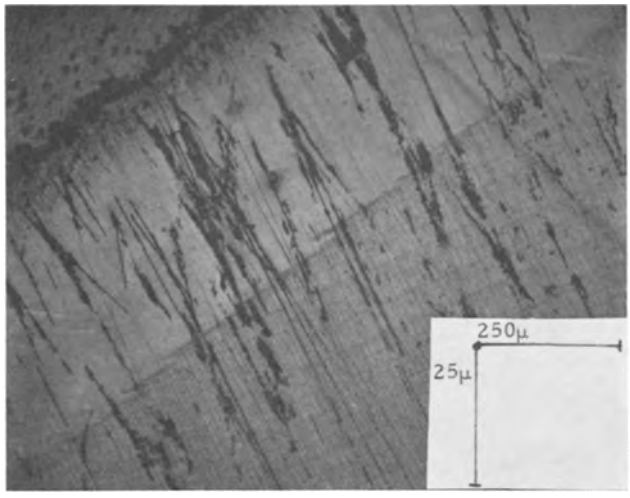

Fig. 9. Bevel-polished and etched under illumination. Surface and diffused portions in left diagonal half of photograph, and undiffused substrate at right. Bevel slope = 0.1. $X_j = 37\mu$. $ZnAs_2$ diffused at 850°C for 3 hr. Note impurity stratification in substrate and consequent jogs in X_j.

Because the absorption of the stimulated emission is not as high in n-type GaAs as it is in p+ type GaAs, this kind of nonflatness is not as deleterious to threshold current as is the first kind. The particular sample shown in Fig. 9 yielded lasers with threshold current densities of 2×10^3 amp/cm^2 at 77°K.

Although Fig. 9 shows definitely that impurity stratification, as well as surface damage, can cause junction nonflatness, Fig. 10 shows just as definitely that there is at least one more cause. This sample is from the same crystal as the one shown in Fig. 9. However, a smaller charge of $ZnAs_2$ was diffused at the same temperature, 850°C, for 16 hr rather than 3 hr. The sample was bevel-polished and etched under illumination. The bevel slope is 0.1; $X_j \sim 75\mu$. The upper portion is the diffused region, and impurity stratification can be seen in the lower undiffused region. It is plainly seen, however, that there is an effect which overrides the impurity-stratification effect. This effect produces a junction

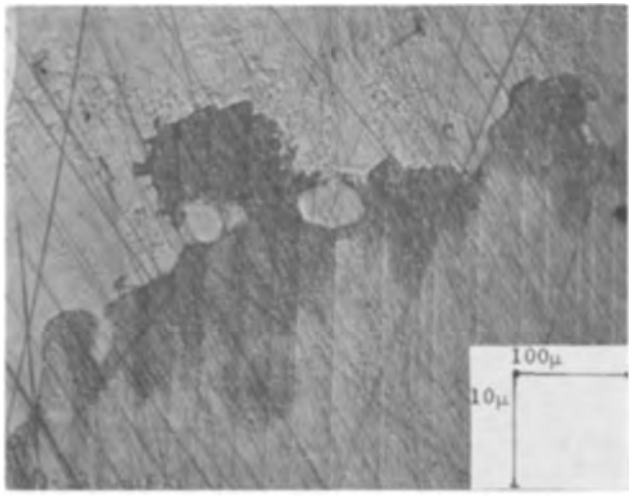

Fig. 10. Bevel-polished and etched under illumination. Bevel slope is 0.1; $X_j \sim 75\mu$. Upper portion is diffused region. Note that another effect overrides junction nonflatness due to effect of impurity stratification. This slice is similar to that of Fig. 9, except that it was diffused with a smaller charge of $ZnAs_2$ at 850°C for 16 hr.

line which appears "amorphous" rather than "polygonal." The sample shown in Fig. 10 did not yield any operable lasers.

In this section, it has been shown that nonflatness can occur in two ways: by an irregular diffusion front and by a nonuniform distribution of dopant in the substrate. Nonflat junction profiles can be of two kinds: "polygonal" and "amorphous." In many cases, the former kind is due to known causes; however, the causes of the "amorphous" kind of profile are not known but possible causes are discussed in the next section.

Discussion of the Possible Causes of "Amorphous" Nonflatness

1. The first question to be asked is: does the cause lie within the crystal itself or the diffusion ambient? Many diffusion runs have been made in which substrates from several crystals have been diffused simultaneously, and some junctions were found to be flat and others nonflat. This is illustrated in Fig. 11.

Both samples were diffused in the same tube at 850°C for 2 hr with a $ZnAs_2$ charge. $N_d - N_a$ for the sample in Fig. 11a was 1 x 10^{17}/cm^3 and 2.3 x 10^{17} for the other. Despite the similarity in doping levels, flatness in the sample in Fig. 11b is much worse than in the other. How these crystals differ will be mentioned below.

It seems, therefore, that the cause of nonflatness lies within the material itself and not in the diffusion ambient.

2. Flatness worsens as the diffusion time or temperature increases. Although most of the photographs shown so far were of samples diffused at 850°C, it can be seen that flatness after about 16 hr diffusion is worse than it is after 3 hr diffusion. By the same token, junctions diffused as long as ~80 hr at 750°C are as flat (and about as deep) as junctions diffused 3 hr at 850°C.

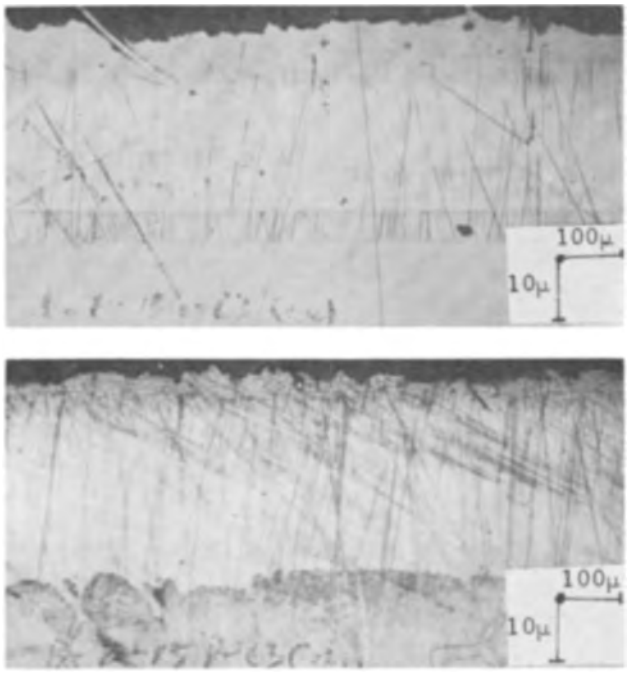

Fig. 11. Bevel-polished and etched under illumination. Bevel slope is 0.1; $X_j \sim 25\mu$. $N_d - N_a$ in the sample in Fig. 11a (top) is 1 x 10^{17}/cm^3 and 2.3 x 10^{17} in the one in Fig. 11b (bottom). Diffused at 850°C for 2 hr with a small charge of $ZnAs_2$ (0.7 mg).

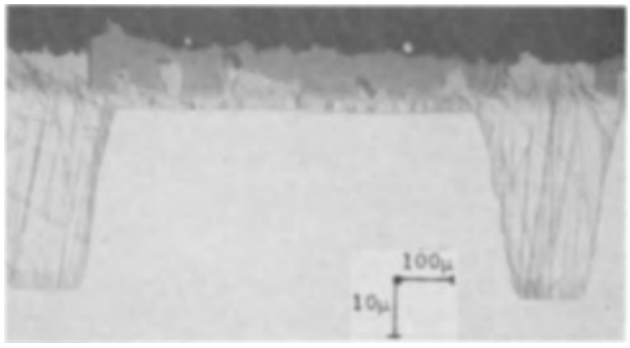

Fig. 12. Bevel-polished and then etched under illumination. $ZnAs_2$ diffused through a slotted SiO mask at 850°C for 2.5 hr. X_j in the slotted regions is 35μ. Some diffusion occurred through the mask, but the junction flatness is approximately the same in all regions.

Actually, it would be difficult to separate the time-temperature effect from a possible depth effect, if the latter exists. However, Fig. 12 affords some information on this question. This is a bevel-polished sample which was etched under illumination. The bevel slope is 0.1. $ZnAs_2$ was diffused for 2.5 hr at 850°C through a slotted mask of SiO. X_j at the slotted regions is 35μ. Some diffusion occurred through the SiO mask, and the junction there is much less deep. However, in both regions the flatness appears to be approximately equal, and therefore it is not likely that depth itself has any effect on flatness.

3. Junction flatness depends on the amount of diffusant in the tube. Relatively small amounts are prone to yield nonflat junctions. Figure 13 com-

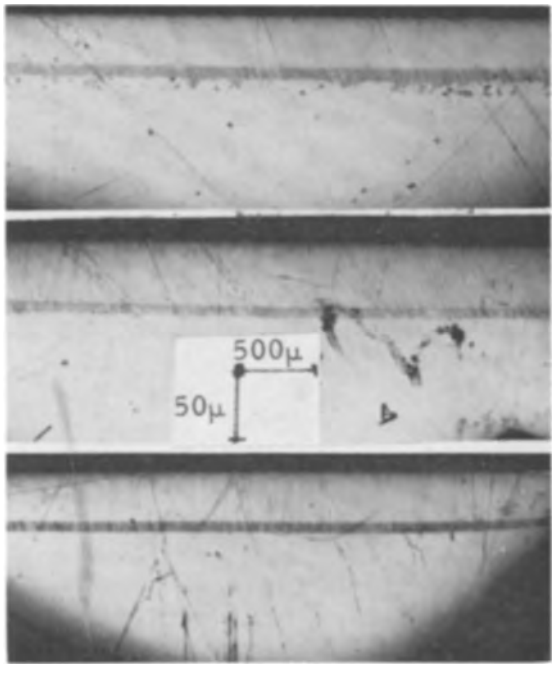

Fig. 13. Bevel-polished gold plated lightly, and etched 15 sec in 10:1:1::H_2O:H_2O_2; bevel slope is 0.1. All slices from same crystal and diffused with $ZnAs_2$ for 850°C for 3 hr. Samples in Fig. 13a (top) and Fig. 13b (center) came from part of crystal at which $N_d - N_a$ = 1 x 10^{17}; Fig. 13c (bottom) from part at which $N_d - N_a$ = 4 x 10^{17}. Figure 13a and 13c had 0.8 mg of $ZnAs_2$ in the 7 cm^3 tube; Fig. 13b had 8 mg. In Fig 13a: $X_j = 45\mu$; $X_j' = 38\mu$. In Fig. 13b: $X_j = 50\mu$; $X_j' = 45\mu$. In Fig. 13c: $X_j = 40\mu$; $X_j' = 34\mu$.

pares two diffusions with different amounts of $ZnAs_2$ in the tubes. The samples were bevel-polished, and then etched under illumination. Both diffusions were carried out at 850°C for 3 hr on substrates from the same crystal ($N_d - N_a \sim 1 \times 10^{17}/cm^3$). The sample in Fig. 13a was diffused in a 7 cm^3 tube with 0.8 mg of $ZnAs_2$ in it, and the sample in Fig. 13b had 10 times as much $ZnAs_2$.

Under the experimental conditions used, ~ 5 mg $ZnAs_2$ charges in the 7 cm^3 tube seemed to be the threshold amount; amounts greater than this yielded no apparent improvement in junction flatness or greater junction depth (some of the $ZnAs_2$ diffusant remains unevaporated at 850°C when more than 5 mg is used). With $ZnAs_2$ diffusant charges less than 5 mg, a tendency toward junction nonflatness became evident. Three mg charges of pure Zn also were used as a diffusant. The junction depths were much greater than when either $ZnAs_2$ or Zn + As were used. This is in agreement with earlier work (2, 3). At diffusion temperatures of 950° and 1020°C, the pure Zn charges resulted in flatter junctions than when $ZnAs_2$ or Zn + As were used. At diffusion temperatures of 850° and 750°C, flatter junctions resulted from the $ZnAs_2$ or Zn + As diffusants than with a pure Zn diffusant.

Incidentally, a 3 mg Cd diffusant charge, in contradistinction to the Zn case, yielded shallower junctions than did Cd_3As_2 or Cd + As diffusant charges.

4. Substrates with lower $N_d - N_a$ values tend to produce nonflat junctions. To be specific, in substrates with $N_d - N_a \sim 10^{17}$ junction nonflatness becomes evident under conditions which still produce flat junctions in higher doped substrates.

Figures 13a and c are typical of this phenomenon. As mentioned earlier, both of these slices were from the same crystal and were diffused with 0.8 mg of $ZnAs_2$ at 850°C for 3 hr. However, the sample in Fig. 13a had an $N_d - N_a$ value of 1×10^{17}, while Fig. 13c had 4.5×10^{17}.

This phenomenon is probably due to the shallow concentration gradient of the Zn in the lower doped samples. However, in referring back to Fig. 11, in which both samples were of approximately the same $N_d - N_a$ and presumably the same concentration gradient, it is seen that nonflatness depends also on something other than the Zn concentration gradient at the junction.

5. Several other miscellaneous possible causes of junction nonflatness have been considered and tentatively eliminated.

(*a*) A sample which was elastically strained during diffusion showed no difference in junction flatness from a nonstrained control sample in the same tube. Another sample was plastically deformed and diffused;[3] it exhibited a junction line quite parallel to the curved surface due to the deformation.

Junctions generally are flatter near the axes of the pulled-crystal substrates than they are at the portions of the crystal near the surface, as shown in Fig. 6. However, dislocation densities have been ~$10^5/cm^2$ in the axis regions, and ~$10^4/cm^2$ near the outer regions. Therefore, flatness does not depend in any direct, clear way on dislocation density.

[3] This experiment was conducted by H. Rupprecht of this Laboratory.

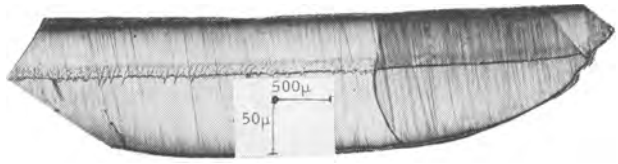

Fig. 14. Bevel-polished, gold plated lightly, and etched in 10:1:1::H_2O:H_2O_2:HF for 15 sec. Bevel slope is 0.1; $X_j \sim 50\mu$; $X_j' = 40\mu$. $ZnAs_2$ diffused at 850°C for 16 hr. Note that X_j' is constant in both grains, while X_j varies slightly, and that flatness is poorer in the main part of the crystal.

(*b*) It does not seem likely that a nonuniform distribution of surface concentration of diffusant is involved in the "amorphous" kind of nonflatness. If such a condition existed, junction flatness would improve with increasing depth, but the general observation has been that deeper junctions exhibit "amorphous" nonflatness.

(*c*) Various etch treatments have been tried, but no effect on junction flatness has been observed.

(*d*) Warming and cooling rates to and from diffusion temperatures have been varied, but again no effect on junction flatness has been observed.

(*e*) The possibility that some unknown matter is diffusing inward or outward during the Zn diffusion and interacting with it is much more difficult to assess. However, various samples have been preheat-treated at diffusion temperatures and higher for times comparable to or longer than ordinary diffusion times, with or without As. These samples were then subjected to standard diffusion procedures with nonheat-treated controls. No difference in junction flatness was observed. Also, other experiments in which H_2 backfilling and O_2 backfilling (~5 mm Hg pressure) were used showed no differences in junction flatness.

(*f*) Copper or copper-like impurities do not have an appreciable effect on junction nonflatness. Figure 14 depicts a sample whose substrate had an extra crystal grain in it. $ZnAs_2$ was diffused at 850°C for 16 hr. The sample was bevel-polished, plated lightly with gold, then etched in 10:1:1::H_2O:H_2O_2:HF for 10 sec. Bevel slope is 0.1; $X_j = 50\mu$; $X_j' = 40\mu$. The fact that the junction is nonflat in the main part of the substrate and flat in the other suggests that a fast-diffusing copper-like impurity is not responsible for the nonflatness.

This nonflatness is of the "polygonal" kind and not of the "amorphous" kind. However, a number of experiments in which Cu, Ni, or Fe impurities were intentionally introduced before, during, and after Zn diffusion failed to effect either kind of nonflatness. Sometimes complete or partial conversion from n-type to p-type would occur, and often junctions would be nonflat, but the flatness was never significantly different in the control samples.

Placing Cu, Ni, or Fe in the tube with $ZnAs_2$ during diffusion resulted in shallower junctions. Very likely, they formed a compound of some sort with the Zn and thereby reduced the Zn vapor pressure in the diffusion tube.

6. Crystals which had some O_2 present during growth show a greater tendency toward "amor-

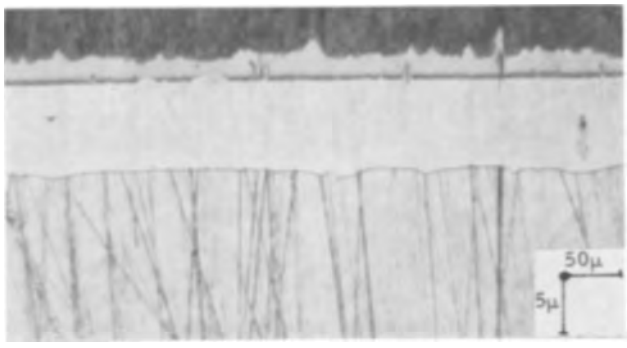

Fig. 15. Bevel-polished and etched under illumination. Bevel slope is 0.1; $X_j = 8\mu$. Se diffused through an SiO mask at 1020°C for 186 hr. Note that nonflatness is of the "polygonal" and not the "amorphous" kind.

phous" nonflatness. Samples shown in Fig. 5 and in Fig. 11b were of this kind.

As stated earlier, it seems that all GaAs crystals will show nonflat junctions if diffused at high enough temperatures or long enough times. This applies more strictly to n-type crystals with acceptor diffusions and the "amorphous" kind of nonflatness. It is probable that there are varying amounts of O_2 present during crystal growth even when reasonable precautions are taken to keep it out, as is the usual case, and it can be conjectured that this accounts for the varying degrees of susceptibility to nonflat junctions.

Whether the effect of the O_2 is a direct chemical effect or an indirect structural effect is, of course, quite speculative. An observation that favors the former mechanism is shown in Fig. 15. This is a bevel-polished sample etched under illumination. The bevel slope is 0.1. $X_j = 8\mu$. Se (a donor) was diffused through a surface layer of SiO into a p-type substrate.[4] To be noted especially are the very high diffusion temperature, 1020°C, and the very long diffusion time, 168 hr. To be sure, the junction is nonflat, but had it been a Zn diffusion into n-type material, the junction flatness would have been much worse. Because a Se-O bond is weaker than a Zn-O bond, it seems possible that a diffusing Zn atom could react chemically with an O atom and remain combined, becoming electrically inactive. If the distribution of O is nonuniform, then the junction could become nonflat.

Summary

It has been shown that n-type GaAs when diffused with an acceptor such as Zn has a tendency to produce nonflat junctions, some crystals having a greater tendency to nonflatness than others, and all much greater than in Ge or Si.

There are two ways in which junction nonflatness can occur, namely, by irregular diffusion front, and by a nonuniform distribution of donors or deep-level impurities in the substrate. There are two kinds of nonflatness, namely, that in which the junction section is "polygonal" and that in which the junction section is "amorphous."

Using any of several etching methods to demarcate junctions, an extra demarcation line not quite as deep as the junction line is observed in most Zn and some Cd diffusions. This extra line apparently is concentration-dependent.

The tendency toward the "amorphous" kind of junction nonflatness is greater in crystals which had some O_2 present during growth.

Using 8 mg of $ZnAs_2$ diffusant in a 7 cm^3 tube and diffusing at 850°C for 3 hr or less generally yields a junction of good flatness in almost all n-type GaAs. Figure 16 is a typical example.

[4] This was done by C. E. Kelly of this Laboratory.

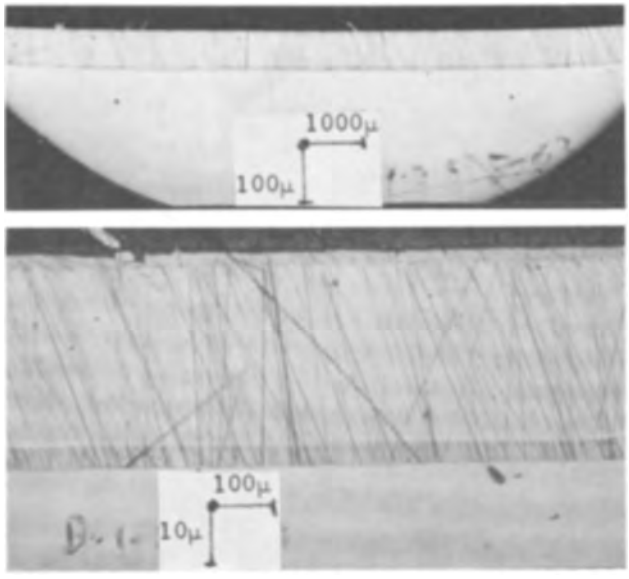

Fig. 16. Bevel-polished and etched under illumination. Bevel slope is 0.1. $X_j = 33\mu$; $X_j' = 28\mu$. 8 mg of $ZnAs_2$ diffused at 850°C for 3 hr. This is a standard structure for fabrication into present-day experimental injection lasers. Fig. 16a (top) is at low magnification; Fig. 16b (bottom) is at higher magnification.

Acknowledgments

The author is indebted to many persons in this Laboratory for their generous help. In particular, he thanks B. J. Canavello for his cooperation throughout all the work, and he thanks H. Rupprecht for many enlightening discussions. Special thanks are due to the Crystal Studies Group, S. E. Blum, N. G. Ainslie, and J. M. Woodall, for supplying the GaAs crystals.

Manuscript received June 13, 1963; revised manuscript received July 30, 1963. This paper was presented at the Pittsburgh Meeting, April 15-18, 1963.

Any discussion of this paper will appear in a Discussion Section to be published in the June 1964 JOURNAL.

REFERENCES

1. J. W. Allen and F. A. Cunnell, *Nature*, **182**, 1158 (1958).
2. F. A. Cunnell and C. H. Gooch, *J. Phys. Chem. Solids*, **15**, 127 (1960).
3. B. Goldstein, *Phys. Rev.*, **18** [4], 1024 (1960).
4. A. E. Michel, E. J. Walker, and M. I. Nathan, *IBM J. of Rev. and Dev.*, **7** [1], 70 (1963).

A Rapid Neutron Activation Method for Determining Chromium in Ruby Maser and Laser Crystals

Joseph R. Weiner, John J. O'Connor,[1] and Bernard Rubin

Air Force Cambridge Research Laboratories, Office of Aerospace Research, L. G. Hanscom Field, Bedford, Massachusetts

In the synthesis of ruby by the Verneuil technique, the question of the possible loss of the chromium due to volatilization during the growth process has arisen. It is the purpose of this work to establish a rapid method for the determination of chromium in ruby and to correlate the chromium content in the final boule with the chromium content of the starting powder mixture.

To date, two methods have been investigated for the analysis of the chromium in ruby: a chemical method (1) and an electron microprobe technique (2). The latter method has been used for determining relative concentrations of chromium in localized volumes of the ruby and for obtaining chromium profiles in a plane normal to the growth axis of the crystal. The chemical method has been used for analyzing the average chromium content of relatively large volumes of the crystal. The effective sample weight was about 10^{-9}g in the electron microprobe technique while the chemical method dealt with samples weighing about 0.02g. There are several inherent sources of error in the chemical method: contamination of the sample by grinding, contamination of the sample from chemical reagents, retention by the container of significant amounts of chromium, and systematic errors associated with the colorimetric technique.

A method for the quantitative determination of chromium in ruby using the neutron activation technique (3-11) has been developed in this laboratory. This involves irradiating the sample with thermalized neutrons in a nuclear reactor and subsequent counting of the emitted gamma rays with a multichannel gamma ray spectrometer. The advantages of this method are: it is a relatively uncomplicated procedure; it is neither time-consuming nor tedious; it yields an absolute value for the chromium content; it eliminates problems from contamination; and it offers the possibility of monitoring each step of the procedure for errors.

Experimental Procedure

Fifteen ruby boules, grown by the Verneuil technique were analyzed by the neutron activation method. From each crystal, three samples were sliced, representing the initial, middle, and last grown portions. The samples ranged in weight from 25 to 200 mg. Each sample was placed in a recessed area on top of a polyethylene cylinder 13.5 mm in diameter and 11 mm long. A chromium standard was inserted into a hole in the bottom of the cylinder so that the distance between sample and standard was only 5 mm. Four such cylinders were tightly stacked into a polyethylene container. The ruby samples were selected on the basis of the chromium content of the starting powder to contain about the same weight of chromium. The irradiation time was adjusted so that the integrated count rate was about 50,000 cpm from the Cr^{51} activity. This was possible for all samples except those whose chromium content was below 10 μg. The samples were then irradiated in the "rabbit" tube of the M.I.T. Reactor for times which varied from 3 min to 24 hr.

To reduce flux depression and the effects of self-shielding, and to minimize the radiation hazard, the chromium standards taken were each less than 8 mg. All weighings of standards were done on a Cahn Electrobalance having an accuracy of $\pm$ 0.1%.

After irradiation, the samples and standards were weighed and transferred to 4 ml glass vials. The standards were dissolved in concentrated HCl and diluted so that 1 ml aliquots contained a convenient amount of activity for counting. To minimize the interference of Na^{24} from the reaction $Al^{27}(n,\alpha)Na^{24}$, the activity in the sample was allowed to decay for several days. One-minute integral counts of the gamma ray spectra were then taken on both sample and standard.

To check the fact that only chromium was being counted, the gamma ray spectra of both the samples and standards were photographed with a Polaroid camera from the oscilloscope display of the instrument. A typical spectrum is shown in Fig. 1. The resulting display is a plot of the logarithm of the gamma ray count rate *vs.* the gamma ray energy. Visual comparison of sample and standard spectra indicates qualitatively that the only significant peaks in the spectrum were those of Cr^{51}.

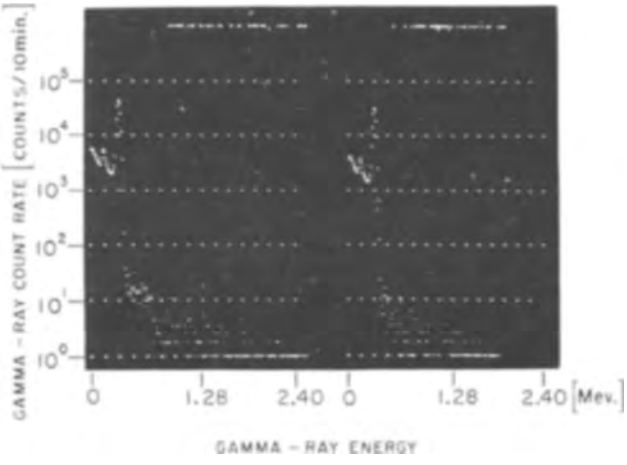

Fig. 1. Typical spectra of a ruby sample (left) and chromium standard (right) with energy full scale set at 2.56 Mev.

[1] Present address: Tracerlab, a Division of Laboratory for Electronics, Inc., Waltham, Massachusetts.

As a further qualitative check on the presence of only Cr^{51}, the samples and standards were allowed to decay for two weeks and 10 min counts were taken. The integral count rates were taken automatically using the data reduction unit of the multichannel analyzer. From the ratio of the integral count-rates, the half-life of the chromium was calculated and was found to agree with that of Cr^{51}.

To confirm the unique presence of Cr^{51}, the ratio of the integral count rate of the original irradiated sample and standard was compared to the ratio of the count rate under the 0.32 Mev peak of sample and standard after a two week decay. The ratios were found to be unchanged, indicating that only Cr^{51} was present.

All counting was done on a 512-channel Nuclear Data Analyzer Computer using a 1¾ in. diameter by 2 in. thick NaI(Tl) crystal with a well ¾ in. in diameter by 1½ in. deep. The crystal was mounted on an EMI 9578B photomultiplier tube.

As a comparative method to determine the chromium content of the ruby, an absorption spectrophotometric procedure was used. The sample that had been irradiated and evaluated was powdered in a boron carbide mortar and fused with sodium bisulfate ($NaHSO_4 \cdot H_2O$) in a platinum crucible. The fusion products were dissolved in 30 ml of water, and four pellets of sodium hydroxide were added, followed by ½ ml of 30% hydrogen peroxide solution. The solution was then boiled for 10 min. The volume was adjusted to 50 ml, and the optical density of the chromate solution was read on a Beckman DK-2 spectrophotometer at 3550Å. Six samples of higher chromium content were analyzed by this technique.

Results

Reference to Table I shows that there is good agreement between the per cent chromium in the ruby samples determined from a 1-min integral count of the whole spectrum and a 10-min integral count taken under the Cr^{51} peak. It therefore is necessary to count for only 1 min after the Na^{24} has disappeared for an accurate determination.

Table I. Results of chromium analyses of synthetic rubies by neutron activation

Sample No.	Wt % Cr as determined from 1-min integral count of whole spectrum			Wt % Cr as determined from 10-min integral count under 0.32 Mev Cr^{51} peak taken at later date			Wt % Cr in starting powder
	Initial portion	Middle portion	Last grown portion	Initial portion	Middle portion	Last grown portion	
1	0.014	0.011	0.012	0.013	0.011	0.012	0.020
2	0.039	0.037	0.041	0.039	0.037	0.040	0.048
3	0.058	0.047	0.042	0.059	0.048	0.040	0.068
4	0.084	0.053	0.055	0.083	0.052	0.054	0.088
5	0.066	0.075	0.080	0.068	0.075	0.079	0.116
6	0.189	0.235	0.212	0.189	0.237	0.216	0.22
7	0.250	0.214	0.227	0.252	0.216	0.231	0.30
8	0.227	0.268	0.243	0.227	0.260	0.251	0.48
9	0.499	0.501	0.470	0.511	0.497	0.470	0.62
10	1.03	0.955	0.886	1.04	0.983	0.880	1.36
11	0.029	0.048	0.047	0.029	0.048	0.048	0.011
12	0.030	0.034	0.036	0.030	0.035	0.036	0.034
13	2.87	2.81	3.20	2.82	2.78	3.21	5.48
14	5.45	5.30	5.36	5.58	5.30	5.54	8.22
15	5.55	6.72	6.47	5.46	6.77	6.34	10.94

Table II. Comparison of neutron activation and absorption spectrophotometric analyses for determining chromium in synthetic ruby

Sample No.	Neutron activation, wt % Cr	Spectrophotometric, wt % Cr
15A	5.46	5.40
15B	6.77	6.71
15C	6.34	6.46
13A	2.82	2.75
13B	2.78	2.78
13C	3.21	3.03

From a comparison of the starting chromium content of the powder mix of Al_2O_3 and Cr_2O_3 and the chromium content of the ruby boule (Table I) it is apparent that random amounts of Cr_2O_3 are lost during the crystal growing process, probably due to vaporization. Furthermore, there is no correlation between the chromium content of a boule and the distance along the growth direction This is probably due to the heterogeneous radial distribution of the chromium (2) along a given slice and the resulting difficulty of carefully controlled sampling for the analysis. It appears as if the Verneuil technique does not yield crystals of sufficient doping uniformity to render a correlation possible.

Reference to Table II indicates that there is good agreement between the absorption spectrophotometric and the neutron activation methods.

To determine the possible sources of error in the neutron activation method the following equation is introduced

$$\left[c/s = \psi \sigma f \frac{m}{A} N^{\circ} S \epsilon e^{-\lambda t} \right] \qquad [1]$$

where c/s is the activity of the activated species in counts per second at the time of counting, ψ is the neutron flux in neutrons/cm^2-sec, σ is the reaction cross section in cm^2, f is the fractional isotopic abundance, m is the mass of the chromium in grams, A is the atomic weight of chromium, N° is Avogadro's number, S is the saturation factor, ϵ is the counting efficiency, λ is the decay constant of Cr^{51} in sec^{-1}, and t is the time in seconds that has elapsed from the end of the irradiation until the counting of the specimen takes place.

Applying Eq. [1] to sample and standard, taking the ratio of both equations, and eliminating common terms, the following relationship is found

$$\frac{(c/s)_x}{(c/s)_y} = \frac{\psi_x}{\psi_y} \cdot \frac{m_x}{m_y} \cdot \frac{\epsilon_x}{\epsilon_y} \qquad [2]$$

where x refers to the sample and y to the standard.

Rewriting the equation, the following is found for the mass of the chromium in the sample

$$m_x = \frac{(c/s)_x}{(c/s)_y} \cdot \frac{\epsilon_y}{\epsilon_x} \cdot \frac{\psi_y}{\psi_x} \cdot m_y \qquad [3]$$

To approximate the accuracy of the activation method used, the contribution of each of the terms above to the over-all error is considered. The error in the activity ratio which is due to statistics can be kept to less than 1% by the choice of a count

rate in the vicinity of 50,000 cpm. The instrumental error in this ratio appears to be small as shown by the excellent agreement between the result obtained for 1-min and 10-min counts (Table I).

The ratio of the counting efficiencies, ϵ_y/ϵ_x, was determined by counting the activity of a 0.1 ml volume of Cr^{51} solution, which is approximately the geometry of the ruby sample. This volume was then diluted to 1 ml, which is the aliquot of the dissolved standard that was used. It was found that the ratio was 1.02 indicating that the counting efficiency does not vary appreciably with volume. Additional dilution studies indicated that the error of this ratio was less than 0.5%.

The error in the ratio ψ_y/ψ_x due to flux gradient was determined to be negligible by comparing the activity of each of the four standards after neutron irradiation. It was found that a difference of 4% in count rate occurred over the maximum distance of 50 mm. The distance between sample and standard was 5 mm, indicating a minimal error from flux gradient.

The error in ψ_y/ψ_x due to the attenuation of the neutron flux has been determined according to the method used by Plumb and Lewis (12). The fractional flux depression F is related to the thermal neutron cross section σ of a sphere of radius a, of a material with N atoms per unit volume by the equation

$$F = \tfrac{3}{4} N\sigma a \qquad [4]$$

Substitution of the relevant data for the chromium metal standard where $\sigma = 3.1$ barns, $N = 8.34 \times 10^{22}$ at./cc, and $a = 0.06$ cm results in a value of F of about 1%. This value is higher than that for the sample because the chromium is dispersed throughout the alumina matrix. There is no appreciable flux depression from aluminum or oxygen because of their low absorption cross sections.

The accuracy of the weighing for the standard on the Cahn Electrobalance is 0.1%. Under the most adverse conditions where the above-mentioned errors might be in one direction and cumulative, the maximum likely error would be about 2.6%.

Comparing the neutron activation method to the spectrophotometric method used, it is apparent that the latter is open to many more sources of error. These arise from the refractory nature of the crystal and the necessity for processing of the crystal and include grinding, fusion, chemical additions, and transferring of solutions. It would appear as if the simplicity of the handling techniques in the activation method make it a more accurate one than spectrophotometry without considering the lack of homogeneity of the chromium.

Conclusions

The neutron activation technique coupled with gamma-ray spectrometry has been found to be a rapid, accurate, and simple method for the determination of chromium in ruby. Results show good agreement with a chemical-spectrophotometric approach. The advantages of the neutron-activation analysis are that it is rapid, processing of the sample is eliminated, handling is minimized, and the method is nondestructive for certain additional types of testing. Gamma-ray counting of the irradiated sample has been found to require only a 1-min duration count. Analysis of rubies with chromium contents in the range of 0.01-5% indicates that there is no correlation with the starting chromium content of powders used in the crystal growth.

Acknowledgments

The authors wish to acknowledge Mr. J. P. Cali for his suggestions and his development of the chemical-spectrophotometric technique. Thanks are given to Captain G. D. Oshesky for his contribution of the ruby samples.

Manuscript received April 25, 1963; revised manuscript received July 31, 1963.

Any discussion of this paper will appear in a Discussion Section to be published in the June 1964 JOURNAL.

REFERENCES

1. E. M. Dodson, *Anal. Chem.*, **34**, 966 (1962).
2. R. R. Dils, G. W. Martin, and R. A. Huggins, *Appl. Phys. Letters*, **1** [4], 75 (1962).
3. O. U. Anders, Gamma-Ray Spectra of Neutron Activated Elements, June 1960, 69 pp., Dow Chemical Co., Midland, Mich.
4. D. H. F. Atkins and A. A. Smales, "Activation Analysis" in "Advances in Inorganic Chemistry and Radiochemistry," **1**, 315-45, Academic Press, New York (1959).
5. V. P. Guinn and C. D. Wagner, *Anal. Chem.*, **32**, 317 (1960).
6. R. C. Koch, Activation Analysis Handbook, Air Force Cambridge Research Center, Rept AFCRC-tr-59-139, 237 pp., December 1958.
7. W. W. Meinke, *Science*, **121**, 177 (1955).
8. W. W. Meinke, *Anal. Chem.*, **31**, 792 (1959).
9. R. L. Heath, Scintillation Spectrometry—Gamma-Ray Spectrum Catalogue, U. S. A. E. C. Rept. IDO-16408, 200 pp., July 1957.
10. C. E. Crouthamel, "Applied Gamma-Ray Spectrometry," 443 pp., Pergamon Press, New York (1960).
11. K. Siegbahn, "Beta and Gamma Spectroscopy," Interscience Publishers, Inc., New York (1955).
12. R. C. Plumb and J. E. Lewis, *Nucleonics*, **13** (8), 42 (1955).

Photogalvanic Effects with Anodized Zirconium and Niobium Electrodes

Robert E. Salomon, George B. Adams,[1] and Wendell M. Graven[2]

Chemistry Department, Temple University, Philadelphia, Pennsylvania

Illumination with ultraviolet light of certain anodized metal electrodes, such as aluminum, niobium, tantalum, and zirconium, causes an alteration in the electrode potential and gives rise to a photocurrent without the application of an external field. These effects may be observed if the electrode is immersed in an electrolytic solution (photogalvanic effect) or if the metal oxide film separates the metal from a solid electrical conductor (photovoltaic effect).

A number of investigations of the photogalvanic behavior of tantalum electrodes have been reported (1-3). Photocurrent measurements have been made with zirconium electrodes (4). A comparative study of the photogalvanic and photovoltaic properties of tantalum and aluminum electrodes has been reported recently (5). Current theories offered in explanation of the behavior of these electrodes under the influence of illumination have emphasized the semiconductor properties of the oxide films.

The present work was undertaken to assist in the elucidation of the nature of these photoeffects by procuring data with anodized zirconium and niobium electrodes. An attempt has been made to establish the effects of a number of pertinent parameters and to correlate the results with several types of electrode systems.

Experimental

Cylindrical bar stock and thin sheet metals were used. Iodide process, hafnium-free, zirconium bar (99.9%) was obtained from U.S. Bureau of Mines, Albany, Oregon. Niobium bar (99.9%) and 0.5 mil foil (99.7%) were obtained from Fansteel Metallurgical Corporation.

For most of the measurements the metal surface was wet-polished with a sequence of canvas, felt, and flannel-covered wheels using a series of progressively finer abrasives. In certain cases the surfaces were chemically polished using an etch solution of 12% HNO_3 and 2.5% HF.

The electrode was mounted on a Teflon support in a thermostatted cell. The level of the electrolyte, which was usually 0.01M $Na_2B_4O_7$ solution, was maintained about 1 cm above the surface of the electrode.

Oxide films of the desired thickness were produced on the electrode surface by controlling the formation voltage with a Heathkit variable-voltage, regulated power supply.

Electrode potentials were measured against a $Hg/Hg_2SO_4/Na_2SO_4$ (sat'd) reference electrode which was separated from the cathode compartment by a salt bridge containing an Agar plug. Potential measurements were made with a L&N millivolt indicator, the output of which was recorded with a L&N Type G, AZAR, indicating recorder.

Current measurements were made with a Millivac micromicroammeter. For measurements at controlled polarizations the potential between specimen and reference electrode was maintained constant by application of the proper voltage between specimen and a platinum cathode.

For ascertaining the effect of wavelength of the incident radiation a 1000w Hanovia Compact Hg-Xe lamp was used together with a Bausch-Lomb grating monochromator. Relative intensities throughout the spectral regions of interest were measured with an Epply thermopile in conjunction with a L & N high sensitivity galvanometer.

In the remainder of the measurements a 250w General Electric Uviarc was used without the monochromator. The intensity of the output of the lamp was monitored at a selected wavelength with a Photovolt photometer.

Results with Anodized Zirconium Electrodes

Photopotentials.—A freshly polished Zr electrode when immersed in solution showed an initial potential, relative to the reference electrode, of about −1.2v. As oxide began to form on the electrode surface the potential became less negative. When the thickness of the oxide layer had increased such that the electrode potential was less negative than −1.0v there occurred a negative shift in potential upon illumination which initially increased with increasing film thickness.

Only the behavior of electrodes with oxide films which were sufficiently thick to produce large negative shifts in potential upon illumination has been examined in the present investigation.

Zirconium electrodes which had been anodized with formation voltages greater than 10v exhibited potentials, relative to the reference electrode, of −0.03 to −0.06v in the absence of illumination. The potentials of the irradiated electrodes relative to the reference electrode (photopotentials) were more negative, in many instances, than −2.0v.

The rise and decay of the photopotentials are shown for several film thicknesses by the chronopotentiograms of Fig. 1. The decay of the photopotential was observed to be approximately a logarithmic function of time. A steady value of the photopotential was usually observed, although the magnitude often differed somewhat from one electrode to another.

[1] Present address: Lockheed Aircraft Corporation, Missiles and Space Division, Sunnyvale, California.

[2] Present address: Aeronutronics, Division of Ford Motor Company, Newport Beach, California.

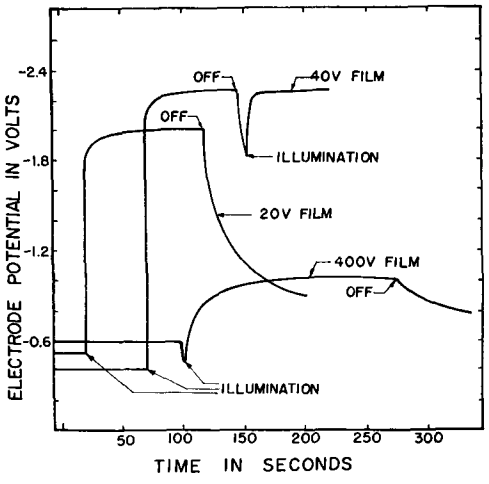

Fig. 1. Photogalvanic chronopotentiograms for Zr electrodes

The effect of film thickness on the steady-state photopotential with a constant incident intensity is shown in Table I. It was observed that the value of the steady-state photopotential is rather insensitive to light intensity and temperature.

An experiment was performed in which a dry electrode was irradiated briefly and then rapidly covered with electrolyte. The observation that the chronopotentiogram was closely similar to the photopotential decay curve of a continuously immersed electrode indicates that a photopotential was produced on the dry electrode.

Photocurrents.—Application to the Zr electrode of a positive polarization voltage, well below the film-formation voltage, produced a small current in the absence of illumination. A considerably larger steady current resulted from illumination of the electrode. The difference between the current measured during illumination and that measured prior to illumination was taken as the photocurrent.

A linear dependence on light intensity and applied field of the photocurrent was observed for films of various thickness. The photoconductance for a given light intensity decreased with increasing film thickness.

The dependence of the photocurrent on the wavelength of the incident light is demonstrated in Table II. Some absorbance indices are also listed for comparison. No significant photocurrent was observed when the wavelength of the incident light was greater than 2550Å. There is a close correlation of spectral sensitivity with the absorption spectra of anodic ZrO_2 films (6).

Table I. Effect of film thickness on steady state photopotential

Formation voltage, v	Photopotential, v
10	—1.91
20	—2.01
40	—2.18
60	—2.19
100	—2.15
200	—1.99
300	—1.22
400	—0.93

Table II. Effect of wavelength of incident light on photocurrent

Wavelength, mμ	Spectral sensitivity, mμ amp/mm	Absorbance index, $cm^{-1} \times 10^{-5}$
255	0.00	0.00
250	0.23	—
245	0.84	—
240	2.60	0.14
238	3.40	—
235	4.40	0.17
233	5.30	—
230	10.50	0.27

Table III. Effect of film thickness on maximum photopotential

Formation voltage, v	Maximum photopotential, v
10	—0.75
20	—0.67
30	—0.51
50	—0.40
100	—0.36

Results with Anodized Niobium Electrodes

Photopotentials.—Niobium electrodes which had been anodized with formation voltages greater than 10v exhibited behavior under illumination which closely resembled that of zirconium electrodes. However, there were certain dissimilarities. The differences between rest potentials and steady-state photopotentials were considerably lower and photocurrents were considerably greater with niobium electrodes. More rapid rise and decay of the photopotentials were observed with Nb electrodes, but the shapes of the chronopotentiograms are similar to those in Fig. 1. For Nb electrodes, also, the photopotential decay appears to be a logarithmic function of time.

Table III demonstrates the dependence of photopotential on film thickness under constant incident intensity.

Photocurrents.—Both "short-circuit" photocurrents and photocurrents with positively polarized Nb electrodes were observed. Photocurrents decreased with increasing film thickness.

A linear dependence of photocurrent on incident light intensity and applied field was observed.

In Table IV the effect of wavelength of incident radiation on the magnitude of the short-circuit

Table IV. Effect of wavelength of incident light on photocurrent

Wavelength, mμ	Spectral sensitivity, mμ amp/mm		Absorbance index, $cm^{-1} \times 10^{-5}$
	20v film	40v film	
375	0	0	—
360	0.034	0.024	—
350	0.098	0.054	—
345	0.16	0.088	—
340	0.25	0.14	0.08
330	0.50	0.32	0.16
315	0.82	0.50	0.38
305	1.2	0.68	—
295	1.8	0.98	0.61
285	2.2	1.3	0.89
280	2.5	1.4	1.42
275	2.8	1.5	—
270	3.0	1.7	—

photocurrent is demonstrated by the computed spectral sensitivities for two electrodes of different thickness. The spectral sensitivities of both electrodes increase with decreasing wavelength, although the magnitude of the photocurrent is greater for the 20v electrode than for the 40v electrode. With light of wavelength greater than 3750Å no significant photocurrent was observed for either electrode. A close correspondence beween the spectral sensitivities of Nb electrodes and the absorption spectra of Nb_2O_5 films (7) is also apparent.

Discussion

Opposing theories have been offered to account for the results obtained with tantalum. A theory proposed by Van Geel *et al.* (5) considers the conditions of electron equilibrium in the three phase system, Ta/Ta_2O_5/electrolyte. An insulating oxide bounded by two contacts having different work functions must be subjected to an electric field at equilibrium. The creation of hole-electron pairs by illumination causes a reduction of this field and a concomitant potential difference (open-circuit photovoltage) between the contacts. A second theory has been proposed by Apker and Taft (2) in which, as a result of the conditions of film growth, the oxide is considered to support a concentration gradient of tantalum ions which in effect requires a p-n junction in the film. A p-n junction is known to exhibit photovoltaic effects.

The similarity between the spectral sensitivity of the short-circuit photocurrent and the absorption spectrum of the oxide is to be noted. Light absorption within the oxide appears to be the primary step, and thus possible photoelectric effects need not be considered. The observed decay of photovoltage with logarithm of time can be predicted theoretically, if the decay is assumed to be due to electron emission over a barrier. However, according to this model the proportionality constant, should be equal to kT. In all cases this constant was found to be much greater than kT. The appearance of a photopotential on a dry electrode indicates that a second contact is not a prerequisite to photogalvanic activity. This would indicate that the source of the emf is within the oxide. Finally, mention may be made of recent experiments at low temperatures with electrodes of the form $Zr/ZrO_2/Sn$ (8). At −175°C this electrode develops a photopotential of 90v. This cannot be reconciled with either of the two theories previously mentioned unless a different mechanism is applicable at low temperatures.

Acknowledgment

The authors wish to thank the U.S. Atomic Energy Commission for financial support for this work.

Manuscript received March 7, 1963; revised manuscript received July 5, 1963.

Any discussion of this paper will appear in a Discussion Section to be published in the June 1964 JOURNAL.

REFERENCES

1. I. Lifschitz and M. Reggiani, *Z. physik. Chem.*, **A155**, 431 (1931).
2. L. Apker and E. A. Taft, *Phys. Rev.*, **88**, 58 (1952).
3. L. Young, *Trans. Faraday Soc.*, **50**, 164 (1954).
4. A. Charlesby, *Acta Met.*, **1**, 348 (1953).
5. W. C. Van Geel, C. A. Pistorius, and P. Winkel, *Philips Research Repts.*, **13**, 265 (1958).
6. R. E. Salomon, W. M. Graven, and G. B. Adams, *J. Chem. Phys.*, **32**, 310 (1960).
7. W. M. Graven, R. E. Salomon, and G. B. Adams, *ibid.*, **33**, 954 (1960).
8. R. E. Salomon and P. N. Ramachandran, *J. Phys. and Chem. of Solids*, **24**, 583 (1963).

Brief Communications

The Use of Close Spacing in Chemical-Transport Systems for Growing Epitaxial Layers of Semiconductors

F. H. Nicoll

RCA Laboratories, Radio Corporation of America, Princeton, New Jersey

The method of chemical transport of materials via a volatile compound such as an oxide or halide has been well established by many workers (1). Furthermore, the method has been successfully applied to a large number of materials for the purpose of growing single crystals and epitaxial layers of semiconductors. In general, transport takes place from a source at one end of a tube to a seed at the opposite end, a suitable temperature difference being maintained by means of a gradient furnace.

In the close-spaced method the source and substrate are separated by only a fraction of a millimeter. Close-spacing of the source and substrate has a number of advantages. If the spacing is less than about 1/10 of the diameter of the source and substrate, then the chemical transport conditions in between are largely independent of conditions elsewhere in the system. This is the case because the transporting agent such as oxygen is not consumed in transporting material and is therefore available between the source and substrate for continued re-use. Re-use of the transporting agent means that deposition conditions are not affected by source and substrate size provided their diameter is

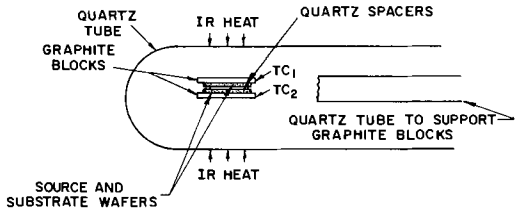

Fig. 1. Diagram of close-spaced system for depositing epitaxial semiconductor layers by chemical transport.

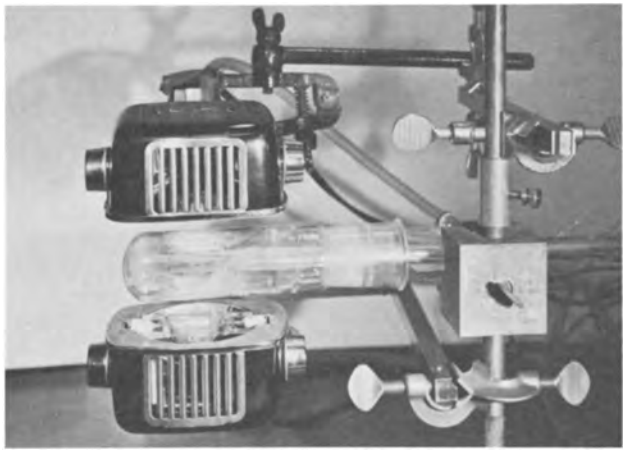

Fig. 2. Photograph of complete close-spaced system for depositing epitaxial semiconductor layers by chemical transport.

greater than 5-10X the spacing. Close-spacing of source and substrate also means direct transport of each component of the material across the space. This is especially advantageous for compounds of elements with widely different physical properties. If infrared heating of source and substrate is used, the system has the added advantage of having a cold wall, and conditions for transport are maintained only at the source and substrate. Finally, this technique can provide a compactness and simplicity of operation not hitherto attained.

Figure 1 shows a diagram and Fig. 2 a photograph of an all-quartz system for deposition of epitaxial layers of semiconductor using the close-spaced concept. The system operates at atmospheric pressure and utilizes water vapor as the transporting medium (2). The water vapor is obtained by passing hydrogen over water at 0°C. This mixture is used at a very low flow rate of less than 1 cc/min. The source and substrate wafers are separated from each other by quartz strip spacers of about 0.25 mm thickness. Two graphite disks are in contact with the wafers on top and underneath and have thermocouples TC1 and TC2 inserted in them for temperature measurement. Heating is done entirely from outside the tube using infrared radiation from two photographic Sylvania Sun Guns of the 625w variety. A suitable temperature is maintained at the source while the substrate is at a temperature about 10-50°C lower. Deposition is satisfactory whether the higher-temperature source wafer is on top or bottom.

Good results have been obtained with this close-spaced system using a number of different semiconductors. Ge, GaAs, and GaP have been deposited in single crystal epitaxial layers on single crystal substrates. Layers of Ge on GaAs and *vice versa* as well as GaP on GaAs have been deposited in single crystal form. An example of GaAs epitaxially deposited

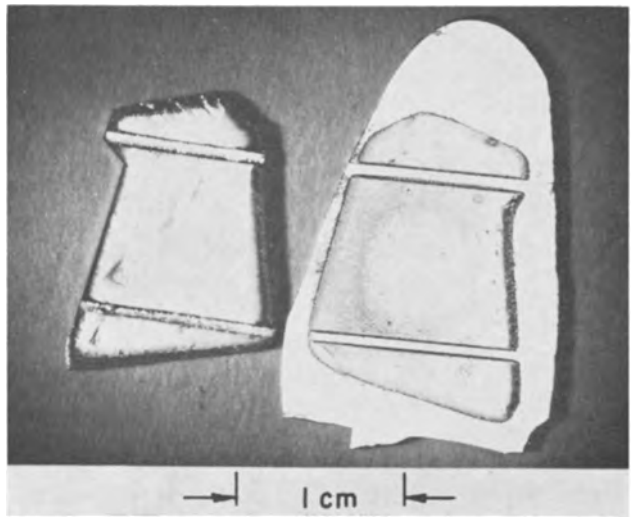

Fig. 3. Photograph of (111) GaAs source wafer on the left and (100) Ge substrate wafer after deposition on the right. Spacer positions are evidenced by nontransport of material from the source wafer and by absence of deposition on the substrate wafer. The area of deposition is seen to be restricted to that covered by the source wafer.

on a (111) Ge substrate is shown in Fig. 3 along with the source wafer which in this case is (100) GaAs. This GaAs layer was grown with 850°C source temperature and 825°C substrate temperature. The time of growth was 1 hr and the thickness about 50μ. The source and substrate show the protected areas under the quartz spacers. It is also clear that the GaAs deposition is confined to approximately the area covered by the source. Good smooth deposition usually occurs in the central region away from the edges. Near the edges the growth is also single crystal, but shows other growth habits such as pyramids. The limited area of growth indicates very little scattering of the transported material and a very high transport efficiency. In actual tests approximately 95% of the material leaving the source arrives at the substrate; thus the loss of material is small and the system remains relatively clean.

An example of single crystal GaP growth on GaAs is shown in Fig. 4 which is a microphotograph of a

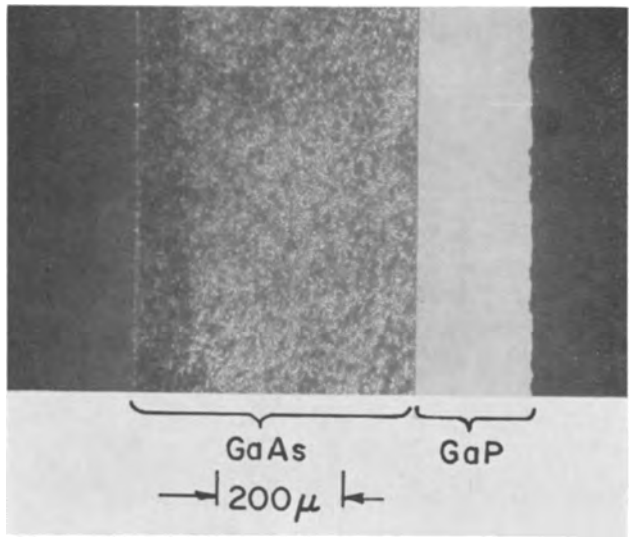

Fig. 4. Cleaved edge of GaP epitaxial layer 200μ thick on a (100) GaAs substrate. The GaAs has been lightly etched to show the boundary.

cleaved edge. This shows the uniformity of the layer and the absence of cleavage differences between the GaAs substrate and GaP layer. In order to show up the interface an extremely light etch with nitric acid was used to change the surface appearance of the GaAs without attacking the GaP. This GaP layer is about 200μ thick. A polycrystalline GaP source wafer was used in this case at a temperature of 945°C, the (100) GaAs substrate being at 905°C. The time required to grow the layer was approximately 2 hr.

The usefulness of the new technique is not restricted to semiconductor wafers or to the use of oxide transport. Powdered source material can be used to grow single crystal layers on single crystal substrates and can also be used to grow polycrystalline layers on quartz or metal. By this means transparent layers of CdS 5 cm^2 have been grown using iodine transport. In addition, matte polycrystalline layers of CdS, ZnS, GaP, and GaAs have been grown in large areas.

Doping can be carried out by transport from the source material or by adding a suitable dopant as a vapor during the growth of the layers. Sulfur doping of GaP has been carried out successfully using H_2S in the water over which the hydrogen is passed.

Acknowledgments

It is a pleasure to acknowledge the contributions of I. J. Hegyi in the early CdS work and P. H. Robinson in the first work with semiconductors. G. Gottlieb was responsible for demonstrating the usefulness of added water vapor. H. Johnson deserves thanks for his continuing support throughout this work.

Manuscript received July 12, 1963.

Any discussion of this paper will appear in a Discussion Section to be published in the June 1964 JOURNAL.

REFERENCES

1. H. Schaefer, "Chemische Transportreaktionen," Verlag Chemie, Weinheim (1962).
2. M. Gershenzon and R. M. Mikulyak, *This Journal*, **108**, 548 (1961).

The Effects of an Electric Field on Epitaxial Vapor Growth

Y. Tarui and H. Teshima

Electrotechnical Laboratory, Tanashimachi, Tokyo, Japan

and Kirokuro Okura and A. Minamiya

Okura Laboratory, Tokyo, Japan

The epitaxial growth of semiconductor has advantages in that it can take place at a lower temperature than from a melt, and in the possibility of geting more uniform impurity distribution. If the energy can be supplied in some other form than heat, the temperature of growth will be lowered and the problem of impurity diffusion during growth will be lessened. And if impurities can be controlled without changing the source vapor, more precise impurity distribution will be possible.

To explore these possibilities, the effects of an electric field on epitaxial growing surfaces were examined and promising results were obtained. Experiments were carried out on germanium and silicon single crystals grown epitaxially by vapor phase deposition in the electric field. The electric field applied to the seed during growth is found to increase the growth rate and the transfer ratio of impurities.

Germanium.—The thermal disproportionation of GeI_2 (1) has been done in quartz tubes with molybdenum electrodes, as shown in Fig. 1. Seed temperature was 400°C, source temperature, 600°C, and iodine density, 0.8 mg/cc. Seeds were 8 to 12x5x1 mm in size, with (111) surfaces and specific resistivity of 10 ohm-cm. Two runs for each condition, *i.e.*, without voltage and with ± 1 kv, were carried out. The duration of deposition was 8 hr in every case.

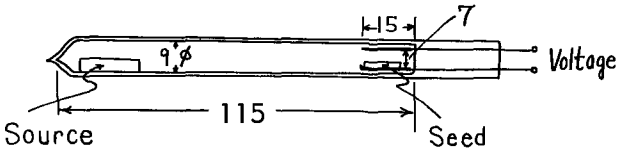

Fig. 1. Apparatus used for vapor growth in electric field

Results for a gallium doped source are shown in Table I in which values of each column are the mean of two runs. In the case of a gallium doped source, the growth rate and the transfer ratio of impurity are increased by the applied electric field; moreover the effect is more noticeable at a negative voltage on the seed than at a positive voltage. The same procedure was carried out with a phosphorus doped source; however, no significant difference in the transfer ratio could be seen. This may come about because phosphorus is more non-ionic than gallium, or because phosphorus is very reactive with iodine.

Silicon.—During silicon deposition by the hydrogen reduction of $SiCl_4$ (2), the electric field was applied between the silicon seed and the opposite electrode, and its effects were investigated. The diameter of the quartz reaction tube was 35 mm. The flow

Table I. Effects of the electric field on germanium deposition (gallium source)

Voltage on the seed, kv	Growth rate, μ/hr	Specific resistivity, ohm-cm
0	3.1	10
+1.0	5.9	5
−1.0	7.1	2

rate of hydrogen gas was 1 liter/min. The temperature of the $SiCl_4$ vessel was kept constant at −30°C, and the impurity dopant was PCl_3 at 10 ppm. Deposition runs were carried out at 1270°C, for 1 hr. The gap between the seed and the opposite electrode was 15 mm.

From the results shown in Fig. 2, it is found that the growth rate of silicon on (111) surfaces increases with the negative voltage on the seeds, and the specific resistivity first decreases and then increases at higher voltages.

To eliminate the errors which are introduced by varying conditions in each run, and to see the effect of the electric field directly, a series of continuous runs was carried out. During each run, the voltage was changed, *e.g.*, 0, −1 kv, 0, −1 kv, every 1 hr. Then the deposited layers were lapped at a 3° angle, and the specific resistivity was checked by the spreading resistance of a point contact.

An example of the resistivity distribution of these wafers expressed by spreading resistance is shown in Fig. 3. The gradual resistivity increase toward the right can be explained by the approach of measuring points to a p-n junction. The dotted line is drawn by averaging the local spreading resistance and using the growth rate ratio of Fig. 2. The fact that the measured points do not exactly fit the dotted line may be explained by impurity diffusion and the averaging and scatter of the spreading resistance measurements. The results obtained from the series of these runs can be summarized as follows: (i) The decrease of the specific resistivity due to the applied electric field is more noticeable at −1 kv than at −2 kv. (ii) Negative voltages on the seed are more effective in decreasing the resistivity than positive voltages. (iii) The growth rate is faster at negative voltage on the seed than at positive voltage, and faster at −2 kv than at −1 kv. These results are in qualitative agreement with the result of Fig. 2.

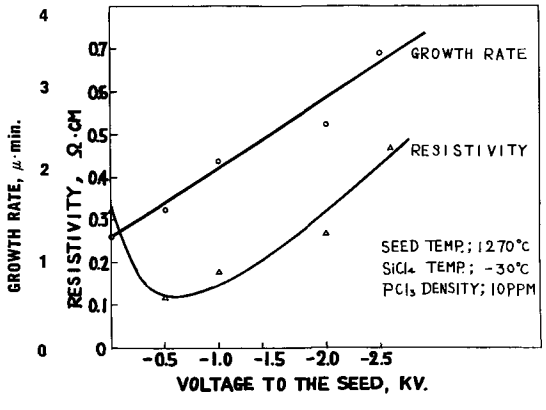

Fig. 2. Growth rate and resistivity as function of voltage; seed temperature, 1270°C; $SiCl_4$ temperature, −30°C; PCl_3 density, 10 ppm.

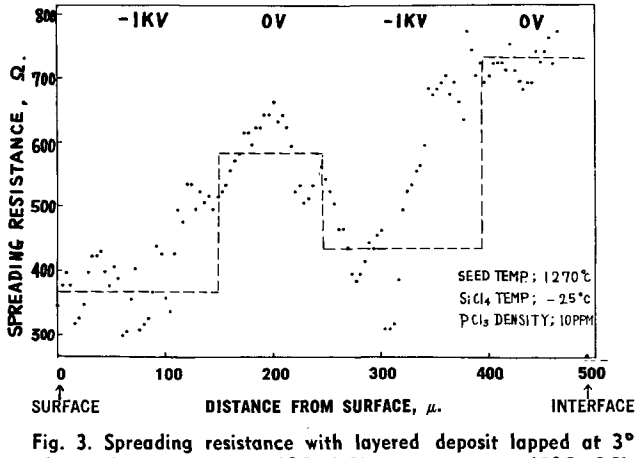

Fig. 3. Spreading resistance with layered deposit lapped at 3° angle; seed temperature 1270°C; $SiCl_4$ temperature, −25°C; PCl_3 density, 10 ppm.

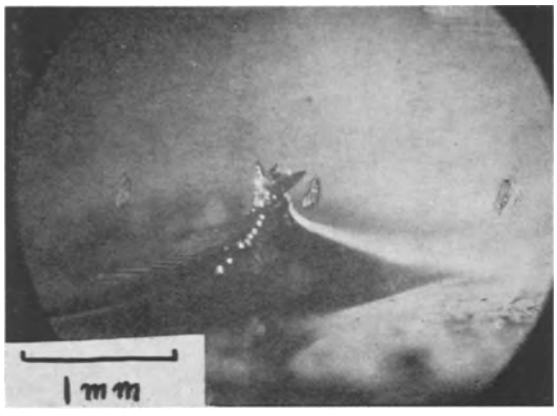

Fig. 4. Growth in electric field with needle electrode

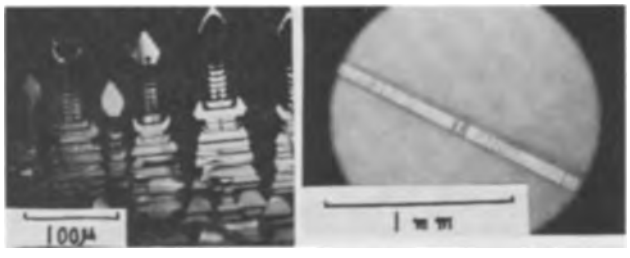

Fig. 5. Dendritic growth of Si in electric field

By mechanisms similar to segregation in growth from a melt, the faster the growth rate is, the more impurity can be incorporated into the crystal. So if the resistivity change resulted from the change of growth rate, resistivity would be lower in the case of −2 kv than −1 kv. Since this is not the case, the electric field seems to have another effect on the mechanism of impurity entering into the crystals.

To visualize the effect on growth rate change, voltage was applied with a needle electrode. The growth was faster just beneath the needle. The deposit was formed in the shape of a mountain with a horn at the top, as shown in Fig. 4.

Singular dendritic growth was observed with the application of an electric field at $SiCl_4$ temperatures higher than −15°C. Figure 5 A, B shows examples of those samples where −2 kv was applied to the seed, showing the possibility of dendritic vapor growth.

To evaluate the mechanism of these effects of the electric field, many experiments with changing temperature, flow rate, and impurities will be necessary. Such experiments are now in progress. It seems apparent that with the apparatus and conditions of epitaxial growth used, the rate-limiting factor of growth cannot be mass transfer of reactant or product molecules, but some process which oc-

curs on the crystal surface. This may be an effect of the electric field on the rate of surface adsorption or the rate of addition to growth steps; and it may involve ionization of the reaction molecules, but this is only speculation.

Acknowledgment

The authors are deeply grateful to Kihichiro Okura, who was president of Okura Laboratory, and many people in the Japan Radio Company and Electrotechnical Laboratory for their encouragement and support of this project.

Manuscript received Aug. 1, 1963.

Any discussion of this paper will appear in a Discussion Section to be published in the June 1964 JOURNAL.

REFERENCES

1. J. C. Marinace, *J. IBM*, **4**, 288 (1960).
2. H. C. Theuerer, *This Journal*, **108**, 649 (1961).
3. E. G. Bylander, *ibid.*, **109**, 1171 (1962).
4. J. M. Charig and B. A. Joyce, *ibid.*, **109**, 957 (1962).

The Properties of the Intermetallic Phases in the System Au-Sn

M. B. McNeil

Materials Research & Development Laboratory, Texas Instruments Incorporated, Dallas, Texas

The equilibrium phase diagram of the system Au-Sn has been investigated by a number of workers [see bibliography in (1)] and is generally regarded as fairly well established, although some question remains as to the details of the Au-rich side (1, 2). However, no data appear to be available on the mechanical properties of the three intermetallic compounds, AuSn, $AuSn_2$, and $AuSn_4$, whose existence appears to be firmly established. Not only would these data be of practical interest because of the use of Au-Sn in semiconductor devices, but in the light of recent work (3) relating the hardness of intermetallic compounds to their electronic structure, they might be of some theoretical interest as well.

AuSn has a B8 structure homologous with NiAs (4); the structure of $AuSn_2$ has not been completely determined, but its translation group is orthorhombic primitive (5); $AuSn_4$ has a complicated structure with a large unit cell having orthorhombic translational symmetry (6, 7).

AuSn, $AuSn_2$, and $AuSn_4$ are all thought to have very narrow ranges of homogeneity (1, 2).

The specimens used in this work were made up from stoichiometric quantities of 99.99% Au and 99.9% Sn and were cast in alundum in a helium atmosphere. The AuSn was furnace cooled; because of the lack of a congruent melting point in the cases of $AuSn_2$ and $AuSn_4$, these ingots were quenched from the melt and annealed; they appeared to be one-phase on microscopic examination, and the powder patterns showed no lines of extraneous phases.

The microhardness of finely polished slices of the compounds was measured on a Bleeker superficial hardness tester belonging to the Texas Instruments Standards Laboratory. The results of these studies are embodied in Fig. 1, 2, and 3 and Table I.

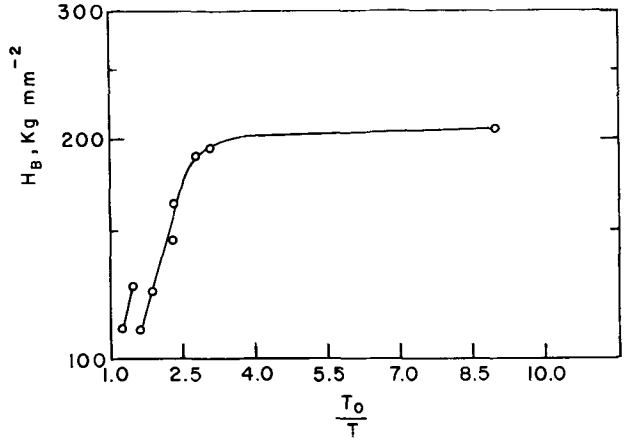

Fig. 1. AuSn : T, temperature in °K; T_0, 691°K

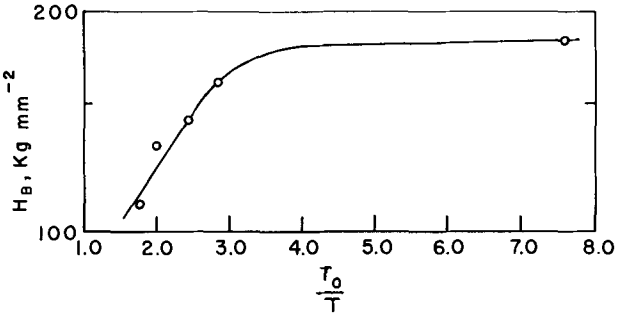

Fig. 2. $AuSn_2$: T, temperature in °K; T_0, 582°K

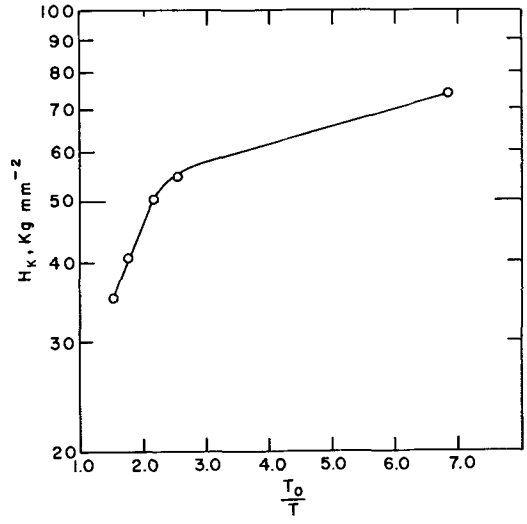

Fig. 3. $AuSn_4$: T, temperature in °K; T_0, 525°K

Table I. Hardness measurements

AuSn hardness measured as Brinell hardness in kilograms per square millimeter:

Temp, °K	Hardness	Temp, °K	Hardness
77	207	366	124
223	195	430	110
248	190	476	126
297	175	535	110
304	146		

$AuSn_2$ hardness as Brinell hardness in kilograms per square millimeter:

Temp, °K	Hardness	Temp, °K	Hardness
77	185	291	133
207	161	334	110
243	145		

$AuSn_4$ hardness as Knoop hardness in kilograms per square millimeter:

Temp, °K	Hardness	Temp, °K	Hardness
77	74.0	298	41.5
206	55.0	348	35.2
244	50.5		

The hardness curve for AuSn, the most interesting of the three compounds, shows a discontinuity at a value of T_0/T corresponding to 200°C. This discontinuous behavior is reversible, as was verified by repeating the measurements a number of times on a single sample.

Bernstein (8) has observed a reversible discontinuity in the coefficient of thermal expansion of Au-AuSn eutectic alloys at 200°C. This may be presumed to be due to the same effect that causes the change in hardness, but so far no success has been achieved in detecting the nature of the effect. If it is an order-disorder transformation, the superlattice lines must be relatively faint, since no change was detected in a powder pattern above and below this temperature.

Acknowledgment

The author desires to thank Dr. D. P. Miller for his assistance in this investigation.

Manuscript received July 6, 1963.

Any discussion of this paper will appear in a Discussion Section to be published in the June 1964 JOURNAL.

REFERENCES

1. M. Hansen, "Constitution of Binary Alloys," 2nd ed., McGraw-Hill Book Co., New York (1958).
2. C. J. Smithells, "Metals Handbook," 3rd ed., Vol. 1, Butterworths, London (1962).
3. G. M. Schwab, "The Electronic Factor in Mechanical Strength" in "Mechanical Properties of Intermetallic Compounds" (Symposium Proceedings), J. Wiley & Sons, Inc., New York (1960).
4. S. Stenbeck and A. Westgren, *Z. physik. Chem.*, **B14**, 91 (1931).
5. K. Schubert and U. Rösler, *Naturwissenschaften*, **40**, 437 (1953).
6. K. Schubert and U. Rösler, *Z. Metallukunde*, **41**, 298 (1950).
7. K. Schubert and U. Rösler, *Z. Naturforschung*, **5a**, 127 (1950).
8. L. Bernstein, *Semiconductor Products*, **4**, 29 (1961).

Capacity Measurements on Rapidly Polarized Germanium Electrodes

P. J. Boddy and W. J. Sundburg

Bell Telephone Laboratories, Incorporated, Murray Hill, New Jersey

When the germanium-electrolyte interface is polarized, the observed change in potential across the system (ΔV_E) is the sum of the changes across three regions; the space charge region in the semiconductor ($\Delta\Psi_S$), the space charge region in the solution ($\Delta\Psi_{sol}$), and the Helmholtz region (ΔV_H). For the electrolyte concentrations considered here, $\Delta\Psi_{sol}$ is much smaller than $\Delta\Psi_S$ and may be neglected. Hence $\Delta V_E \doteqdot \Delta V_H - \Delta\Psi_S$. Further, since Ψ_S may be determined by analyzing the interfacial capacity (1) or the photovoltaic response (2), ΔV_H may be calculated with an error of up to a few millivolts due to neglect of $\Delta\Psi_{sol}$.

In previous experiments (1) a constant polarizing current was applied, and the capacity of the interface was measured by means of a superimposed short duration constant current pulse. The resulting voltage response (V_C) was observed on an oscilloscope while V_E was measured on a high impedance voltmeter. This process took from 1 to 2 sec. The polarizing current was then switched off, the current source adjusted to a new value, and the process repeated.

It was found that at high current densities V_E changed more rapidly than the variation in Ψ_S deduced from capacity measurements. This variation may be explained by changes in the potential difference across the Helmholtz region. Further, it was determined experimentally that the magnitude of ΔV_H was a function of the charge that flowed through the system, *i.e.*, was time dependent at constant current.

Since a certain range of current is needed to polarize the system to obtain sufficient data, the only feasible way to reduce the charge is to reduce the time that the system is subject to polarization. One means of doing this is to sweep the polarizing current rapidly through the required range while the capacity signal (V_C) described above and the electrode potential are continuously recorded.

Figure 1A shows a typical oscilloscope presentation of the potential across the system when a con-

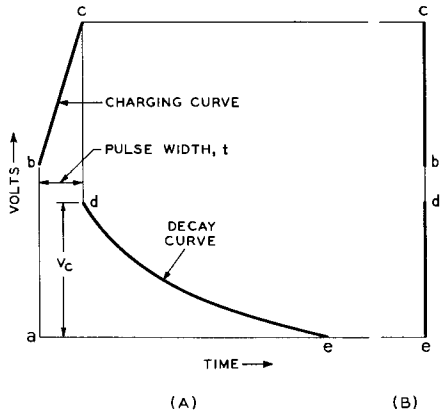

Fig. 1. (A) Representation of the potential *vs.* time across a germanium-electrolyte interface when a constant current pulse (duration *t*) is passed through it; (B) the same representation with no time reference.

stant current pulse is passed through it (1). The capacity of the interface is inversely proportional to V_C providing the lifetime of the decay curve, τ, is long compared with the pulse width, t. If there is no horizontal sweep, the presentation will consist of two vertical lines bc and de as in Fig. 1B. The upper line, bc, represents the magnitude of the charging curve, and the lower line, de, is the magnitude of V_C. Because the slope of ab and cd is so great these lines will appear very faintly or not at all.

If the electrode potential is used to drive the horizontal amplifier of the oscilloscope while the polarizing current is automatically varied through a given range, the resulting presentation will be two envelopes. The upper one will be the magnitude of the charging curve and the lower one will be V_C, both as a function of the electrode potential. The magnitude of the two envelopes will be the same at any one value of electrode potential. In Fig. 1B one can see that there may be difficulty in separating cb and de if point d lies above point b. In practice ab and cd are quite large due to the series resistance of the germanium and solution; therefore, the upper envelope is generally projected off the screen. If, however, the inherent resistance is not sufficient to do this, an external resistance can be placed between the germanium and ground. This will have no effect on the magnitude of V_C.

An experiment of this nature has been carried out with a (110) oriented 30 ohm-cm p-type germanium electrode (apparent surface area 1.46 cm^2) in neutral potassium sulfate solution. Polarizing current was swept from 0 to 200 μa and back to zero in 10 sec. This current was nonlinear with time, being supplied by application of a triangular voltage sweep applied to a tube operated near cut-off. This arrangement gave an approximately linear electrode potential sweep and, hence, approximately equal intensity of the image across the screen. The capacity measuring pulse was 100 μa applied for 5 μsec at 1 millisec intervals.

The oscilloscope trace was photographed (Fig. 2) and analyzed to give interfacial capacity *vs.* electrode potential curves (Fig. 3). The curve denoted by the triangles is the calculated interfacial capacity

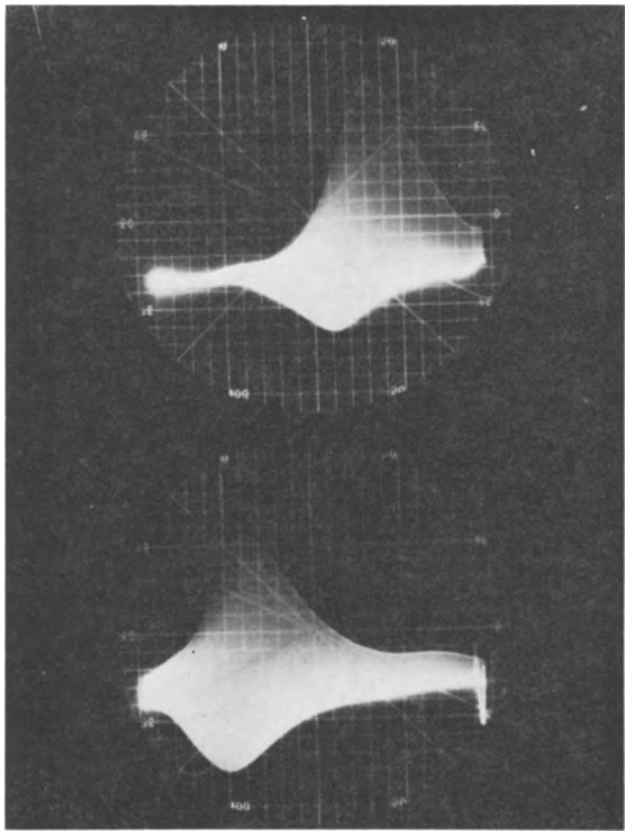

Fig. 2. V_C *vs.* the electrode potential. In (a) (top) the polarizing current was varied from 200 μa to 0; in (b) (bottom) it was varied from 0 to 200 μa. In both instances the vertical scale was 4.3 x 10^{-3} v/large div. and the horizontal scale was 1.2 x 10^{-1} v/large div.

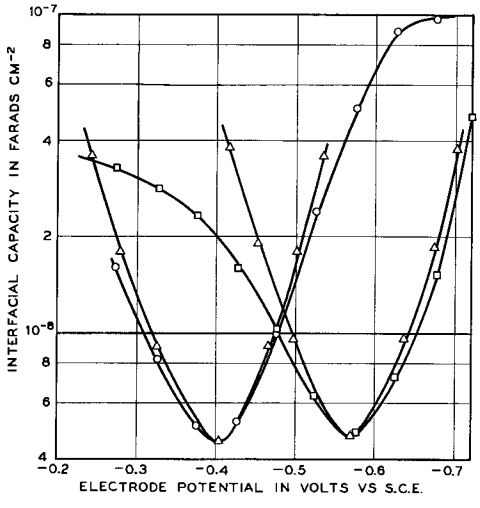

Fig. 3. Electrode potential *vs.* the interfacial capacity. The circles and squares were obtained from the photograph in Fig. 1. The triangles were calculated and normalized to the experimental minimum capacity. □, 0-200 μa; ○, 200-0 μa; △, theoretical.

normalized to the experimental minimum and assuming $\Delta V_E = -\Delta\Psi_S$. It may be observed that the theoretical and experimental curves agree favorably over a wide range of polarization indicating that ΔV_E and $-\Delta\Psi_S$ are equal. This agreement may be compared with that of the curves in Fig. 4, in which the data were taken point by point, where the electrode potential changes by a greater amount than the theoretical Ψ_S. This indicates a much

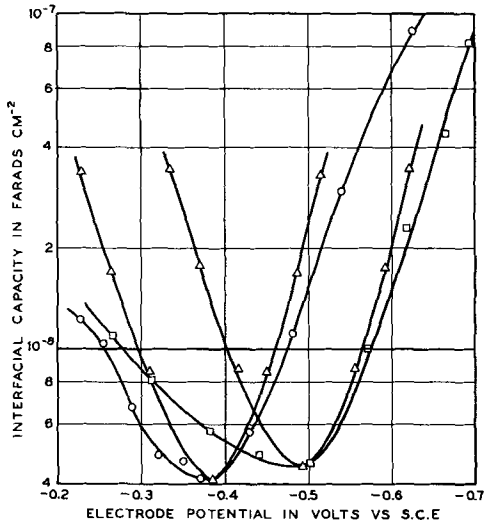

Fig. 4. Electrode potential *vs.* the interfacial capacity. The circles and squares were obtained by the point by point method. Theoretical values were calculated and normalized to the experimental minimum capacity. □, 0-200 μa; ○, 200-0 μa; △, theoretical.

larger change in the Helmholtz potential than is evident with the more rapidly applied polarization.

The effect observed is similar to that of slow surface states which are formed at the germanium-gas interface. However, it is believed that such slow states occur in or on thick oxide films which are not present under the conditions of our experiment. We have previously interpreted the change in Helmholtz potential on prolonged polarization as being due to the removal of adsorbed oriented water molecules (3, 4). The present system provides a means of systematically studying the kinetics of the phenomenon.

The data described here extend the similar data of Brattain and Boddy (1) to a wider polarization range and substantially confirm the observations of Harten and Memming (5) who concluded, on the basis of surface conductivity measurements, that changes in V_E and Ψ_S were equal in magnitude over a considerable range of rapidly applied anodic polarization.

Manuscript received July 3, 1963.

Any discussion of this paper will appear in a Discussion Section to be published in the June 1964 JOURNAL.

REFERENCES

1. W. H. Brattain and P. J. Boddy, *This Journal*, **109**, 574 (1962).
2. P. J. Boddy and W. H. Brattain, *Ann. N. Y. Acad. Sci.*, **101**, 683 (1963).
3. P. J. Boddy and W. H. Brattain, *This Journal*, **110**, 570 (1963).
4. W. H. Brattain and P. J. Boddy, *Proc. Nat. Acad. Sci.*, **48**, 2005 (1962).
5. H. U. Harten and R. Memming, *Phys. Letters*, **3**, 95 (1962).

Ion Exchange Membrane Properties—Their Effect on the Development of the Dual Membrane Fuel Cells

Robert M. Lurie,[1] Carl Berger,[2] and Hans Viklund[1]

Ionics Incorporated, Cambridge, Massachusetts

ABSTRACT

The operation and construction of dual ion exchange membrane fuel cells are described, and data are given for the operating characteristics of dual and single membrane cells. Membranes of varying diffusivity, thickness, and composition are compared. The strong effect of electrode construction is noted. Particular attention has been given to the changes that occur during long time operation, and the importance of water and electrolyte transfer is discussed.

In the last few years fuel cell research has crystallized into four distinct areas. These are represented by the caustic electrolyte-graphite electrode cell (1), the intermediate range temperature-nickel electrode-caustic electrolyte cell (2), the high-temperature solid electrolyte fuel cell (3), and the ion membrane fuel cell. It is the latter that has been the subject of research efforts in these laboratories (4).

The single ion membrane fuel cell (SIMFC) is represented in Fig. 1A. The membrane is a cross-linked polystyrene matrix into which conductive SO_3H groups have been introduced. Conduction through these resins may take place by the transfer of hydrogen ions through the resin, or the membrane may be equilibrated with salts or bases so that conduction occurs mainly by cations such as sodium or potassium (4). While it is possible for anionic transfer to be used in SIMFC, due to problems related to resin stability and diffusion rates (to be discussed below), the cation membrane is the preferred form at the present time. Two membranes separated by a liquid layer may also be used with great advantage in place of the single membrane (Fig. 1B). This configuration is called a dual membrane cell.

The catalyst electrode assembly may be constructed in a number of ways. Noble metal catalyst powder may be imbedded into the membrane and electronic conduction maintained with a collector contacting the powder; sintered assemblies of catalyst and waterproofing agents may be applied to the membrane; or, finally, the system used in our experimental models, the deposition on a platinum screen of a noble metal catalyst which is then pressed against the membrane. Oxygen or air is introduced into the cathode and the reaction

$$O_2 + H_2O + 2e^- \rightarrow HO_2^- + OH^-$$

has been postulated (1) as occurring, indicating that O_2 is utilized in the cell through a peroxide mechanism, a hypothesis which explains the less than theoretical open-circuit potential obtained for such oxygen electrodes *vs.* the standard hydrogen electrode.

[1] Present address: Research and Advanced Development Division, Avco Corporation, Lowell, Massachusetts.

[2] Present address: Astropower, Inc., Newport Beach, California.

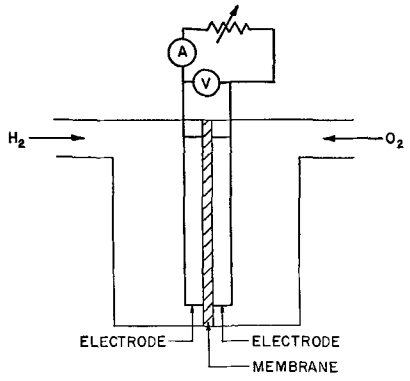

Fig. 1A. Single membrane cell

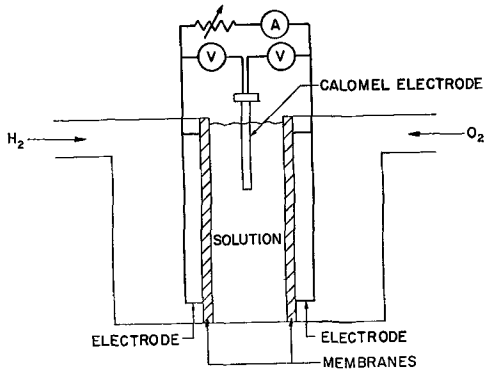

Fig. 1B. Hydrogen and oxygen voltage-current characteristics (dual membrane cell).

Experimental

Membranes.—The cationic membranes used were produced by impregnating dynel cloth, 0.020 in. in thickness, with a mixture of styrene, divinyl benzene, and diethyl benzene. The wet cloth was laid between glass plates for 16 hr at 60°C. The glass plates were stripped and the resinous "board" soaked in methanol. The resultant product was treated by sulfonation to yield a product with a capacity of 3 meg per dry gram. Anionic membranes are produced in a similar fashion except that chloromethylation and subsequent amination produce quaternary ammonium groups.

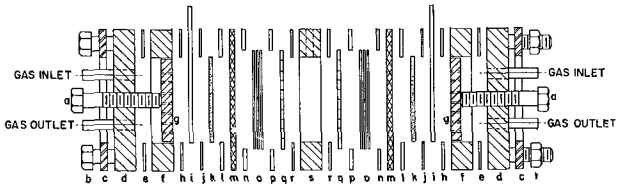

Fig. 2. Exploded view, fuel cell, dual membrane; a, pressure screw; b, tie down bolt; c, metal flange; d, Lucite end plate; e, thin pvc gasket; f, Lucite spacer; g, perforated Lucite backup plate; h, thin pvc gasket; i, Pt-Ti grid; j, thin pvc gasket; k, Pt electrode; l, Teflon gasket; m, membrane; n, Teflon gasket; o, 3 Saran screens; p, thick pvc gasket; q, expanded Ta grid; r, thin pvc gasket; s, Lucite center compartment; t, nut.

Electrodes.—One of the techniques used in preparing electrodes for our cells utilized a platinum screen, 80 mesh. A paste of platinum black and water was spread onto the screen and pressure was applied in a press. When dried, a sufficiently cohesive structure was obtained for use as an electrode.

Assembly procedure.—The cell components are shown in Fig. 2. The center compartment has three holes drilled in it, one for a heater, one for a thermometer, and one for a calomel electrode. The backup section, made of expanded titanium or tantalum, is placed next to the center compartment. This expanded material is gasketed with polyvinyl chloride. Three thicknesses of Saran screening cover the expanded screen. After this, in order of their use, is a Teflon gasket, an ion exchange membrane, another Teflon gasket, a platinum electrode, a thin pvc gasket, a current collector, and finally another pvc gasket. A gas compartment equal in dimension to the catalyst is then provided. A backup plate is inserted in the gas compartment against the surface of the current collector followed by a gasket which is placed on top of the gas compartment followed by an end plate which contains a screw in the middle, the purpose of which is to apply pressure to the backup plate. The end plate also has gas inlet and outlet openings. The end piece is a metal flange.

Experimental procedure.—Pure H_2 and O_2 were allowed to flow into the H_2 and O_2 electrode compartments, respectively. Total current discharge characteristics were studied by altering the external resistance in the fuel cell circuit. As the resistance was varied, readings were made from open circuit in 4 ma/cm^2 intervals until polarization was noted. Steady state was achieved at each reading by waiting several minutes. As the current was measured, half cell voltage measurements were made between a calomel electrode immersed in the central electrolyte compartment and the hydrogen and oxygen electrodes, utilizing a Beckman Model G millivoltmeter. In this manner comparative performance of O_2 and H_2 electrodes could be studied throughout the effective operating range of the fuel cell.

Results and discussion.—Single ion membrane hydrogen-oxygen fuel cells are attractive in concept but have practical limitations with respect to dehydration and water balance problems and safety considerations in critical space missions. Other important problem areas are related to electrode type and configuration, membrane thickness, and demineralization at electrode-membrane interfaces.

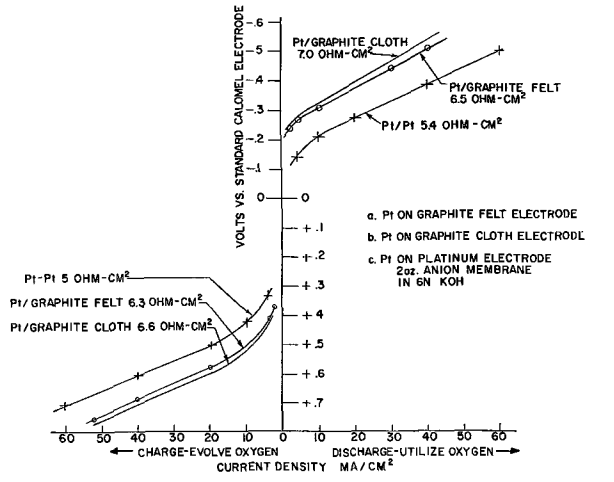

Fig. 3. Oxygen utilization and evolution

One of the more important research areas investigated pertinent to both SIMFC and the DMFC is the proper selection of an electrode-collector assembly, not only on the basis of its physical properties such as contact area but also on its chemical characteristics. Some of the differences noted can be found in Fig. 3, where the charge and discharge curve of the several different forms of oxygen electrode have been examined. It is clear that distinct differences in irreversible phenomena occur when comparing platinum electrode collectors with various forms of graphite electrode collectors. On the discharge portion of the curve the difference amounts to about 0.1v and includes open-circuit conditions. A smaller, yet substantial difference is also noted when the electrode catalyst assembly evolves O_2. The reasons for this behavior are not clear.

From a purely technical point of view the problem of resistance of membranes is not a pressing one. It is likely that thinning of membranes would eliminate much of this problem. In addition, it would appear that the choice of backing materials would also affect resistance of the cell and could also be solved readily. Thinner membranes and proper backing materials would solve the resistance problem as can be noted in Table I. However, the chances of getting pinholes in a membrane increase with the reduction of membrane thickness, thereby heightening the possibility of cell failure.

In the final analysis, work on the SIMFC ceased in these laboratories as a result of water balance and desiccation problems. Whether the problems were caused by use of air, thereby causing dehydration of the O_2 electrode or due to imbalance of the entering moisture content *vs.* the vapor pressure of the membrane surface facing the gas, the only solution to such problems in the SIMFC appears to be mechanical wicks (5). An example of problems en-

Table I. Cation membranes

Weight of backing g	(oz)	Thickness, cm	Resistance, ohm-cm², in 6*N* HCl
57	(2)	0.041	0.49
113	(4)	0.060	0.71
227	(8)	0.052	1.18

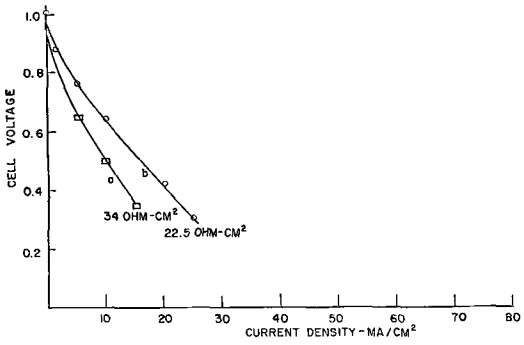

Fig. 4. Hydrogen-oxygen fuel cells: a, single membrane, non-humidified, Pt/graphite felt electrode; b, single membrane humidified, Pt/graphite felt electrode.

countered can be observed in Fig. 4. Using the fuel cell with platinum catalyst on graphite, H_2 and O_2 were fed into the cell. The curve labeled 34 ohm-cm^2 was obtained as the current discharge characteristic of the cell. The gases H_2 and O_2 were then led through humidification apparatus and into the fuel cell. The resultant discharge characteristic is noted in the curve labeled 22.5 ohm-cm^2 and is illustrative of the water balance problems encountered.

The Dual Membrane Fuel Cell concept (DMFC) had been evolved prior to our work on the single membrane cell (6).

The system has a great deal of flexibility in that membranes may be anionic or cationic. In addition, the liquid composition in the central compartment can be varied over a wide range with respect to conductivity, concentration, and vapor pressure, an important consideration in water removal.

Other advantages to be gained from the dual membrane system type are:

1. The problem of membrane dehydration can be eliminated when air is used as a source of O_2. In addition, the H_2 and O_2 chambers need not be filled with fluid or saturated water vapor when stored since the moisture from the central compartment will prevent drying and cracking at the membrane-electrode interface.

2. The possibility of mixing and reacting H_2 and O_2 has been sharply reduced by the presence of two membranes.

3. By the proper selection of membranes, important flexibility is given to this system. Water usually forms on the surface of the electrode, which results in a problem in zero-gravity operation of such a cell. This is the separation of gross droplets of water on the electrode when gravitational forces are absent. However, evaporation of formed water on the H_2 electrode can be effected by passage of relatively dry hydrogen through the compartment. In our system, we have been able to direct the water, which forms, to yield a net flow of water into the central compartment, due to the osmotic pressure difference between the central compartment and the newly formed water on the electrode. In addition, by the proper control of the humidity of entering reactant gases, we have been able to concentrate the solution in the electrolyte chamber. Table II shows the details of one experiment where all of the water formed electrochemically was found in

Table II. Diffusion of electrochemically formed water into dual membrane fuel cell

Initial concentration	6.0*N* KOH
Initial volume	50.0 ml
After 48 hr at 0.4 amp	
Actual concentration	5.30*N* KOH
Calculated concentration	5.33*N* KOH
Actual volume	56.0 ml
Calculated volume	56.4 ml

the central compartment. Essentially, this eliminates the separation problem (H_2 from H_2O in zero gravity field) discussed above and allows us to recover water by simple distillation techniques or newer approaches, such as membrane permeation (7).

Preliminary models of the DMFC were tested and considerable improvements in performance were noted. (Compare Fig. 4 and Fig. 5.) Analogous to the electrode collector problem found in SIMFC, similar characteristics were noted in the DMFC. In Fig. 5, a comparison of the polarization curves of platinum catalyst deposited on graphite felt and platinum deposited on platinum gauze is shown. As previously indicated, performance on the platinum gauze is superior as indicated by a 16.5 ohm-cm^2 slope for graphite *vs.* 10.8 ohm-cm^2 for platinum gauze.

The advantages of utilizing an electrolyte-impregnated membrane in the DMFC are accompanied by the need for maintaining the proper balance between demineralization at the electrode-membrane interface caused by electrically induced migration of ions and diffusion of electrolyte into the depleted area. An example of such depletion is depicted in the performance of the earliest form of our dual membrane cell shown in Fig. 6a. The polarization curve is extremely steep, and single electrode analysis indicated that the hydrogen electrode gave poor performance over this range. The fact that the increase in resistance is due to migration of ions in an electrical field is shown by the fact that, on standing, diffusion has restored the original performance characteristics of the cell. Data accumulated with reference to the demineralization problem indicated that the alteration of the membrane could

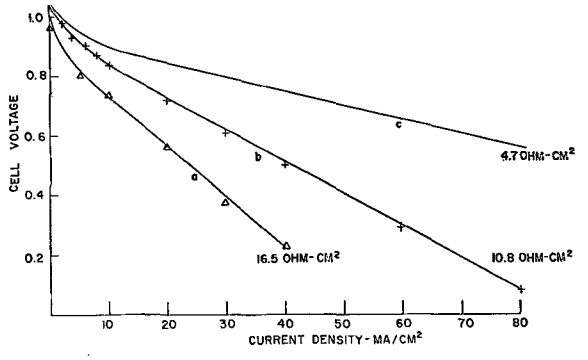

Fig. 5. Hydrogen-oxygen fuel cells: a, dual membrane (3.17 cm electrolyte thickness), Pt/graphite felt electrode; b, dual membrane (3.17 cm electrolyte thickness), Pt/Pt electrode; c, dual membrane (0.1 cm electrolyte thickness, calculated), Pt/Pt electrode.

produce a balance in the electromigration and counterdiffusion of ions.

The conventional membrane in contact with the hydrogen electrode was replaced by a "high diffusivity" membrane, Fig. 6b. As indicated in the graph, the cell performance improved markedly, and the ultimate polarization that occurred was shown to be due to the degradation in performance of the oxygen electrode, still in contact with the conventional membrane.

Finally, replacement of both membranes with high diffusivity components resulted in continued sustained performance, Fig. 6c.

An over-all view of the superiority of the DMFC *vs.* the SIMFC is clearly indicated in life tests of the two varieties. In single membrane cells equilibrated with electrolyte sustained performance for several days could only be obtained at low current densities, about 3 ma/cm^2. It is clear that rapid demineralization occurs in the single membrane cell. When such a mechanism operates in the dual membrane cell, controlled diffusivity from the central chamber aids in maintaining the ion balance at the electrode-membrane interface. It is interesting to note that, in recent life tests, dual membrane cells with thick liquid interlayers, have now run at 16 ma/cm^2 and 0.6v continuously for 120 days, and such tests are continuing.

The flexibility of the dual membrane fuel cell is further exemplified by the possibility that various electrolytes, aqueous and nonaqueous, may be utilized in the central compartment. Typical of electrolytes that can be used are H_2SO_4 and KOH solutions and, in Fig. 7, performance curves are shown for such test cells. It is interesting to note that not only do the performances of the cell vary with electrolyte, but also with electrolyte concentration. Differences may probably be attributed to changes in the conductivity of the solution and membranes. Analogous behavior has been noted when solutions of salts such as potassium phosphate were used in the central chamber. Although open-circuit voltages were high, polarization occurred rapidly on discharge. This subject is still under investigation.

The membranes, of course, must be able to exist in the electrolyte. For example, several membranes

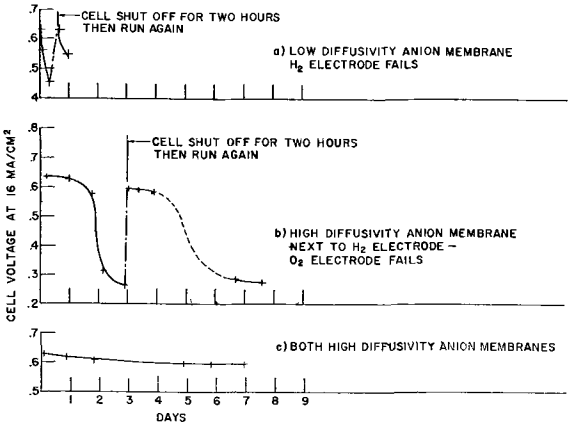

Fig. 6. Life tests, dual membrane cells, 6*N* KOH, cells run at 16 ma/cm^2.

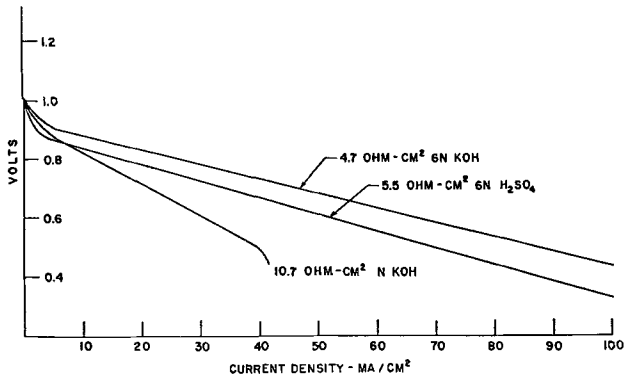

Fig. 7. Dual membrane fuel cell. Different solutions and membranes: 6*N* KOH 2 oz anion membranes; *N* KOH 2 oz anion membranes; 6*N* H_2SO_4 2 oz cation membranes; Pt/Pt electrodes.

have been tested at temperatures of 90°-100°C for over 2000 hr in 3*N* NaOH with less than 10% loss of exchange capacity.

In summary, it appears that the dual membrane fuel cell has a number of advantages.

1. Safety—The chances of burning or explosion due to the catalytic union of H_2 and O_2 are eliminated.

2. Water balance—The problem of retaining a proper water content in membranes to avoid dehydration and potential cracking appears to be well in hand.

3. The dual membrane cell appears to have high-temperature capabilities not heretofore found in ion membrane fuel cells.

4. A flexibility in developing different modes of operation has been developed, due to the possibility of using various membranes and electrolyte solutions.

Acknowledgments

The authors wish to express their appreciation of Vincent J. Masse and Ralph J. Shuman for their contributions to these efforts.

Manuscript received March 7, 1962; revised manuscript received Aug. 8, 1963. This paper was presented at the Detroit Meeting, Oct. 1-5, 1961.

Any discussion of this paper will appear in a Discussion Section to be published in the June 1964 JOURNAL.

REFERENCES

1. K. Kordesh, "The Hydrogen-Oxygen Fuel Cell with Carbon Electrodes," in "Fuel Cells," G. Young, Editor, p. 11, Reinhold Publishing Co., New York (1960).
2. F. T. Bacon, "The High-Pressure Hydrogen-Oxygen Fuel Cell," *op cit.*, p. 51.
3. G. H. J. Broers and J. A. A. Ketelaar, "High-Temperature Fuel Cells," *op cit.*, p. 78.
4. R. M. Lurie, C. Berger, and R. J. Shuman, "Ion Exchange Membranes in Hydrogen-Oxygen Fuel Cells," *op cit.*, Vol. 2, p. 143 (1962).
5. E. Oster, "Cation-Exchange-Membrane Fuel-Cell Batteries," 14th Power-Sources Conference, Atlantic City, May 18, 1960.
6. W. Juda, C. E. Tirrell, and R. M. Lurie, "Fuel Cells with Ion Exchange Membranes," "Energy Conversion for Space Power," N. W. Snyder, Editor, p. 445, Academic Press, New York (1961).
7. R. C. Binning, R. J. Lee, J. F. Jennings, and E. C. Martin, *Ind. Eng. Chem.*, **53**, 45 (1961).

Structure of Oxide Films Formed on Individual Crystal Grains of Stainless Steels

Goro Shimaoka[1]

Department of Physics, Brown University, Providence, Rhode Island

ABSTRACT

Transmission electron microscopy and diffraction studies were made on thin sections of 18Cr-8Ni and 25Cr-20Ni stainless steels oxidized in $\sim 10^{-4}$ mm Hg dry air at 300°-600°C, and on oxide replica films formed on etched surfaces of both steels in a molten nitrate solution at 300°-400°C. The oxide films consisted of spinel phase oxides, near $FeCr_2O_4$ in the low-pressure oxidation and near $NiCr_2O_4$ in the molten nitrate oxidation, and completely parallel growth between these spinel oxides and the austenite crystals was observed in both cases. Electron micrographs of the oxidized thin sections showed anisotropy of oxidation of the austenite crystal, suggesting that the (111) plane is least active and the <110> direction is most active for oxidation.

Many studies have been published on the resistance of stainless steels to corrosion and high-temperature oxidation. Electron diffraction has been used to examine the surface products resulting from the corrosion and the oxidation and has produced much information concerning thin surface layers on these alloys. The structure of oxidation products, such as γ-Fe_2O_3, Fe_3O_4, α-Fe_2O_3, Cr_2O_3, $FeCr_2O_4$, $NiCr_2O_4$, and their solid solutions (1-7), and (Fe, Ni)CrO_4 (8) have been reported. But for a complete understanding of the corrosion resistance of the stainless steels, it is necessary to study not only the chemical stability, but the physical properties of the surface products, for example, the crystallographic relation between the base metal and the oxide lattice. The purpose of the present work is to examine the texture and orientation of oxide crystals formed on individual crystal grains of stainless steels.

Recently electron metallographers have employed extremely thin metallic sections, below several hundreds angstroms in thickness, to directly observe dislocations in metals and alloys (9-14). Techniques of this type were used in the present experiments. The use of thin metallic sections is profitable for studying the growth mechanism of oxide nuclei and the texture and orientation of the oxide on the base metal. Further, structural study on the minor phases of about one micron square is possible by the aid of selected area electron diffraction. In addition, in the present study, oxide film replica techniques were applied to confirm the crystallographic relation between the metal and the oxide.

Though the oxide replica technique has been applied to only a few metals such as aluminum and its alloys (15-17), stainless steels (18, 19), and high nickel alloys (18), etc., up to date, this method is more interesting than other replica methods, because the metallographic observations of the base metal and structure study of the oxide are possible simultaneously in the electron microscope. In the region of observed magnification of the electron microscope used, the stainless steel specimen could be treated as a large grain of its single crystal.

Experimental

Two types of austenitic stainless steel, AISI 304 and 310, were used in this experiment. Their chemical compositions (wt %) were as follows:

	C	Cr	Ni	Si	Mn
AISI 304:	0.07	18.09	8.53	0.49	1.00
AISI 310:	0.04	25.21	21.50	0.52	1.35

Thin sections of the stainless steels were prepared by electrothinning using a technique given by Tomlinson (13) from the sheets of ca. 15 x 40 x 0.3 mm in size. The condition of the electrothinning was as follows: electrolyte, H_3PO_4-H_2SO_4 (3:2 by volume); current density, $\sim$20 amp/dm^2; temperature of the electrolyte, 40°C. After treatment, the specimens were rinsed carefully in methanol-acetone (1:1 by volume) and in ether. Thin specimens below 1000Å thickness, which can be observed by the electron microscope, were easily obtained. Oxidation of the thin sections was carried out inside an electron diffraction specimen chamber of a Hitachi HU-10 electron microscope, in a low pressure of $\sim 10^{-4}$ mm Hg air, dried through silica gel, platinum asbestos, and a liquid air trap, at 300°-600°C. Successive structure changes of the specimen in the process of oxidation were observed by transmission electron diffraction. Details of the experimental technique have been described in a previous paper (20).

Oxide replica films of the stainless steels were prepared by the Mahla-Nielsen method (18). The sheet specimens were polished through 4/0 emery paper and etched in 5% Br_2-methanol solution for about 1 min. After rinsing, the specimens were oxidized in a molten salt bath of $NaNO_3$-KNO_3 (1:1 by volume) for about 10 min at 300°-400°C. The oxide films formed on the specimens were isolated from the base metal by immersing in methanol containing 5-10% bromine, and then were carefully rinsed through fresh methanol and methanol-acetone.

[1] Visiting Professor of Physics, on leave from National Research Institute for Metals, Tokyo, Japan.

The oxidized thin sections and the oxide replica films were examined using the HU-10 electron microscope, by high resolution electron diffraction, transmission electron microscopy, and selected area electron diffraction under an accelerating voltage of 75 or 100 kv. The high resolution electron diffraction experiments were made using a double condenser lens and single focusing lens system, and using an evaporated film of pure gold as a standard for calibration. The transmission electron microscopy was carried out using a three-stage lens system of the electron microscope. A selected area electron diffraction pattern corresponding to a small area of the microscopic image limited with an adjustable aperture was taken by changing the intermediate lens current. The rotation angle between the micrograph and corresponding selected area diffraction pattern arising by the change of the intermediate lens current was calibrated with a carbon replica film of ruled diffraction gratings.

Results

Oxide Films on Thin Sections

Before oxidizing, extremely thin, clean sections of the stainless steels were chosen by transmission electron microscopy. Then the specimens were mounted on the high-temperature electron diffraction specimen holder, and diffraction patterns were taken. Figure 1A shows an example of transmission diffraction patterns from a thin section of 18-8 stainless steel at room temperature. The photograph indicates a cross grating pattern of spots due to a single austenite crystal oriented with the (110) plane parallel to the specimen surface. The observed value of lattice constant was 3.60Å, which agrees well with that of γ-iron. The same specimen was heated inside the electron diffraction specimen chamber, under a pressure of $\sim 10^{-4}$ mm Hg air dried as described above, at 300°-600°C, and diffraction patterns were taken *in situ*. When the specimen was heated at 450°C for about 3 min, a new spot pattern due to a spinel-type oxide superimposed by the austenite pattern was observed. Figure 1B shows an example of this type of diffraction pattern observed at 600°C. A schematic illustration of Fig. 1B is given in Fig. 2. It was found from this diagram that the spinel oxide was oriented in a definite manner with respect to the underlying austenite: the (110) planes of the two lattices were parallel, the [001] direction of the austenite lattice coinciding with the same direction of the oxide lattice.

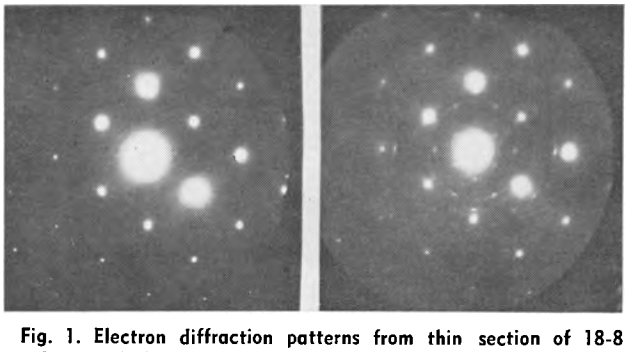

Fig. 1. Electron diffraction patterns from thin section of 18-8 stainless steel. A (left), at room temperature; B (right), at 600°C in $\sim 10^{-4}$ mm Hg dry air.

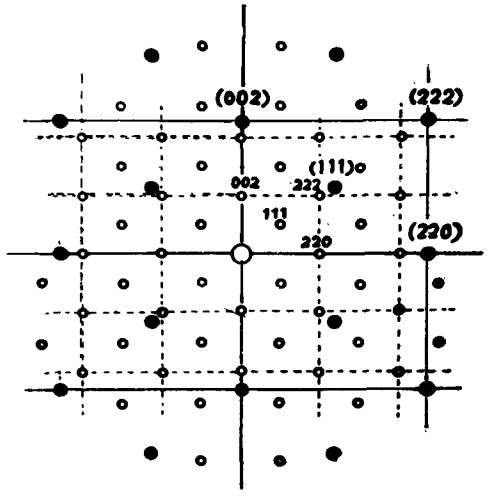

Fig. 2. Diagrammatic representation of Fig. 1B. •, spot due to austenite; ○, spot due to spinel oxide.

After the high-temperature electron diffraction observation the specimen was cooled rapidly to room temperature, and the lattice constant of the spinel oxide was measured by a high resolution electron diffraction technique. As a mean value, 8.366 ±0.005Å was obtained.

The same specimen was then placed in the electron microscope specimen stage, and transmission electron microscopy was used to examine the texture and orientation of the oxide on individual crystal grains of austenite. Figure 3 shows an electron micrograph and a corresponding selected area diffraction pattern from an austenite grain. The bright field of the fringe near the edge was completely oxidized and gave a diffraction pattern of spotted rings due to spinel oxide. However, a relatively thick portion of the dark field showed cross grating patterns due to a combination of spinel oxide and austenite as in Fig. 3B. The diffraction pattern indicates completely parallel growth of the spinel oxide on the (001) plane of austenite.

Figure 4 shows an electron micrograph and a corresponding selected area diffraction pattern from the (111) plane of austenite grain of the same specimen. The oxidized edge, wavy contours near the edge, and extinction contours running parallel with the edge can be seen in the micrograph. By the selected area diffraction method, it was found that the wavy contours lie along the direction of the <110> axis of

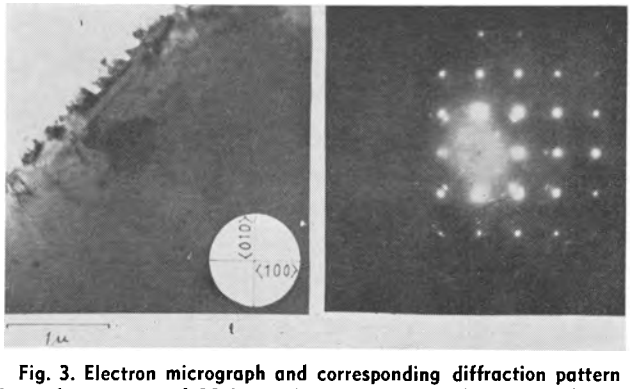

Fig. 3. Electron micrograph and corresponding diffraction pattern from thin section of 18-8 stainless steel oxidized in $\sim 10^{-4}$ mm Hg dry air. (001) plane of austenite crystal; A, left; B, right.

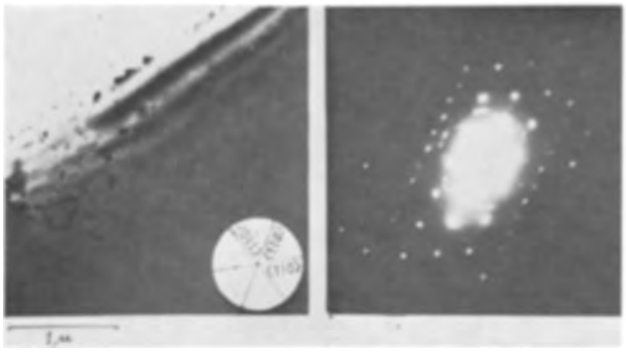

Fig. 4. Electron micrograph, A (left), and corresponding diffraction pattern, B (right), from thin section of 18-8 stainless steel oxidized in $\sim 10^{-4}$ mm Hg dry air. (111) plane of austenite crystal.

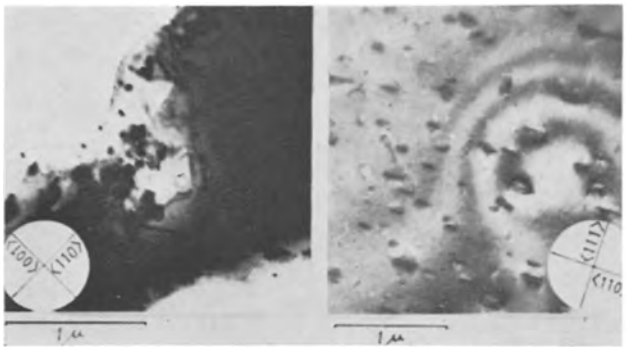

Fig. 5. Oxidized grains of 18-8 stainless steel. A (left) and B (right) are (110) and (211) plane of austenite crystal, respectively.

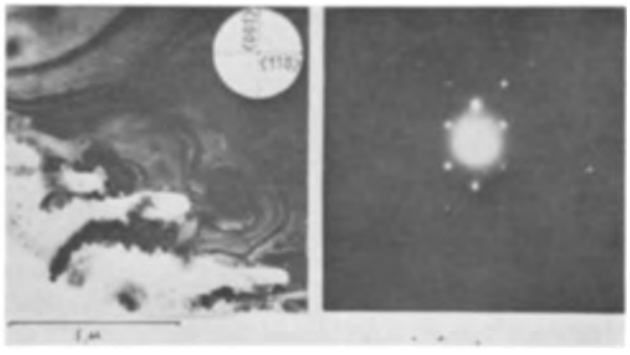

Fig. 6. Electron micrograph, A (left), and corresponding diffraction pattern, B (right), from thin section of 25-20 stainless steel oxidized in $\sim 10^{-4}$ mm Hg dry air. (110) plane of austenite crystal.

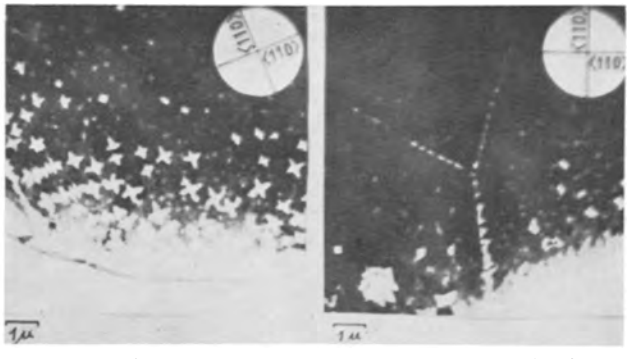

Fig. 7. Oxidized grains of 25-20 stainless steel. A (left) and B (right) indicate preferential oxidation along <110> direction and along grain boundaries, respectively.

the austenite lattice. The selected area diffraction pattern of Fig. 4B shows completely parallel growth of the spinel oxide on the (111) plane of austenite.

Figure 5A is a micrograph showing an oxidation process on the (110) plane of an austenite grain. Contours of the metal grain show the shape characteristic of the (110) plane, and several combinations of the two regular triangles can be seen in the oxidized portions of the bright field. The edges of these triangles run parallel to the <110> directions of the austenite. The corresponding selected area diffraction pattern showed completely parallel growth of the oxide on the base metal. Figure 5B is an oxidation figure on the (211) plane of an austenite grain. Many dislocation lines and protuberances can be seen in the micrograph. These protuberances are formed by triangles, suggesting the octahedrons consisting of the (111) planes of the austenite. The selected area diffraction pattern corresponding to the micrograph indicated also completely parallel growth of the oxide on the base metal.

Similar results were also observed in case of 25-20 stainless steel. Figure 6 shows an electron micrograph and a corresponding selected area diffraction pattern from an austenite grain of 25-20 stainless steel oxidized in the same way as described above. The micrograph shows oxidation figure on the (110) plane of austenite. The edge of the grain is almost completely oxidized and gives a bright field. The oxide layer developing laterally inside the grain runs parallel to the <110> direction of austenite. Many rhombs observed near the oxide layer show the shape characteristic of the (110) plane. Many extinction contours can be seen in the relatively dark field. The corresponding selected area diffraction pattern also shows completely parallel growth of the spinel oxide on the austenite lattice. Figure 7A shows an interesting electron micrograph observed on the (001) plane of an austenite grain in a relatively advanced stage of oxidation. Numbers of oxide nuclei and many cross-like oxide particles can be seen as bright specks in the micrograph. These crosses lie parallel to the direction of the <110> axis of austenite and show a tendency to develop along the same direction inside the austenite grain. The size and density of the oxide nuclei were 300 $\sim$ 2000Å and 5 x 10^8/cm^2, respectively. The selected area diffraction pattern corresponding to the micrograph showed almost continuous rings from spinel oxide superimposed by a cross grating pattern due to austenite. Figure 7B shows an example of oxidation behaviors at grain boundaries. The micrograph indicates that the degree of oxidation at the grain boundaries is greater than inside of the grains. Several oxide nuclei produced on the grain boundaries show a tendency to develop along the <110> direction of austenite.

Oxide Replica Films from Etched Surfaces

Electron micrographs of the oxide replica films from etched surfaces of the stainless steels revealed the texture and orientation of the crystal grains of austenite. Furthermore, selected area diffraction patterns of the replica films themselves gave information concerning crystal structure and orientation of the oxide to the base metal. Figure 8 shows a micrograph and a corresponding selected area diffraction pattern of a replica film from an austenite

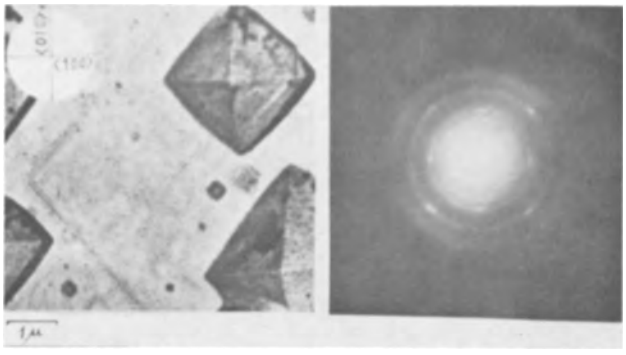

Fig. 8. Electron micrograph, A (left), and corresponding diffraction pattern, B (right), of oxide replica film from etched surface of 18-8 stainless steel. From (001) plane of austenite crystal.

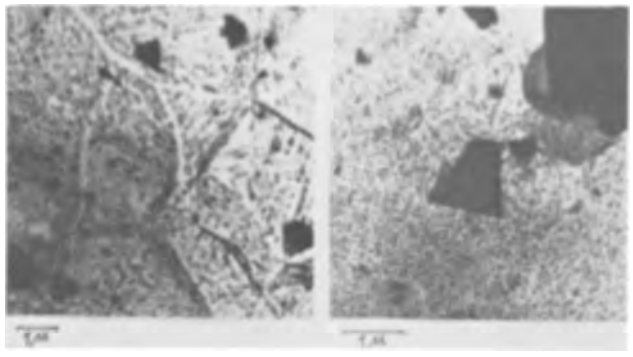

Fig. 11. Nonmetallic inclusions in oxide replica films of 25-20 stainless steel. A (left), chromium carbide; B (right), β-quartz.

grain of 18-8 stainless steel. The micrograph shows the etching figure characteristic of the (001) plane of a single crystal of austenite. Regular octahedrons formed by the (111) planes of austenite are exposed on the surface. Further, relatively thick oxide particles oriented along the <110> direction of austenite can be seen in the micrograph. The corresponding selected area diffraction pattern shows that the replica film consisted of spinel-type oxides oriented with the (001) plane parallel to the film surface. By comparing the results of electron diffraction observation with those of electron microscopy, it was found that the (001) planes of the austenite and the spinel oxide lattices were parallel, the [100] direction of the austenite lattice coinciding with the same direction of the oxide lattice. In the same way, completely parallel growth of the spinel oxide was confirmed on the (110) and the (111) surfaces of austenite grains, as shown in Fig. 9 and 10. In addition,

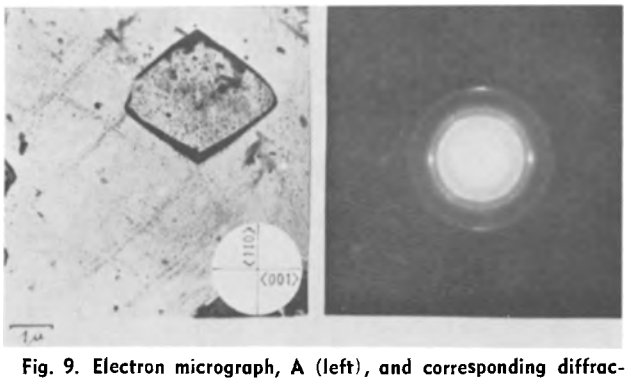

Fig. 9. Electron micrograph, A (left), and corresponding diffraction pattern, B (right), of oxide replica film from etched surface of 18-8 stainless steel. From (110) plane of austenite crystal.

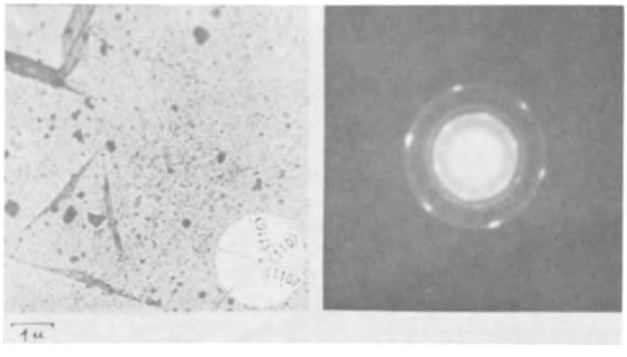

Fig. 10. Electron micrograph, A (left), and corresponding diffraction pattern, B (right), of oxide replica film from etched surface of 18-8 stainless steel. From (111) plane of austenite crystal.

preferential growth of oxide particles along the <110> direction of austenite can be seen in Fig. 9A, and slipping of the (111) plane along the <110> direction of austenite is observed in Fig. 10A. Lattice constant of the spinel oxide was also measured by means of high resolution electron diffraction, and as a mean value, 8.316 ± 0.007Å was obtained.

Similar results were also obtained from the oxide replica films produced on 25-20 stainless steel. Completely parallel growth of spinel oxide on austenite grains was observed on the micrographs of the oxide replica films from the (001), (110), and (111) planes of austenite and their corresponding diffraction patterns.

Several kinds of nonmetallic inclusions were occasionally extracted from the stainless steels in the process of isolating the oxide replica films. Two examples are shown in Fig. 11, which indicate shape, size, and distribution of the inclusions in the austenite. By the aid of selected area diffraction, the inclusions shown in Fig. 11A were identified as chromium carbide ($Cr_{23}C_6$, cubic $a_o = 10.65$Å). These carbide crystals have precipitated not only in the grain boundaries but inside the grains of austenite. This observation is of interest in relation to the mechanism of the grain boundary corrosion of stainless steels. Figure 11B shows a micrograph of thin platelike inclusions identified as β-quartz (β-SiO_2, hexagonal $a_o = 5.12$, $c_o = 5.38$Å). It seems probable that these silica crystals were included in the material of stainless steel, because silicon was used in the "deoxidation" process of the steel making.

Discussion

Structure of oxide films observed.—Results obtained in the present experiments showed that the oxides formed on the 18-8 stainless steels are spinel-type structure with lattice constants of 8.366 ±0.005Å and 8.316 ±0.007Å in the low-pressure oxidation and in the molten nitrate oxidation, respectively. The observed lattice constants are slightly lower than that of Fe_3O_4 (spinel type, $a_o = 8.390$Å or 8.374 kX) (21). In practice, these oxide films were compared with Fe_3O_4 film by means of high resolution electron diffraction in the same condition, and the results also supported the above data. The values of 8.366 and 8.316Å agree well with the lattice constants of $FeCr_2O_4$ (spinel type, $a_o = 8.360$Å or 8.344 kX) and $NiCr_2O_4$ (spinel type, $a_o = 8.315$Å or 8.299 kX) (21), respectively. According to the data

of lattice parameters of spinel phase oxides on nickel-chromium steels reported by Yearian and his co-workers (6, 22), the spinel oxides of lattice constants of 8.366 and 8.316Å correspond to a solid solution named LPS' (spinel phase, lattice parameter between 8.374 and 8.337Å, containing Ni and possibly Cr) and LPS" (spinel phase, lattice parameter between 8.336 and 8.306Å; containing both Ni and Cr), respectively.

These data suggest that the spinel oxides observed in the present study are rather solid solutions of composition near $FeCr_2O_4$ or near $NiCr_2O_4$ than those of unique composition. Similar results also were obtained about the oxide films on 25-20 stainless steel. It seems that the discrepancies of compositions of the oxide films were probably brought about by differences in pretreatments and in oxidation environments of the specimens, because chemical etching treatments often lead to preferential corrosion of the elements of the alloy surface, and also, low-pressure oxidation tends to produce selective oxidation of the alloying elements.

Orientation of oxide films observed.—The observed orientation of the oxides to the base metal is in good agreement in both oxidation environments. Complete parallel growth of spinel oxides on the austenite single crystal was proved. This orientation relationship is illustrated schematically in Fig. 12, in comparison with the α-iron lattice. In case of α-iron, the orientation relation between the metal and spinel oxide (magnetite) is known as follows (23, 24): the (001) planes of the two lattices were parallel, the [110] direction of the iron lattice coinciding with the [100] direction of the oxide lattice. The atomic distance along the face diagonal of the unit cell of α-iron, 4.04Å, is very near the half value of the cube edge of the magnetite lattice, 4.19Å. The magnetite has the "inversed" spinel structure (25-27), but this orientation gives the best correspondence of interatomic distances on the α-iron lattice. In case of stainless steels, the lattice fit of the spinel oxides

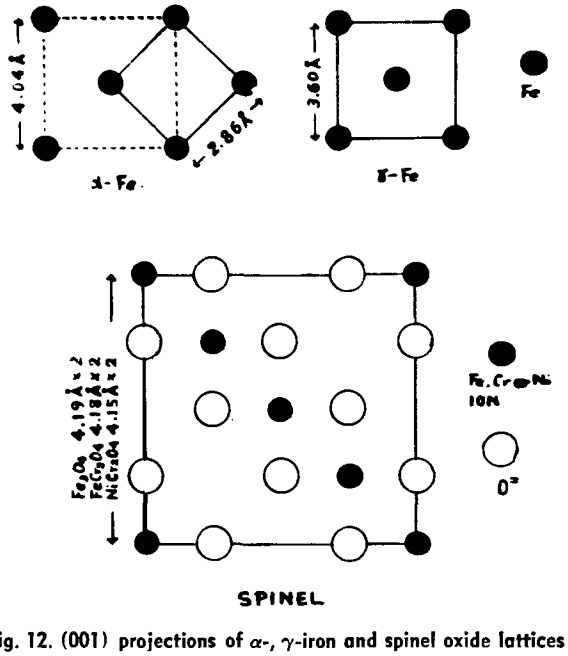

Fig. 12. (001) projections of α-, γ-iron and spinel oxide lattices

on the austenite (γ-iron) crystal is not as good as that on α-iron. There are discrepancies of 15 ~ 16% between the dimensions of these two lattices as is seen from Fig. 12. Important zone axes of both unit cells are parallel to each other, suggesting that the spinel oxide lattice is strongly affected by the orientation of the austenite crystal. Though the oxides of $FeCr_2O_4$ and $NiCr_2O_4$ have the "normal" spinel structure (22) and are known in general as good protective films in oxidation, these results suggest a limitation of protectiveness of the spinel oxide to the austenitic stainless steel.

Oxide nuclei and anisotropy of austenite crystal in oxidation.—Transmission electron microscopy of oxide nuclei formed by a low pressure oxidation of thin sections are of interest from the viewpoint of oxide nucleation of stainless steels. For example, as is seen in Fig. 7, numerous oxide nuclei 300 ~ 2000Å in size are distributed in a discontinuous manner inside the austenite grains and some of them show a tendency to grow into cross-like oxide particles oriented along the <110> direction of austenite, and the grain boundaries are outlined by discontinuous precipitates of oxide particle. As thin sections were used in the present study, these micrographs show the structure of alloy/oxide interface rather than the surface of oxide film. Therefore, these oxide nuclei are thought to be brought about by internal oxidation. The observed value of the density of oxide nuclei suggests that their nucleating sites might be closely related to structural imperfections in the austenite crystal, such as dislocations, stacking faults, and other defects.

These results were also compared with the observations of oxide nodules previously reported by Radavich (28). He has recorded that the process of oxide formation on stainless steels starts with growth of a thin uniform layer of oxide but is followed by growth of the oxide nodules randomly distributed on the oxide film as the oxidation proceeds, and that the nodular formation is dependent on the iron content of the stainless steels. The size of the nodules, quoted from his observations of the stainless steel (Type 310) oxidized in air for 5 min at 600°C, varies from a few hundred Angströms to over a micron. Although it was not clear whether the oxide nuclei observed in the present study were of the same type as those of Radavich, the fact that the size of the oxide nuclei is of the same order of magnitude as that of the oxide nodules is of interest.

In the electron micrographs observed in the present experiments, the (111) plane appeared very often on the chemical etched and on the oxidized grains of austenite crystals. Further, many texture patterns concerning preferential oxidation along the <110> direction of the austenite were shown. These facts indicate that the anisotropy of the crystal lattice has an important role in corrosion and oxidation attack. It is well known that the (111) plane is a slip plane and the slip direction is the <110> in face-centered cubic metals. The (111) is the most densely packed, while the (110) is the most sparsely packed of the three important planes of the face-centered cubic lattice. Therefore, it is suggested that

the (111) plane is least active and the <110> direction is most active for oxidation. The anisotropy of oxidation is an interesting phenomenon in oxidation attack, but its interpretation will require many more detailed examinations.

Summary

1. Electron microscope and diffraction studies were made on the oxide films produced on thin sections of 18-8 and 25-20 stainless steels in $\sim 10^{-4}$ mm Hg dry air at 300°-600°C. The oxide films consisted of spinel type oxide near $FeCr_2O_4$. Completely parallel growth of the oxide crystals on the austenite grains was observed.

2. Oxide replica films formed on etched surfaces of the stainless steels, in a molten nitrate solution at 300°-400°C, were also investigated by the same method. The oxide replica films consisted of spinel type oxide near $NiCr_2O_4$. In this case completely parallel growth of the oxide on the austenite was also observed. Nonmetallic inclusions, such as $Cr_{23}C_6$ and β-SiO_2, were occasionally extracted from the alloys with the oxide replica films.

3. Oxide nuclei and anisotropy of the austenite crystal were observed in the oxidation of the thin sections, the electron micrographs suggesting that the (111) plane was least active and the <110> direction was most active for oxidation.

4. The orientation relationship between the spinel oxides and the austenite was discussed in connection with the protective nature of the stainless steels.

Acknowledgments

The author wishes to thank Dr. F. W. Fink, of Battelle Memorial Institute, and Professor J. A. Dillon, Jr., of Brown University, for their interest and critical reading of this manuscript, and also thanks to Dr. U. Hashimoto, President of the National Research Institute for Metals (Japan), for his encouragement in the course of this study.

Manuscript received Feb. 1, 1963; revised manuscript received June 29, 1963. This paper was presented in part at the Detroit Meeting, Oct. 1-5, 1961.

Any discussion of this paper will appear in a Discussion Section to be published in the June 1964 JOURNAL.

REFERENCES

1. S. Miyake, *Sci. Papers Inst. Phys. Chem. Research (Tokyo)*, **31**, 161 (1937).
2. H. R. Nelson, *J. Chem. Phys.*, **6**, 606 (1938).
3. T. Tokumitu, *Nature*, **145**, 589 (1940); *Sci. Papers Inst. Phys. Chem. Research (Tokyo)*, **38**, 59 (1940).
4. J. W. Hickman and E. A. Gulbransen, *Trans, Am. Inst. Mining Met. Engrs.*, **171**, 344 (1947).
5. H. J. Yearian, E. C. Randell, and T. A. Longo, *Corrosion*, **12**, 515*t* (1956).
6. H. J. Yearian, H. E. Boren, Jr., and R. E. Warr, *ibid.*, **12**, 561*t* (1956).
7. H. J. Yearian, W. D. Derbyshire, and J. F. Radavich, *ibid.*, **13**, 597*t* (1957).
8. S. Yamaguchi, T. Nakayama, and T. Katsurai, *This Journal*, **95**, 21 (1949).
9. R. D. Heidenreich, *J. Appl. Phys.*, **20**, 993 (1949).
10. W. Bollman, *Phys. Rev.*, **103**, 1588 (1956).
11. P. B. Hirsch, R. W. Horne, and M. J. Whelan, *Phil. Mag.*, **1**, 677 (1956).
12. M. J. Whelan, P. B. Hirsch, and R. W. Horne, *Proc. Roy. Soc. (London)*, **240**, 524 (1957).
13. H. M. Tomlinson, *Phil. Mag.*, **3**, 867 (1958).
14. G. Thomas, "Transmission Electron Microscopy of Metals," John Wiley & Sons, New York (1962).
15. H. Mahl, *Z. tech. Physik*, **21**, 17 (1940).
16. F. Keller and A. H. Geisler, *Trans. Am. Inst. Mining Met. Engrs.*, **156**, 62 (1944).
17. G. Thomas and J. Nutting, *J. Inst. Metals*, **85**, 1 (1956).
18. E. M. Mahla and N. A. Nielsen, *J. Appl. Phys.*, **19**, 378 (1948).
19. S. Yamaguchi, *Kagaku Kenkyujo Hokoku* (in Japanese), **25**, 156 (1949); **26**, 160, 228 (1950).
20. G. Shimaoka, *J. Phys. Soc.* (Japan), **17**, Supplement B-II, 306 (1962), "Proceedings of International Conference on Magnetism and Crystallography," Vol. II (1961).
21. R. W. G. Wyckoff, "Crystal Structures," Vol. 1, New York (1948).
22. H. J. Yearian, J. M. Kortright, and R. H. Langenheim, *J. Chem. Phys.*, **22**, 1196 (1954).
23. H. R. Nelson, *ibid.*, **5**, 252 (1937).
24. O. Haase, *Z. Naturforsch.*, **11**, 46 (1956).
25. E. J. W. Verwey and J. H. de Boer, *Rec. trav. chim.*, **55**, 531 (1936).
26. E. J. W. Verwey, P. W. Haayman, and F. C. Romeijin, *J. Chem. Phys.*, **15**, 181 (1947).
27. C. G. Shull, E. O. Wollan, and W. C. Koehler, *Phys. Rev.*, **84**, 912 (1951).
28. J. F. Radavich, Am. Soc. Testing Materials, Special Technical Publication No. 171, 14, 89 (1955).

An Electrochemical pH-Stat and Its Application to Corrosion Studies

F. A. Posey, T. Morozumi, and E. J. Kelly

Chemistry Division, Oak Ridge National Laboratory, Oak Ridge, Tennessee

ABSTRACT

An apparatus has been developed which controls automatically the acidity of unbuffered solutions in the region from *p*H 4 to 10. A potentiostat is used to control the potential of an inert electrode on which the hydrogen gas-hydrogen ion reaction occurs in a solution saturated with hydrogen gas. The inert electrode acts as both a sensing element and a regulating electrode for the control of acidity. Current from the potentiostat passes through the inert electrode and an auxiliary polarizing electrode in an external compartment separated from the main cell by a salt bridge or porous plate. Transients which occur during the regulating action are presented and analyzed. The electrochemical *p*H-stat may be used to measure corrosion rates. Limitations of the device are discussed and a modification is proposed which makes use of a differential amplifier instead of a potentiostat.

Problems in the control of solution acidity occur frequently in studies on the kinetics of homogeneous and heterogeneous reactions which involve the consumption or liberation of hydrogen ions in solution. The decrease of acidity with time during the corrosion of iron or other metals in unbuffered solutions is a notable example. A classical solution to the problem involves the use of buffered solutions in cases where the presence of buffering reagents has no undesirable effect on reaction kinetics. More recently, ingenious devices known as *p*H-stats have been developed (1-5). These electrochemical instruments generally employ the principle of the automatic titrator (6) and utilize the controlled addition of reagents by use of electrically driven burettes or syringe pumps. Similar apparatus has been reported for the control of acidity in processes of industrial importance (7, 8), and a recent review on *p*H and its control is available (9).

A need for a different type of *p*H-stat arose in this Laboratory as a consequence of attempts to measure the polarization behavior of iron and other metals in unbuffered solutions over the *p*H range 4 to 10. The use of buffer mixtures in electrochemical kinetic studies is sometimes undesirable because of the possibility of introduction of extraneous reactions or of specific effects on the kinetics of interfacial processes. In addition, the use of the automatic titrator type of *p*H-stat possesses some disadvantages, particularly in studies requiring the absence of atmospheric oxygen. Besides the effort needed to prepare standard reagents, considerable difficulty may be experienced in deoxygenating and pre-electrolyzing the solutions used, and corrections are necessary for volume changes due to the addition of reagents.

In order to circumvent these difficulties, an apparatus was devised which takes advantage of favorable properties of the hydrogen gas-hydrogen ion reaction on platinum or other inert electrodes. An electronic potentiostat (10, 11) is used to control precisely the potential of a large platinum electrode in a solution saturated with hydrogen gas. The current required for the control of potential passes through an auxiliary polarizing electrode located in a chamber exterior to the primary cell and connected to this cell by use of a salt bridge or porous plate. The large platinum electrode acts both as a sensing element and as a regulating electrode for the addition or removal of hydrogen ions. Within certain limitations, the precision with which the potential of the platinum electrode is controlled determines the degree of control of solution acidity. For electrode systems in which the use of a hydrogen atmosphere can be tolerated, this method of *p*H control possesses certain advantages. No complex electromechanical devices are necessary with their attendant difficulties of regulation, reagent preparation, and deoxygenation. Since no external reagents are added by the controlling device, no solution volume corrections are necessary; this is particularly convenient in long-term experiments. Solution acidity is controlled automatically by the electronic potentiostat, and the *p*H may be changed easily and precisely by merely changing the potential at which the platinum electrode is maintained. Furthermore, the method is most effective in the *p*H region near neutrality, where precise *p*H control is often difficult to obtain in unbuffered solutions. Some results of experiments on the properties of the electrochemical *p*H-stat are presented below, togther with an analysis of the transients encountered during changes of solution acidity. The application of the device to the measurement of corrosion rates is discussed. In addition, a modification of the method is proposed which makes use of a differential amplifier instead of a potentiostat. The differential amplifier type of *p*H-stat uses a glass electrode (or other *p*H-responsive electrode) as the *p*H-sensing element, is not re-

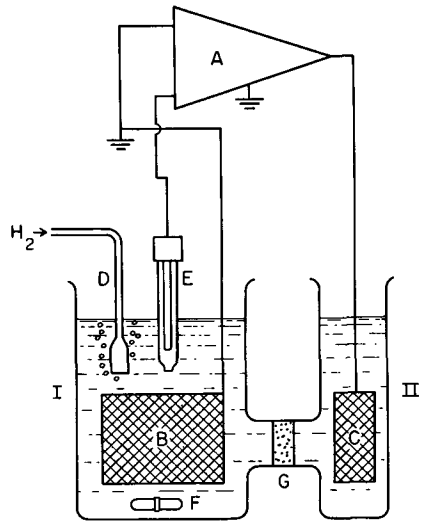

Fig. 1. Schematic diagram of potentiostat type of electrochemical pH-stat. A, Electronic potentiostat; B, large platinum electrode; C, auxiliary polarizing electrode; D, inlet and bubbler for hydrogen gas; E, reference electrode; F, stirrer (magnetic); G, salt bridge or porous disk; I, primary cell; II, exterior polarizing chamber.

stricted to use with systems in which a hydrogen atmosphere is maintained, and possesses improved transient response.

Experimental

A schematic diagram of an experimental cell for the electrochemical pH-stat is shown in Fig. 1. The potential difference between the large platinum electrode (B) and the reference electrode (E) provides the input voltage to the potentiostat. Any difference between this voltage and the reference voltage setting on the potentiostat actuates a flow of current between the platinum electrode and the polarizing electrode in compartment II. The magnitude and direction of current flow are such as to minimize the difference between the input voltage and the potentiostat reference voltage. If the reversible potential of the platinum electrode in the solution in compartment I differs from the potentiostat reference voltage, the flow of current polarizes the electrode to the value of the reference voltage. In a manner depending on the polarization characteristics of the hydrogen gas-hydrogen ion reaction on the electrode and on the ratio of electrode area to solution volume, Faradaic current from the hydrogen gas-hydrogen ion reaction then passes through the electrode interface and the concentration of hydrogen ions in solution increases or decreases with time. When the pH of the solution approaches the value at which the reversible potential equals the potentiostat reference voltage, current flow approaches zero and the pH is subsequently controlled automatically with a precision which depends on the control characteristics of the potentiostat.

The potentiostat used in the present studies permitted precise control of electrode potentials over an extended period.[1] It incorporated a chopper-stabilized operational amplifier of high gain. Maximum output voltage was ±100v and output current could attain ±25 ma. Electrode potentials were constant to within ±0.1 mv at all times when the potentiostat was controlling, as could be observed oscilloscopically. Response time of this type of potentiostat was slow compared to that of the straight-amplifier type, but this was a negligible disadvantage for the present purposes. The experimental cell was constructed of Pyrex glass with a fritted glass disk to minimize diffusion between electrode compartments (cf. Fig. 1). A commercial saturated calomel electrode was employed as reference electrode. Hydrogen gas purified over copper turnings in a tube furnace was effused into the solution and provided some degree of stirring. Additional stirring was provided by use of a Teflon-coated magnetic stirring bar. The pH of the solution was monitored by use of a commercial glass electrode (not shown in Fig. 1). Both the potential of the glass electrode and the current output of the potentiostat were recorded with time. Solutions were prepared with triply distilled water, obtained by redistilling distilled water from the laboratory supply in a two stage quartz still. Analytical reagent grade chemicals were used in the preparation of all solutions

Results

Some experimental results are shown in Fig. 2 for the variation of the glass electrode potential with time during adjustment of solution acidity by the electrochemical pH-stat. Curves A through D correspond to changes of 60 mv in the potentiostat reference voltage. The glass electrode potential changes in an exponential manner with time and finally approaches and maintains the desired potential. Curves E and F exhibit a somewhat different behavior; curve E shows the transient behavior found for a change from pH 4 to pH 9 while curve F shows the

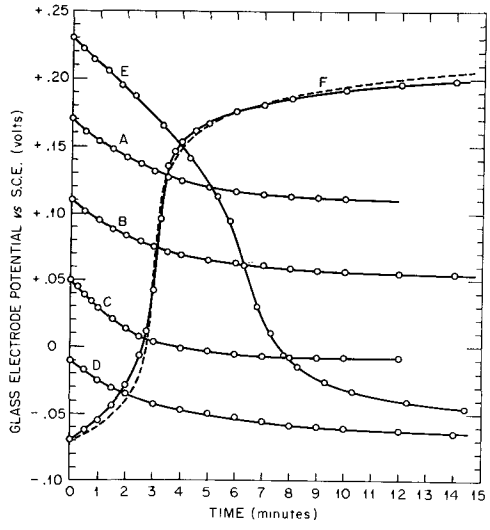

Fig. 2. Variation of glass electrode potential with time during adjustment of solution acidity by electrochemical pH-stat. Solution, 0.5M NaCl; temperature, 25°C; atmosphere, H_2.

Curve	Potential change, mv	pH, approx. Initial	Final
A	—60	5	6
B	—60	6	7
C	—60	7	8
D	—60	8	9
E	—300	4	9
F	+300	9	4

[1] An improved model of this potentiostat is available commercially as the Model 610 Potentiostat-Galvanostat, manufactured by Fairport Instruments, Inc., Oak Ridge, Tennessee.

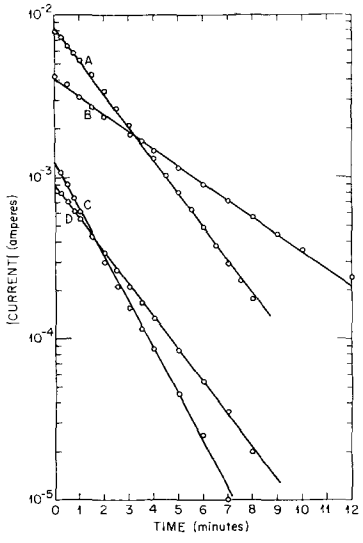

Fig. 3. Variation of current from potentiostat with time during adjustment of solution acidity by electrochemical pH-stat. Solution, 0.5M NaCl; temperature 25°C; atmosphere, H_2.

Curve	Potential change, mv	pH, approx. Initial	Final
A	−60	4	5
B	+60	5	4
C	−60	5	6
D	+60	6	5

behavior observed on readjusting the acidity from pH 9 to pH 4. These curves resemble and are closely related to the usual acid-base titration curves. Inflection points may be noted in curves E and F in the vicinity of pH 7 (glass electrode potential $\cong +0.05$v); these sigmoid curves are obtained when the equivalence point of water is crossed during changes of pH.

Typical variations of current with time during adjustment of pH are shown in Fig. 3. Faradaic current varies exponentially with time and approaches zero as the solution acidity approaches the value determined by the setting of the potentiostat reference voltage. The slopes of the curves in Fig. 3 depend on the value of the platinum electrode potential, on the kinetic parameters of the hydrogen gas-hydrogen ion reaction, and on the ratio of electrode area to solution volume. For example, the slopes of curves A and D are essentially the same, and these transients were obtained at the same electrode potential. Although the data in Fig. 3 correspond to pH transients like those in curves A-D of Fig. 2 (curve C of Fig. 3 corresponds to curve A of Fig. 2), very similar behavior is observed for current transients corresponding to curves E and F.

Other experiments were performed in which solution acidity was changed suddenly by additions of acid or base to the solution. The transients observed during the readjustment action of the potentiostat are similar in every respect to those shown in Fig. 2 and 3. Several experiments were also performed to test the degree of control over an extended period. No significant long-term changes in the value of the glass electrode potential greater than 1 mv were detected, and momentary fluctuations were also no greater than 1 mv. Therefore, the electrochemical pH-stat is capable of controlling pH to approximately ±0.01 pH unit over an indefinite period.

Discussion

Theory of operation.—The forms of the transients in Fig. 2 and 3 may be calculated by use of well-known concepts of electrochemical kinetics (12). The net flux ($v_N(t)$) of hydrogen ions at the interface of the platinum electrode due to the hydrogen gas-hydrogen ion reaction may be expressed by Eq. [1].[2] In Eq. [1], $\bar{k}_a$ and $\bar{k}_c$ are the

$$v_N(t) = \frac{\bar{k}_a C_{H_2} - \bar{k}_c C_{H^+}(t)}{1 + \frac{\delta_a}{D_a}\bar{k}_a + \frac{\delta_c}{D_c}\bar{k}_c} \qquad [1]$$

electrochemical specific rate constants for the anodic and cathodic partial processes, respectively, of the reaction, $2H^+(aq) + 2e^- = H_2(g)$. Equation [1] takes formal account of the existence of limiting currents due to mass transfer of the reactants, dissolved molecular hydrogen (C_{H_2}) and hydrogen ions ($C_{H^+}(t)$). The diffusion coefficients of H_2 and of H^+ are symbolized by D_a and D_c, respectively, and δ_a and δ_c are the corresponding hypothetical thicknesses of the Nernst diffusion layer.

The current as a function of time is given simply by Eq. [2], where

$$i(t) = \mathbf{F}Sv_N(t) \qquad [2]$$

S is the electrode area. It is assumed that the hydrogen gas-hydrogen ion reaction is the only source of Faradaic current at the interface. Equation [2] neglects non-Faradaic currents like those due to charging of the electrical double layer and to adsorption or phase formation or decomposition reactions on the electrode surface. Hydrogen ion concentration in the bulk of the solution may be assumed to change with time according to Eq. [3], where V is the volume of the solution and t_+ is the

$$\frac{dC_{H^+}(t)}{dt} = \frac{S}{V}(1 - t_+)v_N(t) \qquad [3]$$

transference number of hydrogen ions (assumed constant) through the diaphragm which separates electrode compartments (cf. G of Fig. 1).

Equation [3] may be integrated to give Eq. [4] for the variation of

$$C_{H^+}(t) = C_{H^+}(o)e^{-\beta t} + \frac{\bar{k}_a}{\bar{k}_c}C_{H_2}(1 - e^{-\beta t}) \qquad [4]$$

with

$$\beta \equiv \frac{\frac{S}{V}(1 - t_+)\bar{k}_c}{1 + \frac{\delta_a}{D_a}\bar{k}_a + \frac{\delta_c}{D_c}\bar{k}_c}$$

hydrogen ion concentration with time; note that in the new steady state $C_{H^+}(\infty) = \frac{\bar{k}_a}{\bar{k}_c}C_{H_2}$. The current as a function of time is given by Eq. [5]

[2] Equation [1] does not represent any particular mechanism of the hydrogen gas-hydrogen ion reaction. It is used here because it provides an adequate simple approximation to the form of experimental polarization curves in neutral and moderately acid solutions. The theory may be developed also for specific mechanisms of the hydrogen evolution reaction, and in general the resulting equations are considerably more complicated than those presented here.

$$i(t) = \frac{\mathbf{F}S[\bar{k}_a C_{H_2} - \bar{k}_c C_{H^+}(o)]}{1 + \frac{\delta_a}{D_a}\bar{k}_a + \frac{\delta_c}{D_c}\bar{k}_c} e^{-\beta t} \quad [5]$$

which is obtained by combination of Eq. [1], [2], and [4]. Equation [5] is of the form

$$\ln\left[\frac{i(t)}{i(o)}\right] = -\beta t$$

and the results shown in Fig. 3 follow this equation closely. For a constant ratio of electrode area to solution volume, the time constant parameter β varies only with electrode potential; for example, the slopes of curves A and D in Fig. 3 are essentially the same, even though $C_{H^+}(o)$ differs in the two cases.

The time response of the glass electrode potential, $V_g(t)$, is given by Eq. [6]. This equation accounts for results like those of curves A,

$$V_g(t) - V_g(o) = \frac{RT}{\mathbf{F}} \ln \frac{C_{H^+}(t)}{C_{H^+}(o)}$$

$$= \frac{RT}{\mathbf{F}} \ln\left[e^{-\beta t} + \frac{\bar{k}_a C_{H_2}}{\bar{k}_c C_{H^+}(o)}(1 - e^{-\beta t})\right] \quad [6]$$

B, C, and D in Fig. 2, but not for the results of curves E and F, where the neutrality point of water (*p*H 7) is crossed during the adjustment action of the *p*H-stat.

Modification of the treatment to include the effect of the ionization of the aqueous solvent into hydrogen ions and hydroxide ions accounts for the form of curves E and F in Fig. 2. In this case Eq. [3] is modified to include the stoichiometry of the water ionization equilibrium, which may be expressed as usual by $K_w = C_{H^+} \cdot C_{OH^-}$. Integration of the modified form of Eq. [3], with use of the parameter β defined in Eq. [4], leads to Eq. [7] for the variation of hydrogen ion concentration, $C_{H^+}(t)$, with time.

$$\left[\frac{C_{H^+}(\infty) - C_{H^+}(t)}{C_{H^+}(\infty) - C_{H^+}(o)}\right]^{\left[1 + \frac{K_w}{[C_{H^+}(\infty)]^2}\right]} \times \left[\frac{C_{H^+}(t)}{C_{H^+}(o)}\right]^{-\frac{K_w}{[C_{H^+}(\infty)]^2}} \times e^{-\left[\frac{K_w[C_{H^+}(t) - C_{H^+}(o)]}{C_{H^+}(\infty) C_{H^+}(t) C_{H^+}(o)}\right]} = e^{-\beta t} \quad [7]$$

It is assumed in the derivation of Eq. [7] that the transference number of hydrogen ions (and/or hydroxide ions) is negligibly small, so that $(1 - t_+) \cong 1$. Equation [7] reduces to Eq. [4] when the quantity $K_w/C_{H^+}(\infty)$ is sufficiently small. Although Eq. [7] cannot be solved explicitly for $C_{H^+}(t)$ except for certain limiting cases, the variation of the current and the glass electrode potential with time may be calculated by use of Eq. [7] with Eq. [2] and [6]. The dashed line in Fig. 2 (cf. curve F) was calculated by use of Eq. [7], where the constant β was chosen to fit the experimental curve at *p*H 7. The agreement between theoretical and experimental curves is fairly good in view of the approximations made in the derivation. Equation [7] does not describe results like curve E of Fig. 2 because the mechanism of the hydrogen reaction differs in acid and basic regions. The exact form of the transient depends on the particular reaction mechanism and its variation with *p*H. In the basic region, the overall stoichiometry of the electrode reaction may be expressed by $2H_2O + 2e^- = H_2(g) + 2OH^-(aq)$. It is found in this case that the flux equation has a form different from that of Eq. [1], such that the hydrogen ion concentration changes with time according to an expression which is similar in form to Eq. [7], but which has different parameters.

Equations [4], [5], [6], and [7] are good approximations to the experimental behavior provided the potentiostat controls the potential of the platinum electrode at the chosen value. In case the current requirements are such that more current than the maximum output of the potentiostat is needed for the control of potential during a transient, the electrode potential is not controlled, and the current output remains essentially constant at a limiting value (i_L) until control is re-established. During this period, the rate of change of hydrogen ion concentration is given by Eq. [8]. When control is re-established, subsequent variations

$$\frac{dC_{H^+}(t)}{dt} = \frac{(1 - t_+) i_L}{\mathbf{F}V} \quad [8]$$

of $C_{H^+}(t)$ are given, as before, by Eq. [3] and [4] or by Eq. [7].

Optimum conditions for use of the electrochemical *p*H-stat require a large ratio of electrode area to solution volume. The use of platinized platinum electrodes is advantageous in this respect. In general, an excess of inert electrolyte is advantageous, and the theoretical analysis of transient behavior is much simpler in this case because the effect of variations in the transport numbers of hydrogen and hydroxide ions is minimized. Good mechanical stirring improves the performance by decreasing δ_a and δ_c of Eq. [1] and ensures that Eq. [3] is a good approximation. An increase of temperature increases the exchange current density of the hydrogen reaction on the platinum electrode and decreases response time. The *p*H of the solution is varied easily by changing the setting of the potentiostat reference voltage by the appropriate amount; for example, a 59 mv change of the reference voltage at 25°C changes the *p*H by one unit.

Measurement of corrosion rates.—The kinetics of reactions which produce or consume hydrogen ions may be measured at constant acidity by use of the electrochemical *p*H-stat. This capability is particularly valuable in the case of corrosion reactions since the technique provides a continuous measurement of corrosion rate as a function of time without the necessity for weight loss or polarization measurements. In the absence of external polarizing current, the rate of corrosion of an isolated metallic electrode equals the rate of the hydrogen evolution reaction on its surface, provided the reduction of hydrogen ions is the sole cathodic process. For this case, Eq.

[3] may be modified to give Eq. [9], where R_x is the rate of increase of hydrogen ion concentration

$$\frac{dC_{H^+}(t)}{dt} = \frac{S}{V}(1 - t_+)v_N(t) + R_x \qquad [9]$$

in solution due to the corrosion or other reaction (R_x is negative in the case of a corroding metal). The solution of Eq. [9] is given by Eq. [10]

$$C_{H^+}(t) = C_{H^+}(o) + \frac{R_x}{\beta}(1 - e^{-\beta t}) \qquad [10]$$

where the condition that $C_{H^+}(t) = C_{H^+}(o)$ at $t = 0$ has been used. The current transient induced on immersion of the corroding metal electrode is then given by Eq. [11]. In the new steady state, the current passing

$$i(t) = -\frac{\mathbf{F}VR_x}{(1 - t_+)}(1 - e^{-\beta t}) \qquad [11]$$

through the interface of the platinum electrode just compensates the current due to reduction of hydrogen ions on the corroding electrode, so that the measurable current is given by Eq. [12]. In Eq. [12], i_{corr} is

$$i(\infty) = -\frac{\mathbf{F}VR_x}{(1 - t_+)} = \frac{i_{corr}}{(1 - t_+)} \qquad [12]$$

the corrosion current of the metallic electrode in the absence of external polarizing current. Figure 4 shows typical examples of current transients obtained from the pH-stat on immersion of an iron electrode into solution. Data points were taken from recordings of the current transients and the solid lines are fits of Eq. [11] to the data.

The degree of control of solution acidity by the electrochemical pH-stat during the time of immersion of the corroding electrode depends on the rate of the corrosion reaction. The hydrogen ion concentration in the new steady state, $C_{H^+}(\infty)$, is given by Eq. [13], which follows from

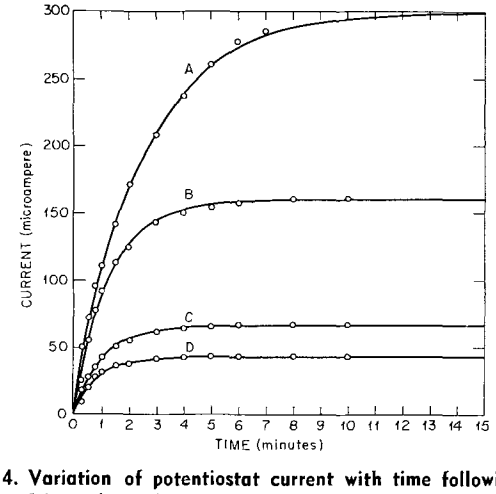

Fig. 4. Variation of potentiostat current with time following immersion of iron electrode into solution. Solution, 0.5M NaCl; Electrode, zone-refined iron; atmosphere, H_2.

Curve	pH	Temp. °C
A	2.9	70
B	3.5	70
C	4.0	50
D	4.5	50

$$C_{H^+}(\infty) = C_{H^+}(o) + \frac{R_x}{\beta} = C_{H^+}(o) - \frac{i_{corr}}{\mathbf{F}V\beta} \qquad [13]$$

Eq. [10] and [12]. Equation [13] may be rearranged to give Eq. [14] for the

$$\frac{C_{H^+}(\infty)}{C_{H^+}(o)} = 1 - \frac{i_{corr}}{\mathbf{F}V\beta C_{H^+}(o)} = 1 - \frac{i_{corr}}{(1 - t_+)i_o} \qquad [14]$$

degree of control of acidity as a function of the corrosion rate of the metallic electrode. In Eq. [14], i_o is the exchange current of the hydrogen gas-hydrogen ion reaction on the platinum electrode prior to immersion of the corroding electrode. This equation shows that the pH change incurred as a consequence of the corrosion reaction may be minimized by increasing the exchange current of the pH-controlling electrode of the pH-stat. For sufficiently small corrosion rates, this effect can be relatively unimportant, particularly if a platinized platinum electrode is used with the pH-stat.[3]

The present method for the measurement of corrosion rates is most useful when the corrosion rate remains essentially constant with time. In the case of corrosion rates which vary with time, the method remains useful provided the time required for a significant variation of i_{corr} is large compared to $1/\beta$. If the corrosion reaction produces metallic ions in solution which undergo appreciable hydrolysis at the pH in question, $i(\infty)$ no longer equals $i_{corr}/(1 - t_+)$, and the treatment must be corrected for this effect. Alternatively, if corrosion rates were known independently, the method might be useful for investigating the hydrolysis of corrosion products. In favorable cases, this method of corrosion rate measurement is capable of providing an independent check on values of corrosion rate estimated by extrapolation of Tafel lines to the corrosion potential or by measurement of the polarization resistance.

Disadvantages and modifications.—Certain disadvantages are inherent in the use of the present device for the control of acidity, particularly in the presence of a corroding electrode on which polarization measurements are desirable. (*a*) The necessity for use of a hydrogen atmosphere limits the utility of the device to systems in which hydrogen can be tolerated. (*b*) The transient response is relatively slow and depends greatly on the characteristics of the hydrogen reaction on the platinum electrode and on the area to volume ratio. (c) The degree of control of pH in the presence of a homogeneous or heterogeneous reaction which produces or consumes hydrogen ions depends on the rate of that reaction (cf. Eq. [14]). (*d*) The large platinum electrode is grounded in the usual potentiostatic configuration, so that use of a second electronic potentiostat or other grounded current source on a corroding (or other) electrode in the same cell is awkward.

A different type of electrochemical pH-stat was designed and constructed which largely eliminates,

[3] The use of platinum electrodes may present difficulties in certain media, especially chloride solutions. The finite dissolution rate of platinum in chloride solutions produces platinum ions which may be reduced on other electrode surfaces in the cell, causing significant changes in the kinetics of reactions occurring at these surfaces. If this effect is troublesome in specific cases, it may be necessary to replace the platinum with a less reactive material (pyrolytic graphite, porous carbon, boron carbide, etc.).

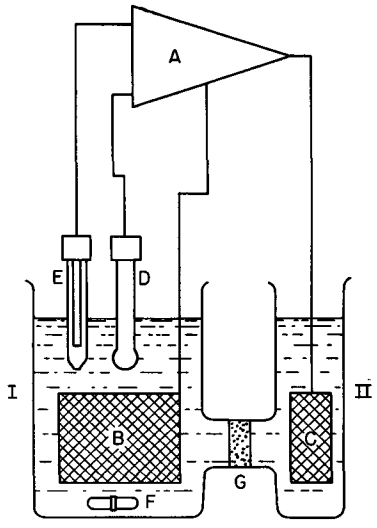

Fig. 5. Schematic diagram of differential amplifier type of electrochemical pH-stat. A, Differential amplifier; B, platinum electrode; C, auxiliary polarizing electrode; D, glass electrode; E, reference electrode; F, stirrer (magnetic); G, salt bridge or porous disk; I, primary cell; II, exterior polarizing chamber.

at least in principle, the difficulties mentioned above. Although the same type of cell as that in Fig. 1 is employed, so that the method of production or consumption of hydrogen ions by an electrochemical reaction at an inert electrode is unchanged, the control of acidity is accomplished by use of a differential amplifier instead of a potentiostat. Figure 5 shows schematically the experimental arrangement. The difference in the potential of a glass electrode (D) (or other pH-responsive electrode) and a reference electrode (E) is the input potential to the differential amplifier (A). This potential is opposed by a reference voltage at the input of the amplifier, in a manner similar to that used in potentiostats. Any difference between the input potential and the reference voltage is amplified by the differential amplifier and drives a current through the circuit consisting of electrodes B and C. The polarity of the current is such that the pH change caused by the equivalent electrochemical reaction at electrode B shifts the potential of the glass electrode in the proper direction to reduce the difference between the input potential and the reference voltage. Current output is zero when the input potential equals the reference voltage setting and any change in acidity as detected by the glass electrode causes immediate corrective action.

A Philbrick Model P2 solid state differential operational amplifier is used in the modified electrochemical pH-stat. Power is supplied from mercury cells (Type TR-136), so that the entire apparatus can be floated with respect to ground potential. By this means, the modified pH-stat may be operated simultaneously with other line-operated instruments without the introduction of ground loops or other related difficulties. The open loop gain of this amplifier is approximately 3 x 10^4, and the input impedance is approximately 10^{10} ohms. The maximum output voltage is ±10v and the maximum output current is ±1 ma; although the output capability is somewhat less than that of conventional differential amplifiers, it is still sufficient to provide good regulating action over the pH range from 4 to 10 when used with cells of moderate size. Feedback resistors of appropriate values may be used to lower the gain of the amplifier in cases where maximum gain is undesirable. The apparatus is constructed so that it may be used also as a conventional potentiostat (cf. Fig. 1) by a slight change in the wiring arrangement.

The differential amplifier type of pH-stat is not limited to use with cells in which a hydrogen atmosphere is maintained. It is capable of controlling pH providing any suitable electrochemical reaction occurs on the platinum electrode which liberates or consumes hydrogen ions in a manner which depends on the direction of current flow. The transient response is not exponential, as in the case of the potentiostatic type of pH-stat. At maximum gain, the full output of the amplifier is obtained when the difference between the input potential and the reference voltage exceeds *ca.* ± 0.3 mv. Under these conditions, the modified pH-stat operates essentially as a "go-no go" device. Current flow stops when the glass electrode potential attains the value determined by the reference voltage setting (see below, however).

When the amplifier is operated at maximum gain, full output is obtained when $\epsilon(t) = V_g(t) - V_R = V_g(t) - V_g(\infty)$ exceeds *ca.* ±0.3 mv; here, $\epsilon(t)$ is the difference betwen $V_g(t)$, the glass electrode potential *vs.* the reference electrode, and V_R, the reference voltage. If the input signal required for full output is designated by ϵ_l, the (constant) current output (i_l) is given approximately by Eq. [15], where $i(t)$ is the current through

$$i(t) = i_l = -\frac{A}{Z}\epsilon_l \qquad [15]$$

electrode B of Fig. 5, A is the gain of the amplifier, and Z is the cell impedance (assumed constant). Hydrogen ion concentration changes with time according to Eq. [16], which gives Eq. [17] on integration.

$$\frac{dC_{H^+}(t)}{dt} = \frac{(1-t_+)}{FV}i(t) = -\frac{(1-t_+)A}{FVZ}\epsilon_l = -\gamma \qquad [16]$$

$$C_{H^+}(t) = C_{H^+}(o) - \gamma t \qquad [17]$$

The concentration of hydrogen ions changes linearly with time because of the constant output current, and the corresponding variation of glass electrode potential is given by Eq. [18]. The time (τ) required for a

$$V_g(t) = V_g(o) + \frac{RT}{F}\ln\frac{C_{H^+}(t)}{C_{H^+}(o)}$$

$$= V_g(o) + \frac{RT}{F}\ln\left(1 - \frac{\gamma}{C_{H^+}(o)}t\right) \qquad [18]$$

change in the glass electrode potential of $V_g(\infty) - V_g(o)$ follows from Eq. [18] as Eq. [19]. For $V_g(\infty) - V_g(o) < 0$, $\epsilon_l > 0$, and $\gamma > 0$; and for $V_g(\infty) - V_g(o) > 0$

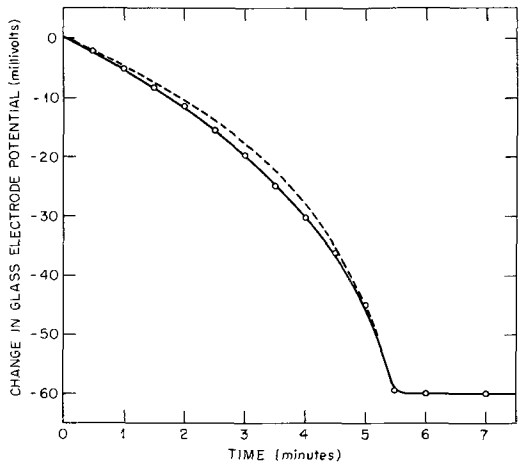

Fig. 6. Variation of glass electrode potential with time during adjustment of solution acidity by differential amplifier type of pH-stat. Solution, 0.5M NaCl; temperature, 25°C; atmosphere, H_2; pH change, 4 to 5.

$$\tau = \frac{C_{H^+}(o)}{\gamma}\left[1 - e^{+\frac{F}{RT}[V_g(\infty) - V_g(o)]}\right] \quad [19]$$

$\epsilon_l < 0$, and $\gamma < 0$. Equations [17], [18], and [19] are approximately correct for the operation of the modified pH-stat at maximum gain, although no account is taken of the effect of the ionization constant of water on the transient behavior in the pH region near neutrality. Figure 6 shows a typical experimental result on the variation of the glass electrode potential with time during the adjustment action at maximum gain. The dashed line in Fig. 6 is a theoretical curve calculated by use of Eq. [18].

Since the amplifier output is independent of pH for $\epsilon(t) > \epsilon_l$, some difficulty may be experienced in the control of acidity near neutrality. Oscillations of pH and of current may occur because of a time lag in the response of the glass electrode to hydrogen ions liberated or consumed at the platinum electrode. A finite time of mixing is unavoidable, and the current "overshoot" produced by this means depends on the rate and mode of stirring and on the output current of the amplifier. Oscillations may be reduced or eliminated by providing more efficient stirring, by increasing the impedance of the cell (with external resistance, if desired) so that less current is produced at full output, or by reducing the gain of the amplifier.

In case the differential amplifier is operated at reduced gain, so that, for example, $\epsilon_l = \pm 10$ mv might be required to produce the full output, the transient behavior differs from that of Eq. [17] and [18] when $\epsilon(t) = V_g(t) - V_R = V_g(t) - V_g(\infty) < \epsilon_l$. The current through the platinum electrode is given by Eq. [20] instead of by Eq. [15], and the rate of

$$i(t) = -\frac{A}{Z}[V_g(t) - V_R] = -\frac{A}{Z}[V_g(t) - V_g(\infty)] \quad [20]$$

change of hydrogen ion concentration follows Eq. [21] instead of Eq. [16].

$$\frac{dC_{H^+}(t)}{dt} = \frac{(1-t_+)}{FV}i(t) = -\frac{(1-t_+)A}{FVZ}[V_g(t) - V_g(\infty)] \quad [21]$$

Integration of Eq. [21] with use of the relation, $V_g(t) = V_g(o) + \frac{RT}{F}\ln\left[\frac{C_{H^+}(t)}{C_{H^+}(o)}\right]$, leads to Eq. [22] for the variation of $C_{H^+}(t)$ with time. In Eq. [22],

$$li\left[\frac{C_{H^+}(t)}{C_{H^+}(o)}e^{+\frac{F}{RT}[V_g(o) - V_g(\infty)]}\right] = li\left[e^{+\frac{F}{RT}[V_g(o) - V_g(\infty)]}\right] - e^{+\frac{F}{RT}[V_g(o) - V_g(\infty)]}\frac{(1-t_+)ART}{F^2VZC_{H^+}(o)}t \quad [22]$$

$li(x) = \int_o^x \frac{d\xi}{\ln \xi}$ is the logarithmic integral (12). For $\epsilon(t) \geqq \epsilon_l$, the transient behavior is given by Eq. [17], while for $\epsilon(t) < \epsilon_l$, Eq. [22] applies.

The degree of control of the modified pH-stat in the presence of a corroding electrode or other reaction which produces or consumes hydrogen ions may be calculated from Eq. [23], where R_x (cf. Eq. [9]) is the rate

$$\frac{dC_{H^+}(t)}{dt} = \frac{(1-t_+)}{FV}i(t) + R_x \quad [23]$$

of increase of solution acidity due to the corrosion (or other) reaction (R_x is negative for a corroding metal). With $i(t) = -\frac{A}{Z}[V_g(t) - V_R] = -\frac{A}{Z}[V_g(t) - V_g(o)] = -\frac{ART}{ZF}\ln\frac{C_{H^+}(t)}{C_{H^+}(o)}$, the degree of control in the steady state attained after immersion of the corroding electrode into solution is given by Eq. [24].

$$\frac{C_{H^+}(\infty)}{C_{H^+}(o)} = e^{+\frac{F^2VZR_x}{(1-t_+)ART}} \quad [24]$$

Equation [24] shows that better control of acidity is obtained at high gain, but this advantage is counterbalanced by an increased tendency toward oscillation, as discussed above. The current in the steady state is given by Eq. [25], which is identical to Eq. [12]; both the potentiostat and the

$$i(\infty) = -\frac{FVR_x}{(1-t_+)} = \frac{i_{corr}}{(1-t_+)} \quad [25]$$

differential amplifier types of electrochemical pH-stat are useful for measuring corrosion rates of metals. The potentiostat type is inherently more stable than the modified or differential amplifier type, although the transient behavior of the latter is superior in certain cases. Both devices should prove to

be useful in situations whether automatic control of pH is important in studies on reaction kinetics.

Manuscript received April 22, 1963; revised manuscript received July 5, 1963. This paper was presented at the New York Meeting, Sept. 29-Oct. 3, 1963. The paper is based on work performed for the Office of Saline Water, U. S. Department of the Interior, at the Oak Ridge National Laboratory, Oak Ridge, Tennessee, operated by Union Carbide Corporation for the U. S. Atomic Energy Commission.

Any discussion of this paper will appear in a Discussion Section to be published in the June 1964 JOURNAL.

REFERENCES

1. J. B. Neilands and M. D. Cannon, *Anal. Chem.*, **27**, 29 (1955).
2. K. I. Wood, *ibid.*, **32**, 537 (1960).
3. M. Murayama, J. M. Conlon, and G. C. Riggle, *ibid.*, **33**, 1454 (1961).
4. L. Josefsson, C. E. Ryberg, and R. Svensson, *ibid.*, **34**, 173 (1962).
5. S. W. Thorne, *J. Sci. Inst.*, **39**, 593 (1962).
6. J. J. Lingane, "Electroanalytical Chemistry," p. 158, Interscience Publishers, Inc., New York (1958).
7. J. E. Breeze, Labs. Natl. Res. Council Can., Radio and Elec. Eng. Div. Rept. No. ERA-166 (1949), N.R.C. No. 1889.
8. W. B. Murray, *J. Am. Water Works Assoc.*, **51**, 1318 (1959).
9. R. G. Bates, *Chimia*, **14**, 111 (1960).
10. H. Gerischer and K. E. Staubach, *Z. Elektrochem.*, **61**, 789 (1957).
11. P. Delahay, in "Advances in Electrochemistry and Electrochemical Engineering," Vol. 1, p. 304, P. Delahay, Editor, Interscience Publishers, Inc., New York (1961).
12. K. J. Vetter, "Elektrochemische Kinetik," Springer-Verlag, Berlin (1961).
13. E. Jahnke and F. Emde, "Tables of Functions," p. 1, Dover, New York (1945).

SYMBOLS

A	gain of differential amplifier
β	convenient combination of kinetic parameters (cf. Eq. [4]), sec^{-1}
$C_{H^+}(t)$	hydrogen ion concentration, moles/cm^3
C_{H_2}	concentration of dissolved molecular hydrogen, moles/cm^3
D_a, D_c	diffusion coefficients of H_2 and H^+, cm^2/sec
δ_a, δ_c	hypothetical thicknesses of Nernst diffusion layer, cm
$\epsilon(t)$	difference between glass electrode potential and reference voltage of differential amplifier, v
ϵ_l	input voltage required for full output of differential amplifier, v
$\mathbf{F}$	Faraday's constant, coulombs/equivalent
γ	convenient combination of parameters (cf. Eq. [16]), moles/cm^3-sec
$i(t)$	net current through electrode interface, amp
i_{corr}	corrosion current of metallic electrode, amp
i_o	exchange current of the hydrogen gas-hydrogen ion reaction, amp
i_L	maximum output current of potentiostat, amp
i_l	maximum output current of differential amplifier, amp
K_w	ionization constant of water, moles^2/cm^6
$\bar{k}_a, \bar{k}_c$	electrochemical specific rate constants of anodic and cathodic partial processes, cm/sec
R	gas constant, joules/°K
R_x	rate of increase of hydrogen ion concentration due to corrosion (or other reaction), moles/cm^3-sec
S	electrode area, cm^2
T	absolute temperature, °K
t	time, sec
t_+	transference number of hydrogen ions
τ	time required to change glass electrode potential by $V_g(\infty) - V_g(o)$, sec
V	volume of solution, cm^3
$V_g(t)$	glass electrode potential *vs.* reference electrode, v
V_R	reference voltage of differential amplifier. v
$v_N(t)$	net flux of hydrogen gas-hydrogen ion reaction, moles/cm^2-sec
Z	cell impedance, ohms

On the Formation of Electrochemical Etch Pits on the (111) Face of Copper

Ugo Bertocci, L. D. Hulett, and L. H. Jenkins
Solid State Division, Oak Ridge National Laboratory,[1] Oak Ridge, Tennessee

ABSTRACT

In an effort to elucidate the role of defects on the anodic behavior of copper single crystals, information has been gathered about the etch pits formed at dislocations on the (111) face. Anodic etching has been carried out in chloride, chloride/bromide, bromide, and chloride/iodide solutions, with and without copper salt added, as well as in CH_3COOH, H_2SO_4, and $HClO_4$. In halide solutions dislocation pits have been found to be formed over a large range of current densities and solution compositions, whereas no preferential nucleation at dislocation intersections has been detected in other solutions. The role of small misorientations of the surface from (111), as well as the etching of (100) and (110) surfaces has also been investigated. The influence of such parameters as current density, solution compositions, and orientation of the copper surface on the formation and characteristics of such pits is discussed.

Several etchants which cause pits to be developed at points where dislocations intersect the surface of copper crystals have been developed (1-3). Although the reaction(s) occurring on the metal surface is electrochemical in character—for while the metal is oxidized to copper ions, an oxidizing agent such as Cu^{++}, Fe^{+++}, Br_2, $S_2O_8^{=}$, etc., is reduced at the surface—successful and reproducible methods for forming etch pits at dislocations by the application of an external emf have only recently been reported (4). Such a method is advantageous for not only can the anodic and cathodic reactions be separated in space, but also the magnitude of the current flowing and potential at the electrode can be controlled and/or measured.

[1] Oak Ridge National Laboratory is operated by Union Carbide Corporation for the United States Atomic Energy Commission.

A study of the correlation between such parameters at current density and electrode overpotential and the structure of metallic single crystals seems a promising method of investigating the role of defect structure upon the surface reactivity of metals. However, before more precise data are obtainable in any system, a certain amount of exploratory work is necessary. The following is a discussion, in rather general terms, of the initial results obtained in a study of some of the parameters affecting the formation of etch pits at dislocations, largely in HCl and HBr mixtures. A more specific and quantitative aspect of the work, the kinetics of the growth of etch pits, has been reported by Young and Hulett (5).

Experimental Method

Solutions used in this study were prepared from reagent grade materials and singly distilled water from a tin-lined still. Copper single crystals, grown from the melt in graphite crucibles, were prepared from polycrystalline 99.999% material supplied by American Smelting and Refining Company. Most of the observations which follow were made on crystals 1 x 2 x 0.1 cm with the preferred orientation on the large 1 x 2 cm area. The dislocation density in an average specimen was $\sim 5 \times 10^6$ cm^{-2}.

The preparation and handling of such samples, including cutting and lapping by acid baths, has been described previously (6, 7). It is only necessary to repeat that the methods used to prepare surfaces for study did not introduce appreciable numbers of new dislocation into the samples. The final treatment given any oriented surface just prior to experimentation consisted of a 30-min polish in an acid copper phosphate bath followed by washing in a stream of distilled water. All the data discussed below were obtained under galvanostatic conditions at room temperature, and all current densities referred to throughout are based on geometric electrode areas.

After electropolishing and washing, the surface being tested was dried in a jet of oxygen, and the sample then was immersed in the solution contained in the test cell. Current was then passed through the system for the desired time, and the sample was removed, washed, dried, and finally the surface examined by optical microscopy.

In some instances it was desirable that the solution be free of any dissolved oxygen. This was accomplished by bubbling Matheson HP grade nitrogen through the system. After oxygen had been removed, the system was momentarily opened and the copper sample inserted quickly while vigorous flow of nitrogen was continued so that re-introduction of oxygen in the solution was held to a minimum.

Experimental Results

Most of the observations which follow relate to the anodic attack of (111) oriented surfaces in mixtures of HCl and HBr, although some data obtained in other solutions and/or from different orientations are included. As was anticipated from chemical etching experiments, pits formed easily at dislocations on surfaces subjected to anodic polarization in the former solutions. Among other parameters, the effects of current density, concentration of solution components, and the influence of slight surface misorientation from a true (111) on the pitting process have been studied.

Current density and solution composition.—In mixtures of HCl and HBr the range of current densities in which pits developed at dislocations—the characteristic pattern of attack in such mixtures—was reasonably wide. At concentrations of HBr between 0.1 and 0.5M, varying the concentration of HCl in the range 2-6M had little detectable effect other than to increase the maximum current density allowable before precipitation occurred at the anode. The minimum current density at which pits could be developed apparently was set by the experimental method since at lower current densities the presence of oxygen in solutions complicated interpretation of results. In HCl-HBr solutions which were free of oxygen, pits have been developed at current densities as low as 0.1 ma cm^{-2}. As stated previously, the maximum current density was determined by the precipitation of salt at the electrode and was therefore dependent on concentrations, stirring, and time. Considering these factors, the maximum current density allowable varied from $\sim$80-150 ma cm^{-2}.

It was also possible to obtain pits at dislocations on surfaces exposed to solution of 2-6M HCl. The range of current densities at which pits could be developed in 2-6M HCl was relatively narrower than in HCl-HBr mixtures. The observed upper limit of $\sim$2-5 ma cm^{-2} was shifted toward the higher values by stirring. This maximum was not limited by salt precipitation, but presumably by the no longer favorable rate of dissolution at the pits as compared with the remainder of the surface. The minimum current density at which pits could be obtained in oxygen-free solutions of HCl was $\sim$50 μa cm^{-2}, slightly lower than in chloride-bromide mixtures.

Solutions of HCl which were free of dissolved oxygen and which contained complex ions of copper in equilibrium with copper metal had an adverse influence on the formation of pits at dislocations. It was determined that a concentration of copper as low as 0.05M in 2M HCl was generally large enough to prevent pit formation. This result is in agreement with the observed effect of stirring, so that it can be surmised that in order to have pitting at dislocations a certain concentration of Cu^+ containing complexes should not be exceeded in the vicinity of the copper surface.

Results very similar to those observed in HCl were obtained in KCl solutions of the same chloride concentration and in which the pH had been adjusted to 1 with HCl.

Solutions of HBr in the range of 2-6M produced results not greatly different from those obtained in mixtures of HCl and HBr, and it was observed that copper concentrations as high as 0.6M in 5M HBr did not prevent pit formation.

Pit geometry.—In all cases the symmetry axis of the pyramid bounding an etch pit was in the [111] direction; that is to say, the axis was independent of

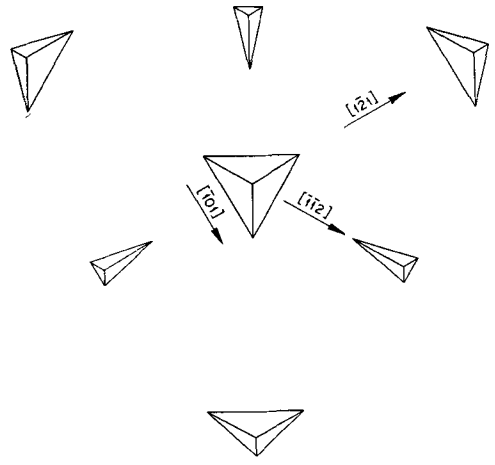

Fig. 1. Schematic diagram of etch pits formed around the (111)

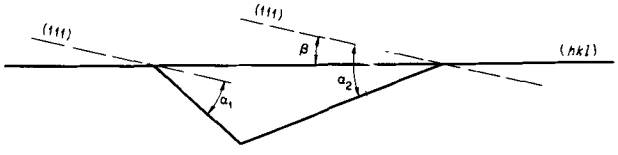

Fig. 2. Relationship between etch pit structure and crystal orientation.

the misorientation of the surface from the true (111). However, the shape of the triangle created on the surface by the intersection of the surface plane with the pit was dependent on slight surface misorientations. The effect of these symmetry limitations on the shapes of etch pits is illustrated schematically in Fig. 1. The center of the diagram represents a pit formed on a surface oriented exactly (111), and the asymmetry of pits formed on surfaces slightly misoriented from the (111) in the directions shown is illustrated. The end result of such symmetry restrictions is that there is an approximately triangular area around the exact (111) orientation on which dislocation pits having threefold symmetry can be formed. This area can be defined in the following way: Consider the profile of a pit (Fig. 2) resulting from the cutting of a pit on a surface by a plane which, in addition to passing through the vertex of the pit, is also normal to the actual (hkl) surface as well as the (111) nearest that surface. The sides of such a pit form angles α_1 and α_2 with the (111) plane which is at an angle β to the (hkl). The value of either α_1 or α_2, the choice being determined by the sign of β, establishes the limit of allowable misorientation since a pit can form on an (hkl) only if β is smaller than the limiting α value.

It was possible to determine experimentally the limits of allowed misorientations. This was accomplished by measuring with the microscope the limited area around the (111) pole of spherical crystals on which etch pits could be developed. Figure 3 illustrates such a typically pitted area. The extent of this restricted area of pit development was termed "angular spread," and its variations with current density and solution compositions were studied. Observations were made in 6M HCl solutions with HBr concentrations ranging from 0.1 to 0.5M. The results of some of the angular spread measurements are shown in Fig. 4. It is readily seen that the area

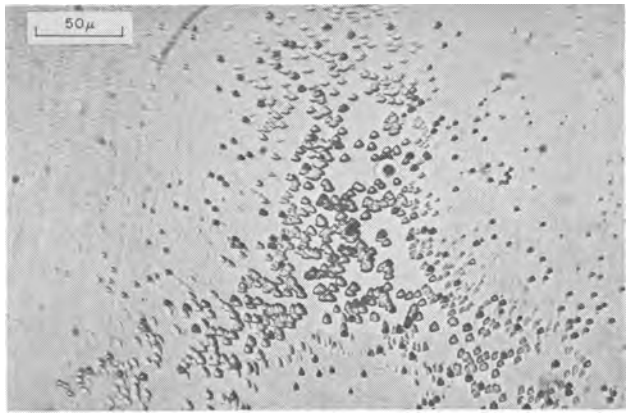

Fig. 3. Pitted area surrounding the (111)

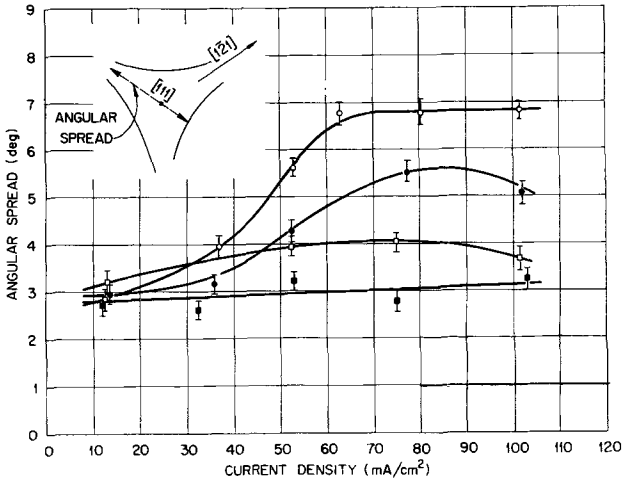

Fig. 4. Extent of pitted area as a function of current density and bromide ion concentration: ■, 6M HCl-1.1M HBr; □, 6M HCl-0.50M HBr; ●, 6M HCl-0.25M HBr; ○, 6M, HCl-0.1M HBr.

over which pits can develop increases with increasing current density and decreasing bromide ion concentration. Also, it appears that a maximum occurs in the range of 80-100 ma cm^{-2}. It should be noted that orientation requirements are rather severe in this system for the greatest allowable deviation from the (111) in any given direction is ~4°.

For any one solution, the applied current density also plays a relevant role in determining the shapes of pits. At low current densities they exhibit a hexagonal contour like that shown in Fig. 5a, whereas at higher current densities the pits approach more closely a true triangular shape (Fig. 5b).

Kinds of pits.—Two types of pits with approximately equal widths, but considerably different depths, were observed. The ratio of the slopes of the two kinds of pits can be measured using interference methods. Such a ratio varies somewhat with experimental conditions, and its average value is about 1.5. If the microscope is fitted with an interference contrast device, the two kinds of pits can be easily recognized by the different colors of their sides. To test whether the two types of pits correspond to aged and fresh dislocations,[2] new dis-

[2] Dislocations introduced in the specimen at near room temperature, and never subjected to annealing, are termed "new" or "fresh"; in particular, they are supposed to have a concentration of impurities around them not significantly different than the concentration in perfect regions of the crystal. For this reason they are sometimes called "clean" dislocations, as opposed to "grown-in" or "aged" dislocations.

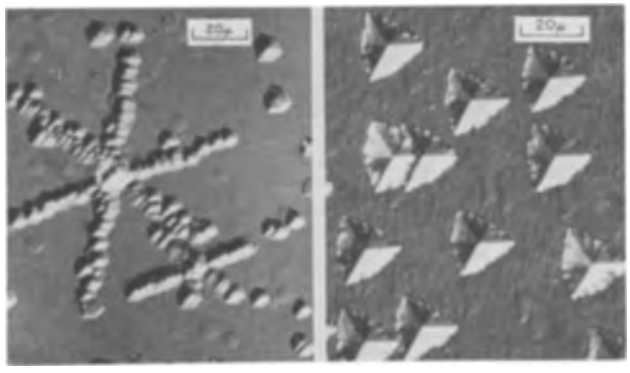

Fig. 5. Etch pits at dislocations obtained in a 4.3M HBr solution containing 0.65M CuBr: (a) (left) after 24 min at a current density of 0.5 ma cm^{-2}; (b) (right) after 25 sec at a current density of 50 ma cm^{-2}.

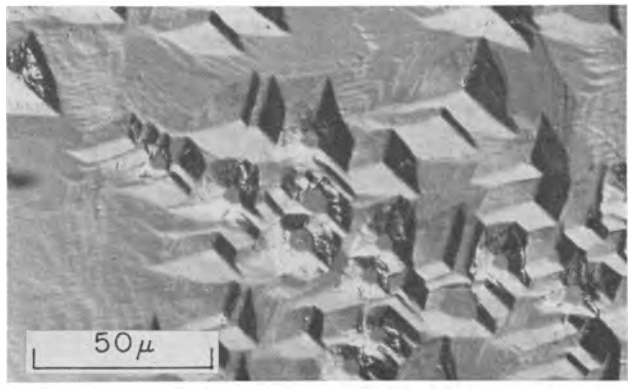

Fig. 6. Pits after dissolution for 2 min in 6M HCl + 0.5M HBr at 2.0 ma cm^{-2} followed immediately by electrolysis for 1 min in 3M HCl at the same current density.

locations were introduced in specimens by dropping carborundum particles on the surface in the manner of Livingston (3). On etching, these new dislocations produced both the shallow and deep pits previously observed. Moreover, the dislocations were arrayed in star-shaped patterns like those obtained by Livingston in which the two different types of pits were interpreted by him to be caused by dislocations of opposite sign. However, since all pits tended to become shallower with decreasing current densities, as the lowest current densities at which pits could be produced were approached, the shallow kind of pits did not develop. Thus, star-shaped arrays of pits (Fig. 5a) could be seen in which the legs of the stars were formed of one, rather than the usual two, row of pits. At any rate, it was clear that the two types of pit did not result from different concentrations of impurities at dislocations.

Also, it was observed that in solutions containing only HCl both fresh and grown-in dislocations caused pits to be formed. However, instead of finding the two kinds of pits found at higher current densities in the HCl/HBr mixtures, all pits appeared to have approximately the same depth and width.

It was found that only dislocations which produce shallow pits in HCl/HBr mixtures give rise to pits in HCl. For instance, if a (111) surface is etched first in HCl and subsequently in a HCl/HBr mixture, new pits are formed in the second etching, all of them of the deep kind, whereas the pits formed in the first etching grow larger during the second electrolysis, but their slopes are smaller than the slopes of the smaller pits. Conversely, if the specimen is first etched in HCl/HBr mixture and then in HCl, pits of the deep kind develop flat bottoms. Figure 6 shows the result of such an experiment. No explanation for such a phenomenon can be advanced at this time, but this point is particularly interesting since one might hope to develop solutions which are selective for certain kinds of structural defects.

Other systems.—Less detailed information has been gathered about other systems. When added to 2-6M solutions of HCl or KCl, concentrations of iodide ion as low as 10^{-5}-10^{-3}M greatly enhanced the ease with which etch pits were nucleated. While pitting was observed in iodide-chloride mixtures at current densities varying from 0.1 to 20 ma cm^{-2}, pit formation was not hindered, as in chloride solutions, by the presence of Cu^{+}.

Pits associated with dislocations also were formed in mixtures of NH_4OH and NH_4Br. For example, well-developed pits were obtained in the range 1.0-50 ma cm^{-2} in a 4.5M NH_4OH solution containing 0.5M NH_4Br. Since $(NH_4)_2S_2O_8$ causes pits to develop at dislocations in solutions containing NH_4OH and NH_4Br (2), the previous result had been anticipated.

Clear-cut results were obtained neither in ammonia or KCN, nor in their mixtures; although there was a tendency to form pits, such pits did not seem to be related to dislocations. $HClO_4$, H_2SO_4, and CH_3COOH were tested for enhanced activity at dislocations with negative results. An interesting experiment consisted of dissolving anodically a Cu (111) surface in a solution which produced pits at dislocations; the current was then stopped, the solution quickly removed and replaced with an $HClO_4$ solution. When the current was switched on again, it was observed (see Fig. 7) that the pits previously formed developed flat bottoms, showing that no preferential nucleation of new steps occurred at the dislocation intersection under the latter conditions. Moreover, the fine structure of the sides of the pits also changed. Since the pits keep growing when the specimen, after removal and rinsing, is put back into a solution where dislocation pits can be formed, the development of flat bottoms cannot be attributed to

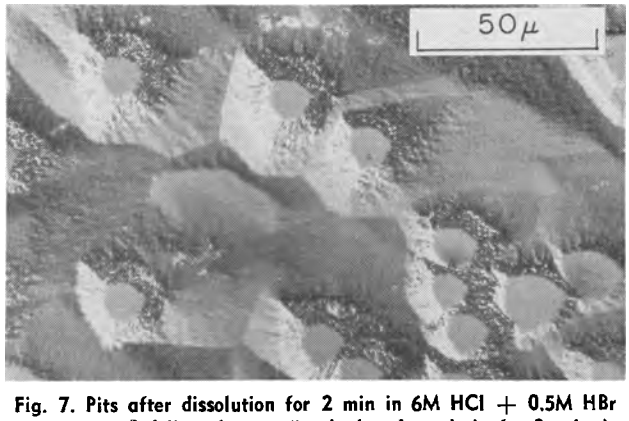

Fig. 7. Pits after dissolution for 2 min in 6M HCl + 0.5M HBr at 5 ma cm^{-2} followed immediately by electrolysis for 3 min in 2M $HClO_4$ at the same current density.

contamination of the surface during the transfer from one solution to another.

In addition to experiments on the (111), some work has been done on (100) and (110) surfaces. Etch pits at dislocations can be developed by anodic attack on these surfaces also. Dissolution of (100) surfaces in an acid chloride-bromide solution produces etch pits at dislocations. However, the pit pattern has a large amount of random faceting which makes interpretation difficult. Subgrain boundaries are clearly delineated as rows of square pits, but isolated pits are sometimes difficult to distinguish from the surrounding square facets. Subgrain boundaries on the (110) were preferentially etched anodically in HCl solutions at current densities ~2 ma cm^{-2}.

Discussion and Conclusions

It has been assumed throughout the previous presentation that there is a correspondence between the dislocations intersecting the surface and the pits developed. This assumption is not as gross as first appears for not only were the pitting patterns Livingston obtained with a chemical etch after dropping carborundum particles on a (111) surface of copper duplicated, but dislocations introduced by surface indentations, bending, etc., could also be detected as etch pits. Moreover, no significant difference in etch patterns was observed whether crystals were etched anodically in the presence of bromide ions or using the chemical etch of Lovell and Wernick (1), which has been shown to produce etch pits at dislocations. It is not certain, however, that all dislocations intersecting the surface were revealed as etch pits, even though it was demonstrated that both clean and aged dislocations, as well as edge dislocations of opposite sign, could form etch pits. It is only reasonable in view of these results and those of others (1-3) to assume that the difference between the number of dislocations present and those forming pits is certainly less than an order of magnitude.

Although considerable effort was expended in attempting to achieve a uniform current density over the electrode, visual inspection of etched surfaces indicated rather clearly that local current densities were highly dependent on small misorientations from a close-packed surface. There seemed to be a direct relationship between local current densities and the number of atom steps on the immediate surface. The latter obviously is a function of the degree of misorientation from a low index face. Therefore, average values of current density which were calculated from current readings and geometric surface areas do not correspond to local values. This is particularly true of experiments performed on single crystalline spheres, but also on flat specimens as well since even in the latter case local fluctuations in orientation of ½° were observed.

The conclusions which can be drawn from experimental observations of the qualitative nature of those reported here must necessarily be rather unsophisticated. However, some comments concerning enhanced dissolution at dislocations and the geometric surface patterns developed can be made. Results obtained in other than halide solutions indicate that the dissolution of copper as Cu^+ is a necessary, but not a sufficient, condition for etch pits to be formed at dislocations. Since in the final analysis a pit is formed only if there is locally an increased rate of dissolution over that of the remainder of the surface, it is not obvious that anodic removal of Cu^+ rather than Cu^{++} would enhance pit formation. A not improbable explanation is that the process is very sensitive to the presence of copper ions near the electrode surface, and a major role of the halides is to serve as complexing agents which effectively reduce the concentration of free copper ions. Such an explanation is in agreement with the observation that the addition of bromide ions, a more effective complexing agent, to the chloride systems promotes the formation of pits.

However, the complete function of bromide ions seems to be much more complex than that of simply decreasing the activity of copper ions in the vicinity of the electrode. Explanations of such phenomena as the appearance of deep pits when bromide was added to a chloride system which had produced pits only of the shallow kind seem to require some concept of a direct interaction between bromide ions and the metal surface. Also, the observations of parameters affecting the angular spread of the pitted area around the (111) pole indicated that approximately equivalent surface changes were obtained if either the current density was increased or the bromide ion concentration decreased. Since bromide ions, in particular, appear to exhibit the most favorable properties for inducing the development of etch pits at dislocations over a reasonably wide range of conditions, either or both of the preceding proposals seem reasonable.

It is also true that the geometry of etch pits and the relationship to small misorientations of the surface from the (111) can be accounted for by equally elementary assumptions such as: the velocity vectors of noninteracting surface steps have the same symmetry as the surface. However, no single approximation accurately describes all the experimental observations. It is most probable that the ultimate explanation will be based on complex interactions of several parameters, and it is hoped that work now in progress in this laboratory will contribute to clarifying the situation and permit a more rigorous and quantitative treatment.

Manuscript received May 7, 1963. This paper was presented at the Boston Meeting, Sept. 16-20, 1962.

Any discussion of this paper will appear in a Discussion Section to be published in the June 1964 JOURNAL.

REFERENCES

1. L. C. Lovell and J. H. Wernick, *J. Appl. Phys.*, **30**, 590 (1959).
2. F. W. Young, Jr., *ibid.*, **32**, 192 (1961).
3. J. D. Livingston, "Direct Observation of Imperfections in Crystals," J. B. Newkirk and J. H. Wernick, Editors, p. 115, Interscience Publishers, New York (1962).
4. B. Sestók, *Czech. J. Phys.*, **9**, 339 (1959); L. H. Jenkins and J. O. Stiegler, *This Journal*, **109**, 467 (1962).
5. F. W. Young, Jr. and L. D. Hulett, In press.
6. L. H. Jenkins, *This Journal*, **107**, 371 (1960).
7. F. W. Young, Jr. and T. R. Wilson, *Rev. Sci. Inst.*, **32**, 559 (1961).

Oxide Structures Produced on Iron-Chromium Alloys by a Dissociative Mechanism

C. T. Fujii and R. A. Meussner

Physical Metallurgy Branch, Metallurgy Division, United States Naval Research Laboratory, Washington, D. C.

ABSTRACT

The oxidation of Fe-Cr alloys (1 to 15 wt % Cr) in a $0.1H_2O$-0.9Ar atmosphere at 700°-1100°C produces a characteristic two-layer scale overlaying a thin subscale. The outer wüstite scale is extensively detached from the inner scale containing an Fe-Cr spinel phase in a wüstite matrix. Phase identification by x-ray diffraction, chemical analyses by conventional and electron microprobe techniques, and detailed metallographic studies have shown these structures to be consistent with the phase equilibria of the Fe-Cr-O constitution diagram. The extensive detachment of the outer wüstite scale layer and the continued high rate of oxidation of these alloys after such detachment occurs suggest that a dissociative process is responsible for the maintenance of this high oxidation rate. The experimental evidence for this process is presented, the importance of such a mechanism is discussed, and examples of other gas-metal systems in which a similar process has been recognized are cited.

The high-temperature oxidation of Fe-Cr alloys, containing insufficient Cr to provide and maintain a protective chromic oxide layer, produces oxides and scale structures which depend greatly on the nature of the oxidizing atmosphere. The scale structures produced in oxygen or air are very complex indeed. Such structures have been described by Birchenall and his colleagues (1) and differ markedly from the uniformly consistent and characteristic scale structure observed when water vapor is the oxidizer. In oxygen, rhombohedral phases of α-Fe_2O_3 and Cr_2O_3 or solid solutions of these two oxides are prominent. These higher oxides generally are not observed in water vapor, but instead wüstite, FeO, appears as the major oxidation product. Only under the most favorable conditions of alloy composition, oxidation temperature, and time are significant amounts of wüstite found in the scales formed in oxygen. In the absence of wüstite, these scale layers of spinel and rhombohedral phases are rather brittle even at the oxidation temperature, and metallographic and kinetic evidence indicate that cracking of the scale occurs during its growth. As a consequence, the oxidation rates are irregular and unpredictable and the structure of the scale is complex and nonuniform (1).

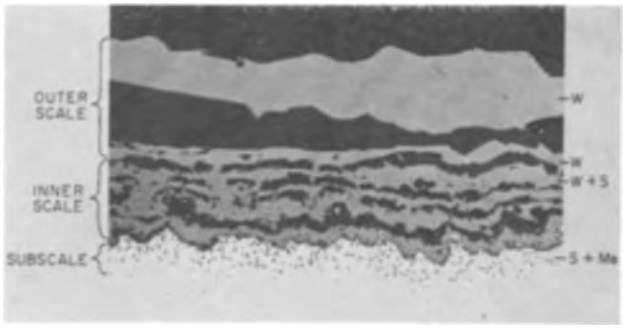

Fig. 1. Oxide structure produced on an Fe-5Cr specimen oxidized for 20 hr at 1100°C in a 0.1 H_2O-0.9 Ar atmosphere. Unetched. Magnification 105X.

In contrast, the scale structures observed in Fe-Cr alloys oxidized in water vapor differ in that a characteristic two-layer oxide structure and a subscale are always produced. Figure 1 is an example of the microstructure of an Fe-5Cr specimen oxidized at 1100°C. Quite similar structures are observed on specimens containing 1-15 weight per cent (w/o) Cr when oxidized in water vapor at temperatures between 700° and 1100°C. As shown in the figure, three distinct oxidation zones are formed: (i) an outer wüstite layer, (ii) an inner, porous, two-phase layer of wüstite and an Fe-Cr spinel, and (iii) a subscale containing Cr rich oxides. Ipat'ev and Sibirskaya (2) have observed this scale structure on Cr steels oxidized in water vapor at 1000°C. Wood and Melford (3) have demonstrated that this characteristic structure is formed in as little as 10-30 min during the oxidation of Fe-14Cr specimens at 950°-1000°C in steam.

The results of a detailed examination of this characteristic scale structure are presented in this paper. While these observations indicate the nature of the oxide growth mechanism, kinetic data (to be presented in a subsequent paper) are required to substantiate the detailed mechanism. The present discussion of the mechanism will thus be limited, and a more complete treatment of this problem will be given in the succeeding paper.

Experimental

Binary Fe-Cr alloys of the compositions shown in Table I were prepared from high-purity electrolytic metals by vacuum melting and casting. The resulting ingots were forged and rolled hot to 1 in. diameter rods which were shown to be homogeneous by chemical analysis of samples obtained from dif-

Table I. Chemical analysis of Fe-Cr alloys

Element	Per cent of element in the alloy				
	Fe-1Cr	Fe-5Cr	Fe-10Cr	Fe-15Cr	Fe-20Cr
Cr	0.99	5.0	9.9	14.8	19.5
S	0.007	0.010	0.010	0.008	0.008
P	0.004	0.004	0.006	0.007	0.003
Si	0.02	0.04	0.05	0.04	0.05
Mn	0.01	0.04	0.06	0.08	0.07
O*	—	0.027	0.024	0.031	0.035
N*	—	0.0010	0.0019	0.0028	0.0037

* The oxygen and nitrogen contents were determined by vacuum fusion. The amount of these elements in the Fe-1Cr alloy were not determined.

ferent radial and longitudinal portions of the rods. The variation in Cr content among these samples of each of the alloys was less than ±0.1%. Metallographic examination of a cross section of each rod revealed no evidence of microsegregation and a low population of chromic oxide particles.

The specimens used for the present studies were 1/16 in. thick disks, 7/8 in. in diameter. The specimens, surface ground on both faces, were vacuum annealed (10^{-5} mm Hg) for 24 hr at 1050°C. Before being oxidized, the specimens were chemically cleaned in a dilute sulfuric-hydrochloric acid solution and rinsed successively in a 5% sodium cyanide solution, water, and acetone.

The oxidation atmosphere was produced by passing purified argon through two water-filled, fritted-disk bubblers, followed by a spray trap, all of which were immersed in a constant temperature bath. The temperature of the bath was 46.2° ± 0.2°C which saturated the argon with water vapor at a pressure of 76 mm Hg or 0.1 atm. Prior to saturation with water vapor, the argon was purified by successive passage through (i) a chromous sulfate solution, (ii) two dry ice-acetone traps, and (iii) an anhydrone-ascarite drying tower. The argon flow rate was regulated at 175 ± 10 ml/min for the experiments in this investigation.

All of the experiments were started by preheating the chemically cleaned specimens to the oxidation temperature in dry argon before admitting the water vapor. The argon was sufficiently purified and dried so that no measurable weight changes in the specimens (±0.5 mg) were detected during the preheating periods of 5-15 min. To terminate an experiment, the water vapor saturator was bypassed and a flow of pure, dry argon was maintained while the specimens were withdrawn into the cool (60°C) end zone of the oxidation chamber.

After examining the external surface structure and removing adequate samples of the two oxide layers for x-ray diffraction and chemical analyses, the remainder of the specimen was vacuum impregnated and mounted in an epoxy resin for metallographic study. This procedure provided samples for the three analytical techniques from the same specimen and thus should avoid any ambiguity among these data.

Observations and Results

During the steady-state growth of the oxides, equilibrium is not attained in all parts of the system.

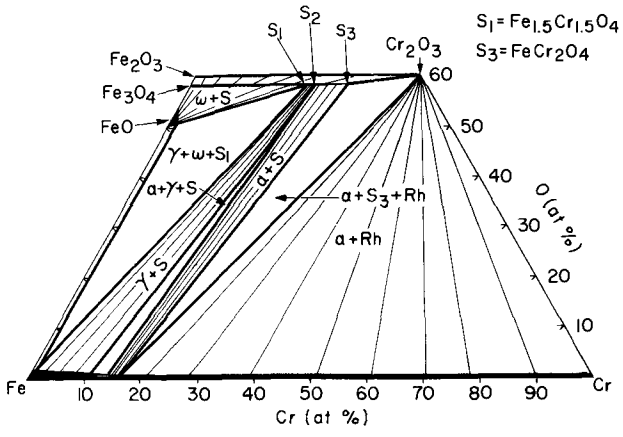

Fig. 2. Phase equilibria in the Fe-Cr-O system for temperatures between 920° to 1300°C.

However, the structures observed in these specimens can be related to the phase equilibria of the Fe-Cr-O constitution diagram. An isothermal section of the diagram, as recently revised by Seybolt (4), is shown in Fig. 2 where α and γ refer to the metallic phases and W, S, and Rh refer to the wüstite, spinel, and rhombohedral oxide phases, respectively. This arrangement of the phase fields is valid at temperatures above 910°C. Between this temperature and 830°C, a four-phase reaction (class II) between the $\alpha + \gamma +$ W and $\gamma +$ W + S_1 three-phase fields occurs producing phase fields of $\alpha +$ W + S_1 and $\alpha + \gamma + S_1$. At approximately 830°C the $\alpha + \gamma + S_1$ and $\alpha + \gamma + S_2$ fields merge as the limiting tie line of the $\gamma +$ S region. Seybolt has determined the compositions of the spinel phase at S_1 and S_3 to correspond to $Fe_{1.5}Cr_{1.5}O_4$ and $FeCr_2O_4$ at 1300°C. Because of the difficulty in determining the composition of the spinel phase from x-ray data alone (5) and because this phase never appeared in the experimental specimens as a single phase layer, the compositions of the spinel have not been determined in this study, but rather, it is assumed that the S_1 and S_3 compositions do not change rapidly with temperature. The solubility of Cr in wüstite has never been determined, but it is generally accepted as being very small (1). Similarly, the exact compositions of the metallic phase in equilibrium with these oxides are not well established. The concentration of Cr in Fe in equilibrium with W (the dilute solution of Cr in FeO) is assumed to be very small[1] and the compositions of the other metallic phases are inferred from the Fe-Cr binary diagram (6).

Microstructures

As shown in Fig. 1, the characteristic oxide structure of these specimens can be conveniently divided into three zones for this discussion of the microstructures. These zones are the subscale, the inner scale, and the outer scale. In addition, the alloy adjacent to the subscale is somewhat depleted of Cr and thus may be considered a reaction zone.

The alloy.—As a consequence of the precipitation of chromium-rich oxides in the subscale, the matrix in that zone is depleted of Cr. Diffusional flow of Cr

[1] The data presented in the paper by Birchenall *et al.* (1) might indicate this composition to be near 0.2 w/o Cr, but the scaling processes in oxygen are very complex.

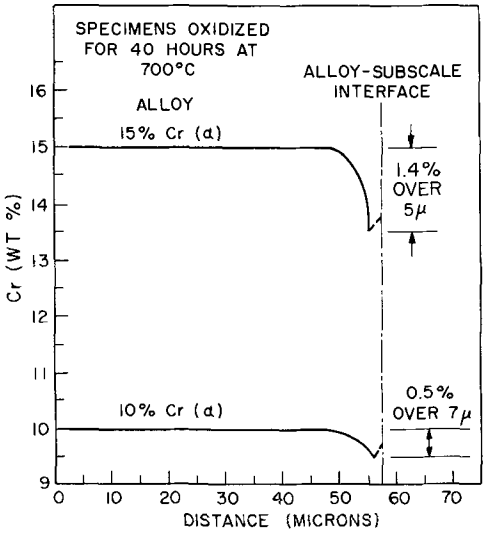

Fig. 3. Summary of electron microprobe data of the Cr depletion in Fe-Cr alloys oxidized for 40 hr at 700°C in a 0.1 H_2O-0.9 Ar atmosphere.

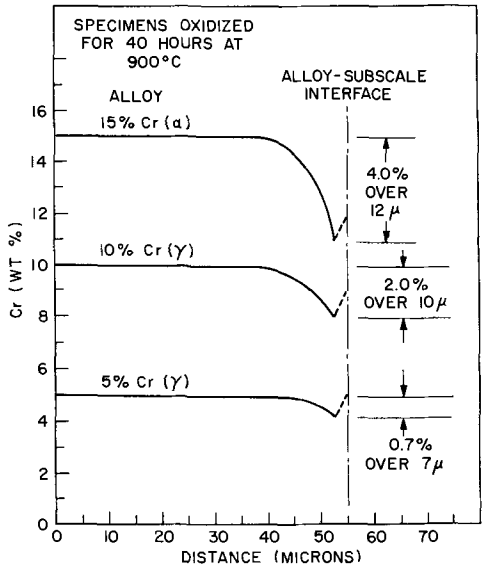

Fig. 4. Summary of electron microprobe data of the Cr depletion in Fe-Cr alloys oxidized for 40 hr at 900°C in a 0.1 H_2O-0.9 Ar atmosphere.

from the interior of the alloy occurs and the growth of the subscale continues. Preliminary electron microprobe analyses of several specimens have shown that the zone beyond the subscale showing Cr depletion is rather narrow. The results from specimens oxidized at 700°, 900°, and 1100°C are summarized in Fig. 3, 4, and 5, respectively. In these figures each curve represents an average of several probe scans normal to the oxide interface.

At 700°C all of these alloys are ferritic and the Cr depletion increases with the Cr content of the alloy. At this temperature, there was no measurable Cr depletion in the Fe-5Cr specimen. At 900° and 1100°C the 5 and 10 w/o Cr alloys are austenitic and again the depletion characteristics reflect the increased driving force of the chemical gradient with increasing Cr content of the alloy. The 15 w/o Cr alloy remains ferritic at all temperatures, but at 900° and 1100°C the depletion of Cr from this alloy generates an austenitic surface layer. The observed

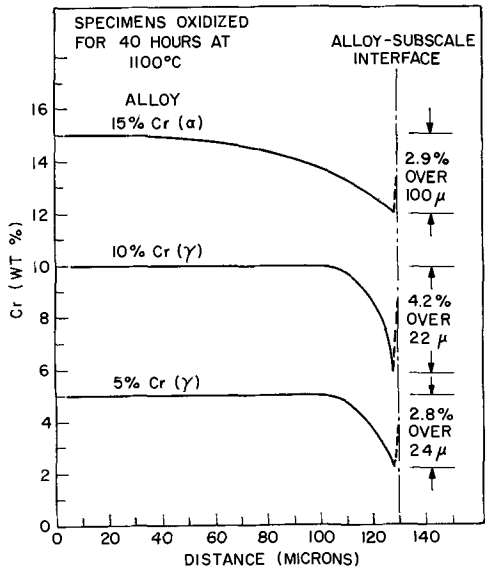

Fig. 5. Summary of electron microprobe data of the Cr depletion in Fe-Cr alloys oxidized for 40 hr at 1100°C in a 0.1 H_2O-0.9 Ar atmosphere.

Cr contents at the alloy:subscale interface for these two specimens, 11.9 and 10.8 w/o Cr at 1100° and 900°C, respectively, agree very well with the compositions of the α : $\alpha + \gamma$ phase boundary of the binary Fe-Cr system (6). Although somewhat complicated by the change in the limiting composition of the ferrite field with temperature, a comparison of the Cr depletion curves for the 15 w/o Cr alloy and those of the 5 and 10 w/o Cr alloys at 900° and 1100°C clearly reflects the higher diffusion rates in the ferritic material (7). These results from this preliminary survey of these oxidation specimens are substantially in accord with the recent microprobe data published by Wood and Melford (3) and Birchenall *et al.* (1).

As indicated in the curves of Fig. 3, 4, and 5, the Cr content detected by the microprobe reached a minimum at a position 3-5μ from the apparent subscale boundary. The uncertainty in the microscopic definition of this boundary and the resolution limits of the microprobe instrument precluded a more precise analysis of the alloy:subscale interface.

The subscale.—The structure within the subscale can be rather complex. Specimens of moderately high Cr contents, when oxidized at high temperatures, may show a sequence of structures indicated by the following phase equilibria: α, α + Rh, [α + Rh + S_3], α + S, [α + S_2 + γ], γ + S, [γ + S_1 + W]. Under the isothermal conditions of these oxidation experiments the three-phase equilibria, enclosed in square brackets above, should appear only as interfaces. The final three-phase field (the first to involve wüstite) is represented by the boundary between the subscale and the inner scale of the specimen. In the alloys used in this study, only the 15 w/o Cr should show the structures indicated by the above sequence of phase equilibria. As the Cr content of the alloy is decreased, fewer of the phase fields are accessible, and the subscale structure should become simplified. Alloys containing 10 w/o Cr or less will be fully austenitic at high tempera-

ture and the subscale will then contain only γ, γ + S, [γ + S_1 + W].

Metallographic studies of the 15 w/o Cr alloys oxidized at 1100°C revealed phase distributions fully in accord with the equilibria of the phase diagram. Etched sections of these, illustrated in Fig. 6, showed evidence of the existence of the γ + S zone during oxidation. Thin sections of these structures, in which the transmission colors and optical characteristics of the oxide particles were examined, confirmed these observations. The oxide particles in the inner zone of the subscale (α + Rh) were green in color and displayed the optical characteristics of the rhombohedral phase in polarized light while the zones nearer the subscale:inner scale boundary (α + S and γ + S) contained orange-brown spinel particles. Some of these particles contained unreacted rhombohedral cores (see Fig. 6a). The wüstite of the inner scale layer was opaque, but the spinel particles in this layer again showed the same orange-brown transmission color.

The alloys of lower Cr contents were examined by these same techniques. No evidence of γ formation in the subscale was detected in etched sections of either the 10 or 5 w/o Cr alloys. While identification of the oxide particles by transmission in thin sections was impaired by the smaller size of the oxide particles in these subscales, where transmission could be observed the orange-brown color indicated that the oxide was the spinel. However, a thin zone containing the green oxide, presumed to be the rhombohedral phase from this color, was detected along the inner edge of the subscale in the 10 w/o Cr alloy. Since the γ + Rh phase field should not be encountered in the oxidation of alloys of such low Cr content, it is suggested that during cooling excess oxygen from the metallic phase may convert this high Cr spinel to the rhombohedral phase of essentially unaltered Fe/Cr ratio.

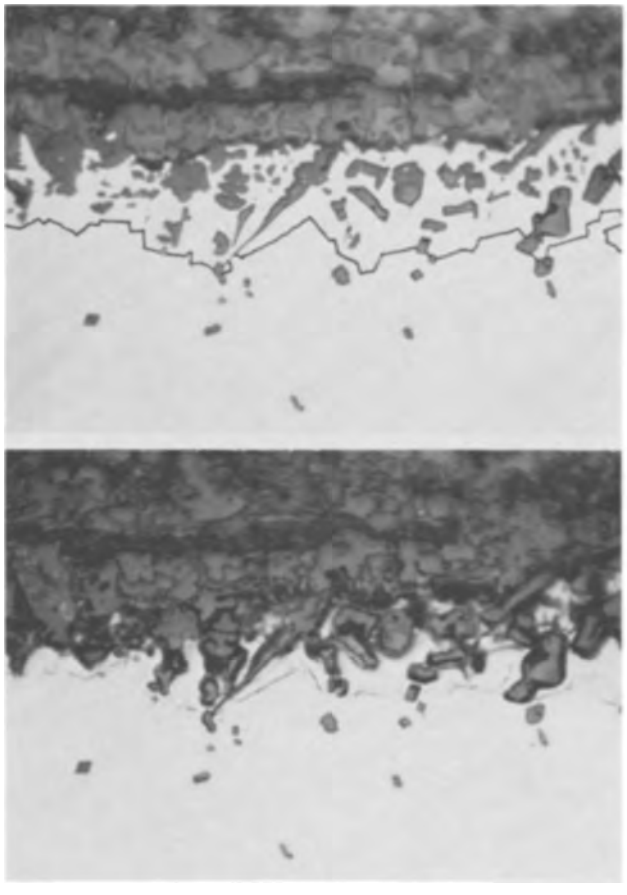

Fig. 6. Microstructure of the subscale region in an Fe-15Cr specimen oxidized for 7 hr at 1100°C in a 0.1 H_2O-0.9 Ar atmosphere. (a) (top) Unetched (with the location of the "γ" boundary of Fig. 6b sketched in): showing the partial conversion of rhombohedral to spinel in the "γ" + S zone; (b) (bottom) etched (1% picral): revealing the location of the α:γ boundary during oxidation. Magnification approximately 500X.

The microstructure of the subscale varied with both the Cr content of the alloy and the temperature of oxidation. The subscale formed at 700°C was very thin and contained only fine oxide particles. With increasing Cr content of the alloy the population of particles increased. In all of the alloys oxidized at this temperature there was a preferential growth of oxides along the grain boundaries and, probably as a consequence of the local Cr depletion, a more rapid conversion of the subscale to inner scale at these sites. At 900°C the subscale was, in general, thicker and the oxide particle size larger but more varied than at 700°C. Again, the population rather than the average particle size appeared to increase with increasing Cr content of the alloy. The strong preference for oxide formation along grain boundaries and the resulting accelerated attack at these sites, so prominent at 700°C, was evident only in the lower Cr alloys. The subscales formed at 1100°C were thick and the oxide particles were rather massive and of irregular form. As a consequence of the large size and low population of the particles the inner boundary of this zone was less clearly defined than in the other specimens, but there appeared to be very little preferential grain boundary oxidation in any of the alloy compositions at this temperature.

The inner scale.—During the growth of the scale layers the matrix of the subscale is converted to oxide and the spinel particles of the subscale are transferred to the inner scale. Although it is suspected that a small amount of Cr dissolves in the wüstite, this should not alter the growth mechanism of this oxide. Since the growth of wüstite is by cation migration, the spinel particles should accumulate at the subscale:inner scale interface. Such an accumulation of these markers does not occur to any appreciable extent. Rather, the growth of wüstite at this interface is disrupted by microspalling or cracking of the oxide, and the spinel markers are carried with the wüstite. The forces responsible for this disruption of the growth of the inner scale arise from many factors. The most obvious are (i) variations in the local oxidation rate caused by variations in the Cr content of the matrix and the differences in population, orientation, and shape of the spinel particles, and (ii) the general recession of the alloy:oxide interface as a consequence of the oxidation process. Since wüstite shows some plasticity at high temperatures (8) the extent of the detachment is somewhat temperature dependent, but the detachment of the initial set of spinel markers occurs so

rapidly at all temperatures that they serve as rather reliable markers of the position of the original specimen interface. Measurements substantiating this observation will be presented in a later section of this report.

The distribution of porosity in this scale indicates the direct effects of oxide plasticity and the spinel particle population in altering the spalling or detachment of the inner scale from the subscale. Specimens with low Cr contents oxidized at high temperatures (low spinel populations and high plasticity of wüstite) produce inner scales containing rather *thick continuous* layers of oxide, as shown in Fig. 7. With increasing Cr content or decreasing temperature of oxidation the porosity is more generally distributed throughout the inner scale, indicating a greater propensity for spalling during the growth of the scale. The effect of the spinel population illustrated by a comparison of Fig. 7 and 8, is equally valid if different temperatures are compared.

Studies of the porosity within the inner scales of all of these specimens have shown that the distribution of the spinel particles is not disrupted by pore formation, that is, the spinel particles project into the pores suggesting that the wüstite matrix was destroyed to enlarge the pores during the growth process. This evidence, abundant and clear when polished sections are examined under dark-field illumination, is discernible but not striking in Fig. 7

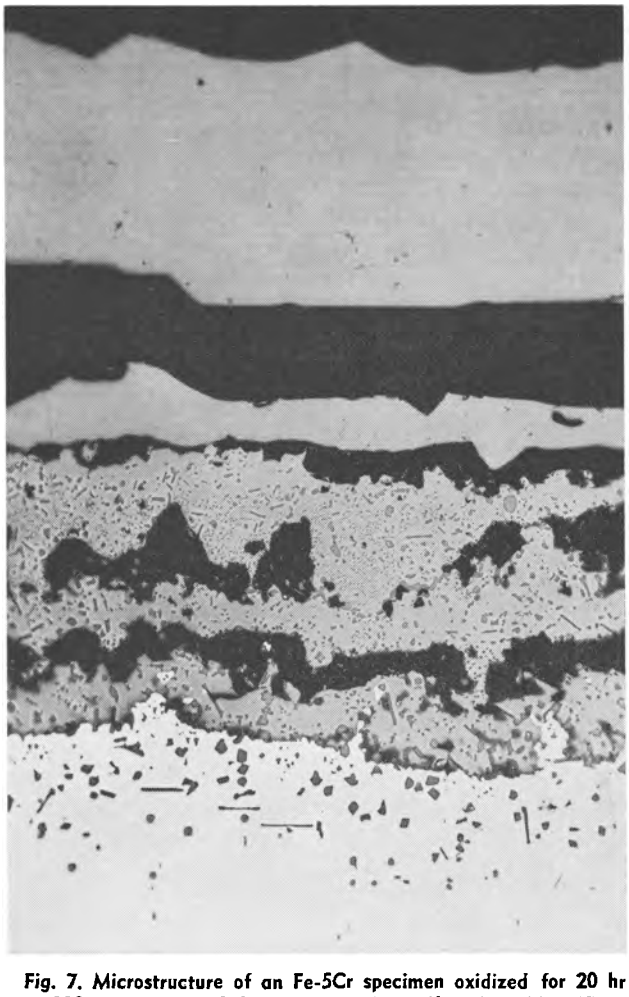

Fig. 7. Microstructure of an Fe-5Cr specimen oxidized for 20 hr at 1100°C in a 0.1 H_2O-0.9 Ar atmosphere. Unetched. Magnification approximately 160X.

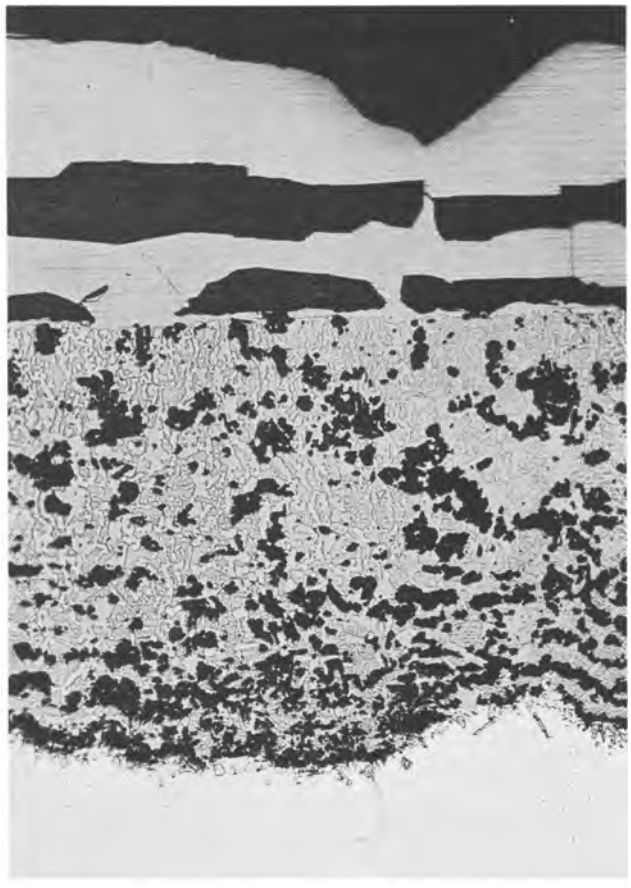

Fig. 8. Microstructure of an Fe-15Cr specimen oxidized for 20 hr at 1100°C in a 0.1 H_2O-0.9 Ar atmosphere. Unetched. Magnification approximately 160X.

and 8. The epoxy mounting material, the dark phase in the figure, fills almost all of the pores in the body of the inner scale, completely surrounding the projecting spinel particles. This indicates that these pores existed in the scale and were *not* formed by fragmentation of the oxide during sectioning or polishing. The shape and distribution of the spinel particles within the inner scale remain very similar to those of the particles of the subscale. This does not mean that there is no change in the composition or total amount of spinel during the growth of the inner scale. Ipat'ev and Sibirskaya (2) have noted the increase in the spinel phase across the inner scale layers produced on their steel specimens. Though less marked in the present study there was ample evidence of the growth of the spinel phase in some specimens.

The outer scale.—During the oxidation process this scale is almost entirely wüstite. When the total oxidation is low a single oxide layer may constitute this scale, but in general it is made up of several layers which are separated by gross voids as shown in Fig. 1, 7-9. However, each of these layers is quite continuous and entirely dense. The connections among the layers of this scale are narrow ridges or small columns of oxide. Thus in section, the layers frequently appear to be completely detached. The outermost wüstite layer of this scale is oxygen rich and, after cooling to room temperature, contains a precipitate of magnetite or may even develop a thin surface layer of magnetite. All of the inner layers

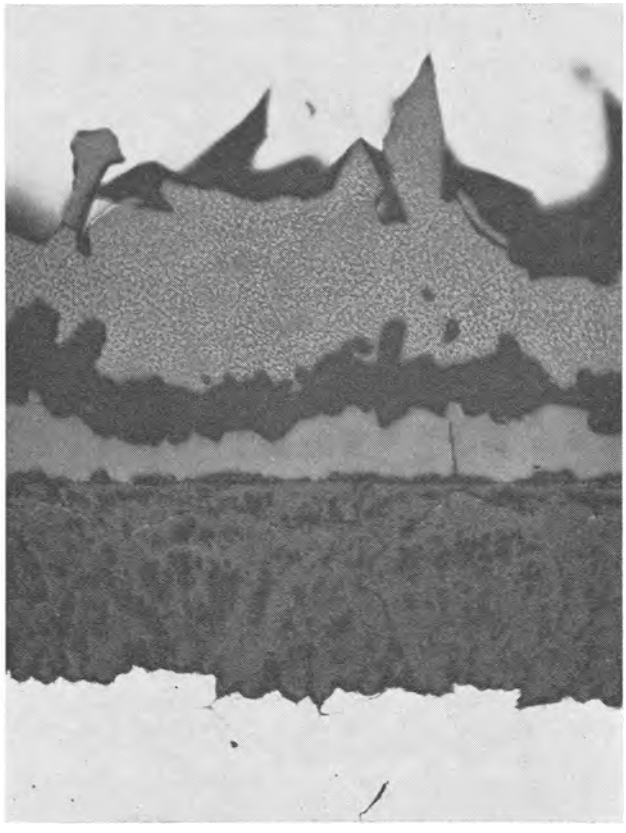

Fig. 9. Microstructure of an Fe-10Cr specimen oxidized for 10 hr at 900°C in a 0.1 H_2O-0.9 Ar atmosphere. Etched (1% picral + HCl). Magnification approximately 150X.

are wüstite showing neither surface layers of higher oxides nor a precipitate of magnetite even though the cooling rates for these inner layers must be less rapid than that of the exterior layer. Thus the composition of these inner layers must be distinctly oxygen lean. This composition difference is illustrated in the etched section of Fig. 9.

The composition and topography of the outer oxide layer are related and are functions of the oxidation temperature. Specimens oxidized at temperatures below 900°C always formed a layer of higher oxides on the external surface of the outer wüstite layer. At 800°C this surface layer was magnetite. At 700°C a thin coat of hematite was produced over the magnetite when the period of oxidation was extended. The magnetite surfaces had a dull gray appearance, and the formation of hematite at the lower temperatures was evident by the appearance of a velvet-like surface coat of short red needles. At 900°C and above no higher oxides were formed on the wüstite surface during the normal oxidation period, and the specimen was a lustrous black. At 900°C the surface had a cinder-like appearance and, metallographic sections of specimens oxidized for long times occasionally revealed a very thin surface layer of magnetite. This thin magnetite layer, as well as the abundance of magnetite within the body of this layer, formed during the cooling of the specimen after the oxidation period. At 1100°C the specimens formed a lustrous black surface of large wüstite grains which had developed well defined crystal facets.

These wüstite surfaces developed needle-like projections. At 900°C these projections were short, stout, spikes and were most profuse along the edges of the specimen. At 1100°C the projections were long thin needles, many of which terminated in long whiskers. Truncated sections of the short needles formed at 900°C are evident in the section of Fig. 9, and an indication of the surface character has been provided in this figure by backlighting the specimen through the transparent mount. Laue patterns of several of the needles formed at 1100°C identified the growth direction of the wüstite as the <110> axis and the surfaces as {100} and {111}.

As illustrated in the photomicrographs of Fig. 7-9, the inner surface of the external layer and the surfaces of subsequent oxide layers all show well developed crystal facets. The faceted form of these surfaces and the non-mating contours of the two surfaces separated by a void indicate that the detachment of these layers is not the result of mechanical spalling alone. Although the edges of the oxide layers in Fig. 9 have been somewhat rounded in polishing, this photomicrograph shows an interesting characteristic of these oxide interfaces. The outer surface of the external layer shows needle-like projections; the inner surface of this layer, "negative needles," *i.e.*, deep narrow holes bounded by well-developed crystal faces. The inner layer of wüstite resembles the outer in that projecting needles are found on its outer surface and holes on the inner surface. These, however, are much less prominent than those of the external oxide layer. The formation of needle-like projections occurs by a growth process and thus the outer surface of each wüstite layer in this outer scale is viewed as a growth surface. The formation of negative crystals is interpreted as evidence of a decomposition process and the inner surface of each layer is viewed as a decomposition surface.

Chemical and X-ray Analyses

Chemical analyses of the outer scale layers showed that these were very low in Cr content. The results from these analyses were: 1100°C, 0.04 to 0.1 w/o Cr; 900°C, 0.03 to 0.27 w/o Cr; and 700°C, 0.1 to 0.8 w/o Cr. The higher values for the oxide from the 700°C specimens are probably erroneous since the outer scale formed on these specimens was always thin and rather adherent to the inner scale. Thus these samples were probably contaminated with the Cr-rich spinel of the inner scale. Though less subject to this sampling error, the high Cr limits for the 900° and 1100°C specimens probably reflect some inner scale contamination since these high Cr contents were generally associated with short time, high Cr, oxidation specimens. These data indicate that the Cr content of the outer scale is probably less than 0.1 w/o and thus confirm the identity of the second phase spinel particles in the outer scale as magnetite. Meaningful Cr analyses of the wüstite of the inner scale was impossible since this scale is known to contain a Cr rich spinel phase.

The data from the x-ray studies of the outer and inner scales formed at 900° and 1100°C are presented in Fig. 10. The percentage of magnetite in the outer scale, formed by precipitation during cooling, increases as the Cr content is raised to 10 w/o.

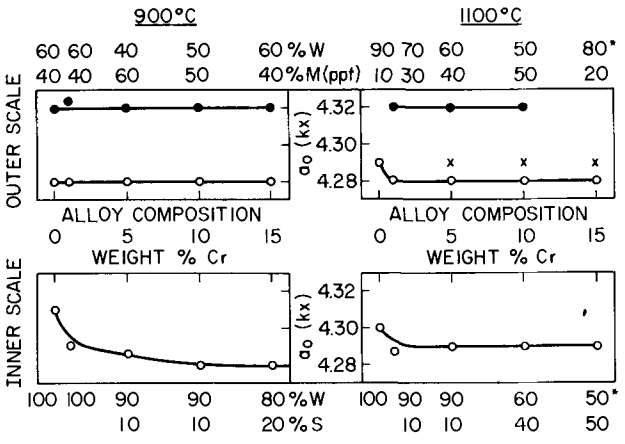

Fig. 10. Summary of the powder x-ray diffraction data showing the composition of the oxides and lattice parameters of the wüstite formed in the outer and inner scales as functions of alloy composition.

The 15 w/o Cr alloy, however, appears to show a reversal of this trend. The powder patterns from these outer scale layers all show distinct doublets for the wüstite phase. Each line of the doublet is sharp indicating that the outer scale contains regions of wüstite with two distinctly different compositions. The regions giving rise to the high lattice parameter, 4.32 kx, are the regions surrounding the magnetite precipitate in which the Fe content of the wüstite has been increased as a result of the precipitation reaction (9). The regions of the matrix wüstite which do not participate in this reaction retain their low Fe content and yield a low lattice parameter value (4.28 kx). The x-ray sample from the 15 w/o Cr specimen oxidized at 1100°C showed no doublets and indicated a low lattice constant characteristic of the low Fe wüstite. Metallographic studies of this specimen indicated that some regions of the external layer of the outer scale were essentially free of precipitated magnetite, while other areas showed the normal high concentration of this precipitate. Thus this x-ray sample was not representative of the entire specimen and the percentage of magnetite reported in Fig. 10 (marked by an asterisk) is based on the metallographic observation. The low lattice parameter for the wüstite sample from this specimen which was free of precipitated magnetite, however, supports the interpretation of the significance of the doublets found in all other specimens. Similarly the interior wüstite layers of the outer scale of the 1100°C specimens, all of which were free of magnetite precipitation, did not produce doublets in the x-ray powder patterns. The lattice parameter of the inner layers of wüstite was 4.29 kx (the "x" symbols in Fig. 10), indicating that this wüstite was richer in Fe than the unreacted wüstite of the outermost layer. The lattice parameter of the wüstite phase of the inner scale formed at 1100°C was essentially identical with that of the inner layers of the outer scale. The lattice parameter of the wüstite of the inner scale formed at 900°C approached 4.29 kx for the 1 and 5 w/o Cr alloys. The significance of the lattice parameter of the wüstite of the inner scale, and variations in this parameter, cannot be easily assessed since this phase may contain Cr as well as Fe and oxygen.

The lattice parameter of the spinel phase in the inner scales of the specimens oxidized at 900° and 1100°C was 8.37 kx and was independent of the Cr content of the alloy. Yearian *et al.* have reported lattice parameter variation as a function of composition for Fe-Cr oxide spinels (5). However, determination of the Cr content of the spinel on the basis of these data is not definitive because the lattice parameters are not single-valued functions of composition. Thus at 8.37 kx, three values for the Cr content are possible for the spinel.

Marker Data and Oxide Growth

In order to obtain data on the relative rates of growth of the inner and outer scales produced in the present study and to define the growth mechanism more accurately, marker experiments were performed and careful measurements of the oxide thicknesses were obtained. Fine platinum wire markers placed on the surfaces of alloy specimens before oxidation were always found at the interface between the inner and outer scales after the oxidation experiments. Also, the spinel phase of the inner scale served as reliable markers. These particles were never transferred into the outer scale and the outermost line of spinel markers coincided with the boundary defined by the platinum wire markers. Thus, the outer scale of wüstite, while frequently containing several detached layers, grew exclusively by the outward migration of cations across the inner: outer scale interface.

The position of the interface between the inner and outer scales coincided almost exactly with the location of the original gas: specimen interface. Ipat'ev and Sibirskaya (2) and Pfeil (10) made similar observations in the studies of the oxidation of Cr steels and various iron base alloys. In the present studies measurements of the total distance between the outermost line of spinel markers on opposite sides of the specimen confirmed this interesting behavior. These data for a series of alloys oxidized at 900° and 1100°C are shown in Fig. 11a. Since the original specimen thickness was not exactly the same for each series, the data are presented as the percentage change in this "thickness measurement" after oxidation. In spite of the complex spalling or detachment processes occurring during the oxidation these interface locations remain virtually unmoved for all alloy compositions and oxidation times at these two temperatures. It is thus apparent that there is no mass transfer across this interface by mechanical strain. Also, the diffusional transport of cations across this interface to form the outer scale must be greater than that required to accommodate the volume change in converting the alloy to the oxides of the inner scale, since a large volume of voids is generated within the bounds of this interface and yet the interface is unmoved.

Measurements of the average thickness of the alloy converted to oxide at each face of the specimen (the average thickness of the inner scale) and the average thickness of the outermost layer of the outer

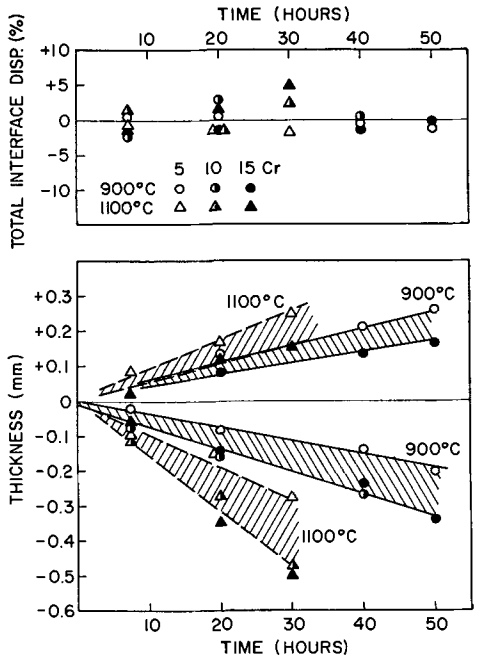

Fig. 11 (a) (top) Percentage total displacement of the inner: outer scale interface as a function of oxidation time; (b) (bottom) increase in thickness of the outermost oxide layer and metal consumption as functions of time.

scale are plotted in Fig. 11b. The upper set of data points shows that the outermost layer of wüstite, although extensively detached from the interior oxide layers of the outer scale, continues to increase in thickness throughout the oxidation period. The lower set of data shows that the rate of conversion of alloy to oxide is apparently a linear function of the oxidation time. Higher oxidation temperatures, naturally, accelerate these processes. These data indicate that the 5 w/o Cr alloy oxidized more slowly than the 10 or 15 w/o Cr alloys, but produced a somewhat thicker external wüstite layer than the higher Cr alloys. This relative oxidation resistance of the alloys was reflected in the weight gain data from these specimens, but the spread in the oxidation rates was very much smaller than that indicated by the metal consumption data. All of the data in Fig. 11 were necessarily obtained from interrupted oxidation tests in which only the initial and final weights were measured. The specimens employed in these tests were full ⅞ in. diameter disks. In subsequent continuous weight gain experiments, employing smaller one-quarter disk specimens, approximately the same rate of weight gain was observed, but the Cr content of the alloy appeared to have little or no effect on this rate. As a consequence of these observations, bands have been shown in Fig. 11b rather than lines which might imply more reliability than is intended for these data. These measurements do, however, indicate two important characteristics of the oxidation process: (i) the rate of metal conversion to oxide is approximately linear with oxidation time, and (ii) in spite of the extensive detachment of the outer oxide layer, a rate of cation delivery to the external scale: gas interface is maintained which permits this wüstite layer to continuously grow at approximately the same rate throughout the oxidation experiment.

The Oxidation Process

The data and observations from this study provide a basis for examining the nature of the oxidation mechanism which produces the characteristic layered scale structures. Both the metallographic observations and the x-ray data indicate that the outer wüstite scale layers are dense, continuous oxide layers and, thus, direct admission of the oxidizing atmosphere is denied to the scale interior. The retention of markers at the inner: outer scale interface indicates that the small concentration of Cr in the outer wüstite layers does not alter the growth mechanism of this phase; *i.e.*, cation migration alone is important, the anions being essentially immobile. Under these growth conditions the detachment of the scales from the metal during oxidation is normally ascribed to the stress system produced by the diminishing volume of the metal as the oxidation proceeds. Also, when cation migration is the only transport process, the detachment of the outer scale should drastically retard the oxidation. Neither of these "normal" events occurs during the oxidation of these Fe-Cr specimens. The inner: outer oxide interface is essentially stationary, and growth occurs at the free external surfaces. Thus the outer oxide should be subjected to very little stress. However, extensive detachment of the outer oxide is observed to occur after rather brief oxidation periods and yet the rate of the oxidation process is only slightly reduced. Under these circumstances a second process involving a gaseous transport appears to be necessary to account for these observations.

The process, or processes, responsible for the detachment of the outer scale is not well understood. While a detailed study of the kinetic data may be of assistance in defining the characteristics of this step in the oxidation, it now appears that the diffusional flow of cations to the oxide: gas interface is not rate determining. Thus the composition of the wüstite at the outer interface is determined by the kinetics of the oxidation process, and the equilibrium oxide composition is not attained. As the scale grows the flux of cations to this surface is reduced by the increased length of the diffusion path and also by the local detachment events occurring at the subscale: inner scale interface. As a consequence, the cation concentration decreases in the outer wüstite and the equilibrium oxygen pressure for this phase rises. A smaller but similar change will occur in the composition of the wüstite surrounding the spinel particles of the inner scale and a growth of the spinel particles will result. Such growth is suggested by the phase equilibria of the W + S field of Fig. 2 which requires an increase in the proportion of spinel, and a large change in its composition, as the surrounding wüstite becomes cation lean. Since the oxide ions are close packed in both wüstite and spinel and since these ions are immobile, spinel growth occurs by the excess cations being rejected into the wüstite phase. The excess cations released by this reaction migrate toward the outer surface and sustain the high oxidation rate. A small volume contraction occurs as wüstite is converted to spinel by this process and under the constraints of the system this volume change may be sufficient to cause the spinel: wüstite

interface to fail. This detachment process, initiated at the outermost line of spinel particles, is progressive and self-perpetuating.

As the cation flow is reduced, the composition of the growing outer scale layer becomes increasingly lean in cations and the equilibrium oxygen pressure rises. Across the voids of the detachment zone a discontinuity in cation concentration in the wüstite is generated and, as a consequence of the difference in the equilibrium oxygen pressures of these two wüstite surfaces, dissociation of the outer cation lean material occurs and oxygen is transferred to the cation rich material. At the dissociation site excess cations are formed and these augment the normal flux toward the outer wüstite:gas interface and sustain the high oxidation rate. Thus the cations liberated in the dissociation process go to form new wüstite at the outer interface. The oxygen liberated moves inward as a gaseous species to form wüstite and higher oxides in the inner scale and subscale of the specimen.

The effect of this dissociative mode of growth is to destroy wüstite at the inner surface of the external layer and create new oxide at the outer surface. Thus the outer oxide layer moves away from the metal specimen. Since the interface between the inner and outer scale is the site of the original detachment, marking the original gas:metal interface, it remains unmoved throughout the oxidation process. The motion of the inner surface of the external wüstite layer relative to this marker is a measure of the contribution of the dissociation process to the over-all oxidation. Measurements of this void volume (planimetric measurements on a series of photomicrographs covering from 7 to 12 mm along the section length) have been made on the series of specimens represented in Fig. 11b. In these measurements the volume occupied by wüstite layers which formed after the initial detachment is counted as void space since these layers represent succeeding generations of the same process. From the weight gain data, which indicated that the oxidation was approximately linear with time, the volume of wüstite formed was calculated. If the detachment of the outer layer occurred very early and if the detachment were complete, cations required for the growth of this wüstite would be supplied entirely by the dissociative process. Under these circumstances a void volume equal to the wüstite volume calculated from the weight gain data would appear between the outer and inner oxide of the specimen. The detachment is known to occur early in the oxidation process, but the detachment is never complete. Thus the ratio of the observed void volume to that calculated for complete detachment is an estimate of the contribution of the dissociative process to the over-all oxidation. At 900°C, where the measured rates of weight gain were 1.1 and 1.6 mg/cm^2 hr for the 5 and 15 w/o Cr specimens, the dissociative process accounted for 10-20% of the oxidation for the 5 w/o Cr specimens and 25-35% for the 15 w/o Cr specimens. At 1100°C where the oxidation rate of both alloys was 3.8 mg/cm^2 hr, 30-40% of the oxidation was attributable to the dissociative process for the 5 w/o Cr specimens and as much as 50% for the 15 w/o Cr specimens. These data show the importance of this type of process in the over-all oxidation. The increasing contribution in the higher Cr alloys is attributable to a more complete detachment. The temperature effect is derived from the increased decomposition pressure and the kinetics of the dissociation and growth processes. These estimates of the vapor transport contribution to the total oxidation process show that even in these extensively detached scales a great proportion of the cation requirement can be supplied by lattice diffusion along the connecting oxide bridges. However, the dissociative process becomes increasingly important as the Cr content of the alloy and the temperature of oxidation are increased.

Discussion

The importance of a vapor transport process in oxidation has not been widely accepted nor extensively studied. Pfeil (10), in discussing his experiments establishing the dominant role of cation diffusion in the growth of wüstite, observed that when scales had become detached ". . . although oxygen could no longer diffuse inwards in solution it could still bridge the gap in the gaseous state, since the enclosing scale envelope would have an appreciable dissociation pressure." The conditions necessary for vapor transport indicated in this early report are: (i) generation of detached or porous scales, (ii) an oxygen activity gradient across the void space to provide a driving force for the process (this condition requires that the phase on one side of the void exists over a range of compositions), and (iii) an appreciable partial pressure of the gaseous species in the voids to permit the process to occur at a measurable rate. The present metallographic and x-ray data confirming the composition difference between the wüstite of the outer and inner scale layers, the difference in morphology of the inner and outer surfaces of the detached wüstite layers, the large displacement of the outer scale layer relative to the original specimen interface, and the continued high oxidation rate of these specimens, show that these conditions are fulfilled and that the dissociative transport process is important in the oxidation of Fe-Cr alloys in water vapor.

Although the dissociative process has not been extensively studied, its importance has been recognized in several other gas-metal reactions. The sulfidization of iron (11), nickel (12), and silver (13) are systems in which this type of process appears to operate. The role of the vapor transport process in these systems and in a number of more complex alloy systems has been discussed by Maak and Wagner (14) and oxidation of Cu-Be alloys, studied by Maak (15), appears to be quite analogous to that of the Fe-Cr alloys.

Since the dissociative process can only occur when porous or detached scales are formed, it is not entirely unexpected that the literature should show so little evidence of this type of reaction. In laboratory studies of gas-metal reactions, a considerable effort is made to adjust the experimental parameters to insure the formation of dense continuous scales. The examples of the reactions involving vapor transport

are either the sulfidization of metals or the oxidation of alloys. In both cases the generation of porous or detached scales is virtually unavoidable. The rapid growth of the sulfides and their poor mechanical properties appear to be responsible for the detachment of scale layers in these materials. While limited plasticity may be responsible for the detachment of oxides formed during alloy oxidation, it is likely that the many complex reactions occurring during this process and the volume change resulting from phase redistribution in the inner multiphase layers play an important part in promoting the detachment process. The detachment may be avoided in carefully contrived and controlled laboratory experiments for some materials. However, these same materials when exposed to varying service conditions may generate porous or detached scales and, if the other requirements for vapor transport are met, quite different scaling rates may be observed as a consequence of the dissociative process.

Because of the high dissociation pressures of the sulfides of iron, nickel, and silver, no problem is involved in basing the transport process on gaseous sulfur. Similarly, as proposed by Maak (15), oxygen can serve as the transport species in porous cuprous oxide. However, in this case a more complex vapor species may be involved for Pfeil (10) and Wood (16) have presented evidence indicating that a vapor phase containing both copper and oxygen may be involved. Maak's observation that large pores in the Cu_2O scale appeared to migrate toward the outer surface and that in a few instances these voids appeared to have reached the outer surface and popped open, suggest that copper as well as oxygen is involved in the inward vapor transport process. In the oxidation of Fe-Cr alloys, the very low dissociation pressure of wüstite (10^{-11} and 10^{-15} atm at 1100° and 900°C, respectively) indicates that a vapor species other than oxygen is necessary to account for the sustained high transfer rate observed. The apparent anomaly that rapid transport of oxygen can be achieved at such low oxygen partial pressures may be dispelled if a gaseous species other than molecular oxygen is considered. In the discussion of the present experimental results it has been tacitly assumed that only oxygen was transported through the gas phase. This has been done as a matter of convenience rather than an assumption basic to the process. Thus the vapor species involved in the transport process in the oxidation of Fe-Cr alloys in water vapor may contain, in addition to oxygen, either iron or hydrogen, or both. The nature of the gaseous species remains to be investigated.

Acknowledgment

The authors gratefully acknowledge the work of Mr. E. J. Brooks in obtaining the electron microprobe data and Mr. A. R. Donaldson in preparing the specimens for metallographic examination. One of the authors (C. T. Fujii) served as a NAS-NRC Postdoctoral Research Associate at the U. S. Naval Research Laboratory during the course of the research.

Manuscript received Feb. 14, 1963; revised manuscript received July 2, 1963. This paper was presented at the Boston Meeting, Sept. 16-20, 1962.

Any discussion of this paper will appear in a Discussion Section to be published in the June 1964 JOURNAL.

REFERENCES

1. D. Lai, R. J. Borg, M. J. Brabers, J. D. Mackenzie, and C. E. Birchenall, *Corrosion*, **17**, 357t (1961).
2. V. V. Ipat'ev and V. V. Sibirskaya, *Uchenye Zapiski Leningrad. Gosudarst. Univ.* im. A. A. Zhdanova No. 227, Ser. Khim, Nauk No. 17, 5-47 (1957).
3. G. C. Wood and D. A. Melford, *J. Iron Steel Inst.*, **198**, 142 (1961).
4. A. U. Seybolt, *This Journal*, **107**, 147 (1960).
5. H. J. Yearian, H. E. Boren, Jr., and R. E. Warr, *Corrosion*, **12**, 561t (1956).
6. M. Hansen, "Constitution of Binary Alloys," p. 527, McGraw-Hill Book Co., Inc., New York (1958).
7. T. Heumann and H. Böhmer, *Arch. Eisenhuttenw.*, **31**, 749 (1960).
8. J. D. Mackenzie and C. E. Birchenall, *Corrosion*, **13**, 783t (1957).
9. W. A. Fischer and A. Hoffmann, *Arch. Eisenhuttenw.*, **30**, 15 (1959).
10. L. B. Pfeil, *J. Iron Steel Inst.*, **119**, 501 (1929).
11. R. A. Meussner and C. E. Birchenall, *Corrosion*, **13**, 677t (1957).
12. S. Mrowec and H. Rickert, *Z. Physik. Chem. N. F.*, **28**, 422 (1961).
13. H. Rickert, *ibid.*, **23**, 355 (1960).
14. F. Maak and C. Wagner, *Werkstoffe u. Korrosion*, **12**, 273 (1961).
15. F. Maak, Doctorate dissertation, "Untersuchungen über die Oxydation von Kupfer-Beryllium-Legierungen bie erhöhter Temperatur," Georg-August Universität, Göttingen (1961).
16. D. L. Wood, *Trans. AIME*, **206**, 1252 (1956).

The Distribution of A-C Resistance in Oxide Films on Aluminum

M. A. Heine and M. J. Pryor

Metals Research Laboratories, Olin Mathieson Chemical Corporation, New Haven, Connecticut

ABSTRACT

Films of γ Al_2O_3 produced by anodizing superpurity aluminum at 20v in neutral ammonium tartrate are thinned uniformly when placed in sodium chromate solution of *p*H range 7-9. During film thinning the metal remains passive and the inherent specific resistance of the film substance is not modified by the dissolution process. Uniform thinning can continue from an initial film thickness of around 240Å down to the passive film thickness 20-25Å. Measurement of capacitance and dielectric loss at frequencies of 1000 to 100,000 cps during thinning has permitted determination of the variation of electronic and ionic resistivity throughout the majority of the thickness of the alumina films. Corrections for a-c resistance of the solution have been found to be unnecessary at 1000 cps but mandatory at 100,000 cps in order to obtain accurate results. The films possess a region of low electronic resistivity up to 60-80Å from the oxide-metal interface. At greater thickness, electronic resistivity is constant. Ionic resistivity is only constant across a central region of the film around 100Å thick. Nearer to the oxide solution interface, the ionic resistivity falls gradually and then rises sharply in the outer 20Å of the film. A defect model is advanced to account for this resistivity distribution.

Two previous investigations (1, 2) were concerned with the determination of the resistivity of γ-Al_2O_3 films formed anodically on high-purity aluminum, together with the changes in resistivity resulting from subsequent immersion in chromate, chloride, and fluoride solutions. In these investigations, the oxide film was compared to a simple electrical analog of a capacitor with a parallel resistance; any electrical effects of the solution and the second electrode were ignored.

Experimental determination of the series capacitance and dielectric loss of the film by an a-c method, in a high conductivity electrolyte, permitted calculation of the average specific resistance or resistivity after immersion in chromate, chloride, or fluoride solutions. More detailed studies of γ-Al_2O_3 films over a wide frequency range (2) and after 8 hr immersion in sodium chloride solution at *p*H 6 indicated that chloride ions were incorporated into the anion lattice of the oxide and resulted in a large decrease in ionic resistivity of the film without detectable, accompanying change in thickness, topography, or crystal structure. However, these earlier studies did not give any indication of the distribution of resistivity through the thickness of the original anodic film, or of the distribution of chloride ions in γ-Al_2O_3 films that had been immersed in sodium chloride solution at *p*H 6. Such information is clearly necessary for a detailed understanding of the conduction mechanism through the original or the exchanged alumina film.

Previous studies also showed that gamma alumina films up to 1000Å could be maintained for several hours without major change in series capacitance or dielectric loss in molar sodium chromate solution with the *p*H adjusted to a value of around 6.0. An earlier investigation (3) had suggested that the dissolution rate of γ-Al_2O_3 films in chromate solution was at a minimum at this *p*H. When the *p*H of the chromate solution was raised above this value the oxide film was dissolved slowly, even though the passive state was maintained through the ability of adsorbed chromate ions to react with aluminum to form additional γ-Al_2O_3.

The work described in the present paper is concerned with the development of a method for studying the distribution of resistivity in γ-Al_2O_3 films formed by anodizing aluminum in neutral ammonium tartrate solution. The method is based on the measurement of the capacitance and dielectric loss of γ-Al_2O_3 films over a range of bridge frequencies, while they are slowly dissolving in a slightly alkaline, passivating chromate solution. The chromate solutions do not appear to introduce additional defects into γ-Al_2O_3 films as they dissolve down to passive film thickness at the appropriate *p*H value. The measurement of capacitance and dielectric loss during film thinning enables calculation of the change in total a-c resistance in the measuring cell. Separate experiments permit determination of the a-c resistance of the solution and associated double layers thereby enabling calculation of the film resistance[1] as a function of thickness. Conduct of the experiments at bridge frequencies of 1000 and 100,000 cps permits the separation of ionic and electronic relaxation effects, due to impurity substitution or departure from stoichiometry, and can throw additional light on the conduction mechanism through these films. The surface topography of the films has also been studied by high resolution electron microscopy during their dissolution; results show that the films are thinned quite uniformly.

Experimental and Results

Materials.—The aluminum used in the low-frequency capacitance and dielectric loss experiments was annealed 2.5 mm diameter wire having a purity

[1] Unless otherwise stated, the term "resistance" will be taken to imply a-c resistance.

of 99.997%. The impurities were 0.001% Si, 0.001% Fe, and 0.001% Cu. Similar superpurity aluminum, in the form of annealed sheet 0.37 mm thick, was used for the high-frequency (100,000-1,000,000 cps) electrical experiments. The aluminum used in the electron optical studies was annealed, 0.5 mm thick sheet having a purity of 99.999%. The chromate solutions were made up from CP chemicals and demineralized distilled water. The pH of molar sodium chromate solution was adjusted by additions of sodium dichromate.

Sample preparation.—Wire specimens for the low-frequency capacitance and dielectric loss measurements were first degreased with benzene and then etched with 1.0*N* sodium hydroxide for 10 min. They were rinsed in demineralized distilled water and methanol and masked with Tygon paint in order to leave a cylindrical surface area of 0.2 cm^2 exposed. The masked specimens were then stored for a period of 24 hr over calcium sulfate before further treatment. Sheet specimens for the high-frequency experiments were similarly etched and then anodized before being masked with the Minnesota Mining and Manufacturing Company's pressure-sensitive Electroplaters Tape No. 470 from which a small hole of 0.02 cm^2 area had been punched.[2]

The anodic films investigated in this study were composed of γ-Al_2O_3 and were formed in an electrolyte consisting of 3% by weight of ammonium tartrate dissolved in demineralized distilled water; the pH of the solution was adjusted to 7.0 by the additions of a few drops of dilute ammonium hydroxide. The γ-Al_2O_3 films were formed using a platinum gauze cathode at 20v (giving a film thickness of around 240Å); one set of specimens was formed at 15v (180Å). The specimen was first placed in the anodizing solution at 25° ± 0.05°C in the absence of applied voltage. The voltage was then raised gradually over a period of approximately 1 min to the required value, keeping the current surge below 5 ma/cm^2. When the potential reached the required value, it was held constant and the current was allowed to decay for a period of 5 min after which stable leakage currents in the range of 15-20 μa/cm^2 were obtained. A maximum value of leakage current of 20 μa/cm^2 was selected as the criterion of an acceptable specimen. If this condition was achieved, the applied voltage was interrupted sharply by removing the specimen from solution.

The 99.999% pure aluminum sheet specimens for the electron optical experiments were pretreated by electropolishing in a cooled perchloric acid-ethyl alcohol electrolyte at 20v, as described earlier (2). The higher purity aluminum was used only to obtain a smoother electropolished surface showing a minimum of structural detail. After electropolishing the specimens were anodized as described above.

Experimental method.—The relaxation times of common impurity defects such as OH′ and Cl′ ions substituted in the anion lattice of γ-Al_2O_3 films are somewhat less than 10^{-5} sec (2). Accordingly, the dielectric loss of the films measured at bridge frequencies of 100,000 cps and above should be sensitive only to the electronic relaxation effects resulting from impurity substitution.[3] Dielectric loss values measured at lower frequencies of 1000 cps are sensitive to both electronic and ionic relaxation effects resulting from impurity substitution. The two a-c measurements, taken together, were used in this investigation to separate the ionic and electronic relaxation effects resulting from impurity substitution and departure from stoichiometry in the oxide films.

The experimental procedure for the electrical experiments was similar to that described in an earlier publication (2). The oxide covered specimen, either in the form of wire or sheet, was immersed in a polyethylene beaker which was in turn placed in a larger beaker lined with aluminum foil. Molar sodium chromate solution was used as the solution electrode and a cylindrical platinum grid (3.2 cm diameter) as the second electrode of the system. The chromate solution was always passivating so that no corrosion of the aluminum occurred. All connecting leads were shielded and guarded, and an aluminum plate covered the outer beaker to provide virtually complete electrical shielding from stray fields.

A General Radio 716-C capacitance bridge was used for experiments within the frequency range of 100-100,000 cps. A constant signal of 50 mvs p-p was always applied to the specimens. Lead and other stray capacitances were eliminated by the use of a General Radio 716-P4 guard circuit which also assists in the development of maximum sensitivity. Some experiments (Fig. 3-5) were conducted at a frequency of 1000 cps using the multiplying range on the 716-C capacitance bridge and a specimen area of 0.2 cm^2. The guard circuit was not used in these experiments because its use is incompatible with that of the multiplying range. However, in all other experiments the guard circuit was used together with the smaller specimen area (0.02 cm^2) and a low loss external series capacitor (0.001 μF), enclosed within the shielded beaker, to bring the capacitance of the series combination within the range that could be measured by the 716-C capacitance bridge.

When the solution resistance was a very small fraction (less than 2%) of the resistance of the oxide film plus solution and double layers, the external series capacitor was eliminated at any given frequency by the equation

$$\frac{1}{C_t} = \frac{1}{C_a} + \frac{1}{C_b} \qquad [1]$$

where C_t is the measured capacitance of the series combination of oxide film and the external series capacitance, C_a is the external series capacitance, and C_b the film series capacitance at the same frequency. The series loss was eliminated at any given frequency by the equation

$$D_b = \frac{C_a D_t - D_a C_t}{C_a - C_t} \qquad [2]$$

where D_t is the measured dielectric loss of the series

[2] The smaller specimen area was necessary at higher bridge frequencies to permit a capacitance balance since the multiplying range in the 716-C capacitance bridge could be used only at a frequency of 1000 cps. However, identical loss values were obtained at 1000 cps with both specimen sizes; the capacitance values were in the proper ratio of 10:1.

[3] Including departure from stoichiometry.

combination of the oxide film and the external series capacitance, D_a is the loss of external series capacitance, and D_b the loss of the oxide film at the same frequency. Under those conditions, where capacitance and resistance effects from the solution were unimportant, the oxide covered aluminum in the chromate solution was treated as a simple capacitor with a parallel resistance. Accordingly, the specific resistance or resistivity of the oxide (ρ) could be calculated from D_b as follows

$$\rho = \frac{R_p A}{\delta} = \frac{4\pi}{K} C_p R_p = \frac{4\pi}{K\omega D_b} \qquad [3]$$

where R_p is the parallel a-c resistance of the film, A is the specimen area, δ is the film thickness, C_p is the parallel capacitance of the film, ω is the angular frequency of the a-c signal, and K is the dielectric constant of γ-Al_2O_3. The film thickness was calculated directly from the series capacitance of the oxide covered aluminum in the chromate solution, since the dielectric loss was low (<0.1) and correction to obtain $C_p(C_p = C_s/1 + D^2)$ from C_s was unnecessary. That the change in capacitance is due to a change in film thickness rather than one in dielectric constant is confirmed by earlier experimental observation (2) that capacitance is inversely proportional to the forming voltage.

When the solution and double layer resistance became a significant fraction (>2%) of the total resistance of the combination of the oxide covered aluminum specimen plus the solution, a more accurate analog was employed which necessitated a different method of calculation. The more accurate analog for the oxide covered aluminum in the chromate solution under these conditions is believed to be two series capacitors each with a parallel resistance. One capacitance-resistance element represents the oxide film on the metal, whereas the other similar element represents the capacitance and a-c resistance of the double layers on the two metal electrodes together with that of the chromate solution. The effect of the external series capacitor (C_a) was eliminated as before, by the use of Eq. [1] and [2]. The parallel a-c resistance of the oxide film, associated double layers, and solution was calculated for the relationship

$$R_p = \frac{1 + D_b^2}{D_b \omega C_s} \qquad [4]$$

where C_s is the series capacitance of the film, double layers, and solution. The parallel resistance values for the solution and double layers were obtained, under the same experimental conditions and at the same frequency, by substituting a similar area of smooth platinum for the oxide covered aluminum. Subtraction of the two parallel resistance values gives a more accurate a-c resistance value for the oxide film alone. Since the dielectric loss of the film alone did not exceed 0.1 (after correction for solution effects film thickness could again be accurately obtained from the series capacitance of the oxide film as described above, provided that suitable correction for the solution effects was first made.

The limited experiments that were conducted at a frequency of 1,000,000 cps were carried out with a General Radio 716-CS1 high-frequency bridge, together with the small (0.02 cm^2) specimen area and the low loss external series capacitor. Since a guard circuit is not available for this bridge, corrections for the capacitance and inductance of the leads were made by the standard methods described earlier (2) before calculating the a-c resistance of the oxide film by the second method.

Results

Cylindrical wire specimens carrying γ-Al_2O_3 films formed at 20v were immersed in 1.0M sodium chromate solutions at 25° ± 0.05°C with the pH adjusted to values of 5.5, 5.9, 6.4, 7.2, and 8.0. After 20 hr immersion in these solutions the specimens were transferred to fresh chromate solutions having the same concentration, temperature, and pH. The series capacitance and dielectric loss of the oxide films were measured in the fresh chromate solutions using the external low loss series capacitor. All electrical measurements made in this investigation were conducted in fresh chromate solutions in order to eliminate any possibility of interference (4) from the minute amounts of aluminum oxide which dissolve during film thinning.

The changes in capacitance and dielectric loss occasioned by 20 hr immersion of the specimens in chromate solutions from pH 5.5 to 8 are shown in Fig. 1 and 2. Each experimental point in these figures is the arithmetical average of measurements on six separate specimens with the scatter being less than ±5%. The curves relating change in capacitance to pH (Fig. 1) exhibit a minimum around pH 6 to 6.5. The frequency dispersion of the capacitance values is small and in the anticipated direction except at the highest pH and at the lowest frequency.

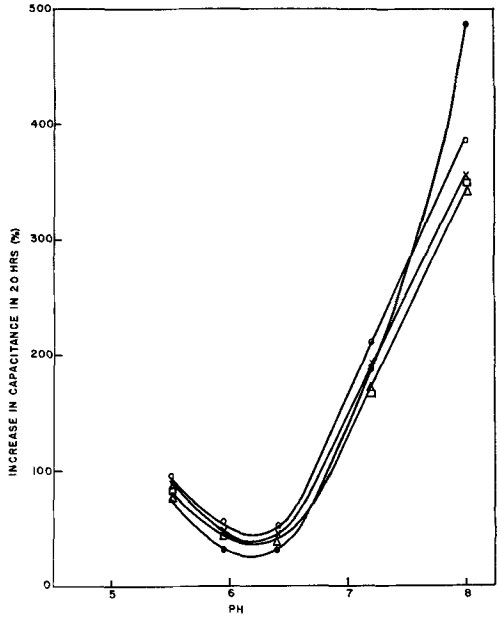

Fig. 1. Change in capacitance (at frequencies from 100 to 1,000,000 cps) of 99.997% pure annealed aluminum wire carrying anodic γAl_2O_3 films formed at 20v in ammonium tartrate solution after immersion for 20 hr in 1.0M sodium chromate solution at 25° ± 0.05°C with the pH adjusted between 5.5 and 8.0. O, 1,000,000 cps; ×, 100,000 cps; □, 10,000 cps; △, 1000 cps; ●, 100 cps.

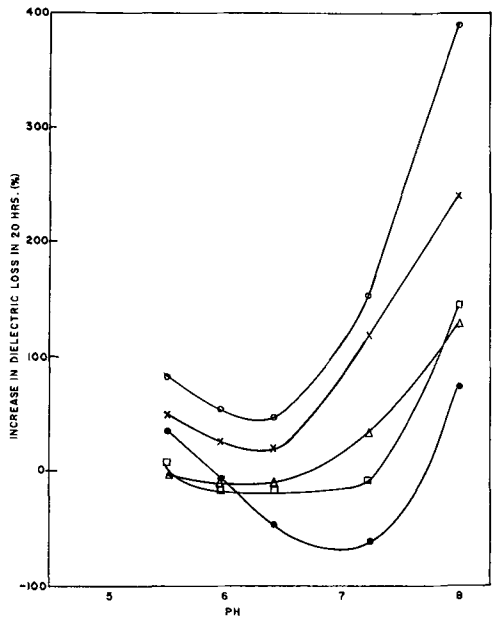

Fig. 2. Change in dielectric loss (at frequencies from 100 to 1,000,000 cps) of 99.997% pure annealed aluminum wire carrying anodic γAl_2O_3 films formed at 20v in ammonium tartrate solution after immersion for 20 hr in 1.0M sodium chromate solution at 25° ± 0.05°C with the pH adjusted between 5.5 and 8.0. O, 1,000,000 cps; ×, 100,000 cps; □, 10,000 cps; △, 1000 cps; ●, 100 cps.

The curves relating the change in dielectric loss of the oxide films to pH (Fig. 2) exhibit the same general characteristics as the capacitance results in Fig. 1, except that the frequency dispersion is greater and the minimum around pH 6 is less sharply defined. In fact, at the lower frequencies, the minimum appears to shift to higher pH values of up to 7.0.

The capacitance increase during immersion of γ-Al_2O_3 films in chromate solutions having pH values above 6.0 appears to confirm an earlier suggestion that film dissolution occurs in this pH range (3). In order to confirm this point, experiments were carried out in which 20v (240Å) γ-Al_2O_3 films were allowed to remain in chromate solutions having pH values of 7.1, 8.0, and 9.0 until steady values of capacitance were attained. The experimental values of capacitance and dielectric loss were, of course, measured in fresh chromate solutions at the same pH.

Experiments at the three pH values were first conducted on wire specimens (0.2 cm^2) at a bridge frequency of 1000 cps which is sensitive to ionic and electronic relaxation effects resulting from impurity substitution in γ-Al_2O_3 (2). The multiplying range on the 716-C capacitance bridge was used in these experiments only, since it permits the measurement of relatively large capacitance values. The results of experiments on triplicate specimens at pH values of 7.1, 8.0, and 9.0 are shown in Fig. 3, 4, 5, respectively. These results confirm that a pH dependent rise in capacitance occurs with time up to constant values

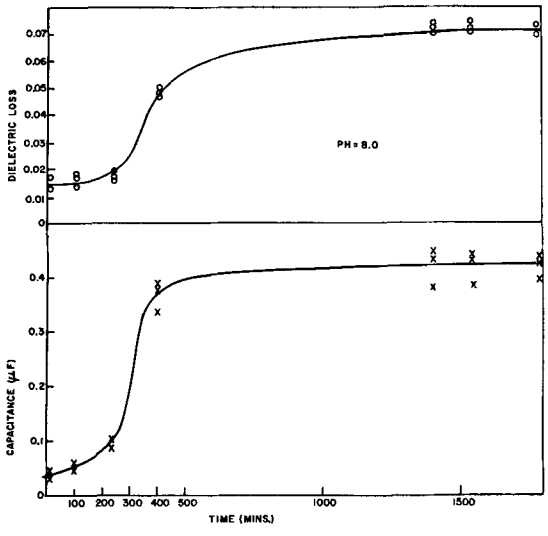

Fig. 4. Increase in capacitance and dielectric loss, at a frequency of 1000 cps of 99.997% pure annealed aluminum wire specimens carrying anodic γAl_2O_3 films formed at 20v in ammonium tartrate solution as a function of time of immersion in 1.0M sodium chromate solution at 25° ± 0.05°C with the pH adjusted to 8.0.

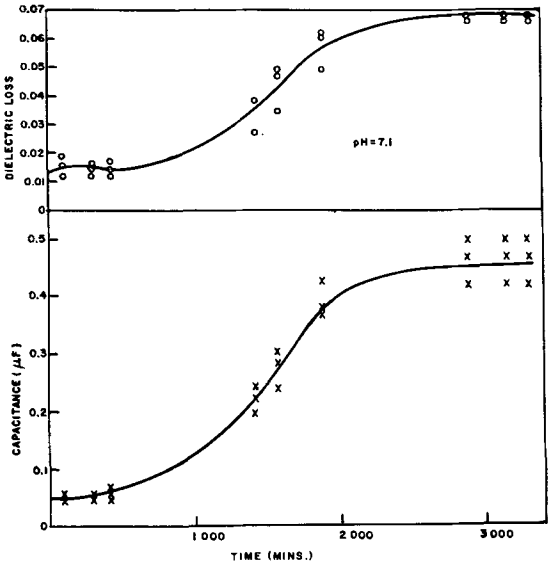

Fig. 3. Increase in capacitance and dielectric loss, at a frequency of 1000 cps of 99.997% pure annealed aluminum wire specimens carrying anodic γAl_2O_3 films formed at 20v in ammonium tartrate solution as a function of time of immersion in 1.0M sodium chromate solution at 25° ± 0.05°C with the pH adjusted to 7.1.

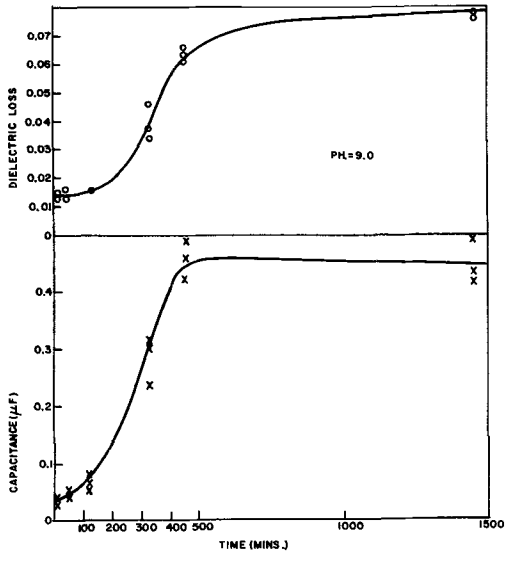

Fig. 5. Increase in capacitance and dielectric loss, at a frequency of 1000 cps of 99.997% pure annealed aluminum wire specimens carrying anodic γAl_2O_3 films formed at 20v in ammonium tartrate solution as a function of time of immersion in 1.0M sodium chromate solution at 25° ± 0.05°C with the pH adjusted to 9.0

within the range of 0.4-0.5 μF (per 0.2 cm^2) together with a similar increase in dielectric loss.

The scatter in capacitance values is due to variations in the projected areas of specimens masked with Tygon paint, together with some variation in dissolution rate of the different oxide films. The area independent dielectric loss (2) does not show as much variation between triplicate specimens and is due primarily to small variations in dissolution rate of the oxide films.

Similar experiments were conducted on 20v γ-Al_2O_3 films formed on 99.997% pure sheet at a bridge frequency of 100,000 cps. These experiments were confined to *p*H 7.1 only and were carried out on the small highly reproducible specimen areas (0.02 cm^2) in combination with the external series capacitor. The results of experiments on duplicate specimens are shown in Fig. 6 which bears a general similarity to the lower frequency results (Fig. 3).

The results in Fig. 1, 3, 4, 5, and 6 strongly suggest that γ-Al_2O_3 films having an initial thickness of 240Å become thinned on exposure to chromate solutions at a rate which increases with increasing *p*H value above 6.0. Figures 3-5 also suggest that the final equilibrium film thickness is not greatly changed as the *p*H of the chromate solution is raised from 7.1 to 9.0.

The surface roughness of a γ-Al_2O_3 film 240Å thick was next studied during thinning in 1.0M sodium chromate at *p*H 7.1 using high-resolution electron microscopy. The purpose of these experiments was to determine whether the dissolution of the oxide is a uniform process or whether significant additional roughening occurs as thinning proceeds. Aluminum sheet, 99.999% pure, was electropolished in a cooled perchloric acid-ethanol bath and then anodized in neutral ammonium tartrate at 20v. The electropolished aluminum surface, the surface of the original γ-Al_2O_3 film formed at 20v and the oxide surface partly thinned by 1700 min immersion and fully thinned by 8000 min immersion in sodium chromate solution at *p*H 7.1 were replicated to produce direct positive replicas by the platinum-carbon method of Bradley (5). The shadowing angles and replica de-

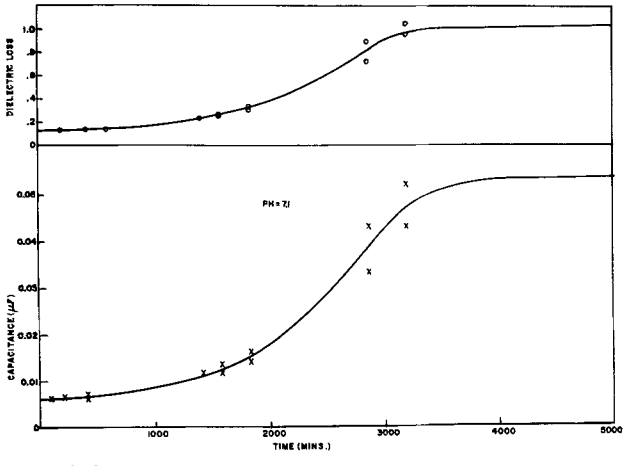

Fig. 6. Increase in capacitance and dielectric loss, at a frequency of 100,000 cps of 99.997% pure annealed aluminum sheet specimens carrying anodic γAl_2O_3 films formed at 20v in ammonium tartrate solution as a function of time of immersion in 1.0M sodium chromate solution at 25° ± 0.05°C with the *p*H adjusted to *p*H 7.1. Capacitance and loss values uncorrected for solution effects.

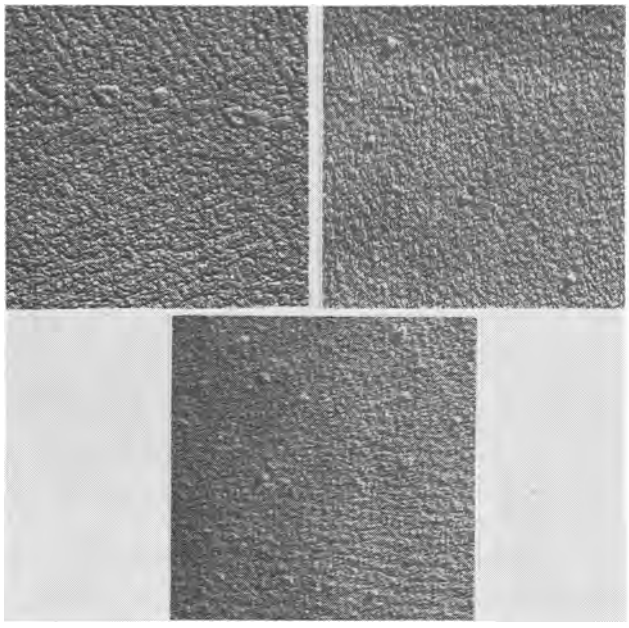

Fig. 7. Electron micrographs of the surface of γ-Al_2O_3 films formed at 20v in ammonium tartrate solution on 99.999% pure annealed aluminum sheet: (a) (top left) original γ-Al_2O_3 surface; (b) (top right) γ-Al_2O_3 film surface after thinning for 1700 min in 1.0M sodium chromate at *p*H 7.1 and 25° ± 0.05°C; (c) (centered) γ-Al_2O_3 film surface after thinning to the maximum degree by 8000 min immersion in 1.0M sodium chromate at *p*H 7.1 and 25° ± 0.05°C. Direct positive platinum replicas. Shadowing angle 20°. Direction indicated by the arrows. Magnification approximately 40,000X.

tachment methods were described in an earlier publication (2). The replicas were then examined at 75 kv in a Metropolitan-Vickers EM6 electron microscope. The original metal surface was similar to that shown in an earlier publication (2) and gave evidence of a slight substructure such as has been described earlier by Altenpohl (6). Figure 7(a), (b), and (c) show the surface of the γ-Al_2O_3 film at a magnification of 40,000 diameters before thinning and after partial and virtually complete thinning in the chromate solution. It may be seen that the original oxide surface, Fig. 7(a), is relatively uniform, except for some shallow isolated mounds of oxide protruding around 50Å above the surface. Similar surface structural detail was also observed earlier (2) in 20v anodic films. After partial thinning of the film by immersion for 1700 min in the chromate solution, the surface roughness and detail Fig. 7(b) appears to be identical to that of the original oxide surface in Fig. 7(a), thereby suggesting that the dissolution is highly uniform in nature. After complete thinning by 8000 min immersion in chromate solution, the thinned oxide surface Fig. 7(c) is again fairly uniform except that there appears to be a somewhat higher density of oxide protrusions than are apparent in the thicker films. The additional oxide protrusions on the fully thinned films give somewhat diffuse reflection electron diffraction patterns of γ-Al_2O_3 similar to that of the original anodic oxide.

Discussion

Dissolution of Aluminum Oxide Films by Sodium Chromate Solutions

The electronoptical results in Fig. 7 show that the thinning of the aluminum oxide films is very uni-

form on a microscale until they approach the passive film thickness where rather more oxide protrusions are apparent. These additional protrusions could either represent isolated locations at which the film dissolves more slowly, or oxide crystals formed by the passivating action of the chromate solution. Previous work on passive films formed in sodium chromate solution showed that small crystals of γ-Al_2O_3 were formed on top of a comparatively uniform γ-Al_2O_3 film. These crystals had a high degree of perfection of crystallographic structure (3) which was manifested in reflection electron diffraction as a series of single crystal spots superimposed on the broader haloes from the underlying γ-Al_2O_3. Reflection electron diffraction from a fully thinned specimen, similar to that whose surface is depicted in Fig. 7(c), shows that these single crystal spots are not obtained. Instead, somewhat diffuse γ-Al_2O_3 patterns similar to that of the original oxide are obtained, thereby suggesting that the additional oxide protrusions are small local areas more resistant to dissolution in the chromate solution. Accordingly, it is considered that the nature of the oxide-metal interface does not change significantly during film thinning in the passivating chromate solution. Because of this factor and because the oxide protrusions only cover a small portion of the specimen surface, no important errors will result from calculation of an average film thickness from capacitance measurements.

Influence of Chromate Solution on Accuracy of Film Resistance Measurements

The dielectric loss values in Fig. 2 run approximately parallel to the capacitance changes in Fig. 1. This behavior is also evident in Fig. 3-6. The loss values can be used to calculate the specific resistance of the oxide directly (from Eq. [3]) provided that the a-c resistance of the chromate solution and double layers is small compared with that of the oxide. Accordingly, the capacitance and dielectric loss of the chromate solution and double layers were determined experimentally at frequencies from 100 to 1,000,000 cps by substituting 0.02 cm^2 of smooth platinum in the experimental cell for the oxide covered aluminum electrode as described earlier. The small signal (50 mvs p-p) and series external low loss capacitor were also employed. External potential control of the platinum specimens was not employed because their potential remained constant at a value of $+0.51 \pm 0.015$v on the hydrogen scale even when different concentrations of chromate were used. Results are shown in Table I with the a-c resistance values of the solution and double layers being calculated from Eq. [4] after correcting for the external series capacitor. Although the total solution resistance might include a small term for the a-c resistance of a very thin oxide film on the platinum specimen, it is not believed that this is a significant portion of the total resistance of the platinum cell. It may be seen from Table I that the total solution resistance decreases by almost three orders of magnitude as the frequency is increased by five decades.

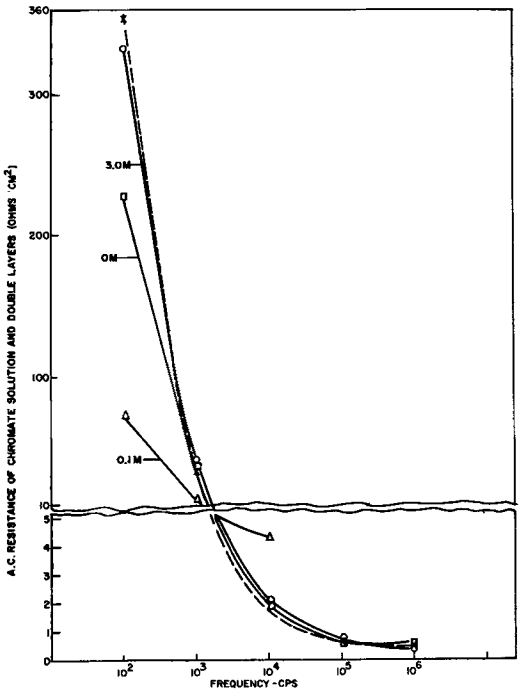

Fig. 8. A-C resistance of the $Pt/Na_2CrO_4/Pt$ cell at 25° ± 0.05°C as a function of sodium chromate concentration at pH = 7.1 and frequency. △, 0.1M Na_2CrO_4; ×, 1.0M Na_2CrO_4 (halved electrode spacing); O, 3.0M Na_2CrO_4; □, 1.0M Na_2CrO_4.

Additional experiments with the smooth platinum specimen were carried out to determine whether either the a-c resistance of the solution itself or that of the double layers on the platinum electrodes was a dominant factor in the total solution resistance results in Table I. One experiment was performed in 1.0M sodium chromate solution at pH 7.1 in which both the solution path between the platinum electrodes and the area of the cylindrical platinum grid were halved by using a cylindrical grid having a diameter of 1.6 cm. The resulting a-c resistance of the $Pt/Na_2CrO_4/Pt$ cell (Fig. 8) at 100,000 cps was little affected by reducing the length of the electrolyte path within these limits and by halving the area of the platinum grid. This result suggests that the a-c resistance of the double layers on the smooth platinum specimen (0.02 cm^2) comprises the largest part of the total solution resistance at high frequency.

This conclusion is further supported by additional experiments, also shown in Fig. 8 in which the concentration of the chromate solution was varied while still maintaining the conventional cell geometry. Although the d-c resistance of the electrolyte increases with increasing dilution, the a-c resistance of the solution plus double layers decreases at low frequency as the chromate concentration is decreased, thereby further indicating that the a-c resistance of the double layers on the small aluminum or platinum specimens has a major influence on total solution resistance. That the total solution resistance is strongly frequency dependent is at variance with some previously assumed (7) frequency independent corrections for the a-c resistance of aqueous solutions and double layers.

Comparison of solution resistance with the total resistance of the same cell containing a 240Å γ-Al_2O_3 film on aluminum (calculated from Eq. [3]) shows that the percentage error introduced by ignoring the solution is insignificant at frequencies below 10,000 cps (Table I). Even with a 25Å γ-Al_2O_3 film at 1000 cps ignoring solution resistance would result in an error of less than 1%. However, at 100,000 and 1,000,000 cps severe errors result if the solution resistance is ignored. Accordingly, ρ may be calculated directly from D at 1000 cps without applying corrections for the solution. At 100,000 and 1,000,000 cps, R_p for the electrode plus solution must be calculated from Eq. [4] and the resistance of the solution from Table I subtracted to give accurate a-c resistance values for the film.

Interpretation of Electrical Results

Figures 2-5 show that the dielectric loss at 1000 cps increases as the capacitance of the specimen increases, *i.e.*, as the film thins.

The increase in dielectric loss with decreasing thickness could be due either to: (*a*) a well-defined resistivity distribution in the oxide film with the film nearest to the oxide-metal interface exhibiting lower resistivities, or (*b*) the introduction of defects into the film during its dissolution, *i.e.*, from the incorporation of hydroxyl or possibly hydrogen ions into the oxide lattice.

Previous work (2) showed that the exchange of Cl′ and OH′ with oxygen ions in the γ-Al_2O_3 lattice created defects which introduced ionic relaxation effects with characteristic relaxation times of slightly less than 10^{-5} sec. Accordingly, the dielectric loss of a film which has been allowed to exchange with Cl′ ions was significantly increased at frequencies of up to 10,000 cps but was unaffected at frequencies of 100,000 cps and above. The fact that an increase in loss is also seen in Fig. 2 at high frequencies of 100,000 and 1,000,000 cps, suggested that the increases in dielectric loss with decreasing film thickness are not due to the introduction of OH′ ions (or H^+) into the film during dissolution.

In order to confirm this conclusion, the results at 1000 cps in Fig. 3-5 were replotted in the form of average resistivity (ohm-cm) *vs.* thickness curves. The average resistivity calculations were made using Eq. [3] and, therefore, by ignoring the solution resistance; from Table I this procedure introduces no significant error at 1000 cps. Actual pairs of capacitance and loss values were used from Fig. 3-5 rather than projected values from the smoothed curves. The resistivity value at any given thickness represents the average resistivity of the film at that appropriate thickness rather than the resistivity of a small element of the oxide at that location. If OH′ ions, for instance, were to enter the anion lattice of γ-Al_2O_3 during its dissolution in passivating chromate solutions, higher dielectric losses and lower resistivities at 1000 cps would be expected in the more alkaline chromate solutions. The results in Fig. 9 show that one single curve accounts accurately for all the measured capacitance and dielectric loss results from Fig. 3-5, *i.e.*, from pH 7.1 to 9.0. Also included in Fig. 9 are the isolated points from the 1000 cps determinations in Fig. 1 and 2. In fact, Fig. 9 incorporates the measurements taken from 27 different specimens.

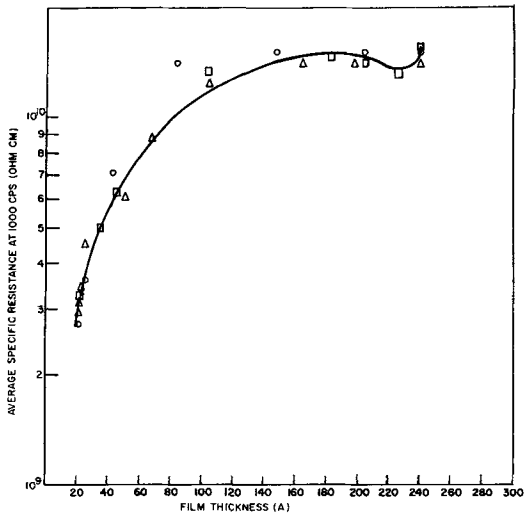

Fig. 9. Relation between average specific resistance at 1000 cps and film thickness of γ Al_2O_3 films formed anodically at 20v in ammonium tartrate solution. □, pH 7.1; △, pH 8.0; O, pH 9.0.

It may be seen that the fit to a single curve in Fig. 9 is more accurate than the reproducibility of the capacitance values in Fig. 3-5 thereby indicating that the errors are subtractive rather than additive. Also, the scatter of experimental points in Fig. 3-5 must be due largely to variations in actual dissolution rates which have no effect on the resistivity *vs.* thickness relationship. When the results in Fig. 9 are taken in conjunction with the observation of loss increases with decreasing film thickness at frequencies high enough to preclude observation of ionic relaxation effects due to impurity substitution, it appears that a well-defined resistivity distribution exists throughout the thickness of γ-Al_2O_3 films formed by anodizing at 20v in neutral ammonium tartrate.

Probable Defect Structure of Aluminum Oxide Films

The results in Fig. 9 include both ionic and electronic relaxation effects due to impurity substitution and departure from stoichiometry. The smoothed curve in Fig. 9 can be recalculated as a curve relating film thickness to the a-c resistance of the film (ohm-cm^2) at 1000 cps. The resulting curve in Fig. 10 shows the calculated a-c resistance values (at 1000 cps) as a function of thickness of the oxide film. The curve can be seen to include four distinct portions as follows:

1. A 60-80Å thick low-resistance portion of the film adjacent to the metal-oxide interface where the resistivity[4] increases with increasing thickness from around 4 x 10^9 ohm-cm at 25Å from the oxide-metal interface to 2 x 10^{10} ohm-cm at 80Å from the oxide-metal interface.

2. A 100Å thick portion of the film from 60Å to around 160Å from the oxide-metal interface where the a-c resistance is a linear function of thickness,

[4] Actual resistivity at a given thickness is obtained by constructing tangents to Fig. 10 at the appropriate thickness.

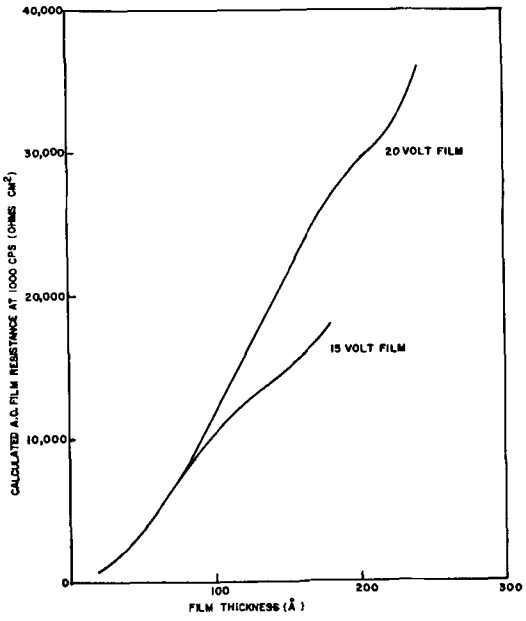

Fig. 10. Relation between calculated a-c resistance at 1000 cps and thickness of γAl_2O_3 films formed anodically at 15 and 20v in ammonium tartrate solution as a function of thickness.

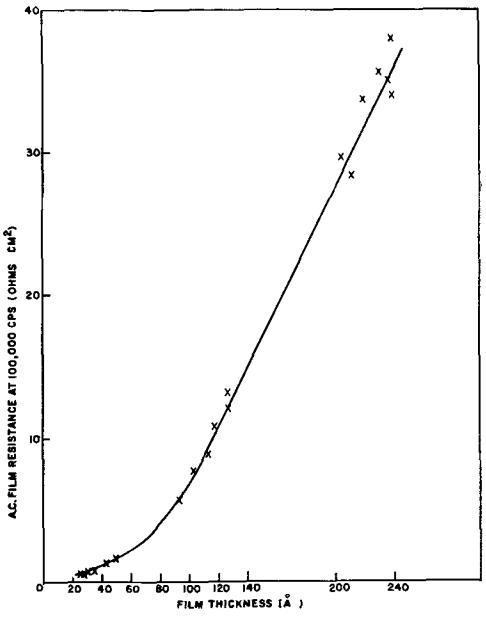

Fig. 11. Relation between a-c resistance at 100,000 cps and thickness of γAl_2O_3 films formed anodically at 20v in ammonium tartrate solution.

i.e., the resistivity is constant at a value of around 2×10^{10} ohm-cm.

3. A 60Å thick portion of the film located from 160 to 220Å from the oxide-metal interface, having a much lower resistivity decreasing to as little as 5×10^9 ohm-cm. This accounts for the constant and the decreasing portions of the average resistivity *vs.* thickness curves in Fig. 9.

4. A 20Å thick portion of the film adjacent to the oxide-solution interface where the resistivity is very high (around 5×10^{10} ohm-cm at 1000 cps) which accounts for the sharp rise in average resistivity at the oxide-solution interface in Fig. 9.

If the a-c resistance *vs.* thickness curves are analyzed for individual specimens, portions 1, 2, and 3 are obtained with great regularity and reproducibility. However, the high resistivity in the region of the oxide-solution interface (portion 4) is strongly dependent on the method of formation of the anodic film and to a larger extent on the pH of the thinning solution. If slower rates of anodizing voltage rise or lower peak anodizing current surges are permitted, portion 4 of Fig. 10 is partly or completely suppressed. This high resistivity portion also tends to be suppressed as the total film thickness decreases. For instance, Fig. 10 contains a resistance *vs.* thickness curve for a 15v (180Å thick) film formed in neutral ammonium tartrate. The central linear resistance region, 2, is severely reduced, and the resistivity in the outer 20Å is much lower than that in the 20v film. The other portions, 1 and 3, are essentially unchanged in reducing the forming voltage from 20 to 15v.

In order to determine whether the features of Fig. 10 are due to electronic or ionic relaxation effects, resulting from impurity substitution or departure from stoichiometry, the relationship between a-c resistance and thickness was calculated from the 100,000 cps results in Fig. 6 by the use of Eq. [4]. The total a-c resistance of the oxide film plus solution was then corrected by subtracting the a-c resistance of the solution and double layers at 100,000 cps from Table I. The results are shown in Fig. 11 which contains the experimental values from Fig. 6. Using Fig. 11, a smoothed curve relating calculated average specific resistance at 100,000 cps to thickness may be obtained (Fig. 12).

It may be seen from Fig. 11 that a low a-c resistance is again obtained in the 60-80Å of oxide film adjacent to the oxide-metal interface. In this region the high-frequency resistivity is around one-fourth of that at any other location in the film more

Table I. Capacitance and a-c resistance of 1.0M Na_2CrO_4 solution and associated double layers at pH — 7.1, temperature 25° ± 0.05°C; platinum electrode area 0.02 cm², a-c signal ± 25 mv

Frequency, cps	Cs, μF	D	A-C resistance of solution & double layers, ohms cm²*	Total a-c resistance of 20v γAl_2O_3 film plus solution & double layer, ohms cm²	Error resulting from ignoring solution resistance, %
100	0.6040	0.249	224	330,000	0.07
1,000	0.4183	0.277	29.6	36,000	0.08
10,000	0.3429	0.340	1.89	1,080	0.19
100,000	0.2973	5.87	0.65	35.5	1.8
1,000,000	0.0747	13.55	0.58	1.24	53

* Based on the area of the smooth Pt electrode.

distant from the oxide-metal interface. However, at greater thicknesses than 80Å, the a-c resistance of the oxide film measured at 100,000 cps is a linear function of the thickness thereby showing that the remainder of the anodic film has a constant high-frequency resistivity (2.2×10^7 ohm-cm). Similar results can be obtained when the electrical measurements are conducted at a frequency of 1,000,000 cps, although, of course, the a-c resistance is lower due to the frequency effect, and the results are less sensitive because of the greater relative contribution afforded by resistance effects from the solution (Table I).

Since it has been previously shown that defects resulting from anion impurity substitution (such as from Cl′ and OH′) in γ-Al_2O_3 have relaxation times of slightly less than 10^{-5} sec, the foregoing results can be analyzed to throw light on the defect structure of the anodic films formed in neutral ammonium tartrate solution.

The low a-c resistance and resistivity values obtained at 1000 and 100,000 cps in the 60-80Å region of the γ-Al_2O_3 films adjacent to the oxide-metal interface (Fig. 9 to 12) appear to be due primarily to electronic relaxation effects resulting from departure from stoichiometry since they are unaffected by raising the signal frequency to 10^5 cps and above. This low resistivity region is considered to be due to the proximity of the metal interface and to represent an n-type region of excess metal ions in the oxide film as has been suggested previously by several investigators in the field (7, 8). Presumably, this region is similar to that studied in the photosensitized electron emission experiments of Grunberg and Wright (9) who hypothesized that excess metal ions existed as missing oxygen ions in the lattice with two electrons trapped at each anion vacancy. Such an n-type defect structure would be expected to contribute to enhanced high- and low-frequency conduction in the region of the oxide-metal interface such as is observed in Fig. 9-12. The present work

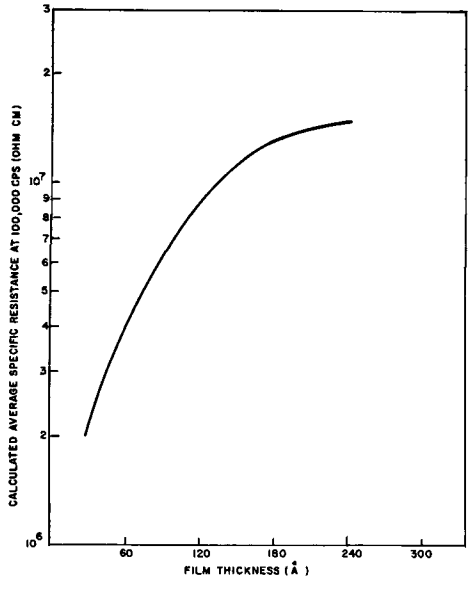

Fig. 12. Relation between calculated average specific resistance at 100,000 cps and film thickness of γAl_2O_3 films formed anodically at 20v in ammonium tartrate solution.

does not permit deduction of whether the ionic resistivity is constant in this region because of the effect of frequency on a-c resistance. However, comparison of Fig. 10 and 11 would certainly strongly suggest that the major effect of the metal interface is on electronic relaxation effects due to departure from stoichiometry.

At greater thicknesses than 60-80Å linear relationships between a-c resistance and thickness are obtained both at 1000 and 100,000 cps (Fig. 10 and 11). At 100,000 cps this linear relationship persists out to the oxide-solution interface thereby indicating that specific resistance is constant when the film thickness becomes greater than 60-80Å and the influence of the oxide-metal interface disappears. Constant specific resistance at 1000 cps is only obtained in a narrower, 100Å thick section of the oxide formed at 20v and is not obtained at all in the 15v film (Fig. 10). This is because of the existence of another diffuse zone of the oxide film, some 60Å thick which shows a lower specific resistance and which is overlayed by a sharp zone of very high specific resistance oxide immediately adjacent to the solution interface (Fig. 10). Since these two effects are only seen at frequencies below 100,000 cps, they are considered to be due to ionic relaxation effects resulting from either impurity substitution or nonstoichiometry. Accordingly, these are considered to be zones of variable ionic resistivity.

The more diffuse zone of lowered ionic resistivity some 60Å thick (Fig. 10) was invariably observed in this investigation. It is believed to be primarily due to the presence of OH′ ions in the γ-Al_2O_3 lattice in the outer portion of the films. Hydroxyl ion substitution should also give an n-type defect structure in γ-Al_2O_3 [5] of the same type that was assumed to result from exchange of Cl′ ions with equal numbers of O″ ions from the oxide lattice (1, 2). The entry of OH′ into the outer portion of the anodic film should be assisted by the field applied during formation of the anodic oxide. The proposed OH′ ion entry in this fashion is supported by the recent experiments of Davies *et al.* (10) who showed, by the use of Xe 125 as an inert marker, that an appreciable inward anion migration must be anticipated during the anodic formation of barrier layer films on aluminum with the proportion of anion migration increasing as the forming voltage decreases. The ionic relaxation effects, accompanying OH′ ion entry into the outer third of the aluminum oxide film, are persistent effects in that no significant change in the low-frequency resistance distribution through this area of the film is induced by annealing in vacuum (10^{-6} Torr) for 24 hr at 350°C.

The outer 20Å of the 20v anodic films, near the oxide solution interface, exhibits a high resistivity at 1000 cps (Fig. 10) which is some two-and-a-half times greater than that characteristic of the bulk of the film itself. Since this effect is not seen at higher frequencies of 100,000 cps and above (Fig. 11), it appears to be a region of high ionic resistivity. The existence of this region is strongly influenced by the method of anodic film formation. For instance, this

[5] When one hydroxyl ion replaces one oxygen ion.

region is either not detected, or is not so pronounced, when the forming voltage is raised more slowly, when lower current surges are permitted, or when thinner, lower voltage films are formed (Fig. 10).

It is believed that this high resistance region is the result of the strongly oxidizing conditions existing at this region during anodic film formation. The high ionic resistance could well result from an anion lattice completely "saturated" or filled with oxygen ions so that few or no anion vacancies exist. This would normally require presence of a number of bound positive holes, *i.e.* a more p-type defect structure assumed to exist at this location by several other investigators (7, 8, 11). This outer layer defect structure, when stabilized by the forming voltage, should impede cation or anion migration and lead to high resistivity values at low frequency. This outer layer structure is quite similar to the one first postulated by one of the authors (12) for the defect structure of the outer portion of thin anodic oxide films formed on iron in sulfuric acid and for which some experimental support was later obtained by Nagayama and Cohen (13). It follows, by analogy, that the high ionic resistance of the outer 20Å of the γ-Al_2O_3 is a consequence of the sharp interruption of the polarizing voltage and that migration of the mobile carriers between the outer high resistance p-type layer and the underlying low resistance n-type layer would be expected ultimately to produce redistribution of ionic resistance in these outer layers.

The foregoing investigation is considered to establish that passivating chromate solutions are well suited to determining the distribution of ionic and electronic relaxation effects due to impurity substitution and departure from stoichiometry throughout the thickness of single phase oxide films on aluminum. The film thinning can be performed at any constant pH values between 7.0 and 9.0, depending on the duration of the experiment that is desired. This method clearly does not permit determination of the a-c resistance distribution throughout the total thickness of the film and instead is limited to determining resistance distribution down to a distance of around 20-25Å from the oxide-metal interface, *i.e.*, to the passive film thickness in slightly alkaline chromate solutions. Conduct of the experiments at lower pH values closer to 6.0 results in a slower rate of thinning and maximum experimental sensitivity. If the dielectric loss measurements are conducted at a frequency of 1000 and 100,000 cps, the distribution of the ionic and electronic components of the film resistance resulting from impurity substitution or departure from stoichiometry may be estimated. The high-frequency measurements of film resistance are relatively sensitive only because the a-c resistance of the chromate solution and associated double layers drops remarkably rapidly with increasing frequency, an observation which is at variance with the assumption of many investigators who have carried out a-c measurements on porous films containing electrolytically conducting paths.

Acknowledgments

The authors wish to thank the Metals Division of the Olin Mathieson Chemical Corporation for their support of this study, Mr. A. F. Beck for conducting the electronoptical experiments and Professor T. J. Gray for his many helpful discussions and contributions.

Manuscript received Feb. 14, 1963. This paper was presented at the New York Meeting, Sept. 29-Oct. 3, 1963.

Any discussion of this paper will appear in a Discussion Section to be published in the June 1964 JOURNAL.

REFERENCES

1. J. J. McMullen and M. J. Pryor, Proceedings of the First International Congress on Metallic Corrosion, p. 52, Butterworths (1961).
2. A. F. Beck, M. A. Heine, D. S. Keir, D. van Rooyen, and M. J. Pryor, *Corrosion Sci.*, **2**, 133 (1962).
3. M. J. Pryor, *Z. Elektrochem.*, **62**, 782 (1958).
4. K. F. Lorking, *J. Appl. Chem.*, **10**, 449 (1962).
5. D. E. Bradley, *Proc. Intern. Conf. Electron Microscopy, London*, 478 (1954).
6. D. Altenpohl and W. Hugi, *Aluminium*, **33**, 774 (1957).
7. J. W. A. Scholte and W. Ch. Van Geel, *Philips Research Repts.*, **8**, 47 (1953).
8. J. Sasaki, *Phys. Chem. Solids*, **13**, 177 (1960).
9. L. Grunberg and K. R. H. Wright, *Proc. Roy Soc. (London)*, **A236**, 68 (1956).
10. J. A. Davies, J. P. S. Pringle, R. L. Graham, and F. Brown, *This Journal*, **109**, 999 (1962).
11. A. P. Belova, L. G. Gorskaya, and L. N. Zakgeim, *Soviet Physics-Solid State*, **3**, 1348 (1961).
12. M. J. Pryor, *This Journal*, **106**, 557 (1959).
13. M. Nagayama and M. Cohen, *ibid.*, **107**, 781 (1962).

Critical and Passive Current Densities for Copper-Nickel-Zinc Alloys in Sulfuric Acid

N. D. Stolica and H. H. Uhlig

Corrosion Laboratory, Massachusetts Institute of Technology, Cambridge, Massachusetts

ABSTRACT

The critical composition for passivity in Cu-Ni-Zn solid solution alloys containing 32-45% Ni was determined from potentiostatic measurements of critical and passive current densities in 1*N* H_2SO_4. The alloys fall into two groups. The first group behaves as does copper, a true passive current is not observed, and the alloys are, therefore, not passive. The second group exhibits passive current densities which lie appreciably below the critical current densities for anodic passivation and behaves more like passive nickel. Calculations in accord with the electron configuration theory show that the critical composition separating passive from active alloys corresponds to filling of the surface d electron vacancies or unfilled d orbitals of nickel by electrons donated from both Cu and Zn. Each Zn atom contributes two electrons, and each copper atom one electron, to 1.6 unfilled surface d orbitals per atom of Ni. The data support the view that passivity in Ni-Cu and similar alloys is related to uncoupled d electrons or unfilled d orbitals of transition metal components, and that donor electrons induce a shift from passive to active properties at a critical alloy composition.

A study of passivity in alloys contributes to scientific understanding of the passive phenomenon in general, including passivity in pure metals. Passive alloys are also of interest because of their practical importance, as is evident by the widespread use of stainless steels.

Passivity and the corresponding improved corrosion resistance in alloys is typically established beyond a critical alloy composition. This critical composition may vary with the medium in which corrosion resistance is measured, often caused by sensitivity of the cathodic reaction rate to factors of the environment which determine whether or not the critical anodic current density for passivity is exceeded or not. Thus the critical composition for the Cr-Fe alloys is at 12% Cr in neutral media, but moves to 20% Cr in $FeSO_4$ solution and to 7% Cr in 33% nitric acid. The critical composition as measured by the critical or minimum anodic current density to produce passivity, on the other hand, is less sensitive to pH and electrolyte concentration, as was demonstrated for the Cr-Fe and the Cr-Ni binary alloy systems (1, 2). It is well-known that the corrosion rate of passive metals is controlled by the anodic reaction (hence the usual noble corrosion potentials of passive metals). Correspondingly, the critical anodic current density for passivity is a reasonable measure of the tendency for any metal to become passive, and this is not influenced by any factors affecting cathodic reaction rates. For this reason, the critical composition for passivity in the present Cu-Ni-Zn ternary alloys was determined by measurements of anodic polarization rather than by corrosion rates.

The critical composition for passivity in the Cu-Ni binary alloys comes at about 30-40 weight per cent (w/o) Ni. This was first established by measurements of corrosion rates in 4% NaCl and in sea water (3), and later more exactly by critical current densities for passivity in 3% Na_2SO_4 (3) or in 1*N* H_2SO_4 (4). According to the electron configuration theory, the critical alloy composition should correspond to the equivalence of uncoupled or vacant d electrons in nickel at the surface of the alloy (0.6 vacancy per Ni atom plus 1 vacancy created by surface oxygen or some other passivator) to the number of available donor electrons from copper (1 donor per Cu atom). The calculated critical composition is 38.5 atomic per cent (a/o) or 36.6 w/o Ni as calculated from the relation: atomic per cent element A in alloy AB at which the d band is just filled equals $100/[(v/n) + 1]$ where v is the number of uncoupled or vacant d electrons per atom of A, and n is the number of electrons per atom donated to A by element B of the alloy. The calculated value agrees reasonably well with the observed value.

The theory predicts, furthermore, that if a bivalent metal, such as zinc, is alloyed with Cu-Ni alloys so as to form a single-phase solid solution, and the zinc contributes 2 electrons per atom, then the uncoupled or vacant d electrons of Ni become filled so much the sooner compared to equal atomic percentages of Cu. Saturation magnetic moments of nickel alloys have shown that zinc contributes two electrons to Ni compared to one electron from copper (5), and it is expected that passive properties of the nickel alloys would follow a similar pattern. Accordingly, to check this matter, ternary alloys of Cu-Ni-Zn were prepared and the critical current densities for passivity were measured. The proportion of alloyed Ni atoms containing coupled d electrons or filled d orbitals expressed as per cent orbital-filled is given by the ratio (a/o Cu + 2 a/o Zn)100/(1.6 a/o Ni). Alloys for which this ratio is

less than 100 are expected to show some degree of passivity, whereas alloys for which the ratio is greater should behave as nonpassive metals, much the same as Cu in sulfuric acid.

Preparation of Alloys

In order to check the effect of zinc on passive properties of the Ni-Cu alloys, two conditions had to be met. The first was that maximum alloyed zinc should supply electrons sufficient to fill the d band of Ni. The second was that the amount of added zinc should not exceed solubility limits for a single-phase alloy; otherwise galvanic interaction of the separate phases tends to destroy passivity and complicates interpretation of the measurements. Hence, the Ni content for most alloys was chosen to average 44 w/o which is about 7% above the composition at which the d band is filled in Ni-Cu alloys. The required amount of zinc calculated to supply electrons just enough to fill the d band for a 44 w/o Ni, balance Cu alloy, is about 21 w/o. Alloys in this composition range are all single-phase as was shown by examining polished and etched specimens under the microscope. The phase diagram (6) indicates that solid solution α phase exists at low temperatures up to 27% Zn.

The appreciable volatility of zinc at the melting point of 44% Ni-Cu alloys (1280°C) made it difficult to obtain the required compositions. In general, alloys were prepared employing a partially covered alumina crucible into which pieces of electrolytic copper, carbonyl nickel, and analytical reagent grade zinc sticks were placed. Alloys were melted under an argon or helium atmosphere employing an induction furnace. The melt was drawn into 7 mm Vycor tubes and quenched in water. More zinc was then added and castings again obtained after the zinc had melted and had been stirred into the alloy. Several alloys were prepared by melting in sealed 13 mm diameter quartz (or Vycor) tubes, pieces of electrolytic copper, electrolytic nickel, and high-purity zinc.[1] This proved to involve a time-consuming and tedious procedure. The tubes, evacuated and sealed off, were placed in an iron pipe which was capped at both ends. The pipes were then placed in a furnace at 1100°C overnight, followed by treatment at 1250°-1300°C for 4 hr. Mixing was accomplished by rotating the alumina furnace tube with a large pair of tongs and also by moving the tubes back and forth. The pipes containing the melt were finally quenched in water and the castings swaged to 7 mm diameter rod. Some melts prepared in this manner had not mixed completely and were discarded.

The rods by either method of preparation were homogenized by heating in an evacuated Vycor tube at 1000°C overnight. After homogenization, specimens were mounted, polished, etched with Marbles reagent, and observed under the microscope. Small cylinders of approximately 1.5 cm long and 0.4 cm in diameter were machined from the rods. The cylinders were drilled and tapped at one end, and screwed onto a threaded brass shank which was soldered to a nickel wire. The wire was enclosed by an 8 mm diameter glass tube using a Teflon gasket to maintain a water-tight seal between the electrode and the glass at one end, with constant contact effected by means of a screw, nut and rubber grommet attached to the wire at the other end. Only Teflon and alloy made contact with the electrolyte. Chemical analyses of the alloys are given in Table I. Alloys 4 and 6 were prepared by melting within a quartz tube; all others were prepared in an open crucible under an inert atmosphere.

[1] From American Smelting and Refining Co.

Table I. Composition of Cu-Ni-Zn alloys

	Weight per cent			Atomic ratio	
	% Cu	% Ni	% Zn	$\left(\frac{Cu + 2Zn}{Ni}\right)$	% Orbital filled
1	55.59	(44.41)*	—	1.156	72.3
2	51.23	44.21	4.60	1.253	78.4
3	47.84	43.75	8.36	1.355	84.8
4	41.51	43.85	(14.64)	1.472	92.1
5	41.36	43.40	(15.24)	1.512	94.5
6	36.55	44.06	(19.39)	1.555	97.4
7	32.65	44.76	(22.59)	1.583	98.8
8	44.3	41.0	(14.7)	1.648	103
9	52.1	37.4	(10.5)	1.793	112
10	61.9	32.2	(5.9)	2.095	131

* Values in brackets obtained by difference.

Experimental Procedure

Polarization curves for the alloys were determined potentiostatically in deaerated 1*N* H_2SO_4 using a Wenking electronic potentiostat. Deaeration was accomplished by bubbling nitrogen through the acid for at least 1 hr, the gas being previously purified over copper turnings at 450°C. The electrodes were pickled in 6*N* HNO_3 at 60°C for 5 min, then placed in the cell and further cleaned by anodic polarization at 50 ma/cm^2 for 5 min. A Luggin capillary containing 1*N* H_2SO_4 was placed close to the alloy surface and the capillary in turn made contact with a saturated calomel reference electrode. After the corrosion potential was established, polarization was started, changing the impressed potential at the rate of 53 mv/min using a motor-driven potentiometer. Current was recorded automatically. Alloys were polarized to an ultimate potential of 1400 mv cathodic with respect to the saturated calomel electrode. In most cases, the polarization curve was repeated, starting at 1400 mv cathodic to saturated calomel electrode and proceeding in the active direction to a final potential corresponding to the corrosion potential. The electrolyte was renewed at the beginning of each run in order to maintain as low a concentration of contaminating metal ions as possible.

Results and Discussion

Polarization curves as recorded for electrolytic copper are shown in Fig. 1, and for the alloy containing 44.3% Cu, 41.0% Ni, 14.7% Zn (103% orbital-filled) in Fig. 2, and for the alloy containing 47.8% Cu, 43.8% Ni, 8.4% Zn (85% orbital-filled) in Fig. 3. Curves for other alloys are similar. Values of critical current densities, i (critical), and for passive current densities, i (passive), averaged from data

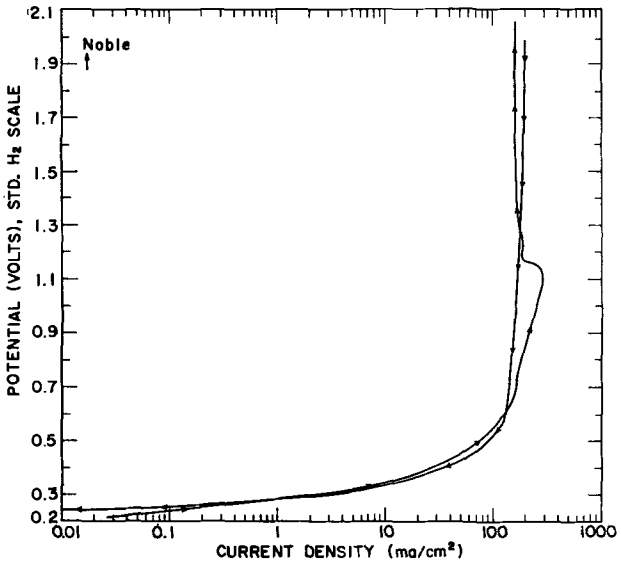

Fig. 1. Potentiostatic anodic polarization curve for electrolytic copper in 1*N* H_2SO_4, 25°C.

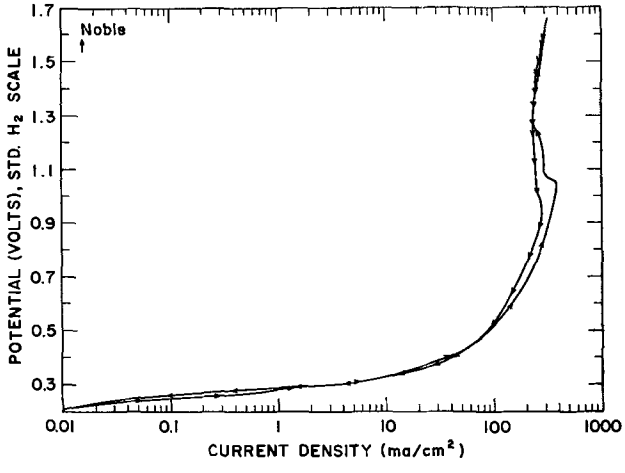

Fig. 2. Potentiostatic anodic polarization curve for 44.3% Cu, 41.0% Ni, 14.7% Zn alloy (103% orbital-filled) in 1*N* H_2SO_4, 25°C.

going from the active to the passive region and vice versa, are shown in Fig. 4. In Fig. 1 for copper, the change of slope for current *vs.* potential, which becomes pronounced beginning at about 100 ma/cm², is caused by concentration polarization. A slight drop in value of current beyond the maximum change of slope is probably caused by visible film formation on the copper surface. A thin red film, probably basic copper sulfate or cuprous oxide, sometimes became detached at higher current densities. For the nickel alloys, the corresponding visible film was black. The alloys of less than 100% orbital-filled composition showed a much greater reduction in current near the change of slope, typical of passivity, than did alloys of greater than 100% orbital-filled, including copper. The former group of alloys exhibited passivity whether or not a visible film was present.

Points of Fig. 4 show that *i* (passive) and *i* (critical) tend to intersect at an atomic ratio of 1.65 (103% orbital-filled). Thereafter, the difference between the two current densities is no greater from that for copper, and, hence, it is concluded that

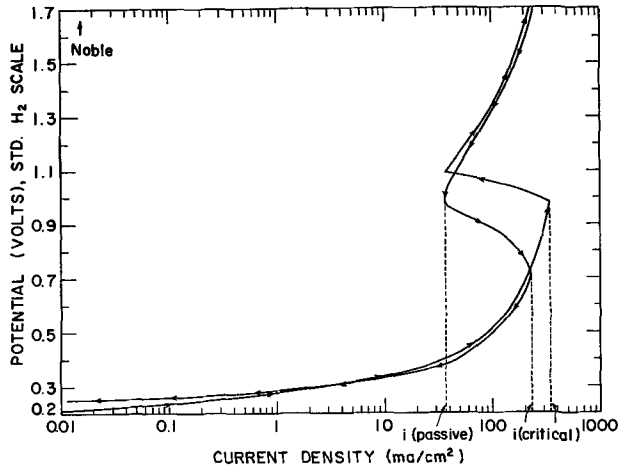

Fig. 3. Potentiostatic anodic polarization curve for 47.8% Cu, 43.8% Ni, 8.4% Zn alloy (85% orbital-filled) in 1*N* H_2SO_4, 25°C.

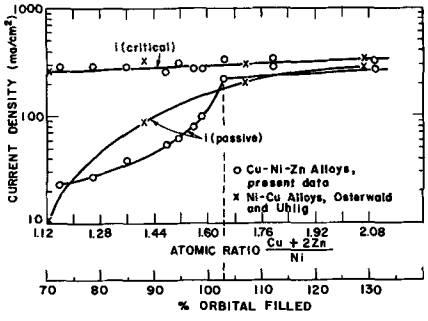

Fig. 4. Critical and passive current densities for Cu-Ni and Cu-Ni-Zn alloys in 1*N* H_2SO_4, 25°C.

properties of passivity are not common to alloys of atomic ratio greater than 1.65. Data for the binary Ni-Cu alloys in 1*N* H_2SO_4 previously reported by Osterwald and Uhlig (4) are also shown in Fig. 4. Critical current densities for the two alloy systems are in good agreement. They are not very sensitive to alloy composition in the range of critical composition. Passive current densities, on the other hand, are more sensitive to composition. For both alloy series, passive current densities approach critical current densities as Ni content decreases, but the shapes of the curves differ. Other than the fact that fewer points were available for the Ni-Cu alloy system in the region of convergence, the difference may be caused by Zn being a component of the alloys reported presently. Also, the change of potential with time for Osterwald and Uhlig's experiments was 7 to 50 mv/min compared to the present 53 mv/min. These differences notwithstanding, the critical composition for passivity occurs approximately at 100% orbital-filled alloy compositions for both alloy series. It should be considered in this respect that the difference between *i*(critical) and *i*(passive) for Osterwald and Uhlig's data at compositions corresponding to their 107% and 129% orbital-filled alloys are probably the same within experimental error of determining such values.

The good correspondence of the observed critical composition for passivity (103% orbital-filled alloy 8) to the theoretical 100% contributes support to the electron configuration theory of passivity. If, for example, zinc were to contribute only one electron per

atom instead of two, the critical composition would have been observed in the present alloys at an atomic ratio of 1.32 instead of 1.65. The results definitely point, therefore, to a contribution of two electrons per zinc atom and one electron per copper atom to the unfilled orbitals of Ni in the ternary Ni-Cu-Zn alloys. This composition, corresponding to orbitals just filled by electrons donated from Cu and from Zn, marks a transition from passive to nonpassive properties.

Acknowledgment

This research was supported by the Shell Oil Companies in the U. S. to whom the authors express their appreciation.

Manuscript received April 19, 1963. This paper was presented at the New York Meeting, Sept. 29-Oct. 3, 1963.

Any discussion of this paper will appear in a Discussion Section to be published in the June 1964 JOURNAL.

REFERENCES

1. A. P. Bond and H. H. Uhlig, *This Journal*, **107**, 488 (1960).
2. P. King and H. H. Uhlig, *J. Phys. Chem.*, **63**, 2026 (1959).
3. H. H. Uhlig, *Z. Elektrochem.*, **62**, 700 (1958).
4. J. Osterwald and H. H. Uhlig, *This Journal*, **108**, 515 (1961).
5. N. F. Mott and H. Jones, "The Theory of the Properties of Metals and Alloys," p. 197, Clarendon Press, London (1936).
6. "Metals Handbook," p. 1263, American Society for Metals, Cleveland (1948).

Phase Equilibria and Manganese-Activated Luminescence in the System $Zn_3(PO_4)_2$-$Cd_3(PO_4)_2$

Jesse J. Brown and F. A. Hummel

Department of Ceramic Technology, College of Mineral Industries,

The Pennsylvania State University, University Park, Pennsylvania

ABSTRACT

The phase equilibrium diagram for the system $Zn_3(PO_4)_2$-$Cd_3(PO_4)_2$ was constructed from quench and DTA data. Approximately 15 mole % $Cd_3(PO_4)_2$ is soluble in β-$Zn_3(PO_4)_2$ at 950°C, but less than 1 mole % is soluble in α-$Zn_3(PO_4)_2$ at 900°C. Three intermediate solid solution series A, B, and C have compositional limits of stability from 2 to 7, 20 to 37, and 56 to 80 mole % $Cd_3(PO_4)_2$, respectively. The A solid solution series has a maximum temperature limit of stability of 910°C and the "gamma" $Zn_3(PO_4)_2$ structure. The cathodoluminescence of the five significant solid solution regions was systematically investigated using molar substitutions of divalent manganese as an activator. Spectral distribution curves are shown for each solid solution series. Previous work by Smith and Power on this system is discussed in view of the new phase equilibria and cathodoluminescence data.

This paper is the first of a series intended to establish the phase equilibrium relationships in a portion of the system ZnO-CdO-P_2O_5. A second purpose of this work was to investigate the manganese-activated luminescence of compounds and solid solutions that exist in this ternary system.

The work by Smith (1), which introduced the alpha, beta, and "gamma" zinc orthophosphate nomenclature, eventually led to the development of the "red" fluorescing β-$Zn_3(PO_4)_2$:Mn T. V. phosphor. Katnack and Hummel (2) reported that the low-temperature (α) form of $Zn_3(PO_4)_2$ undergoes a sluggish reversible inversion to the high-temperature (β) form at 942°C. Hummel and Katnack (3) and Sarver, Katnack, and Hummel (4) found that "gamma" zinc orthophosphate is not a polymorph of $Zn_3(PO_4)_2$ but various solid solutions with structures very similar to that of the compound $Mg_3(PO_4)_2$.

Smith and Power (5) investigated the manganese-activated cathodoluminescence of various compositions in the $Zn_3(PO_4)_2$-$Cd_3(PO_4)_2$ system, but it was not clear from this work which phase or phases were responsible for the emission results.

Experimental Procedure

Phase relationships.—The equilibrium relationships in the system were established using the twenty-seven compositions listed in Table I. The raw materials used were Phosphor Grade ZnO and $CdCO_3$ and C.P. grade ammonium dihydrogen phosphate, $NH_4H_2PO_4$. The batch materials for quench and DTA work were reacted in air at 800°C for 24 hr, remixed, and reacted again at 800°C for 24 hr. Under these conditions of preparation loss of CdO and P_2O_5 due to vaporization was negligible according to weight loss determinations.

Although the system is nonglass forming, the phase relationships could be determined easily by quench techniques in every region except that immediately above the solidus temperatures. In this especially difficult region DTA determinations and a special technique were used to estimate the relationships. The special technique consisted of simple visual observations at room temperature of the condition of quenches using recrystallized fragments as the starting material. For most compositions it was possible to distinguish between unmelted and partially or completely melted material. It is

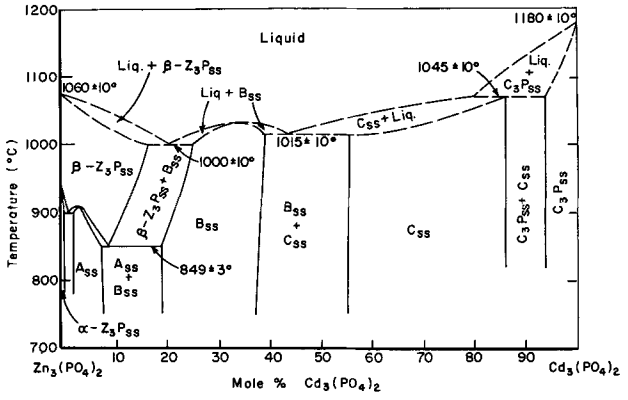

Fig. 1. Phase relationships on the $Zn_3(PO_4)_2$-$Cd_3(PO_4)_2$ join

obvious that the accuracy and reliability of these data for the solidus and liquidus temperatures are not as great as for those obtained for the remainder of the system. The dashed lines in Fig. 1 indicate this uncertainty.

A Norelco x-ray diffractometer employing nickel-filtered CuKα radiation, operating at 40 kv and 15 ma, was used for phase identification.

Luminescence.—All phosphors were activated by 1.0 mole % manganese, using Phosphor Grade $MnCO_3$ as the source of manganese. Sample preparations were essentially the same as for the phase equilibria preparations except that the temperature of the final heat-treatment was determined from the temperature stability region of the phase under consideration.

Spectral distribution curves were obtained using a demountable cathode-ray tube operating at 16 kv anode potential, 1.0 μa/cm^2 beam current density of a standard scan T. V. raster of 65 cm^2 area. Brightnesses under these conditions were measured with an eye-corrected foot-lambert meter.

Experimental Results

Phase Relationships in the $Zn_3(PO_4)_2$-$Cd_3(PO_4)_2$ *System*

The quench and DTA data used to establish the phase relationships in the $Zn_3(PO_4)_2$-$Cd_3(PO_4)_2$ binary join (Fig. 1) are shown in Table I. The DTA data were employed primarily to locate the approximate solidus temperatures. The solidus temperatures were subsequently determined more accurately by the special quench technique previously described. It was observed that the DTA temperatures were in some cases as much as 75°C below those indicated by the more accurate quench data.

It was found that the β-$Zn_3(PO_4)_2$ structure will accept up to 15 mole % Cd^{2+} isomorphously substituting for Zn^{2+}. In the pure form, β-$Zn_3(PO_4)_2$ is stable only above 942°C; however, the addition of 8 mole % $Cd_3(PO_4)_2$ in solid solution decreases the lower temperature limit of stability to 850°C.

Stable below 942°C, α-$Zn_3(PO_4)_2$ will accept a vanishingly small amount of $Cd_3(PO_4)_2$ in solid solution.

Between 2 and 7 mole % $Cd_3(PO_4)_2$ the solid solution series labeled "A_{ss}" in Fig. 1 is stable. This small intermediate solid solution region has an upper temperature limit of stability of 910°C which

Table I. Compositions and subsolidus heat treatments in the system $Zn_3(PO_4)_2$-$Cd_3(PO_4)_2$

No.	Composition, mole % $Cd_3(PO_4)_2$	Composition, mole % $Zn_3(PO_4)_2$	Temp, °C	Time, hr	Phases
1	1	99	854	48	α-Z_3P_{ss} + A_{ss}
			881	48	α-Z_3P_{ss} + A_{ss}
			893	48	α-Z_3P_{ss} + A_{ss}
			898	48	β-Z_3P_{ss}
			922	48	β-Z_3P_{ss}
2	2	98	855	48	α-Z_3P_{ss} + A_{ss}
			881	48	α-Z_3P_{ss} + A_{ss}
			916	48	β-Z_3P_{ss}
3	3	97	820	48	A_{ss}
			864	48	A_{ss}
			869	48	β-Z_3P_{ss} + A_{ss}
			882	48	β-Z_3P_{ss}
			936	48	β-Z_3P_{ss}
4	4	96	854	48	A_{ss}
			864	48	β-Z_3P_{ss} + A_{ss}
			869	48	β-Z_3P_{ss}
5	5	95	852	48	β-Z_3P_{ss} + A_{ss}
			927	48	β-Z_3P_{ss}
6	6	94	834	48	A_{ss}
			852	48	β-Z_3P_{ss} + A_{ss}
			864	48	β-Z_3P_{ss} + A_{ss}
			869	48	β-Z_3P_{ss}
7	7	93	780	48	A_{ss}
			834	48	A_{ss}
			866	48	β-Z_3P_{ss}
			932	24	β-Z_3P_{ss}
8	8	92	827	48	A_{ss} + B_{ss}
			846	48	A_{ss} + B_{ss}
			879	48	β-Z_3P_{ss}
			936	24	β-Z_3P_{ss}
9	9	91	714	48	A_{ss}
			827	48	A_{ss} + B_{ss}
			840	48	A_{ss} + B_{ss}
			879	48	β-Z_3P_{ss}
			931	24	β-Z_3P_{ss}
10	10	90	828	48	A_{ss} + B_{ss}
			848	48	A_{ss} + B_{ss}
			851	48	β-Z_3P_{ss} + B_{ss}
			878	48	β-Z_3P_{ss} + B_{ss}
			931	24	β-Z_3P_{ss}
11	12	88	904	48	β-Z_3P_{ss} + B_{ss}
			932	24	β-Z_3P_{ss}
12	14	86	924	24	β-Z_3P_{ss} + B_{ss}
13	15	85	838	48	A_{ss} + B_{ss}
			977	½	Crystalline
			992	½	Crystalline
			1017	½	Liquid
14	18	82	841	48	A_{ss} + B_{ss}
15	20	80	843	48	B_{ss}
			870	48	B_{ss}
			904	48	β-Z_3P_{ss} + B_{ss}
			924	24	β-Z_3P_{ss} + B_{ss}
16	30	70	850	48	B_{ss}
17	40	60	850	48	B_{ss} + C_{ss}
			996	½	Crystalline
			1011	½	Crystalline
			1020	½	Liquid

(Table continued on p. 1220)

Table I. Continued.

No.	Composition, mole % $Cd_3(PO_4)_2$	$Zn_3(PO_4)_2$	Temp, °C	Time, hr	Phases
18	50	50	850	48	B_{ss} + C_{ss}
			1009	½	Crystalline
			1019	½	Crystalline
			1029	½	Partially liquid
			1040	½	Liquid
19	60	40	850	48	C_{ss}
			999	½	Crystalline
			1019	½	Crystalline
			1028	½	Crystalline
			1030	—	Solidus (DTA)
			1044	½	Liquid
			1052	½	Liquid
20	70	30	850	48	C_{ss}
			1003	½	Crystalline
			1021	½	Partially liquid
			1022	—	Solidus (DTA)
			1044	½	Liquid
21	80	20	850	48	C_{ss}
			1030	—	Solidus (DTA)
			1045	—	Crystalline
			1058	—	Crystalline
			1071	—	Crystalline
			1080	—	Liquid
22	85	15	850	48	C_{ss}
			882	48	C_{ss}
			930	40	C_{ss}
23	87	13	800	48	C_{ss} (trace C_3P_{ss})
			932	40	C_{ss}
24	90	10	850	48	C_{ss} + C_3P_{ss}
			882	48	C_{ss} + C_3P_{ss}
			930	40	C_{ss} + C_3P_{ss}
25	93	7	800	48	C_{ss} + C_3P_{ss}
			932	40	C_3P_{ss} + (trace C_{ss})
26	95	5	850	48	C_3P_{ss}
			994	—	Solidus (DTA)
27	100	0	1166	10 min	Crystalline
			1178	10 min	Crystalline
			1181	10 min	Liquid
			1192	10 min	Liquid

α-Z_3P_{ss} = α-zinc orthophosphate solid solution series.
β-Z_3P_{ss} = β-zinc orthophosphate solid solution series.
C_3P_{ss} = cadmium orthophosphate solid solution series.
A_{ss} = "A" solid solution series.
B_{ss} = "B" solid solution series.
C_{ss} = "C" solid solution series.

decreases as Cd^{2+} is substituted for Zn^{2+}. The x-ray diffraction powder data indicate that this structure is very similar to that of the compound $Mg_3(PO_4)_2$ (sometimes referred to as the "gamma" zinc orthophosphate structure).

The "B" and "C" solid solution series appear to have very similar if not identical structures; however, they are separated by an immiscibility gap as indicated by Fig. 2 where the *d*-values of two reflections are plotted as a function of composition. The x-ray diffraction data used to construct these curves were obtained using a scanning rate of ¼°-2θ/min and silicon metal powder as an internal standard. Both of these curves show sharp inflections at approximately 37 and 56 mole % $Cd_3(PO_4)_2$ which were interpreted as the phase boundaries of the two phase (B_{ss} + C_{ss}) region at 850°C. The solidus curve between 20 and 80 mole % $Cd_3(PO_4)_2$ is relatively flat, varying from 1000° to 1050°C. The most probable solidus-liquidus configuration is shown in Fig. 1.

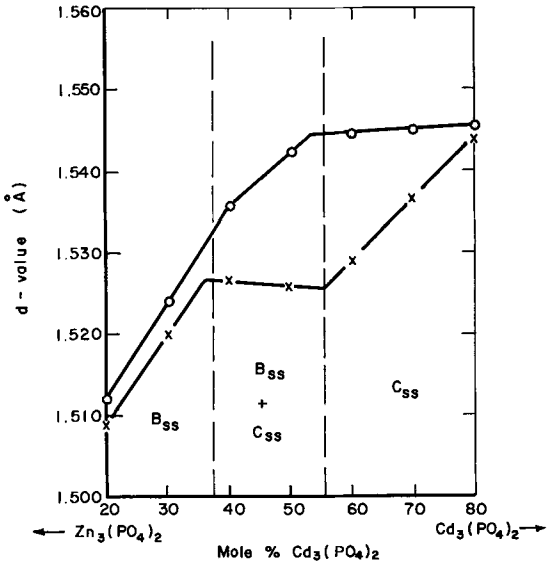

Fig. 2. Plot of *d*-value as a function of composition between 20 and 80 mole % $Cd_3(PO_4)_2$ (compositions quenched from 850°C).

$Cd_3(PO_4)_2$ melts congruently at 1180°C, and a maximum of 6 mole % $Zn_3(PO_4)_2$ is soluble in this structure.

The D.T.A. curves for various compositions between 40 and 100 mole % $Cd_3(PO_4)_2$ all indicated a small endothermic heat effect which varied between 850° and 950°C. High-temperature x-ray diffraction data obtained above and below this temperature range did not show any new reflections but did indicate some intensity changes. It, therefore, appears that neither the "C" nor the $Cd_3(PO_4)_2$ solid solution series have more than one crystalline modification; however the intensity changes could be an indication of an order-disorder phenomenon.

Table II shows the characteristic x-ray diffraction powder data for the various single phases in the orthophosphate system. These data were obtained using a scanning rate of 1° -2θ/min. The x-ray data obtained for $Cd_3(PO_4)_2$ agree with that previously reported by Ropp, Mooney, and Hoffman (6). The x-ray data for α and β-$Zn_3(PO_4)_2$ were given by Katnack and Hummel (2).

Luminescence in the $Zn_3(PO_4)_2$-$Cd_3(PO_4)_2$ *System*

The compositions, heat-treatments, equilibrium phases, and cathodoluminescence emission results for the fifteen phosphors prepared in the $Zn_3(PO_4)_2$-$Cd_3(PO_4)_2$ system are shown in Table III. These phosphors were prepared assuming that in each 1.0 mole % divalent manganese would substitute for Cd^{2+} and Zn^{2+} and maintain the RO/P_2O_5 molar ratio at 3/1 where *RO* represents the molar sum of the basic oxides. It was found by visual examination that these phosphors were only weakly responsive to 3650 and 2537Å u.v. radiation. It should be noted that Ropp (7) has shown that the response of

Table II. X-ray diffraction data for A, B, and C solid solution series

A_{ss} $(Zn_{0.95},Cd_{0.05})_3(PO_4)_2$			B_{ss} $(Zn_{0.80},Cd_{0.20})_3(PO_4)_2$			$(Zn_{0.70},Cd_{0.30})_3(PO_4)_2$			$(Zn_{0.40},Cd_{0.60})_3(PO_4)_2$			C_{ss} $(Zn_{0.30},Cd_{0.70})_3(PO_4)_2$			$(Zn_{0.20},Cd_{0.80})_3(PO_4)_2$		
2θ	d	I/I₀	2θ	d	I/I₀	2θ	d	I/I₀	2θ	d	I/I₀	2θ	d	I/I₀	2θ	d	I/I₀
15.9	5.6	20	21.33	4.2	15	21.16	4.2	10	21.19	4.2	20	21.24	4.2	15	21.25	4.2	15
20.5	4.3	100	22.84	3.89	10	22.71	4.92	10	22.33	4.0	30	22.23	4.0	30	22.14	4.0	30
22.3	4.0	85	24.34	3.66	35	24.26	3.67	30	24.06	3.70	20	23.99	3.71	15	23.92	3.72	15
23.1	3.85	40	24.82	3.59	20	24.65	3.61	20	24.42	3.65	10	24.27	3.67	5	24.13	3.69	5
24.1	3.69	15	25.42	3.50	95	25.11	3.56	75	24.68	3.61	50	24.70	3.60	50	24.78	3.59	50
26.1	3.41	100	27.90	3.20	10	27.66	3.23	10	27.13	3.29	15	27.03	3.30	15	26.98	3.32	15
27.6	3.23	40	28.87	3.09	10	28.63	3.12	10	28.08	3.19	10	28.02	3.18	5	27.98	3.19	5
29.5	3.03	50	30.00	2.988	30	29.81	2.998	30	29.78	3.00	50	29.57	3.02	30	29.22	3.06	20
30.7	2.912	25	30.46	2.935	90	30.20	2.959	45	29.98	2.981	50	29.67	3.01	65	29.60	3.02	35
31.9	2.805	55	30.86	2.897	40	30.53	2.929	35	30.00	2.979		30.00	2.979	30	30.03	2.976	30
32.9	2.722	35	31.14	2.882	100	30.93	2.892	100	30.26	2.954	40	30.29	2.958	50	30.24	2.955	35
33.9	2.644	30	31.34	2.854	50	31.00	2.885		30.82	2.901	100	30.70	2.912	100	30.37	2.944	40
35.7	2.515	75	31.45	2.844	50	31.48	2.842	30	30.89	2.883	40	30.70	2.912		30.59	2.923	100
35.9	2.501	75	32.50	2.755	75	32.37	2.766	54	31.93	2.803	20	31.96	2.800	20	32.06	2.792	20
36.5	2.462	95	32.94	2.712	35	32.55	2.751	27	32.26	2.774	45	32.24	2.777	55	32.21	2.779	30
37.6	2.392	50	Other reflections			Other reflections			Other reflections			Other reflections			Other reflections		
39.0	2.309	20	61.31*	1.512	5	60.76	1.524	5	59.89	1.544	5	59.86	1.545	5	59.83	1.546	5
40.4	2.233	20	61.45*	1.509	5	60.94	1.520	5	60.56	1.529	5	60.17	1.538	5	59.99	1.544	5
41.9	2.156	10															
Other reflections																	

* Reflections used in Fig. 1.

Table III. Compositions, heat-treatments, phases, and manganese-activated cathodoluminescence emission data for phosphors in the $Zn_3(PO_4)_2$-$Cd_3(PO_4)_2$ system

No.	Composition, mole % $Zn_3(PO_4)_2$	$Cd_3(PO_4)_2$	$Mn_3(PO_4)_2$	Temp/time, °C/hr	Phases	Peak wavelength, Å	Brightness, ft-L
1	99.00	0	1.00	950/48	β-Z_3P	6370	23.6
2	94.05	4.95	1.00	950/48	β-Z_3P_{ss}	6350	21.7
3	89.10	9.90	1.00	950/48	β-Z_3P_{ss}	6340	20.2
4	94.05	4.95	1.00	800/48	A_{ss}	6300	20.2
5	79.20	19.80	1.00	850/48	B_{ss}	6150	24.1
6	69.30	29.70	1.00	850/48	B_{ss}	6200	24.9
7	66.33	32.67	1.00	850/48	B_{ss}	6260	26.0
8	62.37	36.63	1.00	850/48	B_{ss}	6340	22.6
9	59.40	39.60	1.00	850/48	B + C_{ss}	6490	17.0
10	49.50	49.50	1.00	850/48	B + C_{ss}	6570	12.3
11	39.60	59.40	1.00	850/48	C_{ss}	6540	13.0
12	29.70	69.30	1.00	850/48	C_{ss}	6510	14.0
13	19.80	79.20	1.00	850/48	C_{ss}	6510	13.8
14	4.95	94.05	1.00	950/48	C_3P_{ss}	6200	19.1
15	0	99.00	1.00	950/48	C_3P	6110	26.0
N.B.S. zinc orthophosphate: Mn						6380	21.0

$Cd_3(PO_4)_2$:Mn to u.v. excitation is dependent on the method of preparation.

The brightness values shown in Table III are not an absolute measure of the brightnesses of the phosphors, but they are meaningful when compared with the brightness of the "red" National Bureau of Standards zinc orthophosphate which was measured under the same experimental conditions.

Figure 3 shows the spectral distribution curves for phosphors in the α-$Zn_3(PO_4)_2$, β-$Zn_3(PO_4)_2$, A, and $Cd_3(PO_4)_2$ solid solution regions.

The results show that the addition of $Cd_3(PO_4)_2$ to β-$Zn_3(PO_4)_2$ slightly reduces both the brightness and peak emission wavelength. The one phosphor examined in the small A solid solution region was not quite as bright or as "red" as the β-$Zn_3(PO_4)_2$ phosphors.

$Cd_3(PO_4)_2$:Mn was found to peak at 6110Å with a brightness of 26.0 ft-L. The addition of $Zn_3(PO_4)_2$ to this compound produced a slight increase in peak emission and a decrease in brightness.

The isomorphous replacement of Zn^{2+} by Cd^{2+} in solid solution series B increases the peak emission from 6150Å to about 6300Å with the brightness remaining around 25.0 ft-L.

The substitution of Cd^{2+} for Zn^{2+} in solid solution series C decreases the peak emission slightly from 6570 to 6510Å and increases the brightness from 12 to 15 ft-L.

Figure 4 shows the spectral distribution curves for seven phosphors prepared in the region from 20 to 80 mole % $Cd_3(PO_4)_2$. Curves 1 and 2 are for B_{ss} phosphors, curves 5, 6, 7 are for C_{ss} phosphors, and curves 3 and 4 are for phosphors in the immiscibility

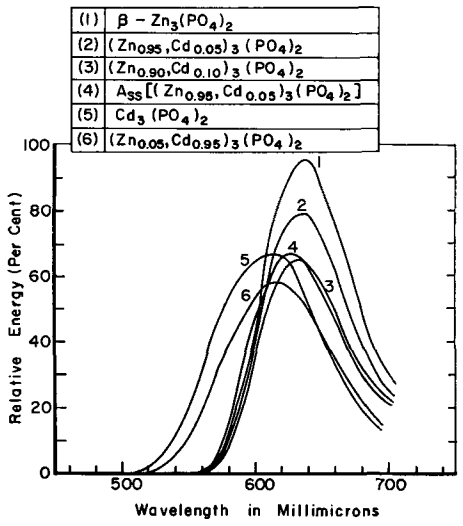

Fig. 3. Cathodoluminescence emission curves for α-$Zn_3(PO_4)_2$, β-$Zn_3(PO_4)_2$ A, and $Cd_3(PO_4)_2$ solid solution series.

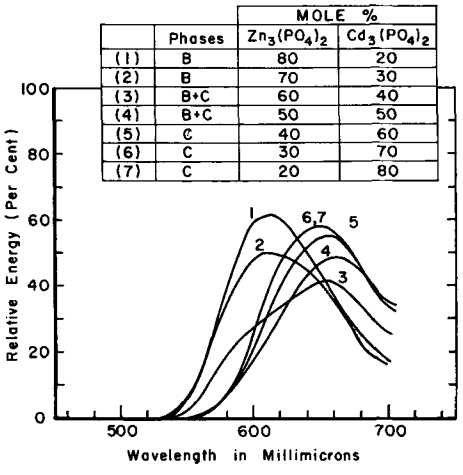

	Phases	MOLE % $Zn_3(PO_4)_2$	MOLE % $Cd_3(PO_4)_2$
(1)	B	80	20
(2)	B	70	30
(3)	B+C	60	40
(4)	B+C	50	50
(5)	C	40	60
(6)	C	30	70
(7)	C	20	80

Fig. 4. Cathodoluminescence emission curves for B and C solid solution series.

gap separating these two solid solution regions. Curve 3 shows two emission bands and confirms the existence of the two-phase (B_{ss} + C_{ss}) region. Curve 4 is predominantly C_{ss}, therefore the secondary emission peak is not resolved.

Discussion

Throughout this investigation the activator concentration was held constant at 1.0 mole % manganese in order to compare one phosphor with another.

In the three solid solution series involving β-$Zn_3(PO_4)_2$, C_{ss}, and $Cd_3(PO_4)_2$, it appears that the peak emission wavelength decreases as Cd^{2+} is substituted for Zn^{2+}, whereas the opposite is true for the B solid solution series. Since Cd^{2+} (1.03Å) is larger than Zn^{2+} (0.83Å), it is reasonable to expect that lattice expansion will produce less perturbation on the activator center and more energetic (shorter wavelength) emission will occur, similar to the results of Klasens, Zalm, and Huysman (8). However, Cd^{2+} is more polarizable than Zn^{2+}, and an antagonistic activator perturbation effect could occur which would result in an increase in peak emission wavelength as Cd^{2+} replaces Zn^{2+}. Such an effect is probably dependent on the kind of crystal structure involved, and the present data show that the relationship between manganese-oxygen distances, polarization effects, and peak emission wavelengths are highly qualitative.

The present phase equilibrium and manganese-activated cathodoluminescence data on phases in the $Zn_3(PO_4)_2$-$Cd_3(PO_4)_2$ system provide a better understanding of the emission results reported by Smith and Power (5). The system does contain six different phases and one of these has the "gamma" zinc orthophosphate structure. They also suggested (from their emission measurements) that most of these phases behaved as solid solution regions. From their emission data they constructed a curve of peak emission wavelength *vs.* composition for the entire orthophosphate join in which inflections occurred at 20, 35, and 85 mole % $Cd_3(PO_4)_2$. Since their phosphors were prepared at 875°C, the inflections are probably caused by the phase changes β-$Zn_3(PO_4)_{2ss}$ to B_{ss}, B_{ss} to C_{ss}, and C_{ss} to $Cd_3(PO_4)_{2ss}$, respectively.

Conclusions

1. The maximum solid solubility of $Cd_3(PO_4)_2$ in β-$Zn_3(PO_4)_2$ is 15 mole % at 950°C. Increasing the $Cd_3(PO_4)_2$ content decreases slightly both the manganese-activated cathodoluminescence peak emission wavelength and brightness.

2. A small intermediate solid solution (A_{ss}) having the magnesium orthophosphate structure exists from 2 to 7 mole % $Cd_3(PO_4)_2$ and has a maximum limit of stability of 910°C. Manganese-activated phosphors (1 mole % Mn^{2+}) in this region are not quite as "red" or as bright as the β-$Zn_3(PO_4)_2$:Mn phosphors.

3. Two solid solution series with similar structures are stable between 20 and 80 mole % $Cd_3(PO_4)_2$ and are separated by an immiscibility gap. B solid solution series exist from 20 to 37 mole % $Cd_3(PO_4)_2$. Phosphors prepared in this region with 1 mole % Mn^{2+} have peak emissions that vary from 6150 to 6300Å and brightnesses of about 25.0 ft-L as Cd^{2+} is substituted for Zn^{2+}. C solid solution series is stable from 56 to 80 mole % $Cd_3(PO_4)_2$. The manganese emission of these phosphors decreases from 6570 to 6510Å as Cd^{2+} replaces Zn^{2+}. The brightnesses of these preparations are relatively low, ranging from 12 to 15 ft-L.

4. $Cd_3(PO_4)_2$ melts congruently at 1180°C and will accept a maximum of 5 mole % $Zn_3(PO_4)_2$ in solid solution. Small amounts of Zn^{2+} substituting for Cd^{2+} increases the peak emission wavelength from 6110 to 6200Å and decreases the brightness from 26.0 to 19.1 ft-L.

Acknowledgment

Emission data were obtained through cooperation of Marjorie Brines of the Chemical Products Plant, General Electric Company, Cleveland, Ohio. This investigation was made possible through the support of the International Lead-Zinc Research Organization.

Manuscript received Jan. 25, 1963. This is part of a paper presented at the Pittsburgh Meeting, April 15-18, 1963. Contribution No. 62-48 from the College of Min-

eral Industries, The Pennsylvania State University, University Park, Pennsylvania.

Any discussion of this paper will appear in a Discussion Section to be published in the June 1964 JOURNAL.

REFERENCES

1. A. L. Smith, *This Journal*, **98**, 363 (1951).
2. F. L. Katnack and F. A. Hummel, *ibid.*, **105**, 125 (1958).
3. F. A. Hummel and F. L. Katnack, *ibid.*, **105**, 528 (1958).
4. J. F. Sarver, F. L. Katnack, and F. A. Hummel, *ibid.*, **106**, 960 (1959).
5. A. L. Smith and A. D. Power, *ibid.*, **101**, 244 (1954).
6. R. C. Ropp, R. W. Mooney, and C. W. W. Hoffman, *Anal. Chem.*, **33**, 1687 (1961).
7. R. C. Ropp, *This Journal*, **109**, 569 (1962).
8. H. A. Klasens, P. Zalm, and F. O. Huysman, *Philips Research Repts.*, **8**, 441 (May 1953).

The Systems BaO-MgO-P_2O_5 and BaO-ZnO-P_2O_5 Compounds and Fluorescence

Mary V. Hoffman

Luminescent Materials Laboratory, Chemical Products Plant, General Electric Company, Cleveland, Ohio

ABSTRACT

The BaO-MgO-P_2O_5 and BaO-ZnO-P_2O_5 systems were investigated, and the ternary compounds, solid solution areas, and compatibility triangles were determined. The ternary compounds were examined for fluorescence, and data on several crystalline phosphors and one fluorescent glass are given. X-ray diffraction data for the ternary compounds are included.

The ternary systems BaO-MgO-P_2O_5 and BaO-ZnO-P_2O_5 were investigated as part of a program of examining alkaline earth phosphate phosphors. The scope of the work reported here was limited to determining the compositions and x-ray patterns of the ternary compounds, examining these compounds for fluorescence with potential activators, and determining the compatibility triangles. The compounds of the binary systems involved in this work have been definitely established although complete work has been reported only on the ZnO-P_2O_5 system. Katnack and Hummel (1) found the compounds $Zn(PO_3)_2$, $Zn_2P_2O_7$, and $Zn_3(PO_4)_2$, each having two forms. In the MgO-P_2O_5 system, the ASTM Powder Data File lists the compounds $Mg(PO_3)_2$, $Mg_2P_2O_7$, and $Mg_3(PO_4)_2$. In the BaO-P_2O_5 system, four compounds are listed: $Ba(PO_3)_2$, $Ba_3P_4O_{13}$, $Ba_2P_2O_7$, and $Ba_3(PO_4)_2$. Data obtained in these tests on $Ba_2P_2O_7$ and $Ba(PO_3)_2$ are not in close agreement with those found in the ASTM files (2). Data obtained for $Ba_2P_2O_7$ by firing $BaHPO_4$ at 1000°C agree more closely with that presented by Ranby for $\delta Ba_2P_2O_7$ (3). Data shown in the appendix for $Ba(PO_3)_2$ were obtained on a sample prepared by firing $BaCO_3$ and $(NH_4)_2HPO_4$ in the mole ratio of 1:2 at 400°C for 16 hr, milling and refiring at 750°C for 16 hr.

In the ternary systems, very little has been reported. Ropp (4) has reported a Sn-activated phosphor in the pyrophosphate region of the BaO-MgO-P_2O_5 system. He included some x-ray data and indicated that a join between the pyrophosphates probably exists. This is the only reference found to either phosphors or compounds in the ternary systems of BaO-P_2O_5 with MgO or ZnO.

Procedure

The materials used in these tests were prepared from chemicals normally used in phosphor preparation. These materials include $BaHPO_4$ and $BaCO_3$ manufactured by the General Electric Company for phosphor use, $3MgCO_3 \cdot Mg(OH)_2 \cdot 3H_2O$ from either Merck and Company or the General Electric Company, and ZnO from New Jersey Zinc Company. In addition, three starting materials were prepared for use in these tests: $Zn_3(PO_4)_2 \cdot 4H_2O$ was made by adding H_3PO_4 to a solution of zinc acetate. $ZnNH_4PO_4$ was made by precipitation from diammonium phosphate and zinc acetate solutions. $MgNH_4PO_4 \cdot H_2O$ was precipitated by a modification of the analytical method using diammonium phosphate and magnesium sulfate solutions with a 10% excess of phosphate. Chemical analyses were made on all precipitated materials to determine the loss on ignition and the cation to phosphate ratio. Where possible, precipitated materials were used as the source of phosphate ion. In compositions lying between the pyrophosphate join and the P_2O_5 apex, an additional source of phosphate is needed and diammonium phosphate was used. These samples were mixed and given a preliminary firing at 500°C for 1 to 2 hr to decompose the diammonium phosphate and initiate the reaction, reducing the possibility of losing phosphate by volatilization or of melting the sample.

The ternary compounds and the compatibility triangles were determined by preparing 10-15g samples of various compositions and firing them for periods of 16-65 hr. Temperatures were varied depending on the melting point of the composition. Samples were examined by x-ray diffraction using the GE XRD-5, with nickel-filtered CuK_α radiation, and with the microscope. The samples were ground and refired if the x-ray patterns showed phases inconsistent with previous tests or in conflict with the phase rule. In order to preclude the formation of any quaternary compounds, no fluxes of any type were used. It was found, for instance, that the inclusion

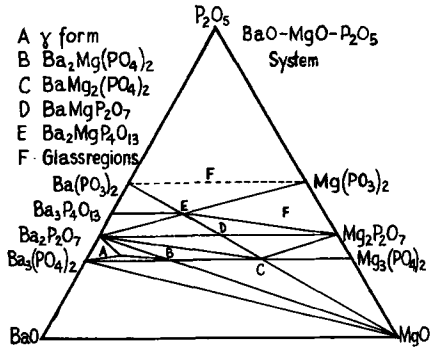

Fig. 1. Compatibility relationships in BaO-MgO-P_2O_5 system

of a fluoride resulted in the formation of a metastable barium apatite structure in many compositions with high Ba content, making it difficult to obtain an equilibrium condition.

Compatibility Diagrams

BaO-MgO-P_2O_5 *system.*—Compatibility triangles for the BaO-MgO-P_2O_5 system are shown in Fig. 1. No tests were made between the metaphosphate join and the P_2O_5 apex, and it is not likely that any ternary compounds that can be formed by solid-state reaction exist in this region. In the area examined, five compounds were found: $Ba_2Mg(PO_4)_2$, $BaMg_2(PO_4)_2$, $BaMgP_4O_{13}$, $BaMgP_2O_7$, and a compound which does not have a simple mole ratio, labeled γ in the compatibility diagram.

$Ba_2Mg(PO_4)_2$.—Differential thermal analyses (DTA) showed no heat effects below 1300°C.

$BaMg_2(PO_4)_2$.—DTA showed two reversible endotherms: a sharp, quickly reversible one at 820°C and a less energetic one at 1080°C. X-ray diffraction data were determined at 25°C and at 900°C, but not above 1080°C because of the corrosive action of the sample on the platinum sample holder of the high temperature x-ray furnace. X-ray data show that at least two crystalline forms of $BaMg_2(PO_4)_2$ exist, but only one is stable at room temperature.

$Ba_2MgP_4O_{13}$.—The DTA curve gave a questionable exothermic reaction at 640°C and a strong endothermic reaction at 900°C. Samples heated at 1000°C were partially melted. When quenched in water they contained glass and $BaMgP_2O_7$, indicating that the 900°C endotherm was due to incongruent melting. At 1100°C, the composition melted and could be quenched in water to a glass.

γ *form.*—This compound has a composition which lies between the ortho- and pyrophosphate. Compounds of similar structure and composition have been found in the SrO-Al_2O_3-P_2O_5 and BaO-Al_2O_3-P_2O_5 systems. The γ forms behave as a ternary compound, but the possibility that they are stabilized high-temperature forms of a binary compound has not been eliminated. A DTA showed no heat effects below the melting point of about 1250°C. A composition of 10 mole % MgO, 27 mole % P_2O_5, and 63 mole % BaO is close to a pure phase of this material and was used to record the x-ray diffraction pattern and to examine the fluorescence. Samples of this composition were melted and recrystallized. Microscopic examination showed uniformly sized crystals with moderate birefringence and an index of refraction of about $\eta = 1.644$. Very little extraneous material was found.

$BaMgP_2O_7$.—This compound is similar to $Mg_2P_2O_7$, and its determination as a separate compound is complicated by the similarity of patterns and also by the tenacity with which $Ba_2P_2O_7$ remains at this composition. The best means of identifying compositions along the $BaMgP_2O_7$-$Mg_2P_2O_7$ join as mixtures of the two end members is by utilizing the inversion of $Mg_2P_2O_7$ at 68°C. X-ray diffraction patterns run on samples which are above 68°C show the high form of $Mg_2P_2O_7$, which gives a pattern which can be distinguished from that of $BaMgP_2O_7$. The ternary compound contains no inversions and melts about 1050°C.

Two areas in which glass formed readily are shown. The metaphosphate "join" could not be definitely established because samples in this area formed crystals plus glass that did not recrystallize when fired as low as 400°C. The glass area between the pyro- and metaphosphate joins was explored more thoroughly for fluorescence and will be discussed in that section of this report.

BaO-ZnO-P_2O_5 *system.*—This system is similar to BaO-MgO-P_2O_5 in some respects and contains the compounds $BaZn_2(PO_4)_2$, $Ba_2Zn(PO_4)_2$, $BaZnP_2O_7$, and the γ form. The compatibility diagram is shown in Fig. 2.

$BaZn_2(PO_4)_2$.—This compound showed only a small reversible endothermic reaction at 550°C on heating in the DTA apparatus, which may have been due to a small amount of extraneous material, since no other evidence could be found to explain it. High-temperature x-ray patterns showed a slight shift in d spacings between 25° and 400°C, but little change at 500° and 600°C. Line intensities did not change on patterns run on a scanning speed of 2° 2θ/min.

$Ba_2Zn(PO_4)_2$.—This differs considerably from the corresponding Mg compound. The DTA curve shows a strong endothermic reaction at 970°C, a smaller endotherm at 1170°C and melting at 1225°C. The two endothermic reactions are sluggishly reversible. The composition has a lower limit of stability at about 970°C, below which $Ba_3(PO_4)_2$ and $BaZn_2(PO_4)_2$ are in equilibrium. X-ray diffraction patterns were run at 1000°C to obtain a pattern of pure β $Ba_2Zn(PO_4)_2$. A second crystallographic form exists above 1170°C. To obtain this form, samples of the composition $Ba_2Zn(PO_4)_2$ were melted and quenched in water. These showed the new pattern

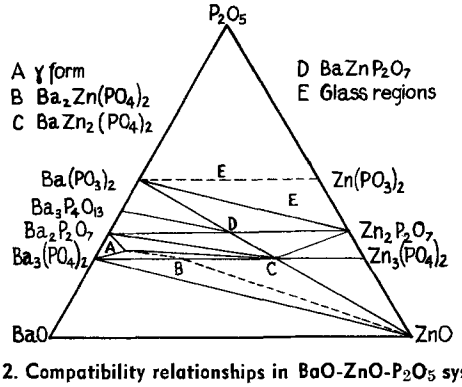

Fig. 2. Compatibility relationships in BaO-ZnO-P_2O_5 system

of the high-temperature form α $Ba_2Zn(PO_4)_2$, which inverted to the β form on reheating below 1170° but above 970°C. The α form could not be obtained in pure form in an air quench.

The γ form.—This has approximately the same mole ratio as the corresponding Mg compound. The DTA curve shows no reaction below the melting point. The x-ray patterns of the γ forms in the two systems are almost identical. The slight difference in the number of lines present in the x-ray patterns as shown in the appendix may be due to some contamination with extraneous phases or to differences in the degree of crystallinity.

$BaZnP_2O_7$.—This compound melts to a glass at about 975°C and shows no heat effects on the DTA curve.

Fluorescence

The ternary compounds were examined for fluorescence by preparing several compositions positioned near the apexes of the compatibility triangles that include the compound being examined. The γ forms were prepared as pure as possible. The compositions were mixed by ball milling and fired at least 16 hr or until x-ray or microscopic examination showed them to contain uniform and well-reacted crystals. These were then ball milled. Activators were added to the fired matrix in amounts on the order of 0.05 mole activator per mole of matrix. The activators were usually added from solutions containing the activator in the desired amount. The slurry was dried, ground, and fired for 1 to 2 hr.

While a number of the matrices gave weak fluorescent response with various activators, those described here were found to have a luminescent response sufficiently strong to warrant making emission and brightness measurements. Variations in activator concentration composition and other parameters were made until no further major improvement in brightness was obtained. Emission measurements were then made on the sample. Emission curves for these phosphors are shown in Fig. 3, 4, and 5. In the phosphors shown in these figures, no change in emission color was detected with variations in activator concentration.

$BaMg_2(PO_4)_2$:Mn.—This phosphor is responsive only to cathode ray excitation, emitting in the deep red. The peak wavelength is at 6800Å, with a half-width of about 1000Å. Brightness was measured to be 2.1 ft-L at 1.0 μa/cm^2. The best brightness was obtained with a slight excess of P_2O_5 and 0.03 moles Mn per mole orthophosphate. Brightness change with Mn is slight. Firings were made at 1075°C for 4 hr.

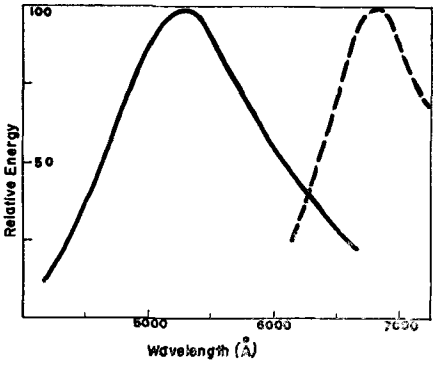

Fig. 3. Spectral distribution curves: ——, $BaMg_2(PO_4)_2$:Sn; — — —, $BaMg_2(PO_4)_2$:Mn; cathode ray excitation.

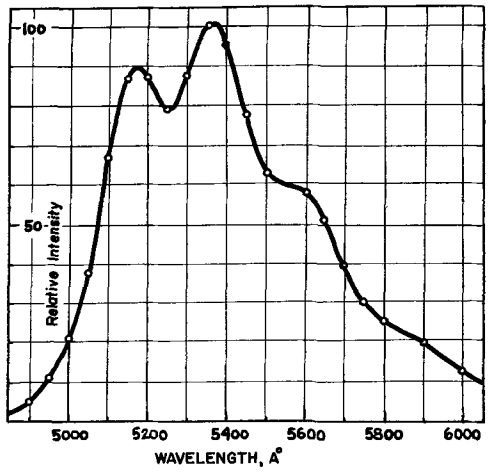

Fig. 4. Spectral distribution curve: $Ba_2Mg(PO_4)_2$:U; 2537Å excitation.

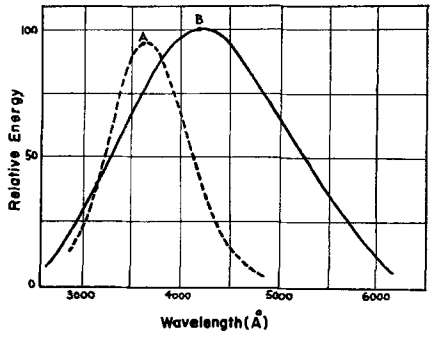

Fig. 5. Spectral distribution curves: ——, BaMg Phosphate:Sn glass; — — — γ BaMg Phosphate:Pb.

$BaMg_2(PO_4)_2$:Sn.—The same composition with Sn activation has a broad greenish-white emission under cathode ray excitation. The peak is at 5250Å with a half-width of 1450Å. Brightness was measured at 7.0 ft-L at 1.0 μa/cm^2. The phosphor was fired in an atmosphere of 0.5% H_2 in N_2 to incorporate the activator as Sn^{+2}.

$Ba_2Mg(PO_4)_2$:U.—This phosphor responds to both 2537 and 3650Å excitation with about equal intensity. The maximum brightness was obtained with compositions containing up to 20 mole % Zn substituted for Mg. Substitutions of Ca or Sr for Ba decreased the brightness. The spectral distribution, which is shown in Fig. 4, did not change in line position with Zn, Ca, or Sr substitution and is similar to those found for U activation in many phosphate matrices. Only compositions containing a slight excess of P_2O_5 fluoresced with U activation. The optimum U content was 0.004 moles U per mole orthophosphate, added from a solution of uranium acetate in methanol. Lower U content gave sharply reduced brightness, while higher contents improved the brightness only slightly but caused considerable sintering.

Maximum brightness obtained was 55% of zinc silicate:Mn, with 86% absorption of 2537Å radiation. The phosphor is damaged by milling, losing about 50% of its brightness with 8 hr milling. This loss is partially restored by refiring and is probably

Table I. Data obtained from 40w lamps

	0 hr	100 hr	500 hr
Lumens	1018	905	785
Lpw	25.0	22.3	19.3
Color, x/y	0.272/0.509	0.269/0.498	0.269/0.479

highly dependent on particle size. A phosphor containing the partial Zn substitution was milled in a suspending medium for 3 hr, and suspension was used to coat fluorescent lamp bulbs. Brightness of the phosphor was 37% of zinc silicate:Mn after milling and 26% as bright after being removed from a lamp that had not been burned. Data obtained from 40w lamps are shown in Table I.

Fluorescence in the γ Forms

These forms gave fluorescence with several different activators. With Sn^{+2}, the γ BaZn phosphate containing form responds to 2537Å excitation, emitting a broad band peaking at 5400Å. Incorporation of Sn^{+2} in a mildly reducing atmosphere resulted in the formation of some $Ba_2P_2O_7$ by partial decomposition of the γ form. This gave some mixed fluorescence so that an exact measure of the emission from the γ form could not be obtained. With U activation, the same form responds to both 2537 and 3650Å excitation. The emission lies in bands from 5100 to 5500Å, but has poor brightness.

Both the Zn and Mg γ forms respond to Pb activation. These phosphors emit in the ultraviolet under 2537Å excitation and are similar in spectral distribution. The spectral distribution curve of γ BaMg phosphate:Pb was measured using a grating monochrometer with a 1P28 photomultiplier as detector, calibrated with a standard tungsten lamp above 3600Å. The emission of this phosphor is shown in Fig. 5. The peak is at 3600Å with a half-width of 950Å. It has no emission beyond 5000Å and very little past 4400Å. Emission intensity was compared with a Pb-activated barium silicate phosphor and found to be only 7% at 3600Å.

Other Phosphors

The crystalline phosphors described above were the brightest found in examining these systems, but they do not represent the only fluorescence observed. A number of other phosphors were found on which only visual evaluations were made because of their low intensity. For instance, Mn gave luminescence under cathode ray excitation in all the compounds. The emission color ranged from a deep red in the orthophosphates to an orange color in the pyrophosphates and $Ba_2MgP_4O_{13}$. Under 2537Å excitation, Pb activation gave a deep blue color in the pyrophosphates but not in the orthophosphates. Incorporation of Sn^{+2} gave blue fluorescence under cathode ray excitation in most of the compounds, but had 2537Å response only in the Zn-containing compounds. With rare earths as activators, the Zn-containing compounds were generally poor, but the Mg-containing compounds responded with the typical emission color, such as salmon with Sm, red with Eu, yellow-white with Dy. Approximately twenty possible activators were examined in each of the compounds found in these systems.

Pyro-meta region.—Ropp's paper (4) on Sn-activated magnesium barium pyrophosphate phosphor is the only work reported that covers these systems in any detail. Ropp reported finding several different Sn-activated phosphors along the $Ba_2P_2O_7$:$Mg_2P_2O_7$ join which were responsive to 2537Å excitation. On the high Ba side, he listed α $Ba_2P_2O_7$:Sn, previously reported by McKeag and Steward (5) as a red phosphor. With the $Mg_2P_2O_7$ content between 20 and 80 mole % and firing temperatures below 1010°C, he reported a blue-green phosphor. At $Mg_2P_2O_7$ contents above 80%, he found a phosphor which emits at 3970Å. Investigation in this laboratory of $BaMgP_2O_7$ and of the area along the join between $BaMgP_2O_7$ and $Mg_2P_2O_7$ with Sn^{+2} activation gave no fluorescent response under 2537Å excitation. The difference is probably attributable to the degree of equilibrium attained. Ropp required precise control over flux content, firing times, and temperatures to obtain maximum brightness, but did not obtain an equilibrium condition. In the examination of the pyrophosphate join with Sn^{+2} activation, an equilibrium condition was obtained in the matrix alone, before addition of the activator and firing in reducing atmosphere.

Examination of the area between the pyro- and metaphosphate joins showed that compositions in this region form stable glasses which can be activated by Sn and emit in the near ultraviolet. It is possible that a mixture of $BaMgP_2O_7$ and the fluorescent glass would form metastably under the firing conditions given by Ropp. Such a mixture would give only the pyrophosphate x-ray diffraction pattern since the glass would not contribute.

The fluorescent glass was prepared with the fired composition 45 parts P_2O_5, 50 parts MgO, and 5 parts BaO, which is midway between the pyro- and metaphosphates as shown in Fig. 1. Compositions higher in pyrophosphate did not remain a pure glass when cooled but contained some crystalline material, $MgBaP_2O_7$. Compositions higher in P_2O_5 had a higher melting point, so that the composition used for the glass is close to a eutectic composition. This composition was milled with SnO and fired at 500°C to decompose the diammonium phosphate, milled with 5 wt % NH_4Cl and melted at 1250°C in a kyanite crucible. NH_4Cl is essential for good brightness, but does not affect the melting point appreciably. Samples melted without NH_4Cl had the same emission, but were only about 30% as bright as those containing chloride. The glass was melted in air with no reducing atmosphere other than that supplied by the decomposition of NH_4Cl. The addition of a mixture of forming gas and nitrogen over the melt did not improve the brightness or change the spectral distribution. Refiring the glass in air or in reducing atmosphere below the melting point resulted in recrystallization and loss of most of the brightness.

The spectral distribution of a glass is shown in Fig. 5. Spectral emission curves made on a number of different samples containing glass plus crystals indicate that two emission bands may be present

in compositions surrounding the glass area, one about 4800Å and another closer to 4000Å. Both are broad bands. Spectral distribution curves of the pure glass were run on duplicate samples without change in distribution or evidence of two emission bands.

Acknowledgments

The author would like to thank Dr. F. J. Studer for making the ultraviolet emission measurements and Miss L. Margolis for assistance in sample preparation.

Manuscript received May 9, 1963; revised manuscript received June 21, 1963. This paper was presented at the Pittsburgh Meeting, April 15-18, 1963.

Any discussion of this paper will appear in a Discussion Section to be published in the June 1964 JOURNAL.

REFERENCES

1. F. L. Katnack and F. A. Hummel, *This Journal*, **105**, 125 (1958).
2. R. P. Langguth, R. K. Osterheld, and E. Karl-Kroupa, *J. Phys. Chem.*, **60**, 1335 (1956); ASTM Powder Data File Cards, 9-45, 9-46 and 12-7.
3. P. W. Ranby, D. H. Mash, and S. T. Henderson, *Brit. J. Appl. Phys.*, Supplement No. 4 S-18.
4. R. C. Ropp, *This Journal*, **109**, 15 (1962).
5. A. H. McKeag and E. G. Steward, *Brit. J. Appl. Phys., Supplement* No. 4, S-26.

APPENDIX

$Ba(PO_3)_2$

d	I/I
4.27	24
4.19	100
3.98	55
3.80	20
3.41	34
3.35	100
3.17	25
3.06	20
2.97	41
2.72	30
2.61	30
2.57	22
2.52	25
2.36	20
2.26	28
2.23	26

γ BaMg Phosphate

d	I/I
4.37	12
4.29	20
4.19	12
3.80	15
3.71	16
3.60	6
3.48	8
3.32	78
3.24	100
3.18	68
3.12	96
2.96	21
2.93	12
2.84	29
2.79	20
2.66	8
2.62	8
2.32	9
2.27	15
2.25	12
2.22	11
2.20	6
2.18	23
2.14	15
2.12	14
2.09	33
2.05	24

γ BaZn Phosphate

d	I/I
4.37	17
4.29	23
4.21	11
3.79	19
3.70	17
3.32	69
3.24	99
3.18	60
3.12	100
2.96	27
2.83	21
2.42	7
2.34	9
2.27	17
2.25	19
2.18	21
2.14	13
2.12	17
2.08	31
2.05	23

$Ba_2Mg(PO_4)_2$

d	I/I
4.50	25
4.37	23
4.23	8
4.02	17
3.46	73
3.40	44
3.30	17
3.11	100
3.02	19
2.97	21
2.88	9
2.75	31
2.64	37
2.53	25
2.17	17
2.09	17
2.04	17
2.01	12
1.97	40

$Ba_2Zn(PO_4)_2$ α form, quenched

d	I/I
4.50	33
4.41	22
4.06	11
3.83	16
3.40	56
3.19	100
2.82	42
2.63	93
2.39	11
2.37	7
2.19	27

$BaZn_2(PO_4)_2$

d	I/I
3.97	100
3.01	100
2.67	8
2.64	40
2.30	8
2.20	31
2.00	8
1.99	10
1.87	30
1.83	8
1.69	11

$Ba_2Zn(PO_4)_2$ β form, at 1000°C

d	I/I
4.27	32
3.85	13
3.78	16
3.72	27
3.63	40
3.53	86
3.46	100
3.30	13
3.22	46
3.17	24
3.16	73
2.84	38
2.71	41
2.64	41
2.13	27

$Ba_2MgP_4O_{13}$

d	I/I
8.42	16
7.08	5
5.57	17
4.95	25
4.79	19
4.04	18
3.98	8
3.59	100
3.35	56
3.21	95
3.07	13
2.89	11
2.81	76
2.74	8
2.69	20
2.64	13
2.54	25
2.50	16
2.44	16
2.38	30
2.31	21
2.24	22
2.18	14
2.16	17
2.12	29
2.05	34
2.03	14
1.97	16
1.94	17

$BaMg_2(PO_4)_2$ At room temperature

d	I/I
4.00	52
3.93	69
3.86	100
3.09	33
3.06	27
3.00	39
2.98	56
2.95	10
2.72	13
2.63	4
2.57	50
2.35	14
2.29	10
2.24	21
2.17	10
2.15	14
2.13	21

At 900°C

d	I/I
8.19	34
3.95	100
3.04	73
2.73	8
2.61	43
2.49	8
2.34	20
2.26	10
2.18	16
2.04	3
1.98	5

$BaZnP_2O_7$

d	I/I
7.31	7
5.71	9
5.27	5
4.62	10
4.41	15
4.19	5
4.07	5
3.86	20
3.63	20
3.55	55
3.34	18
3.10	28
3.00	70
2.95	78
2.90	5
2.86	20
2.70	14
2.64	33
2.56	8
2.55	8
2.50	17
2.42	20
2.38	5
2.31	4
2.23	5
2.20	15
2.18	10

$BaMgP_2O_7$

d	I/I
7.07	14
6.32	35
5.07	22
4.05	16
3.75	13
3.69	15
3.53	8
3.37	69
3.30	14
3.24	5
3.14	16
3.08	30
2.99	40
2.96	45
2.79	14
2.74	32
2.63	22
2.60	8
2.57	8
2.27	17
2.13	16
2.04	20

The Influence of Copper on Structural Transformations in ZnS:Cu,Cl

J. Nickerson, P. Goldberg, and D. H. Baird

General Telephone & Electronic Laboratories, Incorporated, Bayside, New York

ABSTRACT

Chemical analyses and x-ray powder photographs have shown that thermal treatment of hexagonal ZnS:Cu,Cl phosphors in atmospheres of H_2S and of He containing $ZnCl_2$ results in structural transformations and solubility changes of activator and co-activator. The temperature at which these changes occur depends on the copper concentration. Our results demonstrate the role of a separate phase of copper sulfide in promoting the growth of cubic zinc sulfide and thus effecting the hexagonal-to-cubic transformation.

The two crystalline modifications of zinc sulfide are well known. The high-temperature hexagonal and the low-temperature cubic forms exhibit a reconstructive transformation at a transition temperature of approximately 1020°C. In these studies, previously crystallized hexagonal ZnS:Cu,Cl phosphors (ZnS phosphors with Cu activator and Cl co-activator) were thermally treated in either H_2S atmospheres or mixed atmospheres of He and $ZnCl_2$, with or without additional activator present, and the resulting structural and chemical changes were determined by x-ray diffraction and chemical analyses. The results of these experiments demonstrate the role of a separate phase of copper sulfide in promoting the growth of cubic zinc sulfide and thus effecting the hexagonal-to-cubic transformation.

Earlier studies have been made of the influence of foreign atoms and the regions of stability of wurtzite and sphalerite. Work in this area has included that of Skinner and Barton (1) on the effect of oxygen on increasing the stability of wurtzite below the transition temperature. Aven and Parodi (2) have discussed the role of copper and silver in effecting the hexagonal-to-cubic transformation during the crystallization of ZnS phosphors in H_2S.

All of these studies have dealt with transitions encountered during the crystallization of ZnS. It is well known that hexagonal ZnS can persist in the region of cubic stability. Studies have been published on the effect of grinding in causing the hexagonal form to convert to the cubic. Little work has been done on determining chemical factors that influence the transformation. Our research has placed emphasis on the influence of copper on the transformation of previously crystallized hexagonal phosphors subsequently fired in the range of cubic stability.

Experimental Results

Thermal treatment of ZnS:Cu,Cl *in* H_2S.—A family of hexagonal ZnS:Cu,Cl phosphors was prepared with activator concentrations ranging from 0.1-1.75 x 10^{-3}g at Cu/mole ZnS. These were crystallized at 1100°C in air for several hours with 9 wt % chloride flux. The phosphors were then washed with a hot potassium cyanide solution to remove any unincorporated copper and analyzed for copper and chloride. As previously reported (3), the photoluminescence of these materials is green with long decay in the region of 0.1-0.4 x 10^{-3}g at Cu and blue-green and blue with short decay at higher activator concentrations.

Samples of these phosphors were then thermally treated in a stream of H_2S for 1 hr over a range of temperatures. It was found that transformation to the cubic form can occur, the transformation being accompanied by a loss of activator and co-activator. Figure 1 shows the copper concentrations of the phosphors studied plotted along the abscissa, with the concentrations expressed in g at. Cu/mole ZnS retained. Seven principal families of phosphors were studied containing 0.1 to 1.75 x 10^{-3}g at Cu/mole. Along the ordinate is plotted the temperature of the H_2S treatment given the samples. For any one family of phosphors, for instance the one containing 0.75 x 10^{-3}g at Cu/mole, there exists a critical temperature (T_c), in this case 800°C, above which transformation to the cubic structure will occur. The family of phosphors containing 1.6 x 10^{-3}g at Cu/mole will transform at 700°C. The solid line indicates the approximate relationship between T_c and copper concentra-

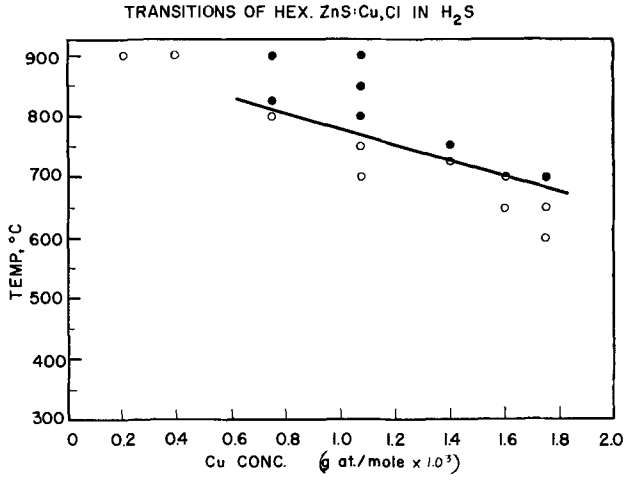

Fig. 1. Transitions of hexagonal ZnS:Cu,Cl in H_2S. ●, Transforms; O, remains hexagonal.

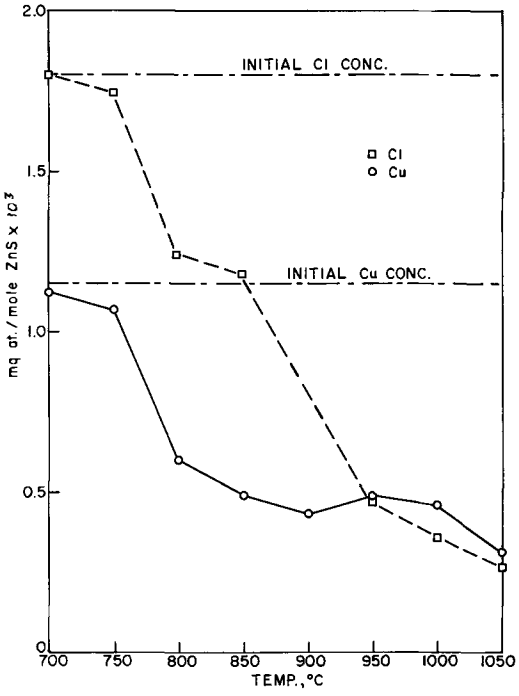

Fig. 2. Copper and chloride retention as a function of temperature

tion. In addition, chemical analyses show that those phosphors treated above T_c lose considerable copper and chloride as shown in Fig. 2. It is believed that the H_2S serves to remove the copper and chloride as copper sulfide and HCl.

Those samples treated at temperatures below the T_c corresponding to their copper concentrations do not transform and show no change in activator or co-activator content. It can be seen in Fig. 1 that an inverse relationship exists between copper concentration and temperature of transformation in the region 0.75-1.75 x 10^{-3}g at Cu/mole. The two families of phosphors whose Cu content is below 0.75 x 10^{-3}g at Cu/mole do not show transformation or loss of copper when fired at temperatures as high as 1000°C. Further, it has been found that the photoluminescence of the phosphors treated above their respective T_c is deep blue with short decay, while that of the phosphors treated below T_c is green with long decay, regardless of initial or final activator concentration.

To study further the role of Cu in influencing the phase transformation, an experiment was conducted with a separate phase of copper sulfide added to two of the phosphors prepared for the previous experiment. 10 x 10^{-3}g at. Cu/mole were added as CuS to hexagonal ZnS:Cu,Cl phosphors containing 0.75 and 1.6 x 10^{-3}g at Cu/mole and these samples were treated in H_2S as before. In this experiment, however, where CuS was added to the phosphors before re-firing, complete transformation to the cubic form was observed at temperatures as low as 600°C for these two Cu concentrations. This is 100°-200° lower than the temperature at which transformation would occur had no additional Cu been present. In addition, the formation of mixed cubic and hexagonal structures was observed after thermal treatment at temperatures as low at 350°C. These samples, when analyzed following a cyanide wash, showed no significant change in incorporated Cu and chloride. Also phosphors containing 0.2 to 0.4 x 10^{-3}g at Cu/mole were fired at 900°C, with 10 x 10^{-3}g at Cu/mole present as CuS, and transformation to the cubic structure was observed. It should be noted that no transformation occurred when these phosphors were treated at 1000°C with no CuS added.

Thermal treatment of ZnS:Cu,Cl *in mixed atmospheres of* He *and* $ZnCl_2$.—The next study involved thermal treatment of a hexagonal ZnS:Cu,Cl phosphor, also with CuS added as a separate phase, but this time the treatment was carried out in an atmosphere that favored incorporation of the activator. Hexagonal ZnS:Cu,Cl containing 1.1 x 10^{-3}g at Cu/mole and 1.5 x 10^{-3}g at Cl/mole ZnS was prepared at 1100°C by the same method used for the other phosphors. Copper was added as CuS (10 x 10^{-3}g at Cu/mole) and the phosphor was fired in an atmosphere consisting of He at about 760 mm pressure and $ZnCl_2$ at 10 mm pressure in the temperature range 600°-700°C. The samples were then washed with hot KCN solution and analyzed for copper and chloride. Table I shows the relationships between activator and co-activator concentrations and structure of the phosphors following this treatment.

At 700°C a sharp increase in activator concentration is seen, coincident with the hexagonal-to-cubic phase transformation. This experiment further demonstrates the role of copper sulfide as a separate phase in effecting the hexagonal-to-cubic transformation. In this case, the transformation occurs under ambient conditions favoring incorporation of Cu (*i.e.*, a chloride-rich environment) as opposed to the H_2S atmosphere experiments which lead to removal of copper and chloride.

Discussion

The above experimental results can be explained by postulating that a separate phase of copper sulfide serves as a nucleating phase for the growth of cubic ZnS and thus promotes the hexagonal-to-cubic transition. In H_2S with no copper added, this phase is formed as a result of the removal of Cu from the lattice as copper sulfide. The rate of the reaction between H_2S and the copper and chloride in the phosphor which forms the copper sulfide is dependent on the initial concentrations of Cu and chloride and on the temperature. At Cu concentrations less than 0.75 x 10^{-3}g at., the rate of this reaction is too slow to form the amount of copper sulfide necessary for initiating the phase transformation, and no transformation occurs. In the experiment where CuS was added to the phosphors prior to the H_2S treatment, transformation was observed at much lower temperatures.

The experiments with $ZnCl_2$-bearing He also demonstrate the role of a separate phase of copper

Table I

Temp, °C	Cu, g at./mole × 10^3	Cl, g at./mole × 10^3	Structure
Initial	1.1	1.5	Hexagonal
600	1.3	3.1	Hexagonal
650	1.5	4.0	Cubic
700	4.4	5.7	Hexagonal

sulfide in initiating the phase transformation. Here the incorporation of copper and chloride is favored by charge compensation. When the transformation occurs, the rate of incorporation of copper and chloride in the lattice is found to increase. Other experiments using crystalline phosphors with cubic structure indicate that the resulting increase in activator and co-activator concentrations is not due to a greater solubility of copper and chloride in the cubic structure. It is, rather, due to an increased rate of diffusion during phase transformation. This phenomenon, in which the reactivity between several phases is increased when one or more of them is undergoing a phase transformation, is commonly known as the Hedvall effect.

Aven and Parodi (2) have discussed the role of Cu in triggering the hexagonal-to-cubic transformation during crystallization in H_2S of ZnS:Cu,Al phosphors. They observe the formation of cubic ZnS in phosphors that contain Cu in amounts that exceed its solubility in the wurtzite lattice. They believe that, after firing, copper sulfide precipitates exothermically from solution in hexagonal ZnS as a result of a lower solubility at lower temperatures and, in so doing, supplies the energy necessary for nucleation of cubic ZnS. Our results indicate that it is the physical presence of copper sulfide as a separate phase, rather than the energy released during its formation, that initiates the observed transformations. There may be a relation between the crystal structure of the copper sulfide formed and its ability to promote the formation of cubic ZnS. Djurle (5) has indicated the compositional and structural complexity of the Cu-S system. High-temperature cubic forms of Cu_2S and Cu_9S_5 have recently been reported by Kullerud and Yund (6) and Morimoto and Kullerud (7).

These experiments have shown the role that Cu plays in effecting the transformation of hexagonal ZnS to the cubic form. The presence of a separate phase of copper sulfide serves to promote the growth of cubic ZnS and thus causes the transformation. This conversion is observed under ambient conditions favoring both precipitation and incorporation of Cu.

There are, of course, other factors influencing the phase transformations studied. As a result of these investigations, some observations might be made on the effects of small amounts of oxygen on the stability of hexagonal ZnS. Skinner and Barton (1) have found that the presence of oxygen leads to the metastable growth of wurtzite in the sphalerite stability field. We believe that oxygen present in the ambient and/or in the phosphor lattice can stabilize the hexagonal structure. The initial crystallization of our phosphors was carried out in air with excess Cu present and resulted in the hexagonal form. Were this synthesis carried out in an H_2S atmosphere as done by Aven and Parodi, cubic ZnS would form. Thus we can see the effect of oxygen on inhibiting the transformation during crystallization in air.

To cite another observation on the inhibiting effect of oxygen, a hexagonal ZnS:Cu,Cl phosphor with a separate phase of copper sulfide present can be given a thermal treatment in air at temperatures below 1020°C and show little or no conversion to the cubic structure. Yet if this treatment were carried out in H_2S or $ZnCl_2$-bearing He, transformation would take place.

Summary

Our experiments have shown the role that copper plays in effecting the transformation of hexagonal to cubic ZnS. The presence of a separate phase of copper sulfide serves to promote the growth of cubic ZnS and thus causes transformation. This conversion is observed under ambient conditions favoring both removal and incorporation of copper.

Acknowledgments

It is a pleasure to acknowledge helpful discussions with G. Gashurov and S. Faria during the course of the research. The authors are grateful to J. Ragusin for preparing many of the samples, C. Creter for providing x-ray data, and R. Weberling for the chemical analyses.

Manuscript received May 7, 1963. This paper was delivered at the Indianapolis Meeting, April 30- May 3, 1961.

Any discussion of this paper will appear in a Discussion Section to be published in the June 1964 JOURNAL.

REFERENCES

1. B. J. Skinner and P. B. Barton, *Am. Mineral.*, **45**, 612 (1960).
2. M. Aven and J. A. Parodi, *J. Phys. Chem. Solids*, **13**, 56 (1960).
3. A. L. Solomon and P. Goldberg, Paper presented at Chicago Meeting of The Electrochemical Soc., (1960).
4. F. A. Kroeger and J. Dikhoff, *Physica*, **16**, 297 (1950).
5. S. Djurle, *Acta Chem. Scand.*, **12**, 1415 (1958).
6. G. Kullerud and R. Yund, Geol. Soc. Amer., Abstracts of Denver Meeting, 143 (1960).
7. N. Morimoto and G. Kullerud, *Am. Mineral.*, **48**, 110 (1963).

Erratum

In the paper "Observations on the Formation of Color Centers in Calcium Halophosphate" by E. F. Apple [*This Journal*, **110**, 374 (1963)] on page 378, Fig. 11; A and B on curves should be interchanged. The lower curve represents the slowly cooled sample and the upper curve the rapidly quenched sample.

The Preparation and Electrical Properties of Bismuth Trisulfide

Alfred C. Glatz and Virginia F. Meikleham

Carrier Research and Development Company, Syracuse, New York

ABSTRACT

The direct synthesis of bismuth trisulfide was investigated by differential thermal analysis. It is demonstrated that bismuth trisulfide forms exothermically at about 285°C and melts at 760° ± 5°C. The probable reasons for the previous detonations in the preparation of this compound are elucidated. The thermoelectric properties of stoichiometric bismuth trisulfide and bismuth trisulfide doped with Pb, Ag, O_2, and Sb were investigated. The thermoelectric figure of merit for stoichiometric bismuth trisulfide measured in the [001] crystallographic direction at 300°K is 2.3 x 10^{-5}/°K. Hall coefficient studies indicate that the mobility of stoichiometric bismuth trisulfide in the same crystallographic direction at 300°K is 21.3 cm^2/volt-sec, and acoustical lattice scattering is probably the predominant scattering mechanism in the temperature range 78°-300°K.

Investigations of the bismuth chalcogenides for thermoelectric cooling applications have been primarily concerned with the compounds bismuth telluride and/or bismuth selenide and their alloys. These materials have been thoroughly studied, and their room temperature electrical properties are quite well known. On the other hand, the compound bismuth trisulfide has been the subject of only a few investigations (1-7), and there are large deviations in the reported electrical properties for this compound. A summary of the reported (room temperature) electrical properties of bismuth trisulfide is given in Table I. It may be observed from this table that there are wide variations in both the electrical resistivity and the thermoelectric power for this compound. The electrical resistivity, for example, varies from 10 milohm-cm to 10^{10} milohm-cm. Part of this variation is probably due to the fact that the first four investigators (all Russian) used pressed and sintered samples and reported higher resistivities than the latter investigators, who used Bridgman lowered samples.

These variations in the electrical properties of bismuth trisulfide are probably due to compositional changes, which are related to the method of preparation and crystal growth. Therefore, a more thorough understanding of the physical chemistry of these processes was required. For this reason, the purpose of this investigation was to study the physiochemical properties of bismuth trisulfide related to its preparation and crystal growth, and to investigate the room temperature thermoelectric properties of stoichiometric and doped samples of bismuth trisulfide.

Experimental

Materials.—Bismuth metal shot (99.999+%) and elemental sulfur (99.999+%) were obtained from American Smelting and Refining Company, and were used in the preparation of the ingots. Bismuth metal powder (99.95%) which was obtained from the J. B. Baker Chemical Company, was appropriately sieved and used to study the bismuth-sulfur reaction. The dopants Ag, Pb, and Sb (99.999+%) were obtained from American Smelting and Refining Company, and Bi_2O_3 (99.0%) was obtained from the J. T. Baker Chemical Company.

Preparation and physiochemical properties.—Probably the most important factors that have limited a really comprehensive thermoelectric investigation of bismuth trisulfide are the difficulties associated with its preparation and crystal growth. Descriptions of detonations in the synthesis of bismuth trisulfide have been commonplace in the literature. When this investigation was initiated, the only available phase diagram, as given in Hanson (8), indicated that bismuth trisulfide was a peritectic

Table I. Reported electrical properties of bismuth trisulfide at 300°K

Investigator	Year	α, μv/°C	ρ, milliohm-cm	K, mw/cm/°C	Form of sample
Hokhberg *et al.* (1)	1937	80	10^4	—	—
Galkin *et al.* (2)	1952	700	10^9-10^{10}	—	Polycrystalline Pressed
Konorov (3)	1956	1300	10^6	—	Pressed
Goriunova (4)	1957	—	2×10^4	—	Polycrystalline
Black *et al.* (5)	1957	750	10	—	Polycrystalline
Franklin Institute (6)	1957	296	48	15	Polycrystalline
Gildart *et al.* (7)	1961	550	850	20.6	Single crystals

compound, with a peritectic reaction temperature of 850°C. All previous measurements on bismuth trisulfide grown from the melt were on samples prepared at this temperature. However, we have found that in a closed system bismuth trisulfide behaves as a congruently melting compound with a melting point of 760°± 5°C. This lower melting point for bismuth trisulfide in a closed system has also been reported by Van Hook (9) and Cubicciotti (10).

Bismuth trisulfide was prepared in minimum void volume, heavy-walled quartz ampoules having an inside diameter of 10 mm and a wall thickness of 3 mm. The appropriate quantity of high-purity sulfur was initially added to the ampoule and melted in a small crucible furnace. High-purity bismuth shot was added to the molten sulfur to form a dispersion of bismuth shot in molten sulfur. The ampoule was then cooled down to room temperature and sealed off as close to the melt line as possible. By proper technique it is possible to maintain a minimum void volume and prevent the vaporization of sulfur during seal-off. The void volume inside the ampoule was minimized to prevent the dissociation of bismuth trisulfide. The ampoule was then placed in a Hevi-Duty tube furnace provided with a rotating mechanism and a Wheelco pyrometer controller for mixing the constituents and varying the temperature. An exothermic reaction was invariably observed at about 285°C that sent the temperature as indicated on the pyrometer controller about 30°-35°C beyond the set point. After this exothermic reaction, the temperature was raised above the melting point of bismuth trisulfide, maintained there for about 30 min, and then cooled down to room temperature. During this heating and cooling procedure the ampoule was continuously rotated at 25 rpm to obtain a homogeneous ingot.

The reaction between elemental bismuth and sulfur was studied by differential thermal analysis (DTA). The DTA thermograms were obtained by the conventional technique of plotting the difference in temperature between an aluminum oxide standard and the sample *vs.* the temperature of the sample on an X-Y recorder. Both the standard and the sample were contained in sealed Vycor ampoules with concentric thermocouple wells and placed symmetrically in a high thermal capacity furnace with the heating rate controlled at 5°C/min.

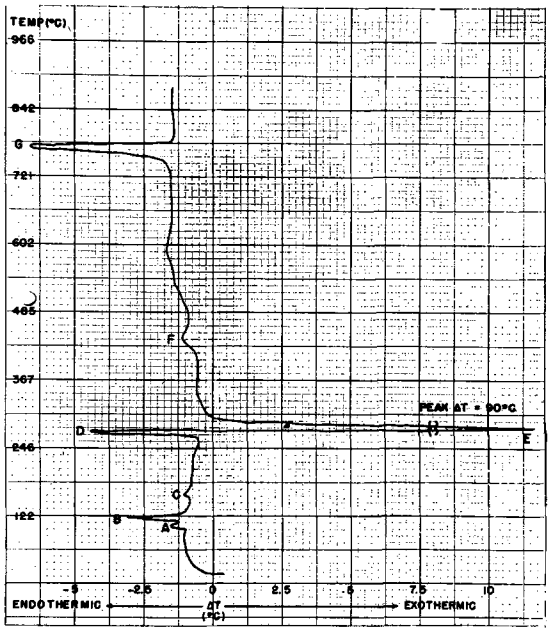

Fig. 1. DTA of bismuth-sulfur reaction with 140 mesh particle size.

A DTA study of the reaction between bismuth and sulfur powders, using 0.8129 and 0.1871g, respectively, sieved to 140 mesh is shown in Fig. 1. The following peaks are observed and explained below:

Peak	*Reason for peak*
A	Conversion of rhombic to monoclinic sulfur
B	Melting of sulfur
C	Conversion of sulfur (S_8) from a ring to a linear molecule
D	Melting of bismuth
E	Exothermic reaction for the formation of bismuth trisulfide
F	Boiling of sulfur
G	Melting of bismuth trisulfide

This DTA curve explains the large exothermic reaction observed at about 285°C in the preparation of bismuth trisulfide. X-ray diffraction, using the Debye-Scherrer powder technique, of the solid formed at this temperature verified the formation of bismuth trisulfide.

The boiling of sulfur, as shown by Peak F on the DTA curve of Fig. 1, indicates that excess sulfur is present after the low-temperature exothermic reaction. This excess sulfur is apparently due to the formation of an impervious layer of bismuth trisulfide surrounding molten bismuth particles at this temperature, leaving some free, unreacted sulfur in the system. At the melting point of bismuth trisulfide the impervious layer melts and the entrapped bismuth is free to react with the excess sulfur. Similar behavior has been reported by Reisman and Berkenblit (11) in the formation of II-VI compounds. By reducing the particle size of the bismuth powder, the amount of unreacted bismuth and sulfur should be correspondingly reduced. This is shown in Fig. 2 in which the particle size of the bismuth and sulfur powders has been reduced to 300 mesh or greater. It may be observed from this graph that the boiling point peak of sulfur is absent, indicating that there is no detectable free sulfur in the system. It may also be observed that the area under the curve corresponding to the melting point of bismuth trisulfide is greater in Fig. 2 than in Fig. 1. This is because the area under the curve in Fig. 1 is reduced by the exothermic reaction in the formation of bismuth trisulfide corresponding to the amount of free sulfur and bismuth in the system.

It appears that three factors have been responsible for the detonations that have been described in the direct synthesis of bismuth trisulfide. These factors are: (i) the fallacious melting point previously reported for bismuth trisulfide, (ii) the low-temperature exothermic reaction, and (iii) the formation of the impervious layer of bismuth trisulfide leaving free, unreacted sulfur in the system.

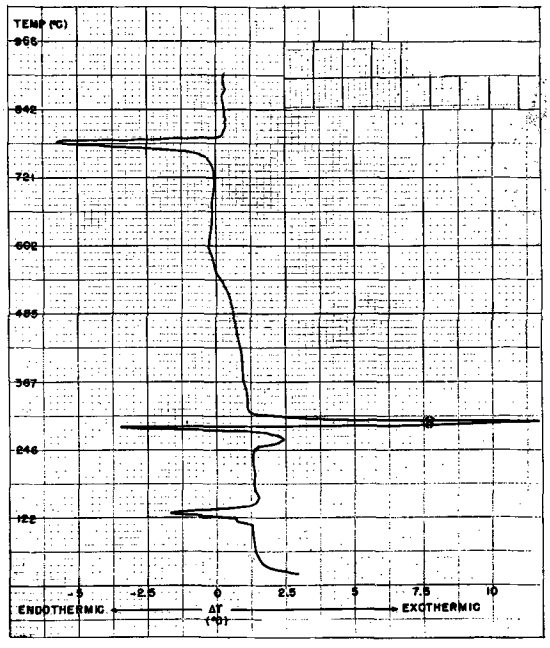

Fig. 2. DTA of bismuth-sulfur reaction with 300 mesh particle size.

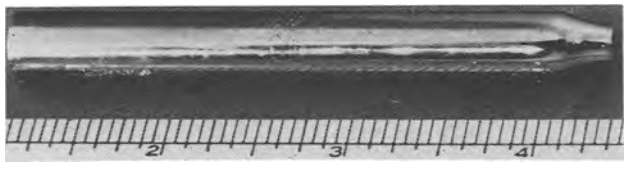

Fig. 3. An ingot of bismuth trisulfide (sample 564)

Crystal growth of bismuth trisulfide.—After the compound Bi_2S_3 was prepared in the rotating-tube furnace as described above, crystals were grown by the Bridgman technique in a special three-zone furnace at growth speeds of ¼ in./hr. This furnace has an upper (preheat), a middle melting, and a lower (post-heat) temperature zone. The preheat and post-heat zones are 11-¼ in. long, and the center melting zone is 2-⅛ in. long. All three furnaces (zones) are wound on a single alundum core and are independently controlled. The temperatures of the zones were measured by thermocouples attached to the inside wall of the alundum tube, 120° apart, in the middle of the respective zones. For the growth of bismuth trisulfide crystals, the preheat and post-heat zones were maintained at 680°C, and the center zone was maintained at 780°C. Under these growth conditions, any sulfur resulting from the decomposition of bismuth trisulfide is maintained in the vapor state. The resulting ingot is annealed in the post-heat zone at a constant chemical potential of sulfur. A photograph of an ingot of bismuth trisulfide prepared and grown in the manner described above is shown in Fig. 3. Bismuth trisulfide crystallizes with an orthorhombic unit cell ($a_o = 11.13$Å, $b_o = 11.27$Å, and $c_o = 3.97$Å) having the P_{bnm} space group (5). The [001] crystallographic direction was found by x-ray measurements to be the direction of crystal growth.

Electrical properties.—Bismuth trisulfide ingots were cut normal to the [001] crystallographic direction for thermoelectric parameter measurements. These measurements were made on samples 1 cm long, having a cross-sectional area of 0.5 cm^2, which were cut from the grown ingots. Electrical contacts were joined to the [001] faces in the following manner: The samples were initially nickel plated, then tin plated, and finally joined to pretinned copper end-blocks with a bismuth-indium eutectic solder. The thermoelectric parameters were measured by the following techniques: Seebeck coefficient by comparison to copper, thermal conductivity by a transient method, and the electrical resistivity by a moving probe profile of the sample. The thermoelectric properties of stoichiometric bismuth trisulfide, prepared and grown in the manner described above, at 300°K (room temperature) are: thermoelectric power (α) = -524 ± 27 μv/°C; thermal conductivity (K) = 16.2 ± 1.8 mw/cm/°C; electrical resistivity (ρ) = 736 ± 51 milliohm-cm. These values were taken from 12 samples using 95% confidence limits from the "student's t" distribution and are very similar to those reported by Gildart *et al.* (7) at the University of Kentucky. Using the average values for the thermoelectric parameters, the calculated thermoelectric figure of merit, Z, for stoichiometric bismuth trisulfide is 2.3×10^{-5}/°K. This is about a factor of 100 below the figure of merit of commercially available bismuth telluride alloys.

Alternating current Hall measurements were made on cleaved crystals of bismuth trisulfide (1 x 3 x 12 mm) using the apparatus described by Milgram (12). The crystals were oriented so that the sample current was passed in the [001] crystallographic direction with the magnetic field and Hall contacts placed mutually perpendicular. The [100] and [010] crystallographic directions, being very similar, were not distinguished for these Hall measurements. Ohmic electrical contacts were joined to the samples with a silver-lead eutectic solder employing the techniques described by Gildart *et al.* (7). A typical graph of the Hall coefficient and electron mobility versus temperature from 78° to 300°K is shown in Fig. 4 for stoichiometric bismuth trisul-

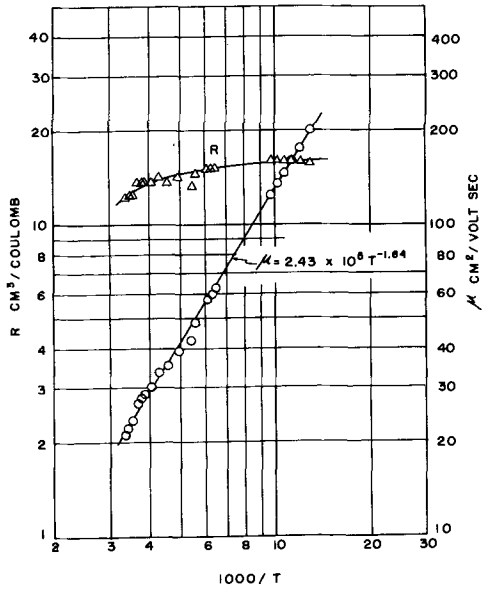

Fig. 4. Temperature dependence of the Hall coefficient and electron mobility of stoichiometric bismuth trisulfide (sample 509-C) from 78° to 300°K.

Table II. Electrical properties of stoichiometric and doped samples of Bi_2S_3 at 300°K

Sample, mole composition	α, μV/°C	K, mw/cm/°C	ρ, milliohm-cm	μ, cm²/volt-sec
Bi_2S_3 (Stoichiometric)	—524	16.2	736	21.3
Bi_2S_3 + 0.00005Pb	—577	19.7	3450	—
Bi_2S_3 + 0.005Pb	—	—	Very high	—
Bi_2S_3 + 0.005Ag	—360	15.7	916	—
Bi_2S_3 + 0.01Ag	—322	16.0	4820	7
Bi_2S_3 + 0.006O_2	—500	19.6	658	15
Bi_2S_3 + 0.012O_2	—520	15.2	2350	—
Bi_2S_3 + 0.01Sb_2S_3	—457	17.5	1460	—

fide (sample 509-C). It may be observed that the Hall coefficient decreases slightly over the temperature range 78°-296°K and the electron mobility varies as $2.43 \times 10^5\ T^{-1.64}$ cm²/volt-sec. The average room temperature electron mobility of stoichiometric bismuth trisulfide prepared and grown in the manner described above is 21.3 cm²/volt-sec and the average carrier concentration is 4.7×10^{17} carriers/cm³.

Bismuth trisulfide was doped with lead, silver, oxygen, and antimony. The average measured electrical properties for these doped samples are presented in Table II. It may be observed from this table that all of these dopants increased the electrical resistivity and generally decreased the electron mobility.

Discussion

It has been demonstrated that bismuth trisulfide forms at a relatively low temperature with a large exothermic reaction and that the true melting point of the compound is 760° ± 5°C. By distributing the heat of the exothermic reaction over the entire ampoule in a rotating furnace, temperature gradients are eliminated, and the compound can be prepared without the detonations that have been previously described in the preparation of this compound.

Crystals of bismuth trisulfide were grown from the melt by the Bridgman technique in sealed heavy-walled quartz ampoules in a special three-zone furnace.

Measurements of the thermoelectric properties of bismuth trisulfide at 300°K and Hall measurements from 78° to 300°K indicate that this compound is an n-type semiconductor. The slight decrease of the Hall coefficient near 300°K indicates that the material is becoming intrinsic. At lower temperatures the carrier concentration is essentially constant. This saturation of the carrier concentration may arise from shallow donor levels associated with deviations from stoichiometry, which are either completely ionized or have broadened and have overlapped the conduction band. The temperature dependence of the electron mobility, $T^{-1.64}$, indicates that in this temperature range acoustical lattice scattering is predominant.

The electrical properties of bismuth trisulfide doped with lead, silver, oxygen, and antimony indicate that these impurities are associated with deep-lying acceptor levels in the band gap, which is reported (7) as 1.2 ev at room temperature, and electrons at room temperature cannot be trapped by these levels. This is also consistent with the fact that a p-type sample of bismuth trisulfide has not been prepared.

Acknowledgments

The authors wish to acknowledge the work performed by Mr. James Endress, Jr. on DTA measurements, Mr. Raymond McDowell on Hall measurements and, in addition, the various members of the Research Department and the Development Department of Carrier Research and Development Company who have contributed their time and effort to this project.

Manuscript received March 18, 1963; revised manuscript received July 3, 1963. This paper was presented at the Boston Meeting, Sept. 16-20, 1962.

Any discussion of this paper will appear in a Discussion Section to be published in the June 1964 JOURNAL.

REFERENCES

1. B. M. Hokhberg and M. S. Sominskii, *J. Exptl. Theoret. Phys. (USSR)*, **7**, 1099 (1937); *Physki Z Sowjetunion*, **13**, 198 (1938).
2. G. Galkin, G. Dolgikh, and V. Yurkow, *Zhur. Tech. Fiz.*, **22**, 1533 (1952).
3. P. P. Konorov, *Zhur. Tekh. Fiz.*, **26**, 1126 (1950) (in Russian); *Soviet Physics, Tech. Phys.*, **1**, 1100 (1957) (in English).
4. N. A. Goriunova, B. T. Kolomiets, and A. A. Mal'Kovam, *Soviet Physics*, Technical Physics, **1**, 1583 (1957).
5. J. Black, E. M. Conwell, L. Seigle, and C. A. Spencer, *Phys. and Chem. Solids*, **2**, 240 (1957).
6. Unpublished Data from "The Thermoelectric Effects Research Program," Franklin Institute, Philadelphia.
7. L. Gildart, J. M. Kline, and D. M. Mattox, *J. Phys. Chem. Solids*, **18**, 286 (1961).
8. "Constitute of Binary Alloys," M. Hanson, Editor, p. 331, McGraw-Hill Book Co., Inc., New York (1958).
9. H. J. Van Hook, "The Ternary System Ag_2S-Bi_2S_3-PbS," Thesis, Pennsylvania State University, 1959.
10. D. Cubicciotti, *J. Phy. Chem.*, **66**, 1205 (1962).
11. A. Reisman and M. Berkenblit, *J. Phy. Chem.*, **67**, 22 (1963).
12. A. A. Milgram, To be published.

Epitaxial Growth of Silicon from the Pyrolysis of Monosilane on Silicon Substrates

B. A. Joyce and R. R. Bradley

Plessey Company (U.K.) Ltd., Caswell Research Laboratories, Towcester, Northants., England

ABSTRACT

Epitaxial films of silicon have been grown on silicon substrates by the pyrolysis of silane. Reaction kinetics have been investigated and the behavior shown to depend on the substrate temperature, being transport controlled above 1100°C and reaction controlled below this temperature. An over-all activation energy and reaction order have been determined in this lower range. The initial mode of growth of the films has been studied by electron microscopy and electron reflection diffraction, which has shown that growth commences by a three-dimensional nucleation process. Finally these results are compared with those obtained from films grown from $SiHCl_3$ in an effort to determine the nature of any mobile surface species.

The preparation of high-purity bulk (polycrystalline) silicon from the pyrolysis of silane has been described by Lewis *et al.* (1), but little or no quantitative data exist for the growth of isoepitaxial silicon films from silane. Carroll, Lever, and Powers (2) have reported attempts to obtain oriented overgrowths on silicon substrates, in which they met with very limited success, and Magdis (3) has given details of the pressure and temperature range over which he observed epitaxy. It is considered, however, that his temperature measurements could be at least 100°C low because of the positioning of the thermocouple with respect to the substrate.

The purpose of this paper is to present some kinetic data for the pyrolysis of silane on a silicon substrate in a flow system under conditions where a perfectly oriented deposit is obtained. From these results some conclusions about the reaction mechanism have been made. Associated with this, work has also been carried out to try to determine the mode of initial nucleation of the films, using electron microscopy and electron reflection diffraction. Finally, the results of this work are compared with those obtained previously from the hydrogen reduction of $SiHCl_3$ on silicon substrates (4, 5) and some rather speculative suggestions made about the nature and relative importance of certain surface processes.

Experimental

Silane was prepared by the reaction between magnesium silicide and ammonium chloride in anhydrous liquid ammonia. The crude material as obtained was purified by water scrubbing to remove ammonia, and dried using a 5A molecular sieve column. The gas was then passed through a series of molecular sieve adsorption columns, and a final purification was achieved by condensing the silane in a stainless steel trap at −196°C, pumping off any remaining gases, and allowing the monosilane to evaporate into a stainless steel tank. Samples were taken from this in 1 liter stainless steel bombs. A typical gas chromatographic analysis of such a sample is: SiH_4, 98.7% ±0.5% by volume; Si_2H_6, less than 0.015% by volume; Ar, 1.3% ±0.5% by volume; PH_3, below the detection limit of 0.5 ppm; B_2H_6, not determinable because of the masking effect of the monosilane peak, but probably less than 1 ppm.

The apparatus is shown schematically in Fig. 1 and consisted essentially of a quartz reactor corrected to hydrogen and silane supplies and a vacuum system. The air space over the rotary pump was purged with argon to remove any silane reaching that part of the system, and the hydrogen was purified by a catalytic deoxygenating unit and a 5A molecular sieve column. Silane pressures were measured with a McLeod gauge to an accuracy of ±1% and initial pressures with an *ionization* gauge. Substrates were supported vertically from their ends with tantalum tapes and heated by a direct resistance method so as to be the hottest part of the system. In this way

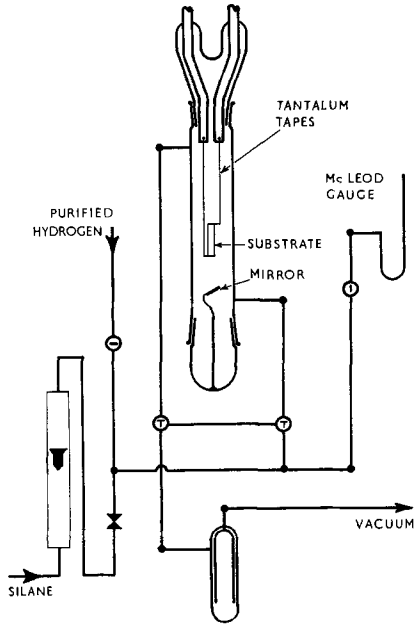

Fig. 1. Schematic diagram of apparatus

practically all of the silicon formed on the substrate, the wall deposit being negligible.

The substrates used were bars 7 mm x 1.5 mm x 6 cm long, and in all cases the 7 mm face was the {110}. Before growth they were chemically polished to a mirror finish, and final oxide removal was carried out in the reactor by treating in hydrogen for 20 min at a temperature of 1260°C. The substrates were all approximately 1 ohm-cm n-type and the layers approximately 20 ohm-cm p-type. Layer thicknesses were obtained by measurement of stacking fault defects (5) since it was felt that for kinetic measurements this would give a more accurate representation of the actual grown layer than a staining technique, which would delineate the electrical junction rather than the grown one. To minimize errors the bars were oriented to within ±6 min of {110}, and unetched defects were measured, using interference contrast microscopy (7). Layer thicknesses were found to be constant to within ±0.5μ both along the length and across the bar. The procedure for each run was as follows: the substrate was heated to 1260°C in a hydrogen stream of 500 ml/min (at atmospheric pressure) for 20 min. After the substrate had cooled rapidly to room temperature, the hydrogen supply was cut off and the system evacuated to about 5 x 10^{-6} mm Hg. The substrate was then quickly heated to the appropriate growth temperature and silane admitted via the needle valve. Readings of flow, pressure, and temperature were recorded frequently during growth. The silane flow rate as recorded on the rotameter, while providing a means of pressure control, did not represent the true volume flow rate, since this was determined essentially by the rotary pump speed (approximately 10 ml/sec at the reactor) and was sensibly constant over the whole pressure range considered. The temperature was measured by means of an optical pyrometer, which had been calibrated at the melting point of silicon, to an accuracy of ±5°C, and, since a slight deposit usually occurred on the reactor walls, readings were taken from an image in a mirror situated at the base of the reactor. A correction for reflection losses was made in each run during the hydrogen cleaning operation.

Kinetic Results and Discussion

The two parameters which have been investigated are the influence of substrate temperature and silane pressure on reaction rate. It was initially established that layer growth rate was a linear function of time after allowing a few seconds for steady-state conditions to be established. The reaction rate was therefore measured in terms of the growth rate of the epitaxial layer.

The substrate temperature range investigated was from 1260° to 920°C at a silane pressure of 1 mm Hg, and completely oriented overgrowths were observed between these limits. However, growth rate behavior fell into two clearly defined regions within this range. From 1260° to 1100°C rate was independent of temperature for a fixed silane pressure. (The actual measured deviation in growth rate was ±0.1 μ/min, which was well within the limit

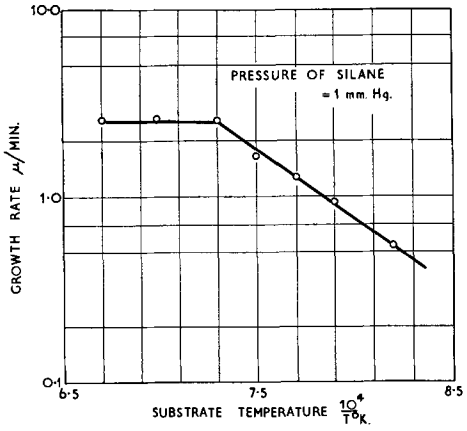

Fig. 2. Temperature dependence of layer growth rate

of experimental error in pressure control and layer thickness measurement.) From 1100° to 950°C growth rate varied exponentially with temperature, the results being shown in Fig. 2, which indicates that the over-all energy of activation for the process is 37 ± 1 kcal/mole. Below 950°C the growth rate was too low for any accurate measurements to be made, but complete orientation was observed down to the lowest temperature used (920°C). The variation of growth rate with pressure similarly showed two types of behavior, depending on whether the temperature was above or below 1100°C. Figure 3 shows the effect of pressure on growth rate for a series of fixed temperatures above 1100°C, from which it is apparent that in this region rate as a function of pressure obeys a relationship of the form

$$\frac{dx}{dt} = k_1(e^{ap} - 1)$$

over the silane pressure range 0.1-1.5 mm Hg, while above this the deposition rate tends to remain constant for further increases in pressure. It is worth noting that even at the highest deposition rate obtained (24 μ/min) complete orientation was still observed.

The rate data for the lower temperature range, at a particular temperature of 1060°C, are shown in

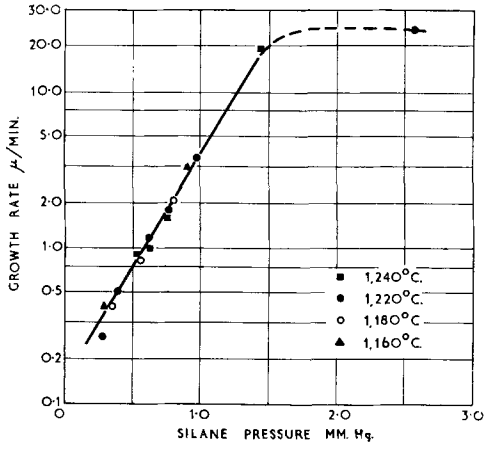

Fig. 3. Effect of SiH_4 pressure on growth rate above 1100°C

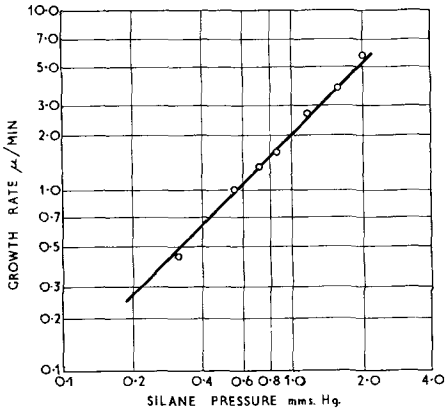

Fig. 4. Effect of SiH_4 pressure on growth rate at 1060°C

Fig. 4, and here the growth rate-pressure relationship is given by

$$\frac{dx}{dt} = k_2 p^n$$

and the slope of the line gives $n = 1.3$.

The reaction conditions were so chosen to suppress completely the homogeneous gas phase reaction and ensure that deposition occurred only on the silicon substrate. Obviously low pressures favor the heterogeneous reaction, and the upper limit in this particular system was found to be about 2 mm Hg. At pressures greater than this some gas phase decomposition occurred, and a fine powder of essentially amorphous silicon was formed. This accounts for the slow-down of deposition rate above 2 mm Hg, since under these conditions not all of the silicon formed was on the substrate. In addition, by measuring the volume of silane admitted per unit time, the proportion which actually reacted could be determined when the total amount of deposit was known. It was found that in the temperature independent region, rather more than 50% reacted, but this fell to less than 5% at the lower end of the temperature controlled region. Since the number of collisions of any particular silane molecule with the substrate would be quite small at the flow velocities used, it seems a reasonable inference that above 1100°C most collisions result in decomposition, but this is not true for the lower temperatures.

The first point of interest is the nature of the overall rate-controlling step for the process. In any heterogeneous reaction the following possibilities exist: (*a*) transport of the reactants to, or products from, the surface, (*b*) adsorption of the reactants, or (*c*) reaction on the substrate followed by desorption of the products. Of these (*b*) and (c) are both activated processes, (*a*) is nonactivated. Clearly, therefore, between 1100° and 1260°C a gas transport process provides the slow step, and in the range 1100°-950°C the rate limitation is imposed either by the chemisorption step or by the reaction and desorption stage.

The nature of the transport process which provides the rate-controlling step over the higher temperature range is open to some speculation. Since most silane substrate collisions result in reaction, growth rate may be equated to rate of gas transport toward the substrate. Over the pressure range considered, however, gas molecules diffuse rapidly, and the small total amount of material present will tend to reduce convective effects. The rate data could perhaps be fitted by the following model, which has previously been suggested for the vapor growth of zirconium by the iodide disproportionation reaction (6). Each silane molecule decomposing at the surface of the silicon substrate will give rise to four hydrogen atoms, and therefore as soon as steady-state conditions have been established a countercurrent of hydrogen will be set up against which the incoming silane must diffuse. The whole system will, however, tend to constant pressure, and thus a concentration gradient with respect to hydrogen will be established around the substrate, which, assuming cylindrical symmetry, decays exponentially with distance from the substrate. The rate increases rapidly with increasing pressure, however, so that it seems probable that convective transport provides the driving force through this barrier. It has not been possible to derive analytically the experimentally determined rate equation, but this does not necessarily invalidate the model, since mathematically it is a highly complex system. Under these conditions, the reactor geometry may well influence the rate data obtained, since both gas diffusion and convection could be dependent on purely geometric factors. Over the range where the rate is reaction controlled however, (as discussed below), geometry will have no influence. Furthermore, as the substrate was heated by a direct resistance method, deposition was confined to the substrate, the wall deposit being negligible. This means that rate data obtained from growth rate measurements should be completely valid.

The rate data presented in Fig. 4 at a temperature of 1060°C indicate that the silicon deposition reaction is of the order of 1.3 with respect to silane. The same order was observed at two other temperatures in the lower range (1000° and 1030°C). The fact that zero order kinetics are not approached indicates that surface coverage is fairly incomplete even at 2 mm Hg. This type of behavior is in fact indicative of a second order heterogeneous reaction retarded by products, since in this case the rate is given by

$$v = k \frac{p_A^2}{p_p}$$

(where p_A is the pressure of reactant and p_p the pressure of retardant) assuming the retardant to be a diatomic molecule adsorbed dissociatively, as is probable in the case of hydrogen on silicon. Thus in the case of silane it could be written that

$$\frac{dx}{dt} = k \frac{p^2_{SiH_4}}{p_H}$$

but since p_H is related to p_{SiH_4}

$$\frac{dx}{dt} = k_2 p^{(2-y)}_{SiH_4}$$

and experimentally it was found that $(2 - y) = 1.3$.

The conclusion which may be drawn therefore is that the pyrolysis of silane on silicon involves re-

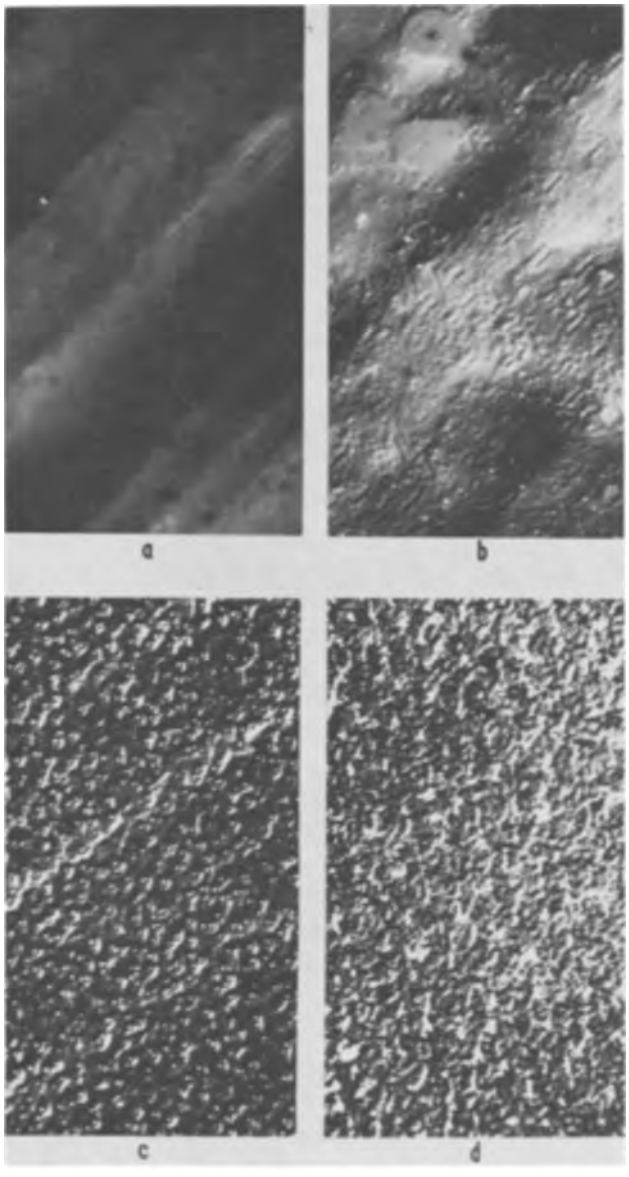

Fig. 5. Interference contrast micrographs showing effect of SiH_4 pressure on layer perfection: (a) 0.9 mm; (b) 0.41 mm; (c) 0.33 mm; (d) 0.27 mm. Magnification 225X.

action between molecules adsorbed on neighboring sites, since the reaction exhibits essentially second order behavior, for which it is necessary to postulate dual sites. Hogness *et al.* (9) have shown the homogeneous decomposition of silane to be first order and to proceed rapidly at 400°C. Up to the highest measured temperature (500°C) the heterogeneous reaction was completely suppressed, and hydrogen was also found to retard the homogeneous reaction, for which the energy of activation was 51.7 ± 2 kcal/mole. Considering this in conjunction with the rate data shown above, it seems most probable that the rate-controlling step in the temperature dependent range is reaction on the surface followed by desorption of the products, rather than chemisorption of the reactants. Similar results have been observed for the decomposition of nitric oxide on platinum (10).

Nucleation and Structure

There were two aspects of this investigation: (*a*) an examination of the initial nucleation mechanism using electron microscopy and electron reflection diffraction, and (*b*) an examination of the effect of silane pressure at a series of fixed temperatures on the ultimate topography of the grown layers. For this interference contrast microscopy (7) was used. Because of its significance with respect to nucleation studies (*b*) will be discussed first.

Figure 5 shows a series of interference contrast micrographs of films grown at 1160° over a range of pressures (decreasing from 5a to 5d). The alternate light and dark bands crossing the micrographs were present in the original substrate material, and probably result from oxygen segregation. Although x-ray diffraction results indicate that all of these films are completely oriented, it is apparent that crystallographic perfection as revealed by surface topography and stacking fault density increases with increasing deposition rate, and this is in fact true for all temperatures. This somewhat anomalous feature will be discussed in more detail after a description of the nucleation results. It was introduced at this stage in order to show that the nucleation results, which must of necessity be obtained at low pressure, may only be completely valid for slow deposition rates. It is most probable, however, that the over-all picture will be similar for all rates.

In order to determine the manner in which growth was initiated it was necessary to examine surfaces on which very limited amounts of growth had taken place. Films were therefore grown at low pressures for different lengths of time so that the growth sequence could be followed, the particular substrate temperature used being 1220°C. Platinum-carbon replicas (8) of these layers were obtained and examined with the electron microscope, and the surfaces themselves were examined by reflection electron diffraction. An electron micrograph of a platinum-carbon replica of a substrate prepared for growth is shown in Fig. 6a, from which it may be seen that the surface is essentially smooth and featureless. The corresponding diffraction pattern (Fig. 7a) shows only strong Kikuchi lines. The absence of any spot pattern indicates that no very small projections exist on the surface, although on a macroscopic scale surface irregularities could be present. As no oxide rings are observed, any oxide layer on the surface must be extremely thin.

The hydrogen treatment did not result in any significant change in the surface topography, since replica micrographs and diffraction patterns were identical to those obtained from a polished surface.

Replica micrographs of a series of layers grown under the same conditions for a range of times are shown in Fig. 6(b)-(d), with the corresponding diffraction patterns in Fig. 7(b)-(d).

It appears that the mode of nucleation of the initial deposit atoms is to form three-dimensional nuclei rather than a continuous monolayer. However, it has not been possible to resolve whether the initial nuclei are randomly distributed or whether they occur at preferential surface sites, principally because of the difficulty in controlling the amount of deposit. The point of particular interest in these micrographs is the very large size and small number of the individual nuclei, especially in comparison

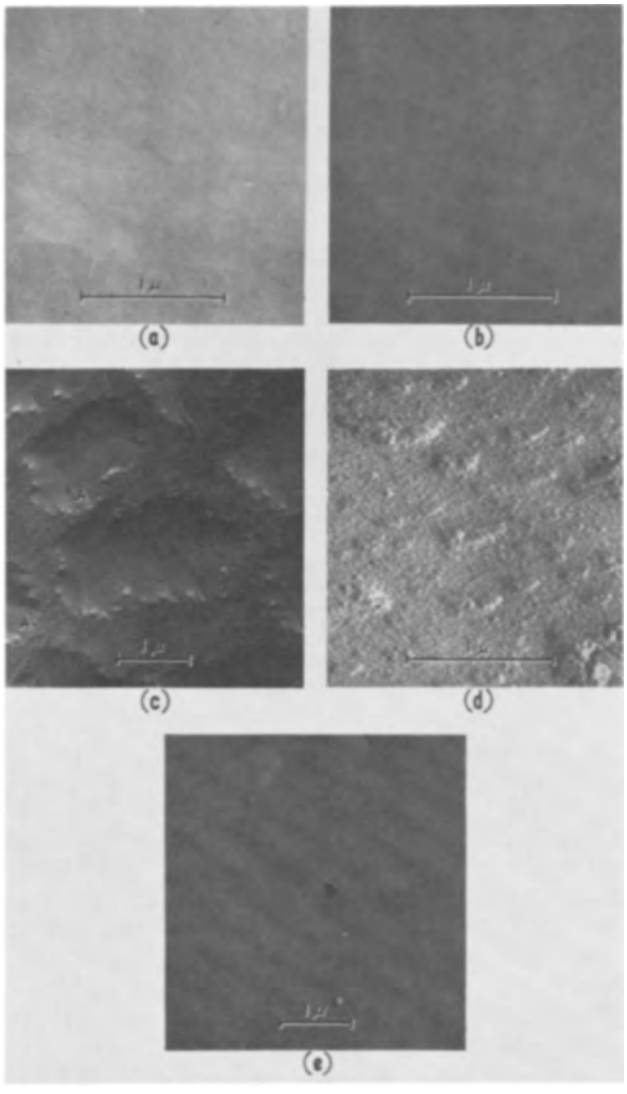

Fig. 6. Pt-C replicas of {110} substrate and growth layer surfaces: (a) substrate: (b) 5 sec growth; (c) 10 sec growth; (d) complete layer, high growth rate; (e) complete layer, slow growth rate. Magnification 10,000X. (c), (e), 40,000X (a), (b), (d).

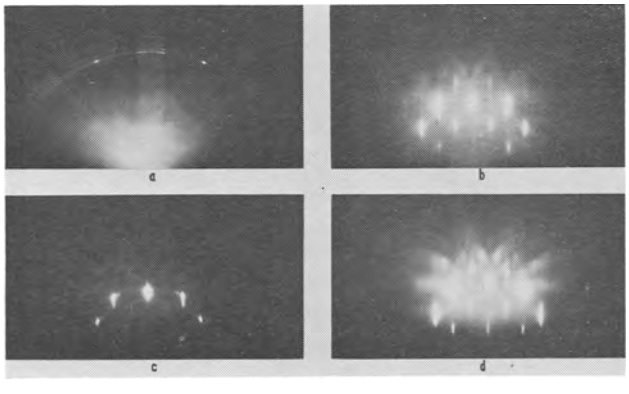

Fig. 7. Diffraction patterns from surfaces shown in Fig. 6(a)-(d), respectively.

with isoepitaxial silicon grown by the hydrogen reduction of $SiHCl_3$ (5). The area marked A in Fig. 6(c) shows the way in which the nuclei apparently grow by coalescence, while at the same time presumably receiving new deposit atoms. Figure 6(d) is a micrograph typical of any complete film (thicker than approximately 0.5μ) grown at a high rate, and Fig. 6(e) a similar film grown slowly. The sequence of diffraction patterns has helped to confirm features of the topography of the growing suface. The absence of spots in the pattern from the substrate, as previously discussed, means that no very small projections exist on the surface. The development of a spot pattern is seen to coincide with the appearance of a comparatively small number of nuclei. These spots are particularly streaked and, while the pattern intensifies somewhat as growth proceeds, the streaked spots are maintained. In terms of surface topography this means that the diffracting sites are rather flat and elongated, and this is apparent from the replica micrographs.

A somewhat surprising feature of these diffraction patterns is the absence of any twin spots, although these always appeared in patterns from layers grown using $SiHCl_3$ (5). Since the same type of defect was present, at least as shown by interference contrast microscopy, it is possible that the equilibrium width of the microtwin region was considerably reduced, and the fact that no chlorine is present in silane grown layers may be associated with this. This point is currently being investigated.

The three-dimensional nucleation process (as opposed to growth by completion of atomic planes) is most probably associated with residual surface contamination, which may well be essentially oxide, on the substrate surfaces. Nuclei as large as those observed are normally indicative of high surface mobility, although the nature of the mobile species is by no means certain. Since the nuclei are so very much larger than those observed in growth from $SiHCl_3$, and in both cases only silicon is being deposited, it is an attractive possibility to consider that the chemisorbed radical is the mobile species. This hypothesis is further substantiated by the reaction mechanism as deduced from kinetic results, since adsorption on neighboring sites is necessary for reaction, and such a process would be aided by surface diffusion. Further, the radical derived from silane is likely to be more mobile than that from $SiHCl_3$, since the chlorine atoms could exert some considerable influence on the latter. It is apparent, however, that the evidence presented here is by no means conclusive, and the different mobilities could perhaps be explained in terms of different impurity contents of the silicon from the two sources. Nevertheless, it is felt that the mobile radical hypothesis, while certainly speculative, does explain the observed results and those obtained with $SiHCl_3$. One much more certain fact concerning the mechanism of epitaxy has, however, emerged from this study. Perfect orientation has been observed at 920°C, and this should finally refute the suggestion that a reversible reaction is necessary for epitaxy to occur.

The final point requiring explanation is the apparent anomaly of greater crystal perfection at higher growth rates. Initially it was thought that this was closely associated with the nucleation mechanism, but a much more likely reason can readily be obtained from elementary gas kinetics. Before silane is admitted to the reactor the pressure is approximately 5×10^{-6} mm Hg. For the sake of simplicity this may be considered to be an oxygen pres-

sure. Silane is then admitted to the appropriate pressure required for growth. Now since the molecular weights of silane and oxygen are equal, it may be shown from kinetic theory that the relative collision frequencies with the substrate will be in the ratio of the partial pressures. Therefore, the higher the pressure of silane the smaller will be the chance of oxygen contamination during growth. Obviously water vapor, hydrocarbons, etc., will have the same effect as oxygen, their relative collision frequencies merely being modified by their respective molecular weights.

Acknowledgments

The authors are indebted to their colleagues J. M. Charig, R. M. Ware, and B. D. Williams for many valuable discussions, and to D. J. Stirland and R. W. Bicknell for the electron micrographs and diffraction results, respectively. The silane was kindly supplied by G. Ord, and R. Kenwright carried out the analysis. Thanks are due to the Plessey Co. (U.K.) Ltd. for permission to submit this paper.

Manuscript received April 18, 1963; revised manuscript received July 1, 1963.

Any discussion of this paper will appear in a Discussion Section to be published in the June 1964 JOURNAL.

REFERENCES

1. C. H. Lewis, H. C. Kelley, M. B. Guisto, and S. Johnson, *This Journal*, **108**, 1114 (1961).
2. T. J. Carroll, R. F. Lever, and J. K. Powers, AFCRC-TR-59-155, AD-216523 "Research directed toward the growth of silicon crystals from silane" Final Report under Contract AF19(609)-4066, 15 May 1959.
3. W. A. Kagdis, Abstract No. 83, paper presented at the Los Angeles Meeting of The Electrochemical Soc., May 1962.
4. J. M. Charig and B. A. Joyce, *This Journal*, **109**, 957 (1962).
5. J. M. Charig, B. A. Joyce, D. J. Stirland and R. W. Bicknell, *Phil. Mag.*, **7**, 1847 (1962).
6. R. B. Holden and B. Kopelman, *This Journal*, **100**, 120 (1953).
7. G. Nomarski and A. R. Weill, *Rev. Mét.*, **52**, 121 (1955).
8. D. E. Bradley, *Brit. J. Appl. Phys.*, **11**, 506 (1960).
9. T. R. Hogness, T. L. Wilson, and W. C. Johnson, J. *Am. Chem. Soc.*, **58**, 108 (1936).
10. P. W. Backman and G. B. Taylor, *J. Phys. Chem.*, **33**, 447 (1929).

The Formation of Metal Oxide Films Using Gaseous and Solid Electrolytes

J. L. Miles and P. H. Smith

Arthur D. Little, Inc., Acorn Park, Cambridge, Massachusetts

ABSTRACT

The growth of oxide films has been observed to occur on the surface of certain metals when they are (*a*) subjected to an oxygen plasma, (*b*) subjected to an oxygen plasma and maintained at a positive potential with respect to the plasma anode, and (*c*) brought into intimate contact with a second metal that has oxygen dissolved in it, and maintained at a positive potential with respect to that metal. Dielectric barriers formed by these methods have been used to construct both active and passive elements in a thin film oscillator-amplifier circuit based on the superconducting tunnel diode.

The process of forming oxide films on metals such as aluminum, tantalum, niobium, etc., by means of anodization in an electrolytic cell employing an aqueous solution is well established in science and industry, the uses of such films extending from protective coatings to capacitor dielectrics.

We have performed experiments in which the anodization process employs either a gaseous or a solid electrolyte rather than the usual aqueous solution. Oxide films formed by these methods are similar, and in certain respects superior to those formed in the usual manner.

The techniques to be described possess certain advantages over "wet" anodization, since they may be applied to the growing field of microminiaturization of electronic circuitry through the application of thin film technology. In particular, the process of gaseous anodization provides a simple, convenient, and reliable method for forming tunneling barriers and thin film dielectrics for use in both active and passive electronic circuit elements. These barriers may be formed over a wide range of thickness and circuits may be fabricated without removing the substrate from the vacuum system.

Theoretical Background

According to the theory of oxidation presented by Mott (1), two things are required in order for the growth of an oxide film to proceed on a metal such as aluminum. One is the availability of oxygen and the second is the existence of an electric field of proper magnitude and sign at the metal-oxide boundary. It is this field which is responsible for dissolving positive metal ions in the oxide already formed, thus allowing them to proceed to the oxide-oxygen interface by a combination of drift in the field and diffusion. Once they reach this interface they react chemically with the oxygen and hence growth of the oxide takes place.

In the case of thermal oxidation, a constant potential is supplied by the adsorbed oxygen ions themselves and hence the field decreases as the oxide

becomes thicker. This limits the oxide growth since metal ions can no longer make their way into the oxide to diffuse to the surface once the field falls below a certain value. On the other hand, in the process of anodization an external potential is supplied which can be varied as the oxide film grows, and hence the thickness is not limited in this manner.

In ordinary "wet" anodization the electrolyte serves both as a source of oxygen ions and as a conducting medium through which an electric potential may be applied across the oxide. In the experiments to be described, the process of anodization is extended to systems utilizing a gaseous electrolyte in the form of an oxygen glow discharge, and to those using a solid electrolyte (metal) in which mobile oxygen atoms are present.

Description of Experiments

While the results to be described here and in the following sections are generally applicable to any metal that can be anodized by normal means, for the sake of simplicity and in view of the fact that most of our work has involved aluminum, this metal has been used as illustrative throughout the entire paper.

In fact, we have successfully anodized by the method involving a gaseous plasma a wide variety of metals and semiconductors including Al, Ta, Mg, Cr, Sb, Bi, Be, Ge, and Si. It is possible that some metals which cannot be anodized in liquid electrolytes due to chemical attack may be anodized by these methods. Be, for example, is difficult to anodize in aqueous solutions since the oxide tends to dissolve in the electrolyte. We have formed anodized Be films with a thickness of 1500Å by the gaseous technique.

Gaseous or Plasma Anodization.—The entire process is carried out inside an ordinary oil diffusion pumped high vacuum system capable of achieving pressures in the 10^{-6} mm Hg range during normal operation. Two liquid nitrogen traps are provided, one between the diffusion pump and the bell jar; the other extending downward into the bell jar. The system is shown schematically in Fig. 1.

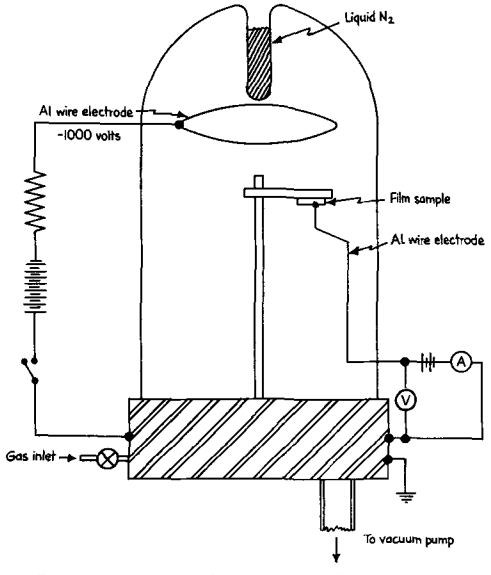

Fig. 1. Schematic of gaseous anodizing system

When the system has pumped down into the 10^{-6} mm Hg range, a film of aluminum approximately 1000Å thick is formed on an ordinary glass microscope slide by evaporating a charge of 99.99% pure material through a suitable mask. After the evaporation is completed, the diffusion pump valve is closed and oxygen gas is admitted through a calcium hydride drying tube to bring the system to a pressure of approximately 50μ Hg.

A glow discharge is then initiated in the system by applying several hundred to one thousand volts negative potential to a pure aluminum wire ring mounted in the bell jar. The metal base plate serves as the ground electrode.

Next, one of two courses is followed. If a relatively thin oxide is desired, the glow is maintained for a few seconds to some tens of minutes; the discharge is then shut off and the diffusion pump valve opened to reduce the pressure to 10^{-6} mm Hg again. We then evaporate a second metal electrode across the first to form a diode structure in the form of a cross.

If on the other hand, a somewhat thicker oxide film is desired, a direct electrical connection is made to the aluminum film in the vacuum system by means of a probe formed of pure aluminum wire. This probe passes outside the system through a vacuum seal, and a small positive d-c potential is applied to it with respect to the system ground. A current is observed to flow in this circuit once contact with the film is established, and this is seen to decay with time in a manner similar to that which prevails in an ordinary aqueous anodizing bath. When the current has decayed, connection is broken, the discharge shut off, and the system pumped down for the evaporation of the second metal electrode as before.

If the anodizing probe is not made of pure aluminum or some other metal which forms an anodized oxide layer, it continues to draw a current which masks the decreasing anodizing current through the specimen.

An oxygen pressure of 50μ is normally used since for this pressure a maximum occurs in the anodizing current and the process proceeds more rapidly. In the neighborhood of 1 mm pressure another maximum in the anodizing current occurs and oxides formed at this pressure seem to be similar to those formed at 50μ.

Solid-state anodization.—In this method the freshly deposited aluminum film is first given a short oxidation. This is accomplished either by exposing the film to a dry oxygen atmosphere for a few minutes, or by maintaining a glow discharge in the system for a few seconds. The top metal electrode is then evaporated to complete the structure. This evaporation is carried out at a system pressure of 10^{-4} mm Hg, the pressure being maintained at this value by a controlled leak of dry oxygen into the system. The metal chosen for the top electrode is one which will readily dissolve relatively large amounts of oxygen, both tin and lead having been used successfully.

We generally evaporate metals so as to form films at the rate of 100-200 Å/sec, but in the evaporation

of the film described above, this rate is kept at about 10-15Å/sec.

When the second electrode evaporation is complete, the sample is removed from the vacuum system and electrical connection is made to each electrode of the assembly. A small d-c potential is then applied across the specimen, the bottom (aluminum) electrode being maintained positive. As in the case of gaseous anodization a current is observed to flow, and this current decays with time, indicating the growth of oxide.

Discussion of Experimental Results

Gaseous anodization—no applied potential.— One hundred individual crossings were deposited on a single 1x1 in. glass substrate. This was accomplished by first evaporating all one hundred aluminum lower electrodes, subjecting these to the discharge for 2 min, evaporating twenty top electrodes, also of aluminum, turning on the discharge for 2 min, evaporating another twenty top electrodes, etc. In this manner five data points were secured on a single specimen, a single point being the average of twenty individual crossings. Figure 2 shows the results of measurements of aluminum oxide thickness made as a function of the time during which a specimen was left immersed in the oxygen glow discharge.

Thickness of the oxide was determined from comparison of the experimentally observed current voltage characteristics with electron tunneling theory (2). Detailed results of this comparison are being treated in a separate publication (3) and are not repeated here.

We have also checked the oxide thickness in some cases by measuring the capacitance of metal-oxide-metal sandwiches. We have approached this method with caution as a result of the work of Mead (4). Mead found that the effective dielectric constant decreased as the thickness of the dielectric decreased, and he postulated this result as being due to a depletion layer in the metal electrode. The effect

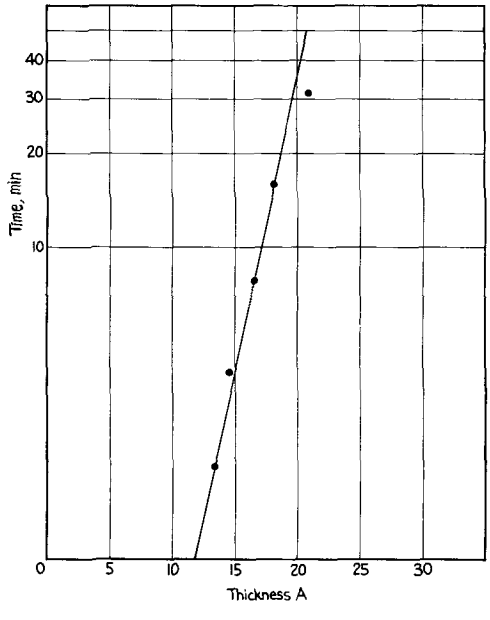

Fig. 2. Thickness *vs.* time for gaseous anodization (without external potential).

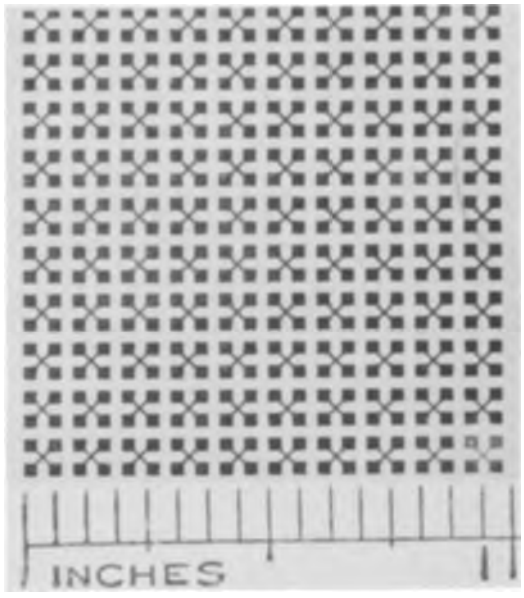

Fig. 3. 100 tunneling samples deposited simultaneously

varied with the electrode material being larger for bismuth than for gold counter electrode.

We have not been able to duplicate Mead's results. Using gas anodized aluminum oxide dielectrics, we deposited samples of size 1x1 mm and measured the capacitance for counter electrodes of Au, Bi, Cu, Ag, and Al. The results were identical for all these counter electrodes. Moreover, if the value of the oxide dielectric constant were taken to be 8, the calculated thickness of the oxide films was found to be 29Å. This is in good agreement with the tunneling results which gave 25Å for these samples.

Further confidence in the measurements results from the very small spread in the observed characteristics for crossings given identical treatment. Figure 3 shows a typical specimen containing 100 identical individual crossings. A contour diagram showing lines of equal tunneling resistance is shown in Fig. 4a, and it is immediately obvious that the variations are both small and regular, *i.e.*, there is little random variation across the sample.

The effect of water vapor on the growth of aluminum oxide layers is very marked. We have noticed that when aluminum is evaporated in a system at a pressure of 10^{-6} mm Hg copious quantities of gas

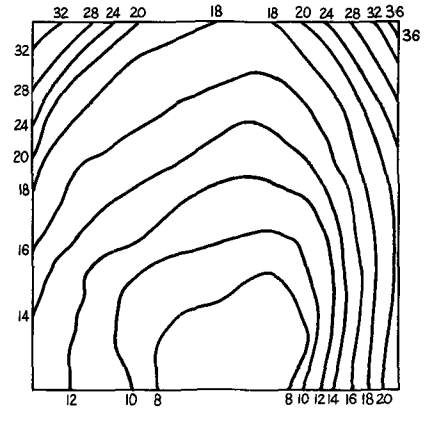

Fig. 4a. Contour map of resistance of tunneling specimen of type shown in Fig. 3.

are evolved and that the system takes up to 5 min to return to 10^{-6} mm. This effect is clearly not due to the release of gas which was dissolved in the aluminum. We believe that the freshly deposited aluminum reacts with the water vapor of the vacuum system and produces aluminum oxide and hydrogen. Since the cold trap in the system pumps water but not hydrogen, the system pressure rises. This phenomenon can be greatly reduced by even a modest bakeout at 100°C overnight. The resistance of tunneling samples deposited directly after such a bakeout are reduced by two to three orders of magnitude over those of our normal samples which indicates that the oxide thickness is perhaps 3-5Å units thinner.

The above effect also explains why the crossings of Fig. 4a have higher resistances at the corners and edges than at the center. During the anodization process water vapor falls on the substrate and moves over the surface until it either re-evaporates or is trapped by reaction with an aluminum film. Aluminum films at the edge and particularly the corner of a specimen trap more water vapor than those in the center and hence the oxide thickness is greater. This explanation is confirmed by the following experiment. Over one half of a substrate an extremely small amount of aluminum was deposited. This aluminum "film" was nonconducting and was presumably broken up into small islands. One hundred crossings were then deposited in the usual manner and their resistances measured. The fifty crossings on the aluminum "film" had resistances within ± 30% whereas those on the glass had resistances within ± 200% (see Fig. 4b). The minute islands of aluminum over half the substrate had acted as traps for surface diffusing water vapor and had thus made the crossing resistances both lower and more uniform than those on the untreated substrate.

These simple experiments show the necessity for controlling water vapor during the formation of the oxide barrier and show that amazing reproducibility of barrier thickness is possible with such control.

Gaseous anodization, external potential applied.— The results of this type of treatment more nearly

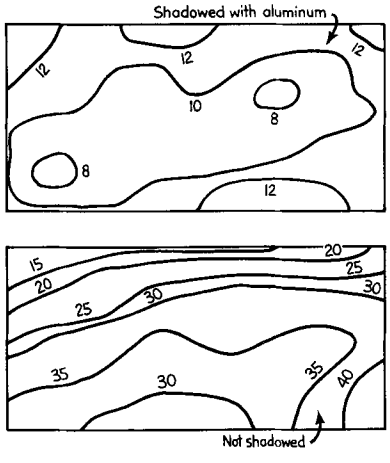

Fig. 4b. Contour map of resistance of tunneling specimen of type shown in Fig. 3 showing effect of shadowing the substrate with aluminum.

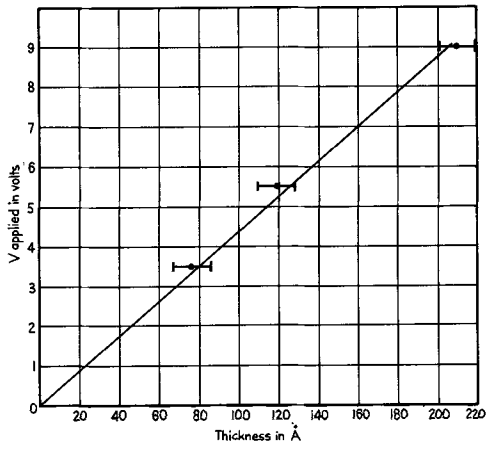

Fig. 5. Oxide thickness of gaseous anodized aluminum single crystals as function of applied anodizing voltage.

parallel anodization in an aqueous electrolyte since a simple linear relationship is found to exist between the applied potential and oxide thickness. Figure 5 shows the results of measurements of oxide thickness *vs.* applied potential. The thickness data in this case were obtained in the following ways. A single crystal of aluminum ¼x¾x1 in. was electropolished in a mixture of methyl alcohol and perchloric acid. After washing and drying, the anodization was then carried out as described earlier with a potential of + 3½v applied to the specimen. After the current had decayed to a small value, the sample was removed from the system and placed in a "wet" anodizing cell, consisting of an aqueous solution containing 1% ammonium citrate and 1% citric acid.

The voltage on the cell was slowly increased to 5½v at which point a current was observed to flow equal to that in the dry system, indicating the initiation of anodic oxide growth. Since the voltage thickness relation for this solution is known to be 14 Å/v, the voltage marking the onset of current flow was taken as a measure of the thickness of oxide which had been produced by the gaseous method. While the crystal was still in the wet cell, the anodic film was increased in thickness to 120Å by increasing the voltage to 8½v. At this point the sample was removed from the cell, rinsed and dried and replaced in the vacuum system. The discharge was initiated and the crystal voltage increased to 5½v at which voltage the onset of current flow was again observed. In this manner the series of points shown in Fig. 5 was determined, and as may be seen from the figure a constant value of approximately 20 Å/v obtained for the slope.

As a check on this relationship, a crystal of aluminum was gas anodized at a potential of 7.4v. The sample was then removed from the system and heated to a temperature of 450°C in a tube furnace. On cooling from this temperature a nucleation of vacancies occurred at the metal-oxide interface resulting in the formation of vacancy pits under the oxide (5). The oxide was removed from over the pits by peeling off a parlodion film formed on the crystal surface (6). Thus a parlodion replica was obtained with a large number of oxide particles adhering to the underside. This was then shadowed

with platinum and a direct measurement of the particle thickness obtained in the electron microscope. In addition, selected area diffraction studies were made on the actual oxide particles themselves and their structure determined.

In this manner it was found that the oxide film was 140±30Å, in agreement with the previous results. Moreover, the oxide was found to be completely amorphous, just as is the case with normal anodized films.

When aluminum films are anodized by this method, the current fall-off is slower than for a bulk sample. For example, an aluminum film anodized at 6v for 5 min achieved a thickness of 100Å, and the current had dropped to 10% of its initial value. After 50 min anodization the current had fallen to 3% and the thickness was 134Å. After 20 hr the current had fallen to 0.1%, and the film thickness was 141Å. This gives a value of 23Å/v applied which agrees with the value for single crystals. These measurements of thickness were made by measuring the capacitance of the samples.

Solid-state anodization—The thickness of the oxide formed by this technique was also measured by comparison of the experimental current-voltage characteristics with tunneling theory. The results are shown in Fig. 6, and it is again seen that a linear relationship exists between anodizing voltage and thickness.

A striking demonstration of the growth of the oxide is provided when the current-voltage characteristics of a sample are displayed on an X-Y oscilloscope with a half wave rectified (60 cps) sweep voltage. If the polarity of the trace is such that the aluminum is negative, then no anodization takes place, and the characteristic is completely stable with time. If, however, the aluminum is made positive, then the characteristic rapidly and smoothly changes as shown in Fig. 7.

Since the change with time is rather rapid when the aluminum is positive, and hence difficult to

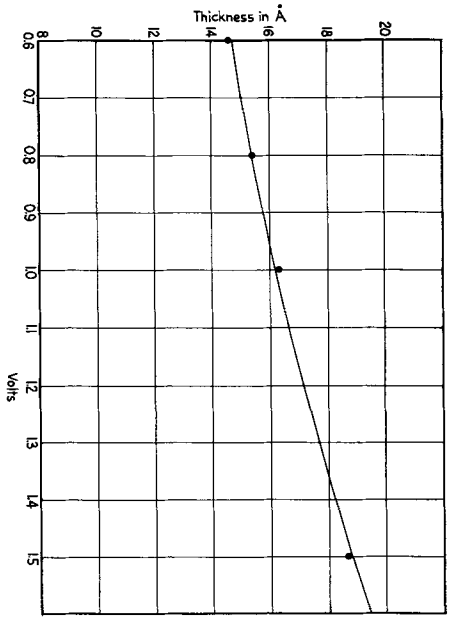

Fig. 6. Oxide thickness as function of applied voltage (solid-state anodization).

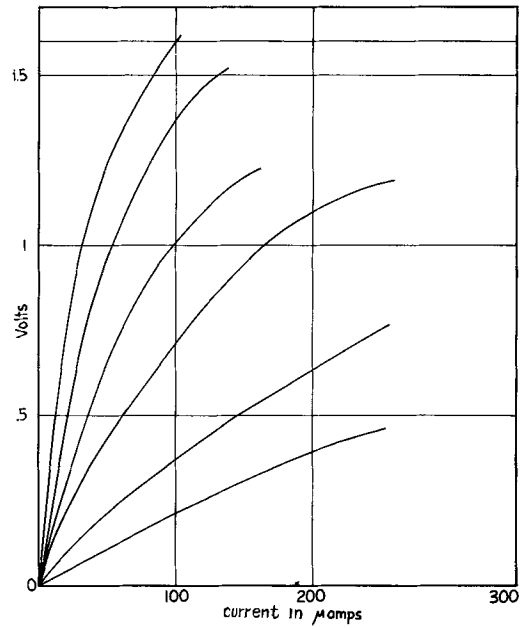

Fig. 7. I-V characteristics for aluminum-tin sample showing growth of oxide resulting from applying a potential across the oxide barrier. The characteristic of the sample changes from curve 1 (bottom) to curve 6 (top) in a few seconds.

photograph, the superimposed characteristics shown in the figure were actually displayed with the aluminum negative, growth between successive curves obtained by reversing the polarity momentarily. A typical crossing with an area 10^{-4} cm^2 having an initial tunneling resistance of 100 ohms can be made to display a resistance (at the origin) of tens of megohms in a few seconds.

The effect is strongly temperature dependent; when the specimens are cooled to 243°K, the oxide growth no longer occurs. The mechanism that inhibits the growth of oxide at low temperature is probably either the cessation of solution of aluminum in the oxide or the immobilizing of the oxygen in the tin. We are, at present, attempting to differentiate between these two possibilities.

An interesting consequence of the sensitivity of the anodization process to the polarity of the applied voltage is the fact that aging effects in Al-Al_2O_3-metal diodes always occur so as to increase their tunneling resistance with time. We interpret this slow increase with time to be due to a gradual build-up in the thickness of the oxide barrier due to the process of solid state anodization. In this case the oxygen is either dissolved in the top metal in the beginning, or diffuses in from the atmosphere with time. The field required for the process derives from the contact potential across such asymmetric diodes. This hypothesis is borne out by the fact that when the counter electrode of tunneling sample is a metal having a higher work function than aluminum, the sample ages more rapidly than do Al-Al_2O_3-Al specimens. This entire question is being treated more completely in a separate publication (3).

Summary and Conclusions

The growth of the oxide films has been observed to occur on the surface of certain metals when they are: (i) subjected to an oxygen plasma atmosphere,

(ii) subjected to an oxygen plasma atmosphere and maintained at a positive potential with respect to the plasma anode, and (iii) brought into intimate contact with a second metal which has oxygen dissolved in it and maintained at a positive potential with respect to that metal.

In (i) above, a thickness *vs.* time relationship has been found to exist which closely resembles that for thermal oxide formation except that the terminal thickness is somewhat greater. The effect of the plasma in this case is most likely merely to provide a more copious supply of ions than would normally exist on the exposed metal oxide surface.

In (ii) and (iii) a comparison has been drawn with the more common process of anodization utilizing an aqueous electrolyte, where the electrolyte is now in one case a plasma of ions, and in the other a metal containing oxygen as an impurity. The existence of a linear relationship between applied voltage and the resulting oxide thickness, and the observation of current fall-off during oxide growth in each case is evidence for the validity of this interpretation.

Oxide films formed by (i) have been found to be particularly useful in tunneling and tunnel emission studies as they are extremely reproducible, allow a very fine control of thickness to be achieved, are quite robust when formed in a dry atmosphere, and obey predictions based on simple electron tunneling theory. Aluminum oxide films formed in this manner have been observed to carry current densities of 1000 amp/cm^2 at 4v before breaking down.

Studies on solid-state anodization (3) have lead to an increased understanding of the mechanism responsible for the aging of tunnel emission diodes.

In view of the fact that method (i) allows the formation of electronic elements in thin film form without the need for either making electrical contact to the substrate or removing it from the vacuum system at any time during the process, it is felt that this technique offers a very convenient and practical means for pursuing circuit miniaturization.

In this connection, the authors have successfully used methods (i) and (ii) to construct an entire thin film oscillator-amplifier circuit, based on the use of a superconducting tunnel diode, including both active and passive circuit elements (7).

Acknowledgments

In conclusion, the authors would like to extend their appreciation to R. S. Davis and P. E. Doherty for supplying the aluminum single crystals used, and for assistance in the thickness determination using the vacancy pit technique.

Manuscript received March 4, 1963; revised manuscript received July 8, 1963. This paper was presented at the Pittsburgh Meeting, April 15-18, 1963.

Any discussion of this paper will appear in a Discussion Section to be published in the June 1964 JOURNAL.

REFERENCES

1. N. F. Mott, *Trans. Faraday Soc.*, 429 (1947).
2. R. Holm, *J. Appl. Phys.*, **22**, 569 (1951).
3. P. H. Smith and J. L. Miles, To be published.
4. C. A. Mead, *Phys. Rev. Letters*, **6**, 545 (1961).
5. P. E. Doherty and R. S. Davis, *Trans. Met. Soc.*, **221**, 737 (1961).
6. P. E. Doherty and R. S. Davis, *J. Appl. Phys.*, **34**, 3 (March 1963).
7. J. L. Miles, P. H. Smith, and W. Schonbein, *Proc. I.E.E.E.*, **51**, 937 (1963).

Properties of HF-H_2O_2 Treated Germanium Surfaces

P. Balk and E. L. Peterson

Thomas J. Watson Research Center,

International Business Machines Corporation, Yorktown Heights, New York

ABSTRACT

Results are given of the measurements of field effect and surface recombination velocity on HF-H_2O_2 treated germanium samples in air, nitrogen, and vacuum. It is found that the quiescent potential, state density, and surface recombination velocity depend on the amplitude of the field voltage at a given frequency. Although it is generally possible to explain the data for the region near the middle of the gap by assuming one discrete set of recombination centers and one discrete set of inactive states, both near the center of the forbidden gap, a continuous distribution cannot be ruled out. n- and p-type samples appear to have different state structures. In addition to the maximum at the center of the gap, which is common to all samples studied, the recombination velocity on n-type samples increases again at more negative surface potentials. For p-type samples indications of a second peak at positive potential are found.

The fast state structure of etched or "real" germanium surfaces has been the subject of several investigations during the last decade (1). Quite generally the experimental data have been fitted to a model with four discrete sets of states at the germanium-oxide interface: one close to the conduction band, one near the valence band, and two in the central region of the forbidden gap. Of the latter two sets, the one just above the center of the gap appears to act as an acceptor-type recombination cen-

ter for excess carriers. Numerical values for energies and densities have been given virtually only for the states in the middle of the gap. There is considerable scatter between data from different sources, but this may be partly explained by differences in surface treatment and crystallographic orientation of the surface.

The present study was aimed at widening the scope of available information through an investigation of a germanium surface prepared by an etch which is rather different from the commonly employed heavily oxidizing type. The etching solution, a weakly oxidizing mixture of HF and H_2O_2 [Ellis' No. 5 etch (2)], dissolves relatively little material, but gives rise to the formation of a surface film of considerable thickness. Both field effect and surface recombination velocity were measured, and the effect of the applied field on the electrical surface properties was investigated. Finally, the possibility of interpreting the data in terms of a discrete state picture was explored.

Theory and Procedures

In a field effect experiment, the amount of charge immobilized in a surface state is determined as a function of the position of the Fermi level at the surface. The theoretical expression for the charge $\Delta\Sigma_{ss}$ trapped in a discrete level is

$$\Delta\Sigma_{ss} = -qN_t\,[1 + \exp\,(E_t - E_i - q\phi_s)/kT]^{-1} \quad [1]$$

Here N_t and E_t stand for the density and energy of the state, E_i is the midgap energy, and ϕ_s is the surface potential ($q\phi_s$ is the difference between the Fermi energy and the midgap energy at the surface). The other symbols have their usual meaning. When more than one set of surface states is present, the charge trapped in the states is given by the sum of a number of expressions like [1].

Surface states may act as recombination centers for excess carriers. The equation describing the surface recombination velocity s attributable to a state as a function of surface potential is

$$s = \frac{N_t c_p\,(p_b + n_b)}{2\,n_i \exp q\phi_o/kT\,[\cosh\,(E_t - E_i - q\phi_o)/kT + \cosh q\,(\phi_s - \phi_o)/kT]} \quad [2]$$

Equation [2] describes a bell-shaped curve centered around $\phi_o = (kT/2q)\,\ln\,(c_p/c_n)$; c_p and c_n are capture constants (products of thermal velocity and cross section) for holes and electrons; p_b and n_b are bulk carrier densities. In general there are two values of E_t that will yield the same curve at a given temperature. Consequently, a single experimental s *vs.* ϕ_s curve does not determine a unique state energy. The most straightforward criterion for selecting the physically significant value for E_t is that this value should fit the field effect data (Eq. [1]). This approach was used here.

In the present work the field was applied using a 0.001 in. aluminum foil field plate with a 0.001 in. mylar spacer. Uniform pressure was exerted on the sample-field plate assembly through a sheet of rubber with a rigid backing plate, resulting in a capacitance of about 100 pfd/cm^2. The sweep frequency and amplitude of the field were chosen such as to avoid hysteresis caused by slow state relaxation and minority carrier lifetime. Because of the rather long sample lifetimes this meant that the frequency had to be limited to 10 or 20 cps at a sweep of 150v peak voltage. While sweeping the field, the sample was illuminated from the side opposite the field plate with a 60 cps square wave of penetrating radiation. Sample conduction in the dark and under illumination were displayed simultaneously on the screen of an oscilloscope as a function of the applied field. The surface recombination velocity was determined from the photoconductance, taking into account the effect of bulk recombination. The injected carrier density was always kept down to a few per cent of the bulk carrier density in order to minimize surface photovoltage. The original data were obtained in the form of smooth curves; the scatter in the points of the figures in this paper has been introduced during the manipulation of the data. Reduced surface mobilities (3) were used in the computations.

For samples with very long lifetimes and pronounced slow state relaxation, as observed in room air and nitrogen, overlap between the frequency regions of slow state relaxation and minority carrier lifetime effects presents a fundamental difficulty to obtaining significant results. Lifetime data were obtained in this case by measuring photoconductance during the application of a square wave field to the sample surface. Subsequently the back surface was lapped, and a field effect experiment was performed in the normal manner. Lapping decreases the sample lifetime by a few orders of magnitude and thus moves minority carrier effects to much higher frequencies if the sample thickness is small compared to the minority carrier diffusion length.

Samples were prepared in the following manner: After cutting and lapping to size (approx. 10 x 5 x 0.2 mm) with S. S. White "Airbrasive" No. 1 and water on glass, the wafers were cleaned ultrasonically in distilled water for several minutes to remove residual particles. The indium doped p- and antimony doped n-type samples had been cut to make the large faces (111) planes; the intrinsic samples were of unknown orientation. Next, they were etched with CP4 which had been "activated" by putting in lapped pieces of germanium from the same ingot. Also, it was hoped that this pretreatment would tend to remove from solution any trace impurities which have a tendency to deposit at the surface of the wafers during the etching process. The reaction was stopped by quenching with distilled water at a point where the activity had diminished to a small fraction of its initial value. The samples were washed thoroughly with distilled water without exposure to air. The water was removed immediately by several washings with methanol and then acetone. The samples, stored under acetone, were dried in a stream of nitrogen just before treating with the No. 5 etch. This etch consists of 40 ml HF (48%), 5 ml H_2O_2 (30%), and 24 ml water (2). The germanium pieces used to pretreat the CP4

were processed in the same manner as the samples and used to test and pretreat the No. 5 etch.

When CP4 etched germanium is treated with No. 5 etch, a colored film is formed on the surface, the growth of which can be followed by observing a sequence of interference colors. The shade and uniformity of color and also the texture of the film can be controlled by varying the composition of the etch and the duration of the treatment. In the course of these experiments, it was observed that low state densities and surface recombination velocities were consistently obtained for films which were uniformly tinted fifth order pale blue or yellow. Less reproducible properties and higher densities were found for films with multicolor patterns, striations, or other visible inhomogeneities. Samples with uniform pale blue or yellow films were studied throughout this investigation; their appearance was adopted as the criterion for acceptability. The desired type of film was often produced by the No. 5 etch as it was originally mixed, with 30 sec etching time. If not, the composition of the mixture and the reaction time were varied slightly; the right conditions were established using CP4 etched test samples. During the process, the sample thickness decreased by only 5μ. It may be noteworthy that an acceptable surface was more difficult to obtain on p-type than on n-type or intrinsic material.

After removal from the etch bath, the samples were washed in methanol, then in acetone, and finally dried in nitrogen. Contact surfaces were made at the ends by lapping with No. 600 abrasive paper and coating with gallium-indium solder. The samples were exposed to HF vapor for 10 sec and placed in the sample holder.

Results and Interpretation

Electrical Measurements in Air and Nitrogen

Very low values of surface recombination velocity at the quiescent surface potential (surface potential at zero field) were found for samples measured in air (relative humidity 30-50%) or in dry nitrogen, in agreement with Ellis' findings (2). For intrinsic germanium at room temperature recombination velocities between 10 and 15 cm/sec were consistently obtained. For 16 ohm-cm n-type and 20 ohm-cm p-type material the values were somewhat higher (around 50 cm/sec). This is not unexpected since the surface recombination velocity is proportional to the bulk carrier density (see Eq. [2]).

As an example, data on field effect and surface recombination velocity obtained on an intrinsic sample at room temperature in a nitrogen atmosphere are presented in Fig. 1. It may be seen that the slope of the surface state charge curve (Fig. 1b) is very small in the central region of the gap; it begins to increase only beyond $\phi_s = +4$. Here, as in the rest of this paper, ϕ_s is expressed in units kT/q. The surface recombination data in Fig. 1a were obtained by sweeping the surface potential with a square wave field. This is a point by point method in which for each value of field excursion only two experimental points are obtained. The surface recombination velocity at zero applied field (where $\phi_s \approx +5$) is indeed between 10 and 15 cm/sec. Also,

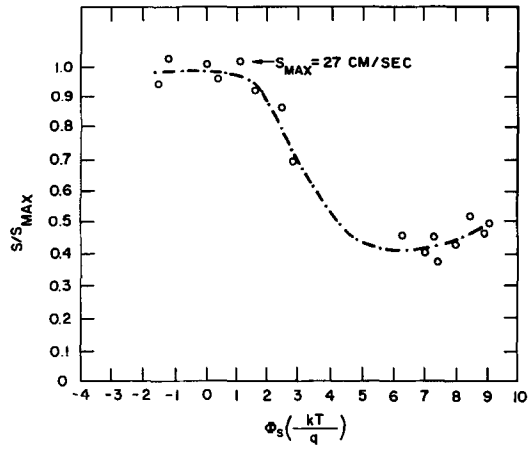

Fig. 1a. Surface recombination velocity for intrinsic germanium at 20°C in nitrogen.

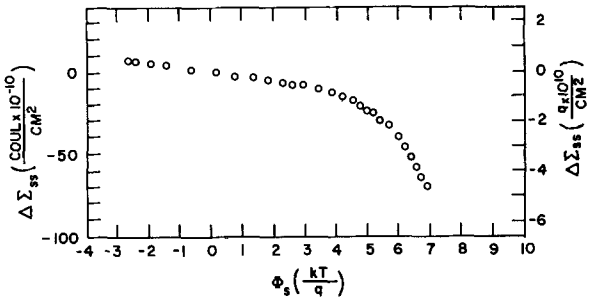

Fig. 1b. Charge in surface states for intrinsic germanium at 20°C in nitrogen.

the maximum value observed in this experiment (27 cm/sec) is very low. At higher positive values s does not go to zero, but levels off at a finite value. Unfortunately only a small part of the s *vs.* ϕ_s curve at negative surface potentials could be observed. When increasing the amplitude of the field voltage the quiescent surface potential shifts toward more positive values, and it is barely possible to swing beyond the conductance minimum. This effect is more pronounced when applying a square wave field than for a sine wave or triangular wave field.

The range of the recombination data is so limited that interpretation in terms of state energy according to Eq. [2] does not seem justified. Therefore, only qualitative conclusions will be drawn from these results. The low maximum recombination and the rather flat surface state charge curve are both indicative of a low state density in the middle of the forbidden gap. The center ϕ_o of the s *vs.* ϕ_s curve must be at a small positive or at a negative value of surface potential, *i.e.*, the state is either weakly acceptor type or it is donor type.

No difference in surface recombination velocity or in the state charge curve was found between samples which had been exposed to HF vapors after the HF-H_2O_2 treatment and those which had not been exposed. However, the quiescent surface potential which was originally for an intrinsic sample at +3 to +4 at room temperature would drift in about a week to +5 or +6; re-exposure would bring the surface potential back to the first value. No significant difference was found between samples exposed to room ambient and samples exposed to nitrogen over

times of the order of a day. When samples were left out in air for over a week a very slow increase in the slope of the state charge curve was observed, indicating that this surface does not have long term stability.

Electrical Measurements in Vacuum

Because of the hysteresis encountered when measuring in air, most experiments were carried out in vacuum. When the sample chamber was evacuated to about 1μ while sweeping the field at some moderate frequency and amplitude (for example, 150v peak at 10 cps), the field effect trace which originally shows a very distinct slow state relaxation loop, gradually begins to close. After a few hours the trace has become a single line. Not only do the slow state effects decrease strongly, but at the same time the density of the fast states in the center of the gap increases, as shown by the increased surface recombination velocity and the larger slope of the state charge curve. These phenomena are not understood at present. It is not clear whether only the number of slow states is affected, the process of communication between slow states and bulk, or both. There generally is some shift in the quiescent surface potential, but it is small (of the order of one kT/q unit to more positive values). The pronounced effect of removing room ambient by evacuating is rather surprising since replacing room ambient by dry nitrogen made little difference. The explanation for this unexpected behavior may be that pressing-on of the mylar-field plate assembly effectively isolates the sample surface from the gas phase. This will only slightly affect evacuation, but make out-diffusion of oxygen and water vapor extremely slow.

Effect of Amplitude of the Field on Surface Characteristics

An increase of the amplitude of the field voltage causes the quiescent surface potential to shift away from the minimum to larger positive values. Also, the slope of the state charge curve increases, indicating an increased state density. Finally, the surface recombination velocity becomes considerably larger. These three effects are reversible. Experimental data on field effect and surface recombination velocity are shown in Fig. 2. Similar results were found by Dousmanis (4) and by Rzhanov *et al.* (5, 6). The extreme parts of the experimental curves have not been worked out since the central region shows the above effects clearly enough. Note that there is an over-all rather than a localized increase in the slope of the charge curves. The irregularities between $\phi_s = +1$ and $\phi_s = 2.5$, *i.e.*, in the region around the conduction minimum, are not significant. These have been introduced during the data reduction; the relative error is largest in this area. An appreciable increase in the maximum surface recombination velocity (about 20%) is observed when changing the peak voltage from 50 to 200v and consequently the field from 2 x 10^4 to 8 x 10^4 v/cm.

It seems plausible that the nonlinear relation between applied field and surface potential is responsible for the change in quiescent potential (4). When increasing the amplitude of the a-c field the

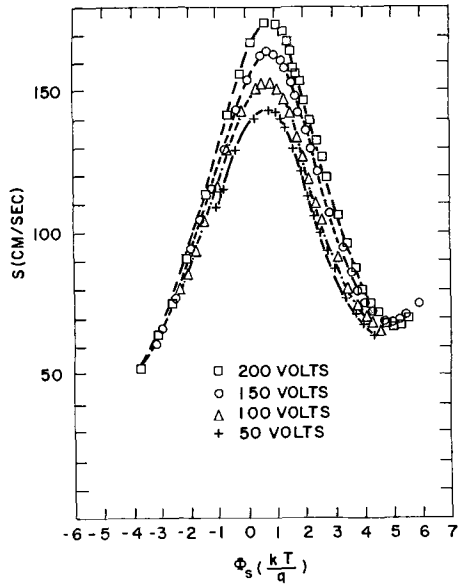

Fig. 2a. Effect of applied field on surface recombination velocity for 20 ohm-cm p-type germanium at 20°C in vacuum.

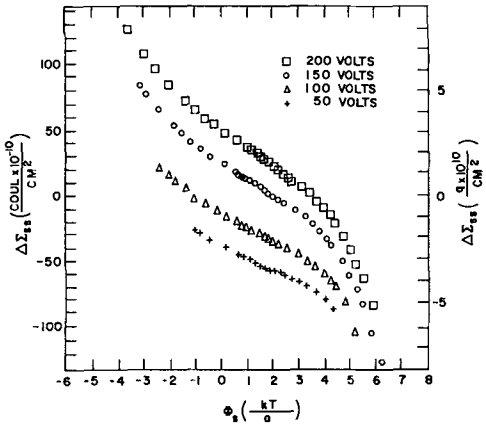

Fig. 2b. Effect of applied field on charge in surface states for 20 ohm-cm p-type germanium at 20°C in vacuum.

average position of the Fermi level at the surface will shift toward the potential of the conductance minimum. Consequently, electrons will leak out of the slow states, and the space charge layer becomes more negative, *i.e.*, the quiescent potential shifts away from the minimum. One has to assume in this explanation that the dependence on the surface potential of the rate of charge transfer from the slow states to the semiconductor is either weak or that it is such that it enhances the above effect. The resulting change in the average voltage across the oxide layer may require a rearrangement of ionic charges resulting in a change in fast state density. Migration of ions has been proposed by other authors (7,8) to explain the increase in fast state density on the application of d-c fields. They assume that in this process some bonds will be freed and thus new fast states created.

Electrical Surface Characteristics in Vacuum

Measurements have been carried out on intrinsic (50 ohm-cm), n-type (16 ohm-cm) and p-type (20 ohm-cm and 11 ohm-cm) samples at different temperatures. Some results are presented in Fig. 3 to 7. For a number of cases the data have been interpreted

in terms of two discrete sets of states in the center of the gap in order to show that it is possible, in principle, to force the data into this model. The solid lines in the graphs are theoretical curves calculated from the values indicated. The recombination data were fitted with a theoretical curve according to Eq. [2]; two possible state energies (one above and one below the center of the gap) and a ratio of cross sections were obtained. Next, it was assumed that only the state at positive surface potential has physical significance. This was done because other workers on etched surfaces have generally concluded that the recombination active state is in the upper half of the gap. The density of this center was found from the fit of a curve as described by [1] to the experimental fast state charge curve.

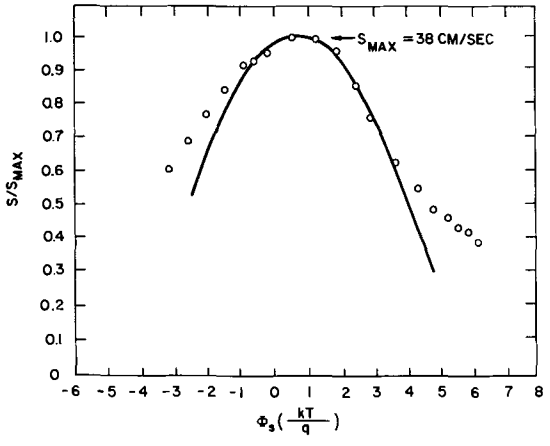

Fig. 3a. Surface recombination velocity for intrinsic germanium at 15°C in vacuum.

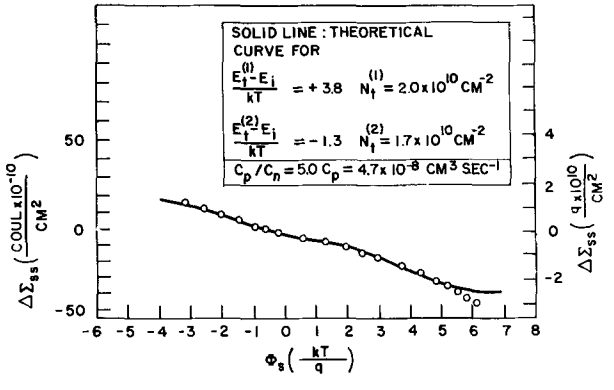

Fig. 3b. Charge in surface states for intrinsic germanium at 15°C in vacuum.

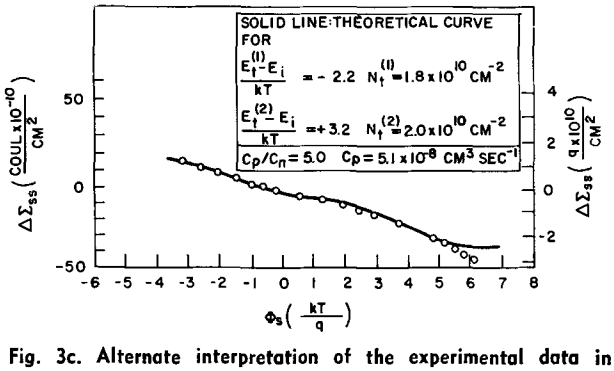

Fig. 3c. Alternate interpretation of the experimental data in Fig. 3a, b

However, by taking for the energy of the center the alternate possibility allowed by the recombination data, an equally satisfactory curve fitting is obtained, as will be demonstrated in two examples. In both cases one has to assume a second set of states (inactive) to explain the remainder of the central part of the state charge curve.

The results for intrinsic germanium at 15°C (Fig. 3) show the very low maximum value of 38 cm/sec for the surface recombination velocity. The alternate interpretation (Fig. 3c) leads to values for stage energies and densities that are not very different.

The data on n-type germanium at 30°C (Fig. 4) may be explained in a similar manner, after subtracting a constant "background" surface recombination velocity. This background was assumed to be 0.52 in terms of the units used in Fig. 4a. In this case the alternate interpretation (Fig. 4d) seems to give a slightly better fit to the field effect data. The data at −15°C (Fig. 5) show very clearly that the recombination velocity goes up again at negative surface potentials, suggesting the presence of a state with strong donor character in the lower part of the gap. This finding is similar to a recent result of Many *et al.* (9) obtained on an n-type sample. It was the only case in the present investigation that a slightly negative value was found for ϕ_o. This may be insignificant since the peak in the center is situated on the slope of the next one, causing its maximum to be shifted toward negative surface potentials. At positive surface potentials the recombination velocity drops off to a very small value. Because of the complex shape of the surface recombination velocity curve, no attempt was made to derive state energies and densities in this case.

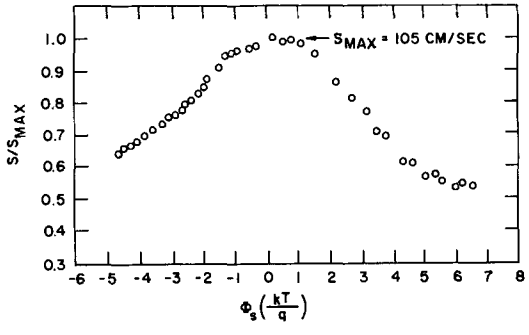

Fig. 4a. Surface recombination velocity for 16 ohm-cm n-type germanium at 30°C in vacuum.

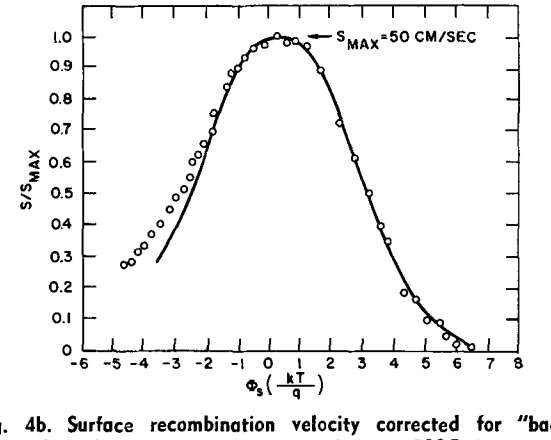

Fig. 4b. Surface recombination velocity corrected for "background" for 16 ohm-cm n-type germanium at 30°C in vacuum.

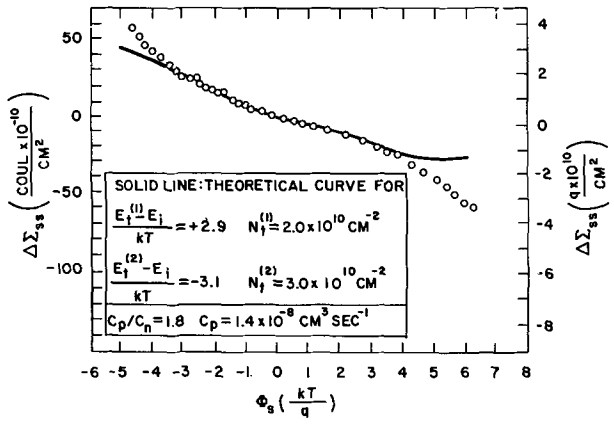

Fig. 4c. Charge in surface states for 16 ohm-cm n-type germanium at 30°C in vacuum.

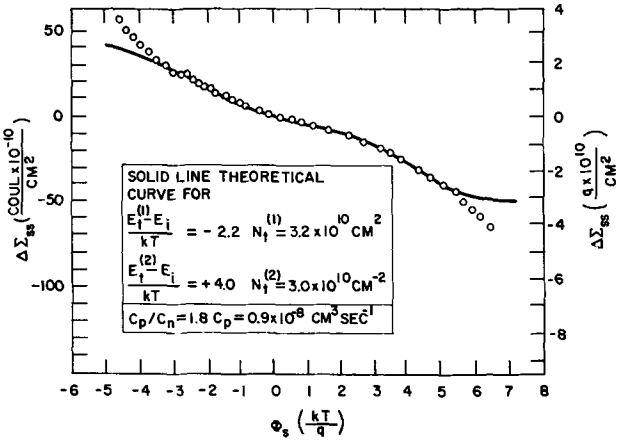

Fig. 4d. Alternate interpretation of the experimental data of Fig. 4a-c.

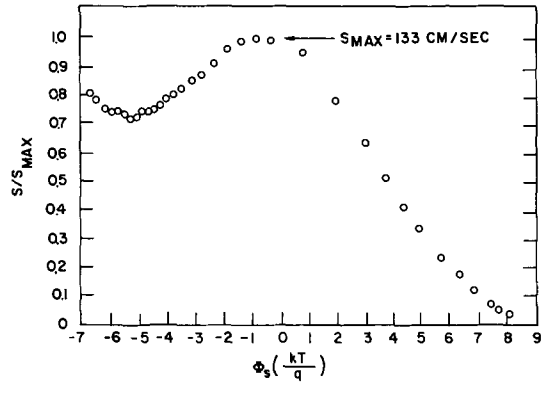

Fig. 5a. Surface recombination velocity for 16 ohm-cm n-type germanium at —15°C in vacuum.

Figures 6 and 7 show data on a 20 ohm-cm p-type sample at 20° and —15°C. The recombination data are again suggestive of a complicated state structure. At both temperatures there is evidence of a second peak in the recombination velocity, now at positive surface potentials. A similar peak was also observed on 11 ohm-cm p-type samples. It suggests the presence of an acceptor state. In all cases the slope of the central peak on the opposite side is not as steep as one would expect for a discrete set of states; this suggests the presence of a third set of recombination centers, possibly with lower density.

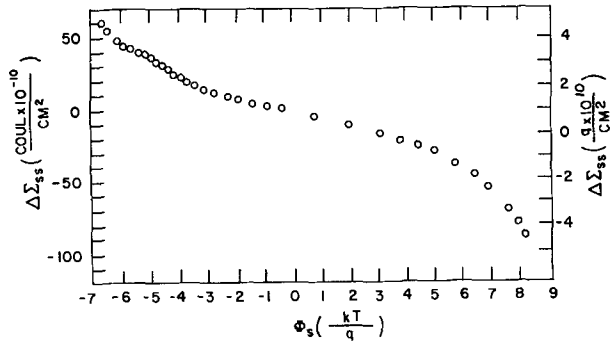

Fig. 5b. Charge in surface states for 16 ohm-cm n-type germanium at —15°C in vacuum.

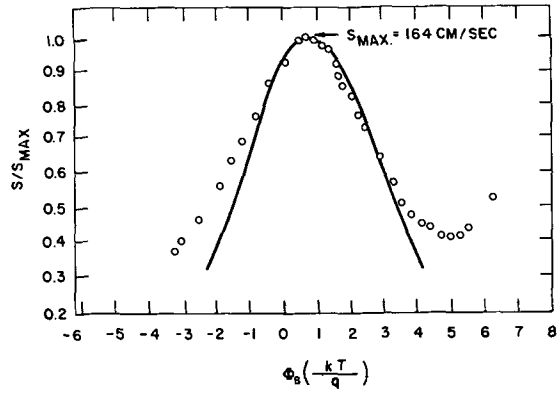

Fig. 6a. Surface recombination velocity for 20 ohm-cm p-type germanium at 20°C in vacuum.

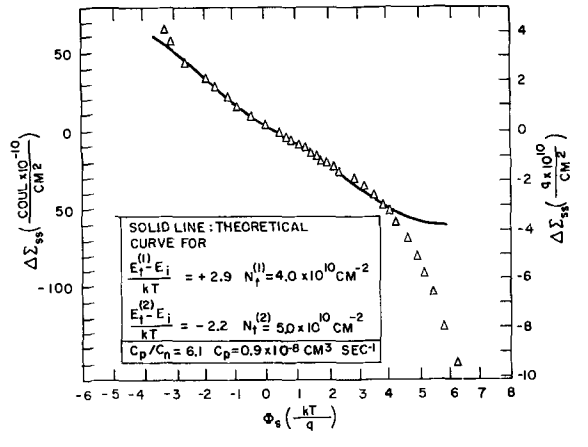

Fig. 6b. Charge in surface states for 20 ohm-cm p-type germanium at 20°C in vacuum.

Field effect and surface recombination velocity data at these temperatures have been interpreted in the discrete state picture. In this interpretation the state densities decrease from 4 x 10^{10} to 2 x 10^{10} and from 5 x 10^{10} to 3 x 10^{10} as the temperature is lowered by 35°C. Also, there is a sizeable increase in state energies (from +2.9 to +3.9 and from —2.2 to —1.0 neglecting a small difference in the kT/q units). The apparent decrease in state density in the central region of the curve could actually result from a decreased effect at lower temperature of states further away from the middle of the gap. For this reason one may doubt the value of trying to explain the present field effect data by assuming only two sets of states with energies in the center of the gap. Low-temperature resistivity and Hall

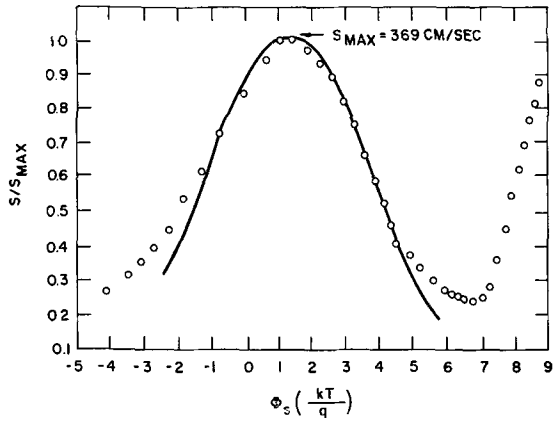

Fig. 7a. Surface recombination velocity for 20 ohm-cm p-type germanium at —15°C in vacuum.

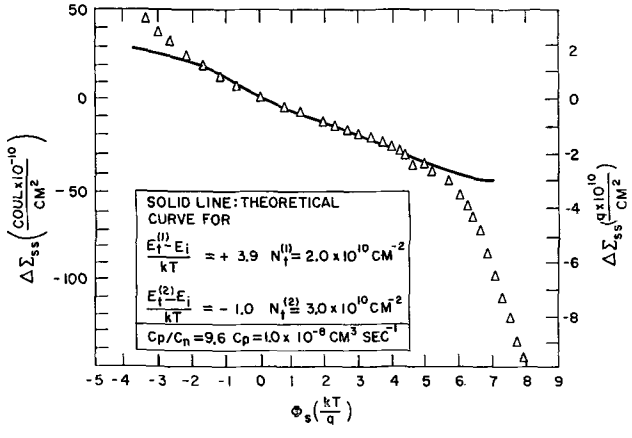

Fig. 7b. Charge in surface states for 20 ohm-cm p-type germanium at —15°C in vacuum.

effect were measured on samples from the same sources; the behavior of these samples was quite normal and the degree of compensation only moderate.

As a possible cause for the specificity of the recombination spectra, the plating-out of bulk impurities at the interface during the etching process may be suggested. Recent investigations by Frankl (10) and by Brattain and Boddy (11) have demonstrated the profound effect of adsorbed ionic species on the electrical surface properties. It is thought that similar effects may play a role in the phenomena observed in the present study.

Discussion

From the foregoing the conclusion emerges that it is impossible in this investigation uniquely to assign energies and densities to the states in the central region of the gap. One even has to allow for the possibility that some or all of these states are continuously distributed over a range of energies. Although a model with one discrete set of recombination active states and one (or sometimes two) discrete sets of inactive states seems to be the accepted pattern of interpretation of field effect and surface recombination data the authors of this paper feel that in some of the cases published in the literature [see *e.g.*, (7)] the workers' faith in the discrete state picture rather than the experimental data was the decisive factor. The experimentalist will have a preference for this model because of its simplicity and also because he realizes that all departures from the ideal uniform field in the experiment will result in an apparent spread of the states over a range of energies. Nevertheless, one should keep in mind that it is possible to approximate any smooth curve as obtained in a field effect experiment by a superposition of curves according to Eq. [1] for E_t values about 4 to 6 kT/q units apart, or even to interpret it in terms of a continuous distribution of varying density. Similarly, any experimental surface recombination velocity *vs.* surface potential plot can be considered as arising from a superposition of curves according to Eq. [2] for a number of values of E_t, N_t, c_p, and ϕ_o or for a range of values of these parameters.

The suggestion that changes in the fast state density under the application of electric fields are related to ion migration, leading to an increase in the numbers of vacancies at the oxide-semiconductor interface, has to be scrutinized more closely. Since the effects of the field on the electrical properties are reversible it seems to follow that the interface is in an equilibrium condition. The problem of ionic migration in oxide layers is worth further investigation, either by itself or in conjunction with the general problem of the mechanism of charge transport through the oxide.

One of the most interesting points revealed in the present study is the difference between the surface characteristics of n and p germanium. Other workers in the field often limit their investigations to samples from the same ingot in order to reduce the load of data reduction. In the present work the effect of the bulk material on surface properties has been studied in a somewhat more systematic manner. Unfortunately, it was necessary to limit the field sweep, and at most half of the forbidden gap could be covered. Finally, it should be mentioned that, except for the rather low state densities and the small values of ϕ_o, the mid gap characteristics of HF-H_2O_2 treated surfaces do not seem to be radically different from those of samples etched in more heavily oxidizing solutions. A fundamental difficulty in comparing results obtained on different surfaces is that one has no proper criterion as to what differences are really significant. This lack of a proper model for the fast interfacial states is probably the most serious weakness in the present state of semiconductor surface physics.

Acknowledgment

The authors are indebted to Mr. D. K. Hartman of the General Electric Company for a gift of two germanium crystals.

Manuscript received May 31, 1963.

Any discussion of this paper will appear in a Discussion Section to be published in the June 1964 JOURNAL.

REFERENCES

1. H. Flietner, *Phys. Stat. Sol.*, **2**, 221 (1962).
2. S. G. Ellis, *J. Appl. Phys.*, **28**, 1262 (1957).
3. R. F. Greene, D. R. Frankl, and J. N. Zemel, *Phys. Rev.*, **118**, 967 (1960).
4. G. C. Dousmanis, *ibid.*, **112**, 369 (1958).

5. A. V. Rzhanov, In. F. Novototskii-Vlasov, and I. G. Neizvestnyi, *Soviet Phys.—Tech. Phys.*, **2**, 2274 (1957).
6. A. V. Rzhanov, N. M. Pavlov, and M. A. Seleznova, *ibid.*, **3**, 2419 (1958).
7. V. G. Litovchenko and V. I. Lyachenko, *Soviet Phys.—Solid State*, **1**, 1470 (1960).
8. Y. Margoninski, *Phys. Rev.*, **121**, 1282 (1961).
9. A. Many, Y. Goldstein, N. B. Grover, and E. Harnik, "Proceedings of the International Conference on Semiconductor Physics," p. 498, Publishing House of the Czechoslovak Academy of Science, Prague (1961).
10. D. R. Frankl, *This Journal*, **109**, 238 (1962).
11. W. H. Brattain and P. J. Boddy, *ibid.*, **109**, 812 (1962).

Epitaxial P-Type Germanium and Silicon Films by the Hydrogen Reduction of $GeBr_4$, $SiBr_4$, and BBr_3

K. J. Miller and M. J. Grieco

Bell Telephone Laboratories Incorporated, Murray Hill, New Jersey

ABSTRACT

Epitaxial p-type films of germanium or silicon with controlled thicknesses and resistivities have been grown on parent substrates using the hydrogen reduction of $GeBr_4$ or $SiBr_4$, respectively, doped with BBr_3. The thermochemistry and kinetics related to the growth of these films are discussed, and some comparisons with film growth from $GeCl_4$ or $SiCl_4$ are presented.

A conventional process for vapor phase deposition of epitaxial germanium or silicon films on parent substrates uses the hydrogen reduction of $GeCl_4$ of $SiCl_4$ (1,2). The object of this paper is to present data on epitaxial deposition on parent substrates using hydrogen reduction of either $GeBr_4$ or $SiBr_4$ and to compare some of the deposition reactions of $GeBr_4$ and $SiBr_4$ with those of $GeCl_4$ and $SiCl_4$. The use of $SiBr_4$ for vapor phase deposition of silicon on silicon filaments was first reported by Sangster *et al.* (3).

Deposition from $GeBr_4$ or $SiBr_4$ and the p-type dopant BBr_3 has eliminated the formation of mixed boron halides and BCl_3 which should be expected in $GeCl_4$-BBr_3 or $SiCl_4$-BBr_3 solutions. Such exchange of halogens has been reported between BCl_3 and BBr_3 and between $SiCl_4$ and $SiBr_4$ (4, 5). Recently, Deal (6) has reported instability of BBr_3 in solution with $SiCl_4$, and Amron (7) has suggested the possibility of halogen exchange between BBr_3 and $GeCl_4$. Doping control of epitaxial films is affected by such halogen exchange reactions because of the high vapor pressure and the greater thermochemical stability of BCl_3, and mixed boron halides, as compared with that of BBr_3.

Experimental Procedure

Film deposition.—The deposition apparatus used was similar to that previously reported (8). The hydrogen gas halide saturator was used in this study with the hydrogen flow over the surface of the liquid, which was stirred with a glass-encapsulated magnetic stirrer. This saturation technique eliminated spray which can result from bubbling. Stirring ensured uniformity of temperature in the liquid. Saturators used for $GeBr_4$ had a 30g capacity and for $SiBr_4$, a 200g capacity. Figure 1 shows a sketch of the type of saturator used.

Electronic grade chemicals were used without further purification. The BBr_3, $GeCl_4$, and $SiCl_4$ were reported to be 99.999+% and $GeBr_4$ 99.99+%; these reagents were obtained from Eagle-Picher Company. The $SiBr_4$ was reported to be 99+% and was obtained from Stauffer Chemical Company.

Substrate samples were single crystal wafers, oriented in the (111) plane, and mechanically polished; in the case of germanium, samples were further chemically polished in concentrated HNO_3-HF in 2:1 ratio. Germanium films have, however, also been successfully deposited on substrates electrochemically polished by the method of Sullivan (9) and subsequently etched in boiling 3% H_2O_2 for 30 sec (10). High resistivity p-type susceptors of

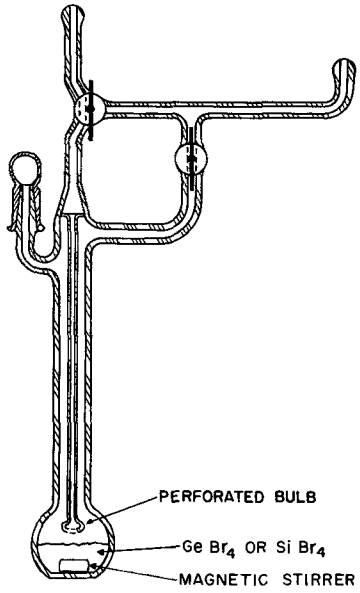

Fig. 1. Tetrabromide saturator for hydrogen carrier gas

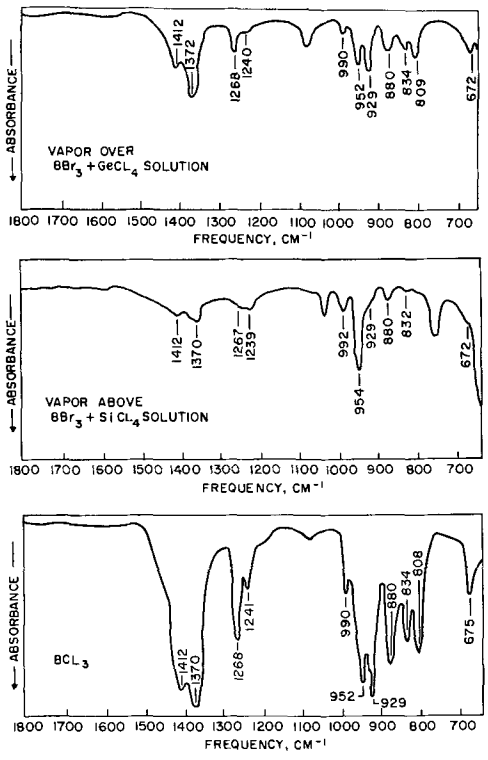

Fig. 2. Infrared spectra of vapor above solutions of BBr_3-$GeCl_4$ and BBr_3-$SiCl_4$ compared with BCl_3 spectrum.

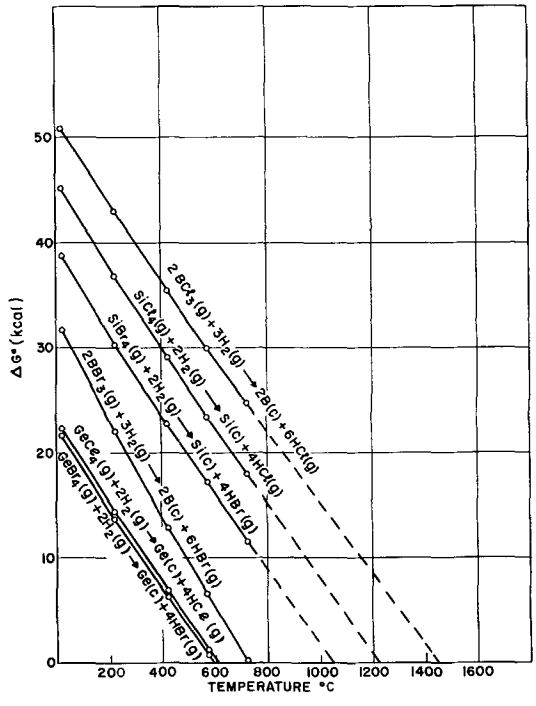

Fig. 3. ΔG° as a function of temperature for some epitaxial reduction reactions.

germanium or silicon were used, and samples of germanium or silicon were placed directly on their respective susceptors. Film thickness was determined by angle lapping, staining, and interferometric examination (11, 12). Substrate samples were approximately ½ in. diameter. Inside diameter of the reaction tube was 2 in. and susceptor diameter was 1 in.

Analysis of products of halogen exchange.—In order to test the theory of halogen exchange between BBr_3 and $GeCl_4$ or $SiCl_4$ in liquid solution, infrared analyses of the vapor above these solutions were made. Approximately 50g each of $GeCl_4$ and BBr_3, and 50g of $SiCl_4$ and 10g of BBr_3 were placed in closed reaction flasks for 60 hr at room temperature. Infrared gas cells were partially filled with the gases above each of these solutions. The characteristic spectrum of BCl_3 observed in the vapors above each of the solutions is shown in Fig. 2 and compared to the spectrum of pure BCl_3. No evidence of BBr_3 was detected in the vapor above either solution. This was indicated by the absence of the characteristic BBr_3 band at 1100 cm^{-1}.

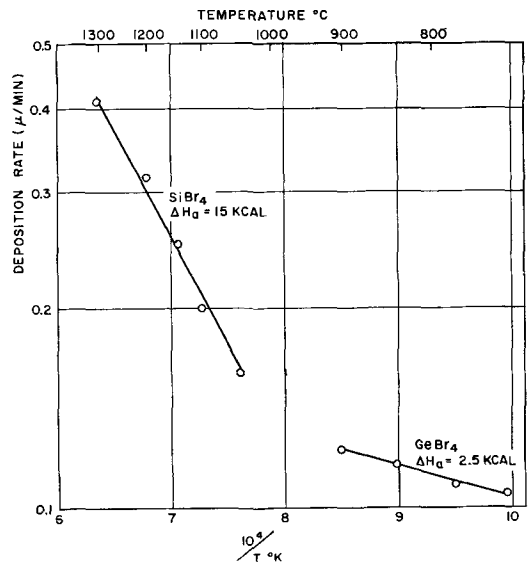

Fig. 4. Temperature dependence of deposition rate for $GeBr_4$ and $SiBr_4$.

Results and Discussion

Temperature dependence of film deposition.—Thermodynamically, there is less energy required for reduction of germanium and silicon tetrabromides as compared with their respective tetrachlorides. This factor could be beneficial for the preparation of epitaxial films. The comparison can be readily seen in Fig. 3 from the calculated (13-18) standard free energy change of the idealized reduction reactions as a function of temperature. The negative free energy change values start at 600°C for $GeBr_4$ as compared with 615°C for $GeCl_4$ and 1050°C for $SiBr_4$ as compared with 1225°C for $SiCl_4$.

Figure 4 shows the temperature dependence of deposition rate for undoped $GeBr_4$ and $SiBr_4$. Hydrogen flow over the stirred tetrabromides was 1 liter/min with an additional 1 liter/min of hydrogen bypassing the halide saturator. The tetrabromides were thermostatted at 30° ± 0.5°C. From these curves the apparent activation energy was determined to be 15 kcal/mole for $SiBr_4$ and 2.5 kcal/mole for $GeBr_4$. Because the binding energy is less for Si-Br bonds, 69.3 kcal/mole (19), as compared with Si-Cl bonds, 85.8 kcal/mole (19), it is reasonable to expect the smaller activation energy found for the $SiBr_4$ reduction reaction as compared with the values of 37 and 30 kcal/mole reported for the $SiCl_4$ reduction reaction by Theuerer (2) and by Kahng *et al.* (20), respectively. The low

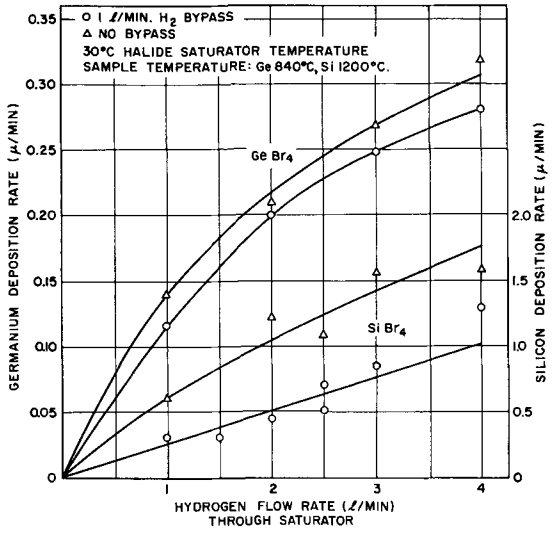

Fig. 5. Deposition rate as a function of hydrogen flow rate for $GeBr_4$ and $SiBr_4$.

activation energy for the deposition of germanium suggests that its rate of deposition is controlled by the rate of diffusion of reactants and products at the reaction surface rather than by the rate of the reaction

$$GeBr_4(g) + 2H_2(g) = Ge(c) + 4HBr(g)$$

Gas flow rate.—Deposition rates of germanium and silicon, from their respective undoped tetrabromides as a function of hydrogen gas flow, are shown in Fig. 5. The dilution of tetrabromide in the reaction chamber by a constant additional flow of 1 liter/min of hydrogen which has bypassed the halide saturator is indicated in the curves by their downward displacement.

An estimate of the saturation of hydrogen carrier gas with tetrabromide has been made by measuring the dew point of the tetrabromide immediately after the saturator. With the type of saturator shown in Fig. 1 held at 30° ± 0.5°C, the dew point at 1 liter/min hydrogen flow was 18.5°C for $SiBr_4$ and 22.3°C for $GeBr_4$, giving approximately 60% hydrogen saturation with $GeBr_4$ and 47% for $SiBr_4$. These dew points remained constant when the tubing between the saturator and the reaction chamber was at either

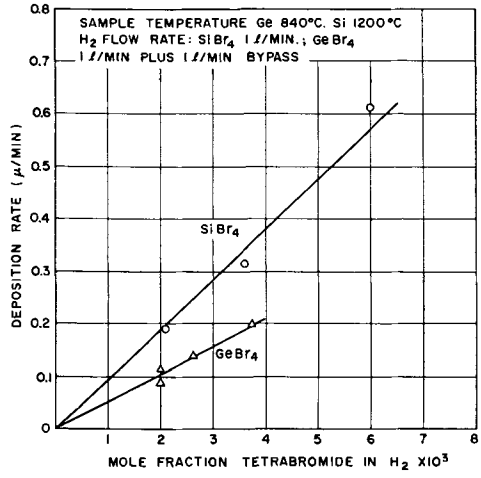

Fig. 6. Deposition rate as a function of tetrabromide concentration for $GeBr_4$ and $SiBr_4$.

24° or 70°C. Van Gelder and Roberts (21) have determined 100% saturation for hydrogen bubbled into $SiCl_4$ as determined by dew point measurements. In this study, it was found possible to obtain 100% hydrogen saturation with $GeBr_4$ or $SiBr_4$ by bubbling also, provided the tubing between the saturator and the reaction chamber was kept at a temperature greater than the saturator temperature.

Tetrabromide concentration.—Figure 6 shows deposition rates of germanium and silicon from undoped $GeBr_4$ and $SiBr_4$ as a function of mole fraction of tetrabromide. The mole fraction was calculated assuming the hydrogen carrier gas was 60% saturated with $GeBr_4$ and 47% saturated with $SiBr_4$. The concentration of $GeBr_4$ was calculated before dilution with the bypass hydrogen flow. Concentration was varied by changing the temperature of the tetrabromide saturator.

Factors affecting film doping.—The stability of BBr_3, when mixed with $GeBr_4$ or $SiBr_4$, was a prerequisite for it to be a controllable dopant. However, BBr_3 in $GeCl_4$ or $SiCl_4$ was found to be unstable as determined by infrared analysis. The halogen exchange reactions indicated in these latter solutions are:

$$4BBr_3(l) + 3GeCl_4(l) = 4BCl_3(g) + 3GeBr_4(l) \quad \Delta H°_{298} = -22.7 \text{ kcal} \qquad [1]$$

$$4BBr_3(l) + 3SiCl_4(l) = 4BCl_3(g) + 3SiBr_4(l) \quad \Delta H°_{298} = -3.5 \text{ kcal} \qquad [2]$$

The greater negative magnitude of the calculated (13, 14) enthalpy change for reaction [1] suggests that this reaction may proceed more readily than reaction [2].[1] Because of these reactions, it is apparent that BCl_3 would be a boron containing specie in such solutions and should be present in gaseous solutions as well. Figure 3 shows that the idealized reduction reaction for BCl_3 cannot proceed spontaneously until 1450°C indicating a greater stability as compared with BBr_3 which can proceed spontaneously at 730°C. Therefore, to obtain a comparable number of deposited boron atoms from BCl_3 as can be obtained from BBr_3 at the same temperature would require a greater concentration of BCl_3 in the vapor phase.

Vapor pressure as a function of temperature for the tetrachlorides and tetrabromides of germanium and silicon and of BCl_3 and BBr_3 are compared in Fig. 7. Vapor pressures have been calculated from data in the literature (13, 22-24). In previous studies (2) BBr_3 was chosen as a dopant for $SiCl_4$ because its vapor pressure was similar to that of $SiCl_4$. However, the halogen exchange reactions described above convert BBr_3 to BCl_3 and mixed halides in $GeCl_4$ or $SiCl_4$. Figure 7 shows that the difference in vapor pressure between BCl_3 and $GeCl_4$ or between BCl_3 and $SiCl_4$ is greater than that between BBr_3 and $GeBr_4$ or between BBr_3 and $SiBr_4$.

It is believed that the bromide solutions remain more constant in composition than the chloride solutions because their lower vapor pressures are experimentally more controllable. However, the vapor pressure of BBr_3 is still higher than that of

[1] Insufficient data were available in the literature from which one could obtain the free energy changes for these reactions.

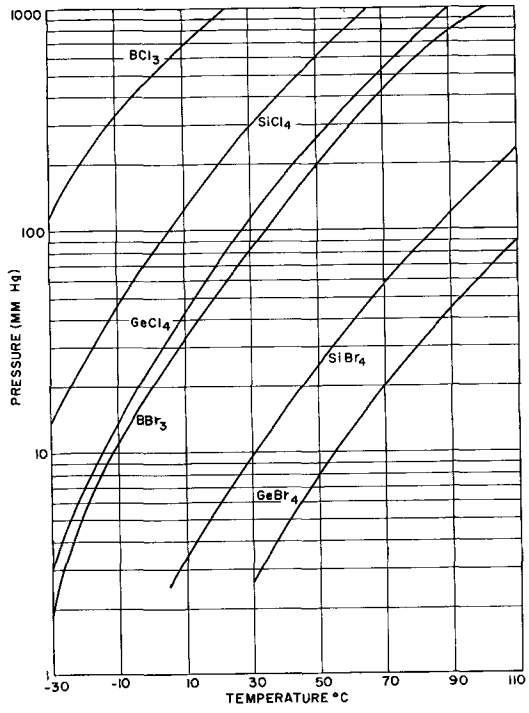

Fig. 7. Vapor pressure curves for some epitaxial reactants

either $GeBr_4$ or $SiBr_4$ and the concentration of BBr_3 in liquid solution with $GeBr_4$ or $SiBr_4$ has apparently varied when fast (1-2 liter/min) hydrogen flow rates have been passed over such solutions. Experiments have shown that doping by a liquid solution of BBr_3 and $GeBr_4$ or $SiBr_4$ and using a single saturator produced films which were progressively less doped with time.

Doping of films was accomplished by using two halide saturators of the type as shown in Fig. 1, one containing undoped $GeBr_4$ or $SiBr_4$ and another containing $GeBr_4$ or $SiBr_4$ doped with BBr_3 depending on the doping level required. Hydrogen was passed over the doped $GeBr_4$ at the rate of 1 cc/min while 1-2 liters/min of hydrogen was passed over the undoped $GeBr_4$, both held at 30°C. Both gas streams entered the reaction chamber at the same time.

Diodes were fabricated from the germanium films for evaluation of impurity profiles of films by the differential capacitance voltage method (25, 26). Diodes had 0.015 in. diameter etched mesas and

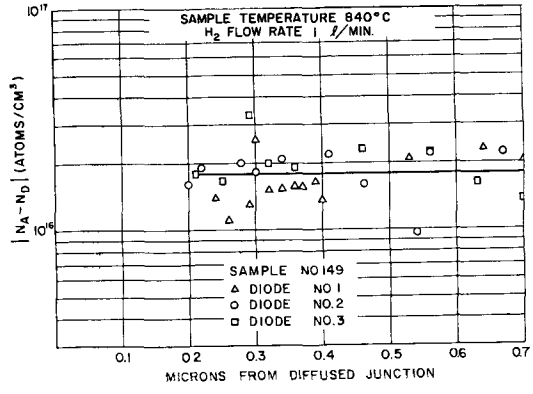

Fig. 8. Doping profile for BBr_3 doped germanium film grown from $GeBr_4$. Film thickness 5.6μ.

were formed by diffusing arsenic 0.5μ into the films. Substrates were p-type with 0.01 ohm-cm resistivities. Breakdown voltages of diodes with film thicknesses greater than their depletion layer widths have been obtained similar to those reported by Miller (27) for bulk germanium of comparable resistivities.

An example of the results of germanium film doping is shown in Fig. 8 where the doping saturator contained 25g of $GeBr_4$ and 20 microliters of BBr_3. The BBr_3:$GeBr_4$ ratio was calculated to be $1:10^8$ in the reactant gases, assuming Raoult's ideal solution law to hold and assuming the hydrogen to be 60% saturated with $GeBr_4$. Figure 8 shows the concentration of uncompensated acceptor atoms as a function of distance from the diffused junction into the film. Of particular interest in Fig. 8 is the constancy of doping level for the 5.6μ thick film over the approximately 0.7μ distance from the diffused junction which could be measured. The average run-to-run deviation of uncompensated acceptor atoms for five consecutive deposits using the same doping procedure was $\pm 0.6 \times 10^{16}/cm^3$ from an arithmetical mean of $1.5 \times 10^{16}/cm^3$. The scatter of values about the curve drawn in Fig. 8 is to a great degree due to the method of measurement used rather than to an actual variation in the doping profile. The arsenic diffusion, carried out at 600°C for 45 min, is believed to be sufficient to anneal out copper contamination to less than $10^{15}/cm^3$. Figure 9 shows the impurity profile with depth for an undoped 7.4μ thick germanium film grown from $GeBr_4$.

Heavily doped silicon was deposited from $SiBr_4$ by using the doping saturator with pure BBr_3 held at −40°C. The rates of deposition and resistivities for these p-type films deposited on 0.06 ohm-cm n-type substrates are shown below for a 1 liter/min H_2 flow rate and a 1200°C sample temperature. Resistivities were determined by four-point probe measurements.

Sample	Resistivity, ohm-cm	Deposition rate, μ/min
49	0.02	0.875
50	0.08	0.785
51	0.04	0.880

The deposition rates of BBr_3 doped silicon films shown above are seen to be almost 30% greater than that of the 0.61 μ/min deposition rate found for films grown under the same conditions from undoped $SiBr_4$. Run-to-run control of deposition rate for undoped films was approximately ±3%. Undoped silicon films were p-type with 1.5 ohm-cm resistivities. Theuerer (2) has observed a more than twofold increase in deposition rate when $SiCl_4$ was heavily doped with BBr_3 and has suggested that the increase involved the following reaction

$$3SiCl_4(g) + 4B(c) = 3Si(c) + 4BCl_3(g)$$

Figure 10 shows that $\Delta G°$ is favorable at 770°C for the above reaction and at 1050°C for the analogous reaction of $SiBr_4(g)$ with B(c). This increase in rate could be due to boron acting as a surface catalyst for silicon tetrahalide reduction, thereby causing a greater number of silicon atoms to be

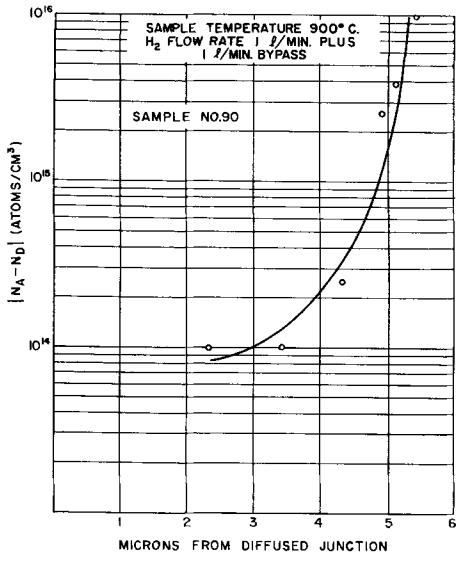

Fig. 9. Doping profile for undoped germanium film grown from $GeBr_4$. Film thickness 7.4μ.

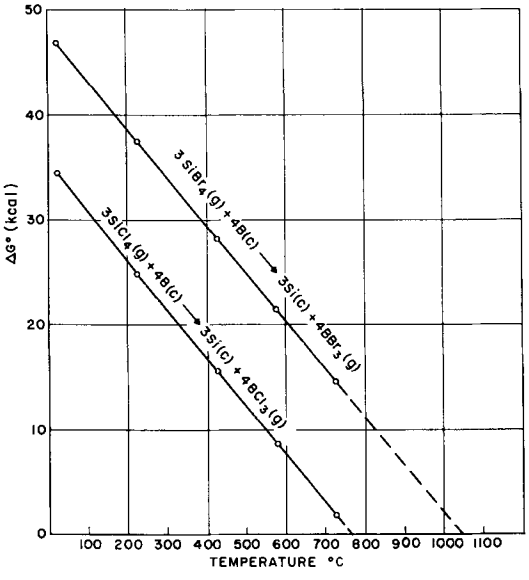

Fig. 10. $\Delta G°$ as a function of temperature for boron reduction of $SiBr_4$ as compared with $SiCl_4$.

deposited than that indicated by the stoichiometry of the above equation. These reactions can be expected to be dependent on the experimental concentrations of the reactants. The values of $\Delta G°$ give, however, a relative thermochemical comparison between the reactions. The concentration of the reactant, B(c), would, in this case, be expected to be rate-determining. Because of the lower deposition temperature of germanium and corresponding decrease in decomposition of BBr_3 at the lower temperature, the concentration of B(c) may be too small to cause a measurable change in the deposition rate of $GeBr_4$. Experimentally, no increase has been observed in the rate of deposition of germanium from BBr_3 doped $GeBr_4$. However, the comparable reaction of $GeCl_4(g)$ with B(c) has a value of $\Delta G°_{298} = -95.4$ kcal as compared with a value of $\Delta G°_{298} = -3.99$ kcal for the reaction of $GeBr_4(g)$ with B(c). The tetrachlorides, therefore, at the same concentration and temperature, may be more reactive with B(c) as compared with the tetrabromides of germanium and silicon.

Summary

An attempt has been made to determine the process parameters for epitaxial p-type film deposition by the hydrogen reduction of $GeBr_4$, $SiBr_4$, and BBr_3. The results obtained suggest an alternate approach to doped germanium and silicon film growth from that of $GeCl_4$ and $SiCl_4$ reduction.

Acknowledgment

It is a pleasure to acknowledge the efforts of J. P. Luongo and Mrs. L. B. Jassie in the infrared analysis, the assistance of G. Reutlinger in resistivity measurements, of W. Van Gelder and J. Roberts in dew point measurements and the stimulating discussions with our colleagues at the Bell Telephone Laboratories.

Manuscript received May 13, 1963; revised manuscript received June 25, 1963. This paper was delivered before the New York Meeting, Sept. 29-Oct. 3, 1963.

Any discussion of this paper will appear in a Discussion Section to be published in the June 1964 JOURNAL.

REFERENCES

1. H. C. Theuerer, J. J. Kleimack, H. H. Loar, and H. Christensen, *Proc. IRE*, **48**, 1642 (1960).
2. H. C. Theuerer, *This Journal*, **108**, 649 (1961).
3. R. C. Sangster, E. F. Maverick, and M. L. Croutch, *ibid.*, **104**, 317 (1957).
4. L. P. Lindeman and M. K. Wilson, *J. Chem. Phys.*, **24**, 242 (1956).
5. G. S. Forbes and H. H. Anderson, *J. Am. Chem. Soc.*, **66**, 931 (1944); **67**, 859 (1945).
6. B. E. Deal, *This Journal*, **109**, 514 (1962).
7. I. Amron, Private communication.
8. K. J. Miller, R. C. Manz, and M. J. Grieco, *This Journal*, **109**, 643 (1962).
9. M. V. Sullivan, D. L. Klein, R. M. Finne, L. A. Pompliano, and G. A. Kolb, *ibid.*, **110**, 414 (1963).
10. K. J. Miller, *ibid.*, **108**, 296 (1961).
11. C. S. Fuller and J. A. Ditzenberger, *J. Appl. Phys.*, **27**, 548 (1956).
12. G. Reutlinger in a private communication gave stain-etch for germanium as: 200 cm³ HF and two drops of 30% H_2O_2.
13. F. D. Rossini, D. D. Wagman, W. H. Evans, S. Levine, and I. Jaffe, "Selected Values of Chemical Thermodynamic Properties," U. S. NBS Circ. 500, Series I and II (1952) and Series III (to date).
14. D. F. Evans and R. E. Richards, *J. Chem. Soc.*, **1292** (1952).
15. D. R. Stull and G. C. Sinke, "Thermodynamic Properties of the Elements," American Chemical Society, Washington, D. C. (1956).
16. J. R. Lacher, L. Casali, and J. D. Park, *J. Phys. Chem.*, **60**, 608 (1956).
17. K. K. Kelley, U. S. Bur. Mines Bull. No. 584 (1960).
18. K. K. Kelley and F. G. King, *ibid.*, No. 592 (1961).
19. L. Pauling, "The Nature of the Chemical Bond," 2nd ed., p. 53, Cornell University Press, Ithaca, N. Y., (1948).
20. D. Kahng, C. O. Thomas, and R. C. Manz, *This Journal*, **110**, 394 (1963).
21. W. Van Gelder and J. Roberts, Private communication.
22. K. K. Kelley, U. S. Bur. Mines Bull. No. 383 (1935).
23. D. R. Stull, *Ind. Eng. Chem.*, **39**, 540 (1947).
24. E. Pohland, *Z. anorg. u. allgem. Chem.*, **201**, 265 (1931).
25. C. O. Thomas, D. Kahng, and R. C. Manz, *This Journal*, **109**, 1055 (1962).
26. M. M. Atalla and D. Kahng, Private communication.
27. S. L. Miller, *Phys. Rev.*, **99**, 1234 (1955).

Evaluating the Effective Resistances of Diaphragms or Electrolytic Separators

Robert E. Meredith
Department of Chemical Engineering, Oregon State University, Corvallis, Oregon

and Charles W. Tobias
Department of Chemical Engineering, University of California, Berkeley, California

ABSTRACT

It is shown that diaphragms or electrolytic separators, such as those commonly made of cloth or fibrous asbestos, can be approximated by a model comprised of rods which are randomly oriented in a two-dimensional lattice. The effective resistance of various arrangements of rods are measured and compared with the data for cloth, asbestos, and spun glass. The theory of electrical potential is employed to derive expressions that relate the effective resistance of such diaphragms to their porosity and the conductivity of the dispersing solution.

Many industrial electrochemical processes employ diaphragms or separators in order to keep the anode and cathode products from mixing. Although these separators are porous and allow current to flow from one compartment to the other, they nevertheless cause an increase of resistance to the flow of electrical current when compared with an equivalent thickness of electrolytic solution.

In the following a discussion is offered on the alternative ways of estimating the effective resistance of diaphragms.

Theoretical

The first approach that one might take toward the solution of this problem would be to evaluate the effective conductivity of the separator, k, in terms of the volume fraction of the nonconducting matter in the diaphragm, f, and the solution conductivity, k_1, by a simple volume averaging technique that gives

$$k = k_1(1 - f) \qquad [1]$$

Although such an approach may appear reasonable, the results obtained can be in error by as much as 100%. Furthermore, as far as cell design is concerned, the error is not in such a direction as to result in a "conservative" calculation (*i.e.*, the true effective resistance is greater than one calculates in this manner).

Obviously a better approach would be to treat the separator as if it consisted of a two-phase dispersion instead of stratified lamina that might obey Eq. [1]. With a model such as this, one could now consider using the work of Maxwell (1), Wagner (2), or Bruggeman (3) which respectively yield

$$k = k_1(2 - 2f)/(2 + f) \qquad [2]$$

$$k = (k_1/2)(2 - 3f) \qquad [3]$$

$$k = k_1(1 - f)^{1.5} \qquad [4]$$

A closer examination, however, shows that Eq. [2], [3], and [4] were derived with the assumption that the dispersed phase consisted of spherically shaped particles, whereas the separator material under consideration (*e.g.*, cloth, spun glass, and asbestos) is better visualized as being composed of cylindrical bodies which are probably preferentially arranged in two dimensions with the long axis of the cylinders aligned normal to the flow of current.

The problem of the effect of shape of the dispersed particle has been treated among others by Rayleigh (4) and Fricke (5) who have developed expressions appropriate to cylinders. However, since Rayleigh treated the case of cylinders aligned in one direction only while Fricke treated the completely random three-dimensional arrangement, it would be fortuitous if either of their equations agreed with our two-dimensional case.

Each of the factors mentioned above, *i.e.*, shape and orientation, are considered in the following treatment.

Expressions for cylindrical arrays.—Although one cannot obtain the effective conductivity of dispersions by volumetrically averaging the conductivities of the components in the system, it is possible, nevertheless, to take advantage of the valid relations that exist among other average properties of the system. For instance, if we denote averages by bars, we may write

$$\bar{i} = \overline{kE} \qquad [5]$$

where i is the current density and E is the electrical field. In practice we seek the effective conductivity of the system which may be defined by k in

$$\bar{i} = k\bar{E} \qquad [6]$$

Thus

$$k = (\overline{kE})/(\bar{E}) \qquad [7]$$

where the averages are defined over the volume, v, by

$$\overline{kE} = \frac{1}{v}\int_v kE\, dv \qquad [8]$$

and

$$\bar{E} = \frac{1}{v}\int_v E\, dv \qquad [9]$$

Denoting the properties of the continuous phase by 1 and the dispersed phase by 2, integration of Eq. [8] and [9] yield

$$\overline{kE} = k_1E_1(1-f) + k_2E_2f \quad [10]$$

and

$$\overline{E} = E_1(1-f) + E_2f \quad [11]$$

Finally, combining Eq. [7], [10], and [11], denoting E_2/E_1 by W, and recalling that $k_2 = 0$, we obtain

$$k = k_1(1-f)/(1-f+Wf) \quad [12]$$

The field ratio, W, has been discussed to some extent by Meredith (6). To obtain it we may employ any one of a number of standard textbooks on electricity and magnetism [for example see ref. (7)]. In our case, the value of W for each dispersed particle depends on the orientation of the rod or cylinder with respect to the electrodes. If we take a rectangular coordinate system and align a cylinder with its long dimension on the z-axis, the components of W become

$$W_x = W_y = (2k_1)/(k_1+k_2) \text{ and } W_z = 1 \quad [13]$$

which, in the case of nonconducting cylinders, reduces to

$$W_x = W_y = 2 \text{ and } W_z = 1 \quad [14]$$

For a completely random dispersion of nonconducting rods or cylinders we calculate the average field ratio from

$$W = (W_x + W_y + W_z)/(3) = 5/3 \quad [15]$$

which, when combined with Eq. [12] yields

$$R_m = \frac{1+(2/3)f}{1-f} \quad [16]$$

While if the mixture is such that the long axes of the rods are always parallel to the electrodes we use

$$W = (W_x + W_y)/(2) = 2 \quad [17]$$

and

$$R_m = (1+f)/(1-f) \quad [18]$$

Here R_m has been used to replace k_1/k. This quantity physically represents the effective resistance of the dispersion when compared with a solution of unit conductivity.

From what has already been stated, we would expect Eq. [16] to hold if the dispersion or diaphragm could be visualized as consisting of a completely random dispersion of rods in three dimensions. If, on the other hand, we consider that the diaphragm contains a random arrangement of rods with the long axis always parallel to the electrodes, we would expect Eq. [18] to fit the data. In general, for any combination of various orientations, we could use

$$R_m = (1+xf)/(1-f) \quad [19]$$

For example, if half of the rods are parallel to the electrodes we have $W = 3/2$ and $x = 1/2$.

In passing, it may be noted that, since W_x and W_y are equal, one obtains Eq. [18] regardless of whether the cylinders are crossed in two dimensions or not. This may be interpreted to mean that the mathematical model employed in deriving the above equations is physically equivalent only to a dilute dispersion of cylinders for which interactions due to rotation in the xy plane are negligible. This restriction arises due to the method of using a single cylinder in calculating the field ratios given in Eq. [12].

Experimentally it is shown below that there is very little difference in the effective resistances of crossed and uncrossed cylinders as long as one is concerned with square arrays. Thus, in spite of the above limitations, Eq. [18] will still have great utility.

Experimental Equipment and Procedure

A series of experiments on ordered arrangements of nonconducting cylinders was made in addition to studies involving material which resembled ordered or random arrangements of cylinders. The reasoning that was involved in planning these experiments is as follows: First, it was desirable to obtain conductivity data on both parallel and crossed cylinders in various arrays in order to test the results of the theories given above. Second, with the above results, it would be possible to make comparisons with data on material such as cloth, spun glass, asbestos pads, etc., which, to some extent, resemble two dimensional patterns of cylinders, and thus ascertain how far the mathematical model could be carried without serious discrepancies.

Equipment Used

Conductivity cells.—The cells used in the study of ordered cylinders consisted of units of rectangular geometry with Lucite walls and silver-plated copper electrodes. One of the cells was designed to act as a reference unit and to give a measurement of the continuous phase or electrolyte. The other cell, which may be called the working cell, contained a unit cell of the geometry that was to be studied. The overflow outlets were arranged in such a manner that the electrode surfaces were each covered to a depth of 5.00 in. The width of the electrodes in both cells was also 5.00 in. The distance between the electrodes in the reference cell was fixed at this same value, but in the case of the working cell this distance was adjustable in steps up to 5.00 in. by using different Lucite spacers. The reference and working cells are shown in Fig. 1.

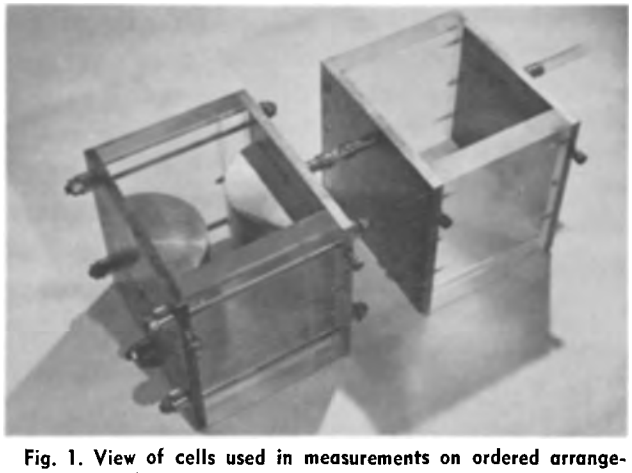

Fig. 1. View of cells used in measurements on ordered arrangements of cylinders.

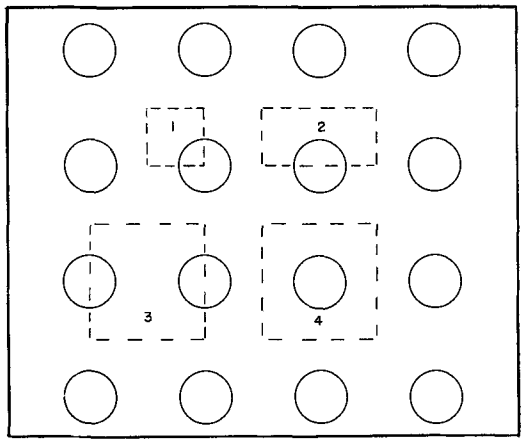

Fig. 2. Examples of unit cells in square arrays

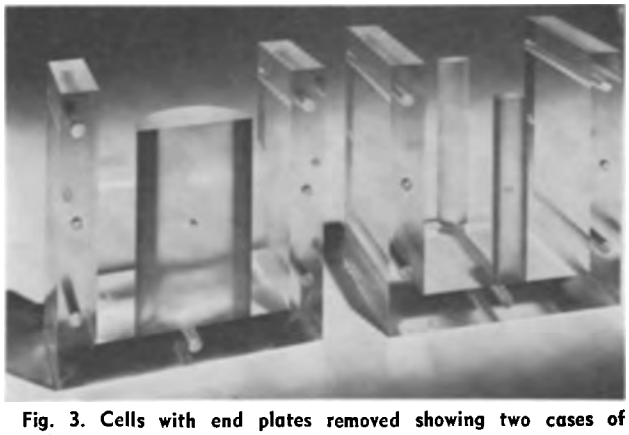

Fig. 3. Cells with end plates removed showing two cases of cylinder geometry.

An enclosed and smaller cell, but one which was nevertheless similar to that described above, was employed in determining the effective conductivity as a function of volume fraction for materials such as cotton cloth, thin sheet asbestos, and pads of spun glass.

Cylinder geometry.—There are several basic sectioning patterns that may be used in studying square arrays of parallel cylinders. Some of these are illustrated in Fig. 2. With the idea in mind that the cell would also be used to obtain data on crossed cylinders, a decision was made to use half cylinders or the third pattern in this figure.

For each volume fraction studied, two carefully machined half cylinders were constructed of Lucite. Threaded screw holes were placed in the center of the flat sides of the half cylinders and were matched with holes in the center of the electrode surfaces. The cylinders to be studied were locked flush against the electrodes in either a parallel or crossed orientation by means of a locking screw (see Fig. 3). The length of the half cylinders exactly matched the width of the cell so that, when a half cylinder was turned crossways in the cell, no conduction could occur between the walls of the cell and the end of the half cylinder.

Conductivity bridge.—The bridge employed to obtain electrical conductivity data was of conventional design (8). Measurements were made at a bridge frequency of 1 kc.

Experimental Procedure

Measurements on cylinders.—The electrodes of the working cell were combined with various Lucite spacers or walls that were to be used in this study and were calibrated against the reference cell. This operation took place before the holes were placed in the electrodes to hold the half cylinders.

Tap water was used as the electrolyte in this study, and prior to making any measurements, the water was circulated between the working cell and the reference cell and allowed to come to equilibrium at room temperature. The liquid level in both cells was carefully brought up to a standard reference mark by using a hypodermic syringe.

At least four measurements were made for every run or data point that appears in the following tables. The typical standard deviation for these runs was less than 1%.

Measurements on other materials.—In the smaller cell studies were made on cotton cloth, thin sheet asbestos, and pads of spun glass. In each case the sample was prepared by cutting the material in squares which exactly matched the dimensions of the cell. Next, the samples were carefully pre-equilibrated with electrolyte and laid in layers within the cell until the distance between the electrodes was fully occupied. All entrained air was displaced with electrolyte, and a conductivity reading was obtained. The conductivity of the electrolyte alone was also determined in the same cell. The volume fractions of the materials were determined in a Cassia flask.

As in the preceding section, multiple measurements were made for each material studied. The resulting standard deviation, in most cases, was less than 1%.

Discussion

Experimental results are given in Tables I, II, and III and are compared in Fig. 4 and 5.

Table I. Effective resistance data on dispersions of nonconducting cylinders arranged in square arrays

Volume fraction, f	Parallel cylinders, R_m	Crossed cylinders, R_m
0.0314	1.056	1.056
0.1226	1.266	1.289
0.2827	1.769	1.804
0.5026	3.084	3.074
0.7088	8.097	8.170

Table II. Effective resistance data on dispersions of nonconducting cylinders arranged with sides in contact

Volume fraction, f	Parallel cylinders, R_m	Crossed cylinders, R_m
0.0745	1.085	1.128
0.1570	1.200	1.302
0.3066	1.540	1.748
0.4712	2.145	2.413
0.6283	3.482	3.792
0.7461	8.271	8.734

Table III. Effective resistance data on materials that resemble cylinders arranged in two dimensions

Material	f	R_m
Pads of spun glass in layers	0.037	1.06
Cotton cloth in layers	0.212	1.55
Cotton cloth in layers	0.258	1.70
Sheet asbestos in layers	0.42	2.34

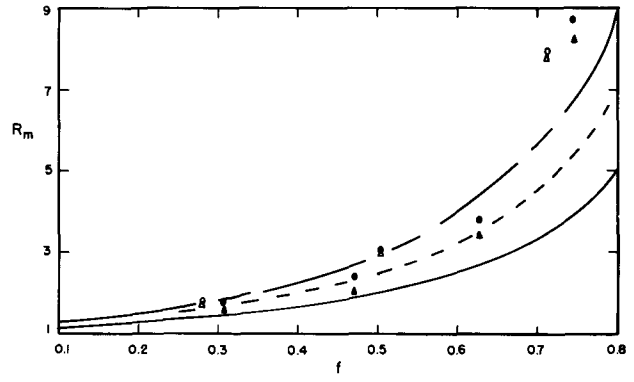

Fig. 4. Effective resistances of dispersions of solid cylinders. ($R_m = k_1/k$). ▲, Parallel cylinders in contact; ●, crossed cylinders in contact; △, parallel cylinders in square arrays; ○, crossed cylinders in square arrays; ———, Eq. [1]; — — — —, Eq. [2]; —— · ——, Eq. [18].

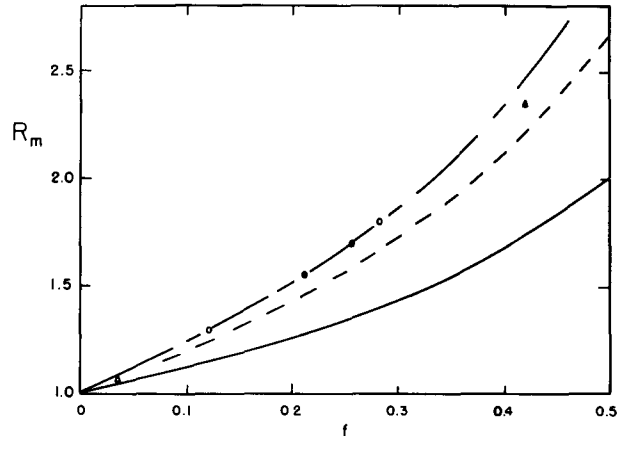

Fig. 5. Comparison of materials which resemble a mixture of solid cylinders arranged in two dimensions. △, Pads of spun glass in layers; ●, cotton cloth in layers; ▲, sheet asbestos in layers; ○, cylinders crossed at right angles in square arrays; ———, Eq. [1]; — — — —, Eq. [16]; —— · ——, Eq. [18].

The data given in Table I are for the case of measurements in a cubic cell and thus have been designated as "square arrays." For this case the crossed cylinders do not touch. Table II summarizes the results obtained when the distance between the electrodes was equal to the diameter of the cylinder being studied. Thus, in this latter case, the parallel or crossed cylinders were always touching or in contact.

All data on cylinders are compared in Fig. 4. Qualitatively the following facts are clear. There is very little difference, in the case of square arrays, between the results obtained for the parallel and crossed cylinders. The crosses, however, do consistently give a slightly higher resistance than their parallel counterparts. In the case of measurements on cylinders in contact, the situation is different. Here the data collected on parallel cylinders in contact seem to agree with measurements that one would obtain with lamina, and thus give results which are close to what one would predict by volume fraction averaging. On the other hand, the crossed cylinders in contact behave intermediate between lamina and true dispersions. This latter fact is as one would expect since the section of the cylinders at the cross would act as pure lamina, while the portion of the cylinders which was some distance away from the cross would act as a dispersion.

The measurements made on clothlike material were surprising inasmuch as the results obtained appear to agree more with cylinders in a "square array" rather than with crossed cylinders in contact (compare Fig. 4 and 5). Although some of the data points deviate in the direction of the crossed cylinders in contact, it is apparent that most of the rods or cylindrical bodies in the materials studied are not in tight contact by comparison with the crossed cylinder geometry. This is in spite of the fact that the cell was firmly packed (certainly to the extent that one would have in the case of diaphragms or separators) before conductivity measurements were made.

It may also be noted, by studying Fig. 5, that separators made from asbestos would appear to give a slightly lower effective resistance than cotton cloth at the same volume fraction of solids. This behavior may be explained by pointing out that the fibers in a layer of asbestos are probably close to being randomly arranged in three dimensions and thus obey Eq. [16], whereas the fibers in cotton cloth would preferentially be ordered according to our two-dimensional model and thus follow Eq. [18].

Acknowledgment

This work was partly performed under the auspices of the U. S. Atomic Energy Commission.

Manuscript received June 26, 1962; revised manuscript received Sept. 5, 1962. This paper was presented at the Los Angeles Meeting, May 6-10, 1962.

Any discussion of this paper will appear in a Discussion Section to be published in the June 1964 JOURNAL.

REFERENCES

1. J. C. Maxwell, "A Treatise on Electricity and Magnetism," 2nd ed., Vol. 1, p. 435, Clarendon Press, London (1881).
2. K. W. Wagner, *Arch. Elektrotech.*, **2**, 371 (1914).
3. D. A. G. Bruggeman, *Ann. Physik*, **24**, 636 (1935).
4. Lord Rayleigh, *Phil. Mag.*, **34**, 481 (1892).
5. H. Fricke, *Phys. Rev.*, **24**, 575 (1924).
6. R. E. Meredith, "Studies on the Conductivities of Dispersions," University of California Radiation Lab. Report 8667 (1959).
7. V. C. A. Ferraro, "Electromagnetic Theory," p. 369, Athlone Press, London (1954).
8. S. Glasstone, "An Introduction to Electrochemistry," p. 33, D. Van Nostrand Co., New York (1942).

Ion Exchange on Single-Crystal Silver and Zinc

Cecil V. King,[1] Todd Simmons, and Alice Berlin

Department of Chemistry, New York University, New York, New York

ABSTRACT

Exchange studies have been made with electropolished single-crystal specimens of silver and zinc immersed in dilute solutions of their salts, using Ag^{110} and Zn^{65} ions as tracers. In 0.02M solutions of the salts, exchange in the surface layer of the metals is rapid and complete, and continued tracer pickup is due to diffusion within the crystals. At lower salt concentrations the tracer pickup is slower, apparently because complete exchange is not maintained in the surface layer of atoms.

In most previous studies of exchange between silver and zinc and their ions in solution, polycrystalline specimens have been used (1-3). This has the disadvantage that both grain-boundary and lattice diffusion occur within the metal. The rate of radiotracer pickup depends on the grain size and grain-boundary area, and only the ratio of the two diffusion coefficients is significant. One run with a silver single crystal was carried out by Gerischer and Tischer (4), who concluded that the behavior was not essentially different from that of polycrystalline specimens. Zinc single crystals were used by Bushmanov and Vozdvizhenskii (5), who found somewhat different exchange rates on base and prism facets. Zinc bicrystals were investigated by Sandor (3), who found that the metal specimens corroded promptly even in well-deaerated solutions.

The purpose of the present investigation was to find whether single-crystal specimens, prepared with minimum surface roughness, would show a consistent and understandable pattern of exchange with their ions in aqueous solution. We find that silver specimens do so, with no complication from corrosion or surface films. On the other hand, zinc is subject to corrosion by water in the absence of oxygen

$$Zn + H_2O \rightarrow ZnO + H_2; \quad \Delta G^\circ = -19 \text{ kcal}$$

A similar free energy value applies if $Zn(OH)_2$ is the product. A polished specimen does not acquire a visible film for a long time in deaerated water; in salt solutions the initiation of visible film formation appears to be accidental and in general occurs sooner, the more concentrated the salt.

Experimental

Single-crystal rods of silver and zinc[2] about 2 cm in diameter were cut into disks 2 mm thick, and a 1 mm hole was drilled near the edge for suspending. After smoothing the surfaces the disks were annealed (silver at 400°, zinc at 120°C) and cooled slowly. Before use each disk was electropolished to remove distorted material and to give a smooth, bright surface (silver in AgCN-NaCN, zinc in phosphoric acid-ethanol). After removal from radioactive solutions the disks were electropolished to remove the active material.

In electropolishing, the disks were suspended on a Pt wire, midway between 2 stainless steel cathodes. Disks were suspended in the radioactive solutions either on glass hooks or on wire hooks coated with insulating lacquer. Solutions of $AgNO_3$ were not deaerated except in a few tests; $Zn(ClO_4)_2$ solutions were deaerated with nitrogen or hydrogen which was passed over hot copper, then through two wash bottles containing solution of the same concentration as the test solution. Immersion cells used for zinc were similar to those described by Gerischer and Tischer (4). All experiments were at room temperature, 20°-25°C, except for one series with silver, carried out in a thermostat at 60°C.

Ag^{110} was obtained as the nitrate in HNO_3; most or all of the acid was removed by evaporation. Zn^{65} was obtained as the chloride in HCl; the calculated amount of $HClO_4$ was added and HCl removed by evaporation. A stock solution of $Zn(ClO_4)_2$ was prepared from the hydrated salt and standardized volumetrically.

After immersion in the tracer solutions the disks were washed in cold water, and their activity was measured by counting under a GM tube. It was necessary to wash the silver samples for 20-30 min in several changes of water to reduce their activity to a minimum; the zinc required less washing. The count was converted to gram atoms of exchange by comparing with calibration disks on which 5 or 10 microliters of each solution was evaporated.

Visible corrosion films nearly always appeared on zinc disks in 0.1M $Zn(ClO_4)_2$, sometimes in a few minutes, sometimes not for several hours. The activity pickup was erratic and was much higher when a film was visible, as found by Sandor (3). Often when no film was visible the pickup was far higher than could be expected from simple exchange, probably indicating that a film was growing. It was found that if 0.02M $Zn(ClO_4)_2$ were adjusted to the pH at which a mere trace of $Zn(OH)_2$ appeared, visible corrosion could be delayed for several days, and exchange seemed to occur normally.

Results with Silver

Figure 1 shows the amount of exchange at room temperature on silver in 0.02M and in 1 x 10^{-5}M

[1] Present address: American Gas & Chemicals, Inc., New York, New York.

[2] Obtained from Monocrystal Company, Cleveland, Ohio.

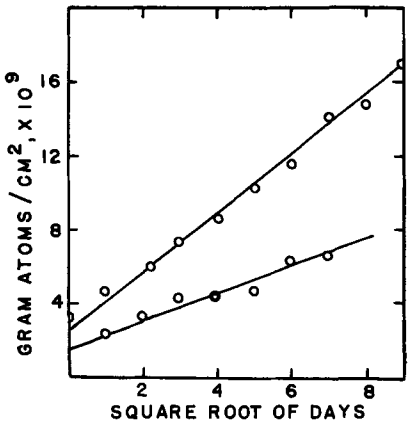

Fig. 1. Exchange on silver in 0.02M $AgNO_3$ (upper line) and in 1 x 10^{-5}M $AgNO_3$ (lower), room temperature.

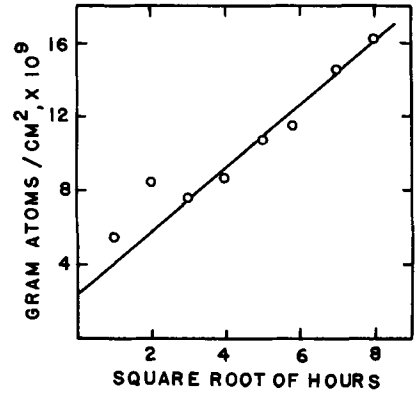

Fig. 2. Exchange on silver in 0.02M $AgNO_3$ at 60°C

$AgNO_3$, plotted *vs.* the square root of time in days. Results at 2 intermediate concentrations are summarized in Table I, and a run at 60° is presented in Fig. 2, were the time unit is hours rather than days. Most of these results are the average from counting the 2 sides of 2 disks. All of these disks were cut from the same silver rod and had surfaces near the (134) plane. A few disks from another rod gave results which differed not more than 20%.

Figure 1 makes it appear that the intercepts at zero time for all room-temperature runs should be different and should be smaller, the smaller the slope. The intercept for 0.02M $AgNO_3$ at both temperatures was taken as 2.5 x 10^{-9} g at./cm², which is the average value for a monolayer in all directions in a silver crystal. The intercept for 10^{-5}M $AgNO_3$ was arbitrarily taken as 1.5 x 10^{-9} g at./cm², which seems reasonable and gives a consistent value of the self-diffusion coefficient. Intercepts for the other solutions are given as zero-time extrapolations in Table I, where the columns headed "slope" give the increase in exchange above the intercept, divided by square root of days (with 10^9 omitted).

Table I. Exchange with silver at room temperature

Days	0.002M $AgNO_3$ g at./cm² x 10^9	slope	0.0002M $AgNO_3$ g at./cm² x 10^9	slope
0	2.0[a]	—	1.75[a]	—
1	4.08	(2.08)	3.44	(1.69)
9	4.45	0.82	3.93	0.76
15	5.06	0.79	5.04	0.85
26	6.27	0.83	5.25	0.69
36	7.96	0.99	6.40	0.77
50	8.52	0.92	8.03	0.88

[a] *Extrapolated.*

Brief immersion gave exchange as follows: 30 sec-3 min in 0.02M $AgNO_3$, 3.2-3.3 x 10^{-9} g at./cm²; the same time in 0.002M $AgNO_3$, 3.0-3.4 x 10^{-9} g at./cm²; in 4 x 10^{-4}M $AgNO_3$, 1.1 x 10^{-9} in 30 sec with gradual rise to 2.6 x 10^{-9} in 30 min. We interpret these results to indicate very rapid surface exchange in 0.02M solution, the excess above 2.5 x 10^{-9} being due to surface roughness, minute surface flaws, and adsorbed salt; but at lower concentrations exchange equilibrium is not reached quickly. The surface concentration of exchange atoms is then never equal to the bulk concentration of the metal; the ratio of radioactive to inactive atoms in the metal surface is never equal to its value in the solution.

Some points at 1 day, and in the 60° run at 1 and 4 hr, are high. In each case 2 disks gave satisfactory agreement, but it is not certain whether a real effect is involved or an unknown experimental mistake. If the effect is real it might have been avoided by pre-equilibrating the disks in inactive $AgNO_3$ solution. The high 1-day slopes are given in parentheses in Table I.

Diffusion coefficient.—To interpret the continuing exchange in terms of self-diffusion in the metal we may use the equation (6)

$$a_t = 2\, c_o\, (Dt/\pi)^{1/2} \qquad [1]$$

Here a_t is the amount of exchange (above the intercept) at time t, in g at./cm², and c_o is the surface concentration of exchanged metal in g at./cm³, both as determined by the tracer. D is the diffusion coefficient in cm²/sec if t is in seconds. Values of D calculated by use of the graphical slopes are given in Table II. In 0.02M $AgNO_3$, $c_o = 0.0973$ g at./cm³ (density of silver divided by atomic weight); in the other solutions $c_o = 0.0973$ x 2.0/2.5, 1.75/2.5, 1.5/2.5 has been used. The values for 0.1M $AgNO_3$ are based on 2 disks which were left in the solution for about 4.5 months. The intercept and c_o were assumed to be the same as in 0.02M solution.

An alternate treatment is to assume a fixed value of D and calculate values of c_o to conform. This would be preferable if the best value of D were known.

Results with Zinc

The exchange for 2 concentrations of $Zn(ClO_4)_2$ at room temperature is shown in Fig. 3, where it is evident that self-diffusion in the metal is much faster than in silver. The average amount of zinc in a monolayer in the crystal is about 2.7 x 10^{-9} g at./cm². Immersions of 30 sec to 1 min gave exchange of 2.3-5 x 10^{-9}, so it was assumed that the intercept

Table II. Self-diffusion coefficients in silver

C_{AgNO_3}, M	D, cm²/sec x 10^{21}	C_{AgNO_3}, M	D, cm²/sec x 10^{21}
0.10	2.2, 4.3	0.002	1.3
0.02	2.4	0.0002	1.4
0.02 (60°)	68	1×10^{-5}	1.5

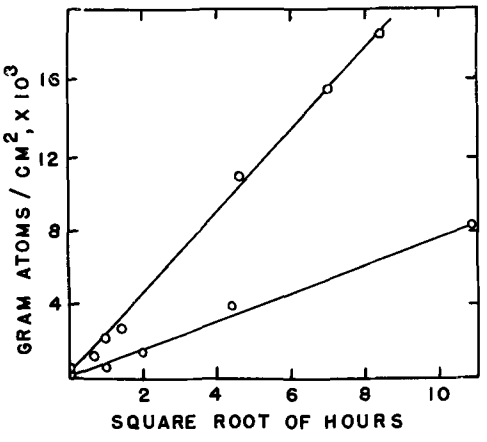

Fig. 3. Exchange on zinc in 0.02M $Zn(ClO_4)_2$ (upper line) and in 5 x 10^{-4}M $Zn(ClO_4)_2$ (lower), room temperature.

should be 2.7 x 10^{-9}, corresponding to $c_o = 0.109$ g at./cm³. Probably the crystal orientation should be taken into account, but the approximation will do for the present purpose. In 5 x 10^{-4}M solution, 30 sec-1 min immersions gave 0.9-1.0 x 10^{-9} g at./cm²; 0.905 x 10^{-9} was used as the intercept, corresponding to $c_o = 0.0365$ g at./cm³. The resulting values for D for the 2 solutions are, respectively, 9.1 x 10^{-18} and 8.8 x 10^{-18} cm²/sec.

Distribution of Exchange in Depth

If the tracer has penetrated deeply enough and thin, uniform layers can be removed from the metal surface, it is possible to find the concentration of exchanged metal c_x at various depths x after a fixed immersion time t. Then D can be found using the equation (6)

$$c_x/c_o = \text{erfc}\,[x/(4Dt)^{1/2}] \qquad [2]$$

where erfc refers to the complement of the error function integral. This procedure was applied to cadmium, where D is much larger (*ca.* 10^{-15} cm²/sec), and the removal of uniform layers by electropolishing appeared to be valid (7).[3] It is of interest to see whether this stripping procedure might be applied to silver.

Two silver disks were immersed in tagged 0.1M $AgNO_3$ for 1.20, 1.26 x 10^7 sec (4.5 months), and exchange occurred to the extent of 18 and 20 x 10^{-9} g at./cm², the equivalent of 7-8 complete monolayers. Let us assume that metal can be removed uniformly until $c_x/c_o = 0.01$, *i.e.*, the concentration of exchanged atoms at depth x is 1% of the surface concentration. From the error function tables, $x/(4Dt)^{1/2} = 1.83$; inserting $D = 2$ x 10^{-21} and $t = 1.2$ x 10^7, we obtain $x = 5.6$ x 10^{-7} cm. This thin layer corresponds to a weight loss of 0.04 mg on the disks used, which had an area of 6.6 cm² including both faces and the edge.

Determination of D by a stripping technique would thus seem impossible with the 2 disks mentioned. It was still of interest to see whether uniform layers could be removed, and two methods were tried: (i) In a solution containing NaCN and H_2O_2 (1), dissolution of 0.08 mg from one disk removed nearly half the activity, but dissolution of 14 mg (in 10 steps) left 20% of the activity. The disk visibly did not etch uniformly. (ii) The other disk was etched anodically in 0.05M NaCN with a current of 10 ma (on 6.6 cm²). Dissolution of 0.14 mg removed 60% of the activity; after removing 3.4 mg, 7% of the activity remained. The appearance of the disk showed that the current density was not uniform over the surface.

It is not possible to remove such thin layers of silver in the regular electropolishing procedure since the metal must go through a cycle of oxide film formation and dissolution. Exchange at a higher temperature and a better stripping method might make it possible to determine D by this method.

Discussion

Since the self-diffusion coefficient D cannot depend on the solution concentration, it is evident that the value of c_o does. Further, c_o must remain constant throughout the exchange experiment to account for the linear plots, and it is not easy to see why incomplete exchange in the surface layer should persist over a long period of time. The exchange current i_o, as measured by conventional polarization methods, is known to decrease with decreasing ion concentration; but since diffusion in the metals is so very slow, i_o would have to be unreasonably small not to maintain equilibrium. A possible explanation of the behavior is that exchange equilibrium is maintained on only a fraction of the surface (active sites?) in solutions of low concentration; this would account for a constant c_o.

The self-diffusion coefficient of silver has been measured by a dry method in the temperature range 450°-950°C (8, 9). If we use the equation (9)

$$D = 0.724 \exp\,(-45{,}500/RT)\ \text{cm}^2/\text{sec} \qquad [3]$$

the value of D for lattice diffusion extrapolated to 25°C is 3.6 x 10^{-34} cm²/sec, in sharp contrast to our value of about 10^{-21} cm²/sec. Further, combination of our values at room temperature and at 60° gives an activation energy of about 20,000 cal/g at. compared to the above value of 45,500 cal. Since there seems to be no pronounced change in the crystal lattice between 60° and 450°C, these discrepancies indicate a sharp difference in the mechanism of diffusion. The high-temperature measurements on polycrystalline silver give an activation energy of 20,000 cal for grain-boundary diffusion (8). It might be suggested that diffusion in the single crystal at low temperatures occurs primarily through connected series of lattice imperfections or networks of dislocation pipes, which would give it some resemblance to grain-boundary diffusion.

The self-diffusion coefficient of zinc has been measured in the temperature range 240°-403°C (10). Extrapolation of equations similar to [3] to 25° gives:

D (parallel to symmetry axis) = 1.3 x 10^{-17} cm²/sec

D (perpendicular to symmetry axis) = 9.1 x 10^{-19} cm²/sec

Our results of 8.8, 9.1 x 10^{-18} are intermediate. Two zinc crystals were used in our work, and accidental fractures, which occur along the basal (perpendicu-

[3] In Tables II, III, and IV of ref. (7), depth should be labelled cm x 10^6 instead of cm x 10^6.

lar) planes, showed that the surfaces used were inclined at 10°-15° to the parallel planes.

In attempting to avoid corrosion of zinc specimens, solutions of $Zn(ClO_4)_2$ in methanol and ethanol were tried. It is doubtful if the anhydrous salt can be prepared, and alcohol solutions of the hydrate led to as much corrosion as aqueous solutions. On evaporating alcohol solutions to dryness no water is lost, the hydrated salt crystallizing out.

Acknowledgment

The work reported here was sponsored by the U. S. Army Research Office (Durham). The authors are indebted to Dr. I. I. Tingley for the silver orientation data.

Manuscript received Feb. 5, 1963; revised manuscript received May 8, 1963.

Any discussion of this paper will appear in a Discussion Section to be published in the June 1964 JOURNAL.

REFERENCES

1. C. V. King and N. E. McKinney, *Can. J. Chem.*, **37**, 205 (1959). Earlier references are given.
2. C. V. King and S. Evans, *J. Phys. Chem.*, **63**, 1816 (1959). Earlier references are given.
3. J. E. Sandor, *Can. J. Chem.*, **39**, 393, 1869 (1961).
4. H. Gerischer and R. P. Tischer, *Z. Elektrochem.*, **58**, 819 (1954).
5. B. N. Bushmanov and G. S. Vozdvizhenskii, *Doklady Akad. Nauk S.S.S.R.*, **114**, 1046 (1957); **124**, 346 (1959).
6. L. S. Darken and R. W. Gurry, "Physical Chemistry of Metals," Chap. 18, McGraw-Hill Book Co., New York (1953).
7. C. V. King, D. S. Newman, and E. Suriani, *This Journal*, **108**, 291 (1961).
8. R. E. Hoffman and D. Turnbull, *J. Appl. Phys.*, **22**, 634 (1951); *Acta Metallurgica*, **2**, 419 (1954).
9. L. Slifkin, D. Lazarus, and T. Tomizuka, *J. Appl. Phys.*, **23**, 1032 (1952).
10. G. A. Shirn, E. S. Wajda, and H. B. Huntington, *Acta Metallurgica*, **1**, 513 (1953).

Heat-Treatment of Anodic Oxide Films on Tantalum

I. The Effects on Dielectric Properties

D. M. Smyth, G. A. Shirn, and T. B. Tripp

Research Laboratory, Sprague Electric Company, North Adams, Massachusetts

ABSTRACT

When anodized tantalum is subjected to temperatures in excess of 200°C, the equivalent series capacitance, equivalent series resistance, and temperature, frequency, and bias dependences of these properties increase. These phenomena are interpreted as resulting from the extraction of oxygen from the dielectric oxide by the tantalum substrate. This process creates an oxygen-deficient region in the oxide whose semiconductivity causes the above-mentioned changes in dielectric properties. Reanodization of the sample removes the effects associated with the conductivity. A small increase in apparent dielectric constant, which also results from heat-treatment, is a permanent effect.

This paper discusses the effects on the dielectric properties of a Ta/Ta_2O_5/aqueous electrolyte/metal capacitor which result from prior heat-treatment of the $Ta\text{-}Ta_2O_5$ portion of the structure. It will be seen that most of the peculiarities of the dielectric behavior of $Ta/Ta_2O_5/MnO_2$ solid electrolyte capacitors can be attributed to the effect of the heat-treatment associated with the application of the MnO_2 to the anodized tantalum by pyrolytic decomposition of $Mn(NO_3)_2$.

Vermilyea has reported that when anodized tantalum is heated at temperatures above about 300°C, there is a marked increase in the capacitance of the film (1). The capacitance increase depends on the time and temperature of heating, and is much more extensive when the heating is carried out in vacuum or hydrogen rather than in air or other oxygen-containing atmospheres. Vermilyea attributes this phenomenon to a short-circuiting of portions of the Ta_2O_5 film due to extraction of some of the oxygen from the oxide film by the tantalum. Sasaki has discussed the effect of conducting regions in the oxide film in greater detail and has concluded that the unheated anodic Ta_2O_5 film has a P-I-N structure due to excess tantalum atoms near the tantalum and excess oxygen atoms adjacent to the electrolyte (2).

Vermilyea has also reported that heat-treatment of anodized tantalum results in a slight sharpening of the x-ray diffraction pattern of the oxide film, indicating that some ordering of the structure has occurred (3).

The evidence reported here will support the conclusions of Vermilyea in general, although some modification of details will be required. Some of the experimental results of Sasaki appear not to be typical of the $Ta\text{-}Ta_2O_5$ system and are discussed in terms of specific experimental procedure.

Experimental

Samples having about 18 cm^2 surface area were cut from 0.010 in. tantalum sheet obtained from the Fansteel Metallurgical Corporation. This material has a minimum tantalum content of 99.9%. Typical impurity contents, furnished by the supplier, are C, 0.005%; O, N, H, not given (maximum 0.02%); Nb, 0.008%; Fe, Ti, Si, Zr, and Mo, 0.001% each. Narrow tabs were left attached to each sample to reduce errors due to variable immersion depth in the measuring electrolyte.

The samples were washed in hot detergent and hot acetone to remove grease. They were then polished for approximately 10 sec in a hot chemical-

polishing solution composed of 5 parts (by volume) 98% H_2SO_4, 2 parts 70% HNO_3, and 2 parts 48% HF. They were then vacuum annealed at 2100°C and $<10^{-4}$ Torr for 30 min. Some samples were electropolished in a 9:1 (by volume) 98% H_2SO_4, 48% HF solution and then leached in boiling concentrated HNO_3 to remove colloidal sulfur prior to vacuum annealing. In all cases, chemically or electrochemically polished samples were leached in boiling demineralized water for several minutes to remove residual fluoride (4). The sample cleaning has been found to be a most important operation. Many strange and erratic effects have been obtained with samples which either were not vacuum annealed or were subjected to any other cleaning treatment between annealing and anodization.

Samples were anodized in a 0.1% by weight (~0.01M) H_2SO_4 solution held at 34.0° ± 0.1°C. The voltage was increased manually, maintaining a nearly constant formation current density not exceeding 1 ma/cm² until the desired formation voltage was reached. The samples were then held at the formation voltage for approximately 1 hr. Except where specifically designated otherwise, all of the data shown are for samples anodized to 75v. These results are typical of a wide range of oxide thicknesses.

Most capacitance measurements were made with a conventional a-c bridge with a General Radio Type No. 1302-A Oscillator and a Rohde and Schwarz Type UBM-BN 12121 Tunable Detector. The bias voltage was supplied from large dry cells. The measuring electrolyte was 40% H_2SO_4. The immersion of the sample in the electrolyte of the measuring cell was adjusted visually since no masking material has been found which did not either disintegrate during heat-treatment or contaminate the tantalum. The reproducibility of the capacitance for successive immersions of the same sample was found to be ±0.2%. All general comparison measurements were made at 34.0° ± 0.1°, 120 cycles, and with no d-c bias. Measurements of the temperature dependence of capacitance were made with a Sprague Model 1W2 Capacitance Bridge at a frequency of 120 cycles. In this case the measuring electrolyte was 38% by weight H_2SO_4 which permits measurements to be made to −70°C.

The heat-treatment was done in air in a furnace controlled to ±5°. A comparison of the results obtained when samples were heated in air with those obtained when the samples were heated in 0.2 atm of dry oxygen showed no detectable difference.

For each sample considered separately, the relative magnitudes of the effects of heat-treatment on the various dielectric properties were consistent, but there was considerable scatter among different samples. Samples cut from the same sheet of tantalum, given identical cleaning treatment, vacuum annealed simultaneously, formed simultaneously and in parallel connection, and heat-treated at the same time in the same oven still gave scattered results.

Results and Discussion

When anodized tantalum is heated to temperatures of the order of 200°C and above, it is found that a permanent increase in capacitance has taken place, but that the interference color of the film has not changed (1). The dependence of capacitance and equivalent series resistance (ESR) on d-c bias, frequency, and measuring temperature for heated and unheated samples are shown in Fig. 1 and 2. It is seen that the heat-treatment creates an "excess capacitance" (and an "excess ESR") which can be decreased by increasing the positive bias on the tantalum, increasing the frequency, or decreasing the measuring temperature. All of these effects are interrelated in that a reduction of capacitance by any one of these variables reduces its sensitivity to the other two. The effect on the ESR is very similar (no correction has been made for the contribution of the electrolyte resistance to the ESR in Fig. 2).

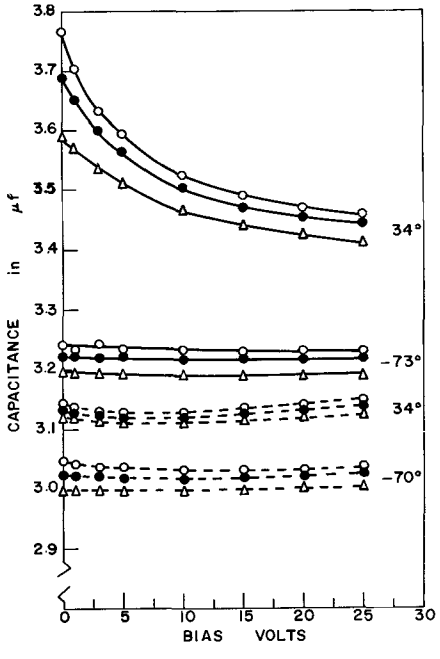

Fig. 1. Bias dependence of capacitance for heated and unheated Ta-Ta_2O_5 at two temperatures and three frequencies: -----, unheated; ———, heated 30 min, 400°C in air; ○, 50 cycles; •, 120 cycles; △, 400 cycles.

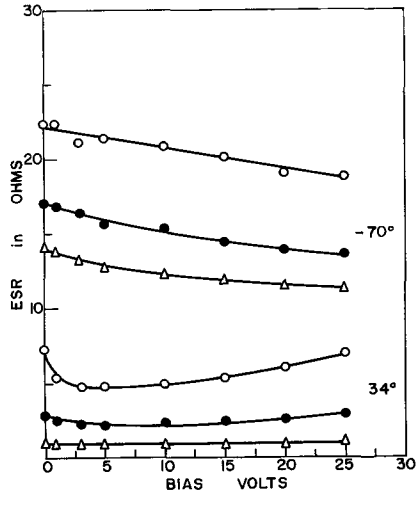

Fig. 2a. Bias dependence of ESR for unheated Ta-Ta_2O_5 at two temperatures and three frequencies. ○, 50 cycles; •, 120 cycles; △, 400 cycles.

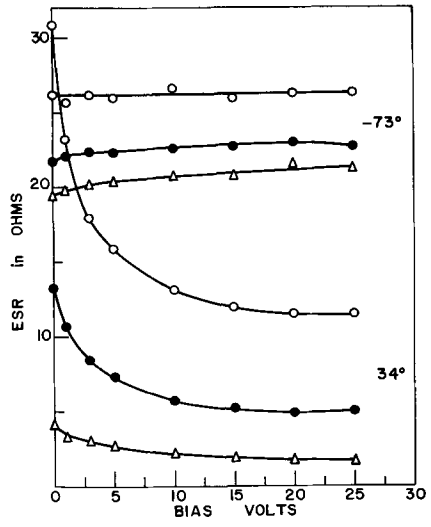

Fig. 2b. Bias dependence of ESR for Ta-Ta_2O_5 heated 30 min in air at 400°C at two temperatures and three frequencies. ○, 50 cycles; •, 120 cycles; △, 400 cycles.

Plots of ESR *vs.* reciprocal frequency for a sample before and after heat-treatment are shown in Fig. 3. The heat-treatment does not significantly affect the ESR intercept at $1/f = 0$, which is characteristic of the series resistance due to leads, electrodes, electrolyte, etc. It does greatly increase the portion of the ESR which is inversely proportional to the frequency; *i.e.*, the portion that is characteristic of dielectric losses in the oxide film as shown by the interpretations of Bernard (5) and McLean (6).

If the heat-treated, anodized tantalum is reanodized in an aqueous electrolyte at the original formation voltage, its properties approach those of an unheated sample, and the interference color of the oxide film remains unchanged. The effects of bias, frequency, and temperature on capacitance and ESR are greatly reduced, and the "excess" capacitance of the sample (measured at 120 cycles, 34°C, no bias) is reduced by about 75%.

All of this evidence indicates that the heat-treatment causes part of the anodic oxide film to assume a conductivity which can be removed by reanodization. We shall now consider the origin of this conductivity and its distribution in the Ta_2O_5 film.

If anodized tantalum is heated in air or oxygen, the capacitance of the sample increases at a rate which depends on the oxide thickness and the heating temperature, and the capacitance ultimately reaches an equilibrium value, as shown in Fig. 4 and 5. Samples which have been heated several hours show a weight increase, an increase in the hardness of the tantalum anode, and an increase in the oxygen content of the tantalum, all of which increase with increasing time of heat-treatment. It is apparent that oxygen from the ambient atmosphere is passing through the oxide film into the tantalum. If the heat-treatment is carried out in vacuum, the capacitance continues to rise until it approaches that which would be observed for unanodized tantalum. In other words, the entire oxide film becomes conducting. This was reported by Vermilyea and has been confirmed here. It thus appears that the tantalum anode extracts oxygen from the Ta_2O_5 film during the heat-treatment, leaving the Ta_2O_5 oxygen-deficient. When the oxygen-deficiency reaches the oxide-air interface, oxygen begins to flow into the film, maintaining a constant composi-

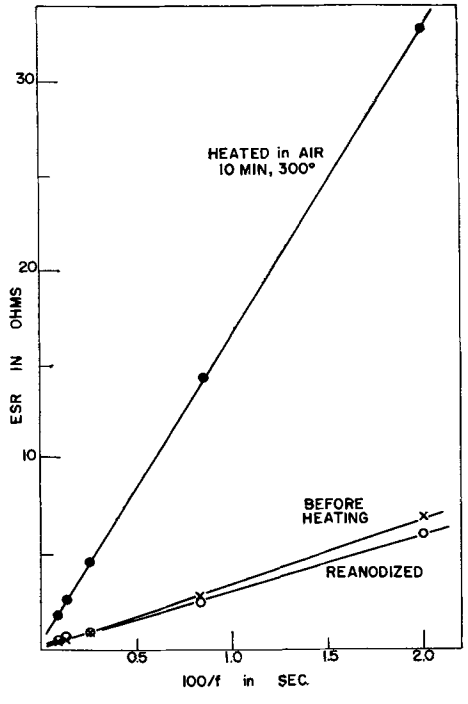

Fig. 3. Frequency dependence of ESR. X, unheated; •, heated 10 min, 300°C in air; ○, reanodized at original formation voltage.

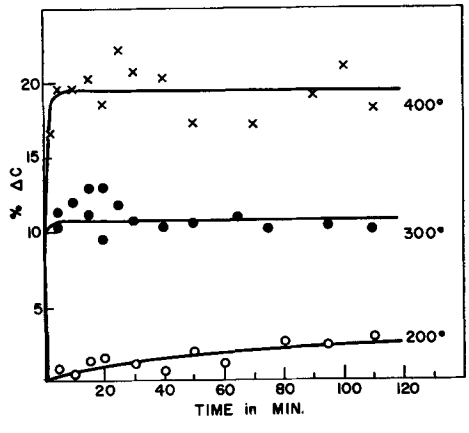

Fig. 4. Percentage increase of capacitance, relative to the preheated capacitance, due to heat-treatment in air.

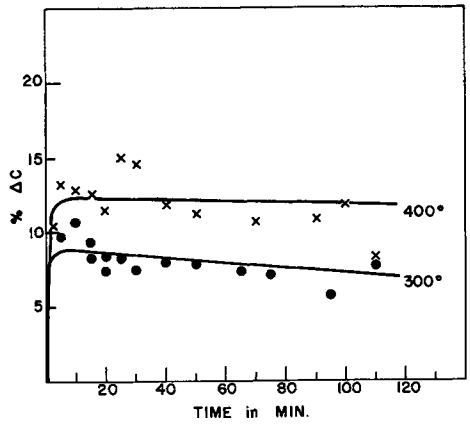

Fig. 5. Percentage increase of capacitance, relative to the reanodized capacitance, due to heat-treatment in air.

tion at this interface. This composition may be a function of the ambient oxygen pressure, since we have found evidence that the capacitance increase due to heat-treatment is pressure dependent.

The increase in oxygen content of the tantalum could occur by passage of oxygen through cracks and pores in the film. This would not, however, explain the effects on the dielectric properties of the system and their removal by reanodization. In addition, if the oxide of a heat-treated specimen is chemically removed and the sample reanodized, it behaves as an unheated sample. Thus, the heat-treatment effects clearly lie in the oxide film (or possibly at the metal-oxide interface). We shall thus continue under the assumption that the flow of oxygen is by diffusion through the oxygen-deficient Ta_2O_5 film.

When equilibrium has been attained during heat-treatment in an oxygen-containing atmosphere, oxygen is entering the oxide, flowing across it, and entering the tantalum at the same rate, and the oxide compositions at the metal-oxide and oxide-air interfaces are fixed. This is analogous to a standard membrane diffusion problem where the concentration of the diffusing species is linear across the film at equilibrium. The transfer of oxygen from the oxide to the metal will leave the film oxygen deficient and we shall refer to this in terms of "oxygen vacancies," according to the definition of Dewald (7). Two electrons must be associated with these oxygen vacancies in order to maintain charge neutrality, and the vacancies can thus be considered as donor centers. Thus the oxygen deficient portions of the Ta_2O_5 will exhibit n-type semiconductivity. It is this conductivity which causes most of the effects on the dielectric properties.

This general picture of deviations from stoichiometry, and the associated conductivity, is similar to that found in single crystal and sintered α-Nb_2O_5 by Greener, Whitmore, and Fine (8), and by Kofstad and Anderson (9), and for Ta_2O_5 by Kofstad (10). The extreme affinity of tantalum for dissolved gases is well-known [see, for example, the work of Gebhardt and Seghezzi (11)]. In a few experiments with anodized niobium we have found similar effects as reported here for tantalum, although much more pronounced.

A gradient of oxygen vacancies across the Ta_2O_5 will result in a gradient of conductivity across the oxide film. For the sake of simplicity we will assume a linear gradient of conductivity, since the exact shape will not affect the discussion. As shown in Table I, as the Ta_2O_5 of a heat-treated sample is

Table I. Change of the bias dependence of capacitance of heat-treated Ta-Ta_2O_5 as the oxide is chemically removed

(Three samples formed to 75v and heated in air for 30 min at 400°C)

Equivalent thickness (formation voltage equivalent of interference color), v	% Capacitance decrease with 10v bias		
	A	B	C
75	5.0	4.3	4.2
70	6.0	5.5	5.8
55	9.1	8.4	7.9
40	13.2	13.1	12.8

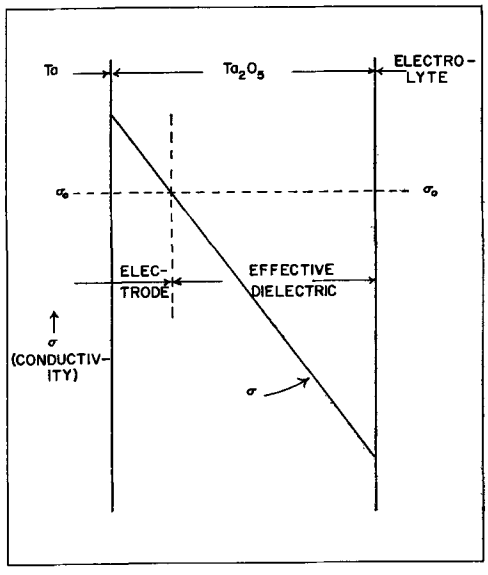

Fig. 6. Schematic representation of the conductivity profile of an anodic Ta_2O_5 film after heat-treatment in air.

step-wise removed by dissolution in hydrofluoric acid, the bias dependence of capacitance becomes increasingly pronounced. This is to be expected if the conductivity is greatest in the oxide adjacent to the tantalum. Thus, in Fig. 6, the linear conductivity profile across the oxide is drawn with the high end adjacent to the tantalum.

Simple dielectric theory predicts that a dielectric containing any distribution of conductivity will have an enhanced series capacitance and series resistance compared with the nonconducting state. It has been found very useful to consider that the conductivity resulting from the nonstoichiometry causes some of the oxide film thickness to be short-circuited. A critical level of conductivity, which we shall call σ_0, determines whether any given increment of film thickness acts as dielectric or as an extension of the adjacent electrode. Thus, the effective electrode-dielectric interface is at the point inside the oxide where the local conductivity equals σ_0. This is shown graphically in Fig. 6. From this simplified representation, the capacitance increase resulting from heat-treatment is due to a reduction of the effective dielectric thickness. This simple model is not a rigorously correct one, since it assumes an abrupt junction between effective dielectric and effective electrode, but its usefulness will be demonstrated.

Sasaki has reported a decrease in capacitance as a result of heating tantalum, anodized to 20v, in oxygen or vacuum for 2 hr between 150° and 330°C (2). Above 330°, he observed a capacitance increase for all heating conditions. Using our cleaning and anodizing procedure we have never observed a capacitance decrease for any heating condition for any heating time in excess of 5 min. We have attempted to resolve this discrepancy, and the results are shown in Table II.

The first three experiments show that our cleaning and anodizing techniques gave a capacitance increase of about 50%. This was reduced to 10% when Sasaki's cleaning technique was used, and was

Table II. Effect of sample preparation on the capacitance change due to vacuum-heating

Exp. No.	Surface preparation*	Formation electrolyte†	Heating temp, °C	Heating time at $1\text{-}3 \times 10^{-5}$ Torr, hr	% Cap. change
1	1	A	300	2	+34
2	1	A	300	2	+59
3	1	A	300	2	+57
4	2	A	300	2	+10.5
5	2	B	300	2	+3.9
6	2	B	270	2	+1.5
7	2	B	260	1	−0.16
8	2	B	260	2	−0.22
9	2	A	260	2	+6.7
10	1	B	260	2	+1.8
11	1	A	260	2	+9.3

* Surface preparation: 1. electropolish and vacuum anneal; 2. anodized at 10v then remove oxide with HF.
† Formation electrolyte: A. 0.01M H_2SO_4; B. 1% $NH_4HB_4O_7 \cdot 3H_2O$ in 3 parts ethylene glycol + 1 part water.

further reduced to 4% when both his cleaning and anodizing techniques were used. When the heating temperature was reduced from 300° to 270°, we obtained, with Sasaki's procedure, an increase of only 1.5%. For a heating temperature of 260°, small capacitance decreases were observed for heating times of 1 and 2 hr for samples prepared by Sasaki's techniques. These lower heating temperatures were used because Sasaki indicates that his temperature measurement may have a maximum error of 30° (12). The last three runs show the relative importance of the cleaning and formation techniques for a heating temperature of 260°.

With our cleaning technique, the electropolishing gives a very smooth surface and the vacuum annealing volatilizes most impurities and relieves mechanical strains. It is interesting to note that Sasaki obtained less capacitance decrease with smoother (chemically polished) samples. The formation electrolyte of Sasaki seems to be the major cause of discrepancy, however. In this regard, we point out that this electrolyte (1% ammonium borate in 3:1 ethylene glycol:water) is very similar to one of the "nonaqueous" electrolytes which Vermilyea found to yield anodic oxide films which have anomalous properties (13).

Effect of D-C Bias

As seen in Fig. 1 and 2, the effect of a low, anodic (Ta+) d-c bias on a heat-treated Ta-Ta_2O_5 sample is to reduce reversibly the series capacitance and ESR. The increase in these two properties with decreasing anodic bias persists through a change of polarity and continues into the region of increasing cathodic bias. This latter effect is particularly apparent in a Ta-Ta_2O_5-MnO_2 capacitor, where a higher cathodic bias can be applied before high current begins to flow. An example of this is shown by Taylor and Haring (14). This behavior is very similar to that of the depletion-layer capacitance of a p-n junction and can be interpreted in an analogous way. The application of an anodic bias to the system as depicted in Fig. 6 causes the conduction electrons to be attracted toward the tantalum anode. Since additional free electrons are not available from the intrinsic and electron-depleted portions of the Ta_2O_5, the effect is to shift the intersection of the conductivity profile with σ_0 toward the tantalum. This causes an increase in the effective dielectric thickness, which results in the observed decrease in series capacitance. If the anodic potential is of the order of half of the formation voltage or more, irreversible effects occur. It is assumed that these result from the field in the depletion region becoming sufficiently large to move ionic defects, thus permanently changing the conductivity profile.

A cathodic bias pushes conduction electrons deeper into the dielectric region, causing a decrease in effective dielectric thickness. One then observes an increase in the series capacitance.

From the bias dependence of capacitance one should be able to calculate the ionic space charge distribution from the Schottky depletion layer theory, suitably modified to fit the boundary conditions appropriate to this case. McDonald has made modifications of this general type (15). Unfortunately, the bias effect with heat-treated Ta-Ta_2O_5 is insufficient to allow such a calculation, since the experimental uncertainty is as large as the anticipated effect.

This pronounced bias dependence of capacitance is a strong argument in favor of the presence of a fixed ionic space charge in the oxide film as required by the proposed model. The fact that the capacitance increases continuously through a change in polarity of the bias indicates that the effect is not due to a mere "locking" of dipoles by the field, since the latter effect should be symmetrical about a maximum capacitance at zero bias.

Sasaki has reported a rather pronounced dependence of capacitance on d-c bias for unheated, anodized tantalum (2). We have found, however, that the effect of bias is negligible for unheated samples when the bias is kept below about 50% of the formation voltage as shown in Fig. 1. At higher bias voltages the capacitance decreases with time, and if the capacitance is then measured at lower bias voltages, a temporary significant dependence is observed. The zero-bias capacitance is then greater than before application of the high bias and slowly decays back toward the original value. This time-dependent behavior is demonstrated in Fig. 7 for an experiment

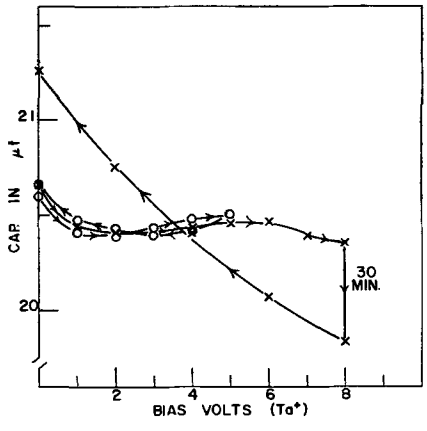

Fig. 7. Bias dependence of capacitance for unheated Ta-Ta_2O_5 (10v formation). O, 0 to 5v to 0; X, 0 to 8v to 0.

designed to reproduce the experimental conditions of Sasaki. For this 10v formation, it is seen that the bias dependence of capacitance is reproducibly small for increasing or decreasing bias up to 5v. While an 8v bias was maintained for 30 min, however, the capacitance dropped 2.5%, and a strong bias dependence was subsequently observed with decreasing bias. The result was a 7.2% increase in capacitance between 8 and 0v bias. Sasaki showed a 4.8% change. We thus believe that his bias effects were a result of this time-dependent behavior and are not representative of equilibrium conditions. This phenomenon is undoubtedly connected with the frequent observation that the capacitance drops slowly with time immediately after anodization; see, for example, Young (16, 17).

Vermilyea (1) proposed that the increase in capacitance which results from heat-treatment is due to "the short-circuiting of some of the film by regions of increased conductivity." He clearly implies, moreover, that the film is partially short-circuited in terms of area (particularly near grain boundaries in the tantalum), while we postulate partial short-circuiting in terms of thickness. The experimental evidence presented here clearly favors the latter, although Vermilyea may be correct in assuming that the diffusion process is more rapid near grain boundaries in the metal substrate. The best evidence against the short-circuiting of areas is the complete reversibility of the effect of d-c bias up to nearly 50% of the formation voltage. If the film were conducting throughout the entire thickness in some areas, then even very small bias voltages should result in some irreversible reanodization of the oxide.

Effect of Temperature

The conductivity of the oxygen deficient Ta_2O_5 will decrease with decreasing temperature as the extent of ionization of electrons from oxygen vacancies decreases. This will lower the conductivity profile across the oxide film and will cause the intersection of this profile with σ_0 to move toward the tantalum anode (see Fig. 6). Thus, the effective dielectric thickness will increase with decreasing temperature until the conductivity at the Ta-Ta_2O_5 interface has reached σ_0. Below this temperature the entire oxide film thickness will act as an effective dielectric, and the change of capacitance with temperature will be determined solely by the temperature dependence of the dielectric constant. Figure 8 shows a plot of capacitance *vs.* temperature for the same sample before and after heat-treatment. After heat-treatment, the temperature dependence of capacitance is much steeper above —33°. Below this temperature, which is that at which $\sigma = \sigma_0$ at the Ta-Ta_2O_5 interface, the line is nearly parallel to that observed prior to heat-treatment. After reanodization at the formation voltage, the steep dependence is removed and the low temperature slope is extended over the entire range of measuring temperature. The oxygen content of the oxide has then been restored and the entire Ta_2O_5 film is an effective dielectric again. (The slight increase in capacitance in the low temperature range which results from reanodization is typical but unexplained.) Both Taylor and Haring (14), and McLean and Power (18) have given slight indications of a lower temperature dependence of capacitance at low temperatures for Ta-Ta_2O_5-MnO_2 capacitors.

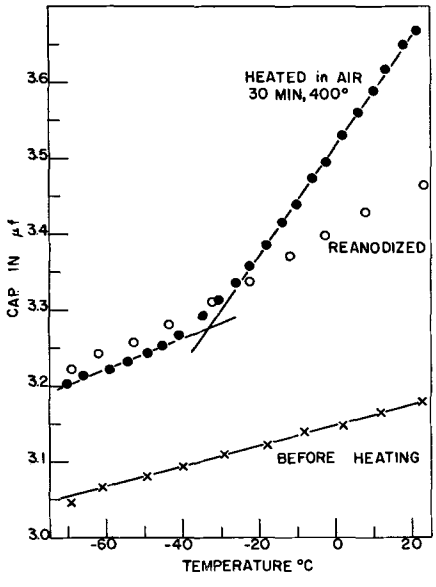

Fig. 8. Temperature dependence of capacitance of unheated, heated, and reanodized Ta-Ta_2O_5.

It is interesting to note that, after heat-treatment and reanodization, the temperature dependence of capacitance is nearly the same as that of the unheated sample, but that the absolute value of the capacitance has been increased. It appears that the dielectric constant of the Ta_2O_5 has been increased by the heat-treatment. This effect is probably related to the increase in crystallinity of anodic Ta_2O_5 observed by Vermilyea after an annealing treatment (3). Thus, the heat-treatment has two effects: it introduces an oxygen deficit and its associated conductivity into the oxide, and it increases the dielectric constant of the oxide by increasing its crystalline order. The former effect can be removed by reanodization; the latter cannot. In Fig. 4, the total increase in capacitance due to heat-treatment is shown, whereas in Fig. 5, only the change due to the conductivity effect is shown; since, in the latter figure, the capacitance increase is related to the capacitance observed after reformation of the heated sample which thus includes the change in dielectric constant.

This technique of measuring the dependence of capacitance on temperature has proved to be very valuable, since, in effect, it is a means of scanning a portion of the conductivity profile in the Ta_2O_5 film. A subsequent publication will deal with this aspect in greater detail (19).

Effect of Frequency

Young (16) and Winkel and de Groot (20) have shown that there is a relationship between the frequency dependence of capacitance and the frequency dependence of ESR such that

$$\frac{\partial 1/C_s}{\partial \ln f} = \frac{4R_s}{1/f}$$

where C_s and R_s are the series capacitance and re-

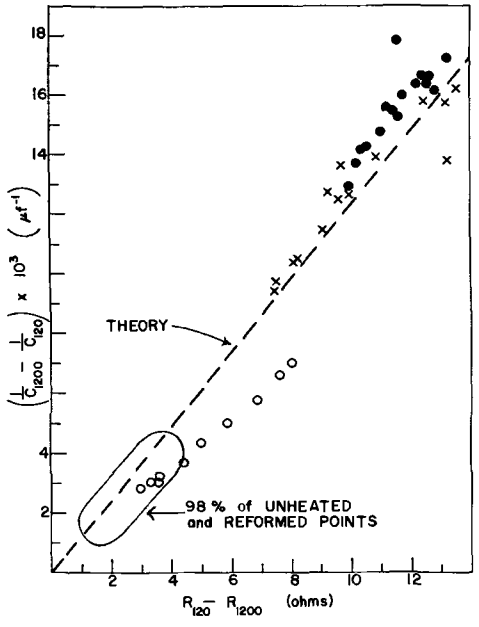

Fig. 9. Frequency dependence of capacitance *vs.* the frequency dependence of ESR for unheated, heated, and reanodized Ta-Ta_2O_5. O, heated at 200°C in air; X, heated at 300°C in air; •, heated at 400°C in air. Different points represent different heating times. Subscripts on C and R represent the frequency of measurement.

sistance, respectively (the latter corrected for the lead and electrolyte resistance which is R_s at $1/f=0$), and f is the frequency of measurement. Figure 9 shows a plot of frequency dependence of capacitance *vs.* the frequency dependence of ESR for formed, heat-treated, and reformed samples. It is seen that all of these cluster around the theoretical line, with formed and reformed samples having similarly small frequency dependences. For some unknown reason, the points for the samples heated at 200° are skewed from the theoretical line. Thus, heat-treatment and the resulting introduction of conductivity into the oxide film do not change this basic relationship.

In the highly conducting part of the oxide film one can consider that each thickness increment has its original dielectric properties with an additional parallel resistance which represents the conductivity. When this parallel resistance is small enough, the equivalent circuit can be approximated as a simple parallel capacitance and resistance combination. For such a circuit the point at which the reactance equals the resistance is the dividing line between predominantly resistive and predominantly capacitive behavior. This point can be represented as

$$\frac{1}{\sigma_c}\frac{dx}{A} = R_c = \frac{dx}{\omega\epsilon\epsilon_0 A} = X_c$$

where σ_c, R_c, and X_c are the critical conductivity, and the resistance and reactance of a dielectric increment of thickness dx and area A where the resistance equals the reactance. This reduces to

$$\sigma_c = \omega\epsilon\epsilon_0$$

The σ_0 introduced in this paper is not necessarily the same as σ_c but should be of the same order of magnitude and should have the same frequency dependence. σ_c for Ta_2O_5 at 120 cycles is 1.8×10^{-9} ohm^{-1} cm^{-1}.

According to this analysis, σ_0 should be proportional to the frequency of measurement, and the effects of frequency on the capacitance and ESR of heat-treated samples can be explained on this basis. The frequency dependence of capacitance at constant temperature thus results from the movement of σ_0 across the conductivity profile, whereas the temperature dependence of capacitance at constant frequency results from the movement of the conductivity profile across σ_0.

Summary

The increases of capacitance and ESR, and of their dependence on d-c bias, temperature, and frequency, for anodized tantalum which has been heated in air are due to a gradient of conductivity across the anodic Ta_2O_5 film. This conductivity is associated with an oxygen deficiency in the Ta_2O_5 which results from the tendency of tantalum to extract oxygen from its own oxide. Neither this heat-treatment, nor subsequent reanodization at the formation voltage, cause any discernable change in the interference color of the oxide film as determined by direct visual comparison. The apparent dielectric constant of the oxide is increased slightly. All of the effects of heat-treatment except the latter, and presumably the change in crystallinity, can be removed by reanodization at the formation voltage.

The significance of these effects on the properties of the so-called solid electrolyte capacitor, based on the Ta-Ta_2O_5-MnO_2 system, is obvious. In fact, the bias, temperature, and frequency dependences of capacitance and ESR of these capacitors (at moderate frequencies) are directly related to the heat-treatment to which the anodized tantalum is subjected during the pyrolytic deposition of the MnO_2. The presence of an MnO_2 counterelectrode rather than an aqueous electrolyte has no direct influence on these properties, since they are determined by the state of the Ta_2O_5 near the tantalum anode. The increase in capacitance due to heat-treatment also explains the observation that solid electrolyte capacitors frequently have a higher capacitance than the same anodes had when measured in an aqueous electrolyte prior to application of the MnO_2. The effects of aging ("life-testing") on the properties of solid electrolyte capacitors can be explained in terms of the migration of the oxygen deficiency within the oxide film under the influence of concentration and potential gradients.

Manuscript received Feb. 28, 1963. This paper was presented at the Pittsburgh Meeting, April 15-18, 1963.

Any discussion of this paper will appear in a Discussion Section to be published in the June 1964 JOURNAL.

REFERENCES

1. D. A. Vermilyea, *Acta Met.*, **5**, 113 (1957).
2. Y. Sasaki, *J. Phys. Chem. Solids*, **13**, 177 (1960).
3. D. A. Vermilyea, *This Journal*, **104**, 485 (1957).
4. L. Young, *Trans. Faraday Soc.*, **53**, 841 (1957).
5. W. J. Bernard, *This Journal*, **108**, 446 (1961).
6. D. A. McLean, *ibid.*, **108**, 48 (1961).
7. J. F. Dewald, *J. Phys. Chem. Solids*, **2**, 55 (1957).
8. E. H. Greener, D. H. Whitmore, and M. E. Fine, *J. Chem. Phys.*, **34**, 1017 (1961).
9. P. Kofstad and P. B. Anderson, *J. Phys. Chem. Solids*, **21**, 280 (1961).

10. P. Kofstad, *This Journal*, **109**, 776 (1962).
11. E. Gebhardt and H. D. Seghezzi, *Z. Metallkunde*, **48**, 503 (1957); *ibid.*, **48**, 559 (1957); *ibid.*, **50**, 248 (1959); *ibid.*, **50**, 521 (1959).
12. Y. Sasaki, Private communication.
13. D. A. Vermilyea, *Acta Met.*, **2**, 482 (1954).
14. R. L. Taylor and H. E. Haring, *This Journal*, **103**, 611 (1956).
15. J. R. McDonald, *J. Chem. Phys.*, **29**, 1346 (1958); *ibid.*, **30**, 806 (1959).
16. L. Young, *Trans. Faraday Soc.*, **51**, 1250 (1955).
17. L. Young, *Acta Met.*, **4**, 100 (1956).
18. D. A. McLean and F. S. Power, *Proc. IRE.*, **44**, 872 (1956).
19. D. M. Smyth and T. B. Tripp, *This Journal*, **110**, 1271 (1963).
20. P. Winkel and D. G. de Groot, *Philips Research Rept.*, **13**, 489 (1958).

Heat-Treatment of Anodic Oxide Films on Tantalum

II. Temperature Dependence of Capacitance

Donald M. Smyth and Terrance B. Tripp

Research Laboratory, Sprague Electric Company, North Adams, Massachusetts

ABSTRACT

The temperature dependence of capacitance for heat-treated, anodized tantalum has been used as a means of scanning the conductivity profile across the Ta_2O_5 film. This conductivity results from the extraction of oxygen from the oxide by the metal during heat-treatment. The results show that subsequent reanodization at the formation voltage is a slow process which proceeds in a stepwise manner from the electrolyte side of the oxide film toward the underlying tantalum. The application of a small anodic d-c bias gives a temporary conductivity profile which is similar to the permanent profile obtained by partial reanodization. Further evidence is given that the oxide conductivity is highest at the Ta-Ta_2O_5 interface.

A recent publication has presented an oxygen depletion layer theory to explain the phenomena observed when anodized tantalum is heated at temperatures above 200°C (1). It was found that under these heating conditions, the capacitance increased and strong bias, frequency and temperature dependences of capacitance were introduced.

It was concluded that when anodized tantalum is heated in air, the metal extracts oxygen from the Ta_2O_5 leaving the oxide oxygen-deficient. After sufficient heating this deficiency reaches the Ta_2O_5-air interface and an equilibrium is established such that an oxygen deficiency gradient is set up in the oxide. This gradient is maintained by the flow of oxygen from the atmosphere through the oxide and into the tantalum. It was proposed that the oxygen deficiency would appear as oxygen vacancies with two trapped electrons, and that these electrons could be thermally ionized thus causing the oxygen deficient portion of the Ta_2O_5 to exhibit n-type semiconductivity. On this basis it was postulated that a gradient of conductivity existed across the film such that it was greatest at the Ta-Ta_2O_5 interface and decreased toward the Ta_2O_5-air interface. For the sake of simplicity this conductivity gradient was assumed to be linear, and a level of conductivity, σ_0, was assumed to exist such that in regions of the film where the conductivity was greater than σ_0 the oxide would act as a pure resistance while in regions where it was below σ_0, the oxide would act as a pure dielectric. This sharp distinction between dielectric and conducting oxide is, of course, an idealization of the actual, continuous gradation. The phenomena observed on heating were then explained on the basis of a short-circuiting of that part of the oxide film where the conductivity was raised above σ_0, and the varying of the thickness of this conducting layer by the application of a bias or a change of the temperature of the measuring electrolyte. This temperature dependence of capacitance has been found to be a very useful tool in studying the shape of the conductivity profile across the oxide of heat-treated, anodized tantalum and this paper will present the details of this work.

Measurements of the temperature dependence of capacitance for the similar system involving the solid electrolyte tantalum capacitor by Taylor and Haring (2), McLean and Power (3), and Fraioli (4) all indicate a slight curvature to the capacitance *vs.* temperature curve, but in no cases were distinct changes in slope of the curves observed. As will be apparent, the shape of the curves would be dependent on the MnO_2 pyrolysis temperature and the extent of reanodization. Because these parameters were not reported, and since little data were taken to determine the curves, it is not possible to conclude that a discrepancy exists between the results on solid units and those reported herein on anodized tantalum foil measured in an aqueous electrolyte.

Experimental

The tantalum foil was obtained from Fansteel Metallurgical Corporation and had a minimum purity of 99.9%. Samples were die cut from the 10 mil stock and had an apparent surface area of approximately 18 cm^2. The samples were designed so that a 3/16 in. tab was left attached to serve as the electrical contact. This small tab also served the more important purpose of minimizing apparent area changes as the measuring electrolyte volume

changed slightly with temperature. The details of the electropolish and vacuum annealing pretreatment are available elsewhere as are the details of the procedure used to anodize the samples to 75v in 0.01M H_2SO_4 (1). The heating was done in a tube furnace whose temperature was controlled manually to approximately ±3°C. The heating atmosphere was air unless specified otherwise.

The cell in which the capacitance measurements were made was immersed in trichloroethylene contained in a large Dewar flask. Provisions were made to stir both the coolant and the cell electrolyte. The measuring electrolyte was a 38% by weight H_2SO_4 solution which permitted measurements to be taken as low as −70°C, and its temperature was measured with a calibrated iron-constantan thermocouple. The capacitance was measured with a Sprague 1W2 capacitance bridge at a frequency of 120 c/sec with no applied bias.

After the temperature of the trichloroethylene was lowered to the desired value with dry ice, the electrolyte in the capacitance cell was stirred until temperature equilibrium was reached. The capacitance, dissipation factor, and temperature were then recorded. The coolant temperature was then lowered further and the desired measurements were repeated at the new temperature. The temperature dependence of capacitance results for two runs on the same sample agreed to within 0.1%.

Results and Discussion

Heat-Treatment in Air

A typical temperature dependence of capacitance curve for an unheated, anodized tantalum sample is shown in Fig. 1 along with the curves obtained after heating ½ hr at 400°C and after reanodization for 4 hr at the formation voltage. Before heating and after reanodization the rate of change of capacitance with temperature is low (~0.002 $\mu f/C°$) and constant over the whole temperature range studied. After heating, however, the temperature dependence of capacitance curve is found to have changed drastically in shape. At temperatures above about −30°C, the rate of change of capacitance with temperature was found to be considerably greater than before heating. A break in the curve occurs at about −30°C, however, and at lower temperatures the slope of the curve decreases to approximately the value observed before heating. Also, the capacitances at low temperatures were found to be higher after heating than before heating.

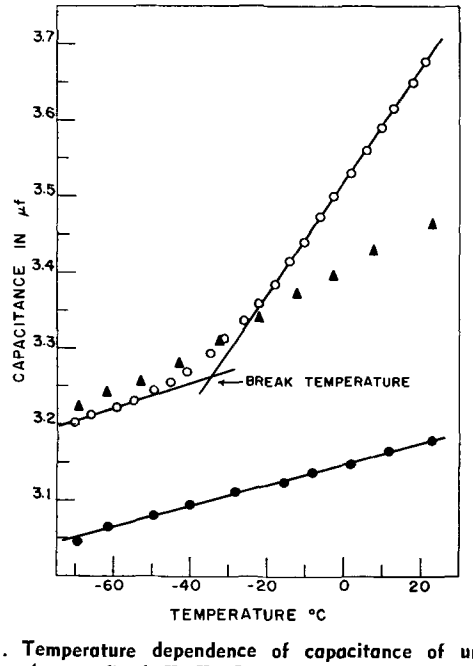

Fig. 1. Temperature dependence of capacitance of unheated, heated, and reanodized Ta-Ta_2O_5. •, Unheated; ○, heated 30 min at 400°C in air; ▲, reanodized 4 hr at formation voltage.

These temperature dependence of capacitance results can be explained with the aid of the simple conductivity profile model previously presented (1). Before heating, the conductivity across the oxide film is uniformly low and the predominant parameter which would cause a temperature dependence of capacitance would be the change of dielectric constant with temperature (and, for this experimental setup, the slight change in sample area due to the change of the electrolyte volume with temperature). This would be expected to produce only a small variation of capacitance with temperature in agreement with the observed results.

According to the simplified model, the conductivity profile across the heat-treated oxide film is as shown in Fig. 2. In this case it is assumed that a linear gradient of conductivity exists across the film and that σ_0 represents a level of conductivity which distinguishes conducting from nonconducting oxide. The level of conductivity at any point in the film is dependent on the concentration of oxygen vacancies, $\boxed{O^=} \cdot 2e^-$, produced by the extraction of oxygen from the oxide by the tantalum during heating, and on the thermal ionization reactions

$$\boxed{O^=} \cdot 2e^- \leftrightharpoons \boxed{O^=} \cdot e^- + e^- \qquad [1]$$

$$\boxed{O^=} \cdot e^- \leftrightharpoons \boxed{O^=} + e^- \qquad [2]$$

Therefore, as the temperature is lowered from T_1 to T_2 the equilibria in Eq. [1] and [2] shift to the

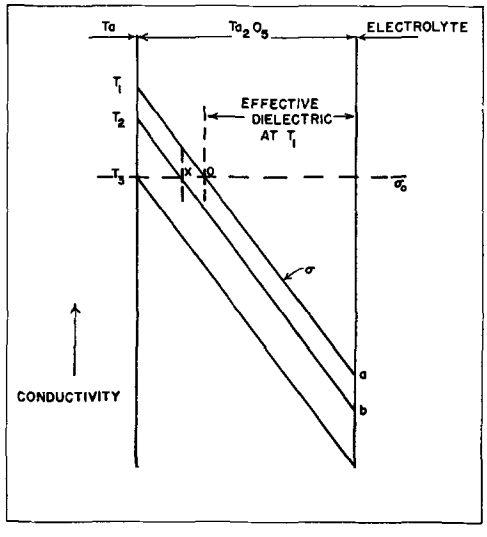

Fig. 2. Schematic representation of the conductivity profile of an anodic Ta_2O_5 film after heat-treatment in air.

left with a corresponding decrease in the concentration of conduction electrons. This has the effect of lowering the conductivity level T_1-a toward the level T_2-b, and as this occurs, the effective thickness of the dielectric oxide increases by the amount o-x. This would cause a strong capacitance decrease which would be superimposed on the change caused by the decrease in dielectric constant. As the temperature is lowered, the level of conductivity of the film drops until, at a temperature T_3, it is at or below σ_0 throughout the entire film. Therefore, at this temperature the whole oxide film may be considered to be nonconducting and no further change in the effective thickness can occur at lower temperatures. This would cause a change in slope of the temperature dependence of capacitance curve since, below this temperature, the only change in capacitance would be due to the temperature dependence of the dielectric constant.

According to a strict interpretation of our simplified model, this change in slope should occur abruptly at a particular temperature, whereas it actually occurs gradually over a range of temperatures. This is a consequence of the fact that there is a gradual transition between conducting and nonconducting oxide rather than a sharp boundary as implied by the model.

During reanodization, oxygen vacancies are eliminated by the migration of oxygen across the film from the electrolyte under the influence of the applied field. This removes the oxygen deficiency and the associated conductivity gradient established during heating and, therefore, the temperature dependence of capacitance would be reduced to the same level as before heating. This is indicated by the results shown in Fig. 1.

The permanent increase in capacitance which persists even after reanodization can tentatively be explained on the basis of an increase in the oxide dielectric constant. It has been shown by x-ray measurements (5, 6) that heating produces a change in the crystallinity of a tantalum oxide film, and this may cause the dielectric constant of the oxide to change also.

Effect of Heating Temperature

The temperature dependence of capacitance results for samples heated at various temperatures are shown in Fig. 3. Reproducibility at each heating temperature was possible only when extreme care was taken to assure uniform sample preparation. The data obtained from two different samples heated at 400°C are presented to give a typical example of reproducibility.

If one extends the two linear segments of the temperature dependence of capacitance curve to their point of intersection, a characteristic temperature as shown in Fig. 1 is obtained. This shall be referred to as the break temperature to denote the break in slope. This break temperature is the hypothetical temperature at which the conductivity of the Ta_2O_5 at the Ta-Ta_2O_5 interface reaches σ_0. Below this temperature the entire oxide thickness is acting as an effective dielectric, whereas above it the effective dielectric thickness is a function of

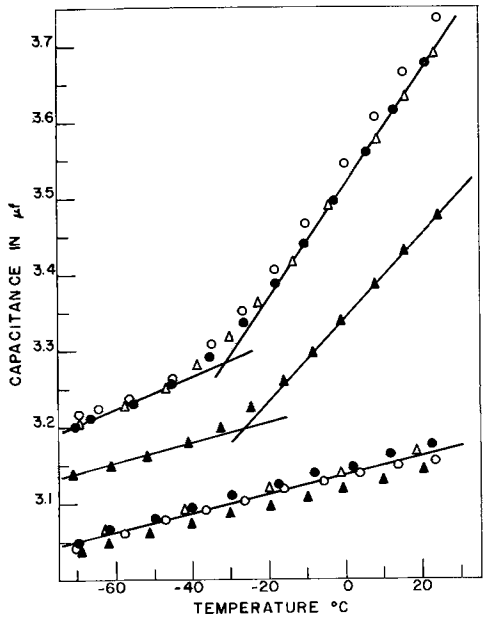

Fig. 3. Temperature dependence of capacitance before and after heating anodized tantalum at various temperatures. ▲, Heated ½ hr at 350°C; △, heated ½ hr at 400°C (sample I); ●, heated ½ hr at 400°C (sample II); ○, heated ½ hr at 450°C.

temperature. The temperature at which this change in slope occurs is indicative of the conductivity of the oxide at the Ta-Ta_2O_5 interface; the higher this conductivity the lower the temperature required to lower it to the level of σ_0.

The results shown in Table I are the break temperatures evaluated from curves obtained from samples heated at temperatures of 350°, 400°, and 450°C, respectively. These values represent the average for three runs at each heating temperature. The individual values deviate from the average by about ±0.3°C. It appears that the conductivity at the metal-metal oxide interface increases substantially when the temperature of heat-treatment is increased from 350° to 400° but that a further increase to 450° has little effect on this property.

An attempt was made to obtain these data by heating an individual sample at each of the three heating temperatures with each heating being followed by a long reformation at the formation voltage. These results did not agree with those presented in Fig. 3, apparently due to the influence of prior heating history. This was confirmed by the fact that when the successive heatings were carried out at the same temperature, it was found that the results after the second heating did not agree with those of the first heating. This dependence on heating history may be related to the change in oxide crystallinity.

Table I. Break temperatures obtained on heat-treatment of anodic oxide films on tantalum at various temperatures

(All samples heated 30 min in air)

Heating temperature, °C	Break temperature, °C
350	—26.6
400	—33.8
450	—34.1

According to the model, the magnitude of the slope of the temperature dependence of capacitance curve above the break is dependent on the angle at which the conductivity profile intersects σ_0. By geometric considerations it can be shown that as the angle of intersection of the conductivity profile with σ_0 is increased, the magnitude of the movement of this point of intersection would have to decrease for a given temperature change. Since it is the magnitude of movement of the point of intersection of the conductivity profile with σ_0 with a given change in temperature which determines the value of the slope of the temperature dependence of capacitance curve, this slope would decrease as the angle of intersection is increased. This analysis would imply that as the heating temperature is increased, the conductivity profile across the film becomes flatter since the slope of the temperature dependence of capacitance curve increases with heating temperature as shown in Fig. 3. It would, therefore, appear that the conductivity level at the Ta_2O_5-electrolyte interface is not fixed and in fact must increase relative to the conductivity at the Ta-Ta_2O_5 interface as the heating temperature is increased. If this were the case, then a dependence of the dielectric effects of heat-treatment on oxygen pressure in the heating atmosphere would be expected and, as stated elsewhere, preliminary results indicate that some oxygen pressure dependence does exist (1).

Reanodization

After a heat-treated, anodized tantalum sample was reanodized at the formation voltage for short periods, it was found that the shape of the temperature dependence of capacitance curve was modified. As shown in Fig. 4, at high temperatures the slope of the temperature dependence curve is reduced to nearly the preheated value but as the temperature is lowered the curve intersects the curve obtained before reanodization and follows its shape throughout

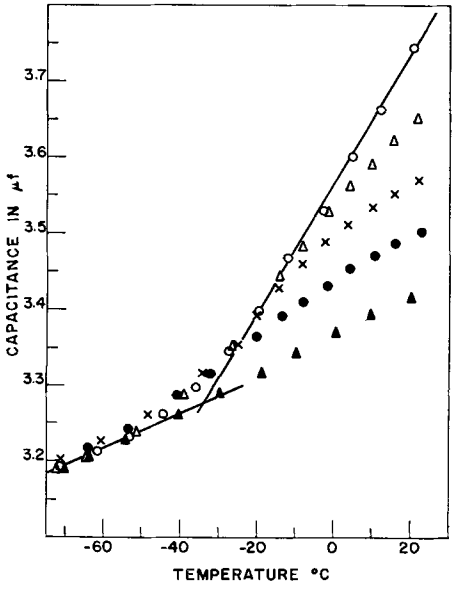

Fig. 4. Temperature dependence of capacitance for anodized tantalum after heating and after reanodization for various times at the formation voltage. ○, Heated ½ hr at 450°C; △, reanodized 6 min; X, reanodized 30 min; ●, reanodized 2 hr; ▲, reanodized 5 hr.

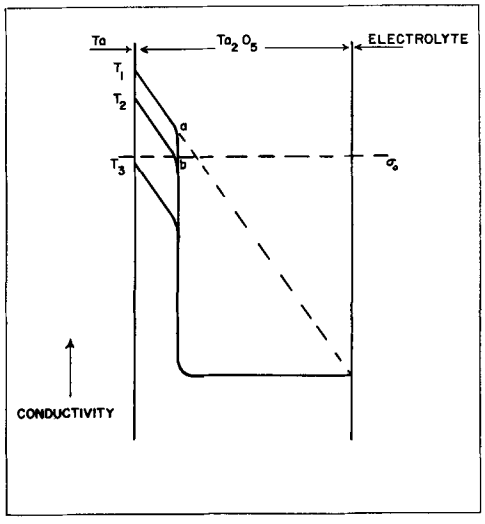

Fig. 5. Schematic representation of the conductivity profile of heat-treated, anodized Ta after a short reanodization.

the rest of the temperature range. As the reanodization time is increased, the level of the high temperature portion of the curve is depressed to lower capacitance values until, after approximately 5 hr of reanodizing a sample heated at 450°, the curve becomes nearly parallel to the preheated curve over the whole temperature range. This process was found to take about 3 hr when the samples were heated to 350°C and approximately 4 hr for samples heated at 400°.

The shape of the temperature dependence of capacitance curve after brief reanodization can be explained with the aid of a modified oxide conductivity profile like that shown in Fig. 5. In this figure the dotted line extension of the T_1-a portion of the conductivity profile represents the original shape of the conductivity profile, *i.e.*, after reanodization the conductivity profile is cut off at the point a. Now, as the temperature drops from T_1 to T_2, the conductivity level T_1-a drops to T_2-b and because of the extreme steepness with which the conductivity profile passes through σ_0, the effective thickness of the dielectric does not change. Therefore, the slope of the temperature dependence of capacitance curve would be like that for an unheated sample. At lower temperatures, the conductivity profile passing through σ_0 is identical to that before reanodization, and over the rest of the temperature range the temperature dependence of capacitance would be identical to that observed before reanodization. As the reanodization progresses, the cut-off of the conductivity profile approaches, and finally reaches, the Ta-Ta_2O_5 interface.

The results described above indicate that, during the reanodization process, the oxygen deficiency in the Ta_2O_5 film is being replenished stepwise from the Ta_2O_5-electrolyte interface. The observation that the temperature dependence in the low temperature region is completely unaffected by reanodization indicates that the oxygen vacancy profile near the tantalum remains unchanged during the initial stages of reanodization. This situation could occur if the reanodization process consisted of a movement of oxygen into the oxide from the electrolyte side.

This could take place by the interstitial transport of oxygen across the film. The recent work of Kofstad (7) indicates that the presence of interstitial, excess oxygen in Ta_2O_5 is not improbable. The observed reformation behavior could also arise from the migration of oxygen vacancies if the nonconducting depletion layer created by the application of the formation voltage did not extend across all of the conducting region of the oxide. Then only those vacancies in the depletion layer would be exposed to the applied field and be accelerated. As reformation proceeded, the conducting layer would narrow and more vacancies would be exposed. This would result in the stepwise removal of the oxygen deficiency in accord with the observed results.

The complete removal of the oxygen deficiency in the oxide by reanodization is seen to be a slow process, requiring, for example, approximately 5 hr for samples heated at 450° for 30 min. The time for complete reanodization increases with the temperature of heat-treatment. It is interesting to note that this time-lag extends to the case where the reanodization voltage is greater than the original formation voltage. For example, when a sample was formed to 75v, heated at 400° for 30 min in air, and then reanodized at 85v, the current remained at a low level (order of 0.1 $\mu a/cm^2$) for about an hour. The current then began a gradual rise and only at this point did the interference color begin to change, indicating a growth of new oxide. The anodization then proceeded normally. With higher "over-voltages" the induction period decreases.

This behavior is analogous to that reported for heat-treated anodized aluminum by Dignam (8). In the case of tantalum it is tempting to suggest that complete restoration of the stoichiometric oxygen content is necessary before the growth of new oxide can begin. However, there is no evidence for the existence of an oxygen deficiency in heat-treated, anodized aluminum.

Effect of D-C Bias

It has been noted previously (1) that when a d-c bias is applied to a heat-treated, anodized tantalum sample, its capacity decreases. This phenomenon was explained on the basis of the movement of the intersection of the conductivity profile with σ_0 toward the Ta-Ta_2O_5 interface because of the attraction of electrons to the Ta electrode by the anodic bias.

The temperature dependence of capacitance curves with 6 and 12v anodic bias (Ta+) applied for a sample heated ½ hr at 400°C is shown in Fig. 6. These results cannot be explained on the basis of a uniform shift of the conductivity profile toward the Ta electrode since this would result in a shift of the entire temperature dependence of capacitance curve to higher temperatures. From the similarity of the curves one would suspect that the conductivity profile would be like that established in a heat-treated sample after short reanodization at the formation voltage. Apparently, when a bias is applied, electrons are drawn into the Ta electrode, and electrons trapped at oxygen vacancies in the outer portion of the oxide move to the sites left vacant by the withdrawn electrons. The extent of electron withdrawal and movement would establish an ionic space charge in the electron depleted portion of the oxide of sufficient strength to counter the external field introduced by the bias.

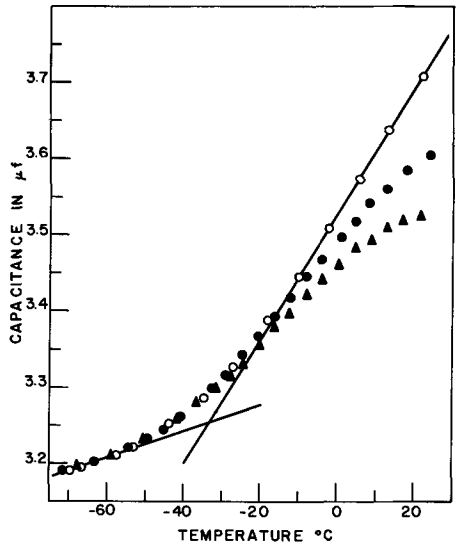

Fig. 6. Temperature dependence of capacitance of heat-treated, anodized tantalum with an anodic d-c bias applied. ○, Heated 30 min at 400°C; ●, 6v d-c bias applied; ▲, 12v d-c bias applied.

The oxide would now have two regions. In the first, near the Ta-Ta_2O_5 interface, the conductivity profile would be essentially unchanged since all conducting electrons drawn to the tantalum electrode would be replaced by electrons from further out in the film. At a distance into the film dependent on the bias voltage, the conductivity would drop very rapidly since all electrons trapped at oxygen vacancies in the rest of the film would have moved to vacant electron sites nearer the Ta electrode. The conductivity profile would now be similar to that established by reanodization with the exception that the outer region of the film is made nonconducting by the temporary and reversible withdrawal of conduction electrons trapped at oxygen vacancies in the former case, while in the latter case oxygen vacancies are permanently eliminated.

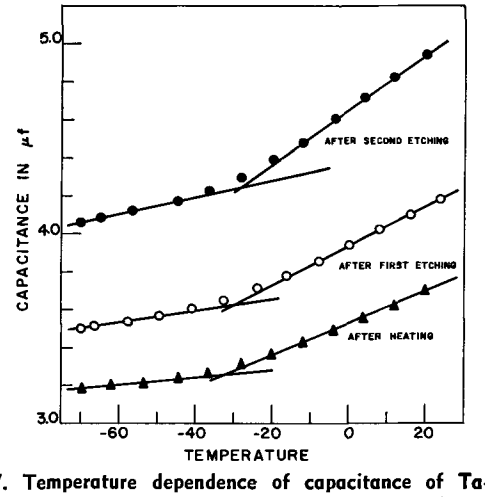

Fig. 7. Temperature dependence of capacitance of Ta-Ta_2O_5 before and after HF dissolution of the heat-treated oxide. ▲, Heated 30 min at 400°C. Oxide dissolved until oxide interference color equivalent to formation to ○ 65v; ●, 55v.

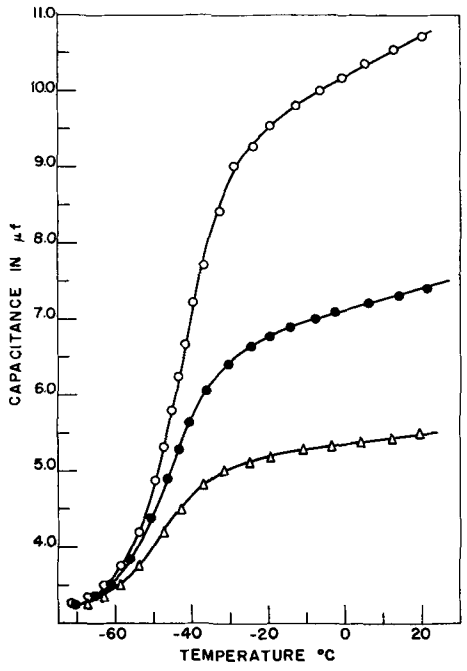

Fig. 8. Temperature dependence of capacitance for Ta-Ta_2O_5 after vacuum heating at 400°C followed by reanodization at various voltages. ○, Reanodized 30 min at 20v; ●, reanodized 30 min at 30v; △, reanodized 30 min at 40v.

HF Dissolution of the Heat-Treated Oxide

In another experiment, a sample was heated for ½ hr at 400°C and the temperature dependence of capacitance was measured before and after the removal of an outer layer of the oxide by treatment in concentrated HF. In Fig. 7 are shown the results of the temperature dependence of capacitance measurements on a heat-treated, anodized tantalum foil before and after the removal of two consecutive layers of the oxide. A thickness of oxide was removed in each case such that the final color of the sample after treatment was equivalent to that for samples formed under the usual conditions to 55 and 65v. The temperature dependence of capacitance increased as the oxide was removed and this indicates that the temperature sensitive region is not at the Ta_2O_5-electrolyte interface. This supports the conclusion, based on the increase of the bias dependence of capacitance as the outer portion of the oxide was removed by HF dissolution, that the oxygen depletion layer is at the Ta-Ta_2O_5 interface (1). The slopes of the curves would be expected to increase as the oxide is removed, as observed, because the relative thickness of the temperature sensitive portion increases with respect to the total oxide thickness as nonconducting oxide is removed from the outer surface of the film.

Heat-Treatment in Vacuum

The temperature dependence of capacitance curves shown in Fig. 8 were obtained with a sample which had been heated at 500°C in vacuum ($1x10^{-5}$ Torr) for 40 hr followed by reanodization at 10, 20, 40, 60, and 75v. It has been reported (1,9) that when anodized tantalum is heated for a sufficient time in vacuum at over 400°C, the oxide becomes conducting throughout. This means that before reanodization the conductivity level in the oxide would be well above σ_0 across the whole film, and on reanodization a portion of the film whose thickness would be dependent on the reanodization voltage and reanodization time would be returned to the nonconducting state by the same process which eliminates oxygen vacancies during the reanodization of a sample heated under standard conditions. The resulting conductivity profile would be similar to that shown in Fig. 5, except that the slopes of the T_1-a and T_2-b portions of the profile would not be as steep. As the measuring temperature is lowered from T_1 to T_2, the effective thickness of the oxide film remains unchanged because of the steepness of the conductivity profile passing through σ_0 and, therefore, the only change in capacitance would be due to changes in the dielectric constant with temperature. When the temperature T_2 is reached, however, the portion of the conductivity profile T_2-b begins to drop below σ_0 and a break in the temperature dependence of capacitance curve occurs, followed by a large rapid drop in capacitance. The extremely high temperature dependence of capacitance between T_2 and T_3 results from the shallow angle with which the conductivity profile intersects σ_0 in the case of this vacuum-heated sample. This causes a large change of effective dielectric thickness with temperature. At T_3 another break in the curve occurs since the whole oxide is now nonconducting and below this temperature further changes in capacitance are due only to changes in dielectric constant. The observed results agree with the curve predicted by the conductivity profile produced in the oxide film.

Manuscript received May 8, 1963. This paper was presented at the Pittsburgh Meeting, April 15-18, 1963.

Any discussion of this paper will appear in a Discussion Section to be published in the June 1964 JOURNAL.

REFERENCES

1. D. M. Smyth, G. A. Shirn, and T. B. Tripp, *This Journal*, **110**, 1264 (1963).
2. R. L. Taylor and H. E. Haring, *ibid.*, **103**, 611 (1956).
3. D. A. McLean and F. S. Power, *Proc. I.R.E.*, **44**, 872 (1956).
4. A. V. Fraioli, I.R.E. Transactions on Component Parts, *CP-5*, 72 (1958).
5. D. A. Vermilyea, *This Journal*, **104**, 485 (1957).
6. L. D. Calvert and P. H. G. Draper, *Can J. Chem.*, **40**, 1943 (1962).
7. P. Kofstad, *This Journal*, **109**, 776 (1962).
8. M. J. Dignam, *ibid.*, **109**, 184 (1962).
9. D. A. Vermilyea, *Acta Met.*, **5**, 113 (1957).

Studies on the Electroreduction of Uranyl (VI) in Molten Equimolar KCl-NaCl by Chronopotentiometric and Electrode Impedance Measurements

R. W. Stromatt

Hanford Laboratories, Hanford Atomic Products Operation,
General Electric Company, Richland, Washington

ABSTRACT

The reduction of $UO_2(VI)$ to UO_2 in molten KCl-NaCl salt at 716°C has been shown by chronopotentiometry to be diffusion controlled at a platinum electrode. Furthermore, the potential-time curves indicated that the reaction occurred in two steps at nearly the same potential. This observation was verified by measuring the pseudo capacity of the polarized cathode as a function of its potential for which a plot of the data shows two peaks in capacity. The first was found to be symmetric with a concentration-independent potential, which is indicative of an electrode reaction producing a soluble product. The second peak was asymmetric with a concentration-dependent potential, which is indicative of an electrode reaction producing an insoluble product. These observations suggested that the electrode reaction proceeds by a reduction of $UO_2(VI)$ to $UO_2(V)$ followed by the reduction of the $UO_2(V)$ to $UO_2(s)$ Additional verification of this mechanism was provided by the reduction of $UO_2(VI)$ by UO_2 to yield a stable solution of $UO_2(V)$. The heterogeneous rate constant for the reduction of $UO_2(VI)$ to $UO_2(V)$ was estimated to be 2 cm sec^{-1}, but a value for the reduction of $UO_2(V)$ could not be determined because of the solid UO_2 deposit. The diffusion coefficient was estimated from the chronopotentiometric data to be 2.2×10^{-5} cm^2 sec^{-1}.

Uranyl(VI) in molten chloride salt solutions can be electrolytically or chemically reduced to UO_2. The electrolytic reduction is under investigation at this laboratory for use in a process to reclaim uranium and plutonium from UO_2-based nuclear fuels (1) and as a method of preparing high quality crystalline UO_2 (2). Part of this research program has been a study of the mechanism and the thermodynamic properties of the reduction.

The electrolytic reduction of UO_2Cl_2 to UO_2 was first described by Hampe in 1888 (3). More recently, Smirnov and Ivanovsky (4) studied the anodic behavior of the UO_2 electrode in the eutectic LiCl-KCl melt. They found only hexavalent uranium in the melt after anodization and determined that the reaction proceeded by direct electron loss rather than through dissolution by anodic chlorine. Their estimate of the oxidation potential of UO_2, compared to a chlorine electrode, was 0.57v. Hill, Perano, and Osteryoung conducted a polarographic investigation of the $UO_2(VI)$ reduction, also in the eutectic LiCl-KCl melt (5). They found that the polarographic wave did not conform to a reversible two-electron process, but that there was a linear relationship between wave height and $UO_2(VI)$ concentration. They plated UO_2 on the microelectrode and measured the open-circuit potential as a function of concentration. The data obtained in this fashion did suggest a reversible two-electron transfer process, and their estimate of the emf for the reaction was close to that obtained by Smirnov and Ivanovsky. Wilks (6) reported a study of the reactions occurring in the UO_2Cl_2-KCl-NaCl melt which would result in stoichiometric and nonstoichiometric UO_2 deposits on electrolysis. He suggested the presence of $UO_2(V)$ to explain some of his observations.

In this laboratory, the electrode reaction mechanism and diffusion properties have been studied by chronopotentiometric and electrode impedance measurement techniques. The studies carried out to date with NaCl-KCl solutions of UO_2Cl_2 are presented in this paper.

Experimental

Solutions.—$UO_2(VI)$ solutions were prepared by adding weighed amounts of $Cs_2UO_2Cl_4$ (7) to a weighed equimolar mixture of reagent grade NaCl and KCl (mp = *ca.* 670°C). Dry chlorine was passed through the mixture while it melted and for 30 min thereafter. Dry helium was then passed through the melt for 30 min to remove the chlorine. This procedure, initially described by Maricle and Hume (8), was found to adequately "dry" the melts. Solutions of $UO_2(VI)$ can also be prepared by reacting chlorine with U_3O_8 dispersed in the NaCl-KCl melt. This is a useful method for the more concentrated solutions.

At the temperature of these studies (716°C) the color of the solutions was observed to vary from a light straw color through an orange to a deep

red as the concentration increased and the charge transfer band shifted.

Cell and electrodes.—The cell body was a 28 by 5.2 cm quartz test tube, with the top flanged and ground flat to provide a seal with the lid. The lid was made of lavite and drilled to accept standard taper joints. The electrodes, thermocouple well, and gas inlets and exit were all fitted with standard taper joints so that a sealed system was provided. The gas exit was connected to a bubbler to protect the solution from the atmosphere.

The counterelectrode was either a ¼ or ⅛ in. spectrographic graphite rod 12 in. long, and was inserted into a compartment isolated from the main body of the melt by a sintered quartz disk. The cathodes for the chronopotentiometric experiments were made from platinum foil spot-welded to fine platinum wire. The measured projected areas of these electrodes were from 0.66 to 2.11 cm^2. The microelectrodes for the impedance (and polarographic) measurements were made by sealing 31 gauge platinum wire into Jena Supremax glass tubing which was sealed to a Pyrex standard taper joint. The platinum wire was then fused to a symmetrical sphere next to the Supremax seal. No imperfections on the surface of the platinum were noted by a microscopic inspection. The measured projected areas for these electrodes were from 1 to 3 mm^2. The reference electrode was a Ag/AgCl (1M in NaCl-KCl) half-cell separated from the UO_2(VI) solution by a Supremax glass membrane as described by Littlewood (9).

Furnace and controls.—The temperature for these experiments was maintained at 716°C by use of a vertical, nichrome wire-wound resistance furnace controlled by a Minneapolis-Honeywell Pyr-O-Vane indicating millivoltmeter. The temperature of the solution, as measured by an alumel-chromel thermocouple, cycled 1.6°C over about 1 hr. A steel cylinder was placed around the cell in the furnace to ground the signal from the windings.

Instruments.—The conventional chronopotentiometer circuit was used (10). Constant current values from 2 to 40 ma were provided by switching ballast resistors, and were determined by measuring the IR drop across standard resistors. A Philbrick R-100B power supply was used as the current source. A Heiland 906C Visicorder with a M1650 galvanometer was used to record the chronopotentiograms. The signal from the reference electrode and cathode was amplified using a Philbrick K-2W plug-in amplifier, and a two transistor stage amplifier to drive the galvanometer of the Visicorder. This arrangement allowed direct recording of chronopotentiograms with transition times down to less than 10 msec. The polarographic studies were made using a Sargent XXI modified for controlled potential polarography, and the Anotrol 4100 potentiostat for the high polarization rates.

The bridge used for the impedance measurements was similar to the one described by Laitinen and co-workers (11, 12). A Hewlett-Packard 200 CD signal generator was used to supply the a-c signal. This signal was amplified by a filtered Philbrick USA-3 M3 amplifier and fed to an oscilloscope to detect bridge balance. The peak to peak potential of the a-c signal was 4 to 6 mv.

Results and Discussion

There are several paths which the cathode reaction could follow to produce UO_2. The following three are the most obvious and likely

$$UO_2(VI) + 2e^- = UO_2(s) \qquad [1]$$

$$UO_2(VI) + e^- = UO_2(V) \qquad [II]$$
$$UO_2(V) = \tfrac{1}{2}\, UO_2(VI) + \tfrac{1}{2}\, UO_2(s)$$

$$UO_2(VI) + e^- = UO_2(V) \qquad [III]$$
$$UO_2(V) + e^- = UO_2(s)$$

Several techniques are known to be useful in elucidating electrode reaction mechanisms, kinetic parameters, and diffusion properties for systems of this type. Electrode polarization techniques such as chronopotentiometry and polarography have been widely utilized for the study of electrode reactions and the diffusion properties of the electrolyzed ion. Electrode impedance measurements have been shown to be very sensitive to the electron transfer process and have been used to estimate kinetic parameters for the electrode reaction.

Chronopotentiometry and polarography.—It was found that polarography could not be used to study this particular electrode reaction. Uranium dioxide is conductive in the temperature range used, and the deposit from dilute UO_2(VI) solutions is dendritic with much branching. Thus, the surface area of the microelectrode changed considerably (more so than for most metal depositions reported in the literature) and a well-defined diffusion plateau was not generally observed at conventional polarization rates (0.22 v/min or less). Polarograms obtained at greater polarization rates (3 to 6 v/min) are somewhat better defined but could not be analyzed quantitatively. Better defined polarograms can also be obtained for lower temperature solvent systems in which the conductivity of the UO_2 is less significant. Chronopotentiometry will yield the same information as polarography, and indeed, Laitinen and Ferguson (13) found the theoretical relationship between transition time and current to hold for metal depositions. It has the advantage over polarography that a comparatively large electrode is used, and the electrolysis time is short enough that the surface area remains effectively constant.

The time-current relationship at constant current for an electrode process with semi-infinite linear diffusion control has been shown to be (10)

$$i_o \tau^{1/2} = \tfrac{1}{2}\, nFD^{1/2} \pi^{1/2} C \qquad [1]$$

where i_o is current density (amp cm^{-2}), τ is the transition time (sec), C is the concentration of the reducible ion (moles cm^{-3}), D is the diffusion coefficient (cm^2 sec^{-1}), and the remaining terms have their usual significance. From this equation it is seen that if the reaction is diffusion controlled the product, $i_o \tau^{1/2}$, remains constant for a given concentration as the current is varied, and that D can be obtained from the slope of a plot of the product *vs.* concentration.

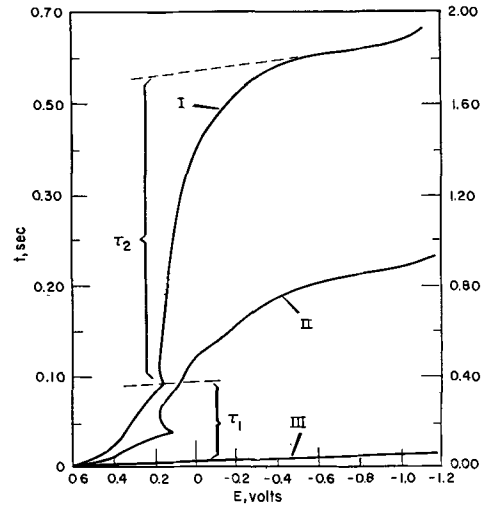

Fig. 1. Chronopotentiograms for the reduction of 5.0 mM UO_2 (VI) at 2.89 (curve I) and 9.92 x 10^{-3} amp cm^{-2} (curve II, L.H. axis), and of the pure melt at 2.89 x 10^{-3} amp cm^{-2} (curve III). Potentials are referred to the Ag/AgCl (1m) half-cell.

Typical chronopotentiograms for the reduction of UO_2(VI) in the KCl-NaCl melt and one for the blank are shown in Fig. 1. The potential overshoot, which divides the reduction waves into two parts, is probably an overvoltage effect. The extent of the overshoot increases with increasing current density and decreasing UO_2(VI) concentration. It is less on graphite than on platinum and there is no overshoot on an electrode previously covered with UO_2, which could explain the return of the potential to that typical for the UO_2 deposition. The first portion of the curve has the appearance expected for a reduction to a soluble product, while the second portion has the appearance expected for a solid product. The two parts of the wave are never sufficiently resolved to determine the transition time accurately for each; however the ratio of the two transition times approaches 1:3 as the resolution is improved. Such an improvement is accomplished for curves having the greatest potential overshoot and for those obtained using the lower concentrations of UO_2(VI). For example, ratios for 3.3 x $10^{-3}M$ UO_2(VI) were 1:3 at 9.7 amp cm^{-2} and 1:4.6 at 1.9 amp cm^{-2}, and for 8.3 x $10^{-3}M$ UO_2(VI) the ratio was 1:3.6 at 9.7 amp cm^{-2}. A ratio of 1:3 would be expected for two successive one-electron reductions from Eq. [2] (10). The $i_o\tau^{1/2}$ product for the total transition time is constant with change in i_o within experimental error ($< \pm 2.5\%$) as shown in Table I; thus the over-all electrode reaction is diffusion controlled.

Table I. Chronopotentiometric data for the reduction of 5.0 x 10^{-3}M UO_2(VI) in molten KCl-NaCl at 716°C

i_o, amp cm^{-2} x 10^3	$i_o\tau^{1/2}$, amp $sec^{1/2}$ cm^{-2} x 10^3
14.5	3.95
9.92	3.94
4.73	3.85
2.89	3.81
1.92	3.94

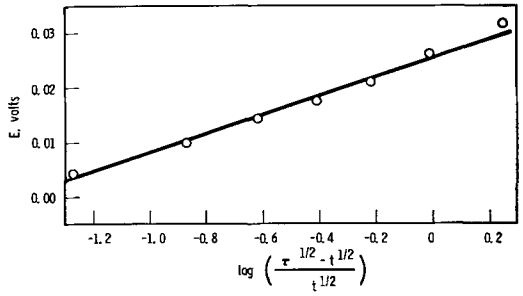

Fig. 2. Potential of the cathode [vs. the Ag/AgCl (1m) reference] as a function of the log term in Eq. [3] for the initial portion of a chronopotentiogram of 3.3 mM UO_2(VI) at 4.72 x 10^{-3} amp cm^{-2}.

$$\tau_2 = \tau_1\left[\left(\frac{n_2}{n_1}\right)^2 + 2\left(\frac{n_2}{n_1}\right)\right] \qquad [2]$$

An analysis of the first part of the wave can be made utilizing Eq. [3], which relates the potential and time for a reaction with a soluble product (10)

$$E = E_{1/4} + \frac{RT}{n\mathbf{F}}\ln\frac{\tau_1^{1/2} - t^{1/2}}{t^{1/2}} \qquad [3]$$

where t is the time (sec) at which the electrode is at a potential E (v), $E_{1/4}$ is the characteristic quarter-wave potential, τ_1 is the transition time (sec) of the first part of the wave as determined by dividing the total transition time by 4, and the remaining terms have their usual significance. Values of n determined from four experiments varied from 0.89 to 0.99 as calculated from the slope of the E *vs.* log term plot as shown in Fig. 2. A comparable treatment of the second portion of the wave is not possible because of its shape.

The diffusion coefficient for UO_2(VI) was calculated from Fig. 3 and Eq. [1] to be 2.2 x 10^{-5} cm^2 sec^{-1}. This compares to values of 7.0 x 10^{-5}, 2.3 x 10^{-5}, 4.5 x 10^{-5}, 1.4 x 10^{-5}, and 3.7 x 10^{-5} cm^2 sec^{-1} for Pb(II), Zn(II), Ag(I), Ni(II), and Cd(II), respectively, as determined by Delimarskii and coworkers (14) for the equimolar KCl-NaCl melt at 710°C. The data at concentrations greater than 6 x 10^{-3}M were reproducible only under exacting conditions (each data point in Fig. 3 is an average of two or more experiments with reproduci-

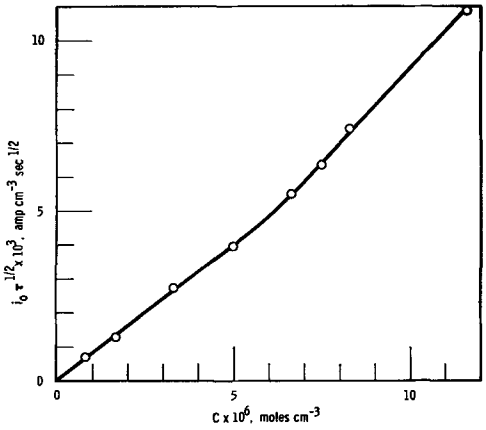

Fig. 3. The i_o $\tau^{1/2}$ product as a function of the UO_2(VI) concentration.

bility better than 5%). Considerable care was required to exclude traces of air or moisture, otherwise a scatter of the $i_o\tau^{1/2}$ values was obtained, although the reaction appeared to be diffusion controlled in each case. It has been the experience at this laboratory that the nature of the UO_2 crystal growth is sensitive to the condition of the melt. Also, it may be that at higher concentrations the growth of the UO_2 deposit may significantly alter the electrode area, which would result in large calculated values of $i_o\tau^{1/2}$, and thus an increase in slope. Then, if there were changes in the melt condition in the high concentration range, the differences in the UO_2 could be significant, and irreproducible results obtained. For this reason it is assumed that the increased slope for the higher concentrations probably does not reflect the true diffusion properties of UO_2(VI).

Impedance Measurements.—Recently several investigations of the electrode impedance at solid electrodes in molten salt solutions have been reported (11, 12, 15). Estimates of kinetic parameters of electrode reactions were obtained using Eq. [4] and [5] (16)

$$AR_r = \frac{RT}{n^2\mathbf{F}^2C}\left[\left(\frac{2}{\omega D}\right)^{1/2} + \frac{1}{k}\right] \qquad [4]$$

$$\frac{A}{\omega C_r} = \frac{RT}{n^2\mathbf{F}^2C}\left(\frac{2}{\omega D}\right)^{1/2} \qquad [5]$$

In these equations, C and D are the geometric means of the concentration (moles cm^{-3}) and diffusion coefficients of the reactant and product ions, ω is the angular frequency (cps) of the alternating current, A is the electrode area (cm^2), k is the heterogeneous rate constant (cm sec^{-1}), C_r and R_r are the capacitance and resistive components of the faradaic impedance, and the remaining terms have their usual significance. By plotting AR_r and $A/\omega C_r$ *vs.* $\omega^{-1/2}$, two straight and parallel lines are obtained with the capacitance component passing through the origin. Their difference is given by subtracting Eq. [5] from [4] to give Eq. [6]

$$AR_r - \frac{A}{\omega C_r} = \frac{RT}{n^2\mathbf{F}^2C}\cdot\frac{1}{k} \qquad [6]$$

The rate constant can then be calculated from this difference. The pseudo capacity is shown as a function of cathode polarization, as well as frequency, in Fig. 4. The symmetric first peak corresponds to what is expected for a reaction with a soluble product. The potential of the first peak is independent of the concentration while that of the second peak is concentration-dependent. This relationship would be expected for reactions with soluble and insoluble products, respectively. The reduction potentials at these two peaks become closer as the concentration increases to about 0.03M at which point the two pseudo capacity peaks are not distinguishable. The change in the potential at the break of the second peak as a function of log [UO_2(VI)] is shown in Fig. 5. The curved line corresponds to values of n between 0.8 and 1.1, increasing as the concentration increases.

The maximum value of the first capacitance peak was reproducible, but it could not be determined

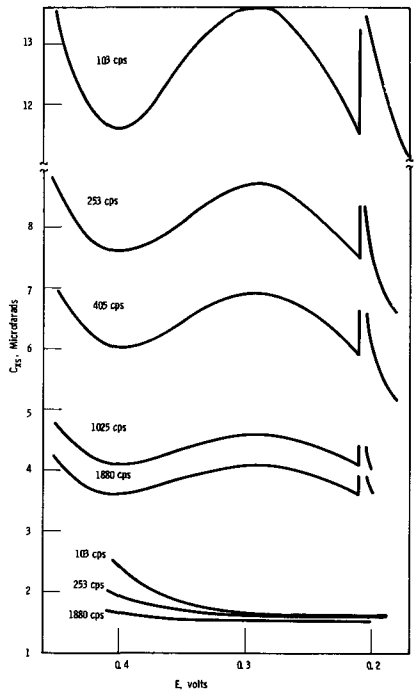

Fig. 4. Pseudo capacity at the Pt microelectrode for the reduction of 10 mM UO_2(VI) and the residual pseudo capacity for the pure melt as a function of cathode potential [vs. the Ag/AgCl (1m) reference].

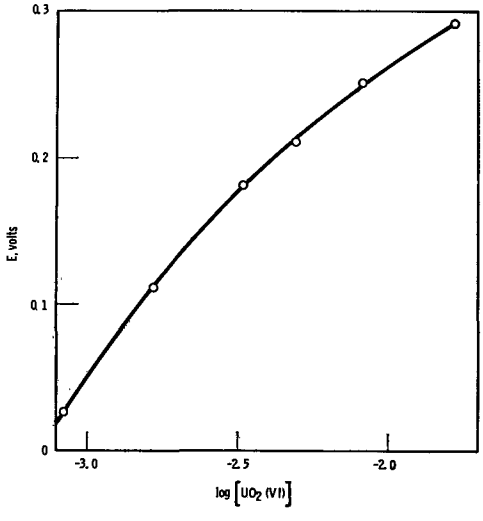

Fig. 5. Potential of the second pseudo capacity peak as a function of the log of the UO_2(VI) concentration. Potentials are referred to the Ag/AgCl (1m) half-cell.

for the second peak. In addition the resistance component did not go through a minimum at the potential of the second capacitance peak as had been expected. This may have been caused by the deposition of the UO_2 which resulted in an increase of the resistance, in effect cancelling the expected minimum. Thus, only the rate constant for the electrode reaction corresponding to the first peak could be estimated. Values of C_r and R_r were calculated from the gross electrode impedance determined from the bridge measurements as described by Laitinen and Randles (17). The impedance components AR_r and $A/\omega C_r$ (solid lines) are shown as a function of $\omega^{-1/2}$ in Fig. 6, but the two lines are not parallel nor does the capacitance component pass through the origin

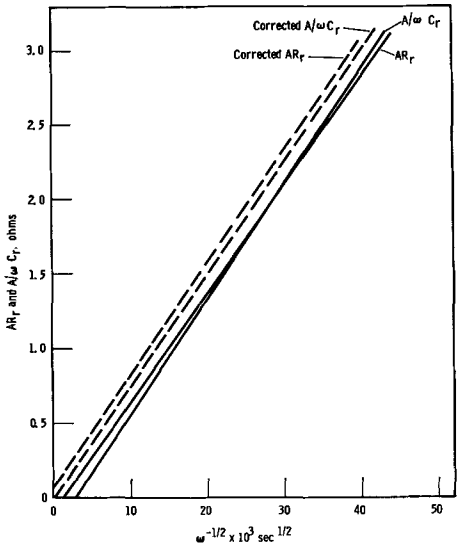

Fig. 6. Uncorrected $A/\omega C_r$ and AR_r data (solid lines) and the corrected data (dashed lines) as a function of $\omega^{-1/2}$ for the reduction of 6.7 mM $UO_2(VI)$.

as defined by Eq. [4], [5], and [6]. This departure from theory has been explained by Laitinen and coworkers (12, 17) as being caused by adsorption of the reducible ion on the electrode surface. In terms of an equivalent circuit, this would insert a series capacitance and resistance, C_a and R_a, in parallel with C_r and R_r. Those authors were able to make arbitrary selections of C_a and R_a and calculate corrected C_r and R_r values which would fit the equations. This technique was used in the present work to correct the data as shown by the dashed lines in Fig. 6. Unfortunately, this technique was found to be somewhat insensitive with the result that precise corrections could not be made, and there was rather large variance in the value of k as calculated for the various experiments. The best rate constant as determined from several concentrations was estimated to be 2 ± 1 cm sec^{-1}.

Reaction of UO_2 with a $UO_2(VI)$ solution.—The electrode potentials of the two reduction steps as seen in Fig. 1 and 4 are such that the reaction

$$UO_2(VI) + UO_2 = 2UO_2(V) \qquad [IV]$$

might be expected to occur. To test this, an excess of powdered stoichiometric UO_2 was added to a 3.3 x 10^{-3}M $UO_2(VI)$ solution, and stirred for about 2 hr with helium. The color of the solution changed from light orange to a light brown color during this time. Cathodic and anodic chronopotentiograms (using a pyrolytic graphite electrode) of the resulting solution are shown in Fig. 7. A reduction wave corresponding to the deposition of UO_2 and an oxidation wave not occurring for $UO_2(VI)$ or U(IV) solutions were observed. This would suggest that reaction [IV] did take place.[1] An analysis of the anodic wave using Eq. [3] is shown in Fig. 8. Values of n calculated in this fashion varied from 0.9 to 1.4. The anodic transition time is slightly less than the cathodic be-

[1] Recently, spectrophotometric evidence for the presence of $UO_2(V)$ in molten salt solutions has been obtained by M. D. Adams (18) at the Argonne National Laboratory and by J. L. Swanson (19) at this laboratory. Additional evidence was obtained for reaction [IV] in the latter work.

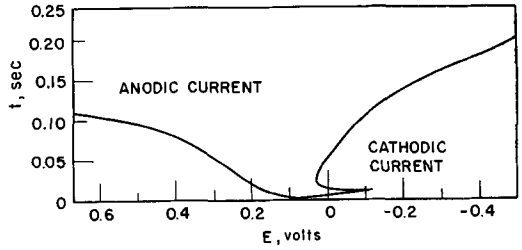

Fig. 7. Anodic and cathodic chronopotentiograms of approximately 7 mM $UO_2(V)$ at a pyrolytic graphite electrode. The current density is unknown, and potentials are referred to the Ag/AgCl (1m) half-cell.

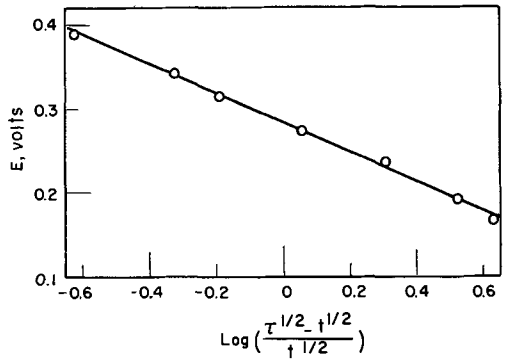

Fig. 8. Potential of the graphite electrode [vs. the Ag/AgCl (1m) reference] for an anodic chronopotentiogram of $UO_2(V)$ as a function of the log term in Eq. [3].

cause of the presence of a small amount of unreduced $UO_2(VI)$.

Conclusions

At the start of this investigation reaction [I] appeared to be the most probable path, since reactions [II] and [III] postulate a $UO_2(V)$ intermediate which had not been shown to exist in molten chloride solutions. A further objection to acceptance of reaction [II] is that UO_2 produced by this mechanism would not be expected to adhere to the cathode. The chronopotentiometric and the electrode impedance data, however, support the third mechanism (reaction [III]). The analysis of the first part of the chronopotentiogram showed a one-electron transfer process, and the symmetry of the first pseudo capacity peak is typical for a reduction to give a soluble product, *i.e.*, the reduction of $UO_2(VI)$ to $UO_2(V)$. The change in potential of the second pseudo capacity peak as a function of concentration showed a one-electron transfer process, and the shape of the second part of the chronopotentiogram and the second pseudo capacity peak are typical of a reduction with an insoluble product, *i.e.*, the reduction of $UO_2(V)$ to $UO_2(s)$. Further confirmation of this mechanism was given by the reduction of $UO_2(VI)$ by UO_2 to yield a stable solution having properties consistent with a $UO_2(V)$ solution.

The reaction was shown to be diffusion controlled. This is not surprising, since the U-O bonds are not broken in the reduction. The rate constant for the reduction of $UO_2(VI)$ to $UO_2(V)$ is quite large, which may be one reason for the insensitivity of the impedance technique. More refined techniques such as the pulse and faradaic rectification methods for determining kinetic parameters will be used for comparison.

Acknowledgments

The author wishes to extend his appreciation to Professor H. A. Laitinen for helpful discussions, and to Mrs. B. B. Lish for laboratory assistance. This work was performed under Contract No. AT(45-1)-1350 for the U. S. Atomic Energy Commission.

Manuscript received Oct. 4, 1962; revised manuscript received May 3, 1963. This paper was presented at the New York Meeting, Sept. 29-Oct. 3, 1963.

Any discussion of this paper will appear in a Discussion Section to be published in the June 1964 JOURNAL.

REFERENCES

1. K. M. Harmon, *Trans. Am. Nuclear Soc.*, **4**, 183 (1961).
2. F. A. Scott and L. K. Mudge, Submitted to *J. Nuclear Materials.*
3. W. Hampe, *Chem. Ztg.*, **12**, 106 (1888).
4. M. V. Smirnov and L. E. Ivanovsky, *J. Gen. Chem.* U.S.S.R., (Eng. Tr.), **27**, 329 (1957).
5. D. L. Hill, J. Perano, and R. A. Osteryoung, *This Journal*, **107**, 698 (1960).
6. R. S. Wilks, United Kingdom Atomic Energy Authority Report AERE-R-3833 (1961).
7. J. Koor, E. Weisskopf, and D. M. Gruen, *J. Inorg. Nuclear Chem.*, **13**, 310 (1960).
8. D. L. Maricle and D. N. Hume, *This Journal*, **107**, 354 (1960).
9. R. Littlewood, *Electrochim. Acta.*, **3**, 270 (1960).
10. P. Delahay, "New Instrumental Methods in Electrochemistry," Interscience Publishers Inc., New York (1954).
11. H. A. Laitinen and R. A. Osteryoung, *This Journal*, **102**, 598 (1955).
12. H. A. Laitinen and H. C. Gaur, *ibid.*, **104**, 730 (1957).
13. H. A. Laitinen and W. S. Ferguson, *Anal. Chem.*, **29**, 4 (1957).
14. J. K. Delimarskii, A. V. Gorodyskii, and V. V. Kuzmic, *Coll. Czech. Chem. Comm.*, **25**, 3056 (1960).
15. G. J. Hills and K. E. Johnson, *This Journal*, **108**, 1013 (1961).
16. J. E. B. Randles, *Discussions Faraday Soc.*, **1**, 11 (1947).
17. H. A. Laitinen and J. E. B. Randles, *Trans. Faraday Soc.*, **51**, 54 (1955).
18. M. D. Adams, Private communication.
19. J. L. Swanson, Private communication.

Technical Note

The Effect of Pressure on the Conductivity of Battery Electrolytes

R. A. Horne, W. J. Bannon, E. Sullivan, and G. R. Frysinger

Arthur D. Little, Inc., Acorn Park, Cambridge, Massachusetts

The electrical conductances of battery electrolytes have been measured at one atmosphere and of relatively dilute solutions of other electrolytes at elevated pressures (1), but inadequate information exists concerning the effect of pressure on the electrical conductance of battery electrolytes such as concentrated KOH and H_2SO_4 solutions.

The high-pressure equipment, conductivity bridge, thermostatic bath, construction of the conductivity cells, and measuring techniques have been described in greater detail in an earlier paper (2).

Concentrated aqueous potassium hydroxide is used as the electrolyte in a number of batteries including the Edison, nickel-cadmium, silver-zinc, silver-cadmium, silver-lead, and zinc-mercury cells. The effect of hydrostatic pressure on the specific electrical conductance of 3.56M KOH is shown in Fig. 1. The molar conductance of KOH at 18°C and 1 atm based on interpolation of our data is in agreement to within 1.5% with values obtained by interpolation of International Critical Tables data. In general, the specific conductance of a strong electrolyte first increases and then decreases with increasing pressure (3); the latter is due to the increasing viscosity of the solvent. In the case of KOH this decrease is much less pronounced than for salts, a fact illustrated by Fig. 1 and by the results of Hamann and Strauss (3). The conductance of OH^- is greater than that of similarly sized anions, and the process which gives rise to this anomalous mobility is apparently enhanced by pressure.

Protons (H_3O^+) exhibit an anomalous mobility considerably greater than that of OH^- ions. Hückel

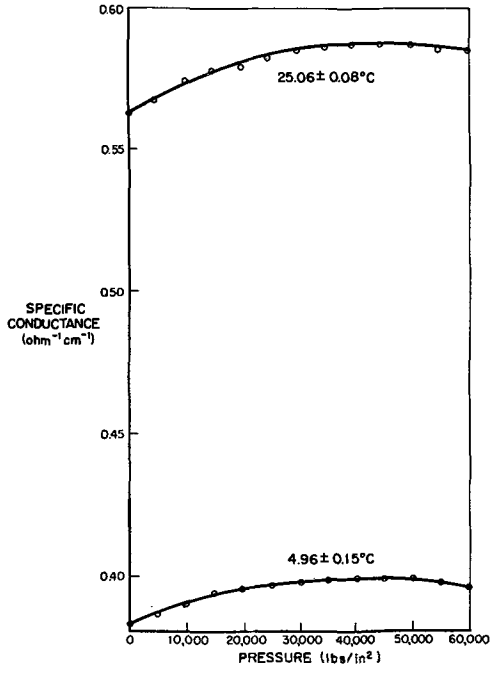

Fig. 1. Effect of pressure on the specific conductance of a 3.56M KOH solution.

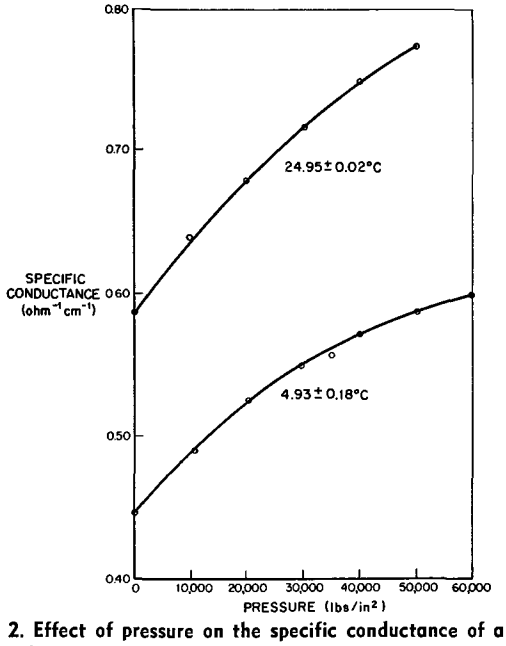

Fig. 2. Effect of pressure on the specific conductance of a 1.55M H_2SO_4 solution.

(4) attributed this phenomenon to proton jumps between adjacent water molecules (the Grotthuss mechanism). Hamann (5) has suggested that pressure might facilitate this process by overcoming the repulsive energy between oxygens. Another important contribution to the relatively large increase in the specific conductance of 1.55M H_2SO_4 solution with pressure (Fig. 2) is the increased ionization of bisulfate ion. The first ionization of H_2SO_4 is presumably complete

$$H_2SO_4 \rightleftharpoons H^+ + HSO_4^- \quad [1]$$

but the second ionization is weak (6)

$$HSO_4^- \rightleftharpoons H^+ + SO_4^=, \quad K = 0.095 \text{ at } 25°C \quad [2]$$

Pressure is known to increase the ionization of weak electrolytes and to facilitate the dissociation of ionic complexes into free ions (7).

The Mg/AgCl and Mg/Cu_2Cl_2 batteries are activated by the admission of sea water which serves as the electrolyte. If the electrolyte is not allowed to flow continuously through the battery or is recirculated, the $MgCl_2$ formed by the reaction is added to the electrolyte. The effect of pressure on the electrical conductivity of sea water has been studied by Hamon (8) and Horne and Frysinger (2).

Figure 3 shows the effect of pressure on the specific conductance of a 0.25M $MgCl_2$ solution at 25.06° ±0.05°C. The maximum in this curve is typical of strong electrolytes. Figure 4 shows the effect of pressure on the specific conductance of $MgCl_2$-NaCl solutions.

Acknowledgment

The authors wish to acknowledge the valuable assistance of Professor R. M. Fuoss of Yale University and Drs. J. H. B. George and M. L. Vidale. This work was partially supported by the Bureau of Ships, Department of the Navy (Contract NObsr-81564).

Manuscript received May 15, 1963; revised manuscript received Aug. 4, 1963. This paper was presented at the New York Meeting, Sept. 29- Oct. 3, 1963.

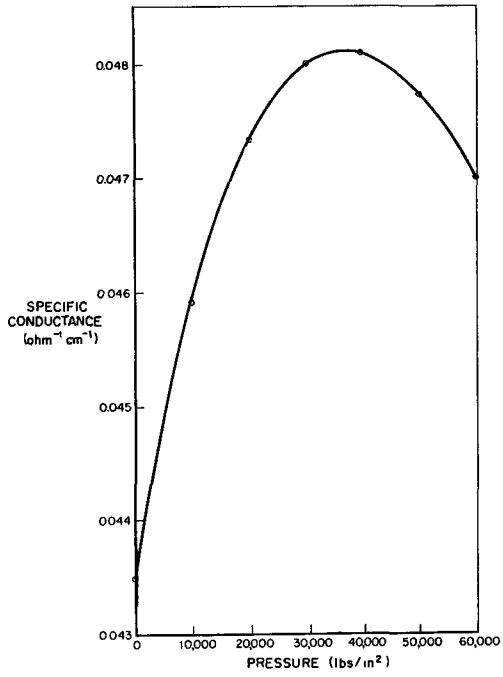

Fig. 3. Effect of pressure on the specific conductance of a 0.25M $MgCl_2$ solution at 25.06° ± 0.05°C.

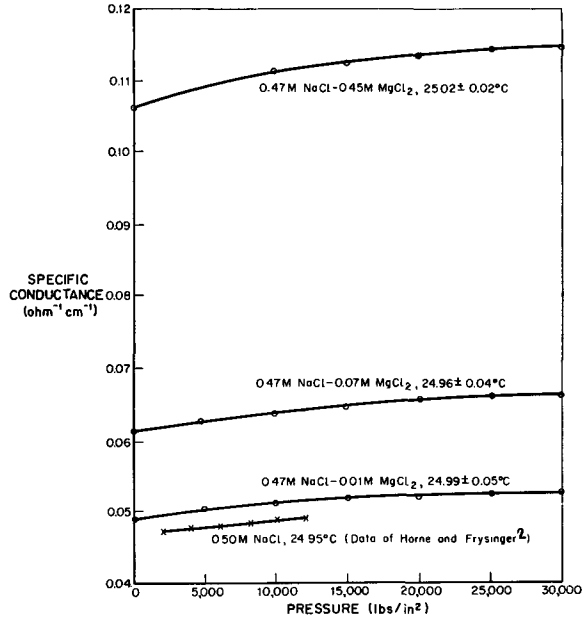

Fig. 4. Effect of pressure on the specific conductance of NaCl-$MgCl_2$ solutions.

Any discussion of this paper will appear in a Discussion Section to be published in the June 1964 JOURNAL.

REFERENCES

1. S. D. Hamann, "Physico-Chemical Effects of Pressure," Butterworths Scientific Pub., London (1957), Ch. 7 and the references cited therein. See also Table 8 in W. Strauss, *Fuel Soc. J. Univ. Sheffield*, **8**, 69 (1957).
2. R. A. Horne and G. R. Frysinger, *J. Geophy. Res.*, **68**, 1967 (1963).
3. See data of S. D. Hamann and W. Strauss, *Trans. Faraday Soc.*, **51**, 1684 (1955).
4. E. Hückel, *Z. Elektrochem.*, **34**, 546 (1928).
5. Ref. 1, pp. 124-126.
6. E. Eichler and S. Rabideau, *J. Am. Chem. Soc.*, **77**, 5501 (1955).
7. Ref. 1, pp. 129-131, 149-158.
8. B. V. Hamon, *J. Marine Res., (Sears Foundation)*, **16**, 83 (1958).

Discussion Section

This Discussion Section includes discussion of papers appearing in the JOURNAL of The Electrochemical Society, Vol. 109, No. 10 (October 1962) and Vol. 110, No. 3-6 (March-June 1963). Discussion not available for this issue will appear in the Discussion Section of the June 1964 JOURNAL.

Oxygen Transport and Reaction Rates at an Air-Depolarized Copper Cathode

H. C. Weber, H. P. Meissner, and D. A. Sama
(pp. 884-889, Vol. 109, No. 10)

P. Hersch[1]: I wish to draw attention to experiments with partly emerging oxygen cathodes[2] which I undertook in view of their bearing on corrosion, galvanic oxygen sensors, and fuel cells. The electrodes were of silver, nickel, and stainless steel; copper was not considered very suitable for the study of the three-phase boundary events because of the fourth oxide phase forming on the air-exposed portion. The experiments revealed the existence and prime importance of an oxygen-gathering zone on the metal surface adjacent to but not part of the meniscus. Under air this band has a width on the order of one millimeter only, therefore it is easy to overlook. It was puzzling to find, however, that under low partial pressures of oxygen the band widens considerably, until, at 10^{-5} atm O_2, portions of the dry, or seemingly dry, surface on the emerging metal several centimeters away from the meniscus still contribute to the process. It was anticipated that the dissolution of hydrogen at a partly emerging platinum anode would similarly benefit from a hydrogen-gathering band. This was recently confirmed by F. G. Will for Pt/H_2SO_4 under 1 atm. H_2.[3]

The efficiency of the oxygen-gathering zone depends on the nature and concentration of the electrolyte, and, more important, on the nature and history of the emerging metal. Therefore, "gas diffusion" electrodes cannot as a rule be limited by a transport process, least of all in fuel cells which are susceptible to catalytic promoters. The active band renders the supply of oxygen molecules so abundant (most probably through surface diffusion), that ionization becomes limiting, even under very low partial pressures of oxygen. Further, diffusion through the bulk of the meniscus wedge on a wettable electrode, and the shape of the meniscus, can only be of secondary importance, since the dry zone effect is conspicuous in air-depolarized porous hydrophobic carbon as it is in porous hydrophilic silver—both cease to work when swamped.

Further insight into the mechanism of partly emerging gas electrodes might come from polarization studies under atmospheres containing the electromotive gas in high dilution, when the active zone becomes macroscopic.

[1] Beckman Instruments, Inc., Scientific & Process Instruments Div., 2500 Harbor Blvd., Fullerton, Calif.

[2] *Nature*, 180, 1407 (1957); *Corrosion Technol.*, 6, 293 (1959).

[3] *This Journal*, 110, 145 (1963).

H. C. Weber, H. P. Meissner, and D. A. Sama: Dr. Hersch[2] discusses experiments which are pertinent to our investigation, and we regret that this work did not come to our attention before publication of our paper. There appears to be agreement between us that oxygen reduction occurs on a narrow zone of active cathode area lying close to the meniscus, but disagreement as to the route or mechanism whereby oxygen reaches this zone. At least three routes are possible:

1. Adsorption of oxygen on the electrode surface projecting into gas phase, followed by migration of the adsorbed oxygen along the surface to the active area.
2. Reaction at the three phase boundary line, restricted to those oxygen molecules reaching this line.
3. Solution of oxygen in the electrolyte at the meniscus, followed by diffusion through the liquid to the active electrode surface.

At an oxygen partial pressure of 0.2 atm, our data and those of Dr. Hersch are similar, but interpretations are different. We concluded that route 3 was predominant, because we obtained equal currents on electrodes of three different metals when these were submerged to an equal degree, and because the current generated did not increase significantly after a three phase boundary line developed as these electrodes were caused to project further from solution. The extent to which an electrode projected could be observed, at least in the case of the copper, by the visible oxide film which covered the exposed surface down to the three-phase boundary line. We further concluded that the active zone was a narrow band lying submerged just below the three phase boundary line, covered by a thin film of the meniscus liquid, and that the maximum current was limited by the rate of oxygen transport through this film. Surface diffusion of oxygen by route 1 and reaction at the three phase boundary line by route 2 might also have been occurring simultaneously, but appeared to make at most only a small contribution to the total current generated.

Dr. Hersch found that at oxygen partial pressures of 10^{-5} atm, the galvanic current varied with the height to which a partially submerged electrode projected out of solution, up to 3 cm or more, and so concluded that oxygen travelled by route 1 under these conditions. We have not explored such extremely low partial pressures, as these do not occur in typical fuel cell electrodes. However, the rate controlling step in a mass transfer process is sometimes pressure dependent, so that route 1 may be predominant at low partial pressures and route 3 at higher partial pressures.

The fact that a "swamped" porous gas diffusion type electrode ceases to generate current when operated in the orthodox fashion with stationary electrolyte in its pores is of course to be expected if route 3 predominates. That is, the diffusional paths through this stagnant electrolyte are now so long that the quantity of oxygen transferred becomes negligible. However, such a swamped electrode can be made to generate current immediately by causing electrolyte containing dissolved oxygen to flow through its pores[4]. Both porous carbon and porous metal electrodes have been made to generate relatively large currents in this way, even though these electrodes contained no unsubmerged area. Mass transfer problems are minimized by such flow operation, since the oxygen is carried into the pores by bulk flow of the electrolyte rather than the much slower process of diffusion, and has a maximum diffusional distance to negotiate equal only to a pore radius.

The recent work by Will[5] with partially submerged platinum electrodes and hydrogen at one atmosphere pressure also shows that a small active zone is responsible for most of the reaction. Dr. Will finds that this active zone is covered by electrolyte, and that diffusion of molecular hydrogen through this electrolyte film is rate determining. The contribution of surface diffusion of adsorbed hydrogen atoms to the current is stated to be negligible. Though Will's work was done with hydrogen, it is interesting to note the correspondence with our findings on oxygen.

On the Defect Structure of ZrO_2 and HfO_2

P. Kofstad and D. J. Ruzicka (pp. 181-184, Vol. 110, No. 3)

P. J. Harrop and J. N. Wanklyn[6]: The interpretation of the electrical properties of oxide compacts in terms of intrinsic point defect mechanisms, as offered by Kofstad and Ruzicka, seems unjustified. Previous work on compacts has yielded conductivities differing by five orders of magnitude and more[7]. The low densities and sintering temperatures reported in the present work must surely enhance the space charge and surface effects which mask the bulk conductivity in polycrystals[8]. Moreover, the "steady" d-c current would measure the magnitude of surface polarization rather than the bulk conductivity. Lidiard[9] has pointed out that this effect can usually be avoided only by the employment of a-c frequencies above 5000 c/s, for a single crystal ionic conductor.

Examination of single crystal Al_2O_3[10] and MgO[11] (which is an ionic conductor under certain conditions[12]) has shown that a mere 100 ppm of impurity can control the electrical properties up to very high temperatures indeed. Active impurities must be kept down to at least this level if intrinsic properties are to be examined and this seems unlikely in the present case. Strain must also be fully annealed[10].

In view of the above, we feel that the explanation of the "complex pressure dependence" obtained must be found in space charge and grain boundary conduction effects that should vary considerably with grain size, sintering temperature, and purity.

The proffered theory also seems unsatisfactory in that (a) it is difficult to imagine an oxygen-oxygen vacancy pair moving any distance in the solid without collapsing. Its electrical neutrality should, in any case, exempt it from being a conductivity component, although it might contribute to diffusion. (b) We are not aware of any evidence for the mobility of a large anion vacancy exceeding that of an electron in such a solid, and we would expect the reverse and (c) surely there is no room for an oxygen interstitial to fit into the monoclinic ZrO_2 lattice[13]?

P. Kofstad and D. J. Ruzicka: We are aware of the fact that measurements on sintered specimens may involve the danger of space charge and surface effects, and it would be most advantageous to employ single crystals in such studies. However, single crystals of ZrO_2 and HfO_2 were not available. In this study—and as we failed to mention in the paper—the measurements of electrical resistance were made as rapidly as possible and also by reversing the polarity.

The authors agree that the question of impurities is extremely important, and there are few, if any, studies on defect structures in oxides with low defect concentrations for which the question of effect and importance of impurities may not be raised. In our opinion the effect of impurities on defect structures and associated properties is a matter of conjecture, and without specifically studying such effects it is difficult to give any discussion of this point.

In the above study an unusual oxygen pressure dependence of the electrical conductance was observed. To explain the pressure dependence it was suggested that ZrO_2 and HfO_2 has an anti-Frenkel defect structure (also proposed for stoichiometric UO_2[14,15]) and that the electrical conductivity reflects a migration of paired or associated defects. This would further imply that the associated defects have a net electrical charge, *i.e.*, that the defects have different electrical charges.

As stated in the paper the interpretation is at this point necessarily qualitative in nature, and we are well aware that many questions may be raised. As to the question of interstitial oxygen the hard-sphere model may not be an accurate method for

[4] H. P. Meissner and A. R. Reti in "Fuel Cells," CEP Technical Manual, 40 (1963).

[5] *This Journal*, 110, 145 (1963).

[6] Atomic Energy Research Establishment, Harwell, Didcot, England.

[7] *See*, for example, J. Pappis and W. D. Kingery, *J. Am. Ceram. Soc.*, p. 459 (1961).

[8] "Semiconductors," N. B. Hannay Ed., p. 542, Reinhold Publishing Corp., New York (1959).

[9] A. B. Lidiard, "Handbuch der Physik," Flugge Ed., "Electrical Conductivity II," p. 312.

[10] P. J. Harrop and R. H. Creamer, *Brit. J. Appl. Phys.* (In press).

[11] S. P. Mitoff, *J. Chem. Physics.*, 31, 1261 (1959).

[12] S. P. Mitoff, *J. Chem. Physics.*, 36, 1383 (1962).

[13] Tennyson Smith, USAEC Report NAA-SR-6267 (1962).

[14] J. Belle and A. B. Auskern, "Kinetics of High-Temperature Processes," p. 44, Technology Press of MIT and J. Wiley & Sons (1959).

[15] B. T. M. Willis, *Proc. Royal Soc.*, 274A, 134 (1963).

evaluating geometrical factors involved, and the size of the interstitial atom is furthermore dependent on its degree of ionization. Presence of interstitial oxygen has, for instance, been suggested to explain results of studies of diffusion of oxygen in NiO[16] and Cu_2O[17]. Excess oxygen in UO_{2+x} most probably involves oxygen in interstitial positions[14,18]. As to ionic conductivity it may be noted that calcia-stabilized zirconia, which is concluded to contain oxygen vacancies, is an ionic conductor[19]. Furthermore, studies of potential measurements on growing ZrO_2-films suggest that the oxygen ion transport number increases from 0.05 to 0.5 from 200° to 750°C[20].

The above paper in no way pretends to be the final word on the defect structure of ZrO_2. On the contrary it should be considered a discussion paper itself, and, as stated in the paper, further studies are necessary to confirm or disprove the proposed interpretation.

In any case, we do hope that the paper and this discussion may stimulate a much greater emphasis on studies of defect structures and transport processes in oxides, the effect of impurities, *etc.*, and that a better understanding may be obtained of such properties of which we today have but an oversimplified and possibly naive picture. We find it surprising that little work has been done on ZrO_2 and that the many interpretations of the oxidation and corrosion mechanism of zirconium and its alloys are based on insufficient knowledge of the defect structure of and transport properties in ZrO_2.

Flaws in Anodic Ta_2O_5 Films

D. A. Vermilyea (pp. 250-262, Vol. 110, No. 4)

K. Huber[21]: In his paper Vermilyea has correctly referred to the importance of oxide film flaws in determining the electrical behavior of formed tantalum anodes. Our own efforts confirm a large part of his results. Although we have many electron micrographs comparable to Vermilyea's, we will content ourselves with only one comparison (Fig. 1 *cf.* Fig. 10 in Vermilyea's paper). [For explanation of figures appearing in this discussion, *see* the table on p. 1289.]

Besides the replica method, another investigation procedure, which goes somewhat farther in its application, has been applied. The method is outlined in the following remarks.

Starting material was electron beam melted tantalum rolled to 0.2 mm under intermediate annealing and finally annealed in vacuo at 10^{-4}—10^{-5} Torr. The analytically determined carbon content was:

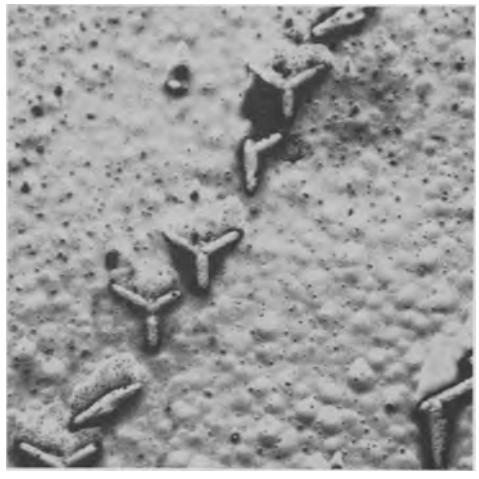

Fig. 1

Final annealing temp. °C	1100	1300	1800	2000
Carbon content ppm	165	140	105	99

The formed anodes were dissolved anodically in a suitable electrolyte. NH_4Br/CH_3OH is an especially useful solution, which has been recommended by Jenny and Ruscetta[22] for etching of tantalum. Tantalum goes into solution as a complex cation. The complex is believed to be of the form $[Ta(OCH_3)_mBr_n]^{p+}$ with $m + n + p = 5$. Other suitable solutions are HCl/CH_3OH, $N(C_2H_5)_4Br/POCl_3$, *etc.*

A black powdery substance and an oxide film are the two kinds of residue left after anodic dissolution.

The black substance can be separated through flotation into two fractions. The coarser fraction consists of tantalum hydrides, which also occur, when the starting material contains only a few ppm hydrogen. The hydrides therefore are formed during the anodic dissolution. The metal is activated as the covering oxide film is loosened from the metal surface. Then besides the anodic dissolution, a chemical reaction of the following type occurs:

$$6\ Ta + 5\ H^+ \rightarrow 5\ TaH + Ta^{5+}$$

The fine particle fraction was identified as Ta_2C through x-ray and electron diffraction as well as through chemical analysis. Its form varies with the annealing temperature. Imperfect hexagonal platelets (Fig. 2) are found in the low-temperature (1100°-1300°) annealed metal and characteristic triplets (Fig. 3) in the high-temperature (1800°-2000°) annealed metal. The triplets consist of three individual triangular leaflets of unequal sides that are joined together along a common side. Their form resembles that of a three winged rocket.

Other foreign phases were not found in the black residue of the tantalum sheet. From sintered pellets, however, other foreign phases were able to be isolated by analogous methods.

[16] M. O'Keefee and W. J. Moore, *J. Phys. Chem.*, 65, 1438 (1961).

[17] W. J. Moore, Y. Ebisuzaki, and J. A. Sluss, *J. Phys. Chem.*, 62, 1438 (1958).

[18] A. Aukrust, T. Forland, and K. Hagemark, "Equilibrium Measurements and Interpretation of Non-Stoichiometry in UO_{2+x}," IAEA Symposium on the Thermodynamics of Nuclear Materials, Vienna, May 1962.

[19] W. D. Kingery, J. Pappis, M. E. Doty, and D. C. Hill, *J. Am. Ceram. Soc.*, 42, 393 (1959).

[20] L. D. Kirkbride and D. E. Thomas, "Ionic Transport in Zirconium Dioxide," Westinghouse Electric Corp., PB No. WADP-T-308.

[21] Universitat Bern, Institut fur Anorganische, Analytische und Physikalische Chemie, Freiestrasse 3, Bern, den, Germany.

[22] A. L. Jenny and R. A. Ruscetta, *This Journal*, 108, 442 (1961).

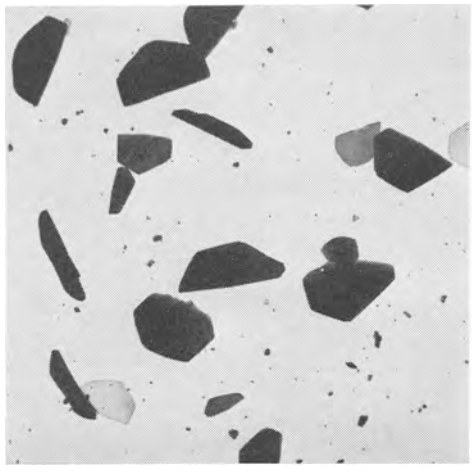

Fig. 2

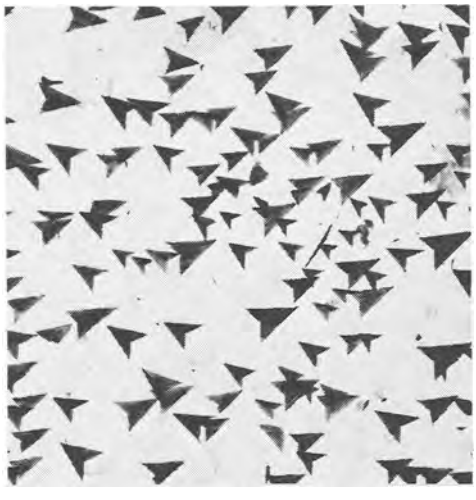

Fig. 3

The results with tantalum sheet are therefore not determined by the method of isolation. The oxide film remains in the ideal case as a bag of the shape of the dissolved tantalum sheet. When the film is very thin, it breaks easily into flakes which, however, are large enough for EM investigation. Anodic formed films of any thickness can be isolated. Sometimes it was even possible to prepare air oxide films. For EM investigation it was found that formation voltages of 10 to 30v were suitable with 20v being the optimum. Thicker films are not easily penetrated by the electron beam; thinner films are mechanically less stable. On thicker films a carbon replica of the metal/oxide film boundary can be made so that these boundaries can also be investigated.

The EM investigation of isolated oxide films gives, as in other analogous cases, two kinds of information: (a) information over the metal, (b) information over the oxide film.

[*Ad (a)*] The anodic formed oxide film is especially suitable, as also with aluminum, for representation of the etch structure (Fig. 4). If the formation process is carried out, so that the foreign phases are not attacked, they stick in the oxide film. The investigation of the oxide film therefore gives information as to the amount and distribution of the foreign phases in the metal as well as to the size,

Fig. 4

shape, and orientation of the single particles and particle aggregates. Selected area diffraction and morphological comparison with the residue of the anodic dissolution served as identification methods.

In the oxide films of the investigated tantalum sheets only Ta_2C or traces of it (Fig. 5 and 6) were found. The Ta_2C triplets appear with different cross sections according to their orientation with respect to the metal surface (*see* also Fig. 8). Without any doubt they are identical to those particles shown in Vermilyea's Fig. 22 and also those particles which caused the three pointed stars in his Fig. 10.

The investigation of oxide films moreover explains the influence of etching before the anodic formation. Planimetry of oxide films of slightly or not etched low-temperature annealed sheets showed

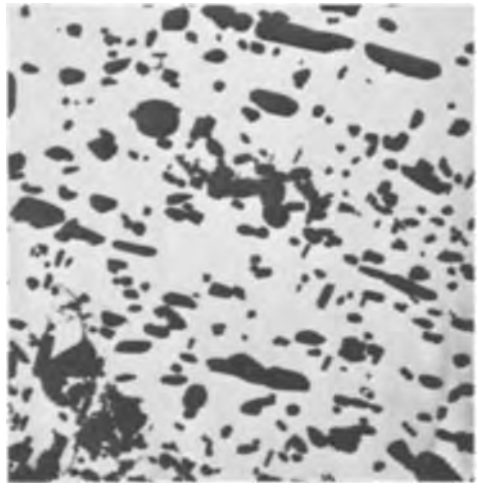

Fig. 5

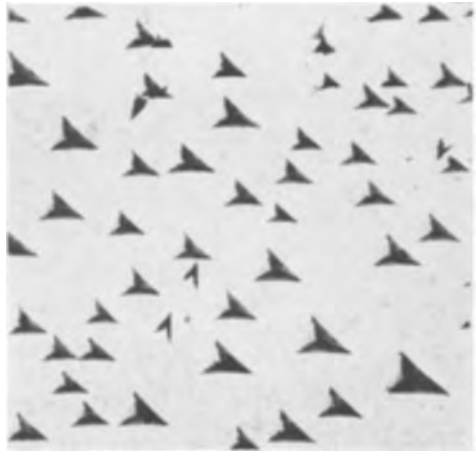

Fig. 6

that the carbides made up 50% and more of the metal surface. When 10 to 30μ were etched away chemically with $H_2SO_4/HNO_3/HF$ or anodically in H_2SO_4/HF or NH_4Br/CH_3OH, the carbide content sank to a few per cent, sometimes even below 1%. At the same time the leakage current decreased by two to three powers of ten.

The investigation of the oxide films also gave some information about the solubility of carbon in tantalum at high-temperature. In the individual crystallites of high-temperature annealed metal the Ta_2C triplets show parallel orientation and are often found concentrated along the crystallite boundaries. From this fact it can be concluded that the triplets were formed only when the recrystallization of the metal was completed. It may therefore be supposed that carbon at 1800°-2000°C was atomically dissolved and during cooling formed Ta_2C.

[*Ad (b)*] Seen apart from the inclusions, the oxide film within the resolving power of the EM (Siemens Elmiskop I) is homogeneous and free of pores. Exceptions are found only under extreme conditions. For example, formation in 30% NaOH (Fig. 7) which obviously has a good dissolving ability for tantalic acid, gives a porous structure like that of the well-known Eloxal films and similar structures formed from Zn/NaOH and Sn/NaOH[23] systems.

If the formation voltage does not exceed 30-50v the oxide films appear amorphous when subjected to x-ray or electron diffraction examination. The films crystallize easily, however, under a heavy electron beam in the EM (Fig. 8) whereby the same pentoxide modification appears as described by Harvey and Wilman[24]. Often it is observed how crystallization starts from foreign particles in the oxide layer. The easy crystallization in the electron beam should be taken into account in diffraction experiments[25].

As seen with the EM, the thickness of the oxide film is constant up to the edge of the inclusions. A lessening thickness towards the flaws, as postulated by Vermilyea, was not observed on the isolated films. In any case, it should be noted that with the EM only films with low formation voltage can be investigated.

[23] K. Huber, *Z. Elektrochem.*, **62**, 675 (1958).
[24] J. Harvey and H. Wilman, *Acta Cryst.*, **14**, 1278 (1961).
[25] H. Mohler and R. G. Hirst, *This Journal*, **108**, 347 (1961).

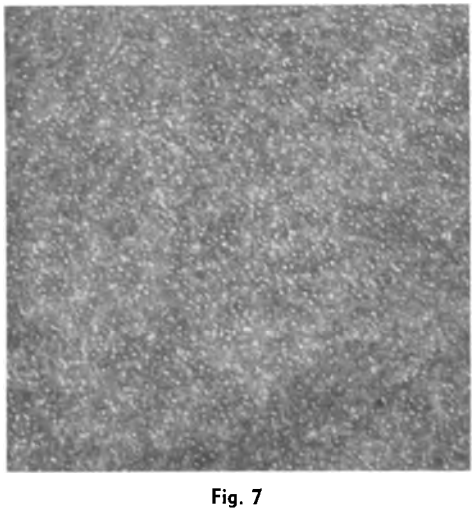

Fig. 7

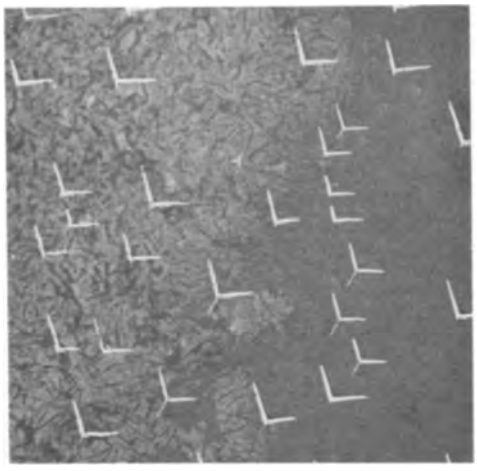

Fig. 8

Of special interest is the behavior of foreign phases during formation, in our case Ta_2C. In diluted aqueous electrolytes, as are most often applied for formation purposes, no noticeable attack on the Ta_2C particles is observed. Only when the potentiostatic time interval lasts for many hours dissolving will begin. Concentrated acids work more quickly as dissolving medium and there appears to exist for every acid an optimum concentration that is rather high. This finding calls to mind a patent[26] in which 80% acetic acid is recommended for supplementary formation. In place of the carbide particles, a sponge-like network remains, whose material is amorphous as determined by selected area diffraction (Fig. 9).

In conclusion it should be mentioned that the described method of investigation can be equally well applied on niobium. Figure 10 shows a typical etch

[26] Western Electric Co., Inc., Ger. Pat. 1108811 Cl.21 g.

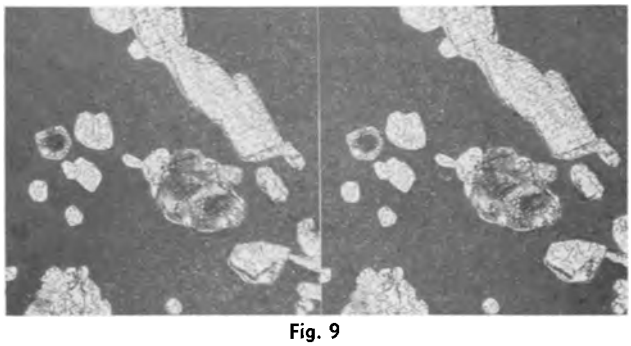

Fig. 9

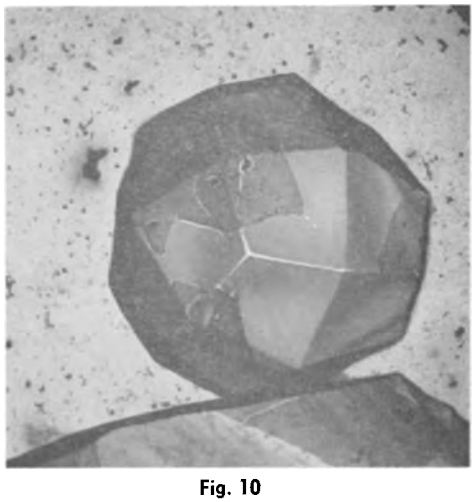

Fig. 10

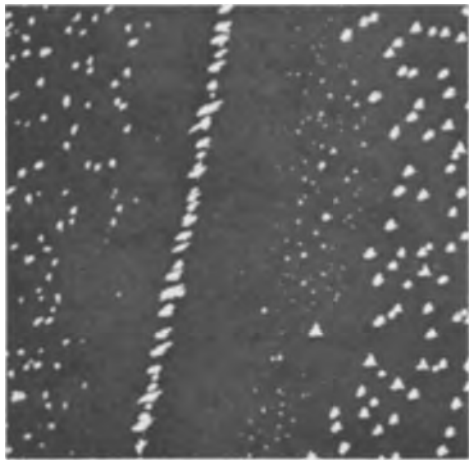

Fig. 11

structure, Fig. 11 an oxide film from niobium, which contained Nb_2C particles.

The above comments to Vermilyea's paper could include only a small part of our results. A complete publication also including the electrical measurements is in preparation.

Our investigations, on which V. Kohl and P. R. Radvila participated, were carried out under grants from CIBA A.G., Basel. We thank Dr. F. A. Schaufelberger for permission to publish and Dr. W. Scheller and Dr. G. J. Korinek for stimulating discussions.

D. A. Vermilyea: I am much indebted to Professor Huber for his stimulating discussion, which has clarified a number of the speculations in my paper. His results that as much as 50% of the surface may consist of carbides after annealing at low temperatures is especially interesting. This fact makes it appear possible that some of the results which I attributed to oxygen may have been caused by precipitation of carbides at the surface. Further studies are needed to clarify this question.

Stresses in Anodic Films

D. A. Vermilyea (pp. 345-346, Vol. 110, No. 4)

D. H. Bradhurst and J. S. Llewelyn Leach[27]: The results obtained by Vermilyea for the stresses in anodic oxide films on aluminum agree qualitatively with the results of similar work at Imperial College[28,29]. In these experiments some evidence has been found showing that the stresses in the anodic oxide films are dependent on the rate of oxidation. This has been interpreted in terms which add fur-

[27] Imperial College of Science and Technology, Royal School of Mines, Prince Consort Rd., South Kensington, London, S. W. 7, England.

[28] D. H. Bradhurst and J. S. Ll. Leach, British Ceramic Soc. Conf. on the Properties of Nonmetallic Crystals and Polycrystals, Hastings, October 16-17, 1962.

[29] D. H. Bradhurst, Reported in *Chem. and Ind. (London)* 473 (1962).

Explanation of figures

Fig.	Object	Enlargement	Metal Heat temp., °C Etch soln.	Anodic electrolyte Anodic voltage Anodic time*
1	Carbon replica	12500	Ta 1800 40% HF, 2½ min	0.01% H_3PO_4 35 V 1 h
2	Isolated Ta_2C-particles	3000	Ta 1100 —	—
3	Isolated Ta_2C-particles	10000	Ta 2000 —	—
4	Oxide layer stereo picture	5000**	Ta 1800 $H_2SO_4/HNO_3/HF$	0.01% H_3PO_4 20 V 1 h
5	Oxide layer with Ta_2C-particles	5000	Ta 1300 —	99% H_3PO_4 20 V 1 h
6	Oxide layer with Ta_2C-particles	10000	Ta 2000 —	40% H_3PO_4 20 V 1 h
7	Oxide layer with pores	40000	Ta 1300 —	30% NaOH 20 V 1 h
8	Oxide layer partially crystallized	10000	Ta 2000 —	40% H_3PO_4 20 V 1 h
9	Oxide layer Ta_2C dissolved stereo picture	20000**	Ta 1300 —	80% Propionic acid 20 V 3 h
10	Oxide layer etch pit	3000	Nb 1900 NH_4Br/CH_3OH anodically	0.01% H_3PO_4 30 V 1 h
11	Oxide layer dissolved Nb_2C particles	10000	Nb 2200 —	0.01% H_3PO_4 30 V 1 h

* Formation always at room temperature.
** Magnification before reduction for publication.

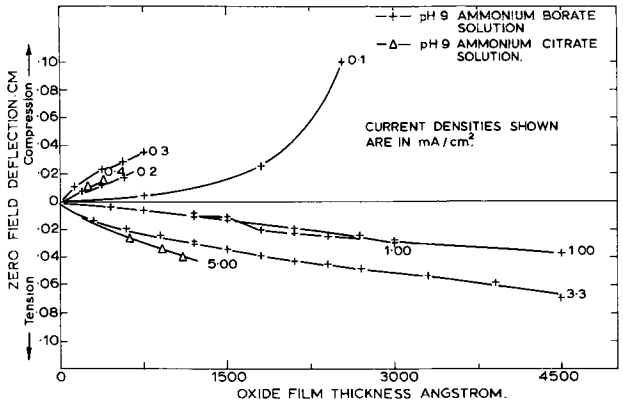

Fig. 1. Deflection of aluminum foil anodized on one side at different current densities.

ther support to the conclusion that "the picture of a uniform, rigid, unchanging oxide film through which only cations move is untenable."

Barrier type films were formed on one side of thin aluminum strips by anodizing at constant current densities in solutions of ammonium borate and of ammonium citrate at pH 9. The current densities used varied in the range 0.1-10 ma/cm^2 and the stresses in the films were measured in terms of the deflection of the free end of the strip.

As can be seen from Fig. 1, at low current densities (0.1-0.5 ma/cm^2) the films formed are in compression whereas at higher current densities (1-10 ma/cm^2) tensile stresses are observed.

Davies[30] has shown by diffusion experiments that, at low current density, anodic film growth on aluminum occurs predominantly by oxygen migration while at higher current density a significant portion of the growth is due to cation movement[31]. Under these circumstances one might expect to find a compressive stress in the oxide at low current densities arising from the growth, at the oxide-metal interface, of an oxide with a volume ratio greater than unity. At higher current densities the increased mobility of the cations might permit the oxide to deform and so relieve the stress or alternatively to grow in a stress-free condition.

Stress-free growth has been postulated for the case of magnetite on iron in water by Potter and Mann[32] where the counter currents of the two ionic species were shown to be precisely those required to produce an unstressed oxide. These observations clearly lend support to a recent suggestion by Evans[33] that the counter current principle deserves to be applied to oxide films other than those formed on iron in boilers. However, it seems likely that even in a given environment the mechanism of oxidation can change with changes in rate.

This work forms part of a study sponsored by the Central Electricity Generating Board whose support is gratefully acknowledged.

[30] J. A. Davies, J. P. S. Pringle, R. L. Graham, and F. Brown, *This Journal*, 109, 999 (1962).

[31] J. P. S. Pringle and J. A. Davies, Contribution to The Electrochemical Society Meeting, Pittsburgh, April (1963).

[32] E. C. Potter and G. M. W. Mann, 1st Int. Cong. Metallic Corrosion, Butterworths, London, 417 (1961).

[33] U. R. Evans, Private Communication, April 1963.

U. R. Evans[34]: Dr. Vermilyea's interesting results seem consistent with those of Bradhurst[35], who found that the stresses in films formed anodically on aluminum were tensile at first and changed to compressive as the film thickened. His data for other metals is welcome. It would aid interpretation to use a method such as that of Hoar and Arrowsmith[36], who measured the stress needed to prevent deflection; if bending is allowed to occur, the stress is different in various layers, producing a complicated situation.

Dr. Vermilyea is right in rejecting the idea of a mechanism based solely on cations moving outwards. Evidence for oxygen moving inwards has been available for 12 years perhaps much longer. In the anodizing of aluminum containing silicon particles as a separate phase, these act as markers, and are found embedded in the oxide; a picture, due to Elssner and reproduced by Machu[37] in 1952, shows the embedded particles.

Counter-current balance as a condition of film-stability, a concept developed by Potter and Mann[38] for boiler films, is probably applicable to other cases. If a film grows solely by oxygen moving into the metal, the film is likely (except on ultra-light metals) to carry compressive stresses, which, while the film is very thin, may aid protective properties, tending to close up gaps, when a certain thickness is passed, failure may be expected[39]. Familiar examples are the "breakaways" on zirconium alloys which trouble Atomic Energy workers, and the sudden fires which sometimes occur without warning in titanium scrap-yards. In contrast, if the films grow solely by cations moving outwards, the vacancies left behind may segregate to produce sizeable voids at the base of the film; several clear demonstrations have been provided by studies of high-temperature oxidation, notably in Fontana's laboratory[40], but anodization at room temperature can produce these gaps between film and basis where there is no penetration of oxygen into the metal. Barnartt[41], subjecting gold to anodic treatment in M/10 sulphuric acid, produced films which developed blisters and then flaked off.

Thus either movement by itself is fatal to lasting protection. By combining the two in the right amounts, both types of collapse should be avoided. Potter and Mann[38] showed that in the case of magnetite films formed in alkaline water, both movements occur in almost equal amount, so that the stresses left in the film are small, and lasting protection is achieved, provided the films are not ill-

[34] Cambridge University, 19 Manor Court, Grange Rd., Cambridge, England.

[35] D. H. Bradhurst, *Chem. and Ind. (London)*, 473 (1963). Fuller results to appear in *Trans. British Ceramic Soc.*

[36] T. P. Hoar and D. J. Arrowsmith, *Trans. Inst. Metal Finishing*, 34, 354 (1957); 36, 1 (1959).

[37] W. Machu, "Nichtmetallische anorganische Uberzuge," p. 19, Abb. 15, Springer, (1952).

[38] E. C. Potter and G. M. W. Mann, p. 417, "1st International Congress Met. Corrosion 1961," Butterworth's (1962); also, p. 103, 2nd International Congress 1963," Extended Abstract.

[39] U. R. Evans, *Trans. Electrochem. Soc.*, 91, 547 (1947).

[40] B. W. Dunnington, F. H. Beck, and M. G. Fontana, *Corrosion*, 8, 2 (1952).

[41] S. Barnartt, *This Journal*, 106, 722 (1959).

treated too much. This is perhaps the reason why Steam Generating Stations—as we know them— are possible!

It may tentatively be suggested that on anodizing aluminum, the barrier film is produced by inward movement, and the porous film—where it occurs at all—by outward movement. The fact that only a few baths (out of all the solutions conceivable) produce films with lasting protective properties, may be that these are the baths which provide the two movements in the right ratios. Probably the best protection may be expected when slight compressional stress is left in the film—such as the film-substance can withstand. Bradhurst[35] showed that the films are more elastic than one would expect from the properties of massive alumina. The outward movement which keeps the compressive stress within a safe range may result in aluminum ions moving into the liquid or in the formation of porous oxide, or both. The first is the "expected reaction" in the sense that it leads directly to the state of lowest free energy; the second may predominate under conditions where activation energy is determinative. The matter has been discussed elsewhere[42] and, for the present argument, it does not matter which type of outward movement prevails.

If the vacancies left in the metal where cations have moved into the film fail to segregate, the effective density of the metal becomes abnormally low, and if later inward movement of oxygen occurs (as anions or otherwise), the oxide might well be in tension. Possibly the tensile stresses observed experimentally might thus be explained, but the suggestion is speculative.

Vacuum Evaporation of Cadmium Telluride

R. Glang, J. G. Kren, and W. J. Patrick
(pp. 407-412, Vol. 110, No. 5)

C. A. Escoffery[43]: In this paper, the authors report that evaporated CdTe films have a high resistivity even if impurities are added to the source material. This is in agreement with our own experience with CdTe films prepared by conventional vacuum evaporation.

The authors, however, conclude that "the high resistivities seriously limit the usefulness of CdTe as a semiconductor material for thin film device applications." While it is true that a high resistivity is undesirable in many applications, there are instances where this property is of value.

On the other hand, it is possible to obtain low resistance CdTe films by vacuum evaporation. Elliot *et al.*,[44,45] have adapted a hot wall bell jar technique to deposit conductive CdTe films on substrates heated to 600°C. Doping is accomplished by coevaporation of suitable impurities such as indium or copper, and n- and p-type films with resistivities less than 10 ohm-cm have been reproducibly obtained. These workers have also investigated the adverse effect of oxygen impurities, confirming earlier work by the Russians[46] and adding new information.

Also, Cusano[47] has reported on conductive CdTe:I films made by a vapor reaction technique utilizing Cd, CdI_2 and Te, to produce 6% efficient CdTe photovoltaic cells.

Finally, studies in progress by us on new ways to prepare II-VI films, indicate that low resistance as well as high resistance films may be controllably obtained.

Growth Twins in the F.C.C. Metals

J. W. Faust, Jr. and H. F. John (pp. 463-464, Vol. 110, No. 5)

G. Poli and L. P. Bicelli[48]: We would like to make a few comments on this very interesting paper. We do not share the opinion of Faust and John that there are "only a few examples of the presence of growth twins" and that, as one might think from a superficial examination of this paper, the only growth twins observed during electrodeposition were on silver.

In fact there are numerous references on twinning occurring during the growth, particularly during electrodeposition, both on a polycrystalline and on a single crystal substrate surface.

We have done research work on the structure of lead[49], copper[50], and cadmium[51] electrodeposited on a single crystal surface of the same nature oriented following determined crystallographic planes. It was shown that between the initial growth layer oriented parallel to the substrate lattice and the randomly oriented polycrystalline layer which develops with increasing deposit thickness at higher current densities, there is an intermediate twinned layer.

The observed twinning planes and directions were the same as those known up to now for deformation twins not only for lead and copper electrodes as found by other authors, but also for cadmium ones as it was shown by us for the first time.

Parallel growth is observed on (100) Pb, (110) Pb, (110) Cu, and on $(11\bar{2}0)$ Cd electrodes in all experimental conditions, while twinning occurs on (111) Pb, (100) Cu, (111) Cu, (0001) Cd, and on $(10\bar{1}0)$ Cd electrodes for certain current densities and thicknesses of the deposits.

At some higher current densities and thicknesses, we found a double twinning of already twinned

[43] U. R. Evans, p. 1, "1st International Congress Met. Corrosion 1961," Butterworth's (1962).

[43] Materials Technology Dept., Hughes Aircraft Co., Culver City, Calif.

[44] J. F. Elliot, R. E. Halsted, and H. D. Coghill, *Proc. 15th Annual Power Sources Conf.*, May 9-11, 1961, pp. 109-110; PSC Publ. Comm., P.O. Box 891, Red Bank, N. J.

[45] J. F. Elliot, Ed., "Unique Photovoltaic Cells," ASD Tech. Rep. 61-242, August 1961, Wright Patterson Air Force Base, Ohio.

[46] Yu. A. Vodakov *et al.*, "Investigation of Surface Layers in Cadmium Telluride Crystals," *Soviet Phys.-Solid State (English Transl.)*, 2, 49 (1960).

[47] D. A. Cusano, Ed., "Polycrystalline Thin Film CdTe Solar Cells," *IRE Trans. of PGED*, p. 504 (1962).

[48] Dept. of Physical Chemistry, Electrochemistry and Metallurgy, Politecnico of Milan, Milan, Italy.

[49] G. Poli and L. Peraldo Bicelli, *La Metallurgia Italiana*, 51, 399 (1959).

[50] G. Poli and L. Peraldo Bicelli, *La Metallurgia Italiana*, 51, 548 (1959).

[51] G. Poli and L. Peraldo Bicelli, *La Metallurgia Italiana*, 54, 497 (1962).

crystals, on (100) Cu electrodes, which gave place to a random polycrystalline region.

J. W. Faust, Jr., and H. F. John: We wish to thank Poli and Bicelli for their interesting discussion, especially for the references to their papers of which we were unaware. We feel that their comment concerning our statement on the literature of growth twins is purely a matter of what one considers the meaning of "only a few." Certainly in growth from processes other than electrodeposition there is indeed only a very few mentioned in the literature; in fact so few that metallurgical texts are careful to point it out.

In relation to the electrodeposition, there is more mention of twinning although in many instances it is not specifically referred to as growth twinning and could, in some cases, conceivably be deformation twinning or in the case of heat treatment following electrodeposition, annealing twinning. One must be careful in distinguishing between the different types of twinning. We did not, however, mean to imply that silver was the only material reported to have growth twins during electrodeposition. Certainly to the best of our knowledge, it was the first time growth twins were shown in electrodeposited dendrites.

The main purpose of this note was to show that f.c.c. metals could grow by the twin plane re-entrant edge mechanism as reported for semiconductors.

The Oxidation of Silicon in Dry Oxygen, Wet Oxygen, and Steam

B. E. Deal (pp. 527-533, Vol. 110, No. 6)

A. G. Revesz and K. H. Zaininger[52]: It is important to realize that the specification of a temperature range alone is not sufficient to draw a final conclusion concerning the oxidation kinetics. As is well known, the oxidation is diffusion controlled (in the sense of the Wagner theory of oxidation) only if the oxide is thicker than the space charge region. Therefore, it is necessary to specify both the temperature and thickness range as well as the conditions of the ambient. For example, it has been determined[53] that oxidation in atmospheric steam at 1000°C is diffusion controlled only if the oxide is thicker than 3000Å, and is definitely not diffusion controlled if the film is thinner than 2000Å.

If diffusion is the controlling mechanism then surface conditions do not determine the rate of oxidation. Therefore, the observed dependence of the oxidation rate on the orientation of the substrate is in complete contradiction with the statement that diffusion controlled oxidation was taking place. It is also quite clear that if one is interested in studying the dependence of the oxidation rate on initial surface conditions (e.g., as a function of the method of surface preparation) the investigations have to be restricted to thin oxide films (*i.e.*, thickness smaller than space charge region) so that the effect is not masked by diffusion through a thick oxide. From this point of view, the conclusion that mechanical polishing does not influence the oxidation is in error since 1μ thick films were used for this study and hence the oxidation was already diffusion controlled. Ellipsometric investigations on thin ($t < 500$Å) SiO_2 films[54] produced by oxidation at 1000°C in dry oxygen show, indeed, that the rate of oxidation is higher for a mechanically polished sample than for a chemically polished one.

B. E. Deal[55]: There does not appear to be any disagreement between our results and those reported here by Revesz and Zaininger. Their first point regarding specification of thickness range is well-taken. Our studies involved oxides in the thickness range 0.20 to 2.00μ. At thicknesses 0.20μ or below we have also noted the change in oxidation mechanism to a non-diffusion-controlled reaction.

Revesz and Zaininger also suggest an apparent contradiction of our data related to surface-orientation dependence and diffusion-controlled oxidation. There should be no confusion here since it is clearly stated (p. 531) that above 1000°C no surface orientation effect was noted where the oxidation is diffusion-controlled. At 1000°C and below, where oxidation undergoes a transition from a diffusion-controlled to a surface controlled reaction, the orientation has an effect in the case of the (100) surface. It has been proposed that this surface has fewer reaction sites, and the rate of SiO_2 formation is enough slower than the diffusion rate to establish a slower over-all oxidation.

Finally no comparison was made in this paper between mechanical and chemical polishing treatments. The purpose of the reoxidation experiments was to determine if the results were reproducible for such a procedure. We stated "It [the results] also demonstrated that any damage of the silicon caused by the mechanical polishing either did not affect oxidation or else provided a constant effect through the 3μ of silicon oxidized." Even though, as Revesz and Zaininger suggest, the actual slope of a thicker oxide thickness-time plot will be equal for different surface treatments, the position of the curve along the time axis could be shifted due to differences during initial oxide formation. This effect was not noted in these experiments. The dependence of oxidation rate on surface preparation for thin oxides has also been noted by us in later experiments.

The Oxidation of Silicon in Dry Oxygen, Wet Oxygen and Steam Supplementary Data

Bruce E. Deal[55]: Silicon oxide thickness measurements, reported in the mentioned paper involved the use of the groove-chord method. Accuracy of this method is $\pm$ 0.02μ. Since that work was conducted, thickness measurements have been repeated using the Tolansky method of multiple beam interferom-

[52] RCA Labs., Radio Corp. of America, Princeton, N. J.

[53] A. G. Revesz and K. H. Zaininger, Colloquium on the Optics of Solid Thin Films, Sept. 1963, Marseilles, France.

[54] A. G. Revesz and K. H. Zaininger, RCA Rev., To be published.

[55] Present address: Fairchild Semiconductor, A Div. of Fairchild Camera & Instrument Corp., Research and Development Lab., Palo Alto, Calif.

etry. Accuracy of the latter type of measurement is $\pm$ 0.002μ. The more precise measurements indicated no significant changes in the original results with but one exception. This involved the dry oxygen thickness data at 1200°C. The corrected data are as follows:

Thickness rate constant, dry oxygen, 1200°C:
$6.95 \times 10^{-4}\mu^2$/min
[*See* Table I]

Time required to obtain 0.5μ dry oxide, 1200°C:
360 min

Time required to obtain 1.0μ dry oxide, 1200°C:
1440 min
[*See* Table II]

Activation energy, dry oxygen thickness data:
29.0 kcal/mole
[*See* Table III]

Apparent oxide density, dry oxygen, 1200°C:
2.24 g/cc
[*See* Table IV]

It can be observed that the corrected activation energy value agrees more closely with the corresponding weight value. Likewise, the corrected 1200° density value for dry oxygen is more in line with the other data. The over-all results and conclusions of the paper have not been affected by these improved thickness determinations.

Surface Energy of Germanium and Silicon

R. J. Jaccodine (pp. 524-527, Vol. 110, No. 6)

G. A. Wolff[56]: In this paper, the author has measured the specific surface free energies of the {111} planes of silicon and germanium. These values are of fundamental importance. The following comment refers to his derivation of the specific surface energy values of the planes {001} and {011} from the experimental specific surface free energy value for {111}. This derivation is based on the assumption that the specific surface free energy value σ_{hkl} is proportional to the number of "dangling" bonds per unit area of the plane {hkl} in diamond structure materials. In all likelihood, this assumption will lead to acceptable values of first approximation accuracy. A refinement of second approximation character would have to consider the possibility that the two bonds "dangling" from a single atom in {001} might contribute less to the surface free energy than two dangling bonds from two atoms in {111} or {011}[57]. The latter planes might also experience an atomic displacement from the ideal structure positions which will lower the respective {111} and {011} values[57,58]. Surface deformations of this type have been verified by low-energy electron diffraction measurements and by other techniques[59,60]. Theoretical estimates will, therefore, only lead to estimates. It is the purpose of this discussion to show that experimental observations should lead to accurate boundary values for specific surface free energy ratios of the various planes, and, by utilizing Jaccodine's σ_{111} value, in turn lead to accurate boundary values of absolute surface free energies for the other planes.

In silicon and germanium, the following crystal planes have been found to appear and coexist during growth, annealing or slow evaporation in the dilute vapor or gaseous phase[61,62]: 1, {111}; 2, {111} and {001}; 3, {111} and {113}; 4, {111}, {113}, and {011} with common apex; 5, {111}, {113}, {011}, and {013} with {113}, {011}, {013} apex.

These data correspond to the following relations: A, $\frac{1}{3} < \frac{\sigma_{001}}{\sigma_{111}\sqrt{3}} < 1$ which follows from observations 1 and 2; B, $\frac{5}{3} < \frac{\sigma_{113}\sqrt{11}}{\sigma_{111}\sqrt{3}} < 3$ and $\frac{5}{9} < \frac{\sigma_{001}}{\sigma_{111}\sqrt{3}} < 1$ which follow from observations 2 and 3; C, $\frac{2}{3} < \frac{\sigma_{011}\sqrt{2}}{\sigma_{111}\sqrt{3}} < 1$ and $\frac{\sigma_{011}\sqrt{2}}{\sigma_{111}\sqrt{3}} - 1 < \frac{\sigma_{113}\sqrt{11}}{\sigma_{111}\sqrt{3}}$ which follow from observation 4; D, $\frac{4}{3} < \frac{\sigma_{013}\sqrt{10}}{\sigma_{111}\sqrt{3}} < 3$ which follows from 5.

The results under 2 and 3 have also been obtained in carefully controlled experiments in vapor phase growth, annealing and evaporation of germanium[62]. The formulas and values for $\frac{\sigma_{hkl}\sqrt{h^2+k^2+l^2}}{\sigma_{111}\sqrt{3}} = R_i$ are, therefore, given below without consideration of conditions 5 and D which would, in any case, affect only a little change. The values given have been arrived at by utilization of Wulff's law $\left(\frac{\sigma_i}{r_i} = \text{const.}\right.$ where σ_i and r_i are the specific surface free energy and central distance of crystal plane i, respectively$\left.\right)$, Gibbs' condition ($\sum_i \sigma_i A_i$ = Minimum where A_i = area of the ith plane) and the fact that the specific surface free energy plot in spherical coordinates is always[63] represented by spheres with their pole in the crystal center (Wulff's point[64]), and their antipole representing maximum values of the crystal[57]. For the planes $l \geq 3\,|k|$; $l \geq 3\,|h|$, $l > R_i > \frac{5}{9}\,l$ holds. Correspondingly, for $3\,k \geq l \geq 2\,|h| + k$, $l > R_i > \frac{1}{6}\,(k + 3l)$ holds, and for $2h + k \geq l \geq k \geq h$, $l > R_i > \frac{1}{3}\,(h + k + l)$ holds.

[56] Erie Technological Products, Inc., Erie, Pa.

[57] G. A. Wolff and J. G. Gualtieri, *Amer. Mineralogist*, 47, 562 (1962).

[58] G. A. Wolff and J. D. Broder, *Acta Cryst.*, 12, 313 (1959).

[59] H. E. Farnsworth, R. E. Schlier, T. H. George, and R. M. Burger, *J. Appl. Phys.*, 29, 1150 (1958).

[60] W. B. Pearson and G. A. Wolff, *Discussions Faraday Soc.*, 28, 142 (1959).

[61] G. A. Wolff, *Amer. Mineralogist*, 41, 60 (1956).

[62] G. A. Wolff, Unpublished results.

[63] In polyhedral crystals, in the absence of rounded convex surface sections.

[64] Wulff's point and crystal center only coincide in crystals with symmetry centers.

It then follows:

	Si (in ergs/cm²)	Ge (in ergs/cm²)
$\left(\frac{2}{3}\right)1 > R_{001} > \frac{5}{9}$	(1420) $2130 > \sigma_{001} > 1185$	(1225) $1835 > \sigma_{001} > 1020$
$1 > R_{011} > \frac{2}{3}\left(\frac{5}{6}\right)$	$1505 > \sigma_{011} > 1005$ (1255)	$1300 > \sigma_{011} > 865$ (1080)
(2) $3 > R_{113} > \frac{5}{3}$	(1290) $1935 > \sigma_{113} > 1075$	(1105) $1660 > \sigma_{113} > 925$

The inequalities are certain for the values which are not given in parentheses. Some experimental evidence points to the narrower limits as given in the brackets. The inequalities also hold true regardless of surface deformations and for the cases R_{001} and R_{113} might also apply to gray tin. These results cannot be applied to diamond, however, since {113} is rather rarely observed in diamond.

Space and time prohibits a more detailed account of the procedure of derivation and its justification. Both are given in the literature quoted. Although the data presented contain much basic information concerning the derivation of the formulas, Fig. 1 may be used for purposes of demonstration. In the figure, it is obviously $\sqrt{3} = \frac{OS}{OP''} > \frac{OR}{OP''} = \frac{a\,\sigma_{001}}{a\,\sigma_{111}} > \frac{OQ}{OP''} = \frac{5}{3}\sqrt{3}$; this is the reported condition for the respective coexistences of {111} and {001}, and of {111} and {113} (*i.e.*, conditions 2 and 3).